4th INTERNATIONAL GRADUATE RESEARCH SYMPOSIUM - IGRS'25

BOOK OF
EXTENDED ABSTRACTS

MAY 12-14, 2025

HYBRID

For more information:
www.igrs2025.com

Dalya

4TH INTERNATIONAL GRADUATE RESEARCH SYMPOSIUM

IGRS'25

BOOK OF **EXTENDED ABSTRACTS**

EDITORS

Fatma Seniha GÜNER, Burçak KARAGÜZEL KAYAOĞLU, Filiz AYAZ

May 12-14, 2025
ITU, Istanbul, Türkiye

4TH INTERNATIONAL GRADUATE RESEARCH SYMPOSIUM

IGRS'25 - E-PROCEEDINGS
May 12-14, 2025 ITU, Istanbul, Türkiye

Editors, Fatma Seniha GÜNER, Burçak KARAGÜZEL KAYAOĞLU, Filiz AYAZ

Istanbul, 2025

e-ISBN 978-975-561-744-2
İTÜ Yayınevi. No: 2025.2/21

© ITU Press
All rights of this book are reserved and all publication rights belong to "ITU Press". All or any part of this book cannot be published, printed, filmed or used indirectly without the permission of the publisher. It cannot be reproduced by dublication, photocopy or any other technique, and cannot be transferred to an environment that can be processed on computers or typesetting machines. The responsibility of all texts and visuals published in the book belongs to the author(s).

International Graduate Research Symposium (4th : 2025 : Istanbul, Türkiye)
4th International Graduate Research Symposium: GRS'25 E-Abstract Book: May 12-14, 2025 ITU, Istanbul, Türkiye / editors, Fatma Seniha Güner, Burçak Karagüzel Kayaoğlu, Filiz Ayaz.-- Istanbul: ITU Press, 2025.
2566 pages. -- (İTÜ Yayınevi. No: 2025.2/21)
Includes bibliographical references
ISBN 978-975-561-744-2
1. Engineering -- Research -- Congresses 2. Engineering--Study and teaching –Congresses 3. Structural stability – Congresses.
TA160.6.T8I88 2025 CIP

ITU PRESS
Certificate Number: 70051
İTÜ Ayazağa Campus

Mustafa İnan Library
34469 Maslak İSTANBUL
0212 285 75 05
www.ituyayinevi.itu.edu.tr / ituyayinevi@itu.edu.tr

PREFACE 37
COMMITTEES 38
SCIENTIFIC PROGRAM 51
EXTENDED ABSTRACTS 71
ORAL PRESENTATIONS 72
AERONAUTICAL AND ASTRONAUTICAL ENGINEERING 73
Aircraft Design, Flight Dynamics And Performance 73
External Store Separation From Fighter Aircraft 74
Sensitivity Analysis of Hypersonic Glide Vehicle Trajectory Under Aerodynamic and Atmospheric Variations 80
Winglet Design, Optimization and Performance Analysis for a Trainer Aircraft 87
Control Systems: Adaptive, Intelligent, Digital, Optimal, Pneumatic-Hydraulic 92
Quadrotor Actuator Fault Detection and Isolation- A Model Based Approach 93
Multi-Agent Reinforcement Learning with Maneuver Primitives for Automatic Ground Collision Avoidance of Fighter Jets 97
Mechanical Vibrations And Structural Dynamics 103
Nonlinear Modeling and Sensitivity Analysis of Oleo-Pneumatic Strut Landing Gear Systems for Aircraft Landing Performance 104
Aeroelastic Optimization with Genetic Algorithm 110
Feed-Forward Neural Network Based Prediction of Flutter Speed of 3 DOF 2D Wing Model 116
Conceptual Modeling of a Multi-Axial Nonlinear Dynamic VibrationAbsorber for Helicopters 124
Rotary Wing Aircraft 130
A Study on Hover and Forward Flight Performance of S70A-28D (UH-60L Black Hawk) Helicopter to Obtain Cruise Chart by Using Momentum and Blade Element Momentum Theory 131
Spacecraft Control, Design And Performance 141
Liquid Propellant Rocket Engine Performance Sensitivity Analysis 142
Theoretical, Computational And Experimental Aerodynamics And Fluid Dynamics 144
A Deep Learning Based Modelling of Axial Turbomachinery 145
Experimental Study on Vortex Gust Encountered by a Flat Plate at 45° Wing Sweep 149
Fully-Coupled k–ω-SST Turbulence Model Implementation for Nonlinear Newton Method in Unstructured Vertex-Based Hemlab Algorithm 153
Digital Twin Approaches in System-Level Modeling for Aerospace and Propulsion Applications of Rocket Engines: A Review 161
Theoretical, Computational And Experimental Structural Analysis And Design 165

Design and Analysis of Isogrid-Stiffened Cylindrical Structures for Launch Vehicles: Mathematical Modelling and Knockdown Factor Correlation with Finite Element Validation 166
Numerical Modeling of Composite Laminates Under Out-of-Plane Impact 169
Investigation Of The Interaction of Carbon Fiber Cylindrical Rocket Bodies With Radial Bolt Joints 176
APPLIED INFORMATICS 183
Computational Electromagnetics 183
Nyström Integral Method for Mode Solving in Optical Waveguides with Arbitrary Geometries 184
Singular Integral Treatment of Nyström Method for Electromagnetic Scattering Problems 189
Data Analysis 194
Optimization Potential of Machine Learning-Based Algorithms in Neonatal Parenteral Nutrition Management: A Systematic Review 195
Medical Image Analysis 201
Deep Learning-Based Breast Tumor Detection in MRI Using Faster R-CNN 202
Prediction of Microsatellite Status Using Deep Neural Network 206
Improving Tumor Segmentation Performance in Breast MRI via U-Net Based Deep Learning Approach 209
ARCHITECTURE 213
Architectural History 213
Spatial Representation In French New Wave Cinema: An Analysis Through Agnès Varda's Cléo De 5 À 7 (1962) Film 214
Legitimisation through Elevation: Romanos' Myrelaion 220
Rural Houses in Renaissance Architecture: Proposals of Sebastiano Serlio According to the Social Hierarchies in his Sixth Book 224
Semi-Open Spaces as a Result of Climate and Culture in Mediterranean Architecture 229
The Historical Layers of Selimpaşa in Constantinople Hinterland Context 232
Furniture Consumption in Istanbul at the Beginning of the 20th Century: The Role of Periodicals 236
Architecture Design Theory 241
The Impact Of Governmental Power On Urban Morphology: A Case Study Of London 242
The Performance of the Archive or Archive as Event: Exhibiting Architecture 249
Typological Transformations and Urban Isolation: Rethinking Architectural Production along Eskişehir Road 252
Conditions of Criticality in Discussions on Architectural Representation 260

Exploring Experiential Learning Design Practices Grounded in Social Responsibility in Mardin 264
Urban Destruction in Malatya's Green Belt Project: A Struggle for Public Space or Capitalist Gain? 266
Reading Architectural Memory Through Cinematic Image: Atatürk Cultural Center 270
Fluid Bodies of Space: Rethinking Architectural Relationality Through The Medusa Head 277
Archival Encounters: Rewriting Istanbul Women's Works Library and its Memory Through Bodily Practices 282
The Potentialities, Displacements, and Spatial Projections of Concepts 289
Soft Matters: (Re)drawing Architecture Through Feminist Material Practices 296
Building Construction Technologies 302
Evaluation of Retrofitting Techniques in Reinforced Concrete Buildings 303
Evaluation of the Seismic Performance of Traditional Akçakese Houses in Relation to Structural Deterioration 306
Evaluation Of Light Steel Structured Housing According To Construction Systems 312
Evaluation of Damage Mechanisms in Stone Structured Houses Due to Earthquakes . 315
Impact of Deterioration Due to Environmental Factors on Seismic Performance of Traditional Timber Buildings in the Historical Peninsula in Istanbul 319
Building Materials and Technologies 323
Developing One-part Geopolymer Binders by Using Ground Granulated Blast-furnace Slag and Ceramic Waste as Precursors 324
Evaluation of Damage Mechanisms of Reinforced Concrete Industrial Structures in Past Earthquakes in Turkey 328
Built Environment Design and Technologies 332
Evaluation of Exterior Cladding Materials in Educational Buildings in Terms of Embodied Energy 333
The Impact of Façade Cladding Materials on Carbon Emissions in Urban Renewal Projects: The Case of Istanbul 337
Conservation and Restoration 341
Ottoman Brick Stamps 342
Examination of the Transformation of Kırklareli Urban Conservation Area and Its Surroundings between 2004 and 2022 in the Context of Conservation and Sustainability 345
The Rural Settlement Structure and the Challenges of Preserving Traditional Housing in Tokat Bağbaşı (İbibse) Village 350
Facade Finishes in Early 20th Century Istanbul: History and State of Conservation ... 356
Environmental Control and Building Technology 361
UrbanReCrete: A Sustainable Approach to Concrete Waste Recycling in Istanbul 362

Reduction of Cooling Loads in Office Buildings in Hot Climates Using Radiant Cooling 365
Multi-Stage Space-Adaptive Shelters: An Alternative to Post-Disaster Shelters 371
Artificial Intelligence in Materials Education for Architecture Opportunities, Challenges and Ethical Considerations..... 381
Project and Construction Management 385
A Literature Review On Organizational Structures In The Construction Industry..... 386
A Systematic Review of BIM and the Circular Economy: Key Research Areas and Findings..... 391
Investigating the Role of Data Management for AI Utilization for Decision-Making in Construction: A Literature Review..... 394
Sustainable Design..... 398
Investigating Circularity in Buildings through Digital Circularity Metric..... 399
ART HISTORY 405
Art and Technology..... 405
The Role of Digital Technologies in Museum Storytelling: Ephesus Experience Museum 406
Art History 409
A Brief Historical Trajectory of Art Collectives as a Commoning Practice in Turkey .. 410
From Functional to Imaginary Forms: Alev Ebüzziya Siesbye's Ceramics..... 413
CHEMICAL ENGINEERING..... 416
Hydrogen Technologies, Fuels Cells, Energy Storage Materials 416
Biomass-Derived Activated Carbon as Electrode Material for Supercapacitors 417
Modelling and Computational Systems..... 420
Machine Learning-Based Prediction of FTIR Spectral Peaks for Biomass Characterization..... 421
CHEMISTRY 424
Inorganic Chemistry 424
The Design And Application of Novel Post-Metallocene Catalysts For Olefin Polymerization..... 425
Nanochemistry..... 428
Investigation of Fluorescence Properties of ZIF-8 Structures Modified with Graphitic Quantum Dots..... 429
Organic Chemistry..... 432
Synthesis Of Polymers Containing Supramolecular Components In The Pendant Or Main Chain 433
Polymer Chemistry..... 437

Dual Radical and Singlet Oxygen Pathways in Polybutadiene Photovulcanization: A Novel Approach Using Phenylacylbromide under UV-A Irradiation for Advanced Crosslinked Films 438
COMMUNICATION SYSTEMS 442
Antennas 442
Design and Inter-Element Spacing Optimization of GNSS Array 443
COMPUTATIONAL SCIENCE AND ENGINEERING 447
Computational Biology 447
Molecular Dynamics Analysis of CHK2 Mutations at the C-lobe of the Kinase Domain 448
Computational Fluid Dynamics 453
Multi-Objective Optimization of Airfoil Geometry for Aerodynamic Efficiency and Noise Reduction Using Bézier Parameterization 454
COMPUTER ENGINEERING 459
Artificial Intelligence 459
An Intelligent Jamming Environment: Reinforcement Learning Approach 460
The Role of Artificial Intelligence in Enhancing Software Quality: A Multivocal Literature Review 469
Multi-Lead ECG Classification Using a Mixture-of-Experts Transformer Model 473
Computer Networks 477
Adaptive Consensus Algorithms for Blockchain Networks 478
Cyber Security 484
Reputation Based Decision Making Consensus Mechanism for UAV Swarms with Ethereum Blockchain 485
Neuromorphic Computing and Memristor-Based Network Attack Detection Systems: New Approaches in Cyber Security 488
Enhancing IoT Botnet Detection: A Streamlined Approach to Feature Selection 495
Embedded Systems 501
Comparison of the Effects of Different Compiler Environments on Communication Signal Detection Software 502
COMPUTER SCIENCE 505
Data Science 505
A Data-Driven Approach to Process Duration Estimation: End-to-End Machine Learning with Process Mining 506
Image Processing 511
PET Image Denoising Using Denoising Diffusion Probabilistic Models (DDPMs) 512
Iterative Reconstruction Applications for Aircraft Image Restoration 514
CONSTRUCTION MANAGEMENT 520

Construction Project Management 520
Inclusion and Gender Equality for Women in the Construction Industry 521
Difficulties Faced by Construction Experts in Construction Sector Cases in the Turkish Justice System 530
Procurement Phases in EPC Projects: A Bibliometric Analysis 533
Determining the Factors Causing Rework in the Turkish Construction Industry 540
IT in Construction 546
Assessing the Level of Digitalization of the Construction Permit Processes in Türkiye 547
Sustainability in Construction 550
Industrialisation of Natural Building Materials for Sustainability in the Built Environment 551
Circular Economy Performance Assessment in Construction: A Critical Review of Firm-Level Models 555
CONTROL AND AUTOMATION ENGINEERING 559
Advances in Automatic Control Engineering 559
Control Surface Failure Management In Dual-System VTOL UAVs 560
4-D Flight Management System Design for the Fighter Jets 563
Lane Change Decision Making For Autonomous Vehicles By Using Adversarial Learning Methods 568
Applications of Control Engineering 571
An Optimization-Based Flight Control Law Design for Fighter Aircraft 572
Enhancing Aircraft Avionics Safety: Integrating STPA With ARP4761 581
Design and Analysis of a Dual Layer Disturbance Observer-Based Controller for Longitudinal Axis in a Fixed Wing Aircraft 585
Fuzzy Gain Decision for Different Types of Aircraft with Dynamic Pitch Control Envelope Cue 591
Enhanced Aircraft Control Throughout Total Energy Control Systems: A Comparative Study with Conventional Autopilots 601
Performance Comparison of Guidance Algorithms for Aerial Vehicles: A Software-In-The-Loop Based Approach 605
Robust Attitude Control of the F-16 Aircraft Using Incremental Nonlinear Dynamic Inversion 610
Adaptive Kalman Filter-Based Gyroscope Error Compensation for IMU Sensors 615
Immersion and Invariance Disturbance Observer-Based Discrete Time Vector Control of BLDC Machines 619
DATA ENGINEERING AND BUSINESS ANALYTICS 628
Big Data Analytics for Decision-Making 628
Automated Plastic Waste Detection on Coastal Areas Using UAVs and Deep Learning 629

Agentic Workflows for Self-Service Analytics Applications in E-Commerce 636
Predictive Analytics and Machine Learning in Business 640
Analyzing Brokerage Firm Trading Behavior via Supervised Learning: A Comparative Study on BIST 10 641
Sentiment Analysis and Opinion Mining 645
Impact of Weekly vs Daily Sentiment Scores on Price Direction Forecast 646
DEFENSE TECHNOLOGIES 649
Remote Sensing 649
A Hybrid Preprocessing Approach Based on Simulation Data for Embedded Object Detection Under an Inhomogeneous Surface 650
Spacecraft Control, Design And Performance 656
Design of a Deployable S-Band Helical Antenna for CubeSats 657
Structural Design and Analysis 661
Optimization and Finite Element Analysis of Metastructures for Vibration Mitigation 662
Parametric Optimization of Semi-Octagon Re-entrant Auxetic Structures for Energy Absorption 667
Finite Element Analysis Of Crack Growth Behavior In The Presence Of Crack-Arresting Holes 672
Design and Modeling of a Nonlinear Bi-Axial Dynamic Vibration Absorber for Helicopter Applications 675
Computational Analysis of Metallic Structures Subjected to Impact Loading Using LS-Dyna 679
Unmanned Vehicles 685
Heuristic Approach to UAV Selection with Fuzzy Logic and MADM Techniques 686
Optimized Visual Odometry and Satellite Image Matching-Based Localization for UAVs in GPS-Denied Environments 689
Comparative Analysis of Object Detection and Tracking Algorithms for UAVs 692
EARTHQUAKE ENGINEERING 696
Artificial Intelligence, Machine Learning, and Deep Learning in Earthquake Engineering 696
Detection of Longitudinal Reinforcement Buckling in Reinforced Concrete Columns by a Deep Learning Method 697
Estimating Equivalent Damping Ratio of Conventional Shear Walls by Machine Learning Methods 702
Experimental Investigation of Reinforced Concrete Building Elements 714
Enhancing Seismic Resilience of Substandard RC Beam-Column Joints with All-Steel Tube-in-Tube Buckling-Restrained Braces: 715
A Shake Table Test 715
Performance-Based Seismic Assessment and Design 719

Seismic Performance Assessment of Irregular RC Structures Using the Extended N2 Method 720
Structural and Geotechnical Earthquake Engineering 725
Seismic Performance Enhancement of RC Coupling Beams Using Shape Memory Alloy Devices 726
Preliminary Study on St. Ilyas Church Damaged in the Kahramanmaraş Earthquakes 732
Design and Comparison of Different Types of Reinforced Concrete Slab Systems for Multi-Storey Buildings 743
ECOLOGY AND EVOLUTION 747
Anthropocene 747
Exploring the Biodiversity Patterns of Anatolia Under Changing Climatic Conditions 748
Defining the Character of Turkey's Biodiversity Policies 752
ECONOMY 755
Financial Crises and Macroprudential Policies 755
Financial Contagion: Dynamic Correlations Approach 756
ELECTRICAL ENGINEERING 762
Electric Power & Energy Systems 762
Techno-Economic Integration of Nuclear Energy Towards Achieving Net-Zero Emissions 763
Electrical Machines 767
Investigation of the Effect of Space Vector PWM Technique on Zero-Sequence Voltage Formation in Open-End Windings 768
Determination of Altitude Dependent Insulation Breakdown of Brushed DC Starter Generators 773
Electrical Vehicles 775
Development And Validation Of A Dynamic Energy Consumption Model For A 12-Meter Electric Bus Using SORT-2 Test Data 776
Power Electronics 779
Three Phase LLC Resonant DC/DC Charger for Railway Applications 780
A Real-Time Resonance Detection and Mitigation Method for Shunt Active Power Filters 784
Smart Grids 786
Adaptation of a Generalized Observer Scheme for False Data Injection Detection in Load Frequency Control Systems 787
Cyber-Resilient Real-Time Transient Stability Prediction for Modern Power Systems 791
ELECTRONICS AND COMMUNICATION ENGINEERING 800
Analog/Mixed-Signal/Microwave Circuits 800

22-nm FD-SOI Internal Power Management Unit for Frequency-Modulated Continuous Wave Lidar 801
Design of a Low-power Phase-Frequency Detector in 65 nm CMOS Technology Suitable for 5G Mobile Applications 804
Bio-Medical, Bio-Inspired Circuits/Systems 812
Thermoplastic Microfluidic Platform for 3D Cell Culturing and Imaging 813
A Deep Learning Network for Automatic Grade Classification of Renal Cell Carcinoma 818
Image Reconstruction and Restoration with Diffusion Network 822
Customizable Fluidic and Anisotropic Vocal Fold Phantom for Biomechanical Analysis 826
Development of Multi-Capsule Endoscopy via Spring-Assisted Distance Control 831
Effect of Wavelength, Intensity, and Eye Color on Pupil Detection in Infrared-Based Eye Tracking Systems 836
Multi-Class Classification for Skin Lesions Using Deep Learning Techniques 844
Digital Circuits and Systems 849
Hardware Implementation of FALCON's ffSampling Algorithm 850
Embedded Systems 853
Design of a Clutchless Automated Gear Control System for Electric Tractors 854
VLSI Systems and Applications 857
Logic Locking-Based FPGA System Design for Third-Party IP Protection 858
ENERGY SCIENCE AND TECHNOLOGY 862
Computational Fluid Dynamics 862
Numerical Investigation of the Effects of Interfacial Contact Resistance in PEM Fuel Cells with Coated Metal Bipolar Plates 863
Computational Heat and Mass Transfer 869
Numerical Investigation of Engine Cooling Using Nanofluids 870
A State-of-Charge Based Experimental and Numerical Investigation of Li-Ion Battery Heat Generation and Temperature Distribution 873
Electrochemical and Thermal Modeling of Lithium Batteries for 878
Temperature Distribution Based on Cathode Materials 878
Flow Control and Thermal Behavior of Bearings Using a Proportional Valve in a Closed-Loop Lubrication System for Turbofan Engines 884
Energy Conversion and Storage Technologies 888
Sustainable GSM Base Station Energizing Using Portable Radioisotope ThermoelectricGenerator (RTG) Design 889
The Lifespan Comparison of an NMC811 Pouch Cell Based High Voltage Battery with Silicone and Polyurethane Foam Usage 892

Energy Conversion and Sustainability 896
Energy Efficiency Potential Analysis of SMEs In Türkiye's Fertilizer Sector 897
Renewable Energy 900
Feasibility Assessment of Hydrogen Fuel Cell Integration in the Dornier 228 Aircraft with the Structural and Operational Considerations 901
Sustainable Energy 905
The Effect Of Seawater On The Electrodecomposition Of Hydrogen Sulfide To Hydrogen And Polysulfides 906
ENVIRONMENTAL ENGINEERING 910
Air Pollution and Control 910
Effects of Air Pollutant Parameters on Respiratory Diseases in Edirne 911
Membrane Technologies 916
Enhancing Reverse Osmosis Performance: A CFD-Based Study of Randomized Feed Spacer Geometries 917
FOOD ENGINEERING 921
Food Bioactive Compounds 921
Extraction of Phenolic Compounds from Grape Pomace; Potential Application Packaging Materials 922
Functional Foods 925
Plant-Based Proteins in Instant Soups: Comparison of Sensory, Functional, and Bioactive Properties 926
Composition and technofunctional properties of Aquafaba from Local Legume 931
Novel Food Processes 933
Effects of Audible-Range Sound Treatment on the Microbiological Quality of Strawberry During Post-Harvest Storage 934
Sustainable Foods 938
Development and Characterization of Biodegradable Films Enriched with Protein Extracted from Agro-Industrial Pea Waste and By-Products 939
GAME AND INTERACTION TECHNOLOGIES 944
AI in Gaming 944
A Comparative Study For Analyzing LLM Performance in Bluff-Based Card Games 945
Preliminary Study on the Feasibility of Neural Network-Based Generative AI Models in Video Game Music Production 948
Game Design 951
Optimizing Level Production in Hidden Object Games Using YOLO Object Detection 952
A Systematic Approach to Ludonarrative Harmony: Methods for Aligning Interactive Gameplay and Storytelling 955

Impossible Spaces in Games: Using Anamorphic Projection in Space Interactions to Explore Possibilities of New Game Mechanics 959
Understanding Player Behavior: The Role of Intrinsic and Extrinsic Motivations in Bartle Player Types 965
Game Production 971
RNBO for Game Development: A Framework for Dynamic and Adaptive Audio Design 972
Gamification 975
Procedural Entity Generation For Simulated Ecosystems 976
Interaction Technologies 979
Naval History Reconstruction Through 3D Modeling and Simulation 980
Series Games 985
Mechanics To Design Virtual Reality Cognitive Training Games 986
User Studies 989
An Analysis of Gaming Behavior Through Bartle's Player Model & Human Psychology 990
GEOGRAPHIC INFORMATION TECHNOLOGIES 993
Artificial Intelligence and Machine Learning in Remote Sensing Analysis 993
Current Challenges in Port Management and Common Approaches from Geographic Information Technologies (GIT) 994
Spatial Data Algorithms and Visualization and 3D GIS Technologies 997
Tactile Map Production Processes And Application Areas For Visually Impaired 998
Spatial Planning and Management with GIS Applications 1002
Analysis of Customer Complaints in Mobile Communication Networks with GIS 1003
City Model Production With LIDAR Technology And Integration Of Urban Transformation With GIT: The Example Of Zeytinburnu District 1006
Mitigating Urban Heat Island Effects through Nature-Based Solutions: The Case of Istanbul 1008
GEOLOGICAL ENGINEERING 1012
Rock Mechanics 1012
Detachments Induced By Thermal Cycling At Grain Boundaries of Fine Grained Marble 1013
GEOMATICS ENGINEERING 1019
Geodesy 1019
On the Role of Earth Observations and Geodetic Data in Environmental and Climate Change 1020
Geographic Information Systems 1023
Spatial Problems And Effective Factors In Hospital Campus Structure 1024

Social Vulnerability Analysis of the Cities Affected by the February 6 Turkey Earthquake 1029
Spatial Analysis and Optimization of E-Commerce Company's Parcel Collection Operations: The Case of Esenyurt, Istanbul 1032
Transformation of Solid Waste Management in Baku: A GIS-Based MCDM Approach to Landfill Site Selection Beyond Balakhani 1040
Natural Hazards 1045
Flood Risk Analysis with Geospatial Artificial Intelligence Techniques 1046
Seismic Hazard Assessment of Kahramanmaraş Region: Analysis of Earthquake Sources and Probabilistic Seismic Risk 1050
Photogrammetry 1057
Generating a High-Definition Map (HD Map) via YOLO (You Only Look Once) Deep Learning-Based Object Detection Model 1058
Remote Sensing 1061
Investigation of Anthropogenic Effects in Protected Wetlands Using Remote Sensing and Geographic Information Systems: A Case Study of Manyas Bird Lake and Bird Paradise National Park 1062
Aircraft Contrails Detection with Deep Learning Methods on Remote Sensing Images 1068
Enhancing Sentinel-1 SAR Geolocation Accuracy: The Impact of DEM on Orthorectification Performance 1071
Offshore Wind Turbine Site Selection in the Aegean Sea 1075
Evaluating The Temporal Consistency Of Sar And Optical Vegetation Indices For Cotton Monitoring Using Sentinel-1 And Sentinel-2 1078
HEAT FLUID 1084
Fluid Mechanics 1084
Generation of Proper Inflow Conditions with Hydrodynamic Stability Approach: A Case Study For An Axially-Rotating Pipe Flow 1085
HISTORY OF SCIENCE AND TECHNOLOGY 1092
History of Engineering 1092
The Transformation of Armored Vehicles as a Response to Amphibious Warfare: A Comparative Analysis of the Dieppe Raid and the Normandy Landings 1093
History of Physics 1095
Scientific Tendencies in Early Nineteenth-Century Britain: William Sturgeon and The Annals of Electricity, Magnetism and Chemistry 1096
History of Sciences 1099
Brief History Of Artificial Intelligence Approaches 1100
HYDRAULICS AND WATER RESOURCES ENGINEERING 1104
Hydrology 1104

Spatio-Temporal Analysis of Long-Term Rainfall Erosivity Trends and Climate Impacts on Erosion Potential 1105
INDUSTRIAL DESIGN 1112
Historical, Cultural and Social Context of Design 1112
Discovering The Choir Members' Practices: An Initial Understanding of The Intersection of Design, Music, and Community 1113
Decoding Toxic Attachment Between Design Products and the Users: Understanding by using Metaphors 1115
Product Design 1119
Testing the Aesthetic Responses to Small Household Appliances in The Context Of Incremental Innovation 1120
Theory and Methodology in Industrial Design 1126
User Narrative as Antenarrative: A Brief Overview 1127
Prompt 'Design the Perfect Product': A Literature Review on AI Incorporation in Industrial Design Processes 1130
Exploring Emotions in Design Research: An Initial Mapping of Emotion-based Concepts 1134
Understanding Creativity: A Survey-Based Investigation into the Psychology of Designers' Creativity during the Ideation Phase 1140
INDUSTRIAL ENGINEERING 1143
Decision Making 1143
Multi Criteria Decision Making For Selecting Best Banking Service Channel 1144
A Comparative Analysis of Machine Learning and MCDM Sorting Methods in Electric Vehicle Selection 1147
A Bayesian Network-Based Approach for Analyzing Railway Accidents 1150
Engineering Management 1154
Impact of Organizational Life Cycle on R&D Project Prioritization Criteria 1155
Structuring Challenges for Textile Industry in Adopting the Digital Product Passport 1160
Sector-Specific Supplier Evaluation Based on LARGS Dimensions 1164
Customer Preferences For Mobile Operating Systems In Smartphones Using Conjoint Analysis 1168
Industrial Data Analytics 1172
Predicting the Closing Time of Debt Files in Legal Stage Using Machine Learning and Deep Learning Methods 1173
Knowledge Management 1175
Understanding University Reputation: A Stakeholder-Centered Model for Reputation 1176
Manufacturing Management 1180

Analysing the Automotive Production: A Bibliometric Analysis on Lean-Green Management 1181
Improvement Study In The Inner Door Production Area With Lean Production Approach 1184
INFORMATICS 1191
Computational Design Tools and Methods 1191
A Decision Support Model Proposal For Urban Green Space Site Selection Problem Based on Multi-Criteria Decision Making 1192
Computational Memorability Model Based on Object Size 1198
INTERNATIONAL MASTER OF INTERIOR ARCHITECTURAL DESIGN 1204
Interior Architecture 1204
Use of Mycelium-Based Materials as an Interior Design Component: A Digital Fabrication Approach 1205
Technology in Interior Design 1211
A Strategy for Dataset Preparation in AI Model Training: The Case of Hotel Room Interiors 1212
LANDSCAPE ARCHITECTURE 1216
Heritage and Identities 1216
From Tradition to Globalization: The Conceptual Transformation of Korean Landscape in Global City Seoul 1217
Innovative Technologies for Landscape Design and Management 1220
The Use of Computer Vision in Observing Human Behavior in Landscape Architecture 1221
Landscape Design 1224
Understanding Play: How Playground Exuipment Shapes Cognitive, Social, and Pyhsical Behaviors in Children Aged 3-12: A Case Study in Maltepe Orhangazi City Park 1225
MANAGEMENT 1228
Economics 1228
Central Bank Digital Currencies (CBDCs): a countermeasure to Anti-Money Laundering (AML) challenges posed by cryptocurrencies? 1229
Finance 1234
Investor Attention and Asymmetric Conditional Volatility: Evidence from GARCH-X and GJR-GARCH-X Models 1235
How Was Financial Performance Affected by ESG In The After- Covid Era? A Global Analysis 1240
Human Resource Management 1246
Remote Work and Virtual Presenteeism: Insights from the Turkish Organizational Context 1247
Marketing 1252

Navigating the Paradox of Connectivity and Isolation: Impacts on Digital Nomads' Psychological Well-Being 1253
Organization 1261
Organizing Through Code: A Bibliometric Review of Algorithms in Organizational Contexts 1262
Production Management 1267
Supplier Performance Evaluation with Balanced Scorecard 1268
Performance Evaluation Model Based on Balanced Scorecard for Industry 4.0 Applications in the Fast Moving Consumer Goods Sector (FMCG) 1272
MANAGEMENT ENGINEERING 1277
Finance 1277
The Effect of ESG Ratings on Firm's Financial Performance in Borsa Istanbul 1278
TEFAS's Effect on the Turkish Mutual Funds Landscape 1281
Marketing 1285
Adoption of Smart Small Home Appliances: An Analysis of Social and Behavioral Factors 1286
Understanding Consumer Acceptance and Purchase Intentions in Unmanned Retail Stores 1289
MARITIME STUDIES 1295
Maritime Human Resources 1295
Importance of Safety Awareness and Safety Culture Onboard with Alternative Fuels 1296
MATERIAL SCIENCE AND ENGINEERING 1300
Ceramics, Glass, Refractory Materials 1300
Improvement of the Selenium Retention and Control of the Color Stability in Selenium Containing Glasses 1301
Nanomaterials 1305
A Study About Tin Nanoparticles and Production of Core-shell Structure 1306
MATHEMATICAL ENGINEERING 1310
Applied Mathematics 1310
Symmetry Analysis on Rosenau Type Equations 1311
Exploring Rayleigh Waves in Layered Media 1314
Understanding Predator- Prey Dynamics Through Equilibrium State Classification. 1317
Effects of Weak Heterogeneity on Nonlinear Love Wave Interactions 1320
Data Science and Machine Learning 1323
A Case Study in Time Series Classification Using Machine Learning and Deep Learning 1324
Mathematical Modeling 1327

Modeling Rare Metal Market Dynamics: A Nonlinear Approach withInvestment and Geopolitical Risk..... 1328
MECHANICAL ENGINEERING 1330
Additive Manufacturing 1330
Evaluation of Mechanical Properties of SLM AlSi10Mg Alloy Produced with Different Production Parameters 1331
Automotive 1335
Optimizing Urban Micro-Mobility: Ergonomic Design, Structural Integrity, and Dynamic Analysis of Electric Kick Scooter 1336
Electrification of Heavy Commercial Truck: Vehicle Modeling with Using MATLAB/Simulink, Energy Efficiency Analysis and Economic Comparison with Conventional Diesel Engine 1346
ANN-Based PID Tuning Mechanism For A Vehicle Control SystemConsidering Improved Path Following 1354
Combustion Model Analysis on Validation Purpose of a Spark Ignition Engine 1358
Computational Fluid Dynamics 1363
Multi-Objective Aerodynamic Shape Optimization of Helicopter Nose..... 1364
Analysis of Effects of Tip Clearance on Axial Pump Performance..... 1369
Aerodynamic Performance Enhancement of a 27-Inch Apc Propeller Through Geometric Modifications 1375
Process Optimization of Polymer Melt Impregnation Systems by Extrusion Method 1380
Investigation of Thermal-Flow Performance in Close Circuit Cooling Towers..... 1388
Computational Solid Mechanics 1396
A Novel Approach for Robust Identification and Characterization of Mechanical Shock Loads for Structural Durability Assessment..... 1397
Modeling Hydrogen-Induced Failure of AISI 4135 Steel by Finite Element Analysis . 1405
A Comparative Modal Analysis of Homogenized and Full-Scale FE Models of Sandwich Composite Structures with Re-entrant Auxetic Core.....1411
Parametric Investigation of Mechanical Properties for Laser Powder Bed Fusion Processed Inco718 Auxetic Metamaterials 1417
Hybrid Optimization Method for I-Section Beams: A Comparative Study with Detailed FEM 1422
Structural Optimization of LPDC Aluminum Wishbone for Sheet Metal Design in Rear Suspension System for Electric C-SUV Vehicles 1426
Post-Buckling Behavior of Metallic Panels 1430
Machine Design..... 1437
Weight and Volume Optimization of Two Stage Wolfrom Planetary Gear Mechanism 1438

Examining the Impact of Groove Profiles and Dimensional Parameters on Shear Pin Strength 1443
Machine Dynamics, Vibration, and Acoustic 1448
Investigation and Optimization of the Effect of Different Profile Modifications on Gear Noise and Strength in the Gearbox with Single-Stage Spur Gear 1449
Semi-Analytical Investigation of Nonlinear Tuned Mass Dampers Using the Multi-Term Harmonic Balance Method 1454
Investigating the Use of Crash Dummies as Human Body Models for Whole-Body Vibration Evaluation 1461
Comparison of Time and Frequency Domain Approaches for Fatigue Life Estimation Using the Finite Element Method 1465
Analytical Investigation of Modal Curvatures of Damaged Beams 1470
System Dynamics and Control 1480
Nonlinear System Identification of a 2-DOF Gimbal System 1481
Trajectory Analysis of a Medium-Range Ballistic Missile Threat via Design and Simulation 1487
MECHATRONICS ENGINEERING 1490
Autonomous Vehicles 1490
WaveDrive: A Pipeline for Gesture Recognition Using Hands Coordinates 1491
Robotics 1496
A Study on the Performance of GNN, PDA, and JPDA in a ROS-Based Tracking Framework 1497
Vehicle Design 1503
Steer-by-Wire System Modeling and Control Using Optimal PID Controller 1504
METALLURGY AND MATERIALS ENGINEERING 1509
Composite and Polymer Materials 1509
Characterization of Talc and Reduced Graphene Oxide Reinforced Polypropylene Composites: Thermal, Mechanical and Structural Properties 1510
Thermal and Mechanical Properties of Reduced Graphene Oxide Reinforced Polypropylene Composites 1513
Corrosion and Wear 1516
Fabrication of Al Matrix MMC Cold Spray Coatings on AZ31 Magnesium Alloy 1517
Extractive Metallurgy 1521
Investigation of Reduction of Chromite Ore with Hydrogen 1522
Production and Characterization of Lanthanum Hexaboride Powder 1526
Mechanical Metallurgy 1530
Effects of Stress Relief Annealing Time on Mechanical Properties and Operating Cost in Lamellar Graphite Cast Iron Engine Blocks 1531

Metals and Alloys 1538
Precious Metal (Au, Pd, Pt, Rh) Recovery Using Torrefied Biomass Species Such As Forest, Marine And Agricultural Biomass 1539
Effect of Heat Treatment on Inconel 718 Superalloy Produced by Cold Spray Additive Manufacturing 1542
Effect of Niobium Addition on the Microstructural Features of Titanium Alloys for Dental Implants 1545
Recycling-Driven Variations in Mechanical Properties and Weldability of 6XXX Series Aluminium Alloys for Electric Vehicle Structural Parts 1549
Surface Treatment and Coatings 1555
Effect of Pack Aluminizing on Hydrogen Charging Behavior of Ti6Al4V Alloy Fabricated by Selective Laser Melting 1556
A Comparative Study of Ni-SiC and Micro-Arc Oxidation Coatings Produced on the Al-Si Casting Alloy 1559
Enhancing CMAS and Hot Corrosion Resistance of YSZ Thermal Barrier Coatings via Aluminium Cold Spray 1562
A Comparative Study Of Anodized Coating And Micro-Arc Oxidation Coatings Produced On The Al-Si Casting Alloy 1565
METEOROLOGICAL ENGINEERING 1568
Atmosphere, Meteorology 1568
Heatwave Analysis Approach 1569
Renewable Energy 1576
Repowering at Türkiye's Leading Power Plant: An Analysis of Energy Production Increase 1577
MINING ENGINEERING 1580
Excavation Mechanics 1580
Machine Learning-Based Prediction of Thrust Force in Tunnel Boring Machines 1581
MOLECULAR BIOLOGY - GENETICS AND BIOTECHNOLOGY 1585
Metagenomics and Protein Engineering 1585
Recombinant Production of Two Novel Ferredoxin-NADP^{+} Reductases from Pseudomonas mandelii KGI_MA19 1586
Site-Directed Mutagenesis on Inactive CYP102A178 from Hydrothermal Hot Spring Hisaralan-Balıkesir 1591
MUSIC 1596
Ethnomusicology 1596
Sonified Memory of the 2020 Aegean Sea Earthquake 1597
Music Business and Management 1602
Music Memes and the Relationship Between Music Marketing and Humor in Turkey: The Past, Present, and Future 1603

Music Performance **1606**

Challenging Conventions: Clara Wieck's Op. 20 and the Gendered Landscape of 19th-Century Music **1607**

Messiaen as Liturgist: A Contextual Reading of the Vingt Regards sur l'Enfant-Jésus **1610**

The Relentless Clash of Dissonant Harmonies and Lyric Melodic Lines… An Extensive Look into the Sound of Sergei Prokofiev **1613**

Music Theory **1615**

Effects of Performance Space on Free Improvisation Practices **1616**

Cyclic Unity and Romantic Expression in Robert Schumann's Fantasiestücke, Op. 12: A Schenkerian Perspective **1619**

Sonic Arts **1622**

Exploring Dance Floor Tactility: Sonic Ethnography and Artistic Inquiry through Audio Paper **1623**

Sound Engineering and Design **1625**

Spatial Auditory Masking in 3D Audio: Challenges, Experimentation and Implications for Immersive Sound **1626**

Methodology on Participatory Media Analysis: Insights from the Audio Modding Scene on Nexus Mods **1629**

Transformation of Digital Audio from Metaverse to Web3 ..... **1632**

MUSICOLOGY AND MUSIC THEORY **1635**

Ethnomusicology **1635**

Ecomusicological Methods in Soundscape Research: Analyzing Sounds on the Water in Haliç **1636**

Historical Musicology **1639**

Analysis Of Some Makams From The Arabic Music Conference 1932 ..... **1640**

Music as Refuge From Reality: Schopenhauerian Aesthetics Revisited **1643**

Music Theory **1646**

Folk Music and Classical Composition: A New Framework in Scottish Music Based on Bartok's Three Folk Music Categorizations **1647**

Harmony in Brouwer's Late Period: Use of Extended Tonality in the First Movement of Del Pensador **1651**

Analysis of Vertical Structures in the Context of Set Theory in Ivan Wyschnegradsky's 24 Preludes in Quarter Tone System for Two Pianos, Op. 22 ..... **1658**

Exploring Perde-Çeşni Transformations in Tanburi Cemil Bey's Nikriz Makam **1667**

Popular Music **1669**

The Issue of "Originality" in Arabesk Music: Analysis of Musical Borrowings, Similarities, and Production Practices from Arab music **1670**

It's Corn!: From Everyday Life's 'Sound' to Viral Musical Meme **1675**

NANOSCIENCE AND NANOENGINEERING 1678
Nanoparticles 1678
Radiation Attenuation of MWCNT and Magnetic Nanoparticle 1679
Reinforced PMMA Comparative Analysis of Coefficient 1679
Polymer and Nano Composites 1688
Thermo-responsive PNIPAAM Based Hydrogels with Bio-inspired Additives for Biomedical Applications 1689
PETROLEUM AND NATURAL GAS ENGINEERING 1692
Geothermal Engineering 1692
Utilization of Carbon Dioxide Gas (CO_2) for Gas Lift Systems In Geothermal Wells. 1693
Natural Gas Engineering 1698
Natural Gas Hydrate Modelling 1699
Reservoir Engineering 1705
Comparison of Thermophysical Gas Properties 1706
A Machine Learning Approach to Forecast Production Performance of Hydraulically Fractured Horizontal Wells in Tight Oil Sandstone Reservoirs 1713
PHYSICS ENGINEERING 1719
High Energy and Particle Physics 1719
Dynamo Process in Proto-Neutron Stars 1720
Constraints on New Physics with Light Mediators and Generalized Neutrino Interactions via Coherent Elastic Neutrino Nucleus Scattering 1722
Mathematical Physics 1728
Investigation of Structural and Optoelectronic Properties of metal/ZnS Junction under Density Functional Theory (DFT) 1729
Optics and Photonics 1733
Imaging Ellipsometry for Material Characterization and Defect Analysis 1734
POLITICAL STUDIES 1738
Political and Social Thought 1738
State Construction of the “Othering” Mechanisms Leading to Stigmatization and Discrimination 1739
Political Philosophy 1742
An Evaluation of Socrates, Plato and Aristotle Regarding Their Conceptualizations of Political Legitimacy 1743
POLYMER SCIENCE AND TECHNOLOGY 1746
Material Science 1746
Synthesis and Characterization of Sulfonated Polysulfone for Proton Exchange Membrane Fuel Cells 1747
RAILWAY SYSTEMS ENGINEERING 1752

Railway Systems Engineering 1752
Fiber Bragg Grating Sensor: Princibles, Applications, and Emerging Trends 1753
Signaling Systems in Railways 1756
Energy Efficiency Optimization through Metro Scheduling: Mixed-Integer Linear Programming (MILP) and Genetic Algorithm Approaches 1757
A Safety-Critical Railway Interlocking Architecture Based on SCADE and HIMA PLCs with Python-Driven Simulation and Control 1759
REAL ESTATE DEVELOPMENT 1763
Real Estate Development 1763
An Event-Driven Architecture in Real Estate Development 1764
SCIENCE, TECHNOLOGY AND SOCIETY 1768
Communication of Science and Technology 1768
A Bibliometric Analysis of Metaverse Technologies in Healthcare Services 1769
Social and Ethical Dimensions of AI 1772
Unintended Consequences of Generative AI in Product Ideation: A Product Management Perspective 1773
Social Dimensions of Science and Technology 1777
The Impact of Music Platforms on Music Production and Taste Profiles in Türkiye: The Case of Spotify 1778
SHIPBUILDING AND OCEAN ENGINEERING 1783
Hydrodynamics of Marine and Offshore Structures 1783
The Penglai 19-3 Incidents: Failures, Response, and Regulatory Lessons 1784
SOIL MECHANICS AND GEOTECHNICAL ENGINEERING 1792
Environmental Geotechnics 1792
Evaluation of Geotechnical Characteristics of Recycled Concrete Aggregate-EAF Slag Mixtures 1793
Geotechnical Earthquake Engineering 1802
Dynamic Site Response Analyses For A Site With A Deep Cut 1803
Geotechnics 1810
Modelling Lateral Spreading in a Sandy Soils 1811
STRUCTURAL ENGINEERING 1817
Bridges 1817
Investigation of the Effects of Vibration Dampers Positioned on Hanger Cables of an Existing Suspension Bridge 1818
Finite Element Methods 1822
Artificial Intelligence Based Surrogate Models for Stiffened Plate Buckling Analysis 1823
Finite Element Analysis of Symmetrical Laminated Sandwich Plates with Stress Singularities Using Gradient Elasticity Theory 1829

Effect of Strut Shape and Relative Density on the Homogenized Material Properties and Anisotropy of Octet-Truss Unit Cell 1835
Reinforced Concrete Structures 1844
Using parametric design software to optimize hyperbolic paraboloid reinforced concrete shells in an example model 1845
A Preliminary Comparison of Turkish Seismic Design Code and the Draft Seismic Design Communiqué based on the Outputs of Structural Analyses of Mid-Rise RC Buildings 1848
Effect of Heat Aging on the Axial Behaviour of PET FRP Confined Low-Strength Concrete 1853
Seismic Performance 1858
Seismic Performance Evaluation and Comparison of Different Structural Systems Using Nonlinear Time History Analysis 1859
Steel Structures 1861
Seismic Performance of Gravity Frames with Flush End-Plate 1862
Beam-to-Column Connections 1862
Effect of Initial Imperfections in Short Link Beams on Frame Behavior 1866
Blast-Resistant Steel Modular Structures Design with the Comparison of Dynamic Analysis Methods: SDOF and MDOF Systems 1873
Structural Damages 1877
Vibration Fatigue-Based Optimization of Open Hole Design in Stiffened Panels 1878
SUSTAINABILITY 1883
Climate Change Mitigation 1883
Assessing Decarbonization Strategies and Decoupling Trends of Türkiye's Private Sector Companies 1884
The Relationship between Sustainable Finance and The Carbon Border Adjustment Mechanism (CBAM): A Policy Impact Assessment and Hypothetical Case Study of A Cement Plant 1887
Life Cycle Assessment 1889
The Intersection Infrastructure of LCA-BIM Inegration: Applicability in Turkey and Europe 1890
Reinforced Concrete Structures 1895
Effects Of Using Waste Glass Powder And Rice Husk Ash As A Partial Replacement With Cement In Mortar Productions 1896
Smart and Sustainable Cities 1899
Investigation of Green Buildings Towards Net Zero Carbon Cities: Example in ITU Ayazağa Campus 1900
An Inclusive Digital Accessibility Policy for Individuals with Disabilities 1902
Sustainable Development Goals 1907

Enhanced Efficiency of PLA-Based Membranes via Optimizing Coagulation Bath Temperature 1908
Water and Waste Management 1913
Evaluating the Water Footprint of Textile Products: A Comparative Study of Wool and Cotton in Türkiye 1914
TEXTILE ENGINEERING 1919
Sustainability in Textile and Fashion Industries 1919
Statistical Analysis of Short Fiber Content and Tenacity Using Exponential Regression 1920
Textile Clothing and Fashion Design 1923
Real Time Production Management in Garment Manufacturing Using IoT-Based Process Monitoring Devices (PMDs) 1924
TRADITIONAL DANCES 1932
Dance, Traditional Dances in Terms of its Role in İnterdisciplinary İnteraction in Performance Areas 1932
The Reinterpreting Choreographic Art Through 1933
Traditional Dances in Turkey: The Shaman Dance '7EDI' Project 1933
URBAN AND REGIONAL PLANNING 1936
Climate Change and Planning 1936
Climate Change Adaptation in Urban Heritage Sites: The Case Of Istanbul Historic Peninsula 1937
Smart Cities, Digitalization, and Data Science 1941
City Information Modeling: Identifying Knowledge Gaps and Research Priorities 1942
Deprivation Analysis In Turkey And Its Provinces: A Study Based On English Index Of Deprivation And Turkish Statistical Institute 1946
Sustainability, Ecology, and Energy in Planning 1950
Rethinking Heritage-Tourism Relations: Critical Perspectives and Sustainable Futures for Cultural Sites 1951
Transportation Planning and Urban Infrastructure 1955
Determination of Saturation Flow Rate Right-Turn Adjustment Factor for Large Radii in Istanbul 1956
Towards Walkable and Green University Campuses: Observational Assessment of ITU Maslak Campus for Advancing the Sustainable Development Goals 1962
URBAN DESIGN 1970
Design and Evaluation of Public Spaces 1970
The Transformative Effect of Digital Art Installations on Public Spaces: The Case of Border Tuner 1971
The Impacts of Building-Street Interaction on Behavior: A case Study on Privacy in Kadıköy 1973

Urban Conservation 1977
A Study Of Meaning In Ruins: Ancient Cities As Open-Air Museums 1978
Urban Image and Identity 1983
The Impact of Space on Sound Perception: The Relationship Between Sound and Context 1984
Urban Resilience 1987
Pedestrianization as a Tool to Create Resilient Cities Through Open Space Networks 1988
POSTER PRESENTATIONS 1994
AERONAUTICAL AND ASTRONAUTICAL ENGINEERING 1995
Rotary Wing Aircraft 1995
Effect of Twist Distribution on Rotor Performance and Twist Applications for Rotor Blades 1996
Span-Morphing Rotorcrafts: Performance Analysis and Mechanism Selection 2002
Theoretical, Computational And Experimental Structural Analysis And Design 2007
Optimization Of Aluminum Plate Under Impact Loading 2008
Optimum Rudder Torque Tube Design for a Light Training Aircraft 2013
Structural Design and Analysis of Engine Mount Structure for Propeller Training Aircraft 2017
APPLIED INFORMATICS 2023
Data Analysis 2023
Comparing Fractional Calculus And LSTM For Greenhouse Gas Emission Forecasting: Insights For Policy And Strategy 2024
ARCHITECTURE 2031
Architectural History 2031
Civil Architecture in Pieter Coecke van Aelst's Depictions from His Journey to Istanbul 2032
Architecture Design Theory 2037
Fiction And Reality In Architectural Representation: Spatial Readings In Graphic Novels 2038
Deconstruction of Clothing: Clothing as a Spatial and Embodied Medium 2042
The Interpretation of the Metaverse through Rhizome Philosophy 2047
Evaluation of Social Performance in Public Squares Through Social Media Images : A Case Study of Taksim Square and Beyazıt Square 2051
Architectural Representation in the New Media Era and Lateness 2057
The Mask as an Instrument of Spatial Construction 2061
Conservation and Restoration 2064

Tracing a Cultural Heritage from the Ottoman Era to the Present: A Study on the Conservation of Kepenekçi Sinan Mosque 2065
Documentation and Conservation Proposalofa 19th Century Ottoman Heritage: Kececizade Fuat Pasha Mosque 2070
Environmental Control and Building Technology 2076
The Role of System Sections in Architectural Competitions: 2077
From Conceptual Design to Construction 2077
ART HISTORY 2080
Modern and Contemporary Art 2080
Valorizing Cultural Heritage through Art and Movement: Spatial and Bodily Experience in a Promenade Performance 2081
CHEMICAL ENGINEERING 2087
Hydrogen Technologies, Fuels Cells, Energy Storage Materials 2087
Preparation and Characterization of Polysulfone Membranes for Proton Exchange Membrane Fuel Cells 2088
Modelling and Computational Systems 2091
Computational Simulation of Corn Wet Milling for Starch Production: Revisiting a Conventional Biotechnological Process 2092
Nanotechnology, Surface Coatings and Films 2099
Fabrication and Characterization of Plant Extract-Added Bilayered Nanofiber Wound Dressing 2100
CHEMISTRY 2105
Analytical Chemistry 2105
Method Development and Validation for Simultaneous Determination of Six Nitrosamines in Different Pharmaceutical Dosage Forms by GC-MS/MS Equipped with Headspace 2106
Biochemistry 2109
Preparation of Peptide-GelMA Composite Hydrogel-Based Wound Dressing with 3D Printer and Its Physical Characterization 2110
Preparation of 3D-Printed Peptide-Based Hydrogel Wound Dressing with GHK-Cu for Chronic Wound Treatment 2115
Drug Design & Drug Delivery (Computational and Experimental) 2120
Synthesis and Characterization of Liposomal Formulations of Biguanide Derivative Active Pharmaceutical Ingredient 2121
Energy Materials (Synthesis, Characterizations, Applications) 2127
Immobilization of Cobalt Wastes in Ceramics for The Long-Term Storage in Deep Radioactive Waste Repository 2128
Organic Chemistry 2130

Stimuli-Responsive Polymers Based on Calix[4]pyrrole and Pillar[5]arene Molecular Recognition 2131
Physical Chemistry 2135
Determination of Solubility of p-aminobenzoic Acid (PABA) Derivative Active Pharmaceutical Ingredient in Non-Aqueous Binary Mixture 2136
Polymer Chemistry 2144
MUF Resin with Low Formaldehyde Emissions for Wood-Based Panel Industry 2145
COMPUTATIONAL SCIENCE AND ENGINEERING 2148
Computational Biology 2148
Identification of Inhibitors Targeting Two-component Regulatory System in Acinetobacter baumannii Called AdeRS 2149
Molecular Dynamics Simulations of CHK2 Kinase Domain Mutants 2154
COMPUTER ENGINEERING 2158
Internet of Things 2158
Effect of Topology on Energy Consumption in Low Power Wireless Sensor Networks 2159
Neural Networks 2166
Performance Comparison of PECNET as Financial Time Series Feature Extraction with Respect to TimeGPT, TSMixer, and Prophet 2167
Software Engineering 2172
A Gamified Hybrid Application for Sports Club Fans: Development and Implementation 2173
COMPUTER SCIENCE 2176
Data Analysis 2176
Comparative Analysis of Large Language Models for Natural Language to SQL and Visualization Code Generation 2177
CONSTRUCTION MANAGEMENT 2182
IT in Construction 2182
Developing An Ontology For Artificial Intelligence Assisted Quality Control Systems In Mega Projects 2183
Usage of Large Language Models in the Construction Industry: A Literature Review and Evaluation 2188
Risk Management in Construction 2193
Artificial Intelligence-Supported Risk Management and Visualization Techniques in the Construction Industry 2194
CONTROL AND AUTOMATION ENGINEERING 2197
Advances in Automatic Control Engineering 2197
Comparison Of Anti-Windup Methods for Fractional Order PI Controllers 2198
Applications of Control Engineering 2203

DESIGN AND CONTROL OF A 120-TON CAPACITY TRANSPORTATION SYSTEM FOR INDUSTRIAL APPLICATIONS 2204
DATA ENGINEERING AND BUSINESS ANALYTICS 2209
Big Data Analytics for Decision-Making 2209
Value-Based Strategy Development for AI Adoption in IT: A Means-End Chain Approach ... 2210
DISASTER AND EMERGENCY MANAGEMENT 2214
Debris Management 2214
Post-Disaster Debris Recycling: Mobile Recycling Units and On-Site Separation 2215
ECOLOGY AND EVOLUTION 2221
Anthropogenic Impacts 2221
Ecological Restoration Potential of Istanbul: Opportunities, Challenges and Risks ... 2222
ELECTRICAL ENGINEERING 2226
Electric Power & Energy Systems 2226
Load Frequency Control of Two Area Hybrid Power System Using a Neural Network-based Gradient Descent Method 2227
Electrical Vehicles 2233
Contributions to the Determination of Optimized Driving Strategies with ML-Based Methods for Electric Vehicles 2234
Power Electronics 2239
Conceptual Power Conversion Architecture for Unmanned Aerial Vehicles Utilizing BLDC Motor as Both Starter and Generator 2240
ENERGY SCIENCE AND TECHNOLOGY 2243
Energy Management and Planning 2243
Comparative Analysis of LSTM and LightGBM for Short-Term Electricity Consumption Forecasting 2244
Building Energy Efficiency: A Data-Driven Machine Learning Approach for Energy Management and Planning 2247
Sustainable Energy 2251
Optimization of Ground Heat Exchangers for Sustainable Heating Solutions: A Case Study Approach 2252
ENVIRONMENTAL ENGINEERING 2257
Air Pollution and Control 2257
Carbon Capture and Utilization in the Cement Industry: Opportunities for Methanol and Urea Production from Process Emissions – A Systematic Literature Review 2258
FOOD ENGINEERING 2261
Food Microbiology 2261
Postharvest Application Of Cold Plasma On Fresh Spices And Evalution Of Major Changes 2262

Food Science 2265
Evaluation of Pasting and Rheological Properties of Modified Starches for Use in Plant-Based Products 2266
Functional Foods 2268
Use of Chlorella Vulgaris in Development of a Functional Ice Cream 2269
Novel Nutritional Yeast Formulation as a Functional Ingredient 2271
for Healthy Snacks 2271
Sustainable Foods 2274
Production and Characterization of a Functional Food Additive from Lemon Peel ... 2275
From Waste to Packaging: Biodegradable Films from Artichoke Products Phenolics via Subcritical Water Extraction 2278
GEOMATICS ENGINEERING 2284
Geographic Information Systems 2284
Earthquake Risk Analysis of Water Transmission Lines in Istanbul 2285
Spatial Estimation of Potential Utilization Performance of Electric Vehicle Charging Stations in Türkiye Using Machine Learning 2288
Geographic Information System-Based Accessibility Analysis of Disaster and Emergency Assembly Areas: The Case of Esenyurt District 2293
HISTORY OF SCIENCE AND TECHNOLOGY 2298
History of Mathematics 2298
The Impact of Gödel's Incompleteness Theorem on Artificial Intelligence: The Roger Penrose Approach 2299
INDUSTRIAL DESIGN 2302
Product Design 2302
Manufacturability for Industrial Design: Mass Production and Design 2303
INDUSTRIAL ENGINEERING 2306
Engineering Management 2306
Analysis of Organizational Capabilities of Companies in Construction Industry Using a Multi-Criteria Decision-Making Approach 2307
MANAGEMENT 2312
Marketing 2312
Value Co-Creation in Banking: Service-Dominant Logic and Service 2313
Logic Perspectives via Electronic Wallets 2313
MANAGEMENT ENGINEERING 2316
Quantitative Methods 2316
Selection of an Electronic Marketplace for Micro-Exports by SMEs: A Hierarchical IFS-WASPAS Approach 2317
MARITIME STUDIES 2323

Maritime Security 2323
Advancing Maritime Security With Unmanned Maritime Systems 2324
MATERIAL SCIENCE AND ENGINEERING 2331
Materials Synthesis and Processing 2331
Structural and Mechanical Characterization of Repair Welded Steels 2332
Synthesis of Boron Carbon Nitride Particles for Adsorptive Heavy Metal Removal 2337
MECHANICAL ENGINEERING 2341
Automotive 2341
Combustion Simulation of HCNG Fueled Single-Cylinder Research Engine Using Fractal Combustion Model 2342
CFD Analysis of The Effects Of Hydrogen Addition On The Performance And Emissions Of A Natural Gas-Fuelled Single-Cylinder Internal Combustion Engine 2348
Machine Design 2355
Design Optimization of Crane Hook by using Generative Design Approach 2356
Hyperelastic Characterization, Modeling and Testing Under Compression Stress Relaxation of a Sealing Component 2362
Design and Analysis of the Drive System Prototype for a Wire Rope Fatigue Test Setup 2370
Creep Behavior of Polyglass Band Used in Electrical Transformer Cores 2374
MECHATRONICS ENGINEERING 2378
Control Systems 2378
Development Of A Deep Reinforcement Learning-Based Flight Control System For F-16 Aircraft 2379
METALLURGY AND MATERIALS ENGINEERING 2386
Energy Materials 2386
The Impact of Different Dispersing Agents Used in Ball Milling onto The Electrochemical Performance of Spinel $LiNi_{0.5}Mn_{1.5}O_4$ Cathode Material 2387
Efficient Leaching of Valuable Metals from NMC Cathodes of Li-Ion Batteries with Green Deep Eutectic Solvents 2392
Metals and Alloys 2398
Development of NiCoCrTiAl Alloy's High Temperature Deformation Resistance With Refractory Alloying 2399
Surface Treatment and Coatings 2403
Investigation of the Properties of Micro-Arc Oxidation Coating on Selective Laser Melted AlSi10Mg Alloy 2404
METEOROLOGICAL ENGINEERING 2409
Aviation Meteorology 2409

Batman Airport Fog Analysis and The Relationship of Long-Term Fog With Low-Level Jets 2410
MINERAL PROCESSING ENGINEERING 2421
Critical and Strategic Raw Materials 2421
Li Recovery from Clayey Boron Plant Tailings Through Mechanical Activation and Saline Water Leaching 2422
Industrial Raw Materials 2427
Effect of Particle Size on Obtaining High-Quality Silica by Flotation Method 2428
MOLECULAR BIOLOGY - GENETICS AND BIOTECHNOLOGY 2432
Bioimaging 2432
Characterization of Cell Features and Trajectories Using Adaptive Tracking Integrated with Learning-based Segmentation Method 2433
Drug and Vaccine Development 2439
Vaccinomics to Design Chimeric Vaccine Candidate Against Four *Bordetella* Species 2440
Metabolic and Evolutionary Engineering 2443
Analysis of Oxidative Stress Response of Stress-Resistant Saccharomyces cerevisiae Strains Obtained by Evolutionary Engineering 2444
Investigation of Caffeine Metabolism in Saccharomyces cerevisiae 2449
Comparative Whole Genome Sequencing and Bioinformatic Analysis of an Aluminum-Resistant, Industrial *Saccharomyces cerevisiae* Strain 2453
Nanobiotechnology 2456
Saccharomyces cerevisiae-Based Silver Nanoparticle Biosynthesis 2457
Production of Silver Nanoparticles by Green Synthesis 2460
NANOSCIENCE AND NANOENGINEERING 2463
Nanotechnology for Energy Systems 2463
A Comparative Evaluation of Copper-Based Electrocatalysts as Potential Candidates for Effective and Selective Electrochemical Conversion of CO_2 2464
NUCLEAR RESEARCH 2468
Radiation Detection and Measurement 2468
Neutron Reflection Method for Element Analysis Using GEANT4 2469
PHYSICS ENGINEERING 2473
Condensed Matter Physics 2473
Two-Body Problem In a Periodic Potential with a Complex Interaction 2474
High Energy and Particle Physics 2477
Neutrino Particle Direction Estimation Using Transformer-Based Deep Learning 2478
POLITICAL STUDIES 2484
Political Philosophy 2484
Understanding Epistemic Injustice Through Speech Act Theory 2485

POLYMER SCIENCE AND TECHNOLOGY 2488
Porous Materials 2488
Adsorption Performance of Hydrophilic PolyHIPE on Removal of Methylene Blue Dye 2489
Material Science 2494
Preparation of Novel Lignin-Based Hydrogels, Properties, and Adhesive Application 2495
Effect of Talc on Carbon Black Reinforced Natural Rubber Compound 2499
RAILWAY SYSTEMS ENGINEERING 2506
Railway Systems Engineering 2506
Railway Positioning and Fiber Optic Sensor Fusion: Integrating GNSS, IMU, and FOS for Enhanced Train Localization 2507
Signaling Systems in Railways 2511
Development of a Control System for Enhanced Safety and Efficiency in a Two-Switch Railway Station Area 2512
Traction Systems in Railways 2516
Fiber Optic Sensing Applications in Railway Systems 2517
SHIPBUILDING AND OCEAN ENGINEERING 2522
Hydrodynamics of Marine and Offshore Structures 2522
Numerical and Experimental Study of The Effect of The Hull Vane on The Total Resistance of The Catamaran 2523
SOIL MECHANICS AND GEOTECHNICAL ENGINEERING 2528
Foundation Engineering 2528
Comparison of Different Methods for Dynamic Earth Pressures on a Retaining Wall 2529
STRUCTURAL ENGINEERING 2533
Reinforced Concrete Structures 2533
Effect of Fly Ash on Chloride Permeability and Sulfate Resistence of Concrete 2534
Structural Damages 2539
High-Temperature Performance of Concrete Containing Calcium Aluminate and Portland Cements 2540
SUSTAINABILITY 2546
Biodiversity 2546
A Multidisciplinary Approach to Sustainable Agriculture: The Impact of Microbial and Organomineral Fertilization on Soil Bacteria, Crop Yield, and Farmer Adoption 2547
Life Cycle Assessment 2552
Life Cycle Assessment in a Zinc Oxide Recovery Plant Using the Waelz Process: Evaluation of Environmental Impacts from a Sustainability Perspective 2553
TEXTILE ENGINEERING 2557
Smart and Functional Textiles 2557

The Impact of Ski Jumping Suit Aerodynamics on Flight and Performance 2558
Textile Clothing and Fashion Design 2562
Simple And Timeless Woven Fabrics Design 2563

SPONSORS

aselsan BAYKAR

ORGANIZATION COMPANY

Dalya
KONGRE & ORGANİZASYON
DAHLIA TOUR

PREFACE

Dear Colleagues, Students and Distinguished Participants,

It is a great pleasure and honor for Graduate School of Istanbul Technical University to invite you to the 4th International Graduate Research Symposium: IGRS'25, to be held between 12th and 14th of May 2025, which will be organized as an hybrid event.

The symposium will present the findings of the most recent graduate researches from a diverse range of disciplines from basic sciences, engineering, and architecture to art and social sciences. We aim to bring together students, staff, alumni and industry from a diverse background to foster the interdisciplinary discussions, exchange of ideas, expand the knowledge, construct professional interactions and discuss the future perspectives. The symposium program will feature keynote presentations as well as poster sessions.

This symposium will demonstrate ITU's Graduate School's strategic commitment to innovation, academic excellence and leadership in higher education.

We hope that you will join the symposium and distribute this invitation to the staff and students across your institutions.

Many thanks
Best regards,

Chair of the Organizing Committee
Dean of Graduate School
Istanbul Technical University

Prof. Dr. F. Seniha Güner

COMMITTEES

HONORARY CHAIR

Prof. Dr. Hasan Mandal, Rector of İstanbul Technical University

ORGANIZING COMMITTEE CHAIR

Prof. Dr. Fatma Seniha Güner, Istanbul Technical University

ORGANIZING COMMITTEE

Prof. Dr. Burçak Karagüzel Kayaoğlu, Istanbul Technical University (Coordinator)
Prof. Dr. Sevil Yücel, Yildiz Technical University
Assoc. Prof. Dr. Ayça Bal Öztürk, Istinye University
Assoc. Prof. Dr. Onur Ferhanoğlu, Istanbul Technical University
Assoc. Prof. Dr. İlke Gürol, TUBITAK Marmara Research Centre
Dr. Res. Asst. Serhat Boynukalın, Istanbul Technical University
Res. Asst. Filiz Ayaz, Istanbul Technical University (Coordinator)
Res. Asst. Kıymet Kaya Ünal, Istanbul Technical University (Coordinator)
Res. Asst. Ahmet Yazıcı, Istanbul Technical University
Res. Asst. Arife Eymen Karabulut, Istanbul Technical University
Res. Asst. Asude Bolat, Istanbul Technical University
Res. Asst. Aycan Kızılkaya, Istanbul Technical University
Res. Asst. Bilal Korkmaz, Istanbul Technical University
Res. Asst. Görkem Giray, Istanbul Technical University
Res. Asst. Hatice Tuğba Karayama, Istanbul Technical University
Res. Asst. İlknur Akça, Istanbul Technical University
Res. Asst. İsrafil Kırmızı, Istanbul Technical University
Res. Asst. Mehmet Onur Demir, Istanbul Technical University
Res. Asst. Mustafa Erdem, Istanbul Technical University
Res. Asst. Nihan Zorlu Başel, Istanbul Technical University
Res. Asst. Nuran Irapoğlu, Istanbul Technical University
Res. Asst. Nurşen Sönmez, Istanbul Technical University
Res. Asst. Ozan Vahit Altınpınar, Istanbul Technical University
Res. Asst. Ömer İmir, Istanbul Technical University
Res. Asst. Özgür Altınışık, Istanbul Technical University
Res. Asst. Seda Tepe, Istanbul Technical University
Res. Asst. Şevki Samet Kaplan, Istanbul Technical University
Res. Asst. Volkan Er, Istanbul Technical University

SCIENTIFIC COMMITTEE

AERONAUTICAL AND ASTRONAUTICAL ENGINEERING

Prof. Dr. İbrahim Özkol, Aeronautical and Astronautical Engineering, Istanbul Technical University
Prof. Dr. Hülya Cebeci, Aeronautical and Astronautical Engineering, Istanbul Technical University
Prof. Dr. Melike Nikbay, Aeronautical and Astronautical Engineering, Istanbul Technical University
Prof. Dr. Metin Orhan Kaya, Aeronautical and Astronautical Engineering, Istanbul Technical University
Prof. Dr. Zahit Mecitoğlu, Aeronautical and Astronautical Engineering, Istanbul Technical University
Prof. Dr. Fırat Oğuz Edis, Aeronautical and Astronautical Engineering, Istanbul Technical University
Prof. Dr. Vedat Ziya Doğan, Aeronautical and Astronautical Engineering, Istanbul Technical University
Prof. Dr. Bayram Çelik, Aeronautical and Astronautical Engineering, Istanbul Technical University
Prof. Dr. Okşan Çetiner Yıldırım, Aeronautical and Astronautical Engineering, Istanbul Technical University
Assoc. Prof. Dr. Özge Özdemir, Aeronautical and Astronautical Engineering, Istanbul Technical University
Assoc. Prof. Dr. Mete Budaklı, Aeronautical and Astronautical Engineering, Istanbul Technical University
Assoc. Prof. Dr. Baha Zafer, Aeronautical and Astronautical Engineering, Istanbul Technical University
Asst. Prof. Dr. Ali Tatar, Aeronautical and Astronautical Engineering, Istanbul Technical University
Asst. Prof. Dr. Duygu Erdem, Aeronautical and Astronautical Engineering, Istanbul Technical University
Asst. Prof. Dr. Saliha Banu Yılmaz, Aeronautical and Astronautical Engineering, Istanbul Technical University
Asst. Prof. Dr. Oğuzcan İnal, Aeronautical and Astronautical Engineering, Istanbul Technical University
Asst. Prof. Dr. Demet Çilden Güler, Aeronautical and Astronautical Engineering, Istanbul Technical University
Asst. Prof. Dr. Barış Başpınar, Aeronautical and Astronautical Engineering, Istanbul Technical University
Asst. Prof. Dr. Cuma Yarım, Aeronautical and Astronautical Engineering, Istanbul Technical University
Asst. Prof. Dr. Demet Balkan, Aeronautical and Astronautical Engineering, Istanbul Technical University
Asst. Prof. Dr. Seher Eken, Aeronautical and Astronautical Engineering, Istanbul Technical University
Asst. Prof. Dr. Ramazan Yeniçeri, Aeronautical and Astronautical Engineering, Istanbul Technical University
Dr. Bülent Tutkun, Aeronautical and Astronautical Engineering, Istanbul Technical University
Dr. Kaan Yıldız, Aviation Institute, Istanbul Technical University

APPLIED INFORMATICS

Prof. Dr. Behçet Uğur Töreyin, Informatics Institute, Istanbul Technical University
Assoc. Prof. Dr. Volkan Müjdat Tiryaki, Informatics Institute, Istanbul Technical University
Asst. Prof. Dr. Mehmet Akif Yazıcı, Informatics Institute, Istanbul Technical University
Azizjon Meliboyev, Digital Technologies and Mathematics, Kokand University

ARCHITECTURE

Prof. Dr. Seden Acun Özgünler, Architecture , Istanbul Technical University
Assoc. Prof. Dr. Francisco Abarca, Urban and Spatial Planning, University of Granada
Prof. Dr. Ozan Önder Özener, Architectural Design, Istanbul Technical University
Assoc. Prof. Dr. Aslıhan Şenel, Architectural Design, Istanbul Technical University
Assoc. Prof. Dr. Bihter Almaç, Architectural Design, Istanbul Technical University
Prof. Dr. Fatih Yazıcıoğlu, Environmental Control and Building Technology, Istanbul Technical University
Assoc. Prof. Dr. Tarık Serhat Bozkurt, Environmental Control and Building Technology, Istanbul Technical University
Assoc. Prof. Dr. Halet Almıla Büyüktaşkın, Environmental Control and Building Technology, Istanbul Technical University
Prof. Dr. Ecem Edis, Building Sciences, Istanbul Technical University
Assoc. Prof. Dr. Caner Göçer, Building Sciences, Istanbul Technical University
Assoc. Prof. Dr. Filiz Akşit, Building Sciences, Istanbul Technical University
Prof. Dr. Elçin Filiz Taş, Project and Construction Management, Istanbul Technical University
Prof. Dr. Hakan Yaman, Project and Construction Management, Istanbul Technical University
Assoc. Prof. Dr. Bahriye Ilhan Jones, Architecture and Built Environment, Northumbria University
Assoc. Prof. Dr. Fatma Pınar Çakmak, Project and Construction Management, Istanbul Technical University
Prof. Dr. Yegan Kahya, Conservation and Restoration, Istanbul Technical University
Assoc. Prof. Dr. Işıl Polat Pekmezci, Conservation and Restoration, Istanbul Technical University
Assoc. Prof. Dr. Umut Almaç, Conservation and Restoration, Istanbul Technical University

Assoc. Prof. Dr. Gül Cephanecigil, Architectural History , Istanbul Technical University
Assoc. Prof. Dr. Bilge Ar, Architectural History , Istanbul Technical University
Assoc. Prof. Dr. Işıl Çokuğraş Bağdatlıoğlu, Architectural History , Yıldız Technical University
Assoc. Prof. Dr. Çağhan Keskin, Architectural History , İstanbul University
Asst. Prof. Dr. Mustafa Kaan Sağ, Architectural History , İstanbul University
Assoc. Prof. Dr. Nisa Semiz, Architectural History , Abdullah Gül University
Asst. Prof. Dr. Mejrema Zatric-Sahovic, Architectural History , International University of Sarajevo
Dr. Ayşe Ercan Kydonakis, Architectural History , Simon Fraser University
Dr. Batu Bayülgen, Architectural History , Istanbul Technical University
Prof. Dr. Mine Özkar Kabakçıoğlu, Building Information Modelling, Istanbul Technical University
Prof. Dr. Figen Gül, Building Information Modelling, Istanbul Technical University
Prof. Dr. Meryem Birgül Çolakoğlu, Building Information Modelling, Istanbul Technical University
Assoc. Prof. Dr. Derya Güleç Özer, Building Information Modelling, Istanbul Technical University
Assoc. Prof. Dr. Lana Kudumovic, Architecture, Istanbul Technical University
Assoc. Prof. Julia Nerantzia Tzortzi, Landscape Architecture, Politecnico di Milano

ART HISTORY

Prof. Dr. Zeynep Kuban, Architecture, Istanbul Technical University
Assoc. Prof. Dr. Aslıhan Erkmen, Graduate School, Istanbul Technical University
Assoc. Prof. Dr. Ebru Yetişkin, Faculty of Science and Letters, Istanbul Technical University
Assoc. Prof. Dr. Fariba Afkari, History of Art, Tahran University

CHEMICAL ENGINEERING

Prof. Dr. Ayşegül Meriçboyu, Chemical Engineering, Istanbul Technical University
Prof. Dr. Ş. Birgül Tantekin-Ersolmaz, Chemical Engineering, Istanbul Technical University
Assoc. Prof. Dr. Neslihan Alemdar, Chemical Engineering, Marmara University
Asst. Prof. Dr. Sadiye Velioğlu, Nanotechnology Institute, Gebze Technical University
Prof. Dr. Begüm Tokay, Chemical and Environmental Engineering, University of Nottingham

CHEMISTRY

Prof. Dr. Turan Öztürk, Chemistry, Istanbul Technical University
Prof. Dr. İsmail Yılmaz, Chemistry, Istanbul Technical University
Assoc. Prof. Dr. Caner Ünlü, Chemistry, Istanbul Technical University
Prof. Dr. Mustafa Gazi, Physics and Chemistry, Eastern Mediterranean University

CLIMATE AND MARINE SCIENCES

Prof. Dr. Hakkı Baltacı, Earth and Marine Sciences Institute, Gebze Technical University
Asst. Prof. Dr. Cihangir Köyceğiz, Civil Engineering, Konya Technical University
Assoc. Prof. Dr. Hu Liu, Northwest Institute of Eco-Environment and Resources, Chinese Academy of Sciences
Asst. Prof. Dr. Semih Sami Akay, Architecture and Urban Planning, İstanbul Topkapı University

COASTAL SCIENCES AND ENGINEERING

Prof. Dr. Şevket Çokgör, Civil Engineering, Istanbul Technical University
Prof. Dr. Mehmet Cüneyd Demirel, Civil Engineering, Istanbul Technical University
Assoc. Prof. Dr. Yavuz Selim Güçlü, Civil Engineering, Istanbul Technical University
Asst. Prof. Dr. Erdal Kesgin, Civil Engineering, Istanbul Technical University
Asst. Prof. Dr. Mehmet Melih Koşucu, Civil Engineering, Istanbul Technical University
Abderrahmane Benabdesselam, Hydraulics, University of Batna
Manousos Valyrakis, Civil Engineering, Aristotle University of Thessaloniki

COMMUNICATION SYSTEMS

Prof. Dr. Erdem Topsakal, Electrical and Computer Engineering, Virginia Commonwealth University
Prof. Dr. Filiz Sertel, Geomatics Engineering, Istanbul Technical University

Prof. Dr. Şinasi Kaya, Geomatics Engineering, Istanbul Technical University
Asst. Prof. Dr. Sebahattin Eker, Informatics Institute, Istanbul Technical University

COMPUTATIONAL SCIENCE AND ENGINEERING

Dr. Birkan Tunç, Computational Science & Engineering in Psychiatry, University of Pennsylvania
Asst. Prof. Dr. Süha Tuna, Computational Science and Engineering, Istanbul Technical University
Prof. Dr. F. Aylin Sungur, Computational Science and Engineering, Istanbul Technical University
Prof. Dr. M. Serdar Çelebi, Computational Science and Engineering, Istanbul Technical University

COMPUTER ENGINEERING

Prof. Dr. Mustafa Kamaşak, Computer Engineering, Istanbul Technical University
Assoc. Prof. Dr. Ahmet Cüneyd Tantuğ, Computer Engineering, Istanbul Technical University
Assoc. Prof. Dr. Yusuf Yaslan, Computer Engineering, Istanbul Technical University
Asst. Prof. Dr. Yaşar Erenler, Computer Engineering, Istanbul Technical University
Asst. Prof. Dr. Tolga Ensari, Computer and Information Science, Arkansas Tech University
Academic Dr. Meriç Yücel, Computer Engineering, Istanbul Technical University
Res. Assis. Dr. Kadir Özlem, Computer Engineering, Istanbul Technical University

COMPUTER SCIENCE

Assoc. Prof. Dr. Sefer Baday, Informatics Institute, Istanbul Technical University
Assoc. Prof. Dr. Volkan Müjdat Tiryaki, Informatics Institute, Istanbul Technical University
Asst. Prof. Dr. Mehmet Akif Yazıcı, Informatics Institute, Istanbul Technical University
Em. Prof. İzzet Kale, School of Computer Science and Engineering, University of Westminster

CONSTRUCTION MANAGEMENT

Prof. Dr. Esin Ergen, Civil Engineering, Istanbul Technical University
Assoc. Prof. Dr. Deniz Artan, Civil Engineering, Istanbul Technical University
Assoc. Prof. Dr. Atilla Damcı, Civil Engineering, Istanbul Technical University
Assoc. Prof. Dr. Onur Tokdemir, Civil Engineering, Istanbul Technical University

CONTROL AND AUTOMATION ENGINEERING

Semih Beyçimen, Control and Automation Engineering, Istanbul Technical University
Asst. Prof. Dr. Erhan Yumuk, Control and Automation Engineering, Istanbul Technical University
Asst. Prof. Dr. Abdurrahman Yılmaz, Control and Automation Engineering, Istanbul Technical University
Dr. İbrahim Beklan Küçükdemiral, Applied Science, Glasgow Caledonian University

DATA ENGINEERING AND BUSINESS ANALYTICS

Assoc. Prof. Dr. Mücahit Çevik, Department of Mechanical, Industrial, and Mechatronics, Toronto Metropolitan University
Asst. Prof. Dr. Mehmet Yasin Ulukuş, Data Science and Analytics, Istanbul Technical University
Asst. Prof. Dr. Mehmet Ali Ergün, Data Science and Analytics, Istanbul Technical University
Assoc. Prof. Dr. Ömer Faruk Beyca, Data Science and Analytics, Istanbul Technical University

DEFENSE TECHNOLOGIES

Dr. Şükrü Akif Ertürk, National Fighter Aircraft Technologies, TUSAŞ
Dr. Tanyel Çakmak, National Fighter Aircraft Product Directorate, TUSAŞ
Dr. Latif Akçay, Electrical and Electronics Engineering, Bayburt University
Prof. Dr. İbrahim Özkol, Aeronautical Engineering, Istanbul Technical University
Prof. Dr. Hülya Cebeci, Aeronautical Engineering, Istanbul Technical University
Assoc. Prof. Dr. Emre Koyuncu, Aeronautical Engineering, Istanbul Technical University
Dr. Alptekin Yıldız, Aviation Institute, Istanbul Technical University
Dr. Kaan Yıldız, Aviation Institute, Istanbul Technical University

Dr. Ramazan Yeniçeri, Aeronautical Engineering, Istanbul Technical University
Dr. Murat Şimşek, Electrical Engineering and Computer Science, University of Ottawa
Dr. Mehmet Akif Özkan, Cadence Design Systems

DISASTER AND EMERGENCY MANAGEMENT

Asst. Prof. Dr. Hikmet İskender, Disaster Management Institute, Istanbul Technical University
Assoc. Prof. Dr. Çağlar Göksu Akkaya, Disaster Management Institute, Istanbul Technical University
Assoc. Prof. Dr. Abdullah Can Zülfikar, Disaster Management Institute, Istanbul Technical University
Mitra Mohammadi, Environmental Science, Kheradgarayn Motahar Institute of Higher Education

EARTHQUAKE ENGINEERING

Prof. Dr. Ufuk Yazgan, Civil Engineering, Istanbul Technical University
Assoc. Prof. Dr. Reşat Oyguç, Civil Engineering, Istanbul Technical University
Prof. Dr. Ercan Yüksel, Earthquake Engineering, Istanbul Technical University

ECOLOGY AND EVOLUTION

Michael Barton, Human Evolution and Social Change, Arizona State University
Isaac Ullah, Anthropology, San Diego State University
Selin Gür, Archaeology, Swiss Archaeological Institute
Assoc. Prof. Dr. Orkan Özcan, Ecology and Evolution, Istanbul Technical University
Prof. Dr. Bülent Arıkan, Ecology and Evolution, Istanbul Technical University

ECONOMICS

Prof. Dr. Ahmet Faruk Aysan, Islamic Economics and Finance, Hammad Bin Khalifa University
Prof. Dr. Bülent Güloğlu, Economics, Istanbul Technical University
Prof. Dr. Resul Aydemir, Economics, Istanbul Technical University
Assoc. Prof. Dr. Aysun Hızıroğlu Aygün, Economics, Istanbul Technical University

ELECTRICAL ENGINEERING

Prof. Dr. Mustafa Bağrıyanık, Electrical Engineering, Istanbul Technical University
Assoc. Prof. Dr. Salih Barış Öztürk, Electrical Engineering, Istanbul Technical University
Assoc. Prof. Dr. Derya Ahmet Kocabaş, Electrical Engineering, Istanbul Technical University
Assoc. Prof. Dr. Duygu Bayram Kara, Electrical Engineering, Istanbul Technical University
Assoc. Prof. Dr. Ramazan Çağlar, Electrical Engineering, Istanbul Technical University
Assoc. Prof. Dr. Suat İlhan, Electrical Engineering, Istanbul Technical University
Asst. Prof. Dr. Lale Erdem Atılgan, Electrical Engineering, Istanbul Technical University
Asst. Prof. Dr. Cavit Fatih Küçüktezcan, Electrical Engineering, Istanbul Technical University
Dr. Ayman El-Hag, Electrical and Computer Engineering, University of Waterloo

ELECTRONICS AND COMMUNICATION ENGINEERING

Prof. Dr. Ender Mete Ekşioğlu, Electronics and Communication Engineering, Istanbul Technical University
Assoc. Prof. Dr. Nil Tarım, Electronics and Communication Engineering, Istanbul Technical University
Assoc. Prof. Dr. Mustafa Berke Yelten, Electronics and Communication Engineering, Istanbul Technical University
Prof. Dr. Edoardo Bonizzoni, Electrical, Computer and Biomedical Engineering, University of Pavia
Prof. Dr. Mattia Frasca, Electrical, Electronics and Computer Engineering, University of Catania
Prof. Dr. Cüneyt Güzeliş, Electrical-Electronics Engineering, Yaşar University
Prof. Dr. Serkan Topaloğlu, Electrical and Electronics Engineering, Yeditepe University
Prof. Dr. Arda Deniz Yalçınkaya, Electrical and Electronics Engineering, Boğaziçi University
Prof. Dr. Günhan Dündar, Electrical and Electronics Engineering, Boğaziçi University
Prof. Dr. Burak Acar, Electrical and Electronics Engineering, Boğaziçi University
Assoc. Prof. Dr. Muhammed Fatih Toy, Electronics and Communication Engineering, Istanbul Medipol University

Prof. Dr. Mustafa Altun, Electronics and Communication Engineering, Istanbul Technical University
Asst. Prof. Dr. Faik Başkaya, Electronics and Communication Engineering, Boğaziçi University
Assoc. Prof. Dr. Yiğit Dağhan Gökdel, Electronics and Communication Engineering, Istanbul Bilgi University
Prof. Dr. Tufan Kumbasar, Electronics and Communication Engineering, Istanbul Technical University
Assoc. Prof. Dr. Tufan Coşkun Karalar, Electronics and Communication Engineering, Istanbul Technical University
Assoc. Prof. Dr. İsa Yıldırım, Electronics and Communication Engineering, Istanbul Technical University

ENERGY SCIENCE AND TECHNOLOGY

Assoc. Prof. Dr. M. Suha Yazıcı, Energy Institute, Istanbul Technical University
Asst. Prof. Dr. Sevan Karabetoğlu, Energy Institute, Istanbul Technical University
Asst. Prof. Dr. M. Berker Yurtseven, Energy Institute, Istanbul Technical University
Prof. Dr. Arjan Korpa, Chemistry, University of Tirana

ENVIRONMENTAL BIOTECHNOLOGY

Prof. Dr. Özlem Karahan, Environmental Engineering, Istanbul Technical University
Prof. Dr. Mahmut Altınbaş, Environmental Engineering, Istanbul Technical University
Assoc. Prof. Dr. Börte Köse Mutlu, Environmental Engineering, Istanbul Technical University
Assoc. Prof. Dr. Mahmut Ekrem Karpuzcu, Environmental Engineering, Istanbul Technical University

ENVIRONMENTAL ENGINEERING

Prof. Dr. Vahid Vatanpour, Chemistry, Kharazmi University
Asst. Prof. Dr. Ramazan Keyikoğlu, Environmental Engineering, Istanbul Technical University
Asst. Prof. Dr. Mehmet Sadık Akca, Environmental Engineering, Istanbul Technical University
Asst. Prof. Dr. Hazal Gülhan Eksin, Environmental Engineering, Istanbul Technical University

FOOD ENGINEERING

Prof. Dr. Pervin Başaran Akocak, Food Engineering, Istanbul Technical University
Asst. Prof. Dr. Evren Demircan, Food Engineering, Istanbul Technical University
Prof. Tuba Esatbeyoğlu, Food Science and Human Nutrition, Leibniz University Hannover
Dr. Francesca Giampieri, Food Science and Human Nutrition, Universita Politecnica delle Marche

GAME AND INTERACTION TECHNOLOGIES

Asst. Prof. Dr. Aslı Kanan, Architecture, Istanbul Technical University
Assoc. Prof. Dr. Gökhan İnce, Computer Engineering, Istanbul Technical University
Asst. Prof. Dr. Mehmet Tahir Sandıkkaya, Computer Engineering, Istanbul Technical University
Asst. Prof. Dr. Ahmet Gün, Architecture, Istanbul Technical University
Prof. Halil Erhan, Interactive Arts & Technology, Simon Fraser University

GEOGRAPHIC INFORMATION TECHNOLOGIES

Dr. Mehmet Furkan Celik, Geomatics Engineering, Twente University
Prof. Dr. Taşkın Kavzoğlu, Geomatics Engineering, Gebze Technical University
Assoc. Prof. Dr. Muzaffer Can İban, Geomatics Engineering, Mersin University
Asst. Prof. Dr. Ozan Öztürk, Civil Engineering, Recep Tayyip Erdoğan University

GEOLOGICAL ENGINEERING

Asst. Prof. Dr. Zeynep Döner, Geological Engineering, Istanbul Technical University
Dr. Alp Ünal, Geological Engineering, Istanbul Technical University
Asst. Prof. Dr. Bala Ekinci Şans, Geological Engineering, Istanbul Technical University
Prof. Dr. Haibo Zou, Geosciences, Auburn University

GEOMATICS ENGINEERING

Prof. Dr. Bihter Erol, Geomatics Engineering, Istanbul Technical University
Assoc. Prof. Dr. Uğur Algancı, Geomatics Engineering, Istanbul Technical University
Assoc. Prof. Dr. M. Oğuz Selbesoğlu, Geomatics Engineering, Istanbul Technical University
Dr. Penjani Hopkins Nyimbili, Geomatics Engineering, The University of Zambia

GEOPHYSICAL ENGINEERING

Prof. Dr. Hülya Kurt, Geophysical Engineering, Istanbul Technical University
Prof. Dr. Doğa Doğan, Geophysical Engineering, Istanbul Technical University
Asst. Prof. Dr. Ümit Avşar, Geophysical Engineering, Istanbul Technical University
Dr. Nordiana Binti Mohd Muztaza, Geophysics, Universiti Sains Malaysia

HEAT FLUID

Prof. Dr. Ayşegül Abuşoğlu, Mechanical Engineering, Istanbul Technical University
Assoc. Prof. Dr. Sertaç Çadırcı, Mechanical Engineering, Istanbul Technical University
Assoc. Prof. Dr. Abdussamet Subaşı, Mechanical Engineering, Istanbul Technical University
Assoc. Prof. Dr. Amjad Anvari-Moghaddam, Mechanical Engineering, Aalborg University

HISTORY OF SCIENCE AND TECHNOLOGY

Prof. Dr. Aytekin Çökelez, Humanities and Social Sciences, Istanbul Technical University
Prof. Dr. Tuncay Zorlu, Humanities and Social Sciences, Istanbul Technical University
Assoc. Prof. Dr. Burak Barutçu, Renewable Energy, Istanbul Technical University
Asst. Prof. Dr. Mehmet Ali Doğan, Sociology, Istanbul Technical University
Darina Martykanova, Contemporary History, Universidad Autónoma de Madrid

HYDRAULICS AND WATER RESOURCES ENGINEERING

Prof. Dr. Şevket Çokgör, Civil Engineering, Istanbul Technical University
Prof. Dr. Mehmet Cüneyd Demirel, Civil Engineering, Istanbul Technical University
Assoc. Prof. Dr. Yavuz Selim Güçlü, Civil Engineering, Istanbul Technical University
Asst. Prof. Dr. Erdal Kesgin, Civil Engineering, Istanbul Technical University
Asst. Prof. Dr. Mehmet Melih Koşucu, Civil Engineering, Istanbul Technical University
Abderrahmane Benabdesselam, Hydraulics, University of Batna
Dr. Manousos Valyrakis, Civil Engineering, Aristotle University of Thessaloniki

INDUSTRIAL DESIGN

Prof. Dr. Gülay Hasdoğan, Industrial Design, Middle East Technical University
Assoc. Prof. Dr. Aykut Coşkun, Media and Visual Arts, Koç University
Prof. Dr. Piera Maresca, Industrial Design, Universidad Politécnica de Madrid
Prof. Dr. Ahmet Zeki Turan, Industrial Design, Mimar Sinan Fine Arts University

INDUSTRIAL ENGINEERING

Prof. Dr. Mehmet Güray Güler, Industrial Engineering, Istanbul Technical University
Assoc. Prof. Dr. Hatice Tekiner Moğulkoç, Industrial Engineering, Istanbul Technical University
Asst. Prof. Dr. A. Elvan Bayraktaroğlu, Industrial Engineering, Istanbul Technical University
Assoc. Prof. Dr. Çağatay İris, Management, University of Liverpool
Assoc. Prof. Dr. Velichka Traneva, Natural Sciences, Assen Zlatarov University
Assoc. Prof. Dr. Stoyan Tranev, Social Sciences, Assen Zlatarov University
Assoc. Prof. Dr. Venelin Todorov, Mathematics and Informatics, Assen Zlatarov University
Asst. Prof. Dr. Slavi Georgiev, Mathematics and Informatics, Assen Zlatarov University

INFORMATICS

Asst. Prof. Dr. Benay Gürsoy, Architecture, Pennsylvania State University
Prof. Dr. Özgür Ediz, Architecture, Bursa Uludağ University
Prof. Dr. Neşe Çakıcı Alp, Architecture, Kocaeli University
Asst. Prof. Dr. Gamze Gündüz, Architecture, Istanbul Bilgi University

INSTRUMENT - VOICE

Prof. Dr. Cihat Aşkın, Instrumental Performance, Istanbul Technical University
Prof. Dr. Tolgahan Çoğulu, Instrumental Performance, Istanbul Technical University
Prof. Kandemir Basmacıoğlu, Instrumental Performance, Istanbul Technical University
Dr. Reuben de Lautour, Music Technology, Istanbul Technical University
Prof. Dr. Münir Nurettin Beken, Instrumental Performance, University of California

INTERNATIONAL MASTER OF INTERIOR ARCHITECTURAL DESIGN

Prof. Dr. Suzie Attiwill, Interior Design, RMIT University
Prof. Dr. Özge Cordan, Interior Architecture, Istanbul Technical University
Prof. Dr. Banu Garip, Interior Architecture, Istanbul Technical University
Assoc. Prof. Dr. Demet Arslan Dinçay, Interior Architecture, Istanbul Technical University

LANDSCAPE ARCHITECTURE

Prof. Dr. Hayriye Eşbah Tunçay, Landscape Architecture, Istanbul Technical University
Prof. Dr. Elif Kutay Karaçor, Landscape Architecture, Istanbul Technical University
Assoc. Prof. Dr. Melih Bozkurt, Landscape Architecture, Istanbul Technical University

MANAGEMENT

Prof. Dr. Suat Teker, Management, Işık University
Prof. Dr. Nimet Uray, Management, Kadir Has University
Prof. Dr. Gül Tekin Temur, Industrial Engineering, Bahçeşehir University
Prof. Dr. Ephraim Clark, Management, Middlesex University

MANAGEMENT ENGINEERING

Assoc. Prof. Dr. Fuat Kosanoğlu, Management Engineering, Istanbul Technical University
Assoc. Prof. Dr. Ahmet Göncü, Management Engineering, Istanbul Technical University
Assoc. Prof. Dr. Ayşe Aylin Bayar, Management Engineering, Istanbul Technical University
Assoc. Prof. Dr. Ahmet Atıl Aşıcı, Management Engineering, Istanbul Technical University
Assoc. Prof. Dr. Adnan Veysel Ertemel, Management Engineering, Istanbul Technical University
Assoc. Prof. Dr. Öznur Özdemir Akyıldırım, Faculty of Management, University of Bradford
Assoc. Prof. Dr. Tuncay Özcan, Management Engineering, Istanbul Technical University
Assoc. Prof. Dr. Kaya Tokmakcıoğlu, Management Engineering, Istanbul Technical University
Prof. Dr. Elif Karaosmanoğlu, Management Engineering, Istanbul Technical University
Prof. Dr. Raziye Selim, Management Engineering, Istanbul Technical University
Prof. Dr. Oktay Taş, Management Engineering, Istanbul Technical University
Prof. Dr. Hür Bersam Bolat, Management Engineering, Istanbul Technical University
Asst. Prof. Dr. İdil Vedia Evcimen, Management Engineering, Istanbul Technical University
Prof. Dr. Mehmet Erçek, Management Engineering, Istanbul Technical University
Prof. Dr. Ferhan Çebi, Management Engineering, Istanbul Technical University

MARITIME STUDIES

Assoc. Prof. Dr. Pelin Bolat, Maritime, Istanbul Technical University
Prof. Dr. Levent Kırval, Maritime, Istanbul Technical University
Prof. Dr. Funda Yercan, Maritime, Piri Reis University

Dr. Christos Kontovas, Engineering and Technology, Liverpool John Moore University
Dr. George Gabedeva, Management, Batumi Navigational Teaching University

MARITIME TRANSPORTATION ENGINEERING

Prof. Dr. Yasin Arslanoğlu, Basic Sciences, Istanbul Technical University
Assoc. Prof. Dr. Burak Zincir, Marine Engineering, Istanbul Technical University
Asst. Prof. Dr. Gizem Kayışoğlu, Maritime Transportation and Management Engineering, Istanbul Technical University
Asst. Prof. Dr. Onur Yüksel, Faculty of Engineering and Technology, Liverpool John Moores University

MATERIAL SCIENCE AND ENGINEERING

Asst. Prof. Dr. Erçin Çağan Duran, Metallurgical and Materials Engineering, Istanbul Technical University
Asst. Prof. Dr. Faiz Muhaffel, Metallurgical and Materials Engineering, Istanbul Technical University
Assoc. Prof. Dr. Aytekin Uzunoğlu, Metallurgical and Materials Engineering, Istanbul Technical University
Prof. Dr. Ahmet Alpas, Mechanical, Automotive & Materials Engineering, University of Windsor

MATHEMATICAL ENGINEERING

Asst. Prof. Dr. İzzet Göksel, Mathematics Engineering, Istanbul Technical University
Prof. Dr. Seher Melike Aydoğan, Mathematics Engineering, Istanbul Technical University
Prof. Dr. Murat Sarı, Mathematics Engineering, Istanbul Technical University
Prof. Dr. Nigar Aslanova, Vice-Rector for Science and Innovation Issues, Azerbaijan University of Architecture and Construction

MECHANICAL ENGINEERING

Prof. Dr. Aliihsan Koca, Mechanical Engineering, Istanbul Technical University
Prof. Dr. Senem Kurşun, Mechanical Engineering, Istanbul Technical University
Assoc. Prof. Dr. Raşit Ahmet Yıldız, Mechanical Engineering, Istanbul Technical University
Asst. Prof. Dr. Akif Yavuz, Mechanical Engineering, Istanbul Technical University
Prof. Dr. Özgen Akalın, Mechanical Engineering, Istanbul Technical University
Prof. Dr. Mesut Kırca, Mechanical Engineering, Istanbul Technical University
Prof. Dr. Erkan Günpınar, Mechanical Engineering, Istanbul Technical University
Assoc. Prof. Dr. Sertaç Çadırcı, Mechanical Engineering, Istanbul Technical University

MECHATRONICS ENGINEERING

Prof. Dr. Volkan Sezer, Robotics and Autonomous Systems Engineering, Istanbul Technical University
Assoc. Prof. Dr. Zeki Yağız Bayraktaroğlu, Mechanical Engineering, Istanbul Technical University
Asst. Prof. Dr. Kerem Altun, Automation and Control Engineering, Yıldız Technical University
Assoc. Prof. Libor Pekař, Automation and Control Engineering, Tomas Bata University

METALLURGY AND MATERIALS ENGINEERING

Assoc. Prof. Dr. Billur Deniz Karahan, Metallurgical and Materials Engineering, Istanbul Technical University
Assoc. Prof. Dr. Aytekin Uzunoğlu, Metallurgical and Materials Engineering, Istanbul Technical University
Assoc. Prof. Dr. Yakup Yüretürk, Metallurgical and Materials Engineering, Bursa Technical University
Prof. Dr. Süleyman Can Kurnaz, Metallurgical and Materials Engineering, Sakarya University
Dr. Łukasz Maj, Metallurgy and Materials Science, Polish Academy of Sciences

METEOROLOGICAL ENGINEERING

Assoc. Prof. Dr. Bahtiyar Efe, Meteorological Engineering, Istanbul Technical University
Prof. Dr. Anthony Lupo, Environmental Sciences, Missouri University
Prof. Dr. Barış Önol, Meteorological Engineering, Istanbul Technical University
Assoc. Prof. Dr. Elçin Tan, Meteorological Engineering, Istanbul Technical University

MINERAL PROCESSING ENGINEERING

Prof. Dr. Feridun Boylu, Mineral Processing Engineering, Istanbul Technical University
Prof. Dr. Fırat Burat, Mineral Processing Engineering, Istanbul Technical University
Asst. Prof. Dr. Ş. Beste Aydın, Mineral Processing Engineering, Istanbul Technical University
Dr. Behzad Vaziri Hassas, Earth and Environmental Engineering, Columbia University

MINING ENGINEERING

Assoc. Prof. Dr. Cüneyt Atilla Öztürk, Mining Engineering, Istanbul Technical University
Assoc. Prof. Dr. Muhammet Mustafa Kahraman, Mining Engineering, Istanbul Technical University
Asst. Prof. Dr. Emre Avunduk, Mining Engineering, Istanbul Technical University
Dr. Özge Akyıldız, Geoscience, Norwegian University of Science and Technology

MOLECULAR BIOLOGY - GENETICS AND BIOTECHNOLOGY

Prof. Dr. Bahtiyar Yılmaz, Visceral Surgery and Medicine, University of Bern
Prof. Dr. Gamze Torun Köse, Genetics and Bioengineering, Yeditepe University
Prof. Dr. Ayten Karataş, Molecular Biology and Genetics, Istanbul Technical University
Asst. Prof. Dr. Abdulhalim Kılıç, Molecular Biology and Genetics, Istanbul Technical University

MUSIC

Assoc. Prof. Dr. Taylan Özdemir, Turkish Music State Conservatory, Istanbul Technical University
Asst. Prof. Dr. Emmanouil Ekmektsoglou, Turkish Music State Conservatory, Istanbul Technical University
Dr. Paul Whitehead, Centre for Advanced Studies in Music, Istanbul Technical University
Dr. Alexandros Charkiolakis, Friends of Music Society, Ionian University
Asst. Prof. Dr. Ozan Sarıer, Music, Istanbul Technical University

MUSICOLOGY AND MUSIC THEORY

Prof. Dr. Nilgün Doğrusöz Dişiaçık, Turkish Music State Conservatory, Istanbul Technical University
Prof. Dr. Burcu Yıldız, Turkish Music State Conservatory, Istanbul Technical University
Prof. Dr. Ozan Baysal, Turkish Music State Conservatory, Istanbul Technical University
Assoc. Prof. Eliot Bates, Music, City University of New York

NANOSCIENCE AND NANOENGINEERING

Prof. Dr. Nilgün Baydoğan, Energy Institute, Istanbul Technical University
Prof. Dr. Nilgün Karatepe Yavuz, Energy Institute, Istanbul Technical University
Assoc. Prof. Dr. Birgül Benli, Mineral Processing Engineering, Istanbul Technical University
Asst. Prof. Dr. Abdulhalim Kılıç, Molecular Biology and Genetics, Istanbul Technical University
Asst. Prof. Dr. Elif Öztürk Er, Chemical Engineering, Istanbul Technical University

NAVAL ARCHITECTURE AND MARINE ENGINEERING

Prof. Dr. Şakir Bal, Naval Architecture and Marine Engineering, Istanbul Technical University
Prof. Dr. Ahmet Ergin, Naval Architecture and Marine Engineering, Istanbul Technical University
Prof. Dr. Gökdeniz Neşer, Marine Sciences and Technology, Dokuz Eylül University
Dr. Tahsin Tezdoğan, Ship Science, Southampton University

NUCLEAR RESEARCH

Assoc. Prof. Dr. Tayfun Akyürek, Energy Institute, Istanbul Technical University
Prof. Dr. Üner Çolak, Energy Institute, Istanbul Technical University
Prof. Dr. Nilgün Baydoğan, Energy Institute, Istanbul Technical University

PETROLEUM AND NATURAL GAS ENGINEERING

Prof. Dr. Ö. İnanç Türeyen, Petroleum and Natural Gas Engineering, Istanbul Technical University
Prof. Dr. Gürşat Altun, Petroleum and Natural Gas Engineering, Istanbul Technical University
Asst. Prof. Dr. Şenol Yamanlar, Petroleum and Natural Gas Engineering, Istanbul Technical University
Prof. Dr. Murat Çınar, Petroleum and Natural Gas Engineering, Istanbul Technical University
Assoc. Prof. Dr. Hasan Özgür Yıldız, Petroleum and Natural Gas Engineering, Istanbul Technical University
Asst. Prof. Dr. Burak Kulga, Petroleum and Natural Gas Engineering, Istanbul Technical University
Asst. Prof. Dr. Emine Didem Korkmaz Başel, Petroleum and Natural Gas Engineering, Istanbul Technical University

PHYSICS ENGINEERING

Prof. Dr. Ahmet Levent Subaşı, Physics Engineering, Istanbul Technical University
Prof. Dr. Oğuzhan Gürlü, Physics Engineering, Istanbul Technical University
Prof. Dr. Hakan Özgür Özer, Physics Engineering, Istanbul Technical University

POLAR SCIENCES

Assoc. Prof. Dr. Bilge Tutak, Shipbuilding and Ocean Engineering, Istanbul Technical University
Assoc. Prof. Dr. Fatma Elif Genceli Güner, Chemical Engineering, Istanbul Technical University
Assoc. Prof. Dr. Deniz Bozkurt, Climate Science and Meteorological Engineering, Universidad de Valparaíso (Chile)

POLITICAL STUDIES

Assoc. Prof. Dr. Ayşe Serdar, Political Studies, Istanbul Technical University
Prof. Dr. Gürcan Koçan, Political Studies, Istanbul Technical University
Res. Asst. Dr. Görkem Giray, Political Studies, Istanbul Technical University
Dr. Yufei Xu, School of Marxism, Xihua University

POLYMER SCIENCE AND TECHNOLOGY

Dr. Natasha Shirshova, Engineering, Durham University
Assoc. Prof. Dr. Nesrin Köken, Chemistry, Istanbul Technical University
Prof. Dr. Ahmet Akar, Chemistry, Istanbul Technical University
Prof. Dr. Nilgün Kızılcan, Chemistry, Istanbul Technical University

RAILWAY SYSTEMS ENGINEERING

Asst. Prof. Dr. S. Ergün Bozdağ, Mechanical Engineering, Istanbul Technical University
Dr. Serhat Boynukalın, Rail Systems Engineering, Istanbul Technical University
Assoc. Prof. Dr. Hüseyin Onur Tezcan, Civil Engineering, Istanbul Technical University
Dr. Tarık Dündar, Transportation Engineering, Istanbul Technical University

REAL ESTATE DEVELOPMENT

Dr. Christopher Hannum, Global Economics, University of Central Asia
Prof. Dr. Ali Hepşen, Finance, İstanbul University
Prof. Dr. Evren Özus, Industrial Product Design, Beykent University
Prof. Dr. Mehmet Topçu, Urban and Regional Planning, Konya Technical University
Prof. Dr. Şevkiye Şence Türk, Urban and Regional Planning, Istanbul Technical University
Assoc. Prof. Dr. Kerem Yavuz Arslanlı, Urban and Regional Planning, Istanbul Technical University

SCIENCE, TECHNOLOGY AND SOCIETY

Assoc. Prof. Dr. Aslı Öğüt Erbil, Science and Letters, Istanbul Technical University
Assoc. Prof. Dr. Ebru Yetişkin Doğrusöz, Science and Letters, Istanbul Technical University

Asst. Prof. Dr. Sevil Hatice Baltalı Tırpan, Science and Letters, Istanbul Technical University
Asst. Prof. Alessandra Cenci, IT and Design, Aalborg University Copenhagen

SHIPBUILDING AND OCEAN ENGINEERING

Asst. Prof. Dr. Bilge Baş, Civil Engineering, Bilgi University
Assoc. Prof. Dr. Emre Peşman, Naval Architecture and Marine Engineering, Karadeniz Technical University
Asst. Prof. Dr. Ahmet Gültekin Avcı, Naval Architecture and Maritime, Yıldız Technical University
Dr. Bülent Düz, Maritime Research Institute Netherlands
Assoc. Prof. Dr. Sevil Deniz Yakan Dündar, Shipbuilding and Ocean Engineering, Istanbul Technical University
Assoc. Prof. Dr. Ceren Bilgin Güney, Shipbuilding and Ocean Engineering, Istanbul Technical University
Assoc. Prof. Dr. Şafak Nur Ertürk Bozkurtoğlu, Shipbuilding and Ocean Engineering, Istanbul Technical University
Asst. Prof. Dr. Burak Karacık, Shipbuilding and Ocean Engineering, Istanbul Technical University

SOIL MECHANICS AND GEOTECHNICAL ENGINEERING

Prof. Dr. Musaffa Ayşen Lav, Civil Engineering, Istanbul Technical University
Assoc. Prof. Dr. Müge Balkaya, Civil Engineering, Istanbul Technical University
Assoc. Prof. Dr. Ece Bayat, Civil Engineering, Istanbul Technical University
Prof. Dr. Erol Tutumluer, Civil Engineering, University of Illinois

SOLID EARTH CHAIR

Prof. Dr. Gültekin Topuz, Eurasia Institute of Earth Sciences, Istanbul Technical University
Prof. Dr. Tolga Görüm, Eurasia Institute of Earth Sciences, Istanbul Technical University
Prof. Dr. Oğuz Göğüş, Eurasia Institute of Earth Sciences, Istanbul Technical University
Dr. Jiamin Wang, Geology & Geophysics, Chinese Academy of Science

STRUCTURAL ENGINEERING

Prof. Dr. Bülent Akbaş, Civil Engineering, Gebze Technical University
Prof. Dr. Bilge Doran, Civil Engineering, Yıldız Technical University
Prof. Dr. Serdar Soyöz, Civil Engineering, Boğaziçi University
Prof. Dr. Özkan Şengül, Civil Engineering, Istanbul Technical University
Prof. Dr. Yılmaz Akkaya, Civil Engineering, Istanbul Technical University
Prof. Dr. Yasin Fahjan, Civil Engineering, Istanbul Technical University
Prof. Dr. Nihal Eratlı, Civil Engineering, Istanbul Technical University
Prof. Dr. Hakan Nuri Atahan, Civil Engineering, Istanbul Technical University
Prof. Dr. Ünal Aldemir, Civil Engineering, Istanbul Technical University
Prof. Dr. Kutlu Darılmaz, Civil Engineering, Istanbul Technical University
Prof. Dr. Tülay Aksu Özkul, Civil Engineering, Istanbul Technical University
Assoc. Prof. Dr. Kadir Özakgül, Civil Engineering, Istanbul Technical University
Assoc. Prof. Dr. Osman Bulut, Civil Engineering, Istanbul Technical University
Asst. Prof. Dr. Cem Demir, Civil Engineering, Istanbul Technical University
Asst. Prof. Dr. Tuba Gürbüz Büyükkayıkçı, Civil Engineering, Istanbul Technical University
Asst. Prof. Dr. Ayda Şafak Ağar Özbek, Civil Engineering, Istanbul Technical University
Asst. Prof. Dr. Hasan Nuri Türkmenoğlu, Civil Engineering, Istanbul Technical University
Assoc. Prof. Dr. Kadir Özakgül, Structural Engineering, Istanbul Technical University

SUSTAINABILITY

Prof. Dr. Fatoş Germirli Babuna, Environmental Engineering, Istanbul Technical University
Prof. Dr. Emrah Acar, Architecture, Istanbul Technical University
Asst. Prof. Dr. Emrah Çoraman, Eurasia Institute of Earth Sciences, Istanbul Technical University
Assoc. Prof. Anders Damgaard, Environmental and Resource Engineering, Denmark Technical University
Asst. Prof. Dr. Ebru Acuner Türet, Sustainability, Istanbul Technical University
Assoc. Prof. Dr. Başak Demires Özkul, Sustainability, Istanbul Technical University

Prof. Dr. İsmail Koyuncu, Sustainability, Istanbul Technical University
Assoc. Prof. Dr. Göksenin İnalhan, Architecture, Istanbul Technical University

TEXTILE ENGINEERING

Prof. Dr. Nazan Okur, Textile Engineering, Istanbul Technical University
Assoc. Prof. Dr. Ali Kılıç, Textile Engineering, Istanbul Technical University
Asst. Prof. Dr. Pelin Altay, Textile Engineering, Istanbul Technical University
Prof. Dr. Yordan Kyosev, Assembly of Textile Products, Dresden Technical University

TRADITIONAL DANCES

Paul-Alexandru Remeş, Romanian Academy, Institute Archive of Folklor and Babeş, Bolyai Üniversity from Cluj- Napoca
Prof. İlknur Bektaş, Turkish Music State Conservatory, Turkish Folk Dance Department, Istanbul Technical University
Prof. Eyüp Uzunkaya, Turkish Music State Conservatory, Turkish Folk Dance Department, Istanbul Technical University
Prof. Nihal Cömert, Turkish Music State Conservatory, Turkish Folk Dance Department, Istanbul Technical University
Prof. Dr. Mehmet Öcal Özbilgin, State Turkish Music Conservatory, Turkish Folk Dance Department, Ege University
Prof. Dr. Kamil Perçin Akgül, Turkish Music State Conservatory, Turkish Folk Dance Department, Gaziantep University

URBAN AND REGIONAL PLANNING

Prof. Dr. Tüzin Baycan, Urban and Regional Planning, Istanbul Technical University
Assoc. Prof. Dr. Eda Yücesoy, Urban and Regional Planning, Istanbul Technical University
Assoc. Prof. Dr. Gülden Demet Oruç Ertekin, Urban and Regional Planning, Istanbul Technical University
Prof. Dr. hab. Jadwiga Biegańska, Urban Studies and Sustainable Development, Nicolaus Copernicus University

URBAN DESIGN

Assoc. Prof. Dr. Eren Kürkçüoğlu, Urban and Regional Planning, Istanbul Technical University
Assoc. Prof. Dr. Melih Bozkurt, Landscape Architecture, Istanbul Technical University
Assoc. Prof. Dr. Ozan Önder Özener, Architecture, Istanbul Technical University

SCIENTIFIC PROGRAM

12.05.2025 | MONDAY | ONLINE

MAIN HALL

10:00 – 11:00

Opening Remarks:
Prof. Dr. Fatma Seniha GÜNER , Institute Director, Istanbul Technical University
Prof. Dr. Hasan MANDAL, Rector, Istanbul Technical University
KEYNOTE SPEAKER: "An Academic Journey From Chemical Engineering to Robotics and Multidisciplinary Impressions of a Scientist"
Prof. Dr. Berna ÖZKALE EDELMANN, Technical University of Munich

11:00 – 12:00

Chair: Assoc. Prof. Dr. Abdullah Aydoğan

CHEMISTRY
Inorganic Chemistry
"The Design and Application of Novel Post-Metallocene Catalysts For Olefin Polymerization"
Önder Güneş, Ozan Sanlı Şentürk - Istanbul Technical University
Nanochemistry
"Investigation of Fluorescence Properties of ZIF-8 Structures Modified With Graphitic Quantum Dots"
Hilal Nazan Ağar, Caner Ünlü- Istanbul Technical University
Organic Chemistry
"Synthesis Of Polymers Containing Supramolecular Components In The Pendant Or Main Chain"
Hafize Reva Bayraktar, Abdullah Aydoğan -Istanbul Technical University
Polymer Chemistry
"Dual Radical and Singlet Oxygen Pathways in Polybutadiene Photovulcanization: A Novel Approach Using Phenylacylbromide under UV-A Irradiation for Advanced Crosslinked Films"
Ragib Talha Uzun, Barış Kiskan - Istanbul Technical University

13:00 – 14:00

Chair: Asst. Prof. Dr. Berna Doğan, Asst. Prof. Dr. Hüseyin Enis Karahan

CHEMISTRY
Drug Design & Drug Delivery (Computational and Experimental)
"Exploring New MAO-B Selective İnhibitors Through in-silico Methods"
Ali Aksu, Mine Yurtsever, Fethiye Aylin Sungur - Istanbul Technical University
CHEMICAL ENGINEERING
Hydrogen Technologies, Fuels Cells, Energy Storage Materials
"Biomass-Derived Activated Carbon as Electrode Material for Supercapacitors"
Damla Kökmen , Anıl Yılmaz, Nahid A. Keshtiban, Ali Gelir, Nil Özbek, Hanzade Açma, Serdar Yaman - ITU
Modelling and Computational Systems
"Machine Learning-Based Prediction of Ftir Spectral Peaks for Biomass Characterization"
Talha Sağiş, Anıl Yılmaz, Hanzade Haykırı-Açma, Serdar Yaman - Istanbul Technical University

14:00 – 15:00

Chair: Assoc. Prof. Dr. Ahmet Gün, Asst. Prof. Dr. Süha Tuna

INFORMATICS
Computational Design Tools and Methods
"A Decision Support Model Proposal For Urban Green Space Site Selection Problem Based on Multi-Criteria Decision Making"
Erdal Kondakcı, Gülen Çağdaş - Istanbul Technical University
"Computational Memorability Model Based on Object Size"
Fatma Seven, Sema Alaçam - Istanbul Technical University
COMPUTATIONAL SCIENCE AND ENGINEERING
Computational Fluid Dynamics
"Multi-Objective Optimization of Airfoil Geometry for Aerodynamic Efficiency and Noise Reduction Using Bézier Parameterization"
Ali İhsan İşgüder, Baha Zafer, Melike Nikbay - Istanbul Technical University
Computational Biology
"Molecular Dynamics Analysis of CHK2 Mutations at the C-lobe of the Kinase Domain"
Cihan Uğur Otçu, Clara Xazal Buran, Gizem Dinler Doğanay, Levent Doğanay, Mert Gür - Istanbul Technical University

15:00 – 16:00

Chair: Assoc. Prof. Dr. Volkan Müjdat Tiryaki

APPLIED INFORMATICS
Medical Image Analysis
"Improving Tumor Segmentation Performance in Breast MRI via U-Net Based Deep Learning Approach"
Alptuğ Şeref Ayyıldız,İbrahimAkduman, AleksandarJanjic-Istanbul Technical University
"Deep Learning-Based Breast Tumor Detection in MRI Using Faster R-CNN"
Şeyma Nur Tufan, Aleksandar Janjic, İbrahim Akduman - Istanbul Technical University
"Prediction of Microsatellite Status Using Deep Neural Network"
Fatma Vildan Engin, Ender Mete Ekşioğlu - Institute of Science and Technology
Data Analysis
"Optimization Potential of Machine Learning-Based Algorithms in Neonatal Parenteral Nutrition Management: A Systematic Review"
Sümeyye Nalbat, Mustafa Alpkan Çiçek, Serkan Türkeli, Mustafa Doğan - Istanbul Technical University

16:00 – 17:00

Chair: Asst. Prof. Dr. Mehmet Akif Yazıcı

APPLIED INFORMATICS
Computational Electromagnetics
"Singular Integral Treatment of Nyström Method for Electromagnetic Scattering Problems"
Faik Yaman, Mehmet Çayören - Istanbul Technical University
"Integral Equation based Eigenmode Solution of Optical Waveguides with Arbitrary Cross Section"
Mücahit Hüseyin Özdilekler, Mehmet Çayören - Istanbul Technical University
Cybersecurity
"Usability of Token-based and Remote Electronic Signatures: A User Experience Study"
Ömer Ege, Kemal Bıçakcı - Istanbul Technical University

12.05.2025 | MONDAY | ONLINE

HALL - I

Chair: Dr. Demet Aydoğmuş

METALLURGY AND MATERIALS ENGINEERING

Composite and Polymer Materials

11:00
12:00

"Thermal and Mechanical Properties of Reduced Graphene Oxide Reinforced Polypropylene Composites"
Cemile Gürer, Yeliz Köse, İrem Düzenli, Fatma Seniha Güner - Istanbul Technical University

"Characterization of Talc and Reduced Graphene Oxide Reinforced Polypropylene Composites: Thermal, Mechanical and Structural Properties"
İrem Düzenli , Yeliz Köse, Cemile Gürer, Yavuz Emre Yağcı, Fatma Seniha Güner - Istanbul Technical University

Extractive Metallurgy

"Investigation of Reduction of Chromite Ore with Hydrogen"
Ayse Deniz, Çağdaş Ekin Zöhra, Selçuk Kan, Ceren Imer, Gökhan Basman, Yavuzhan Kaya, Onuralp Yücel - Istanbul Technical University

"Production and Characterization of Lanthanum Hexaboride Powder"
Deniz Nalcı, Mehtap Arslan-Kaba, Güldem Kartal Şireli, Kürşat Kazmanlı - Istanbul Technical University

---

Chair: Dr. Yonca Alkan Göksu

METALLURGY AND MATERIALS ENGINEERING

Metals and Alloys

13:00
14:00

"Precious Metal (Au, Pd, Pt, Rh) Recovery Using Torrefied Biomass Species Such As Forest, Marine And Agricultural Biomass"
Cansu Kargı, Mahmut Ercan Açma, Hanzade Haykırı Açma, Nil Özbek, Serdar Yaman - Istanbul Technical University

"Effect of Niobium Addition on the Microstructural Features of Titanium Alloys for Dental Implants"
Sena Burcu Hayırcı, Faiz Muhaffel, Hüseyin Çimenoğlu- Istanbul Technical University

"Effect of Heat Treatment on Inconel 718 Superalloy Produced by Cold Spray Additive Manufacturing"
Serra Bayram, Erdem Balcı, Aptullah Karakaş, Murat Baydoğan - Istanbul Technical University

"Recycling-Driven Variations in Mechanical Properties and Weldability of 6XXX Series Aluminium Alloys for Electric Vehicle Structural Parts"
Zeynep Tutku Özen, Necip Ünlü - Istanbul Technical University

---

Chair: Asst. Prof. Dr. Cevat Fahir Arısoy

METALLURGY AND MATERIALS ENGINEERING

Surface Treatment and Coatings

14:00
15:00

"Enhancing CMAS and Hot Corrosion Resistance of YSZ Thermal Barrier Coatings via Aluminium Cold Spray"
Ahmed Emin Tok, Faiz Muhaffel, Muhammed Karabaş - Istanbul Technical University

"Effect of Pack Aluminizing on Hydrogen Charging Behavior of Ti6Al4V Alloy Fabricated by Selective Laser Melting"
Belgin Ataman, Burak Bayram, Erdem Balcı, Murat Baydoğan - Istanbul Technical University

"Comparative Evaluation of Surface Treatments: Anodizing and Micro-Arc Oxidation for Al-Si Cast Alloys"
FurkanTezer, Faiz Muhaffel- Istanbul Technical University

"A Comparative Study of Ni-SiC and Micro-Arc Oxidation Coatings Produced on the Al-Si Casting Alloy"
Özkan Karaman, Faiz Muhaffel - Istanbul Technical University

Chair: Asst. Prof. Dr. Erçin Çağan Duran

METALLURGY AND MATERIALS ENGINEERING

Corrosion and Wear

15:00
16:00

"Fabrication of Al Matrix MMC Cold Spray Coatings on Magnesium Alloy AZ31"
Efecan Madazlı, Hüseyin Çimenoğlu, Sezgin Cengiz, Faiz Muhaffel, Erdem Balcı - Istanbul Technical University

Mechanical Metallurgy

"Effects of Stress Relief Annealing Time on Mechanical Properties and Operating Cost in Lamellar Graphite Cast Iron Engine Blocks"
Furkan Üstün, Ali Kalyon - Yalova University

MATERIAL SCIENCE AND ENGINEERING

Nanomaterials

"A Study About Tin Nanoparticles and Production of Core-shell Structure"
Ayşe Zuhal Karakaş, Ş. Samet Kaplan, M. Şeref Sönmez - Istanbul Technical University

Ceramics, Glass, Refractory Materials

"Improvement of the Selenium Retention and Control of the Color Stability in Selenium Containing Glasses"
Elif Fagiye Yaylacı, Merve Akdemir Kutluğ, Ahmet Caner Kayaalp, Reha Yavuz - Istanbul Technical University

---

Chair: Prof. Dr. Barış Kışkan, Assoc. Prof. Dr. Birgül Benli

POLYMER SCIENCE AND TECHNOLOGY

Material Science

16:00
17:00

"Preparation and Characterization of Sulfonated Polysulfone for Proton Exchange Membrane Fuel Cells"
Turan Can Özmen - Istanbul Technical University

NANOSCIENCE AND NANOENGINEERING

Nanoparticles

"Radiation Attenuation of MWCNT and Magnetic Nanoparticle Reinforced PMMA Comparative Analysis of Coefficient"
Deniz Hande Aydın, Nilgün Baydoğan - Istanbul Technical University

Polymer and Nano Composites

"Thermo-responsive Pnipaam Based Hydrogels with Bio-inspired Additives for Biomedical Applications"
Rabia Yılmaz, Özgür Yılmaz, Birgül Benli - Istanbul Technical University

12.05.2025 | MONDAY | ONLINE

HALL - II

11:00 - 12:00

Chair: Asst. Prof. Dr. Saeed Tasouji Hassanpour

MANAGEMENT ENGINEERING

Marketing

"The Adoption of Smart Small Home Appliances: An Integrated Model of Consumer Acceptance and Behavior"
Betül İmamoğlu, Huriye Şebnem Burnaz - Istanbul Technical University

"Understanding Consumer Acceptance and Purchase Intentions in Unmanned Retail Stores"
Gözde Erdoğan - Istanbul Technical University

Finance

"The Effect of ESG Ratings on Firm's Financial Performance in Borsa Istanbul"
Alper Ataker, Oktay Taş - Istanbul Technical University

"TEFAS's Effect on the Turkish Mutual Funds Landscape"
Mehmet Sami Boz - Boğaziçi University

13:00 - 14:00

Chair: Asst. Prof. Dr. Saeed Tasouji Hassanpour

Economics

"Central Bank Digital Currencies (CBDCs): a countermeasure to Anti-Money Laundering (AML) challenges posed by cryptocurrencies?"
Albina Gaisina, Matthias Finger - Istanbul Technical University

Finance

"Investor Attention and Asymmetric Conditional Volatility: Evidence from E-GARCH-X and GJR-GARCH-X Models"
Müge Özdemir, Oktay Taş - Istanbul Technical University

"Return Predictability and Attention-Based Trading Strategies: Casual and Time-Varying Volatility Dynamics in Borsa Istanbul"
Müge Özdemir, Oktay Taş - Istanbul Technical University

"How Does Firm Esg Impact Financial Performance After Covid-Era? A Worldwide Analysis"
Sırma Şeker, Cumhur Ekinci - Istanbul Technical University

14:00 - 15:00

Chair: Asst. Prof. Dr. Saeed Tasouji Hassanpour

MANAGEMENT

Human Resource Management

"The Impact of Remote Work on Presenteeism During the COVID-19 Pandemic"
Deniz Mat Artun, Fatma Küskü - Istanbul Technical University

Marketing

"Navigating the Paradox of Connectivity and Isolation: Impacts on Digital Nomads' Psychological Well-Being"
Mahin Farshbaf Maherian, Adnan Veysel Ertemel - Istanbul Technical University

Organization

"Organizing Through Code: A Bibliometric Review of Algorithms in Organizational Contexts"
Hakan Sarı - University of Glasgow

15:00 - 16:00

Chair: Asst. Prof. Dr. Saeed Tasouji Hassanpour, Asst. Prof. Dr. Umut Kuruüzüm

MANAGEMENT

Production Management

"Performance Evaluation Model Based on Balanced Scorecard for Industry 4.0 Applications in the Fast Moving Consumer Goods Sector (FMCG)"
Ceren Dilbaz, Hür Bersam Sidal Bolat - Istanbul Technical University

"Supplier Performance Evaluation with Balanced Scorecard"
Hanife Özcan, Hür Bersam Sidal - Istanbul Technical University

"A Quantitative Approach To Sustainability: Applying Multi-Criteria Decision-Making Techniques And Data Envelopment Analysis Models"
Musa Aktaş, Ferhan Çebi - Istanbul Technical University

ECONOMY

Financial Crises and Macroprudential Policies "Financial Contagion: Dynamic Correlations Approach"
Esra Çakır - Istanbul Technical University

16:00 - 17:00

Chair: Prof.Dr. Şevkiye Şence Türk, Prof. Dr. Levent Kırval, Assoc. Prof. Dr. Ceren Bilgin Güney

REAL ESTATE DEVELOPMENT

Geospatial Analysis in Real Estate

"A Spatial and Investment-Oriented Site Selection Model for EV Charging Stations: The Case of Istanbul"
Handan Kaplan,Kerem Yavuz Arslanlı-IstanbulTechnicalUniversity

Real Estate Development

"An Event-Driven Architecture In Real Estate Development"
Özlem Sertbaş, Hakan Yaman - Istanbul Technical University

MARITIME STUDIES

Maritime Human Resources

"Importance of Safety Awareness and Safety Culture Onboard with Alternative Fuels"
Aysel Camci, Firat Bolat - Istanbul Technical University

SHIPBUILDING AND OCEAN ENGINEERING

Marine Environmental Impact and Pollution Control "The Penglai 19-3 Incidents: Failures, Response, And Regulatory Lessons"
Gulled Makaran, Ceren Bilgin Güney - Istanbul Technical University

12.05.2025 | MONDAY | ONLINE

HALL - III

Chair: Assoc. Prof. Dr. Sefer Baday

DATA ENGINEERING AND BUSINESS ANALYTICS

Predictive Analytics and Machine Learning in Business

"Analyzing Brokerage Firm Trading Behavior via Supervised Learning: A Comparative Study on BIST 10"

Kubilay Karaçam - Istanbul Technical University

11:00

Sentiment Analysis and Opinion Mining

"Impact of Weekly vs Daily Sentiment Scores on Price Direction Forecast"

12:00

Ahmet Berkay Gültekin, Alp Üstündağ -Istanbul Technical University

Big Data Analytics for Decision-Making

"Automated Plastic Waste Detection on Coastal Areas Using UAVs and Deep Learning"

Hesam Hatamzadeh Khanghahi, Şule Itır Satoğlu - Istanbul Technical University

"Agentic Workflows for Self-Service Analytics Applications in E-Commerce"

Taylan Yurtsever - Istanbul Technical University

Chair: Prof. Dr. Seher Melike Aydoğan

MATHEMATICAL ENGINEERING

Applied Mathematics

"Effects of Weak Heterogeneity on Nonlinear Love Wave Interactions"

13:00

Berna Yavaş, Semra Ahmetolan, Ali Demirci-Istanbul Technical University

"Understanding Predator- Prey Dynamics Through Equilibrium State Classification"

14:00

Kerime Nur Kavadar, Ali Demirci - Istanbul Technical University

"Exploring Rayleigh Waves in Layered Media"

Tuğçe Sezer, Semra Ahmetolan, Ayşe Peker Dobie, Ali Demirci - Istanbul Technical University

"Symmetry Analysis on Rosenau Type Equations"

Tuğçe Sezer, Cihangir Özemir - Istanbul Technical University

Chair: Prof. Dr. Seher Melike Aydoğan

MATHEMATICAL ENGINEERING

Data Science and Machine Learning

14:00

"A Case Study in Time Series Classification Using Machine Learning and Deep Learning"

15:00

Barış Küçük, Atabey Kaygun - Istanbul Technical University

Mathematical Modeling

"Modeling Rare Metal Market Dynamics: A Nonlinear Approach with Investment and Geopolitical Risk"

Furkan Emre Işık, Ali Demirci- Istanbul Technical University

Chair: Prof. Dr. Esra Özkan Zayim

PHYSICS ENGINEERING

Optics and Photonics

"Imaging Ellipsometry for Material Characterization and Defect Analysis"

Furkan Yıldız, Esra Zayim, Muharrem Aşar - Istanbul Technical University

15:00

High Energy and Particle Physics

"Dynamo Process in Proto-Neutron Stars"

16:00

İrem Bakır, Kazım Yavuz Ekşi - Istanbul Technical University

"Constraints On New Physics With Light Mediators And Generalized Neutrino Interactions Via Coherent Elastic Neutrino Nucleus Scattering"

Sevgi Karadağ, Muhammed Deniz, Henry T. Wong - Istanbul Technical University

Mathematical Physics

"Investigation of Structural and OptoelectronicProperties ofmetal/ZnS Junction under Density Functional Theory (DFT)"

Haris Kulosmanovic, Murat Çalışkan - Yıldız Technical University

---

Chair: Prof. Dr. Nazan Okur

TEXTILE ENGINEERING

Textile Clothing and Fashion Design

16:00

"Real Time Production Management in Garment Manufacturing Using IoT-Based Process Monitoring Devices (PMDs)"

17:00

Bülent Koç, Selin Hanife Eryürük - Istanbul Technical University

Sustainability in Textile and Fashion Industries

"Statistical Analysis of Short Fiber Content and Tenacity Using Exponential Regression"

Çağdaş Aslan,Selin Hanife Eryürük,Michael Will-Istanbul Technical University

12.05.2025 | MONDAY | ONLINE

HALL - IV

Chair: Asst. Prof. Dr. Ayşe Elvan Bayraktaroğlu

INDUSTRIAL ENGINEERING

Decision Making

11:00
12:00

"A Bayesian Network-Based Approach for Analyzing Railway Accidents"
Derya Cephe, Umut Asan - Istanbul Technical University

"A Comparative Analysis of Machine Learning and MCDM Sorting Methods in Electric Vehicle Selection"
Mehmet Demir, Umut Asan - Istanbul Technical University

"Multi Criteria Decision Making for Selecting Best Banking Service Channel"
Mustafa Akça - Istanbul Technical University

Engineering Management

"Customer Preferences For Mobile Operating Systems In Smartphones Using Conjoint Analysis"
Cansu Aksu - Istanbul Technical University

Chair: Assoc. Prof. Dr. Umut Asan

INDUSTRIAL ENGINEERING

Engineering Management

13:00
14:00

"Impact of Organizational Life Cycle on R&D Project Prioritization Criteria"
Furkan Yasin Taksim, Cafer Erhan Bozdağ - Istanbul Technical University

"Sector-Specific Supplier Evaluation Based on LARGS Dimensions"
Gözde Çinkay, Şeyda Serdarasan - Istanbul Technical University

"Structuring Challenges for Textile Industry in Adopting the Digital Product Passport"
Sena Nur Dursun, Şeyda Serdarasan- Istanbul Technical University

Knowledge Management

"Understanding University Reputation: A Stakeholder-Centered Model for Reputation"
Orhan Dursun, Çiğdem Altın Gümüşsoy - Istanbul Technical University

---

Chair: Assoc. Prof. Dr. Seda Yanık

INDUSTRIAL ENGINEERING

Industrial Data Analytics

14:00
15:00

"Predicting the Closing Time of Debt Files in Legal Stage Using Machine Learning and Deep Learning Methods"
Şeyda İrem Bilgehan, Başar Öztayşi - Istanbul Technical University

Manufacturing Management

"Analysing the Automotive Production: A Bibliometric Analysis on Lean-Green Management"
Ayşe Melissa Ergün, Hür Bersam Sidal Bolat - Istanbul Technical University

"Improvement Study In The Inner Door Production Area With Lean Production Approach"
İsa Emre Gül, Seda Yanık - Istanbul Technical University

Chair: Asst. Prof. Dr. Saltuk Duran

HISTORY OF SCIENCE AND TECHNOLOGY

History of Engineering

15:00
16:00

"From Dieppe to Normandy: Technological Innovations and the Reclamation of Offensive Initiative in World War II"
Göktuğ Berk Çakı - Istanbul Technical University History of Sciences

"Brief History of Artificial Intelligence Approaches"
İlkem Ahu Şahin, Aytekin Çökelez - Istanbul Technical University

History of Physics

"Scientific Tendencies in the Context of the Annals of Electricity, Magnetism, and Chemistry (1836-1843) in England"
Tuğçe Esenduran - Istanbul Technical University

12.05.2025 | MONDAY | ONLINE

HALL - V

Chair: Asst. Prof. Dr. Murat Yeşiloğlu

CONTROL AND AUTOMATION ENGINEERING

Advances in Automatic Control Engineering

11:00
12:00

"Lane Change Desicion Making for Autonomous Vehicles By Using Adversarial Learning Methods"
Aytuğ Onurhan Efil, Mustafa Doğan - Istanbul Technical University

"Control Allocation Strategies for Dual-System VTOL UAVs Under Control Surface Failures: Enhancing Fault Tolerance and Flight Stability"
Bilal Badur, Fikret Çalışkan - Istanbul Technical University

"New Generation 4-D Flight Management System Design for the Fighter Jets"
Kaan Tellioğlu, Fikret Çalışkan - Istanbul Technical University

Applications of Control Engineering

"Fuzzy Gain Decision for Different Type Aircrafts with Dynamic-pitch-control Envelope Cue"
Ali Karaduman, İlker Üstoğlu - Istanbul Technical University

Chair: Asst. Prof. Dr. Erhan Yumuk

CONTROL AND AUTOMATION ENGINEERING

Applications of Control Engineering

13:00
14:00

"Performance Comparison of Guidance Algorithms for Aerial Vehicles: A Software-In-The-Loop Based Approach"
Alper Makaraç, Mustafa Doğan- Istanbul Technical University

"An Optimization Based Flight Control Law Design for Fighter Aircraft"
Bora Akaryıldız, Yaprak Yalçın - Istanbul Technical University

"Adaptive Kalman Filter-Based Gyroscope Error Compensation Using Magnetometer and Accelerometer Data for IMU Sensors"
Mehmet Eren Savaştürk, Mustafa Doğan - Istanbul Technical University

"Design and Analysis of a Dual Layer Disturbance Observer Based Controller for Suppressing Internal and External Disturbances for Longitudanel Axis in a Fixed Wing Aircraft"
Merve Demiroğlu, İlker Üstoğlu, Yusuf Sıncak - Istanbul Technical University

---

Chair: Assoc. Prof. Dr. Ahmet Onat

CONTROL AND AUTOMATION ENGINEERING

Applications of Control Engineering

14:00
15:00

"Enhanced Aircraft Control Through Total Energy Control Systems: A Comparative Study with Conventional Autopilots"
Rumeysa Kökoğlu, Müjde Güzelkaya - Istanbul Technical University

"Enhancing Aircraft Avionics Safety: Integrating STPA with ARP4761 Analysis"
Şükrü Can Sulak - Istanbul Technical University

"Robust Attitude Control of the F16 Aircraft Using Incremental Nonlinear Dynamic Inversion"
Yasin Şahin, İlker Üstoğlu- Istanbul Technical University

"Immersion and Invariance Disturbance Observer based Discrete Time Vector Control of BLDC Machines"
Ziya Cem Salış - Istanbul Technical University

Chair: Asst. Prof. Dr. Ali Yeşilyurt

EARTHQUAKE ENGINEERING

Artificial Intelligence, Machine Learning, and Deep Learning in Earthquake Engineering

15:00
16:00

"Detection of Longitudinal Reinforcement Buckling in Reinforced Concrete Columns by a Deep Learning Method"
Bahadır Güleşmen, Ömer Tuğrul Turan - Istanbul Technical University

"Estimating Equivalent Damping Ratio of Conventional Shear Walls by Machine Learning Methods"
Siamak Tahaei Yaghoubi, Zeynep Tuna Deger - Istanbul Technical University

Performance-Based Seismic Assessment and Design

"Seismic Performance Assessment of Irregular RC Structures Using the Extended N2 Method"
Zekeriya Semih Aygün,Reşat Atalay Oyguç - Istanbul Technical University "Seismic Performance of Irregular RC Frames Retrofitted with TnT BRBs"
Zeynep Orman, Resat Oyguc - Istanbul Technical University

Chair: Res. Asst. Mustafa Mert Eyüpgiller

EARTHQUAKE ENGINEERING

Experimental Investigation of Reinforced Concrete Building Elements

16:00
17:00

"Enhancing Seismic Resilience of Substandard RC Beam-Column Joints with All-Steel Tube-in-Tube Buckling Restrained Braces: A Shake Table Test"
Evrim Oyguç, Abdul Hayır, Reşat Oyguç, Onur Şeker, Bülent Akbaş - Istanbul Technical University

Structural and Geotechnical Earthquake Engineering

"Design and Comparison of Different Types of Reinforced Concrete Slab Systems For Multi-storey Buildings"
Ahmet Jabban, Kadir Güler - Istanbul Technical University

"Seismic Performance Enhancement of RC Coupling Beams Using Shape Memory Alloy Devices"
Ali Attariyan, Beyza Taşkın, Kıvanç Taşkın - Istanbul Technical University

"Preliminary Study on St. İlyas Church Damaged in the Kahramanmaraş Earthquakes"
Kerem Kurnaz, Yunus Arca, Elif Durgut, Sinan Acikgöz, Medine İspir Arslan - Istanbul Technical University

12.05.2025 | MONDAY | ONLINE

HALL - VI

Chair: Prof. Dr. Sevinç Asilhan, Asst. Prof. Dr. Emre Avunduk

METEOROLOGICAL ENGINEERING

Atmosphere, Meteorology

"Heatwave Analysis Approach"

Anıl Eken, Sevinç Asilhan - Istanbul Technical University

11:00
12:00

Renewable Energy

"Repowering at Türkiye's Leading Power Plant: An Analysis of Energy Production Increase"

İpeknur Hazar, Mehmet Özkan Başar, Elçin Tan - Istanbul Technical University

MINING ENGINEERING

Excavation Mechanics

"Machine Learning-Based Prediction of Thrust Force in Tunnel Boring Machines"

Hadi Alizadeh, Ömür Acaroglu - Istanbul Technical University

Chair: Asst. Prof. Dr. Ramazan Yeniçeri

DEFENSE TECHNOLOGIES

Structural Design and Analysis

"Finite Element Analysis Of Crack Growth Behavior In The Presence Of Crack-Arresting Holes"

Buse Yaşın Aydın, İbrahim Özkol, Mustafa Tolga Yavuz - Istanbul Technical University

13:00
14:00

Unmanned Vehicles

"Heuristic Approach to UAV Selection with Fuzzy Logic and MADM Techniques"

Emre Yüksek-Istanbul Technical University

"Comparative Analysis of Object Detection and Tracking Algorithms for UAVs"

Merve İsmailvelioğlu, Mustafa Doğan - Istanbul Technical University

"Optimized Visual Odometry and Satellite Image Matching-Based Localization for UAVs in GPS-Denied Environments"

Ömer Sefa Öztürk, Alptekin Yıldız - Istanbul Technical University

---

Chair: Asst. Prof. Dr. Ramazan Yeniçeri

DEFENSE TECHNOLOGIES

Structural Design and Analysis

"Optimization and Finite Element Analysis of Metastructures for Vibration Mitigation"

Elif Nur Yaşar, Kaan Yıldız - Istanbul Technical University

14:00
15:00

"Parametric Optimization of Semi-Octagon Re-entrant Auxetic Structures for Energy Absorption"

Şenay Yener, Kaan Yıldız - Istanbul Technical University

"Design and Modeling of a Nonlinear Bi-Axial Dynamic Vibration Absorber for Helicopter Applications"

Resmiye Ağan, Vedat Ziya Doğan, Halit Süleyman Türkmen, Ali Tatar - Istanbul Technical University

"Computational Analysis of Metallic Structures Subjected to Impact Loading Using LS-Dyna"

Ümran Türkan, Vedat Ziya Doğan- Istanbul Technical University

---

Chair: Asst. Prof. Dr. Ramazan Yeniçeri, Dr. Abdülkadir Ünal

DEFENSE TECHNOLOGIES

Remote Sensing

"A Hybrid Preprocessing Approach Based on Simulation Data for Embedded Object Detection Under an Inhomogeneous Surface"

Ali Batuhan Bağcacier, Ali Yapar - Istanbul Technical University

15:00
16:00

RAILWAY SYSTEMS ENGINEERING

Railway Systems Engineering

"Fiber Bragg Grating Sensor: Principles, Applications, and Emerging Trends"

Serhat Boynukalın, Kemal Atakan Kırca - Istanbul Technical University

Signaling Systems in Railways

"A Safety-Critical Railway InterlockingArchitecture Based on SCADE and HIMA PLCs with Python-Driven Simulation and Control"

Serhat Boynukalın, Feride Berra Köseoğlu, Erdem Kısaç - Istanbul Technical University

"Energy Efficiency Optimization through Metro Scheduling: Mixed-Integer Linear Programming (MILP) and Genetic AlgorithmApproaches"

Mustafa Karaipek, Abdurrahman Yılmaz - Istanbul Technical University

---

Chair: Asst. Prof. Dr. İhsan Burak Kulga

PETROLEUM AND NATURAL GAS ENGINEERING

Geothermal Engineering

"Utilization of Carbon Dioxide Gas (CO2) for Gas Lift Systems in Geothermal Wells"

Force Lugembe Ndege, Ömer İnanç Türeyen - Istanbul Technical University

16:00
17:00

Natural Gas Engineering

"Natural Gas Hydrate Modelling" Devrim Başar Han - Istanbul Technical University

Reservoir Engineering

"A Machine Learning Approach to Forecast Production Performance of Hydraulically Fractured Horizontal Wells in Tight Oil Sandstone Reservoirs"

Ferhat Yurttagül, Burak Kulga - Istanbul Technical University

"Comparison of Thermophysical Gas Properties"

Nariman Valiyev, Ömer İnanç Türeyen - Istanbul Technical University

13.05.2025 | TUESDAY | ONLINE

MAIN HALL

09:00 - 10:00

Chair: Asst. Prof. Dr. Recep Gül

MUSICOLOGY AND MUSIC THEORY

Music Theory

"Exploring Perde-Çeşni Transformations in Tanburi Cemil Bey's Instrumental Works within Nikriz Makam"
Burak Kesgin - Istanbul Technical University

"Analysis Of Vertical Structures In The Context Of Set Theory In Ivan Wyschnegradsky's 24 Preludes In Quarter Tone System For Two Pianos, Op. 22"
Selçuk Canberk Dağtekin - Istanbul Technical University

"Folk Music And Classical Composition: A New Framework in Scottish Music Based on Bartok's Three Folk Music Categorizations"
Senay Yilmaz - Istanbul Technical University

"Harmony in Brouwer's Late Period: Use of Extended Tonality in the First Movement of Del Pensador"
Tamer Çelik, Recep Gül - Istanbul Technical University

10:00 - 11:00

Chair: Prof. Dr. Burcu Yıldız

MUSICOLOGY AND MUSIC THEORY

Popular Music

'It's Corn': From Everyday Life's 'Sound' to Viral Musical Meme"
Cevher Sarıgül - Istanbul Technical University

"The Issue of "Originality" in Arabesk Music: Analysis of Musical Borrowings, Similarities, and Production Practices from Arab Music"
Yiğit Sarıgül - Istanbul Technical University

Historical Musicology

"Analysis Of Some Makams FromThe Arabic Music Conference 1932"
Mohamed Mostafa Ahmed Mohamed - Istanbul Technical University

"Music as 'Refuge' From Reality: Schopenhauerian Aesthetics Revisited"
Selim Güre - Istanbul Technical University

11:00 - 12:00

Chair: Prof. Dr. Burcu Yıldız

MUSICOLOGY AND MUSIC THEORY

Ethnomusicology

"Evaluating Sounds on the Water from an Ecomusicological Perspective: The Case of Haliç"
Semin Tunalı-Istanbul Technical University

13:00 - 14:00

Chair: Assoc. Prof. Dr. Gökhan Deneç

MUSIC

Sound Engineering and Design

"Transformation of Digital Audio from Metaverse to Web3"
Günsel Işık Gruson, Taylan Özdemir - Istanbul Technical University

"Methodology on Participatory Media Analysis: Insights from Audio Modding Scene on Nexus Mods"
Başar Ünder, Taylan Özdemir-Istanbul Technical University

"Spatial Auditory Masking in 3D Audio: Challenges, Experimentation and Implications for Immersive Sound"
Emre Tenker - Istanbul Technical University

Music Business and Management

"Music Memes and the Relationship Between Music Marketing and Humor in Turkey: The Past, Present, and Future"
Alp Timuçin Bulut - Istanbul Technical University

14:00 - 15:00

Chair: Dr. Jane Harrison

MUSIC

Music Theory

"Effects of Performance Space on Free Improvisation Practices"
Aslıhan Adlin - Istanbul Technical University

"Cyclic Unity and Romantic Expression in Robert Schumann's {Fantasiestücke}, Op. 12: A Schenkerian Perspective"
Doğucan Temizel - Istanbul Technical University

Ethnomusicology

"Sonified Memory of the 2020 Aegean Sea Earthquake"
Doruk Başoğlu - Istanbul Technical University

Music Performance

"Challenging Conventions: Clara Wieck's Op. 20 and the Gendered Landscape of 19th-Century Music"
İrem Hayrioğlu-Istanbul Technical University

15:00 - 16:00

Chair: Dr. Robert Oliver Beahrs

MUSIC

Music Performance

"Messiaen as Liturgist: A ContextualReadingofthe Vingt Regards sur l'Enfant-Jésus"
Robert McDonald - Istanbul Technical University

"The Relentless Clash of Dissonant Harmonies and Lyric Melodic Lines… An Extensive Look into the Sound of Sergei Prokofiev"
Selçuk Ener-Istanbul Technical University

Sonic Arts

"Exploring Dance Floor Tactility: Sonic Ethnography and Artistic Inquiry through Audio Paper"
Gazele Aydın- Istanbul Technical University

16:00 - 16:45

KEYNOTE SPEAKER

"*Reconstructing A Turkish Identity in Boston: Jazz, Mehter, Byzantine Music and the Process of Internalization*"
Prof. Dr.Mehmet Ali SANLIKOL, New England Conservatory - Boston

17:00 - 18:00

Chair: Prof. Dr. Kamile Perçin Akgül, Dr. Görkem Giray

TRADITIONAL DANCES

Dance, Traditional Dances in terms of its role in interdisciplinary interaction in performance areas

"The Reinterpreting Choreographic Art Through Traditional Dances in Turkey: The Shaman Dance 'JEDI' Project"
Gülce Su Gümüş - Istanbul Technical University

POLITICAL STUDIES

Political and Social Thought

"State's Construction of "Othering" Mechanisms: Stigmatization and Discrimination Processes"
Ela Gülboy - Istanbul Technical University

Political Philosophy

"An Evaluation of Socrates, Plato and Aristotle Regarding Their Conceptualizations of Political Legitimacy"
Giray Çavdar- Istanbul Technical University

13.05.2025 | TUESDAY | ONLINE

HALL - I

09:00 - 10:00

Chair: Assoc. Prof. Dr. Umut Almaç

ARCHITECTURE
Conservation and Restoration
"The Rural Settlement Structure and the Challenges of Preserving Traditional Housing in Tokat Bağbaşı (İbibse) Village"
Eva Köker, Zeynep Eres Özdoğan - Istanbul Technical University
"Examination of the Transformation of Kirklareli Urban Conservation Area and Its Surroundings between 2004 and 2022 in the Context of Conservation and Sustainability"
Zeynep Gökçen, Zeynep Eres Özdoğan - Istanbul Technical University
"Facade Finishes in Early 20th Century Istanbul: History and State of Conservation"
Berru Çelik, Işıl Polat Pekmezci - Istanbul Technical University
"Ottoman Brick Stamps"
Nevriye Öztürk, Gülnin Tanyeli - Istanbul Technical University

10:00 - 11:00

Chair: Dr. Görkem Günay

ARCHITECTURE
Architectural History
"Rural Houses in Renaissance Architecture: Proposals of Sebastiano Serlio according to the Social Hierarchies in his Sixth Book"
E. Merve Aksoy Oral, Aygül Ağır - Istanbul Technical University
"Spatial Representation in French New Wave Cinema: An Analysis Through Agnès Varda's Cléo De 5 À 7 (1962) Film"
Mivaç Kaykılı, Demet Arslan Dinçay - Istanbul Technical University
"Legitimisation through Elevation: Romanos' Myrelaion"
Ömer Faruk Ulusoy, Bilge Ar - Istanbul Technical University
"Furniture Consumption in Istanbul at the Beginning of the 20th Century: The Role of Periodicals"
Sezin Dirihan, V. Gül Cephanecigil - Istanbul Technical University

11:00 - 12:00

Chair: Dr. Ebru Şevkin

ARCHITECTURE
Architectural History
"The Historical Layers Of Selimpaşa In Constaninople Hinterland Context"
Nil Ceren Karagülle, Bilge Ar - Istanbul Technical University
"Semi-Open Spaces As A Result of Climate And Culture in Mediterranean Architecture"
Furkan Sağdıç - Istanbul Technical University
Building Materials and Technologies
"Developing One-part Geopolymer Binders by Using Ground Granulated Blast-furnace Slag and Ceramic Waste as Precursors"
İlar Berfin İlbeyi, Ünal Anıl Doğan - Istanbul Technical University

13:00 - 14:00

Chair: Assoc. Prof. Dr. Bihter Almaç

ARCHITECTURE
Architecture Design Theory
"Soft Matters: (Re)Drawing Architecture Through Feminist Material Practices"
Beyza Nergis Özbek, Sıdıka Aslıhan Şenel -Istanbul Technical University
"Fluid Bodies of Space: Rethinking Architectural Relationality Through the Medusa Head"
Esra Yüksek, Sıdıka Aslıhan Şenel - Istanbul Technical University
"Urban Destruction in Malatya's Green Belt Project: A Struggle For Public Space Or Capitalist Gain?"
Furkan Evliyaoğlu, Nurbin Paker Kahvecioğlu - Istanbul Technical University
"Archival Encounters: Rewriting Istanbul Women's Works Library and Its Memory Through Bodily Practices"
Seray Rusçuklu, Sıdıka Aslıhan Şenel - Istanbul Technical University

14:00 - 15:00

Chair: Prof. Dr. Ozan Önder Özener

ARCHITECTURE
Architecture Design Theory
"The Performance of the Archive or Archive as Event: Exhibiting Architecture"
Derya Yıldız, Funda Uz - Istanbul Technical University
"Reading Architectural Memory through Cinematographic Image: Atatürk Cultural Center"
İsmail Gökkaya , Funda Uz - Istanbul Technical University
"Conditions of Criticality in Discussions on Architectural Representation"
Burçe Karadağ, Nurbin Paker Kahvecioğlu - Istanbul Technical University
"The Impact of Governmental Power On Urban Morphology: A Case Study of London"
Hande Nur Çalışkan Yüksel, Tan Kamil Gürer - Istanbul Technical University

15:00 - 16:00

Chair: Assoc. Prof. Dr. Aslıhan Şenel

ARCHITECTURE
Architecture Design Theory
"The Potentialities, Displacements, and Spatial Projections of the Concept"
Umran Aydın-Beykoz University
"Typological Transformations and Urban Isolation: Rethinking Architectural Production along Eskişehir Road"
Ahmet Günel, Celal Abdi Güzer - Middle East Technical University
"Exploring Experiential Learning Design Practices Grounded in Social Responsibility in Mardin"
Betül Toy, Yüksel Demir - Istanbul Technical University
"A Comparative Study on the Physical Quality of Başakşehir Deprem Konutları (Başakşehir Earthquake Housing) and Metrokent Site"
Sena Betül Demircan, Şayeste Tülin Görgülü-Istanbul Technical University

17:00 - 18:00

Chair: Asst. Prof. Dr. Ecem Tezel

ARCHITECTURE
Project and Construction Management
"A Literature Review On Organizational Structures In The Construction Industry"
Ece Gamze Sentuna, F. Pınar Çakmak - Istanbul Technical University
"Investigating the Role of Data Management for AI Utilization for Decision-Making in Construction: {A Literature Review}"
Hansa Eusmanaga, Fatma Pınar Çakmak - Istanbul Technical University
"A Systematic Review of BIM and the Circular Economy: Key Research Areas and Findings"
Merve Cellek, Fatma Pınar Çakmak -Istanbul Technical University
Sustainable Design
"Investigating Circularity in Buildings through Digital Circularity Metric"
Burcu Kumet , Meryem Birgül Çolakoğlu - Istanbul Technical University

18:00 - 19:00

Chair: Assoc. Prof. Dr. Orkan Zeynel Güzelci

INTERNATIONAL MASTER OF INTERIOR ARCHITECTURAL DESIGN
Interior Architecture
"Use of Mycelium-Based Materials as an Interior Design Component: A Digital Fabrication Approach"
Müge Özkan, Orkan Zeynel Güzelci - Istanbul Technical University
Technology in Interior Design
"A Strategy for Dataset Preparation in AI Model Training: The Case of Hotel Interiors"
Yaren Cengiz, Orkan Zeynel Güzelci, Derya Göleç Özer, Koray Kutlu - Istanbul Technical University

13.05.2025 | TUESDAY | ONLINE

HALL - II

09:00 - 10:00

Chair: Assoc. Prof. Dr. Almula Büyüktaşkın

ARCHITECTURE

Building Construction Technologies

"Impact of Deterioration Due to Environmental Factors on Seismic Performance of Traditional Timber Buildings in the Historical Peninsula in Istanbul"
Abdüllatif Sarıkaya, Caner Göçer - Istanbul Technical University

"Evaluation Of Damage Mechanisms Of Reinforced Concrete Industrial Structures In Past Earthquakes In Turkey"
Bahar Şevli, Caner Göçer - Istanbul Technical University

"Evaluation of Light Steel Structured Housing According to Construction Systems"
Burçin Fırtına, Caner Göçer - Istanbul Technical University

"Evaluation of Damage Mechanisms in Stone Structured Houses Due to Earthquakes in Turkey and Surrounding Areas"
Sarvin Iravani Ghadim, Caner Göçer - Istanbul Technical University

---

10:00 - 11:00

Chair: Assoc. Prof. Dr. Tarık Serhat Bozkurt

ARCHITECTURE

Building Construction Technologies

"Evaluation of Retrofitting Techniques in Reinforced Concrete Buildings"
Sinan Sarvan, Caner Göçer - Istanbul Technical University

"Evaluation of the Seismic Performance of Traditional Akçakese Houses in Relation to Structural Deterioration"
Zeynep Dikyer, Caner Göçer - Istanbul Technical University

Built Environment Design and Technologies

"Evaluation of Exterior Cladding Materials in Educational Buildings in Terms of Embodied Energy"
Dilfuruz Kara, Caner Göçer - Istanbul Technical University

"The Impact of Façade Cladding Materials on Carbon Emissions in Urban Renewal Projects: The Case of Istanbul"
Ikranur Sena Akkaya, Caner Göçer - Istanbul Technical University

---

11:00 - 12:00

Chair: Assoc. Prof. Dr. Feride Şener Yılmaz

ARCHITECTURE

Environmental Control and Building Technology

"MUrbanReCrete: A Sustainable Approach to Concrete Waste Recycling in Istanbul"
Başak Akarsu Akdemir, Fatma Sultan Bozkurt, Gizem Aluçlu Armutcu - Istanbul Technical University

"Multi-Stage Space-Adaptive Shelter: An Alternative for Post-Disaster Shelters"
Furkan Berke Çileziroğlu, Oğuz Cem Çelik - Istanbul Technical University

"Integration of Artificial Intelligence into Materials Education in Architecture: Opportunities, Challenges and Future Perspectives"
Peyam Başer, Seden Acun Özgünler, Mine Topçubaşı - Istanbul Technical University

"Reduction of Cooling Loads in Office Buildings in Hot Climates Using Radiant Cooling"
Yasemin Kılıçoğlu, Gülten Manioğlu - Istanbul Technical University

---

13:00 - 14:00

Chair: Prof. Dr. Hatice Ayataç

URBAN AND REGIONAL PLANNING

Transportation Planning and Urban Infrastructure

"Towards Walkable and Green University Campuses: Observational Assessment of ITU Maslak Campus forAdvancing the Sustainable Development Goals"
Amira Maway, Hatice Ayataç - Istanbul Technical University

"Determination of Saturation Flow Rate Right-Turn Adjustment Factor for Large Radii in Istanbul"
Ozan Emekter, Kemal Selçuk Öğüt - Istanbul Technical University

Sustainability, Ecology, and Energy in Planning

"Rethinking Heritage-Tourism Relations: Critical Perspectives and Sustainable Futures for Cultural Sites"
Büşra Yalçın, Turgay Kerem Koramaz - Istanbul Technical University

---

14:00 - 15:00

Chair: Assoc. Prof. Dr. Başak Demirez

URBAN AND REGIONAL PLANNING

Smart Cities, Digitalization, and Data Science

"City Information Modeling: Identifying Knowledge Gaps and Research Priorities"
Abdalrahman T. Y. Alashi, Özhan Ertekin - Istanbul Technical University

"Deprivation Analysis In Turkey And It's Provinces: a Study Based On English Index Of Deprivation And Turkish Statistical Institute"
Abdalrahman T. Y. Alashi, Özhan Ertekin - Istanbul Technical University

Climate Change and Planning

"Climate Change Adaptation in Urban Heritage Sites: The Case of Istanbul Historic Peninsula"
Turgay Kerem Koramaz, Tugce Turk - IstanbulTechnicalUniversity

---

15:00 - 16:00

Chair: Prof. Dr. Hayriye Eşbah Tunçay

LANDSCAPE ARCHITECTURE

Innovative Technologies for Landscape Design and Management

"The Use of Computer Vision in Observing Human Behavior in Landscape Architecture"
Gizem Yağmur Gölbaşı, Melih Bozkurt - Istanbul Technical University

Landscape Design

"Understanding Play: How Playground Equipment Shapes Cognitive, Social and Physical Behaviors in Children Aged 3-12: A Case Study in Maltepe Orhangazi City Park"
İçim Gündoğan Ata - Istanbul Technical University

Heritage and Identities

"From Tradition to Globalization: The Conceptual Transformation of Korean Landscape in Global City Seoul"
Mülkiye Kurt, Ebru Erbaş Görler - Istanbul Technical University

---

17:00 - 18:00

Chair: Assoc. Prof. Dr. Merve Tomaç

FOOD ENGINEERING

Food Bioactive Compounds

"Production of Phenolic Compounds from Grape Pomace by Enzyme-Assisted Extraction"
Ayşe Nilay Yıldırım, Derya Kahveci Karıncaoğlu - Istanbul Technical University

Functional Foods

"Composition and Technofunctional Properties of Aquafaba from Local Legume"
Nurullah Zekeriya Akar, Meral Kılıç Akyılmaz- IstanbulGelisimUniversity

"Plant Based Proteins In Instant Soups: Comparison of Sensory, Functional and Bioactive Properties"
Ceren Çakır - Istanbul Technical University

18:00 - 19:00

Chair: Prof. Dr. Neşe Şahin Yeşilçubuk, Asst. Prof. Dr. Çiğdem Yılmaz Çelak

FOOD ENGINEERING

Sustainable Foods

"Development and Characterization of Biodegradable Films Enriched with Proteins Extracted from Agro-Industrial Fes Waste and By-Products"
Nihal Sultan Bayar, Neşe Şahin Yeşilçubuk, Hande Yenipazar, Ayşe Saygün - Istanbul Technical University

Novel Food Processes

"Effects of Audible-Range Sound Treatment on the Microbiological Quality of Strawberry During Post-Harvest Storage"
Deniz Çavdar,Gürbüz Güneş-Istanbul Technical University

MOLECULAR BIOLOGY - GENETICS AND BIOTECHNOLOGY

Metagenomics and Protein Engineering

"Site-directed mutagenesis oninactive CYP102A178 fromhydrothermalhot spring Hisaralan-Balıkesir"
Elif Mehvej Özer, Başak Birdal, Kaan Dizer, Hande Mumcu, Nevin Gül Karagüler - Istanbul Technical University

"Recombinant Production of Two Novel Ferredoxin-NADP Reductases from {Pseudomonas mandelii} KGI_MA19"
Kaan Dizer, Hande Mumcu, Elif Mehvej Özer, Nevin Gül Karagüler-Istanbul Technical University

13.05.2025 | TUESDAY | ONLINE

HALL - III

09:00 - 10:00

Chair: Assoc. Prof. Dr. Özge Özdemir

AERONAUTICAL AND ASTRONAUTICAL ENGINEERING

Aircraft Design, Flight Dynamics And Performance

"External Store Separation From Fighter Aircraft"
Ahmet Kutsay Dere, Hayri Acar - Istanbul Technical University

"Winglet Design, Optimization and Performance Analysis for a Trainer Aircraft"
Çağlar Yakın, Hayri Acar, Serhat Yılmaz- Turkish National Defence University

"Sensitivity Analysis of Hypersonic Glide Vehicle Trajectory Under Aerodynamic and Atmospheric Variations"
Ekin Gözükaya, Halil Ersin Söken - Middle East Technical University

Rotary Wing Aircraft

"A Study on Hover and Forward Flight PerformanceofS70A-28D(UH-60L Black Hawk) Helicopter to obtain Cruise Chart by using Momentum and Blade Element Momentum Theory"
Mehmet Tayfun Ülbegi, Özge Özdemir - Turkish National Defence University

---

10:00 - 11:00

Chair: Assoc. Prof. Dr. Emre Koyuncu

AERONAUTICAL AND ASTRONAUTICAL ENGINEERING

Control Systems: Adaptive, Intelligent, Digital, Optimal, Pneumatic-Hydraulic

"Multi-Agent Reinforcement Learning with Maneuver Primitives for Automatic Ground Collision Avoidance of Fighter Jets"
Fatih Erol, Hayri Acar, Emre Koyuncu - Istanbul Technical University

"Quadrotor Actuator Fault Detection and Isolation. A Model-Based Approach"
Muhammed Arslan, Gökhan Inalhan- Istanbul Technical University

Spacecraft Control, Design And Performance

"Design of a Deployable S-Bant Helical Antenna for Cubesats"
Rümeysa Üstüncan -Istanbul Technical University

"Liquid Propellant Rocket Engine Performance Sensitivity Analysis"
Turan Copuroglu, Fırat Oğuz Edis - Istanbul Technical University

---

11:00 - 12:00

Chair: Asst. Prof. Dr. Ali Tatar

AERONAUTICAL AND ASTRONAUTICAL ENGINEERING

Mechanical Vibrations And Structural Dynamics

"Aeroelastic Optimization With Genetic Algorithm" Ahmet Güver, Seher Eken - Istanbul Technical University

"Feed-Forward Neural Network-Based Prediction of Flutter Speed of 3 DOF 2D Wing Model"
Osman Dağlı, Metin Orhan Kaya- Istanbul Technical University

"Conceptual Modeling of a Multi-Axial Nonlinear Dynamic Vibration Absorber for Helicopters"
Özkan Karayiğit, Ali Tatar, Vedat Ziya Doğan, Halit Süleyman Türkmen -Istanbul Technical University

"Nonlinear Modeling and Sensitivity Analysis of Oleo-Pneumatic Strut Landing Gear Systems for Aircraft Landing Performance"
Sadık Utku Gulek, Kaan Yıldız - Istanbul Technical University

---

13:00 - 14:00

Chair: Prof. Dr. Mehmet Şahin

AERONAUTICAL AND ASTRONAUTICAL ENGINEERING

Theoretical, Computational And Experimental Aerodynamics And Fluid Dynamics

"Fully-Coupled k–ω-SST Turbulence Model Implementation for Nonlinear Newton Method in Unstructured Vertex BasedHEMLABAlgorithm"
Atakan Okan, Mehmet Şahin - Istanbul Technical University

"Ground Wind Loads on Launch Vehicles"
Ece Saykan, Fırat Oğuz Edis -Istanbul Technical University "

A Deep Learning Based Modelling of Axial Turbomachinery"
Mehmet Fatih Reyhan, Yavuz Selim Mehel, Baha Zafer - Istanbul Technical University

"Experimental Study on Vortex Gust Encountered by a Flat Plate at 45° Wing Sweep"
Ozan Ibrahimagaoglu, Oksan Cetiner- Istanbul Technical University

---

14:00 - 15:00

Chair: Asst. Prof. Dr. Saliha Banu Yılmaz

AERONAUTICAL AND ASTRONAUTICAL ENGINEERING

Theoretical, Computational And Experimental Aerodynamics And Fluid Dynamics

"Digital Twin Approaches in System-Level Modeling for Aerospace and Propulsion Applications of Rocket Engines: A Review"
Yasir Şimes, İbrahim Özkol - Istanbul Technical University

Theoretical, Computational And Experimental Structural Analysis And Design

"Design and Analysis of Isogrid-Stiffened Cylindrical Structures for Launch Vehicles: Mathematical Modelling and Knockdown Factor Correlation with Finite Element Validation"
Hakan Atkan, Atkan Altınkaynak - Istanbul Technical University

"Investigation of the Interaction of Carbon Fiber Cylindrical Rocket Bodies with Radial Bolt Joints"
Kubilay Sazan - Istanbul Technical University

"Numerical Modeling of Composite Laminates Under Out-of-Plane Impact"
Vuslat Sena Avcı - Istanbul Technical University

15:00 - 16:00

Chair: Assoc. Prof. Dr. Ramazan Çağlar

ELECTRICAL ENGINEERING

Smart Grids

"Adaptation of a Generalized Observer Scheme for False Data Injection Detection in Load Frequency Control Systems"
Arslan Mete Baybars, Fikret Çalışkan, Istemihan Genç - Aselsan Inc., Istanbul Technical University

"Cyber-Resilient Real-Time Transient Stability Prediction for Modern Power Systems"
Kemal Aygül,Anurag K.Srivastava, Mostafa Mohammadpourfard, Istemihan Genç - IstanbulTechnicalUniversity

Power Electronics

"Three Phase LLC Resonant DC/DC Charger for Railway Applications"
Murat Gümüş, Abdulkadir Balıkçı - Gebze Technical University Electrical Vehicles

"Development And Validation Of A Dynamic Energy Consumption Model For A 12-Meter Electric Bus Using SORT 2 Test Data"
Mehmed Demirtaş, Mehmet Onur Gülbahçe - Istanbul Technical University

---

17:00 - 18:00

Chair: Assoc. Prof. Dr. Salih Barış Öztürk

ELECTRICAL ENGINEERING

Electric Power & Energy Systems

"Techno-Economic Integration of Nuclear Energy Towards Achieving Net-Zero Emissions"
Serdar Hudayberdiyev, Lale Erdem Atılgan - Istanbul Technical University

Power Electronics

"A Real-Time Resonance Detection and Mitigation Method for Shunt Active Power Filters"
Ramazan Berkan Tut, Veysel Tutku Buyukdegirmenci, Mustak Erhan Yalçın-Istanbul Technical University

Electrical Machines

"Investigation of the Effect of Space Vector PWM Technique on Zero-Sequence Voltage Formation in Open-End Windings"
Arda Tüfekçi, İlker Şahin, Derya Ahmet Kocabaş- Aselsan Inc., Istanbul Technical University

"Determination of Altitude Dependent Insulation Breakdown of Brushed DC Starter Generators"
Ayşe Nur Köklü Ulusoy - Istanbul Technical University

13.05.2025 | TUESDAY | ONLINE

HALL - IV

09:00 - 10:00

Chair: Prof. Dr. Mehmet Murat Monkul

SOIL MECHANICS AND GEOTECHNICAL ENGINEERING

Geotechnics

"Modelling of Lateral Spreading of Sandy Soils"
Hamed Feizollahzadeh Arabili - Istanbul Technical University

Environmental Geotechnics

"Evaluation of Geotechnical Characteristics of Recycled Concrete Aggregate-EAF Slag Mixtures"
Seyedsina Norouzian, Bilal Korkmaz, Aslı Yalçın Dayıoğlu - Istanbul Technical University

Geotechnical Earthquake Engineering

"Dynamic Site Response Analyses for A Site with A Deep Cut"
Yusuf Şahin, Gürkan Özden - Istanbul Technical University

10:00 - 11:00

Chair: Assoc. Prof. Dr. Deniz Artan

CONSTRUCTION MANAGEMENT

Construction Project Management

"Difficulties Faced by ConstructionExperts in Construction Sector Cases in the Turkish Justice System"
Bekir Haktanır, Murat Kuruoğlu, Onur Behzat Tokdemir - Istanbul Technical University
"Determining The Factors Causing Rework in Turkish Construction Industry"
Eda Nur Erdem, Gülden Gümüşburun Ayalp - Adana Alparslan Türkeş Science and Technology University
"Inclusion and Gender Equality for Women in the Construction Industry"
Elif Kılıç, Fatma Pınar Irlayıcı Çakmak - Istanbul Technical University
"Procurement Phases in EPC Projects: A Bibliometric Analysis"
Hasan Utku Uygun, Zeynep Işık - Yıldız Technical University

11:00 - 12:00

Chair: Assoc. Prof. Dr. Onur Behzat Tokdemir

CONSTRUCTION MANAGEMENT

Construction Project Management

"The Role of Cloud-Based Construction Management Software in Enhancing Project Efficiency"
Hazal Tokdemir, Deniz Artan - Istanbul Technical University

IT in Construction

"Assessing the Level of Digitalization of Construction Permit Processes in Türkiye" Gamze Nur İşeri Çetin, Esin Ergen Pehlevan - Istanbul Technical University

Sustainability in Construction

"Industrialisation of Natural Building Materials for Sustainability in the Built Environment"
Merve Guven, Deniz Artan - Istanbul Technical University
"Circular Economy Performance Assessment In Construction: A Critical Review Of Firm-Level Models"
Mohammed Alhallaq, Deniz Artan - Istanbul Technical University

---

13:00 - 14:00

Chair: Asst. Prof. Dr. Ömer Tuğrul Turan

STRUCTURAL ENGINEERING

Steel Structures

"Seismic Performance of Gravity Frames with Flush End-Plate Beam-to-Column Connections"
Alper Demir, Cüneyt Vatansever - Istanbul Technical University
"Effect of initial imperfections in short link beams on frame behavior"
Bünyamin Mutlu, Cüneyt Vatansever - Istanbul Technical University
"Blast-Resistant Steel Modular Structures Design with the Comparison of Dynamic Analysis Methods: SDOF and MDOF Systems"
Nur Doger, Barlas Ozden Cağlayan - Istanbul Technical University

Structural Damages

"Vibration Fatigue-Based Optimization of Open Hole Design in Stiffened Panels "
Görkem Aşçı - Istanbul Technical University

14:00 - 15:00

Chair: Assoc. Prof. Dr. Murat Yılmaz

STRUCTURAL ENGINEERING

Finite Element Methods

"Finite Element Analysis of Symmetrical Laminated Sandwich Plates with Stress Singularities Using Gradient Elasticity Theory"
Azir Mert Yavuz, Ülkü Hülya Çalık Karaköse - Istanbul Technical University
"Effect of Strut Shape and Relative Density on the Homogenized Material Properties and Anisotropy of Octet Truss Unit Cell"
Soheil Gholibeygi, Hale Ergün,Bahar Ayhan- Istanbul Technical University
"Artificial Intelligence Based Surrogate Models for Stiffened Plate Buckling Analysis"
Hasan Kıyık, Metin Orhan Kaya - Istanbul Technical University

Bridges

"Investigation of the Effects of Vibration Dampers Positioned on Hanger Cables of an Existing Suspension Bridge"
Muhammed Emin Demir, Kadir Özakgül - Istanbul Technical University

---

15:00 - 16:00

Chair: Assoc. Prof. Dr. Enes Zengin

STRUCTURAL ENGINEERING

Reinforced Concrete Structures

"A Preliminary Comparison of Turkish Seismic Design Code and the Draft Seismic Design Communiqué based on the Outputs of Structural Analyses of Mid-Rise RC Buildings"
Halit Emre Uygun, Çağlar Göksu Akkaya, Alper İlki - Istanbul Technical University
"Using Parametric Design Software to Optimize Hyperbolic Paraboloid Reinforced Concrete Shells in an Example Model"
İzel Ece Yılmaz, Kutlu Darılmaz - Istanbul Technical University
"Effect of Elevated Temperature on the Compressive Behavior of PET FRP Confined Low Strength Concrete Columns"
Mirsaeid Razavi, Birdal Koçak, Medine Işpir Arslan, Korhan Deniz Dalgıç , Alper İlki - Istanbul Technical University
"Effects Of Using Waste Glass Powder And Rice Husk Ash As A Partial Replacement With Cement In Mortar Productions"
Mohamad Alaa Shurbaji, Özgür Ekincioğlu - Istanbul Technical University

---

17:00 - 18:00

Chair: Assoc. Prof. Dr. Enes Zengin

STRUCTURAL ENGINEERING

Seismic Performance

"Seismic Performance Evaluation and Comparison of Different Structural Systems Using Nonlinear Time History Analysis"
Volkan İygen, Konuralp Girgin - Istanbul Technical University

HYDRAULICS AND WATER RESOURCES ENGINEERING

Hydrology

"Spatio-Temporal Analysis of Long-Term Rainfall Erosivity Trends and Climate Impacts on Erosion Potential"
Ahmet Faruk İpek, Ercan Kahya - Istanbul Technical University

GEOLOGICAL ENGINEERING

Rock Mechanics

"Detachments Induced By Thermal Cycling At Grain Boundaries of Fine Grained Marble"
Dilek Karapınar, Yılmaz Mahmutoğlu, Orhan Apaydın - Istanbul Technical University

13.05.2025 | TUESDAY | ONLINE

HALL - V

09:00 - 10:00

Chair: Prof. Dr. Üner Çolak

ENERGY SCIENCE AND TECHNOLOGY

Computational Heat and Mass Transfer

"A State-of-Charge Based Experimental and Numerical Investigation of Li-Ion Battery Heat Generation and Temperature Distribution"
Barış Işıklar, Ceyda Kök, Nergiz Gürbüz Karslıoğlu, Hasan Celal Malkoç, Sevan Karabetoğlu, Senem Şentürk Lüle, Rahim Jafari, Tuba Okutucu Özyurt - Istanbul Technical University

"Numerical Investigation of Engine Cooling Using Nanofluids"
Metehan Duman, Tuba Okutucu Özyurt, Zafer Dursunkaya - Istanbul Technical University

"Electrochemical and Thermal Modeling of Lithium Batteries for Temperature Distribution Based on Cathode Materials"
Sıdıka Vişne, Tuba Okutucu Özyurt, Sevan Karabetoğlu, Rahim Jafari - Istanbul Technical University

"Flow Control and Thermal Behavior of Bearings Using a Proportional Valve in a Closed-Loop Lubrication System for Turbofan Engines"
Yasin İnce, İlhan Kocaarslan - Istanbul Technical University

10:00 - 11:00

Chair: Asst. Prof. Dr. Sevan Karabetoğlu

ENERGY SCIENCE AND TECHNOLOGY

Energy Conversion and Storage Technologies

"Sustainable GSM Base Station Energizing Using Portable Radioisotope Thermoelectric Generator (RTG) Design"
Erdem Hayat, İskender Atilla Reyhancan - Istanbul Technical University

"The Lifespan Comparison of an NMC811 Pouch Cell Based High Voltage Battery with Silicon and Polyurethane Foam Usage"
Serhat Soyer - Istanbul Technical University

Energy Conversion and Sustainability

"Multi Criteria Decision Analysis For The Selection Of Alternative Marine Fuels In The Shipping Industry"
Emre Uz- Istanbul Technical University

"Energy Efficiency Potential Analysis of SMEs In Türkiye's Fertilizer Sector"
Sude Karabağ, Ebru Acuner - Istanbul Technical University

11:00 - 12:00

Chair: Asst. Prof. Dr. Sevan Karabetoğlu, Prof. Dr. Hakan Ali Çırpan

ENERGY SCIENCE AND TECHNOLOGY

Renewable Energy

"Feasibility Assessment of Hydrogen Fuel Cell Integration in The Dornier 228 Aircraft with the Structural and Operational Considerations"
Caner İlhan, Mehmet Suha Yazıcı - Istanbul Technical University

Sustainable Energy

"The Effect of Seawater on The Electrodecomposition of Hydrogen Sulfide to Hydrogen And Polysulfides"
Faezeh Nazari, Alper Sarioglan, Mehmet Suha Yazıcı - Istanbul Technical University

Computational Fluid Dynamics

"Numerical Investigation of Interfacial Contact Resistance in PEM Fuel Cells with Coated Metal Bipolar Plates"
Özgün Önen, Mehmet Suha Yazıcı, Dilek Kumlutaş, Utku Alp Yücekaya - Istanbul Technical University

COMMUNICATION SYSTEMS

Electrical Vehicles

"Design and Inter-Element Spacing Optimization of GNSS Array"
Muhammed Yusuf Şahin, Meave Kartal - Istanbul Technical University

---

13:00 - 14:00

Chair: Assoc. Prof. Dr. Onur Ferhanoğlu

ELECTRONICS AND COMMUNICATION ENGINEERING

Bio-Medical, Bio-Inspired Circuits/Systems

"Customizable Fluidic and Anisotropic Vocal Fold Phantom for Biomechanical Analysis"
Afarin Sarrafzadeh, Onur Ferhanoğlu, Ahmet C. Erten - Istanbul Technical University

"Development of Multi-Capsule Endoscopy via Spring-Assisted Distance Control"
Erfan Parsaei, Furkan Peker, Ali Fuat Ergenç, Onur Ferhanoğlu - Istanbul Technical University

"Effect of Wavelength, Intensity, and Eye Color on Pupil Detection in Infrared-Based Eye Tracking Systems" Murat Teksin, Onur Ferhanoğlu - Istanbul Technical University

"Image Reconstruction and Restoration with Diffusion Networks"
Onur Parapan, Ender Mete Ekşioğlu - Istanbul Technical University

---

14:00 - 15:00

Chair: Prof. Dr. Ece Olcay Güneş

ELECTRONICS AND COMMUNICATION ENGINEERING

Bio-Medical, Bio-Inspired Circuits/Systems

"Thermoplastic Microfluidic Platform for 3D Cell Culturingand Imaging"
Özlem Koçoğlu, Umut C. Coşkun, Berna Morova, Alper Kiraz, Kemal Baysal, Ahmet C. Erten - Istanbul Technical University

"A Deep Learning Network for Automatic Grade Classification of Renal Cell Carcinoma"
Süeda Kaya, Mürvet Kırcı - Istanbul Technical University

"Multi-Class Classification for Skin Lesions Using Deep Learning Techniques"
Ümmühan Kopal, Mürvet Kırcı - Istanbul Technical University

Embedded Systems

"Design of a Clutchless AutomatedGearControlSystem for Electric Tractors"
Bertuğ Bingöl, Ece Olcay Güneş, Murat Gündoğdu, Bertuğ Bingöl - Istanbul Technical University

---

15:00 - 16:00

Chair: Prof. Dr. Berna Örs Yalçın

ELECTRONICS AND COMMUNICATION ENGINEERING

Analog/Mixed-Signal/Microwave Circuits

"Design of a Low-power Phase-FrequencyDetectorin65nmCMOSTechnology Suitable for 5G Mobile Applications"
Bora Batuhan Işgör, Nil Tarım - Istanbul Technical University

"22-nm FD-SOI Internal Power Management Unit for FMCW lidar"
Mahmut Coban, Ahmet Tekin - Istanbul Technical University

VLSI Systems and Applications

"Logic Locking-Based FPGA System Design for Third-Party IP Protection"
Teyyar Açar, Fatih Tiryakioğlu, Sıddıka Berna Örs Yalçın - TÜBİTAK BİLGEM

Digital Circuits and Systems

"Hardware Implementation of FALCON's ffSampling Algorithm"
Yasin Yılmaz, Sıddıka Berna Örs Yalçın, Mustafa Mert Esen- Istanbul Technical University

---

17:00 - 18:00

Chair: Prof. Dr. Volkan Sezer

MECHATRONICS ENGINEERING

Robotics

"Comparison Of MPC Based Motion Control Algorithms On MuJoCo Hybrid Platform"
Ayşe Kızıldemir Kılıç, Hakan Temeltaş - Istanbul Technical University

"A Study on the Performance of GNN, PDA, and JPDA in a ROS-Based Tracking Framework"
Nurettin Özçelik, Volkan Sezer- Istanbul Technical University

Vehicle Design

"Steer-by-Wire System ModelingandControlUsing Optimal PID Controller"
Seyitcan Şahin, Erhan Yumuk - Istanbul Technical University

Autonomous Vehicles

"WaveDrive: A Pipeline for Gesture Recognition Using Hands Coordinates"
Abdülkerim Sipahi, Erdinç Altuğ - Istanbul Technical University

13.05.2025 | TUESDAY | ONLINE

HALL - VI

09:00 - 10:00

Chair: Assoc. Prof. Dr. Ersin Sayar

MECHANICAL ENGINEERING

Computational Fluid Dynamics

"Optimization of Thermal-Flow Performance in Close Circuit Cooling Towers"
Efe Gürle, Tahsin Engin - Istanbul Technical University

"Analysis of Effects of Tip Clearance on Axial Pump Performance"
Mehmet Deniz Papacı, Levent Kavurmacıoğlu - Istanbul Technical University

"Aerodynamic Performance Enhancement of a 27-inch APC Propeller Through Geometric Modifications"
Mehmet Emin Arslan, Sertaç Çadırcı-Istanbul Technical University

"Optimization of Polymer Melt Impregnation Systems by Extrusion Method"
Mehmet Usta, Ali İhsan Koca, Mustafa Doğu - Istanbul Technical University

10:00 - 11:00

Chair: Asst. Prof. Dr. Korhan Şahin

MECHANICAL ENGINEERING

System Dynamics and Control

"Nonlinear System Identification of A 2-Dof Gimbal System"
Batuhan Kalkan, Ayhan Kural - Istanbul Technical University

"Trajectory Analysis of a Medium-Range Ballistic Missile Threat via Design and Simulation"
Doruk Ünal, İlker Murat Koç, Ukte Aksen - Istanbul Technical University

Machine Design

"Weight and Volume Optimization of Two Stage Wolfrom Planetary Gear Mechanism"
Kadir Kanat, Ali İmre Aydeniz, Cevat Erdem İmrak - Istanbul Technical University

"Examining the Impact of Groove Profiles and Dimensional Parameters on Shear Pin Strength"
Mehmet Ozan Yitim, Cevat Erdem Imrak, Adem Candas - Istanbul Technical University

11:00 - 12:00

Chair: Prof. Dr. Erdinç Altuğ

MECHANICAL ENGINEERING

Machine Dynamics, Vibration, and Acoustic

"Comparison of Time and Frequency Domain Approaches for Fatigue Life Estimation Using the Finite Element Method"
Ahmet Fatih Turhan, Osman Taha Şen - Istanbul Technical University

"Semi-Analytical Investigation of Non-Linear Tuned Mass Dampers Using the Multi-Term Harmonic Balance Method"
Okan Çengel, Osman Taha Şen - Istanbul Technical University

"Analytical Investigation of Modal Curvatures of Damaged Beams"
Ozan Ürel, Uğurcan Eroğlu - Istanbul Technical University

"Investigating the Use of Crash Dummies as Human Body Models for Whole-Body Vibration Evaluation"
Safa Eren Pepeç, Özgen Akalın - Istanbul Technical University

13:00 - 14:00

Chair: Prof. Dr. Ata Muğan

MECHANICAL ENGINEERING

Computational Solid Mechanics

"Hybrid Optimization Method for I-Section Beams: A Comparative Study with Detailed FEM"
Ahmet Aktaş, Hacı Abdullah Taşdemir - Istanbul Technical University

"Structural Optimization of LPDC Aluminum Wishbone for Sheet Metal Design in Rear Suspension System for Electric C-SUV Vehicles"
Alparslan Erdirençelebi - Istanbul Technical University

"A Novel Approach for Robust Identification and Characterization of Mechanical Shock Loads for Structural Durability Assessment"
Doğukan Elibol, Mesut Kırca - Istanbul Technical University

"Post-Buckling Behavior of Metallic Panels"
Taha Çimen, Ata Muğan - Istanbul Technical University

14:00 - 15:00

Chair: Prof. Dr. Ata Muğan

MECHANICAL ENGINEERING

Computational Solid Mechanics

"Parametric Investigation of Mechanical Properties for Laser Powder Bed Fusion Processed Inco718 Auxetic Metamaterials"
Kubilay Özgönül, Hacı Abdullah Taşdemir - Istanbul Technical University

"Modeling Hydrogen-Induced Failure of AISI 4135 Steel by Finite Element Analysis"
Dorukhan Güngör, Emin Sünbüloğlu - Istanbul Technical University

"A Comparative Modal Analysis of Homogenized and Full-Scale FE Models of Sandwich Composite Structures with Re-entrant Auxetic Core"
Özgür Değirmenci, Kadir Günaydın, Halit Süleyman Türkmen, Şafak Yılmaz - Istanbul Technical University

Additive Manufacturing

"Evaluation of Mechanical Properties of SLM AlSi10Mg Alloy Produced with Different Production Parameters"
Hasret Baş, Rasid Ahmed Yıldız - Istanbul Technical University

15:00 - 16:00

Chair: Asst. Prof. Dr. Alper Tolga Çahk

MECHANICAL ENGINEERING

Automotive

"Effect of injection timing on performance of port injection hydrogen engine"
Hilmi Ersin Oktar, Muammer Özkan - Yıldız Technical University

"Combustion Model Analysis on Validation Purpose of A Spark Ignition Engine"
Akay Delihasan, Ahmet Yapmaz,Barış Doğru-Istanbul Technical University

"ANN-Based PID Tuning Mechanism for A Vehicle Control System Considering Improved Path Following"
Başar Zaman, Volkan Bekir Yangın, Özgen Akalın- Istanbul Technical University

"Optimizing Urban Micro-Mobility: Ergonomic Design, Structural Integrity, And Dynamic Analysis of Electric Kick Scooter"
Kadir Rıdvan Düzelli, Mehmet Oğuz Mutlu - Istanbul Technical University

17:00 - 18:00

Chair: Assoc. Prof. Dr. Alaadin Burak Irez

MECHANICAL ENGINEERING

Automotive

"Electrification of Heavy Commercial Truck: Vehicle Dynamics Modelling, Energy Efficiency Analysis, and Economic Comparison with Conventional Diesel Engine"
Kadir Rıdvan Düzelli, Osman Taha Şen - Istanbul Technical University

"Investigation and Optimization of the Effect of Different Profile Modifications on Gear Noise and Strength in the Gearbox with Single Stage Spur Gear"
Hakan Yardımcı, Ali Gökşenli,Ali İmre Aydeniz- Istanbul Technical University

HEAT FLUID

"Generation of Proper Inflow Conditions with Hydrodynamic Stability Approach: A Case Study For An Axially Rotating Pipe Flow"
Taha Günaydın, İ. Bedii Özdemir-Istanbul Technical University

"Multi-Objective Aerodynamic Shape Optimization of Helicopter Nose"
Yiğit Can Özdemir, Sertaç Çadırcı - Istanbul Technical University

14.05.2025 | WEDNESDAY | ONLINE

MAIN HALL

Chair: Prof. Dr. Bihter Erol

09:00
10:00

GEOMATICS ENGINEERING
Geographic Information Systems
"Estimating Vessel-Based Carbon Emissions in the Ambarlı Port Region Using AIS and GIS Data"
Fırat Bolat, Hande Demirel - Istanbul Technical University
"Social Vulnerability Analysis of the Cities Affected by the February 6 Turkey Earthquake"
Hilal Akın, Himmet Karaman - Istanbul Technical University
"Transformation of Solid Waste Management in Baku: A GIS-Based MCDM Approach to Landfill Site Selection Beyond Balakhani"
Kanan Alakbarlı, Dursun Zafer Seker - Istanbul Technical University
"Spatial Problems and Effective Factors in Hospital Campus Structure"
Özgür Elmas, Rahmi Nurhan Çelik - Istanbul Technical University

---

Chair: Prof. Dr. Bihter Erol

10:00
11:00

GEOMATICS ENGINEERING
Remote Sensing
"Aircraft Contrails Detection with Deep Learning Methods on Remote Sensing Images"
Çağatay Yıldırım, Hande Demirel - Istanbul Technical University
"Investigation of Anthropogenic Effects in Protected Wetlands Using Remote Sensing and Geographic Information Systems: A Case Study of Manyas Bird Lake and Bird Paradise National Park"
İlyas Bursa, Adalet Dervişoğlu- Istanbul Technical University
"Enhancing Sentinel-1 SAR Geolocation Accuracy The Impact of DEM on Orthorectification Performance"
Sena Oğuzhanoğlu, Filiz Sunar - Istanbul Technical University
"Offshore Wind Turbine Site Selection in the Aegean Sea"
Şule Feride Arıkç, Adalet Dervişoğlu - Istanbul Technical University

---

Chair: Prof. Dr. Bihter Erol

11:00
12:00

GEOMATICS ENGINEERING
Natural Hazards
"Seismic Hazard Assessment of Kahramanmaraş Region: Analysis of Earthquake Sources and Probabilistic Seismic Risk"
Sajjad Alghezi, Abdullah Can Zülfikar - Istanbul Technical University
"Flood Risk Analysis with Geospatial Artificial Intelligence Techniques"
Miraç Taha Derman, Muhammed Oğuzhan Mete - Istanbul Technical University
Geodesy
"On the Role of Earth Observations and Geodetic Data in Environmental and Climate Change"
Solmaz Farnad, Bihter Erol - Istanbul Technical University
Photogrammetry
"Generating a High-Definition Map (HD Map) via YOLO (You Only Look Once) Deep Learning-Based Object Detection Model"
Yasin Memi, Hande Demirel - Istanbul Technical University

HALL - I

Chair: Asst. Prof. Dr. Abdulkerim Çapar

09:00
10:00

COMPUTER SCIENCE
Data Science
"A Data-Driven Approach to Process Duration Estimation: End-to-End Machine Learning with Process Mining"
Burak Batıbay, Barışmert Günal, Hakan Yıldırır, İsmail Çağatay Bilgin, Serkan Günal, Emre Çimen - **Eczacıbaşı**
Informatics Image Processing
"PET Image Denoising Using Denoising Diffusion Probabilistic Models (DDPMs)"
Emine Pacci, Isa Yildirim - Istanbul Technical University
"Iterative Reconstruction Applications For Aircraft Image Restoration"
Emirhan Gül, Ender Mete Ekşioğlu - Istanbul Technical University

---

Chair: Dr. Meriç Yücel

10:00
11:00

COMPUTER ENGINEERING
Artificial Intelligence
"Multi-Lead ECG Classification Using a Mixture-of-Experts Transformer Model"
Atalay Çelik, Mehmet Ali Ergün - Istanbul Technical University
"The Role of Artificial Intelligence in Enhancing Software Quality: A Multivocal Literature Review"
Melis Toksoy, Murat Yilmaz - Gazi University
"An Intelligent Jamming Environment: Reinforcement Learning Approach"
Ömer Faruk Dikmen, Hasari Çelebi - Gebze Technical University
Computer Networks
"Adaptive Consensus Algorithms for Blockchain Networks"
Esin Küpükmeriç, Adnan Ozsoy - Hacettepe University

Chair: Assoc. Prof. Dr. Şerif Bahtiyar

11:00
12:00

COMPUTER ENGINEERING
Cyber Security
"Reputation Based Decision Making Consensus Mechanism for UAV Swarms with Ethereum Blockchain"
Mustafa Tosun, Şerif Bahtiyar - Istanbul Technical University
"Enhancing IoT Botnet Detection: A Streamlined Approach to Feature Selection"
Nilüfer Uslan, Şerif Bahtiyar- Istanbul Technical University
"Neuromorphic Computing and Memristor-Based Network Attack Detection Systems: New Approaches in Cybersecurity"
Yusuf Etka Köylü, İlhan Kocaarslan - Istanbul Technical University
Embedded Systems
"Comparison of the Effects of Different Compiler Environments on Communication Signal Detection Software"
Mustafa İmeci, Onur Göksel, Bilge Minisker, Sergen Çetin - Aselsan

14.05.2025 | WEDNESDAY | ONLINE

HALL-II

09:00 – 10:00

Chair: Prof. Dr. Bülent Arıkan

ECOLOGY AND EVOLUTION

Anthropocene

"Exploring The Biodiversity Patterns Of Anatolia Under Changing Climatic Conditions"
Batuhan Atıf Tunç, Emrah Çoraman- Istanbul Technical University

"Defining the Character of Turkey's Biodiversity Policies"
Süleyman İlteber Upar - Istanbul Technical University

Paleo-Ecology

"The Geoarchaeology of The Ambar Basin (Diyarbakir) In the Light of GIS and Geomorphological Data"
Alaaddin Al, Kemal Koçakli - Dicle University

"Exploring the Evolution of Socio-Ecological Systems Through Agent-Based Modeling in Resuloğlu Höyük (North Central Anatolia) During the Early Bronze Age (4300–4100 BP)"
Kemal Kocakli, Bülent Arıkan, Neriman Erdem - Istanbul Technical University

---

10:00 – 11:00

Chair: Asst. Prof. Dr. Recep Kaya

ENVIRONMENTAL ENGINEERING

Air Pollution and Control

"Effects of Air Pollutant Parameters on Respiratory Diseases in Edirne"
Kutlay Özdemir, Burçak Kaynak - Istanbul Technical University

Membrane Technologies

"Preliminary Experimental Investigation of Nanofiltration and Reverse Osmosis Processes for Desalinating Seawater"
Hande Gulcan, Derya Y. Koseoglu Imer - Istanbul Technical University

"Enhancing Reverse Osmosis Performance: A CFD-Based Study of Randomized Feed Spacer Geometries"
Rabiya Karalı Türker, Halil Ekici, Cemanur Aydınalp- Istanbul Technical University

---

11:00 – 12:00

Chair: Asst. Prof. Dr. Ebru Acuner Türet

SUSTAINABILITY

Climate Change Mitigation

"Assessing Decarbonization Strategies and Decoupling Trends of Türkiye's Private Sector Companies"
Aslı Ceydanur Akbaba, Kadriye Elif Maçin, Börte Köse Mutlu - Istanbul Technical University

"The Relationship between Sustainable Finance and the Carbon Border Adjustment Mechanism (CBAM): A Policy Impact Assessment and Hypothetical Case Study of a Cement Plant"
İnci Nur Çetin - Istanbul Technical University

Smart and Sustainable Cities

"Investigation of Green Buildings Towards Net Zero Carbon in Cities: Example in ITU Ayazaga Campus"
Merve Maçin, İsmail Toröz - Istanbul Technical University

"An Inclusive Digital Accessibility Policy for Individuals with Disabilities"
Oylum Bülbül, Hatice Ayataç - Istanbul Technical University

HALL - III

09:00 – 10:00

Chair: Assoc. Prof. Dr. Adalet Dervişoğlu

GEOMATICS ENGINEERING

Geographic Information Systems

"Spatial Analysis and Optimization of E-Commerce Company's Parcel Collection Operations: The Case of Esenyurt, Istanbul"
Fatma Reyyan Sarıkaya, Adalet Dervişoğlu- Istanbul Technical University

Remote Sensing

"Evaluating The Temporal Consistency Of SAR And Optical Vegetation Indices For Cotton Monitoring Using Sentinel-1 And Sentinel-2"
Alp Eren Furkan Demirci, Ayşe Filiz Sunar- Istanbul Technical University

GEOGRAPHIC INFORMATION TECHNOLOGIES

Artificial Intelligence and Machine Learning in Remote Sensing Analysis

"Current Challenges In Port Management And Common Approaches From Geographic Information Technologies (GIT)"
Cemre Fazilet Aldoğan, Hande Demirel - Istanbul Technical University

Remote Sensing Applications in Natural Disaster and Natural Resource Management

"Spatiotemporal Change Analysis and Future Projections of Wetlands in Central Anatolia, Türkiye"
Hilal Daşdemir - Istanbul Technical University

10:00 – 11:00

Chair: Prof. Dr. Himmet Karaman

GEOGRAPHIC INFORMATION TECHNOLOGIES

Spatial Data Algorithms and Visualization and 3D GIS Technologies

"Tactile Map Production Processes and Application Areas for Visually Impaired"
Ayça Eraslan - Istanbul Technical University

Spatial Planning and Management with GIS Applications

"Mitigating Urban Heat Island Effects through Nature-Based Solutions: The Case of Istanbul"
Gizem Baydı, Fatih Terzi - Istanbul Technical University

"City Model Production with Lidar Technology and Integration of Urban Transformation with GIS: The Example of Zeytinburnu District"
Merve Altın Çetinkaya, Mustafa Yanalak - Istanbul Technical University

"Analysis of Customer Complaints in Mobile Communication Networks with GIS"
Merve Tanır, Rahmi Nurhan Çelik - Istanbul Technical University

---

11:00 – 12:00

Chair: Assoc. Prof. Dr. Börte Köse Mutlu

SUSTAINABILITY

Life Cycle Assessment

"The Intersection Infrastructure of LCA–BIM Integration: Applicability in Turkey and Europe"
Tuğba Ayvaz - Istanbul Technical University

Sustainable Development Goals

"Enhanced Efficiency of PLA-Based Membranes via Optimizing Coagulation Bath Temperature"
Rana Memarzadeh, Vahid Vatanpour, Mohhamadreza Nofar - Istanbul Technical University

Water and Waste Management

"Evaluating the Water Footprint of Textile Products: A Comparative Study of Wool and Cotton in Türkiye"
Gizem Aydın, Börte Köse Mutlu - Istanbul Technical University

14.05.2025 | WEDNESDAY | ONLINE

HALL-IV

Chair: Asst. Prof. Dr. Elif Küçüksayraç

09:00
10:00

INDUSTRIAL DESIGN
Historical, Cultural and Social Context of Design
"Decoding Toxic Attachment Between Design Products and the Users: Understanding by using Metaphors "
Bilge Ceren Ay, Özge Çelikoğlu - Istanbul Technical University
"Discovering the Choir Members' Practices: An Initial Understanding of the Intersection of Design, Music, and Community"
Gürkay Aydoğmuş, Koray Gelmez - Istanbul Technical University
Product Design
"Testing the Aesthetic Responses to Small Household Appliances in the Context of Incremental Innovation"
Fatma Cizrelioğlu Karaer, H. Tengüz Ünsal - Marmara University

---

Chair: Assoc. Prof. Dr. Koray Gelmez

10:00
11:00

INDUSTRIAL DESIGN
Theory and Methodology in Industrial Design
"Understanding Creativity: A Survey-Based Investigation into the Psychology of Designers' Creativity during the Ideation Phase"
Naz Feryal Cezayirli, Aysun Ateş Akdeniz - Istanbul Technical University
"User Narrative as Antenarrative: Exploring New Possibilities"
Fulden Ateş, Özge Merzali Çelikoğlu - Istanbul Technical University
"Exploring Emotions in Design Research: An Initial Mapping of Emotion-based Concepts"
Gamze Uğurlukişi, Koray Gelmez - Istanbul Technical University
"Prompt 'Design the Perfect Product': A Literature Review on AI Incorporation in Industrial Design Processes"
Sude Kartalbaş, Aysun Ateş Akdeniz - Istanbul Technical University

HALL - V

Chair: Asst. Prof. Dr. Ebru Acuner Türet

09:00
10:00

GAME AND INTERACTION TECHNOLOGIES
Game Design
"Understanding Player Behavior: The Role of Intrinsic and Extrinsic Motivations in Bartle Player Types"
Muhammet Sinan Çavdar, Derya Güleç Özer, Hüseyin Kutay Tinç- Istanbul Technical University
"Optimizing Level Production in Hidden Object Games Using YOLO Object Detection"
Ekin Demircan, Sema Alaçam - Istanbul Technical University
"Impossible Spaces in Games: Using Anamorphic Projection in Space Interactions to Explore Possibilities of New Game Mechanics"
İrem Aydındoğan, Sema Alaçam - Istanbul Technical University
"A Systematic Approach To Ludonarrative Harmony: Methods For Aligning Interactive Gameplay and Storytelling"
Cem Çelik, Ayşegül Akçay Kavakoğlu - Istanbul Technical University

---

Chair: Assoc. Prof. Dr. Derya Güleç Özer

10:00
11:00

GAME AND INTERACTION TECHNOLOGIES
User Studies
"An Analysis of Gaming Behavior Through Bartle's Player Model & Human Psychology"
Asena Ersoy, Leman Figen Gül - Istanbul Technical University
Game Production
"RNBO for Game Development: A Framework for Dynamic and Adaptive Audio Design"
Deniz Koçak, Ozan Sarıer - Istanbul Technical University
AI in Gaming
"Preliminary Study on the Feasibility of Neural Network-Based Generative AI Models in Video Game Music Production"
Ülkü Nur Nar, Ozan Sarıer - Istanbul Technical University
"A Comparative Study for Analyzing LLM Performance in Bluff-Based Card Games"
İrem Şalk, Sanem Sarıel - Istanbul Technical University

Chair: Assoc. Prof. Dr. Derya Güleç Özer

11:00
12:00

GAME AND INTERACTION TECHNOLOGIES
Gamification
"Procedural Entity Generation For Simulated Ecosystems"
Gazi Muhammet Canbolat, Selçuk Sümengen, Sema Alaçam - Istanbul Technical University
Interaction Technologies
"Naval History Reconstruction Through 3D Modeling and Simulation"
Deniz Çakır, Gökdeniz Neşer- Dokuz Eylül University Series Games
"Mechanics To Design Virtual Reality Cognitive Training Games"
Evrim Kabadayı, Leman Figen Gül - Istanbul Technical University

14.05.2025 | WEDNESDAY | ONLINE

HALL-VI

Chair: Assoc. Prof. Dr. Mehmet Emin Şalgamcıoğlu

09:00
10:00

URBAN DESIGN

Design and Evaluation of Public Spaces

"The Transformative Effect of Digital Art Installations on Public Spaces: The Case of Border Tuner"
Gülay Didir, Eren Kürkçüoğlu - Istanbul Technical University

"Effects Of Building And Street Interaction On Behavior: An Examination Through Privacy In Kadiköy"
İrem İncetuzcu, Gülden Demet Oruç - Istanbul Technical University

Urban Image and Identity

"The Impact of Space on Sound Perception: The Relationship Between Sound and Context"
Kübra Türk, Meltem Erdem Kaya - Istanbul Technical University

---

Chair: Assoc. Prof. Dr. Mehmet Emin Şalgamcıoğlu

10:00
11:00

URBAN DESIGN

Urban Conservation

"A Study of Meaning in Ruins: Ancient Cities as Open-Air Museum"
Bahar Çalışkan, Mehmet Emin Şalgamcıoğlu - Istanbul Technical University

Urban Resilience

"Shaping Resilient Cities: Pedestrianization as a Tool for Open Space Networks"
Ilgın Yılmaz, Meltem Erdem Kaya - Istanbul Technical University

---

Chair: Assoc. Prof. Dr. Aslıhan Erkmen

11:00
12:00

ART HISTORY

Art History

"A Brief Historical Trajectory of Art Collectives as a Commoning Practice in Turkey"
Ezgi *Ceren Tuncaelli Çakmak, Ebru Belgin Yetişkin Doğrusöz* - Istanbul Technical University

"From Functional to Imaginary Forms: Alev Ebüzziya Siesbye's Ceramics"
Funda Türeli, Aslıhan Erkmen - Istanbul Technical University

Art and Technology

"The Role of Digital Technologies in Museum Storytelling: Ephesus Experience Museum"
Hilal Kesikci, Zeynep Kuban Tokgöz - Istanbul Technical University

---

*** THE PRESENTATION DURATION IS DEFINED AS 15 MINUTES, INCLUDING Q-A (ONLY FOR ORAL PRESENTATIONS)**

14.05.2025 | WEDNESDAY | IN-PERSON

ITU Süleyman Demirel Arts and Conference Center, Ayazağa Campus

GROUND FLOOR and FIRST FLOOR - IN PERSON

09:00
12:45

POSTER SESSION

CONFERENCE HALL - IN PERSON

10:00
11:30

"3 MINUTE THESIS" Competition

WORKSHOP HALL - IN PERSON

09:00
10:00

Chair: Prof. Dr. Aydan Turanlı

SCIENCE, TECHNOLOGY AND SOCIETY (STS)

Communication of Science and Technology

"A Bibliometric Analysis of Metaverse Technologies in Healthcare Services"
Seçkin Damar, Gülşah Hançerlioğulları Köksalmış, Istanbul Technical University

Social Dimensions of Science and Technology

"The Impact of Music Platforms on Music Production and Taste Profiles in Turkey: The Case of Spotify"
Mert Sarıkaya, Ebru Yetişkin, Istanbul Technical University

Social and Ethical Dimensions of AI

"Unintended Consequences Of Generative AI In Product Ideation: A Product Management Perspective"
Tuğçe Gültekin Atlı, Deniz Tunçalp, Istanbul Technical University

---

KEYNOTE SPEAKER STS - Talk

11:15
12:00

"Democratic Science And Participation in the Digital Era: Insights from Citizen Science Projects in the Environmental And Marine Sciences"

Asst. Prof. Allesandra Cenci, Aalborg University - Denmark

* The distinguished speaker is hosted within the scopus of ERASMUS+ programme.

12:45
12:00

CLOSING REMARKS

Prof. Dr. Fatma Seniha GÜNER , Institute Director, Istanbul Technical University

---

13:00
14:00

CONCERT AND PERFORMANCE PROGRAMME

CONFERENCE HALL - Istanbul Technical University
Turkish Music State Conservatory

EXTENDED ABSTRACTS

Oral Presentations (72-1993)

Poster Presentations (1994-2564)

ORAL PRESENTATIONS

AERONAUTICAL AND ASTRONAUTICAL ENGINEERING

Aircraft Design, Flight Dynamics And Performance

Control Systems: Adaptive, Intelligent, Digital, Optimal, Pneumatic-Hydraulic

Mechanical Vibrations And Structural Dynamics

Rotary Wing Aircraft

Spacecraft Control, Design And Performance

Theoretical, Computational And Experimental Aerodynamics And Fluid Dynamics

Theoretical, Computational And Experimental Structural Analysis And Design

External Store Separation From Fighter Aircraft

Ahmet Kutsay Dere[a], Hayri Acar[b]

[a] Istanbul Technical University, Graduate School, Aeronautical and Astronautical Engineering Program, Turkiye
[b] Istanbul Technical University, Faculty of Aeronautics and Astronautics Department of Aeronautical Engineering, Turkiye
derea15@itu.edu.tr

Keywords: Safe Separation, Eglin Test Case, F-22, Fifth Gen Aircraft, Grid Method, Simulation.

Aim

Developing a new aircraft consists of many challenging topics including carrying and employing of stores. Aircraft must be designed to enable safe seperation of new designed or currently used stores. Designed store must be certified to demonstrate that it is suitable for effective separation. Store separation can be tested in three different ways. First one is the flight test which is highly risky for manned flight and it is expensive. Second way is wind tunnel testing which is also expensive and time consuming. The most cheapest and safest method is using store separation simulations.
The stores can be divided into two categories: bombs and missiles, and differ in their release mechanisms. The stores can be carried in internal stations or external stations which are under the wings. In this study safe separation of Eglin store geometry from a fifth generation fighter aircraft modelled and tested for different flight conditions. The ultimate goal of the fighter jet and store development projects is to hit a targeted point in the most effective way. In order to hit the target accurately, the flight conditions and the aerodynamic and inertial properties of the store must be taken into consideration and the release must be made in the most suitable position and flight conditions. An important criterion in determining the release moment is to prevent the store from collision to the aircraft during its separation. For this purpose, maneuvering the aircraft during the release moment can be a solution. A more effective one is to decide on the correct release moment with simulations to be performed before the flight.
The store examined in this study is an uncontrolled (free-falling) bomb and will be dropped from external stations (under the wing). The aim is to determine the correct release moment for the store to be safely separated from the aircraft. Also ejector force profile will be determined for safe separation.
Separation from inner stations is more challenging than separation from outer stations. Aerodynamic phenomena are more effective in separation from inner stations due to the unsteady characteristics of the flow inside the cavity. Cavity flow is not the subject of this study.

Material and Method

In this study, releases will be performed under different flight conditions using the Eglin store geometry and a generic 5th generation fighter jet (similar to the F-22 geometry)[3]. The correct release points will be determined based on the scenarios where safe separations occur. The 6-DOF model used for the simulations to be performed was verified using the Eglin test case and the verification results were given in Figure 1.
Then, the pylon and store geometries of the Eglin test case were placed under the wing of the generic fighter jet and aerodynamic analyses were performed. The aerodynamic data obtained using the grid method gives the aerodynamic effects that the store will be exposed to during separation from the aircraft. (The aerodynamic analyses obtained with the grid method used in this study were provided by TUSAS and were obtained using open-source geometries that are not subject to any restrictions. For this contribution, I would like to thank my company.)
Another force that the store will be exposed to during separation from the aircraft is the ejector forces. Due to limited data, the ejector forces given in the Eglin test case were used as ejector forces. While ejector profile of the Eglin test case is 2400-

9600 lbf on the forward and aft ejector, in this study different profile will be attempted.

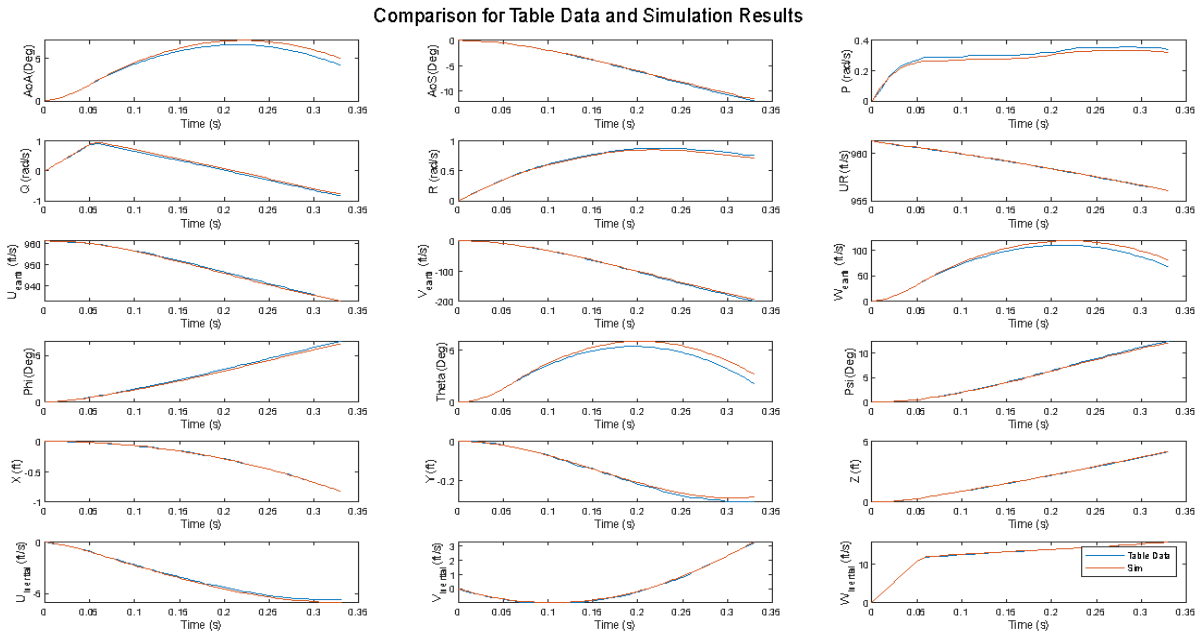

Figure 1. Comparison of simulation results and experimental CTS data on literature [2].

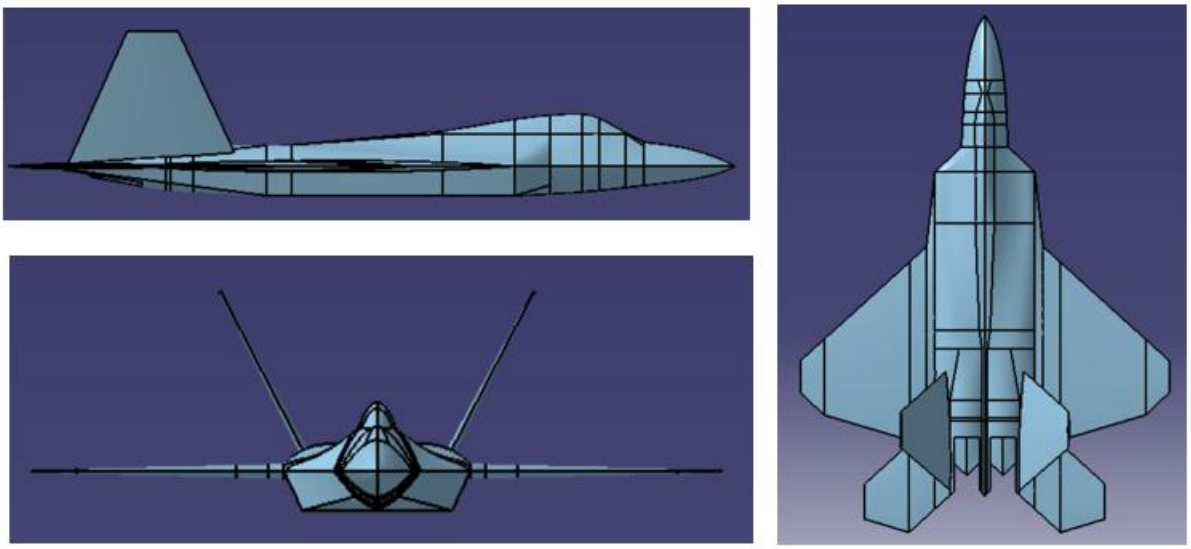

Figure 2. Fifth-Generation High-Performance Aircraft [3].

Degree Of Freedom Equations Of Motions

Store separation equations of motions are very similar to the conventional aircraft equations of motion. Equations of motion for store separation can be found in the literature. For this study equations of motions are derived by using [2].

1. Translational Kinematics

(Equation 1)
(Equation 2)

(Equation 3)

2. Rotational Kinematics

$$\dot{\phi} = p + (qsin(\phi) + rcos\phi)tan(\theta) \quad \text{(Equation 4)}$$

$$\dot{\theta} = qcos(\phi) - rsin(\phi)$$

$$\dot{\psi} = (qsin(\phi) + rcos(\phi))sec(\theta) \cdot \cos(\psi)\sin(\phi)\sin(\theta)) + w(\sin(\phi)\sin(\psi) + \cos(\phi)\cos(\psi)\sin(\theta))$$

$$\dot{y} = v(\cos(\phi)\cos(\psi) + \sin(\phi)\sin(\psi)\sin(\theta)) - w(\cos(\psi)\sin(\phi) - \cos(\phi)\sin(\psi)\sin(\theta)) + u\cos(\theta)\sin(\psi) \quad \text{(Equation 5)}$$

$$\dot{z} = w\cos(\phi)\cos(\theta) - usin(\theta) + v\cos(\theta)sin(\phi) \quad \text{(Equation 6)}$$

3. Translational Kinematics

$$\dot{u} = F_x/m \ - gsin(\theta) - qw + rv \quad \text{(Equation 7)}$$

$$\dot{v} = F_y/m \ + pw - ru \ + gcos(\theta)sin(\phi) \quad \text{(Equation 8)}$$

$$\dot{w} = F_z/m \ - pv + qu \ + gcos(\phi)cos(\theta) \quad \text{(Equation 9)}$$

4. Rotational Dynamics

$$\dot{p} = (I_{xx}I_{zz} - I_{xz}^2)^{-1}[\mathrm{I_{xz}M_z} + \mathrm{I_{zz}M_x} + (\mathrm{I_{yy}I_{zz}} - \mathrm{I_{xz}^2} - \mathrm{I_{zz}^2})\mathrm{qr} + (\mathrm{I_{xx}I_{xz}} - \mathrm{I_{xz}I_{yy}} + \mathrm{I_{xz}I_{zz}})\mathrm{pq}] \quad \text{(Equation 10}$$

$$\dot{q} = I_{yy}^{-1}[M_y - I_{xz}p^2 + I_{xz}r^2 - I_{xx}pr + I_{zz}pr] \quad \text{(Equation 11)}$$

$$\dot{r} = (I_{xx}I_{zz} - I_{xz}^2)^{-1}[I_{xz}M_x + I_{xx}M_z + (I_{xz}I_{yy} - I_{xx}I_{xz} - I_{xz}I_{zz})qr + (I_{xx}^2 + I_{xz}^2 - I_{xx}I_{yy})pq] \quad \text{(Equation 12)}$$

Findings

The separation analysis was performed under the conditions shown in the Table 1 and the effect of the application rates of the ejector forces on the separation analysis was investigated. The results given in the literature [3] give a ratio of 1/4 (2400-9600 lbf) between the forward and aftward ejector forces. It should be noted that this ratio may change since the Eglin pylon and store geometries were installed on another aircraft in this study.

Table 1. Performed Store Separation Conditions.

Mach	Altitude (kft)	Ejector Profile 1	Ejector Profile 2	Ejector Profile 3
0.8	10-20-30	9600-4800 lbf	4800-4800 lbf	4800-9600 lbf

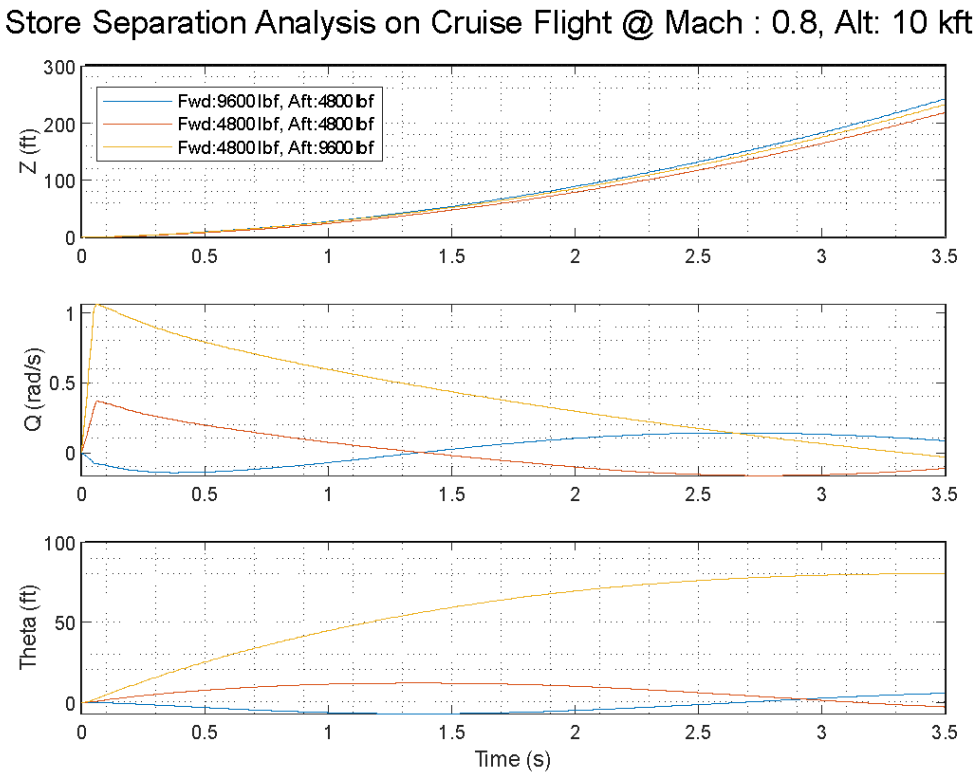

Figure 4. Store Separation Analysis Result on Mach: 0.8, Alt: 10 kft.

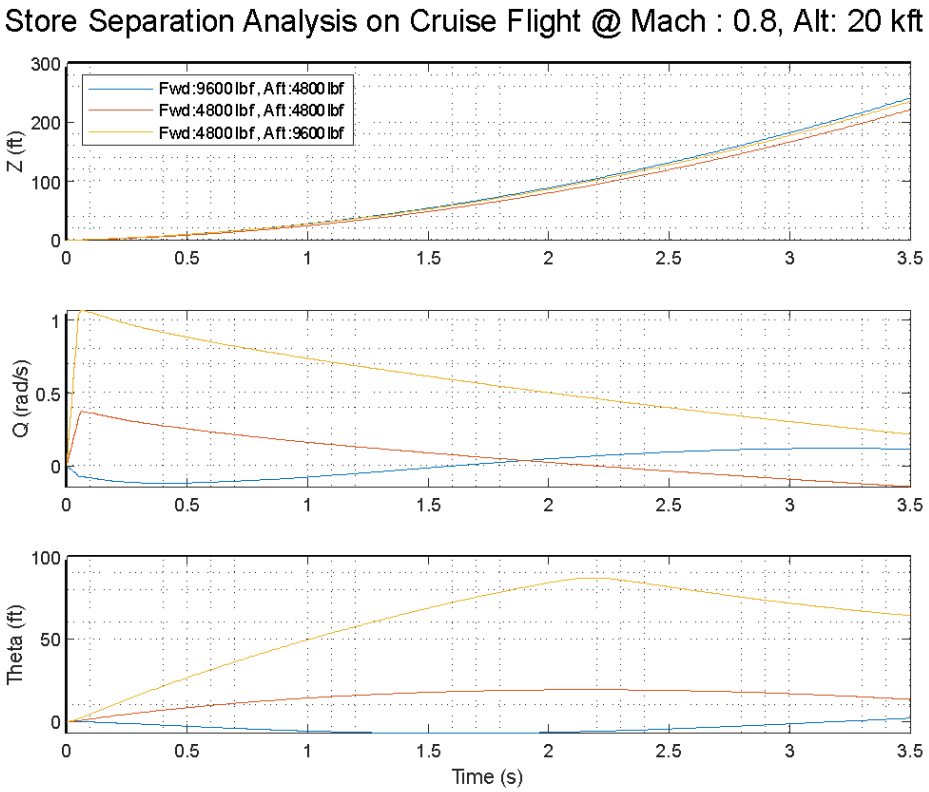

Figure 5. Store Separation Analysis Result on Mach: 0.8, Alt: 20 kft.

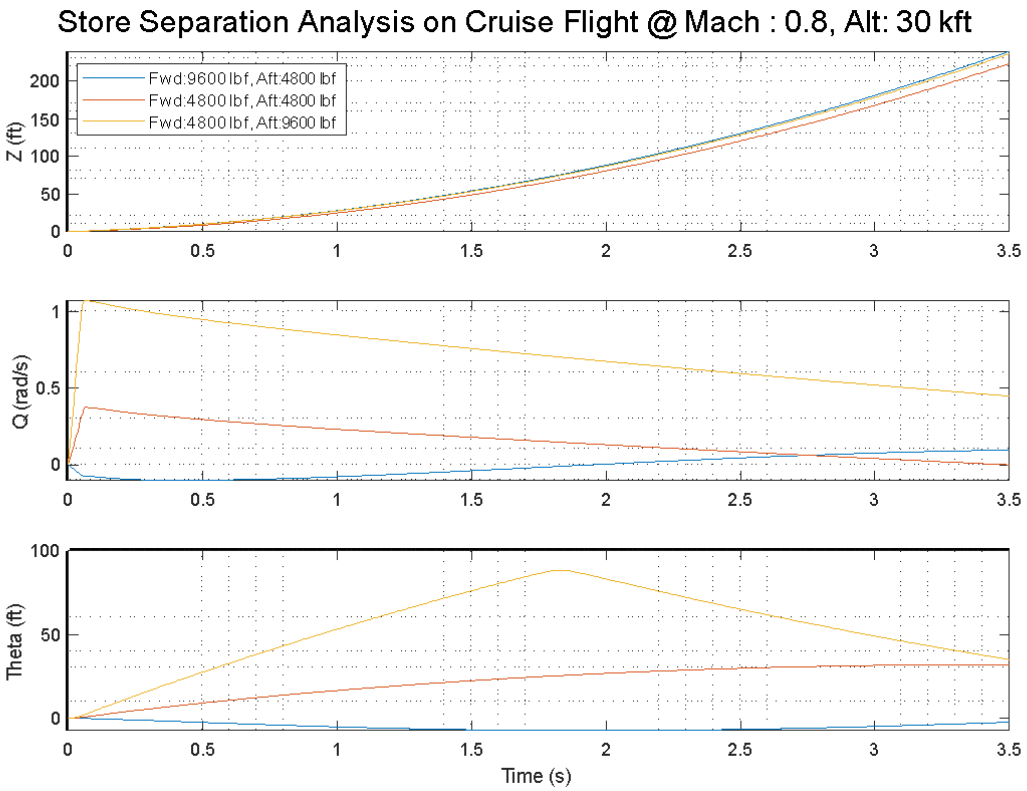

Figure 6. Store Separation Analysis Result on Mach: 0.8, Alt: 30 kft.

Conclusion

In order to test whether the separation was carried out safely, it was decided that the store should not make a pitch up moment until a certain altitude change. This altitude change was determined to be approximately 50 ft (15 m). When the figures above are examined, it is seen that the store reaches the safe distance in approximately 1.5 seconds. When ejector profile 1 is applied for all 3 altitudes, it is seen that the store has a pitch down moment up to 1.5 seconds and the pitch angle is negative. For ejector profile 2 and ejector profile 3, it is seen that it makes a pitch up before 1.5 seconds and the pitch angle is positive. Based on these results, it was decided that the ejector profile to be applied should be ejector profile 1.

References

Heim, E. R. (1991) CFD Wing/Pylon/Finned Store Mutual Interference Wind Tunnel Experiment, Calspan Corporation/AEDC Operations, Final Report for Period September 1-17,1990

Carter. R. E. (2012) Store Separation Equations of Motion, AIAA Atmospheric Flight Mechanics Conference 13 - 16 August 2012, Minneapolis, Minnesota

Giannelis, N.F.; Bykerk, T.; Vio, G.A. A Generic Model for Benchmark Aerodynamic Analysis of Fifth-Generation High-Performance Aircraft. Aerospace **2023**, 10, 746. https://10.3390/aerospace10090746

Sensitivity Analysis of Hypersonic Glide Vehicle Trajectory Under Aerodynamic and Atmospheric Variations

Ekin Gözlükaya[a,b], Halil Ersin Söken[a]

[a] Middle East Technical University, Faculty of Engineering, Department of Aerospace Engineering, Türkiye
[b] TÜBİTAK SAGE, Ministry of Industry and Technology, Türkiye
ekin.gozlukaya@metu.edu.tr

Keywords: HGV, Trajectory Optimization, Sensitivity Analysis.

Aim

Hypersonic glide vehicles (HGVs) are aerial vehicles which glide at hypersonic speeds toward their destination after being launched by a rocket into extreme velocities and high altitudes. HGVs have attracted significant interest both in the military field (e.g., strategic strike weapons) and in civilian applications (e.g., intercontinental passenger or cargo transport). However, HGVs' extremely high speeds and complex, unpredictable aerodynamic environments make sensitivity analysis critical, especially for parameters such as heat transfer rate, dynamic pressure, and load factor. These quantities are highly sensitive to variations in aerodynamic coefficients and atmospheric conditions, significantly affecting performance, vehicle safety, and structural integrity. These sensitivities necessitate statistical analysis for mission-level reliability. In this study, sensitivity of the main parameters of HGVs (flight time, terminal velocity, maximum heat flux, maximum dynamic pressure) for the uncertainties of aerodynamic coefficients and environmental parameters are investigated. A Monte Carlo-based statistical analysis is conducted to evaluate the influence of these uncertainties on trajectory performance and to highlight the most critical parameters for robust design considerations.

Hypersonic glide vehicles (HGVs) are primarily accelerated to high speeds and to space by boosters after that the booster is released. Then the HGV re-entries into the atmosphere and glides through the desired destination while satisfying the constraints and accomplishing mission requirements. In the gliding phase these vehicles have speeds around Mach 5-20 which causes extreme heat transfer rates and structural loads. Moreover, the effects of extreme shock waves, plasma formation, and ionization of air causes severe uncertainties in the aerodynamic coefficients and atmospheric parameters (Lampis, 2024). Therefore, it is critical to analyze the effect of these uncertainties on trajectory parameters, structural and thermal loads. The aim of this study is to analyze the sensitivity of hypersonic glide vehicle trajectory parameters (range, flight time, heat transfer exposure, dynamical pressure etc.) to the changes, uncertainties in the aerodynamic coefficients (lift, drag coefficients) and atmospheric uncertainties (density, temperature). Moreover, to provide a statistical representation of deviations in trajectory, identifying the most influential uncertainty sources on flight time, altitude, range, thermal loads and structural loads. The results are beneficial to be used in robust trajectory optimization strategies.

Material and Method

In this study to evaluate the uncertainties in aerodynamic coefficients and atmospheric properties on the HGV dynamics, a 3-DoF dynamic model of a HGV used together with a trajectory optimization tool. The state variables for 3-DoF dynamic model are latitude (φ), longitude (λ), and altitude (h), and the control inputs are angle of attack (α) and bank angle (σ). The equations of motion are given below (Zhou et al. 2019).

$$\frac{dr}{dt} = V sin\gamma$$

$$\frac{d\theta}{dt} = \frac{V cos\gamma sin\psi}{r cos\phi}$$

$$\frac{d\phi}{dt} = \frac{V cos\gamma cos\psi}{r}$$

$$\frac{dV}{dt} = -\frac{D}{m} - gsin\gamma$$

$$\frac{d\gamma}{dt} = \frac{1}{V}[\frac{Lcos\sigma}{m} + \left(\frac{V^2}{r} - g\right)cos\gamma]$$

$$\frac{d\psi}{dt} = \frac{1}{V}[\frac{Lsin\sigma}{mcos\gamma} + \frac{V^2}{r}cos\gamma sin\psi tan\phi]$$

Where r is the distance from the center of the Earth to the vehicle, θ is the latitude angle, ϕ is the azimuth angle, V is the magnitude of velocity, D is drag force, L is lift force, γ is flight path angle, ψ is the heading angle, σ is the bank angle, g is the gravity constant and m is mass of HGV. For trajectory optimization, the angle of attack and bank angle are used as control inputs. Even though, angle of attack does not exist in the equations of motion, it affects the lift and drag forces since the lift and drag coefficients are functions of angle of attack. The definition of aerodynamic forces is given below.

$$L = \frac{1}{2}\rho V^2 S_{ref} C_L(\alpha, M)$$

$$D = \frac{1}{2}\rho V^2 S_{ref} C_D(\alpha, M)$$

The mass, reference area, C_L and C_D coefficients are dependent on the vehicle geometry. The geometry used in the analysis is CAV-H. The physical parameters for CAV-H are given in Table 1.

Table 1. Physical Parameters of CAV-H adopted from Duan et al. (2010).

Parameter	Unit	Value
Diameter/Width	(m)	1.2192
Weight	(kg)	907.2
Reference Area	(m²)	0.4839

The lift and drag coefficient of CAV-L is modeled as a function of angle of attack and Mach (Duan et al., 2010). The relations are given below.

$$C_L = C_{L1}\alpha + C_{L2}\ exp\ exp\ (C_{L3}M)\ + C_{L0}$$

$$C_{L1} = 0.0513, C_{L2} = 0.2945, C_{L3} = -0.1028, C_{L0} = -0.2317$$

$$C_D = C_{D1}\alpha^2 + C_{D2}\ exp\ exp\ (C_{D3}M)\ + C_{D0}$$

$$C_{D1} = 7.24e-4, C_{D2} = 0.406, C_{D3} = -0.323, C_{D0} = 0.024$$

Where C_L is lift coefficient, and C_D is drag coefficient. The atmosphere model used in analysis is COESA standard atmosphere model, and the gravitational acceleration is assumed to be constant and equal to 9.81 m/s^2.

To obtain an optimal trajectory, the Sequential Convex Programming (SCP) method is applied because this method is capable of obtaining feasible solutions even when the initial trajectory and control input guesses are inaccurate (Malyuta et al. 2022). By this approach, the originally non-convex trajectory optimization problem is converted into a series of convex subproblems to obtain a solution. The SCP method iteratively solves convex approximations of the non-convex problem until convergence is reached.

To analyze the effects of atmospheric uncertainties, a Monte-Carlo simulation framework is implemented. Uncertainty is introduced in C_L, C_D and density. The nominal values are multiplied by a gain which is determined using gaussian distributions. Used distributions are given in Table 2. 400 simulations are completed for the same mission and according to the resultant trajectories of these simulations the heat transfer rate, dynamic pressure, normal accelerations, maximum

altitude and flight time are obtained. Then the effect of C_L, C_D and density on these parameters are compared, analyzed and statistically evaluated.

Table 2. Distributions in C_L, C_D and Density.

Parameter	Range	Distribution
Density	±%10	Gaussian [1σ=%3]
C_D	±%30	Gaussian [1σ=%10]
C_L	±%30	Gaussian [1σ=%10]

Findings

400 Monte-Carlo simulations with perturbations on CL, CD and density are completed using the mission stated in Table 3. For all the simulations the flight time is minimized when satisfying the given final conditions. The resultant states are presented in Figure 1. As can be seen most trajectories closely follow the nominal (red) path, maintaining feasibility throughout the glide phase. Velocity generally decreases smoothly with time and the altitude profiles varies. In some cases, jumps in the altitude profiles are observed, however mostly the altitude decreased with a stable flight path angle. To further examine how variations in aerodynamic coefficients affect trajectory feasibility, Figure 2 illustrates the distribution of feasible and non-feasible (final conditions could not be satisfied) simulations in the CD–CL parameter space. This visualization enables a clearer understanding of which combinations of lift and drag gains lead to mission failure, offering insight into the bounds of aerodynamic robustness for the vehicle. According to this graph, over 85% of the simulations resulted in feasible trajectories, indicating strong robustness under moderate variations in aerodynamic parameters. Infeasibility arises predominantly in cases with low CL and high CD, due to insufficient lift and excessive drag, preventing the vehicle from reaching the desired range. Conversely, high CL with low CD can lead to insufficient energy dissipation during flight, preventing the vehicle from descending effectively and reaching the destination altitude.

Table 3. Mission Boundary Conditions and Objective.

Parameter	Value
Initial Altitude	60 km
Initial Latitude	0 deg
Initial Longitude	0 deg
Initial Velocity	6000 m/s
Initial Flight-Path Angle	-2 deg
Initial Heading Angle	0 deg
Final Altitude	Sea Level
Final Latitude	12 deg
Final Longitude	75 deg
Objective	Minimize Time

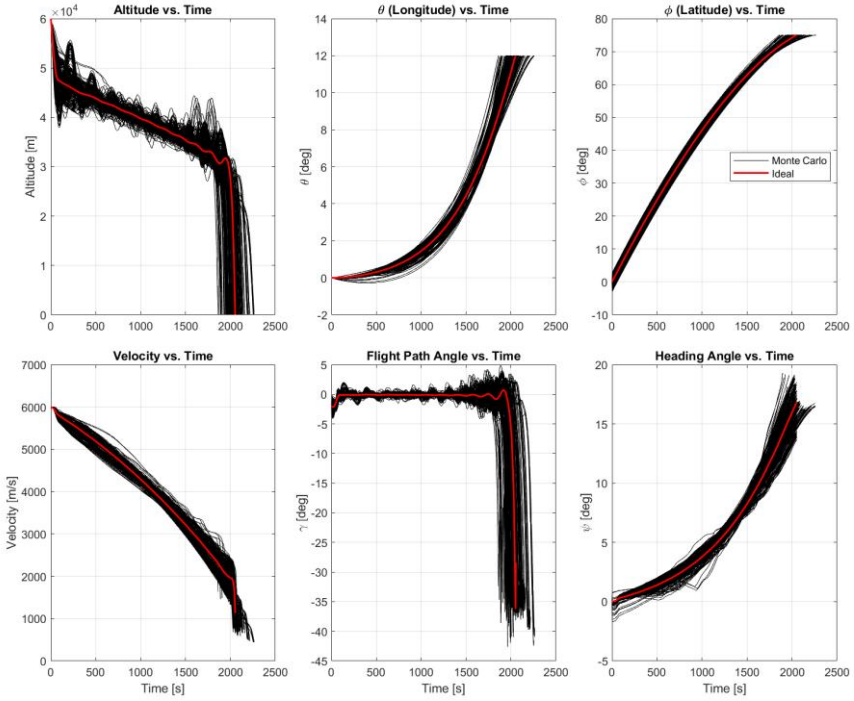

Figure 1. Monte-Carlo Trajectory Results.

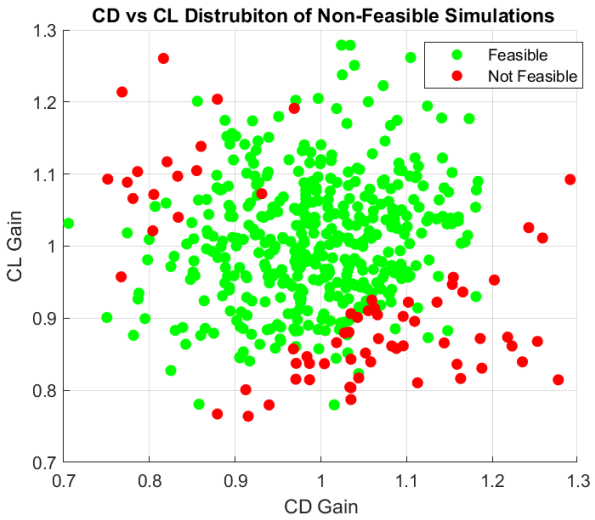

Figure 2. Effect of Aerodynamic Perturbations on Feasibility.

After determining the effect of perturbations on feasibility, the effect of perturbations on flight time, terminal velocity, maximum heat flux and maximum dynamic pressure (above 20 km) are obtained. The effect of perturbations on flight time and terminal velocity are given in ***Figure 3***-***Figure 4*** and the effect of perturbations on heat flux and dynamic pressure are given in ***Figure 5***. In the figures, the x-axis represents the gain applied to each respective parameter, and the y axis represents the value of the parameter which was examined for sensitivity analysis. Each dot represents one simulation, and the black dashed lines show the linear trend (fit) across all simulations for each parameter. According to these results, for flight time it is noteworthy that increasing lift (CL) and density (ρ) tends to reduce final time by enabling more control in trajectory. On the other hand, changes in drag (CD) have an insignificant impact on flight time. Final velocity is strongly influenced

by aerodynamic coefficients, higher CD leads to greater deceleration and lower final speeds, while higher CL helps the vehicle maintain altitude and speed, resulting in higher final velocities. Increased atmospheric density (ρ) also slightly increases final velocity due to greater dynamic pressure enhancing lift generation. Maximum heat flux is most sensitive to the drag coefficient CD, as CD increases the vehicle decelerates rapidly, leading to lower velocities and consequently reduced heat flux. Moreover, a slight downward trend with increasing CL is observed, due to improved altitude control which reduces exposure to denser atmospheric layers. Atmospheric density (ρ) shows a minimal effect on maximum heat flux, indicating that aerodynamic properties dominate heat flux variation for this scenario. Lastly for the dynamic pressures above 20 km, higher CD values lead to significantly lower maximum dynamic pressures due to earlier deceleration in less-dense atmospheric layers. Conversely, increasing CL and ρ both correlate with higher maximum dynamic pressures, due to decreased energy dissipation.

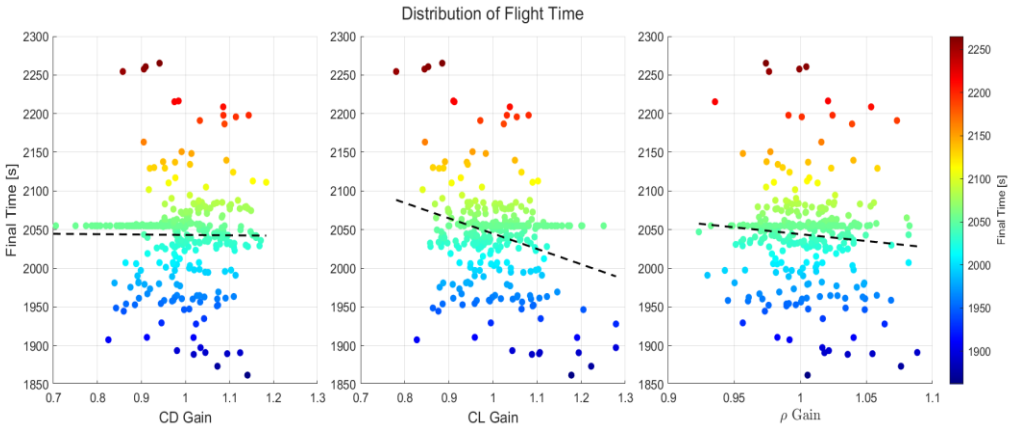

Figure 3. Effect of Perturbations on Flight Time.

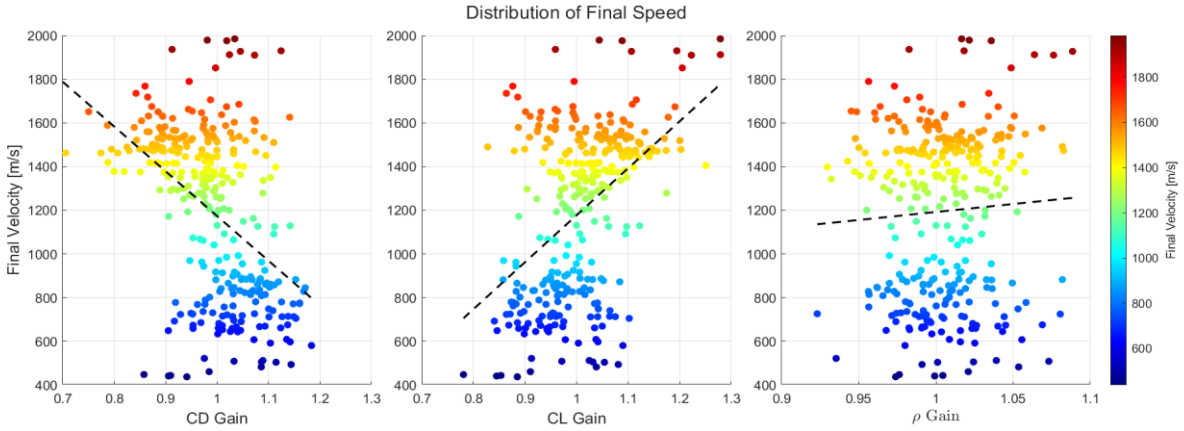

Figure 4. Effect of Perturbations on Terminal Speed.

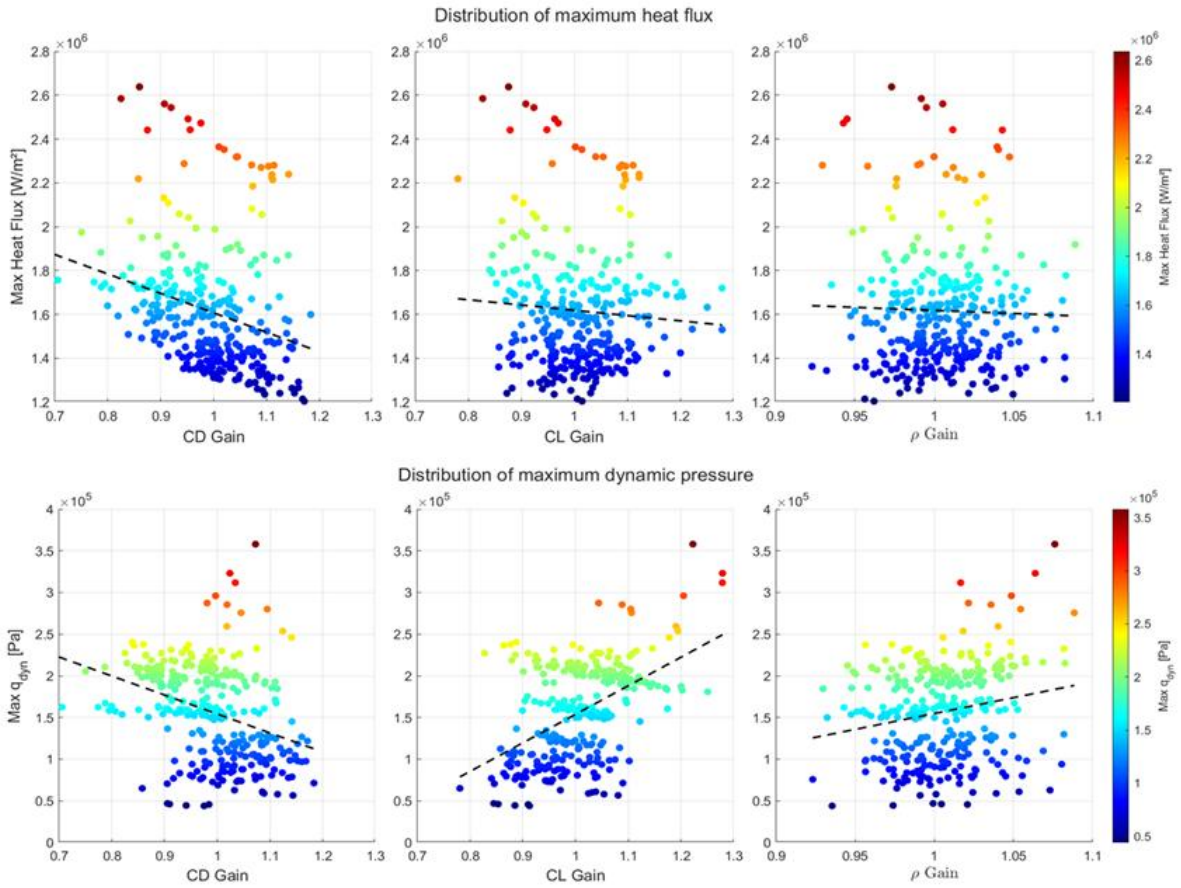

Figure 5. Effect of Perturbations on Dynamic Pressure (Above 20 km) and Maximum Heat Flux.

Conclusion

Sensitivity analysis on the trajectory performance of a hypersonic glide vehicle (HGV) under parametric uncertainties in aerodynamic coefficients and atmospheric density is performed. A total of 400 Monte Carlo simulations were conducted by perturbing drag coefficient (CD), lift coefficient (CL), and atmospheric density (ρ) to assess their impact on key performance indicators such as flight time, final velocity and heat flux, and dynamic pressure. Results demonstrate that approximately 85% of the simulations remained feasible under uncertainty. Infeasible cases were mainly concentrated in scenarios with low CL and high CD—leading to insufficient range—or with excessively high CL and low CD, which hindered energy dissipation and descent. Among the perturbed parameters, CL and ρ had the most significant influence on flight time and thermal loads, while CD showed a relatively minor effect on timing but contributed notably to the reduction of heat flux and dynamic pressure due to earlier deceleration. Maximum heat flux and dynamic pressure distributions reveal that increasing CD reduces aerodynamic loads effectively, whereas increased CL and ρ lead to higher thermal and structural stress. These findings highlight the critical importance of accounting for aerodynamic and environmental uncertainties in trajectory planning and provide guidance for future robust optimization strategies in hypersonic vehicle design.

References

Duan, G., Sun, Y., Zhang, M., Zhang, Z., & Gao, X. (2010). Aerodynamic coefficients models of hypersonic vehicle based on aero database. *In 2010 First International Conference on Pervasive Computing, Signal Processing and Applications*. IEEE.

El-Kebir, H., & Ornik, M. (2020). *In-flight air density estimation and prediction for hypersonic flight vehicles*. University of Illinois at Urbana-Champaign & Delft University of Technology.

Lampis, L. (2024). *Modeling of a hypersonic glide vehicle during a re-entry phase* (Master's thesis, Politecnico di Milano, Italy).

Malyuta, D., Szmuk, M., Vaskov, E., Wolf, M. T., & Acikmese, B. (2022). Convex optimization for trajectory generation: A tutorial on generating dynamically feasible trajectories reliably and efficiently. *IEEE Control Systems Magazine, 42*(5), 40–113.

Zhou, H., Wang, X., & Cui, N. (2019). Glide trajectory optimization for hypersonic vehicles via dynamic pressure control. *Acta Astronautica, 164*, 376–386.

Url-1 http://dx.doi.org/10.3969/j.issn.2096-0204.2021.03.0249, date retrieved 24.03.2025

Winglet Design, Optimization and Performance Analysis for a Trainer Aircraft

Çağlar Yakın[a], Hayri Acar[b], Serhat Yılmaz[a]

[a] Turkish National Defence University, Turkish Air Force Academy, Department of Aerospace Engineering, Turkey
[b] Istanbul Technical University, Faculty of Aeronautics and Astronautics, Department of Aeronautical Engineering, Turkey
caglar.yakin@msu.edu.tr

Keywords: Optimization, Tornado VLM, Winglet Design.

Aim

This study has been conducted to design, optimize, and analyze the performance of winglets for the MFI-395 Super Mushshak military training aircraft, which is recorded in the inventory of the Turkish Air Force. The primary objective of the study is to enhance aerodynamic efficiency, reduce drag, and improve overall flight performance of the aircraft. Within the scope of the research, an optimized winglet design will be developed using a computational method Vortex Lattice Method (VLM). Additionally, the impact of different winglet configurations on aircraft performance parameters has been evaluated.

Material and Method

Winglets are aerodynamic surfaces installed at the wingtips of fixed-wing aircraft to reduce induced drag (D_i) caused by wingtip vortices. By mitigating these vortices, winglets increase lift-to-drag ratio, improve fuel efficiency, increase range, and contribute to lower emissions, making them crucial for both economic and environmental performance. The main geometric parameters considered in winglet design are winglet length, cant angle, toe angle, sweep angle, and taper ratio. The parameters are illustrated schematically in Figure 1 [1].

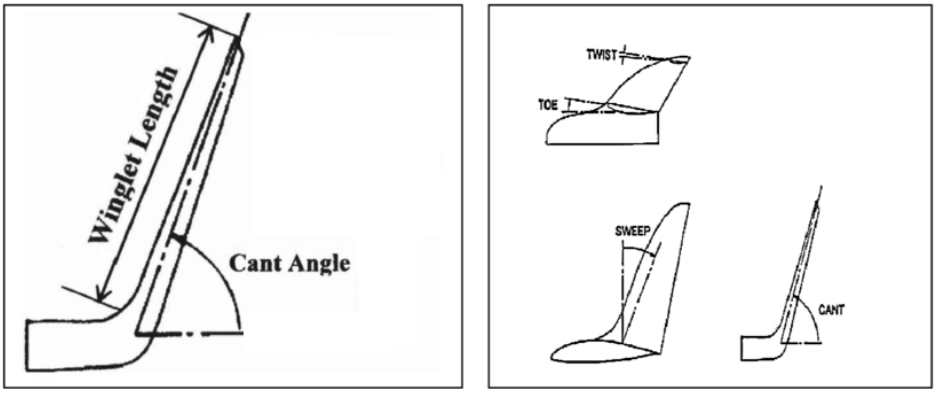

Figure 1. Winglet geometry parameters.

MFI-395 Super Mushshak has been derived from MFI-17 Mushshak military trainer aircraft; however, main updates have been made in engine performance, avionics systems, and missile integration systems [2]. Therefore, geometric properties have been obtained from MFI-17 Mushshak due to data accessibility considerations. The aircraft has a wingspan of 8.85m, root chord length of 1.5m, taper ratio of 1, negative sweep angle of 5°, incidence angle of 0°, dihedral angle of 0° and twist angle of 0° [3]. Main wing airfoil of the aircraft is "NACA23012MOD" with thickness ratio of 10% [4]. The airfoil has been illisturated in Figure 2.

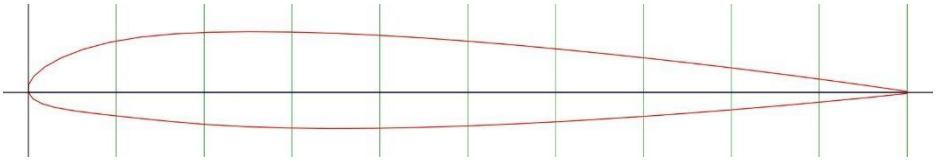

Figure 2. NACA23012MOD airfoil.

In this study, the Vortex Lattice Method (VLM) has been preferred due to its efficient, low-order computational analysis, which makes it both quick and cost-effective. It has been widely used in aerodynamic modeling, offering advantages in design optimization and multi-objective studies. Compared to conventional CFD, VLM is faster, cheaper, and ideal for preliminary aerodynamic analysis [5]. Tornado VLM, which is an open-source code implemented in MATLAB and developed by Tomas Melin, has been used for winglet performance analysis [6]. Tornado VLM code has a user-friendly interface. The code prompts the user for the geometry parameters, sends them to the solution function and presents the results to the user as tables and graphs in separate pop-up windows.

Before the winglet design studies, the main wing geometry without winglet has been analyzed using the Tornado VLM code. The results of this analysis are presented in Table 1. All analyses have been conducted under the MFI-17 Mushshak cruise flight conditions, corresponding to a speed of 210 km/h and an altitude of 4100 meters [3]. The angle of attack was set to 6° to ensure sufficient lift generation during cruise. Winglet optimization studies have been carried out based on these results.

Table 1. Main wing results.

Lift Force (N)	Induced Drag Force (N)	Lift Coefficient (C_L)	Induced Drag Coefficient (C_{Di})	L/D_i
9237	255	0.5105	0.0141	36.21

The geometry of the wing without winglet is illustrated in Figure 3.

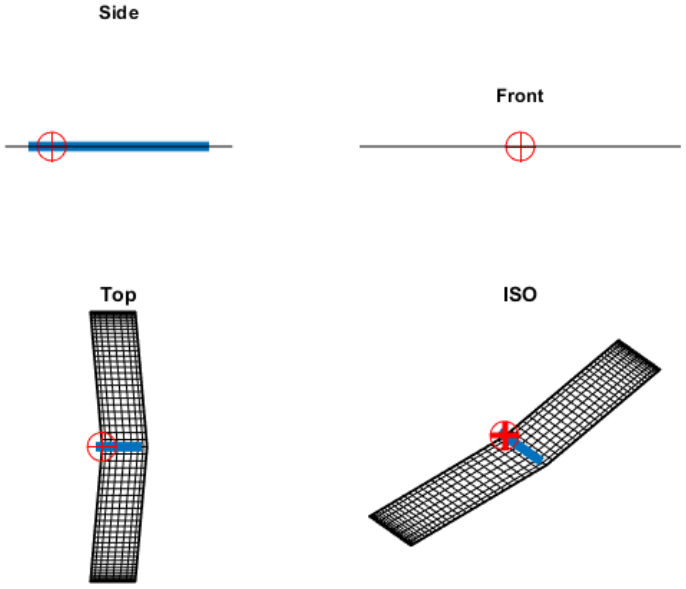

Figure 3. Main wing geometry.

The Tornado VLM code has a user interface. The code prompts the user for the geometry parameters. To accelerate the winglet analysis process, the Tornado VLM code has been modified and automated. The functions within the code have

been regenerated, and all the input functions have been removed. This modification has been made it possible to computationally generate results by varying the winglet parameters within the desired ranges. In this study, toe and twist angles have been assumed to be zero, and the other parameters along with their value ranges have been specified in Table 2. The airfoil of the winglet has been assumed to be the same as that of the main wing, "NACA23012MOD".

Table 2. Winglet geometry parameters.

Parameters	Lower Limit	Upper Limit	Step Size
Cant Agle (deg)	0	90	10
Length (m)	0.1	1	0.1
Sweep Angle (deg)	0	60	10
Taper Ratio	0.1	1	0.1

To obtain consistent and realistic results in VLM, it is required to determine the number of panels both for the main wing and the winglet. The number of panels in the Vortex Lattice Method strongly affects aerodynamic accuracy; higher panel density improves flow representation but increases computational cost [7]. The code has been run multiple times with different panel configurations, and the results have been analyzed. The most consistent panel configuration, considering computational cost, with minimal data noise has been identified and presented in Table 3. Panel distributions of the main wing and the winglet are shown in figure 3 and figure 4.

Table 3. Panel configuration.

Wing Section	Chordwise Panel	Spanwise
Main Wing	10	30
Winglet	10	5

Findings

The results have been exported to Excel and analyzed. Many winglet configurations in which the lift-to-induced drag ratio increases have been identified in the analysis results. In most of the configurations, the improvement in the lift-to-induced drag ratio has been attributed to an increase in lift rather than a reduction in induced drag. Therefore, it has been necessary to apply filtering to the analysis results. In this context, based on the main wing analysis results presented in Table 1, The primary objective of this study is to reduce the induced drag force. Significant increases in lift are not desired; however, increases comparable to the approximate structural weight added by the winglets are considered acceptable. Based on the analysis results, the top three most efficient winglet configurations have been identified and shown in Table 4.

Table 4. Winglet optimization results.

Cant Angle (deg)	Length (m)	Sweep Angle (deg)	Taper Ratio	L (N)	D_i (N)	C_L	C_{Di}	L/D_i	Increment of L/D_i (%)
0	0.3	20	0.3	9327	225	0.5154	0.0124	41.45	14.46
0	0.4	50	0.4	9412	232	0.5201	0.0128	40.59	12.10
0	0.3	50	0.1	9320	231	0.5151	0.0128	40.29	11.27

According to the results, the most efficient winglet configurations have the cant angle of zero. It has been observed that an increase in winglet length leads to a higher lift force. The wing geometry with the highest lift-to-drag ratio is illustrated in Figure 4. This configuration enables 14.46% improvement in the aerodynamic efficiency of the wing.

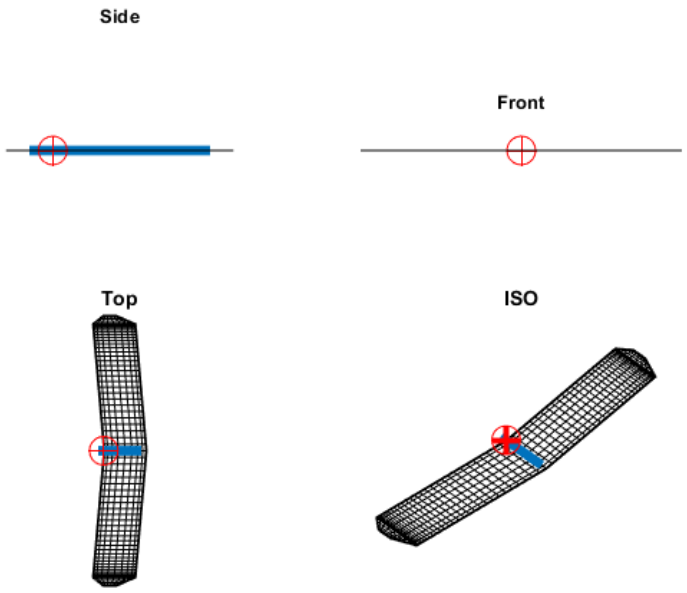

Figure 4. The most efficient winglet configure.

Conclusion

In this study, winglets have been designed, optimized, and analyzed for the MFI-395 Super Mushshak military trainer aircraft in order to improve its aerodynamic performance. The main objective has been to reduce induced drag and increase the lift-to-drag ratio (L/D), contributing to more efficient flight. Various winglet configurations have been tested using the Vortex Lattice Method (VLM), and their impacts on performance have been evaluated. It has been observed that several configurations have provided significant improvements in aerodynamic efficiency. The most efficient design has achieved

a 14.46% increase in L/D_i ratio. Winglets with a cant angle of 0°, short length, and specific sweep angles have been found to be the most effective. The results have demonstrated that well-optimized winglets can lead to enhanced flight performance, reduced fuel consumption, extended range, and lower environmental impact. The potential of winglet applications on trainer aircraft like the MFI-395 has been clearly shown.

Future work may focus on experimental validation, further refinement using high-fidelity CFD methods or wind tunnel testing and exploring additional improvements through detailed aerodynamic studies.

References

Airforce Technology. (n.d.). *MFI-395 Super Mushshak trainer aircraft.* Retrieved March 19, 2025, from
Url-1 https://www.airforce-technology.com/projects/mfi-395-super-mushshak-trainer-aircraft/

Gao, W., Liu, Y., Li, Q., & Lu, B. (2023). Aerodynamic Modeling and Simulation of Multi-Lifting Surfaces Based on the Unsteady Vortex Lattice Method. *Aerospace*, *10*(2).
Url-3 https://doi.org/10.3390/aerospace10020203

Home. (n.d.). Retrieved March 15, 2025, from
Url-4 https://tornado.redhammer.se/

Joshi, H., & Thomas, P. (2023, March). *Unsteady Vortex Lattice Method in Tornado: A Fast and Cost-Effective Solver for Dynamic Analysis of Supersonic Lifting Surfaces*.
Url-5 https://doi.org/10.13009/EUCASS2023-092

Pakistan Aeronautical Complex Kamra - Mushshak Aircraft. (n.d.).

The Incomplete Guide to Airfoil Usage. (n.d.). Retrieved March 20, 2025, from
Url-2 https://m-selig.ae.illinois.edu/ads/aircraft.html

Whitcomb, R. T. (1976). *A Design Approach And Selected Wind-Tunnel Results At High Subsonic Speeds For Wing-Tip Mounted Winglets*.

AERONAUTICAL AND ASTRONAUTICAL ENGINEERING

Aircraft Design, Flight Dynamics And Performance

Control Systems: Adaptive, Intelligent, Digital, Optimal, Pneumatic-Hydraulic

Mechanical Vibrations And Structural Dynamics

Rotary Wing Aircraft

Spacecraft Control, Design And Performance

Theoretical, Computational And Experimental Aerodynamics And Fluid Dynamics

Theoretical, Computational And Experimental Structural Analysis And Design

Quadrotor Actuator Fault Detection and Isolation- A Model Based Approach

Muhammed Arslan[a], Gokhan Inalhan[a]

[a] Istanbul Technical University, Aerospace Department, Aerospace, Turkey
darwish16@itu.edu.tr

Keywords: Control, FDI, Quadrotor, UAV.

Aim

Unmanned Aerial Vehicles (UAVs), particularly quadrotors, are increasingly integrated into various fields, including surveillance, agriculture, inspection, and delivery services, due to their vertical take-off and landing (VTOL) capabilities and mechanical simplicity. Their dynamic nature, however, makes them highly susceptible to actuator faults—failures in any of the four motors can lead to loss of stability, degraded control authority, or total mission failure. Various Fault Detection and Isolation (FDI) methods have been developed to address this vulnerability, which are typically categorized into three main approaches: data-driven methods (e.g., machine learning), model-based approaches (e.g., observers and parity space methods), and feedback-based methods. While data-driven techniques are effective in handling complex environments, they often require large amounts of labelled data and are difficult to interpret in real-time safety-critical systems. On the other hand, hardware that includes feedback systems increases system cost, which may not be practical or cost-effective for compact UAV platforms.

Model-based observers offer a good compromise by using a mathematical model of the system to detect inconsistencies between expected and measured outputs. However, many of the existing model-based approaches in the literature depend on linearization approaches. Linearizing the system around an operating point may not be efficient in a naturally unstable system like the quadrotors. Furthermore, several existing FDI strategies show limitations in detecting time-varying actuator degradations or a lack of robustness against disturbances. In this research, we address actuator fault detection in quadrotor UAVs through a model-based approach that does not require feedback from actuators or redundant sensors.

The primary objective of this study is to develop, implement, and validate a robust non-linear model-based fault detection and isolation (FDI) method for actuator/motor faults in quadrotor Unmanned Aerial Vehicles (UAVs) without requiring actuator feedback or redundant sensors. A nonlinear Thau observer-based method is proposed for the detection and isolation of actuator faults. This observer leverages the quadrotor's nonlinear dynamics to track time-varying LOE faults, improving upon traditional observers' static detection limits. The approach prioritizes robustness against noise and unmodeled dynamics. Additionally, this research explores combining this observer with dynamic inversion residual analysis to enhance fault-type identification under realistic conditions, validated through simulations.

Material and Method

Simulation Environment and Platform

The simulation was conducted in MATLAB/Simulink using a fixed-step solver (ode3). The study uses a standard X-configuration quadrotor UAV with a total mass of 2.3 kg. Its inertial properties are as follows: Ixx = 0.0088 kg.m2, Iyy =0.0125 kg.m2, and Izz = 0.0122 kg.m2. The quadrotor has the X configuration with four DC motors, where motors 1 and 3 rotate clockwise, and motors 2 and 4 rotate counterclockwise, as shown in Figure 1.

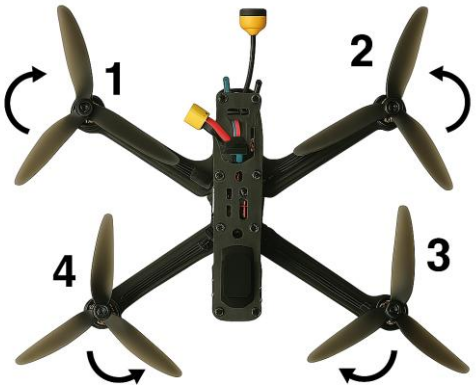

Figure 1. Quadrotor configuration.

System Dynamics

The quadrotor's dynamics are modelled using the Euler-Lagrange formalism as a nonlinear 6-degree-of-freedom system (assuming rigid body, rigid propeller, and symmetric design) with 12 states as shown in Equation 1.

$$x = \left[x, y, z, v_x, v_y, v_z, \phi, \theta, \psi, p, q, r \right]^T$$

The translational dynamic of the system is modelled as shown in Equation 2. While the rotational dynamics is modelled as shown in Equation 3.

$$m\,\ddot{x} = R * [0;\ 0;\ T]^T - [0;\ 0;\ mg]^T + F_{ext}$$

$$I\ \dot{\omega} + \omega \times (I\ \omega) = \tau$$

R is the Direction Cosine Matrix (DCM) mapping body frame to inertial frame. The thrust is the total vertical thrust generated by all four rotors. The Euler angle kinematics are as shown in the following equation

$$\dot{\phi} = p + q\ sin(\phi)\ tan(\theta) + r\ cos\ (\phi)\ tan\ (\theta)$$

$$\dot{\theta} = q\ cos\ (\phi) - r\ sin\ (\phi)$$

$$\dot{\psi} = (q\ \ sin\ sin\ (\phi\ ) + r\ \ cos\ cos\ (\phi\ ))\ cos\ cos\ (\theta)$$

Control Strategy

A model-based cascaded control architecture is employed to ensure the stability and robustness of the system. The outer loop of the controller controls the position (x, y, z) by generating desired accelerations based on a second-order system response with required damping ratio and natural frequency. These accelerations are mapped to reference angles (phi, theta) for stabilization. The inner loop controls the attitude angles, generating a moment command which being transferred to motor angular velocity commands. The overall control strategy is illustrated in in Figure 2.

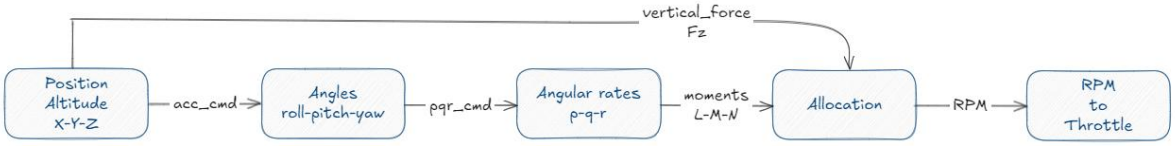

Figure 2. Controller Architecture.

Observer Design

A nonlinear Thau observer-based method is proposed for the detection and isolation of actuator faults. The observer mathematical model is illustrated in the following equation

$$\hat{\dot{x}} = f(\hat{x}, u) + K(y - \hat{y})$$

Where r(t) is the residual vector representing the discrepancy between measured and estimated outputs. The f(xhat,u) function describes the system's full nonlinear dynamics. Observer equations are derived from the same translational and rotational equations described above. The gain K is computed via the Lyapunov equation, ensuring stability.

$$A^T P + P A = -Q$$

Residuals are generated for outputs x,y,z,ϕ,θ,ψ. The residuals are being evaluated continuously, comparing them to thresholds. Faults are detected when residuals exceed thresholds. Then comes the process of isolating the faulty actuator. The overall observer structure is illustrated in Figure 3.

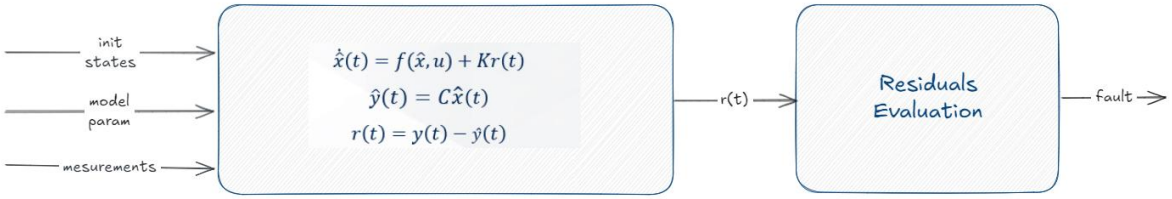

Figure 3. Observer Structure.

To enhance the performance, we implement a dynamic inversion-based complementary observer based assuming that the moments and forces are directly related to the linear and angular acceleration, as illustrated in the equations

$$\tau_{est} = I\dot{\omega}_{meas}$$

$$F_{est} = m\, a_{meas}$$

$$RPM_{est} = [F\ L\ M\ N]^T\ x\ A$$

The residual of this complementary observer is being generated by comparing the estimated motor RPM with the desired motor RPM, assuming the motors are able to generate the desired RPM, as well as neglecting the model uncertainties. When the residuals exceed a specific threshold, the motor fault is detected.

Findings

The proposed fault detection system was successfully integrated into a high-fidelity nonlinear quadrotor simulation built in MATLAB/Simulink. Through a series of test cases, including nominal flight and fault injection scenarios, the system demonstrated high sensitivity to actuator degradations and disturbances. Under fault-free operation, the residual signal remained close to zero, with minor fluctuations due to model uncertainties and unmodeled external disturbances. The observer successfully tracked all 6 measurements, demonstrating rapid convergence and numerical stability under a wide range of flight conditions.

The fault scenarios introduced a sudden partial loss of efficiency or a time-varying degradation in one of the motors. In both cases, the fault detection mechanism triggered a noticeable increase in residuals, allowing for successful detection. The observer remained robust even when small parameter mismatches (in mass and inertia) were introduced and was able to detect the fault with acceptable delay.

The complementary dynamic inversion module played a crucial role. By estimating the actuator torque vector using the measured angular acceleration, and reconstructing motor RPMs through the relationship mentioned before. it was possible to cross-validate the controller's motor commands against the expected actuator performance. This dual detection

mechanism, based on both state residuals and actuator-level discrepancies, enhanced the system's ability to distinguish between modelling errors, sensor noise, and true actuator faults.
The observer was further evaluated under multiple simulation runs with varying levels of input noise and uncertainties in model parameters.
, the observer system was capable of:

- Detecting and isolating single actuator effectiveness loss (LOE).
- Estimating the direction and type and magnitude of fault through combined state and actuator residuals.
- Responding rapidly to fault initiation without additional sensor feedback.

Conclusion

This work demonstrates a robust and practical model-based fault detection system for quadrotor UAVs, leveraging a nonlinear Thau observer and a complementary dynamic inversion observer. The simulation results confirm that the detection system estimates system states and identifies actuator degradations under various conditions, including parameter uncertainties and external disturbances.
The dual-residual approach improves both detection speed and fault interpretability by combining state estimation discrepancies with actuator-level analysis. The observer operates effectively without the need for motor feedback, which is valuable for lightweight UAV platforms. These findings indicate that the proposed method can offer a solution for fault detection in real-world UAV applications and pave the way for future development of fault-tolerant control strategies.
Future work includes implementing the system in a real-time embedded environment, testing with more complex multi-fault scenarios, and exploring adaptive gain tuning to further improve robustness.

References

Freddi, A., Longhi, S., & Monteriù, A. (2010). Actuator fault detection system for a mini-quadrotor. Proceedings of the IEEE International Symposium on Industrial Electronics, 2055-2060.
Freddi, A., Longhi, S., & Monteriù, A. (2009). Fault detection and isolation for a quadrotor UAV using a bank of observers. 2009 IEEE International Conference on Control Applications, 40–45.
Freddi, A., Longhi, S., & Monteriù, A. (2010). Actuator fault detection and isolation for a quadrotor UAV. Journal of Intelligent & Robotic Systems, 57(1–4), 137–157.
Url-1 https://doi.org/10.1007/s10846-009-9369-3
Guillermo Valencia-Palomo , Mohammed Chadli, Madain Pe´rez-Patricio. (2019). Actuator fault detection and isolation on a quadrotor unmanned aerial vehicle modeled as a linear parameter varying system. Vol. 52(9-10) 1228–1239.
Khattab, A., Alwi, H., & Edwards, C. (2019). Mitigating total rotor failure in quadrotor using LPV based sliding mode control scheme. 2019 4th Conference on Control and Fault Tolerant Systems (SysTol), 98-103.
Isermann, R. (2006). Fault-Diagnosis Systems: An Introduction from Fault Detection to Fault Tolerance. Springer-Verlag.
Yuxue Li; Xiaoyuan Zhu. (2023). Observer-based actuator fault detection for quadrotor UAV with experimental validation.
Julio Alberto Guzma´n-Rabasa, Francisco Ronay Lo´pez-Estrada, Brian Manuel Gonza´lez-Contreras, Z. Cen, H. Noura .(2013).An Adaptive Thau Observer for Estimating the Time-varying LOE Fault of Quadrotor Actuators. Conference on Control and Fault-Tolerant Systems (SysTol). Nice, France.

Multi-Agent Reinforcement Learning with Maneuver Primitives for Automatic Ground Collision Avoidance of Fighter Jets

Fatih Erol[a], Hayri Acar[a], Emre Koyuncu[a]

[a] Istanbul Technical University, Aeronautics and Astronautics, Aeronautical and Astronautical Engineering, Türkiye
erolfa@itu.edu.tr

Keywords: Multi Agent, Reinforcement Learning, Maneuver Primitive, Ground Collision Avoidance, Fighter Jets.

Aim

Current automatic ground collision avoidance (AGCAS) systems rely on executing a zero-wing-level maneuver followed by a 5G pull-up when a collision is detected (Swihart, et al., 2011). However, this approach is not always optimal, particularly in challenging terrain with significant elevation changes, such as mountainous regions or canyons, where leveling the wings before pulling up could be counterproductive. In such cases, a lateral maneuver may provide a more effective solution for avoiding ground collisions (Neidhardt, 2021).To account for this, recent methods employ predefined maneuver sets, evaluating whether a pull-up at different roll angles can successfully mitigate terrain impact (Kirkendoll, 2021). However, this process requires extensive computational power and multiple trajectory estimations, making real-time implementation challenging.

We aimed to develop an intelligent collision detection and avoidance framework capable of performing collision checking with a single simulation run and autonomously taking control upon detecting a potential collision, even in highly rough environments such as canyons or Cont. In contrast to prior methods that require multiple simulation runs to evaluate predefined maneuver sets for collision avoidance, our approach enables intelligent, sequentially executed evasive maneuvers within a single simulation run.

The intelligent collision detection framework begins with predicted states 0.5 seconds ahead, assuming the real aircraft continues its current behavior during that interval like previous methods (Swihart, et al., 2011). It runs the intelligent simulation using these initial conditions and output the resulting trajectory to the real aircraft. If a collision is detected, it indicates that no viable avoidance trajectory will remain available after 0.5 seconds. Under such circumstances, the AI takes control of the aircraft to execute an evasive maneuver and prevent the collision.

The multi-agent framework facilitates the decomposition of the problem into simpler sub-problems by assigning different tasks to each agent, while the maneuver primitive structure enables the generation of meaningful and interpretable maneuver sequences.

In this study, we aimed to develop intelligent automatic ground collision avoidance (AGCAS) strategies that can handle challenging terrain environments. Our approach enables more effective ground collision avoidance unpredictable conditions, making automatic ground collision avoidance systems more adaptable and efficient.

Material and Method

In Multi-Agent Reinforcement Learning, we aimed to replicate how pilots execute maneuvers sequentially, first adjusting the roll angle, followed by a pull-up maneuver (Kirkendoll, 2021), as illustrated in Figure 1. In this framework, we utilize two distinct agents: the first agent controls the roll angle, while the second agent controls vertical velocity. Both agents operate at a 1 Hz frequency, with the vertical velocity controller agent incorporating a 0.5 second phase shift relative to the roll angle selector agent, enabling sequential decision making.

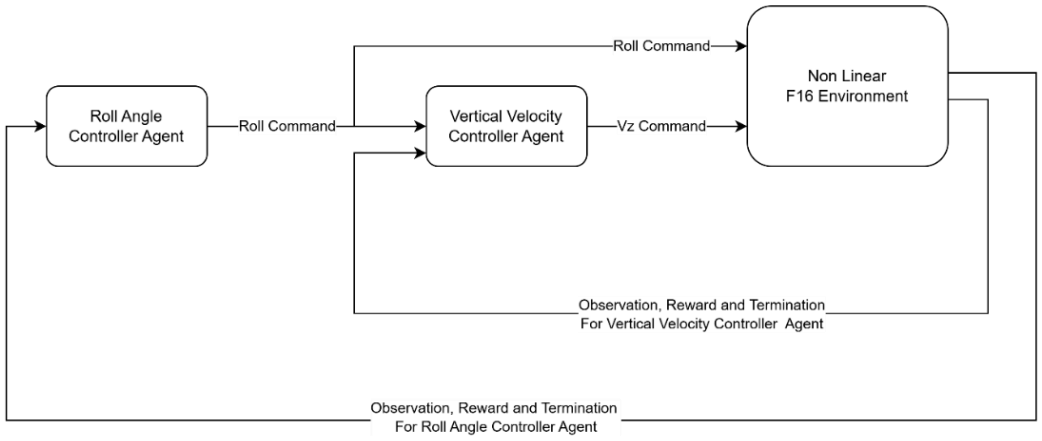

Figure 1. Sequential multi-agent reinforcement learning scheme.

The Multi-Agent framework enables more goal-oriented improvements by allowing each agent to be updated with different observations and rewards. For instance, angle of attack exceedance is primarily the responsibility of the vertical velocity controller agent. This approach prevents unnecessary parameter increases for the roll angle controller agent, ensuring a more efficient and structured learning process.

The Non-Linear F-16 is used as the environment. This model includes post-stall characteristics and features an incremental nonlinear dynamic inversion-based (INDI) autopilot, which controls rotation rates (p, q, r) through an inner loop, while an outer loop manages roll and vertical velocity control. For reinforcement learning (RL), the primary control inputs are the roll angle command and the vertical velocity command.

The action space consists of a discrete set of commands for roll angle ϕ and vertical velocity. Specifically:

- The roll angle command set includes −75°, 0°, and +75°.
- The vertical velocity command set consists of 0 m/s, 20 m/s, and 50 m/s.

The observation space is largely shared between the two agents, with slight variations. The common observations include:

- The loiter point's spherical coordinates in the body-fixed frame shown in Figure 3,
- The lengths of the lidar rays shown in Figure 3,
- Fundamental states of aircraft which are angle of attack, sideslip angle, roll angle, pitch angle, and body angular rates. (α, β, ϕ, θ, p, q, r)

In addition to these, the vertical velocity controller agent has an extra observation: vertical velocity.

To ensure numerical stability, all distances are normalized to the [0,1] range, and angles are expressed in sine and cosine form to prevent discontinuities.

The reward function is composed of two main components: global and local rewards. This structure is one of the key advantages of Multi-Agent RL, as each agent can have distinct reward function. For instance: terrain collision penalty affects both agents, while angle of attack exceedance penalty impact only vertical velocity controller agent.

The total instantaneous reward for the roll controller agent is given by r_{roll} as shown in Equation (1) where $r_{collision}$ penalizes terrain collisions, r_{alive} rewards survival, and r_{ϕ} penalizes excessive roll angles.

$$\begin{aligned} r_{roll} &= r_{collision} + r_{alive} + r_{\phi} \\ r_{collision} &= -1 \\ r_{alive} &= 0.1 \\ r_{\phi} &= \begin{cases} -1, & if\ |\phi| \geq 0.1 \\ 0, & otherwise \end{cases} \end{aligned} \tag{1}$$

The total instantaneous reward for the vertical velocity controller agent is given by r_{VCC} is shown in Equation (2) where $r_{collision}$ penalizes terrain collisions, r_{alive} rewards survival, and r_{G} penalizes excessive load factor and r_{α} penalizes excessive angle of attack.

$$\begin{aligned} r_{VVC} &= r_{collision} + r_{alive} + r_{G} + r_{\alpha} \\ r_{collision} &= -1 \end{aligned} \tag{2}$$

$$r_{alive} = 0.1$$

$$r_G = \begin{cases} -1, & if\ G \geq 5 \\ 0, & otherwise \end{cases}$$

$$r_\alpha = \begin{cases} -1, & if\ \alpha \geq 15° \\ 0, & otherwise \end{cases}$$

Agents are trained using Proximal Policy Optimization (PPO) (John Schulman, 2017) with synchronized update intervals. Both the actor and critic networks are designed with two hidden layers comprising 400 neurons in the first layer and 300 in the second with each layer using the Rectified Linear Unit (ReLU) activation function. The critic network produces a single output value, while the actor network ends with a softmax layer that outputs a probability distribution over the available actions. The PPO parameters for Multi-Agent RL are shown in Table 1.

Table 1. PPO parameters for multi agent RL.

Experience Horizon	100
Clip Factor	0.2
Entropy Loss Weight	0.05
Number of Epoch	5
Advantage Estimate Method	gae
GAE Factor	0.95
Discount Factor	0.997
Sample Time [sec]	1
Mini Batch Size	20
Max. Mini Batch per Epoch	4

Throughout the training process, a consistent increase in cumulative reward can be observed in Figure 2.

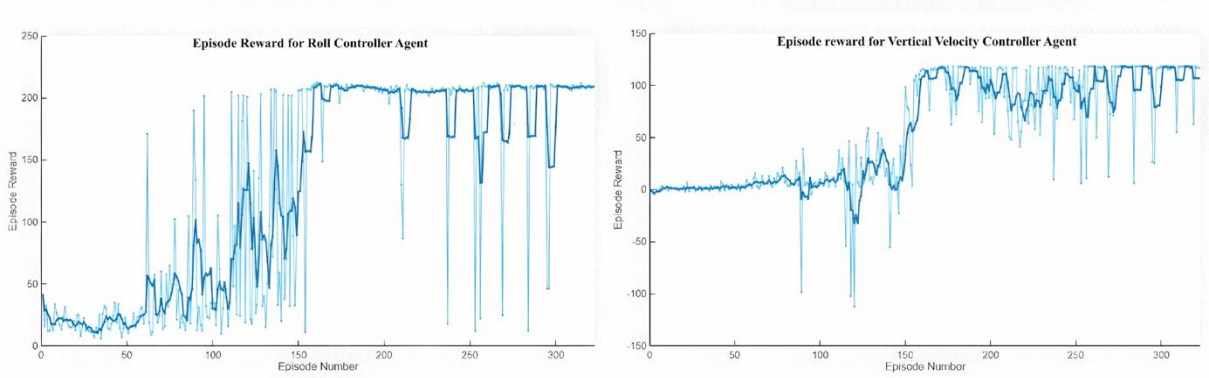

Figure 2. Training results.

All computations, including the nonlinear F-16 model, autopilot, and agent training, are conducted in Matlab Simulink. For visualization, Unity is utilized, as shown in Figure 3, to enable real-time rendering of the aircraft, terrain, LIDAR rays, loiter positions, and trajectory visualization.

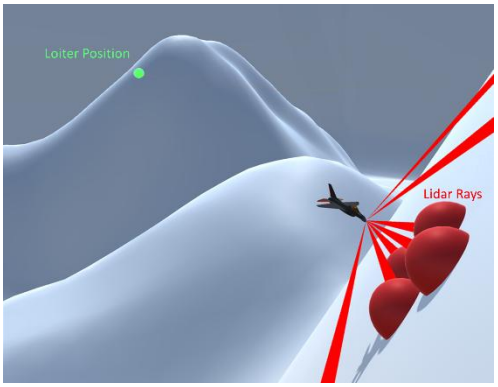

Figure 3. Visualization with Unity.

Terrain generation is achieved by processing digital terrain elevation data (DTED) (Agency, 2022) in MATLAB and meshing it within Unity, or alternatively, by generating procedural terrains using Blender.
Since both methods allow for terrain generation, they provide the flexibility to create diverse environments for RL training, enhancing the model's adaptability and robustness.

Findings

The proposed Multi-Agent RL approach was evaluated across multiple terrain environments with varying elevation profiles and demonstrated successful performance in all tested scenarios.
The RL-based system significantly outperformed traditional AGCAS in highly variable terrains, particularly in regions with steep elevation changes and narrow canyon-like formations. Unlike conventional systems that rely on fixed maneuvers, the RL-based approach adapted dynamically, selecting maneuvers based on the terrain profile as shown in Figure 4, Figure 5 and Figure 6.

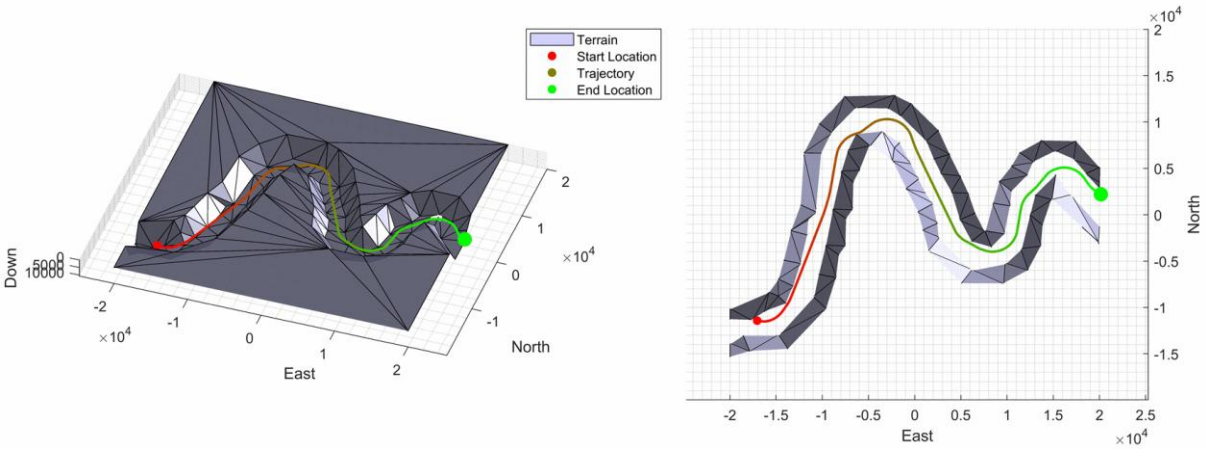

Figure 4. Canyon scenario 1 of multi-agent RL.

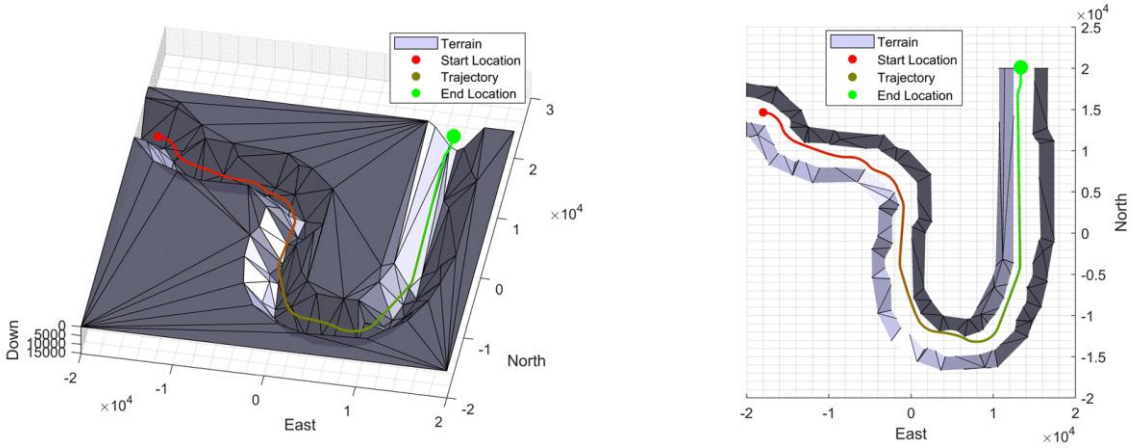

Figure 5. Canyon scenario 2 of multi-agent RL.

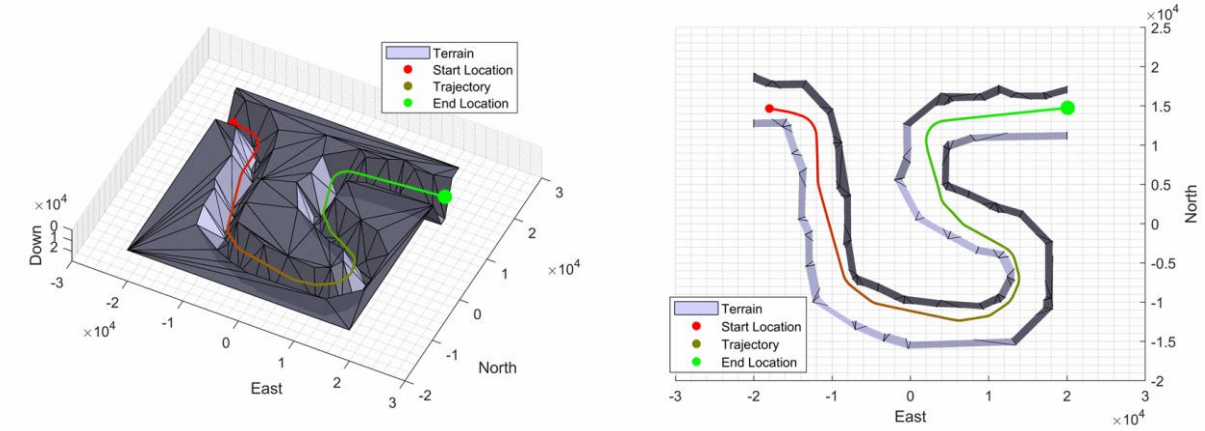

Figure 6. Canyon scenario 3 of multi-agent RL.

The proposed single-pass decision-making approach eliminated the need for multiple trajectory estimations, reducing computational complexity by approximately 80% compared to deterministic predefined maneuver sets. The system successfully delayed intervention until the last feasible moment, allowing the pilot to retain control longer while ensuring safety. This behavior closely mimics human pilot decision-making, providing a more natural and efficient AGCAS response.

Conclusion

This study introduces a novel Multi-Agent Reinforcement Learning approach for AGCAS, addressing the limitations of traditional deterministic maneuver-based methods. Unlike predefined AGCAS techniques that rely on fixed trajectory estimations, our approach enables adaptive, significantly enhancing ground collision avoidance in complex and unpredictable terrain environments. This method offers several key advantages, including a significant reduction in computational complexity, making real-time implementation feasible, improved collision avoidance success rates, particularly in scenarios where traditional pull-up strategies are ineffective, and minimized unnecessary pilot intervention, ensuring that AGCAS decision-making aligns with human pilot strategies, resulting in a more natural and effective safety system. These findings indicate that the Multi-Agent Reinforcement Learning approach provides substantial advancements over conventional AGCAS methodologies, especially in cases where terrain variations necessitate more adaptive and non-traditional avoidance strategies with intelligent, sequentially executed evasive maneuvers within a single simulation run can be seen in Figure 7.

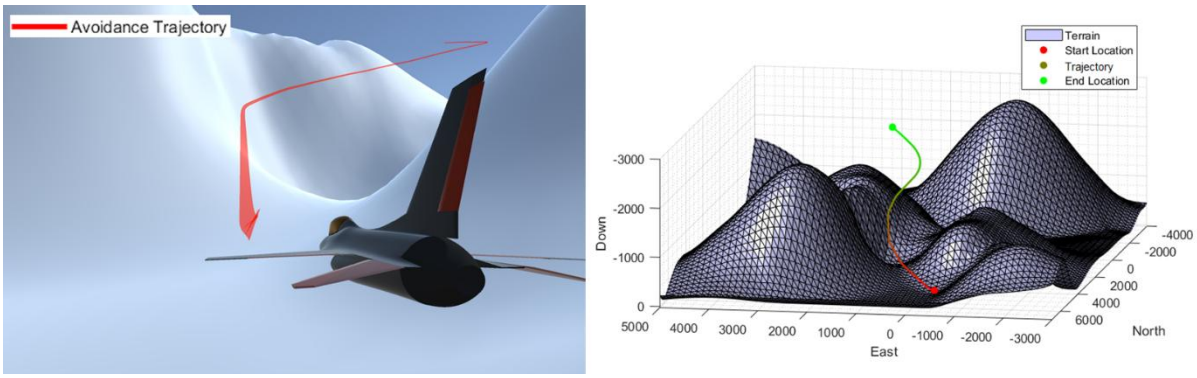

Figure 7. Proposed intelligent avoidance trajectory (with single simulation run).

References

Agency, N. G.-I. (2022, 10 02). Digital Terrain Elevation Data (DTED). National Geospatial-Intelligence Agency: **Url-1** https://earth-info.nga.mil adresinden alındı

John Schulman, F. W. (2017). Proximal Policy Optimization Algorithms. 2-6.

Kirkendoll, Z. a. (2021). Automatic Ground Collision Avoidance System Trajectory Prediction and Control for General Aviation. 2021 IEEE/AIAA 40th Digital Avionics Systems Conference (DASC), 1-10.

Neidhardt, T. a. (2021). Development of an Automatic Ground Collision Avoidance System for a General Aviation Aircraft. 2021 IEEE/AIAA 40th Digital Avionics Systems Conference, 1-10.

Swihart, Barfield, D. E., Griffin, A. F., Lehmann, E. M., Whitcomb, R. C., Flynn, S. C., . . . E, K. (2011). Automatic ground collision avoidance system design, integration, & flight test. IEEE Aerospace and Electronic Systems Magazine, 4-11.

Swihart, D. E. (2011). Automatic Ground Collision Avoidance System Design, Integration, & Flight Test. IEEE Aerospace and Electronic Systems Magazine, 5-11.

AERONAUTICAL AND ASTRONAUTICAL ENGINEERING

Aircraft Design, Flight Dynamics And Performance

Control Systems: Adaptive, Intelligent, Digital, Optimal, Pneumatic-Hydraulic

Mechanical Vibrations And Structural Dynamics

Rotary Wing Aircraft

Spacecraft Control, Design And Performance

Theoretical, Computational And Experimental Aerodynamics And Fluid Dynamics

Theoretical, Computational And Experimental Structural Analysis And Design

Nonlinear Modeling and Sensitivity Analysis of Oleo-Pneumatic Strut Landing Gear Systems for Aircraft Landing Performance

Sadık Utku Gulek[a], Kaan Yıldız[b]

[a] Istanbul Technical University, Faculty of Aeronautics and Astronautics, Aeronautics and Astronautics Engineering Master of Science, Türkiye

[b] Istanbul Technical University, Aviation Institute, Türkiye

gulek15@itu.edu.tr

Keywords: Aircraft Landing Gear Touchdown Dynamics, Landing Gear Systems, Non-Linear Mass-Spring-Damper Dynamic System, Oleo-Pneumatic Strut, Simulink Model.

Aim

Landing gear systems support the aircraft throughout ground operations and play a crucial role in absorbing impact forces at touchdown. In today`s modern landing gears, mostly oleo-pneumatic struts are utilized as the shock-absorber component in the landing gear system since it has the maximum efficiency to weight ratio of about 80% among all the conventional landing gears [1]. The aim of this study is to conduct a sensitivity analysis to evaluate the effects of oleo-pneumatic strut landing gear design parameters on the key performances such as energy absorption capacity and aircraft maximum vertical acceleration.

Material and Method

The vertical motion of a landing gear system can be analytically modeled as a double mass-spring-damper system as shown in Figure 1 [2], capturing the dynamics of both the aircraft and the landing gear system as separate masses: upper or sprung mass and lower or unsprung mass respectively. The upper and lower masses are connected to each other with the oleo-pneumatic strut that can be modeled as one spring and one damper, and the tire-ground interaction can be modeled as one spring. Also, the lift acts on the aircraft wings because of the horizontal speed during the aircraft landing operation. The lift is usually taken equal to the total weight of the aircraft at touchdown. After touchdown, the lift decreases as the horizontal speed decreases during the landing operation [3,4]. The equations of motion for the upper and lower masses are shown in Equation 1 and Equation 2 where y_1 and y_2 are vertical displacements of the upper and lower masses, indicated as m_1 and m_2, respectively. The forces on the right-hand side of the equations of motion are F_s (the total strut force in its axis), F_{Na} (force normal to axis of shock strut at the tire axle), F_{vg} (vertical ground force applied to the tire), L (lift force) and Weights, shown as W_1 and W_2 for the upper and lower masses, respectively. The angle between the shock-strut axis and vertical, shown in Figure 2 [4], is also considered for the equations of motions. Using geometric relations and assuming the lower mass concentrated at the axle, F_{Na} can be expressed by Equation 3 where F_{Hg} is the horizontal ground force applied to the tire.

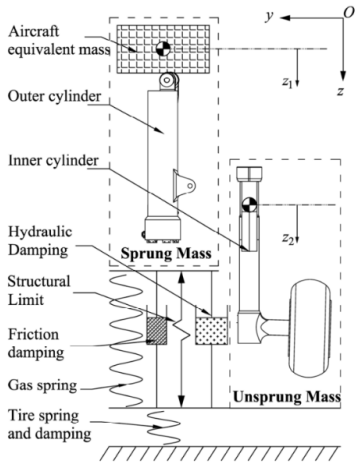

Figure 1. Schematic of the landing gear system as a mass-spring-damper system [2].

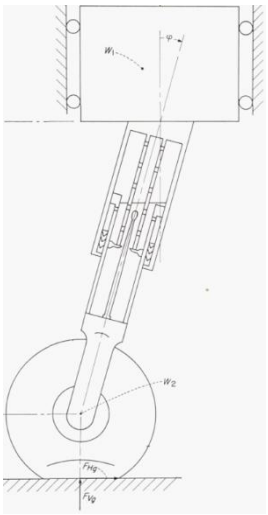

Figure 2. Demonstration of the rake angle (the angle between the oleo-strut axis and the vertical) [4].

An oleo-strut generally refers to a piston-cylinder assembly where the cylinder and piston are generally connected to the upper mass and lower mass respectively. During aircraft landing operation, the oleo strut compresses under load or extends as the load is relieved. A typical oleo-strut consists of two chambers separated by a plate with an orifice. The upper chamber is typically filled with gas like nitrogen or air and the lower chamber is filled with highly viscous fluids like oil, shown in Figure 3 [4]. As the oleo-strut compresses or extends, the damping force in the oleo strut is generated by the flow of viscous fluid into the orifice and the spring force is produced by the compressed air in the upper chamber. The vertical displacement difference between the upper mass and the lower mass is defined as the strut stroke. Similarly, the stroke velocity is the relative vertical velocity of the upper and lower masses. The stroke and stroke velocity can be obtained by utilizing Equation 4 and Equation 5 respectively [4]. The pneumatic spring force (F_p) and the hydraulic damping force (F_h) of the oleo strut total force (Equation 6), given in Equation 7 and Equation 8 respectively [5,6], nonlinearly depend on the strut's stroke and stroke velocity. Other than the stroke and stroke velocity, the spring and damping characteristics of the oleo-strut depend on the pneumatic and hydraulic chamber areas (A_a and A_h), orifice area (A_n), orifice discharge coefficient (C_d), initial gas pressure (P_0), polytropic exponent (n) and the density of the viscous fluid (d_{fluid}). The non-linearity in the strut's spring and damping behavior arises from the complex interactions between these parameters, with the force-displacement and force-

velocity relationships varying dynamically under different loading conditions. The non-linearity in the strut's spring and damping characteristics introduces additional complexities in the analysis and modeling of the landing gear system [3,4].

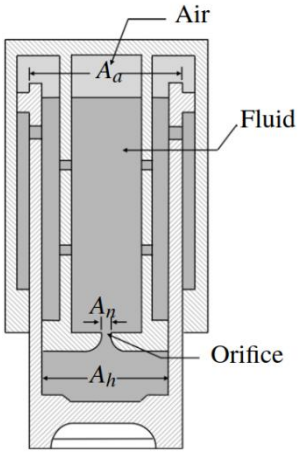

Figure 3. Schematic view of the oleo-pneumatic shock strut [8].

When the aircraft touches down, the tire compresses as it contacts the ground. The vertical force generated is the result of the aircraft's weight and vertical deceleration forces acting on the landing gear. The magnitude of this force mainly depends on the tire's mechanical properties and the vertical touchdown velocity of the aircraft. The higher the touchdown velocity, the greater the force exerted on the tire and, consequently, the landing gear system. Tire force-deflection curves, typically provided by tire manufacturers, offer a detailed relationship between the vertical deflection of the tire and the ground force. These curves generally exhibit exponential variation with vertical deflection, shown in Equation 9 where m' and rtire are tire constants and d_{tire} is tire overall diameter. This relationship is crucial for predicting the behavior of the landing gear during landing impacts, as the non-linearities in the force-deflection response significantly affect the overall shock-absorbing performance of the system [3,4].

In addition to the oleo-strut forces and tire vertical ground forces, the friction forces may play a non-negligible role during the vertical motion of a landing gear system. The friction forces within the oleo-strut itself arise from the bearing friction forces (F_{nf}) and seal friction force (F_{sf}) (Equation 10) [2,7]. These friction forces can be expressed by Equation 11 and Equation 12 where l1 and l2 are axial distance between upper and lower bearings and axial distance between tire axle and lower bearing for fully extended shock strut [2,4]. Other parameters reflect the friction coefficient for the bearing-chamber or seal-chamber contacts. Furthermore, the friction between the tire and the runway surface is another crucial factor that affects the behavior of the landing gear system. This friction is particularly relevant in the context of the horizontal tire-ground force. As a preliminary estimate, the instantaneous friction force can be considered equal to the vertical ground reaction force multiplied by an appropriate friction coefficient, as given in Equation 13, while the tire skids from the moment of touchdown until it stops skidding and spins up [4]. The instant at which the wheel stops skidding can be determined using a simple impulse-momentum relationship, given in Equation 14 where I_w, V_{H0}, r_d and t_{su} are polar momentum of inertia of the wheel, initial horizontal velocity, radius of the deflected tire and time of wheel spinning-up, respectively [4,7]. Especially for shock struts with a rake angle —defined as the angle between the oleo-strut axis and the vertical— the frictional forces between the tire and the runway surface can also affect the forces transmitted to the upper and lower masses of the landing gear system [3]. These frictional effects of internal strut contacts and the tire-ground contact introduce further non-linearities into the system's response, making the analysis of landing gear dynamics more complex [2,4].

Findings

Considering all the variants on the spring effects, damping characteristics and forces caused by the friction, the vertical motion of a landing gear system demonstrates a complex and non-linear behavior [2,3,4]. In this study, a Simulink-based model for the dynamics of an aircraft landing gear with an oleo-pneumatic strut is developed based on the non-linear mass-spring-damper system presented in [4]. The Simulink model includes the oleo strut non-linear responses as well as non-linear tire-ground interactions, summarized in Equations from 1 to 14. The model is validated with experimental data given in [4] and Figure 4 shows that the results from the model and the experimental data are aligned with each other.

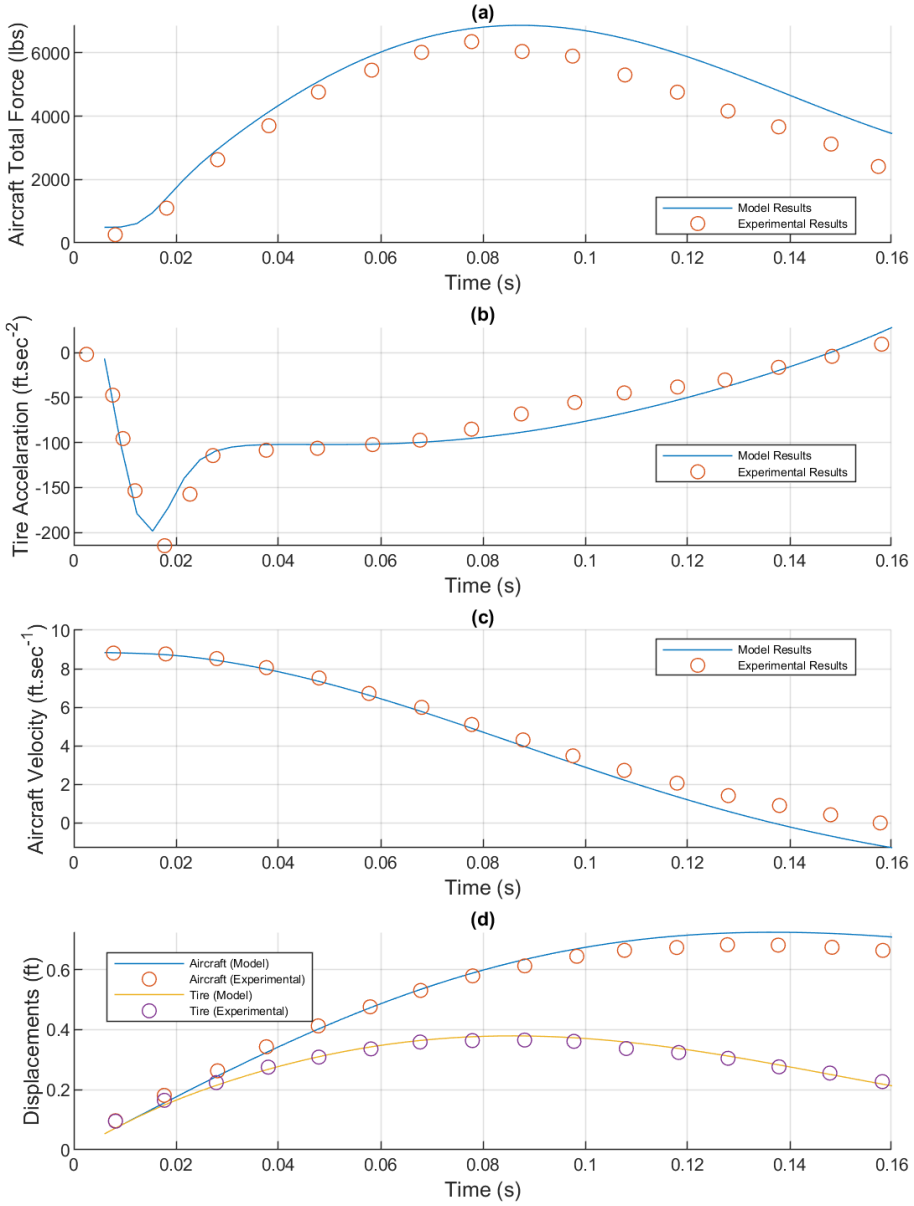

Figure 4. Comparison of model predictions and experimental data for aircraft landing gear dynamics: (a) Aircraft total force; (b) Tire acceleration; (c) Aircraft velocity; and (d) Displacements of the aircraft and tire.

Conclusion

In conclusion, this study provides a sensitivity analysis of the key design parameters of oleo-pneumatic strut landing gear systems, focusing on their impact on energy absorption capacity and maximum vertical acceleration during aircraft touchdown. The developed Simulink model successfully captures the non-linear dynamics of the system, including the complex and non-linear relationships for the oleo strut tire-ground forces. By validating the model with experimental data, it demonstrates the accuracy of the simulated responses in representing real-world behavior. The purpose of this study is to develop an approach to model the dynamics of aircraft landing gear and to provide in-depth discussion of the validation process, including comparisons between simulated and experimental results. Lastly, the study provides a comprehensive parametric study, analyzing the effects of key design parameters on the system's performance.

Summary of Equations used in the Model

$$m_1 * \ddot{y}_1 = -F_S * co(\varphi) - F_{Na} * si(\varphi) - L + W_1 \ \#(1)$$

$$m_2 * \ddot{y}_2 = F_S * co(\varphi) + F_{Na} * si(\varphi) - F_{vg} + W_2 \ \#(2)$$

$$F_{Na} = F_{Vg} * sin\ sin\ (\theta) - F_{Hg} * cos\ cos\ (\theta) + W_2 * \ddot{y}_1 * sin\ sin\ (\theta) - W_2 * sin\ sin\ (\theta) \ \#(3)$$

$$S = \frac{y_1 - y_2}{cos\ cos\ (\varphi)} \ \#(4)$$

$$\dot{S} = \frac{\dot{y}_1 - \dot{y}_2}{cos\ cos\ (\varphi)} \ \#(5)$$

$$F_S = F_p + F_h + F_f \ \#(6)$$

$$F_p = P_0 * A_a * \left[\frac{V_0}{V_0 - A_a * S}\right]^n \ \#(7)$$

$$F_h = d_{fluild} * \left[\frac{A_h^3}{2 * A_n^2 * C_d^2}\right] * |\dot{S}| * \dot{S} \ \#(8)$$

$$F_{vg} = m' * \left(\frac{y_2}{d_{tire}}\right)^{r_{tire}} \ \#(9)$$

$$F_f = F_{nf} + F_{sf} \ \#(10)$$

$$F_{nf} = \frac{\dot{S}}{|\dot{S}|} * |F_{Na}| * \left[(\mu_1 + \mu_2) * \frac{l_2 - s}{l_1 + s} + \mu_1\right] \#(11)$$

$$F_{sf} = -\mu_{sf} * F_a * sgn(\dot{S}) \ \#(12)$$

$$F_{Hg} = F_{vg} * \mu \ \#(13)$$

$$\int_0^{t_{su}} F_{Hg}\, dt = \mu \int_0^{t_{su}} F_{vg}\, dt = \frac{I_w * V_{H0}}{r_d^2} \#(14)$$

References

Ahmad, M. A., Shah, S. I. A., Shams, T. A., Javed, A., & Rizvi, S. T. U. I. (2021). Comprehensive design of an oleo-pneumatic nose landing gear strut. Proceedings of the Institution of Mechanical Engineers, Part G: Journal of Aerospace Engineering, 235(12), 1605–1622.

Gan, S., Fang, X., & Wei, X. (2021). Parametric Analysis on Landing Gear Strut Friction of Light Aircraft for Touchdown Performance. Applied Sciences (2076-3417), 11(12), 5445.

Pecora, R., & Botez, R. M. (2021). A Rational Numerical Method for Simulation of Drop-Impact Dynamics of Oleo-Pneumatic Landing Gear. Applied Sciences (2076-3417), 11(9), 4136.

Milwitzky, B., & Cook, F. E. (1953, January 1). Analysis of Landing-Gear Behavior. NASA Technical Reports Server (NTRS).

Url-1 https://ntrs.nasa.gov/citations/19930092181

Nicola, P. (2013). An Automatic Procedure for the Landing Gear Conceptual Design of a Light Unmanned Aircraft. SAE International.

Beachkofski, B. K. (1999). Elementary Model of Nose Gear Retraction and Oleo-Pneumatic Strut Compression. Georgia Inst Of Tech Atlanta DTIC AND NTIS.

ZEYNEP GEDIKOGLU et al. Shock absorber system dynamic model in model-based environment. [s. l.], 2022.

Li, Y., Jiang, J. Z., Sartor, P., Neild, S. A., & Wang, H. (2017). Including Inerters in Aircraft Landing Gear Shock Strut to Improve the Touch-down Performance. Procedia Engineering, 199, 1689–1694.

Aeroelastic Optimization with Genetic Algorithm

Ahmet Güver[a], Seher Eken[a]

[a] Istanbul Technical University, Aeronautics and Astronautics Engineering Program, Türkiye

guvera16@itu.edu.tr

Keywords: Aeroelasticity, Genetic Algorithm, Optimization.

Aim

After the Wright brothers' first successful flight attempt, the idea that humans could fly with machines was strengthened. Primitive aircraft were manufactured worldwide by entrepreneurs and companies for both military and civilian purposes. The early examples of these aircraft were made from wood and fabric. The wood was primarily used for structural purposes, while the fabric was used for the surface of the wings and stabilizers. Despite the successful attempts, there were also failures. Nine days before Orville and Wilbur Wright success Samuel P. Langley failed to fly his aerodrome with using a catapult mechanism due to wing torsional divergence. Some of these failures occurred because the aircraft structures lacked the static stiffness that necessary to resist wing bending. Additionally, as wing designs became more slender, dynamic instability issues arose, known as flutter. Flutter is an interdisciplinary subject that involves three disciplines: "Elasticity", "Aerodynamics", and "Dynamics (Inertia)". The Collar Triangle in Figure 1. expresses the relationship between these three scientific fields (Collar, 1946).

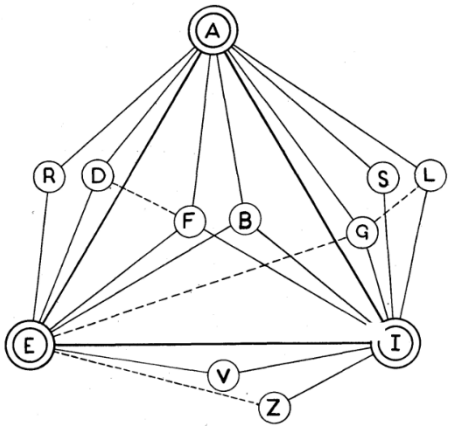

Figure 1. Collar Triangle (Collar, 1946).

The letters "E", "A" and "I" at the corners of triangle are represent the science fields respectively and the other letters at the middle and outside the edges are for inter disciplines. The meanings of these letter can be seen in Table 1.

Table 1. Collar Triangle Letters.

Letters	Interdisciplines
R	Reversal of Control
D	Divergence
V	Vibrations (Mechanical)
Z	Impact
G	Gust
S	Stability and Control
L	Loading
F	Flutter
B	Buffeting

The Collar Triangle also has simpler and more complicated versions that frequently quoted in academic publications. When "Control" added to the triangle servo-aeroelasticity and "Thermal Effects" added with "Control" thermo-servo-aeroelasticity can be defined as inter disciplines.

After World War I and II, there was a growing expectation for aircraft to fly faster and weight less. The need for structural strength to achieve higher flutter speeds required the use of more materials. However, the development of new high-strength materials can help reduce the structural weight, but a suitable design for high flutter speeds is still necessary. These design parameters are interdependent, and even a small change in one of them can cause significantly affect the dynamic stability of the aircraft. The complex nature of the flutter phenomenon can be overcome through design optimization methods. The primary aim of this project is optimize the aeroelastic flutter speed with GA optimization method.

Material and Method

Optimization is defined as "an act, process, or methodology of making something (such as a design, system, or decision) as fully perfect, functional, or effective as possible" (Optimization, 2025). There are two primary types of optimization methods mathematically. The first type of the methods is Gradient-based optimization methods. These methods rely on the derivatives of the system's governing equations. By using the gradient of the objective function, these methods adjust the decision variables in the direction of the steepest descent (or ascent) to reach an optimal solution. These methods require the objective function to be differentiable. Common examples include gradient descent and its variations. The second kind of methods is Gradient-free optimization methods. These methods do not require the calculation of derivatives. They are typically used when the objective function is non-differentiable, noisy, or difficult to compute. Examples of gradient-free methods include Particle Swarm Optimization (PSO) and Genetic Algorithms (GA), both of are metaheuristic, population-based techniques.

The genetic algorithm is founded by John H. Holland in his Adaptation in Natural and Artificial Systems book dated 1975 (Holland, 1992). Genetic algorithm optimizations are evolution based algorithms that structured on concepts like mutation, crossover and selection of elites in a population with respect to their fitness values. The inputs coded to binary strings and mutation and crossover done to this binary string. The mechanism of the genetic algorithm have been resembled to Darwin's Evolution by many researchers, also the binary string similar to the one string of a gene spiral with its mutation and

crossover capability. The crossover is the swap the binary code part between two parents after a particular point. That point can be called crossover point. The crossover can be seen in Figure 2.

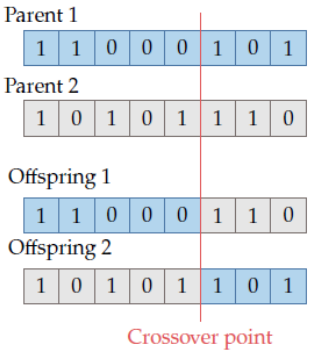

Figure 2. Crossover Procedure (Joaquim & Andrew, 2021).

The other method to create offspring in GA is mutation. The one or more binary code in string randomly changed to opposite and generate a new input. The change can be seen in Figure 3.

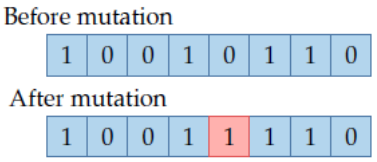

Figure 3. Crossover Procedure (Joaquim & Andrew, 2021).

In each iteration elites are chosen for mutation and crossover procedures with respect to their outputs (fitness value) in objective function. The inputs give the lower fitness value in a population are not used after. In other words become extinct. The elite ratio defines that how many design point remain after elimination. The higher elite ratio means less design point eliminated. The elites and their offspring are become new population and this procedure goes over and over until the goal have been reached.

For this project calculation of flutter speeds and genetic algorithm coded with python. The genetic algorithm optimization main function has three sub-functions for: one for crossover, one for mutation, and one for finding the best fitness value in a population of that generation, also a function is defined for flutter speed calculation for used for each design points in a generation. For calculation of fitness values for each design point parallel processing have endorsed for faster results. After initial population are randomly created the elites are chosen for next generation based on their fitness value. The crossover and mutations are done to elites and parents and children are become new population. The iterations continue to converge or reached to predetermined number of iteration limit. The inputs that give the optimum fitness value are the candidates for design points for wing design process.

Findings

There are flutter functions used in this project; K method, PK Method and Beam method. Although there are multiple modes for Galerkin method depends on mode number, for K method 2 and for PK 4 modes are present. For three methods flutter speed can be indicated with finding the lowest velocity that has zero damping. The negative damping ratio is where the

system is stable. When damping ratio is zero, the point is called stability border and for this specific problem "flutter". The velocity damping graph for Golan Wing can be seen in Figure 4.

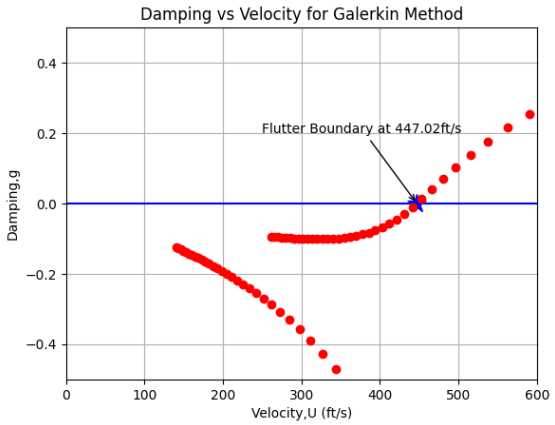

Figure 4. Velocity Damping Graph for Goland Wing.

The functions that used for this project find this velocity and return it when function called for population of each generation. For validate our function the results are compared with the (Lin & Iliff, 2000). The Goland Wing properties can be seen in Table 2.

Table 2. Goland Wing Properties.

Parameters	Definition	Values
m	Mass per unit span	0.746 *slug/ft*
Sy	Static mass moment per unit length about the elastic axis	0.447 *slug/ft/ft*
Iy	Mass moment of inertia about the elastic axis	1.943 *slug/ft2/ft*
EI	Elastic rigidity	23.6x10^6 *lb/ft*
GJ	Torsional rigidity	2.39x10^6 *lb/ft*
α	Location of the elastic axis	-1/3
l	Span of the wing	20 *ft*
b	Half chord	3 *ft*

The flutter speed for Golang Wing compared with Lin and Iliff's results (Lin & Iliff, 2000) in Table 3.

Table 3. Flutter Speed Comparison.

Functions and Reference	Flutter Speed	Difference
(Lin & Iliff, 2000)	447	-
Galerkin Method	447.02	≅0%

The improvement for generations are can be seen in Figure 5. This simplicity the population are 8 and generation is 25 for this graph. The two graphs show that the improvements can evolve different. While the increase in first graph in previous generation, in second graph the flutter speed increase after 10th iteration.

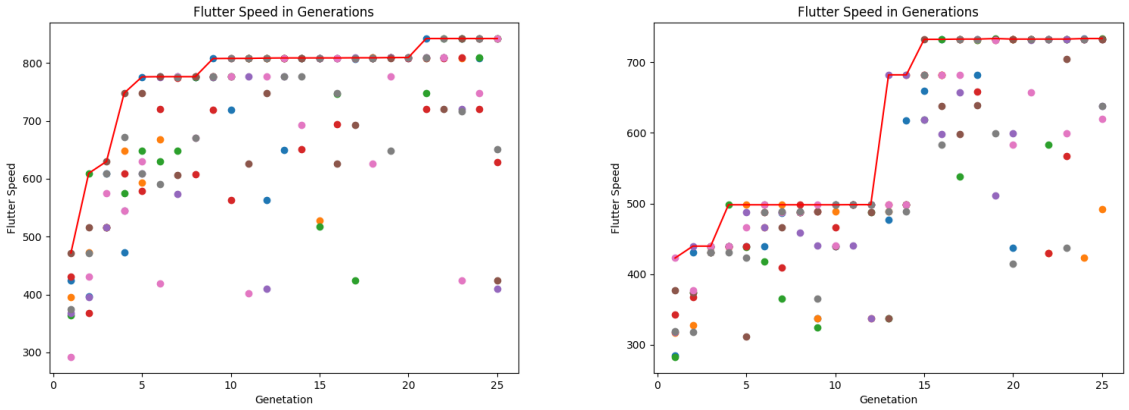

Figure 5. Flutter Speed in Generations.

The scatters on the graphs are represents the fitness values for population members. The fitness values in same generation share same x axis. The highest fitness value are connected with red line for showing the improvement on the flutter speed. Although the random crossover and mutation operations search for more optimum result, offspring can give lower fitness values than their parents. This is because the chaos nature of genetic algorithm. The random procedures can generate strong and weak offsprings but with the nature of genetic algorithm this lower fitness value design points are eliminated from the procedure. Eventually the final result is improved and lower fitness value design points are extinct in the system

Conclusion

Due to the complex nature of aeroelastic responses for design points its unpredictable to from just looking the design point values. Even a small change in values the response can change the dynamic stability characteristics severely, therefore an optimization procedure endorsed for finding the optimum design value. Genetic algorithm has been chosen for this optimization problem because the differentiability and continuity are not present for this problem which is essential for gradient based optimization methods. The results show that in each iterations the flutter speed improved or conserved. In some generation there are relatively high increase in response or small or not increase at all. This is because random operation in crossover and mutation procedures. After desired number of iterations the improvement of the objective results are achieved.

References

Collar, A. R. (1946). The Expanding Domain of Aeroelasticity. Journal of the Royal Aeronautical Society, 613-636.

Holland. (1992). Adaptation in Natural and Artificial Systems. Cambridge: The MIT Press.

Joaquim, R. R., & Andrew, N. (2021). Engineering Design Optimization. Cambridge University Press.

Lin, J., & Iliff, K. W. (2000). Aerodynamic Lift and Moment Calculations Using a Closed-Form Solution of the Possio Equation. NASA/TM-2000-209019.

Loring, S. J. (1941). Outline of General Approach to the Flutter Problem. Society of Automotive Engineering Journal, 345-356.

Optimization. (2025). Retrieved from Merriam-Webster

Url-1 https://www.merriam-webster.com/dictionary/optimization

Feed-Forward Neural Network Based Prediction of Flutter Speed of 3 DOF 2D Wing Model

Osman Dağlı[a], Metin Orhan Kaya[a]

[a] Istanbul Technical University, Aeronautical and Astronautical Engineering Department, Aeronautical and Astronautical Engineering Program, Türkiye
dagli17@itu.edu.tr

Keywords: Aeroelasticity, Feed-Forward Neural Network, Flutter, Wing Model.

Aim

Aeroelastic flutter arises from the interaction of aerodynamic, elastic, and inertial forces, significantly impacting aircraft structures like wings and tails. It occurs when these forces combine to induce self-excited oscillations, which can compromise structural integrity. Given the complexity of flutter analysis, artificial intelligence (AI) has become an effective tool in predicting flutter speed and responses. This study explores artificial neural networks (ANNs) as a computationally efficient method for addressing aeroelastic flutter problems [1-3].
This paper describes a typical 2D airfoil model with a control flap. This model is developed in Theodorsen's unsteady aerodynamics theory and represents a typical section of a wing. The model can be seen in Fig. 1.

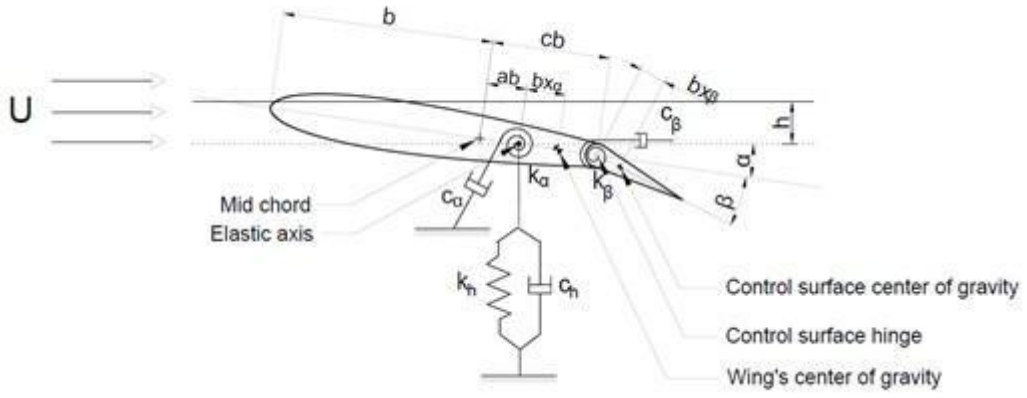

Figure 1. 2D 3 DOF Aeroelastic Typical Section.

Also, the aeroelastic equations of motion is in Eq. 1. To develop a robust dataset for ANN-based flutter prediction, this research integrates the state-space representation method with Theodorsen's unsteady aerodynamics theory.

$$m\ddot{h} + mx_\alpha b\ddot{\alpha} + mx_\beta b\ddot{\beta} + c_h\dot{h} + k_h h = L$$

$$I_\alpha\ddot{\alpha} + mx_\alpha b\ddot{h} + \left[mx_\beta b^2(c-a) + I_\beta\right]\ddot{\beta} + c_\alpha\dot{\alpha} + k_\alpha\alpha = M_\alpha \qquad \text{Eq. 1}$$

$$mx_\beta b\ddot{h} + \left[mx_\beta b^2(c-a) + I_\beta\right]\ddot{\alpha} + I_\beta\ddot{\beta} + c_\beta\dot{\beta} + k_\beta\beta = M_\beta$$

The nondimensionalized form of equations of motion obtained in Eq. 2. The state-space model represents physical systems through input, output, and state variables, while Theodorsen's theory provides insights into unsteady aerodynamic forces.

$$[\bar{M}_s - \bar{M}_a]\begin{bmatrix}\ddot{h}\\ \ddot{\alpha}\\ \ddot{\beta}\end{bmatrix} + [\bar{D}_s - \bar{D}_a]\begin{bmatrix}\dot{h}\\ \dot{\alpha}\\ \dot{\beta}\end{bmatrix} + [\bar{K}_s - \bar{K}_a]\begin{bmatrix}h\\ \alpha\\ \beta\end{bmatrix} = \bar{L}_\delta \begin{bmatrix}\ell_1\\ \ell_2\end{bmatrix} + \bar{L}_c[\beta_c] \quad \text{Eq. 2}$$

The state- space form is given in Eq. 3. Together, these methods create a dataset that captures flutter behavior under varying conditions. A multi-layer ANN architecture is employed, enhancing the predictive capability by processing different aspects of flutter data [4-9].

$$\dot{x} = Ax + Bu \quad \text{Eq. 3}$$

Recent studies demonstrate ANN's effectiveness in flutter analysis. Research leveraging Reduced Order Models (ROMs) and deep learning, including Long Short-Term Memory (LSTM) networks, has shown improved accuracy and reduced computational costs compared to traditional methods. Studies indicate that ANN can identify the most influential geometric parameters affecting flutter speed, with frequency ratio being the most critical factor [10-15]. Zhang et al. introduced Time Delay Recurrent Neural Networks (TDRNNs) for modeling nonlinear aeroelastic systems, further confirming ANN's reliability [16-18].

This study develops an ANN-based approach, specifically using Feedforward Neural Networks (FFNNs), to predict flutter speeds efficiently. The mathematical output of a node in an FFNN is determined based on the input it receives through these weighted connections as in Eq. 4. MATLAB is utilized for implementation, with results validated against theoretical predictions. The findings highlight ANN's potential in accurately modeling aeroelastic flutter, making it a valuable tool for aerospace engineering applications.

$$y_i = \varphi_i\left(\sum_{j=1}^{n^i} w_j^i z_j^i + b^i\right) \quad \text{Eq. 4}$$

The main aims of the study are:

- It provides a trustworthy dataset for flutter speed prediction based on state-space representation and Theodorsen's unsteady aerodynamic theory.
- Development and training of an FFNN model that can have good estimates in flutter speeds through key aeroelastic parameters are possible.
- To compare the ANN-based predictions with numerical results obtained by eigenvalue analysis and previous experimental studies.
- The use of machine learning in aeroelastic analysis for the purpose of establishing whether this can replace or supplement the conventional methods.
- It provides an example for a continuously developing field, namely AI-driven aerospace engineering, and points out the potentiality of using neural networks in modeling complicated aerodynamic behavior in order to reduce the reliance on costly experimental setups and high-fidelity numerical simulations.

Material and Method

In this work, an attempt has been made to predict the flutter speed by utilizing a data-driven approach using Feed-Forward Neural Network-FFNN, a kind of Artificial Neural Network-ANN. These procedures contain different steps such as dataset generation, the selection of neural network architecture, training, validation, and testing.

1. Dataset Generation

In this respect, the state-space representation and Theodorsen's unsteady aerodynamic theory will be implemented for the generation of the comprehensive data set of flutter. The aeroelastic parameters which are used in this work given in Table 1.

Table 1. System Parameters for Aeroelastic Analysis [11].

Geometric Parameters		**Stiffness Parameters**	
Chord	0.254 m	K_α, per span	14861 1/s^{-2}
Span	0.52 m	K_β, per span	155 1/s^{-2}
Semi-chord, b	0.127 m	K_h, per span	1809 1/s^{-2}
Elastic axis, a	-0.5		
Hinge line, c	0.5		
Mass Parameters		**Damping Parameters**	
Mass of the wing, m_α	0.62868 kg	ζ_α, log-dec	0.01626
Mass of the flap, m_β	0.18597 kg	ζ_β, log-dec	0.0115
Mass/length of the wing-flap	0.1558 kg/m	ζ_h, log-dec	0.0113
Mass of the support blocks	0.47485*2 kg		
Inertial Parameters		**Jones' Approximation Parameters**	
S_α, per span	0.08587 kg.m	λ_1	0.014
S_β, per span	0.00395 kg.m	δ_1	0.165
x_α	0.434	λ_2	0.32
x_β	0.01996	δ_2	0.335
I_α, per span	0.01347 kg.m^2		
I_β, per span	0.0003264 kg.m^2		
r_α	0.7321		
r_β	0.11397		

Both of those are mathematical methodologies which analyze the so-called aeroelastic system under various conditions. The dataset comprised flutter speed corresponding to the wide range of wing parameters; therefore, the generalization of the neural network could be pretty effective. The parameters used as dataset for flutter speed prediction are given in Table 2.

Table 2. Parameters Used as Dataset for Flutter Speed Prediction.

	C.G. Location	**E.A. Location**	**Mass of Wing Structure**	**Semi-chord Length**
Parameters	e	a	m	b
Range	-0.9, 0.4	-0.9, 0.4	0.4, 4	0.125, 0.25

The state-space form of representation casts the equations of motion that govern aeroelastic flutter in a matrix form that explicitly admits numerical eigenvalue analysis for determination of flutter speeds. Theodorsen's unsteady aerodynamic theory includes both circulatory and non-circulatory aerodynamic effects, hence it represents the most realistic model of aerodynamic forces acting on the wing.
The data comprises 625 samples of the parameters, which are location of CG, e; location of EA, a; wing structure mass, m; and semi-chord length, b.
These were selected to be influential in the dynamics of flutter and also for their easy applicability in FFNN models. The data were then split into training, validation, and testing subsets in the ratio 70:15:15, respectively, to give a robust model evaluation. The FFNN model used in this work is illustrated in Fig. 2.

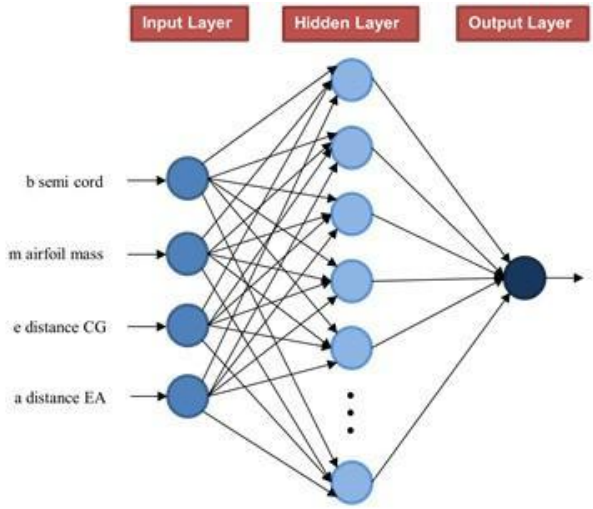

Figure 2. The Suggested Feed-Forward Neural Network Model.

2. Neural Network Architecture

The FFNN model comprises three layers which are:
Input Layer: Accepts four input parameters (e, a, m, b).
Hidden Layer: Utilizes sigmoid activation functions and contains 25 neurons, a value determined through experimental tuning.
Output Layer: Produces a single output, representing the predicted flutter speed.
The network is trained using a very powerful optimization technique for the training of neural networks: the Levenberg-Marquardt algorithm. The loss used was the Mean Squared Error (MSE) for ensuring that minimal prediction errors could be obtained from the model. It can be seen in Eq. 5 [19-21].

$$MSE = \frac{1}{n}\sum_{i=1}^{n}\left(Y_i - \hat{Y}_i\right)^2 \qquad \text{Eq. 5}$$

3. Training and Validation

In the training of the network, this iterative process was followed to continuously update the weights with the aim of minimizing the prediction error. This nonlinear relationship between aeroelastic parameters and flutter speed is learned during this training. The validation set can be used during training to monitor model performance in order to avoid

overfitting. Later, the generalization capability of the trained model was tested on unseen data. Regression coefficient R^2 was considered for measuring the correlation between predicted and actual flutter speed.

Findings

The aeroelastic analysis results and related flutter speed values are verified with the findings in the literature. The comparison between the results of this work and Conner et al.'s work is presented in the Table 3.

Table 3. Validation And Error Rates with Literature [11].

Results	Dağlı	Conner	Error Rate
Flutter Speed (m/s)	23.96	23.9	0.25%
Flutter Frequency (Hz)	6.12	6.112	0.13%
Pitching Nat. Freq. (Hz)	9.128	9.128	0%
Plunging Nat. Freq. (Hz)	19.44	19.44	0%
Flapping Nat. Freq. (Hz)	4.455	4.455	0%

The regression coefficient of the FFNN model thus trained was 0.92, which implied a very good correlation between the predicted and actual flutter speeds. The model predicted the flutter speed for different configurations of wings with very high accuracy.

FFNN predicted the flutter speed as 23.96 m/s at a frequency of 6.12 Hz. These values matched very well with numerical and experimental results, confirming the reliability of the model. This is visualized in Fig. 3 and Fig. 4.

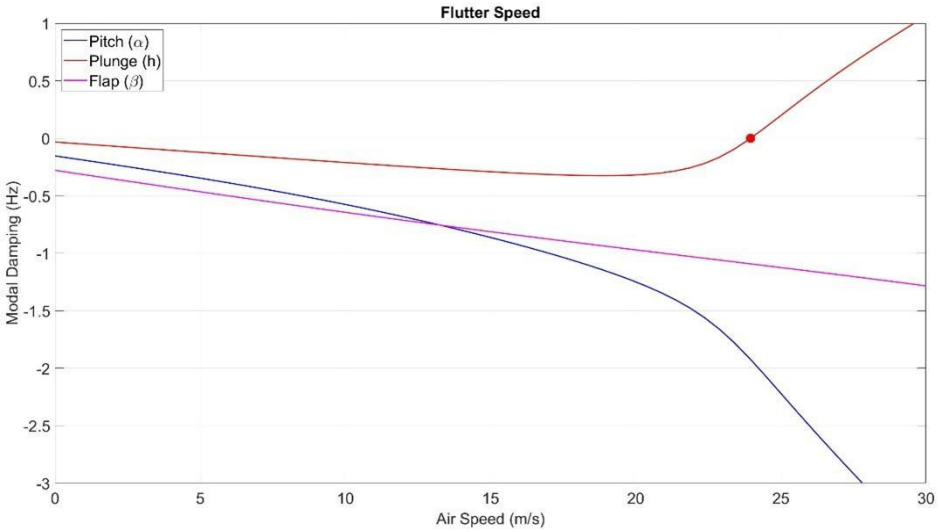

Figure 3. Flutter Speed Detection in U-G Plot.

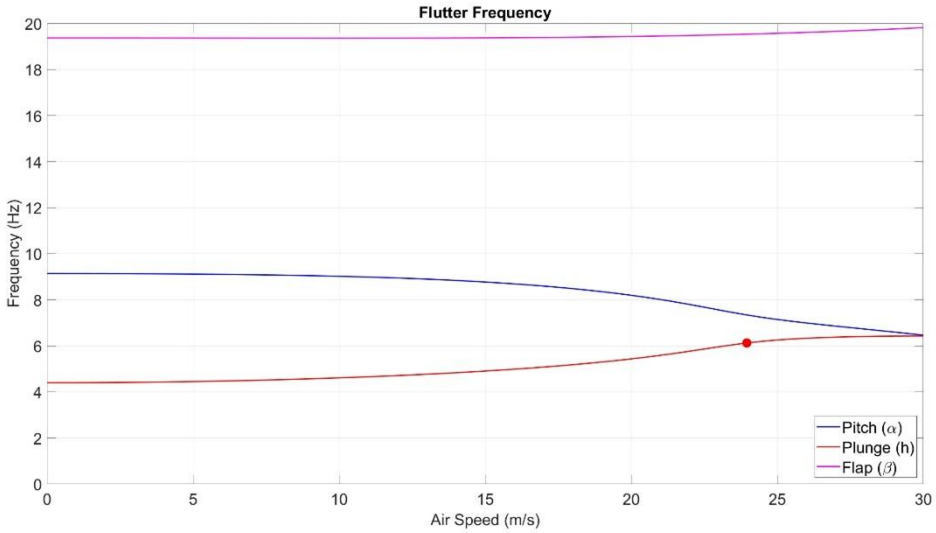

Figure 4. Flutter Frequency Detection in U-Frequency Plot.

Performance Metrics are found as:
Training Regression Value (R^2): 0.9479
Validation Regression Value (R^2): 0.8232
Testing Regression Value (R^2): 0.9043
Overall Regression Value (R^2): 0.9169
The results from the FFNN model matched previous experimental and numerical studies, thus proving its accuracy. The result for the present study predicted the flutter speed, showing good agreement with the numerical result presented by Conner et al. at 23.9 m/s, corresponding to 6.112 Hz. It is this very good agreement which confirms that the FFNN-based flutter speed prediction is an effective alternative for the conventional computational procedure since it is considerably faster and efficient. The results are illustrated in Fig. 5 which are attached.

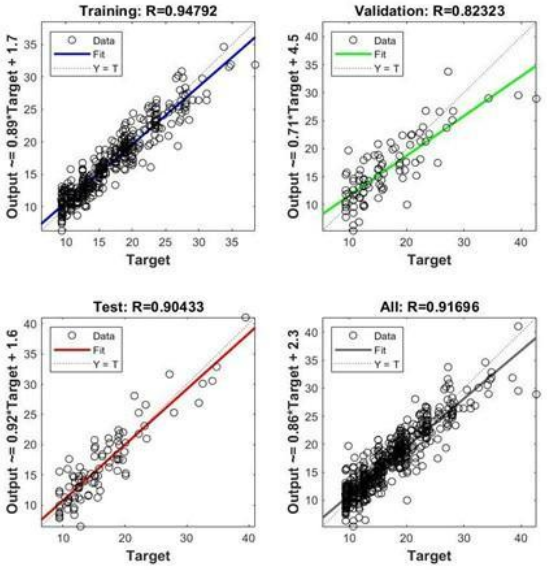

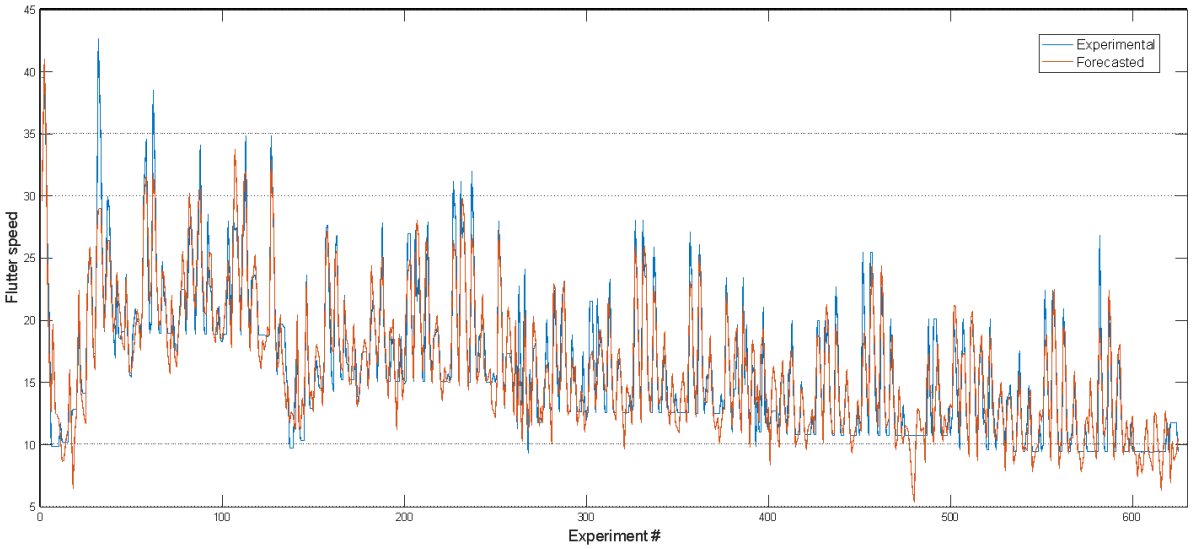

Figure 5. Comparison of Numerical and Forecasted Flutter Speed Values.

Conclusion

The research developed and validated an FFNN-based approach for the estimation of flutter speeds of aeroelastic systems. It shows the potential of machine learning in the advanced field of aerospace engineering, mainly due to reductions in computationally expensive CFD simulations and wind tunnel testing.

These results demonstrate that AI-driven approaches can significantly enhance aeroelastic analyses by giving fast and reasonably accurate predictions. This network gave a very high regression accuracy of 0.92 and thus proved to be pretty effective in estimating the flutter speed of an airfoil. The model predictions matched reasonably well with the experimental and numerical results, hence verifying their reliability. Besides, the proposed methodology here is economically viable and can be easily extended to other aeroelastic stability problems like flutter suppression and structural damping optimization.

This paper thus presents the viability of machine learning as an alternative to conventional aeroelastic analysis methods. The FFNN model was able to predict the flutter speeds successfully, hence reducing expensive and time-consuming simulations. As AI technology continues to advance, its application will become paramount in optimizing aircraft performance and safety.

References

Hodges, D., & Pierce, G. (2011). Introduction to structural dynamics and aeroelasticity. Cambridge University Press.

Dowell, E. (2015). A modern course in aeroelasticity. Springer.

Haudrich, D. P., & Pitt, D. M. (2004, April 19–22). Artificial neural network for multiple aeroelastic analysis [Conference presentation]. 45th AIAA/ASME/ASCE/AHS/ASC Structures, Structural Dynamics & Materials Conference, Palm Springs, CA.

Torregrosa, A. J., Garcia-Cueavs, L. M., Quintero, P., & Cremades, A. (2021). On the application of artificial neural network for the development of a nonlinear aeroelastic model. Aerospace Science and Technology, 115, 106845.

Natarajan, A., Inman, D. J., & Kapania, R. K. (2002, September 4–6). Dynamic aeroelastic response of adaptable airfoils using neural networks [Conference presentation]. 9th AIAA/ISSMO Symposium on Multidisciplinary Analysis and Optimization, Atlanta, GA.

Voitcu, O., & Wong, Y. S. (2003). Neural network approach for nonlinear aeroelastic analysis. Journal of Guidance, Control, and Dynamics, 26(1).

Natarajan, A., Inman, D. J., & Kapania, R. K. (2004). Analysis of time-variant aeroelastic systems using neural network. AIAA Journal, 42(9), 1933–1936.
Chen, C. H., Wu, J. C., & Chen, J. H. (2008). Prediction of flutter derivatives by artificial neural networks. Journal of Wind Engineering and Industrial Aerodynamics, 96, 1925–1937.
Theodorsen, T. (1935). General theory of aerodynamic instability and the mechanism of flutter (Report No. 496). National Advisory Committee for Aeronautics.
Edwards, J. W., & Breakwell, J. (1979). Unsteady aerodynamic modeling for arbitrary motions. AIAA Journal, 17(4), 365–374.
Conner, M. D., Tang, D. M., Dowell, E. H., & Virgin, L. N. (1997). Nonlinear behavior of a typical airfoil section with control surface free play: A numerical and experimental study. Journal of Fluids and Structures, 11(1), 89–109.
Sousa, W., & De Marqui Jr, C. (2014). Effect of pseudoelastic hysteresis of shape memory alloy springs on the aeroelastic behavior of a typical airfoil section. Journal of Intelligent Material Systems and Structures, 27(1), 1–17.
Prabhu, L., & Srinivas, J. (2014). Flutter prediction using neural networks-based hybrid optimization scheme. International Journal of Research in Aeronautical and Mechanical Engineering, 2(4), 127–137.
Torregrosa, A. J., Garcia-Cueavs, L. M., Quintero, P., & Cremades, A. (2021). On the application of artificial neural network for the development of a nonlinear aeroelastic model. Aerospace Science and Technology, 113, 106845.
Wang, Y., & Wang, Y. (2021). Flutter speed prediction by using deep learning. Advances in Mechanical Engineering, 13(11), 1–15.
Zhang, B., Han, J., & Chen, C. (2018). Nonlinear aeroelastic system identification based on neural network. Applied Sciences, 8(10), 1916.
Li, W., Gao, X., & Liu, H. (2021). Efficient prediction of transonic flutter boundaries for varying Mach number and angle of attack via LSTM network. Aerospace Science and Technology, 110, 106451.
Li, W., Laima, S., Jin, X., & Li, H. (2020). A novel long short-term memory neural-network-based self-excited force model of LCOs of nonlinear flutter for various aerodynamic configurations. Nonlinear Dynamics, 100, 2071–2087.
Chamoli, S. (2015). ANN and RSM approach for modeling and optimization of designing parameters for a V-down perforated baffle roughened rectangular channel. Alexandria Engineering Journal, 54(3), 429–446.
Hagan, M. T., Demuth, H. B., & Beale, M. H. (1995). Neural network design. PWS Publishing.
Wackerly, D., Mendenhall, W., & Scheaffer, R. L. (2008). Mathematical statistics with applications. Thomson Brooks/Cole.

Conceptual Modeling of a Multi-Axial Nonlinear Dynamic VibrationAbsorber for Helicopters

Özkan Karayiğit[a], Vedat Ziya Doğan[b], Halit Süleyman Türkmen[b], Ali Tatar[b]

[a] Istanbul Technical University, Aeronautics and Astronautics, M.Sc. Program, Türkiye
[b] Istanbul Technical University, Faculty of Aeronautics and Astronautics, Türkiye
karayigit23@itu.edu.tr

Keywords: Helicopter Fuselage Vibration Control, Multi-Axial Vibration Absorber, Nonlinear Dynamic Vibration Absorber, Optimization-Based Vibration Mitigation, Polynomial Nonlinear Stiffness Model.

Aim

Dynamic vibration absorbers (DVAs), which are an effective method for reducing vibrations caused by rotor, aerodynamic, and structural interactions in helicopters, are widely implemented in helicopter structures. DVAs are devices designed to minimize vibration amplitudes by adapting to the operating frequencies of a system. They were first introduced by Frahm [1] as a mass-spring system and later refined by Ormondroyd and Den Hartog [2], leading to their widespread use in different engineering applications. Over time, these absorbers have been further developed and integrated into various helicopter parts. In particular, bifilar and pendulum absorbers have been employed in rotor heads and blades, while fuselage-integrated vibration absorbers have demonstrated significant effectiveness. Today, DVAs continue to be widely used in many helicopter designs as highlighted in the reviews by Reichert [3] and Welsh [4]. As auxiliary mass is added to the main system, DVAs offer a practical and cost-effective solution without requiring major structural modifications.

Fuselage-integrated vibration absorbers are typically designed to operate in a single direction, predominantly targeting vertical (z-axis) vibrations. These absorbers are tuned to specific frequencies to effectively reduce structural vibrations in the fuselage. However, during dynamic flight conditions, such as maneuvers and varying aerodynamic loads, significant vibrations can also occur in the longitudinal (x-axis) direction. Additionally, conventional linear DVAs are only effective within a narrow frequency range, limiting their robustness against fluctuating excitation forces. These challenges necessitate the development of more adaptive and effective vibration control solutions.

To address these limitations, this study proposes a conceptual model for a multi-axial nonlinear DVA that can be integrated into the helicopter fuselage to mitigate vibrations in both the x and z directions. Unlike conventional linear absorbers, nonlinear DVAs can operate over a broader frequency range, enhancing vibration attenuation capabilities and adaptability to varying flight conditions. Most nonlinear vibration absorbers in the literature are modeled using various nonlinear stiffness formulations, such as polynomial, piecewise, hysteretic, and geometric nonlinearities. These different modeling approaches are discussed in detail in studies by Zheng Lu [5] and Balaji [6]. While many works, like Alsuwaiyan [7], have adopted cubic stiffness systems due to their simplicity and tunability, this study defines the absorber's stiffness characteristics as a polynomial function. This approach offers greater flexibility in shaping the force-displacement behavior, allowing for a more tailored response to varying excitation conditions. To achieve an optimal design, the polynomial coefficients of the stiffness function will be determined through an optimization process in MATLAB. This approach will enable the development of a nonlinear spring with customized stiffness properties, ensuring effective vibration mitigation across a wider frequency range.

Material and Method

In this study, a multi-axial nonlinear dynamic vibration absorber (DVA) is modeled as a two-degree-of-freedom mass-spring-damper system with nonlinear restoring forces in both the x and z directions. The nonlinear restoring forces are represented by third-degree polynomial functions, defined respectively for the x and z axes as follows:

$$f_{non,x} = a_1(x_2 - x_1)^3 + a_2(x_2 - x_1)^2 + a_3(x_2 - x_1) + a_4$$

$$f_{non,z} = b_1(z_2 - z_1)^3 + b_2(z_2 - z_1)^2 + b_3(z_2 - z_1) + b_4$$

The coefficients a_1, a_2, a_3, a_4 and b_1, b_2, b_3, $b_4$determine the force-displacement behavior of the absorber and will be optimized to maximize vibration attenuation. The excitation forces in both directions are modeled as harmonic sinusoidal loads and defined respectively for the x and z axes as follows:

$$F_x(t) = F_{0x} sin(\omega_x t - \varphi_x)$$

$$F_z(t) = F_{0z} sin(\omega_z t - \varphi_z)$$

Where F_{0x} and F_{0z} are the maximum force amplitudes, ω_x and ω_z are the excitation frequencies for x and z directions, and φ_x and φ_z represent the phase angles corresponding to these excitations, respectively. Same parameters are used for both axes to ensure the consistency of theoretical analyses and to validate the dynamic behavior of the system. The equations are numerically solved in MATLAB using the Runge-Kutta method. To compare the performance of the proposed nonlinear absorber, a conventional linear DVA model is also developed by replacing the nonlinear stiffness components with linear stiffness elements, k_{2x} and k_{2z}, in the x and z directions. The effectiveness of both models is evaluated by analyzing displacement-time responses under harmonic excitation.

Findings

The conceptual model of the multi-axial nonlinear DVA has been developed, and its analysis has been conducted using MATLAB. Additionally, results for the linear DVA have been obtained, providing a basis for comparison and further evaluation. In the preliminary analysis, the nonlinear model was constructed using unoptimized values for the coefficients, and the corresponding results were obtained. The values used for the analysis are shown in Table 1, with Figure 2 illustrating the displacement-time graph for the nonlinear model and Figure 3 comparing the initial results for both the linear and nonlinear models. Results are shown for the x direction only since the same values are used for both the x and z directions.

Conclusion

The conceptual model of the multi-axial nonlinear DVA shows promising results in mitigating helicopter vibrations in both x and z directions. The nonlinear stiffness function allows for better adaptability to varying operational conditions, enhancing the effectiveness of the absorber. Further studies will focus on optimizing the stiffness coefficients to maximize vibration suppression across a wider range of frequencies. Additionally, the proposed nonlinear DVA will be compared with existing fuselage-integrated absorbers to evaluate potential improvements in vibration mitigation. In addition, the enhanced adaptability demonstrated by the nonlinear system provides a solid foundation for future research on integrating smart control strategies. This advancement could lead to a new generation of vibration absorbers that dynamically adjust to real-time flight conditions, further improving helicopter safety and performance.

The authors would like to express their gratitude to Turkish Aerospace Industries (TUSAŞ) for providing the necessary resources and support throughout this study. Their financial and technical assistance have been instrumental in the successful completion of this study.

References

Alsuwaiyan, A. S. (2014). Design and analysis of a simple nonlinear vibration absorber. IOSR Journal of Mechanical and Civil Engineering, 11(2), 84–90.

Balaji, P. S., & Selvakumar, K. K. (2021). Applications of nonlinearity in passive vibration control: A review. Journal of Vibration Engineering & Technologies, 9, 183–213.

Frahm, H. (1911). Device for damping vibrations of bodies. U.S. Patent #989958.

Ormondroyd, J., & Den Hartog, J. P. (1928). The theory of the dynamic vibration absorber. Journal of Fluids Engineering, 49, 1-10.

Reichert, G. (1981). Helicopter vibration control—A survey. Vertica, 5(1), 1–20.
Welsh, W. A. (2018). Helicopter vibration reduction. In A. A. Baker, L. R. F. Rose, & R. Jones (Eds.), Morphing wing technologies (pp. 865–892). Elsevier.

Table 1. Parameters of the proposed nonlinear dynamic vibration absorber.

Parameter	Value	Specifications
m_1	100	Primary structure mass (kg)
m_2	2	Absorber mass (kg)
k_{1x} , k_{1z}	10^6	Stiffness of the primary structure in the x and z direction (N/m)
k_{2x} , k_{2z}	18050	Stiffness of the linear absorber in the x and z direction (N/m)
c_{1x} , c_{1z}	200	Damping coefficient of the primary structure in the x and z direction (kg/s)
c_{2x} , c_{2z}	3.8	Damping coefficient of the absorber in the x and z direction (kg/s)
ω_x , ω_z	15.12	Excitation frequency for x and z direction (Hz)
F_{0x} , F_{0z}	200	Maximum amplitude of the excitation force in the x and z direction (N)
φ_x , φ_z	0	Phase angles of the excitation force in the x and z direction (rad)
a_1 , b_1	10^6	First coefficients of the polynomial stiffness function in the x and z directions (N/m)
a_2 , a_3 , a_4	0	Other coefficients of the polynomial stiffness function in the x direction (N/m)
b_2 , b_3 , b_4	0	Other coefficients of the polynomial stiffness function in the z direction (N/m)

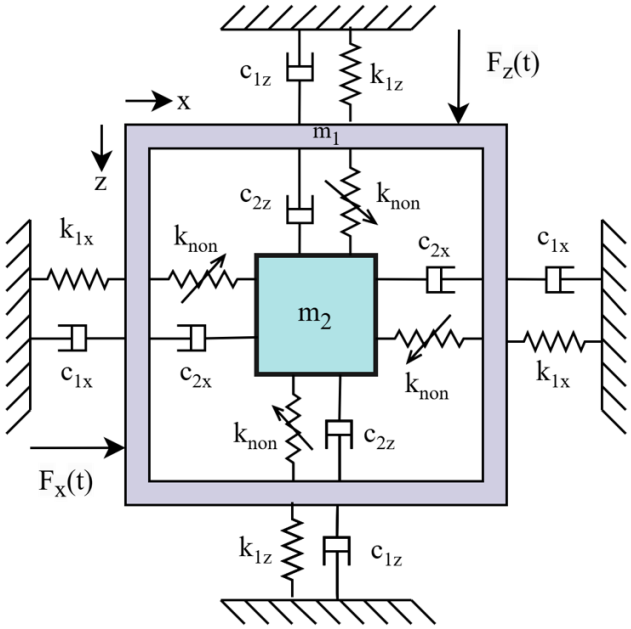

Figure 1. Schematic representation of the proposed multi-axial nonlinear dynamic vibration absorber model.

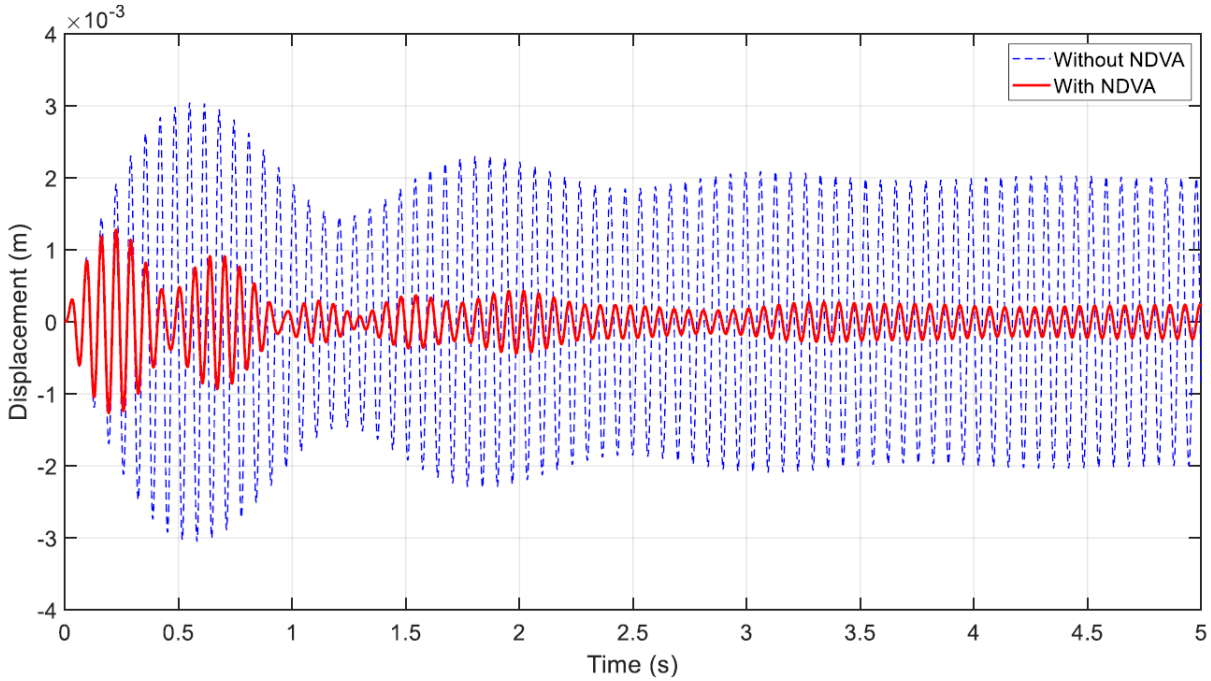

Figure 2. Time Displacement of the Main Mass in the X Direction with and without Nonlinear Dynamic Vibration Absorber (NDVA).

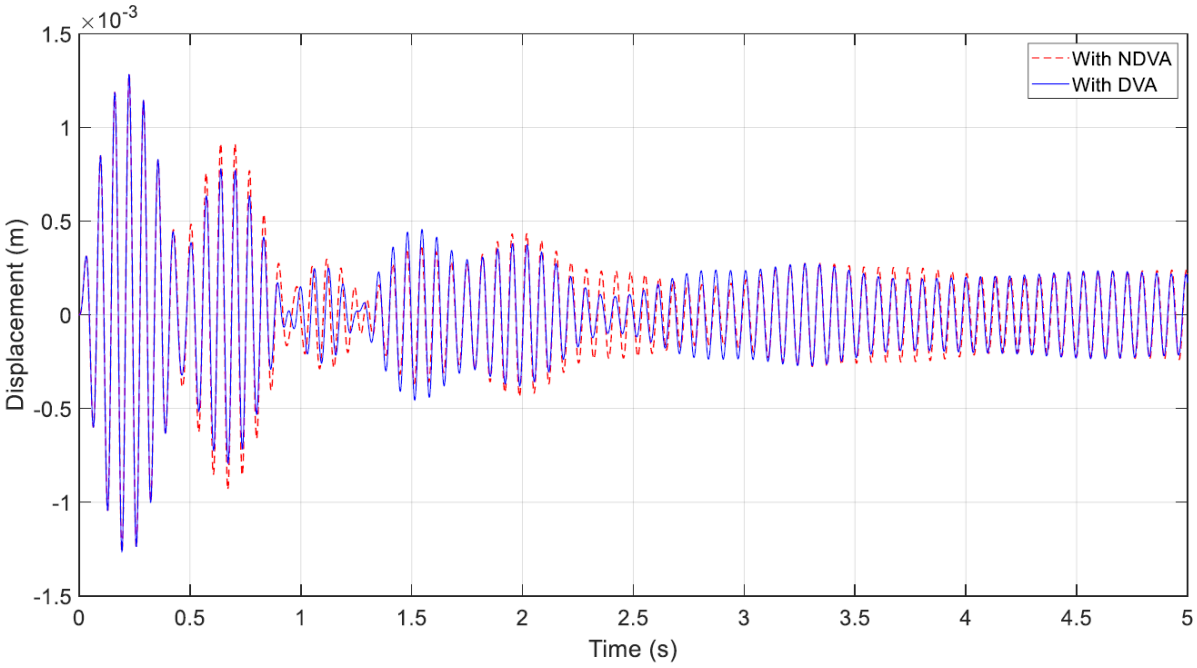

Figure 3. Time Displacement of the Main Mass in the X Direction with and without Nonlinear Dynamic Vibration Absorber (NDVA).[1]

AERONAUTICAL AND ASTRONAUTICAL ENGINEERING

Aircraft Design, Flight Dynamics And Performance

Control Systems: Adaptive, Intelligent, Digital, Optimal, Pneumatic-Hydraulic

Mechanical Vibrations And Structural Dynamics

Rotary Wing Aircraft

Spacecraft Control, Design And Performance

Theoretical, Computational And Experimental Aerodynamics And Fluid Dynamics

Theoretical, Computational And Experimental Structural Analysis And Design

A Study on Hover and Forward Flight Performance of S70A-28D (UH-60L Black Hawk) Helicopter to Obtain Cruise Chart by Using Momentum and Blade Element Momentum Theory

Mehmet Tayfun Ülbegi[a], Özge Özdemir[b]

[a] Turkish National Defence University, Department of Aerospace Engineering, Master of Science of Aeronautical Engineering Program, Türkiye
[b] Istanbul Technical University, Faculty of Aeronautics and Astronautics, Department of Astronautical Engineering, Türkiye
m_tayfun_69@yahoo.com

Keywords: Helicopter, S70A-28D (UH-60L Black Hawk) Main Rotor Efficiency, Cruise Chart, Momentum Theory, Blade Element Theory

Aim

The aim of this study is:

- To obtain Sea Level and +15°C Cruise Chart of S70A-28D (UH-60L,Black Hawk) Helicopter by using Momentum and Blade Element Momentum Theory for hover and forward flight conditions for 23.500, 22.000, 20.000, 18.000, 16.000, 14.000 and 13.000 pound Take off Gross Weight [1] and
- To compare the manufacture's data with the obtained.

What is Cruise Chart

The chart gives:

- The fuel flow rate and fuel consumption rate per hour,
- True airspeed for various combinations of pressure altitude, temperature, and engine percent power,

Speed of;

- Maximum endurance and best rate of climb, where L/D is maximum.
- Maximum range speed, which provides the longest range during cruise, where fuel consumption is minimum, allowing an aircraft to travel the farthest possible distance on a given amount of fuel when the engine is operating at its most fuel-efficient point,
- Maximum level flight, which refers to the maximum airspeed while maintaining level flight at a specific altitude and configuration. It represents the highest speed at which the aircraft's thrust equals its drag in a steady, level flight condition [2].

Material and Method

In order to obtain the sea level +15°C cruise chart of the manufacturer's S70A-28D (UH-60L, Black Hawk) Helicopter, interpolations of;

- The temperature of the +10°C and +20°C cruise charts,
- Max level speed, max range speed,
- Max level speed, max endurance and rate of clımb, lift-to-drag ratio L/D maxımum (Figure 4),
- Torque need to be made interpolated (Figure 1) [2].

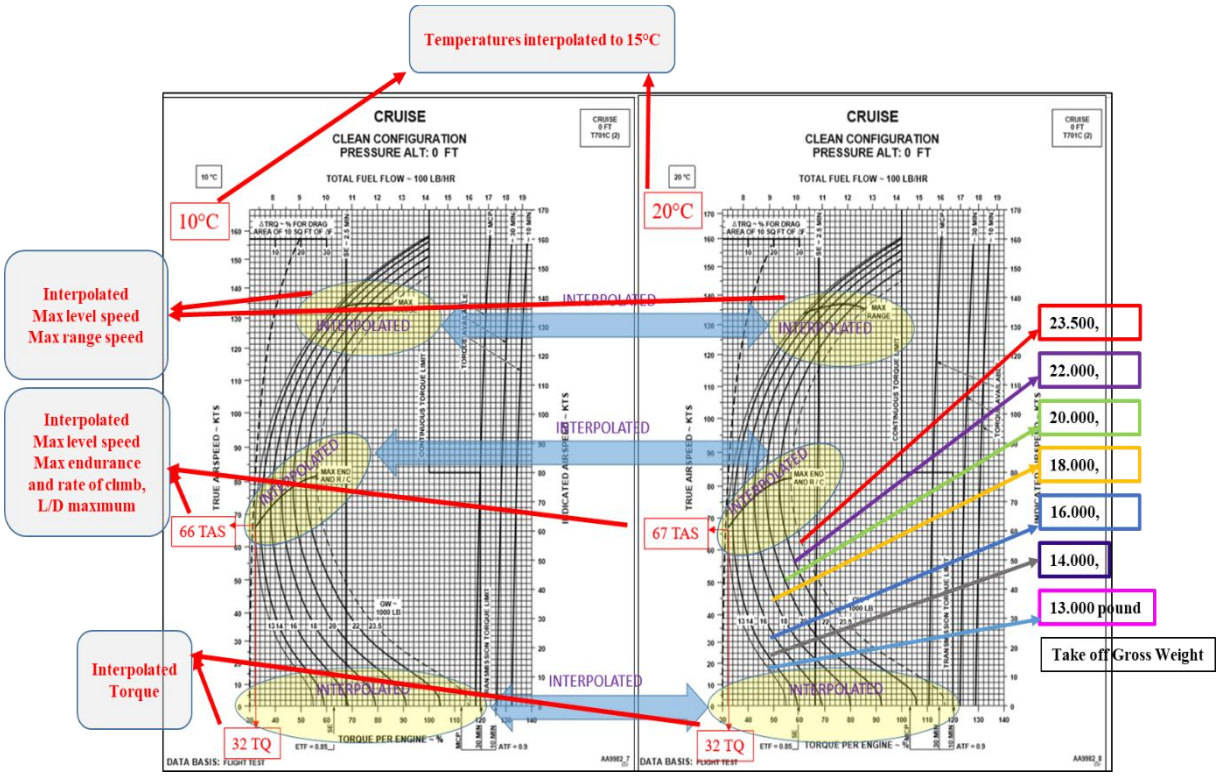

Figure 1. Cruise chart [1].

Interpolated data was prepared in advance and placed in the comparison table. At the end of the study, the obtained data will be placed in the comparison table and the differences between the two data will be evaluated. Accordingly, it will be determined how close we are to the manufacture's cruise chart (Table 1).

Table 1. Comparison table.

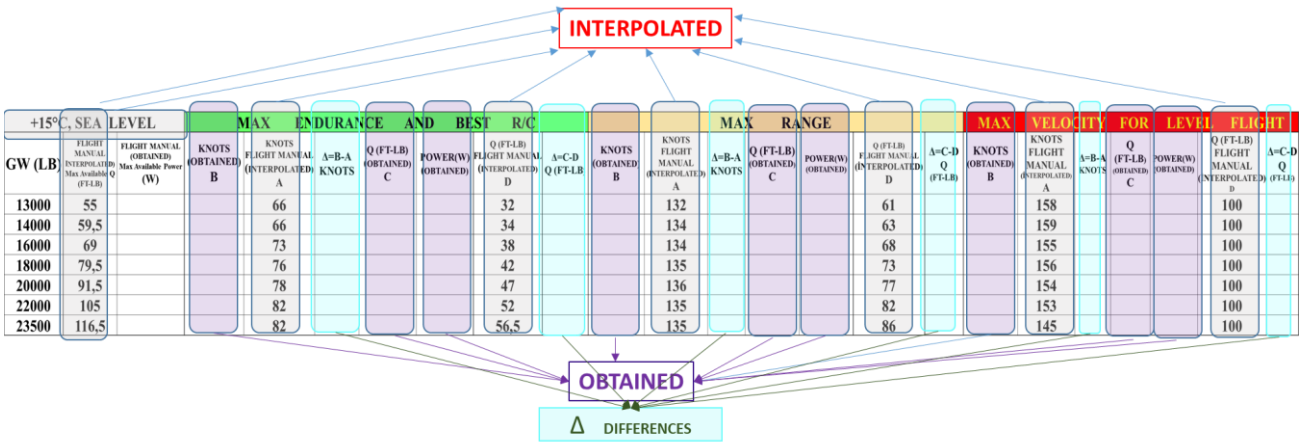

+15°C, SEA LEVEL			MAX ENDURANCE AND BEST R/C							MAX RANGE						MAX VELOCITY FOR LEVEL FLIGHT					
GW (LB)	FLIGHT MANUAL INTERPOLATED Max Available Q (FT-LB)	FLIGHT MANUAL (OBTAINED) Max Available Power (W)	KNOTS (OBTAINED) B	KNOTS FLIGHT MANUAL (INTERPOLATED) A	Δ=B-A KNOTS	Q (FT-LB) (OBTAINED) C	POWER(W) (OBTAINED)	Q (FT-LB) FLIGHT MANUAL (INTERPOLATED) D	Δ=C-D Q (FT-LB)	KNOTS (OBTAINED) B	KNOTS FLIGHT MANUAL (INTERPOLATED) A	Δ=B-A KNOTS	Q (FT-LB) (OBTAINED) C	POWER(W) (OBTAINED)	Q (FT-LB) FLIGHT MANUAL (INTERPOLATED) D	Δ=C-D Q (FT-LB)	KNOTS (OBTAINED) B	KNOTS FLIGHT MANUAL (INTERPOLATED) A	Δ=B-A KNOTS	Q (FT-LB) (OBTAINED) C	POWER(W) (OBTAINED)	Q (FT-LB) FLIGHT MANUAL (INTERPOLATED) D	Δ=C-D Q (FT-LB)
13000	55			66				32			132				61			158				100	
14000	59,5			66				34			134				63			159				100	
16000	69			73				38			134				68			155				100	
18000	79,5			76				42			135				73			156				100	
20000	91,5			78				47			136				77			154				100	
22000	105			82				52			135				82			153				100	
23500	116,5			82				56,5			135				86			145				100	

Momentum Theory in Hover

Momentum theory assumes;
- A smooth,
- Incompressible,
- With zero vorticity across the rotor disk.

It is based on three basic systems of fluid mechanics;
- Conservation of mass,
- Conservation of momentum,
- Conservation of energy.

Momentum theory accounts for;
- Thrust generation,
- Induced velocity,
- Mass flow rate,
- Power required,
- Energy conservation in actuator rotor disc.

The theory aims to **identify three unknowns**:
- Inflow velocity, λ,
- Wake,w, downstream velocity in the far field below the rotor disk,
- The fully contracted flow area, A4 [3][4][5].

To **summarize ;**
- The Momentum theory assists in the preliminary evaluation of a rotor and helps in the comparison of various rotors. However, the theory does not help directly with the design of a rotor.

The hovering efficiency of the rotor is defined as:

$$\text{Figure of Merit} = \frac{(\text{Minimum Power Required to Hover (ideal power)}(P_i = Tv_i)}{(\text{Actual Power in Hover } (P = \rho A\,(\Omega R)^3\ C_p)} \quad (2.1)$$

- The downwash in the far wake is twice the induced velocity at the rotor disk, $\mathbf{w}=\mathbf{2}v_i$,
- Momentum theory gives an expression for induced velocity at the rotor disk,
- It also gives an expression for consumed by a rotor of specified dimensions.

The flow characteristics around a rotor in hover are illustrated in Figure 1 and assumed pressure jump across rotor disk is uniform. Figure 1 summarizes momentum theory in hover. There are four stations, which are:
- Station 1: far feld upstream,
- Station 2: actuator rotor disc, rotor disc area (πR^2),where R radius of blade,
- Station 3: below the rotor disc,
- Station 4: far-field downstream.

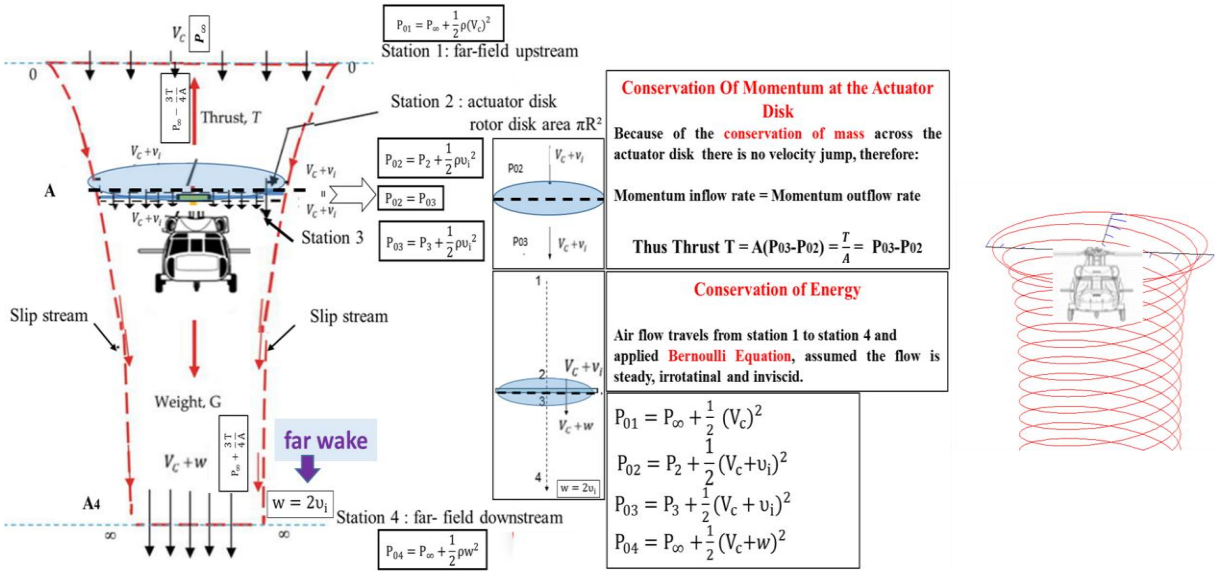

Figure 2. Air flow around rotor actuator in hover [3] [11].

Blade Element Momentum Theory in Hover

Blade element theory includes effects of rotor RPM and blade surface area. It examines the aerodynamic characteristics of an element of the rotor blade by utilizing methods that close mimic airfoil theory. In some cases, it is helpful to combine it with momentum theory in order to reach the necessary equations. Momentum theory and blade element theory are only adequate for conceptual and preliminary design and not for advanced blade design [3][4][5].

Momentum Theory limitations are;
- It provides no information on how rotor blades should be designed to produce a given thrust
- It does not account for
  - rotor rpm, number of blades, nor blade area,
  - airfoil characteristics (lift, drag, angle of zero lift),
  - blade planform (taper, sweep, root cut-out),
  - blade twist distribution,
  - compressibility effect.
- Profile – drag losses are ignored,
- Blade Element Theory provide ways to reduce these limitations.

Drawbacks of Blade Element Theory [5] [6]:
- It assumes that the induced velocity v_i is uniform,
- The predicted power is sometimes empirically corrected for these losses by using K_h=1.15,
- It does not handle tip losses,
- It does not account for swirl losses.

Momentum Theory in Forward Flight

The assumptions are:
- The rotor induced power in forward flight is obtained by a momentum theory,
- A uniformly loaded actuator disk is used to represent the rotor,
- In a forward flight such an actuator disk can be viewed as with a forward tilted, α, circular wing,

- Actuator disk operating at velocity resultant velocity,V_R with the angle of attack α between the free stream velocity and the rotor disk [1] (Figure 3).

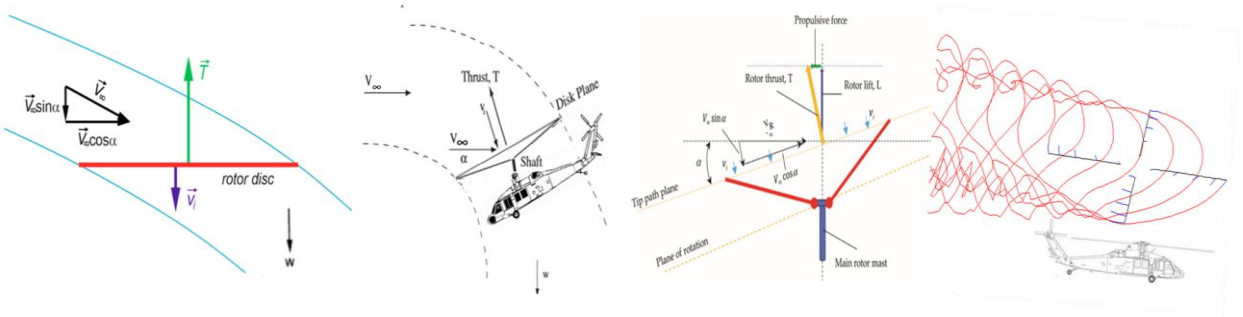

Figure 3. Forward flight [1]

Blade Element Momentum Theory in Forward Flight

Main Rotor Power Required:
The total power required at the rotor, P, can be expressed by the equation (Figure 4);

$$P = P_i + P_o + P_p + P_{tr} \quad (2.2)$$

Where

P_i = induced power,

P_o = profile power required to overcome viscous losses at the rotor,

P_p = parasitic power required to overcome the drag of the helicopter profile,

P_{tr} = tail rotor thrust [7].

$P_i = K_f T v_i$ Where $K_f = 1.2$,

$$P_o = \frac{\sigma C_{d_0}}{8} \rho A(\Omega R)^3 (1 + 4.65\,\mu^2)$$

$$P_p = \frac{1}{2}\rho f_v (V_V)^3 + \frac{1}{2}\rho f_f (V_f)^3 \quad (2.3)$$

$$T_{tr} = \frac{(P_i + P_0 + P_p)_{main\ rotor}}{\Omega_{mr}\, l_{tr}} \quad (2.4)$$

Where σ is the solidity, C_{d_0} is coefficient of zero-drag, μ is the advance ratio, f_v flat plate area in vertical is flight and f_f is flat area in forward flight [8], V_V is vertical velocity, V_f is vertical velocity, Ω is the angular velocity of the main rotor and l_{tr} is the tail rotor moment arm about the main rotor shaft.

$$P_{tr} = P_{i_{tr}} + P_{o_{tr}} + P_{p_{tr}} \quad (2.5)$$

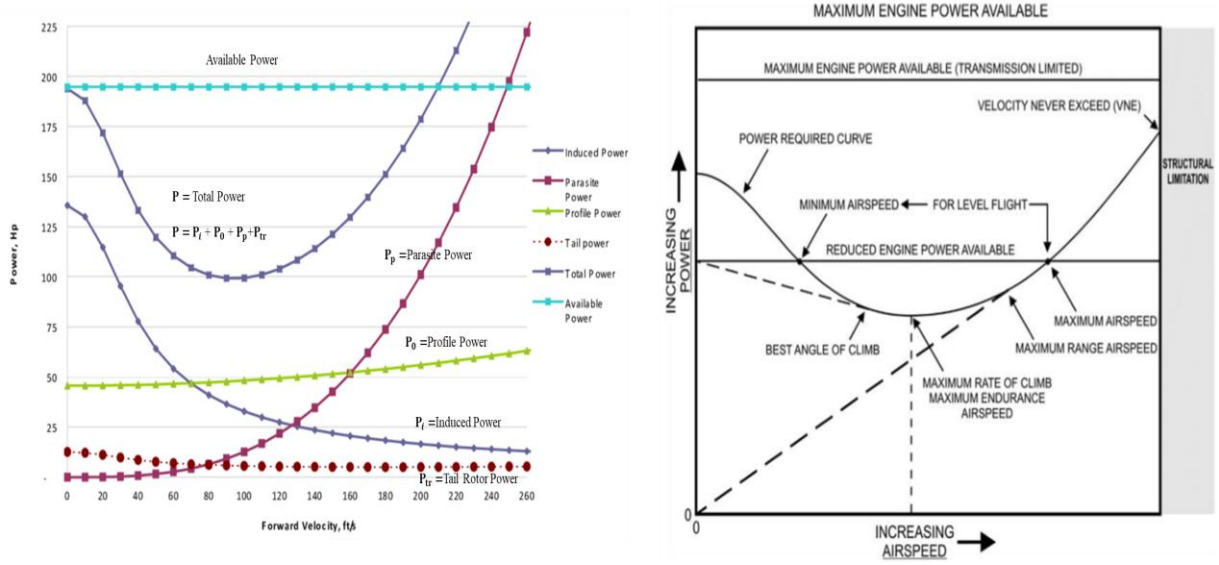

Figure 4. Main rotor power required in forward flight [9] [10]

Findings

The findings are divided into two sections, hover and forward flights.

Hover

Hover findings are shown in Table 2.

Table 2. Hover calculation of main and tail rotor [14, 15] Calculation of the required power of main rotor

S70A-28D (Black Hawk, UH-60L) Helicopter, Main Rotor								
C_{d0}	Nb	c (m)	σ=(Nb c)/πR	A (m²)=πR²	Ω (rad/s)	R (m)	Vtip (m/s)=ΩR	T=TOGW (lb)
0,0092	4	0,5334	0,083182812	209,6285362	27	8,16864	220,55328	23500

SEA LEVEL				
	$D_0 = C_{d0} 2\rho A(\Omega R)^2$	$P_i = \frac{T^{3/2}}{2\rho_0 A} = Tv_i$	$P_0 = \frac{\sigma C_{d0}}{8}\rho A(\Omega R)^3$	$P_{main}=P_i + P_0$
C_{d0}	D_0 (N)	P_i (kW)	P_0 (kW)	P_{main} (kW)
0,0092	57460,75972	1715,906078	263,5472514	1979,45333

SEA LEVEL			
$C_{T_0} = \frac{T_0}{\rho_0(\Omega R)^2 A}$	$C_{P_{i0}} = \frac{K_h C_T^{\frac{3}{2}}}{\sqrt{2}}$	$C_{P_0} = \frac{\sigma C_{d_0}}{8}$	$C_{P_{main}} = C_{P_i} + C_{P_0}$
C_{T_0}	C_{Pi_0}	C_{P_0}	$C_{P_{main}}$
0,008371226	0,000622826	9,56602E-05	0,000718486

Table 2. Hover calculation of main and tail rotor (continue)

Calculation of the Tail Thrust and the required power and power coefficient of the tail rotor

S70A-28D (Black Hawk, UH-60L) Helicopter, Tail Rotor					
Nb_tail	c_tail (m)	σ_tail=(Nb c)/πR	A_tail (m²)	Ω_tail (rad/s)	R_tail (m)
4	0,246888	0,187513022	8,828891762	127	1,6764

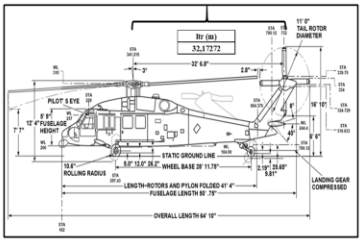

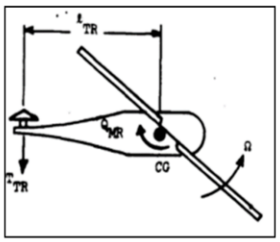

tail rotor moment arm				
feet to	m	inch to	m	ltr (m)
32	9,7536	6,8	0,17272	**9,92632**

$$Q_{main_h0} = \frac{P_{main_h0}}{\Omega_main} \qquad T_{tail_0} = \frac{Q_main_h_0}{l_tr}$$

SEA LEVEL	Q (Nm)	
Q_main_h_0	$Q = C_Q \rho A R(\Omega R)^2$	
73313,08629	73313,08629	

SEA LEVEL	Q (Nm)
Q_main_h_0	T_tail_0 (N)
73313,08629	7385,726663

SEA LEVEL						
$P_{i_tail_0} = \frac{T_{tail_0}^{3/2}}{\sqrt{2\rho_0 A}}$	$P_{0_tail} = \frac{\sigma_{tail} C_{d0_tail}}{8} \rho_0 A_{tail} (\Omega R)_{tail}^3$	$P_{tail_0} = P_{i_tail_0} + P_{0_tail}$	$C_{T_0_tail} = \frac{T_{tail}}{\rho_0 A_{tail} (\Omega R)_{tail}^2}$	$C_{P_{i_tail_0}} = \frac{K_h C_{T_tail}^{3/2}}{\sqrt{2}}$	$C_{P_{0_{tail_0}}} = \frac{\sigma C_{d_{0_tail_0}}}{8}$	$C_{P_{tail_0}} = C_{P_{i_{tail_0}}} + C_{P_{0_{tail_0}}}$
$P_{i_tail_0}$(W)	P_{0_tail} (W)	P_{tail_0} (W)	C_{T_0}	$C_{P_{i_tail_0}}$	$C_{P_{0_{tail_0}}}$	$C_{P_{tail_0}}$
156946,4686	22506,89959	179453,3682	0,015034847	0,001499103	0,00021564	0,001714743

Calculation of the excess power $\Delta P_0 = P_{available} - [(P_{main})_h + (P_{tail})_h$

SEA LEVEL			
$P_{available}$(W)	$(P_{main})_h$ (W)	$(P_{tail})_h$ (W)	ΔP_0 (W)
2106900,418	1979453,33	179453,3682	-52006,27954

Calculation of the figure of merit $FOM = \frac{P_{i_main} + P_{i_tail}}{P_{main} + P_{tail}}$

SEA LEVEL				
P_{i_main} (kW)	P_{i_tail} (kW)	P_{tail} (kW)	P_{main} (kW)	FOM
1715,906078	156,9464686	179,4533682	1979,45333	**0,867500457**

Effect Altitude in Hover (SEA LEVEL)		
Altitude	**(m)**	**Sea Level**
Air density	**(kg/m³)**	**1,225**
Available power	**(W)**	**2106900,418**
Required induced power (main rotor)	**(W)**	**1715906,078**
Required profile power (main rotor)	**(W)**	**263547,2514**
Required induced power (tail rotor)	**(W)**	**156946,4686**
Required profile power (tail rotor)	**(W)**	**22506,89959**
Excess power	**(W)**	**-52006,27954**
Figure of Merit		**0,867500457**
Q_main	**(Nm)**	**73313,08629**
Q_tr	**(Nm)**	**7385,726663**

Forward Flight

The advance (μ) and inflow ratio (λ), calculated, are used for non-dimensionalized forward flight power coefficient calculation to obtain proper power curved diagram, otherwise it is impossible to achieve cruise chart. The curved diagram and iterations obtained are shown in Table 3.

Table 3. Advance ratio iteration

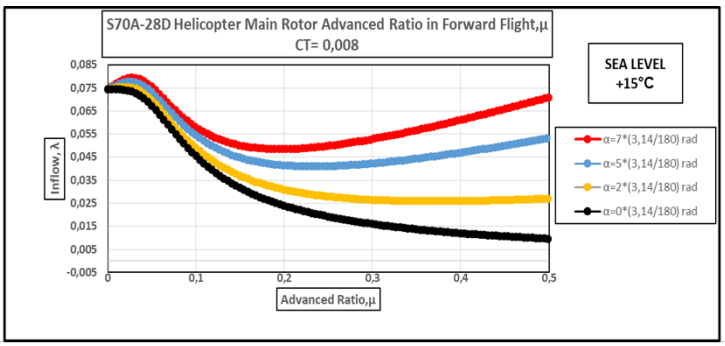

S70A-28D (Black Hawk, UH-60L) Helicopter

ρ=	1,225	kg/m³			
T=MTGW=	23500	lb/pound	10659,42	kg	104568,9 T (N, kg m/s²)
Ω=	27	rad/s			
R=	8,16864	m			
A=π*R²=	209,6285	m²			
Vtip=Ω*R=	723,6	m/s			

$$CT = \frac{T}{A*\rho*Vtip^2} = 0{,}008368$$

$$\mu = \frac{V\infty \cos\alpha}{\Omega R} \qquad v_i = \frac{\frac{T}{2\rho A}}{\sqrt{(V_\infty \cos\alpha)^2 + (V_\infty \sin\alpha + v_i)^2}} = \frac{v_h^2}{\sqrt{(V_\infty \cos\alpha)^2 + (V_\infty \sin\alpha + v_i)^2}}$$

$$\lambda_i = \frac{V_\infty \sin\alpha + v_i}{R\Omega} \qquad \lambda_\mu = \mu \tan\alpha + \lambda_i \qquad \lambda_i = \mu \tan\alpha + \frac{\kappa_f C_T/2}{\sqrt{\mu^2 + \lambda_i^2}}$$

ITERATION	A (m²)	ρ (kg/m³)	T (N, kg m/s²)	α=7*(3,14/180) rad	V∞ (m/s)	R(m)	Ω rad/s	Kf	CT	Advanced Ratio,μ	vi	λi	λi	Inflow Ratio,λi
1	209,6285362	1,225	104568,917	0,122111111	0	8,16864	27	1,15	0,008368	0	14,268984	0,064696314	0,064696314	0,074375117
2	209,6285362	1,225	104568,917	0,122111111	1	8,16864	27	1,15	0,008368	0,00450029	14,114675	0,185804537	0,18635682	0,075555293
3	209,6285362	1,225	104568,917	0,122111111	2	8,16864	27	1,15	0,008368	0,00900058	13,900025	0,30663917	0,307743736	0,076686997
4	209,6285362	1,225	104568,917	0,122111111	3	8,16864	27	1,15	0,008368	0,01350087	13,633337	0,427237863	0,428894713	0,077706888
380	209,6285362	1,225	104568,917	0,122111111	362	8,16864	27	1,15	0,008368	1,629104943	0,5593304	44,09698436	44,29691087	0,202880154

By using the total 360 of iteration, power required curves are obtained for the take-off gross weight of between 23.500 and 13.000 pounds (Table 4).

Table 4. Power required curves

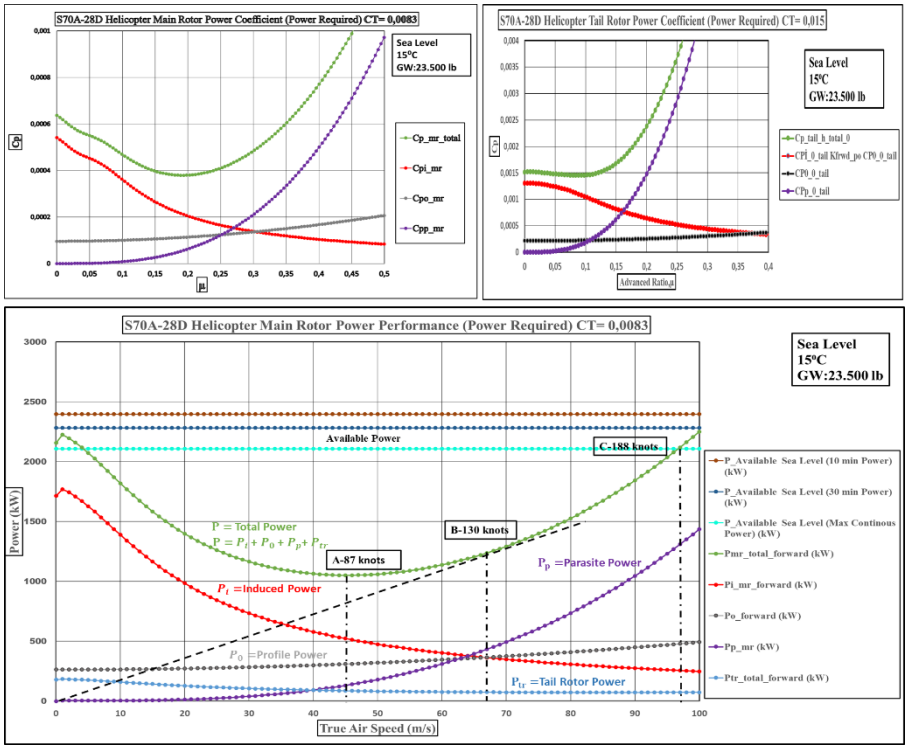

The power required obtained for each the take-off gross weight of between 23.500 and 13.000 pounds are combined in one TRUE AIRSPEED versus POWER (kW) and then it is converted by interpolating into TRUE AIRSPEED versus TORQUE PER ENGINE (%Q), which is percent system in the cockpit (Table 5).

Table 5. Cruise chart obtained

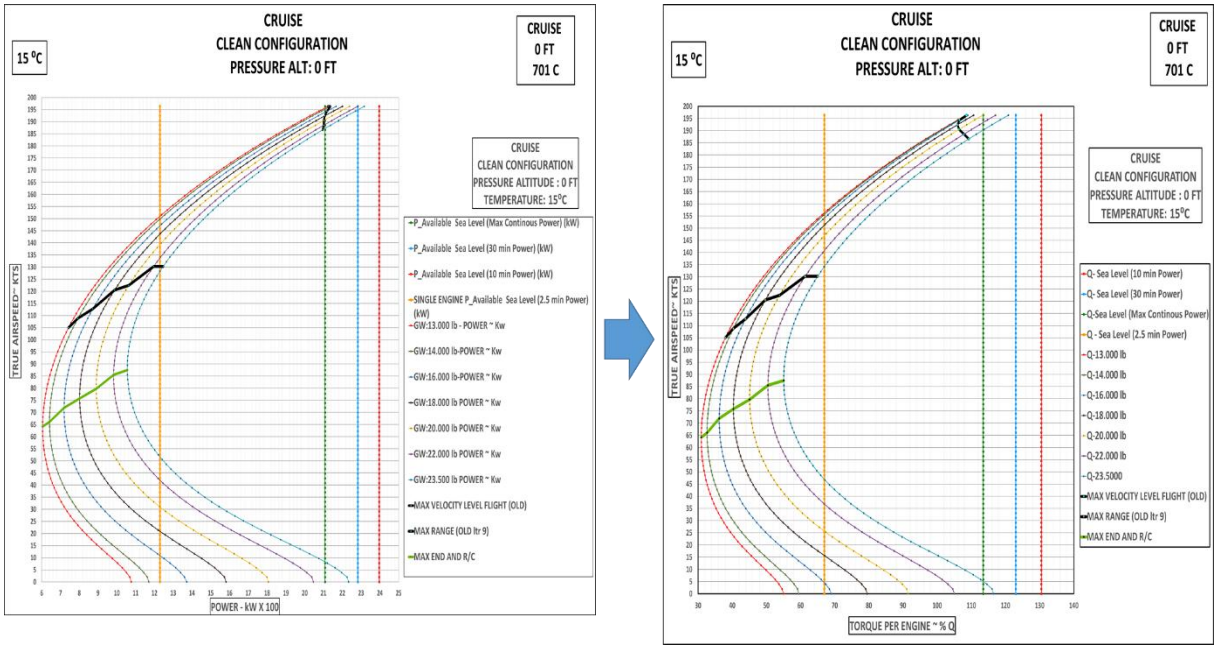

The obtained,

- Max level speed, max range speed,
- Max level speed, max endurance and rate of climb, lift-to-drag ratio L/D maxımum,
- Torques are put into excel sheet (Table 1).

Table 1. Comparison table

+15°C, SEA LEVEL			MAX ENDURANCE AND BEST R/C							MAX RANGE							MAX VELOCITY FOR LEVEL FLIGHT						
GW (LB)	FLIGHT MANUAL INTERPOLATED Max.Available Q (FT-LB)	FLIGHT MANUAL (OBTAINED) Max.Available Power (W)	KNOTS (OBTAINED) B	KNOTS FLIGHT MANUAL (INTERPOLATED) A	Δ=B-A KNOTS	Q (FT-LB) (OBTAINED) C	POWER(W) (OBTAINED)	Q (FT-LB) FLIGHT MANUAL (INTERPOLATED) D	Δ=C-D Q (FT-LB)	KNOTS (OBTAINED) B	KNOTS FLIGHT MANUAL (INTERPOLATED) A	Δ=B-A KNOTS	Q (FT-LB) (OBTAINED) C	POWER(W) (OBTAINED)	Q (FT-LB) FLIGHT MANUAL (INTERPOLATED) D	Δ=C-D Q(FT-LB)	KNOTS (OBTAINED) B	KNOTS FLIGHT MANUAL (INTERPOLATED) A	Δ=B-A KNOTS	Q (FT-LB) (OBTAINED) C	POWER(W) (OBTAINED)	Q (FT-LB) FLIGHT MANUAL (INTERPOLATED) D	Δ=C-D Q (FT-LB)
13000	55	1076,489	64,1	66	-2	30,9	605	32	-1,1	105	132	-27	37,96	743	61	-23	196,3	158	38	108,49	2123,4	100	8,49
14000	59,5	1170,162	66	66	0	32,7	642	34	0	109	134	-25	40,33	793,2	63	-23	196,3	159	37	108,65	2136,8	100	8,65
16000	69	1371,867	71,9	73	-1	36,2	719	38	-2	113	134	-21	43,87	872,2	68	-24	194,4	155	39	106,58	2119	100	6,58
18000	79,5	1581,011	75,8	76	-0	40,3	802	42	-2	121	135	-14	49,68	988	73	-23	192,4	156	36	105,95	2107	100	5,95
20000	91,5	1806,986	79,7	78	1,7	45,1	890	47	-2	122	136	-14	53,87	1064	77	-23	190,5	154	36	106,39	2101	100	6,39
22000	105	2045,954	85,5	82	3,5	50,5	983	52	0	130	135	-4,8	61,36	1196	82	-21	188,6	153	36	107,83	2101,2	100	7,83
23500	116,5	2233,446	87,5	82	5,5	55,1	1056	56,5	-1,4	130	135	-4,8	65,03	1247	86	-21	186,6	145	42	109,27	2094,9	100	9,27

V∞ (knots)	Advanced Ratio,μ
64,14687	0,148509567
66,09071	0,153009857
68,03456	0,157510146
69,9784	0,162010436
71,92225	0,166510726
73,86609	0,171011016
75,80994	0,175511306
77,75378	0,180011596
79,69762	0,184511886
81,64147	0,189012176
83,58531	0,193512466
85,52916	0,198012756
87,473	0,202513045

Conclusion

It can be seen as the forward speed increases from hover, the power initially decreases up to a forward speed of about μ = 0.14 - 0.2, which is between 64 and 88 knots (between 23.500 and 13.000 lb.) on the cruise chart referring mainly to the velocity of best endurance and rate of climb section, which represents the maximum L/D point and then the power increases drastically with forward speed.

The initial decrease in power requirement is mainly due to the reduction in induced flow through the main rotor as the helicopter increases its speed from hover.

As the speed increases for max range velocity and max velocity for level flight, the parasite drag power of the helicopter, $P_p = \frac{1}{2}\rho\, f_v(V_V)^3 + \frac{1}{2}\rho\, f_f(V_f)^3$ increases in cubic power of forward speed and the differences between findings and flight manual's gaps gets bigger.

The accuracy of this study is valid for lower speed and the data obtained can give an idea for conceptual and preliminary design process.

For more accurate output and solutions, there should be a thorough analysis of the underlying data, careful calibration of the models used, and the use of more sophisticated software tools to account for all relevant variables and complexities during test flight phase.

The C_{d0} value was used in calculating P_0, $P_o = \frac{\sigma C_{d_0}}{8}\rho\, A(\Omega R)^3\,(1 + 4.65\,\mu^2)$ for each TOGW. If the C_{d0} value, which should be calculated for the blade element segments according to blade element momentum theory, was used instead, the μ and V_∞ (knots) values would be lower than the delta value at forward speeds.

For speeds above 60 knots, a combination of momentum and blade element theory generally offers a sufficiently accurate foundation for routine engineering practice. This accuracy is enhanced when performance predictions made using this approach are validated with flight test results or compared with more precise theoretical methods, such as those based on vortex theories [12].

Therefore for the future study to obtain more precise data for max range and max velocity for level flight combined blade element momentum should be applied for each segment of the blades with accurate tip losses model.

References

Chopra, I., & Datta, A. (2011). Helicopter dynamics, ENAE,633, pp.10-16,71.
Command, N. A. T. (2014). Flight Training Instruction. Texas: Nas Corpus Christi. Constantin, pp 1-34.
Davis, J. (2021, April 5). Helicopter controls. Retrieved from
Url-4 https://www.spinningwing.com/ date retrieved 01.05.2025.
Ibrahim, A. A. S., & Jaafar, M. N. M. (2008). Power estimation for four seater helicopter. Jurnal Mekanikal.Mekanikal.
Introduction to Helicopter Aerodynamics TH-57, Naval Air Traning Command, 2022, pp. 9-10.
Keys, C. N., & Stephniewski, W. Z. (1979). Rotary-wing aerodynamics. Volume 2: Performance prediction of helicopters (No. NASA-CR-3083), pp 78.
Layton, D. M. (1984). Helicopter Performance. Matrix Publishers, Incorporated, pp 137.
Leishman, G. J. (2006). Principles of Helicopter Aerodynamics with CD Extra. Cambridge University Press, pp. 55-169,189-194, 214,212-240, 495.
Leishman, G. J. (2022). Helicopters & Vertical Flight. In Introduction to Aerospace Flight Vehicles.
Url-1 https://doi.org/10.15394/eaglepub.2022.1066.9, date retrieved 01.05.2025.
Sankar,L., 'Hover Performance Prediction Methods',
Url-2 https://www.sankar.gatech.edu/?q=rotoraero,
Url-3 https://www.sankar.gatech.edu/sites/default/files/Actuator_Disk_Model.pdf, date retrieved 01.05.2025.
TM 1-70-28D-10, (2004). Operators Manual for Sikorsky S70-A Helicopter 28D Glass Cockpit Helicopter. pp 7-31,7-32, 2-6,2-8,2-80.
UH-60A/L Blackhawk Performance Planning Card DA Form 5703- R, Version 1.0, November 2003., pp 43-52.

AERONAUTICAL AND ASTRONAUTICAL ENGINEERING

Aircraft Design, Flight Dynamics And Performance

Control Systems: Adaptive, Intelligent, Digital, Optimal, Pneumatic-Hydraulic

Mechanical Vibrations And Structural Dynamics

Rotary Wing Aircraft

Spacecraft Control, Design And Performance

Theoretical, Computational And Experimental Aerodynamics And Fluid Dynamics

Theoretical, Computational And Experimental Structural Analysis And Design

Liquid Propellant Rocket Engine Performance Sensitivity Analysis

Turan Çopuroğlu[a], Fırat Oğuz Edis[a]

[a] Istanbul Technical University, Department of Aeronautical and Astronautical Engineering, Türkiye
copuroglut16@itu.edu.tr

Keywords: Engine Performance Fine-Tuning, Liquid Propellant Rocket Engine, Mixture Ratio Control.

Aim

Liquid propellant rocket engine is designed to ensure the stringent performance launch vehicle system requirement. In initial stages of project, there are a lot of uncertainties belongs to subsystem component designs. Variation in fluid thermophysical and thermodynamical properties and component manufacturing tolerances change engine performance outputs. Even small deviations in engine performance may cause significant deviation of launch vehicle operation. Engine performance map must be remained within the acceptable launch vehicle system requirement envelope. Otherwise, launch vehicle cannot perform success mission. For this reason, uncertainties regarding to engine sub-component performance must be considered at the engine initial design stage [1].

Analytical methods used in component design processes, computational fluid dynamic analysis results and manufacturing tolerances causes errors and differences in pre-determined performance. Therefore, each liquid propellant rocket engine subsystem has its performance margins individually.

In the early stages of liquid propellant rocket engine system design, all subsystem margins have to be considered to determine and optimize key parameters which have crucial impact on the engine performance. This enables to more manageable design process with controlled uncertainty as project progresses. Thus, the engine performance fine-tuning can be performed more robust and reliable to be met more precisely in the development stages.

In this study, Gas-generator cycle rocket engine is focused on. Gas-generator cycle is an open cycle rocket engine. The gas-generator cycle rocket engine consists of thrust chamber, feed system, turbopump, gas generator, valves and orifices [2].

For on-design conditions of engine, nominal inputs lead to the expected engine performance output. In order to examine key parameters changing effects on the engine performance, three parameters variations on performance dispersion were investigated. Pump efficiency, turbine efficiency, valve flow coefficient variations were examined. In these parameters, variation effects are investigated to analyze on chamber pressure, gas generator pressure, turbine inlet temperature, main chamber mixture ratio. It is aimed to examine not only the relationship between inputs and outputs but also the outputs effects interdependency. This study is also focused on determining pressure drop margins for orifices which are located in gas generator and thrust chamber feed lines [3]. Orifices, passive control components, are used to liquid propellant rocket engine fine-tuning [4].

Material and Method

The study involves performance calculations of the liquid rocket engine components, including the thrust chamber, turbopump, gas generator, oxidizer valves, fuel valves, feed lines, and orifices.

Engine performance map is derived after each component performance calculations performed. In order to obtain performance map, fluid dynamic and thermodynamic equations are solved. These equations provide the relation between pressure, mass flow rate, temperature, fluid thermophysical properties for all sub-components in the system. These parameters affect on the engine's overall performance are shown using developed zero-dimensional calculation program. This program provides a robust calculation for determining performance variations in the engine system. Thanks to this methodology, manageable design stages can be achieved during engine development process.

Findings

The mode analysis provides to obtain liquid propellant rocket engine performance for different conditions [5]. Variations in the three parameters lead to several important findings that impacted the overall engine performance. Changes in pump

efficiency were found to directly affect the pressure at the thrust chamber and gas generator combustion pressure and this affects overall engine performance. Similarly, since turbine efficiency governs the power transferred to the pumps, leading to scatterings in engine performance map. For higher the turbine efficiency, power generated turbine is increased and this leads the higher pump discharge pressures. Thus, better engine performance is provided. However, lower turbine efficiency causes to reduced pump discharge pressure and engine performance is reduced. The shifting pump curves causes to change engine operating condition because intersection with system curve is changed.

Changes in the valve flow coefficient also played a significant role in the system performance, as they directly influenced the pressure drop margins within the hydraulic system. These fluctuations resulted in adjustments to the flow rates within the engine, affecting the performance regime of the system. A higher valve flow coefficient lead to lower pressure drop across the valve, lower valve coefficient higher pressure drop across the valve. For this reason, system curve shift in response to changes in the valve flow coefficient. Furthermore, the relation between system curve and pump curve determines the engine operating point. Therefore, engine operating conditions may be changed with these small deviations on the valve coefficient.

Using randomness margins of three parameters, engine performance map was created. Visualization of overall impact of these parameter variations on the chamber pressure, gas generator pressure, turbine inlet temperature, main chamber mixture ratio was derived. In order to compensate engine performance deviations, orifice pressure drop margins were determined. It enables fine-tuning of the system to meet performance requirements more precisely. The introduction of controlled pressure losses using determined orifice margins allowed the system to compensate for performance variations and ensure engine performance requirements across different engine modes.

Conclusion

This study highlights the importance of considering performance dispersion factors during the design and development of gas-generator cycle liquid rocket engines. Investigating key parameters variations, the study provides a comprehensive understanding of how these factors influence engine performance. Through mode calculation program and detailed performance mapping, it was possible to visualize the impact of parameter variations and evaluate potential system uncertainties before they affect the final system performance. The orifice pressure drop margins derivation indicates the importance of fine-tuning sub-components to achieve precise performance requirements. In rocket engine development processes, the performance resolution of sub-components is increased through component tests and uncertainties in the system are reduced. Using the orifices pressure drop margins, system calibration can be achieved. This comprehensive approach ensures that the engine can perform reliably under a range of expected conditions.

In conclusion, the findings of this study contribute to the development of more robust and reliable liquid rocket engines. System engineers can enhance the engine's efficiency, stability and overall reliability with minimizing development risks using zero-dimensional calculation tool. This provides the opportunity to engine designer for suitable the demanding performance requirements of launch vehicle systems and ensures mission success.

References

Cho, W. K., & Kim, C. I. (2018). Comparison of effectiveness for performance tuning of liquid rocket engine. International Journal of Aerospace System Engineering, 5(2), 16–22.

Huzel, D. K. (1992). Modern engineering for design of liquid-propellant rocket engines (Vol. 147). American Institute of Aeronautics and Astronautics.

Nam, C. H., Kim, S. H., Kim, C. W., & Seol, W. S. (2007). A study on dispersion analysis and calibration of gas generator cycle liquid rocket engine. Journal of Aerospace Technology, 6(1), 120–127.

Park, S. Y., & Cho, W. K. (2008). Program development for the mode calculation of gas-generator liquid rocket engine. Proceedings of the 2008 KSPE Fall Conference, 366–370.

Sutton, G. P., & Biblarz, O. (2001). Rocket propulsion elements (7th ed.). John Wiley & Sons, Inc.

AERONAUTICAL AND ASTRONAUTICAL ENGINEERING

Aircraft Design, Flight Dynamics And Performance

Control Systems: Adaptive, Intelligent, Digital, Optimal, Pneumatic-Hydraulic

Mechanical Vibrations And Structural Dynamics

Rotary Wing Aircraft

Spacecraft Control, Design And Performance

Theoretical, Computational And Experimental Aerodynamics And Fluid Dynamics

Theoretical, Computational And Experimental Structural Analysis And Design

A Deep Learning Based Modelling of Axial Turbomachinery

Mehmet Fatih Reyhan[a], Yavuz Selim Mehel[b], Baha Zafer[a]

[a] Istanbul Technical University, Türkiye
[b] TEI Tusaş Engine Inc., Türkiye
reyhanm17@itu.edu.tr

Keywords: Axial Turbomachinery, CFD, Deep Learning.

Aim

Computational Fluid Dynamics (CFD) has been the standard for aerodynamic performance evaluation in turbomachinery design. However, traditional CFD simulations are computationally expensive and time-consuming, often requiring hours to analyze a single design iteration. This computational bottleneck significantly limits the number of design alternatives that can be explored within practical engineering timelines. As modern turbomachinery design increasingly demands high-fidelity simulations due to the nature of the complex physics, the need for a faster, data-driven alternative becomes crucial. Deep learning has emerged as a useful tool to overcome these computational limitations by providing rapid aerodynamic performance predictions based on previously simulated data. Deep learning models can learn the patterns behind turbomachinery flow physics and output the aerodynamic parameters within milliseconds once trained.This capability significantly increases the number of design iterations that can be evaluated in a given time, accelerating the overall design process while maintaining a high level of accuracy. As an example, pressure losses are predicted using generative adversarial networks architecture by taking the airfoil geometry as input [1].
This study aims to develop and evaluate a deep learning-based model capable of predicting CFD results for various turbomachinery geometries, significantly reducing computational costs while maintaining prediction reliability. The model takes as input geometric configurations of axial fan blades and predicts key aerodynamic. By integrating deep learning into the design workflow, this research demonstrates how artificial intelligence can revolutionize turbomachinery design by enabling faster, more data-driven engineering decisions.

Material and Method

In this study, the dataset is provided by TEI and consists of the blade and flowpath geometries as well as the CFD results. The dataset consist of 1800 separate CFD results including different rotational speeds, designs, number of rows and downstream static pressure (matching on speedline). NUMECA Software is used for pre-processing, solving and post-processing. Mesh resolution is determined such that y+ values remain under 5. Total pressure and temperature are set for the inlet boundary condition, while static pressure is set for the outlet boundary condition at different RPM values. The four parameters mentioned are used as input parameters for the deep learning model. As blade parameters should be investigated on each streamtube for the more precise investigations of turbomachinery flows, a post-processing algorithm to split rotor-stator interaction planes have been implemented. For each of the CFD results, all planes at the upstream and downstream of the rows are detected, and then divided into 15 parts in radial direction that contains the same amount of the mass flow rate. The physical quantities then exported for the divided streamtube planes.
Fan designs have been made using the AxStream software and the geometry information is exported as the "geomTurbo" format. The geometry dataset contains Cartesian Coordinates of the blades suction and pressure sides and axial-radial coordinates of the hub and shroud flowpath. Before preparation of the input tensor, blade geometries are converted to the Polar Coordinate system.
The input tensor for geometry is a 10-channel tensor consisting of:

- R theta Z coordinates for the suction side (3 channel)
- R theta Z coordinates for the pressure side (3 channel)
- R Z coordinates for Hub and shroud (2 channel)

- Number of blades (1 channel)
- Rotor or Stator information (1 if rotor, -1 if stator) (1 channel)

Height and width of the input tensor depends on the export parameters selection. Height represents the number of sections of the exported blade geometries. Width contains the number of rows and number of exported points for each airfoil section. To clarify, when the number of points exported for each of the suction and pressure sides is 200 and the number of rows is 4, the width of the tensor becomes 800. Typical setup for the datased used in this study is 15 sections and 225 points for the airfoil coordinates.

The Vision Transformer (ViT) is emerging architecture designed specifically for image processing tasks, employing attention mechanism for image input [2]. The model can outperform the other image recognition models based on convolutional neural networks and have many variants including different approaches.

Model used in this study is a combination of a Vision Transformer for geometrical input tensor and a standard transformer architecture for the boundary conditions input. Patch embedding and positional embedding blocks takes the geometry tensor as input and outputs the embedded vector with size defined by the patch size. In parallel, the simple transformer model processes the boundary condition information. After the boundary conditions and geometry is processed, resulting tensors are multiplied and becomes input for the attention blocks.

At the final stage, models forward head module results physical parameters for each streamtube and row. Resulting physical parameters areAbsolute Static Pressure and Temperature, Absolute and Relative Mach Numbers, three normalized velocity component in polar coordinates.

Absolute Total Pressure and Temperature are calculated using the isentropic relations inside the model to provide additional feedback from total quantities and reduce the model error and speed up the convergence. On the other hand, modelling the physical relations inside the model instead of adding as a penalty term during training, ensure the model gives phsically consistent results, specifically for the testing the unseen data, however, it is not possible to perform this strategy for each constraint.

As an additional constraint, the conservation of mass is imposed by calculating the mass flow rate at planes and standart deviation of the calculated mass flow rate values are added as the penalty term in training.

Findings

Model trained using 1800 CFD results and 80 percent of the datased used as a training and the remaining part is used for the test. The training phase converged to below 1% error for both the training and test datasets, as shown in Figure 1.

Figure 1. Train and test error.

Figure 2 shows the performance map results of an unseen axial fan geometry at design speed. Mass flow rate is calculated as the average of the rotor-stator stations. As seen in the figure, the model predicts the mass flow rate and pressure ratio with an error below 0.5%. However, most of the error comes from the mass flow rate deviation at choke and stall conditions.

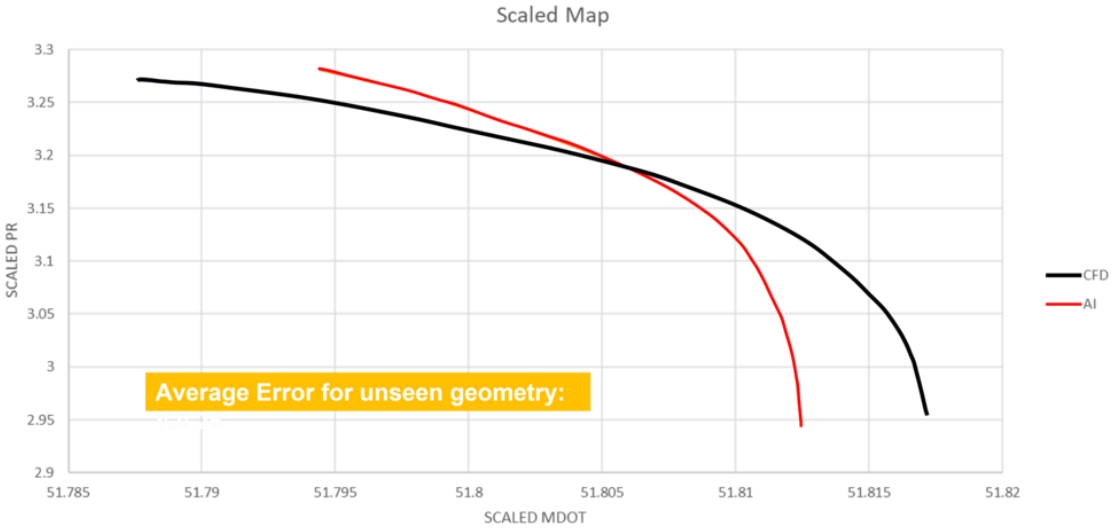

Figure 2. Performance map comparision.

In Figure 3, radial distribution of physical quantities for a single row is shown. Model successfully predicts the radial profile behaviour even at the endwalls, however there is a small deviation specifically on endwalls.

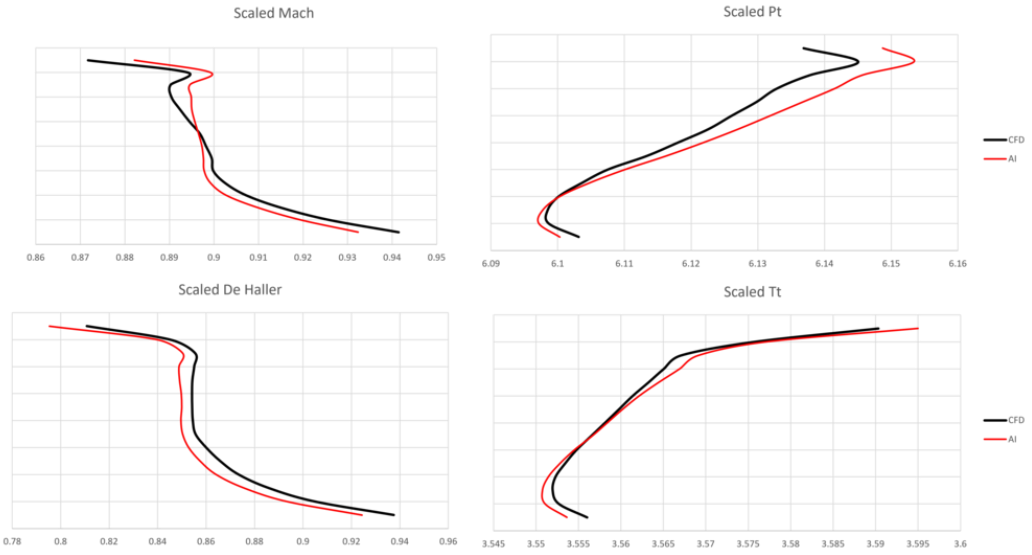

Figure 3. Radial profile for single row.

Conclusion

This study shows the potential of deep learning for predicting CFD results in turbomachinery applications. By leveraging a Vision Transformer-based approach, geometric features are mapped to aerodynamic performance parameters, significantly reducing computational costs and time compared to traditional CFD simulations. While the model performs well for general aerodynamic trends, its sensitivity to small-scale geometric variations remains a challenge for now. Future

work will focus on enhancing feature representation techniques and incorporating novel deep learning architectures to improve accuracy and generalization across turbomachinery geometries.

References

Dosovitskiy, A., Beyer, L., Kolesnikov, A., Weissenborn, D., Zhai, X., Unterthiner, T., ... & Houlsby, N. (2020). An image is worth 16x16 words: Transformers for image recognition at scale. arXiv preprint arXiv:2010.11929.
Feng, Y. et al. (2023) 'Physics-informed Deep Learning Cascade Loss Model', Aerospace Science and Technology, 134, p. 108165. doi:10.1016/j.ast.2023.108165.

Experimental Study on Vortex Gust Encountered by a Flat Plate at 45° Wing Sweep

Ozan Ibrahimagaoglu[a], Oksan Cetiner[b]

[a] Istanbul Technical University, Aeronautical Engineering, Turkey
[b] Istanbul Technical University, Astronautical Engineering, Turkey
ibrahimagaoglu16@itu.edu.tr

Keywords: Gust, Swept Wing, Vortex.

Aim

A considerable amount of research has been recently devoted to the study of massive separation and its control caused by large-scale discrete gusts [1]. Among the three major categories in discrete gust encounters [2], vortex gusts are probably the best representing the real-life scenario where only single direction velocity fluctuations are not possible to observe. Most of the investigations up to now, either experimental or numerical, are focused on quasi two-dimensional gust encounters. However, three-dimensionality is another important issue to be addressed to understand the flow physics for gust mitigation in civil and/or military applications considering that operations in extreme weather conditions become more important and necessary nowadays. As pointed out in recent studies [3, 4], knowledge on the physics of three-dimensional gust encounters is lacking and the aerodynamic response of finite-span wings with sweep angles encountering gust is of a great interest. Therefore, the main objective of this study is to investigate the three-dimensional flow structure interactions in a massively separated flow over a swept wing. The wing tip shape is also considered to include the misalignment of the tip with the flow.

Material and Method

This study is based on the previous experimental investigations where a vortex gust encounters a flat plate, aspect ratio of AR=4 wing [5, 6]. An upstream plate is used to generate a negative vortex gust with its half rotation around its center chord and different rotation rates (half rotation durations of 3s, 4s and 6s) are used to control the vortex gust and velocity profile gradient distance [7]. The positioning perpendicular to the freestream direction of the gust generator and the model is also considered as another parameter to control the encounter path of the vortex gust. T = 4s and $\Delta y = -36$mm constitutes the base case. For $\Delta y = -36$mm, the vortex gust moves aligned with the chord line of the model, therefore h/c = 0. Another trajectory where $\Delta y = -111$mm (h/c = −0.75) is also considered to study a weaker interaction. The flow speed is kept constant to have Re = 10 000 as in the previous experiments. The test model at 0° angle of attack throughout this investigation. In this study the flat plate is at a 45-degree sweep angle and with the same aspect ratio of 4 as before. 2D2C Digital Particle Image Velocimetry (DPIV) is used for the visualization of the flow structures, along with force measurements with an F/T sensor attached to the rod passing through the leading edge of the wing root.

Findings

Quantitative flow visualization results show that there is a non-linear shift in time for the occurrence of similar flow structures observed in the gust encounter. Figure 1 shows the vorticity plots of swept wing case in comparison with the previous study on 2D wing. Upstream camera results indicate that the generated vortex gust is not very affected by the wing being swept. However, the positive leading-edge vortex interacting with the positive vortex shed from the gust generator with comparable size and location obtained at t = 2s for the 2D case is now observed at 3s < t < 4s for the swept wing. It should be noted that the convective time, t*, is equal to t in these experiments $t^* = tU/c$ and the leading edge of the root section is at the same location as that of the 2D wing. Therefore, with the freestream speed, it would take a second for the negative vortex gust to encounter the leading edge of the illuminated plane. On the other hand, previous studies [8] showed that the negative vortex gust does not convect downstream at the freestream speed, rather its convection speed is approximately half of the freestream speed. As can be seen in Fig. 2, the lift transient for the base case (half rotation in 4s

and) occurs later in time in agreement with the quantitative flow visualizations and has considerably lesser effect for the swept wing. On the other hand, the flow structures are very similar at the minimum peak value of the lift coefficient. Although it is for transverse gusts, it has been shown that the occurrence of the peak transient shifts in time and the peak reduces down with increasing sweep angle [4]. In this study on the three-dimensionality and sideslip in strong transverse gust encounters, the rectangular wing is rotated to obtain a sweep angle and misalignment with the cross-flow jet [4]. As a consequence, a swept wing may have a sharp tip and a tip cross-section not aligned with the flow direction. For the current study on vortex gusts, Fig. 3 shows the results on the wing tip shape effect for the gust encounter in close interaction case ($\Delta y = -36$mm). Whether the tip of the swept wing is aligned with the flow or not, as long as the planform area is correctly considered, there are no major differences in the lift transient for all gust generator rotation speeds.

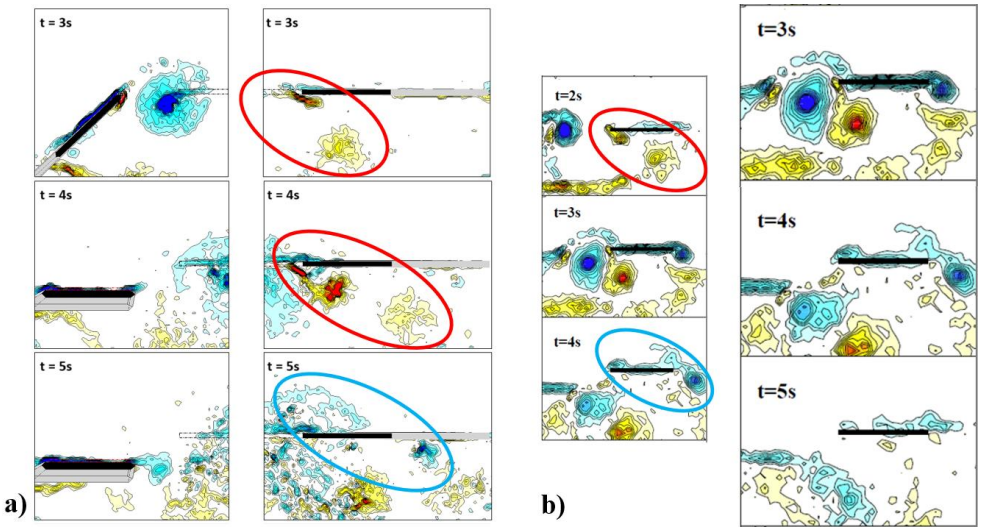

Figure 1. Vorticity plots for $\Delta y = -36$mm and T= 4s, a) swept wing, b) 2D wing.

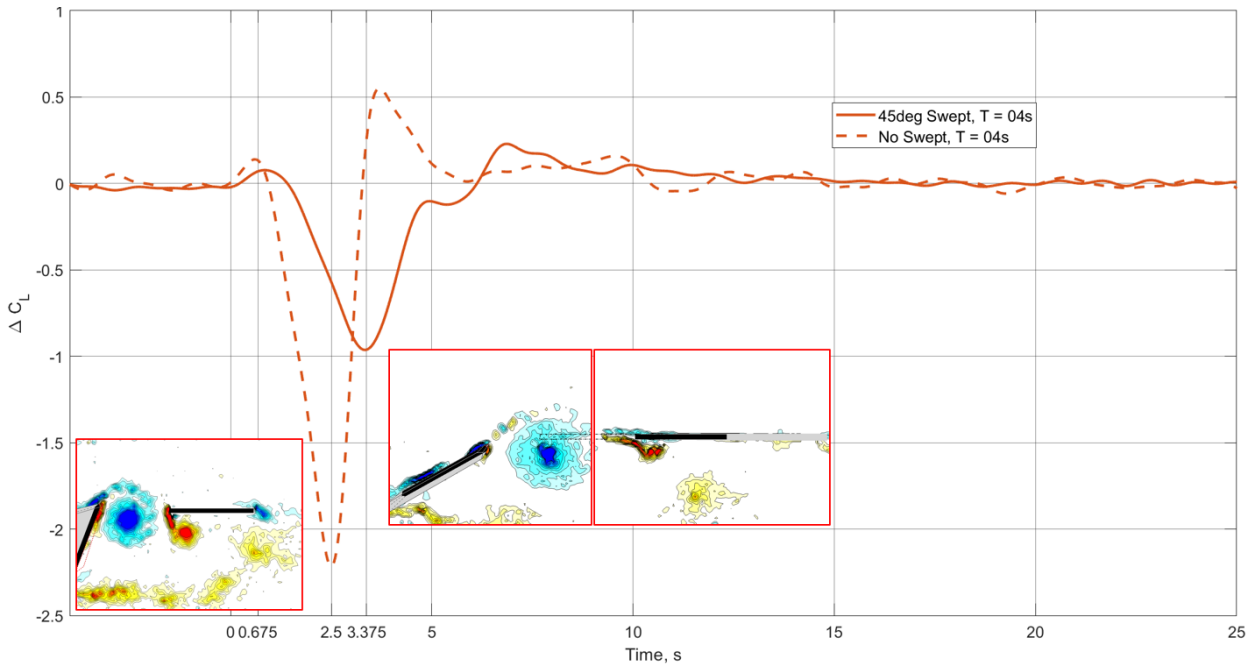

Figure 2. Lift variation for the base case (half rotation in 4s and h/c=0) for 45˚ swept and 2D wings.

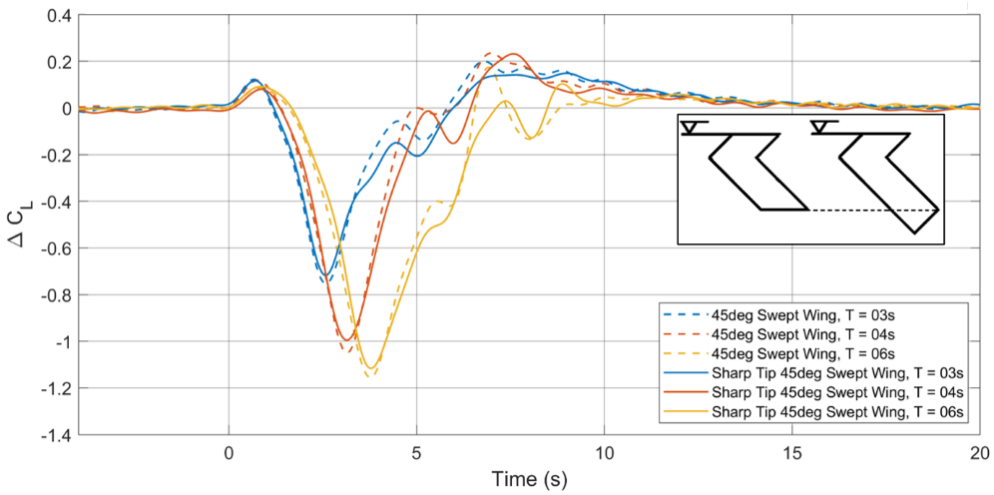

Figure 3. Lift variation for 45˚swept wings with different tip shape (Δy = −36mm).

Conclusion

As a conclusion, the force measurement results show that the lift transient observed in a vortex gust encounter is reduced and delayed for the swept wing at AoA=0° in all cases investigated. The occurrence of the peak value shifted in time can be also predicted from the flow visualization results. The tip shape of the swept wing does not make any difference in the force variations; however, it should be noted that although the flow is not aligned in the sharp tip cases, the cross section is not different for a thin flat plate (thickness of 5%). For future studies, the use of wings with airfoil cross section is recommended to investigate the tip shape effects or in other words, the flow misalignment at the wingtip.

It should be also noted that in the current experiments, the free-surface is either at the symmetry axis or at the 15% of the right wing from the symmetry axis (as seen in the inserts of Fig. 3), to study the effect of the three-dimensional structures emanating from the fuselage or the tip/nose in this case. However, as the wing is at 0° angle of attack for all cases investigated, the results are not much different, the effects are expected to become obvious in future studies when the wing is at an angle of attack or in pitching maneuver.

References

Biler, H., Sedky, G., Jones, A. R., Saritas, M., and Cetiner, O., "Experimental Investigation of Transverse and Vortex Gust Encounters at Low Reynolds Numbers," *AIAA Journal*, Vol. 59, No.3, 2021, pp.786-799. doi: 10.2514/1.J059658

Gloutak, D., Jansen, K. E., and Farnsworth, J. A., "Aerodynamic Performance of Swept Wings in Unsteady Streamwise Flow", *AIAA Scitech 2023 Forum*, 2023, p.1231. doi: 10.2514/6.2023-1231

Jones, A. R., Cetiner, O., and Smith, M., "Physics and Modeling of Large Flow Disturbances: Discrete Gust Encounters for Modern Air Vehicles," *Annual Review of Fluid Mechanics*, Vol. 54, 2022, pp. 469-493. doi:10.1146/annurev-fluid-031621-085520

Jones, A. R., and Cetiner, O., "Overview of NATO AVT-282: Unsteady Aerodynamic Response of Rigid Wings in Gust Encounters," *AIAA Scitech 2020 Forum*, 2020, p.0078. doi: 10.2514/6.2020-0078

M. Saritas, "Flow Structures, Loading and Mitigation for a Large-Scale Discrete Vortex Gust Encounter", *Ph.D. Thesis (submitted)*, Istanbul Technical University, 2025.

Soy, K., Tugan, E., Acar, E., and Cetiner-Yildirim, O. N., "Experimental Investigation of Discrete to Continuous Vortex Gust Encounters," *AIAA Scitech 2023 Forum*, 2023, p. 1621. doi: 10.2514/6.2023-1621

Tilki, B., Saritas, M., & Cetiner, O., "Girdap Turu Tekil Saganaklarin Karakterizasyonu," *9. Ulusal Havacilik ve Uzay Konferansi*, UHUK-2022-142, Izmir, Turkey, 2022.

Wild, O., Gementzopoulos, A., and Jones, A. R., "Navigating Unsteady Airwakes: Three-Dimensionality and Sideslip in Strong Transverse Gust Encounters," *AIAA Scitech 2024 Forum*, 2024, p. 1120a.
doi: 10.2514/6.2024-1120a

Fully-Coupled k–ω-SST Turbulence Model Implementation for Nonlinear Newton Method in Unstructured Vertex-Based Hemlab Algorithm

Atakan Okan[a], Mehmet Şahin[a]

[a] Istanbul Technical University, Faculty of Aeronautics and Astronautics, Astronautical Engineering, Turkey
okan15@itu.edu.tr

Keywords: Fully-coupled, non-linear Newton method, SST.

Aim

Industrial RANS simulations demand efficient solvers & mesh generation is still a major bottleneck. Although adaptive mesh refinement can resolve this, it requires stable solvers for complex geometries. Explicit solvers are easier to program; however they have slow convergence for stiff problems (Blazek, 2001), requiring implicit methods. SST model is often implemented loosely-coupled, preventing quadratic convergence for Newton method. If fully-coupling is enabled with exact Jacobians, solvers can achieve machine-precision level residuals (Sukaş & Şahin, 2025; Thompson & O'Connell, 2019).

Therefore, aim of present study is implementing Menter's k-omega Shear Stress Transport (kω-SST) turbulence model for Reynolds-Averaged Navier–Stokes (RANS) equations in a fully coupled (monolithic) and implicit manner to nonlinear Newton solver algorithm in density-based, unstructured, vertex-centered HEMLAB code for robust and efficient solution of external aerodynamics problems where achieving machine-precision residual tolerance is desired.

In order to achieve higher CFL values for rapid convergence of Newton method (as solution approaches steady state via pseudo-transient continuity (PTC)), rather than approximate methods for Jacobian contributions of turbulence-model source terms, it is intended to construct exact Jacobians using analytical derivatives of source terms in turbulence model equations. Another main goal is to investigate implementation accuracy on benchmark flat plate case and test convergence characteristics of fully coupled kω-SST implementation when combined with more challenging aerodynamic problems such as subsonic airfoil at 10 and 15 degrees of angle of attack.

Material and Method

To begin with, two-equation kω-SST Reynolds-Averaged Navier–Stokes (RANS) turbulence model (Menter, 1994) was non-dimensionalized using compressible, conservative form of equations with production limiter included for k-equation. According to NASA Langley Research Center (n.d.) format, model equations are written as follows:

$$\frac{\partial(\rho k)}{\partial t} + \nabla\cdot(\rho u k) = P_{lim} - \frac{Re_\infty}{Ma_\infty}\beta^*\rho\omega k + \frac{M_\infty}{Re_\infty}\nabla\cdot[(\mu+\sigma_k\mu_t)\nabla k] \#(1)\ \frac{\partial(\rho\omega)}{\partial t} + \nabla\cdot(\rho u\omega) = \frac{M_\infty}{Re_\infty}\gamma\rho S^2 - \frac{Re_\infty}{Ma_\infty}\beta\rho\omega^2 + \frac{M_\infty}{Re_\infty}\nabla\cdot[(\mu+\sigma_w\mu_t)\nabla\omega] + \frac{M_\infty}{Re_\infty}2(1-F_1)\frac{\rho\sigma_{w2}}{\omega}\nabla k\cdot\nabla\omega \#(2)\ P_{lim} = min\left(\frac{M_\infty}{Re_\infty}\mu_t S^2, \frac{Re_\infty}{Ma_\infty}20\beta^*\rho\omega k\right)\#(3)\ \mu_t = \frac{\rho a_1 k}{max\left(a_1\omega, \left(\frac{M_\infty}{Re_\infty}\right)\Omega F_2\right)}\#(4)\ S = \sqrt{2(S\cdot S)}\#(5)\ S = \frac{1}{2}(\nabla\cdot u + (\nabla\cdot u)^\top)\#(6)\ \Omega = \sqrt{2(W\cdot W)}\#(7)\ W = \frac{1}{2}(\nabla\cdot u - (\nabla\cdot u)^\top)\#(8)$$

$$F_2 = tanh\ tanh\ (arg_2^2)\ \#(9)\ arg_2 = max(2\Gamma_1, \Gamma_2)\#(10)\ \Gamma_1 = \frac{M_\infty}{Re_\infty}\frac{\sqrt{k}}{\beta^*\omega d}\#(11)\ \Gamma_2 = \left(\frac{M_\infty}{Re_\infty}\right)^2\frac{500\nu}{d^2\omega}\#(12)\ F_1 = tanh\ tanh\ (arg_1^4)\ \#(13)\ arg_1 = min(\Gamma_3, \Gamma_4)\#(14)\ \Gamma_3 = max(\Gamma_1, \Gamma_2)\#(15)\ \Gamma_4 = \frac{4\rho\sigma_{w2}k}{CD_{k\omega}d^2}\#(16)\ CD_{k\omega} = max\left(2\rho\sigma_{w2}\frac{1}{\omega}\nabla k\cdot\nabla\omega, 10^{-10}\right)\#(17)$$

where intermediate terms based on blending functions F_1 and F_2, and model calibration constants are shown below in Eq. 18 to 23:

$\sigma_k = F_1\sigma_{k1} + (1-F_1)\sigma_{k2}\#(18)\ \sigma_w = F_1\sigma_{w1} + (1-F_1)\sigma_{w2}\#(19)\ \beta = F_1\beta_1 + (1-F_1)\beta_2\#(20)\ \gamma = F_1\gamma_1 + (1-F_1)\gamma_2\#(21)\ a_1 = 0.31\ \beta^* = 0.09\ \kappa = 0.41\ \gamma_1 = \frac{5}{9}\ \gamma_2 = 0.44\#(22)\ \sigma_{k1} = 0.85\ \sigma_{k2} = 1.0\ \sigma_{w1} = 0.5\ \sigma_{w2} = 0.856\ \beta_1 = 0.075\ \beta_2 = 0.0828\#(23)$

For k and ω equations in Eq. 1 & 2, left-hand side of equalities denotes time derivative and convective terms while right-hand side shows production, destruction, and diffusion terms. Only extra term is cross-diffusion in ω equation which reduces freestream sensitivity of original k − ω model (Wilcox, 1988). Blending functions F_1 and F_2 in Eq. 9 & 13 help recover k − ω behavior towards no-slip wall and k − ϵ formulation near boundary layer edge towards freestream. Production limiter in Eq. 3 is recommended for cases involving stagnation points and to handle extreme turbulent kinetic energy production in adverse pressure gradient flows (Menter, 1994).

Due to stiffness of high-Re CFD simulations - requiring very small time steps to resolve boundary-layer gradients near walls —explicit methods are generally infeasible for industrial applications (Blazek, 2001). This necessitates matrix-based implicit methods where large-scale problems can be tackled more effectively thanks to fewer time step restrictions, therefore enabling faster convergence. Although they are more costly per timestep with increased memory requirements and more challenging to program, benefits owing to a proper linear matrix solver and effective preconditioner selection still outweigh the cons in the long run.

If residual vector of coupled equation system for node-based FVM approach using median-dual cells is given by R in Eq. 24, where F_i is inviscid fluxes and F_v is viscous fluxes and backward Euler implicit 1st-order time integration is used as pseudo-time continuation (PTC) strategy in steady-state, following consistent Newton method is obtained (Sukaş & Şahin, 2025) where pseudo-time is added to RHS residual as well in Eq. 25:

$$R(Q) = \frac{\partial}{\partial t}\iiint_{\Omega} Q dV + \iint_{\partial\Omega} n\cdot F_i dS - \iint_{\partial\Omega} n\cdot F_v dS = 0\#(24)\ \frac{\partial R}{\partial Q}\Delta Q^{m+1} = \left[\frac{M}{\Delta t} + J\right]\Delta Q^{m+1} = -R(Q^m) = -\left[\frac{Q^m - Q^n}{\Delta t}V + \sum \quad n\cdot F_i(Q^m)S - \sum \quad n\cdot F_v(Q^m)S\right]\#(25)$$

where Q is state-vector, n is outward face normals of dual volume faces around primal mesh vertices, J is flux Jacobian, ΔQ is solution update, M is mass matrix, V is dual-cell volume, S is dual-volume face area, m is mth Newton subiteration and Δt is pseudo-timestep in steady-state in Eq. 25.

Due to nonlinearity of RANS equations, having an implicit system does not immediately result in an unconditionally stable matrix where pseudo-timestep can be driven to infinity during steady-state problems if simulation undergoes unphysical transients (Blazek, 2001; Thompson & O'Connell). This is exacerbated by approximations in Jacobian construction or ineffective preconditioner selection (Sukaş & Şahin, 2025).

Therefore, a more consistent Newton's method was sought with a "line-search" technique to guarantee that nonlinear residual decreases at each pseudotime by adding time terms to both Jacobian and residual functions (Sukaş & Şahin, 2025; Thompson & O'Connell, 2019). In light of these, HEMLAB is a node-based FVM algorithm for hybrid-unstructured meshes with edge-based data structures for cache efficiency (Sukaş & Şahin, 2025). It is based on a consistent, nonlinear Newton method for robust and efficient solution of fully-coupled system of RANS equations where machine precision tolerance is sought. Nonlinear Newton method is implemented using PETSc Scalable Nonlinear Equations Solvers (SNES) with line-search (Balay et. al.,2018). This method allows both Jacobian-free finite-difference method as well as direct Jacobian construction for Jacobian-vector product.

In order to capture high-gradient regions more effectively, "pyAMG" anisotropic mesh refinement library by Inria (n.d) and "refine" library by NASA (n.d.) is integrated with HEMLAB for mesh adaptation. pyAMG works in metric space where generated mesh corresponds to a highly stretched anisotropic mesh in physical space (Loseille, 2016). In HEMLAB, target adaptation sizes, minimum edge lengths and L_2 and L_4-norms can be specified for Mach & distance-based refinement sensors (Sukaş & Şahin, 2025).

For inviscid flux reconstruction, blending of upwinding with central approach is utilized. At cell interfaces, flux-difference splitting of Roe (1982) is used. Other schemes such as HLLC, AUSM+up and AUSM+M are also available. Left/right state

vectors are obtained with unweighted least-squares approach. In addition, gradients of primitive variables in viscous fluxes are obtained at edge midpoints with Green-Gauss theorem. For convective terms of SST model, first order upwinding is used. Non-dimensional BCs in Eq. 26 to 29 are recommended for k and ω (Menter, 1994; NASA Langley Research Center (n.d.)):

$$k|_{wall} = 0 \#(26)\ k|_{farfield} = 9 \times 10^{-9} \#(27)\ \omega|_{wall} = \left(\frac{M_\infty}{Re_\infty}\right)^2 \frac{60\nu_{wall}}{0.075(\Delta y_1)^2} \#(28)\ \omega|_{farfield} = 1 \times 10^{-6} \#(29)$$

where ν_{wall} is wall kinematic viscosity, and Δy_1 is nearest wall normal distance away from wall in Eq. 33. Wall BC is only for the case with no wall functions where $y+ < 3$ (Menter, 1994). However, it was observed that BC in Eq. 33 is problematic due to quadratic nature of ω near wall and causes grid dependence due to Δy_1 term which is unacceptable for anisotropic refinement due to extremely stretched cells near wall. Since positivity of k and ω needs to be ensured for model stability in flux calculations at edge midpoints (Langer & Swanson, 2024), a transformed k-ω model which is called k-q SST is implemented in HEMLAB. A variable transformation from ω to q is used where Eq. 30 & 31 show transformation relation and wall BC for new q variable, respectively. Here, A is a positive constant for controlling residual equation for new q variable:

$$\omega = \frac{A}{q^2} \#(30)\ q|_{wall} = 0 \#(31)$$

High CFL numbers are critical in Newton methods for quadratic convergence, where accurate Jacobians are required. Automatic differentiation-based source code transformation library Tapenade by Inria (n.d.) is integrated with HEMLAB for exact Jacobians of inviscid fluxes. For turbulence equations' source term contributions to Jacobians, analytical derivatives of source terms in SST model is derived. Therefore, fully-coupling of Navier-Stokes system is achieved for higher CFL numbers. This is not preferred in most solvers due to implementation difficulty in implicit approach and computational cost associated with Jacobian matrix where usually approximate factorization methods are used. Finally, most SST model implementations use a loosely-coupled method of coupling Navier-Stokes equations while solving turbulence equations as segregated (Content, Outtier, & Cinnella, 2013; Langer & Swanson, 2024).

Findings

Validation on zero-pressure-gradient flat plate at Re = 5000000 and $Ma_\infty = 0.2$ was conducted using structured meshes (NASA Langley Research Center (n.d)). Focus was on behavior of k and ω in boundary layer to verify coupled SST implementation. Fig. 1 & 2 indicate that local k & ω behaviour in boundary layer is in good agreement with FUN3D solver. Only discrepancy is at outlet due to lack of "outflow" BC in HEMLAB solver. In addition, rapid residual convergence is observed in Fig. 3 with CFL reaching 10000. Finally, Table 1 shows both solvers are within 1 drag count difference.

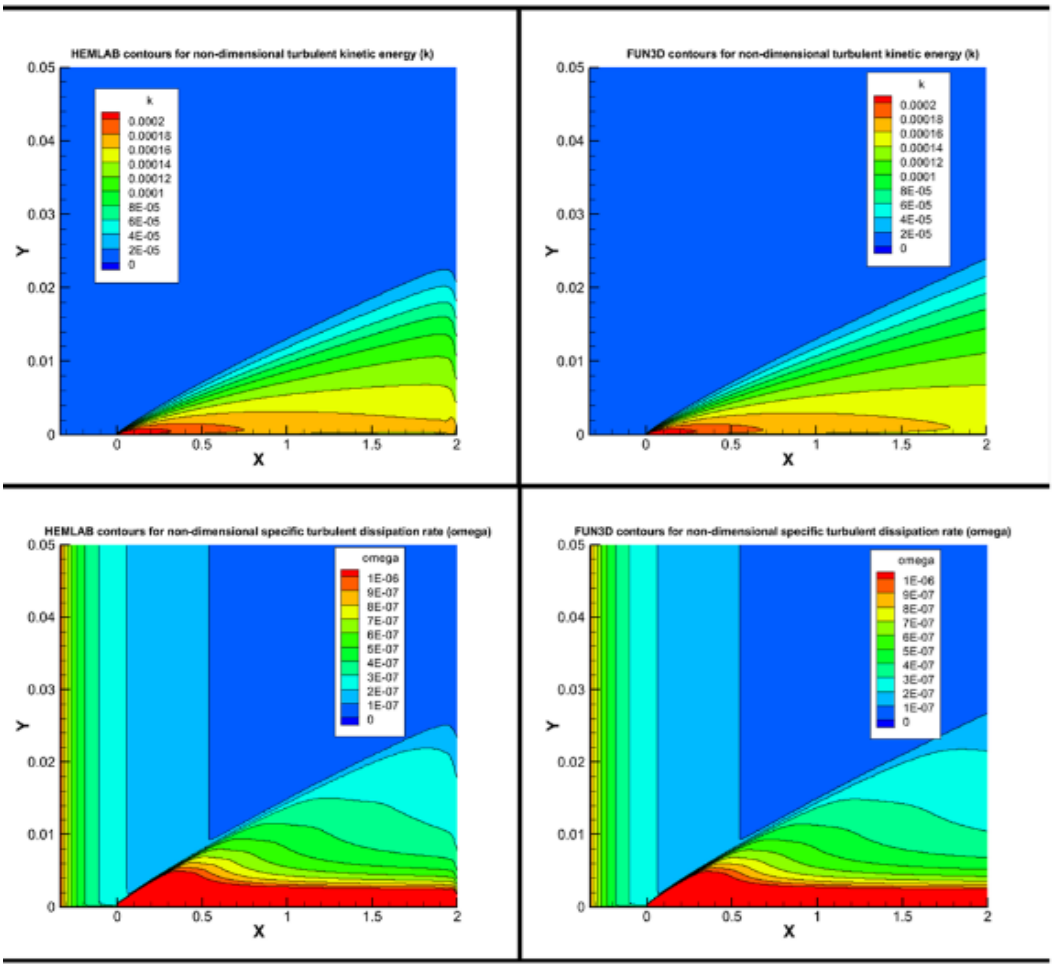

Figure 1. Comparison of HEMLAB and FUN3D (NASA Langley Research Center (n.d.)) contours of k and w in boundary layer for flat plate.

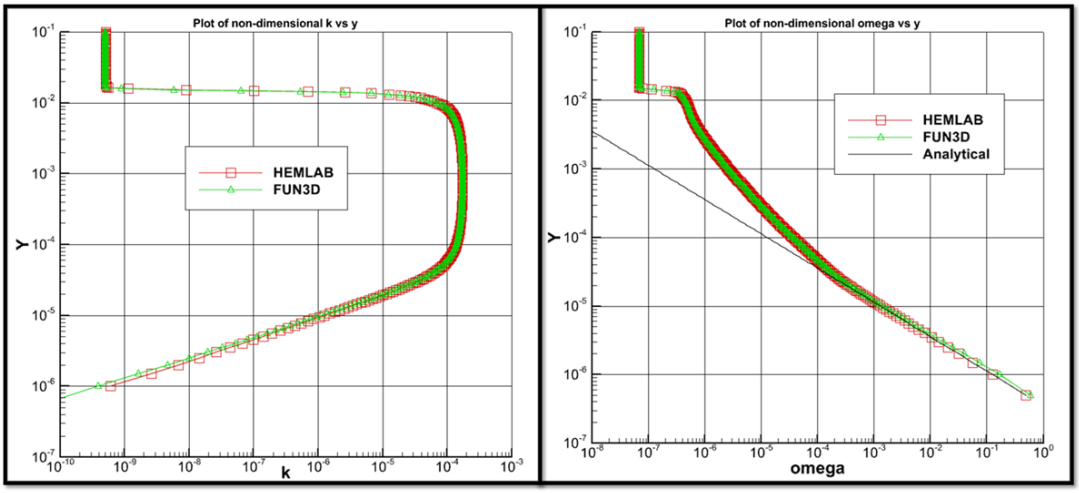

Figure 2. Comparison of HEMLAB and FUN3D (NASA Langley Research Center (n.d.)) profiles for k and w at x=0.97 section of flat plate.

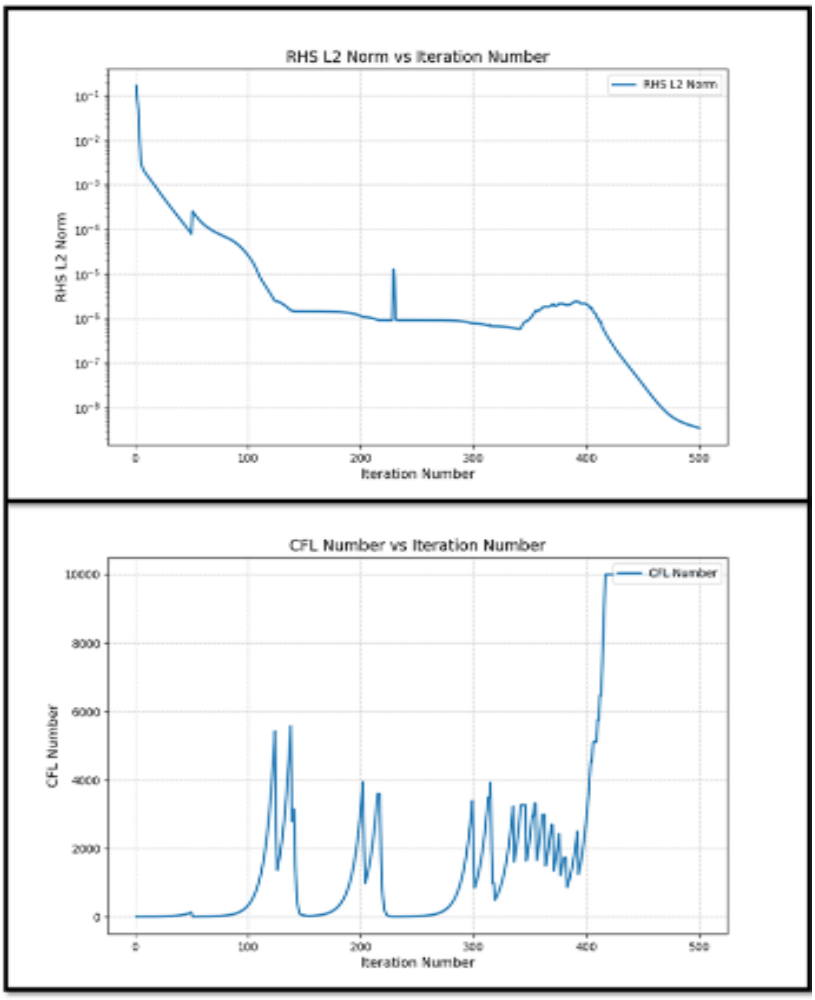

Figure 3. Convergence history of HEMLAB fully-coupled SST implementation for flat plate case.

Table 1. Comparison of HEMLAB and FUN3D (NASA Langley Research Center (n.d.)) turbulence model drag coefficient results for flat plate case.

Solver	Turbulence Model	Drag Coefficient
FUN3D	SA-neg	0.00285
FUN3D	SST-Vm	0.00283
HEMLAB	SA-neg-noft2	0.00296
HEMLAB	SST-m	0.00295

Furthermore, verification on NACA-0012 airfoil at Re = 6000000 and Ma_∞ = 0.15 at 0, 10 and 15 degrees of AoA was conducted. Focus was on robustness of coupled SST implementation in case of practical external-aerodynamics flows. In Fig. 4, mesh independency study comparing HEMLAB SA-neg and SST implementations is shown for structured o-grid, where number of airfoil surface nodes varies from 100 to 500, farfield extent is 500c and first layer height is 2e-6 m. Mesh level 4 was chosen for subsequent runs with 93000 grid nodes. Finally, as shown in Fig. 5, SST C_p plot at AoA=10 matches

well with the experiment and convergence is as robust as flat plate case with CFL reaching 10000 and residual dropping to 1e-10.

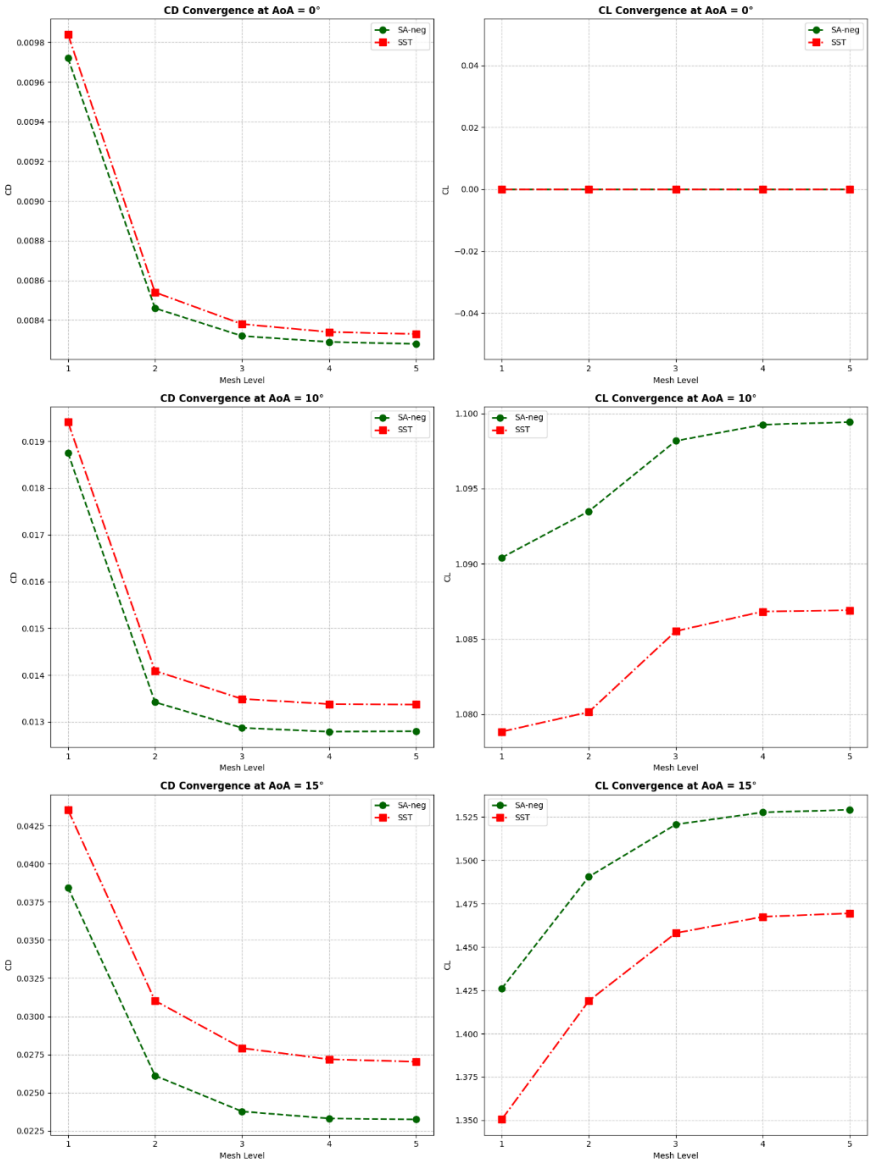

Figure 4. Mesh independency study for NACA-0012 case at all angles of attack.

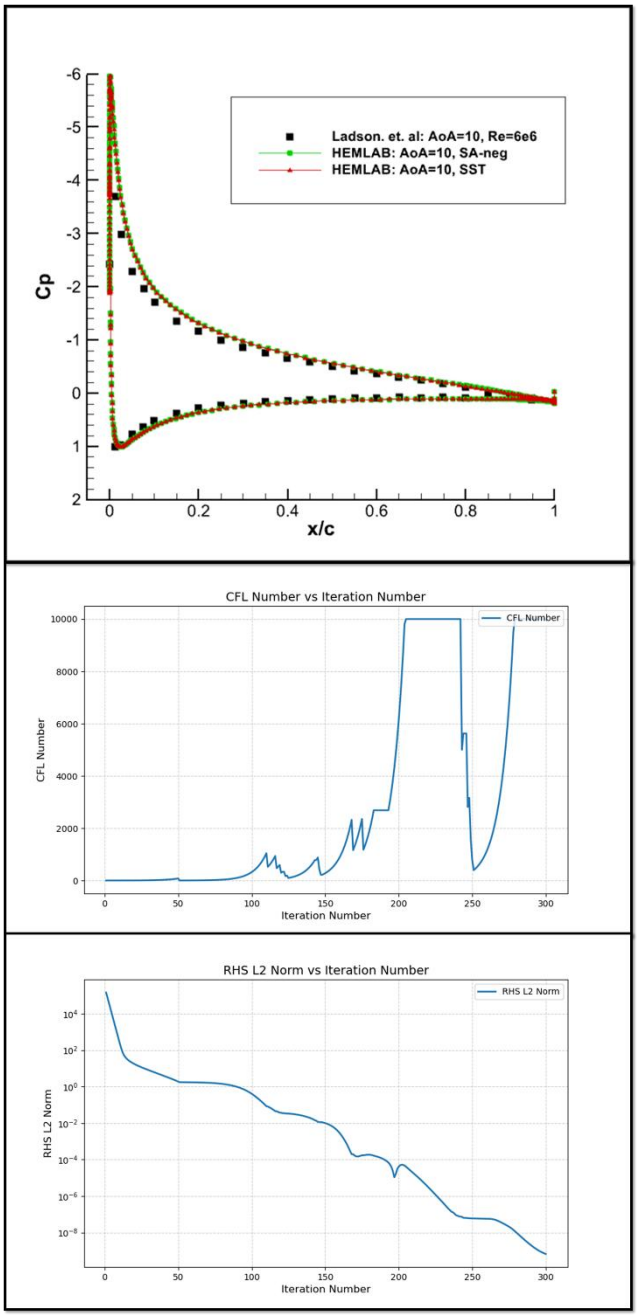

Figure 5. Pressure distribution for NACA-0012 case at AoA=10 and and convergence history of HEMLAB coupled SST implementation.

Conclusion

As a conclusion, k-ω SST model is implemented in HEMLAB in fully-coupled fashion with transformed form as k-q SST model. Exact Jacobians were used for turbulence model source terms. Implementation accuracy was verified based on boundary layer profiles for flat plate case. 2D subsonic cases achieved CFL around 10000 and residual norms of 1e-10. Airfoil flow physics at varying angles of attack did not negatively impact performance. As future work, 3D cases with mesh adaptation need to be assessed for robustness and accuracy as well as transonic & supersonic flows.

References

Balay, S. et. al. (2018). PETSc/TAO Users Manual, ANL-21/39 - Revision 3.23, 2025.

Url-1 https://doi.org/10.2172/2476320,
Url-2 https://petsc.org/release/docs/manual/manual.pdf
Blazek, J. (2001). *Computational fluid dynamics: Principles and applications*. Elsevier.
Content, C., Outtier, P.-Y., & Cinnella, P. (2013). Coupled/uncoupled solutions of RANS equations using a Jacobian-free Newton-Krylov method. In 21st AIAA Computational Fluid Dynamics Conference (AIAA Paper 2013-2423). American Institute of Aeronautics and Astronautics.
Url-3 https://doi.org/10.2514/6.2013-2423
Inria. (n.d.). Tapenade Automatic Differentiation Engine. Retrieved 23.03.2025, from
Url-4 https://team.inria.fr/ecuador/en/tapenade/
Langer, S., & Swanson, R. C. (2024). Implementation, realization and an effective solver of two-equation turbulence models. Journal of Scientific Computing, 98(8).
Url-5 https://doi.org/10.1007/s10915-023-02394-0
Loseille, A. (2016). Metric-orthogonal anisotropic mesh generation. Procedia Engineering, 163, 403–415.
Menter, F. R. (1994). Two-equation eddy-viscosity turbulence models for engineering applications. AIAA Journal, 32(8), 1598–1605.
Url-6 https://doi.org/10.2514/3.12149
NASA. (n.d.). NASA Refine: Mesh Adaptation Library. Retrieved March 24, 2025, from
Url-7 https://github.com/nasa/refine
NASA Langley Research Center. (n.d.). NASA Turbulence Modeling Resource. Retrieved 23.03.2025, from **Url-8** https://turbmodels.larc.nasa.gov
Roe, P. L. (1981). Approximate Riemann solvers, parameter vectors, and difference schemes. Journal of Computational Physics, 43(2), 357–372.
Sukas, H., & Sahin, M. (2025). A robust monolithic nonlinear Newton method for the compressible Reynolds averaged Navier–Stokes equations. Computers & Fluids, 289.
Url-9 https://doi.org/10.1016/j.compfluid.2025.106549
Thompson, K. B., & O'Connell, M. (2019). Streamlined convergence acceleration for CFD codes. In AIAA Aviation 2019 Forum (AIAA Paper 2019-3709). American Institute of Aeronautics and Astronautics.
Url-10 https://doi.org/10.2514/6.2019-3709
Wilcox, D. C. (1988). Reassessment of the scale-determining equation for advanced turbulence models. AIAA Journal, 26(11), 1299–1310.
Url-11 https://doi.org/10.2514/3.10041

Digital Twin Approaches in System-Level Modeling for Aerospace and Propulsion Applications of Rocket Engines: A Review

Yasir Şimes[a], İbrahim Özkol[a]

[a] Istanbul Technical University, Faculty of Aeronautics and Astronautics, Department of Aerospace Engineering, Türkiye
shemis17@itu.edu.tr

Keywords: Digital Twin, System-level Modeling, Rocket Propulsion, Virtual Prototyping, Predictive Maintenance.

Aim

Digital Twin (DT) technology enables creation of high-fidelity, continuously updated virtual replicas of physical systems. In rocket propulsion, DTs offer a unified framework to simulate multi-domain interactions—including thermodynamics, fluid dynamics, structural mechanics, and control systems—under operational conditions. This review surveys the evolution of DTs, outlines system-level modeling methodologies, highlights key applications in design optimization and health management for rocket engines, and discusses challenges and future directions for advancing DTs in propulsion systems. The concept of a Digital Twin in aerospace traces back to mirrored simulators on Apollo 13 in 1970, formalized by Grieves in 2002 and Vickers in 2010, and has since matured through agency and industry efforts. Table 1 summarizes these key milestones.

Material and Method

A comprehensive literature survey identified rocket-engine digital-twin studies published from 2010 to 2025 that couple at least two physics domains (fluid, thermal, structural, control) and report validation errors ≤ 5 % against hot-fire or test-stand data (Grieves, 2002; Glaessgen & Stargel, 2012; Jiménez Mena et al., 2019; Satoh et al., 2020; Tao et al., 2018). Initial database queries returned 120 candidate papers; after title/abstract and full-text screening, 45 met our inclusion criteria.

From this corpus, we distilled a system-level co-simulation workflow: high-fidelity submodels of turbomachinery, feed lines, combustion chambers, actuated valves, and convergent–divergent nozzles are developed in Siemens Simcenter Amesim or Modelica (Mena et al., 2019; Orbi & Martin, 2020). Fluid–dynamics solvers capture transient mass-flow and pressure waves; thermal modules resolve heat-transfer and hot-wall soak effects; structural mechanics predict cyclic stresses; and control-logic blocks sequence valve and throttle commands (Lin et al., 2023; Zhang & Yue, 2021). To enable real-time execution, full-order physics components are replaced by reduced-order surrogates—via proper-orthogonal decomposition or neural-network approximations—that maintain overall simulation error within 1–5 % (Tao et al., 2018).

A continuous digital thread ingests live sensor streams (pressure transducers, thermocouples, accelerometers, rotor-speed encoders) through edge-computing gateways. Extended Kalman filters fuse these measurements with model states, and AI-based estimators iteratively calibrate uncertain parameters (combustion kinetics, heat-transfer coefficients) against historical test-stand and flight data until residual errors fall within prescribed tolerances (Satoh et al., 2020; National Academies of Sciences, Engineering, and Medicine, 2024).

Hardware-in-the-loop validation closes the loop by interfacing actual engine-control electronics—including fuel-valve drivers and ignitor circuits—with the virtual engine model. In benchmark studies on the RL10 expander-cycle engine, closed-loop tests of startup sequences, throttle ramps, and shutdown transients reproduced valve timing, chamber-pressure overshoots, and thermal spikes within a 1–5 % margin of empirical data (Mena et al., 2019; Satoh et al., 2020). Figure 1 shows the overall architecture of the rocket-engine digital twin, from physical test-stand through sensor fusion, multi-physics co-simulation, reduced-order surrogates, and hardware-in-the-loop validation.

Findings

Digital-twin methodologies have delivered up to 60 % reduction in hot-fire campaigns and ≈ 50 % shorter development schedules by enabling early virtual prototyping and in silico design iterations (National Academies of Sciences, Engineering, and Medicine, 2024; Tao et al., 2018). The RL10 expander-cycle twin in Simcenter Amesim reproduced startup valve sequences, chamber-pressure overshoot, and thermal spikes within 1–5 % of test-stand data, guiding injector and nozzle optimizations without additional hardware tests (Jiménez Mena et al., 2019).

Predictive-maintenance frameworks built on the "living twin" extend inspection intervals by 30–50 % through remaining-useful-life estimation, deferring borescope checks and cutting lifecycle costs (Lin et al., 2023; Zhang & Yue, 2021). Rolls-Royce's IntelligentEngine analogue reports similar gains—deferring routine inspections by one flight cycle in three—via real-time fusion of pressure, temperature, and vibration data with physics-based models and Kalman filters (cio.com, 2021; Satoh et al., 2020). When embedded in six-degree-of-freedom ascent simulations, propulsion twins sharpen gimbal-authority margins and payload-injection accuracy—for example, coupling the RL10 twin to a Delta IV model improved lateral-control margin by ~12 % and reduced injection error from 0.35 % to 0.08 % across Monte Carlo runs (Jiménez Mena et al., 2019; Liu et al., 2024).

Hybrid physics–AI surrogates—proper-orthogonal decomposition models and neural-network regressors—accelerate critical submodels (combustion chamber, turbopump) by two orders of magnitude while keeping global error below 5 %, enabling on-board twins running at 20 Hz for autonomous in-flight fault response (Tao et al., 2018; Orbi & Martin, 2020). Collectively, these results confirm that system-level digital twins—anchored in validated physics, continuously synchronized via digital threads, and reinforced with HIL validation—deliver quantifiable benefits in design efficiency, operational reliability, and lifecycle economy, charting a clear path toward fully integrated rocket-propulsion programs.

Table 1. Key milestones in the evolution of digital-twin technology.

Year	Development
1970	Apollo 13 "living model" ground simulators used for in-flight anomaly diagnosis
2002	Michael Grieves introduces the "Digital Twin" concept in product-lifecycle management
2010	John Vickers formally defines the Digital Twin for aerospace systems at NASA
2012	Glaessgen & Stargel publish the DT paradigm for future NASA and U.S. Air Force vehicles
2020s	Rapid explosion of digital-twin research and the emergence of nascent industry standards

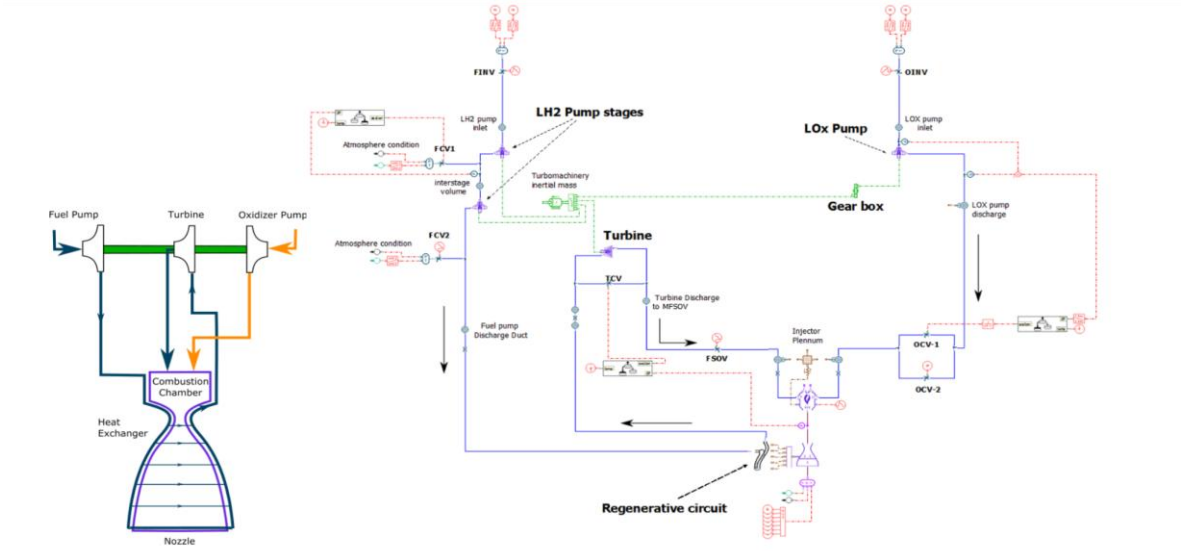

Figure 1. Architecture of the rocket-engine digital twin, showing sensor data ingestion, multi-physics co-simulation with reduced-order surrogates via the Functional Mock-up Interface (FMI), and hardware-in-the-loop validation (Jiménez Mena et al., 2019).

Conclusion

Digital Twin methodologies present a transformative approach for rocket engine development and operation by integrating multi-domain physics models with real-time data. They accelerate design cycles, enhance predictive maintenance, and enable comprehensive mission simulations. Future work should focus on AI-augmented models, lifecycle digital-thread integration, standardization, and onboard implementations to support autonomous operations and virtual certification, thereby reducing cost and risk in advanced propulsion systems.

References

Glaessgen, E., & Stargel, D. (2012). The digital twin paradigm for future NASA and U.S. Air Force vehicles. In Proceedings of the 53rd AIAA/ASME Structures, Structural Dynamics, and Materials Conference (Paper AIAA 2012-1818). Honolulu, HI.

Grieves, M. (2002). Digital twin: Manufacturing excellence through virtual factory replication [White paper]. University of Michigan.

Jiménez Mena, D. J., Pluchart, S., Mouvand, S., & Broca, O. (2019). Rocket engine digital twin – Modeling and simulation benefits (TFAWS Paper ID-04). In Proceedings of the Technical Forum on Avionics and Software Systems. NASA. Retrieved from

Url-1 https://tfaws.nasa.gov/wp-content/uploads/TFAWS19-ID-04.pdf

Lin, R., Yang, J., Huang, L., Chen, X., & Zhao, Y. (2023). Review of launch vehicle engine PHM technology and analysis methods research. Aerospace, 10(6), 517.

Url-2 https://doi.org/10.3390/aerospace10060517

Liu, X., Wang, Y., Chen, Z., & Zhou, K. (2024). Digital twin of space environment: Development, challenges, and opportunities. Remote Sensing, 16(16), 3023.

Url-3 https://doi.org/10.3390/rs16163023

Mena, D. J., Pluchart, S., Mouvand, S., & Broca, O. (2019, August). Rocket engine digital twin – Modeling and simulation benefits. In AIAA Propulsion and Energy Forum.

Url-4 https://doi.org/10.2514/6.2019-4114

National Academies of Sciences, Engineering, and Medicine. (2024). Foundational research gaps and future directions for digital twins. Washington, DC: National Academies Press. Retrieved May 10, 2025. **Url-5** https://www.nap.edu/catalog/26705/foundational-research-gaps-and-future-directions-for-digital-twins

O'Leary, M. (2023). Virtual certification: Regulatory acceptance of digital-twin evidence for aerospace systems. Journal of Aerospace Regulation, 5(2), 45–52.

Orbi, J., & Martin, L. (2020). The digital twin concept: A definition attempt. International Journal of Production Research, 58(12), 3546–3566.

Url-6 https://doi.org/10.1080/00207543.2019.1683578

Satoh, D., Ogura, K., Takahashi, Y., & Fujimoto, H. (2020). Integrating model-based and data-driven simulators for health management of a reusable rocket engine. Proceedings of the Prognostics and Health Management Society Annual Conference, 12(1), 1–9.

Tao, F., Cheng, J., Zhang, M., & Qi, H. (2018). Digital twin-driven product design, manufacturing and service with big data. International Journal of Advanced Manufacturing Technology, 94, 3563–3576. **Url-7** https://doi.org/10.1007/s00170-017-0233-1

Zhang, S., & Yue, M. (2021). A rocket health management system for vehicle testing and launching based on digital twin. Computer Measurement & Control, 29(8), 8–14.

science.nasa.gov. (2023). Why does the world (and NASA) need digital twins? Retrieved November 1, 2024. **Url-8** https://science.nasa.gov/biological-physical/resources/explainers-infographics/

cio.com. (2021, June 10). Rolls-Royce turns to digital twins to improve jet engine efficiency. Retrieved November 5, 2024. **Url-9** https://www.cio.com/article/3630789/rolls-royce-turns-to-digital-twins-to-improve-jet-engine-efficiency.html

ornl.gov. (2024). Trillion Pixel Challenge workshop explores digital twins & foundational AI models. Retrieved May 15, 2025.

Url-10 https://www.ornl.gov/news/trillion-pixel-challenge-workshop-explores-digital-twins-foundational-ai-models

AERONAUTICAL AND ASTRONAUTICAL ENGINEERING

Aircraft Design, Flight Dynamics And Performance

Control Systems: Adaptive, Intelligent, Digital, Optimal, Pneumatic-Hydraulic

Mechanical Vibrations And Structural Dynamics

Rotary Wing Aircraft

Spacecraft Control, Design And Performance

Theoretical, Computational And Experimental Aerodynamics And Fluid Dynamics

Theoretical, Computational And Experimental Structural Analysis And Design

Design and Analysis of Isogrid-Stiffened Cylindrical Structures for Launch Vehicles: Mathematical Modelling and Knockdown Factor Correlation with Finite Element Validation

Hakan Atkan[a], Atakan Altınkaynak[b]

[a] İstanbul Technical Universtiy /Graduate School, Defense Technologies, Turkey
[b] İstanbul Technical Universtiy /Faculty of Mechanical Engineering, Turkey
atkanh@itu.edu.tr

Keywords: Buckling, Cylindrical Structures, Isogrid, Knockdown Factor, Launch Vehicle.

Aim

Launch vehicle structures are subject to extreme mechanical environments, where mass efficiency must be balanced against safety and reliability. One structural configuration that has proven effective in this regard is the isogrid-stiffened cylindrical shell. These structures are widely used in aerospace engineering, particularly in interstages, skirts, and payload adapters. The key advantage of isogrid designs lies in their triangular rib pattern, which provides high stiffness-to-weight efficiency and near-isotropic structural properties. However, due to their thin-walled nature, such structures are also highly susceptible to buckling phenomena under axial, bending, and pressure loads.

Traditionally, engineers have used global knockdown factors (KDFs) to compensate for the discrepancy between idealized analytical predictions and the actual behavior of imperfect structures. These factors such as those presented in NASA SP-8007 [2] are widely accepted and applied in industry. However, they tend to be overly conservative and do not distinguish between the various buckling mechanisms present in stiffened shells. This over-conservatism often results in weight penalties and missed opportunities for optimization in structural design.

Recent advancements in research have introduced a more refined, mode-specific approach. Instead of applying a single global knockdown factor, different constants are proposed for distinct failure modes: c_0 for global shell buckling, c_1 for skin panel instability, and c_2 for stiffener (rib) crippling [4]. These updated knockdown factors offer a more accurate and physically meaningful framework for evaluating buckling resistance. However, applying these factors still requires caution, especially with skin buckling, where the interaction between panel aspect ratio, boundary conditions, and imperfections makes standardized correction factors less reliable.

This study aims to present a comprehensive analysis of isogrid-stiffened cylindrical structures by incorporating updated knockdown factors into classical shell theory and validating their performance using nonlinear numerical methods. Particular attention is given to the application and interpretation of skin-specific knockdown factors (c_1), which, unlike global knockdown values, cannot always be reduced to a fixed empirical constant and often require case-by-case analysis.

Material and Method

The methodology includes two main components: (1) analytical modelling based on thin-shell buckling theory, extended to include updated knockdown factors, and (2) finite element validation using nonlinear static analysis with geometric imperfections.

1. Analytical Formulation

The theoretical model is based on classical cylindrical shell buckling theory, extended to accommodate stiffening patterns and imperfection sensitivity. Three primary loading scenarios are considered:

- Axial compression, representing the majority of in-service launch vehicle load cases,
- Bending moment, simulating flight-induced bending loads and lateral thrust offsets,
- Internal pressure, relevant for structures integrated with pressurized tanks.

For each case, the ideal critical load is calculated using classical equations. Then, this value is modified using mode-specific knockdown factors:

$P_{actual} = c \cdot P_{ideal}$

where:

- P_{ideal} is the elastic critical load of a perfect geometry,
- c is the knockdown factor, selected from $\{c_0, c_1, c_2\}$ based on the dominant failure mode.

These constants originate from the Shell Buckling Knockdown Factor (SBKF) Project [4], which has provided a framework for applying them based on geometry, boundary conditions, and imperfection sensitivity. The global buckling factor (c_0) tends to be conservative and is often used for preliminary sizing. However, for skin buckling (c_1), no single value can be reliably applied across all geometries. Instead, skin buckling knockdowns depend on panel aspect ratio, loading configuration, edge support, and manufacturing imperfections.

As such, in this study, c_1 is not treated as a constant but rather as a design parameter to be evaluated through parametric and numerical methods. While empirical guidelines are available, especially for flat and rectangular panels, their application to cylindrical shell segments requires caution. This observation is crucial because underestimating c_1 may lead to non-conservative designs, while overestimating it results in unnecessary mass penalties.

2. Finite Element Modelling

Nonlinear simulations are performed to validate the analytical predictions. Finite element models are created to represent isogrid-stiffened cylindrical shells, including:

- Skin and ribs with representative aerospace materials (e.g., 2219-T87 aluminum),
- Boundary conditions approximating those found in real vehicle structures,
- Multiple geometric configurations with varying rib depths, panel lengths, and skin thicknesses.

To simulate realistic behavior, geometric imperfections are introduced into the models using the first buckling mode from linear analysis. The imperfection amplitude is typically scaled to 20% of the shell thickness, a standard practice in aerospace design.

Nonlinear static analysis using arc-length control methods is used to trace the load-displacement behavior until instability occurs. The simulations aim to identify:

- The critical buckling load,
- The location and nature of buckling (global, skin, or rib failure),
- Stress concentration areas and post-buckling stiffness.

Simulation outputs, including mode shapes and load-deflection curves, are then compared directly to the analytical predictions corrected with knockdown factors.

Findings

The updated knockdown-factor-based analytical model showed strong correlation with the results of nonlinear simulations across all loading cases.

1. Axial Compression:

Axial loading consistently produced buckling in either the shell (global) or skin (local panel) regions. When global buckling dominated, the c_0 factor predicted failure within 5–8% of the simulated critical load. When local panel instability governed, c_1 provided reasonable predictions, though slightly more variable, with discrepancies within 10–12%. These variations highlight the complexity of skin buckling and its dependence on panel geometry and boundary conditions.

It is important to emphasize that c_1 is not universally conservative. In some configurations, particularly those with long narrow panels or interrupted rib paths, the skin buckled earlier than predicted by generalized c_1 values from literature. This suggests that skin buckling must be evaluated case by case, using parametric analysis or detailed simulation rather than relying solely on catalogued constants.

Under pure bending, instability was more likely to initiate near structural transitions, such as weld lands or rib terminations. Here, combined effects of global and local deformation were observed. In these cases, both c_0 and c_1 needed to be considered. Predictions based on c_0 alone tended to underrepresent the contribution of localized buckling.

3. Internal Pressure*:*

In pressurized configurations, skin wrinkling under compressive hoop stress was the dominant mechanism. Although pressure generally stabilizes shell structures under axial load, it can exacerbate local instabilities when pressure loading is not symmetric or when pre-existing axial compression is present. The analytical model, adjusted with c_1, aligned well with simulation results, particularly when aspect ratio effects were included.

4. Rib Crippling:

For structures with high rib slenderness or under concentrated loads, rib crippling (c_2) was identified as the dominant failure mode. Predictions using c_2 matched simulation results within 6–9%. This agreement confirms the value of the rib-specific correction factor, especially in designs where rib height and thickness are optimized independently of skin stiffness.

Conclusion

This study demonstrates that mode-specific knockdown factors significantly improve the accuracy and reliability of structural buckling predictions for isogrid-stiffened cylindrical shells. While general knockdown values like c_0 are useful and generally conservative, skin-specific knockdown factors (c_1) require more nuanced application. The behavior of the skin under axial, bending, and pressure loading is influenced by several parameters, and generalized values may not always provide adequate safety margins.

Consequently, it is not appropriate to assign fixed values to skin knockdown factors. Instead, each cylindrical configuration should be evaluated individually, using empirical correlations, numerical simulations, or a combination of both. The findings suggest that incorporating updated knockdown factors into early-phase structural design enables mass savings without compromising safety.

The results validate the use of c_0, c_1, and c_2 as effective tools for refining theoretical models of stiffened shell behavior. Simulation outputs confirmed that these parameters not only yield improved accuracy but also help in identifying the dominant failure mechanism and its sensitivity to geometry and loading.

Future work may explore the integration of optimization routines for weld land transitions, the inclusion of thermal and dynamic effects, and the experimental validation of these findings using scaled structural test articles.

References

Douglas Aircraft Company. (1973). Isogrid Design Handbook (NASA CR-124075). NASA Contractor Report.

NASA. (1968). Buckling of Thin-Walled Circular Cylinders (NASA SP-8007). National Aeronautics and Space Administration.

Steeve, B. E. (1996). Verification of Orthogrid Finite Element Modeling Techniques (NASA TM-19970001271). NASA Technical Memorandum.

Url-1 https://ntrs.nasa.gov/citations/19970001271

Hilburger, M. W., Nemeth, M. P., & Starnes, J. H. (2020). Shell Buckling Knockdown Factor (SBKF) Project Overview. NASA Langley Research Center.

Url-2 https://ntrs.nasa.gov

Numerical Modeling of Composite Laminates Under Out-of-Plane Impact

Vuslat Sena Avcı[a]

[a]Istanbul Technical University, Departmant of Aeronautical and Astronautical Engineering, Master of Science Program, Turkey
avciv18@itu.edu.tr

Keywords: Composite laminates, Out-of-plane Impact Behavior, Numerical Modeling Of Composite Damage, Cohesive Zone Method For Delamination.

Aim

The increasing use of composite materials in the aerospace industry is driven by their advantages in weight reduction, structural efficiency, and tailorability to specific load-bearing requirements. However, composite structures are highly sensitive to impact loading, which can induce complex failure mechanisms, including delamination, matrix cracking, and fiber breakage. These damage modes can significantly compromise structural integrity, leading to reduced mechanical performance and long-term durability.

Understanding the response of composite laminates to out-of-plane impact loading is crucial for ensuring their reliability in aerospace applications. The impact behavior of these structures is influenced by several factors, including impact velocity, energy, angle, and the stacking sequence of the composite layers. These parameters determine the nature of damage initiation and propagation, as well as the overall failure characteristics of the structure. Moreover, strain rate effects play a significant role in the dynamic response of composites, affecting their deformation and fracture mechanisms under out-of-plane impact conditions.

This study aims to numerically investigate the impact behavior of composite laminates subjected to out-of-plane loading using LS-DYNA. The analysis will focus on the influence of key parameters such as impact velocity, energy, angle, and stacking sequence on damage initiation and progression. Cohesive zone modeling (CZM) and appropriate composite damage criteria [1]will be employed to accurately capture the failure mechanisms. The findings of this study will provide valuable insights into the structural response of composite plates under out-of-plane impact loading, contributing to the optimization of composite material design for aerospace applications.

Material and Method

The impact model employed in this study is illustrated Figure 1. A cylindrical impactor with a hemispherical lower section, made of structural steel, is modeled as rigid to simulate realistic impact conditions. The impactor strikes the center of the composite laminate at two different velocities (10 m/s and 40 m/s) and two different impact angles (0° and 45°). The composite laminate measures 200 mm in length and 200 mm in width, with 2.944 mm and 4.416 mm thicknesses for the 16-layer and 24-layer configurations. The laminate is fully constrained along all four edges, restricting all six degrees of freedom (DOF) to prevent displacement and rotation. Constraints are marked in red in Figure 1.

[1] avciv18@itu.edu.tr

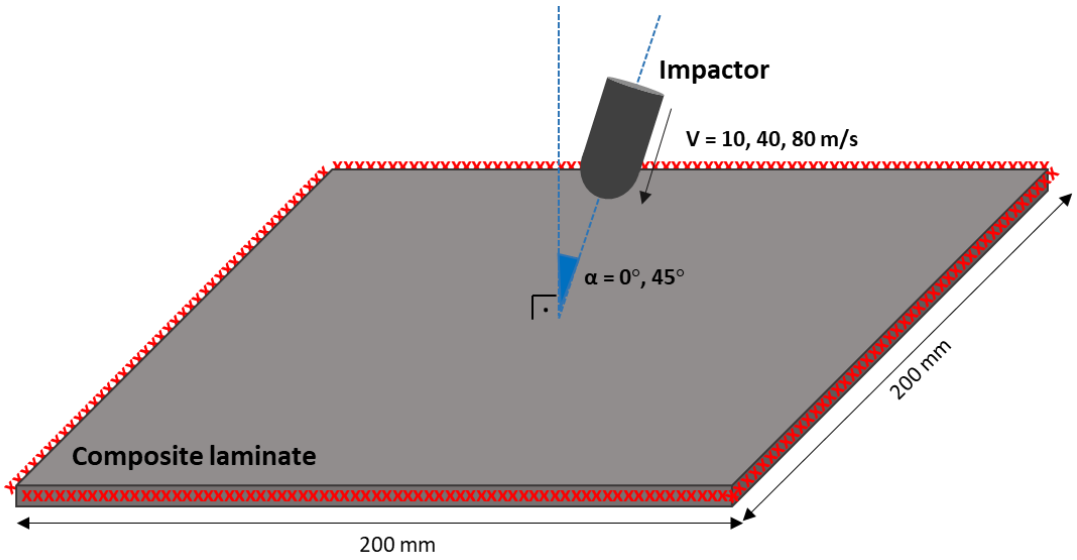

Figure 1. Geometry and boundary conditions for the simulation of out-of-plane impact on composite laminate.

An eroding contact is defined between the impactor and the composite laminate's top surface to accurately capture damage evolution, penetration, and material removal during impact. This setup allows for a detailed investigation of the influence of impact velocity and angle on failure mechanisms such as delamination, matrix cracking, and fiber breakage.

The composite material considered in this study is AS4/8552, a unidirectional carbon fiber/epoxy prepreg with a fiber area weight of 134 g/m². To assess the effect of fiber orientation on impact resistance, different stacking sequences are analyzed, including unidirectional (UD), quasi-isotropic (QI), and cross-ply (CP) configurations. All layups are designed symmetrically to ensure a balanced structural response. Two laminate thicknesses are examined: 16-ply and 24-ply. The 16-ply configurations, with a thickness of 2.944 mm, are defined as $[0°]_{8s}$ for UD, $[0°/45°/-45°/90°]_{2s}$ for QI, and $[0°/90°]_{4s}$ for CP. Similarly, the 24-ply laminates, with a thickness of 4.416 mm, follow $[0°]_{12s}$ for UD, $[0°/45°/-45°/90°]_{3s}$ for QI, and $[0°/90°]_{6s}$ for CP. These variations enable a comprehensive evaluation of stress distribution, damage initiation, and overall structural integrity under impact loading.

The material properties of the AS4/8552 composite, including elastic moduli, Poisson's ratios, shear moduli, strength values, and fracture energies, are presented in Table 1. These parameters are essential for accurately modeling the impact behavior of the composite laminates. The material coordinate system is defined such that the 1-direction corresponds to the fiber axis, the 2-direction represents the in-plane transverse direction, and the 3-direction denotes the through-thickness direction of the laminate.

Table 1. The material properties of AS4/8552 unidirectional composite prepreg.

Properties	Value	References
Density, ρ	1580 kg/m^3	(Karnati, 2014; Mohammadi et al., 2020; Vaidya et al., 2006)
Thickness, t	0.184 mm	(Perogamvros & Lampeas, 2015)
Elastic modulus in the 1-direction, E_1	135 GPa	(Ding et al., 2016; Lopes et al., 2009; Perogamvros & Lampeas, 2015)
Elastic modulus in the 2-direction, E_2	9.5 GPa	(Ding et al., 2016)

Elastic modulus in the 3-direction, E_3	9.5 GPa	(Ding et al., 2016)
Poisson's ratio in the 12-plane, ν_{12}	0.3	(Ding et al., 2016)
Poisson's ratio in the 13-plane, ν_{13}	0.3	(Ding et al., 2016)
Poisson's ratio in the 23-plane, ν_{23}	0.45	(Ding et al., 2016)
Shear modulus in the 12-plane, G_{12}	4.9 GPa	(Ding et al., 2016)
Shear modulus in the 13-plane, G_{13}	4.9 GPa	(Ding et al., 2016)
Shear modulus in the 23-plane, G_{23}	3.275 GPa	(Ding et al., 2016)
Tensile strength in the 1-direction, S_{1T}	2207 MPa	(Karnati, 2014; Lopes et al., 2009)
Compressive strength in the 1-direction, S_{1C}	1531 MPa	(Karnati, 2014; Lopes et al., 2009)
Tensile strength in the 2-direction, S_{2T}	81 MPa	(Lima et al., 2023; Lopes et al., 2009)
Compressive strength in the 2-direction, S_{2C}	199.8 MPa	(Lima et al., 2023; Lopes et al., 2009)
Shear strength in the 12-plane, S_{12}	114.5 MPa	(Lima et al., 2023; Lopes et al., 2009)
Pure mode I critical fracture energy, G_{IC}	274.2 (±29.1) J/m^2	(Mollón et al., 2013)
Pure mode II critical fracture energy, G_{IIC}	738.0 (±103.8) J/m^2	(Mollón et al., 2013)

The impact behavior of composite laminates subjected to out-of-plane loading is numerically investigated using LS-DYNA. To model the composite laminate, each layer is individually represented using solid elements to accurately capture the material's mechanical response. The interaction between layers is represented by cohesive zone elements, simulating the bonding interface where delamination may occur due to interlaminar shear or normal stress. These elements track damage initiation and progression based on stiffness and fracture toughness. Two different unidirectional configurations with 16 and 24 layers were developed, as has been done so far. The side views of both configurations are presented in Figure 2 and Figure 3, respectively. The 16-layer configuration is constructed as $[0°]_{8s}$, while the 24-layer configuration follows $[0°]_{12s}$.

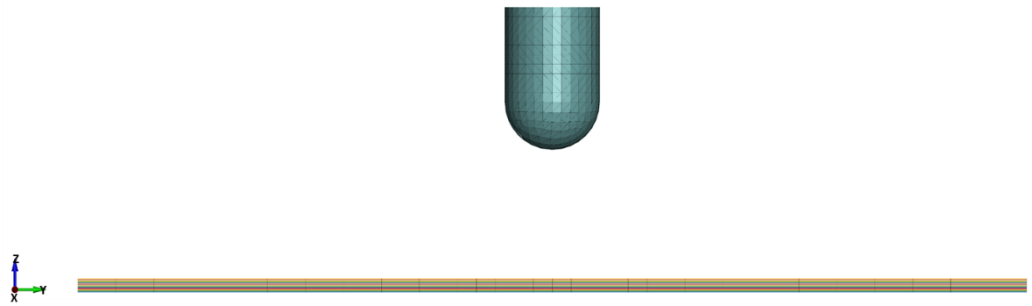

Figure 2. Side view of 16-layer UD composite laminate with $[0°]_{8s}$ stacking sequence.

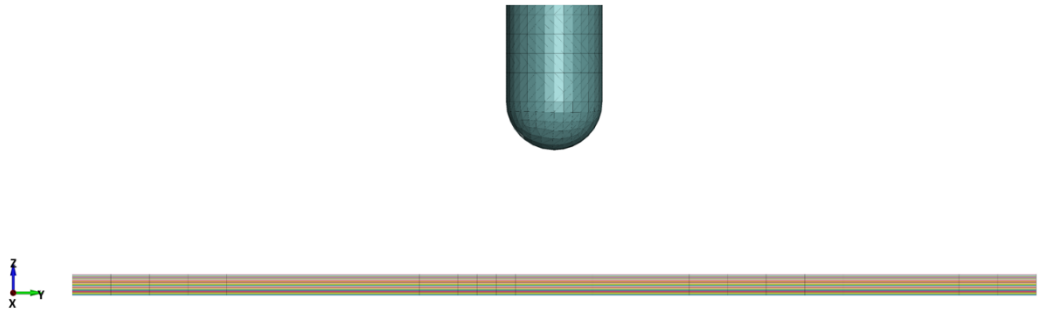

Figure 3. Side view of 16-layer UD composite laminate with $[0°]_{12s}$ stacking sequence.

The custom view of the model, as shown in Figure 4, illustrates the fiber orientations in the longitudinal (x-direction), transverse (y-direction), and through-thickness (z-direction) directions. A downward initial velocity is applied along the negative z-direction to simulate the impact, ensuring a realistic representation of the out-of-plane loading condition. The global mesh size is set to 8 mm with an aspect ratio of approximately 1:44, while a refined mesh of 4 mm with an aspect ratio of approximately 1:22, both determined based on the laminate thickness, is employed in the impact region to better capture localized deformation and stress concentrations, thereby enhancing the accuracy of the laminate's response under dynamic loading conditions.

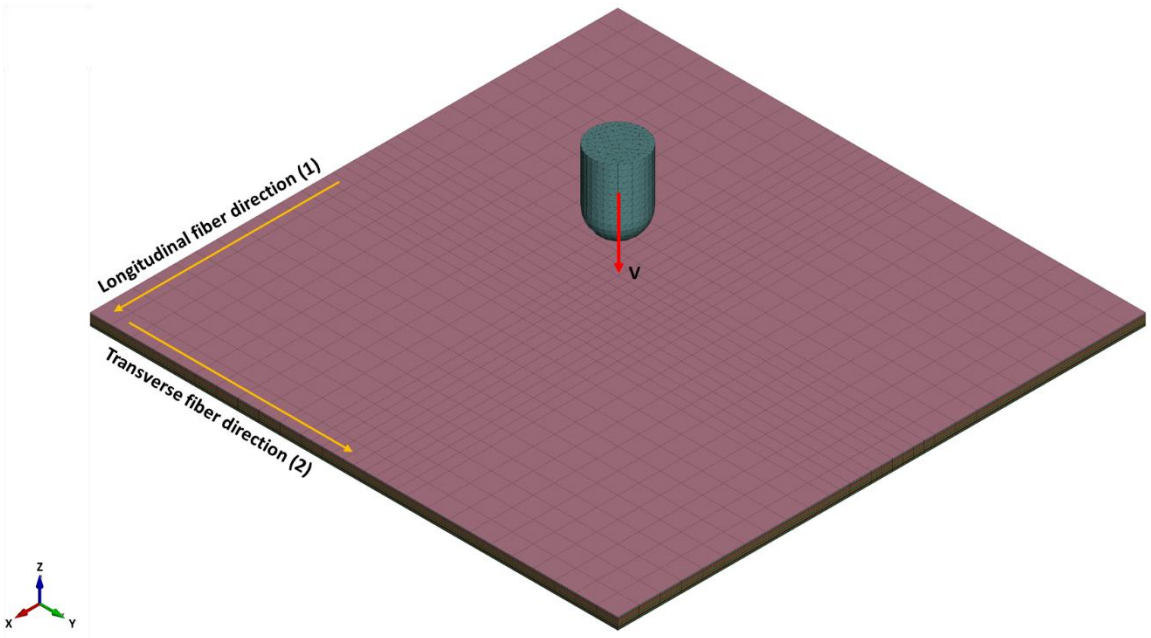

Figure 4. Custom view of 16-layer UD composite laminate with $[0°]_{12s}$ stacking sequence.

Findings

Although the study is still in progress, preliminary results obtained for the $[0°]_{8s}$ stacking sequence have already yielded valuable insights into the impact behavior of composite laminates. Experimental investigations from the literatüre suggest that impact velocity, energy, and angle will significantly influence damage initiation and progression, affecting failure mechanisms such as delamination, matrix cracking, and fiber breakage (Vaidya et al., 2006; Yang et al., 2024). Furthermore, the influence of different stacking sequences will be systematically analyzed, as variations in layer orientation are expected to significantly affect stress distribution, energy absorption, and overall damage tolerance.

Moreover, the stress profile obtained from the finite element model indicates that stress concentrations occur differently depending on the stress direction. For instance, in the x-direction (representing the longitudinal axis of the layered structure), compressive stresses develop along the upper surface of the laminate, while tensile stresses are observed along the lower surface.

Figure *5* illustrates the variation of the impactor's total energy throughout the impact event with the composite laminate. The initial high energy rapidly decreases as energy is transferred to the laminate through deformation and damage, followed by a slight recovery as the impactor rebounds. The stabilized energy level afterward reflects the residual energy remaining after the impact.

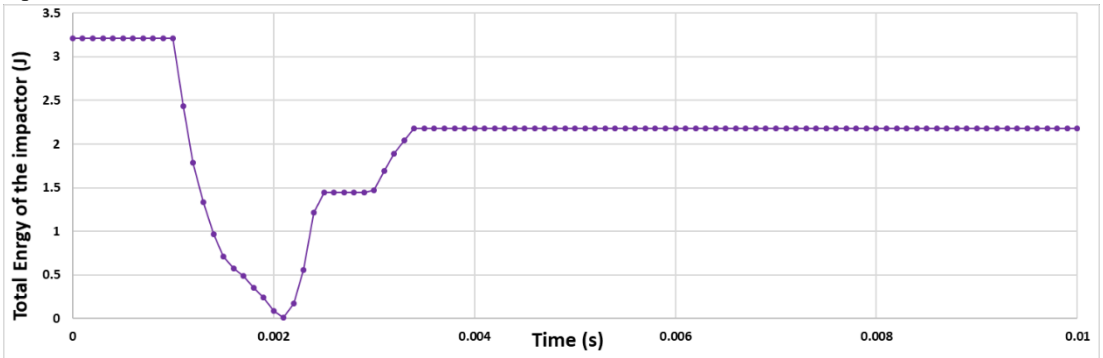

Figure 5. Total energy variation of the impactor during the impact with the composite laminate.

The graph presented in Figure 6 illustrates the stress distribution over 16 elements located in the upper lamina at the impact region throughout the impact event. The maximum stress occurs between 0.0021 and 0.0023 seconds, with the stress in the x-direction (representing the longitudinal axis of the layered structure) reaching up to 110 MPa. Figure 7 presents detailed stress contour plots for three representative time steps within this interval, providing a clear visualization of the stress evolution.

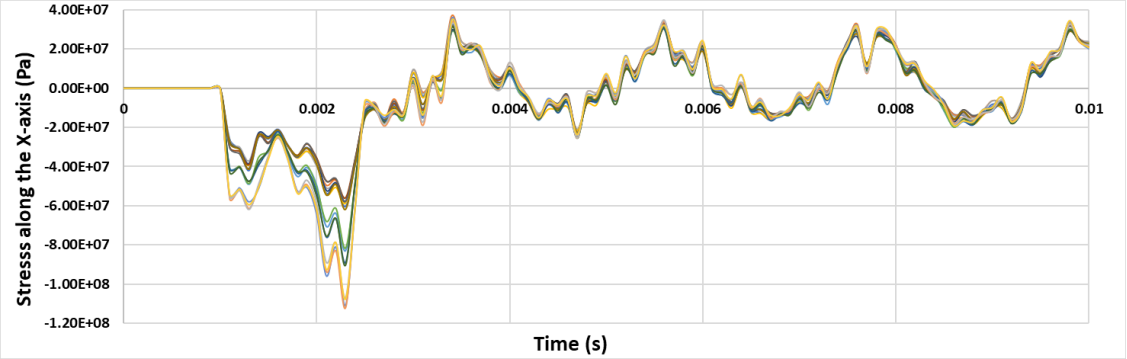

Figure 6. X-direction stress distribution in the upper lamina at the impact region.

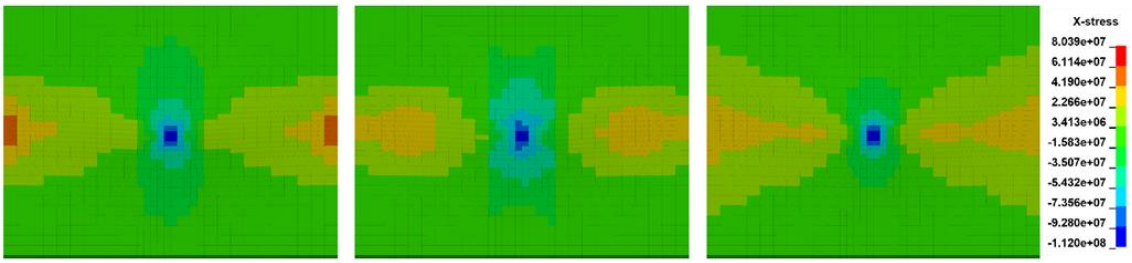

Figure 7. X-direction stress contour plots in the upper lamina at three time steps, from left to right: 0.0021 s, 0.0022 s, and 0.0023 s.

The graph presented in Figure 8 illustrates the stress distribution over 16 elements located in the upper lamina at the impact region throughout the impact event. The maximum stress occurs between 0.0021 and 0.0023 seconds, with the stress in the y-direction (representing the transverse axis of the layered structure) reaching up to 105 MPa. Figure 9 presents detailed stress contour plots for three representative time steps within this interval, providing a clear visualization of the stress evolution.

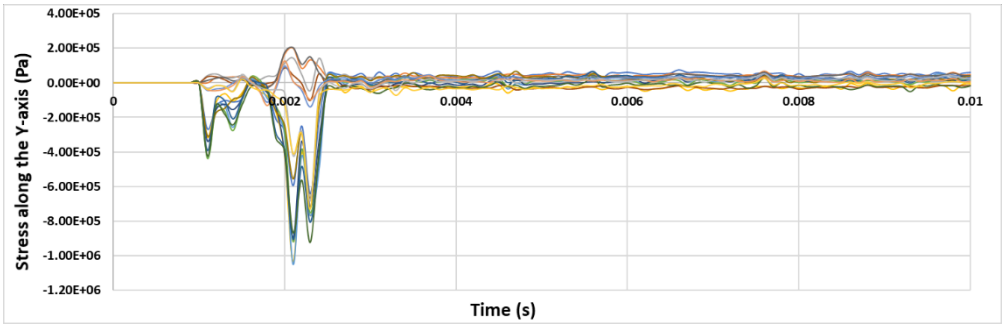

Figure 8. Y-direction stress distribution in the upper lamina at the impact region.

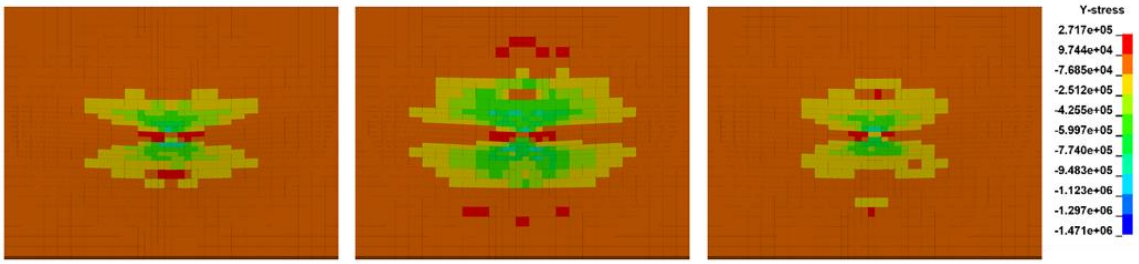

Figure 9. Y-direction stress contour plots in the upper lamina at three time steps, from left to right: 0.0021 s, 0.0022 s, and 0.0023 s.

Conclusion

Understanding the interplay between impact parameters and composite configurations is essential for predicting damage evolution and improving structural performance. This study establishes key correlations between stacking sequence, strain rate, and failure mechanisms, providing valuable insights into composite behavior under out-of-plane impact. The findings contribute to the optimization of composite materials, enhancing their durability and efficiency in aerospace applications.

References

Ding, A., Li, S., Wang, J., Ni, A., Sun, L., & Chang, L. (2016). Prediction of Process-Induced Distortions in L-Shaped Composite Profiles Using Path-Dependent Constitutive Law. Applied Composite Materials, 23(5), 1027-1045.
Url-1 https://doi.org/10.1007/s10443-016-9501-8
Karnati, S. R. (2014). A Mixed-Mode (I-II) Fracture Criterion for AS4/8552 Carbon/Epoxy Composite Laminate.
Lima, R. A. A., Tao, R., Bernasconi, A., Carboni, M., Carrere, N., & Teixeira de Freitas, S. (2023). Uncovering the toughening mechanisms of bonded joints through tailored CFRP layup. Composites Part B: Engineering, 263, 110853.
Url-2 https://doi.org/https://doi.org/10.1016/j.compositesb.2023.110853
Lopes, C. S., Seresta, O., Coquet, Y., Gürdal, Z., Camanho, P. P., & Thuis, B. (2009). Low-velocity impact damage on dispersed stacking sequence laminates. Part I: Experiments. Composites Science and Technology, 69(7), 926-936.
Url-3 https://doi.org/https://doi.org/10.1016/j.compscitech.2009.02.009
Mohammadi, R., Najafabadi, M. A., Saghafi, H., & Zarouchas, D. (2020). Mode-II fatigue response of AS4/8552 carbon /epoxy composite laminates interleaved by electrospun nanofibers. Thin-Walled Structures, 154, 106811.
Url-4 https://doi.org/https://doi.org/10.1016/j.tws.2020.106811
Mollón, V., Bonhomme, J., Viña, J., & Argüelles, A. (2013). Fracture and Failure Mechanisms for Different Loading Modes in Unidirectional Carbon Fibre/Epoxy Composites. In (pp. 227-255).
Url-5 https://doi.org/10.1002/9781118535288.ch10
Perogamvros, N. G., & Lampeas, G. N. (2015). Experimental and numerical investigation of AS4/8552 interlaminar shear strength under impact loading conditions. Journal of Composite Materials, 50(19), 2669-2685. **Url-6** https://doi.org/10.1177/0021998315610899
Vaidya, U. K., Gautam, A. R. S., Hosur, M., & Dutta, P. (2006). Experimental–numerical studies of transverse impact response of adhesively bonded lap joints in composite structures. International Journal of Adhesion and Adhesives, 26(3), 184-198.
Url-7 https://doi.org/https://doi.org/10.1016/j.ijadhadh.2005.03.013
Yang, M., Xuan, H., Qin, T., Wang, Y., Zhou, Y., & Zhang, W. (2024). Numerical and experimental study of the residual strength of CFRP laminate single-lap joint after transverse impact. International Journal of Adhesion and Adhesives, 130, 103593.
Url-8 https://doi.org/https://doi.org/10.1016/j.ijadhadh.2023.103593

Investigation Of The Interaction of Carbon Fiber Cylindrical Rocket Bodies With Radial Bolt Joints

Kubilay Sazan[a]

[a] Istanbul Technical University, Aeronautical and Astronautical Engineering, Turkiye
sazan19@itu.edu.tr

Keywords: CFRP, Finite Element Analysis, Mechanical Joint, Mechanical Strength.

Aim

Rockets are generally designed with cylindrical bodies to have more aerodynamically efficient performance. In this context, radial bolt connections are mostly preferred in the structural connections of rocket bodies. Bolt heads are hidden with special cut-outs to reduce aerodynamic drag in rocket bodies made of metals. However, this method causes deterioration of fiber integrity and reduction in structural stiffness in carbon fiber reinforced polymer (CFRP) material bodies.
In this study, the effects of radial bolt connections and bolt head clearance depth on structural stiffness of two-cylinder structures made of CFRP were investigated. Analyses were performed in Ansys ACP module using the finite element method. The effects of different connection configurations on stiffness were compared in terms of their stiffness. As a result of the study, it was determined that structural stiffness decreased with the deepening of bolt head cuts.
In the literature, CFRP and mechanical connection modeling have generally been examined with plates. In this study, it is aimed to provide a different perspective to the literature by through the analysis of cylindrical structures. In future studies, it is expected that the study will be detailed by adding flight conditions such as vibration and temperature to this connection area.

Material and Method

The usage of metal materials is a common practice due to high structural and thermal strength requirements in rocket designs (Khan et al., 2025). However, advances in material technology have made the usage of composite materials increasingly common, especially in applications which requires weight reduction. Although, composite materials are notable for their high specific strength, the use of these materials must design to meet high structural and thermal strength requirements. In this context, the usage of composite materials in rocket designs provides advantages over metal materials, but at the same time, the need to optimize the structural and thermal performance of these materials poses a challenge.
The designs of rockets are formed according to the main mission decided upon in the conceptual design phase in line with the user's demand. Example of this design mission is, to shoot down an aircraft, hit a ballistic target, or destroy a tank target. Rockets consist of various subsystems in line with their main mission (Hongxing et al., 2023). Each subsystem is a mechanical or avionic subunit that performs a specific function so that the rocket can fulfill its main mission. As can be seen form Figure 1. depending on their sizes and functional requirements, subsystems can be located separately on the rocket or as integrated units to cover a specific area. In this study, it is aimed to model the fracture and bending behavior of a 24 kg subsystem area under rocket maneuver.

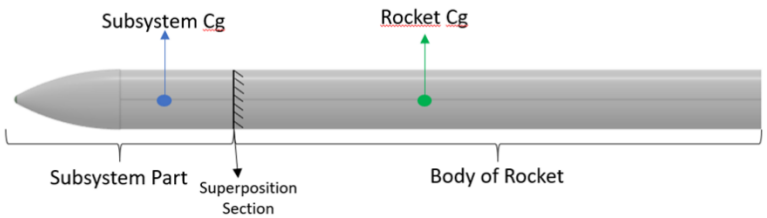

Figure 1. Rocket Body and Subsystem.

This study aims to investigate the effect of the shear and bending forces that a subsystem region will create under the maneuver to which the missile will be subjected, on the shear and bending forces that will occur in the connection area on the composite missile body. The maneuver to which the missile will be subjected is assumed to be 40 g. In the study, the type of coupling joint commonly used in rockets was preferred can be seen in Figure 2. Due to the shape connection they create, coupling joints are frequently preferred in order to provide a safe and rigid connection in applications requiring high stiffness.

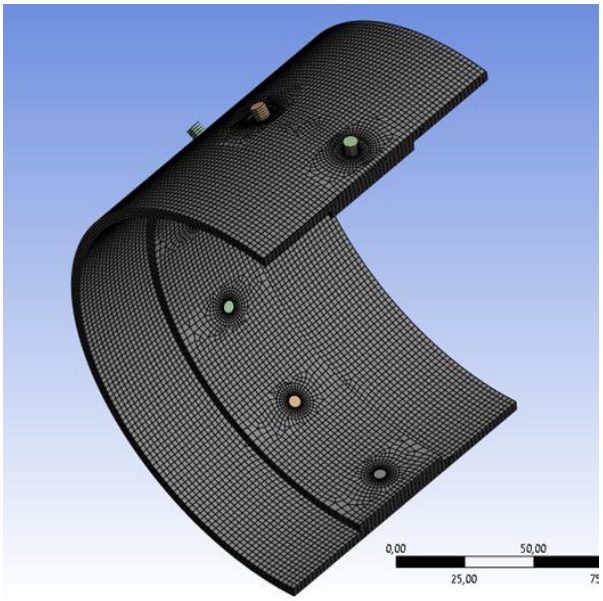

Figure 2. Ansys Workbench Mesh and Layer Solid Model.

In the coupling joint of rocket bodies, bolts or pins are used to limit the degree of freedom in the flight direction. In these types of connections, radial bolts drilled along the body section are mostly preferred to provide ease of assembly. In the scope of this study, it was preferred to fix the bodies with radial bolts. In the placement of radial bolts, the distance between the bolts and the distance of the bolts to the body edge are critical factors that directly affect structural stiffness. In this context, the W(distance)/D (bolt diameter) ratio plays a critical role in structural stiffness (Aktas et al., 2003). In this study, the use of 12 bolts with a diameter of 6 mm was preferred. It is anticipated that this choice provides a suitable solution in order to keep the structural strength high.

Different bolt types can be used in designs according to assembly requirements. Bolts are classified according to a series of features such as their heads, lengths, diameters, and thread types (Jack, 2013). In cylindrical rocket designs, it is preferred to embed the bolt heads in the body in order to prevent extra drag. In composite bodies, embedment of bolt heads reduces structural stiffness by disrupting fiber orientation locally. This study examines the strain, stress, and structural integrity of fibers in the connection areas of a composite body with a wall thickness of 4 mm with different embedment amounts (1 mm, 2 mm, and 3 mm) and no embedment.

Carbon fiber material is generally preferred in line with high structural and thermal requirements, in designs of rocket. Carbon fiber materials are quite suitable materials in terms of structural safety of rockets due to their high specific strength properties. However, due to the high production costs and certain performance deficiencies of other alternative materials, the usage of Kevlar and glass fiber materials is generally not preferred. In this study, MAT_162 UD fabric, which has been characterized as a material, was used (Lee et al., 2011).

First, the selected material information is defined in the material information section in the Ansys ACP (Advanced Composite Pre-Post) module. In the analyses performed, the basic mechanical properties of the material, young's modulus, Poisson ratio, shear modulus, tensile strength, compressive strength, shear strength, the modeling type will be layer-based

and the failure criterion information are defined. The specified material properties are defined according to the x, y and z axes (xy, yz, xz for shear modulus).

The design model to be loaded must be in shell format. The ANSYS application accepts each shell as a layer and layers these shells in the specified orientation when switching to the solid model. The geometry in shell form is meshed before being transferred to ACP. Since the analysis will focus on the hole perimeters, the mesh density around the holes must be fine. Within the scope of the analysis, the surroundings of the holes were divided into equal parts as ± 6°. Mesh was also assigned as course mesh to the non-hole areas in between and the parts of the bodies outside the connection area. As the Figure 2 shows, 2 mm mesh size was preferred for flat parts, the mesh size was reduced to 0.35 mm around the holes. Since fiber agents are seen more around the holes, these areas were left with a larger mesh size. As a mesh type, the analysis time was short and a more rectangular element was preferred.

Within the scope of this study, Figure 1 and Figure 2 shows the connection area to be analyzed was examined by making it independent from the center of gravity of the rocket with the superposition method. With this method, the body close to the center of gravity was locked by selecting a fixed support. On the other side, a 21 kg load was applied from the center of gravity of the subsystem which shown in Figure 3.

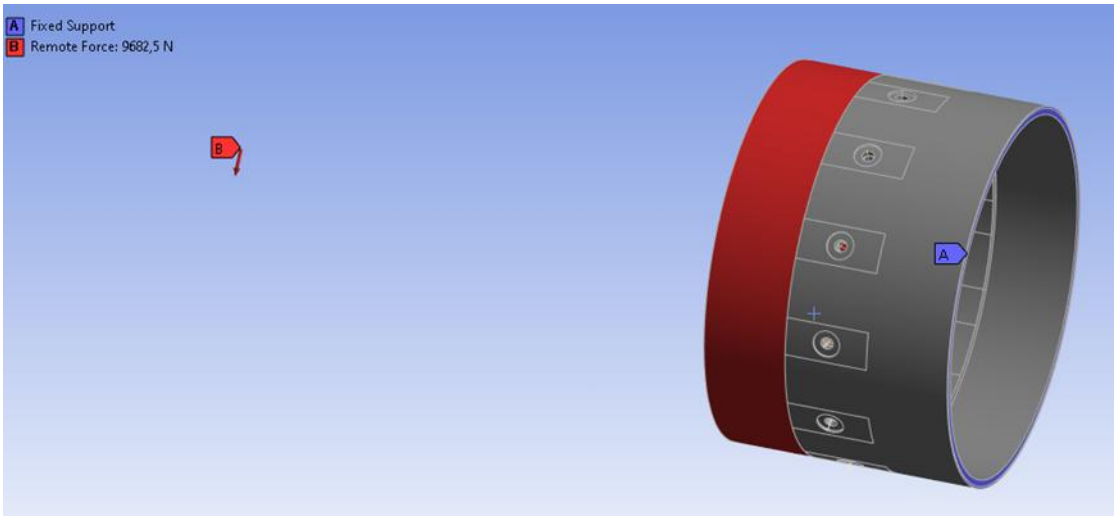

Figure 3. Support and Force Modelling in Ansys.

Finally, the obtained stress and strain values obtained and failure evaluation was made.

Findings

Within the scope of this study, analyses were performed on 4 different designs. The maximum stress, maximum deformation and the number of failing elements for the layer in contact with the bolt head are shared in Table 2.

The information in Table 3 shows the change in body stiffness depending on the increase in hole depth in percent in the column in Table 2.

Table 1. Material Features of MAT_162 UD (Lee et al., 2011).

Young's Modulus X direction (GPa)	122.51	**Tensile Strength X direction (MPa)**	1835.4	**Shear Modulus XY direction (GPa)**	4.76
Young's Modulus Y direction (GPa)	8.4	**Tensile Strength Y direction (MPa)**	40.5	**Shear Modulus YZ direction (GPa)**	1.5
Young's Modulus Z direction (GPa)	8.4	**Tensile Strength Z direction (MPa)**	40.5	**Shear Modulus XZ direction (GPa)**	1.5
Poisson's Ratio XY	0.1	**Compressive Strength X direction (MPa)**	700	**Shear Strength XY direction (MPa)**	41.5
Poisson's Ratio YZ	0.2	**Compressive Strength Y direction (MPa)**	184.2	**Shear Strength YZ direction (MPa)**	55
Poisson's Ratio XZ	0.2	**Compressive Strength Z direction (MPa)**	184.2	**Shear Strength XZ direction (MPa)**	55

Table 2. Analyze Results for maximum stress, maximum deformation and the number of failing elements for the layer in contact with the bolt head.

Hole Depth	Max Stress (MPa)	Total Displacement (mm)	Max. Num. Hole Element Fails
No Hole	903.79	0,6054	108
1mm	792.01	0,568	73
2mm	720.7	0,714	82
3mm	953.94	0,8758	159

Table 3. Comparisons of Deformation Change Percentage.

	No Hole to 1 mm	1mm to 2mm	2mm to 3mm
Deformation Change Percentage (%)	6,2	25,7	23,0

According to shared tables, it is possible to make the following outcomes,

- Figure 4. Shows the stress values observed for the design without embedment for the bolt head is higher than the configuration with 1mm embedment. The reason for this situation is that the bolt head, which has a flat surface, crushes the cylindrical body until it absorbs the load. Since it first provides point contact with the surface it crushes, it causes very high deformation and fiber failure for local elements.

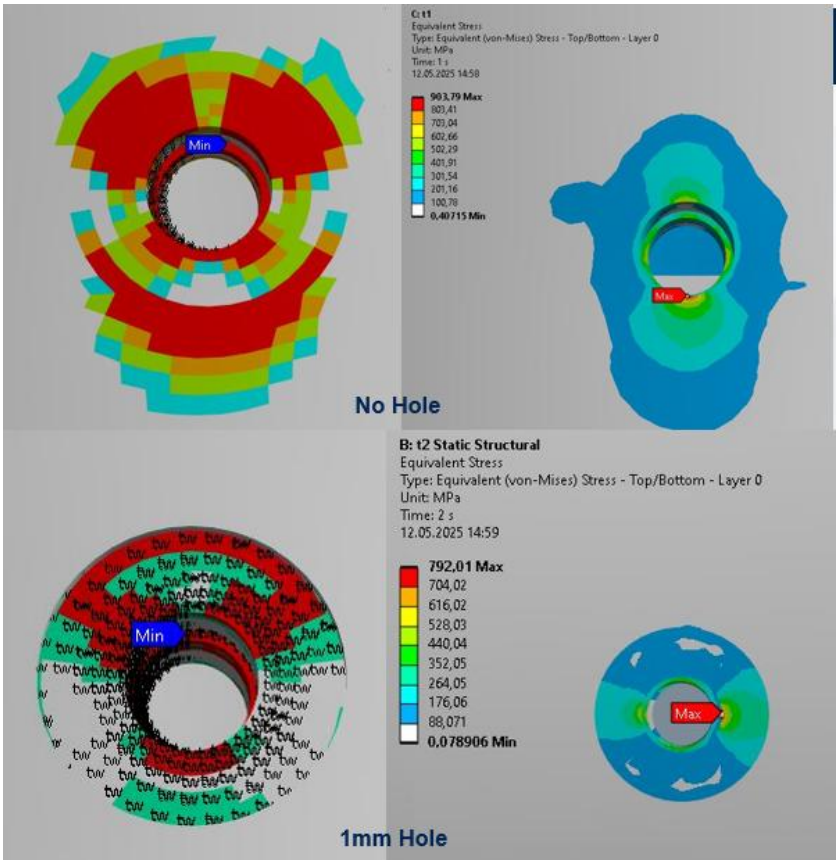

Figure 4. Stress and Failure Around Top Hole for No Hole and 1mm Hole Analyzes.

- As the bolt head embedment depth increases, although an aerodynamically efficient structure is formed, it has been observed that the stiffness decreases by approximately 18.3% for each mm of depth. When we plot the changing deformation due to the decrease, the graph shown in Table 3 can be obtained.
- As can be seen in Figure 5, the bolt tensions decrease as the approaches the neutral axis of the bending force. If the rocket's stiffness requirements were not directed towards maneuver in all directions, the amount of unloading in the bolts in the regions close to the neutral axis could be increased.

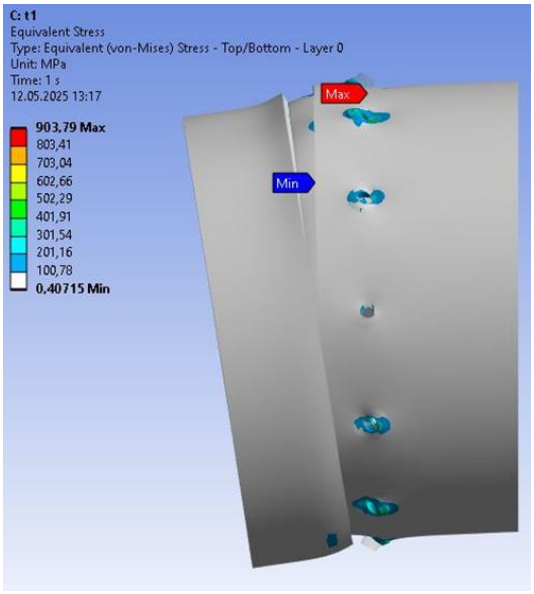

Figure 5. Stress Distribution for Each Hole from Top to Mid for no Hole Depth.

- Finally, if the desired maneuver in different direction is defined differently in the design requirements, there is not the same that the depths of the holes of embedment bolt head be the same as can be seen in Figure 5. In addition, incorrect assembly in the designs can be prevented in this way.

Conclusion

Composite materials are frequently used in applications such as aircraft which weight reduction is required. The sizes of composite structures used in aircraft are extremely high compared to their wall thickness. This situation causes, modeling and analysis are examined on flat plates for these structures. Within the scope of this study, the analysis of mechanical joint methods for a cylindrical body is a first in the literature.

Although radial bolted connection type provides ease of assembly for rocket designs, the drag caused by bolt heads is of critical importance. On the other hand, the use of radial bolts creates drag due to bolt heads and therefore they must be embedded in the body. In composite material bodies, embedding bolt heads creates an average of 18.3% stiffness loss for each mm of discharge.

In the analyses, it was assumed that the bolts did not fail under load, there was no stripping on the threaded surfaces, there was no assembly clearance for antennas, sensors or other structural parts in the bodies and the load was static. These assumptions cause the analyses to deviate from the real.

Rockets heat up excessively during the flight condition and enter low-pressure envelopes. In further studies, it is possible to study how high temperature affects this stiffness, the behavior of the body under low pressure, and the manufacturability, sustainability and pricing of this structure.

References

Aktas, A., & Dirikolu, M. H. (2003). The effect of stacking sequence of carbon epoxy composite laminates on pinned-joint strength. Composite Structures, 62(1), 107–111. doi:10.1016/s0263-8223(03)00096-5

Hongxing, Z., Fei, Z., Hang, X., Xiaowen, X., & Shi, H. (2023). Modular design of missile electrical system. Journal of Physics. Conference Series, 2460(1), 012144. doi:10.1088/1742-6596/2460/1/012144

Jack, H. (2013). Mechanical Design. In Engineering Design, Planning, and Management (pp. 469–545). doi:10.1016/b978-0-12-397158-6.00012-7

Khan, B., Ali, S. A., Gupta, R. K., Srivastava, S. K., & Kumar, P. (2025). Structural Design and Fabrication of a Rocket. doi:10.13140/RG.2.2.14979.62242
Lee, S.; Byun, J.; Cho, H. In Progressive damage structural analysis of carbon/epoxy composite laminates, The 18th International Conference of Composite Materials, ICC Jeju, Korea, 2011; pp 21-26.

APPLIED INFORMATICS

Computational Electromagnetics

Data Analysis

Medical Image Analysis

Nyström Integral Method for Mode Solving in Optical Waveguides with Arbitrary Geometries

Mücahit Hüseyin Özdilekler[a], Mehmet Çayören[a]

[a] Istanbul Technical University Faculty of Electrical and Electronics Engineering, Department of Electronic and Communication Engineering, Türkiye
ozdilekler18@itu.edu.tr

Keywords: Eigenmode Solution, Integral Equations, Nyström Method, Optical Waveguides.

Aim

The analysis of modes supported by optical waveguides is a crucial step in photonic system design. Optical waveguides serve as the backbone of photonic circuits and communication systems, making the accurate computation of supported modes essential. Various numerical methods, such as the Finite-Difference Time-Domain (FDTD) method, Finite Element Method (FEM), and Mode Matching techniques, are commonly employed to determine waveguide modes (Fallahkhair, Li, & Murphy, 2008). However, integral equation methods provide an alternative, often more efficient approach, particularly when dealing with complex geometries. In this study, we aim to solve the mode structure of arbitrarily shaped optical waveguides using the Nyström integral method. Unlike conventional discretization-based approaches, the Nyström method offers an efficient solution by discretizing integral equations rather than differential equations, providing improved accuracy and computational efficiency in certain cases (Wang, Cox, & Friedman, 1998).

Material and Method

To determine the mode profiles in optical waveguides with arbitrary geometries, we adopt an integral equation formulation of Maxwell's equations. The standard approach involves solving the Helmholtz equation, which describes the propagation of electromagnetic waves in waveguides. By converting the wave equation into an integral form, we can employ the Nyström method for discretization and numerical solution (Colton, Kress, & Kress, 1998).
The Nyström method is an efficient numerical approach for solving integral equations. It relies on quadrature rules to discretize the integral equation, leading to a system of linear equations that can be solved for the unknown field values. This method is particularly advantageous for problems involving complex geometries, as it avoids the need for mesh generation, which is a computational bottleneck in FEM and FDTD-based solvers.
In this study, we apply the Nyström method to optical waveguides with arbitrary shapes, including those with sharp corners and highly rounded geometries. We investigate the accuracy of the method by comparing solutions for different geometric representations, ensuring that mode solutions remain consistent across various approximations. For waveguides with sharp corners, we approximate the geometry using superelliptical shapes, allowing for smoother numerical treatment while preserving the essential mode characteristics.

Governing Equations and Boundary Integral Formulation

The foundation of our analysis begins with the two-dimensional Helmholtz equation, which governs the behavior of the modal field ψ in optical waveguides. The domain is partitioned into the core region Ω, characterized by a refractive index n_1, and the cladding region Ω^c, with refractive index n_2. Within each of these regions, the field satisfies a distinct Helmholtz equation, parameterized by the propagation constant β. These formulations (Equations 1 and 2) provide the starting point for mode analysis by describing the spatial variation of the guided fields.
To transform the problem into a more tractable numerical form, we invoke Green's third identity, which allows the Helmholtz equation to be reformulated as a boundary integral equation. This leads to two integral representations: one valid for points located within the core (Ω) and the other for points in the cladding (Ω^c). These expressions (Equations 3 and 4) recast the modal field in terms of boundary values alone, thereby eliminating the need to discretize the full domain. This

property is particularly advantageous for waveguides with complex boundaries, as it underpins the efficiency of boundary element methods such as the Nyström technique.

At the heart of this formulation lies the Green's function for the two-dimensional Helmholtz equation (Equation 5). This function is expressed via the Hankel function of the second kind, $H_0^{(2)}$, which captures the appropriate outgoing wave behavior in open domains. Serving as the kernel of the integral operators, the Green's function encapsulates the response of the system to point sources and allows for the coupling of boundary values across the domain.

Inserting the Green's function into the integral identities yields a Fredholm integral equation of the second kind (Equation 6), in which the field on the boundary is related to itself through two kernel functions, $L(t,\tau)$ and $M(t,\tau)$. This equation serves as the basis for applying the Nyström method, enabling the discretization of the boundary and the formation of a solvable linear system. This approach follows the classical methodology presented in Colton & Kress, adapted here for waveguide mode analysis.

A central challenge in solving the resulting boundary integral equation lies in the treatment of singularities in the kernel functions. The Green's function exhibits a logarithmic singularity as the source and field points coalesce, complicating numerical integration. To address this, the kernels are analytically decomposed (Equations 7 and 8) into singular and smooth parts. Specifically, the logarithmic singularity is isolated using the trigonometric identity, which naturally arises in periodic boundary parameterizations. The remaining components of the kernels, denoted L_1, L_2, M_1, M_2, are smooth and well-behaved, enabling the accurate application of quadrature rules. This singularity separation is critical for achieving high-order accuracy and numerical stability in the Nyström discretization.

Together, these equations establish a robust mathematical foundation for the boundary-integral-based mode solver. They enable the computation of guided modes with high precision, even in geometrically intricate waveguide configurations.

Equations

$$\nabla^2\psi + (n_1^2k^2 - \beta^2)\psi = 0 \quad \text{in } \Omega, \tag{1}$$

$$\nabla^2\psi + (n_2^2k^2 - \beta^2)\psi = 0 \quad \text{in } \Omega^c, \tag{2}$$

$$\psi(\mathbf{r}) = -\int_{\partial\Omega} \frac{\partial G_1(\mathbf{r},\mathbf{r}')}{\partial n'}\psi(\mathbf{r}')dl' + \int_{\partial\Omega} G_1(\mathbf{r},\mathbf{r}')\frac{\partial\psi(\mathbf{r}')}{\partial n'}dl' \quad \text{in } \Omega, \tag{3}$$

$$\psi(\mathbf{r}) = \int_{\partial\Omega} \frac{\partial G_2(\mathbf{r},\mathbf{r}')}{\partial n'}\psi(\mathbf{r}')dl' - \int_{\partial\Omega} G_2(\mathbf{r},\mathbf{r}')\frac{\partial\psi(\mathbf{r}')}{\partial n'}dl' \quad \text{in } \Omega^c, \tag{4}$$

$$G(\mathbf{r},\,\mathbf{r}') = H_0^{(2)}(k_0|\mathbf{r}-\mathbf{r}'|)/(4i) \tag{5}$$

$$\psi(t) - \int_0^{2\pi} \{L(t,\tau) + i\eta M(t,\tau)\}\,\psi(\tau)\,d\tau = g(t), \quad 0 \le t \le 2\pi, \tag{6}$$

$$L(t,\tau) = L_1(t,\tau)\ln\left(4\sin^2\frac{t-\tau}{2}\right) + L_2(t,\tau), \tag{7}$$

$$M(t,\tau) = M_1(t,\tau)\ln\left(4\sin^2\frac{t-\tau}{2}\right) + M_2(t,\tau), \tag{8}$$

Findings

Our results demonstrate that the Nyström method effectively computes the modes of optical waveguides with arbitrary geometries. By approximating waveguides with sharp corners using highly rounded superelliptical shapes, we achieve the same level of accuracy as models that explicitly include corners. This finding is significant, as it suggests that a smooth approximation can simplify numerical computations while preserving essential mode properties.

As seen in Table 1, the Nyström method finds 7 different β values for a multimode step-index fiber, compared with analytical solutions (Ghatak & Thyagarajan, 1998). Moreover, Table 2 shows the exact transcendental equation for scalar modes of rectangular dielectric waveguides compared with our presented well-rounded corner approach (Smartt, Benson, & Kendall, 1994). As seen in Table 2, our findings are highly consistent. Our well-rounded corner approximation is consistent and requires fewer computational steps compared to the graded mesh method (Colton, Kress, & Kress, 1998).

Table 1. Comparison of β values obtained using the Nyström method (N = 32) and analytical solutions for a multimode step-index fiber. Excellent agreement is observed across all guided modes.

Mode Name	Analytical Solution (β)	Nyström (N = 32)	Error
LP_{01}	0.897699	0.8976988159	0.0000001841
LP_{02}	0.475182	0.4751823521	0.0000003521
LP_{11}	0.742163	0.7421627509	0.0000002491
LP_{12}	0.179216	0.1792163591	0.0000003591
LP_{21}	0.541097	0.5410969649	0.0000000351
LP_{31}	0.300334	0.3003342698	0.0000002698
LP_{41}	0.027816	0.0278157872	0.0000002128

Table 2. Comparison of β values from the Nyström method (N = 192) and operator method for scalar modes of rectangular waveguides. The results demonstrate strong consistency across varying normalized heights.

Normalized Waveguide Height (h = V / π)	Operator Method (β)	Nyström (N = 192)	Error
0.4	0.0361	0.0360714601	0.0000285399
0.5	0.1117	0.1117341833	0.0000341833
0.6	0.2047	0.2047199080	0.0000199080
0.7	0.2962	0.2962512635	0.0000512635
0.8	0.3788	0.3788450870	0.0000450870
0.9	0.4507	0.4507618400	0.0000618400
1.0	0.5127	0.5125175506	0.0001824494

In Figure 1, the field intensity distributions of the same waveguide mode are presented using two different approaches. On the left, results from commercial software (Lumerical) are shown, while on the right, our implementation using Green's third identity is displayed. It can be observed that both distributions closely match, confirming the correctness of our numerical method.

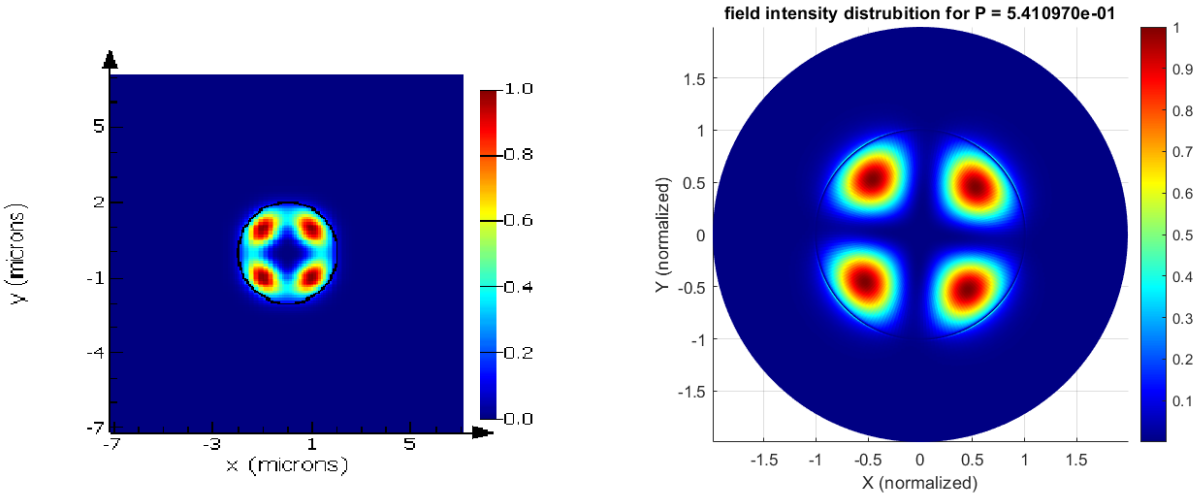

Figure 1. Field intensity from Lumerical (left) vs. Nyström method (right). The close match validates our numerical implementation.

In Figure 2, we present the computed E_{42} mode of a rectangular optical waveguide using the Nyström integral method. The rectangular geometry is defined with a normalized height h = 4 and an aspect ratio a/b = 2. The figure shows the transverse field intensity distribution corresponding to the propagation constant P = 0.602868. As expected, the pattern exhibits four maxima along the x - axis and two maxima along the y - axis, consistent with the modal index E42. The distribution closely matches reference results reported in Goell (1969), validating both the numerical accuracy and physical correctness of our implementation.

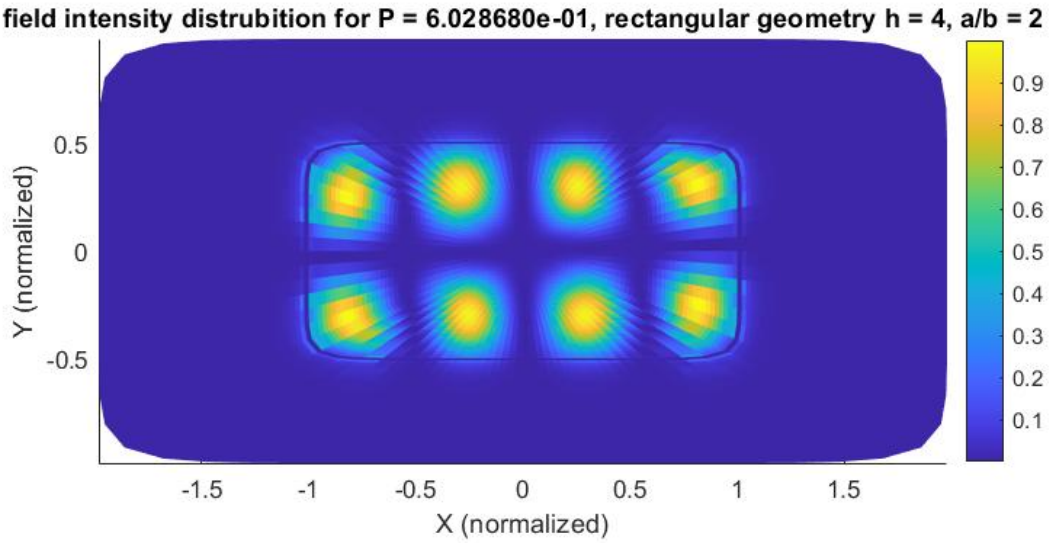

Figure 2. E_{42} mode field distribution in a rectangular waveguide ($h = 4$, $a / b = 2$). Results match the reference mode structure.

Moreover, the Nyström method exhibits improved convergence compared to traditional differential equation solvers. The integral formulation inherently captures the boundary conditions without requiring additional enforcement, leading to a

more stable numerical solution. The computational efficiency of the method is also evident, as it requires fewer discretization points to achieve high accuracy compared to mesh-based solvers.
Through extensive numerical simulations, we validate our approach by comparing computed mode profiles with reference solutions obtained from FEM-based solvers. The agreement between the results confirms the reliability of the Nyström method for solving waveguide mode problems.

Conclusion

This study presents the Nyström integral method as an effective approach for solving the mode structure of arbitrarily shaped optical waveguides. By leveraging the integral equation formulation, we achieve accurate and computationally efficient solutions without the need for extensive meshing. Our findings indicate that approximating sharp-cornered waveguides with highly rounded geometries, such as superelliptical shapes, does not compromise solution accuracy. This insight simplifies numerical computations and broadens the applicability of the method to various photonic waveguide designs.
Future work may focus on extending this approach to three-dimensional waveguides, exploring layered waveguide types, incorporating additional material properties, and investigating hybrid methods that combine the strengths of integral and differential equation solvers. The results of this study contribute to the development of more efficient computational tools for photonic system design, facilitating advancements in optical communication and integrated photonic circuits.

References

Colton, D. L., Kress, R., & Kress, R. (1998). Inverse acoustic and electromagnetic scattering theory (Vol. 93, pp. xii+-334). Berlin: Springer.
Fallahkhair, A. B., Li, K. S., & Murphy, T. E. (2008). Vector finite difference modesolver for anisotropic dielectric waveguides. Journal of Lightwave Technology, 26(11), 1423-1431.
Ghatak, A. K., & Thyagarajan, K. (1998). An introduction to fiber optics. Cambridge University Press.
Goell, J. E. (1969). A circular-harmonic computer analysis of rectangular dielectric waveguides. Bell System Technical Journal, 48(7), 2133-2160.
Smartt, C. J., Benson, T. M., & Kendall, P. C. (1994). Exact transcendental equation for scalar modes of rectangular dielectric waveguides. Optical and Quantum Electronics, 26, 641-644.
Wang, L., Cox, J. A., & Friedman, A. (1998). Modal analysis of homogeneous optical waveguides by the boundary integral formulation and the Nyström method. Journal of the Optical Society of America A, 15(1), 92-100.

Singular Integral Treatment of Nyström Method for Electromagnetic Scattering Problems

Faik Yaman[a], Mehmet Çayören[a]

[a] Istanbul Technical University, Faculty of Electrical and Electronics Engineering, Department of Electronics and Communications Engineering, Turkey
yamanfai@itu.edu.tr

Keywords : Electromagnetic Scattering, Hadamard Finite Part, Nyström Method, Singular Integral.

Computational Electromagnetics (CEM) is a widely used approach for solving electromagnetic scattering problems, a phenomenon central technologies such as biomedical imaging and radar. CEM methods are generally classified as analytical or numerical. Analytical methods solve scattering for simple geometries, whereas numerical methods are preferred for complex ones. In this study, an integral equation-based model is used. The Method of Moments (MoM), a traditional technique, is commonly employed for solving such equations. However, Nyström Method (NM) is preferred for this study instead of MoM. The idea behind using NM is that it does not require basis functions unlike MoM. Nevertheless, the NM involves hypersingular integrals due to Dyadic Green's Function (DGF). This approach provides solutions to electromagnetic scattering problems involving conducting and arbitrary-shaped objects. The proposed strategy is based on numerical solution of surface integral equations using NM. The main contribution of this study is the development of a novel numerical approach for the accurate and stable evaluation of hypersingular integrals.

Aim

The aim of this study is to solve electromagnetic scattering problems using surface integral equations. This type of integral equation generally consists of two types of integrals: non-singular and singular integrals. Non-singular integrals can be solved using standard quadrature rules. Nevertheless, quadrature rules are not applicable to singular integrals. Singular integrals require new techniques due to their complex form. Singular integrals, which arise from the DGF, play a critical role in achieving stable and accurate solutions. However, there is limited research on the numerical treatment of singular integrals in the context of electromagnetic problems. Therefore, a new Nyström-based approach is proposed to solve singular integrals numerically and accurately.

Material and Method

As previously stated, the aim of this study is to solve the electromagnetic scattering problem for arbitrarily shaped perfectly electrically conducting (*PEC*) surfaces using *NM*. This section consists of four main parts: Electric Field Integral Equation (*EFIE*), Nyström Method (*NM*), the application of *NM* to *EFIE*, and the treatment of singular integrals.

1. Electric Field Integral Equation (EFIE)

EFIE is a widely used equation in electromagnetics. Derived from Maxwell's equations, it applies to both open and closed geometries. EFIE defines the relation between surface current density and scattered electric field. The integral kernel is the DGF, which includes second derivatives of the free-space Green's function. To apply EFIE, boundary conditions, the incident field, and the source and observation coordinates must be known. The EFIE for PEC surfaces is given as in Equation (1).

$$\vec{t}.j\,w\,\mu \int_s \left[1+\frac{1}{k^2}\nabla\nabla.\right] g(r,r').\vec{J}(r')dS = \vec{t}.\vec{E}^i(r) \quad \#(\,SEQ\ Denklem\ \backslash *\ ARABIC\ 1)$$

In Equation 1, $\vec{t}$ denotes the tangential unit vector, w is the angular frequency, μ is the permeability, k is the wave number, r and r' are the coordinates of the observation and source points, $\vec{J}(r')$ represents the surface current density at the source point, and $\vec{E}^i(r)$ is the incident electric field at the observation point. The scalar Green's function $g(r, r')$ describes wave propagation between source and observation points in free space. The DGF includes second derivatives of the free-space Green's function, making the integral more complex.

2. Nyström Method (NM)

NM is a numerical method for solving integral equations. Although it is a classical technique, its use in electromagnetics is relatively recent. It utilizes quadrature rules, which approximate integrals by summing weighted function values at specific points (Çalışkan, 2004). Various quadrature rules exist, such as Gauss-Legendre, Gauss-Lobatto, Tanh-Sinh, and Chebyshev. This study employs the Gauss-Legendre rule, which determines sampling points and weights using the roots of Legendre polynomials. In NM, the surface is divided into small elements (meshes), and integrals are evaluated over each mesh (Tong & Chew, 2020). The application of *NM* to a mesh element is given as in Equation (2).

$$\int_s f(x,y)dxdy = \sum_{i=1}^{N} w_i\, f(x_i,y_i)J(x_i,y_i) \quad \#(SEQ\ Denklem\ \backslash *\ ARABIC\ 2)$$

In Equation (2), f represents the kernel function, n is the total sampling points on a mesh element, w_i shows weight of the sampling point, J is the jacobian, x_i and y_i are the coordinates of the sampling points.

3. The application of NM to EFIE

In this section, the EFIE is applied using the NM. As discussed previously, the NM converts integrals into summations via quadrature rules, which evaluate integrals at sampling points. The surface is divided into small mesh elements, and sampling points are placed within each. Quadrilateral planar meshes are used in this study. In practice, the EFIE is applied twice: first to compute the surface currents, and second to obtain the scattered field. In NM, currents are defined only at the sampling points. The EFIE in Nyström form is given as in Equation (3).

$$\vec{E}_{inc}(r_i) = j\mu w \sum_{i=1}^{n} \sum_{j=1}^{n} \left[1 + \frac{1}{k^2}\nabla\nabla\right] g(r_i, r_j).\vec{J}(r_j) w_{ij} J_{ac,j} \quad \#(SEQ\ Denklem\ \backslash *\ ARABIC\ 3)$$

In the third equation, n is the total number of sampling points, $J_{ac,j}$ represents the jacobian value corresponding to the jth sampling point. w_j denotes the quadrature weight corresponding to the jth sampling point. The double summation covers for all combinations of observation index i and source index j. All combinations of the source and observation points are required to be considered in order to account for all electromagnetic interactions. The free-space Green's Function can be written as in Equation (4).

$$g(r_i, r_j) = \frac{e^{-jk|r_i - r_j|}}{4\pi|r_i, r_j|} \quad \#(SEQ\ Denklem\ \backslash *\ ARABIC\ 4)$$

In Equation 4, the free-space Green's function depends on the distance between the source and observation points. If the distance is zero, a singularity occurs (to be addressed in the next section). Otherwise, the Green's function and its derivatives have valid values usable in NM. When computing the scattered field from surface currents, all terms remain non-singular since the distance is non-zero (Tong & Chew, 2020).

Dyadic terms come from second derivatives of the Green's function. To reduce computational cost, local coordinates are used. The u and v components are unit tangential directions defined per mesh and may vary across elements. Equation (5) shows the dyadic matrix structure.

$$[g_{uu}\, g_{uv}\, g_{vu}\, g_{vv}][J_u\, J_v] = [E_u\, E_v] \quad \#(SEQ\ Denklem\ \backslash *\ ARABIC\ 5)$$

In the fifth equation, the dyadic matrix is a 2×2 matrix since it represents the *u* and *v* tangential components. The surface current and electric field vectors are 2×1 vectors containing the corresponding components. If the total number of sampling points is *n*, the global dyadic matrix becomes a $2n \times 2n$ matrix, while the surface current and electric field vectors become $2n \times 1$ vectors (Kılınç, 2010).

4. The Treatment of Singular Integrals

When the observation and source points coincide, DGF integrals become undefined. Standard quadrature rules fail in such cases, requiring alternative techniques like Duffy's or Radial transform (Hayami & Brebbia, 1987). This study uses the Hadamard Finite Part (HFP) method to evaluate singular integrals. Before addressing their treatment, the first DGF component expression is given in Equation (6).

$$g_{uu}(r) = g(r) + \frac{1}{k^2}\frac{\partial^2}{\partial u^2}\, g(r) \quad \#(SEQ\ Denklem\ \backslash *\ ARABIC\ 6)$$

In Equation (6), $r = \sqrt{u^2 + v^2}$ represents the local distance between the observation point and the source point, expressed in the local tangential coordinate system. To accurately calculate the singular integrals, the Taylor series expansion of the DGF is required. After expanding the DGF up to the first three terms, the first dyadic component can be written as follows in Equation (7).

$$g_{uu}(r) = \frac{1}{4\pi}\left[\frac{u^2 + 0.5v^2}{r^3} + \frac{2u^2 - v^2}{k^2 r^5} - \frac{2jk}{3} - \frac{k^2 r}{3} + \frac{jk^3 v^2}{6} + \sum_{n=4}^{\infty} \frac{(-jk)^n r^{n-1}}{n!} + \sum_{n=4}^{\infty} \frac{(-jr)^n k^{n-2}}{n!}\left(\frac{2u^2 - v^2}{r^5} + jk\frac{2u^2 - v^2}{r^4} - \frac{k^2 u^2}{r^3}\right)\right] \quad (SEQ\ Denklem\ \backslash *\ ARABIC\ 7)$$

The remaining components can be derived in a similar manner. These expressions will be used in the singular part of the integral computations, which will be handled by the HFP method.

4.1 Hadamard Finite Part Technique

HFP method is a variant of the Cauchy Principal Value (CPV) used to evaluate singular integrals. It follows a similar approach to CPV but retains only the finite part, discarding divergent terms. Unlike CPV, HFP provides physically meaningful, finite results (Chan, Fannjiang, Paulino, & Feng, 2007; Selçuk, 2014). The HFP part is denoted by H. An example is shown in Equation (8).

$$H\int_{-1}^{1} \frac{dt}{t^2} = \left(\int_{-1}^{-\varepsilon} \frac{dt}{t^2} + \int_{\epsilon}^{1} \frac{dt}{t^2}\right) = \left(\frac{1}{\varepsilon} - 1 - 1 + \frac{1}{\varepsilon}\right) = -2 \quad \#(SEQ\ Denklem\ \backslash *\ ARABIC\ 8)$$

The Equation (8) demonstrates the HFP concept. If a singular integral has an antiderivative, its analytic solution can be obtained using HFP. A numerical example over a square mesh is presented next.

4.2 Application of HFP to EFIE

In this study, the Gauss-Legendre quadrature rule is used, valid for integrals over the reference square $[-1,1]\times[-1,1]$. Sampling points are located within small mesh elements, and their coordinates are obtained by mapping the reference square. Therefore, singular integrals are evaluated using the HFP method on the reference square. The aim is to compute the singular terms in Equation (7) individually. The summation terms are non-singular and can be evaluated via standard quadrature (Selçuk, 2014). As an example, the second singular term in Equation (7) will be evaluated.

In Equation (9), u and v are the coordinates of the observation point, while u' and v' represent those of the source points. Thus, terms like $u-u'$ and $v-v'$ express the relative distance between these points. To simplify integration over the reference square, a coordinate transformation is applied: $A=u-u'$ and $B=v-v'$. This centers the singularity at the origin (0,0), making integral more manageable for numerical evaluation via the HFP method.

$$I = H\int_{-1}^{1}\int_{-1}^{1}\frac{2(u-u')^2-(v-v')^2}{((u-u')^2+(v-v')^2)^{\frac{5}{2}}}dudv \quad \#(SEQ\ Denklem\ \backslash *\ ARABIC\ 9)$$

$$I = H\int_{A=-1-u'}^{1-u'}\int_{B=-1-v'}^{1-v'}\frac{2A^2-B^2}{(A^2+B^2)^{\frac{5}{2}}}dAdB \qquad \#(SEQ\ Denklem\ \backslash *\ ARABIC\ 10)$$

The aim is to calculate the singular integral given in Equation (10). To achieve this, the integral is split into two parts as in Equation (11) and Equation (12): P and T. While evaluating P, an inner integral denoted as $I(A)$ arises, which is computed using the HFP method. During this process, the terms involving the $\frac{1}{\varepsilon}$ variable are disregarded. As a result, $I(A)$ can be expressed as shown in Equations (14), (15), and (16). The numeric values of P and T can be evaluated easily. Similarly, the remaining singular terms of the *DGF* can be evaluated using the same procedure. In Equation (15), C is $1-v'$ and D is $-1-v'$.

$$P = \int_{A=-1-u'}^{1-u'}\int_{B=-1-v'}^{1-v'}\frac{2A^2}{(A^2+B^2)^{\frac{5}{2}}}dAdB \qquad \#(11)$$

$$T = \int_{A=-1-u'}^{1-u'}\int_{B=-1-v'}^{1-v'}\frac{B^2}{(A^2+B^2)^{\frac{5}{2}}}dAdB \qquad \#(12)$$

$$I = 2P - T \qquad \#(13)$$

$$I(A) = \int_{B=-1-v'}^{1-v'}\frac{A^2}{(A^2+B^2)^{5/2}}dB \qquad \#(14)$$

$$I(A) = \frac{2C^3 + 3A^2C}{3A^2(C^2 + A^2)^{3/2}} - \frac{2D^3 + 3A^2D}{3A^2(D^2 + A^2)^{3/2}} \qquad \#(15)$$

Findings

In this study, singular integral arising in the EFIE formulation were evaluated using the HFP method over a reference square. All steps of the computation were carried out analytically by mapping each singular term to standard domain [-1,1]x[-1,1]. This approach allows for the accurate and stable evaluation of hypersingular terms, particularly those originating from the DGF. Table (1) presents the numeric evaluation of the singular integral like Equation (9). The source point is taken as $u' = 0.2$ and $v' = 0.4$ in the first case, and $u' = -0.6$ and $v' = -0.8$ in the second. The results are computed using the HFP and compared with those obtained via Mathematica.

Table 1: Numeric Evaluation of Singular Integrals using HFP and Mathematica.

Source Location	Method	$(2u^2\text{-}v^2)/r^5$
(u'=0.2, v'=0.4)	HFP	2.84069575921
(u'=0.2, v'=0.4)	Mathematica	2.840695759209953
(u'=-0.6, v'=-0.8)	HFP	4.103154172505319
(u'=-0.6, v'=-0.8)	Mathematica	4.103154172505318

Conclusion

In this study, HFP method was applied to evaluate singular integral arising in the EFIE formulation. By mapping the integration domain to a standard reference square and applying analytical techniques, hypersingular term originating from DGF were successfully computed. The numerical results obtained using the HFP method were compared with those computed by Mathematica, and an excellent agreement was observed. This confirms the validity and accuracy of the proposed approach. The findings confirm that HFP is a reliable and efficient method for the stable evaluation of singular integrals in computational electromagnetics. Future work will focus on applying the model to practical RCS computations.

References

Chan, Y. S., Fannjiang, A. C., Paulino, G. H., & Feng, B. F. (2007). Finite part integrals and hypersingular kernels. *Advances in Dynamical Systems*, *14*(S2), 264–269.

Çalışkan, F. (2004). *Electromagnetic analysis of planar layered structures* [Doctoral dissertation, Georgia Institute of Technology].

Hayami, K., & Brebbia, C. A. (1987). A new coordinate transformation method for singular and nearly singular integrals over general curved boundary elements. In C. A. Brebbia, W. L. Wendland, & G. Kuhn (Eds.), *Boundary elements IX: Vol. 1. Mathematical and computational aspects* (pp. 375–382). Springer-Verlag Berlin Heidelberg GmbH.

Kılınç, S. (2010). *Solution of electromagnetic scattering problems with the locally corrected Nyström method* [Master's thesis, Bilkent University].

Selçuk, G. (2014). *Application of Nyström method for the solution of time domain electric field integral equation* [Doctoral dissertation, Middle East Technical University].

Tong, M. S., & Chew, W. C. (2020). *The Nystrom method in electromagnetics*. John Wiley & Sons.

APPLIED INFORMATICS

Computational Electromagnetics

Data Analysis

Medical Image Analysis

Optimization Potential of Machine Learning-Based Algorithms in Neonatal Parenteral Nutrition Management: A Systematic Review

Sümeyye Nalbat[a], Mustafa Alpkan Çiçek[b], Serkan Türkeli[c], Mustafa Doğan[d]

[a]İstanbul Technical University, Electronics and Communication Engineering Graduate School, Biomedical Engineering Master of Science Program, Türkiye
[b]Marmara University, Faculty of Health Sciences,Health Management Doctorate Program, Türkiye
[c]Marmara University, Faculty of Health Sciences, Health Informatics and Technologies Department Head, Türkiye
[d]İstanbul Technical University, Faculty Of Electrical And Electronics Engineering, Control and Automation Engineering Department, Türkiye
korkmazs@itu.edu.tr

Keywords: Parenteral Nutrition, Infant, Machine Learning.

Aim

Total parenteral nutrition is a way of feeding patients who cannot use their digestive system properly. In this method, nutrients are given directly through a vein using a peripheral line or a central venous catheter. It was first used in the 1930s, but it became more common in the 1960s as scientists learned more about how the circulatory system works and how nutrients interact with metabolism and the immune system (Dudrick & Palesty, 2011).

In the late 1970s, parenteral nutrition started to be used for newborns. This made it possible to help premature babies survive, even when their chances were very low before. Total parenteral nutrition (TPN) has helped increase the survival rates of newborns by supporting their growth. It is especially useful for babies who are born too early, have an underdeveloped digestive system, or suffer from conditions like sepsis, malabsorption, short bowel syndrome, or breathing problems (Brine, 2004).

For infants with very low birth weight, the timing of initiating parenteral nutrition within the first hours after birth is crucial, as they exhibit lower weight gain due to hypermetabolism at the time of discharge from intensive care (Specht et al., 2020). In intensive care, the daily vital signs of newborns must be closely monitored to ensure proper nutrition and medication management. Patient information and the data on parenteral nutrition (PN) helps guide adjustments to the treatment plan (Brine, 2004).

It is still unclear whether the nutritional requirements of premature infants after birth depend on their gestational age or birth weight; moreover, there are different opinions regarding the concentrations of the required nutrients (Rizzo et al., 2022). Machine learning methods have been widely accepted and studied in fields requiring data-driven decision-making, such as dialysis (Burlacu et al., 2020). Research on data-driven decision support systems in neonatal intensive care has focused on sepsis, mortality, and discharge weight. However, more studies are needed to explore their use in determining the nutritional composition (Yalçın et al., 2023; Derakhshandara et al., 2024).

In this study, publications focusing on the adjustment of nutrient content in parenteral nutrition management through machine learning methods have been reviewed.

The aim of this study is to answer the question: "Is it possible to effectively use machine learning algorithms to optimize parenteral nutrition management in neonates?" It also aims to highlight the gap in TPN data management that needs to be addressed to enable more effective research in neonatal intensive care units (NICUs) in the future.

Material and Method

This was achieved with a systematic review of research on total parenteral nutrition (TPN) using machine learning. Using the keywords "parenteral nutrition," "infant," and "machine learning," searches were conducted in the PubMed and Scopus databases to identify the publications. Each search was carried out in English, and there were no time restrictions. Table 1 lists all of the inclusion and exclusion criteria.

Table 1. All of the inclusion and exclusion criteria.

Inclusion Criteria	Exclusion Criteria
Article on the analysis of the use of Machine learning with the Parenteral Nutriton	Studies in the form of cohort study, reviews, guidelines, book,congress proceedings
Open-access and fully available studies that have been published on the subject.	Studies that are not available in full text
Articles published in 1996 and up to and including Jan (5th) of 2025	Studies before 1995 and after Jan (5th) of 2025
Articles in English	Article in other languages

The study followed evidence-based review guidelines known as PRISMA. Two databases were searched and the details are shown in Figure 1.

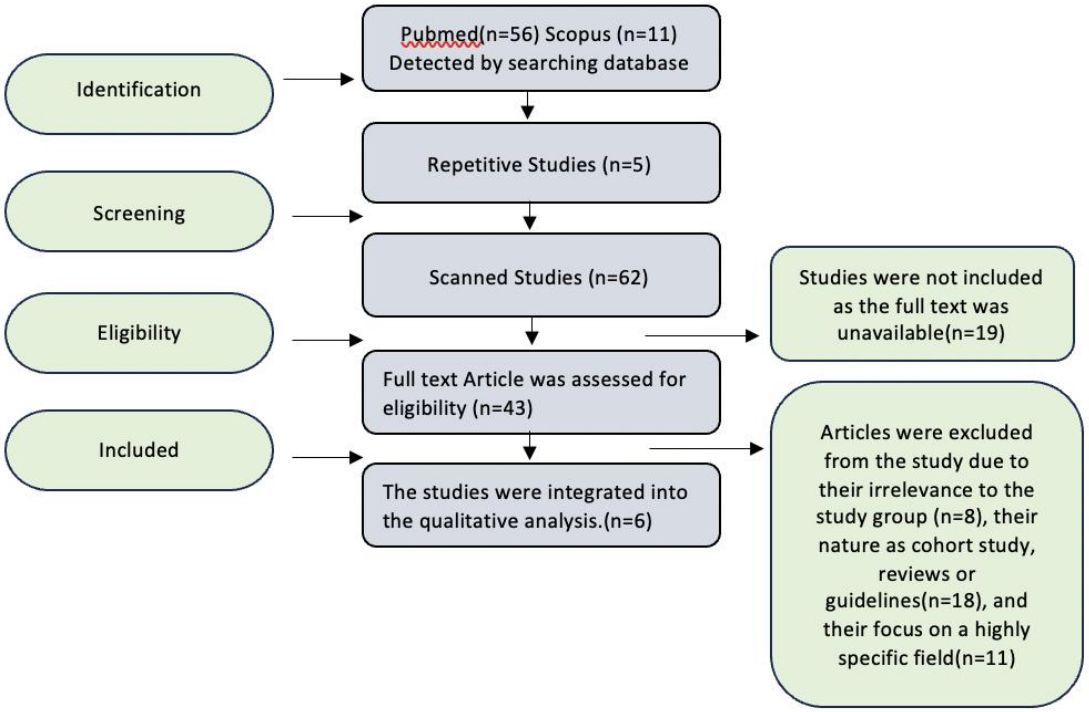

Figure 1. Databases that were searched at and details.

The PICO (Population, Intervention, Comparison, Outcome) technique was employed to determine the study's goal. Sackett and associates created the PICO method in the 1990s as an organized technique for creating research questions and carrying out methodical literature reviews. The following are the PICO criteria for this systematic review based on this methodology showed table 2.

Table 2. PICO criteria for this systematic review.

P(Population-based) :	Infants
I(Intervention) :	Parenteral nutrition control with machine learning support
C(Comparison) :	Manual parenteral nutrition control
O (The outcome) :	Weight gain, less nutritional errors, and a shorter hospital stay

A total of 67 articles were identified from the initial search, including 56 from PubMed and 11 from Scopus. After removing duplicate studies (n=5), articles without full-text access (n=19), cohort study, reviews, guidelines, and conference proceedings (n=18), irrevelant to the study group (n=8), and their focus on a highly specific field(n=11) a total of 43 full-text articles met the inclusion criteria. Following a thorough analysis of the full-text articles, the number of studies accepted into the systematic review (n = 6) was established, with preference given to those that were appropriate for the study's objectives (Table 3).

Findings

As a result of the systematic analysis, six articles were selected based on the inclusion criteria and their relevance to the research field. Of these six articles, five were based on neonatal data, whereas one study was conducted on an adult patient group. However it was included in the review since it focused on computer-assisted parenteral nutrition (PN) management. Since parenteral nutrition (PN) is delivered through an intravenous route, it is regarded as a high-risk procedure due to both the interaction between the patient and the nutritional components and the infection risk linked to the administration process. However, PN remains essential for neonates, particularly for those with an immature digestive system, where proper growth plays a crucial role in recovery. Some studies have indicated that physicians often lack confidence when prescribing PN (Van den Broucke & Deleenheer, 2022; Lenders et al., 2014; Adams et al., 2010). In a pre-post randomized study conducted in Belgium, the impact of decision support systems on physicians' prescribing behavior and their ability to guide physicians was examined. As a result, it was stated that decision support systems could alter the physician's initial PN planning, but no direct impact was observed (Van den Broucke & Deleenheer, 2022).

Physicians' clinical experience, their familiarity with parenteral nutrition (PN) guidelines, and differences in assessing the clinical conditions of infants can lead to variations in PN prescriptions. A study comparing standardized, computer-assisted ready TPN orders (based on ASPEN and with physician-modifiable options) and manually prepared PN orders found that while there was no difference in the length of hospital stay among infants, there was a difference in calorie intake and weight gain. Infants who received computer-assisted PN were found to have gained more weight (Skouroliakou & Koutri, 2009).

When assessed in terms of error rates and time efficiency, parenteral nutrition (PN) is a time-intensive process and is susceptible to errors at every stage, including prescription, order review, preparation, labeling, distribution, and administration (MacKay & Anderson et al., 2016). A survey conducted between 2003 and 2013 on the use of parenteral nutrition (PN) identified that the main factor contributing to error rates was the lack of implementation of computerized prescriber order entry (CPOE) (MacKay & Anderson et al., 2016). In a study conducted in Greece, a TPN Formulation Automated Assistant was developed, which calculated recommended nutrient values based on the entered parameters of the infant. These values were then compared with manually prepared ones. The error rates were found to be very low, and the system required significantly less time, with the results being statistically significant (Skouroliakou & Koutri, 2005).

Newborns typically lose some weight after birth, and how much time it takes to go back to their birth weight can be a sign of adequate nutrition. This process may take longer in preterm infants, indicating possible nutritional challenges. In a study conducted by Kyle A. Franco and Keliana O'Mara at a neonatal center in Florida, the time to regain birth weight, hyperglycemia episodes, and electrolyte imbalances were compared between pre-CPOE and post-CPOE groups in infants born weighing less than 1750 grams. The study revealed that in the CPOE-assisted TPN order group, the achievement rate

of target macronutrient levels improved, the requirement for order corrections declined, and the occurrence of electrolyte imbalances was positively impacted (Franco & O'Mara, 2016). CPOE practices were designed based on protocols for baseline, minimal, and gradually increasing amounts of nutritional components or by using predefined minimum and maximum values set according to newborn weight range thresholds (Franco & O'Mara, 2016; MacKay & Anderson et al., 2016).

In a study where machine learning techniques were applied, machine learning methods trained on a 17-year dataset were compared in predicting macronutrient amounts. The random forest (RF), gradient boosting machine (GBM), support vector machine (SVM), and multilayer perceptron (MLP) techniques were compared in terms of rmse and r^2 values to predict pn volume, protein, lipid, and carbohydrate amounts. The results showed that RF and GBM were the most interpretable and explainable models (Derakhshandara et al., 2024).

Table 3. Studies accepted into the systematic review.

	Title	Year	Article Accsess	Subject	Purpose Of Study	Conclusion
1	Comparison of two types of TPN prescription methods in preterm neonates (Skouroliakou & Koutri, 2009)	2009	PubMed	60	Standardized, computer-assisted ready TPN orders (based on ASPEN and with physician-modifiable options) were compared with manually prepared PN orders.	There was no difference in the length of hospital stay among infants, there was a difference in calorie intake and weight gain.
2	Computer assisted total parenteral nutrition for pre-term and sick term neonates(Skouroliakou & Koutri, 2005)	2005	PubMed	96	A study developed a TPN Formulation Automated Assistant that generated recommended nutrient values based on infant parameters and compared them with manually prepared values.	The study compared error rates between the manual and computerized methods, finding a statistically significant difference.
3	Offering Guidance and Learning to Prescribers to Initiate Parenteral Nutrition using a Validated Electronic Decision TREE (OLIVE TREE)(Van den Broucke & Deleenheer, 2022)	2022	PubMed	73	The impact of decision support systems on physicians' prescribing behavior and their ability to guide physicians was examined.	In this study, it was found that 53% of PN initiation could be prevented. The preliminary results of the conceptual evidence analysis conducted in this study indicated a potential impact (16.4%) on preventing PN use, but no directly effective outcome was observed.
4	Impact of Computerized Provider Order Entry on Total Parenteral Nutrition in the Neonatal Intensive Care Unit(Franco & O'Mara, 2016)	2016	PubMed	91	The study aimed to compare between pre-CPOE and post-CPOE groups in infants born weighing less than 1750 grams.	The study found that CPOE-assisted TPN orders improved macronutrient target achievement, reduced order corrections, and positively impacted electrolyte balance.
5	Machine Learning Decision Support for Macronutrients in Neonatal Parenteral Nutrition(Derakhshandara et al., 2024)	2024	Scopus	17 years data	The study aims to investigate the potential of evidence-based decision support systems implemented with machine learning as a valuable tool for predicting nutritional outcomes in neonatal clinical practice.	The results showed strong estimation capabilities, with R-squared values consistently above 0.7, confirming machine learning's potential as a valuable tool for predicting nutritional outcomes in neonatal care.

6	Frequency and Severity of Parenteral NutritionMedication Errors at a Large Children's Hospital AfterImplementation of Electronic Ordering and Compounding(MacKay & Anderson et al., 2016)	2016	PubMed	PN orders within a specific time period	According to the ASPEN guidelines, nutrition recommendation data generated using an integrated CPOE system was compared with errors reported in the existing literature.	This resulted in a significant cost reduction and a lower error rate compared to those reported in the literature.

Conclusion

Few studies have been conducted on decision support systems in the context of managing newborn parenteral feeding. Only one research which conducted to estimate 4 values of TPN employing machine learning methods has been carried out in this field so far.

In order to increase the diversity of the TPN data pool and enhance algorithm models that make use of this field, more research is also required.

The nutritional care of newborns with a variety of real-life medical disorders is not well supported by current decision support systems, despite the fact that they offer clinical recommendations based on values provided in medical guidelines. Given the significant degree of heterogeneity in the newborn population, the number of subjects that have been investigated in decision support system research is still insufficient, as seen in Table 3. Physician knowledge, previous nutrition prescriptions, and their results must be documented and organized as a usable data source for these systems to improve newborn nutrition management. Machine learning-based decision support systems, which can integrate historical data and medical expertise, are the most practical way to close this knowledge gap.

References

Adams, K. M., Kohlmeier, M., Powell, M., & Zeisel, S. H. (2010). Nutrition in medicine: Nutrition education for medical students and residents. *Nutrition in Clinical Practice, 25*(5), 471–480.

Brine, E. (2004). Total parenteral nutrition for premature infants. *Neonatal Network*, *23*(3), 21–26.

Url-2 https://doi.org/10.1053/j.nainr.2004.03.006

Burlacu, A., Iftene, A., Jugrin, D., Popa, I. V., Lupu, P. M., Vlad, C., & Covic, A. (2020). Using artificial intelligence resources in dialysis and kidney transplant patients: A literature review. *BioMed Research International, 2020*, Article 9867872.

Url-3 https://doi.org/10.1155/2020/9867872

Derakhshandara, S., Franzoni, V., Mezzetti, D., & Poggioni, V. (2024). Machine learning decision support for macronutrients in neonatal parenteral nutrition. *IEEE Access, 12*, 170001–170010.

Url-4 https://doi.org/10.1109/ACCESS.2024.3498059

Dudrick, S. J., & Palesty, J. A. (2011). Historical highlights of the development of total parenteral nutrition. *Surgical Clinics of North America, 91*(3), 693–717.

Url-5 https://doi.org/10.1016/j.suc.2011.02.009

Franco, K. A., & O'Mara, K. (2016). Impact of computerized provider order entry on total parenteral nutrition in the neonatal intensive care unit. *Journal of Pediatric Pharmacology and Therapeutics, 21*(4), 339–345.

Url-6 https://doi.org/10.5863/1551-6776-21.4.339

Lenders, C. M., Deen, D. D., Bistrian, B., Edwards, M. S., Seidner, D. L., McMahon, M. M., et al. (2014). Residency and specialties training in nutrition: A call for action. *American Journal of Clinical Nutrition, 99*(5 Suppl), 1174S–1183S.

Url-7 https://doi.org/10.3945/ajcn.113.073528

MacKay, M., & Anderson, C., et al. (2016). Frequency and severity of parenteral nutrition medication errors at a large children's hospital after implementation of electronic ordering and compounding. *Nutrition in Clinical Practice, 31*(2), 195–206.

Url-8 https://doi.org/10.1177/0884533615591606

Rizzo, V., Capozza, M., Panza, R., Laforgia, N., & Baldassarre, M. E. (2022). Macronutrients and micronutrients in parenteral nutrition for preterm newborns: A narrative review. *Nutrients, 14*(7), 1530.
Url-9 https://doi.org/10.3390/nu14071530
Skouroliakou, M., & Koutri, K. (2005). Computer assisted total parenteral nutrition for pre-term and sick term neonates. *Pharmacy World & Science, 27*(4), 305–310.
Url-10 https://doi.org/10.1007/s11096-005-2462-x
Skouroliakou, M., & Koutri, K. (2009). Comparison of two types of TPN prescription methods in preterm neonates. *Pharmacy World & Science, 31*(2), 202–208.
Url-11 https://doi.org/10.1007/s11096-009-9281-4
Specht, R. C. V. L. P., Barroso, L. N., Machado, R. C. M., Santos, M. S. D., Ferreira, A. A., Chacon, I., & Padilha, P. C. (2020). Enteral and parenteral nutrition therapy for neonates at a neonatal unit: A longitudinal retrospective study. *Journal of Maternal-Fetal & Neonatal Medicine, 35*(17), 3323–3329.
Url-12 https://doi.org/10.1080/14767058.2020.1818212
Van den Broucke, E., & Deleenheer, B. (2022). Offering guidance and learning to prescribers to initiate parenteral nutrition using a validated electronic decision TREE (OLIVE TREE). *Journal of Medical Systems, 46*(5), Article 35.
Url-13 https://doi.org/10.1007/s10916-022-01835-x
Yalçın, N., Kaşıkcı, M., Çelik, H. T., Demirkan, K., Yiğit, Ş., & Yurdakök, M. (2023). Development and validation of machine learning-based clinical decision support tool for identifying malnutrition in NICU patients. *Scientific Reports, 13*(1), 5227.
Url-14 https://doi.org/10.1038/s41598-023-32570-z

APPLIED INFORMATICS

Computational Electromagnetics

Data Analysis

Medical Image Analysis

Deep Learning-Based Breast Tumor Detection in MRI Using Faster R-CNN

Şeyma Nur Tufan[a,b], Aleksandar Janjic[b], İbrahim Akduman[c,b]

[a] Istanbul Technical University, Graduate School, Satellite Communications and Remote Sensing, Türkiye
[b] InfiWave Diagnostics Software Limited Company, Türkiye
[c] Istanbul Technical University, Faculty of Electrical and Electronics, Electronics and Communication Engineering, Türkiye
tufan19@itu.edu.tr

Keywords:Biomedical Imaging, Breast Tumor Detection, Deep Learning, Faster R-CNN, Magnetic Resonance Imaging.

Aim

Breast cancer is one of the most prevalent malignancies among women worldwide and continues to be a leading cause of cancer-related mortality (Siegel, Miller, Wagle, & Jemal, 2023). If breast cancer is diagnosed at an early stage, the five-year survival rate exceeds 90% (American Cancer Society, 2016). Traditional imaging methods such as mammography and ultrasound, though widely used, may have limitations in detecting tumors, particularly in dense breast tissue. In contrast, Magnetic Resonance Imaging (MRI) has emerged as a powerful and widely utilized imaging modality for breast cancer screening and diagnosis, owing to its superior sensitivity in detecting malignant lesions, especially in high-risk patients (Mann, Kuhl, Moy, Baron, Borelli, Goerres, & Weinstein, 2019). Therefore, this emphasizes the importance of MR imaging in breast cancer screening.

Recent advances in artificial intelligence (AI) have significantly impacted the field of medical imaging and cancer detection. Detecting lesions or regions of interest in medical images is a crucial and labor-intensive task for clinicians, often requiring the positioning and identification of small lesions across the entire image. Convolutional neural networks (CNNs), a common deep learning-based model, are widely used in computer-aided detection systems and help to automate lesion detection and improve diagnostic accuracy or shorten the time needed by experts (Litjens, Kooi, Bejnordi, Setio, Ciompi, Ghafoorian & van der Laak, 2017). AI-assisted detection systems can assist radiologists by identifying subtle patterns in imaging data, reducing interpretation time and minimizing human error. These models have shown great potential in detecting breast cancer in early stages, enabling timely interventions and improving patient outcomes. A study by McKinney et al. (2020) showed that AI systems can detect cancers earlier than conventional methods. Furthermore, analysis of the localization performance of the AI system reveals its potential to flag suspicious sites for examination by specialists. As AI continues to evolve, its integration into clinical workflows is expected to enhance diagnostic efficiency, optimize resource utilization, and ultimately contribute to improved patient care. For this study, one of the widely preferred detection algorithm Faster R-CNN, was used. Faster R-CNN improves upon previous region-based models by introducing a Region Proposal Network (RPN) that shares convolutional features with the detection network, enabling nearly cost-free region proposals. As explained by Ren, He, Girshick, and Sun (2015), the region proposal network (RPN) is a fully convolutional architecture designed to generate object bounding boxes and estimate the likelihood of objects being present at each location. This design allows Faster R-CNN to efficiently generate high-quality region proposals and refine them for precise object detection, making it a widely adopted model in various detection applications.

The aim of this study is to develop an advanced deep learning model for breast cancer detection using MRI scans. The proposed model is developed by obtaining the parameters of the Faster R-CNN model through a hyperparameter tuning process with Optuna. In addition, the model is designed to track tumor locations along slices. This provides a comprehensive detection framework that can be applied to real-world clinical settings. The developed model was also used and tested to track the tumor location in other slices when it is marked in one slice.

Material and Method

1. Dataset:

In this study, a comprehensive breast MRI dataset was used to train and evaluate the proposed model. The dataset consists of 6,670 tumor-containing breast MRI scans obtained from the Duke Breast Cancer MRI dataset, which is available through The Cancer Imaging Archive (TCIA). Additionally, an independent dataset comprising 3,146 healthy breast MRI scans was retrospectively collected from a private medical center, under appropriate ethical approval, to ensure a balanced representation of non-cancerous cases. For model evaluation, a separate test set was curated, including 208 tumor-containing MRI scans and 177 healthy MRI scans.

2. FasterRCNN:

In this study, Faster R-CNN was utilized as the object detection model for identifying tumor regions in breast MRI scans. The model employs a ResNet-50 backbone combined with a Feature Pyramid Network (FPN) to enhance multi-scale feature representation, improving its ability to detect tumors of varying sizes. The Faster R-CNN architecture was trained from scratch, rather than using pre-trained weights, to ensure that the model learns directly from the medical imaging data without biases introduced from non-medical datasets. This approach allows for better adaptation to the unique characteristics of breast MRI scans, potentially improving detection performance.

A crucial aspect of developing a deep learning model is addressing the optimization problem defined by the loss function. Stochastic Gradient Descent (SGD) is one of the most widely used algorithms for tackling these optimization challenges (Ketkar, 2017). In this study, SGD was used for model optimization. The learning rate, weight decay, and momentum values were fine-tuned through Optuna-based hyperparameter optimization, ensuring optimal convergence.

3. Hyperparameter Tuning:

Hyperparameter optimization plays a crucial role in enhancing the performance and generalization capability of deep learning models. For this study, Optuna, was employed to systematically tune key parameters of the Faster R-CNN model. The selected hyperparameters learning rate, weight decay, and momentum were optimized.

The learning rate is one of the most critical hyperparameters influencing model convergence and performance (Smith, 2017). The search space for the learning rate was chosen as the range that gave the highest accuracy after testing with 10 epochs.

The weight decay parameter helps prevent overfitting by penalizing large weight values during training (Krog & Hertz, 1992). Prior research has shown that selecting an appropriate weight decay value can significantly improve generalization (Zhang et al., 2017).

Momentum is used in SGD to reduce oscillations and accelerate convergence by taking into account previous gradients. This helps the model to reach the optimum point more smoothly and quickly (Seyyarer, Ayata, Uçkan, & Karci, 2020). As in this study, values of 0.9 or higher are generally preferred for momentum (Shi, 2024).

By leveraging Optuna's Bayesian optimization approach, the best-performing hyperparameter combination was identified, leading to improved model accuracy and robustness. The tuning process enabled a more efficient exploration of hyperparameter space while reducing computational cost compared to exhaustive grid search methods (Akiba, et al., 2019).

4. Testing:

The proposed Faster R-CNN model was evaluated on a test set consisting of 208 tumor-containing MRI scans and 177 healthy MRI scans. Model performance was assessed using a confusion matrix, and key evaluation metrics were computed to measure detection accuracy.

To quantify the model's effectiveness, sensitivity, specificity, and Intersection Over Union (IoU) were calculated. Sensitivity reflects the model's ability to correctly detect tumor-containing slices, while specificity indicates how well the model distinguishes healthy slices from tumor-containing ones. IoU measures the overlap between the predicted bounding box and the ground truth, with a higher IoU value indicating better localization of the tumor.

These evaluation metrics together provide a comprehensive assessment of the model's performance in detecting and distinguishing tumor-containing and healthy slices, as well as its ability to localize tumors accurately.

Findings

The performance of the proposed Faster R-CNN model was evaluated using 208 tumor-containing MRI scans and 177 healthy MRI scans. Detailed evaluation results, including sensitivity, specificity, and IoU, are presented in Table 1.

Table 1. Accuracy results of the model according to different metrics.

Metrics	Results (%)
Specifity	88
Sensitivity	93
IOU	68

While the model demonstrated relatively high sensitivity, indicating its effectiveness in detecting tumor-containing slices, there remains a small chance of missing tumors. The specificity score of 88% suggests that the model is reasonably good at distinguishing healthy slices from tumor-containing ones, though there could still be instances of false positives. The IoU score of 68% reflects the overlap between predicted and ground truth bounding boxes, suggesting that while the model performs well, further refinement is needed to improve localization accuracy. These results indicate that, although the model is effective overall, there is room for improvement, particularly in reducing false positives and increasing detection accuracy across all cases.

Conclusion

In this study, we developed a Faster R-CNN-based deep learning model for breast tumor detection using MRI scans. The model demonstrated promising performance, achieving a sensitivity of 93%, a specificity of 88%, and an IoU score of 68% on the test dataset. These results suggest that the model is effective at identifying tumor-containing slices and distinguishing healthy tissues. However, there is still potential for improvement in minimizing false positives and enhancing accuracy, particularly in complex or ambiguous cases.

Future work could focus on refining the model's ability to generalize across a broader set of data, potentially by incorporating larger and more diverse datasets or exploring different network architectures. Additionally, using carefully annotated training and test datasets, where tumor regions are precisely marked by experts, can enhance the model's performance and contribute to a more reliable evaluation. Overall, the results of this study highlight the potential of deep learning models like Faster R-CNN in assisting radiologists with breast cancer detection, but further development is needed to make these models more robust and reliable for clinical use.

References

Akiba, T., Sano, S., Yanase, T., Ohta, T., & Koyama, M. (2019, July). Optuna: A next-generation hyperparameter optimization framework. In Proceedings of the 25th ACM SIGKDD International Conference on Knowledge Discovery & Data Mining (pp. 2623–2631).

American Cancer Society. (2016). Cancer facts & figures, The Society, New York,NY, USA, 2016.

Ketkar, N. (2017). Stochastic gradient descent. In Deep learning with Python. Apress, Berkeley, CA. **Url-1** https://doi.org/10.1007/978-1-4842-2766-4_8

Krogh, A., & Hertz, J. A. (1992). A simple weight decay can improve generalization. Advances in Neural Information Processing Systems, 4, 950–957.

Litjens, G., Kooi, T., Bejnordi, B. E., Setio, A. A. A., Ciompi, F., Ghafoorian, M., ... & van der Laak, J. A. W. M. (2017). A survey on deep learning in medical image analysis. Medical Image Analysis, 42, 60–88. **Url-2** https://doi.org/10.1016/j.media.2017.07.005

Mann, R. M., Kuhl, C. K., Moy, L., Baron, P., Borelli, C., Goerres, G., & Weinstein, S. (2019). Breast MRI: State of the art. JAMA Oncology, 5(9), 1369–1378. **Url-3** https://doi.org/10.1001/jamaoncol.2019.0649

McKinney, S. M., Sieniek, M., Godbole, V., Godwin, J., Antropova, N., Ashrafian, H., ... & Suleiman, M. (2020). International evaluation of an AI system for breast cancer screening. Nature, 577(7788), 89–94. **Url-4** https://doi.org/10.1038/s41586-019-1799-6

Ren, S., He, K., Girshick, R., & Sun, J. (2015). Faster R-CNN: Towards real-time object detection with region proposal networks. Advances in Neural Information Processing Systems, 28, 91–99. **Url-5** https://doi.org/10.48550/arXiv.1506.01497

Seyyarer, E., Ayata, F., Uçkan, T., & Karci, A. (2020). Derin öğrenmede kullanılan optimizasyon algoritmalarının uygulanması ve kıyaslanması. Computer Science, 5(2), 90–98.

Shi, B. (2024). On the hyperparameters in stochastic gradient descent with momentum. Journal of Machine Learning Research, 25(236), 1–40.

Siegel, R. L., Miller, K. D., Wagle, N. S., & Jemal, A. (2023). Cancer statistics, 2023. CA: A Cancer Journal for Clinicians, 73(1), 17–48. **Url-6** https://doi.org/10.3322/caac.21763

Smith, L. N. (2017). Cyclical learning rates for training neural networks. In IEEE Winter Conference on Applications of Computer Vision (WACV) (pp. 464–472). **Url-7** https://doi.org/10.1109/WACV.2017.58

Zhang, Y., Bengio, S., Hardt, M., Recht, B., & Vinyals, O. (2017). Understanding deep learning requires rethinking generalization. International Conference on Learning Representations (ICLR).

Prediction of Microsatellite Status Using Deep Neural Network

Fatma Vildan Engin[a], Ender Mete Ekşioğlu[a]

[a] Istanbul Technical University, Electronics and Communication Engineering Department, Türkiye
enginfvildan@gmail.com

Keywords : Colorectal Cancer, Deep Learning, Digital Pathology, Microsatellite Instability, Whole Slide Image.

Aim

Microsatellite instability (MSI) is an important biomarker for colorectal cancer (CRC). Due to cost and time issues, many patients remain untested for MSI. However, recent studies illustrated that patients with MSI respond better to immunotherapy (Kather et al., 2019a). Hence, segmentation for MSI in CRC patient images stands out as an important problem. In this study, hematoxylin and eosin (H&E) whole slide image samples from The Cancer Genome Atlas (TCGA) are used to develop a model for MSI segmentation. Additionally, data augmentation is applied to the used dataset. Two distinct models have been trained in a sequential setting. The first model realizes the segmentation of tumor and non-tumor tissues, whereas the second model is applied for the classification of MSI status. aim section should be written in Times New Roman font, justified-alignment and in 10-point size.

Material and Method

Tissue segmentation and classification are two separate problems. Therefore, two different datasets were used in the study. For segmentation, public tissue images are used, and these are labeled into three classes. The first class is ADIMUC, which consists of adipose tissue and mucus, and it is known as loose non-tumor tissue. The second class is STRMUS, which consists of stroma and muscle, and it is also called dense non-tumor tissue. The third and final class is TUMSTU, which consists of colorectal cancer epithelial tissue and stomach cancer epithelial tissue (Su et al., 2022). Microsatellite instability occurs in tumor tissues. Hence, tissues classified as TUMSTU are significant for microsatellite status detection, while the other classes are not important for further steps. The dataset for segmentation includes approximately 12,000 tissue images, which were split to train and test subsets with a ratio of 0.8 and 0.2. material and method section should be written in Times New Roman font, justified-alignment and in 10-point size.

The second dataset used for microsatellite status classification consists of whole slide tissue images from The Cancer Genome Atlas (TCGA). The samples from whole slide images belonging to TCGA-READ and TCGA-COAD were used because TCGA-CRC specifically focused on colon adenocarcinoma and rectum adenocarcinoma. A whole slide image involves both tumor and non-tumor tissue. For microsatellite status detection, only tumor tissues are essential. Each whole slide image is divided into image tiles. These patches are then classified as adipose tissue, stroma tissue, or tumor tissue. Tumor tissues were considered meaningful for microsatellite status detection. The classifier for the segmentation task was created by using the ResNet-18 architecture. ResNet-18 utilized in this study has 71 layers in total. ResNet-18 model was trained using transfer learning by building upon a model pre-trained on the ImageNet dataset. The end layers of the model need to be re-arranged for our particular application, hence, these layers were fine-tuned using the dataset. The initial learning rate was chosen as 0.00001 . Such a small learning rate necessitates a rather large number of epochs (Jepkoech et al., 2021). Hence, 100 epochs were applied.

After the classification, tumor tissues for colorectal cancer were obtained. To obtain image patches, n = 1922 whole slide images belonging to 1687 patients were acquired. After division and elimination, considering the tumor or non-tumor tissue, patches were acquired. These patches are considered significant for MSI status because the classification of MSI status can be determined for tumor tissues. Therefore, non-tumor tissues such as adipose or stroma were eliminated.

Then, color normalization was applied to these image patches to normalize the pixel values. For color normalization, the Macenko method was used (Macenko et al., 2009). This method is utilized to overcome the color variation problem in histopathology. The method uses a reference image to normalize the pixel values (Macenko et al., 2009). A vital information

for microsatellite status detection is the location of the pixel. This can be determined by the colors of pixels. Because H&E staining was used in pathology images, in this staining technique,blue staining represents the nucleus while red parts are used for coloring the rest of the cell. Thus, the locations of pixels are determined. Color normalization kept important pixels while removing or blurring the insignificant pixels of the image.

After the color normalization, images are augmented to improve the model's performance. Every tissue image has similar textures. There is a homogeneous distribution within the image. For the augmentation purpose, cut-out and cut-mix methodologies have been used. These techniques both determine a certain part of the image. This part was chosen as a square area for both models. The cut-out technique suggests filling this area with zero padding, while the cut-mix suggests filling it with a patch from another image (Rao et al., 2023). A sample of the application of the cut-mix technique for an image from the dataset is shown in Figure 1.

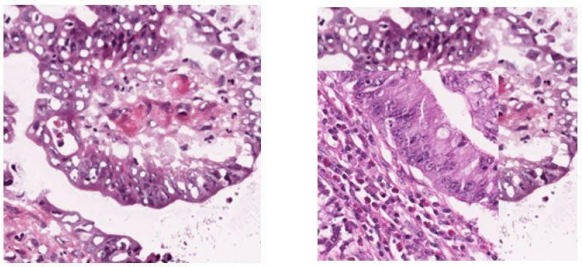

Figure 1. A sample of Cut-mix Application.

Finally, the obtained dataset was divided into train, test, and validation sets with a ratio of 0.7, 0.2, and 0.1. Also, patient labels are considered for splitting into the test and train subsets. All patients have more than one patch because of the whole slide image division (Kather et al., 2019b). Also, for some cases, the same patient might have more than one whole slide image, which leads to more image patches. These image patches should be considered in the same class to determine if the patient has MSI. Thus, the labels for each case were kept. Then, a pre-trained ResNet-18 model was used for microsatellite status prediction. The last layers of the architecture were fine tuned, while the other layers were fixed

Findings

This study aimed to detect microsatellite status on colorectal cancer images using the Resnet-18 model. The utilized performance evaluation criterion was based on the Reciever Operating Characteristic curve. The area under the curve (AUC) was calculated as 0.88, as seen in Figure 2. This result suggests that our model performed rather well for the whole slide tissue image classification problem under consideration.

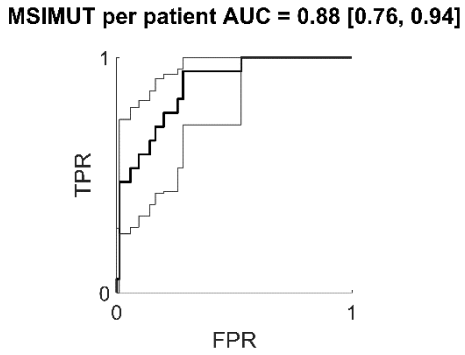

Figure 2. ROC Curve for Microsatallite Status Prediction Model.

Additionally, accuracy, sensitivity, precision, and f1 score were also calculated, which can be seen in Table 1. These additional results confirm the performance of our developed model.

Table 1. Evaluation Metrics of the Model.

Evaluation Metric	Results
Accuracy	0.95484
Sensitivity	0.95484
Precision	0.82738
F1 Score	0.88655

Conclusion

The purpose of this study was to predict microsatellite status models in colorectal cancer (CRC) tissue slides by using deep learning. The AUC result and additional evaluation metrics demonstrated the performance of the utilized ResNet-18 model and also the importance of data augmentation. The proposed model would be a beneficial asset for pathologists. The model also provides a fast and accurate approach to cancer tissue segmentation. The model can be extended in a rather straightforward manner to the images for other types of cancer patients.

References

Kather, J. N., Krisam, J., Charoentong, P., Luedde, T., Herpel, E., Weis, C. A., Gaiser, T., Marx, A., Valous, N. A., Ferber, D., & Jansen, L. (2019). Predicting survival from colorectal cancer histology slides using deep learning: A retrospective multicenter study. PLOS Medicine, 16(1), e1002730. **Url-1** https://doi.org/10.1371/journal.pmed.1002730.

Su, F., Li, J., Zhao, X., Wang, B., Hu, Y., Sun, Y., & Ji, J. (2022). Interpretable tumor differentiation grade and microsatellite instability recognition in gastric cancer using deep learning. Laboratory Investigation, 102(6), 641–649. **Url-2** https://doi.org/10.1038/s41374-022-00742-6.

Jepkoech, J., Mugo, D. M., Kenduiywo, B. K., & Too, E. C. (2021). The effect of adaptive learning rate on the accuracy of neural networks. International Journal of Advanced Computer Science and Applications, 12(8). **Url-3** http://dx.doi.org/10.14569/IJACSA.2021.0120885.

Macenko, M., Niethammer, M., Marron, J. S., Borland, D., Woosley, J. T., Guan, X., Schmitt, C., & Thomas, N. E. (2009, June). A method for normalizing histology slides for quantitative analysis. In 2009 IEEE International Symposium on Biomedical Imaging: From Nano to Macro (pp. 1107–1110). **Url-4** https://doi.org/10.1109/ISBI.2009.5193250.

Rao, A., Lee, J. Y., & Aalami, O. (2023). Studying the impact of augmentations on medical confidence calibration. In Medical Imaging with Deep Learning (Vol. 236, pp. 2624–2643). **Url-5** https://proceedings.mlr.press/v236/rao23a.html.

Kather, J. N., Pearson, A. T., Halama, N., Jäger, D., Krause, J., Loosen, S. H., Marx, A., Boor, P., Tacke, F., Neumann, U. P., Grabsch, H. I., Yoshikawa, T., Brenner, H., Chang-Claude, J., Hoffmeister, M., Trautwein, C., & Luedde, T. (2019). Deep learning can predict microsatellite instability directly from histology in gastrointestinal cancer. Nature Medicine, 25(7), 1054–1056.

Url-6 https://doi.org/10.1038/s41591-019-0462-y.

Improving Tumor Segmentation Performance in Breast MRI via U-Net Based Deep Learning Approach

Alptuğ Şeref Ayyıldız[a,b], İbrahim Akduman[b,c], Aleksandar Janjic[b]

[a] Istanbul Technical University, Graduate School, Satellite Communication and Remote Sensing, Türkiye
[b] InfiWave Diagnostics, Software Limited Company, Türkiye
[c] Istanbul Technical University, Electrical and Communication Engineering, Türkiye
ayyildiza19@itu.edu.tr

Keywords: Biomedical Imaging , Breast Tumor Segmentation , Deep Learning , Magnetic Resonance Imaging, U-Net.

Aim

Breast cancer is one of the most common invasive cancer types worldwide and is a leading cause of cancer-related deaths among women (Bray et al., 2018; Siegel et al., 2019). Early diagnosis in breast cancer is critically important for the success of the treatment process, and for this purpose, medical imaging techniques are extensively utilized. Magnetic Resonance Imaging (MRI) is a widely preferred imaging method in the diagnosis of breast cancer and the detailed morphological analysis of tumors (Yousaf, Dervenoulas, & Politis, 2018). Manual annotation of tumor regions in MRI images, which is essential for training artificial intelligence (AI) based diagnostic models, is a time-consuming process that requires significant effort and radiological expertise (Jiang, Diao, & Yao, 2022). This step, typically carried out by expert radiologists, is crucial for preparing high-quality labeled datasets needed for developing automated diagnostic systems. This manual process can affect the accuracy of segmentation among different observers, potentially leading to incomplete evaluations. In this context, the development of automatic or semi-automatic segmentation methods to reduce radiologists' workload, ensure segmentation consistency, and improve the accuracy of diagnostic processes has emerged as an important research topic in the field of medical imaging.
The main objective of this study is to enhance the accuracy and efficiency of tumor segmentation in breast MRI images by utilizing a U-Net-based approach. The proposed method aims to improve segmentation performance by addressing the limitations of existing fully automatic models.

Material and Method

1. Dataset

In this study, two different datasets were used for the segmentation of breast cancer lesions: the Mama Mia Breast MRI Dataset (Garrucho et al., 2024) and the Zenodo Breast MRI Dataset (Zhang, 2023). Both datasets include segmentation masks that indicate the tumor regions.
The Mama Mia dataset is a research-oriented dataset containing breast MRI data from a total of 1506 patients. This dataset includes dynamic contrast-enhanced MRI (DCE-MRI) images captured at different time points for breast cancer diagnosis. In the study, only the last post contrast images from the Mama-Mia dataset were used in the dataset.
The breast MRI dataset obtained from the Zenodo platform contains breast MRI data from a total of 100 patients. For each patient, the dataset includes six types of images in total, consisting of pre-contrast and post-contrast scans. Both image types were used in the study. Subtracted images, which are obtained by subtracting pre-contrast and last post-contrast images from each other, are used to analyze which image format the model performs better in segmentation. Accordingly, the model was trained with both post-contrast and subtracted images separately and performance comparisons were made. Based on the findings, the image type with higher performance was identified and this dataset was combined with post-contrast images from the Mama-Mia dataset to create a hybrid training set.
To enable data analysis and enhance the effectiveness of the segmentation models, a comprehensive data preprocessing step was carried out. In the initial stage, the minimum rectangular area (bounding box) that best encloses the tumor regions was calculated, and each image was cropped based on this bounding box. This approach allowed the models to focus only on

the tumor-containing regions, preventing background information from negatively affecting model performance. However, to better model the boundary areas between tumorous and healthy tissues and to gain a deeper understanding of the transitions between tissues, the bounding box areas were expanded by 10% and 20%, respectively, and the resulting images containing surrounding healthy tissue were also included in the training process.
Subsequently, the datasets were individually optimized according to the input size requirements of the segmentation models to be used. The images prepared for the U-Net model were resized to 256x256 pixels.

2. Methodology

In this study, a segmentation pipeline is proposed to accurately delineate tumor regions in breast MRI images. Initially, the dataset was prepared for the training and testing processes through the application of various data augmentation techniques. Subsequently, the model's performance was evaluated using two different image types—post-contrast and subtracted images—exclusively on the Zenodo dataset. Based on the comparative results, the image format that yielded a higher Dice score was selected. In the final step, the U-Net model was trained using a combination of the Mama Mia and Zenodo datasets, utilizing the selected image type to enhance segmentation accuracy.
The U-Net model is a type of fully convolutional network (FCN) that is widely used for medical image segmentation and follows an encoder-decoder architecture (Azad et al., 2024). In the encoder phase, the model processes the input image at multiple resolution levels to learn deep and semantic features. In the decoder phase, it reconstructs the original resolution by enriching the high-level features obtained from the encoder with detailed information. This process provides the ability to capture global contextual information while preserving fine details, which is particularly important for segmenting small and irregularly shaped structures such as tumors (Du et al., 2020).
In this study, the U-Net model was trained using the Dice Loss function. Dice Loss is a loss function commonly used in segmentation models and is particularly effective in cases of imbalanced class distributions; it aims to improve segmentation accuracy by maximizing regional overlap (Zhao et al., 2020). The AdamW optimization algorithm was employed to ensure stable progression during the learning process.
In addition, to increase the diversity of tumor shapes and enhance the model's generalization ability to different tumor morphologies, an affine transformation—a two-dimensional geometric transformation method—was applied in this study. This method involves a combination of operations such as translation, rotation, scaling, and shearing applied to the images (Stearns & Kannappan, 1995). Through this data augmentation technique, the model gains the ability to better recognize tumors with varying shapes and locations that may not be present in the training dataset, thereby enabling stronger generalization to diverse tumor morphologies in real clinical settings.

Findings

To assess the impact of image selection on segmentation performance, two different input strategies were compared: subtracted images (obtained by subtracting pre-contrast from last post-contrast images) and last post-contrast images alone. The evaluation was conducted using the Zenodo dataset, and the results are presented in Table-1 and Table-2:

Table 1. Dice Score (%) for the Subtracted Images Dataset.

Dataset	Dice Scores (%)
Validation	77
Test	76

Table 2. Dice Score (%) for the Last Post-Contrast Images Dataset.

Dataset	Dice Scores (%)
Validation	90
Test	83

The comparison reveals a clear performance advantage when using last post-contrast images. Specifically, a 13% increase in Dice score was observed on the validation set and a 7% increase on the test set, demonstrating that last post-contrast images offer better lesion visibility and enable more accurate segmentation.
Based on these observations, last post-contrast images were selected for the construction of the hybrid dataset used in the proposed approach. The U-Net model was trained on tumor positive images with the application of various data augmentation techniques. The performance on this hybrid dataset is reported in Table-3:

Table 3. Dice Score (%) for the Hybrid Dataset.

Dataset	Dice Scores (%)
Validation	83
Test	84

These results indicate that the U-Net model, when trained under the specified conditions, achieves high segmentation accuracy and generalizes well across different patient data. The combination of contrast-enhanced image selection, targeted training, and data augmentation played a crucial role in obtaining these performance levels.

Conclusion

This study aimed to improve tumor segmentation performance in breast MRI images by leveraging a U-Net-based approach trained under a carefully designed pipeline. The results demonstrate that the proposed method achieved high segmentation accuracy and efficiency, particularly when trained on tumor-positive images augmented with appropriate data augmentation techniques. The U-Net model exhibited a strong learning capacity, effectively capturing and delineating tumor regions with precision.
An important finding emerged from the comparative analysis of subtracted images (pre-contrast subtracted from last post-contrast) and last post-contrast images. The model performed considerably better on last post-contrast images, achieving higher Dice scores and more accurate segmentations. This insight guided the selection of last post-contrast images for the composed dataset used in this study, contributing significantly to the model's improved performance.
Moreover, integrating multiple datasets to form a composite training set enhanced the model's generalization capability. This hybrid dataset enabled the U-Net model to adapt effectively to a variety of imaging characteristics, leading to robust and consistent results across different data distributions.
These findings indicate that both selective training on tumor-present images and the incorporation of diverse, contrast-enhanced datasets are key to improving segmentation accuracy. Overall, the proposed training strategy has proven effective and highlights the potential of the U-Net architecture as a reliable and generalizable tool for breast tumor segmentation in both clinical and research contexts.

References

Azad, R., Aghdam, E. K., Rauland, A., Jia, Y., Avval, A. H., Bozorgpour, A., ... & Merhof, D. (2024). Medical image segmentation review: Thesuccess of u-net. IEEE Transactions on Pattern Analysis and Machine Intelligence.
Bray, F., Ferlay, J., Soerjomataram, I., Siegel, R. L., Torre, L. A., & Jemal, A. (2018). Global cancer statistics 2018: GLOBOCAN estimates ofincidence and mortality worldwide for 36 cancers in 185 countries. CA: a cancer journal for clinicians, 68(6), 394-424.
Du, G., Cao, X., Liang, J., Chen, X., & Zhan, Y. (2020).Medical image segmentation based on U-net: A review. Journal of Imaging Science & Technology, 64(2).
Garrucho, L., Reidel, C. A., Kushibar, K., Joshi, S., Osuala, R., Tsirikoglou, A., ... & Lekadir, K. (2024). Mama-mia: A large-scale multi-centerbreast cancer dce-mri benchmark dataset with expert segmentations. arXiv preprint arXiv:2406.13844.
Jiadong Zhang. (2023). Breast_Cancer_DCE-MRI_Data [Data set]. Zenodo.
Url-1 https://doi.org/10.5281/zenodo.8068383

Jiang, H., **Diao, Z., & Yao, Y. D.** (2022). Deep learning techniques for tumor segmentation: a review. The Journal of Supercomputing, 78(2),1807-1851.
Siegel RL, Miller KD, Jemal A (2019) Cancer statistics, 2019. CA Cancer J Clin 69:7– 34. 10.3322/ caac.21551 [PubMed: 30620402]
Stearns, C. C., & Kannappan, K. (1995). U.S. Patent No. 5,475,803. Washington, DC: U.S. Patent and Trademark Office.
Yousaf, T., **Dervenoulas, G., & Politis, M**. (2018). Advances in MRI methodology. International review of neurobiology, 141, 31-76.
Zhao, R., Qian, B., Zhang, X., Li, Y., Wei, R., Liu, Y., & Pan, Y. (2020, November). Rethinking dice loss for medical image segmentation. In2020 IEEE international conference on data mining (ICDM) (pp. 851-860). IEEE.

ARCHITECTURE

Architectural History

Architecture Design Theory

Building Construction Technologies

Building Materials and Technologies

Built Environment Design and Technologies

Conservation and Restoration

Environmental Control and Building Technology

Project and Construction Management

Sustainable Design

Spatial Representation In French New Wave Cinema: An Analysis Through Agnès Varda's Cléo De 5 À 7 (1962) Film

Miraç Kaykulu [a], Demet Arslan Dinçay[b]

[a] Istanbul Technical University, Department of Architecture, Architectural History Program, Turkey
[b] Istanbul Technical University, Department of Interior Architecture, Turkey
kaykulu22@itu.edu.tr

Keywords: Cinematic Space, France New Wave Cinema, Post War II, Contextual Analysis, Semantic Analysis.

Aim

Space, the primary subject of architecture, is also a fundamental component of cinema. According to Pallasmaa, architecture, much like cinema, exists in the dimensions of time and movement. Designing and interpreting a building takes place through sequential spatial experiences. Constructing a building involves anticipating and composing the effects of contrasts and connections experienced within the spatial flow. When considering a building as a continuous plan/sequence, the architect essentially works with cuts, montages, framing, and openings. (2012) In this regard, architectural and cinematic space intersect in their exploration of time and human experience.

The New Wave was a cultural movement that emerged in the 1950s as a result of the economic, political, aesthetic, and social developments in post-war France. (Neupert, 2007) This movement developed a complex relationship with architecture, as filmmakers created a new cinematic language that reflected the cultural context of post-war France. By focusing on Paris's built environment, they revealed its cultural, social, and aesthetic dimensions, presenting a panoramic urban view.

This study investigates the use of space in French New Wave Cinema, with a specific focus on Agnès Varda's Cléo de 5 à 7 (1962). Varda's innovative use of space in the film will be analyzed, showing how its settings document Paris's urban fabric and how cinematic space conveys the narrative and the characters' experiences.

Material and Method

This study employs a qualitative analysis to explore the use of space in Cléo de 5 à 7, focusing on both semantic and contextual aspects. The theoretical framework is grounded in a review of the socio-political, cultural, artistic, and architectural conditions in post-World War II France, which influenced the rise of French New Wave Cinema. The analysis progresses from broad urban landscapes—reflecting socio-cultural dynamics in public spaces—to more intimate, personal interiors that align with the character's internal journeys within the film's narrative.

Findings

1. Post-World War II France

According to Hoffmann, post-world War II France experienced not only a crisis but also a political and social reconstruction process (1961). The colonial wars in Algeria and Indochina deeply affected France's national identity, setting the stage for May 1968 protests, which led to significant cultural changes (Wolin, 2010).

The cultural and artistic environment following World War II saw a dynamic shift where traditional structures were dismantled, and experimental approaches emerged. Hopkins notes that this period marked the rise of modern art movements in France (2000). Similar innovation was observed in architecture. The devastating effects of the war led to a severe housing crisis, bringing issues of reconstruction and repurposing to the forefront. At the same time, debates about balancing the preservation of historical heritage with modernization took place. While the historic fabric of Paris was prioritized for preservation, modern development was concentrated in the city's suburbs. Modernism, led by figures such as Le Corbusier and Auguste Perret, influenced urban planning projects. However, these experimental projects remained largely conceptual

and were only implemented on a limited scale (Ragon, 2010). Notable examples of modernist planning include the La Défense project and Le Corbusier's Cité Radieuse and Unité d'Habitation projects (Cohen, 2013).
Similarly, cinema also saw new developments, with the French New Wave emerging in this context. André Bazin's Cahiers du Cinéma (1951) played a key role in spreading the French New Wave. Alexandre Astruc developed the ‘‘auteur’’concept, viewing cinema as a language and form of expression in the ‘‘camera-stylo’’ era (Makal, 1996). According to Kovacs, French New Wave auteurs positioned themselves as representatives of modern cinema in France and Europe. In their films, they used sound, music, and dialogue in ways that contrasted with visual storytelling, thus developing a new aesthetic approach where meaning was conveyed predominantly through visuals (2010).

2. Cléo de 5 à 7 (1962)

In Cléo de 5 à 7, the film depicts the two-hour internal journey of the singer Cléo as she awaits her hospital test results, unfolding almost in real-time (Mennel, 2019). The narrative centers on the character's emotional state, exploring themes such as the fear of death, mental distractions, and the rapid process of reinterpreting life from a new perspective. Space plays a crucial role in enhancing the narrative. The film's settings will be analyzed in three sections: urban spaces, public interiors, and personal interiors, with semantic and contextual analyses.

2.1. Urban Spaces

The urban landscapes reflect real life. The character is static in one sense, awaiting test results for a possible cancer diagnosis, while in another, she is dynamic, walking through Paris, navigating taxis, cars, and buses (Stark, 2012). This contrast emphasizes the tension between her internal stillness and the city's external movement, enriching her emotional journey.

2.1.1. Semantic Analysis

In the 1962 Paris city panorama, the architecture of the city center reflects historical influences rather than modernist ones (Figure 1) (Url-1). This period coincides with the acceleration of modern construction and mass housing on the city’s outskirts. In the film’s public spaces, locations such as Parc de Montsouris and Hôpital de la Salpétrière are featured (Figure 2). Varda uses the city's streets, avenues, parks, and dynamic spaces as stages in the film. Long takes, wide-angle shots, and over-the-shoulder tracking shots highlight the character’s continuous interaction with the city, emphasizing movement and change.

Figure 1. The urban spaces of the film, the panorama of the city of Paris.

Figure 2. Hôpital de la Salpétrière ve Parc de Montsouris.

2.1.2. Contextual Analysis

According to Mennel, commercial areas like Rue de Rivoli and Boulevard Montparnasse symbolize Cléo's initial consumption-driven world. In contrast, Parc de Montsouris represents natural, open public spaces where Cléo begins to experience freedom and connect with others (2019). Varda presents Paris not only as an aesthetic backdrop but as a dynamic space where socio-political events unfold. The details Cléo encounters while walking, taking a taxi, riding a bus, or traveling in her friend's car reflect the political climate of the time.

2.2. Public Interior Spaces

2.2.1. Semantic Analysis

In examining the public interior spaces in the film, while modernism had not yet influenced mass architecture in 1960s Paris, it began to emerge in interior design through rational furnishings, functional solutions, and the use of mirrors. In the opening tarot scene, Cléo encounters her reflection in a mirror as she exits the fortune teller's room; in another mirror in the lobby, she questions her youth and beauty. After leaving the fortune teller, Cléo sits with Angèle at a café in front of a mirror; as she gazes into it, she begins to cry. This mirror reflects not only Cleo and Angèle but also the café interior and the street outside. In a hat store, mirrors fragment the space and multiply Cléo's image, emphasizing her dominance in the space while the city fades into the background . Later, at Le Dôme café, reflections in glass mirrors and modern paintings stand out. When Cléo visits her friend's sculpture studio, both the interior and exterior are shown from different angles. Finally, at the cinema, a falling mirror shatters, with Cléo's reflection symbolizing her confrontation with herself (Figure 3).

Figure 3. Public Interior Spaces.

2.2.2. Contextual Analysis

The public interior spaces in the film offer a glimpse into Cléo's daily life. Amid the vibrant surroundings, the fear and anxiety brought on by shifting circumstances are reflected through mirrors placed in these spaces. Mennel notes that mirrors in public spaces extend the perceived boundaries of the environment and enable the multiplication of characters. The split-screen effect created by mirrors emphasizes a space where private life is revealed in the public domain (2019). The mirrors symbolize Cléo's confrontation with herself.

2.3. Cléo's Flat

2.3.1. Semantic Analysis

In areas like Montmartre and Montparnasse, artist studios rapidly multiplied, and building complexes such as La Ruche and Le Bateau Lavoir were constructed. In these areas, it is common to find artist studios with glass roofs opening onto courtyards of buildings with classical façades (Delanoe, 2001). Cléo's apartment is located on Rue Huyghens, near the

Montmartre district (Url-2). Upon examining the features of Cléo's home, it could be considered one of the artist studios mentioned above.

The interior of the apartment is a single space with high ceilings and white walls. In the interior, a Jacobin-style wooden bed and table stand out. The style includes vertically oriented chain-effect load-bearing elements. Additionally, there is a Neo-Baroque pair of armchairs next to the bed. The apartment also features Michael Thonet's rocking chair model no.1 (1862) and chair model no.14 (1859) (Url-3). The furnishings do not form a cohesive composition within the interior but are displayed individually. Within the spatial furnishings, attention is drawn to the mirrors (a freestanding singular mirror, a vanity mirror, and several mirrors hanging on the wall) as well as the collection of numerous clocks arranged side by side on the shelf (Figure 4).

Figure 4. Cleo's Flat.

2.3.2. Contextual Analysis

Cléo's apartment interior reflects her fantasy world, with furnishings arranged without cohesion, mirroring the fragmented state of her mind as she faces death. The Jacobin-style furniture, representing the past, contrasts with rational pieces symbolizing the future. Items like wigs, wings, mirrors, and clocks further embody her complex mental state.

The fluted carriers on the furniture resemble chains, symbolizing her captivity to illness. The duality of the Neo-Baroque armchairs and two Thonet chairs highlights the life-death dichotomy. Mirrors on the walls symbolize her confrontation with reality, while the clocks emphasize the passage of time and the life-death process.

Kitsch accessories such as feathered wings and costumes suggest her immersion in fantasy. She does not use the rational furniture, which is instead used by others (e.g., her assistant or friends), while she sits in the rocking chair. This may symbolize her subconscious desire to escape into her fantasy world.

Conclusion

Cléo de 5 à 7 is a key example in French New Wave Cinema, where emotion-driven storytelling is placed in a spatial context. The narrative centers on the chaos in the protagonist's mind. The film uses spaces, from urban public areas to personal interiors, as a tool that enhances the narrative.

The public spaces reflect Cléo's connection to life, while her home symbolizes detachment from reality. Through urban landscapes, public interiors, and Cléo's apartment, the film captures 1960s Paris's architectural structure and explores the emotional transformation of the character. The spaces are not just a backdrop but an active part of the narrative, with Paris's urban fabric carrying the story. Through cinema, architectural space becomes a reinterpretable text. In this sense, Cléo de 5

à 7 is more than a film; it exemplifies how cinematic space integrates with the narrative, shedding light on the socio-cultural and architectural context of the time.

References

Cohen, J. L. (2013). Le Corbusier: An Atlas of Modern Landscapes. Thames & Hudson Publishing.
Delanoë, B. (2001). Lofts of Paris. Tectum Publishers, (pp. 11-12). Belgium: Antwerp.
Hoffmann, S. (1961). The Effects of World War II on French Society and Politics. Duke University Press, (Vol. 2, No. 1, pp. 1).
Hopkins, D. (2000). After Modern Art 1945-2000. Oxford University Press.
Kovács, A. B., & Yılmaz, E. (2010). Modernizmi Seyretmek: Avrupa Sanat Sineması, 1950-1980. De Ki Yayınları, (pp. 231-332).
Makal, O. (1996). Fransız Sineması. Kitle Yayınları. (pp. 97-109).
Mennel, B. (2019). Cities and cinema. Routledge Publishing, (pp. 61-80).
Neupert, R. (2007). A History of The French New Wave Cinema. University of Wisconsin Press., (2nd ed., pp. 3)
Pallasmaa, J. (2001). The architecture of image: Existential space in cinema. Rakennustieto Publishing, (pp. 17).
Ragon, M. (2010). Modern mimarlık ve şehircilik. Kabalcı Yayınevi. (Vol. 351).
Stark, K. (2012). The Modern Flâneur: Representations of Walking and Driving in French New Wave Cinema (Doctoral dissertation). University of California, Berkeley, (pp. 34-43)
Vialard, A. (2023). Intelligibility of Post-War Reconstruction in French Bombed Cities. Urban Planning, (Vol. 8 pp., 226-230)
Wolin, R. (2010). The Wind From the East: French Intellectuals, The Cultural Revolution, and The Legacy of The 1960s. Princeton University Press.
Url-1 https://archive.org/details/cleo.-from.-5.-to.-7.1962.1080p, date retrieved 16.02.2025.
Url-2 https://www.bfi.org.uk/features/agnes-varda-cleo-from-5-7-paris-locations?utm, date retrieved 16.02.2025.
Url-3 https://collection.design-museum.de/#/en/search?_k=9u5zjd, date retrieved 16.02.2025.

Legitimisation through Elevation: Romanos' Myrelaion

Ömer Faruk Ulusoy[a], Bilge Ar[a]

[a] Istanbul Technical University, Department of Architecture, Architectural History Program, Turkey
ulusoyo17@itu.edu.tr

Keywords: Legitimisation, Myrelaion, Patronage, Romanos I Lekapenos, Visibility.

Aim

This study constitutes the transformation of a conceptual practice concerning the external perception of the Myrelaion structure into a scholarly research project. It represents a line of thought that proceeds from the externally observable architectural features of the structure toward the possible intentions of the patron who financed its construction. Although not all externally perceived characteristics of the building may have been consciously designed, it is certain that some were intentionally crafted to evoke specific impressions in viewers. In this respect, buildings serve as intermediaries between patrons and the perceptions they aim to instill in people.

The Myrelaion Church was constructed on a platform that radically increased the building's height. This deliberate manipulation of the topography evidently contributed significantly to enhancing the visibility of the structure. However, the external perception of Myrelaion has been profoundly altered due to the radical transformation of its surrounding physical environment in recent centuries. Today, the tall apartment buildings surrounding the site have erased its once-dominant position within the urban fabric and greatly diminished its visibility. Nevertheless, due to its dominant position in the topography of Constantinople and the substantial substructure elevating it, Myrelaion must have been a much more visible and prominent structure at the time of its construction.

Some complexes built on the sloped topography of Constantinople were erected on substructures designed to create flat surfaces for construction (Janin, 1964). These substructures typically generated level platforms accessible from higher ground. In the case of Myrelaion, however, the substructure rises from all directions, preventing pedestrian access to the church's platform. Therefore, unlike other examples, the sole purpose of Myrelaion's substructure cannot have been merely to produce an accessible flat surface on sloping terrain. In the literature, it is commonly stated that the reason for Myrelaion's elevation was to align the church with the elevation of the adjacent palace (Striker, 1968). However, like the church, the palace also rises on a substructure and is similarly inaccessible from street level. Considering that the adjacent palace was also commissioned by Romanos Lekapenos, the patron of Myrelaion, it is likely that the patron played a role in this unconventional architectural approach.

Based on existing studies in the literature, it can be suggested that Romanos was an emperor who sought to establish legitimacy through various means (Runciman, 1969). In this study, Romanos' patronage and his quest for legitimacy will be examined specifically through the example of Myrelaion—his only surviving architectural work today. While the structural features of this building have previously been analyzed in detail, this study adopts a different approach, treating the church's architectural and locational characteristics as the result of intentional decisions. By investigating the underlying motivations that led the builders to such outcomes, a conceptual framework is constructed, moving from the structure's physical features toward the patron's potential intentions.

Material and Method

The unique substructure of Myrelaion, uncommon in its period, suggests a deliberate and exceptional architectural choice likely tied to the patron's personal intentions. Its execution by builders unfamiliar with such forms reinforces this view. To explore this relationship, the study compares Myrelaion to other elevated religious buildings from the same period—namely the Monastery of St. Mary Peribleptos, Hagia Georgios in Mangana, and the Gül Mosque.

Another approach to understanding Myrelaion's distinct architectural form involves examining other structures commissioned by Romanos. While many are now lost, the Chalke Chapel—described in reliable sources—shares similar elevated and inaccessible features. This suggests a consistent architectural strategy across Romanos's projects.
Understanding the motivations behind these design choices also requires insight into Romanos's political career and personal ambitions. Primary sources, particularly Theophanes Continuatus, offer valuable context.
This study follows a conceptual framework moving from Myrelaion's external perception to its design rationale and patronal intention. The investigation began by asking why the church was elevated without any evident topographical necessity. Since the surrounding environment has changed considerably, historical maps and travel accounts—especially those of 16th-century visitor Pierre Gilles—were used to reconstruct the structure's original visual prominence.

Findings

Although it is currently impossible to comprehend due to the high-rise buildings surrounding Myrelaion, the study has demonstrated—based on visual and textual sources—that Myrelaion was, at the time of its initial construction, a highly visible structure occupying a dominant position within its surroundings. This pronounced visibility was partly the result of the strategically chosen dominant location and, undoubtedly, also a consequence of the unconventional form of the substructure upon which the building was erected. Through a comparative analysis of the substructure employed in Myrelaion with those of other contemporaneous constructions, the unique nature of its architectural solution has been identified. Moreover, by including other buildings commissioned by the same patron in the scope of the study, it has been established that this distinctive architectural approach was a recurring practice in the constructions associated with Romanos.
Comparable examples of churches built on substructures include the Monastery of St. Mary Peribleptos, Hagios Georgios in Mangana, and the Gül Mosque, likely built slightly later. All were elevated on substantial platforms that enhanced their visibility.
Of Peribleptos, only the substructure survives, with a later church built above. Set on a slope, it was accessible from the higher side, while its lower façade rose impressively on a massive base. The 17th-century traveler Simeon described it as "on a high place overlooking the sea," likely referring to this effect.
Hagios Georgios, now lost, was rebuilt multiple times. Its final form rested on deepened foundations with added columns (Psellos, 1953), also rising on a slope with support from below.
The Gül Mosque, of uncertain original identity, was built atop a leveled hilltop. Its platform meets the ground at only one point, making it accessible only there, while its retaining walls become increasingly prominent from a distance.

Conclusion

In the sloped topography of Constantinople, it was common to build substructures to create level construction platforms. In the examples above, these substructures primarily served to counteract the slope and provide accessible flat surfaces. Myrelaion, too, stands on a massive substructure. Pierre Gilles, who visited Istanbul in the 16th century, wrote: "Above the Blancha to the North, there stands a temple upon an eminence, called Myreleos; in the inside of which was a cistern, the roof of which is supported with about sixty marble pillars" (Gilles, 1555). This substructure significantly shaped the external appearance of the building. Unlike the other examples, the Myrelaion is raised on all sides and its upper platform is inaccessible on foot, suggesting that the purpose of its elevation was not only to create a flat surface accessible on foot.
Myrelaion was constructed simultaneously with Romanos' adjacent palace, which itself was built atop the ruins of an ancient rotunda—the largest in Constantinople at the time. Romanos converted this rotunda into a cistern by filling it with columns and building his palace on top (Striker, 1968). Like the church, the palace platform is elevated and inaccessible by foot from any direction. This inaccessibility distinguishes Romanos' architectural approach from that of his contemporaries. It suggests that his intent was not only to create flat ground but also to elevate the structures symbolically and visually.
The same principle appears in Romanos' Chalke Chapel. Though the structure no longer survives, it is described in primary sources. Cedrenus (1839) notes that the chapel was built atop the Chalke Arch. Deacon Leon described it as "a narrow chapel that could accommodate at most fifteen people, reached by spiral staircases, difficult to access, almost like a labyrinth

or a hiding place" (Talbot & Sullivan, 2005). These descriptions confirm that the chapel was elevated above ground level and accessible only by a long, winding staircase.

The unique architecture of the Chalke Chapel represents an exceptionally singular implementation. The peculiarity of its location choice for a chapel was even criticized in contemporary sources. However, we are fortunate that one event, recorded in a primary source from the period, helps illuminate why such a location may have been chosen. In the Chronicle of Theophanes Continuatus, there is an account of Romanos delivering a speech to the people in front of the Chalke Chapel, publicly announcing one of his charitable acts.

"On the other hand, Emperor Romanos was striving to repay his obligations to the city and to win the favor of the people. To this end, he annulled all public debts and ordered the official debt registers to be torn up. These documents were publicly burned at the Chalke Gate, and the people applauded the gesture with great enthusiasm." (Theophanes Continuatus, 1838, p. 429).

This account describes Romanos standing on the terrace and publicly declaring his philanthropic act in a highly political display. Despite the small size of the chapel, its elevated position made it easily visible from a distance. Romanos, speaking from the terrace, could also be clearly seen by the gathered crowd. Behind him stood a physical embodiment of his piety and generosity — the chapel he had built.

The repetition of this unusual architectural choice in both Myrelaion and the Chalke Chapel—structures commissioned by the same patron— strongly suggests that elevation was a personal preference of Romanos.

What might have motivated Romanos to favor this solution? Understanding this requires consideration of his career and political ambitions. Romanos came from a peasant background and rose through the ranks of the Byzantine navy, eventually usurping the throne from the young Emperor Constantine VII Porphyrogenitus. He later declared his own sons as heirs. Romanos was attempting to build a dynasty while facing serious legitimacy issues. Constantine described Romanos as "a common illiterate fellow... not of imperial and noble stock" (Constantine VII Porphyrogenitus, 1967). Another source that reflects Romanos' efforts to legitimize his rule is the correspondence of Patriarch Nicholas Mystikos, which includes personal anecdotes about him (Marić, 2013).

The elevation technique used in Romanos' buildings undoubtedly enhanced their visibility from afar and ensured they appeared more monumental when seen up close. Although it seems to be an exceptional feature in Myrelaion, the fact that we see the same approach in the lost Chalke Chapel strengthens the argument that this was a deliberate strategy. By elevating his buildings, Romanos may have aimed to draw daily attention to these impressive structures, prompting discussions about their patron.

Romanos' speech in front of the Chalke Chapel may serve as a key to understanding these elevated structures, which are otherwise difficult to interpret—particularly due to their deliberate inaccessibility. In this instance of overt political propaganda, a chapel built under his patronage formed the backdrop. This architectural form can be seen as part of Romanos' broader campaign to reinforce his legitimacy and authority. The buildings he commissioned were not merely structures, but instruments of political messaging and visual expressions of imperial power.

References

Andreasyan, H. D. (Ed. & Trans.). (1964). Polonyalı Simeon'un Seyahatnâmesi (1608–1619). İstanbul Üniversitesi Edebiyat Fakültesi Yayınları.

Cedrenus, G. (1838). Corpus scriptorum historiae Byzantinae (B. G. Niebuhr, Ed.). Academia Litterarum Regia Borussica.

Constantine VII Porphyrogenitus. (1967). De administrando imperio (Gy. Moravcsik, Ed.; R. J. H. Jenkins, Trans.; New, rev. ed.). Dumbarton Oaks, Harvard University.

Gilles, P. (1729). The antiquities of Constantinople (J. Ball, Trans.). London: Printed for the benefit of the translator. (Original work published ca. 1544).

Janin, R. (1964). Constantinople Byzantine: Développement urbain et répertoire topographique. Paris: Institut Français d'Études Byzantines.

Marić, I. (2013). Legitimizing usurpation: Romanos I Lekapenos and Nikolaos I Mystikos (Master's thesis, Central European University). Central European University Repository.

Mango, C., & Talbot, A.-M. (1991). Mangana. In A. P. Kazhdan et al. (Eds.), The Oxford Dictionary of Byzantium (Vol. 2, p. 1283). Oxford University Press.
Theophanes Continuatus. (1838). Theophanis Continuati libri I–IV (I. Bekker, Ed.). In Corpus Scriptorum Historiae Byzantinae (p. 429). Bonn: Weber.

Rural Houses in Renaissance Architecture: Proposals of Sebastiano Serlio According to the Social Hierarchies in his Sixth Book

E. Merve Aksoy Oral[a], Aygül Ağır[b]

[a] Istanbul Technical University, Graduate School, Architectural History Program, Turkey
[b] Istanbul Technical University, Faculty of Architecture, Department of Architecture, Turkey
aksoyem@itu.edu.tr, agiray@itu.edu.tr

Keywords: Renaissance Architectural Treatises, Sebastiano Serlio, Domestic Architecture, Rural Houses, Social Classes.

Renaissance architectural treatises are invaluable documents that provide deep insights into the architectural culture and social classes of the period. Among Renaissance theorists, Leon Battista Alberti (1404-1472) defined cities in relation to their houses, describing the house as a "miniature city," thus indicating that houses are concrete examples reflecting the dynamics of cities (Alberti, 1:9, 1988). This perspective highlights that domestic spaces do not merely serve residential purposes but also reflect the social and spatial dynamics of the city on a smaller scale.

Architecture, in this context, does not merely accommodate social stratification—it plays an active role in visualizing and legitimizing it. Vitruvius's architectural principles, particularly the concept of *decorum*, served as a primary reference for Renaissance architects and patrons in domestic architecture (Pellecchia, 1992). Accordingly, the application of *decorum* ensured that domestic spaces were aligned with the owner's social status.

The architectural treatises written during the Renaissance period reflect the existing social stratification in a strict hierarchical order. However, housing for low-income groups has often been overlooked in architectural treatises, despite their significance in reflecting social hierarchy. In this context, Sebastiano Serlio's (1475–1554) Sixth Book is remarkable for its systematic approach to housing across different social strata, establishing a valuable resource for understanding the architectural expression of class distinctions (Fiore, 1994; Rosenfeld, 1996). Serlio proposed a wide range of housing designs, from humble thatched cottages for the poorest to grand palaces for the nobility, aiming for designs that were comprehensible not only to the educated but also to the "average person" (Fiore, 1994; Rosenfeld, 1996).

The necessity of designing country houses according to social status and specific needs is a recurring theme in rural architecture and agricultural treatises of the period. This notion can be found in works such as Crescenzi's *De Agricultura* (1495), Alberti's *De re Aedificatoria* (1485), and Anton Francesco Doni's *Le Ville del Doni* (1566) (Lazzaro, 1985, p. 346). Doni, for instance, categorizes country houses based on five social classes, referring to "functional huts" (*capanna dell'utile*) for peasants, in contrast to villas for the nobility, which are described primarily as spaces for retreat and leisure (*podere di spasso*). Correspondingly, Serlio designs a modest hut for the poorest peasant, which aligns with Doni's description of a simple shelter for the lower classes. However, Serlio takes this concept further by introducing different layers within the peasant class, categorizing them into economic strata.

Aim

The study examines Serlio's rural house designs for the peasants, focusing on the social hierarchy he established in housing for the lower classes. Through a critical reading of Renaissance literary sources regarding farmhouses and villas, the study aims to explore how the agricultural economy influenced rural architecture and Serlio's interpretations of ancient and local traditions.

Material and Method

This study employs a comparative analysis of theoretical texts and illustrations presented in Serlio's Sixth Book. The research also contextualizes Serlio's designs within the broader framework of rural architecture, considering the socio-economic and agricultural factors that shaped his approach. Additionally, the study investigates the influence of ancient and local traditions on Serlio's interpretations by comparing textual descriptions with visual depictions in contemporary sources.

Findings

In the 16th century, class distinctions became increasingly pronounced even within the peasant class. Wealthier peasants—typically landowners or long-term tenants—came to form a "peasant aristocracy," whereas short-term tenants and wage laborers constituted a poorer group with limited economic power (Brocchieri, 2020, p. 245). Some of the affluent peasants portrayed by Serlio likely belonged to the urban aristocracy, as indicated by the social profiles depicted in Andrea Palladio's *I Quattro Libri dell'Architettura* (The Four Books of Architecture), one of the most influential works of the period (Palladio, 1997). The size of landowning peasant groups varied depending on land rental agreements (Waley & Dean, 2021). Within this system, short-term tenants were employed either permanently or seasonally by wealthier peasant families. Social stratification in rural areas was also reflected in living spaces. In the Veneto region, impoverished peasants resided in modest rural houses called *casóne*, which typically consisted of a simple living space and a stable under a thatched roof. In contrast, wealthier peasants lived on farms that featured a two-story main house with an attic used as a granary, a stable, and a porticoed barn (Cosgrove, 2000).

During the Renaissance, rural houses were also influenced by traditional vernacular architecture as well as ancient Roman architecture (Forster, 1974). In the Venetian countryside, simple rural houses typically consisted of the landowner's residence, *barchesse* (utility buildings for agricultural use), and dovecote towers. While these structures were generally dispersed within the landscape in the 15th century, by the 16th century, rural settlements had evolved into more cohesive complexes organized around a quadrangular courtyard (Suitner Nicolini, 1973) (Figure 1).

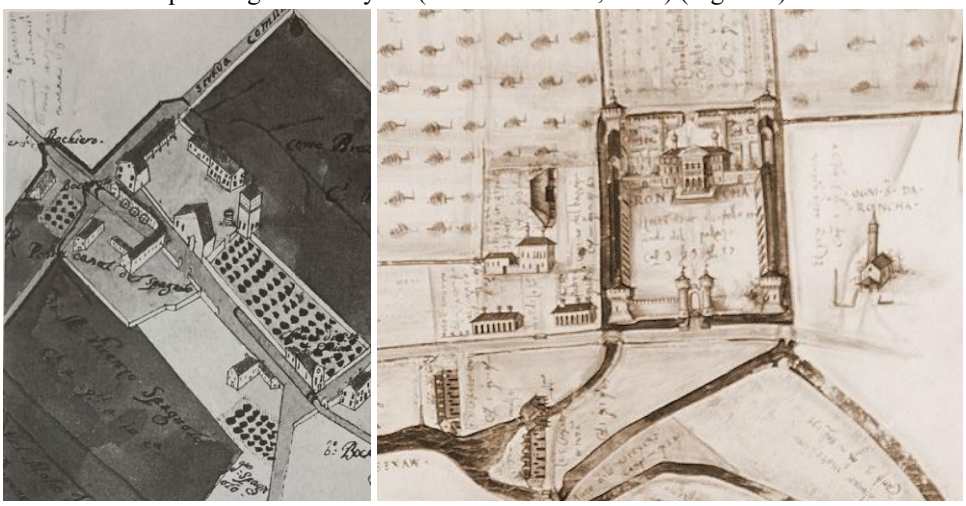

Figure 1: 15th century Farmhouse, Marano, Vicenza (from a 18th century drawing, Ackerman, 1990); Villa Giustiniani, Roncade (1511-1522) (Burns, 2012).

Accordingly, Serlio designed rural houses with careful consideration of living conditions, the economic status of their inhabitants, and their social standing. Having categorized peasants into three economic categories—poor, middle-class, and wealthy—and Serlio designed three different rural houses to match these distinctions. Interestingly, his designs also exhibited variations within these categories based on degrees of wealth (*gradi di ricchezza*). These rural houses generally featured a main residential unit—occupied by either the peasant or the landowner—organized around a courtyard, accompanied by service structures related to agricultural activities and additional wings integrated into the main building.

Serlio defined the poorest peasant as "a person who owns a small piece of land, can manage their own work, and is self-sufficient," and accordingly, he developed a design consisting of a minimal living space and a hearth (Serlio, fol. 1v) (Figure 2). This design is reminiscent of the thatched-roofed houses that preceded the porticoed and towered villa typology in Venice and the Veneto region (Forster, 1974) (Figure 3).

The rural house of the mid-level peasant was designed according to three different wealth levels. The core unit opens from its porticoed front façade into a small hall (*saletta*), which provides access to the surrounding spaces. Interestingly, Serlio suggested that if the mid-level peasant required additional rooms for a more comfortable life (*per esser più agiato*), two

rooms could be added to the sides of the core unit, depending on the width of the farm. This flexibility illustrates Serlio's sensitivity to varying farmhouse needs and spatial comfort. His rural house for the "mid-level" peasant reflects the influence of Late Roman architecture, particularly the U-shaped villa with projecting blocks and a central loggia (Ackerman, 1990). As Forster (1974) pointed out, Serlio's plan bears a resemblance to the Late Roman Villa of Theodoric in Galeata, which was discovered through archaeological excavations in 1541–42, as well as the rural traditions of the Veneto region (Figure 4).

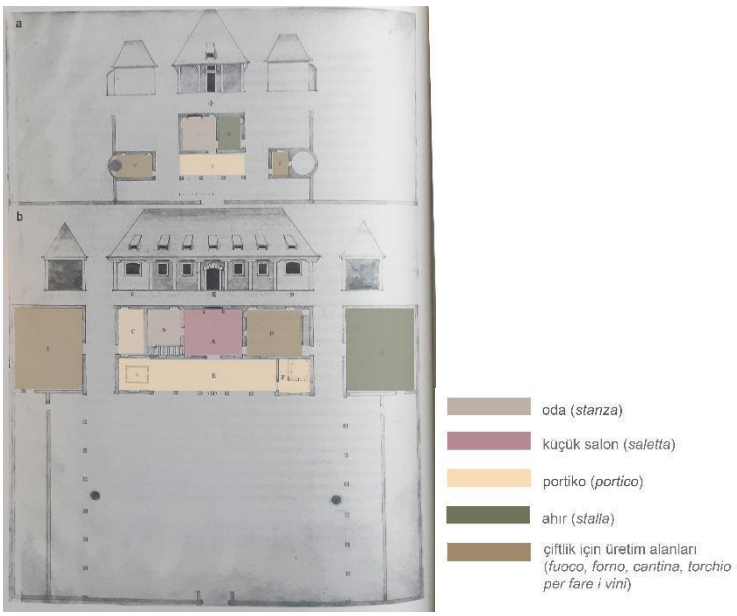

Figure 2: Serlio, (top) Rural house for the poorest peasant (*casa del povero contadino*) (bottom) Rural house for the middle-class peasant (*casa del mediocre contadino*) (Munich manuscript, Fiore, 1994, adapted from plate 1).

Figure 3: Thatched cottage, unknown date, Rosara di Codevigo, Padova (Kubelik, 1986).

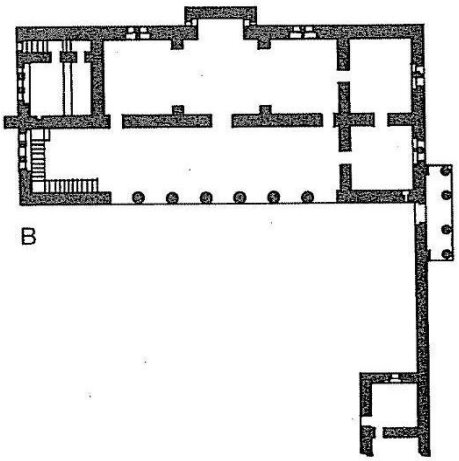

Figure 4: Villa of Theodoric in Galeata, c. 500 (Ackerman, 1990).

At the upper end of the hierarchy, Serlio depicts the wealthy peasant as a "village prince" (*rustico principe*), a figure he observed in many Italian cities (Serlio, fol. 2v, 1994). This depiction aligns with the concept of a "peasant aristocracy" within the peasant classes. The representation of the wealthy peasant as a "village prince" can be interpreted as a continuation of the feudal system organization, which was beginning to dissolve in Italy. This interpretation also finds its expression in architecture: the wealthy peasant's rural house is carefully structured to accommodate both residential and agricultural functions. Distinct side wings are dedicated to wine and olive oil production, incorporating additional spaces for agricultural activities (Figure 5). The inclusion of production tools in Serlio's plan is a significant detail, reflecting a holistic approach to farm organization. Behind the house, stables for cattle and poultry are located, with cultivated land (*il bruolo e i campi*) extending further beyond. The core unit, which functions as the owner's living quarters, is two stories high and features a central common room (*sala comune*), echoing earlier designs.This space serves as a gathering place for the farm's inhabitants around the hearth, where the family head keeps the farm's key. Through its integrated layout, Serlio's design creates a more harmonious connection between the dwelling and the agricultural wings—a notable contrast to the spatial configuration observed in Villa Giustiniani.

Figure 5: Serlio, Rural house for wealthy peasants (*abitazione del ricco contadino per tre gradi di ricchezza*) (Munich manuscript, Fiore, 1994, adapted from plate 2).

Conclusion

Serlio's rural house designs span a wide spectrum, ranging from the most basic structures that provided minimal shelter for the poorest peasants to the more elaborate dwellings of wealthy landowners, often referred to as "village princes". These proposals reveal a gradual increase in spatial complexity, carefully aligned with the economic status and specific needs of their inhabitants. While Serlio's designs may not fully reflect the realities of land ownership of the period, they nonetheless represent a significant effort to give architectural form to the social and cultural dynamics of 16th-century Italy. By incorporating hierarchical distinctions within the peasant class and highlighting them through design, Serlio developed a spatial vocabulary that both expressed and reinforced social stratification. Through this approach, his work provides valuable insight into the multi-layered nature of Renaissance rural society.

References

Ackerman, J. S. (1990). *The Villa. Form and ideology of country houses*. New Jersey: Princeton University Press.
Alberti (1988). *On The Art of Building in Ten Books.* (trans. J. Rykwert, N. Leach& R. Tavernor). Cambridge, Mass.: MIT Press.
Azzi Visentini, M. (1995) *La villa in Italia: Quattrocento e Cinquecento*, Milano: Electa.
Brocchieri, V. H. B. (2020). Ekonomi ve Toplum: Köylüler, *16. Yüzyıl Rönesans Çağı* (U. Eco, ed.). 243-247. İstanbul: Alfa.
Cosgrove, D. (2000). Il *Paesaggio Palladiano La trasformazione geografica e le sue rappresentazioni culturali nell'Italia del XVI secolo*, F. Vallerani (ed.). Verona: Cierre Edizioni.
Fiore, F. P. (1994). Introduzione, in *Architettura Civile. Libri Sesto, Settimo e Ottavo nei manoscritti di Monaco e Vienna*. Milano: Il Polifilo.
Forster, K. (1974). Back To The Farm- Vernacular Architecture And Development Of The Renaissance Villa. *Architectura. Zeitschrift für Geschichte der Baukunst* 4, pp. 1-12.
Hart, V. (2003). Of little or even no importance to the architect': on absent ideals in Serlio's drawings in the Sixth Book, on domestic architecture, in *The Rise of the image: essays on the history of the illustrated art book*, pp. 87-104. Burlington, VT: Ashgate.
Kubelik, M. (1986). Palladio's Villas in the Tradition of the Veneto Farm, Assemblage, 1, pp. 90-115.
Lazzaro, C. (1985). Rustic Country House to Refined Farmhouse: The Evolution and Migration of an Architectural Form, *JSAH*, 44(4); 346-367.
Palladio, A. (1997). *The Four Books of Architecture on Architecture*. Cambridge, Mass.: MIT Press.
Pellecchia, L. (1992). Architects Read Vitruvius: Renaissance Interpretations of the Atrium of the Ancient House, *JSAH,* 51(4); 377-416.
Rosenfeld, M. N. (1996). *Serlio on Domestic Architecture*. New York: Dover Publications, Inc.
Suitner Nicolini, G. (1973) Per una lettura urbanistica delle ville venete. Proposta di una tipologia territoriale, *Bollettino CISA*, XV; 447-465.
Waley, D., Dean, T. (2021) *İtalyan Şehir Cumhuriyetleri*, İstanbul: İş Bankası Kültür Yayınları.

Semi-Open Spaces as a Result of Climate and Culture in Mediterranean Architecture

Furkan Sağdıç[a]

[a] Istanbul Technical University, Graduate School, Architectural History Program, Turkey
sagdicf@itu.edu.tr

Keywords: Mediterranean, Palace Building, Semi-Open Space.

Aim

This research aims to investigate whether the common living practices that emerged as a result of the interaction of different ethnic, religious and cultural structures throughout history in the Mediterranean geography can be traced through architectural elements. In particular, the reflections of the commercial and cultural relations that accelerated in the Mediterranean between the 14th and 17th centuries on the 'loggia/exterior sofa', one of the semi-open space types, are analysed. While the natural and human geography of the Mediterranean region necessitates semi-open spaces that provide shade and air circulation due to the hot and dry summers, different communities' understanding of privacy and use of space has created diversity in the design and functions of these spaces. The main purpose of the research is to reveal whether the 'loggia/exterior sofa' as a semi-open space is one of the indicators of a common architectural culture in the Mediterranean. In this direction, the relationship between more introverted spaces such as courtyards and the extroverted natural and human environment is also questioned, and how the lifestyles of Mediterranean societies shape architecture is analysed.

Material and Method

In this research, the approaches of different disciplines (history, geography, sociology, architecture, etc.) examining the Mediterranean are analysed and the common features and/or differences in the Mediterranean are determined within the scope of the subject. From this point of view, the interaction between architecture and the natural and human environment is discussed. Academic sources on the place of the concept of semi-open space in Mediterranean architecture, its definitions, purposes of use and historical development are analysed. The existing literature on how similar semi-open spaces are named in different geographies, what kind of functions they undertake and what formal characteristics they have is reviewed. The use of semi-open spaces in both Mediterranean vernacular architecture and Modern architecture has been analysed in the existing literature. With a special focus on the period between the 14th and 17th centuries, the buildings built during this period were identified and the buildings to be analysed were selected based on their state of preservation and representativeness. Based on different studies, the Mediterranean is culturally divided into seven regions. Although these seven regions are located on different continents, they have been in intense interaction in the historical process since they are located on the Mediterranean coast. The examples selected from each region constitute examples of palaces or residences that have been preserved to a certain extent to the present day and have the potential to represent the local residential culture in the most qualified way. The buildings are analysed in terms of plan types, relationship with the building, formal features, usage functions and courtyard relationship. The similarities and differences between the sample buildings are revealed.

Findings

The research has revealed that climatic conditions in the Mediterranean basin support the prevalence of semi-open spaces, but the design and use of these spaces may vary from region to region. In particular, the loggia/exterior sofa element has been found to assume both an 'introverted' identity associated with the courtyard that fulfils the need for privacy and an 'extroverted' identity that facilitates interaction with the natural and human environment by opening outwards.
Although the names and design details of the loggia/exterior sofa spaces may vary in the seven regions analysed in this study, the common point is the functions of providing shade and increasing air circulation. These spaces have become an

important part of daily life in the Mediterranean climate, where summers are hot, and provide semi-public or semi-private gathering spaces that increase social interaction. On the other hand, the positioning and shaping of these spaces have varied in line with the privacy perceptions of different cultures. For example, in some regions, the loggia/exterior sofa was designed as an inward-oriented element as a continuation of the courtyard, while in other regions it was transformed into a living space that opens to the outside and establishes a relationship with the landscape or street.

Between the 14th and 17th centuries, political, commercial and technological developments in the Mediterranean accelerated architectural interaction. As a result of this interaction, while regional differences were preserved, spaces sharing similar functional and formal characteristics also emerged. It has been determined that the loggia/exterior sofa element exists under different names, but basically responds to similar needs. This situation provides important clues that a common architectural culture can be traced in the Mediterranean.

Conclusion

The findings of the research show that despite the existence of different political, religious and cultural structures in the Mediterranean basin, common architectural elements have developed with the influence of historical interactions as well as the requirements of climate and geography. Semi-open spaces, defined as loggia/exterior sofas, stand out with their features that support both privacy and social interaction by acting as a threshold between interior and exterior spaces. Despite their different names and design variations, these spaces, which are shaped around functions such as providing shade, coolness and social communication, can be considered as one of the clear indicators of the shared living culture in the Mediterranean.

Through analyses of buildings constructed between the 14th and 17th centuries, this study reveals that the concept of a 'shared architectural culture' in the Mediterranean can be discussed. The findings show that beyond climatic and geographical conditions, centuries of interaction between different societies played an important role in the shaping of architectural elements. Thus, it is concluded that the living practices and spatial understanding specific to the Mediterranean are part of a multi-layered cultural heritage with the balance it establishes between inward and outward use.

References

Abulafia, D. (2005). Tarih boyunca Akdeniz uygarlıkları. Oğlak Yayıncılık.

Ağır, A. (2006). Yapı ve mekan olarak loggia. Sanat Tarihi Defterleri, 10, 151-164.

Arıkan, F. D. (2015). Tracking continuities between the modern and vernacular architecture: Courtyard in the west Mediterranean architecture as a case study (Doctoral dissertation). Middle East Technical University.

Bloom, J. M. (2020). Architecture of the Islamic West: North Africa and the Iberian Peninsula, 700-1800. Yale University Press.

Braudel, F. (2019). Akdeniz ve Akdeniz dünyası 2. Doğu Batı Yayınları.

Braudel, F. (2021). Akdeniz ve Akdeniz dünyası 1. Doğu Batı Yayınları.

Braudel, F. (2021). Akdeniz ve Akdeniz dünyası 3. Doğu Batı Yayınları.

Contadini, A., & Norton, C. (Eds.). (2018). Rönesans ve Osmanlı dünyası. Koç Üniversitesi Yayınları.

Göksoy, B. (1999). Tracing continuities within the Mediterranean space (Doctoral dissertation). Middle East Technical University.

Malaktou, E., Philokyprou, M., Michael, A., & Savvides, A. (2016). Environmental behaviour of semi-open spaces in Mediterranean vernacular architecture: The case of rural traditional dwellings of Cyprus. Renewable Energy and Power Quality Journal (RE&PQJ), 14, 1-7.

Ögel, S. (1981). Hayat (Sofa) Köşkü ve Tahtseki. Sanat Tarihi Yıllığı, 9-10, 227-240.

Petruccioli, A. (2008). Bellek yitiminin ardından: Akdeniz İslam kent dokusunun öğrettikleri. YEM Yayınları.

Poggi, C. (2015). Potenzialità di uno spazio di transizione microclimatica: Il portico nel clima mediterraneo-temperato (Master's thesis). Politecnico di Milano.

Saoud, R. (2004). The impact of Islam on urban development in North Africa. Foundation for Science, Technology and Civilisation. 16.

Ulusoy, M., & Kanlı, B. (2023). Eski Kahire geleneksel konut mimarisi: "Hilmiye ve Seyide Zeynep konutları örneği". Mimarlık Planlama ve Tasarım Alanında Uluslararası Teori, Araştırma ve Derlemeler, 37-50, Serüven Yayınevi.
Yılmaz, E. C. (2009). İstanbul'da yazılı ve görsel kaynaklara göre 15. ve 16. yüzyılda (1453-1559) Osmanlı sivil mimarlığı üzerine bir değerlendirme: Gurfe örneği (Doctoral dissertation). Istanbul Technical University.

The Historical Layers of Selimpaşa in Constantinople Hinterland Context

Nil Ceren Karagülle[a], Bilge Ar[b]

[a]Istanbul Technical University, Graduate School, Architectural History Program
[b]Istanbul Technical University, Faculty of Architecture, Department of Architecture
karagulle15@itu.edu.tr, bar@itu.edu.tr

Keywords: Constantinople Hinterland, Thrace, Road Networks, Land Use Continuity.

Aim

The aim of this study is to examine the town of Selimpaşa, located in Silivri region in Istanbul, through historical research with architectural and regional analysis. This study will explore the role of Selimpaşa in Constantinople's hinterland in Thrace, focusing on it as one of the satellite settlements and trade networks that sustained the imperial capital. The definition of the hinterland will be explored in detailed historical context, with its structural and economic functions in relation to Constantinople. Several settlements in Thrace, positioned along key commercial routes, served as supply areas, providing agricultural goods and other essential resources. Among these, some locations, due to their size and historical documentation, allow for a more comprehensive analysis of their economic and logistical contributions to the capital.
The chosen case study will represent a typical example of such settlements rather than an exceptional or unique site. By studying Selimpaşa, the aim is to reconstruct the broader dynamics of regional trade and resource distribution in Thrace. Unlike Selymbria (modern Silivri), which was a highly trafficked and well-documented urban center directly on the main trade route, the selected Selimpaşa offers insight into a more localized and decentralized network of provisioning systems. While Selymbria played a direct role in supplying Constantinople, its surrounding settlements were further divided into smaller subunits, each operating within a specific economic and ecological framework.

Material and Method

This study will be examined by using a comparative approach, analysing the selected settlement of Selimpaşa alongside neighbouring sites and its connections with Selymbria and Constantinople. Through this, the aim is to reconstruct and understand the economic and logistical framework of medieval Thrace, particularly along its trade routes. The study will also assess continuity and transformation in settlement patterns, tracing their evolution from antiquity to the Middle Ages. While some settlements experienced disruptions during the transition from the ancient to medieval periods, many have shown continuity since the 9th century CE, therefore this will be a major analysis point for the study.
The continuity analysis will incorporate factors such as land use, climatic conditions, and geographical features, including river systems and fertile plains of Thrace, demonstrating how these elements shaped settlement sustainability from the Byzantine to the Ottoman period and beyond.

Findings

Throughout history the Byzantine capital had been supported by its hinterland, the surrounding rural areas, economically, militarily, and logistically. The hinterland borders varied over time, consisting from parts of Thrace in the west and Bithynia and Anatolia in the east. These regions have been vital for food supplies, materials, trade networks and manpower, ensuring the city's sustainability and strategic importance (Mango & Dagron, 1995).
Western hinterland of Constantinople is the region of Thrace, which today is split between Türkiye, Greece, and Bulgaria. The historical region of Thrace, located in the southeast Balkans, is defined as the area bordered between the Balkan Mountains to the north, the Aegean Sea to the south, the Black Sea, and the Sea of Marmara to the east and is named after Thracians tribes that inhabited the area. During the Middle Ages the region was interchangeably ruled by the Byzantine Empire, Bulgarian and Serbian medieval states until it became part of the Ottoman Empire in the 14th and 15th centuries.

Thrace was the immediate hinterland for fifteen centuries and one of the prime sources for the grain supply for the capital (Magdalino, 2006).

One of the most important settlements of the immediate Thracian hinterland was Selymbria, todays Silivri. Throughout time Selymbria, located by the coast Marmara, and about 60 km west of Constantinople, played a significant role in trade, defence and regional administrations. For trade context, Via Egnatia one of the major routes, passed through Selymbria and made the town became important hub for trade (Külzer, 2019). For defence, Selymbria had a major role for having fortification that is today known as the Silivri Castle (Çiçek, 2019) and being close to Anatasian Walls. Anastasian Walls or Long Wall, was a significant late Roman and Byzantine fortification stretched from the Black Sea near Karacaköy to the Sea of Marmara near Selymbria. The wall originally extended for 45 km, though much of it has deteriorated over time. It was constructed with a curtain wall, outer works, and a system of forts and towers, a major defensive barrier against outsider attacks (Crow & Ricci, 1997).

The focus of this paper will be about Selimpaşa (formerly known as Bigados and Epivates/Epibatai) one of the smaller settlements located in this region. Laying 13 km to the east of Selymbria (47 km east of Constantinople), Epivates was a town with agricultural life and trade and where several historical events took place. Such as the meeting of Emperor Andronikos II and his grandson Andronikos III in 1322 to end their disputes over control of the empire, during the civil war, with a peace treaty that lasted for five years (Külzer, 2008). Epivates also was one of the last centers of Byzantium power in Eastern Thrace; with the final conquest by the Turks only taking place after February or March of 1453 (Külzer, 2008).

The first survey and excavations on Selimpaşa were done by D. H. French in 1960s (Eyice, 1969). The tell (höyük) of Selimpaşa is identified as the last remaining tell on the western side of Istanbul (Aydıngün, Ş., Heyd, V., Güldoğan, E., & Öniz, H., 2014). Most recent excavations showed remains from various historical periods, notably from: Chalcolithic Age, Bronze Age Iron Age, Classical Antiquity, Byzantine Period. Surveys and excavations have identified ceramic fragments and tone tools. The site is registered as a cultural heritage site.

Between 1453 -1923 Ottoman rule of the town, the name of Epivates slowly came to known as Bigados and have been referred to as such in official documents and maps. According to two mukataa (parcels of land owned by the Ottomans) tax records dated 1476 and 1479, the Istanbul and Galata customs office covered the area from opposite Yoros to Bigados on the Rumelian side and from Yoros to Aydıncık (Edincik) on the Anatolian side (Anhegger & Inalcık, 1956). In other words, the document showed that the Bosphorus and a part of the Marmara coast were within the area of this customs office (Bulunur, 2013).

British clergyman and traveller John Covel visited Istanbul in 1675 and later wrote about his travels in his books. Covel stopped by the town of Pebatos (Πεβάτος), and he described it as a pleasant market town with a harbor for small boats, called Epivates in Greek (Külzer, 2008). He stated that although most of the people living there were Greek, he saw many Turks on the streets and adds that there was a small fortress with thick walls here and that it was used as a granary (Covel, 1998). But claimed it was not possible to see the walls that once surrounded this town as they have completely disappeared.

In Verdic Registers (Ahkam Defterleri) about Bigados in 18th century shows the continuing agricultural activities (Tabakoğlu, 1994). In majority of the registration documents, Bigados is referred as a village under Çekmece-i Kebir (Büyükçekmece) or Silivri.

One of the ways to track land use continuity can be done by looking at the history of the Church of St. Paraskeva. The earliest written source about the building is from Anthony the archbishop of Novgorod, who visited Constantinople in 1200 and wrote about what he saw in his pilgrimage book named "Kniga Palomnik" (Majeska, 2002). He mentioned about a church dedicated to St. Paraskeva in his writings as "a day's journey from Constantinople", therefore it can be identified with the one in Epivates (Külzer, 2008). Until its destruction in 1980, it was a three-naved church built in the same location as the original in 1884 (Han, 2000). The following verdict that was found in Directorate of State Archives with following title translation "July 7, 1884, construction of a church for the Greek community in the village of Bigados in Silivri.". This document serves as evidence to how residents continued the land usage for the church (BOA.İ.DH.923/73182).

After the foundation of Turkish Republic, in accordance with the Ankara Treaty signed in 1924, population exchange between Greeks and Turks made the Greek inhabitants of Bigados migrate to Greece in 1926. Following years the name of

the town was changed to Selimpaşa. This name came from the former Ottoman Grand Vizier Mehmet Selim Sırrı Paşa, who had visited and stayed in the town and had the İkizli Fountain built to his name 1828 (Taşkın, 2002).

Conclusion

This research will demonstrate that Constantinople's hinterland was not merely a passive supplier but an active and organized economic system with hierarchical settlement structures, efficient trade networks, and sustainable agricultural practices. Hinterland settlements functioned as interconnected units, supporting both local economies and the larger provisioning needs of Constantinople.

The presence of major trade routes, particularly the Via Egnatia, facilitated economic integration and ensured the movement of goods across Thrace. Settlement continuity from the 9th century onward indicates a stable economic framework, with medieval land-use patterns persisting into the Ottoman period. Thrace's temperate climate and favourable agricultural conditions ensured long-term settlement continuity, supporting the study's hypothesis regarding sustained land-use patterns. By integrating environmental and historical perspectives, this research contributes to a deeper understanding of Constantinople's hinterland and its enduring functionality over centuries.

And among these satellite settlements in hinterland of Thrace, Selimpaşa (Epivates/Bigados) was not a unique region but showcased a typical example with its existence and therefore will be able enhance understandings and to open space for further studies about the areas involved and historical periods.

References

Anhegger, R., & İnalcık, H. (1956). Kanunname-i Sultani ber muceb-i örf-i Osmani: II. Mehmed ve II. Bayezid devirlerine ait yasakname ve kanunnameler. Türk Tarih Kurumu Yayınları.

Aydıngün, Ş., Heyd, V., Güldoğan, E., & Öniz, H. (2014). İstanbul'un batısında kalan son höyük: Selimpaşa. In Engin Özgen'e armağan (pp. 47–50). Asitan Kitap Yayınevi.

Bulunur, K. İ. (2013). Osmanlı Galatası (1453–1600) (Yayımlanmış doktora tezi). Sakarya Üniversitesi Sosyal Bilimler Enstitüsü.

Çiçek, M. (2019). Selymbria (Silivri) Kalesi ve Nekropolü üzerine arşiv belgeleri ışığında yeni değerlendirmeler (Yüksek lisans tezi). İstanbul Teknik Üniversitesi Fen Bilimleri Enstitüsü.

Crow, J., & Ricci, A. (1997). Investigating the hinterland of Constantinople: Interim report on the Anastasian Long Wall. Journal of Roman Archaeology, 10, 235–262.

Covel, J. (1998). Voyages en Turquie, 1675–1677 (J.-P. Grélois, Ed. & Trans.; Preface by C. Mango). Institut Français d'Études Anatoliennes.

Eyice, S. (1969). Trakya'da Bizans devrine ait eserler. Belleten, 33(131), 325–358.

Han, B. (2000). Silivri-Selimpaşa tarihsel sit alanı ve Arhigenya Kız Öğretmen Okulları araştırma ve değerlendirme projesi (Yüksek lisans tezi). Yıldız Teknik Üniversitesi Fen Bilimleri Enstitüsü.

Külzer, A. (2008). Ostthrakien (Europe). Tabula Imperii Byzantini 12. Verlag der Österreichische Akademie der Wissenschaften.

Külzer, A. (2019). Production and trade in Late Antique and Byzantine Eastern Thrace. In O. Dumankaya (Ed.), Çağlar boyunca üretim ve ticaret: Prehistorya'dan Bizans Dönemi'ne (pp. 643–650). Türkiye İş Bankası Kültür Yayınları.

Külzer, A. (2011). The Byzantine road system in Eastern Thrace: Some remarks. In 4th International Symposium on Thracian Studies: Byzantine Thrace Evidence and Remains, Komotini, 18–22 April 2007 (pp. 179–202). Verlag Adolf M. Hakkert.

Magdalino, P. (2006). The grain supply of Constantinople, ninth to twelfth centuries. In Studies on the history and topography of Byzantine Constantinople (pp. 35–47). Ashgate.

Majeska, G. (2002). Russian pilgrims in Constantinople. Dumbarton Oaks Papers, 56, 93–108.

Martin, J. (1996). Medieval Russia. Cambridge University Press.

Mirsky, D. S. (1958). A history of Russian literature. Knopf.

Mango, C., & Dagron, G. (Eds.). (1995). Constantinople and its hinterland: Papers from the Twenty-Seventh Spring Symposium of Byzantine Studies, Oxford, April 1993 (1st ed.). Routledge.
Tabakoğlu, A., Kal'a, A., Aynural, S., & Kara, İ. (Eds.). (1994). İstanbul ahkâm defterleri: İstanbul tarım tarihi 1 (1743–1757). Türkiye Ekonomik ve Toplumsal Tarih Vakfı.
Taşkın, S. (2002). Silivri-Selimpaşa kentsel sit alanında tarihsel çevre korumaya yönelik bir araştırma ve küçük kilise koruma projesi (Yüksek lisans tezi). Yıldız Teknik Üniversitesi Fen Bilimleri Enstitüsü.

Furniture Consumption in Istanbul at the Beginning of the 20th Century: The Role of Periodicals

Sezin Dirihan[a], V. Gül Cephanecigil[a]

[a] Istanbul Technical University, Graduate School, Architectural History, Turkey
dirihan16@itu.edu.tr

Keywords: Furniture, Consumption, Periodicals, İstanbul, Ottoman Empire.

Aim

This study examines how furniture was represented in everyday life in early twentieth-century Istanbul, and how these representations were connected to changing patterns of consumption. Drawing on advertisements and content from contemporary periodicals, it aims to understand how furniture—beyond its functional role—became associated with concepts such as social identity, belonging, and status. The period under examination was marked by significant social and cultural transformations, including industrialisation, increased access to imported goods, and the growing influence of Western-oriented ideas of modernity. Within this context, furniture emerged not only as a reflection of these shifts but also as a medium through which new forms of taste and identity were constructed and communicated.

Material and Method

The conceptual framework of the study is informed by theoretical approaches that understand consumption not only as an economic act but also as a culturally and symbolically meaningful practice. Various theories have discussed how consumption reflects not just material need but also social positioning, aesthetic preferences, and distinctions of taste. For instance, Thorstein Veblen's notion of conspicuous consumption highlights how the display of goods—such as furniture—functions as a marker of refinement and status.[2] Pierre Bourdieu has emphasized how taste operates as a form of social differentiation shaped by class habitus, while Jean Baudrillard draws attention to the symbolic function of objects in constructing identity through systems of signs.[3] These perspectives together provide a conceptual lens through which the study interprets how furniture was represented in periodicals as both a reflection of social aspiration and a means of cultural expression.

The main sources of this study are periodicals published in early twentieth-century Istanbul. These publications include content related to consumption culture, domestic life, and practices of social representation, offering valuable insight into the cultural and economic changes of the period. The main periodicals examined in the study are Servet-i Fünun, Hanımlara Mahsus Gazete, Şehbal, Mahasin, and Süs. In addition to these, other periodicals that contained relevant content about domestic life and social imagery were also used. These publications were selected because of their regular circulation, the variety of their content, and their extensive use of commercial advertising.

This study uses a qualitative approach to explore how furniture was represented in early twentieth-century periodicals. Advertisements, visual content, and selected articles were examined through close attention to language and imagery, with a focus on how meanings related to taste, identity, and social roles were constructed. The aim is to understand how furniture functioned not only as a material object, but also as a cultural expression that reflected and shaped emerging forms of consumption and modern identity.

[2] Veblen, T. (1994). *The Theory of the Leisure Class*. New York: Dover Publications. (Original work published 1899).

[3] Bourdieu, P. (1984). *Distinction: A Social Critique of the Judgement of Taste*. Cambridge, MA: Harvard University Press. Also see Baudrillard, J. (1998). *The Consumer Society: Myths and Structures*. London: Sage Publications. (Original work published 1970)

Findings

In the periodicals examined, references to the West often appear as a clear marker of distinction in the representation of furniture. Expressions like "American style," "London-made," or "English marocain" frequently appear in advertisements. These phrases do more than indicate the origin of the products—they also suggest associations with quality, taste, and a certain lifestyle.

Such language was also deliberately used by furniture producers of the time. In the advertisements of firms like Narlıyan, Baker, and Psalty, the European or American origin of the products is often emphasized (Figure 1, 2). Items such as bedroom sets, armchairs, or sofas—especially those placed in the more visible parts of the home—are given particular attention. At the same time, women's magazines from the period often featured decoration advice and illustrations for spaces like living rooms and bedrooms. These examples suggest that furniture for these areas was not only seen as functional, but also carried strong symbolic value. References to Western origins served as signs of good taste and modern identity, but also reflected a broader belief that Europe and America represented a more advanced and respectable way of life. In the context of early twentieth-century Istanbul, aligning with Western styles implied access to a more advanced, rational, and prestigious way of living. For this reason, Western labels became signs of social status and helped people show where they belonged—or wanted to belong—in the social hierarchy.

Although some advertisements and articles mentioned specific origins—such as American, British, or Austrian—these references rarely served to differentiate between distinct stylistic traditions. Instead, they contributed to a broader, idealised image of "the West" as a unified cultural construct associated with refinement, modernity, and prestige. In this context, Western styles functioned less as nationally distinct aesthetics and more as a symbolic language of civilisation, shaped by the discourse of taste and aspiration.

Expressions such as European elegance[4], civilised ornamentation[5] and Western civilisation[6] used in various publications made a clear link between aesthetic taste and the ideal of civilisation. In an article published in Servet-i Fünun, the yacht of the Egyptian Khedive Sefai-Bahir was described as an example of refined British design, its ornate furniture and sophisticated interior praised and presented as a perfect example of cultural refinement.[7] Similarly, an article on wicker chairs in Austria and Germany emphasised Europe's sense of continuous improvement, arguing that it manifested itself even in everyday objects and contributed to a more relaxed and enjoyable lifestyle.[8] These descriptions reveal that design and taste were seen not only as aesthetic concerns but as reflections of a broader ideal of civilisation. In this context, Western elegance was framed as a sign of moral and intellectual superiority - qualities believed to be readable in even the most ordinary furniture.

Many of the periodicals examined suggest that furniture carried cultural meanings and became part of how people positioned themselves socially. Advertisements presented these products not just as functional or decorative objects, but as reflections of personal taste and lifestyle. The language of "elegance," "refinement," and "refined and cultivated taste" described not only the furniture, but also the type of person who would choose it. In this context, furniture was imagined not only as a possession, but as an object of cultural appreciation. Through these preferences, one's social and aesthetic position was subtly communicated.

This kind of narrative was especially visible in advertisements published in popular women's magazines and commercial periodicals of the time. For example, in an advertisement for the Psalty store, elegant and durable furniture was described as suitable for every taste and budget, but it also stated that such items would be chosen with satisfaction and approval refined taste and elegance. Similarly, in an advertisement for the Selanik Bonmarşesi, it was implied that the target

[4] *zarâfet-i Avrupa*

[5] *tezyinat-ı medenîye*

[6] *medeniyet-i garbiye*

[7] "Séfai Al Bahir," *Servet-i Fünun*, no. 229.

[8] "Yeni Hasır İskemleler," *Mahasin*, no. 10.

customers were not only those seeking quality products, but also those who had the aesthetic capacity to appreciate them.[9] The combination of refinement and affordability made it possible to present a privileged lifestyle as both desirable and accessible. These examples show how taste, access, and identity were closely linked in the language of furniture consumption.

In some publications, the arrangement of the home and the choice of objects were directly linked to personal identity, emotional state, and social belonging. This connection was especially visible in content associated with women. In Süs magazine, for example, home decoration was described not only as a visual or practical act, but as a space where a woman's personality was realized. The shape, placement, and style of furnishings were presented as tools through which personal ideals and emerging notions of taste could be expressed. This kind of discourse shows how interior design and furniture became ways to shape and communicate one's identity, especially within the broader desire to be modern.

Conclusion

The findings of this study suggest that furniture in early twentieth-century Istanbul was more than a set of domestic objects; it was deeply intertwined with contemporary discourses on taste, identity, and modernity. Advertisements and articles in periodicals did not merely promote products but participated in shaping a symbolic language through which social roles, aspirations, and cultural values were expressed. The frequent references to European and American origins, the emphasis on refinement and affordability, and the association of furniture with personal character and modern lifestyle all indicate that furniture became a medium through which both aesthetic ideals and social distinctions were negotiated.

Rather than highlighting clear stylistic differences between national traditions, the materials examined tended to present a composite image of "the West" as a unified symbol of civilisation, elegance, and progress. This symbolic construction of Westernness served to legitimise certain tastes and ways of living as modern and desirable. Overall, the study shows that periodicals were not only platforms for promoting consumer goods but also active agents in the cultural redefinition of domestic life, where material choices became intertwined with broader social transformations.

Figure 1. Baker Mağazası Reklamı (Servet-i Fünun Supplement Politique, No. 460, p. 144.).
Figure 2. Psalty Mağazası Reklamı (Hanımlara Mahsus Gazete, No. 9, p. 3.).

[9] "Selânik'te bir mevki-i mümtâz ihraz etmiş bulunan 'Selânik Bonmarşe' müesseseleri, bu kere Dersaadet'te [...] mağazalarını, zevk-i selîm sahibi nefîs-perverân ahâlîmiz için her türlü emtiâ-yı nefîse ile [...] küşâd etmiş bulunmaktadır." (Servet-i Fünun, no. 570).

References

Ahmetoğlu, S. (2007). From the Unionist actualité to the mass popularity: Şehbâl (1909–1914) (Master's thesis). Boğaziçi University, Institute for Graduate Studies in Social Sciences.
Barber, P. (2008). The power of word of marketing: Library communication strategies, a workshop for the Library Association [Self-published].
Barthes, R. (2005). Göstergebilimsel serüven [The semiotic adventure] (M. Rifat & S. Rifat, Trans.). Istanbul, Turkey: Yapı Kredi Yayınları.
Batı, U. (2005). Bir anlam yaratma süreci ve ideolojik yapı olarak reklamların göstergebilim bir bakış açısıyla çözümlenmesi [Creating meaning and ideology in advertisements: A semiotic perspective]. Cumhuriyet Üniversitesi Sosyal Bilimler Dergisi, 29(2), 175–190.
Batı, U. (2012). Reklamın dili [The language of advertising]. Istanbul, Turkey: Alfa Yayınları.
Baudrillard, J. (1998). The consumer society: Myths and structures (C. Turner, Trans.). London, United Kingdom: Sage Publications.
Duben, A., & Behar, C. (2002). Istanbul households: Marriage, family and fertility, 1880–1940. Istanbul, Turkey: Istanbul Bilgi University Press.
Dumont, P. (1993). Said Bey – The everyday life of an Istanbul townsman at the beginning of the twentieth century. In A. Hourani, P. Khoury, & M. C. Wilson (Eds.), The modern Middle East (p. 36). London, United Kingdom: I.B. Tauris.
Edwards, C. (2017). Turning houses into homes: A history of the retailing and consumption of domestic furnishings. London, United Kingdom: Routledge.
Faroqhi, S. (1999). Consumption and elite status in the eighteenth and nineteenth centuries: Exploring the Ottoman case. In R. Motika, C. Herzog, & M. Ursinus (Eds.), Studies in Ottoman social and economic life (pp. 141–169). Heidelberg, Germany: Heidelberger Orientverlag.
Faroqhi, S. (2014). Ottoman culture and daily life: From the Middle Ages to the twentieth century. Istanbul, Turkey: Tarih Vakfı Yayınları.
Göçek, F. M. (1996). Rise of the bourgeoisie, demise of empire: Ottoman Westernization and social change. New York, NY: Oxford University Press.
Günaydın, B. (2017). Modernization and women in Turkey: The case of Şehbal magazine (1909–1914) (Master's thesis, Trakya University, Institute of Social Sciences). Edirne, Turkey.
Hall, S. (Ed.). (1997). Representation: Cultural representations and signifying practices. London, United Kingdom: Sage Publications.
Koloğlu, O. (1999). Reklamcılığımızın ilk yüzyılı (1840–1940) [The first century of advertising in Turkey]. Istanbul, Turkey: Reklamcılık Vakfı Yayınları.
Köse, Y. (2016). Dersaadet'te tüketim (1855–1923) [Consumption in Dersaadet (1855–1923)]. Istanbul, Turkey: Tarih Vakfı Yurt Yayınları.
McCracken, G. (1988). Culture and consumption: New approaches to the symbolic character of consumer goods and activities. Bloomington, IN: Indiana University Press.
McKee, A. (2003). Textual analysis: A beginner's guide. London, United Kingdom: Sage Publications.
Quataert, D. (1999). Consumption studies and the history of the Ottoman Empire, 1550–1922. Albany, NY: SUNY Press.
Rose, G. (2016). Visual methodologies: An introduction to researching with visual materials (4th ed.). London, United Kingdom: Sage Publications.
Ünalan, Y. (2007). Mehmet Rauf's women's magazines: Mehasin and Süs (Analysis and selected texts) (Master's thesis, Erciyes University, Institute of Social Sciences). Kayseri, Turkey.
Veblen, T. (1991). The theory of the leisure class. Fairfield, NJ: A. M. Kelley.

Primary Sources (Periodicals)

Hanımlara Mahsus Gazete (1908–1925). Istanbul, Ottoman Empire.
Mahasin (1908–1910). Istanbul, Ottoman Empire.

Ma'lûmat (1894–1923). Istanbul, Ottoman Empire.
Servet-i Fünun (1891–1944). Istanbul, Ottoman Empire.
Süs (1923–1924). Istanbul, Turkey.
Şehbal (1909–1914). Istanbul, Ottoman Empire.
Tanin (1908–1942). Istanbul, Ottoman Empire.

ARCHITECTURE

Architectural History

Architecture Design Theory

Building Construction Technologies

Building Materials and Technologies

Built Environment Design and Technologies

Conservation and Restoration

Environmental Control and Building Technology

Project and Construction Management

Sustainable Design

The Impact Of Governmental Power On Urban Morphology: A Case Study Of London

Hande Nur Çalışkan Yüksel[1] , Tan Kamil Gürer[1]

Istanbul Technical University

caliskan18@itu.edu.tr

Keywords: Change, London, Power, Typomorphology, Urban Morphology

Introduction and Aim

Urban form is inherently dynamic and can only be comprehended by examining it within its historical context; it is not feasible to define it as a finished object (Moudon, 1997). According to Lefebvre, space is a social construct, continuously reproduced through social relations (Lefebvre, 2014). Throughout history, changes in a country's ruling powers are reflected in the structure of its cities. Therefore, analyzing a city's layout is essential for understanding the spatial influence of administrative power. As argued by David Harvey (1997), cities are shaped in accordance with the interests of capital and power, which in turn defines the class structures and economic networks of space. Public spaces, monumental structures, and symbolic projects materialize the power of ruling authorities in the urban fabric. City plans are shaped by ideological and economic strategies. Shifts in power manifest in urban plans through the construction of monumental buildings, the emergence of new building types, the formation of axes, squares, statues, and street names (Colombijn, 2006). While administrative power is predominantly held by the state, it can sometimes be in the hands of religious or aristocratic classes. Individuals seeking to benefit from this power tend to physically position themselves near these groups. This proximity reinforces social status and provides economic advantages.

In line with the sociological and ideological transformations of the city, structures representing central authority and power significantly influence the shaping of urban form and contribute to its evolving character over time. The most tangible examples of this governmental power and urban space relationship are capital cities. Capitals of countries with a long-standing historical presence offer a robust framework for observing this temporal transformation. With a two-thousand-year history, London, the capital of the United Kingdom, has been chosen as the study area for this research.

The aim of this study is to examine the influence of administrative power on the urban morphology of London throughout its historical evolution. In this context, the study analyzes the physical transformation of the Strand axis—which links the city's dual-centered urban structure—along with its associated spatial components, using the typomorphology method. The research seeks to reveal how changes in power are reflected in urban plans by evaluating building typologies, parcellation systems, and road networks, thereby demonstrating how urban form has evolved in its historical context.

Material and Method

The morphological examination of the Strand axis, which connects the London and Westminster districts, and the identification of its morphological character will be conducted using the typomorphology method in architecture. Typomorphology is a fundamental analytical method used to reveal the principles and rules of urban design when studying the city as a human living environment. This method enables the conceptualization of the complexity of physical form and allows for a deeper understanding of how cities grow and develop (Oliveira, 2022). The study will analyze the morphological structure of London and Westminster by utilizing the taxonomy developed by M.R.G. Conzen, a historical geographer and one of the key figures in typomorphology. His methodology examines urban morphology through town-plan analysis. In this approach, the basic spatial components of the city—street networks, building blocks, and parcellation systems—are classified and analyzed.

By applying this methodology, the study aims to systematically interpret the morphological characteristics of the urban space at different scales. This will facilitate a deeper understanding of how the social needs of communities along the Strand have changed over time in relation to administrative structures and how they have reshaped the physical environment around them. To achieve this, the research will quantitatively examine the building routes (streets) connected to the Strand matrix route, the parcellation system along this route, and the building texture and density within the parcellation system. It will also statistically demonstrate the mathematical relationships between these systems, analyzing the functions, land use, and building types along the Strand.

The study will present the historical dimension of the area's urban development from its foundation to the present by consulting various sources. The morphological transformations of the study area and the social content driving these changes will be documented using these sources. Simultaneously, the physical changes will be demonstrated through the analysis of historical maps. The current morphological condition will be identified using zoning maps, aerial photographs, street photographs, personal archives, and on-site observations. Thus, the historical morphological analyses will be compared with current data to reveal the physical transformations caused by administrative power over time.

Historical Background and Findings

As a continuous settlement and center of power from the Roman era to the modern period, London offers an ideal research area for understanding the spatial impacts of ruling powers throughout history. The city was founded by the Roman Empire in 48 AD under the name Londinium. Initially, access to the city was provided by the London Bridge, followed by the construction of a basilica and a forum, establishing the administrative center. The city was planned as a typical Roman town, featuring marketplaces, religious, and cultural structures. It was connected to other major cities through the Roman road network, quickly becoming the capital of Britannia province (Morris, 1982).

After the Romans abandoned Britain in the 4th century, Celtic uprisings and Viking raids inflicted significant damage on London. Although it was not used as a settlement for a long period by the Anglo-Saxons, its location on the Roman road network allowed it to retain its commercial importance. During the late medieval period, increasing attacks led to the city's restructuring into a fortified settlement. Numerous ports were built, strengthening trade with Europe. Following a brief Viking occupation in the 9th century, the city was fortified with castles and walls as part of a general planning strategy to protect it from future attacks.

After the Normans conquered England in the mid-11th century, they constructed the Tower of London (White Tower) as a symbol of military power, reinforcing the city's defense system. However, as the Tower's administrators gained influence, London moved toward becoming an autonomous entity, culminating in the signing of the Magna Carta, which marked the beginning of parliamentary monarchy in England. This event represents a significant example of the relationship between power and urban morphology.

One of the most influential factors in the city's morphological transformation was the Norman kings' decision to abandon their itinerant government system and establish a monastery and palace in Westminster, where they chose to reside. This decision transformed the area into the administrative and religious heart of the United Kingdom. Consequently, Westminster (The City of Westminster) became the administrative center, while intra-muros London (The City of London) remained the capital of commerce and economy (Inwood, 1998). These two centers were connected by the Strand axis, forming Greater London (Figure 1).

Figure 1

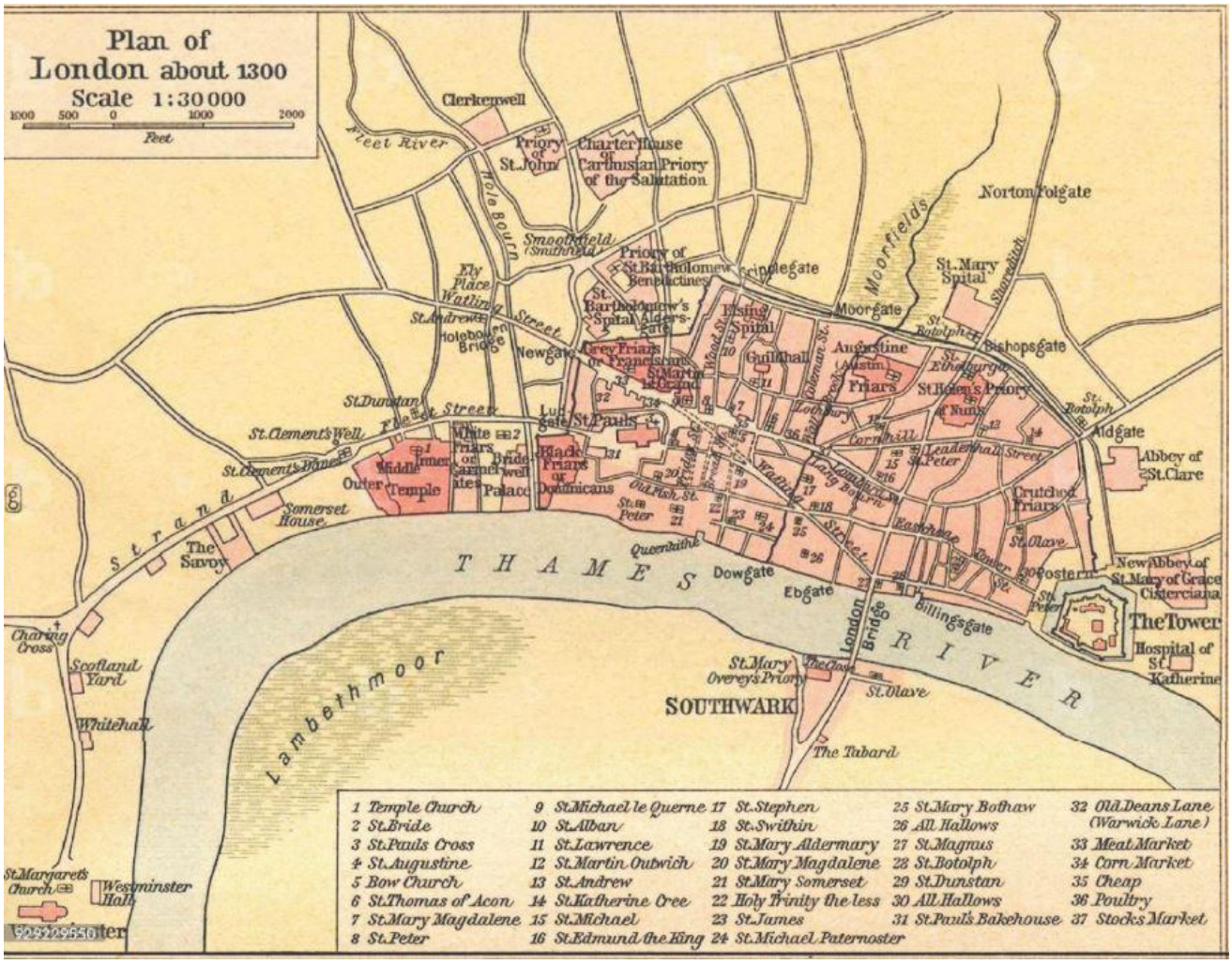

Figure 1. The Strand axis developing between London and Westminster (Historical Atlas, 1923).

Over time, new palaces and administrative buildings were rapidly constructed along the Strand axis. These included Somerset House, Savoy Palace, and Whitehall Palace, alongside bishop's residences for clergy members seeking proximity to the royal court—Durham, Bath, Chester, Carlisle, Exeter, Norwich, Worcester, and York Bishop's Palaces. In addition, noble estates such as Albemarle, Bedford, Berkeley, Burghley, Clare, Drury, Hungerford, and Northumberland Mansions were established along the axis (Figure 2) (Croot, 2014).

Figure 2

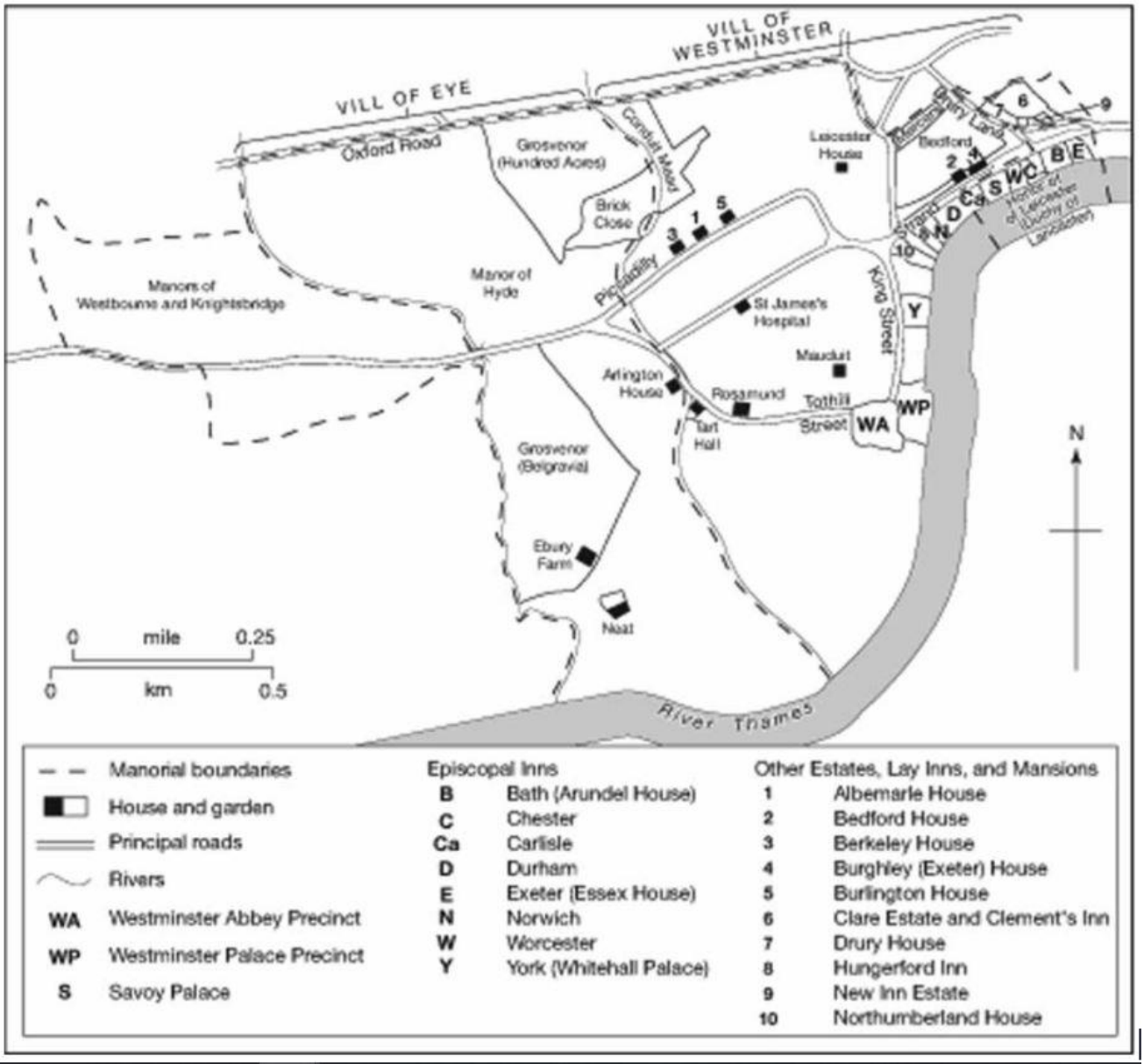

Figure 2. London and Westminster in the Early Modern Period (Croot, 2014, s. 87).

By the 12th century, historical records indicate that 75 buildings belonging to leading nobles and bishops were located in this area (Inwood, 1998). These manors and palaces created a significant marketplace for London merchants, boosting the trade of luxury goods with Europe. Consequently, the development of Westminster also enhanced London's international commercial influence. In the modern period, with the transition to parliamentary monarchy and the royal court's relocation to Buckingham Palace, Westminster was repurposed as the House of Government (Parliament Building) and has maintained its position as the administrative center ever since. According to Hanson (1989), new commercial spaces emerged around Westminster to meet the needs of the royal court. The study also focuses on the typologies of buildings that emerged while examining the urban plan of the region, including palaces, mansions, churches, hotels, offices, and public buildings (Figure 3).

Figure 3

Figure 3. Whitehall Palace (Danckerts, 2016)

Notably, during the periods of Roman, Anglo-Saxon, and Norman rule, and the subsequent transfers of power between various noble families, the formation of road networks and the differentiation of the building block system in the city were observed. It is understood that the city responded to historical events and interventions of power. At the end of this historical process, the Strand axis has become one of the most important regions of London, today lined with ministries, administrative and military offices, luxury hotels, and commercial buildings (Figure 4).

Figure 4

Figure 4. Westminster, Whitehall, Savoy Palaces on the Strand axis (mapping.cityoflondon.gov.uk, 2025).

Conclusion

It is understood that urban form is continuously evolving and that this evolution is directly connected to the power relations in its historical context. This study demonstrates how spatial interventions and strategic decisions of power have shaped the city form through the example of London. The strategies of power throughout history have directly affected the organizational structure of the city, and spatial decisions have determined the morphological characteristics of the urban form. In this process, the existence of a dual-center city structure and the main axis connecting these centers has emerged as one of the most significant urban characteristics of London today. The study offers an analytical framework for understanding the historical evolution of cities by examining the relationship between power and the city from a typomorphological perspective. Studying the spatial organization of cities in relation to administrative powers, evaluating the city as a reflection of the socio-cultural structure of these powers, brings a historical perspective to urban architecture. As in the case of London, considering the historical and social context is of great importance in understanding the identity of modern cities. This study also highlights the necessity of planning processes that will contribute to the evolution of cities while preserving their identity, demonstrating how modern powers' decisions can influence urban development. The analysis of the morphological transformation of the Strand axis concretely reveals the impact of spatial interventions of power on urban form and emphasizes that such axes can be used as an analytical model for investigating how administrative power leaves its mark in the physical space of modern city planning strategies.

References

Colombijn, F. (2006). Chapter 6 Planning and social tension in Indonesian cities. Global Bioethics, 19(1), 73-84. https://doi.org/10.1080/11287462.2006.10800886

Croot, P. (2014). A Place in Town in Medieval and Early Modern Westminster: The Origins and History of the Palaces in the Strand. The London Journal, 39(2), 85-101. https://doi.org/10.1179/0305803414Z.00000000042

Danckerts, H. (2016). The Old Palace of Whitehall [Graphic]. https://commons.wikimedia.org/w/index.php?curid=298524

Hanson, J. M. (1989). ORDER AND STRUCTURE IN URBAN SPACE: a Morphological History of the City of London. University of London.

Harvey, D., & Savran, S. (1997). Postmodernliğin Durumu. Metis.

Historical Atlas. (1923). Plan of London, England c. 1300 [Map]. Historical Atlas.

Inwood, S. (1998). A history of London. Carroll & Graf Publishers.

Lefebvre, H. (2014). Mekanın üretimi (Işık. Ergüden, Çev.; İkinci Baskı: Eylül 2014). Sel Yayıncılık.

Mapping.cityoflondon.gov.uk.(2025,Mart22).mapping.cityoflondon.gov.uk. https://www.mapping.cityoflondon.gov.uk/geocortex/mapping/?viewer=compass

Morris, J. (1982). Londinium: London in the Roman Empire (S. Macready, Ed.). Weidenfeld and Nicolson.

Moudon, A. V. (1997). Urban Morphology as an emerging interdisciplinary field. Urban Morphology, 1(1), Article 1. https://doi.org/10.51347/jum.v1i1.4047

Oliveira, V. (2022). Urban Morphology: An Introduction to the Study of the Physical Form of Cities. Springer International Publishing. https://doi.org/10.1007/978-3-030-92454-

The Performance of the Archive or Archive as Event: Exhibiting Architecture

Derya Yıldız[a], Funda Uz[b]

[a] Istanbul Technical University, ITU Graduate School, Architectural Design Doctor of Philosophy Program, Turkey
[b] Istanbul Technical University, Faculty of Architecture, Department of Architecture, Turkey
yildizd18@itu.edu.tr

Keywords: Architectural Archives, Exhibition as Performance, Collective Memory, Institutional Mediation.

Aim

This study treats the concept of the archive in architecture not merely as a repository for historical documents but rather as a dynamic event or "performance." Building on Derrida's (1996) emphasis on the self-preserving nature of archives and Foucault's (1972) view of archives as frameworks that shape knowledge, the paper discusses how exhibitions function as primary sites where archival materials are activated and reinterpreted. Focusing on architectural exhibitions, it argues that archival practices in architecture are not confined to storage and retrieval but instead manifest as performances that are socially and spatially enacted. Consequently, the archive informs not only our perception of architectural history but also how collective memory is continually constructed, revised, and transformed.

Reflecting on the relationality between "archive" and "event" in the title, this discussion centers on exhibitions and the venues that host them. Exhibitions are highlighted because they render archives tangible for diverse audiences and bring together different actors through curatorial strategies and visitor experiences within institutional contexts such as museums, architecture centers, and schools. This multiplicity in performance largely depends on the mediation of cultural and research institutions. The overarching aim of the study is to demonstrate how architectural exhibitions, by underscoring the ever-changing and context-dependent nature of archival materials, become catalysts for new modes of knowledge production and secure a place in collective memory through spatial practices.

Material and Method

This research adopts an interdisciplinary approach, integrating perspectives from archival studies, architectural history, and memory theory. Derrida's (1996) views on archives highlight how meaning is generated through both preservation and selective omission, while Foucault's (1972) "archaeology of knowledge" provides a historical foundation for understanding the archive as a basis for discursive structures. Deleuze's concept of the "event" resonates with the "multiplicity" that shapes both archives and exhibitions. Maurice Halbwachs's (1992) notion of "collective memory" and Pierre Nora's (1989) concept of "sites of memory" (lieux de mémoire) further clarify the role of space in generating memory and in shaping how archives are preserved and transmitted. Additionally, key texts on architectural exhibitions (Forty, 2008; Cohen, 1999; Colomina, 2013) are examined to trace how the definition and content of exhibitions have evolved. Museum studies literature is also incorporated to analyze the function of exhibitions as a form of research (Herle, 2013).

The study uses a comparative analysis method. First, the classifications proposed by Adrian Forty (2008) and Jean Louis Cohen (1999) are employed to explain the diversity of architectural exhibitions in terms of form (full-scale vs. representational) and content (e.g., forgotten works, thematic displays, paradigm-shifting shows). Then, it evaluates selected institutions that organize, archive, and exhibit architectural documents. By referencing both international and local cases, the study explores how architectural exhibitions interact with archival processes and, in contexts with limited archival infrastructure, how they can function as de facto repositories.

This methodological framework reveals how exhibitions, understood as "archival performances," continually rewrite and reinterpret architectural discourse within specific contexts. The dimension of institutional mediation is also integrated into this approach, clarifying how the archive is performed through multiplicity.

Findings

The first key finding is that exhibitions are more than mere displays of objects; they serve as unique platforms for architectural research. Forty (2008) points out that architecture is not confined to "building" alone but appears in multiple media. Exhibitions integrate different types of materials — models, drawings, photographs, digital projections — within a spatial narrative, offering a highly immersive experience. Consequently, the production and circulation of architectural knowledge is enriched through exhibitions.

From a performance theory perspective (Schechner, 2013), exhibitions reorganize archived materials to generate new narratives. Decisions about selection, sequencing, and thematic emphasis can reinforce or challenge canonical discourse. This process echoes Derrida's (1996) notion of "archive fever," highlighting the intertwining urges to preserve and rewrite.

A third finding is that the multiplicity that characterizes the performance of the archive largely relies on the mediating role of institutions. Museums, research centers, and architecture schools — such as the Canadian Centre for Architecture (CCA), Het Nieuwe Instituut (HNI), SALT, and VEKAM — preserve and digitize archives, curate exhibitions, and organize public events that open up new interpretive possibilities. For instance, SALT activates diverse archives of Istanbul and its surroundings, while HNI hosts research on how the digital era influences both architectural practice and archiving. The CCA focuses on global architectural heritage, using archival exhibitions and publications to evolve into an international research hub. VEKAM, meanwhile, expands and sustains Ankara-centered archives through public programs, thus contributing to spatial memory research. In academic settings (e.g., ITU and METU), exhibitions compensate for limited archival infrastructures by enriching institutional memory.

Exhibitions are frequently supplemented by symposia, panels, workshops, and publications that regenerate archives. The photographs, documents, and critical essays arising from these events re-enter the archive, expanding it and providing additional resources for further investigation. Each exhibition thus leaves a lasting "trace" on institutional and societal memory.

Lastly, following the democratization of architectural culture in the 1960s (Okumuş Solmaz & Doğrusöz, 2022), exhibitions play a decisive role in making architectural discourse more accessible. Forgotten or fragmented works (Cohen, 1999) become visible once again through exhibition formats, thus enlarging the architectural canon by foregrounding alternative design histories. This inclusivity expands the audience and fosters engagement with a collective architectural heritage.

Conclusion

The perspective of "the performance of the archive" and institutional mediation underscores how pivotal architectural exhibitions are in archival processes. Far from being passive repositories, archives become dynamic processes that are ceaselessly reinterpreted and reactivated in space. Consequently, our understanding of architectural history undergoes continual renewal, while collective memory is enriched through novel forms of engagement and encounter.

In particular, architecture faculties and research centers introduce exhibitions into their educational and public programs, bringing previously undocumented materials to light and stimulating new discussions. Institutional efforts toward digitization, participatory practices, and open access transform archives from static collections into sustainable "archival landscapes." This approach underscores not merely the "construction" of the archive but its "performance." As a result, the roles of exhibitions and institutions broaden our view of how architecture is recorded, recalled, and reshaped, prompting critical reflection on the policies and curatorial strategies that inform these collective endeavors.

References

Cohen, J. L. (1999). Exhibitionist revisionism: Exposing architectural history. Journal of the Society of Architectural Historians, 58(3), 316–325.

Colomina, B. (2013). Exhibitionist architecture. Texte zur Kunst, 92, 80–93.

Deleuze, G. (1990). The Logic of Sense. Columbia University Press.

Derrida, J. (1995). Archive fever: A Freudian impression (E. Prenowitz, Trans.). Diacritics, 25(2), 9.

Foucault, M. (1972). The Archaeology of Knowledge & The Discourse on Language. Pantheon Books.

Forty, A. (2008). Ways of knowing, ways of showing: A short history of architectural exhibitions. In P. Sparke & **D. Sudjic** (Eds.), Representing Architecture. New Discussions: Ideologies, Techniques, Curation (pp. 42–61). Design Museum.
Halbwachs, M. (1992). On Collective Memory. University of Chicago Press.
Herle, A. (2013). Exhibitions as research: Displaying the technologies that make bodies visible. Museum Worlds, 1(1), 113–135.
Nora, P. (1989). Between Memory and History: Les Lieux de Mémoire. Representations, 26, 7–24.
Okumuş Solmaz, G., & Doğrusöz, U. (2022). Mimarlığı "okulsuzlaştırmak": Mimarlık kültürünün demokratikleşme sürecinde Fransa ve çağdaş mimarlık müzeleri. MSGSÜ Sosyal Bilimler, 1(25), 39–67.
Schechner, R. (2013). Performance Studies: An Introduction (3rd ed.). Routledge.
Url-1 https://doi.org/10.2307/991524
Url-2 https://doi.org/10.2307/465144
Url-3 https://doi.org/10.56074/msgsusbd.1123724

Typological Transformations and Urban Isolation: Rethinking Architectural Production along Eskişehir Road

Ahmet Günel[a], Celal Abdi Güzer[a]

[a] Middle East Technical University, Department of Architecture, Architecture Design Theory, Türkiye
ahmet.gunel@metu.edu.tr

Keywords: Urbanisation in Turkey, Urban-scale Building, Urban and Architecture Relationship, Urban Transformation, Eskişehir Road in Ankara.

This study is based on the author's master's thesis conducted at the Department of Architecture at Middle East Technical University (METU)under the supervision of Prof. Dr. Celal Abdi Güzer. The presented research is derived and adapted from the thesis titled "Re-Mapping Contemporary Architecture in Turkey Based on the Relationship Between Urbanisation and Architecture: Eskişehir Road Development in Ankara". The key arguments and findings of the thesis have been restructured for this paper, with some sections directly reproduced. In line with academic integrity principles, proper attribution to the original work is provided throughout. All intellectual rights, data, methodological framework, and analyses belong to the author. Unauthorized use without citation whether partial or full reproduction is prohibited and constitutes a violation of academic ethics. All academic rights are reserved.

Aim

This study aims to investigate the relationship between architecture and urbanisation through some examples with a focus on the transformative impacts on each other and the problems of contemporary situation. By examining this relationship, it is intended to evaluate and demonstrate the transformation of architectural typologies and productions. In this sense, the significant aims in this study are exemplifying and mapping the emerging typologies, the changes in the use of existing typologies, the reflections of typological multiplicity on urban scale, and the determinative relationship between architecture and city.

The study also seeks to re-map the existing theoretical discussion from a different perspective, offering an interpretive framework for analysing, understanding and evaluating contemporary architecture within urban context. A wider meaning of context will be carried out through the study extending beyond the physical environment to include political, social, ideological, economic, physical, urban development and planning dimensions. The gap between urban and architectural scales is examined to propose an alternative ground to new models through theoretical background, concepts, architectural productions and the case study representing the contemporary situation of Turkey.

Material and Method

The method of this research is based on the examination of an area as the case study which has great representative potential. In other words, the contemporary architecture in Turkey is examined through the situation of this specific example representing Turkey. The case study as the main research material consists of new building typologies which come together and form an urban fabric through their coexistence. It will be analysed through the observed problems which continuously occur in architectural and urban scales. Therefore, the repetitive patterns and determinative situation of architecture in Turkey will be discussed.

It is aimed to examine and evaluate a specific area of Eskişehir Road in Ankara as an urban part of the city, while architectural concepts and building typologies are used as important discussion topics in the methodology to investigate and test the urban scale of contemporary Turkish architecture and to understand the relationship of architecture with urbanisation, context, and city. In addition, the coexistence of the buildings on this corridor leads to form integrity in terms of urban fabric. Thereupon, the methodology incorporates to examine whether these typologically large-scale urban buildings really contribute to the city or not. Accordingly, the main concern is to evaluate the new understanding of

urbanization in Turkey through this case study as a representative example of the contemporary situation. For this reason, changes and transformations of the contemporary architecture in Turkey will be discussed through the analysis of Eskişehir Road.

This area will be analysed through its impacts on urbanisation, urban scale, architecture and Ankara, focusing on:

- Building typologies,
- Relationship of buildings with each other,
- Site plan characteristics and complex-wise architectural organization,
- Their contributions to city,
- Integration with infrastructure, traffic, pedestrian, public transportation, car parking,
- Forms of representation of some architectural concepts.

The methodology of this research is based on the examination of a certain area with concepts and typologies. This area representing almost completed new development zone, accommodating large-scale public buildings and different typologies, serves as the main axis of this research.

Figure 1.a. The case study area along Eskişehir Road, Ankara [Source: Google Maps, https://www.google.com/maps (accessed on 26.12.2018) The image is edited and drawn by the author].

Figure 1.b. Developments and impacts on the case study area [Source: Google Maps, https://www.google.com/maps (accessed on 26.12.2018) The image is edited and drawn by the author].

Selected area (Figure 1.a) can be considered as an appropriate corridor where lots of new buildings come together rapidly in Ankara. The public buildings along this area are selected and evaluated. Selected contemporary buildings were built after 2000, representing the transformation and new developments in Turkey. They will be scrutinized and discussed to support and embody the main discussion framework. It is not intended and aimed to criticise the buildings on single scale but rather to discuss with concepts through urban and architecture relationship. In addition, there are three important focal points having significant impacts on the case study area with regards to developments and densities coming from these points (Figure 1.b).

Findings

Contemporary architecture in Turkey demonstrates a limited interaction in terms of feeding and feeding from urban scale, despite a significant increase in new architectural productions and process in building scale. Therefore, architecture does not contribute enough to city and is not sufficiently fed from urban data, urban dynamics, and context. This aligns with Aldo van Eyck's call for a reciprocal understanding: "the time has come to conceive of architecture urbanistically and urbanism architecturally." (as cited in Ellin, 2006, p.17).

Considering many factors and changes, contemporary architecture has undergone some certain transformations all around the world; and a new state has inevitably emerged which is effective on all scales. The fundamental problems observed among these emerged situations are:

- understanding of planning approach in urban scale,
- understanding of design with values in architectural scale,
- continuity between values is no longer a necessity,
- introversion of architectural productions,
- many of the projects try to maintain their own existence as an "entity" in urban scale.

These affect not only the urban state, but also typology, scale, identity and language of architectural productions, their relationship with each other, city, silhouette, and density. Within this perspective, many of the urban problems stem from this transformation.

As Rossi (1984, p.22) states "destruction and demolition, expropriation and rapid changes in use as a result of speculation and obsolescence, are the most recognizable signs of urban dynamics." The rapid change of production, urban fabric and urbanisation in Turkey has become inevitable with the increase of these large-scale introverted buildings as new urban dynamics. Since urban dynamics "refers to any process capable of transforming the urban or social morphology of a certain space" (Mahmoud, 2017, p.434), fifteen-year evolution of Eskişehir Road is analysed, indicating how urban fabric changes with the emergence of new building typologies (Figure 2).

Large-scale buildings emerge in such an eclectic way and are independent of each other, forming an urban fabric through their coexistence. This causes an increase of density and traffic since these typologies host and undertake city-center functions. 1990 Master Plan's decentralization of public institutions further contributes to this density.

This main artery hosts ministries, public institutions, shopping malls, many residential projects and office buildings forming a radial development along this corridor. From another perspective, a corridor can spontaneously form in time by itself and can be a focal development as it develops as a metamorphosis. This can be observed on different scales and in different cities. For this reason, it has become a representative example for Turkey.

Within this area, seven different types of building typologies are examined as case studies. Figure 3 indicates their location, density, scale, and their coexistence in the area. This map is significant in terms of how such a coexistence of multi-functionality regenerates each other as a repetitive pattern in case study area.

It is observed that the case study area represents the features including restricted urban accessibility, creating urbanism within itself, introversion, scale, the discontinuity between local zoning plan and main plan, eclectic and partial planning, and functional multiplicity. (Figures 4-5).

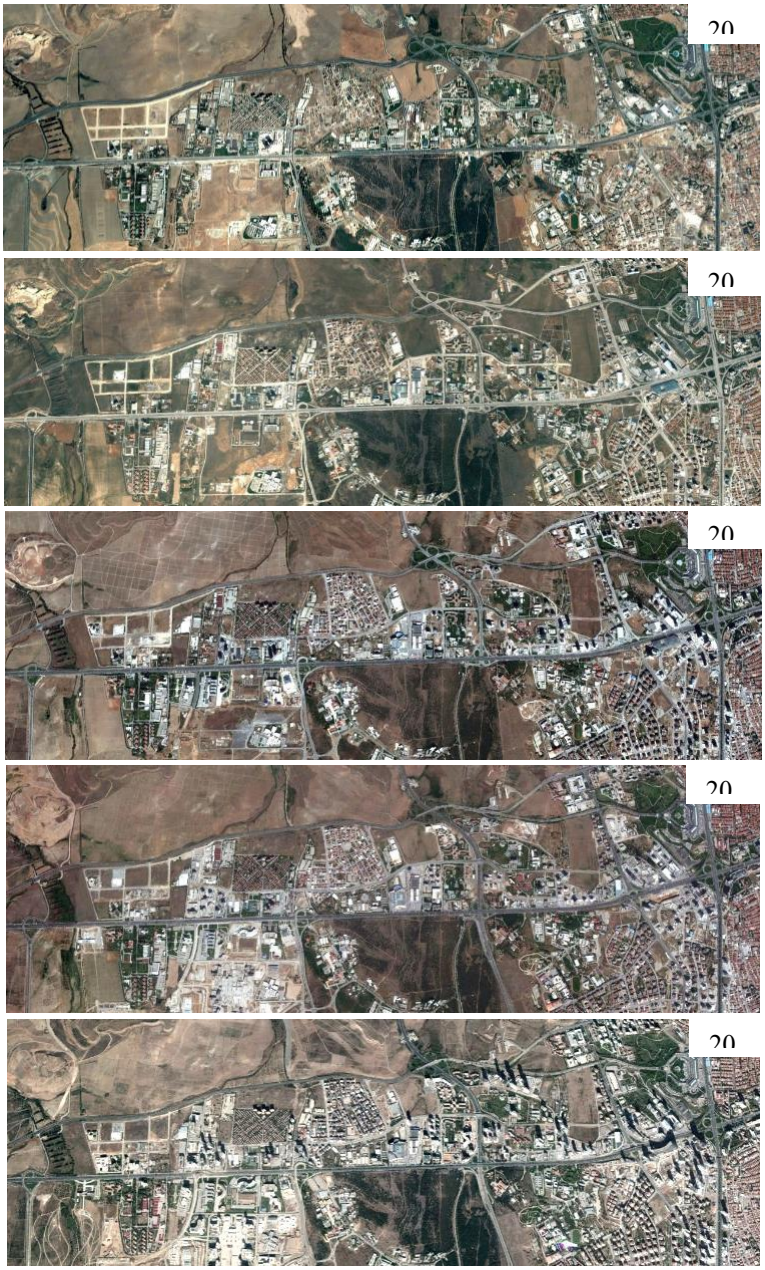

Figure 2. Urban transformation in Eskişehir Road [Source: Google Maps, https://www.google.com/maps (accessed on 26.12.2018)].

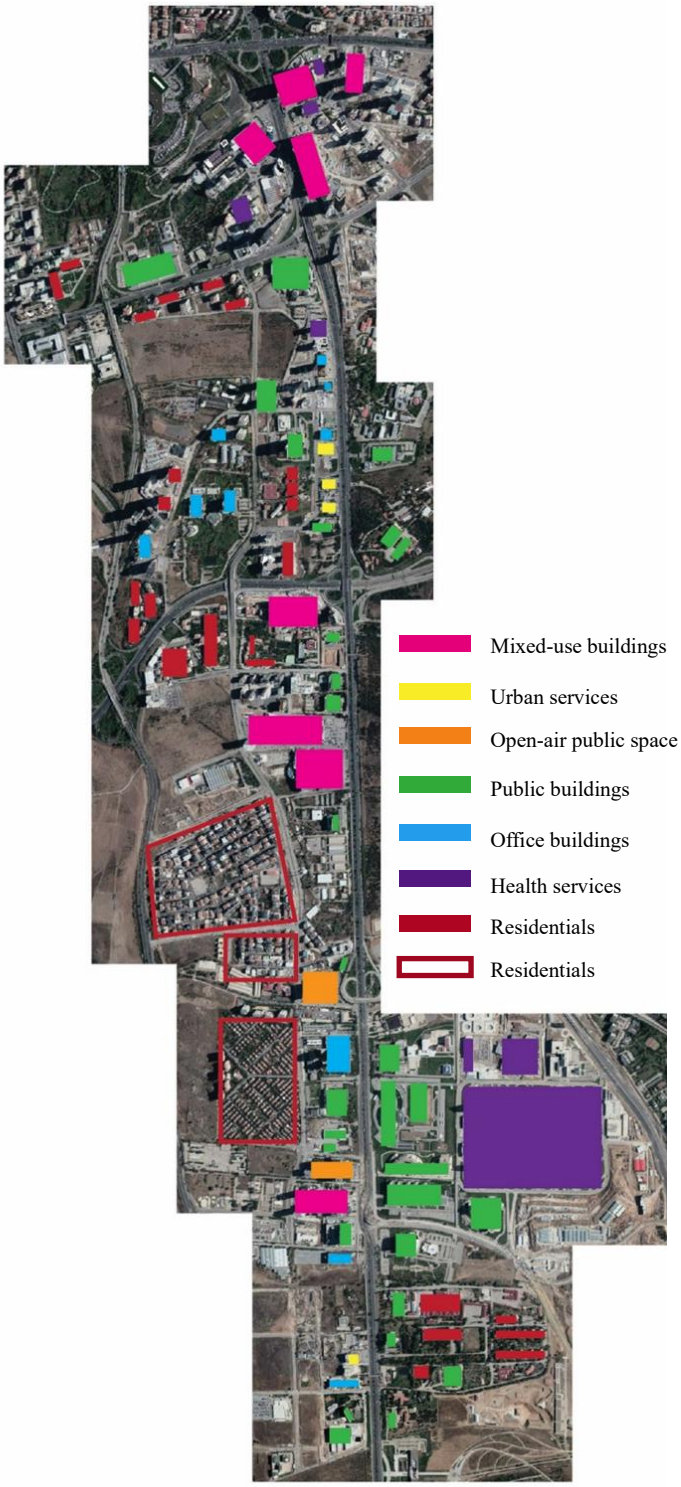

Figure 3. Typologies along Eskişehir Road [Source: Google Earth, (accessed on 26.12.2018) (The image is dited and drawn by the author)].

Figure 4.a. Restricted urban accessibility: The transition between two points with security check in Armada [Source: Youtube, https://www.youtube.com/watch?v=w5dIJeHOAm8 (accessed on 6.12.2019) The image is edited and drawn by the author].

Figure 4.b. Introversion, Scale: YDA Center, Ulusoy bus terminal and Vatan computer center [Source: Youtube, https://www.youtube.com/watch?v=ZJix7TOtTn4 (accessed on 6.12.2019) The image is edited and drawn by the author].

Figure 4.c. Eclectic and partial planning: The eclectic coexistence of buildings with different densities, heights, scales, and functions along the same axis [Source: Twitter, https://twitter.com/vedat1910/status/1053251907903459329 (accessed on 10.10.2019) The image is edited by the author].

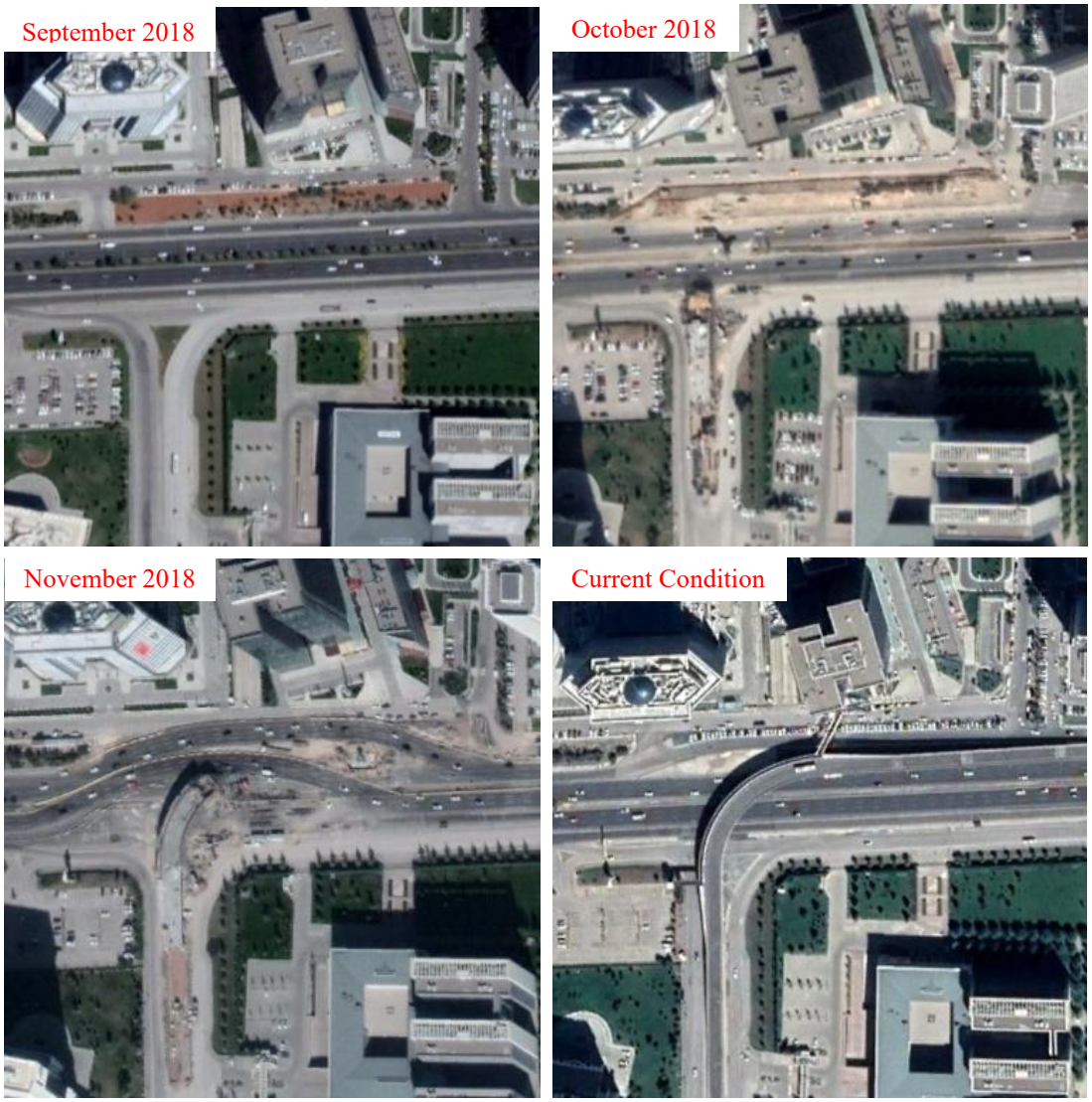

Figure 5. Eclectic and partial planning: Transformation process of Eskişehir Road due to city hospital [Source: Google Earth,(accessed on 3.11.2019) The image is edited by the author].

Conclusion

Introverted large-scale urban buildings exclude relationship with context and isolate themselves. For this reason, these can be located anywhere and become a prototype without giving contextual, historical and cultural references. This points out the creation of cities where car transportation forms the boundaries, social relations become spatially impossible, and public spaces are commercialized and privatised. In this way, cities start to consist of such clusters which have become isolated and create their own world within themselves through introversion and their bigness. This is because urban-scale buildings change and transform cities. Without the need for a city, these gated entities create their own urbanity and fulfil all functions inside in a self-sufficient way which refers directly to being competitive of city, simulating the urban life by accommodating all urban facilities inside, and replacing the public nature of city. As a result, architecture becomes an object as a commodification of consumer society to be consumed and reused again. Some of the increasing results of such urban-scale buildings are as follows:

- They are introverted, enclosed, and tautological. They neither contribute to city, nor take advantage from the city. This weakens their relationship with context pointing out placelessness.

- When these buildings do not have a relationship with concepts of memory, belonging, and identity, their presence does not contribute to the city in terms of urban identity.
- Their planning approach is not based on local and contextual problems, but rather on the priorities of the marketing strategies.
- Instead of integrating with urban life, they form gated entities that simulate urbanity.
- They are independent from their contexts that make architecture be reproduced in anywhere regardless of surrounding, built environment and city.

As an urban impact, the concept of city-center has been transformed along Eskişehir Road. It took on a central function suddenly and in an unplanned way. Although it is not appropriate to be a city-center; lots of state buildings, shopping malls, business centers have been built which create huge density. There is a common tendency towards creating isolated and gated entities rather than urban space, which represents disconnection of architecture from city because each entity creates its own urbanity within itself whereas "architecture takes its function and program from the city" (Mutlu, 2006). Many of the buildings as 'closed-boxes' simulate the city with functional multiplicity, which causes the relationship between city and architecture to diminish and isolation from urban life. These make architectural productions be forced to a typology which is isolated. Introversion of privileged architectural productions demonstrates their lack of reference to the built environment. This problem is directly related to the understanding of eclectic and partial planning since the formation of urban fabric is based on parcels rather than a main plan, which leads to the following observations in the case study area:

- Multiple shopping malls next to each other,
- Large-scale city hospital without planning,
- Understanding of city-center is changed,
- Buildings are surrounded by vehicle traffic around parcels and have weak relationships with each other,
- Transportation-oriented, car-dependent, introverted urban habitat developments.
- Exclusion of greenery and open-public spaces.

In conclusion, there is a transformative relationship between urban and architectural scales as a new understanding of urban dynamics in Turkey. Eskişehir Road reveals not only a physical transformation of the cityscape, but also a deeper shift in the way architectural productions interact or fail to interact with their built environments. The case study exemplifies a broader situation that large-scale building typologies are increasingly detached from urban context and collective spatial experience. The emergence of typologically repetitive, introverted, isolated, self-sufficient urban entities reflects a transformation from contextual responsiveness to self-referentiality, where architecture operates in isolation from the socio-urban fabric. This tendency results in placelessness and weakening of the role of architecture in shaping urban life. Thus, rethinking performative role of architecture within the urban realm becomes imperative for envisioning more inclusive and integrated built environments.

References

Ellin, N. (2006). Integral urbanism. Routledge.
Mahmoud, R. (2017). New Cairo's urban dynamics: Redefining gentrification as a main actor of social resilience. Procedia Environmental Sciences, 37, 429-441.
Mutlu, Ö. (2006). Understanding city as an architectural and non-architectural program: Learning from Ankara (Master's thesis, Middle East Technical University).
Rossi, A. (1984). The architecture of the city (D. Ghirardo & J. Ockman, Trans.). MIT Press.

Conditions of Criticality in Discussions on Architectural Representation

Burçe Karadağ[a], Nurbin Paker Kahvecioğlu[b]

[a] Istanbul Technical University, Graduate School, Architectural Design Program, Türkiye

[b]Istanbul Technical University/Graduate School, Department of Architecture,

Architectural Design Program, Türkiye

karadag17@itu.edu.tr

Keywords: Architectural Representation, Critical Representation, Conditions of Representation.

Aim

The aim of the study is to seek and understand the conditions of criticality in order to reveal the possibilities and challenges of architectural representation. The study provides an understanding of the history of architectural representation in order to discover the context of current discussions and different positions related to this area of research. Through the literature review, it has been seen that the 15th century, 18th century, and the second half of the 20th century act as three primary thresholds in the history of architectural representation. The parallels between scientific representation, representation of thought, and architectural representation are discussed at these thresholds. However, it has been argued that the current break is characterized by the transition from the representational to the performative. Through this break, critical approaches to architectural representation mediated a field of discussion within their current context. The aim of transformation, the relationship between knowledge production, power dynamics and ethics, and the disconnection between thought and action have been observed as common themes of criticality. Particularly in the field of architecture, the social and cultural structure of criticality, the differences between criticality and criticism, the possibilities of other ways of making, and the creative potential of criticality have become significant.

Material and Method

This study approaches "representation" as an active, co-constructive process, rather than a passive depiction, and considers "criticality" as inherently contextual, situated, and relational, rather than fixed by a singular definition. A broad historical framework is employed deliberately, as much of the current discourse on architectural representation tends to concentrate on specific time periods, historical or contemporary, often overlooking the longer evolution of representational practices. By tracing this historical trajectory, the study aims to foreground the ways in which "ways of making" have shaped the relationship between representation and the represented. Recent examples from critical cartography are examined not only to illustrate contemporary practices but also to highlight the need for a deeper discussion of critical approaches. This perspective invites renewed attention to the conditions under which architectural representation operates and suggests that a more expansive temporal and conceptual framework is essential for understanding its evolving role within spatial practices.

Findings

In discussions of criticality in architectural representation; established ideas of architectural representation, thresholds that mediate the questioning and challenging of established ideas, predictions of other ways of making, and qualities of a critical representation were encountered. In order to question the scope of representation, attention has been drawn to the distinction between representation and the reality it represents. This approach problematized the premise of drawing as a neutral tool that conveys absolute information and highlighted the role of drawings in producing and maintaining power dynamics. The position of representation in perceiving and making sense of the world has been considered for its power to change, hide, reveal, and reproduce the things it represents. These dynamics have exposed the creative potential of representation as well

as the visibility of its restrictive structure. The transformation of drawing into a field of discovery has mediated the search for other ways of representation and enabled the evaluation of issues such as authority, precision, and fragmentation. These discussions on representation made it possible to move from the question of representation to the conditions of representation. The parallels between media theory and critical architectural representation have been observed and evaluated within this scope. Such studies did not remain only in the conceptual field but also problematized the techniques, technologies, tools, and mediums, as well as the power dynamics they involve and their relations with ethics and discipline of architecture.

Along with the thresholds determined through studies examining the history of architectural representation, it is thought that the most recent break, as stated by Vidler (2002), is the adoption of a performative approach in productions instead of a representational one. Through this break, a paradigm shift occurred in architectural representation, and the association or relationship between representation and non-representation began to be questioned. Additionally, this break emphasized the idea that works in the category of representation are viewed as entities in themselves, rather than merely representations of something else, which was pivotal for the productions of this period. Regarding the relationship of architectural drawings with architecture, Van Gerrewey (2021) suggests that architectural drawings always point to what the architect can do in the future, refer to something other than themselves, and are related to something beyond their own scope. Discussions on criticality in architectural representation problematize these established ideas about production processes by questioning such assumptions. Although criticality debates frequently emerge in the field of architecture, it appears that the accepted notions of architectural drawing and representation can still be reproduced in current studies. This indicates that criticality may not begin to infiltrate production processes and transform them if it remains limited to the content of the productions.

Critical approaches to architectural representation have revealed the determining factors of representation and, therefore, the problem of the conditions of representation. This transition becomes visible in studies that bring the space of representation into focus. Especially in the last twenty years, studies in the field of cartography that discuss the space of representation have increased and supported this transition. By looking at what maps do instead of what they represent, the emphasis on action in the field of cartography has become significant. The transition from map to mapping was not only a conceptual leap, rather made the actions involved in mapping visible. Especially in studies referred to as counter or critical mapping, many qualities such as bringing the neutrality of representation into question, mediating transformation, revealing hierarchies, and the relationship between academic and non-academic form similarities with critical approaches to architectural representation. In studies where the conditions of representation are questioned, the methods, techniques, mediums, tools of representation, as well as the scope and content, and the relations between these elements have been opened to discussion, where the search for new forms of production and the interactions in these processes become visible.

Conclusion

Among the concepts included in the study, thresholds express certain periods that are encountered. There have been common perspective changes at these thresholds, and these changes have occurred simultaneously in multiple areas of study. Breaks, such as the transition from the representational to the performative, are accepted as intervals that are present and opened to discussion. Unlike thresholds, breaks have not been observed in more than one area simultaneously. Breaks include fractures, disintegrations, proliferations, and differentiations, making it impossible to express them in a linear narrative. Conditions, another concept included in the study, involve the ongoing search to understand the domain of the concept discussed, such as representation or criticality. The conditions were chosen to identify the common approaches to the concept evaluated in different fields of study and research. In studies where the conditions of representation are questioned, the methods, techniques, mediums, tools of representation, as well as the scope and content, and the relations between these elements have been opened to discussion, where the search for new forms of production and the interactions in these searches become visible. Through this study, it has been argued that the conditions of criticality in representation hold a creative and transformative potential, which does not reside in the disciplinary boundaries but in the shared space of representation.

References

Aureli, P. V. (2005). After Diagrams. Log, 6, 5-9, Anyone Corporation.

Corner, J. (2012). The Agency of Mapping: Speculation, Critique and Invention. The Map Reader: Theories of Mapping Practice and Cartographic Representation, (ed.) M. Dodge, R. Kitchin & C. Perkins, John Wiley & Sons.

Desimini, J. (2019). Cartographic Grounds: The Temporal Cases. Mapping Landscapes in Transformation, (ed.) T. Coomans, B. Cattoor & K. De Jonge, Leuven University Press.

Dovey, K. (2007). 'I Mean to be Critical, But ... '. Critical Architecture, (ed.) J. Rendell, J. Hill, M. Fraser & M. Dorrian, Routledge.

Doucet, I. & Janssens, N. (2011). Transdisciplinarity, the Hybridisation of Knowledge Production and Space-Related Research, Transdisciplinary Knowledge Production in Architecture and Urbanism, Towards Hybrid Modes of Inquiry, (ed.) I. Doucet & N. Janssens, Springer.

Emmons, P. (2007). Drawn to Scale: The Imaginative Inhabitation of Architectural Drawings. From Models to Drawings: Imagination and Representation in Architecture, (ed.) M. Frascari, J. Hale & B. Starkey, 64-78, Routledge.

Evans, R. (1982). 1975-1980 Projects: From Axes to Violins. AA Files, 115-20, Architectural Association School of Architecture.

Evans, R. (1984). In Front of Lines That Leave Nothing Behind. AA Files, 89-96, Architectural Association School of Architecture.

Evans, R. (1989). Architectural Projection. Architecture and Its Image, (ed.) E. Blau & E. Kaufman, MIT Press.

Frascari, M. (1990). A New Angel/Angle in Architectural Research: The Ideas of Demonstration. Journal of Architectural Education, 44(1), 11-19, Taylor&Francis.

Frascari, M. (2007). A Reflection on Paper and its Virtues within the Material and Invisible Factures of Architecture. From Models to Drawings: Imagination and Representation in Architecture, (ed.) M. Frascari, J. Hale & B. Starkey, 23-33, Routledge.

Frascari, M. (2008). Elegant Curiosity. Log, 12, 66-79, Anyone Corporation.

Frascari, M. (2009). Lines as Architectural Thinking. Architectural Theory Review, 14(3), 200-212, Taylor&Francis.

Fraser, M. (2007). The Cultural Context of Critical Architecture. Critical Architecture, (ed.) J. Rendell, J. Hill, M. Fraser & M. Dorrian, Routledge.

Hewitt, M. (1984). Representational Forms and Modes of Conception: An Approach to the History of Architectural Drawing. Journal of Architectural Education, 39(2), 2-9, Taylor&Francis.

Heynen, H. (2007). A Critical Position for Architecture?. Critical Architecture, (ed.) J. Rendell, J. Hill, M. Fraser & M. Dorrian, Routledge.

Kulper, P. (2020). A (drawn) practice(d) construction: Relational Structuring, Chased. Expanding Fields of Architectural Discourse and Practice: Curated Works from the P.E.A.R. Journal, (ed.) M. Butcher & M. O'Shea, UCL Press.

Manolopoulou, Y. (2020). Open Score Architecture. Expanding Fields of Architectural Discourse and Practice: Curated Works from the P.E.A.R. Journal, (ed.) M. Butcher & M. O'Shea, UCL Press.

Mesquita, A. (2018). Counter-Cartographies Politics, Art and the Insurrection of Maps. This is Not an Atlas, transcript Verlag.

Perez-Gomez, A. (1982). Architecture as Drawing. Journal of Architectural Education, 36(2), 2-7, Taylor&Francis.

Perez-Gomez A., & Pelletier, L. (1992). Architectural Representation Beyond Perspectivism. Perspecta, 27, 20-39, The MIT Press.

Perez-Gomez, A. (2012). The Historical Context of Contemporary Architectural Representation. Persistent Modelling, (ed.) P. Ayres, 13-25, Routledge.

Rattenbury, K., Cook, C., & Hill, J. (2002). Iconic Pictures. This is not Architecture: Media Constructions, (ed.) K. Rattenbury, 57-90, Routledge.

Rendell, J. (2007). Critical Architecture Between Criticism and Design. Critical Architecture, (ed.) J. Rendell, J. Hill, M. Fraser & M. Dorrian, Routledge.

Rendell, J. (2020). Hotspots and Touchstones: From Critical to Ethical Spatial Practice, Architecture and Culture, Routledge.

Siegert, B. (2011). The Map is the Territory. Radical Philosophy, 169, 13-16.

Spiller, N. (2013). The Magical Architecture in Drawing Drawings. Journal of Architectural Education, 6(2), 264-269, Taylor&Francis.

Stoppani, S. (2007). Translucent and Fluid: Piranesi's Impossible Plan. From Models to Drawings: Imagination and Representation in Architecture, (ed.) M. Frascari, J. Hale & B. Starkey, 99-108, Routledge.

Van Gerrewey, C. (2021). Drawing Rescues Architecture. Log, 9-18, Anyone Corporation.

Vesely, D. (1985). Architecture and the Conflict of Representation. AA Files, 8, 21-38, Architectural Association School of Architecture.

Vidler, A. (2000). Diagrams of Diagrams: Architectural Abstraction and Modern Representation. Representations, 72, 1-20, University of California Press.

Yaneva, A. (2011). From Reflecting-in-Action Towards Mapping of the Real, Transdisciplinary Knowledge Production in Architecture and Urbanism, Towards Hybrid Modes of Inquiry, (ed.) I. Doucet & N.Janssens, Springer.

Exploring Experiential Learning Design Practices Grounded in Social Responsibility in Mardin

Betül Toy[a], Yüksel Demir[a]

[a] Istanbul Technical University, Architectural Design PhD Programme, Türkiye
toyb20@itu.edu.tr

Keywords: Experiential Learning, Social Responsibility-Based Learning, Community-Engaged Learning, Social Benefit.

Aim

The study aims to explore strategies to strengthen students' understandings of social responsibility through the outcomes of ITU Mardin design studies, which extends beyond the design studio space in schools and tackles non-hypothetical, real issues through processes conducted directly in the field. This aspect of ITU Mardin design studies (onwards, ITU Mardint) also has the potential to bridge the gap between society and architecture schools. Accordingly, the research mainly focuses on ITU Mardint design studies conducted in Mardin, Türkiye, between 2005 and 2012, which comprise a series of interdisciplinary and integrated design studios, including the application project studio supervised by Cem Altun, the survey and restoration studio supervised by Yegan Kahya et al., as well as landscape studios, all developed in coordination with the architectural design studio.

The concept of social responsibility can be briefly defined as the obligation to take into account the interests of society rather than individual interests. Architecture, as a social action field with a direct impact on society, holds a significant place in this regard. Berman (1990) states that social responsibility for the well-being of society will not develop spontaneously; it requires intention, interest and time. Therefore, architectural education should intentionally and continuously engage students with issues of social responsibility, providing both the time and context necessary for this awareness to emerge and deepen.

The study has been conducted to structure the research in a way that ensures the transfer of a process previously carried out at ITU to future generations in alignment with these objectives, questioning its sustainability, exploring its positive and negative feedback through actors' individual experiences, investigating its socio-spatial contributions to the society, and helping to develop social responsibility-based approaches in architectural education through the expansion of such initiatives as practice research centers, associations, studios, etc. The primary research question of the study is: "What are the socio-spatial impacts of ITU Mardint studios in terms of social responsibility, considering experience, communication and collaboration, reflection, and social benefit?" The study has been structured based on Kolb's (2015) experiential learning paradigm, which has been restructured and expanded in light of the field data from ITU Mardint. Thus, the learning cycle has been redefined around four key components-experience, communication & collaboration, reflection, and social benefit-within the context of social responsibility.

Material and Method

The method of this research can be described as "experience-based action research" methodology, within the theoretical framework of Kolb's (2015) learning paradigm and the methodological framework of action research design. It can be considered, in a sense, as the overlap of methodology and theoretical background that intersect ontologically.

Prepared in alignment with the research question, the semi-structured interview questions constitute the primary method of data collection in this study. Accordingly, data were primarily gathered through reflective interviews conducted with groups composed of (former) students, academic staff, the people of Mardin, and representatives of stakeholder institutions (or institution representatives, onwards), alongside various documents such as researcher and practitioner notes, student projects, posters, booklets, etc. The data obtained from these interviews are analyzed using qualitative analysis methods to explore the complex and context-specific nature of social responsibility. The interview data were examined through content analysis. The analysis of interviews was conducted using MAXQDA to deeply examine participants' reflective thoughts

through code-subcode models and facilitate the identification of patterns, themes, and relationships within the data. Among the ITU Mardint participants reached through the snowball sampling method, 42 out of a total of 132 individuals voluntarily participated in the research, including 21 out of approximately 36 students, 10 out of 26 academic staff, 5 out of 30 individuals from Mardin, and 6 out of 40 institution representatives.

Findings

The findings are analyzed to reveal the students' thoughts on social responsibility in architecture and its role in enhancing their skills such as encountering real problems, collaborating, using regional data, integrating it into their designs, etc. At the same time, these analyses provide an opportunity for the evaluation of the perspectives of academic staff on the studies, the experiences of institution representatives, and the socio-spatial contributions of these studies to the people of Mardin. Participant responses were examined through multiple perspectives of actors using code-subcode models, and the findings contributed significantly to the conclusions of the study. The analysis revealed that people of Mardin primarily addressed issues related to socio-spatial contributions; institutional representatives focused on communication and collaboration; whereas faculty members and students emphasized ITU Mardint's non-hypothetical, proactive, and reactive approaches.
Overall, 88% (n=42) of participants found the experience satisfactory, 5% reported dissatisfaction, and 7% stated they were moderately satisfied. It has been determined that dissatisfaction arises from factors such as lack of communication, insufficient information and publicity, as well as disruptions in project implementation. Participants also stated that they had the chance to explore the region and experience various aspects of Mardin such as its unique geography, daily lifestyle, and climate. Additionally, it has been determined in the study that when the student responses were analyzed, the incorporation of daily life and local data was evident in addressing design problems, with an emphasis on user-centered solutions and communication reflected with the people of Mardin and other stakeholders. When examined in terms of social benefit, it was observed that all participants from Mardin stated that the studies contributed to the preservation of the historical fabric and fostered a change in the perception of the city as a socio-spatial contribution.

Conclusion

In the study, various strategies have been proposed based on the areas where ITU Mardint is lacking. It was revealed that issues such as communication breakdowns, discontinuation of collaborations, and a lack of information sharing must be addressed. It has been revealed that, although challenges such as the discontinuation of the studies, communication gaps, insufficient information, and the non-application of projects were encountered, the majority of participants held positive views regarding the process, contributing to the development of social awareness and facilitating the establishment of university-community collaboration. The feedback received has shown a significant need for university-community collaborative studies, particularly the need for an agile, circular, and sustainable model that integrates academy with the society. The findings of the study indicate that more permanent and systematic strategies need to be developed to sustain community–university collaborations. The development and sustainability of such studies will be crucial for the advancement of experiential learning based on social responsibility & community-engaged learning, which is the primary focus of the research.

References

Berman, S. (1990). Educating for Social Responsibility. Educational Leadership, 48(3), 75-80.
Kolb, D. (2015). Experiential Learning: Experience as the Source of Learning and Development. New Jersey: Pearson Education, Inc.

Urban Destruction in Malatya's Green Belt Project: A Struggle for Public Space or Capitalist Gain?

Furkan Evliyaoğlu[a], Nurbin Paker Kahvecioğlu[b]

[a] Istanbul Technical University, Graduate School, Architectural Design, Türkiye
[b] Istanbul Technical University, Faculty of Architecture, Department of Architecture, Türkiye
evliyaoglu16@itu.edu.tr

Keywords: Green Belt Project, Malatya, Public Space, Urban Demolition, Urban Memory.

Aim

This study examines the partially implemented "Green Belt Project" in the Battalgazi district of Malatya. Initiated by then-mayor Selahattin Gürkan, who described it as his "greatest dream," the project aims to expand the existing Hürriyet Park northward, creating a continuous green zone within the dense urban fabric. Marketed as an unprecedented initiative in Turkey, this park aspires to be Malatya's "Hyde Park" or "Central Park" (Url-1).

However, to expand Hürriyet Park and implement the "Green Belt Project," the demolition of several public and semi-public buildings was necessary, including the State Hydraulic Works (DSI) Service Building and Residences, Malatya İnönü Stadium, Atatürk Indoor Sports Hall, an indoor swimming pool, Şehit Kemal Özalper Vocational and Technical Anatolian High School, and Atatürk Girls' High School. As part of this process, a new municipal building was constructed on the former DSI Service Building and Residences' site, while the DSI facilities were relocated to another part of the city. After the relocation, the old structures were demolished. Similarly, a new stadium was built on the city's outskirts, and upon its completion, the old İnönü Stadium and Atatürk Indoor Sports Hall were demolished. The former stadium site was transformed into the "Nation's Garden." Finally, Atatürk Girls' High School was relocated due to seismic concerns, and its original structure was replaced with the "Nation's Library." The Şehit Kemal Özalper Vocational and Technical Anatolian High School remains standing, as it is a registered historical building (Figure 1).

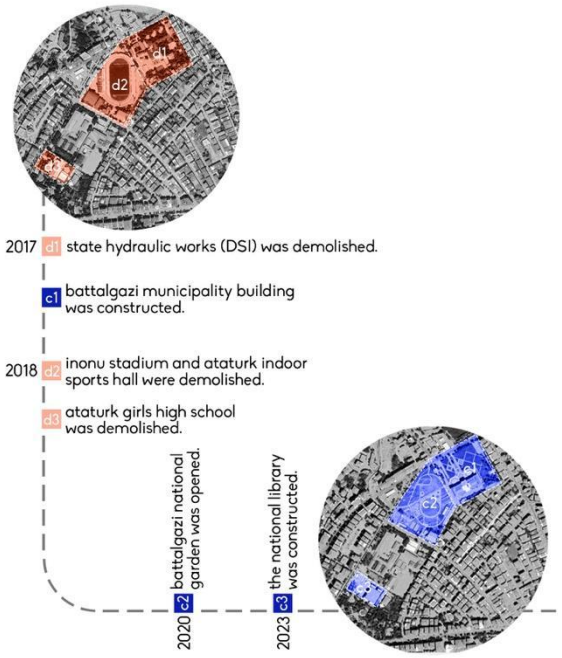

Figure 1. A diagram describing the destruction process (Evliyaoğlu, 2025).

Although the "Green Belt Project" ostensibly aims to create a public recreational space, it has led to the demolition of several significant structures, including the stadium, which held a strong place in urban memory. This study hypothesizes that the project, framed as a struggle to create public space, embodies diverse ideological motivations. Instead of prioritizing public access, the transformations align with broader aspirations such as positioning Malatya as a global city or a branded city. Consequently, these urban spaces have been commodified and instrumentalized for consumption, essentially serving as tools for economic gain (Harvey, 2013). Moreover, projects such as the "Nation's Garden" and "Nation's Library" have been utilized as election campaign promises. The demolition of structures embedded in the city's memory can also be interpreted as a deliberate attempt to erase urban history.

The primary motivation of this study is to decipher the ideological underpinnings of these transformations carried out by state actors. In other words, the research aims to expose the panorama of urban demolitions as a tool of political struggle and to test the hypotheses regarding their underlying motivations.

Theoretical Framework

Public space is generally defined as parks, streets, squares, and recreational coastal areas under public ownership and administration, which urban residents use to meet various needs such as relaxation and socialization (Aksoy & Firidin Özgür, 2020). Beyond these functions, public space is also a site of interaction and encounter, bringing society together and granting visibility to urban dwellers (Akkar Ercan, 2016; Lefebvre, 2014). As such, the public spaces of a city are essential components of the public sphere, serving as arenas for political action and engagement among different social groups and individuals (Bilsel, 2006).

With the rise of neoliberal capitalism, high-value public spaces in city centers have increasingly been transformed into pseudo-public spaces—such as shopping malls and theme parks—designed for consumption and serving only specific segments of society (Smith, 2005). As a consequence of privatization, these spaces no longer function as shared public areas accessible to all but have instead become exclusive domains claimed by particular social groups (Bilsel, 2006).

Material and Method

The demolitions in question involve various actors, including state mechanisms, capital-related stakeholders, and social actors. However, rather than focusing on the perpetrators of these demolitions, this study centers on the urban residents who were affected by them. Therefore, this study is based on qualitative content and discourse analysis of a variety of user comments gathered from Malatya-based local news platforms, media outlets (e.g., Malatya Haber), social media, and from users associated with the physical spaces under study—such as the demolished stadium, schools, and public facilities affected by the "Green Belt Project." The data were gathered through a purposive sampling strategy, focusing specifically on comments related to the demolition of key structures. The analysis followed a thematic framework, aiming to identify recurring discursive patterns—particularly those reflecting nostalgia, ideological critique, and urban memory shaped by environmental transformation. This analysis provides insight into both the political authorities' perspectives and the responses of Malatya's residents.

Findings

Public reactions to the project varied across different segments of society. For instance, some citizens criticized the decision to construct the Battalgazi Municipality Building on the former site of the DSI Service Building and Residences rather than on vacant land, labeling it an example of profiteering. They argued that the reported project cost was misleading, as it failed to include the expenses for constructing the new DSI facilities elsewhere. Others, however, defended the project, asserting that the expenditure was justified.

Beyond the demolition of existing buildings, the project also faced criticism for cutting down numerous monumental trees within the so-called "Green Belt" area. Additionally, incorporating the municipal building into the space, rather than solely preserving it as a green zone, sparked further disapproval.

Similar criticisms were directed at the "Nation's Garden," which replaced the demolished stadium. Initially, many citizens welcomed the project, emphasizing the need for green spaces in an increasingly concrete-filled city. However, one resident

argued that the stadium should have been preserved, as it could have been used for morning exercises, rallies, and concerts. Others suggested that the indoor sports hall and swimming pool should not have been demolished and should have been integrated into the "Nation's Garden." Many users also expressed concerns that the new park would become unsafe at night. Some residents opposed relocating the stadium to the city's periphery, arguing that this decision undermined the city's football culture. Others lamented the loss of personal memories associated with the stadium. One resident, for instance, recalled participating on April 23rd performances as a child and attending football matches with their father, expressing sadness over the demolition.

A significant portion of the comments were ideological. Many believed that the demolitions were politically motivated, pointing out that the stadium bore the name "İnönü" and the sports hall was named "Atatürk." The removal of these names from the new structures intensified public backlash. Critics argued that the demolitions targeted Malatya's historical and cultural values.

Even after the project was completed, criticism persisted, particularly regarding the insufficient number of trees and green areas in the park. Many users claimed that the park was overly dominated by concrete structures and lacked essential recreational elements. Additionally, the park's children's play areas were deemed inadequate, and the presence of surrounding walls was another major point of contention.

The last demolished structure in the project area was Atatürk Girls' High School, which had been deemed structurally unsound before the 2023 Kahramanmaraş earthquakes. The school was relocated, and the "Nation's Library" was built on its former site. However, unlike other transformations, the architecture of the new library drew significant criticism. Many compared it to a prison or a military barracks, arguing that its design bore no resemblance to traditional library typologies. Additionally, residents questioned the rationale behind demolishing the school only to construct a much larger building in its place. Some sarcastically asked, "If you were going to build a library, why demolish the school?" or "Wasn't this supposed to be a green park?"

Conclusion

The "Green Belt Project" was presented by political actors as a series of ambitious initiatives. The Battalgazi Municipality Building was promoted as a "green and smart" structure, the "Nation's Library" was introduced as "Turkey's largest indoor library," and the "Nation's Garden" was marketed as a major public space initiative. However, despite its overarching goal of creating a green belt within the city, the project ultimately fell short. The newly created green spaces remained limited, and multiple concrete structures were added within the area. Moreover, the envisioned seamless integration of green zones with Hürriyet Park was not achieved, resulting in a fragmented and restricted green corridor.

In summary, the project received widespread public criticism. The first major concern was its excessive cost, with many citizens believing that the outcome did not justify the expense. The second major criticism was that the project failed to fulfill its mission of providing a public breathing space, as the park's landscaping elements, such as tree cover, walking paths, and recreational facilities, were deemed inadequate. Lastly, the project was seen as an attack on urban memory, with critics arguing that demolishing structures such as the stadium and schools erased Malatya's historical identity. Additional concerns included the deliberate erasure of names associated with "Atatürk" and "İnönü," reinforcing the perception that these demolitions were ideologically motivated and systematically targeted at Republican-era structures.

References

Akkar Ercan, Z. M. (2016). Endüstri-sonrası kentlerin değişen ve dönüşen kamusal mekânları. Planlama, 26(3), 193-203.

Aksoy, O. A., & Firidin Özgür, E. (2020). Ekonomik, siyasi, toplumsal çekişme alanı ve kamusal bir olgu olarak (kamusal) mekân: "Halk plajı"ndan "Millet bahçesi"ne Ataköy kıyı alanı: Ataköy kıyı alanı'nda 1960'lardan günümüze kamusallık. Tasarım+ Kuram, 16(30), 37-60.

Bilsel, C. F. (2006). Kentsel dönüşüm, çözülen kentler ve parçalanan kamusal alan. Mimarlık, 327(42), 33-34.

Harvey, D. (2013). Asi şehirler: Şehir hakkında kentsel devrime doğru (A. D. Temiz, Trans.). Metis Yayınları.

Lefebvre, H. (2014). Mekânın üretimi (I. Ergüden, Trans.). Sel Yayıncılık.

Smith, N. (2005). The new urban frontier: Gentrification and the revanchist city. Routledge.

Url-1 www.milliyet.com.tr/yerel-haberler/malatya/yesil-kusak-projesinin-ilk-etabi-hayata-geciriliyor-12027743, date retrieved 23.03.2025.

Reading Architectural Memory Through Cinematic Image: Atatürk Cultural Center

İsmail Gökkaya[a], Funda Uz[b]

[a] Istanbul Technical University, Graduate School, Architectural Design Program, Turkey

[b] Istanbul Technical University, Faculty of Architecture, Department of Architecture, Turkey

gokkaya17@itu.edu.tr

Keywords: Architectural Memory, Cinematic Montage, Architectural Representation, AKM.

Aim

The Atatürk Cultural Center (AKM) has maintained its place in urban and collective memory despite its tumultuous history, including a 23-year-long design and construction process, destruction in a 45-minute fire, reopening in 1978, and closure in 2008 for renovations. As Boysan (2005) aptly stated, AKM is a building that has been influenced by "countless people." This study does not seek to document the present state of AKM but rather to explore how its multilayered memory can be traced through cinematic images. Contrary to the traditional understanding of architectural history, the study searches for a memory by following the traces of numerous ignored time-space experiences, not only through conventional representation tools (plans, sections, facades, etc.). The aim is to reconstruct the memory of Atatürk Cultural Center through photographs, narratives, texts, and archives with cinematographic images and to present a narrative far from linear historiography.

Material and Method

The representation of AKM through cinematic montage involves assembling different fragments, images captured at various points in time, and even speculative visualizations of the building before its construction. This research methodologically examines the architectural memory of AKM under three main themes: Memory, Memory of Representation, and Representation of Memory. These categories are designed to explore how the building's memory can be reconstructed and understood through a cinematic perspective. The study employs a range of montage strategies to investigate the intersection of memory, space, and representation. The Atatürk Cultural Center is reimagined as a living archive, where images, written narratives, and layered temporal fragments interact continuously through the lens of the present. Examining AKM in this manner helps reveal the intricate and evolving memory embedded in the building. The different design processes that AKM has gone through—construction, idle waiting, and redevelopment—not only make it a physical structure that exemplifies the architecture of the 20th-century Republic but also a constantly transforming image in Istanbul's collective memory. Its direct relationship with the city and its monumental facade's connection to Taksim Square reinforce its layered historical significance. This layered structure between the past and the present can be revealed with cinematographic montage techniques.

Findings

The idea of constructing an opera house in Taksim first emerged in 1939, within the urban plan developed by French architect and urban planner Henri Prost. As a spatial embodiment of the newly established republic's national identity, the project carried significant symbolic value. While Auguste Perret initially proposed a design in 1939, the foundation was laid in 1946 based on plans by Günay and Kip. The foundation of the building, laid in 1939 based on Prost's proposal and Günay and Kip's plans in 1946, initially reflected the "neoclassical architectural language". The neoclassical architectural language of the period is generally characterized by monumentality, symmetry, classical proportions, and prominent façade features such as columned entrances or arched windows. These early designs aimed for a more traditional, grandiose, and

representative structure, seeking to spatially embody the national identity of the newly established Republic. Although these earlier designs reflected a neoclassical architectural language, economic constraints delayed construction progress.

When Hayati Tabanlıoğlu was commissioned in 1956, the project was redesigned with the modernist approach of the period. The 'Istanbul Cultural Palace' (as it was known at the time), which was the 2nd largest opera house in Europe and the 4th largest in the world when it was opened in 1969, was rendered unusable by a fire that broke out in November 1970 during a performance of The Crucible. After repair and renovation works in 1973-78, it was reopened as the Atatürk Cultural Center. Due to the constraints imposed by the previously constructed concrete frame, Tabanlıoğlu had to adhere to this existing structure (Ganiç, 2016). However, in contrast to earlier monumental design proposals, he envisioned a transparent facade facing Taksim Square, which became a defining feature of the building. As Tabanlıoğlu stated, "This facade was designed to be unlike any other existing building facade in the world, yet it possesses an artistic identity" (Ganiç, 2016, p. 68). Tabanlıoğlu's modernist approach, in contrast to the previous neoclassical grandeur, was distinguished by functionality, transparency and the use of industrial materials. The existing reinforced concrete frame influenced Tabanlıoğlu's design decisions and imposed certain restrictions on him. This led to the adoption of modernist and fluid solutions in the general form and interior arrangement of the building, in line with what the existing structure allowed.

The Atatürk Cultural Center has a very rich archive in terms of historical and spatial memory. The Tabanlıoğlu Archive, especially located in Salt Galata, is valuable in that it contains documents from different periods of the structure. This archive includes not only architectural plans and drawings but also detailed process photographs related to the structure. When such archive materials are brought together using the cinematographic montage method, the memory and transformation processes of the Atatürk Cultural Center can be examined in their entirety. Cinematic montage, as an analytical tool, employs various techniques derived from Eisenstein's montage theory, including intellectual montage, rhythmic montage, tonal montage, and speculative montage. Intellectual montage traces the building's urban footprint and its evolving relationship with the city through aerial imagery from different periods, categorizing it into three layers: pre-construction, original structure, and reconstructed building. Rhythmic montage visually documents the architectural and experiential differences among the various design phases. Overtonal montage explores the spatial atmosphere of AKM, particularly its monumental facade facing Taksim Square. Finally, speculative montage generates digitally manipulated and collaged images of AKM, enabling alternative temporal and spatial readings (Eisenstein, 2014).

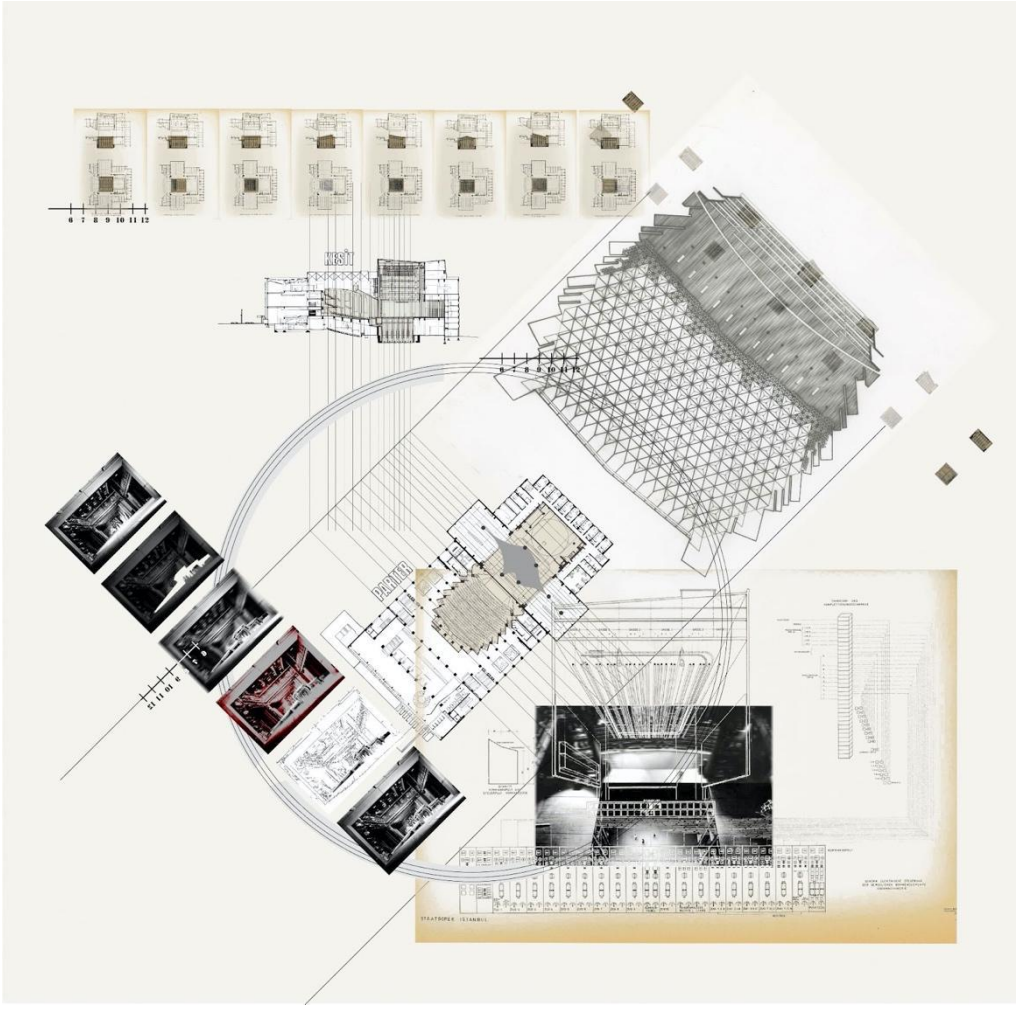

Figure 1. Rhythmic Montage (İsmail Gökkaya, 2025).

One example of a cinematic image study (Figure 1) focuses on the main hall of AKM, particularly the stage-audience relationship. The study visualizes the movement and temporal sequences of the mechanical and electrical stage systems, creating a dynamic representation of spatial memory. The interior configuration of AKM, especially the stage-audience relationship in the main hall, is the architectural expression of the functional heart of the building. The gradual rise of the audience area, the central location of the stage and the acoustically optimised ceiling and wall details are designed to ensure that the performance is perceived as an interactive experience. The complex mechanical and electrical structure of the stage systems demonstrates not only a technical functionality but also that the stage is a living space that transforms within itself. Visualising the temporal sequences of these systems allows the space to be perceived not only as a static volume but also as a dynamic 'performance machine'.

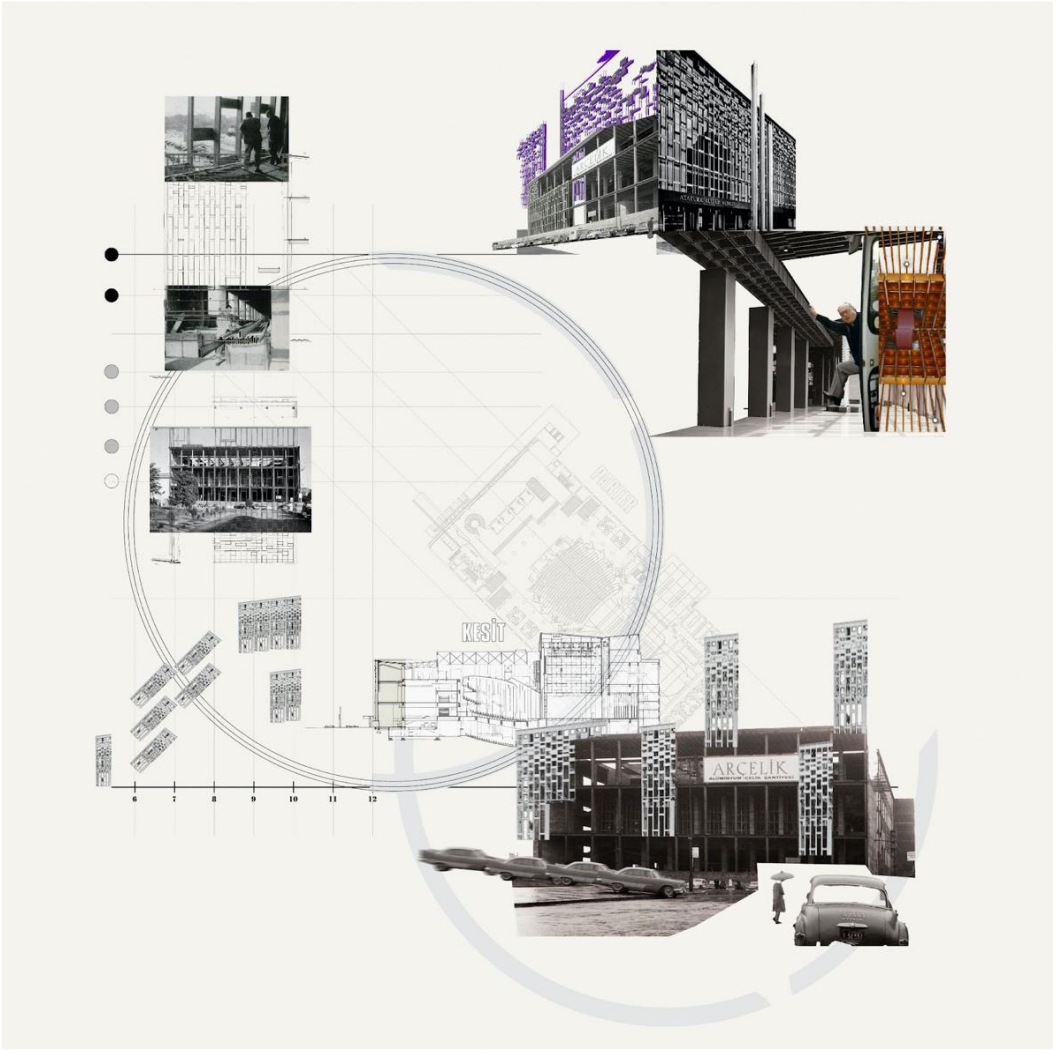

Figure 2. Overtonal Montage (İsmail Gökkaya, 2025).

Another experiment (Figure 2) examines the iconic steel-aluminum facade, which serves as both a backdrop and an active participant in the city's theatrical life. The monumental façade of the AKM overlooking Taksim Square is the most striking expression of Hayati Tabanlıoğlu's modernist vision. Steel and aluminum materials were preferred in its design with the intention of creating a constantly changing surface with light and reflections. This transparency opened the interior of the building to the outside, creating not only a performance space, but also a dynamic urban interface that participated in the city's own 'real life drama' as a stage and audience. The fact that the initial concept of the façade was created by Tayman, implemented in collaboration with Boysan and Arçelik Construction Department, and produced in Arçelik workshops with technical support from Germany (Aluminium-Walzwerke Singen) shows that this architectural element is not only aesthetic, but also the product of a complex production and industrial cooperation process. The fact that it was completely rebuilt in Türkiye by the Türkeli company after the 1971 fire emphasizes that the façade is not only a design but also an indicator of national construction capacity (Uz, 2017). As Akcan (2013) asserts, "AKM is as much a stage for the performances inside as it is a backdrop and spectator for the real-life drama unfolding in Taksim. The spatial atmosphere and architectural expression of this monumental façade are deeply investigated through the overtonal montage technique. Overtonal montage questions how the façade has produced an image in different periods. By examining both the façade's installation and its

relationship with the square, it is clarified how the façade is perceived not only as a physical boundary but also as a dynamic part of the city and a focal point of emotional connection.

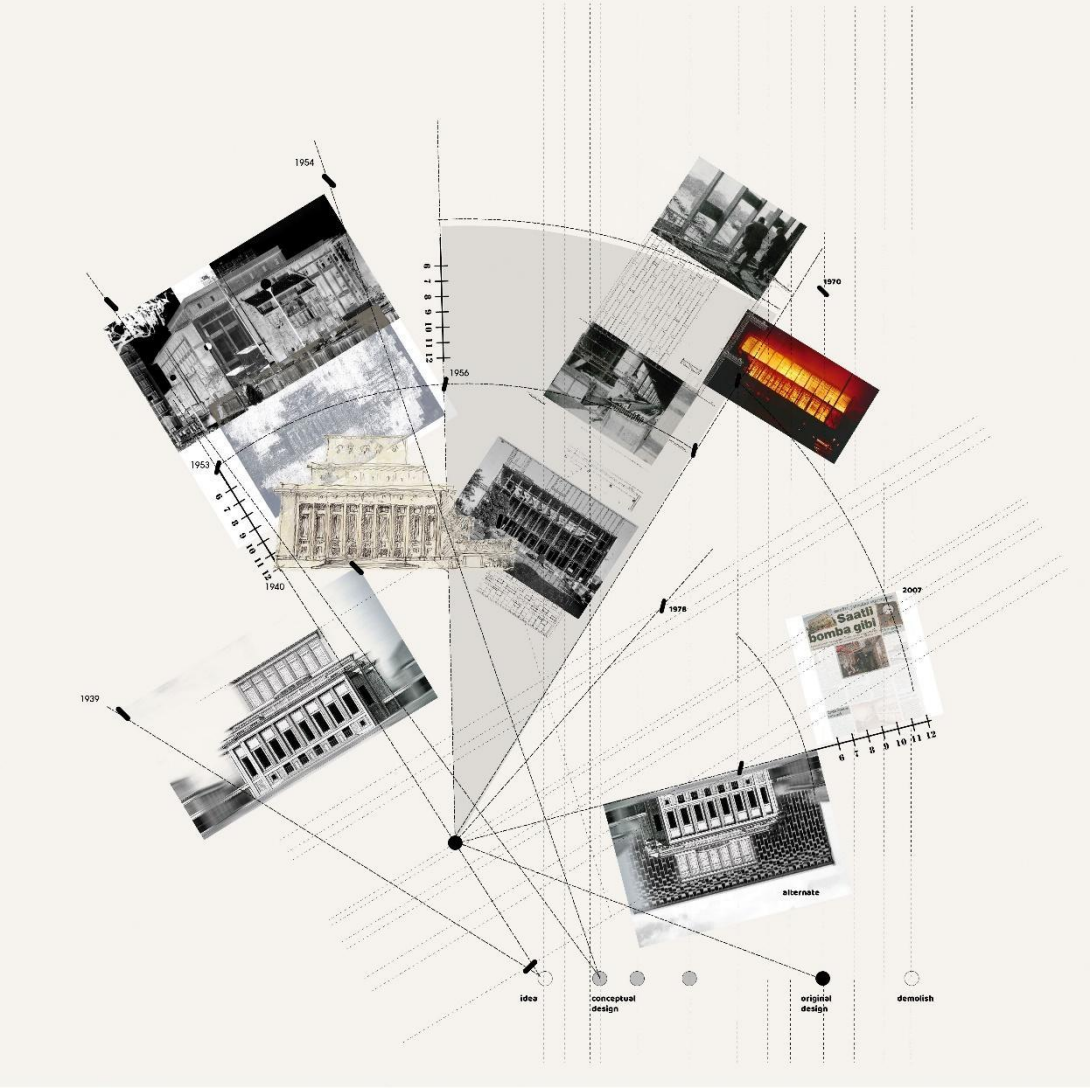

Figure 3. Speculative Montage (İsmail Gökkaya, 2025).

Speculative montage (Figure 3) allows for different thought experiments on the architectural composition and spatial potentials of the AKM. This technique combines existing archival materials (plans, photographs) with digital manipulations to visualize unbuilt versions of the building, alternative uses or hypothetical states in different time periods. For example, it explores architectural scenarios such as how spatial arrangements in early plans could be integrated into the present-day structure or how a different design approach in post-fire restoration could change the spatial flow of the building. This shows that the AKM is not only a completed building, but also a spatial archive that can be continuously re-imagined.

Conclusion

In the previous sections, the place of the Atatürk Cultural Center (AKM) in collective memory, its historical processes and spatial transformation were discussed. The study examined not only the transformation of the Atatürk Cultural Center as a physical structure but also how it exists as a constantly evolving image in the cultural memory of Istanbul. Many layered

elements, from the design and construction process of the building to its history interrupted by fire, reconstruction processes and the strong relationship it establishes with Taksim Square with its transparent façade, were analyzed with cinematographic montage techniques. An image inventory of the AKM was made using archive photographs, plans, written narratives and digital collages, and its memory was reconstructed through elements such as the stage-space relationship and façade design. In this context, the research conducted with Eisenstein's montage techniques revealed the AKM as a memory space that is constantly reshaped in terms of time and space, rather than a static structure. In conclusion, the findigs demonstrates how cinematic montage serves as a powerful analytical tool for reconstructing architectural memory. By moving beyond linear historiography and integrating archival imagery, textual narratives, and speculative visualizations, AKM's evolving identity is revealed as a continuous dialogue between past and present. This method not only offers an alternative way of perceiving AKM but also provides a broader framework for understanding architecture as a dynamic and temporal entity within urban memory.

Acknowledgments

This paper is based on a master's thesis supported by the Scientific and Technological Research Council of Turkey (TÜBİTAK) – BİDEB 2210-A National Graduate Scholarship Programme.

References

Akcan, E. (2013). Bir cepheyi paylaşmak: Parşömen olarak AKM ve toplumsal bellek [Sharing a facade: AKM as a parchment and collective memory]. Mimarist, 13(48), 85.

Boysan, A. (2005). Ne güzel günlermiş!: yaşantı [What beautiful days!: A memoir] (Vol. 662). Yapı Kredi.

Eisenstein, S. (2014). Film form: Essays in film theory. Houghton Mifflin Harcourt.

Ganiç, K. (2016). Kentsel yapıtlar üzerinden bir mekansal bellek okuması: Atatürk Kültür Merkezi (AKM) [A spatial memory reading through urban works: Atatürk Cultural Center (AKM)] (Doctoral dissertation, Fen Bilimleri Enstitüsü [Institute of Science]).

SALT Research. (n.d.). Gültekin Çizgen Archive. Retrieved May 23, 2025, from https://archives.saltresearch.org/handle/123456789/87140

Tabanlıoğlu Family. (n.d.). SALT Research Archive. Retrieved May 23, 2025, from https://archives.saltresearch.org/handle/123456789/214862

Tabanlıoğlu Family. (n.d.). SALT Research Archive. Retrieved May 23, 2025, from https://archives.saltresearch.org/handle/123456789/214784

Tabanlıoğlu Family. (n.d.). SALT Research Archive. Retrieved May 23, 2025, from https://archives.saltresearch.org/handle/123456789/214786

Tabanlıoğlu Family. (n.d.). SALT Research Archive. Retrieved May 23, 2025, from https://archives.saltresearch.org/handle/123456789/214877

Tabanlıoğlu Family. (n.d.). SALT Research Archive. Retrieved May 23, 2025, from https://archives.saltresearch.org/handle/123456789/214889

Tabanlıoğlu Family. (n.d.). SALT Research Archive. Retrieved May 23, 2025, from https://archives.saltresearch.org/handle/123456789/215002

Tabanlıoğlu Family; Günay, R. (n.d.). SALT Research Archive. Retrieved May 23, 2025, from https://archives.saltresearch.org/handle/123456789/214851

Uz, F. (2019). Alüminyum ile tasarlamak: 1970'lerde Ankara mimarlığında alüminyum [Designing with aluminum: Aluminum in 1970s Ankara architecture]. Journal of Ankara Studies/Ankara Araştırmaları Dergisi, 7(1).

Fluid Bodies of Space: Rethinking Architectural Relationality Through The Medusa Head

Esra Yüksek[a], Sıdıka Aslıhan Şenel[a]

[a] Istanbul Technical University, Faculty of Architecture, Architectural Design Program, Türkiye
yuksek18@itu.edu.tr

Keywords: Spatial Ecology, Fluid Bodies, Relationality, Vulnerability.

Aim

It always begins with the Medusa Head, catching me in the garden of the Istanbul Archaeological Museums. She's not tucked away in some sterile gallery but sits out there, majestic yet fragile, her stone face shifting under rain, plants, fungi, and time. Each visit shows a new face of her. Myths, the space it occupies, the keystone of an old structure—all of its relationships intertwine, and new states of being, fluid bodies, emerge. She's my way into this research, a quiet call to rethink architectural space not as the fixed, invulnerable volumes we're taught to design, but as fluid bodies, open to wounds and transformation. This study aims to explore how spaces, especially this museum, live through their entanglements, challenging the static ideals of architectural design with a feminist lens that's personal and porous. As a young woman, architect, researcher, and student, I ask: what if we design for relationality, for vulnerability, instead of control? Rooted in feminist research methods and pedagogy, this isn't abstract theory. It's a dialogue with the museum, a 250-year-old complex that's more than a repository or static archive, but a spatial ecology of social, material, fictional, and trans-temporal dynamics (Figure 1.).

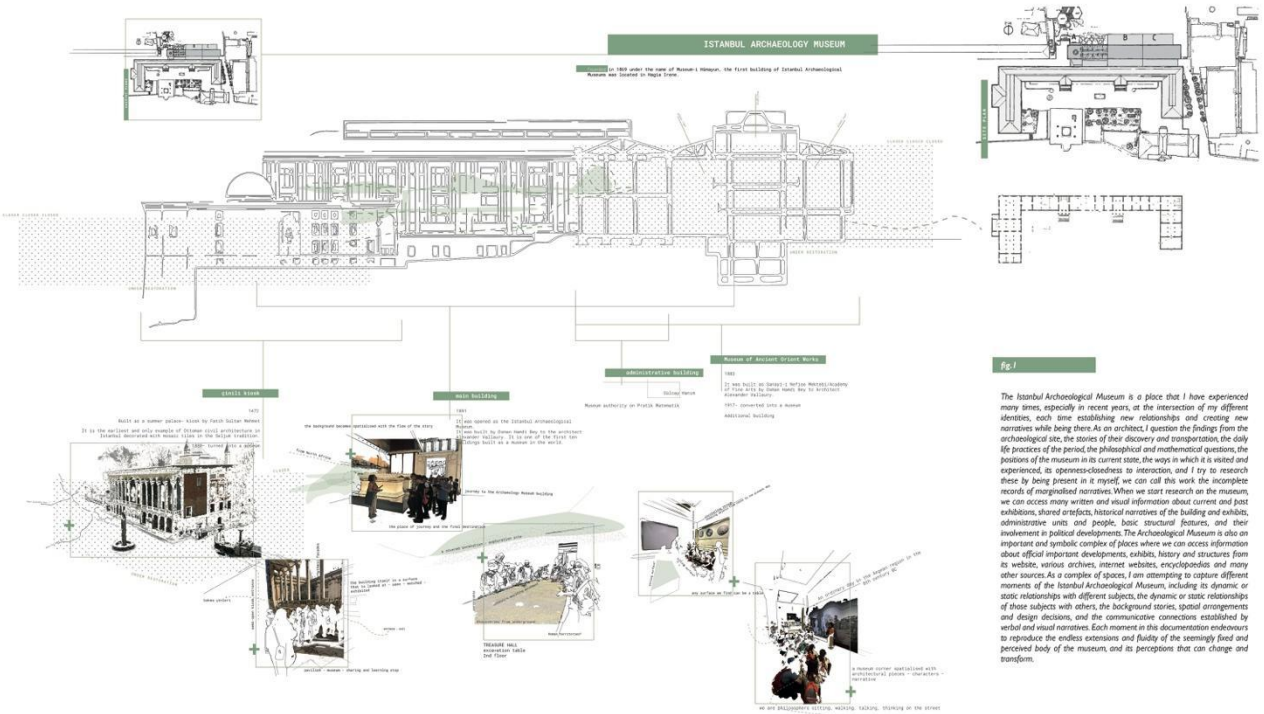

Figure 1. Multi-layered and multi-relational mapping trials about the Istanbul Archaeology Museum.

Material and Method

The Medusa Head stands in contrast to the museum's imagined autonomy: a sterile, regulated space that architectural norms might demand. My methodology, like the spaces that are the subjects of the research, defines a multi-layered, variable, and fluid production process. It's not a precise blueprint or a key solution to an architectural problem; it's about wandering the museum space, sketching at the corners, and looking for alternative methods. Later, I dig into archives and research, weaving with on-site mappings, architectural drawings, narratives, and performances to construct altering stories of the space. With students, I've led "Mathematics in the Museum" events, pausing at corners like the sarcophagus hall, where Osman Hamdi Bey's excavated finds from the Sidon site. How these massive pieces moved from Lebanon to Istanbul, and how the hall's layout and visual narratives shape their story. It's a method of co-creation, not observation. I'm not outside this but part of it, my identities are intersecting with the museum's actors, from artifacts to visitors (Figure 2.).

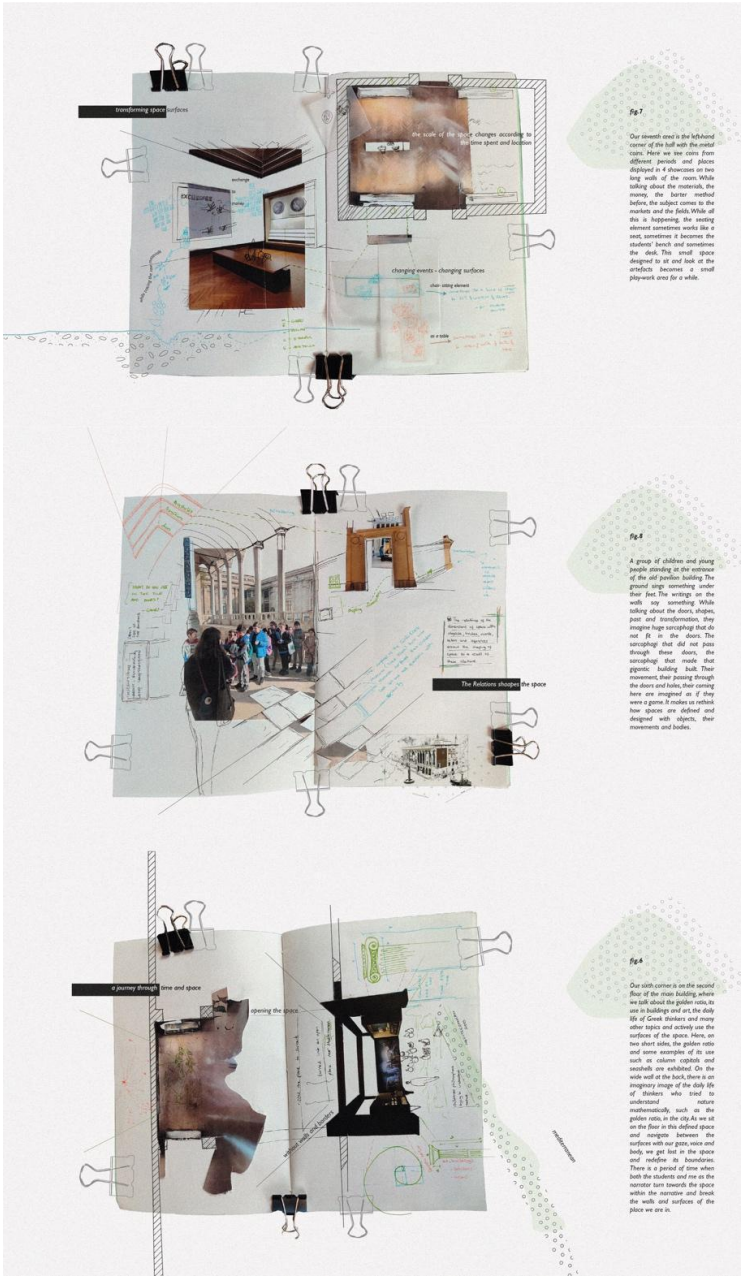

Figure 2. Istanbul Archaeology Museum's reproduced multi-layered fluid bodies I.

Neimanis (2019) guides my research practice here, rejecting "we" for "I'm a body of water," urging us to ask not just what a space is, but where, how, when, and with what it flows. Trying to think and make sense of architecture and space with such a fluid concept of the body makes it possible to critically reconsider our view of them and to be aware of the potential of a more relational, dynamic, nomadic, fluid space and spatial installation as opposed to static-autonomous perceptions of architecture. Rich (1984) adds that there's no single state of being. The Museum's halls and corners change dynamically, shifting their bodies like a body of water. Along with feminist literature, research about agency plays a critical role in this research-design study. In his text Reassembling the Social, Bruno Latour uses the Actor-Network Theory (ANT) to show that the social world consists of dynamic relations rather than a static structure. With this approach, Latour (2013) argues that the subject-object distinction in social studies should be overcome and that each actor should be given real importance. When talking about space, it may be a critical nodal point to think about the whole network of relations established with human and non-human, 'other' actors, and to see the care relations established by the actors in this network of relations with each other in a non-hierarchical manner as valuable. Thanks to the care-oriented collaborations established by the actors with each other, the space tries to live a hybrid life together with them, not despite them. Without seeking stability, it continues its existence in an unpretentious manner and by transforming between different body states.

Findings

These fluid bodies take shape through mappings that are transformed across scales and senses. In the sarcophagus hall, students and I construct narratives of objects and spaces that brought those heavy relics here, their display blurring boundaries between continents and times. The excavation site corner recreates digging gestures indoors, its surfaces and tools forming a small ecology of fluid narratives of excavating actions. In the Troy room, a 3D animation plane and a cross-section of a mound allow us to imagine between scales and temporal plans that overlap with the physicality of the museum, revealing how perception changes with the relationships between actors. These multi-layered mappings are not just recordings; they construct the body of the museum, making its intersectionality and fluidity visible.

Neimanis' figurations (2019) fuel this, opening up planes where space is fragmented and reshaped, while Stengers' ecology of practices (2011) frames it as a living network of actions and subjects. I'm not pinning the space down; I'm producing with its ecology, seeing its wounds as strengths, building situated knowledge that's feminist, embodied, and never universal. This subject I am discussing is trying to turn conventional, rigid, static architectural design on its head and make the possibility of other potentials possible. We're taught to design spaces that are resistant, durable, controlled, and human-centric. But the Istanbul Archaeological Museum's fluid bodies, also Medusa's, describe other kinds of spaces. Its physical structure may not shift daily, yet its interior is constantly becoming through artifacts' narratives, visitors' steps, and restoration's touch. The sarcophagus hall's design doesn't just hold relics; it leaps across geographies, its fluid body mixing past and present. The olive tree corner redesigns a corridor into a multi-temporal commons, its spatiality alive with imagined uses. The excavation site's ecology redraws boundaries, letting us inhabit archaeological time through design gestures. The Troy room's layered scales show how design can multiply a space's states, not fix them.

Conclusion

These findings reveal the museum as a vibrant, reshaping entity, its boundaries transgressible, its control an illusion. Tsing's Matsutake (2015) finds a resonance here; survival is not about stability but adaptation, a lesson for architectural design practices where fluidity is more potential than permanence. The museum's fluid bodies, documented through these corners, challenge static norms, offering a design practice that bends with its ecology, not against it (Figure 3.).

This research reimagines architectural design through relationality and vulnerability, with the Istanbul Archaeological Museums as a spatial ecology. It's not a monolith but a series of spaces, alive with me, Medusa, movement, time, and countless actors. My conclusion isn't a rulebook; it's a call to design spaces that reflect this interplay, that embody historical and contemporary dynamics through openness. Feminist objectivity anchors this, valuing the situated over the universal, my voice as architect and educator threading through (Haraway, 1988). For the conference, I bring a museum that's more than its walls, a fluid, evolving design where every crack, every relation, tells a story. It's a bit wild, a bit poetic, but that's an architectural narrative in between theory and practice.

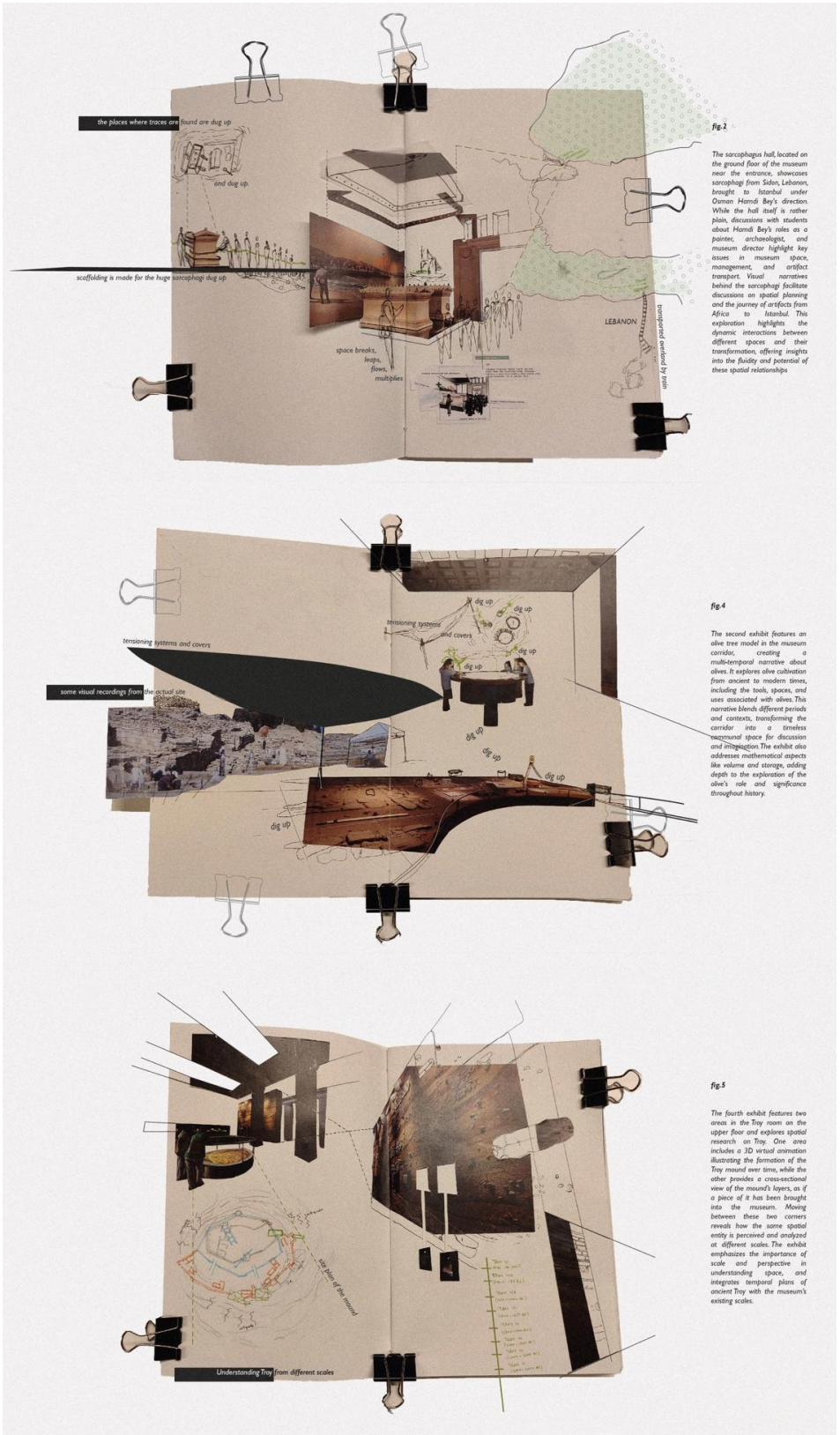

Figure 3. Istanbul Archaeology Museum's reproduced multi-layered fluid bodies II.

References

Haraway, D. (1988). Situated Knowledges: The Science Question in Feminism and the Privilege of Partial Perspective, Feminist Studies, Vol. 14(3), pp. 575-599.
Latour, B. (2013). Reassembling the Social. An Introduction to Actor-Network-Theory. Journal of Economic Sociology, National Research University Higher School of Economics, Vol. 14(2), 73-87.
Neimanis, A. (2019). Bodies of Water: Posthuman Feminist Phenomenology. Bloomsbury Academic.
Rich, A. (1984). Notes Toward a Politics of Location, Lewis, R. and Mills, S. (eds.), Feminist Postcolonial Theory. Routledge, 29-42.
Stengers, I. (2011). Cosmopolitics. University of Minnesota Press.
Tsing, A.L. (2015). The Mushroom at The End of The World. Princeton University Press.
Url-1 https://archives.saltresearch.org/, date retriewed 20.11.2024.

Archival Encounters: Rewriting Istanbul Women's Works Library and its Memory Through Bodily Practices

Seray Rusçuklu[a], Sıdıka Aslıhan Şenel[b]

[a] Istanbul Technical University, Graduate School, Architectural Design Program, Türkiye
[b] Istanbul Technical University, Faculty of Architecture, Department of Architecture, Türkiye
ruscuklu17@itu.edu.tr

Keywords: Feminist-Objective Knowledge, Library, Archive, Spatial Dialogue.

Aim

In architecture, research space is often seen as a controlled, rational structure that produces objective knowledge through predetermined inputs and singular outcomes. This reinforces a hierarchical dynamic, positioning the researcher as the active subject and the research object as passive, leading to a singular, absolute conception of knowledge. The knowledge produced is definitive and singular, establishing a one-sided, hierarchical relationship between the researcher and the research object, placing the object in a passive position within the research space. The precise production process of objective knowledge eliminates room for error and does not allow for any deviation. This normative approach thus reduces the research space to a linear framework aimed at ensuring predictable outcomes in the research process. This paper's aim is to examine the potential of a non-human-centered gaze in the research space and its multi-layered architectural representation. The study challenges the linear and predictable nature of research space by examining how rethinking the relationship between the controlled research interior and the exterior realm of shared knowledge can embrace uncertainty, fostering more dynamic and exploratory environments through the research by design.

Material and Method

As a critical dimension of the discussion, feminist theory and research by design emerge as potential methods for questioning the nature of knowledge process and its architectural representation. Donna Haraway's "situated knowledge" critiques claim of objectivity, arguing that knowledge is always produced from specific positions. She challenges traditional views of science as neutral, emphasizing that diverse backgrounds shape knowledge itself (Haraway, 1988). In such a framework, the research space that perpetually evolves, the researcher and the research object are no longer distinct; they transform into, learn from, and influence one another.

Fiction, as research by design method, serves as a critical tool for rethinking the interior of the research space, where feminist-objective knowledge is produced and continuously multiplied through overlooked narratives. Le Guin's fiction weaves layered temporalities, using narrative as a political tool to critique contemporary worlds rather than imagining unreal spaces (Naimon&Le Guin, 2018). Rather than only constructing imaginary worlds, it serves as a tool for critical engagement with contemporary realities. In literature, fiction functions as a feminist-political instrument, creating alternative modes of writing. Similarly, incorporating fiction into architectural practice and representation becomes essential for amplifying marginalized voices and generating alternative forms of architectural knowledge.

Using fiction as a creative method in architectural representation is essential for amplifying the voices of marginalized agents and generating alternative forms of architectural representation. Stead and Frichot also introduce fiction in architecture as another creative thinking method. Ficto-criticism is a writing practice that combines essay, criticism, and storytelling (Stead&Frichot, 2020, pp.15-16). As actions shift between reality and fiction within spaces, unexpected spatial and temporal intersections arise, exposing the diverse agents engaged in feminist-objective knowledge production. These dynamics manifest through the body's engagement with space. These relationships will unfold through the body's movements in, around, and beyond space within the specific context of the work with the help of creative spatial dialogues.

Findings

The laboratory, frequently depicted in fiction literature, serves both as a physical space and a metaphor, offering a critical framework for analyzing the interaction between research subjects and objects. This study explores the laboratory in two dimensions: first, as a physical space that facilitates experimentation, and second, as a conceptual catalyst that, through its fictional nature, inspires new spatial possibilities for feminist knowledge production. In the novel Frankenstein, Mary Shelley envisioned a researcher creating "a hideous creature". The ethical tensions between researcher (Mr. Frankenstein) and subject (the monster), both sharing the same name, exemplify the complex dynamics between agents within the research space (Shelley, 2017). Shelley defines the space where Frankenstein was created as a laboratory rather than a room, emphasizing the experimental nature of the process and its unpredictable results (Shelley, 2017, p.143).

On the other hand, Latour and Woolgar consider laboratory practice as a literary writing and translation system (Latour&Woolgar, 2013, p.246). Translation typically understood as the researcher's application of symbolic representation onto the research object implies a hierarchical relationship, thereby neglecting the significance of bodily movements and actions within the laboratory. The study questions the potential of translation as an architectural act that takes place within the research space through bodily practices. Writing and recording thus becomes a way of communicating with the research object through research space. Information does not transfer directly from the laboratory bench to the world; it carries its own temporality and spatiality. The involvement of human and non-human agents in the research process, as well as their interactions within the research space, is frequently overlooked. In contrast, feminist knowledge resists de-historicization by recognizing research outcomes as one of many possible truths. Informal communications and the documentation of bodily practices further politicize and feminize the research process and its architectural representation.

The research extends to the Women's Works Library and Information Center in Istanbul, the first and only women's library and information center in Türkiye. Situated within an 18th-century Fener House, the library serves as an evolving research laboratory, shaped by the embodied and archival practices of its users. Housing a diverse collection of letters, photographs, and documents from women artists, writers, researchers, and activists, the archive-library actively integrates women into history by preserving their narratives. This process extends visibility to non-human agents involved in archival practices, emphasizing the dynamic and embodied nature of research within the archive. The main research question arises from the library space: "How can alternative narratives of agents and their relations, obscured in normative history, reframe the archive-library's temporal spatiality through female bodily archival practices?"

Karen Barad's concept of intra-action challenges conventional notions of interaction, asserting that objects, people, and forces emerge through entanglements (Barad, 2007, p.33). Grounded in Piaget's notion of spatial engagement, this study reframes act-ings on space through Barad's lens as creative spatial dialogues, constructing the research space's temporality through fiction. Spatial knowledge is acquired through movement in space (Piaget, 1964, p.179). This study proposes that research, as demonstrated in spatial sequences drawn from within the library (Figure 1.), creates tangible connections with architectural elements such as stone arches, reinforced wooden staircases, niches, and windows. These features shape the physical movement of bodies and objects, influencing the research process and imbuing it with spatial actuality. Building on this idea, research space is continuously reconstructed through the actions of human and non-human agents.

Figure 1. Spatial Dialogue Frames and Creative Spatial Dialogues Between Library and Bodies As An Alternative Method for Architectural Representation (Rusçuklu, 2023).

To illustrate this, the study employs a fiction-construction method, layering archival research with speculative narratives to generate alternative architectural representations of the research space and its often-overlooked characteristics. Sculptor Zerrin Bölükbaşı, whose works are found within the Library's archive, is examined to explore how the subject within the research space is constructed through bodily practices. The Women's Library is read in conjunction with Bölükbaşı's archival materials, revealing how sculpture, research, and archival practices intertwine across different temporal layers. The creative spatial dialogues established between the researcher and the research object (Figure 2. and Figure 3.) dissolve traditional hierarchies, proposing an alternative approach to architectural representation and construction. In this way, it is found that constructing creative spatial dialogues enables a multi-temporal and layered architectural representation of the research space, transcending normative archiving practices (Figure 4. and Figure 5.).

Figure 2. Non-Human Agencies in the Library (Rusçuklu, 2024).

Figure 3. Bodily Practices in the Library (Rusçuklu, 2024).

Figure 4. Transcending the Normative Archiving Practices (Rusçuklu, 2025).

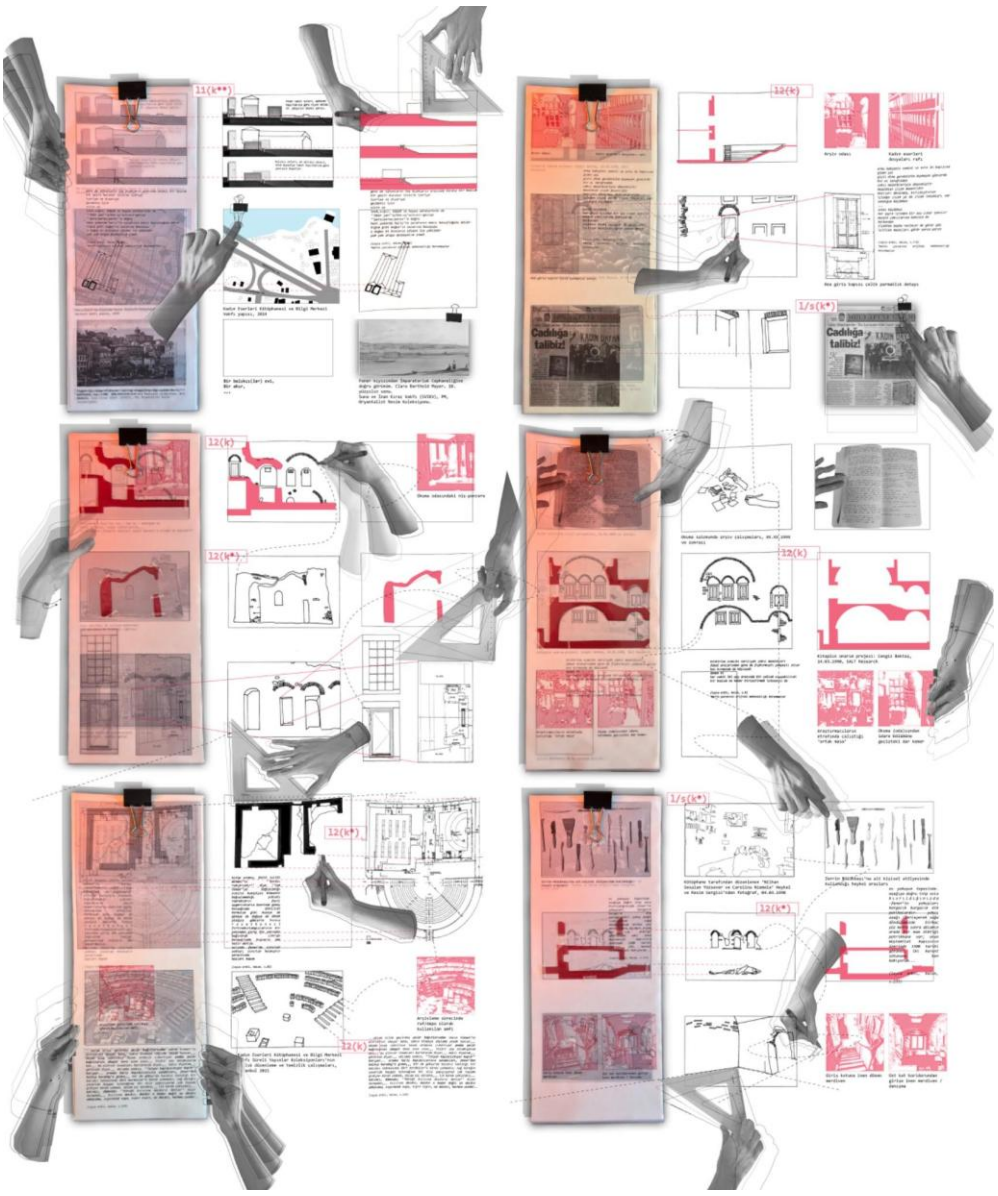

Figure 5. Transcending the Normative Archiving Practices-2 (Rusçuklu, 2025).

Conclusion

Consequently, the paper challenges the hierarchical and static nature of research spaces by proposing a non-human-centered gaze and exploring the entanglement of human and non-human agents in knowledge production. Through feminist-objective knowledge, fiction, and bodily archival practices, the research repositions the archive-library as an evolving laboratory, where spatial and temporal dynamics unfold beyond normative frameworks. By employing a fiction-construction method and mapping bodily interactions, the study demonstrates how alternative representations can reveal the temporality of research space. Ultimately, this approach offers a multi-layered architectural representation that disrupts conventional research methodologies, fostering a more dynamic and inclusive framework.

References

Barad, K. (2007). Meeting the Universe Halfway: Quantum Physics and the Entanglement of Matter and Meaning. Duke University Press.
Frichot, H. and Stead, N. (Eds.). (2020). Writing Architectures: Ficto-Critical Approaches. Bloomsbury Visual Arts.
Latour, B., Salk, J. and Woolgar, S. (2013). Laboratory life: The Construction of Scientific Facts. Princeton University Press.
Le Guin, U. K. and Naimon, D. (2018). Ursula K. Le Guin: Conversations on Writing. Tin House Books.
Piaget, J. (1964). Cognitive Development in Children. Journal of Research in Science Teaching, 2(2), 176-186.
Shelley, M. (2017). Frankenstein: Annotated for Scientists, Engineers, and Creators of All Kinds. Mit Press.

The Potentialities, Displacements, and Spatial Projections of Concepts

Ümran Aydın[a]

[a] Beykoz University, Department of Architecture, Turkey
umranaydin@beykoz.edu.tr

Keywords: Aesthetics, Conceptualization, Spatial Layer, Spatial Transformation, Tectonics.

Aim

The space, which is both the primary tool and object of architectural production, describes a multi-layered dimension through the elements it contains and the possibilities it provides. In other words, space points to a realm beyond its mathematical boundaries: how do we perceive through the mediation of space? What is the social, communal, and intrinsic knowledge produced by this perception? What potentials and healing aspects does this knowledge bring to the surface? In short, what does space mediate in its purest form, and how, why, and to what end? In order to bring the complexity generated by this question to a reasonable level, space is subjected to a deconstruction within the context of work. This deconstruction is necessitated by the fact that the more we touch space, the more it dares to approach us in the same way; as we alter the space, the space changes us. The first layer of space is unfolded through the existing: it is analyzed through its material and immaterial, real and virtual, physical and atmospheric components. How space provides a foundation and time and the components through which it achieves this are examined. The relationships within the tectonic structure of space manifest themselves in this layer, appearing as a structure, a stage, or a foundation. In the second layer, the perceptual and sensory dimensions of space on the individual are unraveled: perception enables space to produce meaning, here, space is taken beyond mere existence and acquires an aesthetic dimension that can be both learned and felt. The third layer is the meaning-driven knowledge that is unfolded: in this realm, the inputs and outputs of space in the social dimension through power relations, decision processes, agents, and authors are explored. The political potentials of space not only generate knowledge in this layer but also transform and redistribute it. With this tripartite deconstruction, answers are sought to the question of what the possibilities of space are in terms of affect, by weighing the distribution of being, meaning, and knowledge within space. On the other hand, this deconstruction reveals that when space reaches a certain fullness in its tectonic, aesthetic, and political layers, it gains the ability to offer perception, produce emotion, and distribute knowledge. Thus, space assumes an authoritative position.

These deconstructions can be elaborated as follows:

- Ontological-Layer, Tectonic — What exists in space?
- Phenomenological-Layer, Aesthetic — What is the meaning produced by what exists?
- Epistemological-Layer, Political — What knowledge does the produced meaning offer?

Material and Method

The tripartite conceptual deconstruction begins with the meaning code attributed to the material in the tectonic aspect. This corresponds to Semper's (1989) description of the four elements and the harmony it creates with perception. This initiative incorporates an anthropological perspective on the origins of architecture. These four elements, which also allow similar readings in the traces of traditional arts, carry a presentation beyond the pure form of being. In other words, the aforementioned origins, which are not treated materially, trigger certain behaviors and shape communications; on the other hand, they have already emerged from here. For example, the hearth, being central, statically describes the beginning, where people gather, meet, form alliances, and organize; enclosure, by marking a boundary, completes the instinct for protection that inherently thrives within its material presence. For instance, a stone on the sidewalk, beyond its materiality, invites people to stop, wait, and can even become the focus and trigger of a potential conversation. As a cast, space leans on the aesthetic concept with its movements and perceptible states. In this case, aesthetics does not present itself as a form of beauty; it integrates as an experience and a mode of perception into space (Rancière & Gage, 2019). In this way, space

becomes an area where affect and sensation spread. The aesthetic perspective emphasizes the meanings added to an object rather than its materiality (Perniola, 2013). This perspective makes the world perceptible and facilitates the organization of social structures, the shaping of behavioral patterns, and the direction of communication preferences. A simple illustration of this is the paving stone; its materiality invites bodily actions and suggests possibilities.

Rancière's (2019) ideas about the interaction between perception and sensation offer another dimension of the potential enabled by space. Here, the capacity of politics rises, incorporating the interaction between space and body. The micro-decisions space makes about where we will see, hear, or walk evolve into macro-level practical ideas and creative emotions after perception. Aesthetics, by dispersing the senses, can transform social order; its autonomy surpasses issues of representation or expressing knowledge systems. In this way, space becomes a place of organization, presenting a political narrative. Aesthetics is the configuration of experience, and thus, it shakes, wraps, and redistributes knowledge. Decisions made regarding the relationships to be established, the places to be seen, are political, and the state of being observed is hidden within the perceptible stimuli emitted by space (Rancière, 2020). The relationship between aesthetics and epistemology, when considered in the context of space, is fundamental in a philosophical sense, as aesthetics invokes curiosity about knowledge, making it a primary authority. Aesthetics serves as a tool, desire, or curiosity for accessing knowledge of a situation triggered by a spatial condition. This inquisitive nature and questioning of truth position aesthetics at the forefront and allow us to read it through its relationalities (Young, 2019).

Findings

The lexicon, which serves as a tool for expanding the distribution of emotions, focuses on the reflections and potentials of the concept within space. The goal is to gain access to the meaningful role of the concept in the spatial distribution of emotion and its potential within the toolset created by the concept and its selected pool. The main structure of the lexicon is formed by thresholds; the primary support lies on the vertical axis. Thresholds encompass the time, narrative, or event during which concepts undergo transformation. The transformation of concepts here is unveiled through the sub-concepts that describe them. The attempt to bring these hidden transformations of the threshold to the surface is conceptually framed within the sub-concepts of the concept. This section is situated on the secondary supports in the horizontal axis, where the possibilities of the concept intersect with those of space.

Exploratory Framework:

- Main-Concepts: What is the concept that reveals the presentation/possibility of space in the ontological/tectonic, aesthetic/phenomenological, and political/epistemological context?
- Sub-concepts: What sub-concepts open up in the narrative of the main concept?
- Thresholds: How do these sub-concepts evolve in the context of architectural tools and transformations?

The Seyrantepe Auto Industry Complex, designed by Architect Seyfi Arkan in 1957 and completed in 1959, emerges as a significant example reflecting both spatial and economic transformation in Turkey's modernization process. The complex, consisting of 350 workshops and garages, encapsulates modern architecture's clean geometry, modular units, strip windows, and a sense of linear continuity through its original system solutions and typological design approach. Initially conceived as an isolated production area on the northern periphery of Istanbul, the complex has, over time, become a socio-cultural hub as surrounding residential developments and social amenities have expanded. The site has led to the formation of a neighborhood transforming it into a communal space beyond just an industrial site. Today, the Seyrantepe Auto Industry Complex, situated in Istanbul's urban center, holds a significant position due to its architectural elements of group value, social amenities, and contribution to the cultural urban landscape, although its continued existence is threatened by rapid urban transformation in the surrounding area. This situation enables a multi-layered reading of the spatial history of the building and its environment (Bereket & Aydoğan, 2020).

The lexicon that aims to reveal how space mediates the spread of emotional resonance opens the discussion through the Seyrantepe Auto Industry Area. As a collective production space, the industrial site was initially experienced as a place with clearly defined boundaries and a self-contained spatial cycle due to the low density of settlement in Istanbul's northern outskirts when it was established. However, as construction increased in the surrounding areas, various intersections emerged within its boundaries. These transformations in boundaries have, over time, been interwoven with the social and

cultural structures of the era, architectural principles, and environmental mentality, adding new layers to the modern architectural lines. We are presented with various sections and breaking points regarding the transformation of space (Figure 1):

Figure 1. Threshold 1: Environmental Constriction, Main Concepts: Boundary, Encounter, Society.

The initially defined and expansive boundaries of the structure have narrowed, become more permeable, and more complex with the addition of residential areas. This situation has created a new network of interactions, where encounters have increased instead of individual isolation, transforming the social information produced by the structure from a singular and autonomous form into a relational dynamic resembling a neighborhood (Figure 2).

Figure 2. Threshold 2: Integrated Surfaces, Main Concepts: Tectonics, Continuity, Intervention.

The tectonic purity of the structure has fragmented over time with the integration of additional floors, projections, and interventions, adopting a plural and heterogeneous language. These integrations have disrupted the visual and experiential continuity of the space, causing interruptions in perception, and generating a new form of knowledge production that reveals the political and social responses of the structure to interventions.

Figure 3. One of the lexicon page and its description.

The production rituals inherent in traditional craftsmanship have been transformed by modern technological interventions, leading to ruptures in the continuity created by the union of hand, mind, and space. This rupture has altered the trace of spatial production, changing the content of the craftsman's knowledge and evolving into anonymous new production practices. In traditional craftsmanship, the relationship between manual labor and space is strong; every movement and decision holds meaning, and the process operates like a ritual. However, with the influence of technology, these rituals are disrupted, and the direct interaction between manual labor and space diminishes. Instead, production processes become more anonymous, mechanized, and standardized. Technological interventions create a mechanical production process, and the knowledge and experience offered by space also undergo a transformation. This shift allows traditional forms of knowledge to give way to a more industrial and systematic form of knowledge. As a result, the craftsman's personal skill and deep connection to space evolve into a more generalized, colder, and more anonymous form of production (Figure 3).

Conclusion

These thresholds deeply transform the ways in which space mediates the dissemination of emotional experience. Environmental constriction allows for a shift from individual isolation to collective encounters and interactions, breaking down previously distinct boundaries. This reshapes the social context of space, providing emotional transitions and a sense of closeness between layers. Integrated surfaces, through interventions that disrupt the functional and visual continuity of space, blur the boundaries between perception and emotions. These interruptions make the spatial experience more complex, allowing space to begin to be 'written', with emotions shaped according to this writing. Production rhetoric, through the ruptures between technological and traditional practices, transforms the emotional traces and atmosphere created by space. This rupture presents emotional separations and reconnections at each step of the production process, enhancing the depth of the connection space establishes with its users. These thresholds reshape the emotional aspects of the spatial experience, shaking and redistributing previously unobservable, layered, and multidimensional emotional activities within space.

References

Bereket, C. K., & Aydoğan, E. (2020). 1950'lerin saklı moderni: Seyrantepe Oto Sanayi Sitesi. Betonart, 65.
Perniola, M. (2013). Aesthetics and feeling. In M. Verdicchio (Trans.), 20th century aesthetics: Towards a theory of feeling. Bloomsbury.
Rancière, J., & Gage, M. F. (2019). Politics equals aesthetics: A conversation between Jacques Rancière and Mark Foster Gage. In M. F. Gage & M. Shaw (Ed.), Aesthetics equals politics (ss. 9-26). The MIT Press.
Rancière, J. (2000). The politics of aesthetics (G. Rockhill, Ed.). (pp. 7-42).
Semper, G. (1989). The four elements of architecture and other essays. (H. F. Mallgrave & W. Hermann, Trans.). Cambridge University Press.
Young, M. (2019). The aesthetics of abstraction. In M. F. Gage & M. Shaw (Eds.), Aesthetics equals politics (pp. 127-150). The MIT Press.

Soft Matters: (Re)drawing Architecture Through Feminist Material Practices

Beyza Nergis Özbek[a], Sıdıka Aslıhan Şenel[a]

[a] Istanbul Technical University, Graduate School, Architectural Design Program, Türkiye

ozbekbe@itu.edu.tr

Keywords: Architectural Drawing, Ecological Creative Practices, Intra-Action, Soft Materiality.

Aim

The paper begins with a desire to investigate the material-semiotic, discursive and corporeal entanglements between tools, bodies and materials in the practice of architectural drawing, entities that are simultaneously assigned to represent, while also being entangled in representation and the matter/environment they inhabit. These interactions are explored through the framework of an ontology of relationality, which posits that selves do not pre-exist drawing but rather emerge within the "intra-actions" they enact (Barad, 2007). Rather than treating drawing as a fixed representational tool, the study approaches architecture as a practice operating within "ecologies of creative practices" (Frichot, 2019) embracing embodiment, material agency and relationality. In this context, it questions the habitual structures of architectural representation and suggests alternative ways of thinking through drawing.

The research unfolds through an inquiry into the limits of architectural drawing encountered while attempting to trace the material, corporeal, and discursive imprints of soft components such as curtains, cushions and fabrics within the Giritli Mustafa Pasha Han, a 19th-century trade inn in Istanbul. The observations made in this inn emphasize the importance of craft practices that resist mass production and the necessity of documenting them with their spatial counterparts. Incoming orders, bodies folding fabrics, the accelerating rhythms of sewing machines, and the transformation of materials into inhabitable forms render space as constantly in mobility. Attempts to document these processes reveal the limitations of conventional drawing tools, leading to the central question: "how can mobility, interiority, soft materiality be represented?". Building on this, the study aims to examine soft components through materials, bodies, and forms of relationality that remain excluded from architectural representations and spatial imaginaries.

Throughout the study, objects such as curtains, cushions, and fabrics are referred to as soft components, a term adopted to foreground their material characteristics, such as lightness and flexibility, and to approach them with what Lloyd Thomas (2007) defines as "material attention". This concept, as defined by Llyod Thomas (2007, p. 5), is a reminder of the need to question "the material as part of a network of forces and actions and a collective rejection of a purely visual (static) contextualization of the material".

Material and Method

A theoretical framework for this study is provided by philosophy of science studies (Stengers, 2010), material-semiotic approaches (Haraway, 1988; Barad, 2007), which emphasize that knowledge objects are generative and their boundaries are illusory and fluid, and agential realism (Barad, 2007), which provides a causal account of how discursive practices relate to material phenomena. This theoretical framework enables a critical examination of architectural production processes by challenging traditional notions of representation and materiality. In order to argue that the object of architecture is only a small part of what constitutes the highly differentiated discipline, architecture is reconceptualized as operating within "ecologies of creative practices" (Frichot, 2019).

The boundaries encountered in the drawing essays open up a relational discussion on how the hard, structural, and measurable historically marking the normative permanence of architecture are intertwined with the soft, ephemeral, and interior. This entanglement raises questions about how they co-constitute one another and how exclusion is maintained. Grounding the argument in the binary oppositions of the hard, structural and measurable, which signify permanence in architecture, versus the soft, ephemeral and domestic, as Haraway puts it, "misrepresents in a critical way the positions of embodied objectivity" (1988, p. 588). With this approach, instead of creating oppositional positions such as soft-hard, permanent-impermanent, inside-outside, the study advocates for a careful reading of the traces of difference created by materials, bodies, tools, and discourses, in order to explore how knowledge is produced, interpreted, and made meaningful. In this context, the study proposes to reflect on the meanings created based on Emmons's (2019, p. 13) claims that "architectural drawings are indexes of construction" for limitations of architectural drawing to incorporate soft components into its representational systems.

As Emmons (2019, p. 13) critiques, the rationalized theory of architectural drawing derived from Cartesianism rejected the implicit embodied approach that was once defined drawing practices. While architectural drawings initially functioned as "iconic indexes" of construction in direct parallel to the building, they have been reduced to abstracted symbols under the dominance of linguistic models (Emmons, 2019, p. 13). In my thesis, I extend the discussion to the corporeal, material and instrumental indexes in drawing, including their soft components, mobility, materiality, and interiority, although this paper focuses specifically on instrumental indexes. Emmons (2019, p. 33) further argues that architectural drawing tools originate in construction tools. However, it is important to recognize that drawing tools are not merely technical instruments to which specific actions are attributed, they also possess "agency". Barad's (2007) proposition of "intra-action" refers to the mutual constitution of entangled agents and challenges the assumption that agents exist as separate individual agents prior to their intra-action. In this understanding, drawing tools are not just extensions of the designer's intention, but as co-constitutive agents that emerge through entanglement with materials, environments and users actively engaged in ecologies of creative practices.

An ecology of practices utilizes tools to think through and with a situation, making sense of what is happening. As Stengers (2005, p. 185) argues,"where we take up our tools for thinking, habit must be resisted" highlighting that the act of passing or receiving a tool creates a meaningful relation between the tool, its user, and the context in which it is applied. Considering drawing as a representational tool that generates architecture through its material-semiotic relationships, and examining the habits embedded in architectural drawing, provides critical insights into how we think and produce with this tool. Emmons (2019, p. 166) explores the relationship between architectural drawing tools and drawing practice beyond a simple matter of instrumentality, embedded in a reflexive relationship that transcends simple subject–object dualism. This approach emphasizes that drawing tools should not be considered passive instruments, but rather as active components within the interplay of relational engagement.

Findings

Drawing tools are also active components in the creative process. In the work titled "Lost in Translation" (Figure 1.), representational experiments were conducted through the remains of an abandoned wooden structure, using the analogy between drawing and sewing. These experiments explored the material interactions into which the tools used during the act of drawing enter, beyond their attributed instrumentality. Drawing attempts that began with an ink pen on the fabric in a fixed position produced various deviations on a smooth surface, while narratives concerning both the fabric and the structure were developed through drawing–sewing methods. The layers of the wooden remnant began to be processed by sewing on the two-dimensional surface, engaging movements of the drawing body, different visual angles toward the wooden forms, and material interactions formed by folding the fabric and stretching the threads.

Figure 1. Lost in Translation, Material encounters beyond instrumentality (Özbek, 2023).

The documentation of the soft components of the inn draws on Evans's (1997) analysis of 18th-century furniture maker's drawings, in which architectural elements are represented orthographically, while furniture and decorative objects, often classified as interior materials, are represented in perspective. These examples highlight opposing positions within representational systems of dichotomies such as interior/exterior, structure/fill, solid/soft. In the representational work conducted at the inn, these dichotomies are challenged through representational deviations that explore the ambiguity of such boundaries (Figure 2.). While the workshops that produce soft components are spatially organized around a courtyard, material movements such as the flow of fabrics, the entry and exit of materials, and the hanging of cloth on the surrounding railings blur spatial boundaries. In this system of representation, collage techniques have been adopted to express the complex spatial entanglements, rather than to depict such binary conditions.

Figure 2. (Re)drawing Soft Components: Plan unfolding as a method for unsettling spatial hierarchies (Özbek, 2024).

While drawing the plan, measurements were made using leftover fabric pieces from the inn's production process and transferred to paper by approximating the proportions of elements captured in photographs. At the same time, the fabric surface itself functioned both as a measurement tool and a tactile documentation medium, recording the textures of surrounding materials. In the documentation drawings of the inn, the bodily actions of a curtain seamstress such as standing on a chair to measure curtain lengths with reference to her own body, hanging a piece of leftover fabric from a railing to

deliver completed orders to the ground floor, placing another piece at the threshold to cover, separate, and soften the passage, or using her favorite golden scissors beside the sewing machine are recorded as part of the spatial interactions of soft components (Figure 3. and Figure 4.). These experiments attempt to trace the complex intra-actions between tools, materials and spatial gestures through the traces of soft components, relationships that are largely unrecognized in architectural drawing practices.

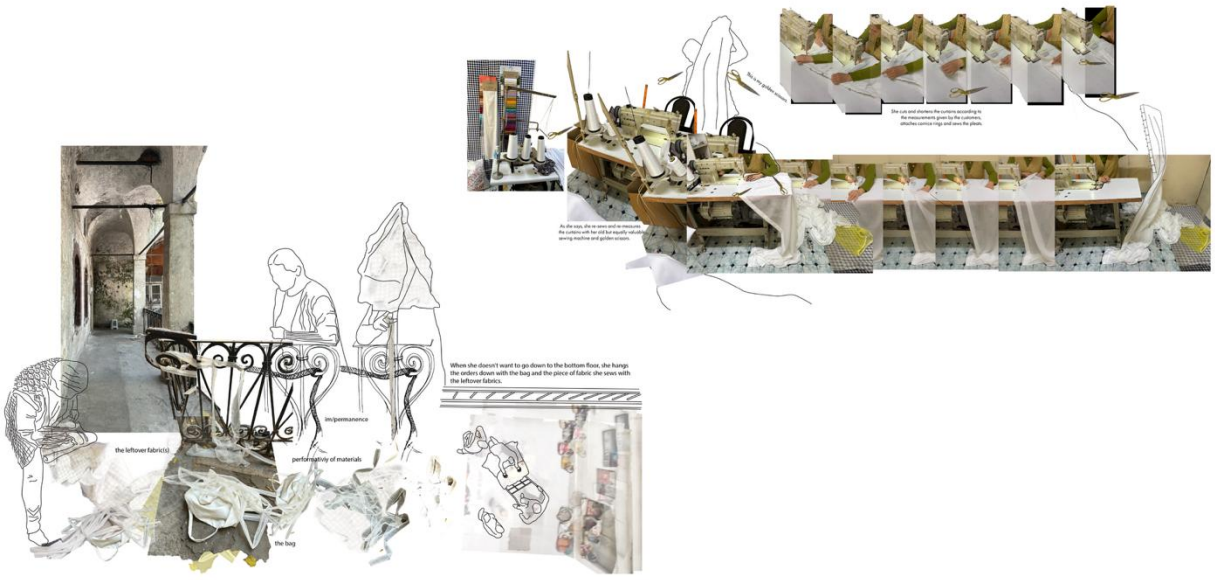

Figure 3. (Re)drawing Soft Components: Tracing mobility and repetition in sewing-based spatial production (Özbek, 2024).

Figure 4. (Re)drawing Soft Components: Everyday soft materialities and improvised spatial arrangements (Özbek, 2024).

Conclusion

While the practice of architecture is constituted in interaction with bodies, materials and tools, addressing the affinities of these components with representation draws attention to the network of material-representational, discursive and corporeal relations that interact with drawing. The possibility of witnessing what systems of representation relate to, their tools and how they function is one of the methods of embodied feminist objectivity (Haraway, 1988).

These habits of representation are deeply embedded within normative structures that sustain specific power relations and ideological assumptions. As Haraway (2016, p. 12) says, "it matters what issues we use to think about other issues; it matters what stories we tell to tell other stories; it matters what knots are tied, what thoughts think thoughts, what definitions define definitions, what ties bind ties". Therefore, questioning the habitual structures of architectural representation is crucial for exploring alternative ways of knowing and making.

The representational attempts (Figure 5.) in this work may be described as fragments of an ongoing research process. The knowledge gathered through different visits to the inn, composed of situated moments and partial narratives as manifestations of drawing, reveals relationships that are not yet fully visible. This study aims to continue the work with mixed media through further experiments that allow for material interaction. The experiments thus far have been shaped by the question of why soft components remain absent from architectural drawings. Architectural drawing, then, becomes not merely a representational technique, but also a critical tool a means of questioning how space, materials, and knowledge are constructed, and who or what is excluded in the process. Rather than assuming that architectural drawing exists solely to construct, this paper proposes drawing as a practice that is relational, speculative, open-ended, soft, partial, and capable of engaging with that which is not yet.

Figure 5. (Re)drawing Soft Components: Fragments of soft spatiality and unfinished stitching (Özbek, 2024).

References

Barad, K. (2007). Meeting the universe halfway: Quantum physics and the entanglement of matter and meaning. Duke University Press.

Emmons, P. (2019). Drawing imagining building: Embodiment in architectural design practices (1st ed.). Routledge. https://doi.org/10.4324/9781315567600

Evans, R. (1997). The developed surface: An enquiry into the brief life of an eighteenth-century drawing technique. In R. Evans (Ed.), Translations from drawing to building and other essays (pp. 195–231). MIT Press.

Frichot, H. (2019). Creative ecologies: Theorizing the practice of architecture. Bloomsbury Visual Arts.

Haraway, D. (1988). Situated knowledges: The science question in feminism and the privilege of partial perspective. Feminist Studies, 14(3), 575–599. https://doi.org/10.2307/3178066

Haraway, D. (1999). The promises of monsters: A regenerative politics for inappropriate/d others. In J. Wolmark (Ed.), Cybersexualities (pp. 314–366). Edinburgh University Press. https://doi.org/10.1515/9781474473668-022

Haraway, D. (2016). Staying with the trouble: Making kin in the Chthulucene. Duke University Press.

Lloyd Thomas, K. (2007). Introduction: Architecture and materials. In K. Lloyd Thomas (Ed.), Material matters: Architecture and material practice (pp. 1–12). Routledge.

Stengers, I. (2010). Cosmopolitics I. University of Minnesota Press.

Stengers, I. (2013). Introductory notes on an ecology of practices. Cultural Studies Review, 11(1), 183–196. https://doi.org/10.5130/csr.v11i1.3459

ARCHITECTURE

Architectural History

Architecture Design Theory

Building Construction Technologies

Building Materials and Technologies

Built Environment Design and Technologies

Conservation and Restoration

Environmental Control and Building Technology

Project and Construction Management

Sustainable Design

Evaluation of Retrofitting Techniques in Reinforced Concrete Buildings

Sinan Sarvan[a], Caner Gocer[b]

[a] Istanbul Technical University, Graduate School, Environmental Control and Construction Technologies, Türkiye
[b] Istanbul Technical University, Faculty of Architecture, Department of Architecture, Türkiye
sarvan17@itu.edu.tr

Keywords: Retrofitting Techniques, Reinforced Concrete Buildings, Environmental Sustainability, Carbon Footprint, Cost-Benefit Analysis.

Aim

It is not possible to rebuild all reinforced concrete residential buildings in earthquake-prone areas due to city conditions. Therefore, strengthening the durability of buildings is of critical importance in terms of ensuring life and property safety. However, since a significant portion of the existing building stock was constructed according to outdated regulations, therefore, reconstruction or reinforcement works are a necessity. Strengthening existing structures has various advantages and disadvantages in terms of cost, sustainability and technical feasibility. This process offers the opportunity to extend the service life of structures and to minimize possible structural risks by increasing their durability. However, each strengthening method creates different economic and environmental impacts depending on the type of material used, labor requirements and long-term performance. In this context, the evaluation of strengthening strategies in terms of their technical adequacy and sustainability is important for the preservation of the existing building stock. This research analyzes in detail the techniques for strengthening reinforced concrete structures with different storey heights. The study aims to determine the most efficient option by comparing the economic and environmental effects of various strengthening methods. The evaluation process focuses on sustainability and durability criteria and takes into account the requirements of international environmental standards and building codes. In this context, it is aimed to develop optimal solutions for the protection and improvement of the existing building stock.

In recent years, the importance of sustainable retrofitting strategies has been increasingly emphasized due to their potential to reduce environmental impact and enhance the seismic resilience of urban areas (Shao & Billington, 2019). Studies suggest that reinforcement practices, when aligned with energy efficiency improvements, can generate significant lifecycle benefits compared to complete demolition and rebuilding (Comerio, 2004). Furthermore, environmental assessments indicate that targeted reinforcement methods often produce substantially lower embodied carbon emissions, especially when recyclable and low-carbon materials are prioritized (Colavitti & Usai, 2015). International guidelines also recommend that such strategies be cost-effective, performance-oriented, and adaptable to varying structural conditions, making them highly relevant for policymakers and urban planners (Kappos, 1996).

Material and Method

The main purpose of this study is to analyze different renovation methods applied in reinforced concrete structures in terms of cost and benefit and to compare them with the reconstruction process. The research considers three different building height groups: (1) low-rise, (2) mid-rise and (3) high-rise reinforced concrete residential buildings. For each group, techniques such as cladding, reinforcement with steel elements, use of fiber-reinforced polymer (FRP) and carbon fiber-reinforced polymer (CFRP), addition of shear walls, bracing with internal or external frames and foundation reinforcement are examined. These analyses are carried out on the basis of field studies, cost estimates and comprehensive literature reviews. The evaluation process is carried out based on international building safety standards such as Eurocode 8, ACI 318 and FIB.

Additionally, carbon footprint analyses of reinforcement techniques and reconstruction processes revealed significant differences in terms of environmental impacts. The indexing system created in line with the obtained data provided a comparative framework for sustainability assessments. In the context of environmental sustainability, examination of green

building certification criteria such as LEED and BREEAM revealed the importance of evaluating the ecological impacts of reinforcement methods. In order to minimize environmental damage, reinforcement strategies should be compatible with international sustainability standards, use low-carbon emission materials and be supported by energy-efficient solutions. With this way, detailed cost analyses were conducted to evaluate the structural performance of reinforced structures under different seismic scenarios, and the amount of carbon footprint was examined in detail, taking into account the production methods of the structural elements used. In this context, buildings were divided into three groups according to their heights and comprehensive calculations were made on the selected structures for each category.

Findings

This research aims to determine the most suitable reinforcement methods for buildings of different heights. In low-rise buildings, lightweight and economical solutions such as jacketing and carbon fiber reinforced polymer (CFRP) applications come to the fore. In medium-rise buildings, the addition of shear walls and the use of steel frame systems have been shown to be more effective in increasing structural strength. In the case of high-rise buildings, the application of foundation reinforcement and steel-supported systems provides the most successful results in terms of preserving structural integrity.

Recent studies have shown that reinforced concrete buildings with irregular geometries may not achieve sufficient structural improvement with standard strengthening methods. Such structures require specially developed solutions instead of generalized strengthening strategies due to irregularities in their load-bearing systems. In particular, it has been determined that methods such as the addition of shear walls and base isolation significantly increase structural strength in buildings with soft story effects. In this context, a unique analysis process is required for each building and detailed engineering evaluations are required to select the optimum strengthening technique.

Cost analyses show that in some cases, strengthening existing structures offers a more economical option than reconstruction, but under certain conditions, demolition and reconstruction may be a more viable solution. In particular, in cases where the costs of strengthening exceed 50% of the costs of reconstruction, reconstruction may become a more economically sustainable alternative in the long term, considering the advantages of increased structural durability and energy efficiency. However, when the production processes of the building materials used, the manufacturing of the elements required for storage, the emissions from industrial facilities, the environmental impacts of logistics activities and the implementation processes of all these elements at the building scale are taken into account, carbon footprint analyses may yield negative results. This situation may require a re-evaluation of a method that is considered advantageous in terms of environmental sustainability.

Carbon footprint analyses show that structural renovation is a more sustainable alternative in most cases, but this effect varies depending on the type of materials used. In general, renovation practices are associated with lower natural resource consumption and reduced greenhouse gas emissions compared to reconstruction. However, the environmental advantages of renovation can be significantly reduced when high-carbon materials such as steel and concrete are used. According to international environmental standards, the preference for recyclable and low-carbon materials increases the sustainability potential of renovation processes. For instance, composite materials such as FRP and CFRP, although they require high energy consumption in the production stages, can provide long-term environmental benefits by extending the service life of structures.

In addition, studies show that energy efficiency improvements can be integrated with structural renovation processes. In particular, the implementation of modern facade designs that increase insulation systems and thermal performance can contribute to the reduction of operational carbon emissions. Such improvements can make renovation methods more advantageous in terms of sustainability, providing both environmental and economic benefits in the long term.

Conclusion

Studies have shown that the most appropriate reinforcement methods vary depending on the height of the building and its current structural condition. While lightweight and easy-to-implement solutions are preferred for low-rise buildings, comprehensive and durability-enhancing reinforcement techniques are needed for taller buildings (Table 1). Cost-benefit analyses show that reinforcement is economically advantageous in some cases, while reconstruction offers a more suitable

solution in terms of long-term durability and sustainability for certain buildings. These analyses show that when reinforcement costs remain at approximately 50% of the reconstruction cost, reinforcement methods are a more rational option. However, when reinforcement costs approach the reconstruction cost, reconstruction becomes more advantageous in terms of longevity and energy efficiency.

In the context of environmental sustainability, reinforcement techniques generally result in lower carbon emissions, but the production processes of the materials used may increase this effect. The use of materials that comply with international environmental standards and are recyclable increases the sustainability of reinforcement methods by reducing the environmental burden caused by construction processes. In addition, integrating seismic reinforcement works with energy efficiency-enhancing measures can significantly improve the overall sustainability performance of buildings. In particular, the use of advanced insulation systems and high-performance façade technologies can contribute to minimizing environmental impacts throughout the building life cycle by reducing operational carbon emissions.

As a result, a holistic approach to evaluating cost, benefit and carbon footprint analyses reveals the need for a decision support system that will determine the most appropriate retrofit method for building owners and engineering firms. This system determines the most effective methods for different building types, allowing the implementation of the most economically and environmentally sustainable solutions. This decision support tool, which will be developed using mathematical modeling and formulation-based approaches, can support scientifically based decision-making processes for urban planners, architects and policy makers by providing real-time evaluation of various retrofit and reconstruction scenarios.

Table 1. Earthquake Resistant Concrete Structures (Kappos 1996).

TECHNIQUE	INITIAL COST LEVEL	DURABILITY IMPACT	CARBON FOOTPRINT	MATERIAL SOURCEABILITY
Steel Jacketing	High	High	High	Moderate
FRP/CFRP Wrapping	Moderate	Moderate-High	Low	Moderate-High
Shear Wall Addition	Moderate-High	High	High	Easy
Base Isolation	Very High	Very High	Moderate	Limited
External Bracing (Steel Frames)	Moderate	Moderate-High	Moderate	Moderate

References

Comerio, **M. C. (2004).** Public policy for reducing earthquake risks: a US perspective. Building Research & Information, 32(5), 403-413. DOI: 10.1080/0961321042000221052

Colavitti, A. M., & Usai, A. (2015). Partnership building strategy in place branding as a tool to improve cultural heritage district's design: The experience of UNESCO's mining heritage district in Sardinia, Italy. Journal of Cultural Heritage Management and Sustainable Development, 5(2), 150–165.

Kappos, A. (1996). Earthquake resistant concrete structures (1st ed.). CRC Press.

Shao, Y., & Billington, S. L. (2019). Predicting the two predominant flexural failure paths of longitudinally reinforced high-performance fiber-reinforced cementitious composite structural members. Engineering Structures, 199, 109581.

Url-1 https://doi.org/10.1108/JCHMSD-03-2014-0011

Url-2 https://doi.org/10.1201/9781482271300

Url-3 https://doi.org/10.1016/j.engstruct.2019.109581

Evaluation of the Seismic Performance of Traditional Akçakese Houses in Relation to Structural Deterioration

Zeynep Dikyer [a], Caner Göçer [b]

[a]Istanbul Technical University, Graduate School, Environmental Control and Construction Technologies, Türkiye
[b]Istanbul Technical University, Faculty of Architecture, Department of Architecture, Türkiye
dikyer22@itu.edu.tr

Keywords: Earthquake, Timber-Framed Structures, Akçakese Houses, Wattle And Daub Wooden Houses, Timber Structure Deterioration.

Aim

Turkey's location in a high seismic risk zone makes the preservation of traditional buildings and cultural heritage in regions along active fault lines a critical issue. Traditional residential buildings in Anatolia, constructed with timber-framed structural systems over generations, not only reflect local architecture and craftsmanship but also contribute to the sustainability of historical, socio-cultural, and economic structures (Göçer & Erarslan, 2020; Arun, 2012; Gündoğan, 2018). Preserving such buildings is of great importance not only in terms of aesthetics but also in ensuring the transmission of architectural heritage to future generations.

The traditional houses located in the Akçakese village of Şile are characterized by their wattle and daub infill technique and possess unique architectural features that are well adapted to the region's climate, geography, and locally available materials (Göçer & Erarslan, 2020). Chestnut wood, which is abundant in the region, has been used as the main material for the timber frame, contributing to the lightweight and flexible nature of these structures (Figure 1). Over time, however, these buildings have deteriorated due to environmental factors, leading to various structural damages. As a result, their overall structural integrity has begun to decline. Especially in the face of sudden and severe natural disasters such as earthquakes, these structural weaknesses pose a significant risk. Furthermore, the preservation of these buildings should not be viewed solely as an aesthetic or cultural concern but as an essential component of disaster risk reduction strategies within communities. With ongoing urbanization and the dominance of modern construction techniques, the conservation of traditional buildings has become increasingly challenging. Many such houses have been abandoned due to neglect. At this point, evaluating the seismic performance of traditional Akçakese houses becomes a crucial topic for scientific inquiry, as it contributes both to maintaining historical continuity and minimizing the potential impacts of future earthquakes.

Figure 1. Traditional Akçakese Houses, Göçer C.

The primary objective of this study is to comprehensively evaluate how the seismic performance of traditional timber-framed houses in Akçakese village has been affected over time due to deterioration caused by atmospheric and other

environmental factors. Within the scope of the study, the original construction techniques, material properties, and the wattle and daub infill system employed in these structures were thoroughly examined. Furthermore, an estimation was made regarding the seismic behavior of these buildings by considering the structural degradations that have occurred over time.

Material and Method

The materials utilized in this study include literature reviews, archival photographic documentation, and on-site observations. In order to understand the structural anatomy of the buildings, the durability of the materials used, the quality of the joints at connection points, and the deterioration that has occurred over time were analyzed in detail. Additionally, traditional buildings that sustained damage during past earthquakes were examined, and comparative assessments were made with the structures under study (Bozkurt, 2018).

As a methodological approach, the study evaluates the deterioration of traditional timber structures over time and assesses how these deteriorations compromise their resistance against seismic loads under current conditions. Initially, a comprehensive literature review was conducted on similar buildings in the region, followed by an examination of the observed damages. The types of damage, causes of deterioration, and structural weaknesses were thoroughly analyzed to identify vulnerabilities in the load-bearing systems. Throughout this process, the progressive degradation of timber elements and its influence on the seismic performance of the buildings were systematically evaluated.

Findings

Based on a literature review, the damages observed in traditional timber structures during the 1970 Gediz (Kütahya) earthquake, the Afyon (2002), Bingöl (2003), and Erzurum (2004) earthquakes, the 1999 Marmara (Kocaeli) earthquake, and most recently, the February 6, 2023 earthquakes centered in Pazarcık and Elbistan districts of Kahramanmaraş, have been examined. The analysis focuses on the type and causes of damage according to different structural classifications of traditional wooden buildings.

Figure 2. A rusty building damaged in the Gediz Earthquake, Güçhan, 2005.

The first image presents an observation of a traditional hımış structure damaged during the 1970 Gediz Earthquake. In this case, the lack of adequate connection elements between the structural systems prevented effective interaction between the building and the adjacent structure. This deficiency resulted in what is known as the "pounding effect," caused by the stiffness difference and pendulum-like movement between neighboring buildings during seismic excitation. The lightweight and flexible nature of the hımış structure rendered it

insufficiently resistant to such lateral impacts; the absence of proper connections led to displacement or damage of the exterior walls. This case serves as a significant example underscoring the importance of structural connections and adequate spacing between adjacent buildings in traditional architecture (Figure 2).

Figure 3. Partially demolished Timber-framed structure with infill, Aksoy D., Ahunbay Z.

The second image illustrates significant material degradation of the structural elements due to prolonged exposure to atmospheric conditions such as rain, humidity, temperature fluctuations, and UV radiation. In particular, biological deterioration—including decay, fiber separation, and loosening—has occurred in the wooden beams and columns located beneath the oriel (projecting bay) that supports the overhanging section on the exterior façade. This degradation process has led to a reduction in the structural load-bearing capacity, ultimately resulting in the failure and collapse of the oriel. In traditional buildings, when proper maintenance and protective measures are not implemented, wooden elements tend to lose their structural integrity, posing a serious threat to the overall safety of the building (Figure 3).

Figure 4. Demolished Timber-framed structure with infill, Göçer C., 2023.

The third image depicts a traditional hımış structure that sustained severe damage during the 2023 Kahramanmaraş Earthquake. It is observed that the external walls, particularly in the short direction, collapsed out-of-plane and separated from the main structure. Such a failure typically results from the insufficient stiffness of the infill material (adobe or brick), lack of composite action between the frame and the infill, and weakness

at the connection points. The image clearly shows not only the disintegration of the infill but also the failure of some joints within the timber frame, indicating a loss of structural integrity in the load-bearing system. This case reveals the inherent weaknesses of traditional construction systems in terms of seismic performance and highlights the necessity of reevaluating their behavior under lateral forces (Figure 4).

When reviewing past earthquake damage cases, it can be stated that Akçakese houses, built with chestnut timber known for its lightweight and flexible properties, exhibit a degree of resistance to earthquakes under normal conditions. Timber displays a ductile behavior under seismic loads, enabling energy dissipation and resulting in less damage compared to heavy masonry structures (Tomaževič, 1999; Ceccotti, 2008). Moreover, the wattle and daub infill system contributes to seismic resilience by providing a lightweight and flexible wall structure. However, it has been identified that over time, environmental factors have caused deterioration in various structural components. Timber elements have been found to decay, loosen, crack, or deform due to moisture, temperature fluctuations, and other external influences (Figure 5). Failures and loosenings in timber joints further compromise the overall stability of the building. Additionally, it has been observed that the mortar used in the infill has fallen off, negatively affecting the structural continuity of the walls.

Figure 5. Rotten wooden structural element detail, Göçer C.

The load-bearing systems of these houses are composed of timber members connected to each other primarily through nailing techniques. However, the absence of reinforcing components such as steel wedges or triangular wooden blocks at the joints results in weakened connection points. In order to mitigate this weakness in the walls, diagonal braces were implemented between the main vertical posts and bottom beams. These braces increased the in-plane stiffness of the walls and improved their seismic performance under lateral earthquake loads (Figure 6).

In addition to the braces, timber cladding panels made of chestnut wood also contributed to the structural behavior by acting as rigid diaphragms during seismic events, thus enhancing the overall stability of the buildings under horizontal loading (Figure 6). Field observations revealed that due to material degradation, some brace connections had loosened, and partial detachment of façade cladding was also identified. These forms of deterioration negatively affected the seismic performance of the structures.

Figure 6. Buttress and wood cladding detail, Göçer C.

In traditional masonry structures, the deterioration and cracking of the mortar binding the stone blocks due to atmospheric effects over time have resulted in a significant reduction in lateral stiffness. Particularly, intense rainfall and freeze–thaw cycles have caused erosion of the mortar joints in stone walls, leading to partial collapse in some structures. As a consequence of such deterioration, these buildings have become increasingly vulnerable to horizontal seismic forces.

Conclusion

The deterioration of Akçakese houses due to environmental effects negatively impacts their earthquake resistance. Although the lightweight and flexible structural system offers certain advantages under seismic loads, material degradation, weakened connections, and deformations in load-bearing elements compromise this advantage over time. Therefore, a scientifically grounded and conservation-conscious approach must be adopted in restoration practices to protect these structures from ongoing environmental damage.

First, structural components affected by deterioration should be identified and documented. Then, in accordance with conservation principles, repairs and reinforcements should be performed using timber materials of similar species. Strengthening of timber joints, replacement of decayed members, and reinforcement of critical load-bearing elements will enhance the long-term durability of the structures. Moreover, combining traditional building techniques with modern engineering principles in accordance with restoration ethics will not only preserve the authenticity of these buildings but also improve their seismic resilience.

It is essential for local authorities, academic institutions, and civil society organizations to collaborate and develop policies aimed at preserving traditional buildings. While the current Turkish Seismic Code provides comprehensive regulations for reinforced concrete and steel structures, expanding its scope to include timber structures is of great importance. Timber, with its low weight and inherent flexibility, can offer superior seismic performance, yet without proper design and construction standards, it may fail to meet expectations. Therefore, the seismic design provisions should incorporate detailed engineering assessments for timber buildings, standardized connection details, and robust material performance criteria.

In conclusion, preserving and strengthening the traditional timber houses of Akçakese is not only vital for transferring cultural heritage to future generations but also critical for ensuring public safety. The conservation of these structures contributes not only to the continuity of tangible heritage but also to sustainable local development.

References

Aksoy D., Ahunbay Z., (2005). Geleneksel ahşap iskeletli Türk Konutu'nun deprem davranışları, itüdergisi/a, Cilt:4, Sayı:1, 47-58 Mart

Arun, G. (2012). Ahşap Yapılar ve Restorasyonu. Mimar Sinan Güzel Sanatlar Üniversitesi Yayınları. **Bozkurt, İ. (2018).** Yapısal Analiz Yazılımlarının Karşılaştırılması.

Ceccotti, A. (2008). New technologies for construction of medium-rise buildings in seismic regions: The XLAM case. Engineering Structures, 30(9), 2336–2343.

Göçer, C., & Erarslan, A. (2020). Geleneksel Ahşap Yapı Sistemlerinde Sepet Örgü Dolgu Teknikleri: Şile Akçakese Örneği. Yapı ve Mimarlık Dergisi, 5(2), 33–50.

Gündoğan, Ü. (2018). Anadolu'da Geleneksel Ahşap Yapılar ve Yapım Teknikleri. Mimarlık ve Kentleşme Araştırmaları Dergisi, 7(1), 41–58.

Şahin Güçhan N.,(2005), Observations on earthquake resistance of traditional timber-framed houses in Turkey, Building and Environment 42 (2007) 840–851

TS 647. (1982). Yapılarda Kullanılan Kerestelerin Sınıflandırılması. Türk Standardları Enstitüsü.

TBDY. (2018). Türkiye Bina Deprem Yönetmeliği. AFAD, Ankara.

Tomaževič, M. (1999). Earthquake-Resistant Design of Masonry Buildings. Imperial College Press.

Evaluation Of Light Steel Structured Housing According To Construction Systems

Burçin Fırtına[a], Caner Gocer[a]

[a]Istanbul Technical University/Graduate School, Architecture, Environmental Control and Construction Technologies, Turkey
firtina22@itu.edu.tr

Keywords: Light Steel Systems, Industrial Construction Systems, Residential Construction System, Building Construction Methods.

Aim

Light steel bearing systems, which emerged in the USA and Europe in the mid-20th century and whose production accelerated especially in the housing sector in North America after the 1970s, are one of the innovative construction systems increasingly preferred in today's construction sector. The system, which is based on the method of assembling coating materials on a carcass skeleton consisting of cold-formed light steel galvanized profiles, has various advantages over other traditional construction systems. Due to its basic features such as reducing the weight of the building, accelerating the construction process, continuity of the quality control system originating from industrial production and being made of recyclable materials, it provides various advantages such as cost effectiveness, energy efficiency, earthquake resistance and minimizing errors. Light steel structured housing constitutes the most common area of use. It offers an important opportunity to meet the increasing housing need, especially in cities, in a fast, economical, high-quality and sustainable way. (Harini et al., 2020; Veljkovic& Johansson, 2007)
The aim of this study is to examine in detail the different construction systems of light steel structured housing, to reveal the differences of these systems in terms of architecture, structure and economy, and to make a comparative assessment to determine the most suitable construction system that meets certain needs.

Material and Method

The data used in the research is based on literature review, sector research and field observations. This data was evaluated through qualitative and quantitative analysis; parameters such as cost, durability, time, energy efficiency and sustainability of different construction systems were examined comparatively. In the analyses, cold-formed galvanized light steel profiles, coating materials and insulation materials, which constitute the main materials of light steel structured housing structures, were evaluated.

Figure 1. Light Steel Framed Housing (Url-1).

Findings

Three different systems are used as a construction system in the production of light steel structured housing: linear (frame or rod) systems, panel systems and modular (cell) systems. (Ekinci, 2006; Yıldırım, 2010) In linear systems, horizontal and vertical carrier elements pre-produced in the factory are brought together on site to form carrier components. The production of linear systems is based on the construction site; The assembly phase is taken into consideration more than the production phase. In panel systems, structural elements such as floors and walls, which have been pre-installed in a factory, are transported as a whole or in parts and directly to the application area and assembled in a short time. Walls and floors can be manufactured as a single piece or as multi-piece modules. Panels can be brought to the construction site as a frame with one side coated, two sides coated or uncoated. The system based on the principle of producing the parts of a structure in the size of the space and then assembling them on the construction site is called the cellular system. This system, which emerged as a result of the development of linear and panel systems, has a high production percentage level in the factory. The structural working principles of the system are the same as the light steel frame system. However, each unit forms a rigid frame within itself. The structural rigidity of the building system is provided by the combination of the units. In the cell construction system, the units are in the form of "closed cells" or "open cells". In closed modular cells, all sides of the unit are completely limited and the space size is determined. The size of the cell is limited by the possibility of transportation. The width of the cells can be as much as the traffic laws allow during transportation by road. In this case, the length of the modules in one direction should not be more than 2.40 m. or 3.30 m. Since the space dimensions will be dependent on this width, it is generally more suitable for residential buildings. In open cells, the cells are not completely limited. The limited sides can be a load-bearing wall or a load-bearing interior wall. The unrestricted side of the cells allows for a larger space to be created by merging with the other cell. The purpose of this is to facilitate the transportation of the modular cell or to provide planning flexibility starting from a unit space consisting of a single cell module to large spaces formed by a large number of combined cells. Compared to linear and panel systems, the cellular system provides a large amount of labor and time savings during the assembly phase, although the production process in the factory is longer. As we move from linear systems to module systems, the level of industrialization increases, the production process in the factory is extended while the assembly process on the construction site is shortened.

Linear systems are more advantageous than other production types in terms of providing design flexibility and being able to cover wider openings. Linear systems are preferred in residential projects where flexibility of use, special designs and larger openings are required. However, due to the large number of assemblies on the construction site, the construction period is long and the rate of being affected by seasonal conditions is high in linear system housing production. Since it is the production type with the longest construction period, labor and construction site costs are also the highest. Thanks to its lightness and elements developed against earthquake loads, the linear system has at least as high resistance properties as other systems. At the same time, it is the most disadvantageous of all systems in terms of quality control processes. Panel systems have more flexible design opportunities compared to modular systems. The construction site process is shorter and labor costs are lower compared to the linear system. Transportation costs are more advantageous when compared to the modular system. High energy efficient detail solutions are possible. It has high durability performance with appropriate detail solutions. Thanks to prefabrication processes, material losses are lower and the quality control process is more effective compared to linear systems. The most important advantages of modular (cell) systems are the possibility of assembly in a short time, controlled production in a factory environment, reduced labor costs and low material losses. It is preferred in terms of time and cost in mass housing production, especially in post-disaster situations that require rapid production. The most important disadvantages can be seen as the high transportation costs and the logistical difficulties in transporting large modules and the flexibility limitations in the design. It has high performance in terms of durability, low material losses and a production system with high energy efficiency are important in terms of sustainability.

Conclusion

Research findings have shown that light steel structures are more resistant to earthquakes due to their lighter weight than traditional building systems. It has been determined that these systems reduce material loss and accelerate the construction process thanks to continuous quality control mechanisms. (Vitale et al., 2018) At the same time, it has been determined that

thanks to pre-production, significant time savings are achieved in production and assembly processes, but initial investment costs can be higher in some cases compared to traditional structures. In terms of energy efficiency, it has been observed that light steel construction systems can show high performance with the right insulation and insulation details. Using appropriate materials and producing effective detail solutions to ensure sound insulation and fire resistance can make the use of light steel construction systems, especially in residential structures, widespread. As a result, each production type can be more advantageous for certain usage scenarios. While cellular systems are an ideal option for residential projects that require fast and mass production, panel systems offer more flexible and economical solutions. Considering the advantages and disadvantages of these different systems, the most suitable production type should be selected depending on the project requirements.

References

Ekinci, S. (2006). Light steel construction systems: An analysis in terms of structural system, building physics effects, and architectural design principles. Master's Thesis, Mimar Sinan University, Turkey. (in Turkish)

Harini, B., Lingeshwaran, N., Perumal, K., Aravinthan, K. (2020). Sustainable design of cold formed steel. Materials Today: Proceedings, 33:881-885

Veljkovic, M., Johansson, B. (2007). Light steel framing for residential buildings. Thin-Walled Structures, 44:1272–1279

Vitale, P., Spagnuolo, A., Lubritto, C., Arena, U. (2018). Environmental performances of residential buildings with a structure in cold formed steel or reinforced concrete. Journal of Cleaner Production, 189:839-852

Yıldırım, S.G. (2010). Light steel construction systems: Semi-open light steel construction system proposal for low-rise housing in Turkey. Doctoral Thesis, Istanbul Technical University, Turkey. (in Turkish).

Url-1, www.lsf-association.co.uk, date retrieved 22.05.2025.

Evaluation of Damage Mechanisms in Stone Structured Houses Due to Earthquakes

Sarvin Iravani Ghadim[a], Caner Göçer [a]

[a] Istanbul Technical University, Graduate School Institute, Environmental Control and Construction Technologies Program, Türkiye
ghadim22@itu.edu.tr

Keywords: Earthquake, Masonry Buildings, Earthquake Damage, Earthquake Damage Assessment, Stone Structures.

Aim

Turkey and its surroundings are tectonically very active and are located in the Alpine-Himalayan earthquake zone, one of the most important earthquake zones in the world. There are many fault lines in this region between the Anatolian plate, Eurasian and African plates. Masonry stone structures, especially those located in rural areas, come to serious damage during these earthquakes. At least one earthquake with a magnitude between Mw=5.0-6.0 occurs every year (AFAD 2025; Bikçe, 2017).

More than 100,000 people have lost their lives due to the devastating effects of earthquakes in Turkey in the past 60 years. 269 earthquakes have occurred in Turkey since 1900, causing loss of life or damage. The largest earthquakes in terms of loss of life are the 2023 Kahramanmaraş, 1939 Erzincan and 1999 Gölcük centered Marmara Earthquakes, respectively. Throughout the historical process, major earthquakes have occurred in the Aegean Sea and its surroundings. These earthquakes are, respectively, 1688 Izmir, 1739 Foça, 1778 Izmir, 1865 and 1867 Lesvos Island, 1880 Samos Island, 1883 Çeşme, 1899 Izmir, 2014 Gökçeada, 2017 Lesvos Island, and 2020 Samos Island Earthquakes (Güleç, 2023).

Stone masonry structures are traditional construction systems that commonly used in rural and historical regions of Turkey. In addition to their cultural and historical value, buildings constructed with stone material also ensure the effective use of local materials (Olğun & Karatosun, 2019). Ensuring the sustainability of architectural heritage is an important issue, considering that until the 1970s, stone was widely used as a structural material in building construction in rural areas of Turkey. After the 1970s, the increasing population and rising land costs led to the widespread construction of multi-story buildings and the use of fast construction systems. Accordingly, the construction of buildings with reinforced concrete skeleton structure systems has has become more dominant. Stone-structured buildings, often constructed without engineering services, suffer severe damage even from moderate earthquakes (Binici & Yakut, 2010). Therefore, evaluating the damage mechanisms caused by seismic effects in stone buildings is of great importance.

In this study, the effects of earthquakes that occurred in the last 50 years in Türkiye and its surroundings on stone-structured houses were analyzed and the resulting damage mechanisms were evaluated.

Material and Method

Within the scope of this study, the evaluation of damage mechanisms in stone masonry residential buildings due to the effects of moderate and large earthquakes in Turkey and its surroundings has been conducted based on literature data. First, the types and degrees of damage were identified, and then the possible causes of these damage types were evaluated. The number of stories, architectural plan characteristics, structural system, interior wall materials and system, type, form, and size of the stone material, masonry system, and mortar used in the masonry system were among the elements that were taken into consideration when conducting the assessments. Possible causes of damage associated with different damage types were identified and evaluated based on literature data, Turkish Earthquake Code (TEC), and comparative analysis principles.

Findings

The effects of past earthquakes have shown that stone masonry structures exhibit five different levels of damage: slight damage, moderate damage, severe damage, partially collapsed, and completely collapsed. In "slightly damaged" buildings, the types of damage observed include vertical fine cracks in the load-bearing interior and exterior walls, as well as diagonal fine cracks at the corners of door and window openings. Cracks defined as "thin" have a width of less than 10 mm. In slightly damaged buildings, stone fragmentation and dislodgement have been observed in the upper sections of chimneys. In the chimney areas of the exterior wall, some stones have detached from the thinned wall section. The vertical and diagonal cracks in "moderately damaged" buildings are 10 to 25 mm wide.

In buildings with the same damage level, the load-bearing wall is observed to have thinned due to stone detachment in the parapet below the window opening and the lintel area above it. In cracks wider than 25 mm, separations within the wall plane are observed. This condition elevates the damage level to a destructive category classified as "severe." Another type of damage seen in "severely damaged" buildings is the out-of-plane overturning of the exterior wall. In damage levels defined as "partially collapsed," the out-of-plane overturning of the exterior wall has occurred in two directions. As a result, it has been found that the wooden roof structure in buildings with the same damage level has also partially collapsed. In two-story buildings, along with out-of-plane overturning damage, partial fragmentation damage has been observed in the wooden construction floors and interior partition walls. Buildings with a damage level of "complete collapse" have been rarely detected (Figure 1).

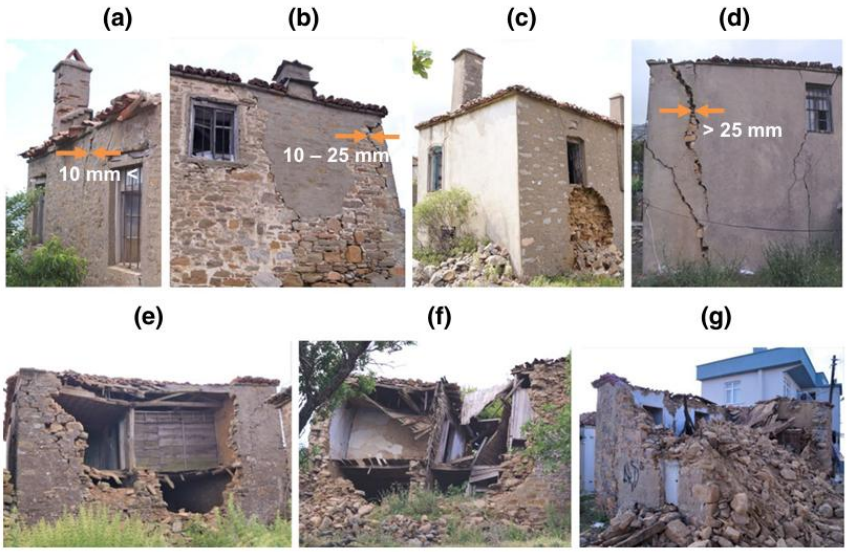

Figure 1. Building examples of the masonry structure according to the level of damage: a slightly damaged, b, c moderately damaged, d, e heavily damaged, f, g partially collapsed, (Göçer, 2020).

Conclusion

Evaluating the causes of the damage types based on the damage levels listed above is crucial both for strengthening the existing building stock with similar characteristics and for taking the necessary precautions in new constructions. In slightly damaged buildings, when the direction of the earthquake force is parallel to the wall, diagonal cracks occur, while horizontal and vertical cracks appear when the force is perpendicular to the wall. Cracks have occurred in high-tension zones. Shear stress, which occurs perpendicular to or along the plane of the wall, is the cause of the diagonal cracks that have developed at the corners of door and window openings.

The form of the stone blocks in the load-bearing wall, irregularities in the masonry system, and the lack of lintels on the load-bearing walls have caused vertical plane separations at some of the exterior wall corner joints due to the effects of the earthquake. According to the TEC (2018), there are certain limitations and dimensional characteristics for masonry structure

systems. According to the TEC (2018), in masonry buildings, reinforced concrete lintels must be applied at each floor level of the load-bearing walls, with a minimum width equal to the wall and a height of 30 cm.
Additionally, to ensure the "rigid diaphragm effect" in masonry buildings, the floor system must be made of reinforced concrete with a minimum thickness of 10 cm. At the junctions of exterior walls, stresses caused by horizontal forces become concentrated. No damage has been observed at the wall corners where large rectangular stone blocks are used. However, separation damage has occurred in some corner joints due to the use of smaller-sized stones. In buildings with lintel beams at intermediate levels, such damage is generally not observed. Another reason for this type of damage is the inadequate shear strength and wear resistance of the earth mortar that binds the stone blocks together.
In buildings with plastered exterior surfaces, protecting the mud mortar from water and moisture helps prevent a reduction in the mortar's strength. In structures with similar design features, where the masonry system uses cement mortar, the load-bearing walls generally show little or no damage, with only fine cracks that can be defined as slight damage.
In partially collapsed buildings, the main causes of the destructive effects can be listed as the absence of rigid lintels at the floor and roof levels of the load-bearing exterior walls, the use of rubble stone in the wall components, the non-homogeneity of the stone block size, the irregular masonry system, the low ductility of the mortar in the masonry system, and the presence of wooden construction for the interior partition walls.
In some buildings, due to the weak connection between the stone exterior wall and the wooden interior wall on the upper floors, the unsupported length of the load-bearing wall has been observed to reach levels of 6.00 - 8.50 meters in plan. This value exceeds the limit specified in the TEC (2018) (maximum 5.50 m). Destructive damage has also occurred due to the unidirectional load transfer of the wooden construction floor and roof structure. In the case of a floor and roof system that exhibits rigid diaphragm behavior, it can be said that the out-of-plane overturning of the exterior wall would be prevented.
Complete collapse damage in stone-structured masonry buildings due to earthquake effects is rarely observed. The main reason for this is the inflexible behavior of the non-homogeneous and brittle wall system.
The formation of damage mechanisms varies depending on the number of damage causes, plan characteristics, and certain structural features. According to the plan characteristics, an increase in the length of the unsupported load-bearing wall has led to the development of more destructive damage mechanisms in residential buildings.
In general, the lack of engineering services and the construction of most stone buildings in rural areas without supervision according to TEC principles are significant factors in the formation of destructive damage. The results of evaluating the damage mechanisms in stone-structured masonry buildings due to the effects of medium and large earthquakes in Turkey and its surroundings are important for the assessment of similar buildings under earthquake threat and for taking necessary precautions.

References

AFAD (Disaster and Emergency Management Authority). (2025). Preliminary assessment report on current seismic activity observed around the Santorini and Kolumbo Volcano in the Aegean Sea. Ankara: Earthquake Department, Disaster and Emergency Management Authority.
Bikçe, M. (2017). Taken and need to take precautions in Turkey's earthquakes. International Journal of Engineering Research and Development, 9(2), 25–31.
Binici, B., & Yakut, A. (2010). Earthquake hazard and damage on traditional rural structures in Turkey. Natural Hazards and Earth System Sciences, 10(3), 605–614. https://nhess.copernicus.org/articles/10/605/2010/
Göçer, C. (2020). Structural evaluation of masonry building damages during the April 24, 2014 Gökçeada earthquake in the Aegean Sea. Bulletin of Earthquake Engineering, 18(12), 3459–3483. https://doi.org/10.1007/s10518-020-00833-z
Güleç, A. (2023). Investigation of the effects of the Kahramanmaraş earthquakes on masonry structures. Journal of Engineering Sciences, 10(1), 634–650.
Olğun, T. N., & Karatosun, M. B. (2019). Rural architectural heritage conservation and sustainability in Turkey: The case of Karaca village of Malatya region. International Journal of Sustainable Development and Planning, 14(3), 237–246. https://doi.org/10.2495/SDP-V14-N3-237-246

Turkish Earthquake Code. (2018). Specifications for buildings to be built in seismic areas [in Turkish]. Ministry of Public Works and Settlement.

Impact of Deterioration Due to Environmental Factors on Seismic Performance of Traditional Timber Buildings in the Historical Peninsula in Istanbul

Abdüllatif Sarıkaya[a], Caner Göçer[b]

[a] Istanbul Technical University, Graduate School, Environmental Control and Construction Technologies, Türkiye
[b] Istanbul Technical University, Faculty of Architecture, Department of Architecture, Türkiye
sarikayaab@itu.edu.tr

Keywords: Timber Structure, Seismic Performance, Architectural Heritage, Traditional Architecture, Deterioration in Timber Buildings.

Aim

The Historical Peninsula is one of the key centers of Istanbul's cultural and historical heritage. The peninsula is included on the UNESCO World Heritage List. It is located within the administrative borders of Fatih district in İstanbul, at present. The Historical Peninsula is often referred to as "Sur İçi" (Inside the Walls). The peninsula is surrounded by the Sea of Marmara to the south, the Golden Horn to the north and the districts of Zeytinburnu and Eyüp to the west. Due to it is bordered by water on three sides, strong city walls were built throughout history to protect it. The land walls between Yedikule and Ayvansaray are still exist and have an important role in protecting the historical identity of the area. The area is significant for its civil and monumental buildings from both the Byzantine and Ottoman periods. This makes the peninsula an important place within the scope of global cultural heritage. Timber structures exhibiting characteristic features of traditional residential architecture possess significant architectural and historical value. Because of that, these structures are essential elements that require protection (Seçkin, 2012). These timber structures are not only important for their design but also for their symbolic meaning. These buildings reflect traditional construction techniques and give information about the craftsmanship, material choices and daily life of humans. These structures are seriously damaged because of environmental factors over time. Timber is sensitive to temperature and humidity changes, air pollution and damage from living organisms. This makes it risky to preserve these buildings for a long time (Wang et al., 2018; Lanata, 2015). This study aims to assess the long-term effects of environmental factors on the load-bearing elements of traditional timber buildings within Istanbul's Historical Peninsula, a site of significant architectural heritage. Focusing on how environmental deterioration compromises the seismic performance of these structures, the study offers preliminary recommendations to support the preservation of their structural integrity and architectural legacy.

Material and Method

In this study, the deterioration of traditional timber structures in Istanbul's Historical Peninsula, caused by environmental factors, was examined through fieldwork, on-site observations and a comprehensive literature review. An initial field survey was carried out across the Historical Peninsula to gain a general understanding of the condition of traditional timber buildings. Following this preliminary assessment, 24 buildings were subjected to detailed analysis. These buildings were selected based on visible signs of deterioration, such as material deformation, surface wear, and color changes. The common types of deterioration were identified during the study. A detailed assessment was then conducted to examine the relationship between environmental factors such as humidity, temperature fluctuations and air pollution. The impact of biological agents on the observed damages was also evaluated. The findings from the fieldwork were documented and compared with existing studies in the literature to highlight any recurring patterns of deterioration and to establish a deeper understanding of how environmental factors impact the structural integrity of these buildings. Furthermore, historical documents and previous research were reviewed to analyze how these buildings have withstood or succumbed to environmental conditions over time. This historical perspective allowed for a better understanding of the long-term effects of environmental stress on timber structures. The study also explored the impact of these deterioration processes on the earthquake performance of the buildings. The weakening of structural elements due to environmental damage was assessed

based on the collected data, taking into consideration both the current state of the buildings and their historical resilience to such factors. Lastly, based on the observations and the analysis of the deterioration processes, suggestions for conservation strategies were proposed. These recommendations aim to improve the sustainability and seismic resilience of these historic timber structures, emphasizing the importance of regular maintenance, moisture control, and the use of appropriate materials for restoration. The goal is to provide a comprehensive approach to the preservation of these culturally significant buildings, ensuring their longevity and structural safety in the face of environmental challenges.

Findings

Timber structures located in the Historical Peninsula are exposed to physical, chemical and biological deterioration over time as a result of environmental factors. These damage processes cause the structural parts to change shape. They also weaken the load-bearing system and reduce the overall strength of the structure. Among the primary factors directly influencing the durability of these timber buildings are humidity, temperature fluctuations, atmospheric pollutants and biological organisms (Yagci and Mazlum, 2016). Rain, snow, hail and frost cause physical damage to timber, leading to cracks, surface erosion and color changes. Because timber absorbs moisture, changes in humidity cause it to swell or shrink, which reduces the strength and stability of the load-bearing parts. Long exposure to sunlight causes the timber surface to lose its color and makes the fiber structure weaker over time. Chemical damage in timber structures is linked to air pollution and harmful gases like sulfur dioxide (SO_2) and nitrogen oxides (NO_x). These react with the timber and reduce its strength. This problem is worse in the peninsula because of increased pollution and traffic. Biological damage happens because high humidity helps fungi, insects and microorganisms grow, harming the timber. While they enter the building, water and moisture are big risks causing the timber to absorb water, deform and weaken.

Poor insulation, bad drainage, ignored condensation and hidden plumbing leaks make timber more open to fungi. If facade and roof damage are not repaired soon, the damage spreads to the load-bearing parts. Decay is common in parts like studs, sills, braces, floor joists and claddings, while metal fasteners usually suffer corrosion. This weakens the load-bearing system, making the building structurally deficient. To reduce moisture damage, moisture sources inside should be found and removed, timber parts dried well and timber kept away from damp surfaces. Proper insulation should be used to protect timber from moisture. In the traditional timber buildings of the historical peninsula, structural damage typically originates from deformations occurring in the roof covering and the failure to repair these deformations in a timely manner (Figure 1). The loss of the roof's functionality allows rainwater to infiltrate the structure. This situation accelerates moisture-induced deterioration in the timber load-bearing elements. Other components of the structure are subjected to various forms of damage. Moreover, the loosening of timber joints leads to the separation of structural elements. When this process continues without intervention, partial collapses have been frequently observed. Many buildings in the area have suffered complete structural failure over time because they were not properly maintained (Günay, 2007).

Figure 1. Inappropriate roof coverings.

Traditional timber frame systems are flexible and have some advantages in earthquakes. However, long-term exposure to weather weakens the connection points of the structural parts. Repeated loads and environmental effects reduce the stiffness

of timber over time, making it less effective. Floor coverings, staircases and joinery parts get worn out because of frequent use and friction and it weakens them. Insects and larvae that feed on timber damage it by making it porous. It leads to reducing the size of timber parts and their load-bearing strength. Timber exposed to sunlight, weather and air pollution for many years shows darkening, aging and loss of brightness. This mostly affects appearance and has less effect on earthquake performance. Long-term heat also causes expansion, texture separation and lower mechanical strength because of reduced density.

Poor workmanship and lack of maintenance cause damage in timber parts, such as cracking, splitting, and breaking, especially under side loads. Using materials that do not match the original during renovation, especially in cladding and wet areas, adds extra weight and speeds up the deterioration of timber elements. A related issue is the use of sheet metal on façades. Although it may protect the building from weather, adding sheet metal increases the load on timber structures and can accelerate deformation and damage. Therefore, careful consideration is needed when adding such materials to historic timber buildings (Figure 2). Effective moisture control, preventive measures against biological deterioration and appropriate fire safety strategies are of critical importance for ensuring both the sustainability and seismic performance of these traditional structures.

Figure 2. Extra load from inappropriate façade material replacement.

Conclusion

In the repair of timber structural elements, interventions can either replace damaged components or address issues in existing timber. When damage is detected in structurally significant timber elements, factors such as the extent of the damage, cost, aesthetic considerations, and reversibility should be carefully evaluated to ensure minimal disruption to the building's overall integrity. Decay-damaged timber requires the removal of compromised or weakened sections. These sections should then be replaced with treated, well-dried timber that matches the original in type, quality, and moisture content. If removal isn't possible, preservatives should be applied, and injection techniques used if necessary. However, many buildings in the Historical Peninsula are poorly maintained. Improper repairs weaken their structural integrity, particularly affecting seismic performance.

Interventions on historic timber structures should aim to preserve the building's original identity and integrity. Prior to intervention, the structure's current condition and load-bearing system must be thoroughly analyzed. The choice of methods, materials and chemicals must prioritize the building's preservation, avoiding harmful actions. Regular maintenance and periodic inspections are essential to detect and prevent deterioration early.

Traditional timber structures in the Historical Peninsula have suffered significant structural damage due to environmental factors, weakening load-bearing systems and decreasing overall durability. This damage affects the performance of buildings against dynamic loads such as earthquakes, posing a threat to both their safety and sustainability. Field studies show that timber materials deform from moisture, water, and atmospheric conditions, further compromising structural integrity. To protect these buildings and ensure their longevity, preservation strategies must be developed.

While the 12th Section of the Türkiye Building Earthquake Code provides detailed structural guidelines for traditional timber buildings, it lacks conservation principles focused on the long-term preservation and seismic performance of these

structures. Although the regulation specifies load-bearing system dimensions and connection details, it does not offer guidance on maintenance, repair, or material durability, which are crucial for ensuring the seismic performance of these structures.

The Timber Buildings Regulation, which came into force in 2025, takes a more complete approach to improving the performance of buildings, especially addressing deterioration through waterproofing. It emphasizes preventing water and moisture penetration in light-frame timber systems and building components exposed to environmental factors by ensuring the impermeability of the building envelope. Detailed solutions are proposed to avoid water ingress from the external environment into interior spaces, including proper design of facade slopes to ensure effective drainage and architectural features such as eaves and projections to redirect water away from the facade.

The preservation recommendations can be outlined as follows. Regular maintenance and inspections should be conducted, with periodic checks for early detection of deterioration. Moisture levels should be constantly monitored, and sources of water ingress should be eliminated. Decayed timber elements should be removed and replaced with similar, well-dried timber. Effective waterproofing should be applied, and roof covering should be regularly inspected. Preservatives should be applied to decayed timber to prevent further biological damage. Restoration methods should align with traditional techniques and scientific standards. Facade elements and drainage systems should be properly designed to prevent water accumulation.

In conclusion, insulation measures, improved drainage, and regular roof inspections are critical for preserving structural elements against moisture. Timber parts that are damaged by decay should be replaced with treated materials to enhance their resistance to biological damage. Restoration efforts should use methods compatible with traditional construction practices, prioritizing the structure's historical integrity. Preserving historic timber buildings ensures the sustainability of cultural heritage, and conservation efforts must adopt an interdisciplinary approach, supported by long-term strategies for the reinforcement and preservation of these buildings.

References

Günay, R. (2007). Geleneksel Ahşap Yapılar: Sorunları ve Çözüm Yolları. Birsen Yayınevi. İstanbul.

Yagci, S. F. & Mazlum, D. (2015). Traditional Timber Houses of Istanbul: Heritage Values and Preservation Problems. Journal of Architectural Conservation, 21(3), pp. 160-177.

Seçkin, N. P. (2012). An Assessment on Traditional Timber Structures in Süleymaniye and Zeyrek Districts of Historical Peninsula. ITU A | Z, 9(1), pp. 56-69.

Wang, J. Y., Stirling, R., Morris, P. I., Taylor, A., Lloyd, J., Kirker, G., Lebow, S., & Mankowski, M. E. (2018). Durability of Mass Timber Structures: A Review of The Biological Risks. Wood and Fiber Science, 50, pp. 110-127.

Lanata, F. (2015). Monitoring The Long-Term Behaviour of Timber Structures. Journal of Civil Structural Health Monitoring, 5, 167-182.

ARCHITECTURE

Architectural History

Architecture Design Theory

Building Construction Technologies

Building Materials and Technologies

Built Environment Design and Technologies

Conservation and Restoration

Environmental Control and Building Technology

Project and Construction Management

Sustainable Design

Developing One-part Geopolymer Binders by Using Ground Granulated Blast-furnace Slag and Ceramic Waste as Precursors

İlar Berfin İlbeyi[a], Ünal Anıl Doğan[a]

[a] Istanbul Technical University, Graduate School, Structural Engineering Program, Türkiye
ilbeyi17@itu.edu.tr

Keywords: Ceramic Waste, GGBS, One-part Geopolymer, Solid Activator, Waste Glass.

Aim

Concrete is the most widely used building material due to its durability, low cost and ease of handling. The main binding component of the concrete is Portland cement. According to studies, 0.8 tonnes of CO_2 are emitted into the atmosphere for each tonne of cement produced (Mohamada et al., 2022). Released greenhouse gas amount is 1.5 billion tonnes due to Portland cement production for each year (Singha et al., 2020). Since Portland cement has negative impact on the environment, improving an alternative greener material is very important. One of the promising option which can reduce consumption of Portland cement is using geopolymer binders. Geopolymers are formed by treating of aluminosilicate containing precursors with alkaline solutions or solids, known as activators. Geopolymers are classified as one-part and two-part according to the form of the alkali content. If the activator used in the geopolymer binder is solid, it is defined as one-part geopolymer, while if it is liquid, it is defined as two-part geopolymer. Using one-part geopolymers are more advantageous than that of two-part geopolymers in terms of ease of use and commercialization potential. The aim of this study is to develop one-part geopolymer binders, that can be a greener alternative to Portland cement, by using the waste materials.

Material and Method

Within the scope of this study, precursors and activator, which are the main components of the geopolymers, are derived from waste materials. Ground granulated blast-furnace slag (GGBS) and ceramic wastes were used as precursor materials, replacing each other in various proportions, while waste glass and NaOH were used for activator production. Instead of the hydrothermal method, which produces the activator in solution form, the thermochemical method was used to produce the activator in solid form.

According to the literature, for producing a solid activator used in one-part geopolymer, different molar ratio of SiO_2/Na_2O (silicate modulus), heating temperature and heating duration were examined. Studies have shown that, geopolymer mortars containing activator produced with silicate modulus of 1,0 and heating temperature between 150-300 ˚C, achieve higher compressive strength results (Vinai et al., 2019; Delgado Plana et al., 2024).

In this study, preliminary tests were conducted to observe the efficiency of solid activator. Different activators with silicate modulus of 0,5, 1,0 and 1,5 is produced at different temperatures of 150 ˚C, 250 ˚C, 350 ˚C and heating durations of 30, 75, 120, 150 and 180 minutes for preliminary tests. For making the NaOH and waste glass mixture homogenized, water was added to the blend by 25% wt of total mass of NaOH and waste glass. The efficiency of the produced activators were examined using geopolymer mortars containing only GGBS. The strength results of the geopolymer mortars produced to determine the appropriate temperature and duration for activator production are shown in Table 1.

Table 1. Strength results of mortars containing only slag, prepared with activators having different molar ratios, heating temperatures, and durations**.**

Mixture	$nSiO_2/nNa_2O$	Heating Temperature (ºC)	Heating Duration (min.)	Activator (wt.)	Flexural Strength (MPa)			Compressive Strength (MPa)		
					7th Day	14th Day	28th Day	7th Day	14th Day	28th Day
1	1,5	150	30	8,00 %	0,23	0,35	0,50	0,43	0,78	1,00
2	1,5	250	75	8,00 %	0,21	0,30	0,52	0,37	0,62	1,21
3	1,5	350	120	8,00 %	0,22	0,27	0,58	0,48	0,65	1,31
4	1,0	150	75	8,00 %	0,21	0,44	0,62	0,46	0,58	1,10
5	1,0	250	120	8,00 %	0,50	5,39	4,71	1,11	6,90	19,48
6	1,0	350	30	8,00 %	0,24	2,34	3,81	0,50	2,76	8,12
7	0,5	150	120	8,00 %	1,34	3,76	6,48	2,38	8,69	20,91
8	0,5	250	30	8,00 %	1,37	5,66	7,41	2,63	12,05	20,23
9	0,5	350	75	8,00 %	2,22	6,53	6,03	4,02	13,91	17,66
10	0,5	250	120	8,00 %	0,69	2,33	5,69	1,57	4,33	12,73
11	0,5	250	150	8,00 %	0,43	1,69	-	0,89	2,60	8,78
12	0,5	250	180	8,00 %	0,69	1,91	3,75	1,22	4,07	10,12

Twelve different mortars were prepared with a water/binder ratio of 0,45, containing 8% activator by weight, and were kept at room temperature until the testing age. After determining the flexural and compressive strengths of the mortars at 7, 14, and 28th day, it was found that the highest strength results were achieved with activators obtained by heating NaOH and waste glass at 250°C for 120 minutes, with a silicate modulus (SM) of 0,5 and 1,0.

After determining the optimum method for producing the activator with preliminary tests, ceramic wastes were introduced to the mixture as precursor in addition to GGBS. The obtained ceramic wastes were ground in a ball mill until it turned into powder and were made ready to use in the mixtures.

Precursor materials, waste ceramic and GGBS, were used to prepare geopolymer mortars by replacing each other at ratios of 20%, 40%, 60%, and %80 by weight. The water/binder ratio was fixed as 0,45, and the activator content in the mixture was kept constant as 15% by weight. The mixtures were produced for both silicate moduli of 0,5 and 1,0. Mix proportions of 8 different produced mixtures are given in Table 2.

Table 2. Mix proportions of geopolymer mortars containing GGBS and waste ceramics.

Mixture	GGBS (%wt)	Ceramic Waste (%wt)	$nSiO_2/nNa_2O$ (SM)
K1	80	20	0,5
K2	60	40	0,5
K3	40	60	0,5
K4	20	80	0,5
K5	80	20	1,0
K6	60	40	1,0
K7	40	60	1,0
K8	20	80	1,0

During the preparation of the mortars, the precursors and the activator were first mixed in dry form. Then, water was added to prepare the paste, and finally, sand was added to obtain the geopolymer mortar. Prepared mortars were placed in steel molds with the dimensions of 40x40x160 mm, and stored at room temperature until the testing age.

Findings

Figure 1 shows the compressive strength results of geopolymer mortars at 7, 14 and 28th day containing activator with SM of 0,5 and 1,0. The sample K1, containing an activator with a silicate modulus of 0,5 and a precursor composition of 80% blast furnace slag and 20% waste ceramics reached compressive strength of 20 MPa on the 28th day. The mortar produced with the same precursor composition but with a silicate modulus of 1,0, which was named as K5, achieved compressive strength of 12,4 MPa on the 28th day.

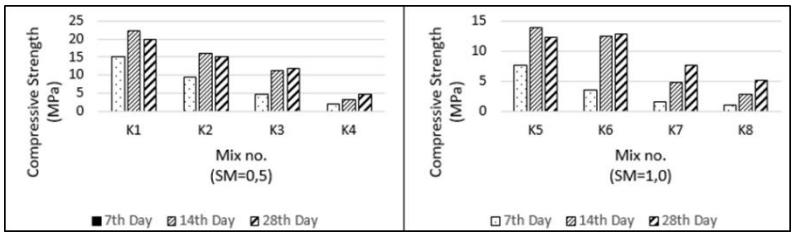

Figure 1. Compressive strength results of geopolymer mortars at 7, 14, and 28th day.

When comparing the strength values at 14th and 28th days, it was observed that mixtures produced with activators having a SiO_2/Na_2O molar ratio of 0,5 and a precursor composition containing 40%, 60%, and 80% GGBS, largely completed the geopolymerization reaction by the 14th day. From Figure 1, it can be seen that K1, K2 and K3 mixtures, containing 80%, 60%, and 40% GGBS, respectively, did not gain strength after 14th day, while mixture K4, having GGBS %20 by weight, gained 30% of its total strength after 14th day. Among the samples produced with an activator having silicate modulus of 1,0, K5 and K6, containing 80% and 60% slag by weight, respectively, did not gain strength after 14th day, while the K7 and K8 samples, containing 40% and 20% slag, respectively, gained 38% and 46% of their total strength after the 14th day.

Conclusion

This study aims to develop geopolymer binders by utilizing waste materials. The optimal silicate modulus and production process for the activator, using NaOH and waste glass, were determined through mixtures prepared with blast furnace slag. Mortars were prepared using waste ceramics and blast furnace slag as precursors, and their mechanical properties were assessed with flexural and compressive strength tests. As a result of the study, it was determined that the most suitable activator composition for blast furnace slag based mixtures was obtained with a silicate modulus of 0.5 and 1.0, with heating process at 250°C for 2 hours. It was seen that, increasing GGBS proportion in precursors results in higher strength values. It was also observed that increasing waste ceramic content in the precursor reduced early-age strength but, it allowed strength development at later ages.

Further studies should be conducted to commercialize geopolymer mortars, which are being developed as an alternative to reduce cement production.

This study includes the preliminary work of the project numbered 223M280, supported by TÜBİTAK.

References

Delgado-Plana, P., Bueno-Rodriguez, S., Pérez Villarejo, L. & Eliche-Quesada, D. (2024). Synthesis of solid sodium silicate from waste glass and utilization on one part alkali activated materials based on spent oil filtering earth. Environment Science and Pollution Research, https://doi.org/10.1007/s11356-024-33368-w

Mohamada, N., Muthusamy, K., Embong, R., Kusbiantoro, A., & Hashim, M. H. (2022). Environmental impact of cement production and solutions: A review. Materials Today: Proceedings, 48, 741-746.

Singha, N.B., Kumarb M., Raic S. (2020). Geopolymer cement and concrete: Properties. Materials Today: Proceedings, 29, 743-748.

Vinaia, R., Soutsos, M. (2019). Production of sodium silicate powder from waste glass cullet for alkali activation of alternative binder. Cement and Concrete Research, 116, 45-56.

Evaluation of Damage Mechanisms of Reinforced Concrete Industrial Structures in Past Earthquakes in Turkey

Bahar Şevli[a], Caner Göçer[b]

[a] İstanbul Technical University, Graduate School, Environmental Control and Building Technology Program, Turkey
[b] İstanbul Technical University, Faculty of Architecture, Department of Architecture, Turkey
sevli20@itu.edu.tr

Keywords: Past Earthquakes, Industrial Structure, Reinforced Concrete Earthquake Damage, Earthquake Performance, Structural Irregularity.

Aim

The fact that earthquakes are a sudden natural event and cause a large number of loss of life and property are the main reasons why earthquakes are seen as a greater threat than other natural disasters (Ataman & Tabban,1977). In the last thirty years, many earthquakes with magnitudes greater than M:6.0 have occurred in areas close to fault lines in different regions of Turkey. These large earthquakes have caused many casualties and many buildings to be destroyed or heavily damaged, resulting in large economic losses (Erdik vd., 2000). When the earthquakes in Turkey are analysed, it is understood that the industrial zones, which are the locomotive of the country, were also greatly damaged by the earthquake. In these industrial areas, which constitute a large share of the country's population and economy, significant structural damages, destruction, demolitions and loss of labor were experienced in industrial buildings. The fact that most industrial zones in Turkey are built on active fault lines necessitates the analysis of the earthquake performance of industrial structures in these regions. Especially the earthquake readiness of industrial buildings in the Marmara Region, which hosts about half of the industry in Turkey, should be determined.

Material and Method

Past major earthquakes provide important data to understand the causes of damage that the industry clustered in and around İstanbul, one of the most important cities in Turkey with its high population density and consequently a large number of buildings, industrial and commercial activities, may be exposed to in the face of a possible major earthquake. For this purpose, in this study, the types and causes of damage in reinforced concrete (RC) industrial structures in past earthquakes were examined. The main subject of the study is the evaluation of the architectural and structural earthquake performance and damage mechanisms of RC industrial buildings, especially in the earthquakes experienced in recent centuries. In this study, it is aimed to determine the structural irregularities in the horizontal and vertical directions in industrial buildings, structural faults that may affect the seismic performance of the structure and to reveal the important factors that cause damage and to emphasize earthquake-resistant building design.

Findings

The results of the research on the damage mechanisms of industrial structures affected by the 1999 Gölcük and Düzce earthquakes and the 2023 Pazarcık and Elbistan earthquakes provide important data that should be taken into consideration for the analysis of the seismic performance of industrial areas in Istanbul under the threat of earthquakes (Sezen vd., 2003). When the data on these damage mechanisms are analysed, it is seen that the damages in industrial buildings exhibit similar characteristics. In the field work carried out after the earthquake, destructive damages occurred in many buildings that were constructed in low standards and without receiving engineering services, especially without complying with the principles of the Turkish Earthquake Code (TEC). In regions with high earthquake risk, the most important feature required for structures is earthquake safety and ductile behaviour, adequate strength and limited lateral drift (lateral rigidity) conditions should be provided for earthquake performance. As it can be understood from the field investigations and research reports

in the past earthquakes, the design phase of the structures and the production process of the structure have a great importance in the RC structures to meet these conditions (Işık vd., 2024;Sagbas vd., 2024).

Ground and structure interaction should be carefully considered in building design and ground conditions should be accurately determined by in-situ geotechnical tests. Soil liquefaction led to settlement of structures in Adapazarı in the 1999 Kocaeli earthquake (Scawthorn &Johnson, 2000). In-situ observation studies and researches conducted in buildings that have experienced earthquakes show the importance of the behaviour of the ground in earthquakes and the need to consider the structure-ground interaction.

Major reinforcement failures such as missing or incorrect stirrup connections at joints, insufficient wrapping, incorrect clamping, etc. are the cause of devastating damage to structures in the 2023 Pazarcık and Elbistan earthquakes (Figure 1). 'According to TEC (2007), in all earthquake zones, columns of all RC systems with high or normal ductility level, column-beam joints, It is stated that the stirrups used in curtain end zones and beam hugging zones are special seismic stirrups and there must be 135 degree curved hooks at both ends of special seismic stirrups' and 'According to TEC (2018), It is stated in the regulation that the diameter of the transverse reinforcement should not be less than 8 mm and the spacing should not exceed 150 mm in enclosed joint and the diameter of the transverse reinforcement should not be less than 8 mm and the spacing should not exceed 100 mm in non-enclosed joint'. In most of the reinforced concrete structures examined after the earthquake, inadequate reinforcement ratio, weak reinforcement anchors, weak reinforcement detailing in column-beam joints, stirrup spacing up to 25-30 cm in column-beam joints and 90 degrees at the end of the seismic stirrups, insufficient length hooks are observed. Inadequate transverse reinforcement spacing in the plastic joint region and the absence of transverse reinforcement in column beam connections caused serious damage to the structures of industrial buildings.

Figure 1. Reinforcement failures (Sagbas vd.,2024).

Field data from the 1999 Gölcük and Düzce earthquakes show that deficiencies arising from the construction phase of RC buildings such as low concrete quality, unribbed reinforcement bars, corrosion and workmanship defects can also cause

different levels of damage. Many problems occurred in concrete mixing due to the use of unsuitable aggregates such as smooth and large sizes, high water/cement ratios and inadequate curing. In all earthquake zones, it is mandatory to use quality controlled, maintained and vibrator placed concrete according to the definition in TS-500. The use of vibrator is important in order to prevent segregation in concrete, otherwise excessive amount of air void remains in the concrete and this situation adversely affects the strength of concrete. Along with poor concrete quality, the use of unribbed bars in RC structures has further reduced the interlocking mechanisms between concrete and reinforcement details, leading to significant bond problems. In earthquake reports in relation to RC industrial buildings, severe corrosion was observed in most buildings, causing cracking and spalling of the concrete cover and exposing the reinforcement.

Structural irregularities seen in almost every earthquake zone are the main cause of earthquake damages and destructions. According to TEC (2018), structural irregularities are analysed in two groups as plan plane and vertical direction. Plan irregularities are A1-torsional irregularity, A2-floor discontinuity and A3-protrusions on the plan. Vertical irregularities are B1-weak floor irregularity, B2-soft floor irregularity and B3-discontinuity of vertical elements of the structural system. Soft storey, defined as the rigidity irregularity between adjacent floors, is a common cause of damage in RC industrial structures in past earthquakes. If the ground floor height in the structure is higher than the upper floors and the use of infill walls is removed on any floor, a sudden rigidity change occurs in the horizontal load distribution in the structure. The use of mezzanine floors, especially on the ground floor, seen in RC industrial buildings, causes floor discontinuity and soft floor irregularity. In past earthquakes, increasing the gap ratio on the ground floor facades of RC industrial buildings and reducing the use of infill walls to allow the use of large workshop areas caused weak floor irregularity, which negatively affected the earthquake performance. In order to prevent the complete collapse of RC buildings and to provide a ductile and strong structural behaviour, it is essential that the columns are stronger than the beams. This issue becomes more important especially in structures that are fragile due to soft and weak floors. One of the main reasons for pancake type collapse of structures in earthquakes is weak column- strong beam applications. The use of band windows, which is frequently encountered in industrial buildings, causes short column damages. Short column damage is one of the most important causes of damage in RC industrial buildings in past earthquakes (Figure 2). Joint gaps are left between adjacent building blocks due to different ground settlements and earthquake effects. 'According to TEC (2018), the minimum joint gap to be left considering temperature change, height difference and ground conditions shall be at least 30mm up to 6m height and at least 10 mm shall be added to this value for every 3m height after 6m'. In the design of adjacent buildings, sufficient joint space is left between the RC buildings to allow free displacement of the buildings during an earthquake. Otherwise, if there is not enough space between two buildings, these buildings collide and damage each other. Especially in adjacent buildings with different floor levels, examples of the floor slab at the floor level of one building causing serious damage to the column of the other building are encountered in earthquake field reports. As can be understood from the examples observed in the recent 2023 Pazarcık and Elbistan earthquakes, the use of mezzanine floors, single storeys at two storey heights, soft storey and weak storey damage mechanisms due to the difference in the infill wall ratio between the storeys and short column damage mechanisms due to the use of band windows in RC industrial buildings are the main reasons for the destructive effects on the structures and the decrease in the earthquake performance of the structures. In addition, inadequate functioning of the building control mechanism and incorrect applications due to lack of control are important factors in the occurrence of earthquake damages.

Figure 2. Short column damage (left) and soft- weak storey damage (right).

Conclusion

Important industrial cities such as İstanbul, Tekirdağ, Kocaeli and Bursa are under the threat of the northern fault. Most of the industrial buildings, which constitute a large share of Turkey's economic power, are located in these areas with high earthquake risk, and the fact that the majority of the population lives in this region increases the size of the danger. Although there are studies on determining the seismic performance of RC buildings, there is great benefit in enriching the literature on the subject with comprehensive research and studies by analysing the seismic performance of RC industrial buildings. In past earthquakes, the evaluation of the seismic performance of RC industrial buildings, which constitute a significant share of the building stock in Turkey, is very important in order to examine and understand the effects of structural features and irregularities on the seismic performance of existing RC industrial buildings. The evaluation data obtained after the researches in the past earthquakes are important in terms of strengthening the existing structures and taking the necessary precautions for the new structures to be built.

References

Afet ve Acil Durum Yönetimi Başkanlığı. (2018). Türkiye Bina Deprem Yönetmeliği. Resmî Gazete. https://www.resmigazete.gov.tr/eskiler/2018/03/20180318M1-1.htm

Ataman, O., Tabban, A., (1977), Türkiye'de Yerleşme Alanlarının Doğal Afetler İle İlişkileri, Mimarlık, 4 (25).

Erdik, M., Durukal, E., & Sesetyan, K. (2000). 1999 Kocaeli Depremi'nin Zemin Sıvılaşmasına Etkisi Üzerine Gözlemler. Boğaziçi Üniversitesi Kandilli Rasathanesi.

Işık, E., Avcil, F., Hadzima-Nyarko, M., İzol, R., Büyüksaraç, A., Arkan, E., Radu, D., & Özcan, Z. (2024). Seismic Performance and Failure Mechanisms of Reinforced Concrete Structures Subject to the Earthquakes in Türkiye. Sustainability, 16(15), 6473. https://doi.org/10.3390/su16156473

Sagbas, G., Sheikhi Garjan, R., Sarikaya, K. et al. (2024). Field reconnaissance on seismic performance and functionality of Turkish industrial facilities affected by the 2023 Kahramanmaras earthquake sequence. Bull Earthquake Eng **22**, 227–254 (2024). https://doi.org/10.1007/s10518-023-01741-8

Scawthorn C. & Johnson G.S. (2000). Preliminary report Kocaeli (Izmit) earthquake of 17 August 1999, Engineering Structures 22 (2000) 727-745.

Sezen, H., Whittaker, A. S., Elwood, K. J., & Mosalam, K. M. (2003). Performance of reinforced concrete buildings during the 1999 Düzce and Kocaeli, Turkey earthquakes, and their implications for seismic design of RC moment frames. Structural Journal, 100(4), 861–877.

ARCHITECTURE

Architectural History

Architecture Design Theory

Building Construction Technologies

Building Materials and Technologies

Built Environment Design and Technologies

Conservation and Restoration

Environmental Control and Building Technology

Project and Construction Management

Sustainable Design

Evaluation of Exterior Cladding Materials in Educational Buildings in Terms of Embodied Energy

Dilfuruz Kara[a], Caner Göçer[b]

[a] Istanbul Technical University/Graduate School Institute, Environmental Control and Construction Technologies Program, Türkiye
[b] Istanbul Technical University, Department of Architecture, Environmental Control and Construction Technologies Program, Türkiye
sahar22@itu.edu.tr, gocercan@itu.edu.tr

Keywords: Educational Buildings, Facade Cladding Materials, Environmental Impact, Carbon Emissions, Sustainable Architecture.

Aim

Türkiye is a geographically diverse country that encompasses various climate zones. This diversity makes it inevitable for climatic factors to have a direct influence on material selection in building design. In particular, exterior cladding materials are determined not only by aesthetic expectations but also by technical requirements such as climate conditions, durability, and energy efficiency. However, the increasing population and demand for construction have led to significant energy consumption in the production processes of building materials, resulting in considerable carbon emissions. In this context, it is of critical importance to develop strategies aimed at reducing carbon emissions associated with the production of exterior cladding materials, which constitute the largest surface area of the building envelope (IEA, 2023; Republic of Türkiye Ministry of Environment, Urbanization and Climate Change, 2023). A visual representation of this situation is provided in Figure 1.

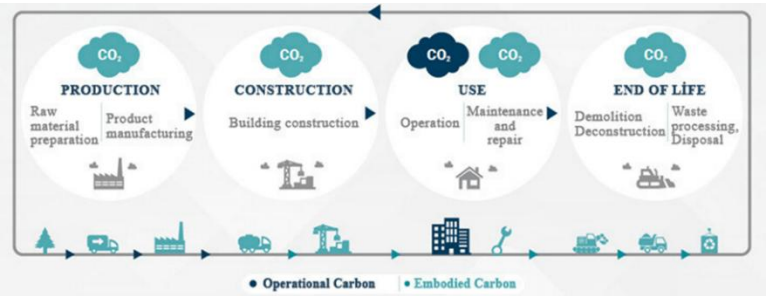

Figure 1. Decarbonization Roadmap for Türkiye's Building Sector, (Url 1).

As illustrated in Figure 2, the construction sector accounts for approximately 40% of global energy consumption and 36% of carbon emissions (IEA, 2023). These figures necessitate the adoption of sustainability-oriented material selection in the building industry.

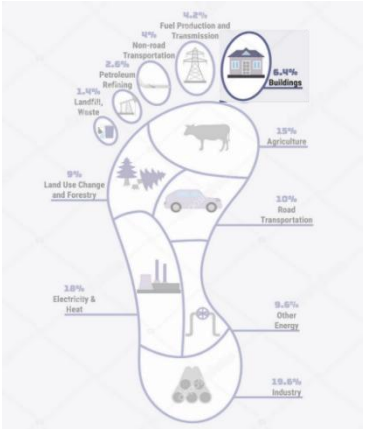

Figure 2. CO_2 Ecological Footprint Diagram (Url 2).

The environmental impacts of buildings are not limited to their direct energy consumption; they are also significantly influenced by the energy consumed during the production, transportation, and processing of materials—a factor referred to as embodied energy. Therefore, identifying and quantifying embodied energy values provides a scientific foundation for selecting environmentally friendly materials in the construction sector (Dixit et al., 2010).

Educational buildings, in particular, should be addressed with a focus on energy efficiency due to their significant share within the building stock and the high rate of user circulation they accommodate (Gökçen Akkurt et al., 2015). The exterior cladding materials used in such buildings should be evaluated not only based on physical attributes such as aesthetics, durability, and maintenance but also in terms of their environmental impacts. In this context, the use of materials with low embodied energy has become increasingly important (González & Navarro, 2006).

The primary aim of this study is to determine the embodied energy values associated with the production processes of exterior cladding materials used in educational buildings in Turkey, and to present an evaluation framework for sustainable material selection based on these data. By comparatively analyzing the carbon emissions produced during the manufacturing stages of various materials, the study seeks to support environmentally responsible design decisions.

Material and Method

In this study, the analysis was conducted by modeling the exterior façade surface of a typical classroom unit found in educational buildings in Turkey. The dimensions of the referenced façade module were assumed to be 7 × 4 meters (28 m²), with a transparency rate of 30%. Accordingly, calculations were based on a net 20 m² of opaque surface area. Material analyses were performed using the LCA One Click software. This tool provides data based on Life Cycle Assessment (LCA) methodology and calculates energy consumption during the production processes of building components in units of $kgCO_2e$.

To ensure realistic system modeling, not only the exterior cladding material but also all layers constituting the building envelope—including substructure systems, adhesives, fasteners, thermal insulation, and plaster layers—were incorporated into the calculation. In this way, the total embodied energy of the cladding systems was comprehensively determined. Figure 3 presents a screenshot from the software interface showing the layers included in the analysis.

Building Part	Resource Name	Details	Quantity	Unit	Thickness mm	Comment
External walls and facade	Aluminium profile (updated dataset), 2700 kg/m3, EN15804+A1, ref. year 2018		120	kg		
External walls and facade	Aerated concrete, 500 kg/m3, non-reinforced, P4 05, EN15804+A1, ref. year 2018		4	m3		
External walls and facade	Stone wool (mineral wool) insulation, unfaced, L = 0.03 W/mK, R = 1 m2K/W, 30mm, 2.1 kg/m2, 70 kg/...		20	m2	30	
External walls and facade	Gypsum plaster for interior applications, 10 mm, 8 kg/m2, 1004.74 kg/m3, Rimano UNI (Saint-Gobain ...		18	m2		
External walls and facade	Aluminum composite panel, curtain walling/facade, mineral filled, 4 mm, 5.85 kg/m2, B2 (Saray)		20	m2	4	

Figure 3. Screenshot taken from the LCA One Click Interface.

The exterior cladding materials evaluated in this study are as follows:

- Cement plaster
- Aluminum composite panel
- Solid wood cladding
- Wood composite panel
- Granite cladding
- Ceramic cladding
- Sinterflex

Given that educational buildings constitute a significant portion of the building stock in Turkey, the environmental performance of the materials used in these structures is crucial—both for reducing the current carbon footprint and for defining long-term sustainability strategies. Therefore, in this study, a system cross-section was developed for each analyzed material, and the associated carbon emissions were comparatively examined through the software interface.

Findings

According to the calculations, cement plaster exhibited the lowest level of embodied energy consumption among the exterior cladding materials analyzed. Cement plaster was found to emit only 1257 $kgCO_2e$ of carbon emissions. In contrast, aluminum composite panels ranked highest, with a carbon emissions value of 4522 $kgCO_2e$. This significantly high figure is attributed to the aluminum production processes, which require intense heat and complex refinement procedures.
Materials with medium levels of carbon emissions are as follows:

- Solid wood: 1393 $kgCO_2e$
- Wood composite: 3625 $kgCO_2e$
- Ceramic cladding: 2818 $kgCO_2e$
- Granite cladding: 2495 $kgCO_2e$
- Sinterflex: 3565 $kgCO_2e$

These values are illustrated in the graph presented in Figure 4 below.

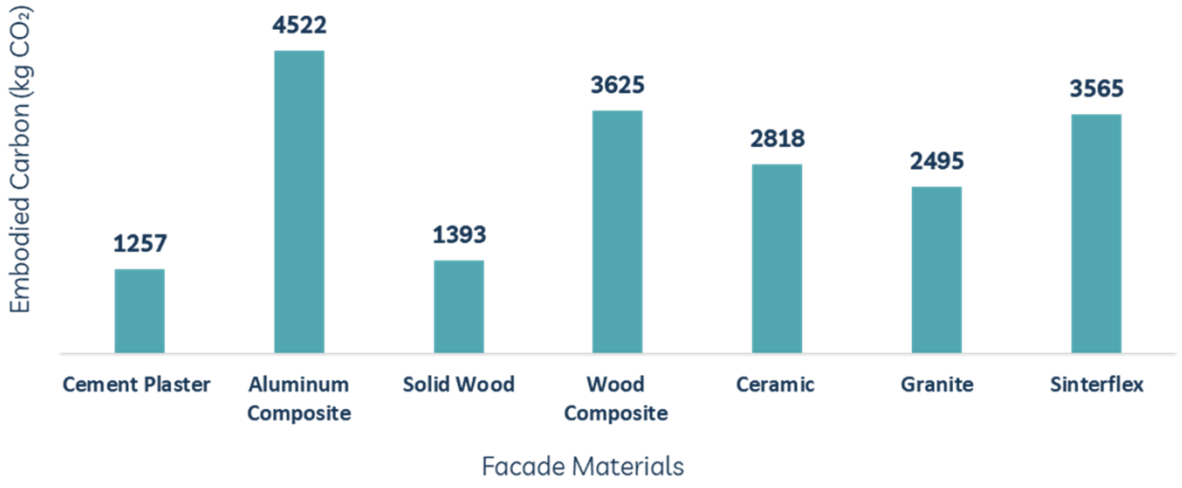

Figure 4. Carbon Emissions Totals for a 20 m² Classroom Unit.

These findings indicate that wood-based materials derived from natural sources are environmentally advantageous due to their lower carbon emissions during the production process. On the other hand, materials such as ceramic and sinterflex, despite exhibiting higher levels of carbon emissions, may offset this impact through performance-related advantages such as durability, ease of maintenance, and longevity.

Therefore, material selection should not be based solely on carbon emissions; rather, the overall contributions of materials throughout their life cycle must be considered holistically.

Conclusion

The results obtained reveal significant variations in the carbon emissions generated during the production processes of exterior cladding materials. The lowest carbon emission value was observed in cement plaster, whereas the highest value was recorded for aluminum composite panels. This disparity is primarily due to the intensive thermal treatments and refinement processes required in aluminum production. Materials such as solid wood, wood composite, granite, ceramic, and sinterflex exhibited moderate levels of embodied energy consumption.

Comparative analysis indicates that cement plaster produces approximately 72.2% less carbon emissions than aluminum composite, solid wood 69.2% less, granite 44.8% less, ceramic 37.7% less, and sinterflex 21.2% less. These figures highlight the critical importance of using low-carbon-emission materials in the building envelope to reduce environmental impacts.

Furthermore, the intensive usage of educational buildings necessitates that selected materials be evaluated not only in terms of energy performance but also through multidimensional criteria such as durability, maintenance requirements, longevity, recyclability, and fire resistance. Therefore, sustainable architectural approaches must encompass holistic performance goals beyond merely low carbon emissions.

In conclusion, material selection strategies that incorporate embodied energy considerations in exterior cladding represent a vital tool for reducing the environmental burden of the construction sector. Conscious choices in educational buildings will contribute significantly to both short-term energy savings and long-term carbon reduction targets.

References

Dixit, M. K., **Fernández-Solís, J. L.**, **Lavy, S.**, & **Culp, C. H.** (2010). Identification of parameters for embodied energy measurement: A literature review. Energy and Buildings, 42(8), 1238–1247.

Gökçen Akkurt, G., Aydın, D., & Hassouneh, K. (2015). Architectural and environmental performance evaluation of schools: A case study from Turkey. Sustainable Cities and Society, 17, 1–10.

González, M. J., & Navarro, J. G. (2006). Assessment of the decrease of CO_2 emissions in the construction field through the selection of materials: Practical case study of three houses of low environmental impact.

International Energy Agency (IEA). (2023) Energy Technology Perspectives 2023.

International Organization for Standardization (ISO). (2006). ISO 14040: Environmental management — Life cycle assessment — Principles and framework. Geneva: ISO.

Straube, J., & Burnett, E. (2005). Building science for building enclosures. Building Science Press.

One Click LCA. (2024). Life cycle assessment software.

T.C. Çevre, Şehircilik ve İklim Değişikliği Bakanlığı (ÇŞİDB). (2023). Binalarda enerji performansı yönetmeliği. Ankara: Resmî Gazete.

Url-1 https://www.oneclicklca.com

Url-2 https://thecityfixturkiye.com, date retrieved 10.05.2025.

Url-3 www.istockphoto.com, date retrieved 10.05.2025.

The Impact of Façade Cladding Materials on Carbon Emissions in Urban Renewal Projects: The Case of Istanbul

İkranur Sena Akkaya[a], Caner Gocer[a]

[a] Istanbul Technical University, Department of Architecture, Environmental Control and Building Technology Program, Turkey
akkayaik23@itu.edu.tr

Keywords: Urban Renewal, Façade Cladding Materials, Embodied Energy, Carbon Emissions, Environmental Sustainability.

Aim

The rapid growth of cities and population growth have significantly increased energy demand. Increased energy consumption leads to a substantial increase in carbon emissions. Consequently, ensuring environmental sustainability has become a primary agenda item for expanding urban areas (Durguter, 2012). It is emphasized that the negative effects on the environment should be reduced with sustainable urbanization policies, especially the need to protect natural ecosystems and transform existing areas in accordance with sustainability principles (Hamurcu and Buldurur, 2017; Tezangi, 2014).
The main aim of urban renewal projects is to renovate buildings that pose earthquake risks and have reached the end of their physical lifespan and to build more safer and modern buildings in accordance with zoning regulations. However, energy consumption and environmental impacts must also be considered during the urban renewal process. Existing buildings often have inadequate thermal insulation in their exterior walls, leading to high energy consumption for heating and cooling (Lo, 2015). Urban renewal projects have the potential to address this issue by offering energy-efficient exterior wall systems. In addition, the production phase of the construction materials can lead to consumes a significant amount of energy and high carbon emissions. Therefore, the selection of materials, which constitute the majority of the building envelope is an important issue to be considered in urban renewal projects and requires a detailed evaluation in terms of sustainability.
The selection and production processes of façade cladding materials hold significant importance in terms of sustainability. The majority of carbon emissions in the construction sector occur during the production phase of building materials. Therefore, the energy consumption and carbon emissions in the production processes of facade cladding materials are key factors for making more environmentally sustainable material choices. This study aims to calculate and compare the embodied energy of commonly used façade cladding materials in urban renewal projects in Istanbul. Design parameters in residential buildings—such as plan typologies, façade arrangements, and building heights—directly influence the volume of the external shell, leading to variations in embodied energy ratios. Therefore, this study analyze and compare the embodied energy values of selected façade cladding materials under different architectural parameters. Developing strategies to reduce the impact of the building sector on global carbon emissions and establishing a scientific basis for sustainable architectural approaches are also among the main objectives of the research.

Material and Method

This study examines a total of 169 buildings from low-rise, mid-rise, and high-rise urban renewal projects in Istanbul. The commonly used façade cladding materials in these buildings were identified, and their floor plans and façade arrangements were analyzed.
The most commonly used aluminum composite, wood composite, ceramic coating and sinterflex panels were evaluated in the facades of the buildings examined. Within the scope of the calculations, the energy consumption per unit volume of the materials was determined and the unit production energies were calculated in accordance with the researches and standards accepted in the literature. According to the data, the embedded energy values of the materials examined are: Aluminum Composite (150 MJ/kg), Wood Composite (12 MJ/kg), Ceramic Cladding (12 MJ/kg), and Sinterflex (14 MJ/kg).

In this study, using the manual calculation method, the analyses were carried out by multiplying the building facade areas with the embedded energy values of the materials. The façade area was determined based on the impact of architectural parameter variations on the volume of the external shell, and calculations were performed accordingly.
The architectural parameters identified in the analysis of buildings were classified: linear and square forms in terms of building shape; parapeted and non-parapeted window types in terms of façade arrangement; and , frame-vertical band, horizontal band, and flat façade layouts in terms of façade elements.
Façade arrangements were categorized into eight different scenarios based on combinations of , frame-vertical band, horizontal band, and parapeted/non-parapeted window designs. Plan typologies were classified into two scenarios: linear and square forms. Building height was categorized as low-rise, mid-rise, and high-rise, with corresponding heights of 4, 8, and 16 stories, respectively, while the floor height was assumed to be 3.20 meters.
Since these parameters directly influence the volume of the building envelope, they were used as fundamental variables in carbon emission calculations. In the scenarios created with the manual calculation method, the structural properties of the wall layers are kept constant and calculations are made only for each façade cladding material. The embodied energy per unit area of the materials are calculated to determine the total carbon emissions for different building scenarios.
Different façade materials were compared based on design parameters, and solutions with the lowest carbon footprint are identified. Additionally, the differences in carbon emissions among various material types have been analyzed for their impact on architectural design decisions.

Findings

The initial findings of the study clearly demonstrate the impact of façade cladding materials, building design, and façade arrangements on carbon emissions.
The calculation data shows that there are significant differences in the embodied energy values of façade cladding materials. Aluminum composite exhibited the highest embodied energy value, making it the material with the greatest carbon burden. Conversely, ceramic cladding and sinterflex panels offered more environmentally friendly alternatives due to their lower embodied energy values.
Plan typology, building height, and façade arrangement variables directly affect embodied energy values. Notably, embodied energy levels increased significantly in high-rise buildings. This phenomenon can be explained by the increase in façade surface area and the corresponding rise in the amount of cladding material used as building height increases.
While flat façade designs exhibited lower embodied energy values compared to other façade elements, non-parapeted façades with , frame-vertical band resulted in lower carbon emissions than other design solutions. However, scenario that include parapeted-horizontal bands and frame-vertical bands exhibited higher embodied energy consumption. This situation can be explained by the use of additional facade elements, such as horizontal band and frame-vertical band, which increase the exterior surface area of the building and, consequently, the amount of material used.
Regarding building shape, square-plan buildings had slightly lower embodied energy values than linear-plan buildings due to their more compact structures.
Figure 1 shows the embodied energy values for each scenario and material used in the study. The corresponding design scenarios are defined and coded in Table 1, based on variations in architectural design parameters such as building form, height, façade arrangement, and parapet presence.

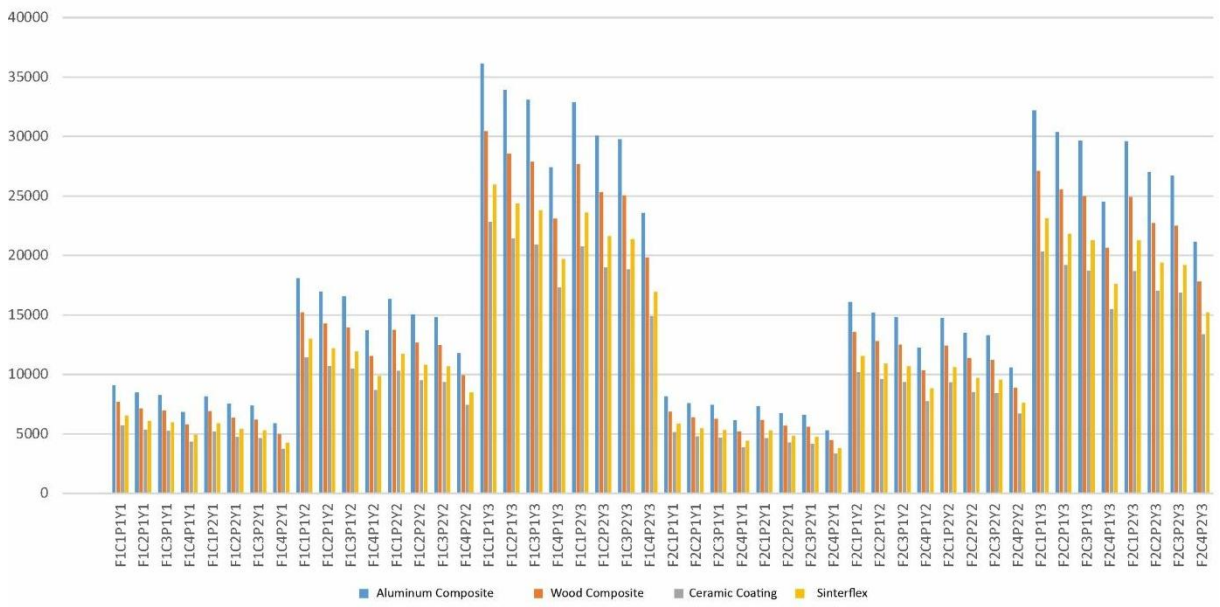

Figure 1. Embodied energy values of each scenario and material.

Table 1. Scenario Definitions Based on Architectural Design Parameters.

Design Parameters	Scenarious
parapet present (h:85 cm)	P1
no parapet	P2
horizontal-vertical band	C1
horizontal band	C2
vertical band	C3
flat façade	C4
linear form	F1
square form	F2
4 story (h:12.8 m)	Y1
8 story (h:25.6 m)	Y2
16 story (h:51.2 m)	Y3

Conclusion

This study highlights that material selection is a critical factor in sustainable building design, and embodied energy values must be considered. Replacing high-embodied-energy materials such as aluminum composite with alternatives like ceramic cladding and sinterflex panels, which have lower carbon footprints, will support environmental sustainability.

It was determined that design decisions related to building height, geometric form, and façade arrangements directly impact energy consumption and carbon emissions. More compact square-plan buildings enhance energy efficiency and reduce the use of unnecessary façade elements, thereby minimizing embodied energy consumption. In this context, the use of low-embodied-energy materials and the adoption of simplified façade designs in sustainable urban transformation projects will significantly contribute to reducing environmental impact.

Future research should not be limited to embodied energy but should also comprehensively examine operational energy consumption. The total carbon emissions of a building are directly related not only to the embodied energy of materials used during construction but also to the energy consumed throughout the building's lifespan. Therefore, heating, cooling, and other operational energy components should be analyzed in detail within sustainable building design processes.

Considering that façade materials' thermal insulation performance, site placement, and architectural characteristics significantly influence operational energy consumption, material selection should not only prioritize low embodied energy but also enhance energy efficiency.

In conclusion, achieving a sustainable construction process requires selecting low-carbon-emission materials, optimizing building geometry and façade design for energy efficiency, and implementing strategies to minimize natural resource consumption. This holistic approach will help reduce the environmental impact of the construction sector and contribute to the development of more sustainable and livable cities.

References

Durguter, H. (2012). Kent modelleri ve sürdürülebilir kent yönetimi. Turkish Studies, 7(3), 1053-1065.

Lo, K. (2015). The "Warm Houses" program: Insulating existing buildings through compulsory retrofits. Sustainable Energy Technologies and Assessments, 9, 63–67. **Url-1** https://doi.org/10.1016/j.seta.2014.12.003

Tezangi, N. R. (2014). Sustainable urbanism: Analysis of sustainable environment principles in practical urban form. Journal of Engineering and Architecture, 2(2).

Ulubaş Hamurcu, A., & Aysan Buldurur, M. (2017). Sürdürülebilir kentsel dönüşüm için performans göstergeleri. Planlama (TMMOB Şehir Plancıları Odası Yayını), 27(3), 222-235.

ARCHITECTURE

Architectural History

Architecture Design Theory

Building Construction Technologies

Building Materials and Technologies

Built Environment Design and Technologies

Conservation and Restoration

Environmental Control and Building Technology

Project and Construction Management

Sustainable Design

Ottoman Brick Stamps

Nevriye Öztürk[a], Gülsün Tanyeli[b]

[a] Istanbul Technical University/Graduate School, Department of Architecture, Restoration Program, Türkiye
[b] Istanbul Technical University/Faculty of Architecture, Department of Architecture (Emeritus), Türkiye
ozturkn@itu.edu.tr

Keywords: Ottoman Bricks, Flat and Modern Bricks, Brick Stamps, Inscriptions and Symbols of the Stamps.

Aim

Bricks have been one of the fundamental construction materials, which were used by various civilizations throughout the ages. This durable material, which could be easily, inexpensively, and rapidly produced, was also employed during all periods of Ottoman architecture.

Studies associated with the Ottoman bricks have been mainly carried out in the academic field of architectural history, and the building elements and masonry bonding techniques in which bricks were used have been examined. Whereas, the majority of brick related studies, which have been conducted in the academic discipline of restoration, have determined the current condition and the existing problems of brick masonry structures and developed conservation proposals for these buildings. The scholars and specialists, who have published research on Ottoman architecture, have devoted very little attention to the brick material itself and its properties. Their interest in the material has been limited to brick sizes, and the relationship between these dimensions and the periods of Ottoman architecture. However, there are other characteristics of Ottoman bricks that need to be focused on and investigated. The brick stamps, in particular, have not been sufficiently researched. The first scholar who revealed the existence of the practice of stamping bricks during the Ottoman era was Semavi Eyice in the early 1980s. He stated that the presence of various stamps on Byzantine bricks had been widely known, but there had been no evidence of Ottoman brick stamps and no publications on the subject until that time. He also pointed out that researchers should conduct studies on these stamps in the future, and emphasized that it would be possible to obtain detailed information about the Ottoman brick industry by increasing the number of studies on this matter (1981). Since then, stamped bricks of Ottoman era have attracted increasing attention from both private collectors and researchers. While a few articles related to this topic were published, it must nevertheless be pointed out that, no comprehensive and systematic study has been conducted on the issue at hand.

Ottoman stamps are significant and merit further research because they provide diverse, robust and reliable data about the historical bricks on which they appear. The first-hand information gained from the stamp is essentially related to the production of that brick. For instance, the place, the facility, and sometimes the date of manufacturing can be determined from the inscriptions of Ottoman brick stamps. Therefore, the inscriptions have the ability to confirm a certain place and, in rare examples, a certain time. It is considered that by benefiting from stamped bricks' potential for validation, even unstamped ones can be associated with the details of their production. One can argue that the data received from Ottoman brick stamps may constitute a credible reference for research undertaken in other fields (history of architecture, archaeology, building materials and technologies, etc.), other periods (Byzantine era bricks, etc.), and other materials (tiles, archaeological ceramics, etc.) as well.

Ottoman bricks have two main types: one of which is flat bricks in the form of thin plates with a square or rectangular plan, and the other one is modern bricks in the form of rectangular prisms. These two fundamental types of bricks differ from each other not only in their shapes but also in their sizes, subordinate types and production technologies. However, stamps can be observed on both of them. These stamps range from simple finger markings to sophisticated inscriptions and symbols.

The aim of this article is to examine and classify the Ottoman brick stamps in terms of form and content.

Material and Method

In order to achieve the goals of the study, field work and archival research methods were used and documentation was made. A number of private collectors were interviewed, several collections were evaluated, and on-site examinations of brick masonry buildings were made within the scope of field work. Historical documents, periodicals and books with regard to the Ottoman bricks and their manufacturing were found and translated from French, Italian, and Ottoman Turkish into contemporary Turkish in the context of archival research. For the purpose of identifying the characteristics of the stamps; brick samples were collected from masonry buildings and procured from different people and institutions, photographs were taken, and detailed survey drawings of the samples were made.

Findings

After examining hundreds of bricks, the stamped brick types, distinct positions of the stamps, characteristics of inscriptions, and symbols were determined.

Flat and modern bricks have numerous subtypes, but not all of them were stamped. An attempt was made to identify the stamped ones by using archival research and fieldwork. It is stated in a 19th century document that brickmakers were instructed to imprint stamps on Beylik, Çarşu, Topaç, and Kebir bricks (BOA.C.İKTS.9/428). The only stamped flat brick sample that was found was broken, so its exact dimensions and form could not be specified. But it is thought that it could be a Beylik or Çarşu brick. The other stamped flat brick example that was observed in Eyice's article has a rectangular form (1981). From its shape and dimensions, it is thought that it could be a half brick, which is called "kuzu tuğla" in Ottoman terminology. Pressed, yard, machine, chamfered, and frogged bricks are subtypes of solid modern bricks, and three and six holed bricks are subtypes of perforated modern bricks, on which stamps were encountered during the fieldwork. However, it is thought that the stamped flat and modern brick types are not limited to these. Since brick is a material used in the load-bearing system, stamp detection is difficult and generally possible in partially or completely damaged structures and during restoration.

There are three main positions where stamps were applied on brick surfaces: the upper bed face, the bottom bed face, and the stretcher face. The detected stamps of flat bricks were positioned only on their upper bed faces. However, on modern bricks, stamps can be observed on all three faces.

Inscriptions can be classified into five categories depending on their content and the information they provide. These categories are inscriptions with names, letters, numbers, places, and statements. The names in the inscriptions may be the name and surname of the manufacturer or the name of the company. The two capital letters in the inscriptions are the initials of the brickmaker's name. Inscriptions with 1-, 2-, and 4-digit numbers were encountered during research. One- and two-digit numbers are thought to be some kind of identification numbers given to the brickyards to distinguish their products from others in regions where many manufacturers were located together. Four-digit numbers indicate a year that may represent the production time of the brick. The place names seen in the inscriptions indicate the locations of factories or brickyards. Some examples include the names of the cities, while others provide more details, such as district names or even the full addresses. Some inscriptions consist of promotional and complimentary expressions. These statements can be considered as advertisements placed on the product.

The symbols can be divided into five groups according to their form: symbols that include animals, floral patterns, celestial bodies, geometrical shapes, and common objects. It can be said that the most preferred symbols were the bee, the butterfly and the moon and star.

The compiled information also led to secondary findings regarding the Ottoman brick making industry. Important brick production centres, especially the hubs in which industrial establishments were accumulated, were specified. Moreover, the names of high-profile manufacturers and companies in the Ottoman brick industry were distinguished. Additionally, a catalogue that consists of the photographs, the dimensions, and detailed information of the bricks that were subjected to inspection was prepared. The entire catalogue in question will be included in the appendix section of the relevant PhD thesis from which this article was created.

Conclusion

In conclusion, Ottoman brick stamps can be classified into different groups according to their location, content and form. But more importantly, the value of the data received from Ottoman brick stamps should be underlined. Finally, it should be pointed out that this study was carried out with the hope that it would contribute to a better understanding of the Ottoman bricks and brick industry, as suggested by Eyice nearly half a century ago.

References

Eyice, S. (1981). Osmanlı Devri Türk Yapı Sanatında Damgalı Tuğlalar. Sanat Tarihi Yıllığı (Vol. IX-X, pp. 155-162). İstanbul Üniversitesi

Türkiye Cumhuriyeti Cumhurbaşkanlığı Devlet Arşivleri Başkanlığı Osmanlı Arşivi (BOA), Cevdet İktisat Fonu (C.İKTS.), Dosya no: 9, Gömlek no: 428 (9/428).

Examination of the Transformation of Kırklareli Urban Conservation Area and Its Surroundings between 2004 and 2022 in the Context of Conservation and Sustainability

Zeynep Gökçen [a], Zeynep Eres Özdoğan [b]

[a] Istanbul Technical University, Graduate School, Restoration Program
[b] Istanbul Technical University, Faculty of Architecture, Department of Architecture
gokcenz20@itu.edu.tr, eresze@itu.edu.tr

Keywords: Kırklareli, Yayla Square, Urban Conservation Area, Architectural Conservation, Restoration.

Aim

According to the Architectural Heritage Conservation Charter of ICOMOS Turkey, urban sites are areas that contain cultural and natural environmental elements (such as structures, gardens, vegetation, settlement patterns, walls) that have architectural, historical, artistic, and local characteristics, and their value increases due to their presence together and their integrity [1]. The urban fabric of Yayla Square and the surrounding neighborhoods constitute the traditional historical settlement of the Kırklareli province. With the decision taken by the Edirne Regional Council for the Conservation of Cultural Heritage in 1996, Yayla Square and its surroundings were designated as an Urban Conservation Area. Following this designation, in 2000, a Conservation Zoning Plan and Implementation Provisions were prepared at scales of 1:1000 and 1:500. With the Conservation Plan, some buildings were registered as examples of civil architecture that should be preserved. In the decisions regarding the site area, there are decisions made for registered structures, traditional structures, new structures, and their surroundings. In 2004, within the scope of the Conservation Project-II course of the ITU Restoration Master's Program, detailed analytical studies were carried out on the basis of street textures and parcels in and around the Urban Conservation Area, and as a result, a conservation project was created. The site protection project carried out for Yayla Square and its surroundings, which has undergone changes over the years, constitutes an important data for evaluating the current site area decisions and practices, identifying the transformation in the area, and detecting the structures that have not survived to the present day.

In this study, research and fieldwork started in 2022. Analytical studies at a 1:1000 scale were conducted based on inventory, documentation, and map drawing. In 2004, an evaluation was conducted by comparing the fieldwork and parcel-based analytical studies carried out as part of the ITU Conservation Project-II course within the scope of the ITU Restoration Master's Program with the analytical studies performed in 2022. This paper aims to present the transformation processes of the area by comparing the data from 2004 to 2022 and to develop recommendations for sustainable conservation planning for the future. These recommendations aim to preserve the cultural heritage values found in the urban site and its surroundings.

Material and Method

In this study, Yayla Square and its surroundings have been considered at the scale of the site. The study area encompasses the site area and its surroundings (Figure 1). Research and fieldwork were conducted in 2022. Documentation work was carried out through observations and photographs. It was determined that the cadastral map of Yayla Neighborhood and its surroundings does not accurately reflect the current situation. The area's plan was updated by processing the 2021 aerial photograph obtained from the Directorate General For Mapping. To document the transformation in the area, analytical studies were conducted at a 1:1000 scale. The analytical studies include environmental condition analysis, cadastral and inventory data, fill-gap analysis, floor count analysis, construction system analysis, registration status analysis, property status analysis, usage status analysis, function and preservation status analysis.

An evaluation was made by comparing the fieldwork and parcel-based analytical studies conducted in 2004 as part of the ITU Restoration Master's Program Conservation Project-II course with the analytical studies performed in 2022. In addition

to these studies, the conservation zoning plan and implementation provisions were examined, along with aerial photographs taken between 1956 and 2021, obtained from the Directorate General for Mapping, to assess the development and transformation of the urban conservation area.

The decisions made by the Edirne Regional Council for the Conservation of Cultural Heritage, approved projects and inventory forms have been reviewed. There are numerous written sources related to Kırklareli province and Yayla Neighborhood. Academic studies containing the texture of the urban site area, civil architectural elements, and restoration works applied have been examined. The book Kırklareli and Traditional Houses, prepared as part of the summer school project conducted by the Architectural Restoration Program of Mimar Sinan Fine Arts University, with its survey drawings, has served as a reference source.

Studies prepared in the field of architectural and urban conservation have been reviewed to understand the concept of urban conservation areas, their architecture, and construction techniques. Additionally, laws, regulations, and agreements related to architectural conservation have been examined to assess the current situation in the area.

Figure 1. Urban Conservation Area and Study Area (Adapted from a 2021 aerial photograph [2]).

Findings

The urban site area located in the central district of Kırklareli province is part of the Yayla and Demirtaş neighborhoods. Yayla Square is situated at the border of these the two neighborhoods. Yayla Square has been used as a gathering and event space from the 19th century to the present day [3]. Around the square, there are photographs from the time of gathering in a building that was used as a school during its period.

The site area and its surroundings contain buildings made with different architectural traditions, including masonry construction systems, wooden frame systems, and mixed construction systems (Figure 2). In addition to the majority of two-story houses with gardens, single-story buildings showing the character of rural settlements with courtyards have also been observed. Most of the buildings are currently used as residences. It has been observed that some of the traditional buildings are no longer in use. To protect the unused buildings from external factors, garden walls have been raised, and the entrances to the buildings have been closed (Figure 3).

Figure 2. Examples of Masonry and Timber Frame Construction Systems.

Figure 3. Example of Traditional Building with Closed Entrances.

As a result of the comparison of the analytical studies prepared within the scope of the ITU Restoration Master's Program, it has been observed that the residential function density has been preserved in the buildings. Although some buildings suffer from the problem of becoming ruins due to neglect, it has been observed that many buildings have been re-functionalized and are in use through restoration and reconstruction practices (Figure 4). It has been determined that most of these buildings have been converted into museums. An example of restoration practice is the transformation of Vali Faik Üstün Primary School into a hotel after its restoration (Figure 5). Although the conservation project suggested maintaining the same function, it has created an important accommodation area for visitors from outside the city and abroad in the area.

Figure 4. Neglect and Deterioration of Buildings Example.

Figure 5. Example of a Restored Building.

It has been observed that the existing terrace roofs have been closed. The analysis revealed that the original paving, which was shown as road coverings, has not survived to the present day. Additionally, the majority of courtyard pavings in registered and traditional buildings have also not survived. The demolition of the building along with its courtyard, the removal of the courtyard paving, and the pouring of concrete are among the reasons for this. Although most of the traditional garden walls have been preserved to the present day, some have had brick or concrete block additions made on top of them. In the new buildings constructed within the site area, it has been observed that the number of floors is three, including the ground floor. It has been observed that the rural character buildings surrounding the site area have gradually been demolished and replaced with high-rise structures. Some buildings have been demolished due to neglect, and their plots remain vacant (Figure 6).

Figure 6. Registered Parcel.

The compared analyses have been evaluated in line with the conservation zoning plan and implementation provisions. These provisions include a decision to prevent the construction of terrace and attic floors in newly built structures. Although there has been a decrease in the number of existing terrace roofs, there is also an example of a terrace roof application in the new building. Additionally, there are buildings where the condition of using traditional roof tiles as roofing material has not been applied. It has been observed that changes have been made in the area designated for preserving the road paving, and the original material is no longer present. It has also been determined that the garden gates, which were to be preserved, have not survived to the present day. In the new construction outside the site area, it has been found that the number of floors has increased, and no buffer zone has been designated in the zoning plan for these areas. A decision was made to relocate the transformer building in Yayla Park to another location, but it has been determined that no changes have been made in the current situation.

Conclusion

It has been observed that the cultural heritage value of the Kırklareli Urban Conservation Area has been maintained, while significant changes and various conservation issues have arisen in the area, particularly due to new constructions in recent years. Thanks to the conservation project prepared in the past, inventory studies, and published academic works, the transformation of Yayla Square and its surroundings over the past eighteen years has been examined. Based on the data obtained from the research, the conservation issues within the site area have been identified. Although zoning decisions have been made for buildings with a rural settlement character, they have not been registered, leading to conservation issues. The non-use of traditional buildings, along with neglect, has initiated the process of decay and demolition. These buildings have been proposed for registration to ensure the protection and transfer of cultural values for the future. Additionally, the concepts of "Interaction-transition zone" in Law No. 2863 and "Buffer zone" in the Valletta Principles should be included in the site area decisions [4][5]. As a result of decisions made under these concepts, a transition area in line with the conservation approach should be created from the site area to its surroundings.

References

Akın, N. (2006). Kırklareli'nde Kentsel Belgeleme ve Koruma, Historical Researchment at Strandza Mountains & in their Vicinity, 22–25 May 2006, Kırklareli (pp. 55-63)

General Directorate of Mapping. (2021). Aerial photograph of Kırklareli

ICOMOS Turkey Architectural Heritage Conservation Charter / 2013. https://www.icomos.org.tr, date retrieved 22.06.2024.

ICOMOS The Valletta Principles for the Safeguarding and Management of Historic Cities, Towns and Urban Areas. 2011. https://www.icomos.org.tr, date retrieved 22.06.2024.

Law No. 2863 Kültür ve Tabiat Varlıklarını Koruma Kanunu. (1983) T.C. Resmi Gazete, 18113, 23 July 1983.

The Rural Settlement Structure and the Challenges of Preserving Traditional Housing in Tokat Bağbaşı (İbibse) Village

Erva Köşker[a], Zeynep Eres Özdoğan[b]

[a] Istanbul Technical University, Graduate School, Restoration Program, Turkey
[b] Istanbul Technical University, Faculty of Architecture, Department of Architecture, Turkey
kosker16@itu.edu.tr, eresze@itu.edu.tr

Keywords: Bağbaşı, Conservation, Cultural Heritage, Restoration, Tokat.

Aim

Bağbaşı (İbibse) Village is a rural settlement located in the central district of Tokat province. The village's old name is recorded as "İbibse" or "İlbis" in sources. The name "İbibse" is still used by the local population. It is believed that a city from the Roman period existed in this region and that the village name originates from there. During the Republican period, village names began to be changed to Turkish names. The village took the name "Bağbaşı" due to the abundance of vineyards and gardens. It is located 20 km from the central city of Tokat. The village is situated between two creek beds that feed the Yeşilırmak River, and its settlement pattern is oriented towards the north, built on a sloping area. The historical street layout and traditional buildings have been preserved to this day. Recently, archaeological remains from the Roman period were discovered in a region within the village settlement. Therefore, it can be said that the village is a multi-layered rural settlement area. Due to its representation of rural settlement, Bağbaşı Village has been considered worthy of examination in this paper.

The villagers make their living through agriculture and small-scale livestock farming. Each family also provides its daily needs with vegetables and fruits grown in their gardens. The population of Bağbaşı Village has significantly decreased because the majority of its residents have migrated to the city center. Those who remain in the village are mostly abandoning their traditional houses and building new living spaces on the outer edges of the historical settlement area. Most of the new buildings are used seasonally. The abandoned structures are mostly used as storage, and over time, these neglected buildings deteriorate.

This paper aims to define the historical significance of Bağbaşı Village, identify the cultural values that need to be preserved, document its historical settlement fabric, and propose sustainable conservation recommendations for the preservation of the rural settlement. In this context, the physical, social, and economic characteristics of the village and the central district of Tokat, to which the village is affiliated, as well as the historical development process, are examined.

Material and Method

In this study, the historical settlement fabric of Bağbaşı Village has been documented, with both its architecture and traditional village life considered together. Through field studies conducted in 2023, the architectural layout of the village and the physical characteristics of the buildings were examined, and analytical maps at the site scale were created. The entire study area was documented with photographs between 2023 and 2024. It was determined that the cadastral map of Bağbaşı Village is up to date, and new buildings constructed in recent years have been added. The built environment, architectural, and rural elements were thoroughly analyzed, and a 1/500 environmental condition analysis was developed. To reveal the architectural identity of the area and its conservation issues, 1/1000 scale analytical studies were conducted.

In addition to the analysis of the historical settlement, the architectural features of traditional houses have also been studied at the scale of individual buildings. A total of 24 traditional buildings, selected from those at risk of destruction, were examined in detail. The buildings were documented using traditional survey techniques and original floor plans were completed at a 1/100 scale, while rural architecture inventory forms were filled out. The architectural features, such as the positioning and orientation of the buildings, building entrances, and additionals, have been examined. Typology have been

conducted to better interpret the documented buildings in the village. By examining the architectural changes of traditional buildings over time, conservation issues were explained.
Documents related to the village were scanned at the Presidential Archives of the Republic of Turkey, and the "Temettuat Defteri" was translated from Ottoman Turkish to Turkish and examined. Historical maps covering the province to which the village belongs and documents regarding the change of the village's name were reviewed in the relevant sources. Oral interviews were conducted with the villagers, and information was gathered about the village's history and buildings. Traditional rural architecture, construction techniques, and building materials were interpreted by reviewing previous studies prepared in the field of conservation.

Findings

The traditional single-storey buildings in Bağbaşı Village are generally constructed using stone materials. In two-storey buildings, the ground floor consists of stone walls, while the upper floor features a timber frame system with adobe filling. The buildings' plots include attached or separate structures such as barns and haylofts. The village settlement is oriented to the north, and there are entrances to the buildings from every facade.
The Georgian House, known to be the oldest structure within the historical settlement fabric, consists of a two-storey construction with stone and timber frame system. There is a barn attached to the building. According to oral sources, the original windows on the building's facade has been changed and recently the building has been divided to accommodate two families. However, the original doors on the upper floor and the closets in the rooms have been preserved to this day. The building is currently used seasonally.
The migration of the majority of the village population to the city center has had significant effects on traditional buildings. This particularly caused changes in village life and the abandonment of traditional buildings. Due to neglect, these traditional structures have deteriorated and become unusable over time. As a result, traditional buildings are increasingly at risk of destruction. Some villagers, however, have chosen not to completely abandon village life but instead have constructed new houses using modern construction techniques and materials on their own plots. The abandoned traditional buildings on the same plots are typically used as storage. Some users who continue to live in the village seasonally have abandoned traditional structures and built new living spaces outside the historical settlement area. These new settlements, built on agricultural land, are causing a transformation in the traditional structure of the village and historical settlement fabric.
The village settlement includes a mosque, primary school, village wedding hall and a health clinic. The old mosque of the village has collapsed over time. However, the minaret, built using traditional construction techniques with bricks, has been preserved to this day. Recently, a new mosque has been constructed on the site of the old mosque. The primary school, located at the entrance of the historic settlement area. Afterward, children from the village continue their education at schools in the city center. An archaeological excavation in the schoolyard has recently uncovered pots and artifacts dating back to the Late Roman Empire. This area has been registered as a 3rd Degree Archaeological Conservation Site. On the opposite side of the archaeological site, there are wall remains believed to belong to an inn. The village wedding hall and health clinic have lost their functionality in recent times.
The water channels found in the study area hold significant importance in the village settlement and agricultural lands. They are primarily used for irrigation in traditional village life. The water channels are generally open, but in locations where roads pass over them, they have been covered. The old mill located to the south of the historical settlement area has been lost to the present day. There is a pool near that area. Two different water sources, one in the southeast and one in the southwest outside the settlement area, have endured to the present day.
The main source of income for the villagers is agriculture and their daily life is largely spent working in the fields. They also provide their daily needs from the vegetable gardens within the village settlement. In addition to agriculture, small-scale livestock farming is also common.

Figure 1. The Historical Settlement Fabric of Bağbaşı Village.

Figure 2. Traditional Houses in Bağbaşı Village.

Figure 3. Traditional Houses in Bağbaşı Village.

Figure 4. An Example of Traditional House in Bağbaşı Village.

Figure 5. An Example of Traditional House in Bağbaşı Village.

Figure 6. The Interior of the Georgian House in Bağbaşı Village: Original Examples of Closets and Doors.

Figure 7. An Example of Traditional House Interior in Bağbaşı Village.

Conclusion

Based on the data obtained from the research, the architectural conservation issues of Bağbaşı Village have been identified. The easy access to electricity and water for the villagers has significantly impacted the traditional way of life. The interior structure of the houses is being changed to adapt to new requirements. Some buildings are being modified with additions that are far removed from traditional materials and techniques, or existing spaces are being reshaped. This results in the destruction of the original architecture of the interior. Roof repairs made with new materials and the replacement of windows and doors with new materials of different sizes on the facade are among the repairs made without proper consideration.
In the development of the conservation approach for Bağbaşı Village, ICOMOS's Charter on The Built Vernacular Heritage (1999) has been examined. The traditional houses and barns identified within the historic settlement will be proposed for registration. Inappropriate additions that disrupt the facade design and do not conform to the architectural layout should be removed. Additions should be made in accordance with new requirements, without altering the original form of the traditional structure.

After the large-scale migration to the city center, the abandoned traditional houses are left neglected and are at risk of destruction over time. Many families living in the village are abandoning their traditional structures and building new living spaces on the outer edges of the historical settlement. These new settlements are being constructed without the use of traditional materials and techniques. As a result, they are disrupting the historical settlement fabric. However, new settlement should be designed in a way that does not damage the historical settlement fabric and does not affect agricultural land. The agricultural economy of the village should be revitalized. In this way, different incentives should be provided to motivate the population who moved to the city center to return to their village.

References

Erdem, F. (2024). Tokat ili merkez köylerinden derlenen yeradlarının halk etimolojisi ve toponimi bağlamında incelenmesi. (Yüksek Lisans Tezi). Samsun Üniversitesi, Lisansüstü Eğitim Enstitüsü, Samsun.
Mat, Z. (2016). Temettüat Defterlerine Göre Kazabadkazasının Sosyal ve İktisadi Yapısı (1844-1845). (Yüksek lisans tezi). Gaziosmanpaşa Üniversitesi.
Sönmez, S. (2023). XV. Yüzyıl Ortasında Tokat Nahiyesi: İskân ve Nüfus. Sosyal Bilimler Metinleri, 2023(2), 189-208. DOI: 10.56337/sbm.1358381.
ICOMOS Geleneksel Mimari Miras Tüzüğü
T.C. Cumhurbaşkanlığı Devlet Arşivleri, Tapu Tahrir Defteri (T.T.d.), No: 2, Tokat Defteri, 859 (1455).

Facade Finishes in Early 20th Century Istanbul: History and State of Conservation

Bersu Çelik[a], Işıl Polat Pekmezci[b]

[a] Istanbul Technical University, Graduate School, Restoration Program, Türkiye
[b] Istanbul Technical University, Faculty of Architecture, Department of Architecture, Türkiye
celikb17@itu.edu.tr

Keywords: Architectural heritage, Modern building materials, Renders.

Aim

Discussions on authenticity have significantly influenced architectural conservation theory. Material authenticity is now internationally recognized. Since the Venice Charter of 1964, various documents have presented the importance of original materials in the preservation of cultural heritage (Polat-Pekmezci, 2024). An important example of these documents is the 'Nara Document on Authenticity'.

Today, architectural conservation theory has a perspective that covers buildings, materials and construction techniques from all periods. Conservation interventions are being carried out on twentieth-century buildings and widely used cement mortars as they are the documents of the modern construction culture. The Madrid New Delhi document of ICOMOS ICS20C is an important guide on 20th century buildings. According to the document the 20th century was characterized by innovative structural solutions, building materials and construction techniques and there is a need to research and develop specific repair methods to modern buildings (Docomomo International, 2017). More than a hundred twentieth-century buildings are on the World Heritage List and the preservation of these structures is on the agenda. When carrying out conservation efforts on modern buildings, it is essential to determine a suitable function for re-use and also to sustain the material characteristics of the buildings. The effective conservation of 20th century buildings requires a comprehensive knowledge of the materials used. This paper aims to document, analyze, and discuss the current state of conservation and the potential for conserving materials used in the architectural surfaces and finishes of modern architectural heritage in Istanbul, Türkiye.

Material and Method

The study focuses on buildings constructed in the first half of 20th century in the districts of Beyoğlu, Şişli, Fatih, and Kadıköy where the registered buildings of the Republican period are prominent in İstanbul (Kudde, 2024).

The research methodology was divided into three stages. In the first stage, academic sources from the relevant period were compiled and evaluated to gather information on the construction techniques, materials used, and architectural details. The primary source of information was the architectural journal, Mimar/Arkitekt, which offered valuable insights into the building materials and construction methods through its articles and photographs.

The second stage involved examining the current condition of the materials referenced in the publications, enabling a better understanding of the terminology and techniques used during that period. Fieldwork included locating the buildings, capturing detailed photographs, and creating sketches to document construction techniques and details. The final stage involved assessing the conservation status of the buildings by comparing their original condition with their current state.

Findings

The Arkitekt Journal, established in the 1930s, is a valuable resource for information on modern buildings, their materials and construction techniques. In the early years, the focus was predominantly on residential buildings, with architects Abidin Mortaş, Seyfi Arkan, Mimar Hüsnü, Adil Denktaş, Zeki Sayâr, Emin Onat, and Rebii Gorbon contributing to the design and construction. Multi-storey apartment buildings were common in neighborhoods like Ayazpaşa, Maçka and Nişantaşı, while two-storey garden houses were built in Suadiye, Kalamış and Moda. The buildings are constructed using reinforced concrete systems and cementitious materials. The floors are finished with decorative cement tiles, terrazzo or terrazzo tiles especially

in circulation and wet areas. Prefabricated stair treads can be made of cement mortar containing colorful aggregates. The facades were enhanced with various application techniques (Shown in Figure 1.).

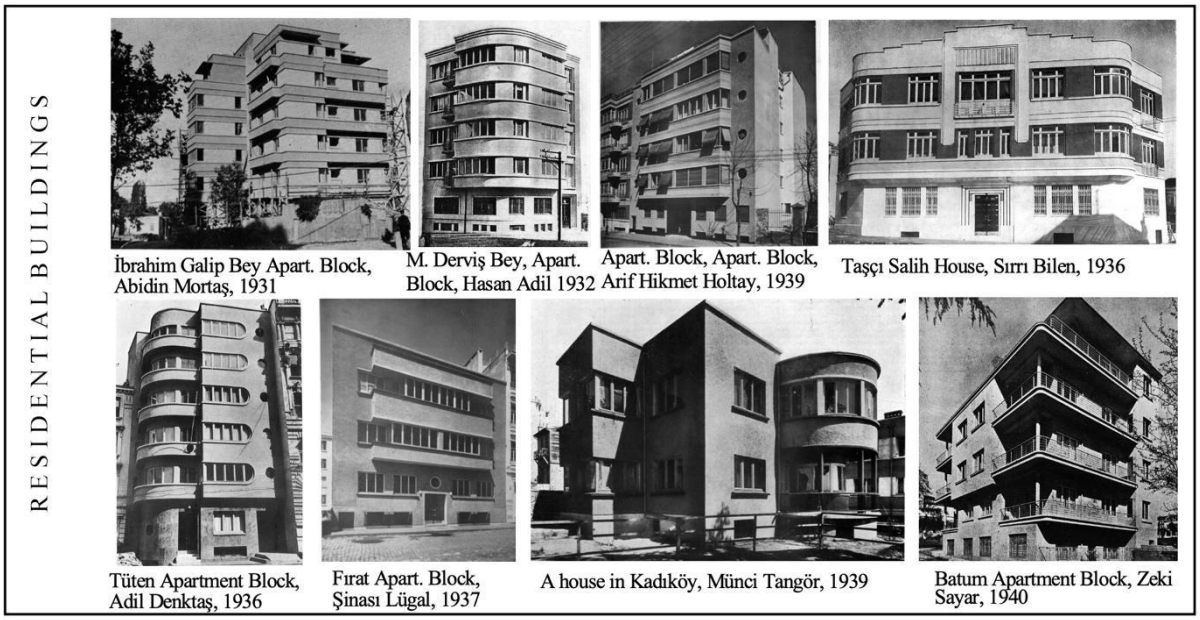

Figure 1. Examples of residential buildings constructed between 1930-1950 (Source: Arkitekt Journal).

In the 1940s, the focus shifted to the construction of commercial and public buildings including ministerial buildings, telephone central offices and public facilities. Notable structures from this period were the Valide Hanı in Sirkeci, Şişli Telephone Central and Zeki Sayâr's apartment building in Kadıköy. The ministerial buildings were constructed with similar materials and construction techniques by Construction Offices of the Ministry (Anonim, Hocapaşa Maliye Şubesi, 1938) (Anonim, Telefon Santralı Binası, 1940). Unlike residential buildings, the facades of public buildings lack projections but they feature curvilinear corners, horizontal lines and rhythmic window arrangements, as illustrated in Figure 2.

Figure 2. Examples of public buildings constructed between 1930-1950 (Source: Arkitekt Journal).

The first issue of Arkitekt Journal, published in 1932 featured an article that highlighted the significance of color composition in modern architecture. The author emphasized the use of exterior plasters to achieve the desired color effect. Painting lime or cement plaster or adding various crushed stone powder or mineral paint into the mortar are suggested as affordable solutions (Shown in Figure 3.). Terranova and Edelputz plasters gained popularity in Ankara, Bursa, and Istanbul in the 1930s and were favored for their crack resistance, color retention, breathability, and water repellent properties (Mimar Hüseyin, 1932).

Figure 3. Façade textures (Mimar Hüseyin, 1932).

The article published in Arkitekt in 1941 is a translated version of Eduard Jobst Siedler's "Lehre vom Neuen Bauen" and 1937-12 issue of "Deutsche Bauzeitung". The text provides insights into the various aspects of plastering, including the tasks performed by exterior plasterers, the requirements for good plastering, and the composition, application, and color of plaster mortar. The text also describes dry mortars, which are high-quality plasters manufactured in factories and then applied on-site by adding water. These dry mortars contain water-repellent additives. Additionally, the article describes renders that are processed by stonemasons. Notably, the recipes used by manufacturers in Germany are registered, and the hardness of these renders can exceed that of natural stones (Anonim, Binalarda Dış Sıva Tekniği, 1941).

Figure 4. Original surfaces of 20th century heritage.

36 articles containing significant information about buildings from Beyoğlu, Şişli, Kadıköy and Fatih districts have been selected. Today, 30% of these buildings are in situ and most of the preserved buildings are located in Beyoğlu. Amongst these buildings all of them except 5 are residential. 16 of them are garden houses, 15 of them are apartment blocks.
Façade finishing materials may vary on the ground and upper floors. Typically, marble stone and less commonly, cement plaster were used for ground floor façades. In contrast, all upper levels were covered with cement plaster. A smooth surface was generally created for the sills, moldings and jambs. On the front façades, various cement mortars were employed to produce different textures. Terranova, Edelputz and stone imitation plasters were widely used on the exterior facades of these buildings. Surfaces were created by craftsmen with hand tools. The facade design of these buildings includes a range of textures and color choices (as shown in Figure 4).
Cement plasters were made with colorful mortars. Color information of the buildings from 30's also compiled from articles. According to the articles in Arkitekt Journal, colorful finishing mortars were commonly in cream, beige, and grey tones. While some buildings utilized a pure cement color without any color additives, others showcased monochromatic surfaces (Sayâr, 1937) (Gorbon, 1937) (Denktaş, 1936). Additionally, there were examples of polychromatic surfaces (Adil, 1932) (Santur & Mortaş, 1932) (Anonim, İstiklâl Apartmanı, 1932).

Conclusion

Modern buildings have different kind of conservation problems from older buildings. Firstly, they are not yet protected in the way they deserve, as they are often not evaluated as heritage by decision-makers. It was observed that the facades of the buildings exemplified in the text have been painted over the original material, which disrupted their authenticity. Furthermore, the additional layers of paint can conceal structural and material deteriorations, allowing significant problems to develop unnoticed.
When making any interventions, it's important to consider the original materials, textures, and colors to ensure that the buildings maintain their historical value. Original materials used in the interior or exterior facades of modern buildings should be preserved to sustain modern architectural characteristics. Yet, various methods have been tried to protect surfaces of modern buildings. The World Heritage Site, Walter Gropius's Bauhaus Dessau of 1926 (Markgraf, 2006), and the buildings of Le Corbusier and Pierre Jeanneret (Fentzloff & Arnold, 2013) (Balletti, 2017) exemplifies projects that focus on preserving original surfaces. Similarly, Adalberto Libera's Malaparte House constructed in 1938, demonstrates an archaeological approach when planning intervention to 20th century buildings (Pittaluga & Quiros Castillo, 2024). These vibrant surfaces are not only aesthetic, but also important documents that convey the building techniques and material knowledge of the period. Such details play a decisive role in understanding modern architectural heritage.

References

Abidin, M. (1931). Mühendis İbrahim Galip B. Apartmanı - Ayaspaşa. Arkitekt, 355-364.
Adil, H. (1932). Mühendis Derviş Bey Apartmanı. Arkitekt, 243-247.
Anonim. (1932). İstiklâl Apartmanı. Arkitekt 11-12, 308-309.
Anonim. (1938). Hocapaşa Maliye Şubesi. Arkitekt Sayı: 91, 179-181.
Anonim. (1940). Telefon Santralı Binası. Arkitekt Sayı: 09-10, 196-197.
Anonim. (1941). Binalarda Dış Sıva Tekniği. Arkitekt 5-6 Sayı:125-126, 127-134.
Balletti, C. (2017). Vılla Stein-De-Monzie By Le Corbusier (1926-1928): Conservation Strategies Between Research And Education.
Denktaş, A. (1936). Kira Evi. Arkitekt 65-66, 139-141.
DOCOMOMO_International. (2017). Madrid-New Delhi Document: Approaches To The Conservation of Twentieth-Century Cultural Heritage, (https://isc20c.icomos.org/wp-content/uploads/2022/03/MNDD_Full-Document.pdf) date retrieved (23.04.2020)
Fentzloff, A., & Arnold, M. (2013). Restauración De La Casa Doble De Le Corbusier En La Weissenhofsiedlung. Loggia N.26, 100-124.
Gorbon, R. (1937). Elektrik Evi. Arkitekt, 1-4.

Kudde, E. (2024). 20. Yüzyıl ve Cumhuriyet Dönemi Mimari Mirasının Korunması Yönünde Çabalar. ICOMOS Türkiye Bülteni Sayı:1, 25-26.
Mühendis Livas. (1932). Bosfor Apartmanı. Arkitekt Sayı:10, 277-279.
Markgraf, M. (2006). Conservation and Preservation of the Bauhaus Building in Dessau. In M. P. Ed. Jörg Haspel, The Soviet Heritage and European Modernism (pp. 108-111). ICOMOS.
Mimar Hüseyin. (1932). Yapıda Haricî Sıva. Arkitekt 13, 22-23.
Pittaluga, D., & Quiros Castillo, J. (2024). Surfaces of 20th-Century Façades: Reflections on Their Archaeological Awareness. Technologies Engineering Materials Architecture Vol.10, No.1, 112-125.
Polat-Pekmezci, I. (2024). Venedik Tüzüğü'nden Günümüze Kültürel Mirasın Korunmasında Malzemenin Önemi ve Korunması Üzerine İlkesel Açılımlar. Mimarist Cilt:24, Sayı:81, 94-99.
Santur, F., & Mortaş, A. (1932). Melek Apartmanı. Arkitekt, 311-316.
Sayâr, Z. (1937). Kalamış'da Bir Villa. Arkitekt, 129-133.
Sayâr, Z. (1937). Suadiye'de Bir Villa. Arkitekt, 269-274.

ARCHITECTURE

Architectural History

Architecture Design Theory

Building Construction Technologies

Building Materials and Technologies

Built Environment Design and Technologies

Conservation and Restoration

Environmental Control and Building Technology

Project and Construction Management

Sustainable Design

UrbanReCrete: A Sustainable Approach to Concrete Waste Recycling in Istanbul

Başak Akarsu Akdemir[a], Fatma Sultan Bozkurt[a], Gizem Aluçlu Armutcu[a]

[a] Istanbul Technical University, Faculty of Architecture, Department of Landscape Architecture, Türkiye
akarsuba@itu.edu.tr

Keywords: Concrete Waste Management, Smart Recycling Systems, Sustainable Building Technology, Urban Environmental Control.

Aim

The construction industry is responsible for major contributions to the global economic development of a nation, however, is also one of the leading causes of environmental degradation. Urban cities such as Istanbul generate high levels of urbanization, urban renewal work, and constant building activities that yield enormous amounts of construction and demolition (C&D) waste. Studies indicate that 3-5 million tons of concrete waste are created annually in Istanbul. With the anticipated large-scale urban transformation projects, especially considering the city's vulnerability to earthquakes, this number could rise dramatically, potentially reaching 320 million tons.

Despite the magnitude of the waste amount, existing waste management practices remain inefficient. The conventional methods are high in cost, environmentally damaging and logistically impractical. Current recycling processes often require extensive land use, involve high transportation costs, and increase significantly to carbon emissions. Furthermore, conventional recycling processes do not recover the cement content of concrete, resulting in more CO2 emissions and wasted material. The aim of this study is to introduce an entrepreneurship proposal named "UrbanReCrete" as a greener alternative to conventional recycling practices. UrbanReCrete proposes a new vision that recycles demolition waste back into reusable materials of concrete that have lower carbon emissions and increased efficiency in construction waste management. This research examines the potential of UrbanReCrete's approach, evaluates its economic and environmental benefits, and presents a roadmap for its implementation in Istanbul's construction field.

Material and Method

UrbanReCrete as an entrepreneurship project proposal has an approach that is based on a comprehensive examination of the state of affairs concerning construction and demolition waste management, using the contrast between traditional practices and emerging technologies, to assess their economic and environmental impacts. The approach is developed with a mixed-method study including four key components: Quantitative Analysis of the Current Scenario, Comparison of Traditional Methods and Contemporary Technology, Analysing Its Economic and Environmental Benefits, Strategic Plan for Large-Scale Valorisation.

The study takes into account the volume of construction waste generated annually in Istanbul and its anticipated growth due to urban transformation. Quantitative analysis provides a precise image of the scale of the problem. A comparative analysis of traditional recycling techniques and UrbanReCrete's SmartCrusher technology is provided. Traditional and modern methods are compared in terms of efficiency, environmental and financial aspects. The economic viability of the deployment of SmartCrusher technology in terms of opportunity in the marketplace, computational costing, operating model, and financial viability is also considered. Furthermore, the way its implementation could contribute to ensuring sustainability goals in terms of a reduction in carbon emissions and resource utilization is addressed. UrbanReCrete's valorisation roadmap facilitates industry integration through policy support and incentives, leveraging SmartCrusher technology to optimize concrete recycling, reclaim cement fines, and reduce CO2 emissions.

Findings

The findings of this study indicate that the use of UrbanReCrete's SmartCrusher technology presents significant environmental, economic, and logistical advantages. Current concrete recycling methods are inefficient due to high capital

needs, energy-intensive processes, and no capacity to recover cement fines. UrbanReCrete overcomes these shortcomings by a technologically advanced, mobile, and cost-effective system.

The key aspects of the strategies developed by UrbanReCrete, an entrepreneurship project proposal, can be listed as mobile recycling units, increased material recovery, sustainability incentives and carbon footprint reduction. Unlike conventional recycling plants that require significant infrastructure and fixed bases, UrbanReCrete mobile units enable on-site treatment. This reduces transportation costs significantly and greenhouse gas emissions from trucking construction waste to distant recycling plants. SmartCrusher technology recovers high-quality aggregate and fine particles to be reused in new concrete production, achieving the highest level of material efficiency with minimal use of virgin resources. Through being aligned with government policies and sustainability programs, UrbanReCrete is rewarded with fiscal incentives such as tax credits and green funding incentives. Cement fines recovery results in significant CO2 savings. For example, with a processing rate of 80,000 tons annually, UrbanReCrete can recover up to 11,200 tons of CO2-free cement fines annually, offsetting cement plant emissions directly. In addition, the methodology considers economic and logistic aspects, assuring sustainability in the regulatory framework of Istanbul. UrbanReCrete collaborates with İSTON, a municipal construction subsidiary, to ensure the utilization of recycled concrete in municipal infrastructure projects. Cost-benefit analysis and return on investment is conducted to determine economic feasibility.

The estimated revenue stream model created based on these feasibility studies consisted of service fees that recycle waste concrete for İSTON and generate revenue from the recycling services themselves; and recycling fees aimed at selling recycled aggregates and cement-sand components to contractors based on municipal policies that encourage contractors to consume recycled concrete in construction. The model operates with an annual revenue of more than 135% of its total costs, with profitability and payback period of just 1.6 years. Additionally, UrbanReCrete also has sustainability benefits like reduced urban disturbance, better waste management, and lower carbon emissions. As the construction sector is being more and more entrusted with meeting sustainability goals, adopting UrbanReCrete's approach is also aligned with industry and government initiatives towards circular economy strategies. On the other hand, UrbanReCrete's ecological impact is likely its biggest selling point. Cement production accounts for roughly 8% of worldwide CO2 emissions. With the potential to recycle cement fines through SmartCrusher technology, these emissions are reduced and UrbanReCrete is an essential tool in climate change protection. The reduced amount of natural aggregates used also cuts down on habitat loss and resource consumption, adhering to broader sustainability goals.

From a commercial point of view, the market for green building materials is increasing very rapidly. The global market for green building materials is projected to grow each year at 9.5% until 2031, which is a very good opportunity for UrbanReCrete. Because Istanbul is undergoing large-scale urban renewal, the city is a significant market for green building solutions.

Conclusion

UrbanReCrete provides an innovative entrepreneurship to the construction waste management challenges of Istanbul. Using the latest technology, mobile recycling capability, and environmentally friendly business models, the scheme has the potential to reduce carbon emissions enormously, make recycling more efficient, and support urban sustainability goals. The scalability of this approach goes beyond Istanbul and offers a template that can be rolled out for other metropolitan cities with comparable waste management issues.

UrbanReCrete's future potential lies in the rationalization of the SmartCrusher technology to enhance efficiency and reduce costs, increasing market coverage through collaboration with municipalities and the private sector, and integrating automation and artificial intelligence-based sorting technologies to optimize recycling processes. By addressing both economics and environmental factors, UrbanReCrete presents a new solution for circular economy interventions in the construction sector, minimizing the environmental impact of urbanization while promoting sustainable development.

Acknowledgements

This study was produced under the instruction of Dr. Zeynep Erden Bayazıt within the scope of LEE 901E Academic Entrepreneurship course in the Spring Semester of Istanbul Technical University Graduate Institute 2023-2024 Academic

Year. This study was produced as a group study and with the contributions of Ekrem Kaynar, Göktuğ Özdemir and Serkan Şenel in addition to the authors.

References

Arredondo-Rea, S., Higuera, R., Gómez-Soberón, J., Gámez-García, D., Bernal, J., Rosas-Casarez, C., … & Ungsson-Nieblas, M. (2019). Durability parameters of reinforced recycled aggregate concrete: case study. Applied Sciences, 9(4), 617.

Circular Ecology. (2024). Concrete embodied carbon footprint calculator. Retrieved from

Demir, İ. (2009). İnşaat yıkıntı atıklarının beton üretiminde kullanımı ve beton özelliklerine etkisi. AKÜ Fen Bilimleri Dergisi, 9(2), 105-114.

Fraile-Garcia, E., Ferreiro-Cabello, J., & López-Ochoa, L. (2017). Study of the technical feasibility of increasing the amount of recycled concrete waste used in ready-mix concrete production. Materials, 10(7), 817.

Güllü, G. (2022). İstanbul'da Kentsel Dönüşüm, İnşaat ve Yıkıntı Atıkları. Cihannüma Teknoloji Fen ve Mühendislik Bilimleri Akademi Dergisi, 1(1), 39-72.

Inel, M., Senel, S., & Ün, H. (2008). Experimental evaluation of concrete strength in existing buildings. Magazine of Concrete Research, 60(4), 279-289.

Jiménez, L. F., Domínguez, J. A., & Vega-Azamar, R. E. (2018). Carbon footprint of recycled aggregate concrete. Advances in Civil Engineering, 2018, 7949741.

Li, Y., Lu, X., Guan, H., & Ye, L. (2011). An improved tie force method for progressive collapse resistance design of reinforced concrete frame structures. Engineering Structures, 33(10), 2931-2942.

SlimBreker. (2024). Groen betonrecycling - c2c - milieuvriendelijk met de SmartCrusher. Retrieved from

Url-1 https://doi.org/10.3390/app9040617

Url-2 https://circularecology.com/concrete-embodied-carbon-footprint-calculator.html

Url-3 https://doi.org/10.3390/ma10070817

Url-4 https://doi.org/10.1680/macr.2007.00091

Url-5 https://doi.org/10.1155/2018/7949741

Url-6 https://doi.org/10.1016/j.engstruct.2011.06.017

Url-7 https://www.slimbreker.nl/

Reduction of Cooling Loads in Office Buildings in Hot Climates Using Radiant Cooling

Yasemin Kılıçoğlu[a], Gülten Manioğlu[b]

[a] Istanbul Technical University, Graduate School, Environmental Control and Construction Technologies Program
[b] Istanbul Technical University, Faculty of Architecture, Department of Architecture
kilicoglu23@itu.edu.tr, manioglugu@itu.edu.tr

Keywords: Radiant cooling, Chilled Ceiling, Cooling Load.

Aim

The increase in global average temperatures due to the effects of global warming has led to a rise in cooling demands in buildings to ensure occupant comfort. Consequently, energy consumption for cooling purposes has significantly increased. Office buildings, due to their high internal heat gains resulting from a large number of occupants and extensive use of equipment, tend to be energy-inefficient. This inefficiency is further exacerbated by contemporary façade designs, which frequently incorporate a high proportion of glazed surfaces. Excessive heat gains through these façades contribute to elevated indoor temperatures, necessitating the operation of active cooling systems to maintain thermal comfort, particularly in office buildings located in hot climates. As a result, a considerable amount of energy is consumed for cooling purposes.

It is well known that 38% of the total global energy consumption is attributed to meeting the cooling demands of buildings. With the increase in the number of buildings and, consequently, rapid urbanization, the rising demand for cooling has led to the continuous expansion of cooling system usage. According to energy efficiency reports, more than 66% of the energy consumed in the building sector is used for HVAC systems and lighting. Since cooling systems release the heat extracted from buildings into the surrounding environment, they contribute to the enhancement of the urban heat island effect. As a result, rising temperatures due to global warming are further exacerbated by the waste heat generated from active cooling systems, leading to an even greater dependence on cooling technologies. This increasing reliance on cooling systems creates a self-reinforcing cycle, highlighting the need for innovative solutions to break this pattern.

The Sustainable Development Goals (SDGs), particularly SDG 7 under the theme of "Affordable and Clean Energy," encourage universities to develop sustainable solutions. One such sustainable approach aims to reduce high energy consumption in buildings while ensuring thermal comfort through efficient cooling strategies (Villar-Ramos et al., 2022). In this context, research has been conducted on passive cooling systems as potential alternatives to conventional HVAC systems.

One of these passive systems, radiant systems, can provide heating and cooling through pipes filled with cold or hot water. In these systems, ventilation and humidity control requirements are met by a DOAS (Dedicated Outdoor Air System). In offices, conditioning and ventilation of spaces account for 41-51% of the total energy load. The use of water to transport and remove heat in a building is more efficient than air, which makes it possible to reduce this energy expenditure with radiant systems. Water transfers thermal energy approximately 7 times more effectively than air (Ali & Naik, 2016). There are different versions of radiant cooling, and their types can be integrated into building components (Vivek & Balaji, 2023). Ceiling-based radiant cooling is more energy-efficient for cooling in summer. The direction of convection currents developed is consistent with the temperature gradient, meaning that cold air falls, facilitating the upward movement of warmer air from the heat source at the floor level (Fairconditioning, n.d.).

The Chilled Ceiling system is a ceiling-mounted system designed to cool the space beneath it in a silent, draught-free manner. Each unit consists of small-diameter chilled water pipes arranged in an S-shape, which are attached to the upper surface of a ceiling panel. The ceiling panels are typically made of thin metallic material, though they may also be made of gypsum board. In some systems, the chilled water pipes are embedded within the ceiling panel. During operation, the panel is cooled through contact with the chilled water piping and cools the space through convective and radiant heat transfer (approximately 40% of the cooling is radiant). Chilled ceiling systems require a separate ventilation system for the supply

of fresh air. Condensation of air within or on the chilled ceiling can be prevented by cutting off the chilled water flow, depending on the room's dew point (DesignBuilder Software, n.d.-a).
The study area is determined as the Bayraklı district of İzmir. Bayraklı is known as a developing business center in İzmir. The region predominantly consists of office buildings, and high-rise buildings with curtain wall facades are commonly constructed. In this context, the increasing number of curtain-wall office buildings in the İzmir Bayraklı region is considered a significant issue in terms of cooling. The lack of sufficient decisions regarding passive design strategies, such as the materials used for office building facades, the orientation of the building, and the thermal performance of the building envelope as determined by regulations, has led to office buildings becoming increasingly dependent on ventilation systems and air conditioning units, further exacerbating cooling loads. Therefore, this study aims to develop solutions to reduce the cooling loads of office buildings in a hot, humid climate region such as İzmir. To achieve this goal, the chilled ceiling system, which provides ceiling-based radiant cooling, will be compared with the commonly preferred Fan Coil system in office buildings.

Material and Method

This study aims to propose solutions to reduce cooling loads for office buildings in the İzmir Bayraklı District by creating façade options with different material choices. To achieve this goal, various scenarios have been developed, and simulations have been conducted through the DesignBuilder simulation program, which is an extension of EnergyPlus.
Primarily, a three-story office building with dimensions of 20x20m and a floor height of 3.5m. Plan is shown on Figure 1. The ofice building was modeled in the DesignBuilder program. The building features a 90% glazing façade on the north, east, south, and west sides. The perspective view of the design builder model is shown in Figure 2.

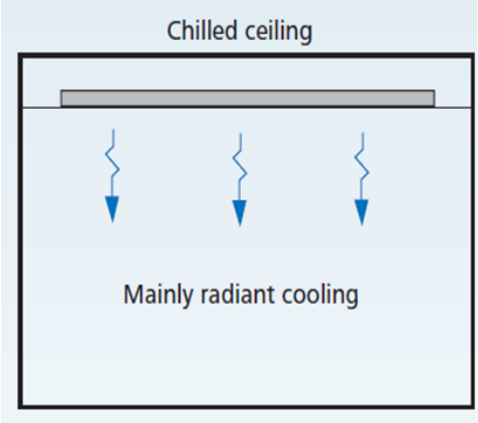

Figure 1. Chilled ceiling schematic representation
Note. Reprinted from Editing zone chilled ceiling, by DesignBuilder Software, n.d., https://designbuilder.co.uk/helpv7.2/Content/Detailed%20HVAC/EditingZoneChilledCeiling.htm. © DesignBuilder Software.

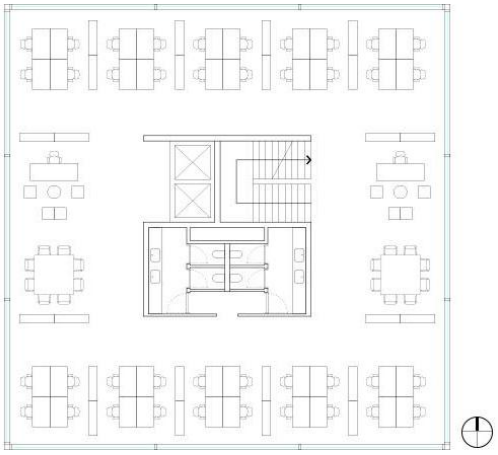

Figure 2. Open Ofice Plan.

Designed as an open office, the building includes enclosed areas only for the stairs, elevator, and restrooms. The walls of these areas were defined as adiabatic surfaces in the DesignBuilder software. Adiabatic surfaces prevent heat transfer through them and are generally applied to simulate interfaces with other spaces whose temperatures are approximately equal to that of the zone (DesignBuilder Software, n.d.-b). Office working hours are set from 8:00 AM to 6:00 PM on only weekdays, and the simulation period is defined to represent the cooling season from May 15th to September 15th. The office building model was simulated using two different types of glazing (G1: Double Glass, G2: Double LoE Elec Ref Bleached) (Table 1) with Fan Coil and Chilled Ceiling systems. The set points were determined according to the ASHRAE adaptive comfort model standard, where comfort levels range between 26°C and 28°C for cooling and between 19°C and 21°C for heating (ASHRAE, 2020).

Table 1. Glazing Options.

Transparent Material	Window Glass Type	Glass U-value (W/M2k)	Solar Heat Gain Coefficient (SHGC)	Light Transmittance	Frame Material	Frame Material U-value (W/M2k)
Glazing 1	Double Glass	1,609	0,629	0,698	Aluminum	5,881
Glazing 2	Dbl LoE Elec Ref Bleached	1,616	0,426	0,634	Aluminum	5,881

Table 2. Opaque Components.

Transparent Material	Opaque Components	Materials	Thermal Conductivity (W/mK)	Thickness (m)	U (W/m2K)
Facade	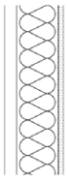	1.Painted Glass 2.Glass Wall 3.Gypsum Board	1,6 0,085 1	0,035 0,12 0,015	0,62
Ground Floor	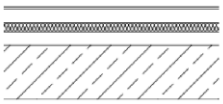	1.PVC Flooring 2.Screed 3.Thermal Insulation 4.Leveling Screed 5.Lightweight Concrete	0,23 1,4 0,035 1,4 0,16	0,005 0,03 0,02 0,03 0,12	0,64
Roof	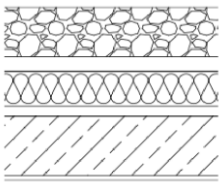	1.Gravel 2.Screed 3.Extruded Polystyrene Foam (XPS) 4.Screed 5.Reinforced Concrete 6.Plaster	0,81 1,4 0,035 1,4 2,5 0,35	0,1 0,03 0,07 0,02 0,12 0,01	0,42

Materials were defined in the simulation program according to the U-values specified for Zone 1 in the TS825 (2013) Standard, which includes İzmir. The U-value for the walls in Zone 1 is 0.66 W/m²K, the U-value for windows is 1.8 W/m²K, the U-value for the floor is 0.66 W/m², and the U-value for the roof is 0.43 W/m²K (Turkish Standards Institution, 2013). The U-values specified are shown in Tables 2.

For the first mechanical system main office zone, a "fan coil air-cooled chiller was selected as a suitable system for İzmir's climate. Fan coil units operate through a water loop connected to chillers and boilers, providing hot or chilled water for heating and cooling. An air handling unit was added to the system. The fan coil datas was simulated as autosize in DesignBuilder.

The second mechanical system evaluated is the chilled ceiling system. For the chilled ceiling system, parameters such as hydronic tubing length and maximum chilled water flow rate were set to autosize in DesignBuilder. The hydronic tubing inside diameter was specified as 0.013 meters. Additionally, the zone temperature control type was set to operative temperature.

The .epw format Typical Meteorological Year (TMY) 2007-2021 weather data file for İzmir was imported from the Climate.org website and used for energy calculations in the simulation tool (Climate Institute, n.d.). It is assumed that the building under consideration is located on a flat terrain and is not shaded by any surrounding structures.

Findings

The office building model created for İzmir was simulated separately for two different types of glass with Fan Coil and Chilled Ceiling systems. According to the calculation results, when the G1 option is used, the total energy consumption for cooling is 165,873.1 kWh with the Fan Coil system and 146,721.42 kWh with the Chilled Ceiling system. This indicates

that the Chilled Ceiling system reduces the total cooling energy by 11.54% for G1. When the G2 option is used, the total cooling energy consumption is 125,213.55 kWh with the Fan Coil system and 104,581.24 kWh with the Chilled Ceiling system. This shows that the Chilled Ceiling system reduces the total cooling energy by 16.47%. The calculation results are shown in Figure 3. The highest cooling load was observed in the Fan Coil and Glaze 1 configurations, while the lowest cooling load was observed in the Chilled Ceiling and Glaze 2 configurations.

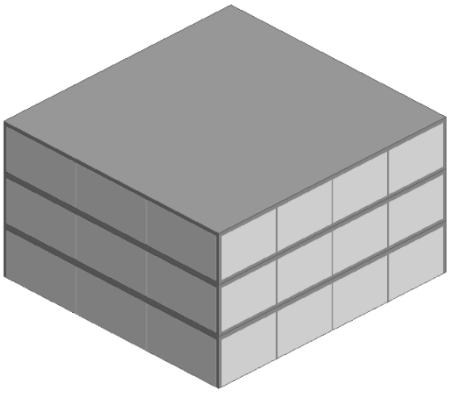

Figure 3. Building Perspective.

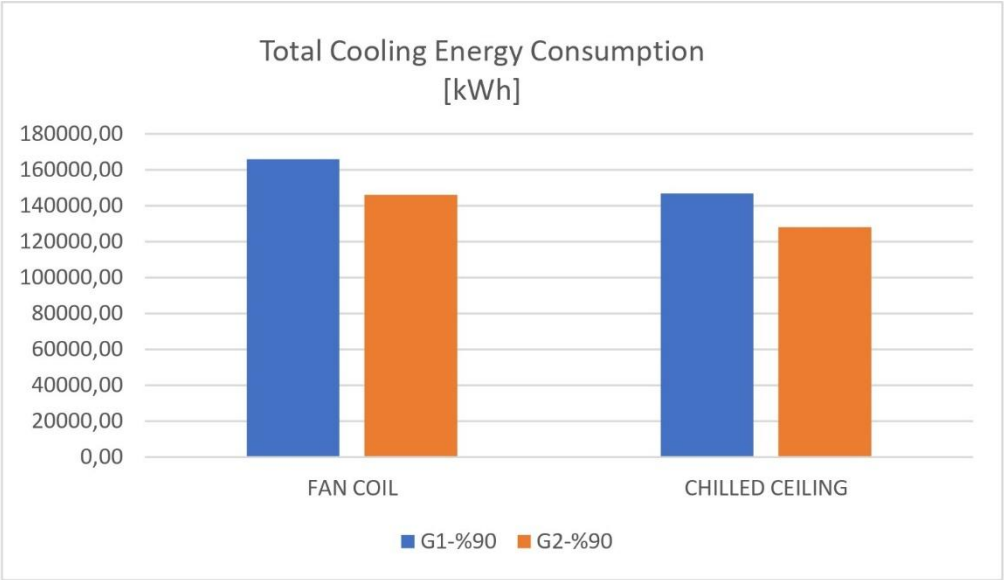

Figure 4. Total Cooling Energy Electricity Consumption.

Conclusion

In hot climate regions, cooling is regarded as a basic necessity that directly influences the quality of life. User comfort is significantly affected by high temperatures. In buildings, effective cooling strategies are required to maintain indoor temperatures at acceptable levels. With the ongoing effects of increasing urbanization and global warming, cooling demands are being continuously raised. However, serious problems are caused when this demand is met through traditional, energy-dependent methods. Therefore, the development of cooling solutions that enhance energy efficiency in hot climate regions is considered highly important.

As a result, it has been observed that the Chilled Ceiling system is an energy-saving system compared to the Fan Coil HVAC system. It was found that the type of glass can be even more critical than mechanical systems in affecting the building's cooling loads. When a better glass with a lower Solar Heat Gain Coefficient value is selected, it has been shown that this ratio can achieve even better results.

As limitations and possible directions for further research, different types of glass with varying transparency levels can be compared. Other façade systems used in office buildings could also be examined. The study focused on a building type with open facades on all four sides (N-S-E-W), but this could be expanded by simulating the building with different orientations. Additionally, the study could be conducted for various climate types.

References

Ali, S. M., & Naik, B. B. (2016). Energy efficient HVAC system designing and simulation of radiant cooling system. International Journal of Scientific & Engineering Research, 7(6). Retrieved from http://www.ijser.org

American Society of Heating, Refrigerating and Air-Conditioning Engineers. (2020). ANSI/ASHRAE Standard 55-2020: Thermal environmental conditions for human occupancy. ASHRAE.

Climate Institute. (n.d.). Climate solutions through global partnerships. Retrieved March 20, 2025, from https://climate.org/

DesignBuilder Software. (n.d.). Editing zone chilled ceiling. Retrieved March 20, 2025, from https://designbuilder.co.uk/helpv7.2/Content/Detailed%20HVAC/EditingZoneChilledCeiling.htm

DesignBuilder Software Ltd. (n.d.). Component block. Retrieved March 20, 2025, from https://designbuilder.co.uk/helpv7.0/Content/Component_Block.htm

Fairconditioning. (n.d.). Radiant cooling. Retrieved March 20, 2025, from https://fairconditioning.org/knowledge/sustainable-cooling-technologies/radiant-cooling/#1500296799628-e5546709-43d950c2-af0b

Turkish Standards Institution. (2013). TS 825: Energy efficiency in buildings—Thermal insulation requirements for buildings (Version 2013).

Villar-Ramos, M. M., Hernández-Pérez, I., Aguilar-Castro, K. M., Zavala-Guillén, I., Macias Melo, E. V., Hernández-López, I., & Serrano-Arellano, J. (2022). A review of thermally activated building systems (TABS) as an alternative for improving the indoor environment of buildings. Energies, 15(17), 6179. https://doi.org/10.3390/en15176179

Vivek, T., & Balaji, K. (2023). Heat transfer and thermal comfort analysis of thermally activated building system in warm and humid climate – A case study in an educational building. International Journal of Thermal Sciences, 183, 107883. https://doi.org/10.1016/j.ijthermalsci.2022.107883

Multi-Stage Space-Adaptive Shelters: An Alternative to Post-Disaster Shelters

F. Berke Cilesizoglu [a], Oguz C. Celik [b]

[a] Istanbul Technical University, Graduate School, Environmental Control & Construction Technology, Turkey
[b] Istanbul Technical University, Faculty of Architecture, Structural & Earthquake Engineering Unit, Turkey
cilesizoglu22@itu.edu.tr

Keywords: Space-Adaptive Structure, Post-Disaster Shelter, Computational Design.

Aim

On February 6th, Earthquake doublets of M_w=7.8 Pazarcık and M_w=7.6 Elbistan/Ekinözü (Ding et al., 2023) have devastated the southeast Turkey by damaging the existing building stock and urban infrastructure, affecting nearly 13.5 million people living in the region. (Celik et al., 2024) A reconnaissance has taken place in the aftermath of the earthquakes to assess the damage and disaster-relief sheltering situation. The immediate need for shelters in abundance caused a strain on manufacturing and construction, with tents and containers being the main solutions. After 2 years, official documents show that 650.000 people still live in 395 container sites in the region, which shows that emergency actions taken in face of catastrophes can have long-lasting effects (Presidency of Strategy and Budget, 2025).

There are various widely recognized post-disaster shelter types offering solutions to different sheltering issues such as emergency, upgradability, durability or comfort. (IFRC/RCS, 2013) In the context of this research, sheltering can be summarized in three important and distinct stages based on both core and recent literature (Quarantelli, 1982; UNHCR, 2021). An immediate stage that answers the emergency need for sheltering, deployed quickly and intended to be habitable for a short time. An interim stage that answers basic requirements and partial comfort until next stage. Finally, an intermediate stage offering temporary housing with adequate comfort conditions. While current solutions suffice the requirements for each stage, their temporary nature and immense numbers creates an abundance of material waste, energy waste and occupied plots (Rios et al., 2015). Ongoing studies aim to bridge the gap between stages; however, an all-encompassing solution is not available due to unique properties of each stage (Abu-Aridah & Ligler, 2024; Shahkar, 2022). Authors aim to improve the workflow of disaster-relief sheltering by offering an alternative sheltering solution based on space-adaptive systems that progressively answer the aforementioned three stages. Multi-Stage Space-Adaptive Structures (MSSAS) are structures that can respond to the changing needs and environmental effects whose spatial qualities can be altered through their structural parts, deployment or replacement. Authors aim to employ MSSAS and their inherent adaptive attributes (Abdullah & Al-Alwan, 2019; Maierhofer & Menges, 2019; McCoy & Duffy, 2022) to answer different needs and challenges of these stages using computational design methods, and a combination of durable high-tech materials and local low-tech materials (Antonini et al., 2020).

Material and Method

Adaptability (Kronenburg, 2013; Matheou et al., 2023; Mitsimponas & Symeonidou, 2024; Schmidt III & Austin, 2016) serves as a crucial aspect of architectural practice to respond to environmental (Loonen et al., 2013) and social transformations (van Ellen et al., 2021), emerging crisis situations (Valcárcel, 2024) and other unforeseen circumstances. Computational design (Caetano & Leitão, 2024; Menges & Ahlquist, 2011) represents a methodology that incorporates generative algorithms, integrated structural analysis and computational design tools into the creative process (Fleischmann et al., 2012; Menges & Ahlquist, 2011; Yazici & Tanacan, 2020). This method proves suitable for adaptive design frameworks, as this approach aligns with the concept of designing systems with multiple variations and configurations that can respond to changing parameters. MSSAS are intended to be established both theoretically and technically by research-through-design method (Roggema, 2016).

A case study is designed for Buruncayir Village in Adiyaman, southeastern Turkiye, in order to observe the effects of site-specific design elements: soil, earthquake, wind and climate. Design was created in NURBS-based CAD environment

(Rhinoceros3D) with visual algorithm tools (Grasshopper) and integrated multi-objective optimization, and structural analysis tools (Karamba3D). Functionality and transformation of structure were tested using a 3D-printed PLA functional prototype. In order to evaluate applicability and feasibility of the case study, spatial, material and construction standards, has been established through analysis of universally accepted guidelines (Sphere Association, 2018), local regulations (TS498, 2021; TBEC, 2018) and 53 well-documented works (IFRC/RCS, 2011, 2013; UNHCR, 2016, 2021) built in the 21st Century (Table 1.).

Table 1. Requirements (maximum values) for three sheltering stages.

	Immediate Stage	Interim Stage	Intermediate Stage
Lifespan	1 Year	5 Years	10 Years
Construction Time	1 Day	7 Days	10 Days
Cost	€500	€2000	€2500
Covered Living Area	12 m^2- 18 m^2	12 m^2- 24 m^2	16 m^2- 24 m^2
Cargo Weight	5000 kg	10000 kg	50000 kg
Cargo Volume	5 m^3	10 m3	40 m3
CO_2 Footprint	1000 kg	5000 kg	10000 kg
Cost/ Lifespan	€500/ year	€400/ year	€250/ year
Cost/ Lifespan/ Area	€40/ year/ m^2	€20/ year/ m^2	€5/ year/ m^2
Cargo Weight/ Area	300 kg/ m^2	500 kg/ m^2	2000 kg/ m^2

Cargo Volume/ Area	0.3 m^3/ m^2	0.4 m^3/ m^2	1.6 m^3/ m^2
CO_2/ Lifespan/ Area	50 kg/ year/ m^2	40 kg/ year/ m^2	30 kg/ year/ m^2
Construction	Pre-fabricated	In-situ	In-situ
Earthquake Resistance	Lightweight Structure/ Adequate Rigidity		
Wind Resistance	Deep Foundation		
Flood Resistance	Elevated Floor		
MEP Services	Not Mandatory	Mandatory	Mandatory

Findings

MSSAS is a deployable progressive structure with modular elements and reconfigurable parts. MSSAS is deployed to create a self-supporting single-layer shell structure **(Figure 1)**. Main structural elements are steel tubular elements and steel hinge connections. The hinged connection details were designed in a way to accommodate eight connections in four axes and, when in free motion, rotation around X-axis in order to fold/unfold the structure. Z-axis allows direct connection to cladding, effectively transferring the loads directly to the joints (**Figure 2)**. Form finding algorithms based on hanging chain model were computed using multi-objective optimization algorithm with minimum weight, minimum displacement (in relation to minimum stresses), maximum living area goals. The structural elements are parametrically generated through their geometric relationality according to site-specific needs. Due to its modularity and transformable form, different-sized shelters for different functions can be built with the same elements **(Figure 3**).

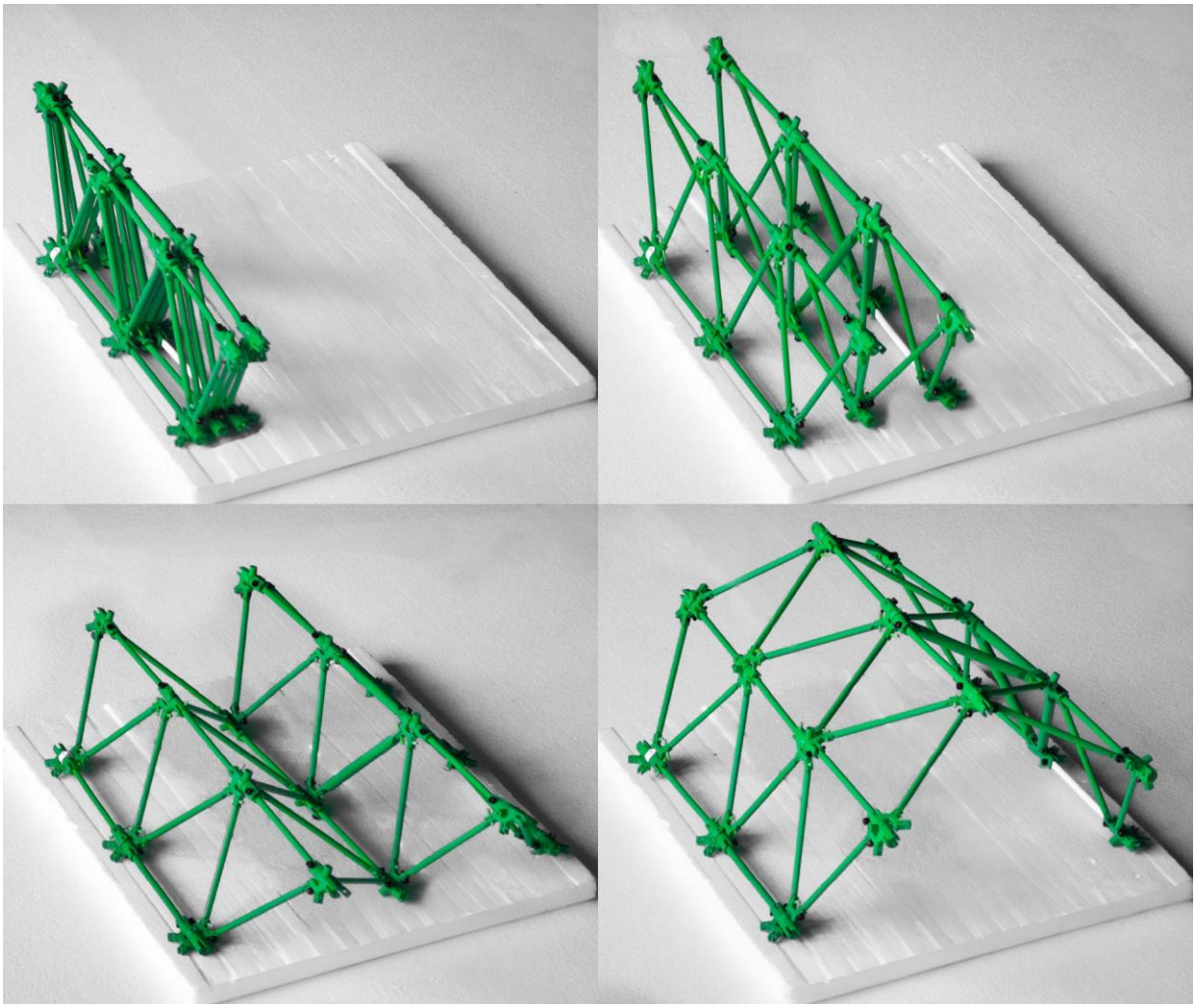

Figure 1. 3D printed functional prototype.

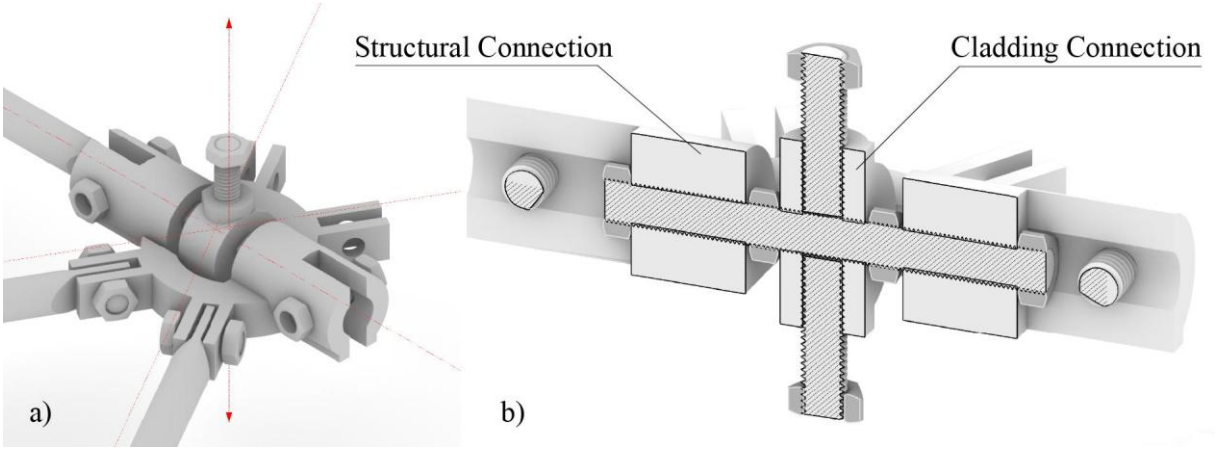

Figure 2. (a) Axonometric perspective, (b) section of detail.

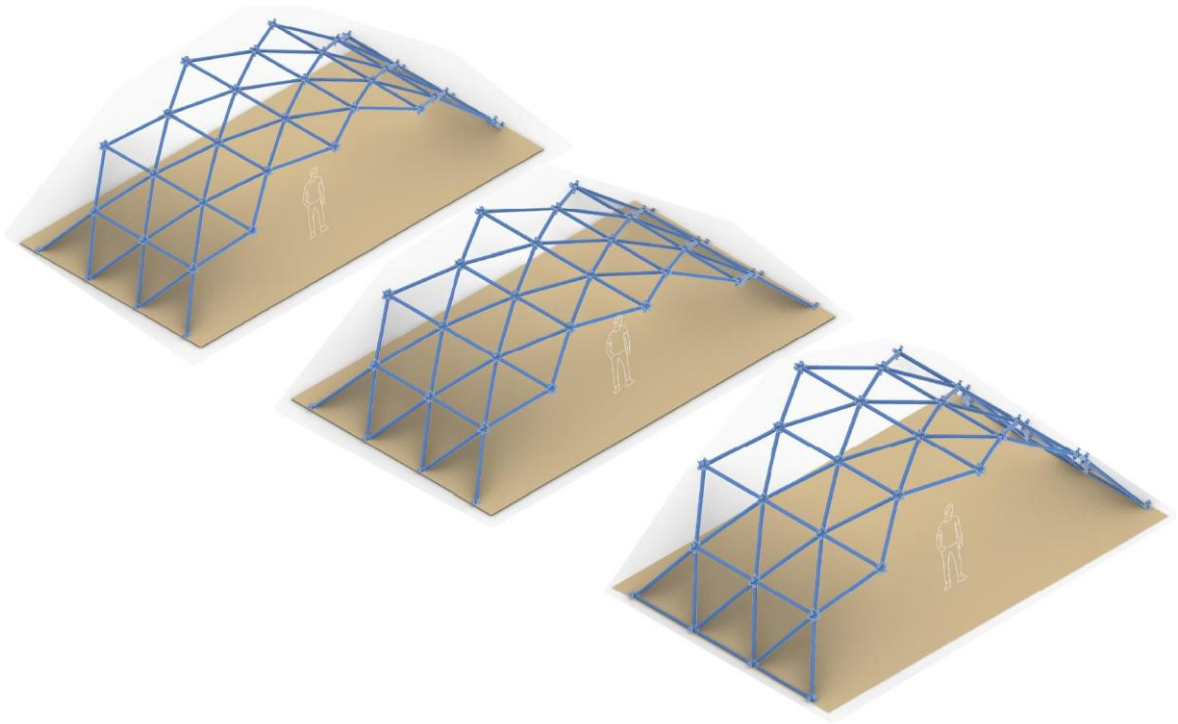

Figure 3. Diagrams showing different forms created by the same modules.

The floor must be elevated using adjustable steel footing to level living area, provide flood protection and create crawl space to be used for MEP installation in interim stage. Immediate stage, consists of deployable shell with lightweight cover, like plastic sheeting, and basic cladding. Deployment mechanism of the structure accelerates the construction, offering the advantage of quality-controlled detailing and construction, which helps with avoiding problems associated with poor workmanship. Interim stage, utilizes common or low-tech materials to upgrade the structure and improve living conditions. Thatching can be used for roof, while plywood, bamboo, and straw mats can be used for both flooring and cladding. Intermediate stage brings living conditions close to a temporary housing standard. Bracings are added increase stability of the structure. Double-layered cladding and roofing with insulation enhance climate conditions for the shelter. A second MSSAS can be added to create rooms, kitchen, and bathroom areas. MSSAS, supplies all the basic needs of three stages **(Figure 4)** while remaining feasible **(Table 2)**.

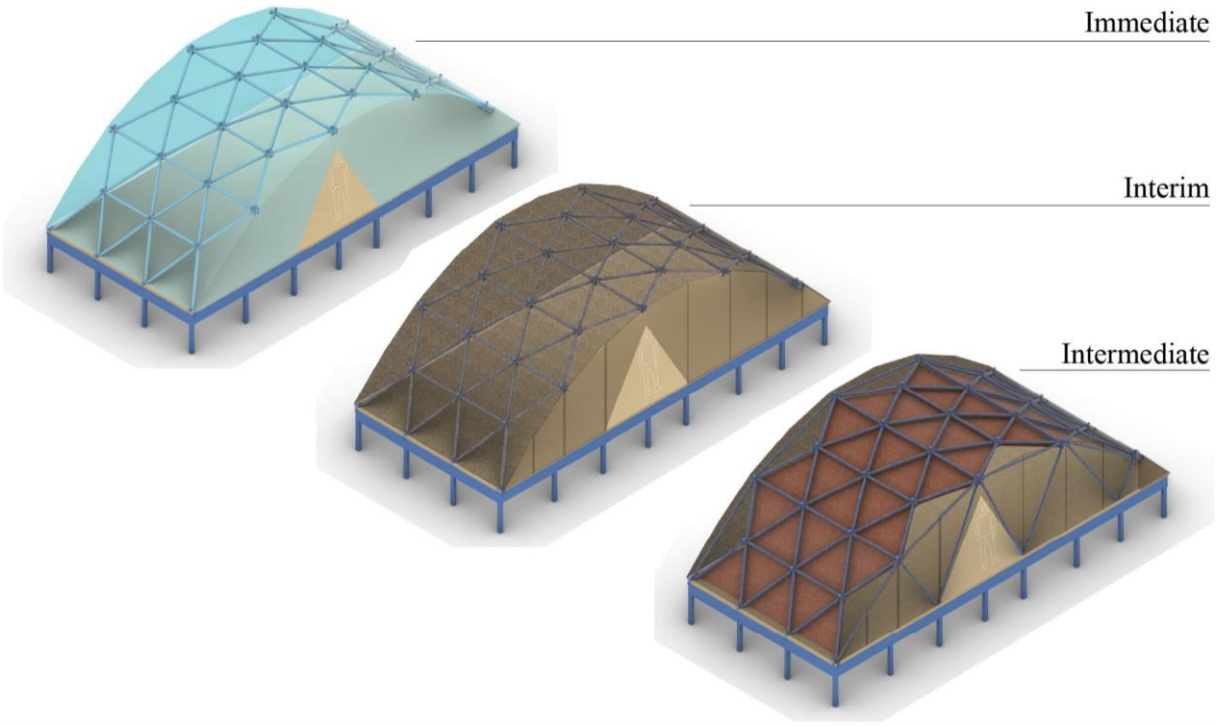

Figure 4. Immediate, interim and intermediate stages.

Table 2. Evaluation of MSSAS.

	MSSAS Initial	MSSAS Total	Three Stages Total
Lifespan	1 Year	15 Years	15 Years
Construction Time	1 Day	7 Days	15 Days
Cost	€2000	€4000	€5000
Covered Living Area	26 m^2		24 m^2
Cargo Weight	3000 kg	5000 kg	50000 kg

Cargo Volume	9 m^3	15 m3	50 m3
CO_2 Footprint	5000 kg	9000 kg	15000 kg
Cost/ Lifespan	€ 250/ year		€ 350/ year
Cost/ Lifespan/ Area	€ 10/ year/ m^2		€ 15/ year/ m^2
Cargo Weight/ Area	200 kg/ m^2		2000 kg/ m^2
Cargo Volume/ Area	0.6 m^3/ m^2		2 m^3/ m^2
CO_2/ Lifespan/ Area	25 kg/ year/ m^2		40 kg/ year/ m^2

The case study is designed for Burunçayır Village in Adıyaman. Gridshell consists of steel tubes (50mm diameter and 5mm wall thickness) and it spans 8 meters. NPI220 and NPI180 beams are used for floor beams. Structure has 26 m^2 living area with additional 16 m^2 covered areas reserved for storage and installation. Structural analysis (FEA) was conducted with Karamba3D for S235 steel material (σ=23,5 [kN/cm²], E=21000[kN/cm²], and checked for displacement ($\delta < L/250$), axial stress and buckling **(Figure 5).** Dead loads (self-weight), live loads (2 kN/m^2), snow loads (1 kN/m^2) and wind loads (28 m/s) were calculated according to TS498 (2021). Earthquake loads were calculated per TBEC (2018) (soil condition ZD, building importance coefficient BKS=3, building height value BYS=8) for DD-3 values received from AFAD Seismic Map (S_S=0.349, S_1=0.088, S_{DS}=0.531, S_{D1}=0.211, PGA=0.153 PGV=8.879).

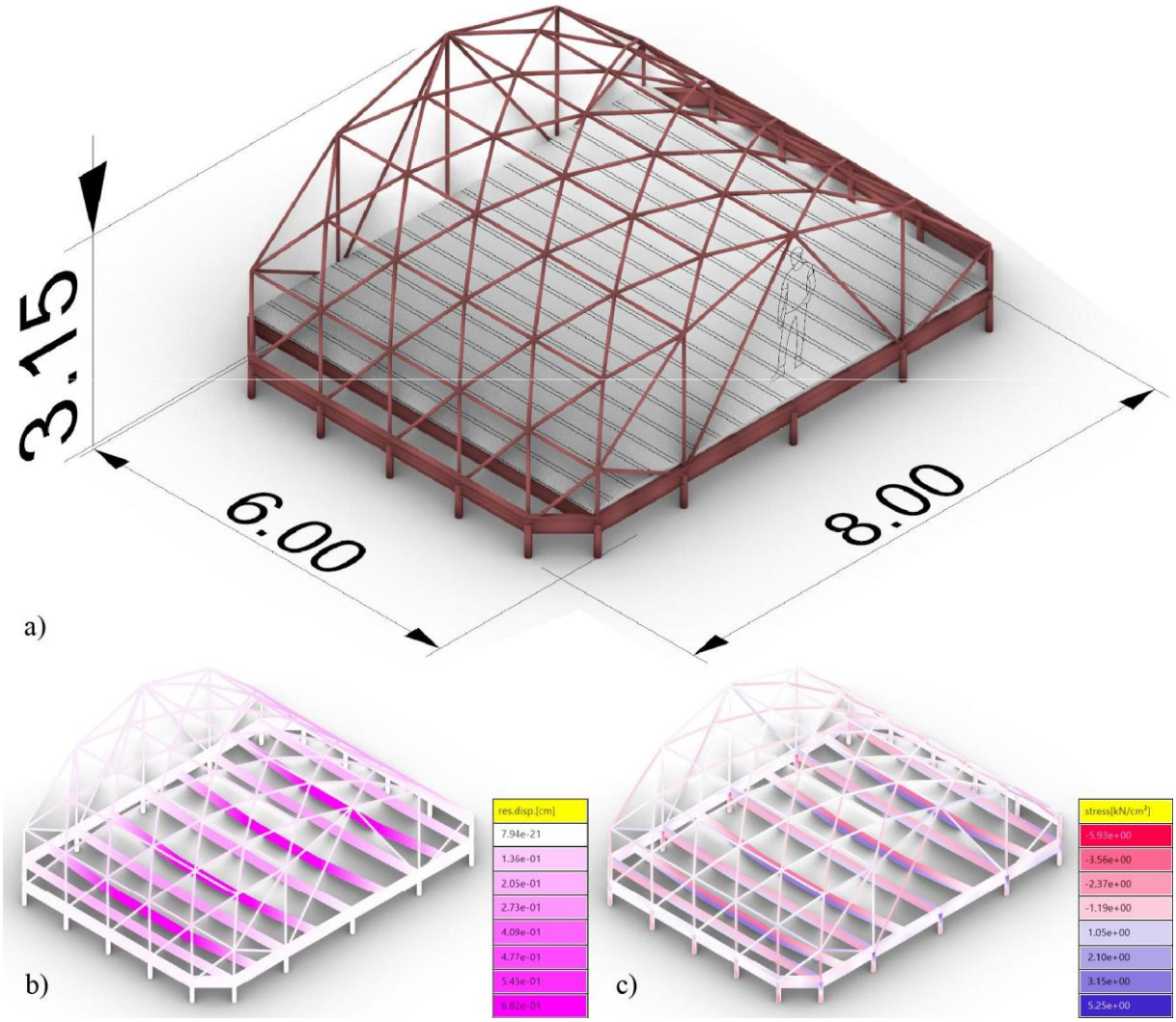

Figure 5. (a) Case study for Buruncayir Village, (b) displacement analysis, (c) stress analysis.

Conclusion

MSSAS displays that deployability with an embedded capacity for progressiveness improves the sheltering workflow. Though initial cost, transportation volume, mass and material usage for SAS are higher than regular emergency shelters, design itself accommodates multiple stages, addresses multiple settlement situations and multiple socio-spatial parameters in one single modifiable structure. When compared to three individual shelters combined, it is estimated that MSSAS decreases costs, transported volume, transported mass, and carbon footprint by a considerable amount. Although available materials and costs can change based on location and situation, study represents a design principle. In conclusion, MSSAS's ease of transportation, usage of local materials and engineered structural and climate performance make it a durable, ecologically and socially sustainable and psychologically sensitive alternative to current shelters.

References

Abdullah, Y. S., & Al-Alwan, H. A. S. (2019). Smart material systems and adaptiveness in architecture. Ain Shams Engineering Journal, 10(3), 623–638. https://doi.org/10.1016/j.asej.2019.02.002

Abu-Aridah, D., & Ligler, H. (2024). Shape grammars and self-built refugee communities: The transformation from tent shelter to customized structure in Irbid Camp. International Journal of Architectural Computing, 22(1), 149–172. https://doi.org/10.1177/14780771241229854

Antonini, E., Boeri, A., & Giglio, F. (2020). Technologies for Building After Disaster: A Critical Review (pp. 27–58). https://doi.org/10.1007/978-3-030-55969-4_2

Caetano, I., & Leitão, A. (2024). Connecting design and fabrication through algorithms: current and future prospects for AEC. Automation in Construction, 164, 105445. https://doi.org/10.1016/j.autcon.2024.105445

Celik, O. C., Ulker, M. B. C., Gocer, C., Guntepe, S., Koz, O., Eyupgiller, M. M., Aksu, M., & Yaz, A. (2024). Multidisciplinary reconnaissance investigation covering structural, geotechnical, and architectural based damage to mid-rise residential buildings following the February 6th, 2023 Kahramanmaraş, Türkiye earthquake doublets (Mw 7.8, Mw 7.6). Soil Dynamics and Earthquake Engineering, 182, 108738. https://doi.org/10.1016/j.soildyn.2024.108738

Ding, H., Zhou, Y., Ge, Z., Taymaz, T., Ghosh, A., Xu, H., Irmak, T. S., & Song, X. (2023). High-resolution seismicity imaging and early aftershock migration of the 2023 Kahramanmaraş (SE Türkiye) MW7.9 & 7.8 earthquake doublet. Earthquake Science, 36(6), 417–432. https://doi.org/10.1016/j.eqs.2023.06.002

Elmokadem, A., Ekram, M., Waseef, A., & Nashaat, B. (2018). Kinetic Architecture: Concepts, History and Applications. International Journal of Science and Research (IJSR), 7(4), 750–758. https://doi.org/10.21275/ART20181560

Fleischmann, M., Knippers, J., Lienhard, J., Menges, A., & Schleicher, S. (2012). Material Behaviour: Embedding Physical Properties in Computational Design Processes. Architectural Design, 82(2), 44–51. https://doi.org/10.1002/ad.1378

Geneva: International Federation of Red Cross and Red Crescent Societies. (2011). Transitional shelters: Eight designs.

Geneva: International Federation of Red Cross and Red Crescent Societies. (2013). Post-disaster shelter: Ten designs.

Loonen, R. C. G. M., Trčka, M., Cóstola, D., & Hensen, J. L. M. (2013). Climate adaptive building shells: State-of-the-art and future challenges. Renewable and Sustainable Energy Reviews, 25, 483–493. https://doi.org/10.1016/j.rser.2013.04.016

Maierhofer, M., & Menges, A. (2019). Towards integrative design processes and computational design tools for the design space exploration of adaptive architectural structures.

McCoy, C., & Duffy, T. A. (2022). The deployable tectonic: mechanization and mobility in architecture. Architecture, Structures and Construction, 2(4), 613–628. https://doi.org/10.1007/s44150-022-00045-w

Menges, A., & Ahlquist, S. (Eds.). (2011). Computational Design Thinking. John Wiley and Sons.

Quarantelli, E. L. (1982). General and particular observations on sheltering and housing in American disasters. Disasters, 6(4), 277–281. https://doi.org/10.1111/j.1467-7717.1982.tb00550.x

Presidency of Strategy and Budget of the Republic of Türkiye. (2025). Kahramanmaraş and Hatay earthquakes reconstruction and
development report. Ankara, Turkey.

Republic of Turkey Ministry of Environment and Urbanization. (2018). Turkish building earthquake code (TBDY 2018). Ankara, Turkey.

Rios, F. C., Chong, W. K., & Grau, D. (2015). Design for Disassembly and Deconstruction - Challenges and Opportunities. Procedia Engineering, 118, 1296–1304. https://doi.org/10.1016/j.proeng.2015.08.485

Roggema, R. (2016). Research by Design: Proposition for a Methodological Approach. Urban Science, 1(1), 2. https://doi.org/10.3390/urbansci1010002

Schmidt III, R., & Austin, S. (2016). Adaptable Architecture. Routledge. https://doi.org/10.4324/9781315722931

Shahkar, A. (2022). POST-DISASTER TEMPORARY HOUSING ALTERNATIVES FOR ENHANCED STRUCTURAL, CONSTRUCTIONAL, AND ARCHITECTURAL PERFORMANCES.

Sphere Association. (2018). The Sphere Handbook: Humanitarian Charter and Minimum Standards in Humanitarian Response.
TSI. (2021). TS 498: Design loads for buildings. Ankara, Turkey: TSE.
UNHCR. (2016). Shelter Design Catalogue.
UNHCR. (2021). Shelter and Sustainability.
Valcárcel, J. P. (2024). Emergency Modular Buildings in Developed Countries: CODEMOSCH Project. Current Trends in Civil & Structural Engineering, 11(1). https://doi.org/10.33552/CTCSE.2024.11.000754
van Ellen, L. A., Bridgens, B. N., Burford, N., & Heidrich, O. (2021). Rhythmic Buildings- a framework for sustainable adaptable architecture. Building and Environment, 203, 108068. https://doi.org/10.1016/j.buildenv.2021.108068
Yazici, S., & Tanacan, L. (2020). Material-based computational design (MCD) in sustainable architecture. Journal of Building Engineering, 32. https://doi.org/10.1016/j.jobe.2020.101543

Artificial Intelligence in Materials Education for Architecture Opportunities, Challenges and Ethical Considerations

Peyam Başer[a], Seden Acun Özgünler[b], Mine Topçubaşı[c]

[a] Istanbul Technical University, Graduate School, Environmental Control and Construction Technologies, Türkiye
[b] Istanbul Technical University, Faculty of Architecture, Department of Architecture, Türkiye
[c] Gebze Technical University, Faculty of Architecture, Department of Architecture, Türkiye
baserp22@itu.edu.tr

Keywords: Artificial Intelligence, Review, Education, Building Materials.

Aim

Artificial intelligence (AI) has been present in various areas of human life for many years; although it has been perceived as a "science fiction product" for many years, it has recently become an ordinary part of everyday life. Efforts to imitate human intelligence through machines began with great hopes, but the progress has been paused periodically for various reasons. Nevertheless, over time, AI has been adopted as an important transformation tool in a wide range of fields.
In this study, the features to be used in the context of architectural materials education were examined and discussed through the findings based on literature research. The historical development of the concept of AI since it first emerged, how the capacity of AI changed over time and how AI was applied especially in education were discussed. In addition, the contributions of AI to educational processes, the opportunities it offered and the limitations that may have been encountered, ethical and legal regulations regarding the use of AI in education were examined within the scope of the literature study findings and it is aimed to discuss the requirements for the sustainable and reliable implementation of this technology.

Material and Method

This study is based on literature review findings to discuss the historical development of AI, the phases and sub-concepts of its capability, current practices that can be taken as examples for integration into material education in architecture, the opportunities it offers as well as the limitations that may be encountered, and the ethical and legal regulations regarding the use of AI in education.
The main sources are academic articles, reports, international regulations, scientific research on past and current AI applications and studies on the use of AI in various fields. The data were categorized and evaluated in terms of types of AI, learning models, its use in education, ethical/legal dimensions, and the opportunities and risks it presents.

Findings

Although the concept of AI was previously expressed under different names, it became widespread at the Dartmouth Workshop in 1956. The workshop was an important turning point where the theoretical foundations of AI were established. (Nilsson, 2005; p.77-79) Within the scope of the workshop, the concept of AI was addressed by McCarthy as the problem of creating machines that behave similarly to human intelligence. (McCarthy et al., 1955)
This early period witnessed significant advances in research on symbolic AI, focusing on cognitive processes. Alan Turing proposed the Turing Test, which assesses a machine's ability to behave intelligently at a level indistinguishable from a human, and the test was used as a standard benchmark for years. (Turing, 1950) Studies such as Samuel's checkers program and Newell and Simon's General Problem Solver (GPS) demonstrated the development potential of AI in learning and problem solving. (Samuel, 1959; Newell et al, 1963) In Turkey in 1959, Cahit Arf's conference titled "Can Machines Think and How Can They Think?" offered insights for AI and the future (Uğur et al, 2025).
The first International Conference on AI (IJCAI) in 1969 was an indication of its growth. In the same period, there was an increase in courses and literature on AI, and academic communities began supporting AI studies. However, during the

1970s, the Mansfield Amendment in the US and the Lighthill Report in the UK resulted in funding challenges for AI researches, which led to a slowdown in the progress (Nilsson, 2005).

Although these difficulties, funding continued thanks to the interest in applications, and expert systems attracted great interest. The period 1975-1985 was considered a "boom period" for AI. The revival period and the successes achieved increased the interest of researchers. With this increasing interest, the American Association for Artificial Intelligence (AAAI) was founded and large companies invested in AI. Although interest in the field increased worldwide, there was a setback in the 1980s when AI failed to deliver the promised success, and this period was called the "AI Winter." (Nilsson, 2005)

In the late 1980s, a revival period began with the development of machine learning technologies. Studies on the applicability of biological structures to machine learning and the development of multilayer neural networks led to significant developments. In the 1990s, artificial neural networks started to give successful. The early 21st century represents the beginning of a new era in AI, the era of deep learning. With advances in computing power and technical capabilities, especially the development of powerful graphics processing units (GPUs), deep learning has enabled the identification of complex patterns from big data using multilayer artificial neural networks (Burkov, 2019; Doğan et al, 2019; Kaplan et al, 2019).

Neural networks provide solutions to various types of problems with supervised, unsupervised and reinforcement learning methods. While supervised learning aims to make predictions using labeled data, unsupervised learning aims to make sense of unlabeled data sets. Reinforcement learning focuses on learning the best strategy through reward mechanisms. Unsupervised learning is used in speech recognition applications such as Apple's Siri or Amazon's Alexa, while Reinforcement learning is used in Microsoft's MSN.com headline selection (Burkov, 2019; Kaplan et al, 2019).

Today, these networks are used in many areas such as classification, prediction, diagnosis and diagnosis, and different models are preferred according to the structure of the data and the type of problem. Deep learning has led to groundbreaking developments in a wide range of fields such as computer vision, classification, object detection, audio processing, medical image analysis and industrial processes (Doğan et al, 2019).

The advancements in technology in the 21st century have significantly impacted educational practices as well. One of the notable developments is the emergence of generative AI, which uses machine learning to create new content based on analysis of existing content. Two key generative AI models are Generative Adversarial Networks (GAN) and Generative Pre-Trained Transducers (GPT). GAN utilizes two neural networks to distinguish between real and artificial content and has found widespread use in visual and audio production. GPT models, on the other hand, employ natural language processing techniques to produce human-like text by analyzing large datasets. These GPT-based models have diverse applications, including customer service chatbots and character development in video games. In recent years, tools like ChatGPT have gained attention in various fields, from education to engineering, journalism, medicine, and economics. (Baidoo-Anu et al., 2023)

AI is being used in various universities and positive results are being achieved. At Georgia Tech University, an AI-based virtual teaching assistant is used to answer student questions; AI-powered chatbots are used to speed up teaching processes at Berlin Technical and Carnegie Mellon Universities. Major academic publishers such as Elsevier and LexisNexis use AI to automate systematic literature searches, detect plagiarism and identify statistical misuse. In online education, facial expressions from webcams can be analyzed to determine which students are paying attention to the lecture and which are not. It is thought that in the future, the RENNE system can support faculty members in determining the most effective coaching strategies or detecting cheating in exams by reading student emotions. Studies show that AI in education has the potential to enrich teaching and learning methods, offer students a more in-depth learning experience, and provide instructors with more effective process management. AI has the potential to revolutionize education by providing personalized learning experiences and automating tasks such as grading. This allows teachers to focus more on individual interactions with students. (Kaplan et al., 2019; Zawacki-Richter et al., 2019; Baidoo-Anu et al., 2023; Kovari, 2025).

On the other hand, there are still uncertainties and ethical concerns surrounding the use of AI in education. It is unclear if students will prefer AI-driven education, if universities will view AI as a substitute for human teachers, and how the quality of education will be affected. To address these concerns, it is recommended that universities offer courses on "AI and

Humanity" to explore issues such as ethics, privacy, and data ownership in AI education. By addressing these issues, the potential benefits of AI in education can be maximized while safeguarding the well-being and values of students. (Kaplan et al., 2019).

Globally, advancements in AI are rapid, but legal frameworks are still developing (Bird et al., 2020). The European Union (EU) established its first international AI strategy in 2018 and published ethical guidelines for trustworthy AI in 2019 (European Commission, 2019). EU member states continue to develop national strategies (European Commission, 2021). In Turkey, the "2021-2025 National AI Strategy" and ethical guidelines by the Council of Higher Education (YÖK) promote responsible AI use in education and research (URL-1; URL-2; URL-3; URL-4; URL-5; URL-6; URL-7). AI's integration into education gives rise to challenges such as data privacy, algorithmic biases, and ethical risks. Ensuring fair, transparent, and responsible AI integration in education is imperative (Zhang et al, 2021).

While AI is developing rapidly around the world, legal regulations have not kept pace. The European Commission established its first international AI strategy in 2018 and set ethical criteria for trusted AI in 2019. In developing their national strategies, EU countries are investing in AI applications in various sectors such as health, education, transportation. For example, Finland aims to use AI in public services, while Germany is focused on developing data protection and ethical frameworks. The United Kingdom has established a data ethics and innovation center that promotes the safe and ethical use of AI (Bird et al., 2020). The European Union adopted its AI regulation in 2021. The regulation, which is the first AI law adopted in the world, focuses on protecting human rights and prohibits harmful AI systems while encouraging socially beneficial applications. In the field of education, ethical use is supported. (Url-1; Url-2; Url-3; Url-4; Url-5)

In Turkey, the "2021-2025 National Artificial Intelligence Strategy", prepared in cooperation with the Presidential Digital Transformation Office and the Ministry of Industry and Technology, has entered into force. This strategy promotes the development and application of AI technologies in areas such as health, industry, education and public administration. Furthermore, the Council of Higher Education (YÖK) published a guideline in 2024 setting out ethical principles for the productive use of AI in scientific research and publication activities (Url-6; Url-7).

AI brings challenges such as data privacy and ethical risks. Issues such as data breaches and student-teacher autonomy are important ethical issues to be considered in the use of AI in education. Therefore, it is of great importance to use AI in education in a fair, transparent and responsible manner (Zhang & Aslan, 2021).

Conclusion

AI refers to the development of algorithms to perform tasks that require human intelligence. The goal of AI is to create software that mimics and, if possible, even surpass human cognitive abilities. Just like the replacement of human muscle power with machines in the Industrial Revolution, the AI transformation enables the automation of cognitive processes and their execution by machines.

Wide range of applications shows that AI will become even more widespread in the future and will play a transformative role in many disciplines such as materials education in architecture. It is seen that it can enrich education with personalized learning experiences, automated tasks and adaptive feedback systems as well as simulating material behavior, predicting performance based on material properties and function, and providing efficient feedback to help students make design decisions with materials that are appropriate for project requirements.

However, in the integration of AI into material education, issues such as data privacy, variability of information according to the data being processed, and over-dependence on technology should be considered. It is important that AI should be used as a tool which plays a complementary role to human abilities by supporting critical thinking and creativity in architectural education.

In conclusion, AI has the potential to transform material education in architecture, enhancing learning and decision-making processes and becoming a helpful, supportive tool for students and instructors when integrated responsibly and ethically. Successful integration of AI in education depends on strengthening ethical and legal frameworks. In this process, collaboration between educators, researchers and policy makers will play a critical role to maximize the potential of AI in education while minimizing potential risks.

References

Baidoo-Anu, D., & Owusu Ansah, L. (2023). Education in the era of generative artificial intelligence (AI): Understanding the potential benefits of ChatGPT in promoting teaching and learning. Journal of AI, 7(1), 52–62. https://doi.org/10.61969/jai.1337500

Bird, E., Fox-Skelly, J., Jenner, N., Larbey, R., Weitkamp, E., & Winfield, A. (2020). The ethics of artificial intelligence: Issues and initiatives. European Parliamentary Research Service.

Burkov, A. (2019). The hundred-page machine learning book. Andriy Burkov.

Doğan, F. & Türkoğlu, İ. (2019). Derin öğrenme modelleri ve uygulama alanlarına ilişkin bir derleme. Dicle Üniversitesi Mühendislik Fakültesi Mühendislik Dergisi, 10(2), 409-445. https://doi.org/10.24012/dumf.411130

Kaplan, A., & Haenlein, M. (2019). Siri, Siri, in my hand: Who's the fairest in the land? On the interpretations, illustrations, and implications of artificial intelligence. Business Horizons, 62(1), 15-25. https://doi.org/10.1016/j.bushor.2018.08.004.

Kovari, A. (2025). A systematic review of AI-powered collaborative learning in higher education: Trends and outcomes from the last decade. Social Sciences & Humanities Open, 11, 101335. https://doi.org/10.1016/j.ssaho.2025.101335

McCarthy, J., Minsky, M. L., Rochester, N., & Shannon, C. E. (1955). A proposal for the Dartmouth Summer Research Project on Artificial Intelligence.

Newell, A., & Simon, H. A. (1963). GPS, a program that simulates human thought. Computers and Thought (pp. 109-124). McGraw-Hill.

Nilsson, N. J. (2005). The quest for artificial intelligence. Cambridge University Press. https://ai.stanford.edu/~nilsson/QAI/qai.pdf. 26 Mayıs 2024.

Samuel, A. L. (1959). Some studies in machine learning using the game of checkers. IBM Journal of Research and Development, 3(3), 210–229.

Turing, A. M. (1950). Computing machinery and intelligence. Mind, LIX(236), 433-460. https://doi.org/10.1093/mind/LIX.236.433.

Uğur, S. & Usta, İ. (2025). Yapay zekânın eğitimde kullanımı ile ilgili Türkiye'de yapılan lisansüstü tezlerin bibliyografik analizi. Manas Sosyal Araştırmalar Dergisi, 14 (1), 143-163. doi:10.33206/mjss.1587252

Zawacki-Richter, O., Marín, V. I., Bond, M., & Gouverneur, F. (2019). Systematic review of research on artificial intelligence applications in higher education – where are the educators? International Journal of Educational Technology in Higher Education, 16(39). https://doi.org/10.1186/s41239-019-0171-0

Zhang, K., & Aslan, A. B. (2021). AI technologies for education: Recent research & future directions. Computers and Education: Artificial Intelligence, 2, 100025. 1 https://doi.org/10.1016/j.caeai.2021.100025

Url-1 https://www.ab.gov.tr/yapay-zek-yasasi-avrupa-parlamentosunda-kabul-edildi_53752.html, date retrieved 26.05.2024.

Url-2 https://www.aa.com.tr/tr/dunya/avrupa-parlamentosu-yapay-zeka-yasasini-onayladi/3163480, date retrieved 26.05.2024.

Url-3 https://www.europarl.europa.eu/news/en/press-room/20240308IPR19015/artificial-intelligence-act-meps-adopt-landmark-law, date retrieved 26.05.2024.

Url-4 https://epthinktank.eu/tag/artificial-intelligence, date retrieved 26.05.2024.

Url-5 https://www.europarl.europa.eu/doceo/document/TA-9-2024-03-13-TOC_EN.html, date retrieved 26.05.2024.

Url-6 https://cbddo.gov.tr/uyzs, date retrieved 26.05.2024.

Url-7 https://cbddo.gov.tr/SharedFolderServer/Genel/File/TR-UlusalYZStratejisi2021-2025.pdf, date retrieved 26.05.2024.

ARCHITECTURE

Architectural History

Architecture Design Theory

Building Construction Technologies

Building Materials and Technologies

Built Environment Design and Technologies

Conservation and Restoration

Environmental Control and Building Technology

Project and Construction Management

Sustainable Design

A Literature Review On Organizational Structures In The Construction Industry

E. Gamze Sentuna[a], F. Pinar Cakmak[a]

[a] Istanbul Technical University, Architecture, Project and Construction Management Program, Turkey
sentuna16@itu.edu.tr

Keywords: Construction Industry, Construction Project Management, Literature Review, Organizational Structure.

Aim

A company's organisational structure can have a pronounced impact on its performance. It influences a wide array of metrics such as productivity, decision-making agility, information sharing, employee retention, and problem-solving ability, all of which directly or indirectly impact the organization's profitability. The construction industry's project-based nature means that the organization's profitability is often determined at the project level, thus making understanding how organizational structures influence projects crucial.

This research focuses on organizational structures and their impacts on the construction industry. Given the industry's project-based nature, understanding how organizational structures influence projects is crucial. By examining existing research on organizational design, this paper explores the fundamental principles, key characteristics, and implications of different structures within a specific industry context.

Existing studies on construction industry organizational structures have approached the topic from multiple perspectives. While project stakeholders operate within their respective organizations, simultaneously, they function within temporary project organizations. As a result, research on the topic often examines structures at the project team level.

Turner and Muller (2003) redefine projects by emphasizing the project team as an organization: "a project is a temporary organization to which resources are assigned to undertake a unique, novel and transient endeavor managing the inherent uncertainty and need for integration in order to deliver beneficial objectives of change".

Unlike permanent organizations, temporary project organizations exhibit certain characteristics, such as temporariness, uniqueness, heterogeneity, short-term orientation, and lack of organizational routines, which pose challenges to management (Hanisch and Wald, 2011). These traits contribute to the inherent complexity of temporary organizations (Geraldi et al., 2011).

Organizational structure by Daft (2007) is stated as ''social entities that are goal-oriented and deliberately designed to coordinate activities so as to link the system to the external environment." Organizational structure by Mahmoudsalehi (2012) is "a formal allocation of work roles and administrative mechanisms for controlling and integrating work activities". Noorderhaven (1995) argues that organizational structure is "the formal pattern of how jobs are allocated to people and divisions, how communication flow is structured and how hierarchical relationships between people are connected". As the primary output of construction projects is the product delivered, project success is inherently linked to the effectiveness of the organizational structure.

Purpose of the Study:

This paper aims to systematically map and analyse existing academic contributions on organizational structures in the construction industry. Rather than presenting new empirical findings, it synthesizes prior research to identify key structural dimensions, thematic patterns and dominant research methods. It is aimed to establish a foundation for further empirical investigation - specifically to develop a research framework for evaluating how organizational structures influence project outcomes in real-world construction settings. To achieve this, the paper first details the research methodology and approach to gathering literature. Then, it presents the findings, categorizing the reviewed literature in terms of levels of analysis, research methods, and key recurring concepts in the topic.

Material and Method

A comprehensive literature search was conducted using Scopus, a database providing access to over 23,500 peer-reviewed titles from more than 5,000 international publishers covering science and social science subjects (Leiringera, 2021).
The search string is as follows: TITLE-ABS-KEY ("organizational structure") AND TITLE-ABS-KEY ("construction industry" OR "construction sector" OR "construction management") AND (LIMIT-TO (DOCTYPE, "ar")). This search yielded 153 articles related to the topic for further review. These articles have been reviewed and categorized depending on their relevance to the research question.

Findings

Out of the 153 identified articles, 52 articles have been deemed relevant to the research topic. Of these, 30 articles have been cited in the thesis draft. The remaining 22 articles provided contextual background without directly contributing to the research question.
Out of the 30 articles, 17 articles examine construction project organizations as temporary entities where multiple actors collaborate for a limited time. The other 13 articles focus on internal organizational structures within individual construction companies. In the thesis research, temporary project organizations are the focus.

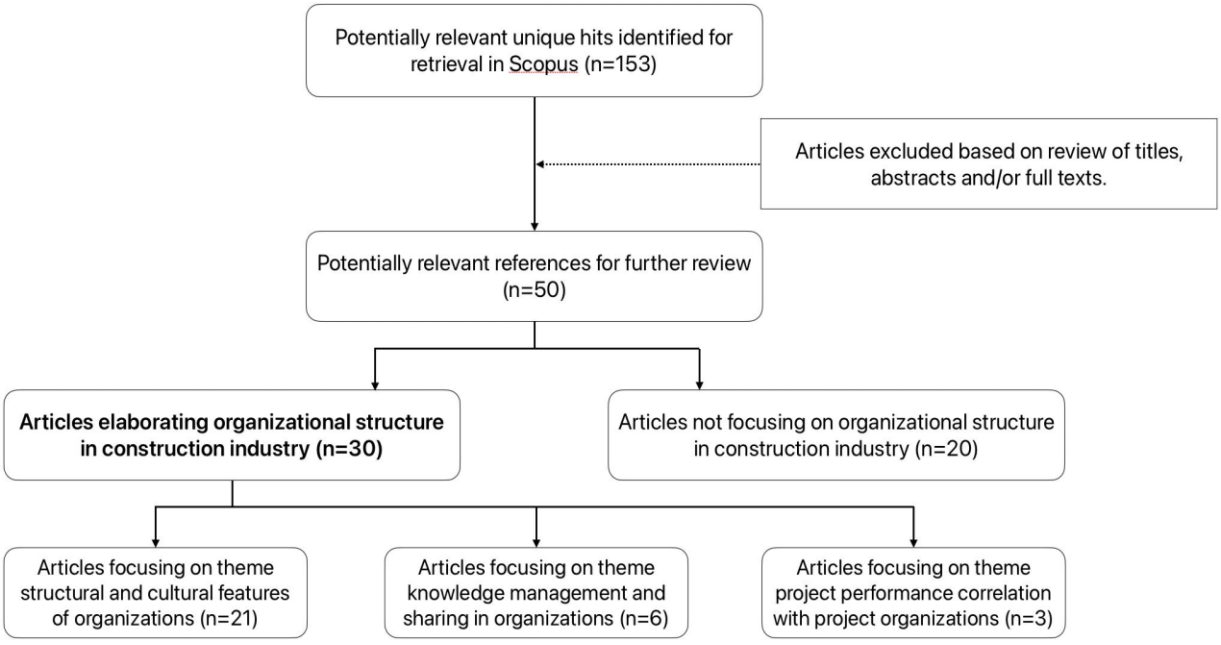

Figure 1. Flow diagram of sample selection process.

As captured in Figure 1, three dominant research themes have been identified within the sample of articles explicitly mentioning organization structures in the construction industry. Out of the 30 key articles, 21 studies explore theoretical frameworks such as centralization, formalization, specialization, complexity, horizontal and vertical schemes, network organizations, and relationships.
The second theme in six articles is knowledge management and sharing practices in project organizations and how organizational structures facilitate or hinder these. Only a small subset of studies (three articles) explicitly investigates the link between organizational structures and project performance outcomes.

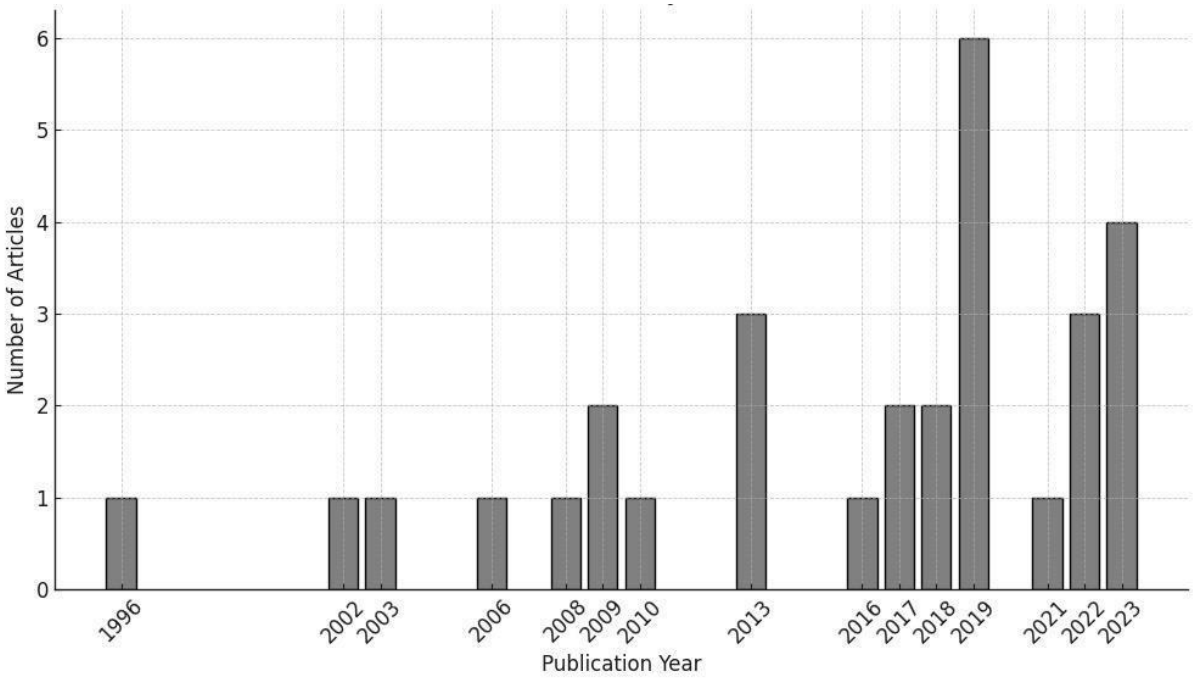

Figure 2. Distribution of articles based by publication year.

Most studies on organizational structure in construction have been published after 2013, reflecting a growing interest in recent years (Figure 2). The project-based organizations (PBO) are mostly reviewed in articles after 2019.

Table 1. Distribution of articles based on level of analysis and research method.

Level of Analysis (n=30)	
1. Individual Level	1
2. Project Level	6
3. Organisational Level	10
4. Multi-level (combining individual, project and organizational levels)	13
Research Method (n=30)	
1. Case Study	4
2. Survey	18
3. Mixed Method	8

The articles analyse the concept of organizational structure at several different levels, i.e., individual, project, and organisational. Approximately one-third of the articles in the sample focus on the organizational level, while 60% employ survey-based research methods (Table 1). Sample survey selection often includes clients, contractors, consultants, subcontractors, manufacturers and other project stakeholders.

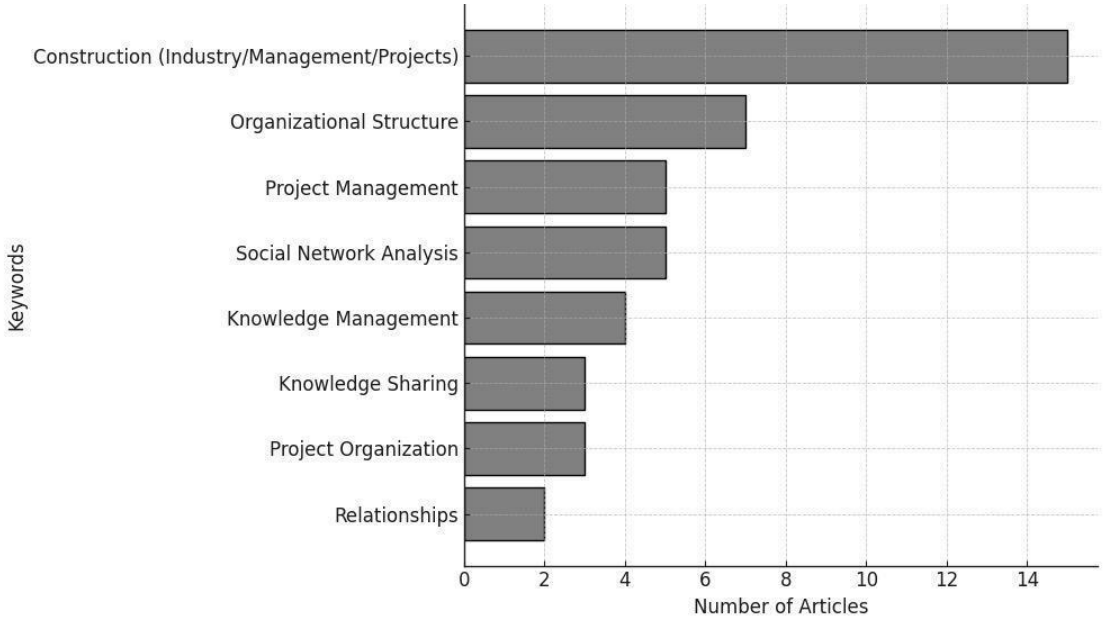

Figure 3. Distribution of most frequently used keywords in sample articles (n=30).

As reflected in Figure 3, 50% of the articles focus on construction organizations, emphasizing their structural and managerial strategies. 23% of the literature highlights knowledge sharing and management, underlining their importance in project organizations' success. Relationships among actors is another function that influences the organizational structures in construction projects.

Conclusion

This literature review provides an initial systematic analysis of research on organizational structures in the construction industry, highlighting key themes, methodologies, and gaps. Over 90% of the articles in the sample have an empirical component, utilizing various data collection methods.

A number of observations can be made as follows: Most research is quantitative, with case studies and surveys being the dominant methodologies. The research focus and objectives vary significantly, with limited evidence of knowledge accumulation or theory building. The majority of studies target the organisational level. 'Enhanced' performance is commonly alluded to, but most articles do not define performance outcomes explicitly or show how the outcomes are in direct correlation with organizational structures.

The insights gained from this review will support the thesis study on the research question: Is there a correlation between organizational structure and project outcomes? The categorization of themes, level of analysis, and research methods derived from this review will directly inform the design of the thesis research. Specifically, it will guide the development of a theoretical framework and the data collection, such as survey questionnaire, to evaluate how organizational structures influence performance in temporary project organizations.

A notable limitation of this review is that the literature search is still ongoing, and relevant references cited within reviewed articles have not yet been fully explored. As the thesis progresses, additional studies may provide further depth and support the refinement of the research approach.

References

Daft, R. (2007). Organization theory and design (9/e.) Mason. OH: Thomson South-Western. 0.1016/j.jbusres.2012.02.023

Geraldi, J., Maylor, H., Williams, T. (2011). Now, let's make it really complex (complicated). A systematic review of the complexities of projects. International Journal of Operations and Production Management (31, pp. 966–990).

Hanisch, B., Wald, A. (2011). A project management research framework integrating multiple theoretical perspectives and influencing factors. Project Management Journal (42, pp.4–22).
Leiringera R., Sujuan Zhang S. (2021) Organisational Capabilities and Project Organising Research. International Journal of Project Management (Vol. 39, pp.422-436).
Mahmoudsalehi, M., Moradkhannejad, R. and Safari, K. (2012). How knowledge management is affected by organizational structure. The Learning Organization (Vol. 19 No. 6, pp. 518-528).
Noorderhaven (1995) Strategic Decision Making, Addison-Wesley, Wokingham.
Turner J.R., Muller R. (2003). On the nature of the project as a temporary organization, International Journal of Project Management (Vol. 21, pp.1–8).

A Systematic Review of BIM and the Circular Economy: Key Research Areas and Findings

Merve Cellek[a], Fatma Pınar Çakmak[a]

[a] Istanbul Technical University, Graduate School, Project and Construction Management, Turkey
cellek19@itu.edu.tr

Keywords: Building Information Modelling (BIM), Circular economy, Literature review.

Aim

In the modern construction industry, the circular economy is becoming increasingly prominent in reducing resource consumption and increasing sustainability. Circularity aims to efficiently use materials and resources, minimizing waste and promoting reuse throughout the life cycle of buildings. In this context, digital technologies such as Building Information Modeling (BIM) significantly contribute to circularity by supporting material tracking, life cycle analysis and sustainable design processes. This meta-analysis aims to systematically assess the academic literature examining the integration of BIM with the circular economy, categorizing the main research areas, methods used and prominent findings.

Material and Method

First of all, Scopus was used to examine the existing studies on BIM and circularity. A systematic data selection procedure based on the keywords TITLE-ABS-KEY("building information model*" OR "BIM" OR "bim") AND TITLE-ABS-KEY("construction sector" OR "construction industr*" OR "construction manage*") AND TITLE-ABS-KEY("circularity") OR TITLE-ABS-KEY("circular economy") was adopted. The search resulted in 137 articles, two of which were removed because they were not in English, leaving 135. The oldest article was published in 2019, and new ones will continue to appear until 2024. We selected 30 articles that addressed the transition to circularity and the inclusion of digitalization. A meta-classification system was developed for the reviewed articles based on research output, data source and content variables. The meta-analysis framework is shown in Table 1 below:

Table 1: Meta-analysis framework.

Category	Attributes Included
Article Info	Article Name, Publication Date, Keywords, Number of Citations
Author & Journal Info	Author(s), Author(s) Background, Country, Journal Name, Publisher
Content & Methodology Info	Research Focus, Topics, Gaps, Methods, Outputs, Data Sources, Geographical Distribution, Recommended Research Areas

Findings

The publications are primarily in sustainability and environmental journals, published in 20 journals and two conference series. The number of publications on BIM, sustainability and circularity is rapidly increasing, with significant increases expected in 2022 and 2024. This increase results from concerns about environmental sustainability and global climate change, which are increasing the importance of circularity and related technologies such as BIM. The increase in 2024 suggests that these topics will continue to be important focuses of future studies.

As stated in Figure 1, keywords such as BIM, circular economy, and life cycle assessment (LCA) are among the most commonly used. Among other keywords, sustainability and waste management also stand out in frequency.

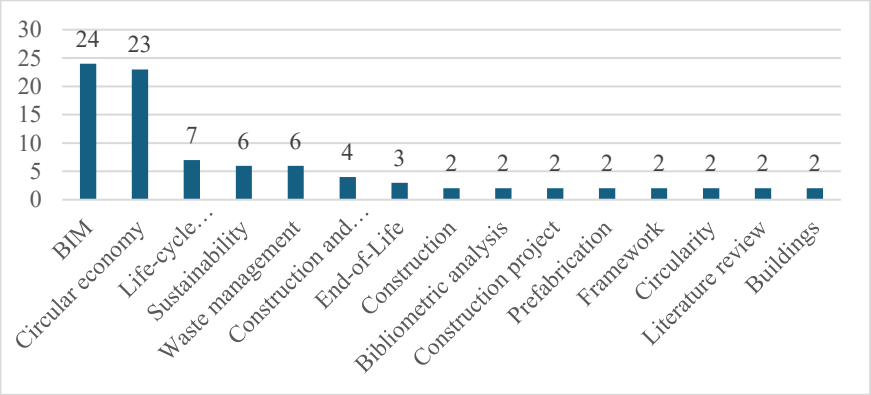

Figure 1: Keyword frequency.

The most cited paper, "Uses of building information modeling for overcoming barriers to a circular economy" received 109 citations. Papers focusing on circular economy, digital transformation and construction supply chain processes significantly impact other research. In particular, studies on the challenges and opportunities of circular economy adoption supported by digital transformation serve as key references. These citation trends highlight the growing importance of the circular economy and digital transformation in the construction industry and their impact on academic research.

In order to classify the research focus, the articles were classified into six categories according to their content. Some articles were included in 2 areas as they were suitable for two categories. The most popular topic, circular economy integration with BIM, was examined in 11 of the 30 articles. These papers are mainly about developing theoretical BIM-based frameworks and exploring BIM use cases supporting circular economy applications (Charef, 2024). The second popular topic is construction, demolition, and waste management with BIM, which was analyzed in 8 papers. These articles generally cover the integration of BIM and JIT to develop environmentally friendly and efficient methods in construction demolition processes (Andriyani et al., 2024), BIM-Lean interaction for developed demolition processes (Torgautov et al., 2021). The third category includes circular economy and strategies, with six articles. These articles generally include identifying circular economy strategies in the construction sector and the factors affecting them (Chen et al., 2022). The fourth category is asset management and life cycle assessment, with five articles on this topic. These papers generally discuss topics such as developing a flexible life cycle assessment framework with a high level of detail (LOD) (Mowafy et al., 2023). The fifth category is circular economy barriers and challenges, with three articles. The articles in this category mainly address the barriers of the circular economy approach in the construction industry (Charef et al., 2021). The last category, named other, includes green business models, integrated/mixed Technologies (Lamptey et al., 2020), and bibliometric analysis (Linglin, 2023). Table 2 shows the categories, articles and years of publication.

Table 2: Research focus distribution by years.

Research Focus	2019	2020	2021	2022	2023	2024	Total
Circular Economy and Strategies		1	1	3		1	6
Circular Economy Integration with BIM	1	1	1	2	1	5	11
Construction Demolition and Waste Management with BIM	1	1		1	2	3	8
Circular Economy Barriers and Challenges			2	1			3
Asset Management and Life Cycle Assessment			2	1	1	1	5
Other (Green Business Models and Integrated/Mixed Technologies, Bibliometric Analyses, etc.)		1			3		4
Total	2	4	6	8	7	10	37

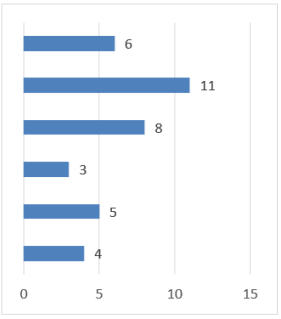

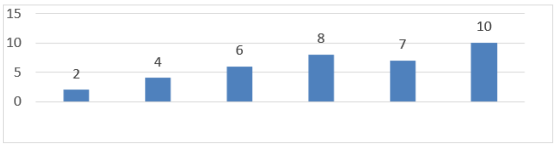

Among the data sources used in the articles, reviews, and surveys are among the leading sources. Reviews showed an increase after 2019, reaching 19 articles in 2024, followed by 12 articles based on surveys. Analysis of the articles by data sources reveals that most of the data used in this field is secondary data and/or data collected from sector professionals.

The 30 publications of the meta-analysis were divided into four categories: statistical results (4 articles), general views (9 articles), experimental/prototype model (8 articles), and conceptual/theoretical model (10 articles). Despite the increase in articles, the categories of research outputs did not change significantly over time.

The 30 articles analyzed were prepared in 16 countries, on a global scale and within the European Union, revealing the global interest in the field. Globally, 11 articles, four articles in the UK, Australia and Italy with two articles each, and Brazil, Indonesia, Ghana and India with one article each, indicating global interest and growing research on the topic.

Conclusion

BIM strengthens circular economy concepts in the construction industry by facilitating efficient management in areas such as material recovery, waste management and life cycle assessment. Research shows that BIM-based component tracking and data management support circularity. Through assessments, interviews and case studies, the literature contributes to the body of knowledge for further studies by investigating how BIM and the circular economy can work together.

References

Andriyani, N., Suprobo, P., Adi, T. J. W., Aspar, W. A. N., Jatmiko, A. D., & Santoso, A. D. (2024). Integrating urban building information modeling and circular economy framework for green sustainability. Global Journal of Environmental Science and Management, 10(3), 1313-1332.

Charef, R. (2024). A digital framework for the implementation of the circular economy in the construction sector: Expert opinions. Sustainability, 16(14), 5849.

Linglin, Z. (2024). A bibliometric review of zero waste in the built environment using VOSviewer: evolution, hotspots, and prospects. Frontiers in Environmental Science, 11, 1326458.

Mowafy, N., El Zayat, M., & Marzouk, M. (2023). Parametric BIM-based life cycle assessment framework for optimal sustainable design. Journal of Building Engineering, 75, 106898.

Torgautov, B., Zhanabayev, A., Tleuken, A., Turkyilmaz, A., Mustafa, M., & Karaca, F. (2021). Circular economy: Challenges and opportunities in the construction sector of Kazakhstan. Buildings, 11(11), 501.

Investigating the Role of Data Management for AI Utilization for Decision-Making in Construction: A Literature Review

Hansa Eusmanaga[a], Fatma Pınar Çakmak[a]

[a] Istanbul Technical University, Graduate School, Project and Construction Management, Turkey
eusmanaga23@itu.edu.tr

Keywords: Artificial Intelligence, Machine Learning, Construction Management, Decision Support, Data Management.

Aim

The integration of Artificial Intelligence (AI) and Machine Learning (ML) in the construction industry has gained attention due to its ability to support the leverage of advanced technologies, enhance decision-making, analyze data, optimize project execution, automate processes, improve safety and mitigate risks (Chenya et al., 2022). However, the effectiveness of AI-driven decision models is highly dependent on the quality, structure, availability and management of data related to construction (Chenya et al., 2022).

This study aims to examine how AI and machine learning applications can be effectively implemented in the construction industry in general through enhanced data management strategies and, more particularly, to improve on-site decision-making processes in construction management. The study collects findings from 62 scholarly articles and identifies AI applications based on their use in optimizing workflows, enhancing risk assessment, and improving predictive analytics. The paper focuses on primary enablers, challenges, and future opportunities in AI-powered data management for the construction industry.

This extended abstract contains the literature review for a thesis study about the applications of AI and ML in the construction management industry. It provides the foundation for understanding the recent progress and identifying the gaps for future studies. The following work will build upon these insights and explore the topic in-depth, thus potentially proposing a structure for handling data for construction management AI and ML integration.

Material and Method

A systematic literature review was conducted, analyzing 62 peer-reviewed articles. A Scopus database was used to search the articles using a keyword-based search; the keywords used were "construction management," "artificial intelligence," and "decision-making." The search was refined to include only English-language journal articles published between 2013 and 2025 to ensure that the works are up-to-date and have high-quality research contributions.

Initially, 203 articles were identified through the structured search. The first screening phase involved analyzing abstracts to determine relevance to AI applications in construction, reducing the selection to 102 articles. The second phase involved a more in-depth evaluation based on the information that can benefit the search, data-driven AI applications, and relevance to data management in construction, resulting in 62 final articles. These selected papers offer a comprehensive perspective on AI integration in construction, covering risk management, decision support systems, cost optimization, site monitoring, digital twin applications, scheduling improvements, and explainable AI models. While most of the selected papers focus on AI applications within the construction industry, some articles are from manufacturing and supply chain management. These industries were included because they provide valuable insights into AI-driven data integration, decision support, and risk management strategies, which can be adapted to enhance AI applications in construction. By leveraging cross-industry findings, this study broadens its scope to identify best practices in AI implementation and benefit from other industries.

The selected papers were categorized into seven thematic areas: AI and ML for risk management and safety, AI-based decision support systems (DSS), AI in construction cost management, AI for site monitoring and process automation, AI and digital twin integration, AI for construction scheduling and resource optimization, and Explainable AI (XAI) in construction decision-making.

Key technological enablers, methodologies, and challenges were extracted from each article and synthesized to develop a framework for AI-driven data management in construction. Figure 1 shows the overall process of the structured literature review.

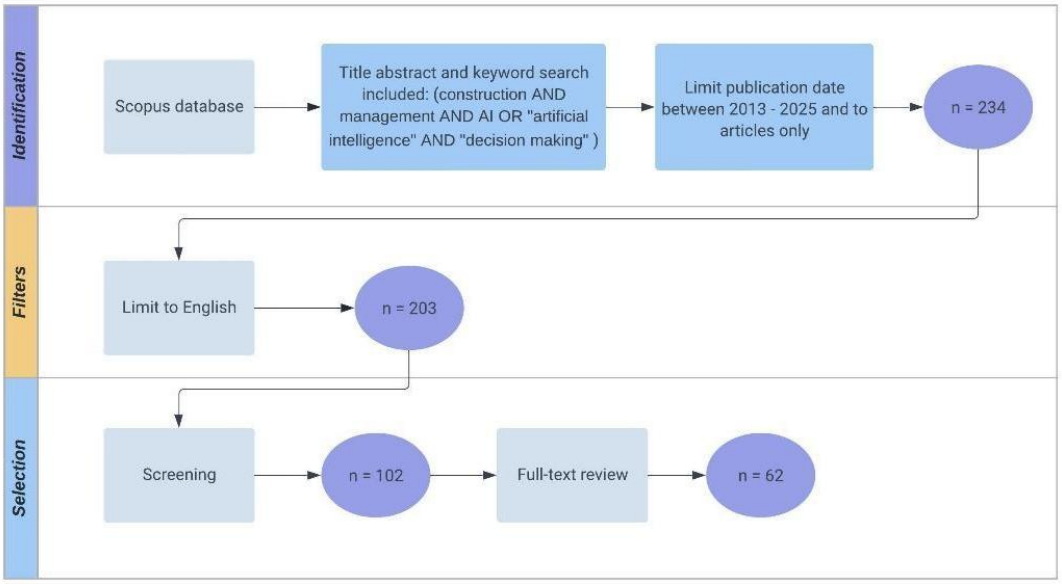

Figure 1: The process of the systematic review.

Findings

The analysis revealed key insights into AI-driven data management in multiple areas. AI-driven risk prediction models using ML and neural networks significantly improve accident prevention and hazard identification (Chenya et al., 2022). However, the lack of structured safety data limits AI model accuracy and makes it more difficult to integrate on a large scale. Data management frameworks that standardize safety data collection and ensure real-time accessibility can significantly improve the effectiveness of AI models.

Explainable AI (XAI) can also enhance model transparency, ensuring reliability in risk assessment and making data-driven insights more interpretable for decision-makers (Love et al., 2024). AI-based DSS enhance construction planning by integrating predictive analytics and real-time site monitoring (Love et al., 2024). However, the effectiveness of these systems is often compromised by inconsistent data formats and missing project information. Proper data management procedures can overcome these constraints, such as real-time data synchronization and standardized reporting systems.

AI-driven cost estimation models using neural networks outperform traditional financial forecasting techniques (Yi & Luo, 2024). However, challenges in data standardization and integration with existing financial systems hinder widespread AI adoption. Implementing a structured database that combines historical project costs and integrates real-time financial data from multiple sources can enhance the predictive accuracy of AI models, ultimately improving budgeting and financial planning.

AI-based computer vision and IoT-enabled monitoring systems improve real-time construction site tracking (Bozorgzadeh & Umar, 2023) (Rafsanjani & Nabizadeh, 2023). The primary obstacle to their scalability lies in fragmented data sources and a lack of integration with BIM systems. Establishing a centralized data-sharing platform that merges real-time site data with BIM models can facilitate predictive maintenance and workflow optimization. However, high computational costs remain a concern, requiring further research into cost-efficient AI processing solutions.

AI-enhanced Digital Twin models facilitate real-time construction monitoring and lifecycle management (Rafsanjani & Nabizadeh, 2023). The biggest challenge in leveraging digital twins is the interoperability between Digital Twin, AI, and BIM platforms, which leads to fragmented insights and inefficient decision-making. A standardized data exchange protocol

that enables seamless data flow between these systems can significantly enhance decision-making capabilities. Additionally, ensuring data accuracy and consistency across different platforms will be key to the success of AI-driven Digital Twins in construction.

AI-powered scheduling models optimize construction timelines by analyzing historical data and project constraints. However, many scheduling models lack real-time adaptability due to delays in data updates and information gaps between on-site activities and digital planning tools (Yi & Luo, 2024). By integrating AI scheduling models with IoT-enabled real-time data feeds, construction managers can make more informed, data-driven adjustments to project timelines, reducing delays and cost overruns.

Table 1 provides an overview of the mentioned AI applications in construction, highlighting their impact, used technologies, and the critical data-related challenges that affect their implementation in the industry.

Table 1. Key AI Applications, Challenges, and Their Impact on Construction Management.

AI Application Area	Impact on Construction	Key Technologies Used	Challenges
Risk Management & Safety	Enhances hazard prediction and safety compliance	Machine Learning, Explainable AI (XAI)	Limited availability and quality of risk data
Decision Support Systems	Optimizes planning and resource allocation	Neuro-Fuzzy Models, Predictive Analytics	Inconsistent data formats and missing project details
Cost Management	Improves budget accuracy and financial forecasting	Neural Networks, Ensemble Learning	Lack of standardized cost data and integration issues
Site Monitoring	Real-time tracking and predictive maintenance	Computer Vision, IoT, BIM	Fragmented real-time data sources and high processing costs
Digital Twin & BIM	Enhances lifecycle management and project visualization	AI-Driven Digital Twins, Smart Sensors	Interoperability and data exchange limitations
Scheduling	Reducing delays and cost overruns	Machine Learning, IoT	Real-time data gaps

Conclusion

This study highlights the transformative impact of AI and ML in construction management, emphasizing the importance of adapting data management frameworks to maximize AI efficiency.

To effectively deploy AI in construction, the following must be addressed: standardized data management to ensure consistency in data formats across AI applications, integration of AI with BIM and IoT to enhance real-time monitoring and predictive analytics, and adoption of Explainable AI to increase transparency and stakeholder trust in AI-driven decision-making. Future research should improve AI model adaptability to unstructured construction data and enhance interoperability between AI, Digital Twin, and BIM platforms. The findings contribute to developing a structured approach to managing data within the construction industry to adapt the use of advanced technologies such as AI-enabled decision support systems.

References

Bozorgzadeh, A., & Umar, T. (2023). Automated progress measurement using computer vision technology in UK construction. Proceedings of the Institution of Civil Engineers: Smart Infrastructure and Construction, 176(4), 165–182. https://doi.org/10.1680/jsmic.22.00026

Chenya, L., Aminudin, E., Mohd, S., & Yap, L. S. (2022). Intelligent risk management in construction projects: Systematic literature review. IEEE Access, 10, 72936–72954. https://doi.org/10.1109/ACCESS.2022.3189157

Love, P. E. D., Matthews, J., Fang, W., Porter, S., Luo, H., & Ding, L. (2024). Learning to comprehend and trust artificial intelligence outcomes: A conceptual explainable AI evaluation framework. IEEE Engineering Management Review, 52(1), 230–247. https://doi.org/10.1109/EMR.2023.3342200

Rafsanjani, H. N., & Nabizadeh, A. H. (2023). Towards digital architecture, engineering, and construction (AEC) industry through virtual design and construction (VDC) and digital twin. Energy and Built Environment, 4(2), 169–178. https://doi.org/10.1016/j.enbenv.2021.10.004

Yi, Z., & Luo, X. (2024). Construction cost estimation model and dynamic management control analysis based on artificial intelligence. Iranian Journal of Science and Technology – Transactions of Civil Engineering, 48(1), 577–588. https://doi.org/10.1007/s40996-023-01173-z

ARCHITECTURE

Architectural History

Architecture Design Theory

Building Construction Technologies

Building Materials and Technologies

Built Environment Design and Technologies

Conservation and Restoration

Environmental Control and Building Technology

Project and Construction Management

Sustainable Design

Investigating Circularity in Buildings through Digital Circularity Metric

Burcu Kısmet[a,b], Meryem Birgül Çolakoğlu[c]

[a] Istanbul Technical University, Graduate School, Architectural Desing Computing, Turkiye
[b] Beykoz University, Department of Architecture, Turkiye
[c] Istanbul Technical University, Faculty of Architecture, Department of Architecture, Turkiye
kismet@itu.edu.tr, burcukismet@beykoz.edu.tr

Keywords: Built environment, Case study, Circularity assessment tool, Circular economy, Sustainability.

Aim

Although the circular economy (CE) has garnered increasing global interest within the AECO industry, its applications largely remain confined to conceptual frameworks and literature reviews. This highlights a critical gap in the translation of circular economy principles into structured design strategies. In this regard, there is a need to develop comprehensive frameworks that integrate circular design strategies and its components, enabling practical implementation and fostering systemic change within the industry. This study aims to develop an assessment tool to measure the circularity of the buildings; to implement circular strategies and design thinking into the built environment, particularly to the buildings.

According to the literature, circularity assessments are developed at four systemic levels: starting from the macro-level (cities, urban areas); followed by meso-level (buildings), micro level as building components, product components, and at the nano-level which is materials, individual products elements (EASAC, 2016; Tecchio et al., 2017; Boyer et al., 2021; Shevchenko et al., 2022). However, existing tools have some certain limitations: some of them (Giorgi et al., 2019; Zhai, 2020) only focus on waste and / or energy, and some of them are only conceptual circular design tools.

This study focuses on developing meso-level building scale circularity assessment tool. Moreover, developing a circularity assessment tool will increase the applicability and awareness of CE among the AECO community which will open the way to wider adoption of CE on the built environment. The overall perspective of this study is to contribute in smartening and improving the built environment with digital technologies within the current and future projection of climate change and energy crises.

The novelty of this study lies in its holistic approach to circular economy within the built environment, emphasizing architectural characteristics such as plan layouts, detail drawings as key determinants of the circularity. Unlike existing studies that primarily focus on energy efficiency or material choices, this research evaluates alternative life scenarios and the reuse potential of buildings, components and materials. By integrating these dimensions, the study aims to provide a more comprehensive framework for assessing and enhancing the adaptability, resiliency, and circularity of architectural designs.

Material and Method

Methodology of this study consists of three stages: (1) Evaluating buildings according to the Shearing Layers, (2) Developing a novel CE-integrated metric, and (3) Implementing the Method on a case study and reaching the building Circularity Score. The workflow of the methodology is shown in the Figure 1.

As the first step of the Methodology, buildings are analysed considering the Brand's (1994) Shearing Layers: Site, Structure, Skin, Services, Space Plan, Stuff. Sub-categories are developed for each layer as criteria for circularity score. Duffy (1992) distinguished building layers into four: Shell, Services, Scenery and Set which was called 4S. Shell is the structure; Services are the Mechanical-Electrical-Plumbing (MEP) related functions; Scenery is the internal partitions and finishings; Set is the furniture. Brand (1994) extended Duffy's 4S model into "Shearing Layers" concept with 6S: Site, Structure, Skin, Services, Space Plan and Stuff. Site is considered eternal. Structure is the load-bearing elements of the buildings that last fifty to three hundred years depending on the structural material. Skin is the façade, roof and the external layers which can last twenty-thirty year. Services are related to MEP: wiring, plumbing, fire sprinkler systems, HVAC, and circulations like elevators and escalators, with a lifespan of 15-20 years. Space Plan is the general layout—the spatial functionality of the

interiors which last long approximately 30 years depending on the buildings' function. Stuff is the elements of daily life, mainly furniture.

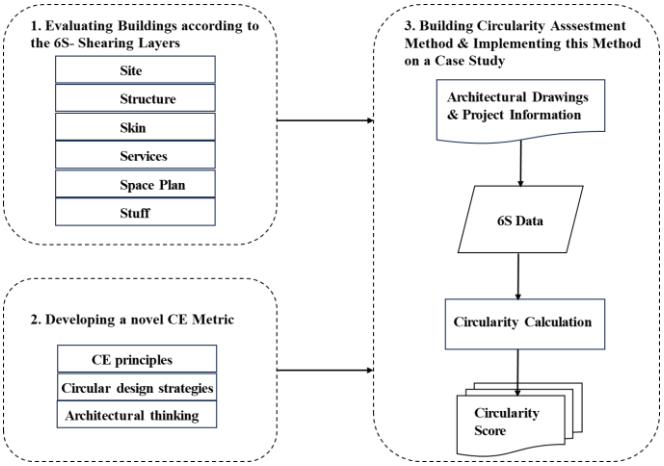

Figure 1. Workflow of the study.

For the second stage of the Methodology, 6S principles divided into sub-categories (Figure 2) considering the circular design strategies, such as designing the end-of-life cycle, reuse and repair potential, disassembly, sharing potential. All the sub-categories have certain value, 1 or 0 that will turn into a scoring system in calculation circularity score.

SITE	Empty	Green Area
		Construction Area
	Demolition	
	Excavation	
STRUCTURE	Life Span	<50-60 years, >60 years
	Material	Bio-based or technical
		GHG value
		Reused material
	Dissassembly	
	End-of-Life Cycle	Reuse as a component
		Reuse as a material
		Recycle
	Safety	Lateral forces, earthquake
SKIN	Life Span	<20-30 years, >30 years
	Material	Bio-based or technical
		GHG value
		Reused material
		Repair potential
	End-of-Life Cycle	Reuse as a component
		Reuse as a material
		Recycle
	Thermal Comfort	Wall section
	Ventilation	Cross ventilation, wind chimney, double skin env.
	Energy Production	
SERVICES	Life Span	<15-20 years, >20 years
	Flexibility	Zoning, modularity, seperate sys., premade instal.
	Material	Dissassembly
		Reused material
		Repair potential
	Smart Digitalized Systems	
	End-of-Life Cycle	Reuse as a component
		Reuse as a material
		Recycle
	Water Management	
	Energy Production	
SPACE PLAN	Function	Residential / Office / Public / Industrial
	Life Span	Residential: <30 years, 30-50 years, >50 years
		Office: <30 years, 30-60 years, >60 years
		Public: <75 years, 75-100 years, >100 years
		Industrial: <25 years, 25-50 years, >50 years
	Dissassembly	Wall Systems
		Floor Systems
	Material	GHG value for wall material
		GHG value for floor material
		Reused material
		Repair potential
	Sharing Potential	Multi-user
		Multi-function
STUFF	Furnitures	Local
	Second Hand	
	End-of-Life Cycle	Reuse potential
		Repair potential
		Remanufacture potential

Figure 2. Criteria and sub-categories of the metric.

Site has the following sub-criteria: situation and status, being empty (green area (0) or construction area (1)) or demolished (valuable (0) or weak (1)) and excavation information (few (1) or sloped area- many (0)). Structure has five sub-categories and nine sub-subcategories: material (bio-based (1) or technical (0); GHG value <100 (1) or >100 (0); reused / waste material (1), not (0)); life-span (<50-60 years (0), >60 years (1)); disassembly (yes (1), no (0)); end-of-life cycle (reuse a component (1 or 0), reuse a material (1 or 0), recycle (1) or waste (0)); safety (1 or 0) is related to being resistance to lateral forces such as earthquake, wind. Skin has six sub-categories and eleven sub-subcategories: material (bio-based (1) or technical (0); GHG value <100 (1) or >100 (0); reused / waste material (1), not (0), repair potential (1 or 0)); life-span (<20-30 years (0), >30 years (1)); energy production (yes (1), no (0)); end-of-life cycle (reuse a component (1 or 0), reuse a material (1 or 0), recycle (1) or waste (0)); thermal comfort according to wall section (1 or 0); natural ventilation (1 or 0) is related to cross ventilation, wind chimneys, double skin envelope. Services has seven sub-categories and eleven sub-subcategories: life-span (<15-20 years (0), >20 years (1)); flexibility (zoning / modularity / separate systems / premade installations (1), none (0)); material (disassembly (1 or 0); reused / waste material (1), not (0), repair potential (1 or 0)); water management system (1 or 0); energy production (yes (1), no (0)); end-of-life cycle (reuse a component (1 or 0), reuse a material (1 or 0), recycle (1) or waste (0)); smart digitalized systems (1 or 0). Space Plan has five sub-categories and ten sub-subcategories: selecting the function (residential / office / public / industrial); according to the function life-span will be marked (shown as Figure 2); disassembly (for walls (1 or 0) and for the floors (1 or 0)); material (GHG value for wall,

GHG value for floor, reused / waste material (1), not (0), repair potential (1 or 0)); water management system (1 or 0); energy production (yes (1), no (0)); sharing potential (multi-user (1 or 0), multi-function (1 or 0). Stuff has three sub-categories and five sub-subcategories: furniture (local (1) or not (0)); second-hand usage (1 or 0); end-of-life cycle (reuse potential (1 or 0); repair potential (1 or 0); remanufacture potential (1 or 0)).
The final stage of the Methodology is Implementing the method on a case study and reaching the building Circularity Score. Calculating the circularity score depends on the core principles of mathematics and the measuring tool is applied by using Python. The scoring based on a binary system as 1 / 0 or yes / no. This is called closed-ended dichotomous scale, and have certain advantageous on providing a straightforward and easily quantifiable response. According to the criteria on the Figure 2, site can take up to 2, structure up to 9, skin up to 11, services up to 11, space plan up to 9 and stuff up to 5 points.

Findings

The selected case study is steel frame 6 storey office building (Figure 3) which is completed in 2015, constructed on an empty construction area. Spanning six floors, the structure is steel, made of HEB240 columns and IPE200 beams ensuring durability while complying with seismic performance standards. Table 1 and Figure 3 describe the buildings' characteristics- materials, building elements, systems, etc.

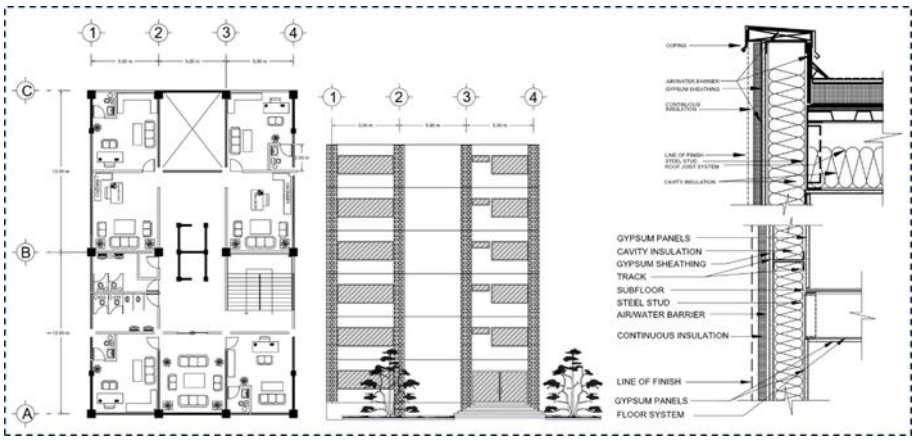

Figure 3. Plan, section and detailed drawings of the selected case study.

The facade features glass panels combined with brick cladding and painting. Internally, modular panel partitions made of gypsum are chosen for the walls and ceilings. The building integrates centralized HVAC systems including zoning and premade wirings, smart lighting solutions, enhancing user comfort and energy efficiency. Each room or area act as a thermal zone. 40% of wall area is window opening for each four façades; and the glass-frame ratio is 10%. Wirings are copper; plumbing is PVC, and ventilations are galvanized steel. Rainwater harvesting system and grey water transformation are adapted as part of water management. For the furniture, local suppliers are used.

Table 1. Project information of the selected case study.

Function:	Office Building
Construction Year:	2015
Number of Floors:	6
Construction Area	2300m2
Site Status:	Construction Area
Excavation:	2500m3
Structure:	HEB240 Steel Columns, IPE200 Steel Beams
Facade:	Brick + Painting + Glass

Insulation:	XPS (8cm) + Air Barrier
Interior Partition:	Vinyl Gypsum Modular Wall Panels
	Vinyl Gypsum Modular Ceiling Panels
MEP:	Centralized Heating / Cooling + Zoning + Premade Wiring
Lightening:	Smart + Led
Water Management:	Rain water harvesting + Smart Control
Energy Production:	No.
Furniture:	Local suppliers.

Implementation of the framework and answers for each criteria are shown in Figure 4. Based on the results; from site 2 points, from structure 7 points, from skin 3 points, from services 8 points, from space plan 6 points and from stuff 4 points are gathered. Considering the circularity percentage calculation in the Methodology, the analysed case study is 59,55 % circular according to the proposed framework. According to EU (2015), EMF (2014), CCD (2024); reaching 40-45% circular is an achievement. In this regard, the selected case study can be accepted as a circular for the analysed aspects.

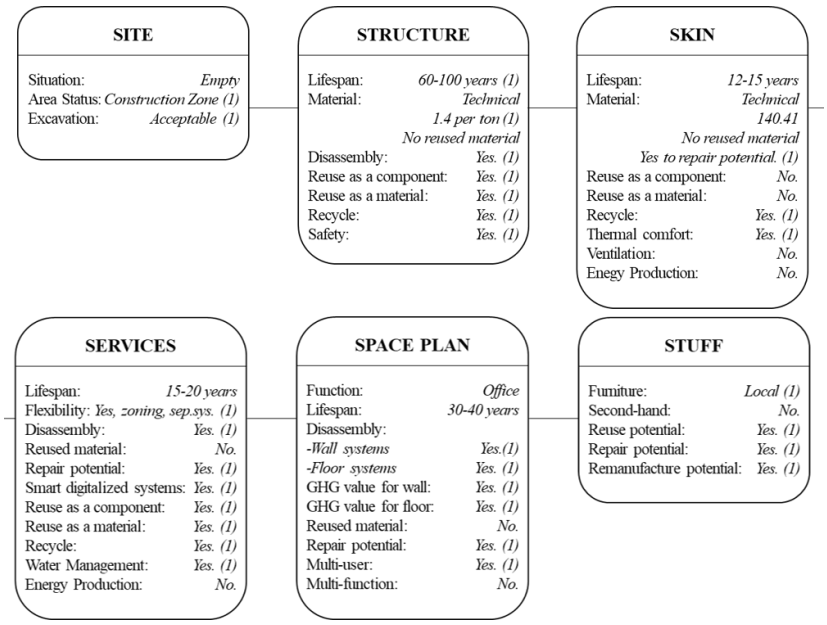

Figure 4. Implementation of the metric on the case study.

Conclusion

To conclude, this study investigates the possibility of developing a building circularity assessment tool in order to contribute circular built environment vision. In this study, circular built environment is considered as "restorative or regenerative by intention and design". Therefore, the building assessment tool is structured focusing on 6S Shearing layers and circularity design strategies such as assembly, disassembly, reuse potential, repair potential, lifespan, for each building layers. The proposed assessment is applied on a new construction steel frame office building and the final circularity score, 59,55%, is considered as acceptable.

This study's insights aim to provide valuable guidance on circular design and inspiration for the future research. This circularity assessment framework aims to be used by architects, policy makers, and the other professionals of the AECO industry that targets to learn the current conditions of the existing buildings or design the new buildings considering the circular economy. The subsequent research will compare the projects with different structural materials and functions, especially comparison of reinforced concrete, steel and timber frame buildings are expected to highlight the heavy effect of

the structure and materials in circularity. Also, existing material database can be extended. This process could retain the diversity of buildings during circularity assessment.

Acknowledgement

The first author is supported by the Scientific and Technological Research Council of Turkey (TÜBİTAK) 2209-A. This study is developed as a part of the first author's Ph.D. studies at Istanbul Technical University, Architectural Design Computing.

References

Boyer, R., Mellquist, A.-C., Williander, M., Whalen, K. (2021). Three-dimensional product circularity. Journal of Industrial Ecology, Early View (7). https://doi.org/10.1111/jiec.13109.

Brand, S. (1994). How buildings learn: What happens after they're built. Viking Penguin.

Circular Cities Declaration (CCD). (2024). Circular cities declaration report 2024. ICLEI Europe. https://circularcitiesdeclaration.eu/fileadmin/user_upload/Resources/CCD-Report-2024.pdf

Duffy, F. (1992). The changing workplace. Phaidon Press.

EASAC. (2016). Indicators for a circular economy. German National Academy of Sciences Leopoldina Publications. https://easac.eu/fileadmin/PDF_s/reports_statements/Circular_Economy/EASAC_Indicators_web_complete.pdf

Ellen MacArthur Foundation (EMF). (2014). Towards the circular economy Vol. 3: Accelerating the scale-up across global supply chains. Last accessed date: 26.10.2024.

European Union(EU). (2015). Closing the loop: Commission adopts ambitious new Circular Economy Package [Press release]. European Commission Press Corner. https://ec.europa.eu/commission/presscorner/detail/en/memo_15_6204

Giorgi, S., Lavagna, M., & Campioli, A. (2019). LCA and LCC as decision-making tools for a sustainable circular building process. IOP Conference Series: Earth and Environmental Science, 296(1), 012027. https://doi.org/10.1088/1755-1315/296/1/012027.

Shevchenko, T., Saidani, M., Ranjbari, M., Laitala, K., & Lab: Circular Economy Lab. (2022). Consumer behavior in the circular economy: Developing a product-centric framework. Journal of Cleaner Production, 384(2), 135568. https://doi.org/10.1016/j.jclepro.2022.135568.

Tecchio P, McAlister C, Mathieux F, Ardente F. (2017). In search of standards to support circularity in product policies: A systematic approach. J Clean Prod. 1(168), 1533-1546. doi: 10.1016/j.jclepro.2017.05.198. PMID: 29200663; PMCID: PMC5656090.

Zhai, X., Cheng, Z., Chang, S., Ai, X., & Zhang, X. (2020). An analysis on the current situation of energy development and its environmental problems in Yulin City. Energy Reports, 6(1), 15–20. https://doi.org/10.1016/j.egyr.2019.08.011.

ART HISTORY

Art and Technology

Art History

Modern and Contemporary Art

The Role of Digital Technologies in Museum Storytelling: Ephesus Experience Museum

Hilal Kesikci[a], Zeynep Kuban Tokgöz[b]

[a] Istanbul Technical University/Graduate School, Art History Program, Istanbul, Türkiye
[b] Istanbul Technical University/ Faculty of Architecture, Architecture, Istanbul, Türkiye
kesikci23@itu.edu.tr

Keywords: Cultural Heritage, Digital Storytelling, Experience Museum, Interactive Exhibitions, Visitor Engagement.

Aim

Museums are places where cultural heritage is preserved and presented, offering visitors a glance into the past through artifacts, documents, and exhibitions. In recent years, the role of museums has expanded beyond static displays, focusing on creating immersive and engaging visitor experiences. This shift has led to the emergence of a new category known as "experience museums." Experience museums use advanced technologies such as Augmented Reality (AR), Virtual Reality (VR), 3D modeling, and interactive installations to go beyond traditional exhibitions. They aim to transform storytelling by actively engaging visitors, allowing them to connect with historical, cultural, or scientific narratives on a deeper, often emotional level. Unlike traditional museums, where visitors are mainly observers, experience museums place them at the center of the story, making them active participants. One of the most notable examples in Turkey is the Ephesus Experience Museum, which combines cutting-edge digital tools with Ephesus's rich archaeological history. It seeks to recreate the past in a way that is both captivating and informative. This study explores the role of digital techniques in transforming storytelling in museums, focusing on the Ephesus Experience Museum as a case study. It examines how these museums are conceptualized and designed, their goals, and how effectively they achieve them. The research aims to analyze the broader impact of digital storytelling in museums by comparing archaeological and non-archaeological contexts and evaluating the economic and cultural factors influencing their development.

Material and Method

The research employs a qualitative approach based on literature review, expert interviews, and comparative analysis. Data were collected through interviews with museum professionals, exhibition designers, and a game designer working on cultural heritage projects. Each interview focused on key topics such as the role of digital technologies in storytelling, the challenges of integrating digital tools into museums, and visitor engagement strategies. The questions explored various aspects, including how digital technologies enhance storytelling in museums, the balance between traditional curation and digital innovation, the challenges faced during digital experience design, and the impact of digital experiences on visitor engagement and education. A thematic analysis was conducted on the interview responses, identifying recurring themes such as immersive engagement, accessibility concerns, and content-driven approaches in digital museum experiences. This analysis helped shape the findings of the study. Publications from the creators of the Ephesus Experience Museum were examined, alongside statistics from the Izmir Provincial Directorate of Culture and Tourism, which supported the interpretation of the findings. Additionally, a review of various digital storytelling techniques employed by museums worldwide was conducted. Key terms such as "digital archaeology," "museum storytelling," and "visitor experience and technology" were used to search relevant databases. The study also compares museums that offer a "digital experience" to explore different storytelling approaches in cultural institutions.

Findings

Digital technologies are widely used in museum storytelling, transforming visitor experiences from passive observation to interactive engagement. Ephesus Experience Museum serves as a case study illustrating this transformation. In order to analyze the museum, first examining the narrative and presentation methods was the beginning of the shaping of the

findings. The museum is housed in a newly constructed building located right next to the ancient city of Ephesus. It employs digital projections, sound, and interactive installations to reconstruct elements of ancient Ephesus. The storytelling follows a structured sequence presented through three immersive rooms. The first room introduces myths associated with Ephesus, such as the Oracle of Delphi (Pythia) and the goddess Artemis. The second room represents the Roman period, offering a digital reconstruction of the ancient streets of Ephesus. The final room focuses on Artemis, highlighting her role in the city's spiritual heritage. One of the key findings is that despite utilizing advanced digital techniques, the museum has notable limitations. The experience is entirely projection-based, relying on pre-designed content rather than interactive or participatory elements. Unlike museums that integrate physical artifacts or allow visitors to explore at their own pace, the Ephesus Experience Museum follows a fixed narrative sequence, restricting independent discovery. As well, the historical context provided is minimal, making it difficult for visitors to fully understand the broader archaeological significance beyond the visual displays.

Interviews conducted to further elaborate the findings were also effective. A common perspective gathered from the interviews is the necessity of avoiding applications that use digital technologies as tools without placing humans at the center. Striking a balance between digital tools and content depth will create a more comprehensive and educational experience for visitors. Additionally, the interviews provided a different perspective while reviewing the literature, helping to refine the comparative approach in a more accurate direction. In the literature, the Ephesus Experience Museum is often compared to other digital or immersive museums, such as the Van Gogh The Immersive Experience, which uses large-scale digital storytelling techniques. In this example, comparisons can only be made in terms of the technologies used. However, considering its location within an archaeological site, a more suitable comparison would be with visitor centers at similar heritage locations. Visitor centers typically provide background information, historical context, and sometimes physical exhibits as an introduction to the archaeological site. Among the examples considered, the Çatalhöyük Visitor Center stands out due to both its architectural design and the interactive experiences it offers. This comparison is crucial in assessing whether digital storytelling alone is sufficient in effectively conveying cultural heritage or if complementary elements are necessary. From another perspective, visitor centers also play a role in increasing visitor numbers at archaeological sites. According to the statistics published by the Izmir Provincial Directorate of Culture and Tourism, Ephesus Ancient City already accounts for more than half of all cultural and tourism activities in Izmir. Currently there is statistical data until July 2023. Interpreting future statistics to see the impact of the Ephesus Experience Museum, which opened in October 2023, will also be an important finding.

Besides, the term "experience museum" in Turkish presents conceptual challenges. It may imply that traditional museums do not provide experiences, which is not entirely accurate. In the case of the Ephesus Experience Museum, "experience" mainly refers to digital engagement rather than broader museum practices. This distinction is important when discussing the effectiveness of digital storytelling in museums. A museum established under the title of experience museum should clearly state in its name exactly what experience it offers. A good example of this, naming it "Schloss Schönbrunn VR" to describe the digital experience offered to visitors within Schönbrunn Palace. This example, which is not near an archaeological site, can be compared in terms of its location and naming within a historical architectural structure.

Conclusion

In conclusion, the study highlights the impact of digital technologies on museum storytelling. Ephesus Experience Museum demonstrates the potential of immersive digital tools in engaging audiences and enhancing historical narratives. However, for digital storytelling to be effective, it must balance technology with meaningful content. Museums should prioritize visitor engagement through well-structured narratives rather than relying solely on technological innovations. Digital storytelling should not be viewed as a mere addition to exhibitions but as an integrated approach that enriches the visitor experience. Future developments in digital museum experiences should focus on accessibility, interactivity, and content-driven storytelling to maximize educational and cultural impact. Museums should consider hybrid approaches that combine traditional exhibition methods with cutting-edge technology, ensuring that historical authenticity is maintained while offering modern engagement strategies. By striking this balance, museums can enhance visitor understanding, foster deeper emotional connections, and create lasting impressions that extend beyond the physical museum space. The success of digital

storytelling depends not only on the technology used but also on how well it aligns with the museum's educational and cultural mission.

References

Bedford, L. (2001). Storytelling: The real work of museums. Curator, 44(1), 27-34.
Chen, H., Hale, J., & Hanks, L. (2024). Archive or exhibition?: A comparative case study of the real and virtual Pitt Rivers Museum. Digital Applications in Archaeology and Cultural Heritage, 32, e00305. https://doi.org/10.1016/j.daach.2023.e00305
Coblence, E., Sabatier, V. (2015), Articulating Growth and Cultural Innovation in Art Museums: The Louvre's Business Model Revision, International Studies of Management & Organization 44 (4), 9-25.
Heath, C., & Vom Lehn, D. (2008). Configuring 'interactivity': Enhancing engagement in science centres and museums. Social Studies of Science, 38(1), 63–91. https://doi.org/10.1177/0306312707084152
Johnsson, E. (2006). Telling tales: A guide to developing effective storytelling programmes for museums (C. Adler, Ed.).
Kahraman, Ö., & Katlan Candan, D. (2024). Experience museology and Ephesus Experience Museum. Yedi: Sanat, Tasarım ve Bilim Dergisi, Digitalism in Art Special Issue, 115-127. https://doi.org/10.17484/yedi.1504176
Milano, C., & Falchetti, E. (2013). Diamond – Dialoguing Museums for a New Cultural Democracy. International Conference The Future of Education 3rd Edition, Seville, Spain.
Roussou, M., Pujol, L., Katifori, A., Chrysanthi, A., Perry, S., Vayanou, M. (2015). The museum as digital storyteller: Collaborative participatory creation of interactive digital experiences. MW2015: Museums and the Web . January
Vallejo, C. (2024). Experience museum stories- part 5: Digital content production [Video]. YouTube. Url-1 www.youtube.com/watch?v=ooh0Jgg94PU, date retrieved 2024.
Vargün, Ö. (2022). Teknolojinin belirleyiciliğinde müzelerde dijitalleşme süreci ve insan odaklı tasarım yaklaşımları. İdil, 92, 565–584. https://doi.org/10.7816/idil-11-92-09
Wyman, B., Smith, S., Meyers, D., & Godfrey, M. (2011). Digital storytelling in museums: Observations and best practices. Curator: The Museum Journal, 54(4), 419–434. https://doi.org/10.1111/j.2151-6952.2011.00110.x
Url-1 www.astel.com.tr, date retrieved 18.12.2024.
Url-2 www.atelier-brueckner.com/de, date retrieved 16.12.2024.
Url-3 www.demmuseums.com/tr/dem-museums-deneyim-muzesi/, date retrieved 2024.
Url-4 www.dijitaldeneyimmuzesi.com/, date retrieved 2024.
Url-5 www.icom.museum/en/resources/standards-guidelines/museum-definition/, date retrieved 20.12.2024.
Url-6 www.infinitylumieres.com/, date retrieved 2024.
Url-7 www.izmir.ktb.gov.tr/, date retrieved 25.12.2024.
Url-8 www.muzeverse.com.tr/, date retrieved 15.12.2024.
Url-9 www.sozluk.tdk.gov.tr/, date retrieved 18.12.2024.
Url-10 www.museumnext.com/article/how-museums-can-tell-stories-online-that-people-want-to-hear/, date retrieved 14.12.2024.
Url-11 www.schoenbrunn.at/unsere-tickets-touren/schloss-schoenbrunn-virtual-reality, date retrieved 20.12.2024.

ART HISTORY

Art and Technology

Art History

Modern and Contemporary Art

A Brief Historical Trajectory of Art Collectives as a Commoning Practice in Turkey

Ezgi Ceren Tuncaelli Çakmak[a], Ebru Belgin Yetişkin Doğrusöz[b]

[a] Istanbul Technical University, Graduate School, Art History, Türkiye
[b] Istanbul Technical University, Faculty of Science and Letters, Sociology, Türkiye
tuncaelli22@itu.edu.tr

Keywords: Art Collectives, Turkish Art History, Commoning, Commons.

This study critically examines the historical trajectory of art collectives in Turkey, analyzing their evolution through the lens of commoning practices. Commoning refers to the collective management of resources through participatory and decentralized governance. Within the sphere of contemporary art, commoning is not merely the redistribution of material assets but an ongoing process that fosters relational dynamics, community-driven sustainability, and alternative forms of artistic labor. By exploring early collective artistic movements in Turkey, such as the Community Centers (*Halkevleri*), the Independent Painters and Sculptors Association (*Müstakil Ressamlar ve Heykeltıraşlar Birliği*), the Newcomers Group (*Yeniler Grubu*), the Ten's Group (*Onlar Grubu*), the d Group and the Attic Painters (*Tavanarası Ressamları*), this research investigates the structural, ideological, and artistic continuities and fractures that have shaped contemporary art collectives since the founding of the Turkish Republic in 1923.

Aim

The primary aim of this research is to analyze how Turkish art collectives have historically navigated socio-political and economic structures while developing collective practices of artistic production, resistance, and sustainability. By investigating historical ground, the study seeks to identify patterns of collaboration, resource sharing, and communal engagement that have either persisted or transformed over time. This examination situates Turkish art collectives within broader global discourses on the commoning, artistic labor, and collective agency in cultural production.
The emergence of art collectives in Turkey, particularly in the late 20th and early 21st centuries, reflects a broader global tendency towards participatory and collaborative artistic practices. However, these collectives operate within a distinct socio-political and economic framework, shaped by local conditions and historical contingencies. By exploring the motivations, organizational structures, and artistic strategies of these collectives, this study aims to reveal the ways in which they negotiate autonomy, sustainability, and visibility within the Turkish art scene. Unlike institutionalized art platforms, collectives prioritize horizontality, non-hierarchical decision-making, and fluid membership structures. This study argues that such practices align with the principles of commoning, where resources, knowledge, and creative labor are collectively generated, managed, and distributed. By analyzing pioneering examples of early Turkish art collectives, this research investigates how they develop mechanisms of shared authorship, co-creation and collective agency by challenging conventional narratives of artistic production.

Material and Method

This study employs a multi-method qualitative approach to provide a comprehensive understanding of the historical dynamics of art collectives in Turkey. This research integrates historical analysis, literature review, and case study methodologies. The study is structured around four primary components. The primary methodological component includes historical analysis, which is an examination of archival materials, including state records, exhibition catalogs, and artist manifestos, to reconstruct the ideological, aesthetic, and organizational frameworks of early Turkish art collectives.This literature review systematically examines theoretical and empirical studies on Turkish art collectives, commoning practices, and alternative cultural economies. Drawing from perspectives in art history, sociology, and political theory, it aims to

provide a comprehensive understanding of how these collectives function and evolve over time. In the case study section, a comparative analysis of selected Turkish art collectives from different historical periods will be conducted. This analysis will focus on their modes of operation, their engagement with commoning practices, and how they have responded to socio-political shifts. By highlighting these aspects, the study seeks to reveal the dynamic nature of art collectives and their role in shaping alternative cultural economies in Turkey. By synthesizing these methodologies, the study constructs a historical and theoretical framework that situates Turkish art collectives within a broader discourse on commons-based cultural production.

Findings

The findings highlight significant continuities and ruptures in the history of Turkish art collectives. While early Turkish art collectives were often state-supported or embedded within nationalist cultural policies, they nevertheless laid the groundwork for alternative and cooperative artistic production models. The Community Centers (*Halkevleri*), established in the early Republican period, functioned as an enlightenment project that sought to integrate art into public life. Though state-led, these centers emphasized art as a public good, a notion that closely aligns with contemporary commoning principles. Similarly, the *Müstakil Ressamlar ve Heykeltıraşlar Birliği* and *Yeniler Grubu* pioneered non-institutional exhibition practices, challenging the centralization of artistic production and prefiguring the DIY ethos of today's independent art collectives. Another critical finding is the evolving conceptualization of commoning in artistic contexts. Early Turkish art collectives engaged with commoning primarily through shared physical resources (such as exhibition spaces and studios). By situating Turkish art collectives within the global discourse on commoning, this study underscores their role in reconfiguring artistic agency, community-building, and knowledge production beyond traditional institutional frameworks.

Conclusion

In conclusion, this study underscores both the continuities and transformations within Turkish art collectives, illustrating how past artistic movements have influenced contemporary commoning practices. While early collectives functioned within centralized structures, today's initiatives prioritize decentralized, grassroots organizational models. This shift reflects broader transformations in artistic labor, cultural production, and strategies for sustainability amid increasing institutionalization. By historicizing Turkish art collectives through the lens of commoning, this research contributes to ongoing debates on cultural production, artistic precarity, and collective agency. By bridging historical and contemporary perspectives, this study provides valuable theoretical and practical insights into the evolving role of commoning within artistic practice in Turkish Art History. By historicizing Turkish art collectives through the lens of commoning, this research contributes to ongoing debates on cultural production, artistic precarity, and collective action.

Finally, this research critically examines early Turkish art collectives within the framework of commoning, revealing how they functioned as pioneering models of artistic collaboration and social engagement. Emerging in the early to mid-20th century, these collectives were often formed in response to political, economic, and cultural challenges, positioning themselves as counter-narratives to dominant institutional structures. They operated through shared artistic production, collective authorship, and an ethos of mutual support, laying the groundwork for contemporary formations. Groups such as the *Yeniler Grubu* and *On'lar Grubu* exemplified an early commitment to artistic solidarity, navigating state policies, economic constraints, and shifting ideological landscapes to sustain alternative creative spaces.

The study thus provides valuable insights into the transformative potential of collective artistic practices in contemporary Turkey and beyond, demonstrating their capacity to reshape the landscape of cultural production while fostering a sense of solidarity within artistic communities. By linking these historical precedents to present-day collectives, this research underscores the persistent relevance of commoning as a mode of resistance, innovation, and artistic renewal.

References

Atakan, N. (2008). *Sanatta alternatif arayışlar.* İzmir: Karakalem Kitapevi.
Başkan, S. (2014). Türk resminde yeni eğilimler ve kavramsallık arayışları: 1960–1980. *Zeitschrift für die Welt der Türken/Journal of World of Turks, 6*(3), 99-114.
Bollier, D. (2012). The commons rising: How digital innovation is transforming politics and culture. In F. Aydoğdu & E. Ertan (Eds.), *Paratactic commons* (pp. 116–128). Istanbul, Turkey: Body-Process Art Association.
Bollier, D., & Helfrich, S. (Eds.). (2015). *Patterns of commoning.* Amherst, MA: The Commons Strategies Group.
Bunulday, S. (2013). *Türkiye'de sanat üretimi 1975-2005.* İstanbul: Parşömen Yayınları.
Bunulday, S. (2021). Türkiye'deki sanatçı kolektifleri üzerine. *Kültür Araştırmaları Dergisi, 10*, 233-244. https://doi.org/10.46250/kulturder.974799
Bursalı, E. A. (2013). *Sanatçı inisiyatifleri ve sanatçılar tarafından yürütülen mekânların İstanbul güncel sanat alanındaki rolü* (Yüksek lisans tezi). Bilgi Üniversitesi Sosyal Bilimler Enstitüsü, İstanbul.
Dolmacı, S. (2006). *1939-1950 yılları arasında Devlet Resim ve Heykel sergileri* (Yüksek lisans tezi). Hacettepe Üniversitesi Sosyal Bilimler Enstitüsü, Ankara.
Escobar, A. (2015). Commons in the pluriverse. In D. Bollier & S. Helfrich (Eds.), *Patterns of commoning.* Amherst, MA: The Commons Strategies Group. Retrieved from http://patternsofcommoning.org/commons-in-the-pluriverse/
Fournier, V. (2013). Commoning: On the social organization of the commons. *M@n@gement, 16*(4), 433–453. https://doi.org/10.3917/mana.164.0433
Genç, M. A. (2012). D Grubu ressamlarının Türk resim sanatının gelişimine olan katkıları. *İdil Sanat ve Dil Dergisi, 1*(05), 405-417.
Helfridge, S. (2017). Commoning: Dimensions of transformational force. In K. Aßmann, M. Bader, R. Talevi, Raumlaborberlin, & U. K. Ruhr (Eds.), *Explorations in urban practice: Urban school ruhr series* (pp. 96-119). Barcelona, Spain: dpr-barcelona.
Keser, N. (2006). *Tek parti döneminde Türk resim sanatının ideolojik üretimi.*
Keskin, C. (2014). I. Dünya Savaşı ve sonrası Türkiye'de kültür-sanat ortamı ve Türk resmi. *Gazi Akademik Bakış, 14*, 263-179.
Kılıç, E. (2002). Türk resminde sorgulama: Çağdaşlaşma sorunu, *Müstakiller ve D Grubu. Güzel Sanatlar Enstitüsü Dergisi, 9*.
Öndin, N. (2002). *Cumhuriyet dönemi (1923-1950) kültür politikalarının Türk resim sanatı üzerindeki yansımaları.*
Ostrom, E. (1990). *Governing the commons: The evolution of institutions for collective action.* New York, NY: Cambridge University Press.

From Functional to Imaginary Forms: Alev Ebüzziya Siesbye's Ceramics

Funda Türeli[a], Aslıhan Erkmen Birkandan[b]

[a] Istanbul Technical University / Graduate School, Art History Program, Türkiye

[b] Istanbul Technical University, Faculty of Science and Letters, Department of Sociology, Türkiye

tureli23@itu.edu.tr

Keywords: Pot, Ceramic Art, Alev Ebüzziya Siesbye, Imaginary Expression, Functional Form.

Aim

Throughout the history of civilisation, pot and ceramic objects are important mediums that are the carriers of the culture in which they are produced. The place of ceramics among small handicrafts, which started with the production of pots and vessels from the B phase of the Neolithic Age and paved the way for mass production with the invention of the potter's wheel, is undeniable. While ceramics initially stood out with its purely functional characteristic, in time it transformed into a decorative object and became an important part of human life. It is one of the important research areas of archaeology and art history as its raw material is clay, the ancient methods used in its processing, shaping and decoration are passed down from generation to generation, and it is the earliest material used in every region of the world other than wood and stone. In a sense, the history of ceramics is also the history of humanity and technology, and the relationship between ceramics and craftsmanship should not be overlooked.

In this paper, first of all, the definition of 'functional object' is clarified. Then the concept of 'imaginary' is analysed. The theoretical framework is shaped in the context of Heidegger's views that categorise objects into types. According to Heidegger, there are three types of object groupings which dominate the Western thought: the pure object, the equipment and the art object. These types are three states of being that appear in different forms. The pure object is that which exists in nature in its own state. An equipment is an object of use produced with appropriate material selection and correct design. The art object, on the other hand, is distinguished from other objects by its characteristic of an act of knowing that includes imagination. (Heidegger, 2011: 24). For Heidegger, a work is the recreation of the essence of a being. This 'essence' of the work of art is recreated by the artist, the 'techne' is revealed by means of [tékʰnɛː]. (Heidegger, 1998: 53). In a general sense, "the word techne, as used by Plato, is a "making" activity in ancient Greek culture in which the distinction between craft and art, as we do today, is not in question, and it includes a basis based on direct knowledge (episteme)." (Haşlakoğlu, 2016:17) Techne is defined as any state of making; the rational method used to produce an object or to realise a goal or purpose. This concept emerged in Ancient Greece at a time when there was not yet a distinction between craft and art and covers everything produced by hand. In this paper, the art practice of Alev Ebüzziya Siesbye (b. 1938), one of the artists who uses the pot form in its simplest form as a way of imaginative expression, will be discussed in the context of imaginative expression.

Material and Method

The minimalist and conceptual approach in the artist's ceramic works will be evaluated; how she transforms the pot form, a traditional object of use, into an art object will be analysed. Biography, work analysis, formal analysis and comparison methods will be used in this analysis which focuses on the transformation of the pot from a functional object into an imaginary object. In addition, oral history practice will also be used by obtaining first-hand data through an interview with the artist.

Findings

In the research, which is limited in scope with ceramic artifacts, the effects of the relationship between the object of use and the material on the process of imaginary form creation are discussed. Since the early periods, ornamental elements have been added to ceramics with various methods. The evaluation of ceramics as a work of art rather than an object of daily life is associated with Modernity. The emergence of imaginative expression forms in ceramics started with Modernity. The history of ceramics, which is obtained by firing 'clay', a natural and easily shaped raw material, dates back to 30,000-32,0000 years ago. The first finds are small-sized objects such as figurines found in excavations in Central Europe and idols thought to be used as talismans. The first examples of ceramic objects used as pots and vessels made 19.000 years ago are found in Central Asia. (Yoleri, H. and Öztürk, Ş. 2023: 57)

In this paper, the concept of image is important. Its literal meaning is 'something conceived in the mind and longed to be realised; imagination'. Imaginary is an adjective derived from this word. The analysis of the transformation of ceramics, an object of use with a certain function, into an imagined form is a process that can only be analysed by plastic evaluation methods. Some evaluation criteria used in ceramic art are raw material, space-occupancy, volume, balance, colour. In this context, first of all, artists who have chosen the path of expression with pure imaginary forms in ceramic art have been analysed. These people work on the transformation from function to image, sometimes intuitively and sometimes planned. Among ceramic forms, the pot stands out. Because the earliest functional ceramic is defined as 'pot', which is also an archaeological term. In his work "The Meaning of Art' (2014), Herbert Read says of ceramic, 'ceramics (pot) is the most difficult because it is the most abstract form of art". (Read, 2014: 22). Although it is one of the simplest forms, it is the most difficult to specialise in, and studies on the pot are concentrated in areas such as form, decoration and glaze.

Alev Ebüzziya Siesbye who will be discussed in the context of imaginative expression was born in 1938 in Istanbul, studied sculpture at the İstanbul State Academy of Fine Arts and ceramics at the Füreya Workshop between 1956-58. In the following years, she continued her studies at the Eczacıbaşı Ceramic Factory in Istanbul and the Royal Danish Porcelain Factories in Copenhagen. In 1969, Ebüzziya established her own studio in Copenhagen and moved her studio to Paris in 1987. Her artistic career spans more than fifty years and she has around three thousand works in various collections, including the Royal Collections in Denmark and England, the Imperial Palace of Japan, the Boymans van Beuningen Museum and the Victoria & Albert Museum. In her exhibition in Denmark in 1974, Siesbye transformed pots, which are functional objects and have been visible for thousands of years, into an imaginary form.

The main subject of this paper is Alev Ebüzziya Siesbye's works from 1974, when she had her first solo exhibition as an artist, until 2024, as a result of the compilation of publications on her pots. While analysing the elements that influenced Alev Ebüzziya Siesbye's works produced between 1974 and 2024 and their reflections on her pots, the place of the concepts of form, space, lightness, simplicity and time in the artist's approach is also discussed. Ebüzziya Siesbye reproduces ceramic pots in their simplest form, without differentiating them with any additional decorative elements; in the process of creation, she carries the pot form to the imaginary level with the concepts of negative space, volume and repetition; she uses these concepts as plastic elements. Her unique 'levitating pots' are the group of works that will be analysed formally and semantically in this paper. In addition, the concepts of imaginative expression, artistic creation process, minimalism and conceptual art will be traced in Alev Ebüzziya Siesbye's art practice. The change, transformation and development of the artist's 'levitating pots' over a period of half a century will be observed retrospectively and the research will deal with the visual analysis of the artist's works with a qualitative method. Qualitative analysis contributes to the evaluation of Ebüzziya Siesbye's works in terms of colour, texture and glaze in addition to form, material and space.

Conclusion

In conclusion, the content of this study reveals how Alev Ebüzziya Siesbye presents an original interpretation on the axis of tradition, Minimalism and Conceptual Art by transforming the pot form, a functional object, into an artwork. The artist, who builds a bridge between thousands of years ago and contemporary art, invites the viewer to think about form, space

and existence through objects that have been de-functionalised. Ebüzziya Siesbye's ceramics not only present a visual aesthetic, but also bring new insights into the meaning of the art object.

References

Bakırcı, G. (2008). 20. yüzyıl Türk Seramik Sanatçılarının Kültürel Üretimlerindeki Düşünsel Altyapılar. (Yüksek Lisans Tezi).Marmara Üniversitesi, Güzel Sanatlar Enstitüsü, İstanbul

Clark, G., & Siesbye, A. (1999). Alev Ebüzziya Siesbye. Kale.

Diller, J. D. (1971). On the limits of pottery. The Ohio State University.

Dostoğlu, H., & Cramer A. (Ed.). (2016). Alev: Alev Ebüzziya Siesbye. Finansbank, İstanbul.

During, N. (2000). Alev Ebuzziya Siesbye. Ceramics Monthly, 48(10), 57-59.

Haşlakoğlu, O. (2016). Platon Düşüncesinde Tekhne. Sanat ve Felsefenin Ortak Kökeni Üzerine Bir İnceleme. İstanbul: Sentez Yayınevi.

Heidegger, M. (1997). Sanatın Doğuşu ve Düşüncenin Yolu. H. Ü. Nalbantoğlu (Yay. Haz.). Patikalar Martin Heidegger ve Modern Çağ. Ankara: İmge Kitabevi Yayınları.

Heidegger, M. (1998). Tekniğe İlişkin Soruşturma (çev. D. Özlem). İstanbul: Paradigma Yayınları.

Heidegger, M. (2011). Sanat Eserinin Kökeni. (Çev. F. Tepebaşılı). 2. Baskı. Ankara: De ki Basım Yayım Ltd. Şti. Ankara.

Kura, N., Dostoğlu, H., Clark, G., De Cramer, A., Melek, L., Yentürk Karapınar, Serra, & İstanbul Galeri Nev. (2016). Alev: Alev Ebüzziya Siesbye.İstanbul Galeri Nev.

Onur, A. & Aygenc, E. (2023). The existential signs through the works of Alev Ebuzziya Siesbye. Semiotica, 2023(250), 235-250.

Read, H. (2014). Sanatın Anlamı (çev. N.Asgari). İstanbul: Hayalperest Yayınevi

Yoleri, H. ve Öztürk, Ş. (2023). Seramik Tekniklerinin Kökeni. yedi: Sanat, Tasarım ve Bilim Dergisi, 30, 5770. doi:10.17484/yedi.1095330

Url-1 www.galerinevistanbul.com/artists/31-alev-ebuzziya-siesbye/works/ date retrieved 02.01.2025

CHEMICAL ENGINEERING

Hydrogen Technologies, Fuels Cells, Energy Storage Materials

Modelling and Computational Systems

Nanotechnology, Surface Coatings and Films

Biomass-Derived Activated Carbon as Electrode Material for Supercapacitors

Damla Kökmen[a], Anıl Yılmaz[a], Nahid A. Keshtiban[b], Ali Gelir[b], Nil Özbek[a], Hanzade Açma[a], Serdar Yaman[a]

[a] Istanbul Technical University, Faculty of Chemical and Metallurgical Engineering, Department of Chemical Engineering, Türkiye
[b] Istanbul Technical University, Faculty of Science and Letters, Department of Physics Engineering, Türkiye
kokmen23@itu.edu.tr

Keywords: Activated Carbon, Biomass, Chemical Activation, Supercapacitor Electrode.

Aim

The increasing demand for energy is leading to the rapid depletion of fossil fuels and environmental pollution. To meet energy demand, it is essential to use renewable energy sources such as solar and wind energy. However, these sources are often intermittent, requiring energy storage solutions (Aziz & Shah, 2023). Supercapacitors, as an energy-storage device bridging the gap between batteries and conventional capacitors, offer advantages such as long cycle life, high power density, and fast charging/discharging (Zhang & Li, 2023). Light rail systems, military services, wind turbine systems, aerospace, and electric vehicles are some of their applications (Aziz & Shah, 2023). The electrochemical performance of a supercapacitor is directly related to the capacitive performance of its electrode material. Carbon materials with hierarchical macro/meso/micropores, used as electrode materials, enhance supercapacitor performance (Xu et al., 2021). Macropores, mesopores, and micropores each play distinct roles in the electrochemical charge/discharge process. Macropores serve as ion storage reservoirs for mesopores and micropores, while mesopores provide transport channels for ion diffusion. Although some regions of micropores may be inaccessible for ion adsorption, they affect the charge state by controlling ion diffusion and exhibiting molecular sieve effects (Yang et al., 2019). Activation is the key method to obtain a hierarchical structure with a large specific surface area (Xu et al., 2021). Commercial activated carbons are still the most commonly used electrode materials today; unfortunately, they are mostly derived from fossil fuels, and their precursors are not environmentally friendly and are expensive (Zhang & Li, 2023). Biomass waste is being extensively investigated as high-performance supercapacitor materials due to its abundance, availability, low cost, and environmental friendliness (Yue et al., 2022). For this purpose, activated carbon was produced from waste biomass under different activation temperatures and using various activator ratios. To evaluate the effect of various operating conditions on porosity, analyses were performed on activated carbon samples, and electrochemical performance tests were conducted on supercapacitor electrodes prepared from activated carbon (Zhang et al., 2022).

Material and Method

Corn stalk (CS), one of the three main agricultural waste products worldwide, was used as the biomass precursor. Potassium hydroxide (KOH) was used for the chemical activation. Figure 1 shows the preparation process of activated carbon from corn stalk. To obtain activated carbon from corn stalk, carbonization was first performed, followed by chemical activation. The corn stalk was ground to a particle size of ≤250 μm. It was heated to 600 °C at a rate of 10 °C/min in a tube furnace under a nitrogen atmosphere and subjected to pre-carbonization by keeping at this temperature for 1 hour. The carbonized corn stalk and KOH were mixed in a 1:3 ratio. The mixture was then heated to the desired temperature (600, 700, 800, 900 °C) at a rate of 10 °C/min in a tube furnace under a nitrogen atmosphere and subjected to chemical activation by keeping at this temperature for 1 hour. The electrochemical measurements of these four samples were conducted, and since better results were obtained at 800°C, subsequent productions were carried out at this temperature. The carbonized corn stalk and KOH were mixed in the determined ratios (1:1, 1:2, 1:3, 1:4) and heated in a tube furnace under a nitrogen atmosphere at a rate of 10 °C/min to 800 °C, keeping at this temperature for 1 hour. The activated carbon was first washed with 1 M HCl to remove residual chemicals, then washed with distilled water until the pH became neutral. It was then left to dry in an oven at 60 °C overnight. The samples were named according to the activation temperature and activation chemical ratio as

CS-600, CS-600-K3, CS-700-K3, CS-800-K3, CS-900-K3, CS-800-K1, CS-800-K2, and CS-800-K4. To observe the effect of activation on the material, the CS-600 sample was only subjected to carbonization without activation. The characterization of the activated carbon samples is being carried out using FTIR, TGA, SEM, Raman Spectroscopy, XRD, XPS, and BET analyses. The proximate, elemental and structural analysis of corn stalk was carried out. For the preparation of the supercapacitor electrode, a weight ratio of 8:1:1 of activated carbon, carbon black, and PVDF was used. First, PVDF was dissolved in NMP using a magnetic stirrer at 30 °C. Then, activated carbon and carbon black were added to the mixture and stirred further. PVDF, carbon black, and NMP were used as a binder, conductivity enhancer, and solvent, respectively. The resulting mixture was drop-cast onto a stainless-steel current collector and dried in an oven at 60 °C. Electrochemical measurements of the electrodes were performed in a three-electrode cell. For the three-electrode cell, Ag/AgCl was used as the reference electrode, Pt as the counter electrode, and a 6 M KOH aqueous solution as the electrolyte. Cyclic voltammetry (CV), galvanostatic charge-discharge (GCD), and electrochemical impedance spectroscopy (EIS) were used to measure the electrochemical performance of the electrodes.

Figure 1. The preparation process of electrode from corn stalk.

Findings

The capacitance values, calculated from the GCD curves shown in Figure 2, were used to evaluate the electrochemical performance of the samples. It was found that the CS-600-K3, CS-700-K3, CS-800-K3, and CS-900-K3 samples, obtained at different temperatures, exhibited specific capacitance values of 43 F/g, 111 F/g, 170 F/g, and 100 F/g, respectively, at a current density of 0.5 A/g. The highest specific capacitance was achieved with the sample produced at 800 °C. Further optimization was conducted at this temperature by varying the KOH ratio in the activation process. The CS-800-K1, CS-800-K2, and CS-800-K4 samples, with different KOH ratios, showed specific capacitances of 105 F/g, 208 F/g, and 129 F/g, respectively, at the same current density of 0.5 A/g. The highest specific capacitance was achieved with the sample produced with a 1:2 KOH ratio at 800 °C. It was also found that the specific capacitance of the non-activated CS-600 sample was 3 F/g at 0.5 A/g. The non-activated sample showed a much lower specific capacitance, confirming the

importance of the activation process in improving the material's electrochemical properties. The activation increased the surface area and charge accumulation by enhancing the porosity, resulting in an extended CV behavior. The GCD curves indicated enhanced charge/discharge performance in activated carbon samples, attributed to increased ion diffusion and storage capacity.

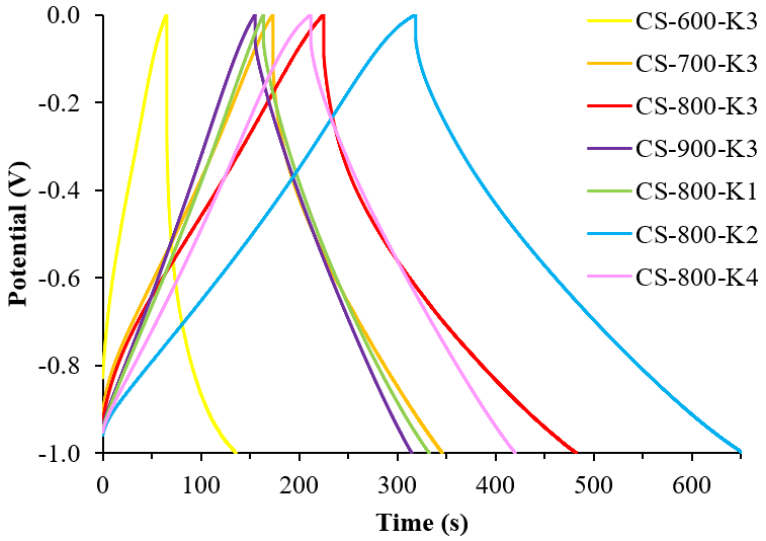

Figure 2. GCD curves at 0.5 A/g.

Conclusion

These results demonstrated that corn stalk-derived activated carbon can serve as a sustainable and cost-effective electrode material for supercapacitors. The findings showed that the activation temperature and activator ratio significantly influenced the porosity and electrochemical performance of the resulting carbon material. Among the tested samples, CS-800-K2, produced at 800 °C with a 1:2 KOH ratio, achieved the highest specific capacitance of 208 F/g at 0.5 A/g, highlighting the optimal activation conditions for corn stalk. In conclusion, this study highlights the potential of biomass-derived activated carbon as a promising alternative to conventional electrode materials, contributing to the development of sustainable energy storage technologies.

References

Aziz, M. A., & Shah, S. S. (Eds.). (2023). Biomass-Based Supercapacitors: Design, Fabrication and Sustainability. John Wiley & Sons.

Xu, H., Zhang, Y., Wang, L., Chen, Y., & Gao, S. (2021). Hierarchical porous biomass-derived carbon framework with ultrahigh surface area for outstanding capacitance supercapacitor. Renewable Energy, 179, 1826-1835.

Yang, H., Ye, S., Zhou, J., & Liang, T. (2019). Biomass-derived porous carbon materials for supercapacitor. Frontiers in Chemistry, 7, 274.

Yue, X., Yang, H., Cao, Y., Jiang, L., Li, H., Shi, F., & Liu, J. (2022). Nitrogen-doped cornstalk-based biomass porous carbon with uniform hierarchical pores for high-performance symmetric supercapacitors. Journal of Materials Science, 57(5), 3645-3661.

Zhang, T., & Li, J. (2023). Mild and Efficient One-Step Synthesis of Nitrogen-Doped Multistage Porous Carbon for High-Performance Supercapacitors. Molecules, 28(24), 8136.

Zhang, Y., Zhao, Y. P., Qiu, L. L., Xiao, J., Wu, F. P., Cao, J. P., ... & Liu, F. J. (2022). Insights into the KOH activation parameters in the preparation of corncob-based microporous carbon for high-performance supercapacitors. Diamond and Related Materials, 129, 109331.

CHEMICAL ENGINEERING

Hydrogen Technologies, Fuels Cells, Energy Storage Materials

Modelling and Computational Systems

Nanotechnology, Surface Coatings and Films

Machine Learning-Based Prediction of FTIR Spectral Peaks for Biomass Characterization

Fahreddin Talha Sağiş[a], Anıl Yılmaz[a], Hanzade Haykırı-Açma[a], Serdar Yaman[a]

[a] Istanbul Technical University/Graduate School, Faculty of Chemical and Metallurgical Engineering, Chemical Engineering Program, Türkiye

sagis22@itu.edu.tr

Keywords: Biomass Characterization, FTIR Spectroscopy, Machine Learning, Multi-Label Classification, Spectral Peak Prediction.

Aim

This extended abstract focuses on accelerating lignocellulosic biomass characterization by integrating Fourier Transform Infrared (FTIR) spectroscopy with machine learning (ML) techniques. Lignocellulosic biomass is composed primarily of cellulose, hemicellulose, and lignin, plus minor constituents like extractives and ash, all of which influence its suitability for bioenergy or bioproduct applications. Conventional chemical analyses—such as Soxhlet extraction for extractives, the Klason method for lignin, and other gravimetric or chromatographic assays—are accurate but demand significant time and labor. Hence, there is a pressing need for rapid, high-throughput analytical methods capable of capturing biomass composition. FTIR meets this need by producing spectra (4000–450 cm^{-1}) that reveal chemical "fingerprints" in the form of characteristic absorption bands for O–H, C=O, and aromatic ring vibrations. However, overlaps among these bands, baseline drifts, and broad peaks complicate manual interpretation.

To address these challenges, this study leverages machine learning models that can parse and interpret FTIR data more efficiently. Specifically, we investigate three distinct phases. In Phase 1, multi-output regression models (Partial Least Squares, Ridge Regression, Random Forest, and Multi-Layer Perceptron) aim to predict every wavenumber intensity (~3551 points) from a small set of nine input features (including moisture, ash, volatile matter, lignin, and holocellulose). Phase 2 transitions to a more tractable approach: broad-range classification, where each defined spectral interval (e.g., 3700–3000 cm^{-1}) is labeled as "peak present" or "peak absent." Finally, Phase 3 narrows the classification scope to only three chemically pivotal windows (e.g., 1800–1500 cm^{-1}), hypothesized to yield clearer relationships between known functional groups and predicted outcomes. By comparing model performance across these phases, we clarify how the level of spectral detail—ranging from entire-spectra regression to interval-based classification—impacts accuracy, interpretability, and computational feasibility.

Material and Method

We acquired 56 biomass samples from woody, herbaceous, and agricultural residues to cover a wide range of lignocellulosic compositions. Each sample underwent proximate analysis to determine moisture, ash, volatile matter, and fixed carbon, followed by compositional assays for holocellulose, lignin, and extractives. FTIR spectra were recorded between 4000 and 450 cm^{-1} at a resolution that yielded approximately 3551 wavenumbers per sample.

Preprocessing involved baseline correction to remove sloping artifacts from inhomogeneities or ATR contact issues (Mokari et al., 2023), followed by normalization to zero-mean, unit-variance so that features with large numeric ranges (e.g., percent ash or extractives) would not skew training. An optional polynomial feature expansion was also tested to capture non-linear interactions among numeric inputs, such as moisture–ash synergy.

In Phase 1 (Full-Spectrum Regression), we used nine input features per sample to predict all 3551 wavenumbers of the FTIR spectrum. We compared Partial Least Squares (PLS), which creates latent factors maximizing covariance with high-dimensional outputs; Ridge Regression, a fundamentally linear model that applies L2 regularization; Random Forest Regressor, an ensemble of decision trees designed to capture non-linear relationships; and an MLP Regressor, a neural network with hidden layers (using ReLU or tanh activation) and a final linear output layer for multi-output tasks, with hyperparameters tuned via grid search.

For Phase 2 (Broad-Range Classification), we converted spectral outputs into 8–10 wide intervals (e.g., 4000–3700 cm^{-1}, 3700–3000 cm^{-1}), labeling each interval as "1" if a strong absorbance peak crossed a chosen threshold or "0" otherwise. We then applied multi-label classification using Classifier Chain wrappers on Logistic Regression, Random Forest, Gradient Boosting, and SVM (RBF kernel).

Phase 3 (Narrow-Interval Classification) targeted three narrower intervals (3000–2800, 1800–1500, 1150–900 cm^{-1}), each closely associated with critical functional groups such as aliphatic C–H, lignin/carbonyl signals, or carbohydrate bands. Models were again multi-label classifiers distinguishing "peak" from "no-peak." Across all phases, we used five-fold cross-validation. Phase 1 results were evaluated by RMSE and R^2, while Phases 2 and 3 were assessed by Hamming Accuracy (1 − Hamming Loss), Micro-F1, and confusion matrices.

Findings

Phase 1 (Full-Spectrum Regression) demonstrated the challenge of mapping only nine input features onto 3551 wavenumber intensities. Among the models, Ridge Regression had the highest RMSE (~1.10) and the lowest R^2 (~0.04), suggesting that a purely linear approach with L2 penalty fails to capture non-linear or interaction effects in spectral data. PLS performed moderately better (RMSE ~1.03, R^2 ~0.17) by extracting latent factors tailored to spectral variance. Random Forest improved over Ridge (RMSE ~1.06, R^2 ~0.13), but still faced difficulties with the large output space. MLP achieved the best scores (RMSE ~1.00, R^2 ~0.21), albeit the R^2 remained relatively small, highlighting the complexity of full-spectrum predictions.

Phase 2 (Broad-Range Classification) saw a jump in multi-label accuracy compared to Phase 1's direct intensity mapping. Logistic Regression sometimes led with a Hamming Accuracy of ~0.75 and Micro-F1 ~0.79, indicating more reliable detection of peak presence/absence in broad spectral ranges. Random Forest and SVM also posted competitive performance, though the choice of parameters (e.g., C and gamma for SVM, max_depth for Random Forest) influenced results. Some intervals (like 3700–3000 cm^{-1}) were less frequently misclassified, presumably due to distinct O–H stretching peaks, whereas intervals with more overlap or fewer "1" samples (like ~2000–1800 cm^{-1}) showed greater confusion.

Phase 3 (Narrow-Interval Classification) targeted intervals known to correlate strongly with lignocellulosic traits: 3000–2800 cm^{-1} (aliphatic C–H), 1800–1500 cm^{-1} (aromatic/carbonyl signals linked to lignin), and 1150–900 cm^{-1} (carbohydrate fingerprint). Random Forest excelled, reaching ~0.81 Hamming Accuracy and ~0.88 Micro-F1. Confusion matrices revealed fewer false positives/negatives in these constrained windows, implying a sharper chemical link between input features and FTIR dips. Even if MLP and SVM were close behind, the ensemble-based approach of Random Forest often captured subtle non-linearities beneficial in narrower spectral domains.

Overall, Phase 1's comprehensive goal proved the hardest with limited data. Aggregating or restricting spectral outputs in Phases 2 and 3 yielded progressively better classification metrics, supporting the strategy of simplifying the output space to major or high-value spectral signals.

Conclusion

This study confirms that integrating FTIR spectroscopy with machine learning can expedite and refine biomass characterization. Predicting the entire FTIR spectrum (Phase 1) underlined the challenge of a massive output space: while

an MLP outperformed other models, absolute R^2 remained modest, indicating that hundreds of samples or more advanced modeling might be needed for highly accurate full-spectrum regression. By transitioning to broad-interval classification in Phase 2, the modeling complexity reduced significantly, leading to higher accuracies in detecting whether a peak existed in each region. Phase 3's targeted classification approach further improved results and interpretability, as focusing on narrower intervals strongly linked to functional groups (e.g., lignin's aromatic region) delivered the best classification metrics.

From an industrial or research standpoint, these findings suggest that if one only requires confirmation of certain functional groups (e.g., lignin presence around 1510 cm^{-1}), narrower intervals with an ensemble classifier (Random Forest) or a well-tuned neural network can yield a fast, robust solution. On the other hand, if a complete spectral reconstruction is desired, more sophisticated or data-intensive approaches may be necessary. Future expansions could include deeper architectures, transfer learning between different biomass categories, or larger multi-feedstock datasets to enhance generalizability. In essence, this multi-phase methodology spotlights a flexible framework: from exhaustive spectrum modeling to selective peak detection, enabling a range of FTIR-based solutions that balance accuracy, speed, and interpretability.

References

Acquah, G. E., Via, B. K., Billor, N., Fasina, O. O., Eckhardt, L., & Hammel, S. (2016). Rapid near infrared modeling of pyrolysis products using forest residue feedstocks. Journal of Analytical and Applied Pyrolysis, 121, 93–100.

Dai, F., Zhuang, Q., Huang, G., Deng, H., & Zhang, X. (2023). Infrared spectrum characteristics and quantification of OH groups in coal. ACS Omega, 8(19), 17064–17076.

Mokari, B., Shojaei, A., & Koohi, A. (2023). Baseline correction in FTIR spectroscopy: A new automated approach. Chemometrics and Intelligent Laboratory Systems, 234, 104744.

Pushpa, R., Smitha, S. V., & Mondal, S. (2024). Multi-feedstock composition prediction using infrared-based ANN models. Renewable Energy, 205, 1361–1372.

Zhuang, Q., Li, J., Wang, Q., & Zhou, D. (2020). FTIR study on functional group changes in cellulose and lignin of biomass under carbonization. Bioresource Technology, 318, 124083.

CHEMISTRY

Analytical Chemistry

Biochemistry

Drug Design & Drug Delivery (Computational and Experimental)

Energy Materials (Synthesis, Characterizations, Applications)

Inorganic Chemistry

Nanochemistry

Organic Chemistry

Physical Chemistry

Nanotechnology, Surface Coatings and Films

Polymer Chemistry

The Design And Application of Novel Post-Metallocene Catalysts For Olefin Polymerization

Önder Güneş[a], Ozan Sanlı Şentürk[a]

[a] İstanbul Technical University, Departmant of Chemistry, Türkiye
guneso18@itu.edu.tr

Keywords: Catalysts, Polyolefins, Post-Metallocene, Tailor-Made-Polymer.

Aim

Polyolefins are macro molecules that are made of many smaller molecules which contain C=C in their structure. Those polymeric materials possess properties like being durable, resistant towards harsh chemicals and heat according to their molecular structure. It is also known that polyolefins are one of the major plastics that is made for many applications in a wide range. Although, plastic materials are among the most widely produced man-made products, with nearly 400 million tons manufactured annually. It is estimated that around 150 million tons of polyethylene (PE) and 85 million tons of polypropylene (PP) account for the vast majority of these polymeric materials.

The distibution of produced plastics are; 21% low density polyethylene (LDPE), 18% of poly(vinyl chloride) (PVC), 17% poly(ethylene teraphthalate) (PET), 15% polypropylene (PP), 14% lineer low density polyethylene (LLDPE), 10% high density polyethylene (HDPE) and 5% polystyrene (PS) which shows the polyolefins as a group are the main backbone of the arrangement.

This research focuses on designing and synthesizing new post-metallocene catalysts for producing tailor-made polyolefins with ultra-high molecular weights (UHMW). UHMWPE is a kind of plastic that has a molecular weight over 1,5 million Da (Malpass, 2010). Within this high of a molecular weight, it has the potential of producing extra strong and durable materials. However, production of UHMWPE requires special kinds of methods. Since it is a polymer within a specific molecular weight (tailor-made), its synthesis necessitates a prescribed pathway (Severn and Chadwick, 2008).

To synthesize polyethylene with ultra-high molecular weights, three key components are needed, the monomer (ethylene gas), the catalyst and a co-catalyst (Kaminsky et al. 1985). All three compounds must be as pure as possible to achieve the maximum catalytic activity. The polymerisation yield is also dependent on other factors like pressure of ethylene gas and temperature of reaction chamber. When these criteria are met, a successful polymerisation can be done according to Natta et al. (1957). Among all of these, most important component in this scenario is the catalyst, since this polymerisation is exceptional when it is compared to the traditional methods. Within a proper catalyst, not only homopolymers but also co-polymers with different olefins can be obtained (Severn and Chadwick, 2008).

Synthesis of UHMWPE can be achieved with presence of a sharp catalyst such as post-metallocene catalysts. According to Matsugi and Fujita, these catalysts are called as 'Constrained Geometry Catalysts' due to their molecular structure (2008). In these molecules, there is a transition metal centre that is surrounded by an organic. When this structure is investigated, it is seen that organic ligand has two main duties. First, it makes the molecule soluble in organic solvents. Second, it balances the electronic interaction in coordination complex. The ligand must also contain electron donating and electron withdrawing groups because coordination polymerisation mechanism involves steps that requires both of them (Johnson et al. 1995).

One of the factors that affect the activity of these catalysts is the energy gap between the highest occupied molecular orbital (HOMO) and lowest unoccupied molecular orbital (LUMO) energy levels. Therefore, the design of the ligand and selection of centre atom takes a critical place according to the ligand field theory. In this context, a coordination complex that consist of a tetradentate organic ligand to coordinate transition metals titanium, zirconium and hafnium is designed in this work. The organic ligand has two imine and two pyrrole functional groups having nitrogen atom as a donor in a chelate form. It is believed that, this structure provides the electronical flexibility to the complex while having the proper energy gap between HOMO and LUMO when it is compared to the literature (Check the previous work in appendices 1-3).

Aim of this research is actualisation of synthesis, characterisation and proving the activity of new post-metallocene catalyst and comparing their activity with corresponding literature examples.

Material and Method

Production of post-metallocene catalyst heavily relies on air-free methods such as, Schlenk Technique and employment of glove box. The reason behind this requirement is this kind of molecules are highly air and moisture sensitive. To prevent losing their activity, all synthesis, analysis and purification works are done under nitrogen atmosphere.
To synthesize the ligand, following chemicals are used:
- Pyrrole-2-carboxyaldehyde
- 1,2-ortho-phenylene diamine
- Ethyl alcohol
- Diethyl ether

This is carried out in Schlenk flask with nitrogen atmosphere. In first step a determined amount of pyrrole-2-carboxyaldehyde and 1,2-ortho-phenylene diamine was weighted according to 1:2 molar ratio (1 eq. Of diamine and 2 eqs. Of pyrrole). After that, solid materials are dissolved in ethyl alcohol in the flask and stirred overnight at room temperature. Continuity of reaction is investigated with thin layer chromatography. To terminate the reaction, firstly, the solvent was evaporated via application of vacuum with heating. When remaining solid was cooled to the room temperature, cooled diethyl ether was added to the flask. Final desired product precipitated from solution as yellowish-white solid and filtered through filter paper and washed several times with diethyl ether again. NMR and IR analysis results showed that product is highly pure and reaction yield is around 55%.

Findings

In this work, afore-mentioned ligand is successfully synthesized and characterized. Characterisation of this molecule is done by the 1H-NMR, 13C-NMR and IR analyses. When results are compared, it could be said that mentioned compounds are highly pure according to cross-comparing different methods. It is believed that, this ligand is ready to be used in further reactions to synthesize novel post-metallocene catalyst which is not done yet. In future, it is aimed to synthesize the desired coordination compound and use it for polymerisation reaction afore mentioned before.

Conclusion

In conclusion, it could be said that, electronically flexible and constrained geometry ligands are decisive elements of production of UHMWPE. This work is focused on synthesis and characterization of the ligand which would be used in later for production of post-metallocene catalyst. When this is achieved, our proposal will be accepted for synthesis of polymeric materials which is promising for many uses in a wide range of industries such as chemistry, automotives, material and mechanical engineering, agriculture, naval and defense industry.

Appendices

1) "Yeni Mühendislik Plastik Ürünler için Yeni Bütansülfonilhidrazon Fragmenti İçeren Postmetalosen Katalizörler", **Ozan Sanlı ŞENTÜRK, Fatma HAMURCU,** Patent Başvuru No: 2017/07426
2) "Yeni Mühendislik Plastik Ürünler için Yeni Pirol-imin ve İndol-imin Fragmenti İçeren Postmetalosen Katalizörler", **Ozan Sanlı ŞENTÜRK, Sibel KILIÇ**, Patent Başvuru No: 2017/07436;
3) "Yeni Mühendislik Plastik Ürünler için Yeni Furan-İmin, Tiyofen-İmin ve Etilendiamin Türevi İçeren Postmetalosen Katalizörler", **Ozan Sanlı ŞENTÜRK, İsmail Hakkı YÜCEL ve Kerem KAYA**, Patent Başvuru No: 2017/07439.

References

Johnson, L. K., Killian, C. M. & Brookhart, M. New Pd(ii)- and Ni(ii)-based catalysts for polymerization of ethylene and α-olefins. J. Am. Chem. Soc. 117, 6414–6415 (1995).

Kaminsky, W. (2012). Discovery of Methyl aluminoxane as Cocatalyst for Olefin Polymerization. Macromolecules, 45(8), 3289–3297. https://doi.org/10.1021/ma202453u

Kaminsky, W., Külper, K., Brintzinger, H. H., & Wild, F. R. W. P. (1985). Polymerization of Propene and Butene with a Chiral Zirconocene and Methylalumoxane as Cocatalyst. Angewandte Chemie International Edition in English, 24(6), 507–508. https://doi.org/10.1002/anie.198505071

Malpass D.B. (2010). Introduction to Industrial Polyethylene. Properties: Catalysts, and Processes. Wiley.

Matsugi, T., & Fujita, T. (2008). High-performance olefin polymerization catalysts discovered on the basis of a new catalyst design concept. Chemical Society Reviews, 37(6), 1264. https://doi.org/10.1039/b708843b

Natta,G., Pino, P., Mazzanti, G., Giannini, U., Mantica, E., Peraldo,M., "The nature of some soluble catalysts for low pressure ethylene polymerization" , J. Polym. Sci., 26:120 (1957).

Severn, J. R., & Chadwick, J. C. (2008). Tailor-Made Polymers: Via Immobilization of Alpha-Olefin Polymerization Catalysts (1st ed.). Wiley-VCH.

CHEMISTRY

Analytical Chemistry

Biochemistry

Drug Design & Drug Delivery (Computational and Experimental)

Energy Materials (Synthesis, Characterizations, Applications)

Inorganic Chemistry

Nanochemistry

Organic Chemistry

Physical Chemistry

Nanotechnology, Surface Coatings and Films

Polymer Chemistry

Investigation of Fluorescence Properties of ZIF-8 Structures Modified with Graphitic Quantum Dots

Hilal Nazan Ağar[a], Caner Ünlü[a]

[a] Istanbul Technical University, Faculty of Science and Letters, Department of Chemistry, Türkiye
agar16@itu.edu.tr

Keywords: Graphitic Quantum Dots, ZIF-8, Fluorescence, Surface Properties, Nanomaterials.

Aim

In recent years, studies in the field of nanotechnology have offered significant opportunities for the synthesis and development of next-generation materials. Graphitic quantum dots (GQDs) have attracted considerable interest in various areas such as sensors, optoelectronic devices, and biomedical applications due to their excellent optical properties, large surface areas, high photoluminescence efficiency, and chemical stability (Li et al., 2021). These unique characteristics make GQDs promising candidates for a wide range of scientific and industrial applications, including biosensors, energy conversion, and drug delivery. Modifying the structures of GQDs to form hybrid systems with different materials is an important strategy contributing to the development of functional materials. Metal-organic frameworks (MOFs) are widely used in applications such as gas storage, catalysis, drug delivery, and separation technologies, owing to their high surface areas, regular porous structures, and chemical flexibility (Zhou et al., 2020). Among these, the zeolitic imidazolate framework (ZIF-8) stands out due to its high thermal and chemical stability. However, the optical properties of ZIF-8 are limited, and enhancing its fluorescence characteristics is important for sensor and optoelectronic applications (Wang et al., 2019). In this study, it was aimed to fluoresce ZIF-8 structures using GQDs and investigate their effects on surface properties.

Material and Method

GQDs, with their small sizes, high photoluminescence efficiency, and chemical stability, can modify the optical and surface properties when integrated into MOF matrices. ZIFs (zeolitic imidazolate frameworks), known for their porous structures and chemical stability, are a class of MOFs used in various applications such as gas storage, separation, and catalysis. The combination of GQDs and ZIF-8 structures is significant in enhancing fluorescence properties and improving surface characteristics. In this context, rendering ZIF-8 structures fluorescent through GQDs and investigating their absorbance properties presents an important approach for the development of potential applications. Evaluating the effects of GQD integration into ZIF-8 structures on fluorescence properties also highlights the importance of characterizing surface features. The integration of GQDs into ZIF-8 structures not only reveals their fluorescence properties but also enables the arrangement of active groups on their surfaces. These active groups facilitate the formation of interactions and catalysts for targeted applications. Such interactions play a crucial role in applications requiring selective adsorption, controlled release, and enhanced photocatalytic activity. The interaction between GQDs and ZIF-8 not only improves optical properties but can also optimize the porous structure within the material, increasing its gas storage capacity (Wu et al., 2019). This combination offers broad application potential, especially in areas such as environmentally friendly technologies and sustainable energy production.

GQDs were synthesized via a microwave-assisted method using boric acid, urea, and varying amounts of citric acid. The microwave method offers high efficiency and low energy consumption, making it advantageous for controlled synthesis (Zhao et al., 2022). Varying the amount of citric acid demonstrated that the fluorescence behavior could be tuned by affecting the distribution of GQDs within the structure and their optical properties.

The synthesized GQDs were dissolved in methanol and incorporated into the ZIF-8 synthesis process. ZIF-8 structures were synthesized via controlled precipitation of 2-methylimidazole and zinc acetate dihydrate. The integration of GQDs into the ZIF-8 matrix and the resulting optical and structural changes were examined. Careful control over synthesis parameters

ensured uniform GQD dispersion and optimal interaction with the ZIF-8 framework. During synthesis, the pre-prepared GQD solution was added to the system in appropriate ratios to integrate them into the ZIF-8 matrix. ZIF-8 structures were synthesized using GQDs containing different citric acid ratios to investigate the effect of GQD concentration on the modification.

The obtained pure and GQD-modified ZIF-8 structures were analyzed using various characterization techniques, including X-ray diffraction (XRD), Fourier-transform infrared spectroscopy (FTIR), scanning electron microscopy (SEM), photoluminescence (PL), and UV-Vis spectroscopy.

Findings

FTIR and XRD analyses confirmed the presence of the ZIF-8 crystal structure with GQDs, while SEM analyses revealed changes in surface morphology. XRD was conducted to examine changes in the crystal structure. FTIR was used to determine alterations in chemical bonding structures. SEM was applied to study surface morphology and structural changes. UV-Vis spectroscopy was employed to evaluate fluorescence properties and analyze dye adsorption behavior. The characterization results demonstrated successful integration of GQDs into the ZIF-8 structure. XRD results indicated that GQD incorporation did not significantly alter the crystal structure of ZIF-8 but could affect its porosity.

FTIR analyses confirmed that the characteristic vibration bands of imidazole groups were preserved in the GQD-modified ZIF-8 structures. SEM images revealed significant changes in surface morphology due to GQD addition, especially in the porous surface structure. UV-Vis spectroscopy analyses showed that the fluorescence properties of ZIF-8 structures were significantly enhanced with the inclusion of GQDs. The fluorescence emission intensity could be controlled by changing the GQD concentration, allowing tunability in optical properties. This suggests that the modified structures may be suitable for sensor and optoelectronic applications. Dye adsorption experiments showed that the inclusion of GQDs altered the ability of ZIF-8 to adsorb dye molecules. Particularly, analyses using methylene blue (MB) dye demonstrated that GQD-modified structures exhibited higher adsorption capacity compared to pure ZIF-8. This is attributed to the increased surface area and altered electrostatic interactions due to modification.

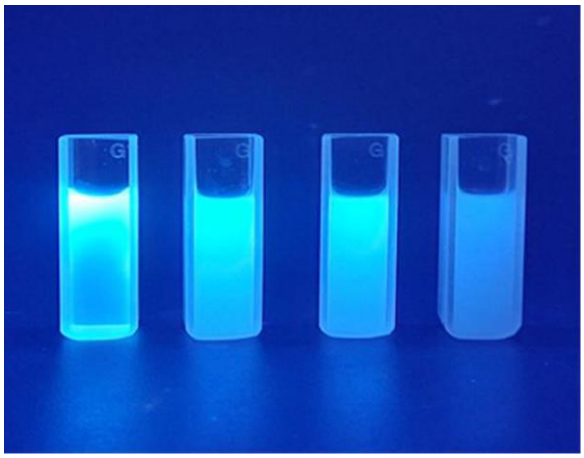

Figure 1. The emission color of carbon dots fluorescent under GQD, ZIF8-GQDs I, ZIF8-GQDs II, ZIF8-GQDs III are shown from left to right, respectively.

Conclusion

This study comprehensively investigated the changes in optical and surface properties of ZIF-8 structures modified using GQDs. The results showed that GQD incorporation significantly imparted fluorescence properties to ZIF-8 and altered its surface to improve dye adsorption capacity. The findings highlight the potential of such hybrid materials for developing efficient adsorbents, photocatalysts, and luminescent probes. Non-fluorescent ZIF-8 structures were converted into fluorescent materials through this method. Such hybrid structures have broad application potential in sensor technologies,

optoelectronics, and environmental pollutant removal. Future studies may focus on further enhancing material properties using different types of GQDs and MOF combinations, enabling more detailed optical tuning and investigation of selective adsorption mechanisms. This study highlights the improvements in optical properties of ZIF-8 structures modified with GQDs and their potential applications in fields such as sensing, optoelectronics, and dye technologies.

References

Li, X., Zhang, Y., Liu, T., Chen, H., & Wang, J. (2021). Graphitic quantum dots for advanced applications. Nanotechnology, 30(24), 1–15.

Wang, S., Liu, F., Zhao, Y., Chen, M., & Xu, Z. (2019). Zeolitic imidazolate frameworks for optoelectronic applications. Journal of Materials Chemistry C, 8, 4567–4578.

Wu, J., Lin, Y., Gao, P., Huang, L., & Li, R. (2019). Enhancement of gas storage and sensing properties of metal-organic frameworks by functionalized graphene quantum dots. Nanoscale, 11(12), 5418–5428.

Zhao, M., Chen, Q., Wang, L., Hu, S., & Li, Y. (2022). Microwave-assisted synthesis of graphitic quantum dots. Materials Letters, 279, 1–10.

Zhou, H., Li, D., Sun, Q., Tang, X., & Yang, W. (2020). Metal-organic frameworks: Properties and applications. Chemical Reviews, 112(2), 673–702.

CHEMISTRY

Analytical Chemistry

Biochemistry

Drug Design & Drug Delivery (Computational and Experimental)

Energy Materials (Synthesis, Characterizations, Applications)

Inorganic Chemistry

Nanochemistry

Organic Chemistry

Physical Chemistry

Nanotechnology, Surface Coatings and Films

Polymer Chemistry

Synthesis Of Polymers Containing Supramolecular Components In The Pendant Or Main Chain

Hafize Reva Bayraktar[a], Abdullah Aydogan[a]

[a] Istanbul Technical University, Faculty of Science and Letters, Department of Chemistry, Turkey
rebayraktar@itu.edu.tr

Keywords: Polymer, Polyurethane, Supramolecular Chemistry.

Aim

The aim section should be written in Times New Roman font, justified-alignment and in 10-point size. Supramolecular chemistry differs fundamentally from classical covalent chemistry by emphasizing non-covalent interactions and complexation, including hydrogen bonding, π-π stacking, van der Waals forces, and metal coordinations. These dynamic and reversible interactions enable the spontaneous self-assembly of intricate molecular architectures, a key feature that underpins the development of advanced functional materials. One particularly significant application of supramolecular chemistry is in the design of self-healing materials, where non-covalent bonds facilitate autonomous repair mechanisms. By incorporating host–guest interactions and hydrogen bonding networks, these materials can undergo reversible cross-linking, allowing structural integrity to be restored after damage shown in figüre 1. This inherent adaptability and responsiveness make supramolecular systems highly promising for applications in biomaterials, soft robotics, and smart coatings (Sinawang et al., 2020).

Calix[4]pyrroles (C4Ps) were initially synthesized by Baeyer in 1886 through a condensation reaction between pyrrole and acetone, with hydrochloric acid serving as the catalyst. The cyclic tetrameric structure was later proposed by Chelintzev and Tronov (Gale et al., 1998) . In 1955, the synthesis process by substituting the catalyst with methane sulfonic acid is enhenced (Rather et al., 2019). The study of it's ion recognition and binding properties gained attention in 1996 (Gale et al., 2001) , (Rather et al., 2019b) . Calix[4]pyrroles (CPs), including octamethylcalix[4]pyrrole shown in Figure 2, and their derivatives are easily synthesized and functionalized. These compounds selectively bind anions in organic solvents. The selectivity order for anion binding by CPs is as follows: $F^- > CH_3COO^- > Cl^- > Br^- > CN^- > NO_3^-$. (Akar & Aydogan, 2005).

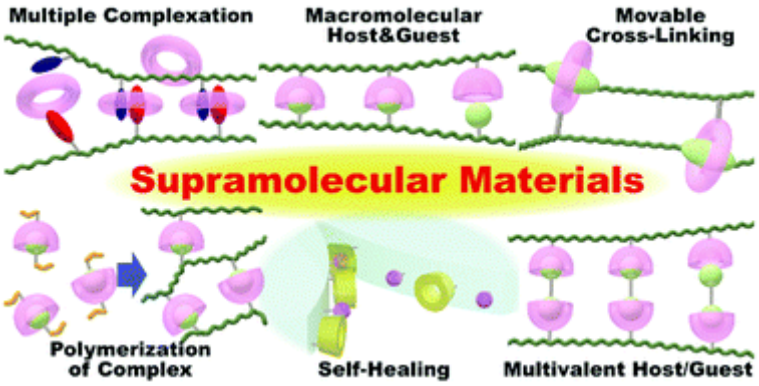

Figure 1. Cartoon representations illustrating the supramolecular complexation concepts (Gale et al., 1998).

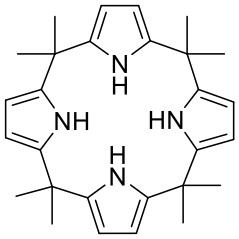

Figure 2. Octamethylcalix[4]pyrrole.

Researchers have continuously investigated the use of polyurethane for the removal, pre-concentration, and separation of various substances such as phenols, phthalates, polychlorinated biphenyls, carboxylic acids, pesticides, and dyes. The use of polyurethane as an adsorbent for organic dyes traces back to the 1990s .The extraction of azo dyes using polyester- and polyether-based types of polyurethane foam has been studied. Now, there are numerous independent reports on the use of polyurethane for the treatment of textile waste water with both model and real waste (Werbowesky & Chow, 1996) .
In this study, polyurethane polymers containing calix[4]pyrrole (C4P) units in the main chain or as pendants, cross-linked either physically or covalently, will be synthesized. The resulting polymer will be used in the extraction studies of organic dye waste,in the formation of supramolecular polymer gel networks and self-cross linking supramolecular polymers. The structural analysis and properties of the new polymers will be carried out using NMR spectroscopy, FTIR spectroscopy, viscosity and conductivity measurements, UV-VIS spectroscopy, and rheological measurements.

Material and Method

The material and method section should be written in Times New Roman font, justified-alignment and in 10-point size. First, the CP-Diester compound, which has an ester functional group at the meso position and serves as a starting compound to bis-alcohol-calix[4]pyrrole (C4P) monomer was synthesized for the preparation of calix[4]pyrrole-based polyurethanes. The obtained CP-Diester was then reduced to a diol monomer for use in polyurethane synthesis. Polyurethanes are formed through a polyaddition reaction between diisocyanates (e.g., TDI, MDI) and polyols (e.g., ethylene glycol, propylene glycol). The reaction between isocyanate (-NCO) and hydroxyl (-OH) groups results in the formation of urethane bonds (-NH-COO-). The properties of the resulting polymer can be tuned by varying the types and ratios of reactants. The synthesis was carried out in dry THF solvent in the presence of dibutyltin dilaurate (DBTDL) as a catalyst. Viscous reaction solution was then diluted with THF and precipitated into hexane, filtered, and washed with hexane, dried under vacuum. Resulting product was a pale yellow powder like solid.The characterization of P-CP was performed using NMR and FTIR techniques. In this study, the diisocyanates IPDI, MDI and TDI were used.

Findings

The findings section should be written in Times New Roman font, justified-alignment and in 10-point size. One of the methods used to demonstrate the formation of suprapolymers is NMR spectroscopy. NMR is used to determine molecular structure and functional groups. The reaction between calix[4]pyrrole-diol and various diisocyanates (IPDI, MDI) occurs between isocyanate groups (-NCO) and hydroxyl groups (-OH), forming urethane bonds (-NH-COO-). This technique is used to identify the –NH and –CH2– groups in the polyurethane structure.
The most significant indication of polymerization is the disappearance of isocyanate group peaks and the appearance of urethane bond peaks in the NMR spectrum. In addition FTIR spectroscopy is used to confirm the presence of functional groups. To analyze polyurethane formation, the presence of characteristic functional groups specific to the polyurethane structure and the disappearance of other groups during the reaction process is examined.
Post-Reaction (Polyurethane Formation):
^{1}H-NMR detects the protonic groups (–H) of the polymer. Below are the key peaks indicating the progress of the polyurethane synthesis based on calix[4]pyrrole-diol and various diisocyanates: Urea (NH) groups:The urea bonds formed in the polyurethane structure generally produce a broad and sharp peak around 4.0–7.0 ppm. This indicates that the

isocyanate has reacted with the diol to form urea bonds. Recently formed –NH–CH2– groups:The protons of these groups appear in the range of 3.0–4.0 ppm. Aliphatic bonds –CH2–CH2–: Due to polymerization with isocyanate, the protons of aliphatic methylene (–CH2–) groups between urea bonds may appear in the region of 2.5–3.5 ppm. The isocyanate group (–NCO) shows a peak in the FTIR spectrum around 2270-2250 cm-¹. This peak will disappear when polymerization is complete. The NH groups will form a broad band in the range of 3300-
3500 cm-¹ upon polyurethane bond formation. The urethane carbonyl groups (–NH–C=O) will produce a peak between 1640–1730 cm-¹ confirming the formation of the polyurethane structure. Additionally, characteristic peaks of aromatic rings and alcoholic hydrogens should appear in the FTIR spectrum. FTIR used to determine whether the isocyanate is present in the reactant and whether polyurethane bonds have formed.

Conclusion

The conclusion section should be written in Times New Roman font, justified-alignment and in 10-point size. In this study, polyurethane polymers incorporating calix[4]pyrrole (C4P) units in the main chain or as pendant groups were successfully synthesized using diisocyanates (IPDI, MDI). The reaction between hydroxyl (-OH) and isocyanate (-NCO) groups resulted in the formation of urethane bonds (-NH-COO-), as confirmed by structural characterization techniques. Characterization via ¹H-NMR spectroscopy provided key evidence for polymer formation by identifying shifts in chemical shifts corresponding to –NH, –CH_2, and aromatic protons. The disappearance of the isocyanate (-NCO) peak and the emergence of urethane (-NH-COO-) and urea (-NH) bond signals confirmed successful polymerization. Complementary FTIR spectroscopy further validated the reaction progress, demonstrating the loss of the isocyanate functional group at 2270-2250 cm-¹ and the appearance of characteristic peaks for polyurethane structures, including broad NH stretching bands at 3300-3500 cm-¹ and carbonyl (C=O) peaks at 1640-1730 cm-¹. The polymer properties were influenced by the choice of diisocyanate and polyol, allowing tunability in terms of viscosity, cross-linking density, and mechanical behavior.Further studies will explore the potential applications of these polymers in supramolecular gel networks, self-cross-linking polymer systems, and organic dye waste extraction.
Overall, this research provides a foundational approach to designing calix[4]pyrrole-based polyurethane materials with tunable properties for specific applications. Future studies aim to focus on optimizing polymer properties by varying monomer ratios, assessing mechanical stability, and exploring real-world applications such as micropollutant adsorption.The synthesized supramolecular polyurethane materials will be evaluated to the broader field of functional supramolecular polymers and their role in environmental benefits in the removal of micropollutants and organic dyes.

References

Akar, A., & Aydogan, A. (2005). Synthesis of meso-tetra acid and ester functionalized calix[4]pyrroles. *Journal of Heterocyclic Chemistry*, *42*(5), 931–934. https://doi.org/10.1002/jhet.5570420527

Chow, A. (1990). Sorption of organic dyes by polyurethane foam. *Talanta*, *37*(4), 407–412. https://doi.org/10.1016/0039-9140(90)80232-5

Gale, P. A., Anzenbacher, P., Jr, & Sessler, J. L. (2001). Calixpyrroles II. *Coordination Chemistry Reviews*, *222*(1), 57–102. https://doi.org/10.1016/s0010-8545(01)00346-0

Gale, P. A., Sessler, J. L., & Král, V. (1998). Calixpyrroles. *Chemical Communications*, *1*, 1–8. https://doi.org/10.1039/a706280j

Rather, I. A., Wagay, S. A., Hasnain, M. S., & Ali, R. (2019a). New dimensions in calix[4]pyrrole: the land of opportunity in supramolecular chemistry. *RSC Advances*, *9*(66), 38309–38344. https://doi.org/10.1039/c9ra07399j

Rather, I. A., Wagay, S. A., Hasnain, M. S., & Ali, R. (2019b). New dimensions in calix[4]pyrrole: the land of opportunity in supramolecular chemistry. *RSC Advances*, *9*(66), 38309–38344. https://doi.org/10.1039/c9ra07399j

Sinawang, G., Osaki, M., Takashima, Y., Yamaguchi, H., & Harada, A. (2020). Supramolecular self-healing materials from non-covalent cross-linking host–guest interactions. *Chemical Communications*, *56*(32), 4381–4395. https://doi.org/10.1039/d0cc00672f

Werbowesky, R., & Chow, A. (1996). Extraction of azo dyes by polyurethane foam. *Talanta*, *43*(2), 263–274. https://doi.org/10.1016/0039-9140(95)01770-4

CHEMISTRY

Analytical Chemistry

Biochemistry

Drug Design & Drug Delivery (Computational and Experimental)

Energy Materials (Synthesis, Characterizations, Applications)

Inorganic Chemistry

Nanochemistry

Organic Chemistry

Nanotechnology, Surface Coatings and Films

Physical Chemistry

Polymer Chemistry

Dual Radical and Singlet Oxygen Pathways in Polybutadiene Photovulcanization: A Novel Approach Using Phenylacylbromide under UV-A Irradiation for Advanced Crosslinked Films

Ragib Talha Uzun[a], Baris Kiskan[a]

[a]Istanbul Technical University, Department of Chemistry, Türkiye
uzunr17@itu.edu.tr

Keywords: Oxidation, Phenylacyl Bromide, Photo-crosslinking, Polybutadiene.

Aim

Polybutadiene (pBD) is extensively utilized in various industrial sectors due to its excellent elasticity, abrasion resistance, and durability, making it indispensable for automotive tires, conveyor belts, footwear, and other industrial products [1]. Traditional methods for crosslinking polybutadiene, such as thermal vulcanization, rely heavily on energy-intensive conditions, including elevated temperatures, prolonged reaction times, and high-pressure setups, resulting in increased operational costs and environmental impacts [2]. Consequently, there is a growing need for alternative methods that provide more sustainable and efficient pathways to achieve similar or enhanced material properties.

Photocrosslinking has emerged as a promising solution, offering milder reaction conditions, reduced energy consumption, shorter processing times, and better environmental compatibility [3]. Nevertheless, conventional photoinitiators predominantly facilitate either radical-induced crosslinking or oxidation-based reactions separately, limiting the overall effectiveness and versatility of these methods. Thus, the development of multifunctional photoinitiators capable of simultaneously triggering both radical and oxidative mechanisms represents an important advancement in photocrosslinking technology.

Polybutadiene contains highly reactive pendant 1,2-vinyl groups and sensitive allylic positions in its 1,4 segments, making it particularly susceptible to radical-induced and oxidation-mediated crosslinking reactions [4–6]. This study builds upon previous research by investigating an improved photocrosslinking strategy utilizing phenylacylbromide (phABr) as a novel photoinitiator under UV-A irradiation. PhABr uniquely combines direct radical generation via homolytic cleavage and indirect generation of singlet oxygen through its photodegradation product, acetophenone [7]. Our research aims to explore the dual-mechanism functionality of phABr comprehensively, evaluating its potential to produce advanced polybutadiene films with superior mechanical, thermal, and surface characteristics suitable for demanding industrial applications.

Material and Method

Polybutadiene (pBD M_n = 5000, %80 cis-trans %20 vinyl, Sigma-Aldrich),2-bromoacetophenone (phenacyl bromide) (phABr, Sigma-Aldrich, 98%), acetophenone (Sigma-Aldrich, >98%), chloroform ($CHCl_3$, Sigma-Aldrich, 99.8%) deuterated chloroform ($CDCl_3$, Sigma-Aldrich, 99.8% atom % D, contains 0.03% (v/v) TMS), potassium bromide (KBr, Sigma-Aldrich, >99%), were all used as received.

Polybutadiene and phABr mixtures (1 g pBD, 25–100 mg phABr) were dissolved in chloroform under dark conditions to prevent premature initiation. Films were formed by solvent casting onto a Petri dish and dried initially in air for 45 minutes, followed by vacuum drying at 40 °C to eliminate residual solvents. UV-A irradiation was performed using Philips TL-36W BLB lamps emitting at 365 nm with an intensity of approximately 100 $mW \cdot cm^{-2}$, and reaction progress was monitored at predetermined intervals (0, 15 min, 30 min, 1 hr, and 2 hrs). Real-time spectroscopic monitoring was conducted via ^{1}H and ^{13}C NMR spectroscopy (Agilent VNMRS 500 MHz, in $CDCl_3$ at 25 °C) and FTIR spectroscopy using KBr pellet and ATR techniques. Film properties will be extensively characterized, including thermogravimetric analysis (TGA), differential scanning calorimetry (DSC) rheological testing, mechanical testing (strain-stress analysis), morphological assessment (scanning electron microscopy, SEM), and wettability evaluation via contact angle measurements with water and olefins.

Findings

Real-time ^{1}H NMR spectroscopy provided detailed insights into the reaction mechanism of polybutadiene (pBD) photocrosslinking under UV-A irradiation with phenylacylbromide (phABr). As can be seen at Figure 1. initial spectra (t=0) revealed only characteristic peaks of $CDCl_3$, 80% cis-trans pBD, and phABr. Upon 15 minutes of irradiation, new signals emerged at 2.63, 7.47, 7.58, and 7.98 ppm, indicative of acetophenone formation. This formation was further confirmed by comparison with reference spectra, showing slight downfield shifts attributed to increased polarity in the reaction medium. Over the reaction period, the gradual disappearance of the methylene peak at 4.48 ppm (phABr) and concurrent rise of the acetophenone-related methylene peak at 2.63 ppm clearly demonstrated phABr consumption and acetophenone production.

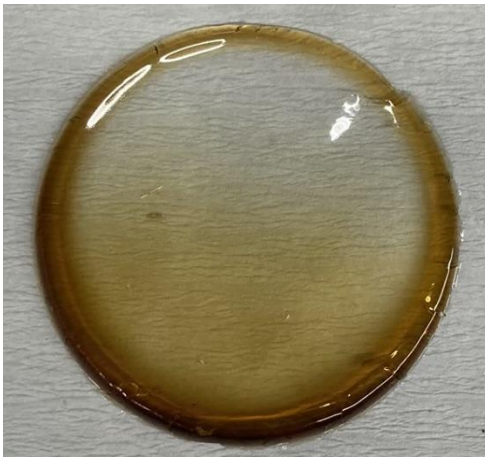

Image 1. Crosslinked film within 2 hours of irradiation.

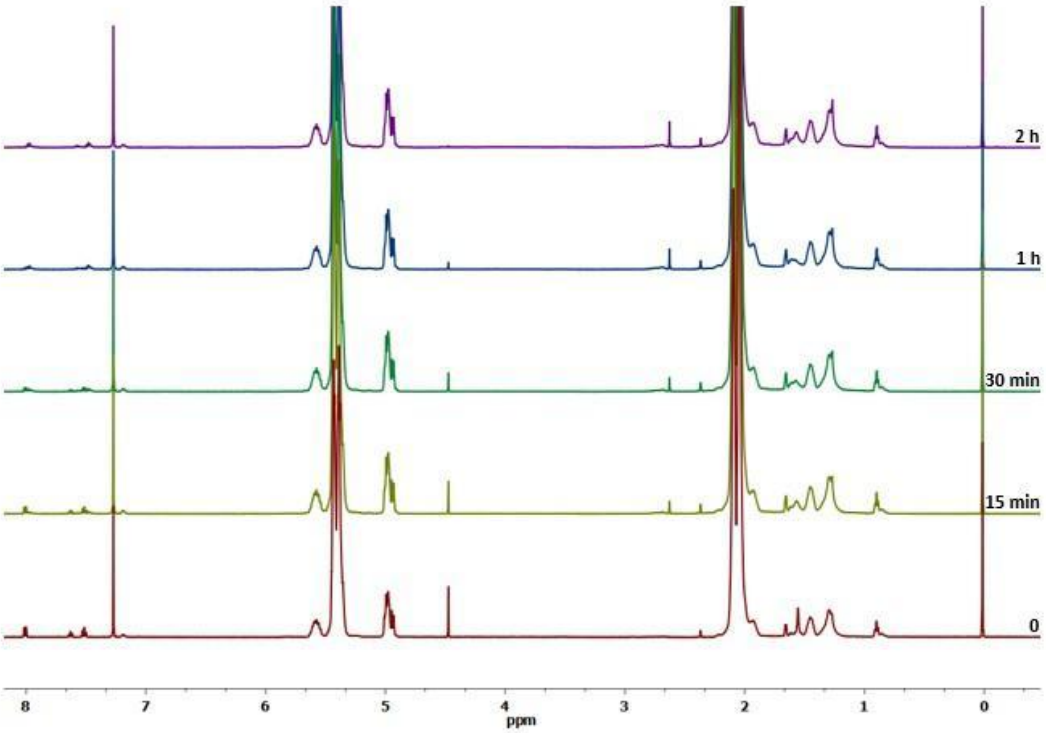

Figure 1. Real-time ^{1}H-NMR investigation of photovulcanization of pBD irradiation with phABr in d-Chloroform.

Analysis of characteristic hydrogen peaks from the 1,2-vinyl double bonds showed a decrease in the non-terminal double bond signal at 5.58 ppm, while an unexplained increase was noted at the terminal double bond at 4.98 ppm, highlighting the crucial role of the 1,2-vinyl units in crosslinking. Additionally, systematic monitoring of cis-to-trans isomerization via ^{1}H NMR exhibited a distinct reduction in cis-alkene signals at 5.39 ppm and an increase in trans-alkene signals at 5.43 ppm. This phenomenon, systematically observed here for the first time by NMR spectroscopy, emphasizes the reactivity of cis units in the photocrosslinking process.

Complementary ^{13}C NMR studies (see Figure 2.) corroborated the ^{1}H NMR findings, with the methylene peak of phABr at 30.83 ppm gradually decreasing and new signals at 26.6 ppm and 133.07 ppm confirming acetophenone formation. The spectral data further showed significant intensity changes, particularly a notable decrease in cis-1,4 methylene groups at 27.39 ppm and a slight increase in trans-1,4 groups at 32.71 ppm. Olefinic carbon signals associated with the 1,2-vinyl unit (114.31 ppm and 142.69 ppm) both exhibited reduced intensity, underscoring their active role in network formation. Additionally, the cis-olefinic carbon peak at 128.42 ppm diminished considerably, while the trans-olefinic peak at 130.13 ppm slightly increased, further validating the cis-to-trans isomerization mechanism.

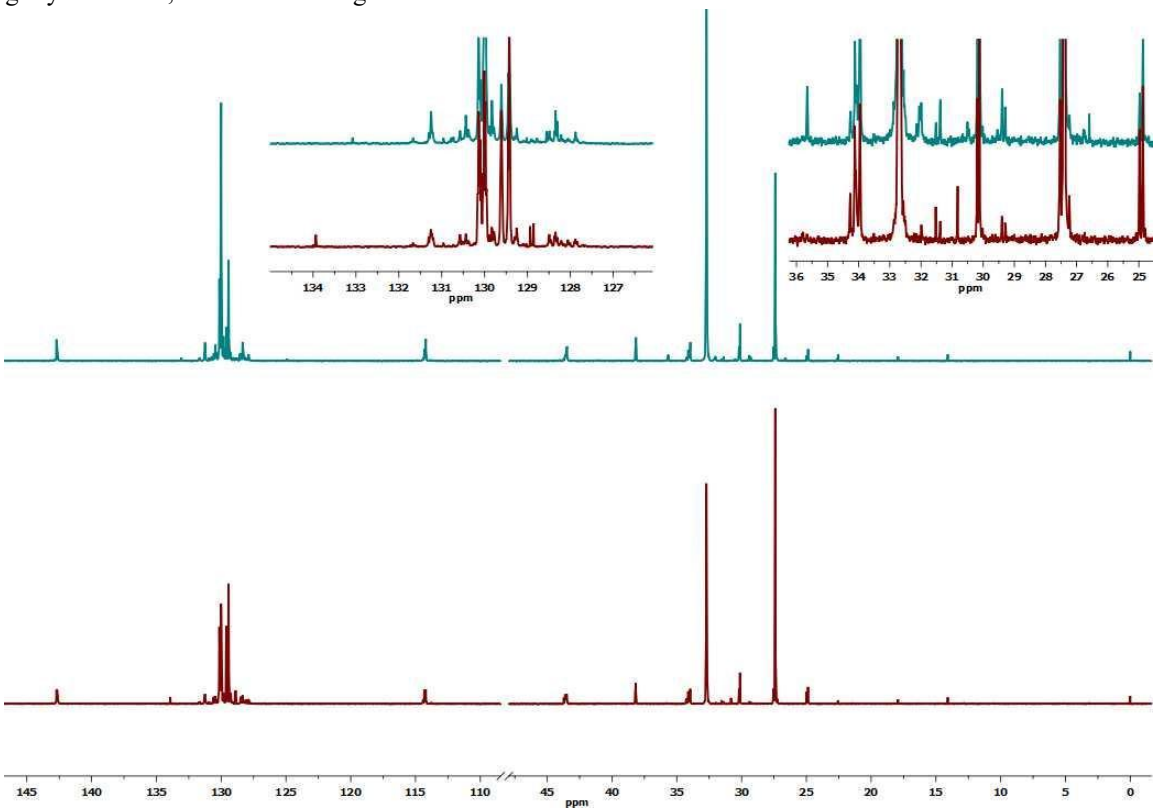

Figure 2. ^{13}C NMR investigation of photovulcanization of pBD irradiation with phABr in d-Chloroform; while the lower spectrum represents the sample at 0 h (before irradiation),the upper spectrum corresponds to the sample after 2 h of irradiation.

FTIR spectroscopy, utilizing KBr pellet method, provided complementary evidence supporting NMR results and offered additional mechanistic clarity. Gradual disappearance of phABr-specific bands (C–Br at 551 cm^{-1} and aromatic C–H bending at 729, 709, and 694 cm^{-1}) indicated its full photolysis within 2 hours. Concurrently, the emergence of a new carbonyl stretching band at 1720 cm^{-1} reflected the formation of saturated ketone oxidation products. Moreover, an increase in the broad O–H stretching band (3200–3600 cm^{-1}), coupled with intensified C–O stretching at 1075 cm^{-1}, confirmed the formation of oxidative functionalities, highlighting the involvement of radical and singlet oxygen pathways.

To conclude, the combined ^{1}H, ^{13}C NMR, and FTIR analyses distinctly characterized the complex dual-mechanism photocrosslinking process involving radical initiation and singlet oxygen-mediated oxidation. The detailed spectral changes demonstrated active participation and structural evolution of polybutadiene, confirming the efficiency of the novel phABr photoinitiator system in achieving robust crosslinked networks suitable for advanced material applications. Comprehensive mechanical and thermal analyses will be conducted in subsequent studies to further evaluate the performance and practical applicability of these crosslinked materials.

Conclusion

This study successfully demonstrated the dual radical and singlet oxygen-mediated photocrosslinking of polybutadiene using phABr under UV-A irradiation, highlighting phABr's exceptional multifunctional characteristics as a novel photoinitiator.. Real-time spectroscopic analyses confirmed the distinct roles of radical and singlet oxygen pathways, enhancing our understanding of photocrosslinking mechanisms. This dual-mechanism approach provides a versatile and efficient alternative to traditional thermal vulcanization methods, opening pathways for advanced elastomeric applications.

References

S. Kohjiya, Y. Ikeda, A short history of natural rubber research, in: Chemistry, Manufacture, and Applications of Natural Rubber, Elsevier, 2021: pp. 407–427. https://doi.org/10.1016/B978-0-12-818843-9.00006-0.

M. Akiba, Vulcanization and crosslinking in elastomers, Progress in Polymer Science 22 (1997) 475–521. https://doi.org/10.1016/S0079-6700(96)00015-9.

R. Bongiovanni, S.D. Vacche, A. Vitale, Photoinduced Processes as a Way to Sustainable Polymers and Innovation in Polymeric Materials, Polymers 13 (2021) 2293. https://doi.org/10.3390/polym13142293.

I. Schopov, N. Kassabova, G. Kossmehl, Oxidation of cis-1,4-polybutadiene by singlet oxygen, Polymer Degradation and Stability 25 (1989) 31–38. https://doi.org/10.1016/0141-3910(89)90121-3.

J.F. Rabek, J. Lucki, B. Rånby, Comparative studies of reactions of commercial polymers with molecular oxygen, singlet oxygen, atomic oxygen and ozone—I. Reactions with cis-1,4-polybutadiene, European Polymer Journal 15 (1979) 1089–1100. https://doi.org/10.1016/0014-3057(79)90042-9.

L.M.J. Moore, V.M.Q. Saludo, O.H. Grasdal, K.M. Smith, T.J. Kolibaba, J.C. Marcischak, J.P. Killgore, J.J. Snyder, G.R. Yandek, K.B. Ghiassi, Polybutadiene Click Chemistry: A Rapid and Direct Method for Vat Photopolymerization, ACS Appl. Polym. Mater. 5 (2023) 9138–9146. https://doi.org/10.1021/acsapm.3c01601.

Y.B. Cakir, R.T. Uzun, H.C. Kiliclar, K. Kaya, S. Jockusch, Y. Yagci, B. Kiskan, Efficient Photolytic Breakdown of Waste Polystyrene Foam Using an "All-in-One" Photo-HAT Reagent at Ambient Conditions, ACS Sustainable Chem. Eng. 12 (2024) 9978–9986. https://doi.org/10.1021/acssuschemeng.4c02871.

COMMUNICATION SYSTEMS

Antennas

Design and Inter-Element Spacing Optimization of GNSS Array

Muhammed Yusuf Şahin[a], Mesut Kartal[a]

[a] Istanbul Technical University, Faculty of Electrical and Electronics Engineering, Department of Telecommunication Engineering, Turkey
sahiny15@itu.edu.tr

Keywords: GNSS, Patch Antenna, Antenna Array, Circular Polarization, Mutual Coupling.

Aim

In this study, a compact GNSS antenna array operating in the GPS L1 frequency band (1575.42 MHz) is designed and optimized for applications requiring small form factor and robust signal performance. GNSS signals are inherently weak, so antennas must provide sufficient gain and have right-hand circular polarization (RHCP) with a good axial ratio. Furthermore, there is an increasing need to install these GNSS antennas on compact platforms such as unmanned aerial vehicles (UAVs), autonomous ground vehicles, and other small devices. To meet the demands for size, gain, and bandwidth, antenna designs must aim to reach the theoretical limits of miniaturization. Mutual coupling is one of the challenges that compact GNSS antennas must overcome after design. Although it is ideal for the distance between antenna elements to be less than half of the wavelength, this can lead to mutual coupling and its effects. These effects include reduced antenna array performance, distorted antenna patterns, the loss of signal-to-interference-plus-noise ratio (SINR), and steering vector non-compliance. Mutual coupling also negatively affects the jammer suppression ratio and degrades beam-nulling performance and null depth, especially in compact GNSS arrays used for CRPA applications. This study aims to design a compact GNSS antenna with high bandwidth, high gain, and low mutual coupling. The goal is to achieve high performance while ensuring suitability for GNSS applications, particularly in size-constrained environments.

Material and Method

The antenna structure employs a single-layer patch element fabricated on a high-dielectric Rogers TMM10 substrate (εr = 9.8, $\tan\delta$ = 0.002), which allows for significant miniaturization without sacrificing bandwidth or gain. The RHCP behavior is realized through corner truncations on the patch and further enhanced by an extra upper-left corner cut to improve impedance bandwidth. Four rectangular slots are added along the patch edges to improve the axial ratio and extend the circular polarization bandwidth. A substrate thickness of 2.5 mm is selected to support bandwidth needs. CST Microwave Studio is used for simulation and optimization of both the unit element and the antenna array. The optimized unit patch serves as the building block for a 4-element array. The unit elements are spaced at intervals between 50 mm and 70 mm and rotated 90 degrees for sequential rotation-based feeding. Two feeding schemes are considered: independent excitation and simultaneous excitation. The latter accounts for mutual coupling effects and enables more realistic performance analysis through active S-parameters.

Findings

The optimized unit antenna exhibits strong performance at 1575.42 MHz with axial ratio consistently below 3 dB and a realized gain exceeding 4 dBi. When integrated into the 4-element array and excited simultaneously with phase differences, the system demonstrates RHCP gain over 8 dBi. The radiation pattern remains stable, and axial ratio variation within the 3 dB beamwidth is minimized. Mutual coupling is found to significantly degrade array performance when element spacing is less than 60 mm. Optimal spacing is identified near 65 mm, balancing compactness and electromagnetic performance. Simulations of active reflection coefficients (S11) show close agreement between the array-fed and standalone element behaviors. The 90° phase-shifted excitation improves axial ratio distribution across the beam coverage. These findings confirm that compact GNSS arrays can maintain beam integrity and polarization quality when element spacing and excitation strategy are carefully optimized.

Table 1. Single Element Antenna Parameters.

Notation	Defination	Value
s_w	Substrate Width	40 mm
s_l	Substrate Length	40 mm
p_w	Patch Width	29.68 mm
p_l	Patch Length	29.68 mm
g_w	Ground Plane Width	$3 \times p_w$
g_l	Ground Plane Length	$3 \times p_l$
h_s	Substrate Height	2.5 mm
t	Feed Inset	9.78 mm
c_{rhcp}	Truncation Width for Circular Polarization	2.76 mm
c_m	Truncation Width for Matching	1.29 mm
rld	Right and Left Slot Depth	0.74 mm
rlw	Right and Left Slot Width	0.62 mm
tbd	Top and Bottom Slot Depth	0.65 mm
tbw	Top and Bottom Slot Width	1.30 mm
e_r	Relative Permittivity	9.8
tan δ_k	Tangent Loss of Dielectric	0.002

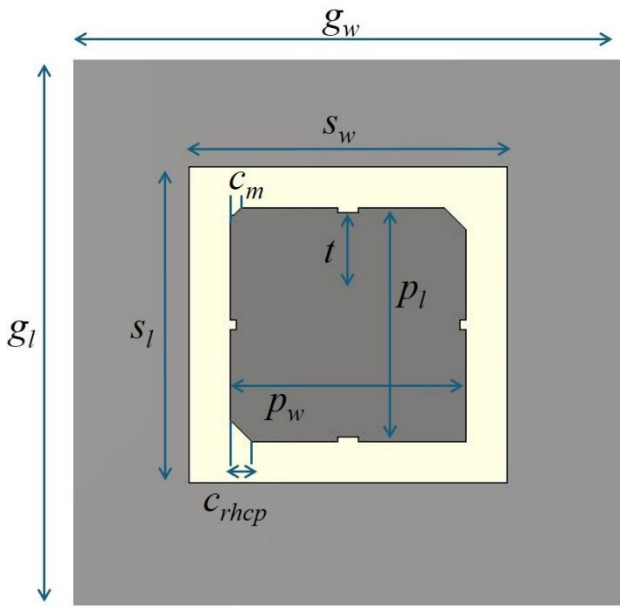

Figure 1. Single-Element Patch Antenna.

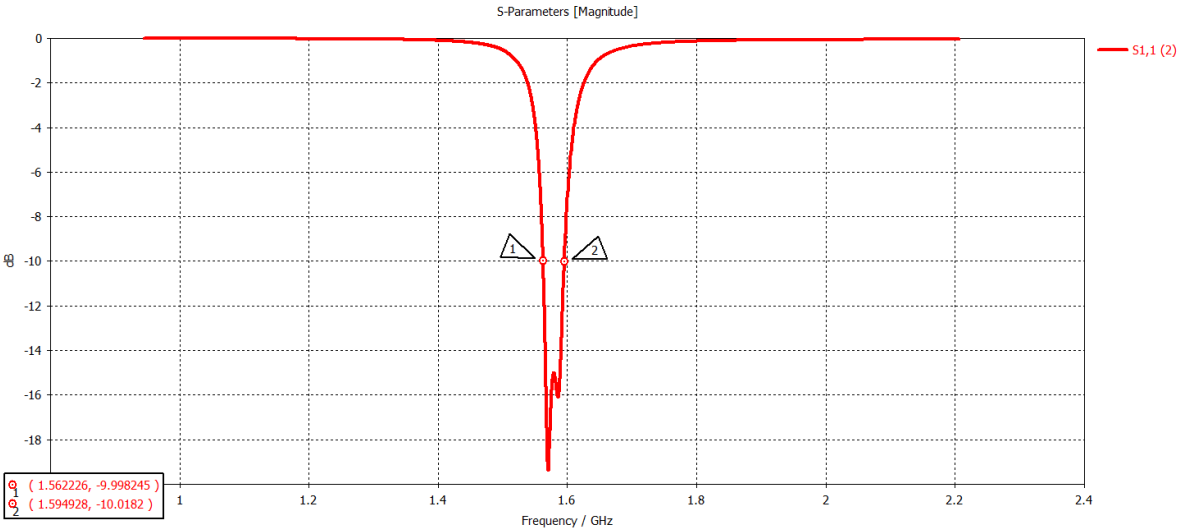

Figure 2. Input reflection coefficient of single element GNSS antenna (S11).

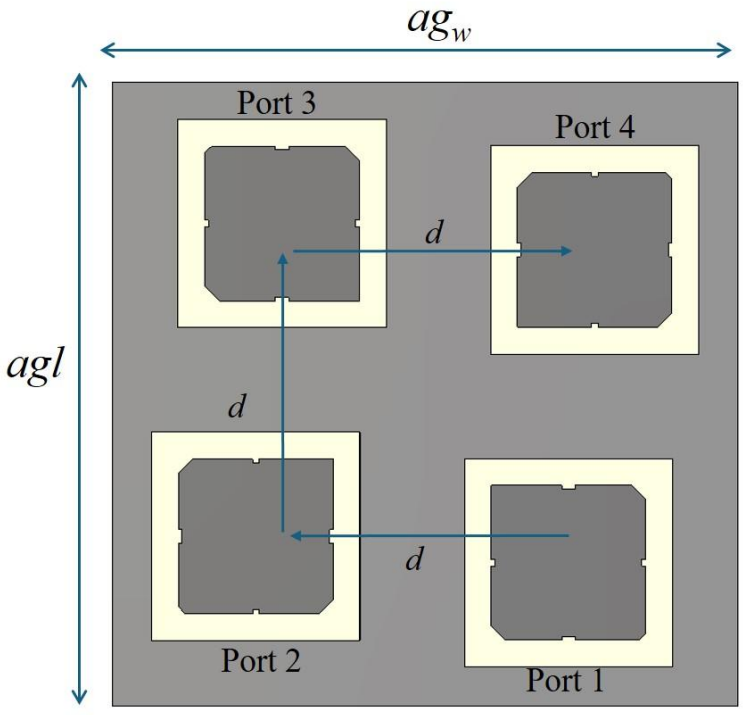

Figure 3. Sequentially Rotated Square Array with Four Elements.

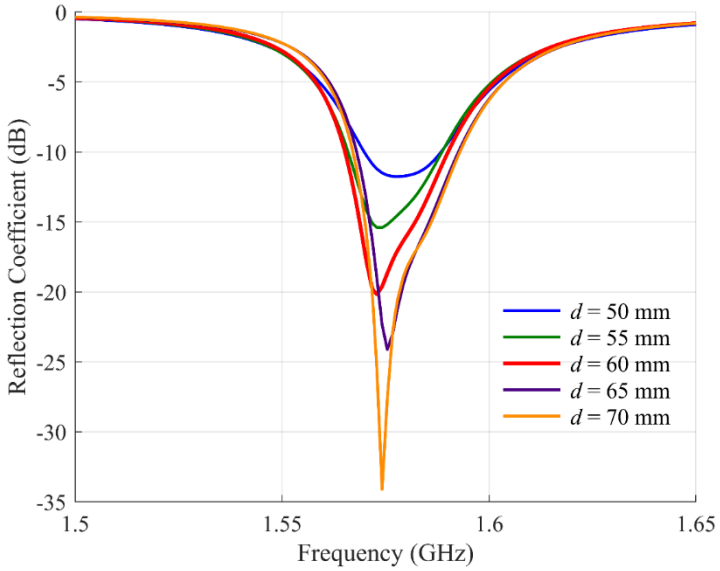

Figure 4. Effect of inter-element spacing on reflection Coefficient (S11) for Distances Between 50 mm and 70 mm in GNSS Array.

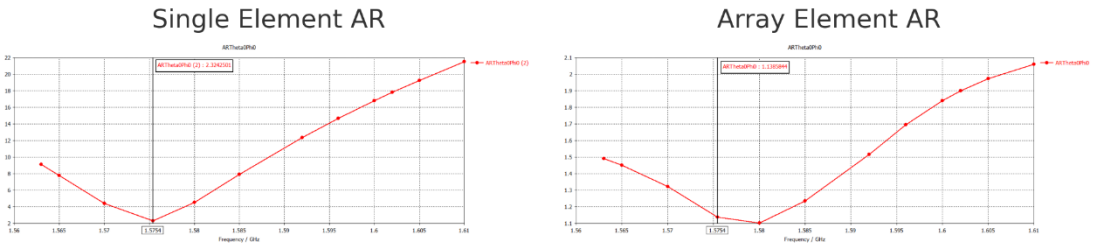

Figure 5. Maximum Axial Ratio of Single Element Antenna vs 4-Element Antenna Array.

Conclusion

A high-performance, compact GNSS antenna array operating at the GPS L1 frequency band is developed, featuring high gain, wide bandwidth, and strong RHCP performance. The combination of high-dielectric substrate selection, patch geometry optimization, and controlled inter-element spacing leads to a compact design suitable for integration into UAVs and other small-scale GNSS platforms. Mutual coupling effects are mitigated through optimized spacing and excitation schemes, resulting in a reliable antenna array capable of maintaining stable radiation patterns and polarization integrity under constrained deployment conditions.

References

Balanis, C. A. (2016). *Antenna Theory: Analysis and Design*. John Wiley & Sons.

Friel, E. M., & Pasala, K. M. (2000). Effects of mutual coupling on the performance of STAP antenna arrays. *IEEE Transactions on Aerospace and Electronic Systems, 36*(2), 518–527.

Hui, H. T. (2002). Reducing the mutual coupling effect in adaptive nulling using a re-defined mutual impedance. *IEEE Microwave and Wireless Components Letters, 12*(5), 178–180.

Valakis, J. L., O'Brien, A. J., & Chrn, C.-C. (2016). Small and adaptive antennas and arrays for GNSS applications. *Proceedings of the IEEE, 104*, 1221–1232.

COMPUTATIONAL SCIENCE AND ENGINEERING

Computational Biology

Computational Fluid Dynamics

Molecular Dynamics Analysis of CHK2 Mutations at the C-lobe of the Kinase Domain

Cihan Uğur Otçu[a], Clara Xazal Buran[a], Gizem Dinler Doğanay[b], Levent Doğanay[c], Levent Doğanay[d], Mert Gür[e],

[a] Istanbul Technical University, Molecular Biology-Genetics and Biotechnology Master of Science Program, Türkiye
[b] Istanbul Technical University, Molecular Biology-Genetics and Biotechnology, Türkiye
[c] VM Pendik Medicalpark Teaching Hospital/Gastroenterology and Hepatalogy, Türkiye
[d] Bahcesehir University/Internal Medicine, Türkiye
[e] University of Pittsburgh, Computational and Systems Biology, Unites States
otcu18@itu.edu.tr

Keywords: Breast Cancer, *CHK2*, DNA Repair, DNA Mutations, Molecular Dynamics Simulations.

Aim

Checkpoint kinase 2 (CHEK2) is an emerging tumor suppressor gene that plays a critical role in maintaining genomic stability and preventing DNA damage. It encodes the CHK2 protein, a serine/threonine kinase involved in DNA repair pathways and cell cycle regulation. CHK2's importance is underscored by its participation in the cellular response to DNA damage as a central mediator in the DNA damage checkpoint pathway. Mutations in CHK2 have been linked to several cancers, including breast, colon, kidney, prostate, and thyroid, making it a promising target for cancer therapy.

Human CHK2 is a single-chain protein of approximately 65 kDa, composed of 543 amino acids. It contains three principal functional domains: The serine-glutamine (SQ) and threonine-glutamine (TQ) cluster domain (SCD), the forkhead-associated (FHA) domain, and the serine/threonine kinase domain (KD*)* (Cai et al., 2009;).The SCD domain is located at the N-terminus of CHK2, and its SQ and TQ motifs are phosphorylated by phosphoinositide 3-kinase–related kinases (PIKKs), such as ATM and ATR (Buscemi et al., 2006;). The FHA domain mediates interactions with phosphorylated proteins, including the phosphorylated SCD of another CHK2 molecule, and demonstrates high specificity for phosphorylated threonine(Almawi et al., 2017; Zannini et al., 2014). At the C-terminal of the protein there is a kinase domain (KD) between residues 213-501. The kinase domain (KD), located at the C-terminus (residues 213–501), adopts a typical Ser/Thr kinase fold consisting of an N-terminal lobe (residues 213–305), which is rich in β-sheets, and a larger, mostly α-helical, C-terminal lobe (residues 306–501). The ATP-binding site lies in the cleft between these two lobes (C lobe; residues 306-501) mostly α-helical (Cai et al., 2009).

Under normal conditions, CHK2 exists as an inactive monomer in the nucleus. Upon DNA double-strand breaks, CHK2 is phosphorylated by ATM, causing significant structural rearrangements that include homodimerization and A-loop phosphorylation upon ATP binding. These events lead to further conformational changes and subsequent dissociation of the CHK2 homodimer into fully active monomers, enabling CHK2 to carry out its DNA repair and cell cycle checkpoint functions effectively.

Molecular dynamics (MD) methods are widely used computational tools for investigating the structural and dynamic properties of proteins at atomic-level spatial and femtosecond-level temporal resolutions. MD simulations model the spatiotemporal behavior of all atoms within a molecular system—including proteins, surrounding water molecules, ions, and ligands—by utilizing physics-based force fields. These simulations provide detailed, real-time molecular insights that are often challenging to obtain through experimental methods alone. In this study, all-atom MD simulations were conducted to examine five point mutations located in the C-lobe of the kinase domain (KD) of CHK2: D438Y, R474H, R318C, R318H, and T476M (Akcay et al., 2021; Baloch et al., 2014; Kleiblová et al., 2019; Momozawa et al., 2018; Xie et al., 2018). The primary aim of these simulations and hence our study was to investigate how these specific mutations affect the structural stability and dynamic behavior of the CHK2 kinase domain, thus enhancing our understanding of their potential roles in tumorigenesis and cancer progression.

Material and Method

To generate the active wild-type (WT) CHK2 structure, an initial structural model for MD simulations was created by integrating structural information obtained from the crystal structures with PDB identifiers 3I6U (Cai et al., 2009) and 2CN5 (Oliver et al., 2006). Specific residues (S379, T383, T387, and T389) within the activation loop of CHK2 were phosphorylated. Moreover, an ADP molecule, two Mg^{2+} ions, and crystallographic water molecules extracted from the 2CN5 structure were incorporated into the model. Structures carrying mutations (D438Y, R474H, R318C, R318H, and T476M) were generated using the Mutator plugin in VMD (Humphrey et al., 1996). All structures were solvated in a TIP3P water box with padding dimensions of 28 Å (x-axis), 20 Å (y-axis), and 28 Å (z-axis). Systems were neutralized, and ionic concentrations were set to 210 mM KCl and 20 mM NaCl. All systems were prepared by using VMD.

All simulations were carried out in NAMD 3.0 (Phillips et al., 2020), and CHARMM36 all-atom additive protein force field (Best et al., 2012). A 12 Å cutoff was applied for van der Waals interactions, and a 2 fs time step was used. Long-range electrostatic interactions were calculated using the particle-mesh Ewald (PME) method. The simulations were run under NPT conditions at 310 K and 1 atm. Temperature was maintained using Langevin dynamics with a damping coefficient of 1 ps^{-1}, and pressure was controlled via the Langevin Nosé-Hoover method with an oscillation period of 100 fs and a damping time scale of 50 fs.

To assess structural stability and flexibility differences between mutant and WT CHK2 proteins, Root Mean Square Deviation (RMSD) (Phillips et al., 2020) and Root Mean Square Fluctuation (RMSF) (Karplus & McCammon, 2002) analyses were performed. RMSD measures the average structural deviation of atoms from a reference structure over the simulation trajectory, quantifying overall conformational stability. RMSD is calculated using the formula:

$$RMSD(t) = \sqrt{\frac{1}{N}\sum_{i=1}^{N} \left(r_i(t) - r_i(0)\right)^2}$$

Equation 1: RMSD equation

where N represents the total number of atoms considered, $\mathbf{r}_i(t)$ denotes the position of atom i at time t, and $\mathbf{r}_i(\text{ref})$ is the position of atom i in the reference structure. Higher RMSD values indicate greater structural deviations from the initial conformation.

RMSF measures the local flexibility and dynamic behavior of individual atoms or residues over the course of the simulation. RMSF is defined as:

$$RMSF = \sqrt{\frac{1}{T}\sum_{t=1}^{T} \left\|r_i(t) - \langle r_i \rangle\right\|^2}$$

Equation 2: RMSF equation

where T represents the total number of trajectory frames analyzed, $\mathbf{r}_i(t)$ is the position of atom i at time t, and $\langle \mathbf{r}_i \rangle$ is the average position of atom i over the entire simulation period. Higher RMSF values reflect increased flexibility or movement, while lower values indicate structural rigidity.

Both RMSD and RMSF calculations enabled comparison of mutant and WT CHK2 proteins, providing valuable insights into how the studied mutations may influence the structure, stability, and dynamic properties of the CHK2 kinase domain. For the RMSD and RMSF analyses, only the coordinates of C_α atoms were considered. The reference structure is the initial build CHK2 protein structure that was build as a combination of crystal structures having PDB IDs 3I6U and 2CN5.

Findings

Two independent sets of MD simulations, each lasting 300 ns, were performed for every mutant. RMSD and RMSF analyses were conducted separately for each MD trajectory. From RMSD analyses (Figure 1), the D438Y, T476M, and R474H mutants showed higher RMSD values compared to the WT CHK2 protein, suggesting structural deviations compared to WT.

RMSD

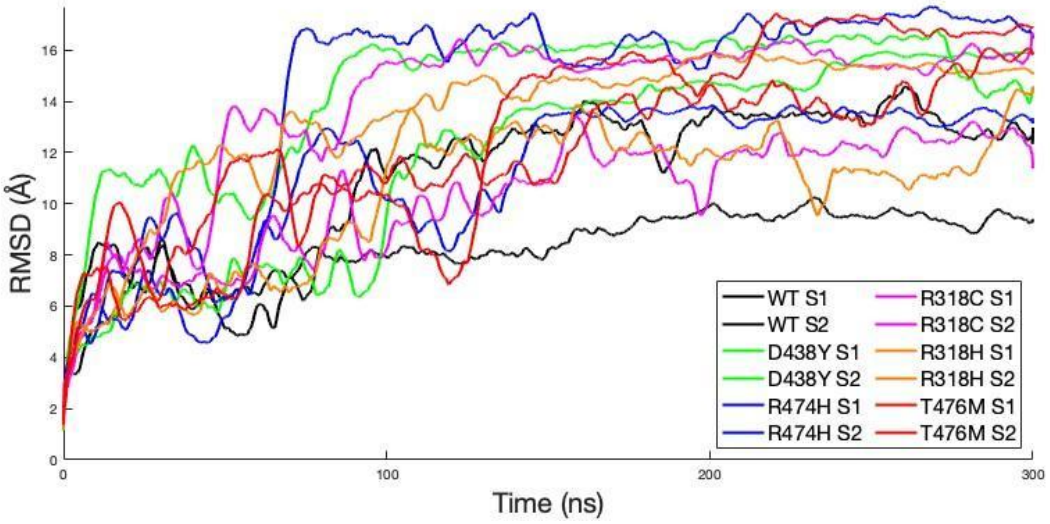

Figure 1. RMSD calculations of mutant and wild type proteins.

Figure 2 shows the RMSF analysis of WT and mutant CHK2 proteins. The R318H mutant exhibited reduced RMSF values between residues 96 and 160. Similarly, in the residue range 208–266, the R318H and T476M mutants demonstrated lower RMSF values compared to WT. Within the residue range 257–264, the R318C mutant showed increased RMSF, whereas the other mutants (R474H, D438Y, R318H, and T476M) exhibited decreased RMSF values. Additionally, in the residue range 371–391, all mutants displayed higher RMSF values relative to the WT. Overall, the R318H mutant displayed consistently lower RMSF values throughout the entire protein compared to the other mutants.

RMSF

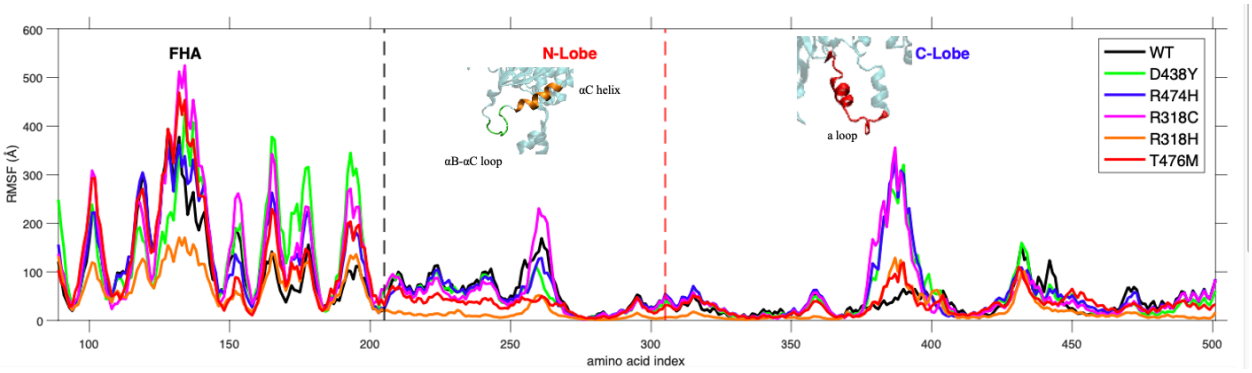

Figure 2. RMSF calculations of wylde type and mutant proteins.

Conclusion

This study utilized all-atom MD simulations to investigate the structural and dynamic consequences of five cancer-associated point mutations (D438Y, R474H, R318C, R318H, and T476M) located in the C-lobe of the CHK2 kinase domain. RMSD analyses indicated that the D438Y, T476M, and R474H mutations induced considerable structural deviations, which may impact protein stability and function. Furthermore, distinct alterations in protein dynamics were also observed through RMSF analysis. In particular, the R318H mutant displayed pronounced dynamic changes throughout nearly the entire protein structure. All five mutations altered RMSF profiles compared to WT CHK2, with notable changes concentrated in the residue ranges 257–264 and 371–391. Within the residue range 208–266, the R318H and T476M mutants exhibited greater dynamic alterations than the other studied mutants. Collectively, these simulations highlight how specific mutations in the CHK2 kinase domain's C-lobe can profoundly influence protein structure and dynamics. These findings provide molecular insights into potential mechanisms through which CHK2 variants may contribute to cancer progression, contributing to guiding future experimental validation and informing potential therapeutic strategies.

Acknowledgement. M.G. gratefully acknowledges support from TUBITAK Award No. 318S129.

References

Akcay, I. M., Celik, E., Agaoglu, N. B., Alkurt, G., Kizilboga Akgun, T., Yildiz, J., Enc, F., Kir, G., Canbek, S., Kilic, A., Zemheri, E., Ezberci, F., Ozcelik, M., Dinler Doganay, G., & Doganay, L. (2021). Germline pathogenic variant spectrum in 25 cancer susceptibility genes in Turkish breast and colorectal cancer patients and elderly controls. *International Journal of Cancer*, *148*(2), 285–295. https://doi.org/10.1002/IJC.33199

Almawi, A. W., Matthews, L. A., & Guarné, A. (2017). FHA domains: Phosphopeptide binding and beyond. *Progress in Biophysics and Molecular Biology*, *127*, 105–110. https://doi.org/10.1016/J.PBIOMOLBIO.2016.12.003

Baloch, A. H., Daud, S., Raheem, N., Luqman, M., Ahmad, A., Rehman, A., Shuja, J., Rasheed, S., Ali, A., Kakar, N., Naseeb, H. K., Mengal, M. A., Awan, M. A., Wasim, M., Baloch, D. M., & Ahmad, J. (2014). Missense mutations (p.H371Y, p.D438Y) in gene CHEK2 are associated with breast cancer risk in women of Balochistan origin. *Molecular Biology Reports*, *41*(2), 1103–1107. https://doi.org/10.1007/S11033-013-2956-X

Best, R. B., Zhu, X., Shim, J., Lopes, P. E. M., Mittal, J., Feig, M., & MacKerell, A. D. (2012). Optimization of the additive CHARMM all-atom protein force field targeting improved sampling of the backbone φ, ψ and side-chain χ(1) and χ(2) dihedral angles. *Journal of Chemical Theory and Computation*, *8*(9), 3257–3273. https://doi.org/10.1021/CT300400X

Buscemi, G., Carlessi, L., Zannini, L., Lisanti, S., Fontanella, E., Canevari, S., & Delia, D. (2006). DNA damage-induced cell cycle regulation and function of novel Chk2 phosphoresidues. *Molecular and Cellular Biology*, *26*(21), 7832–7845. https://doi.org/10.1128/MCB.00534-06

Cai, Z., Chehab, N. H., & Pavletich, N. P. (2009). Structure and Activation Mechanism of the CHK2 DNA Damage Checkpoint Kinase. *Molecular Cell*, *35*(6), 818–829. https://doi.org/10.1016/J.MOLCEL.2009.09.007

Humphrey, W., Dalke, A., & Schulten, K. (1996). VMD: Visual molecular dynamics. *Journal of Molecular Graphics*, *14*(1), 33–38. https://doi.org/10.1016/0263-7855(96)00018-5

Karplus, M., & McCammon, J. A. (2002). Molecular dynamics simulations of biomolecules. *Nature Structural Biology 2002 9:9*, *9*(9), 646–652. https://doi.org/10.1038/nsb0902-646

Kleiblová, P., Stolařová, L., Křížová, K., Lhota, F., Hojný, J., Zemánková, P., Havránek, O., Vočka, M., Černá, M., Lhotová, K., Borecká, M., Janatová, M., Soukupová, J., Ševčík, J., Zimovjanová, M., Kotlas, J., Panczak, A., **Veselá, K., Červenková, J., … Kleibl, Z.** (2019). Germline CHEK2 Gene Mutations in Hereditary Breast Cancer Predisposition - Mutation Types and their Biological and Clinical Relevance. *Klinicka Onkologie : Casopis Ceske a Slovenske Onkologicke Spolecnosti*, *32*(Supplementum2), 2S36-2S50. https://doi.org/10.14735/AMKO2019S36

Momozawa, Y., Iwasaki, Y., Parsons, M. T., Kamatani, Y., Takahashi, A., Tamura, C., Katagiri, T., Yoshida, T., Nakamura, S., Sugano, K., Miki, Y., Hirata, M., Matsuda, K., Spurdle, A. B., & Kubo, M. (2018). Germline pathogenic variants of 11 breast cancer genes in 7,051 Japanese patients and 11,241 controls. *Nature Communications*, *9*(1). https://doi.org/10.1038/S41467-018-06581-8

Oliver, A. W., Paul, A., Boxall, K. J., Barrie, S. E., Aherne, G. W., Garrett, M. D., Mittnacht, S., & Pearl, L. H. (2006). Trans-activation of the DNA-damage signalling protein kinase Chk2 by T-loop exchange. *The EMBO Journal*, *25*(13), 3179–3190. https://doi.org/10.1038/SJ.EMBOJ.7601209

Phillips, J. C., Hardy, D. J., Maia, J. D. C., Stone, J. E., Ribeiro, J. V., Bernardi, R. C., Buch, R., Fiorin, G., Hénin, J., Jiang, W., McGreevy, R., Melo, M. C. R., Radak, B. K., Skeel, R. D., Singharoy, A., Wang, Y., Roux, B., Aksimentiev, A., Luthey-Schulten, Z., … Tajkhorshid, E. (2020). Scalable molecular dynamics on CPU and GPU architectures with NAMD. *The Journal of Chemical Physics*, *153*(4), 044130. https://doi.org/10.1063/5.0014475

Xie, Y., Li, G., Chen, M., Guo, X., Tang, L., Luo, X., Wang, S., Yi, W., Dai, L., & Wang, J. (2018). Mutation screening of 10 cancer susceptibility genes in unselected breast cancer patients. *Clinical Genetics*, *93*(1), 41–51. https://doi.org/10.1111/CGE.13063

COMPUTATIONAL SCIENCE AND ENGINEERING

Computational Biology

Computational Fluid Dynamics

Multi-Objective Optimization of Airfoil Geometry for Aerodynamic Efficiency and Noise Reduction Using Bézier Parameterization

Ali İhsan İşgüder[a], Assoc. Prof. Baha Zafer[b], Prof. Dr. Melike Nikbay[b]

[a]Istanbul Technical University, Computational Science and Engineering, Türkiye
[b] Istanbul Technical University, Aeronautical and Astronautical Engineering, Türkiye
isgudera@itu.edu.tr

Keywords: Aeroacoustic, Aerodynamic, Computational Fluid Dynamics, Multi-Objective Optimisation.

Aim

In many turbomachinery applications, such as wind turbines, military and industrial aerospace applications, computer fans, and even cooling fans in electric vehicles (Qin et al., 2020), which cause the highest noise generation, both high aerodynamic performance and low noise level, thus high aeroacoustic performance have become important. Many aerodynamic optimisation studies have been conducted to achieve high C_l (lift coefficient) and high C_l/C_d (aerodynamic efficiency) values (Hicks et al., 1974; Obayashi & Takanashi, 1996). In addition to aerodynamic performance, there have also been studies to improve aeroacoustic performance by predicting flow separation (hence laminar separation bubbles, LSB) or trailing edge induced noise. However, this study was undertaken because it was observed that studies that address both aerodynamic and aeroacoustic concerns have rarely been carried out.

However, with the inherent contradiction between both aerodynamic and aeroacoustic objectives, optimisation studies create a multidimensional design problem. Increasing the lift force results in increased surface flow velocities. However, flow separation in the boundary layer induces turbulence, resulting in stronger noise generation in the far field, whereas noise improvements can be achieved by sacrificing aerodynamic concerns. Although multi-objective optimisation studies have been studied until recently (Lyu & Xie, 2016), the integration of aerodynamic and aeroacoustic optimisations, especially using flexible geometry parameterisations, is still limited.

As mentioned in the review article by Salunke et al (2014), there are many airfoil parameterisations in the literature such as NACA and PARSEC. In this study, Bezier curves are used and the geometry is left free by using only control points. This study aims to make 4 main contributions. The first is to provide airfoil shape manipulation with Bezier curves. The second is the integration of aerodynamic and aeroacoustic outputs. The third is the use of genetic algorithms for multi-objective optimisation in aerodynamic and aeroacoustic optimisation. Fourth and lastly, pareto-optimal solutions between the obtained results and C_l, C_l/C_d and SPL values are found.

Material and Method

In this study, two different independent Bezier curves were used for the suction and pressure surfaces of the airfoil geometry (Figure 1). In both curves, the points PLE and PTE, which define the traling edge and leading edge, are kept constant. On the other hand, as a preliminary assumption, the position of the intermediate points on the chord axis was kept fixed, while their vertical position was left free within the optimisation limits.

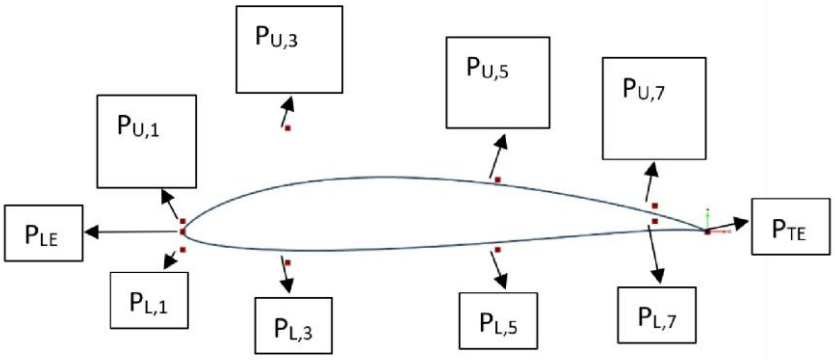

Figure 1. Bezier control points on airfoil, as upper and lower.

In contrast to definitions such as NACA 4-Digit, airfoils defined by Bezier curves can be parameterised more flexibly. In addition, although alternative parametrisation methods are presented in the paper compiled by Salunke et al. (2014), Bezier points are directly included in the optimisation to directly observe the effects of each control point on the optimisation outputs.

In the first stage, Sobol sequences were used to extract the design space. Sobol sequences were first introduced by Ilya Sobol in 1976, and the use of Sobol sequences in the computational environment of high-order applications and optimisation methods was introduced by Bratley and Fox (1988). They showed that by creating low-dispersion and homogeneously distributed solution points with Sobol sequences, the solution space can be created in a large and balanced way without increasing the sampling density. NSGA-II, used in the second and third stages of this study, is a genetic algorithm commonly used in multi-objective optimisation applications (Coello Coello et al., 2007). In addition to preserving optimisation and diversity, it allows to create a new Pareto front in each generation thanks to the mutation parameter while transferring good designs between generations thanks to the 'crowding distance' mechanism (Deb et al., 2002). In the third stage, the final optimisation process was completed by defining constraints on C_l, C_l / Cd and SPL values. With this structure, the solution quality focused on increasingly narrower regions in the design space was improved and the interaction between global exploration and locale improvements was analysed. Unlike single-objective optimisation, multi-objective optimisation searches for a Pareto optimal set of parameters. Genetic algorithms such as NSGA-II are convenient tools for multi-objective optimisation problems such as aerodynamics and aeroacoustics, as they can provide a population of solutions, as opposed to the single solution point search of traditional optimisation algorithms (Obayashi et al., 1997).

Aerodynamic analyses were carried out with XFOIL, an open source panel method commonly used for performance measurement of low and medium Reynolds number wing airfoils. (Drela, 1989). Acoustic analyses were performed using NAFNoise (NREL AirFoil Noise), an open source software that is adept at acoustic measurements by analysing boundary layer and far field properties. Since NAFNoise is a code written with data obtained from experimental studies, it is particularly successful in analysing turbulent boundary layer trailing-edge noise and separated flow noise. In this study, the acoustic signal was measured from a single point and the microphone was placed at theta = 90° and r = 8 chords away on the trailing edge of the airfoil.

Finally, all this work was carried out on a commercial optimisation tool called CAESES. CAESES contains three main parts: Parametric design, software connection and optimisation. It was used in this study as it automates the updating of geometry variables, running the software, setting up the optimisation loop to minimise manual effort while trying to achieve the main objectives of the study.

Findings

At the end of the three-stage optimisation process, significant results on the behavioural effects between the aerodynamic and aeroacoustic outputs were obtained. Design space sampling using the Sobol array yielded 300 airfoil designs, with a wide range of geometric characteristics, angle of attack and performance metrics. C_l values ranged between 0.4 and 1.6,

while the C_l/C_d ratio was between 40 and 150. SPL values were mostly above 130 dB, but a wide range of results was obtained. On the other hand, when the interaction between the control points defining the airfoil and the performances is analysed, the performance metrics showed higher sensitivity to the points on the suction side (airfoil hump, thickness and thus flow separation), although the correlations of the points controlling the pressure side of the airfoil were low. In particular, increasing U_{y3} led to positive effects on both C_l and C_l/C_d output , while increasing U_{y5} and U_{y7} led to a negative effect on SPL output (Figure 2). However, it was observed that the performances were sensitive to these parameters, whether positive or negative.

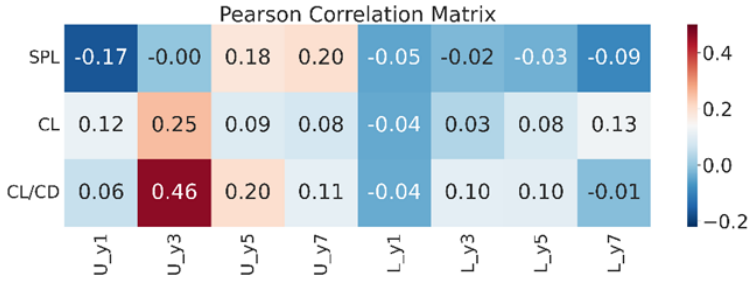

Figure 2. Pearson correlation matrix of SPL, C_l and C_l/C_d targets with upper and lower surface geometric control points (U_{y1} – L_{y7}). Positive correlations are shown in red, negative correlations in blue. Each cell contains the correlation coefficient between the corresponding control point and the target metric.

The second phase of the study analysed the effects between the performance metrics and the pareto surfaces of 1200 design points obtained with NSGA-II without constraints. While analysing the correlations of the performance metrics in this scan, significant clustering was observed. At different ranges of the angle of attack (AoA), the behaviour of the SPL varied in response to both the angle of attack and metrics such as C_l and C_l/C_d.

The SPL values, which have a non-monotonic behaviour (Figure 3), show high values (>60 dB) at relatively low AoA (0° – 6°), while at relatively high AoA (9° – 12°) they show a downward trend at intermediate levels (<60 dB). This can be explained by the appearance of the Laminar Separation Bubble (LSB) effect as the angle of attack increases. The unstable structure caused by LSB in the wake region can cause stronger noise at low angles of attack. As the angle of attack increases, the turbulent flow in the wake can transform this tonal noise into a more balanced noise with broadband character. This behaviour demonstrates the consistency of SPL values that a separation-oriented acoustic solver such as NAFNoise can analyse.

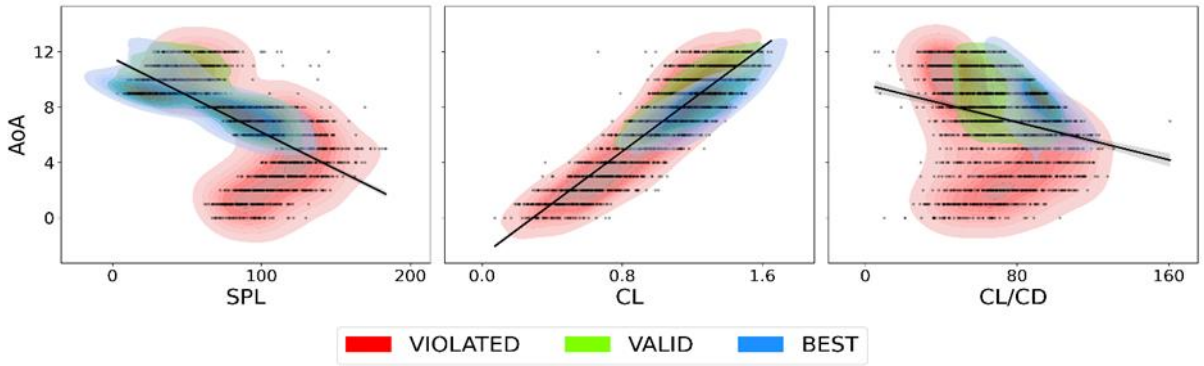

Figure 3. Scatter plots showing the relationships between angle of attack (AoA) and SPL, C_l, and C_l / C_d targets. Dots are shown in black, with KDE (density) clusters for each class colored: red (VIOLATED), green (VALID), blue (BEST). Black lines represent regressio.

In the third stage, some constraints were applied. C_l value min 1.0, C_l/C_d value min 80 and SPL value max 120 dB were started to search for more feasible results. The 120 dB limit for SPL is recommended as an acceptable upper limit for the design of small-scale UAVs. Thanks to the NSGA-II algorithm, non-constraint inputs are penalised and constrained inputs are passed on to the next generation. The designs marked in red are the penalised ones, the green ones are the ones close to the constrain values, and the ones marked in blue are the best design points (Figure 4).

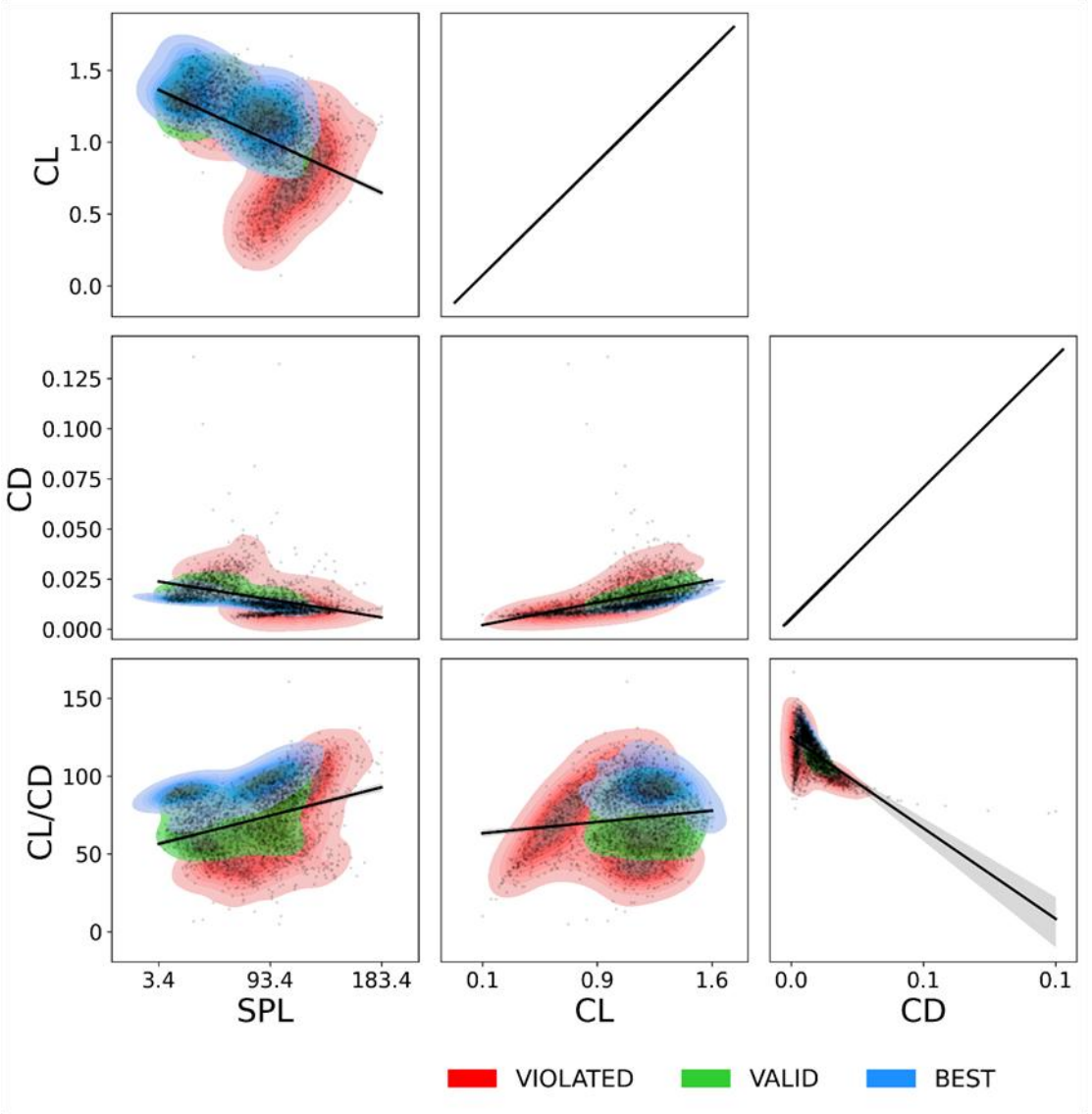

Figure 4. Scatter and intensity plots showing the pairwise relationships between SPL, C_l, C_d, and C_l/C_d targets.

Conclusion

In this study, both aerodynamic (C_l, C_d, and C_l/C_d) and aeroacoustic (SPL) performances of airfoils defined by Bezier curves are examined together in the optimisation process and both geometric and fluid parameters (only angle of attack in this study) are presented as input to the optimisation. The results obtained in this study show that only aerodynamic concerns are not sufficient in airfoil designs where acoustic concerns are pursued, and aeroacoustic objectives should also be taken into consideration.

In particular, the fact that the SPL follows different phenomena at different ranges of the angle of attack is a point to be considered in turbomachinery design. It was also observed that the geometrical design of the suction side, in particular, dominates the results. The nature of the fluid and the airfoils can lead to unexpected positive results.
This study also shows that parameterised and automated processes, such as genetic algorithms or local minimum/maximum searches, can lead the researcher to innovative and unexpected points in order to obtain the design space.
For future studies, additional research could be carried out in several different directions. SPL measurements of pre-designed airfoils obtained from aeroacoustic analyses can be made with higher accuracy with LES or RANS (RANS may be sufficient in this study since measurements are made at farfield) turbulence models in a FVM-based CFD solver. Finally, in geometry parameterisation, control points can be increased; instead of Bezier curves, alternative methods such as NURSB or Free Form Deformation (FFD) can be tried.

References

Bratley, P., & Fox, B. L. (1988). Algorithm 659. ACM Transactions on Mathematical Software, 14(1), 88–100. https://doi.org/10.1145/42288.214372
Chen, S., Lyu, Z., Kenway, G. K. W., & Martins, J. R. R. A. (2015). Aerodynamic shape optimization of common research model Wing–Body–Tail configuration. Journal of Aircraft, 53(1), 276–293. https://doi.org/10.2514/1.c033328
Coello Coello, C. A., Lamont, G. B., & Van Veldhuizen, D. A. (2007). Evolutionary Algorithms for Solving Multi-Objective Problems. In Springer eBooks. https://doi.org/10.1007/978-0-387-36797-2
Deb, K., Pratap, A., Agarwal, S., & Meyarivan, T. (2002). A fast and elitist multiobjective genetic algorithm: NSGA-II. IEEE Transactions on Evolutionary Computation, 6(2), 182–197. https://doi.org/10.1109/4235.996017
Drela, M. (1989). XFOIL: an analysis and design system for Low Reynolds number airfoils. In Lecture notes in engineering (pp. 1–12). https://doi.org/10.1007/978-3-642-84010-4_1
Hicks, R. M., Murman, E. M., & Vanderplaats, G. N. (1974, July 1). An assessment of airfoil design by numerical optimization. NASA Technical Reports Server (NTRS). https://ntrs.nasa.gov/citations/19740020369
Obayashi, S., & Takanashi, S. (1996). Genetic optimization of target pressure distributions for inverse design methods. AIAA Journal, 34(5), 881–886. https://doi.org/10.2514/3.13163
Obayashi, S., Yamaguchi, Y., & Nakamura, T. (1997). Multiobjective Genetic Algorithm for Multidisciplinary Design of Transonic Wing Planform. Journal of Aircraft, 34(5), 690–693. https://doi.org/10.2514/2.2231
Qin, Y., Tang, X., Jia, T., Duan, Z., Zhang, J., Li, Y., & Zheng, L. (2020). Noise and vibration suppression in hybrid electric vehicles: State of the art and challenges. Renewable and Sustainable Energy Reviews, 124, 109782. https://doi.org/10.1016/j.rser.2020.109782
Salunke, N. P., A, J. a. R., & Channiwala, S. (2014). Airfoil Parameterization Techniques: a review. American Journal of Mechanical Engineering, 2(4), 99–102. https://doi.org/10.12691/ajme-2-4-1.

COMPUTER ENGINEERING

Artificial Intelligence

Computer Networks

Cyber Security

Embedded Systems

Internet of Things

Neural Networks

Software Engineering

An Intelligent Jamming Environment: Reinforcement Learning Approach

Ömer Faruk Dikmen[a], Hasari Çelebi[a]

[a] Gebze Technical University, Computer Engineering, Türkiye
o.dikmen2023@gtu.edu.tr

Keywords: Adaptive Jamming, Dynamic Spectrum Access, Intelligent Jammer, Reinforcement Learning.

Aim

In wireless communication systems, which are indispensable in today's life, information is subject to deliberate various types of intentional or unintentional jamming as it is carried on electromagnetic waves along communication channels. Deliberate jamming attemps to reduce signal-to-interference plus noise (SINR) ratio as much as possible so that the information is partially or completely prevented from reaching the receiver [3]. On the other hand, the transmitter side aims to transmit information to the receiver in the safest and fastest way possible. This situation, known as electromagnetic spectrum (EMS) confrontation, makes the signal distortion problem in wireless communications an important area of research and study. Traditional strategies such as fixed frequency, comb type, barrage, and sweeping [1] are insufficient in a dynamic EMS environment, particularly when considering today's 5G and near future 6G communication technologies. Smarter systems are required. The literature predominantly features investigations on anti-jamming techniques [2]. Because wireless communication systems in highly dynamic environment only access the EMS at short intervals, a jammer can capture only a minimal amount of data. The question then becomes: Is it possible to have a real-time model that learns continually by interacting with the environment, without the requirement for labeled data, and so adapts to variations?
In this work, we seek a response to the aforementioned question and focus on the most appropriate strategy for intelligent jammer tuning. For this objective, the Q-Learning methodology, one of the RL methods, is tested in four EMS simulation scenarios and simultaneously contrasted with four conventional jamming techniques.

Material and Method

The simulation environment is presented in Figure 1. Here, the agent is an intelligent model that is always learning and making decisions. To facilitate calculation and analysis, the communication time is separated into equal discrete time periods Each time slot has N channel sets C = {0,1,2,....,N}, with each element being a frequency channel index that the CU and jammer can select. To avoid the jammer, the CU employs a frequency-hopping approach. In each time slot, the transmitter sends data over the next communication channel in a predetermined sequence (Figure 2).

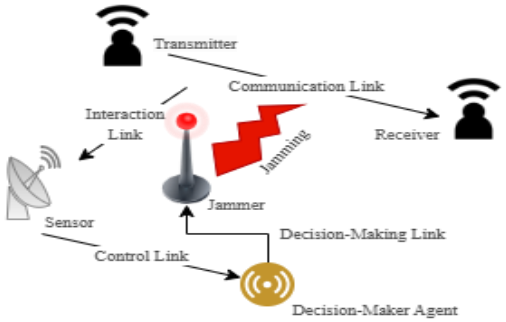

Figure 1. System Model.

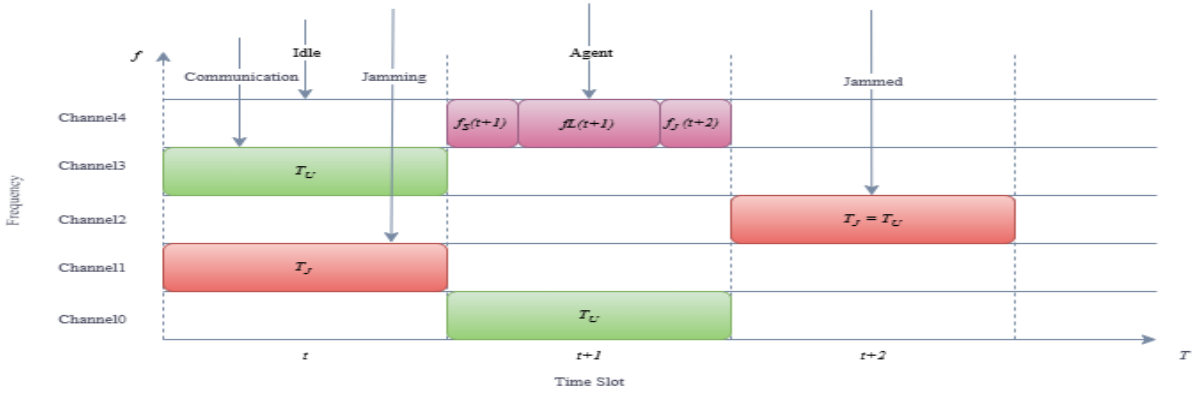

Figure 2. Spectrum model.

Five jamming mechanisms were used in the simulations: comb, sweeping, dynamic, pseudo-random, and RL. Comb jammers provide jamming signals to many communication bands at the same time. Sweeping jammers scan a specific range of communication bands at a set speed; dynamic jammers use both comb and sweeping techniques; pseudo-random jammers determine a target based on randomly generated values in a specific sequence; and RL-driven jammers learn by continuously interacting with the environment in real time without prior knowledge. The simulation assumes that both the transmitter and the jammer send signals across the same communication channel. If the signal emitted by the jammer to the frequency range chosen by the decision-maker agent's communication channel set overlaps with the communication channel of the CU, the SINR ratio is calculated. Since the scenario assumes one jammer and constant noise for each channel, the SINR formula can be simplified as shown in Equation 1. The SINR ratio is compared to a predetermined threshold value to create the indicator function. g_u is the transmitter's channel gain ratio, and p_u is its power value. On the divisor side, n represents channel noise, g_j represents the jammer's channel gain ratio, and p_j represents the jammer's power level.

$$SINR = \frac{g_u p_u}{n + g_J p_J} \tag{1}$$

If the indicator function value exceeds or equals the SINR threshold value, it is set to one; otherwise, it is set to zero (Equation 2). Here, β is the threshold value and $I(t)$ is the indicator function at time t. If the value of $I(t)$ is one, the transmission is successful, otherwise it is unsuccessful.

$$I(t) = \{1, SINR \geq \beta \; 0, SINR < \beta \tag{2}$$

The main goal of jammer is to minimise the value of the target function Λ in total (Equation 3). $\gamma \in (0,1)$ is the discount factor used to reduce the added value of future indicator values.

$$min\ \Lambda\ =\ \sum_{t=0}^{\infty}\quad \gamma^t I(t) \tag{3}$$

The suggested model is designed to learn the CU's frequency hopping technique by constant interaction with the environment, with no prior knowledge. As illustrated in Figure 2, the green signal represented by T_U is transmitted by the CU, while the orange signal represented by T_J is sent by the jammer. The figure clearly shows that T_J equals T_U. The purple colour represents the jammer's agent phase as a training phase, which consists of the sensor's spectrum sensing f_s, the agent's CU communication channel prediction in the previous time slot t compared to the actual communication channel detected, rewarding and punishing the agent, updating the Q-value at time t, and predicting the communication channel on which the jamming signal will be sent in the next time slot. Learning is denoted by f_L, and prediction by f_J.. This method is repeated until the Q-values for each communication channel are finalised. The Q-values for each communication channel are kept in a Q-table. The Q_values are updated using the formula in Equation 4.

The convergence of the Q-values indicates that the jammer has learnt the CU's communication strategy and has exited the learning process. It then determines whether it needs to synchronise its time slot with the CU's time slot.

The symbol A_{t+1} in Equation 4 represents all action options in the state at time $t+1$, which in our case is the CU's communication channel, and this is where Equation 4 takes its maximum. The sensor continuously analyses the surroundings to ensure that the channel of the mixing signal matches the current channel. If a mismatch is discovered in two consecutive time slots, the jammer switches to learning mode and begins learning the new model.

$$Q(s_t,a_t) \leftarrow Q(s_t,a_t)+\alpha[r+\gamma maxQ(s_{t+1},A_{t+1})-Q(s_t,a_t)] \tag{4}$$

Findings

In the experiments, the full frequency bandwidth for both CU and jammer is assumed to be 40MHz and the signal transmission bandwidth is assumed to be 4MHz. Thus, there are ten communication channels $C = \{0,1,2,3,4,5,6,7,8,9\}$ corresponding to a frequency bandwidth (Table 1).

Table 1. Bandwidth frequencies and frequency hopping sequence.

Channel Index	0	1	2	3	4	5	6	7	8	9
Cntre Frequency (MHz.)	2	6	10	14	18	22	26	30	34	38
Current Frequency (MHz)	2	6	10	14	18	22	26	30	34	38
Next Hop (MHz.)	18	10	2	34	38	26	22	14	30	6

Communication link parameters are set to p_u = 30dBm, p_j = 30dBm, n = -100dBm and β = 10dBm. If more than one communication channel is jammed in the same time period, as in the case of Comb-type jamming, the value of p_j is automatically reduced for each channel. The values of g_u and g_j are randomised in the range (0.1, 1.0) for each experiment run.

The comb jammer is intended to jam 6MHz, 14MHz, 22MHz, and 30MHz concurrently. Sweeping jammer speed was set to 0.8 GHz/s. Every 100 milliseconds, the dynamic jammer switches from comb jamming to sweeping jamming. The random jammer jams at random in each time period. The RL-driven jammer, on the other hand, lacks a pre-plan and instead learns the CU pattern through interaction with the environment before developing an adaptive jamming approach. The settings are as follows: ε = 1.0 for epsilon initial value, ε_{decay} = 0.90 for epsilon decay, ε_{min} = 0.01 for minimum epsilon, α = 0.1 for learning rate, and γ = 0.9. The waterfall spectrograms of conventional jammers are shown in Figure 4a.

Experiment 1: The CU frequency hopping sequence was initiated at 18 MHz (Table 2). After 24 iterations, Q values converged, and the RL-driven jammer model learnt the entire sequence (Figure 3). The waterfall spectrogram in Figure 4c shows how the RL focussed jammer behaves. Every 30 iterations, the success rate of each jammer is monitored to determine its performance. The RL jammer's first 30-slice moving average success rate is little less than 0.6 and quickly approaches

1.0. Conventional jammers remain at 0.2 or below (Figure 5a-5b). The RL jammer resulted in 983 successful jammings, compared to 200 or less for the other traditional approaches (Table 2).

Experiment 2: We employed the same frequency hopping mapping as in the prior experiment, but varied the hopping sequence's initial frequency every 20 iterations. The goal here was to see if the RL agent could learn the pattern completely correctly. The results demonstrated that the model could continue jamming without any issues. The jammer success rate also tended to approach 1.0 (Figure 5c). Figure 4b clearly depicts the model's change in behaviour. The prior experiment's success was 0.95, which became 0.98, and the objective function remained at the expected level of 7.50 (Table 2). Figure 5d shows a 1/10 scaled target function plot.

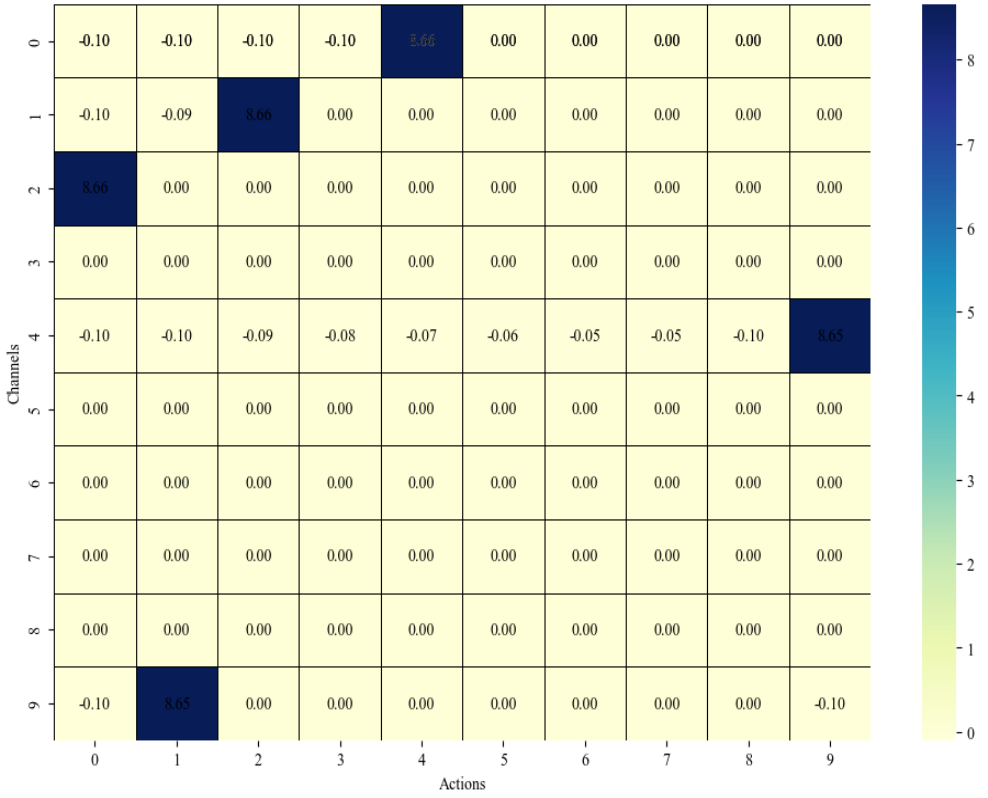

Figure 3. Spectrum Model.

Table 2. Performance table of jammers for experiment 1-2-3.

Experiment 1	Number of Success jams	Succes Rate of Jammer	Target Function
RL Driven Jammer	983	0.98	6.55
Random Jammer	113	0.11	9.52
Comb Jammer	200	0.20	9.99
Sweep Jammer	100	0.099	9.47
Dynamic Jammer	200	0.20	9.53
Experiment 2			
RL Driven Jammer	951	0.95	7.50
Random Jammer	101	0.10	8.21
Comb Jammer	600	0.60	9.99
Sweep Jammer	50	0.05	9.56
Dynamic Jammer	599	0.59	9.60
Experiment 3			
RL Driven Jammer	511	0.51	7.75
Random Jammer	84	0.08	9.75
Comb Jammer	376	0.38	9.99
Sweep Jammer	72	0.07	9.99
Dynamic Jammer	375	0.38	9.99

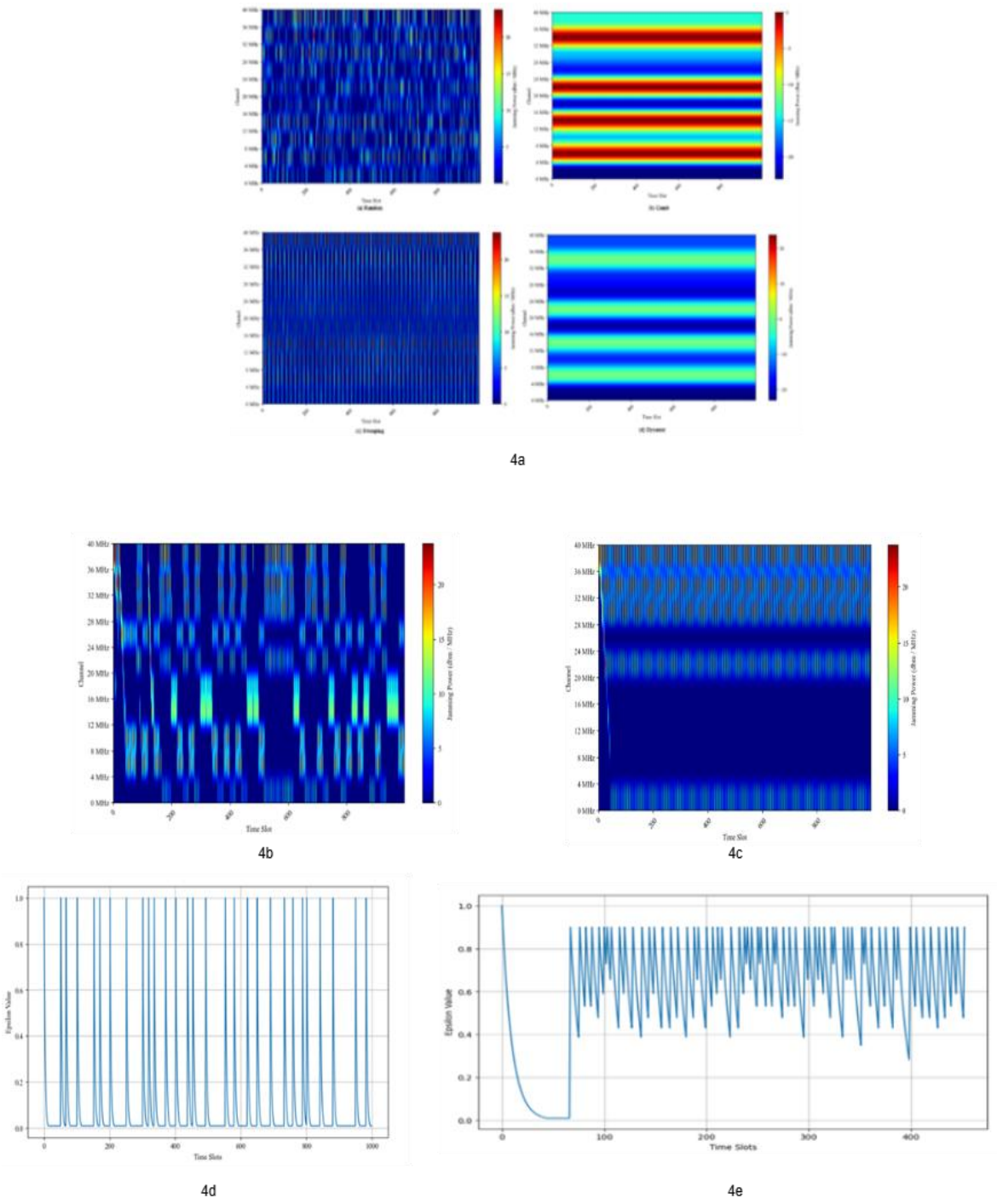

Figure 4. Waterfall spectrograms of jamming techniques and epsilon behaviours.

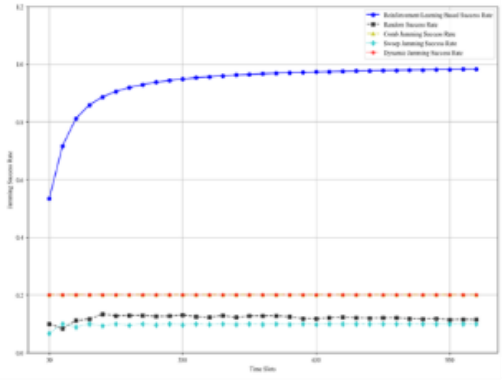

5a

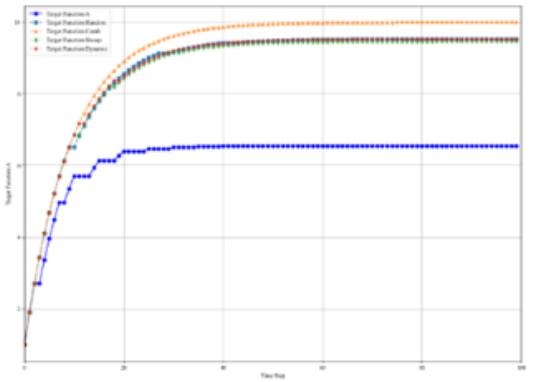

5b

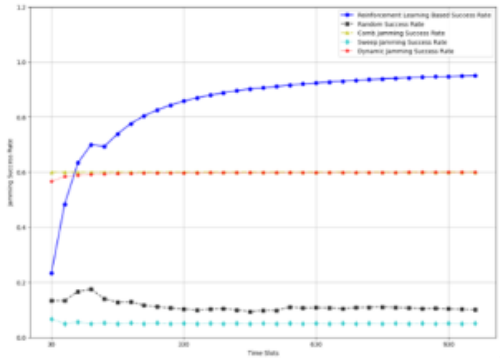

5c

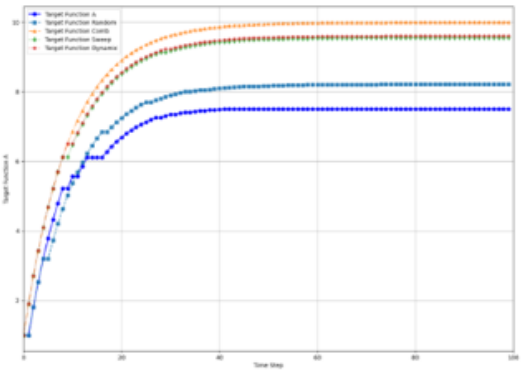

5d

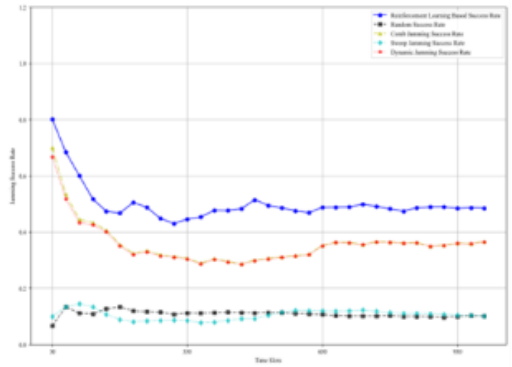

5e

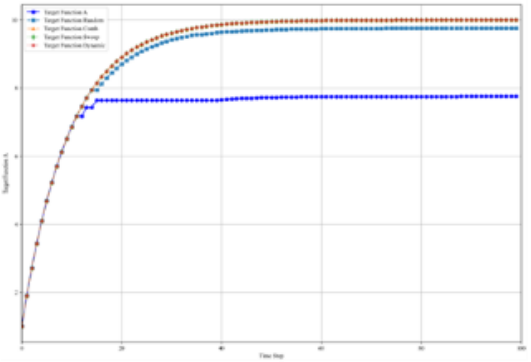

5f

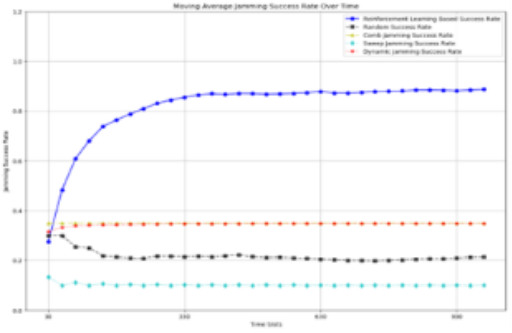

5g

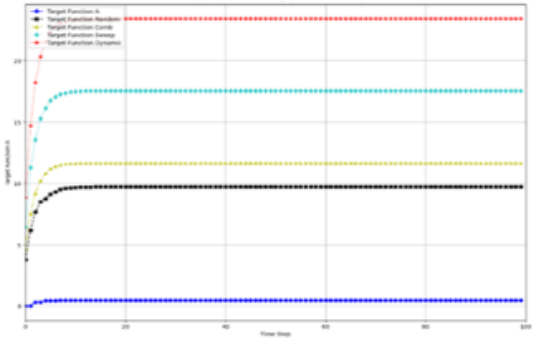

5h

Figure 5. Performance comparison of jamming techniques.

Experiment 3: In this experiment, to imitate a continually changing environment, the frequency hopping mappings were modified every 40 iterations. Thus, it was determined how adaptable the RL jammer was, and it was also compared to other approaches. The RL jammer agent's ε_{decay} was adjusted to 0.7, limiting exploration and enhancing model adaption. The agent's ε is set to 1.0 after two consecutive incorrect predictions (Figure 4d).

When the experiment's findings are evaluated, it is clear that, while the number of correct predictions and success rate has decreased significantly, it is still far more successful than other conventional methods. It was discovered that it created a 12% difference compared to the second successful one (Table 2). The values for comb, sweep, and dynamic jammer overlap on the target function graph in Figure 5f.

Experiment 4: In this experiment, two pairs of CUs are supposed to be operating in the spectrum, implying that the transmitters occupy two different frequency bands at the same time. Tables 3 describe the frequency hopping approach of two CUs. While traditional jammers follow the same technique as in prior studies, the RL jammer agent must estimate two distinct frequency bands at the same time. In this case, there are 100 action sets and a 100x100 matrix for the Q-table. Of course, the RL jammer is unaware of the scenario. First, the agent must identify which channels are currently active. It can accomplish this by arranging two Q-tables in a hierarchical structure.

Table 3. Frequency hopping sequences for communication user 1-2.

Current Frequency (MHz)	2	6	10	14	18	22	26	30	34	38
Next Hop (MHz.)	6	34	22	10	38	30	18	14	2	26
Current Frequency (MHz)	2	6	10	14	18	22	26	30	34	38
Next Hop (MHz.)	34	2	18	6	38	22	30	10	26	14

The number of simultaneously occupied channels will be estimated first, followed by a determination of which channels are occupied. For the sake of simplicity, it will be assumed that the number of channels employed is first determined and remains constant throughout the communication process, which in this experiment consists of two channels operating simultaneously. Because the action set is 100, the agent first initiates the learning process and begins jamming when it has learnt 40% of the pattern. Two incorrect predictions in a row means starting the learning process all over again.

The learning process raises ε to 0.90 (Figure 4e). The first transmitter's initial frequency is 34 MHz, while the second is 26 MHz (Table 3). After 1000 cycles, RL Jammer completed 858 successful jams, comb jammer 350, dynamic jammer 349, random jammer 214, and sweeping jammer 100 (Table 4). As shown in Figure 5g, the RL jammer outperformed other conventional approaches, with an 86% success rate. Because it did not jam during the learning period, the objective function value was near to zero, at 0.47 (Figure 5h).

Table 4. Performance table of jammers For experiment 4.

Performance Table of Jammers	Number of Success jams	Succes Rate of Jammer	Target Function
RL Driven Jammer	858	0.86	0.47
Random Jammer	214	0.21	9.71
Comb Jammer	350	0.35	11.72
Sweep Jammer	100	0.10	17.56
Dynamic Jammer	349	0.35	23.45

Conclusion

In the experiments, as many different environments as possible were created, and it was investigated whether the reinforcement learning model, particularly the Q-learning model, can provide a good solution for the design of an intelligent jammer that can quickly adapt to variability and work in real time without prior knowledge in varying environments. Four tests demonstrated that reinforcement learning offers significant potential as a solution to this problem. This study also provides a good platform for future research into developing intelligent anti-jamming devices to combat intelligent jammers.The conclusion section should be written in Times New Roman font, justified-alignment and in 10-point size.

References

Jaitly, S., Malhotra, H., & Bhushan, B. (2017, July 1–2). Security vulnerabilities and countermeasures against jamming attacks in wireless sensor networks: A survey. In *Proceedings of the International Conference on Computer, Communications and Electronics* (pp. 559–564). Jaipur, India.

Wang, X., Wang, J., Xu, Y., et al. (2020). Dynamic spectrum anti-jamming communications: Challenges and opportunities. *IEEE Communications Magazine, 58*(2), 79–85.

Zhou, Q., & Niu, Y. (2024). From adaptive communication anti-jamming to intelligent communication anti-jamming: 50 years of evolution. *Advanced Intelligent Systems, 6*(2024), 2300853.

The Role of Artificial Intelligence in Enhancing Software Quality: A Multivocal Literature Review

Melis Toksoy[a], Murat Yılmaz[b]

[a] Gazi University, Informatics Institute, Department of Information Systems, Türkiye
[b] Gazi University, Faculty of Engineering, Department of Computer Engineering, Türkiye
melis.toksoy@gazi.edu.tr

Keywords: Artificial Intelligence, Software Engineering, Software Quality.

Aim

With the rapid advancement of technology, software has become a critical component of modern technological products and the fundamental building block of technological systems (Thota, Shajin, & Rajesh, 2020). As software plays such a significant role, the necessity for it to be error-free and of high quality has increased. Low-quality software not only negatively affects system performance but also creates various risks such as security vulnerabilities and data loss. Especially in safety-critical domains such as healthcare, aviation, and automotive, software errors can severely disrupt system operations and lead to large-scale operational losses. Software engineering is a dynamic discipline that encompasses methods, tools, and techniques for the design, development, testing, and management of software products (Yu, 2018). Software engineers aim to not only develop software that works properly, but also to design reliable, scalable, and user-friendly systems. As software development processes become increasingly complex, changing requirements and increasing quality standards make traditional methods inadequate (Syed Adnan Afaq, 2023). This situation causes companies to turn to new technologies to make their software development processes more efficient in an increasingly competitive environment. At this point, artificial intelligence comes into play as a powerful solution partner for software engineers. Artificial intelligence (AI), which was founded with Turing's idea of "thinking machines" and gained a scientific identity with McCarthy's term "artificial intelligence", was initially based on a theoretical framework, but today it is creating significant change in different industries with its concrete applications (Turing, 2007; McCarthy, 1959). In the software development life cycle, various AI-based algorithms are effectively used at different stages. For example, machine learning algorithms are widely preferred to predict software errors and anticipate user needs (Yüksel & Çetin, 2020). Natural language processing technology is an artificial intelligence discipline that aims to transform human language into a form that computers can understand, process, and produce (Geetha, Gomathy, Yagn, & Praneesh, 2023). This technique extracts and interacts with text or audio data by analyzing grammar rules, word meanings, and context relationships. Deep learning and artificial neural networks are used to detect software errors at early stages and accelerate software optimization by processing more complex data sets (Shrestha, Krishna, & Von Krogh, 2020). These AI-based algorithms significantly enhance software quality by making the development process faster and more efficient. AI-powered tools enhance the efficiency of software development processes by making significant contributions in areas such as error detection, test automation, and predictive analysis. While traditional software engineering focuses more on functionality and performance, AI expands this focus, enabling software systems to become more intelligent and adaptable. Thus, software developers have the opportunity to design more flexible, dynamic, and continuously improving systems. Some of the AI-powered tools widely used in software development processes today are: SonarLint is a tool that detects security vulnerabilities and quality issues at an early stage by performing static analysis of the code. In this way, developers can make their software more reliable and maintainable by developing it in accordance with quality standards Yeboah & Popoola, 2023). GitHub Copilot is an AI-powered code assistant powered by OpenAI's Codex model and accelerates the software development process by offering features such as automatic code completion, function suggestions, and direct code generation (Baralla, Ibba, & Tonelli, 2024).These tools not only save software developers time, but also facilitate long-term maintenance of software projects by improving the readability, maintainability, and quality of the code. This study aims to comprehensively address

the contributions of artificial intelligence to software development processes and software quality. Although research on the integration of artificial intelligence into software development and quality assessment processes is increasing, a comprehensive study that addresses the effects of this technology on software processes and quality with a holistic approach has not yet been included. The current gap is not limited to academic literature but also leads to inadequate evaluation of applied knowledge and practical experiences. In this context, this study aims to present a systematic analysis by bringing together leading research on the subject and to contribute to the development of the field.

Material and Method

In this study, the Multivocal Literature Review (MLR) method will be applied. This method aims to better understand the different dimensions and practical applications of the subject by expanding the traditional Systematic Literature Review (SLR) approach and using gray literature sources such as industry reports, technical blogs, and industry articles in addition to academic literature (Ogawa & Malen, 1991). The literature review will enable us to evaluate the potential of AI to contribute to software quality from a broad perspective. This approach will provide a deeper understanding of AI's impact on software quality by bridging the gap between academic and industry perspectives. The data to be used in the study will be collected from the following sources: Academic Databases: IEEE Xplore, ScienceDirect, ACM Digital Library, Springer, Google Scholar academic databases will be scanned for peer-reviewed articles on artificial intelligence and software quality. The articles collected from these databases will form the scientific basis of the study and will allow us to evaluate the quality-enhancing effects of artificial intelligence in software development processes. Gray Literature: It refers to materials containing sector-specific information that are not included in official academic publications (Akl et al., 2019). This type of literature can be examined at three different levels of reliability:

1. First-level gray literature (high reliability): Books, journals, government reports, technical reviews.
2. Second-level gray literature (medium reliability): Annual reports, news articles, presentations, videos, Q&A platforms, and Wiki content.
3. Third-level gray literature (low reliability): Blogs, emails, social media posts (Adams, Smart, & Huff, 2016).

Research Questions and Search Strategy

In accordance with the MLR methodology, the search will be carried out according to the following steps: Determining research questions, defining search terms, searching academic databases, searching Google and other search engines, removing duplicate articles, determining inclusion/exclusion criteria, data extraction, data synthesis. The main research questions are listed in Table 1.

Table 1. Research questions.

ID	Question	Search Strings
RQ1	In which phases of the software development lifecycle are AI techniques most commonly applied?	("Artificial Intelligence" OR "AI Techniques" OR "Machine Learning" OR "Deep Learning") AND ("SDLC" OR "Software Engineering Phases" OR "Agile Development")
RQ2	How do AI techniques impact software quality metrics?	("AI Techniques " OR "Machine Learning") AND ("Software Quality Metrics" OR "Software Quality" OR "Quality Assurance")
RQ3	How do AI-powered tools impact software developer's productivity?	("AI-powered tools" OR "Machine Learning tools") AND ("Developer productivity" OR "Software development efficiency" OR "AI in software development productivity")

Inclusion and Exclusion Criteria

The literature to be included in this study consists of peer-reviewed journal articles, conference papers, and industry reports published between 2010 and 2025, as well as gray literature sources in both English and Turkish. The sources used must address the impact of artificial intelligence techniques on the software development lifecycle and software quality. Literature to be excluded includes studies published before 2010, articles written in languages other than English and Turkish, and content that does not address the research questions. Considering the reliability level of gray literature, only industry-contributing works directly related to the topic will be included.

Findings

To answer the research questions, the integration of artificial intelligence into software development processes will be examined comprehensively. The use of AI in various stages such as requirements analysis, design, coding, testing, and maintenance will be investigated, and the reasons behind its application in each stage will be explored. The advantages provided by AI in each phase will be explained in detail. Based on the initial research, the contributions of artificial intelligence to different stages of the software development lifecycle have been identified. In the requirements analysis phase, AI-based natural language processing techniques analyze user feedback, enabling more accurate and comprehensive requirements to be gathered. In the design and coding processes, AI-powered tools guide developers in code optimization by predicting errors, thus improving code quality. In the testing and debugging phase, AI-supported automated testing tools assist manual testing processes, accelerating error detection and enhancing software reliability. Finally, in the maintenance and deployment stages, AI-powered predictive analytics can identify potential issues that may degrade system performance in advance, ensuring an uninterrupted user experience. It has been observed that artificial intelligence techniques have a positive impact on software quality metrics. These effects may vary depending on the type of AI techniques used, the quality of the data, and the system integration. Therefore, the impact of AI on software quality may not be at the same level in every case, but generally, beneficial outcomes are expected in this area. In the context of the third research question, the effects of AI-powered tools on the productivity of software developers will be evaluated. AI-based tools enhance productivity by enabling developers to accomplish more in less time through features such as automatic code completion suggestions, providing tips, and conducting risk analysis with pre-error warnings. Additionally, AI-based predictive analytics guide developers in project management and resource planning, supporting decision-making processes.

Conclusion

This study aims to provide a valuable source of information that will guide software teams in developing higher-quality, reliable, and high-performance software by examining the effects of integrating artificial intelligence into software development processes. Literature reviews and initial findings show that AI techniques and AI-powered tools bring significant advancements in various stages of the software development lifecycle and can enhance software quality. The study is expected to contribute to a better understanding of the role of AI in software development processes and serve as a guiding resource for both academic research and industrial applications. The outcome of the study is anticipated to introduce a holistic perspective on the relationship between artificial intelligence and software, raise awareness about the impact of AI on software quality, and provide insights for future research.

References

Adams, R. J., Smart, P., & Huff, A. S. (2016). Shades of grey: Guidelines for working with the grey literature in systematic reviews for management and organizational studies. *International Journal of Management Reviews, 19*(4), 432–454. https://doi.org/10.1111/ijmr.12102

Akl, E., Altman, D., Aluko, P., Beaton, D., Berlin, J., Bhaumik, B., & Young, C. (2019). *Cochrane handbook for systematic reviews of interventions*.

Baralla, G., Ibba, G., & Tonelli, R. (2024). Assessing GitHub Copilot in Solidity development: Capabilities, testing, and bug fixing. *IEEE Access, PP*, 1–1. https://doi.org/10.1109/ACCESS.2024.3486365

Geetha, V., Gomathy, C. K., Yagn, M. D. V. Y., & Praneesh, S. (2023). The role of natural language processing. *International Journal of Scientific Research in Engineering and Management, 07*(11), 1–11. https://doi.org/10.55041/ijsrem27094

McCarthy, J. (1959). Programs with common sense.

Ogawa, R. T., & Malen, B. (1991). Towards rigor in reviews of multivocal literatures: Applying the exploratory case study method. *Review of Educational Research, 61*(3), 265–286. https://doi.org/10.3102/00346543061003265

Shrestha, Y. R., Krishna, V., & Von Krogh, G. (2020). Augmenting organizational decision-making with deep learning algorithms: Principles, promises, and challenges. *Journal of Business Research, 123*, 588–603. https://doi.org/10.1016/j.jbusres.2020.09.068

Syed Adnan Afaq, E. A. (2023). Exploring software development change analysis with an emphasis on requirements. *International Journal on Recent and Innovation Trends in Computing and Communication*.

Thota, M. K., Shajin, F. H., & Rajesh, P. (2020). Survey on software defect prediction techniques. *International Journal of Applied Science and Engineering, 17*, 331–344.

Turing, A. M. (2007). Computing machinery and intelligence. In *Springer eBooks* (pp. 23–65). https://doi.org/10.1007/978-1-4020-6710-5_3

Yeboah, J., & Popoola, S. (2023). Efficacy of static analysis tools for software defect detection on open-source projects. *2021 International Conference on Computational Science and Computational Intelligence (CSCI)*, 1588–1593. https://doi.org/10.1109/csci62032.2023.00262

Yu, T. (2018). Software engineering method in the application of computer software development analysis.

Yüksel, A., & Çetin, D. D. A. (2020). Yinelenen hata kayıtlarının makine öğrenmesi ve derin öğrenme yöntemleri ile tespit edilmesi. *Mühendislik Bilimleri ve Tasarım Dergisi, 8*(5), 45–51. https://doi.org/10.21923/jesd.826251

Multi-Lead ECG Classification Using a Mixture-of-Experts Transformer Model

Atalay Çelik [a], Mehmet Ali Ergün [a]

[a] Istanbul Technical University, Data Engineering and Business Analytics, Big Data and Business Analytics Program, Türkiye
celika17@itu.edu.tr

Keywords: Classification, Ecg, Moe, Transformer.

Aim

The aim of the study is to conduct and experiment with a transformer-based mixture-of-expert (MoE) model architecture in the health field to classify electrocardiography (ECG) records into their possible diagnosis. The records are time-based data that vary in length and frequency.

Material and Method

The dataset to be used in the study is one of the datasets used in the Physio Challenge 2020 (Alday et al., 2020) called the CSPC dataset (Liu et al., 2018). George B. Moody PhysioNet Challenges are challenges prepared annuay about specific questions or use cases about ECG records. The Physio Challenge 2020 primarily focused on the classification of the ECG records for diagnosis. These records are ECG signals that are taken from 12 different nodes that are placed on the human body at different specific positions. These nodes measure the signal of the electrical activity around it and record the signal strengths to observe the heart activity or irregularities.
The records are labeled with diagnosis with a specific coding schema called the SNOMED CT Code (SNOMED International, n.d.). These codes refer the specific diagnosis. Across 5,570 records a total of 8 different unique SNOMED CT codes, hence diagnoses are present in the dataset. A single record can be labeled with multiple diagnosis. The dataset characteristics are given in Table 1. All the records have a metadata attach to it to read the diagnosis and other metadata in a specific format WFDB header file format (Moody, 2022).

Table 1. Diagnosis distributions.

SNOMED CT	Diagnosis Name	Number of Records
426783006	Sinus Rhythm	918
164889003	Atrial Fibrillation	1221
270492004	1st Degree Av Block	722
59118001	Right Bundle Branch Block	1857
284470004	Premature Atrial Contraction	616
164909002	Left Bundle Branch Block	236

In the dataset, the length of the records are 15.4 seconds in average. The frequency of the records is 1000 Hz. To feed into the model all the records preprocessed to have the same time interval and frequency by resampling, cropping or padding the records. Records are cropped if they are longer than 10 seconds. This results in all the records having the same number of samples. The time interval is decided by the most common time interval for all the datasets. The frequency is decided by doing an analysis of the signal-to-noise (SNR) ratio for different frequency options. Since these records are electrical signal

there are inherent and outside noise present in the records. To denoise the records filters such as Butterworth filter and finite impulse response (FIR) are used. Resampling and filtering steps are further analyzed in combination to select the best set of parameters to preprocess the records based on SNR values.

Some record show unidentifiable patterns or peaks that indicate a clear mismeasurement, these patterns are detected by a combination of three methods; Z-score for ECG records, principal component analysis (PCA) and Isolation Forest. These three methods vote on possible outliers and if there are records that have 2 out of 3 votes they are flagged as outlier. The methods are applied separately for different diagnosis. For the diagnosis that have more than 20 records the outlier analysis is done within the diagnosis group, but for rare diagnosis that have less than 20 records are grouped together and analyzed as a group. These filtering steps ensure that the data is similar across the same diagnosis and are detached from any outside effect.

Some diagnosis codes are representing similar diagnosis, for this reason they are concatenated to be a single diagnosis. These diagnosis pairs are taken from Physio Challenge evaluation repositories. (Alday, 2020) As a result, 6 unique diagnoses are present if diagnosis pairs are counted as one diagnosis.

Transformer architecture is a commonly used state-of-the-art architecture in fields such as large language models and image processing tasks. Since its first appearance it the literature by Vaswani et al., it has impacted the deep learning architectures with its subcomponents (Vaswani et al., 2017). Even though several subcomponents have changed since its first version, the main design has remained the same. One of the most significant alteration in the architecture has become the mixture-of-expert and router approaches (Shaazer et al., 2017). Original transformer implementation uses a dense model, where every neuron is used for a single inference cycle; however, with the MoE models the models are used sparsely to activate only a portion of the model. This mechanism is applied with the router logic. The router, routes the inputs to different experts according to its characteristics. The experts are fully connected layers that do the computation work. In the context of LLMs, these inputs represent tokens. The MoE architecture also introduces new loss components to ensure the uniform activation of routers and distribution of inputs across the experts.

Adoption of this architecture to the time series domain is still being actively explored in recent studies (Shi et al., 2024). However, most of the studies are focusing on the forecasting scenarios. The classification of the time series with an MoE architecture is still a developing area. The ECG classification task has become a great experimentation area for any classification-based implementation. The multi-feature characteristic of the data, a wide range of diagnosis with different characteristics, and the importance of the field due to critical health implications of a diagnosis present a great challenge.

In this study, a mixture-of-expert transformer model with an auxiliary loss that predicts the possible diagnosis of multi-lead ECG records is worked on.

The model architecture is a transformer architecture multi-head attention and RoPe positional encoding. layers that alternate between normal feed forward layers and MoE layers, the first and third layers are feed forward and second and last layers are MoE layers.

The model consists of multiple specialized experts and a learned routing network that dynamically assigns inputs in the sequence to the most appropriate experts. To mitigate the effect of expert collapsing, where only a small subset of experts receives the majority of sequence tokens, auxiliary losses is added to penalize the routing inefficiencies. The z-loss (Zoph et al, 2022) is implemented to inhibit the extreme routing to some experts and balance loss (Shaazer et al., 2017) is applied for uneven expert utilization, resulting in more efficient use of model capacity.

The architecture also includes a classification token (CLS) similar to BERT class models (Devlin et al., 2019), where a learned token is prepended to the input sequence and used for final classification in the last step of the model. The age and sex features are fed to the model with a projection layer to the model dimension. The training includes several optimization techniques to ensure stability, such as learning rate warmup, cosine annealing for learning rate, early stopping, and gradient clipping. The material and method section should be written in Times New Roman font, justified-alignment and in 10-point size.

Findings

The model which the architecture of it has been described has been trained for 30 epochs. The model is configured with a dimension of 48 and utilizes 4 attention heads across 4 layers. The Feed Forward Network (FFN) size is set to 192, and the model employs 8 experts. Regularization includes a Z-loss coefficient of 0.001 and a balance loss coefficient of 0.005. Training parameters include a batch size of 64, with gradient accumulation over 2 steps with early stopping. The initial learning rate is set to 7e-5 with 100 warm-up training iterations.
To find the best candidate hyperparameters, several runs are conducted for each parameter combination and it is concluded that a model with lower number of parameters learn the representations of the model better than a larger model. The results of the evaluation on the test set are presented at Table 2.

Table 2. Evaluation metrics of the model.

Component	Value
Exact Match Accuracy	54.93 %
Top 1 Accuracy	66.05 %
Top 2 Accuracy	85.06 %
Top 3 Accuracy	93.54 %
F1 Score	72.20 %

The experts that are present for the layers one and three are further analyzed to observe their utilization rate as seen in Figure 1.

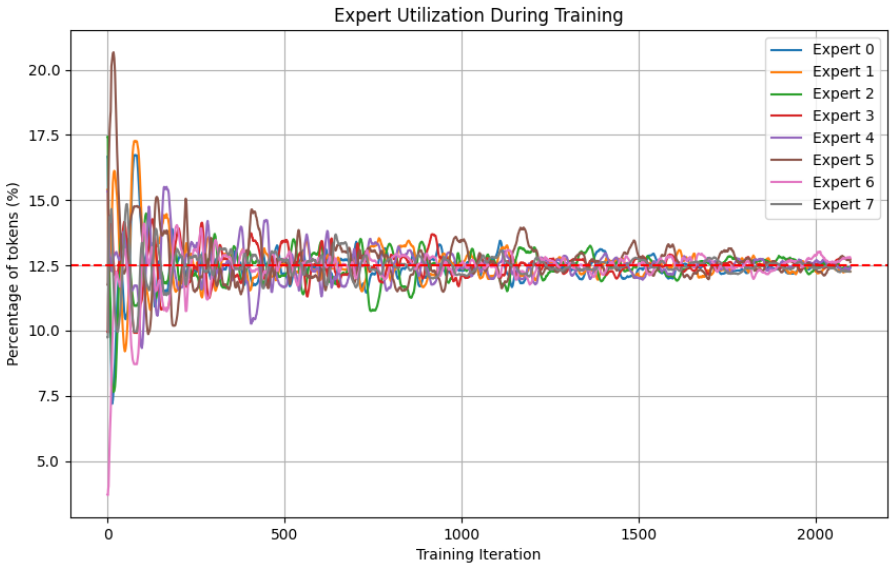

Figure 1. Expert utilization rates during training.

The model exhibits an adequate level of exact diagnosis detection and a high degree of accuracy for the top 3 predictions.

Conclusion

The mixture-of-expert approach to a time sequence data for classification is a great challenge to test this approach in the time series domain. One of the main challenges of this problem is the presence of multi-label diagnosis for the records. The model training demonstrated that it has the capability to learn to recognize different diagnosis with experts in place. Future research topic includes ingestion of extracted features from the ECG records, and implementation of further training on a larger dataset.

References

Alday, E. A. P., (2020). PhysioNet/CinC Challenge 2020 Evaluation Metrics. Retrieved January 13, 2025 from https://github.com/physionetchallenges/evaluation-2020/blob/master/dx_mapping_scored.csv

Alday, E. A. P., Gu, A., Shah, A. J., Robichaux, C., Wong, A. K. I., Liu, C., Liu, F., Rad, A. B., Elola, A., Seyedi S., Li, Q., Sharma, A., Clifford, G. D. & Reyna, M. A. (2020). Classification of 12-lead ecgs: the physionet/computing in cardiology challenge 2020. Physiological measurement, 41(12), 124003.

Devlin, J., Chang, M. W., Lee, K., & Toutanova, K. (2019). Bert: Pre-training of deep bidirectional transformers for language understanding. In Proceedings of the 2019 conference of the North American chapter of the association for computational linguistics: human language technologies, volume 1 (long and short papers) (pp. 4171-4186).

Liu, F., Liu, C., Zhao, L., Zhang, X., Wu, X., Xu, X., Liu, Y., Ma, C., Wei, S., He, Z., Li, J. & Ng, E. YK. (2018). An open access database for evaluating the algorithms of electrocardiogram rhythm and morphology abnormality detection. Journal of Medical Imaging and Health Informatics, 8(7), 1368-1373.

Moody, G. B., (2022). WFDB header file format. Retrieved August 25, 2024, from https://physionet.org/physiotools/wag/header-5.htm

Shazeer, N., Mirhoseini, A., Maziarz, K., Davis, A., Le, Q., Hinton, G., & Dean, J. (2017). Outrageously large neural networks: The sparsely-gated mixture-of-experts layer. arXiv preprint arXiv:1701.06538.

Shi, X., Wang, S., Nie, Y., Li, D., Ye, Z., Wen, Q., & Jin, M. (2024). Time-moe: Billion-scale time series foundation models with mixture of experts. arXiv preprint arXiv:2409.16040.

SNOMED International. (n.d.). Use SNOMED CT. Retrieved January 22, 2025, from https://www.snomed.org/use-snomed-ct

Vaswani, A., Shazeer, N., Parmar, N., Uszkoreit, J., Jones, L., Gomez, A. N., Kaiser, L. & Polosukhin, I. (2017). Attention is all you need. Advances in neural information processing systems, 30.

Zoph, B., Bello, I., Kumar, S., Du, N., Huang, Y., Dean, J., Shazeer, N. & Fedus, W. (2022). St-moe: Designing stable and transferable sparse expert models. arXiv preprint arXiv:2202.08906.

COMPUTER ENGINEERING

Artificial Intelligence

Computer Networks

Cyber Security

Embedded Systems

Internet of Things

Neural Networks

Software Engineering

Adaptive Consensus Algorithms for Blockchain Networks

Esin Küçükmeriç[a], Adnan Ozsoy[a]

[a] Hacettepe University, Computer Engineering, Master's Program, Turkey
esinkucukomeroglu@hacettepe.edu.tr

Keywords: Dynamic Consensus, Hyperledger Fabric, Kafka, Parallel Channel Approach, Raft.

Aim

Blockchain technology has garnered significant attention in recent years due to its ability to provide reliability and transparency in distributed systems. However, one of its most critical components, consensus algorithms, directly impacts the performance and flexibility of the network. It is important to note that consensus algorithms exhibit varying priorities, such as speed, security, and capacity. This diversity complicates achieving an optimal balance between performance and security in different application scenarios. For instance, a financial application requiring high transaction throughput may prioritize speed and scalability, whereas a supply chain management system processing sensitive data may place greater emphasis on security and the fault tolerance of the consensus mechanism. In conventional blockchain architectures, addressing these diverse requirements with a single consensus algorithm often necessitates compromises in one area [7]. Ideally, a system capable of dynamically selecting the most appropriate consensus mechanism based on the network's current state and requirements could enhance both efficiency and security. For example, the system could prioritize speed during peak hours and subsequently prioritize security. Thus, in enterprise-level blockchain platforms like Hyperledger Fabric, the need to dynamically switch consensus algorithms arises [1, 2]. Although Hyperledger Fabric provides a modular and extensible blockchain infrastructure, its current architectural design does not support dynamically changing the consensus mechanism after the blockchain network has been initiated. As clearly stated in the official Hyperledger Fabric documentation, the chosen consensus algorithm is considered a foundational component of the orderer nodes' configuration at network startup and remains constant throughout the lifecycle of the blockchain network. Therefore, if there is a requirement to change the consensus mechanism, it necessitates fully stopping the running network, cleaning the previous configuration thoroughly, and restarting the network with new settings.This study focuses on a parallel channel architecture to overcome these existing limitations and provide a more flexible solution. This approach allows the network to switch between different consensus algorithms without downtime while maintaining transaction consistency and performance [5, 6]. This study aims to overcome the inherent limitations of dynamic consensus algorithm switching in blockchain networks, with Hyperledger Fabric as our selected use case. Currently, Fabric does not support changing the consensus algorithm, such as from Raft to Kafka or vice versa, without restarting the network [6]. This limitation introduces significant latency and operational overhead, making it impractical for real-time applications that require flexibility in consensus mechanisms based on varying workloads or network conditions. To overcome this challenge, we propose a novel parallel channel architecture where two channels—one using Raft and the other using Kafka—run simultaneously. This approach aims to enable seamless consensus switching while minimizing latency, ensuring transaction consistency, and maintaining high availability across channels. Additionally, we aim to quantify the latency introduced by consensus switching and synchronization between channels, providing a comprehensive analysis of the proposed solution's performance. This study also explores the potential of this architecture to support other consensus algorithms in the future, further enhancing the flexibility of blockchain networks [5, 6].

Material and Method

In the initial setup, a Hyperledger Fabric network is configured with Raft as the consensus algorithm. Chaincode operations are performed to establish a baseline for transaction processing latency and throughput. Kafka is then integrated into the network to evaluate the feasibility of consensus switching [3, 4]. The process of changing the consensus algorithm consists

of several critical stages, as illustrated in Figure 1 and Figure 2. The first stage involves cleaning up ("cleanup"), which includes stopping the current network's Docker containers, removing associated configuration files, and deleting previously generated cryptographic materials. This stage is represented in the "Cleanup" step in the graphics. The second step involves generating cryptographic materials ("crypto generation") tailored specifically for the newly selected consensus mechanism, as seen in the "Crypto Generation" phase. Subsequently, the initial state of the blockchain, represented by the genesis block, is generated ("genesis block generation"), followed by the creation of configuration files necessary for channel formation ("channel TX generation"). These stages are represented in the "Genesis Block Generation" and "Channel TX Generation" sections of the graphs.

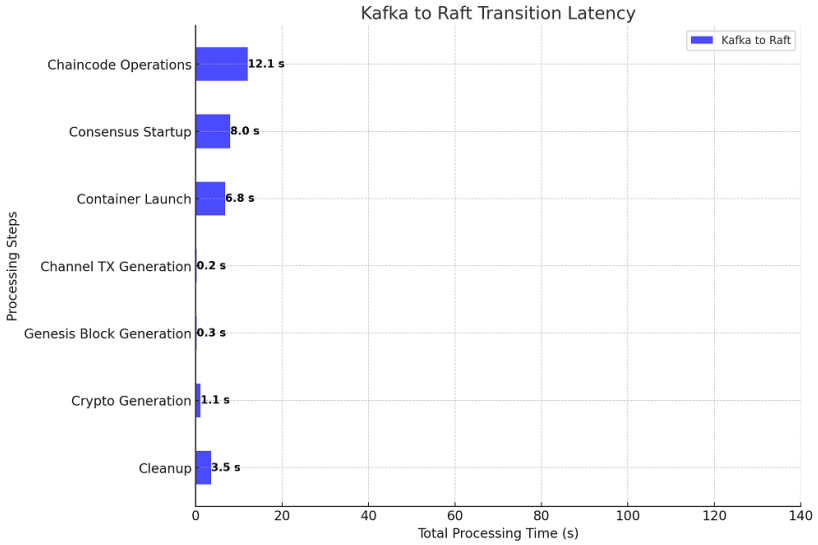

Figure 1. Kafka to Raft transition latency.

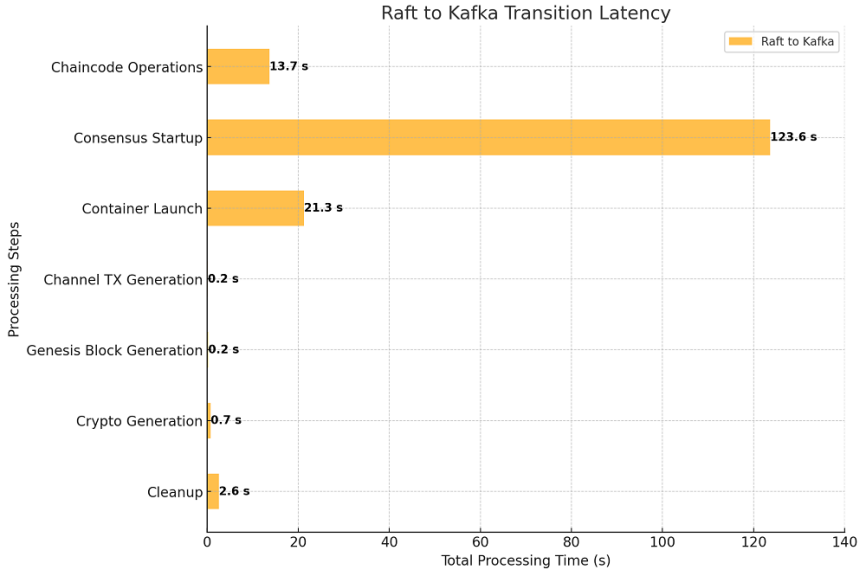

Figure 2. Raft to Kafka transition latency.

In the next phase ("container launch"), the network containers are started using Docker Compose configurations specific to the selected consensus mechanism, which is illustrated in the "Container Launch" phase. Following these general configuration steps, additional mechanism-specific preparations are required depending on the consensus type. For instance,

when initializing a Kafka- based network, the system waits until all Kafka brokers have fully become operational. During this waiting period, the statuses of Kafka brokers are periodically verified to ensure their readiness before initiating any blockchain transactions or channel creations. Similarly, a Raft- based network requires a leader election process among the orderer nodes to become operational. During this stage, periodic checks are performed on the orderer nodes' logs to confirm that a leader node has been successfully elected. This leader election phase is crucial for ensuring that the new consensus algorithm can reliably handle and order transactions across the network. These additional preparation steps significantly contribute to latency during consensus transitions. Once these foundational configuration stages were completed, chaincode operations became essential to bring blockchain functionality online. Chaincode operations involve four primary steps: packaging the chaincode ("chaincode package"), installing it on nodes of relevant organizations ("install"), organizations approving the installed chaincode ("approveformyorg"), and finally committing the chaincode to make it operational on the network ("commit"). After these operations, the chaincode became active, initial states (e.g., creating assets named A and B) were defined, and a simple token transfer was executed to verify the chaincode functionality. This process included instantiation ("instantiate"), asset initialization ("initialize assets"), invoking a transaction ("invoke"), and finally querying ("query") the assets to confirm transaction correctness. However, during these transitions, the necessity of shutting down and restarting the blockchain network inevitably leads to service interruptions. Such disruptions pose serious risks, particularly for blockchain applications requiring high availability and continuous operation. Network outages negatively affect service continuity, potentially reduce network reliability, degrade performance, and diminish user trust. Additionally, interruptions may result in increased transaction delays, growth in transaction queues, and elevated risks of data inconsistency.

As shown in Figure 1 and Figure 2, the latency introduced during the transition phases, especially in the "Consensus Startup" step, contributes significantly to overall transition time. To mitigate the high latency and negative impacts of these network interruptions, a parallel network operation approach has been proposed. In this approach, two separate blockchain networks—one using Raft consensus and the other Kafka consensus—are simultaneously launched and operated.

As shown in Figure 3, the Raft and Kafka networks operate independently but in parallel, with each network performing transaction processing simultaneously. Specifically, one network (the active network) processes transactions, which involve chaincode operations such as asset creation, token transfer, and querying, and immediately writes the processed transaction data into a file. The other network (the passive network) continuously reads the transaction data from this file and synchronizes these transactions internally, ensuring consistency across both networks. This parallel architecture allows for continuous operation during consensus transitions, with both networks mirroring each other's transaction processing and maintaining synchronization. The active network handles transaction processing and records it, while the passive network ensures that the state of both networks remains consistent by processing the same data from the file, effectively mirroring the operations of the active network. This methodology reduces latency, prevents service interruptions, and enhances overall system performance and reliability during consensus algorithm transitions.

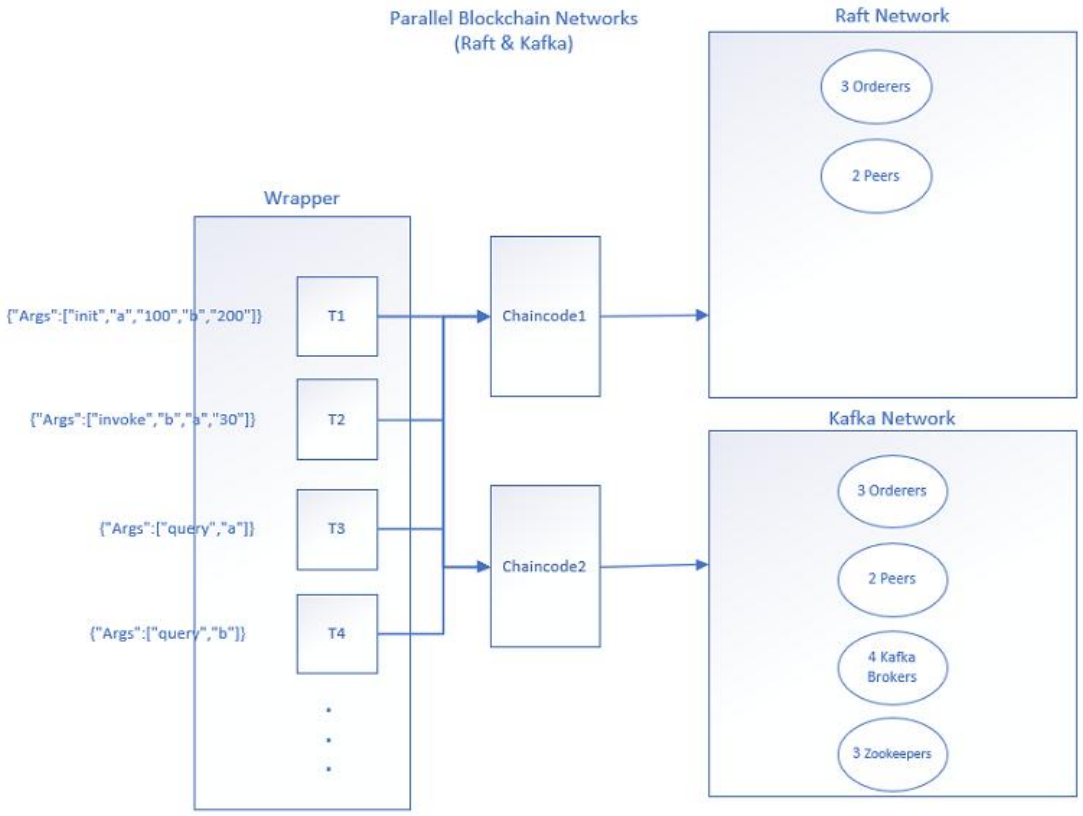

Figure 3. Parallel blockchain networks (Raft & Kafka).

Figure 4 illustrates the performance of this parallel approach, where transaction processing in both networks occurs simultaneously, minimizing overall latency and ensuring continuous operation during the consensus switching process. Performance analysis of these parallel-operating blockchain networks clearly demonstrates that parallelization significantly reduces the latency typically incurred through complete reconfiguration during consensus transitions. Results reflected in experimental measurements indicate a notable reduction in latency and improved system reliability and availability. Building upon this parallel approach, an automated mechanism was implemented to handle active-passive channel switching. The system dynamically selects the active channel based on predefined criteria such as workload or network conditions. This transition is further optimized by implementing a buffer-based approach to manage incoming transactions during the switching process. For instance, if a surge in transactions occurs—such as receiving 1000 transactions at once—the system temporarily stores these transactions in a buffer. Once the new active channel is ready, the transactions are processed from the buffer, ensuring minimal downtime and maintaining optimal transaction consistency. This development addresses the challenge of handling transaction bursts during the active-passive channel switching process, improving both efficiency and transaction handling under varying network conditions.

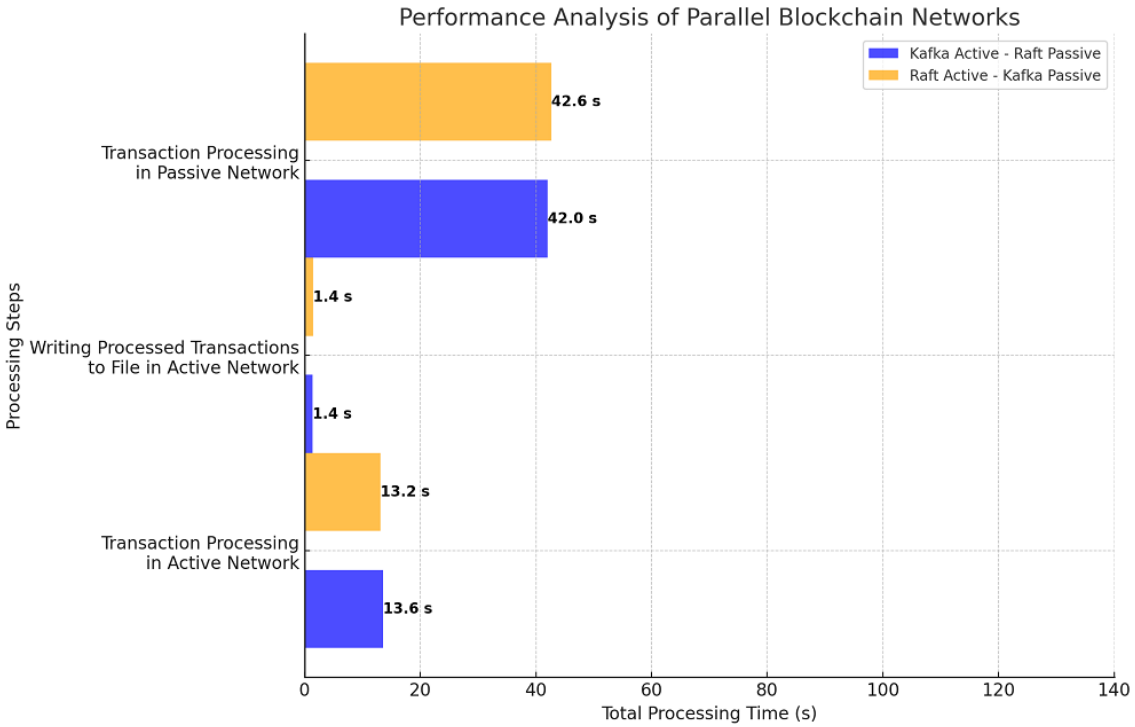

Figure 4. Performance analysis of parallel blockchain networks.

Findings

This research highlights significant drawbacks associated with switching consensus algorithms, such as transitioning from Raft to Kafka, by restarting blockchain networks. Restarting introduces substantial latency, operational complexity, and downtime, severely affecting high- availability and real-time applications. Downtime halts transaction processing, negatively impacting user experience, especially in high- volume scenarios. Moreover, reconfiguring nodes, updating channels, and resynchronizing networks require extensive resources and increase the risk of human error. Raft provides lower latency and simplicity, making it ideal for rapid transaction processing; however, its leader-based structure makes it less effective for high-throughput scenarios. In contrast, Kafka excels in handling massive transaction volumes with high fault tolerance but incurs higher per-transaction latency. Thus, selecting between Raft and Kafka depends on various factors, including the specific performance requirements, scalability considerations, and operational priorities of the application [1,7]. The parallel channel architecture proposed in this research addresses these challenges effectively. By simultaneously operating Raft and Kafka channels, the system dynamically selects the optimal consensus algorithm based on real-time network demands and application-specific priorities, ensuring uninterrupted transaction processing. The network maintains consistency through file-based synchronization, and the automated active-passive channel management mechanism enables seamless switching. This approach significantly enhances performance compared to traditional single-channel approaches, offering superior latency, throughput, and operational flexibility.

Conclusion

In conclusion, this study demonstrates that dynamic consensus switching in Hyperledger Fabric can be achieved through a parallel channel architecture. By running Raft and Kafka channels simultaneously and implementing an automated switching mechanism, the limitations of consensus algorithm switching can be mitigated. The proposed approach reduces latency, ensures transaction consistency, and provides a scalable solution for real-time blockchain applications. The findings highlight the potential of parallel channel architectures to enhance the flexibility and performance of blockchain networks. Future work will focus on optimizing the synchronization process, integrating additional consensus algorithms, and

evaluating the proposed solution in large-scale, real-world deployments. This research opens new avenues for improving the adaptability of blockchain systems in dynamic environments.

References

Androulaki, E., Barger, A., Bortnikov, V., Cachin, C., Christidis, K., De Caro, A., Enyeart, D., Ferris, C., Laventman, G., Manevich, Y., Muralidharan, S., Murthy, C., Nguyen, B., Sethi, M., Singh, G., Smith, K., Sorniotti, A., Stathakopoulou, C., Vukolić, M., ... & Yellick, J. (2018). Hyperledger Fabric: A Distributed Operating System for Permissioned Blockchains. EuroSys '18: Proceedings of the Thirteenth EuroSys Conference. https://doi.org/10.1145/3190508.3190538

Cachin, C., & Vukolić, M. (2017). Blockchain Consensus Protocols in the Wild. arXiv preprint arXiv:1707.01873. https://doi.org/10.48550/arXiv.1707.01873

Hyperledger. (2020). Hyperledger Fabric documentation (Release 2.5). Retrieved May 25, 2020, from https://hyperledger-fabric.readthedocs.io/en/release-2.5/

Krgko, K. (n.d.). krgko/Kafka-Fabric-Network [GitHub repository]. Retrieved March 22, 2025, from https://github.com/krgko/Kafka-Fabric-Network/tree/master

Rajeev Sakhuja. (n.d.). Hyperledger Fabric network design and setup [Udemy course]. Retrieved March 22, 2025, from https://www.udemy.com/course/hyperledger-fabric-network-design-setup/

LFDecentralizedTrust. (n.d.). Fabric topics. Retrieved March 22, 2025, from https://lists.lfdecentralizedtrust.org/g/fabric/topics? sidebar=true

Wang, W., Hoang, D. T., Hu, P., Xiong, Z., Niyato, D., Wang, P., & Kim, D. I. (2019). A survey on consensus mechanisms and mining management in blockchain networks. IEEE Access, 7, 22328–22370. https://doi.org/10.1109/ACCESS.2019.2896108

COMPUTER ENGINEERING

Artificial Intelligence

Computer Networks

Cyber Security

Embedded Systems

Internet of Things

Neural Networks

Software Engineering

Reputation Based Decision Making Consensus Mechanism for UAV Swarms with Ethereum Blockchain

Mustafa Tosun[a], Şerif Bahtiyar[b]

[a] Istanbul Technical University, Department of Cybersecurity Engineering, Türkiye
[b] Istanbul Technical University, Department of Computer Engineering, Türkiye
tosunmu17@itu.edu.tr, bahtiyars@itu.edu.tr

Keywords: Blockchain, Decision, Swarm, UAV, Voting.

Aim

Blockchain technology within drone swarm systems gained a huge impact in recent years for several domains, within military, commercial, and political contexts (Koulianos & Litke, 2023).
Byzantine fault tolerance (BFT) is a critical aspect of UAV systems, especially in networked environments where security and reliability are paramount. In order to reduce the impacts of Byzantine UAVs in the swarm, blockchain based consensus mechanisms are being proposed by researchers (Cheng et al., 2022) (Alsamhi et al., 2023).
This study proposes a blockchain based consensus mechanism for autonomous target selection in military drone swarms. The system integrates reputation weighted voting and Byzantine fault tolerance to enable decentralized decision making. Dynamic thresholds (60% for normal missions, 70% for critical missions) and timeout mechanisms ensure the robustness of the system. This study bridges the gap between decentralized trust and real time operational efficiency in autonomous warfare systems.
The integration of voting based consensus mechanisms into UAV swarms revolutionizes autonomous decision making by addressing critical challenges in military operations, such as Byzantine (faulty/malicious) node resilience, decentralized trust, and real time adaptability.
This study aims to enhance the efficiency, security, and reliability of swarm drone operations with the help of blockchain technology for decentralized decision making. The study will explore how reputation systems can be integrated into swarm Unmanned Aerial Vehicles (UAV) to improve consensus and decision making processes, ultimately leading to more effective and resilient UAV swarms.

Material and Method

The proposed system will utilize Ethereum's blockchain technology to implement a decentralized decision making mechanism for swarm drones. This system will incorporate a reputation based consensus algorithm to ensure efficient and secure operations.
The proposed system contains a smart contract programmed in Solidity language to manage the voting process and dynamically re-evaluate the reputation scores of UAVs. With the help of smart contract, the system creates trust in no trust contracting contexts (Eenmaa-Dimitrieva, H., & Schmidt-Kessen, 2023) (Rouhani, S., & Deters, R., 2019).
The workflow of the proposed system can be seen in Figure 1. Firstly, an administrator user sets the criticality level at the beginning of mission. During mission, highest reputation UAV suggests a target. Other UAVs in the swarm evaluates this suggestion and based on their own sensors and capabilities, they cast votes as yes or no. Smart contract calculates each UAV's vote weight based on their reputation. Calculated votes will be added to blockchain as a transaction. After all UAVs cast their votes, voting will end. Based on the criticality level (60% for normal missions, 70% for critical missions) , if consensus achieved align with the highest reputation UAV's suggestion, the target will be approved for engagement. Otherwise, it will not ensure mission success and safety. After the voting process concludes, each UAV's reputation (including the highest reputation UAV) will be re-evaluated. The re-evaluation system provides a dynamic reputation for each UAV in the swarm based on the accuracy of previous votes.

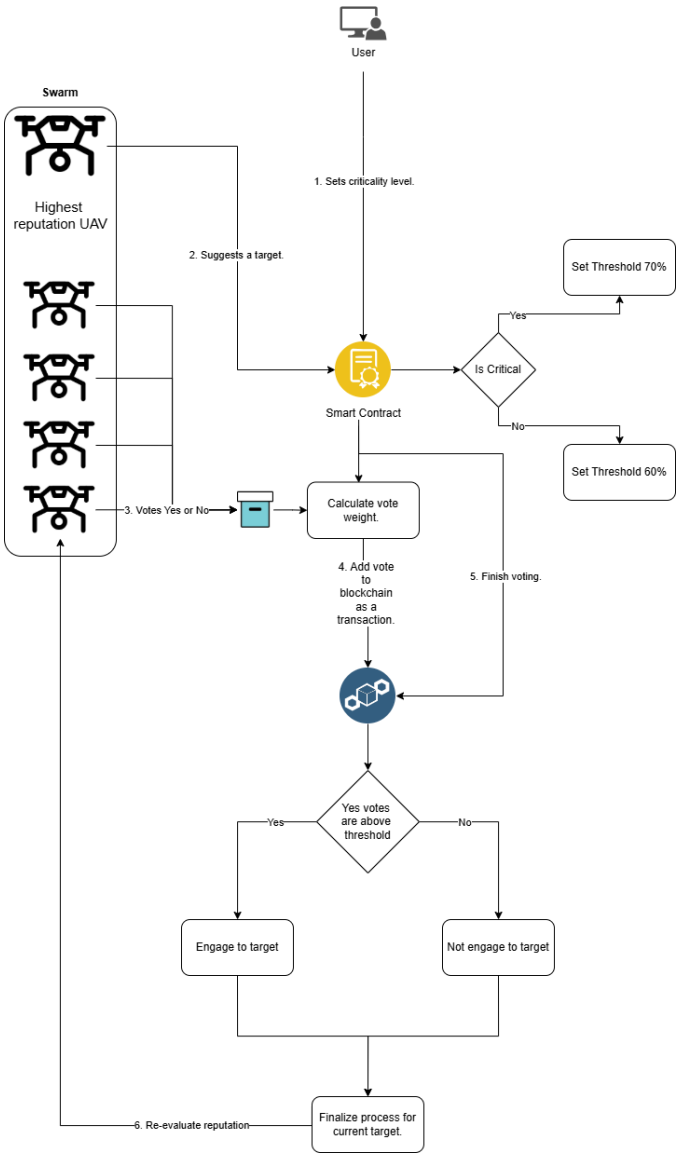

Figure 1. Workflow.

The re-evaluation process will be applied as follows: Reputation of UAVs with accurate votes will be increased by 10 points, Reputation of UAVs with inaccurate votes will be decreased by 5 points. UAVs that did not vote will have their reputations decreased by 2 points. After the re-evaluation process, there is a possibility that the highest reputation UAV may also change due to re-evaluation.

After the process is completed for the current target, the highest reputation UAV may suggest another target. Whenever a new target is suggested, the voting process will be started again.

Some UAVs may cast their vote after a certain amount of time. This may cause the mission to be delayed or result unsuccessfully. The timeout duration will be set as 5 seconds to prevent that problem. In case voting is not completed within 5 seconds, if consensus is not achieved, voting will be restarted. Restarting operation will be applied a maximum of 3 times. If the voting process fails to reach a consensus after 3 attempts, the system will not engage to current target.

Findings

The study is expected to yield several key findings related to the implementation and effectiveness of the proposed system. The use of blockchain technology is anticipated to enhance the security and reliability of the decision making process by providing a decentralized platform.

The reputation based consensus mechanism is expected to improve the efficiency of swarm operations by prioritizing input from drones with higher reputations.

The proposed system aims to enhance the reliability and efficiency of UAV operations by utilizing reputation scores to inform collaborative decision making processes among UAVs, ensuring that actions are taken based on trustworthiness and accuracy of previous votes. By integrating this reputation based approach, the system minimizes the risks associated with unreliable sensors and Byzantine UAVs, ultimately enhancing mission success rates across diverse operational environments.

Conclusion

In this study, we present a new system to carry out decision making process for target engagement in UAV swarms. The integration of Ethereum blockchain technology with a reputation based decision making consensus mechanism offers a promising approach to enhancing the integrity and reliability of swarm UAV operations. With the help of blockchain's decentralized nature, along with a reputation system, the proposed system improves decision making processes and ensures more effective swarm operations. The study's findings will contribute to the growing body of research on blockchain applications in swarm UAV applications, highlighting the potential for innovative solutions in this field.

References

Alsamhi, S. H., Shvetsov, A. V., Shvetsova, S. V., Hawbani, A., Guizani, M., Alhartomi, M. A., & Ma, O. (2023b). Blockchain-empowered security and energy efficiency of drone swarm consensus for environment exploration. IEEE Transactions on Green Communications and Networking, 7(1), 328–338. https://doi.org/10.1109/tgcn.2022.3195479

Cheng, C.-F., Srivastava, G., Lin, J. C.-W., & Lin, Y.-C. (2022). A consensus protocol for Unmanned Aerial Vehicle Networks in the presence of Byzantine faults. Computers and Electrical Engineering, 99, 107774. https://doi.org/10.1016/j.compeleceng.2022.107774

Eenmaa-Dimitrieva, H., & Schmidt-Kessen, M. J. (2019). Creating markets in no-Trust Environments: The law and economics of smart contracts. Computer Law & Security Review, 35(1), 69–88. https://doi.org/10.1016/j.clsr.2018.09.003

Koulianos, A., & Litke, A. (2023). Blockchain Technology for Secure Communication and Formation Control in Smart Drone Swarms. Future Internet, 15(10), 344. https://doi.org/10.3390/fi15100344

Rouhani, S., & Deters, R. (2019). Security, performance, and applications of Smart Contracts: A systematic survey. IEEE Access, 7, 50759–50779. https://doi.org/10.1109/access.2019.2911031

Neuromorphic Computing and Memristor-Based Network Attack Detection Systems: New Approaches in Cyber Security

Yusuf Etka Köylü[a], İlhan Kocaarslan[b]

[a] Istanbul Technical University, Department of Mechatronics Engineering Graduate Program, Türkiye
[b] Istanbul Technical University, Department of Mechatronics Engineering Program, Türkiye
koylu22@itu.edu.tr , kocaarslani@itu.edu.tr

Keywords: Neuromorphic Computing, Network Security, NSL-KDD Dataset, Zero-Day Attack Detection, Cyber Security.

Aim

The increasing complexity of digital infrastructures has led to the rapid evolution of cyber security threats. Traditional Intrusion Detection Systems (IDS) and Intrusion Prevention Systems (IPS) are becoming inadequate against increasingly sophisticated cyber attacks [1]. This study aims to integrate neuromorphic computing and memristor-based architectures into cyber security solutions to improve attack detection efficiency, reduce false positives, optimize energy consumption, and develop real-time threat mitigation mechanisms [2].

Neuromorphic processors, which mimic the neural structure of the human brain, offer higher computational efficiency and rapid adaptation capabilities to dynamic environments compared to traditional computing systems [3]. Processors such as Intel's Loihi and IBM's TrueNorth simulate biological neural networks, enabling real-time analysis of large datasets with high efficiency and low power consumption [4,5]. Other significant neuromorphic projects like SpiNNaker have also demonstrated the potential of brain-inspired computing architectures [6]. The structure of the neuromorphic processor is shown in Figure 1. Intrusion Detection and Prevention Systems

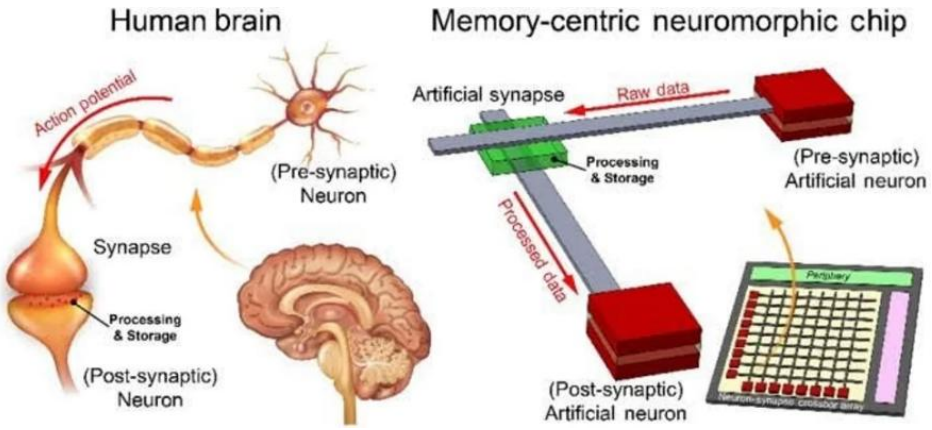

Figure 1. Human brain and memory-centric neuromorphic chip.

Intrusion Detection Systems (IDS) and Intrusion Prevention Systems (IPS) are critical components of modern cyber security infrastructures [7]. These systems continuously analyze network traffic to detect anomalies and enable measures against potential security breaches.

IDS systems are primarily divided into two categories:

- Signature-Based IDS: Detects known threats by searching for predefined attack patterns but is inadequate in identifying new types of attacks.

• Anomaly-Based IDS: Uses machine learning algorithms to detect deviations by creating models of normal network behavior, providing the advantage of detecting previously unseen attacks. Deep belief networks have shown particular promise in this area [8].

The similarities and differences between IPS and IDS are described in detail in Table 1.IPS systems combine the detection capability of IDS with active intervention capacity. These systems conduct comprehensive traffic monitoring, use advanced attack detection mechanisms, and provide automatic intervention when threats are detected.

Table 1. Comparison of IDS and IPS.

Comparison Parameters	IDS	IPS
Full Form	Intrusion Detection Systems	Intrusion Prevention Systems
Release to Market	Released between 1984 and 1986	Released in the mid-2000s
Definition	A system that detects files passing through the gateway for any malware	Software that detects malware according to a defined set of rules and can even block them
Type	A passive software type	An active software
Operation	Involves detecting and reporting malware and errors	Does not require human intervention or participation of other software as it solves the problem on its own
Performance	Does not affect network performance due to offline deployment	Slows down the network due to detection process
Communication	Out-of-band communication	Compatible with data communication
Advantage	Detects malicious traffic	Drops, alerts, and cleans malicious traffic

Materials and Methods

The research methodology evaluates the effectiveness of existing IDS/IPS systems against current cyber threats through comprehensive comparative analysis. Two important datasets were used to objectively measure the performance of neuromorphic IDS models:

1. CIC-IDS2017 Dataset: A comprehensive resource that includes modern attack types such as DoS, ransomware, phishing, and data leakage [9]. This dataset was created by the Canadian Institute for Cybersecurity at the University of New Brunswick in 2017 and contains network traffic data captured over a five-day period. The dataset includes benign traffic and attack scenarios executed in a controlled environment, comprising over 80 network flow features extracted from pcap files. The CIC-IDS2017 features realistic background traffic generated using the B-Profile system, which creates profiles of abstract behaviors for different user groups.

It contains a diverse range of attacks including Brute Force FTP, Brute Force SSH, DoS, Heartbleed, Web Attack, Infiltration, Botnet and DDoS, making it particularly valuable for evaluating modern IDS systems.

2. NSL-KDD Dataset: A standard reference in the classification of network-based attacks, developed to address the inherent problems in the original KDD Cup 99 dataset [10]. The NSL-KDD dataset eliminates redundant records from the original KDD dataset to prevent biased classification towards frequent records and includes a reasonable number of records in both training and testing sets, making performance evaluation more consistent and comparable.

Key characteristics of the NSL-KDD dataset include:

Attack Categories: The dataset classifies attacks into four main categories:

- Denial of Service (DoS): Attempts to make resources unavailable to legitimate users (e.g., SYN flood, Neptune, Smurf)
- Probe: Surveillance and scanning activities to gather information or find vulnerabilities (e.g., portsweep, nmap, satan)
- User to Root (U2R): Unauthorized access attempts to gain superuser privileges (e.g., buffer overflow, rootkit)
- Remote to Local (R2L): Unauthorized access from a remote machine (e.g., password guessing, ftp_write)

Feature Composition: Each record contains 41 features categorized as:

- Basic features (1-9): Derived from TCP/IP connection information
- Content features (10-22): Domain knowledge-related attributes like number of failed login attempts
- Time-based traffic features (23-31): Computed using a two-second time window
- Host-based traffic features (32-41): Historical features examining connections with the same destination host.

Dataset Statistics: The training set contains 125,973 records while the test set has 22,544 records, with different attack distributions between the sets to provide a more challenging and realistic evaluation environment.

Advantages: The NSL-KDD dataset removes redundant and duplicate records, includes a balanced proportion of different attack classes, and has a reasonable number of records that makes it feasible to run experiments on complete datasets without sampling.

The NSL-KDD dataset remains a vital benchmark for evaluating intrusion detection systems despite being somewhat dated, as it allows direct comparison with numerous prior studies and contains attack patterns that remain relevant to contemporary security research.

Data Processing Techniques and Optimization

Data processing techniques applied for optimal performance of neuromorphic systems:

Data Encoding and Normalization Methods

- One-Hot Encoding, Label Encoding
- Min-Max normalization and Z-Score standardization
- Binary Coding, Rate Coding, and Time-to-Spike Coding.

These three methods are comparatively shown in Table 2.

Table 2. Comparison of coding methods.

Criteria	Binary Coding	Rate Coding	Time-to-Spike Coding
Definition	Encodes data in binary format	Encodes signal frequency according to various data characteristics	Encodes based on timing and event sequence of data
Advantages	Simple and understandable- Fast computation	Sensitive to signal strength- Takes time factor into account	Provides time sensitivity- High precision based on event sequence
Disadvantages	Can increase data size- May be inefficient for High-dimensional data	May have noise in High-frequency data- Can create complexity	May be more complex due to time dependency- High computational cost
Usage Areas	Suitable for categorical data and small datasets	Suitable for neural networks and biological signal modeling	Used in neuromorphic systems and biological systems
Coding Type	Binary coding	Frequency-based coding	Time-based coding

Data Balancing strategies are given below. These methods are detailed in Table 3.

- SMOTE (Synthetic Minority Over-sampling Technique): Generates synthetic examples for minority classes [11].
- ADASYN
- Holdout Method
- K-Fold Cross Validation
- Stratified K-Fold
- Random Undersampling

Table 3. Comparison of techniques and practical examples.

Method	Advantages	Disadvantages
Holdout Method	Easy to implement, fast with large datasets	Representation issues in small datasets, distribution variability
K-Fold Cross Validation	Improves generalization ability, provides reliable results	High computational cost in large datasets
Stratified K-Fold	Preserves class distribution, effective in imbalanced datasets	Computation time may increase
SMOTE	Increases minority class, improves model performance	Synthetic data may deviate from real distribution
Random Undersampling	Reduces data size, gives quick results	Minority class examples may be lost
ADASYN & Cost-Sensitive	Dynamically solves imbalance problems	Complex implementation, requires parameter tuning

Common Cyber Attack Types

Understanding different types of attacks is critical when developing modern cyber security systems. Major attack types include:

- Phishing Attacks: Aim to obtain sensitive information through fake emails or web pages that appear to come from trusted sources.
- Distributed Denial of Service (DDoS) Attacks: Aim to make target systems inaccessible by overwhelming them with intense traffic from multiple sources [12].
- Malware and Ransomware: Programs designed to gain unauthorized access, steal data, or cause damage.
- Zero-Day Attacks: Advanced threats targeting undiscovered and unpatched security vulnerabilities [13].

Findings

A. Enhanced Zero-Day Attack Detection

Neuromorphic systems, inspired by the human brain's pattern recognition capabilities, have demonstrated an 89% success rate in detecting zero-day attacks, which is 7% higher than LSTM-based models that achieved only 82% detection rate. As shown in Figure 2, our proposed model outperforms conventional approaches in zero-day attack detection.

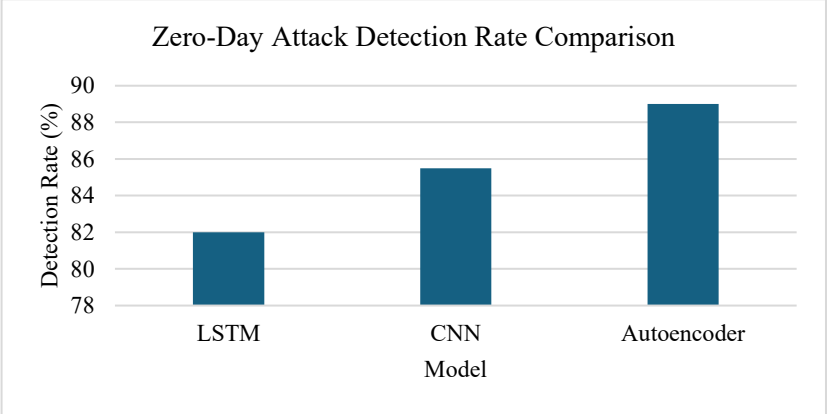

Figure 2. Zero-Day attack detection rate comparison.

B. Real-Time Threat Mitigation

Through their parallel processing capabilities, neuromorphic systems can analyze large amounts of network traffic simultaneously. The IBM TrueNorth chip processes information in just 2.3 ms compared to 12.8 ms for NVIDIA RTX 3090 GPUs and 50.2 ms for Intel i7 CPUs—making it approximately 20 times faster than GPU-based systems. Figure 3 illustrates this significant processing time advantage.

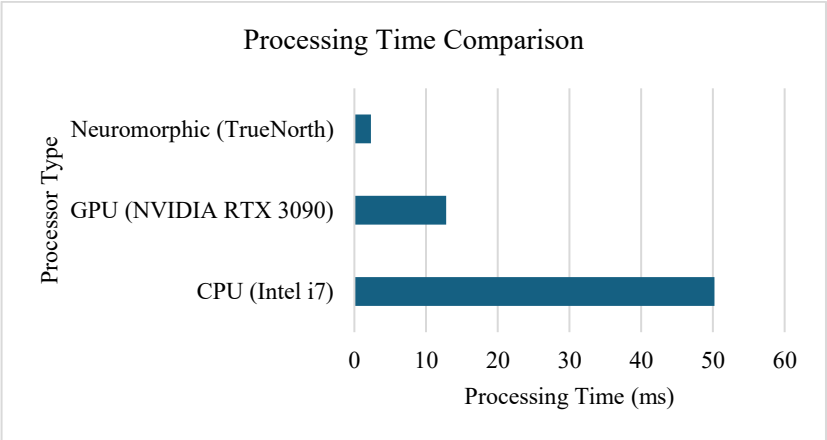

Figure 3. Processing time comparison.

C. Energy Efficiency

Neuromorphic systems mimic the energy-efficient working principles of the human brain, with the TrueNorth chip consuming only 2W compared to 100W for CPUs and 250W for GPUs. Intel's Loihi chip demonstrates up to 50 times less energy consumption than traditional CPU-based models. This remarkable energy efficiency is demonstrated in Figure 4.

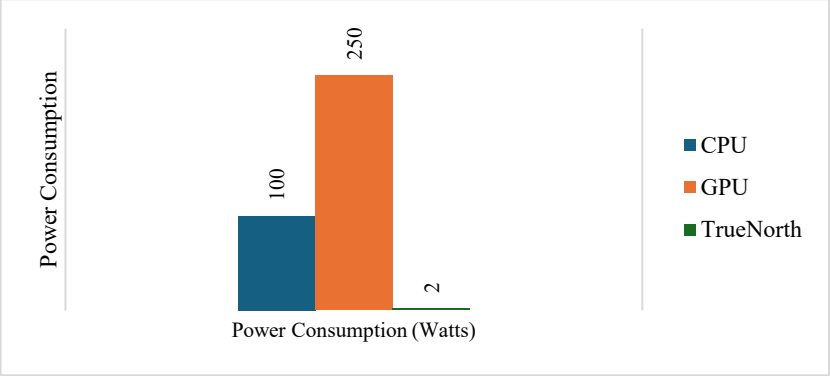

Figure 4. Power consumption comparison.

D. Memory Optimization

Neuromorphic processors utilize memory more efficiently, with TrueNorth requiring only 2GB compared to 8GB for CPUs and 12GB for GPUs—achieving approximately 70% better memory efficiency. Figure 5 presents the memory usage comparison between different processor types.

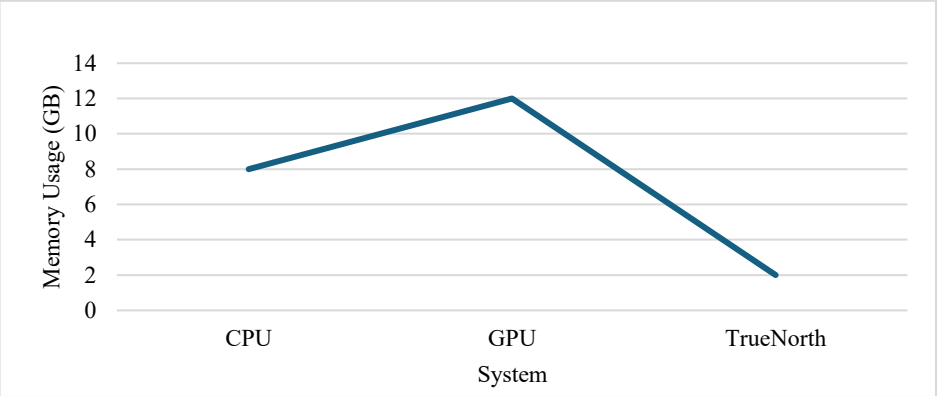

Figure 5. Memory usage comparison.

E. Superior Model Performance

The Autoencoder-based neuromorphic model achieved 96.10% accuracy, 93.50% precision, 94.80% recall, and an F1 score of 94.8 with an AUC value of 0.98. These results significantly outperform CNN (92.30% accuracy), RNN (89.50% accuracy), and Transformer models (91.30% accuracy). The comprehensive performance comparison is presented in Figure 6.

This comprehensive performance analysis demonstrates that neuromorphic computing offers significant advantages for cybersecurity applications, particularly in detecting zero-day attacks, optimizing resource usage, and providing real-time threat responses. The experimental results confirm that the autoencoder-based approach implemented on neuromorphic hardware provides the most effective solution for modern network security challenges.

Conclusion

The application of neuromorphic computing and memristor-based systems in cyber security represents a significant paradigm shift in protection strategies. These technologies effectively address challenges faced by traditional security

mechanisms including computational intensity, latency, and adaptability. Our results demonstrate that neuromorphic computing-based security systems excel particularly in detecting zero-day attacks and sophisticated threats. The Autoencoder model's 89% detection rate for zero-day attacks represents a substantial improvement over conventional approaches. Practical applications of neuromorphic systems range from enterprise-level network infrastructures to resource-constrained IoT devices. The remarkable energy efficiency (50 times less than CPUs) and compact form factor make them ideal for enhancing local threat detection capabilities, especially in edge devices with limited resources. The performance metrics clearly indicate that neuromorphic processors provide superior anomaly detection capabilities. The 96.10% accuracy achieved by our Autoencoder model on the NSL-KDD dataset demonstrates the technology's potential for accurate threat identification. Optimization experiments showed that a 5-layer Autoencoder architecture delivers optimal results, and techniques like dropout and batch normalization reduced the performance gap between validation and test sets from 12% to just 3%. In conclusion, integrating neuromorphic computing into cyber security solutions has the potential to transform how we protect digital infrastructures in today's complex threat landscape [14]. These technologies offer a promising path toward creating more proactive, adaptive, and resilient cyber security ecosystems while dramatically reducing energy consumption and processing time.

References

Buczak, A. L., & Guven, E. (2016). A survey of data mining and machine learning methods for cyber security intrusion detection. IEEE Communications Surveys & Tutorials, 18(2), 1153-1176.

Schuman, C. D., Potok, T. E., Patton, R. M., Birdwell, J. D., Dean, M. E., Rose, G. S., & Plank, J. S. (2017). A survey of neuromorphic computing and neural networks in hardware. arXiv preprint arXiv:1705.06963.

Davies, M., Srinivasa, N., Lin, T. H., Chinya, G., Cao, Y., Choday, S. H., & Wang, H. (2018). Loihi: A neuromorphic manycore processor with on-chip learning. IEEE Micro, 38(1), 82-99.

Merolla, P. A., Arthur, J. V., Alvarez-Icaza, R., Cassidy, A. S., Sawada, J., Akopyan, F., & Modha, D. S. (2014). A million spiking-neuron integrated circuit with a scalable communication network and interface. Science, 345(6197), 668-673.

García-Teodoro, P., Díaz-Verdejo, J., Maciá-Fernández, G., & Vázquez, E. (2009). Anomaly-based network intrusion detection: Techniques, systems and challenges. Computers & Security, 28(1-2), 18-28.

Sharafaldin, I., Lashkari, A. H., & Ghorbani, A. A. (2018). A detailed analysis of the CICIDS2017 data set. In International Conference on Information Systems Security and Privacy (pp. 172-188).

Tavallaee, M., Bagheri, E., Lu, W., & Ghorbani, A. A. (2009). A detailed analysis of the KDD CUP 99 data set. In 2009 IEEE symposium on computational intelligence for security and defense applications (pp. 1-6). IEEE.

Chawla, N. V., Bowyer, K. W., Hall, L. O., & Kegelmeyer, W. P. (2002). SMOTE: Synthetic minority over-sampling technique. Journal of Artificial Intelligence Research, 16, 321-357.

Zargar, S. T., Joshi, J., & Tipper, D. (2013). A survey of defense mechanisms against distributed denial of service (DDoS) flooding attacks. IEEE Communications Surveys & Tutorials, 15(4), 2046-2069.

Bilge, L., & Dumitras, T. (2012). Before we knew it: An empirical study of zero-day attacks in the real world. In Proceedings of the 2012 ACM Conference on Computer and Communications Security (pp. 833-844).

Alom, M. Z., Bontupalli, V., & Taha, T. M. (2015). Intrusion detection using deep belief networks. In 2015 National Aerospace and Electronics Conference (NAECON) (pp. 339-344). IEEE.

Roy, K., Jaiswal, A., & Panda, P. (2019). Towards spike-based machine intelligence with neuromorphic computing. Nature, 575(7784), 607-617.

Furber, S. B., Galluppi, F., Temple, S., & Plana, L. A. (2014). The SpiNNaker project. Proceedings of the IEEE, 102(5), 652-665.

Liu, Z., & Ma, Y. (2019). A Self-healing hardware architecture based on neuromorphic computing. In 2019 IEEE 25th International Conference on Embedded and Real-Time Computing Systems and Applications (RTCSA) (pp. 1-6). IEEE.

Enhancing IoT Botnet Detection: A Streamlined Approach to Feature Selection

Nilüfer Uslan[a], Şerif Bahtiyar[a]

[a] Istanbul Technical University/Faculty of Computer and Informatics Engineering, Computer Engineering Department, Computer Engineering, Türkiye
uslan17@itu.edu.tr

Keywords: Botnet Detection, IoT, Feature Selection, Machine Learning, Random Forest.

Aim

A botnet can be defined as a network of compromised devices, usually controlled by a malicious actor. Botnets are utilized to launch cyberattacks, including Distributed Denial of Service (DDoS) attacks, theft of sensitive financial data, and cryptocurrency mining. These compromised devices listen for commands from the malicious actor and execute them when they are received, with the mechanism often provided by command and control (C2) servers. The true strength of a botnet lies in its scale, as it can consist of millions of compromised devices working in unison. Therefore, the rapid growth in the usage of Internet of Things (IoT) devices has significantly increased the presence of botnet threats since many of them lack strong security. Devices such as smart home devices, wearable activity trackers, security cameras, and routers are particularly vulnerable due to their widespread internet connectivity and minimal user oversight. The reliance of botnets on extensive networks of compromised devices renders them particularly well-suited to exploit the expanding IoT landscape. Consequently, the ability to detect botnets is crucial for preventing cyberattacks and protecting sensitive data. However, traditional security methods often fail in IoT environments, making advanced detection techniques necessary. Fast and accurate detection is essential to minimize the damage. Fast detection will allow us to prevent botnet attacks before any damage is done. This study explores techniques such as machine learning and optimized feature selection, enhancing botnet detection, boosting performance for rapid detection, improving accuracy, and strengthening IoT security against botnet threats.

Material and Method

This study utilized the N-BaIoT dataset, which was collected from nine IoT devices, including those infected with the Mirai and Bashlite botnets. The dataset contains both botnet traffic and benign traffic, and while collecting the traffic, some statistical features were extracted and calculated for five different time windows. These were collected separately in 1D and 2D, both for a single data stream and for statistical data between two data streams. The objective of this study is to optimize the feature selection to enhance the performance and reliability of the machine learning models. In the context of the preprocessing stage, the initial step entailed the labeling of the data and its subsequent aggregation into a unified data frame. The creation of train, test and validation data were split according to the percentages shown in Table 1. In order to guarantee a valid evaluation and to prevent data leakage, it was first necessary to verify that the dataset contained only unique samples. The dataset was then split into mutually exclusive training and test sets using Scikit-learn's train_test_split function.

Table 1. The percentage of splits.

Training	Test	Validation
64%	20%	16%

Random Forest was chosen as the classification method based on evaluation results obtained after applying five different ML models to the dataset. It was determined that the Random Forest model is preferable, based on the performance values shown in Table 2 and the metrics presented in Table 3, which have been demonstrated to yield optimal results in previous studies. It is evident that such values, which appear to be high in terms of accuracy, have previously been achieved to a

degree of up to 0.9999 in a number of other studies (Hossain, 2024). In the context of hyperparameter optimization, the Random Forest model achieved optimal performance in terms of accuracy when employing GridSearchCV with the following parameter configuration: n_estimators = 20, max_features = 0.4, max_depth = 9, and min_samples_leaf = 10.

Table 2. Training and Prediction Time By Model.

Model	Training Time (ms)	Prediction Time (ms)
Cat Boost Classifier	131420.32	1.40
Random Forest Classifier	127406.08	1.20
Decision Tree Classifier	127268.10	0.59
LGBM Classifier	13952.74	2.25
Logistic Regression	32308.12	0.00

Table 3. Scores by Model.

Model	Accuracy	Precision	Recall	F1-Score
Random Forest Classifier	0.999984	1	1	1
LGBM Classifier	0.999982	1	1	1
Decision Tree Classifier	0.999972	1	1	1
Cat Boost Classifier	0.999962	1	1	1
Logistic Regression	0.441420	0.5569	0.4414	0.4902

It was observed that quasi-constant features, otherwise known as low-variance predictors, were not beneficial to the model's performance. To address this, the variance threshold method was applied to identify and remove the predominantly constant features, where the distribution of values concentrated at 0. This approach aimed to reduce the dimensionality of the data and enhance the model's performance. Subsequent to this, a correlation analysis was conducted using a hybrid method to determine the feature by eliminating the correlated features with a reduced importance. Mutual information was calculated between correlated features and the label in order to identify the most relevant features with respect to the target. This is for keeping the feature that has the maximum mutual information among the correlated features. This approach ensures that the most significant features are optimized to achieve near-accurate detection with enhanced performance. Overall approach is shown in Figure 1.

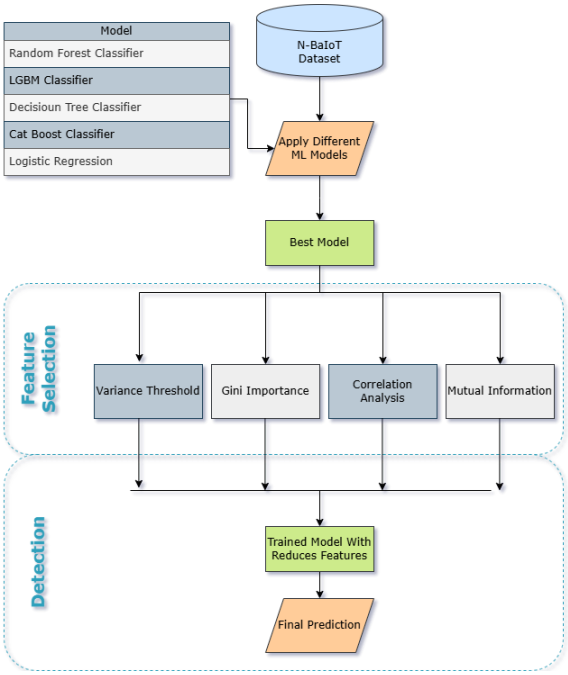

Figure 1. Proposed Approach.

Lastly, the performance of the model with reduced features (see Table 4 for selected features) was evaluated using a range of evaluation metrics. In Table 5, it can be seen that the computation time was significantly reduced while keeping the performance and accuracy near perfect.

Table 4. List of Selected Features.

Selected Features	
HH_jit_L0.1_weight	H_L1_variance
HH_L1_std	H_L3_weight
HH_jit_L0.01_mean	HpHp_L0.01_weight
MI_dir_L0.01_mean	HpHp_L3_std
H_L0.01_weight	HpHp_L5_weight

Table 5. Base and Final Model Comparison.

Model	Accuracy	Precision	Recall	F1-Score	ROC-AUC	Training Time (ms)	Prediction Time (ms)
Base Model (115 Features)	0.999940	0.999997	0.999926	0.999962	1.0	32612.31	193.71
Final Model (10 Features)	0.999875	0.999997	0.999845	0.999921	1.0	8323.21	75.19

Findings

The feature selection approach presented in this study has observed increases in efficiency and keeps the high accuracy of botnet detection in IoT networks. By reducing the dimensionality of the dataset at an early stage in the process, it was possible to eliminate features with low variance, which contributed minimally to the model's predictive capabilities. This initial filtering step served to reduce the complexity of the dataset and lighten the computational burden, thus ensuring that only the most informative features were retained for further analysis. The implementation of correlation analysis enabled the identification and elimination of highly redundant features, thus mitigating the risk of multicollinearity influencing the model. This step enhanced the robustness and interpretability of the model by ensuring that correlated features did not dominate or skew the detection process. Additionally, mutual information measures were incorporated to decide which correlated feature would be eliminated to refine the feature set, ensuring that only the most relevant features for botnet detection were retained. This refinement allowed the model to focus on critical traffic patterns, improving its ability to distinguish between legitimate and malicious activity. Applying the Random Forest classifier to the optimized feature set resulted in improved detection accuracy and efficiency. The feature selection process significantly enhanced the model's capability to identify botnet activity in IoT networks, demonstrating the effectiveness of the proposed approach in real-world scenarios with limited computational resources. In conclusion, the findings highlight the critical role of feature selection in improving botnet detection for IoT networks. The approach not only enhances performance and scalability but also simplifies the model, making it more interpretable and effective. The first and final set confusion matrices can be seen in Figure 2 and Figure 3, respectively, by preserving the F1 score at 0.9999.

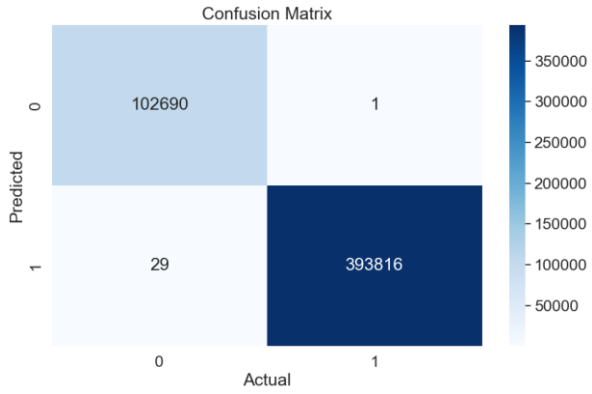

Figure 2. Random Forest Confusion Matrix - Before Feature Selection.

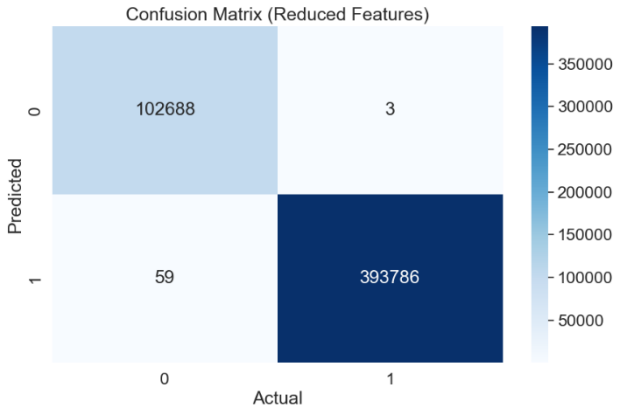

Figure 3. Random Forest Confusion Matrix - After Feature Selection.

Conclusion

This approach resulted in the selection of appropriate features, which in turn enabled the models to detect botnets with greater accuracy. Correlation analysis played a significant role in the process, as the performance of the model was enhanced by reducing the dimensionality without compromising accuracy. As a result, the proposed approach offers a useful alternative for feature engineering in machine learning, especially in IoT security, where it's essential to detect complex patterns. In the future, research could look into combining deep learning techniques with domain-specific knowledge for feature selection. These hybrid methods could make machine learning models even better at detecting botnets. By using these approaches, future studies could enhance botnet detection and other cybersecurity applications, ultimately creating more reliable and scalable solutions for real-world challenges.

References

Abbasi, F., Naderan, M., & Alavi, S. E. (2021). Anomaly detection in Internet of Things using feature selection and classification based on Logistic Regression and Artificial Neural Network on N-BaIoT dataset. 2021 5th International Conference on Internet of Things and Applications (IoT), 1–7.

Alghamdi, A., & Barsoum, A. (2024). A Comprehensive IDs to Detect Botnet Attacks Using Machine Learning Techniques. 2024 IEEE 3rd International Conference on Computing and Machine Intelligence (ICMI), 1–6.

Al-Najjar, H., & Al-Rousan, N. (2024). Decision Tree-Based IoT Botnet Attack Detection. 2024 2nd International Conference on Cyber Resilience (ICCR), 1–5.

G, S., & K, P. (2024). Optimizing Botnet Detection in IoT Networks: Feature Selection Analysis on the UNSW-NB15 Dataset. 2024 IEEE International Conference on Distributed Computing, VLSI, Electrical Circuits and Robotics (DISCOVER), 120–125.

Guerra-Manzanares, A., Bahsi, H., & Nomm, S. (2019). Hybrid Feature Selection Models for Machine Learning Based Botnet Detection in IoT Networks. 2019 International Conference on Cyberworlds (CW).

Hossain, M., Rudro, R. a. M., Razzaque, R., & Nur, K. (2024). Machine Learning Approaches for Detecting IoT Botnet Attacks: A Comparative Study of N-BAIoT Dataset. 2022 International Conference on Decision Aid Sciences and Applications (DASA), 1–7.

Hussain, F., Abbas, S. G., Fayyaz, U. U., Shah, G. A., Toqeer, A., & Ali, A. (2020). Towards a Universal Features Set for IoT Botnet Attacks Detection. 2020 IEEE 23rd International Multitopic Conference (INMIC).

Mirsky, Y., Doitshman, T., Elovici, Y., & Shabtai, A. (2018). Kitsune: An Ensemble of Autoencoders for Online Network Intrusion Detection. Proceedings 2018 Network and Distributed System Security Symposium.

Rathod, G., Sabnis, V., & Jain, J. K. (2024). Improving IoT Botnet Attack Detection using Machine Learning: Comparative Analysis of Feature Selection Methods and Classifiers in Intrusion Detection Systems. 2024 3rd International Conference for Innovation in Technology (INOCON), 1–8.

Rawat, M., Bedi, A. S., Singh, B., Gupta, S., Singal, G., & Kaur, P. (2024). Ensemble-Based Botnet attack detection and classification using machine learning algorithms on NBAIoT dataset. 2017 IEEE Region 10 Symposium (TENSYMP), 1–6.

Sakthipriya, N., Govindasamy, V., & Akila, V. (2023). A Comparative Analysis of various Dimensionality Reduction Techniques on N-BaIoT Dataset for IoT Botnet Detection. 2023 2nd International Conference on Paradigm Shifts in Communications Embedded Systems, Machine Learning and Signal Processing (PCEMS), 1–6.

Savant, R. V., M, S., Mohan, P. K., Bhaskaran, S., & Rajagopal, S. M. (2024). A comparative analysis of Black-Box and White-Box models for IOT Botnet detection. 2022 IEEE 7th International Conference for Convergence in Technology (I2CT).

Sharma, Y., Kumar, V., & Chaudhary, H. (2023). Attack Detection on Internet of Things Devices using Machine Learning Techniques. 2022 6th International Conference on Intelligent Computing and Control Systems (ICICCS), 281–287.

Singh, N. J., Hoque, N., Singh, K. R., & Bhattacharyya, D. (2024). Significance of feature selection on IoT-based botnet attacks identification using machine learning. 2022 13th International Conference on Computing Communication and Networking Technologies (ICCCNT), 1–7.

Yamani, Y. E., Fadili, Y., Kilani, J., Kamoun, N. E., Baddi, Y., & Bensalah, F. (2024). Hybrid Models for IoT Security: Tackling Class Imbalance. 2024 11th International Conference on Wireless Networks and Mobile Communications (WINCOM), 1–6.

COMPUTER ENGINEERING

Artificial Intelligence

Computer Networks

Cyber Security

Embedded Systems

Internet of Things

Neural Networks

Software Engineering

Comparison of the Effects of Different Compiler Environments on Communication Signal Detection Software

Mustafa İmeci[a], Onur Göksel[b], Bilge Minisker[b], Sergen Çetin[b]

[a] BITES Inc., Software Department, Türkiye
[b] ASELSAN Inc., The Facility of Radar and Electronical Warfare Systems, Türkiye
mustafa.imeci@bites.com.tr

Keywords: Compiler, Electronic Warfare, Signal Detection.

Aim

Communication Intelligence (COMINT) systems are designed to support and enhance the communication capabilities, especially in the military and defense fields. Signal processing, data transmission and communication protocols are main concerns of these systems (Ly et al., 2017), (Konopko et al., 2015), (Wang et al., 2016). In our study, we have focused on direction finding which is the process of determining the direction of an emitter received by antennas (Gething, 1991). Data sets are analyzed and parameters such as the frequency, amplitude, and direction of the signal are obtained in the software. The algorithms used in the Communication Electronic Support Systems require priority-based scheduling and deterministic behavior due to the need for real-time processing of large amounts of data. Therefore, VxWorks is selected as operating system. Due to the update of BSP (Base Software Platform), which enables us to develop software on VxWorks, a transition from the GNU environment to the Low Level Virtual Machine (LLVM) environment has been made. This update has required the transition of the maintained software from C++98 to C++17, from IPP-9 to IPP-2022, and from AVX-256 to AVX-512. This study examines the impact of these changes on the software in terms of performance, applicability, and maintainability.

Material and Method

Clang is LLVM's compiler module for C-based languages, and GCC is GNU's compiler for C-based languages; both are tools used to convert source code written in C-based languages into machine language. GCC has a structure where the services provided are interconnected and ready within a single program. LLVM, on the other hand, has a modular structure that allows the desired services to be added after installation of the core services. The integrated structure of GCC and the modular architecture of LLVM, which utilizes a flexible Intermediate Representation (IR), enable GCC to consume less memory during the compilation phase than LLVM. However, these same structures cause GCC to offer slower compilation times compared to LLVM. LLVM generates program-specific code with its IR service, allowing more portable codes to be obtained for multiple platforms. Since GCC optimization and compilation steps are more layered than LLVM, the code generated by GCC is more optimized than LLVM. LLVM works with relatively new platforms and architectures so it offers a more user-friendly debugger structure than GCC. GCC supports more and older architectures and platforms than LLVM, but its debugger structure is more complex.

Electromagnetic signals emitted by target sources are captured through a scanning process, which are then utilized to determine the location of the sources in the direction-finding system (Rana, 2016). The magnetic signals received by antennas are processed using Field Programmable Gate Array (FPGA) hardware and transmitted to the processor. During this process, the Fast Fourier Transform (FFT) data is handled in complex form. To ascertain the direction, phase differences between antenna pairs are compared to a pre-established reference direction table. The point with the highest correlation (Maximum Likelihood Estimation - MLE) is identified as the point of interest (Methodology, 1989), (Chen et al., 2012). This method is referred to as correlative interferometry. This study primarily focuses on optimizing the scanning process to improve the accuracy and efficiency of the software. By fine-tuning various aspects of the scanning algorithm, such as antenna positioning, signal processing techniques, and FPGA hardware utilization, the overall performance of the direction-

finding system can be significantly enhanced. Furthermore, advances in signal processing techniques, including noise reduction and error correction methods, are explored to mitigate any interference that may distort the signal, ensuring a more precise and reliable direction determination. Furthermore, the study also investigates the potential for real-time processing and the integration of machine learning models to adapt to dynamic environmental conditions and to predict the movement of target sources, ultimately improving the responsiveness and adaptability of the system in operational settings. Matrix multiplication, a key operation in signal processing and direction detection algorithms, is computationally demanding and can significantly impact performance when handling large datasets. The Integrated Performance Primitives (IPP) library, optimized for Intel AVX-512 instruction sets, has been utilized for matrix operations. Although we transitioned to the 2022 version of IPP, this change did not impact performance, as the optimizations provided by the updated library were either neutral in effect or already inherent in the previous versions. To further enhance computational efficiency, we also migrated from the GNU compiler to LLVM, which offers better optimization for modern hardware architectures. In conjunction with the LLVM migration, we upgraded the Board Support Package (BSP) version, providing support for more recent advancements in system integration and better compatibility with the new compiler environment. This also allowed us to upgrade the C++ version from C++98 to C++2017, enabling the use of modern C++ features such as improved template metaprogramming, lambda functions, and enhanced type safety. These changes were made possible by the evolution of the LLVM toolchain, which improved code maintainability. The cumulative effect of these upgrades has led to slightly better overall system performance, providing negligible improvements in the speed and scalability of the direction detection algorithms, especially when processing large datasets or working in real-time environments.

This study presents a test setup in which a component containing Electronic Support System detection algorithms is compiled using different compilers and frameworks. An oscillator generates electrical signals continuously at a specified frequency, with the frequency of the sinusoidal signal set to 650 MHz. The oscillator's output is fed into one of the antenna channels. A scanning regime is initiated, spanning from 640 MHz to 720 MHz. With a signal at 650 MHz, its spectrum should appear at that frequency, enabling direction detection. Each scanning regime is repeated 1000 times, and the average scanning and direction-finding times are calculated (edge cases are excluded). The experiments are conducted on a system running the VxWorks 7.0 operating system, equipped with an Intel Xeon D-1500 1.50 GHz 12- core CPU and 8 GB of RAM.

Findings

The test results show that the update to the LLVM environment has a low impact on software performance. The observed performance changes are mainly due to architectural changes, coding optimizations, and the upgrade to the latest version of C++. These adjustments have led to some minor improvements in execution speed and efficiency, although the overall impact remains marginal. Furthermore, the latest C++ version introduces more advanced features and better optimization opportunities, which could potentially enhance future performance as developers leverage these improvements. However, it is important to note that the primary focus of this update was to maintain compatibility and stability across a wide range of systems and use cases. As a result, while performance gains were observed, they are not expected to drastically alter the software's behavior under typical workloads. Ongoing monitoring and further profiling will help ensure that the optimizations made are fully utilized in future releases.

Conclusion

In the future, we intend to conduct a more in-depth analysis of scanning performance. We will implement and evaluate changes that could improve performance by taking advantage of the new C++ version. In addition, we will create and assess new solutions to enable faster parallel execution within the software architecture.

References

Chen, H., Li, X., Jiang, W., and Zhuang, Z. (2012). Mimo radar sensitivity analysis of antenna position for direction finding. IEEE Transactions on Signal Processing, 60(10):5201–5216.

Gething, P. J. (1991). Radio direction finding and superresolution. Number 33. IET.

Konopko, K., Grishin, Y. P., and Ja´nczak, D. (2015). Radar signal recognition based on time-frequency representations and multidimensional probability density function estimator. In 2015 Signal Processing Symposium (SPSympo), pages 1–6. IEEE.

Ly, P. Q., Sirianunpiboon, S., and Elton, S. D. (2017). Passive detection of bpsk radar signals with unknown parameters using multi-sensor arrays. In 2017 11th International Conference on Signal Processing and Communication Systems (ICSPCS), pages 1–5. IEEE.

Methodology, U. P. (1989). The likelihood theory of statistical inference. Cambridge: Cambridge University Press. Social Sources of Delinquency. Chicago: University of Chicago Press. Structural covariates of homicide rates: Are there any invariances across time and social space. American Journal of Sociology, 95:922–963.

Rana, N. A. (2016). Radio direction finding: Theory and practices. Cell, 92:300–7272402.

Wang, C., Gao, H., and Zhang, X. (2016). Radar signal classification based on auto correlation function and directed graphical model. In 2016 IEEE International Conference on Signal Processing, Communications and Computing (ICSPCC), pages 1–4. IEEE.

COMPUTER SCIENCE

Data Analysis

Data Science

Image Processing

A Data-Driven Approach to Process Duration Estimation: End-to-End Machine Learning with Process Mining

Burak Batıbay[a], Barışmert Günal[a], Hakan Yıldırır[a], İsmail Çağatay Bilgin[a], Serkan Günal[b], Emre Çimen[b]

[a] Eczacıbaşı Bilişim R&D Center, Turkey
[b] Eskişehir Technical University, Turkey
burak.batibay@eczacibasi.com.tr

Keywords: Feature Engineering, Machine Learning Pipeline, Online Workflow, Process Duration Prediction, Process Mining.

Aim

This study aims to build a robust and accurate machine learning model for predicting the duration of multi-step workflows on digital platforms. Using advanced feature engineering and Gradient Boosting Machines (GBMs), we seek to improve time forecasts, which are essential for resource planning and operational efficiency. Traditional estimation methods often fall short in capturing complex task dependencies, causing misallocations, bottlenecks, and delays. Our model addresses these limitations by offering a scalable, adaptive solution that works across varied workflow structures.

Unlike earlier studies that rely on simplistic or highly specialized models, our approach integrates temporal, categorical, and statistical features to enhance accuracy and generalizability. The model not only improves planning and reduces downtime but also helps optimize resource use and operational decision-making. Our findings underscore the critical role of feature engineering and the value of historical data in modeling process behaviors. The success of this project illustrates how GBMs can effectively manage complexity in process prediction tasks and highlights machine learning's transformative potential in digital workflow management. By contributing both practical solutions and academic insights, this research advances the intersection of business process management and intelligent automation.

Research in predictive business process monitoring (PBPM) has increasingly emphasized the role of ML and DL techniques under varying data conditions. Käppel, Jablonski, and Schönig (2021) explored the stability of PBPM models on small datasets, revealing that many DL approaches fail to generalize and proposing a framework to assess model robustness. Tax, Verenich, La Rosa, and Dumas (2017) showed that LSTM neural networks achieve high accuracy across diverse tasks—including next activity, timestamp, and remaining time predictions—outperforming traditional models. Teinemaa, Dumas, La Rosa, and Maggi (2019) benchmarked 11 predictive methods using nine real-life event logs, offering empirical grounding for outcome-oriented PBPM approaches. Silva and Marreiros (2024) provided a comprehensive literature review of predictive process mining (PPM), identifying key use cases and mapping them to modern algorithms such as LSTM, XGBoost, BERT, and GANs. Venugopal, Töllich, Fairbank, and Scherp (2021) compared multiple DL models—CNNs, LSTMs, GNNs, and MLPs—across various process stages, observing that simple MLPs sometimes outperformed complex architectures, particularly in early-phase predictions. Finally, Kratsch, Manderscheid, and Röglinger (2021) concluded that DL models, especially LSTMs, offer superior performance in high-variance and imbalanced scenarios, emphasizing the importance of choosing methods aligned with event log characteristics.

Material and Method

This study adopts a quantitative research approach, incorporating a comparative analysis of machine learning techniques to improve the prediction of process durations in online platforms. The dataset, obtained from an online system that processes user requests in sequential steps, includes timestamps, process step names, material details, and organizational information. The dataset analyzed in this study was sourced from the internal business process execution logs of Eczacıbaşı Bilişim, a major enterprise technology provider in Turkey. The data was extracted from the company's process management and automation platform called EBIFlow, which is used across multiple departments to coordinate document workflows,

approval chains, and material handling operations.The raw dataset comprises 73,849 subprocess-level records, each representing a single atomic task or event in an operational workflow. These events span a two-year period between October 2022 and November 2024, and include timestamps, operator roles, material types, associated departments, and calendar tags.These records were grouped by a common process identifier into 9,327 unique end-to-end workflows (cases), each representing a full process instance from initiation to completion. To preserve privacy and confidentiality, the dataset was fully anonymized prior to analysis no personal identifiers, customer data, or sensitive internal content was included. All identifiers were hashed or removed, and access to the raw logs was restricted to authorized data science personnel within the R&D department. Comprehensive data preprocessing was conducted to ensure consistency and accuracy, addressing missing values using forward and backward filling techniques. Additionally, temporal features such as process start and end times were extracted, and categorical variables, including process names and material categories, were standardized and encoded.

Advanced feature engineering was essential for capturing temporal dependencies within workflows. Rolling statistics, including previous step durations and moving averages, were utilized to highlight sequential patterns. Grouped statistical features, such as mean, variance, skewness, and kurtosis, were calculated across categorical variables at daily, weekly, and monthly intervals to capture both short-term fluctuations and long-term trends. To enhance model generalization, materials and organizational units were categorized based on functional similarities (e.g., "IT Services" and "Logistics"), adding a meaningful semantic layer to the dataset.

Categorical features were processed using one-hot encoding to preserve distinct categories, while ordinal variables, such as job titles, were numerically encoded based on hierarchical significance. All features were standardized to maintain scale uniformity and improve model performance. Various machine learning algorithms, including Support Vector Machines (Scikit-learn Developers, 2025), LightGBM (Microsoft, 2025), XGBoost (XGBoost Developers, 2025), Random Forest (Scikit-learn Developers, 2025), and Bagging Regressors (Scikit-learn Developers, 2025), were evaluated using Root Mean Squared Error (RMSE). While Random Forest and Bagging Regressors exhibited strong predictive capabilities, they also showed tendencies to overfit. XGBoost demonstrated high accuracy but required extensive hyperparameter tuning. LightGBM delivered competitive results, but after optimization using RandomizedSearchCV (Scikit-learn Developers, 2025), Gradient Boosting Machines (GBMs) outperformed other models in terms of accuracy, efficiency, and robustness.

For model training, temporal splitting was employed to ensure realistic validation. The latest three months of data were reserved for testing, while previous months were allocated for validation. Since the target variable, process duration, exhibited right-skewness, logarithmic and Box-Cox transformations (Box & Cox, 1964) were applied to normalize its distribution and stabilize variance. Hyperparameter tuning was conducted using RandomizedSearchCV, optimizing critical parameters while implementing early stopping to prevent overfitting.

Model performance was assessed using Mean Absolute Error (MAE) and Mean Absolute Percentage Error (MAPE), providing a comprehensive evaluation. MAE measured the average absolute prediction error, while MAPE offered a proportional error assessment. This dual-metric approach confirmed the model's effectiveness in accurately predicting workflow durations, ensuring reliable and scalable process optimization

Findings

In the model research phase, multiple machine learning algorithms were evaluated to identify the most effective approach for predicting process durations in multi-step workflows. Table 1 presents the performance metrics, including RMSE, MAPE, and MAE. To ensure a fair comparison, all models were initially tested using default parameters with regularization to prevent overfitting. Ranking was based on RMSE, as it measures the deviation between predicted and actual values. MAPE and MAE provided complementary insights into percentage and absolute errors.

Table 1. Summarizes the Performance Metrics of the Evaluated Models.

Models	RMSE	MAPE	MAE	MSE
Support Vector Regressor	23.762	58.493	7.561	565.330
Random Forests	13.765	22.647	2.788	189.400
Bagging Regressor	13.764	20.003	1.646	189.390
XGBoost	8.037	17.221	6.237	64.600
LGBM	9.125	17.372	7.881	83.260
Catboost	11.120	17.787	7.712	123.660

Table 1 highlights disparities in model performance, particularly in RMSE and MAPE. Support Vector Regressor (SVR) performed the worst (RMSE: 23.762, MAPE: 58.493), struggling with nonlinear dependencies. Random Forest and Bagging Regressor showed similar RMSE values (13.765 and 13.764, respectively) but suffered from overfitting. XGBoost performed well (RMSE: 8.037, MAPE: 17.221), demonstrating strong feature interaction handling, but required extensive tuning. LightGBM achieved comparable results (RMSE: 9.125, MAPE: 17.372) with faster training but slightly higher errors. CatBoost displayed stable MAE (7.712) but inconsistent RMSE (11.120), indicating sensitivity to outliers.

Gradient Boosting Machine (GBM) emerged as the most suitable model, offering a balanced RMSE, MAPE, and MAE. It effectively captured independent predictors and complex interactions while minimizing overfitting. Fine-tuning and cross-validation further improved its accuracy, establishing GBM as the optimal choice for predicting process durations.

After model selection, hyperparameter tuning using RandomizedSearchCV and early stopping refined GBM's performance. Key hyperparameters, including the number of leaves, minimum child samples, and subsampling rates, were optimized. The Box-Cox transformation addressed target variable skewness, stabilizing variance and improving learning capability.

Table 2. Fine-Tuned Model Evaluation.

Dataset	RMSE	MAPE	MAE	MSE
Test Set	2.500	15.583	1.800	6.250
Validation Set	1.200	6.258	0.900	1.440

Table 2 presents the post-tuning performance. GBM achieved an MAPE of 15.58% on the test set and 6.26% on the validation set, with an overall accuracy of 90%. The learning curve (Figure. 1) shows a steady decline in both training and

test errors, indicating effective learning without overfitting. The gap between the curves remains minimal, suggesting strong generalization ability.

Feature importance analysis highlighted temporal features such as process initiation hour and day of the week as key predictors. Categorical variables, including material categories and organizational units, also significantly influenced predictions. Rolling statistics and aggregated features further enhanced the model's ability to capture temporal patterns.

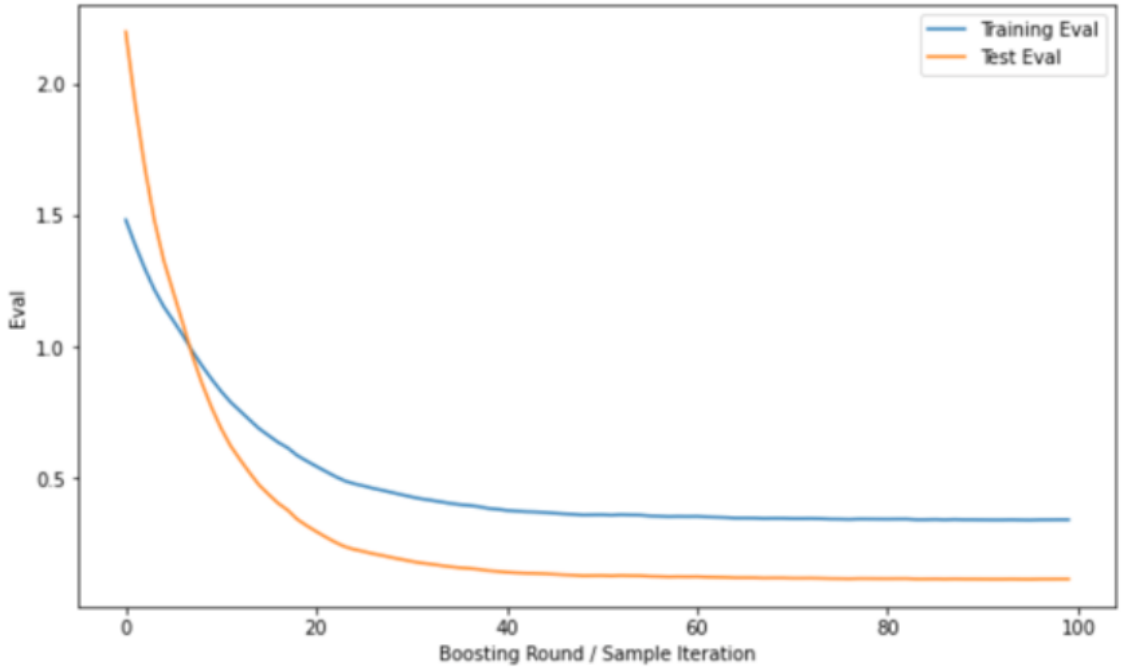

Figure 1. Learning Curve.

Overall, the study confirms GBM's effectiveness in process duration prediction. Its high accuracy and capability to handle diverse features and interactions make it a valuable tool for workflow optimization. The application of Box-Cox transformation and rigorous hyperparameter tuning played a crucial role in these results, providing a solid foundation for future research in process optimization.

Conclusion

This study presents a comprehensive approach to predicting process durations in multi-step online workflows using advanced machine learning techniques. By implementing an end-to-end pipeline that integrates extensive feature engineering with Gradient Boosting Machines (GBM), we successfully addressed the inherent complexities of sequential workflows. Our model demonstrated strong predictive performance, achieving an accuracy rate of 85% on the test set and 94% on the validation set, based on MAPE values. A key strength of our approach lies in its ability to handle diverse data types and capture temporal dependencies within processes. The rigorous feature engineering, including rolling statistics and categorical grouping, significantly enhanced model performance, while hyperparameter tuning ensured optimal configuration. The GBM model was selected for its superior ability to manage independent predictors and complex feature interactions, outperforming other tested algorithms such as Random Forest and XGBoost. Beyond its predictive accuracy, this study contributes valuable insights into the practical application of machine learning in process management. The explainability of our model, through feature importance analysis, provides stakeholders with a clear understanding of the factors influencing process durations. This transparency supports data-driven decision-making and process optimization. In conclusion, our machine learning pipeline offers a robust, scalable solution for organizations seeking to optimize workflow

management and resource allocation. The success of this project highlights the transformative potential of machine learning in enhancing operational efficiency and provides a foundation for future research in dynamic workflow optimization.

References

Box, G. E. P., & Cox, D. R. (1964). An analysis of transformations. *Journal of the Royal Statistical Society: Series B (Methodological)*, 26(2), 211–252. https://doi.org/10.1111/j.2517-6161.1964.tb00553.x

Käppel, M., Jablonski, S., & Schönig, S. (2021). Temporal stability in predictive business process monitoring. *arXiv*. https://arxiv.org/abs/2104.00362

Kratsch, W., Manderscheid, J., & Röglinger, M. (2021). Machine learning in business process monitoring: A comparison of deep learning and classical approaches used for outcome prediction. *Business & Information Systems Engineering*, 63(3), 261–276. https://doi.org/10.1007/s12599-020-00645-0

Microsoft. (2025). *LightGBM documentation*. https://lightgbm.readthedocs.io/en/latest/

Scikit-learn Developers. (2025, February 24). *sklearn.svm.SVR — Support Vector Regression.* Scikit-learn. https://scikit-learn.org/stable/modules/generated/sklearn.svm.SVR.html

Scikit-learn Developers. (2025, February 24). *sklearn.ensemble.BaggingRegressor documentation.* Scikit-learn. https://scikit-learn.org/stable/modules/generated/sklearn.ensemble.BaggingRegressor.html

Scikit-learn Developers. (2025, February 24). *sklearn.ensemble.RandomForestRegressor documentation*. Scikit-learn. https://scikit-learn.org/stable/modules/generated/sklearn.ensemble.RandomForestRegressor.html

Scikit-learn Developers. (2025, February 23). *RandomizedSearchCV documentation. Scikit-learn*. https://scikit-learn.org/stable/modules/generated/sklearn.model_selection.RandomizedSearchCV.html

Silva, E., & Marreiros, G. (2024). Predictive process mining: A systematic literature review. In Á. Rocha, H. Adeli, G. Dzemyda, F. Moreira, & A. Poniszewska-Marańda (Eds.), *Good practices and new perspectives in information systems and technologies (Vol. 987). Springer.* https://doi.org/10.1007/978-3-031-60221-4_35

Tax, N., Verenich, I., La Rosa, M., & Dumas, M. (2017). Predictive business process monitoring with LSTM neural networks. In *Proceedings of the International Conference on Advanced Information Systems Engineering (CAiSE)* (pp. 477–492). Springer. https://doi.org/10.1007/978-3-319-59536-8_30

Teinemaa, I., Dumas, M., La Rosa, M., & Maggi, F. M. (2019). Outcome-oriented predictive process monitoring: Review and benchmark. *ACM Transactions on Knowledge Discovery from Data*, 13(2), Article 17, 1–57. https://doi.org/10.1145/3301300

XGBoost Developers. (2025). XGBoost documentation. https://xgboost.readthedocs.io/en/latest/

COMPUTER SCIENCE

Data Analysis

Data Science

Image Processing

PET Image Denoising Using Denoising Diffusion Probabilistic Models (DDPMs)

Emine Pacci[a], İsa Yıldırım[b]

[a] Istanbul Technical University, Graduate School, Biomedical Engineering Program, Türkiye
[b] Istanbul Technical University, Department of Electronics and Communication Engineering, Türkiye
pacci20@itu.edu.tr

Keywords: Denoising Diffusion Probabilistic Models (DDPM), Low-Dose PET Imaging, Medical Image Denoising, Positron Emission Tomography (PET).

Aim

Positron Emission Tomography (PET) is a nuclear medicine imaging modality that enables the visualization of physiological processes in living organisms without invasive intervention. It is widely used in the diagnosis and treatment monitoring of cancer patients. A radiotracer tailored to the target physiological function is administered to the patient, and as it distributes throughout the body, it undergoes radioactive decay. The emitted energy is detected and mathematically reconstructed to generate an image representing the spatial distribution of the radiotracer. PET imaging offers the ability to track molecular activity at the picomolar (pmol) level. However, due to the inherently low number of detected events, PET images often suffer from high noise levels and lower spatial resolution compared to other imaging modalities such as CT and MRI. To minimize radiation exposure, PET scans are typically performed with low-dose radiotracers and short acquisition times, resulting in limited signal counts. These limitations, along with statistical uncertainty and the nature of the reconstruction process, contribute to the noisy appearance of PET images.
In recent years, advancements in Artificial Intelligence and Deep Learning have enabled significant improvements in PET imaging without requiring additional hardware. These techniques have led to reduced noise, enhanced spatial resolution, shorter acquisition times, and lower radiation doses for patients. While supervised learning approaches require paired datasets consisting of both noisy and noise-free images, the acquisition of such data in PET imaging is challenging due to radiation safety concerns and the high dimensionality of PET scans. As a result, Unsupervised and Self-Supervised learning methods have become increasingly valuable in PET image enhancement.

Material and Method

This study proposes an Unsupervised learning-based approach for PET image denoising using Denoising Diffusion Probabilistic Models (DDPMs). DDPMs operate in two stages: in the forward diffusion process, Gaussian noise is gradually added to a clean image over a series of steps until it becomes indistinguishable from random noise. In the reverse diffusion process, the model learns to progressively denoise the image and reconstruct the original signal. The proposed model was applied to axial lung PET images and demonstrated substantial improvements in image quality, achieving visually clearer outputs and higher Signal-to-Noise Ratio (SNR), while preserving fine anatomical details. By producing high-quality images from low-dose PET scans using a limited amount of training data, the method offers a practical solution for reducing radiation exposure, thus providing a significant advantage in both diagnostic and therapeutic settings.

Findings

In this project, 2D DDPM model has used for PET image enhancement. PET slices (in 2D format) were corrupted by synthetic Gaussian noise to simulate low-dose imaging scenarios.
The model was trained to learn the reverse diffusion process, progressively reconstructing high-quality images. A UNet-based architecture was employed as the noise prediction network within the diffusion framework. Training was performed using a mean squared error loss between the predicted and actual noise.
The dataset consists of PET axial lung images. It was separated as 75% train and 25% test. In order to better evaluate the success of the model, a comparison was made with the classical CNN model (Table 1).

Table 1. The omparison of the DDPM and CNN models.

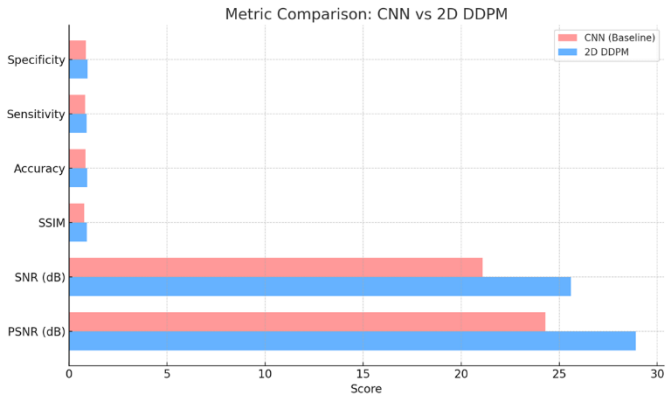

Conclusion

The proposed model has been tested in different modalities and has proven successful, and has recently been adapted to PET images. Since PET images contain Poisson noise, a model can be developed to provide denoising appropriate to this noise. In addition, advanced studies can be conducted using 3D images.

References

Gong, K., Johnson, K., El Fakhri, G., Li, Q., & Pan, T. (2024). PET image denoising based on denoising diffusion probabilistic model. *European Journal of Nuclear Medicine and Molecular Imaging*, 51(2), 358–368.

Schwenck, J., Sonanini, D., Cotton, J. M., Rammensee, H. G., la Fougère, C., Zender, L., & Pichler, B. J. (2023). Advances in PET imaging of cancer. *Nature Reviews Cancer*, 23(7), 474–490.

Yu, B., Ozdemir, S., Dong, Y., Shao, W., Pan, T., Shi, K., & Gong, K. (2025). Robust whole-body PET image denoising using 3D diffusion models: Evaluation across various scanners, tracers, and dose levels. *European Journal of Nuclear Medicine and Molecular Imaging*, 1–14.

Iterative Reconstruction Applications for Aircraft Image Restoration

Emirhan Gül[a], Ender Mete Ekşioğlu[b]

[a] Istanbul Technical University, Graduate School, Electronics Engineering Program, Türkiye
[b] Istanbul Technical University, Electronics and Communication Engineering Department, Türkiye
gulemi22@itu.edu.tr

Keywords: Aircraft Images, Expectation Maximization, Image Restoration, Iterative Reconstruction, Maximum Likelihood Restoration.

Aim

Image Restoration is a popular concept in Digital Image Processing. It is the process of improving the quality of an image by removing distortion, noise, or degradation that occurs during the capture, transmission, or storage of the image. In image restoration process, the main goal is to restore the image to a state as close as possible to its original or to enhance it for better interpretation or use. There are several methods to perform image restoration properly. This study aims to perform aircraft image restoration by implementing Iterative Reconstruction (IR) as the fundamental method and show simulation outputs. To be able to implement IR for aircraft image restoration, Maximum Likelihood Expectation Maximization (ML-EM) has been used as the chosen algorithm. The dataset that has been used in this study is unique and it includes various aircraft images that all have been taken from satellites around the globe. The implementation results have been given in detail.

Material and Method

The newly created dataset that has been used in this study is comprised of five aircraft images that are unique and all have been taken from satellites around the globe. These images are the materials used in this study.
In the context of this study, IR is the fundamental method to perform aircraft image restoration. To be able to implement IR for aircraft image restoration, ML-EM has been used as the chosen algorithm. Also, the new dataset comprised of five aircraft images taken from satellites around the globe has been created for the implementation phase of the study.

Findings

A. Iterative Reconstruction

IR is a process that involves repeatedly refining an initial estimate of an image through a sequence of iterations, each involving the comparison of the estimated image to the actual measurements or data. The method iteratively adjusts the image based on discrepancies between the predicted and observed data, typically by minimizing a defined objective function or cost function. This process helps reduce artifacts and improve the resolution and accuracy of the reconstructed image.
IR is used in imaging, particularly in the fields of medical imaging (e.g., Computed Tomography (CT), Magnetic Resonance Imaging (MRI), and Positron Emission Tomography (PET)) and other areas like signal processing. The goal of IR is to improve image quality and reduce noise while using fewer data samples or lower radiation doses.
There are some important concepts regarding IR. These concepts have been given below:
Initial Estimate: The starting point in the reconstruction process, often a rough or low-quality image.
Forward Model: A mathematical model that describes how the data (such as projection data in CT) is generated from the image.
Objective Function: A mathematical expression that quantifies the difference between the observed data and the data predicted by the current image estimate. The goal is to minimize this difference through iterative refinement.
Optimization: At each iteration, the chosen algorithm adjusts the image to reduce the discrepancy between the observed data and the data generated by the current image.

Convergence: The process continues iteratively until the solution stabilizes, meaning the image quality does not change significantly with further iterations.
The types of IR techniques have been given below.
Algebraic Reconstruction Technique (ART): Involves updating image values by solving a system of linear equations based on measured projection data (Nikazad, 2008, p. V).
Simultaneous Iterative Reconstruction Technique (SIRT): An extension of ART where all projection data are used to update the image simultaneously rather than sequentially (Wei, Biwen and Jiexian, 2013, pp. 42-43).
Expectation Maximization (EM): A probabilistic method, commonly used in PET imaging, that iterates between estimating the image and the system model to maximize a likelihood function.
By iterating and refining the reconstruction process, IR techniques offer advantages over traditional analytical methods like Filtered Back Projection (FBP), especially in terms of noise reduction, artifact suppression, and better resolution with limited or low-quality data.

B. The Chosen Iterative Reconstruction Algorithm: Maximum Likelihood Expectation Maximization

ML-EM refers to the application of the EM algorithm to maximize the likelihood function for models with hidden or missing data. In the context of this process, the goal is to estimate the parameters of a probabilistic model that best explains the observed data, assuming that the model has some unobserved or latent variables. The EM algorithm iterates between estimating the expected values of the latent variables (E-step) and optimizing the parameters to maximize the likelihood given those expectations (M-step).
ML-EM is a mix of two different but related statistical methods: Maximum Likelihood Estimation (MLE) and EM (Nuyts, Michel and Dupont, 2001, pp. 365-366).
These two statistical methods have been explained below:
1) Maximum Likelihood Estimation:
MLE is a statistical method for estimating the parameters of a probabilistic model. The idea behind MLE is to find the parameter values that maximize the likelihood function, which measures how likely it is to observe the given data under different parameter values.
Likelihood Function: This function gives the probability of observing the data given the parameters. In practice, this is often the joint probability density or mass function, depending on whether the data is continuous or discrete.
Maximum Likelihood Estimation Procedure: To find the parameters that maximize the likelihood of the observed data, we compute the log-likelihood.
The MLE for the parameter is typically done using optimization techniques such as gradient ascent or numerical methods, since the likelihood is often complex and not easily solvable analytically.
2) Expectation Maximization:
EM is an iterative algorithm used for parameter estimation in models with incomplete or latent (unobserved) data. The method is a generalization of MLE that is useful when some of the data is missing or when the model has latent variables that need to be inferred.
In the EM algorithm, the data consists of observed data X and latent (hidden) data Z. The goal is to estimate the parameters θ of a probabilistic model when the joint distribution of X and Z is unknown, or when Z is not directly observed.
The joint likelihood $P(X,Z|\ \theta\ )$ of both observed and latent variables is generally difficult to compute directly. The EM algorithm iterates between two steps. These steps have been given below.
Expectation Step (E-Step): In this step, we compute the expected value of the latent variables Z given the observed data X and the current estimate of the parameters θ^t. This is equivalent to calculating the conditional probability distribution of the latent variables.
Maximization Step (M-Step): In the M-step, we maximize the expected log-likelihood function obtained from the E-step with respect to the parameters θ. The M-step updates the parameter estimates based on the expected value of the complete data log-likelihood. The EM algorithm alternates between the E-step and M-step until convergence, i.e., when the parameter estimates stabilize. The algorithm is guaranteed to increase the likelihood at each iteration, though it may converge to a

local maximum, not necessarily the global maximum. As it has been explained above, MLE and EM combine to operate as the ML-EM algorithm.

C. Implementation Phase

To be able to perform IR implementation for aircraft image restoration, Figure 1 (Maxar, 2024) has been chosen from the newly created dataset as the original satellite image of airplanes.

Figure 1. Original Satellite Image of Airplanes (Maxar, 2024).

ML-EM has been used as the IR algorithm in the implementation code (Figure 2).

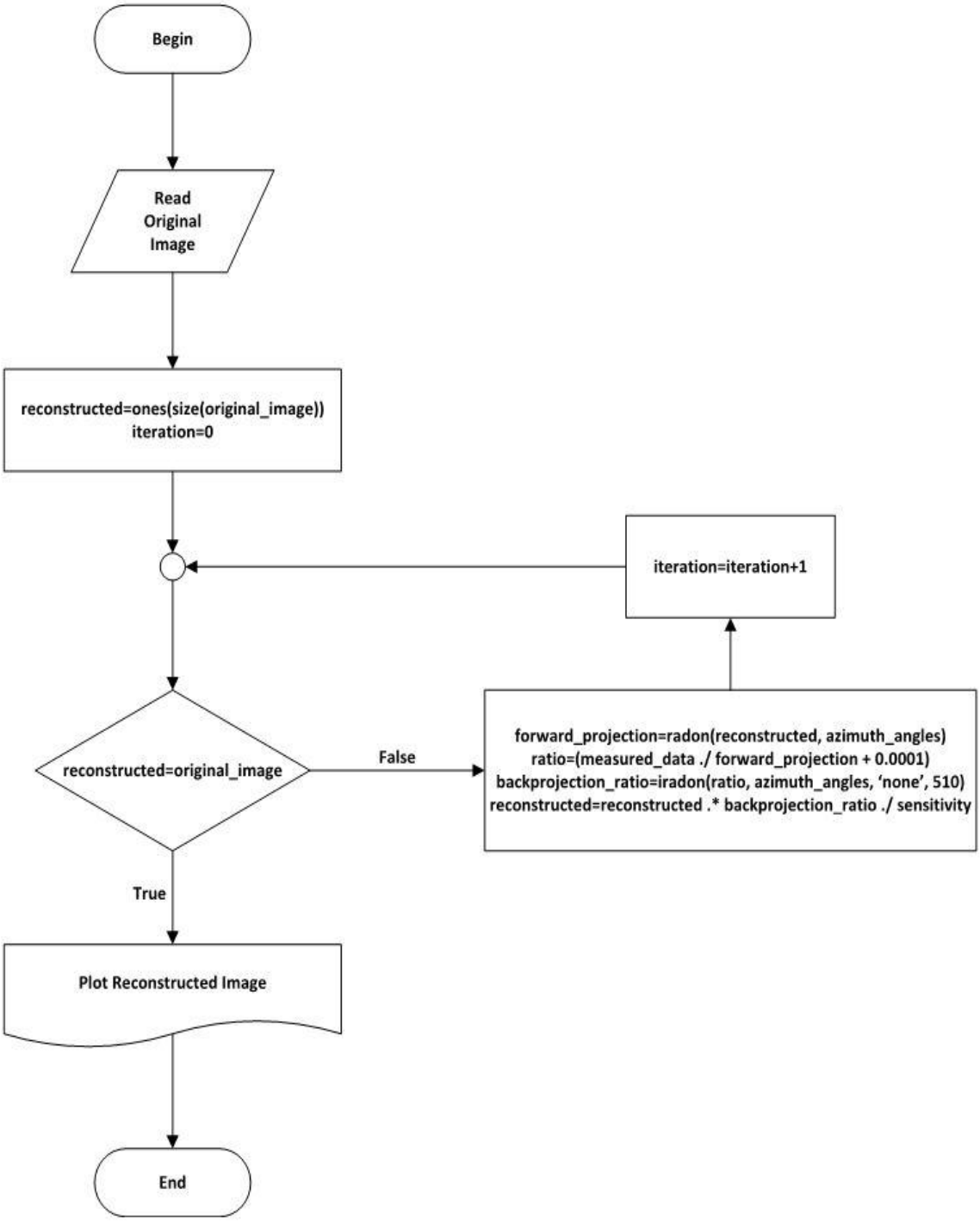

Figure 2. Algorithmic Flowchart for Implementation.

Figure 3. Reconstructed Image After First Iteration.

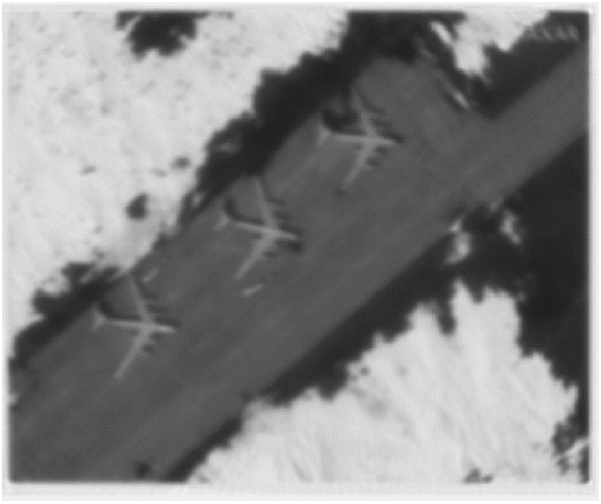

Figure 4. Reconstructed Image After 100 Iterations.

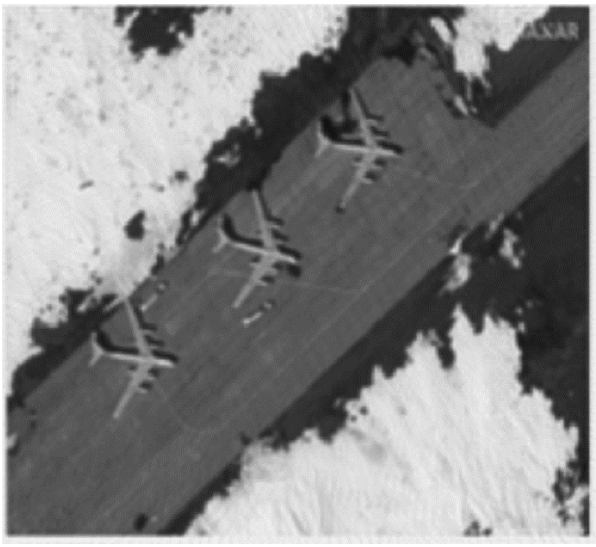

Figure 5. Reconstructed Image After 1000 Iterations.

Conclusion

Image Restoration is one of the popular concepts in Digital Image Processing. It is the process of improving the quality of an image by removing distortion, noise, or degradation that occurs during the capture, transmission, or storage of the image. The main goal of the image restoration process is to restore the image to a state as close as possible to its original or to enhance it for better interpretation or use. There are several methods to perform image restoration properly. In the context of this study, it has been shown that IR is the fundamental method to perform aircraft image restoration. To be able to implement IR for aircraft image restoration, ML-EM has been used as the chosen algorithm. Also, the probabilistic background of ML-EM has been explained in detail. The dataset that has been used in this study is unique and it includes various aircraft images that all have been taken from satellites around the globe. This study has also shown the original satellite image of airplanes, algorithmic flowchart for implementation, reconstructed image after first iteration, reconstructed image after 100 iterations and reconstructed image after 1000 iterations as parts of the implementation process. The implementation outputs (Figure 3, Figure 4 and Figure 5) have revealed that reconstructed image quality primarily depends on the maximum number of iterations and the convergence behavior of the algorithm used. The higher number of iterations up to well-chosen stopping criterion or well-converging algorithms tend to produce higher quality reconstructed images whereas the insufficient number of iterations or poorly converging algorithms produce poor quality reconstructed images.

References

Nikazad, T. (2008). Algebraic Reconstruction Methods. *Linköping*: LiU–Tryck.

Nuyts, J., Michel, C. and Dupont, P. (2001). Maximum-Likelihood Expectation-Maximization Reconstruction of Sinograms with Arbitrary Noise Distribution Using NEC-Transformations, *IEEE Transactions on Medical Imaging*. Vol. 20(5), 365-375.

Wei, W., Biwen, Y. and Jiexian, W. (2013). Application of a simultaneous iterations reconstruction technique for a 3-D water vapor tomography system, *Geodesy and Geodynamics.* Vol. 4(1), 41-45.

Url-1 www.maxar.com, date retrieved 13.12.2024.

CONSTRUCTION MANAGEMENT

Construction Project Management

IT in Construction

Risk Management in Construction

Sustainability in Construction

Inclusion and Gender Equality for Women in the Construction Industry

Elif Kılıç[a], Fatma Pınar Irlayıcı Çakmak[a]

[a]Istanbul Technical University, Department of Architecture, Project and Construction Graduate Program, Türkiye
kilice23@itu.edu.tr

Keywords: Gender, Women, Diversity, Construction, Equality.

Aim

This research seeks to provide a thorough understanding of the systemic challenges impeding women's full inclusion in the construction workforce. Despite incremental efforts to encourage diversity, women remain significantly underrepresented and often marginalized. Through an in-depth literature review, the study explores core issues including unequal access to leadership roles, implicit gender biases in hiring and promotion, and the absence of institutional support mechanisms. It also evaluates effective interventions—such as mentorship programs and equity-focused HR practices—that have shown promise in reducing these disparities. The findings serve not only to illuminate the existing landscape but also to offer concrete recommendations aimed at improving representation, equity, and opportunity for women in the built environment professions.

Material and Method

This research employs a **systematic literature review** methodology to critically examine scholarly discourse on women's roles in the construction industry. The review was designed with a structured and replicable approach to ensure both breadth and depth of coverage. The Scopus database was selected due to its comprehensive index of high-quality, peer-reviewed research across relevant academic disciplines.

A total of **8,853** records published between **1997 and 2021** were initially retrieved using keywords such as "gender," "diversity," "women," and "construction." Following rigorous filtering based on relevance, peer-review status, and disciplinary focus, **216 articles** were shortlisted for thematic categorization. This subset was then further refined to **26 high-impact studies**, which underwent in-depth content analysis.

The methodological framework guiding this review (see **Figure 1**) facilitated the classification of articles based on several dimensions: publication year, journal of origin, research scope, citation frequency, and methodological rigor. The classification matrix used (see **Table 1**) enabled a comprehensive comparison of thematic focus areas and helped identify key research gaps.

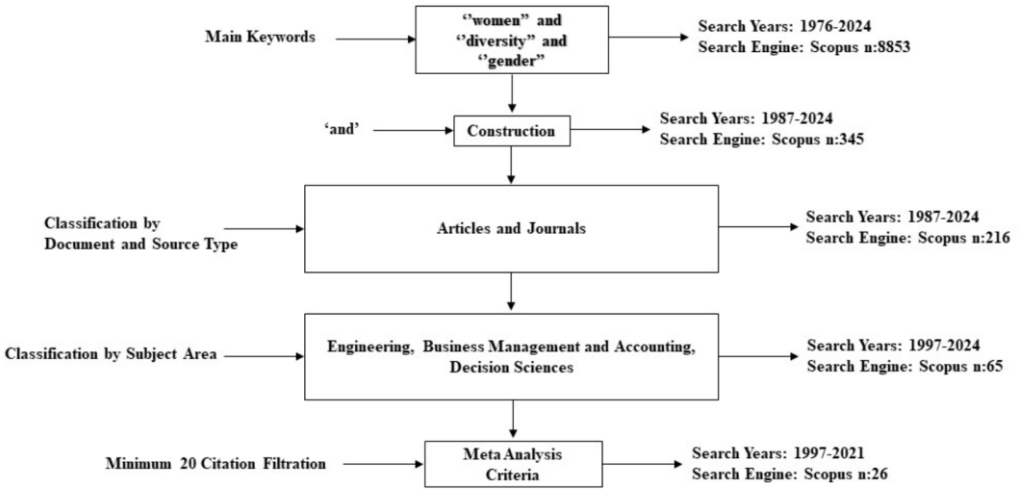

Figure 1.

Table 1.

Category	Details
Key Actors	Female professionals in the construction industry, including engineers, architects, site managers, project leaders, and technical personnel.
Publication Years	1997 – 2021
Source Journals	*Journal of Management in Engineering*, *Construction Management and Economics*, *Equality, Diversity and Inclusion: An International Journal*, and others.
Research Database	Scopus
Keywords	Gender, Diversity, Women, Construction, Construction Industry, Equality
Minimum Citation Threshold	≥ 20 citations (as a filter for academic relevance)
Challenges Identified	Gender-based discrimination, unequal career advancement opportunities, wage disparities, occupational stress, underrepresentation in leadership roles.
Clarity of Research Agenda	Clearly defined across all selected studies; each article articulates its objectives, methodology, and contributions to the field.
Tools and Technologies Used	Systematic literature review methodology, bibliometric analysis tools, citation tracking, and keyword frequency analysis.

Core Themes (Content)	Gender Diversity and Equality; Women's Employment and Career Development; Women's Experiences in Construction; Women in Management and Communication.
Research Areas	Social Sciences, Business and Management, Engineering, Arts and Humanities
Sectoral Focus	Primarily private and public construction sectors, with some research focused on professional associations and educational institutions.
Level of Research Scope	Global, national, and organizational levels; some studies targeted specific firms, projects, or demographics.
Author Country of Origin	Primarily United Kingdom, United States, Australia, Canada, and Italy
Methodologies Applied	Literature Review (dominant), Case Study (1), System Analysis (1)
Information Sources	Peer-reviewed academic publications, sectoral reports, institutional surveys, and governmental policy analyses.
Types of Research Outputs	General Information, Statistical Results, Conceptual Frameworks, and Practical Models
Author Backgrounds	Predominantly academic researchers, supported by contributions from industry practitioners and policy consultants.
Construction-Related Focus	Yes – all selected studies are directly related to the construction industry context.

Findings

The meta-analysis of 26 carefully selected academic sources uncovered several recurring themes that shape the experience of women in the construction industry. A key takeaway is the transformative effect of comprehensive workplace equality policies. For example, Webb (1997) highlighted that well-structured gender policies can serve as foundational tools to dismantle institutional biases and foster organizational cultures rooted in equity.

Another prominent theme emerging from the literature is the impact of occupational stress on gender diversity. According to Sunindijo and Kamardeen (2017), women are disproportionately affected by the psychological demands of construction work, often due to isolation and lack of peer support in male-dominated environments. This view is echoed by Sang et al. (2007), who link elevated stress levels to systemic gender imbalances in professional settings like architecture.

Women's progression into leadership roles also received significant attention. Research conducted by Arena et al. (2015) and Morello, Issa, and Franz (2018) emphasizes that despite growing awareness of the issue, female leadership remains limited due to both overt and subtle structural constraints. Cultural stereotypes, limited mentorship, and unequal access to career development resources collectively contribute to the underrepresentation of women in senior positions across the construction value chain.

Moreover, the literature consistently identified long-standing barriers embedded in the industry's culture. Worrall et al. (2010) provided a critical examination of these obstacles in the UK context, outlining how discriminatory norms persist in both formal and informal workplace interactions. Wright (2013) added nuance to this discourse by exploring how overlapping aspects of identity—such as gender and sexuality—compound the exclusion women face, necessitating an intersectional approach to policy design.

Mentorship programs and inclusive practices have been frequently cited as effective countermeasures. Lingard and Francis (2005), for instance, emphasized the importance of work-life balance frameworks and supportive managerial cultures in enhancing job satisfaction and career longevity for women. Such practices were seen not merely as accommodations, but as strategic tools for retaining talent and promoting innovation through diversity.

Substantial attention was also given to persistent pay gaps and employment inequalities. Manesh et al. (2020) and Shrestha et al. (2020) conducted spatial and quantitative analyses revealing significant wage disparities across roles traditionally occupied by men versus those where women are more likely to be hired. These patterns underscore the broader structural imbalances within the labor market of the construction sector.

In terms of academic coverage, the most prolific journals contributing to this field include the *Journal of Management in Engineering*, *Construction Management and Economics*, and *Equality, Diversity and Inclusion: An International Journal* (see **Table II**). These outlets serve as key platforms for advancing scholarly discussions on gender-related topics in construction.

Table 2.

	1997	1998	1999	2000	2001	2002	2003	2004	2005	2006	2007	2008	2009	2010	2011	2012	2013	2014	2015	2016	2017	2018	2019	2020	2021	TOTAL
Journal of Construction Engineering and Management																					1					**1**
Management Learning				1																						**1**
Construction Management and Economics									1		1						2							1		**5**
Tourism Recreation Research							1																			**1**
Journal of Management in Engineering																								5	1	**6**
Gender, Work and Organization	1			1						1																**3**
Equality, Diversity and Inclusion: An International Journal															1											**1**
Corporate Governance (Bingley)																			1							**1**
International Journal of Gender and Entrepreneurship																					1					**1**
Data Base for Advances in Information Systems												1														**1**
Equality, Diversity and Inclusion															1											**1**
Accounting, Auditing and Accountability Journal																				1						**1**
Journal of Professional Issues in Engineering Education and Practice																						1				**1**
Engineering, Construction and Architectural Management														1												**1**
Howard Journal of Communications																			1							**1**
TOTAL	1	0	0	2	0	0	1	0	1	1	1	1	0	1	2	0	2	0	2	1	2	1	0	6	1	**26**

Keyword frequency analysis revealed that terms such as **"gender"**, **"diversity"**, **"women"**, and **"construction industry"** were dominant across the reviewed studies (see **Table III**), reflecting the sustained thematic focus on inclusion and equity. Citation analysis further indicated that foundational works like those by Webb (1997), Sunindijo and Kamardeen (2017), and Colgan and Ledwith (2000) have had lasting influence on the academic and professional discourse (see **Table IV**).

Table 3.

KEYWORDS	NUMBER OF USED	FREQUENCY OF USED
Gender	20	76,92%
Diversity	11	42,31%
Women	7	26,92%

Construction	5	19,23%
Construction industry	4	15,38%
Equality	3	11,54%
Gender differences	2	7,69%
Gender diversity	2	7,69%
Leadership	2	7,69%
Lesbian	2	7,69%
Sexual orientation	2	7,69%
Sexuality	2	7,69%
Equality and diversity	2	7,69%

Table 4.

TITLE	AUTHORS AND YEARS	CITATION NUMBER
The politics of equal opportunity	Webb J.(1997)	98
Work Stress Is a Threat to Gender Diversity in the Construction Industry	Sunindijo R.Y.; Kamardeen I.(2017)	97
Diversity, identities and strategies of women trade union activists	Colgan F.; Ledwith S.(2000)	87
Teaching Managers about Masculinities: Are You Kidding?	Sinclair A.(2000)	84
Gender: A risk factor for occupational stress in the architectural profession?	Sang K.J.C.; Dainty A.R.J.; Ison S.G.(2007)	72
Barriers to women in the UK construction industry	Worrall L.; Harris K.; Stewart R.; Thomas A.; McDermott P.(2010)	65
Uncovering sexuality and gender: an intersectional examination of women's experience in UK construction	Wright T.(2013)	64
Women on board: Evidence from a masculine industry	Arena C.; Cirillo A.; Mussolino D.; Pulcinelli I.; Saggese S.; Sarto F.(2015)	63
Exploratory Study of Recruitment and Retention of Women in the Construction Industry	Morello A.; Issa R.R.A.; Franz B.(2018)	62
Gender in the Construction Industry: Literature Review and Comparative Survey of Men's and Women's Perceptions in UK Construction Consultancies	Harris J.; Naoum S.G.; Rizzuto J.; Egbu C.(2020)	56
Environmental Influences on Gender in the IT Workforce	Trauth E.M.; Quesenberry J.L.; Yeo B.(2008)	50
Gender and the limits to diversity in the contemporary British Army	Woodward R.; Winter P.(2006)	45

From a geographic standpoint, the majority of the reviewed studies originated in the **United Kingdom**, **United States**, and **Australia**, highlighting these regions as leaders in gender-focused construction research (Figure 2). A surge in publication activity during the year **2020** was also observed (Figure 3), likely driven by increased global interest in workplace equality in response to broader social movements and policy shifts.

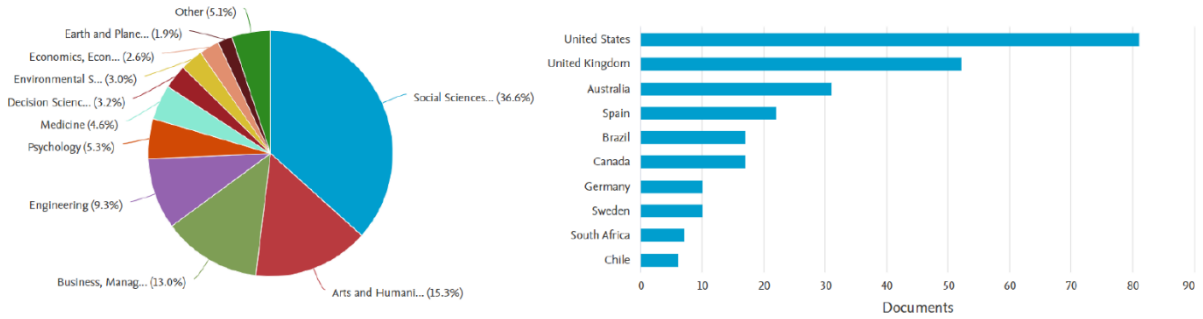

Figure 2.

	1997	1998	1999	2000	2001	2002	2003	2004	2005	2006	2007	2008	2009	2010	2011	2012	2013	2014	2015	2016	2017	2018	2019	2020	2021	TOTAL
Gender Diversity and Equality	1	1	1	3	3	3	3	3	3	4	4	5	5	5	6	6	7	7	8	8	9	9	9	9	10	10
Women's Employment and Career Development in the Construction Industry	0	0	0	0	0	0	0	0	0	0	0	0	0	0	0	0	0	0	0	0	0	1	1	6	6	6
Women's Experiences in the Construction Industry	0	0	0	0	0	0	0	0	1	1	2	2	2	3	3	3	4	4	4	4	4	4	4	5	5	5
Women in Management and Corporate Communication	0	0	0	0	0	0	1	1	1	1	1	1	1	2	2	2	2	2	3	4	5	5	5	5	5	5
TOTAL	1	1	1	3	3	3	4	4	5	6	7	8	8	10	11	11	13	13	15	16	18	19	19	25	26	26

Figure 3.

With respect to methodology, **literature reviews** were by far the most common approach, demonstrating a scholarly preference for synthesis and meta-analysis in studying systemic issues (Figure 4). The main types of research outputs included **statistical analyses** and **conceptual models**, illustrating a balanced emphasis on both empirical data and theoretical development (Figure 5).

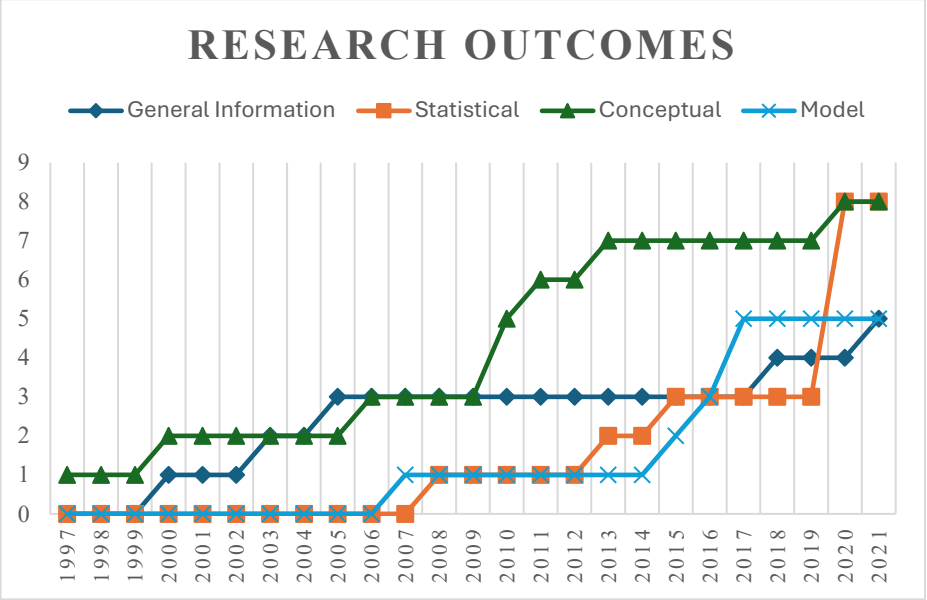

Figure 4.

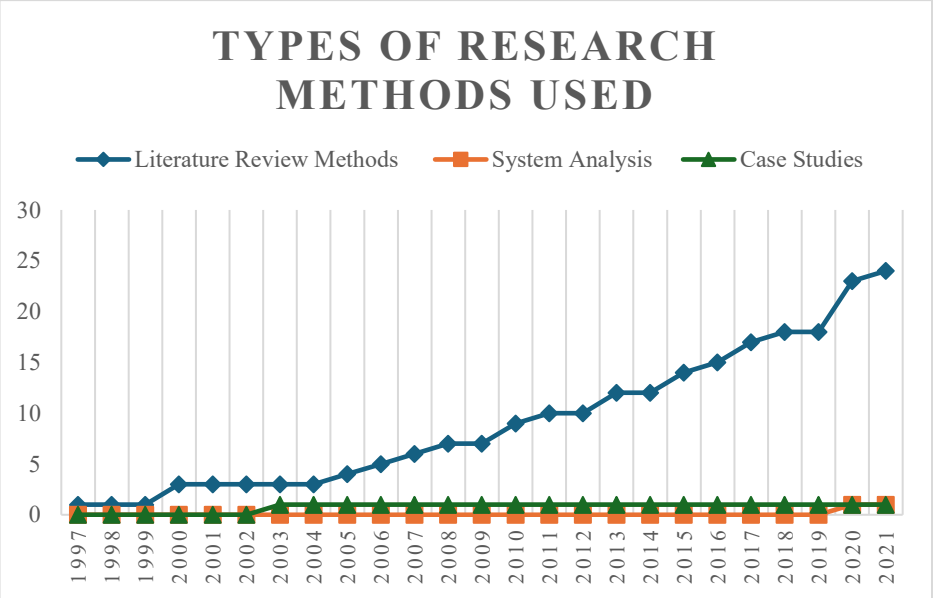

Figure 5.

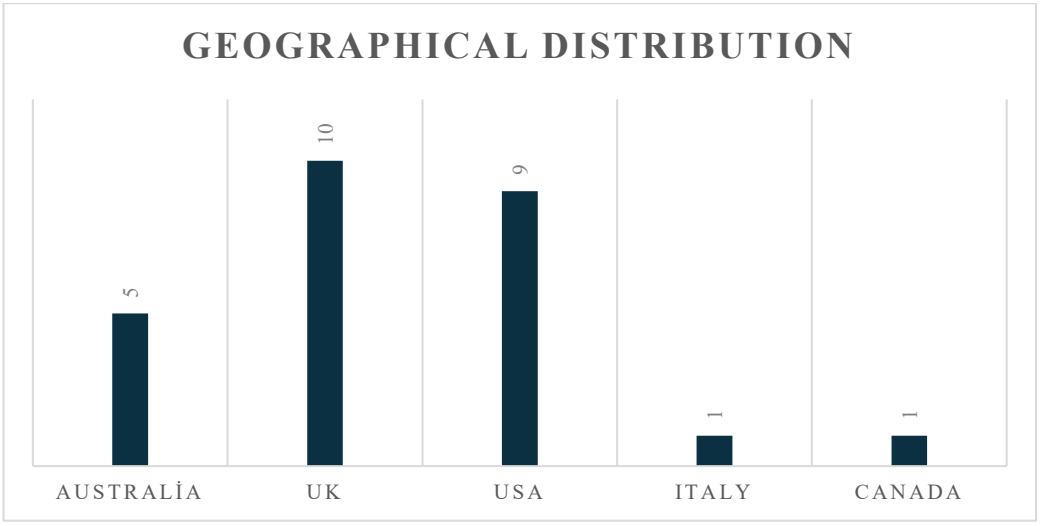

Figure 6.

Conclusion

This systematic review has presented a detailed synthesis of the academic landscape concerning gender dynamics in the construction industry. Despite decades of discussion around inclusion, the findings reaffirm that women remain underrepresented and face a unique set of obstacles, ranging from unequal access to leadership roles and mentorship, to institutionalized wage disparities and psychological stress linked to exclusionary workplace cultures.

By analyzing 26 high-impact studies, this research identified that while initiatives such as gender equality policies, mentorship programs, and inclusive work environments show measurable benefits, their practical implementation often falls short. In particular, the disconnect between policy creation and on-the-ground realities continues to limit women's ability to participate meaningfully and sustainably in construction-related roles.

Importantly, several studies highlighted the necessity of considering intersecting identities—such as race, class, and sexuality—in future inclusion efforts. This intersectional approach is crucial to designing policies that address the full spectrum of discrimination that women may encounter.

The rise in academic interest—particularly visible in the surge of publications around 2020—demonstrates that gender diversity in construction is gaining global attention. Yet, for this awareness to result in tangible change, collaboration between academia, industry leaders, and policymakers must intensify. Initiatives must move beyond symbolic gestures and be grounded in measurable targets and accountability frameworks.

In conclusion, this review offers a foundational reference for future research and policy reform, emphasizing the importance of translating academic insight into actionable strategies. The road to gender equity in construction requires sustained effort, rigorous monitoring, and the commitment of all stakeholders to build not just structures, but fair and inclusive environments within them.

References

Arena, C., Cirillo, A., Mussolino, D., Pulcinelli, I., Saggese, S., & Sarto, F. (2015). *Women on board: Evidence from a masculine industry*. Corporate Governance.

Atewologun, D., & Singh, V. (2010). *Challenging ethnic and gender identities: An exploration of UK black professionals' identity construction*. Equality, Diversity and Inclusion: An International Journal.

Baker, M., French, E., & Ali, M. (2021). *Insights into ineffectiveness of gender equality and diversity initiatives in project-based organizations*. Journal of Management in Engineering.

Chan, P. W. (2013). *Queer eye on a 'straight' life: Deconstructing masculinities in construction*. Construction Management and Economics.
Colgan, F., & Ledwith, S. (2000). *Diversity, identities and strategies of women trade union activists*. Gender, Work and Organization.
Harris, J., Naoum, S. G., Rizzuto, J., & Egbu, C. (2020). *Gender in the construction industry: Literature review and comparative survey of men's and women's perceptions in UK construction consultancies*. Journal of Management in Engineering.
Hickey, P. J., & Cui, Q. (2020). *Gender diversity in US construction industry leaders*. Journal of Management in Engineering.
Lingard, H., & Francis, V. (2005). *The decline of the 'traditional' family: Work-life benefits as a means of promoting a diverse workforce in the construction industry of Australia*. Construction Management and Economics.
Loosemore, M., Alkilani, S., & Mathenge, R. (2020). *The risks of and barriers to social procurement in construction: A supply chain perspective*. Construction Management and Economics.
Manesh, S. N., Choi, J. O., Shrestha, B. K., Lim, J., & Shrestha, P. P. (2020). *Spatial analysis of the gender wage gap in architecture, civil engineering, and construction occupations in the United States*. Journal of Management in Engineering.
Morello, A., Issa, R. R. A., & Franz, B. (2018). *Exploratory study of recruitment and retention of women in the construction industry*. Journal of Professional Issues in Engineering Education and Practice.
Perrenoud, A. J., Bigelow, B. F., & Perkins, E. M. (2020). *Advancing women in construction: Gender differences in attraction and retention factors with managers in the electrical construction industry*. Journal of Management in Engineering.
Sang, K. J. C., Dainty, A. R. J., & Ison, S. G. (2007). *Gender: A risk factor for occupational stress in the architectural profession?* Construction Management and Economics.
Shrestha, B. K., Choi, J. O., Shrestha, P. P., Lim, J., & Manesh, S. N. (2020). *Employment and wage distribution investigation in the construction industry by gender*. Journal of Management in Engineering.
Sinclair, A. (2000). *Teaching managers about masculinities: Are you kidding?* Management Learning.
Sunindijo, R. Y., & Kamardeen, I. (2017). *Work stress is a threat to gender diversity in the construction industry*. Journal of Construction Engineering and Management.
Trauth, E. M., Quesenberry, J. L., & Yeo, B. (2008). *Environmental influences on gender in the IT workforce*. Data Base for Advances in Information Systems.
Tremblay, M.-S., Gendron, Y., & Malsch, B. (2016). *Gender on board: Deconstructing the "legitimate" female director*. Accounting, Auditing and Accountability Journal.
Webb, J. (1997). *The politics of equal opportunity*. Gender, Work and Organization.
Wheadon, M., & Duval-Couetil, N. (2017). *Entrepreneuring gender diversity in entrepreneurship through critical theory and reflexivity*. International Journal of Gender and Entrepreneurship.
Woodward, R., & Winter, P. (2006). *Gender and the limits to diversity in the contemporary British Army*. Gender, Work and Organization.
Worrall, L., Harris, K., Stewart, R., Thomas, A., & McDermott, P. (2010). *Barriers to women in the UK construction industry*. Engineering, Construction and Architectural Management.
Wright, T. (2011). *A "lesbian advantage"? Analysing the intersections of gender, sexuality and class in male-dominated work*. Equality, Diversity and Inclusion.
Wright, T. (2013). *Uncovering sexuality and gender: An intersectional examination of women's experience in UK construction*. Construction Management and Economics.

Difficulties Faced by Construction Experts in Construction Sector Cases in the Turkish Justice System

Bekir Haktanır[a], Murat Kuruoğlu[a], Onur Behzat Tokdemir[a]

[a] İstanbul Technical University, Faculty of Civil Engineering, Department of Construction Management, Turkey
haktanirb17@itu.edu.tr

Keywords: Construction Expert, Technical and Legal Classification of Construction Cases, Turkish Justice System.

Aim

The construction-related lawsuits in the Turkish justice system face prolonged litigation processes and significant difficulties in decision making due to differences between the technical classification system used by technical experts and the legal classification system employed by legal professionals. The technical classification system is more detailed and specialized, focusing on the specific sub-disciplines of construction, whereas the legal classification is more general, abstract, and normative. These differences cause issues in clearly defining the types of construction lawsuits, understanding the technical aspects of the disputes, and lead to differences in perception and approach between technical experts and legal professionals. As a result, the case may be misjudged, which extends the litigation process and increases the number of appeals. The thesis aims to explore the relationship between these two classification systems and help create a common understanding, enabling both technical experts and legal professionals to better understand each other's perspectives and improve their collaboration.

The Turkish justice system is founded on the principle of separation of powers, in which the legislative, executive, and judicial branches function independently, within the framework of a democratic state governed by the rule of law (Tanrıver, 2023). The normative foundation of this system is established by the Constitution of the Republic of Turkey, which was adopted through a public referendum on November 7, 1982, and remains in force today. The Constitution guarantees the independence and impartiality of the judiciary while also emphasizing the protection of individual rights and freedoms as one of its core objectives. Structurally, the Turkish legal system adheres to the continental European legal tradition, particularly influenced by the French and German legal systems, and is characterized by the primacy of codified legal norms. Judicial bodies render decisions in accordance with the hierarchy of norms, including the Constitution, laws, bylaws, and regulations (Gözler, 2024). The primary objective of this thesis is to examine the reasons behind the prolonged duration of construction related legal proceedings adjudicated by the judiciary within the Turkish legal system, particularly in courts, and to identify the underlying factors contributing to these delays. In this context, a comparative analysis was conducted between the 'legal classification of construction lawsuits' utilized by legal practitioners and the 'technical classification' employed by expert technical consultants in the field of construction. As a result of this analysis, it was determined that the legal classification comprises 66 distinct types of cases under 27 main categories, whereas the technical classification encompasses 215 distinct types of construction-related disputes under 54 main categories. This numerical disparity highlights not only a methodological divergence in classification approaches but also reveals significant differences in perspective and interpretation between legal professionals and technical experts throughout critical stages of the judicial process, including issue identification, evaluative reasoning, and the rendering of judgments. The findings of this thesis aim to elucidate the nature of the relationship between the technically detailed and expertise-driven classifications used by technical experts and the more generalized legal classifications employed by legal practitioners. Furthermore, the study seeks to contribute meaningfully to the discourse on how this relationship impacts both the duration and effectiveness of judicial proceedings (Arditi & Tokdemir, 1999).

Material and Method

In the process of developing the technical and legal classifications presented in this study, a comprehensive literature review was conducted, drawing on both national and international academic and professional sources relevant to the subject matter. During the technical classification phase, an in-depth examination was carried out of academic studies at the master's and doctoral levels, primarily sourced from university thesis databases, as well as peer-reviewed scientific articles published in scholarly journals and relevant periodicals in the field. For the legal classification, foundational and supplementary legal texts authored by expert jurists were consulted, along with precedent-setting judicial decisions issued by high courts. Additionally, insights were obtained from practitioners with extensive professional experience and sector-specific knowledge. This multidisciplinary and integrative approach has ensured that the classification framework is grounded on a robust foundation, both theoretically and practically.

Findings

The research findings clearly indicate a significant disparity between the number of case types in the legal classification and the technical classification. This quantitative difference holds substantial importance not only in terms of the scope of the classification systems but also due to its direct impact on the functioning of the judicial process. Indeed, the challenges faced by judges in making decisions in construction related cases, along with the increased number of appeals against the decisions and the subsequent prolongation of the trial duration, are concrete manifestations of this disparity. As identified in the study, there is no direct overlap between the 66 case types used by legal professionals and the 215 technical case types defined by technical experts; in fact, in many cases, a single case type in the legal classification corresponds to multiple subtopics with significantly different technical characteristics. This misalignment complicates the accurate understanding of the case content and hinders the full integration of technical details into the judicial process (Arditi, Oksay, & Tokdemir, 1998). A topic that is highly specific from a technical expert's perspective is often placed into a more general legal category in the court, leading to discrepancies in the manner of case adjudication, the criteria for evaluation, and consequently, the rendered decision. As a result, the decisions are often not fully aligned with the technical realities of the case, prompting appeals from the adversely affected parties and thus extending the duration of the trial. The most effective solution to this issue is the inclusion of experts who possess both technical knowledge and legal expertise in the process. However, despite the growing need for such multidisciplinary experts—i.e., technical consultants with legal knowledge and legal professionals with technical expertise—the limited number of specialists with these qualifications presents a significant structural barrier in the resolution of construction-related disputes in Turkey.

Conclusion

Construction-related lawsuits in the Turkish justice system face prolonged litigation processes and significant challenges in decision-making due to structural and conceptual differences between the technical classification system developed by technical experts and the legal classification framework employed by legal professionals. The classification system used by technical experts is more detailed, specialized, and application-oriented, taking into account the sub-disciplines specific to the construction field. In contrast, the legal classification of construction lawsuits is approached in a more general, abstract, and normative manner. This disparity in scope results in the inability to clearly express the meaning of the types of construction lawsuits presented to the court, a lack of comprehensive understanding of the technical aspects of the dispute, and the emergence of perceptual and approach differences between technical experts and legal professionals. Such communication and conceptual misalignments often lead to the incomplete or incorrect evaluation of the case, which in turn prolongs the judicial process and frequently results in appeals against the decisions. This thesis aims to reveal the relationship between the technical classification system used by technical experts and the legal classification framework relied upon by legal professionals, fostering the development of a shared understanding between both parties. The findings aim to contribute to the establishment of a conceptual bridge that will enable technical experts to better assess legal perspectives and allow legal professionals to more effectively engage with technical details.

References

Arditi, D., Oksay, F. E., & Tokdemir, O. B. (1998). Predicting the outcome of construction litigation using neural networks. Computer Aided Civil and Infrastructure Engineering, 13(2), 75-81.
Arditi, D., & Tokdemir, O. B. (1999). Using case based reasoning to predict the outcome of construction litigation. Computer Aided Civil and Infrastructure Engineering, 14(6), 385-393.
Duman, İ. H. (2023). İnşaat hukuku. Seçkin Kitabevi, (12), 9-40.
Gözler, K. (2024). Hukuka Giriş. Seçkin.
Karadaş, İ. (2013). Eser (İnşaat Yapım) Sözleşmeleri. Adalet Yayınevi, (3), 13-23.
Tanrıver, S. (2023). Türk Yargı Teşkilatı. Yetkin.

Procurement Phases in EPC Projects: A Bibliometric Analysis

Hasan Utku Uygun[a], Zeynep Işık[a]

[a] Yıldız Technical University, Departmant of Civil Engineering, Construction Management, Turkey
utku.uygun@std.yildiz.edu.tr

Keywords: EPC, Procurement, Bibliometric Analysis.

Aim

The construction industry plays a significant role in the global economy, with various approaches developed to ensure financial and temporal efficiency in project management. Construction companies aim to select the most suitable construction method and contract type based on project nature, budget, and past experience. Engineering, Procurement, and Construction (EPC) contracts integrate design, procurement, and construction into a streamlined process, widely used in large-scale infrastructure and industrial projects due to their efficiency in risk allocation and cost management (Dissanayake et al., 2022; Yeo & Ning, 2002).

The procurement phase is crucial to EPC projects, ensuring the timely acquisition of materials, equipment, and services. It bridges engineering and construction, supporting the flow between office and site (Jianhua & Yeo, 2000). This study conducts a bibliometric analysis of the procurement phase in EPC projects, identifying research trends and critical areas for further investigation. Using publications from the Scopus database and VosViewer network analysis, the research provides a comprehensive overview of procurement challenges and management strategies in EPC projects.

Material and Method

The methodology adopted in this study follows a systematic bibliometric approach. The research process starts with the identification of relevant publications from the Scopus database using predefined keywords (procurement, EPC, project, construction) related to procurement in EPC projects. The initial dataset was refined by filtering for subject areas (Engineering, Business, Management and Accounting, Decision Sciences), document types (article, conference paper) and language (English). As a result of this search, 417 studies were examined and 115 of them were found to be related to the researched topic and these studies were included in the analysis.

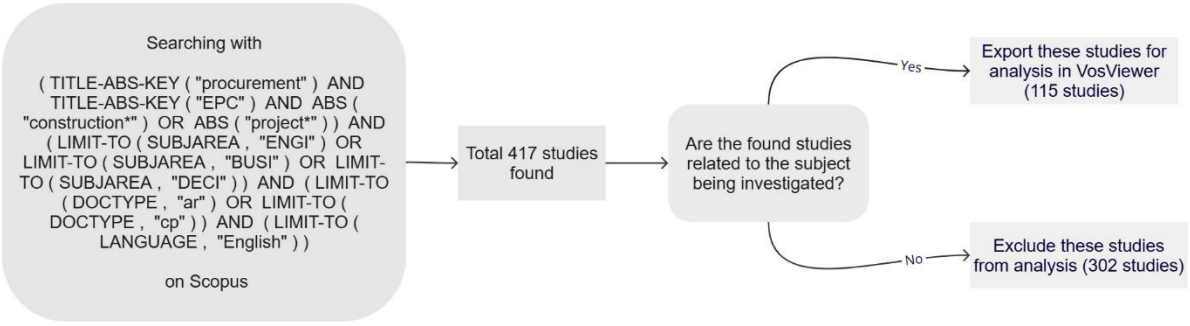

Figure 1. Flow diagram of searching and analyzing progress.

Table 1. Searching criteria.

Title - Abstract - Keyword
procurement
EPC
Abstract
project
construction
Subject Area
Engineering
Business, Management and Accounting
Decision Sciences
Document Type
Article
Conference Paper
Language
English

Subsequently, a detailed bibliometric analysis was conducted using VosViewer software to assess key parameters such as publication trends, keyword co-occurrence patterns, geographical distribution of research outputs, and the most influential journals in this domain.

Findings

A. Research Trends and Key Findings

The analysis of 115 selected articles revealed a steady growth in research activity related to EPC procurement since the early 2000s. Keyword co-occurrence analysis indicated a strong focus on four critical areas: risk management, supply chain management, contract administration, and delay analysis with cost-overrun issues. These thematic areas have significant implications for the efficiency and success of EPC projects.

Figure 2. Mapping of keyword analysis.

Table 2. Keyword analysis result.

Keyword	Occurences	Total Link Strength
project management	12	51
epc	12	43
procurement	8	40
risk management	7	23
epc projects	6	22
supply chain	6	20
engineering	5	28
construction	5	26
delay	3	16
construction industry	3	14
supply chain management	3	13
epc project	3	12
procurement risk	3	12
construction projects	3	10
epc contract	3	10
supply chain configuration	2	11
anp	2	10
business intelligence	2	10

cost overrun	2	10
exploratory research	2	9

Financial, technical, logistical, and operational risks are all present in EPC projects, and they must be effectively managed by early detection, in-depth assessments, and proactive response. It is essential to manage a worldwide supply chain, which includes digital tracking systems, logistics, inventory optimization, and supplier selection. Automation and digital transformation developments can improve the transparency and resilience of the supply chain. Future study will concentrate on novel approaches including performance-based incentives and flexible dispute resolution procedures. Clear, flexible contracts are crucial for outlining roles, risk-sharing, and performance criteria. In EPC projects, delays and cost overruns are still frequent problems. By examining these issues using statistical techniques and historical data, the underlying causes can be identified. Key areas for additional research include improved planning, financial monitoring, and early corrective action.

B. Geographical Distribution of Research Output

The bibliometric analysis shows that research on EPC procurement is mostly concentrated in countries with strong construction industries and advanced technology. China stands out as a major contributor, with many publications on procurement risks and cost management in EPC projects. According to the 2024 ENR rankings, six of the top 20 global construction firms are based in China, reflecting its large-scale infrastructure investments and focus on EPC contracting in international markets.

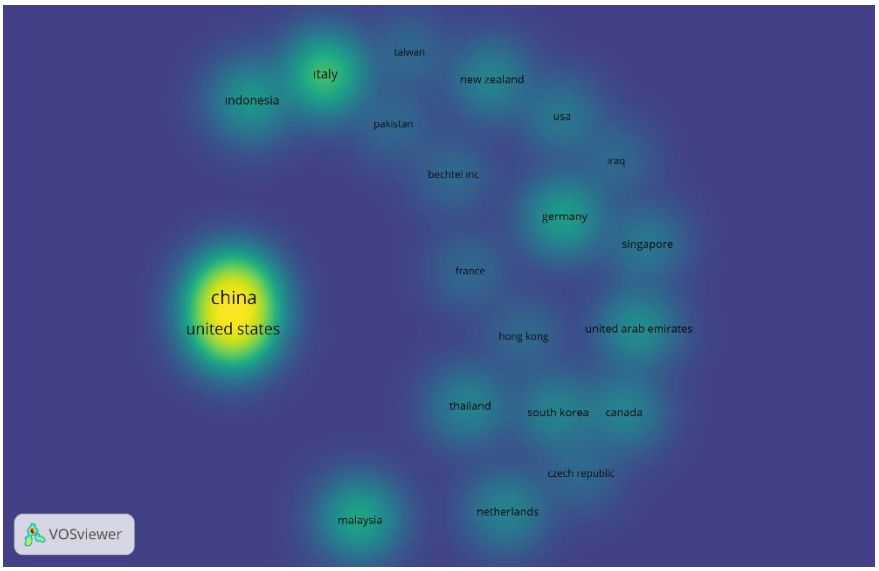

Figure 3. Distribution of the number of studies carried out by contries.

Table 3. Country analysis result.

Country	Documents	Citations
China	29	167
United States	17	261
India	12	70
Italy	7	124
United Kingdom	5	93

Iran	5	41
Indonesia	5	20
Australia	3	87
Canada	3	76
Germany	3	74
Japan	3	29
South Korea	3	25
Thailand	3	20
United Arab Emirates	3	12
Singapore	2	173
Denmark	2	68
Malaysia	2	44
Saudi Arabia	2	40
New Zealand	2	11
Vietnam	2	3

C. Most Cited Study in EPC Procurement Research

Among the analyzed articles, the most frequently cited study is "Integrating Supply Chain and Critical Chain Concepts in Engineer-Procure-Construct (EPC) Projects" which has been referenced 168 times (Yeo & Ning, 2002). Conducted in Singapore, this study explores the integration of supply chain management principles with critical chain project management in EPC projects. It provides a framework for optimizing procurement processes and mitigating risks associated with supply uncertainties, highlighting the importance of aligning procurement strategies with overall project objectives.

Table 4. Source analysis result ranked on citations.

Source	Documents	Citations
International Journal of Project Management	3	290
Buildings	6	111
Engineering Construction and Architectural Management	4	77
Journal of Management in Engineering	2	73
Engineering Economics	1	62
Management Research News	1	58
Infrastructures	1	46
Supply Chain Management	1	44
AACE International. Transactions of the Annual Meeting	1	43
Mathematical Problems in Engineering	1	40

Journal of Construction Engineering and Management	4	39
International Journal of System Assurance Engineering and Management	1	39
Production Planning and Control	2	38
Journal of Purchasing and Supply Management	1	32
International Journal of Production Economics	1	24

D. Discussions

The bibliometric analysis highlights the strengths and weaknesses of procurement in EPC projects. Developed countries, like the United States and China, dominate the publication landscape, aligning with the large-scale cash flow requirements of EPC projects.

Supply chain and procurement are often confused, but supply chain is a broader process that includes procurement (Azambuja et al., 2014). Future research should explore studies combining both terms while recognizing their differences.

Common keywords include risks such as delays and cost overruns, which are significant challenges for EPC projects (An & Shuai, 2010; Hatmoko & Khasani, 2019). Additionally, "risk management," "risk control," and "risk analysis and evaluation" are frequently associated with risk (He & Han, 2022; Wang & Wang, 2022). Given the complexity of risk, there is room for further research in this area.

Although Singapore has fewer publications, it ranks second in citations, mainly due to the 168 citations of the article "Integrating supply chain and critical chain concepts in EPC projects" (Yeo & Ning, 2002). This paper is crucial for future researchers in this field, as it provides valuable insights into integrating supply chain and critical chain concepts in EPC projects.

Conclusion

This study presents a comprehensive bibliometric analysis of procurement research in EPC projects, highlighting key themes, research trends, and knowledge gaps. The analysis reveals the dominance of research contributions from countries with strong construction industries. It also emphasizes the need for further studies to bridge the gap between academic research and industry practices. Future research could focus on developing predictive models for procurement risk assessment, improving contract frameworks, and exploring artificial intelligence in EPC procurement. Strengthening these areas could lead to more efficient procurement strategies and better project outcomes in the global construction industry.

References

Dissanayake, N., Xia, B., Skitmore, M., Trigunarsyah, B., & Menadue, V. (2022). Ranked generic criteria for EPC contractor selection. Engineering, Construction and Architectural Management.

Yeo, K. T., & Ning, J. H. (2002). Integrating supply chain and critical chain concepts in engineer-procure-construct (EPC) projects. International Journal of Project Management, 20(4), 253-262.

Jianhua, N., & Yeo, K. T. (2000, November). Management of procurement uncertainties in EPC projects-applying supply chain and critical chain concepts. In Proceedings of the 2000 IEEE International Conference on Management of Innovation and Technology. ICMIT 2000.'Management in the 21st Century'(Cat. No. 00EX457) (Vol. 2, pp. 803-808). IEEE.

Azambuja, M. M., Ponticelli, S., & O'Brien, W. J. (2014). Strategic procurement practices for the industrial supply chain. Journal of Construction Engineering and Management, 140(7), 06014005.

An, H., & Shuai, Q. (2010, November). Study on cost management of the general contractor in EPC project. In 2010 3rd International Conference on Information Management, Innovation Management and Industrial Engineering (Vol. 2, pp. 478-481). IEEE.

Hatmoko, J. U. D., & Khasani, R. R. (2019, August). Mapping delay risks of EPC projects: a case study of a platform and subsea pipeline of an oil and gas project. In IOP Conference Series: Materials Science and Engineering (Vol. 598, No. 1, p. 012095). IOP Publishing.
Wang, Q. E., & Wang, J. (2022). Research on Key Risk Factors and Risk Transmission Path of Procurement in International Engineering Procurement Construction Project. Buildings, 12(5), 534.
He, J., & Han, D. (2022). Evaluation of key factors of logistics risks for overseas EPC projects. Advances in Civil Engineering, 2022.

Determining the Factors Causing Rework in the Turkish Construction Industry

Eda Nur Erdem[a], Gülden Gümüşburun Ayalp[b]

[a]Adana Alparslan Türkeş Science and Technology University, Department of Architecture, Building Construction, Türkiye
[b] Hasan Kalyoncu University, Department of Architecture, Architecture, Türkiye
enerdem@atu.edu.tr

Keywords: Construction Rework, Project Performance, Statistical Analyses.

Aim

The construction sector is a critical backbone of economic growth and national development, particularly in developing countries like Turkey. Despite its economic significance, the industry often suffers from inefficiencies such as cost overruns, delays, and quality deviations—issues frequently arising from construction rework (Fayek et al., 2003; Josephson et al., 2002; Love, 2002; Yap et al., 2020). Rework is the unnecessary effort to correct tasks initially performed incorrectly (Love & Edwards, 2004a). It is a persistent and costly problem that can occur at any project stage (Love & Edwards, 2004b). Its late detection, often due to errors, omissions, or last-minute changes, significantly undermines project performance and efficiency (Trach et al., 2019). Although rework is a well-known global issue, its specific impact and underlying causes in the Turkish construction industry have not been thoroughly investigated. This study aims to fill that gap by identifying the primary factors leading to rework, assessing their frequency and significance, and offering data-driven recommendations to mitigate them. By shedding light on the most common and influential causes of rework, the research seeks to enhance project outcomes, minimize waste, and support sustainable improvement in the performance and quality of the Turkish construction sector.

Material and Method

The study employed a systematic literature review to identify potential rework causes, then gathered empirical data via a survey of 209 industry professionals including architects, engineers, and contractors. A total of 43 rework criteria were categorized into six groups: client-related, design team-related, project management-related, implementation team-related, project conditions, and general/external factors (Table 1).

The survey utilized a 5-point Likert scale to assess the impact of each criterion. The SPSS 22.0 program and Monte Carlo simulation were used for data analysis. Since the skewness and kurtosis values of the dataset are between -2 and +2, it has been determined that the entire dataset follows a normal distribution, and therefore, parametric tests have been used. Data analysis included descriptive statistics, reliability analysis, relative importance index (RII) (Equation 1), One-Way ANOVA as hypothesis testing, and explanatory factor analysis (EFA). Specifically, to test the hypothesis that there is a statistically significant difference between the types of projects participants were involved in (residential, public, commercial, and others) and the reasons for rework, a one-way ANOVA was conducted. RII was calculated using the following equation: W is the weighting given to each factor by participants (ranging from 1 to 5); A is the highest weight (i.e., 5 in this case); and N is the total number of participants (Pallant, 2007).

Relative importance index (RII) formula:

$$\mathrm{RII} = \frac{\Sigma W}{(A \times N)} \quad (1)$$

The findings obtained from the analyses were evaluated within a scientific framework by comparing them with existing literature, and the validity of the results and their contributions to the sector were thoroughly discussed.

Table 1. Identification and Classification of the Rework Causes.

Cause Group	Cause Code	Rework Cause Definition
Client Related Factors	C1	Client directed changes
	C2	Poor communication
	C3	Client choice and low-cost contractor
	C4	Lack of client involvement
	C5	Inadequate or weak feasibility study
Design Team Related Factors	D1	Incomplete design
	D2	Errors and omissions in design
	D3	Design changes
	D4	Insufficient coordination
	D5	Lack of constructability review
	D6	Poor communication
	D7	Design management failure
	D8	Drawing not clear
	D9	Lack of using modern technology and tools
Project Management Related Factors	PM1	Lack of experience of project manager
	PM2	Inability to perform adequate document review
	PM3	Poor planning and coordination
	PM4	Poor workload planning
	PM5	Inefficient management
Implementation Team Related Factors	IT1	Lack of worker skills
	IT2	Time pressure
	IT3	Poor workmanship
	IT4	Non-compliance with specifications
	IT5	Shortage of skilled laborers required to complete task
	IT6	Lack of motivation
Project Conditions	PC1	Poor site condition

Related Factors	PC2	Congestion of trades
	PC3	Increase in work due to interferences
	PC4	Increase in project changes or the number of trade subcontracts on site
	PC5	Lack of safety enforcement in the site
General Related Factors	G1	Schedule pressure
	G2	Poor communication
	G3	Poor coordination
	G4	Change in project scope
	G5	Inadequate as-built documentation
	G6	Unavailability of materials
	G7	Delivery of construction materials in short supply
	G8	Wrong initial budget
	G9	Change of economic condition and ineffectiveness of follow-up
	G10	Change of contractors
	G11	Change in construction laws of the country
	G12	Natural disasters
	G13	Change in construction method

.

Findings

The statistical analysis of the collected data revealed the following findings: Among the 43 potential criteria evaluated by participants as causes of construction rework, the most significant factors were identified as changes in project scope, modifications initiated by the employer, late design changes, employer-driven adjustments to project scope or schedule, and communication failures between teams. This highlights the critical role of late-stage changes in projects within the Turkish construction sector, demonstrating that rework-inducing modifications negatively impact project performance and significantly reduce productivity.

The influence of rework-related criteria varies depending on project type, with a statistically significant relationship found between six of the 43 factors and specific project categories through a One-Way ANOVA. In commercial buildings, key issues include poor employer communication, scope or schedule changes imposed by the employer, insufficient employer involvement, inadequate feasibility studies, and weak workload planning, all perceived as more problematic than residential projects. In other project types (industrial buildings, socio-cultural structures, etc.), limited time allocated to design teams for task completion and deficient feasibility studies emerge as more prominent concerns. Consequently, the nature of rework risks requiring managerial intervention differs across project types.

Finally, according to the results of the EFA, critical factors contributing to construction rework in the Turkish construction sector were determined and named based on thematically related causes that led to rework occurrence. The analysis was conducted on a survey dataset consisting of 209 responses, evaluating 36 variables with factor loadings greater than 0.5. The parallel analysis using Monte Carlo simulation statistically supported the extraction of five factors. Considering both the distribution of the items and their conceptual alignment with the literature, the factor structure was limited to five, each with an eigenvalue greater than 1.

Based on the underlying variables they comprise (as per the EFA results), the five critical factors were named, and their order of importance (determined by analyzing the mean RII) is as follows (Table 2.):

1. Factor 3 – Communication gaps and lack of coordination (consisting of 6 variables),
2. Factor 4 – Errors due to personnel expertise and knowledge deficiencies (consisting of 5 variables),
3. Factor 5 – Late changes made by the employer (consisting of 5 variables),
4. Factor 1 – Inadequate design and project management (consisting of 12 variables)
5. Factor 2 – Weaknesses in project documentation and difficulties accessing project requirements (consisting of 8 variables).

Table 2. Factor Groups and Related Values Obtained from Exploratory Factor Analysis.

Definition of Rework Factors and Related Causes		**Loads of Causes**	**Eigenvalue**	**% of Variance**	**Avg. RII**	**Factor Importance Rank Order**
Factor 1	**Inadequate design and project management**		**13,04**	**18,51**	**73,39**	**4**
D4	Insufficient experience	0,78				
D1	Incomplete design	0,72				
PM5	Ineffective management	0,71				
PM1	Lack of experience of project manager	0,70				
D2	Errors and omissions in design	0,70				
D3	Design changes	0,69				
D6	Poor contract execution	0,68				
PM2	Failure to perform adequate document control	0,67				
PM3	Poor planning and coordination	0,66				
D7	Design management failure	0,65				
D5	Lack of understanding of user	0,65				
PM4	Poor workload planning	0,55				

Table 2. Factor Groups and Related Values Obtained from Exploratory Factor Analysis (cont.)

Factor 2	**Weaknesses in project documentation and difficulties accessing project requirements**		**3,13**	**13,66**	**68,38**	**5**
G7	Shortage of construction materials in market	0,81				
G8	Wrong initial budget	0,80				
G9	Lack of technological equipment and Ineffective use of technology	0,68				
G10	Change of laws	0,67				
G11	Economic situation of the country	0,59				
G5	Inadequacies in contract documentation	0,57				
G6	Use of poor-quality materials	0,55				
PC4	Increase in project changes as the number of project stakeholders grows	0,55				
Factor 3	**Communication gaps and lack of coordination**		**2,73**	**11,35**	**77,15**	**1**
G1	Schedule pressures	0,72				
G2	Poor communication	0,71				
PC2	Complexity of design	0,61				
G3	Poor information flow	0,61				
G4	Changes in project scope	0,60				
PC1	Poor site condition	0,58				
Factor 4	**Errors due to personnel expertise and knowledge deficiencies**		**2,22**	**8,88**	**74,72**	**2**
IT1	Lack of labour skills	0,81				
IT3	Poor workmanship	0,77				
IT5	Shortage of skilled labours required to complete work tasks	0,74				
IT4	Non-compliance with specifications	0,70				
IT2	Time pressure	0,52				

Factor 5	**Late changes made by the employer**		**1,78**	**7,90**	**74,51**	**3**
C2	Poor communication	0,80				
C3	Client directed plan and scope extensions	0,71				
C4	Lack of client involvement	0,66				
C1	Client directed changes	0,59				
C5	Inadequate or weak feasibility study	0,51				
Total Explained Variance				**60,31**		

* Footnote: Rotation method = Varimax
* Footnote 2: Variables with factor loadings above 0.5 are displayed.

Conclusion

This study systematically identifies and categorizes the factors causing rework in the Turkish construction sector, providing valuable insights. The empirical findings of this study strongly align with those of prior research. These research outcomes revealed that stakeholders in the Turkish construction sector must recognize these critical rework drivers and prioritize preventive measures to mitigate their impact. Proactive strategies addressing these factors are essential to enhancing project efficiency and reducing avoidable costs and delays. The study recommends several strategies to reduce construction rework in Turkey. Key measures include improving communication and coordination through regular team meetings, implementing continuous quality monitoring to catch and correct these issues early, and establishing robust quality control systems. It also advises early contractor involvement to enhance constructability, using BIM for clash detection, and providing training in project management areas such as risk analysis and cost control. Additionally, introducing incentive programs for workers can further minimize errors and rework. By adopting these measures, construction firms can reduce rework, enhance efficiency, and improve project outcomes, ultimately contributing to sustainable growth.

References

Fayek, A. R., Dissanayake, M., & Campero, O. R. (2004). Developing a standard methodology for measuring and classifying construction field rework. Canadian Journal of Civil Engineering, 31(6), 1077–1089. https://doi.org/10.1139/l04-068

Josephson, P., Larsson, B., & Li, H. (2002). Illustrative Benchmarking Rework and Rework Costs in Swedish Construction Industry. Journal of Management in Engineering, 18(2), 76–83. https://doi.org/10.1061/(asce)0742-597x(2002)18:2(76

Love, P. E., & Edwards, D. J. (2004a). Determinants of rework in building construction projects. Engineering, Construction and Architectural Management, 11(4), 259– 274. https://doi.org/10.1108/09699980410547612

Love, P. E. D., & Edwards, D. J. (2004b). Forensic project management: The underlying causes of rework in construction projects. Civil Engineering and Environmental Systems, 21(3), 207–228. https://doi.org/10.1080/10286600412331295955

Pallant, J. F. (2007). SPSS survival manual: a step-by-step guide to data analysis using SPSS for Windows. http://ci.nii.ac.jp/ncid/BA83963567

Trach, R., Pawluk, K., & Lendo-Siwicka, M. (2019). Causes of Rework in Construction Projects in Ukraine. Archives of Civil Engineering, 65(3), 61–74. https://doi.org/10.2478/ace-2019-0034

Yap, J. B. H., Rou Chong, J., Skitmore, M., & Lee, W. P. (2020). Rework Causation that Undermines Safety Performance during Production in Construction. Journal of Construction Engineering and Management, 146(9). https://doi.org/10.1061/(asce)co.1943-7862.0001902

CONSTRUCTION MANAGEMENT

Construction Project Management

IT in Construction

Risk Management in Construction

Sustainability in Construction

Assessing the Level of Digitalization of the Construction Permit Processes in Türkiye

Gamze Nur İşeri Çetin [a], Esin Ergen Pehlevan [b]

[a] Istanbul Technical University, Faculty of Civil Engineering, Construction Management Division, Türkiye
[b] Istanbul Technical University, Graduate School, Department of Civil Engineering, Türkiye
iserig@itu.edu.tr

Keywords: Automated Permit Approvals, Digital Construction Permit Procedures, Digital Transformation in Construction Industry, e-Permitting Systems.

Aim

Digital transformation has become one of the leading subjects of progress in the construction industry with Building Information Modelling (BIM) at the forefront. Digitalization appears in numerous process-focused areas, such as urban planning and construction permit procedures (Olsson et al., 2018). In this context, one of the significant advancements in the digitalization of the construction sector is electronic permitting (e-Permitting). E-Permitting procedures include document submissions, project controls and the assessments that need to be carried out, from the permit application stage until the issuance of the construction permit. It includes processes such as electronic applications, electronic submission of project documents, submission of BIM projects and IFC files in addition to two-dimensional project submissions, automated compliance controls of architectural, structural, mechanical and other properties of the projects, as well as defining and checking the spatial relations of the buildings with their surroundings through three-dimensional, real-time city models. The primary objectives of e-Permitting are to minimize human error, reduce the reliance on physical documentation, accelerate the permit approval process and overall to increase the efficiency of the construction permitting procedures (CHEK, 2023).

In Türkiye, e-Permitting is not being implemented nationwide and there are limited studies on building permit processes at the national level, as well as studies on the development of e-Permitting systems. Although some municipalities have taken steps towards the digitalization of the construction permitting procedures, there is no national framework that facilitates and guides the transition to the nationwide adoption of e-Permitting systems. In order for institutions to adopt e-Permitting, certain adaptations should be implemented in the existing systems. It is primarily necessary to resolve several legal issues in order to accomplish implementing an automated and model-based e-permitting structure, some of which can present significant challenges (Shahi et al., 2019). Submission of BIM models as part of the construction permit processes are required for different types of projects in countries like Singapore, Norway and the UK (Kim et al., 2020), however it is not a widespread practice worldwide. Studies on the realisation of automatic code compliance controls and the integration of geoinformation usage are currently ongoing. The most extensively researched topic is the automated regulation compliance controls and it has the potential to achieve higher maturity. However, significant gaps remain in the use of geoinformation, particularly in relation to BIM and exchangeable conversions (Noardo et al., 2024). Several governments and municipalities worldwide have adopted different levels of e-Permitting procedures and numerous pilot projects take place which incorporate the submission of BIM models and perform the automated code controls for different aspects of the projects (Srinivasan et al., 2020). Considering the global advancements and ongoing research, it is important to understand and assess Türkiye's position in digital permitting procedures. Therefore, the aim of this study is to identify the current digital transformation applications in the building permit processes of municipalities in Türkiye and to develop a roadmap for transition to e-Permit processes.

Material and Method

To achieve this aim, a systematic review of the literature was carried out in the first step. Initially, studies focusing on worldwide e-Permit applications were reviewed, different levels of digital maturity in e-Permit procedures were defined, and e-Permit applications implemented globally were examined. Within the global practices, the steps that were taken to improve the digitalization of the permitting procedures were analysed. Then, studies on the automatic regulation (code) control used in e-Permit practices were investigated.

In the second step of the study, research which focuses on the 30 metropolitan municipalities in Türkiye was conducted to assess the digitalization levels of construction permitting processes. As part of the research, digitalized services and construction permit issuance procedures of a total of 519 district municipalities were investigated and analysed. The research investigated the municipalities that have implemented digital solutions, the extent of digitalization in construction permit issuance, as well as the degree to which municipalities are integrated with national digital systems related to the construction sector. In line with the local digital developments, national services that serve for the digitalization of the construction sector and their impact on the local construction permit procedures were investigated and their further potentials have been analysed. In the third step of the study, interviews were conducted with main stakeholders of the e-Permitting procedures, including e-Permit software and system developers, construction permitting experts from metropolitan district municipalities and experts from metropolitan city municipalities in Türkiye. These interviews provided an understanding of the building permit processes implemented locally and the level of adoption of e-Permitting procedures.

Findings

By analysing the results obtained, the challenges of the building permit issuance processes in both national and local contexts in Türkiye have been identified. The research on metropolitan district municipalities showed disparities between the adoption of digitalization, and while some regional similarities were observed, no clear coordinated approach could be identified. It has been observed that although more than two-thirds of the district municipalities have adopted the digitalization of the systems for general municipal services, different levels of e-Permitting applications and infrastructures have been identified in fewer than one-fifth of the district municipalities. Based on the results obtained from the stakeholder interviews conducted, key challenges against the nationwide implementation of e-Permitting systems included regulatory gaps and legal barriers, lack of standardization across municipalities, lack of trained personnel and technical infrastructure, and lack of planning and organisational structuring. Despite the identified challenges and certain bureaucratic and technical barriers still affecting the implementation process, no explicit and direct resistance against the adoption of e-Permit systems has been reported. Furthermore, legal regulation attempts and local efforts to include BIM models within construction permitting procedures were defined.

Conclusion

Based on the findings of the global studies in the field of e-Permitting, data collected through the research of metropolitan district municipalities and stakeholder interviews, a roadmap for the development of e-Permitting applications in Türkiye has been proposed. The proposed roadmap consists of key phases including the establishment of national regulatory guidelines, development of technical infrastructure, organizational capacity building, and implementation of pilot e-Permitting projects to establish the adoption of nationwide e-Permitting procedures.

The academic contribution of this study is to determine the levels of digitalization and the development of e-Permitting procedures in 519 metropolitan district municipalities for the evaluation of the national and local e-Permitting efforts within the construction sector and the proposal of an e-Permit roadmap. By using the e-Permit roadmap, nationwide e-Permit implementation could be attained in Türkiye and localised solutions for e-Permit applications can be developed.

References

CHEK. (2023). *Code of practice for the digital building permit* [Brochure]. CHEK Digital Building Permit. Retrieved March 4, 2025, from https://chekdbp.eu/wp-content/uploads/2023/04/EN_CoP.pdf

Kim, I., Choi, J., Teo, E. A. L., & Sun, H. (2020). Development of KBIM E-Submission prototypical system for the OpenBIM-based building permit framework. *Journal of Civil Engineering and Management, 26*(8), 744–756. https://doi.org/10.3846/jcem.2020.13756

Noardo, F., Guler, D., Fauth, J., Malacarne, G., Ventura, S. M., Azenha, M., Olsson, P. O., & Senger, L. (2022). Unveiling the actual progress of digital building permit: Getting awareness through a critical state of the art review. *Building and Environment, 213*, 108854. https://doi.org/10.1016/j.buildenv.2022.108854

Olsson, P.-O., Axelsson, J., Hooper, M., & Harrie, L. (2018). Automation of building permission by integration of BIM and geospatial data. *ISPRS International Journal of Geo-Information, 7*(8), 307. https://doi.org/10.3390/ijgi7080307

Shahi, K., McCabe, B. Y., & Shahi, A. (2019). Framework for automated model-based e-permitting system for municipal jurisdictions. *Journal of Management in Engineering, 35*(6), 04019025. https://doi.org/10.1061/(ASCE)ME.1943-5479.0000712

Srinivasan, J., Orellana Tamez, E., Clark-Chakaroun, K., Umarov, F., & Onofri, L. (2020). *From paper to the cloud: Improving building control through e-permitting* (Vol. 1, *Doing Business Case Studies* No. 2). *World Bank Group.* http://documents.worldbank.org/curated/en/705331592344507733

CONSTRUCTION MANAGEMENT

Construction Project Management

IT in Construction

Risk Management in Construction

Sustainability in Construction

Industrialisation of Natural Building Materials for Sustainability in the Built Environment

Merve Guven[a], Deniz Artan[b]

[a] Istanbul Technical University/Institute of Informatics, IT in Construction Management Program, Türkiye
[b] Istanbul Technical University/Faculty of Civil Engineering, Department of Civil Engineering, Türkiye
guvenme23@itu.edu.tr

Keywords: BIM, Industrialisation, Natural Building Materials, Sustainable Construction, Sustainable Development.

Aim

Construction sector has a significant impact on environmental pollution.(Murtagh, Scott, & Fan, 2020). Natural building materials such as earth, wood and straw bale offer sustainable alternatives but face challenges in industrialisation and standardisation(Dams, et al., 2023). Buildings constructed with natural building materials offer an eco-friendly approach that harmonises with ecosystems by reducing their environmental footprint. While traditional construction materials contribute to high carbon emissions and depletion of natural resources, natural building materials are renewable, biodegradable and can be produced with low energy consumption.(Yahia,A.K.M, et al., 2024). For example, bamboo is a sustainable and durable building solution thanks to its fast growth cycle and high strength.(Abera, 2024). Biomaterials like mycelium, a fungal substance, enhance energy efficiency by offering insulation and structural support, making buildings more resilient to extreme weather conditions (Al-Qahtani,S. et al., 2023). ,Furthermore, organic structures, combining traditional ecological knowledge with modern engineering, harmonise with nature.(Balducci, Camilli, 2022). Thus, buildings made with biological materials not only reduce carbon emissions but also become more flexible and resilient in the face of future climate uncertainties. Despite their benefits, research on natural building materials is still limited. Abera (2024) also emphasizes the significance of advancing hybrid materials and conducting innovative research on natural materials to facilitate the incorporation of traditional ecological knowledge.
This study examines the requisite conditions for the industrialization of natural materials through a literature review, industry surveys, and expert interviews. In this context, their resilience and economic feasibility are assessed for their integration into modern structures. The role of Building Information Modelling (BIM) in their adoption and standardization is also considered. Barriers to their widespread adoption were examined, including economic and perceptual challenges and regulations.

Material and Method

A mixed-method strategy was employed to collect qualitative and quantitative data. A structured online survey was administered, collecting responses from 64 industry professionals, including architects, engineers, constructors, and end users. The survey explored awareness and perceptions of natural materials, including commonly used materials and their related applications, as well as barriers to adoption and possible solutions. In-depth interviews were performed with four material producers and two building professionals to obtain perspectives on practical uses, industrialization problems, and potential policy interventions.

Findings

The interview respondents include producers of natural building materials and practitioners who have utilized these materials in construction projects. The interviews aimed to gather qualitative insights into practical work with natural materials, including production challenges, market trends, and experiences of use. The inquiries aimed to elucidate the specific circumstances favoring the use of natural materials, the technical and economic obstacles to industrialization, and the performance of these materials in daily life concerning durability and health effects. Thematic analysis was utilized on

qualitative data obtained from the interviews to delineate prevalent themes and insights that would enhance the quantitative results from the survey.

Seventy percent of the respondents are engaged in the construction sector, with the majority indicating their involvement in residential and commercial projects. 56.5% of this section within the construction sector reported utilizing natural building materials, while the remaining portion indicated either non-use or uncertainty over their use. The predominant materials utilized are wood and stone. Subsequently, earth and clay-based materials are addressed. Natural materials are extensively utilized as facades, structural components, and interior architectural finishes.

The results of the survey show that when evaluating the performance of natural building materials against natural disasters, individuals who know the materials find them more effective. Participants stated that the study provides a general evaluation, but it would be more accurate and necessary to consider each material separately. It was generally agreed that natural materials are more resistant to earthquakes and fire, but less effective for flood and hurricane resistance, although to varying degrees. In addition, there was a common view that these materials have positive effects on life and human health (Figure 1).

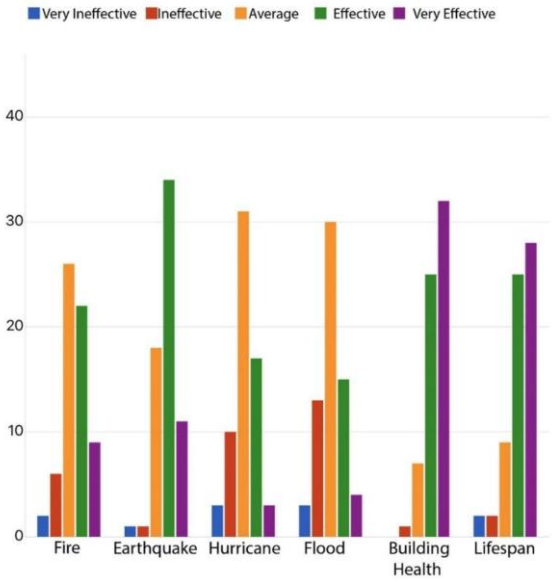

Figure 1. The effects of natural building materials.

Forty-five percent of participants highlighted the lack of standards and high costs as the primary concerns, while forty-one percent cited insufficient training and awareness. The simplicity of usage and the insufficiency of current production capacities were identified as crucial factors.

About 30% of respondents reported using Building Information Modelling (BIM) and about 30% of BIM users reported that they actively incorporate natural building materials as data in BIM and use them in various building analyses. Furthermore, survey results reveal that the majority rely on national material libraries from other countries or modify existing materials, often favoring pre-fabricated library components. Consequently, the establishment of a local natural building material library within the BIM system would be advantageous.

The majority of participants who responded affirmatively or negatively to the preceding questions regarded the prospects of natural building materials as favorable or highly favorable. The research audience is optimistic in this regard. Concerning hybrid building materials, 46.8% of respondents deemed them an optimal choice in terms of durability. 38.7% indicated they could be suitable during the transition phase, while 33.9% expressed concerns over the chemical constituents utilized. Furthermore, 19.4% indicated the risk of greenwashing.

Furthermore, 35.5% indicated that they perceive it as a chance to fulfill the EU Green Deal objectives.

In material-based interviews with manufacturers and practitioners, it has been observed that end-user trends have increased after the pandemic, and materials have proven their durability despite disasters such as floods and earthquakes in applications. For example, the BKM film plateaus, which were manufactured with rammed earth, were exposed to flooding twice; it is observed that there was no deformation on the walls after the disaster and there was no color change(Figure 2). Although it is argued that compacted soil becomes rocky over time, it can be said that there is a need for scientific evidence-based research in this field.

Figure 2. Earth Rammed Techniques & Resillience Interview Alişan,E. (2024).

Conclusion

Despite the overall favorable inclination toward natural construction materials, a notable disparity exists in the methodologies employed by experts who are adept in utilizing these materials and those who lack such expertise. This suggests that resources need to be better recognised and integrated more effectively into training and courses. The pertinent departments inadequately assess building biology and health-related concerns. Conversely, they ought to be incorporated more efficiently by evaluating creative sustainable strategies, including Environmental Social and Governance objectives and the EU Consensus. Considering that one of the main difficulties in the use of natural building materials is that outdoor weather variable factors, such as fluctuations in relative humidity and temperature, create variable results, it can be said that it is a very important factor in front of industrialisation for standardisation and wider application. Anticipating identical functionalities and durability from current chemical materials is impractical and overlooks the health and ecological advantages of natural construction materials. Nonetheless, while it is encouraging to assess durable performance and resilience through appropriate techniques and methodologies, further evidence-based analysis, evaluation, and practical examples are requisite in this domain. This requires appropriate policies and incentives for support. In this regard, while it is anticipated that the non-governmental organization and initiatives of the Natural Building Materials Association will make substantial contributions, additional projects should get support through incentives and research. The study's scope was finalized in two months; it would be advantageous to extend the research with a more exhaustive literature survey, a thorough contextual analysis utilizing BIM, and a more profound investigation of the applications.

References

Abera, Y. A. (2024). Sustainable building materials: A comprehensive study on eco-friendly alternatives for construction. Composites and Advanced Materials, Volume 33:1-17. DOI: 10.1177/26349833241255957.

Url-1
https://www.researchgate.net/publication/380701193_Sustainable_building_materials_A_comprehensive_study_on_eco-friendly_alternatives_for_construction.

Alişan,E. (2024). Earth Rammed Techniques & Resillience Interview.

Url-2 https://erkanalisan.com/proje/bkm-film-platosu, data retrieved 29.07.2024.

Al-Qahtani,S., Koç,M. , Isaifan, R.J. (2023).Mycelium-Based Thermal Insulation for Domestic Cooling Footprint Reduction: A Review. Sustainability. 15(17). 13217.
Url-3 https://doi.org/10.3390/su151713217. https://www.mdpi.com/2071-1050/15/17/13217.
Balducci,B., Camilli,F. (2022). Designing ecology. The organic as a possible paradigm of a sustainable and resilient architecture. Researchgate. n.11. 84-93. doi.org/10.19229/2464-9309/1172022.
Url-4
https://www.researchgate.net/publication/361795729_Designing_ecology_The_organic_as_a_possible_paradigm_of_a_sustainable_and_resilient_architecture.
Dams, B., Maskell, D., Shea, A., Allen, S., Cascione, V., & Walker, P. Upscaling bio-based construction: challenges and opportunities. Building Research & Information, 51:7, 764-782. DOI: 10.1080/09613218.2023.2204414. https://doi.org/10.1080/09613218.2023.2204414.
Url-5 https://www.researchgate.net/publication/370415210_Upscaling_bio-based_construction_challenges_and_opportunities.
Murtagh, N., Scott, L., & Fan, J. (2020). Sustainable and resilient construction: Current status and future challenges. Journal of Cleaner Production. Volume 268. 122264. https://doi.org/10.1016/j.jclepro.2020.122264.
Url-6 https://www.sciencedirect.com/science/article/abs/pii/S0959652620323118.
Yahia, A.K.M., Rahman,M., Shahjalal, M., Morshed,A. (2024). Sustainable materials selection in building design and construction. International Journal of Science and Engineering. 1(04): 106-119. Doi: 10.62304/ijse.v1i04.198.
Url-7 https://globalmainstreamjournal.com/index.php/IJSE/article/download/199/159/496.

Circular Economy Performance Assessment in Construction: A Critical Review of Firm-Level Models

Mohammed Ahallaq[a], Deniz Artan[a]

[a] Istanbul Technical University, Faculty of Civil Engineering, Department of Civil Engineering, Construction Management Program, Turkey
alhallaq21@itu.edu.tr

Keywords: Circular Economy, Performance Assessment, Construction Industry, Firm-Level Performance, CE Indicators.

Circular Economy (CE) concepts have gained increasing attention as industries search for more sustainable ways to use resources. In construction, the urgency is particularly clear: the sector consumes vast amounts of raw materials and generates a high volume of waste (Gasparri et al., 2023). Using CE ideas could make a real difference here by improving how materials are sourced, reused, and managed. Yet, putting CE principles into action in construction settings is often anything but straightforward. This industry tends to work through one-off projects, with various parties involved and site-specific decisions, all of which make systematic changes harder to implement (Kristoffersen et al., 2020).
What makes things more complicated is the lack of common tools to measure how "circular" a construction firm actually is. A lot of the models out there were originally designed for other industries, especially manufacturing, and don't match the day-to-day reality of construction work (Núñez-Cacho et al., 2018). They also rarely account for the shifting conditions across projects or the regulatory landscape construction firms must navigate (Berglund-Brown et al., 2022). Because of this, there's no widely accepted way for construction firms to assess CE performance at the firm level, and that creates a barrier to progress.

Aim

In this work, we reviewed existing models used to evaluate Circular Economy performance, paying close attention to how relevant they are to construction firms. Rather than proposing a new model at this stage, our goal was to better understand how these frameworks were designed, what they measure, and whether they could realistically be adapted for use in construction. This review is also part of a broader PhD project that aims to eventually build a practical, firm-level CE assessment tool specifically for the construction industry.

Material and Method

A systematic literature review was conducted to identify relevant CE performance assessment models. The selection process involved keyword-based searches across academic databases, focusing on circular economy assessment, sustainability metrics, and firm-level indicators in construction and related industries. Databases such as Scopus, Web of Science, and Google Scholar were utilized, with keywords including "Circular Economy Performance Assessment," "Construction Industry," "Firm-Level Circularity," and "Sustainability Metrics." Models lacking a structured assessment methodology or focused solely on macro-level policy analysis were excluded to ensure applicability at the firm level
The selected models were categorized into three structured tables to facilitate comparison:

- **Table 1:** Overview of Circular Economy Performance Assessment Models – Summarizes the year, model type, sector, and key contributions.
- **Table 2:** Theoretical Methodologies of CE Performance Assessment Models – Includes models based on literature reviews and conceptual frameworks.
- **Table 3:** Empirical Methodologies of CE Performance Assessment Models – Covers models that apply case studies, surveys, or industry validation.

Each model was analyzed based on key methodological parameters, including scope, validation approach, and sectoral application. The analysis also considered the strengths and weaknesses of each model, particularly in how well they address construction-specific challenges such as material circularity, lifecycle impacts, and regulatory compliance.

Findings

As we read through the 14 CE performance models, we noticed a recurring trend. Many were designed with manufacturing in mind, where systems tend to repeat and data is easier to track (Baratsas et al., 2022; Kristoffersen et al., 2020). But construction doesn't work that way, it's based on temporary projects, varying sites, and complex stakeholder arrangements. These characteristics make it harder to apply many of the existing CE models directly to construction settings. The workflow and data availability in construction are fundamentally different from manufacturing, which leads to compatibility issues when using standardized performance frameworks.

Out of the four models we found that connect to construction, just two used real-world data from construction companies. The Importance–Adoption Analysis model developed by Lee et al. (2023) focuses on how construction companies perceive and prioritize CE strategies. Similarly, the Circular Information Flow (CIF) model proposed by Shooshtarian et al. (2022) maps how information related to circular practices flows between actors in industrialized construction. These models helped us understand things like awareness levels and communication patterns, but they stopped short of offering practical tools for performance assessment. The other two construction-related models, such as the Circular Business Model review and the Circular Economy Index by Núñez-Cacho et al. (2018), were more conceptual. They provided useful frameworks but lacked clear performance indicators, sector-specific benchmarks, or systematic processes for firm-level tracking.

Something else that became apparent during our review was the limited attention to design-stage planning and lifecycle thinking. Only a handful of models mentioned these aspects, despite their crucial importance in construction. Design decisions, such as material selection, modularity, and adaptability, can directly impact the feasibility of circular practices like reuse and disassembly (Ghisellini et al., 2016; Shooshtarian et al., 2022). Ignoring the early planning phase weakens the overall effectiveness of CE models, especially in a sector where initial design often dictates long-term sustainability outcomes.

Another notable gap was the underuse of digital tools in construction-focused CE models. In other industries, CE frameworks are increasingly integrated with advanced technologies, including the Internet of Things (IoT), artificial intelligence (AI), and big data analytics (Kristoffersen et al., 2020). These tools support real-time tracking of material flows, performance metrics, and environmental impact. However, we found that the construction-specific models largely ignore these technologies, even though the sector generates large volumes of process data. This suggests that the construction industry may be underutilizing available digital tools that could otherwise support circular performance measurement.

While reviewing models designed for general or cross-sectoral use, we also identified certain structural ideas that could potentially be adapted to construction. For example, maturity models like C-METRIC (Holly et al., 2024) and modular indicator frameworks used in MICRON (Baratsas et al., 2022) offer structured approaches that allow firms to assess and compare their progress. However, these models tend to assume controlled environments and consistent data availability. Such assumptions may not hold in the construction sector, where project variability, decentralized data, and regulatory constraints present real challenges.

Taken together, these observations highlight a significant research gap. Despite the diversity of CE models and their growing refinement in various sectors, there is currently no established model that effectively addresses CE performance measurement at the firm level within the construction industry. Most of the models are either too generic or too focused on narrow aspects of circularity, such as material reuse or awareness tracking. For firms operating in the construction sector, this lack of a comprehensive and practical tool limits their ability to benchmark performance, identify areas for improvement, and align with broader sustainability goals. Addressing this gap is a necessary step toward enabling more effective implementation of CE principles in the built environment.

Conclusion

Through this review, we aimed to understand whether current CE performance models are suitable for application in construction firms at the firm level. After analyzing 14 different models, it became evident that while the interest in CE continues to grow, practical tools for performance evaluation in construction are still missing. Existing models are often designed for manufacturing or broader multi-sectoral use. Their structures tend to rely on assumptions such as operational uniformity, centralized data collection, and stable production environments, conditions that are rarely found in construction. Even the four models we identified as relevant to the construction industry had limited value when it came to firm-level performance measurement. Two models were grounded in empirical data, but their scope was confined to perceptions and information flows (Lee et al., 2023; Shooshtarian et al., 2022). The other two offered conceptual insights, but lacked actionable indicators or implementation frameworks (Núñez-Cacho et al., 2018). As a result, construction firms still lack a method to systematically assess and improve their CE performance.

We also noted a significant gap in how existing models deal with early-stage design and digital technologies. These are both critical in construction but are either ignored or only superficially addressed in current CE frameworks. The absence of lifecycle-based thinking and real-time tracking tools limits the effectiveness of existing models when applied to complex, project-based operations.

What this review reveals is more than just a list of what's missing. It clarifies where future efforts should be directed. There is a clear need for a new CE performance assessment model that takes into account how construction firms operate—one that is flexible, measurable, and grounded in real project workflows. Such a model would need to integrate key aspects like firm-level indicators, lifecycle thinking, and the use of digital tools to track performance over time.

This study reinforces the urgency of developing a tailored framework for CE performance measurement in the construction industry. Doing so would not only fill a gap in academic research but also support practitioners and firms aiming to improve their sustainability outcomes. The insights gathered here will directly support the next phase of this PhD research, which focuses on building and validating a sector-specific assessment tool for construction.

Acknowledgement

This study is part of the ongoing Ph.D. research of Mohammed Alhallaq, conducted under the supervision of Deniz Artan at Istanbul Technical University.

References

Baratsas, S. G., Pistikopoulos, E. N., & Avraamidou, S. (2022). A quantitative and holistic circular economy assessment framework at the micro level. *Computers and Chemical Engineering, 160*, 107697. https://doi.org/10.1016/j.compchemeng.2022.107697

Berglund-Brown, J., Kedir, F., Riabova, A., & Hall, D. (2022). Assessing circular information flow in industrialized construction: A framework for evaluating data for circular construction. In *IOP Conference Series: Earth and Environmental Science* (Vol. 1078, No. 1, p. 012005). IOP Publishing. https://doi.org/10.1088/1755-1315/1078/1/012005

Durdyev, S., Koc, K., Tleuken, A., Budayan, C., Ekmekcioğlu, Ö., & Karaca, F. (2023). Barriers to circular economy implementation in the construction industry: Causal assessment model. *Environment, Development and Sustainability*, 1–37. https://doi.org/10.1007/s10668-023-04061-8

Gasparri, E., Arasteh, S., Kuru, A., Stracchi, P., & Brambilla, A. (2023). Circular economy in construction: A systematic review of knowledge gaps towards a novel research framework. *Frontiers in Built Environment, 9*, 1239757. https://doi.org/10.3389/fbuil.2023.1239757

Ghisellini, P., Cialani, C., & Ulgiati, S. (2016). A review on circular economy: The expected transition to a balanced interplay of environmental and economic systems. *Journal of Cleaner Production, 114*, 11–32. https://doi.org/10.1016/j.jclepro.2015.09.007

Holly, F., Schild, C., & Schlund, S. (2024). Development of an assessment model for measuring mechanical engineering companies' circularity and maturity levels. *Journal of Circular Economy*, *2*(1). https://doi.org/10.55845/XUPF2540

Kristoffersen, E., Blomsma, F., Mikalef, P., & Li, J. (2020). The smart circular economy: A digital-enabled circular strategies framework for manufacturing companies. *Journal of Business Research, 120*, 241–261. https://doi.org/10.1016/j.jbusres.2020.07.044

Lee, P.-H., Juan, Y.-K., Han, Q., & de Vries, B. (2023). An investigation on construction companies' attitudes towards importance and adoption of circular economy strategies. *Ain Shams Engineering Journal*, *14*, 102219. https://doi.org/10.1016/j.asej.2023.102219

Núñez-Cacho, P., Górecki, J., Molina, V., & Corpas-Iglesias, F. A. (2018). New measures of circular economy thinking in construction companies. *Journal of EU Research in Business*, 2018, 1–16. https://doi.org/10.5171/2018.909360

Shooshtarian, S., Maqsood, T., Caldera, S., & Ryley, T. (2022). Transformation towards a circular economy in the Australian construction and demolition waste management system. Sustainable Production and Consumption, 30, 89–106. https://doi.org/10.1016/j.spc.2021.11.032

Stucki, T., Woerter, M., & Loumeau, N. (2023). Clearing the fog: How circular economy transition can be measured at the company level. *Journal of Environmental Management, 326*, 116749. https://doi.org/10.1016/j.jenvman.2022.116749

CONTROL AND AUTOMATION ENGINEERING

Advances in Automatic Control Engineering

Applications of Control Engineering

Control Surface Failure Management In Dual-System VTOL UAVs

Bilal Badur[a], Fikret Çalışkan[a]

[a] Istanbul Technical University, Faculty of Electrical and Electronics, Department of Control and Automation Engineering, Türkiye
Badur22@itu.edu.tr

Keywords: Control Allocation, Control Surface Failures, Dual-System VTOL UAVs, Fault Tolerant Control, Fault Detection and Isolation.

Aim

The primary objective of this study is to design, develop, and implement a comprehensive fault-tolerant control (FTC) strategy for dual-system Vertical Take-Off and Landing (VTOL) Unmanned Aerial Vehicles (UAVs) that ensures stable flight performance under fault conditions, particularly during the cruise phase. One of the main challenges in dual-system VTOL UAVs is the loss of control authority due to control surface failures, which can lead to instability and loss of mission effectiveness. To address this issue, the proposed FTC strategy leverages vertical motors, which remain inactive during cruise flights, as auxiliary actuators to compensate for these failures and maintain UAB stability.
The study also presents a real-time fault detection system that can immediately identify and categorize surface failures. Moreover, an adaptive control allocation method is designed to distribute control commands between conventional aerodynamic surfaces and vertical motors according to the failure scenario. A nonlinear dual-system VTOL UAV model created in MATLAB/Simulink is used to simulate dual-system VTOL UAV dynamics and evaluate the performance of the proposed control architecture under multiple failure conditions.

Material and Method

The study is conducted using a comprehensive nonlinear dual-system VTOL UAVs model, developed in Simulink, which features a hybrid dual-system architecture integrating both fixed-wing and rotary-wing components. The dual-system VTOL UAV model consists of a single horizontal motor for forward flights, four vertical motors primarily used for takeoff, landing, and hover but repurposed for fault compensation in cruise, and an inverted V-tail and two ailerons as primary control surfaces for fixed-wing flights.
To ensure accurate representation of real-world flight conditions, the nonlinear flight dynamics of the dual-system VTOL UAVs are rigorously modelled, incorporating aerodynamic forces, moments, actuator dynamics, and limitations. A cascade PID control architecture is employed, featuring separate controllers for rotary-wing and fixed-wing configurations, allowing independent tuning for each mode. One key challenge in the control design arises from the difference in response times between the fixed-wing control surfaces and the vertical motors. The control surfaces exhibit faster response times, whereas the vertical motors introduce slower dynamics. This discrepancy necessitates careful tuning of the fixed-wing controller gains to maintain stability, especially when vertical motors are activated as additional actuators in the event of control surface failures.
A model-based fault detection system is integrated into the study to detect faults that may occur in the control surfaces. This system estimates the expected behavior of each control surface using control surface commands and servo feedback. It then analyzes the deviations that occur in the control surfaces, considering the aerodynamic loads. When this deviation exceeds a predefined deviation threshold, the system perceives this as a fault. The severity of the fault is classified and evaluated, and based on this evaluation, it is decided whether to activate the vertical motors.
Control allocation is performed adaptively, distributing commands between aerodynamic surfaces and vertical motors according to the fault's magnitude. This strategy ensures continued stability and performance, even under substantial actuator failures.

Findings

Extensive simulations in MATLAB/Simulink were carried out to assess the performance of the proposed FTC strategy. The results show that the fault detection system accurately identifies and classifies control surface failures in real time, enabling timely corrective actions. Moreover, the system assesses the severity of each fault and activates the vertical motors only when necessary, conserving energy while preserving control authority.

The controller can maintain flight stability in the event of a failure in either one of the ailerons or one of the inverted V-tail control surfaces. However, if both surfaces fail, the remaining control effectors are insufficient to ensure stable flight. In such cases, the control allocation algorithm engages vertical motors to restore controllability and maintain flight stability.

This control allocation strategy guarantees reliable operation even under severe failure conditions. The cascade PID structure, featuring independently tuned controllers for rotary-wing and fixed-wing modes, provides robust and responsive performance across all phases of flight. Simulation results confirm the system's resilience against various fault scenarios, including isolated aileron failures, inverted V-tail malfunctions, and complete loss of aerodynamic control surfaces.

Conclusion

This study introduces a fault-tolerant control (FTC) strategy for dual-system VTOL UAVs that combines vertical lift motors, a model-based fault detection system, and a control allocation method. Simulation results show that the proposed approach enhances the dual-system VTOL UAV's ability to manage control surface failures during cruise, thereby improving overall flight safety and reliability. By employing vertical motors as auxiliary actuators, the system reduces the risk of mission failure and loss of control, ensuring continued operation under fault conditions. If there is a failure in the aileron or inverted V-tail control surfaces, the dual-system VTOL UAV cannot maintain its attitude with the current controller. However, by using a control allocation algorithm, the vertical motors take over the function of the faulty surfaces and allow the dual-system VTOL UAV to continue its mission.

The cascade PID architecture, with independently tuned gains for different flight modes, provides accurate and responsive control throughout the mission. In addition to improving fault resilience, the strategy reduces dependence on primary aerodynamic control surfaces, making it a practical solution for both civilian and military dual-system VTOL UAV applications.

In future work, vertical motor support will be enhanced in fixed-wing modes to improve the dual-system VTOL UAV's ability to maintain hover and stabilize its attitude angles.

References

Beard, R. W., & McLain, T. W. (2012). *Small unmanned aircraft: Theory and practice*. Princeton University Press.

Bossert, D. E., Morris, S. L., Hallgren, W. F., & Yechout, T. R. (2003). *Introduction to aircraft flight mechanics: Performance, static stability, dynamic stability, and classical feedback control*. American Institute of Aeronautics and Astronautics.

Fourlas, G. K., & Karras, G. C. (2021). A survey on fault diagnosis and fault-tolerant control methods for unmanned aerial vehicles. *Machines, 9*(9), 197. https://doi.org/10.3390/machines9090197

Gu, H., Lyu, X., Li, Z., Shen, S., & Zhang, F. (2017, June). Development and experimental verification of a hybrid vertical take-off and landing (VTOL) unmanned aerial vehicle (UAV). *In 2017 International Conference on Unmanned Aircraft Systems (ICUAS)* (pp. 160–169). IEEE. https://doi.org/10.1109/ICUAS.2017.7991313

He, A., Zhang, Y., Zhao, H., Wang, B., & Gao, Z. (2022). Adaptive fault-tolerant control of a hybrid VTOL UAV against actuator faults and model uncertainties under fixed-wing mode. *International Journal of Aerospace Engineering, 2022*, 8191154. https://doi.org/10.1155/2022/8191154

Mancinelli, A., Voß, N., & Smeur, E. (2025). Fault tolerant control in over-actuated hybrid tilt-rotor unmanned aerial vehicles. *In AIAA SCITECH 2025 Forum* (p. 0317). https://doi.org/10.2514/6.2025-0317

Mizrak, I., Alwi, H., & Edwards, C. (2022, May). Sliding mode FTC of an octoplane UAV transition mode. *In 2022 8th International Conference on Control, Decision and Information Technologies (CoDIT)* (Vol. 1, pp. 978–983). IEEE. https://doi.org/10.1109/CoDIT55151.2022.9803987

Mousaei, M., Geng, J., Keipour, A., Bai, D., & Scherer, S. (2022, October). Design, modeling and control for a tilt-rotor VTOL UAV in the presence of actuator failure. *In 2022 IEEE/RSJ International Conference on Intelligent Robots and Systems (IROS)* (pp. 4310–4317). IEEE. https://doi.org/10.1109/IROS47612.2022.9981615

Ozdemir, U., Aktas, Y. O., Vuruskan, A., Dereli, Y., Tarhan, A. F., Demirbag, K., ... & Inalhan, G. (2014). Design of a commercial hybrid VTOL UAV system. *Journal of Intelligent & Robotic Systems, 74*, 371–393. https://doi.org/10.1007/s10846-013-9956-6

Prochazka, K. F., & Stomberg, G. (2020, July). Integral sliding mode-based model reference FTC of an over-actuated hybrid UAV using online control allocation. *In 2020 American Control Conference (ACC)* (pp. 3858–3864). IEEE. https://doi.org/10.23919/ACC45564.2020.9147827

Puchalski, R., & Giernacki, W. (2022). UAV fault detection methods, state-of-the-art. *Drones, 6*(11), 330. https://doi.org/10.3390/drones6110330

Rehan, M., Akram, F., Shahzad, A., Shams, T. A., & Ali, Q. (2022). Vertical take-off and landing hybrid unmanned aerial vehicles: An overview. *The Aeronautical Journal, 126*(1306), 2017–2057. https://doi.org/10.1017/aer.2022.44

Salem, W. A., Mohamady, O., Draz, M., & El-bayoumi, G. (2024). Promoting the maneuverability and fault-tolerant control capabilities of dual-system/hybrid VTOL UAVs. *Arabian Journal for Science and Engineering, 49*(5), 7411–7429. https://doi.org/10.1007/s13369-023-08068-6

4-D Flight Management System Design for the Fighter Jets

Kaan Tellioğlu[a], Fikret Çalışkan[a]

[a]Istanbul Technical University/ Faculty of Electrical and Electronics Engineering, Department of Control and Automation Engineering, Turkiye
telliogluk19@itu.edu.tr

Keywords: Flight Management, Guidance, Navigation, Route Management

Aim

The new generation of fighter jets, called the 5th generation, began a new era in the military aviation industry. In particular, multirole jets are capable of performing both air-to-air and air-to-ground missions. These complex and expensive aircraft carry huge avionics such as different types of radars and sensor suites. The system supplies vast amounts of information to the pilots. A fighter jet pilot must fly the aircraft through the route, perform tasks in the mission, and return to the base safely. Most of all, they need to evaluate various sensor information on the way to the success of the mission. This sophisticated and stressful environment is a challenge for pilots.

The goal of this study was to describe the design and simulation of a four-dimensional flight management system (FMS) for fighter jets. Current fighter jets have a basic flight management system (FMS) that is just capable of navigating an aircraft between waypoints in the lateral direction. Our FMS manages the flight route of an aircraft in four dimensions: longitudinal, lateral, vertical, and time. The algorithm performs distance, fuel, time, and speed calculations by means of a performance database of the aircraft in considering mission tasks. Besides this, it generates optimization of the current route to overcome undesired situations, such as meteorological conditions, geographical height, and threats, when necessary.

The idea behind the new-generation FMS is to reduce the workload of the pilot in terms of navigation, support for the decisions, and allow the pilot to focus on subtasks more to increase the success of the mission and return to the base safely.

Material and Method

A six-DOF nonlinear F-16 fighter jet model was developed using parameters obtained from previous studies (Stevens & Lewis, 2003; Russell, 2003), such as aerodynamic parameters, size, mass, and inertia. The aerodynamic database has validity between 0.3 Mach and 0.6 Mach.

Table 1. Aircraft States.

States	Description	Type	Unit
δ_a	Aileron Command	input	deg
δ_e	Elevator Command	input	deg
δ_r	Rudder Command	input	ft
δ_t	Thrust	input	ft
ϕ	Latitude	output	deg
λ	Longitude	output	deg
Npos	North Position	output	ft
Epos	East Position	output	ft
h	Altitude	output	ft
ϕ	Roll Angle	output	rad
θ	Pitch Angle	output	rad
ψ	Yaw Angle	output	rad
Vt	Total Velocity	output	ft/s
α	Angle of Attack	output	rad
γ	Flight Path Angle	output	rad
β	Sideslip Angle	output	rad
P	Roll Rate	output	rad/s
Q	Pitch Rate	output	rad/s
R	Yaw Rate	output	rad/s
CM	AC Weight	output	kg
FCR	Fuel Consumption Rate	output	kg/s
RF	Remaining Fuel Amount	output	kg

The Cascade controller strategies are required for navigation purposes. Our F-16 model is unstable. Therefore, in the inner loop, the stability augmentation system (SAS) is designed for the roll, pitch, and yaw axes of the aircraft to enhance stability (Cook, 2015; McLean, 1990). SAS is a PID-based state feedback controller that damps unstable aircraft rate dynamics. In the middle loop, various cascade autopilots are designed for the roll, pitch, and yaw axes of the aircraft to control attitudes. In the lateral axis, the P controller was used for the Roll Attitude hold autopilot. In the outer loop, the P controller is designed to control the aircraft cross-track (XTK), which is the deviation of the aircraft from the defined route. P-based track angle controller is designed to maintain the aircraft's track angle through the desired route. The XTK and track angle controllers operate in parallel as the outer loop of the roll autopilot (Stevens & Lewis, 2003).

In the longitudinal axis, in the pitch axis, a PI controller is used for the gamma hold autopilot. P controller altitude hold autopilot is used as the outer loop of the gamma hold controller. The P controller is designed for the speed autopilot of the aircraft to keep the air speed constant. VNAV (vertical navigator) is a P-based controller that supplies altitude deviation to the altitude hold autopilot and target speed to the speed hold autopilot.

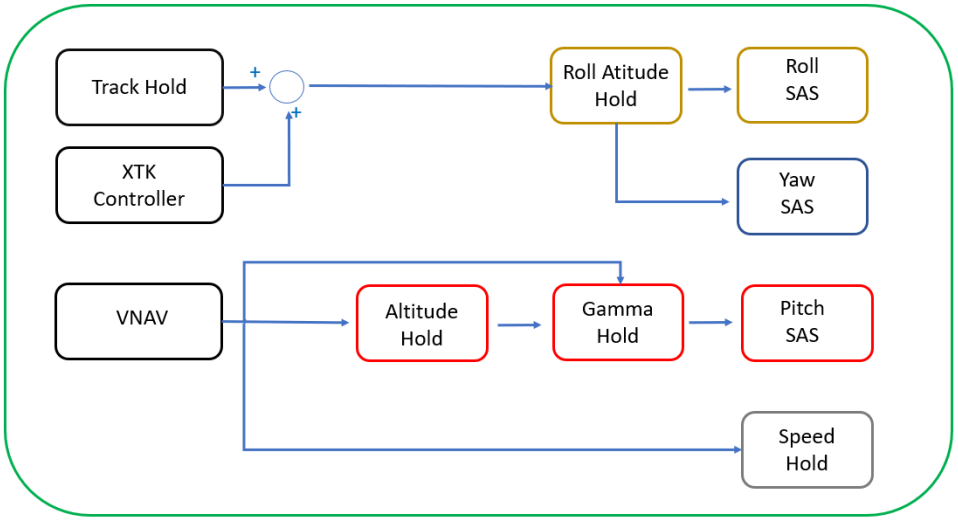

Figure 1. Cascade Controller Loop.

Our FMS consists of four parts, which are planning, execution, editing, and evaluation, respectively. In the planning stage, the distance between waypoints and the desired track of the leg calculations related to the selected route is generated. For this purpose, flat calculations and great circle calculations are used. The proposed FMS uses planning procedures (Slattery & Zhao, 1995). Time calculations were performed using the reference cruise speed information. The estimated time of arrival, estimated leg time, and total route time were the main time variables meaningful to the pilot. An offline performance database was used to calculate the approximate climb, cruise, and descent performance of the aircraft for fuel calculations (Kaminer et al., 1998). The required fuel, estimated on-board fuel, and consumed fuel calculations are crucial for pilots. In the execution part, the XTK and the desired track parameters are generated to navigate autopilots to follow the desired route. In addition, speed and fuel calculations were performed repeatedly in the case of deviation from the planned route and planned speed. In editing mode, the pilot may change the route completely between the active and standby routes. He is also able to add, change, and delete any waypoints on the current route. Planning was necessary after each editing. After automatic planning, the pilot was informed about the changes in the time and fuel of the new route. In the evaluation section, meteorology, geography, and thread in the route information were evaluated. An optimization algorithm offers route updates to overcome unsafe situations during flight, considering the fuel consumption and flight time. For the alternative route generation graph method is used. In this method, the connection between the corners of the restricted area is connected to each other for the purpose of generating a leg. If the corner points are able to reach each other without touching the restricted area, they are accepted as a leg. From the initial point to the final point corner legs are connected to each other to construct alternate routes. The shortest route is offered to the pilot as an alternate route.

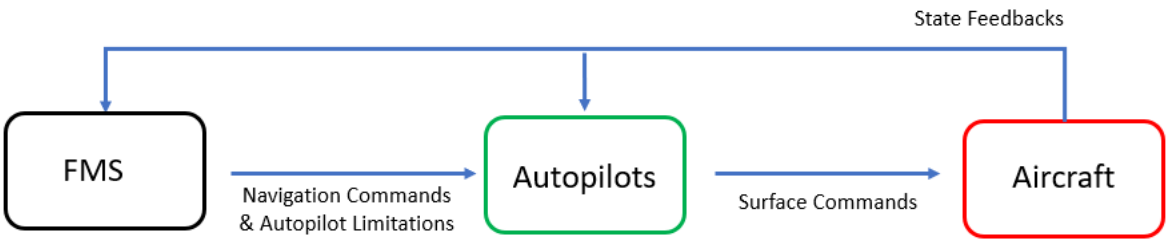

Figure 2. Modelling Scheme.

Findings

The six-DOF F-16 aircraft nonlinear model is trimmable between 0.3 – 0.6 Mach. A three-axis SAS was developed to control the aircraft's attitude in the roll, pitch, and yaw axes. The designed altitude autopilot allows controlling the altitude of the aircraft to reach the selected value without any overshoot and undershoot, and holds the value within less than 100 ft of steady-state error. The designed heading-hold autopilot allows the control heading of the aircraft to reach a selected value without any overshoot or undershoot and hold the value within less than 0.2 degrees of steady-state error. The designed speed-hold autopilot allows the speed of the aircraft to reach a selected value without any overshoot or undershoot and holds the value within less than 5 knots of steady-state error.

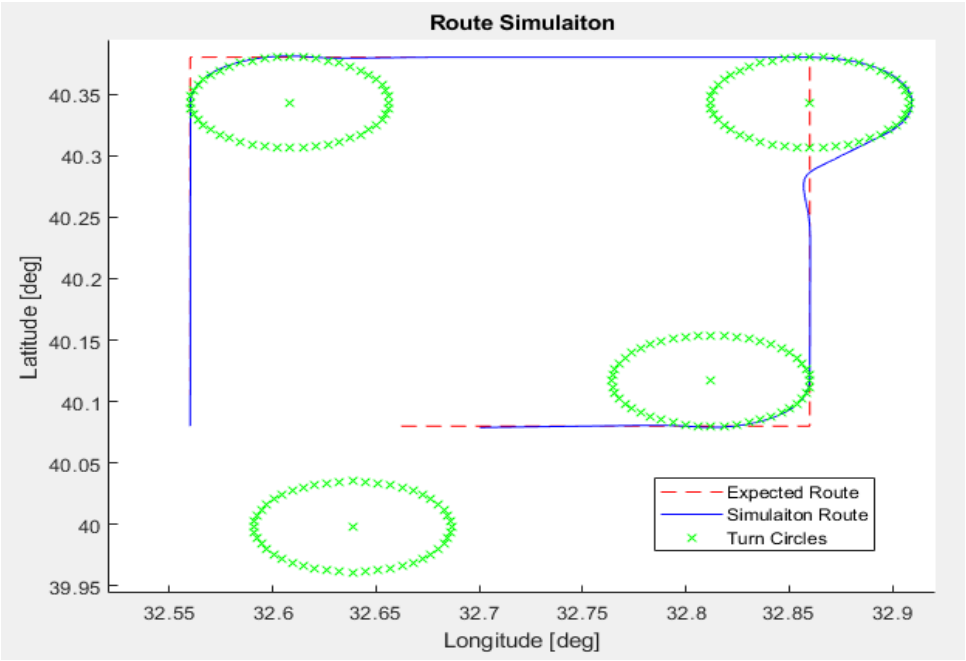

Figure 3. Route Simulation.

The FMS plans the route distance under one-foot error using the great circle algorithm. Fly-by and fly-over transitions were successfully achieved for wide and narrow turn angles. The time calculation deviations between planning and replanning were less than 2 minutes for 2 hours of flight simulations for each waypoint. Fuel calculation deviations are a maximum %3 for 2 hours of flight simulations for each waypoint. The XTK controller holds an XTK of less than 50 feet in the lateral direction. The desired Track controller holds the track less than 0.4 degrees. Route optimization works successfully and offers non-dangerous route waypoints by considering fuel and time. When the return-to-home function is enabled, an automatic path is generated to the emergency airfield.

If the aircraft route passes through any restricted area, the optimization algorithm generates an optimum route and offers it to the pilot (Figure 4).

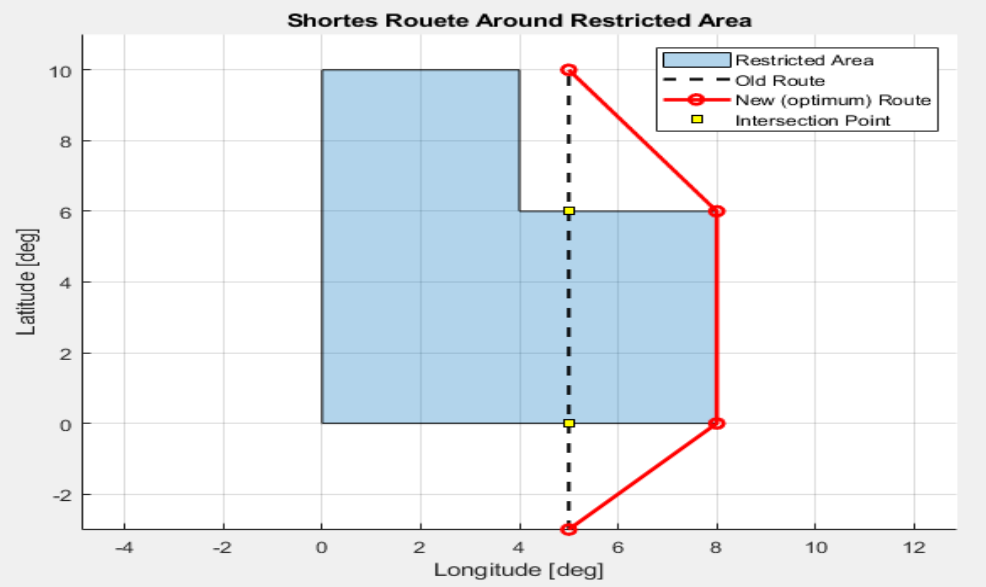

Figure 4. Optimized Route Around Restricted Area.

Conclusion

In conclusion, this study offers a new four-dimensional flight management design approach that involves planning, execution, editing, and evaluation to reduce pilot workload on critical missions to manage aircraft navigation through the performance database. The automatic planning and optimization feature of the FMS increases pilot awareness and consolidates the safety of the flight and the success of the mission. In future works,

References

Cook, M. V. (2015). *Flight dynamics principles* (2nd ed.). Elsevier.
Kaminer, I., Pascoal, A., Hallberg, E., & Silvestre, C. (1998). Trajectory tracking for autonomous vehicles: An integrated approach to guidance and control. *Journal of Guidance, Control, and Dynamics, 21*(1), 29–38. https://doi.org/10.2514/2.4234
McLean, D. (1990). *Automatic flight control systems* (1st ed.). Prentice Hall.
Russell, R. S. (2003). *Non-linear F-16 simulation using Simulink and MATLAB* [Master's thesis, University of Minnesota].
Slattery, R. A., & Zhao, Y. (1995). En-route descent trajectory synthesis for air traffic control automation. In *Proceedings of the 1995 American Control Conference* (pp. 3430–3434). IEEE.
Spitzer, C. R., Ferrell, U., & Ferrell, T. (2015). *Digital avionics handbook* (3rd ed.). CRC Press.
Stevens, B. L., & Lewis, F. L. (2003). *Aircraft control and simulation* (2nd ed.). John Wiley & Sons.

Lane Change Decision Making For Autonomous Vehicles By Using Adversarial Learning Methods

Aytuğ Onurhan Efil[1], Mustafa Doğan[1]

[1] Istanbul Technical University, Control and Automation Engineering Program, Türkiye
efil21@itu.edu.tr

Keywords: AIRL, Autonomous Driving, CARLA, GAIL, GAN.

Aim

The primary purpose of this thesis is to analyze the effectiveness of generative adversarial imitation learning and adversarial inverse reinforcement learning in typical highway driving scenarios. The current consensus within the literature indicates that data-based techniques such as IL and IRL, when combined with adversarial approaches, can produce satisfactory results for autonomous driving on highways. Hence, the central hypothesis is: Can data-driven reinforcement learning through adversarial inverse reinforcement learning or generative adversarial imitation learning produce reasonable behavior in a highway driving environment? This research adds to the knowledge base by combining inverse reinforcement learning and imitation learning using a generative adversarial network for autonomous driving in highway driving.

Material and Method

Initially, a highway driving simulation environment was created using CARLA (Dosovitskiy et al., 2017) and Highway-env (MathWorks, n.d.) to generate the datasets required to train the imitation learning and inverse reinforcement learning models. A human driver performed multiple driving maneuvers. Highway-Env environment was initially trained and validated for simple tasks and to generate various driving scenarios. This environment basically mimics highway conditions and helps in the analysis of vehicle dynamics and interactions. The capability of the developed models to generalize and their performance were evaluated by testing under different traffic conditions and driving scenarios. As a next step, CARLA's detailed scenario modeling, autonomous driving validation capabilities were combined with Highway-env's policy testing and driving maneuver generating capability to create a thorough validation of autonomous driving algorithms. The recorded data suitable for offline learning (Hourigan, n.d.) was stored in a dataset after filtering outliers. Then, the imitation learning and inverse reinforcement learning models were trained of ne using these datasets. To further improve the vehicle's performance, a generative adversarial network (GAN) (Goodfellow et al., 2014) deep neural architecture was used. Within the combination of the methods, Generative Adversarial Imitation Learning (GAIL) (Ho & Ermon, 2016) and Adversarial Inverse Reinforcement Learning (AIRL) (Fu et al., 2017) models were achieved. The trained models were then transferred to an ego vehicle in a highway driving environment using a policy-based approach. Proximal policy optimization (PPO) (Schulman et al., 2017) was utilized to perform this task and to improve the learning performance. At each step, the agent receives the distance to the nearest vehicle in each lane, along with the lane number of the ego vehicle, and decides whether to change lanes or stay in its current lane. Each state-action pair represents the expected future reward. After simulating a finite number of steps, the rewards converge to constant values. In the test phase, the model selects the maneuver with the highest expected reward to achieve its goal, which is closely aligned with human-controlled driving behavior. The complexity of highway driving tasks in the context of autonomous vehicles was analyzed, and evidence was provided in the form of state-action rewards and collision measurements to validate the analysis. Moving to a realistic simulation environment that includes modules that provide a mathematical representation of the ego vehicle's environment validated the practical benefits of the research conducted in the study.

Findings

One of the most significant parts of autonomous driving is autonomous lane change during highway driving, with decision-making. Almost all car makers and suppliers develop autonomous driving strategies to come up with reasonable decision-making based on the context of the traffic. Over the last few years, Reinforcement Learning algorithms have been able to produce discrete actions in both discrete and continuous environments. The Highway-Env environment was used initially to train and validate for simple tasks and to generate various driving scenarios. Later on, we trained our model in CARLA and performed our test in the CARLA environment since it is capable of simulating critical safety scenarios that are necessary for assessing collision risks and for improving the performance of autonomous driving systems (Gu et al., 2024). We applied the mentioned GAIL and AIRL algorithms together with PPO in this thesis for the decision-making planning of highway controls in autonomous vehicles. Finally, we compare the results of two different offline learning approaches and assess the appropriateness of their use.

Conclusion

The primary contribution of this thesis to the research literature is the approach to evaluate two different but similar reinforcement learning paradigms in an autonomous driving environment. Instead of applying the methods used in this study to tasks unrelated to autonomous driving, this research contributes to the existing knowledge by integrating inverse reinforcement learning and imitation learning through adversarial learning networks. The results of the performance measurements and the rewards (Figure 1) obtained during training, together with the crash assessments in the highway environment and the generalization assessments, support the hypothesis that data-driven learning methods (inverse reinforcement learning and imitation learning) can be used as effective learning approaches in advanced applications. With this approach, it was observed that the vehicle can learn a policy similar to a human driver's policy to avoid collision with other vehicles (Figure 2). However, challenges may arise due to driving maneuvers that were not sufficiently represented in the training dataset.

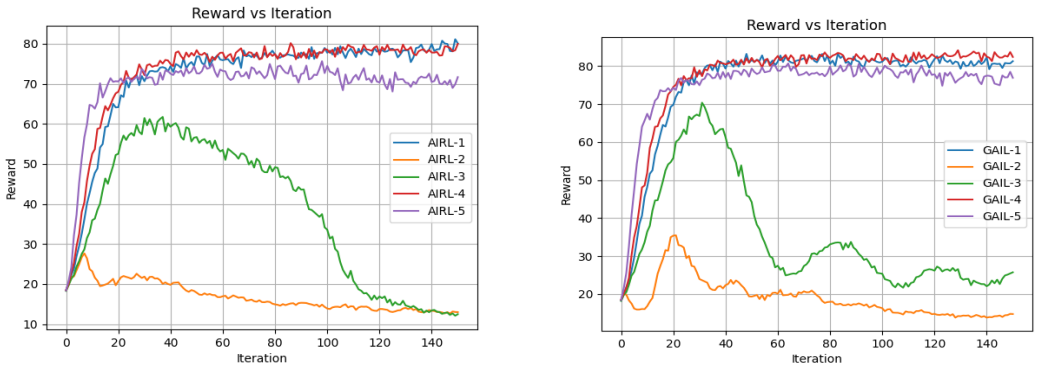

Figure 1. Reward Rate versus Iteration for AIRL and GAIL.

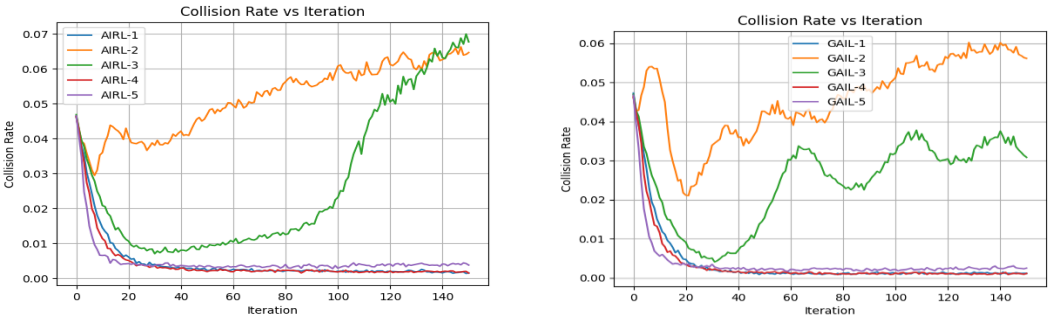

Figure 2. Collision Rate versus Iteration for AIRL and GAIL.

The study focuses on a specific driving task, enabling a meaningful and domain-specific application of reinforcement learning. Additionally, we demonstrate the feasibility and benefits of comparing driving tasks in a minimalist environment.

References

Dosovitskiy, A., Ros, G., Codevilla, F., Lopez, A., & Koltun, V. (2017, October). CARLA: An open urban driving simulator. In *Conference on Robot Learning* (pp. 1–16). PMLR.

Fu, J., Luo, K., & Levine, S. (2017). Learning robust rewards with adversarial inverse reinforcement learning. *arXiv preprint* arXiv:1710.11248. https://arxiv.org/abs/1710.11248

Goodfellow, I., Pouget-Abadie, J., Mirza, M., Xu, B., Warde-Farley, D., Ozair, S., ... & Bengio, Y. (2014). Generative adversarial nets. *Advances in Neural Information Processing Systems, 27*.

Gu, X., Yin, X., Li, Y., Jin, X., & Li, Y. (2024, February). Autonomous driving hazard scenario extraction and safety assessment based on crash reports and CARLA simulation. In *International Conference on Smart Transportation and City Engineering (STCE 2023)* (Vol. 13018, pp. 162–171). SPIE. https://doi.org/10.1117/12.3204297

Ho, J., & Ermon, S. (2016). Generative adversarial imitation learning. *Advances in Neural Information Processing Systems, 29*.

Hourigan, B. (n.d.). Deep reinforcement learning and imitation learning for autonomous driving in a minimalist environment [Unpublished manuscript].

MathWorks. (2025, January 12). *Highway-env documentation.* https://highway-env.farama.org

Schulman, J., Wolski, F., Dhariwal, P., Radford, A., & Klimov, O. (2017). Proximal policy optimization algorithms. *arXiv preprint* arXiv:1707.06347. https://arxiv.org/abs/1707.06347

CONTROL AND AUTOMATION ENGINEERING

Advances in Automatic Control Engineering

Applications of Control Engineering

An Optimization-Based Flight Control Law Design for Fighter Aircraft

Bora Akaryıldız[a], Yaprak Yalçın[a]

[a] Istanbul Technical University, Faculty of Electrical and Electronics Engineering, Control and Automation Engineering, Turkey
akaryildiz17@itu.edu.tr

Keywords: Flight Control Law, Flying and Handling Qualities, Stability and Performance Robustness.

Aim

Flight control law design for modern fighter aircraft must meet strict FHQ requirements while ensuring robustness against aerodynamic and inertial uncertainties. The challenge arises due to large flight envelopes where airframe dynamics change with dynamic pressure, Mach number, and mass-inertia properties, necessitating a multi-stage gradient-based optimization scheme to achieve Level 1 handling qualities with stability robustness in a cost-effective manner.
This paper applies a three-stage optimization scheme inspired by industrial applications for designing a lateral-directional flight control law of a fighter aircraft. The control law architecture includes stability axis roll rate, sideslip angle rate, and lateral acceleration feedback, commonly used in flight control applications. Actuators, noise filters, and time delays are modelled to better represent phase lag effects in the flight control system. The objective is to achieve predicted Level 1 handling qualities and ensure stability robustness using a linear control law.

Material and Method

The optimization follows CONDUIT's strategy (Tischler et al., 2017), structured into three sequential stages as given in Table 1. The requirements are mapped into the optimization functions such that, a "good" value corresponds to predicted Level 1 handling qualities, while a "bad" value represents Level 2 or inadequate stability robustness as depicted in Eq. 1. Various algorithms are used for this problem, for example in (Tischler et al., 2017) FSQP is used for control law design applications for both fixed and rotary wing platforms. In (Moritz & Osterhuber, 2006), the SLLSQP algorithm is utilized for the control law design activities of EF 2000. In (Joos & Finsterwalder, 1999), SQP is used for LQR-based control law design of a transport aircraft by optimizing the Q and R matrices based on design specifications. And in (Park & Tahk, 1998), CEALM is utilized for control law design of a fighter-type aircraft. In this study, MATLAB's interior-point algorithm is used as the solver for its compatibility with nonlinear constraint optimization, fast convergence, and good feasibility properties.

$$f_{h,s_i}(K) = f_{map}\left(f_{req.i}(K)\right) \tag{1}$$

Table 1. Optimization stages.

Stage 1	$solve\ f_{hard}(K) \leq 0$
Stage 2	$solve\ f_{soft}(K) \leq 0, \quad while\ f_{hard}(K) \leq 0$
Stage 3	$minimize\ f_{sum}(K), \quad while\ f_{cons}(K) \leq 0$

In the first stage, the objective function is defined as the maximum of hard objectives that consist of stability requirements as given in Eq. 2. By decreasing the maximum value to the "good" value, all of the requirements are satisfied. This min-max strategy has the advantage of reducing time and computational cost by decreasing the size of the Jacobian matrix,

making it a time-effective strategy for control law design. As soon as the objective function recedes to a "good" value second stage of the optimization scheme starts.

$$f_{hard}(K) = \left(f_{h_1}, f_{h_2}, \dots f_{h_n}\right) \quad (2)$$

In the second stage, soft objectives that consist of FHQ or generic requirements are defined as the objective function given in Eq. 3, and the same min-max strategy is utilized. The maximum value of hard objectives is taken as the constraint function, and the maximum value of soft objectives is minimized until it recedes to a "good" value. Again, as soon as the "good" value is reached, the third stage starts.

$$f_{soft}(K) = max\ (f_{s_1}, f_{s_2}, \dots, f_{s_n}) \quad (3)$$

In the third stage, the maximum of all the soft and hard objectives that are satisfied in prior stages is taken as the constraint function as depicted in Eq. 4, and a designer-defined objective function f_{sum} is minimized. In (Berger & Tischler, 2013), this stage consists of functions that are related to control surface usage and the optimization scheme aims to satisfy all requirements with minimum control effort, whereas in (Moritz & Osterhuber, 2006), this stage consists weighted sum of several functions.

$$f_{cons}(K) = \left(f_{soft}, f_{hard}\right) \quad (4)$$

Flight Control Law Architecture

Flight control law consists of stability axis roll rate feedback to aileron, with aileron to rudder interconnect, washed out sideslip angle rate to rudder, and lateral acceleration feedback to rudder loops. The commanded control variable in the lateral axis is stability axis roll rate, for which a proportional control with K_p gain is used in the forward path. And an interconnect gain K_{ARI} is used for turn coordination. In the directional axis, lateral acceleration is used to minimize the sideslip angle. The hard, soft, and summed objectives used for the design are explained as follows.

Hard Objectives

The minimum gain and phase margin requirement from (U.S. Department of Defense, 2006) is taken as one of the hard objectives with a minimum phase and gain margin of 45°, 6dB, respectively. However, in order to address simultaneous gain and phase variations in loop transfer functions a more generic measure for stability is used by defining the maximum sensitivity peak value to be less than 6dB, which corresponds to guaranteed phase margin of 30° and gain margin of 6dB (Blight et al., 1983). A time to double requirement is added with a maximum value of 20s.

Soft Objectives

Minimum Dutch-roll damping of 0.4 is taken as recommended from (U.S. Department of Defense, 1997). Northrop criterion in (Innocenti & Bava, 1991), which is a measure of Dutch-roll pole-zero cancellation in the roll response, is chosen as one of the objectives. This ensures that the Dutch-roll contamination in the roll response is not objectionable to the pilot and helps achieve a first-order-like response in the roll axis.

Sideslip angle excursion criteria is added to minimize sideslip angle for stick input and its boundaries are taken from the recommended values of (U.S. Department of Defense, 1997). Disturbance rejection criteria is added for the roll rate loop to minimize the aircraft's response to gusts with a maximum gain of -8dB for around 1rad/s of sensitivity function. In order to address linear PIO tendency, Gibson's average phase rate criteria (Gibson, 1999) and attitude quickness criteria (Klyde et al., 1995) are added to the soft objectives with their recommended values.

Summed Objectives

For the last stage, sideslip angle excursion for stick input is added in order to minimize sideslip angle, and sideslip angle build-up for pedal input is added to increase the disturbance rejection performance of lateral acceleration feedback. Crossover frequency for the aileron loop is added in order to minimize aileron control surface activity.

Findings

Lateral-directional flight control law for a fighter aircraft is designed using the three-stage optimization scheme with MATLAB's interior-point algorithm with the linear state-space models of a fighter aircraft that are obtained by linearizing the nonlinear 6-DOF model of the subject aircraft with aerodynamic data acquired from (Nguyen et al., 1979). The design process involved equivalent airspeeds (EAS) 150 to 400 knots and altitudes 0 to 20kft, where gains are scheduled with respect to EAS and altitude.

Designed gains as an output of the optimization process are given in Figure 1, where it can be seen that all the gains form a smooth trend with respect to EAS and altitude. Here, K_{DC} is the gain that is used to achieve a unit response and K_{ARI} is the interconnect gain that is designed prior to the optimization.

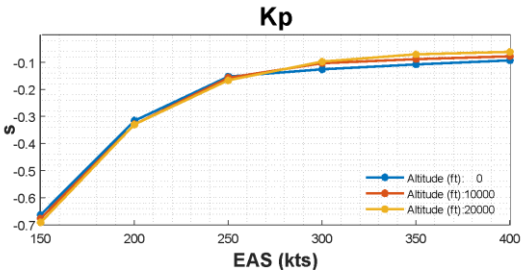

Figure 1.1 Stability axis roll rate gain schedule.

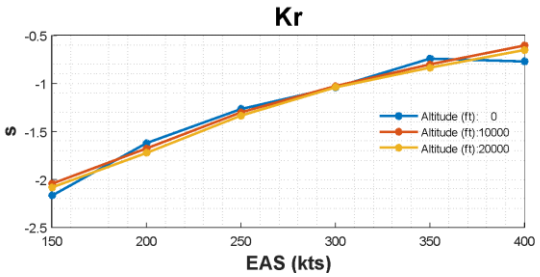

Figure 1.2 Sideslip rate gain schedule.

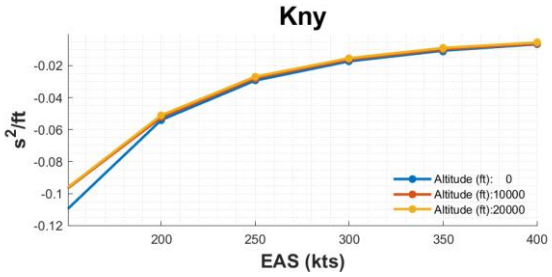

Figure 1.3 Lateral acceleration gain schedule.

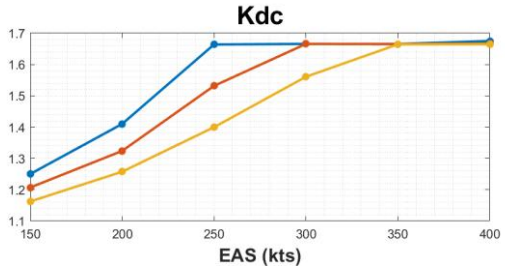

Figure 1.4 "DC" gain schedule.

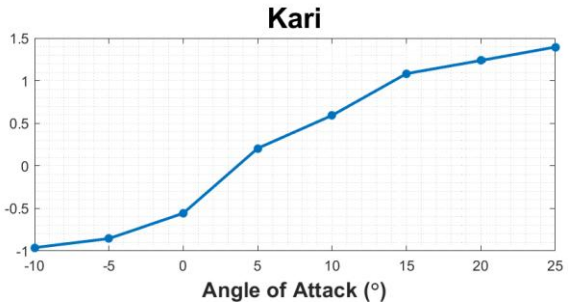

Figure 1.5 Aileron to rudder gain schedule.

As can be seen in Figure 2, all of the hard objective functions are below 0, indicating that all of the stability requirements are satisfied.

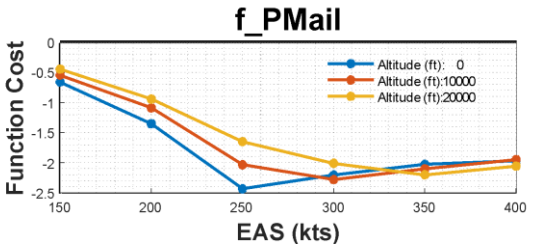

Figure 2.1 Aileron loop phase margin cost value.

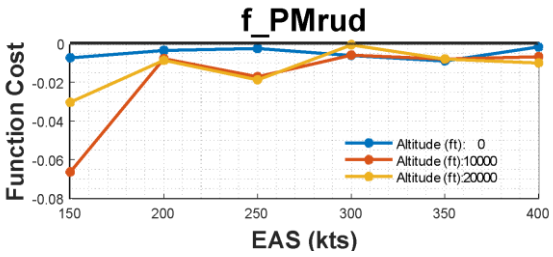

Figure 2.2 Rudder loop phase margin cost value.

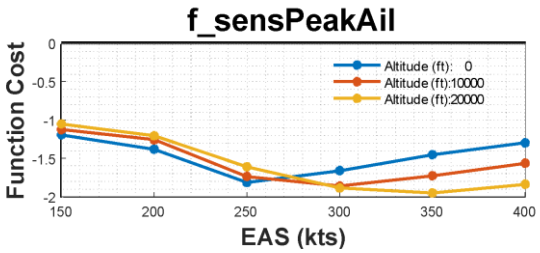

Figure 2.3 Aileron loop sensitivity function peak cost value.

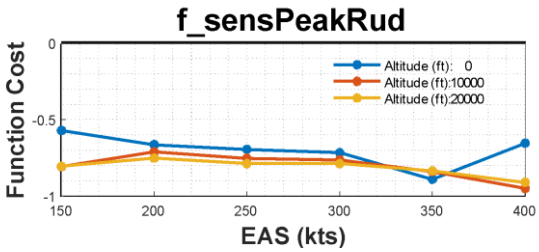

Figure 2.4 Rudder loop sensitivity function peak cost value.

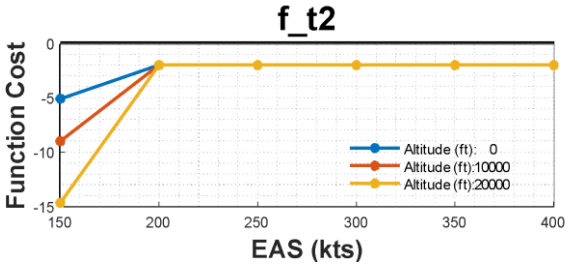

Figure 2.5 Time to double the cost function.

Also, as can be seen from Figure 3, all of the soft objectives are satisfied, indicating a predicted Level 1 FHQ. It can be seen that the disturbance rejection function is around zero for EAS higher than 250kts. Since crossover frequency is minimized in the last stage, the algorithm decreases the roll rate gain K_p which degrades the disturbance rejection performance until it reaches its good value.

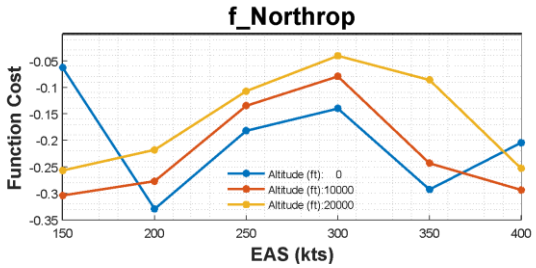

Figure 3.1 Northrop criterion cost value.

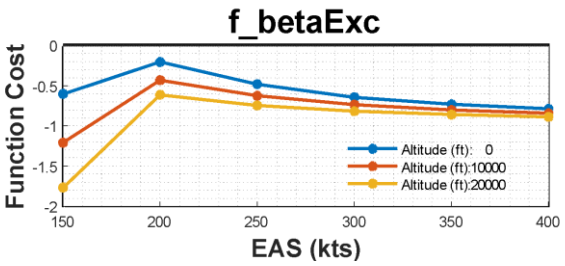

Figure 3.2 Sideslip excursion cost value.

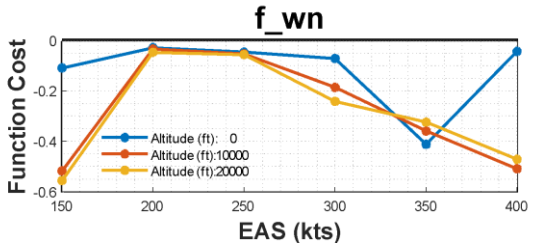

Figure 3.3 Dutch roll frequency cost value.

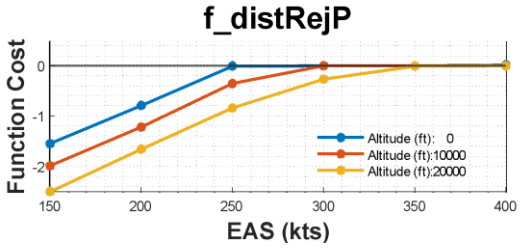

Figure 3.4 Roll rate output sensitivity gain cost value.

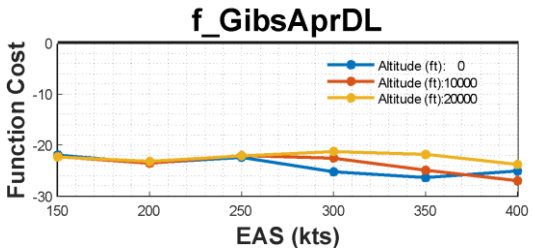

Figure 3.5 Gibson average phase rate cost value.

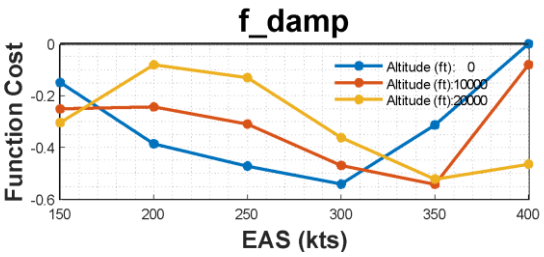

Figure 3.6 Dutch roll damping ratio cost value.

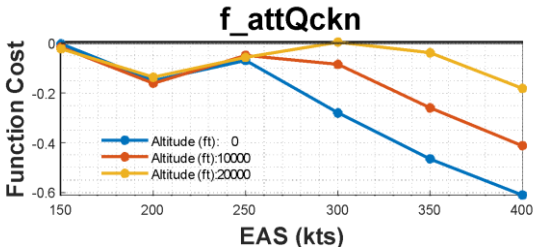

Figure 3.7 Attitude quickness cost value.

In addition, loop transfer functions obtained from actuator inputs and sensor outputs indicate stability robustness against uncertainties as none of them violate the Nichols boundary and satisfy at least 50° of phase margin as depicted in Figure 4.

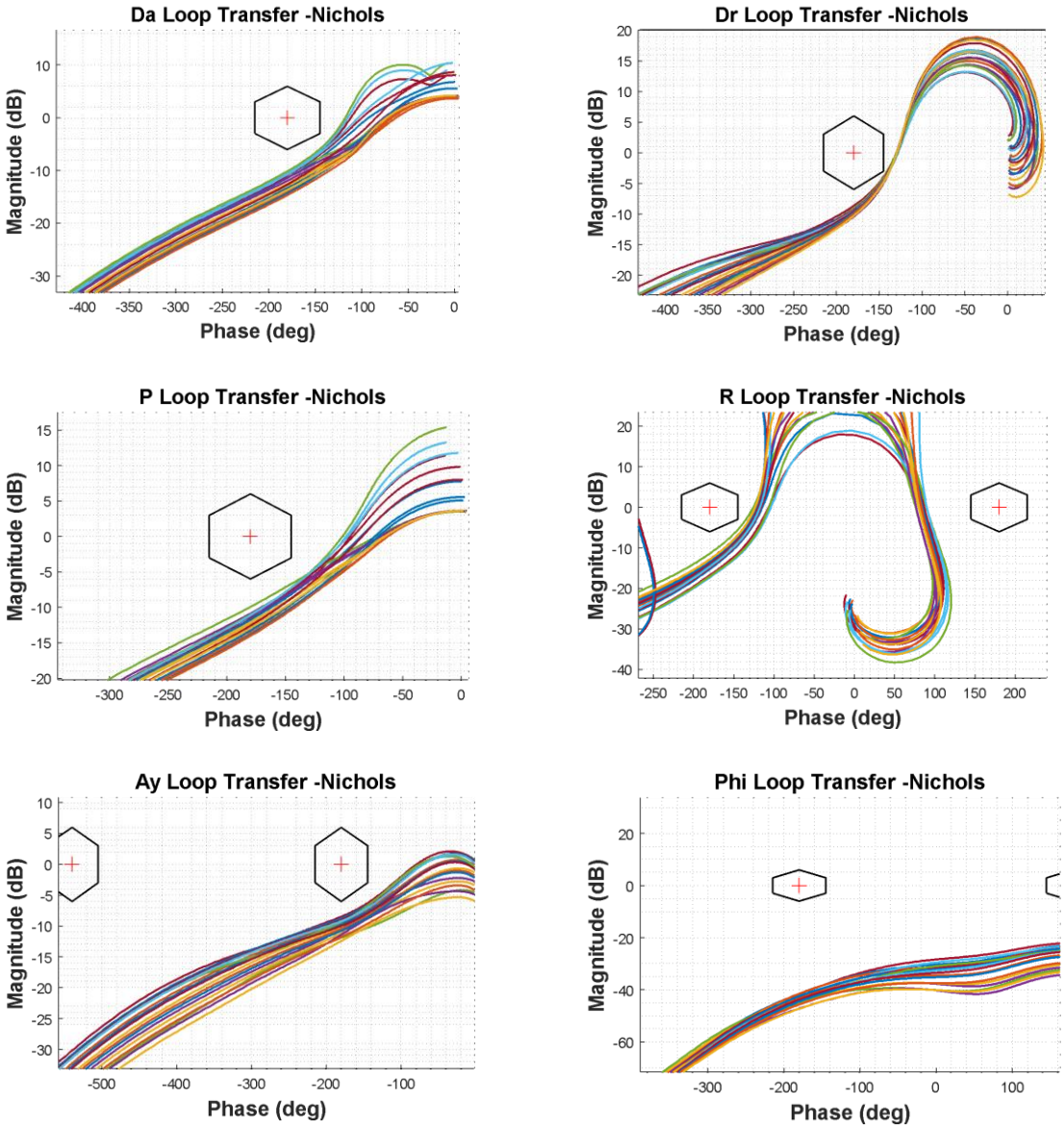

Figure 4. Nichols Exclusion Zone results for actuator input and sensor output loop transfer functions.

As can be seen from the frequency response of the sensitivity function for roll rate output in Figure 5, maximum magnitude around 1 rad/s is -8dB, which is a good value chosen for this criterion. Both frequency responses of loop transfer and sensitivity functions show satisfactory disturbance rejection characteristics around frequencies of interest with good stability robustness.

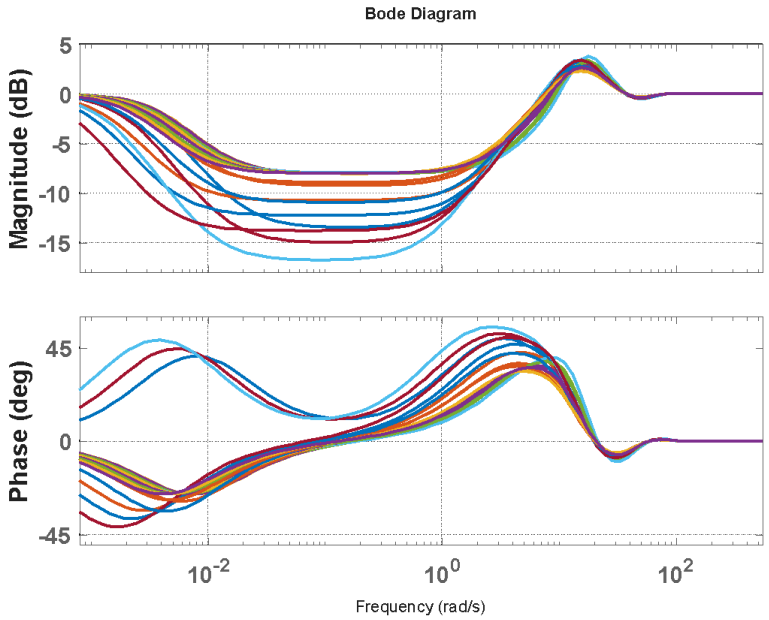

Figure 5. Sensitivity function frequency response of stability axis roll rate output.

It can be seen in FHQ analyses plots, as depicted in Figure 6, that bandwidth and average phase rate criteria indicate a PIO-I free solution as all of the points in the design envelope lie within the Level-I boundaries. There is near-perfect Dutch-roll pole-zero cancellation as solutions lie within the optimal region in the Northrop criterion, and the LOES cost for the roll rate response is well below the Level-I boundary, showing an almost identical response to that of a first-order system that can also be seen in Figure 7. In attitude quickness criteria, some points lie right at the boundary for small stick inputs; however, they move into the Level-I region as the amount of stick input increases. Lastly, for the sideslip excursion criteria,

all of the solutions lie well within the Level-I boundary.

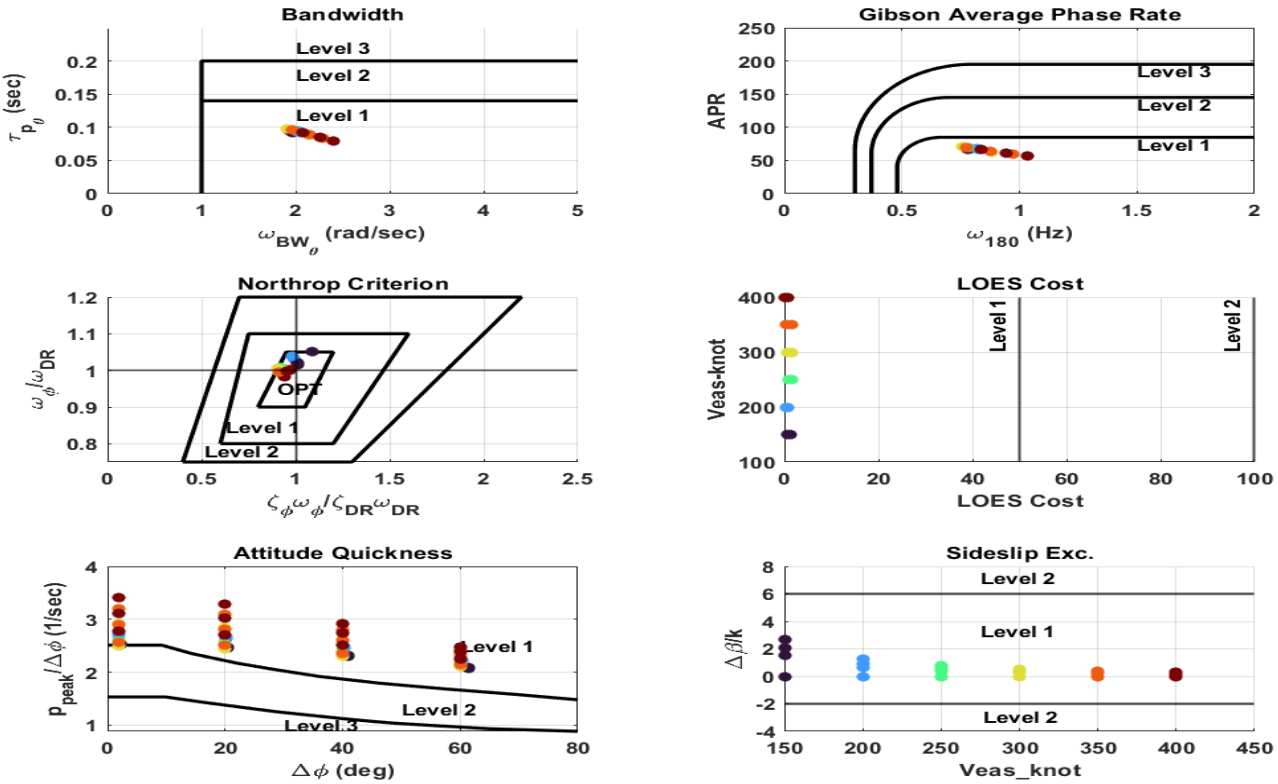

Figure 6. FHQ analysis results.

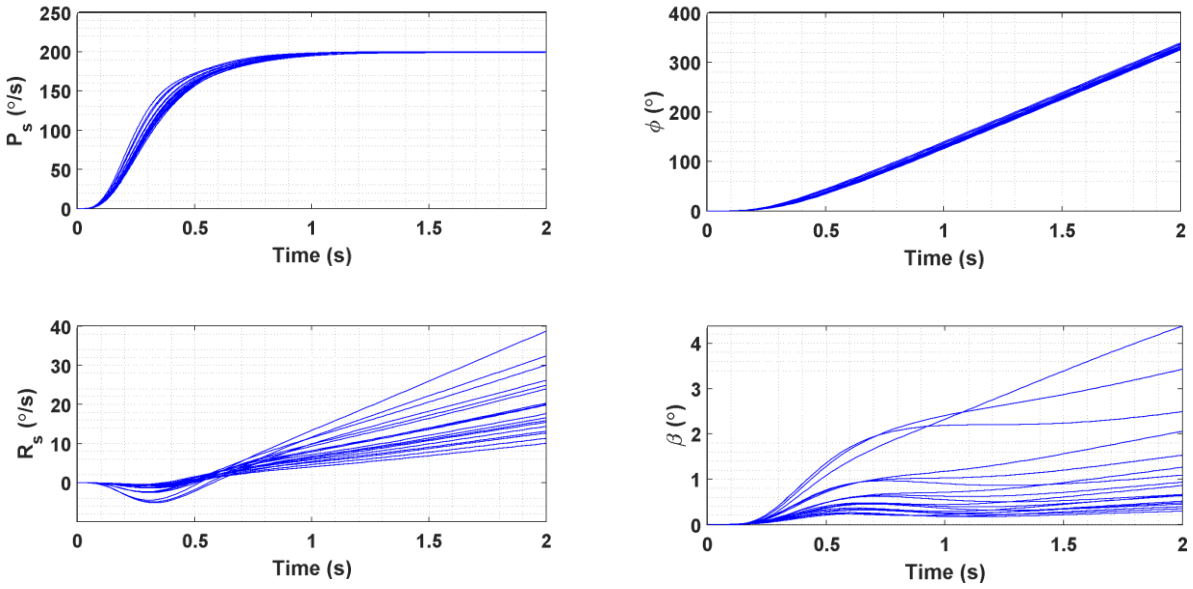

Figure 7. Closed-loop time responses for step input.

Conclusion

An optimization-based flight control law design process is applied to a fighter aircraft by utilizing a min-max strategy with MATLAB's interior-point solver. The design process produced consistent controller gains with respect to EAS and altitude and a smooth gain schedule. The cost functions indicate satisfaction of all of the criteria, although there are several points at the good value limit due to the last stage minimization. Loop transfer functions and sensitivity functions for roll rate output indicate both stability, robustness, and satisfactory disturbance rejection performance. Also, FHQ analyses indicate a PIO-I free, first-order-like roll response with minimal sideslip angle build-up, showing a predicted Level-I FHQ.

References

Berger, T., & Tischler, M. B. (2013). Lateral/directional control law design and handling qualities optimization for a business jet flight control system. *In Proceedings of the AIAA Guidance, Navigation, and Control Conference and Exhibit* (pp. 1–12). American Institute of Aeronautics and Astronautics.

Blight, J. D., Dailey, R. L., & Gangsaas, D. (1983). Practical control law design for aircraft using multivariable techniques. *International Journal of Control, 38*(1), 93–109.

Gibson, J. C. (1999). *Development of a methodology for excellence in handling qualities design for fly-by-wire aircraft*.

Innocenti, M., & Bava, R. (1991). Lateral-directional tracking requirements from simulation data. *Journal of Guidance, Control, and Dynamics, 14*(6), 1346–1353.

Joos, H., & Finsterwalder, R. (1999). Multi-objective design assessment and control law synthesis tuning for flight control development. *In Proceedings of the 1999 IEEE International Symposium on Computer Aided Control System Design*. IEEE.

Klyde, D. H., Aponso, B. L., Mitchell, D. G., & Hoh, R. H. (1995). Development of roll attitude quickness criteria for fighter aircraft. *In Proceedings of the AIAA Guidance, Navigation, and Control Conference* (pp. 824–834). American Institute of Aeronautics and Astronautics.

Moritz, N., & Osterhuber, R. (2006). Three-stage gradient-based optimization scheme in design of feedback gains within Eurofighter primary control laws. *In Proceedings of the AIAA Guidance, Navigation, and Control Conference and Exhibit*. American Institute of Aeronautics and Astronautics.

Nguyen, L. T., Ogburn, M. E., Gilbert, W. P., Kibler, K., Brown, P. W., & Deal, P. L. (1979). *Simulator study of stall/post-stall characteristics of a fighter airplane with relaxed longitudinal static stability* (NASA Technical Paper 1538). NASA Langley Research Center.

Park, C. H., & Tahk, M. J. (1998). A coevolutionary minimax solver and its application to autopilot design. *In Proceedings of the AIAA Guidance, Navigation, and Control Conference and Exhibit*. American Institute of Aeronautics and Astronautics.

Tischler, M. B., Berger, T., Ivler, C. M., Mansur, M. H., Cheung, K. K., & Soong, J. Y. (2017). *Practical methods for aircraft and rotorcraft flight control design: An optimization based-approach*. American Institute of Aeronautics and Astronautics.

U.S. Department of Defense. (1997). *Flying qualities of piloted aircraft (MIL-STD-1797A)*. U.S. Government Printing Office.

U.S. Department of Defense. (2006). *Detail specification: Flight control systems—Design, installation, and test of piloted aircraft, general specification for (MIL-DTL-9490E)*. U.S. Government Printing Office.

Enhancing Aircraft Avionics Safety: Integrating STPA With ARP4761

Şükrü Can Sulak[a], Mehmet Turan Söylemez[a]

[a] Istanbul Technical University, Faculty of Electrical and Electronics, Department of Control and Automation Engineering, Türkiye
sulak22@itu.edu.tr

Keywords: ARP 4761, Flight Management System, Vertical Navigation (VNAV), System-Theoretic Process Analysis (STPA), Functional Hazard Assessment.

Aim

Safety engineering has repeatedly proven its importance through unfortunate events throughout history and across various fields. For instance, in 2018 and 2019, due to the malfunction of the Maneuvering Characteristics Augmentation System (MCAS) on Boeing 737 Max aircraft, the crashes of Lion Air Flight 610 and Ethiopian Airlines Flight 302 resulted in the loss of 346 lives (Barshi et al., 2023). Another example is the crash of American Airlines Flight 965 in December 1995, which was caused by a malfunction of the Flight Management System (FMS) that misdirected the pilots, resulting in 163 fatalities (National Transportation Safety Board [NTSB], 1996).

The Federal Aviation Administration (FAA) and the European Aviation Safety Agency (EASA) do not mandate specific practices for certification; rather, they issue advisory circulars that identify acceptable methods for aircraft development and certification. SAE Aerospace Recommended Practice (ARP) 4754A is an accepted development assurance process as endorsed by Advisory Circular, AC 20-174. SAE ARP 4761A, on the other hand, is an important document that supports ARP 4754A by outlining the safety assessment processes that should be followed (Leveson et al., 2014a). Although ARP 4761A is not explicitly referenced by any advisory circular, it is widely used in the industry.

With the increasing prevalence of software-containing equipment in modern systems and the growing complexity of tasks performed by intercommunicating algorithms, the comprehensiveness of the safety analyses described in ARP 4761A is being questioned. Indeed, the traditional safety analysis methods mentioned in ARP 4761A—such as Fault Tree Analysis (FTA), Failure Mode and Effects Analysis (FMEA)—were developed long ago to identify failure-related losses in electromechanical systems and are based on reliability theory. However, to identify the hazardous scenarios that have not occurred due to a failure of a component involved in the system of today's complex, software-intensive systems, newer analysis methods are needed (Ishimatsu et al., 2014).

This study aims to show that a new hazard analysis method called System-Theoretic Process Analysis (STPA) can be used as a complementary method to traditional ones suggested in SAE ARP 4761A to uncover additional hazardous scenarios and prevent them by developing safety requirements.

Material and Method

Aircraft safety assessment is a process that occurs in tandem with design and other processes. ARP 4754 employs the V-Model, a well-known systems engineering approach, to frame the development process.

The V-Model can be decomposed into three primary stages, regardless of the area under consideration. The following phases were identified: Concept Phase, Design Phase, and Verification Phase. The outcomes of the safety analysis are transmitted to system engineers, who incorporate these requirements into their designs. Finally, after the hardware and software designs are finished, the integration and verification process begins. Integration starts with low-level products (e.g., components) while verifying them, and finishes when all systems are integrated to create an aircraft.

Functional Hazard Assessment (FHA) is the initial analysis to determine failure conditions that may result in hazards and classify them according to their severity values. Fault Tree Analysis and Failure Mode and Effects Analysis are two recommended safety analysis methods that focus on reliability and probability theory to assess the causes of failure

conditions identified in FHA. However, an aircraft consists not only of elements that may have a failure rate or availability rate, such as software-intensive components. In these cases, Development Assurance Level (DAL) requirements are derived from FHA severity classifications and allocated to software items and their host component hardware. After DAL allocations, item development can be carried out under the guidance of DO-254 (for hardware) and DO-178 (for software). However, DO-178 states that a safety assessment process is not required for software items if the system-level safety requirements are complete. This makes ARP 4761 and its assessment method, FHA, inadequate for evaluating modern software-intensive systems (Rong & Dong, 2019).
According to STPA, safety is primarily a control issue rather than a matter of reliability (Leveson & Thomas, 2018). Fundamentally, STPA consists of two main steps: Identification of Unsafe Control Actions (UCAs) and Development of Loss Scenarios. Below, the main steps are given with brief descriptions:

1. Identification of UCAs: Potential unsafe control actions can be considered as triggering reasons for accidents. UCAs shall be identified and need to be eliminated or controlled to prevent accidents. These UCAs can be analyzed in four main categories:

    a. A control action required for safety is not provided.
    b. An unsafe control action is provided that leads to a hazard.
    c. A potentially safe control action is provided too late, too early, or out of sequence.
    d. A safe control action is stopped too soon or applied too long (Fleming & Leveson, 2014).
2. Development of Loss Scenarios: For each UCA identified in Step 1, there should be causal scenarios explaining how these unsafe conditions might arise (Leveson, 2011).

As a result of STPA, the following can be provided as input requirements to the design phase, along with high-level safety requirements and DAL requirements defined by FHA, and to the verification phase to enhance verification performance: generated safety constraints from UCA and their corresponding loss scenarios, and their corresponding test requirements.

Although STPA is an analysis that can be performed in the concept phase, its outputs can contribute to the design and verification phases.

Findings

In this study, STPA was chosen to reveal additional hazardous scenarios of the Vertical Navigation (VNAV) Function of the Flight Management System (FMS), as the FMS is one of the highly software-integrated systems of a commercial aircraft. The FMS is a complex system that relies heavily on software and has a critical impact on flight safety. VNAV's main duty is to control an aircraft's vertical trajectory from the climb phase until the landing phase by generating a vertical flight plan according to airspace constraints (such as speed and altitude) and generating thrust and pitch control signals for the auto throttle computer and autopilot computers. It is an excellent system to show how STPA can contribute to FHA. Its critical role during a flight, especially during critical phases such as climb and approach, means that even minor anomalies can lead to accidents.
To apply FHA, VNAV functions are defined as follows:

1. Profile Generation
2. Constraint Handling
3. Climb Management
4. Auto throttle / Flight Director Coupling
5. Cruise Management
6. Descent Planning
7. Reversion and Degraded Modes

Each VNAV function is assessed in FHA with the following guidewords: Total Loss, Partial Loss, Erroneous, and Inadvertent. As a result of the FHA, 80 failure conditions are generated from 7 different functions in different flight phases. An example from FHA is given below.

Total Loss Reversion and Degraded Modes

Flight Phase: All flight phases

Effect: Due to total loss of Reversion and Degraded Modes, VNAV will stay active even if a failure occurs in a different function of VNAV. Total loss of Reversion and Degraded Modes means loss of detection and degraded mode capability of both FMCs. Depending on the failure, total loss of Reversion and Degraded Modes may lead to stall, CFIT, or violation of altitude and speed constraints. Repercussion is considered CAT.

Possible Crew Action: The Crew needs to disengage VNAV and manage the related flight phase manually

Severity: Catastrophic
Example Functional DAL requirement and other generated requirements for "Total Loss Reversion and Degraded Modes in Flight" with respect to ARP 4754 and ARP 4761 are given below.

1. Reversion and Degraded Mode function shall be developed with DAL-A.
2. Total loss of Reversion and Degraded Modes in flight shall be less than 10^{-8} per flight.
3. No single event shall lead to total loss of the Reversion and Degraded Mode function.

In parallel, STPA is applied to "Inhibit Command – Profile Generation" Control Action that goes from the Reversion and Degraded Modes function to the Profile Generation function. "Inhibit Command – Profile Generation" signal is used to disable a VNAV function when a critical fault is detected, and it is provided to Profile Generation. It includes the VNAV Disable command, the target module, severity flag. Unsafe Control Actions and their corresponding Loss Scenarios are given below.

1. Not Providing Causes Hazards: Reversion & Degraded Modes function does not provide " Inhibit Command – Profile Generation " to Profile Generation function during approach with detected failure. A/C continues erroneous descent profile.
2. Providing Causes Hazard: Reversion & Degraded Modes function provides " Inhibit Command – Profile Generation " to Profile Generation function during nominal operation. A/C unexpectedly exits VNAV, and the crew is confused.
3. Too Soon: Reversion & Degraded Modes function provides " Inhibit Command – Profile Generation " too soon to Profile Generation during descent. A/C disables VNAV before profile failure is confirmed for TBD ms.
4. Too Late: Reversion & Degraded Modes function provides " Inhibit Command – Profile Generation " too late for Profile Generation during climb. A/C applies incorrect pitch/thrust before inhibition takes effect.
5. Stopped Too Soon: UCA-146: Reversion & Degraded Modes function continues providing " Inhibit Command – Profile Generation" to Profile Generation after failure is resolved. A/C remains in degraded mode.
6. Too Late: Reversion & Degraded Modes function stops providing " Inhibit Command – Profile Generation " too soon to Profile Generation during approach. A/C changes back to faulty vertical path generation.

The following safety constraints are generated regarding UCAs given in the 3rd, 4th, 5th, and 6th sections above, since FHA misses timing-related failures because it does not individually consider timing issues.

1. Reversion and Degraded Modes shall not issue an Inhibit Command to Profile Generation until a profile-generation failure has been positively detected and held for ≥ TBD ms.
2. Until the inhibitor takes effect, the flight-control computers shall limit commanded pitch and thrust to values that preserve positive energy margins.

3. If inhibition persists longer than the scheduled maximum dwell time after Profile Generation recovery, the system shall generate a Level B crew alert.
4. Below 1,000 ft AGL, automatic removal of the inhibit shall be disallowed unless explicitly commanded by the crew.

Conclusion

This study analyses the VNAV of a commercial aircraft using FHA in SAE ARP 4761 and STPA. STPA can identify additional hazardous scenarios related to timing interaction and complex software behaviour that FHA cannot capture. STPA was able to find 4 new causal paths that FHA was overlooking. These new causal paths lead to new requirements that are different than FHA-generated requirements. STPA treats safety as a control problem, so an existing design is not required to perform the analysis. This means the analysis and design can proceed in parallel, each supporting the other [4]. This advantage of STPA should also be considered when considering the implementation of safety analysis for systems with complex software behaviours.

References

Barshi, I., Degani, A., Mauro, R., & Mumaw, R. J. (2023). *Analyses of the Boeing 737MAX accidents: Formal models and psychological perspectives*. Human Systems Integration Division, NASA Ames Research Center; GM Advance Technology Center; Decision Research and University of Oregon; San Jose State University Research Foundation.
Fleming, C. H., & Leveson, N. G. (2014). Improving hazard analysis and certification of integrated modular avionics. *Journal of Aerospace Information Systems, 11*(6), 1–12. https://doi.org/10.2514/1.I010164
Ishimatsu, T., Leveson, N. G., Thomas, J. P., Fleming, C. H., Katahira, M., Miyamoto, Y., Ujiie, R., Nakao, H., & Hoshino, N. (2014, March–April). Hazard analysis of complex spacecraft using systems-theoretic process analysis. *Massachusetts Institute of Technology; Japan Aerospace Exploration Agency; Japan Manned Space Systems Corporation.*
Leveson, N. G. (2011). *Engineering a safer world: Systems thinking applied to safety*. The MIT Press.
Leveson, N., Wilkinson, C., Fleming, C., Thomas, J., & Tracy, I. (2014, June). The relationship between ARP 4761 and STPA. *Massachusetts Institute of Technology.* http://sunnyday.mit.edu/papers/ARP4761-Comparison-Report-final-1.pdf
Leveson, N. G., & Thomas, J. P. (2018, March). *STPA handbook*. Massachusetts Institute of Technology.
National Transportation Safety Board. (1996, October 16). *Safety recommendation regarding the American Airlines Flight 965 accident (A-96-90 to A-96-106).* Washington, DC.
Rong, H., & Dong, H. (2019). Incorporating model-based safety design into development process of civil aircraft systems. *In 2019 International Conference on Communication Technology (ICCT)* (pp. 1291–1295). IEEE. https://doi.org/10.1109/ICCT46805.2019.8947119

Design and Analysis of a Dual Layer Disturbance Observer-Based Controller for Longitudinal Axis in a Fixed Wing Aircraft

Merve Demiroğlu[a], İlker Üstoğlu[a], Yusuf Sıncak[b]

[a] Istanbul Technical University, Graduate School, Department of Control and Automation Engineering, Türkiye
[b] Turkish Aerospace Industries Inc., Unmanned Aerial Vehicle Division, Türkiye
ormanci18@itu.edu.tr

Keywords: Dual Layer Disturbance Observers, Autopilot, Robust Control

Aim

In control design, a frequent discrepancy exists between the mathematical model and the actual system. This distinction between them arises from several factors. Such as including the inherent uncertainties in the system's behavior, the neglect of higher-order dynamics, and the linearization of nonlinear dynamics. Furthermore, when aerodynamic and atmospheric disturbances are factored in, the level of uncertainty in the system increases significantly, which must be considered in the system. All these factors negatively affect the stability and performance of control systems, generating an urgent necessity to lessen the effect of these uncertainties to enhance system stability and performance. PID control is one of the conventional control methods which widely used in the industry due to its simple structure and ease of implementation. However, the PID control approach might lack adequate robustness in the face of external disturbances and uncertainties within the system. Therefore, enhancing the robustness of the PID controller by integrating it with various advanced control strategies can provide significant improvements in terms of performance and stability.

In this study, observer design is considered to enhance the effectiveness of the PID controller against disturbances and achieve a more robust control. Observers estimate unknown and unobservable state variables or external disturbances in a system, allowing the control system to compensate for these disturbances and allow the system to operate more precisely. If control algorithms rely solely on directly observable data, they may overlook such variables, which can weaken control performance. Therefore, by estimating unknown or unmeasurable states affecting the system, observers enable control algorithms to function more accurately. In this study, a Disturbance Observer (DOB) structure is employed as the observer. This observer estimates both internal and external disturbances occurring in the system and adds an appropriate compensation signal to the control input, making the system more resilient to internal and external disturbances. The integration of the Disturbance Observer with the PID controller enhances the dynamic performance of the system and provides a more stable structure against unexpected disturbances. This approach offers a significant advantage, particularly in applications requiring precise control, such as aerospace, by effectively suppressing disturbance effects.

This study aims to evaluate the sensitivity of autopilot systems based on DOB-supported PID controllers against uncertainties and disturbances and to demonstrate how they can enhance stability in flight control systems. In this way, the potential and advantages of the DOB structure in modern aircraft autopilot systems will be revealed.

Material and Method

In this study, a PID controller was implemented as the controller, and the Disturbance Observer method was used as the observer for the scaled model of the delta-winged B2-Spirit bomber aircraft. All design and analysis steps were carried out in the MATLAB and Simulink environments.

PID control is one of the most widely used feedback control strategies in engineering applications and has been preferred for many years due to its simplicity, ease of implementation, and reliable performance. The PID controller produces a control signal using three different components by analyzing the system's current error. The first component is the Proportional (P) component. It provides an immediate response based on the magnitude of the error. The second one is the Integral (I) component. It considers past error values to improve the system's long-term accuracy. The last one is the

Derivative (D) component, and it predicts the system's future behavior and reacts to sudden changes. However, one of the major disadvantages of PID controllers is their sensitivity to modeling uncertainties and external disturbances. Especially in rapidly changing systems and nonlinear dynamics, traditional PID controllers may exhibit insufficient performance. Therefore, enhancing PID controllers with an additional method, such as the Disturbance Observer, to improve their robustness is proposed within the scope of this study.

The Disturbance Observer method is a significant technique used in control systems to estimate and compensate for the effects of external disturbances and modeling uncertainties. The difference between the actual system model $\left(P(s)\right)$ and the nominal model $\left(P_n(s)\right)$ is considered an internal disturbance. When calculating this difference, the inverse transfer function of the nominal model $\left({P_n}^{-1}(s)\right)$ is typically used in conjunction with a low-pass filter $\left(Q(s)\right)$ to ensure system stability and prevent algebraic loops (Schrijver & van Dijk, 2002). The total disturbance effect is obtained by summing this difference with the effects of external disturbances, and this calculation is fed back as a cancellation signal to suppress the disturbance effects.

Thus, DOB is regarded as a method for achieving robust control. In other words, DOB transforms a basic, non-robust feedback controller into a robust one. The fundamental controller is designed for a nominal plant model without external disturbances, noise, or uncertainties. When DOB is added to the inner feedback loop, the nominal stability and performance achieved by the basic controller and the nominal plant can be approximately recovered even in the presence of disturbances and uncertainties.

A general DOB structure for a Single Input Single Output (SISO) plant is illustrated in the upper part of Figure 1. Here, r represents the reference command input, u_r is the control input, d is the external disturbance input, y is the model output, and n represents the sensor noise. $P(s)$ represents the physical plant to be controlled, $P_n(s)$ is the nominal plant model, and $C(s)$ is the feedback controller. Finally, $Q(s)$ is a transfer function that is designed as a low-pass filter to prevent algebraic loops.

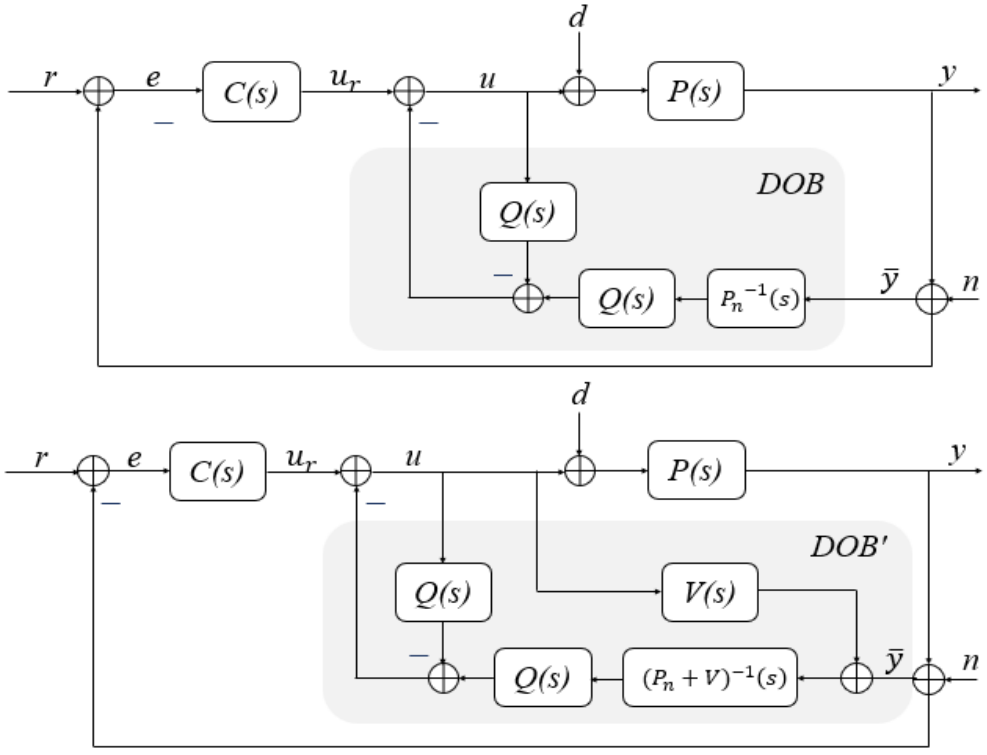

Figure 1. Minimum phase and non-minimum phase DOB structure.

In the Disturbance Observer, disturbance rejection is achieved by directly feeding back the difference between u_r and u, assuming that this difference represents an estimate of the total disturbance. However, the direct feedback of the estimated disturbance signal ($\hat{d}$) cannot be implemented because using the inverse plant model is not an appropriate approach. Additionally, direct feedback leads to an algebraic loop. Therefore, the Q-Filter is used. With this approach, the DOB design can be reduced to the design of the Q-Filter. However, since the selection of Q-Filter requires a trade-off between disturbance rejection and noise rejection, the design must be carried out carefully. In Figure 2, it can be seen that as the cutoff frequency of the low-pass filter increases, the disturbance estimation capability improves, but the noise sensitivity also increases.

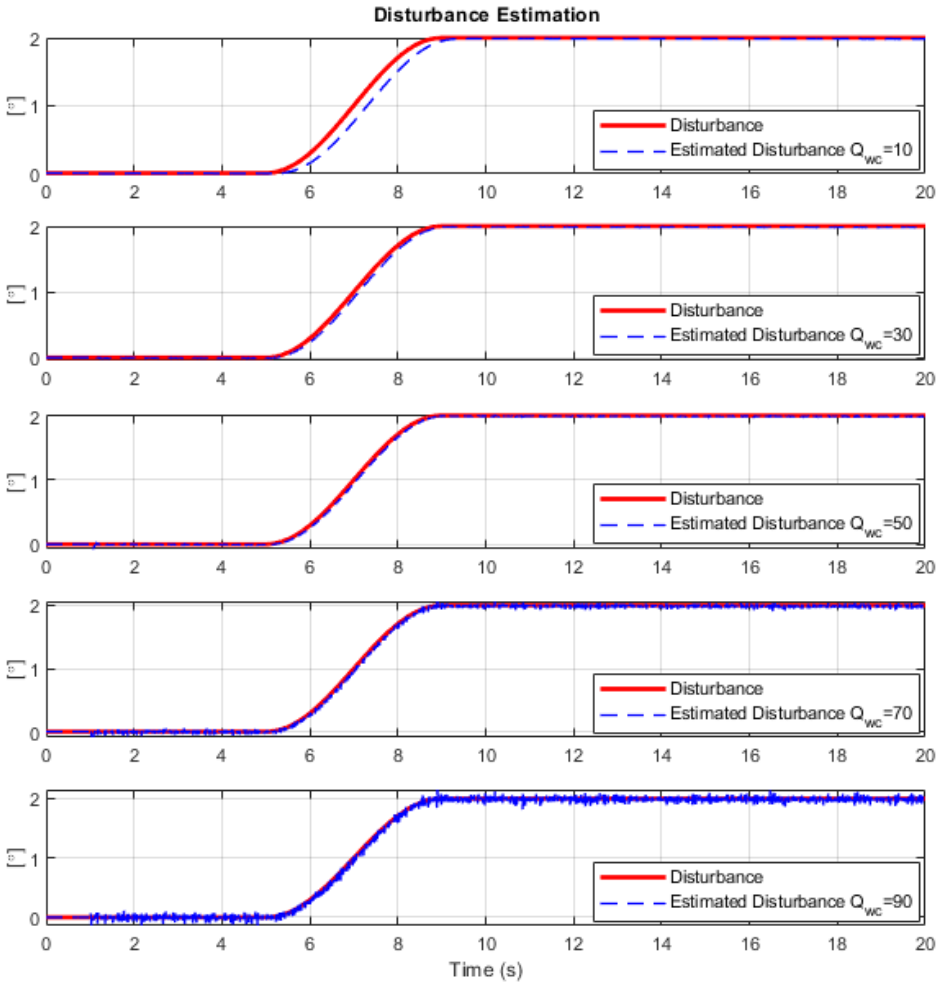

Figure 2. Disturbance estimation performance at different cutoff frequencies under noise.

Although the Disturbance Observer method is effective in suppressing disturbances, some challenges arise when applying it to a non-minimum phase system. If the nominal model $P_n(s)$ has unstable right-half-plane (RHP) zeros, the inverse transfer function ${P_n}^{-1}(s)$ used in the inner feedback loop of the DOB will cause these unstable zeros to transform into unstable poles. As a result, the system response may diverge to infinity. To eliminate this issue and apply the DOB method to such systems, a new parallel filter is added to the given system, modifying the classic DOB method (Shim et al., 2007). Non-minimum phase DOB structure can be seen in the lower part of Figure 1.

This additional filter, called the V-Filter, is designed to ensure that the inverse of the nominal model used in the inner feedback loop of the DOB becomes minimum-phase. With the inclusion of the V-Filter, the classical DOB method becomes applicable to non-minimum phase systems. The key feature of this new structure is the design of a V-Filter that transforms the parallel connection in the DOB feedback loop $(P_n(s) + V(s))$ into a minimum-phase system.

The control design for longitudinal axes consists of two separate controllers, namely the inner loop and outer loop controllers. Inner loop controllers are typically responsible for controlling faster-changing variables that require a higher bandwidth. In this loop, variables such as attitude, angular rate, or velocity are monitored, and quicker responses are generated for the control surfaces. The outer loop, on the other hand, is responsible for controlling slower-changing variables that define the overall flight profile. Variables such as altitude, position, or heading are addressed in the outer loop. This loop provides reference values to the inner loop and ensures that overall flight objectives are achieved. In this study, the disturbance observer design is employed in the inner loop for pitch angle control and in the outer loop for altitude control. In the inner loop, due to the structure of the disturbance observer method, the disturbance affecting the system includes servo errors or errors arising from the control surface interface. With the design of the outer loop controller, atmospheric disturbances affecting the aircraft are directly introduced to influence the attitude angles.

During the PID controller design phase, the inner loop controller was initially designed using a linearized model. While designing the controller, care was taken to ensure that the percent overshoot did not exceed 20%, and the settling time did not exceed 3 seconds. Control surface commands were also examined, and it was confirmed that they remained within the actuator limits. The PID controller gains were obtained using an optimization method based on the Integral of Squared Error criterion, which also considered percent overshoot, phase margin, and gain margin. These initially obtained gains were then manually fine-tuned based on the system's response. After the controller design, a Classical Disturbance Observer was designed and integrated into the inner loop. In the outer loop, a PI controller was first designed similarly, and then a Non-Minimum Phase Disturbance Observer was designed and integrated into the system.

By designing a disturbance observer for both the inner and outer loops, it is aimed to suppress all types of disturbances affecting the aircraft. The longitudinal autopilot architecture incorporating the disturbance observer method is presented in Figure 3.

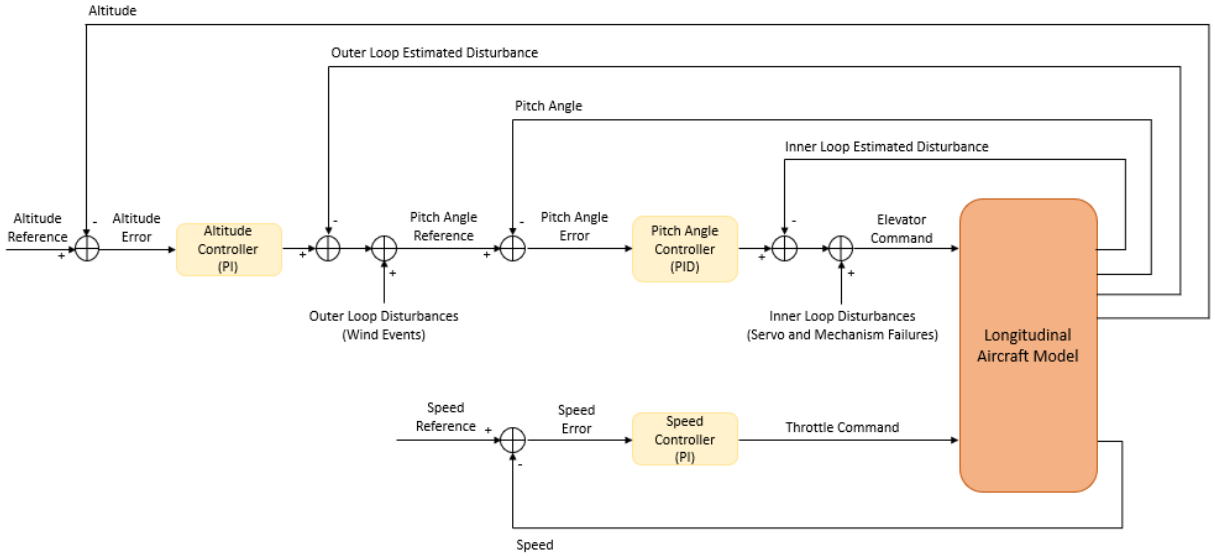

Figure 3. Longitudinal autopilot architecture.

Findings

All design and analysis processes were carried out in the MATLAB and Simulink environments. In the inner loop, a PID controller was initially designed for pitch angle control, and later, the classical disturbance observer structure was added. To evaluate the system's performance, the $P_n(s)$ model was modified by changing the coefficients C_l, C_m and C_n by 25% to obtain a new linear model, which was then incorporated into the system as $P(s)$. Additionally, 0.2° white noise was introduced into the pitch angle feedback signal, and an internal disturbance was simulated by assuming a servo jam that begins at 5 seconds and gradually leads to a 2° blockage over time. The inner loop performance evaluation is shown in Figure 4.

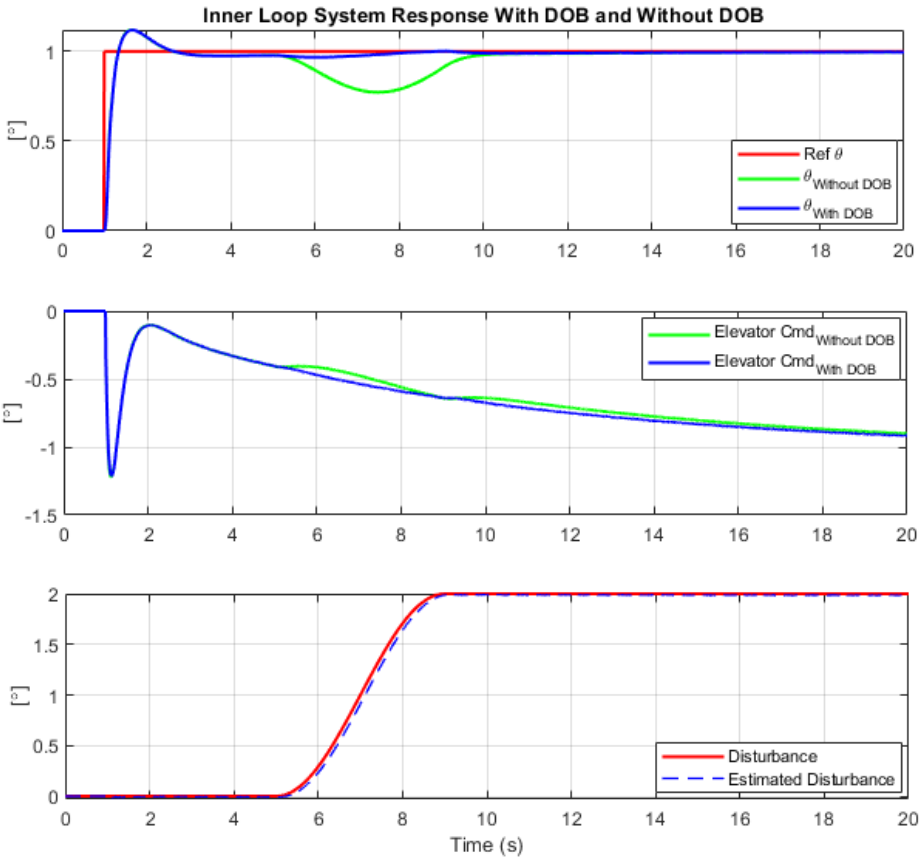

Figure 4. Inner loop performance.

In the outer loop, the pitch angle reference signal is generated. In this loop, altitude is controlled, thereby enabling the investigation of the effects of wind disturbances on altitude and the compensatory effect of the DOB structure during the desired phase of flight. For this purpose, a PI controller was designed. When designing the DOB, it was noted that the $P_n(s)$ model obtained for the outer loop is a non-minimum phase system. Therefore, a V-Filter was added to the DOB structure to ensure proper design for such systems.

To assess system performance, 0.2 m white noise was introduced into the altitude feedback signal. Additionally, as an external disturbance, a wind gust of 13 m/s was applied at 30 seconds, causing a 5° pitch angle deviation, and its effect diminished at 40 seconds. The performance results of the PI controller supported by the outer loop DOB are presented in Figure 5.

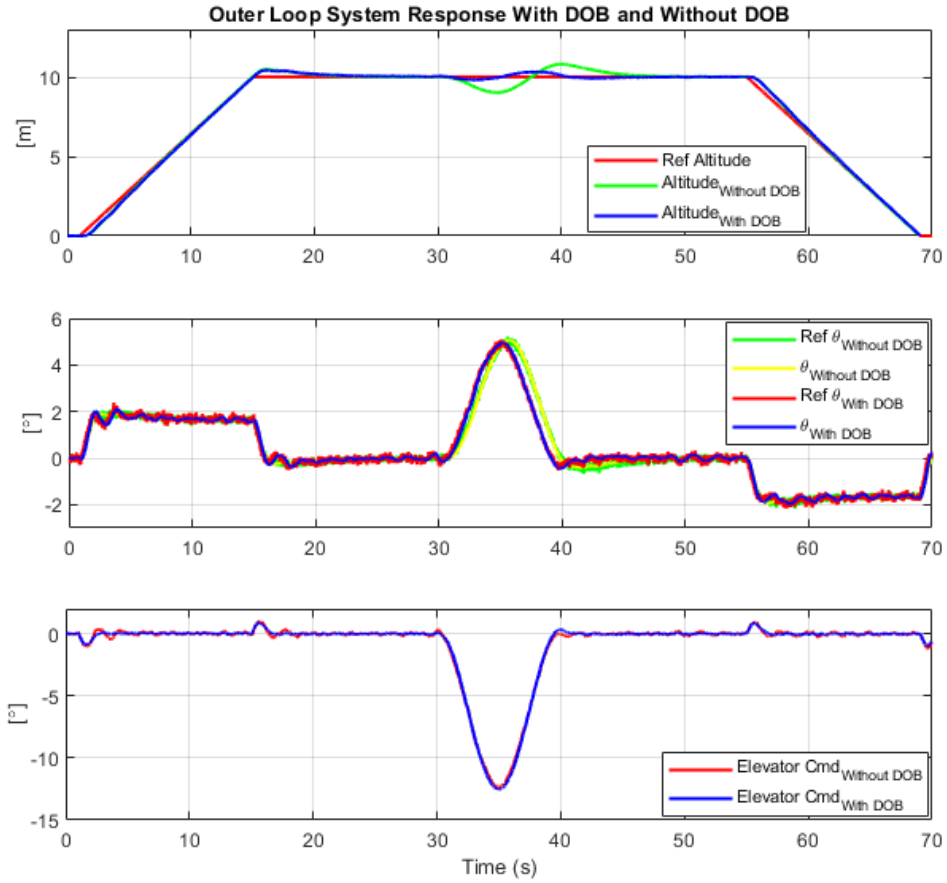

Figure 5. Outer loop performance.

Conclusion

It has been shown that the Disturbance Observer-supported PID controller makes the fixed-wing aircraft less affected by disturbances in the longitudinal axis compared to the PID controller without an observer. Thanks to the Dual-Layer Disturbance Observer structure, all disturbances, including modeling-sourced disturbances, internally sourced disturbances such as servo errors, and externally sourced disturbances such as wind gusts, are simultaneously estimated and eliminated from the system. As a result, a more robust and stable controller resistant to all disturbance effects has been achieved.

References

Schrijver, E., & van Dijk, J. (2002). Disturbance Observers for Rigid Mechanical Systems: Equivalence, Stability, and Design. Journal of Dynamic Systems, Measurement, and Control, 124(4), 539–548.

H. Shim, Y.-I. Son, N.H. Jo. (2007). Disturbance Observer (DOB) Can Be Applied to Non-minimum Phase Systems. Technical Report of CDSL, Seoul National University.

Fuzzy Gain Decision for Different Types of Aircraft with Dynamic Pitch Control Envelope Cue

Ali Karaduman[a], İlker Üstoğlu[a]

[a]Istanbul Technical University, Control and Automation Engineering Program, Turkey

karaduman23@itu.edu.tr

Keywords: Aviation; Pilot-İnduced-Oscillations; Flight Envelope; Fuzzy Logic.

Aim

Loss of control in flight is one of the most critical safety problems in aviation. The main objective of this study is to design and validate an envelope cueing strategy that improves flight safety by dynamically adjusting controller gain parameters in response to pilot behavior and system feedback. Dynamic-pitch-control envelope cueing method was developed to evaluate the oscillations caused by the pilot to minimize PIO risk. Fuzzy modeling was used to include the fuzziness of human behavior, and pilot responses within the control envelope were also modeled using fuzzy logic to assess cueing method performance with a human pilot model. The proposed cueing method can help reduce control loss incidents resulting from pilot-aircraft system oscillations.

Material and Method

I. Dynamic Pitch Control Envelope Cue

The pitch axis is the axis on which the aircraft can maneuver nose down or nose up. Figure 1 shows the axes of the aircraft. A dynamic pitch control envelope is created depending on elevator deflection and dynamic pitch attitude. Dynamic pitch attitude is obtained by adding the pitch angle and its derivative. The dynamic pitch attitude equation is given in Eq. (1).

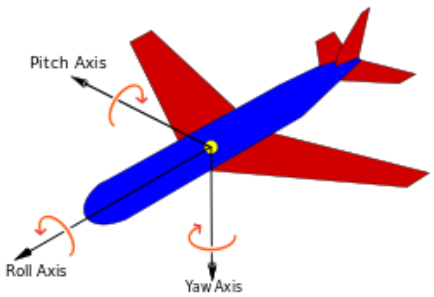

Figure 1. Aircraft principal axes [2].

$$\theta' = \theta + \dot{\theta} \tag{1}$$

This flight envelope, which is created depending on the dynamic pitch attitude and the control authority of the pitch axis, is given in Figure 2. The dynamic pitch control envelope can also be presented in 3D in a membership value manner. This representation is given in Figure 2.

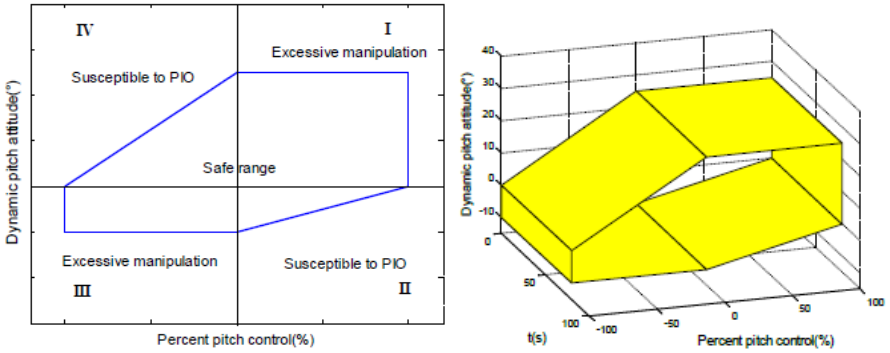

Figure 2. Dynamic pitch control envelope and with envelope with membership function [6].

II. Modelling

The pilot-aircraft model is formed by the combination of several systems. These are the human-pilot model, interceptor, and aircraft system. The block diagram of the pilot-aircraft system with dynamic pitch control envelope cue is given in Figure 3.

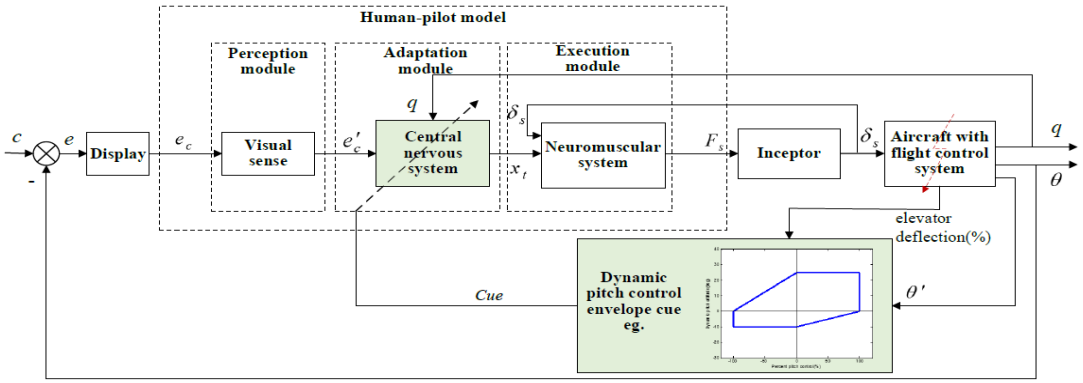

Figure 3. The block diagram of the pilot-aircraft system with dynamic pitch control envelope cue [3].

As seen in Figure 3, the input of the system is pitch angle θ (it is given as c in the figure), and the system output is pitch angle θ and pitch rate q. Error (e) is calculated by taking feedback from the output to the input, and this error signal enters the display. The e_c signal coming from the display is transmitted to the human-pilot model.

The aircraft system with the inceptor model consists of two parts. The first one is the inceptor module, and the other one is the aircraft system module.

1) Inceptor Model

The transfer function of the feel system is obtained with the parameters that are given in Table 1. The transfer function can be found as Eq. (2).

Table 1. Feel System Dynamics Parameters [5].

Parameter	Value
Spring gradient (N/m)	400
Damping ($N \cdot s \cdot m^{-1}$)	28.28
Mass (kg)	1
Control system gearing	1

$$\frac{400}{s^2+28s+400} \tag{2}$$

2) Aircraft System

Two different types of aircraft dynamics were used for testing in this paper. The first one is the configuration dynamics, which is used in the simulation tests, and its transfer function is shown in Eq. (3). The second one is the linear configuration dynamics of the Boeing-747 aircraft.

$$\frac{\theta}{\delta_e} = \frac{31520(s+0.02379)(s+1.246)}{(s^2+2\times0.2389\times0.05637s+0.05637^2)(s^2+2\times0.702\times4.571s+4.571^2)(s^2+2\times0.7\times75s+75^2)} e^{-0.10s} \tag{3}$$

This transfer function is obtained with the input elevator and the output pitch angle. Therefore, the parameters of the flight control system are given in Table 2.

Table 2. Parameters of Flight Control System [5].

Flight control system	Form	Parameter value
Rate limit ((°)/s)	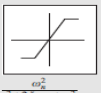	$V_L = \begin{cases} 10\ (°)/s \text{ failure} \\ 100\ (°)/s \text{ baseline} \end{cases}$
Surface actuator	$\frac{\omega_n^2}{s^2+2\xi\omega_n s+\omega_n^2}$	$\omega_n = 44$ rad/s, $\xi = 0.707$
Surface position limit	$\delta_{e_{max}}$	30°

The linear configuration dynamics of the Boeing 747 are also calculated. Firstly, it is linearized by trimming at a selected point. Subsequently, the state-space representation of longitudinal motion is obtained. This representation is given in Eq. (4).

$$[\Delta\dot{u}\ \Delta\dot{w}\ \Delta\dot{q}\ \Delta\dot{\theta}\ ] = \begin{bmatrix} X_u & X_w & 0 & -g \\ Z_u & Z_w & u_0 & 0 \\ M_u + M_{\dot{w}}Z_u & M_w + M_{\dot{w}}Z_w & M_q + M_{\dot{w}}u_0 & 0 \\ 0 & 0 & 1 & 0 \end{bmatrix} [\Delta u\ \Delta w\ \Delta q\ \Delta\theta\ ] + \begin{bmatrix} X_\delta \\ Z_\delta \\ M_\delta + M_{\dot{w}}Z_\delta \\ 0 \end{bmatrix} [\Delta\delta_e\ ] \tag{4}$$

Then the characteristic parameters of the short mode were determined. In this direction, the transfer function between the pitch rate and the elevator for the short period was found. This transfer function is given in Eq. (5).

$$\frac{\Delta q(s)}{\Delta\delta e(s)} = \frac{-0.553s-0.3886}{s^2+1.639s+0.82} \tag{5}$$

3) Simulink Models

The entire structure can be seen in Figure 4. The sum-of-sines function was created so that the model receives an input test signal. It can be seen in Eq. (6).

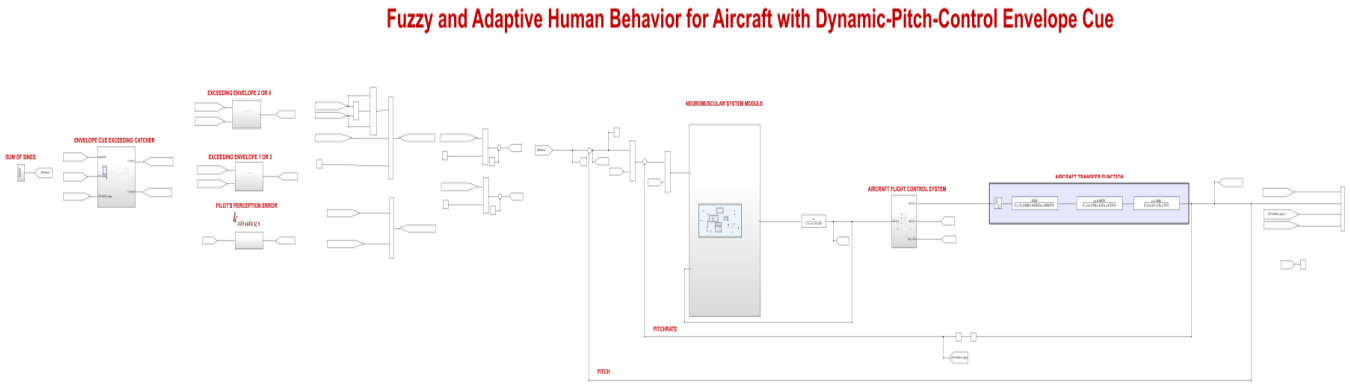

Figure 4. The entire structure in SIMULINK.

$$\sum \quad A\,sin(2\pi f + \phi) = Sum\ of\ sines \tag{6}$$

The envelope cue membership value was obtained in Figure 5. The structure that determines whether the envelope is in zone 2 or 4, or zone 1 or 3, is set up as shown in Figure 6. The freezing process is carried out in the same way for both regions. The structure of the freezing process is shown in Figure 6.

By inserting the error signal into the system's fuzzy logic, the $k_{strategy}$ parameter, which is the strategy variation coefficient of the pilot, is obtained. This structure is given in Figure 6.

The Fuzzy Logic app is used to create a file to evaluate fuzzy decisions. The smallest of the maximum was chosen as the defuzzification method. The app settings and the obtained $k_{strategy}$ output are shown in Figure 7. Then, ΔK_r and ΔK_p parameters were calculated as shown with Eq (7) and Eq (8).

$$\Delta K_r = k_{tuning_1} * k_{strategy} \tag{7}$$

$$\Delta K_p = 0.35 * k_{strategy} * (k_{tuning_1} + k_{tuning_2}) \tag{8}$$

Finally, these parameters were integrated into the system by giving initial values.

The neuromuscular system, with its components, is modeled as seen in Figure 8. The feel system, with its input and output, and the aircraft flight control system are seen in Figure 9. The transfer function given in Eq. 4 has been added to the model. The pitch angle, which is the output of the aircraft transfer function, is fed back into the model. In addition, the transfer function of the Boeing 747 aircraft has been added to the model.

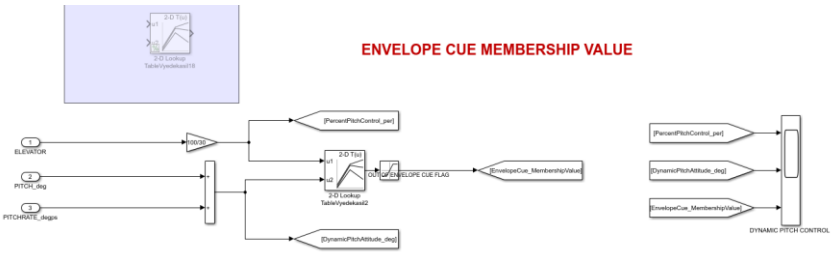

Figure 5. Envelope Cue Membership Value in SIMULINK.

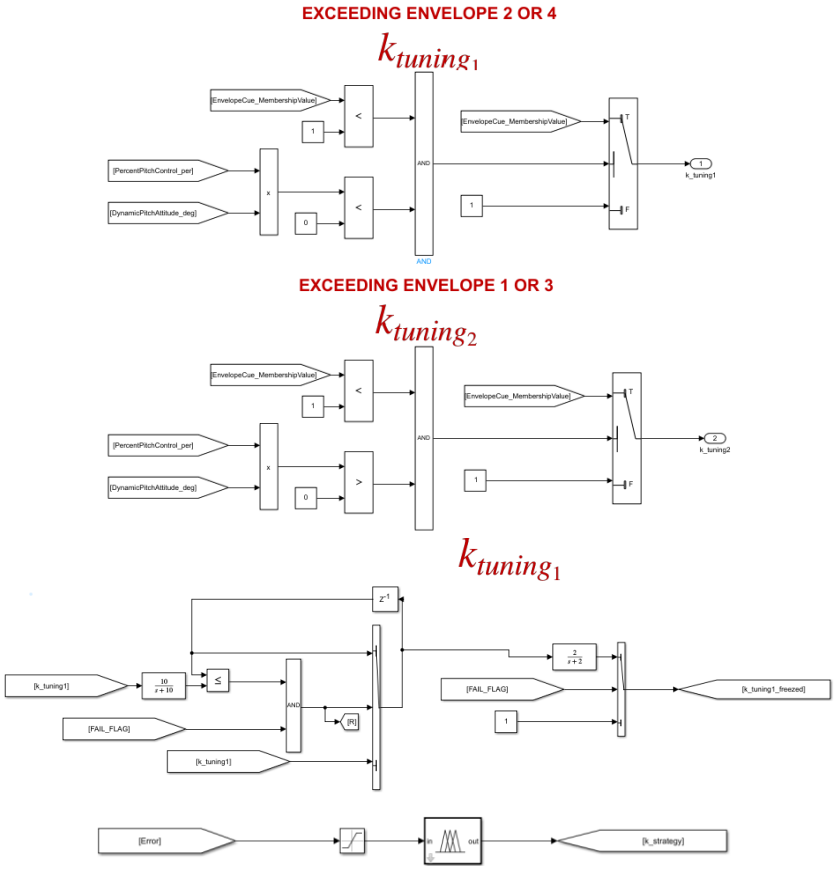

Figure 6. Decision of Envelope Zones, freezing, and obtaining $k_{strategy}$.

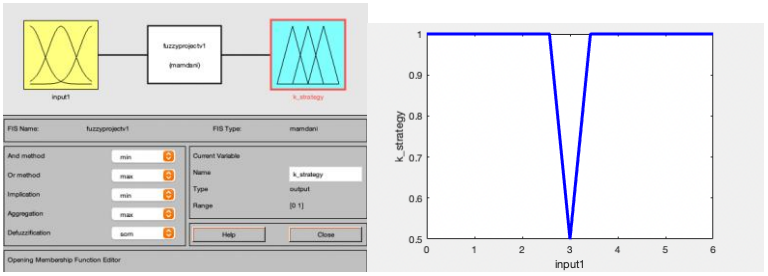

Figure 7. Fuzzy Logic Application and $k_{strategy}$ Output.

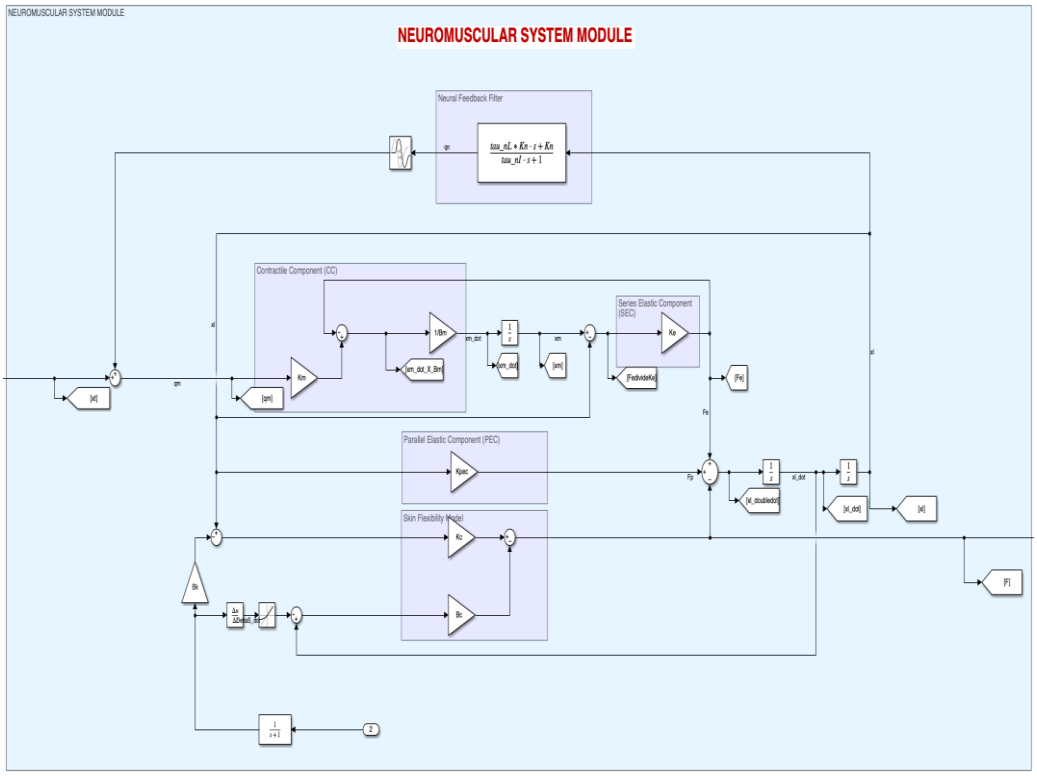

Figure 8. Neuromuscular System Model.

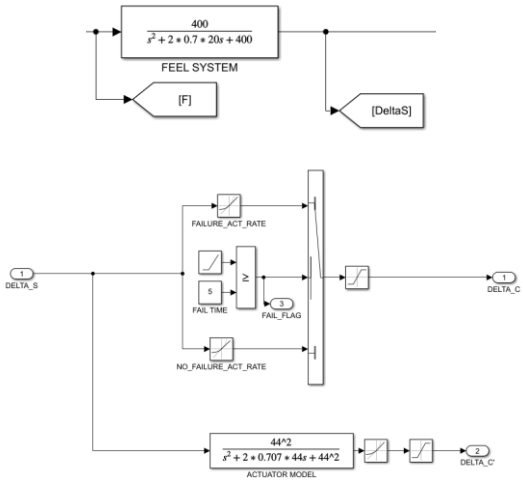

Figure 9. Feel the system and aircraft flight control system model in SIMULINK.

Findings

I. Simulation Results

In these simulations, the system's response to Pilot Induced Oscillation (PIO) is analyzed, and methods for its recovery are explored. The system was designed to enter PIO at the fifth second of the simulation through a switch in the model. Initially, the rate limit of the control surfaces of the system, which enters the PIO, was reduced from ±100 degrees to ±10 degrees. Once the system entered the PIO, the K_p and K_r values were adjusted to ensure the recovery of the system.

By adjusting the $K_p$and K_r coefficients, the system was able to recover from PIO effectively. The system was evaluated using three different test cases. In the first test case, the gap in the envelope cue is narrow, in the second test case, it is wider, and in the third test case, the system behavior of Boeing-747 aircraft is examined.

The 2-D and 3-D envelope cues of the first test case, the impact of K_p and K_r coefficients on system performance, and the variations in the K_p and K_r parameters are illustrated in Figure 10.

In addition, the envelope cues obtained with fixed gain and gain adjustment were compared. The corresponding envelope graphs are presented in Figure 11.

As seen in the figures, the system successfully adjusted the gains and enabled recovery. It was also observed that narrowing the envelope cue reduced the gains faster; however, this adjustment occurred prematurely.

Subsequently, the 2-D and 3-D envelope cues of the second test case, the impact of K_p and K_r coefficients on the system, and the variations in the K_p and K_r parameters are seen in Figure 12. The envelope graphs of the second test case, obtained with fixed gain and with gain adjustment, are presented in Figure 13. In Test 2, K_r value decreases only when the stick and dynamic pitch have opposite signs, while K_p decreases whenever the signal goes out of range.

Finally, simulation results of the tests conducted with Boeing-747, including gain variation and envelope cues with and without gain adjustment, are presented in Figure 14. If Boeing-747 had not implemented dynamic pitch control, the aircraft would have experienced oscillations, but it remained stable when the system used the gain regulator.

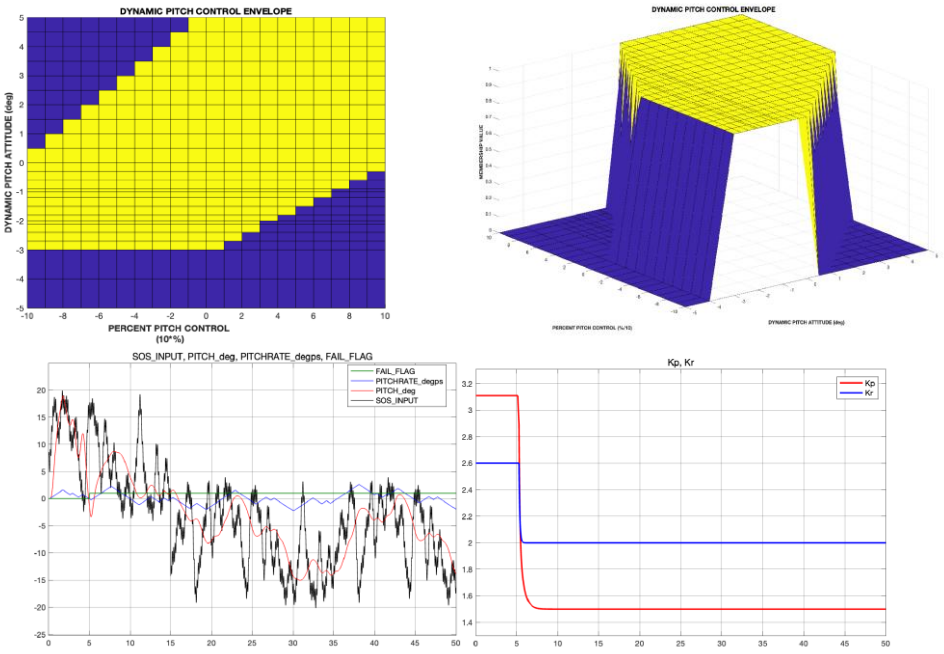

Figure 10. The 2-D, 3-D envelope cues and simulation results of the first test case.

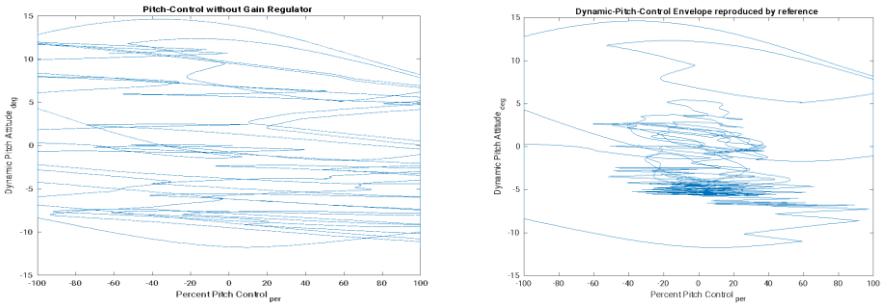

Figure 11. Envelope with and without Gain Regulator for the first test case.

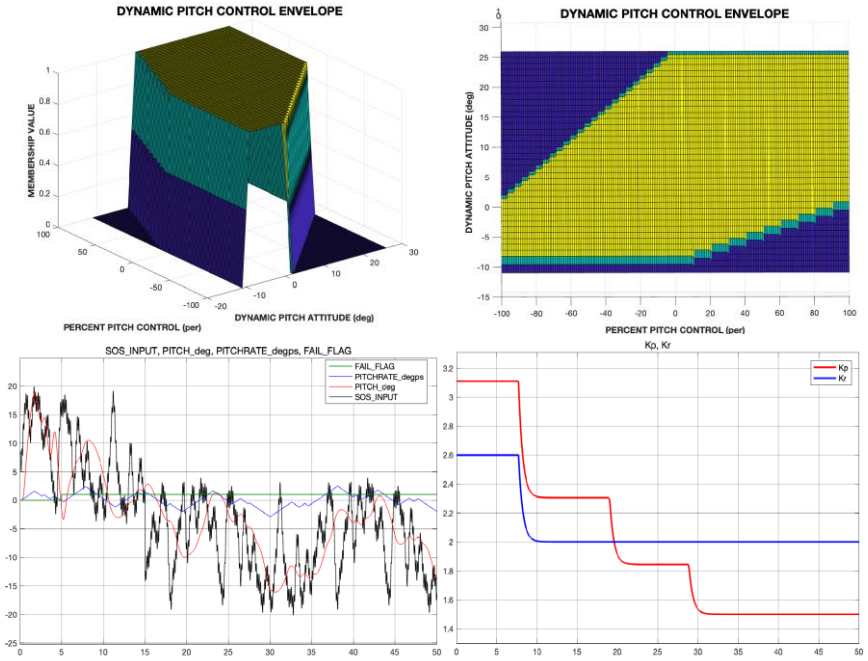

Figure 12. The 2-D envelope cue of the second test case.

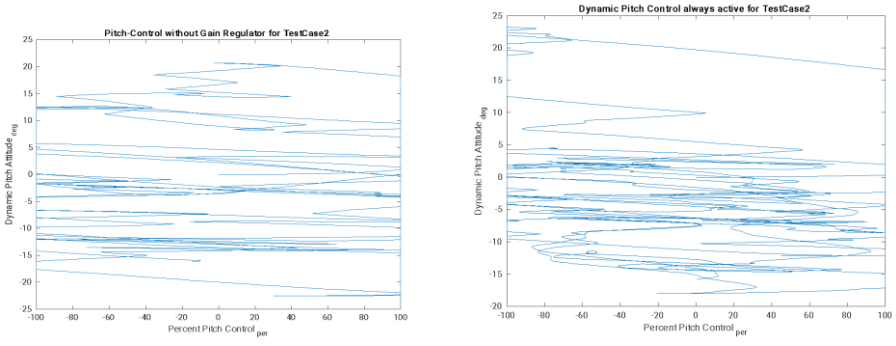

Figure 13. Envelope with and without Gain Regulator for the second test case.

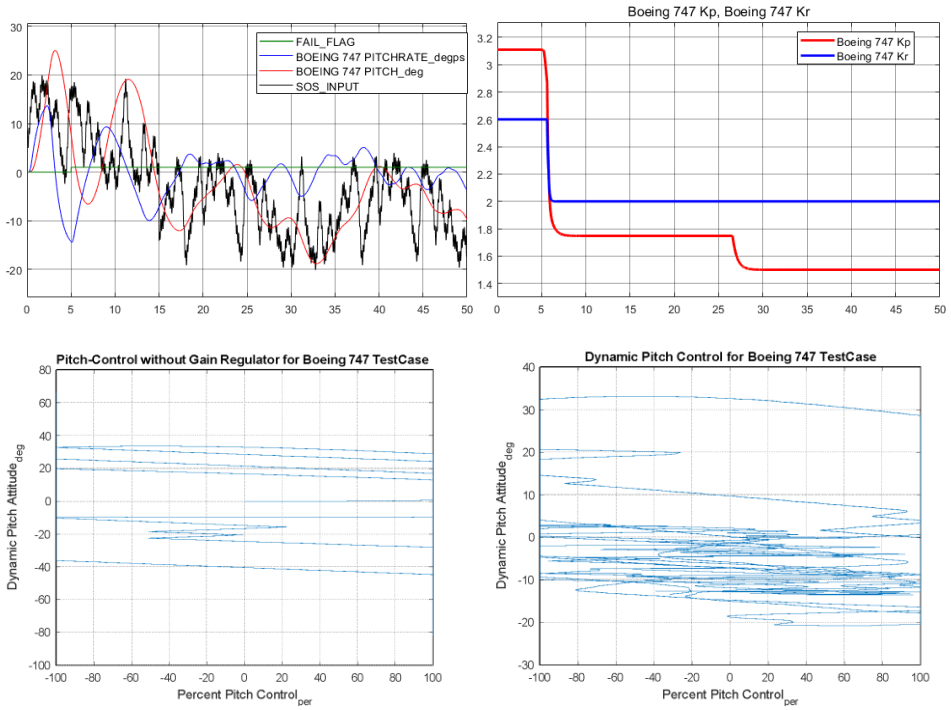

Figure 14. Simulation Results of the Third Test Case.

Conclusion

As a result, the human pilot model was implemented in the SIMULINK environment, and the relevant tests were conducted. By inserting the system into a PIO condition, the corresponding gain values were adjusted in a fuzzy and adaptive manner, enabling the system to recover. All tests demonstrate how significantly our system contributes to preventing oscillation conditions.

However, designing this system to rely only on pitch would require generating different envelope cues, as each altitude, weight, angle of attack, pitching moment coefficient C_m, lift coefficient C_l, dynamic pressure ,and velocity would correspond to different trim points. This would make it difficult to apply the method across all trim conditions. As a suggestion, an envelope cue based on $\frac{N_z}{\alpha}$ could be developed. In this way, a single envelope cue could potentially cover the entire flight envelope.

References

Ackerman, K. A., Talleur, D. A., Carbonari, R. S., Xargay, E., Seefeldt, B. D., Kirlik, A., Hovakimyan, N., & Trujillo, A. C. (2017). Automation situation awareness display for a flight envelope protection system. *Journal of Guidance, Control, and Dynamics, 40*(4), 964–980. https://doi.org/10.2514/1.G002243

Entzinger, J. O., & Suzuki, S. (2010). Modeling of the visual approach to landing using neural networks and fuzzy supervisory control. *Aerospace Science and Technology, 14*(2), 118–125. https://doi.org/10.1016/j.ast.2009.07.008

Xu, S., Tan, W., Qu, X., & Zhang, C. (2019). Prediction of nonlinear pilot-induced oscillation using an intelligent human pilot model. *Chinese Journal of Aeronautics, 32*(12), 2592–2611. https://doi.org/10.1016/j.cja.2019.03.006

Stepanyan, V., Krishnakumar, K., Dorais, G., Reardon, S., Barlow, J., Lampton, A., & Hardy, G. (2017). Loss-of-control mitigation via predictive cuing. *Journal of Guidance, Control, and Dynamics, 40*(4), 831–846. https://doi.org/10.2514/1.G002124

Van Baelen, D., Ellerbroek, J., van Paassen, M. M., Abbink, D., & Mulder, M. (2020, January 6–10). Using

asymmetric vibrations for feedback on flight envelope protection. In *Proceedings of the AIAA Scitech 2020 Forum* (p. 0409). Orlando, FL, USA. https://doi.org/10.2514/6.2020-0409

Xu, S., Tan, W., Wu, Y., & Sun, L. (2022). Modeling fuzzy and adaptive human behavior for aircraft with dynamic-pitch-control envelope cue. *Drones, 6*(5), 121. https://doi.org/10.3390/drones6050121

Enhanced Aircraft Control Throughout Total Energy Control Systems: A Comparative Study with Conventional Autopilots

Rumeysa Kökoğlu[a], Müjde Güzelkaya[a]

[a] Istanbul Technical University, Faculty of Electrics and Electronics Engineering, Department of Control and Automation Engineering, Türkiye
kokoglu16@itu.edu.tr

Keywords: Energy Control, Longitudinal Autopilots, Small UAV Control.

Aim

Longitudinal control of aircraft involves regulating altitude and airspeed. Conventionally, longitudinal control has been achieved using separate autopilot systems. These systems typically use the elevator to maintain altitude and engine thrust to control airspeed. This Single Input, Single Output (SISO) approach simplifies control design and is widely preferred in aviation because it is easy to implement. However, this approach ignores the coupled effects between altitude and airspeed dynamics (Brockhaus, Alles, & Luckner, 2011; Stevens, Lewis, & Johnson, 2016). When an aircraft is set to a certain altitude by elevator input, the airspeed is inevitably affected by the aircraft's total energy distribution and the coupled effects between altitude and airspeed. For example, when an aircraft maneuvers to gain altitude, some of its kinetic energy is converted to potential energy, causing a short-term speed decrease. Conversely, when the aircraft performs a maneuver that will decrease its altitude, potential energy is converted into kinetic energy, causing the airspeed to increase. Ignoring this energy exchange can lead to slower responses, excessive deviations, and the system performing more control actions to correct unwanted deviations. Conventional autopilots rely on separate control loops that do not take into account energy distribution/transfer, coupled effects, and therefore, adjusting one parameter, such as airspeed or altitude, can cause unintended changes to the other, resulting in efficiency and performance losses. In order to overcome these problems, the Total Energy Control System (TECS) has been proposed in the literature. TECS has been proposed as an advanced control architecture that integrates the coupled effects between altitude and airspeed by considering the total energy of the aircraft and the energy distribution rates (Lambregts, 1983, 1984). The purpose of this study is to compare the results of the TECS with conventional autopilots and to highlight the advantages of TECS.

Material and Method

Total Energy Control System (TECS) is a Multi-Input Multi-Output (MIMO) control architecture that can simultaneously control the airspeed and altitude of an aircraft. This system works by considering the kinetic and potential energy of the aircraft. The basic principle of TECS is to control the total energy rate with the engine thrust (throttle) and manage the energy distribution rate with the elevator. Unlike conventional autopilots, TECS optimizes control inputs more efficiently by considering the interaction and coupled effects between kinetic and potential energy. While the total energy rate is controlled using the throttle, the energy distribution is rearranged between kinetic and potential energy via the elevator. This method minimizes cross-coupling effects and increases tracking performance, robustness against disturbances, and control efficiency. This principle, introduced by Lambregts in the 1980s, was developed to improve flight path and speed control.

For an aircraft modeled as a point mass, the total energy (ET) is the sum of the kinetic and potential energy, and the rate of change is affected by both altitude and speed.

$$E_T = \frac{1}{2}mv^2 + mgh$$

$$\dot{E}_t = mv\dot{v} + mg\dot{h}$$

where m is mass, g is gravitational acceleration, h is altitude, and v is speed. Dividing $\dot{E}$ by mgv yields the non-dimensional specific energy rate $\dot{E}_s$, which is controlled by the throttle.

$$\dot{E}_s = \frac{\dot{v}}{g} + \frac{\dot{h}}{v} = \frac{\dot{v}}{g} + \gamma$$

To manage the energy distribution between kinetic and potential forms, TECS uses the Lagrangian L , defined as the difference between kinetic and potential energy.

$$L = \frac{1}{2}mv^2 - mgh$$

$$\dot{L} = mv\dot{v} - mg\dot{h}$$

Dividing by mgv gives the specific energy distribution rate $\dot{L}_s$, is controlled by the elevator.

$$\dot{L}_s = \frac{\dot{v}}{g} - \frac{\dot{h}}{v} = \frac{\dot{v}}{g} - \gamma$$

Where γ is the flight path angle. TECS employs proportional-integral (PI) control loops to minimize the errors in both $\dot{E}_s$ and $\dot{L}_s$. The throttle command δ_{T_c} and pitch command θ_c are determined as follows.

$$\delta_{T_c} = K_{TI}\int\left(\dot{E}_{s_{cmd}} - \dot{E}_s\right)dt + K_{TP}\dot{E}_s$$

$$\theta_c = K_{EI}\int\left(\dot{L}_{s_{cmd}} - \dot{L}_s\right)dt + K_{EP}\dot{L}_s$$

where K_{TI} and K_{EI} are integral gains, and K_{TP} and K_{EP} are proportional gains. This dual-loop architecture ensures that the aircraft's total energy is adjusted primarily through throttle modulation, while the elevator redistributes energy between kinetic and potential forms, reducing cross-coupling effects.

The unmanned aerial vehicle DEHA (Experimental Aircraft) is a high-performance experimental platform for evaluating advanced flight control systems. The aircraft has a fuselage length of 2.14 meters and a wingspan of 2.21 meters. It is equipped with a jet engine capable of providing 12 kilograms of thrust and is capable of performing high-speed flight operations. Primary control surfaces include ailerons for roll, elevators for pitch, and rudders for yaw. In addition, DEHA has retractable landing gear that improves performance by minimizing aerodynamic drag during flight. DEHA has extensive flight experience, having conducted over 200 sorties under various flight conditions. This extensive flight history has allowed for detailed system identification tests, which have enabled the development of a high-fidelity, six-degree-of-freedom (6DOF) nonlinear simulation model of DEHA. This model, created in a MATLAB/Simulink environment, provides a reliable virtual testbed for evaluating control algorithms by accurately simulating the aerodynamic and dynamic properties of DEHA. The simulation model includes realistic aerodynamic forces, engine dynamics, and deflections of control surfaces to reflect actual flight behavior closely. In this study, conventional longitudinal autopilots and Total Energy Control System (TECS) architecture were implemented within this simulation framework. The accuracy and reliability of the model allowed detailed performance comparisons to be made in various flight scenarios such as altitude step changes, speed adjustments, and combined maneuvers.

Findings

To evaluate the performance of the TECS architecture with conventional longitudinal autopilots, a series of flight maneuvers were simulated using the DEHA's 6-degree-of-freedom (6DOF) model. In the tested maneuver, the aircraft aimed for a 10-meter climb while performing a coordinating turn with 60 degrees of bank angle and simultaneously reducing its airspeed by 5 m/s. As shown in Figure 1, the results show that the TECS architecture performed better in tracking performance than conventional autopilots. In particular, the results of TECS reached the target altitude faster and showed less overshoot while adjusting to the reference airspeed. In addition, the throttle input generated by TECS is significantly less than that of the conventional autopilot, making energy management more efficient. These results show that the TECS architecture takes into account the coupled effects between altitude and airspeed, resulting in better performance.

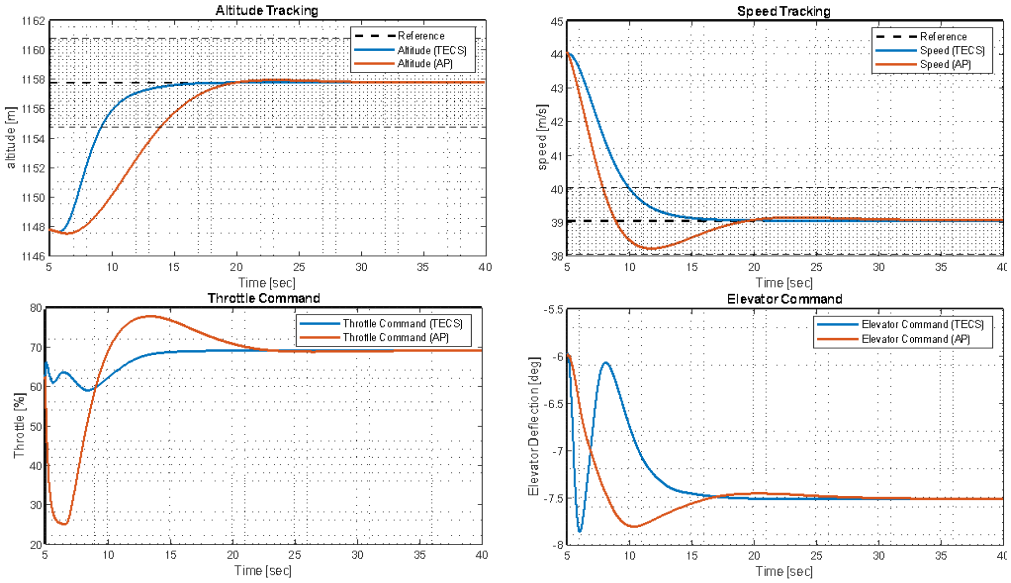

Figure 1. 10m Climb & 5m/s Deceleration ~ 60-degree Bank.

Conclusion

In conclusion, the comparative analysis of TECS with conventional longitudinal autopilots shows that TECS provides higher performance thanks to its energy-based approach. Unlike conventional autopilot systems, TECS takes into account the coupled effects between altitude and airspeed, providing faster response times, less overshoot, and smoother control inputs. Including the effects of both control inputs on airspeed and altitude allows TECS to maintain precise altitude and airspeed tracking even during sudden maneuvers and external disturbances. In addition, TECS produces fewer control inputs and exhibits less activity during engine thrust and elevator deflections compared to conventional autopilots. These advantages make TECS particularly suitable for applications where energy efficiency, performance, and reliability are critical.

References

Argyle, M. E., & Beard, R. W. (2016). Nonlinear total energy control for the longitudinal dynamics of an aircraft.
Bauer, P. (2023). A modified total energy control scheme for unmanned aircraft.
Brockhaus, R., Alles, W., & Luckner, R. (2011). *Flugregelung* (4th ed.). Springer.
Degaspare, T. G., & Kienitz, K. H. (2020). More integrated total energy control law for longitudinal automatic flight control system design. In *AIAA Scitech 2020 Forum*, 0205.
Lambregts, A. A. (1983, 1984). Total energy based flight control system.
Spark, H., González, P. J., et al. (2021). An assessment of aircraft control via SISO control loops and total energy

control. In *2021 AIAA Aviation Forum*.
Stevens, B. L., Lewis, F. L., & Johnson, E. N. (2016). *Aircraft control and simulation: Dynamics, controls design, and autonomous systems* (3rd ed.). Wiley.
Weiser, C., Looye, G., & Ossmann, D. (2024). Flight testing total energy control autopilot functionalities for high altitude aircraft. In *AIAA Scitech 2024 Forum*.

Performance Comparison of Guidance Algorithms for Aerial Vehicles: A Software-In-The-Loop Based Approach

Alper Makaraç[a], Mustafa Doğan[a]

[a] Istanbul Technical University, Control and Automation Engineering, Türkiye
makarac22@itu.edu.tr

Keywords: Guidance, PNG, TPNG, APNG, MPNG.

Aim

The main aim of this research is to evaluate the performance of different guidance algorithms for aircraft, which are designed to reach specific target coordinates. The main algorithms explored include Proportional Navigation Guidance (PNG), Augmented Proportional Navigation Guidance (APNG), Modified Proportional Navigation Guidance (MPNG), True Proportional Navigation Guidance (TPNG), and similar algorithms. These are studied together under different conditions to evaluate their responsiveness and reliability. A software-in-the-loop (SITL) simulation was established by incorporating aerodynamic coefficients—derived via DATCOM—into JSBSim, thus creating an accurate mathematical model of the missile. This model was linked with Ardupilot via UDP communication, enabling real-time interplay between flight simulation and guidance commands. Additionally, the simulation experience was improved by integrating Unreal Engine 5.0, which offers high-quality, real-time visualization of the missile's flight dynamics and target interception movements. The main goal is to understand the strengths and weaknesses of these guidance methods, especially in situations with stationary, constant-speed, and accelerating targets, as well as under aerodynamic disturbances. Figure 1 illustrates the data flow between different software components. Using this data flow, guidance algorithms can be tested by implementing aerodynamic effects and control surface commands.

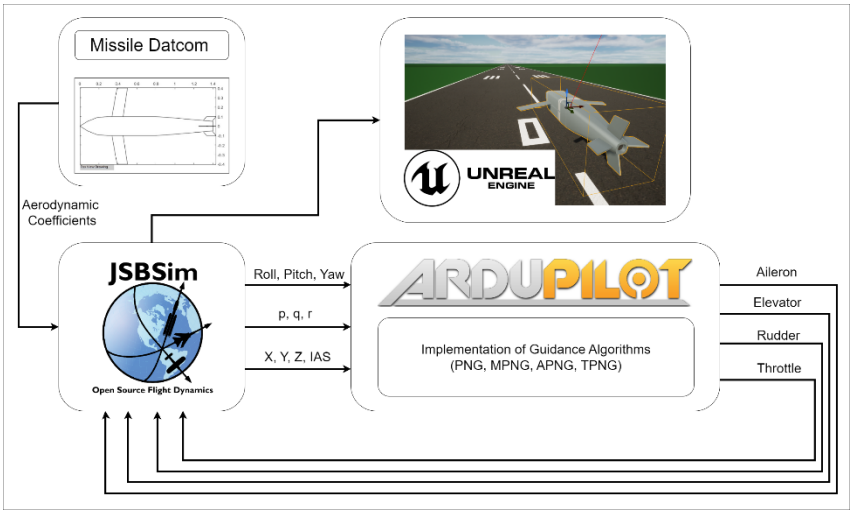

Figure 1. Simulation System Architecture.

Material and Method

The study was initiated by generating aerodynamic coefficients for the cruise missile using the DATCOM tool. *Figure 2* visualizes the physical properties of the aircraft transferred to the DATCOM model. Aerodynamic moments and derivatives of the aircraft shown in this figure were obtained and utilized in the simulation. These coefficients were carefully

implemented into JSBSim software, forming the foundational mathematical model. This step ensured that the simulation environment accurately reflected real-world aerodynamic forces and moments acting on the missile. Once the JSBSim model was established, the development advanced toward integrating Ardupilot via a UDP-based data exchange. Within this SITL configuration, JSBSim delivers updated state variables such as position, velocity, orientation, and angular rates to Ardupilot. Concurrently, Ardupilot produces guidance and control commands (for example, control surface deflections and thrust commands), which are then streamed back into JSBSim. This continuous transfer of data allows the simulation loop to approximate real-flight conditions while giving researchers the flexibility to test, refine, and analyze various guidance algorithms.

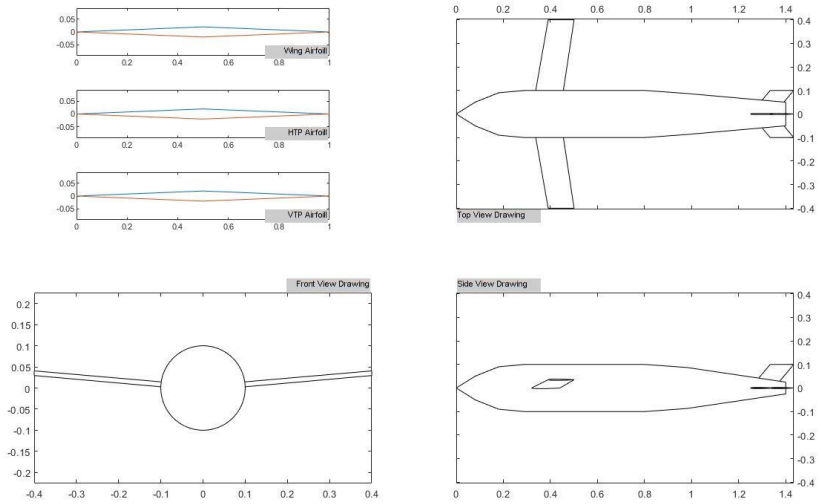

Figure 2. Appearance of the Datcom Model.

In parallel, Unreal Engine 5.0 was employed to provide an immersive, high-resolution visualization layer. By rendering 3D scenarios that reflect real-time flight states, Unreal Engine aids in better interpreting the missile's trajectory and how it responds to algorithmic instructions. As seen in *Figure 3*, the situation between the aircraft and the target can be easily observed in the 3-dimensional simulation environment.

Figure 3. Unreal Engine Implementation.

Using this comprehensive framework, the following guidance algorithms were examined:

1. Proportional Navigation Guidance (PNG): PNG is a classical missile guidance technique where missile acceleration commands are proportional to the rate of change of the line-of-sight (LOS) angle to the target. This method is known for its effectiveness in intercepting relatively predictable targets due to its straightforward and efficient nature (Siouris, 2004). However, PNG can show significant limitations when targets undertake high acceleration maneuvers, as its assumptions of target predictability and constant velocity may lead to larger miss distances (Yanushevsky,2007).
2. Augmented Proportional Navigation Guidance (APNG): APNG is an advanced guidance law that builds upon the standard PNG by incorporating additional feedback channels or corrective terms. These augmentations are designed to enhance the system's ability to compensate for target maneuverability and environmental disturbances, such as wind or sensor noise, making APNG more robust and adaptable in complex engagement scenarios. For instance, APNG often includes acceleration feedback or predictive terms to account for the target's future motion, which improves interception accuracy against highly maneuverable targets (Zarchan, 2012). Additionally, APNG can integrate adaptive control techniques to dynamically adjust its parameters in real-time, further improving performance in uncertain or rapidly changing environments (Lin, 1991). This adaptability makes APNG particularly suitable for modern missile systems and autonomous vehicles operating in challenging conditions.
3. Modified Proportional Navigation Guidance (MPNG): MPNG enhances traditional PNG to effectively address real-world combat scenarios involving highly maneuverable or high-speed targets. Unlike PNG, which assumes constant velocities and ideal dynamics, MPNG employs adaptive gain adjustments, additional correction terms, cross-range compensators for improved observability, and sophisticated filtering techniques to enhance robustness and accuracy (Lin et al., 2010). Additionally, it includes advanced techniques such as lead-bias commands, improving missile interception accuracy by targeting specific interception points (Moharampour et al., 2010). Moreover, MPNG dynamically accounts for missile velocity variations, particularly useful during significant speed changes like boost phases (Dohi et al., 2004).
4. True Proportional Navigation Guidance (TPNG): TPNG is an advanced form of the PNG, characterized by generating acceleration commands perpendicular to the instantaneous missile-target line-of-sight (LOS), proportional to the LOS rate and closing velocity. TPNG provides distinct advantages over standard PNG, especially in scenarios demanding high accuracy and minimized overshoot, as it can be analytically easier to

handle and offers improved predictability in missile-target engagements (Ghose, 1994). Additionally, in three-dimensional engagements, TPNG is effectively implemented by decomposing the guidance problem into three orthogonal planes (xy, yz, and xz), independently solving pursuit scenarios within these planes, and then integrating the computed acceleration commands back into three-dimensional space. This method enhances missile performance significantly in terms of interception accuracy and effectiveness against high-g maneuvering targets (Moran, 2005).

All four guidance approaches were tested under three distinct target profiles:

- Stationary Target: The target remains at a fixed coordinate, allowing initial validation of the algorithms and baseline performance measurements.
- Constant Velocity Moving Target: The target moves linearly at a steady speed, evaluating each algorithm's ability to track and intercept a uniformly moving object.
- Accelerating Target: The target undertakes varying acceleration profiles, creating highly dynamic and unpredictable engagement conditions that stress-test each guidance method's adaptability.

To further challenge the algorithms' resilience, aerodynamic disturbances, including wind gusts, turbulence, and control surface defects, were introduced in JSBSim. Monitoring how quickly and effectively the missile guidance re-acquired accurate interception trajectories revealed the comparative robustness of each algorithm. Unreal Engine 5.0's rich visualization played a key role here, facilitating real-time observation of subtle trajectory deviations and flight path corrections.

Findings

In analyzing extensive simulation datasets, notable distinctions emerged in how each guidance method addressed varying target and environmental complexities:

- **Performance of PNG:** PNG successfully intercepted stationary and constantly moving targets. It works well by following the LOS rate, creating a direct path when the target moves steadily. However, its performance dropped significantly with accelerating targets, causing the missile to react more slowly. This led to longer flight times and larger miss distances, especially when the target moved sideways with high acceleration.
- **Strengths of APNG:** APNG outperformed standard PNG in most scenarios involving maneuvering targets. By integrating additional feedback loops or calibration factors, APNG compensated more effectively for abrupt target trajectory changes and aerodynamic disturbances, maintaining tighter control over the intercept path.
- **Advantages of PNG:** MPNG demonstrated improved tracking performance compared to standard PNG, particularly against maneuvering targets. By incorporating adaptive gain adjustments or correction factors, it responded more effectively to rapid target accelerations. This resulted in shorter reaction times and reduced miss distances. However, its effectiveness depended on proper parameter tuning, and in highly dynamic environments, it still faced challenges in maintaining optimal intercept trajectories.
- **Effectiveness of TPNG:** TPNG demonstrated a balanced performance profile that bridged some of the gaps found in basic PNG. By adjusting specific gain factors and introducing refined handling of abrupt target maneuvers, TPNG exhibited quicker response times in intercept calculations. Although not as robust as APNG in every scenario, TPNG significantly mitigated issues encountered by standard PNG, particularly under moderate target accelerations.
- **Influence of Environmental Disturbances:** Wind gusts, variable atmospheric conditions, and minor control surface anomalies introduced additional challenges. PNG and LOS guidance were generally more susceptible to

becoming unstable, requiring longer to reorient intercept solutions. APNG and TPNG held up better, with APNG showing the smallest average miss distance under high-disturbance simulations.

Conclusion

In summary, the comparative study highlights that the optimal choice of guidance algorithm depends on the anticipated target motion and existing environmental conditions. PNG stands out for simpler engagements but encounters perceptible limitations against agile or unpredictable targets. TPNG modifies the classical PNG framework with more flexible gain parameters, delivering improved results over pure PNG in moderately dynamic conditions. MPNG, while an improvement over standard PNG, can still be insufficient when dealing with highly unpredictable or aggressively maneuvering targets. APNG shows the highest adaptability and resilience, a feature that is particularly advantageous against high-acceleration targets or significant aerodynamic disturbances.

The integration of Unreal Engine 5.0 within the SITL environment was a practical solution, allowing for a detailed visual inspection of missile flight behaviors under diverse conditions. This approach improved the interpretability of algorithmic performance and highlighted pathways for further refinement. Prospective research directions may focus on incorporating real sensor feedback, thereby reducing reliance on ideal seeker or tracker assumptions. Additionally, advanced machine learning models can be explored to dynamically tailor guidance laws to evolving scenarios, potentially unlocking further performance gains. Ongoing improvements in aerodynamic modeling, weather simulation fidelity, and real-time disturbance injection can also enhance the fidelity of SITL setups.

References

Dohi, N., Baba, Y., & Takano, H. (2004). Modified proportional navigation for a missile with varying velocity. In *24th International Congress of the Aeronautical Sciences*.

Ghose, D. (1994). Capture region for true proportional navigation guidance with nonzero miss-distance. *Journal of Guidance, Control, and Dynamics, 17*(3), 627–628. https://doi.org/10.2514/3.21214

Lin, C.-F. (1991). *Modern navigation, guidance, and control processing*. Prentice Hall.

Lin, Y.-P., Lin, C.-L., & Huang, C.-W. (2010). Design of a 3-D modified proportional navigation guidance law. In *Proceedings of the 8th IEEE International Conference on Control and Automation* (pp. 888–893). IEEE. https://doi.org/10.1109/ICCA.2010.5524299

Moharampour, A., Poshtan, J., & Khaki Sedigh, A. (2010). A modified proportional navigation guidance for accurate target hitting. *Iranian Journal of Electrical & Electronic Engineering, 6*(1), 20–30.

Moran, İ. (2005). *Three plane approach for 3D true proportional navigation* (Master's thesis, Turkish Naval Academy, Istanbul).

Siouris, G. M. (2004). *Missile guidance and control systems*. Springer. https://doi.org/10.1007/b138594

Yanushevsky, R. (2007). *Modern missile guidance*. CRC Press. https://doi.org/10.1201/9781420067296

Zarchan, P. (2012). *Tactical and strategic missile guidance* (6th ed.). American Institute of Aeronautics and Astronautics.

Robust Attitude Control of the F-16 Aircraft Using Incremental Nonlinear Dynamic Inversion

Yasin Şahin[1], İlker Üstoğlu[1]

[1] Istanbul Technical University, Control and Automation Engineering, Control and Automation Engineering Program, Turkiye
sahinyas18@itu.edu.tr

Keywords: F-16 , Modelling , NDI , INDI.

Aim

It is necessary for modern fighter planes, such as the F-16 Fighting Falcon, to have flight control systems that are exceptionally responsive and resilient in order to ensure that the aircraft maintains its stability and mobility in challenging flight conditions. Additionally, the F-16 is dependent on a technology known as fly-by-wire (FBW), which involves digital flight controllers continuously modifying control surfaces. This technology is inherently unstable. Traditional Proportional-Integral-Derivative (PID) controllers find challenges due to the nonlinear and time-varying features of such aircraft, requiring the adoption of more complicated control algorithms.
This research contrasts two prevalent nonlinear control methodologies, Nonlinear Dynamic Inversion (NDI) and Incremental Nonlinear Dynamic Inversion (INDI), for the attitude control of an F-16 aircraft. NDI depends on a precise model of aircraft dynamics, whereas INDI reduces model dependency through real-time incremental updates. The primary objectives of this research are to construct a comprehensive model of the F-16 aircraft by incorporating its aerodynamic characteristics, actuator mechanisms, and control system dynamics; to devise and execute both NDI and INDI controllers specifically for attitude stabilization; to assess and compare the robustness of these controllers with respect to the effects of external disturbances such as wind gusts and sensor noise; and ultimately, to deliver a quantitative evaluation of control performance based on essential criteria including attitude tracking accuracy, control effort, and system stability. Through the utilization of simulations and a comprehensive comparison examination, this study contributes to the enhancement of the optimization of existing flight control methods, specifically for future high-performance aircraft.

Material and Method

A complex nonlinear model of the aircraft is developed to evaluate the attitude control effectiveness of the F-16. This model incorporates aerodynamic forces and moments based on traditional F-16 flight dynamics equations, actuator dynamics considering control surface deflections and physical limitations, and external disturbances like wind gusts and sensor noise to enable a thorough assessment of the system's robustness. The overall closed-loop structure implemented for both NDI and INDI controllers is illustrated in Figure 1, emphasizing the integration of the F-16 aircraft dynamics, control laws, and feedback paths.

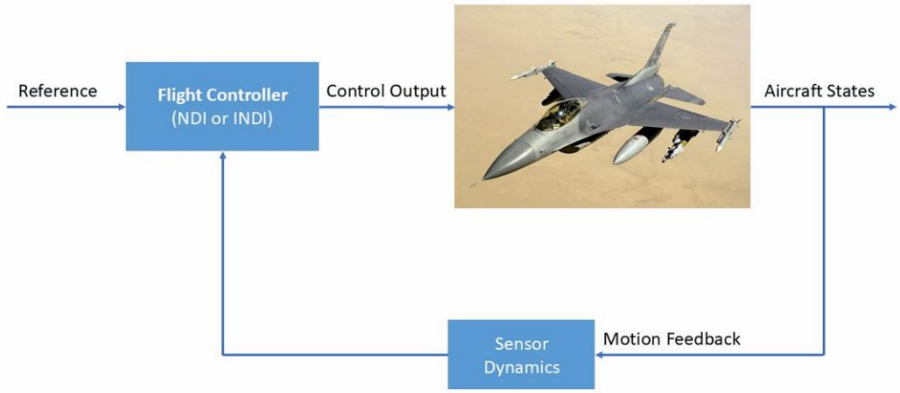

Figure 1. Closed-loop control architecture of the F-16 fighter utilizing NDI or INDI flight controllers.

a. Nonlinear Dynamic Inversion (NDI) Approach

NDI is a prevalent nonlinear control methodology that depends on the precise cancellation of nonlinear components in an aircraft's dynamic model to attain a linearized system response. The primary control law for NDI is articulated as follows:

$$u = A^{-1}(v - f(x))$$

where u is the control input, A denotes the control effectiveness matrix, v represents the virtual control input, and $f(x)$ encompasses the system's nonlinear dynamics.

A significant constraint of NDI is its pronounced reliance on a precise model of airplane dynamics. Modelling inaccuracies or external perturbations might lead to substantial performance deterioration. Moreover, actuator limitations and sensor noise generate uncertainties that diminish the robustness of pure NDI systems. NDI necessitates a precise understanding of the aircraft's dynamics, rendering it extremely sensitive to fluctuations in aerodynamic coefficients, control surface efficacy, and actuator latencies. Furthermore, it presupposes the existence of the inverse of the control effectiveness matrix, which may not be applicable in instances of actuator failures or saturation. The resilience of NDI has been thoroughly examined, and several improvements, including adaptive NDI and disturbance observer-based NDI, have been proposed to address its shortcomings. NDI is typically efficient when precise aerodynamic models are accessible; nevertheless, its efficacy diminishes considerably in real-world scenarios where aerodynamic factors fluctuate. This has resulted in the creation of incremental control approaches that depend on sensor-based feedback instead of the explicit inversion of the aircraft's dynamic model.

b. Incremental Nonlinear Dynamic Inversion (INDI) Approach

Incremental Nonlinear Dynamic Inversion (INDI) is a control strategy that improves robustness by minimizing dependence on an accurate aircraft model. In contrast to Nonlinear Dynamic Inversion (NDI), which relies on precise model inversion, INDI utilizes real-time sensor data to estimate unmodeled dynamics and emphasizes incremental modifications in control inputs.

The rotational dynamics of an aircraft are governed by:

$$J\dot{\omega} = M_{tot}$$

where J is the moment of inertia, ω is the angular velocity, and M_{tot} is the total moment acting on the aircraft. The total moment consists of aerodynamic, control, and external moments: $M_{tot} = M_{aero} + M_{prop} + M_{ext}$ where M_{aero} represents aerodynamic moments, M_{prop} accounts for propulsion effects, and M_{ext} includes external disturbances.

Rather than calculating the complete control input u, INDI emphasizes incremental control updates Δu, resulting in the control formulation:

$$\Delta u = J^{-1}(M_{cmd} - M_{prev})$$

where M_{cmd} is the commanded moment from the controller and is M_{prev} the previously estimated moment.
To enhance resilience, inbuilt gyroscopes and accelerometers quantify angular acceleration, facilitating real-time estimation of the unknown moments: $\omega_{meas} = J^{-1}M_{meas}$ where M_{meas} is the measured moment based on sensor feedback. The ultimate INDI control law, which includes real-time adaptation, is articulated as:

$$u = u_{prev} + J^{-1}(M_{cmd} - M_{meas})$$

This guarantees that INDI consistently adjusts for unmodeled dynamics and disturbances, providing enhanced adaptability compared to conventional NDI. In contrast to NDI, which necessitates predetermined aerodynamic characteristics, INDI adaptively modifies control inputs according to real-time aircraft performance, rendering it far more robust against uncertainties, actuator latencies, and environmental perturbations. The internal structure and signal flow of the Incremental Nonlinear Dynamic Inversion (INDI) controller are depicted in Figure 2, outlining the real-time computation of incremental control inputs.

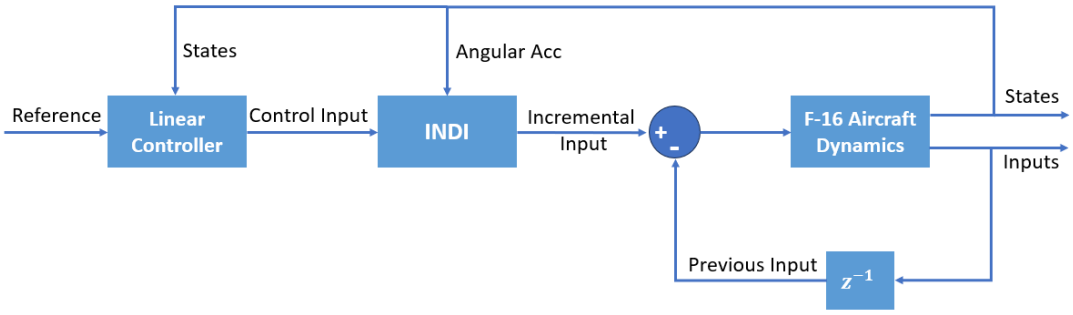

Figure 2. General block diagram of an INDI controller.

Findings

The simulation findings of this work demonstrate that the Incremental Nonlinear Dynamic Inversion (INDI) controller has superior performance compared to the Nonlinear Dynamic Inversion (NDI) method, especially for disturbance rejection. The disparity in performance is apparent across multiple essential aspects. The INDI controller constantly demonstrates superior precision and enhanced stability in sustaining the correct pitch and roll angles in terms of attitude tracking performance. Both Figure 3 and Figure 4 provide evidence that INDI ensures greater stability and accuracy in angular response, particularly when model fidelity is compromised. Conversely, the NDI-based system demonstrates more significant divergences from reference trajectories, particularly during dynamic flight conditions. Secondly, regarding control effort, INDI necessitates less actuator burden and produces smoother, more continuous control surface inputs, hence enhancing overall system efficiency and prolonging actuator lifespan. Ultimately, the INDI controller exhibits enhanced adaptability to fluctuating aerodynamic circumstances and unmodeled dynamics, rendering it a more feasible and pragmatic option for real-time flying applications characterized by uncertainty and environmental unpredictability.

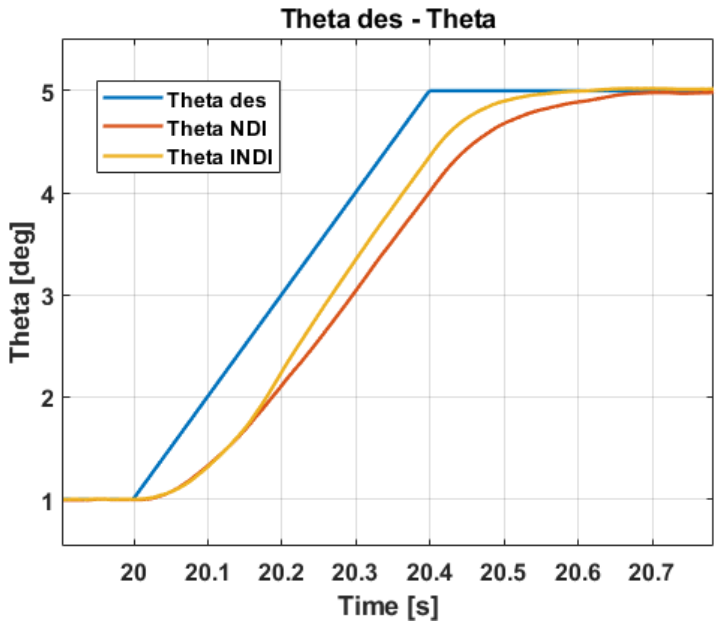

Figure 3. Pitch angle (θ) tracking response under model uncertainty using NDI and INDI controllers.

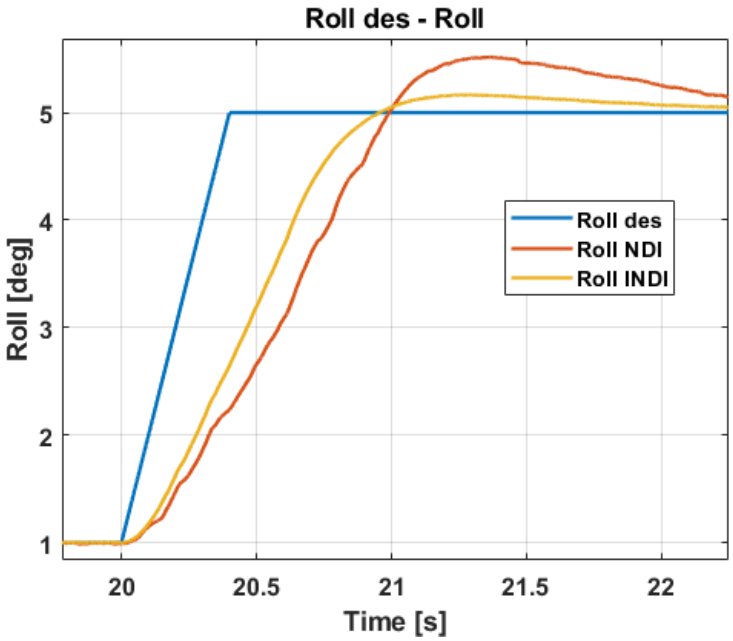

Figure 4. Roll angle (φ) tracking response under model uncertainty with NDI and INDI controllers.

Conclusion

This paper provides a comprehensive comparison of NDI and INDI controllers for F-16 attitude regulation, illustrating that INDI achieves superior tracking accuracy and demonstrates effective mitigation of external disturbances. In contrast, NDI is highly dependent on precise modelling, which limits its effectiveness in uncertain or unpredictable flight environments. Moreover, while INDI demands higher computational resources, this requirement is compensated by improved flight stability and robustness.

These findings highlight the potential of INDI-based control architectures as a promising approach for next-generation fighter aircraft. Future studies are planned to investigate the real-time implementation of such methods within embedded flight control systems.

References

Beard, R. W., & McLain, T. W. (2012). *Small unmanned aircraft: Theory and practice.* Princeton University Press.
Bittner, A. C., & Champney, P. C. (2015). Human factors in aviation. In S. K. Card, J. D. Mackinlay, & B. Shneiderman (Eds.), *Readings in information visualization: Using vision to think* (pp. 45–60). Morgan Kaufmann.
Chester, R. (2002). Materials selection and engineering. In A. A. Baker, L. R. F. Rose, & R. Jones (Eds.), *Advances in the bonded composite repair of metallic aircraft structure* (2nd ed., Vol. 1, pp. 19–40). Wiley.
Dole, C. E., & Lewis, J. E. (2000). *Flight theory and aerodynamics: A practical guide for operational safety* (2nd ed.). Wiley.
Gibbs, J. W. (2004). Thermodynamics and statistical mechanics. In M. Green (Ed.), *Classical and statistical thermodynamics* (pp. 123–145). Academic Press.
Hale, F. J. (2012). *Introduction to aircraft performance, selection, and design.* Wiley.
Kumar, V., & Garg, R. (2018). Advances in composite materials for aerospace applications. In P. K. Mallick (Ed.), *Fiber-reinforced composites: Materials, manufacturing, and design* (3rd ed., pp. 567–589). CRC Press.
Moir, I., & Seabridge, A. (2008). *Aircraft systems: Mechanical, electrical, and avionics subsystems integration* (3rd ed.). Wiley.
Nelson, R. C. (1998). *Flight stability and automatic control* (2nd ed.). McGraw-Hill.
Raymer, D. P. (2012). *Aircraft design: A conceptual approach* (5th ed.). AIAA Education Series.
Roskam, J. (2000). *Airplane design: Part I–VIII.* DARcorporation.
Sadraey, M. H. (2012). *Aircraft design: A systems engineering approach.* Wiley.
Stinton, D. (2001). *The design of the aeroplane* (2nd ed.). Blackwell Science.
Torenbeek, E. (2013). *Advanced aircraft design: Conceptual design, analysis, and optimization of subsonic civil airplanes.* Wiley.
Wells, A. T., & Rodrigues, C. C. (2013). *Commercial aviation safety* (5th ed.). McGraw-Hill Education.

Adaptive Kalman Filter-Based Gyroscope Error Compensation for IMU Sensors

Mehmet Eren Savaştürk [a], Mustafa Doğan [b]

[a] Istanbul Technical University, Department of Electronics Engineering, Master of Science Program, Turkiye
[b] Istanbul Technical University, Department of Control and Automation Engineering, Turkiye
savasturk22@itu.edu.tr, mustafadogan@itu.edu.tr

Keywords: Adaptive Kalman Filter, Gyro Bias, IMU, Prefilter.

Aim

This research aims to compensate gyro errors of an inertial measurement unit (IMU) by using magnetometer and accelerometer measurements of the same IMU sensor. IMU devices usually have three types of sensors, which are accelerometers, gyroscopes, and magnetometers. So, IMU's can measure the movement of the object that the IMU has been integrated into. However, these sensors are noisy and have fixed or time-varying biases. All these sensors have different types of noise or biases that can be eliminated by different methods. So, a cross-check between these sensors has become possible, and error compensation can be applied to sensor data.

This research focuses on gyro data, which has a major impact on navigation solutions. Gyroscope data can cause divergence in the navigation solution easily because even accelerometer data is integrated by using attitudes (Groves, 2013). So, a correction on Gyroscope's data can lead to a significant enhancement in the navigation solution. This error correction is based on magnetometer and accelerometer data that have been collected from the same IMU device. Thus, an inertial navigation solution is still possible with one device.

This research aims that correct gyro errors by using accelerometer and magnetometer measurements and makes IMU which have low-performance gyroscopes usable for inertial navigation solutions. So, size, weight, power, and cost advantages of IMU devices like MEMS IMU's can be used for reliable navigation solutions, and cheap navigation can become more common.

Material and Method

Simulated IMU measurements were used for this research. Matlab's IMU model is selected as a simulation tool (MathWorks, n.d.). This model includes magnetometer, accelerometer, and gyroscope data. The type and magnitude of error are determined for each sensor type separately. Constant bias, bias instability, random walk error, and axis misalignment were taken into account during the data generation process for the accelerometer and gyroscope. On the other hand, constant bias error and noise density parameters were determined for the magnetometer and added to the simulated data. The IMU data rate was selected as 100 Hz. Simulation was run for 100 seconds, and the generated data were used in algorithms.

Simulated data was chosen in this study because in studies using real-world data, it is difficult to determine an accurate ground truth, which makes performance evaluation challenging.

After simulated data were created, different methods were tested. There were 3 different types sensor measurements, and some data that were derived from measurements were used as the state vector for the Kalman Filter. Different combinations of parameters generate different state vectors, and the succession of different methods is examined. Methods requiring low computational power are preferred in this study, as navigation applications are real-time systems and low-cost IMU devices are often paired with simple processing units. Therefore, an Adaptive Kalman Filter approaches were examined (Hashlamon & Erbatur, 2013). The adaptive Kalman filter was combined with basic low-pass filters. While methods such as the Extended Kalman Filter (EKF) could also be used, they demand significantly more processing power. Moreover, EKF is highly dependent on the system model, meaning that system and measurement noises must be modeled with high precision (Simon, 2006). In contrast, this study focuses on adaptive methods that operate based on real-time data, aiming to reduce dependency on precise modeling.

1. Adaptive Kalman Filter by using gyroscope measurements and attitude change is examined. In this method, the IMU device's attitude has been calculated by using magnetometer and accelerometer measurements. A new parameter, which has been named attitude change, is derived. The system state vector has been chosen as gyroscope measurements and gyro biases. The measurement noise covariance matrix has been updated by using the difference between gyro measurements and the rotation rate derived from magnetometer measurements. An adaptive Kalman filter has been implemented for the updated measurement noise covariance matrix. Gyro measurements and gyro biases have been estimated as the output of the filter. The algorithm is illustrated with a flowchart in Figure 1.

2. Adaptive Kalman Filter by using gyroscope measurements and prefiltered attitude is examined. A low-pass prefilter process has been applied for both accelerometer and magnetometer data (Toroslu & Doğan, 2018). The moving average method was used as a prefilter because navigation applications are generally used in real time. So, a method that does not require too much processing power but is still effective against white noise is needed. The moving average method matched these requirements. IMU device attitude has been calculated by using filtered magnetometer and accelerometer measurements. As a result, more accurate and less noisy attitude data is calculated. The system state vector has been chosen as gyroscope measurements and sensor attitude. The difference between prefiltered IMU sensor attitude data and estimated IMU sensor orientation was used to update the measurement noise covariance matrix of the Adaptive Kalman Filter. So, a cross-check between sensors is possible. Then, adaptive Kalman filtering is applied to the generated IMU device attitude data and gyroscope measurements. The algorithm is illustrated with a flowchart in Figure 2

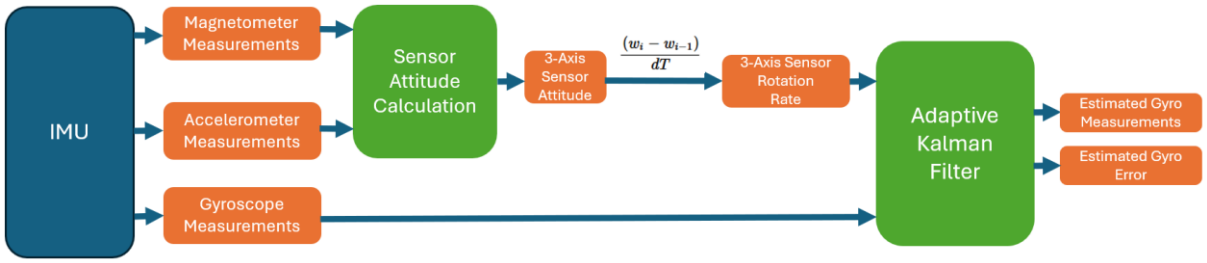

Figure 1. Adaptive Kalman Filter by Using Gyroscope Measurements and Rotation Rate Data.

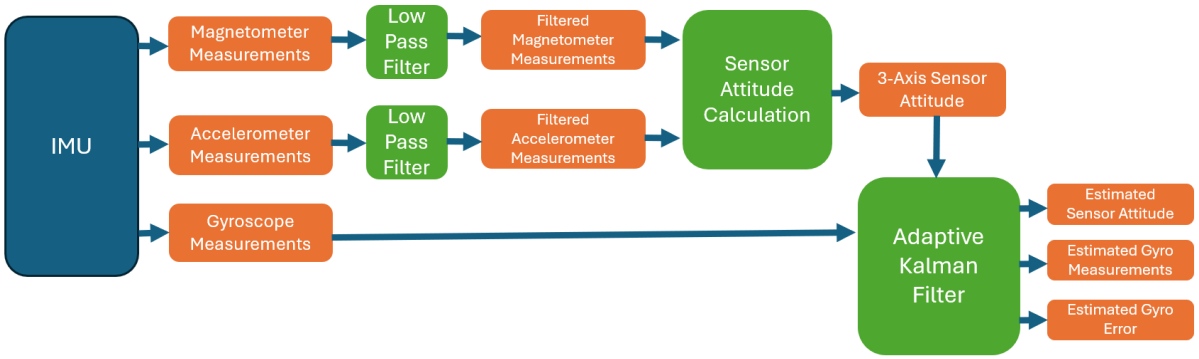

Figure 2. Adaptive Kalman Filter by Using Gyroscope Measurements and Prefiltered Attitude Data.

Findings

In the first method, accelerometer and magnetometer measurements have been used without prefiltering. Accelerometer and magnetometer data are noisy, and the random walk error has a dominant effect for both these sensors. When this data is used without prefiltering to calculate attitude, a very noisy attitude data is generated. On the other hand, the difference between attitude data is used to update the measurement noise covariance matrix, but the random walk on the data hinders

an appropriate update for the matrix. There is a random difference that cannot reflect real attitude change because of the random walk error.

In the second method, a low-pass filter is implemented for magnetometer and accelerometer data. A moving average filter has been used as a low-pass filter. So, the random walk error was removed from measurements. IMU sensor attitude is calculated by using filtered magnetometer and accelerometer measurements. On the other hand, the state vector consisted of three-axis IMU sensor orientations and three-axis gyroscope measurements. Using sensor orientations instead of orientation changes proved to be a more advantageous choice in terms of gyro error compensation. This way, it became possible to estimate gyro errors more accurately. The difference between prefiltered IMU sensor attitude data and estimated IMU sensor orientation was used to update the measurement noise covariance matrix of the Adaptive Kalman Filter. This method seems more usable for estimating gyro biases and attitude change for IMU devices.

Conclusion

This study demonstrates that if you have an IMU device capable of producing accelerometer, gyroscope, and magnetometer data along all three axes, it becomes possible to compensate for IMU gyro errors. By feeding an adaptive Kalman filter with sensor orientation information, along with gyro measurements, a better solution with error compensation for gyro data is possible. There are two steps to improve gyro error estimation. The first of them is prefiltering the accelerometer and magnetometer data. When a low-pass filter is applied to sensor data, the random walk effect is mostly removed from measurements. So, more accurate attitude data can be available for the sensor. At this point, this study focused on the rotation rate instead of absolute attitude accuracy. So, the rotation rate can be compared with gyro measurement, and gyro biases or gyro errors can be estimated. Of course, gyro errors can be time-varying errors. At this point, the adaptive Kalman filter is implemented, and the measurement covariance matrix is updated according to measurement differences. Measurement differences have been calculated between generated sensor attitude data and gyroscope measurements, so a cross-check between sensors becomes possible. According to the simulation, gyroscope errors were estimated with an average error of less than 4% across all three axes, and estimated gyro measurements provide more accurate data for inertial navigation.

By using these two steps, derivative gyro measurements have been generated, and this data can be replaced with raw gyro measurements. For inertial navigation solutions, gyroscope errors are the most critical error type. Gyroscope measurements affect not only attitude, but also acceleration, velocity, and position calculations. Because acceleration, velocity, and position updates are based on sensor attitude. According to this study, using compensated gyro data instead of raw gyro measurements can provide a better navigation solution. All data for the method that is described in this research can be provided by only one IMU sensor, so this method guarantees simplicity in hardware and better gyro data. So, better navigation data is possible with a low-performance gyro sensor.

As a direction for future work, gyro bias estimation can also be performed using the Extended Kalman Filter, and the strengths and weaknesses of EKF compared to the methods proposed in this study can be investigated.

References

Groves, P. D. (2013). *Principles of GNSS, inertial, and multisensor integrated navigation systems* (2nd ed.). Artech House.

Hashlamon, I., & Erbatur, K. (2013). An improved real-time adaptive Kalman filter with recursive noise covariance updating rules. *Turkish Journal of Electrical Engineering and Computer Sciences, 24*(5), 524–540. https://doi.org/10.3906/elk-1309-60

MathWorks. (n.d.). IMUSensor system object. *MathWorks.* https://www.mathworks.com/help/nav/ref/imusensor-system-object.html

Simon, D. (2006). *Optimal state estimation: Kalman, H∞, and nonlinear approaches.* Wiley-Interscience.

Toroslu, I., & Doğan, M. (2018). Effective sensor fusion of a mobile robot for SLAM implementation. In *2018 4th*

International Conference on Control, Automation and Robotics (ICCAR) (pp. 76–81). IEEE. https://doi.org/10.1109/ICCAR.2018.8384648

Immersion and Invariance Disturbance Observer-Based Discrete Time Vector Control of BLDC Machines

Ziya Cem Salış[a], Yaprak Yalçın[a]

[a] Istanbul Technical University, Department of Control & Automation Engineering, Turkey
salis21@itu.edu.tr

Keywords: BLDC Machine, Discrete Time Control, Disturbance Observer, Immersion and Invariance, Vector Control.

Aim

The performance of BLDC machines can be adversely affected by disturbances, parameter uncertainties, and inherent system nonlinearities. To mitigate these challenges, Nonlinear Disturbance Observers (NDOs) have been developed, offering the capability to estimate and compensate for unknown disturbances in real time.
Many control approaches based on NDO exhibit significant complexity and sensitivity to modeling assumptions. In contrast, Immersion and Invariance (I&I) observers ensure asymptotic convergence of the estimation error to zero and can be flexibly adapted to accommodate a wide range of nonlinear dynamic models, while preserving a straightforward structure and ease of implementation. Consequently, in this paper, we propose an I&I Observer-Based Vector Control strategy specifically tailored for BLDC Machines. This proposed strategy is intended to enhance the system's robustness against external disturbances and model uncertainties. The primary focus of our approach lies in its structural simplicity, real-time applicability, and, critically, the formulation of a systematic method for applying the I&I framework to BLDC machines—an area that has not yet been addressed within the existing academic literature.
The key contributions of this work are as follows:

1. Design of a Reduced-Order I&I Disturbance Observer: The proposed observer is specifically tailored to accommodate the dynamic characteristics of BLDC machines, ensuring accurate disturbance estimation.
2. The I&I disturbance observer is integrated into a vector control strategy.
3. The effectiveness of the proposed approach is demonstrated through simulation results.

Material and Method

The BLDC machine model is first established, and disturbances are systematically formulated. A modified state-space equation is derived to facilitate the design of an I&I observer. The proposed observer is then integrated into a Vector control framework to mitigate the effects of disturbances through the incorporation of a feedforward term. The performance of the proposed control structure is evaluated through simulation studies.

1. BLDC Machine Model

To implement the I&I framework, it is essential to utilize an accurate BLDC machine model, as outlined in (Rashid, 2013; Krause et al., 2013). The parameters employed in this study are presented in Table 1.

Table 1. Used parameters.

Parameter	**Description**	**Unit**
V_x	Phase Voltage	V
R	Phase Resistance	Ohm
i_x	Phase Current	A
is_{max}	Maximum Stator Phase Current	A
Ls	Phase Inductance	Henry
e_x	Back Electromotive Force (EMF)	V
K_e	Back EMF Constant	Vs/rad
W_{elec}	Electrical Angular Speed	rad/s
Q_{elec}	Electrical Angular Position	rad
J	Inertia	Kg m^2
T_e	Electromagnetic Torque	Nm
T_l	Load Torque	Nm
B	Fluid Friction Coefficient	Nm s/rad
W_{mech}	Mechanical Angular Speed	rad/s
Q_{mech}	Mechanical Angular Position	rad
pp	Pole Pair	-
K_t	Torque Constant	Nm/A
T	Sampling Time	s

1.1. Electrical model

In the electrical model, electromagnetic field generation is achieved by passing current through the phase conductors of the machine. The equations governing these circuitries are presented below.

$$V_a = Ri_a + L\frac{di_a}{dt} + e_a \quad (1)$$

$$V_b = Ri_b + L\frac{di_b}{dt} + e_b \quad (2)$$

$$V_c = Ri_c + L\frac{di_c}{dt} + e_c \quad (3)$$

Back EMF is the voltage potential generated because of rotational motion, which acts to oppose the current flowing within the circuitry. The corresponding equations are provided below.

$$e_a = K_e W_{elec} sin(Q_{elec}) \tag{4}$$

$$e_b = K_e W_{elec} sin(Q_{elec} + \frac{2\Pi}{3}) \tag{5}$$

$$e_c = K_e W_{elec} sin(Q_{elec} - \frac{2\Pi}{3}) \tag{6}$$

1.2. Mechanical Model with Disturbance

Disturbances can be categorized into two types: measurable disturbances and non-measurable disturbances. Non-measurable disturbances include factors such as friction in bearings, variations in phase resistance or inductance due to manufacturing imperfections, and temperature differences. These disturbances are incorporated into the mechanical equations with the parameter du.

$$J \frac{dW_{mech}}{dt} = T_e - T_l - BW_{mech} - du \tag{7}$$

In the Equation (8), T_e denotes the generated torque by machine.

$$T_e = pp\ K_t\ (i_a\ sin(Q_{elec}) + i_b\ sin(Q_{elec} + \frac{2\Pi}{3}) + i_c\ sin(Q_{elec} - \frac{2\Pi}{3})) \tag{8}$$

1.3. State Space Model

The state-space representation of the given system can be expressed as follows.

$$\frac{d}{dt}\ [i_a\ i_b\ i_c\ W_{mech}\ Q_{elec}\ ] = \left[-\frac{R}{L}\ 0\ 0\ 0\ 0\ 0\ -\frac{R}{L}\ 0\ 0\ 0\ 0\ 0\ -\frac{R}{L}\ 0\ 0\ 0\ 0\ 0\ -\frac{B}{J}\ 0\ 0\ 0\ 0\ pp\ 0\right][i_a\ i_b\ i_c\ W_{mech}\ Q_{elec}\ ] +$$
$$\left[\frac{1}{L}\ 0\ 0\ 0\ 0\ 0\ \frac{1}{L}\ 0\ 0\ 0\ 0\ 0\ \frac{1}{L}\ 0\ 0\ 0\ 0\ 0\ -\frac{1}{J}\ \frac{1}{J}\ 0\ 0\ 0\ 0\ 0\right][V_a\ V_b\ V_c\ T_l\ du\ ] + \left[-\frac{1}{L}\ 0\ 0\ 0\ -\frac{1}{L}\ 0\ 0\ 0\ -\frac{1}{L}\right][e_a\ e_b\ e_c\ ] \tag{9}$$

The primary challenge in applying the I&I framework arises from the treatment of back EMF. Specifically, the back EMF is inherently dependent on rotational speed and position, leading to non-constant matrix coefficients. This variability hinders the direct application of the I&I framework. To address this issue, we propose a novel approach involving the utilization of update functions external to the state-space representation. These updated equations are formulated as presented in Equations (10) to (11).

$$U_x = V_x - e_x = R\ i_x + L \frac{di_x}{dt} \tag{10}$$

$$T = T_e - T_l \tag{11}$$

The update functions will be computed externally from the state-space equations, and their outputs will be supplied to the state-space representation. This approach yields Equation (12).

$$\frac{d}{dt}\ [i_a\ i_b\ i_c\ W_{mech}\ Q_{elec}\ ] = \left[-\frac{R}{L}\ 0\ 0\ 0\ 0\ 0\ -\frac{R}{L}\ 0\ 0\ 0\ 0\ 0\ -\frac{R}{L}\ 0\ 0\ 0\ 0\ 0\ -\frac{B}{J}\ 0\ 0\ 0\ 0\ pp\ 0\right][i_a\ i_b\ i_c\ W_{mech}\ Q_{elec}\ ] +$$
$$\left[\frac{1}{L}\ 0\ 0\ 0\ 0\ 0\ \frac{1}{L}\ 0\ 0\ 0\ 0\ 0\ \frac{1}{L}\ 0\ 0\ 0\ 0\ 0\ -\frac{1}{J}\ 0\ 0\ 0\ 0\ 0\ \frac{1}{J}\right][U_a\ U_b\ U_c\ T_l\ du\ ] \tag{12}$$

2. I&I Disturbance Observer Design

This method has been described in (Adıgüzel & Yalçın, 2021, 2022; Astolfi & Ortega, 2003; Astolfi et al., 2010; Yalçın, 2015; Yalçın & Astolfi, 2012) and is summarized below. It is important to note that this method operates under the assumption that unknown constant or time-varying disturbances vary at a significantly slower rate compared to the system dynamics. The disturbance estimation error can be defined as follows.

$$z(k) = \hat{\theta}(k) - \theta + \beta(x(k-1))\, x(k) \tag{13}$$

The variable θ(k) represents the estimated disturbance, which will be updated according to a specified update rule. The parameter β is a free design variable that allows for controlling the behavior of the observer. The time difference of the error dynamics, considering the system equations, can be expressed as follows.

$$z(k+1) - z(k) = \hat{\theta}(k+1) - \hat{\theta}(k) + \beta(k)\left(x(k) + T\left(Ax(k) + Bu(k)\right)\right) - \beta(k-1)x(k) + \beta(k)\, T\,(\hat{\theta}(k) + \beta(k-1)x(k) - z(k)) \tag{14}$$

The update rule for the disturbance estimation is selected as follows,

$$\hat{\theta}(k+1) = \hat{\theta}(k) - \beta(k)\,(x(k) + T(Ax(k) + Bu(k)) + \beta(k-1)\, x(k) - \beta(k)\, T\,(\hat{\theta}(k) + \beta(k-1)x(k)) \tag{15}$$

yields to following error dynamics,

$$z(k+1) = (1 - \beta(k)\, T)\, z(k) \tag{15}$$

Selecting β(k)= diag(α) I_5, where I_5 is the identity matrix with dimension 5, and selecting $0 < \alpha < 2$ makes these dynamics asymptotically stable.

3. Vector Controller and I&I Disturbance Observer Control Structure

Vector control, also referred to as Field Oriented Control (FOC), is a technique employed to achieve effective control over the entire torque and speed range. The most utilized control modes within FOC are speed control and torque control (Blaschke, 1972; Bose, 2002; Vas, 1990). However, due to the presence of disturbances within the system, it becomes challenging to achieve the desired reference value. To address this issue, we incorporate the previously developed I&I disturbance observer into the control loop in a feedforward configuration (as indicated by the red-marked section) as illustrated in Figure 1.

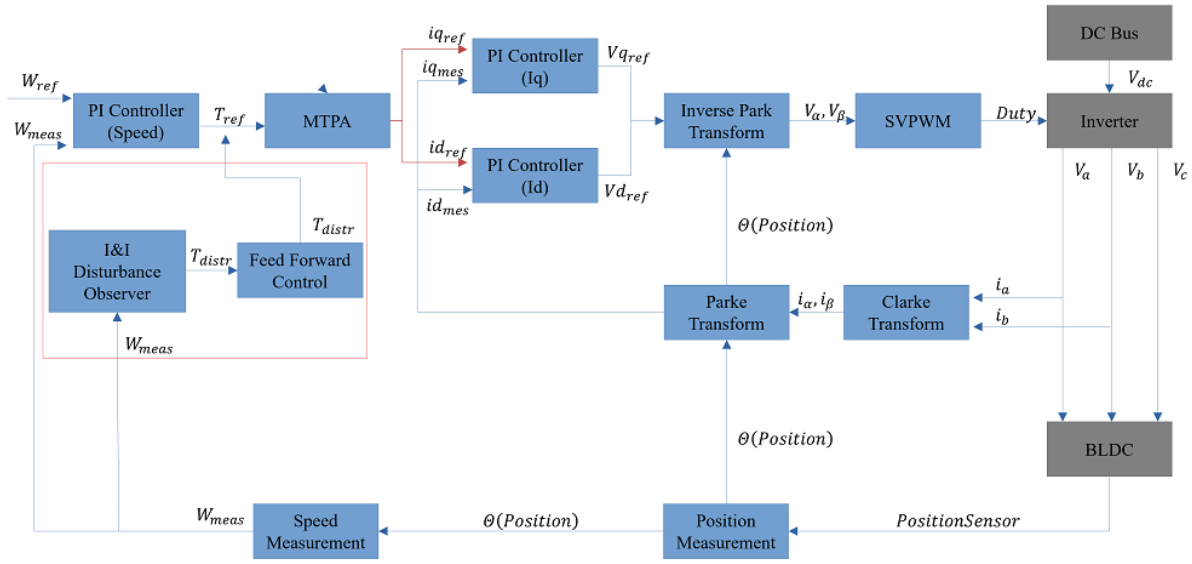

Figure 1. Proposed control loop.

Findings

To evaluate the performance of the proposed method, a simulation environment was developed using the Simulink platform. A BLDC machine characterized by the parameters listed in Table 2 is utilized.

Table 2. BLDC machine parameters.

Parameter	is_{max}	pp	R	L	K_e	K_t	J	T
Value	30	2	0.416	1.365e-3	0.0957	0.0957	2e-3	0.0001

The simulation environment adopts a control structure like that depicted in Figure 1. The performance of the system is evaluated under the following scenarios:

1. Performance under different β, constant disturbance, and speed

In the simulations, the constant parameters du=1.5 and W_{ref}=1000 are employed, while different values of β (0.1, 0.25, 0.5, 1) are selected. The objective of this test is to assess system performance and determine the optimal value of β for use in subsequent simulations.

The simulation results, illustrating the tracking of disturbance values, are presented in Figure 2. The parameter β influences both the estimation speed and the overshoot of the system. It is observed that selecting a larger β results in improved disturbance attenuation and reduced overshoot during estimation.

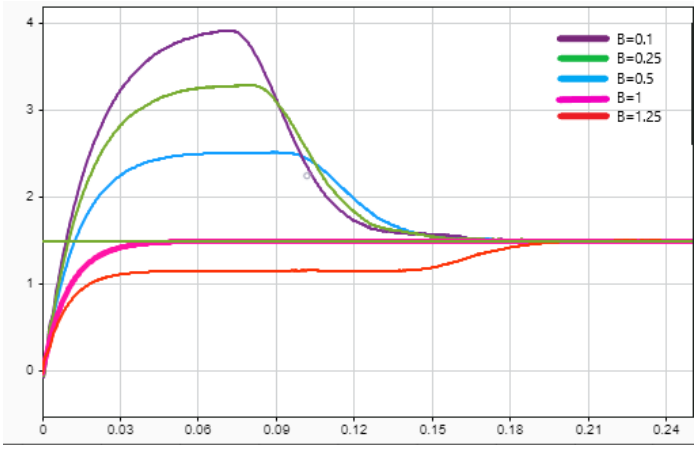

Figure 2. Observer performance for different β.

It can be claimed that parameter tuning of the proposed method is easy with the β parameter; with this free design parameter, settling time and overshoot characteristics can be directly influenced. This means that in practical implementations, this free design parameter can be adjusted on the side to meet the desired output characteristics.

2. Performance under different β, constant disturbance, and speed

The constant parameters β=1 and W_{ref}=1000 is utilized. Various disturbance profiles, including ramp and sinusoidal functions, are introduced to the system to evaluate its performance under time-varying disturbances. Ramp function disturbance and the system's tracking performance are illustrated in Figure 3.

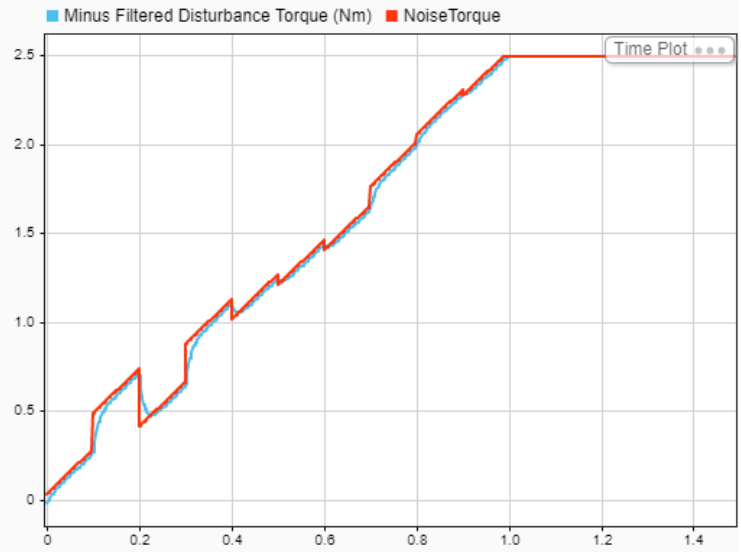

Figure 3. Disturbance tracking with ramp disturbance.

The sinusoidal disturbance and tracking performance for this case are depicted in Figure 4.

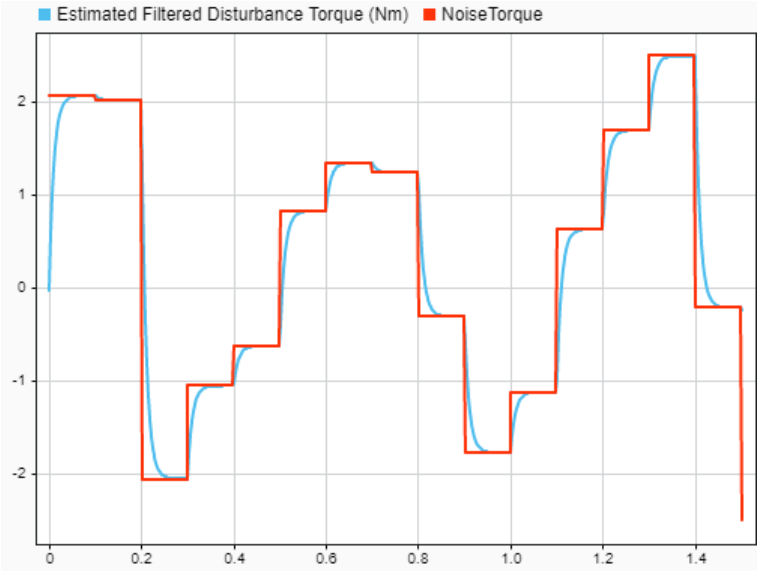

Figure 4. Disturbance tracking with sinusoidal disturbance.

The ramp disturbance profile emulates the most dominant disturbance source of friction-based disturbances to the system; thus, it increases as the speed increases and settles at a constant disturbance torque once the machine settles down to a constant speed. In traction applications motor experiences acceleration and deceleration also experiences sudden changes in disturbances because of the ever-changing conditions of the road. A sinusoidal disturbance emulates this behavior. The proposed I&I disturbance observer effectively tracks the time-varying injected disturbances, exhibiting minimal delay and negligible overshoot.

3. Comparison with or without feed forward I&I Disturbance Observer control present in the system

The constant parameters β=1 and W_{ref}=1000 are utilized, and a sinusoidal disturbance profile is introduced. The primary objective of this test is to assess the impact of feedforward I&I Disturbance Observer control on the system. The tracking performance is presented in Figure 5.

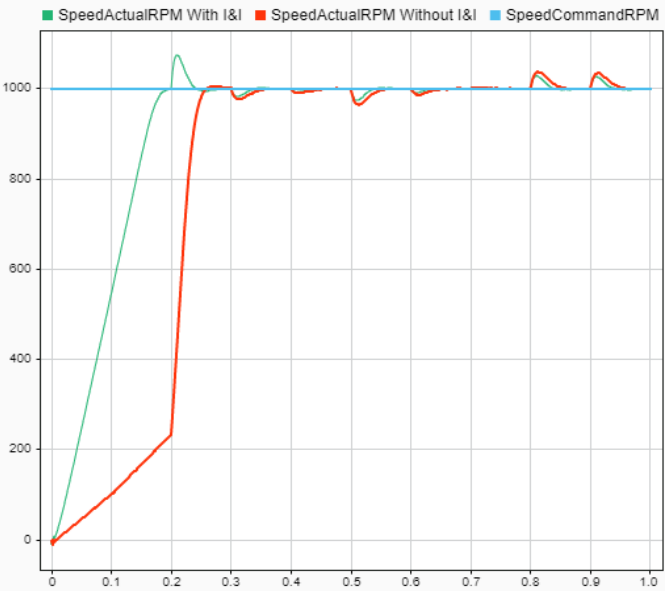

Figure 5. Tracking performance with sinusoidal disturbance.

In a detailed analysis, performance evaluation can be divided into:

1. Transient Part: A System without feedforward control exhibits a significantly slower response in achieving the desired speed compared to the system with feedforward control. At the instance of 0.2 seconds machine shows an unwanted acceleration which is not desirable in a practical application. Feedforward experiences the same sudden drop in disturbance torque, but the acceleration is less critical and less severe, and lasts for a considerably smaller time.

2. Steady-State Part: In the absence of feedforward control, the system experiences a reduction in the magnitude of disturbance, leading to improvement in control quality. This highlights the effectiveness of the feedforward I&I Disturbance Observer in maintaining steady-state performance despite the presence of disturbances.

In practical applications, the proposed observer and the feedforward control structure improve and enable quicker settling time, and reduce disturbance effects on the system.

Conclusion

In this paper, a dynamic model of a BLDC machine subjected to disturbances is developed. To address unmeasured disturbances, a disturbance estimator design based on the I&I observer approach is proposed. The FOC method for BLDC machines is integrated into the control strategy. This approach leverages estimated disturbance information to mitigate the impact of disturbances through a feedforward control mechanism and is formulated within a discrete-time framework.

The proposed method is implemented in a Simulink environment to evaluate its applicability. Performance tests are conducted through simulations under various scenarios, demonstrating that the proposed I&I disturbance observer, combined with feedforward control, effectively attenuates unmeasured disturbances.

In future work, the proposed control structure will be implemented in hardware and tested on a physical BLDC motor to further validate its effectiveness.

References

Adıgüzel, F., & Yalçın, Y. (2021). Discrete-time backstepping control with nonlinear adaptive disturbance attenuation for the inverted-pendulum system. Transactions of the Institute of Measurement and Control, 43(5), 1068–1076.
Adıgüzel, F., & Yalçın, Y. (2022). Immersion and invariance disturbance observer-based nonlinear discrete-time control for fully actuated mechanical systems. International Journal of Systems Science, 53(2), 388–401.
Astolfi, A., & Ortega, R. (2003). Immersion and invariance: A new tool for stabilization and adaptive control of nonlinear systems. IEEE Transactions on Automatic Control, 48(4), 590–606. https://doi.org/10.1109/TAC.2003.809820
Astolfi, A., Ortega, R., & Venkatraman, A. (2010). A globally exponentially convergent immersion and invariance speed observer for mechanical systems with non-holonomic constraints. Automatica, 46(1), 182–189. https://doi.org/10.1016/j.automatica.2009.10.027
Blaschke, F. (1972). The principle of field orientation as applied to the new transvector closed-loop control system for rotating-field machines. Siemens Review, 34(3).
Bose, B. K. (2002). Modern power electronics and AC drives. Prentice Hall.
Krause, P. C., Wasynczuk, O., & Sudhoff, S. D. (2013). Analysis of electric machinery and drive systems (3rd ed.). Wiley-IEEE Press.
Rashid, M. H. (2013). Power electronics: Circuits, devices and applications (4th ed.). Pearson.
Vas, P. (1990). Vector control of AC machines. Oxford University Press.
Yalçın, Y. (2015). Discrete-time immersion and invariance adaptive control via partial state feedback for systems in block strict feedback form. European Journal of Control, 25, 27–38. https://doi.org/10.1016/j.ejcon.2015.05.002

Yalçın, Y., & Astolfi, A. (2012). Immersion and invariance adaptive control for discrete-time systems in strict feedback form. Systems & Control Letters, 61(12), 1132–1137. https://doi.org/10.1016/j.sysconle.2012.09.010

DATA ENGINEERING AND BUSINESS ANALYTICS

Big Data Analytics for Decision-Making

Predictive Analytics and Machine Learning in Business

Sentiment Analysis and Opinion Mining

Automated Plastic Waste Detection on Coastal Areas Using UAVs and Deep Learning

Hesam Hatamzadeh Khanghahi [a], Şule Itır Satoğlu [b]

[a] Istanbul Technical University, Faculty of Management, Big Data and Business Analytics, Türkiye
[b] Istanbul Technical University, Industrial Engineering Department, Faculty member, Türkiye
khanghahi23@itu.edu.tr

Keywords: Waste Detection, UAV, YOLO, Real-Time Monitoring, Convolutional Neural Network.

Aim

Plastic pollution is a major threat to coastal ecosystems, wildlife, and human health. Beaches, as dynamic interfaces between land and sea, are particularly vulnerable to plastic litter. Traditional methods of plastic waste clean-up face significant limitations due to being slow and labor-intensive. However, advancements in drone technology and deep learning offer promising alternatives [1]. This project aims to develop an automated system for detecting, identifying, and classifying plastic waste on beaches using drone images and deep learning models like YOLO [2]. By leveraging this approach, we aim to enhance clean-up prioritization, reduce human labor reliance, and support environmental conservation efforts.[3]
Plastic pollution poses significant threats to biodiversity, ecosystem functionality, and public health. Beaches are particularly susceptible to plastic litter due to their dynamic nature as interfaces between land and sea [4]. Traditional methods of addressing plastic waste, while effective on a small scale, are limited by labor intensity and inefficiency when scaled to large coastlines. Advances in drone technology and deep learning have paved the way for more efficient monitoring and detection systems.
Drones provide large-scale surveillance with high-resolution imagery, enabling precise identification of plastic waste [5][6]. Coupled with models like YOLO (You Only Look Once) [2], these technologies facilitate real-time detection and classification, supporting cleanup and conservation initiatives [7]. Various studies have explored AI-driven waste detection systems, including the development of specialized datasets such as the FloW [8] Dataset for floating waste detection and UAV-BD for drone-based plastic bottle recognition. These studies highlight the importance of multimodal data fusion and orientation-aware detection but also expose challenges related to scalability and computational demands.
A UAV-based real-time marine trash monitoring system integrating YOLO detection and data management frameworks has demonstrated the feasibility of autonomous waste monitoring. However, issues such as false positives in complex environments and the need for improved standardization persist. This paper builds upon these advancements by integrating multiple deep learning models to enhance plastic waste detection on beaches. [9][10]

Material and Method

Dataset

The dataset for this project includes drone-captured images of waste materials on beaches [11]. It is organized into three subsets: test, train, and validation, with categories such as plastic bottles, takeaway cups, retort pouches, tin and aluminum cans, glass, and takeaway containers. The original dataset, sourced from Roboflow [12], contains 1,151 labeled images, while the created dataset expands this to 2,072 labeled images using augmentation techniques as shown in Figure 1. These techniques include: Saturation adjustments (±50%), Brightness adjustments (±25%), Exposure adjustments (±10%), Blur (up to 5.7px), Noise (up to 2% of pixels).

Figure 1. A sample image that represent the dataset [11]

Method

Deep learning-based object detection methods are mainly divided into:

- One-Stage Detectors: Predict object locations and classes in a single step, offering high speed for real-time use.
  - YOLO: Processes the entire image in one pass for fast detection, though it may struggle with small objects [2].
- Two-Stage Detectors: First generate region proposals, then classify them more accurate but slower.
  - Faster R-CNN: Uses a Region Proposal Network (RPN) for precise detection at the cost of speed [13].

Comparison of Methods

Table 1. Comparison of YOLO and Faster R-CNN [14].

Model	Type	Speed	Accuracy	Pros	Cons
YOLO	One-Stage	Fast	Moderate	Real-time performance, low latency	Struggles with small objects
Faster R-CNN	Two-Stage	Slow	Very High	High detection accuracy	Not suitable for real-time use

Table 1 shows a comparison between YOLO and Faster R-CNN models in terms of type, speed, accuracy, advantages, and limitations.

Workflow

Overall workflow of the proposed waste detection system using drone imagery, from data collection to model deployment and cleanup guidance as shown in Figure 2.

1. Image Preprocessing: Images are evaluated for quality parameters like resolution, brightness, and noise. Low-quality images undergo preprocessing, including denoising, brightness adjustment, and color enhancement.
2. Exploratory Data Analysis (EDA): Insights such as class distributions, object dimensions, and heatmaps are analyzed to optimize the dataset.
3. Model Training: The YOLOv8 pre-trained model is employed. Training occurs over 25 epochs using GPU computation, and the best-performing model is selected for predictions. Other methods also trained in same way.
4. Validation: Ground truth labels are compared against predictions to evaluate model accuracy and prioritize cleaning efforts.

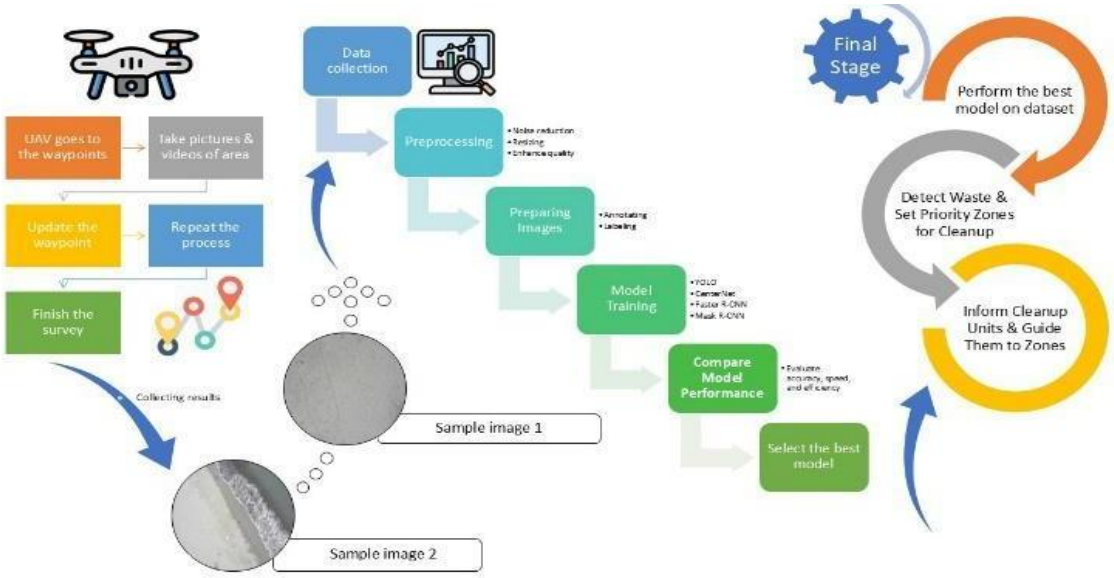

Figure 2. Workflow.

Findings

A. Dataset Metrics

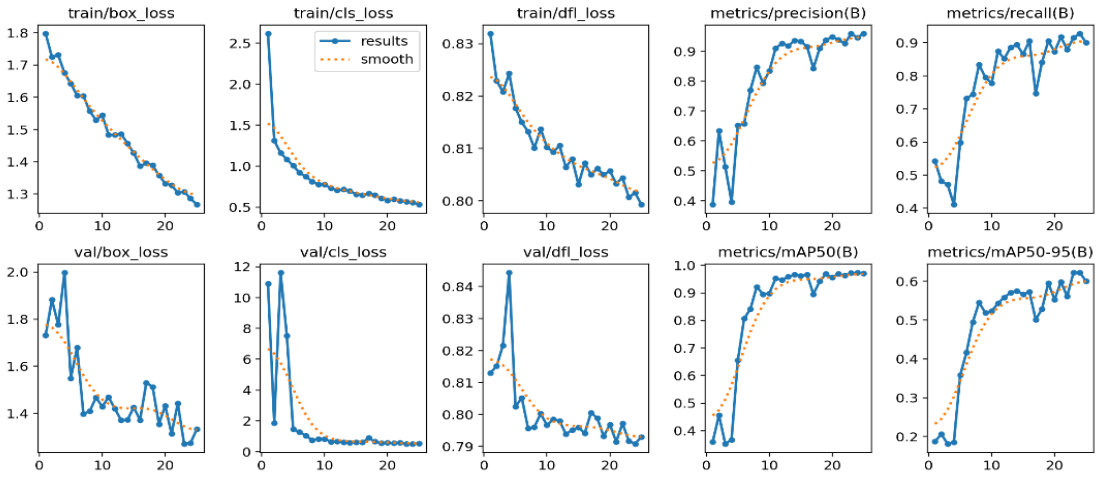

Figure 3. Dataset metrics for train and validation session.

Figure 3 presents the training and validation loss curves and performance metrics over the training epochs. Loss Metrics (a–f):

(a) train/box_loss: Measures training loss for object localization. A steady decline indicates improved bounding box accuracy.

(b) val/box_loss: Same as (a) for validation data; fluctuations suggest varying generalization.

(c) train/cls_loss: Tracks training classification loss; decreasing values show better class differentiation.

(d) val/cls_loss: Validation classification loss; divergence from training loss may signal overfitting.

(e) train/dfl_loss & (f) val/dfl_loss: Distribution focal loss for refining box predictions in training and validation, respectively.

Performance Metrics (g–j):

(g) Precision: Proportion of correct predictions; higher values mean fewer false positives.
(h) mAP@50: Mean Average Precision at 50% IoU; a key detection performance metric.
(i) Recall: Rate of correctly identified objects; higher recall means fewer misses.
(j) mAP@50–95: mAP across IoU thresholds (0.50–0.95); a broader performance indicator.

Interpretation: Training losses (a, c, e) decrease consistently, while validation losses (b, d, f) fluctuate but trend downward—suggesting good generalization. Metrics (g–j) improve, reflecting enhanced detection accuracy.

B. Model Performance:

Table 2. Comparison of YOLOv8 detection performance on different dataset configurations.

Dataset\Metrics	Precision	Recall	F1	mAP-50
Raw dataset Without pre-processing	0.9669	0.8916	0.9277	0.974
Enlarged dataset Without pre-processing	0.9629	0.9047	0.9329	0.985
Enlarged dataset with pre-processing	0.9682	0.9057	0.9359	0.988

Interpretation of Results (Table 2):

1. Raw Dataset Without Pre-processing:
   - High precision (0.9669) indicates the model is good at avoiding false positives.
   - Recall is slightly lower (0.8916), meaning some objects were missed.
   - mAP-50 is already strong at 0.974, showing good detection capability even without modifications.
2. Enlarged Dataset Without Pre-processing:
   - Slightly lower precision (0.9629) but improved recall (0.9047), meaning the model detects more objects but at the cost of slightly more false positives.
   - The F1-score improves slightly, showing a better balance between precision and recall.
   - mAP-50 jumps to 0.985, indicating the model benefits from having more training data.
3. Enlarged Dataset with Pre-processing:
   - The best overall performance.
   - Precision (0.9682) increases slightly, meaning fewer false positives compared to the enlarged dataset without pre-processing.
   - Recall (0.9057) remains strong, showing the model still detects a high percentage of objects.
   - The highest F1-score (0.9359), indicating the best balance between precision and recall.
   - mAP-50 reaches 0.988, the highest value, meaning pre-processing further improves detection accuracy.

Table 3. YOLOv8 model configuration and execution time breakdown.

Model specs	Ultralytics 8.3.58 Python-3.11.7 torch-2.5.1+cu118 CUDA:0 (NVIDIA GeForce RTX 3080 Laptop GPU, 16384MiB)
Model summary	365 layers, 43,634,466 parameters, 43,634,450 gradients, 165.4 GFLOPs
Pre-Processing execution time	176.85 seconds
Train execution time	1659.04 seconds
Val execution time	27.36 seconds
Test execution time	11.42 seconds

Table 3 provides detailed specifications of the YOLOv8 model, including the computing environment, model architecture, and the execution times for preprocessing, training, validation, and testing phases.

Figure 4. Detected objects in pictures with their corresponding confidence score.

Figure 4 shows the detection results of the trained model, where objects such as takeaway cups, containers, and glass are accurately identified across various beach images, each labeled with their confidence scores. The consistent detection with high confidence (mostly ≥0.7) indicates reliable model performance in real-world scenarios.

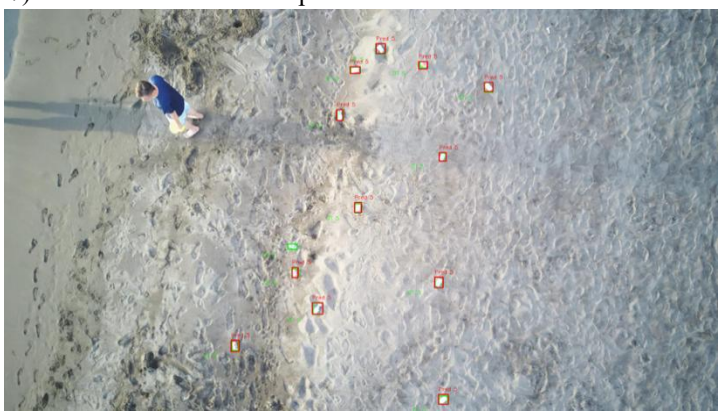

Figure 5. Predicted objects(Red labels) and ground truth(Green labels) comparison.

Many predictions match the ground truth, indicating good performance as shown in Figure 5. However, some false positives and missed detections are present, suggesting room for improvement.

Conclusion

Enlarging the dataset through augmentation resulted in a more robust and richer dataset, which also led to increased mean average precision, accuracy, and recall. On the other hand, while pre-processing slightly improved performance, it is more time-consuming compared to other methods. Therefore, for faster, real-time detection, we may need to sacrifice some accuracy for speed.

This study demonstrates the potential of integrating drone technology and deep learning for effective monitoring and detection of plastic waste on beaches. The system's high accuracy and efficiency in identifying and classifying waste types can significantly enhance cleanup prioritization and resource allocation. However, challenges such as improving algorithms for aerial imagery interpretation, expanding datasets, and incorporating additional data like thermal imaging remain areas for future research.

Future work will focus on:

- Enhancing real-time detection: Optimizing deep learning models to balance speed and accuracy for practical deployment.
- Improving dataset diversity: Incorporating additional environmental conditions and image types (e.g., thermal imaging) for robust model generalization.
- Developing an improved model: Exploring hybrid architectures that combine the strengths of one-stage and two-stage models.
- Implementing real-time applications: Deploying the system on edge devices for autonomous waste detection and classification.

By addressing these areas, we aim to develop a more efficient and scalable solution for environmental monitoring and beach cleanup prioritization.

References

Liao, Y.-H., & Juang, J.-G. (2022). Real-time UAV trash monitoring system. Applied Sciences, 12(4), 1838. Applied Information Technology, 102(11), 4735–4745. https://doi.org/10.3390/ app12041838

Ultralytics. Ultralytics documentation. Retrieved from https://docs.ultralytics.com/, date retrieved 2025, February 12

Manivannan, C., Virgin, J., Suseendran, S., & Vani, K. (2024). Garbage monitoring and management using deep learning. ISPRS Annals of the Photogrammetry, Remote Sensing and Spatial Information Sciences, X-1, 1–6. https://doi.org/10.5194/isprs-annals-X-1-2024-163-2024

Yandouzi, M., Grari, M., Berrahal, M., Elmiad, A. K., Badaoui, M., Barkaoui, A., & Zarhloule, Y. (2024). Elevating plastic litter surveillance: Drones and deep learning for efficient detection. Journal of Theoretical and Applied Information Technology, 102(11), 4735–4745.

Wang, J., Guo, W., Pan, T., Yu, H., Duan, L., & Yang, W. (2018). Bottle detection in the wild using low-altitude unmanned aerial vehicles. In 2018 21st International Conference on Information Fusion (FUSION).
https://doi.org/10.3390/ drones6120401

Taddia, Y., Corbau, C., Buoninsegni, J., Simeoni, U., & Pellegrinelli, A. (2021, November). UAV approach for detecting plastic marine debris on the beach: A case study in the Po River Delta (Italy). Drones, 5(4), 140.
https://doi.org/10.3390/drones 5040140

Kumar, M. G. V., Kumar, M., Rao, K. N., Rao, P. S., Tirumala, A., & Patnala, E. (2024). Advanced YOLO-based trash classification and recycling assistant for enhanced waste management and sustainability. In Proceedings of the 2nd International Conference on Intelligent Cyber Physical Systems and Internet of Things (ICoICI), 1–6.

Cheng, Y., Zhu, J., Jiang, M., Fu, J., Pang, C., Wang, P., Sankaran, K., Onabola, O., Liu, Y., Liu, D., & Bengio, Y. (2021). FloW: A dataset and benchmark for floating waste detection in inland waters. In 2021 IEEE/CVF International Conference on Computer Vision (ICCV).

Pfeiffer, R., Valentino, G., D'Amico, S., Piroddi, L., Galone, L., Calleja, S., Farrugia, R. A., & Colica, E. (2023). Use of UAVs and deep learning for beach litter monitoring. Electronics, 12(1), 198. https://doi.org/10.3390/electronics12010198

Taddia, Y., Corbau, C., Buoninsegni, J., Simeoni, U., & Pellegrinelli, A. (2021, December). UAV approach for detecting plastic marine debris on the beach: A case study in the Po River Delta (Italy). Drones, 5(4), 140. https://doi.org/10.3390/drones 5040140

Aerial Beach Waste Dataset. Roboflow Universe. Retrieved from https://universe.roboflow.com/national-cheng-kung-university-wjot1/aerial-beach-waste-dataset-xpzsi, date retrieved 2025, January 20

Roboflow. Retrieved from https://roboflow.com/, date retrieved 2025, January 20

PyTorch. Faster R-CNN. Retrieved from https://pytorch.org/vision/main/models/faster_rcnn.html, date retrieved 2025, January 20

Liu, L., Ouyang, W., Wang, X., Fieguth, P., Chen, J., Liu, X., & Pietikäinen, M. (2020). Deep learning for generic object detection: A survey. International Journal of Computer Vision, 128(2), 261–318. https://doi.org/10.1007/s11263-019-01247-4

Agentic Workflows for Self-Service Analytics Applications in E-Commerce

Taylan Yurtsever[a]

[a] Istanbul Technical University, Graduate School, Big Data and Business Analytics, Türkiye
yurtsever15@itu.edu.tr

Keywords: Large Language Models, LLM Agent, Model Context Protocol, Self-Service Business Intelligence and Analytics.

Aim

Recent years have seen widespread adoption of large language models for a variety of business tasks (Singla, 2025), including use cases in the analytics space (Zhang, 2024). Efforts on enhancing the capabilities of these models led to reasoning models (Huang, 2023) and more recently tool development frameworks for use by large language models. On the business side e-commerce has been one of the sectors that require fast decision making it an ideal candidate for self-service analytics due to its promise of faster turnaround times (Bani-Hani, 2017). The aim of this study is to provide a framework for agentic workflow use in e-commerce leveraging recent developments from in reasoning models and tool development frameworks to address shortcomings of prior research on LLM use for self service analytics. First one being the lack of context for ad-hoc tasks with basic chat applications such as ChatGPT, and second one being the lack of structured integration of execution solution for generated artifacts. Viability of this approach is tested through a set of analytics tasks.

Material and Method

Analysis of data gathered from different operational and analytical sources is a challenging problem for non-technical users with little to no experience beyond basic business intelligence tools such as spreadsheet software (Bani-Hani, 2019). As such any solution to self-service business analytics requires a careful balance between flexibility and complexity.

Recent advances in large language models allow for creation of code for use with analytical systems such as basic analysis code and SQL queries, achieving this through a chat-only interface brings two major limitations. First limitation in usage of chat-only LLM applications for analytics use cases arise from the lack of context. With no context available the model makes assumptions about the organization of data, including where it is stored, how it is stored and what information is kept within. Providing this manually while possible, is a tedious process and might result in non-repeatable analyses with erroneous results (Ouyang, 2025). Furthermore this approach requires business user to have a deep understanding of the data infrastructure. Second limitation comes from the open ended execution of any suggested steps. Besides risking correctness, any output of a chat-only large language model requires execution by the user leading to problems in security, system performance and usability.

The solution proposed for above given problems is to integrate tool use capabilities combined with self-prompting models to achieve low-level autonomy on the technical side, guided by high level user requests. This can be achieved through use of a recent tool development framework open-sourced by AI services company Anthropic called Model Context Protocol (MCP). Model Context Protocol allows developers to predefine prompts to guide, resources the model can access to and tools that can perform various operations, providing flexibility beyond static prompting while reducing the degree of freedom for structured execution and safe use. Model Context Protocol is based on a client-server architecture, where users interact with MCP compatible client that can make calls to MCP servers, that contain various tools, resources and prompts. Resources can be operational, analytical databases as well as log streams as presented in Figure 1. for an example case from an e-commerce platform.

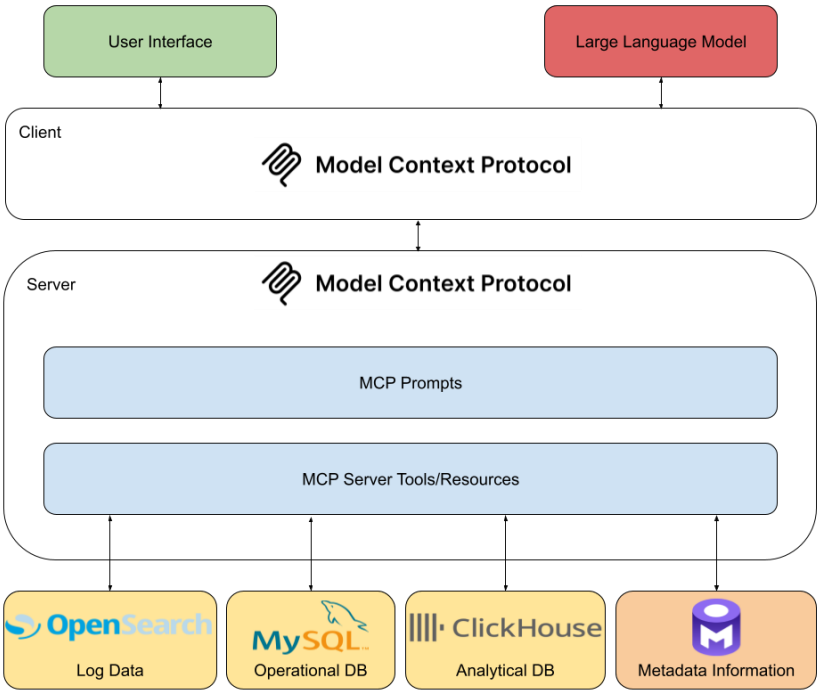

Figure 1. E-commerce data architecture incorporating MCP.

Starting from the bottom up, the first and one of the most important components of the proposed architecture is the metadata information source such as Openmetadata as shown in the diagram. Metadata and data quality management is one of the key areas of data management (Retwisch, 2017). Openmetadata with its functionality for managing metadata and ensuring data quality is one of the platforms of choice for data management (Boukraa, 2024). This component allows for detailed annotation of data sources and organization, providing needed context to LLM for further task planning and execution. With initial analysis request from user relayed via MCP client and server to the LLM, metadata server provides detailed information and notes about different data sources inside the data infrastructure. This step allows LLM model to decide which sources to use and how to use them effectively instead of manual descriptions provided by user.

The second group of components are the actual data sources which the LLM gets its data for analysis. For the case of an e-commerce platform these include operational OLTP (online transaction processing) databases, online analytical processing (OLAP) databases as well as log storage solutions such as OpenSearch for log and event processing on the platform. OLTP databases form the backbone of the data operations for non-analytical tasks for the majority of E-Commerce systems (Yang, 2024). These databases hold normalized data on inventory, pricing, transactions and other information related to daily operations of the business. OLAP databases provide specialized data structures for efficient execution of queries regularly encountered during data analysis tasks (Ansari, 2001). And finally, a search engine such as OpenSearch compliments other databases with its document storage and query capabilities allowing a detailed look into user behavior and experience across the platform via logs and events collected (Poggi, 2013). The combination of these data sources allows for tracking of customer experience from landing page to payment and also provides capabilities of historical analysis of their behavior.

The third component of focus is the MCP Server with its three primitives: prompts, resources, and tools. Prompts provide efficient interaction workflow to the resources and tools by use of predefined message templates. Resources provide the data from the systems in a predefined structured way such as execution of a SQL query with a filter accepting a parameter from the model. Tools can provide both a more flexible way to access the data and also perform operations beyond data fetching, such as creating a view or an index on a database.

The final component of the architecture is the MCP Client that orchestrates user input, MCP server connection and communication with the LLM. Client is the first point of entry for both the user and the model to the MCP context.

Findings

Across 15 tasks in a simulated e-commerce environment, agentic workflows provide correct analyses by utilizing metadata and tools integrated with MCP. Requiring only natural language queries with no information on data organization or steps to take, the system autonomously utilizes its tools to retrieve and process data from multiple data sources.

The integration of MCP with LLMs significantly enhances analytics capabilities for non-technical business users by providing a structured and accessible interface for interacting with complex data systems. Structured contextual information improves the accuracy and relevance of query results, while predefined tooling facilitates ease of access, reliability, and repeatability of analytics processes. The structured approach offered by MCPs also significantly reduces complexity and enhances user confidence in leveraging analytics tools, driving faster, more informed decisions.

In the context of e-commerce, rapid decision-making is essential to maintaining competitive advantage. Efficient self-service business intelligence, enhanced by MCP-driven structured data interactions, accelerates decision-making processes as shown in Figure 2., enabling organizations to swiftly respond to market changes, optimize marketing strategies, manage inventory efficiently, and enhance customer experiences.

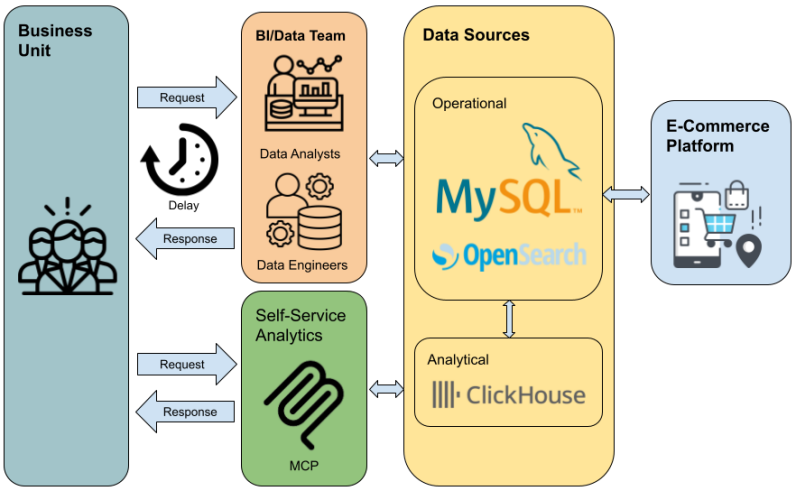

Figure 2. Agentic workflows remove organizational bottlenecks.

Conclusion

Combining advanced LLMs with Model Context Protocols significantly elevates the capability of self-serve analytics, particularly in dynamic and rapidly evolving e-commerce contexts. MCPs specifically address limitations inherent to plain LLMs by providing structured context and standardized data access mechanisms, thus empowering business users with improved accuracy, operational efficiency, and decision-making agility.

Further research should explore scalability, real-time analytical capabilities, and deeper integration with enterprise-wide governance and analytics infrastructures. Additionally, future studies should investigate critical areas such as data governance, privacy, and security implications of MCP-enhanced analytics workflows, ensuring responsible and compliant use of AI-driven analytics solutions.

References

Ansari, S., Kohavi, R., Mason, L., & Zheng, Z. (2001). Integrating e-commerce and data mining: Architecture and challenges. In Proceedings 2001 IEEE International Conference on Data Mining (pp. 27-34). IEEE.

Bani-Hani, I., Deniz, S., & Carlsson, S. (2017). Enabling organizational agility through self-service business intelligence: The case of a digital marketplace. In 21st Pacific Asia Conference on Information Systems: Societal Transformation Through IS/IT, PACIS 2017.

Bani-Hani, I., Tona, O., & Carlsson, S. (2019). Modes of engagement in SSBA: a service dominant logic perspective. In Proceedings of Americas Conference on Information Systems. Association for Information Systems.

Boukraa, D., Bala, M., & Rizzi, S. (2024). Metadata Management in Data Lake Environments: A Survey. Journal of Library Metadata, 24(4), 215-274.

Huang, J., & Chang, K. C. C. (2023). Towards Reasoning in Large Language Models: A Survey. In Findings of the Association for Computational Linguistics: ACL 2023 (pp. 1049-1065).

Ouyang, S., Zhang, J. M., Harman, M., & Wang, M. (2025). An empirical study of the non-determinism of chatgpt in code generation. ACM Transactions on Software Engineering and Methodology, 34(2), 1-28.

Poggi, N., Muthusamy, V., Carrera, D., & Khalaf, R. (2013). Business process mining from e-commerce web logs. In Business Process Management: 11th International Conference, BPM 2013, Beijing, China, August 26-30, 2013. Proceedings (pp. 65-80). Springer Berlin Heidelberg.

Rethwisch, David G. (2017). DAMA-DMBOK: Data Management Body of Knowledge (Second Edition).

Singla, A. (2025). The State of AI. https://www.mckinsey.com/capabilities/quantumblack/our-insights/the-state-of-ai, date retrieved 18.03.2025

Yang, A., & Wiratama, J. (2024). Empowering Data Transformation: Transforming Raw Data into A Strategic Planning for E-Commerce Success. Journal of Information Systems and Informatics, 6(1), 339-348.

Zhang, W., Shen, Y., Lu, W., & Zhuang, Y. (2024). Data-Copilot: Bridging Billions of Data and Humans with Autonomous Workflow. In ICLR 2024 Workshop on Large Language Model (LLM) Agents.

DATA ENGINEERING AND BUSINESS ANALYTICS

Big Data Analytics for Decision-Making

Predictive Analytics and Machine Learning in Business

Sentiment Analysis and Opinion Mining

Analyzing Brokerage Firm Trading Behavior via Supervised Learning: A Comparative Study on BIST 10

Kubilay Karaçam[a], Mehmet Yasin Ulukuş[b]

[a] Istanbul Technical University, Big Data and Business Analytics Program, Türkiye
[b] Istanbul Technical University, Industrial Engineering Program, Türkiye
karacamk@itu.edu.tr

Keywords: Brokerage Firms, Stock Market, Supervised Learning, Technical Indicators.

Stock transactions in financial markets and the dynamics behind these transactions have always been an interesting research topic for academics and investors. The complexity of financial markets arises from the interplay of multiple factors, including investor sentiment, macroeconomic conditions, and institutional trading strategies [1]. Among these factors, the behavior of brokerage firms plays a crucial role in shaping market trends and influencing price movements. Brokerage firm behavior is believed to have significant effects on price discovery, market liquidity, and overall market stability [2]. Understanding the mechanisms through which brokerage firms execute trades, manage risks, and respond to market signals is essential for both regulators and investors aiming to navigate financial markets effectively.

Therefore, it is believed that understanding the trading strategies and behavioral patterns of brokerage firms can provide valuable information and insights for both market participants and regulators. In particular, analyzing the relationship between brokerage firms' trading decisions and technical indicators may offer predictive power in forecasting future market movements [3]. In light of this information and insights, it is of great importance to understand the buying and selling behavior of brokerage firms in order to carry out an effective decision-making process in financial markets. By integrating machine learning methodologies with traditional financial analysis, it is possible to develop more sophisticated models that can capture hidden patterns in brokerage firm trading behavior [4]. This study represents a pioneering effort in the specific context of the Turkish stock market, being the first to systematically model the trading behavior of specific, major Turkish brokerage firms using a comprehensive set of technical indicators and advanced supervised learning techniques.

Aim

The main objective of this study is to model the trading behavior of two different brokerage firms, Merrill Lynch Yatırım Bank A.Ş. (MLB) and Yapı Kredi Yatırım Menkul Değerler A.Ş. (YKR), on 10 different stocks with the codes AKBNK, BIMAS, EREGL, ISCTR, KCHOL, SAHOL, SISE, TCELL, THYAO and TUPRS. By focusing on these specific brokerage firms and stocks, the study aims to capture firm-specific and stock-specific trading patterns that may not be evident in broader market analyses. This modeling is performed using buy and sell signals generated from 7 different technical indicators and 9 different supervised learning methods. The selection of technical indicators is based on their widespread use in financial analysis and their ability to capture momentum, trend, and volatility-based signals [5].

The study aims to reveal the relationship between the decision-making mechanisms of brokerage firms and technical indicators and to determine the most effective forecasting models. By identifying the most influential technical indicators for each brokerage firm, this research can contribute to the development of more precise trading strategies. As a result of the analysis, it is aimed to learn how the technical indicators used in the study affect the trading strategies of brokerage firms. This knowledge can help investors refine their strategies by aligning their decisions with those of institutional players.

Material and Method

The study was conducted using a historical data set of 587 trading days between January 2022 and June 2024. This period was chosen to ensure that the data set captures a variety of market conditions, including both bullish and bearish trends. By incorporating a sufficiently long-time span, the study aims to mitigate the effects of short-term anomalies and provide a more generalized model of brokerage firm behavior. The data set used in the study includes brokerage firms' trading volumes, net positions and buy and sell signals generated by 7 different technical indicators with RSI, MACD, BBANDS, SMA, STOCH, WILLR and ROC codes. Each of these indicators captures different aspects of market behavior, ranging from momentum oscillations to mean reversion tendencies [6]. For each technical indicator, buy and sell signals are generated using individually optimized thresholds.

In the data preprocessing stage, missing data were checked and completed and features were standardized to be suitable for classification. The target variable for classification is the daily net trading decision for each specific brokerage firm on each specific stock, derived from their daily net trading volume (positive net volume: buy, negative net volume: sell, near-zero net volume: hold). This provides a clear, three-class categorical variable representing the firm's directional bias on a given day for a specific asset. The process of cleaning and normalizing the data is critical to improve the accuracy of the modeling phase. A robust preprocessing pipeline was implemented to ensure data integrity and consistency across different stocks and time periods.

In the modeling phase, 9 different supervised learning algorithms such as Logistic Regression, Decision Tree, Random Forest, Support Vector Machines, XGBoost, K-Nearest Neighbor, Multilayer Perceptron, Gaussian Naive Bayes and Gradient Boosting were used [7]. These models were selected based on their ability to handle classification problems with structured financial data. The performance of the models was evaluated using the F_1-score metric, which balances precision and recall. By prioritizing F_1-score over accuracy, the study ensures that both false positives and false negatives are minimized, leading to more reliable predictions.

Findings

The experimental results show that different supervised learning models perform optimally for different stocks. This finding highlights the importance of model selection in financial prediction tasks, as no single model consistently outperforms others across all scenarios. It is observed that the most appropriate model for the brokerage firm with MLB code is Logistic Regression. This suggests that MLB's trading behavior aligns well with linear decision boundaries, making Logistic Regression a suitable choice. Similarly, the most appropriate model for predicting the trades of the brokerage firm with the code YKR is the Decision Tree. Decision Trees' ability to capture nonlinear relationships may explain their superior performance in modeling YKR's trading patterns.

The stocks and models with the highest F_1-score for the MLB coded brokerage firm are EREGL (Logistic Regression: 0.5424), AKBNK (Logistic Regression: 0.5169), TCELL (XGBoost: 0.5085). The stocks and models with the highest F_1-score for the brokerage firm with YKR code are AKBNK (Logistic Regression: 0.5254), KCHOL (Support Vector Machines: 0.5254), BIMAS (Decision Tree: 0.5085). These results suggest that while some stocks are better modeled using linear techniques, others require more complex decision boundaries to capture the underlying patterns effectively. When these findings are analyzed, it can be concluded that different modeling techniques are more appropriate for different stocks. Crucially, these performance levels significantly exceed the 0.33 baseline expected from random chance in a three-class problem. Given the inherent complexity, noise, and stochastic nature of financial markets, especially when modeling the behavior of individual institutional players, these F_1-scores indicate substantial predictive power and demonstrate the model's effectiveness in capturing meaningful patterns beyond random guessing.

The study concludes that supervised learning methods are an effective tool for modeling the behavior of brokerage firms. In addition, another result of the study is that the decision-making processes of brokerage firms can be explained by using technical indicators. In particular, the Logistic Regression method was found to be more successful in capturing market dynamics compared to other models. The findings may help investors to interpret market signals more effectively and may also contribute to the development of early warning systems by regulators to ensure market stability. The combination of technical indicators and supervised learning models provides deeper insights into the analysis of broker trades.

Practical Implications

The practical implications of this study are direct and actionable. Firstly, it provides investors with valuable insights into the potential drivers behind the trading decisions of two major market participants, MLB and YKR. By understanding which technical indicators are statistically linked to the buy/sell behavior of these firms on specific stocks, investors can potentially anticipate directional pressure or liquidity changes, thereby making more informed trading decisions. Secondly, for regulators, the developed models offer a concrete quantitative framework for monitoring the trading activities of significant brokerage firms. Deviations from the modeled 'expected' behavior, based on prevailing technical signals, could potentially serve as flags for further investigation, aiding in the detection of anomalous trading patterns or contributing to oversight mechanisms designed to prevent market manipulation and ensure market stability. Increased use of supervised learning algorithms in market analysis, as demonstrated here, is expected to increase transparency and predictability in financial markets.

Future Studies

Future studies that will aim to predict the behavior of brokerage firms with higher accuracy can achieve their goals by using time series analysis, deep learning and reinforcement learning models. Time series analysis allows for a better understanding of trends and cycles in market data [9]. Deep learning models can be used to identify more complex relationships, especially when analyzing dynamics in large data sets [10]. Reinforcement learning models, on the other hand, dynamically adapt to market conditions, enabling the development of more effective forecasting models [11]. In future studies, the accuracy of the models is expected to increase by including more stocks and brokerage firms in the analysis.

In addition, the inclusion of macroeconomic variables in the model in order to analyze the impact of economic and political factors on market movements in more detail is thought to increase the accuracy of the results to be obtained. The predictive power of the models can be increased by determining the impact of factors such as interest rates, inflation, exchange rate changes and global economic developments on the decision-making processes of brokerage firms. By integrating such variables into supervised learning and other learning models, a more comprehensive market analysis will be possible.

Conclusion

As a result, as the first study of its kind focusing on modeling the behavior of specific major Turkish brokerage firms (MLB and YKR) on key stocks using technical indicators and machine learning, this study takes an important step forward in understanding the impact of brokerage firms on the market. In particular, the combination of technical indicators and supervised learning algorithms provides a powerful framework for modeling the behavior of brokerage firms trading in financial markets. The achieved F_1-scores, while reflecting the challenging nature of the prediction task in noisy financial markets, demonstrate the feasibility and practical utility of this approach, significantly outperforming random chance. The findings are expected to help market participants make more informed decisions and help regulators supervise markets more effectively. Future research aims to further improve the models used and increase their effectiveness in financial markets. In addition, the scope of the models can be expanded by including macroeconomic factors affecting market dynamics in the analysis, which will enable a more comprehensive modeling strategy to be developed and a deeper understanding of the trading patterns in financial markets will be possible. Ultimately, this line of research holds significant potential to increase market transparency, reduce risks and create a more efficient trading environment.

References

Shiller, R. J. (1981). Do stock prices move too much to be justified by subsequent changes in dividends? *The American Economic Review, 71*(3), 421-436.

Kyle, A. S. (1985). Continuous auctions and insider trading. *Econometrica: Journal of the Econometric Society*, 1315-1335.

Lo, A. W., Mamaysky, H., & Wang, J. (2000). Foundations of technical analysis: Computational algorithms, statistical inference, and empirical implementation. *The Journal of Finance, 55*(4), 1705-1765.

Bishop, C. M. (2006) *Pattern recognition and machine learning*. Springer Verlag.

Murphy, J. J. (1999). *Technical analysis of the financial markets: A comprehensive guide to trading methods and applications*. Penguin.
Achelis, S. B. (2013). *Technical Analysis from A to Z, 2nd Edition*. McGraw-Hill Education.
Hastie, T., Tibshirani, R., & Friedman, J. (2009). *The elements of statistical learning: Data Mining, Inference, and Prediction, Second Edition.* Springer Science & Business Media.
Aggarwal, R. K., & Wu, G. (2006). Stock market manipulations. *The Journal of Business, 79*(4), 1915-1953.
Box, G. E., Jenkins, G. M., Reinsel, G. C., & Ljung, G. M. (2015). *Time Series analysis: Forecasting and Control*. John Wiley & Sons.
Goodfellow, I., Bengio, Y., & Courville, A. (2016). *Deep learning*. MIT Press.
Sutton, R. S., & Barto, A. G. (2018). *Reinforcement Learning, second edition: An Introduction*. MIT Press.

DATA ENGINEERING AND BUSINESS ANALYTICS

Big Data Analytics for Decision-Making

Predictive Analytics and Machine Learning in Business

Sentiment Analysis and Opinion Mining

Impact of Weekly vs Daily Sentiment Scores on Price Direction Forecast

Ahmet Berkay Gultekin[a], Alp Ustundag[b]

[a]Istanbul Technical University, Data Engineering and Business Analytics, Big Data and Business Analytics, Turkey
[b]Istanbul Technical University, Industrial Engineering, Industrial Engineering, Turkey
gultekinah@itu.edu.tr

Keywords: Sentiment Analysis, Financial News, Asset Price Prediction, ChatGPT, Trading Strategy.

The integration of sentiment analysis within financial forecasting has attracted considerable scholarly interest in contemporary research. For example, Halder (Halder, 2022) introduced the FinBERT-LSTM model, which synergizes the sentiment derived from financial news with stock price data to augment predictive accuracy. In a similar vein, Zhu and Yen (Zhu & Yen, 2024) employed BERTopic to conduct an in-depth examination of stock market discourse, consequently integrating sentiment analysis with advanced deep learning architectures to improve the efficacy of stock price forecasting results. Furthermore, a study conducted by Srinivas (Srinivas et al., 2023) developed a theoretical model that analyzes a comprehensive collection of news articles, demonstrating that the incorporation of sentiment analyses derived from financial journalism can significantly affect the predictions regarding stock price movements. Collectively, these studies highlight the potential of employing sophisticated natural language processing techniques and sentiment analysis to more effectively anticipate asset price fluctuations. Recent advancements in large language models (LLMs) have further augmented the capacity to interpret sentiment within financial news articles, yielding enhanced accuracy and contextual comprehension. While traditional sentiment analysis methodologies typically depend on pre-established lexicons or machine learning classifiers, LLMs present a more dynamic and adaptable approach to deriving sentiment scores from intricate financial texts. The application of sentiment analysis in the context of financial markets holds significant relevance for traders and investors who seek to enhance their trading methodologies by leveraging real-time market sentiment. This scholarly investigation aims to assess the effectiveness of sentiment analysis in predicting fluctuations in asset prices triggered by financial news. Specifically, it investigates how sentiment scores, extracted from financial articles and macroeconomic reports, may be utilized to predict both short-term and medium-term market fluctuations. By employing LLM models to generate sentiment assessments, this study explores the correlation between sentiment polarity and actual asset price movements. Additionally, it scrutinizes whether aggregated sentiment scores enhance predictive accuracy and investment performance across diverse time intervals. Through the examination of news data associated with high-volume trading assets in the S&P 100 index, along with macroeconomic reports relevant to the United States economy, this study provides valuable insights into the practical implementation of sentiment-driven trading strategies. The research seeks to address crucial questions about the forecasting effectiveness of sentiment-based models and the potential benefits of time-based aggregation of sentiment information.

Aim

The primary objective of this study is to assess the efficacy of sentiment analysis in predicting asset price variations that are influenced by financial news. By employing large language models to evaluate sentiment assessments derived from news articles, this research aims to enhance trading methodologies for short-term investment horizons, including daily and weekly price direction predictions. The methodology encompasses both asset-specific and macroeconomic news to formulate predictions predicated on sentiment analysis. Furthermore, this study investigates the impact of cumulative sentiment ratings on the precision of predictions and the performance of investments over extended periods.

Material and Method

The dataset encompasses essential financial news acquired from Eikon, which includes ten high-volume trading assets spanning diverse sectors within the S&P100 index over a temporal horizon of approximately 15 months. Additionally, macroeconomic news relevant to the United States is also incorporated. For the purpose of daily forecasts, news articles are aggregated up to 30 minutes prior to the market's opening time (09:30 AM). A Cosine Similarity filter (threshold: 0.98) is employed to exclude redundant news entries. The refined news articles, alongside macroeconomic and sector-specific data, are subsequently processed through ChatGPT to yield a sentiment score that ranges from -1 (indicative of negativity) to 1 (indicative of positivity). The accuracy of the forecasts is confirmed by comparing the sentiment score's direction with the real market path, determined by the difference between opening and closing prices. If the anticipated trajectory corresponds with the actual motion, the degree of accuracy is documented as 1; conversely, in the event that it does not correspond, it is recorded as 0. The calculation of return on investment is derived from the absolute differential in price, whereby inaccurate forecasts lead to adverse returns. The methodology for weekly forecasting utilizes a similar framework, synthesizing information from the initial business day of the prior week to the initial business day of the present week. The same cosine similarity threshold and sentiment scoring methodology are applied. Weekly accuracy and returns are determined in an identical manner to that of daily predictions. Furthermore, cumulative sentiment scores are calculated by summing over designated rolling periods for both daily and weekly frequencies to evaluate their impact on prediction accuracy and return performance.

Findings

The results indicate that forecasts driven by sentiment exhibit superior accuracy for weekly transactions in comparison to daily transactions. Specifically, differentiated sentiment assessments provided more reliable indicators for weekly price variations. The computation of cumulative sentiment scores appeared to have minimal influence on the precision of daily forecasts, yet demonstrated improvements under specific market circumstances. Nevertheless, in the context of weekly predictions, cumulative sentiment scores significantly enhanced the effectiveness of the model during particular temporal intervals. This suggests that the aggregation of sentiment data over time can augment the reliability of predictions, particularly for trades with an extended time frame (see Figure 1).

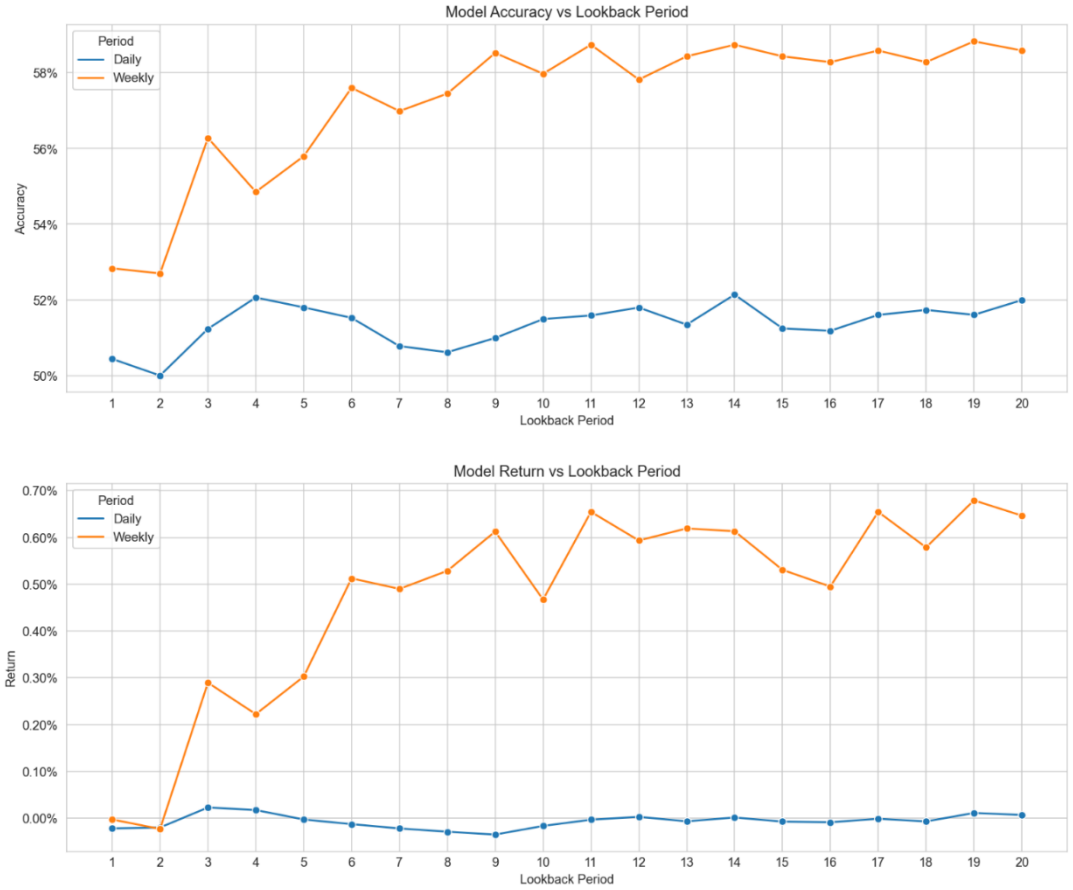

Figure 1. Model Performances.

Conclusion

This research investigates the capabilities of sentiment analysis through the application of large language models (LLMs) to anticipate variations in asset valuations as impacted by financial news. Although daily sentiment assessments exhibited a limited capacity for prediction, weekly sentiment forecasts were determined to be more effective, with aggregated sentiment evaluations considerably improving accuracy within designated temporal spans. These findings underscore the importance of incorporating historical sentiment trends to optimize trading strategies. Subsequent scholarly investigations may delve into sophisticated sentiment aggregation methodologies and alternative machine learning paradigms to further enhance predictive efficacy.

References

Halder, S. (2022). FinBERT-LSTM: Deep Learning based stock price prediction using News Sentiment Analysis. arXiv.Org, abs/2211.07392. https://doi.org/10.48550/arXiv.2211.07392

Srinivas, R., Gadela, R. B., Sabu, R., Das, A. R., Nath, G., & Datla, V. (2023). Effects of Daily News Sentiment on Stock Price Forecasting. arXiv.Org, abs/2308.08549. https://doi.org/10.48550/arxiv.2308.08549

Zhu, E., & Yen, J. (2024). BERTopic-Driven Stock Market Predictions: Unraveling Sentiment Insights. arXiv.Org, abs/2404.02053. https://doi.org/10.48550/arxiv.2404.02053

DEFENSE TECHNOLOGIES

Remote Sensing

Spacecraft Control, Design And Performance

Structural Design and Analysis

Unmanned Vehicles

A Hybrid Preprocessing Approach Based on Simulation Data for Embedded Object Detection Under an Inhomogeneous Surface

Ali Batuhan Bağcacier [a], Ali Yapar [b]

[a]Istanbul Technical University, Department of Defence Technologies, Türkiye
[b] Istanbul Technical University, Faculty of Electrical and Electronics Engineering, Department of Electronics and Communication Engineering, Türkiye
bagcacier19@itu.edu.tr

Keywords: GPRMax, Ground Penetrating Radar, CNN Pre-processing, Background Subtraction, Hyperbola Detection.

Introduction

Ground Penetrating Radar (GPR) is a powerful technology. It images the subsurface using electromagnetic waves, with applications in construction, geophysics, and other fields. It is vital in defense for detecting objects like buried landmines. However, GPR data interpretation is challenging. Complex data arise from ground conditions, noise, and varied subsurface structures. Usually, interpretation of this data is performed by people, but this can be slow and person-dependent. Machine Learning (ML) can address these issues.

This study aims to systematically compare and analyze the effect of different preprocessing techniques on GPR data, to gain an in-depth understanding of their impact, and to determine how the most suitable input data for Machine Learning models can be prepared.

Applied preprocessing steps are evaluated via comparative visualizations and histogram analyses of the processed data, and an optimized preprocessing process for GPRMax simulation data is presented. Results indicate the proposed methods significantly improve signal clarity, making data more suitable for CNN-based analysis.

Aim

Due to difficulties in collecting and labelling real GPR data, GPR simulations are crucial for the investigation of subsurface structures. For this reason, GPRMax simulation data was used in this study. GPRMax models electromagnetic wave propagation, enabling analysis of signal behavior under various ambient conditions. However, simulation outputs are often unsuitable for direct analysis due to:

- May contain high amplitude reflections arising from the air-soil interface,
- Hyperbolas can be blurred due to noise and low signal-to-noise ratio (SNR),
- Since the amplitude distribution is not standard, it needs to be normalized for machine learning algorithms.

The role of pre-processing is to refine this raw data, in particular to clarify reflections from embedded targets and to provide a "cleaned" input to the Machine Learning model. In this study, a comprehensive pre-processing process is developed for optimizing the GPRMax data prior to a CNN-based analysis. Specifically, background removal methods are compared for their effect on preserving hyperbola structures. It is also evaluated how different preprocessing combinations can affect the discriminative properties of radargram images in convolutional neural network (CNN) algorithms.

Material and Method

Raw GPRMax simulation data often contains high noise, artefacts due to air-soil transfer, and variable amplitude distributions. This hinders meaningful data inferences. For deep learning models to work correctly, high-quality input data is required.

This study is distinguished by its use of complex, diversified test scenarios. While single-layer homogeneous environments are commonly preferred in the literature, in this study, scenarios involving multi-layer (up to 4 layers) and heterogeneous

materials, such as PEC-plastic mixtures, were investigated. These more realistic, complex environments demonstrate that the proposed hybrid preprocessing method is effective even in challenging conditions. Beyond the results obtained in single-layer homogeneous media, satisfactory results are obtained even in multilayer media, proving the reliability of the method. The proposed preprocessing process aims to optimize the *.out files generated by GPRMax prior to analysis. Key pre-processing categories include Background Subtraction, Filtering, Time Gain application, Noise Reduction, and feature-emphasizing techniques. In this context, the following steps have been implemented:

1. Background Subtraction

Many background subtraction methods in the literature are based on ideal laboratory conditions. Unlike conventional methods, the hybrid preprocessing approach proposed in this study has the potential to be used in real-time applications. The air-ground transition can mask deep structures as it contains high-amplitude reflections. Different background removal methods are tested and compared to reduce this effect:

a. **Average-based background subtraction:** Pixel averages were calculated on the horizontal axis, and these average values were subtracted from each row. Used alone, this method may produce false artefacts by creating black shadows around the hyperbola.
b. **Gaussian Filter:** Reduces high-frequency random noise while preserving low-frequency components. Used alone, this approach may cause hyperbola details to be blurred because high-frequency components are not preserved.
c. **Grey Opening:** With the morphological opening process, large structures are preserved while small noise structures are removed. This method is effective in suppressing non-structural random noise.
d. **SVD Filter (Singular Value Decomposition):** By performing singular value decomposition of the radargram matrix, components with a low significance level are eliminated, and only the most dominant structural features are preserved.
e. **High-pass Filter:** High-pass filtering, especially in the horizontal axis, was used to suppress broad, low-frequency background fluctuations and emphasize fine, sharp structures.
f. **Curvature Enhanced Filter (CEF):** It uses the second derivative information of the signal to suggest low-amplitude structures in the data. By emphasizing the geometric features of weak signals, the target is made more prominent.

2. Whitening

Whitening normalizes amplitude and equalizes the frequency spectrum by reducing low-frequency signal components. This makes target structures more distinct.

3. Time Gain

Time Gain increases signal amplitude to compensate for its attenuation with depth.

- The underlying structures should become more prominent,
- Since exponential gain is applied, different contrast levels should be seen.

4. Normalization

For consistent CNN results, the entire data set should be processed with the same scaling. Two normalization methods are compared:

- **Min-Max Normalization:** Compresses the data in the range [0,1]. It provides better visualization by preserving hyperbola edges.
- **Z-Score Normalization:** Normalizes data by mean and standard deviation. It increases sensitivity in dense signal regions but may cause loss of detail in low-amplitude regions.

5. Noise Filtering

Only the Non-Local Means (NLM) filter is used in this study. This aims to prevent detail loss during noise reduction.

Findings

The proposed preprocessing method's effectiveness was analyzed via visual comparisons of raw and processed data.
Figure 1 illustrates how pre-processing yields varying results for targets at different depths. For deeper targets (top image, target depth 30mm, even below the second layer), noise is reduced, background subtraction is successful, and the signal is clean.
However, for shallower targets (lower image), it was noticed that unwanted residuals persisted after background subtraction. This indicates that preprocessing performance varies with technique, target depth, and position.

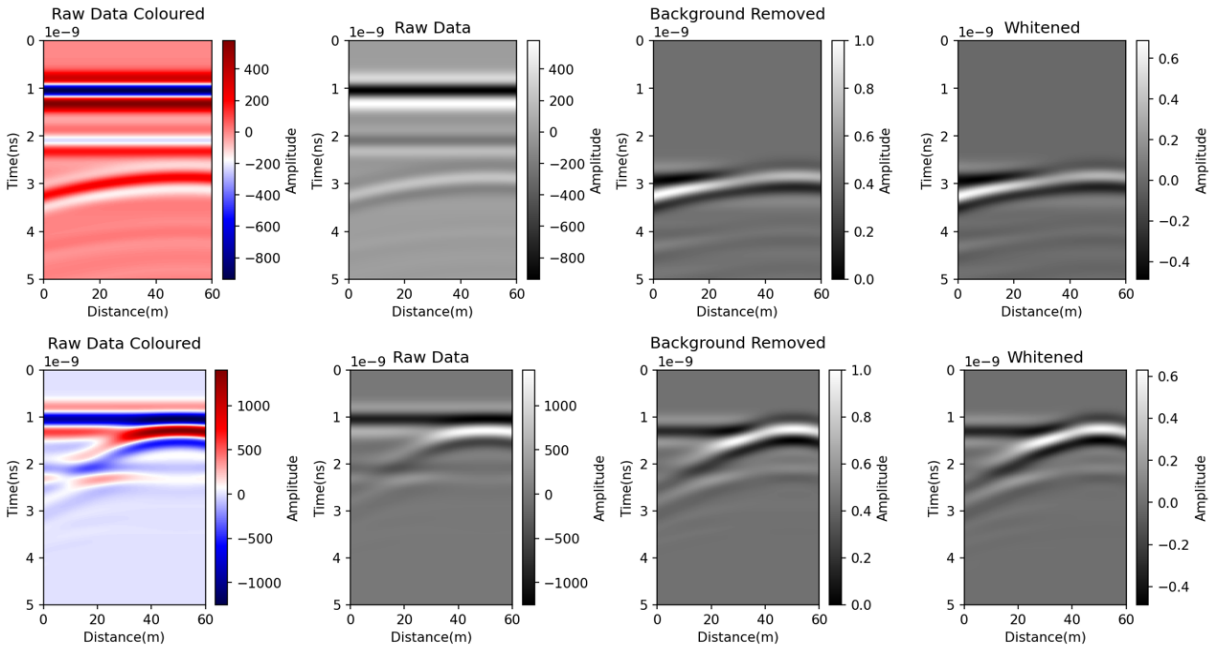

Figure 1. Target depth 30mm and 150mm /Depths of two layers:100mm and 170mm.

In the B-scan of both figures, the curved event that appears at a later time (lower on the vertical axis) below the main hyperbola is a repeated reflection from the target (multiple reflection). These common multiple reflections are considered data-cluttering 'noise'.
A second comparison involves results from different Background Removal techniques. Background removal is a fundamental step in GPR to remove strong, horizontal reflections, such as air-surface.
Figure 2 shows the final images obtained when four different background subtraction techniques (Mean, Grey Opening, SVD, and Gaussian Filter) are applied to the same raw data (keeping the other pre-processing steps the same). Image differences are striking. The techniques yielded significantly different results in background removal and target (hyperbola) highlighting.

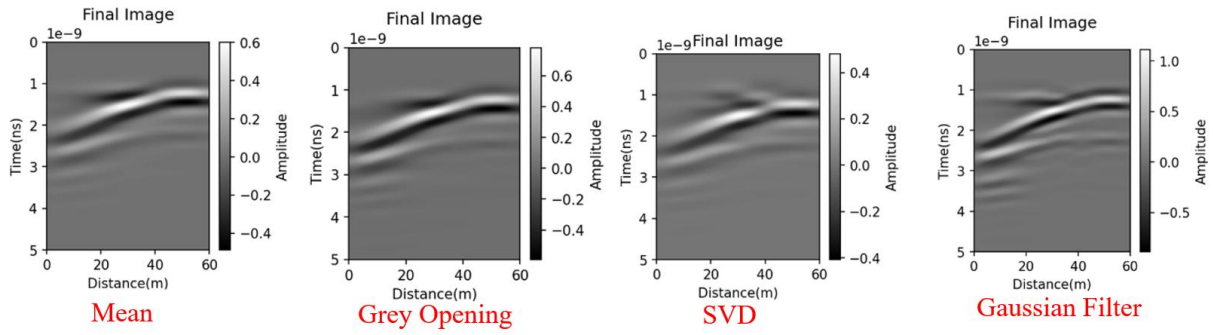

Figure 2. Asphalt and dry sand (two-layer) media, Plastic and PEC mix material.

The effect of the preprocessing step order is also compared. In Figure 3, the results obtained when the location of two specific processing steps, Whitening and Background Removal, is changed are seen.

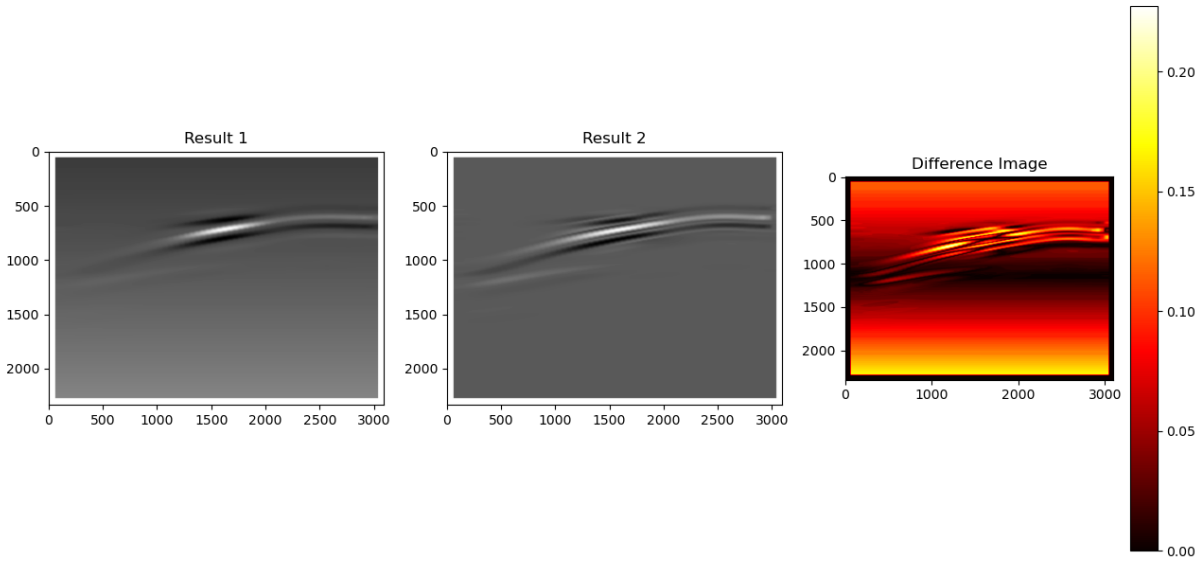

Figure 3. Difference Image.

a. **Whitening first (Result 1):** Whitening normalizes the data and reduces low-value noise. In this case, when the background is removed from the whitened data, the results may be clearer because the targets are already more distinct. However, since whitening changes the data dynamics, background modelling may be affected. Result 1 shows that the reflection around the hyperbola is much smaller. However, when compared to Result-2, it clearly shows that the hyperbola structure is distorted at the peak, where the reflection is the strongest.
b. **Performing background subtraction first (Result 2):** The effectiveness of the whitening process may be reduced because the effect of the background removed during the whitening process may reappear. However, in this approach, the background is first removed from the raw signal, thus improving the dynamic range and target clarity. This allows the hyperbola to be better optimized for CNN analysis.

A key finding was the significant visual differences in the final radargram images produced by the different preprocessing methods. Figure 3 shows the difference between the two approaches: the amount of variation in background components and hyperbola structure is represented by a color intensity diagram. In particular, the shape, amplitude, and contrast of the target reflections with the background vary significantly between the methods.

The difference image and color bar show pixel amplitude differences up to 0.20.
In the histogram analysis in Figure 4, the classical method is shown as Result-1, while the hybrid model is shown as Result-2. This compares pixel intensity distributions of the two methods. There are some differences between the two histograms:

- "Result 2" (orange) has a higher peak and a slightly narrower distribution.
- "Result 1" (blue) has a wider distribution.

This indicates the method makes off-target background regions numerically more homogeneous and stable.

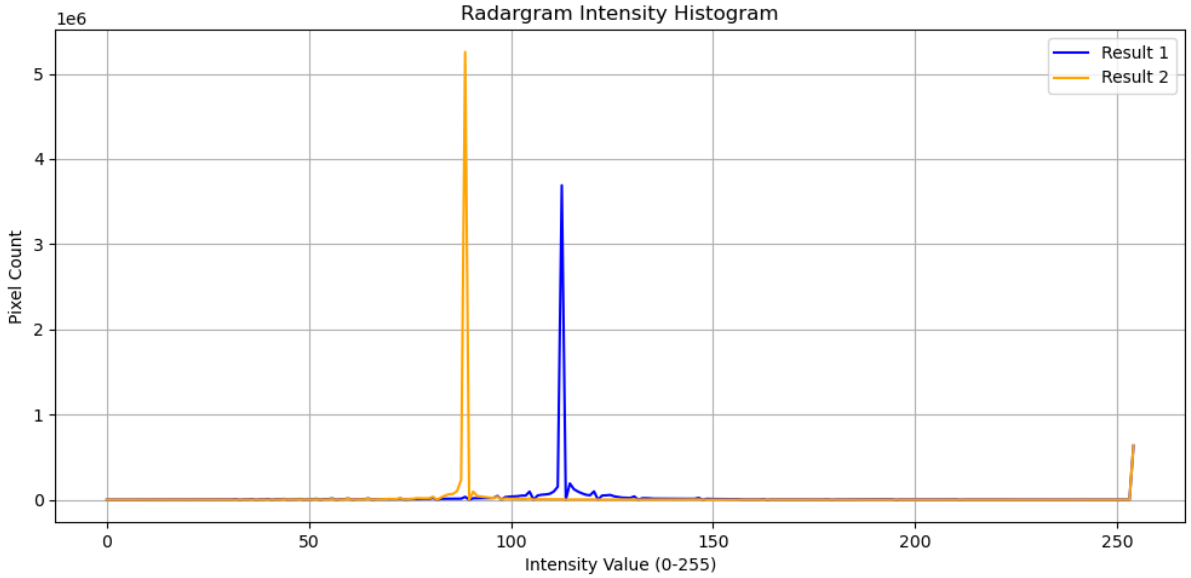

Figure 4. Histogram Analysis.

This is important for CNN models. For the CNN algorithm:

- 'Result 2' appears to have sharper contrasts and more pronounced features.
  If background pixels have very stable and predictable values, the CNN can more easily learn this standard background pattern and focus on target signals (deviations from background). Thus, background stabilization efficacy can be as crucial for Machine Learning performance as signal region brightness.
- 'Result 1' has a wider dynamic range and could potentially have more detail. This could enable finer features to be preserved.

These visual and statistical comparisons demonstrate that different preprocessing steps, sequences, and parameters significantly affect the result. Furthermore:

- The best preprocessing is not a single step or a fixed chain, but may vary depending on the target and the ground.
- High-pass methods for high-contrast applications, SVD-based methods for preserving structural information, and Gaussian filtering for noise robustness have been emphasized.
- As deep learning models readily learn sharp edges and intensity differences, a hybrid preprocessing approach was developed to enhance deep structure visibility.

Based on these observations, an optimized GPRMax preprocessing process combining the most promising steps is presented. This method includes Background subtraction, high-pass filter, Time Gain, Curvature Enhancement, Whitening, and Noise reduction steps.

Figure 5 shows that processing steps significantly improved signal clarity when this hybrid method is applied step by step to a single raw dataset. The raw GPRMax data shows high amplitude reflections and low contrast hyperbolas due to the air-soil transition. In the final image, horizontal components are reduced, and hyperbola structures are emphasized.

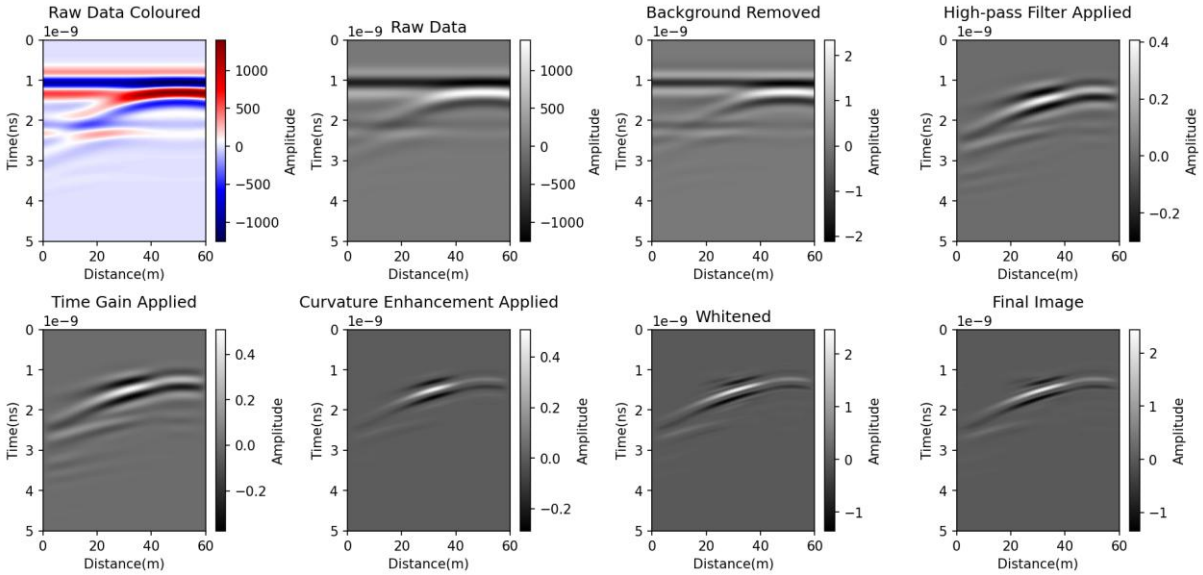

Figure 5. Hybrid Preprocessing Approach.

Conclusion

The key contribution is that Preprocessing methods applied to GPR data radically alter final data representation, and their choice directly impacts ML model success.

This shows that for CNN-based GPRMax data optimization, the correct preprocessing order is crucial for target detection, as incorrect ordering can cause significant information loss.

Different methods or implementations uniquely emphasize or suppress signal features, noise, and target reflections. The sequence of preprocessing steps, the parameters used, and even the target position/depth can significantly change the results. A major challenge is preprocessing sensitivity to different geometries.

The main consequence of this is the following: To achieve the best Machine Learning performance, carefully selecting and optimizing the preprocessing chain that best suits the nature of the data set is the key to success.

References

Abhinaya, A. (2021). Using machine learning to detect voids in an underground pipeline using in-pipe ground penetrating radar (Master's thesis, University of Twente).

Aydin, E., & **Erdem, S. E. Y.** (2019, May). Transfer and multitask learning using convolutional neural networks for buried wire detection from ground penetrating radar data. In Detection and Sensing of Mines, Explosive Objects, and Obscured Targets XXIV (Vol. 11012, pp. 259–270). SPIE.

Melor, C. K. N. A. H. C. K., **Joret, A.**, **Ponniran, A.**, **Sulong, M. S.**, **Omar, R.**, & **Razali, M.** (2021). Signal processing technique for pulse modulation (PM) ground penetrating radar (GPR) system based on phase and envelope detector technique. In Proceedings of the 11th National Technical Seminar on Unmanned System Technology 2019: NUSYS'19 (pp. 659–669). Springer Singapore.

Sharma, P., **Kumar, B.**, **Singh, D.**, & **Gaba, S. P.** (2017). Critical analysis of background subtraction techniques on real GPR data. Defence Science Journal, 67(5).

DEFENSE TECHNOLOGIES

Remote Sensing

Spacecraft Control, Design And Performance

Structural Design and Analysis

Unmanned Vehicles

Design of a Deployable S-Band Helical Antenna for CubeSats

Rümeysa Üstüncan[a], Alim Rüstem Aslan[b]

[a] Istanbul Technical University, Graduate Research Institute, Department of Defense Technologies, Turkiye
[b] Istanbul Technical University, Faculty of Aeronautics and Astronautics, Defense Technologies Program, Turkiye
ustuncan23@itu.edu.tr

Keywords: CubeSat, Helical Antenna, Deployment, Satellite Communication.

CubeSats are small satellite systems to access and benefit opportunities in space in a cost-effective and accessible way for universities, companies, and student groups, which are assigned various missions such as ground observation, telemetry, data transfer, and payload access. These capabilities are only possible when reliable communication between ground systems and the spacecraft is provided. The key elements to enable efficient communication are antennas, which convert electromagnetic waves into electrical signals, making data transmission possible.
The mission of a CubeSat determines the required characteristics of its antenna. For instance, omnidirectional antennas provide wide-area coverage, while directional antennas concentrate energy into a specific region for stronger signals. So, in the process of an antenna, the type of antenna is crucial since each type of antenna has its own specific characteristics. High-gain antennas improve communication quality and speed. Helical antennas promise high gain, wide bandwidth, which is needed for CubeSat communication, which has a structure that requires a deployment system. Deployable antennas are particularly challenging to design; however, successfully implemented versions significantly enhance communication capabilities and overall CubeSat performance, which are the key considerations. Since antennas are initially stowed inside the spacecraft and deploy once in space, ensuring a reliable deployment mechanism is crucial.

Aim

This project aims to design, prototype, fabricate, simulate and test a high-gain, circularly polarized, deployable helical antenna with a large front-to-back ratio, wide bandwidth, and optimized radiation pattern, to prepare the antenna space communication mission and to achieve a gain of 10 dB with an operational frequency range of 2 - 4 G Hz which contains S Band which is a very common band for CubeSat communication. Helical antennas have the advantage of inherently exhibiting circular polarization due to their curved form and helical structure. This project aims Designated frequency, defines most of the antenna's structural and electrical characteristics such as wavelength of antenna, diameter of antenna and ground plane of antenna which is a necessity for helical antennas to provide directivity and target the satellite to ground station and other characteristics are determined as requirements of communication like gain, directivity and spacing limitations such are antenna measures and placement in the CubeSat structure since CubeSats have limited space, which makes balancing antenna size, gain, and directivity particularly challenging and essential approach.
The antenna system consists of multiple materials, which are divided into the helix antenna and the deployment system. Candidate materials for the antenna wire include aluminum, gold-coated titanium, copper, spring steel, phosphor bronze, and beryllium copper, and structural Teflon, PTFE, and carbon fiber composites can be assigned for the mechanical system. The selected materials should not negatively interfere with signal transmission. Material selection is critical for space applications, as components must withstand harsh environmental conditions in space. Beryllium copper is widely used due to its favorable electrical properties, while Teflon is preferred as it does not affect electromagnetic waves. Accessibility and manufacturability are also key factors in material selection.

Material and Method

The primary method used for antenna selection is comparison between several types of antennas, such as patch, helical, conical, log-periodic, quadrifilar helix (QHA), and other deployable configurations. Patch antennas are simpler and more cost-effective, making them a practical choice for many applications. However, helical antennas offer inherent circular

polarization, higher gain, and wider bandwidth, making them more suitable for high-performance communication missions. Helical antennas can provide superior performance with a well-designed and optimized deployment mechanism. Theoretical calculations with fundamental antenna equations help determine the initial results and optimize dimensions and performance characteristics. To refine the geometry to enhance structural stability and to maximize deployment reliability and efficiency CATIA modelling program is used. Catia Kinematics digital mockups have been made to design the mechanism and define the relationship with the CubeSat components, structure, and constraints, also to simulate the deployment mechanism and movements. Deployment of the antenna is also physically evaluated by prototyping with 3D Printing to see the weak points of the design and improve. Besides, testing the antenna in an anechoic chamber to assess real-world performance and validate by comparing with analysis results will contribute helical antenna validation process. Also, the TVAC vacuum chamber is used to test to examine the antennas and deployment mechanisms' space performance with vacuum cycling, outgassing testing, and functional testing.

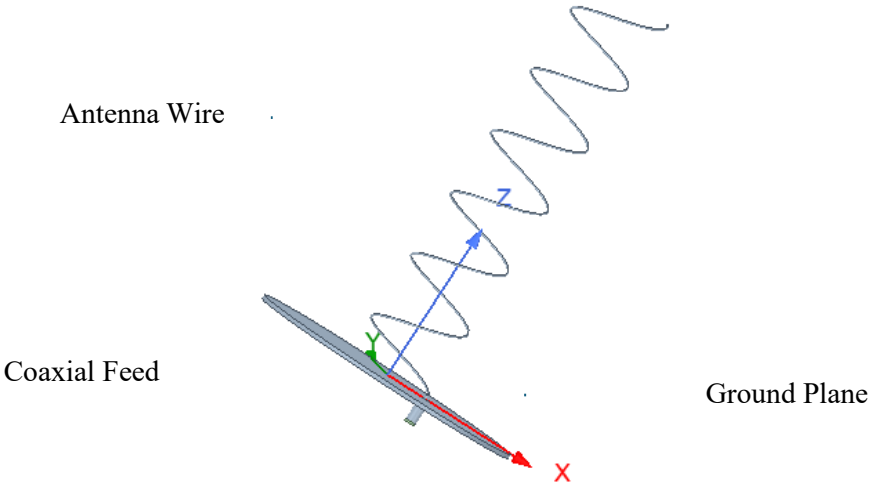

Figure 1. Initial Helical Antenna Model in HFSS.

Table 1. Physical Properties (mm).

Wavelength	132.3
Diameter of ground plane	132.3
Spacing between each turn	33.2
Total length of antenna	231.3
Number of turns	7
Helix Diameter	42.1
Circumference of helix	132.3
Length of coaxial feed	10

Thickness of ground plane	2
Total Length of Wire	954.1
Distance between feed and helix	2

Findings

For radiation performance stability directly impacts communication, analysis is conducted in ANSYS HFSS to analyze radiation characteristics, generate radiation patterns, and evaluate key parameters such as return loss (S11) to ensure that the antenna meets the mission requirements and attempts to achieve the smallest antenna while maintaining performance. Some initial S11 plots are obtained with the defined design parameters.

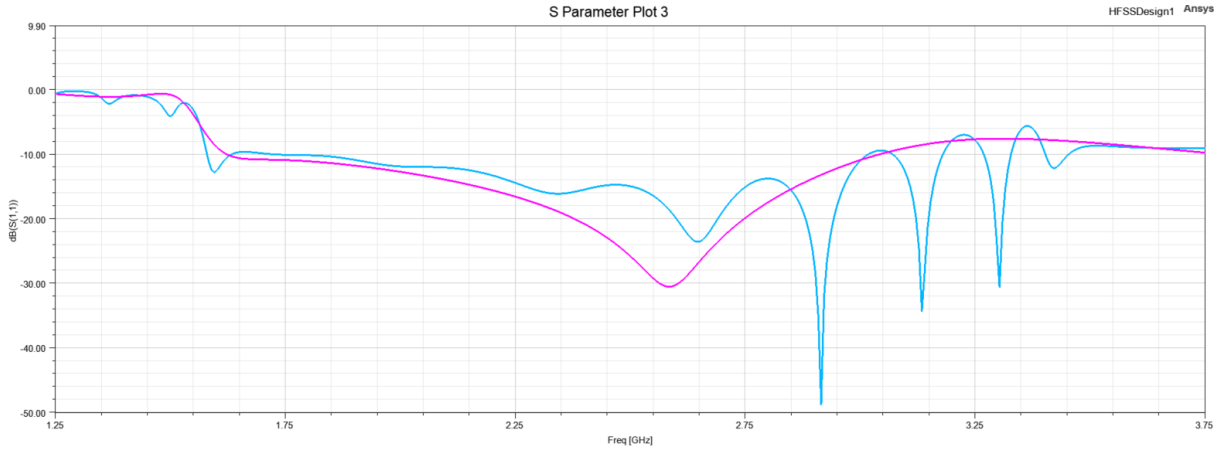

Figure 2. S Parameter of the antenna.

This configuration exhibits a clear resonance at a particular frequency, marked by a significant dip in S11, indicating efficient impedance matching and minimal power reflection. The impedance matching is optimized within a moderate bandwidth, allowing the antenna to operate effectively over a defined frequency range.

The antenna is initially stowed within the satellite and deployed once in orbit. The deployment mechanism is based on a coaxial system that utilizes the strain energy stored in the helical wire since the helix naturally is a spring. When the restraining wire is cut, this stored elastic potential energy is converted into kinetic energy, allowing the antenna to deploy. The initial design for the deployment mechanism is a telescopic structure, where nested parts extend using an internal spring for actuation. Additionally, the structure is enclosed with origami-inspired clothing, an ancient Japanese art of folding, that offers superior deployment capabilities. Origami-based deployment systems are already widely used in space applications, for example, the James Webb Space Telescope, as the clothing helps support telescopic structures and maintain spacing between sections, and antenna wire will be integrated with the origami structure, which is executed with space-qualified polyamide (Kapton) material.

Conclusion

To conclude, this study discusses the design considerations for a deployable helical S Band antenna for CubeSats. It has been found that helical antennas offer circular polarization, high gain, and impressive performance for space communication. However, QHA, log-periodic, and egg-beater antennas remain strong candidates in terms of directivity and gain. Simplicity, cost, and accessibility are major factors in antenna selection. Additionally, the choice of deployment mechanism plays a crucial role in ensuring a reliable and efficient operation in space. Finding the right balance between radiation characteristics and antenna size is key to designing an optimal CubeSat antenna.

References

Abulgasem, S., Tubbal, F., Raad, R., Theoharis, P. I., Lu, S., & Iranmanesh, S. (2021). Antenna designs for CubeSats: A review. *IEEE Access, 9*, 45289–45324.
Balanis, C. A. (2016). *Antenna theory: Analysis and design*. John Wiley & Sons.
Cisco Systems, Inc. (2007). *Antenna patterns and their meaning*. Cisco Systems, Inc.
Costantine, J., Tawk, Y., Maqueda, I., Sakovsky, M., Olson, G., Pellegrino, S., & Christodoulou, C. G. (2016). UHF deployable helical antennas for CubeSats. *IEEE Transactions on Antennas and Propagation, 64*(9), 3752–3759. https://doi.org/10.1109/TAP.2016.2588458
Dolapçı, T. (2020). *Design, simulation, and fabrication of CubeSat antenna systems* (Master's thesis, Middle East Technical University). Graduate School of Natural and Applied Sciences, Middle East Technical University.
Fang, H., Zhang, Y., & Wang, K. W. (2017). Origami-based earthworm-like locomotion robots. *Bioinspiration & Biomimetics, 12*(6), 065003. https://doi.org/10.1088/1748-3190/aa9112
Slade, B. (2015). *The basics of quadrifilar helix antennas*. Orban Microwave Inc.
Sureda, M., Sobrino, M., Millan, O., Aguilella, A., Solanellas, A., Badia, M., Munoz-Martin, J. F., Fernandez, L., Ruiz-De-Azua, J. A., & Camps, A. (2021). Design and testing of a helix antenna deployment system for a 1U CubeSat. *IEEE Access, 9*, 66103–66114. https://doi.org/10.1109/ACCESS.2021.3077373
Tariq, S., & Baktur, R. (2015, July). Circularly polarized UHF up- and downlink antennas integrated with CubeSat solar panels. In *2015 IEEE International Symposium on Antennas and Propagation & USNC/URSI National Radio Science Meeting* (pp. 1424–1425). IEEE. https://doi.org/10.1109/APS.2015.7305154
Yao, S., Georgakopoulos, S., Cook, B., & Tentzeris, M. (2014). A novel reconfigurable origami accordion antenna. In *Proceedings of the IEEE MTT-S International Microwave Symposium (IMS), Tampa Bay, FL, USA*. https://doi.org/10.1109/MWSYM.2014.6848571

DEFENSE TECHNOLOGIES

Remote Sensing

Spacecraft Control, Design And Performance

Structural Design and Analysis

Unmanned Vehicles

Optimization and Finite Element Analysis of Metastructures for Vibration Mitigation

Elif Nur Yaşar[a], Kaan Yıldız[b]

[a] Istanbul Technical University, Defense Technologies Master of Science, Turkey
[b] Istanbul Technical University, Aviation Institute & Aerospace Research Center, Turkey
yasare17@itu.edu.tr

Keywords: Metastructure, Vibration Mitigation, Optimization, Absorbers, Design.

Aim

Metastructures are designed to include distributed absorbers, a tunable approach to vibration damping in advanced engineering systems. Metastructures are exhibiting significant engineering advantages over traditional structures. Metastuctures are made possible by shifting the natural frequency to the desired range and directing vibrations without changing the total mass. A comparison between a baseline structure without vibration absorbers and a Metastructure with integrated absorbers is the typical method to measure the effectiveness of Metastructures. Optimization of structural parameters allows higher efficiency in vibration reduction to be achieved. The structural efficiency of Metastructures to enhance system performance while maintaining mass efficiency is considered a significant advantage in the aerospace, automotive, and defense industries. The development of new systems incorporating smart materials, adaptive Metastructures, and data-driven optimization approaches is anticipated to make significant contributions to engineering applications (Kovacic et al., 2024). The main aim of the study is to achieve maximum damping performance while preserving the total mass of the structure, through the optimization of Metastructure design parameters using the PSO algorithm.

Material and Method

Metastructures' dynamic characteristics are evaluated and validated via finite element analysis (FEA) (He et al., 2016). The validation process ensures the consistency of theoretical models with practical applications while demonstrating the effectiveness of Metastructure designs under real-world conditions. By integrating optimization techniques into vibration engineering, more innovative solutions are provided compared to traditional methods. Metastructures are designed for customization in specific applications and are applied across various fields. In this study, a discrete system model under uniaxial vibrations was developed in MATLAB to enable fast simulations due to its simplicity. In the modeling process, the parameters that were varied include the mass ratio (μ) in equation 1, defined as the ratio of the total absorber mass to the total system mass, the number of absorbers (n), and the natural frequencies assigned to the absorbers. These parameters were utilized as optimization variables in the study. Upon completion of the optimization, the obtained results have been utilized as design inputs for the MATLAB finite element model. In the baseline structure, the mass of each element is defined as m_0. These elements are referred to as the main structure within the Metastructure, and their mass is updated to m_i shown in Equation 1. The m_i value depends on the mass ratio. The total mass of both structures was kept constant. In the initial stage, the host structure without any absorbers was modeled as a system that is free to move only in the axial direction using discrete mass, spring, and damper elements, and this configuration was defined as the baseline structure. In the second stage, a finite element model of the Metastructure was developed as an absorber system with multiple degrees of freedom, consisting of multiple resonators modeled as spring-mass oscillators, as illustrated in Figure 1. The Metastructure was constructed for a model with two absorbers and another configuration with ten absorbers. In both configurations, the natural frequencies of all absorbers were tuned to the natural frequency of the baseline structure. The mass ratio was set to μ=0.3. To analyze the dynamic response of the structure, the mass (M), stiffness (K), and damping (D) matrices were constructed. Based on these matrices, the frequency response function (FRF), H(s), was calculated as shown in Equation 2. The matrix A represents the system, and the axial displacement is denoted by q.

$$\mu = \frac{n * m_{absorber}}{m_{total}}$$

$$H(j\omega) = [-\omega^2 M + j\omega D + K]^{-1} \rightarrow \omega = 2\pi f$$

Findings

To optimize structural parameters, PSO algorithms were applied. The structural design is improved through the use of the PSO algorithm. PSO has been extensively utilized in a wide range of engineering problems, including structural optimization, control systems, and signal processing (Alam, 2016), and has been effectively implemented in Metastructure designs to enhance vibration attenuation, stability, and overall performance (Reichl & Inman, 2017a). The H_2 norm, as defined in Equation 3, was selected as the performance criterion, representing the total area under the FRF curve (Reichl & Inman, 2017b). The objective was to determine the configuration that maximizes the reduction in the H_2 value compared to the baseline structure. In the first configuration, the natural frequency of the baseline structure was calculated to be 613.884 Hz. All absorbers were tuned to match this fundamental frequency, 613.884 Hz. The results showed that the resonance peak in the baseline structure was split into two, effectively reducing its magnitude, as illustrated in Figure 1. It is also observed that the change in the H_2 performance value is relatively small between the cases with 2 absorbers and 10 absorbers. The H_2 reduction values obtained from the two configurations are presented in Table 1. To achieve maximum reduction in the H_2 performance index (Zhu et al., 2014), the natural frequencies of the absorbers were defined as variable values. This was implemented by linearly distributing the natural frequencies of 10 absorbers within an optimized frequency range determined through the optimization process shown in Table 2. An optimization was conducted to determine the minimum and maximum tuning frequencies of the absorbers. The mass ratio was also included as a design variable in the optimization process. The FRF graph of the Metastructure with linearly varying absorber frequencies reveals improvement in the system's dynamic response, as illustrated in Figure 3.

$$H_2 = \| H(s) \|_2^2 = \left(\frac{1}{2\pi}\right) \int_{-\infty}^{+\infty} tr\left(H^*(j\omega) H(j\omega) \right) d\omega$$

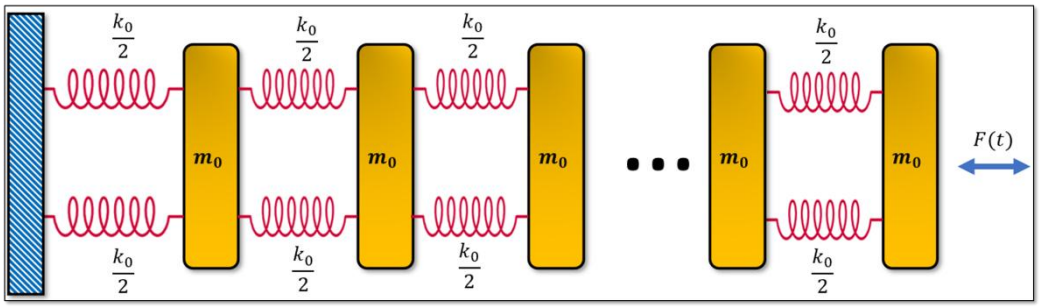

Figure 1.1: Baseline Structure.

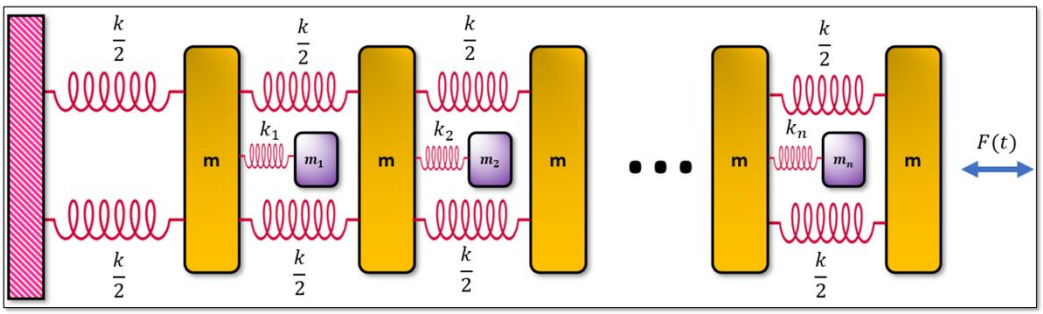

Figure 1.2: Metastructure.

Figure 1. Schematic representations of two structural configurations used in the study: the baseline structure (top), consisting of repeated mass-spring units with identical parameters, and the Metastructure (bottom), which incorporates internal resonators to enhance vibration attenuation performance.

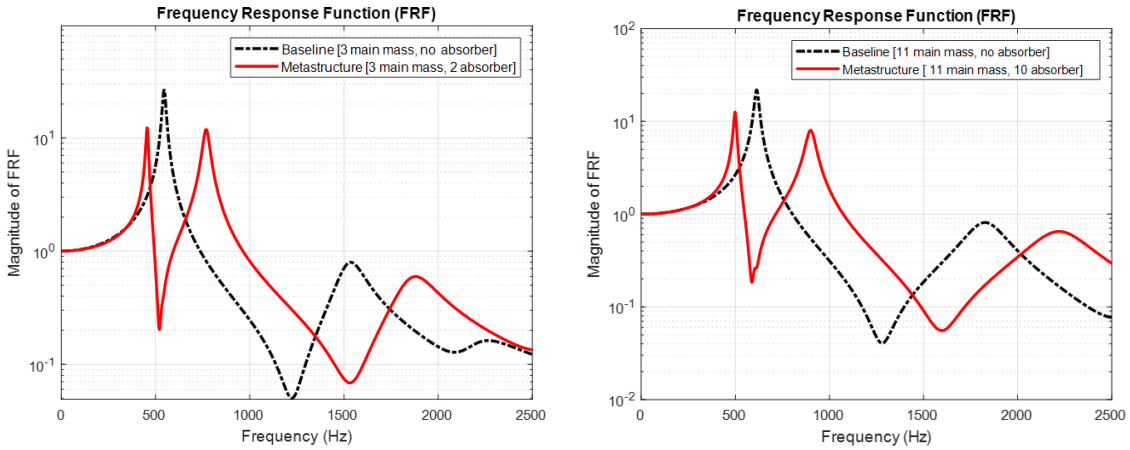

Figure 2. FRF graphs of two configurations are presented: the system with 2 absorbers is shown on the left, and the system with 10 absorbers, tuned to the same frequency, is shown on the right. All absorbers are tuned to the natural frequency of the baseline structure at 613.844 Hz, within the frequency range of 0-2500 Hz.

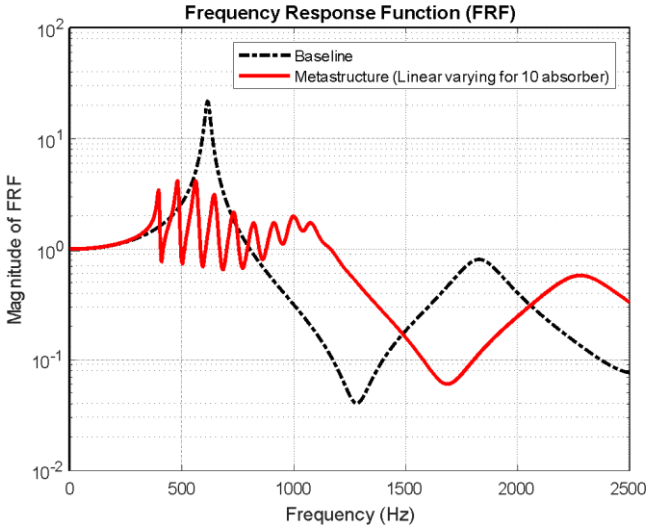

Figure 3. FRF graph of a structure with absorbers having linearly varying frequencies within 0-2500 Hz. The absorber frequencies range between 407-1254 Hz. The total mass of both structures is equal.

Table 1. Different absorber configurations are compared based on their frequency range and effectiveness in reducing the H_2 norm. three configurations are presented: absorbers tuned to the baseline fundamental frequency (with 2 and 10 absorbers) and absorbers optimized with respect to the H_2 norm, where stiffness varies linearly. The results show that the reduction in the H_2 norm increases as the number of absorbers increases and the frequency range is optimized, with the highest reduction (58.74%) achieved when stiffness varies linearly.

Configuration	Number of Absorbers, n			Absorber Frequency (Hz)	H_2 Reduction
Set to Baseline Fundamental Frequency	2			545.887	25.74 %
Set to Baseline Fundamental Frequency	10			613.844	27.50 %
Optimized with Respect to H_2 Norm (Stiffness Varies Linearly)	10			407-1254	58.74 %

Table 2. Optimization results obtained using the PSO algorithm for different iteration numbers and population sizes for 10 absorbers. The table presents the iteration number, population size, mass ratio, minimum and maximum frequency values, H_2 performance metric for each case. The results illustrate the impact of population size and iteration count on solution quality and computational efficiency.

	Iteration Number	Population Size	Mass Ratio	Min. Frequency [Hz]	Max. Frequency [Hz]	H_2 Reduction
Run 1	20	50	0.301	406	1254	59.291
Run 2	40	50	0.302	407	1254	59.293
Run 3	20	100	0.299	404	1256	59.292
Run 4	20	100	0.336	374	1316	59.170

Conclusion

At the final stage, an analysis of H_2 reduction amount showed that the optimized absorber system achieved a 50-60% improvement in vibration mitigation compared to the baseline structure. A certain level of improvement is achieved by tuning the absorbers to the fundamental frequency of the main structure; however, significantly greater enhancement is obtained when varying natural frequencies are assigned to the absorbers, as illustrated in Table 1. The final parameters have been incorporated into the design, enabling the modification of resonance regions without increasing the total mass. Evaluation of the dynamic performance of metastructures under varying conditions demonstrates superior vibration attenuation compared to the baseline structure. In the additional optimization studies, it has been identified that maintaining an adequate population size and a sufficient number of iterations is essential to ensure convergence. The Particle Swarm Optimization (PSO) algorithm has demonstrated the capability to simultaneously optimize more than one parameter.

References

Kovacic, I., **Kanovic, Z.**, **Rajs, V.**, **Teofanov, L.**, & **Zhu, R.** (2024). Reaching a desirable metastructure for passive vibration attenuation by using a machine learning approach. *Nonlinear Dynamics, 112*(23), 20661–20676.
He, Y., **Ma, W. J.**, & **Zhang, J. P.** (2016). The parameters selection of PSO algorithm influencing on performance of fault diagnosis. In *MATEC Web of Conferences* (Vol. 63, p. 02019). EDP Sciences.
Alam, M. N. (2016). Particle swarm optimization: Algorithm and its codes in MATLAB. *ResearchGate, 8*(1), 10.
Reichl, K. K., & **Inman, D. J.** (2017a). Lumped mass model of a 1D metastructure for vibration suppression with no additional mass. *Journal of Sound and Vibration, 403*, 75–89.
Reichl, K. K., & **Inman, D. J.** (2017b). Constant mass meta-structure with vibration absorbers of linearly varying natural frequencies. In *Topics in Modal Analysis & Testing, Volume 10: Proceedings of the 35th IMAC, A Conference and Exposition on Structural Dynamics 2017* (pp. 153–158). Springer International Publishing.
Zhu, R., **Liu, X. N.**, **Hu, G. K.**, **Sun, C. T.**, & **Huang, G. L.** (2014). A chiral elastic metamaterial beam for broadband vibration suppression. *Journal of Sound and Vibration, 333*(10), 2759–2773.

Parametric Optimization of Semi-Octagon Re-entrant Auxetic Structures for Energy Absorption

Şenay Yener[a], Kaan Yıldız[b]

[a]Istanbul Technical University, Faculty of Aeronautics and Astronautics, Türkiye
[b] Istanbul Technical University Aviation Institute & Aerospace Research Center, Türkiye
yeners21@itu.edu.tr

Keywords: Auxetic Structures, Re-Entrant Unit Cells, Sandwich Panels, Finite Element Analysis, Energy Absorption.

Aim

In recent years, with the advancements in the defense and aerospace industries, the development of new material designs has gained significant importance to meet the needs of these sectors. One of the most innovative designs in these fields is sandwich structures, which stand out due to their high impact resistance and lightweight properties (Reis & Rizkalla, 2008). Traditional sandwich structures, widely used in defense and aerospace applications, consist of a cellular core placed between two thin, rigid, and durable outer layers. These outer layers are generally made of high-strength materials such as aluminum alloys or fiber-reinforced composites, while the core is composed of cellular structures (Schaedler & Carter, 2016).
The deformation behaviors of unit cell structures under mechanical loading can be systematically classified based on their Poisson's ratio into three main categories: Positive Poisson's Ratio (PPR) structures, Zero Poisson's Ratio (ZPR) structures, and Negative Poisson's Ratio (NPR) structures. The majority of conventional engineering materials and structural configurations typically exhibit a positive Poisson's ratio, indicating a tendency to contract laterally when subjected to uniaxial tensile forces. However, in 1987, a novel class of materials characterized by a negative Poisson's ratio was discovered (Lakes, 1987). These materials, known as "auxetic," exhibit the counterintuitive behavior of lateral expansion under tensile loading. Auxetic materials possess several remarkable mechanical properties, including enhanced energy absorption capacity, superior impact resistance, and improved structural stability (Lakes & Elms, 1993; Imbalzano et al., 2018; Liu et al., 2016).

Material and Method

This study focuses on optimizing the mechanical performance of Semi-Octagon Re-entrant (SOR) auxetic core structures designed based on the geometric motifs of the Isfahan Jameh Mosque (Etemadi, Bashtani, & Hu, 2024). The SOR structures consist of modified re-entrant unit cells with a semi-octagonal geometry, providing advantages such as more homogeneous load distribution and enhanced impact resistance. The findings are expected to contribute to the development of next-generation lightweight and high-performance materials for applications in ballistic protection, blast-resistant panels, aerospace armor, and other advanced engineering fields.
Figure 1(a) presents a detailed design of the unit cell structure used in this study. This design encompasses the geometric features and fundamental structural elements of the unit cells. Additionally, Figure 1(b) illustrates the configuration of the lattice structure in which the unit cells are laterally connected through node points (Etemadi et al., 2024). The lattice structure comprises a total of 35 unit cells.

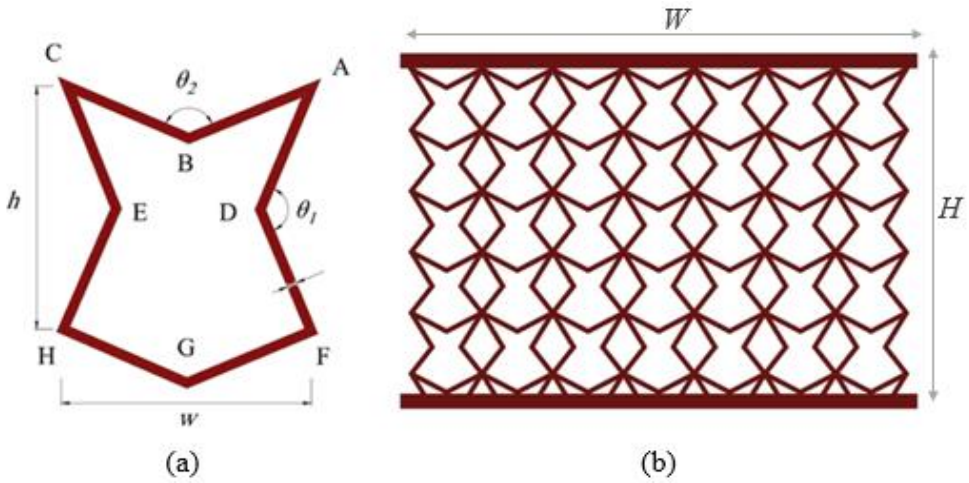

Figure 1. The design parameters (a) unit cell and design parameters of the SOR unit cell (b) auxetic structure with SOR unit cell arrangement (Etemadi et al., 2024).

The dimensions of all design parameters, along with the θ_1 and θ_2 angles presented in Figure 1, are provided in Table 1. In Figure 1(b), the width (W), height (H), and depth (b) of the arranged SOR lattice structure are illustrated. All dimensions are given in millimeters.

Table 1. Design parameters of the SOR structure.

Parameters	t	w	θ_1	θ_2	t	H	W	b
SOR	12	12	110°	125°	1	70.07	102.38	7

In this study, Finite Element Analysis (FEA) was performed using the Abaqus software, with PLA+ selected as the core material. The stress–strain curve of the PLA+ material used in the simulations is presented in Figure 2, while its mechanical properties are listed in Table 2. To analyze the mechanical behavior under compressive loading, a dynamic-explicit solver was employed. The general contact algorithm was applied to model the interactions between structural components, and the coefficient of friction between contact surfaces was set to 0.1. The bottom surface was fixed, while axial displacement loading was applied to the top surface.

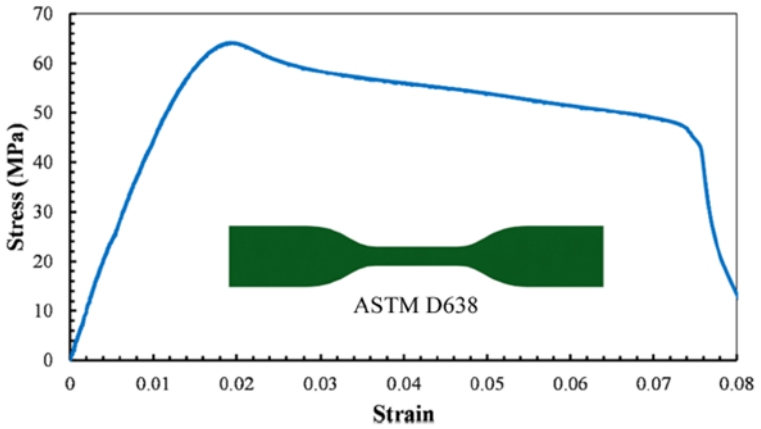

Figure 2. The stress–strain diagram of PLA+ material (Etemadi et al., 2024).

Table 2. Mechanical properties of PLA+ material (Etemadi et al., 2024).

Density (ρ)	1.21 g/cm³
Young's Modulus (E)	3.65 GPa
Poisson's Ratio (ν)	0.35
Yield Strength (σ_y)	64 MPa

To ensure numerical accuracy and computational stability, a mesh size of 0.5 mm was adopted, as shown in Figure 3. For meshing the structures, the C3D8R (solid, reduced integration) element type was used to achieve a balance between computational efficiency and result accuracy.

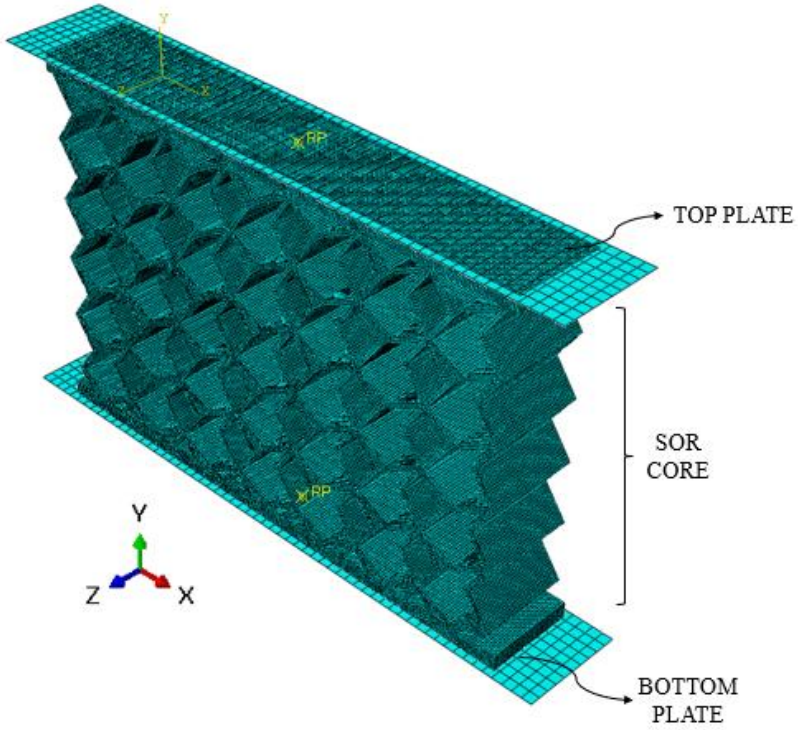

Figure 3. Finite element mesh of the SOR auxetic structure.

Energy Absorption Calculations: The total energy absorption (U) of the auxetic sandwich structures under compressive loading was calculated by integrating the area under the stress-strain curve up to the end of the second region, known as the plateau stage. Energy absorption is considered a critical parameter for evaluating the durability and performance of the structure against mechanical loads such as impact and compression. In this study, the total energy absorption was determined using the method specified in Equation 1 (Li, Liao, Dai, & Xie,2019). $U = \int_0^{\varepsilon} \sigma d\varepsilon \quad \#(SEQ\ Denklem \setminus * ARABIC\ 1)$

Additionally, the Specific Energy Absorption (SEA) was calculated using Equation 2. This parameter represents the amount of energy absorbed per unit mass of the structure and serves as an important measure for evaluating the lightweight and energy absorption performance of materials. In the equation, Δρ denotes the relative density of the structure, which is defined as the ratio of the material density to the total volume of the structure. SEA is widely used to compare the energy absorption capacity of lightweight materials and structural designs (Li et al., 2019). $SEA = \frac{U}{\rho \Delta \rho} \quad \#(2)$

Findings

The stress-strain curve obtained in this study has been compared with reference studies available in the literature (Etemadi et al., 2024). The graph presented in Figure 4 illustrates the mechanical behavior of the SOR auxetic structure under compressive loading examined in this study. Within the scope of the study, numerical analyses will be conducted to thoroughly investigate the mechanical performance of auxetic core sandwich structures. Through simulations, the effects of variations in unit cell angle and cell width on the stiffness and energy absorption capacity of the structure will be comprehensively examined. Additionally, the impact of cell size on structural densification and overall integrity will be evaluated in detail.

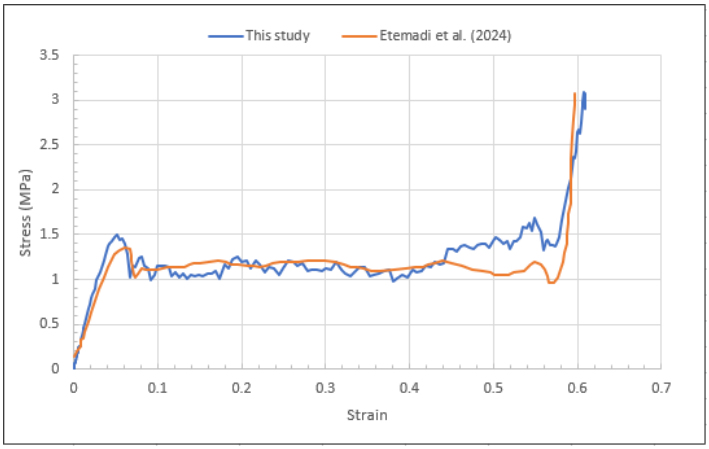

Figure 4. Comparison of the stress-strain curves of the Etemadi et al. (2024) and this study.

Conclusion

At this stage, experimental validation has not been conducted; however, the numerical analyses are expected to provide a solid basis for future physical testing. Based on literature data, Semi-Octagon Re-entrant (SOR) auxetic structures demonstrate significant potential for engineering applications, with geometric parameters playing a decisive role in mechanical performance.

The mechanical behavior of sandwich structures incorporating SOR cores has been shown to offer advantages over conventional re-entrant auxetic designs due to the unique semi-octagonal geometry. Increased energy absorption capacity provides notable benefits for high-performance fields such as defense and aerospace. The prominence of SOR structures stems from their distinctive geometric configuration, which enables a more balanced and efficient mechanical response compared to traditional auxetic structures. These characteristics contribute to enhanced structural stability under high-energy loads and optimized material utilization. Unlike conventional auxetic structures, the SOR configuration absorbs energy more effectively while maintaining structural integrity.

References

Etemadi, E., **Bashtani, M.**, & **Hu, H.** (2024). Novel auxetic metamaterials inspired from geometry patterns of an Iranian mosque with improved energy absorption capability. *Materials Today Communications, 41*, 110470.

Imbalzano, G., **Linforth, S.**, **Ngo, T. D.**, **Lee, P. V. S.**, & **Tran, P.** (2018). Blast resistance of auxetic and honeycomb sandwich panels: Comparisons and parametric designs. *Composite Structures, 183*, 242–261.

Lakes, R. (1987). Foam structures with a negative Poisson's ratio. *Science, 235*(4792), 1038–1040.

Lakes, R. S., & **Elms, K.** (1993). Indentability of conventional and negative Poisson's ratio foams. *Journal of Composite Materials, 27*(12), 1193–1202.

Li, D., **Liao, W.**, **Dai, N.**, & **Xie, Y. M.** (2019). Comparison of mechanical properties and energy absorption of sheet-based and strut-based gyroid cellular structures with graded densities. *Materials, 12*(13), 2183.

Liu, W., **Wang, N.**, **Luo, T.**, & **Lin, Z.** (2016). In-plane dynamic crushing of re-entrant auxetic cellular structure. *Materials & Design, 100*, 84–91.

Reis, E. M., & **Rizkalla, S. H.** (2008). Material characteristics of 3-D FRP sandwich panels. *Construction and Building Materials, 22*(6), 1009–1018.

Schaedler, T. A., & **Carter, W. B.** (2016). Architected cellular materials. *Annual Review of Materials Research, 46*(1), 187–210.

Finite Element Analysis Of Crack Growth Behavior In The Presence Of Crack-Arresting Holes

Buse Yasin Aydin[a], Ibrahim Ozkol[b], Mustafa Tolga Yavuz[b]

[a] Istanbul Technical University, Defense Technologies, Turkiye
[b] Istanbul Technical University, Faculty of Aeronautics and Astronautics, Turkiye
yasin21@itu.edu.tr

Keywords: Crack Arrest, Crack Propagation, Fracture Mechanics, Wing Structures, XFEM.

Aim

In materials science, crack propagation refers to the process in which a void forms within a material and gradually expands over time (Anderson, 2017). This phenomenon is particularly significant in industries such as aerospace, defense, the automotive sector, and machinery production. The reason is that cracks can critically impact the structural integrity and safety of vehicles and machines.

In the aviation industry, crack propagation significantly compromises the structural integrity of aircraft, particularly in the wings, wing components, and where the wings meet the fuselage. This reduces the load-carrying capacity and increases safety risks (Reymer et al., 2023). During flight, wings are subjected to vibrations, aerodynamic forces, and repeated mechanical and thermal loading, which generate high-stress concentrations. These stresses cause material fatigue, facilitating the initiation and progression of micro-cracks that ultimately compromise material performance and strength (Reymer et al., 2023; Shah et al., 2014; Zeng et al., 2018). This issue is critical in aircraft structures, especially fighter aircraft, in which high maneuverability and sudden load changes require early crack detection to prevent structural failure. Improper management and monitoring of crack propagation can lead to catastrophic failures. Both civil and military aviation have experienced severe consequences from unchecked crack propagation. For example, in 1988, an Aloha Airlines Boeing 737-200 had cracks on the upper side of the fuselage near the cockpit on riveted joints, which had gone unnoticed during maintenance. The high-stress environment of the aircraft led to these cracks expanding and caused a structural failure. An 18-foot-long section of the upper fuselage was torn away from the airplane, critically compromising its integrity and endangering lives. This incident highlights the need for proper crack detection procedures (National Transportation Safety Board, 1988). Similarly, a U.S. Air Force F-111A fighter jet experienced fatigue cracks caused by micro defects in the wing pivot joint during production, which eventually led to a sudden fracture of its wing in-flight. Similar cases throughout history have resulted in damage to both civilian and military aircraft due to crack formation and propagation (Molent, 2010). For these reasons, various academic and industrial research efforts are conducted to better understand the mechanisms of crack propagation, perform risk analyses, develop new monitoring technologies, and investigate methods to arrest cracks.

This study aims to investigate how incorporating holes and other geometric shapes into structures might affect crack propagation and also, possibly, how these new designs can delay crack growth. The research explores how such design modifications can enhance structural durability and reduce the risks associated with crack propagation. Specifically, the study focuses more on controlling and analyzing crack propagation in the wings of all types of aircraft, particularly in fighter jets, and investigates the key parameters that govern the crack behavior.

Within this research, the effects of various parameters in aircraft wing components are examined for crack propagation. The study evaluates the crack-arresting potential of incorporating holes and other geometric modifications while also analyzing the influence of material properties and structural thickness. It further investigates how variations in hole diameter, the use of multiple holes, different hole configurations, and the incorporation of various geometric shapes affect crack propagation. Additionally, the research considers diverse boundary conditions to provide a comprehensive understanding of how these factors interact with crack growth.

After conducting a literature review of similar studies, the initial phase of this research involved developing a basic model characterized by standard circular holes and an initial crack (Fageehi & Alshoaibi, 2024). This model served as a foundation for investigating how holes influence stress intensity distribution and also how they affect the crack propagation path. In later cases, various scenarios were created; an increased number of holes, optimizing the placements of these holes. This allows for a better understanding of how these factors affect crack behavior. Additionally, the study examines different types of high-performance alloys such as Ti-6Al-4V, Al 7050, and Al 2050 to determine their effects on crack progression. These materials are commonly used in aircraft wing components and fuselage (Yavuz & Ozkol, 2024; Dursun & Soutis, 2014). Samples with different plate thicknesses were also tested to assess the influence of thickness on crack development.

Material and Method

To accurately capture crack initiation and propagation, analyses were conducted using the Extended Finite Element Method (XFEM). Analyses for the study were done using a software program, ABAQUS. With the help of XFEM, detailed analyses were performed to monitor crack initiation, track crack growth, and evaluate changes in crack orientation under varying conditions.

Findings

Preliminary study results showed that, in samples with holes, cracks were attracted toward the holes, whereas in samples without holes, cracks propagated without deflection, ultimately leading to fracture. Furthermore, higher Von Mises stresses were observed in samples without holes compared to those with holes, indicating that the holes help redistribute stress and lower stress concentrations. These findings lay the groundwork for investigating the effect of circular holes on crack propagation behavior and their potential as crack stoppers.

Conclusion

The expected contributions of this study are comprehensive, offering insights from various perspectives. First, the research provides a detailed investigation for future literature on how different material types, structural thickness, geometric shapes and their dimensions, different boundary conditions, and various configurations of integrated shapes affect crack propagation. Additionally, in the aviation industry, cut-outs are incorporated in aircraft wings for weight reduction, to facilitate maintenance and inspection access, and for fuel cable and pipe passages (De, 2017). This shows that our study can be further included in both the aviation and defense industries. The findings contribute to improved monitoring and management of crack propagation, offering guidelines that could help maintain the structural integrity of wing components and extend their fatigue life. This, in turn, aids in preventing large, unexpected structural failures and minimizes mission risks. Finally, the development of a robust analytical framework to explain the effects of various design modifications on crack propagation not only provides a perspective for future studies but also serves as a roadmap for subsequent research.

References

Anderson, T. L. (2017). *Fracture mechanics: Fundamentals and applications* (4th ed.). CRC Press–Taylor & Francis Group.

De, S. (2017). *Structural modeling and optimization of aircraft wings having curvilinear spars and ribs (SpaRibs)* [Doctoral dissertation, Virginia Polytechnic Institute and State University].

Dursun, T., & Soutis, C. (2014). Recent developments in advanced aircraft aluminium alloys. *Materials & Design (1980–2015), 56*, 862–871. https://doi.org/10.1016/j.matdes.2013.12.002

Fageehi, Y. A., & Alshoaibi, A. M. (2024). Investigating the influence of holes as crack arrestors in simulating crack growth behavior using finite element method. *Applied Sciences, 14*(2), Article 2. https://doi.org/10.3390/app14020897

Molent, L. (2010). Fatigue crack growth from flaws in combat aircraft. *International Journal of Fatigue, 32*(4), 639–649. https://doi.org/10.1016/j.ijfatigue.2009.09.002

National Transportation Safety Board. (1988). *Aircraft accident report: Aloha Airlines, Flight 243, Boeing 737-200,*

N73711, near Maui, Hawaii (Report No. NTBS/aar-89/03). United States Government.
Reymer, P., Leski, A., & Kurdelski, M. (2023). Sensitivity analysis of the Nasgro equation based on the PZL-130 TC-II Orlik trainer aircraft full scale fatigue test. *Fatigue of Aircraft Structures, 2022*(14), 8–17. https://doi.org/10.2478/fas-2022-0002
Shah, S. R., Pryce, I. L., John, T. B. S., & Greer, J. M. (2014). Effect of environmental corrosion on fatigue crack growth morphology: A detailed investigation of the boundary between fatigue and corrosion control regimes. *Advanced Materials Research, 891–892*, 278–285. https://doi.org/10.4028/www.scientific.net/AMR.891-892.278
Yavuz, M. T., & Ozkol, I. (2024). Thermal structural design aspects of military aircraft. *Journal of Aeronautics and Space Technologies, 17*(1), Article 1.
Zeng, W., Yang, S.-Q., & Tian, W.-L. (2018). Experimental and numerical investigation of brittle sandstone specimens containing different shapes of holes under uniaxial compression. *Engineering Fracture Mechanics, 200*, 430–450. https://doi.org/10.1016/j.engfracmech.2018.08.016

Design and Modeling of a Nonlinear Bi-Axial Dynamic Vibration Absorber for Helicopter Applications

Resmiye Ağan[a], Vedat Ziya Doğan[a], Halit Süleyman Türkmen[a], Ali Tatar[a]

[a] Istanbul Technical University, Faculty of Aeronautics and Astronautics, Defense Technologies, Türkiye
doganre@itu.edu.tr

Keywords: Cubic Nonlinear Stiffness Approach, Helicopter Vibration Control, Nonlinear Dynamic Vibration Absorber.

Aim

Helicopter structures are inherently exposed to complex and multi-directional vibration sources, stemming primarily from main rotor dynamics, tail rotor interactions, fuselage resonance, gearbox transmission, and engine-induced oscillations. These vibrational forces vary in direction, amplitude, and frequency over time, leading to considerable challenges in maintaining flight stability, structural durability, and overall system performance. In particular, fuselage vibrations may adversely affect the precision of avionics, increase pilot fatigue, and amplify internal cabin noise levels, compromising both safety and comfort.

Historically, linear dynamic vibration absorbers have been deployed in aerospace and rotorcraft structures to alleviate such oscillations. However, these devices are inherently limited by their narrow operational frequency bands, requiring exact tuning to match the dominant excitation frequency. When the system experiences variable operational conditions such as changes in rotor speed, mass distribution, or maneuvering-induced loads, the excitation frequencies may drift, causing linear absorbers to lose effectiveness. In practical rotorcraft missions, such variations are common, leading to the need for vibration suppression solutions that are more adaptive and capable of functioning across a wide frequency spectrum.

To address these challenges, this study explores the design and modeling of a nonlinear dynamic vibration absorber (NDVA) equipped with a polynomial stiffness component—specifically, a cubic nonlinear spring connecting the primary and absorber masses. The nonlinear element allows for amplitude-dependent stiffness behavior, making the absorber effective over broader frequency ranges and under diverse loading conditions. This characteristic makes it suitable for rotorcraft environments, where multi-axial and time-varying vibrations are expected. The research begins with a single-axis NDVA configuration and transitions into a more advanced bi-axial setup capable of mitigating vibrations in both vertical and lateral directions. This progression allows a comparative understanding of absorber performance and sets the stage for further integration into helicopter fuselage structures.

Material and Method

To understand the dynamic response of the NDVA, both analytical modeling and numerical simulations were performed. A base dynamic system was constructed using MATLAB, incorporating a mass-spring-damper configuration with a cubic nonlinearity introduced into the restoring force. This setup consists of a primary mass representing the helicopter component and a secondary mass acting as the vibration absorber. The governing equation includes linear and nonlinear stiffness terms, damping, and an external harmonic excitation force. Time-domain simulations were conducted using numerical solvers to observe the system's transient and steady-state responses under different excitation frequencies and amplitudes. The Fast Fourier Transform (FFT) was employed to evaluate frequency-domain behavior, enabling the identification of resonance, sub-harmonic, and super-harmonic components.

In parallel with analytical modeling, a finite element (FE) model of a cantilever plate resembling a simplified helicopter fuselage panel was created in ANSYS. This beam-like structure was designed using shell elements, and the appropriate material properties were assigned to reflect aerospace-grade components. A comprehensive modal analysis was performed first to identify the structure's natural frequencies and mode shapes. Subsequently, harmonic response analyses were conducted both with and without the absorber to quantify the effectiveness of the NDVA.

To explore the impact of placement and force direction on absorber efficiency, the NDVA was attached at multiple points along the cantilever plate. Simulations were repeated for various attachment locations under harmonic excitations applied in different directions, mimicking different loading conditions. This allowed assessment of how absorber placement relative to mode shape nodes and antinodes affects energy dissipation performance. Both single-axis and bi-axial absorber configurations were simulated to evaluate improvements in performance and directional effectiveness.

Findings

The simulation results clearly demonstrated the enhanced performance of the nonlinear absorber compared to its linear counterpart. In the single-axis setup, the NDVA was able to reduce vibration amplitudes significantly, with reductions exceeding 90% under resonant excitation. In the bi-axial configuration, the absorber maintained similar levels of suppression in both vertical and lateral directions, confirming the benefit of extending the model to account for multi-directional vibrations typical of helicopter fuselage dynamics.

In MATLAB simulations, the cubic stiffness coefficient was varied to observe its effect on system response. It was found that while a properly tuned nonlinear stiffness greatly improved performance, an incorrectly selected coefficient could result in minimal gains or even amplification at certain frequencies. This highlights the importance of parameter sensitivity and the need for optimization algorithms in future stages of this research. The FFT results confirmed the presence of sub- and super-harmonic peaks in nonlinear cases, suggesting complex energy transfer mechanisms that contribute to improved damping. In ANSYS simulations, the cantilever plate exhibited six primary modes within the frequency range of 1.56 Hz to 53.72 Hz. When the absorber was positioned at locations aligned with peak modal displacements (antinodes), the vibration mitigation effect was significantly enhanced. Conversely, placement near modal nodes showed reduced effectiveness. Changing the direction of excitation also affected absorber performance, with lateral excitations being better suppressed in the bi-axial setup. These results offer valuable design insights for future implementations of NDVAs in full-scale helicopter fuselages.

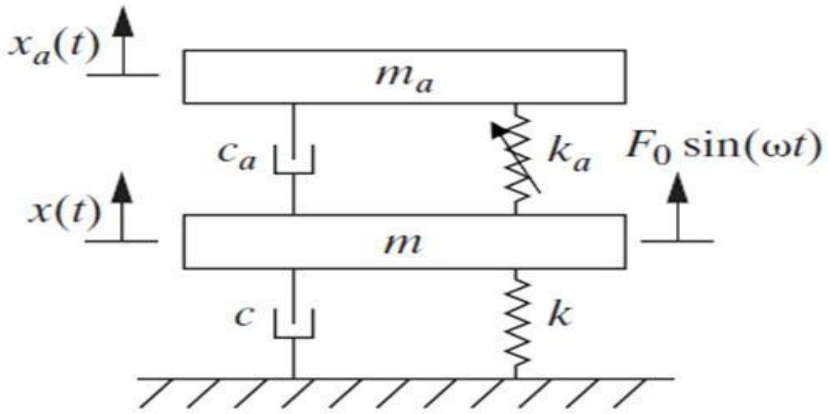

Figure 1. Schematic representation of a nonlinear vibration absorber model.

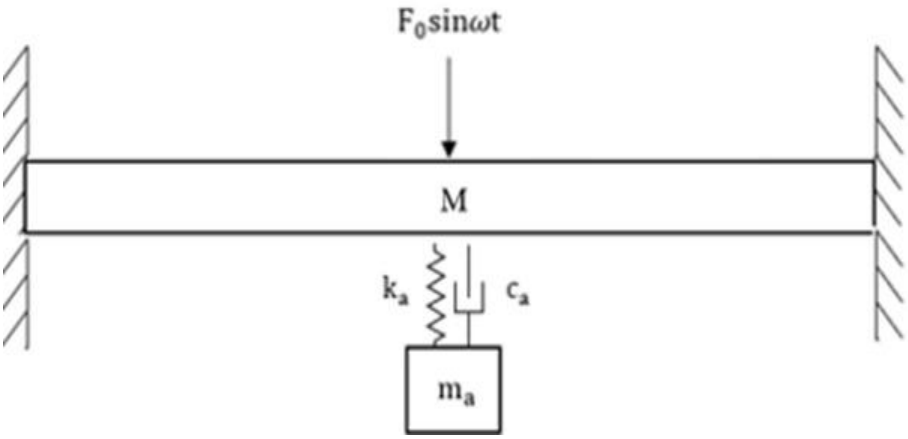

Figure 2. Schematic representation of the absorber and force application point.

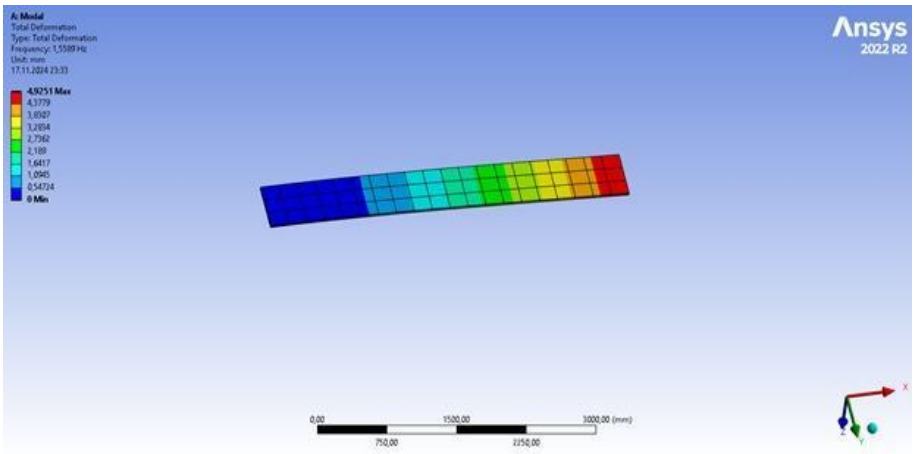

Figure 3. Out-of-Plane Bending System Behavior Analysis of a Beam Model Using Finite Element Method in ANSYS (Mode Shape 1).

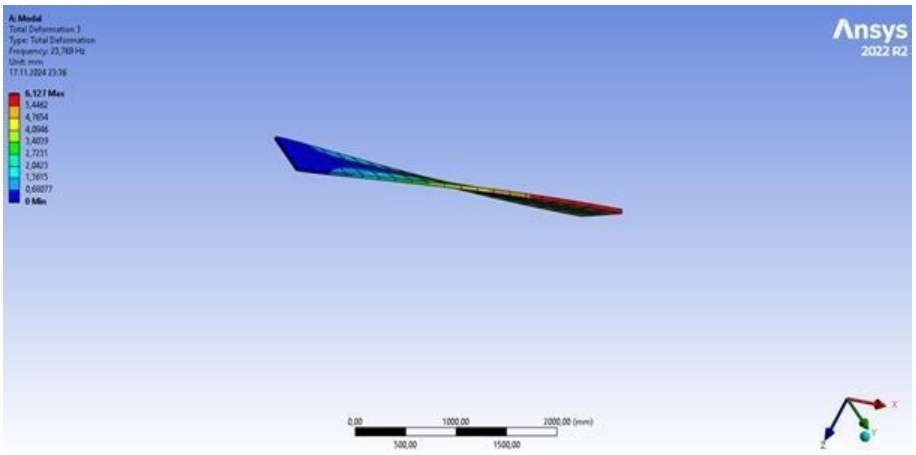

Figure 4. Torsion System Behavior Analysis of a Beam Model Using Finite Element Method in ANSYS (Mode Shape 3).

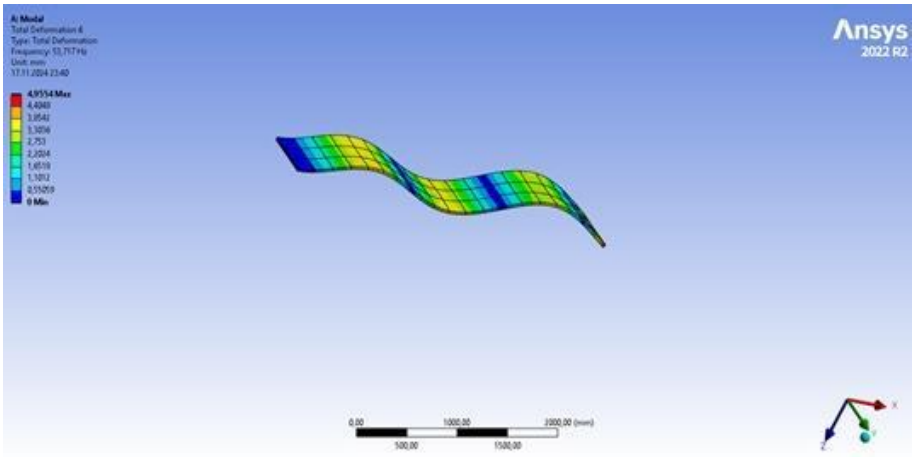

Figure 5. Out-of-Plane Bending System Behavior Analysis of a Beam Model Using Finite Element Method in ANSYS (Mode Shape 6).

Conclusion

This study reinforces the potential of nonlinear dynamic vibration absorbers as a superior alternative to conventional linear systems for rotorcraft vibration control. By transitioning from a single-axis to a bi-axial configuration, the absorber gains the ability to respond to complex, multi-directional excitation environments typically experienced in helicopter operations. The inclusion of a cubic stiffness element extends the effective operational bandwidth, allowing the device to maintain performance even as excitation frequencies drift due to flight maneuvers, payload changes, or other in-flight variations.

The combination of analytical modeling in MATLAB and detailed finite element analysis in ANSYS provides a holistic understanding of system dynamics. The effects of absorber positioning, nonlinear parameter tuning, and loading direction were systematically studied, revealing critical insights that will inform future design and optimization strategies. This research lays the foundation for enhancing structural safety, passenger comfort, and component longevity in rotorcraft systems.

References

Chen, Z., Chen, Z., & Wei, Y. (2022). Quasi-zero stiffness-based synchronous vibration isolation and energy harvesting: A comprehensive review. *Energies, 15*(19), 7066. https://doi.org/10.3390/en15197066

Ding, H., & Chen, L. Q. (2020). Designs, analysis, and applications of nonlinear energy sinks. *Nonlinear Dynamics, 100*(4), 3061–3107. https://doi.org/10.1007/s11071-020-05645-7

Lu, Z., Wang, Z., Zhou, Y., & Lu, X. (2018). Nonlinear dissipative devices in structural vibration control: A review. *Journal of Sound and Vibration, 423*, 18–49. https://doi.org/10.1016/j.jsv.2018.02.039

Ma, Z., Zhou, R., & Yang, Q. (2022). Recent advances in quasi-zero stiffness vibration isolation systems: An overview and future possibilities. *Machines, 10*(9), 813. https://doi.org/10.3390/machines10090813

Welsh, W. A. (2018). Helicopter vibration reduction. In D. Brei (Ed.), *Morphing wing technologies* (pp. 865–892). Butterworth-Heinemann. https://doi.org/10.1016/B978-0-08-100544-6.00029-3

Computational Analysis of Metallic Structures Subjected to Impact Loading Using LS-Dyna

Ümran Türkan[a], Vedat Ziya Doğan [b]

[a] Istanbul Technical University/ Department of Defense Technologies, Defense Technology M.Sc. Program, Turkiye
[b] Istanbul Technical University/ Faculty of Aeronautics and Astronautics, Aeronautics and Astronautics Program, Turkiye
turkan22@itu.edu.tr, doganve@itu.edu.tr

Keywords: Metals, Impact, LS-Dyna.

Aim

There is a wide variety of materials utilized by engineers in the construction of structures, machine components, and various other applications. Among these materials, metals are particularly significant due to their versatile range of uses. In many situations, metals are subjected to loads, which can result in deformation. This deformation may be either elastic or plastic, depending on the nature of the applied force. This study aims to examine material models that are used to investigate the behavior of metals under high-strain-rate deformations, such as those occurring in impact, shock waves, and explosions. Using LS-Dyna.

Material and Method

This study investigates analytical and parametric material models that define the plastic properties of materials. Among the material models found in the literature, particular attention has been given to the Johnson-Cook material and damage model. Based on the obtained information, the material properties of Ti-6Al-4V, a titanium alloy according to the Johnson-Cook approach, have been sourced from the literature, and a material model has been created using the LS-DYNA MAT_015 (LS-DYNA, 2024) material card. The developed material model was defined as a plate with dimensions 250mm × 250mm × 3mm, and the scenario where a sphere with a diameter of 20mm strikes this plate perpendicularly at a velocity of 10 m/s was simulated.

Table 1. Mechanical Properties of Ti-6Al-4V.

Symbol	Description	Value	Unit	Ref.
σ_{uts}	Ultimate stress	1062 +/-11	MPa	(Prakash et al., 2023)
σ_y	Yield stress	972 +/-10	MPa	(Prakash et al., 2023)
ε_{break}	Elongation at break	25	%	(Prakash et al., 2023)
E	Young modulus	114	GPa	(Hu et al., 2020)
ν	Poisson ratio	0,33		(Hu et al., 2020)
G	Shear modulus	44	GPa	(ASM, 2024)
τ_u	Shear stress	550	MPa	(ASM, 2024)

Findings

Material Models

In the literature, there is a variety of mathematical models that describe the plastic behavior of materials. These models can be classified into five categories, which are (Banerjee, 2005):

1. Specific heat model
2. Equation of State Models
3. Melting Temperature Models
4. Shear Modulus Models
5. Flow Stress Models

Studies focusing on Flow stress models are frequently found in the literature. Additionally, "Flow Stress Models" are based on five distinct approaches, which include:

a. Johnson-Cook Model (JC)
b. Steinberg-Cochran-Guinan-Lund Model (SCGL)
c. Zerilli-Armstrong Model
d. Mechanical Threshold Stress (MTS) Model
e. Preston-Tonks-Wallace (PTW) Mode

Johnson-Cook Model (JC)

This study focuses on the Johnson-Cook model, as it is the most widely used model in the literature for metals.
The Johnson-Cook model consists of a Material Model equation (Fig. 1) and a Damage Model equation (Fig. 3). It is a parametric model that utilizes experimental results to construct the equations. (Banerjee, 2005; Johnson, 1983)
JC Material Model (Banerjee et al., 2015; Johnson, 1983):

$$\sigma_{eq} = \left(A + B\left(\varepsilon_{eq}^{pl}\right)^{n}\right)\left(1 + C\, ln\left(\frac{\dot{\varepsilon}}{\dot{\varepsilon_o}}\right)\right)\left(1 - \left(\frac{T - T_o}{T_{melt} - T_o}\right)^{m}\right)$$

Fig. 1 JC Material Model.

JC Material model, in which A, B, n, C, and m represent the reference yield strength, the effect of work hardening, the exponent for thermal softening, the effect of the deformation rate, and the effect of thermal softening, respectively.

The Johnson-Cook material model considers stress as a function of three terms. These terms are strain hardening effect, Strain rate effect, and thermal softening effect.

First term of equation is representing the strain hardening effect:

$$\left(A + B\left(\varepsilon_{eq}^{pl}\right)^{n}\right)$$

Second term of equation represents the Strain rate effect:

$$\left(1 + C\ ln\ ln\ \left(\frac{\dot{\varepsilon}}{\dot{\varepsilon}_0}\right)\right)$$

And third term of equation represents the Thermal softening effect:

$$\left(1-\left(\frac{T-T_0}{T_{melt}-T_0}\right)^m\right)$$

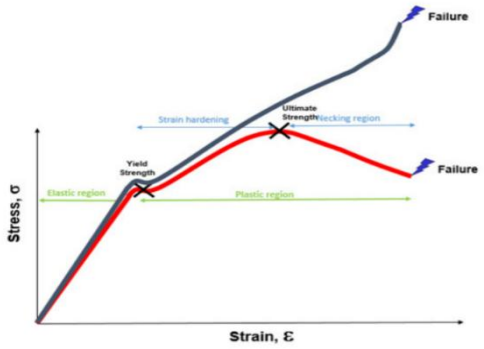

Fig. SEQ Fig. * ARABIC 2: The Presentation of Flow Curve

The coefficients of the Johnson-Cook material model are calculated using engineering stress-strain curves obtained from tensile tests. Since the aim is to examine the material's plastic behavior, the area between the yield strength and the maximum tensile strength points on the curve, referred to as the "flow curve," is considered. (Fig. 2)

JC Damage Model (Banerjee et al., 2015; Johnson, 1983)

The Johnson-Cook damage model (Fig. 3) links the damage phenomenon in the material to the triaxial stress ratio, temperature, and deformation rate. As can be seen from the equation, the first term is related to the triaxial stress, the second term is related to the deformation rate, and the third term is dependent on temperature change/thermal softening.

$$\varepsilon_f = [D_1 + D_2 \exp D_3\sigma^*][1 + D_4 \ln \dot{\varepsilon}^*][1 + D_5 T^*]$$

Fig. 3 JC Damage Model.

JC Damage Model, in which ε_f represents the fracture strain, D_1 is the initial fracture strain, D_2 is the exponential factor, D_3 is the triaxiality factor, D_4 is the strain rate parameter, and D_5 is the temperature parameter. σ_m is the mean stress, and σ_{eq} is the equivalent stress ($\sigma^* = (\sigma_m/\sigma_{eq})$) is known as the stress triaxiality, and $T^* = \frac{T-T_{ref}}{T_m-T_{ref}}$

All constants and coefficients described in the damage model can be calculated from experimental results. These experiments should involve different samples with varying triaxiality properties.

LS- Dyna Material card for JC model

Ansys LS-DYNA is the explicit simulation software used for applications like drop test, impact and penetration, smashes and crashes, occupant safety, and more. Within LS-DYNA, there are 10 material models based on the Johnson-Cook equations. These are shown in Table 2

Table 2 LS-Dyna JC based Material Models (LS-DYNA, 2024).

No	MAT Code	Description
1	MAT_015	JOHNSON_COOK
2	MAT_110	JOHNSON_HOLMQUIST_CERAMICS
3	MAT_111	JOHNSON_HOLMQUIST_CONCRETE
4	MAT_241	JOHNSON_HOLMQUIST_JH1
5	MAT_107	MODIFIED_JOHNSON_COOK
6	MAT_098	SIMPLIFIED_JOHNSON_COOK
7	MAT_099	SIMPLIFIED_JOHNSON_COOK_ORTHOTROPIC_DAMAGE
8	MAT_224	TABULATED_JOHNSON_COOK
9	MAT_224_GYS	TABULATED_JOHNSON_COOK_GYS
10	MAT_264	TABULATED_JOHNSON_COOK_ORTHO_PLASTICITY

In this study, MAT_015 has been studied. MAT_015 can be applied in cases where the deformation rate varies significantly, and softening mechanisms are activated due to the increase in adiabatic temperature. It is suitable for high deformation rates for many metals. The MAT_015 card is shown in Fig. *4*.

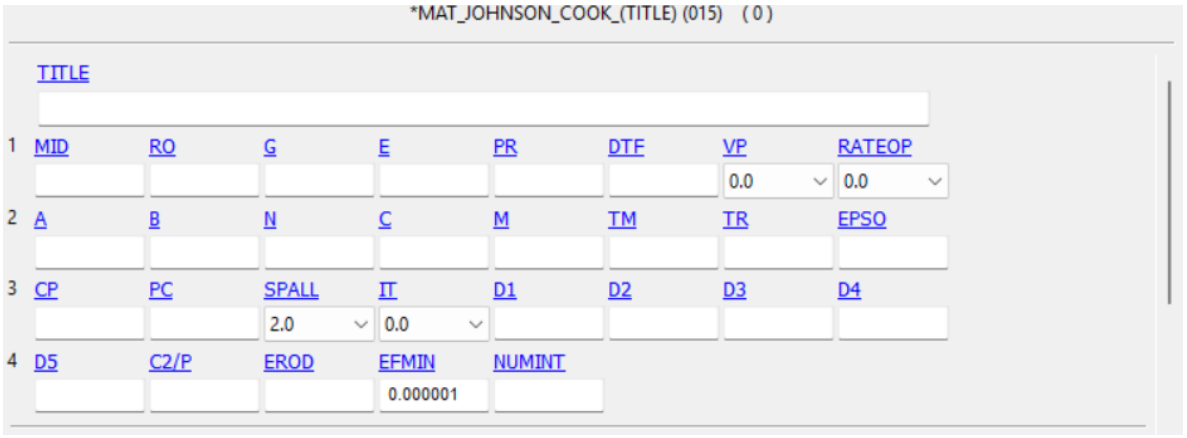

Fig. 4 MAT_015 Material Card. The description of codes can be found on (LS-DYNA, 2024).

Results

Using the information obtained from the literature, the MAT_015 material card was defined (Fig. 6), and an impact analysis was conducted using the LS-DYNA program. The developed material model was defined as a plate with dimensions 250mm × 250mm × 3mm, and the scenario where a sphere with a diameter of 20mm strikes this plate perpendicularly at a velocity of 10 m/s was simulated (Fig. 7). The ball is described as a steel and elastic material. (Fig. 7).
Time duration is 0.1 seconds, and the interval between steps is 0.001. The maximum stress follows at step 5 (t=0,005) and the value is 123.4 MPa at the impact zone (Fig. 8).

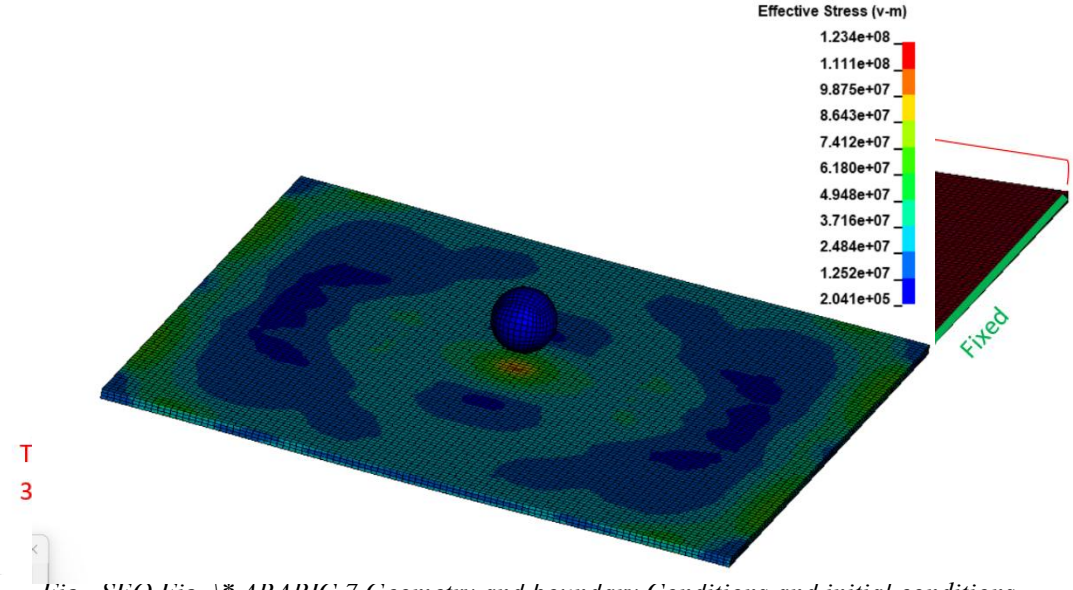

*Fig. SEQ Fig. * ARABIC 7 Geometry and boundary conditions and initial conditions.*

Fig. SEQ Fig. * ARABIC 8 Maximum Stress on The Plate

	TITLE							
	Ti64-Flextural							
1	MID	RO	G	E	PR	DTF	VP	RATEOP
	1	4430.0000	4.400e+10	1.140e+11	0.3300000	0.3300000	0.0	0.0
2	A	B	N	C	M	TM	TR	EPSO
	1.546e+09	3.164e+10	1.3360000	0.0098353	0.0098353	1604.0000	23.000000	0.0010000
3	CP	PC	SPALL	IT	D1	D2	D3	D4
	526.29999	0.0	2.0	0.0	0.0431050	0.0469390	0.0495880	0.0395260
4	D5	C2/P	EROD	EFMIN	NUMINT			
	0.0	0.0	0	1.000e-06	0.0			

*Fig. SEQ Fig. * ARABIC 6 MAT_015 Card of Ti-6Al-4V ADDIN EN.CITE*

*MAT_ELASTIC_(TITLE) (001) (1)

	TITLE						
	Steel						
1	MID	RO	E	PR	DA	DB	NOT USED
	4	7830.0000	2.100e+11	0.3300000	0.0	0.0	0.0

*Fig. SEQ Fig. * ARABIC 5 Elastic Material Card of steel for Ball Units: m, N, Pa, s, kg, i*

Additionally, we can track the history of the kinetic energy of the ball before and after impact. Initially, as per the initial conditions, the ball has 1.6 Joules of kinetic energy (which can be calculated analytically). After the impact, the ball has 0.107 Joules of kinetic energy (Fig. 9).

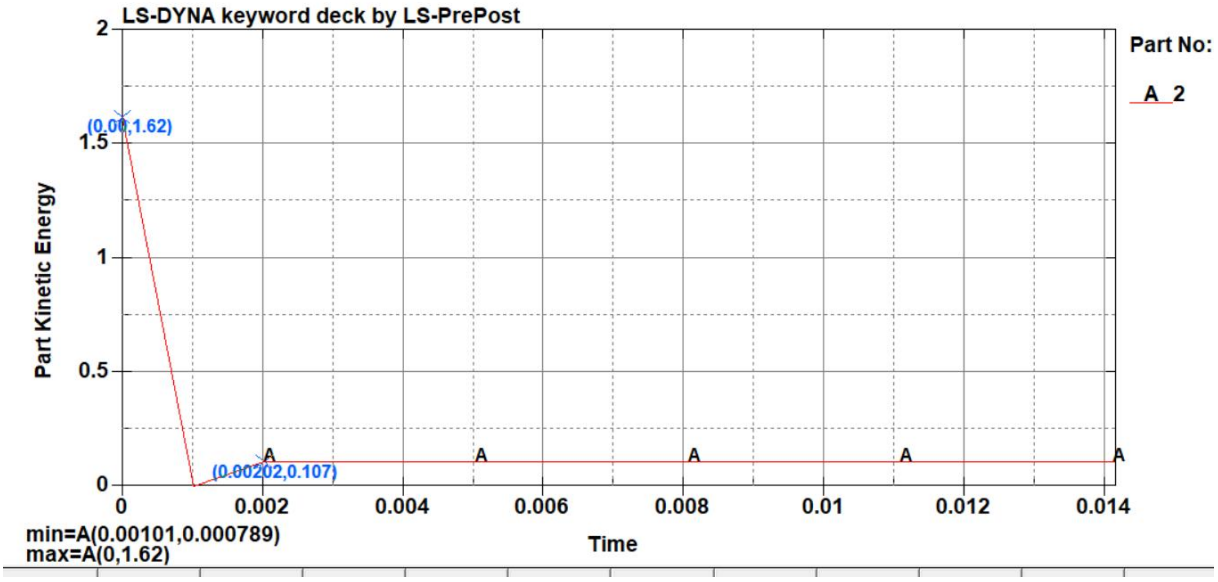

Fig. 9 Kinetic Energy Traction of The Ball.

The results obtained are consistent with the general consensus and analytical calculations, which demonstrate the reliability of the model.

Conclusion

- Metals under high strain rate flow at a high stress level, which can be calculated mathematically.
- The Johnson and Cook model gives a reasonable result for impact loads
- LS-Dyna software allows us to logically model multiple materials and scenarios

References

Banerjee, A., Dhar, S., Acharyya, S., Datta, D., & Nayak, N. (2015). Determination of Johnson cook material and failure model constants and numerical modelling of Charpy impact test of armour steel. Materials Science and Engineering: A, 640, 200-209.

Banerjee, B. (2005). An evaluation of plastic flow stress models for the simulation of high-temperature and high-strain-rate deformation of metals. arXiv preprint cond-mat/0512466.

Hu, H., Xu, Z., Dou, W., & Huang, F. (2020). Effects of strain rate and stress state on mechanical properties of Ti-6Al-4V alloy. International Journal of Impact Engineering, 145, 103689.

Johnson, G. R. (1983). A constitutive model and data for metals subjected to large strains, high strain rates and high temperatures. Proceedings of the 7th International Symposium on Ballistics, The Hague, Netherlands, 1983,

LS-DYNA. (2024). LS-DYNA® KEYWORD USER'S MANUAL VOLUME II Material Models.

Prakash, G., Singh, N., & Gupta, N. (2023). Flow behaviour of Ti-6Al-4V alloy in a wide range of strain rates and temperatures under tensile, compressive and flexural loads. International Journal of Impact Engineering, 176, 104549.

DEFENSE TECHNOLOGIES

Remote Sensing

Spacecraft Control, Design And Performance

Structural Design and Analysis

Unmanned Vehicles

Heuristic Approach to UAV Selection with Fuzzy Logic and MADM Techniques

Emre Yüksek[a], Cengiz Kahraman[b]

[a] Istanbul Technical University, Defence Technologies, Strategy Development, Türkiye
[b] Istanbul Technical University, Industrial Engineering, Türkiye
yuksek20@itu.edu.tr, kahramanc@itu.edu.tr

Keywords: Fuzzy AHP, UAV Selection, Multi Criteria Decision Making, Fuzzy Logic, Sensitivity Analysis

Aim

The aim of this study is to apply the Fuzzy Analytic Hierarchy Process (Fuzzy AHP) methodology to address the complex UAV (Unmanned Aerial Vehicle) selection problem under multiple criteria. Given the increasing use of UAVs in military and civilian applications, selecting the most suitable UAV requires careful consideration of various operational, technical, and economic factors. These factors include payload capacity, range, endurance, maximum altitude, and maximum speed. The goal is to develop an optimized decision-making framework that incorporates both subjective judgments and quantitative analysis. This study not only provides a ranking of different UAV alternatives but also evaluates the robustness of the decision-making process by performing a sensitivity analysis on the criteria weights. The Fuzzy AHP method used in this study follows the extent analysis method proposed by Chang (1996).

Material and Method

In this study, a comprehensive decision-making process based on Fuzzy AHP is used to select the most appropriate UAV from a list of alternatives. The following steps were followed in the methodology:
Criteria Definition: The primary criteria for selecting UAVs were defined as:
• Payload Capacity: The maximum weight the UAV can carry.
• Range: The maximum operational distance.
• Endurance: The maximum operational time.
• Maximum Altitude: The maximum height the UAV can reach.
• Maximum Speed: The maximum speed at which the UAV can fly.
The data were obtained from the relevant technical documents and websites of the UAVs (Baykar, n.d.; TUSAŞ, n.d.; Elbit Systems, n.d.; Army Technology, n.d.). Fuzzy Pairwise Comparisons: Decision-makers provided pairwise comparisons of the criteria using linguistic variables such as "very low," "low," "medium," "high," and "very high." These linguistic terms were then converted into fuzzy triangular numbers, which represent the subjective judgment of decision-makers about the relative importance of each criterion. Fuzzy numbers were used to account for the inherent uncertainty in human judgment (Chang, 1996; Liu & Rodríguez, 2013). Fuzzy Consistency Check: To ensure the logical consistency of the pairwise comparisons, a consistency check was performed. The consistency ratio (CR) was calculated to assess whether the judgments provided by the decision-makers were consistent enough to support a reliable final ranking (Lin & Hung, 2011). Weight Calculation: The fuzzy weights of the criteria were calculated using the Fuzzy AHP method. These weights reflect the relative importance of each criterion and serve as the foundation for the UAV ranking. The fuzzy weights were defuzzified to obtain crisp values for further evaluation.(Buckley, 1985).
Alternative Evaluation: Each UAV alternative (Bayraktar Akıncı, Aksungur, MQ-9 Reaper, TUSAŞ ANKA-S, Elbit Hermes 900, and MQ-1C Gray Eagle) was evaluated based on the defined criteria. Fuzzy ratings were assigned to each UAV for each criterion based on expert assessments, capturing both the objective data and subjective evaluations (Abrahart & See, 2000).

Final Ranking: The final UAV ranking was determined by calculating the overall scores of each UAV using the weighted fuzzy evaluations. The UAV with the highest score was identified as the most suitable for selection based on the defined criteria.

Sensitivity Analysis: To ensure the robustness of the model, a sensitivity analysis was performed. This analysis assessed how changes in the criteria weights affected the final UAV ranking. By varying the weights, the sensitivity of the model was tested, providing insight into how the decision-making process could be influenced by different scenarios.(Tavana, Azadeh, & Behzadian, 2013; Lin & Hung, 2011).

Findings

The implementation of the Fuzzy AHP methodology resulted in the following findings:
Ranking of UAVs: Based on the fuzzy evaluations and the derived criteria weights, the UAVs were ranked as follows:

1. MQ-9 Reaper
2. Bayraktar Akıncı
3. MQ-1C Gray Eagle
4. Aksungur
5. Elbit Hermes 900
6. TUSAŞ ANKA-S

Discussion on Findings: The MQ-9 Reaper emerged as the most suitable UAV, due to its high performance across multiple criteria, especially in payload capacity, range, and endurance. Bayraktar Akıncı followed closely, with its high payload capacity and range, making it a competitive alternative. MQ-1C Gray Eagle, while slightly lower in range, also performed well in terms of endurance and payload capacity. UAVs such as Aksungur and TUSAŞ ANKA-S were ranked lower due to their relatively shorter endurance and lower maximum speed compared to the higher-ranking UAVs.
Sensitivity Analysis Results: The sensitivity analysis revealed that the final ranking was particularly sensitive to changes in the "Endurance" and "Maximum Speed" criteria. For example, increasing the weight of Endurance slightly shifted the ranking, making Bayraktar Akıncı outperform MQ-9 Reaper due to its higher operational time. Conversely, increasing the weight of Maximum Speed led to MQ-9 Reaper regaining the top position, reflecting its higher speed. These results underscore the importance of carefully considering the weight assignment during decision-making, as small changes in these critical criteria can significantly impact the UAV selection (Chang, 1996; Lin & Hung, 2011).
Detailed Sensitivity Observations:

- A 10% increase in the weight of Endurance resulted in a ranking change where Bayraktar Akıncı and MQ-1C Gray Eagle moved up the ranks.
- A 15% increase in the weight of Maximum Speed caused a noticeable shift in favor of MQ-9 Reaper, which highlighted its superior speed.

Consistency of Results: The fuzzy pairwise comparison matrix was evaluated for consistency, with the consistency ratio (CR) falling within an acceptable range, indicating that the decision-makers' judgments were reasonably consistent (Saaty, 1980). The Fuzzy AHP methodology's ability to handle subjective assessments with imprecision contributed to the robustness of the decision making process (Zadeh, 1965; Buckley, 1985).

Conclusion

The Fuzzy AHP approach provided a reliable and structured framework for UAV selection, effectively handling multiple conflicting criteria and incorporating expert judgments through fuzzy logic (Chang, 1996; Sabo & Cohen, 2012). The results demonstrated that MQ-9 Reaper was the most suitable UAV for selection, based on the defined criteria. However, the sensitivity analysis highlighted that the final ranking is highly dependent on the weightings of key criteria such as Endurance and Maximum Speed (Tavana, Azadeh, & Behzadian, 2013). This reinforces the need for careful weight assignment and consideration of decision-maker preferences in complex decision making problems (Wang, Jing, Zhang, & Zhao, 2009).
In practical terms, the study underscores the importance of utilizing fuzzy decision-making models in selecting UAVs, especially in defense and aerospace applications where uncertainty is inherent, and decisions are often influenced by subjective judgments (Ramirez-Atencia, Rodriguez Fernandez, & Camacho, 2020). The results also suggest that the Fuzzy AHP model could be further improved by incorporating additional criteria, such as operational adaptability or stealth

capabilities, which could provide a more holistic evaluation of UAVs (Qamar, Sarfraz, Rahman, & Ghauri, 2023; Bai et al., 2024).

References

Abrahart, R. J., & See, L. (2000). Comparing neural network and autoregressive moving average techniques for the provision of continuous river flow forecasts in two contrasting catchments. Hydrological Processes, 14, 2157–2172.
Url-1 Army Technology. (n.d.). MQ-1C Gray Eagle UAS – US Army. Retrieved from https:// www.army-technology.com/projects/mq1c-gray-eagle-uas-us-army, date retrieved 17.05.2025.
Url-2 Baykar. (n.d.). İnsansız Hava Aracı Sistemleri. Baykar. Retrieved from https:// baykartech.com/tr/insansiz-hava-araci-sistemleri/, date retrieved 17.05.2025.
Buckley, J. J. (1985). Fuzzy hierarchical analysis. Fuzzy Sets and Systems, 17(3), 233-247.
Chang, D. Y. (1996). Applications of the extent analysis method on fuzzy AHP. European Journal of Operational Research, 95(3), 649-655
Url-3 Elbit Systems. (n.d.). Hermes 900. Elbit Systems. Retrieved from https://elbitsystems.com/product/hermes-900/, date retrieved 17.05.2025.
Lin, K. P., & Hung, K. C. (2011). An efficient fuzzy weighted average algorithm for the military UAV selecting under group decision-making. Journal of Systems Engineering and Electronics, 22(3), 535-547.
Liu, H., & Rodríguez, R. M. (2013). A fuzzy envelope for hesitant fuzzy linguistic term set and its application to multicriteria decision making. Expert Systems with Applications, 40(10), 3956-3966
Qamar, R. A., Sarfraz, M., Rahman, A., & Ghauri, S. A. (2023). Multi-criterion multi-UAV task allocation under dynamic conditions. Journal of King Saud University - Computer and Information Sciences, 35(6), 101734
Ramirez-Atencia, C., Rodriguez-Fernandez, V., & Camacho, D. (2020). A revision on multi criteria decision making methods for multi-UAV mission planning support. Expert Systems with Applications, 165, 113708
Saaty, T. L. (1980). The Analytic Hierarchy Process: Planning, Priority Setting, Resource Allocation. New York: McGraw-Hill.
Sabo, C., & Cohen, K. (2012). Fuzzy logic UAV (Unmanned Aerial Vehicle) motion planning. Advances in Fuzzy Systems, 2012(Article ID 989051)
Url-4 SavunmaTR. (n.d.). MQ-9 Reaper İHA Nedir? Özellikleri Nelerdir? Retrieved from https:// www.savunmatr.com/mq-9-reaper-iha-nedir-ozellikleri-nelerdir, date retrieved 17.05.2025.
Tavana, M., Azadeh, A., & Behzadian, M. (2013). A fuzzy inference system with MADM methods for UAV mission planning. International Journal of Systems Science, 44(4),
677-695
Url-5 TUSAŞ. (n.d.). Operatif & Stratejik İHA Sistemleri. TUSAŞ. Retrieved from https:// www.tusas.com/urunler/iha/operatif-stratejik-iha-sistemleri, date retrieved 17.05.2025.
Wang, J. J., Jing, Y. Y., Zhang, C. F., & Zhao, J. H. (2009). Review on multi-criteria decision analysis aid in sustainable energy decision-making. Renewable and Sustainable Energy Reviews, 13(9), 2263-2278.
Zadeh, L. A. (1965). Fuzzy sets. Information and Control, 8(3), 338-353

Optimized Visual Odometry and Satellite Image Matching-Based Localization for UAVs in GPS-Denied Environments

Ömer Sefa Öztürk[a], Alptekin Yıldız[b]

[a]Istanbul Technical University, Defence Technologies, Turkey
[b] Istanbul Technical University, Aviation, Turkey
ozturko15@itu.edu.tr

Keywords: Custom UAV Dataset, Satellite Image Matching, UAV, Visual Navigation, Visual Odometry.

Aim

Unmanned Aerial Vehicles (UAVs) are increasingly required to operate in environments where Global Positioning System (GPS) signals are unreliable or unavailable, such as urban canyons or areas subjected to intentional GPS jamming. Traditional navigation systems that rely heavily on GPS often fail in such scenarios, necessitating alternative methods for accurate localization. This study aims to develop and evaluate an innovative visual navigation system for UAVs that integrates continuous visual odometry (VO) with satellite image matching to produce accurate, real-time position estimates. The key contributions include the development of a novel UAV dataset by synchronizing high-rate camera frames with low-rate GPS data, an enhanced VO performance through the optimization of ORB-SLAM3 parameters (DeTone, Malisiewicz, & Rabinovich, 2018), the integration of the Monodepth algorithm (Campos, Elvira, Gómez Rodríguez, Montiel, & Tardós, 2021)

to mitigate scale ambiguity, and the creation of a map retrieval interface for accessing high-resolution satellite maps to determine absolute UAV positions through image matching.

Material and Method

UAV flights were conducted using a DJI Mavic Air 2 over various outdoor locations. The drone's downward-facing camera recorded video at 30 frames per second (FPS), while GPS data was logged at 1 Hz. The GPS coordinates (latitude and longitude) were converted to local North-East-Down (NED) coordinates. Linear interpolation was applied to the GPS timestamps so that every video frame received an accurate ground truth pose, achieving synchronization within ±10 milliseconds. This procedure yielded a unique dataset of ground truth trajectories at 50–100 meters altitude. Visual odometry was implemented by processing the video frames with an optimized version of ORB-SLAM3 (DeTone, Malisiewicz, & Rabinovich, 2018)—a state-of-the-art feature-based Simultaneous Localization and Mapping (SLAM) system. The camera was calibrated to provide the necessary intrinsic parameters, and ORB-SLAM3 extracted Oriented FAST and Rotated BRIEF (ORB) features to track the camera's pose continuously. The algorithm was fine-tuned to the dataset to ensure robust and accurate VO. To address the scale ambiguity inherent in monocular VO, the Monodepth algorithm (Campos, Elvira, Gómez Rodríguez, Montiel, & Tardós, 2021), which estimates depth from single images using deep learning techniques, was integrated to provide scale-consistent depth information. For absolute localization, high-resolution satellite imagery of the flight area was acquired and geo-referenced. Keypoints were detected using SuperPoint (Godard, Mac Aodha, & Brostow, 2017), and correspondences with the satellite map were established via SuperGlue (Sarlin, DeTone, Malisiewicz, & Rabinovich, 2020). These matches allowed the estimation of an absolute drone pose through the Perspective-n-Point (PnP) algorithm, assuming a planar ground. Although this approach provided drift-free position estimates, updates were intermittent, occurring only when a sufficient number of feature matches were detected. Additionally, a user-friendly interface was developed to enable the free download of high-resolution maps, ensuring access to current satellite imagery essential for the matching process. Finally, the estimated trajectories from both the optimized ORB-SLAM3 (VO) and the satellite matching approach were compared against the ground truth using the Robotics and

Perception Group (RPG) trajectory evaluation library, with key metrics (including RMSE for position and orientation) computed.

Findings

The optimized ORB-SLAM3-based visual odometry provided continuous, high-frequency pose estimates with an average error of approximately 2 meters. Despite the dataset-specific optimization enhancing VO performance, the trajectory exhibited cumulative drift over longer distances without global correction. Fig.1 The optimized ORB-SLAM3 model was tested on the custom UAV dataset to assess its accuracy in trajectory estimation. Figure 1 illustrates a comparison between the predicted trajectory and the ground truth for one of the test sequences. The results show that the optimized model provides a smoother trajectory, though some drift is observed over longer distances. In contrast, the integration of Monodepth successfully addressed the scale ambiguity, resulting in more accurate and scale-consistent VO estimates. Satellite image matching, while delivering absolute localization with minimal drift and an average error of about 4 meters, produced updates intermittently. The complementary nature of these methods suggests that combining continuous VO with periodic satellite-based corrections can reduce cumulative drift and improve UAV navigation in GPS-denied environments.

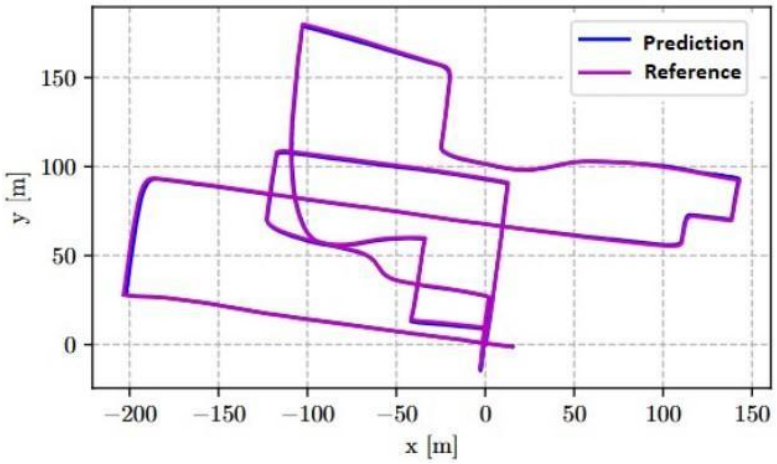

Figure 1. Reference vs. Predicted Trajectory using Visual Odometry.

Conclusion

This study demonstrates that a combined visual navigation system leveraging both optimized visual odometry (via ORB-SLAM3) and satellite image matching can significantly enhance UAV navigation in GPS-denied conditions. The creation of a novel, fully annotated dataset with synchronized ground truth at mid-altitude contributes to the research community and opens new possibilities for sensor fusion strategies. The integration of depth estimation algorithms like Monodepth addresses the scale ambiguity issue, further improving VO accuracy, while the map retrieval interface facilitates the acquisition of necessary satellite imagery for absolute localization. Table 1 presents the quantitative comparison of the two navigation methods. While visual odometry provides continuous real-time motion estimation, it suffers from cumulative drift over long distances. In contrast, satellite image matching provides globally referenced absolute position fixes but at an intermittent rate. However, the current method still has limitations. Its performance can be sensitive to environmental variability—such as changes in lighting, terrain, or the landscape's appearance—which may degrade matching accuracy. Additionally, the approach relies on the availability of high-quality, up-to-date satellite data and assumes a relatively planar ground, conditions that might not hold universally. Future work will focus on enhancing the method's robustness by implementing real-time sensor fusion algorithms (e.g., extended Kalman filtering) and incorporating additional sensors (such as an Inertial Measurement Unit (IMU) and barometer) to complement visual data. Moreover, adapting the image matching process to be more invariant to environmental changes and periodically updating the reference maps could further improve the system's reliability and performance in diverse GPS-denied environments.

Table 1. Comparison of Visual Odometry and Satellite Image Matching Methods.

Method	Average Position Error	Drift Over Distance	Update Frequency	Absolute Accuracy
Optimized ORB-SLAM3 (VO)	~2 m	Increases over time	Continuous (every frame)	No absolute reference
Satellite Image Matching	~4 m	No drift	Intermittent (~every few seconds)	Geo-referenced

References

DeTone, D., Malisiewicz, T., & Rabinovich, A. (2018). SuperPoint: Self-supervised interest point detection and description. In *Proceedings of the IEEE/CVF Conference on Computer Vision and Pattern Recognition Workshops*.

Godard, C., Mac Aodha, O., & Brostow, G. J. (2017). Unsupervised monocular depth estimation with left-right consistency. In *Proceedings of the IEEE Conference on Computer Vision and Pattern Recognition (CVPR)* (pp. 6602–6611).

Campos, C., Elvira, R., Gómez Rodríguez, J. J., Montiel, J. M. M., & Tardós, J. D. (2021). ORB-SLAM3: An accurate open-source library for visual, visual-inertial and multi-map SLAM. *arXiv preprint* arXiv:2007.11898.

Sarlin, P.-E., DeTone, D., Malisiewicz, T., & Rabinovich, A. (2020). SuperGlue: Learning feature matching with graph neural networks. In *Proceedings of the IEEE/CVF Conference on Computer Vision and Pattern Recognition (CVPR)* (pp. 4938–4947).

Comparative Analysis of Object Detection and Tracking Algorithms for UAVs

Merve İsmailvelioglu[a], Mustafa Doğan[b]

[a]İstanbul Technical University, Defense Technologies Graduate Program, Türkiye
[b]İstanbul Technical University, Faculty of Electrical and Electronics Engineering, Türkiye
ismailvelioglu22@itu.edu.tr, mustafadogan@itu.edu.tr

Keywords: Object Detection, Tracking Algorithms, Real-Time Performance.

Modern defense technologies are a rapidly developing field with the use of UAVs (unmanned aerial vehicles). Although UAVs used in the defense field generally have limited computational resources, they need to detect and track objects in real-time in highly dynamic and variable environments. Although existing object detection and tracking algorithms provide high accuracy in such environments, they are not optimized in terms of processing speed and resource usage. Solving these problems is of vital importance in terms of increasing the effectiveness of defense systems and ensuring operational security. This study investigates the optimization of object detection and tracking algorithms specifically designed for unmanned aerial vehicles by evaluating their performance through the application of state-of-the-art machine learning models. Experiments have shown that YOLOv8m achieves the highest accuracy with 0.971 mAP@0.5 and 0.709 mAP@0.5:0.95 values. ByteTrack, one of the tracking algorithms, exhibited optimized performance for real-time applications with 50.5 FPS and 0.926 MOTP. The results reveal that the combination of YOLOv8m and ByteTrack offers a balanced solution in UAV-based systems. These findings contribute to improving the effectiveness and reliability of object detection and tracking for UAV systems in complex operational environments.

Aim

The main objective of the study is to increase the sensitivity and speed of object detection and tracking in images obtained from UAVs, to compare the performance of algorithms used in this field with quantitative metrics, and to develop optimization suggestions. In particular, the behavior of YOLOv8 models of different sizes on an extended dataset and the real-time performance of tracking algorithms are analyzed. The study aims to fill the gap in the literature and provide a practical guide for algorithm selection in UAV operations.

Material and Method

Dataset

The dataset, initially consisting of 4415 datasets, is optimized for object detail and tracking, especially in UAV systems. The images include examples of objects taken from different angles, objects of various sizes, and real-world conditions. The data is also manually labeled in COCO format.

In order to increase the overall capacity of the dataset and to ensure that the model gives more robust results, data augmentation techniques were used. These techniques are rotation, reflection, scaling, stretching, and color changing. In this way, the number of data points was doubled, and the model's ability to learn under different conditions was strengthened. As a result of the applied techniques, two examples of the data in the dataset and their augmented versions are shown in Figure 1. The dataset is divided into training (80%), validation (10%), and testing (10%) subsets.

Figure 1. Examples of data and augmented data.

Hardware and Software Infrastructure

All experiments were performed in a Google Colab Pro environment with an A100 GPU (40 GB RAM) and 83.5 GB RAM. The Ultralytics YOLOv8 (v8.0.143) library was used for object detection (Jocher et al., 2023). PyTorch (v2.1.0) and OpenCV (v4.7.0) based codes were optimized for the implementation of tracking algorithms.

Object Recognition Algorithm

YOLO (You Only Look Once) architecture is a widely preferred deep learning model for real-time object detection. In this study, five different models belonging to the YOLOv8 family were used as object detection methods. The models used were developed with different dimensions and effects, and the performance differences were shown for comparison purposes. These models are as follows:

YOLOv8n: The smallest model, notable for its fast processing time and low memory usage. However, it can generally exhibit lower accuracy rates.

YOLOv8s: Slightly larger than YOLOv8n, this model provides intermediate accuracy and speed.

YOLOv8m: This model has high accuracy rates and provides overall results in terms of processing time. According to the research results, this model is the one that exhibits the best overall performance with our dataset.

YOLOv8l: It is a larger model, and although it provides very high accuracy rates, it has a more intensive structure in terms of processing time and resource consumption.

YOLOv8x: It is the largest model in the YOLOv8 family, and although it provides the highest accuracy rates, it creates a significant burden in terms of processing time and memory usage in large data sets.

At each stage of training, Adam Optimizer was preferred as the backup schedule used. The training time of the model varied depending on the size of the model used and the size of the dataset**.**

Object Tracking Algorithms

The main purpose of the tracking programs is to ensure that moving products are stored correctly and to minimize detection errors. The tracking algorithms in the study are as follows:

SORT: Tracks objects using a Kalman filter. It is profitable with its simple structure and fast processing time, but low accuracy may be exhibited.

DeepSORT: Transmits vectors of detected features and makes their registration more robust. This solution uses deep learning models to increase the accuracy of object detections.
ByteTrack: It is a lighter and faster tracking algorithm. Although not complex, it can be preferred in certain applications with its fast processing time and low programming rates.

Evaluation Metrics

Evaluation metrics for object detection algorithms are as follows:

- **Mean Average Precision (mAP):** Evaluates the overall performance of the model by combining the accuracy and coverage rates of detected objects.
- **Precision:** Indicates how many of the detected objects are accurate.
- **Recall:** Indicates how many correct objects have been detected.
- **Inference Duration (ms):** It refers to how much time the model spends making predictions on an image.

Evaluation metrics for tracking algorithms are as follows:

- **FPS:** Real-time processing speed.
- **MOTP:** Estimated and actual bounding average IoU (Intersection over Union) between boxes (Zhang et al., 2022).
- **Tracked Object:** Specifies the number of objects that tracking algorithms have successfully tracked.

Findings

The Impact of Data Augmentation

Data augmentation significantly improved model generalization; the risk of overfitting was reduced by 22%. The validation mAP@0.5 value of YOLOv8m reached **0.971** on the augmented dataset, which increased **by 8.3%** compared to the baseline dataset.

Performance of YOLOv8 Models

Table 1. Evaluation of YOLOv8 Models.

Model	mAP@0.5	mAP@0.5:0.95	Precision	Recall	Inference Duration (ms)
YOLOv8n	0.928	0.656	0.938	0.86	4.91
YOLOv8s	0.960	0.677	0.927	0.93	4.99
YOLOv8m	**0.971**	**0.709**	0.946	**0.93**	**4.92**
YOLOv8l	0.959	0.702	0.986	0.87	5.16
YOLOv8x	0.960	0.698	**0.989**	0.91	5.53

The performance results of the models are as shown in Table 1 below. According to the results obtained, **YOLOv8m** stands out with its balance of both accuracy **(0.971 mAP@0.5)** and speed **(4.92 ms/inference)**. YOLOv8x, 98.9% it can be used in special scenarios with precision but its high resource consumption limits practical use.

Performance of Tracking Algorithms

Table 2. Evaluation of Tracking Algorithms.

Algorithm	Avg. FPS	MOTP	Tracked Object
ByteTrack	**50.5**	**0.926**	632
SORT	49.99	0.905	616
DeepSORT	26.89	0.755	**749**

The performance results of the algorithms are as shown in Table 2 below. According to the results obtained, **ByteTrack** has demonstrated ideal performance for real-time applications with high **FPS (50.5)** and **MOTP (0.926)**. DeepSORT has the most comprehensive tracking capability with 749 objects despite low FPS.

Conclusion

This study showed that the combination of YOLOv8m and ByteTrack is optimal for object detection and tracking in UAV images. Data augmentation significantly increased the model's accuracy. YOLOv8m provides high mAP values with low resource consumption, while ByteTrack provides real-time performance and stable tracking. Large models (YOLOv8l/x) can be preferred in missions requiring high precision. These findings provide the basis for future developments in autonomous UAV systems where efficient and accurate detection and tracking are critical for mission success.

References

Bochkovskiy, A., **Wang, C.**, & **Liao, H.** (2020). *YOLOv4: Optimal speed and accuracy of object detection* (arXiv:2004.10934). arXiv. https://arxiv.org/abs/2004.10934

Jocher, G., **Chaurasia, A.**, & **Qiu, J.** (2023). *Ultralytics YOLOv8* [Computer software]. GitHub. https://github.com/ultralytics/ultralytics

Redmon, J., **Divvala, S.**, **Girshick, R.**, & **Farhadi, A.** (2016). You only look once: Unified, real-time object detection. In *Proceedings of the IEEE Conference on Computer Vision and Pattern Recognition (CVPR)* (pp. 779–788). https://doi.org/10.1109/CVPR.2016.91

Shorten, C., & **Khoshgoftaar, T. M.** (2019). A survey on image data augmentation for deep learning. *Journal of Big Data, 6*(1), Article 60. https://doi.org/10.1186/s40537-019-0197-0

Zhang, Y., **Sun, P.**, **Jiang, Y.**, **Yu, D.**, **Weng, F.**, **Yuan, Z.**, ... & **Wang, X.** (2022). *Bytetrack: Multi-object tracking by associating every detection box* (arXiv:2110.06864). arXiv. https://arxiv.org/abs/2110.06864

Wojke, N., **Bewley, A.**, & **Paulus, D.** (2017). Simple online and real-time tracking with a deep association metric. In *Proceedings of the IEEE International Conference on Image Processing (ICIP)* (pp. 3645–3649). https://doi.org/10.1109/ICIP.2017.8296962

EARTHQUAKE ENGINEERING

Artificial Intelligence, Machine Learning, and Deep Learning in Earthquake Engineering

Experimental Investigation of Reinforced Concrete Building Elements

Performance-Based Seismic Assessment and Design

Structural and Geotechnical Earthquake Engineering

Detection of Longitudinal Reinforcement Buckling in Reinforced Concrete Columns by a Deep Learning Method

Bahadir Gulesmen[a], Omer Tugrul Turan[b]

[a]Istanbul Technical University, Graduate School, Structural Engineering Program, Türkiye
[b] Istanbul Technical University, Civil Engineering Departmant, Türkiye
gulesmen21@itu.edu.tr

Keywords: Deep Learning, Post-earthquake Assessments, Reinforced Concrete Buildings, Reinforcement Buckling.

Aim

The objective of this study is to utilize deep learning methodologies to detect longitudinal reinforcement buckling in the columns of reinforced concrete buildings following seismic events. The February 6, 2023, Turkey–Syria earthquakes (Mw 7.8 and Mw 7.5), with epicenters in Pazarcık and Elbistan [1], resulted in significant structural damage and loss of life, thereby underscoring the critical need for structural health monitoring (SHM) systems. This study aims to demonstrate that even with a limited dataset, a deep learning approach based on transfer learning can reliably detect localized damage, such as reinforcement buckling. This, in turn, facilitates post-disaster assessments and assists in emergency and rehabilitation efforts.

Material and Method

The data for this study were collected during field investigations conducted in the aftermath of the February 6, 2023, earthquake. The dataset consists of high-resolution images of damaged reinforced concrete columns, with particular emphasis on sections exhibiting longitudinal reinforcement buckling. Image dimensions were standardized to minimize the effect of variable imaging conditions [2]. A total of 110 images were collected, in which 458 instances of longitudinal reinforcement buckling were identified. These images were annotated to label visible buckling zones, using bounding boxes to indicate their positions. The dataset was then divided into three subsets—training, validation, and test—using an 80:10:10 split. The training set comprised 88 images, while the validation and test sets each contained 11 images. These were associated with 351, 50, and 57 reinforcement buckling instances, respectively.

It is important to note that the dataset size and variability pose certain limitations. Since all images were captured within a limited time frame during post-earthquake site visits, variations in natural lighting—ranging from direct sunlight to overcast conditions—may have affected the visual clarity of the reinforcement details. In some cases, shadows or inconsistent illumination could obscure critical features. Moreover, several reinforcement bars showed signs of surface corrosion or rust, potentially altering the appearance of the buckling zones and influencing model perception.

The Faster R-CNN architecture was employed due to its proven effectiveness in balancing speed and localization accuracy. Its Region Proposal Network (RPN) is known to improve capture efficiency by generating high-quality region proposals [3]. The model utilized a pre-trained ResNet-101 backbone, further enhanced through transfer learning from the COCO dataset. Training was conducted with a batch size of 8 and a cosine decay learning rate schedule beginning at 0.01—an approach shown to prevent premature convergence and promote better generalization [4]. Data augmentation methods included random horizontal flips, hue/contrast/saturation adjustments, and random square cropping with a scale factor between 0.6 and 1.3, all of which increased dataset diversity and model robustness to real-world variability [5].

In addition to the Faster R-CNN model, the YOLOv8 architecture was employed to leverage its capability for real-time object detection with high spatial precision. The unified architecture of YOLOv8 eliminates the necessity for separate region proposal stages, thereby enabling end-to-end detection at substantially accelerated inference speeds while maintaining competitive accuracy [6]. The training process was executed for 200 epochs, employing a batch size of 16 and a 640×640 input image resolution. The Stochastic Gradient Descent (SGD) optimizer, with a momentum value of 0.9, was utilized to ensure stable convergence. Furthermore, advanced data augmentation strategies such as mosaic augmentation (applied at

every batch), mixup with a 50% probability, horizontal flipping (50%), and vertical flipping (20%) were incorporated. These techniques enhance the variability of the training samples and contribute to the model's robustness against scale, orientation, and illumination changes [7], thereby improving its generalization ability in real-world applications. A high patience value (300) was defined to allow extended learning without premature early stopping, a critical consideration when leveraging complex augmentations and extensive training epochs.

The performance of the model was evaluated using standard metrics including Intersection over Union (IoU), precision, and recall. Precision was calculated according to Equation (1) and recall according to Equation (2).

$$Precision = \frac{TP}{TP + FP} \tag{1}$$

$$Recall = \frac{TP}{TP + FN} \tag{2}$$

To ensure precise detections, a 50% IoU threshold was implemented, which indicates that if the IoU between the predicted and ground-truth bounding boxes exceeds 0.5, the detected box is designated as a true positive (TP). Subsequently, precision and recall values were calculated by identifying false positives (FP) and false negatives (FN). In addition to these metrics, we incorporated complementary metrics such as the F1-score (Equation (3)) and the Average Precision (AP) (Equation (4)) to more accurately evaluate the model's detection performance. These metrics offer a quantitative assessment of the model's accuracy and its capacity to identify patterns in test data that the model has not previously observed.

$$F1 = \frac{2\ x\ Precision\ x\ Recall}{Precision + Recall} \tag{3}$$

$$AP = \sum_{i=1}^{N} (R_i - R_{i-1})P_i \tag{4}$$

Findings

The performance of the Faster R-CNN-based deep learning model was evaluated on the test dataset, and the results demonstrated that it performed considerably well. Following several optimizations, the model achieved its highest accuracy at the 90th epoch. An Intersection over Union (IoU) threshold of 0.5 was employed to assess detection accuracy. Within the 11 test images containing 57 ground truth annotations, the model produced 51 true positives (TP), 14 false positives (FP), and 6 false negatives (FN). A precision score of 0.78 indicates that approximately 78% of the model's predictions were correct, while a recall value of 0.89 reflects the model's ability to identify nearly 89% of all reinforcement buckling instances present in the data. The high recall rate is particularly critical for civil infrastructure monitoring applications, where undetected damage (FN) can lead to severe safety risks. Notably, a recent study emphasized that models with a recall lower than 0.85 may be insufficient for deployment in disaster-prone regions [8].

The F1-score, which is the harmonic mean of precision and recall values, was found to be approximately 0.84, thereby supporting the balanced performance of the model. It is crucial to maintain this balance in applications where both false positives and false negatives can lead to significant operational costs[9]. Furthermore, the Average Precision (AP) of 0.88 supports the model's success in the reinforcement buckling detection task. Recent studies underline that AP values above 0.85 are indicative of robust performance in industrial defect detection systems[10].

The model's predictions on the images in the test dataset and the ground-truth buckling regions are presented in Figure 1. Prediction boxes are delineated by orange dashed lines, while ground-truth regions are indicated by blue lines. Additionally, the prediction score is indicated above the prediction boxes, and the IoU value is specified below.

Figure 1. Faster R-CNN Prediction and ground-truth regions.

The YOLOv8 model was also assessed using the test dataset to determine its effectiveness in detecting reinforcement buckling. An IoU threshold of 0.5 was applied for the evaluation process. Out of 57 ground truth instances across 11 images, the model successfully identified 45 true positives, while producing 5 false positives and missing 12 cases (false negatives). With a precision of 0.898, the model demonstrated strong reliability in its predictions, accurately identifying most of the positive cases. The recall rate of 0.772, though slightly lower, indicates a solid capability in detecting the majority of actual buckling events. This balance between minimizing incorrect alerts and capturing real damage is essential in practical field applications.

The calculated F1-score of approximately 0.83 reflects a harmonious trade-off between precision and recall, underscoring the model's stable and consistent performance. Additionally, the mAP@0.5 value of 0.8574 further supports its overall effectiveness in this task, confirming the model's potential for use in automated damage detection systems. Figure 2 illustrates the comparison between predicted regions and ground-truth boxes, where prediction boxes are outlined in orange

dashed lines and reference annotations are marked in blue. Each prediction box is labeled with the confidence level above and the IoU score below, providing insight into the model's detection accuracy and reliability.

Figure 2. YOLOv8 Prediction and ground-truth regions.

Comparatively, the results indicate that while Faster R-CNN achieved higher recall, YOLOv8 delivered better precision. This contrast is rooted in architectural differences: Faster R-CNN's two-stage design enables deeper analysis but requires more computation, whereas YOLOv8's single-stage pipeline offers faster, more efficient performance, well suited for real-time or mobile applications.

Conclusion

This study demonstrates the effectiveness of deep learning in detecting reinforcement buckling in reinforced concrete columns. Despite a limited dataset, the models achieved strong precision and recall, supporting their use in post-earthquake damage assessment. Compared to traditional inspections, this approach offers speed, consistency, and objectivity. While

one model offered broader coverage and the other higher precision, both highlighted the need to align model choice with specific operational goals.

Faster R-CNN and YOLO reflect two different detection strategies. The former provides more precise localization through a two-stage process, while the latter prioritizes speed and efficiency with a single-stage design—making it better suited for real-time, resource-limited applications.

These models also show great potential for integration into UAV-based inspections and edge-device deployments. Their lightweight, fast-inference design makes them ideal for mobile toolkits used in disaster zones, enabling quick on-site evaluations without relying on cloud connectivity.

References

Chen, Y., Zhang, X., & Wang, H. (2021). Advances in Image Standardization Techniques for Deep Learning Applications. *IEEE Transactions on Neural Networks and Learning Systems*, 32(4), 1523-1534.

Gupta, A., et al. (2023). Benchmarking average precision thresholds for industrial defect detection. *International Journal of Computer Vision, 131*(4), 789-805.

Jocher, G., Chaurasia, A., Qiu, J., & Stoken, A. (2023). YOLO by Ultralytics [Computer software]. GitHub. https://github.com/ultralytics/ultralytics

Loshchilov, I., & Hutter, F. (2016). SGDR: Stochastic gradient descent with warm restarts. *International Conference on Learning Representations (ICLR)*.

Martinez, G., et al. (2023). Recall thresholds for seismic damage detection: A regulatory and technical review. *Earthquake Engineering & Structural Dynamics, 52*(8), 2319-2335.

Patel, S., & Nguyen, T. (2020). Balancing precision and recall in safety-critical computer vision systems. *Journal of Machine Learning Research, 21*(1), 1-25.

Ren, S., He, K., Girshick, R., & Sun, J. (2015). Faster R-CNN: Towards real-time object detection with region proposal networks. *Advances in Neural Information Processing Systems*.

Shorten, C., & Khoshgoftaar, T. M. (2019). A survey on image data augmentation for deep learning. *Journal of Big Data, 6*(1), 60.

US Geological Survey (USGS). (2023). M7.8 – Turkey Earthquake. Available from: https://earthquake.usgs.gov/earthquakes/eventpage/us6000jllz. Date retrieved March 15, 2025.

Zhang, H., Cisse, M., Dauphin, Y. N., & Lopez-Paz, D. (2018). mixup: Beyond empirical risk minimization. *International Conference on Learning Representations (ICLR).* https://arxiv.org/abs/1710.09412

Estimating Equivalent Damping Ratio of Conventional Shear Walls by Machine Learning Methods

Siamak Tahaei Yaghoubi[a], Zeynep Tuna Deger[a]

[a] Istanbul Technical University, Earthquake Engineering and Disaster Management Institute, Türkiye
tahaeiyaghoubi@itu.edu.tr

Keywords: Equivalent Damping Ratio, Machine Learning, Reinforced Concrete Shear Walls.

Aim

A deep insight into the damping properties of structures and structural components is crucial for understanding their behavior under dynamic loads. Nonetheless, estimating the damping properties is a challenging task compared to identifying other structural parameters (e.g., stiffness, dynamic frequencies, etc.) This is because many mechanisms influencing the damping are not comprehensively understood and structural components may show different levels of damping depending on their deformations and experienced damage levels. The equivalent damping ratio is a simplified representation of complex structural damping mechanisms with broad application in the analysis and design purposes due to its straightforward formulation and convenient calculation. The present study aims to estimate the equivalent damping ratio of conventional RC shear walls at 1.0% drift ratio using machine learning-based methods. A dataset of 161 rectangular conventional shear walls subjected to quasi-static cyclic loading was assembled for this purpose. Five different machine learning (ML) methods, namely, Regularized Least Squares Linear Regression (RLR), K-Nearest Neighbor Regression (KNNR), Kernel Ridge Regression (KRR), Support Vector Regression (SVR), and Gaussian Process Regression (GPR) were examined. Analysis results revealed that Gaussian Process Regression exhibited superior prediction performance with a mean coefficient of determination (R^2) of about 0.89, a relative root mean square error (RELRMSE) of about 0.14 and a mean absolute percentage error (MAPE) of 10.44%.

Material and Method

RC shear walls are one of the most commonly used lateral load-resisting mechanisms worldwide. They have been broadly employed to enhance stiffness and reduce lateral deformations of medium-rise and tall buildings. These key structural components may undergo inelastic deformations during their service life due to loads imposed by seismic events or strong winds.

Employing inaccurate values of equivalent damping ratio may result in misleading evaluation of the ductility and energy dissipation capacity of structures. Due to the increasing popularity of displacement and energy-based design methodologies, the equivalent damping ratio of structures and structural components must be estimated properly at deformations beyond the elastic limit. This study uses machine learning techniques to evaluate the equivalent damping ratio of conventional RC shear walls at displacements corresponding to 1.0% lateral drift ratio. The selected reference deformation is the maximum allowable drift level by many building standards for several types of buildings (e.g., Eurocode 8 Part 1 for the ultimate limit state of buildings with non-structural elements, FEMA 356 for life safety limit state performance level of concrete wall structures, etc.)

The formulation used for quantifying equivalent damping ratio ξ_{eq} is based on the method proposed by (Jacobsen, 1930). According to this method, the dissipated energy in a vibrating cycle by the original structure is equated to the energy dissipated by an equivalent linear system with viscous damping under sinusoidal excitation. In resonance conditions, this definition leads to Equation 1:

$$\xi_{eq} = \frac{1}{4\pi}\frac{E_D}{E_{so}} \quad (1)$$

where E_D, the cyclic dissipated energy, is the area of the hysteresis loop and E_{s0} is the elastic strain energy (Figure 1). The latter parameter is calculated as $E_{so} = 0.5 f_0 u_0$ where u_0 is the maximum displacement and f_0 is the corresponding lateral force (Chopra, 2020).

As listed in Table A.1, this study uses a database of 161 rectangular RC shear walls from laboratory experiments carried out around the world to train and validate the ML models. All gathered specimens have concentrated rebars at their extreme ends and a height limit of 3.25 m to represent the common structural walls in Turkish stock. In terms of the failure mechanism, 54 walls failed in shear while 67 and 40 walls experienced respectively flexural and shear-flexural failure modes.

Table 1. Statistical properties of the output parameters.

Output parameter	Minimum	Maximum	Range	Mean	Standard deviation	Coefficient of Variation (%)
f_0 (kN)	15.2	2028.9	2013.7	544.9	507.6	93.2
E_D (kN.m)	0.45	25.74	25.29	5.42	4.41	81.4
ξ_{eq}(%)	3.02	26.6	23.6	11.1	4.9	43.8

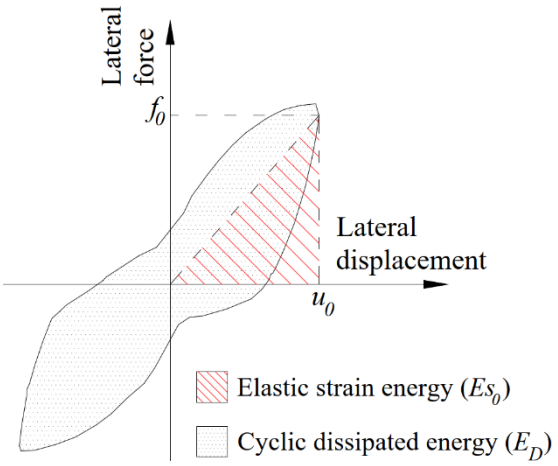

Figure 1. Definition of the elastic strain and cyclic dissipated energy.

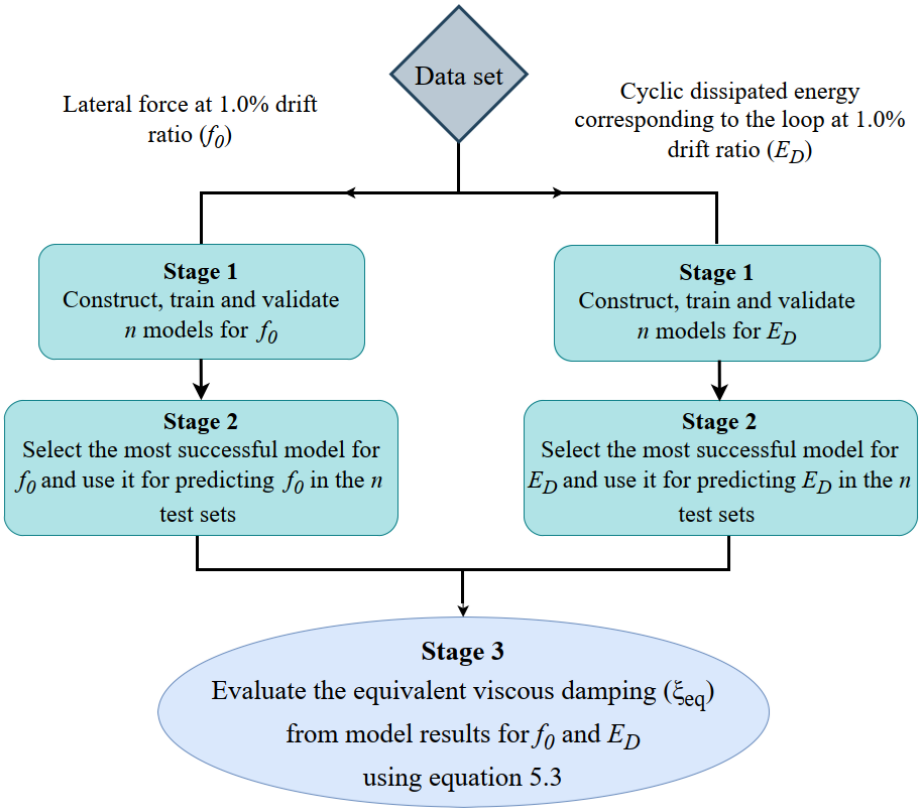

Figure 2. The algorithm for ML-aided evaluation of ξ_{eq}.

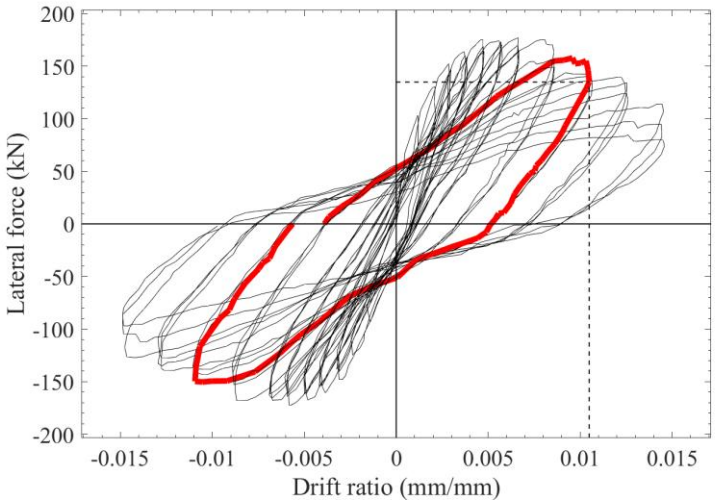

Figure 3. ξ_{eq} by Jacobsen's method (Specimen MSW3, (Salonikios et al., 1999)).

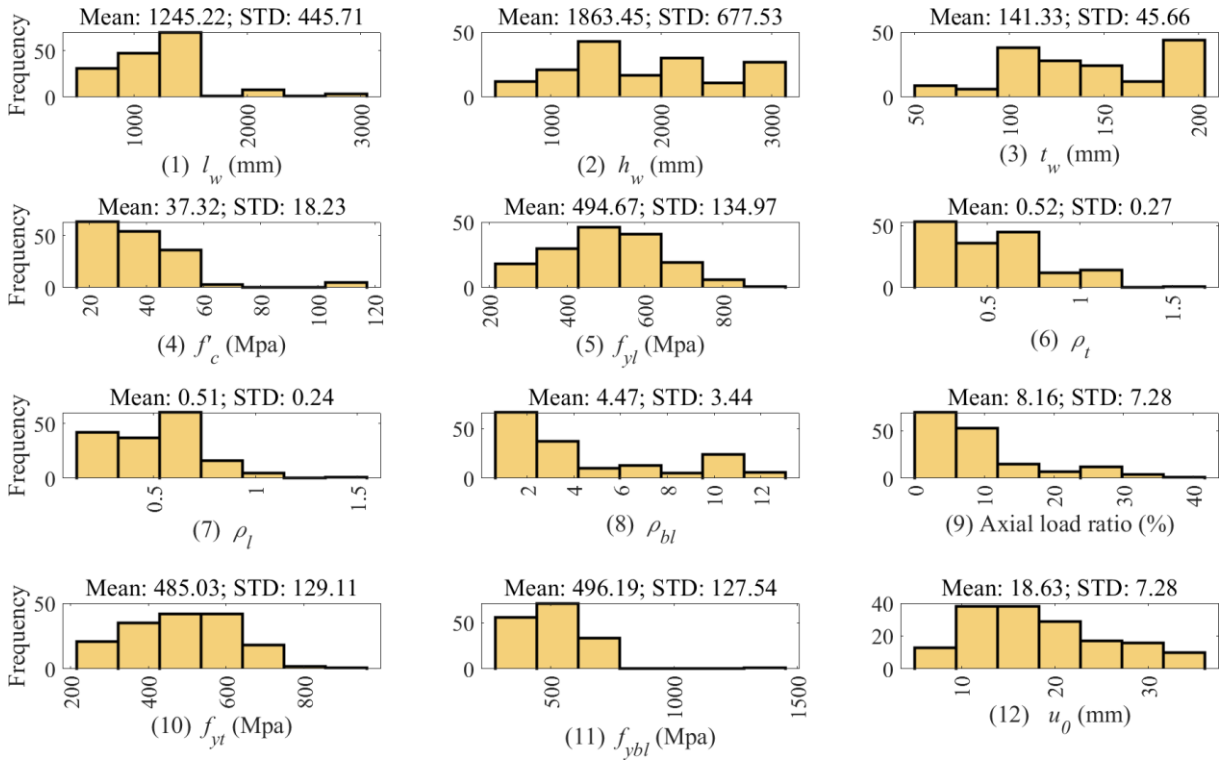

Figure 4. Frequency distribution of input variables (features).

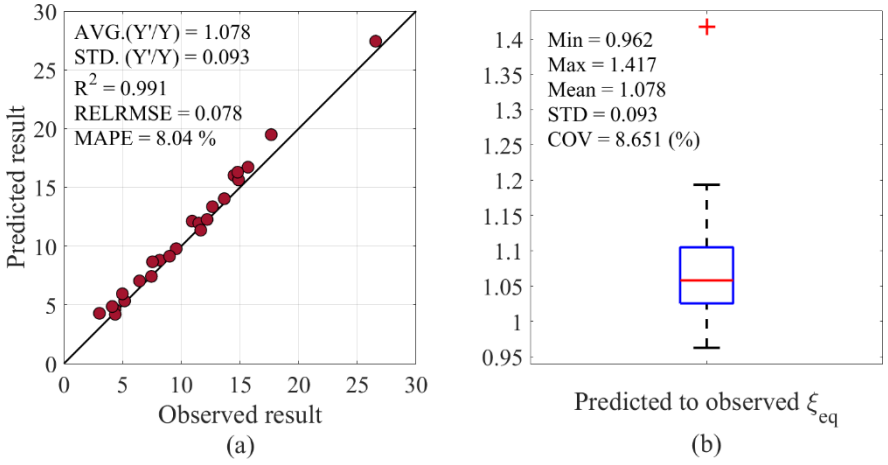

Figure 4. a) Results of the proposed model predicting ξ_{eq}; b) Distribution of the predicted to observed values.

Considering that the damping properties of structures and structural components are influenced by their level of damage (Chopra (2020)), a study was carried out to identify the damage status of the database shear walls at the reference drift level (i.e., 1.0% drift ratio). The damage status of shear walls was determined using their damage evolution reports, pre-failure photographs/figures and lateral load-displacement hysteresis curves. It was found that 18%, 62% and 20% of the walls had respectively experienced moderate, heavy and major damages at 1.0% drift ratio according to the ATC-13 damage index. Code conformity of the database specimens was controlled against the provisions of ACI 318-11 standard, revealing that the vast majority of the database specimens were substandard with only 10 out of 161 walls fully meeting the ACI 318-11

requirements considering the minimum wall reinforcement, boundary element provisions for special structural walls, the minimum material strength, etc.

Developing the machine learning-based model was initiated by defining the equivalent damping ratio as the output variable and its direct evaluation using different ML techniques. However, numerous attempts using various ML algorithms with assorted input variables (features) failed to establish a good correlation between the observed and predicted ξ_{eq} values. Consequently, an algorithm (schematically shown in Figure 2) consisting of two stages was established which treats f_0 and E_D as the intermediate outputs while ξ_{eq} (the final output) is computed according to Jacobsen's method using the approximated f_0 and E_D values in the first phase.

The input variables (feature sets) of the ML algorithms predicting f_0 and E_D were selected based on domain knowledge in the literature review. To this end, parameters known to influence the lateral load and energy dissipation capacity of shear walls were determined from scientific resources. The models predicting f_0 and E_D employ 10 and 11 features respectively, representing geometrical and mechanical properties of the database walls. The feature set for predicting f_0 includes: 1- wall length (l_w); 2- wall height (h_w); 3- wall thickness (t_w); 4- axial load ratio defined as the applied compressive load *P* divided by the wall cross-sectional area (A_g) and concrete compressive strength (f_c'); 5- concrete compressive strength (f_c'); 6- yield strength of longitudinal web rebars (f_{yl}); 7- transverse web reinforcement ratio (ρ_t); 8- longitudinal web reinforcement ratio (ρ_l); 9- longitudinal boundary reinforcement ratio (ρ_{bl}) and 10- yield strength of transverse web rebars (f_{yt}). The feature set for the model predicting E_D includes the first nine features of the model predicting f_0 and the two additional variables of longitudinal boundary rebars yield strength (f_{ybl}) and maximum lateral displacement of the hysteretic loop (u_0). The last feature (u_0) is introduced to provide the model with the actual maximum displacement data of the hysteresis loop. This is because, as demonstrated in Figure 3 for specimen MSW3 (Salonikios et al., (1999)), for some walls the measured deformation may have slight deviations from the reference deformation of 1.0% drift level. Statistical properties of the 12 features and 3 output variables are shown in Figure 4 and Table 1, respectively.

Subsequently, the collinearity of features (the situation when there is a strong correlation between two or more variables) was studied by looking at the Variance Inflation Factor (VIF) parameter:

$$VIF = \frac{1}{1 - R^2} \tag{2}$$

Table 2 summarizes the VIF values for the multicollinearity control. Considering that for VIF values smaller than 10 collinearity is not a significant issue (Hair, JR. et al., (2003)), it is concluded that collinearity only exists between h_w and u_0 in the feature set of the model estimating E_D. Despite this observation, both features (i.e., u_0 & h_w) were retained because their contribution to the prediction efficacy was confirmed through trial and error, and considering that their strong association is expected due to the definition of u_0 (i.e., $u_0 \approx 0.01 h_w$).

Logarithmic transformation of input and output variables was carried out so that their distributions fit the normal distribution in a better manner. Coefficient of determination (R^2), relative root mean square error ($RELRMSE$) and mean absolute percentage error ($MAPE$) were employed as statistical measures to evaluate the performance of the ML models (Equation 3 to 5). In these equations, n is the data number, Y is the observed value and Y' is the predicted value.

Table 2. Collinearity statistics of the input variables.

f_0			E_D		
Feature	R^2	*VIF*	Feature	R^2	*VIF*
l_w	0.61	2.58	l_w	0.62	2.60
h_w	0.32	1.47	h_w	0.95	20.77
t_w	0.70	3.37	t_w	0.84	6.21
f'_c	0.39	1.63	f'_c	0.28	1.39
f_{yt}	0.81	5.32	f_{ybl}	0.65	2.85
f_{yl}	0.80	4.99	f_{yl}	0.63	2.71
ρ_t	0.65	2.83	ρ_t	0.63	2.67
ρ_l	0.68	3.08	ρ_l	0.17	1.21
ρ_{bl}	0.13	1.14	ρ_{bl}	0.59	2.45
ALR (%)	0.39	1.63	*ALR (%)*	0.39	1.64
-	-	-	u_0	0.95	19.97

$$R^2 = \left[\frac{n\sum YY' - (\sum Y)(\sum Y')}{\sqrt{n(\sum Y^2) - (\sum Y)^2} \times \sqrt{n(\sum Y'^2) - (\sum Y')^2}}\right]^2 \quad (3)$$

$$RELRMSE = \sqrt{\frac{1}{n}\sum (Y - Y')^2} \Big/ \left(\frac{1}{n}\sum Y'\right) \quad (4)$$

$$MAPE = \frac{100\%}{n}\sum \left|\frac{Y - Y'}{Y}\right| \quad (5)$$

Findings

The performance of the five machine learning algorithms (RLR, KNNR, KRR, SVR & GPR) was evaluated after carrying out 10 analysis trials. Each trial was repeated 1000 times, and in each repeat, the database was randomly split into training and validation sets with a train/validation ratio of 85%-15%.

The kernelized methods (KRR, SVR and GPR) all use the radial basis function (RBF) kernel. Hyperparameter optimization for RLR, KRR, SVR and KNNR methods (i.e., shrinkage factor in RLR, the Gaussian kernel variance and penalty parameter in KRR, threshold, penalty and γ parameters in SVR, the number of nearest neighbors in KNNR) was carried out using grid search, while GPR hyperparameters (including the length/scale parameter, the signal and noise variance) were optimized via the conjugate gradient method (Rasmussen & Nickisch (2010)) by maximizing log marginal likelihood. The

Gaussian Process Regression algorithm (Rasmussen (2004)) exhibited significantly superior performance in comparison to the other four ML algorithms estimating the intermediate and final outputs.

Table 3 summarizes the regression analysis results on the validation set by the GPR-based model. Figure 5 demonstrates the performance of the model with the highest R^2 in predicting ξ_{eq} ($R^2 = 0.991$). The regression results for the four remaining ML methods are omitted for brevity.

Table 3. Performance scores of the GPR-based model.

Output Parameter	Maximum R^2	Mean R^2	Mean RELRMSE	Mean MAPE (%)
f_0	0.997	0.939	0.231	24.47
E_D	0.982	0.818	0.354	28.49
ξ_{eq}	0.991	0.890	0.141	10.44

Table A.1. List of database specimens.

Author(s)	Specimens
Abdulridha & Palermo (2017)	W1-SR
Alarcon et al., (2014)	W1, W2, W3
Altin et al., (2013)	1 (Reference)
Athanasopoulou (2010)	S1, S4, S6, S9
Baek et al., (2017a)	NS2, HS2, NS2L, HS2L, NF2, HF2, HF2-500, HF2-600
Baek et al., (2017b)	NS1M, HS1M, NF1M, HF1M, HF1M-B, NF1T-B, HF1T-B, NS0.5M, HS0.5M, HF0.5M-B
Baek et al., (2018)	SW1, SW2, SW3, SW4, SW5, SW6, FW1, FW2, FW3, FW4
Cheng et al., (2016)	M60, M115, H60, H115, H60X
Christidis & Trezos (2017)	W7, W9, W11
Cortés-Puentes & Palermo (2018)	SQ2
Deng et al., (2008)	HPCW-01, HPCW-02, HPCW-03, HPCW-04
Elnashai & Pinho (1998)	Original
Ghazizadeh & Cruz-Noguez (2018)	Control Wall
Ghorbani-Renani et al., (2009)	A2C, B2C
Gu et al., (2019)	XQB-1
Han et al., (2002)	W2, W3
Hidalgo et al., (2002)	1, 2, 4, 6, 7, 8, 9
Hube et al., (2014)	W4, W5, W7, W8, W9

Jiang (1999)	SSW-T, DSW-T
Jiang et al., (2013)	SW7
Kuang & Ho (2007)	M-1.0-H, M-1.0-2H, M-1.0-SH, M-1.0-J, M-1.0-T
Lefas & Kotsovos (1990)	SW33
Lombard et al., (2000)	1' (Control Wall)
Lu et al., (2016a)	SW-1, SW-2
Lu et al., (2016b)	C5, C6
Lu et al., (2018)	M1, M2, M3, M4
Luna et al., (2015)	SW11, SW12
Ma et al (2013)	SW1, SW2, SW3, SW4
Massone et al., (2009)	WP-T5-N0-S1, WP-T5-N0-S2, WP-T5-N5-S2, WP-T5-N10-S2
Massone et al., (2019)	W1
Oh et al., (2002)	WR-20, WR10, WR-0
Park et al., (2015)	S1, S2, S3, S5, S6, S7, S8
Paulay et al., (1982)	Wall 1
Peng et al., (2016)	SW1
Pilakoutas & Elnashai (1995)	SW4, SW5, SW6, SW7, SW8, SW9
Qiao et al., (2017)	W1
Quiroz et al., (2013)	MFIEN3EP
Ren et al. (2018)	RC-W
Salonikios et al., (1999)	MSW1, MSW2, MSW3, MSW6
Shen et al., (2017)	SHW0
Tasnimi (2000)	SHW1
Terzioğlu, (2011)	T2-S2-3, T2-S3-4, T3-S1-5, T4-S1-6, T5-S1-7, T6-S1-8, T1-S2-9, T1-N5-S1-10, T1-N10-S1-11, T1-S1-2
Tran & Wallace (2015)	RW-A20-P10-S38, RW-A20-P10-S63, RW-A15-P10-S51, RW-A15-P10-S78, RW-A15-P2.5-S64
Tripathi et al., (2019)	SWD-1, SWD-2
Yan et al., (2008)	SW-1, SW-2, SW-3, SW-4, SW-5
Yuan et al., (2018)	SW-1, SW-2
Zhang & Wang (2000)	SW7, SW8, SW9

Zhang (2007)	SW1-1, SW1-2, SW1-3
Zhang et al., (2014)	SW-2, SW-3, SW6-1, SW6-3
Zhou et al., (2004)	SW1, SW2

Conclusion

The possibility of estimating the equivalent damping ratio of conventional RC shear walls at 1.0% drift ratio using machine learning-based methods was investigated using five different ML methods.

A database including 161 planar RC shear walls with a height limit of 3.25m subjected to quasi-static cyclic loading was assembled. The database mostly consists of substandard experimental walls with a relatively homogenous distribution of shear, flexural and shear-flexural failure mechanisms. All specimens had experienced beyond elastic deformations at 1.0% drift ratio with 82% undergoing heavy or major damage levels according to ATC-13 damage index. The equivalent damping ratio values of the gathered experimental walls were quantified using their lateral load-displacement hysteresis curves at displacements corresponding to 1.0% drift ratio. The calculated equivalent damping ratios had a minimum of 3%, a maximum of 26.6% and the mean value of 11.1%.

An algorithm based on predicting the equivalent damping ratio (final output) using the estimated values of cyclic dissipated energy and lateral force (intermediate outputs) was developed. The GPR-based model showed superior performance over other examined methods in terms of establishing a strong correlation between the observed and predicted values of both the intermediate and final outputs.

Future efforts will include enhancing the model's interpretability and explainability. In particular, SHAP (SHapley Additive exPlanation), a model-agnostic method, is of interest due to its efficiency in describing the contribution of each feature to the model's prediction.

References

ACI Committee 318. (2011). *Building Code Requirements for Structural Concrete (ACI 318-11) and Commentary*. Farmington Hills, MI, USA: American Concrete Institute.

Applied Technology Council. (1985). *ATC-13, Earthquake Damage Evaluation Data for California*. Redwood City, CA.

Chopra, A. K. (2020). *Dynamics of Structures: Theory and Applications to Earthquake Engineering (Fifth Edition in SI Units). Harlow*, United Kingdom: Pearson Education Limited.

European Committee for Standardization. (2004). *Eurocode 8: Design of Structures for Earthquake Resistance - Part 1: General Rules, Seismic Actions and Rules for Buildings (EN 1998-1).* Brussels, Belgium: CEN.

Federal Emergency Management Agency. (2000). *Prestandard and Commentary for the Seismic Rehabilitation of Buildings*. Washington, DC

Hair, JR., J. F., Bush, R. P. & Ortinau, D. J. (2003). *Marketing Research Within a Changing Information Environment*. New York, NY, USA: McGraw-Hill.

Jacobsen, L. S. (1930). Steady Forced Vibrations as Influenced by Damping. *ASME Transactions*, 52(1), 169-181.

Rasmussen, C. E. (2004). Gaussian Processes in Machine Learning. In O. Bousquet, U. V. Luxburg, & G. Rätsch, *Advanced Lectures on Machine Learning* (pp. 67-75). Springer, Berlin, Heidelberg.

Rasmussen, C. E., & Nickisch, H. (2010). Gaussian Processes for Machine Learning (GPML) Toolbox. (S. Sonnenburg, Ed.) *Journal of Machine Learning Research*, 11, 3011-3015.

Salonikios, T. N., Kappos, A. J., Tegos, I. A., & Penelis, G. G. (1999). Cyclic Load Behavior of Low-Slenderness Reinforced Concrete Walls: Design Basis and Test Results. *ACI Structural Journal*, 96(4), 649-661.

References (experimental specimens)

Abdulridha, A., & Palermo, D. (2017). Behaviour and modelling of hybrid SMA-steel reinforced concrete slender shear wall. *Engineering Structures*, 147, 77-80.

Alarcon, C., Hube, M.A., & de la Llera, J.C. (2014). Effect of Axial Loads in the Seismic Behavior of Reinforced Concrete Walls with Unconfined Wall Boundaries. *Engineering Structures*, 73, 13-23.

Altin, S., Kopraman, Y., & Baran, M. (2013). Strengthening of RC walls using externally bonding of steel strips. *Engineering Structures*, 49, 686-695.

Athanasopoulou, A. (2010). *Shear Strength and Drift Capacity of Reinforced Concrete and High-Performance Fiber Reinforced Concrete Low-Rise Walls Subjected to Displacement Reversals.* (Doctorate Thesis). The University of Michigan.

Baek, J-W., Park, H-G., Shin, H-M.,& Yim, S-J. (2017a). Cyclic Loading Test for Reinforced Concrete Walls (Aspect Ratio 2.0) with Grade 550 MPa (80 ksi) Shear Reinforcing Bars. *ACI Structural Journal*, 114(3), 673-689.

Baek, J. W., Park, H. G., Lee, J. H., & Bang, C. J. (2017b). Cyclic Loading Test for Walls of Aspect Ratio 1.0 and 0.5 with Grade 550 MPa (80 ksi) Shear Reinforcing Bars. *ACI Structural Journal*, 114(4).

Baek, J-W., Park, H-G., Choi, K-K., Seo, M-S., & Chung, L. (2018). Minimum Shear Reinforcement of Slender Walls with Grade 500 MPa (72.5 ksi) Reinforcing Bars. *ACI Structural Journal,* 115(3), 761-774.

Cheng, M. Y., Hung, S. C., Lequesne, R. D., & Lepage, A. (2016). Earthquake-Resistant Squat Walls Reinforced with High-Strength Steel. *ACI Structural Journal*, 113(5), 1065-1076.

Christidis, K., & Trezos, K. (2017). Experimental Investigation of Existing Non-Conforming RC Shear Walls. *Engineering Structures*, 140, 26-38.

Cortés-Puentes, W. L., & Palermo, D. (2018). Performance of pre-1970s squat reinforced concrete shear walls. *Canadian Journal of Civil Engineering*, 45(11), 922-935.

Deng, M., Liang, X., & Yang, K. (2008). Experimental Study on Seismic Behavior of High Performance Concrete Shear Wall with New Strategy of Transverse Confining Stirrups. *The 14th World Conference on Earthquake Engineering*, (pp. 1-8). Beijing, China.

Elnashai, A. S., & Pinho, R. (1998). Repair and retrofitting of RC walls using selective techniques. *Journal of earthquake engineering*, 2(04), 525-568.

Ghazizadeh, S., & Cruz-Noguez, C. A. (2018). Damage-Resistant Reinforced Concrete Low-Rise Walls with Hybrid GFRP-Steel Reinforcement and Steel Fibers. *Journal of Composites for Construction*, 22(2).

Ghorbani-Renani, I., Velev, N., Tremblay, R., Palermo, D., Massicotte, B., & Léger, P. (2009). Modeling and Testing Influence of Scaling Effects on Inelastic Response of Shear Walls. *ACI Structural Journal*, 160(3), 358-367.

Gu, Q., Dong, G., Wang, X., Jiang, H., & Peng, S. (2019). Research on pseudo-static cyclic tests of precast concrete shear walls with vertical rebar lapping in grout-filled constrained hole. *Engineering Structures*, 189, 396-410.

Han, S. W., Oh, Y.-H., & Lee, L.-H. (2002). Seismic Behaviour of Structural Walls with Specific Details. *Magazine of Concrete Research*, 54(5), 333–345.

Hidalgo, P. A., Ledezma, C. A., & Jordan, R. M. (2002). Seismic behavior of squat reinforced concrete shear walls. Earthquake Spectra, 18(2), 287-308.

Hube, M.A., Marihuén, A., de la Llera, J.C.,& Stojadinovic, B. (2014). Seismic Behavior of Slender Reinforced Concrete Walls. *Engineering Structures*, 80, 377–388.

Jiang, H. (1999). Shear walls R01~R02. In State Key Lab. of Disaster Reduction in Civil Eng., SLDRCE database on static tests of structural members and joint assemblies (pp. 69-85). Shanghai, China,: Tongji University (September, 2008).

Jiang, H., Wang, B., & Lu, X. (2013). Experimental Study on Damage Behavior of Reinforced Concrete Shear Walls Subjected to Cyclic Loads. *Journal of Earthquake Engineering*, 17, 958–971.

Kuang, J. S., & Ho, Y. B. (2007). Enhancing ductility of non-seismically designed RC shear walls. *Proceedings of the Institution of Civil Engineers-Structures and Buildings*, 160(3), 139149.

Lefas, I. D., Kotsovos, M. D., & Ambraseys, N. N. (1990). Behavior of reinforced concrete structural walls: strength, deformation characteristics, and failure mechanism. *Structural Journal*, 87(1), 23-31.

Lombard, J., Lau, D. T., Humar, J. L., Foo, S., & Cheung, M. S. (2000). Seismic strengthening and repair of reinforced concrete shear walls. In *Proc., 12th World Conf. on Earthquake Engineering (12WCEE)* (pp. 1-8). Auckland, New Zealand: New Zealand Society for Earthquake Engineering.

Lu, X., Wang, L., Wang, D., & Jiang, H. (2016a). An innovative joint connecting beam for precast concrete shear wall structures. *Structural Concrete*, 17(6), 972-986.

Lu, Y., Henry, R. S., Gultom, R., & Ma, Q. T. (2016b). Cyclic Testing of Reinforced Concrete Walls with Distributed Minimum Vertical Reinforcement. *Journal of Structural Engineering*, 143(5).

Lu, Y., Gultom, R. J., Ma, Q. Q., & Henry, R. S. (2018). Experimental Validation of Minimum Vertical Reinforcement Requirements for Ductile Concrete Walls. *ACI Structural Journal*, 115(4), 1115-1131.

Luna, B., Whittaker, A., & Rivera, J. (2015). Seismic behavior of low aspect ratio reinforced concrete shear walls. *ACI Structural Journal*, 12(5), 593-604.

Ma, H., Zhang, H., & Zhai, Y. (2013). Experimental Study on Seismic Performance of RC Shear Wall with High-Strength Rebars. *Sixth China-Japan-US Trilateral Symposium on Lifeline Earthquake Engineering* (pp. 505-512). Chengdu, China: ASCE Press.

Massone, L. M., Orakcal, K., & Wallace, J. W. (2009). Modelling of Squat Structural Walls Controlled by Shear. *ACI Structural Journal*, 106(5).

Massone, S. L., Díaz, S., Manríquez, I., Rojas, F., & Herrera, R. (2019). Experimental Cyclic Response of RC Walls with Setback Discontinuities. *Engineering Structures*, 178, 410–422.

Oh, Y-H., Han, S. W., & Lee, L-H. (2002). Effect of Boundary Element Details on the Seismic Deformation Capacity of Structural Walls. *Earthquake Engineering and Structural Dynamics*, 31, 1583–1602.

Park, H. G., Baek, J. W., Lee, J. H., & Shin, H. M. (2015). Cyclic loading tests for shear strength of low-rise reinforced concrete walls with grade 550 MPa bars. *ACI Structural Journal*, 112(3), 299-310.

Paulay, T., Priestley, M. J. N., & Synge, A. J. (1982). Ductility in earthquake resisting squat shearwalls. *ACI Journal,* 79(4), 257-269.

Peng, Y-Y., Qian, J-R., & Wang, Y-H. (2016). Cyclic Performance of Precast Concrete Shear Walls with a Mortar–Sleeve Connection for Longitudinal Steel Bars. *Materials and Structures*, 49, 2455–2469.

Pilakoutas, K., & Elnashai, A. (1995). Cyclic Behavior of Reinforced Concrete Cantilever Walls, Part I: Experimental Results. *ACI Structural Journal*, 92(3), 271-281.

Qiao, Q., Cao, W., Qian, Z., Li, X., Zhang, W., & Liu, W. (2017). Cyclic behavior of low rise concrete shear walls containing recycled coarse and fine aggregates. *Materials*, 10(12), 1400.

Quiroz, L. G., Maruyama, Y., & Zavala, C. (2013). Cyclic behavior of thin RC Peruvian shearwalls: Full-scale experimental investigation and numerical simulation. *Engineering Structures*, 52, 153-167.

Ren, F., Chen, J., Chen, G., Guo, Y., & Jiang, T. (2018). Elements, Seismic Behavior of Composite Shear Walls Incorporating Concrete-Filled Steel and FRP Tubes as Boundary. *Engineering Structures*, 168, 405-419.

Salonikios, T. N., Kappos, A. J., Tegos, I. A., & Penelis, G. G. (1999). Cyclic Load Behavior of Low-Slenderness Reinforced Concrete Walls: Design Basis and Test Results. *ACI Structural Journal*, 96(4), 649-661.

Shen, D., Yang, Q., Jiao, Y., Cui, Z., & Zhang, J. (2017). Experimental investigations on reinforced concrete shear walls strengthened with basalt fiber-reinforced polymers under cyclic load. *Construction and Building Materials*, 136, 217-229.

Tasnimi, A. A. (2000). Strength and deformation of mid-rise shear walls under load reversal. *Engineering Structures*, 22(4), 311-322.

Terzioğlu, T. (2011). *Experimental evaluation of the lateral load behavior of squat structural walls*. (MSc thesis). Boğaziçi University.

Tran, T. A., & Wallace, J. W. (2015). Cyclic Testing of Moderate-Aspect-Ratio Reinforced Concrete Structural Walls. *ACI Structural Journal*, 112(6), 653-666.

Tripathi, M., Dhakal, R. P., & Dashti, F. (2019). Bar buckling in ductile RC walls with different boundary zone detailing: Experimental investigation. *Engineering Structures*, 198.

Yan, S., Zhang, L. F., & Zhang, Y. G. (2008). Seismic Performances of High-strength Concrete Shear Walls Reinforced with High-strength Rebars. In W. K. Binienda (Ed.), *Earth & Space 2008: Engineering, Science, Construction, and Operations in Challenging Environments,* (pp. 1-8). Long Beach, California, USA.

Yuan, W., Zhao, J., Sun, Y., & Zeng, L. (2018). Strands, Experimental Study on Seismic Behavior of Concrete Walls Reinforced by PC. *Engineering Structures*, 175, 577-590.

Zhang, Y., & Wang, Z. (2000). Seismic Behavior of Reinforced Concrete Shear Walls Subjected to High Axial Loading. *ACI Structural Journal*, 97(5), 739-750.

Zhang, H. (2007). Shear Wall R11. In State Key Lab. of Disaster Reduction in Civil Eng., SLDRCE database on static tests of structural members and joint assemblies (pp. 169-188). Shanghai, China: Tongji University (September, 2008).

Zhang, H., Lu, X., Duan, Y., & Zhu, Y. (2014). Experimental Study on Failure Mechanism of RC Walls with Different Boundary Elements under Vertical and Lateral Loads. *Advances in Structural Engineering*, 17(3), 361-379.

Zhou, G. (2004). Shear Wall (R08). In State Key Lab. of Disaster Reduction in Civil Eng., SLDRCE database on static tests of structural members and joint assemblies (pp. 139-146). Shanghai, China: Tongji University (September, 2008).

EARTHQUAKE ENGINEERING

Artificial Intelligence, Machine Learning, and Deep Learning in Earthquake Engineering

Experimental Investigation of Reinforced Concrete Building Elements

Performance-Based Seismic Assessment and Design

Structural and Geotechnical Earthquake Engineering

Enhancing Seismic Resilience of Substandard RC Beam-Column Joints with All-Steel Tube-in-Tube Buckling-Restrained Braces: A Shake Table Test

Evrim Oyguc[a], Abdul Hayır[b], Resat Oyguc[a], Onur Seker[c], Bulent Akbas[c]

[a] Istanbul Technical University, Institute of Disaster Management, Earthquake Engineering Program, Türkiye
[b] Istanbul Technical University, Faculty of Civil Engineering, Department of Civil Engineering, Türkiye
[c] Gebze Technical University, Faculty of Civil Engineering, Department of Civil Engineering, Türkiye
eoyguc@itu.edu.tr

Keywords: Seismic Retrofitting, Buckling-Restrained braces, Substandard RC Beam-Column Joints, Shake Table Testing.

Aim

The seismic vulnerability of reinforced concrete (RC) frames, particularly those constructed prior to the implementation of modern seismic codes, continues to pose a significant risk to built environments. Many existing RC buildings, characterized by limited ductility and inadequate detailing, are inherently deficient when subjected to the dynamic loads generated during moderate to severe earthquakes (Oyguc et al., 2018). The financial impracticality of demolishing and reconstructing these structures necessitates the development of cost-effective and efficient retrofitting techniques. This study investigates the efficacy of employing an all-steel tube-in-tube buckling-restrained brace (TnT-BRB) system as a retrofit strategy for substandard RC frames. The primary aim is to evaluate whether the integration of TnT-BRBs can substantially improve the lateral strength, stiffness, energy dissipation capacity, and overall seismic performance of deficient RC frames while mitigating damage during intense seismic events.

The research leverages a state-of-the-art experimental approach involving shake table tests on one-third-scale specimens representing typical non-seismically detailed RC frames. One specimen serves as a control (bare frame), while the other is retrofitted with a diagonal TnT-BRB. Through this comparative investigation, the study seeks to elucidate the potential of TnT-BRB systems to function as primary seismic energy dissipation devices, thereby reducing excessive drift demands and preventing structural damage during earthquake excitations. This extended abstract further discusses the design rationale behind TnT-BRBs, details the experimental protocol including similitude requirements and instrumentation, and synthesizes the key findings that underscore the benefits and limitations of this retrofit technique.

The ultimate goal is to provide a rigorous, evidence-based recommendation for the adoption of TnT-BRBs as a feasible seismic retrofit solution that can be generalized for application in real-world scenarios, particularly for older RC buildings in seismically active regions.

Material and Method

To address the seismic deficiencies of substandard RC frames, an experimental program was designed and executed at the Allianz Teknik Earthquake and Fire Test and Training Center in Istanbul, Türkiye. Two one-story, one-bay RC frame specimens, scaled down to one-third of the prototype dimensions, were constructed based on the similitude rules derived from dimensional analysis and Buckingham's π theorem (1914). The control specimen (Specimen 1) represents a typical RC frame lacking seismic detailing, while the retrofitted specimen (Specimen 2) is enhanced with a single diagonal TnT-BRB system. Figure 1 shows the details of the specimens.

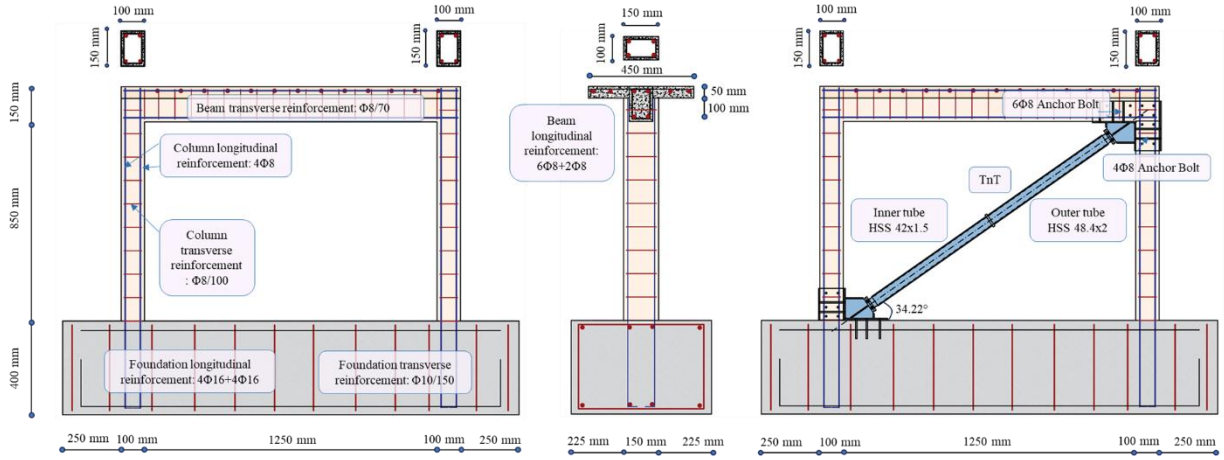

Figure 1. Details of the specimens.

The TnT-BRB, which is the cornerstone of this retrofit strategy, is an all-steel brace consisting of a load-bearing inner tube and an outer tube that functions as a buckling restrainer. The inner tube is fabricated from a circular hollow structural section (HSS) that is designed to undergo significant plastic deformations under seismic loading. The outer tube, segmented and attached via a ring-shaped stopper plate, provides continuous lateral support along the length of the brace to prevent global buckling. Notably, a deliberate gap between the two tubes allows the load-bearing tube to deform independently under axial loads while ensuring that the outer tube does not contribute to the compressive capacity. Connector plates and end connection assemblies, reinforced with pretensioned bolts, facilitate the integration of the TnT brace with the RC frame without imposing excessive additional stiffness on the structural elements.

The experimental protocol incorporated dynamic shake table tests for global stability evaluation. The shake table, equipped with hydraulic actuators and capable of delivering accelerations up to 1g across a frequency range of 0–50 Hz, was used to subject both specimens to scaled ground motion records. The primary seismic input was derived from the 2023 Kahramanmaraş earthquake (AFAD, 2023), and its time-history record was carefully scaled according to the similitude law established during the experimental design phase. In particular, the scaled acceleration time histories were applied to simulate various seismic intensity levels, from moderate (0.35g) to full-scale (1g) excitations, thus allowing for a detailed comparison between the bare and retrofitted frames. The physical variables are detailed in Table 1.

Table 1. Calculated physical quantities for shake table tests.

Physical Quantity	Scale Factor
Length, l_r	3
Modulus of elasticity, E_r	1
Time, t_r	1.732
Gravitational acceleration, g_r	1
Strain, ε_r	1
Acceleration, a_r	1
Frequency, ω_r	0.577
Velocity, v_r	1.732

Instrumentation played a critical role in capturing the dynamic response of the specimens. Linear voltage displacement transducers (LVDTs) were strategically placed at the top of the frame and along the length of the TnT brace to monitor lateral displacements and axial elongations. Accelerometers were deployed at key locations on the foundation, slab, and shake table surface to record the acceleration responses during testing. In addition, strain gauges embedded within the RC frame provided valuable data on the distribution of strains during dynamic loading. These measurement systems were synchronized with a computer-aided data acquisition system, ensuring high-resolution recording of transient responses and allowing for subsequent signal processing, such as baseline correction and low-pass filtering, to remove noise artifacts.

Findings

The shake table tests revealed a marked difference in the performance of the bare RC frame (Specimen 1) compared to the TnT-retrofitted frame (Specimen 2). Under a moderate excitation of 0.35g, Specimen 1 exhibited significant damage in the form of shear cracks at the beam-column connections and spalling of concrete at the lower portions of the columns. In contrast, Specimen 2, equipped with the TnT brace, demonstrated a nearly elastic response with only minor hairline cracks observed at similar excitation levels. The experimental data indicate that the TnT-BRB system effectively reduced lateral displacements: while Specimen 1 recorded a maximum lateral displacement corresponding to a story drift ratio of approximately 0.055 radians, Specimen 2 exhibited displacements well below the damaging threshold, with a drift ratio near 0.02 radians even under a full-scale 1g ground motion.

Quantitative analysis of the recorded acceleration responses further substantiated the benefits of the TnT retrofit. The damping ratios calculated via the half-power bandwidth method revealed that Specimen 2 had a significantly lower acceleration amplification factor compared to Specimen 1. This reduction in vibrational response is directly attributed to the energy dissipation mechanism of the TnT brace, which yielded symmetrically in both tension and compression. Axial displacement measurements from the LVDTs on the TnT brace indicated that the load-bearing tube experienced minimal elongation, remaining within the elastic range at 0.35g and achieving a peak ductility demand of less than three under 1g excitation. These observations confirm that the brace not only provides additional lateral stiffness but also acts as a controlled fuse that dissipates seismic energy, thereby protecting the primary RC frame from excessive stress.

Furthermore, the base shear force recorded for Specimen 2 was notably higher than that for Specimen 1 under similar ground motion levels. At 0.35g excitation, the bare frame's peak shear force was measured at approximately 18.17 kN, whereas the retrofitted frame experienced a peak force of 30.65 kN. Although the absolute shear force increased with the retrofit, the corresponding reduction in story drift ratio indicates a more favorable distribution of forces, with the TnT brace effectively absorbing and redirecting the seismic energy. The results suggest that, by acting as the primary seismic line of defense, the TnT-BRB system mitigates the adverse effects of horizontal forces on the main structural components. This conclusion is further reinforced by post-test inspections, which revealed that the retrofitted specimen maintained the integrity of its beam-column connections and overall structural configuration even after exposure to high-intensity ground motion.

A detailed comparison of the cyclic responses, illustrated in Figure 2, demonstrates that the TnT brace maintained stable, symmetrical hysteretic behavior throughout the testing cycles. This behavior is critical for ensuring that the brace can reliably dissipate energy without suffering premature failure due to local buckling or connection deficiencies.

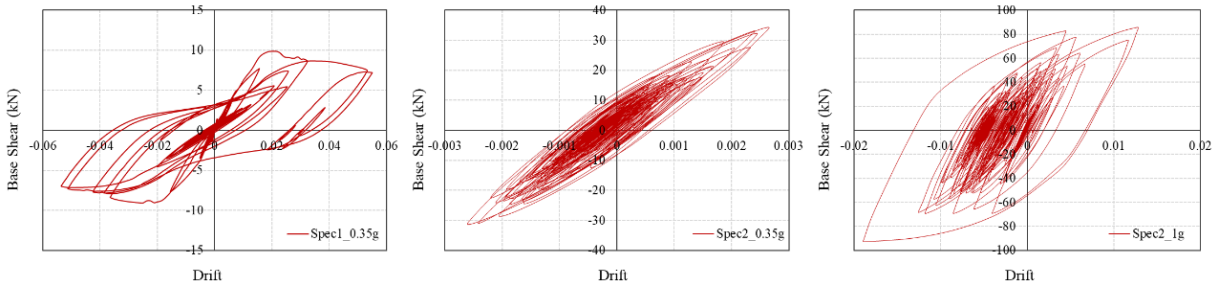

Figure 2. Hysteretic response of the specimens.

Additional insight was provided by the detailed analysis of the damage patterns observed during and after testing. Specimen 1 exhibited significant cracking and spalling, particularly in the vicinity of beam-column joints, a common failure mechanism in inadequately detailed RC structures. In contrast, Specimen 2, with the TnT retrofit, showed minimal superficial cracking and no evidence of damage in the critical joint regions. The absence of such damage underscores the potential of the TnT-BRB system to maintain structural integrity under severe seismic loading. Furthermore, the minimal axial elongations recorded along the TnT brace imply that the retrofit does not impose undue stress on the connected RC frame, thus ensuring that the primary structure can continue to perform effectively during subsequent seismic events.

Conclusion

The experimental investigation demonstrates that retrofitting substandard RC frames with all-steel tube-in-tube buckling-restrained braces markedly improves seismic performance. The TnT-BRB system not only enhances lateral stiffness and energy dissipation but also significantly reduces excessive lateral displacements and associated damage under seismic loading. The shake table tests, corroborated by finite element simulations, confirm that the TnT brace serves as an effective primary seismic defense mechanism, thereby protecting critical structural elements from inelastic deformations and catastrophic failure.

In summary, the incorporation of TnT-BRBs into RC frames offers a promising retrofit strategy for aging and deficient structures in seismically active regions. The retrofit enhances the overall ductility and resilience of the frame while maintaining cost-effectiveness and ease of installation. Future work should focus on large-scale and three-dimensional testing to further generalize these findings and to address additional uncertainties related to multi-directional seismic inputs. The present study provides a robust experimental and analytical basis for the widespread adoption of TnT-BRB systems in seismic retrofitting applications.

References

AFAD (Disaster and Emergency Management Presidency), *Ministry of Internal Affairs of the Republic of Turkey, 2023, Turkish Accelerometric Database and Analysis System*. Available online: https://tadas.afad.gov.tr/ (accessed on 15 December 2024).

Buckingham, E. (1914). On physically similar systems; illustrations of the use of dimensional equations. *Phys. Rev.*, **4**, 345–376. https://doi.org/10.1103/PhysRev.4.345.

Oyguc, R., Oyguc, E., Tonuk, G. (2018). Case study on seismic behavior of aseismically designed reinforced concrete frame structures. *Bull. Earthq. Eng*., **16**, 3057–3080. https://doi.org/10.1007/s10518-017-0300-x.

EARTHQUAKE ENGINEERING

Artificial Intelligence, Machine Learning, and Deep Learning in Earthquake Engineering

Experimental Investigation of Reinforced Concrete Building Elements

Performance-Based Seismic Assessment and Design

Structural and Geotechnical Earthquake Engineering

Seismic Performance Assessment of Irregular RC Structures Using the Extended N2 Method

Zekeriya Semih Aygün[a], Reşat Atalay Oyguç[a]

[a] Istanbul Technical Unıversity, Institute of Disaster Management, Department of Earthquake Engineering, Earthquake Engineering Program, Türkiye
aygun21@itu.edu.tr

Keywords: Extended n2, Higher Mode Effect, Irregular Buildings, Nonlinear Dynamic Analysis, Pushover Anaylsis.

Aim

Earthquakes have been among the most devastating natural disasters throughout human history and will continue to cause significant destruction in the future. The losses caused by earthquakes are not limited to casualties but also extend to economic and social dimensions, clearly indicating that the impact of this hazard will not diminish in the coming years. From past to present, numerous scientific studies and engineering solutions have been developed in the field of earthquake engineering, particularly focusing on earthquake-structure interaction. Throughout history, significant advancements have been made in seismic codes, and extensive academic research has been conducted on the design of earthquake resistant structures.

The fundamental philosopy of earthquake resistant design is based on ensuring that structures experience little to no damage during frequent small earthquakes, sustain repairable damage during moderate earthquakes, and maintain their structural integrity to preserve life safety during rare, large scale seismic events. Following the 1994 Northridge and 1995 Kobe earthquakes, the concept of performance based earthquake engineering emerged, proposing that structures should meet different performance objectives under varying levels of seismic hazard.

The nonlinear analysis and performance assesment methods used in performance based design aim to provide practical yet realistic results by combining the nonlinear static pushover analysis of multi degree of freedom (MDOF) models with the spectral analysis of equivalent single degree of freedom (SDOF) systems. One of these methods, and the basis of this study, is the N2 method developed by Fajfar (1999) at the University of Ljubljana. In conventional pushover based methods like the N2 method, it is assumed that the structure primarily vibrates in a single mode, typically the first mode. While this approach can yield accurate results for structures where higher mode effects are negligible, it may not provide satisfactory results for tall, irregular, asymmetric structures where torsional and higher mode effects are significant.

To address these limitations, Fajfar et al. (2005) proposed and extended N2 method, which accounts for plan-wise higher mode effects and can be applied to asymmetric structures. More recently, Kreslin and Fajfar (2011) introduced a further extension of the method to consider higher mode effects in the vertical (height) direction.

The aim of this study is to compare the story drift results obtained from Incremental Dynamic Analysis (IDA) -a more realistic analysis method- for two plan-irregular structures an done vertically irregular structure, with the results obtained from the conventional N2 method and extended N2 method considering higher mode effects. In this context, the study evaluates whether the extended N2 method can predict seismic demands more accurately than the conventional N2 method.

Material and Method

Within the scope of this study, a total of three reinforced concrete building models were developed, two of which are plan-irregular and one vertically irregular. All structures are four-story buildings, with material strengths selected as C16 for concrete and S420 for reinforcement steel. Irregularity parameters were calculated according to Eurocode 8 standards, and values such as eccentricities, torsional radii, and radii of gyration were determined for both X and Y directions.

For the Incremental Dynamic Analysis (IDA) of the structures, acceleration records from the Pazarcık (Table 1) earthquake (M_w 7.7) and the Elbistan (Table 2) earthquake (M_w 7.6), which bot occurred on February 6, 2023, were utilized. The shallow focal depths of these earthquakes (8.6 km and 7.0 km, respectively) significantly intensified the ground shaking.

Furthermore, the occurrence of two major earthquakes within a 9-hour interval severely challenged the performance levels of structures, leading to the complete collapse of many buildings that had already sustained moderate or severe damage after the first event. These characteristics highlight the importance of analyzing these earthquakes from the perspective of performance based earthquake engineering.

Table 1. Pazarcık earthquake records.

	Station	R_{jb} (km)	R_{rup}(km)	R_{epi}(km)	PGA_{EW}(cm/s^2)	PGA_{NS}(cm/s^2)	Soil Type	Vs_{30}
Pazarcık	3129	75,71	75,71	146,39	1209,572	1353,023	B	447
	3125	70,82	70,82	142,15	1121,948	822,160	B	448
	3135	66,18	66,18	142,15	1372,071	740,971	B	460
	3123	72,58	72,58	143,00	593,940	655,571	B	469
	3142	38,09	38,09	106,49	749,514	646,630	B	538
	3132	73,08	73,08	143,12	514,634	515,309	B	377
	3131	74,95	74,95	144,98	366,051	363,033	B	567
	6304	74,19	55,38	130,27	238,228	210,897	B	376

Table 2. Elbistan earthquake records.

	Station	R_{jb} (km)	R_{rup}(km)	R_{epi}(km)	PGA_{EW}(cm/s^2)	PGA_{NS}(cm/s^2)	Soil Type	Vs_{30}
Elbistan	4405	60,32	66,23	100,81	158,052	155,411	B	579
	2308	177,65	180,07	185,23	48,254	69,798	B	450
	3144	104,09	78,92	162,37	78,108	59,115	B	485
	0127	112,56	112,56	119,52	62,723	56,093	B	583
	7901	87,32	102,59	153,88	49,814	50,910	B	463
	3138	98,71	73,95	156,81	68,715	49,268	B	619

The selection of earthquake records for IDA analyses is critically important for obtaining accurate and reliable results. Parameters such as the epicentral distance (R_{epi}), the closest distance to the surface projection of the fault (R_{jb}), and the closest distance to the rupture (R_{rup}) were considered. To avoid near-fault effects and pulse like ground motions, short distance records were not preferred. Additionally, the shear wave velocities (V_{s30}) of the recording stations were selected within the range of 360-800 m/s, corresponding to soil class B as defined in Eurocode 8.

The selected ground motion records were obtained from the AFAD database and processed using the SeismoSignal software. To preserve the authenticity of ground motions, no spectral mathcing to a target design spectrum was performed. Instead, all records were scaled based on the Accelaration value corresponding to the average of the first two mode periods of the structure. This approach allowed the scaling process to be performed without altering the original frequency content of the records (Figure 1).

The building models were subjected to nonlinear time history analyses with increasing intensity under the selected ground motions using the SeismoStruct software. The results obtained from these analyses were evaluated using Excel software. Additionally, eigenvalue analyses were performed for each building model to determine parameters such as mode shapes, natural periods, and modal participation factors.

For the application of the N2 method, nonlinear static pushover analyses were first conducted on the building models. During these analyses, the structures were pushed under a predefined lateral load pattern until significant plastic behavior developed, and the capacity curves of the structures were obtained. These capacity curves were then transformed into equivalent single-degree-of-freedom (SDOF) capacity curves using modal transformation techniques to simplify the multi-degree-of-freedom (MDOF) system behavior.

The equivalent SDOF capacity curves were then compared with the elastic demand spectrum defined in Eurocode 8. The intersection point between the capacity curve and the demand spectrum was used to determine the target displacement and

the corresponding performance level of the structure. In the conventional N2 method, only the first mode of vibration was considered. While this approach yields sufficient accuracy for low-rise and regular structures, it may be inadequate for irregular, high-rise, or torsionally sensitive structures (Figure 1).

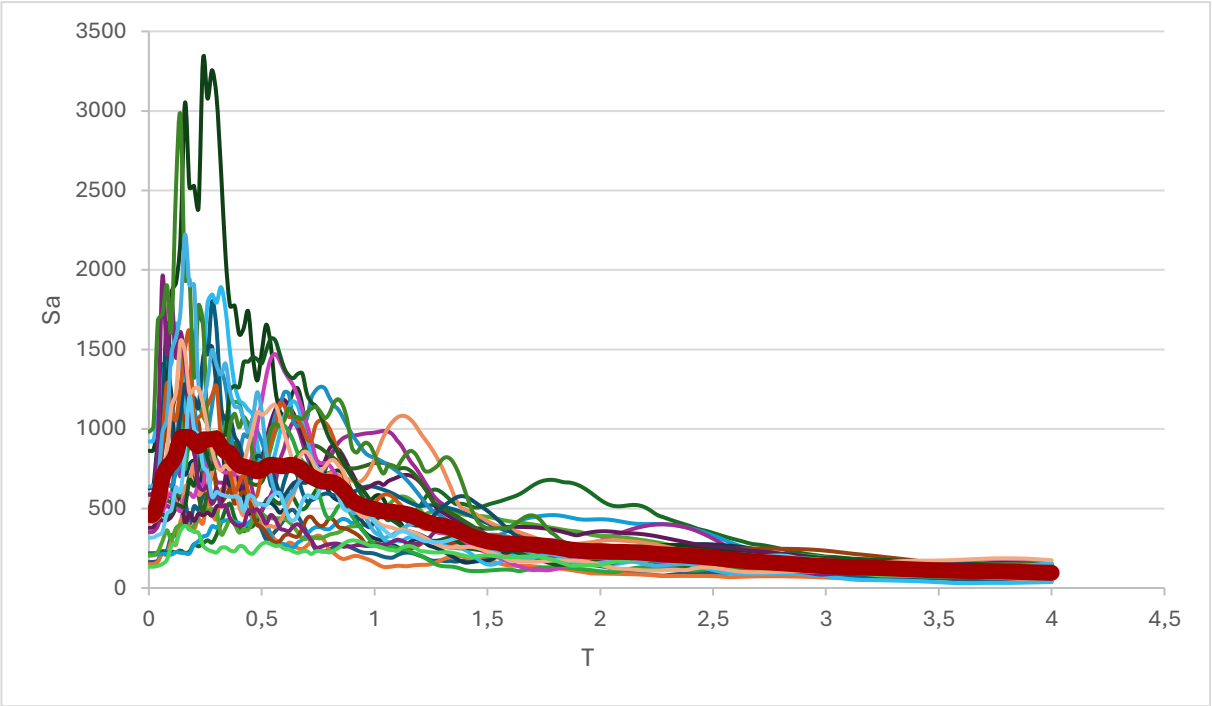

Figure 1. Sa (cm/s^2) – T (s) graph for different earthquake stations.

Therefore, in the later stages of the study, the extended N2 method, which accounts for higher mode effects, was applied. In this method, correction factors obtained from the elastic modal analyses were utilized to calculate the contribution of higher mode effects, particularly on the demands at the upper stories, and the existing capacity curve was updated accordingly. This approach ensured a more realistic assessment of structural performance by incorporating higher mode contributions. Finally, displacements and story drift obtained from both the conventional and extended N2 methods were compared with the IDA results to evaluate the accuracy of these methods (Figure 2).

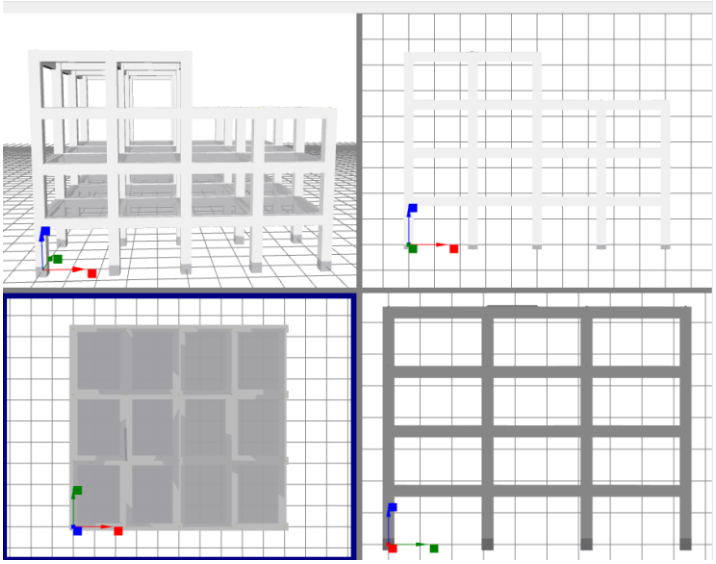

Figure 2. Vertically irregular structure.

Findings

The findings obtained from the analyses are summarized as follows:

- It was observed that story drift values increased significantly, particularly at the upper stories, as the degree of irregularity increased.
- It was found that the extended N2 method provided story drift predictions closer to the IDA results compared to the conventional N2 method, especially at the upper stories. The use of correction factors in the extended N2 method improved the accuracy of results for structures where higher mode effects were significant.
- In the vertically irregular structure, the effects of the second and third vibration modes became more pronounced, significantly influencing the distribution of story drifts throughout the structure.
- As the level of irregularity increased, a notable rise in residual displacement values was also observed in the structures.
- It was concluded that in structures with advanced irregularities, due to the intensified interaction between different modes, predictions made using single-mode approaches were insufficient, confirming the necessity of considering multi-mode effects.
- It was observed that in structures with plan irregularities, increased torsional effects led to irregular distributions in story drift and interstory drift ratios, particularly at the corner regions of the structures.

Conclusion

Based on the results obtained, the following general conclusions were drawn:

- Existing irregularities in structures, especially under conditions dominated by higher mode effects, led to significant changes in story drift distributions and damage patterns. In particular, in the vertically irregular structure, higher mode effects became markedly more significant, causing deviations from the predictions of the conventional N2 method. Therefore, employing analysis approaches that account for higher mode effects is critically important.
- Torsional effects in plan-irregular structures locally amplified story drift demands, and these amplifications were not adequately represented in the conventional N2 method.
- The extended N2 method, by considering higher mode effects, provided more accurate predictions compared to the conventional N2 method, yielding story drift values closer to IDA results, particularly at the upper stories (Figure 3).
- An increase in the degree of irregularity led to greater residual displacements, highlighting the necessity of developing performance assesment methods tailored for irregular structures.
- Overall, considering higher mode effects in the performance based evaluation of plan irregular and vertically irregular structures, and enhancing conventional methods, is crucial for achieving safer and more accurate engineering predictions.

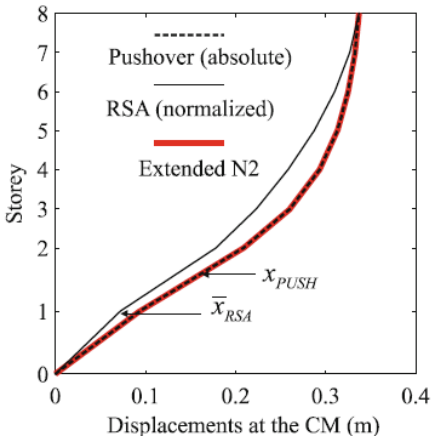

Figure 3. Higher mode effects in elevation (Kreslin and Fajfar, 2011).

References

AFAD Disaster and Emergency Management Presidency. (2018). *Turkey Earthquake risk map*. https://tdth.afad.gov.tr/

Bertero, V. (1997). Performance based seismic engineering: A critical review of proposed guidelines. In P. Fajfar & H. Krawinkler, *Seismic design methodologies for the next generation of codes*. AA Balkema.

Elnashai, A.S., & Sarno, L.D. (2008). *Fundamentals of earthquake engineering.* John Wiley & Sons, Ltd.

CEN. (2006). Eurocode 8: design of structures for earthquake resistance. *Part 1: general rules seismic actions and rules for buildings:* EN 1998-1, CEN, Brusselss, December 2004.

Kreslin, M., & Fajfar, P. (2011). The extended N2 method taking into account higher mode effects in elevation. *Earthquake Engineering & Structural Dynamics*, 40(13), 1571-1589.

Kreslin, M., & Fajfar, P. (2012). The extended N2 method considering higher mode effects in both plan and elevation. *Bulletin of Earthquake Engineering*, 10(2), 695-715.

Seismosoft. (2024). SeismoSignal – A computer program for signal processing of strong motion data (Version 2024) [Computer software]. *Seismosoft*. https://seismosoft.com/seismosignal

Seismosoft. (2024). SeismoStruct – A computer program for static and dynamic nonlinear analysis of framed structures (Version 2024) [Computer software]. *Seismosoft*. https://seismosoft.com/seismostruct

EARTHQUAKE ENGINEERING

Artificial Intelligence, Machine Learning, and Deep Learning in Earthquake Engineering

Experimental Investigation of Reinforced Concrete Building Elements

Performance-Based Seismic Assessment and Design

Structural and Geotechnical Earthquake Engineering

Seismic Performance Enhancement of RC Coupling Beams Using Shape Memory Alloy Devices

Ali Attariyan [a], Beyza Taşkın [b], Kıvanç Taşkın [c]

[a] Istanbul Technical University, Disaster Management Institute, Earthquake Engineering Department, Türkiye
[b] Istanbul Technical University, Civil Engineering Faculty, Civil Engineering Department, Türkiye
[c] Eskisehir Technical University, Engineering Faculty, Civil Engineering Department, Türkiye
attariyan17@itu.edu.tr

Keywords: Reinforced Concrete Coupled Beams, Replaceable Components, Shape Memory Alloy (SMA).

Aim

This study investigates the potential of shape memory alloys (SMAs) to improve the seismic performance of reinforced concrete (RC) coupled beams. In conventional systems, permanent damage and difficult post-earthquake repairs highlight the need for replaceable and resilient components. This study explores the feasibility of using SMAs as replaceable diagonal reinforcement in coupled beams. Superelastic (SE) and shape memory effect (SME) properties were evaluated via tensile testing, along with connection techniques such as laser welding, TIG welding, and mechanical splicing. Findings showed SME materials were unsuitable due to heat activation requirements, whereas SE materials exhibited desirable mechanical behavior. Welding methods proved unreliable, while mechanical splicing—particularly double splicers—offered effective performance. SE SMA wires, when properly shaped and mechanically connected, are concluded to be suitable for seismic applications in RC coupled beams.

Introduction

Reinforced concrete (RC) shear walls play a crucial role in resisting lateral forces in structures. To enhance lateral stiffness and meet architectural needs, they are often designed as coupled systems. However, conventional RC coupled beams can run into construction and performance issues, mainly due to the complex reinforcement detailing, especially when it comes to diagonal bars that need proper confinement (Foroughi & Yuksel, 2024; Han et al., 2022; Subramanian, 2021). To address these issues, replaceable coupling beams (RCBs) have been identified as viable options. The RCBs are specifically designed to localize damage during seismic events, thereby preserving the main structural system and facilitating cost-effective post-earthquake repair. Research shows that RCBs improve energy dissipation, lessen the force demand on shear walls, and postpone wall yielding, ultimately enhancing overall seismic performance (Chen et al., 2017; Lü et al., 2014; Lu et al., 2018; Sun, 2021).

Incorporating SMAs into RCBs further improves energy dissipation and re-centering. Used as diagonal reinforcement, SMAs reduce damage to beams and adjacent walls and minimize residual displacements (Ghassemieh, Rezapour, et al., 2017). Studies showed that SMA dampers enhance nonlinear seismic behavior in RC frame-wall systems (Mao et al., 2013). Also, the numerical studies confirming superior dynamic performance compared to conventional steel reinforcement (Ravi & Krishnan, 2019). Moreover, SMAs contribute to better energy dissipation and reduced residual deformations during earthquakes (Ghassemieh et al., 2012; Ghassemieh, Nojoumi, et al., 2017).

Material and Method

There are many types of SMAs, but the most common are those that contain nickel and titanium (NiTi), commonly referred to as Nitinol, known for its favorable mechanical properties. SMAs show two main behaviors: the SME and SE. SMAs with SME undergo plastic deformation and keep their deformed shape upon loading. The shape returns to the original upon heating. Conversely, SMAs with SE recover to their original shape upon unloading, without heating.

Additionally, using SMAs in coupled beams incurs some challenges, which depend on the properties of the SMAs. Materials with (SME) require heating to return to their original shape. However, it is almost impossible to apply heat to the SMA

during loading in a real structure. On the other hand, (SE) SMAs do not need heating, but they have other issues. One challenge is shaping the material correctly before using it. Another challenge involves developing reliable connection techniques between SMA wires.

The shape of the SMA can be set by using a proper mold and heating the material to around 500°C. The mold can be arbitrarily dimensioned based on manufacturability considerations and made of steel for adequate strength and thermal resistance. For connecting the wires, welding methods or mechanical splicers can be used.

In this study, both types of SMAs were tested to understand their mechanical behavior and select the most suitable one for use in a replaceable coupled beam. Standard tensile tests were performed on several specimens to measure their ultimate tensile strength (UTS) and Young's modulus. These tests help identify the failure point and provide a reference for future experiments.

Experimental Test

Tensile tests were carried out on SMA materials to identify their basic mechanical properties of different types and compared different welding methods with mechanical splicing to help solve practical challenges. The tested specimens are summarized in Table 1.

Table 1. Test program.

Specimen	SMA Property	Number of Specimens	Explanation*
SME	SME	3	Wire
SE	SE	3	Wire
SE-LW-2	SE	3	Wires connected using 2 cm laser welding
SE-LW-4	SE	3	Wires connected using 4 cm laser welding
SE-TW	SE	1	Wires connected using TIG welding
SE-O-1-1	SE	1	single oval with single splice
SE-O-1-2	SE	1	double oval with single splice
SE-O-2-1	SE	1	single oval with double splice
SE-O-2-2	SE	1	double oval with double splice

* All wire specimens have identical dimensions: 18 cm in length and 2 mm in diameter.

The SME and SE wires were first tested using a simple tensile test to understand their mechanical behavior. Owing to equipment limitations and the absence of advanced control systems, advanced tests could not be conducted. However, critical data such as ultimate stress and strain, and the material's ductility were successfully observed in the simple tensile test (Figure 1).

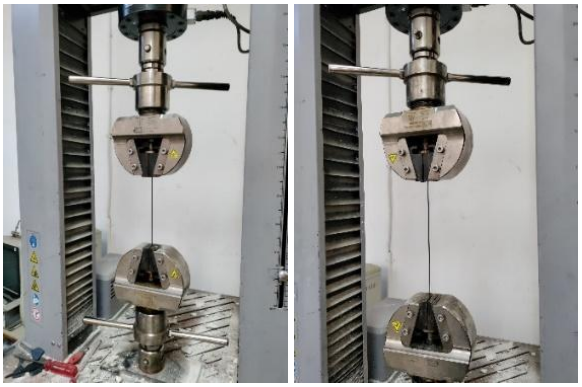

(a) (b)

Figure 1. (a) SME and (b) SE specimens.

After selecting the SE material as suitable for use in the coupled beam, several methods were used to connect the wires. Initially, the well-known laser welding method was employed to connect the SMA wires. Three specimens were welded using a 2 cm supporting section in the welding zone. Another three specimens were welded using a 4 cm supporting section in the welding zone (Figure 2).

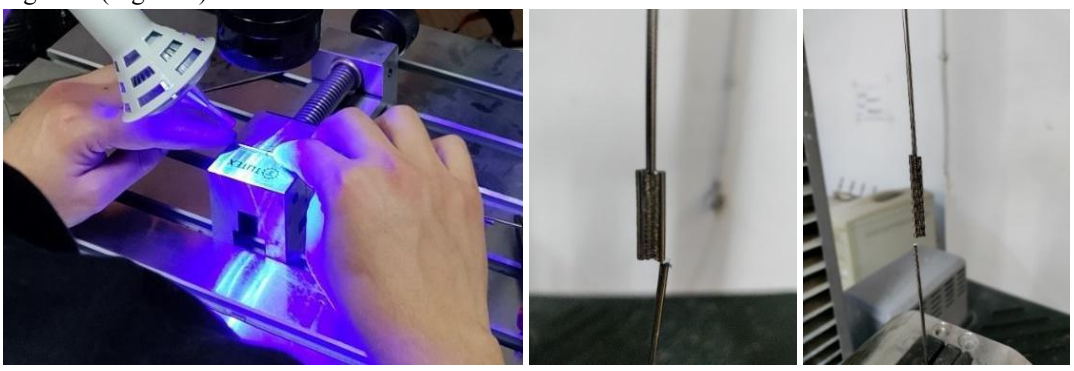

(a) (b) (c)

Figure 2. (a) laser welding, (b) 2 cm laser welding specimen and (c) 4 cm laser welding specimen.

Secondly, TIG welding, which uses inert gas with non-consumable tungsten electrode, was employed to join the SMA wires while minimizing contamination in the weld zone, (Figure 3).

Figure 3. Specimen connected with TIG welding method.

Finally, a mechanical method was employed to connect the wires. To achieve this, a mold was designed with an oval shape to better accommodate splicing, to limit stress concentrations, and to remove the need to connect the SMA wires to other elements. The dimensions of the mold were arbitrarily chosen based upon considerations of how to actually make it, and the mold was manufactured in steel for sufficient strength and thermal resistance. The SMA wires were heated to approximately 500°C and then cooled to retain the desired shape. This heating and cooling thermal treatment retains the superelastic property and provides mechanical stability when loaded. (Figure 4). Subsequently, oval specimens with splicers were tested (Figure 5).

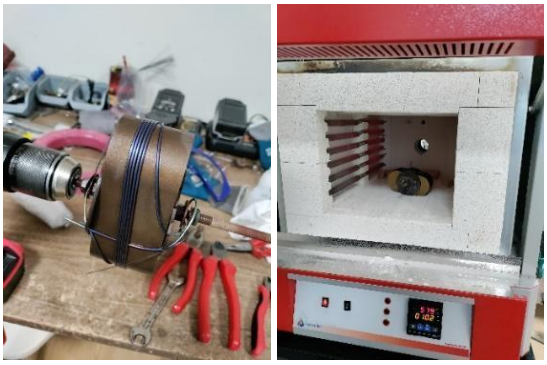

Figure 4. Reshaping the SMA wire.

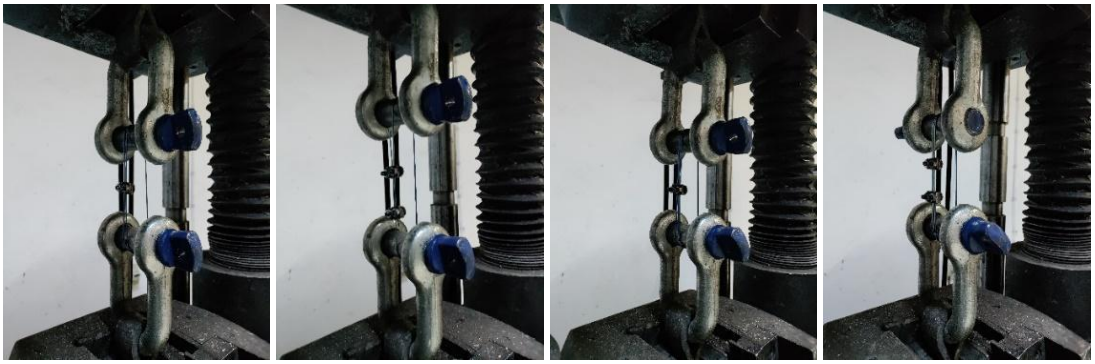

Figure 5. The oval specimen tensile tests.

Findings

To evaluate the mechanical properties of the tested specimens, force–displacement and stress–strain diagrams were obtained. The diagrams of the wire tests are shown in Figure 6. The SME specimens exhibited superior ductility, as evidenced by a gradual stress increase and an extended plateau. In contrast, SE-type specimens demonstrated higher initial strength but lower ductility, with a sudden drop in stress after reaching peak values. As illustrated in the diagrams, it is seen that none of the welded specimens withstood significant loading due to premature fracture, confirming the inadequacy of welding methods.Figure 7 shows the results of specimens connected with mechanical splicers. The results indicate that specimens SE-O-1-1 and SE-O-2-2 displayed higher peak stresses and extended strain capacities, suggesting improved ductility behavior compared to SE-O-2-1, which failed prematurely. SMAs connected with double splicers achieved an acceptable level of performance in both diagrams.

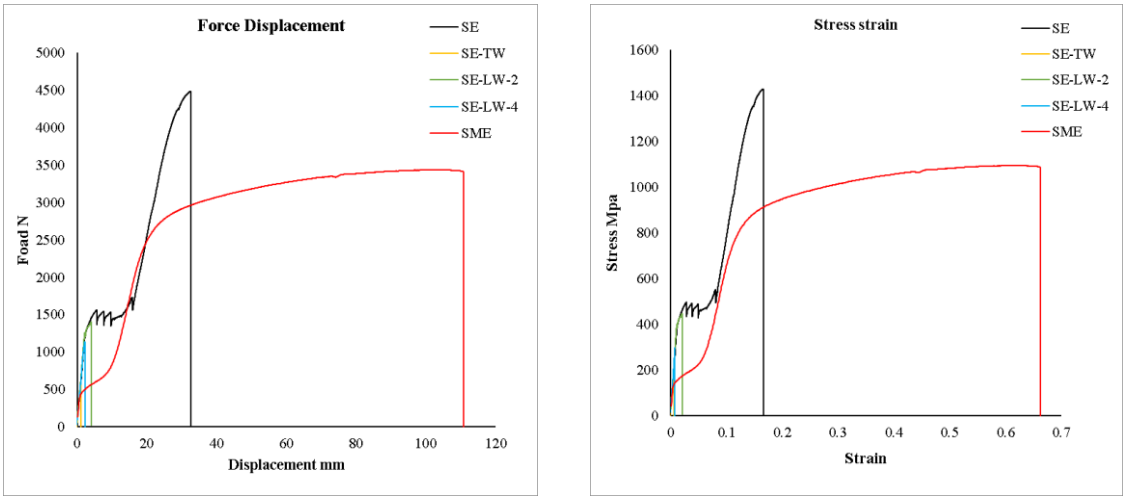

Figure 6. The force-displacement and stress strain diagrams of wire specimens.

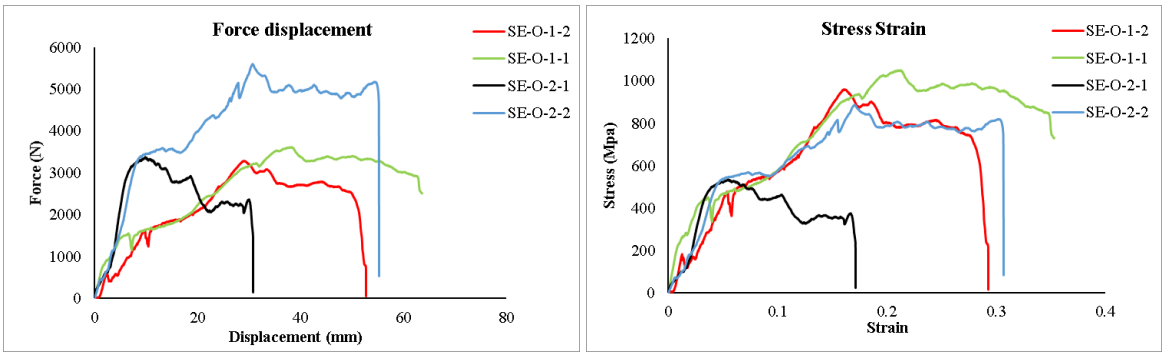

Figure 7. The force-displacement and stress strain diagrams of oval specimens.

Conclusion

This study concludes that while SME SMAs possess favorable ductility, their reliance on heat activation makes them impractical for seismic applications. In contrast, SE SMAs offer suitable mechanical properties without requiring external heat. Welding methods such as laser and TIG welding led to embrittlement and early failure. Mechanical splicing emerged as the most effective connection technique, particularly with double splicers, due to improved stress distribution and enhanced ductility. To incorporate SMA coupling mechanisms into seismic design standards, future research should focus on cyclic, low-cycle fatigue, or pseudo-dynamic tests, which require high-performance actuators, real-time data acquisition, accurate loading control. Further numerical research should involve in nonlinear time-history simulations and detailed finite element modeling to predict the seismic performance of SMA-based coupling systems at a structural scale. Comparative studies between conventional steel-reinforced and SMA-integrated coupling beams are also recommended to develop performance-based design guidelines and repair strategies.

Acknowledgment

The authors gratefully acknowledge Assist. Prof. Dr. Oğuz Güneş and Dr. Kerem Peker for their guidance. Experimental tests were conducted at the ITU Materials Laboratory with support from the staff. SMA materials were provided by Aksoz Arge Mühendislik.

References

Chen, C., Lu, X., & Li, X. (2017). Shaking table tests of RC structure with replaceable coupling beams. *International Conference on Advances in Experimental Structural Engineering,* 2017-September, 153–161. https://doi.org/10.7414/7aese.T2.34

Foroughi, S., & Yuksel, S. B. (2024). Nonlinear Behaviour of the Concrete Core of the Diagonally Reinforced Coupling Beams. *Gazi University Journal of Science*, 37(1), 119–135. https://doi.org/10.35378/gujs.1233545

Ghassemieh, M., Mostafazadeh, M., & Sadeh, M. S. (2012). Seismic control of concrete shear wall using shape memory alloys. *Journal of Intelligent Material Systems and Structures*, 23(5), 535–543. https://doi.org/10.1177/1045389X12436731

Ghassemieh, M., Nojoumi, S. A., Kari, A., & Bahaari, M. R. (2017). Upgrading of concrete shear wall system using shape memory alloys. *Proceedings of the 11th International Conference on Inspection, Appraisal, Repairs and Maintenance of Structures*, 175–180.

Ghassemieh, M., Rezapour, M., & Sadeghi, V. (2017). Effectiveness of the shape memory alloy reinforcement in concrete coupled shear walls. *Journal of Intelligent Material Systems and Structures*, 28(5), 640–652. https://doi.org/10.1177/1045389X16657200

Han, S. W., Jang, J., & Kim, T. (2022). Effect of HPFRCC on Cyclic Behavior of Diagonally Reinforced Coupling Beams. In *RILEM Bookseries* (Vol. 34, pp. 259–266). https://doi.org/10.1007/978-3-030-76465-4_23

Lu, X., Chen, C., Jiang, H., & Wang, S. (2018). Shaking table tests and numerical analyses of an RC coupled wall structure with replaceable coupling beams. *Earthquake Engineering and Structural Dynamics*, 47(9), 1882–1904. https://doi.org/10.1002/eqe.3046

Lü, X., Chen, Y., & Jiang, H. (2014). Experimental study of seismic performance of coupled shear wall structure with replaceable coupling beams. *Tongji Daxue Xuebao/Journal of Tongji University*, 42(2), 175–182. https://doi.org/10.3969/j.issn.0253-374x.2014.02.002

Mao, C., Zhang, Y., Li, B., Wang, Z., Li, H., & Ou, J. (2013). Nonlinear analysis of reinforced concrete frame-shear wall structure with shape memory alloy dampers in coupling beams. *Harbin Gongye Daxue Xuebao/Journal of Harbin Institute of Technology*, 45(12), 70–77.

Ravi, V., & Krishnan, P. A. (2019). Effect of Replacing Steel with Shape Memory Alloy in Shear Wall Systems. *Materials Today: Proceedings*, 11, 1088–1093. https://doi.org/10.1016/j.matpr.2018.12.043

Subramanian, N. (2021). Constructability and detailing of rc coupling beams. *Indian Concrete Journal*, 95(8), 45–55.

Sun, F. (2021). Research progress of replaceable steel coupling beam. *Journal of Physics: Conference Series*, 2029(1). https://doi.org/10.1088/1742-6596/2029/1/012064

Preliminary Study on St. Ilyas Church Damaged in the Kahramanmaraş Earthquakes

Kerem Kurnaz[a], Yunus Arca[b] , Elif Durgut[b], Sinan Açıkgöz[c] , Medine İspir Arslan[d]

[a] Istanbul Technical University, Graduate School, Earthquake Eng. Program, Türkiye
[b] Istanbul Technical University, Graduate School, Structural Eng. Program, Türkiye
[c] University of Oxford, Department of Engineering Science, England
[d] Istanbul Technical University, Faculty of Civil Engineering , Department of Civil Eng., Türkiye
kurnazk22@itu.edu.tr

Keywords: Cultural Heritage, Finite Element Model, Natural Stone, Non-destructive Test, Seismic Damage.

Aim

The aim of this study is to describe preliminary experimental and numerical investigations conducted on a historical church as part of an ongoing comprehensive study to understand the behaviour of historical churches that were affected by the 2023 Kahramanmaraş Earthquakes.

Material and Method

St. Ilyas Greek Orthodox Church, which is the subject to the study, is located in Hatay province of Türkiye. It is understood from the inscription at the main entrance of the church that the church was built in the late 1800s. The photograph of the historical structure is presented in Figure 1. Post-earthquake field studies were carried out to determine the load-bearing system of the building and damage status, to reveal its structural elements and components, and to determine its geometric dimensions and material properties. The load-bearing system of the church consists of unreinforced irregular stone masonry walls, pillars, vaults and arches.

Figure 1. The photograph of St. Ilyas Greek Orthodox Church.

Studies on Creating a 3D Model of the Church:
Point clouds obtained from terrestrial laser scanning and photogrammetry (Figure 2) were utilized to extract an accurate 3D model of structural geometry and to assess damage. Two different scanners, Faro Focus S70 and M70, were used for the terrestrial laser scanning. The resulting point cloud included 44 million points with a point spacing of 6 mm. The manufacturer of the laser scanning reports that the accuracy of each point is 2 to 3 mm at a ranging distance of 25 m. In

addition to laser scanning, a Canon EoS 6D Mark II camera and a Mavic 2 Pro drone (Figure 2) were used for complementary point clouds of the church. Details of this measurement system are available in Yang et al. (2024).

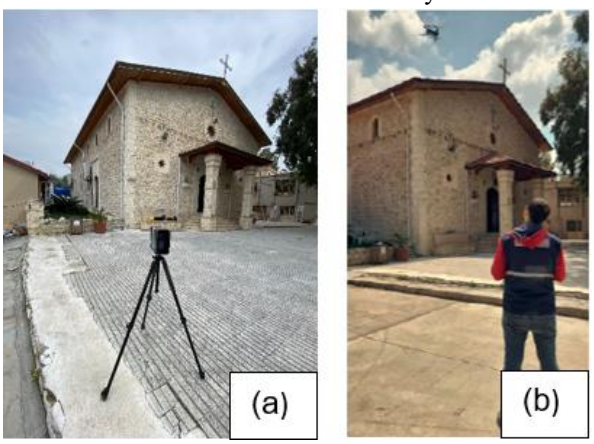

Figure 2. (a) the terrestrial laser scanning and (b) aerial photogrammetry (modified from Bozyigit et al., 2024).

Material Characterization with In-Situ Tests:
A Schmidt rebound hammer (SRH) with a mushroom plunger was used for non-destructive stone compressive strength estimation. During the application of the SRH, the instructions of ASTM C805/C805M-18 was followed whenever possible.

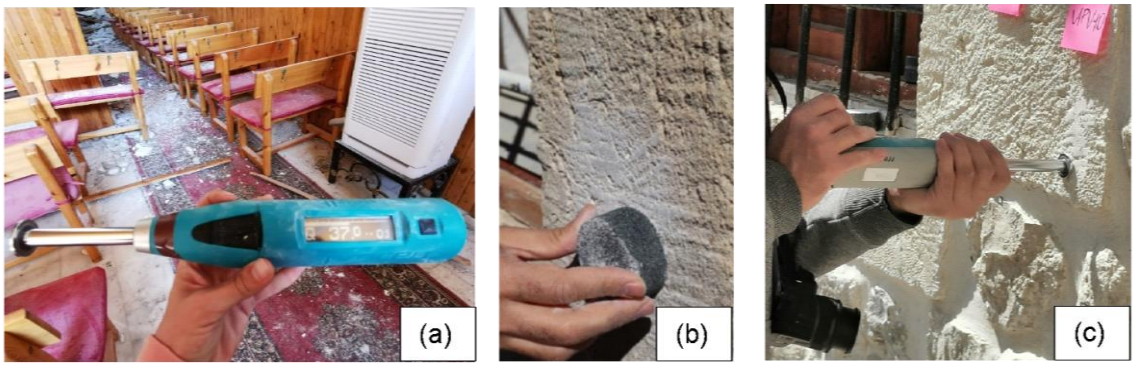

Figure 3. Application of Schmidt rebound hammer on stone unit.

The Proceq Silver Schmidt Hammer was used, Figure 3a. Before applying SRH to the specified small surface of the stone unit, the surface was cleaned and 10 readings of the Q value were taken by applying SRH in this surface (Figure 3b-c). This procedure was applied to 11 different stone samples. The median of these readings was used to estimate the compressive strength of the stone units (f_s) using Equation 1:

$$f_s = 0.0108Q^2 + 0.2236Q \quad (MPa) \tag{1}$$

Equation 1 is applicable solely for values of Q ranging from 13 to 44, which are associated with compressive strengths of approximately 5 MPa and 31 MPa, respectively (Kocáb et al 2019).
Mortar penetrometer (MP) tests are non-destructive and slightly destructive test techniques, conducted to estimate the compressive strength of the mortar which is based on the dynamic penetration of a steel needle (Gambilongo et al 2023; Žalskỳ et al 2023). The test measures the response of the mortar to needle penetration and relates the measurement to the compressive strength of the mortar (f_m). In this study, Diagnostic Research Company's (DRC) MP device shown in Figure 4 was used to perform mortar penetrometer tests.

Figure 4. Mortar penetrometer test device and its use in the field.

The tests of nine different bed/head mortar joints were performed. Following manufacturer guidance, each test was performed by striking the needle 10 times and measuring the penetration depth (d_m). Using Equation 2, the compressive strength of the mortar was estimated as in the studies of Bozyigit et al. (2024) and Gambilongo et al. (2023).

$$f_m = \frac{5970-\sqrt{(1.58d_m-5.3)10^6}}{1580} \quad (2)$$

Compressive strength and elasticity modulus values of masonry are needed for finite element analysis studies. Compressive strengths of stone and mortar determined by non-destructive test methods were used to estimate the mean compressive strength of stone masonry (f_{mas}). For the characteristic compressive strength estimation ($f_{ck,mas}$), Equation 3 recommended by Eurocode 6 was used and then the calculated value was divided by 0.67 to obtain the mean strength (f_{mas}).

$$f_{ck,mas} = 0.45 f_s^{0.7} f_m^{0.3} \quad (3)$$

The modulus of elasticity was calculated as 750 times the mean compressive strength of the masonry according to TSC (2018).

Establishing the Finite Element Model and Modal Analysis:
The finite element model of the church was created using the software Abaqus. A macro modelling approach was adopted for the structural components of the church and they were modelled using shell elements (S4R). A mesh sensitivity analysis was conducted to decide mesh size. The finite element model is shown in Figure 5.

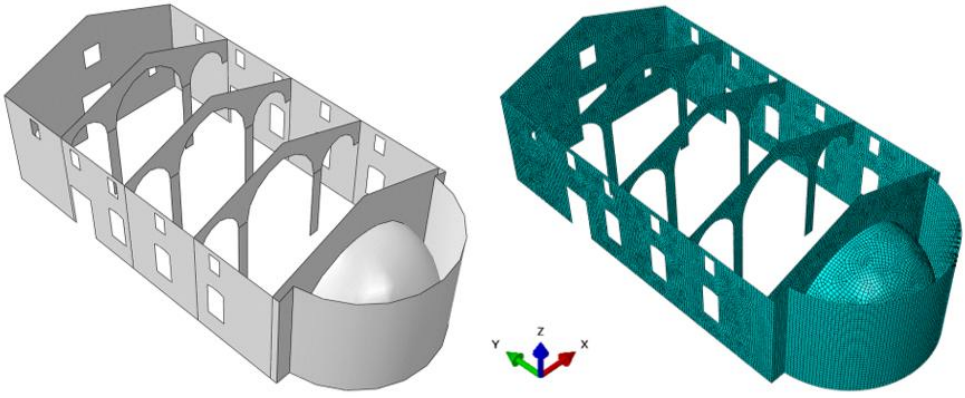

Figure 5. Finite element model views of the church.

After the church finite element model was completed, the above-mentioned elasticity modulus values were assigned to the relevant elements for modal analysis. The frequency values and corresponding mode shapes of the church were obtained from modal analysis.

Findings

On-site experimental and preliminary numerical studies are used to provide a general description of the existing damage, construction details, geometry, material and seismic behaviour of the historic church.

Damage Status:

The damage to the church was determined through observations made after the earthquake. The locations of the visible cracks on the exterior walls and the localized collapse on the roof are indicated in Table 1. It was also observed that some arches had cracks and that the voussoirs had slid.

Table 1. Damages due the 2023 Kahramanmaraş Earthquakes.

Damage location	Damage photograph	Note
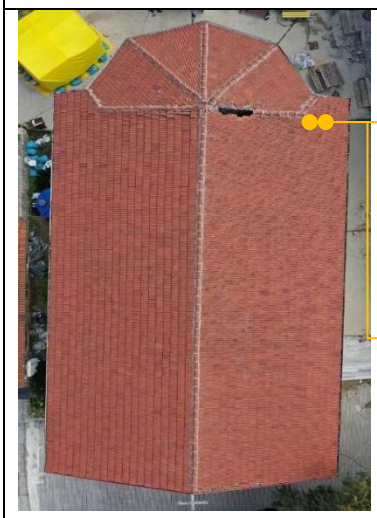	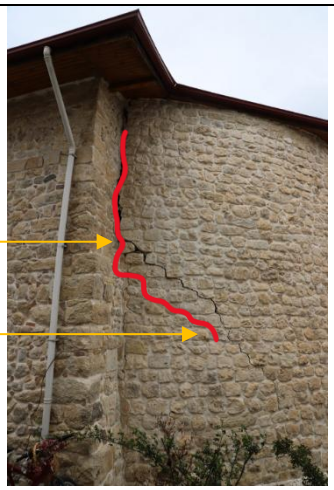	The separation between the apse and the external wall The stepped diagonal crack on apse
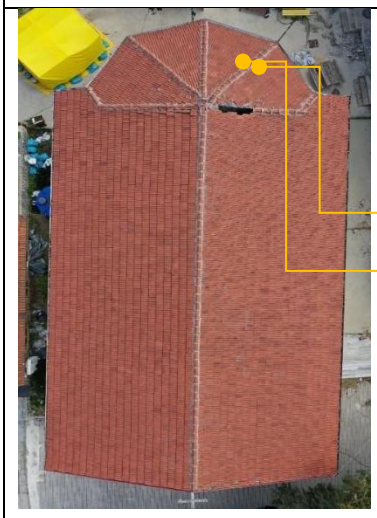	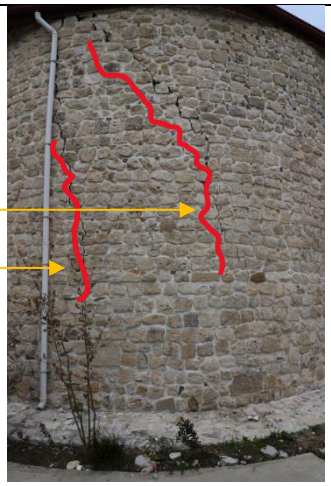	Approximately vertical crack following head mortar joints Approximately diagonal crack

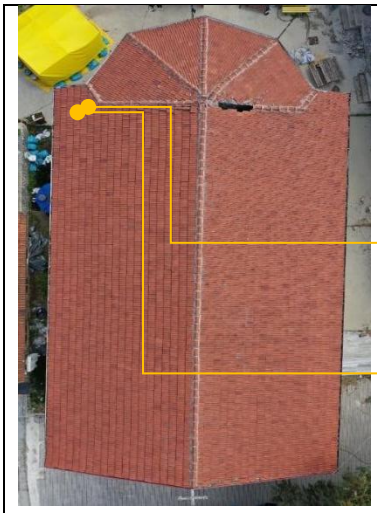	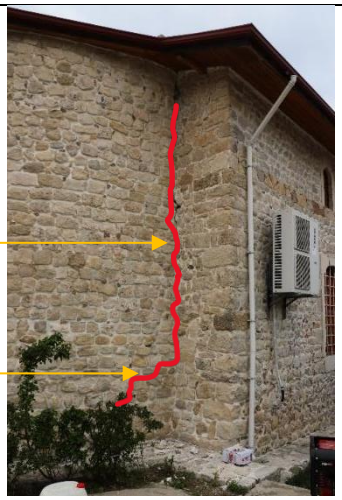	The separation between the apse and the external wall The stepped diagonal crack
		Approximately vertical crack between window openings
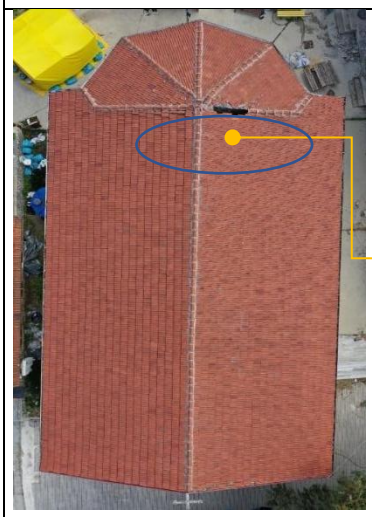	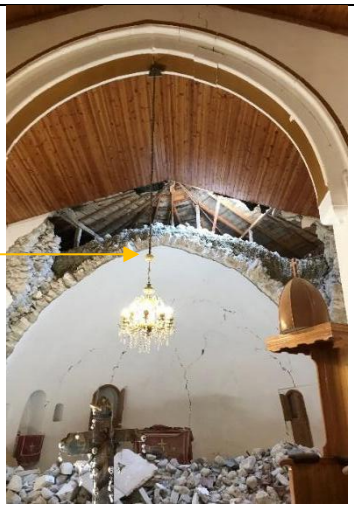	Partial collapse of the spandrel wall above the apse

Masonry wall type :
The church has unreinforced stone masonry structural components. The faces of the walls are made of irregular stonework, Figure 6. The pillars were constructed with cut stone units without mortar joints.

Figure 6. Face appearances of masonry walls.

Geometric Dimensions :
Point cloud data obtained by terrestrial laser scanning and photogrammetry were processed using the Cloud Compare program. The 3D and plan views of the church and the transverse arched frame system are shown in Figures 7-9.

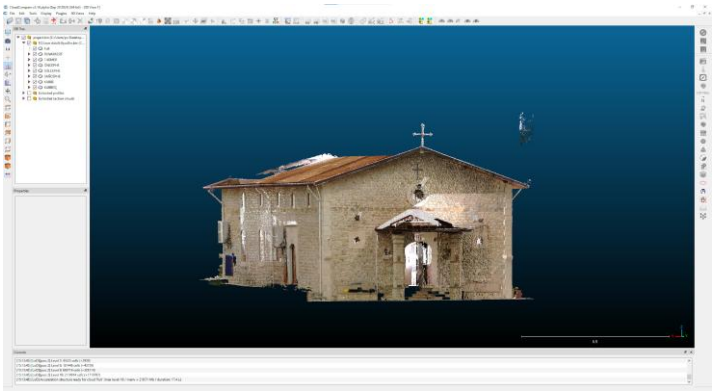

Figure 7. 3D view of the church.

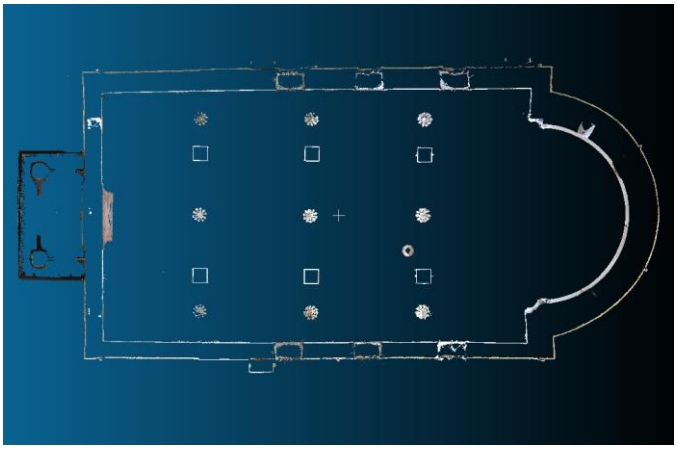

Figure 8. Plan view of the church.

The plan dimensions of the church are obtained from the Cloud Compare program as 11.38 m and 22.89 m. The average wall thickness was measured as 750 mm. The cross-sectional size of each pillar was determined as 550×550 mm.

Figure 9. An arched frame system along the building transverse axis.

Material Characteristics:
In order to determine the compressive strength of the stone units, SRH tests were carried out. Based on the Q values obtained from these tests, the compressive strengths were calculated using Equation 1. Table 2 shows the Q values obtained from the SRH readings, the calculated compressive strengths, and descriptive statistics (average and standard deviation).

Table 2. Compressive strength values of stone units.

Stone ID	Q	f_s (MPa)
STİLY-1	31.15	17.44
STİLY-2	26.5	13.51
SS2	31.25	17.53
SS4	39.5	25.68
SS7	42.5	29.01
Average	34.18	20.64
Standard Deviation	6.60	6.45

The average results of Mortar penetrometer (MP) tests are listed in Table 3. The compressive strengths of mortar (f_m) was calculated using Equation 2. The penetration depths, the compressive strengths, and descriptive statistics (average and standard deviation) of mortar are listed in Table 3.

Table 3. Compressive strength values of mortar.

Test ID	d_m (mm)	f_m (MPa)
MP2	15	1.06
MP3	8	2.06
MP4	5	2.76
MP6	8	2.06
MP8	17	0.84
Average	10.6	1.76
Standard deviation	5.13	0.79

As a result of the tests, the average compressive strengths of the stone and mortar were determined as 20.64 MPa (Table 2) and 1.76 MPa (Table 3), respectively. To use Equation 3, the masonry wall was accepted as homogeneous material. In Equation 3 and the coefficient of 0.67 is applied, the average compressive strength of the wall masonry is obtained as 6.6 MPa. The modulus of elasticity is calculated as 4950 MPa, which is 750 times the compressive strength. The compressive strength of the dry-stone pillars was calculated as 9.3 MPa, taking 0.45 times the average compressive strength of the stone units considering the study of Demir (2012). The modulus of elasticity of the pillars was calculated as 6975 MPa using the coefficient of 750 adopted for the masonry wall.

Dynamic characteristics:

Finite element model of the church was created using shell elements in the Abaqus program. The masonry material was accepted as a homogeneous material and was defined with its modulus of elasticity in the program. After a sensitivity analysis was performed to find the appropriate mesh size, resulting in a mesh size of 150 mm. By performing modal analysis of the FEM of the church, frequency values and mode shapes were obtained. The first ten frequency/period values are given in Table 4.

Table 4. Frequency and period values.

Mode No	Frequency (Hz)	Period (s)
1	6.2776	0.159
2	6.3297	0.158
3	6.3626	0.157
4	7.4213	0.135
5	8.8731	0.113
6	10.695	0.094
7	14.850	0.067
8	15.596	0.064
9	15.857	0.063
10	16.097	0.062

Mode shapes of the church, along with mass participation ratios, are illustrated in Table 5. Except for Mode 4, the modes given in the table show the existence of local behaviours. This situation manifests itself in lower mass participation ratios. The mode shapes indicate that out-of-plane behavior can be expected in the transverse arched frame systems and gable walls. In structures such as churches with large openings or high walls, it has been observed that mode shapes are mostly formed on individual walls rather than on the entire structure (Kılıç, 2025; Illimpas et al., 2020; Valente&Milani, 2018; Betti&Vignoli, 2011).

Table 5. Mode shapes, periods and mass participation ratios**.**

Mode number	Mode shape	Period (s)	Mass participation ratio (%)
Mode 3	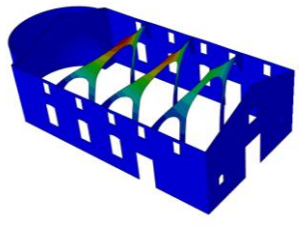	0.157	5.6
Mode 4	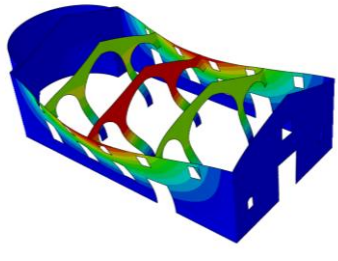	0.135	28.2
Mode 5	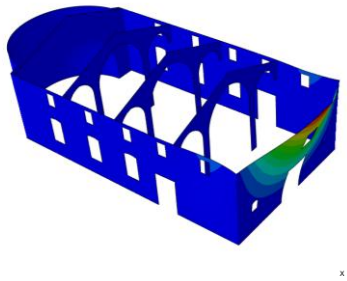	0.113	8.6
Mode 8	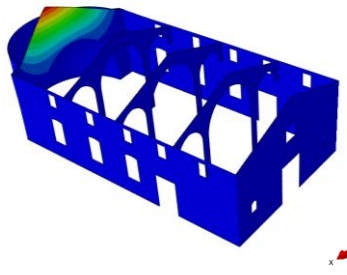	0.064	4.0

Conclusion

In this study, preliminary experimental and numerical investigations carried out in a historical church affected by the 2023 Kahramanmaraş Earthquakes are described. The study ensures the attainment of the following main outputs.

- The 3D geometric model of the church was created using terrestrial laser scanning and photogrammetry.
- The damage to the church was understood through on-site observations.
- The compressive strengths of stone and mortar were obtained from non-destructive tests performed on these materials.
- A FEM model of the church was created using geometric and material data obtained from field measurements, and modal analysis of the church model was performed to obtain mode shapes and corresponding frequency values.

In future work, the church structure can be modeled with the micromodel approach and finite element analysis can be performed under real ground motion acceleration data.

Acknowledgments

The authors would like to thank Baran Bozyiğit, Anıl Özdemir, Kökcan Dönmez, Korhan Deniz Dalgıç, Cennet Yeşilyurt, Yavuz Dizgin, Canan Yıldeniz, İdris Bedirhanoğlu and Yasemin Didem Aktaş for their help and support in the studies carried out in the field.
The authors gratefully acknowledge Shirley Underwood of Screening Eagle/Proceq for the provision of NDT equipment used in this study. Appreciation is also extended to DRC Italia for supplying additional equipment on short notice. The authors thank FARO UK for generously providing software licenses that facilitated the processing of laser scan data. Processed datasets were kindly provided by University of Oxford PhD students Yilong Yang, Yixiong Jing, and Zheng-You Zhang.
We would like to express our sincere gratitude to Dimyan Emektaş for facilitating our field work. The authors are also grateful to Misel Uyar (Nehna) and Ahmet Cakmak (Istanbul Metropolitan Municipality) for their invaluable logistical support.
They would like to express their sincere gratitude to our academic collaborators, Prof. Heather Viles, Prof. Alper Ilki, Prof. Bora Pulatsu, Prof. Eser Cakti, Prof. Paulo Lourenco, and Dr. Pascal Lava, for their invaluable

References

Abaqus (2017). Abaqus Analysis User's Manual 6.13. Dassault Systèmes Simulia Corp., Providence, RI, USA.
ASTM C805/C805M-18 (2019). *Standard Test Method for Rebound Number of Hardened Concrete*. American Society for Testing and Materials, Philadelphia, PA.
Betti, M., & Vignoli, A. (2011). Numerical assessment of the static and seismic behaviour of the basilica of Santa Maria all'Impruneta (Italy). *Construction and Building Materials*, 25(12), 4308-4324.
Bozyigit, B., Ozdemir, A., Donmez, K., Dalgic, K.D., Durgut, E., Yesilyurt, C., Dizgin, Y., Yıldeniz, C., Ispir, M., Bedirhanoglu, I, Aktas, Y.D. and Acikgoz, S (2024). Damage to monumental masonry buildings in Hatay and Osmaniye following the 2023 Turkey earthquake sequence: The role of wall geometry, construction quality, and material properties. *Earthquake Spectra*, 40(3), 1870-1904.
Demir, C. (2012). *Seismic behaviour of historical stone masonry multi-leaf walls.* PhD thesis, Istanbul Technical University, Istanbul.
European Committee for Standardization (2005) *Eurocode 6: Design of masonry structures-Part 1-1: General rules for reinforced and unreinforced masonry structures*.
Gambilongo, L., Barontini, A., Silva, RA., Lourenco, PB. (2023). Evaluation of non-destructive techniques for mechanical characterisation of earth-based mortars in masonry joints. *Construction and Building Materials* 392: 131960.
Illampas, R., Ioannou, I., & Lourenço, PB. (2020). Seismic appraisal of heritage ruins: The case study of the St. Mary of Carmel church in Cyprus. *Engineering Structures*, 224, 111209.
Kılıç, R. (2025). Determination of earthquake resistance of historical masonry inn with finite element analysis. *Bulletin of Earthquake Engineering*, 1-25.
Kocáb, D., Misák, P., Cikrle, P. (2019). Characteristic curve and its use in determining the compressive strength of concrete by the rebound hammer test. *Materials* 12(17): 2705
Turkish Seismic Code (2018). *The Disaster and Emergency Management Presidency of Turkey,* (AFAD), Ankara.

Valente, M., & Milani, G. (2018). Seismic response and damage patterns of masonry churches: seven case studies in Ferrara, Italy. *Engineering Structures*, 177, 809-835.
Yang, Y., Durgut, E., Ispir, M., Pulatsu, B., Acikgoz, S. (2024). Use of Post-Earthquake Point Cloud Data for Forensic Evaluation of Failures in Masonry Structures. *Bulletin of Earthquake Engineering* (under review).
Žalskỳ, J., Vokáč, M., Hrabánek M., Hurtig, K. (2023). Development of a new nondestructive method for the in-situ determination of mortar strength. *Buildings* 13(2): 273.

Design and Comparison of Different Types of Reinforced Concrete Slab Systems for Multi-Storey Buildings

Ahmet Jabban[a], Kadir Güler[b]

[a]Istanbul Technical University, Graduate School, Earthquake Engineering Program,Türkiye.
[b]Istanbul Technical University, Civil Engineering Department, Türkiye
aljabban23@itu.edu.tr

Keywords: Dynamic Behavior, Multi-storey, Reinforced Concrete, Slab System.

Aim

The escalating demand for multi-storey buildings is a global phenomenon driven by relentless population growth, proliferation of smaller family units, and increasing preference for individual housing solutions. This trend is particularly acute in densely populated metropolitan regions such as Istanbul, where the imperative for efficient land utilization is paramount. The concentration of urban populations necessitates vertical expansion to accommodate residential and commercial needs, thereby mitigating encroachment on valuable land resources. Recent seismic events in Türkiye have highlighted critical vulnerabilities in structural design practices, underscoring the urgent need for reassessment of construction methodologies. The catastrophic earthquake of February 6, 2023, triggered a comprehensive investigation by Turkish scientists and engineers to meticulously identify design flaws and formulate strategies to prevent their recurrence. Properly engineered multi-storey buildings, incorporating advanced seismic resistance features, offer a viable solution for urban renewal and transform aging infrastructure into resilient, modern structures. Furthermore, these tragic events reinforced the indispensable role of rigorous numerical analyses and strict adherence to building codes to safeguard urban populations against seismic hazards. The enduring consequences of inadequate earthquake-resistant designs are profound, potentially impacting communities for generations.

The objective of this study is to conduct a comparative analysis of different slab designs in multi-storey reinforced concrete buildings, assess their respective seismic performance without undertaking a full design process, and explore the influence of diverse slab systems on structural behavior. The primary objective is to analyze the impact of slab design on critical structural parameters, ensuring compliance with the Turkish Building Earthquake Code 2018 (TBEC 2018), TS 498, TS 500 standards, and related American standards, including ASCE 7-16 and ACI 318. A comparative analysis of the distinct design methodologies for slabs, as delineated in these standards, will be conducted to highlight their respective strengths and limitations. A strength-based design approach utilizing the ETABS software will be employed to develop detailed three-dimensional building models, enabling a comprehensive assessment of structural behavior under seismic loads. Specifically, this study aims to determine the optimal slab system for seismic performance, as defined by TBEC 2018, and to evaluate the performance variations of different systems under a spectrum of earthquake intensities. For instance, while flat slab construction offers advantages in terms of rapid on-site construction speed in terms of preparing to pour concrete and architectural flexibility such as divide the internal space in different way or change it later, its contraction with unwanted characteristics, such as increased structural weight, necessitates a thorough comparison with alternative systems such as two-way slabs.

Material

The primary construction material utilized in this study was reinforced concrete of class C50, conforming to the stringent specifications outlined in TS 500. This material selection ensured a robust structural framework capable of withstanding significant loads. Steel reinforcement, specifically B500C, was employed for all primary structural components, including shear walls, columns, beams, and slabs. This high-grade reinforcement provided essential tensile strength and ductility, enhancing the overall seismic resistance of the building. The rebar steel specifications adhered meticulously to TS 708, guaranteeing data reliability and providing detailed guidelines on the mechanical properties and strength characteristics of

the materials used in the structural models. Adherence to established standards ensured the accuracy and validity of the research findings. The applied loads included a dead load of 2 kN/m² for the ground floor and 3.5 kN/m² for upper floors. The live load was 5 kN/m² on the ground floor and 2 5 kN/m² on upper floors, while 3.5 kN/m² was used in corridors and near staircases.

Method

A strength-based design methodology was implemented using ETABS software to develop comprehensive three-dimensional models of multi-storey the buildings. The structures consist of 17 floors with a total height of 58.9 meters and the general layout for all model as in (Figure 1). Four distinct models were created that differed only in the slab design each slab system have different thickness as list in (Table 1), and the other variables were kept the same, each characterized by unique vibration periods, weights, and dynamic behaviors. These variations allow for a thorough investigation of the influence of slab systems on structural response. Initial analyses were conducted to determine the internal forces within the structural elements using a strength-based method. Subsequently, the fundamental natural vibration period was determined and employed in the equivalent seismic load method. This method, utilizing DD-2 earthquake parameters derived from TBEC 2018, serves as the principal method for comparing storey displacements and evaluating structural performance. Finally, response spectrum analysis was performed by incorporating model combination techniques to achieve realistic and representative results. This comprehensive analytical approach ensured the reliability and accuracy of the findings.

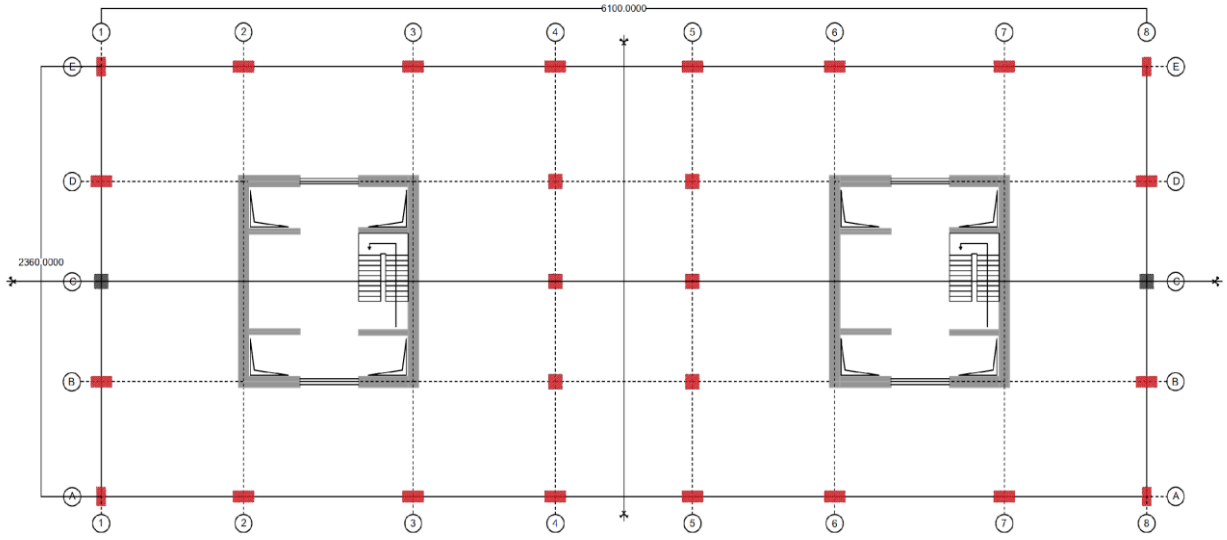

Figure 1. General structural layout.

Table 1. Model types and thicknesses of slab.

Model	Type of slab	Thickness
First	Flat slab without edge beams	32 cm
Second	Flat slab with edge beams	30 cm
Third	2-way slab	22cm
Fourth	2-way slab with cross beam	18cm

Findings

The study revealed that slab design exerts a profound influence on the rigidity and weight of structural systems, significantly affecting free vibration periods as illustrated for the first three mode in (Figure 2), and, consequently seismic behavior. Given that slabs constitute a substantial portion of a building's mass and area, their design critically affects the overall structural weight and rigidity. Notably, ACI 318 provides more detailed and nuanced specifications for flat slabs with perimeter beams compared to TS 500 and related standards, which treats flat slabs with or without beams in a generalized manner. This study demonstrated the advantages and disadvantages of each slab system with respect to storey drifts, weight, free vibration periods, and dynamic behavior. For example, flat slabs without spandrel beams exhibit lower rigidity, leading to increased story drifts and potentially compromising the structural stability under seismic loads. Conversely, two-way slab systems demonstrate enhanced resistance to deformation and story drift, indicating a superior seismic performance.

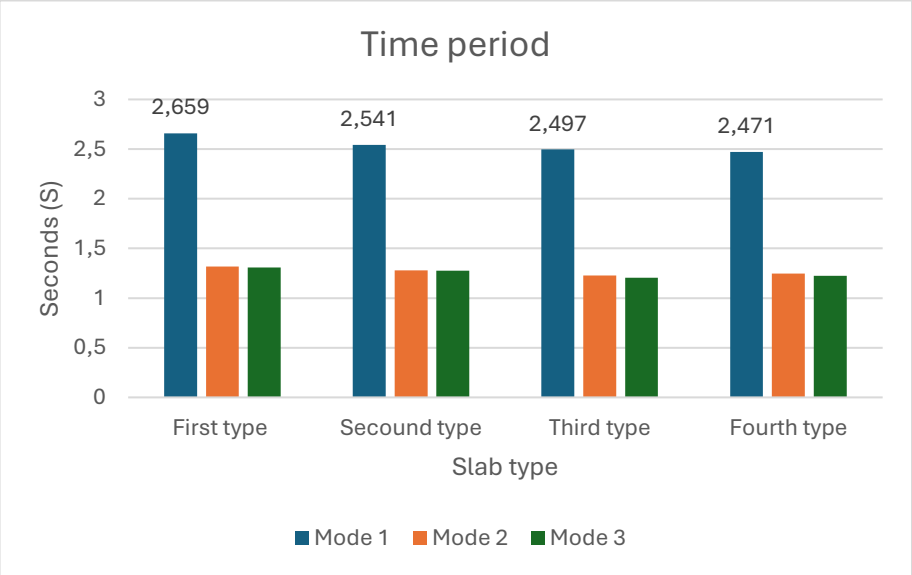

Figure 2. Free vibration mode periods for different slab types.

Conclusion

The findings of this research confirm the important role of rigidity and weight in structural systems, particularly in relation to free-vibration periods and seismic responses. This study provides a comprehensive analysis of the advantages and disadvantages of various slab systems, focusing on their impacts on story drifts, weight, free vibration periods, and dynamic behavior. Specifically, flat slabs without spandrel beams have lower rigidity and higher weight on the other hand adding spandrel beams to flat slab give the structural more resistance and lateral stability as, whereas two-way slab systems show superior resistance to deformations and story drifts with far less weight. As illustrated in (Figure 3 and 4**)**. Detailed comparisons and data illustrating the performance characteristics of each system were provided to enhance the understanding of the critical impact of slab design choices on structural performance and seismic resilience. This research provides valuable insights into the optimization of multi-storey building design, fostering the development of safer and more resilient urban infrastructures. Further studies are required to develop more information on each slab design, their effect on the nonlinear characteristics and dynamic behavior of each slab system, and how this will affect design decisions. Future research would benefit significantly from the inclusion of pushover or nonlinear time-history analyses to provide a more comprehensive understanding of the structural behavior of different slab systems under seismic loading. While the current study offers valuable insights based on linear elastic analysis methods, pushover analysis would enable the evaluation of progressive structural yielding and failure mechanisms specific to each slab system when subjected to incrementally increasing lateral loads. Additionally, nonlinear time-history analyses using suites of ground motion records would capture the complex dynamic responses and energy dissipation characteristics that are not fully represented in equivalent static or response spectrum methods.

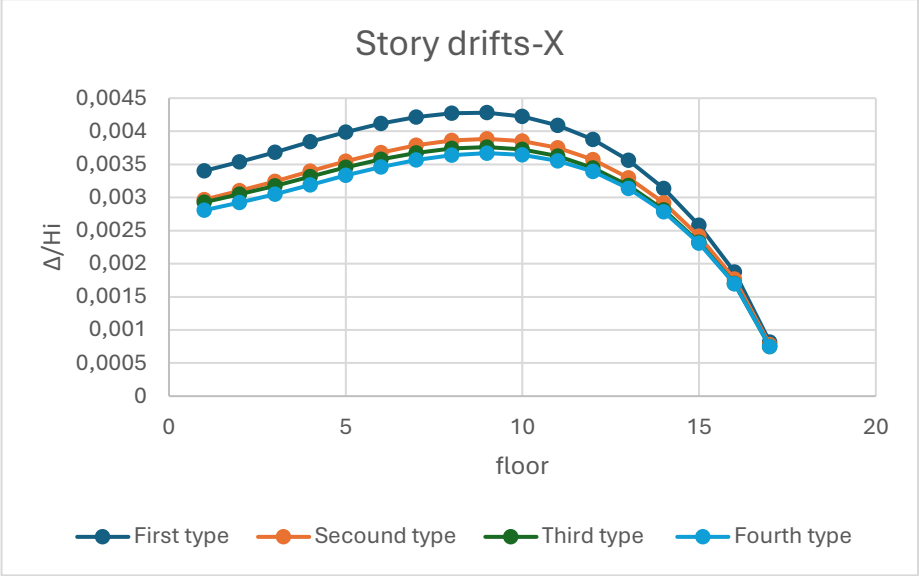

Figure 3. Story drifts in x direction for different slab types.

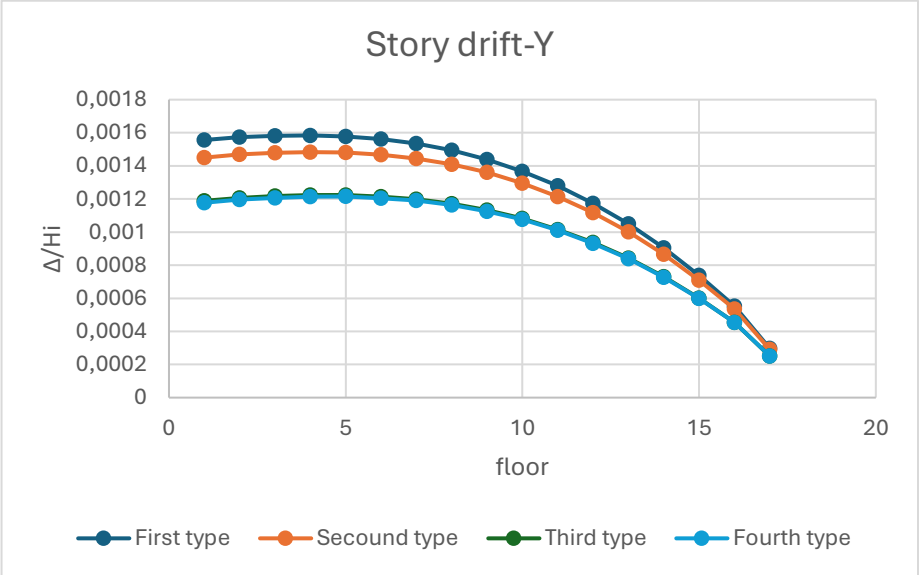

Figure 4. Story drifts in Y direction for different slab types.

References

American Concrete Institute. (2019). *ACI 318-19: Building Code Requirements for Structural Concrete and Commentary. Farmington Hills*, MI: American Concrete Institute.

American Society of Civil Engineers. (2017). *ASCE/SEI 7-16: Minimum Design Loads and Associated Criteria for Buildings and Other Structures.* Reston, VA: American Society of Civil Engineers.

Ministry of Environment and Urbanization. (2018). *Turkish Building Earthquake Regulation (TBDY 2018).* Ankara, Türkiye.

Turkish Standards Institute. (2000). *TS 500: Requirements for Design and Construction of Reinforced Concrete Structures*. Ankara, Türkiye.

Turkish Standards Institute. (2010). *TS 708: Steel Bars for Concrete Reinforcement.* Ankara, Türkiye.

Turkish Standards Institute. (2021). *TS 498: Design Loads for Buildings*. Ankara, Türkiye.

ECOLOGY AND EVOLUTION

Anthropocene

Anthropogenic Impacts

Exploring the Biodiversity Patterns of Anatolia Under Changing Climatic Conditions

Batuhan Atıf Tunç[a], Emrah Çoraman[b]

[a] Istanbul Technical University/Eurasia Institute of Earth Sciences, Climate and Marine Sciences, Earth System Science, Türkiye
[b] Istanbul Technical University/Eurasia Institute of Earth Sciences, Ecology and Evolution, Türkiye
tuncb23@itu.edu.tr

Keywords: Biodiversity , Climate Change , Spatial Ecology , Species Distribution Models.

Aim

Global change and ecological crises are pressing issues threatening Earth's systems. Climate change and its effects on biodiversity present an urgent challenge to contemporary ecological research (Pereira et al., 2012). Anatolia, with its rich biodiversity, faces considerable uncertainty regarding how its ecosystems will respond to the challenges posed by global change (Ohlemüller et al., 2008; Trew & Maclean, 2021). The biodiversity of Anatolia remains underexplored, particulary in spatial terms. And we believe that spatial analyses provide crucial contributions to global change studies.
We aim to assess spatial biodiversity patterns of Anatolia and how these patterns evolve under changing climatic conditions. These assessments, though biologically coarse, are geographically detailed, and aim to explore climate-biodiversity relationships, inform conservation efforts, and most critically address the spatial biodiversity knowledge gap in Anatolia.

Materials and Methods

Correlative methods play a central role in analyzing the relationships between organisms and their environment. Among these, ecological niche modeling has been widely used by ecologists to model species distributions. Ecological niche models are mathematical frameworks that relate species occurrence records to environmental predictors, thereby allowing researchers to quantify and project species distributions (Guisan & Thuiller, 2005). Given its established utility in the field, we employed ecological niche models to examine the spatial biodiversity distribution patterns in Anatolia. We obtained biodiversity data from the Global Biodiversity Information Facility, an open-access repository that integrates datasets from various sources, including field studies and citizen science observations. The dataset consists of presence-only species occurrence records for Türkiye, covering amphibians, birds, insects, mammals and plants (GBIF.org, 2024a, 2024b, 2024c, 2024d, 2024e).
The environmental predictors in this study consist of 19 bioclimatic variables, which provide biologically meaningful representations of temperature and precipitation patterns. We obtained bioclimatic data from WorldClim 2 as the averages for the years 1970-2000 at 2.5 arc-minutes resolution (Fick & Hijmans, 2017). Future projections include the time periods 2041-2060 and 2081-2100, and the shared socio-economic pathways SSP1-2.6, SSP2-4.5, SSP3-7.0, SSP5-8.5 (Calvin et al., 2023). Future climate data were sourced from CMIP6 by averaging the outputs of six different models (Boucher et al., 2018; Peano et al., 2020; Shiogama et al., 2019; Tang et al., 2019; Volodin et al., 2019; von Storch et al., 2017). We chose these six models with the aim of representing different climate modeling approaches such as earth system models which take an holistic outlook to modeling and include many processes such as biogeochemical cycles, and global circulation models which model how air moves through the atmosphere, focusing on the physics of vortices.
After preparing the data, we fitted ecological niche models using split sample cross-validation with statistical and machine learning methods. The modeling approaches employed included Maxent, random forests, and boosted regression trees which are top performing methods in multi model benchmarks.

Maxent is a Bayesian inference method that provides the least biased probability distribution of the target variable given specified constraints set by the modeler (Jaynes, 1957a, 1957b; Phillips et al., 2006; Phillips & Dudík, 2008). Random forests are decision-tree based methods, in which multiple trees, that are fitted to bootstrapped subsamples of training data with random subsamples of predictor variables, are combined into an ensemble model (Breiman, 2001). Similarly, boosted regression trees are also decision-tree based models. However, in this approach, simpler trees are iteratively fitted, with each subsequent tree focusing on the remaining unexplained variance (Elith et al., 2008; Schapire, 2003).
We repeated the modeling process for each species and combined successful models into ensembles. The results were then aggregated by higher taxa to construct a biodiversity metric representing species richness. Finally we projected the models to future time periods under different climate scenarios and analyzes shifts in biodiversity patterns.

Findings

The results consist of ecological niche models for 519 species, including 5 amphibians, 118 birds, 126 insects, 5 mammalians, and 265 plants. These models reveal broad patterns of high biodiversity concentrated along the coastal regions of Türkiye, with notable variations in distribution patterns across taxonomic groups. In contrast, the inner Anatolia and southeastern Anatolia exhibit relatively low biodiversity. Among the taxa, insects exhibit the most pronounced deviations in biodiversity patterns, displaying particularly high biodiversity in northeastern Anatolia.
From a geographic perspective, the results highlight strong associations between high biodiversity patterns and environmental features such as water bodies, forested areas, and topographical complexity. When compared to biodiversity range maps from the International Union for Conservation of Nature (IUCN) (IUCN (International Union for Conservation of Nature), 2024)—despite fundamental differences in their objectives and methodologies—the two approaches show considerable agreement (Figure 1).

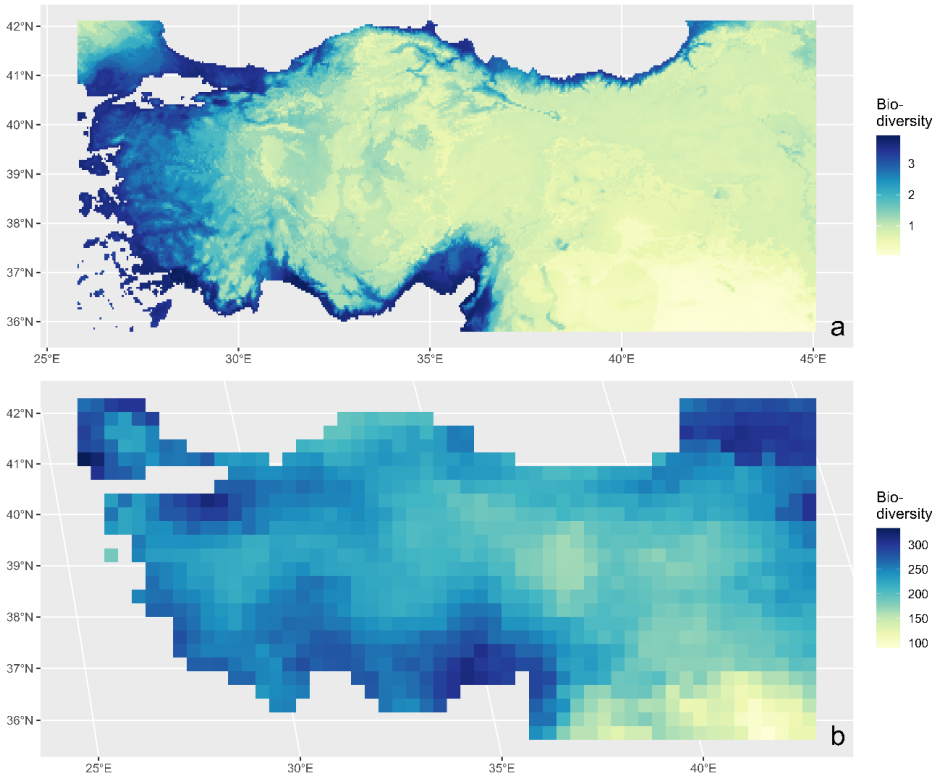

Figure 1. Species richness patterns in Anatolia based on a) ecological niche models for amphibians, birds, insects, mammals, reptiles; and b) IUCN biodiversity maps for amphibians, birds, mammals, reptiles. Note the differences in coordinate systems; this study employs WGS84, whereas the IUCN maps use the Mollweide projection.

Model projections under future climatic conditions indicate a general northward and northeastward shift in biodiversity patterns. These shifts become more pronounced over successive time periods and climate scenarios. Additionally, complex biodiversity patterns emerge around elevation gradients, water bodies, and forest cover, suggesting that these features play a critical role in shaping biodiversity patterns under changing climatic conditions.

Conclusion

In this study, we employed ecological niche models to map the spatial biodiversity patterns of Türkiye, addressing a notable gap in spatial approaches to biodiversity analyses in Anatolia. Our results highlight the coastal regions of Türkiye as high biodiversity areas and the inner Anatolia and southeastern Anatolia as low biodiversity areas across different taxa. Projections under future climate scenarios indicate biodiversity shifts toward the north and northeast. Additionally, geographical features such as elevation gradients, water bodies, and forest cover play a critical role in shaping biodiversity patterns, particularly in the context of climate change. This study contributes to our understanding of how climate change may shape the spatial distributions of biodiversity in Anatolia.We anticipate that this study will contribute to future research, enhance biodiversity studies in Anatolia, and support conservation decision-making.

References

Boucher, O., Denvil, S., Levavasseur, G., Cozic, A., Caubel, A., Foujols, M.-A., Meurdesoif, Y., Cadule, P., Devilliers, M., Ghattas, J., Lebas, N., Lurton, T., Mellul, L., Musat, I., Mignot, J., & Cheruy, F. (2018). IPSL IPSL-CM6A-LR model output prepared for CMIP6 CMIP [Dataset]. Earth System Grid Federation. https://doi.org/10.22033/ESGF/CMIP6.1534

Breiman, L. (2001). Random Forests. Machine Learning, 45(1), 5–32. https://doi.org/10.1023/A:1010933404324

Calvin, K., Dasgupta, D., Krinner, G., Mukherji, A., Thorne, P. W., Trisos, C., Romero, J., Aldunce, P., Barrett, K., Blanco, G., Cheung, W. W. L., Connors, S., Denton, F., Diongue-Niang, A., Dodman, D., Garschagen, M., Geden, O., Hayward, B., Jones, C., … Péan, C. (2023). IPCC, 2023: Climate Change 2023: Synthesis Report. Contribution of Working Groups I, II and III to the Sixth Assessment Report of the Intergovernmental Panel on Climate Change [Core Writing Team, H. Lee and J. Romero (eds.)]. IPCC, Geneva, Switzerland. (First). Intergovernmental Panel on Climate Change (IPCC). https://doi.org/10.59327/IPCC/AR6-9789291691647

Elith, J., Leathwick, J. R., & Hastie, T. (2008). A working guide to boosted regression trees. Journal of Animal Ecology, 77(4), 802–813. https://doi.org/10.1111/j.1365-2656.2008.01390.x

Fick, S. E., & Hijmans, R. J. (2017). WorldClim 2: New 1-km spatial resolution climate surfaces for global land areas. International Journal of Climatology, 37(12), 4302–4315. https://doi.org/10.1002/joc.5086

GBIF.org. (2024a). Occurrence Download (p. 700210415) [Darwin Core Archive,text/tab-separated-values,application/zip]. The Global Biodiversity Information Facility. https://doi.org/10.15468/DL.QXYMSD

GBIF.org. (2024b). Occurrence Download (p. 34842630) [Darwin Core Archive,text/tab-separated-values,application/zip]. The Global Biodiversity Information Facility. https://doi.org/10.15468/DL.XN3HKN

GBIF.org. (2024c). Occurrence Download (p. 52998736) [Darwin Core Archive,text/tab-separated-values,application/zip]. The Global Biodiversity Information Facility. https://doi.org/10.15468/DL.QAMGT7

GBIF.org. (2024d). Occurrence Download (p. 1184042) [Darwin Core Archive,text/tab-separated-values,application/zip]. The Global Biodiversity Information Facility. https://doi.org/10.15468/DL.9ZFWTY

GBIF.org. (2024e). Occurrence Download (p. 823197540) [Darwin Core Archive,text/tab-separated-values,application/zip]. The Global Biodiversity Information Facility. https://doi.org/10.15468/DL.Q7GTGJ

Guisan, A., & Thuiller, W. (2005). Predicting species distribution: Offering more than simple habitat models. Ecology Letters, 8(9), 993–1009. https://doi.org/10.1111/j.1461-0248.2005.00792.x

IUCN (International Union for Conservation of Nature). (2024). The IUCN Red List version 2024-2 Species Richness. (Spatial data) [Dataset]. https://www.iucnredlist.org

Jaynes, E. T. (1957a). Information Theory and Statistical Mechanics. Physical Review, 106(4), 620–630. https://doi.org/10.1103/PhysRev.106.620

Jaynes, E. T. (1957b). Information Theory and Statistical Mechanics. II. Physical Review, 108(2), 171–190. https://doi.org/10.1103/PhysRev.108.171

Ohlemüller, R., Anderson, B. J., Araújo, M. B., Butchart, S. H. M., Kudrna, O., Ridgely, R. S., & Thomas, C. D. (2008). The coincidence of climatic and species rarity: High risk to small-range species from climate change. Biology Letters, 4(5), 568–572. https://doi.org/10.1098/rsbl.2008.0097

Peano, D., Lovato, T., & Materia, S. (2020). CMCC CMCC-ESM2 model output prepared for CMIP6 LS3MIP [Dataset]. Earth System Grid Federation. https://doi.org/10.22033/ESGF/CMIP6.13165

Pereira, H. M., Navarro, L. M., & Martins, I. S. (2012). Global Biodiversity Change: The Bad, the Good, and the Unknown. Annual Review of Environment and Resources, 37(1), 25–50. https://doi.org/10.1146/annurev-environ-042911-093511

Phillips, S. J., Anderson, R. P., & Schapire, R. E. (2006). Maximum entropy modeling of species geographic distributions. Ecological Modelling, 190(3), 231–259. https://doi.org/10.1016/j.ecolmodel.2005.03.026

Phillips, S. J., & Dudík, M. (2008). Modeling of species distributions with Maxent: New extensions and a comprehensive evaluation. Ecography, 31(2), 161–175. https://doi.org/10.1111/j.0906-7590.2008.5203.x

Schapire, R. E. (2003). The Boosting Approach to Machine Learning: An Overview. In D. D. Denison, M. H. Hansen, C. C. Holmes, B. Mallick, & B. Yu (Eds.), Nonlinear Estimation and Classification (Vol. 171, pp. 149–171). Springer New York. https://doi.org/10.1007/978-0-387-21579-2_9

Shiogama, H., Abe, M., & Tatebe, H. (2019). MIROC MIROC6 model output prepared for CMIP6 ScenarioMIP [Dataset]. Earth System Grid Federation. https://doi.org/10.22033/ESGF/CMIP6.898

Tang, Y., Rumbold, S., Ellis, R., Kelley, D., Mulcahy, J., Sellar, A., Walton, J., & Jones, C. (2019). MOHC UKESM1.0-LL model output prepared for CMIP6 CMIP [Dataset]. Earth System Grid Federation. https://doi.org/10.22033/ESGF/CMIP6.1569

Trew, B. T., & Maclean, I. M. D. (2021). Vulnerability of global biodiversity hotspots to climate change. Global Ecology and Biogeography, 30(4), 768–783. https://doi.org/10.1111/geb.13272

Volodin, E., Mortikov, E., Gritsun, A., Lykossov, V., Galin, V., Diansky, N., Gusev, A., Kostrykin, S., Iakovlev, N., Shestakova, A., & Emelina, S. (2019). INM INM-CM5-0 model output prepared for CMIP6 ScenarioMIP [Dataset]. Earth System Grid Federation. https://doi.org/10.22033/ESGF/CMIP6.12322

von Storch, J.-S., Putrasahan, D., Lohmann, K., Gutjahr, O., Jungclaus, J., Bittner, M., Haak, H., Wieners, K.-H., Giorgetta, M., Reick, C., Esch, M., Gayler, V., de Vrese, P., Raddatz, T., Mauritsen, T., Behrens, J., Brovkin, V., Claussen, M., Crueger, T., … Roeckner, E. (2017). MPI-M MPIESM1.2-HR model output prepared for CMIP6 HighResMIP [Dataset]. Earth System Grid Federation. https://doi.org/10.22033/ESGF/CMIP6.762

Defining the Character of Turkey's Biodiversity Policies

Süleyman İlteber Uçar[a]

[a]Istanbul Technical University, Eurasia Institute of Earth Sciences, Geoanthropology Program, Türkiye
ucars22@itu.edu.tr

Keywords: Biodiversity Policies of Turkey, International Agreements, Policy Adoption, Semi-Periphery, World-Systems Analysis.

Aim

This study aims to examine the characteristics of Turkey's biodiversity policies and assess its adoption process of international biodiversity agreements. In order to do that, the study analyzes the international agreements to which Turkey has signed, assessing the extent and pace of their implementation. Furthermore, using World-Systems Analysis as a framework, this study investigates whether Turkey's semi-peripheral position in the global economic system influences its approach to biodiversity-related policies. By doing so, it seeks to deepen our understanding of how economic dynamics shape societies' relationships with the environment. In other words, this study aims to demonstrate that the position and role of countries within the global economic system are key factors influencing environmental policies, particularly biodiversity policies, in the case of Turkey.

Material and Methods

This study examines the extent and pace of Turkey's implementation of international biodiversity agreements by analyzing official documents, national policy reports, and external evaluations. The agreements under review include but are not limited to the Ramsar Convention, the Convention on Biological Diversity (CBD), and CITES.

The research focuses on three key aspects. First, the signing and ratification timelines of the agreements. The study examines the years in which Turkey signed and ratified these agreements to determine whether it has acted as an early or late adopter in comparison to other nations. Second, performance of implementation. The study reviews national reports published by the Turkish government, including policy documents, strategy reports, and implementation updates, to assess the extent to which commitments under these agreements have been fulfilled. Additionally, independent evaluations conducted by international organizations and research institutions are considered to provide a broader assessment of Turkey's compliance. Third, using World-Systems Analysis as an analytical framework. The study applies Wallerstein's classification of world systems to contextualize Turkey's policy adoption behavior. A literature review is being conducted on World-Systems Analysis to examine how Turkey's position as a semi-peripheral country influences its biodiversity policies.

The analysis follows a qualitative approach, utilizing document analysis to track Turkey's policy progress. Key indicators outlined in each agreement are examined to measure the degree of implementation, considering factors such as the number of completed policy actions, established conservation targets, and compliance with reporting obligations. Additionally, the timing of implementation is assessed by comparing the gap between ratification and concrete policy action that helps to identify whether commitments were fulfilled promptly or delayed over extended periods. By integrating World-Systems Analysis, this study examines whether Turkey's delayed adoption of biodiversity policies results from structural constraints tied to its semi-peripheral status in the global system or other internal political and economic factors. This framework allows for a deeper understanding of whether Turkey's position in the world economy has contributed to its classification in biodiversity governance.

Findings

The preliminary findings suggest that Turkey has signed some agreements generally close to other semi-peripheral countries like Argentina, Brazil, and Spain. For instance, Turkey ratified the CBD in 1996, making it the 166th country to do so, while Argentina, Brazil, and Spain ratified it in 1993 and 1994 (Convention on Biological Diversity, n.d.). Similarly, Turkey ratified the CITES in 1996, whereas Argentina, Brazil, and Spain signed it in 1981, 1975, 1986 respectively (CITES, n.d.). In the case of the Ramsar Convention, Turkey became a party in 1994, while Argentina, Brazil, and Spain joined in 1992, 1993, 1982 respectively (Ramsar Convention, 2023). Although these ratification dates are generally close among semi-peripheral countries, Turkey has approved these agreements later than core countries, reflecting a pattern of delayed commitment. Although legal regulations and policies have been introduced to fulfill the obligations of these agreements, there are gaps in implementation (OECD, 2019). The country often falls behind the targets set by these agreements, and sometimes policies that contradict these targets are also adopted. For example, while protected areas have been designated for wetland conservation, new projects that could put pressure on these areas continue to be proposed (Arslan, Çiçek, Döndüren, Ernoul, 2021; Doğa Derneği, 2024). This situation may be explained by Turkey's limited institutional capacity and the priority given to economic development goals.

World-Systems Analysis explains the hierarchical structure of the global economy. According to this approach, the world is divided into core countries, which have advanced industries and strong institutions; peripheral countries, which are low-income, dependent economies based on raw material trade; and semi-peripheral countries, which share characteristics of both. These countries have progressed in industrialization but are not as politically strong as core countries, and their environmental policies are often shaped by economic priorities (Wallerstein, 2004).

From a World-Systems Analysis perspective, the economic development efforts of semi-peripheral countries have a significant impact on their environmental performance. Frame (2019) suggests that industrialization pressures in semi-peripheral countries increase raw material production and trade, leading to greater environmental degradation. Turkey is classified as a semi-peripheral country (Babones, 2005; Cairó-i-Céspedes & Palacios Cívico, 2022), and its development model, which prioritizes economic growth, may explain why environmental and biodiversity policies lag behind. Its participation in international agreements is also shaped by economic concerns and limited institutional capacity (Turhan, Cerit Mazlum, Şahin, Şorman, & Gündoğan, 2016).

Conclusion

The findings indicate that Turkey's adoption of international biodiversity agreements aligns with other semi-peripheral countries but lags behind core nations. While legal and policy frameworks have been established to meet international commitments, implementation remains inconsistent. I argue that these challenges may stem from limited institutional capacity and the dominance of economic development priorities.

Using World-Systems Analysis as a framework, this study suggests that Turkey's semi-peripheral status influences its biodiversity policies. Similar to other semi-peripheral countries, Turkey faces industrialization pressures that drive resource exploitation, potentially hindering effective environmental governance. The analysis highlights how economic position within the global system can shape a country's commitment to biodiversity policies. By examining Turkey's case, this study seeks to deepen our understanding of how economic dynamics shape societies' relationships with the environment, demonstrating that biodiversity governance is not solely a matter of policy choices but also of broader economic structures.

References

Arslan, D., Çiçek, K., Döndüren, Ö., & Ernoul, L. (2021). Threat ranking to improve conservation planning: An example from the Gediz Delta, Turkey. *Land, 10*(12), 1381. https://doi.org/10.3390/land10121381

Babones, S. (2005). The country-level income structure of the world-economy. *Journal of World-Systems Research, 11*(1), 29–55. https://doi.org/10.5195/jwsr.2005.392

Cairó-i-Céspedes, G., & Palacios Cívico, J. C. (2022). Beyond core and periphery: The role of the semi-periphery in global capitalism. *Third World Quarterly, 43*(8), 1950–1969. https://doi.org/10.1080/01436597.2022.2079488

Frame, M. (2019). The role of the semi-periphery in ecologically unequal exchange: A case study of land investments in Cambodia. In R. S. Frey, P. K. Gellert, & H. F. Dahms (Eds.), *Ecologically unequal exchange* (pp. 75-91). Palgrave Macmillan. https://doi.org/10.1007/978-3-319-89740-0_4

OECD. (2019). *OECD environmental performance reviews: Turkey 2019*. OECD Publishing. https://doi.org/10.1787/9789264309753-en

Turhan, E., Cerit Mazlum, S., Şahin, Ü., Şorman, A. H., & Cem Gündoğan, A. (2016). Beyond special circumstances: Climate change policy in Turkey 1992–2015. *WIREs Climate Change*, *7*(3), 448–460. https://doi.org/10.1002/wcc.390

Wallerstein, I. (2004). *World-systems analysis: An introduction.* Duke University Press.

Url-1 https://www.cbd.int/information/parties.shtml, date retrieved 21.03.2025.

Url-2 https://cites.org/eng/disc/parties/index.php, date retrieved 21.03.2025.

Url-3 https://www.ramsar.org/sites/default/files/documents/library/annotated_contracting_parties_list_e.pdf, date retrieved 21.03.2025.

Url-4 https://dogadernegi.org/izmir-gediz-deltasina-jeotermal-tehdidi/, date retrieved 21.03.2025.

ECONOMY

Financial Crises and Macroprudential Policies

Financial Contagion: Dynamic Correlations Approach

Esra Çakır[a]

[a] Istanbul Technical University, Economics Program (MA), Türkiye
cakires19@itu.edu.tr

Keywords: Dynamic Correlations, Financial Contagion, Stock Markets, Volatility Transmission.

Aim

Globalization has strengthened financial market linkages over time. However, this development has also increased the vulnerability of the global financial system to cross-market shock transmission. In this context, the following questions become crucial for market participants, policymakers, and academicians: Do shocks in one market lead to greater volatility in others? Is volatility transmitted across financial assets? Are the effects of positive and negative shocks symmetric? Do correlations change over time, particularly during crises?

Despite the extensive literature on asset market linkages and shock transmission, there is no single definition of financial contagion. Generally, both theoretical and empirical studies define contagion as "a significant increase in cross-market linkages after a shock" (Claessens, S., & Forbes, K., 2013, p.44). Broadly, three main approaches have been employed to test for contagion: correlation analysis, ARCH-type models and copula-based models. A wide body of research has examined contagion effects across countries and periods by using different methodologies and focusing on various financial shocks, analyzing equities, bonds, currencies, and commodities (see King & Wadhwani, 1990; Baig & Goldfajn, 1999; Longin & Solnik, 1995; Dimitriou et al., 2013).

The existence of a higher degree of co-movement in the financial markets during the period of instability leads to several challenges for agents since the lower correlation between financial assets means higher diversification benefit and the lower the portfolio risk (Porras, E. R., 2016). Therefore, understanding these additional linkages (if it exists) which emerge during the crisis periods is crucial. In this context, this study aims to investigate the presence of financial contagion by modeling time-varying correlations between the U.S. and Fragile Five stock markets using a DCC-MGARCH framework. The empirical analysis focuses on two episodes of financial turmoil: the Global Financial Crisis (GFC) and the post-COVID-19 Federal Reserve policy shock.

Material and Method

Volatility modeling originated with the Autoregressive Conditional Heteroskedasticity (ARCH) model introduced by Engle (1982) and subsequently extended to the Generalized ARCH (GARCH) model by Bollerslev (1986). Over time, these models have evolved into a broad family of ARCH-type frameworks that are widely applied in financial market analysis (Bollerslev, 2008).

Multivariate GARCH (MV-GARCH) models have been widely used to model volatility transmission. These models enable the analysis of interrelationships between financial markets by capturing not only the mean but also the variance of the variables (Aydemir, 2021). Building on Bollerslev's (1990) constant correlation model, Engle (2002) introduced the DCC-GARCH framework, which allows for the analysis of time-varying correlations.

In this framework, the DCC-MGARCH model is employed to examine contagion between the U.S. and Fragile Five stock markets using daily return data from January 2007 to December 2022. The analysis focuses on two crises: the Global Financial Crisis (*September 2008)* and the 2022 Fed Policy Shock (*March 2022*), which followed the COVID-19 pandemic and marked the beginning of an aggressive monetary tightening cycle. These periods were selected due to their origin in the U.S., which allows for the examination of potential contagion from the U.S. to the Fragile Five economies. The stock indices analyzed include the BIST 100 (Turkey), BOVESPA (Brazil), SENSEX (India), IDX (Indonesia), FTSE/JSE (South Africa), and the S&P 500 (U.S.). Data obtained from DataStream.

Findings

Firstly, the daily returns are calculated as a percentage log difference. Figures 1 and 2 display the price and returns of the stock indices.

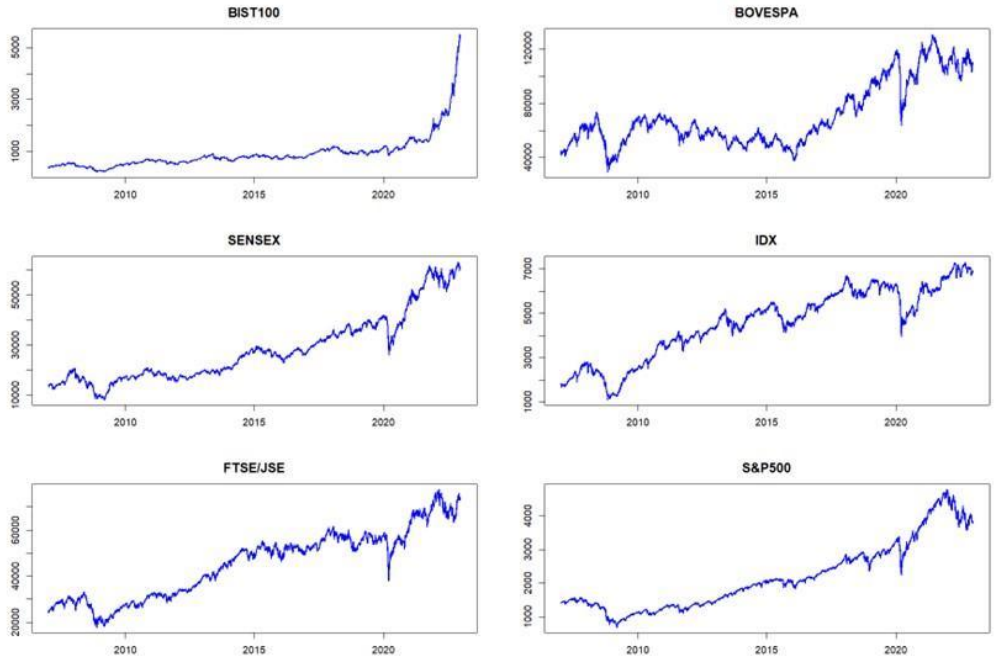

Figure 1: Time series plots of stock indices for S&P 500 and Fragile Five.

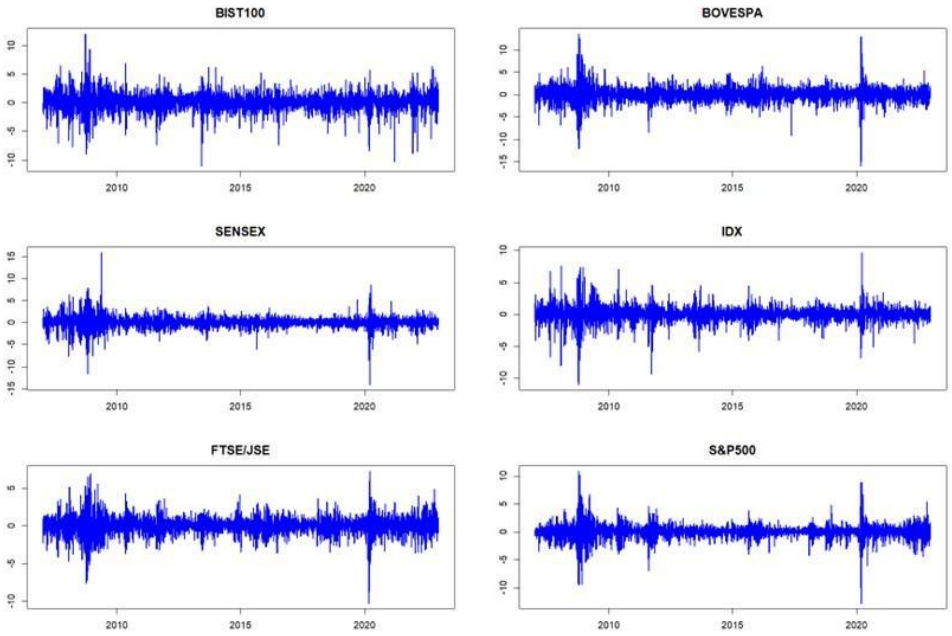

Figure 2: Time series plots of stock returns for S&P 500 and Fragile Five.

Descriptive statistics for the return series are presented in Table 1. The return series demonstrate common characteristics observed in financial time series: they are stationary, non-normally distributed, and exhibit negative skewness and excess kurtosis. The Jarque-Bera tests confirm the departure from normality, while the Augmented Dickey-Fuller (ADF) tests indicate stationarity. Additionally, the Box-Ljung tests applied to both raw returns and squared returns reveal the presence of serial correlation and volatility clustering, respectively. Furthermore, significant ARCH effects detected by ARCH-LM tests suggest the presence of conditional heteroskedasticity. These findings strongly justify the use of GARCH-type models.

Table 1: Descriptive statistics of return series.

Index	BIST 100	BOVESPA	SENSEX	IDX	FTSE/JSE	S&P 500
Mean	0.0633	0.0216	0.0356	0.0319	0.0258	0.0239
Median	0.0672	0.0000	0.0000	0.0289	0.0129	0.0343
Maximum	12.1281	13.6782	15.9899	9.7041	7.2614	10.9572
Minimum	-11.0633	-15.9938	-14.1017	-10.9540	–10.2268	-12.7652
Std. Dev.	1.6014	1.7096	1.3511	1.2305	1.2096	1.2797
Skewness	-0.4840	-0.4464	–0.2168	-0.5516	–0.3403	-0.5216
Kurtosis	4.9005	10.0963	13.37089	9.5323	5.6430	12.3475
Jarque-Bera	4340.7 [0.000]	17871 [0.000]	31133 [0.000]	16019 [0.000]	5620 [0.000]	26711 [0.000]
ARCH	318.71 [0.000]	1306.4 [0.000]	590.49 [0.000]	554.94 [0.000]	1140.9 [0.000]	1256 [0.000]
Q (20)	33.154 [0.032]	63.01 [0.000]	93.31 [0.000]	84.43 [0.000]	68.08 [0.000]	140.88 [0.000]
Q^2 (20)	835.82 [0.000]	5021.4 [0.000]	1946.9 [0.000]	2142.7 [0.000]	5029.4 [0.000]	5956.1 [0.000]
ADF stats	-43.42	-46.47	-45.19	-42.88	-46.23	-48.76
Observations	4175	4175	4175	4175	4175	4175

Notes: Square brackets report p-values. Null hypotheses: normality (JB), unit root (ADF), no autocorrelation (Box-Ljung), and no ARCH effects (ARCH-LM).

Table 2 shows the estimation results of DCC-GARCH models for each US-Fragile Five country pairs. An AR(1)-GARCH(1,1) specification is employed for all return series for simplicity. Also, DCC parameters, which are obtained the conditional standard deviations derived from the first stage, are presented. Model adequacy is assessed based on parameter significance, diagnostic test outcomes, and theoretical constraints such as the positivity of variance parameters. Since normal distribution hypothesis is rejected for all returns, student t distribution is used. The changes in DCC during the crisis periods can be observed in Figure 3.

Table 2: DCC model estimation results.

	SP500–BIST		SP500–BOVESPA		SP500–SENSEX		SP500–IDX		SP500–FTSE/JSE	
	US	BIST	US	BOVESPA	US	SENSEX	US	IDX	US	FTSE
Panel A: Mean and Variance Equation Estimates										
Constant (Mean)	0.0699	0.1075	0.0699	0.0484	0.0699	0.0732	0.0699	0.0471	0.0699	0.0496
	[0.0000]	[0.0000]	[0.0000]	[0.0199]	[0.0000]	[0.0000]	[0.0000]	[0.0007]	[0.0000]	[0.0006]
AR(1)	-0.0689	0.0093	-0.0689	-0.0422	0.8933	-0.0956	-0.0689	0.0234	0.8933	-0.8493
	[0.0001]	[0.5923]	[0.0001]	[0.0083]	[0.0000]	[0.7929]	[0.0001]	[0.1939]	[0.0000]	[0.0000]
Constant (Variance)	0.0286	0.0925	0.0286	0.0687	0.0282	0.0152	0.0286	0.0236	0.0282	0.0195
	[0.0000]	[0.0080]	[0.0000]	[0.0000]	[0.0000]	[0.0004]	[0.0000]	[0.0216]	[0.0000]	[0.0002]
ARCH (Alpha)	0.1453	0.0878	0.1453	0.0750	0.1442	0.0861	0.1453	0.0899	0.1442	0.0839
	[0.0000]	[0.0000]	[0.0000]	[0.0000]	[0.0000]	[0.0000]	[0.0000]	[0.0000]	[0.0000]	[0.0000]
GARCH (Beta)	0.8372	0.8771	0.8372	0.8965	0.8385	0.9066	0.8372	0.8944	0.8385	0.9020
	[0.0000]	[0.0000]	[0.0000]	[0.0000]	[0.0000]	[0.0000]	[0.0000]	[0.0000]	[0.0000]	[0.0000]
Panel B: DCC Estimates										
Average Corr.	0.2555		0.5260		0.2499		0.1135		0.3317	
	[0.0000]		[0.0000]		[0.0000]		[0.0000]		[0.0000]	
DCC α	0.0030		0.0399		0.0000		0.0047		0.0049	
	[0.0767]		[0.0001]		[0.0000]		[0.1334]		[0.0067]	
DCC β	0.9954		0.9461		0.8428		0.9848		0.9925	
	[0.0000]		[0.0000]		[0.0358]		[0.0000]		[0.0000]	
Panel C: Diagnostic Tests										
Q(20)	22.65	29.78	20.17	15.78	22.71	26.62	23.64	33.24	24.41	36.72
	[0.3065]	[0.0735]	[0.4474]	[0.7304]	[0.3033]	[0.1462]	[0.2584]	[0.0317]	[0.2251]	[0.0126]
$Q^2(20)$	14.29	10.04	12.36	11.83	18.47	16.23	15.78	11.83	14.87	21.32
	[0.8153]	[0.9674]	[0.9033]	[0.9219]	[0.5560]	[0.7025]	[0.7301]	[0.9219]	[0.7837]	[0.3785]

Note: For the SP500–FTSE/JSE and SP500–SENSEX models, an AR(2,1)–GARCH(1,1) specification was used, but only the AR(1) parameter is reported here to save space. Values in square brackets are *p*-values.

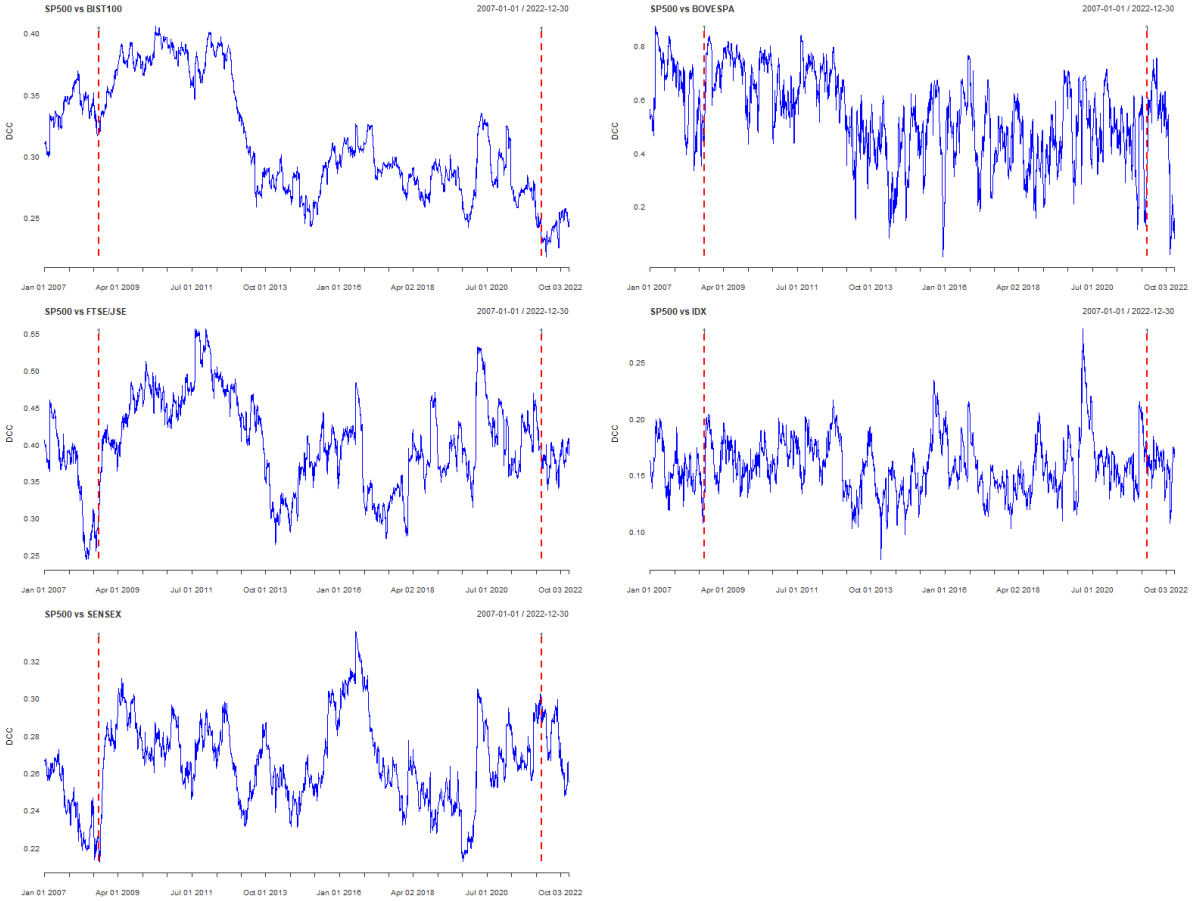

Figure 3: DCCs for stock returns.

Conclusion

The empirical findings of this study provide strong evidence of financial contagion from the U.S. to the Fragile Five stock markets. The DCC-GARCH model results indicate statistically significant increases in dynamic correlations across most market pairs. The DCC plots visually confirm these findings, with notable spikes in correlations. During the Global Financial Crisis, sharp increases are observed across nearly all markets, particularly for Brazil, India and South Africa. Similarly, the 2022 Fed policy shock is associated with moderate increases in correlations, most notably in Brazil and South Africa, indicating some sensitivity to U.S. market movements, though less pronounced than during the Global Financial Crisis.

However, the standard symmetric GARCH (1,1) model may not fully capture volatility behavior, especially in emerging markets. During periods of financial instability, returns often respond differently to positive and negative shocks. A more flexible model, such as EGARCH or APARCH, which allows for asymmetry in volatility, may capture these effects more accurately and improve models.

Future research could also examine how other shocks impact the Fragile Five, as well as how contagion patterns evolve across different stages of a crisis (e.g., early, peak, recovery). It would also be interesting to explore the determinants of dynamic conditional correlations - one of the major debates in literature. For example, examining the role of different types of funds and other financial intermediaries could be interesting, particularly in emerging markets, to assess the presence of financial panics or herding behavior during the crisis periods.

References

Aydemir, R., Guloglu, B., & Saridogan, E. (2021). Volatility spillovers and dynamic correlations among foreign exchange rates and bond markets of emerging economies.
Panoeconomicus, *68*(1), 99-127.
Baig, T. and Goldfajn, I. (1999). Financial market contagion in the Asian crisis, IMF staff papers, 46(2), 167–195.
Bollerslev, T. (1986). Generalized autoregressive conditional heteroskedasticity, Journal of econometrics, 31(3), 307–327.
Bollerslev, T. (2008). Glossary to arch (garch), CREATES Research paper, 49.
Claessens, S., & Forbes, K. (Eds.). (2013). *International financial contagion*. Springer Science & Business Media.
Dimitrios, D., Dimitris K., Theodore S. (2013), Global financial crisis and emerging stock market contagion: A multivariate FIAPARCH–DCC approach, International Review of Financial Analysis, Volume 30, Pages 46-56.
Engle, R.F. (1982). Autoregressive conditional heteroscedasticity with estimates of the variance of United Kingdom inflation, Econometrica: Journal of the econometric society, 987–1007.
Engle, R. (2002). Dynamic conditional correlation: A simple class of multivariate generalized autoregressive conditional heteroskedasticity models, Journal of Business & Economic Statistics, 20(3), 339–350.
Forbes, K. and Rigobon, R., (2001). Measuring contagion: conceptual and empirical issues, International financial contagion, Springer, pp.43–66.
Forbes, K.J. and Rigobon, R. (2002). No contagion, only interdependence: measuring stock market comovements, The journal of Finance, 57(5), 2223–2261.
King, M.A. and Wadhwani, S. (1990). Transmission of volatility between stock markets, The Review of Financial Studies, 3(1), 5–33.
Porras, E. R. (2016). *Bubbles and Contagion in Financial Markets, Volume 1: An Integrative View*. Palgrave Macmillan UK.
Soebhag, A. (2018). Investor Sentiment: Too Contagious to Ignore?. *Applied Finance and Accounting*, *4*(1), 54-72.
Soylu, P. K., & Güloğlu, B. (2019). Financial contagion and flight to quality between emerging markets and US bond market. *The North American Journal of Economics and Finance*, *50*, 100992.

ELECTRICAL ENGINEERING

Electric Power & Energy Systems

Electrical Machines

Electrical Vehicles

Power Electronics

Smart Grids

Techno-Economic Integration of Nuclear Energy Towards Achieving Net-Zero Emissions

Serdar Hudayberdıyev [a], Lale Erdem Atılgan [a]

[a] Istanbul Technical University, Departmant of Electrical Engineering, Electrical Engineering Program, Türkiye
hudayberdiyev20@itu.edu.tr

Keywords : Nuclear Energy, Net-Zero Emissions, PLEXOS, Energy Security, Grid Stability.

Aim

The global pursuit of net-zero emissions has intensified the demand for reliable, low-carbon energy sources. Nuclear energy, characterized by stable, dispatchable electricity generation, emerges as a critical solution. Nuclear energy accounts for approximately 9% of global electricity production, generating around 2,600 TWh annually and preventing approximately 2.1 billion tons of CO_2 emissions each year, playing a critical role in the transition to low-carbon energy (World Nuclear Association, 2024). This study evaluates the importance of nuclear energy and its potential contributions to Türkiye's energy transition process.

Türkiye's electricity generation is largely dependent on fossil fuel imports. Although renewable energy accounts for approximately 42% of electricity generation, energy supply security remains a significant concern (Republic of Türkiye Ministry of Energy, 2023). Fluctuations in fossil fuel prices and supply disruptions threaten energy security. To address these issues, Türkiye aims to achieve net-zero emissions by 2053. As part of this target, the Akkuyu Nuclear Power Plant (4,800 MW) is being commissioned, and once fully operational, it is expected to meet approximately 10% of Türkiye's electricity demand (Güler & Kavaz, 2023). Additionally, the İğneada Nuclear Power Plant is also planned, with a total capacity of 5,300 MW, further enhancing Türkiye's clean energy capacity and supporting the country's net-zero ambitions.

This study investigates the techno-economic integration of nuclear energy into Türkiye's electricity system, specifically focusing on the Akkuyu and İğneada Nuclear Power Plants. Using PLEXOS, a sophisticated energy modeling tool, the research assesses the impact of nuclear power on energy security, fossil fuel dependency, and grid stability. The analysis includes scenario-based simulations, exploring various configurations of nuclear and renewable energy. Findings indicate that nuclear power enhances energy reliability while supporting Türkiye's net-zero goals.

This study aims to evaluate the techno-economic integration of nuclear energy into Türkiye's electricity grid, with a specific focus on the Akkuyu and İğneada Nuclear Power Plants. This project does not advocate for a pro-nuclear approach; instead, it objectively and scientifically analyzes the advantages and disadvantages of nuclear energy. The objectives are to:

- Assess the role of nuclear energy in enhancing energy security and grid stability.
- Investigate the economic viability of nuclear energy in the Turkish context.
- Analyze the potential of nuclear energy to reduce carbon emissions. The analysis is conducted using PLEXOS, leveraging real-world data from EPİAŞ, TEİAŞ, and international energy reports.

Material and Method

This study employs the PLEXOS software platform, a robust tool for power system optimization, to explore the impact of nuclear energy integration within Türkiye's electricity system. The analysis begins with the development of three scenarios: a base scenario without nuclear energy, a scenario integrating the Akkuyu Nuclear Power Plant, and a third scenario including both Akkuyu and İğneada Nuclear Power Plants. These scenarios are designed to capture the range of possible outcomes, from a non-nuclear future to a nuclear-dominated energy mix.

The model incorporates fixed capacities for existing power plants across various fuel types, including coal, natural gas, hydro, solar, wind, and nuclear. These capacities are held constant for 2024, while electricity demand is projected to grow at an annual rate of 3.49%, as indicated by the TR-Power Report (Kat, 2021). Real-world data from EPİAŞ and TEİAŞ provide insights into generation and consumption patterns, while international sources, such as the International Energy Agency (IEA), inform fuel prices and demand forecasts (IEA, 2022).

The optimization process utilizes a combination of Linear Programming (LP) for cost minimization, Mixed-Integer Programming (MIP) for generator scheduling, and Quadratic Programming for complex growth modeling. Shadow pricing is applied to co-optimize energy and reserves.

The outputs of the model include generation profiles, offer prices, pool revenue, net revenue, and CO_2 emission intensity for each scenario. These results provide a comprehensive understanding of the economic and environmental implications of nuclear energy integration in Türkiye.

Findings

The scenario analysis reveals the following numerical results (2024-2049):

Table 1. Comparative Analysis of Scenario-Based Results for Türkiye's Electricity System (2024-2049).

Scenario	Average Offer Price ($/MWh)	Total Pool Revenue ($ Billion)	Total Net Revenue ($ Billion)	CO_2 Emission Intensity (tCO_2/GWh)
Base With Nuclear (Akkuyu)	84.67	6.51	4.83	473.24
Base With Nuclear (Akkuyu + İğneada)	75.43	6.60	4.93	460.87
Base Without Nuclear (NoN)	62.15	5.91	5.34	482.51

Table 2. Annual Electricity Generation for the Base Without Nuclear Scenario (2024-2049).

Base Without Nuclear NoN_medGR	Fiscal Year	2024	2025	2026	2027	2028	2029	2030	2031	2032	2033	2034	2035	2036	2037	2038	2039	2040	2041	2042	2043	2044	2045	2046	2047	2048	2049
	Generation (TWh)	361	371	381	391	402	411	420	430	440	448	458	467	478	486	496	505	516	524	534	543	554	562	572	581	592	600

Table 3. Annual Electricity Generation for the Base With Nuclear Scenario (Akkuyu) (2024-2049).

Base With Nuclear BAU_medGR Akkuyu	Fiscal Year	2024	2025	2026	2027	2028	2029	2030	2031	2032	2033	2034	2035	2036	2037	2038	2039	2040	2041	2042	2043	2044	2045	2046	2047	2048	2049
	Generation (TWh)	361	371	381	392	402	411	420	430	440	449	458	467	478	487	496	506	517	526	536	547	559	568	579	589	602	611

Table 4. Annual Electricity Generation for the Base With Nuclear Scenario (Akkuyu + İğneada) (2024-2049).

Base With Nuclear BAU_medGR Akkuyu + İğneada	Fiscal Year	2024	2025	2026	2027	2028	2029	2030	2031	2032	2033	2034	2035	2036	2037	2038	2039	2040	2041	2042	2043	2044	2045	2046	2047	2048	2049
	Generation (TWh)	361	371	381	392	402	411	420	430	440	449	458	472	490	501	511	521	533	541	552	562	574	584	594	605	618	628

In the "Base With Nuclear BAU_medGR Akkuyu" scenario, the presence of Akkuyu Nuclear Power Plant ensures consistent and substantial electricity production over the years. As a stable and reliable baseload source, nuclear energy provides continuous generation, unaffected by external factors like fuel price volatility or weather conditions. This stability translates into a steady increase in production, supporting energy security and maintaining grid reliability.

The "Base With Nuclear BAU_medGR Akkuyu + İğneada" scenario further amplifies this effect by incorporating the İğneada Nuclear Power Plant, leading to a significant boost in total electricity generation, particularly after 2035 when İğneada is fully operational. The combined output of the two nuclear plants not only enhances energy supply security but also increases the overall share of low-carbon electricity in the generation mix. This dual-nuclear setup demonstrates the critical role of nuclear energy in achieving consistent and reliable electricity supply.

In contrast, the "Base Without Nuclear NoN_medGR" scenario exhibits a more volatile production pattern. This is primarily due to the reliance on a mix of fossil fuel and renewable energy sources. Fossil fuel plants are susceptible to market price fluctuations, while renewable sources such as wind and solar are inherently variable, depending on weather conditions. This combination leads to irregular production patterns, with lower overall generation compared to the nuclear scenarios. The lack of nuclear energy's stable baseload contribution highlights the challenges of achieving a balanced and secure energy supply without nuclear power.

The scenario-based average offer prices reveal notable differences between the nuclear and non-nuclear scenarios. In the "Base With Nuclear BAU_medGR Akkuyu" scenario, the average offer price is $84.67/MWh, reflecting the high fixed costs associated with nuclear power, including construction, maintenance, and staffing. Although nuclear plants provide stable and continuous generation, their inflexibility in adjusting prices results in higher average offer prices.

The addition of the İğneada Nuclear Power Plant in the "Base With Nuclear BAU_medGR Akkuyu + İğneada" scenario leads to a reduced average offer price of $75.43/MWh. This reduction is due to the higher total production, which helps spread the fixed costs across more generated electricity, effectively lowering the cost per unit.

In contrast, the "Base Without Nuclear NoN_medGR" scenario exhibits the lowest average offer price at $62.15/MWh. This is primarily because fossil fuel and renewable energy plants can operate with more flexible pricing strategies. Renewables, such as wind and solar, generate electricity at nearly zero marginal cost, contributing to a lower overall average offer price in this scenario.

Total pool revenue is highest in the scenario with both Akkuyu and İğneada, benefiting from increased production capacity. However, net revenue is slightly lower in nuclear scenarios due to the high fixed costs associated with nuclear plants, including construction and maintenance expenses. Despite this, the nuclear scenarios exhibit significantly lower CO_2 emission intensity, highlighting their environmental advantage. The Akkuyu + İğneada scenario achieves the lowest emission intensity, demonstrating the significant role of nuclear energy in reducing carbon emissions and enhancing sustainability.

Conclusion

Nuclear energy significantly contributes to Türkiye's energy transition by providing stable, low-carbon electricity. This study demonstrated that integrating nuclear power, particularly through the Akkuyu and İğneada Nuclear Power Plants, offers notable benefits for energy security, grid stability, and carbon emission reduction. Scenario analysis revealed that nuclear-inclusive scenarios deliver higher average electricity generation and lower CO_2 emissions compared to non-nuclear scenarios, supporting Türkiye's net-zero target for 2053.

Despite high fixed costs, nuclear energy maintains competitiveness due to its stable generation and high capacity factors. The analysis highlighted a trade-off between reliable electricity supply and economic profitability, with nuclear scenarios having slightly lower net revenues due to their significant capital costs.

Environmental benefits were evident, with the lowest CO_2 emission intensity in the scenario including both Akkuyu and İğneada. This supports Türkiye's climate targets and emphasizes nuclear power's role in decarbonization. The PLEXOS model further demonstrated that nuclear energy enhances grid reliability, providing a stable supply regardless of external conditions, unlike the variability of renewable sources.

Future research should refine the model by incorporating capacity growth rates for each power plant, enhancing cost analysis with dynamic CO_2 shadow prices, and improving simulation accuracy using regional demand growth rates. Scenario-specific CO_2 emission factors should be developed, and machine learning techniques could be employed to model growth rates of demand and power plant capacities.

Overall, this study offers a balanced evaluation of nuclear energy's potential in Türkiye's electricity system, highlighting its benefits for energy security and emission reduction while acknowledging its economic and regulatory challenges.

Acknowledgements

The results of this study were obtained using the PLEXOS software provided by Energy Exemplar pursuant to a research license.

References

Güler, M. Ç., & Kavaz, İ. (2023). Türkiye'nin Nükleer Enerji Politikası: Akkuyu Nükleer Güç Santrali Örneği. İn B. Durgun & F. Durgun (Eds.), Makro Boyutlarıyla Enerji Ekonomisi. Özgür Yayınları. https://doi.org/10.58830/ozgur.pub299.c1444

International Energy Agency (IEA). (2022). World Energy Outlook 2022 (World Energy Outlook) [Annual Report]. International Energy Agency (IEA). https://www.iea.org/reports/world-energy-outlook-2022

Kat, B. (2021). Renewable energy transition in the Turkish power sector: A techno-economic analysis with a high-resolution power expansion model, TR-Power (Report No. 346).

Republic of Türkiye Ministry of Energy and Natural Resources. (2023). 2023 Activity Report [Activity Report]. Republic of Türkiye Ministry of Energy and Natural Resources.
https://enerji.gov.tr/Media/Dizin/SGB/tr/Faaliyet_Raporlari/2023/ETKB2023FR.pdf

World Nuclear Association. (2024). World Nuclear Performance Report 2024. World Nuclear Association. https://world-nuclear.org/images/articles/World-Nuclear-Performance-Report-2024.pdf

ELECTRICAL ENGINEERING

Electric Power & Energy Systems

Electrical Machines

Electrical Vehicles

Power Electronics

Smart Grids

Investigation of the Effect of Space Vector PWM Technique on Zero-Sequence Voltage Formation in Open-End Windings

Arda Tüfekçi[a,b], İlker Şahin[b] , Derya Ahmet Kocabaş[a]

[a] Istanbul Technical University, Electrical Engineering, Turkey
[b] Aselsan Inc., Turkey
tufekci22@itu.edu.tr

Keywords : Circulating Current, Open-end Windings, Zero-sequence Voltage.

Open-end winding Permanent Magnet Synchronous Machine (OEW-PMSM) drives offer several advantages over traditional star-connected configurations, making them a preferred choice in various high-performance applications. Their benefits include an extended modulation range, multilevel voltage characteristics, and enhanced fault tolerance, all of which contribute to improved system performance and reliability. However, these advantages come with increased complexity, particularly in the form of zero-sequence voltage (ZSV) formation and its associated zero-sequence current (ZSC). ZSV arises due to multiple factors, including modulation strategies, dead-time effects, machine harmonics, and inverter nonlinearities [1]. If not properly controlled, ZSV can lead to circulating currents, increased power losses, and degraded machine efficiency. In non-isolated systems where the inverters share a common DC bus, the presence of ZSV exacerbates these issues, making it a critical factor in system design and control.

Aim

The primary aim of this study is to analyze the formation of ZSV in OEW-PMSM drives under different modulation strategies and identify key sources contributing to its occurrence. Specifically, the research seeks to investigate how one of the most commonly used pulse- width modulation (PWM) techniques influence ZSV generation, examine the effects of different modulation angle pairs (0-120°, 0-150°, and 0-180°) between the inverters on ZSV behavior, and identify the contributions of dead-time effects, machine harmonics, and inverter nonlinearities to ZSV formation [1,2]. Additionally, the study aims to validate these findings through experimental testing to determine optimal strategies for minimizing ZSV. By addressing these objectives, this study provides valuable insights into the underlying mechanisms of ZSV formation and offers guidance on selecting effective modulation strategies to mitigate its impact. Understanding these interactions is essential for improving the efficiency and operational stability of OEW-PMSM drives, enabling their wider adoption in applications where high performance and reliability are paramount.

Material and Method

The OEW-PMSM drive system consists of an Open-end Winding Permanent Magnet Synchronous Machine (PMSM), supplied by two independent voltage source inverters (VSIs). The two inverters (inverter-1 and inverter-2) operate synchronously to generate the desired voltage waveforms while maintaining precise control over the motor's torque and speed. The experimental setup consists of an OEW-PMSM drive controlled by a dual-inverter configuration. An oscilloscope, high voltage differential probes were used to measure ZSV levels, as well as a current probe to capture phase current.

$$u_{a12} = (u_{a10} - u_{a20}) \quad (1)$$
$$u_0 = (u_{a12} + u_{b12} + u_{c12})/3 \quad (2)$$

In (1), ua10 is the voltage of phase-to-ground for phase a of inverter-1. (2) is used for scope captures, u0 is the zero-sequence voltage from inverter-side which equals to sum of voltage of phases across machine divided by three.

Key Contributors to ZSV Formation

To systematically analyze ZSV formation, several key sources were considered, including dead-time effects, machine harmonics, and inverter nonlinearities. Dead time is introduced in inverter switching to prevent short circuits between power devices, but it causes voltage distortions that lead to unwanted ZSV components. Machine harmonics, particularly the third harmonic in back-EMF, contribute to circulating currents and additional ZSV, further degrading system performance. Additionally, inverter nonlinearities such as switching device voltage drops and non-ideal switching transitions introduce small but significant distortions, further influencing ZSV behavior. After presenting key contributors of zero-sequence voltage, equation for ZSV is provided below.

$$u_0 = R_s i_0 + L_0 \frac{di_0}{dt} - 3\omega_r \psi_0 \, sin \, sin \, (3\theta_e) \, i_0 \qquad (3)$$

In (3), u0 is zero-sequence voltage (ZSV), i0 is circulating current (ZSC), L0 is zero-sequence inductance, ψ0 is the amplitude third-harmonic flux linkage, Rs is stator resistance, ωr is rotor angular velocity, θe is electrical angle.

Modulation Strategies

The study focuses on the most common modulation technique: Space Vector PWM (SVPWM), which is an advanced technique that optimizes switching sequences to improve voltage utilization and overall system performance. In this study, three different SVPWM modulation angle pairs between the inverters: 0-120°, 0-150°, and 0-180° modulation [3]. Each angle pair affects the synchronization and interaction between the two inverters, significantly impacting the resulting ZSV levels and the operational efficiency of the OEW-PMSM drive.

Influence of Dead-Time Effects

Despite improvements achieved through modulation angle selection, dead-time effects remain a persistent source of ZSV. Dead-time voltage errors are highly dependent on current polarity and switching sequence, leading to the introduction of unwanted ZSV components at every switching cycle [4]. Therefore, the magnitude of dead-time-induced ZSV varies with switching frequency and dead-time itself, making it a dynamic challenge in system performance. Even with optimal modulation strategies, dead-time effects cannot be fully eliminated, emphasizing the need for compensation techniques to mitigate their impact and improve overall drive efficiency.

Contribution of Machine Harmonics to ZSV

Machine harmonics, particularly third harmonic components in back-EMF, introduce additional circulating currents, which contribute to ZSV formation [3]. The study finds that the presence of third harmonic components increases ZSV ripple, negatively impacting system performance. Additionally, these harmonics interact with inverter switching states, sometimes amplifying the effects of dead-time distortions, further exacerbating ZSV issues. To mitigate these effects, filtering or compensation techniques may be necessary to suppress harmonic-induced ZSV, ensuring improved drive efficiency and stability.

Findings

The analysis of the three SVPWM modulation angles reveals that 0-120° modulation provides the lowest ZSV RMS values making it the most effective choice for minimizing ZSV formation. In contrast, 0-150° and 0-180° modulations result in higher ZSV due to increased switching interactions and harmonic content which amplify circulating currents and voltage distortions. These findings emphasize that proper modulation angle selection plays a crucial role in reducing ZSV, demonstrating that choosing the right SVPWM modulation angle is just as important as the modulation technique itself in optimizing OEW-PMSM drive performance.

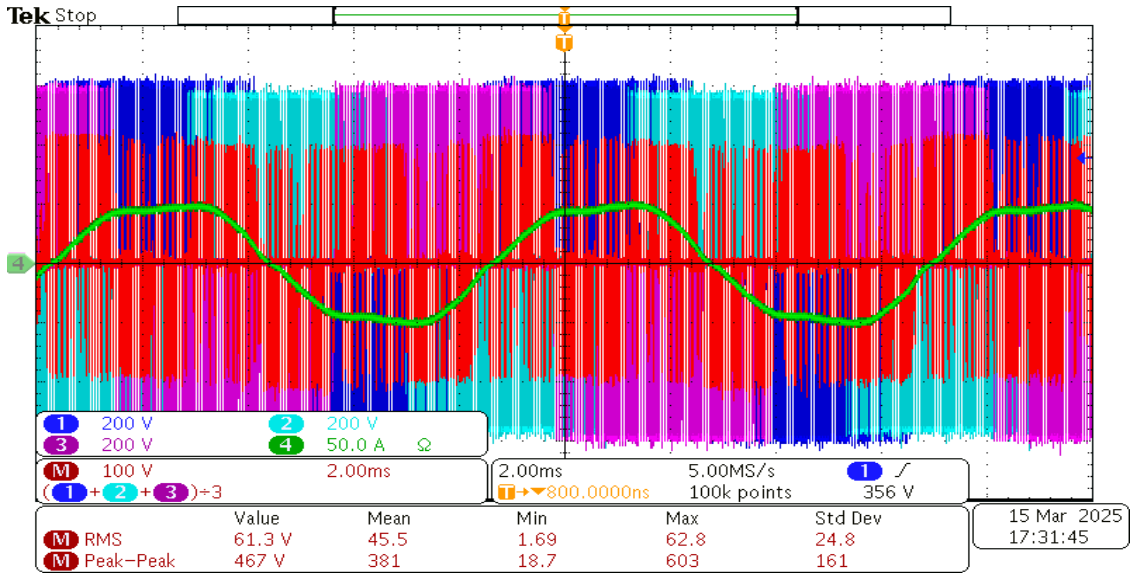

Figure 1. Space Vector PWM with 0-120°.

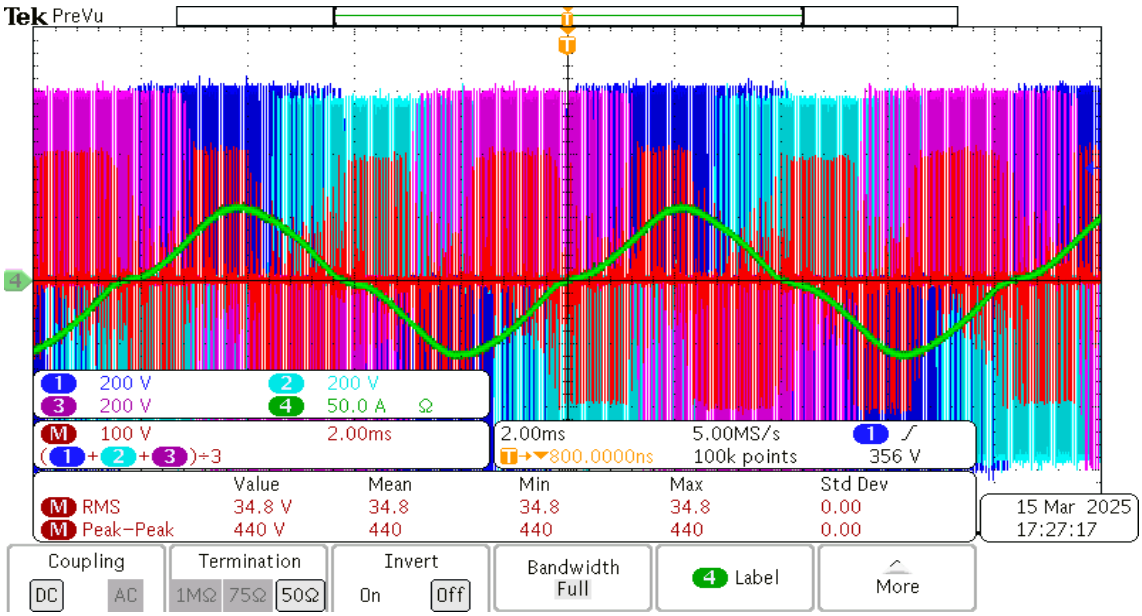

Figure 2. Space Vector PWM with 0-150°.

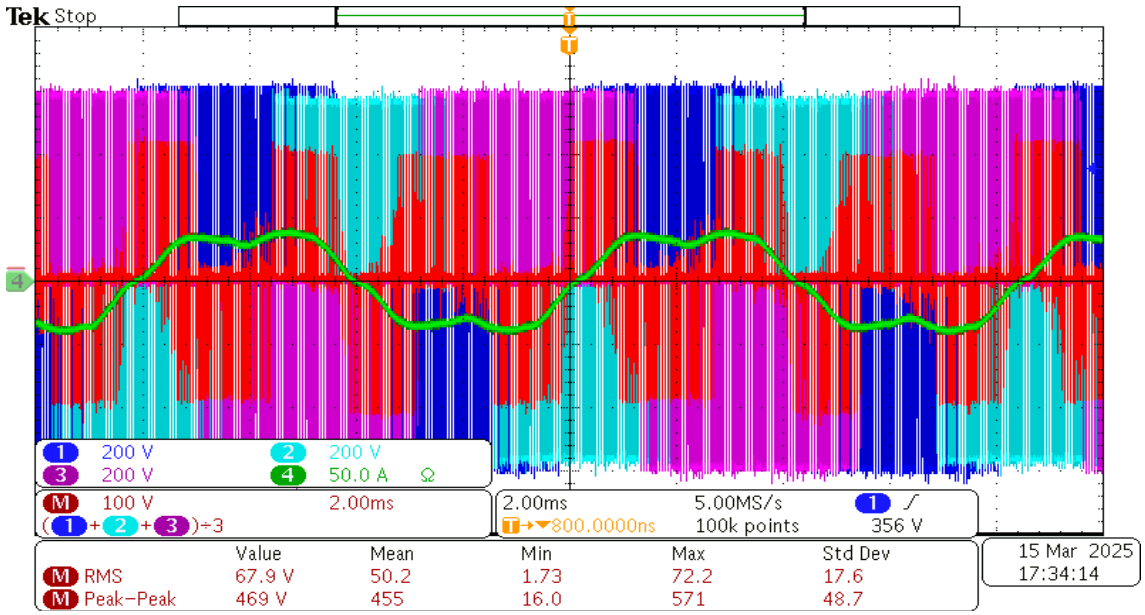

Figure 3. Space Vector PWM with 0-180°.

Table 1: Comparison of Modulation Angles.

Modulation	ZSV RMS (V)	ZSV PP (V)
SVPWM 0-120°	34.8	440
SVPWM 0-150°	61.3	467
SVPWM 0-180°	67.9	469

Conclusion

This study systematically investigates the formation of zero-sequence voltage (ZSV) in open-end winding PMSM drives, analyzing the effects of different modulation strategies and identifying key contributors to ZSV generation. The findings demonstrate that: Modulation strategy significantly affects ZSV formation, with 0-120° modulation providing the lowest RMS ZSV values. Dead-time effects remain a persistent challenge, introducing unavoidable ZSV components due to switching delays in the inverter legs. Selecting the appropriate modulation angle pair (e.g., 0-120°) is crucial for minimizing ZSV, as it helps balancing inverter switching states and reducing unwanted interactions. While 0-120° modulation was found to be the most effective in reducing ZSV, although it does not completely eliminate it. Future research should explore dead-time compensation techniques, advanced harmonic suppression methods, and alternative inverter topologies to further mitigate ZSV and enhance OEW-PMSM drive performance. Additionally, adaptive control strategies that dynamically adjust modulation parameters based on operating conditions could provide further improvements in minimizing ZSV-related issues. Understanding the interactions between modulation strategies, machine harmonics, and inverter nonlinearities is essential for optimizing OEW-PMSM drives. By carefully selecting modulation parameters and compensating for known sources of ZSV and ZSC, engineers can enhance system efficiency, reduce power losses, and

improve the reliability of OEW-PMSM-based applications.

References

Apurva Somani, Ranjan K. Gupta, Krushna K. Mohapatra, and Ned Mohan, 2013. "On the Causes of Circulating Currents in PWM Drives With Open-End Winding AC Machines". In: *IEEE Transactions on Industrial Electronics* 60.9 (2013), pp. 3670–3678. DOI: 10.1109/TIE.2012.2208430.

M.R. Baiju, K.K. Mohapatra, R.S. Kanchan, and K. Gopakumar, 2004. "A dual two-level inverter scheme with common mode voltage elimination for an induction motor drive". In: *IEEE Transactions on Power Electronics* 19.3 (2004), pp. 794–805. DOI: 10.1109/TPEL.2004.826514.

Hanlin Zhan, Zi-qiang Zhu, and Milijana Odavic, 2017. "Analysis and Suppression of Zero Sequence Circulating Current in Open Winding PMSM Drives With Common DC Bus". In: *IEEE Transactions on Industry Applications* 53.4 (2017), pp. 3609–3620. DOI: 10.1109/TIA.2017.2679678.

Q. An, J. Liu, Z. Peng, L. Sun and L. Sun, 2016. "Dual-Space Vector Control of Open-End Winding Permanent Magnet Synchronous Motor Drive Fed by Dual Inverter," in IEEE Transactions on Power Electronics, vol. 31, no. 12, pp. 8329-8342, Dec. 2016, doi: 10.1109/TPEL.2016.2520999.

Determination of Altitude Dependent Insulation Breakdown of Brushed DC Starter Generators

Ayşe Nur Köklü Ulusoy[a], Derya Ahmet Kocabaş[a]

[a] Istanbul Technical University/Department of Electrical Engineering, Turkey
koklu15@itu.edu.tr

Keywords: DC Starter Generator, Altitude-dependent, Insulation Breakdown, Electrostatic Analysis.

Aim

Brushed direct current (DC) machines have a widespread market application in Unmanned Aerial Vehicles (UAVs) and small-scale aircraft because of their compact size, economical price, and easily controllable capabilities. Brushed DC machines are mostly used as starter generators in aircraft engine starters and electrical power generation systems. Aircraft operate at different altitudes, which presents several changes in environmental conditions. Aircraft must be able to operate all components safely at all operating altitudes. Therefore, it is important that starter generators can operate safely under variable environmental conditions, maintaining both functionality and insulation integrity. Change in altitude, air pressure, ambient temperature, and relative humidity result in significant insulation breakdowns, and poses a great danger to the reliability and safety of operation.

This study aims to examine the potential consequences of attitude dependent environmental changes on the winding insulation of brushed DC starter generators from an electrostatic view which is one of the most important components of aircraft electrical power systems. The objective is to understand the relationship between altitude-dependent environmental variables and brushed DC starter generator insulation failures like winding-to-winding and winding-to-frame insulation failure.

Material and Method

This study presents a simulation-based approach. ANSYS Maxwell 2D Electrostatic solution is used as a simulation environment. ANSYS Maxwell 2D is a Finite Element Method (FEM) based simulation software used to perform two-dimensional analysis of electromagnetic devices, especially effective in the design and optimization of systems based on magnetic fields such as motors, transformers, and actuators. FEM is used in numerical solutions to engineering and physics problems. It helps to model the characteristics of the components in complex systems by dividing the structure or system into many small and finite element parts and solving differential equations on these elements.

In the simulation, a two-dimensional model of a separately excited brushed DC machine was created. In the electric machine model, field windings, armature windings, and auxiliary windings were detailed. Various insulation defects were created separately in the field, as well as in the armature and auxiliary windings. Insulation defects were simulated as gaps, tears, and microcracks between the winding and between the winding and the body.

These insulation defects were analyzed in terms of electric fields at different altitudes. The altitude variable was simulated by the dielectric constant of the insulator materials in the brushed DC starter generator design. The environmental conditions changing with altitude were determined as air pressure, temperature, and relative humidity. The dielectric constant of the insulator materials was calculated for each altitude level depending on the air pressure, temperature, relative humidity parameters in the air gap, and the relative humidity parameter in the winding insulators and simulations were performed. Polyimide material, which is frequently used in space and aviation applications, was preferred for winding insulations. The reason for performing the analysis of the polyimide material only depending on the humidity parameter is that the temperature and air pressure parameters do not cause a significant change in the polyimide dielectric constant. International Standard Atmosphere data were used for the altitude-dependent humidity, temperature, and ambient pressure data. The dielectric coefficient calculation of the air gap was performed with the formula given in Equation 1, which is also based on

the International Standard Atmosphere data. Simulations were performed for altitudes of 10,000 ft, 20,000 ft, 30,000 ft, and 40,000 ft, and the electric field distributions in various parts of the machine at these levels were examined.

$$\varepsilon_{hava} = \varepsilon_0 \cdot \left[1 + \frac{311}{T}\left(P + \frac{48\,P_s}{T}\,RH\right)10^{-6}\right] \quad (1)$$

Findings

Various damages were created in the windings of the brushed shunt DC starter generator and simulations were performed at different altitudes with these damages to investigate the electric field distributions. The electric field distributions were compared for each deformation and altitude value. The results showed that insulation deterioration was significantly affected by altitude changes. Analysis results showed that as altitude increases, the dielectric strength of the air decreases, thus decreasing the insulating properties and increasing the possibility of an insulation breakdown at lower voltages compared to ground level. In addition, it was observed that the dielectric strength of the winding insulations decreased to a certain altitude and then increased up. The dielectric strength of the winding insulation material polyimide is directly related to the relative humidity, and as the humidity increases, the dielectric constant increases. While the relative humidity decreases up to 30,000 ft, it increases from 30,000 ft to 40,000 ft. Therefore, the dielectric strength of polyimide decreases up to 30,000 ft and increases from 30,000 ft to 40,000 ft.

When this situation is evaluated in terms of starter generators, it is predicted that the possibility of insulation damage will increase due to high currents passing through the armature windings in cases where the engine needs to be started at high altitudes. It has been evaluated that this situation may cause the starter generator to become unable to start the engine and may negatively affect flight and operational safety by not being able to start the engine. In addition, it has been evaluated that the possibility of a short circuit in the windings and frame increases when the starter generators are in generator operating mode, which may lead to system failures and power loss.

Conclusion

The study confirms that altitude changes play a critical role in insulation defect induced breakdown and short circuit events in brushed shunt DC starter generators, which are commonly used in aviation. These findings highlight the need for improved insulation materials or protective coatings that can withstand variable altitude and therefore variable weather conditions. The results demonstrate the importance of selecting advanced insulation materials for high altitude applications and suggest that predictive maintenance strategies can help extend the operational life of starter generators and increase reliability.

Future studies should focus on developing predictive models using machine learning techniques to assess insulation degradation trends in real time. Additionally, research should continue the use of advanced nanocomposites and hybrid insulation systems to increase insulation life and reliability. Implementation of real time monitoring systems to monitor insulation health will help prevent electrical failures that may occur during flight by providing early fault detection.

References

DuPont. (2022). *Kapton® summary of properties* (Publication No. EI-10142). DuPont de Nemours, Inc.

Jiang, J., Li, Z., Li, W., Ranjan, P., Wei, X., Zhang, X., & Zhang, C. (2023). A review on insulation challenges towards electrification of aircraft. *High Voltage, 8*(2), 209–230.

Mendez-Astudillo, J., Lau, L., Yu Fat Lun, I., Tang, Y.-T., & Moore, T. (2021). Urban heat island monitoring with Global Navigation Satellite System (GNSS) data. In *Urban Science and Engineering for Smart Cities* (pp. 37–65). https://doi.org/10.1007/978-981-33-4050-3_3

Ren, X., Chen, Z., Du, R., & Feng, M. (2024). Design and performance analysis of windings considering high frequency loss and connection mode of a starter generator.*Energies*,*17*(20), 5124. https://doi.org/10.3390/en17205124

Santo Zarnik, M., & Belavic, D. (2012). An experimental and numerical study of the humidity effect on the stability of a capacitive ceramic pressure sensor. *Radioengineering, 21*(1), 201–206.

ELECTRICAL ENGINEERING

Electric Power & Energy Systems

Electrical Machines

Electrical Vehicles

Power Electronics

Smart Grids

Development And Validation Of A Dynamic Energy Consumption Model For A 12-Meter Electric Bus Using SORT-2 Test Data

Mehmed Demirtaş[a], Mehmet Onur Gülbahçe[a]

[b] Istanbul Technical University, Department of Electrical Engineering, Türkiye
demirtasm15@itu.edu.tr

Keywords: Dynamic Modelling, Electric Bus, Energy Consumption Model, Sustainable Transportation.

Aim

The growing use of electric buses in the transportation sector presents a significant opportunity to reduce environmental impacts, particularly in urban areas where air pollution and carbon emissions from traditional vehicles are a major concern. However, to fully utilize their potential, accurate and reliable consumption calculations are necessary.

The aim of this study is to develop a dynamic model of a 12-meter electric bus and to compare its energy consumption with SORT-2 data to validate the model's accuracy. By building a comprehensive model that represents the electric bus's energy usage, this study aims to verify how closely the predicted consumption aligns with actual test data. Modeling the energy efficiency of electric buses accurately provides critical insights for both manufacturers and consumers. This can contribute to designing more efficient buses, enhancing battery life, and lowering operational costs. In this context, one of the primary objectives of the study is to validate the model by comparing its output with real-time data from actual bus operations, focusing on driving cycles that reflect real-world conditions. Another objective of this study is to adapt the model to different driving profiles and road conditions. By incorporating realistic driving scenarios into the model, a more robust and reliable understanding of energy consumption patterns can be achieved.

Material and Method

The bus dynamic model is developed in this study in MATLAB. The input parameters of the model represents energy consumption in kWh and km. Additionally, a comparison between the developed model and the real-world data collected during SORT-2 tests will be conducted.

Energy consumption calculations for electric buses are usually validated using specific tests and standards. For passenger vehicles, the WLTP (Worldwide Harmonized Light-Duty Vehicles Test Procedure) standard is commonly used, while for buses, SORT (Standardized On- Road Test) tests are utilized. The SORT tests are divided into three categories: SORT 1, SORT 2, and SORT 3 (UITP, 2017). In this study, the real data collected during the SORT 2 test will be used for the 12-meter electric bus.

In the model, it is essential to calculate the distance traveled by the bus to determine the energy consumption accurately. Average speed and the time the bus has been in motion will be used as input parameters. The model will integrate these parameters with SORT test data to ensure that the simulation reflects real-world driving behavior.

Moreover, the model primarily calculates energy consumption by analyzing the bus's instantaneous voltage and the current flowing into and out of the battery. Energy consumption in electric buses depends largely on the electrical components of the drive system, including the battery, electric motor, power electronics, thermal management systems. The model will take into account these components' performance under different operational conditions, such as acceleration, deceleration, and cruising.

During motion, vehicles encounter various resistance forces that must be overcome by engine power. Reducing these resistances enhances energy efficiency and extends the driving range in electric vehicles. A vehicle experiences four primary resistance forces: aerodynamic resistance, rolling resistance, hill resistance, and acceleration resistance. To replicate real-world driving conditions, these resistances are applied during operation (Karakaş, Şeker, & Solmaz, 2021). The effect of

wind, which directly influences the vehicle's energy consumption, has been neglected in this study which aligns with the SORT-2 test conditions. Since the SORT-2 test is conducted on a flat road, gradient resistance is neglected, and the model has been developed accordingly. Moreover, the application of different driving dynamics will increase the vehicle's energy consumption due to the forces caused by the road gradient. On inclined roads, the gradient can be included as an input parameter in the model, allowing for its impact on energy consumption to be assessed.

A study has investigated the impact of internal losses in high-voltage lithium-ion batteries on EV range estimation and proposed a method to predict these losses by integrating a vehicle consumption model with trip-based data and a battery model that accounts for future losses based on the control strategy's predicted energy use (Enthaler & Gauterin, 2013). In the battery model of this study, a battery cell with the same chemistry as that used in the 12-meter electric bus was tested under different temperatures. The Hybrid Pulse Power Characterization (HPPC) test was conducted. Although various types of HPPC tests are defined in the literature, the methodologies described in the study by Christophersen (2015) were adopted for this study.

For accurate energy consumption estimation, an appropriate relationship between electric motor power and applied force must be established. Efficiencies of the electric motor, the inverter for the electric motor, and the DC-DC converter are also taken into account. Furthermore, there are other high-voltage components that may influence energy consumption, such as HVAC (heating, ventilation, and air conditioning), pre-heater, and BTMS (battery thermal management system). However, these components are not considered in the SORT-2 test.

Findings

The model developed and tested according to the SORT-2 duty cycle data. Comparison between the model and the SORT-2 data is essential since it allows to identify any discrepancies between the predicted energy consumption and the actual performance of the bus.

The results show that there is a 4.55% difference between the energy consumption obtained from the vehicle's dynamic model and the SORT-2 data. Despite a minor discrepancy, the model demonstrates a high level of accuracy in predicting energy consumption based on the SORT-2 test. It is important to note that discrepancies between modeled and measured data can arise from factors such as sensor calibration, road conditions, and real-time adjustments that are difficult to replicate in simulations. Nonetheless, the close match suggests that the model provides a reliable estimate of the energy consumption for the 12-meter electric bus.

Conclusion

This study developed a bus dynamic model to predict the energy consumption of a 12-meter electric bus. The model's accuracy was successfully tested by comparing the results with real-world data from the SORT-2 test. This validation demonstrates the model's reliability and usefulness for manufacturers. The findings suggest that accurate energy consumption models can contribute to improved fleet management, better cost forecasting, and a more sustainable transportation infrastructure.

Moving forward, the model's accuracy can be further enhanced using different driving cycles. By incorporating additional real-world data and refining the model through continuous feedback, its predictive capability can be improved. This model will aid in more accurate energy efficiency predictions for electric buses and will serve as a valuable reference for future research in this field. Incorporating additional high- voltage components such as HVAC, pre-heaters, and BTMS into the model would further enhance its accuracy. With continued advancements in data collection and modeling techniques, future models are expected to be even more precise, enabling greater optimization of electric bus fleets and reduced overall energy consumption.

References

Christophersen, Jon P. (2015). Battery Test Manual For Electric Vehicles, Revision 3. https://doi.org/10.2172/1186745

Enthaler, A., & Gauterin, F. (2013). Significance of internal battery resistance on the remaining range estimation of electric vehicles. *2013 International Conference on Connected Vehicles and Expo (ICCVE)*, 94–99. https://doi.org/10.1109/ICCVE.2013.6799776

Karakaş, O., Şeker, U. B., & Solmaz, H. (2021). Modeling of an electric bus Using MATLAB/Simulink and determining cost saving for a realistic city bus line driving cycle. Engineering Perspective, 1(2), 52-62.

UITP. (2017). *Project SORT – Standardised On-Road Test cycles* [Brochure]. Retrieved Feb 24, 2025, from https://www.uitp.org/publications/uitp-sort-e-sort-brochures/

ELECTRICAL ENGINEERING

Electric Power & Energy Systems

Electrical Machines

Electrical Vehicles

Power Electronics

Smart Grids

Three Phase LLC Resonant DC/DC Charger for Railway Applications

Abdulkadir Balikçi[a], Murat Gümüş[a]

[a] Gebze Technical University/Institute of Science, Engineering Department, Electronic Engineering, Turkey
a.balikci@gtu.edu.tr, muratgumus150@gmail.com

Keywords: Three Phase System, LLC Converter , Multiphase Converter.

This study introduces the topology of a three-phase LLC resonant converter design. The three-phase LLC resonant converter retains the advantages of conventional LLC resonant converters, such as zero-voltage switching (ZVS) on the primary side, zero-current switching (ZCS) on the secondary side, high-frequency operation capability, and high efficiency. Additionally, it offers unique benefits beyond those of traditional LLC converters, including reduced output capacitor current ripple, natural current sharing among the three resonant currents, and suitability for high-power applications. Due to these features, LLC topology is widely used in electric vehicle charging systems, server power supplies, and other high-power applications.

However, as power levels increase, the input voltage tends to be higher to reduce conduction losses, and the output current also rises. This creates challenges in transformer design, as higher currents lead to increased core and copper losses, making heat dissipation more difficult. Three phase transformer provides a direct and effective solution to this issue. By employing three phase transformers with primary windings connected in series and secondary windings connected in parallel, primary voltage stress and secondary current stress can be reduced, while output current distribution is improved.

Aim

The traditional LLC resonant converter is among the most widely adopted resonant topologies due to its ability to achieve soft switching and maintain high efficiency across the entire load range. Nonetheless, in high-current scenarios, the single-phase LLC converter exhibits certain limitations. Specifically, the output capacitor is subjected to substantial current ripple, which can impose significant stress. As a result, a large output filter capacitor is typically required to mitigate these ripple effects. To overcome these issues, multiphase LLC resonant converters offer notable benefits over their single-phase counterparts. By distributing the total load current across multiple phases, conduction losses are reduced, and thermal stress on power components is alleviated. Furthermore, when three identical sinusoidal waveforms with 120° phase displacement are rectified, the resulting output exhibits significantly lower ripple, enhancing filter performance. A schematic of the three-phase LLC resonant converter is shown below.

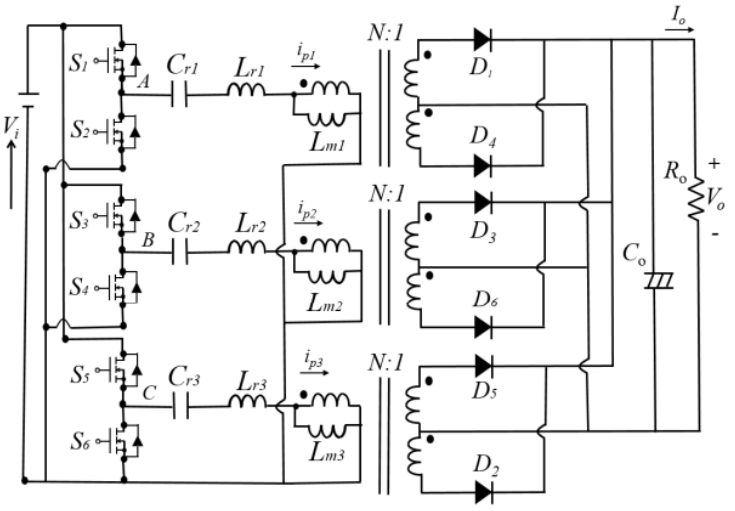

Figure 1. Three-phase LLC resonant converter with three-discrete transformers.

The Resonant Tank system Gain depending on frequency is shown below.

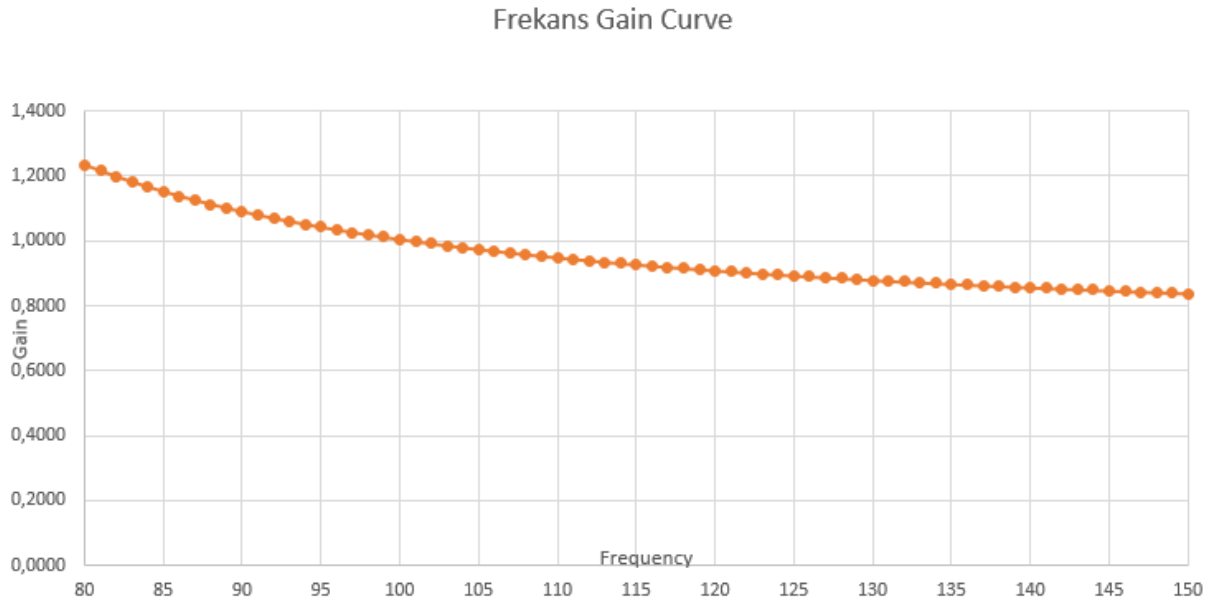

Figure 2. Three-phase LLC resonant converter Gain Curve.

Material and Method

The resonant inductor, capacitor, transformer ratio and other components required for the Three Phase LLC Resonant Converter Design are given in Table 1.

Table 1. Resonance Tank and Other Components.

Component	Value
Resonance Inductance (Lr)	47µH
Resonance Capacitor	56nF
Transformer Ratio	5:1
Operating Frequency Range	80kHz-150KHz
Resonance Frequency	~100KHz
Input Voltage	600V DC
Output Voltage	77.5V-110V
Output Current	60A

As a result of the simulation study performed with the LTspice program with these values, the Transformer Primary Current waveform appears as in the Figure.

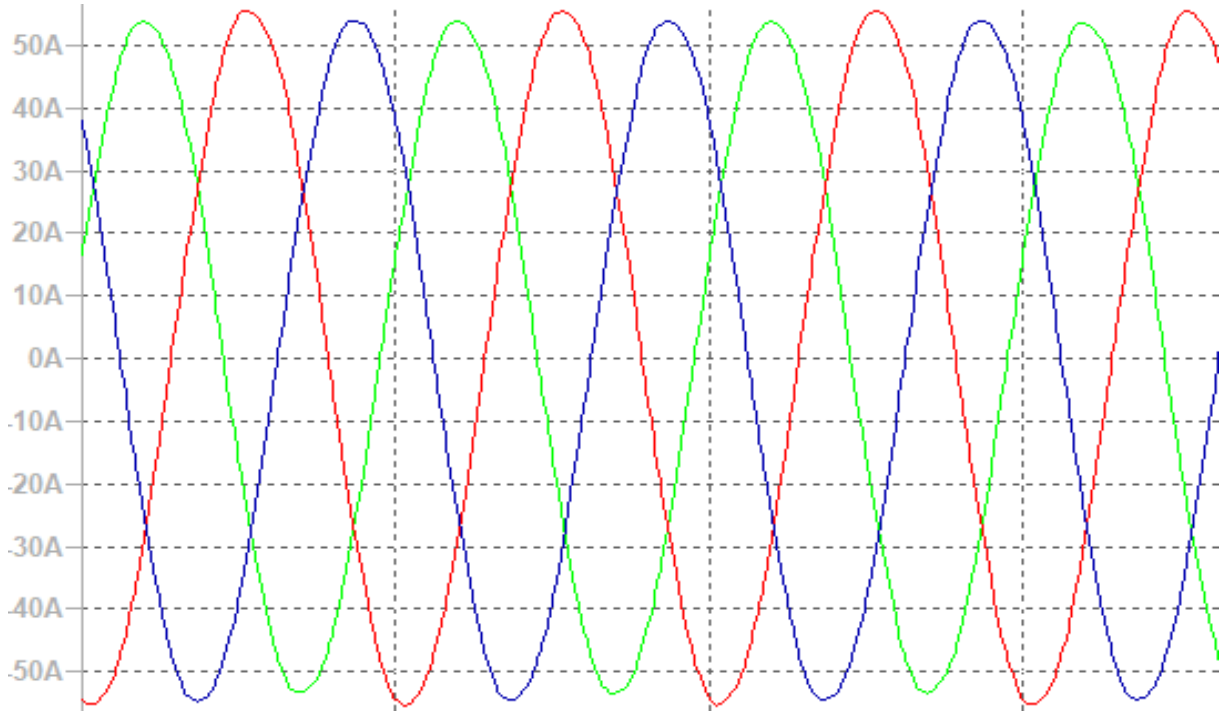

Figure 3. Current Wave of Three Transformer Primary Current.

Findings

Single and three phase LLC Resonant Converter analyses were performed using the LTSpice program. These analyses show that the output load resistance and output capacity of single LLC and three phase LLC Resonant Converters are the same. Therefore, the output current ripple of the three phase Resonant Converter was compared with the single LLC converter. According to the comparison result, the output voltage ripple can be seen in the visual below.

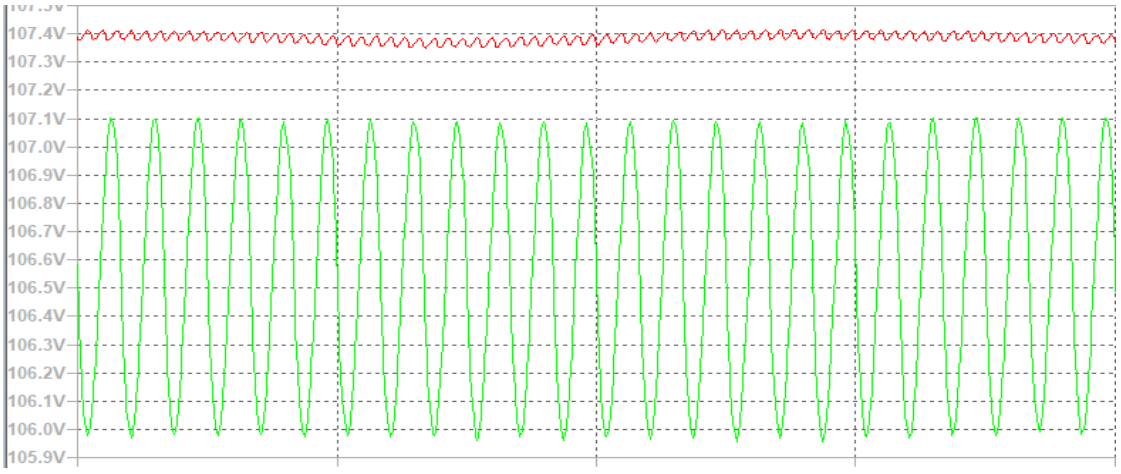

Figure 4. Green: Single Phase LLC Output Voltage Ripple, Red: Three Phase LLC Output Voltage Ripple.

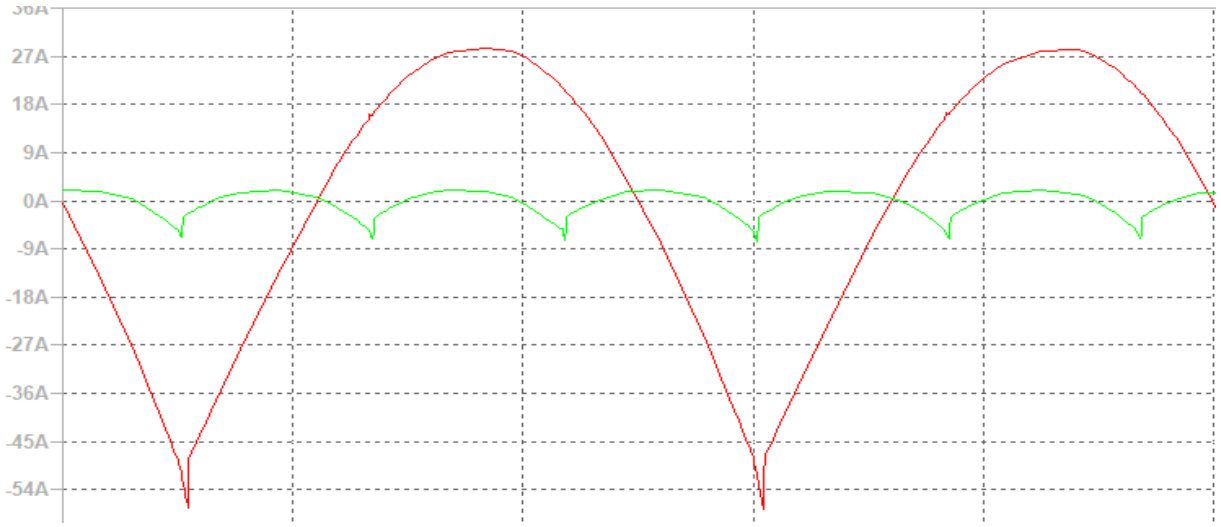

Figure 5. Output Capacitor Current, Green: Three Phase LLC, Red: Single Phase LLC.

Conclusion

As a result of the study carried out using the LTspice program, both input and output current ripple were minimized with the three phase LLC resonant converter. As a result, the capacity requirement used in traditional LLC converters was reduced. As a result, the electrolytic capacity requirement in DCDC converters is eliminated.

References

Chester, R. W. Martinez et al., "Three-phase LLC resonant converter with integrated magnetics," 2016 IEEE Energy Conversion Congress and Exposition (ECCE), Milwaukee, WI, USA, 2016, pp. 1-8,
Url-1 www.wolfspeed.com/products/power/reference-designs/crd30dd12n-k/

A Real-Time Resonance Detection and Mitigation Method for Shunt Active Power Filters

Ramazan Berkan Tut[a], Veysel Tutku Buyukdegirmenci[b], Mustak Erhan Yalcin[c]

[a] Istanbul Technical University, Electronics and Communication Engineering, Graduate Program, Turkiye
tut23@itu.edu.tr

Keywords: Active Power Filter, Harmonic Filtering, Resonance Mitigation, Resonance Damping, Filter Instabilities.

Aim

This study aims to present a novel real-time resonance detection and mitigation technique tailored for shunt active power filters (APFs), which are integral to enhancing power quality in industrial systems. These filters can become unstable in the presence of capacitive and resonant loads, necessitating a dynamic approach to ensure continuous and reliable operation. The primary goal is to develop an adaptive control mechanism that preserves system stability under varying load conditions.

Material and Method

The research is based on the modeling of a three-phase, three-wire power system that includes a supply transformer, a shunt APF modeled as a controlled current source, and nonlinear loads. Resonance conditions were investigated using the following equations:

$SH = 3 * \Sigma(Vh * Ih)$
$Jh = h * HDvh * HDih$

Here, SH represents harmonic apparent power, and Jh is an objective function formed by harmonic distortion components. The proposed method introduces a supervisory control algorithm with closed-loop selective harmonic filtering using finite gain integrators. The filtering rate is adaptively tuned via a perturb-and-observe (P&O) strategy. Validation was performed through both simulations in PLECS and hardware experiments using a 100 kVA laboratory APF prototype.

Findings

Simulation outcomes demonstrate a significant reduction in harmonic distortion under resonant conditions. Specifically, the proposed method enabled the APF to maintain THDi levels below 7%, even with highly capacitive loading. Experimental results supported these findings, showing effective resonance identification and mitigation within two grid cycles. The adaptive control strategy dynamically adjusted the virtual damping resistor and successfully suppressed harmonic amplification.

Conclusion

The proposed method provides a reliable solution to resonance-induced instabilities in shunt APFs. By leveraging a harmonic power-based detection strategy and a dynamic adaptive control framework, the system enhances operational robustness in fluctuating grid environments. This advancement is a step forward for power quality management in modern power electronics. Future work will explore machine learning integration for predictive damping and expansion to multi-inverter systems and microgrid applications.

References

Buyukdegirmenci, V. T., Sozuer, A., Milletsever, O. C., Kozarva, O. F., Oz, T., & Hava, A. M. (2022). Considerations for Inverter Topology Selection and Limitations in Active Power Filtering Applications. In IEEE Power and Energy Conference at Illinois (PECI).

IEEE Std 519-2022 IEEE Standard for Harmonic Control in Electric Power Systems.

Mattavelli, P. (2001). A closed-loop selective harmonic compensation for active filters. IEEE Transactions on Industry Applications, 37(1), 81-89.
Chen, H., Liu, H., Xing, Y., & Hu, H. (2019). Enhanced DFT-Based Controller for Selective Harmonic Compensation. IEEE Transactions on Power Electronics, 34(8), 8017-8030.
Buso, S., Malesani, L., & Mattavelli, P. (1998). Comparison of current control techniques for active filter applications. IEEE Transactions on Industrial Electronics, 45(5), 722-729.

ELECTRICAL ENGINEERING

Electric Power & Energy Systems

Electrical Machines

Electrical Vehicles

Power Electronics

Smart Grids

Adaptation of a Generalized Observer Scheme for False Data Injection Detection in Load Frequency Control Systems

Arslan Mete Baybars[1], Fikret Çalışkan[2], V.M. İstemihan Genç[1]

[1]Istanbul Technical University, Faculty of Electrical and Electronics, Department of Electrical Engineering
[2]Istanbul Technical University, Faculty of Electrical and Electronics, Department of Control and Automation Engineering
baybars@itu.edu.tr, caliskanf@itu.edu.tr, gencis@itu.edu.tr

Keywords : False Data Injection (FDI), Load Frequency Control, Generalized Observer Scheme, Residual Analysis.

Aim

The aim of this study is to adapt and evaluate a Generalized Observer Scheme (GOS), originally designed for sensor fault detection, for the purpose of detecting false data injection (FDI) attacks in a two-area Load Frequency Control (LFC) system. The approach leverages a bank of Unknown Input Observers (UIOs) to monitor critical measurement signals, including frequency deviations in both control areas and tie-line power flow.

By analyzing the behavior of residual norms under various FDI scenarios, the study seeks to determine whether the observer-based framework can successfully identify malicious data injections that target specific measurement channels. Particular attention is given to the structure and interpretability of residual signals, as well as the potential limitations of conventional threshold-based detection logic in detecting stealthy or short-lived anomalies.

The study ultimately aims to demonstrate that observer-based monitoring systems—when properly adapted—can serve as an effective cyber-security layer in modern power systems, capable of enhancing detection robustness without requiring major changes to system architecture.

Material and Method

In this study, a two-area Load Frequency Control (LFC) system is modeled using MATLAB/Simulink to evaluate the capability of an observer-based approach in detecting false data injection (FDI) attacks. Each control area includes primary components of load frequency dynamics, namely the governor, turbine, and generator, as well as frequency deviation feedback and tie-line power exchange between areas. The model tracks three critical measurements: frequency deviations in Area 1 (Δf_1), Area 2 (Δf_2), and the tie-line power flow (ΔP_{12}).

To detect anomalies in these measurements, a Generalized Observer Scheme (GOS) is employed. This structure consists of a bank of Unknown Input Observers (UIOs), where each observer is designed to be insensitive (decoupled) to unknown disturbances such as load changes, but sensitive to anomalies in specific measurement channels. While traditionally applied to sensor fault detection, in this study, the GOS framework is adapted for identifying FDI attacks that mimic sensor anomalies by injecting falsified data into communication channels.

FDI attacks are introduced into the system by artificially manipulating the measurement signals. Each attack scenario targets one signal at a time (Δf_1, Δf_2, or ΔP_{12}) and is implemented as an additive deviation, with controlled amplitude and timing to simulate a stealthy intrusion. These injected values are designed to preserve overall system dynamics superficially, making detection challenging under conventional methods.

The residual output of each observer is continuously monitored, and norms of each residual vector is computed in real-time. Three separate simulation scenarios are carried out, each corresponding to an FDI attack on a different measurement signal. The performance of the detection structure is evaluated by observing the residual norms and analyzing their patterns over time to determine whether the attack has been effectively revealed and isolated.

Findings

To assess the performance of the proposed observer-based structure in detecting cyber-attacks, three separate false data injection (FDI) scenarios were simulated—each targeting a different measurement signal in the two-area LFC system: frequency of Area 1 (Δf_1), frequency of Area 2 (Δf_2), and tie-line power flow (ΔP_{12}). In each scenario, only one measurement signal was corrupted at a time using an additive injection profile with defined amplitude and activation time.

The detection process was carried out using a Generalized Observer Scheme (GOS), consisting of three Unknown Input Observers (UIOs), each responsible for generating a residual signal that ideally remains insensitive to system disturbances (e.g., load changes) but reacts to anomalies in specific measurement channels. The Euclidean norm of each residual was continuously monitored to detect abnormal behavior.

The results revealed distinct detection characteristics depending on the type of attack:

- FDI attacks on Δf_1 and Δf_2 led to a sustained deviation in the residuals associated with the unaffected observers. These residuals exhibited a relatively constant offset during the attack period, while the residual associated with the compromised signal remained near zero due to the inherent decoupling feature of the GOS structure.
- FDI attack on ΔP_{12} (tie-line power flow) produced a significantly different pattern. The residual output showed a brief but sharp transient spike at the moment the attack was triggered. However, this response rapidly decayed and returned to zero within a short time interval. As a result, detection based on simple thresholding logic could easily fail to identify this type of transient anomaly.

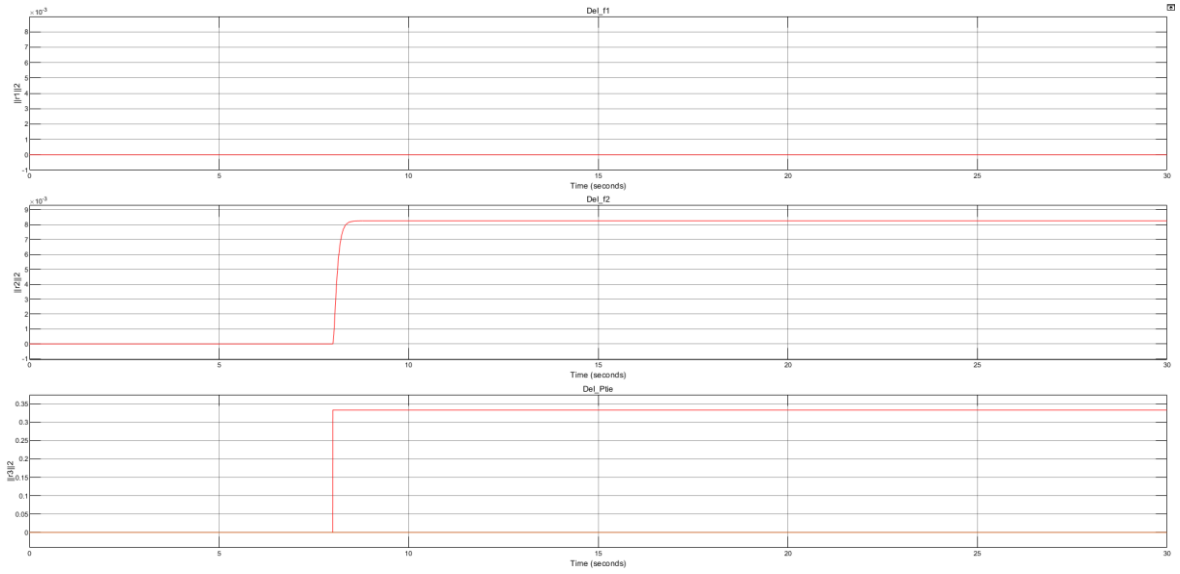

Figure 1. Frequency sensor (Δf_1) under FDI attack condition.

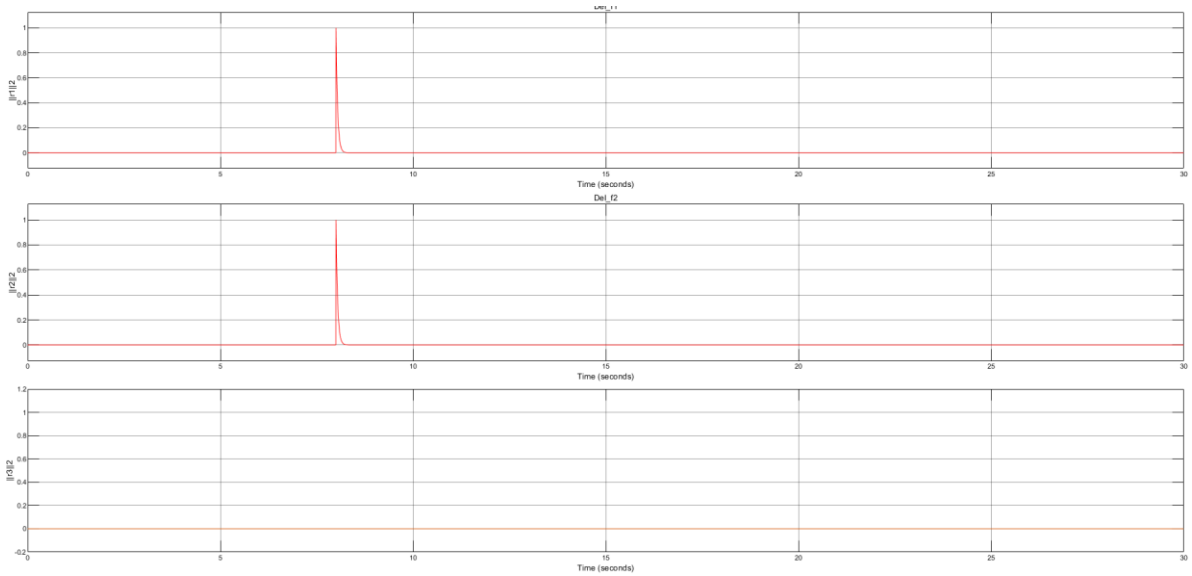

Figure 2. Tie-line power flow sensor (ΔP_{12}) under FDI attack condition.

Overall, the observer structure was able to expose the presence of falsified data through cross-residual reactions; however, the detection capability was highly dependent on the temporal characteristics of the attack and the choice of measurement being targeted. The study emphasizes the need for additional signal-processing layers or logic structures to ensure detection reliability, especially in the case of stealthy or short-duration attacks.

Conclusion

This study has investigated the use of a Generalized Observer Scheme (GOS), originally developed for sensor fault detection, as a detection mechanism for false data injection (FDI) attacks in a two-area Load Frequency Control (LFC) system. By adapting the observer framework to a cyber-security context, the study aims to leverage residual-based monitoring as a lightweight, model-driven layer of protection against data integrity threats.

Simulation results demonstrated that the GOS structure can effectively react to injected anomalies in measurement channels, even when the attack is designed to be stealthy and short-lived. In the case of frequency signal attacks (Δf_1, Δf_2), the system generated stable residual deviations in unaffected observers, indicating the presence of anomalous behavior. However, in the case of tie-line attacks (ΔP_{12}), the residual response was transient and quickly returned to zero—highlighting a fundamental limitation of relying solely on threshold logic for detection.

The key insight from the findings is that the observer structure, due to its decoupling nature, may suppress the very residual in the channel under attack. This behavior is inherent in the GOS methodology and must be accounted for in practical implementations. Relying only on instantaneous thresholds may lead to false negatives, especially in cyber-attack scenarios that exploit system dynamics to remain undetected.

To address this challenge, it is recommended to integrate a discrete-time integrator or cumulative logic block after the threshold comparison, which would accumulate residual energy over time. Such an approach could improve the detection of short-duration anomalies and enhance the robustness of the overall system against cyber threats.

In conclusion, the proposed adaptation of a GOS-based observer framework shows promising results for FDI detection in power systems. With minor structural improvements, it can serve as a scalable and non-invasive cyber-security tool for modern smart grid environments.

References

Chester, R. (2002). Materials Selection and Engineering. In A.A. Baker, L.R.F. Rose, R. Jones (Eds.), Advances in the Bonded Composite Repair of Metallic Aircraft Structure (2nd ed., Vol. 1, pp.19-40). New York: Wiley. **Url-1** www.mohid.com, date retrieved 29.06.2006.

Achaal, B., Adda, M., Berger, M. et al. Study of smart grid cyber-security, examining architectures, communication networks, cyber-attacks, countermeasure techniques, and challenges. Cybersecurity 7, 10 (2024). https://doi.org/10.1186/s42400-023-00200-w

Demirören A., Zeynelgil L., Elektrik Enerji Sistemlerinin Kararlılığı Kontrolü ve Çalışması, İstanbul Teknik Üniversitesi – Elektrik Elektronik Fakültesi, Birsen Yayınevi, İstanbul, 2004, (B. 6, s. 163-203)

E. Drayer and T. Routtenberg, "Detection of False Data Injection Attacks in Smart Grids Based on Graph Signal Processing," *in IEEE Systems Journal*, vol. 14, no. 2, pp. 1886-1896, June 2020, doi: 10.1109/JSYST.2019.2927469

F. Caliskan and I. Genc, "A Robust Fault Detection and Isolation Method in Load Frequency Control Loops," in *IEEE Transactions on Power Systems*, vol. 23, no. 4, pp. 1756-1767, Nov. 2008, doi: 10.1109/TPWRS.2008.2004831.

M. Aldeen and R. Sharma, "Robust detection fault in frequency control loops," *IEEE Trans. Power Syst*.,vol. 22, no.1, pp. 413–422, Feb.2007.

Prabha Kundur (1994), Power System Stability and Control, Electric Power Research Institue, Mc Graw Hill, (Ch. 11, 581-691)

Cyber-Resilient Real-Time Transient Stability Prediction for Modern Power Systems

Kemal Aygul[a], Anurag K. Srivastava[b], Mostafa Mohammadpourfard[c], Istemihan Genc[a]

[a] Department of Electrical Engineering, Istanbul Technical University, Istanbul, Turkiye
[b] Lane Department of Computer Science and Electrical Engineering, West Virginia University, WV, USA
[b] National Wind Institute, Texas Tech University, TX, USA
kemal.aygul@itu.edu.tr

Keywords : False Data Injection Attacks, Machine Learning, Power Systems, State Estimation, Transient Stability.

Aim

Modern power systems are undergoing a significant transformation through the digitalization of the smart grid. The integration of next-generation components—such as phasor measurement units (PMUs), smart relays, and advanced communication networks—has enhanced real-time monitoring and control capabilities. These advancements offer improved operational flexibility and efficiency, yet they also present critical challenges in maintaining transient stability and ensuring robust cybersecurity. Transient stability, defined as the power system's ability to remain synchronized after disturbances, is essential for preventing cascading failures and ensuring uninterrupted power delivery (Lee et al., 2024; Zhu et al., 2020). Traditional stability-assessment methods, which rely on offline simulations or conventional state-estimation techniques, are increasingly inadequate for meeting real-time operational demands, particularly when confronted with sophisticated cyber threats such as false-data-injection attacks (Kazemi et al., 2020).

This study aims to develop and validate a comprehensive, cyber-resilient framework that delivers accurate, real-time transient stability prediction in modern power systems. By integrating advanced state-estimation techniques (Zhou et al., 2014), deep-learning-based anomaly detection (Radhoush et al., 2023), measurement-recovery methods, and an ensemble prediction strategy (Aygul et al., 2023), the proposed framework is designed to sustain high prediction accuracy even in the presence of cyber-attacks. The ultimate objective is to facilitate proactive control measures and enhance the overall security and reliability of grid operations under both normal and adverse conditions.

Material and Method

The proposed methodology is structured as a multi-layer framework that seamlessly integrates wide-area monitoring, dynamic state estimation, cyber-attack detection, measurement recovery, and an ensemble learning based post fault transient stability prediction. Figure 1 illustrates the architecture of the proposed TSP classifier, while Figure 2 provides an overview of the complete framework.

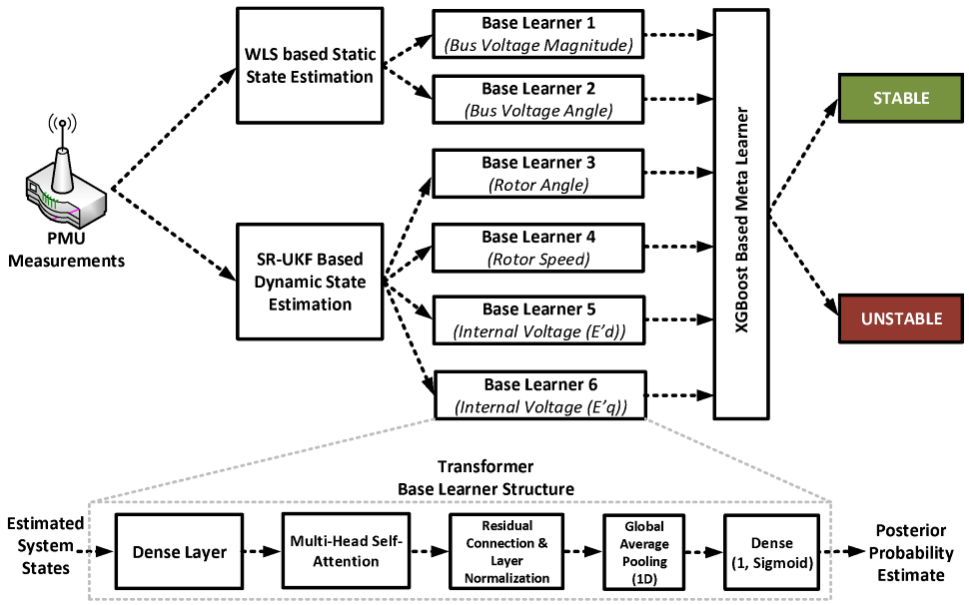

Figure 1. Proposed TSP Classifier Structure.

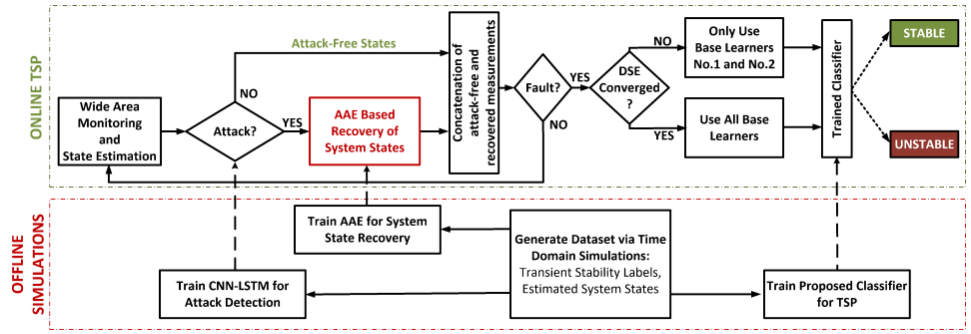

Figure 2. Proposed Framework.

Wide-Area Monitoring and State Estimation:

A. Static State Estimation (SSE):

Synchronized measurements obtained from PMUs are processed using a linear Weighted Least Squares (WLS) estimator. This estimator corrects for measurement inaccuracies and produces rapid snapshots of the power system's state, providing an initial estimate that supports immediate monitoring and control decisions (Radhoush et al., 2023).

B. Dynamic State Estimation (DSE):

To capture the system's dynamic behavior during and after disturbances, the framework employs a Square-Root Unscented Kalman Filter (SR-UKF), which is adept at managing the nonlinear dynamics of power systems and updating state estimates over time (Zhou et al., 2014). While static state estimation (SSE) reliably monitors measurable parameters, the dynamic state estimation (DSE) module is pivotal for providing non-measurable states—such as rotor angle and rotor speed—that are essential for assessing system stability and performance. This combined estimation strategy ensures that both static and dynamic aspects of the system are accurately captured, significantly enhancing the overall predictive capability of the framework.

Cyber-Attack Detection and Measurement Recovery:

A. FDIA Detection via CNN-LSTM:

Modern power systems are vulnerable to FDIAs that subtly manipulate measurement data to evade traditional bad data detection techniques. To address this, the framework incorporates a hybrid Convolutional Neural Network–Long Short-Term Memory (CNN-LSTM) architecture. (Z. Li et al., 2024) The CNN component extracts spatial features from the system states, while the LSTM component captures the temporal dependencies inherent in system dynamics. This combined architecture is highly effective at identifying coordinated and stealthy FDIA patterns, ensuring that compromised data is flagged for further processing.

B. Measurement Restoration using Adversarial Autoencoder (AAE):

Upon detection of an FDIA, the corrupted measurements are not discarded but instead are restored using a Wasserstein GAN-based adversarial autoencoder (AAE). (Y. Li et al., 2019) The AAE maps the compromised data into a latent space and then decodes it to produce reconstructed power system states that closely approximate the true state. The use of Wasserstein loss with gradient penalty ensures that the latent representations are well-regularized, significantly reducing the impact of the cyber-attack on state estimation accuracy.

Ensemble Transient Stability Prediction

A. Base Learners – Deep Transformer Models:

The clean and verified state estimates are then fed into an ensemble classifier designed for transient stability prediction. Multiple Deep Transformer (Y. Li et al., 2024) models are employed as base learners. These models are particularly suited for extracting long-range spatiotemporal features from high-dimensional PMU data, which is critical for understanding the complex dynamics of power systems during transient events.

B. Meta-Learner – XGBoost Aggregation:

The predictions generated by the Deep Transformer base learners are aggregated using an XGBoost meta-learner. This ensemble strategy leverages the strengths of each individual model, combining them to produce a final, robust prediction. The integration of XGBoost (N. Li et al., 2020) helps to mitigate the effects of any residual errors from the base learners and further enhances the accuracy and robustness of the overall TSP module.

Findings

The proposed framework was rigorously validated using simulations on the NPCC 48-machine, 140-bus test system. A comprehensive dataset was generated through time-domain simulations, encompassing both normal operating conditions and scenarios involving various intensities of FDIA. Key experiments were designed to evaluate the performance of each component of the framework under realistic conditions.

State Estimation Performance:

The proposed state estimation approach demonstrated high accuracy under attack-free conditions, with both SSE and SR-UKF providing reliable estimates of system states. However, when subjected to FDIA scenarios, state estimation techniques showed significant degradation in performance, as indicated by increased Mean Absolute Error (MAE) and Root Mean Square Error (RMSE) values in critical state variables such as rotor angles, rotor speeds, and internal voltages. The incorporation of the AAE-based measurement recovery module effectively restored these values to near-normal levels. For instance, under a moderate attack vector, rotor speed RMSE values were reduced by more than 90% after recovery. Tables 1, 2, and 3 summarize the error metrics for the estimated states under attack conditions, both with and without measurement recovery.

Table 1. Error Metrics for Rotor Angle and Rotor Speed.

Attack Vector = 0.05								
PMUs Attacked	**Attacked**				**Reconstructed**			
	Rotor Angle (°)		**Rotor Speed (rad/s)**		**Rotor Angle (°)**		**Rotor Speed (rad/s)**	
	MAE	RMSE	MAE	RMSE	MAE	RMSE	MAE	RMSE
1 PMU	0.746	6.97449	0.78954	3.86885	0.35627	3.57337	0.01449	0.20418
5 PMU	3.562	14.98841	3.94587	8.64691	1.67116	4.69904	0.07667	0.60592
7 PMU	3.973	15.14545	5.51565	10.21468	1.87889	4.77031	0.08225	0.60669
12 PMU	5.122	15.57311	9.43999	13.35147	2.43506	4.86155	0.10142	0.61341
Attack Vector = 0.1								
PMUs Attacked	**Attacked**				**Reconstructed**			
	Rotor Angle (°)		**Rotor Speed (rad/s)**		**Rotor Angle (°)**		**Rotor Speed (rad/s)**	
	MAE	**RMSE**	**MAE**	**RMSE**	**MAE**	**RMSE**	**MAE**	**RMSE**
1 PMU	0.80773	7.48537	1.57909	7.73770	0.46100	3.80389	0.34222	2.19004
5 PMU	3.81460	15.90295	7.89174	17.29382	2.20844	5.34722	1.45132	4.76512
7 PMU	4.17212	16.00396	11.03131	20.42935	2.62390	6.46670	1.48308	4.76743
12 PMU	5.16257	16.29307	18.88000	26.70294	3.73624	6.81081	1.56099	4.77344

Table 2. Error Metrics for d-axis and q-axis Internal Voltages.

Attack Vector = 0.05								
PMUs Attacked	**Attacked**				**Reconstructed**			
	d-axis Voltage (p.u.)		**q-axis Voltage (p.u.)**		**d-axis Voltage (p.u.)**		**q-axis Voltage (p.u.)**	
	MAE	**RMSE**	**MAE**	**RMSE**	**MAE**	**RMSE**	**MAE**	**RMSE**
1 PMU	0.00209	0.01089	0.00088	0.00467	6.409e-05	0.00081	0.00031202	0.00508
5 PMU	0.01114	0.02375	0.00613	0.01322	0.00037620	0.00186	0.00227531	0.01461
7 PMU	0.01460	0.02695	0.00840	0.01569	0.00052809	0.00224	0.00297776	0.01677
12 PMU	0.02601	0.03634	0.01291	0.01895	0.00086440	0.00267	0.00386241	0.01789
Attack Vector = 0.1								

PMUs Attacked	Attacked				Reconstructed			
	d-axis Voltage (p.u.)		q-axis Voltage (p.u.)		d-axis Voltage (p.u.)		q-axis Voltage (p.u.)	
	MAE	RMSE	MAE	RMSE	MAE	RMSE	MAE	RMSE
1 PMU	0.00419	0.02177	0.00177	0.00934	0.00221	0.01210	0.00050	0.00571
5 PMU	0.02228	0.04751	0.01225	0.02645	0.01103	0.02513	0.00344	0.01707
7 PMU	0.02920	0.05389	0.01679	0.03138	0.01660	0.03296	0.00443	0.01932
12 PMU	0.05203	0.07268	0.02583	0.03790	0.02697	0.04282	0.00631	0.02107

Table 3. Error Metrics for Bus Voltage Magnitude and Angle.

Attack Vector = 0.05								
PMUs Attacked	Attacked				Reconstructed			
	Bus Voltage Magnitude (p.u.)		Bus Voltage Angle (p.u.)		Bus Voltage Magnitude (p.u.)		Bus Voltage Angle (p.u.)	
	MAE	RMSE	MAE	RMSE	MAE	RMSE	MAE	RMSE
1 PMU	0.00215	0.01042	0.06879	1.58319	0.00031	0.00597	0.03496	0.25363
5 PMU	0.01054	0.02319	0.36840	3.94362	0.00140	0.01126	0.20439	0.62759
7 PMU	0.01484	0.02745	0.48224	4.33581	0.00192	0.01333	0.26871	0.71151
12 PMU	0.02546	0.03604	0.70994	4.75076	0.00258	0.01419	0.55922	1.03276
Attack Vector = 0.1								
PMUs Attacked	Attacked				Reconstructed			
	Bus Voltage Magnitude (p.u.)		Bus Voltage Angle (p.u.)		Bus Voltage Magnitude (p.u.)		Bus Voltage Angle (p.u.)	
	MAE	RMSE	MAE	RMSE	MAE	RMSE	MAE	RMSE
1 PMU	0.00431	0.02085	0.08032	1.59661	0.00042	0.00944	0.06992	0.50727
5 PMU	0.02108	0.04638	0.42483	3.96606	0.00179	0.01729	0.40877	1.25518
7 PMU	0.02967	0.05491	0.56132	4.37006	0.00248	0.02069	0.53741	1.42302
12 PMU	0.05091	0.07207	0.83328	4.81382	0.00322	0.02199	1.11843	2.06553

FDIA Detection Efficacy:

The CNN-LSTM based detection module achieved exceptional performance, with Precision and Recall metrics approaching 100%. This hybrid model consistently outperformed standalone CNN, LSTM, and GRU architectures in identifying both isolated and coordinated FDIAs. The high detection rate enabled the prompt activation of the measurement recovery

process, preventing erroneous data from adversely impacting the transient stability predictions. Table 4 presents a performance comparison between the proposed FDIA detection method and the benchmark methods.

Table 4. Performance Metrics of FDIA Detection Models.

Model	Precision	Recall	F-Measure
LSTM	0.9918	0.9919	0.9918
GRU	0.9921	0.9921	0.9921
CNN	0.9833	0.9839	0.9836
Transformer	0.8938	0.8749	0.8842
CNN-LSTM	0.9997	0.9997	0.9997

Transient Stability Prediction Accuracy

The ensemble classifier, combining Deep Transformer base learners with an XGBoost meta-learner, maintained high accuracy even under severe cyber-attack conditions. In tests conducted with attack vectors of up to 10%, the ensemble system sustained an overall prediction accuracy above 98%, with only a minimal decline in F1 scores. The robust performance of the ensemble approach is attributed to the effective extraction of spatiotemporal features by the deep transformers and the complementary aggregation provided by XGBoost. Figures 3 and 4 illustrate the impact of FDIA on TSP performance, while Figure 5 demonstrates how recovery via AAE influences the performance of the proposed TSP model.

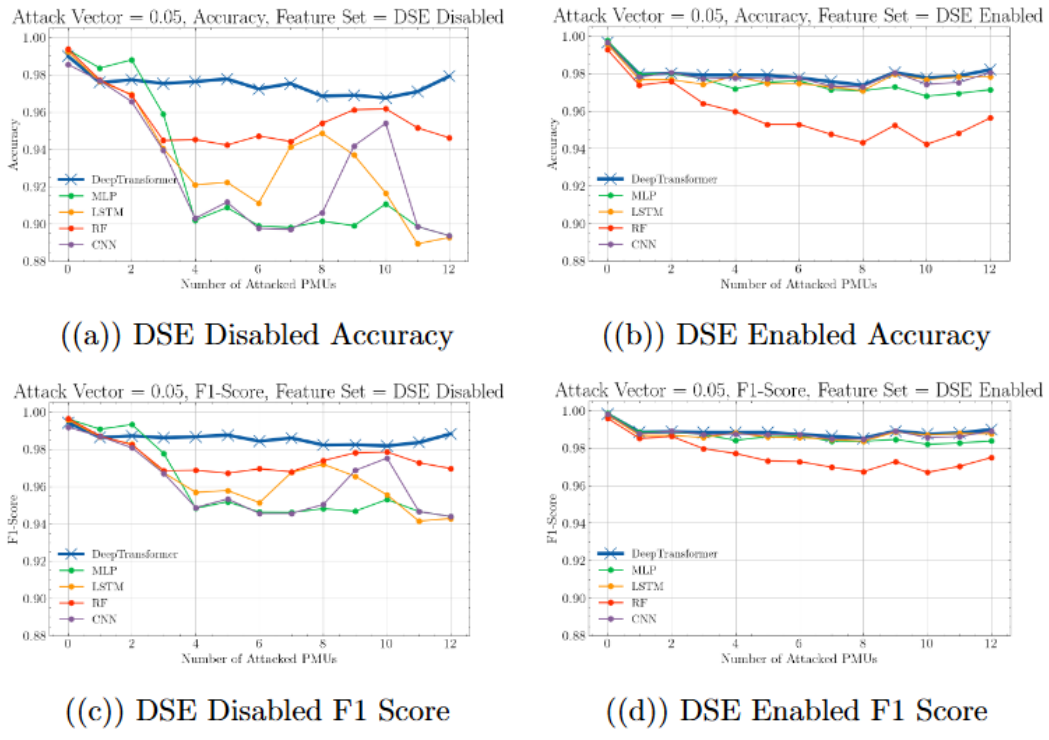

Figure 3. Impact of FDIA (5% Attack Vector) on Accuracy and F1 Score.

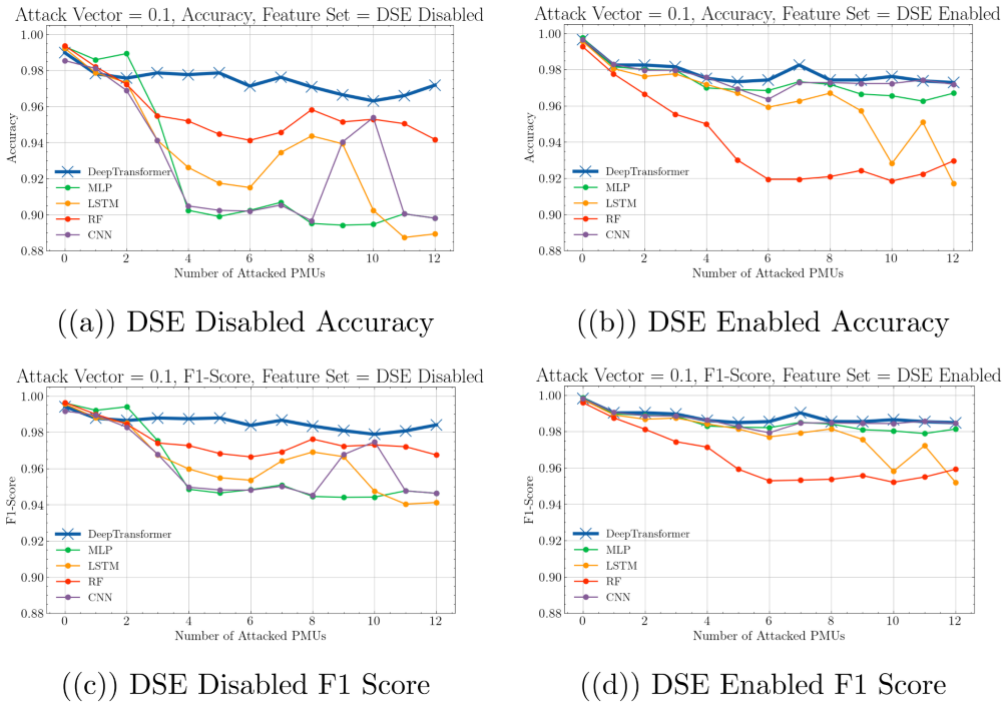

Figure 4. Impact of FDIA (10% Attack Vector) on Accuracy and F1 Score.

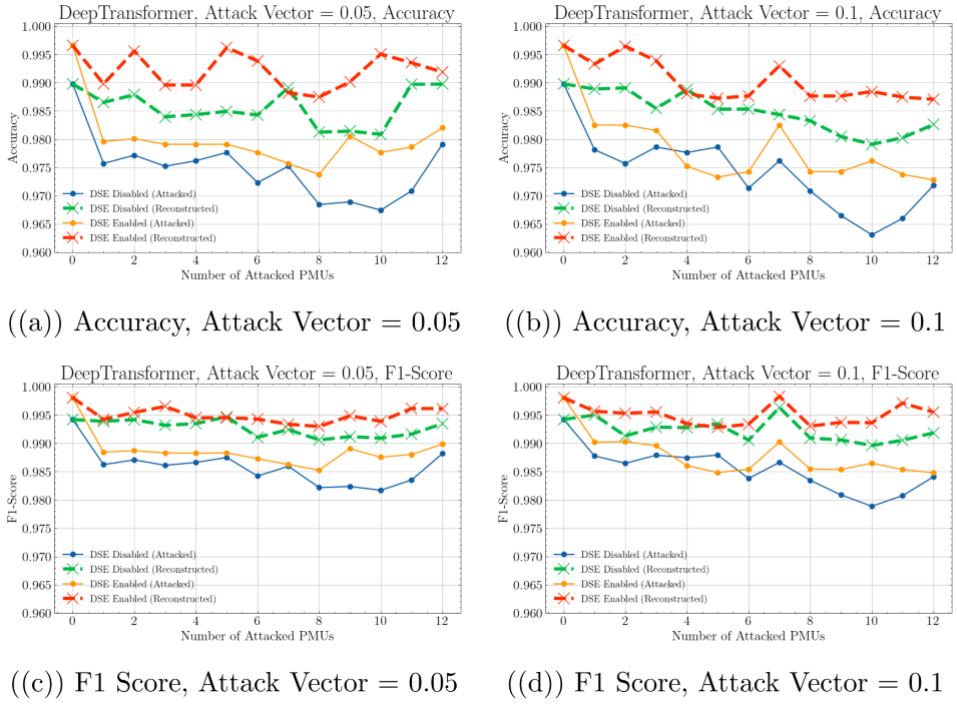

Figure 5. Comparison of TSP performance under different attack intensities with and without AAE-based measurement recovery.

Summary

The experimental results confirm that the proposed cyber-resilient framework significantly enhances both the accuracy and reliability of transient stability prediction in modern power systems.

Key findings include:

- FDIA conditions induce significant state estimation errors, which are largely mitigated by the AAE-based recovery module.
- The hybrid CNN-LSTM model effectively detects subtle, coordinated FDIA patterns, enabling prompt recovery.
- The ensemble TSP classifier—combining Deep Transformer models with an XGBoost meta-learner—consistently achieves over 98% accuracy even under sophisticated cyber-attacks.
- Integrating advanced dynamic state estimation, deep learning-based FDIA detection, and measurement recovery offers a robust enhancement over traditional transient stability prediction methods, addressing both technical and cybersecurity challenges.

Conclusion

This study presents a comprehensive, cyber-resilient framework for real-time transient stability prediction in modern power systems. By integrating the proposed state estimation approach, a hybrid CNN-LSTM detector for FDIA, an adversarial autoencoder for measurement recovery, and an ensemble-based transient stability predictor, the proposed methodology addresses the dual challenges of ensuring rapid and accurate stability assessment while safeguarding against cyber threats.

The validation on the NPCC 48-machine, 140-bus system demonstrates that the framework not only restores compromised measurements and maintains high prediction accuracy under cyber-attacks but also satisfies stringent real-time processing requirements. These results underscore the potential of the proposed methodology to serve as a critical tool for enhancing the resilience and security of modern power grids.

The promising results of this study lay a strong foundation for the development of next-generation, data-driven power system monitoring and control systems that are resilient in the face of both operational disturbances and cyber-attacks.

References

Aygul, K., Mohammadpourfard, M., Kesici, M., Kucuktezcan, F. C., & Genc, I. (2023). Benchmark of machine learning algorithms on transient stability prediction in renewable-rich power grids under cyber-attacks. Internet of Things, 25, 101012. https://doi.org/10.1016/j.iot.2023.101012

Kazemi, Z., Safavi, A. A., Naseri, F., Urbas, L., & Setoodeh, P. (2020). A secure hybrid dynamic state estimation approach for power systems under false data injection attacks. IEEE Transactions on Industrial Informatics, 16(12), 7275–7286. https://doi.org/10.1109/TII.2019.2957242

Lee, G., Park, C., & Kim, D.-I. (2024). Event detection-free framework for transient stability prediction via parallel CNN-LSTMs. IEEE Transactions on Instrumentation and Measurement, 73, 1–10. https://doi.org/10.1109/TIM.2023.3307987

Li, N., Li, B., & Gao, L. (2020). Transient stability assessment of power system based on XGBoost and factorization machine. IEEE Access, 8, 28403–28414. https://doi.org/10.1109/ACCESS.2020.2971415

Li, Y., Wang, Y., & Hu, S. (2019). Online generative adversarial network-based measurement recovery in false data injection attacks: A cyber-physical approach. IEEE Transactions on Industrial Informatics, 16(3), 2031–2043. https://doi.org/10.1109/TII.2019.2936050

Li, Y., Cao, J., Xu, Y., Zhu, L., & Dong, Z. Y. (2024). Deep learning based on transformer architecture for power system short-term voltage stability assessment with class imbalance. Renewable and Sustainable Energy Reviews, 189, 113913. https://doi.org/10.1016/j.rser.2023.113913

Li, Z., Xie, Y., Ma, R., & Wei, Z. (2024). Optimizing CNN-LSTM for the localization of false data injection attacks in power systems. Applied Sciences, 14(16), 6865. https://doi.org/10.3390/app14166865

Radhoush, S., Vannoy, T. C., Liyanage, K., Whitaker, B. M., & Nehrir, H. (2023). Distribution system state estimation and false data injection attack detection with a multi-output deep neural network. Energies, 16(5), 2288. https://doi.org/10.3390/en16052288

Zhou, N., Meng, D., Huang, Z., & Welch, G. (2014). Dynamic state estimation of a synchronous machine using PMU data: A comparative study. IEEE Transactions on Smart Grid, 6(1), 450–460. https://doi.org/10.1109/TSG.2014.2345416

Zhu, L., Hill, D. J., & Lu, C. (2020). Hierarchical deep learning machine for power system online transient stability prediction. IEEE Transactions on Power Systems, 35(3), 2399–2411. https://doi.org/10.1109/TPWRS.2019.2961501

ELECTRONICS AND COMMUNICATION ENGINEERING

Analog/Mixed-Signal/Microwave Circuits

Bio-Medical, Bio-Inspired Circuits/Systems

Digital Circuits and Systems

Embedded Systems

VLSI Systems and Applications

22-nm FD-SOI Internal Power Management Unit for Frequency-Modulated Continuous Wave Lidar

Mahmut Coban[a], Ahmet Tekin[b]

[a] Istanbul Technical University, Electronics and Communication Engineering Department, Türkiye
[b] Bogazici University, Electrical and Electronics Engineering Department, Türkiye
cobanm21@itu.edu.tr

Keywords: Buck Converter, LDO, PMU, Power Managements.

Aim

The primary aim of this study is to develop an efficient internal power management unit (PMU) for a 22-nm Fully Depleted Silicon On Insulator (FD-SOI) process. The designed PMU integrates a Bandgap Reference (BGR) circuit and three Low Dropout (LDO) regulators: a high-voltage LDO, an auxiliary always-on LDO, and a current sink LDO and Buck Converter. Figure 1 illustrates the relationship between these blocks, providing a clear representation of their interactions and dependencies. This PMU autonomously adjusts its operation based on the input supply voltage (1.8V to 3.6V) and ensures stable power distribution while maintaining transistors within the Safe Operating Area (SOA). The system is optimized for minimal power consumption and high efficiency, making it suitable for low-power analog and mixed-signal applications.

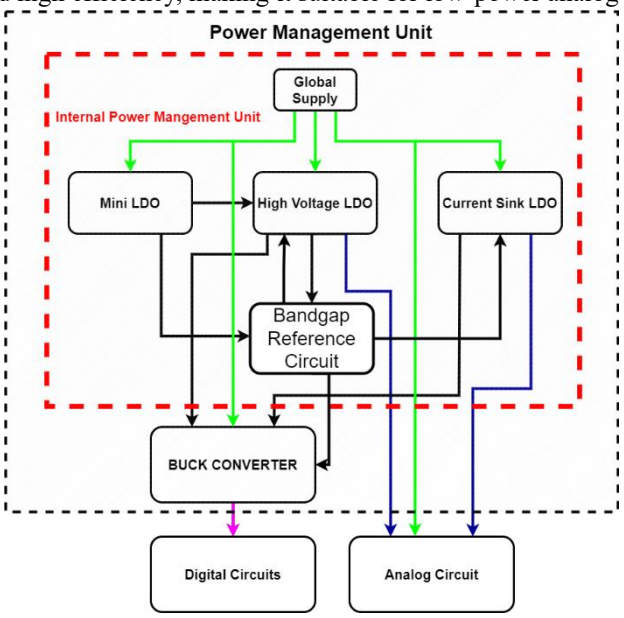

Figure 1. The overall structure of the PMU.

With the increasing demand for efficient power management solutions in modern semiconductor designs, the integration of advanced internal PMUs is essential. Conventional power management architectures often rely on external components, leading to increased complexity, power loss, and design constraints. By incorporating an advanced PMU within the 22-nm FD-SOI process, this study aims to overcome these limitations, offering an integrated solution with enhanced performance, reduced power consumption, and improved voltage regulation across diverse operational conditions. The PMU is designed to provide robust performance while ensuring process scalability and adaptability for various applications. Moreover, the study explores novel techniques for optimizing power efficiency in ultra-low-power systems, ensuring long-term viability for next-generation semiconductor devices.

Material and Method

The PMU is implemented using a 22-nm FD-SOI process, leveraging its inherent advantages such as low leakage current, high efficiency, and enhanced control over transistor behavior. The Bandgap Reference (BGR) [1] serves as the primary voltage and current reference, ensuring stability across variations in Process, Voltage, and Temperature (PVT). The BGR provides a stable output crucial for powering analog and digital sub-circuits within the PMU.

The high-voltage LDO is responsible for maintaining a consistent 1.8V output across a broad input supply range of 1.8V to 3.6V, ensuring optimal performance of low-power circuits. Its design integrates noise-reduction techniques and transient response optimization to enhance reliability. The auxiliary always-on LDO plays a crucial role in the power-up sequence, preventing startup failures and ensuring smooth operation. This LDO operates with an ultra-low quiescent current, making it highly power-efficient while maintaining system integrity during initial startup phases.

The current sink LDO dynamically adjusts ground voltage levels, facilitating stable digital circuit operation across varying supply voltages. This LDO adapts to changes in the power supply while keeping transistor stress within acceptable limits, extending the lifespan of the integrated circuits. The layout design emphasizes compactness, with a total area of 292.4 µm x 98.3 µm, ensuring minimal silicon real estate utilization while maximizing functionality [2-3].

Simulation methodologies include post-layout verification, stability analysis, transient response evaluation, and power supply rejection ratio (PSRR) assessments. Extensive Monte Carlo simulations were conducted to assess variation tolerance and ensure reliability across manufacturing processes. Noise analysis and thermal simulations were also performed to confirm robustness under extreme conditions. Additionally, parasitic extraction analysis was conducted to validate layout-dependent effects, ensuring optimal power distribution efficiency within the PMU [4-8].

Findings

Simulation results demonstrate that the BGR achieves a temperature coefficient of 12.43 ppm/°C, ensuring minimal voltage variation across temperature extremes. This low variation is critical for maintaining consistent performance in temperature-sensitive applications. The high-voltage LDO successfully maintains a stable 1.8V output across varying supply inputs, with a worst-case PSRR of -55 dB at 3.6V, signifying excellent noise immunity. Load regulation analysis reveals minimal voltage deviations under dynamic load conditions, further reinforcing the LDO's effectiveness.

The auxiliary always-on LDO provides reliable startup functionality while consuming less than 1 µA quiescent current, ensuring minimal power overhead. The current sink LDO efficiently adjusts ground voltage levels in digital circuits, eliminating the need for additional external protection circuits. It maintains stable operation across all tested process corners, confirming its adaptability to different manufacturing variations.

Further evaluations of transient responses indicate that the designed PMU successfully mitigates voltage spikes and fluctuations, preserving signal integrity across power-sensitive circuits. The integration of specialized filtering techniques within the PMU enhances PSRR performance, effectively isolating noise from power sources and improving the overall stability of the system. The PMU's ability to sustain a steady voltage level under rapidly changing load conditions highlights its robustness in real-world scenarios, making it suitable for mission-critical applications. Additionally, power efficiency metrics confirm significant reductions in overall power dissipation, contributing to enhanced battery life in portable applications.

Conclusion

The proposed 22-nm FD-SOI internal PMU effectively regulates power across a wide input voltage range while ensuring stability and reliability. Its compact design and autonomous voltage adaptation eliminate the need for external calibration. The integration of high-performance BGR and LDOs enables efficient power management for modern SoCs, reducing external component dependency and overall system complexity.

This study demonstrates that a well-designed PMU can significantly enhance power management efficiency while reducing power loss and layout constraints. The proposed system is suitable for a wide range of applications, including low-power analog and mixed-signal circuits, energy-efficient SoCs, and mobile devices requiring adaptive voltage regulation. The

automated self-adjusting features incorporated into the PMU architecture provide an advantage in minimizing design iterations, improving scalability, and ensuring robust operation under varying power conditions.

The results highlight the potential of the designed internal PMU for widespread adoption in advanced semiconductor technologies. Future work includes further miniaturization, adaptive power-saving techniques, and the integration of machine learning algorithms for real-time power optimization, paving the way for next-generation power management solutions in ultra-low-power applications. Moreover, research into alternative reference generation methods and innovative regulation strategies will be explored to further improve energy efficiency and system resilience in future semiconductor advancements.

References

Banba, H., Shiga, H., Umezawa, A., Miyaba, T., Tanzawa, T., Atsumi, S., & Sakui, K. (1999). A CMOS bandgap reference circuit with sub-1-V operation. IEEE Journal of Solid-State Circuits, 34(5), 670–674. https://doi.org/10.1109/4.760378

Baker, R. J. (2010). CMOS circuit design, layout, and simulation (3rd ed.). Wiley-IEEE Press.

P. Y., & Leung, K. N. (2010). An output-capacitorless low-dropout regulator with direct voltage-spike detection. IEEE Journal of Solid-State Circuits, 45(2), 458–466. https://doi.org/10.1109/JSSC.2009.2034805

Lee, C. F., & Mok, P. K. T. (2004). A monolithic current-mode CMOS DC-DC converter with on-chip current-sensing technique. IEEE Journal of Solid-State Circuits, 39(1), 3–14. https://doi.org/10.1109/JSSC.2003.820870

Kim, M. W., & Kim, J. J. (2021). A PWM/PFM dual-mode DC-DC buck converter with load-dependent efficiency-controllable scheme for multi-purpose IoT applications. Energies, 14(4), 960. https://doi.org/10.3390/en14040960

Lee, T.-J., Hsu, C.-H., & Wang, C.-C. (2019). High efficiency buck converter with wide load current range using dual-mode of PWM and PSM. In 2019 IEEE International Symposium on Circuits and Systems (ISCAS) (pp. 1–4). https://doi.org/10.1109/ISCAS.2019.8702618

Wu, P. Y., Tsui, S. Y. S., & Mok, P. K. T. (2010). Area- and power-efficient monolithic buck converters with pseudo-type III compensation. IEEE Journal of Solid-State Circuits, 45(8), 1446–1455. https://doi.org/10.1109/JSSC.2010.2047451

Tsai, J.-C., Huang, T.-Y., Lai, W.-W., & Chen, K.-H. (2010). Dual modulation technique for high efficiency in high switching buck converters over a wide load range. In Proceedings of 2010 IEEE International Symposium on Circuits and Systems (pp. 3709–3712). https://doi.org/10.1109/ISCAS.2010.5537750

Design of a Low-power Phase-Frequency Detector in 65 nm CMOS Technology Suitable for 5G Mobile Applications

Bora Batuhan Isgor[a], Nil Tarım[a]

[a] Istanbul Technical University/Faculty of Electrical and Electronics, Department of Electronics and Communication Engineering, Programme of Electronics Engineer, Turkey
isgorb20@itu.edu.tr

Keywords: 5G, Blind Zone, Dead Zone, Low-Power, Phase-Frequency Detector.

Aim

This paper improves the development of a low-power CMOS phase frequency detector (PFD) circuit for phase-locked loop (PLL) applications in 5G New Radio (NR) 78 standard. The circuit ensures the detection of phase and frequency variations in the reference signal and input signal (same as PLL, V_{IN}). This work is based on the circuit architecture presented in [1], with a redesign aimed at improving its performance. Specifically, the work is focused on reducing power consumption while maintaining dead zone and blind zone efficiency.

Material and Method

The phase frequency detector (PFD) circuit in a phase-locked loop (PLL) environment is important to ensure locking of the reference signal (V_{REF}) and the input signal (same as PLL input, V_{IN}), thereby providing the best possible oscillation at the frequency of interest. In 5G new radio (NR) 78 mobile applications, the operating frequency is 3.5 GHz with 500 MHz bandwidth [2]. To ensure smooth oscillation at 3.5 GHz, PFD circuit is employed to provide up (Up) and down (Down) signals to the charge pump (CP). The reference signal is chosen to be 10 MHz because most base stations in 5G networks use 10 MHz reference to be compatible with Global Positioning System (GPS) [3]. According to [2], 10 MHz is within allowable bandwidth range in time division duplex (TDD) signal necessary for NR78.
Several PFD architectures are used to resolve main PFD problems such as dead zone and blind zone. PFD experiences a region of near-zero phase difference around phase locking when it is unable to detect this small phase difference and it can cause an increase in phase noise of PLL. The PFD is unable to respond to voltage variations when the phase difference is near zero, a phenomenon known as the dead zone issue. The dead zone is an important specification as it limits operating frequency and introduces jitter to the PLL system. One solution is to introduce a delay at the PFD output to ensure proper reset operation [4]. However, some random glitches occur in this structure. Furthermore, the reset pin limits the maximum operating frequency as depicted in equation 1. Another solution can be to provide delay in both input signals [5]. Although the dead zone is eliminated since it is no longer dependent on the reset signal, power consumption increases significantly.

$$f_max = 1/(2 \times T_reset\ ) \quad (1)$$

The second common issue in PFDs is the blind zone, which occurs near a 2π phase differences when the rising edge of VREF appears moderately after VIN while the reset feedback path is activated. Then, PFD misses this rising edge phase differences and produces a wrong output. The blind zone reduces the PLL acquisition speed, enhances the linearity of PFD, increases energy consumption and degrades phase noise. To solve this issue, the reset path is removed, as designed in [6]. Although this architecture obliterates the blind zone, it leads to an increase in both the dead zone and power consumption.
The PFD is designed in reference to the architecture presented in [1]. The designed PFD, shown in Figure 1, improves the dead zone and the blind zone, eliminates glitches and reduces reference spurs [1]. The PFD operates in both frequency-aligned and non-aligned frequency scenarios under the following conditions: (1) V_{REF} phase leads V_{FB} (2) V_{REF} phase lags V_{FB} and (3) V_{REF} is in-phase with V_{FB}.

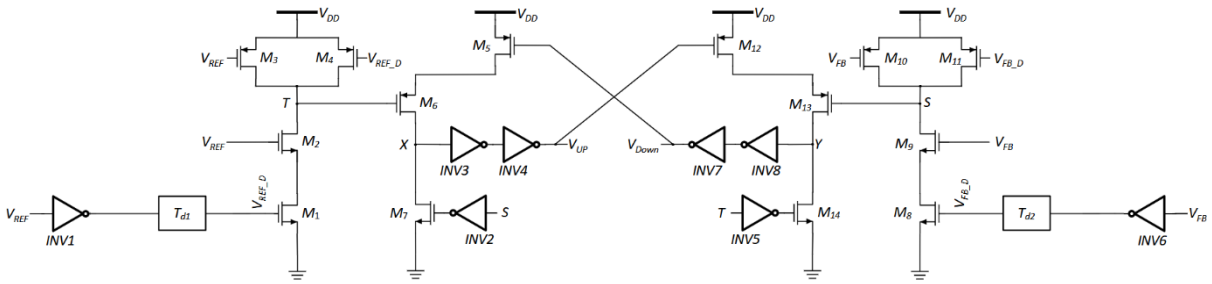

Figure 1. The Designed PFD Architecture.

To explain the working principle of the designed PFD, frequency-aligned condition (1) is selected as an example: When both inputs are logic low, the T node is in the logic high state as switch M_3 pulls this node to V_{DD}. When V_{REF} goes logic high and V_{FB} stays in logic zero, node T is pulled down to ground by M_1 and M_2 on the rising edge, and thus node X reaches the high state when M_6 turns on. After the time delays in T_{d1} and INV1, V_{REFD} goes
low as the rising edge of the reference signal occurs. Therefore, M_1 turns off and forces the T node to reach V_{DD} again. M_6 turns off, and node X holds the logic high. When V_{FB} goes logic high, node S is triggered to pull down by M_8 and M_9, but node Y cannot go to logic high and stays in logic low because M_{12} is off as UP is applied to its gate. After the time delays in T_{d2} and INV6, V_{FB_D} goes to logic low when the rising edge of the V_{FB} signal occurs. Therefore, M_8 turns off and forces the S node to reach V_{DD} again. At this moment, the PFD is reset by the inverted output of S node, which is applied to the gate of M_7. Additionally, nodes X or Y are in a middle state, preventing the establishment of either a logic high or logic low. INV3 and INV4 (INV7 and INV8) are employed to ensure correct switching mechanism of CP. The reader may find Figure 2 helpful for understanding the working principle of the designed PFD. The same analysis can be made further for the other scenarios, which is left for the reader's discretion.

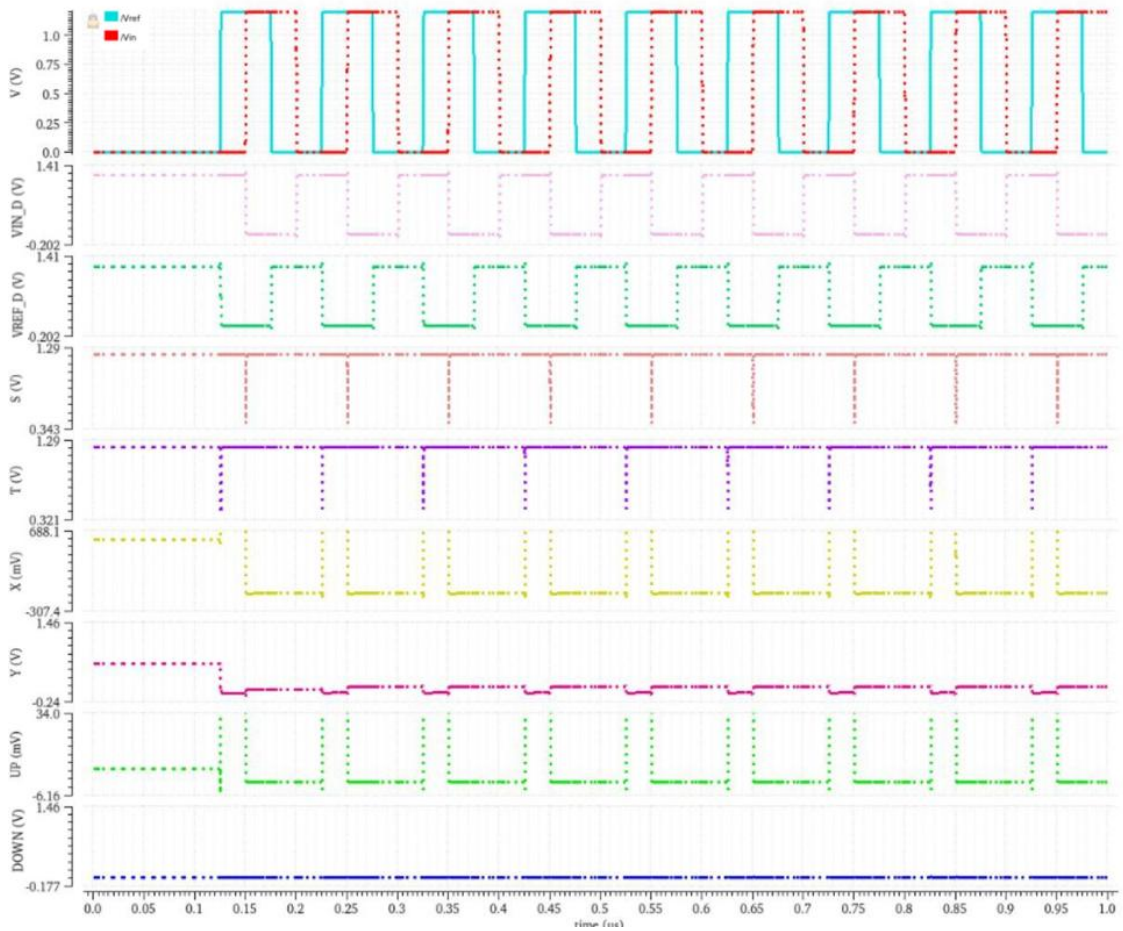

Figure 2. Transient Response of Key Nodes in the Designed PFD Under V_{REF} Leading V_{IN} at the Same Frequency Condition.

It is crucial to emphasize that the time delays, T_{d1} and T_{d2}, are essential in the design, ensuring that the applied V_{REF} and V_{IN} signals are sufficiently delayed to drive M_6 (M_{13}). Additionally, the duration of these delays must be shorter than the reset pulse width to trigger switching pulse width spikes at the nodes in PFD.

Aspect ratios are adjusted to force this architecture to be compatible for 10 MHz input signals. The fundamental idea here is focused on transition time of NMOS devices to voltage changes. Taking as an example, when V_{REF} is leading V_{IN} and its rising edge occurs, M_1 and M_2 needs to react to this change in order to pull node T to ground. M_1 and M_2 need slow transition time to its input signal therefore small aspect ratios are used.

Besides, the frequency of V_{IN} signal can differ between 9 MHz to 11 MHz depending on choice of divider used in the PLL structure. The reason to this difference belongs to 5G NR 78 standard as VCO generates its output signal within a frequency range between 3.3 GHz to 3.8 GHz. Thus, the circuit is also tested for this frequency range.

Lastly, power consumption is another important specification in the design and is closely managed. Power hungry devices in this architecture are M_5, M_6 and M_7 (M_{12}, M_{13} and M_{14}). When the node T (S) is grounded, M_7 (M_{14}) conducts current and creates logic high at node X (Y).

If the width of M_7 (M_{14}) is reduced, using the width and drain current relationship Equation 2, the drive current also decreases. This reduction is managed while ensuring that the correct switching of Up (Down) occurs. Additionally, the aspect ratios of the inverters are lowered to reduce power consumption while ensuring that sufficient invertor gain and bandwidth are maintained for the topology.

$$I_D = \left(\frac{1}{2} \times \mu_n \times C_{ox} \times \frac{W}{L} \times (V_{GS} - V_{th})^2\right) \quad (2)$$

where I_D, μ_n, C_{ox} , W, L, V_{GS} and V_{th} are the drain current of the NMOS transistor, electron mobility, oxide capacitance per unit area, width of the NMOS transistor channel, length of the NMOS transistor channel, gate-source voltage, and threshold voltage of the NMOS transistor, respectively.

Findings

The designed circuit is simulated by Virtuoso tools using TSMC 65 nm CMOS technology. The supply voltage is 1.2 V. The aspect ratios are provided in Table 1. The reference frequency is selected as 10 MHz. As mentioned earlier, the latency applied to the V_{REF} and V_{IN} signals is controlled by T_{D1} and T_{D2}, which introduces delays of 14.2 ps to these signals. Figure 3 illustrates the dead zone analysis of the designed PFD, where V_{REF} leads V_{IN} by 25 ps when the equal 10 MHz frequency signals applied. In this dead zone, the PFD is able to generate correct output signals.

Table 1. Aspect ratio of transistors used in the designed PFD.

Device	W/L
M_1, M_2, M_8, M_9, PMOS transistor of: (INV_3, INV_4, INV_7, INV_8)	1.2 µm/65 nm
M_3, M_4, M_{10}, M_{11}	8 µm/65 nm
M_5, M_6, M_{12}, M_{13}	4.8 µm/65 nm
M_7, M_{14}	1.8 µm/65 nm
PMOS transistor of: (INV_1, INV_6, Td_1, Td_2)	2.2 µm/240 nm
NMOS transistor of: (INV_1, INV_6, Td_1, Td_2)	1.5 µm/240 nm
NMOS transistor of: (INV_2, INV_5)	8 µm/130 nm
PMOS transistor of: (INV_2, INV_5)	12 µm/130 nm
NMOS transistor of: (INV_3, INV_4, INV_7, INV_8)	600 nm/65 nm

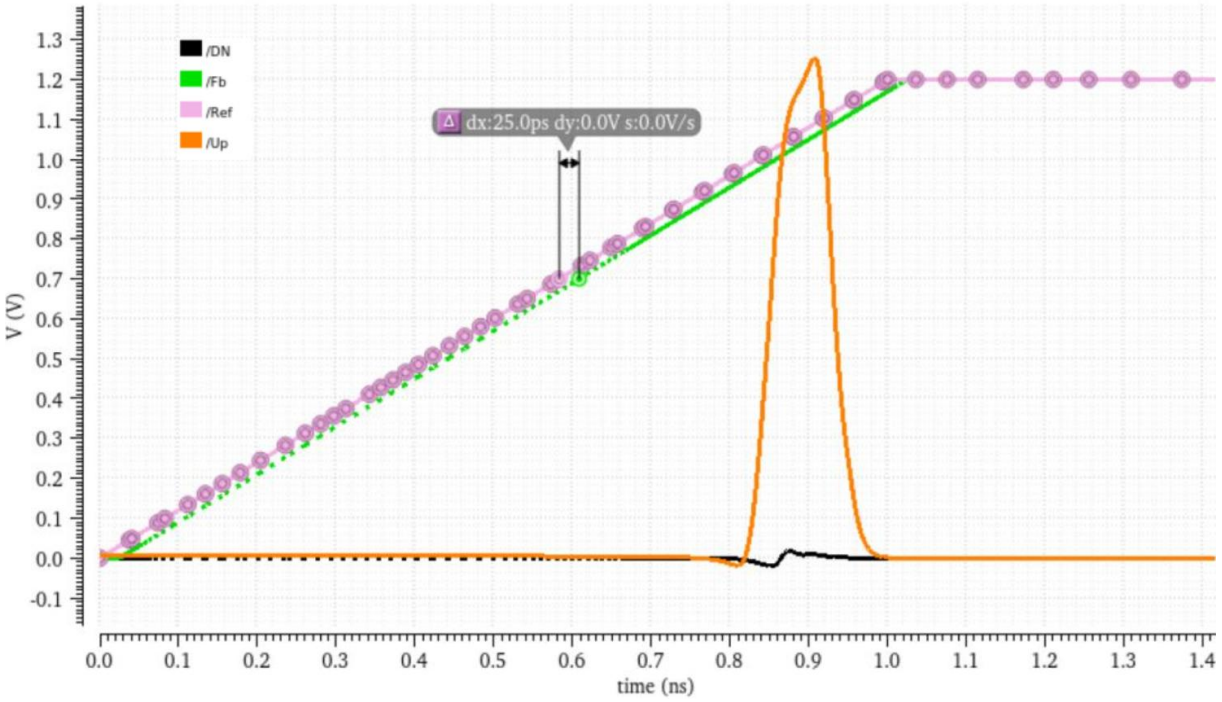

Figure 3. Dead Zone Analysis of the Designed PFD when V_{REF} leads V_{IN} by 25 ps.

The blind zone analysis of the designed PFD is performed. For better view of blind zone analysis, V_{REF} leads V_{IN} by 1 ns is shown in Figure 4. The simulations resulted that the blind zone of the PFD is 39.46 ps.

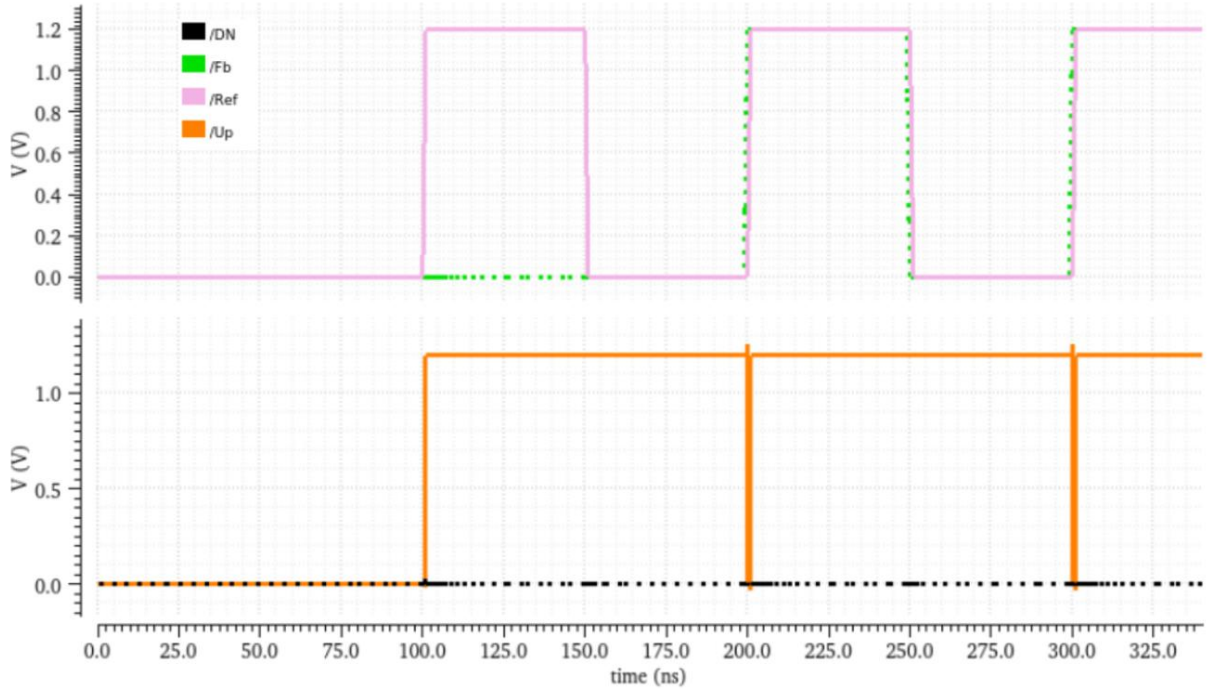

Figure 4. Blind Zone Analysis of the Designed PFD when V_{REF} leads V_{IN} by 1 ns.

The maximum operating frequency of designed PFD is limited by Equation 1. To determine the frequency, we must consider

the maximum delays during the charging and discharging durations of node X. The charging duration of node X is the sum of the maximum delays in INV_1, T_{d1}, INV_3, INV_4 and the required time to charge X node through M_5 and M_6. Similarly, the discharging duration of node X is the sum of the maximum delays in INV_2, INV_3, INV_4, and the required time to discharge X node through M_7. The same analysis applies to the calculation of node Y. Although calculating the duration of reset time is an option, it can be derived by the following equation:

$$f_max = 1/(4 \times max\{T_(dead\ zone),\ T_(blind\ zone)\}) \quad (4)$$

where $T_(dead\ zone)$, $T_(blind\ zone)$ are dead zone and blind zone values, respectively. The maximum operating frequency is calculated as 6.34 GHz and applied to V_{REF} and V_{IN} signals, considering the phase delay that arises in the blind zone. Figure 5 shows that when the rising edge of V_{REF} occurs, up transitions to logic high while Down maintains logic low state. The reset of Up occurs on the rising edge of V_{IN}. In summary, the circuit correctly responds to this frequency as anticipated.

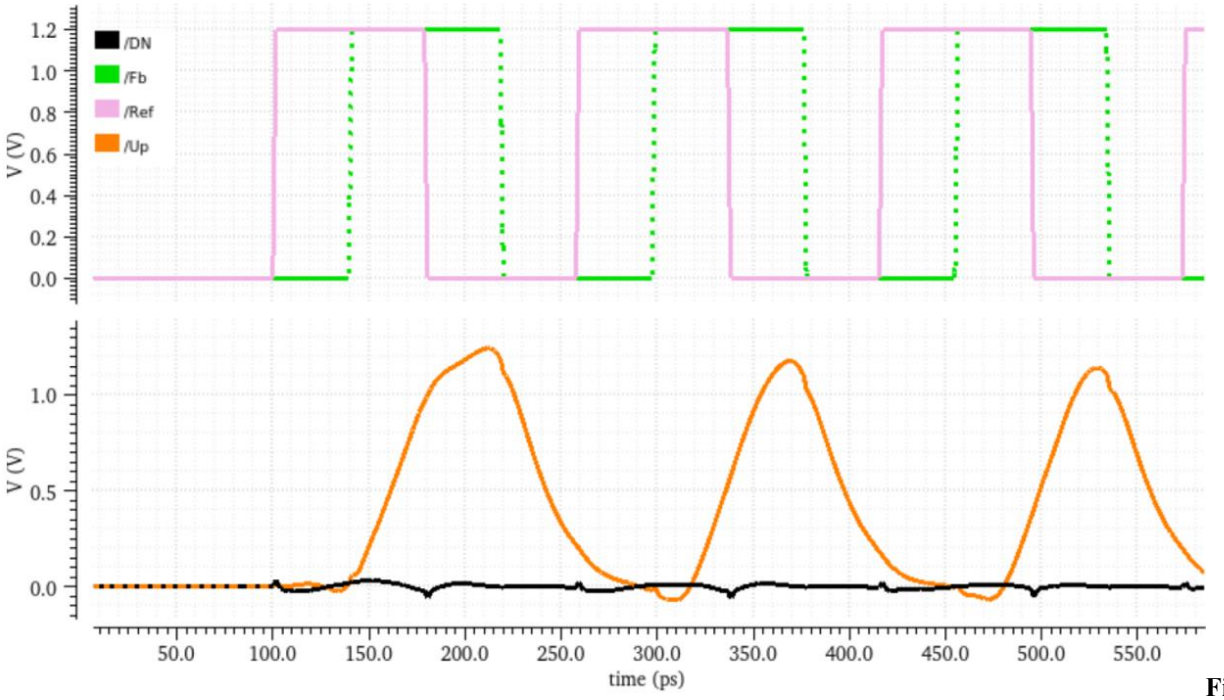

Figure 5. Performance of the Designed PFD at 6.34 GHz when V_{REF} leads V_{IN} by 39.46 ps.

The performance parameters of this work and recent works are depicted in Table 2. Compared to other references, the designed PFD achieves lower power consumption while maintaining detection range, dead zone and blind zone durations within optimal performance limits for the desired application use.

Table 2. Summary and Comparison Table.

Performance parameter	**This work***	[1]*	[7]**	[8]*	[9]*	[10]*	[11]*
		2021	**2010**	**2020**	**2019**	**2006**	**2020**
CMOS technology(nm)	65	65	130	65	130	180	28
Power supply (V)	1,2	1,2	1,2	1,2	1,2	1,5	1
Reference freq.	10 MHz	125 MHz	2,7 GHz	500 MHz	1 GHz	10 MHz	50 MHz
No. of Transistor	38	38	-	38	16	46	>36
Power (μW)	50.88@10 MHz	137@1 GHz	171@2,7 GHz	324@3.44 GHz	76	7000	324
Dead zone (ps)	25	2,5	61	Free	25	-	200
Blind zone (ps)	39,46	20	-	Free	–	–	–
Detection range	$\pm 2\pi$	$\pm 2\pi$	$\pm 2\pi$	$\pm 2\pi$	$\pm 2\pi$	$\pm 2\pi$	$\pm 2\pi$
Max freq. (GHz)	6,34	12,5	5,4	3,44	4,1	5,4	4

** Fabrication, *Simulation

Conclusion

In this work, a low-power CMOS phase frequency detector (PFD) is designed using TSMC 65 nm CMOS technology. The designed PFD is compatible with 5G NR 78 mobile applications and operates with a reference signal at 10 MHz. The designed PFD consumes 50.88 μW, achieves 25 ps dead zone and 39.46 ps blind zone durations under $\pm 2\pi$ detection range. The simulation results validate the advantages of the designed PFD, demonstrating improvements in power consumption and the efficiency of dead zone and blind zone.

References

H. Ghasemian, A. Bahrami, E. Abiri, M. R. Salehi (2021). A New Low-Power Charge Pump with a Glitch-Free PFD for Speedup the Acquisition Process of a PLL in 65 nm CMOS Technology. Circuits, Systems, and Sig. Processing, 40, 2982–3006.

3GPP TS 38.101-1, User Equipment (UE) radio transmission and reception; Part 1: Range 1 Standalone 3rd Generation Partnership Project (3GPP), version 17.5.0 Release 17

3GPP TS 38.211, Physical channels and modulation, 3rd Generation Partnership Project (3GPP), Release 15, 2018.

Johansson, H. (1998). A simple precharged CMOS phase frequency detector. IEEE Journal of Solid-State Circuits, 33(2), 295-299.

A. Dhiman, T. Sharma, B. Kaur (2018). Design and Performance Analysis of Phase Frequency Detector for High Speed Application. 2nd International Conference on Inventive Systems and Control (ICISC), Coimbatore, India, 2018, 161-168.

K. K. A. Majeed and B. J. Kailath (2013). Low power, high frequency, free dead zone PFD for a PLL design. 2013 IEEE Faible Tension Faible Consommation, Paris, France, 2013, 1-4.

Wu-Hsin Chen, Maciej E. Inerowicz, and Byunghoo Jung (2010). Phase Frequency Detector with Minimal Blind Zone for Fast Frequency Acquisition IEEE Transactions on Circuits and Syst.—II: Express Briefs, 57, no. 12, December 2010.

H. Lad Kirankumar, S. Rekha, T. Laxminidhi (2020). A Dead-Zone-Free Zero Blind-Zone High-Speed Phase Frequency Detector for Charge-Pump PLL. Circuits, Syst. Signal Process, 39, 3819–3832.
S. Sofimowloodi, F. Razaghian, M. Gholami (2019). Low-power high-frequency phase frequency detector for minimal blind-zone phase-locked loops, Circuits, Syst. Signal Process. 38(2), 498–511.
Y. -F. Kuo, R. -M. Weng and C. -Y. Liu (2006). A 5.4-GHz Low-Power Swallow-Conterless Frequency Synthesizer with a Nonliear PFD, 2006 IFIP International Conference on Very Large-Scale Integration, Nice, France, 2006, 357-360.
K. Cai and G. Zhang (2020). High-Gain PFD/Charge Pump with Gain Proportional to Slew Rate of Up/Down Signals, 2020 IEEE International Conference on Integrated Circuits, Tech. and App. (ICTA), Nanjing, China, 2020, 1-2.

ELECTRONICS AND COMMUNICATION ENGINEERING

Analog/Mixed-Signal/Microwave Circuits

Bio-Medical, Bio-Inspired Circuits/Systems

Digital Circuits and Systems

Embedded Systems

VLSI Systems and Applications

Thermoplastic Microfluidic Platform for 3D Cell Culturing and Imaging

Özlem Koçoğlu [a], Umut Can Coşkun [b], Berna Morova [c], Alper Kiraz [d], Kemal Baysal [e], Ahmet Can Erten [a]

[a] Istanbul Technical University, Department of Electronics and Communication Engineering, Istanbul/Turkey
[b] Numedyne Informatics and Engineering Inc., Istanbul/Turkey
[c] Istanbul Technical University, Department of Physics Engineering, Istanbul/ Turkey
[d] Koç University, Department of Physics and Department of Electrical and Electronics Engineering, Istanbul/Turkey
[e] Koç University, School of Medicine, Department of Biochemistry, Istanbul/Turkey
kocoglu21@itu.edu.tr

Keywords: 3-D Cell Culture, Microfluidics, PMMA, Thermoplastics.

Aim

Cancer is one of the most critical health problems on a global scale, and early diagnosis and treatment of the disease are of paramount importance in reducing mortality rates. Microfluidic-based cell three-dimensional (3-D) culture systems are instrumental in in vitro cancer research, including observation of angiogenesis and evaluation of cancer cell responses to chemotherapeutic drugs. In the production of these systems, a flexible and biocompatible silicone elastomer such as polydimethylsiloxane (PDMS) [1] or thermoplastic materials such as polymethyl methacrylate (PMMA) [2], cyclic olefin copolymer (COC), cyclic olefin polymer (COP) and polycarbonate (PC) are commonly used. In cell studies, PDMS is often preferred for its flexible, biocompatible, gas-permeable, and transparent properties, which facilitate optical imaging. However, its drawbacks include incompatibility with high-volume manufacturing, limited mechanical stability, and hydrophobicity. In contrast, thermoplastic materials are biocompatible, optically transparent, more hydrophilic than PDMS, and offer organic solvent resistance along with high mechanical strength. These characteristics make them suitable for rapid prototyping techniques such as laser ablation, micromilling, and mass-production methods like injection molding and hot embossing [3].

These platforms utilize hydrogels made from macromolecules like collagen and fibrin, as well as synthetic hydrogels such as Matrigel, to simulate the cellular microenvironment, which facilitates the development of 3D cell cultures. They provide a continuous supply of nutrients, creating a 3D extracellular matrix (ECM) and minimizing sample volumes. This leads to cost-effective systems that provide precise control and faster analysis. The systems may contain different compositions of channels and regions that house the hydrogels. Two or more microchannels can house the hydrogels and replenish the culture media. Cells are added through one of the side channels and the system can also include structures such as microwells [4] or microchambers [5] where cells accumulate. Some designs enable cells to interact and spontaneously form spheroids. Test chemicals, such as anticancer drugs that are targeted to interact with cells, are introduced through the opposing side channel. Separation of interconnected channels and intrachannel structures can be achieved by implementing virtual walls, using structural elements such as micropillars [6]. In the design outlined in this study, virtual walls that divide the channels are created by employing channels that exhibit level differences.

Here, we present a thermoplastic microfluidic cartridge with a groove-based design that supports 3D cell culture and can be easily imaged using a confocal imaging system. PMMA is used for fabrication, and CNC micromilling is used to create three parallel channels and also two grooves for the cells. This cartridge is designed to facilitate the imaging of cells isolated from cancerous tissue and the subsequent examination of their response to the drug. It is intended for use in medical facilities, such as hospitals and cancer centers, to ensure effective medication and treatment for patients.

Material and Method

1. Fabrication of the Microfluidic Cartridges

The channel design in this study is inspired by the design generated in Coşkun et al. from Dr. Ahmet Erten's research group, and uses a groove-based design concept that allows the interface between the hydrogel channel and the side channels to be fully utilized [7]. The design consists of three microchannels: a middle channel with a height of 150 µm and two side channels, each with a height of 400 µm. Two pockets, each with a diameter of 1200µm, are connected to one of the side channels. In addition, a retention groove with a height of 50 µm surrounds the entire design, which helps to form a strong and leakproof seal by the solvent.

The microfluidic cartridge designs were modeled using Computer-Aided Design (CAD) software.To ensure the precise fabrication of the microstructures in the design, Computer Numerical Control (CNC) micromilling is employed (Roland MDX-50) on 75×25×2 mm transparent PMMA substrates (SDS Plastic, Türkiye). After the inlets and outlets of the PMMA microfluidic cartridges are drilled using the DREMEL® Workstation 220, the cartridges undergo a sonication process. The cartridges are then treated with isopropyl alcohol (IPA), rinsed with DI water, and subsequently dried with nitrogen gas. Once these procedures are completed, the final PMMA cartridges are produced using a solvent bonding technique involving a mixture of acetone (ACE-ISOLAB Chemicals) and IPA (ISOLAB Chemicals).

This study uses a solvent mixture comprising 80% IPA and 20% ACE, determined on the basis of the solvent equation and Hildebrand solubility parameters [8]. PMMA substrates are exposed to oxygen plasma for one minute. After this treatment, the solvent mixture is poured onto one of the plasma-treated surfaces. The PMMA substrates are stacked on top of each other with a microscope slide positioned on both the top and bottom surfaces using paper clips. As illustrated in Figure 1, the assembled structure is placed in an oven at 65°C for 10 minutes, followed by an additional 5 minutes at room temperature. After this process, the cartridges are soaked in DI water for one day to remove any residual solvent before being used in cell studies. They are then exposed to nitrogen gas for desiccation prior to utilization. In the final cartridges, a mixture of DI water and dye is introduced into the channels to assess hydrogel confinement. Cartridges that exhibit no confinement issues in this preliminary control test are subsequently prepared for cell culture studies.

Figure 1. Schematic illustration of fabrication process of microfluidic cartridge.

2.Preparation of the Hydrogel and Cell Culture in Cartridges

2.1. Preparation of Hydrogel

In this study, we chose collagen I; a natural component of the ECM, that can readily form a hydrogel that provides a model closer to in vivo conditions by promoting cell attachment, proliferation, and cell-cell interactions. Following their assembly, microfluidic cartridges are sterilized under UV light in a laminar flow cabinet before hydrogel formation and cell culture studies. For filling the middle channel, 1X DMEM, 10X Dulbecco's Modified Eagle's Medium (DMEM, F-12 Ham with 15 mM HEPES and sodium bicarbonate, without L-glutamine, Sigma-Aldrich Inc), $NaHCO_3$ (7.5% w/v, sodium bicarbonate, Sigma-Aldrich), NaOH (1M, sodium hydroxide, Sigma-Aldrich), and collagen (Type-I, bovine, 6 mg/mL, Sigma-Aldrich Inc.) is mixed to make a 3% collagen end concentration on ice. The prepared mixture is introduced in 5 µL volume into the central channel and the cartridges are placed in sterile culture plates. These are incubated in the incubator at 37°C for approximately 1 hour for collagen gelation. Afterward, 10 µL of Trypan blue was applied to each side channel

to test collagen confinement and observed with a microscope. Microfluidic cartridges that pass these confinement tests are used for cell studies [7].

2.2. Gastric Cancer Cell Culture

The gastric cancer cell line SNU 484 was cultured in DMEM/F12 containing 10% fetal bovine serum (FBS) and penicillin/streptomycin in cell culture plates. During collagen gelation, the cells were detached by trypsin and pelleted. The pelleted cells were resuspended in the culture medium and counted. The cell number was adjusted to 30–60 × 10^3 per 100 µL. Following the addition of the cells to the side channel, the cartridges were placed vertically (with the cell channel on top) to aid cell seeding on the collagen surface [7].

2.3. The Response of Cancer Cells to Anticancer Drug 5-FU

In this study, experiments were conducted to investigate the response of gastric cancer cells (SNU-484) to chemotherapeutic drugs when plated in PMMA cartridges. The chemotherapeutic drug 5-fluorouracil (5-FU) was utilized in experiments using SNU-484. Cells were seeded in the side channels of the PMMA cartridges, and 5-FU was added in culture solution (50 µM) to the opposite channel of some cartridges. In the cartridges designated as the control group, incubation was continued without adding any drug to facilitate comparison (Figure 3.II.). Following a 72-hours incubation period, cell viability was analyzed. This analysis used a reduced biohazard cell viability kit, LIVE/DEAD™ (Invitrogen), to mark cells, distinguishing between live and dead cells using a confocal microscope. The LIVE/DEAD™ staining method labels dead cells with red fluorescence, while live cells exhibit green fluorescence. After the labeling step, the cells were incubated at 37°C, and measurements were performed using a confocal microscope (Leica TP8).

Findings

1. Fabrication and Solvent Bonding

In the fabricated microfluidic cartridges, a noticeable surface height difference was observed, which was attributed to machining marks from the micromilling process. This surface unevenness impacted the adhesion profile of the cartridges. To reduce this effect, as the Figure 2C shown that the microstructured PMMAs were sanded using sandpaper. Additionally, the solvent volume used in the solvent bonding technique was optimized to 150 µL, as excessive solvent usage led to significant clogging and residue formation in some cartridges. These modifications in the fabrication process resulted in cartridges with an improved adhesion profile, enhanced optical transparency, and eliminated clogging in the microchannels. As a result of the confinement tests conducted on the cartridges, successful results were achieved, demonstrating that the DI water mixed with dye supplied to the middle channel could fill the channel completely without any gaps and did not overflow into the side channels (Figure 2D).

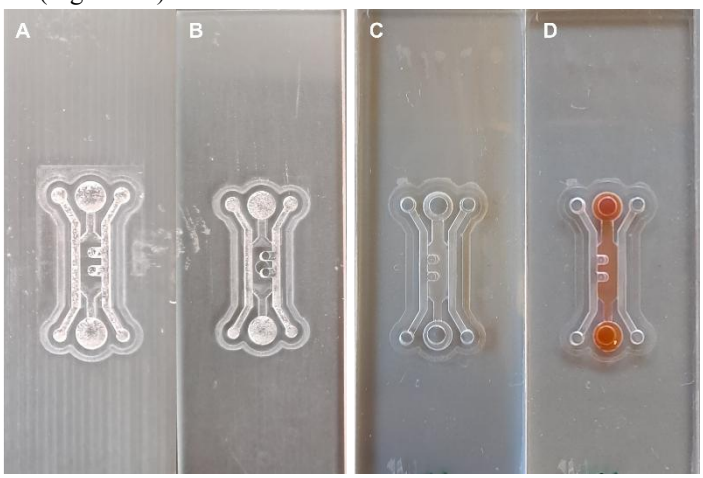

Figure 2. Cartridge images. A: Micromilled PMMA, B: After sandpaper process, C: After. bonding, D: Confinement test.

2. Response of Gastric Cancer Cells to 5-FU

Images were acquired with a confocal microscope to quantify the number of dead and live cells in the cartridges of the control group (Figure 3.II) and those treated with chemotherapeutic drugs (Figure 3.I). The fluorescent labeling method enabled the quantification of dead-to-live cell ratios in SNU-484 cells seeded in PMMA cartridges. As shown in Figure 3, treatment with 5-FU for 72 hours resulted in increased cell death in SNU-484 cells cultured in grooves compared to the control group. Figure 3.I.B exhibits a higher number of dead cells than Figure 3.II.B, whereas Figure 3.II.C presents more live cells than Figure 3.I.C.

In conclusion, these findings demonstrate that PMMA cartridges are effective for studying cellular responses to chemotherapeutic drugs. In experiments carried out in SNU-484 cells, the impact of chemotherapeutic agents such as 5-FU on cell viability and death was effectively analyzed.

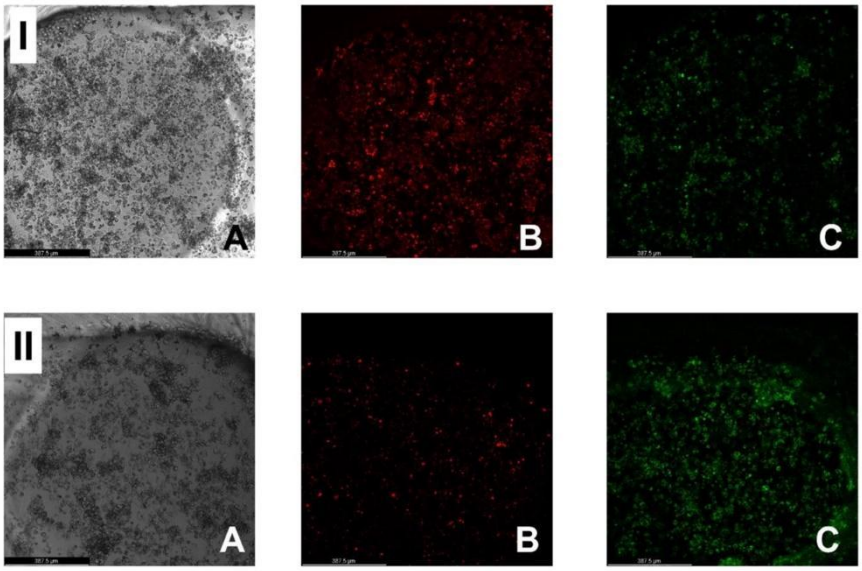

Figure 3. An imaging experiment with SNU 484 cells was performed in the groove channel of the cartridges. Confocal images were taken after a 72-hour experiment in which cells in some cartridges were treated with 5-FU (I) or were untreated as controls (II). Then, SNU-484 cells were labeled using dead-live fluorescence labeling. A : images under a light microscope, B: dead cells, C: live cells.

Conclusion

In this study, we successfully designed and fabricated a thermoplastic microfluidic cartridge to support 3D cell culture for cancer research applications. The groove-based design enables imaging of tumor cells and their interactions with chemotherapeutic drugs, facilitating studies on drug responses. The fabrication process used CNC micromilling, and solvent bonding techniques were optimized to ensure the structural integrity of the device. The results demonstrated that the fabricated PMMA cartridges effectively confined hydrogels, enabling controlled cell culture and drug testing. Preliminary drug response studies with SNU-484 cells confirmed the capability of the platform for in vitro chemotherapeutic testing. Fluorescence-based viability assays provided insights into the effects of 5-FU on cancer cells, highlighting the potential of this system for personalized drug screening. The developed microfluidic cartridge is a promising tool for advancing cancer research by enabling physiologically relevant in vitro models with precise control over the tumor microenvironment.

Acknowledgment

This project was supported by TÜBİTAK ARDEB 1001 with the project number 119E138. The project scholar, Özlem Koçoğlu, was supported by the TÜBİTAK BİDEB 2210-C.

References

Lipreri, M. V., Totaro, M. T., Boos, J. A., Basile, M. S., Baldini, N., & Avnet, S. (2024). A Novel Microfluidic Platform for Personalized Anticancer Drug Screening Through Image Analysis. *Micromachines*, *15*(12), 1521. https://doi.org/10.3390/mi15121521

Madadi, M., Madadi, A., Zareifar, R., & Nikfarjam, A. (2023). A simple solvent-assisted method for thermal bonding of large-surface, multilayer PMMA microfluidic devices. *Sensors and Actuators A: Physical*, *349*, 114077. https://doi.org/10.1016/j.sna.2022.114077

Schneider, S., Brás, E. J., Schneider, O., Schlünder, K., & Loskill, P. (2021). Facile patterning of thermoplastic elastomers and robust bonding to glass and thermoplastics for microfluidic cell culture and organ-on-chip. *Micromachines*, *12*(5), 575. https://doi.org/10.3390/mi12050575

Zhuang, J., Zhang, J., Wu, M., & Zhang, Y. (2019). A dynamic 3D tumor spheroid chip enables more accurate nanomedicine uptake evaluation. *Advanced Science*, *6*(22), 1901462. https://doi.org/10.1002/advs.201901462

Chen, Y., Gao, D., Wang, Y., Lin, S., & Jiang, Y. (2018). A novel 3D breast-cancer-on-chip platform for therapeutic evaluation of drug delivery systems. *Analytica chimica acta*, *1036*, 97-106. https://doi.org/10.1016/j.aca.2018.06.038

Wang, Y., Wang, L., Zhu, Y., & Qin, J. (2018). Human brain organoid-on-a-chip to model prenatal nicotine exposure. *Lab on a Chip*, *18*(6), 851-860. https://doi.org/10.1039/C7LC01084B

Coskun, U. C., Kus, F., Rehman, A. U., Morova, B., Gulle, M., Baser, H., ... & Erten, A. (2022). An Easy-to-Fabricate Microfluidic Shallow Trench Induced Three-Dimensional Cell Culturing and Imaging (STICI3D) Platform. *ACS omega*, *7*(10), 8281-8293. https://doi.org/10.1021/acsomega.1c05118

Tsampanakis, I., & Orbaek White, A. (2021). The mechanics of forming ideal polymer–solvent combinations for open-loop chemical recycling of solvents and plastics. *Polymers*, *14*(1), 112. https://doi.org/10.3390/polym14010112

A Deep Learning Network for Automatic Grade Classification of Renal Cell Carcinoma

Süeda Kaya[a], Mürvet Kırcı[a]

[a] Istanbul Technical University/Graduate School, Electronics and Communication Engineering, Biomedical Engineering, Türkiye
kayasued19@itu.edu.tr

Keywords: CNN, Histopatology Images, Medical Image Classification, Renal Cell Carcinoma.

Aim

Renal Cell Carcinoma (RCC), the most common type of kidney cancer, accounts for approximately 90% of all kidney malignancies and originates from the lining of the proximal convoluted tubule, which is part of the kidney's filtration system. RCC is often asymptomatic in its early stages, making it difficult to detect until it is advanced. Early diagnosis and accurate grading are essential to improving patient outcomes. Therefore, histopathological analysis of tissue samples is a critical step in diagnosing and grading RCC, and grading evaluates the level of abnormality exhibited by cancer cells based on comparison of tissue samples with normal cells under the microscope. Although different grading schemes have been used for RCC to date, this study is based on Fuhrman's four-step grading system (Fuhrman et al., 1982). In Fohrman's system, Grade-1 nuclei closely resemble normal nuclei in terms of their tubular structure and uniformity. Grade-2 nuclei exhibit irregular contours, while Grade-3 nuclei show more pronounced irregularities. Finally, Grade-4 nuclei are characterized by pleomorphic cells, mitoses, and multilobed structures that contain the features observed in Grade-3 nuclei (Moch et al., 2016). Table 1 provides examples of images from each grade taken from the KMC dataset.

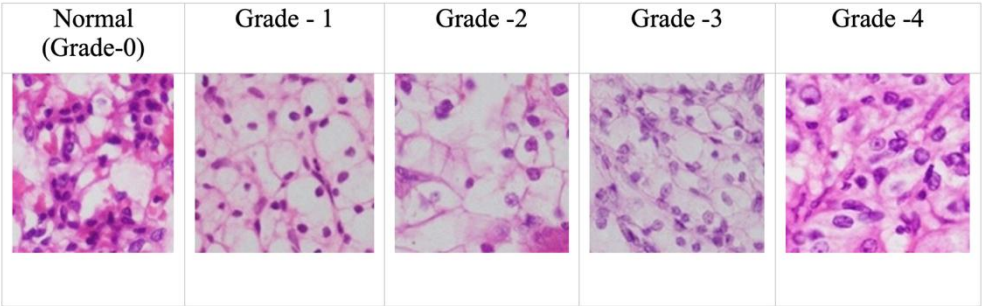

Figure 1. Example patches of kidney tumors of different grades.

Table 1. Class distribution of KMC dataset (Chanchal et al., 2023).

Class	Training	Validation	Test
Grade – 0 (Normal)	693	102	41
Grade – 1	708	104	27
Grade – 2	648	96	25
Grade – 3	735	105	21
Grade – 4	648	96	28
Total	3432	503	142

Pathologists obtain valuable information about the tumor growth rate and metastatic potential based on information about the tumor stage and grade. This information allows the development of personalized treatment strategies for the specific characteristics of the patient's cancer. However, grading complex histological patterns is a challenging and error-prone process that requires the expertise of highly experienced pathologists. Therefore, an automated and accurate system based on histopathology images is essential for grading RCC.

The aim of this study is to demonstrate the success of rapidly developing computer vision methods in the classification of complex histopathological images. In this way, it can support pathologists in their medical decision-making processes (Nahid et al., 2021; Tajbakhsh et al., 2020). Cell detection using convolutional neural networks (CNNs) is an important step in histopathological analysis (Xie et al., 2015).

Material and Method

The KMC kidney histopathology dataset used in our study contains normal (Grade-0) and cancerous (Grade-1 to Grade-4) images of RCC. These images were collected at Kasturba Medical College (KMC), India [8]. The images were labeled by expert pathologists. The preprocessing process was done automatically and except for the area selection, everything was kept the same for all images. Each part of the dataset was obtained by randomly cropping and horizontally and vertically flipping 722 images of 1920×1440. Non-overlapping square parts were extracted and resized to 224 and normalized to zero mean and unit variance before being passed through the deep learning architecture for training and testing (Chanchal et al., 2023; Dong et al., 2018; Moch et al., 2016).

Before the training images were normalized using ImageNet mean (0.485, 0.456, 0.406) and standard deviation (0.229, 0.224, 0.225) values. Data augmentation was applied only to the training set to enhance model generalization.

We implemented a modified U-Net architecture for histopathology image classification. The model features an encoder path with five consecutive down-sampling blocks, each consisting of a max pooling operation followed by two convolutional layers with batch normalization and ReLU activation. Unlike the traditional U-Net, we replaced the decoder path with a classification head that includes:

1. Global average pooling to extract features from the bottleneck layer (1024 channels)
2. A three-layer fully connected network (1024→512→256→5 neurons) with dropout (0.3) between layers to prevent overfitting

The network contains approximately 57 million parameters, with the majority in the encoder's convolutional layers. This architecture leverages U-Net's ability to capture multi-scale contextual information while adapting it for classification tasks. The model was trained for 100 epochs using the RMSprop optimizer with a learning rate of 1e-4, alpha of 0.99, and weight decay of 0. Cross-entropy loss was used as the optimization objective. Training was conducted on an NVIDIA GPU with a batch size of 32. To prevent overfitting, we implemented early stopping with a patience of 10 epochs, saving the model with the highest validation accuracy. Through applied early stopping mechanism effectively identified the optimal model checkpoint at epoch 23, which achieved a validation accuracy of 90.66%.

Table 2. Hyperparameter used in U-Net classification model.

Input Size	224x224x3
Batch Size	32
Optimizer	RMSProp (with alpha: 0.99, epsilon 1e-8)
Learning Rate	1e-4
Loss Function	Cross Entropy
Stopping Epoch	23

Model performance was evaluated using accuracy, F1 score, and confusion matrices. These metrics were chosen to account for potential class imbalance in the histopathology dataset and to provide detailed insights into classification performance across the five grades.

Findings

The final model achieved strong performance on the test set, with an overall accuracy of 91.55% across the five histopathological grades. The confusion matrix (Figure 2) reveals that:

1. Grade 0 samples were classified with the highest precision (39/41 = 95.1%)
2. Grade 1 samples showed good classification performance (26/27 = 96.3%)
3. Grade 2 had the lowest accuracy (20/25 = 80.0%), with 4 samples misclassified as Grade 3
4. Grade 3 achieved 84.0% accuracy (21/25), with 4 samples incorrectly classified as Grade 4
5. Grade 4 showed strong performance (24/28 = 85.7%), with all misclassifications being Grade 3The findings section should be written in Times New Roman font, justified-alignment and in 10-point size.
6.

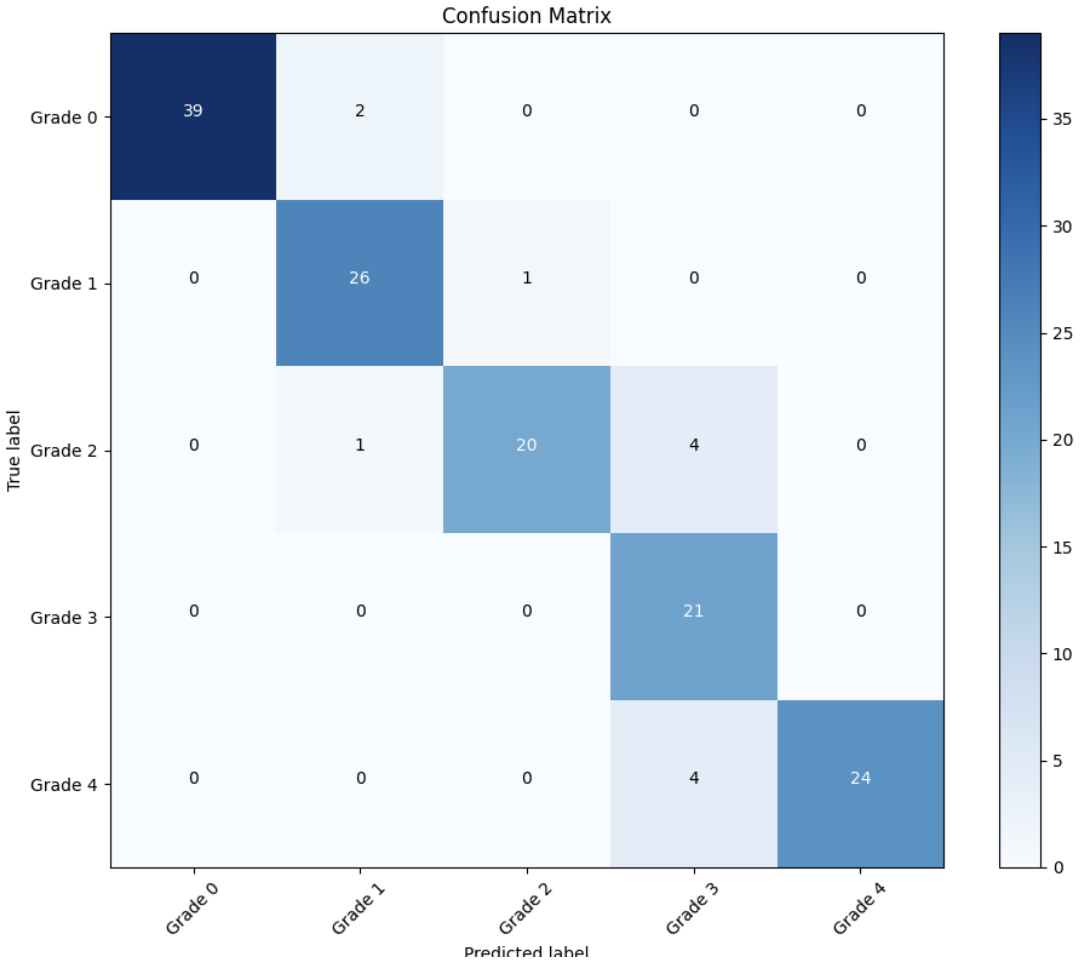

Figure 2. Confusion matrix.

Conclusion

The most common misclassification pattern occurred between adjacent grades (particularly Grades 2-3 and 3-4), which is consistent with the inherent difficulty in distinguishing between proximate histopathological grades.
The macro-averaged F1 score of 0.886 further confirms the model's balanced performance across all grades. This indicates that despite some class-specific variations, the modified U-Net architecture effectively learned discriminative features for histopathological grade classification.
Ablation studies and hyperparameter comparisons performed within the scope of the study are not included in the extended summary and will be presented through tables in the oral presentation.
In the future, the scope of our work will be expanded by training on larger datasets and will also be used for different grading and or classification of histopathology images.

References

Chanchal, A. K., Lal, S., Kumar, R., Kwak, J. T., & Kini, J. (2023). A novel dataset and efficient deep learning framework for automated grading of renal cell carcinoma from kidney histopathology images. *Scientific Reports*, *13*(1), 5728. https://doi.org/10.1038/s41598-023-31275-7

Dong, N., Kampffmeyer, M., Liang, X., Wang, Z., Dai, W., & Xing, E. P. (2018). Reinforced auto-zoom net: Towards accurate and fast breast cancer segmentation in whole-slide images. *Deep Learning in Medical Image Analysis and Multimodal Learning for Clinical Decision Support*, 317–325. https://doi.org/10.1007/978-3-030-00889-5_36

Fuhrman, S. A., Lasky, L. C., & Limas, C. (1982). Prognostic significance of morphologic parameters in renal cell carcinoma. *The American Journal of Surgical Pathology*, *6*(7), 655–663. https://doi.org/10.1097/00000478-198210000-00007

Moch, H., Humphrey, P. A., Ulbright, T. M., & Reuter, V. E. (Eds.). (2016). *WHO Classification of Tumours of the Urinary System and Male Genital Organs* (4th ed., Vol. 8). International Agency for Research on Cancer.

Nahid, A.-A., Kong, Y., & Abd Rahman, S. F. (2021). Histopathological breast-image classification with restricted Boltzmann machine along with backpropagation. *Biomedical Signal Processing and Control*, *66*, 102481. https://doi.org/10.1016/j.bspc.2021.102481

Tajbakhsh, N., Jeyaseelan, L., Li, Q., Chiang, J. N., Wu, Z., & Ding, X. (2020). Embracing imperfect datasets: A review of deep learning solutions for medical image segmentation. *Medical Image Analysis*, *63*, 101693. https://doi.org/10.1016/j.media.2020.101693

Xie, Y., Xing, F., Kong, X., Su, H., & Yang, L. (2015). Beyond classification: Structured regression for robust cell detection using convolutional neural network. *International Conference on Medical Image Computing and Computer-Assisted Intervention*, 358–365. https://doi.org/10.1007/978-3-319-24574-4_43

Image Reconstruction and Restoration with Diffusion Network

Onur Parapan[a], Ender Mete Ekşioğlu[b]

[a] Istanbul Technical University, Telecommunication Engineering, Türkiye
[b] Istanbul Technical University, Electronics and Communication Engineering Department, Türkiye
parapan@itu.edu.tr

Keywords: Image Reconstruction, Image Restoration, Deep Learning, Diffusion Networks, Residual Shifting.

Aim

This study focuses on exploring the effectiveness of diffusion models in addressing two key challenges in digital image processing: image reconstruction and image restoration. The motivation behind this research lies in the frequent occurrence of image degradation in real-world settings. Various types of distortion—such as random noise, motion blur, downsampling, or missing pixels—are commonly encountered in domains like medical imaging, satellite photography, and consumer media.

Diffusion models, originally developed for high-quality image generation, have recently been applied to inverse problems such as denoising and super-resolution (Ho et al., 2020). These models are based on a simple concept: they learn how to reverse a degradation process by modeling how data transitions from a clean state to pure noise, and then teaching a neural network to invert this process.

In particular, this study also examines the role of recent innovations, especially the residual shifting technique (Zhang et al., 2023), which improves denoising performance during inference by modifying the residual flow between time steps. The primary aim is to assess whether such models can serve as effective tools for high-fidelity restoration of degraded images in a variety of settings.

Material and Method

Diffusion models consist of two sequential processes: a forward process that gradually adds noise to clean data, and a reverse process that learns to remove this noise. The forward process is typically fixed and Gaussian, while the reverse process is parameterized by a deep neural network that is trained using gradient-based optimization.

As shown in Figure 1 (see top of the second page), the forward diffusion process transforms a clean image into progressively noisier versions until it becomes indistinguishable from pure noise. The reverse process begins with random noise and reconstructs the original image by iteratively denoising each intermediate result. This bidirectional learning procedure enables the model to learn the entire data distribution.

In this research, a U-Net-based architecture is adopted for the reverse denoising network. The U-Net's encoder-decoder design, along with skip connections, allows the model to capture both fine-grained details and high-level semantics. To improve denoising fidelity, we apply the residual shifting technique as introduced by Zhang et al. (2023). This approach adjusts the model's intermediate denoising steps, improving stability and image clarity.

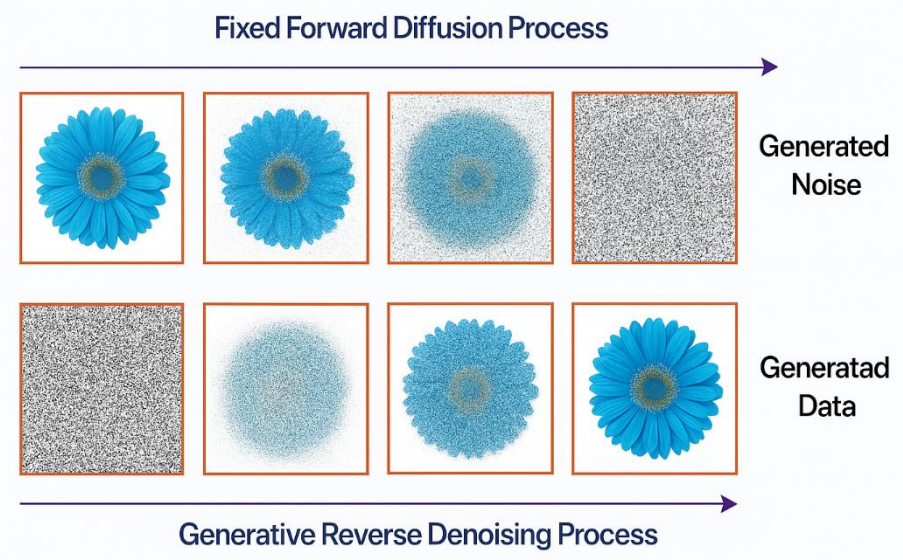

Figure 1. Forward Diffusion (Top) and Reverse Denoising (Bottom) Showing Progressive Degradation and Recovery of an Image.

Training is conducted using synthetic datasets where noise, blur, or missing patches are artificially introduced. The datasets include:

- Synthetic super-resolution data (bicubic downsampled images),
- RealSet65 and RealSet80 datasets for real-world super-resolution,
- Natural and facial image inpainting datasets, where central or random areas of images are removed,
- Blind face restoration data, involving low-resolution, degraded face images.

The models are implemented using PyTorch and trained using Adam optimizer. The loss functions include Mean Squared Error (MSE) and Structural Similarity Index Measure (SSIM) loss. Some experiments also employ perceptual loss to improve visual fidelity.
In addition to the residual shifting-based diffusion model and the standard diffusion model, a baseline U-Net model is also trained using the same datasets and training setup. This comparative framework allows a consistent evaluation of all three models—U-Net, standard diffusion, and ResShift—under identical conditions. This setup provides a clearer understanding of the benefits each model offers, particularly in terms of restoration accuracy, visual quality, and computational efficiency. Performance evaluation includes:

- Peak Signal-to-Noise Ratio (PSNR),
- Structural Similarity Index Measure (SSIM),
- Visual inspection for perceptual quality assessment.

Findings

Experimental results indicate that diffusion models are highly effective in both image restoration and reconstruction tasks. In denoising experiments, the model successfully removed both low- and high-intensity Gaussian noise, yielding clean outputs with minimal artifacts. As shown in Figure 2, in super-resolution settings, the model recovered detailed high-resolution content from severely downsampled inputs.

Figure 2. Super Resolution Processing with ResShift.

Inpainting results were particularly impressive. The model not only restored the missing regions but also generated visually coherent content that matched the surrounding context. When using the residual shifting strategy, structural consistency and edge sharpness improved significantly. For facial image restoration, the model was able to recover facial features that were heavily blurred or occluded in the input.

Table 1 summarizes the model's performance on different tasks, demonstrating high PSNR and SSIM values across the board. In many scenarios, diffusion models outperformed traditional restoration methods such as BM3D (Dabov et al., 2007) and total variation minimization, as well as other deep learning-based methods.

Table 1. Diffusion Model's Performance on Different Tasks**.**

Task	PSNR (↑)	SSIM (↑)
Gaussian Denoising	31.6 dB	0.92
Super-Resolution (x4)	28.4 dB	0.88
Natural Image Inpainting	33.2 dB	0.94
Blind Face Restoration	27.5 dB	0.89

To further evaluate the relative performance of different model types, a comparative analysis was conducted between the U-Net baseline, the standard diffusion model, and the residual shifting-enhanced ResShift model. The results show that:

- The U-Net model provides fast inference and decent restoration, particularly in low-complexity degradation scenarios.
- The standard diffusion model delivers improved perceptual quality and better PSNR/SSIM scores but requires more inference steps and computation.
- The ResShift model significantly reduces the number of sampling steps needed while maintaining or improving quality. It strikes a balance between performance and efficiency, outperforming both the U-Net and standard diffusion in most tasks.

This comparison highlights the superiority of ResShift for complex restoration problems, particularly when computational efficiency is also a priority.

An additional observation is the model's robustness. Even in cases of extreme degradation—such as when more than 50% of the image pixels were missing—the ResShift model was still able to generate plausible and coherent reconstructions. This supports previous findings from the DDRM framework proposed by Wang et al. (2022), where diffusion models are used as flexible priors for solving inverse problems.

Conclusion

This study confirms that diffusion networks can serve as powerful tools for solving image restoration and reconstruction problems. They provide a unified and general-purpose approach capable of addressing various types of degradation without requiring task-specific architectures.

Their performance in denoising, super-resolution, and inpainting tasks is not only competitive but often superior to traditional and even many deep learning-based methods. The inclusion of residual shifting further improves the model's accuracy and robustness, making it suitable for real-world applications.

The direct comparison between U-Net, standard diffusion, and ResShift models further reinforces the value of diffusion-based methods, especially when enhanced with techniques like residual shifting. Overall, diffusion models represent a promising direction for future research in image processing. Further work may focus on reducing computational costs during inference and adapting these models for real-time or mobile applications.

References

Dabov, K., Foi, A., Katkovnik, V., & Egiazarian, K. (2007). Image denoising by sparse 3-D transform-domain collaborative filtering. IEEE Transactions on Image Processing, 16(8), 2080–2095.

Ho, J., Jain, A., & Abbeel, P. (2020). Denoising diffusion probabilistic models. arXiv preprint, arXiv:2006.11239.

Song, Y., & Ermon, S. (2021). Score-based generative modeling through stochastic differential equations. International Conference on Learning Representations (ICLR).

Wang, Y., Zhang, H., Lin, Z., Fang, C., Wang, X., & Luo, J. (2022). DDRM: Denoising Diffusion Restoration Models. Advances in Neural Information Processing Systems (NeurIPS).

Zhang, S., Liu, X., Zhang, L., Liu, Y., & Yang, M. (2023). ResShift: Residual-Shifting Diffusion for Image Restoration. arXiv preprint, arXiv:2309.07301.

Customizable Fluidic and Anisotropic Vocal Fold Phantom for Biomechanical Analysis

Afarin Sarrafzadeh[a], Onur Ferhanoğlu[a], Ahmet C. Erten[a]

[a] Istanbul Technical University, Department of Electronics and Communication Eng., Turkey
Sarrafzadeh22@itu.edu.tr

Keywords: Vocal Fold Phantom, Anisotropy, Young's Modulus, Tunable Biomechanics, Fluid Inclusion.

Aim

The vocal folds, situated within the larynx, play a vital role in the process of phonation. They span across the laryngeal opening, forming a narrow gap that allows airflow from the lungs. As air passes through this gap, it induces self-sustained vibrations of the vocal folds, thereby generating sound [1]. A key mechanical property of the vocal folds is their anisotropy — their material behavior varies depending on the direction of applied force. Specifically, parameters such as Young's modulus change in relation to the direction of airflow originating from the lungs. This directional dependence significantly influences sound production, making it essential to accurately capture this behavior in biomechanical models. Such models are critical for advancing our understanding of vocal fold function and for developing effective treatments for voice disorders [2].

Synthetic vocal fold models have long been utilized to investigate the mechanics of phonation, significantly advancing the understanding of tissue dynamics and vocal pathologies. These models are generally categorized into two main types: membranous and solid elastic [3]. Membranous models, extensively studied by Titze et al. (1995) and Ruty et al. (2005) [4], capture certain vibratory behaviors of human vocal folds but lack precision in structural design. To address this, Thomson et al. (2005) and Murray and Thomson (2012) proposed solid elastic models using soft polymers like silicone to better replicate tissue properties. However, the inherent isotropic nature of these materials limits their ability to accurately mimic vocal fold mechanics [5]. More recently, multilayer silicone models with graded stiffness across layers, introduced by Greenwood and Thompson (2021), have demonstrated improved similarity to native vocal fold structures [6]. Nevertheless, these designs rely on discrete stratification rather than a truly heterogeneous architecture. An alternative approach involving fiber-reinforced hydrogels by Ferri-Angulo et al. (2023) has shown enhanced replication of anisotropic mechanical behavior [7]. Despite these advances, hydrogels pose challenges such as limited long-term durability, susceptibility to dehydration, and overall stability, restricting their use in prolonged phonation studies.

To overcome these limitations, this study introduces a novel approach to achieving anisotropy by embedding a natural latex rubber tube within a polydimethylsiloxane (PDMS) cube representing vocal fold tissue. Unlike previous methods that involve intricate layering or specialized reinforcement, the proposed design offers a simpler and more practical fabrication process. To assess the model's ability to replicate anisotropic behavior, both computational simulations and experimental analyses were performed. The results closely match the anisotropic properties observed in real vocal folds, validating the effectiveness of the proposed phantom for biomechanical phonation research.

Materials and Methods

Computational modeling

Simulations were conducted in COMSOL Multiphysics using the Solid Mechanics module. A cube with 15 mm sides and Young's modulus of 2.401 kPa was modeled. The 15 mm dimension was selected as an average, considering the typical human vocal fold length ranges from 11 mm to 21 mm [1]. Anisotropy was introduced by embedding a natural latex rubber tube, characterized by Young's modulus of 350 kPa, at the center of the cube. To incorporate tunability, the tube was simulated with varying water fill levels, from 0% to 80%, with the remainder filled by air. The bulk modulus was defined as 2.2 GPa for water and 101 kPa for air [8]. A total force of 98 mN was applied in both longitudinal and transverse directions. The resulting displacements were measured to deduce Young's modulus values [9].

Fabrication of Phantoms

Initially, a cubic mold with an internal cavity of 15 mm and wall thickness of 1.1 mm was designed in SolidWorks and fabricated using PLA filament via 3D printing. This mold was used to cast a silicone cube with dimensions of 15 mm × 15 mm × 15 mm. Next, a cylindrical insert measuring 3.1 mm in diameter and 15 mm in height was also designed in SolidWorks and 3D-printed. This insert was positioned at the center of the mold to reserve space for the natural latex rubber, which was introduced after the silicone had fully cured. The mold setup is illustrated in Figure 1.

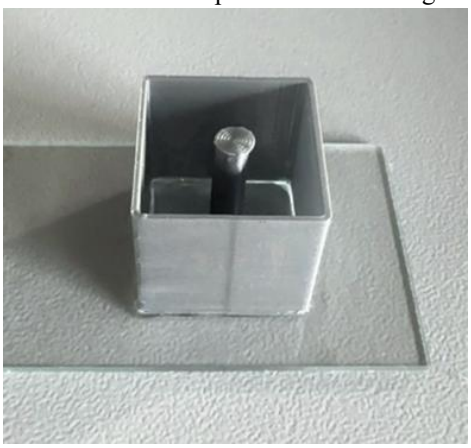

Figure 1. The PLA mold for the vocal fold phantom.

A silicone mixture containing 88% silicone, with Young's modulus of 2.401 kPa, was poured into the prepared mold and allowed to cure for 48 hours. Once the silicone had fully set, the central cylindrical insert was removed to make space for the tube. A natural latex rubber tube—15 mm in height, with an outer diameter of 3.2 mm, an inner diameter of 1.6 mm, and Young's modulus of 350 kPa—was then inserted into the center of the cube. The tube was filled with varying percentages of tap water, which has a bulk modulus of 2.2 GPa [10], to enable tunability. To prevent water leakage, a thin layer of adhesive was applied to both ends of the tube, as shown in Figure 2. Image analysis software, ImageJ, was used to process the captured images and calculate the displacement of each sample under applied force**.**

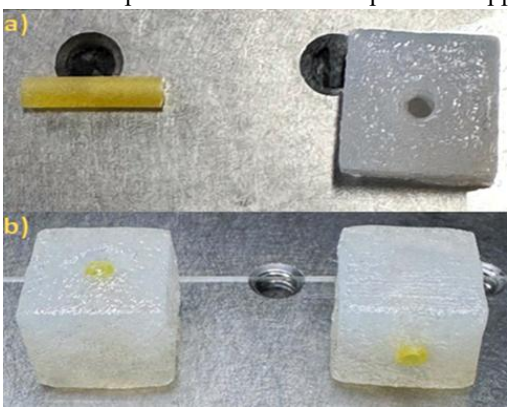

Figure 2. (a) The cured silicone structure with a hole in the center with a latex tube next to it, and (b) two complete vocal fold phantoms with latex tubes inserted.

Experimental setup

The experimental setup consisted of a digital scale and a camera connected to a laptop for image-based displacement measurements. A reference image of each sample was captured prior to loading, and this image was used in ImageJ software to set the initial cube length at 15 mm. A 10-gram weight, corresponding to a force of 98 mN, was then applied to the top

surface of the cube, while the bottom was held fixed. This procedure was carried out for both longitudinal and transverse orientations as shown in Figure 3.

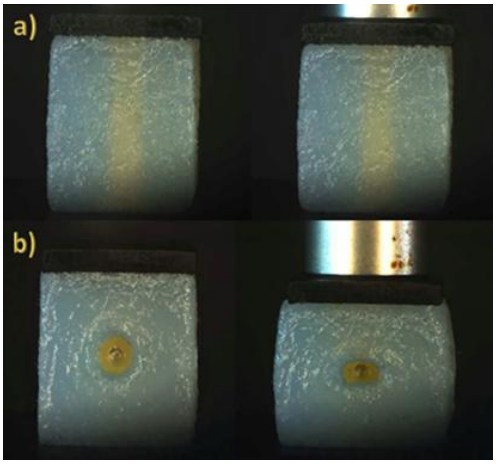

Figure 3. (a) Displacement in the longitudinal direction, and (b) Displacement in the transverse direction.

Following the application of force, a second image was taken to record the deformed state of the sample. The post-deformation length was measured in ImageJ, and displacement was calculated by comparing the initial and deformed lengths. Using this data, the mechanical response of each sample was quantified through the calculation of Young's modulus.

Findings

Simulation

In COMSOL Multiphysics, a compressive force of 98 mN was applied to the cross-sectional area of the cube in both longitudinal and transverse directions. For each configuration, with varying water-to-air ratios inside the latex tube, the resulting displacement was recorded and used to calculate Young's modulus. The Young's modulus in the transverse direction remained constant at 2.6 kPa, while in the longitudinal direction, it varied significantly, ranging from 12.18 kPa to 47.34 kPa, depending on the water content as presented in Table 1.

Table 1. The simulation and experimental results are based on longitudinal displacement (mm), the corresponding Young's modulus (kPa), the transverse displacement (mm), and the corresponding Young's modulus (kPa) for varying water percentages.

		Simulations		**Experiments**	
Sample	**Water %**	**E_L Young's modulus (kPa)**	**E_T Young's modulus (kPa)**	**E_L Young's modulus (kPa)**	**E_T Young's modulus (kPa)**
1	0	12.18	2.6	11.58	2.3
2	20	14.08	2.6	13.9	2.3
3	40	18.88	2.6	18.09	2.3
4	60	26.23	2.6	25.42	2.3
5	80	47.34	2.6	47.68	2.3

Experimental

Using ImageJ software, the displacement of each deformed sample under a 10-gram load was measured. The experimental findings closely match the simulation results, confirming that Young's modulus in the transverse direction consistently remains at 2.3 kPa across all samples. In contrast, variations in the water content within the latex tube significantly influence the longitudinal Young's modulus. Displacement and corresponding Young's modulus values for both directions are also summarized in Table 1. Additionally, a comparison of water content and longitudinal Young's modulus, illustrating both simulation and experimental data, is presented in Figure 4.

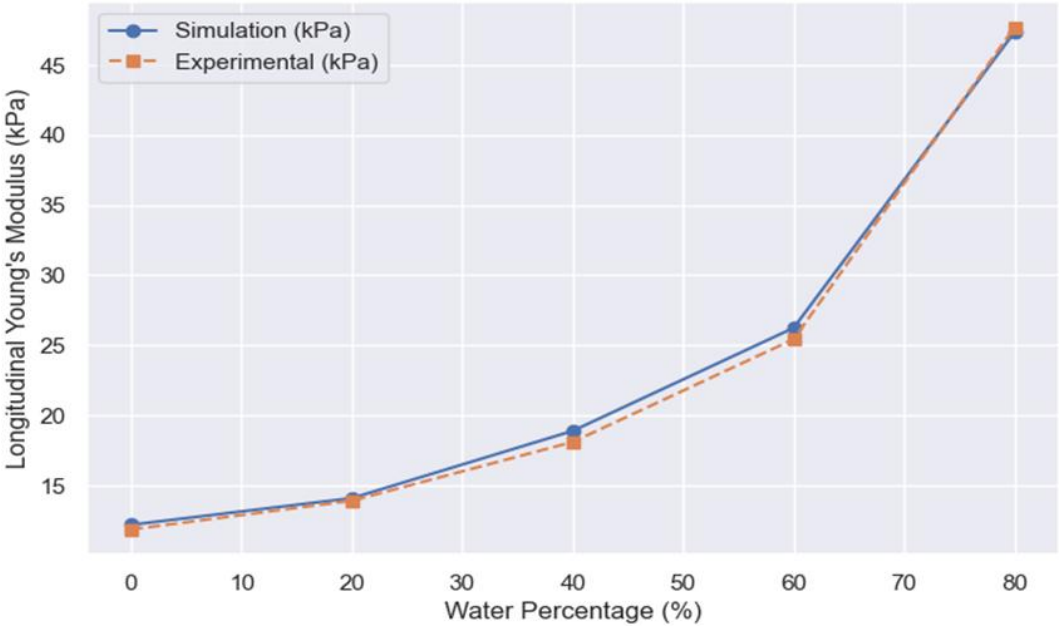

Figure 4. Longitudinal Young's Modulus vs. Water Percentage.

Conclusion

This study successfully presents a tunable vocal fold phantom that effectively replicates the anisotropic characteristics of human vocal folds. The strong correlation between simulation and experimental results confirms the validity and reliability of the proposed method. By embedding a latex tube within a PDMS cube and adjusting the internal water-to-air ratio, the model achieved a tunable Young's modulus range from 2.3 kPa to 47.68 kPa. Notably, modulating the water content between 0% and 75% enables coverage of the physiological stiffness range of human vocal folds (2 kPa to 40 kPa) [11]. Moreover, the ability to remove, refill, and reinsert the latex tube minimizes the need for fabricating multiple samples, thereby reducing both production complexity and preparation time. This simple yet effective approach to mimicking anisotropy and enabling adjustable stiffness offers a practical and versatile tool for studying vocal fold mechanics, advancing phonation research, and investigating voice disorders.

References

Zhaoyan Zhang. Mechanics of human voice production and control. The journal of the acoustical society of america, 140(4):2614–2635, 2016.

Jordan E Kelleher, Thomas Siegmund, Mindy Du, Elhum Naseri, and Roger W Chan. The anisotropic hyperelastic biomechanical response of the vocal ligament and implications for frequency regulation: A case study. The Journal of the Acoustical Society of America, 133(3):1625–1636, 2013.

Scott L Thomson. Synthetic, self-oscillating vocal fold models for voice production research. The Journal of the Acoustical Society of America, 156(2):1283–1308, 2024.

Ingo R Titze, Sheila S Schmidt, and Michael R Titze. Phonation threshold pressure in a physical model of the vocal fold mucosa. The Journal of the Acoustical Society of America, 97(5):3080–3084, 1995.
Preston R Murray and Scott L Thomson. Vibratory responses of synthetic, self-oscillating vocal fold models. The Journal of the Acoustical Society of America, 132(5):3428–3438, 2012.
Taylor E Greenwood and Scott L Thomson. Embedded 3d printing of multi-layer, self-oscillating vocal fold models. Journal of biomechanics, 121:110388, 2021.
Daniel Ferri-Angulo, Hamid Yousefi-Mashouf, Margot Michel, Anne Mcleer, Laurent Org´eas, Lucie Bailly, and J´erˆome Sohier. Versatile fiber-reinforced hydrogels to mimic the microstructure and mechanics of human vocal-fold upper layers. Acta Biomaterialia, 172:92–105, 2023.
Annemie Van Hirtum, Mohammad Ahmad, Raphal Chottin, and Xavier Pelorson. A composite analogy to study the linear elasticity of a pressurized latex tube with application to a mechanical vocal fold replica. International Journal of Applied Mechanics, 15(08):2350068, 2023.
Xiaoming Yuan, Weiqi Wang, Xuan Zhu, and Lijie Zhang. Theoretical model of dynamic bulk modulus for aerated hydraulic fluid. Chinese Journal of Mechanical Engineering, 35(1):121, 2022.
Fariborz Alipour and Sarah Vigmostad. Measurement of vocal folds elastic properties for continuum modeling. Journal of Voice, 26(6):816–821, 2012.
Amir K Miri. Mechanical characterization of vocal fold tissue: a review study. Journal of Voice, 28(6):657–667, 2014.

Development of Multi-Capsule Endoscopy via Spring-Assisted Distance Control

Erfan Parsaei[a], Furkan Peker[a], Ali Fuat Ergenç[b], Onur Ferhanoglu[a]

[a]Istanbul Technical University, Department of Electronics and Communication Eng., Turkey
[b]Istanbul Technical University, Department of Robotics and Autonomous Systems Eng., Turkey
Parsaei22@itu.edu.tr

Keywords: Finite-Element Modeling, Spring Design, Wireless Capsule Endoscopy.

Aim

Capsule endoscopy-assisted GI tract analysis has revolutionized endoscopy procedures since its emergence in 2000, and due to its minimal invasiveness and patient-friendly mechanism, it has been widely adopted by clinicians since then. Early gastrointestinal examinations were performed by endoscopy or/colonoscopy tubes, which involved sedation medications and invasive tube insertions. In contrast to conventional endoscopy and colonoscopy procedures, WCE has introduced a patient-friendly and minimally invasive GI tract examination by providing enhanced imaging techniques. This imaging procedure enables early detection of gastrointestinal diseases such as inflammatory bowel conditions like Crohn's disease, autoimmune diseases like Celiac, obscure bleeding in the intestines, and various tumors [1].

Besides the wireless capsule endoscopy's commercial success, it is limited only to imaging procedures. However, researchers have introduced various techniques through their ongoing studies to develop new capabilities for the capsules, focusing on locomotion and navigation systems. A couple of studies have innovatively been done to improve capsule mobility, including magnetic actuation using external solenoids [3], robotic appendages for controlled movement [4], biomimetic propulsion inspired by jellyfish-like movements reducing tissue damage [5-6], spiral-based motion mechanisms [7], using magnetic soft robotic for MagCap functionality with the integration of drug release capabilities of capsules [8].

Single-capsule endoscopy in conventional procedures struggled to perform complicated medical tasks such as biopsy, drug delivery, and real-time diagnostics due to functionality limitations. To overcome such limitations, literature has revealed other functionalities for WCE, such as a real-time polyp-detection system integrated with WCE based on AI and deep learning algorithms [9], introducing micro positioning and holding mechanics for drug delivery uses in WCE [10], and integration of a robotic device to WCE for biopsy procedures [11].

Besides the broad clinical applications of WCE, the conventional single capsule endoscopy system has space limitations that limit its multifunctionality, however, multiple capsule endoscopy trains can operate in coordination to perform various clinical tasks. Although we previously approached the multi-capsule endoscopy mobility by introducing coil-based inductive power systems [12] and magnetic-based remote actuation locomotion [14], these methods have encountered challenges in navigating the capsule-train through complex GI environment, particularly in sharp radius of curvature (ROC), less than 50mm, transitions. In this study, we introduce a multi-capsule endoscopy train model connected via flexible magnetic springs designed to traverse tight ROCs while maintaining stable inter-capsule connectivity.

This study focuses on the development of the WCE train, mainly on locomotion limitations through sharp GI tract turns, by introducing spiral spring modifications to the capsule's cap that assist the intracapsular connectivity. The primary objectives of our research include:

- Developing a new approach by using magnet-equipped springs that support the capsule connection during sharp turns.
- Analyzing the pre-designed springs' mechanical behaviors by performing COMSOL simulation and physical testing.
- Administering phantom experiments with different intestine-like surfaces to compare different intestinal conditions, mimicking the movement of the capsule trains in realistic simulations.

Materials and Methods

System Design & Components

Our capsule-train system consists of two capsules attached, each equipped with a custom-designed spiral spring. The springs encompass magnets that enable stable attachment between capsules while allowing for necessary flexibility during movement. The capsule train in this study, unlike the designs discussed in the literature, provides a physical connection that can tolerate the natural peristaltic forces when it passes through sharp turns of the GI tract.

- The study overviews three different capsule designs with different spring Characteristics in order to find the most suitable capsule-spring configuration, which is represented in Figure 1.
- Intestinal phantoms with a sharp radius of curvatures, indicated in Figure 2, were designed with a SolidWorks program to simulate the curvature parts of the GI tract.

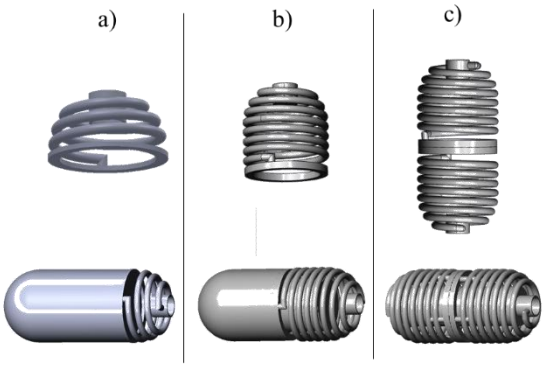

Figure 1. Different capsule-spring prototypes were designed in SolidWorks. (a) A 6 mm spring, 4 coils, 1.1 mm wall thickness integrated with a 22 mm length capsule; (b) A 14 mm spring, 8 coils, 1.1 mm wall thickness with a capsule; (c) The full spring design, which encompasses a 28 mm length spring, 16 coils, 1.1 mm wall thickness with an inter-capsule configuration. These different arrangements were tested to determine their ability to resist the forces while keeping the capsules connected during locomotion.

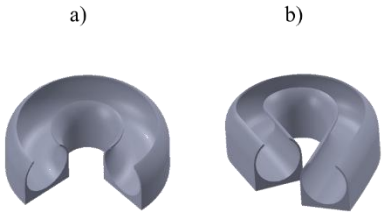

Figure 2. Human bowel designs indicate the curved paths of the GI tract, which multi-capsule endoscopies would face challenges in locomotion. (a) An intestinal model with a 50mm radius of curvature; (b) an intestinal model with a 25mm radius of curvature designed in SolidWorks.

Optimization of the Springs

To ensure the optimal performance of the springs, a finite element analysis based on COMSOL Multiphysics was conducted, and various metrics were tested. Key mechanical characteristics of the spiral springs were tested to attain the most suitable designs for the study.

Spring constant (K) was evaluated to reach a balance between stability and flexibility under peristaltic forces, stress**,** and yield point analysis were executed to prevent the springs from deformation under bowel contractions, and the expected displacement was calculated under the known forces to ensure the avoidance of the tissue damage, these metrics have been shown in Table 1. Finally, by considering all the factors, three of the many spring designs were selected for further experimental analysis.

Table 1. Finite-element analysis of spring information.

Parameters	***Values***
Spring constant	*50.9 N/m*
Stress	*0.0303 GPa*
Young's Modulus	*18.49 MPa*
Displacement	*4.44mm*

An experimental assessment was conducted to compare the printed spring constant ($K_{Simulation}$ = 50.9 *N/m*) with the finite-element analysis. the K constant was calculated by a setup, and the result was $K_{experimental}$ = 40 *N/m***.** The discrepancy between the simulation result and the experimental one is caused by variations in PLA characteristics and the thickness differences between 3D-printed PLA and simulated springs. In Table 2, we tabulate the material properties of the fused-deposition modeling printed capsule and phantom parts.

Table 2. Polylactic acid characteristics.

Parameters	***Values***
E_{pla}	*2636+-330 MPa*
ρ_{pla}	*1250 kg/m³*
v_{pla}	*0.3*

Source: (https://www.iemai3d.com/wp-content/uploads/2021/03/PLA_TDS__EN.pdf)

Experimental Setup

The setup was arranged with a stepper motor connected to a motor driver, which is controlled by an Arduino Uno, and the stepper motor was connected to the capsules with a nylon string as illustrated in Figure 3. Experiments were conducted to ensure the capability of the proposed designs to maintain inter-capsule connectivity through different ROCs. In the first step, bowel phantoms, printed with PLA, were used with a smoothened surface, testing the model accuracy in two different radii of curvatures (50 and 25mm). After getting the expected result from three different spring-capsule configurations, the next step was to imitate the human-like intestinal structure. We introduced a silicon layer with 90% silicon and mimicked a villus-like configuration on the surface of the intestinal phantoms, which were tested under the same setting.

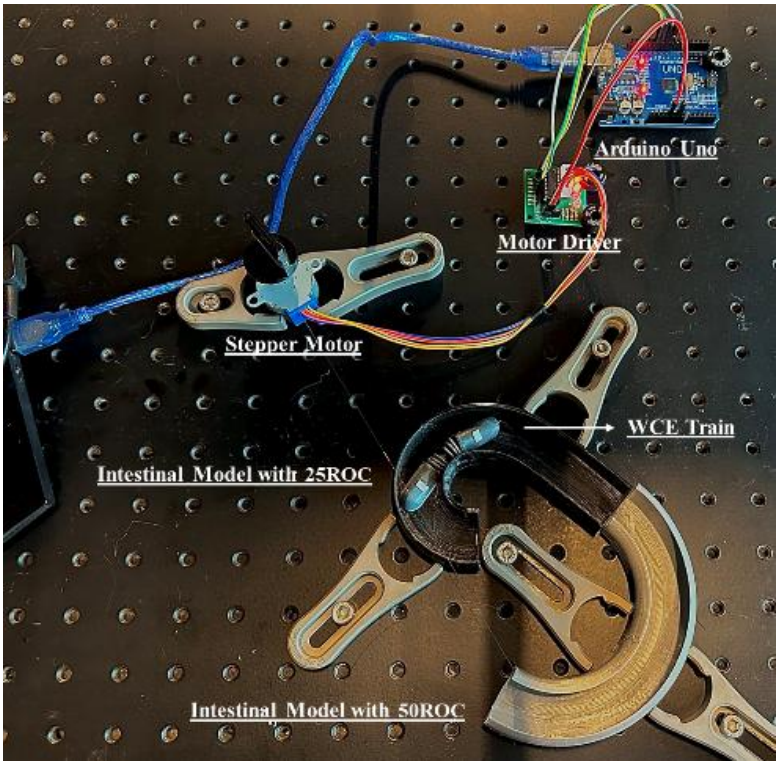

Figure 3. Experimental setup components.

The locomotion of the capsules was mimicked using a stepper motor, which was controlled by an Arduino-uno system; the motor was programmed to pull a fish rope attached to the first capsule. The pulling speed was conducted at 0.1 mm/s, which is a rounded average speed used following the average peristalsis speed of 0.5-4.3 cm/min in humans [15]. Also, 10x peristalsis speed(1mm/s) was used to survey the train mobility in harsh circumstances. Each experiment setup was captured in video recordings and was post-processed using MATLAB-based movement tracking algorithms to assess the capsule-distance variations during passing the bowel model and its attachment stability through sharp turns. The post-processed locomotion process is shown in Figure 4.

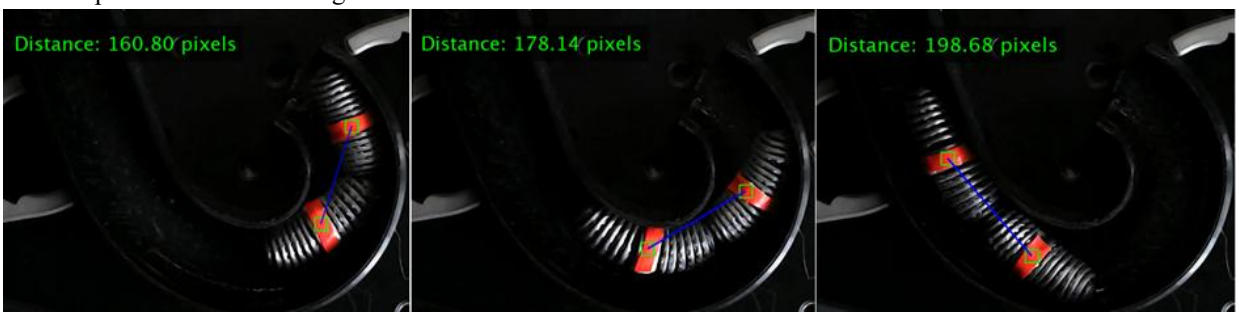

Figure 4. Post-processing shots from the distance evaluation in MATLAB.

Findings

Through all the examinations with various intestinal configurations and capsule-spring models, the results yielded satisfaction when the WCE train navigated through sharp turns with 50 mm and 25 mm ROCs. The evaluation of the capsule train interconnectivity and capsule distance modifications showed success. Also, the distance variation, based on different spring stiffness (K-values) between capsules, reveals that the suggested model supports the development of capsule endoscopy train locomotion.

Conclusion

Our findings suggest that multi-capsule endoscopy trains with magnetic spring connections provide a viable solution for traversing complex intestinal pathways while maintaining stable inter-capsule connectivity. Compared to previous coil-based and passive magnet configurations, which had limitations in ROCs 50mm and below, the proposed design is more adaptable to sharp ROCs and real GI conditions. Future work will focus on integrating advanced sensors, improving real-time control algorithms, and conducting in vivo testing to further validate the approach.

References

H. Adler and A. J. Gostout, "Wireless capsule endoscopy," Hosp. Physician, vol. 39, no. 3, pp. 14–22, 2003.
C. Koulaouzidis, K. I. Plevris, "Wireless capsule endoscopy: A revolution in imaging of the small intestine," Gastrointest. Endosc. Clin. N. Am., vol. 19, no. 4, pp. 747–772, Oct. 2009.
M. Sendoh, K. Ishiyama, and K. Arai, "Fabrication of magnetic actuator for use in a capsule endoscope," IEEE Trans. Magn., vol. 39, no. 5, pp. 3232–3234, Sep. 2003.
H. Liu, X. Liu, L. Dong, and W. Wang, "A robotic capsule endoscope with a novel design for untethered biopsy," IEEE Robot. Autom. Lett., vol. 4, no. 4, pp. 3385–3391, Oct. 2019.
B. Menciassi, M. Quirini, and P. Dario, "Design and development of a biomimetic robotic fish for endoscopic applications," Int. J. Robot. Res., vol. 28, no. 4, pp. 546–558, Apr. 2009.
D. Son et al., "Flexible propulsive endoscopic system inspired by fish locomotion," Bioinspir. Biomim., vol. 15, no. 2, pp. 1–12, Mar. 2020.
H. S. Ryou and C. K. Kim, "Spiral motion microcapsule robot," Sensors Actuators A: Phys., vol. 280, pp. 291–298, Jan. 2019.
Sun, Y., Zhang, W., Gu, J. et al. Magnetically driven capsules with multimodal response and multifunctionality for biomedical applications. Nat Commun 15, 1839 (2024).
Krenzer A, Banck M, Makowski K, et al. A Real-Time Polyp Detection System with Clinical Application in Colonoscopy Using Deep Convolutional Neural Networks. Research Square; 2022. DOI: 10.21203/rs.3.rs-1310139/v1.
Woods SP, Constandinou TG. Wireless capsule endoscope for targeted drug delivery: mechanics and design considerations. IEEE Trans Biomed Eng. 2013 Apr;60(4):945-53. doi: 10.1109/TBME.2012.2228647. Epub 2012 Nov 21. PMID: 23192476.
Kong, Kyoungchul & Yim, Sehyuk & Choi, Sunhee & Jeon, Doyoung. (2012). A Robotic Biopsy Device for Capsule Endoscopy. Journal of Medical Devices. 6. 031004. 10.1115/1.4007100.
Peker, F., Ferhanoğlu, O. Active distance control in multi-capsule endoscopy via closed-loop electromagnetic force between capsules. Med Biol Eng Comput 62, 1153–1163 (2024).
Peker F, Beşer MA, Işıldar E, et al. Towards capsule endoscope locomotion in large volumes: design, fuzzy modeling, and testing. Robotica. 2024;42(1):203-224. doi:10.1017/S026357472300142X
Peker, F., Ferhanoğlu, O. Multi-Capsule Endoscopy: An initial study on modeling and phantom experimentation of a magnetic capsule train. J. Med. Biol. Eng. 41, 315–321 (2021).
Freitas M, Macedo Silva V, Xavier S, et al. Prolonged gastric transit time in small-bowel capsule endoscopy: Which patients are at risk and what implications? Turk J Gastroenterol. 2023;34(3):227-233.

Effect of Wavelength, Intensity, and Eye Color on Pupil Detection in Infrared-Based Eye Tracking Systems

Murat Teksin[a,b], Onur Ferhanoğlu[c]

[a] Istanbul Technical University, Electronics and Communication Engineering, Biomedical Engineering Programme, Turkey
[b] Turkish Aerospace Industry, Turkey
[c] Istanbul Technical University, Electronics and Communication Engineering, Turkey
teksin16@itu.edu.tr

Keywords: Driving Monitoring System, Pupil Detection System, Pupil Diameter Detection, Pupil Tracking System.

Aim

Eye tracking, or pupil tracking, is a key method for monitoring an individual's health. Eye-tracking technology comes up with some optimal solutions to health monitoring, such as noninvasiveness and easy placement for various scenarios. Typically, Eye tracking is achieved with a device that consists of a video camera and generally a constant wavelength and intensity IR light source as hardware. The software component processes captured images to detect the pupil—an aperture at the center of the eyeball—and determine the gaze point. This method can be used to detect both psychological [1] and physiological [2] symptoms. Besides, it can be used for driver monitoring in cars or trucks. Nowadays most high-segment cars have this monitoring system to measure driver tiredness, as shown in the illustration in Image I, drowsiness or gaze location, and the system creates some alerts for unintentional situations to prevent accidents [3]. However, environmental lighting conditions, IR source intensity and even eye color can affect the accuracy of pupil detection. This study aims to compare the quality of pupil detection under varying lighting conditions, eye colors, light source intensities, and wavelengths.

Material and Method

Hardware Setup and Data Collection:

The developed hardware setup includes a webcam and three types of IR LEDs with wavelengths of 730 nm, 850 nm, and 940 nm. Each type includes two 1 W LEDs.The camera used is the Piranha-9635 webcam (shown in Image 2), with its IR filter removed to allow IR light capture. Two eye-tracking techniques—bright pupil and dark pupil methods—exist [4]. This study uses the dark pupil method by positioning the LEDs at a specific distance from the camera sensor.
Images were collected with the lights both on and off, to mimick day and night time conditions. For eye color evaluation, images were taken of blue- and brown-eyed participants under all three wavelengths, with a constant current applied to the LEDs. Participants looked directly at the camera and sequentially at each corner of the screen, as illustrated in Image 3.
Secondly, for intensity examination again, three different wavelengths have been used, and input current has been changed between 0 A and 1.5 A with respect to the LED's specification during environmental lights being on and off. Similarly, the participant looked at 4 points of the screen and camera as seen in Image 4 and Image 5. Additionally, a picture with 10 different dots in it has been shown on the monitor, and the participant has looked at the 10 dots in order.

Image processing:

After collection has been done, the image processing part has been realized. For processing images, a Python script has been created. The image processing package, open computer vision library, has been mainly used in scripts. Color conversion, adaptive thresholding, and edge detection methods have been applied to images. Detected edges classified with respect to their circularity. Finally, the pupil and the pupil center have been marked on the images. A total of 65 pictures have been taken for the eye color study and 451 pictures for the light effect study. The algorithm can detect pupils in 267 images, while 39 of these pictures belong to the eye-color study. In comparison, manual marking has also been done to image center points and pupil diameters generated.

Findings, Results and Discussion

As a result, comparison with respect to the changing wavelengths has been done. Firstly, for different eye color studies, blue eye color has shown a 1.72 pixel error for the center point and a 1.26 pixel error for the pupil diameter value at 730 nm wavelength. In contrast, brown eye color has shown a 2.28 pixel error for the center point of the pupil and a 3.17 pixel pupil diameter error at a 730 nm wavelength. At 850 nm, again the blue-colored eye has given a better result, with 1.14 pixel center point error and 0.90 pixel pupil diameter error, while the brown eye has 3.35 pixels and 1.97 pixels, respectively. Finally, at the 930 nm source wavelength, both eye colors have shown worse results with 5.51 and 5.57 pixel center point error for brown and blue, 5.55 and 4.22 pixel pupil diameter error. With this study, it can be specified that eye color changes the pupil detection method success rate. Secondly, a source current change effect has created a discernible result, as it can be seen in Table I. Considering all-day scenarios, 730 nm sources with currents of 0.60 A and 0.84 A are proposed as the best solution when a center point wants to be detected. When pupil diameter is added as a parameter that is looked for, an 850 nm source with 0.65 A gives the best result and has the most detectable number of images. When Table I is observed, from the total calculations the best result for the diameter error can be seen at 940 nm and 0.79 A. However, 940 nm results mostly stay at the day images. Therefore, 940 nm is not made a part of the best solution for an all-day scenario. Now, it is mentioned, 850 nm wavelength with 0.78 A gives the best result for pupil center estimation for only the daylight condition scenario, while 850 nm wavelength gives the best result for pupil diameter with 1.04 A. In contrast, when night conditions are mentioned, again the 850 nm wavelength source gives the best results but with a 0.65 A current in that situation.

Conclusion

This study demonstrates that variations in LED wavelength and current significantly affect pupil detection performance under different lighting conditions and for different eye colors. To improve driver monitoring systems, adaptable LED configurations with variable voltage control and integrated ambient light sensors are recommended. Furthermore, incorporating eye color information could enhance the robustness and accuracy of real-time driver monitoring.

References

Mele, M.L., Federici, S. (2012). Gaze and eye-tracking solutions for psychological research. Cogn Process 13 (Suppl 1), 261–265

He, D., Wang, Z., Khalil, E. B., Donmez, B., Qiao, G., & Kumar, S. (2022). Classification of Driver Cognitive Load: Exploring the Benefits of Fusing Eye-Tracking and Physiological Measures. Transportation Research Record, 2676(10), 670-681.

F. Vicente, Z. Huang, X. Xiong, F. De la Torre, W. Zhang and D. Levi. (2015). Driver Gaze Tracking and Eyes Off the Road Detection System. IEEE Transactions on Intelligent Transportation Systems, vol. 16, no. 4, pp. 2014-202

Karlene Nguyen, Cindy Wagner, David Koons, and Myron Flickner. (2002). Differences in the infrared bright pupil response of human eyes. In Proceedings of the 2002 symposium on Eye tracking research & applications (ETRA '02). Association for Computing Machinery, New York, NY, USA, 133–138.

Table 1. Comparison of Results.

		Total			Night			Day		
Source Wavelength (nm)	Source Current (A)	Number of Detected Images	Center Point Error (px)	Diameter Error (px)	Number of Detected Images	Center Point Error (px)	Diameter Error (px)	Number of Detected Images	Center Point Error (px)	Diameter Error (px)
730	0.12	3	11.29	4.07	0	-	-	3	11.29	4.0
	0.37	17	1.85	3.29	14	1.79	3.24	3	2.15	3.48
	0.60	17	1.97	3.35	12	1.76	3.60	5	2.49	2.74
	0.84	20	1.92	1.93	14	2.07	2.20	6	1.57	1.56
	1.03	20	2.72	2.48	12	3.33	2.79	8	1.82	2.01
850	0.17	14	7.34	3.55	7	3.02	3.78	7	11.66	3.32
	0.40	20	3.16	2.21	9	3.97	3.36	11	2.49	1.27
	0.65	21	2.03	1.64	9	1.50	1.74	12	2.43	1.56
	0.78	18	3.02	1.87	6	2.61	2.54	12	3.22	1.53
	1.04	16	2.60	2.07	7	3.55	3.77	9	1.87	0.75
940	0.26	14	8.73	2.89	1	9	7.79	13	8.71	2.52
	0.48	12	6.82	4.37	1	6	10.6	11	7.01	3.80
	0.79	11	2.53	1.00	0	-	-	11	2.53	1.00
	1.02	12	3.36	1.35	0	-	-	11	3.36	1.35
	1.50	12	3.33	2.38	0	-	-	12	3.33	2.38

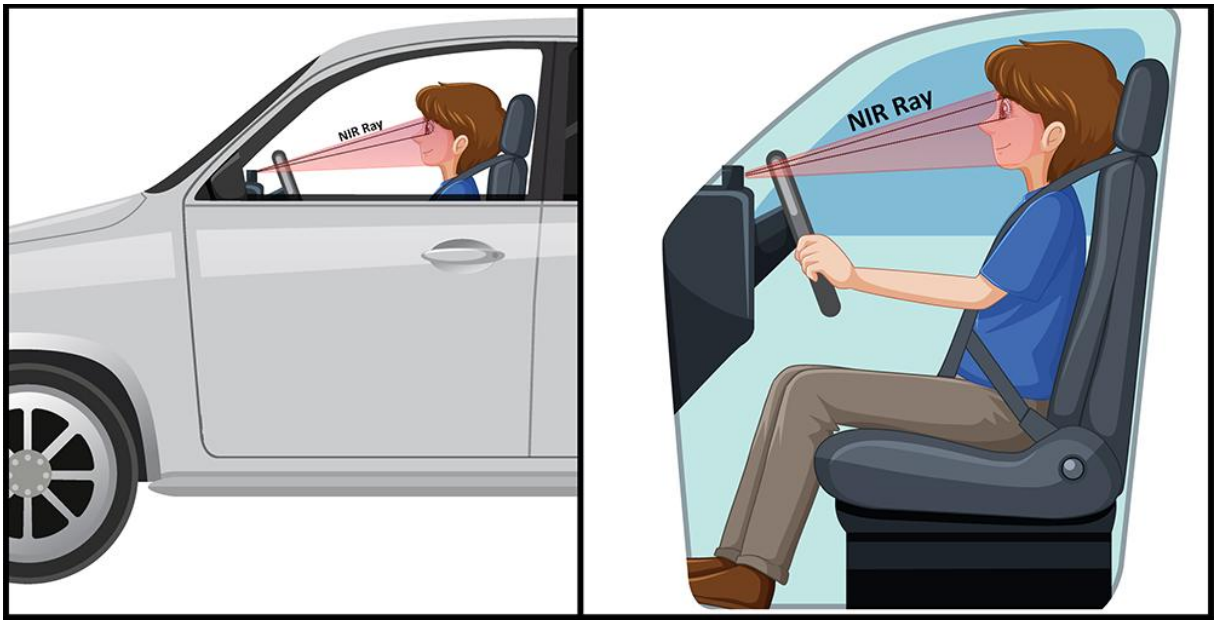

Figure 1. Illustration of driver monitoring system in a car.

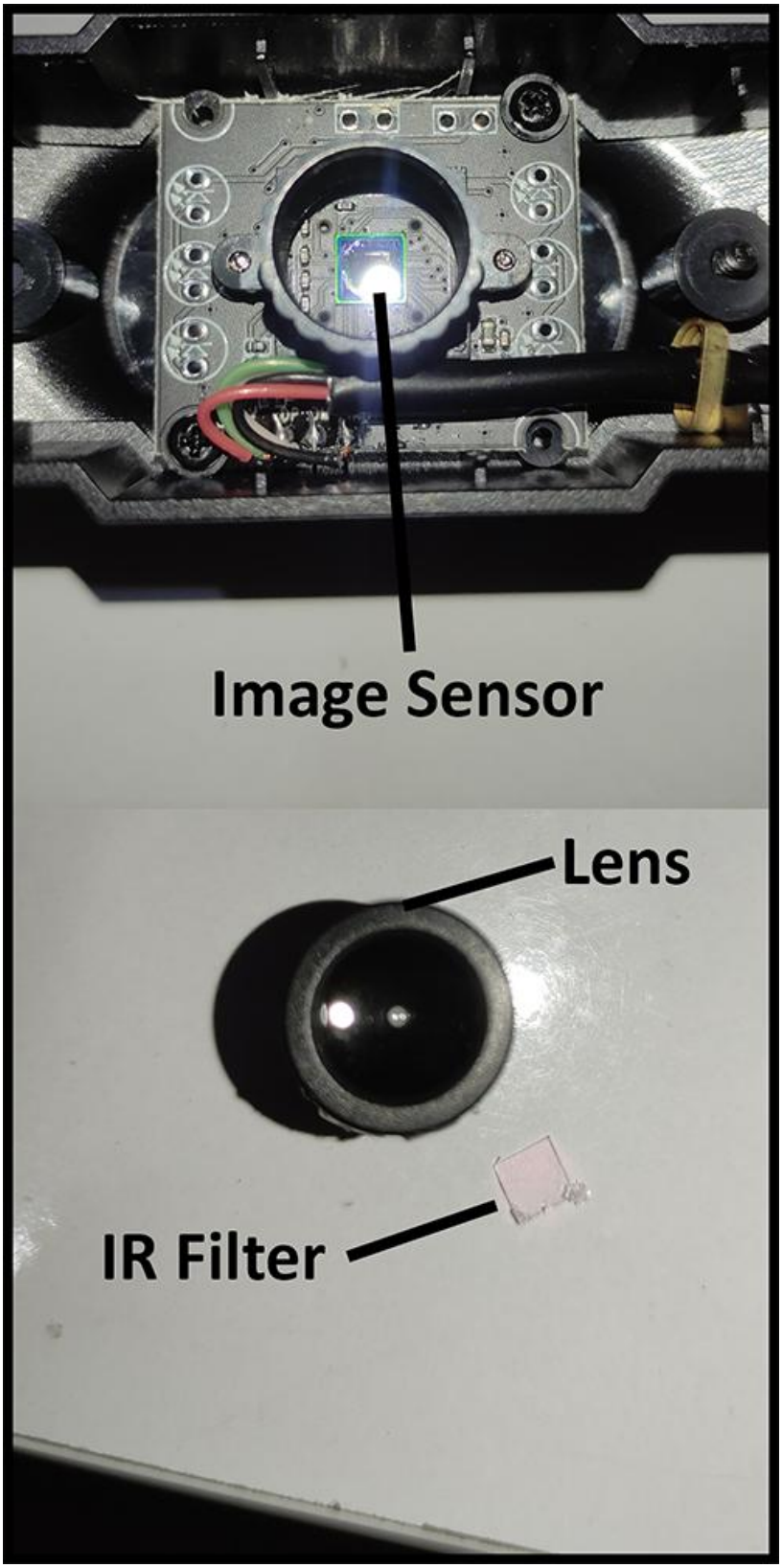

Figure 2. IR filter removal from camera.

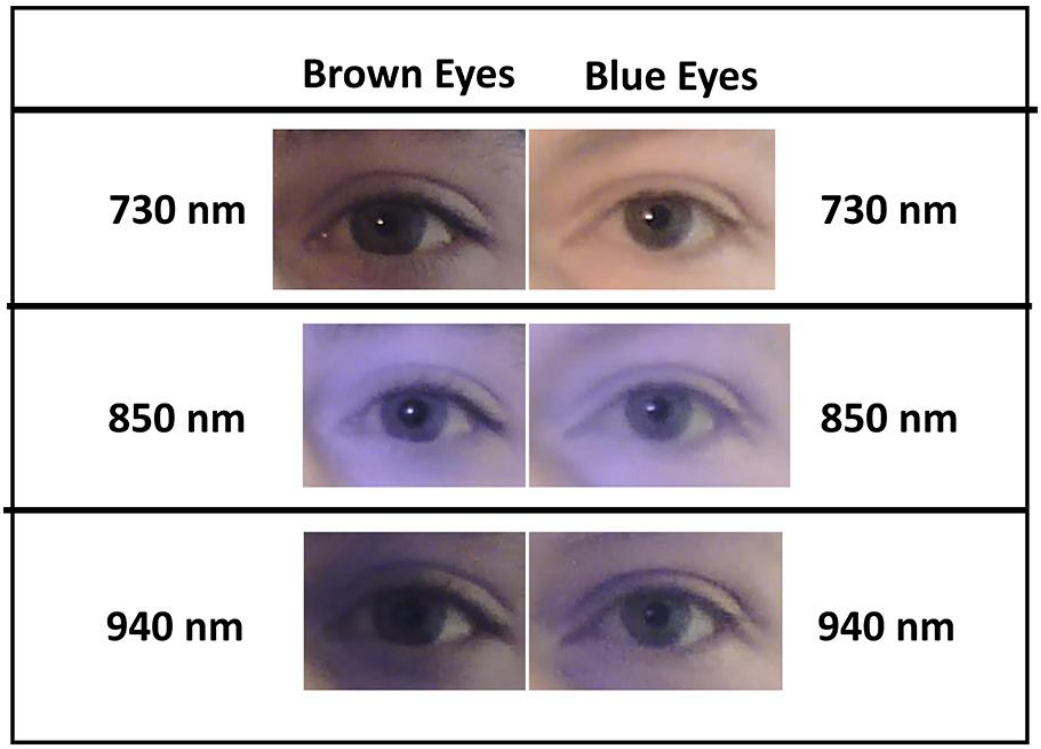

Figure 3. Eye images with different eye color under lights with various wavelength.

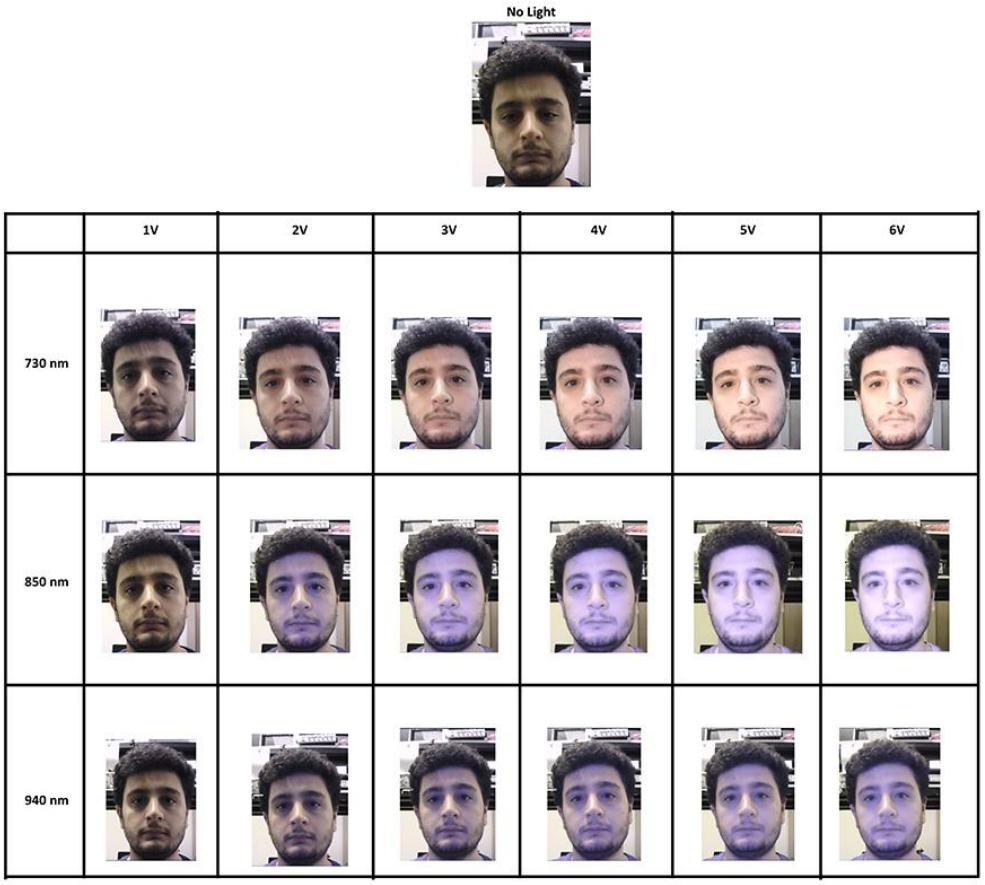

Figure 4. Face images that are lighted by IR LED with various wavelength and intensity.

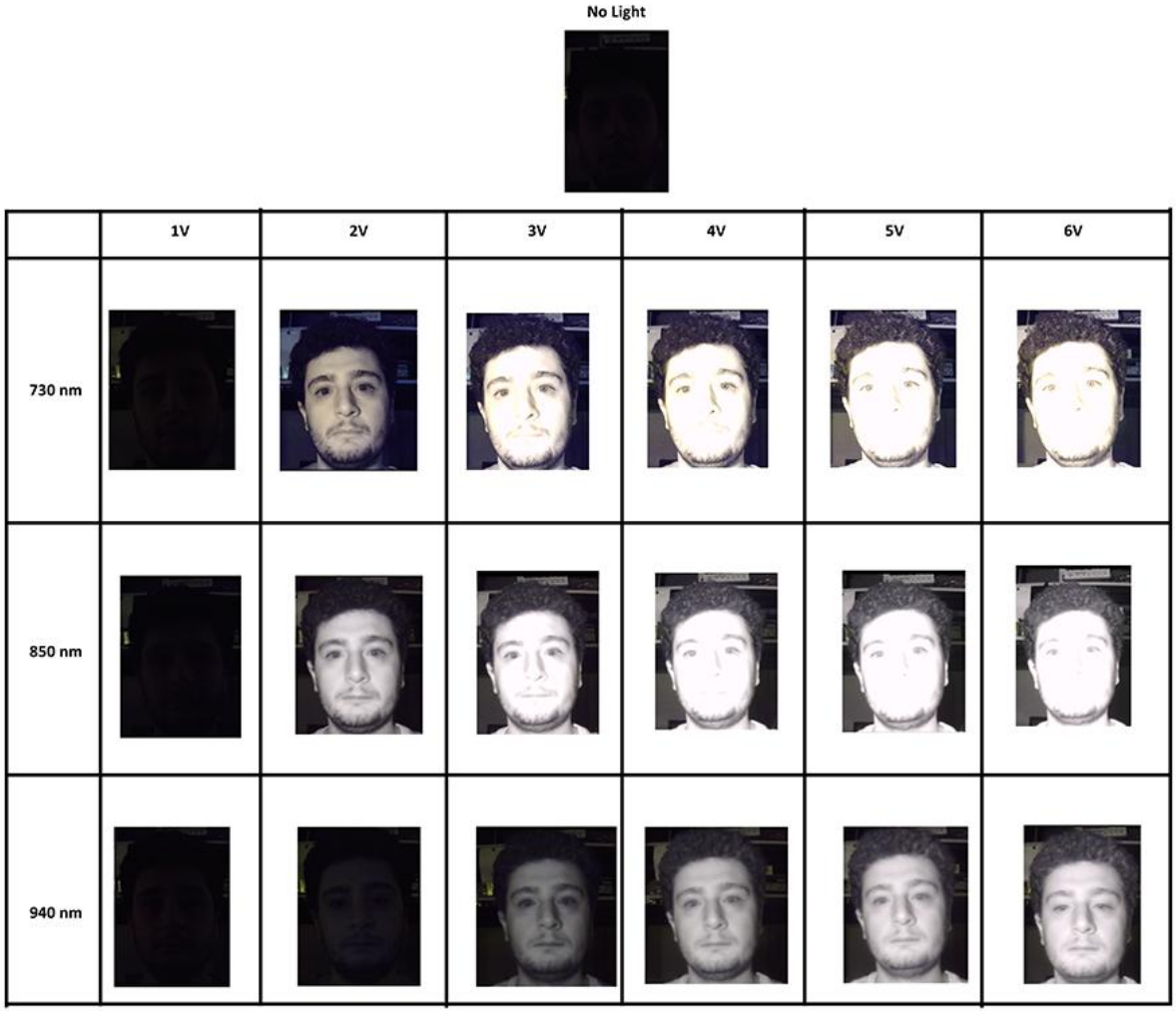

Figure 5. Face images that are lighted by IR LED with various wavelength and intensity in dark environment.

Multi-Class Classification for Skin Lesions Using Deep Learning Techniques

Ümmühan Kopal[a], Mürvet Kırcı[a]

[a] Istanbul Technical University/ Graduate Institute, Department of Electronics and Communication Engineering, Biomedical Engineering Program, Türkiye
kopal21@itu.edu.tr

Keywords: Skin Lesion, Multiclass Classification, Deep Learning.

Aim

Skin cancer is one of the most prevalent and deadly types of cancer globally, with early detection being a critical factor in improving patient outcomes. Traditional diagnostic methods rely heavily on dermatologists' expertise, which can be time-consuming and prone to human error. Recent advancements in deep learning have shown significant promise in automating the classification of skin lesions, thereby aiding in early and accurate diagnosis.(Esteva et al., 2017) This study aims to develop a robust multi-class classification system for skin lesions using deep learning techniques, specifically leveraging the ResNet (Residual Network) architecture. The primary objective is to classify dermoscopic images into multiple categories, including melanoma, basal cell carcinoma, and benign keratosis, using a publicly available dataset such as the ISIC 2019. (Isic2019 dataset, 2023) By employing advanced techniques such as data augmentation and transfer learning, this work seeks to improve the generalization and accuracy of the model, ultimately contributing to more efficient and reliable skin cancer diagnosis.

Material and Method

Dataset: The study utilizes the ISIC archive, a publicly available dataset containing thousands of dermoscopic jpeg images of skin lesions. The dataset includes images labeled with various categories, such as melanoma, basal cell carcinoma, benign keratosis. (Kaggle, 2023)

Model Architecture: The ResNet architecture is chosen due to its proven effectiveness in image classification tasks. ResNet residual blocks address the vanishing gradient problem, enabling the training of deeper networks without performance degradation. A pre-trained ResNet model is fine-tuned using transfer learning to adapt it to the specific task of skin lesion classification.

Data Augmentation: To enhance the model generalization ability and prevent overfitting, data augmentation techniques are applied. These include random rotations, flips, and brightness adjustments, which artificially increase the diversity of the training dataset.

Training Process: The model is trained using a split of the dataset, with 80% allocated for training, 10% for validation and 10% for test. Transfer learning is employed by initializing the model with pre-trained weights from ResNet, followed by fine-tuning on the skin lesion dataset. The model is optimized using the AdamW optimizer. The model was trained for 100 epochs with a mini-batch size of 64 and an initial learning rate of 0.0001. Table 1 demonstrates the hyperparameters of the Resnet-18 classifer used in the experiments.

Table 1. Hyperparameters of the Resnet-18 Model.

Parameters	Values
Input Size	224*224*3
Batch Size	64
Loss Function	Cross Entropy
Activation	ReLU
Optimizer	AdamW
Learning Rate	0.0001
Train/Validation/Test Split	80% / 10% / 10%

The cross-entropy loss is used as loss function. The loss function quantifies the difference between predicted andactual values during training. Lower loss values indicate better model performance. The prediction and actual labels can be seen in Figure 1.

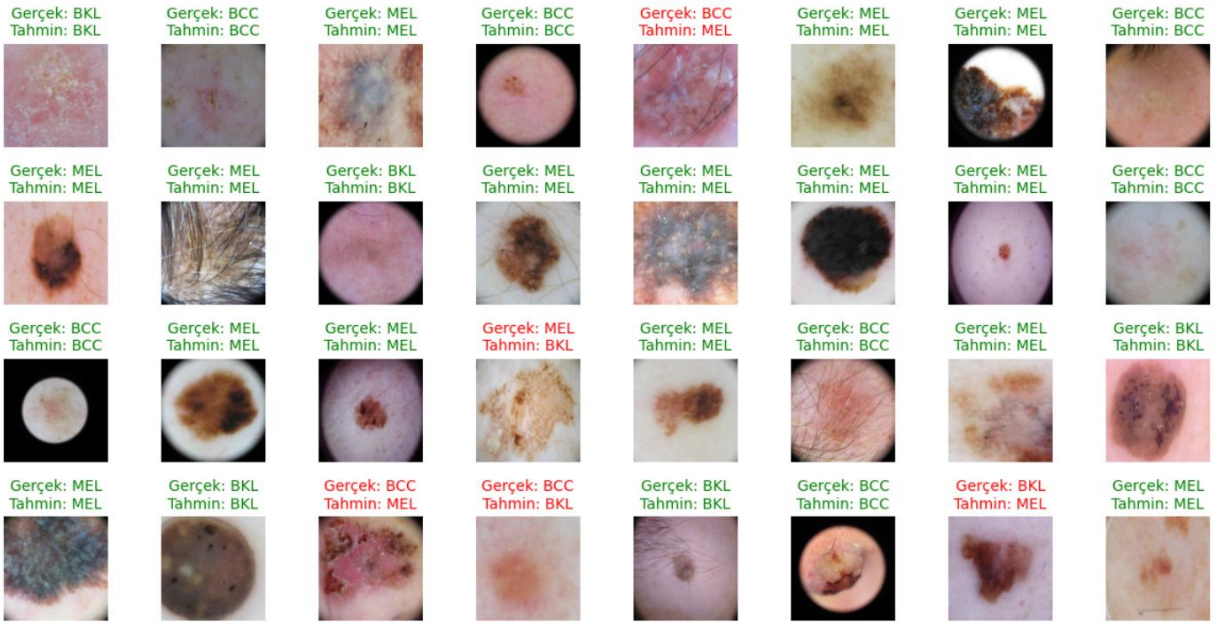

Figure 1. Label and Expected Label Comparison.

Evaluation Metrics: The performance of the model is evaluated using standard metrics such as accuracy, precision, recall, and F1-score. A confusion matrix is also generated to analyze the classification performance across different categories. (Nigar et al., 2022) The confusion matrix results can be seen in Figure 2.

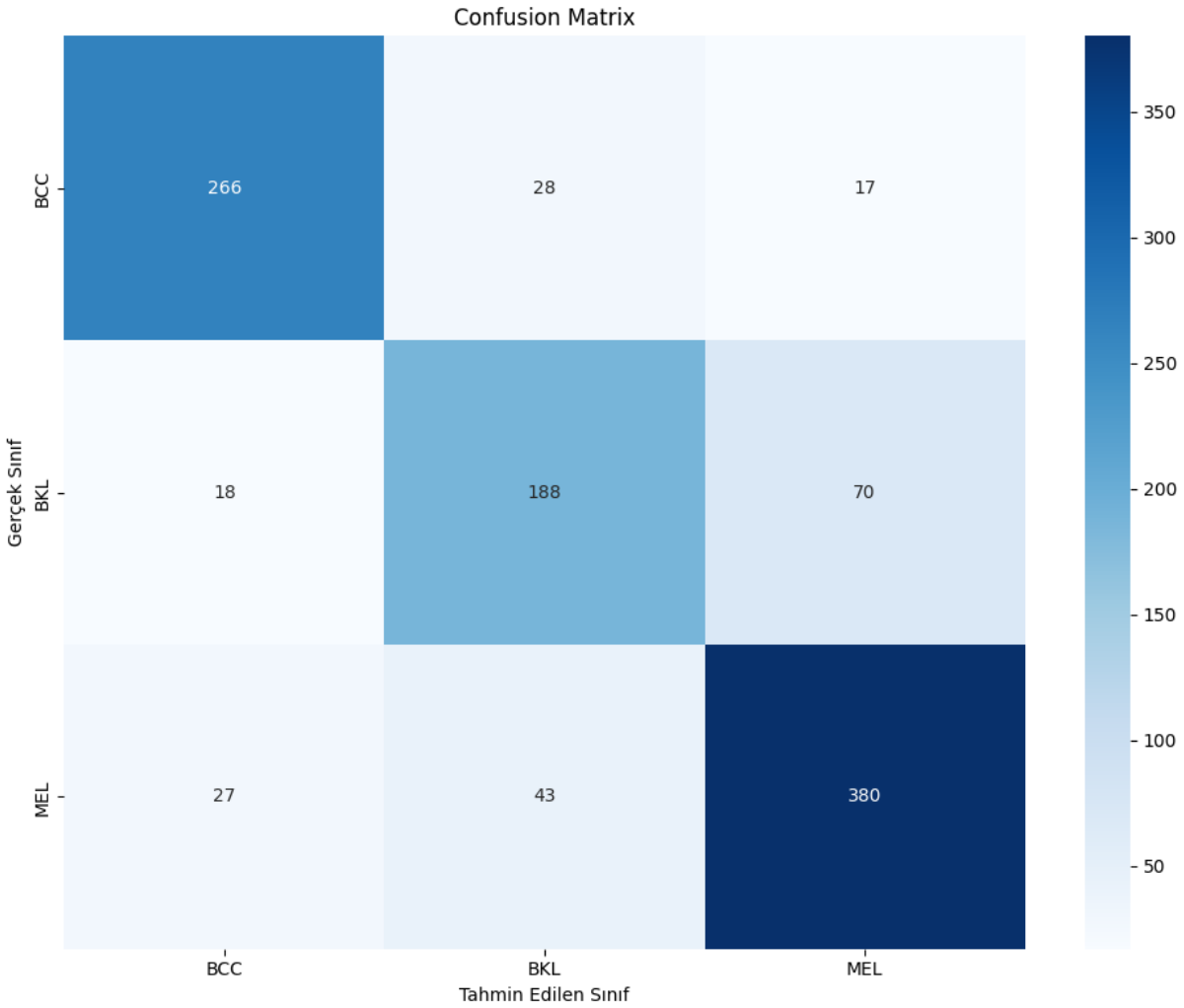

Figure 2. Confusion Matrix of Model.

Findings

The results from the model training and evaluation provide valuable insights into its performance.

Performance Metrics on Test Set

Accuracy: **80.42%**

Accuracy is a metric used to evaluate the overall performance of a classification model. It measures the proportion of correct predictions out of all predictions made (Equation 1)**.**
This is a relatively strong result, suggesting that the model performs well overall. However, in medical applications, accuracy alone may not be sufficient, as it does not account for class imbalances or the specific costs of false positives and false negatives.

$$Accuracy = \frac{TP + TN}{FP + TN + TP + FN} \quad (1)$$

Precision: **80.28%**

Precision is a metric used in classification models to measure how many of the predicted positive instances are actually correct**.** It helps evaluate how well the model avoids false positives (Equation 2).
This indicates that the model has a good ability to avoid false positives. In the context of skin lesion classification, this means that when the model predicts a lesion as malignant (e.g., melanoma), it is correct 80.28% of the time. This is important for reducing unnecessary biopsies or treatments.

$$Precision = \frac{TP}{TP + FP} \quad (2)$$

Recall: **80.42%**

Recall is a classification metric that measures how many of the actual positive instances the model correctly identified**.** It helps evaluate how well the model avoids false negatives (Equation 3).
This is a strong result, indicating that the model is effective at capturing most of the true positive cases. In medical diagnostics, high recall is critical because missing a positive case (e.g., failing to detect melanoma) can have severe consequences.

$$Recall = \frac{TP}{TP + FN} \quad (3)$$

F1 Score: **80.32%**

F1 Score is a metric that combines Precision and Recall into a single value. It is useful when you need a balance between avoiding false positives **(**Precision**)** and avoiding false negatives **(**Recall) (Equation 4).
This score reflects the model's ability to maintain a balance between avoiding false positives (precision) and avoiding false negatives (recall). In the context of skin lesion classification, this is particularly important because both false positives and false negatives carry significant costs.

$$1 = 2\,\frac{(Recall).(Precision)}{Precision + Recall} \quad (4)$$

Class-Based Performance Metrics:

BCC (Basal Cell Carcinoma):
Precision: **85.53%**
Recall: **85.53%**
F1 Score: **85.53%**
The model's performance for this class is excellent. High values were obtained in terms of both precision and sensitivity.

BKL (Benign Keratosis Lesions):
Precision: **72.59%**
Recall: **68.12%**
F1 Score: **70.28%**
The model struggles most with the BKL class, particularly due to its low recall value (68.12%). This suggests that BKL samples are often misclassified, especially as MEL.

MEL (Melanoma):
Precision: **81.37%**

Recall: **84.44%**
F1 Score: **82.88%**
The model also performed very well for this class. Especially the high sensitivity (recall) value shows that it can correctly detect the majority of melanoma cases.

Conclusion

Skin cancer remains one of the most significant health challenges worldwide, and the accurate classification of skin lesions is crucial for early and effective diagnosis. In this study, we developed a ResNet18-based model to classify skin lesions into multiple categories, including melanoma, basal cell carcinoma, and benign keratosis. According to these results, we achieved an accuracy of 80.42%, a precision of 80.28%, a recall of 80.42% and an F1 score of 80.32% with our skin lesions classification model on the test set. The developed multi-class classification system using the ResNet architecture demonstrates promising results in classifying skin lesions. The model is generally successful in the task of classifying skin lesions. An F1 score above 80% indicates that the model has potential for clinical use.
When we evaluate the class-based metrics, the performance of the model is high for the BCC and MEL classes. Especially the detection of a serious condition such as melanoma (MEL) with high recall shows that the model is clinically valuable. The fact that the performance is low for the BKL class compared to other classes indicates that this class should be enriched with more examples or the model should learn the features specific to this class better. Techniques such as oversampling, class weighting, or advanced data augmentation can be applied to improve the model's performance on the BKL class. These results show that the model is promising for clinical use and that performance can be further increased by making improvements, especially for the BKL class.
To enhance model results, several improvements are necessary. Since the results obtained in another study conducted with the same data set were better, we will continue to work on improving the results of our model. (Kassem et al., 2020) These improvements include enhancing data quality through advanced augmentation techniques or additional data collection, implementing regularization techniques to reduce overfitting, addressing class imbalance through methods such as oversampling or class weighting. Furthermore, exploring more advanced architectures, and leveraging transfer learning from suitable datasets could significantly improve the model's performance.
In conclusion, while the current model shows promise, there is substantial area for improvement. We are actively working on refining the model by addressing the identified issues and optimizing its architecture and training process. These efforts aim to enhance the model's classification performance, ultimately contributing to more accurate and reliable skin cancer diagnosis. Future work could focus on implementing more sophisticated data augmentation techniques, exploring ensemble methods, or testing alternative architectures to further enhance performance. These efforts aim to improve the model's classification accuracy and reliability, ultimately contributing to more accurate and efficient skin cancer diagnosis.

References

Esteva, A., Kuprel, B., Novoa, R. A., Ko, J., Swetter, S. M., Blau, H. M., & Thrun, S. (2017). Dermatologist-level classification of skin cancer with deep neural networks. *Nature*, *542*(7639), 115–118. doi: 10.1038/nature21056
Kaggle. (2023). *Isic2019 dataset*. **Url-1** https://www.kaggle.com/datasets/interestingstats/isic2019-dataset, date retrived 24.03.2025
Kassem, M. A., Hosny, K. M., & Fouad, M. M. (2020). Skin Lesions Classification into Eight Classes for ISIC 2019 Using Deep Convolutional Neural Network and Transfer Learning. *IEEE Access*, *8*, 114822–114832. doi: 10.1109/ACCESS.2020.3003890
Nigar, N., Umar, M., Shahzad, M. K., Islam, S., & Abalo, D. (2022). A Deep Learning Approach Based on Explainable Artificial Intelligence for Skin Lesion Classification. *IEEE Access*, *10*, 113715–113725. doi: 10.1109/ACCESS.2022.3217217
Chester, R. (2002). Materials Selection and Engineering. In A.A. Baker, L.R.F. Rose, R. Jones (Eds.), Advances in the Bonded Composite Repair of Metallic Aircraft Structure (2nd ed., Vol. 1, pp.19-40). New York: Wiley. **Url-1** www.mohid.com, date retrieved 29.06.2006.

ELECTRONICS AND COMMUNICATION ENGINEERING

Analog/Mixed-Signal/Microwave Circuits

Bio-Medical, Bio-Inspired Circuits/Systems

Digital Circuits and Systems

Embedded Systems

VLSI Systems and Applications

Hardware Implementation of FALCON's ffSampling Algorithm

Yasin Yılmaz[a], Sıddıka Berna Örs Yalçın[b], Mustafa Mert Esen[c]

[a] Istanbul Technical University, Graduate School, Electronics Engineering Program, Türkiye
[b] Istanbul Technical University, Faculty of Electrical and Electronics, Department of Electrical and Communication Engineering, Türkiye
[c]Secure Information Research (SIR) Team Procenne, Türkiye
yasinxyilmaz@gmail.com

Keywords: Circuit Design, FALCON, FPGA, Post-Quantum.

Aim

The emergence of quantum computing poses a significant threat to classical cryptographic schemes, necessitating the development and implementation of post-quantum cryptographic algorithms. One such algorithm, FALCON (Fast-Fourier Lattice-based Compact Signatures over NTRU), has been selected by the National Institute of Standards and Technology (NIST) for post-quantum cryptography standardization (NIST, 2023). FALCON is a lattice-based digital signature scheme that adheres to the Gentry-Peikert-Vaikuntanathan (GPV) framework, which constructs signatures by sampling short vectors from a lattice using a trapdoor mechanism (Gentry et al., 2008).

At its core, FALCON employs the novel Fast Fourier Sampling algorithm, a variant of the nearest-plane algorithm, a technique introduced by Babai (1986) for solving the closest vector problem (CVP) in lattices. This modified approach ensures that signatures are compact while maintaining security against quantum attacks. To achieve efficient computations, FALCON leverages the Fast Fourier (FFT) for polynomial arithmetic, significantly improving performance over traditional lattice-based schemes. Also, a novel algorithm Fast Fouirer Sampling (Ducas et al., 2018).

This study aims to identify key aspects of FALCON that can be further investigated for efficient implementation through detailed analysis and inspection. Furthermore, it seeks to design and propose a circuit that enhances the performance of FALCON's primary signature generation function, ffSampling, which is the realization of the Fast Fourier Sampling algorithm.

Material and Method

The initial phase of the study involves a comprehensive analysis of the FALCON algorithm, utilizing reference documentation and existing C implementations (NIST, n.d.). A C profiler is employed to quantify the proportion of total execution time attributed to each sub-function within FALCON. This analysis provided insights into the computational workflow, identified performance bottlenecks, and pinpointed critical operations requiring acceleration. Preliminary findings indicate that floating-point operations account for the majority of execution time.

It was aimed to use an open-source RISC-V processor alongside designed circuits on an FPGA platform for the implementation. Accordingly, the reference C code was modified to be compatible with the RISC-V compiler. By utilizing a RISC-V simulator, the required clock cycles for each sub-function's execution within the RISC-V instruction set were measured and analyzed (Spike RISC-V Compiler, n.d.). These measurements will be used as a comparison basis to determine performance improvements of the study.

Both analyses showed that the function ffSampling takes most of the time and clock cycles. The ffSampling function is a Gaussian sampling algorithm that leverages Fast Fourier Sampling to efficiently sample short lattice vectors, which will form the signature. Specifically, ffSampling uses Gram-Schmidt orthogonalization in the Fourier domain to produce samples maintaining Gaussian distribution properties. This function is the core of FALCON and constitutes FALCON's compact signatures and resistance to quantum attacks.

According to the analysis results, ffSampling function was chosen for hardware implementation. Design process started with analyzing the function in depth. The function is constructed in a recursive way, results from the previous call are used in the next recursive call to calculate new results. Consequently, its sub-functions are executed in a structured sequence,

processing relevant data in each recursion step to construct short lattice vectors in the end. Its sub-functions and their calling pattern are inspected using the reference C code. A Python model replicating the ffSampling function is formed and used for further analysis. Sub-functions' calling sequence was unraveled using the model. The model is later used for testing the circuit design methodologies.

The ffSampling sub-functions primarily involve complex number operations, such as complex addition and multiplication, with both real and imaginary components represented as floating-point values. Additionally, the function incorporates floating-point vector operations, like element-wise floating-point addition and multiplication.

With sub-functions and their sequence analyzed, a circuit that will realize the ffSampling function was designed. Firstly, sub-functions are designed using Xilinx's floating-point IPs. These IPs can be used for a variety of operations, and can be configured to construct pipelined structures. To ensure flow of data and therefore high throughput, submodules that realize the subfunctions are designed using the pipelined IPs. These sub-modules are tested separately with test vectors generated using the reference C code.

Following the analysis of sub-functions and their execution order, a hardware circuit to implement the ffSampling function was designed. Initially, sub-functions were implemented using Xilinx's floating-point intellectual property (IP) cores. These IP cores support various mathematical operations and can be configured to establish pipelined architectures. To maintain a steady data flow and ensure high throughput, the submodules implementing the sub-functions were constructed using pipelined IP cores. Each submodule was individually tested using test vectors derived from the reference C code. Subsequently, a control circuitry was developed to manage the data flow to sub-modules from memories in the correct sequence. This control circuitry generates appropriate control signals, mirroring the recursive behavior of ffSampling. Additionally, the control mechanism ensures that results from the sub-modules are correctly stored at designated memory addresses.

With the submodules and control mechanisms finalized, a complete circuit integrating these components and memory components was assembled, effectively realizing the ffSampling function in hardware.

Findings

Through this study, an in-depth understanding of FALCON, particularly its signature generation process and the ffSampling function, has been achieved. Additionally, the significant role of floating-point operations in FALCON's computational performance has been identified.

The proposed hardware circuit was evaluated in terms of execution speed and resource consumption. Given that speed optimization was prioritized over resource efficiency, the design partly serves as a proof-of-concept; however, it remains a viable approach for FPGA-based implementations. The minimum execution time of the circuit was measured using a simulator and subsequently compared to the reference C implementation running on a RISC-V core. A speed-up factor relative to the baseline implementation was computed.

The designed circuit operates at a maximum clock frequency of 200 MHz, executing a single ffSampling function within 316,159 cycles, which corresponds to an execution time of 1.58 ms per computation. In comparison, the ffSampling function, when executed using the reference C implementation on a RISC-V core, requires 8,465,252 cycles when simulated using spike, resulting in an execution time of 84.6 ms at a clock frequency of 100 MHz. When implemented on a RISC-V processor on an FPGA, ffSampling function took 418.1 ms to complete, now accounting events like hazards and branch mispredictions that occur in real implementations.

Based on these results, the proposed hardware implementation achieves an approximate 265× speed-up compared to the reference C code, compared to the used RISC-V core. This performance enhancement is highly promising, as the circuit would significantly accelerate the overall signature generation process when integrated with a RISC-V core in a complete system.

These findings are derived from the first version of the circuit. A detailed analysis of the simulation has identified potential optimizations, such as parallelizing sub-functions where applicable and improving hardware efficiency by designing custom floating-point circuits. Future research will focus on refining both speed and area utilization to further optimize the circuit's performance.

Conclusion

The analysis of FALCON has underscored the extensive utilization of floating-point operations and their impact on computational performance. The study has reaffirmed that the ffSampling function constitutes the core of FALCON's signature generation process and entails a significant number of floating-point calculations. The proposed hardware implementation of ffSampling, which incorporates floating-point IP cores and a memory-based data and control structure, has resulted in a performance improvement in signature generation.

Furthermore, this study highlights the advantages of integrating custom accelerator cores to enhance the efficiency of FALCON. Similar circuit design for many other parts of the algorithm can be designed in the same fashion, accelerating other critical operations. Although the current design prioritizes computational speed over resource efficiency, future research could explore additional optimizations to achieve a more balanced trade-off between speed and hardware resource utilization.

References

Babai, L. (1986). On Lovász' lattice reduction and the nearest lattice point problem. Combinatorica, 6(1), 1–13. https://doi.org/10.1007/BF02579403

Ducas, L., Kiltz, E., Lepoint, T., Lyubashevsky, V., & Stehlé, D. (2018). FALCON: Fast-Fourier Lattice-based Compact Signatures over NTRU. Cryptology ePrint Archive. https://eprint.iacr.org/2018/123

Gentry, C., Peikert, C., & Vaikuntanathan, V. (2008). Trapdoors for hard lattices and new cryptographic constructions. Proceedings of the 40th Annual ACM Symposium on Theory of Computing (STOC), 197-206. https://doi.org/10.1145/1374376.1374407

National Institute of Standards and Technology (NIST). (2023). Post-quantum cryptography standardization process. U.S. Department of Commerce. https://csrc.nist.gov/projects/post-quantum-cryptography

NIST. (n.d.). NIST PQC Round 3 submission for FALCON. Retrieved from https://csrc.nist.gov

Spike RISC-V Compiler. (n.d.). Spike: RISC-V ISA simulator. Retrieved from https://github.com/riscv/riscv-isa-sim on 23.05.2025

ELECTRONICS AND COMMUNICATION ENGINEERING

Analog/Mixed-Signal/Microwave Circuits

Bio-Medical, Bio-Inspired Circuits/Systems

Digital Circuits and Systems

Embedded Systems

VLSI Systems and Applications

Design of a Clutchless Automated Gear Control System for Electric Tractors

Bertuğ Bingöl[a,b], Ece Olcay Güneş[a], Murat Gündoğdu[b]

[a] Istanbul Technical University, Electronics and Communication Eng.,Electronics Program, Türkiye
[b] Turk Traktor and Agricultural Machinery Inc., R&D Department, Türkiye
bingolb21@itu.edu.tr

Keywords: Battery-powered Agricultural Vehicle, Automated Transmission, Drivetrain Control Architecture.

Aim

Replacing fossil fuels with cleaner and more sustainable electric alternatives is crucial for reducing agricultural emissions. Therefore, electrification has become inevitable. In addition to reducing emissions, electrification offers advantages such as improved energy efficiency and easier system control. In particular, electric motors provide constant torque over a wide speed range, enabling more flexible and efficient operation. Moreover, electrification not only enhances motor performance but also improves the reliability and effectiveness of other subsystems within the vehicle architecture.

Conventional tractors powered by internal combustion engines (ICEs) are commonly used in agricultural applications, requiring specific torque and speed values for tasks such as planting and harvesting crops like tomatoes and potatoes. When analyzing the torque-speed characteristics of ICEs, their maximum efficiency is approximately 40% (A. Rajagopalan, 2003). To operate within efficient regions while meeting these torque and speed demands, tractors are often equipped with transmissions featuring up to 32 gears (Elia Scolaro, 2021). However, if appropriate gear ratios are not selected, unnecessary power consumption and fuel waste become unavoidable. In contrast, electric motors of equivalent power can achieve efficiencies of up to 95% based on their torque-speed characteristics.

The primary objective of this study is to achieve the torque-speed characteristics of a 32-speed ICE tractor using only a 2-speed electric tractor. Additionally, by eliminating complex components such as traditional clutch packs, the simplicity and efficiency offered by electrification will be integrated into the gear system as well.

Material and Method

The electric tractor features an architecture that incorporates multiple electronic control units (ECUs). These units are managed by the Vehicle Management Unit (VMU) through the CANBus communication protocol. The tractor used in this study is equipped with a VMU containing a 32-bit NXP SPC5746C microcontroller.

In an electric vehicle, the traction motor's motion is transmitted to the wheels via drivetrain components, including gearboxes with various ratios. From the field, the wheel torque-speed graph of an equivalent ICE tractor was analyzed (Müjdat Ersarı, 2024). To match its torque-speed characteristics using an electric motor with two gears, optimal ratios were determined. This resulted in two gear requirements: a field gear for 0–16 km/h and a road gear for 16–40 km/h. Unlike conventional transmissions, this tractor does not include a clutch or synchronizer. The coupling mechanism that transfers the electric motor's motion to the wheels utilizes a dog clutch mechanism. Consequently, gear engagement in a moving vehicle is achieved by locking two rotating gears together.

The key components of the system include the Vehicle Management Unit (VMU), valve box, position sensor, gear lever, and traction motor.

The valve box is a hydraulic unit with two proportional valves that control high-pressure input. These valves generate the necessary pressure for gear shifting based on the user's selection, moving the shift fork accordingly. In the literature, this is typically done with electrically controlled servo motors in trucks and race cars. The limited research on hydraulic actuator-based shift fork control adds value to this study.

The position sensor reads the analog position of the shift fork responsible for gear shifting. This analog data is transmitted to the VMU, which continuously monitors the position in real time to ensure proper system operation.

The gear lever has buttons for user-selected gear positions, generating digital outputs for field or road mode. These activations are read by the VMU's GPIO units.

A permanent magnet synchronous motor (PMSM) is used as the electric traction motor. Thanks to the field and road gears, the motor power is transmitted to the wheels. Specific requirements must be met for the dog clutch to engage while the vehicle is in motion. The most critical requirement is the synchronization of the motor speed with the transmission speed, as there is no clutch pack or synchronizer. Rapid execution of this synchronization process is essential to minimize torque interruption during gear shifting. The electric motor's ability to be
controlled quickly and precisely makes it more advantageous than ICEs for such applications.
The VMU manages the entire gear-shifting process. The software was developed using the integrated development environment (IDE) provided by the VMU supplier, utilizing the C programming language. In the software, each hardware component is controlled using task loops operating in multiples of a 20ms period.
Fundamentally, the gear-shifting process begins with a user request. The VMU detects the requested gear and then zeroes the electric motor's torque to disengage the currently engaged gears. Once the torque is neutralized, the gear position is set to neutral. Subsequently, the motor control mode switches from torque mode to speed mode. The electric motor speed is then matched with the transmission speed associated with the target gear. If the speed difference between the transmission and the electric motor falls below a specific threshold, the VMU controls the valve box using a PWM signal to initiate the shift fork movement. Once the shift fork movement is complete and the gears are engaged, the motor control mode switches back to torque mode. Finally, the user's torque demand via the gas pedal is transmitted to the wheels.
In this study, two algorithms were tested. In one, speed synchronization was implemented, whereas in the other, speed synchronization was omitted, and gear shifting was performed solely by zeroing the torque.

Findings

Electric tractor testing was conducted using two different test scenarios. The first scenario did not involve active speed synchronization, whereas the second scenario incorporated it. In the first scenario, the tractor was tested on dedicated test rigs in the absence of counter torque. In contrast, the second scenario was conducted under field conditions, where the tractor's wheels were in contact with the ground and counter torque was present.
During testing, all system parameters were recorded and analyzed using Vector CANalyzer. In the first scenario, gear shifts were successfully performed while the vehicle was stationary. However, when shifting gears while the vehicle was in motion, audible squealing noises were detected. This outcome highlighted the importance of speed synchronization.
In the second scenario, the algorithm incorporating active speed synchronization was tested. When the vehicle was stationary, gear shifts were completed successfully. While the vehicle was in motion, the advantages of active speed synchronization became evident. When the target gear's transmission speed was synchronized with the motor speed before shifting, the gear change was completed without generating any disturbing noise.
This observation underscores the effectiveness of the synchronization algorithm in eliminating mechanical stress and enhancing overall gear shift durability.

Conclusion

Although studies in the literature on the feasibility of clutchless and synchronizer-free gear shifting are limited, this study contributes to the literature by evaluating the suitability of a dog clutch gear system in an electric tractor through real-world tests using various control-based approaches.
Dog clutch systems, due to their direct engagement of gears at high relative speeds, can lead to mechanical stress and material wear over time (Mohamed El Morsy, December 2014). However, the design of the gear geometry and the infrequent occurrence of road-to-field gear shifts in agricultural operations provide a practical advantage by minimizing wear and tear within the transmission system.
This study advances transmission systems for agricultural applications by emphasizing the effectiveness and straightforward integration of electric motors in tractor gear shift mechanisms. The proposed architecture enhances user convenience while also providing substantial benefits to the industry, especially in terms of maintenance and aftersales support.

References

El Morsy, M., Achtenova, G., & Pakosta, J. (2014). 13th International CTI Symposium. Smoothness of Maybach dog clutch shift in the automotive gearbox. Berlin, Germany.

Gündoğdu, M., & Ersarı, M. (2024). Engineering Perspective. Tractor transmission gear ratio optimization (1st ed., Vol. 4, pp.95–99).

Rajagopalan, A., Washington, G., Rizzoni, G., & Guezennec, Y. (2003). National Renewable Energy Laboratory. Development of fuzzy logic and neural network control and advanced emissions modeling for parallel hybrid vehicles.

Scolaro, E., Beligoj, M., Perez Estevez, M., Alberti, L., Renzi, M., & Mattetti, M. (2021). IEEE Access Electrification of agricultural machinery: A review (Vol. 9, pp.164520–164541).

ELECTRONICS AND COMMUNICATION ENGINEERING

Analog/Mixed-Signal/Microwave Circuits

Bio-Medical, Bio-Inspired Circuits/Systems

Digital Circuits and Systems

Embedded Systems

VLSI Systems and Applications

Logic Locking-Based FPGA System Design for Third-Party IP Protection

Teyyar Açar[a,b], Fatih Tiryakioğlu[b], Sıddıka Berna Örs Yalçın[c]

[a] Istanbul Technical University, Graduate School, Electronics Engineering Program
[b] TÜBİTAK, BİLGEM, TDD, Türkiye
[c] Istanbul Technical University, Faculty of Electrical and Electronics, Department of Electronics and Communication Engineering, Türkiye
teyyaracar@itu.edu.tr, fatih.tiryakioglu@tubitak.gov.tr, orssi@itu.edu.tr

Keywords: 3rd Party IP, Encrypted Bitstream, FPGA, Logic Locking, Security.

Aim

Nowadays, hardware designs are implemented on Field Programmable Gate Arrays (FPGAs) due to the convenience they offer to users, their diverse capacities, and low costs. With the increasing prevalence of solutions implemented with FPGAs, designers often want to use certain predefined operations as ready-to-use intellectual property (IP) cores to reduce labor and time costs when creating their designs. Some of these ready-to-use IPs are provided by the FPGA development tool, while others may need to be sourced externally. Since a third party is involved with these ready-to-use IPs, they are referred to as third-party intellectual property (3rd party IP). Currently, some 3rd party IPs are provided in an encrypted form through licensing within FPGA development tools. However, when users include the IP in their design, the encryption is decrypted before being loaded onto the FPGA, revealing the structure of the user's design. It has been demonstrated by Zhang et al. (2019) that the netlist, and subsequently the original design, can be extracted from the bitstream file format through reverse engineering.
The aim of this study is to design a security feature for FPGA systems that will protect 3rd party IPs used in FPGAs, based on the logic locking technique used to protect the IP rights of Application Specific Integrated Circuits (ASICs). When the designed solution is applied to the produced FPGAs, 3rd party IPs will be able to be used securely in post-development stages.

Material and Method

Logic Locking Technique:

Logic locking has been described as a holistic countermeasure that protects an integrated circuit (IC) throughout the globalized IC supply chain against hardware-centric threats such as design intellectual property piracy and unauthorized overproduction (Patnaik, Limaye, & Sinanoglu, 2022). Essentially, this technique involves adding an additional key input (K) and integrating XOR/XNOR gates into the existing circuit structure to obfuscate the design. The circuit functions correctly only when the correct key is applied to the K input. Various attacks have been carried out against logic locking, prompting the continuous development of more resilient techniques. Among these, the SAT (Satisfiability) attack is considered one of the most effective, leveraging the scan chain used for testing purposes in ASIC circuits. SAT attack is defined by Subramanyan at al. (2015).

Proposed FPGA Security Architecture Solution:

As a solution, a security module (Logic Unlocker - LUL module) intended to be part of the FPGA system architecture has been designed. The schematic structure of the LUL module is shown in Figure 1. The proposed solution involves the use of the logic locking technique, where the 3rd party IP netlist is locked by the developer and unlocked by the FPGA vendor through cryptographic architectural steps. In this study, the term 'IP' will refer to 3rd party IP.

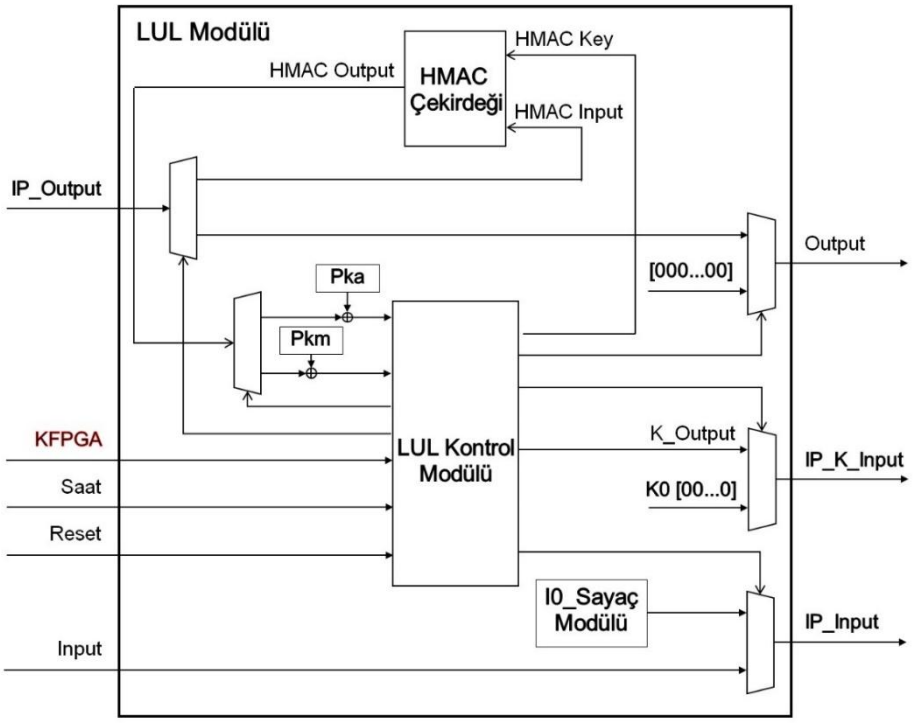

Figure 1. Schematic Design of the LUL Module.

Developer Procedures:

The IP developer obtains IP-L by using a K key of appropriate size corresponding to the number of gates in the IP, applying the logic locking technique. The schematic representation of the IP and IP-L is shown in Figure 2. The developer then sends IP-L and K to the FPGA vendor.

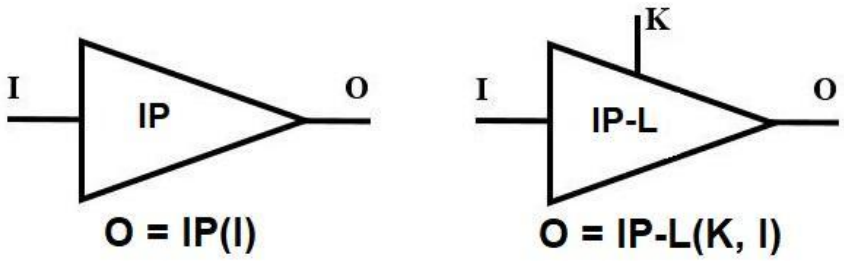

Figure 2. Functional Representation of IP and IP-L Structures.

FPGA Vendor Procedures:

The FPGA vendor performs the cryptographic operations defined below to obtain the key masking parameter (Pkm) and the authentication parameter (Pka). Then, the vendor signs the IP-L file using a Digital Signature Algorithm (DSA) with their private key to generate the signature value Sign(IP-L). The obtained parameters (Pkm and Pka), and the signature value Sign(IP-L) are then sent to the IP developer.

1. The vendor applies the key K_0 and input data I_0 to the IP-L netlist circuit for n clock cycles to obtain the output data sequence O_0^n from IP-L using the following formula (1).

$$O_0^n = IP_L(K_0, I_0) \quad \text{(for n clock cycles)} \qquad (1)$$

Here, K_0 represents the constant key value defined by the FPGA vendor for the K input, and I_0 is the input sequence provided through the I input, starting from 0x00...0 and incrementing by one on each clock cycle up to n (where $n \gg 0$).

2. The vendor calculates the HMAC value of the output data O_0^n from IP-L using the following formula (2)

$$HMAC(IP_L) = HMAC(K_FPGA, O_0^n) \quad (2)$$

Here, K_FPGA represents the secret key defined by the FPGA vendor for logic locking, which is embedded within each FPGA.

3. The vendor computes the key masking parameter Pkm in (3)

$$Pkm = HMAC(IP_L) \text{ xor } K \quad (3)$$

4. Using the key K and the input data I_0 defined in Step 1, the vendor obtains the output data sequence O_1^n from IP-L using the following formula (4).

$$O_1^n = IP_L(K, I_0) \quad \text{(for n clock cycles)} \quad (4)$$

5. The vendor computes the HMAC value of the output data O_1^n from IP-L using the key K_FPGA in (5)

$$HMAC(IP) = HMAC(K_FPGA, O_1^n) \quad (5)$$

6. The calculated value is also used as the authentication parameter Pka in (6)

$$Pka = HMAC(IP) \quad (6)$$

Usage of IP:

When the IP developer presents the IP to the customer, it is sent in the form of IP-L along with the parameters Pkm, Pka, and Sign(IP-L). When the IP customer creates their own IP (C-IP), they use IP-L and the parameters within the Integrated Development Environment (IDE), as shown in Figure 3. During the synthesis of C-IP, the FPGA vendor's IDE first performs a signature verification of the IP-L file. Once the signature verification is successful, the synthesis is carried out, and an FPGA bitstream file is generated.

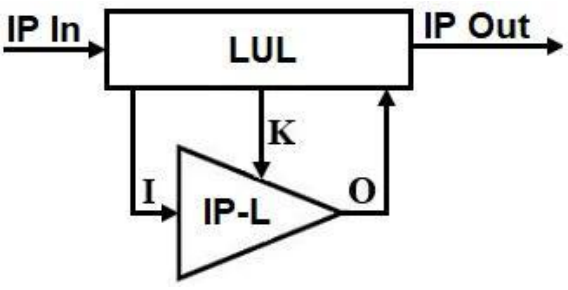

Figure 3. Integration of the LUL Module with IP-L.

When the FPGA is powered on, the LUL module uses the Pkm and Pka parameters to generate the correct K key, ensuring that the IP-L operates in its original form. If the correct K key cannot be derived, the Pka value also cannot be correctly obtained. In this case, the LUL module outputs a sequence of zeros from the IP-L.

Findings

The LUL module has been implemented using VHDL, with ITC99 benchmark circuits in Url-1 used as the IP. The benchmark circuit has been logic locked using the Neos tool in Url-2. Using Xilinx Vivado as the IDE, the locked benchmark and the prepared LUL module were tested through simulation to verify their correct operation, ensuring that the correct K value was obtained and the IP-L functioned properly.

Security Analysis:

The following threat situations and scenarios have been identified for obtaining the IP, and an evaluation of whether the attacks can be carried out using the proposed method is provided below.

Obtaining K_FPGA:
K_FPGA is written to secure memory during the production stage within the FPGA. If the algorithm using K_FPGA is implemented in a way resistant to side channel attacks, it will not be possible to obtain K_FPGA.

Obtaining the K key:

1. Scenario
Obtaining K by generating the K key using a fake IP-L. When the proposed cryptographic architecture is applied, the Pkm and Pka verification will not be successful, so this attack cannot be performed. Additionally, the signature verification process will prevent synthesis.
2. Scenario
Obtaining K by generating the K key using a counterfeit IP-L. By choosing an n value large enough to ensure that IP-L does not fit into the FPGA, this attack becomes impossible. Furthermore, the signature verification process will prevent synthesis.
3. Scenario
Obtaining K by generating the K key using a wrapper IP-L-Plus containing IP-L. Since the signature verification will fail, synthesis cannot be performed, making this attack infeasible.
4. Scenario
Obtaining K by using a SAT attack. A scan chain is required for the SAT attack. Since scan chains are not used in the FPGA environment, this attack cannot be carried out.

Conclusion

With the proposed FPGA architecture, 3rd party IP designs are protected in the stages following the developer. In this approach, FPGA vendors are assumed to be trusted entities. The proposed method does not impose any limitation on the number of times the 3rd party IP can be used. In future work, a solution that also enforces usage restrictions can be explored.

References

Patnaik, S., Limaye, N., & Sinanoglu, O. (2022). Hide and seek: Seeking the (un)-hidden key in provably-secure logic locking techniques. IEEE Transactions on Information Forensics and Security, 17, 3290–3305.
Subramanyan, P., Ray, S., & Malik, S. (2015). Evaluating the security of logic encryption algorithms. In 2015 IEEE International Symposium on Hardware Oriented Security and Trust (HOST) (pp. 137–143). IEEE.
Zhang, T., Wang, J., Guo, S., & Chen, Z. (2019). A comprehensive FPGA reverse engineering tool-chain: From bitstream to RTL code. IEEE Access, 7, 38379-38389.
Url-1 https://github.com/cad-polito-it/I99T, date retrieved 22.05.2025.
Url-2 https://github.com/jinyier/NEOS, date retrieved 22.05.2025.

ENERGY SCIENCE AND TECHNOLOGY

Computational Fluid Dynamics

Computational Heat and Mass Transfer

Energy Conversion and Storage Technologies

Energy Conversion and Sustainability

Energy Management and Planning

Renewable Energy

Sustainable Energy

Numerical Investigation of the Effects of Interfacial Contact Resistance in PEM Fuel Cells with Coated Metal Bipolar Plates

Özgün Önen[a,b], Mehmet Suha Yazıcı[a], Dilek Kumlutaş[b], Utku Alp Yücekaya[b]

[a] Istanbul Technical University, Energy Institute, Turkiye
[b] Dokuz Eylul University, Mechanical Engineering Department, Turkiye
oneno22@itu.edu.tr

Keywords: ICR, Interfacial Contact Resistance, Metal Bipolar Plate, Numerical Analysis, Pem Fuel Cell.

Aim

Fuel cells have emerged as promising next-generation electrochemical energy converters due to their high power density and low emissions, making them attractive for transportation and stationary energy applications (S. Wang et al., 2017) .In particular, replacing conventional internal combustion engines with fuel cells is expected to play a crucial role in transitioning to sustainable energy systems [(Qasem & Abdulrahman, 2024).

Fuel cells comprise various components, including the bipolar plate and membrane electrode assembly. Due to its crucial role in efficient thermal and electrical management, as well as ensuring proper gas distribution and mechanical stability, the bipolar plate is one of the most important components of the system (Xiong et al., 2021).

Graphite, traditionally used as a bipolar plate material, requires a significant volume to achieve adequate mechanical strength, which limits its application in compact fuel cell designs such as automotive systems. To address this challenge, metal bipolar plates offer superior mechanical properties, allowing more fuel cell units to be integrated within the same volume. However, metal bipolar plates suffer from poor corrosion resistance, requiring protective coatings to enhance their durability. These coatings not only provide benefits in terms of corrosion resistance but also have an impact on interfacial contact resistance (ICR) (Xiong et al., 2021).

ICR is an electrical resistance that occurs at the interface between two contacting surfaces in a fuel cell, such as between the bipolar plate and the gas diffusion layer (GDL). It arises due to surface roughness, material properties, and contact pressure (Lædre et al., 2022). Additionally, each coated metal bipolar plate has a different ICR value, which affects the overall performance and efficiency of the fuel cell (Leng et al., 2020).

It has been observed that the ICR of coatings is not typically included in simulations of metal bipolar plate PEM fuel cells. In this study, The numerical model was first validated using data from an experimental study, and then ICR values of three widely used coatings were obtained from the literature and incorporated into the study. The results were presented comparatively.

Material and Method

This study uses Ansys Fluent PEM [6] modules to analyse the effect of ICR on PEM fuel cell performance. Different coating materials are considered, and their influence on interfacial resistance is examined through numerical simulations. The model incorporates key electrochemical and transport phenomena within the fuel cell structure. The numerical model, which has also been used in experimental studies in the literature (L. Wang et al., 2003) , was utilized in this study to examine the effect of coatings on ICR. The numerical model is presented in Figure 1.

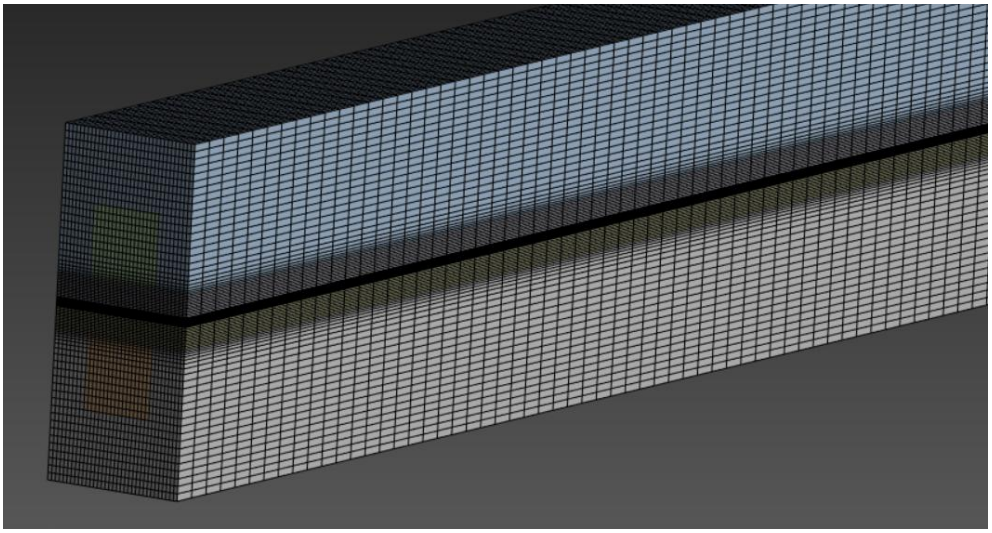

Figure 1: Mesh Structure of PEM Fuel Cell.

The numerical model presented in Figure 1 was meshed using Ansys Meshing (Fluent, A. N. S. Y. S. (2011). Ansys Fluent Theory (2011). The mesh parameters were configured in accordance with the low skewness and high orthogonality values recommended in the literature (Choopanya et al., 2016.). A skewness value of 0 and an orthogonality quality value of 1 were achieved, ensuring the accuracy of the numerical study (Choopanya et al., 2016).

Parameters for numerical study were obtained from the literature study used for validation (L. Wang et al., 2003.). Additionally, the diffusivity values of H_2, O_2, and H_2O reference diffusivity (m^2/s) and Equivalent weight of membrane (kg/kmol) were taken from a study that included the numerical analysis of the uncoated model (Chen et al., 2021). Parameters used in the analyses are presented in Table 1.

Table 1: Parameters used in the PEM fuel cell simulation (Chen et al., 2021; L. Wang et al., 2003).

Parameters	Value	Ref
Operating temperature (K)	343	(L. Wang et al., 2003)
Operating pressure (atm)	2,7	(L. Wang et al., 2003)
GDL porosity	0,4	(L. Wang et al., 2003)
CL porosity	0,4	(L. Wang et al., 2003)
Anode exchange coefficient	0,5	(L. Wang et al., 2003)
Cathode exchange coefficient	2	(L. Wang et al., 2003)
H_2 reference diffusivity (m^2/s)	1.10×10^{-4}	(Chen et al., 2021)
O_2 reference diffusivity (m^2/s)	3.23×10^{-5}	(Chen et al., 2021)
H_2O reference diffusivity (m^2/s)	7.35×10^{-5}	(Chen et al., 2021)
H_2O reference concentration(mol/m^3)	56,4	(L. Wang et al., 2003)
O_2 reference concentration (mol/m^3)	3,39	(L. Wang et al., 2003)

Equivalent weight of membrane (kg/kmol)	1100	(Chen et al., 2021)

The numerical analyses were conducted at 343 K and 2.7 atm pressure, in accordance with the experimental study used for validation. The current density-voltage curve reflects the general electrochemical behavior of the fuel cell and serves as a fundamental tool for validation, enabling a direct comparison between the numerical and experimental performance (Energy S, 2011) Through numerical analyses, current and voltage values were obtained, and the corresponding current density values at different voltage levels were compared with experimental data from the literature (L. Wang et al., 2003.) and presented.

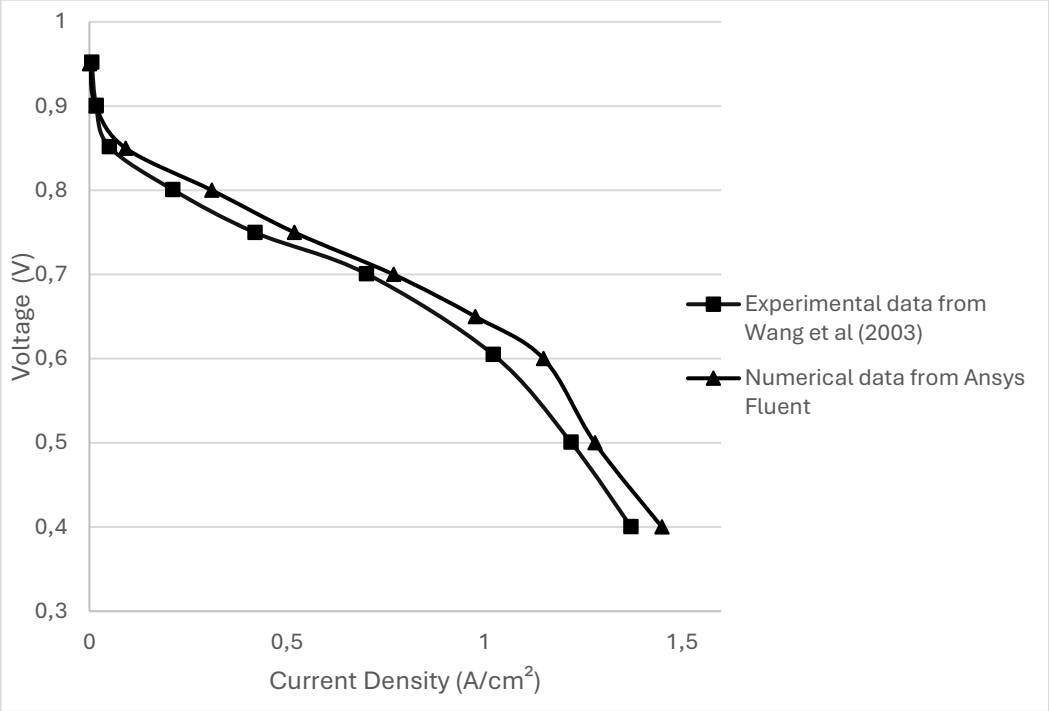

Figure 2: Validation using Data from Experimental Studies.

When examining Figure 2, the analyses were validated with a maximum error of 10% within the operating range of fuel cells, which is between 0.5 V and 0.65 V (Qasem & Abdulrahman, 2024) Using the validated numerical model, ICR definitions were assigned to Using the validated numerical model, ICR definitions were assigned to the interfaces between the bipolar plate and the GDL at surfaces A, B, C, and D, as shown in Figure 3, to investigate the effects of coatings.

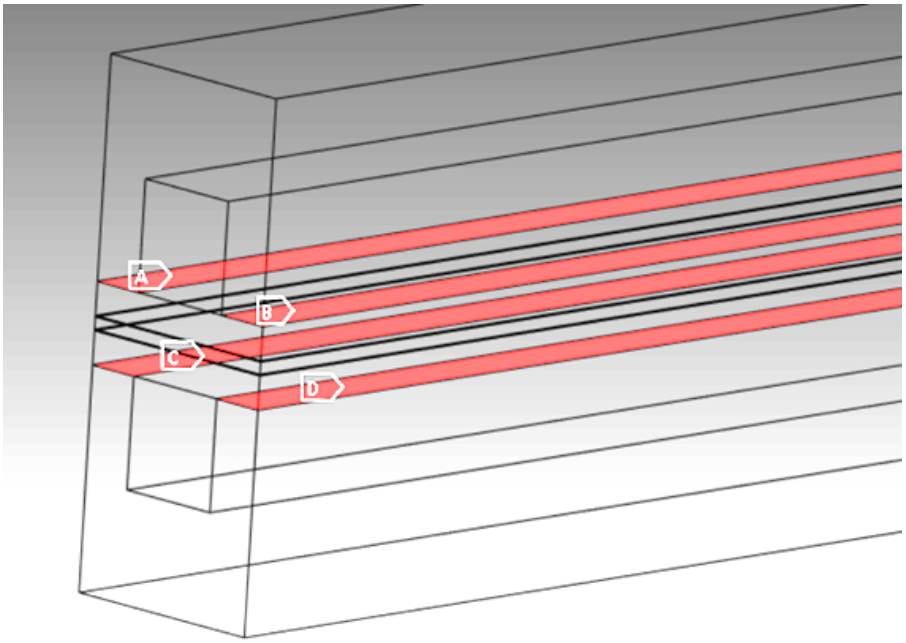

Figure 3: Interfacial Contact Resistance between GDL and Bipolar Plate.

(ICR) assigned to the surfaces shown in Figure 3 vary depending on the coating material. The coating materials used in the literature are CrN (Chromium Nitride), TiN (Titanium Nitride), and Ti/TiN (Titanium/Titanium Nitride), and the corresponding contact resistance values are presented in Table 2.

Table 2: ICR values of coatings used in metal bipolar plates (Haghighat Ghahfarokhi et al., 2016; Jannat et al., 2019; Lee et al., 2013).

Metal Material	Coating	ICR (mΩ·cm²)	References
SS316L	CrN	23	(Lee et al., 2013.)
SS316L	TiN	7,41	(Haghighat Ghahfarokhi et al., 2016)
SS316L	Ti\TiN	11	(Jannat et al., 2019.)

ICR of different coatings presented in Table 2 were defined on PEM module. The results of the numerical analyses are presented in the Findings section.

Findings

As shown in Figure 4, variations in ICR caused by different coating materials influence fuel cell performance. In this study, numerical analyses were conducted to examine how current density varies at a constant voltage level depending on the ICR of the coating material.

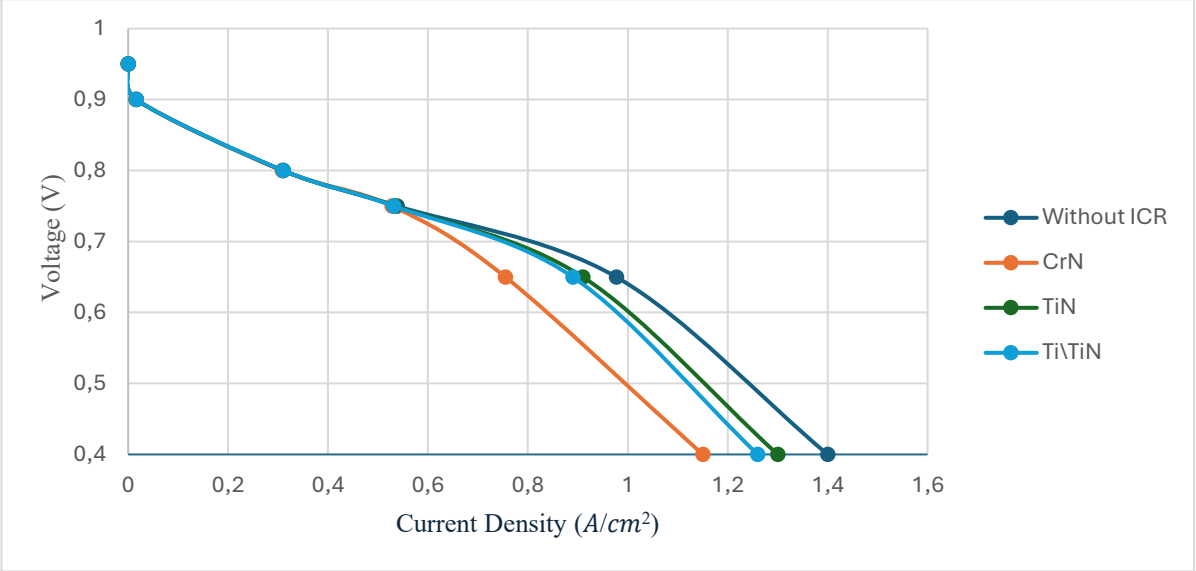

Figure 4: Effect of Electrical Contact Resistance on the Voltage-Current Density Curve.

Figure 4 shows that the ICR of the coatings significantly affects the fuel cell performance. The current density per unit voltage has considerably decreased compared to the case without contact resistance. Consequently, this has led to a significant reduction in the power density per unit area of the single-cell PEM fuel cell.

At an operating voltage of 0.65 V, the current density is 0.97 A/cm² without contact resistance. However, with the application of a CrN coating, it decreases to 0.82 A/cm², while Ti/TiN and TiN coatings result in reductions to 0.89 A/cm² and 0.91 A/cm², respectively.

In the absence of ICR the power density was determined to be 0.63 W/cm² at an operating voltage of 0.65 V. However, due to ICR of the CrN coating, the power density decreased to 0.49 W/cm², while for the Ti\TiN and TiN coatings, it was observed to decrease to 0.57 W/cm² and 0.59 W/cm², respectively. This indicates that the CrN coating has an effect of 24.62%, while the Ti\TiN and TiN coatings have effects of 12.31% and 9.23%, respectively. Additionally, it is noted that the impact of ICR becomes more evident at lower voltage levels (0.4 V - 0.6 V).

Conclusion

The conclusions of this study emphasize the significant impact of ICR on coated metal bipolar plates in fuel cells, affirming that the effect of coatings on ICR should not be neglected, as observed in previous simulation studies. As the voltage decreases, the impact of ICR becomes more pronounced, and its influence on the system becomes increasingly significant. For CrN coating at 0.65 V, there is a 15.46% decrease in current density and a 24% decrease in power density. For TiN and Ti/TiN coatings, current density decreases by 6.19% and 8.25%, while power density decreases by 9.23% and 12.31%, respectively. Furthermore, the results indicate that the influence of the TiN coating is lower compared to the other two coating types, suggesting that TiN is currently the most suitable coating for metal bipolar plate fuel cells.

References

Chen, X., Yu, Z., Yang, C., Chen, Y., Jin, C., Ding, Y., ... & Wan, Z. (2021). Performance investigation on a novel 3D wave flow channel design for PEMFC. *International Journal of Hydrogen Energy*, *46*(19), 11127-11139.
Choopanya, P., & Yang, Z. (2016). An effective mesh strategy for CFD modelling of polymer electrolyte membrane fuel cells. *International Journal of Hydrogen Energy*, *41*(15), 6445-6456.
Fluent, A. N. S. Y. S. (2011). Ansys fluent theory guide. *Ansys Inc., USA*, *15317*, 724-746.
Haji, S. (2011). Analytical modeling of PEM fuel cell i–V curve. *Renewable Energy*, *36*(2), 451-458.

Haghighat Ghahfarokhi, H., Saatchi, A., & Monirvaghefi, S. M. (2016). Corrosion investigation of chromium nitride and chromium carbide coatings for PEM fuel cell bipolar plates in simulated cathode condition. *Fuel Cells*, *16*(3), 356-364.
Jannat, S., Rashtchi, H., Atapour, M., Golozar, M. A., Elmkhah, H., & Zhiani, M. (2019). Preparation and performance of nanometric Ti/TiN multi-layer physical vapor deposited coating on 316L stainless steel as bipolar plate for proton exchange membrane fuel cells. *Journal of Power Sources*, *435*, 226818.
Lædre, S., Craciunescu, C. M., Khoza, T., Vaszilcsin, N., Kellenberger, A., Bolocan, V., ... & Ercuta, A. (2022). Issues regarding bipolar plate-gas diffusion layer interfacial contact resistance determination. *Journal of Power Sources*, *530*, 231275.
Lee, S. H., Kakati, N., Maiti, J., Jee, S. H., Kalita, D. J., & Yoon, Y. S. (2013). Corrosion and electrical properties of CrN-and TiN-coated 316L stainless steel used as bipolar plates for polymer electrolyte membrane fuel cells. *Thin Solid Films*, *529*, 374-379.
Leng, Y., Ming, P., Yang, D., & Zhang, C. (2020). Stainless steel bipolar plates for proton exchange membrane fuel cells: Materials, flow channel design and forming processes. *Journal of Power Sources*, *451*, 227783.
Qasem, N. A., & Abdulrahman, G. A. (2024). A recent comprehensive review of fuel cells: history, types, and applications. *International Journal of Energy Research*, *2024*(1), 7271748.
Wang, L., Husar, A., Zhou, T., & Liu, H. (2003). A parametric study of PEM fuel cell performances. *International journal of hydrogen energy*, *28*(11), 1263-1272.
Wang, S., & Jiang, S. P. (2017). Prospects of fuel cell technologies. *National Science Review*, *4*(2), 163-166.
Xiong, K., Wu, W., Wang, S., & Zhang, L. (2021). Modeling, design, materials and fabrication of bipolar plates for proton exchange membrane fuel cell: A review. *Applied energy*, *301*, 117443.

ENERGY SCIENCE AND TECHNOLOGY

Computational Fluid Dynamics

Computational Heat and Mass Transfer

Energy Conversion and Storage Technologies

Energy Conversion and Sustainability

Energy Management and Planning

Renewable Energy

Sustainable Energy

Numerical Investigation of Engine Cooling Using Nanofluids

Metehan Duman[a,b], Tuba Okutucu-Özyurt[c], Zafer Dursunkaya[d]

[a] Istanbul Technical University, Graduate School, Energy Science and Technology Program, Türkiye
[b] BMC Power Engine and Control Technologies, Türkiye
[c] Istanbul Technical University, Energy Institute, Renewable Energy Division, Türkiye
[d] Middle East Technical University, Department of Mechanical Engineering, Türkiye
dumanm15@itu.edu.tr

Keywords: Engine Cooling, Nanofluids, Internal Combustion Engines, Natural Gas Engine.

Aim

With increasing power densities of internal combustion engines due to the competitive environment of engine technologies and the latest developments in automotive industry, the thermal load on engine components continues to increase. Consequently, reducing temperatures while consuming less hydraulic power has become increasingly critical. Furthermore, improving specific fuel consumption is a crucial factor for advancing environmental sustainability. This study aims to investigate potential benefits of using nanofluids for internal combustion engine cooling, specifically focusing on reducing the critical peak temperatures of engine components by enhancing heat rejection to the engine coolant.

Literature Review

Numerous studies in the literature have explored the wide range of application areas of nanofluids such as heat pipes (Wang, et al., 2021), heat exchangers (Gupta, Verma, & Yadav, 2022), solar energy systems (Yıldırım & Yurddas, 2021), engine cooling (Jadeja, Bumataria, & Chavda, 2022) etc. Several researchers have noticed the potential of using nanofluids for cooling systems of internal combustion engines to improve thermal management efficiency. In recent computational heat transfer (CHT) studies on cylinder engine cooling using nanofluids, the heat addition from combustion has been implemented into the models as a constant heat flux imposed on the combustion chamber walls (Bøthun, 2023) (Alves & Henríquez, 2022). In the present study, a combustion analysis is performed using boundary conditions (BCs) derived from a test bench data. The results of the combustion analysis are then implemented to the model on the combustion chamber walls as heat transfer coefficients and near-wall temperatures to accurately model the heat source.

Material and Method

For potential improvement of cooling performance by using nanofluids, the present numerical study investigates the effects of inlet temperature, base fluid type, nanoparticle type and concentration on the thermal behavior of a single-cylinder natural gas engine. Previously obtained test data on the engine is gathered from a test bench archive in the Automotive Laboratory of Istanbul Technical University (ITU), Faculty of Mechanical Engineering. The research steps involve the examination of the consistency of the existing test data and its suitability for use in the analyses, construction of the computer-aided design (CAD) model of cylinder, and the conduction of combustion and conjugate heat transfer (CHT) analyses to simulate engine behavior. In the initial phase of the study, technical drawings of cylinder, spark plug and CAD data for the cylinder head were sourced from the automotive laboratory. The test data are then used to define the boundary conditions for the combustion and conjugate heat transfer analyses to ensure realistic and accurate results.

Once the computational model is constructed and validated, a series of preliminary CHT analyses are conducted in order to identify the most effective combination of nanoparticle, base fluid type and concentration and inlet temperature in obtaining lower operating temperature, and the corresponding penalty of added pressure loss. The analyses are first conducted on a pipe that is of representative length and diameter. The pipe diameter is the same as the engine's coolant inlet diameter, and analyses are performed under conditions that replicated the engine's heat flux. A total of 60 simulations were conducted to explore various combinations of AlO, CuO, carbon black (CB) nanoparticles suspended in water or ethylene glycol-based fluids. Nanoparticle concentrations of 1%, 2%, 3%, and 4%, along with coolant inlet temperatures of 25°C and 70°C, are

investigated with the aim of determining the optimal nanofluid combination that could provide the most effective heat transfer performance for the engine cooling system. Since preliminary simulations do not require significant computational resources, all environmental points were investigated to comprehensively explore the parameter space. For future studies, it is recommended to consider implementing various Design of Experiments (DoE) methodologies, such as factorial design and response surface methods, to optimize computational effort and enhance the robustness of the analysis.
Further, an in-cylinder combustion analysis was performed to evaluate the heat load within the engine during operation. This analysis provided crucial data on the heat transfer coefficients and near-wall temperatures of the combustion gases in each computational domain cell. These values were then implemented into the conjugate heat transfer simulations as convection coefficients, helping to accurately model the heat exchange between the engine components and the coolant.

Findings

The effects of nanofluid inlet temperature, type of the base fluid, type of nanoparticle and nanofluid concentration on the maximum interface temperature are shown in Figure 1.

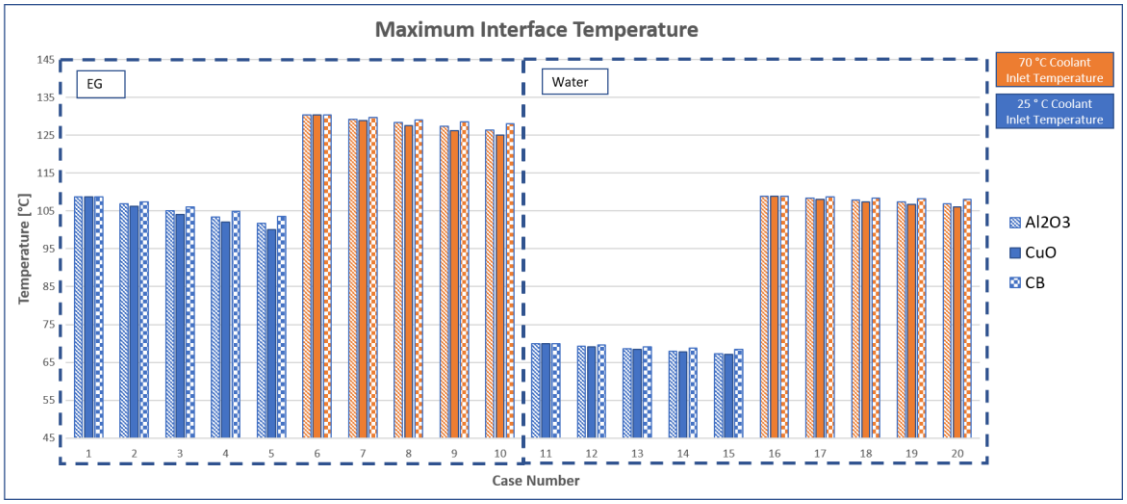

Figure 1. Maximum Interface Temperature Between Solid Pipe and Coolant.

As can be observed from Figure 1, lower inlet temperatures and nanofluids containing CuO provide lower temperatures compared to Al2O3 and CB under the same operational conditions. Due to the higher thermal conductivity of pure water compared to ethylene glycol, the temperatures are lower when pure water is used as the base fluid. As the nanoparticle concentration increases, the temperatures also decrease.

Conclusion

The research includes CHT analyses and combustion simulations to evaluate the heat load of the engine. Data from a natural gas-fueled single cylinder engine test bench were used to define realistic boundary conditions and ensure the accuracy. The results demonstrated improvements in the thermal performance of the engine when using nanofluids. The study showed that nanofluids could slightly enhance heat dissipation from critical engine components. The thermal conductivity of the coolant is enhanced by the use of nanoparticles, which positively influences heat transfer from the wall to the coolant. However, the pressure loss in the system increases due to the higher viscosity ratio compared to the condition without nanoparticles. Additionally, the use of nanofluids may contribute to a reduction in fuel consumption and thus contribute to environmental sustainability. This could potentially lower fuel consumption and contribute to environmental sustainability. In the present study, the nanofluid coolant is considered as single phase, homogeneous and the surface interactions of nanoparticles are neglected. For future research, it is recommended to explore the non-homogeneity of the nanofluid and the surface reactions of nanoparticles.

Acknowledgements

The authors express their sincere gratitude to Dr. Osman Akın Kutlar, the coordinator of the Automotive Laboratory at Istanbul Technical University, Faculty of Mechanical Engineering for providing the hand drawn technical drawings of single-cylinder test engine, cylinder head CAD data, and Dr. Hüseyin Emre Doğan for providing previously collected test data on the engine which are used as boundary conditions in the present study.

References

Alves, L., & Henríquez, J. (2022). Comparative performance analysis of internal combustion engine water jacket coolant using a mix of Al2O3 and CuO-based nanofluid and ethylene glycol. Energy, 250.

Bøthun, L. B. (2023). Numerical Simulation of Nanofluid Cooling in a Single-Cylinder Diesel Engine. Bergen: Western Norway University of Applied Sciences Department of Mechanical and Marine Engineering.

Gupta, S. K., Verma, H., & Yadav, N. (2022). A review on recent development of nanofluid utilization in shell & tube heat exchanger for saving of energy. Materials Today: Proceedings, 54.

Jadeja, K., Bumataria, R., & Chavda, N. (2022). Nanofluid as a coolant in internal combustion engine – a review. International Journal of Ambient Energy.

Wang, X., Luo, L., Xiang, J., Zheng, S., Shittu, S., Wang, Z., & Zhao, X. (2021). A comprehensive review on the application of nanofluid in heat pipe based on the machine learning: Theory, application and prediction. Renewable and Sustainable Energy Reviews, 150.

Yıldırım, E., & Yurddas, A. (2021). Assessments of thermal performance of hybrid and mono nanofluid U-tube solar collector system. Renewable Energy, 171.

A State-of-Charge Based Experimental and Numerical Investigation of Li-Ion Battery Heat Generation and Temperature Distribution

Barış Işıklar[a], Ceyda Kök[b], Nergiz Gürbüz Karslıoğlu[c], Hasan Celal Malkoç[c], Sevan Karabetoğlu[d], Senem Şentürk Lüle[e], Rahim Jafari[f], Tuba Okutucu Özyurt[d]

[a] Istanbul Technical University, Graduate School, Energy Science and Technology Program, Türkiye
[b] Iskenderun Technical University, Department of Electronic and Automation, Mechatronic Program, Türkiye
[c] TÜBİTAK Rail Transportation Technologies Institute (RUTE), Türkiye
[d] Istanbul Technical University, Energy Institute, Renewable Energy Division, Türkiye
[e] Istanbul Technical University, Energy Institute, Nuclear Energy Division, Türkiye
[f] Turkish Aeronautical Association University, Mechanical Engineering Department, Türkiye
isiklar22@itu.edu.tr

Keywords: Equivalent Circuit Model, HPPC Test, Li-Ion Battery, State-Of-Charge, Thermal Management.

Aim

The global shift towards electric vehicles is accelerating due to the long-term economic benefits of Electrical Vehicles (EVs), the global objective of reducing greenhouse gas emissions, and the alignment with environmental policies such as the European Green Deal. For this reason, it is vital that the batteries, which are both one of the most important and most expensive components of electric vehicles, operate safely and efficiently over the long term. Heat generation and temperature distribution in the battery has an important role in battery lifetime and safety. Therefore, battery cooling systems are used to maintain the battery on the optimal operating temperatures. Generally, battery cooling systems are designed considering constant heat generation in the battery during fixed discharge conditions. However, heat generation in batteries is also affected by the state of charge (SoC) of the batteries. This study focuses on obtaining an electrochemical model of the battery to determine heat generation at different SoC levels and to obtain temperature distribution in the battery, in order to develop precise and optimized battery cooling strategies.

Material and Method

In this study, a 168 Ah NMx Li-ion prismatic battery is selected due to its high energy density and stable operating voltage range, making it particularly suitable for electric vehicle applications. The battery geometry is modeled in SolidWorks, and its dimensions are illustrated in Figure 1.

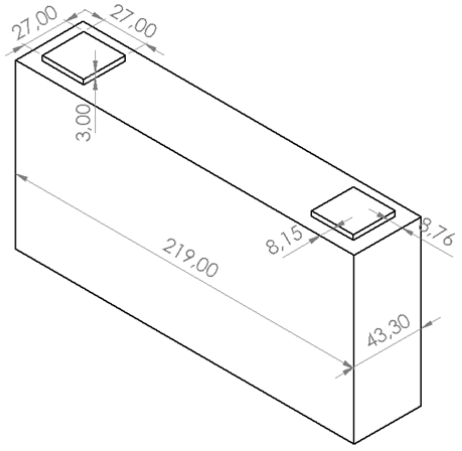

Figure 1. Battery Geometry.

Since the prismatic batteries contain layers of the cathodes, anodes, and separators, the thermochemical properties inside the battery changes with the direction. Therefore, the relevant studies are reviewed to determine specific heat and thermal conductivity of the Li-ion battery in order to obtain accurate heat generation and temperature distribution over the battery. As a result of the researches carried out by taking into account the thermochemical properties of the battery specific heat and orthotropic thermal conductivity of the battery is determined (Cheng et al., 2021; Sheng et al., 2019). The material properties which are used in our study are given in the Table 1.

Table 1. Thermochemical Properties of Materials in the Simulation.

	Density [kg/m^3]	Specific Heat [J/(kg.K)]	Thermal Conductivity In Horizontal Axis [W/(m.K)]	Thermal Conductivity In Vertical Axis [W/(m.K)]	Electrical Conductivity [S/m]
Active Zone Material	2236	1081	1.0341	21.5472	1000000
Aluminum	8978	381	387.6		58000000
Copper	2719	871	202.4		35410000

In the study, the Battery Material is identified as Active Zone Material. Positive Tab Material is identified as Copper. Negative Tab Materials is identified as Aluminum.

Since Li-ion batteries exhibit complex electrical behaviors under varying charge/discharge conditions, it is essential to develop an accurate mathematical model to represent their dynamic behavior. Equivalent Circuit Models (ECMs) are widely used for this purpose due to their balance between computational efficiency and accuracy.

Among different ECM configurations, the 2 RC model was selected in this study as it effectively captures both fast and slow transient effects during charge and discharge cycles. The model consists of internal resistance which represents instantaneous ohmic losses and two RC networks (R_1C_1 and R_2C_2) which capture short-term and long-term transient voltage responses, accounting for polarization and diffusion phenomena (Chen & Rincón-Mora, 2006).

The ECM requires test data that capture the dynamic response of the battery. To obtain the dynamic voltage and current responses across different SoC levels, the Hybrid Pulse Power Characterization (HPPC) test is adopted. A Battery Test Kit was prepared and the test was conducted following the procedure outlined below (URL-1):

1. Charge the battery to 1 SoC.
2. Rest for 1200 seconds.
3. Discharge at 1 C-rate until the desired SoC level is reached.
4. Rest for 1200 seconds.
5. Discharge at 1 C-rate for 10 seconds at the desired SoC level.
6. Rest for 1200 seconds.
7. The steps between 3 and 6 are repeated till the last desired SoC is obtained at Step 5.

Following the development of the electrical model using the ECM, the identified parameters are systematically incorporated into the Multi-Scale Multi-Domain (MSMD) model. The MSMD framework enables a comprehensive representation of electrochemical and electrical processes by integrating multiple spatial scales—ranging from the microscopic structure of electrode materials to the full cell and battery pack levels—as well as various temporal scales to ensure an accurate simulation of battery behavior under different operating conditions (Kim et al., 2011).

By employing this approach, the MSMD model provides a more detailed and physically consistent analysis of battery performance, capturing both the internal dynamics and external electrical responses with high precision. This allows for the

simultaneous evaluation of Joule heating and electrochemical heat generation, along with the resulting temperature distribution across the battery structure. Additionally, key electrical parameters such as voltage, current, and state of charge (SoC) evolution can be accurately monitored during the discharge process. These insights are critical for understanding thermal and electrical interactions within the battery system and optimizing its performance under real-world operating conditions.

Findings

To validate the simulation with experimental tests, five measurement points were selected, as shown in Figure 2, to monitor the temperature. The battery is simulated at a 100% state of charge (SoC) level, with a 0.3 C-rate, using boundary conditions where the battery wall temperature ($T_{boundary}$) is set to 22°C, and the heat transfer coefficient is 5 W/m·K for a duration of 1800 seconds.

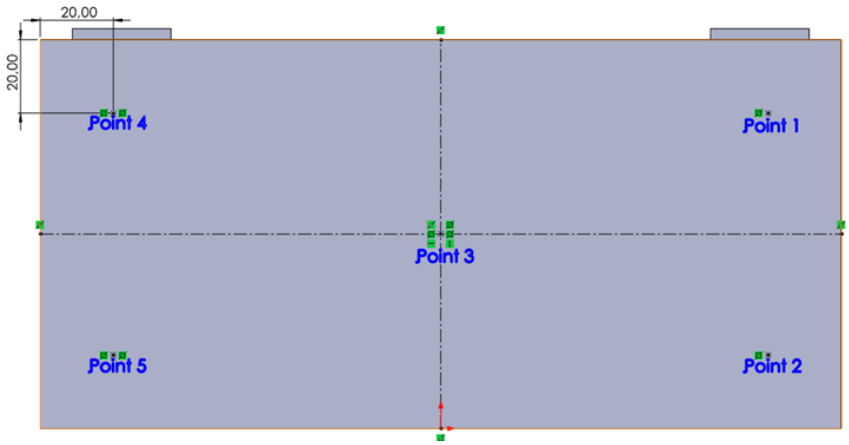

Figure 2. Temperature Measurement Points on the Battery.

After completing the simulation, Neware dataloggers are attached to the same points. The battery environment is set to 22°C, and the battery is charged to 100% state of charge (SoC). Once the battery is fully charged, it is allowed to rest until the temperature monitored by the dataloggers reaches 22°C and stabilizes. Then, the battery is discharged at a 0.3 C-rate for 1800 seconds. During the test, temperature data was obtained from the data loggers on the battery, while voltage values were recorded from the battery test system.
The temperatures obtained from both the experimental and simulation results are compared in Table 2.

Table 2. Comparison of Battery Experiment Test Temperature Results and Simulation Temperature Results in (Temperatures are in °C).

	Point 1		Point 2		Point 3	
seconds	Experimental	Simulation	Experimental	Simulation	Experimental	Simulation
0	22.5	22.0	22.6	22.0	22.6	22.0
200	23.8	23.17	22.9	23.14	23.3	23.15
400	24.9	24.26	23.5	24.21	24.5	24.22
600	25.6	25.33	24.2	25.28	25.5	25.29
800	26.3	26.40	25	26.34	26.4	26.36
1000	27	27.43	25.8	27.36	27.3	27.41
1200	27.7	28.42	26.6	28.35	28.3	28.43
1400	28.3	29.38	27.4	29.31	29.1	29.41
1600	29	30.31	28.2	30.23	30.1	30.38
1800	29.7	31.21	28.9	31.13	31.1	31.31

Table 2. (continued).

	Point 4		Point 5	
seconds	Experimental	Simulation	Experimental	Simulation
0	22.6	22.0	22.7	22.0
200	26.6	23.17	23.4	23.14
400	28.7	24.26	24.8	24.21
600	30.1	25.34	25.9	25.28
800	31.3	26.40	27	26.34
1000	32.6	27.43	28.2	27.36
1200	33.6	28.42	29.2	28.35
1400	35.1	29.39	30.2	29.31
1600	37.2	30.32	31.4	30.23
1800	37.6	31.21	32.5	31.12

Conclusion

This study provides a comprehensive experimental and numerical investigation into the thermal management of high-capacity NMx Li-ion prismatic batteries used in electric vehicle applications. By integrating electrochemical modeling, experimental validation, and computational simulations.

Key findings demonstrate that developed electrochemical and thermal model successfully predicted battery temperature distribution, with experimental validation confirming its accuracy within an acceptable margin. Although deviations were observed under the negative tab due to geometrical and material differences in the internal battery, particularly at higher discharge rates and longer test durations, the model effectively captures the heat generation characteristics and thermal behavior of the battery.

Acknowledgement: This study was supported by the Scientific and Technological Research Council of Türkiye (TUBITAK) under Grant Number 22AG018. The authors thank TUBITAK for the support.

References

Chen, M., & Rincón-Mora, G. A. (2006). Accurate electrical battery model capable of predicting runtime and I-V performance. IEEE Transactions on Energy Conversion, 21(2), 504–511. https://doi.org/10.1109/TEC.2006.874229

Cheng, X., Tang, Y., & Wang, Z. (2021). Thermal Property Measurements of a Large Prismatic Lithium-ion Battery for Electric Vehicles. Journal of Thermal Science, 30(2), 477–492. https://doi.org/10.1007/s11630-021-1398-3

Kim, G.-H., Smith, K., Lee, K.-J., Santhanagopalan, S., & Pesaran, A. (2011). Multi-Domain Modeling of Lithium-Ion Batteries Encompassing Multi-Physics in Varied Length Scales. Journal of The Electrochemical Society, 158(8), A955. https://doi.org/10.1149/1.3597614

Sheng, L., Su, L., Zhang, H., Fang, Y., Xu, H., & Ye, W. (2019). An improved calorimetric method for characterizations of the specific heat and the heat generation rate in a prismatic lithium ion battery cell. Energy Conversion and Management, 180, 724–732. https://doi.org/10.1016/j.enconman.2018.11.030

Url-1 https://www.ansys.com/blog/building-better-batteries, date retrieved 23.03.2025

Electrochemical and Thermal Modeling of Lithium Batteries for Temperature Distribution Based on Cathode Materials

Sıdıka Vişne[a], Sevan Karabetoğlu[b], Rahim Jafari[c], Tuba Okutucu-Özyurt[b]

[a] Istanbul Technical University, Graduate School, Energy Science and Technology Program, Turkiye
[b] Istanbul Technical University, Energy Institute, Renewable Energy Division, Turkiye
[c] Turkish Aeronautical Association University, Mechanical Engineering Department, Turkiye
visne23@itu.edu.tr

Keywords: Lithium-Ion Battery, Electrochemical simulation, Thermal modelling, NMC811, LFP, NCA.

Aim

Due to climate change and restriction of the traditional energy sources, sustainability is a consequential issue. As pollutant gas emissions increase, the earth becomes more exposed to air pollution and greenhouse effect. Land transportation has almost 14% of total greenhouse gas emissions of recent years (Milovanoff et al., 2021). Hence, the modern fossil fuel land vehicles that cause emissions need to evolve the ones which use more sustainable power sourcesand produce less pollutants.Electrical vehicles are designed as one such solution. The main issue in electrical vehicles is the range and the electrical storage. Lithium-ion batteries are the preferred electrochemical storage choice in electrical vehicles (Bharti et al., 2024; Promi et al., 2024). The most significant problem in lithium-ion batteries is the increase in the cell temperature during charging and discharging. The electrochemical reaction that occurs in battery cells, the internal resistance and polarization all contribute to battery heating (Tan et al., 2023). The main parameter that affects battery temperature level and distribution are geometric and chemical structures of the batteries.
This study focuses on the effects of the different positive electrode materials on the temperature level and thermal distribution as a chemical property of batteries.

Material and Method

In this study, different cell cathode materials are compared by using an experimentally verified simulation model. Lithium Nickel Manganese Cobalt Oxide $LiNi_{0.8}Mn_{0.1}Co_{0.1}O_2$ (NMC811), $LiNi_{0.8}Co_{0.15}Al_{0.05}O_2$ (NCA) and Lithium Iron Phosphate (LFP) are the compared cathode materials. The study initially involves the electrochemical modeling in the COMSOL Multiphysics environment by utilizing charging experiments on a commercial battery with known chemical and physical properties.
In the first step of the study, the electrochemical model of the battery was created. To reduce the computational load, the cell geometry in the model was simplified to a one-dimensional environment. Experiments are caried out as charging with 0.3C current. As the electrochemical model built, measured electric potential values were compared with experimental data in Figure-1. Thus, an electrochemical-thermal model has been created. In this model, the NMC811 cathode initially used has been replaced with LFP and NCA cathodes, respectively. In the first step of the study, the electrochemical model of the battery was created. To reduce the computational load, the cell geometry in the model was simplified to a one-dimensional environment. Experiments are caried out as charging with 0.3C current. As the electrochemical model built, measured electric potential values were compared with experimental data in Figure-1. Thus, an electrochemical-thermal model has been created. In this model, the NMC811 cathode initially used has been replaced with LFP and NCA cathodes, respectively.

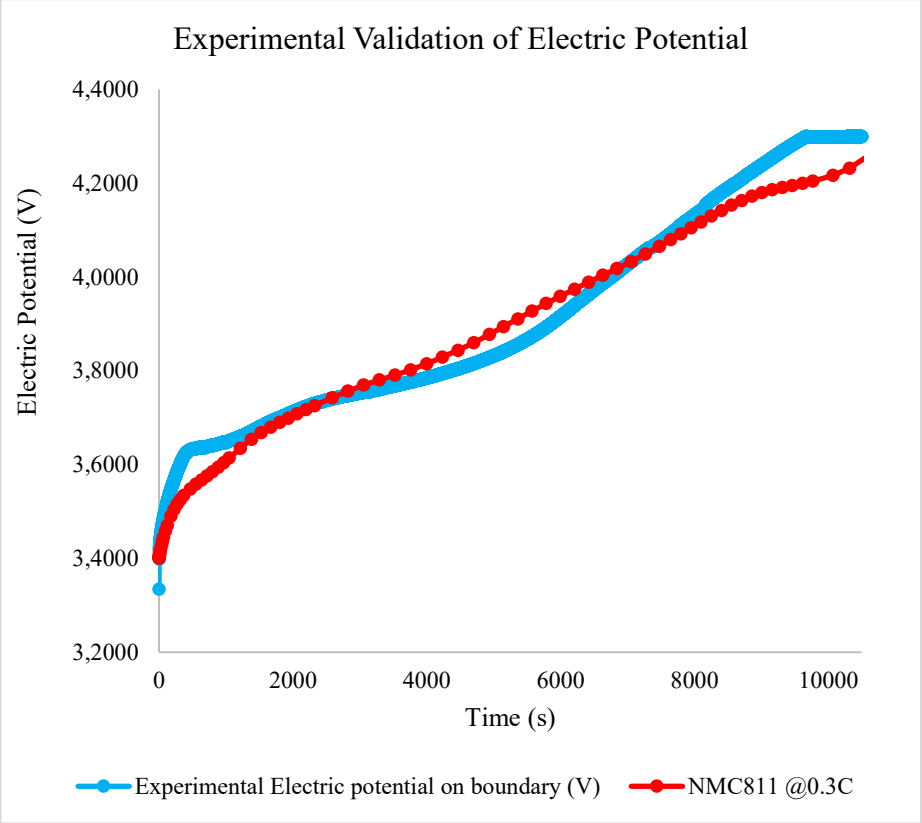

Figure 1: Experimental Validation of Electric Potential.

After validating the voltage values, the second step involved creating the three-dimensional thermal model of the battery and examining the temperature levels. Unlike the one-dimensional model, the three-dimensional thermal model was constructed at the battery pack level, including the case and terminal parts, rather than at the cell level. To simulate the thermal behavior heat transfer in solids and interface is used in 3D component. In the electrochemical model, heat sources are dynamically calculated by using time dependent electrode and electrolyte potentials. The average value of heat sources is used in time dependent thermal model. Both models are run in the same study steps.

Findings

Each cathode material has their own characteristic parameters that affects the temperature levels such as open-circuit voltage graphs, diffusion coefficients, electrical conductivity, insertion particle radius and maximum lithium host capacity. Some of the parameters were shown in Table 1. By changing and optimizing the parameters thermal and electrical behaviors simulated.

The voltage values obtained from running the electrochemical model are provided in Figure-2. Despite all cathodes has different starting voltage level, state of charge (SOC) parameters are all the same as %5.

In the 3D model, the active material of the battery is modeled in bulk, independent of the electrode-based cell structure. The time-dependent heat generation data obtained from the electrochemical model has been assigned as a heat source to the active material. The time-dependent average temperature values in the batteries are shown in Figure-3.

The thermal distribution in the 3D battery shows a relatively homogeneous distribution due to the active battery material being provided in bulk. In Figure 4, the temperature gradients of the batteries are shown by taking a cross-section from the center of the battery.

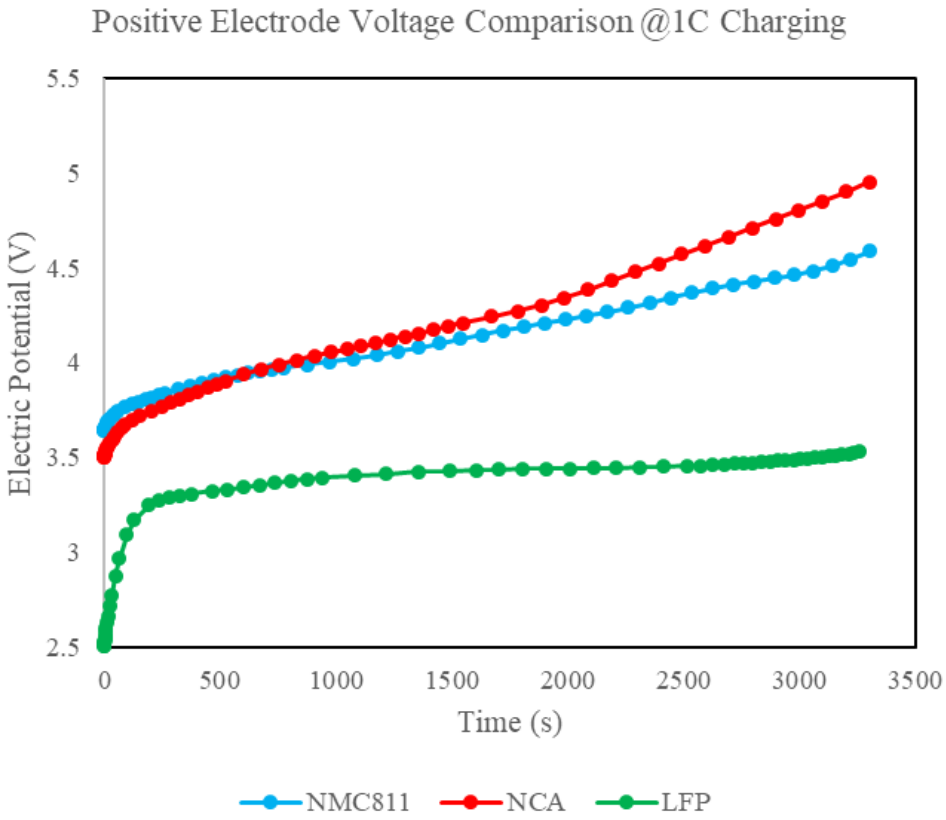

Figure 2: Electric potential values at 1C current charging.

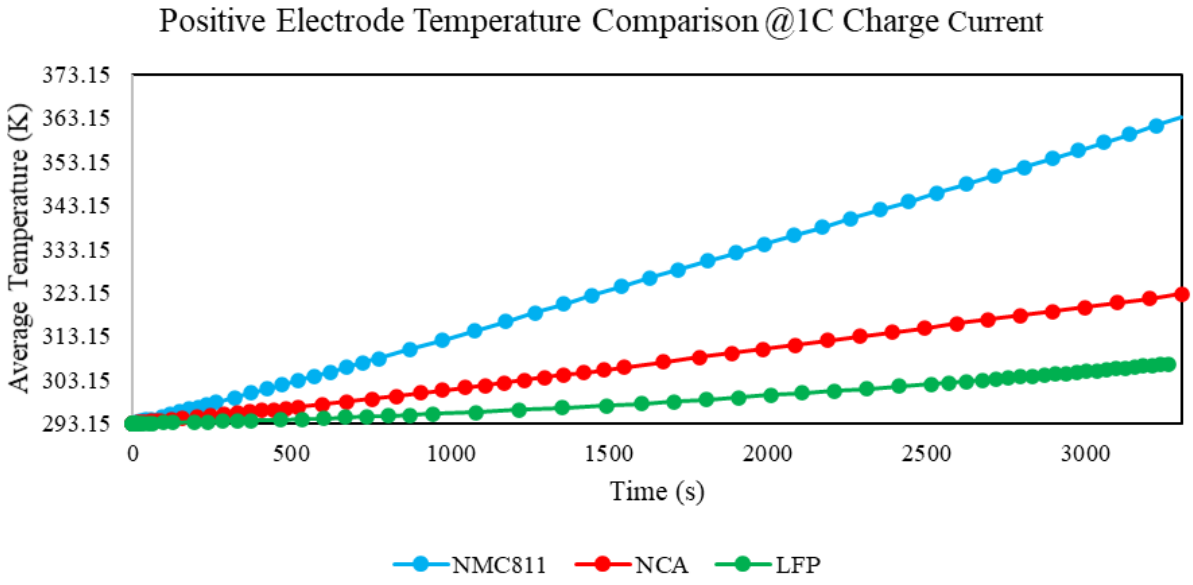

Figure 3: Average temperature levels of simulated batteries.

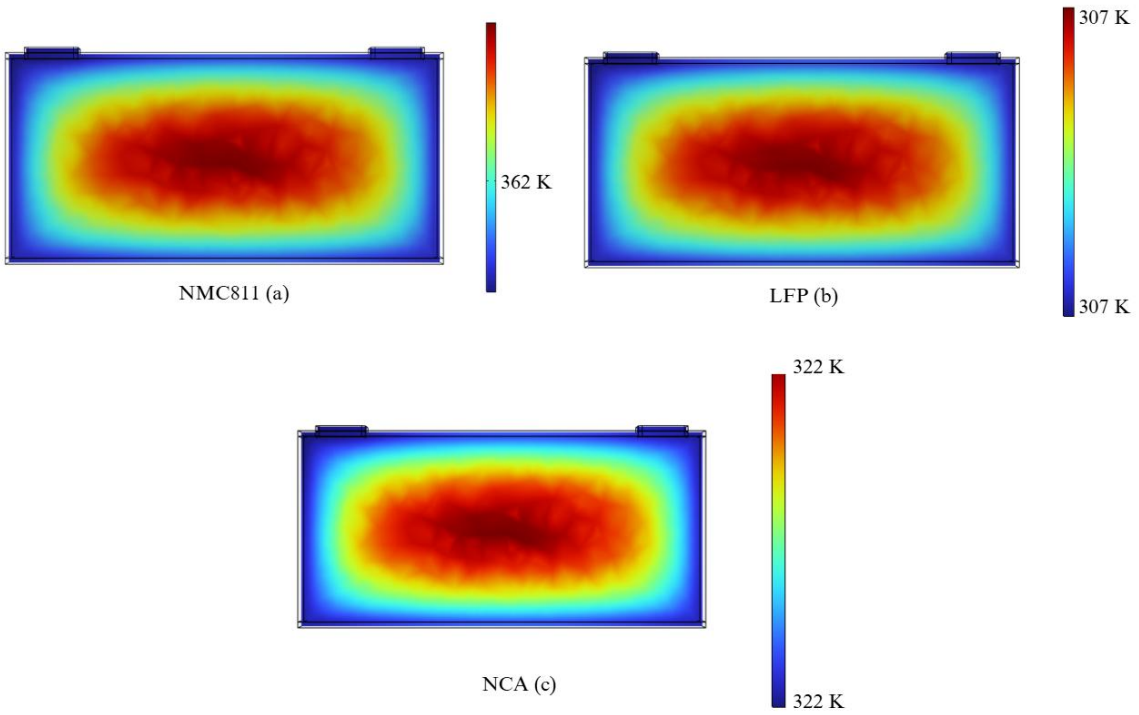

Figure 4: Temperature distirbution after 1C charging (3240s) at cross-section of the simulated batteries.

Conclusion

Three different batteries have been modeled using NMC811, NCA, and LFP as positive electrode materials. The batteries are identical in terms of open circuit voltage curves, dynamic diffusion coefficients, and geometric properties other than the values given in Table-1. Additionally, the separator, electrolyte, negative electrode, housing material, and terminals used in all batteries are identical. The batteries have been compared to examine the effect of the positive electrode's chemical characteristics on electrical potential and average temperature.

As a result of the modeling, the capacity ranking from largest to smallest is NMC811>NCA>LFP; the initial voltage ranking is NMC811>NCA>LFP; the post-charge voltage ranking is NCA>NMC811>LFP; and the temperature level ranking at the last time step is NMC811>NCA>LFP.

As given Table-1, the highest capacity belongs to NMC811 batteries because of its high lithium host capacity and OCV values. LFP has half of the capacity of NMC811, but thanks to its other parameters, shows more stable voltage profile (Figure-2), which is more favorable for battery applications.

Table 1: Characteristic parameters of the compared materials (Brown et al., 2008; Hall et al., 2016; Kasavajjula et al., 2008; Maxisch & Ceder, 2006; Sturm et al., 2019; Yang & Prakash, 2004).

	NMC811	NCA	LFP
Electrical Conductivity	0.17 S/m	91 S/m	91 S/m
Particle Radius	7 um	5 um	5 um
Maximum Ion Host Capacity	43143 mol/m^3	38482	26641
Cell Capacity	9000C	6500C	4500C

Table 2: Obtained results.

	NMC811	NCA	LFP
Start Voltage @0.05 SOC (V)	**3.6419**	3.503	2.4994
Final Voltage	4.5869	**4.9543**	3.5292
Final Temperature (K)	**363.35**	322.86	306.88

Capacity of NCA is moderate, but its high electrical conductivity brings NCA forward in after-charging voltage level. Generally, high-voltage causes high temperatures but the high ion concentration of NMC has been more effective in terms of temperature and has changed the ranking.
Considering the impact of cell temperature on safety and performance, LFP can be a good option. However, the low capacity is quite a challenging issue in land vehicle transportation. Therefore, NMC811 is preferred in some applications, but it should be accompanied by a sufficient and effective cooling system. When examining the prices for 2024, NCA cathode batteries require more cost compared to other batteries. In conclusion, the most suitable battery selection should be made by optimizing performance, safe temperature range, and cost parameters.

References

Milovanoff, A., Cheah, L., Posen, I. D., Maclean, H. L., Balasubramanian, R., & Minet, L. (2021). Greenhouse Gas Emission Mitigation Pathways for Urban Passenger Land Transport under Ambitious Climate Targets. *Environmental Science & Technology*, *55*(12), 8236–8246. https://doi.org/10.1021/acs.est.0c06671
Bharti, A., & Gupta, N. (2024). Electrifying Transportation and Pioneering the Future of Sustainable Electricity Mobility (pp. 80–89). CRC Press. https://doi.org/10.4018/979-8-3693-2611-4.ch005
Promi, A., Meyer, K., Ghosh, R., & Lin, F. (2024). Advancing electric mobility with lithium-ion batteries: A materials and sustainability perspective. *MRS Bulletin*, *49*(7), 697–707. https://doi.org/10.1557/s43577-024-00749-y
Tan, Y., Liu, W., Li, Y., Gu, Y., Fang, J., & Pan, C. (2023). Numerical Study on Heat Generation Characteristics of Charge and Discharge Cycle of the Lithium-Ion Battery. *Energies*, *17*(1), 178. https://doi.org/10.3390/en17010178

Yang, H., & Prakash, J. (2004). Determination of the Reversible and Irreversible Heats of a LiNi0.8Co0.15Al0.05 O 2/Natural Graphite Cell Using Electrochemical-Calorimetric Technique. *Journal of The Electrochemical Society*, *151*, A1222–A1229. https://doi.org/10.1149/1.1765771

Brown, S., Mellgren, N., Vynnycky, M., & Lindbergh, G. (2008). Impedance as a Tool for Investigating Aging in Lithium-Ion Porous Electrodes. *Journal of The Electrochemical Society*, *155*(4), A320. https://doi.org/10.1149/1.2832654

Hall, F., Wussler, S., Buqa, H., & Bessler, W. (2016). On the Asymmetry of Discharge/Charge Curves of Lithium-Ion Battery Intercalation Electrodes. *The Journal of Physical Chemistry C*, *120*. https://doi.org/10.1021/acs.jpcc.6b07949

Kasavajjula, U., Wang, C., & Arce, P. (2008). Discharge Model for LiFePO4 Accounting for the Solid Solution Range. *Journal of The Electrochemical Society*, *155*, A866. https://doi.org/10.1149/1.2980420

Maxisch, T., & Ceder, G. (2006). Elastic properties of olivine LixFePO4 from first principles. *Physical Review B - PHYS REV B*, *73*. https://doi.org/10.1103/PhysRevB.73.174112

Sturm, J., Rheinfeld, A., Zilberman, I., Spingler, F. B., Kosch, S., Frie, F., & Jossen, A. (2019). Modeling and simulation of inhomogeneities in a 18650 nickel-rich, silicon-graphite lithium-ion cell during fast charging. *Journal of Power Sources*, *412*, 204–223. https://doi.org/https://doi.org/10.1016/j.jpowsour.2018.11.043

Flow Control and Thermal Behavior of Bearings Using a Proportional Valve in a Closed-Loop Lubrication System for Turbofan Engines

Yasin Ince[a], Ilhan Kocaarslan[b]

[a] Istanbul Technical University/Energy Institute, Energy,Science and Technology Program, Turkiye
[b] Istanbul Technical University/ Faculty of Electrical and Electronics Engineering, Control and Automation Engineering Program, Turkiye
incey22@itu.edu.tr

Keywords: Turbofan Engine, Bearing Thermal Management, Lubrication, Proportional Valve.

Aim

Effective lubrication and thermal management have become extremely important in modern turbofan engines, under extreme temperatures and high rotational speeds. The bearings in both the cold and hot sections of these engines are subjected to considerable thermal and mechanical stresses and require credible lubrication to reduce wear and avoid early failures (Rolls-Royce, 2005), (MIL-PRF-23699, 2012). Indeed, closed-loop lubrication has become the de facto industry norm in aero-engine designs as it efficiently re-circulates oil, controls heat, and removes contaminants (Winterbone & Turton, 1996). However, the biggest engineering challenge still lies in the proper optimization of oil distribution, especially across regions where there is a difference in thermal load (Hill & Peterson, 2015).
Fixed or manually adjusted components have always been a part of the traditional lubrication system. They do not adequately respond to the dynamic conditions of the engine with varying RPM and sudden thermal excursions during operation (Velásquez & Herrera, 2021).New-age systems try to overcome this limitation by adding active flow control devices like proportional valves that control oil delivery to important parts of the system in real-time (SAE International, 2019). These valves offer very precise control of oil flow, ensuring that the bearing temperatures are kept safe, which ultimately improves the durability of the engine and its operational reliability (Kerlin & Walter, 2010).

The study is directed towards the incorporation of oil flow regulation using proportional valves into a closed-loop lubrication system of a small turbofan engine, rated for approximately 4000 N of thrust . The research investigates two most vital bearings in the engine - one in the cold sector and the other in the hot sector. The bearings thermally responds appropriately to oil distribution changes under different flow scenarios. Moreover, the work contributes to the overall advancement in the aerospace arena in thermal management by showing how adaptive lubrication control could elevate efficiency and safety (Guimaraes & de Oliveira, 2017), (McLean, 2012), (Greitzer, Tan, & Lord,2007).

Material and Method

This study is about a closed-circuit lubrication system in a small-class turbofan engine that produces 4000 Newton thrust at nominal performance and reaches 44000 rpm. This lubrication subsystem consists of an oil pump, oil tank (reservoir) heat exchanger, filter, and two proportional valves separated for 2 separate bearings, cold and hot. This two-channel system provides independent control in the lubrication of each bearing group.
MIL-PRF-23699 synthetic ester oil was selected as the lubricant fluid due to its high thermal stability and low volatility properties. Due to the mentioned properties, MIL-PRF-23699 is a type of oil frequently used in aviation applications.The turbofan engine was examined by dividing it into two groups, basically cold section and hot section. While the bearing in the cold section is located in the compressor assembly where it is exposed to moderate thermal loads, the bearing in the hot section is exposed to much higher thermal loads due to its location in the turbine and combustion chamber.
To evaluate the system performance, a system architecture was designed with parametric simulations and thermal models in MATLAB. Four different valve opening ratios were determined as 25%, 50%, 75% and 100%. The oil flow rate changes

according to these opening ratios. In addition, a relationship was established between the engine speed and the pump output, and the effect of changing flow rates on bearing temperatures was examined.

Findings

Overall, this research has highlighted the importance of using proportional valve controlled lubrication system to improve the basic performance of bearings used in turbofan engines. One of the first findings is the critical relationship between valve opening ratio (%) and oil flow rate, as shown in Fig. 1. Oil flow rate (L/min) increases directly from 0 to 40 liters with valve opening from 0 to 100%. This shows the reliability of using proportional valves to control the flow of lubrication system, no matter how challenging the engine operating conditions are.

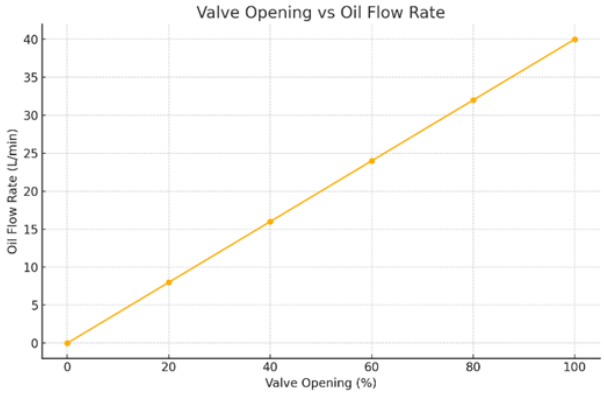

Figure 1: Valve Opening vs Oil Flow Rate.

Figure 2 shows the relationship between the pump oil output and engine speed. The pump performance starts at 10 L/min at 10,000 rpm and delivers 30 L/min at 28,000 rpm, while it delivers 40 liters of oil per minute when it reaches 44,000 rpm. This shows that engine performance and pump performance have a linear relationship under normal operating loads, and that when the maximum engine speed is approached, a regulated oil flow is provided by proportional valves.

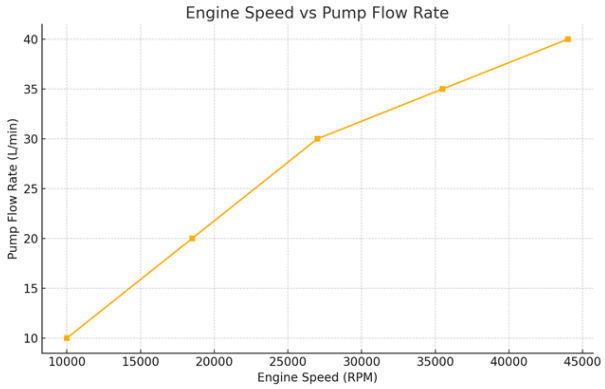

Figure 2: Engine Speed vs Pump Flow Rate.

As seen in Figure 3, the oil flow rate is of great importance in regulating the temperatures of the bearings in the cold and hot sections. The temperature of the bearing located in the cold section decreases from 55 °C to 35 °C with the increase in oil flow. In contrast, the temperature of the bearing in the hot section, which is subject to much higher thermal loads, decreases from 100 °C to 65 °C. These results emphasize the thermal gradient between the two sections and indicate that the oil supply of the system is directed more towards the areas where the cooling requirement is greater.

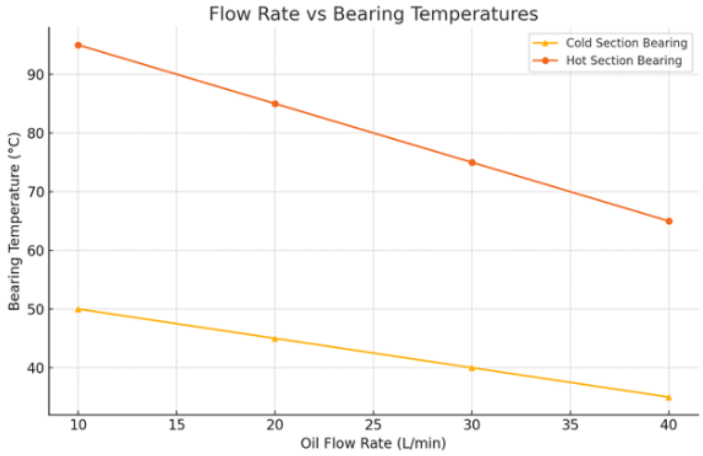

Figure 3: Flow Rate vs Bearing Temperatures.

In addition, Table 1 shows the bearing temperatures in relation to the valve openings. For example, with a 50% valve opening, the bearing temperature in the cold section is fixed at 45 °C, while the bearing temperature in the hot section is fixed at 90 °C. Therefore, these results confirm that the system is actively driven in the cooling process as determined by the local thermal requirements.

Table 1: Valve Opening & Temperature Table.

Valve Opening (%)	Cold Section Temp (°C)	Hot Section Temp (°C)
25	55	100
50	45	90
75	40	80
100	35	65

Conclusion

The results obtained from this study show that proportional valve controlled lubrication systems affect the thermal performance of bearings to a very serious extent. There is also a linear relationship between the life of the engine and the life of the bearings. Engine OEMs (Original Equipment Manufacturers) who want to produce long-life engines attach great importance to the thermal resistance of bearings in particular. Closed-loop lubrication systems create specialized thermal management systems for different performance requirements by regulating the amount of oil delivered to the bearings.

A significant result obtained is that when the oil flow rate delivered to the bearings reaches the highest levels, the bearing temperatures experience a major decrease from 55°C to 35°C in the cold section and from 100°C to 65°C in the hot section when the valve opening is compared with 25% and 100%. This cooling process reduces the thermal stress on the bearings and increases the reliability of the engine.

Moreover, this study reveals the importance of lubrication systems in reducing the energy consumption of propulsion and control systems in aviation engines. In the future, advanced 3D computational fluid dynamics analysis, testing and validation applications can optimize system performance, provide higher levels of thermal stability, and design safer lubrication systems and engines.

References

Greitzer, E. M., Tan, C. S., Lord, M. B. (2007). Internal flow: Concepts and applications. Cambridge University Press.
Guimaraes, G. B., de Oliveira, A. J. (2017). Heat transfer analysis in gas turbine bearing lubrication systems. International Journal of Heat and Mass Transfer, 115, 861–870.
Hill, G., Peterson, M. (2015). Aircraft systems: Mechanical, electrical and avionics subsystems integration (3rd ed.). Wiley.
Kerlin, T. W., Walter, W. H. (2010). Active control of lubricating oil in aero-engine bearing chambers. ASME Turbo Expo.
McLean, D. H. (2012). Automatic flight control systems (4th ed.). Prentice Hall.
MIL-PRF-23699. (2012). *Lubricating oil, aircraft turbine engine, synthetic base* [Specification sheet]. U.S. Department of Defense.
Rolls-Royce. (2005). The Jet Engine (5th ed.).
SAE International. (2019). Lubrication systems for gas turbine engines (SAE Aerospace Information Report AIR 1934C). SAE International.
Velásquez, S. A., & Herrera, J. E. (2021). Control of proportional valves in aircraft lubrication systems. *International Journal of Aerospace Engineering, Article ID 6678159.
Winterbone, D. E., & Turton, R. J. (1996). Advanced thermodynamics for engineers (2nd ed.). Butterworth-Heinemann.

ENERGY SCIENCE AND TECHNOLOGY

Computational Fluid Dynamics

Computational Heat and Mass Transfer

Energy Conversion and Storage Technologies

Energy Conversion and Sustainability

Energy Management and Planning

Renewable Energy

Sustainable Energy

Sustainable GSM Base Station Energizing Using Portable Radioisotope Thermoelectric Generator (RTG) Design

Erdem Hayat[a], İskender Atilla Reyhancan[a]

[a]Istanbul Technical University, Department of Nuclear Researches, Radiation Science and Technology, Türkiye
hayat21@itu.edu.tr

Keywords: Radioisotope Thermoelectric Generator (RTG), Thermoelectric Generators (TEG), GSM Antenna, Disaster Resilience, Decentralized Energy Systems.

Aim

Conventional energy sources often struggle to provide consistent and reliable power to GSM base stations, particularly in rural and remote areas. These regions typically lack the necessary infrastructure for a stable electricity supply, and geographical challenges further complicate energy distribution. For instance, constructing power lines through dense forests and rugged terrains is not only costly but also environmentally detrimental due to deforestation and increased wildfire risks. Additionally, traditional energy sources such as diesel generators require regular maintenance and refuelling, which is often impractical in isolated locations. These challenges underscore the need for innovative and sustainable energy solutions to support remote communication infrastructure.

The primary objective of this research is to design a portable Radioisotope Thermoelectric Generator (RTG) capable of delivering uninterrupted and reliable power to GSM antennas. RTGs are particularly well-suited for this application due to their ability to provide long-term, maintenance-free power. Unlike conventional generators, RTGs lack moving parts, significantly reducing the risk of mechanical failure and ensuring continuous operation even in harsh environmental conditions. This reliability is critical for maintaining essential communication infrastructure during natural disasters or other emergencies. Furthermore, the compact and lightweight design of RTGs facilitates easy transportation and deployment in challenging environments.

Material and Method

The initial phase of RTG design involves the selection of an appropriate radioactive source and thermoelectric (TE) material. Based on the criteria outlined above, particularly the use of a beta-emitter radioisotope, Strontium-90 (^{90}Sr) was chosen as the radioactive source (Shor, 1971, May). The radiation characteristics of 90Sr and its decay product, Yttrium-90 (^{90}Y), are summarized in Table 1 (Abolhasan Khajepour, 2017). For the Radioisotope Heat Source (RHS), the strontium-based composition must exhibit high thermal conductivity, excellent chemical stability, and mechanical strength under high temperatures and pressures.

Table 1. Radiation properties of ^{90}Sr and its daughter ^{90}Y.

Nuclide	Half-life	Maximum E, MeV	Average E, MeV	Abundance, %	Specific power, W/kCi	Particles per W·s
^{90}Sr	28.90 years	0.546	0.1936	100	1.164	5.51×10^{12}
^{90}Y	64.053 hours	2.284	0.9365	100	5.551	5.51×10^{12}
		Total power			**6.715**	

*No alpha, gamma, neutron, or fission.

For the RHS, strontium titanate (SrTiO3) was selected due to its high thermal conductivity, excellent chemical stability, and mechanical strength under high temperatures and pressures. (Shigemasa Enomoto, 1975) These properties are critical for maintaining the structural integrity of the RHS and ensuring efficient heat transfer to the thermoelectric modules.

Table 2. Strontium titanate ($SrTiO_3$) properties at 25 °C.

Properties	Value
Density (g/cm^3)	5.11
Melting point (°C)	2040
Coefficient of thermal expansion ($°C^{-1}$)	12.1×10^{-6}
Specific heat (J/g·K)	0.544
[a] Specific power (W/g), 100% Sr (55%)^{90}Sr	0.247
Specific activity (Ci/g), 100% Sr (55%)^{90}Sr	36.8
Dielectric constant (ε_0)	300

a-By assuming 148.9 Ci/W (thermal), 139 Ci/g or 0.933 W/g (100% 90Sr). (Abolhasan Khajepour, 2017)

The thermoelectric modules used in RTGs rely on the Seebeck effect, which converts temperature differences into electric voltage. The performance of these modules is evaluated based on the figure of merit (ZT), which depends on the material's electrical conductivity, Seebeck coefficient, and thermal conductivity. Materials such as bismuth telluride (Bi_2Te_3) and lead telluride (PbTe) are commonly used due to their optimal ZT values at moderate temperatures. (Rowe, 2006) Recent advancements in material science have led to the development of more efficient thermoelectric materials, such as skutterudites and half-Heusler compounds, which offer higher ZT values and improved energy conversion efficiency.
The shielding design is another critical aspect of RTG development. The shielding must be robust enough to prevent the release of harmful radiation while also being lightweight to facilitate transportation and deployment. Advanced shielding techniques, such as multi-layered designs incorporating both high-Z and low-Z materials, have been developed to minimize radiation exposure and ensure the safety of personnel and the environment.

Findings

The selection of ^{90}Sr and $SrTiO_3$ as the radioactive source and RHS material, respectively, provides a robust and efficient solution for long-term energy generation. The radiation characteristics of ^{90}Sr and ^{90}Y ensure a consistent and reliable heat source, while the thermal and mechanical properties of $SrTiO_3$ enable efficient heat transfer and structural stability. The use of advanced thermoelectric materials, such as skutterudites and half-Heusler compounds, further enhances the energy conversion efficiency of the RTG system. These materials exhibit high ZT values, which are critical for maximizing the efficiency of thermoelectric modules. Additionally, the integration of segmented thermoelectric designs, where different materials are used at varying temperature zones, has shown promising results in optimizing energy conversion.
The shielding design effectively contains the beta radiation emitted by ^{90}Sr, minimizing the risk of radiation exposure. The multi-layered shielding approach, incorporating both high-Z and low-Z materials, provides an additional layer of safety, ensuring that the RTG can be safely deployed in various environments, including residential areas and nature reserves. This design not only protects personnel and the environment but also ensures compliance with international radiation safety standards.
The integration of RTGs into remote communication infrastructure offers several advantages over conventional energy sources. Unlike diesel generators, which require regular refueling and maintenance, RTGs provide a continuous and

maintenance-free power supply. This is particularly beneficial in remote and inaccessible locations where logistical support is limited. Furthermore, the silent operation of RTGs makes them suitable for use in noise-sensitive environments, such as wildlife reserves and urban areas. The absence of moving parts in RTGs significantly reduces the risk of mechanical failure, ensuring reliable operation even in harsh environmental conditions.

The portability of the designed RTG is a critical advantage, particularly in disaster scenarios. In disaster-stricken areas, energy infrastructure is often damaged or completely non-functional. In such cases, RTGs can be quickly transported to the disaster zone and provide a reliable energy source to support communication infrastructure. The silent operation of RTGs eliminates noise pollution, which is crucial for facilitating efficient communication among rescue teams. Additionally, the long energy supply duration of RTGs ensures continuous and uninterrupted power, which is essential for prolonged rescue operations. Unlike traditional energy sources, RTGs do not require personnel for maintenance or operation, making them ideal for hard-to-reach disaster areas. These features make RTGs a vital component of disaster response and recovery efforts.

Conclusion

This study demonstrates that portable RTGs provide a sustainable and reliable alternative to conventional energy sources for powering GSM base stations. The selection of ^{90}Sr as the radioactive source and $SrTiO_3$ as the RHS material provides a robust and efficient solution for long-term energy generation. The integration of advanced thermoelectric materials and shielding techniques further enhances the performance and safety of RTGs. The portability and silent operation of RTGs make them particularly valuable in disaster scenarios, where they can provide uninterrupted power without the need for frequent maintenance or personnel.

The findings of this research highlight the potential of RTGs to revolutionize energy supply in remote and disaster-prone regions. By leveraging the unique advantages of radioisotope decay and thermoelectric conversion, RTGs can provide a sustainable and reliable energy solution for a wide range of applications, including telecommunications, space exploration, and disaster management. Future research will focus on optimizing thermoelectric materials, enhancing radiation shielding techniques, and exploring hybrid energy systems that combine RTGs with renewable energy sources, such as solar and wind power. These advancements will further solidify RTGs as a cornerstone of sustainable energy solutions.

In conclusion, the development of portable RTGs represents a significant step forward in addressing the energy challenges faced by remote and disaster-affected regions. The ability of RTGs to provide reliable, maintenance-free power in the most challenging environments underscores their potential to transform the way we approach energy generation and distribution. As the world continues to grapple with the impacts of climate change and natural disasters, the importance of innovative energy solutions like RTGs cannot be overstated.

References

Enomoto, S., Senoo, M., & Maeda, S. (1975). New method for preparation of a ceramic strontium-90 titanate β-ray source. *The International Journal of Applied Radiation and Isotopes*, 363-366.

Khajepour, A., & Rahmani, F. (2017). An approach to design a 90Sr radioisotope thermoelectric generator using analytical and Monte Carlo methods with ANSYS, COMSOL, and MCNP. *Applied Radiation and Isotopes*, 53.

Rowe, D. (2006). *Thermoelectrics Handbook-Macro to Nano.* Boca Raton: CRC Press.

Shor, R., Robert H. Lafferty, J., & Baker, P. S. (1971, May). STRONTIUM-90 HEAT SOURCES. *Oak Ridge National Lab., Tenn. (USA)*.

The Lifespan Comparison of an NMC811 Pouch Cell Based High Voltage Battery with Silicone and Polyurethane Foam Usage

Serhat Soyer [a]

[a] Istanbul Technical University, Department of Mechanical Engineering, Materials and Manufacturing Programme, Türkiye
soyerser@itu.edu.tr

Keywords: Battery, Foam, Pouch Cell.

Aim

The electric vehicles (EVs) increased its popularity year by year because of; improvments in its technology decreasing of battery pack costs, newly builded infrastructure and increasing level of consciousness on global warming.
So high voltage batteries are getting more and more importance since the powertrain transition of vehicle industry from internal combustion engine to electrical engines is rapidly increasing. It is a well-known fact that the most common high voltage battery cell types nowadays are mainly pouch, prismatic and cylindrical cells. Every cell type has its own advantages and disadvantages.
Cylindrical cells has high mechanical strength but also problematic thermal management systems.Prismatic cells has high energy density which represents their energy density per volume, however they have also high manufacturing cost.
Between those cell types pouch cels are one of the favourite in the vehicle cell market thanks to its high specific energy which represents energy per mass. However, pouch cells has two unignorable disadvantage that these cells has low mechanical strength and tends to swell.
Because of these reasons to prevent high swelling in lifetime and mechanical defetcs, pouch cells must be supported in battery architecture by soft materaials from its swell direction.
Due to commercial and easy applicability reasons silicone foams and polyurethane foams are two main supporter elements to cells in battery trays and selection between these two alternatives is a hot topic in high voltage battery design.
The purpose of this thesis is to prove that those two alternatives can easily be replaced instead of each other after an easy and fast compression test comparison to maintain a continuous pressure on cells to gain same level lifespans.
To understand those phenomena one polyurethane and one silicone commercial foams are selected. At first compressure deflection (CFD) curves of these two foams compared in different speeds. At the second step initial pressure of 36 cell-36 foam module stack forces are calculated from CFD curves, matched, and correlated with stack test data. At the last step the lifespan of 4 cell-4 foam battery mini-modules are tested with charge-discharge loop and their state of health which represents the condition of a cells compared to its ideal condition are measured continuously to make a final evaluation.
According to final evaluation it is proved that both foam types are suitable for use in battery cell stacks and easily replaced with each other if they have same level CFD behaviour from mechanical and lifespan point of view. For both types, the CFD curve can be used to select suitable foam option in battery modules.
The purpose of this research is to prove that two different alternative compression pad can easily be replaced instead of each other in a design after an easy and fast -shorter than a hour- compression test without performing a long and requiring resources lifecycle test.

Material and Method

Mechanically similar one silicone and one polyurethane foam products are chosen to compare. The compression deflection curves are initially compared from technical data sheets and then tested to validate accuracy. Standart test method for rubber properties is named as compression set from American Society for Testing and Materials International. Two test methods are covered as follows:

- Compression Set Under Constant Force in Air
- Compression Set Under Constant Deflection in Air

In this study compression set under constant deflection in air method is used to compare foam compression behaviour. Aufschläger at. al. (2024) shows in their study the compression ratios after 1000kPa will cause a high capacity retention for the pouch cells. In addition to that at higher compression ratios the hardening of foams will be too high unpredictably which might cause a mechanical deformation on pouch cells. Because of this reason design area of the cell stack must be selected to not exceed the 1000kPa load and the assumption of this study is on that direction as well.
Figure 1 showing that the pressure against compression is slightly higher for silicone type foam compared with polyurethane one however the pressure levels are getting closer after 70% compression ratio and almost same after %70 compression level which creating 1000kPa reaction compression.

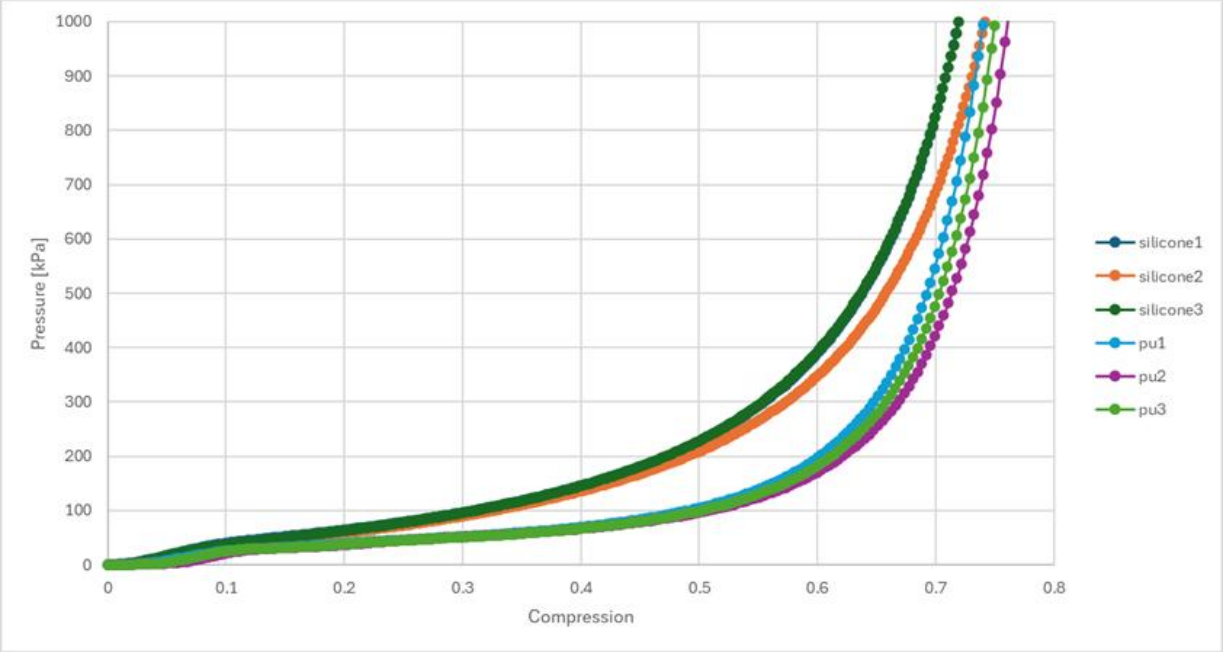

Figure 1: Compression Deflection Curve of Selected Foams.

At second step this study tested one type of module that assembled with pouch cells, compression pad foams, casettes and enclosure plates which shown in below Figure 2.

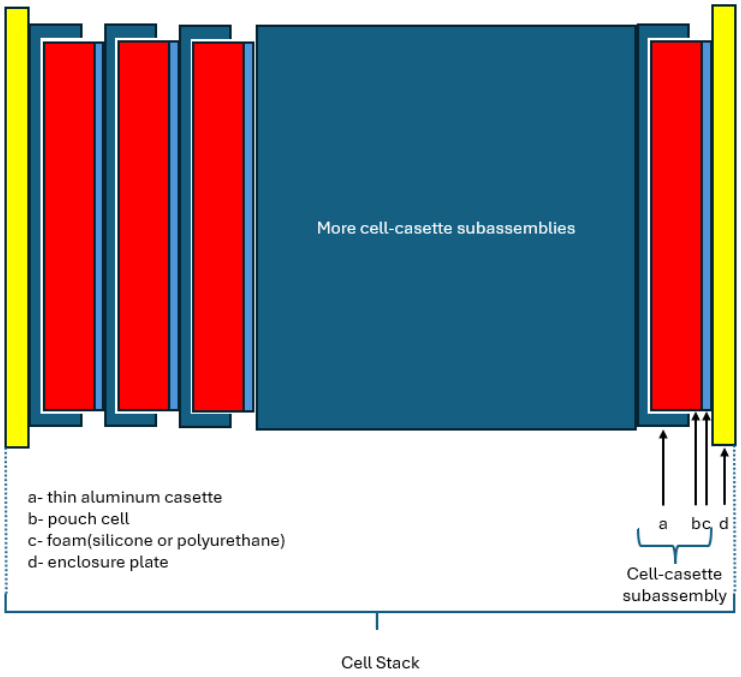

Figure 2: Schematic of Module Stack.

At the and the cycle aging is taken as the main factor to compare between two minimodule which set up with polyurethane and silicone foams.

Findings

Results clearly show that the capacity decreases between two modules which assembled with different foams are almost same in a lifetime. Below Figure 3 shows the comparison between 2 modules.
The deviation between two samples is 2 ‰ which can be negligible. In the case of different foam usage, it might be expected that the state-of-health (SOH) loss would be different because of the pressure onto cells are different. But even if the pressures are different against deformation caused by swelling for selected foams since the pressure level is lower than critical stress levels both cycle aging tests have given same capacity loss.

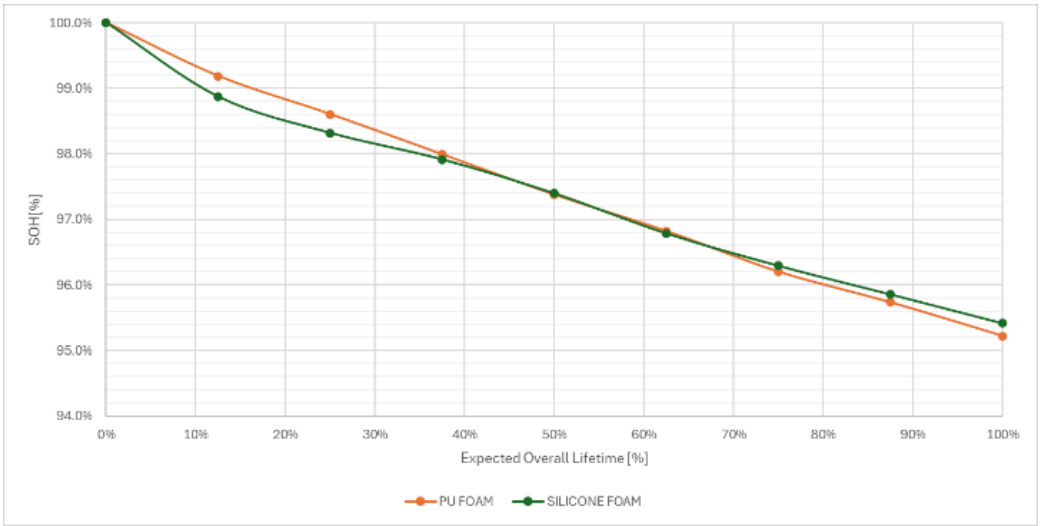

Figure 3: SOH vs. Expected Lifetime Graph.

Conclusion

This research aims to demonstrate that silicone and polyurethane foams can be substituted for one another without compromising performance, provided they exhibit similar behavior in terms of mechanical properties and lifespan. The comparison begins by evaluating the compression deflection (CFD) curves of both foam types at different compression speeds. Next, the initial pressure exerted on a 36-cell, 36-foam module stack is calculated using the CFD curves, with results matched and correlated against actual stack test data. In the final phase, the lifespan of 4-cell, 4-foam mini-modules is tested through charge-discharge cycles, and the state of health of the cells (which indicates how close the cells are to their ideal condition) is continuously monitored. The results confirm that both silicone and polyurethane foams are viable options for use in battery cell stacks. They can be interchanged as long as they exhibit similar CFD behaviors in terms of mechanical properties and lifespan. Thus, the CFD curves can be used as a reliable tool to select the most suitable foam material for battery modules.

References

S. G. Abens, W. C. Merz, C. R. Walk, (1967). *Development of High Energy Primary Batteries Final Report.*, National Aeronautics and Space Administration, PENNSYLVANIA

M. S. Whittingham, (1976). Electrical Energy Storage and Intercalation Chemistry. *Science 192,* 1126-1127. doi: 10.1126/science.192.4244.1126

K. Mizushima, P.C. Jones, P.J. Wiseman, J.B. Goodenough, (1980). LixCoO2 (0<x<-1): A new cathode material for batteries of high energy density. *Materials Research Bulletin, 15-5,* 561-570. doi: 10.1016/0025-5408(80)90135-x.

N. A. Godshall, I. D. Raistrick, Robert A. Huggins, (1980). Thermodynamic Investigations of Ternary Lithium-transition Metal-oxygen Cathode Materials. *Materials Research Bulletin, 15-6,* 783-789. doi: 10.1016/0025-5408(80)90012-4.

R. Fong, U. von Sacken and J. R. Dahn, (1990). Studies of lithium intercalation into carbons using nonaqueous electrochemical-cells. *Journal of The Electrochemical Society, 137 (7),* 2009-2013. doi: 10.1149/1.2086855.

A. Aufschläger, A. Durdel, L. Kraft, A. Jossen, (2024). Optimizing mechanical compression for cycle life and irreversible swelling of high energy and high power lithium-ion pouch cells. *Journal of Energy Storage, 76,* doi: 10.1016/j.est.2023.109883

ENERGY SCIENCE AND TECHNOLOGY

Computational Fluid Dynamics

Computational Heat and Mass Transfer

Energy Conversion and Storage Technologies

Energy Conversion and Sustainability

Energy Management and Planning

Renewable Energy

Sustainable Energy

Energy Efficiency Potential Analysis of SMEs In Türkiye's Fertilizer Sector

Sude Karabağ[a], Ebru Acuner[a]

[a]Istanbul Technical University, Energy Institute, Turkey
karabags18@itu.edu.tr

Keywords: Energy Efficiency, Fertilizer Sector, Green Transformation, SMEs, Sustainability.

Aim

Due to its high energy consumption and heavy reliance on imported raw materials, the Turkish fertilizer industry offers both potential and problems for increasing energy efficiency. The Carbon Border Adjustment Mechanism (CBAM) and the European Green Deal have increased pressure on Small and Medium Size Enterprises (SMEs) in this industry to embrace sustainable production methods. With an emphasis on their involvement in the green transition and the identification of significant challenges and opportunities, this study evaluates the energy efficiency potential of SMEs in the fertilizer sector in Turkey.

Material and Method

SMEs, which make up a sizable portion of the Turkish economy, are essential for long-term change but frequently face obstacles related to funding, access to technology, and regulatory compliance (Özdemir et al., 2007). The study examines trends in sectoral energy use, greenhouse gas emissions, and possible efficiency improvements via cutting-edge strategies including green finance and circular economy models. The results show that although some SMEs have started to adopt energy-saving practices, more industry cooperation, financial incentives, and wider regulatory support are required to hasten the process.

Assessing the energy efficiency potential of SMEs in Turkey's fertilizer industry is the aim of this study, especially in context with the European Green Deal and the Carbon Border Adjustment Mechanism (CBAM). SMEs are underrepresented in the green transition initiatives, although playing a vital role in the Turkish economy. Opportunities and difficulties unique to the fertilizer industry are addressed, with a focus on this energy-intensive and strategically significant sector for agriculture. By identifying the major factors influencing SMEs' transition to sustainable manufacturing, the study adds to the body of literature and aims to give empirical data on their energy efficiency methods.

A survey study specific to the fertilizer sector is planned in the study. This sector-based survey will determine the awareness of many SMEs in the fertilizer sector on the importance of green transformation and the differences in their approaches to sustainability. The survey includes questions to measure the awareness of SMEs in the fertilizer sector regarding CBAM; to identify the difficulties they experience in green transformation and energy efficiency studies and also includes questions necessary for data analysis. Based on the literature review, it is anticipated that certain SMEs have held energy-efficient technologies and improved resource utilization. On the other hand, some may still be reluctant because of financial limitations and insufficient support systems. The Analytical Hierarchy Process (AHP) approach is intended to be utilized to rank the challenges and opportunities highlighted in the survey. SMEs will be asked to rate different factors affecting their energy efficiency potential. This approach helps SMEs understand which aspects (financial, regulatory, technological or awareness-related) play a more important role in their decision-making processes. In this way, the aim is to evaluate the energy efficiency potentials of SMEs operating in the fertilizer sector in Türkiye using the Analytical Hierarchy Process (AHP) method.

Findings

The primary anticipated outcome of this research will be the capability of SMEs to leverage circular economy principles like waste recycling and sustainable resource utilization in their manufacturing processes. By adopting these practices, SMEs are likely to minimize their environmental impact while simultaneously enhancing their economic performance

through long-term reductions in operational expenses. However, a more widespread adoption of green practices requires a change in mindset supported by government policies and sectoral cooperation.
The gathered information will then be evaluated using Life Cycle Assessment (LCA) methods to more thoroughly examine the environmental effects for each sector. This research will act as an important reference to enhance the understanding of SMEs' roles in the transition towards sustainability and assist in setting sustainability objectives for each sector. Also, highlights that SMEs within the fertilizer industry have the capability to facilitate substantial change if provided with appropriate support and incentives. By tackling critical challenges and capitalizing on emerging opportunities, SMEs can not only minimize their environmental impact but also bolster their market position and aid Türkiye's overarching green growth strategy.

Conclusion

By adopting energy efficiency measures and sustainability-oriented policies, small and medium-sized enterprises (SMEs) in the fertilizer industry can improve their competitiveness in global markets while minimizing their environmental footprint. This research provides valuable insights into how SMEs can be assisted in their shift towards a low-carbon economy, in line with Türkiye's wider strategy for green growth.

References

Albayrak, E., & Erensal, Y., (2004). Using Analytic Hierarchy Process (AHP) to İmprove Human Performance: An Application of Multiple Criteria Decision-Making Problem. Journal Of Intelligent Manufacturing, vol.15, no.4, pp. 491-503.
Bilen A., & Solmaz H., (2014). Structural Problems Faced by SMEs and Proposed Solutions (Diyarbakır Example).
C., Sørensen, S.Y., Bjørn Larsen, P., Alexopoulou, S. et al., (2010). SMEs and the Environment in the European Union. Brussels: PLANET SA and Danish Technological Institute for European Commission, DG Enterprise and Industry.
European Commissions, (2024). EU trade relations with Türkiye.
Fertilizers Europe, (2008). Energy Efficiency and greenhouse Gas Emissions In European Nitrogen Fertilizer Production and Use.
General Directorate of Agricultural Research and Policy of Türkiye, (2018). Fertilizer Sector Policy Document.
Gödekmerdan, E. et.al., (n.d.). Border Carbon Adjustment Mechanism and the Future of Agriculture in Turkey: The Perspective of Fermented Fertilizer, Compost, and Biochar. Ege University, Solar Energy Institute.
ISO, (2015). Chemical and Chemical Products Manufacturing Industry. Istanbul Chamber of Industry Economic Research Department.
KOSGEB, (2023). Report on the Place of SMEs in Foreign Trade in Türkiye.
M. Skowroñska ve T. Filipek, (2014) Life Cycle Assessment of Fertilizers: A Review, Int. Agrophys., no. 28, pp. 101-110.
OPDM, (2004). Multi-Criteria Analysis: A Manual.
Özdemir, S., Ersöz, H. Y., & SARIOĞLU, H. İ. (2007). The increasing importance of small entrepreneurship and SMEs in Turkish economy. The Conference Journal of Social Policy, (53).
Republic of Turkey Ministry of Agriculture and Forestry. (2018). Fertilizer Sector Policy Document 2018-2022.
Republic of Türkiye Ministry of Energy and Natural Resources, (2024). Energy Efficiency 2030 Strategy and 2nd National Energy Efficiency Action Plan (2024-2030).
Sarıkahya M., (2012). Effect of State Subsidies Granted to SMEs in Furniture Industry on The Companies (Ankara Example).
T.C. Ministry of Environment, Urbanisation and Climate Change, *(2024).* Climate Change Mitigation and Adaptation Strategy and Action Plans, 2024.
The Union of Chambers and Commodity Exchanges of Türkiye (TOBB), (2014). *Economic Forum, v:*241: p13.
Tosyalı S. B., (1995). The Place of SMEs in the Turkish Economy Izmir Chamber of Commerce.
Turkish Statistical Institute, (2024). Small and Medium Enterprises Statistics, 2023.
Türkiye Exporters Assembly, (2022). Sustainability Action Plan.

Trade Map, (2018). Trade Statistics For İnternational Business Development.
World Bank, (2007). Phosphate Fertilizer Plants, International Finance Corporation, World Bank Group.

ENERGY SCIENCE AND TECHNOLOGY

Computational Fluid Dynamics

Computational Heat and Mass Transfer

Energy Conversion and Storage Technologies

Energy Conversion and Sustainability

Energy Management and Planning

Renewable Energy

Sustainable Energy

Feasibility Assessment of Hydrogen Fuel Cell Integration in the Dornier 228 Aircraft with the Structural and Operational Considerations

Caner İlhan[a], Mehmet Suha Yazıcı[a]
[a] Istanbul Technical University, Energy Institute, Energy Science and Technology Program, Türkiye
ilhan22@itu.edu.tr

Keywords: Conceptual Aircraft Design, Fuel Cell, Hydrogen Propulsion, Sustainable Aviation.

Aim

Since energy demand is increasing worldwide, the aviation industry is committing itself to the development of increasingly sustainable solutions and the meeting of solid emission criteria (IEA, 2023). While gas turbine engines have already been said to be very highly efficient, a completely carbon-neutral solution is impossible due to thermodynamic constraints and operational restrictions (Darecki et al., 2011; IEA, 2022). Aviation CO_2 emissions rose fastest in 2022, outpacing other modes of transport, which is likely to continue in future years (National Academies of Sciences, 2016; Roland Berger, 2020). In view of the objectives set by the European Union for 2050, alternative fuels, as well as new kinds of propulsion systems, have become an inevitable aspect of net-zero emissions flights (IEA, 2022).

To lessen this problem, sustainable aviation fuels (SAF) have been invented to curb the environmental damage associated with the burning of fossil fuels. When substituted for conventional jet fuel, SAF can cut carbon dioxide emissions by as much as 80%. For instance, as much effort may be put into making the use of burning fossil fuel neutral in carbon, it will not be attainable due to the processing and the emissions from combustion (Incer-Valverde et al., 2023). On the other hand, it is possible to use hydrogen for power generation using fuel cells and achieve almost no carbon (McKinsey and Company, 2020). Although, in theory, burning hydrogen does not produce any CO_2, this process does produce NO_x due to increased temperatures. It does have some negative impacts as well, involving excess water vapor at altitudes (Elitzur et al., 2017; Wilcox et al., 2012).

Hydrogen-powered fuel cells are hydrogen-use solutions that emit zero CO_2 and no NO_x, enabling the aviation industry to reach its net-zero targets (Noland, 2021). Most of the literature, including a few design processes for a comprehensive hydrogen and fuel cell aircraft design, is still very limited. It is noticed that ongoing studies are in the preliminary phase, and much more research is needed to carry out their transition towards an implementable full-scale application. This study aims to provide a sustainable and viable propulsion solution by evaluating the potential of hydrogen and fuel cells for use in aviation.

Material and Method

By integrating the hydrogen fuel cells into a CS-23 category aircraft and using the Dornier 228 as a reference, this study is concentrated. By weight and performance, this airplane was chosen to exhibit an ideal conversion to hydrogen cell technology.

The methodology involved assessing flight performance through constraint diagrams, analyzing flight conditions such as take-off, cruise, climb, and stall speed, and evaluating the implications of fuel cell powertrain integration. The powertrain was designed to include a fuel cell stack, a turbo-normalizing compressor, a cooling system, power management and distribution units, and electric motors. Hydrogen storage solutions were also considered, comparing liquid and gaseous hydrogen configurations for their impact on aircraft mass and aerodynamics. The wing and fuselage dimensions were adjusted to accommodate hydrogen tanks while maintaining stability and minimizing aerodynamic penalties.

By running performance simulations with MATLAB and SUAVE, the efficiency of hydrogen planes with respect to power and sustenance was compared and contrasted with that of conventional planes. The experiment established that the fuel cell efficiency of hydrogen planes is respectable and provides an appropriate flight speed without pollution. The method used

here provides a structured method for examining the incorporation of hydrogen in the improvement of aviation and offers valuable suggestions for green aviation in the future.

Findings

This study presents an extensive evaluation of hydrogen fuel cell integration into a CS-23 category aircraft, using the Dornier 228 as the reference model. The findings demonstrate significant structural and performance changes, particularly in weight distribution, energy efficiency, and operational range. One of the key results is the substantial increase in Maximum Take-Off Mass by 63.73% and Operating Empty Mass by 120.78% due to the additional weight of the fuel cell system and hydrogen storage tanks. However, despite these increases, the total fuel weight is reduced by approximately 78.42%, highlighting the superior energy density of hydrogen compared to conventional aviation fuels, as shown in Figure 1.

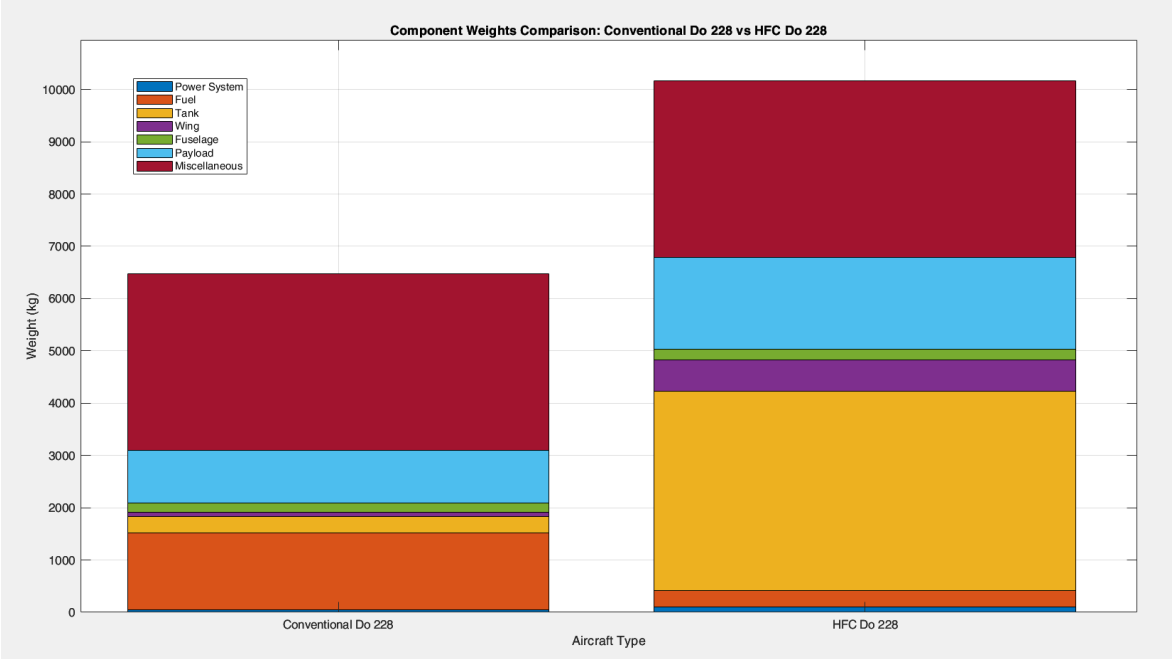

Figure 1: Weight distribution by components of the Conventional and Hydrogen Fuel Cell Dornier 228.

Analyses show that the hydrogen-powered aircraft has a lower range than the conventional version, but optimized structures, such as liquid hydrogen storage, increase operational efficiency. The effect of hydrogen on the shape of the aircraft is the requirement for a longer fuselage and larger wingspan, especially with the increase in fuel tank sizes, as can be seen from Figure 2. The fuselage length was adjusted to accommodate hydrogen tanks, reducing aerodynamic losses and maintaining aircraft stability. Renewable energy-produced hydrogen has 90% potential for sustainable aviation.

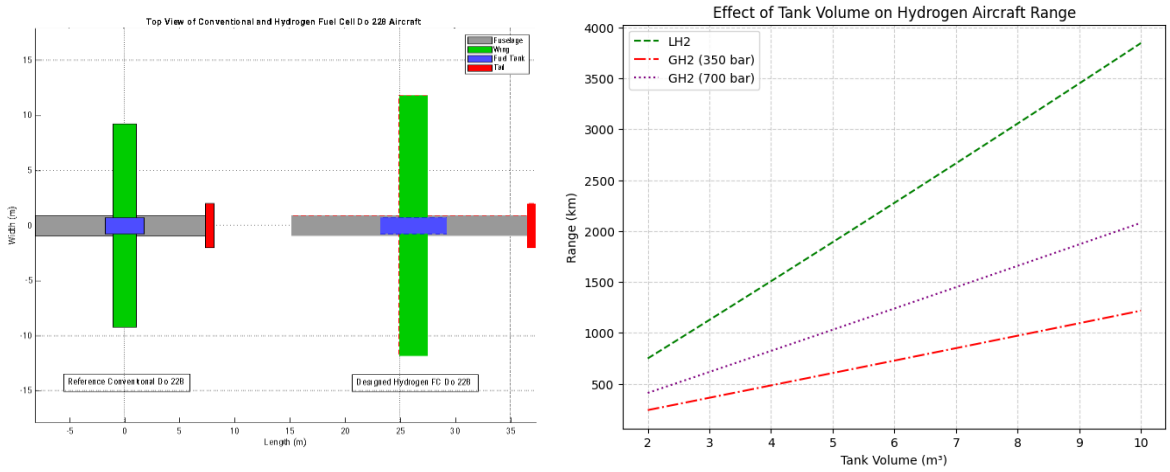

Figure 2: Comparison of Aircraft Dimensions and Range Variation with Tank Volume for the Hydrogen Fuel Cell Dornier 228.

Well-to-wing emissions are 21,995.45 kg-CO_2 for kerosene and 0 kg-CO_2 for LH_2/GH_2 if produced by renewable energy. If not, emissions rise to 366.41 kg-CO_2 for LH_2 and 368.01 kg-CO_2 for GH_2. Hydrogen still has lower emissions than kerosene due to better energy efficiency. For a 4-hour mission, the kerosene range is 1390.97 km with 1470.41 kg of fuel, and the LH_2 range is 404.40 km with 317.32 kg of fuel. When all fuel is consumed, the range increases to 3932.04 km for kerosene and 2598.53 km for hydrogen, showing hydrogen's potential for lower fuel consumption in short/medium-haul flights.

Conclusion

The integration of hydrogen fuel cells into the Dornier 228 showed a 63.73% increase in MTOM and 120.78% in OEM due to the added fuel cell system and tanks. However, fuel weight was reduced by 78.42%, highlighting hydrogen's higher energy density. Performance simulations showed a 4.86% reduction in power-to-weight ratio, with hydrogen-powered aircraft offering lower fuel consumption in short/medium-haul flights. The range for hydrogen was 2598.53 km when all fuel was consumed, compared to 3932.04 km for kerosene. Hydrogen fuel cells can reduce emissions by up to 90% with renewable energy, making them a viable, sustainable solution.

References

Darecki, M., Edelstenne, C., Enders, T., Fernandez, E., Hartman, P., Herteman, J.-P., Kerkloh, M., King, I., Ky, P., Mathieu, M., Orsi, G., Schotman, G., Smith, C., & Wörner, J.-D. (2011). *Flightpath 2050 Europe's Vision for Aviation*.
Elitzur, S., Rosenband, V., & Gany, A. (2017). On-board hydrogen production for auxiliary power in passenger aircraft. *International Journal of Hydrogen Energy*, *42*(19), 14003–14009. https://doi.org/10.1016/J.IJHYDENE.2017.02.037
IEA. (2022). *Global Energy Review: CO2 Emissions in 2021*. https://www.iea.org/reports/global-energy-review-co2-emissions-in-2021-2
IEA. (2023). *Tracking Clean Energy Progress 2023*. https://www.iea.org/reports/tracking-clean-energy-progress-2023
Incer-Valverde, J., Korayem, A., Tsatsaronis, G., & Morosuk, T. (2023). "Colors" of hydrogen: Definitions and carbon intensity. *Energy Conversion and Management*, *291*, 117294. https://doi.org/10.1016/J.ENCONMAN.2023.117294
McKinsey and Company. (2020). *Hydrogen-powered aviation | A fact-based study of hydrogen technology, economics and climate impact by 2050*.
National Academies of Sciences, E. and M. (2016). Commercial Aircraft Propulsion and Energy Systems Research: Reducing Global Carbon Emissions. In *Commercial Aircraft Propulsion and Energy Systems Research: Reducing Global Carbon Emissions*. National Academies Press. https://doi.org/10.17226/23490

Noland, J. K. (2021). Hydrogen Electric Airplanes: A Disruptive Technological Path to Clean up the Aviation Sector. *IEEE Electrification Magazine*, *9*(1), 92–102. https://doi.org/10.1109/MELE.2020.3047173
Roland Berger. (2020). *Hydrogen | A future fuel for aviation?*
Wilcox, L. J., Shine, K. P., & Hoskins, B. J. (2012). Radiative forcing due to aviation water vapour emissions. *Atmospheric Environment*, *63*, 1–13. https://doi.org/10.1016/J.ATMOSENV.2012.08.072

ENERGY SCIENCE AND TECHNOLOGY

Computational Fluid Dynamics

Computational Heat and Mass Transfer

Energy Conversion and Storage Technologies

Energy Conversion and Sustainability

Energy Management and Planning

Renewable Energy

Sustainable Energy

The Effect Of Seawater On The Electrodecomposition Of Hydrogen Sulfide To Hydrogen And Polysulfides

Faezeh Nazari[a], Alper Sarioglan[a], Mehmet Suha Yazici[b]

[a]Istanbul Technical University, Chemical Engineering, Turkey

[b]Istanbul Technical University, Energy Institute, Turkey

syazici@itu.edu.tr

Keywords: Hydrogen Sulfide, Hydrogen Evolution, Electrolysis, Metal-Phthalocyanine.

Aim

The effect of different types of electrolytes on hydrogen sulfide (H_2S) splitting is investigated. The coated cobalt phthalocyanine (CoPc) and nickel phthalocyanine (NiPc) on porous nickel (Ni) are selected as the catalysts for comparison. The linear sweep voltammetry (LSV) and electrochemical impedance spectroscopy (EIS) are measured to understand the behavior of the catalysts and support. NiPc on nickel in NaOH solution has the best response compared to other catalysts and electrolytes. In addition, the presence of sodium chloride decreases the rate of reaction.

The entire amount of H_2S in the Black Sea is estimated to be 4.6 billion metric tons. The anoxic conditions begin in the deeper sections of the basin (below 150-200 meters), where H_2S is believed to be created by sulfur-reducing bacteria at an approximate pace of 10,000 tons per day, which continues to reduce life in the Black Sea (Petrov et al., 2018). H_2S electrolysis involves cathodic H_2 and anodic sulfur oxidation reactions (SOR) at a low cell voltage of 0.14 V (Hakim et al., 2023). Replacing the OER with the SOR reduces the electrolysis potential from 1,23 V (H_2O electrolysis) to 0,14 V (H_2S electrolysis), resulting in significant energy savings for pure H_2 generation (Kumar and Nagaiah, 2022). In the alkali solution H_2S is desolved in the solution (Yang et al., 2019):

$$H2S + OH^- \rightarrow H2O + HS^-$$

And then in the electrolysis reaction:

$$\text{Anode}: 2HS^- \rightarrow S+H2S+2e^-$$

$$HS^- + OH^- \rightarrow S+H2O+2e^-$$

$$\text{Cathode}: 2H2O+2e^- \rightarrow H2 + 2OH^-$$

and then, sulfur rapidly dissolves in the alkaline media forming polysulfides:

$$S+HS^- + OH^- \rightarrow S2^{-2}+H2O$$

In addition, phthalocyanine (Pc) with different central metals has wonderful specifications as a catalyst such as, the ease of large-scale production, distinctive redox behavior, high efficiency, ease of separation, and recyclable nature (Yang et al., 2021).The type of metal center, substitution, support, and aggregation of Pc's are some of the critical parameters that determine the total H_2 production rate for the photo- and electrocatalytic H_2 formation processes of Pc-based catalysts

(Keshipour and Asghari, 2022). For a thorough understanding of the role of the central metal atom in a three-electrode cell electrolysis of H_2S for hydrogen production, CoPc and NiPc were selected for this study.

Material And Method

$Na_2S{\cdot}9H_2O$ (from Carlo Erba) was used as the source of H_2S for its convenience. The original pH values of the Na_2S aqueous solution were adjusted with sodium hydroxide (Riedel-DeHaen and LabKim). CoPc 96% and NiPc 98% (BLD Pharmatech GmbH) were supported on 200 micron 83% porosity nickel fiber (Bekaert).

All electrochemical measurements have done by potentiostat Gamry Instrument Interface 5000e. A conventional three-electrode cell, wherein CoPc and NiPc ($1cm^2$) on diffusion support acts as a working electrode (WE), a platinum wire as counter and 3.5M KCl Ag/AgCl as reference electrodes. The electrolyte solutions were 0.1M NaOH, 0.3M NaCl, and 0.1M NaOH+0.3 MNaCl while 0.1M Na_2S has added as the source of H_2S. The SOR activity of the catalysts was illustrated by performing LSV over a potential range of -0,5 to 0,1 V vs. SHE at scan rate 5 mV/s. The EIS measurements were performed in a frequency range of 100 kHz to 200 mHz at open circuit potential (OCP).

Findings

Electrocatalytic performance is evaluated using LSV at a scan rate of 5 mV/s (Figure 1, 2). The SOR graphs show the different catalyst performances, including NiPc on Ni and CoPc on Ni in 0.1M NaOH, 0.3M NaCl, and 0.1M NaOH+0.3M NaCl electrolyte solutions. As shown in Figure 1a, CoPc on Ni in NaOH solution produces a higher current than in other electrolytes. At 0 V (vs. SHE) in the NaOH solution, the current density is 12.7 mA/cm², while at the same voltage, the current in other electrolytes reaches 2.7 mA/cm². This pattern is also observed for NiPc on Ni. At 0 V (vs. SHE), the NaOH solution results in a current density of 9.8 mA/cm², but the currents decrease to 4.1 and 2.3 mA/cm² for NaCl and NaCl+NaOH, respectively. Moreover, comparing the catalysts CoPc and NiPc shows that in NaOH electrolyte solution, CoPc has a better response, producing 10 mA/cm² at -50 mV (vs. SHE), while NiPc reaches the same value at +37 mV (vs. SHE).z

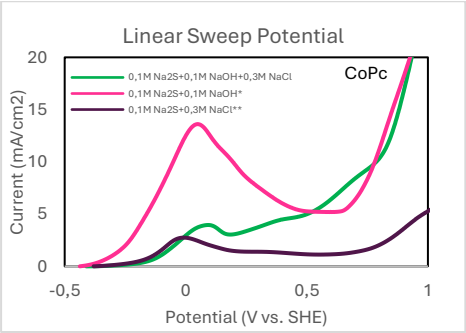

Figure 1: LSV measurement of CoPc at scan rate 5mV/s (in different electrolyte solutions).

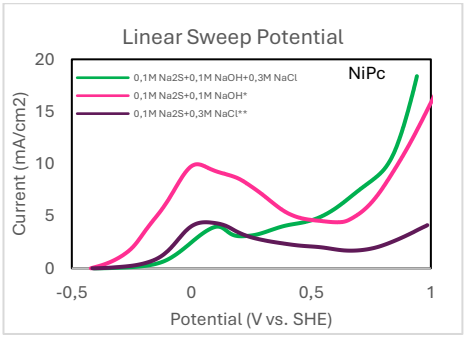

Figure 2: LSV measurement of NiPc at scan rate 5mV/s (in different electrolyte solutions).

Figure 3 reveals the impedance of different electrolytes for both catalysts, NiPc and CoPc. In NaCl and NaOH+NaCl electrolytes, the same patterns can be observed; both electrolytes exhibit lower impedance when the working electrode is CoPc. By comparing different electrolytes with NiPc, it can be concluded that NaOH+NaCl provides high resistance, which results from sluggish kinetics.

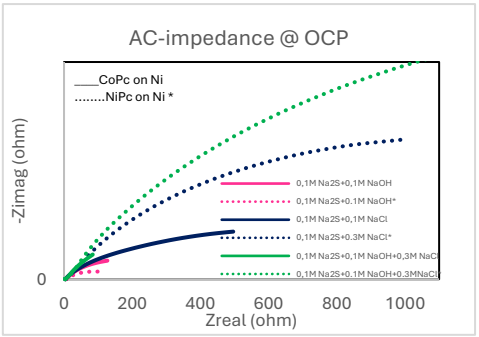

Figure 3: EIS measurement of CoPc and NiPc at OCP (in different electrolyte solutions).

Conclusion

The influence of various electrolytes on H_2S splitting is examined. The catalysts used for comparison are coated CoPc and NiPc on Ni. The LSV and EIS are used to investigate the behavior of the catalysts and support. CoPc on Ni in NaOH solution offers the best response when compared to other catalysts and electrolytes. Additionally, the presence of sodium chloride reduces the rate of reaction.

Acknowledgment

This study was financially supported by Turkish Scientific and Technological Research Council (TUBITAK) under 2502–Research Projects-BAS Bilateral Collaboration program with Grant #123N020.

References

Hakim, L., Sari, R., Fadli, F., Fajar, Safrizal, Selvy, & Emma. (2023). Hydrogen production from seawater using H_2SO_4 catalyst by photovoltaic-electrolysis method. *Materials Today: Proceedings, 87*, 315–320. https://doi.org/10.1016/j.matpr.2023.03.289

Keshipour, S., & Asghari, A. (2022). A review on hydrogen generation by phthalocyanines. *International Journal of Hydrogen Energy, 47*(56), 12865–12881. https://doi.org/10.1016/j.ijhydene.2022.02.058

Kumar, M., & Nagaiah, T. C. (2022). Pure hydrogen and sulfur production from H_2S by an electrochemical approach using a NiCu–MoS_2 catalyst. *Journal of Materials Chemistry A, 10*(25), 13031–13041. https://doi.org/10.1039/D2TA02751H

Petrov, K. P., Dimitrov, D. P., & Uzun, D. R. (2018). *The Black Sea problem – Possible solutions*. LAP LAMBERT Academic Publishing.

Yang, J., Smulders, V., Smits, J. J. T., Mei, B. T., & Mul, G. (2019). Electrochemical oxidation of H_2S on polycrystalline Ni electrodes. *Journal of Applied Electrochemistry, 49*(9), 929–936. https://doi.org/10.1007/s10800-019-01334-x

Yang, S., Yu, Y., Gao, X., Zhang, Z., & Wang, F. (2021). Recent advances in electrocatalysis with phthalocyanines. *Chemical Society Reviews, 50*(20), 12985–13011. https://doi.org/10.1039/D0CS01605E

ENVIRONMENTAL ENGINEERING

Air Pollution and Control

Membrane Technologies

Effects of Air Pollutant Parameters on Respiratory Diseases in Edirne

Kutlay Özdemir[a], Burçak Kaynak[a]

[a] Istanbul Technical University, Faculty of Civil Engineering, Department of Environmental Engineering, Türkiye
ozdemirk18@itu.edu.tr, burcak.kaynak@itu.edu.tr

Keywords: Distributed Lag Non-Linear Model (DLNM), Health Effects, PM, NO2, SO2.

Aim

The association between air pollution and respiratory diseases has gained growing attention in recent years, as air pollution is recognized as one of the leading global risk factors contributing to morbidity and mortality. Increased air pollution can lead to an increase in many diseases, especially respiratory diseases. Edirne, gateway of Türkiye to Europe, with a population of over 400000, its proximity to main highways, and the number of motor vehicles up to 200000, is one of the cities with serious air pollution problems. Based on the number of hospital admissions due to respiratory diseases in Edirne between March 1, 2013 and December 31, 2017, seven different respiratory diseases (shortness of breath, cough, asthma, COPD, sinusitis, bronchitis, and upper respiratory tract infections-URTI) were examined together with the analysis of criteria air pollutants -particulate matters (PM_{10} and $PM_{2.5}$), nitrogen dioxide (NO_2), and sulfur dioxide (SO_2)- between the same dates.

The aim of this study was to evaluate the effect of each 10 μg/m³ increase in criteria air pollutants (PM_{10}, $PM_{2.5}$, NO_2, and SO_2) on respiratory diseases in Edirne/Türkiye during between March 1, 2013 and December 31, 2017. The significant effects of air pollutants on human health were investigated. At the same time, the results will enable more effective and efficient use of decision support systems.

When the relationship between them was investigated, very high levels of sulphur dioxide (SO_2) pollution occurred due to the use of poor-quality coal for residential heating in some districts of Edirne, especially in Keşan. In these years (2013-2017), Keşan was identified as the most polluted location in Türkiye in terms of SO_2. In time, with the widespread use of natural gas, SO_2 pollution has decreased to the limit values specified in the national legislation. However, despite the increase in the number of households subscribed to natural gas, a slight rise in SO_2 levels was observed in 2024. This may be attributed to the preference for cheaper and lower-quality fuels, potentially driven by the ongoing economic crisis in Türkiye.

Material and Method

In this study, the daily average concentrations of criteria air pollutants PM_{10}, $PM_{2.5}$, NO_2, and SO_2, were associated with the number of hospital admissions due to respiratory diseases in Edirne province during the study period (a total of 1767 days / 58 month). In order to investigate the health impacts of air pollutants, a time series analysis of daily hospital admissions for respiratory diseases and air pollutants at various time lags (0-9 days) was performed using a single-pollutant Poisson Generalized Linear Model (Poisson GLM). In this study, the Distributed Lag Non-Linear Model (DLNM) which is the most commonly used statistical methods to evaluate air pollution exposure on human health as a component of GLM was used to account for the delayed effect of air pollution exposure on hospital admissions (Gasparrini, et. al, 2010). This model allows the effects of pollution to be examined on the same day (lag 0), the next day (lag 1), and up to a certain number of days (in this case, 9 days).

Findings

Total hospital admissions for shortness of breath, cough, asthma, COPD, sinusitis, bronchitis and URTI in Edirne were 9625, 43547, 240787, 140539, 12091, 192080 and 1016224, respectively. PM_{10} and $PM_{2.5}$ have been found to be strongly associated with the number of hospital admissions for many respiratory diseases, both in the long term and in the short

term. The comparison of criteria air pollutants (PM_{10}, $PM_{2.5}$, NO_2, SO_2) and the number of daily hospital admissions for respiratory diseases in Edirne are given in Figure 1.

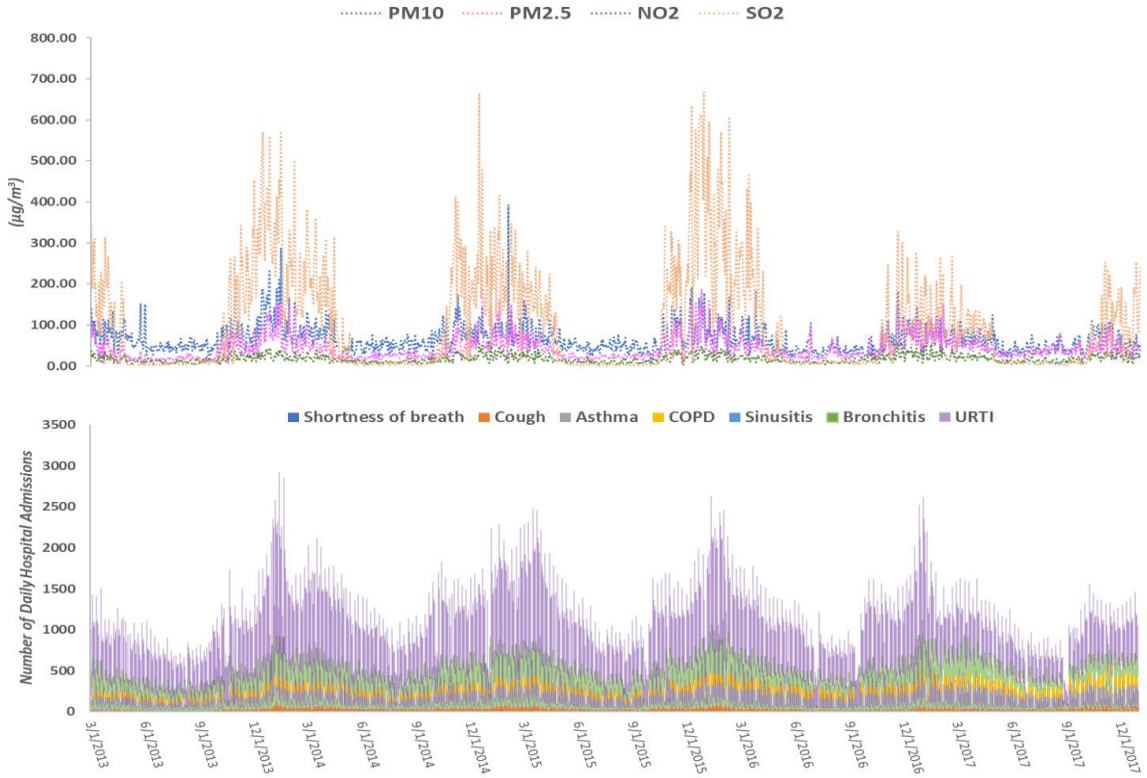

Figure 1: The Comparison of Criteria Air Pollutants (PM_{10}, $PM_{2.5}$, NO_2, SO_2) and The Number of Daily Hospital Admissions for Respiratory Diseases in Edirne between March 1, 2013, and December 31, 2017.

It was observed that hospital admissions for respiratory diseases were significantly higher during the winter months compared to the summer months. In addition to the health effects of air pollution, the air quality of Edirne province (Central and Keşan districts) was examined in detail between 2013-2024, and pollution distribution analyses were performed. Annual mean air pollutants (PM_{10}, $PM_{2.5}$, NO_2, SO_2) of 3 Air Quality Monitoring Stations (AQMSs) in Edirne province for the period between 2013-2024 and their comparison with the limit values were made. For comparison, both the limit value in the Turkish legislation (Air Quality and Assessment Management Regulation, HKDYY) and the European Union (EU) annual limit value for PM_{10} and SO_2, and the EU annual limit values for $PM_{2.5}$ and NO_2, were taken Figure 2.
When the number of natural gas subscriptions of residences in Edirne and its most large district, Keşan, was examined, and a very strong negative correlation between SO_2 pollution and natural gas subscription was observed Figure 3.

A 10 µg/m³ increase in PM_{10} (lag 0–9 days) was associated with a 16.74% [95% Confidence Interval (CI): 2.05–136.70] increase in hospital admissions for sinusitis, a 9.39% [2.63–33.57] increase for shortness of breath and a 2.16% [1.74–2.69] increase for cough. A 10 µg/m³ increase in $PM_{2.5}$ (lag 0–9 days) was associated with a 1.77% [1.29–2.42] increase in hospital admissions for sinusitis, a 1.54% [1.42–1.66] increase for URTI and a 1.45% [0.62–3.37] increase for shortness of breath. A 10 µg/m³ increase in NO_2 (lag 0–9 days) was associated with a 2.20% [1.35–3.59] increase in hospital admissions for shortness of breath, a 1.45% [1.26–1.65] increase for cough and a 1.36% [0.80–2.31] increase for sinusitis. A 10 µg/m³ increase in SO_2 (lag 0–9 days) was associated with a 1.93% [0.99–3.75] increase in hospital admissions for sinusitis, a 1.29% [1.05–1.60] increase for cough and a 1.21% [0.94–1.58] increase for shortness of breath.

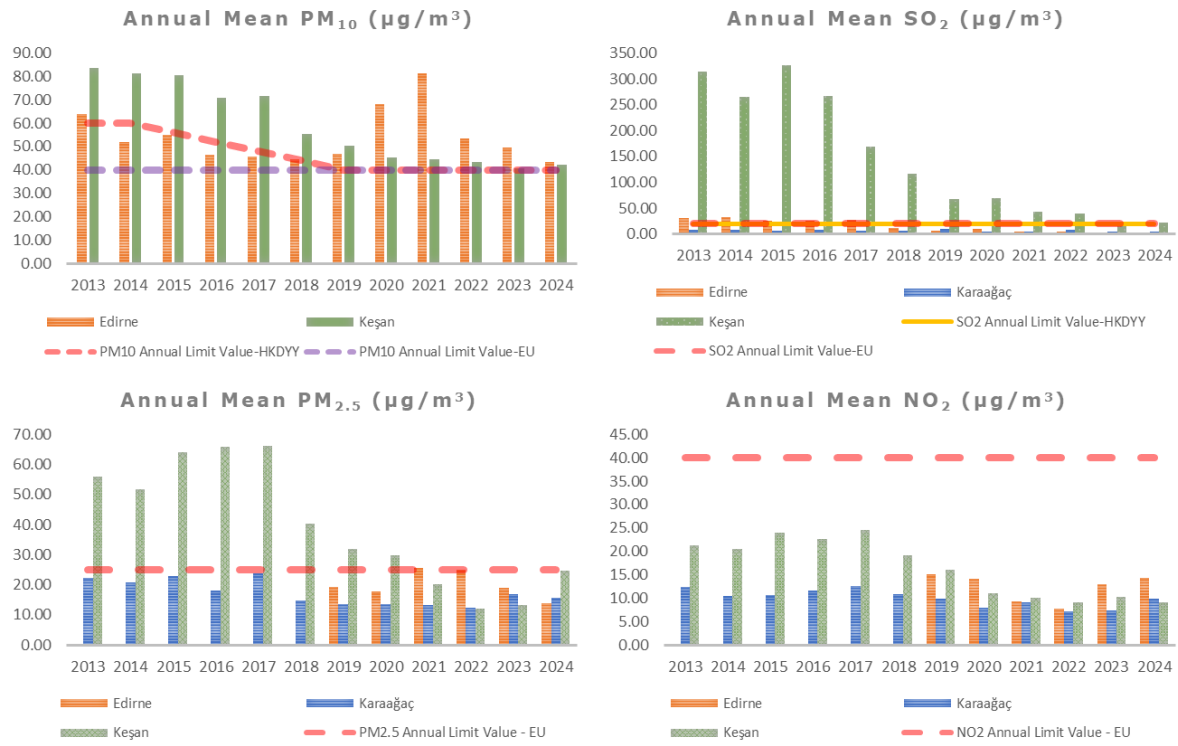

Figure 2: Annual Average Air Pollutants (PM_{10}, $PM_{2.5}$, NO_2, SO_2) of 3 AQMSs in Edirne Province for the Period between 2013-2024 and Comparison with Limit Values.

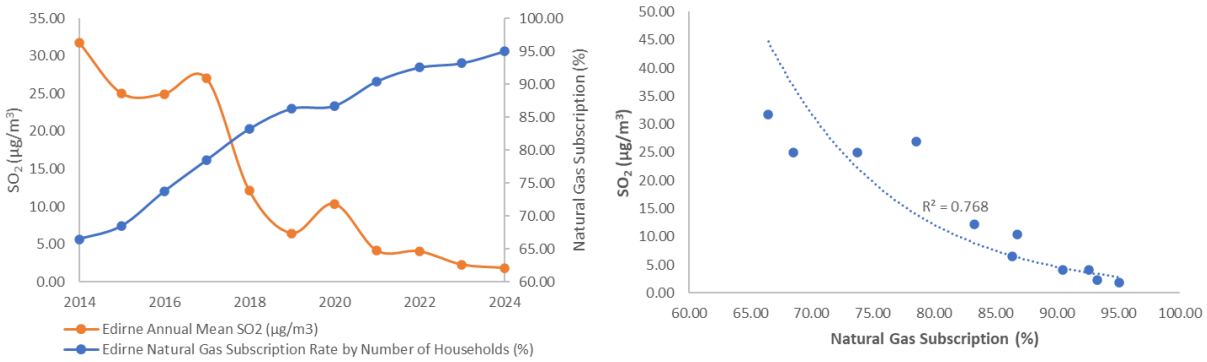

Figure 3: Relationship of SO_2 Concentrations and Natural Gas Subscription Rate by Number of Households (%) in Keşan.

When the cumulative effect was analyzed, every 10 µg/m³ increase in PM_{10} caused a significant increase, especially in sinusitis, shortness of breath and bronchitis; every 10 µg/m³ increase in $PM_{2.5}$ caused a significant increase, especially in sinusitis, cough and asthma; every 10 µg/m³ increase in NO_2 caused a significant increase, especially in shortness of breath and cough; every 10 µg/m³ increase in SO_2 caused a significant increase, especially in URTI, bronchitis and COPD. Cumulative excess relative risk (ERR, %) of hospital admissions associated with a 10 µg/m³ increase in pollutant concentrations over 10 days of lag (lag 0-9) in Edirne is shown in Table 1.

Table 1: Cumulative Excess Relative Risk (ERR, %) of Hospital Admissions Associated with a 10 μg/m³ Increase in Pollutant Concentrations Over 10 Days of Lag (lag 0-9) in Edirne.

	ERR (95% CI) (%)mean			
Health Effects	**PM_{10}**	**$PM_{2.5}$**	**NO_2**	**SO_2**
Shortness of breath	**22.74 [8.62 - 66.27]**	9.31 [5.44 - 16.50]	**10.94 [6.64 - 18.51]**	9.32 [6.69 - 13.12]
Cough	11.51 [8.36 - 16.15]	**10.59 [8.52 - 13.28]**	**12.29 [10.44 - 14.50]**	9.87 [8.59 - 11.36]
Asthma	**10.38 [7.20 - 15.21]**	**10.34 [8.45 - 12.75]**	9.25 [7.86 - 10.89]	10.08 [8.87 - 11.47]
COPD	**10.38 [7.39 - 14.77]**	8.68 [7.07 - 10.71]	9.80 [8.33 - 11.55]	**10.11 [8.97 - 11.42]**
Sinusitis	**25.18 [4.96 - 162.02]**	**10.99 [5.27 - 33.85]**	9.18 [5.40 - 15.78]	9.99 [6.59 - 15.43]
Bronchitis	**12.00 [8.74 - 16.73]**	**10.31 [8.72 - 12.26]**	9.06 [8.00 - 10.28]	10.13 [9.11 - 11.26]
URTI	**10.70 [9.89 - 11.58]**	10.04 [9.58 - 10.53]	9.73 [9.39 - 10.07]	**10.56 [10.26 - 10.87]**

Similarly in the literature; In Klang Valley, an industrial region near Kuala Lumpur, Malaysia's capital, the link between air pollution and acute respiratory infections in children aged 0-14 years was studied, and a significant correlation was found between acute bronchitis and high PM_{10} concentrations (Abdul Rahman et.al, 2017). PM_{10} was shown to significantly increase the risk of 13 different acute respiratory infections subtypes. Among the diseases most impacted by PM_{10} were acute bronchiolitis, acute upper respiratory infection of multiple and unspecified sites, and unspecified acute lower respiratory infection (RR = 1.07, 95% CI = 1.04–1.11 (Abdul Rahman et.al, 2017). Similarly, in a study conducted in Tasmania, Australia between 1992 and 2002, a strong association was found between daily PM_{10} concentrations and hospital admissions for shortness of breath, sinusitis, acute bronchitis and bronchiolitis, but no significant correlation was observed for acute exacerbations of asthma and COPD (Mészáros, D et.al, 2015).

Conclusion

As a result, it has been found that the air pollution parameters PM_{10}, $PM_{2.5}$, NO_2, and SO_2 were found to be closely associated with respiratory diseases, particularly sinusitis and shortness of breath, as well as cough and bronchitis in Edirne. It was found that PM_{10} is the pollutant of primary importance for shortness of breath, sinusitis, COPD, URTI, bronchitis. $PM_{2.5}$ is the pollutant of secondary importance for asthma, NO_2 is the pollutant of secondary importance for cough, SO_2 is the pollutant of secondary importance for URTI.

Although the number of natural gas subscribers has increased in Edirne, many households have been adversely affected by the ongoing economic crisis in Turkey and they have been using cheaper, lower-quality fuels. To prevent the decline in living standards and mitigate the health risks associated with increased air pollution, it is essential for the government to implement support mechanisms such as natural gas subsidies. The economic loss due to respiratory diseases will be much greater than the investments to improve air quality. Public health should be prioritized above other governmental projects or investments.

References

Abdul Rahman, S. R.(2017). A case crossover analysis of primary air pollutants association on acute respiratory infection (ARI) among children in urban region of Klang valley, Malaysia. (Vol. 10, Iss: 1, pp 44), Annals of Tropical Medicine and Public Health, DOI:10.4103/ATMPH.ATMPH_75_17.

Gasparrini, A. (2010). Distributed Lag Non-Linear Models. Statistics in Medicine, (29, 2224-2234). DOI:10.1002/sim.3940

Mészáros, D. (2015). An observational study of PM_{10} and hospital admissions for acute exacerbations of chronic respiratory disease in Tasmania, Australia 1992–2002. *BMJ Journals*. DOI: 10.1136/bmjresp-2014-000063

ENVIRONMENTAL ENGINEERING

Air Pollution and Control

Membrane Technologies

Enhancing Reverse Osmosis Performance: A CFD-Based Study of Randomized Feed Spacer Geometries

Rabiya Karalı Türker[a], Halil Ekici[b], Cemanur Aydınalp[a]

[a] Istanbul Technical University, Department of Electronics and Communication Engineering, Telecommunications Engineering, Turkiye
[b] Izmir Institute of Technology, Department of Chemical Engineering, Chemical Engineering, Turkiye
karalir15@itu.edu.tr

Keywords: Feed spacer geometry, Reverse osmosis, Saltwater desalination.

Aim

Reverse osmosis (RO) is a key technology for desalination, widely applied to treat saline water and provide fresh water for various industrial and domestic uses. The efficiency of RO membranes is often constrained by fouling, leading to performance degradation, increased operational costs, and reduced membrane lifespan. Addressing fouling issues requires strategies such as feed water pre-treatment (Prihasto et al., 2009), membrane surface modifications (Goh et al., 2019), operational optimization (Hoslett et al., 2018), and innovative channel designs (Koutsou et al., 2004). This study investigates the influence of feed channel geometries on RO membrane efficiency, focusing on randomly generated channel structures compared to a pre-examined sinusoidal design (Ling et al., 2021). To achieve this, three different channel designs were created by assigning Bsplines with 10, 15, and 20 random knots while maintaining the same length, allowing a systematic comparison of their impact on flow characteristics and membrane performance. Computational Fluid Dynamics (CFD) simulations were employed to analyze these flow channel configurations, aiming to enhance flow rate and improve mass transfer efficiency. Furthermore, this research will contribute to the body of knowledge by quantitatively assessing how various channel geometries affect the performance parameters of RO systems, specifically targeting enhancements in permeate flux and reduction in fouling. By integrating novel designs with practical engineering applications, the study seeks to pave the way for more sustainable and efficient RO systems.

Material and Method

Computational Fluid Dynamics Simulations

In this study, the CFD simulation was applied to investigate the influence of the feed channel geometry on the performance of RO systems. Water flow profile, membrane fouling, and clean water flow over time were calculated by CFD simulations. The CFD simulations utilize the Navier-Stokes equations to determine the velocity and pressure profiles, while the advection-diffusion equation was used to model the salt concentration distribution in the channel. Additionally, the Langmuir adsorption-desorption equation was applied to the membrane surface to quantify membrane fouling. Lastly, permeate flux equation based on Darcy's law on porous surface, was used to calculate the amount of permeate flux. These equations define the dynamics of fluid flow and the associated mass transfer phenomena within the RO process.

Feed Spacer Design and Simulation Setup

The feed channel geometry design process followed three key steps: (1) feed spacer geometries were designed using CAD software (Salome Platform version 19.4.0), (2) mesh generation was performed for CFD analysis, and (3) simulations were conducted with OpenFOAM (v2412) CFD software. pimpleFOAM solver package of openFOAM was modified to analyze flow, permeate flux, and membrane fouling for various channel geometries. Key parameters such as inflow velocity, pressure, and solute concentration were set to define the boundary conditions for the simulations. This process was repeated for each feed spacer geometry, including three randomly generated designs and one sinusoidal design. Both the randomized channels and the sinusoidal design were generated with a length of 100 mm. The randomized channels used 10, 15, and 20

knots, applying a B-spline algorithm to introduce geometric randomness. For sinusoidal design, the period is selected as 2.4 mm. From these models, the membrane performance parameters, including fouling deposition (surface fouling), fluid flow characteristics, and permeate flux were obtained.

The simulations were performed by introducing bulk concentration, surface concentration, and permeate flux as scalar quantities to pimpleFOAM solver modeling different spacer geometries, and assessing their impact on overall system performance. Residuals for flow velocity, pressure, solute concentration, and flux were set to $1\times e^{-7}$ in CFD solution package to obtain accurate results. Boundary conditions used in CFD simulations are indicated in Table 1.

Table 1. Boundary conditions used in CFD simulations: U represents the three-dimensional velocity vector(m/s), P denotes pressure (bar), C_s refers to the salt concentration on the membrane surface, C_b indicates the mass ratio of salt (1 corresponds to 0.035 kg salt/kg solution) in the solution, and J_w (Lmh) represents permeate flux.

	Input	Output	Walls	Membrane
U	0.15 m/s	dU/dt = 0	0	partial slip
P	dP/dt = 0	40 bar	dP/dt = 0	dP/dt = 0
C_s	0	0	0	$dC_s/dt = 0$
C_b	1	$dC_b/dt = 0$	$dC_b/dt = 0$	$dC_b/dt = 0$
J_w	0	0	0	$dJ_w/dt = 0$

Findings

The study comprised three random models with varying complexities, 10, 15, and 20 knots, alongside a reference model featuring a conventional flat geometry and a sinusoidal model. The comparative analysis of simulation results, as documented in Table 2, clarifies several key observations regarding the performance metrics across different channel designs including the average flux J_w, the average surface fouling C_s, and the end-to-end pressure drop. The performance metrics are independent of surface area, and they are listed in the table as additional information. Moreover, visuals showing the final fouling characteristics of all models are presented in Figure 1.

Table 2. For each channel, the average values at the membrane surface, the membrane surface area, and the calculated pressure difference between the inlet and outlet of the channel.

Models	Average J_w (Lmh) 10^{-3}	Average C_s	Pressure Drop	Models
Reference model	2.75	1.76	0.2	1.00
Random (10)	2.79	1.77	0.37	1.72
Random (15)	2.77	1.78	0.59	1.88
Random (20)	3.30	1.73	1.00	1.78
Sinusoidal	2.83	1.72	1.20	1.00

The findings indicate that all models, including those with random geometries, achieved at least comparable or superior average flux J_w values relative to the baseline established by the reference model. Notably, the Random(20) model exhibited

a significant increase in performance metrics, distinguishing itself, particularly in areas of flux enhancement. This suggests a potential correlation between the complexity of knot configurations and flux performance, although the differences between the 10, and 15 knots models were not pronounced enough to draw definitive conclusions.

In terms of pressure drop, an important factor considering hydraulic performance, the Random(20) model demonstrated advantages over the sinusoidal model, suggesting that higher knot configurations might optimize both mass transfer efficiency and hydraulic resistance. However, the results related to fouling metrics C_s did not significantly differentiate between the models, indicating that this performance aspect might be less sensitive to changes in channel geometry or might require additional experimental data for a more nuanced analysis.

Overall, the simulation outcomes underscore the promising potential of random models, particularly as the number of knots increases. These models not only challenge the traditional efficiency benchmarks set by rectangular and sinusoidal geometries but also hint at an emergent trend where increased geometrical complexity leads to performance gains. To confirm these preliminary findings and to fully figure out the impact of knots on RO system performance, further detailed experiments and analyses are warranted.

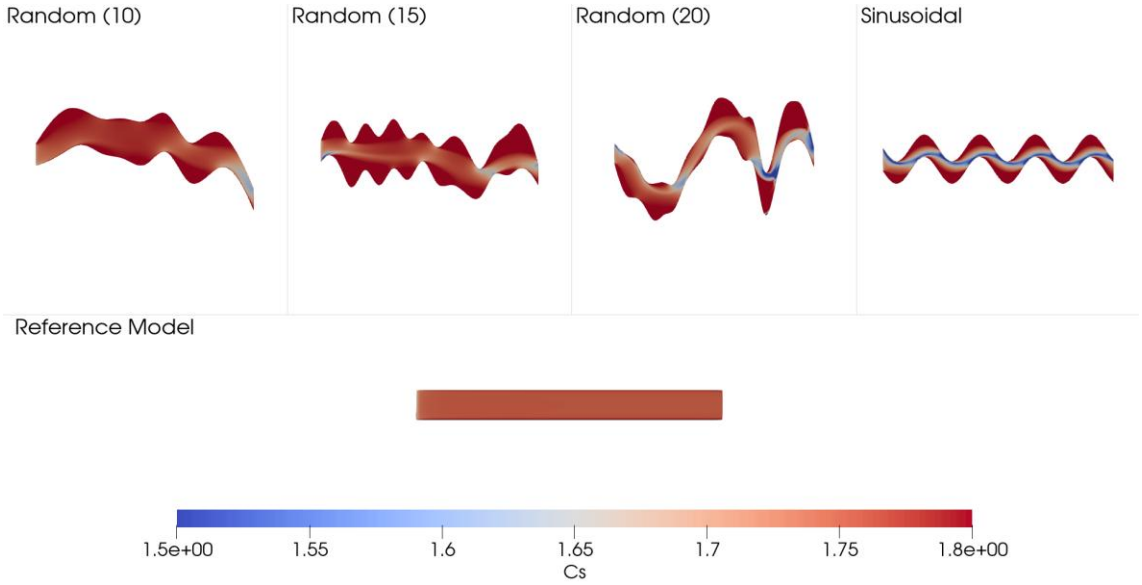

Figure 1. Membrane fouling distribution for channel geometries: 10-knots random, 15-knots random, 20-knots random, sinusoidal model, and reference model.

These insights contribute significantly to the ongoing discourse on optimizing feed spacer designs within reverse osmosis systems, highlighting the critical role of channel geometry in enhancing system efficiency and sustainability.

Conclusion

The study confirms that optimizing the geometry of the feed channel using random generation techniques and CFD simulations can pave the way to improve the performance of the RO system. These advances provide a promising pathway for designing next-generation RO systems that operate more efficiently and sustainably, offering a vital solution to global challenges in water treatment.

References

Goh, P.S., Zulhairun, A.K., Ismail, A.F., Hilal, N. (2019). Contemporary antibiofouling modifications of reverse osmosis desalination membrane: a review. Desalination 468, 114072.

Hoslett, J., Massara, T.M., Malamis, S., Ahmad, D., van den Boogaert, I., Katsou, E., Ahmad, B., Ghazal, H., Simons, S., Wrobel, L., Jouhara, H. (2018). Surface water filtration using granular media and membranes: a review. Sci. Total Environ. 639, 1268–1282.

Koutsou, C.P., Yiantsios, S.G., Karabelas, A.J. (2004). Numerical simulation of the flow in a plane-channel containing a periodic array of cylindrical turbulence promoters. Journal of Membrane Science 231 (1), 81–90.

Ling, B., Xie, P., Ladner, D. & Battiato, I. (2021). Dynamic modeling of fouling in reverse osmosis membranes. Membranes. 11, 349.

Prihasto, N., Liu, Q.-.F., Kim, S.-.H. (2009). Pre-treatment strategies for seawater desalination by reverse osmosis system. Desalination 249 (1), 308–316.

FOOD ENGINEERING

Food Bioactive Compounds

Food Microbiology

Food Science

Functional Foods

Novel Food Processes

Sustainable Foods

Extraction of Phenolic Compounds from Grape Pomace; Potential Application Packaging Materials

Ayşe Nilay Yıldırım[a], Derya Kahveci Karıncaoğlu[a]

[a] Istanbul Technical University, Faculty of Chemical-Metallurgical Engineering, Department of Food Engineering
doldur18@itu.edu.tr, kahvecid@itu.edu.tr

Keywords: Grape Pomace, Phenolic Compounds, Quercetin, Bioactive Compounds, Extraction.

Aim

In the context of functional food and bioactive compound production, the valorization of food industry by-products holds significant importance. Particularly, phenolic compounds such as polyphenols offer health-promoting effects due to their antioxidant activity, enabling the development of high value-added products. The aim of this study is to investigate the effects of sample preparation techniques, solvent concentration, and enzymatic pretreatments on extraction yield, total phenolic content (TPC), total flavonoid content (TFC), and antioxidant activity in phenolic extraction from grape pomace. In future stages of the project, the obtained extracts are intended to be evaluated for food packaging applications.

Material and Method

Extraction of bioactive compounds, primarily quercetin, was performed from red grape pomace, a by-product of wine production. Upon delivery to the laboratory, the pomace was stored at −20 °C until analysis. Prior to extraction, some samples were subjected to freeze-drying at −40 °C for 24 hours. The moisture content of pomace was calculated based on weight differences before and after drying. Fresh or dried pomace samples were ground and homogenized prior to extraction. Ethanol solutions at 50% and 80% (v/v) concentrations were used as solvents, maintaining a solid-to-solvent ratio of 1:10. Extractions were conducted at 65 °C for 1 hour in a shaking water bath.

For enzymatic pretreatments, the pH of homogenized pomace was adjusted to 5.0 using 1 M NaOH after the addition of distilled water. Then, 100 µL of Pectinex®, Celluclast®, or a 1:1 mixture of both enzymes was added per gram of pomace. The mixture was incubated at 50 °C for 2 hours with shaking. Enzymes were inactivated by heating the solution at 100 °C for 1 minute. Subsequently, solvent was added, and the conventional solvent extraction process was initiated. For control groups, all procedures were identical except for the absence of enzyme addition. After extraction, samples were centrifuged at 9000 rpm for 10 minutes, and the supernatants were stored at −4 °C until analysis.

Total phenolic content (TPC), total flavonoid content (TFC), and concentrations of specific phenolic compounds such as quercetin and resveratrol were determined. TPC was measured using the Folin–Ciocalteu method, with absorbance recorded at 765 nm and results expressed as mg gallic acid equivalent (GAE)/mL extract. TFC was determined via aluminum chloride colorimetric assay, absorbance measured at 510 nm, and results expressed as mg quercetin equivalent (QE)/mL extract. To characterize the phenolic profile, HPLC analysis was conducted using a Waters 2695 system with PDA detector. A Supelcosil LC-18 column (25 cm × 4.60 mm) was used, with the mobile phase composed of 0.1% (v/v) formic acid in water (Solvent A) and 0.1% (v/v) formic acid in acetonitrile (Solvent B). A linear gradient elution was applied with a flow rate of 1 mL/min. Chromatograms were recorded at 360 nm, and retention times and UV spectra were compared with those of authentic standards for compound identification.

Findings

Analytical results indicated that freeze-dried samples subjected to enzymatic pretreatment yielded the highest TPC (1.09 mg GAE/mL) and TFC (3.00 mg QE/mL) values. In comparison, fresh samples without pretreatment yielded a TPC of 0.58 mg GAE/mL, demonstrating the significant effect of freeze-drying on extraction efficiency. Antioxidant activity assays (DPPH and CUPRAC) also confirmed higher antioxidant potential in freeze-dried samples.

HPLC-based quantitative analysis confirmed the presence of several flavonoids, notably quercetin and kaempferol. Optimal extraction conditions for quercetin were found to be with dried pomace, without enzymatic pretreatment, and using 50% ethanol. In the following phases of the study, the application of the extract in bio-based packaging systems will be further explored and experimentally evaluated. This study aimed to extract phenolic compounds, particularly quercetin, from grape pomace—an industrial by-product of winemaking—and to enhance extraction yield using enzymatic pretreatments prior to conventional solvent extraction. The findings are consistent with previous reports in the literature. It is well-established that phenolic compounds are predominantly located in the grape seed. According to Deryaoğlu (1997), approximately 62.6% of total phenolics are found in the seed, 33% in the skin, and only 4.1% in the pulp. Therefore, the seed content of grape pomace may significantly influence the total phenolic yield obtained.

In a study by Gomez-Mejía et al. (2022), optimization of extraction parameters from grape seed pomace yielded 112 μg/g of quercetin, supporting the efficacy of similar strategies applied in this study. The use of enzymes such as Pectinex® and Celluclast® facilitates the breakdown of plant cell walls, releasing soluble phenolic compounds. This is further supported by Drevelegka and Goula (2020), who reported enhanced polyphenol extraction efficiency via enzymatic pretreatment of grape pomace. Phenolic compound content varies not only with processing parameters but also with grape cultivar, clone, geographical origin, and environmental factors. Jaworski and Lee (1987) reported considerable variability in phenolic contents among different grape varieties of Vitis labrusca and Vitis vinifera. Similarly, Roggero et al. (1986) observed notable differences in phenolic content among clones of the Syrah grape variety. In this study, enzymes were found to both enhance and reduce extraction yield depending on the sample type. The highest yield was obtained from dried pomace without enzymatic pretreatment; however, enzyme mixtures were found to be effective in fresh pomace samples. These results indicate that factors such as pomace processing (fresh vs. dried), enzymatic treatment, and solvent composition are key determinants of phenolic yield. HPLC analysis proved reliable for profiling specific phenolics in the extracts. Ultimately, the data demonstrate that grape pomace is a valuable source of bioactive compounds and that enzymatic pretreatments can significantly enhance their recovery. Further research with different grape varieties and production residues would offer more comprehensive insights.

Several studies have demonstrated the high potential of quercetin as an active compound in bio-based packaging materials due to its antioxidant, UV-blocking, and antimicrobial properties. When incorporated into biodegradable films, quercetin enhances mechanical strength, UV-barrier capacity, and oxidative stability of the film, which are all critical for food preservation (Roy & Rhim, 2021; Ezati & Rhim, 2021). For example, gelatin- or chitosan-based films doped with quercetin have been shown to significantly reduce microbial growth on perishable items like fish or fresh-cut fruits (Li et al., 2020; Tongdeesoontorn et al., 2021). Additionally, the radical scavenging ability of quercetin-loaded films contributes to the prevention of lipid oxidation in oil-containing products, thereby extending shelf life (Jakubowska et al., 2023).

In the context of this study, the quercetin-rich extract obtained from grape pomace holds considerable promise for further incorporation into biofilms. Based on literature precedents, it is anticipated that the integration of such extracts into biopolymers like gelatin, polyvinyl alcohol, or polylactic acid via electrospinning or solution casting could yield functional films with improved bioactivity. Future work will focus on optimizing the incorporation of this extract into polymer matrices and evaluating the resultant films for physicochemical, mechanical, and antimicrobial properties, aligning with sustainable packaging goals.

Conclusion

This study shows that wine industry by-products such as grape pomace can be effectively valorized for their phenolic content using enzyme-assisted extraction methods. Freeze-drying combined with appropriate enzymatic treatment yielded extracts with high antioxidant capacity and phenolic content, including elevated levels of bioactive compounds such as quercetin. These results suggest that this method may be extended and adapted for the development of functional food ingredients or active packaging materials.

References

Cacciola, F., et al. (2022). Polyphenols in grape pomace: HPLC profiling and potential food applications. Antioxidants, 11(3), 567.

Deryaoğlu, A. (1997). Elazığ yöresinde yetiştirilen siyah şaraplık Boğazkere ve Öküzgözü üzüm çeşitlerinin olgunlaşması sırasında meydana gelen fiziksel ve kimyasal değişmeler. ÇÜ Fen Bilimleri Enstitüsü. Çukurova Üniversitesi Fen Bilimleri Enstitüsü, 148s.

Drevelegka, V., & Goula, A. M. (2020). Recovery of bioactive compounds from olive mill waste: Enzyme-assisted extraction enhanced by ultrasound. Journal of Cleaner Production, 277, 123389.

Ezati, P., & Rhim, J. W. (2021). Active antimicrobial packaging films based on chitosan and gelatin containing quercetin. Food Hydrocolloids, 120, 106899.

Gómez-Mejía, E., Vicente-Zurdo, D., Rosales-Conrado, N., León-González, M. E., & Madrid, Y. (2022). Screening the extraction process of phenolic compounds from pressed grape seed residue: Towards an integrated and sustainable management of viticultural waste. LWT, 169, 113988.

Jakubowska, M., et al. (2023). Chitosan-based films with quercetin and silver nanoparticles: Shelf-life extension of edible oils. Carbohydrate Polymers, 303, 120415.

Jaworski, A. W., & Lee, C. Y. (1987). Fractionation and HPLC determination of grape phenolics. Journal of agricultural and food chemistry, 35(2), 257-259.

Li, M., et al. (2020). Quercetin-functionalized films for enzymatic browning inhibition in apples and potatoes. Journal of Agricultural and Food Chemistry, 68(10), 2952–2960.

Lojková, L., et al. (2023). Influence of drying and solvent polarity on polyphenol extraction from fruit residues. Food Chemistry, 412, 135524.

Roggero, J. P., Coen, S., & Ragonnet, B. (1986). High performance liquid chromatography survey on changes in pigment content in ripening grapes of Syrah. An approach to anthocyanin metabolism. American Journal of Enology and Viticulture, 37(1), 77-83.

Roy, S., & Rhim, J. W. (2021). Quercetin-incorporated chitosan-based functional films for active food packaging. Food Hydrocolloids, 120, 106882.

Tongdeesoontorn, W., et al. (2021). Cassava starch/gelatin-based packaging film infused with quercetin for pork preservation. LWT - Food Science and Technology, 147, 111601.

FOOD ENGINEERING

Food Bioactive Compounds

Food Microbiology

Food Science

Functional Foods

Novel Food Processes

Sustainable Foods

Plant-Based Proteins in Instant Soups: Comparison of Sensory, Functional, and Bioactive Properties

Ceren Çakır[a], Esra Çapanoğlu Güven[a]

[a] İstanbul Technical University, Food Engineering Departmant, Master of Science Program, Türkiye
cakirce@itu.edu.tr

Keywords: Plant Protein, Instant Soup, Phenolic Content, Antioxidant Capacity, Rheology.

Aim

This study aims to develop instant soup formulations enriched with different plant proteins and to evaluate their sensory properties, bioacive properties (total phenolic content and atioxidant capacity), flowability and viscosity characteristics with explore the balance between nutritional value and consumer satisfaction. The objective is to identify plant protein sources that are both nutritionally valuable and acceptable in terms of taste and processing properties for instant soup applications. This research focuses on the potential of rice, chickpea, and pumpkin seed proteins as sustainable, plant-based ingredients in instant tomato and lentil soups. As demand for plant-based foods increases, especially among health-conscious and environmentally aware consumers, the use of novel protein sources in convenient foods such as instant soups is gaining attention (Gamal & MF Albaz, 2024).

Material and Method

Six different plant protein sources were incorporated into instant tomato and lentil soup formulations. Protein powders from different sources were supplied by industrial company. The protein powders used in this study were rice, chickpea, fava bean, pea, oat, and pumpkin seed proteins. Tomato and lentil soups were prepared in the laboratory using with industrial raw materials. Both tomato and lentil soups were prepared with 10% protein powder content (rice, pea, chickpea, fava bean, and pumpkin seed proteins). Samples without protein powder were designated as control(reference) samples. The soup mixtures containing 10% protein powder and control samples were portioned as 18 grams. They were prepared by adding 170 ml of water heated to 100°C and thoroughly mixing for 45 seconds.

Sensory analysis was conducted with 20 trained panelists aged between 22-45, evaluating attributes such as appearance, aroma, taste, mouthfeel, and aftertaste using a 6-point hedonic scale. Panelists scored the samples on a scale of 1 to 6 by comparing them to the control. Based on sensory scores, three proteins with the highest acceptability were selected for further analysis.

In vitro gastrointestinal digestion was simulated using the standardized protocol (Minekus et al., 2014), which includes oral, gastric and intestinal phases. The total phenolic content of initial and digestion samples was determined according to the method of Singleton & Rossi (1965), expressed in mg GAE/g. CUPRAC (Cupric Reducing Antioxidant Capacity) method was used to determine the antioxidant capacities of the samples according to the method proposed by Apak et al. (2009). And finally functional attributes which are flowability (ffc index) and viscosity were assessed. Flowability was expressed as the flow function coefficient (ffc), which is defined as the ratio of consolidation stress to unconfined yield strength. The viscosity of soup samples was measured using a Brookfield RV DV2T viscometer.

Findings

Tomato and lentil soups were compared with control samples in terms of appearance and color, aroma and taste, smell, aftertaste, and consistency parameters. Based on the taste test conducted with 20 panelists, samples containing pumpkin seed (P8), rice (P3), and chickpea (P4) proteins received the highest scores for taste, smell, and consistency (Figure 1). Fava bean protein (P5) altered the soups the most significantly, receiving the lowest score for taste and aroma. Oat protein also negatively affected taste and was excluded from further studies due to its low protein content and high processing costs.

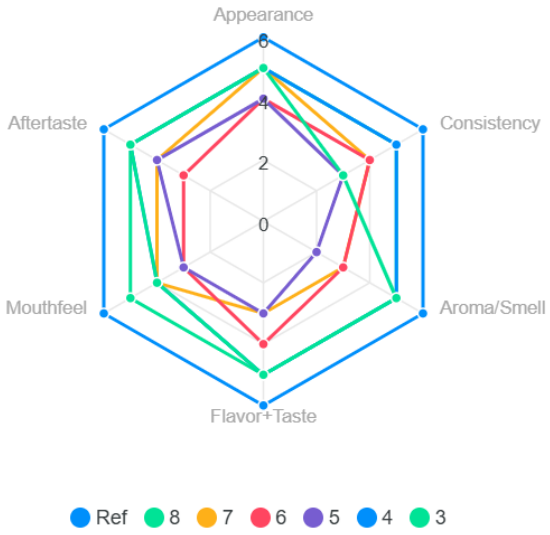

Figure 1. Sensory analysis scores.

For total phenolic content of tomato soup, the control sample showed an increase from 18.93±1.66 mg GAE/g (initial) to 25.59±3.95 mg GAE/g (gastric), but a sharp decrease to 8.18±2.61 mg GAE/g after the intestinal phase. Sample which is enriched by rice protein had the highest gastric TPC (34.25±3.24 mg GAE/g), but dropped to 7.72±1.90 mg GAE/g after intestinal digestion. Adding chickpea protein in tomato soup showed the lowest intestinal phenolic content (2.77±0.08 mg GAE/g). Tomato soup with pumpkin seed protein started with the highest initial TPC (20.50±0.85 mg GAE/g) and retained the highest TPC after intestinal digestion (23.82±3.37 mg GAE/g), suggesting strong phenolic-protein interactions that protect antioxidants during digestion. The control sample of lentil soup had the highest gastric TPC (52.43±1.44 mg GAE/g), but it dropped sharply to 6.95±1.74 mg GAE/g in the intestinal phase. When it is enriched by rice and chickpea protein maintained moderate TPC levels after intestinal digestion (17.05±0.85 and 15.40±2.15 mg GAE/g, respectively). Lentil soup with pumpkin seed protein preserved the highest TPC after intestinal digestion (22.60±5.32 mg GAE/g), outperforming other protein sources.

The antioxidant capacities of the soup samples were determined using the CUPRAC (Cupric Reducing Antioxidant Capacity) method, which measures antioxidant activity at nearly physiological pH and provides a reliable estimate of the total antioxidant potential in complex food matrices (Apak et al., 2008). The control sample of tomato soup showed an increase in antioxidant capacity from the initial (48.52±4.59) to the gastric phase (58.43±0.28), and a further increase in the intestinal phase (75.09±7.08). Among the protein-enriched samples, T+P8 (pumpkin seed protein) demonstrated a remarkable increase, reaching 160.55±8.30 after the intestinal phase. This value was notably higher than both the control and other protein-enriched samples, indicating a strong protective effect of pumpkin seed protein on antioxidant capacity during digestion. Addition rice protein and chickpea protein also maintained relatively high antioxidant capacities after the intestinal phase (63.87±6.97 and 51.82±0.50, respectively), but not as high as pumpkin seed protein. For lentil soup the control sample showed a steady increase from initial (11.14±0.88) to gastric (40.25±0.62) and intestinal phases (77.86±6.80). L+P8 (pumpkin seed protein) again stood out, with an intestinal phase value of 67.05±4.06, which was higher than other protein-enriched lentil samples. Samples which enriched by rice protein and chickpea protein had lower antioxidant capacities after the intestinal phase (38.94±5.51 and 23.37±4.13, respectively).

The viscosity and flowability results of the instant soup samples are presented in Table 2 and Table 3.

Table 1. Nutritional compositon of instant soups.

Composition	Tomato Soup	Lentil Soup
Energy	34 kcal / 143 kJ	34 kcal / 141 kJ
Fat (g)	0.6	0.5
Protein (g)	0.7	1.8
Carbohdrate (g)	6.8	4.7
Dietary fiber (g)	0.6	0.7
Salt (g)	0.5	0.5

Table 2. Viscosity values of soups with protein.

Speed	Samples					
	T + P3	T + P4	T + P8	L + P3	L + P4	L + P8
5	1,40	1,48	2.3	4,32	1,52	4,20
10	832,00	822,00	611,00	2,47	1,08	2,12
15	612,00	634,00	858,70	1,78	712,00	1,02
20	532,00	592,00	682,00	1,43	568,00	900,00
50	302,40	300,30	368,00	703,20	310,40	754,00
100	219,60	211,00	248,80	395,20	210,00	412,00

*The results are expressed in centipoise (cP).

Table 3. Ffc and Rhob values of soups with protein.

Samples	Ffc	Rhob
T	2,65±0,07	571,50±6,36
T + P3	2,35±0,07	561,50±0,73
T + P4	2,30±0,07	540,00±0,80
T + P8	2,50±0,01	477,50±0,71
L	2,03±0,11	672,00±8,48
L + P3	1,68±0,04	649,00±1,41
L + P4	1,66±0,01	633,50±0,71
L + P8	1,70±0,01	635,00±1,01

Ffc: Flow function coefficient
Rhob: Bulk density

Viscosity ranks among the most important functional properties of proteins. Therefore, understanding the flow characteristics of protein-enriched soups is vital for quality control, process design, and equipment selection. Furthermore, rheological properties of liquid foods are critically important and can directly affect sensory quality, thereby influencing consumer preference. However, these properties may be altered by various added components (Yılmaz et al., 2010). This

study evaluated how different plant proteins affected both flowability and viscosity of instant soups, providing valuable insights for industrial applications. Viscosity measurements were performed at different shear rates for both tomato and lentil soup formulations enriched with rice (P3), chickpea (P4), and pumpkin seed (P8) proteins. Tomato soup samples (T+P3, T+P4, T+P8) exhibited very low viscosity at the lowest shear rate (5 rpm), followed by a sharp increase at 10 rpm (up to 832.00 cP). The viscosity then gradually decreased at higher shear rates, indicating a shear-thinning behavior typical for semi-liquid foods. Lentil soup samples (L+P3, L+P4, L+P8) showed different flow patterns. For example, L+P8 reached the highest viscosity (900.00 cP) at 20 rpm, while L+P3 and L+P4 peaked at 50 rpm (703.20 cP and 712.00 cP, respectively). All lentil formulations showed a decrease in viscosity at the highest shear rate (100 rpm).

Maintaining component functionality stability from powder mixing to packaging is critical in industrial production of instant soups. These products consist of various ingredients (salt, flour, starch, oils) that differ in particle size, distribution, and density, resulting in diverse flow properties. Determining these properties is essential to prevent major issues such as agglomeration or poor flow during processing. Flowability, measured by the flow function coefficient (ffc), represents plastic deformation under specific stress and serves as an excellent metric for characterizing powder behavior-higher ffc values indicate better flowability. According to industry standards, powders are classified as non-flowing (ffc<1), very cohesive (1<ffc<2), cohesive (2<ffc<4), flowing (4<ffc<10), or free-flowing (ffc>10) (Schulze, 2008). Ffc values indicated that tomato-based soups had better flowability (Ffc: 2.65–2.50) compared to lentil-based soups (Ffc: 2.03–1.66). Among the protein-enriched samples, the addition of pumpkin seed protein (P8) resulted in the least reduction in flowability for both soup types. Bulk density (Rhob) was higher in lentil-based soups (672.00–633.50 g/L) than in tomato-based soups (571.50–477.50 g/L). Protein addition generally increased the density of tomato soups, while it slightly decreased the density in lentil soups. There was a clear negative relationship between viscosity and flowability, samples with higher viscosity tended to have lower flowability, making them harder to process and serve.

Conclusion

In summary, the results of this study demonstrate that the type of plant protein added to instant soup formulations has a significant impact on sensory properties, flowability, viscosity, total phenolic content, and antioxidant capacity. Among the tested proteins, pumpkin seed protein consistently provided the highest antioxidant retention and total phenolic content after digestion, as well as favorable flow and viscosity characteristics, making it a promising ingredient for functional instant soups. These findings highlight the importance of selecting appropriate protein sources not only for improving nutritional value but also for optimizing technological and sensory qualities in instant soup production. As protein content and functional properties such as water-holding capacity, emulsification, and gelation are critical for product quality and consumer acceptance, further studies will continue to investigate these functional attributes in detail (Zhang et al., 2021).

References

Apak, R., Güçlü, K., Özyürek, M., Bektaş¸ oğlu, B., & Bener, M. (2008). Cupric ion reducing antioxidant capacity assay for food antioxidants: vitamins, polyphenolics, and flavonoids in food extracts. *Advanced protocols in oxidative stress I*, 163-193.

Gamal, A., & MF Elbaz, A. (2024). Production of Vegetables Soup Powder Supplemented with Two Protein Sources. *Food Technology Research Journal*, *5*(2), 110-122.

Minekus, M., Alminger, M., Alvito, P., Ballance, S., Bohn, T. O. R. S. T. E. N., Bourlieu, C., ... & Brodkorb, A. (2014). A standardised static in vitro digestion method suitable for food–an international consensus. *Food & function*, *5*(6), 1113-1124.

Schulze, D. (2008). Stresses. *Powders and Bulk Solids: Behavior, Characterization, Storage and Flow*, 249-289.

Singleton, V. L., & Rossi, J. A. (1965). Colorimetry of total phenolics with phosphomolybdic-phosphotungstic acid reagents. *American journal of Enology and Viticulture*, *16*(3), 144-158.

Yilmaz, M. T., Sert, D., & Demir, M. K. (2010). Rheological properties of tarhana soup enriched with whey concentrate as a function of concentration and temperature. *Journal of Texture Studies*, *41*(6), 863-879.

Zhang, Y., Sharan, S., Rinnan, Å., & Orlien, V. *Survey on Methods for Investigating Protein Functionality and Related Molecular Characteristics. Foods 2021, 10, 2848*.

Composition and technofunctional properties of Aquafaba from Local Legume

Nurullah Zekeriya Akar[a,b], Meral Kılıç Akyılmaz[a]

[a] Istanbul Technical University, Department of Food Engineering, Turkey
[b] Istanbul Gelisim University, Department of Food Technology, Turkey
nzakar@gelisim.edu.tr

Keywords: Aquafaba, Legume, Food Waste, Emulsion, Foam.

Aim

Today, one of the leading global problems is malnutrition, and one of the ways to prevent this is to utilize nutrient-rich agricultural products without loss and to recycle by-products for sustainability. In terms of sustainability in the food sector, there is a need to develop innovative, nutritious, healthy and low-cost products and to utilize waste within circular economy system. Due to problems such as lactose intolerance and milk protein allergy worldwide, the increasing cost of animal production and its effects on the environment, a decrease in animal-based foods and an increase in plant-based foods and proteins are predicted. Legumes such as beans, chickpeas, broad beans, lentils and peas, which contain 20-30% protein, are being investigated as an alternative to animal-based foods. Legumes are among the most important food sources that benefit the sector and sustainable production and consumption due to their nutritional richness, formation of multiple by-products in the process stages, functional and technological properties, and diversity of use in foods. The evaluation of a by-product released from the production of canned legumes is important in terms of the economical use of natural resources, the reduction of waste and the creation of a circular economy system in which waste is evaluated. Soaking and boiling pulses in water before selling them as canned or frozen are processes that use a significant amount of water in the industry. Canning process includes soaking, boiling (85°C for 30 minutes), cooling, filling and adding filling liquid to the can and finally sterilization stages. The remaining process water after boiling is called as aquafaba, which is a significant nutritionally valuable waste and this waste liquid is obtained not only from chickpeas, but also from lentils, peas and different types of beans. Legume process water varies according to the legume type, legume:soaking and boiling water ratio, temperature, pH, time and pressure and has a content of carbohydrates, proteins, phytochemicals, vitamins and minerals. Legume process water has recently been investigated as a structuring additive in plant-based food production studies due to its functional properties such as foaming, emulsification, thickening and gelation. There are very few products that commercial process water is used for. The demand for plant-based products is constantly increasing. The fact that process water is both plant-based and contains surfactants shows that it has high potential. In this study, composition and functional properties of process waters obtained from different local legume species (İspir bean, red lentil, mung bean, grass pea, pigeon pea) were investigated.

Material and Method

Legumes were soaked in distilled water at 25°C for 12 hours with a 1:4 (w/w) legume:water ratio to ensure hydration. Then, the soaking water was separated from the legumes and water was added at a 1:1 (w/w) legumes:water ratio and heated at 85°C for 30 minutes. The resulting mixture was filtered through coarse filter paper to obtain process water samples. The obtained process waters were analyzed for dry matter, ash, protein and carbonhydrate content using standard analytical methods (e.g., Lowry method for soluble protein, gravimetric analysis for dry matter, ash and carbonhydrate). Functional properties such as foaming and emulsion capacity and stability were evaluated by measuring foam overrun and emulsion phase separation over time.

Findings

Process water samples from local legumes contained 2.93–5.69% total solids, 0.33–0.73% ash, 0.27-1.52% protein and 1.60–3.44% carbonhydrate. The lower total solids content compared to the literature is due to the process waters not being cooked for a short duration and under pressure. The composition of process water depended on legume type, cell wall composition and structure. Among the legumes analyzed, mungbean had the highest dry matter, protein, ash and carbonhydrate content and this is probably due to the small size of this legume. Because high surface area increases the extraction efficiency and enables more soluble solid compounds into the process water. Grass pea, ispir bean, pigeon pea and red lentil followed mungbean in terms of dry matter content. The foaming capacity and stability ranged between 54.17 to 145.83% and 31.37 to 63.27%, respectively. Among the process water samples, İspir, red lentil and pigeon pea showed good foaming capacity with overrun values greater than 100%. Red lentil process water was determined to have the highest foaming activity and stability. This is mainly due to high soluble protein content and polysaccharides. Less foaming activity of mung bean with the highest protein content compared to red lentil can be explained by low molecular weight proteins (albumin) and saponin content. Low molecular weight proteins are well-known foaming and surface-active attributes. Pigeon pea, ispir bean, grass pea and mung bean followed red lentil in terms of foaming capasity. The emulsion capacity and stability ranged between 71.88 to 76.39% and 73.61 to 75.35%, respectively. Similar results were observed in terms of emulsion activity and stability among the samples. İspir bean process water was determined to have the highest emulsion activity and stability. Red Lentil, mung bean, grass pea and pigeonpea followed ispir bean in terms of emulsion capasity and stability. The emulsifying properties of aquafaba are attributed to its protein, oligosaccharide, polysaccharide, phenolic, saponin contents, protein- polysaccharide complex and hydrophilic to hydrophobic groups of proteins with emulsifying properties.

Conclusion

In conclusion, it was determined that process waters from local legumes had a nutrient-rich composition with significant foaming and emulsifying activity and stability. While studies on chickpea aquafaba are prevalent in the literature, this study compares the functional properties of process waters obtained from different legumes, including İspir bean, red lentil, mung bean, grass pea, and pigeon pea. Additionally, the industrial potential of these local species is evaluated. The study highlights a substantial potential for the development of novel products, which could contribute to the advancements in the field. In addition, studies on local legumes for our country will pave the way for the production of this low-cost waste by-product as an additive in both liquid and powder form. Future studies could investigate the effects of different cooking temperatures and durations on the functional properties of process water. Additionally, a detailed molecular-level analysis of specific components that enhance foam and emulsion stability could be conducted.

References

Erem, E., Icyer, N. C., Tatlisu, N. B., Kilicli, M., Kaderoglu, G. H., Toker, Ö. S. (2021). A new trend among plant-based food ingredients in food processing technology: Aquafaba, Critical Reviews in Food Science and Nutrition., 63, 1-18.
Kilicli, M. and Toker, O. S. (2022). Some physicochemical and technological properties of cooking water of pulses as a canned industry waste: effect of ultrasound treatment during soaking, International Journal of Food Engineering., 18, 105-118.

FOOD ENGINEERING

Food Bioactive Compounds

Food Microbiology

Food Science

Functional Foods

Novel Food Processes

Sustainable Foods

Effects of Audible-Range Sound Treatment on the Microbiological Quality of Strawberry During Post-Harvest Storage

Deniz Çavdar[a], Gürbüz Güneş[a]

[a] Istanbul Technical University, Faculty of Chemical-Metallurgical Engineering, Department of Food Engineering, Türkiye
cavdard18@itu.edu.tr

Keywords: Frequency, Fruits and Vegetables, Microbiology, Postharvest, Sound Treatment.

Aim

Plants continuously interact with the external environment. They utilize various external factors for growth and development, striving to maintain optimal conditions for survival. However, exposure to factors that disrupt these optimal conditions, stress factors, can make survival more challenging. Stress factors are generally categorized into two types: biotic (e.g., plants, microorganisms, animals, and anthropogenic effects) and abiotic (e.g., temperature, water, sound, minerals, light, chemicals, radiation, etc.) (Levitt, 1980; Lichtenthaler, 1996). To survive, plants develop physiological and metabolic responses to these stress factors (Korkmaz & Durmaz, 2017). It has been suggested that when stress levels are mild, instead of causing harm, they may lead to beneficial changes in plants (Ozkurt & Altuntas, 2018). In response to stress, the secondary metabolites, which play a crucial role in plant defense mechanisms, accumulate, and are influenced by factors including temperature, humidity, light intensity, and mineral availability (Akula & Ravishankar, 2011).

Sound stress, an abiotic stress factor, is a form of mechanical stress that originates from sound waves generated by various sources (Ozkurt & Altuntas, 2018). Sound waves are classified into three main spectral ranges based on their frequency: infrasound (<20 Hz), audible sound (20 Hz-20 kHz), and ultrasound (>20 kHz) (Dikilitaş et al., 2016). The application of sound waves has been studied as non-thermal postharvest preservation method. Although most research in this field has focused on high-frequency "ultrasound" waves, research on audible sound waves has demonstrated their potential effects on plant growth and metabolism. For instance, the application of "green music" consisting of classical music and natural sounds (e.g. birds, water, and insects), for three hours during two growth stages (seedling and mature) of Chinese cabbage was found to increase polyamine levels and oxygen uptake compared to the control group (Qin et al., 2003). Furthermore, sound wave exposure has been suggested to enhance plant resilience to abiotic stresses (Jung et al., 2018). Plant Acoustic Frequency Technology (PAFT) has been reported to stimulate plant growth, improve photosynthesis efficiency, enhance yield and quality, strengthen the immune system, and extend the postharvest shelf life of agricultural products (Hendrawan, 2020).

Some postharvest studies on audible sound waves suggest their potential for preserving fruit and vegetable quality and shelf life. Audible sound treatments have been shown to delay tomato ripening and extend shelf life (Kim et al., 2015), while also preserving the color and texture of broccoli (Asuncion et al., 2020) and white oyster mushrooms (Paclibare Ceejay et al., 2019). However, research on the postharvest effects of audible sound waves on fresh produce remains scarce. Most studies in the literature focus on preharvest applications or ornamental plants. Despite this, the potential impact of audible sound on postharvest preservation should not be overlooked, and further studies are needed to better understand its effects on fruits and vegetables.

The aim of this study is to investigate the use of audible-range sound waves during the postharvest storage of fruits to retard microbial growth and extend their shelf life. In the literature, the use of audible sound waves during the pre-harvest period has been reported; however, there is limited information on their post-harvest applications. This study will contribute to the use of audible sound waves as a food preservation method after harvest.

Material and Method

The effects of sound waves on microbial growth in strawberries were investigated. Fresh strawberries were purchased from a local market and rinsed with water before the sound treatment. The strawberries were stored at 4°C in a cooling unit for 12 days, where sound treatment was conducted at frequency of 250 Hz for 12 hours per day. Analyses were performed on predetermined storage days (0, 3, 5, 7, 10 and 12). Microbiological analyses included total mesophilic aerobic bacteria and mold/yeast counts. Casein-pepton Soymeal-peptone (CASO) Agar was used for total viable bacterial analysis, while Czapek-Dox Sabouraud Dextrose Agar (C-SDA) was utilized for mold and yeast analyses. 10 g of strawberry samples were blended and homogenized with 90 mL of Physiological Saline Solution (PSS), and further dilutions were prepared. While total viable bacterial plates were incubated at 37°C for 48 h, mold/yeast plates were incubated at 30°C for 72 h. Each analysis was conducted in triplicate using three parallel samples. All experimental data were statistically analyzed using Minitab 21.

Findings

The total aerobic mesophilic bacteria count results are presented in Figure 1. Initially, bacterial counts were similar across all groups (~2.69 log CFU/g). However, distinct trends emerged during storage. In the control group, bacterial counts increased to 3.75 log CFU/g by day 12. The 250 Hz treated samples exhibited fluctuations, decreasing to 2.3 log CFU/g on day 10 before slightly rising to 2.75 log CFU/g by day 12. Statistical analyses confirmed significantly lower bacterial counts in the 250 Hz group on days 10 and 12, compared to the control ($p<0.05$).

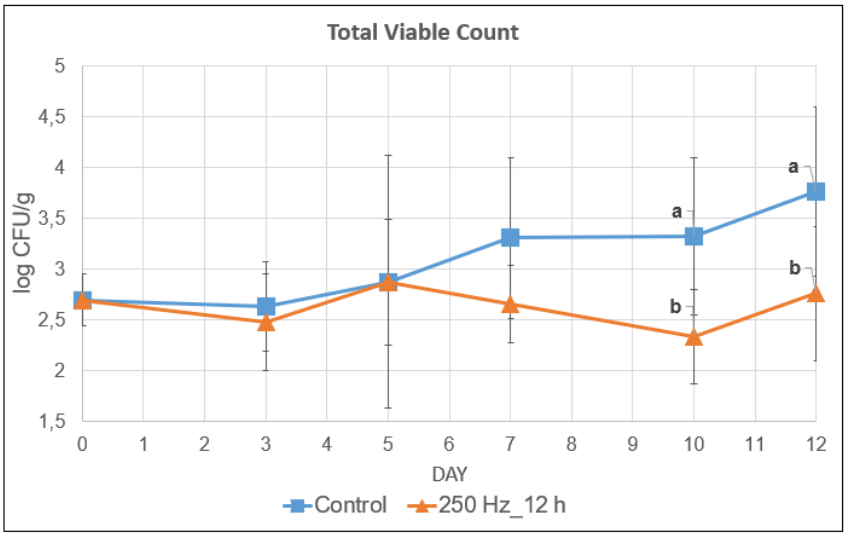

Figure 1. Changes in the total aerobic mesophilic bacterial count in strawberry samples (log CFU/g). Values marked with different letters on the same day are statistically different ($p<0.05$)

Mold and yeast growth results are shown in Figure 2. Unlike bacterial inhibition, the effect of sound treatment on mold and yeast was more limited. Initial counts (~3.18 log CFU/g) were similar across both control and treated samples, and gradually increased throughout storage. By day 12, mold and yeast loads reached 3.91 log CFU/g in the control group, 3.88 log CFU/g in the 250 Hz group. However, no statistically significant differences were observed between groups ($p>0.05$), suggesting that mold and yeast exhibit greater resistance to sound waves compared to bacteria.

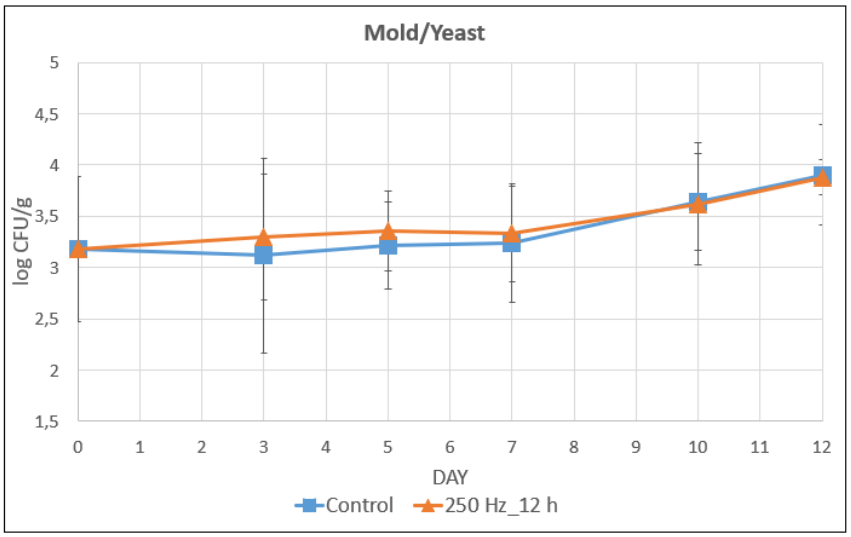

Figure 2. Changes in total mold/yeast count in strawberry samples (log CFU/g). No statistically significant differences were found between values on the same day ($p>0.05$).

Razavizadeh et al. (2024) investigated the effects of sound waves on certain molds that cause food spoilage, including *Aspergillus niger*, *Aspergillus flavus*, *Aspergillus parasiticus*, and *Botrytis cinerea*. Molds inoculated on Potato Dextrose Agar (PDA) medium were exposed to 250 Hz sound at 25°C for 24 hours, and the growth was recorded as colony diameter. The 250 Hz sound application showed an inhibitory activity on different *Aspergillus* species. While the effect was the least on *A. flavus*, the inhibition was the most against *A. niger* by 20.02% compared to the control group. In the case of *B. cinerea*, no significant growth difference was observed compared to the control group ($p > 0.05$). The underlying reason for the lack of the antifungal effect observed in our study can be explained by the fact that different mold species showed different resistance to sound treatment in the study conducted by Razavizadeh et al. (2024). Our study included the natural microbiota of strawberries, rather than specific mold inoculation. The dominant mold species of the natural microbiota may be resistant to sound treatment; however, the antifungal activity may be further investigated by spot or spray inoculation of selected yeasts and molds, and under varied frequencies.

Conclusion

The findings show that sound waves exhibit different effects on microbial growth. The results indicate that sound application within specific frequency ranges can have an inhibitory effect on total viable bacterial load. However, a similar effect was not observed in mold and yeast populations. It is suggested that molds are more resistant due to the durability provided by their spore structures, and the applied sound treatments were not sufficient to suppress these microorganisms effectively. These findings suggest that audible sound frequencies could be considered as an alternative method for food preservation. However, to enhance the effectiveness of sound waves and to better understand their impact on shelf life, it is necessary to optimize different frequencies and treatment durations. In the future, integrating this method with other preservation techniques for industrial applications could be a promising research area for extending shelf life of fruit and vegetables by retarding microbial growth and preserving their freshness.

References

Akula, R., & Ravishankar, G. A. (2011). Influence of abiotic stress signals on secondary metabolites in plants. Plant signaling & behavior, 6(11), 1720-1731.

Asuncion, D. P., Lavarias, J. A., Tuates Jr, A. M., Somera, C. G. G., & Peneyra, R. G. (2020). Influence of Acoustic Waves on the Shelf Life Quality of Broccoli (Bsassica oleracea var. italic).

Dikilitaş, M., Balak, V., & Karakaş, S. (2016). Ses Dalgalarının Tarımsal Ürünlerin Muhafazası Ve Bitki Gelişimi Üzerine Etkileri. Harran Tarım Ve Gıda Bilimleri Dergisi, 20(4), 338-355.

Hendrawan, Y., Putra, A. H., Sumarlan, S. H., & Djoyowasito, G. (2020). Plant acoustic frequency technology control system to increase vegetative growth in red-lettuce. TELKOMNIKA (Telecommunication Computing Electronics and Control), 18(4), 2042-2052.

Jung, J., Kim, S. K., Kim, J. Y., Jeong, M. J., & Ryu, C. M. (2018). Beyond chemical triggers: evidence for sound-evoked physiological reactions in plants. Frontiers in plant science, 9, 25.

Kim, J. Y., Lee, J. S., Kwon, T. R., Lee, S. I., Kim, J. A., Lee, G. M., ... & Jeong, M. J. (2015). Sound waves delay tomato fruit ripening by negatively regulating ethylene biosynthesis and signaling genes. *Postharvest Biology and Technology*, *110*, 43-50.

Korkmaz, H., & Durmaz, A. (2017). Bitkilerin abiyotik stres faktörlerine karşı geliştirilen cevaplar. Gümüşhane Üniversitesi Fen Bilimleri Dergisi, 7(2), 192-207.

Levitt, J. (1980). Responses of plants to environmental stresses. Chilling, freezing, and high temperature stress, 1, 345-447.

Lichtenthaler, H. K. (1996). Vegetation stress: an introduction to the stress concept in plants. Journal of plant physiology, 148(1-2), 4-14.

Ozkurt, H., & Altuntas, O. (2018). Quality parameter levels of strawberry fruit in response to different sound waves at 1000 Hz with different dB values (95, 100, 105 dB). Agronomy, 8(7), 127.

Paclibare Ceejay, O., Lavarias, J. A., Tuates Jr, A. M., Somera, C. G. G., & Peneyra, R. G. (2019). Influence of Acoustic Waves on the Shelf Life Quality of White Oyster Mushroom (Pleurotus Florida).

Qin, Y. C., Lee, W. C., Choi, Y. C., & Kim, T. W. (2003). Biochemical and physiological changes in plants as a result of different sonic exposures. Ultrasonics, 41(5), 407-411.

Razavizadeh, B. M., Shahrampour, D., & Niazmand, R. (2024). Investigating the effect of acoustic waves on spoilage fungal growth and shelf life of strawberry fruit. Fungal Biology, 128(2), 1705-1713.

FOOD ENGINEERING

Food Bioactive Compounds

Food Microbiology

Food Science

Functional Foods

Novel Food Processes

Sustainable Foods

Development and Characterization of Biodegradable Films Enriched with Protein Extracted from Agro-Industrial Pea Waste and By-Products

Nihal Sultan Bayar[a], Neşe Şahin Yeşilçubuk[a], Hande Yenipazar[a], Ayşe Saygün[a]

[a]Istanbul Technical University, Faculty of Chemical and Metallurgical Engineering, Food Engineering, Türkiye
sultan@itu.edu.tr

Keywords: Alkali Extraction, Biodegradable Film, Pea Pod Protein, Ultrasound Pre-Treatment, Valorization.

Aim

Agricultural and agro-industrial production generate substantial volumes of waste and by-products each year. A recent review indicates that the fruit and vegetable industry contributes to around 14.5% of total waste (Pérez-Marroquín et al., 2023). Notably, certain vegetable components like hulls, seeds, stems, leaves, and bagasse are often discarded due to their undesirable taste or texture (Lau et al., 2021). Peas are among the most widely consumed seasonal legumes, available in fresh, frozen, or shelled forms in supermarkets. The pea industry generates approximately 30%–40% of waste from pea pods during processing (Çam et al., 2022). Recently, food scientists have shown increasing interest in utilization of pea pod by-products as functional food ingredients, as they are rich in dietary fiber, carbohydrates, crude proteins, minerals, and bioactive compounds (Nasir et al., 2023). Especially, pea pods have 13% crude protein content (Karabulut et al., 2023). Efficient utilization and valorization of these by-products are essential for environmental sustainability and economic viability.

The objective of this study is to valorize pea by-products for the extraction of pea pod protein and to evaluate its potential in the formation of biodegradable films. In this context, the study aims to characterize the biodegradable films formulated with pea pod protein and to assess its suitability as a film-forming material. By conducting a comprehensive analysis, this research seeks to demonstrate the feasibility of utilizing pea pod protein in biodegradable film production, thereby contributing to the valorization of agricultural by-products and the development of sustainable packaging alternatives.

The study comprised of four steps: preparation of pea pods for protein extraction, extraction of protein, development of biodegradable films incorporating pea-pod protein, and characterization of the films.

Material and Method

Green peas supplied from a local market in Istanbul were separated from their seeds. The remaining parts especially pods were washed, dried and grounded into fine powder for performing alkali extraction. Pea pod protein was extracted from pea pod powder by ultrasound-pretreated alkali extraction method, which is known to enhance protein recovery efficiency (Kumar et al., 2021). Following the extraction process, the obtained protein was subjected to freeze drying procedure to form a uniform powder, ensuring consistency for the subsequent preparation of biodegradable films and further analyses. In order to determine the extraction efficiency, the protein content of both pea pod powder and extracted protein was quantitatively analyzed. Total nitrogen content was analyzed by the Kjeldahl procedure (AOAC Method No. 920.87, 1995). The conversion factor of 6.25 was used to transform nitrogen into protein (Mateos et al., 2010) In order to investigate the film-forming capability of pea pod protein in combination with different materials, various film forming materials were investigated. Agar, fish gelatin and chitosan were determined as main film forming materials which are widely recognized for their structural and functional properties in film development. Following this preliminary assessment, film forming solutions were prepared and development of biodegradable films were carried out using these materials.

Five different film samples that successfully formed films were selected for further analysis. Three of these films contained pea protein, while the other two were selected as controls. These formulations included A (agar-based film), AP (agar-pea pod protein-based film), AGP (agar-gelatin-pea pod protein-based film), C (chitosan-based film), and CP (chitosan-pea pod protein-based film), each representing different combinations of film-forming materials. The agar containing film samples were prepared according to the method specified by Ozhan (2022), while chitosan based film were prepared by Nan et al.

(2022) with some modifications. The production of edible films was conducted utilizing the solvent casting method. Biodegradable films were obtained after drying at 55°C for 24 hours.
For the characterization of the film samples, thickness, transmittance, opacity, moisture content, swelling behavior, color attributes, and antimicrobial activity assays were conducted. A range of instruments was utilized to conduct experimental measurements, including an electronic digital micrometer for film thickness determination, a Nano spectrophotometer for transmittance and opacity measurements, a Chroma meter for color analysis. The antimicrobial activities of all films were investigated for their inhibitory effects towards Gram-positive *S. aureus*, Gram-negative *E. coli* and fungus *A. niger* using the agar disc diffusion method. Statistical analysis was conducted with the use of Minitab Statistical Software.

Findings

Protein extraction was conducted with ultrasound-assisted alkali extraction method. Based on the findings obtained from protein content analysis, the efficiency of the protein extraction process was determined to be 13.20%, indicating the proportion of protein successfully recovered from the original raw material. Karabulut et al. (2023) studied different protein extraction methods from pea pods to maximize protein yield and evaluate the effects of ultrasound and enzyme pretreatments on extraction. Their findings showed that ultrasound-pretreated alkaline extraction achieved the highest protein recovery, 21.1%, which is comparable to the extraction efficiency observed in the current study.
After obtaining the protein, biodegradable film samples were prepared using the selected film formulations. Visual appearances of biodegradable film samples are shown in Figure 1.

Figure 1. Visual appearance of the film samples.

a: A (agar-based film), b: AP (agar-pea pod protein-based film), c: AGP (agar-gelatin-pea pod protein-based film), d: C (chitosan-based film), e: CP (chitosan-pea pod protein-based film)

The developed films were systematically characterized through a series of tests to assess their physical and functional properties. Thickness, transmittance, opacity, moisture content and swelling values of the film samples are shown as in Table 1.

Table 1. Thickness (mm), transmittance (%), opacity (%), moisture content (%) and swelling (%) values of the film samples.

Sample	Thickness (mm)	Transmittance (%)	Opacity (%)	Moisture content (%)	Swelling in water (%)
A	0.041±0.0020^{c}	0.84±0.014^{ab}	4.46±0.535^{a}	20.65±0.275^{b}	761.01±11.812^{b}
AP	0.031±0.0052^{c}	0.88±0.020^{a}	4.25±1.008^{a}	11.77±2.546^{c}	201.26±20.449^{d}
AGP	0.039±0.0039^{c}	0.85±0.026^{ab}	4.08±0.904^{a}	9.30±1.371^{c}	2223.68±37.500^{a}
C	0.132±0.0165^{a}	0.78±0.040^{b}	1.87±0.39^{b}	28.57±3.046^{a}	287.97±14.998^{c}
CP	0.213±0.0165^{b}	0.62±0.105^{c}	2.27±0.776^{b}	28.30±4.036^{a}	169.20±16.478^{d}

A: Agar based film, AP: Agar-protein based film, AGP: Agar-gelatin-protein based film, C: Chitosan based film, CP: Chitosan-protein based film. Results are given as average ± standard deviation. Means within a column followed by different lowercase superscripts (a–d) are significantly different (p<0.05).

Based on the thickness findings, no significant differences were observed among the agar-containing films. (p<0.05) However, the thickness of chitosan-containing films showed a significant difference when compared to agar-containing films (p<0.05). Films containing chitosan were found to be thicker compared to those containing agar. Additionally, CP was measured as the thickest, with a thickness of 0.21±0.02 mm.

The opacity values of the chitosan containing films are significantly different from agar containing films. (p<0.05). Moreover, the transmittance of the agar containing films are not significantly different from each other, while CP which has the lowest transmittance value (0.62±0.11%), is significantly different from the other films. (p<0.05). CP had also the lowest opacity value (2.27±0.78 UA/mm) among protein containing films.

While chitosan films have the highest and similar moisture content, films containing both agar and pea protein have the lowest and similar moisture content (p<0.05). Agar film is significantly different from the other films (p<0.05).

Swelling measurements of the film samples revealed that the addition of pea pod protein reduced the swelling values. While CP exhibited similar moisture content to the control, its swelling value (169.20 ± 16.478) was nearly half that of the control (287.97 ± 14.998). Similarly, the swelling value of AP (201.26 ± 20.449) was lower than that of A (761.01 ± 11.812). In contrast, AGP (2223.68 ± 37.500) showed a significantly higher swelling value compared to AP, indicating the effect of gelatin's hydrophilicity (Ramos, 2016).

According to the color results of the biodegradable films shown in Table 2, in terms of L* values which represents light coefficient, AP is significantly different from all other films and the other films show similarities with each other (p<0.05). b* value of CP is significantly different from AP and AGP through protein containing films. (p<0.05) CP had the highest b* value (4.02±1.247) that indicates dark yellow color is significantly different from the other protein containing films (p<0.05).

Table 2. Color values of the film samples.

Sample	Color parameters		
	L*	a*	b*
A	45.53±1.046[a]	4.27±0.059[a]	-3.18±0.108[c]
AP	38.16±0.567[b]	2.33±0.136[d]	-0.74±0.426[b]
AGP	45.76±2.529[a]	3.45±0.379[b]	-1.01±0.274[b]
C	45.31±1.373[a]	3.60±0.068[b]	-0.32±0.454[b]
CP	43.97±0.554[a]	2.98±0.299[c]	4.02±1.247[a]

A: Agar-based film, AP: Agar-protein-based film, AGP: Agar-gelatin-protein-based film, C: Chitosan-based film, CP: Chitosan-protein-based film. Results are given as average ± standard deviation. Means within a column followed by different lowercase superscripts (a–d) are significantly different (p<0.05).

For antimicrobial activity, the largest inhibition zones (0.39±0.005 mm against *E.coli*, 0.46±0.005 mm against *S.aureus* and 0.72±0.008 mm agains *A. Niger*) were observed in CP among the protein-containing films, likely due to the antibacterial and antifungal properties of chitosan (Manigandan et al., 2018). The results also indicate that pea pod protein reduced the antimicrobial effect of chitosan, though CP films still exhibited promising activity compared to other protein films.

Conclusion

The results demonstrated that pea pod protein-enriched films positively impacted film properties, underscoring their potential as nutritious food packaging alternatives. Furthermore, the findings highlight the role of pea pod protein in reducing agricultural waste while enhancing the sustainability and functionality of edible films in the food industry. No significant adverse effects of pea pod protein were observed, suggesting its suitability for biodegradable film formation. This study recommends further research on the application of these films to selected food products to evaluate their practical use in food packaging.

References

Çam, G., Akın, N., Konak Göktepe, Ç., & Demirci, T. (2023). Pea (Pisum sativum L.) pod powder as a potential enhancer of probiotic Enterococcus faecium M74 in ice cream and its physicochemical, structural, and sensory effects. Journal of the Science of Food and Agriculture, 103(6), 3184–3193. https://doi.org/10.1002/jsfa.12276

Karabulut, G., Yildiz, S., Karaca, A. C., & Yemiş, O. (2023). Ultrasound and enzyme-pretreated extraction for the valorization of pea pod proteins. Journal of Food Process Engineering, 46(12). https://doi.org/10.1111/jfpe.14452

Kumar, M., Tomar, M., Potkule, J., Verma, R., Punia, S., Mahapatra, A., Belwal, T., Dahuja, A ., Joshi, S., Berwal, M. K., Satankar, V.,Bhoite, A. G., Amarowicz, R., Kaur, C., & Kennedy, J. F. (2021). Advances in the plant protein extraction: Mechanism and recommendations. Food Hydrocolloids, 115, 106595. https://doi.org/10.1016/j.foodhyd.2021.106595

Lau, K. Q., Sabran, M. R., & Shafie, S. R. (2021). Utilization of Vegetable and Fruit By-products as Functional Ingredient and Food. Frontiers in Nutrition, 8. https://doi.org/10.3389/fnut.2021.661693

Manigandan, V., Karthik, R., Ramachandran, S., & Rajagopal, S. (2018). Chitosan Applications in Food Industry. In Biopolymers for Food Design (pp. 469–491). Elsevier Inc. https://doi.org/10.1016/B978-0-12-811449-0.00015-3

Mateos-Aparicio, I., Redondo-Cuenca, A., Villanueva-Suárez, M. J., Zapata-Revilla, M. A., & Tenorio-Sanz, M. D. (2010). Pea pod, broad bean pod and okara, potential sources of functional compounds. LWT, 43(9), 1467–1470. https://doi.org/10.1016/j.lwt.2010.05.008

Nan, X., Zhou, Q., Ji, W., Chen, X., Li, J., Wang, H., Dong, L., Meng, X., & Sheng, G. (2022). Development of a pea protein-/chitosan-based bioactive film using Aronia melanocarpa polyphenols as a bioactive ingredient. Journal of Food Processing and Preservation, 46(12). https://doi.org/10.1111/jfpp.17168

Nasir, G., Zaidi, S., Siddiqui, A., & Sirohi, R. (2023). Characterization of pea processing by-product for possible food industry applications. Journal of Food Science and Technology, 60(6), 1782–1792. https://doi.org/10.1007/s13197-023-05718-y

Ozhan, S. (2022). Development of Pea Protein Agar Based Biodegradable Film with The Incorporation of Essentıal Oils. (Master's Thesis). Istanbul Technical University, Food Enginneering Department, Istanbul.

Pérez-Patricio, M., Camas-Anzueto, J. L., Sanchez-Alegría, A., Aguilar-González, A., Gutiérrez-Miceli, F., Escobar-Gómez, E., Voisin, Y., Rios-Rojas, C., & Grajales-Coutiño, R. (2018). Optical method for estimating the chlorophyll contents in plant leaves. Sensors (Switzerland), 18(2). https://doi.org/10.3390/s18020650

Ramos, M., Valdés, A., Beltrán, A., & Garrigós, M. C. (2016). Gelatin-based films and coatings for food packaging applications. In Coatings (Vol. 6, Issue 4). Multidisciplinary Digital Publishing Institute (MDPI). https://doi.org/10.3390/coatings6040041

GAME AND INTERACTION TECHNOLOGIES

AI in Gaming

Game Design

Game Production

Gamification

Interaction Technologies

Series Games

User Studies

A Comparative Study For Analyzing LLM Performance in Bluff-Based Card Games

İrem Şalk[a], Sanem Sarıel[b]

[a]Istanbul Technical University, Game and Interaction Technologies Program, Türkiye
[b]Istanbul Technical University, Artificial Intelligence and Data Engineering Program, Türkiye

Keywords : Artificial Intelligence, Card Game, Game-Playing Agent, Imperfect Information, Probabilistic Problem.

Aim

The aim of this study is to investigate and compare the decision-making performance of multiple agent strategies in a modified bluff-based card game under imperfect information. The study focuses on whether a large language model (LLM) that is prompted through in-context learning (ICL), can generate effective action recommendations when compared to other agents that use traditional rule-based strategies and reinforcement learning in a game where deception plays a critical role. The central hypothesis is that reasoning-driven agents using LLM, can adaptively recommend successful bluff or challenge actions by interpreting structured sets of information despite having no training on game-specific reward signals. Our research question is "Can LLM-driven strategy suggest optimal actions by making predictions and inferences about opponents in a bluff based card game?".

Material and Method

Several studies on AI decision-making have examined the use of Large Language Models (LLMs), reinforcement learning, and Monte Carlo methods in strategic games (Cowling et al., 2015; Duan et al., 2025; Huang et al., 2024; Wu et al., 2024). Zeek and Ben (2025) developed an LLM-based assistant for the game Diplomacy, which has a deceptive game environment, combining language reasoning with computational tools for strategic guidance. An instruction-driven poker engine that provides players a new gameplay experience by generating the whole process of the defined games was created by Wu et al. (2024). A study conducted by Luo and Tan (2023) improved the decision-making process of the game DouDiZhu which is a gambling game popular in China, by combining reinforcement learning with a reward-shaping algorithm. Also, Guo et. al. (2024) conducted a study where they introduced GPT-4 with Theory of Mind (ToM) abilities to predict beliefs, intentions, and strategies of opponents, since these quantities are important for bluffing scenarios in real-life gameplay. They focused on single-move decision-making, where the model predicts opponents' behavior by evaluating their behavior and detecting possible deception using GPT-4 with modular prompts and human-like planning.

This study will contribute to growing research on the application of LLMs in real-time decision-making domains by analyzing the performance of the agents in terms of success rate of actions and win. To do that, the evaluation focuses on the model's ability to reason over game states, player histories, and probabilistic cues to select actions in a bluff-based setting.

The game environment is a modified version of the traditional Bluff (also known as Cheat or BS) card game. The modified version of Bluff game uses a special 24-cards deck which consists of 6 suits and 4 and played by three players (agents). At the start of the game, cards are evenly distributed among all players, the first player is chosen randomly and turns continue with clockwise direction in each game. Players keep their cards hidden from others during the game. A fixed table rank is used throughout the game. During the gameplay, players can perform two actions: challenge and move. When players make a move, they pile face down in the middle and claim to play a certain amount of cards with the table rank and rank value. This feature allows players to bluff their opponents. A bluff move includes at least one card not matching the declared rank while a truthful move in which all cards match the declared rank. To simplify the action selection we limit the challenge phase to one player, as only the next-moving player may perform challenge action. Therefore, a player may challenge the previous move if they believe it does not match the required rank. If the last played move was bluff then the previous player

takes all cards in the pile, otherwise the player who performs the challenge takes all cards in the pile. The first player who discards all the cards in their hand is the winner of the game. The game proceeds in turns until one player wins.
To create a game simulation framework, we first model the gameplay and rules mathematically by using set notation based on our game design. Then, we derive frequency of action selections along with their corresponding outcomes, define dynamic reward-penalty for each action and game conclusion. Next, we model the game which is played by five different agents. Each agent selects actions based on its internal strategy logic, and rewards are distributed based on the success of bluffs and challenges. In this methodology, five distinct agents are implemented:

1. Random Agent: Selects actions uniformly at random without considering game context. Serves as a performance baseline.
2. State Dependent Agent: Uses handcrafted rules based on the current state, such as pile size, card distribution. We modelled the agent with minimal logic and contextual awareness as calculating the probability of occurrence of the matching cards in the opponent's hand.
3. Bayesian Agent: Employs hierarchical priors from historical game data and current game state to evaluate best action for bluffing and challenging. Adapts action preferences based on prior success rates.
4. DQN Agent: A deep reinforcement learning model trained to maximize long-term reward. It maps observed states to derive optimal actions using Q-learning, updating its policy across turns in episodes. To support reinforcement learning, we defined both episode-level rewards (e.g., winning or losing the game) and turn-based rewards for each action type (move and challenge) to guide the learning process of the agent effectively.
5. ICL Agent: A GPT-based language model (GPT-4o) receives a structured prompt describing the rules and instructions, current state, past behaviours, and probabilistic game summaries such as winning rate. In addition, we represented a simple chain of thoughts by instructions and strategy guidelines to analyze opponents behaviors, predict possible outcomes of possible action scenarios and evaluate risk-reward to select an action. It reasons step-by-step internally but outputs only the final action as JSON.

At this stage, we compared the win rate by simulating different player combinations. The most successful player in the baseline strategies was Bayesian Agent. In 900 games,The Bayesian Agent achieved a 42% win rate, followed by the State Dependent Agent with 38%, and the Random Agent with 19%. When we compared the performance of the two most successful players in the baseline strategies with the DQN Agent over 900 games, we observed that ability to adapt through reinforcement learning of the DQN agent proved highly effective with a 74% win rate when we compared the other agents' win rate which are 16% for Bayesian and 10% for State-dependent. As a result of these simulations, learning-based and inference-driven agents show stronger performance trends than rule-based or random strategies.

Findings

Simulation results will be used to analyse different strategy types. The analysis will focus on success in bluffing and challenging decisions, and consistency across repeated trials. Metrics such as win rate and cumulative performance will be used to compare static strategies (Random, State-dependent, Bayesian), learning-based agent (DQN) and reasoning-based agent (LLM). The findings will aim to show how adaptive decision-making contributes to success in environments that involve uncertainty, deception, and player modeling. Findings will provide a comparative analysis of action success rates, adaptability, and overall win rates across all agent types and allow evaluation of performance of LLM-driven strategy.

Conclusion

In conclusion, by comparing the action decisions made by the LLM with those generated by other strategies, the study aims to determine the effectiveness of LLM-driven actions and will assess the relative effectiveness of LLM-driven recommendations. By designing this framework, the study contributes to understanding of how LLMs perform in strategic decision-making in games where uncertainty and deceptiveness are the primary objective.

References

Cowling, P. I., Whitehouse, D., & Powley, E. J. (2015). Emergent bluffing and inference with Monte Carlo tree search. 2015 IEEE Conference on Computational Intelligence and Games (CIG), 114–121. IEEE.
Url 1 - https://doi.org/10.1109/CIG.2015.7317923
Duan, J., Zhang, R., Diffenderfer, J., Kailkhura, B., Sun, L., Stengel-Eskin, E., Bansal, M., Chen, T., & Xu, K. (2024). GTBench: Uncovering the strategic reasoning limitations of LLMs via game-theoretic evaluations (arXiv preprint arXiv:2402.12348).
Url 2 - https://arxiv.org/abs/2402.12348
Guo, J., Yang, B., Yoo, P., Lin, B. Y., Iwasawa, Y., & Matsuo, Y. (2023). Suspicion-agent: Playing imperfect information games with theory of mind aware GPT-4. arXiv preprint arXiv:2309.17277.
Url 3 - https://arxiv.org/abs/2309.17277
Huang, C., Cao, Y., Wen, Y., Zhou, T., & Zhang, Y. (2024). PokerGPT: An end-to-end lightweight solver for multi-player Texas Hold'em via large language model. arXiv preprint arXiv:2401.06781.
Url 4 - https://arxiv.org/abs/2401.06781
Hu, S., Huang, T., Ilhan, F., Tekin, S., Liu, G., Kompella, R., & Liu, L. (2024). A survey on large language model-based game agents. arXiv preprint arXiv:2404.02039.
Url 5 - https://arxiv.org/abs/2404.02039
Jataware. (n.d.). Building an LLM-based assistant for the game of Diplomacy.
Url 6 - https://jataware.com/projects/react-diplomacy
Q. Luo and T. -P. Tan, "RRARSMSDou: Master the Game of DouDiZhu With Deep Reinforcement Learning Algorithms," in IEEE Transactions on Emerging Topics in Computational Intelligence, vol. 8, no. 1, pp. 427-439, Feb. 2024, doi: 10.1109/TETCI.2023.3303251.
Wu, H., Liu, X., Wang, Y., & Zhao, H. (2024). Instruction-driven game engine: A poker case study. arXiv preprint arXiv:2410.13441.
Url 7 - https://arxiv.org/abs/2410.13441

Preliminary Study on the Feasibility of Neural Network-Based Generative AI Models in Video Game Music Production

Ülkü Nur Nar [a], Ozan Sarıer[b]

[a] Istanbul Technical University, Department of Game and Interaction Technologies, Game and Interaction Technologies Program, Turkey
[b] Istanbul Technical University, Department of Turkish Music State Conservatory, Music Technologies Program, Turkey
naru17@itu.edu.tr

Keywords: Generative AI, Video Game Music, Ludomusicology.

Aim

Music is not just a background element for games but also plays a central role in increasing the depth of the narrative, directing the emotional experience of the player, and strengthening the player's engagement (Collins, 2008). With an understanding of the role and importance of music in games, the importance given to game music has increased both in academia and in the game industry as a creative production area.

Kamp, Summers, and Sweeney (2016) stated that video game music studies have developed rapidly in the last half decade. However, they stated that this field addressed basic research questions. In the same study, they mentioned that the concept of "ludomusicology," which is formed by combining the terms "ludology" and "musicology" and refers to video game music research, was proposed by Guillaume Laroche and Roger Moseley in 2013.

The aim of this paper is to present a preliminary study that evaluates the feasibility and possibilities of integrating generative artificial intelligence models into game music workflows. In particular, it aims to make a meaningful contribution to both the ludomusicology sub-discipline and the game industry by providing a theoretical basis for understanding the potential of neural-network-based music production tools in game development.

Material and Method

This study was designed as a preliminary qualitative and theoretical research. Within the scope of this method, the literature and documentation of generative artificial intelligence models were examined, and an observational analysis was conducted on prompts created according to the selected game types and sample outputs obtained from these tools.

The focus of this study is to evaluate the extent to which neural network-based music production tools can meet the creative and technical requirements of game development processes in terms of efficiency, adaptability, and artistic expression and to investigate which functions of these models can be used practically in the game development process.

Traditional AI music production tools are generally parameter based. They request musical input from the user to guide and structure the music production process. Neural networks and deep learning models that emerge later have the potential to produce higher-quality music and resolve more complex relationships within music (Zhu et al., 2023; Herremans et al., 2017).

The nonlinear nature of games is the most important problem faced by game music composers (Collins, 2008). The fact that games are based on complex interactions indicates that such systems have the potential to offer more compatible solutions for game music production.

Based on this potential, only neural network-based generative AI music models were evaluated in this study. Sample music outputs were obtained from the Suno.AI model and Udio neural network-based systems, which provide music and sound production from text, are based on advanced artificial intelligence models and have the ability to produce realistic and expressive musical content (Nugroho & Manggala, 2024).

Three game types were determined within the scope of observational analysis: puzzle, action adventure, and horror. Based on Collins' (2008) statement that "different genres have different types of recording needs," each game type's unique

musical needs were taken into consideration and special prompts were created in line with the in-game atmosphere and musical function.

Puzzle games generally do not contain dialogue; music usually plays a background role that supports concentration, and minimal ambient music is preferred in this genre (Collins, 2008). The prompt for the puzzle game: "Minimal ambient background music for a puzzle level that supports focus and calm thinking."

In most action-adventure games, the music may be soft and calm in areas where there is no conflict, but when conflict begins it may become faster and more energetic, encouraging the player to adventure (Nieves, 2021). The prompt for the action-adventure game: "Fast-paced action music with percussive elements and dramatic tension."

In horror games, the psychological state of the player can be reflected in the music with dissonant tones to increase the tension and make the player tense (Munday, 2007). The prompt for the horror game: "Dark orchestral theme with dissonant harmonies and ambient textures to build suspense and tension."

Findings

Udio (Free) generated Silent Clarity and Quiet Reflections, both with durations of 32 seconds for the puzzle genre. Silent Clarity features a modal tonality, static harmonic progression, minimal melodic content with soft pads, and no discernible rhythm. It creates a calm and meditative atmosphere, and it is not loopable. Quiet Reflections is set in a minor key with subtle harmonic shifts, sparse melodic material, and very low rhythmic density. It conveys a melancholic and introspective tone, and it is not loopable.

It generated *Rising Storm* and *Rushing Shadows*, both with durations of 32 seconds for the action-adventure genre. *Rising Storm* features a minor, electronic tonality, a repetitive and stable harmonic progression, strong percussive patterns. Its lead synth motifs, creates an energetic and tense atmosphere, and it is not loopable. *Rushing Shadows* is also in a minor key, with limited harmonic complexity, prominent percussion, and rapid electronic beats. It layers synth textures, conveying an intense and suspenseful tone, and it is not loopable.

It generated Veil of Shadows 1 and Veil of Shadows 2, both with durations of 32 seconds for the horror genre. Veil of Shadows 1 features a minor tonality, mostly consonant harmonic progression with slight background dissonance and minimal ambient pulses and pads. It creates a dark and atmospheric tone, and it is not loopable. Veil of Shadows 2 also uses a minor key with slightly richer harmonic layering and subtle dissonant touches, very low rhythmic activity. Its ambient flow conveys a dark and slightly tense atmosphere, and it is not loopable.

Suno.AI (Free) generated Puzzle Whisper 1 and Puzzle Whisper 2, both with durations of approximately 2 minutes for the puzzle genre. Puzzle Whisper 1 features a modal tonality, static harmonic progression and soft ambient textures with piano. Its low rhythmic density creates a calm and reflective atmosphere, and it is not loopable. Puzzle Whisper 2 is set in a minor key with gradual harmonic shifts, sparse piano figures, gentle pulses, and light percussive movement. It conveys a calm yet slightly melancholic tone, and it is not loopable.

It generated Action Adventure 1 and Action Adventure 2, both with durations of approximately 2 minutes for the puzzle genre. Action Adventure 1 features a minor tonality, repetitive and stable harmonic progression, strong percussive foundation, metal guitar-like riffs. It creates an energetic and adventurous atmosphere, and it is not loopable. Action Adventure 2 also uses a minor key with a repetitive harmonic structure, percussive drive, electronic pulse, aggressive guitar, and synths. It conveys an intense and dramatic tone, and it is not loopable.

It generated Horror 1 and Horror 2, both with durations of 4 minutes for the horror genre. Horror 1 features a minor tonality with layered dissonant textures, sustained tension, minimal rhythmic activity and ambient noise. It creates a tense and suspenseful atmosphere, and it is not loopable. Horror 2 also uses a minor key with chromatic and slow-moving dissonance, and very low rhythmic activity. Atmospheric layers convey a dark and unsettling tone, and it is not loopable.

Suno.AI (Premium) generated Puzzle 1 and Puzzle 2 for the puzzle genre, with durations of 4 minutes and 1 minute 45 seconds. Puzzle 1 features a modal tonality with static harmonic progression and low rhythmic density. Subtle pulses, piano motifs, and layered ambient pads create a calm and reflective atmosphere. It is partially loopable. Puzzle 2 is set in a minor key with gradual harmonic evolution, soft percussive and piano arpeggios. Ambient textures, and light synth layers convey a calm yet slightly melancholic tone. It is also partially loopable.

It generated Action Adventure 1 and Action Adventure 2 for the action-adventure genre, with durations approximately 3 minutes. Action Adventure 1 features a minor tonality with repetitive, stable progressions, strong percussive drive, metal guitar riffs, orchestral bursts, and synthetic leads. It creates an energetic and dramatic atmosphere. It is partially loopable. Action Adventure 2 also uses a minor key with cyclical, stable progressions and occasional harmonic shifts, fast-paced percussion, layered guitar lines, synth textures, and dynamic orchestral hits. It conveys an intense and suspenseful tone. It is not loopable.

It generated Horror 1 and Horror 2 for the horror genre, both with durations of 4 minutes. Horror 1 features a minor tonality with chromatic dissonance, dissonant layers, slow-moving harmonic tension, minimal rhythm, eerie ambient swells, and dark textures. It creates a tense and unsettling atmosphere. It is not loopable. Horror 2 also employs a minor key with dissonant clusters, a highly unstable harmonic field, and very low rhythmic density. Its layered dissonances, and evolving textures convey a dark, anxiety-inducing tone. It is loopable due to smooth transitions.

Conclusion

In this study, the generated outputs were analyzed for their musical structure and adaptability to game environments in terms of genre suitability.

For the puzzle genre, most outputs, particularly from Udio (Free) and Suno.AI (Free), met the minimum ambient background music requirement to support calmness but were not conducive to concentration. Suno.AI Premium outputs, while partially loopable, introduced more harmonic complexity and movement. They offered richer textures that could have been distracting to players in a typical puzzle environment.

For the action-adventure genre, the outputs, especially in the Suno.AI Premium tracks, effectively captured the fast-paced, percussive, and energetic qualities expected during combat scenes. However, some free-to-play outputs fell short in terms of dramatic tension and orchestral or cinematic depth. In terms of loopability, the AI tools examined did not provide sufficient performance for the game music requirements.

In the horror genre, AI models consistently delivered dark, tense, and dissonant textures. Suno.AI outputs generally showed more layering and atmospheric complexity than Udio, closely matching player expectations for increased tension and excitement. While all models demonstrated a basic capacity to meet genre demands, Suno.AI Premium emerged as the most consistent model in delivering outputs that reflected both the emotional and structural demands outlined in the literature. It was moderately successful in terms of loopability.

Although the outputs are not yet ready for direct integration into game workflows without manual editing, they hold clear value for prototyping and experimentation. Continued research and development will be crucial to improving their use in real-time game music production.

References

Collins, K. (2008). Game sound: an introduction to the history, theory, and practice of video game music and sound design. Mit Press.

Herremans, D., Chuan, C. H., & Chew, E. (2017). A functional taxonomy of music generation systems. ACM Computing Surveys (CSUR), 50(5), 1-30.

Kamp, M., Summers, T., Sweeney, M., & Masse, J. B. (2016). Ludomusicology: Approaches to video game music. Intersections: Canadian Journal of Music/Revue Canadienne de Musique, 36(2), 117-124.

Munday, R. (2007). Music in video games. Music, sound and multimedia: From the live to the virtual, 51-67.

Nieves, A. J. A. (2021). " It's More than a Game, It's an Experience": Eudaimonic Storytelling in the Music of Art Games. The Florida State University.

Nugroho, Y. Y. T., & Manggala, P. P. M. D. (2024, December). The Use of AI in Creating Music Compositions: A Case Study on Suno Application. In 7th Celt International Conference (CIC 2024) (pp. 177-189). Atlantis Press.

Zhu, Y., Baca, J., Rekabdar, B., & Rawassizadeh, R. (2023). A survey of ai music generation tools and models. arXiv preprint arXiv:2308.12982.

GAME AND INTERACTION TECHNOLOGIES

AI in Gaming

Game Design

Game Production

Gamification

Interaction Technologies

Series Games

User Studies

Optimizing Level Production in Hidden Object Games Using YOLO Object Detection

Ekin Demircan[a], Sema Alaçam[b]

[a] Istanbul Technical University, Department of Game and Interaction Technologies
[b] Istanbul Technical University, Faculty of Architecture, Department of Architecture
demircanek@itu.edu.tr

Keywords: Hidden Object Games, Level Design Optimization, Level Generation, Object Detection.

Aim

Hidden object games (HOGs) are a widely recognized subgenre of casual games, characterized by their extensive level-based content. The primary challenge in developing these games lies in optimizing level design while maintaining quality and efficiency. The traditional level production process is a very time-consuming process when done manually. Marking the locations and names of the objects that are desired to be found in the game, which is necessary for tracking the success condition, is a repetitive and time-consuming action for the level designer. This study proposes a level production model, that optimizes the location marking and naming part of the level production process with an object recognition algorithm, YOLO. The main focus of this study is to optimize the level production pipeline, which will be achieved through the training of the YOLO object detection algorithm.

Material and Method

The proposed production model will be tested as a small-scale prototype to test its applicability to the hidden object game. The Level production process for HOG is grouped under four main topics, and the production model's steps are determined accordingly. (1) deciding a game concept and style, (2) placing objects in an environment to create a level composition, (3) marking object positions for possible success conditions, and (4) selecting target objects as objectives of a level to finalize the level.

The production model has been structured to create a sample level. To maintain visual harmony across all level compositions, a photocopy filter will be applied during the concept definition phase. (Figure 1.) Following this, the selected objects will be placed within different environments to construct the level layout, establishing the foundation for object placement. (Figure 2.) In the third step, the Yolo algorithm is utilized for object recognition. The Yolo algorithm contributes to the estimation of the bounding box enclosing an object and determines its location based on its coordinates. (Do,2021, p.11) The YOLO algorithm will be run to detect the positions and labels of objects that can be assigned as tasks within these created compositions. (Figure 3.) In the fourth step, the marked objects will be selected as the level objectives, and the finalized level will be prepared accordingly.

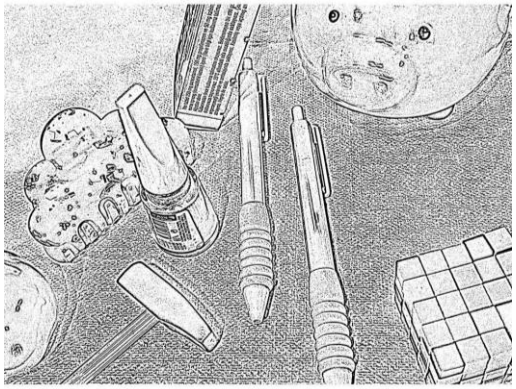

Figure 1.

Figure 2.

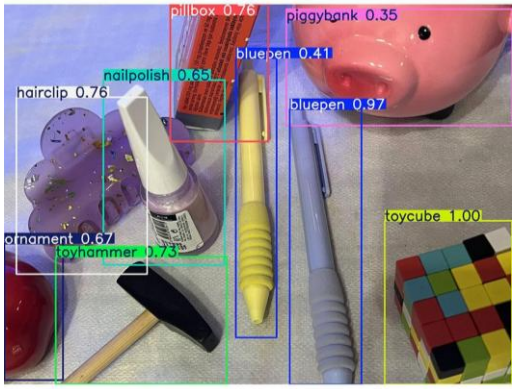

Figure 3.

In the scope of this study, a hidden object game titled June's Journey is utilized for the testing process. June's Journey, one of the most popular mobile games, surpassed 60 million downloads in 2022 (Long, 2022). Its level progression has been taken as a reference, as it serves as a significant example for understanding this widely preferred game structure, making it a suitable choice for this study. In June's Journey, which has been selected as a reference, the early game levels include a hidden object search task with 8 to 10 objects per level. The level progression is designed in a way that presents three words (objects) at a time as tasks to the player. Once an object is found, the next object to be discovered appears in its place. Based on this structure, 10 objects will be selected for a single level, and the model will be initially tested using these objects.
In the context of data collection, a total of 200 photos were taken of 10 selected objects from different angles. These objects were chosen with attention to their distinguishable forms to ensure they could be differentiated from one another. The selected objects are: a piggy bank, ballpoint pen, colorful toy cube, fork, medicine box, toy hammer, decorative pomegranate figurine, nail polish bottle, and decorative elephant figurine. The dataset was annotated and augmented with the use of Roboflow. The augmentation process involved rotating, scaling, and altering the lighting conditions of the objects to create a more robust dataset capable of handling real-world variations. The training process will be conducted using Google Colab, leveraging GPU acceleration to enhance model performance. The dataset was divided into training, validation, and test sets to train the algorithm. Various training epochs, batch sizes, and learning rates will be tested to determine the optimal balance between accuracy and computational efficiency.

Findings

Multiple test environments will be created to validate the model's applicability to the hidden object game. These scenarios will feature backgrounds with varying levels of simplicity and complexity. Model performance will be measured based on how accurately the YOLO-trained algorithm identifies objects within these diverse setups. If the model exhibits low accuracy, the dataset will be expanded, and the factors affecting accuracy will be further examined.

Conclusion

In conclusion, this study aims to present a scalable model that optimizes the level design process by testing a proof of concept. By integrating the object detection algorithm into the proposed model, the goal is to automate one of the stages of the process, eliminating manual workload and improving efficiency. To support scalability, future work should involve expanding and diversifying the dataset. Furthermore, designers should be included in the testing phase to gather feedback on usability and integration into hidden object games. The aim is for this generation model to recognize objects accurately under various lighting and rotation conditions, and across different scenarios, ultimately optimizing the level generation process. The model's scalability will be evaluated based on its detection accuracy. In future stages, designers will be included in the process to evaluate the model's efficiency in generating levels, aiming to reduce the time spent on manual creation. As the number of examples increases, the object recognition algorithm is expected to improve its accuracy. Accordingly, more object images will be added to the dataset based on test results.

References

Do, T. (2021). *Evolution of YOLO algorithm and YOLOv5: The state-of-the-art object detection algorithm* (Bachelor's thesis). Oulu University of Applied Sciences.
Long, N. (2022, October 28). June's Journey hits 60m downloads, over $500m gross lifetime spend. Mobile Gamer. https://mobilegamer.biz/junes-journey-hits-60m-downloads-over-500m-gross-lifetime-spend/, date retrieved 20.03.2025.

A Systematic Approach to Ludonarrative Harmony: Methods for Aligning Interactive Gameplay and Storytelling

Cem Çelik[a], Ayşegül Akçay Kavakoğlu[b]

[a] Istanbul Technical University, Institute of Science and Technology, Department of Game and Interaction Technologies, Turkey
[b] Istanbul Technical University, Faculty of Architecture, Department of Landscape Architecture/Architectural Design Computing, Turkey
celikc15@itu.edu.tr

Keywords: Ludonarrative Harmony, Game Design, Player Agency, Narrative Coherence, Interactive Storytelling.

Aim

Ludonarrative harmony in game design enhances the cohesiveness and enjoyment of the gameplay experience. This work is motivated by a fascination with how interactive gameplay can enhance narrative impact and by a desire to contribute to the development of interactive art. It ensures that the narrative and gameplay elements of a game are effectively integrated. This enhances the game's emotional impact and engages players effectively. Ludonarrative dissonance occurs when gameplay mechanics and narrative elements in video games are incongruent, resulting in a diminished immersive experience and thematic coherence.

This work presents a multi-dimensional evaluation method whereby ludonarrative harmony is seen as a continuum rather than as a binary concept. The proposed paradigm defines three basic dimensions: mechanics-narrative synchronization, player agency and narrative coherence, and systematic storytelling integration, thereby evaluating the degree of coherence between gameplay and narrative. Game designers might use a choice matrix as a theoretical tool to carefully assess and improve ludonarrative alignment in their works.

By taking a methodical approach to comprehending and utilizing ludonarrative harmony, this work seeks to enhance scholarly debate and useful game design techniques. This study combines theoretical frameworks with real-world game development techniques to build a foundation for interactive experiences that are immersive, story-driven, and emotionally powerful.

Material and Method

To create a systematic framework for assessing ludonarrative harmony, this study employs a qualitative research technique. A methodical approach to looking at how gameplay and story interact is shown in this study, which uses a comparative case study analysis and well-known theoretical models.

The technique consists of four primary components:

Literature Review and Theoretical Synthesis

The study starts with a full review of the literature on basic game design theories. Works like The Art of Game Design (Schell, 2008), Ludonarrative Dissonance: Is Storytelling About Reaching Harmony? (Seraphine, 2016), and The Quest for Ludonarrative (Donoghue, 2021) are included. This review lays out the theoretical basis of ludonarrative harmony, showing how it differs from dissonance and pointing out important design issues.

Development of the Ludonarrative Harmony Framework

Drawing from existing research, the study constructs a multi-dimensional evaluation framework that positions ludonarrative harmony on a continuum rather than a binary scale. Three core dimensions are defined to analyze the level of integration between narrative and mechanics:

Mechanics-Narrative Synchronization (MNS): Evaluates whether core gameplay mechanics reinforce or contradict the game's narrative themes.

Player Agency and Narrative Coherence (PANC): Measures the extent to which player choices align with narrative constraints, preventing thematic inconsistencies.

Systemic Storytelling Integration (SSI): Evaluates the impact of environmental and systemic design components on storytelling, eschewing passive exposition.

These criteria are intended to offer a systematic yet adaptable framework for assessing ludonarrative design. This framework does not provide fixed ratings but presents a reproducible process for qualitative evaluation.

Dimension	Definition	Evaluation Criteria	Example
Mechanics-Narrative Synchronization (MNS)	Measures how well gameplay mechanics reinforce narrative themes.	- Do mechanics embody or contradict the game's themes? - Is player interaction aligned with intended emotional responses?	Celeste (gameplay mirrors protagonist's struggle)
Player Agency and Narrative Coherence (PANC)	Assesses the balance between player freedom and narrative integrity.	- Does increased agency disrupt or enhance narrative coherence?	Brothers: A Tale of Two Sons (control scheme reinforces emotional themes)
Systemic Storytelling Integration (SSI)	Evaluates how environmental and systemic design elements contribute to storytelling.	- Does the game world convey narrative meaning through interaction?	Hollow Knight (worldbuilding and lore integrated into exploration)

Table 1. Ludonarrative Harmony Framework.

Comparative Case Study Analysis

A case study analysis was performed to evaluate the applicability of the framework on games demonstrating differing levels of ludonarrative harmony. Titles like Celeste and Brothers: A Tale of Two Sons were scrutinized for their robust integration of gameplay and narrative, whereas Bioshock was evaluated for its thematic contradictions. Each scenario was evaluated utilizing the proposed paradigm, offering specific instances of how mechanics, player agency, and systemic storytelling affect ludonarrative cohesiveness.

Decision Matrix Development

Based on the case study findings, a decision matrix was proposed as a theoretical tool for categorizing games along the ludonarrative harmony spectrum.This matrix serves as a systematic evaluation tool, assisting developers in recognizing possible design discrepancies and enhancing narrative-gameplay cohesion.Despite the lack of quantification in this work, the matrix offers a systematic basis for iterative design methods and future investigations.
This methodology connects academic research with practical application, providing game makers a systematic technique to assess and enhance ludonarrative coherence in interactive games.

Findings

This study introduces a comprehensive evaluation framework that transcends subjective interpretations, providing a systematic approach for assessing ludonarrative harmony and dissonance. The research identifies three key factors influencing ludonarrative cohesiveness.

Mechanics-Narrative Synchronization (MNS): The extent to which game mechanics align with or oppose narrative themes. This evaluation involves analyzing the ways in which core gameplay interactions contribute to the intended narrative experience, referencing texts such as The Art of Game Design (Schell, 2008) and Ludonarrative Dissonance: Is Storytelling About Reaching Harmony? (Seraphine, 2016).

Player Agency and Narrative Coherence (PANC): refers to the equilibrium between player autonomy and the integrity of the narrative. This examines the influence of interactive choices on narrative development, citing research on emergent storytelling (Greenwood, 2022) and structured narrative constraints (Donoghue, 2021).

Systemic Storytelling Integration (SSI): refers to the extent to which environmental design and systemic mechanics enhance narrative meaning independently of non-interactive exposition. This is consistent with studies on diegetic storytelling and structured experience frameworks (Winn, 2008).

A comparative case study analysis was conducted to implement this paradigm, categorizing games along a harmony-dissonance continuum based on these principles. The findings suggest that games with strong alignment between mechanics and narrative themes tend to improve player immersion and emotional engagement, whereas those characterized by mechanical-narrative dissonance often experience a deficiency in thematic coherence.
A choice matrix was created as a theoretical framework to categorize games along the ludonarrative harmony continuum according to these dimensions. This framework is not an empirical scoring system; instead, it is a systematic approach for evaluating narrative-mechanical integration in game design, facilitating further study and iterative game creation. This analytical framework enables a systematic evaluation of ludonarrative integration, providing developers with an organized method to enhance the interaction between narrative and gameplay.

Conclusion

This study demonstrates that ludonarrative harmony is a concrete design principle, rather than an abstract or subjective notion, which can be methodically studied and applied. This research establishes a basis for evaluating and enhancing the interaction between gameplay and narrative by identifying essential dimensions: mechanics-narrative synchronization, structured player agency, and systemic storytelling integration.
The results show that games with good ludonarrative integration make players more immersed and keep the theme consistent. On the other hand, games with mechanical-narrative dissonance may not have the effect they wanted on the story. This paper introduces a choice matrix as a theoretical tool that gives game designers a way to measure ludonarrative harmony that goes beyond subjective assessments. A key contribution of this study is a qualitative, adaptable framework for evaluating ludonarrative harmony in both existing and in-development games. This framework provides practical guidance for designers to align gameplay with narrative, while also serving as a structured method of scholarly inquiry that respects the artistic nature of game design.

References

Donoghue, A. (2021). The Quest for Ludonarrative.
Greenwood, S. (2022). Optional Narratives and Supplemental Storytelling in Behaviour Interactive's Dead By Daylight.
Hocking, C. (2007). Ludonarrative Dissonance in Bioshock: The Problem of What the Game is About.
Schell, J. (2008). The Art of Game Design: A Book of Lenses. Morgan Kaufmann.
Seraphine, F. (2016). Ludonarrative Dissonance: Is Storytelling About Reaching Harmony?
Winn, B. (2008). The Design, Play, and Experience Framework: Handbook of Research on Effective Electronic Gaming in Education.

Impossible Spaces in Games: Using Anamorphic Projection in Space Interactions to Explore Possibilities of New Game Mechanics

İrem Aydındoğan[a], Sema Alaçam[a]

[a] Istanbul Technical University/Graduate School, Department of Game and Interaction Technologies, Game and Interaction Technologies Program, Türkiye
aydindogan@itu.edu.tr

Keywords: Anamorphosis, Non-Euclidean, Optical Illusion, Perspective.

Aim

This study aims to explore Impossible Spaces in games and the potential of anamorphic projection as a spatial game mechanic to create perceptual illusions and exciting level designs. The central research question is: How can anamorphic projection be used to redefine spatial interactions in game environments to challenge the conventional notions of reality and navigation?

Impossible spaces are environments that cannot be experienced within the physical rules of the real world. These spaces feature impossible geometries that are beyond human visualization and consist of spatial configurations that defy the rules of gravity, time, perception and Euclidean geometry. According to Thiering and Mittelberg (2022), game environments of impossible worlds play with players' knowledge and expectations of logic. Using digital tools, it is possible to visualize such spaces, and they are commonly used in movies, games and other digital media. Games can be considered the ideal place to explore such spaces because they offer a unique advantage of being interactive. While movies only allow for observation, games enable true engagement. There is a symbiotic relationship between games and impossible spaces: as digital game environments make them possible to be experienced, these spaces open up new possibilities for exciting game mechanics that enrich game design. Many designers experiment with the creation of surreal and mind-bending game worlds. Often inspired by the works of M.C. Escher, as noted by Orbons and Ruttkay (2008), artists research in the area to create paradoxical and mathematical scenes in virtual 3D environments.

It is evident that games have used a variety of techniques to challenge rules of physics to present new mechanics and experiences, using different impossible spaces as their environments. Broadly speaking, these games can be categorized into two groups. The first group includes games that take place in fundamentally Euclidean spaces but use non-Euclidean manipulations to create the illusion of impossibility. These game spaces include portals, gravity shifts, perspective manipulations, optical illusions, warping and spatial discontinuities that break players' spatial expectations. According to Osudin et al. (2024), these types of games are known as non-Euclidean by the players but those games only appear impossible because they use pieces of Euclidean manifolds combined in a novel way to create these illusions. The second group includes games that take place in truly non-Euclidean spaces, where the geometry of space is redefined and mathematically curved into hyperbolic and spherical worlds.

To better understand the different approaches to the concept of impossible spaces, it is helpful to examine existing games that use a variety of different techniques to represent those worlds. Table 1 provides a comparative overview by categorizing selected games based on whether they take place in Euclidean or non-Euclidean space, their core spatial and perceptual mechanics and the type of game world representation (2D or 3D) they employ. What these have in common is that they challenge the players' intuitive understanding of space through diverse approaches to perception- and space-based mechanics, such as visual illusions, dimensional transformations and time manipulations.

This paper focuses on anamorphic projection as a technique to experiment with possibilities of level design and game mechanic ideas.

Table 1. Comparative Overview of Games Using Impossible Spaces.

Game Title	Publishing Year	Dimension	Game Space Category	Core Mechanic/ Technique
Portal	2007	3D	Spatial Illusion	Portal-based teleportation
Echochrome	2008	2.5 D	Spatial Illusion	Optical illusion, perspective dependent paths
Braid	2008	2D	Time Manipulation	Time reversal, object-time independence
HyperRogue	2011	2D	Non-Euclidean Geometry	Hyperbolic tiling, infinite procedural world
Fez	2012	2.5 D	Dimensional Shift	Rotation between 2D planes in 3D space
Antichamber	2013	3D	Spatial Illusion	Illusions, space rearrangements
Monument Valley	2014	2.5 D	Spatial Illusion	Escher-like illusion, perspective based architectural puzzles
Life is Strange	2015	3D	Time Manipulation	Narrative time manipulation
Fragments of Euclid	2017	3D	Spatial Illusion	Escher-like environment, perspective portals
Superliminal	2019	3D	Spatial Illusion	Forced perspective object scaling
Manifold Garden	2019	3D	Spatial Illusion	Gravity shift, infinite space
Hyperbolica	2022	3D	Non-Euclidean Geometry	Hyperbolic geometry
Viewfinder	2023	3D	Spatial Illusion	Photographic teleportation

Anamorphosis is a term used to describe a distorted or skewed image that appears in its intended form only when observed from a specific angle, or through a reflective surface placed in a correct position and orientation. Araújo (2017) points out that a common way to create surface anamorphosis is by projecting objects onto a plane. Anamorphic projection is a technique that uses geometry and perspective to distort and project the subject onto a surface, creating the illusion of anamorphosis. According to Di Paola et al. (2014), first uses of anamorphosis can be found in art pieces like Pala di Brera by Piero della Francesca (1472) and Hans Holbein's painting The Ambassadors (1533). The Ambassadors painting includes a distorted skull that only becomes visible when viewed from a specific perspective. During the Renaissance, anamorphosis

was often used in murals and ceiling paintings to surprise viewers' perceptions, becoming a tool for exploring perspectives, illusions, and hidden meanings.

In contemporary art, artists use the technique with large-scale pavement drawings that appear three-dimensional when viewed from a precise angle. In architecture, anamorphic projections are used to create spatial illusions that reveal the artwork not only as a visual trick but also as a form of spatial storytelling. Digital installations take this one step further by employing digital tools and projections onto surfaces to boost the effect of the illusion. While anamorphic projection techniques are being used in games, there is still significant untapped potential for their implementation. Unlike static media, games allow anamorphic illusions to become dynamic and interactive.

Material and Method

This paper adopts a research-through design methodology to explore the potential of anamorphic projection in level design to experiment with novel game mechanics that allow players to experience and interact with the environment in non-traditional ways. The core concept of suggested mechanics is to treat the game levels as projected objects, fragments of space that can only be discovered and accessed when the player finds the correct viewpoint. In this environment, perception becomes access: the alignment of the player's perspective acts as a key to solve the puzzles and progress through the game. The project explores the notion that in digital games, perception can be more than a means of observing reality; it can become a mechanism for shaping it. The illusion becomes the structure, what is seen becomes real. Perception shapes reality, acting both as subject and as the primary design tool.

A framework is proposed for implementing anamorphic projection as a spatial mechanic. The method involves the use of portal planes and projection cameras. Two visually connected portal surfaces are placed in two different 3D environments. Portal 1 is located at the entrance of Level 1, and Portal 2 is at the entrance of Level 2. Since the portals are connected, Portal 2 displays a view of Level 1 and Portal 1 displays a view of Level 2. A projection camera is positioned in front of Portal 2, capturing the view of Level 1 through Portal 1. This view is then projected on the surface of Level 2. At the beginning of the game, the player can see the projection, but the object being projected remains hidden. The player's task is to explore the space and find the exact viewpoint that matches the position and orientation of the projection camera. When the correct location and rotation are found, the hidden portal becomes visible and active, allowing the player to pass through into the next level. Figure 1illustrates the logic of the system.

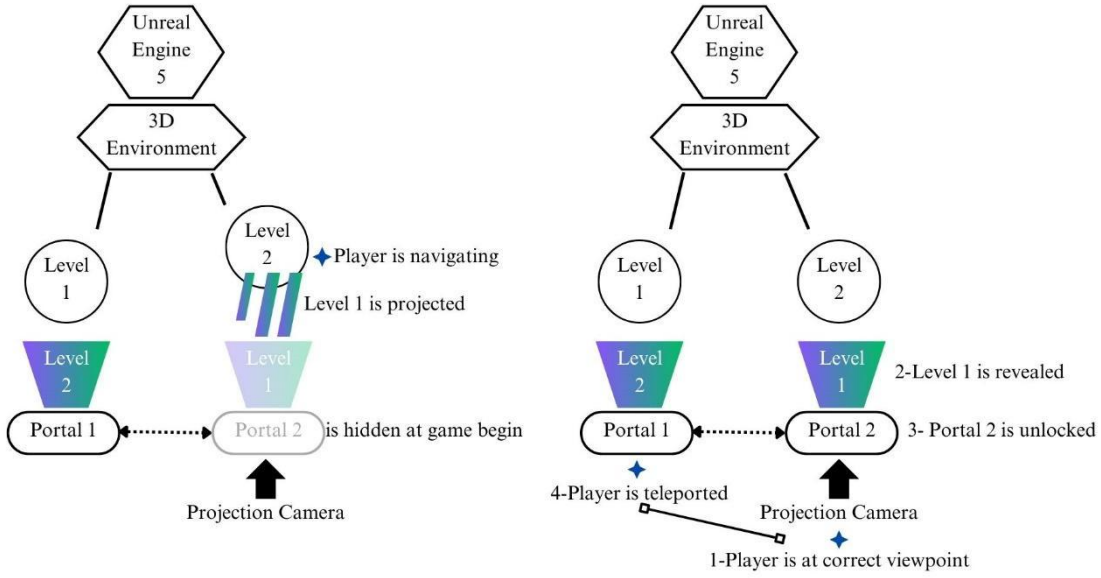

Figure 1. Portal/Projection Setup Diagram.

Using this system a game prototype is developed using Unreal Engine 5. In this prototype, three game levels were created, and the portal/projection systems were implemented within each level. The player's objective is to progress through levels by finding the correct viewpoint. Figure 2 shows the implementation in Unreal Engine 5.

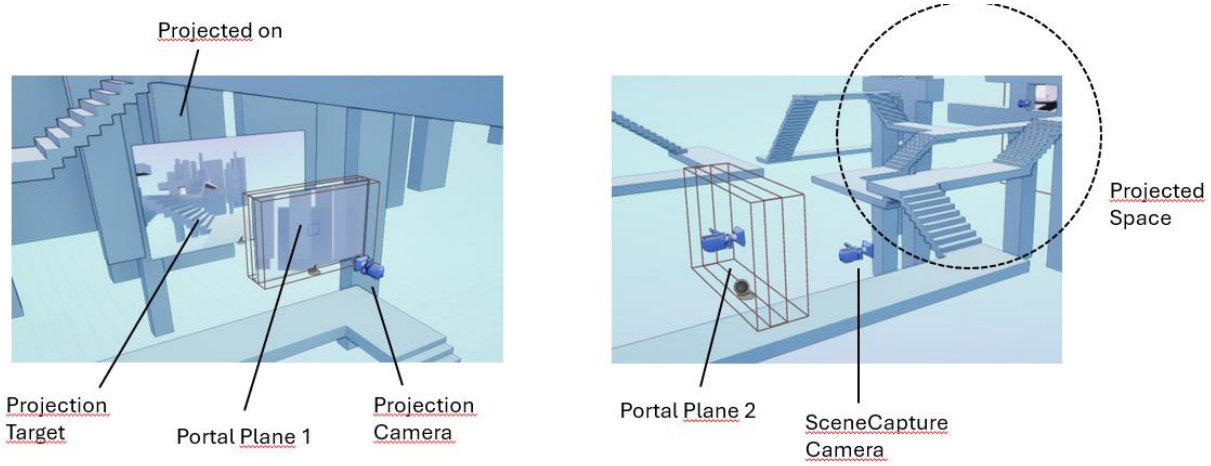

Figure 2. Prototype Implementation of Portal/Projection Logic in Unreal Engine 5.

To evaluate the usability and experiential impact of the mechanic, the study employed the Player Experience Inventory (PXI), developed by Vanden Abeele et al. (2020), to measure both functional and psychosocial consequences of gameplay. Since the aim was to assess both the effectiveness and emotional response, examining functional aspects (Ease of Control, Progress feedback, Audovisual appeal, Goals and Rules, Challenge) as well as psychosocial constructs (Mastery, Curiosity, Immersion, Autonomy, Meaning), the PXI was a valid choice for this study.

A total of 33 participants played the prototype and completed a survey that uses questions from the PXI tool, using a 7-point Likert scale. Six out of ten constructs were selected as they were most relevant to the mechanic: Ease of Control, Goals and Rules, Challenge, Mastery, Curiosity, and Immersion. Most of the participants were familiar with games, as shown in Figure 3., 57.6% play games every day and 30.3% percent play games several times a week.

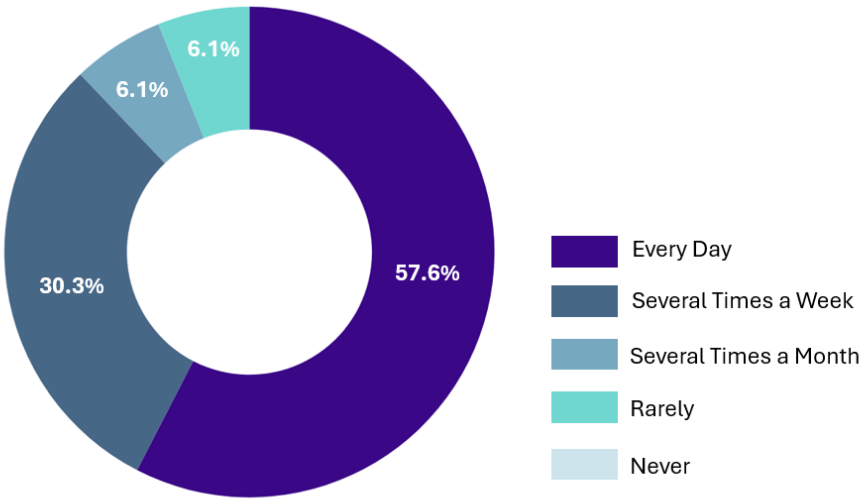

Figure 3. Distribution of Participants by Game Playing Frequency.

Findings

The average scores indicate a consistently positive reception of the mechanic. As shown in Figure 4, Mastery received the highest average score (5.97). This suggests that the players felt successful while interacting with the mechanic. Goals and Rules received the second highest score (5.57), suggesting that the players did not have a problem understanding the objective of the mechanic and the goal was clear. Ease of Control scored the third highest (5.47) which indicated that the controls were manageable. The Curiosity, Challenge and Immersion constructs received a slightly lower score (5.14, 5.09 and 5.06, respectively), which although being lower still indicates a good level of cognitive engagement. One possible reason for this is that the prototype consisted of only three levels designed primarily to introduce the mechanic, and the players did not have the opportunity to apply their understanding in more complex scenarios.

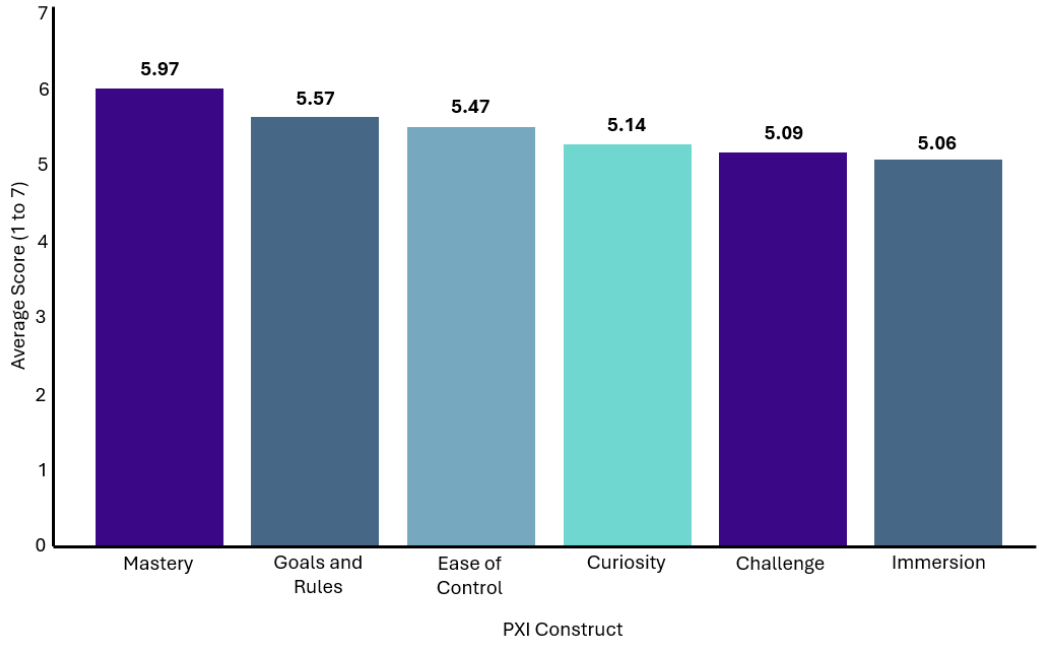

Figure 4. Average PXI Scores for Selected Constructs.

Conclusion

This study explored the use of anamorphic projection as a game mechanic by turning perspective into a key for unlocking new levels. Through the development of a design framework and a prototype to test the system, the findings from the PXI-based evaluation reveal that the players responded positively to the mechanic. The results suggest that the perception can be used as a design tool in games and the mechanic holds foundational potential for future iterations that focus on more emotionally engaging environments.

References

Araújo, A. (2017). Anamorphosis: Optical games with perspective's playful parent. In Proceedings of Recreational Mathematics Colloquium V – G4G (pp. 71–86). Universidade Aberta, Lisbon, Portugal.

Di Paola, F., Pedone, P., Inzerillo, L., & Santagati, C. (2014). Anamorphic projection: Analogical/digital algorithms. Nexus Network Journal,17(1), 253–285. **Url-1** https://doi.org/10.1007/s00004-014-0225-5, date retrieved 15.03.2025.

Orbons, E. M., & Ruttkay, Zs. (2008). Interactive 3D simulation of Escher-like impossible worlds. University of Twente, Department of Computer Science. **Url-2** https://www.researchgate.net/publication/228780258, date retrieved 10.03.2025.

Osudin, D., Denisova, A., & Child, C. (2024). Non-Euclidean video games: Exploring player perceptions and experiences inside impossible spaces. IEEE Transactions on Games.
Url-3 https://doi.org/10.1109/TG.2024.3386816, date retrieved 12.03.2025.
Thiering, M., & Mittelberg, I. (2022). Image and force schemas interacting in digital environments: The computer game Antichamber. In Proceedings of the Sixth Image Schema Day (ISD6), March 24–25, 2022, Jönköping University, Sweden. CEUR Workshop Proceedings.
Url-5 http://ceur-ws.org, date retrieved 15.03.2025.
Vanden Abeele, V., Spiel, K., Nacke, L., Johnson, D., & Gerling, K. (2020). Development and validation of the player experience inventory: A scale to measure player experiences at the level of functional and psychosocial consequences. International Journal of Human-Computer Studies, 135, 102370.
Url-6 https://doi.org/10.1016/j.ijhcs.2019.102370, date retrieved 12.03.2025.

Understanding Player Behavior: The Role of Intrinsic and Extrinsic Motivations in Bartle Player Types

Muhammet Sinan Çavdar[a], Derya Güleç Özer[b], Hüseyin Kutay Tinç[c]

[a] Istanbul Technical University, Graduate School, Game and Interaction Technologies, Türkiye
[b] Istanbul Technical University, Faculty of Architecture, Department of Informatics Architectural Design Computing, Türkiye
[c] MEF University, Faculty of Art, Design and Architecture, Department of Digital Game Design, Türkiye
cavdarm17@itu.edu.tr

Keywords: Core Gameplay Loop, Motivation, Player Typologies, Reward.

Aim

Player engagement is a fundamental aspect of game design, ensuring player continuity, satisfaction and loyalty. What pleases players and what connects them to the game has always been one of the biggest study and research topics in game design. While some players are interested in competition or achievement, others seek exploration, social connection or simply relaxation. To analyze and address the diverse expectations of players, they have been categorized into various typologies over the years.

Richard Bartle's player type model (1996), one of the most well-known typologies, divides players into four main categories, as shown on Chart 1, based on their expectations and desires from games: achievers, explorers, killers, and socializers. According to Bartle, the player typology framework is based on two dimensions: action versus interaction and player orientation versus world orientation.

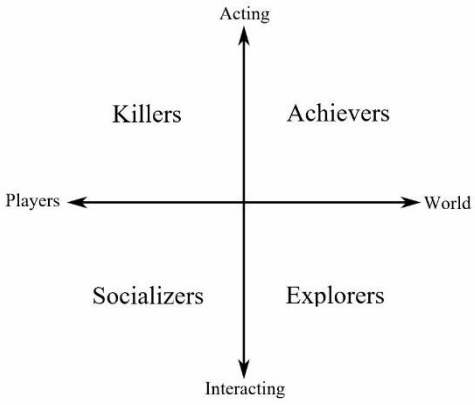

Chart 1. The Bartle taxonomy of player types (Bartle, 1996).

The most important component to meet players different expectations is core gameplay loop. According to Brazie (2023), the structure of a significant majority of core gameplay loops contains three important elements: challenge, actions, and reward. Creating a core gameplay loop that keeps the player engaged and satisfied is a huge challenge. According to Guardiola (2016), the primary goal in game design and game analysis is to define the basic gameplay of a game as a cycle (pp. 2-3). This involves identifying the set of actions that players repeat most often and linking them to certain winning or losing outcomes.

Meaningful play describes the experiences in which players perform actions for a specific purpose and have fun. For gameplay to be meaningful, every action taken by the player must be meaningful and no action must occur without a reason or consequence. As Tekinbas and Zimmerman (2003) explain, for an action to be meaningful, it must be both discernible and integrated. A discernible action allows the player to understand that their actions have consequences. Integrated action

ensures that the consequences are visible and truly effective, sometimes immediately and sometimes as the game experience progresses (p. 12).

In game loops, elements that give feedback to the player about their progress are needed so that they can understand that they are experiencing certain developments. These elements can be called progression mechanics. Butler et al. (2015) highlighted that what keeps players engaged and interesting is not the rules of the game or the interactions they have in the game, but how they combine them in progression in increasingly complex ways. There are many combinations to mix basic concepts, but creating progression while making the game experience engaging and interesting is an enormous challenge (p. 2407).

Player motivation examined under two main headings. These are intrinsic motivation and extrinsic motivation. Intrinsic motivation is the motivation that expresses the situations in which the action they do is interesting to the player and the player enjoys doing this action internally. Extrinsic motivation is the motivation that expresses the situation in which the player does the action entirely for the reward they will receive afterwards, and continues what they do with the desire to receive great items and awards. According to Zubek (2020), intrinsic motivation is hard to analyze and manage, whereas extrinsic motivation is easier to handle, because the player can be satisfied by simply increasing the outcome. However, over time, extrinsic motivation may begin to feel more like a job for the player (pp. 136-137).

The aim of this study is to provide a deep understanding of Bartle's player types, their intrinsic and extrinsic motivations, their expectations and preferences regarding the reward system within the core gameplay loops. The study aims to reveal whether different player types show significant differences in their preferences in the game and their satisfaction levels in terms of whether their expectations are met. By analyzing player behavior through a developed game, this study aims to reveal how much the characteristics of the player types that players define themselves as are truly reflected in the game.

Material and Method

The developed game for this research is designed to include core gameplay loops, decision mechanisms, and reward systems compatible with intrinsic and extrinsic motivations. Players' in-game data is collected based on their preferences, decisions in certain situations, and satisfaction levels for each level.

Players answer certain questions about themselves at the beginning of the game, as seen on Image 1 and Image 2, and they are categorized based on Bartle's player types in line with their own choices.

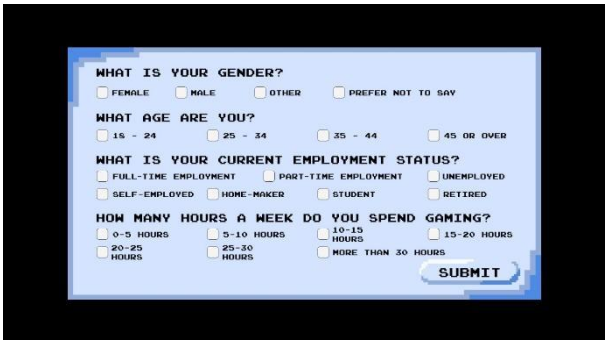

Image 1. Data collected to separate players into categories.

Image 2. Categorizing players by Bartle player types.

During the game, data is collected about players' interactions, preferences, and performances. At the end of each level, a general satisfaction score is obtained from the players. This satisfaction evaluation can be seen on Image 3.

Image 3. Players' overall satisfaction rating within the levels.

When the game is completed, the data sent allows a comparison and analysis between the player types they report and their actual in-game behaviors. According to certain situations, many comparative statistical methods are used to standardize and compare player preferences among different player types.

Findings

The findings of this study provide insights into how different types of players identified by Bartle respond to intrinsic and extrinsic reward systems within core gameplay loops.

A study was conducted with 80 people on the developed game, and players were asked for personal information about themselves in order to conduct a detailed analysis. Information was obtained on which Bartle player type they thought they were suitable for.

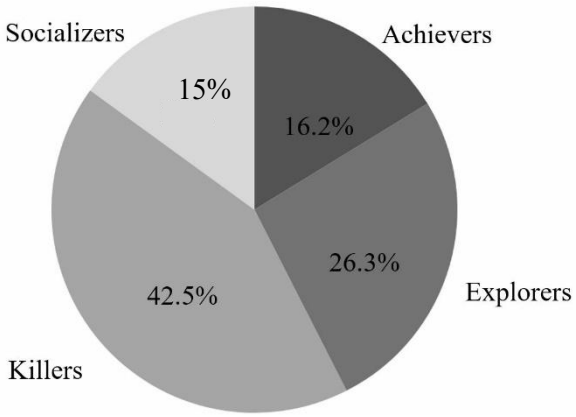

Chart 2. Distribution of 80 participants according to Bartle's player types.

As shown in the Chart 2, 16.2% of the participants identified as achievers, 26.3% as explorers, 42.5% as killers, and 15% as socializers. Before the players played the game, they were told that there would be two separate leaderboards, which would be published publicly for everyone to examine, based on a 'Lost Souls' counter that is kept according to the number of deaths in the game but can be reduced with certain choices, and the time it takes to complete the game. The elements that would motivate players with extrinsic motivation priorities were notified to them in advance.

The game begins with our main character learning that he can bring back a friend who has already died with the help of a portal and thinking that he will go to this portal no matter what. There are 3 sections in the game where players can explore different areas and complete achievements by helping a side character. Players can choose to help these side characters and play, discover new levels and witness different stories. However, when they choose not to play, their 'Lost Souls' number decreases by 5, and since they do not play extra levels, they have a chance to rise in both leaderboards.

Table 1. Correlation between death counts and satisfaction scores at level ends, compared across normal and side levels, based on Bartle's player types.

	Normal Levels	Side Levels	All Levels
Achievers	-0,055	-0,084	-0,058
Explorers	-0,315	-0,421	-0,340
Killers	-0,379	-0,243	-0,357
Socializers	0,088	-0,065	0,056
All Players	-0,202	-0,181	-0,198

According to the data analysis shown on Table 1, it is seen that the satisfaction levels of achievers and socializers are not affected much by dying. The satisfaction levels of explorers and killers are negatively affected due to more deaths. It can be said that explorers aim to gain new experiences by playing without dying and killers are negatively affected by dying in order to rise in the competitive leaderboard. It can also be seen that explorers, unlike killers, are more negatively affected by dying in side levels.

When the portal is reached at the end of the game, our main character learns that if he saves his friend, his 'Lost Souls' number will increase by 20, and therefore they will fall on the leaderboard. Accordingly, the player is asked to make a decision, 'Save the friend of the main character whom they have struggled with throughout the game and fall behind on the leaderboard or leave them as they are and stay where they are on the leaderboard?'.

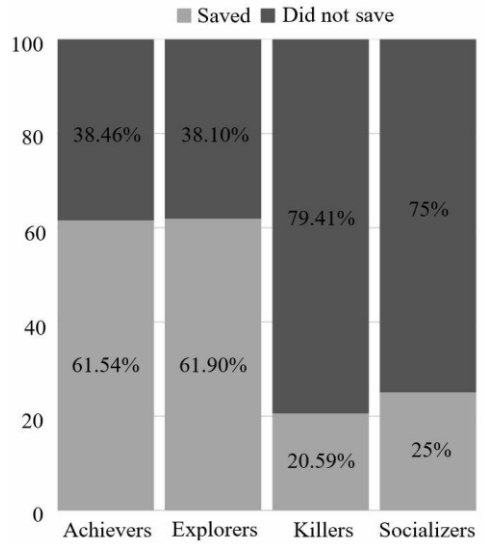

Chart 3. Percentage of players saving the main character's friend at the end of the game by Bartle's player types.

Again, according to the data analysis shown on Chart 3, 61.54% of the achiever players, 61.90% of the explorer players, 20.59% of the killer players and 25% of the socializer players chose to save the main character's friend. The fact that the characters rescue, which is the reward for the effort given throughout the game, is accepted by the achievers at a high rate, and rejected by the killers at a high rate, at the cost of the 'Lost Souls' number increasing by 20 and falling behind on the leaderboard, is exactly the expected data from the player types. The absence of discovery, and it being only a result of the struggle given throughout the game makes it meaningful for the explorer players to make such a decision. Socializer players are clearly interested in climbing the leaderboard and being able to talk about it with their friends.

Conclusion

In conclusion, 80 different people who played the game were expected to make different choices according to their own motivations and expectations during the game, and these preferences were analyzed according to Bartle's player types. Achiever players are more focused on certain achievements and completing different tasks, and they stand out with intrinsic motivation. Explorer players were completely satisfied with the discovery of stories, and their expectations were in this direction, so they focused on completing side missions as much as possible and seeing new and different levels. Killer players were clearly not satisfied with the side missions and focused on finishing the game quickly and climbing the leaderboard as much as possible. Acting in a way that met the expectations of their extrinsic motivation, very few of them eventually saved the main character's friend. Finally, socializers, generally acting similarly to killers, did not focus much on side missions, acting with the insight of climbing the leaderboard, sharing this with their friends, and proving themselves to their friends and few saved the main character's friend at the end of the game. Significant differences have been identified in the intrinsic and extrinsic motivations of various player types, as well as in the types of rewards that effectively satisfy them.

In the future, the findings of this research will offer game developers valuable insights into how to effectively satisfy players of different types by addressing their expectations in terms of intrinsic and extrinsic motivations.

Acknowledgements

This work was supported by TÜBİTAK within the scope of Scientist Support Programs Directorate (BİDEB) 2211-Domestic Postgraduate Scholarship Program.

References

Bartle, R. (1996). Hearts, clubs, diamonds, spades: Players who suit MUDs. Journal of MUD research, 1(1), 19.
Brazie, A. (2023). "Designing the Core Gameplay Loop: A Beginner's Guide." Game Design Skills, gamedesignskills.com/game-design/core-loops-in-gameplay/, date retrieved 10.10.2024.
Butler, E., Andersen, E., Smith, A. M., Gulwani, S., & Popović, Z. (2015). Automatic game progression design through analysis of solution features. In Proceedings of the 33rd annual ACM conference on human factors in computing systems (pp. 2407-2416).
Guardiola, E. (2016). The gameplay loop: a player activity model for game design and analysis. In Proceedings of the 13th International Conference on Advances in Computer Entertainment Technology (pp. 1-7).
Tekinbas, K. S., & Zimmerman, E. (2003). Rules of play: Game design fundamentals. MIT press.
Zubek, R. (2020). Elements of game design. MIT Press.

GAME AND INTERACTION TECHNOLOGIES

AI in Gaming

Game Design

Game Production

Gamification

Interaction Technologies

Series Games

User Studies

RNBO for Game Development: A Framework for Dynamic and Adaptive Audio Design

Deniz Koçak[a], Ozan Sarıer[b]

[a] Istanbul Technical University, Department of Game and Interaction Technologies, Game and Interaction Technologies Program, Turkey
[b] Istanbul Technical University, Department of Turkish Music State Conservatory, Music Technologies Program, Turkey
kocak17@itu.edu.tr

Keywords: Game Audio Design, Audio Programming, RNBO, Interactive Sound.

Aim

Audio is a critical component of games that greatly contributes to player experience. While the visuals shape the game world, audio design enhances immersion by engaging players emotionally and reinforces the game's narrative and gameplay. Commonly, modern game audio relies on middleware tools such as Wwise or FMOD to create interactive soundscapes. Popular and recently released games that use Wwise include Silent Hill 2, Alan Wake 2 and Baldur's Gate 3 (Audiokinetic, n.d.). Some of the popular games that use FMOD are Celeste, Silence of the Lambs, and Sekiro: Shadows Die Twice. Big studios like Activision, Bethesda and Rockstar are also known to use FMOD (FMOD, n.d.). Both AAA and independent studios widely use FMOD and Wwise in their games. Audio middleware tools are powerful audio engines that provide seamless integrations to popular game engines like Unity and Unreal Engine. These middleware tools allow audio designers to create immersive audio environments without scripting, and overall having much more control over the game. However, these software tools mainly rely on pre-recorded samples and pre-configured effects, which limits their interactive responses.

Game audio designers would benefit from a flexible, real-time sound synthesis tool to create dynamic and interactive soundscapes. Unreal Engine has released MetaSound which is a high-performance audio system. MetaSound provides sound designers control over Digital Signal Processor which allows them to generate sound sources. It is a node-based system where sound designers can create audio behaviors with visual scripting. It can be easily integrated with game data and player interactions, creating an immersive experience (Epic Games, n.d.).

Max is a visual programming language for creating music, interactive audio, and multimedia applications. It is used in real-time sound synthesis, sound design, and interactive applications. It allows the sound designer to manipulate samples, or design their own custom synthesizer (Cycling '74, n.d.). RNBO is a patching environment for exporting software made in Max. This allows the user to turn audio patches into standalone plugins, C++ code, or web applications. It's designed for real-time cross platform audio processing and is very useful in interactive applications (Cycling '74, n.d.).

Unlike middleware tools, RNBO provides dynamic sound generation using Digital Signal Processing (DSP). DSP mathematically manipulates audio signals in real-time, enabling features such as live sound synthesis, adaptive effects, and procedural audio generation. By processing audio live, DSP allows the game audio to be in sync with players actions, creates interactive soundscapes and improves immersion.

RNBO has multiple export formats, but none can be directly imported into game engines with ease, limiting its use for sound designers who lack coding experience. Many audio designers are experienced with Max and RNBO, but they don't have the technical background needed to integrate it to game engines, consequently, this limits their ability to take advantage of procedural audio.

This research focuses on developing a tool, using RNBO exports, that enables sound designers to create and implement real-time audio processing in Unity. Creating a native audio plugin for sound designers would give them the freedom to use their skills in a familiar environment like Max and then easily integrate it into game engines. It is expected that this would result in a more dynamic and immersive audio experience by expanding the creative possibilities of in-game sound.

Material and Method

The study begins by researching, analyzing and understanding RNBO's capabilities, focusing on its functionality, real-time audio processing potential, and its integration capabilities with game engines. RNBO works as a visual patching environment inside Max. It allows users to design digital signal processing (DSP) algorithms through a node-based interface. Unlike commonly used sample-based methods, RNBO enables procedural sound synthesis, real-time signal manipulation and effects, making it a perfect tool for interactive game audio.

RNBO provides various export formats, each format was examined to determine if it is suited for game development. This examination was done by looking for factors such as performance, flexibility, and ease of integration to the game engines. The C++ export was prioritized as it offers the most efficient path leading to a low-latency digital signal processing within a game engine. However, since Unity does not support RNBO's output formats natively, additional interface is required. The study identified technical struggles of connecting Unity and RNBO, such as compatibility constraints, performance issues and the need for structured workflow to create smooth integration.

After analyzing various integration methods, it was determined that the JUCE framework provides the most efficient and flexible solution for incorporating RNBO into Unity. JUCE is an open-source C++ framework, which is generally used in audio application and plug-in development. It provides a broad set of tools for building custom digital signal processing (DSP) modules, standalone applications, and audio plug-ins. One of its key advantages is, its ability to export a number of formats such as, VST, AU and AAX, making it a popular choice (JUCE, n.d.). JUCE also integrates well with popular game engines such as Unity.

JUCE serves as an important network for linking RNBO and popular game engines like Unity, enabling seamless integrations for real-time audio processing inside interactive environments. Since RNBO's C++ export provides a raw DSP unit, JUCE can be used to process the DSP code into a native audio plugin for Unity, whether as a VST3, AU, or a custom DSP module. The process begins with designing and exporting a RNBO project which can range from being a procedural sound generator to an interactive effects unit. The RNBO generated code is then integrated into JUCE AudioProcessor, allowing it to operate within a real-time audio environment. Using JUCE Projucer to ensure cross-platform compatibility, the project can be compiled into different formats including plugins compatible with Unity. Once integrated into Unity, these plugins can directly be controlled by C# scripts, enabling adaptive and interactive soundscapes in game environments, enhancing player immersion.

To ensure a smooth integration of RNBO into game engines, this study primarily relies on the official documentation of Unity, JUCE, Max and RNBO. The Unity Engine documentation provides important insights into the game engines native audio system and its support for custom audio plug-ins. To understand how to develop cross-platform audio applications and wrap RNBO exports into formats compatible with Unity, JUCE's extensive documentation is essential. Additionally, Max and RNBO documentations play an important role in understanding the capabilities of RNBO patches, their export options, and how they can be adapted for real-time game audio. With the help of these materials, a roadmap for making a RNBO audio plugin for Unity can be create.

Findings

The research led to several key findings about integrating RNBO into Unity. First, the analysis of RNBO's capabilities confirmed it is a powerful environment for digital audio processing in real time. An essential component of RNBO is its ability to export projects as C++ code, which is a vital step in the tool's development. Second, the analysis of Unity's native audio system showed its support for custom audio plugins, creating a pathway for integration. Nonetheless, Unity's lack of native support for RNBO export format created challenges during initial considerations. This made it clear that an intermediary solution was required. JUCE was found to be a practical and effective way to connect the two. The ability of JUCE to compile C++ code into various plugin formats showed a clear path for creating a RNBO plugin that works with Unity.

At this point, a simple RNBO patch has been successfully exported and compiled within a JUCE plugin structure. Frequency and gain were the two parameters defined in Max/RNBO, which were preserved in the exported code and mapped within

the JUCE processor. This confirms that the C++ export from RNBO can be adapted for real-time DSP inside JUCE. While Unity integration is still in progress, the early tests show that the proposed workflow is technically feasible.

Conclusion

In conclusion, this study aims to provide a practical and user-friendly tool for integrating RNBO into game development environments. By using JUCE to turn RNBO's C++ exports into plugins compatible with Unity, this approach lets sound designers implement real-time procedural audio without needing to write complex codes. The goal is to combine creative audio design and technical implementation, helping to create more dynamic and immersive soundscapes in video games and interactive media. With the early stages of development, the project has strong potential to offer sound artists a better control over the game audio. Future work will involve completing the plugin prototype, examining its performance in a real game setting, and optimizing the workflow.

References

Audiokinetic. (n.d.). Powered by Wwise. Audiokinetic. Retrieved March 24, 2025, from https://www.audiokinetic.com/en/wwise/powered-by-wwise/

Cycling '74. (n.d.). Max. Cycling ’74. Retrieved March 24, 2025, from https://cycling74.com/products/max

Cycling '74. (n.d.). RNBO. Cycling ’74. Retrieved March 24, 2025, from https://cycling74.com/products/rnbo

Epic Games. (n.d.). MetaSounds: The next generation sound sources in Unreal Engine. Unreal Engine Documentation. Retrieved March 24, 2025, from https://dev.epicgames.com/documentation/en-us/unreal-engine/metasounds-the-next-generation-sound-sources-in-unreal-engine

FMOD. (n.d.). Games using FMOD. FMOD. Retrieved March 24, 2025, from https://www.fmod.com/games

JUCE. (n.d.). JUCE: The audio application framework. JUCE. Retrieved March 24, 2025, from https://juce.com

GAME AND INTERACTION TECHNOLOGIES

AI in Gaming

Game Design

Game Production

Gamification

Interaction Technologies

Series Games

User Studies

Procedural Entity Generation For Simulated Ecosystems

Gazi Muhammet Canbolat[a], Selçuk Sümengen[a], Sema Alaçam[a]

[a] Istanbul Technical University, Faculty of Computer and Informatics Engineering, Game and Interaction Technologies, Turkey
canbolat24@itu.edu.tr

Keywords: Computer Graphics, Ecosystem Simulation, Gamification, Procedural Content Generation, Procedural Modeling.

Aim

Procedural Content Generation (PCG) is a common technique in game development and simulations to create dynamic and diverse environments. It allows for the automatic generation of game levels, textures, and characters, reducing manual effort while maintaining variety. Our study demonstrates how procedural modeling approaches can be used to simulate biological ecosystems by dynamically generating entities and their interactions in a structured 3D simulation environment. We enable procedural content generation in our scalable and adaptable simulation environment, resulting in a rich and dynamic simulation that does not require pre-modeled elements. Our 3D simulation utilizes computer graphics principles to enhance visualization and realism, ensuring an immersive experience. As a proof of concept, the presented framework enables the investigation of how procedural modeling might be used to simulate an ecosystem.

Material and Method

Related Work

Procedural modeling plays a crucial role in content generation, allowing for the dynamic construction of objects based on predefined rules. Unlike traditional modeling, where assets are manually designed, procedural modeling enables the algorithmic creation of complex structures with minimal user intervention. PCG is commonly utilized in game development to enhance content diversity and reduce manual workload. It provides a structured approach to content creation, allowing developers to generate interactive environments efficiently.

Hendrikx et al. (2013) propose a six-layered taxonomy for PCG, categorizing it into game bits, game space, game systems, game scenarios, game design, and derived content. From low-level materials like textures and models to high-level game mechanics and narrative frameworks, each of these layers represents a distinct degree of content abstraction.

PCG techniques can also be classified according to their generation process. Togelius et al. (2011) describe three main approaches: constructive, generate-and-test, and search-based. Constructive approaches generate content in a single pass using predetermined rules, providing immediate usability but limiting flexibility. Generate-and-test methods iterate over generated content without structured optimization, whereas search-based techniques refine content over multiple iterations using evaluation functions.

In the realm of game development, procedural techniques have also been successfully integrated into various games. For instance, Spore (Maxis, 2008) and No Man's Sky (Hello Games, 2016) utilize procedural methods to create vast and highly detailed game worlds. By using algorithmic approaches to generate complex environments, these methods enhance scalability and diversity while minimizing the need for manual design effort. No Man's Sky employs procedural methods to generate planets and ecosystems, whereas Spore concentrates on evolutionary simulations and species development. Procedural content generation in Spore and No Man's Sky highlights how PCG enhances adaptability and scalability in interactive simulations.

Simulated Ecosystem

We used procedural modeling to generate biological entities that vary in shape, size, and behavioral characteristics based on predefined rules. The creatures in our simulation environment are divided into three groups depending on their eating habits: producers, herbivores, and carnivores. These classifications align with the ecological structuring described by Schoener et al. (1989), forming the foundation of procedural entity generation.
The entity attributes are classified into three broad categories. The first category contains static physical attributes, including body structure and limb count. The second category contains dynamic features that alter over time, such as entity growth caused by consuming food. The final category contains hereditary traits that carry across generations, impacting how children adjust to environmental limits.
The food chain regulates resource distribution, ensuring that producers sustain herbivores, which in turn support carnivores. When an entity dies from starvation, its remains enrich the soil, allowing new producers to grow and contributing to the ecosystem's nutrient cycle. In our simulation, procedural rules govern how entities consume resources, grow, reproduce, and interact with one another, ensuring that ecosystem balance emerges naturally.

Implementation

In this study, PCG is primarily used for game space and game systems, where interactions and environmental conditions are generated dynamically. The presented simulation framework utilizes a hybrid procedural generation approach. Initial procedural entity creation follows constructive principles, ensuring structural consistency. However, inherited traits introduce indirect selection over generations, allowing for emergent ecological adaptations without the need for explicit optimization. The hybrid approach that we used during entity generation balances structured procedural generation with dynamic environmental interactions, resulting in a self-regulating ecosystem model.
Our simulation environment offers an interactive and customizable framework, incorporating elements of gamification to enhance user engagement and experimentation. Users configure initial population parameters and adjust environmental variables to observe how species adapt over time. Before running the simulation, users can specify the initial number of entities for each species, as well as define value ranges for procedurally assigned attributes such as movement speed, body size, reproduction rate, and energy consumption. As the simulation progresses, new entities inherit certain parameters from their parents, with slight adjustments made by randomization processes. The given parameters have an impact on how entities interact in the environment, including population dynamics and resource competition. Through controlled experimentation, users can analyze the effects of procedural constraints such as energy consumption, predator-prey relationships, and reproduction rates on ecosystem stability. This interactive aspect introduces a gamification element, making the simulation applicable as both a research tool and a procedural game design framework.

Findings

The presented study advances procedural modeling by illustrating how PCG may be used to generate an artificial ecosystem in which elements interact dynamically. Furthermore, our approach lays the groundwork for game developers to incorporate similar procedural entity generation techniques into their projects. Such an approach enhances versatility and scalability in gaming environments.
In our simulation environment:

- A scene graph is used to efficiently handle scene objects, permitting optimized transformations and the effective display of procedural entities.

- PCG eliminates reliance on pre-modeled assets, allowing for dynamic ecosystem generation while significantly reducing data storage requirements.

- The structured procedural generation method uses predefined rules to regulate entity behaviors while allowing for variable ecological interactions, resulting in a scalable and adaptable simulation framework.

Conclusion

As a proof of concept, our simulation framework demonstrates how procedural approaches go beyond traditional game development, giving a systematic foundation for ecological simulations and artificial life studies. The methodology used in our research may be applied to investigate population dynamics by modeling how species interactions and resource availability affect long-term ecosystem stability. By applying procedural modeling principles, our system enables a continuously adapting environment, facilitating in-depth studies of ecological dynamics and providing an engaging framework for interactive applications.

Future Work

Future research may focus on expanding procedural interactions and increasing species diversity. Additional ecosystem categories could introduce more complex ecological relationships. The simulation framework could also be extended to support multiple ecosystems, each with unique environmental conditions and interactions. Further advancements may explore integrating deep learning techniques into the reproduction process, refining trait inheritance, and enhancing biologically inspired adaptation mechanisms. These improvements could elevate procedural modeling applications in artificial life research and game design, contributing to more intricate and realistic ecosystem simulations.

References

Hello Games. (2016). No Man's Sky [Video game]. Hello Games. https://www.nomanssky.com/
Hendrikx, M., Meijer, S., Van Der Velden, J., & Iosup, A. (2013). Procedural content generation for games: A survey. ACM Transactions on Multimedia Computing, Communications, and Applications (TOMM), 9(1), 1-22.
Maxis. (2008). Spore [Video game]. Electronic Arts. https://www.spore.com/
Schoener, T. W. (1989). Food webs from the small to the large. Ecology, 70(6), 1559-1589.
Togelius, J., Yannakakis, G. N., Stanley, K. O., & Browne, C. (2011). Search-based procedural content generation: A taxonomy and survey. IEEE Transactions on Computational Intelligence and AI in Games, 3(3), 172-186.

GAME AND INTERACTION TECHNOLOGIES

AI in Gaming

Game Design

Game Production

Gamification

Interaction Technologies

Series Games

User Studies

Naval History Reconstruction Through 3D Modeling and Simulation

Deniz Çakır[a], Gökdeniz Neşer[a]

[a] Dokuz Eylül University, Institute of Marine Sciences and Technology, Naval Architecture, Türkiye
deniztcakir@gmail.com

Keywords: 3D Modeling, Naval Architecture, Naval History, Realistic Texturing, Warship Visualization.

Aim

The aim of this study is to digitally reconstruct historical and unrealized warships through a visually accurate and technically grounded 3D modeling workflow. This reconstruction supports academic research by providing precise visualizations based on archival documentation, aids in digital preservation of naval heritage, and enhances public engagement by making historically significant vessels accessible in virtual environments. Such digital twins serve as invaluable tools to bridge the gap between historical records and modern audiences, preserving maritime culture in an interactive and immersive way.

Material and Method

This study employs a systematic and structured 3D modeling workflow founded on extensive archival research and careful blueprint analysis. The process begins with collecting primary and secondary source materials, including detailed ship plans, archival photographs, written technical documentation, and where possible, first-hand testimonies or museum records. These materials provide the foundational data for creating geometrically accurate digital models.

The initial modeling phase utilizes polygonal modeling techniques in professional 3D software, where the hull, superstructure, and key components of the ship are recreated with high fidelity. A novel aspect of the workflow is the application of a grid-based topology method during the modeling phase. This approach organizes the mesh into uniform, logically arranged quads that facilitate subsequent UV unwrapping processes. The consistent topology improves texel density distribution, reducing texture stretching and wasted UV space, which is critical when working with high-resolution textures.

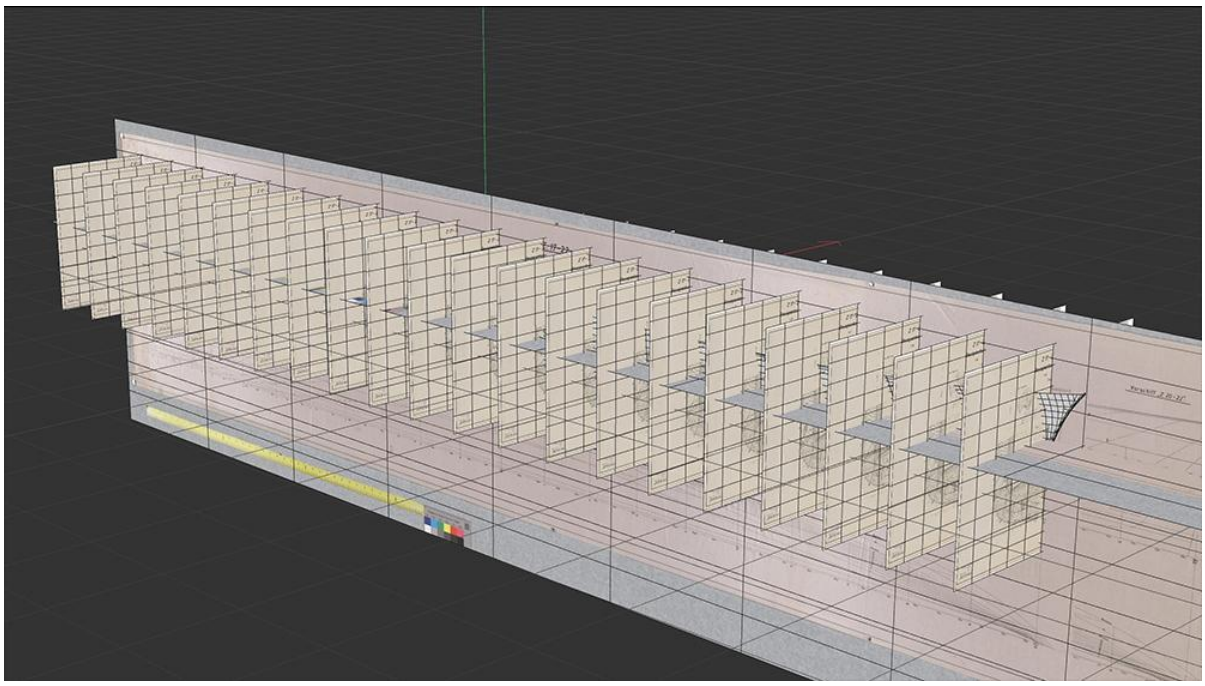

Figure 1. Reference to 3D Model Stage.

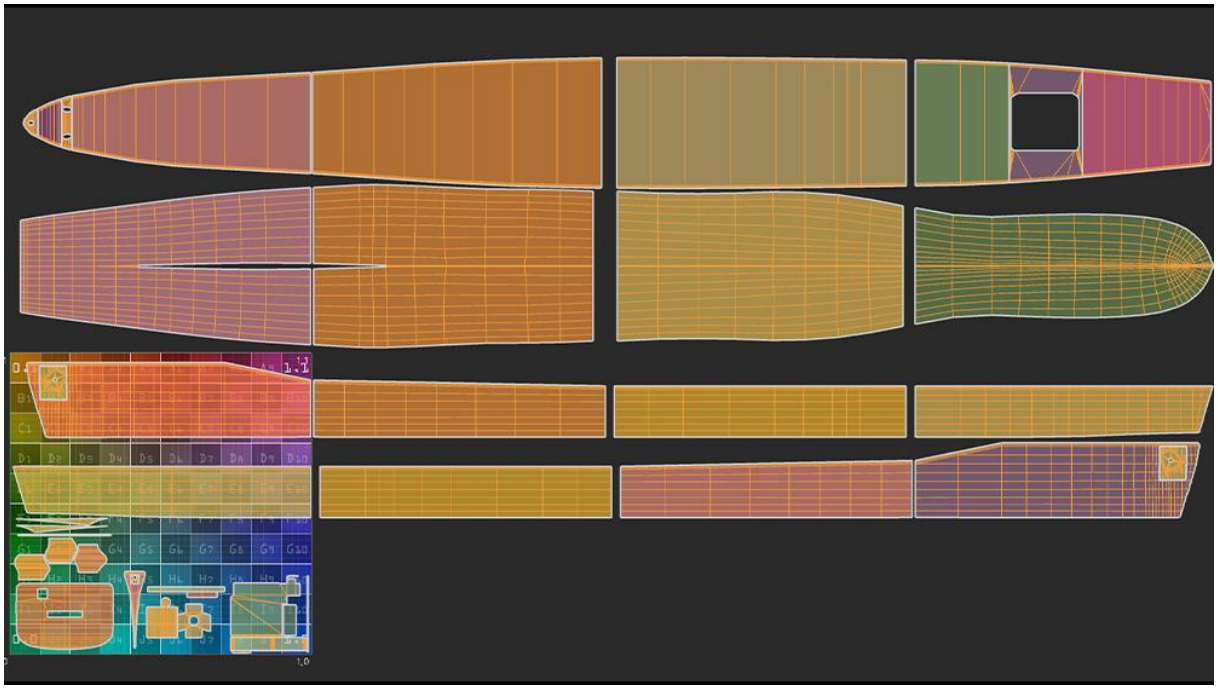

Figure 2. UV Islands.

Texturing is performed using Physically Based Rendering (PBR) techniques in software such as Substance Painter. This approach allows for the realistic simulation of materials under various lighting conditions by accurately replicating physical properties like metalness, roughness, and reflectivity. Surface details such as micro-wear, manufacturing tool marks, environmental weathering effects (e.g., rust, paint chipping), and asymmetries are intentionally integrated. These imperfections enhance visual authenticity, conveying the vessel's history and usage over time.

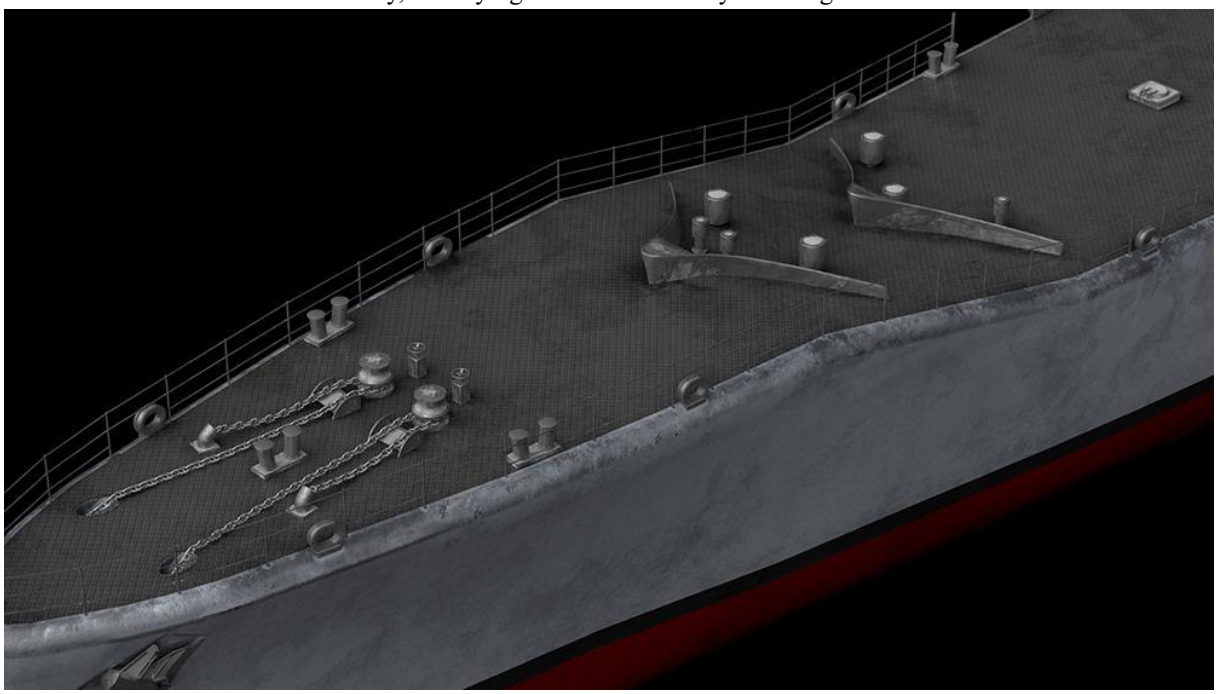

Figure 3. Realistic texturing.

To simulate dynamic elements, Houdini is employed to generate realistic ship wake effects. Using the ship's 3D geometry as input, fluid and particle simulations produce volumetric wake data that can be exported as VDB files. Final composition includes realistic lighting setups, ocean surfaces, and atmospheric effects, with post-processing touch-ups done in Photoshop to enhance color grading and contrast.

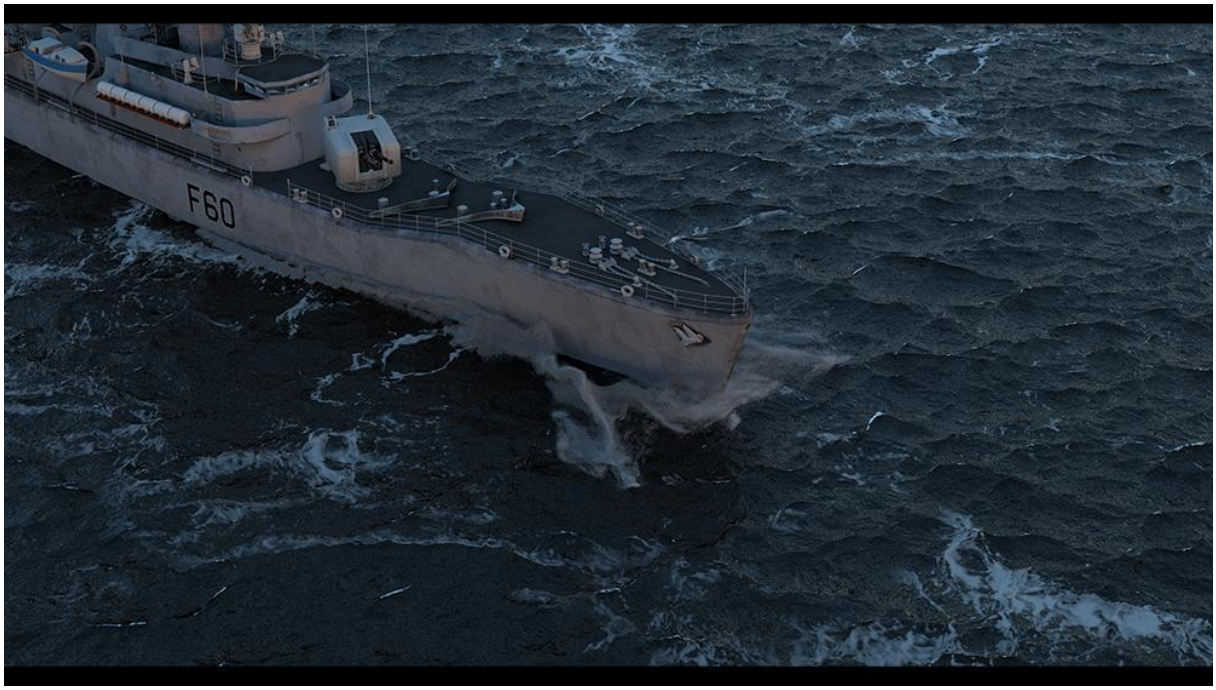

Figure 4. Volumetric Data Wake Imported into Scene.

Importantly, this workflow is versatile enough to digitally realize "never-built" warships from historical plans that were either canceled or remained conceptual, such as the German H-44 class battleships or the Soviet Stalingrad class heavy cruisers. This aspect allows historians and researchers to visualize theoretical designs and assess their feasibility and appearance in ways previously impossible.

Figure 5. Final Scene Render.

One key challenge in this workflow is ensuring the balance between geometric accuracy and computational efficiency. High polygon counts increase detail but can hinder real-time rendering performance, especially for interactive applications such as virtual museums or VR experiences. Thus, strategic use of grid-based topology and texture optimization is critical. The choice of industry-standard software such as Houdini for fluid simulations and Substance Painter for PBR texturing reflects the need for robust tools that can handle complex data while maintaining artistic flexibility.

Additionally, the ability to simulate environmental effects like corrosion, dirt accumulation, and wear patterns allows for more authentic reconstructions that go beyond mere geometric modeling. These effects are essential for conveying the lived history of the vessels, enabling viewers to understand their operational context and aging process.

Findings

The implementation of the grid-based topology method yields significant improvements in UV layout efficiency. Uniform polygon distribution enables optimized use of texture space, preventing common issues like pixel density imbalance and texture distortion. This optimization allows for higher detail levels on critical visual areas without increasing overall texture memory requirements, a crucial factor for real-time visualization and digital exhibitions.

Physically based texturing combined with carefully modeled imperfections results in models with a high degree of visual realism and narrative authenticity. These subtle surface details help viewers subconsciously associate the models with tangible, historical artifacts, increasing immersion and credibility. The integration of realistic wake effects generated through Houdini simulations further enhances dynamic realism, making the scenes more engaging and lifelike.

The final models and scenes are well-suited for use in various contexts such as academic research presentations, digital museum exhibits, educational virtual reality environments, and even entertainment or documentary production. By balancing technical accuracy with artistic detail, the workflow successfully bridges the gap between scientific fidelity and visual storytelling.

Conclusion

This research demonstrates how advanced visual effects tools and techniques traditionally used in the entertainment industry can be effectively adapted to serve the field of naval historical research. The presented workflow offers a reliable and

repeatable method for visualizing both existing and unrealized warships within digital environments. This approach fills a crucial gap in public access to naval heritage, providing detailed and immersive representations that support both academic documentation and popular engagement.

Furthermore, by balancing fidelity, modularity, and realism, the method ensures that digital reconstructions are not only visually compelling but also technically sound, facilitating their integration into a range of applications from virtual museums to interactive simulations. As digital technology evolves, such workflows will become increasingly vital in preserving and reinterpreting maritime history for future generations.

As digital preservation and visualization technologies continue to evolve, workflows like the one presented here will play an increasingly vital role in safeguarding maritime cultural heritage. By making naval history accessible and engaging to a broad audience, these digital reconstructions help foster appreciation and understanding of the past, informing present and future maritime research and conservation efforts.

References

Rodriguez-Garcia, B., Ramírez-Sanz, J. M., Miguel-Alonso, I., & Bustillo, A. (2024). Enhancing learning of 3D model unwrapping through virtual reality serious game: Design and usability validation. Electronics, 13(1972). **https://doi.org/10.3390/electronics13101972,** date retrieved 11.04.2025.

Zhang, X., Liu, W., Liu, B., Zhao, X., & Hu, Z. (2021). Size-adaptive texture atlas generation and remapping for 3D urban building models. *ISPRS International Journal of Geo-Information, 10*(798). **https://doi.org/10.3390/ijgi10120798**, date retrieved 11.04.2025.

Lai, J.-Y., Wu, T.-C., Phothong, W., Wang, D. W., Liao, C.-Y., & Lee, J.-Y. (2018). A high-resolution texture mapping technique for 3D textured model. *Applied Sciences, 8*(11), 2228. **https://doi.org/10.3390/app8112228**, date retrieved 12.04.2025.

Wallin, R., & Stephens, F. (2014). Maintaining authenticity: Transferring patina from the real world to the digital to retain narrative value. Making Futures Journal, 3. University of the Arts London & University of West London. **https://repository.uwl.ac.uk/id/eprint/1788/,** date retrieved 11.04.2025

Di Giuseppantonio Di Franco, P., Galeazzi, F., & Vassallo, V. (Eds.). (2018). Authenticity and cultural heritage in the age of 3D digital reproductions. McDonald Institute for Archaeological Research.

GAME AND INTERACTION TECHNOLOGIES

AI in Gaming

Game Design

Game Production

Gamification

Interaction Technologies

Series Games

User Studies

Mechanics To Design Virtual Reality Cognitive Training Games

Evrim Kabadayı[a], Leman Figen Gül[b]

[a] Istanbul Technical University, Institute of Science and Technology, Department of Game and Interaction Technologies
[b] Istanbul Technical University, Faculty of Architecture, Department of Informatics Architectural Design Computing
kabadayie21@itu.edu.tr

Keywords: Cognitive Training, Virtual Reality, Game Mechanics, Game Design, Serious Games.

Aim

The capacity of humans for cognitive abilities is their best "x-factor" for differentiating themselves from other animals. These skills play an important role not only in managing large-scale actions but also in doing everyday tasks. Cognitive training denotes a systematic array of activities aimed at improving, sustaining, or rehabilitating cognitive processes including memory, attention, problem-solving, and executive functions. These programs are constructed according to neuroscientific and psychological principles, with the objective of enhancing brain pathways and optimizing cognitive efficiency.

Cognitive training is employed in various contexts, including clinical applications for rehabilitating patients with neurodegenerative diseases, brain injuries, or cognitive impairments, as well as non-clinical settings that promote healthy aging, academic achievement, and professional skill enhancement. Traditional cognitive training methods, such as pen-and-paper exercises, have been used for decades to measure, preserve, and enhance these cognitive functions. While cognitive training creates a multibillion-dollar market (Ahuja, 2019), the healthcare industry explores new mediums to find more adaptive methods.

Virtual Reality is seen as a promising alternative, giving immersive and interactive environments for cognitive training for players (Damaševičius et al., 2023). Since then, an increasing number of medical fields have seen the potential of VR for data collection, treatment, and training. (Pawassar & Tiberius, 2021). Unlike conventional training methods, VR enables users to actively participate in exercises that challenge their cognitive functions in a dynamic and responsive setting.

Khaleghi (2021) emphasized that most gamified cognitive tasks are developed by cognitive psychologists rather than professional serious game designers. As a result, researchers tend to prioritize the clinical effectiveness of these tasks while paying less attention to creating engaging and well-structured game design outputs. If clinical outcomes are prioritized over the user experience process -where data is collected, or progress is assessed- the product will lack durability and genuine efficacy.

The extent to which these two methodologies are equilibrated dictates the project's definition. The project may serve as a gamified cognitive task – a replication that disregards new patterns that could be uncovered by technological advancements. Also, it can be a cognitive-based serious game which is produced and refined in the light of the behavioral traces that people give during the content they are exposed to. This highlights the need for collaboration between serious game experts and cognitive scientists to better understand the tension between studied cognitive functions and related game features (Lumsden et al., 2016).

This study aims to explore the game mechanics that contribute to the effectiveness of cognitive training games in VR. By analyzing existing virtual reality cognitive training games, the research seeks to identify common design patterns that have an impact on user experience. This study intends to understand the mechanics of current VRCTs. The main issue of research is how VR cognitive training games use design aspects to improve cognitive functions and what important factors influence their efficacy.

Material and Method

To effectively evaluate the design features of cognitive training games in VR, the Elemental Tetrad (Schell, 2008) framework proves to be a valuable tool. By categorizing design elements into technology, story, mechanics, and aesthetics, this framework provides a structured way to analyze how these components interact within a virtual reality cognitive training environment. Technology plays a significant role in immersion and accessibility, while mechanics determine the effectiveness of cognitive engagement. Story elements, even in minimalistic forms, contribute to motivation and goal setting, whereas aesthetics influence user experience and emotional connection. The framework is used to evaluate the hypothesis that accessible cognitive training games are not engaging and user-friendly, but also functional, addressing critical factors such as usability, interaction, and immersion that are essential for cognitive development process. This study will focus solely on the 'Mechanics' section of the four headings of the framework.

Priority was given to commercial VRTCs during the game selection process over the ones with academic purposes. These games were selected based on their accessibility, focus on cognitive training, and relevance to the study's objectives. A keyword-based search was carried out using the terms "cognitive," "training," and "health" inside the Meta Quest and Steam VR stores to guarantee the selection of pertinent titles.

The only product that appeared in both platforms' search results was Enhance VR. In addition to Enhance VR, other products were found for case analysis: NeuroBoostVR, Optics Trainer, Oroi Cognitive, Mastermind Cognitive Training, XRHealth Physical & Cognitive Space, and REAKT Performance Trainer. Although the usability of these games was determined during the study, some of them was excluded from the study as it could not be accessed through the Meta Store during the process. The selected virtual reality cognitive training games are NeuroBoostVR, Optics Trainer and REAKT Performance Trainer. Following the selection process, playtest sessions are conducted for each of the four VRCTs. The products were analyzed through a comparative analysis under the 'Mechanics' sections, including Game Mechanics, Difficulty Curve, Game Balance, Feedback, Locomotion, and Interaction.

Findings

Players can navigate through menu in Optics Trainer and REAKT Performance Trainer, unlike in NeuroBoostVR. Task objective differ across platforms: NeuroBoostVR provides generic cognitive exercises, Optics Trainer focuses on visual domain-specific tasks, and REAKT Performance Trainer incorporates both cognitive and motor domain-specific components.

In terms of feedback modalities, NeuroBoostVR utilizes auditory and visual cues, whereas both Optics Trainer and REAKT Performance Trainer integrate auditory, visual, and haptic feedback, offering multimodal sensory engagement. A training overview screen is available exclusively in REAKT Performance Trainer.

Structured training systems are absent in NeuroBoostVR, integrated with prescription logic in Optics Trainer, and comprehensively implemented in REAKT Performance Trainer. Competitive mechanics are included only in REAKT Performance Trainer, enabling social comparison and performance benchmarking.

Difficulty settings are not available in NeuroBoostVR, are limited to three levels in Optics Trainer, and consist of ten gradations in REAKT Performance Trainer. Interaction styles remain unspecified for both NeuroBoostVR and REAKT Performance Trainer, and require clarification in Optics Trainer. Session duration control is open-ended in NeuroBoostVR, pre-defined in Optics Trainer, and user-adjustable in REAKT. Spatial orientation is reportedly more difficult to navigate in NeuroBoostVR, whereas Optics Trainer and REAKT provide structured orientation environments.

Conclusion

This study highlights the necessity of connecting academic research with practical game design in VR-based cognitive training. Cognitive training games, although primarily designed with a clinical emphasis, must also prioritize engagement and structured design to enhance their long-term effectiveness and usability.

The development of a common terminology between cognitive scientists and game designers facilitates the creation of advanced, user-focused cognitive training experiences that integrate clinical efficacy with engaging gameplay.

This study provides a foundation for future research and development in the field, offering insights that may inform subsequent iterations of virtual reality cognitive training games. The ongoing evolution of these technologies necessitates a collaboration to fully realize their potential in enhancing and preserving cognitive skills.

References

Ahuja, A. (2019, January 23). An evidence deficit haunts the billion-dollar brain training industry. Financial Times. **Url-1** www.ft.com/content/a0166eea-1e41-11e9-a46f08f9738d6b2b, date retrieved 18.03.2025.

Damaševičius, R., Maskeliūnas, R., & Blažauskas, T. (2023). Serious games and gamification in healthcare: A meta-review. Information, 14(2), 105. https://doi.org/10.3390/info14020105

Khaleghi, A., Aghaei, Z., & Mahdavi, M. A. (2021). A gamification framework for cognitive assessment and cognitive training: Qualitative study. JMIR Serious Games, 9(2), e21900. https://doi.org/10.2196/21900

Lumsden, J., Edwards, E., Lawrence, N., Coyle, D., & Munafò, M. (2016). Gamification of cognitive assessment and cognitive training: A systematic review of applications and efficacy. JMIR Serious Games, 4(2), e11. https://doi.org/10.2196/games.5888

Pawassar, C. M., & Tiberius, V. (2021). Virtual reality in health care: Bibliometric analysis. JMIR Serious Games, 9(4), e32721. https://doi.org/10.2196/32721

Schell, J. (2008). The art of game design: A book of lenses. Burlington, MA: Morgan Kaufmann Publishers.

GAME AND INTERACTION TECHNOLOGIES

AI in Gaming

Game Design

Game Production

Gamification

Interaction Technologies

Series Games

User Studies

An Analysis of Gaming Behavior Through Bartle's Player Model & Human Psychology

Asena Ersoy[a], Leman Figen Gül[b]

[a] Istanbul Technical University/Graduate School, Department of Game and Interaction Technologies, Game and Interaction Technologies Program, Turkey
[b] Istanbul Technical University/Faculty of Architecture, Department of Architecture, Architectural Design Computing Program, Turkey
ersoya16@itu.edu.tr

Keywords: Game Psychology, Bartle Player Types, Virtuality and Identity, Gaming Motivations.

Aim

The aim of this research is to understand the effects of personalities and demographic groups on player motivations. In other words, it is aimed to discover which characteristics of individuals shape their in- game behaviours. Thus, by examining how individuals' real-life characteristics shape their behaviours and motivations in games, it is aimed to show the opportunities that games offer to people. This study, which focuses not only on personality traits but also on the demographic structure of individuals, aims to create an important data source for a better understanding of the reasons for playing games. Players' personality, such as anyone, has a significant impact on how they act or think under certain conditions, suggesting that in-game behaviour is influenced by personality (Quwaider, Alabed&Duwairi, 2019). For this reason, some studies examine and categorize players' personalities and motivations. Bartle (1996), in his study of Multi-User Dungeon players, divided player types into four on a coordinate system: achiever, killer, socializer, and explorer. Also, personalities can be classified according to different models. One of the most broadly used and inclusive classifications of personality types is The Five Factor Model. Divides personalities into five categories: Extraversion, Agreeableness, Conscientiousness, Emotional Stability and Openness (Liu et. al., 2024).

Material and Method

In this study, a questionnaire is used to measure personalities and player types. Validated and tested Turkish questionnaires from different sources are used to determine personality and player types. The personality assessment was based on the model proposed by Tatar (2017), while the player type classification was adopted from the model developed by Hamutoğlu, Topal, Samur, Gezgin, and Griffiths (2020). The questionnaire included demographic questions and two different models: one is used to analyse player types and the other is used to analyse personality traits. Bartle model is preferred for the analysis of player types and Five Factor Model is preferred for the analysis of personality traits. The Bartle model has a simple and widely accepted structure that divides players into four basic groups according to their in-game behaviours. The fact that this model has similar characteristics with the Five Factor Model used for personality analysis enables the examination of the relationships between the two models. Also, the Five Factor Model is a widely studied model with high validity and reliability values. Its measurement of continuous variables enables in-depth analyses of personality traits, while questionnaires of different lengths provide flexibility. Observing the similarities between the personality dimensions in the Bartle model and the Five Factor Model provides an important basis for analysing the relationships between player types and personality traits.

The questionnaire is delivered to the participants online via Google Forms. The questionnaire is delivered to the participants by snowball sampling and it is therefore prepared in Turkish. The questionnaire distribution process lasted for six weeks, and it is important that the participants in the research are gamers and even massive multiplayer online role-playing game players. Therefore, when the questionnaire was to be distributed, massive multiplayer online role-playing game players were first asked to complete the questionnaire and forward it to their communities. Then, academics and students working in the field of Digital Game Design are asked to participate and spread this survey. Likewise, the survey was sent to the

Game Development student communities of schools via WhatsApp. To ensure that the entire sample does not consist of similar demographic groups, the questionnaire is sent to people of different ages, professions and genders. As a result of the survey, a total of 417 people are reached. The majority of the participants are between the ages of 18-30 and most of them are university graduates. Approximately two-thirds of the participants identified themselves as male and the rest as female or other. When the gaming habits of the participants are analysed, there are very few participants who do not play games. Specifically, the number of people who answered the question of how many hours they played a massive multiplayer online role-playing game in total is less than half of the data. The participants in the survey are mostly gamers. When the data are analysed, 6 incorrect entries are detected and these are removed. The analysis is made over 411 data. The data collected from the survey are statistically analyzed and visualized in Python. Correlation analysis, ANOVA test and Tuckey's Honestly Significant Difference tests are applied respectively.

Findings

The findings of the study show that there are significant relationships between individuals' personality traits and their preferences in games. In particular, it is observed that individuals with high openness to experience display an exploration-oriented approach in games and show less interest in tasks and collecting points. When gender differences are examined, it is observed that women who prefer socializing in games are more responsible and disciplined individuals in real life, while men who prefer socializing in games stand out with a compatible and helpful personality structure. This situation can be interpreted as that women consider games as a space to get away from the responsibilities of daily life, while men behave more parallel to their real-life tendencies in in-game social dynamics.

When analyzed in terms of age groups, it is found that emotionally stable young individuals tended to explore the game world, whereas older individuals who were open to experience are more distant from in-game goals and achievement-oriented mechanics. This suggests that emotionally stable younger individuals tend to view games as a way to stimulate a sense of exploration, whereas older individuals may tend to perceive games as an extension of real life. The findings may indicate that in-game behaviours are shaped not only by individual personality traits but also by the developmental dynamics of individuals.

In the analysis in terms of educational level, no significant results are obtained for the group above the university level since the majority of the participants are university graduates. When high school and university level participants are analyzed, similar results are observed with the age analysis. In addition, a negative relationship is found between the personality traits associated with agreeableness, helpfulness and the player type representing competitive and aggressive play style. This finding suggests that compliant individuals tend to avoid causing difficulties to other players in the game. A comprehensive comparison could not be made due to insufficient data on other education levels.

Conclusion

In conclusion, by helping to better understand player motivations and behaviours in the game world, the outputs of this research can help game designers create more effective content that appeals to different demographic groups. The results of this research help us understand how games reflect social structures by revealing how individuals' demographic identities and their roles in the game world overlap or diverge. Furthermore, how games shape how individuals express themselves can be better understood. This study contributes to understanding how games function as part of social identities, rather than simply as a means of entertainment.

References

Bartle, R. (1996). Hearts, clubs, diamonds, spades: Players who suit MUDs. Journal of MUD research, 1(1), 19.

Hamutoğlu, N. B., Topal, M., Samur, Y., Gezgin, D. M., & Griffiths, M. D. (2020). The development of the online player type scale: Construct validity and reliability testing. International Journal of Cyber Behavior, Psychology and Learning (IJCBPL), 10(1), 15- 31.

Liu, Y., Realo, A., Mendonça, M., Baumann, N., Bartmann, P., Räikkönen, K., Heinonen, K., Robinson, R., Marlow, N., Johnson, S., Ni, Y., Kajantie, E., Hovi, P., Tikanmäki, M., & Wolke, D. (2024). The effect of very preterm birth on

the Five-Factor Model of personality traits: A meta- analysis of individual participant data. European Journal of Personality. https://doi.org/10.1177/08902070241280101

Quwaider, M., Alabed, A., & Duwairi, R. (2019). The impact of video games on the players behaviors: A survey. Procedia Computer Science, 151, 575-582.

Tatar, A. (2017). Büyük Beş-50 Kişilik Testinin Türkçeye çevirisi ve Beş Faktör Kişilik Envanteri Kısa Formu ile karşılaştırılması. Anatolian Journal of Psychiatry/Anadolu Psikiyatri Dergisi, 18(1).

GEOGRAPHIC INFORMATION TECHNOLOGIES

Artificial Intelligence and Machine Learning in Remote Sensing Analysis

Spatial Data Algorithms and Visualization and 3D GIS Technologies

Spatial Planning and Management with GIS Applications

Current Challenges in Port Management and Common Approaches from Geographic Information Technologies (GIT)

Cemre Fazilet Aldoğan[a], Hande Demirel[b]

[a] Istanbul Technical University/Informatics Institute, Department of Informatics Applications, Geographic Information Technologies, Türkiye
[b] Istanbul Technical University/Faculty of Civil Engineering, Department of Geomatics Engineering, Türkiye
aldogan17@itu.edu.tr

Keywords: GIT, Maritime Transportation, Port Management.

Ports are key transportation centres for global trade, and they face challenges as the number of ships continues to increase. Efficiency problems in cargo handling, vulnerability of ports to illicit activities such as illegal fishing, terrorism, and trafficking, and pollution from ships are some of the human-induced problems still requiring effective measures. On the other hand, natural disasters as a result of climate change are a serious threat to port security, besides anthropogenic interventions. The infrastructure of ports is prone to being affected by floods and earthquakes, followed by their adverse effects on the economy. A review of methods and solutions regarding these challenges is necessary for identifying gaps for future studies. Thus, this paper aims to discuss common approaches that Geographic Information Technologies (GIT) provide, along with a review of these challenges regarding port management. Aerial, remote sensing, and ground-based instruments as part of GIT offer large volumes of geospatial data to gain insights for potential solutions. Optical and radar remote sensing images supported by computer vision technology facilitate automated surveillance of ports, vessels, and containers. Ship detection in port areas helps authorities to track unauthorized entrances, enabling a more secure environment. Detection of oil spills, clutter, and other types of pollution in ports and open seas is one of the other approaches that GIT reflects for helping form environmental measures. For addressing challenges related to port operations, proprietary and open-source GIS software launch frameworks are used to decrease congestion and support better management of traffic flow. In addition, these maritime frameworks integrated with Automatic Identification System (AIS) act as an adept tool to respond to vulnerability caused by natural and man-made disasters with map visualizations. This paper intends to assess the sufficiency of the aforementioned methods and findings from a critical perspective. It is anticipated that this study will inform researchers about the future directions and contribute to the conduct of further studies.

Aim

Ports serve as critical transportation points where more than 80% of global trade is handled (UNCTAD, 2024). Due to pressure caused by increased shipping activities, a myriad of issues related to port management have emerged, such as congestion in marine environments, disruption in cargo operations, and inadequacy in maintaining port security due to the impracticality of inspecting the conditions of containers. Security is a major concern, especially in large container ports. Since marine environments by nature are difficult to manage, this leaves large container ports vulnerable to terror attacks (Widodo et al. 2024). Moreover, the infrastructure of ports is affected by extreme weather events such as high winds, heavy rainfall, tectonic activities, and tsunamis. Geographic information systems (GIS) tailor solutions to the problems above by collecting, integrating, and analyzing a variety of geospatial data. Therefore, the main aim of this review is to explore what these geospatial solutions are in the current research agenda. In this review, a short body of literature was synthesized to deliver up-to-date approaches.

Material and Method

For a systematic and concise literature review, journal articles featuring port management and GIS technology with a query "Port Management AND GIS" were searched in databases of Web of Science and Scopus. A year filter limitation was applied to each database search to obtain the articles between 2020 and 2025. 165 and 68 articles in total were retrieved from Web of Science and Scopus databases, respectively. After retrieving articles from each database, they were filtered

manually by focusing on specific maritime keywords such as port operations, port infrastructure, environmental risks, and maritime traffic management. Final selection of the articles was completed in this order, following the aim of this paper. As a result, 21 articles were distilled from the entire search. The usage purposes of GIS in these articles are multifaceted. However, many commonalities exist, such as overlaying data sources, multi-criteria decision making, and thematic mapping. Vulnerability and risk assessment studies were observed to share this order in methodology. The articles in which natural disasters and their impact on the functionality of port operations are dominant since nowadays the destructive effects of climate change are distinct (Allen, McLeod, ve Hutt, 2021; Alshareef vd. 2024; Abdelaziz vd. 2024). On the other hand, GIS was observed to be utilized as an auxiliary tool to help design digital twin (DT) and building information modeling (BIM), besides being utilized as a decision support system (Agostinelli vd. 2022).

Findings

It has been revealed that the articles are centered around three research problems such as the health of port infrastructure, shipping traffic, and natural disasters. Infrastructural problems can be summarized as energy efficiency (Agostinelli vd. 2022; Wang vd. 2024), risk of construction damage due to chemical explosions (Lee, Ham ve Jeong, 2022) and aging of port infrastructure (Tsaimou, Sartampakos ve Tsoukala, 2023). As for the problems related to shipping traffic, only a small minority of papers focused on delivering a solution regarding the traffic flow of ships or accidents in general. Because ports are primary places having a high probability of being affected by water-related disasters, the number of papers covering environmental risk assessment for coastal areas is higher.

Conclusion

In this paper, a short body of literature was analyzed to reveal the most recent issues and geospatial practices related to ports. The statements and observations were made to guide the target audience of this paper on corresponding research directions. A future study can be implemented to cover a large body of literature about these issues to discuss them in more detail. An alternative study idea can be based on the comparative advantages and disadvantages of proprietary or open source GIS software regarding the contributions they made to resolving the aforementioned issues. Lastly, a future study can be conducted by applying frequently used spatial analysis techniques to address problems related to shipping traffic as a case study.

References

AbdelAziz, N. M., Eldrandaly, K. A., Al-Saeed, S., Gamal, A., & Abdel-Basset, M. (2024). Application of GIS and IOT Technology-Based MCDM for Disaster Risk Management: Methods and Case Study. *Decision Making: Applications in Management and Engineering*, *7*(1), 1–36. https://doi.org/10.31181/dmame712024929

Agostinelli, S., Cumo, F., Nezhad, M. M., Orsini, G., & Piras, G. (2022). Renewable Energy System Controlled by Open-Source Tools and Digital Twin Model: Zero Energy Port Area in Italy. *Energies*, *15*(5). https://doi.org/10.3390/en15051817

Allen, T. R., McLeod, G., & Hutt, S. (2022). Sea level rise exposure assessment of U.S. East Coast cargo container terminals. *Maritime Policy and Management*, *49*(4), 577–599. https://doi.org/10.1080/03088839.2021.1903597

Alshareef, M. H., Aljahdali, B. M., Alghanmi, A. F., & Sulaimani, H. T. (2024). Spatial Analysis and Risk Evaluation for Port Crisis Management Using Integrated Soft Computing and GIS-Based Models: A Case Study of Jazan Port, Saudi Arabia. *Sustainability (Switzerland)* , *16*(12). https://doi.org/10.3390/su16125131

Lee, J. J., Ham, T. Y., & Jeong, W. S. (2022). Economic risk assessment of ammonium nitrate explosions at the Busan Port by determining the building damage using a 3D explosion simulation. *Heliyon*, *8*(12). https://doi.org/10.1016/j.heliyon.2022.e12285

Tsaimou, C. N., Sartampakos, P., & Tsoukala, V. K. (2023). UAV-driven approach for assisting structural health monitoring of port infrastructure. *Structure and Infrastructure Engineering*. https://doi.org/10.1080/15732479.2023.2290255

Wang, M., Lan, Y., Li, H., Jing, X., Lu, S., & Deng, K. (2024). Spatial–Temporal Differentiation and Trend Prediction of Coupling Coordination Degree of Port Environmental Efficiency and Urban Economy: A Case Study of the Yangtze River Delta. *Land*, *13*(3). https://doi.org/10.3390/land13030374

Widodo, A. M., Widayanti, R., Wisnujati, A., Anwar, N., Bansal, S., Tabassum, F., & Rahaman, M. (2024). Port-to-Port Expedition Security Monitoring System Based on a Geographic Information System. *International Journal of Digital Strategy, Governance, and Business Transformation*, *13*(1), 1–20. https://doi.org/10.4018/ijdsgbt.335897

Url-1 https://unctad.org/publications-search?f%5B0%5D=product%3A393, date retrieved 21.02.2025.

GEOGRAPHIC INFORMATION TECHNOLOGIES

Artificial Intelligence and Machine Learning in Remote Sensing Analysis

Spatial Data Algorithms and Visualization and 3D GIS Technologies

Spatial Planning and Management with GIS Applications

Tactile Map Production Processes And Application Areas For Visually Impaired

Ayça Eraslan[a]

[a] Istanbul Technical University, Applied Informatics, Geographical Information Technologies, Turkiye
eraslana@itu.edu.tr

Keywords: Visually Impaired, Tactile Maps, Accessibility, 3D Printing, Spatial Awareness.

Aim

Visually impaired individuals face significant difficulties in terms of spatial awareness and independent mobility. According to research, 56% of visually impaired individuals state that they have various difficulties in independent mobility (Bahram, 2013). This situation directly affects the social and professional lives of individuals and increases the risk of social exclusion. Therefore, accessible geographic maps play a critical role in ensuring understanding of the city and neighborhood structure and enabling safe and independent mobility.

Traditionally, embossed maps and Braille texts have been used for visually impaired individuals (Brock et al., 2012). However, such tactile maps can provide limited spatial information and are insufficient to include detailed data. In addition, there is an increasing demand for map systems that can be customized according to individual needs (Kern, 2016).

Tactile maps appeal to two main user groups: mobility trainers who create maps and train users, and visually impaired individuals who use these maps to find their way and provide spatial awareness (Rowell & Ungar, 2016). Considering the limitations presented by traditional map designs, the development of new generation tactile maps that offer more accessible and inclusive solutions is of great importance.

In order for visually impaired individuals to use tactile maps effectively, certain design criteria must be taken into consideration. Factors such as the arrangement of the spaces between the signs, material selection, interactive elements and inclusive design directly affect the ease of use of maps. Research shows that visually impaired individuals prefer rough-surfaced papers and Braille-compatible plastic surfaces (Ungar et al., 2005). While voice guidance systems increase the understandability of maps, interactive screens and mobile applications stand out as innovative solutions that support accessibility. In addition, the ability of individuals with or without visual impairments to use the same map offers a more inclusive approach in education and social life.

Increasing automation in the map design process and shortening the production time provide significant advantages in terms of accessibility (Koch, 2012). Increasing the production speed, especially in maps developed for visually impaired individuals, enables faster responses to individual needs. In this context, interactive interfaces and multimodal technologies – such as voice guidance systems, touch screens and mobile applications – offer revolutionary innovations in terms of map design and user experience.

At the same time, the proliferation of large-scale web map systems has made open source data available to wider audiences, which has contributed to the increased adoption of automated cartography solutions (Brock et al., 2015). Thus, it has become possible to produce maps specific to different user groups in a short time and to present these maps in formats that appeal to multiple sensory organs.

Different printing techniques are used in the production of tactile maps. Studies based on user experiences show that rough paper and microcapsule paper are preferred more by visually impaired individuals (Ungar et al., 2005). In addition, voice feedback and mobile applications are considered as key components that increase the accessibility and ease of use of tactile maps.

This study aims to analyze the impact of tactile maps on accessibility and to provide suggestions for the development of existing systems and the implementation of new technologies. In the study, different techniques such as relief maps, 3D printing technologies, thermal expansion method and digital tactile maps were examined and their advantages and limitations were discussed. In addition, innovative applications such as TEKNOFEST "Talking Maps" project and London

Tactile City Map were evaluated and the effects of voice feedback and multimodal interactions on accessibility were discussed.

Material and Method

Accessible solutions such as tactile tube maps and embossed bus station maps are being developed to enable visually impaired individuals to move independently in public transportation and city planning processes. The London Tactile Tube Map is produced by embossing on plastic material and includes various surface textures to distinguish different tube lines. In this study, the methods used in tactile map production and the advantages of these maps in terms of accessibility are analyzed and how they can be made more effective for visually impaired individuals in different application areas are examined. In this context, different types such as embossed maps, maps produced with 3D printing technology, maps prepared with the thermal expansion method and digital tactile maps were evaluated.
Inclusion Criteria: The case study must feature a significant technological advancement in tactile map design, such as 3D printing, digital tactile maps, or integration with voice-guided systems The case studies must be derived from various geographical regions, ensuring a diverse perspective on the use of tactile maps in different cultural and urban environments. The case studies should involve active participation from visually impaired users in the development or testing phase, ensuring the maps are designed with user needs in mind. The case studies must demonstrate how tactile maps improve accessibility in public spaces, transportation systems, or educational environments for visually impaired individuals
Exclusion Criteria: Maps that are purely static and do not offer any form of interactivity, voice guidance, or multi-modal features will be excluded. Case studies that do not include feedback or testing from visually impaired users will be excluded from this analysis, as user-centered design is crucial for assessing the effectiveness of these maps Case studies limited to private use or small-scale applications (e.g., personal devices) that do not address broader societal accessibility needs will be excluded.

Findings

The findings of the study show that smart city applications and automatic map production systems have the potential to increase the spatial awareness of visually impaired individuals. In this context, the integration of new technologies is important to make accessible maps more inclusive and effective. In addition, the dissemination of accessible maps in education, transportation and daily life areas will contribute to the independent movement of visually impaired individuals.

Conclusion

The development of tactile maps that can be customized according to demand will provide solutions that are suitable for individual needs. Digital and voice guidance systems should be made more widespread, mobile applications and smart maps should be made accessible for visually impaired individuals. The use of tactile maps in education should be increased. In order to develop spatial skills of visually impaired students, relief maps and interactive educational materials should be made widespread. Public and private sector collaboration should be encouraged, and municipalities, transportation companies and tourism sectors should be directed to develop accessible map solutions for the visually impaired. In the future, the integration of tactile maps with interactive and smart technologies will provide more accessible and user-friendly solutions for visually impaired individuals.

References

Almeida, B. M., da Silva, R. C. F., da Silva, J. C. A., & Arigoni, L. B. (2021). Evaluation of A Braille-Based Colour Code Proposal For People With Visual Impairment. Human Factors in Design, DOI:10.5965/2316796310202021070.
Araújo, N.S.; Amorim, F.R.; Antunes, A.P.; Marchi, S.R.; Schmidt, M.A.R.; Andrade, A.F.; Delazari, L.S. (2021). An experiment using the graphic variable color and the see color code on isarithmic maps accessible to blind and normally sighted people. Bulletin of Geodetic Sciences. 27(1): e2021006.

Araújo, N. S., Delazari, L. S., Fernandes, V. O., & Júnior, M. A. (2020). A Bibliometric Study of Graphic Variables Used on Tactile Maps. The International Archives of the Photogrammetry, Remote Sensing and Spatial Information Sciences, XLIII-B4-2020, 25–32, https://doi.org/10.5194/isprs-archives-XLIII-B4-2020-25-2020

Bahram, S. (2013). Multimodal Eyes-Free Exploration of Maps: TIKISI for Maps. ACM SIGACCESS Accessibility and Computing, DOI:10.1145/2505401.2505402

Balley, S., Baella, B., Christophe, S., Pla, M., Regnauld, N., Stoter, J. (2014). Map Specifications and User Requirements. Abstracting Geographic Information in a Data Rich World. Lecture Notes in Geoinformation and Cartography. Springer, https://doi.org/10.1007/978-3-319-00203-3_2

Brock, A. M., Truillet, P., Oriola, B., Picard, D., & Jouffrais, C. (2012). Design and User Satisfaction of Interactive Maps for Visually Impaired People. Lecture Notes in Computer Science 7383, DOI:10.1007/978-3-642-31534-3_80

Brock, A. M., Truillet, P., Oriola, B., Picard, D., & Jouffrais, C. (2015). Interactivity Improves Usability of Geographic Maps for Visually Impaired People. Human-Computer Interaction, 30(2), 156–194. DOI:10.1080/07370024.2014.924412.

Cervenka, P., Brinda, K., Hanousková, M., Hofman, P., & Seifert, R. (2016). Blind Friendly Maps, Lecture Notes in Computer Science 9759:131-138, DOI:10.1007/978-3-319-41267-2_18.

Ducasse, J., Macé, M., & Jouffrais, C. (2015). From Open Geographical Data to Tangible Maps: Improving the Accessibility of Maps for Visually Impaired People. ISPRS - International Archives Of The Photogrammetry, Remote Sensing and Spatial Information Sciences, XL-3/W3, 517–523. https://doi.org/10.5194/isprsarchives-XL-3-W3-517-2015

Gkanidi, M. I., & Drigas, A. (2021). Tactile Maps and New Technologies for Blind and People with Visual Impairments. International Journal of Management and Humanities, 5(8), 1–5. DOI:10.35940/ijmh.E1208.045821.

Kane, S. K., Morris, M. R., Perkins, A. Z., Wigdor, D., Ladner, R. E., & Wobbrock, J. O. (2011). Access Overlays: Improving Non-Visual Access To Large Touch Screens For Blind Users. Proceedings of the 24th Annual ACM Symposium on User Interface Software and Technology (pp. 273–282). ACM Press. https://doi.org/10.1145/2047196.2047232

Kane, S. K., Frey, B., & Wobbrock, J. O. (2013). Access Lens: A Gesture-Based Screen Reader For Real-World Documents. Proceedings of the SIGCHI Conference on Human Factors in Computing Systems (pp. 347–350). https://doi.org/10.1145/2470654.2470704

Kern, R. (2016). Cartographie Et Malvoyance - Du Papier Au Numérique. Cartes & Géomatique, 229–230, 167–174.

Koch, W. G. (2012). State Of The Art Of Tactile Maps For Visually Impaired People. True-3D in Cartography, DOI:10.1007/978-3-642-12272-9_9

Kröger, J., Schiewe, J., & Weninger, B. (2013). Analysis And Improvement Of The Open-Streetmap Street Color Scheme For Users With Color Vision Deficiencies. In 26th International Cartographic Conference (p. 17).

Mulder, M. (2024). Tactile Maps Presenting Sdg 6: Clean Water And Sanitation (Doctoral Dissertation, Palacký University Olomouc).

Mościcka, A., Śmiechowska-Petrovskij, E., Wabiński, J., Araszkiewicz, A., & Kiliszek, D. (2024). Methodical Testing Of Tactile Cartographic Signs In Isolation And In Context. Cartography and Geographic Information Science, 1-18.

Rowell, J., & Ungar, S. (2003). The World Of Touch: An International Survey Of Tactile Maps. Part 2: Design. British Journal of Visual Impairment, 21(3), 105–110. https://doi.org/10.1177/026461960302100304.

Sena, C. C. R. G., & Carmo, W. R. (2005). Tactile Map Production for the Visually Impaired User: Experiences in Latin America. University of São Paulo Reports.

Simonnet, M., Bothorel, C., Maximiano, L. F., & Thépaut, A. (2012). Geotablet, Une Application Cartographique Pour Les Personnes Déficientes Visuelles. Proceedings of Handicap (Vol. 7, pp. 8–13), hal-00732475, Paris, France.

Touya, G. (2017). Vers L'automatisation De La Production De Cartes. Habilitation à diriger des recherches (HDR), Thesis, Université Paris-Est.

Ungar, S., Jehoel, R., McCallum, D., & Rowell, J. (2005). Tactualization Of Spatial Information: Towards A Perceptual-Cognitive Approach To Tactile Map Design. In Proceedings of XXII International Cartographic Conference, La Coruña, Spain, ICA.

Vasconcellos, R. (2023). Tactile Mapping for Visually Impaired Children. 31st International Cartographic Conference Proceedings. Cape Town, South Africa.

Van Altena, V., Rijnberk, D., Kuijer, M., Jansen, J., Min, E., Welbergen, A. V., Visser, T., van der Vaart, N., & Nauta, J. (2023). Tailoring Tactile Maps Based on Blind Users' Needs. Proceedings of the International Cartographic Association, 5, 22, DOI:10.5194/ica-proc-5-22-2023.

Voženílek, V., Růžicková, V., Finková, D., Ludíková, L., Němcová, Z., Doležal, J., Vondráková, A., Kozáková, M., & Regec, V. (2012). Hypsometry In Tactile Maps, True-3D in Cartography (pp.153-168), DOI:10.1007/978-3-642-12272-9_10.

Watanabe, T., Yamaguchi, T., Koda, S., & Minatani, K. (2014). Tactile Map Automated Creation System Using OpenStreetMap. In Proceedings of the 14th International Conference on Computers Helping People with Special Needs, Paris, France, DOI:10.1007/978-3-319-08599-9_7.

GEOGRAPHIC INFORMATION TECHNOLOGIES

Artificial Intelligence and Machine Learning in Remote Sensing Analysis

Spatial Data Algorithms and Visualization and 3D GIS Technologies

Spatial Planning and Management with GIS Applications

Analysis of Customer Complaints in Mobile Communication Networks with GIS

Merve Tanur[a], Rahmi Nurhan Çelik[a]

[a] Istanbul Technical University/Graduate School, Department of Geomatics Engineering, Geomatics Engineering PhD Program, Türkiye
korkutanm@itu.edu.tr

Keywords: Big Spatial Data, GIS Applications, Mobile Communication Networks, Spatial Decision Support Systems, Spatial Planning.

Aim

In the telecommunications sector, the correct management of customer complaints, which helps to bring a product or process to higher quality, is seen as one of the biggest criteria of success. The main reason for complaints indicating the existence of deficiencies or malfunctions resulting from many reasons is that the service provided does not satisfy the customer. In order to resolve customer complaints quickly and accurately, the tools and methods used must be sufficient and appropriate to take rapid and accurate actions (Alabay, 2012). Since mobile communication networks have a dynamic and spatial structure, it is important that complaint management, which will be discussed within this scope, is also examined in a dynamic and spatial dimension (Zhu et al, 2019). The increasing market volume day by day brings with it increasing customer complaints. Considering the total number of mobile subscribers, including machine-to-machine communication (M2M) subscribers, reaching 94.5 million, corresponding to a penetration rate of 110.7% by the end of the third quarter of 2024 in Türkiye, the volume that can arise when each subscriber creates at least one complaint record reveals the importance of proper complaint management. The total number of subscribers to UMTS technology, which was launched in July 2009, reached 65.9 million by the end of March 2016. With the LTE technology that was put into service in April 2016, there was a transition period from UMTS subscription to LTE subscription. At the end of the third quarter of 2024, the number of UMTS subscribers was 4.6 million, while the number of LTE subscribers reached 87.5 million. When we consider the number of complaints submitted through the Online Consumer Complaint System of Information and Communication Technologies Authority in Türkiye on a quarterly basis, we see that among the consumer complaints made within the scope of mobile access at the end of the third quarter of 2024, the ratio of complaints regarding coverage area/service quality to total complaints was 21.2%. In addition, three mobile operators in Türkiye made investments of ₺6.1 million, ₺7.1 million, and ₺17.2 million respectively in 2023, reaching a total mobile investment value of approximately ₺30.5 million (BTK, 2024). In order for customer complaints to be resolved as quickly and correctly as possible, it is essential that every stage of complaint management is carried out meticulously. In this context, complaints must be understood correctly, categorized correctly, directed to the right places, and workflows must be adapted accordingly. In a dynamic mobile network structure, using customer complaints as a dynamic system input is very valuable in terms of planning and investment. Proper mobile network planning means making the right mobile investment. The fact that investment is being made in the right places in an effective, demand-driven mobile network planning process is an indicator of the effective use of mobile investment costs. New base stations installed to provide maximum benefit with minimum quantity are a powerful weapon in increasing customer satisfaction and reducing complaints, as well as increasing customer loyalty and increasing mobile market share. Customer loyalty, which is an important factor for companies to achieve a sustainable competitive advantage, is one of the keys to both company performance and growth (Kim et al, 2004).

Material and Method

This study will present an approach to analyze the complaints about mobile communication network design in GIS (Geographic Information Systems) environment and use these complaints as an input for future mobile communication network planning. Within the scope of the study, it will be analyzed from which perspective and how customer complaints obtained through different channels are evaluated in mobile network planning with UMTS (Universal Mobile

Telecommunications System) and LTE (Long-Term Evolution) technology. The spatial data subject to the study does not belong to any telecommunications company and consists of sample datasets produced entirely for academic purposes. This preference was intended to increase the objectivity and reliability of the scientific study. In this context, many different datasets such as customer complaint dataset for a one-year period, Türkiye province map, Türkiye geographical regions map, UMTS coverage map, LTE coverage map, land use map and settlement map were used. It is aimed to produce a comprehensive and rapid solution for this large spatial data by using GIS tools and methods. Due to the need to confirm the locational accuracy of customer complaint data obtained through different channels, data cleaning was performed by first eliminating data that was not located within the administrative borders of Türkiye. Complaints submitted for different reasons were classified according to the reason for which they were received and it was decided from which perspective the problem should be addressed. In this framework, questions such as which base station the customer complaint locations should be associated with in the GIS environment, in which time period the complaints increased the most, in which provinces and regions the most problems were experienced, in which land use areas the most problems were experienced, whether the location subject to the complaint was inside or outside the settlements were analyzed in detail. In addition, UMTS and LTE coverage maps were used to obtain signal levels at complaint locations separately for each technology. For both technologies, signal levels were divided into three different classes as good, medium and bad, and it was determined which level had more coverage complaints. After all the analyses, it was decided that the problems declared by the customer should be used as input in the next mobile planning phase as a result of matching the same problems on the technical side.

Findings

Within the scope of the study, two hundred thousand customer complaints collected from different channels within a one-year period were analyzed. It was observed that the rate of records falling outside the administrative borders of Türkiye was 1% after the process of removing records containing incorrect coordinate information from the data set for various reasons. The complaint type was divided into two classes as call and internet. Call type complaints had a distribution of 28%, while internet type complaints had a distribution of 72%. The sub-details of the problem types were divided into eight different groups. The problem detail with the highest rate was the lack of indoor coverage with a rate of 58%. The month in which the highest complaint occurred was January, while the city with the highest complaint was Istanbul with a rate of 15%. The region with the highest complaint rate among the seven geographical regions was the Marmara Region with a rate of 25%. The main cluster with the highest complaint was dense urban with a rate of 38%, while the sub-cluster was the city center with a rate of 65%. By looking at the distance of the existing base station near the place where the complaints occurred, the problem was tried to be addressed to one of the existing base stations. In this context, it was seen that the presence of an existing base station 150 meters or closer to the location of the problem was 15%. On the other hand, the rate of the place subject to the complaint being located within a settlement is 83%. Considering the presence of technology-based coverage in the complaint locations, the rates for UMTS outdoor, UMTS indoor, LTE outdoor, LTE indoor are 96.5%, 91.2%, 99.9, 99.5%, respectively. As can be understood from these results, the places subject to the complaint mostly indicate UMTS indoor coverage problems. According to the signal levels divided into three classes as good, medium, and bad, it was seen that 93% of the complaints came from places with good coverage, 5% from places with medium coverage, and 2% from places with poor coverage.

Conclusion

The impact of the solutions produced within the scope of this study on the sector will be of great benefit both technically and commercially. The fact that the benefits provided can be felt by both telecommunications companies and customers increases the importance of the study. It is important for companies to be able to analyse customer complaints at a spatial level in order to correctly identify the source of the complaint, take the right action and identify areas for improvement (Tanur et al, 2024). On the other hand, responses to complaints that are satisfactory and understandable to the customer, as well as feedback such as providing an estimated time for resolution, increase the sense of trust in the customer and positively support customer loyalty. The approach of this study on how to analyze customer complaints, which is one of the spatial inputs in mobile communication network planning in the telecommunications sector, with GIS is framed only with UMTS

and LTE technology since 5G technology is not yet available in Türkiye. Once 5G technology starts to be used actively in Türkiye, it will be necessary to examine similar processes from different perspectives. One of the things that is essential to ensure rapid adaptation to the 5G ecosystem is to create a scalable and sustainable infrastructure (Deloitte, 2022). In this regard, more base stations will be needed to achieve the desired level of 5G performance and effectiveness. Thus, the prediction that future complaints about the coverage and capacity of 5G technology will be greater than current complaints will further reveal the need for rapid action to be taken with GIS tools and methods of large spatial data. Since the customer satisfaction indicators of 5G technology (higher speed, lower latency, etc.) will be higher than the current UMTS and LTE technologies, it will be necessary and beneficial for different academic researchers to further enrich the scope of this study for 5G technology.

References

Alabay, M. N. (2012). Müşteri Şikâyetleri Yönetimi. Uluslararası Yönetim İktisat Ve İşletme Dergisi, 8(16), 137-157.

BTK (Bilgi Teknolojileri ve İletişim Kurumu). (2024). Türkiye Elektronik Haberleşme Sektörü Üç Aylık Pazar Verileri Raporu:2024 2. Çeyrek. https://www.ttyatirimciiliskileri.com.tr/media/dycmehnn/btk-raporu-2c-24.pdf, date retrieved 07.04.2025.

BTK (Bilgi Teknolojileri ve İletişim Kurumu). (2024). Türkiye Elektronik Haberleşme Sektörü Üç Aylık Pazar Verileri Raporu:2024 3. Çeyrek. https://www.ttyatirimciiliskileri.com.tr/media/rdbghhcx/btk-raporu-3ç_24.pdf, date retrieved 07.04.2025.

Chen, Q. & Chen, S. & Guo, W. & Li, J. (2013). An Efficient Approach and Procedure to Solve Customer Complaints Based on Combined Rasterization of Geography Information System. TELKOMNIKA Indonesian Journal of Electrical Engineering. 11. 10.11591/telkomnika.v11i9.2279.

Choi, C. (2018). Predicting Customer Complaints in Mobile Telecom Industry Using Machine Learning Algorithms. Open Access Theses. 1365. https://docs.lib.purdue.edu/open_access_theses/1365

Crié, D. (2003). Consumers' complaint behaviour. Taxonomy, typology and determinants: Towards a unified ontology. Journal of Database Marketing & Customer Strategy Management, 11(1), 60-79

Deloitte. (2022). Yeni Nesil Bağlantının Gücü: 5G Teknolojisinin Türkiye için Ekonomik ve Sosyal Faydaları. https://www2.deloitte.com/content/dam/Deloitte/tr/Documents/technology-media-telecommunications/Deloitte-Vodafone-5G-Etki-Analizi.pdf, date retrieved 07.04.2025.

Garín-Muz , T., Pérez-Amaral, T., Gij , C., & L ez, R. (2016). Consumer complaint behaviour in telecommunications: The case of mobile phone users in Spain. Telecommunications Policy, 40(8), 804-820.

Ibrahim, H. & Al-hakim, M. (2021). Predicting customer complaints in Mobile Telecom Industry based on supervised machine learning. Journal of Environmental Science, Computer Science and Engineering & Technology. 127-137. 10.24214/jecet.B.10.3.12737.

Jacoby, J., & Jaccard, J. J. (1981). The sources, meaning, and validity of consumer complaint behavior: A psychological analysis. Journal of retailing.

Kim, M.K., Park, M.C., & Jeong, D.H. (2004). "The effects of customer satisfaction and switching barrier on customer loyalty in Korean mobile telecommunication services", Telecommunications Policy, 28, 145–159.

Nimako, S. G., & Mensah, A. F. (2012). Motivation for customer complaining and noncomplaining behaviour towards mobile telecommunication services. Asian Journal of Business Management, 4(3), 310-320.

Özsoy, T. (2021). Türkiye'de Telekomünikasyon Sektörü Hizmet Sağlayıcılarına İlişkin Tüketici Şikayetleri: Sorunlar ve Çözüm Önerileri. 4. 1-19.

Santouridis, I., & Trivellas, P. (2010). Investigating the impact of service quality and customer satisfaction on customer loyalty in mobile telephony in Greece. The TQM Journal, 22(3), 330343.

Tanur M., Çelik R.N., & Güney C. (2024). Mobil Planlamada CBS Tabanlı Müşteri Şikayetlerinin Değerlendirilmesi. TMMOB 8. Coğrafi Bilgi Sistemleri Kongresi.

Zhu, L., Zhao, J., Wang Y., Feng J., Deng, C., & Li H. (2019). Smart Prediction of the Complaint Hotspot Problem in Mobile Network. Proceedings of the 2019 Workshop on Network Meets AI & ML - NetAI'19.

City Model Production With LIDAR Technology And Integration Of Urban Transformation With GIT: The Example Of Zeytinburnu District

Merve Altın Çetinkaya[a], Mustafa Yanalak[b]

[a] Istanbul Technical University, Informatics Institute, Department of Geographic Information Technologies, Istanbul.
[b] Istanbul Technical University, Faculty of Civil Engineering, Department of Geomatics Engineering, Istanbul.
altin22@itu.edu.tr

Keywords: LIDAR Technology, 3D City Model, Urban Transformation, Point Cloud, Urban Analysis.

Aim

In the past, with the migration of people living in the east of the country to Istanbul in the hope of finding work, the need for housing close to the areas where the migrants would work emerged. With the number of residential buildings in Istanbul being low compared to the incoming population, housing production came to the agenda. As a result of the rapid migration to the city and the fact that the people coming to the city for work purposes mostly belonged to low or middle-income households in terms of economic status, the way for the process of shantytowns was paved in order to meet the need for housing. With this wave of migration, some districts in Istanbul received more migration than other districts. Zeytinburnu district was one of the districts with the highest population in Istanbul during the period when migration from east to west began. It was observed that the number of houses produced as a result of shantytowns in the district after the wave of migration was quite high. When the existing building stock in the district is examined, it is concluded that there are quite a few illegal constructions in the buildings built in that period, and that buildings that are in need of transformation in terms of urban transformation and that carry earthquake risk should be subject to transformation.
Urban transformation works in the district are increasing day by day in order to increase the quality of life in the district and to create qualified and healthy housing structures. Urban transformation projects are implemented with the aim of both making existing structures safe and creating more livable areas. These transformation projects are carried out with the support of the public and private sectors, and a series of analysis and evaluation studies are required within the scope of the preparation processes in these processes. The transformation preparation processes are carried out by the relevant persons, institutions or organizations before the demolition and renovation processes of these structures, which are transformed by both the persons authorized to build by the parcel owners and the authorized institutions and organizations. The preliminary preparation processes in urban transformation are basically grouped under two headings: urban analyses that will include analyses regarding the existing building stock in the transformation area and cost calculations to be created together with these analyses. In line with these headings, studies should be carried out within the scope of the phase specified as the preliminary preparation phase, where all the analysis, research and calculation data needed are evaluated. In order to obtain the mentioned data at this stage, it is seen that it needs to be accelerated due to reasons such as the high number of relevant institutions and organizations from which data requests will be made through applications, the time-consuming processes of processing the obtained data and obtaining a feasibility study by making an evaluation. Within the scope of the study, it is aimed to accelerate the processes of obtaining these stages and to develop more reliable data collection by feeding with technological developments.

Material and Method

When urban transformation processes are examined in detail, it is seen that the stage that needs to be accelerated in urban transformation preliminary preparation processes is the collection of data obtained through field research, not obtained from relevant institutions, and this stage takes too much time, causing time loss in urban transformation studies. Trying technological methods that will minimize this time loss and being able to obtain preliminary preparation processes with less time, cost and damage is an important step for the acceleration of urban transformation. It is foreseen that by facilitating the collection of data in a short time without performing one-to-one measurements and photography on the relevant land

where urban transformation will be carried out, the loss of time will be prevented and healthier studies will be carried out as a result of providing fast and reliable data for the necessary urban analysis and feasibility studies in the preliminary preparation phase If we are to talk about the device, the measurements were made using a drone, which is an unmanned aerial vehicle, and this device is equipped with a LIDAR sensor.

Findings

An urban transformation area declared as a risk area in the district has been determined as a study area. It is thought that by measuring with a drone containing advanced laser scanning technology and producing 3D point cloud data and using this data in the production of a 3D city model, the resulting model and point cloud cluster will be used in the preliminary preparation studies to obtain information such as current area size, function, number of floors, urban voids, illegal construction, type and material information, and to produce base studies such as the current situation, thus providing direct savings in the number of personnel to be assigned in the field and time, and the margin of error in the obtained data will be less than collecting one-to-one data in the field, except for the margin of error obtained as a result of the measurement. In order to evaluate the quantitative accuracy of the studies, laser scanning technology is used to send laser beams to urban surfaces in the area determined within the scope of the study and to obtain a point cloud cluster with the X, Y, Z values obtained from the data reflected from this energy and to compare the obtained point cloud data with the current application project data and to investigate its statistical accuracy. By conducting ground-based measurements at four points around a randomly selected area, the obtained coordinates were matched with their corresponding points within the 3D point cloud data in the 3D Survey software, and error margin calculations were performed. Upon examining the results, it was determined that the error margin for the point cloud data corresponding to these four points was less than one.With this comparison study, the results regarding how close the measurements made with LIDAR technology are to the truth have been revealed. In particular, it is very important to determine the margin of error rate and prove the reliability of the study in estimation studies such as the distribution of the construction to the rightful owners and the approximate size of the construction area to be built. For this reason, the error rate in the study conducted using LIDAR technology was determined by considering the margin of error in the current application studies.

Conclusion

As a result, the time spent while carrying out urban transformation works in cities with earthquake risk such as Istanbul is of vital importance. It is seen that minimizing the time spent in implementing urban transformation works in the most healthy way is quite important when the multitude of structures in need of urban transformation are taken into consideration. For this reason, in order for these projects to be successful, technological methods should be used more effectively and data collection processes should be accelerated. In this study, important solutions are presented for accelerating the urban transformation pre-preparation processes of the construction areas that will be subject to urban transformation where risky structures are dense in order for urban transformation to be carried out successfully. In summary, the study demonstrates that with low cost and minimal manpower, it is possible to access up-to-date information with a low margin of error. It is anticipated that studies like this one will contribute to future research, regardless of changes in the location of the study area. Determining the ways of using the dataset obtained as a result of the study in a way that will contribute to urban transformation and design processes by creating a solid model, presenting the program and determining which urban analyzes that will guide urban transformation pre-preparation works together with this study as a final product will have a significant impact on the institutions and organizations responsible for accelerating urban transformation processes. This structure created to accelerate urban transformation pre-preparation works is an important step in terms of providing development in the field of urban transformation and improving time and economy management.

References

Bediroğlu, Ş. (2018). CBS Tabanlı 3 Boyutlu Kent Modellerinin Geliştirilmesi ve Bulut Bilişim İle Sunulması. (Doktora Tezi). Karadeniz Teknik Üniversitesi Fen Bilimleri Enstitüsü. Trabzon.

Güler, B. E. (2023). Level of Detail Optimization For 3D City Models. (DoktoraTezi). Dokuz Eylül Üniversitesi. İzmir.

Mitigating Urban Heat Island Effects through Nature-Based Solutions: The Case of Istanbul

Gizem Baydı[a], Prof. Fatih Terzi[b]

[a] Istanbul Technical University, Geographical Information Technologies, Türkiye
[b] Istanbul Technical University, Department of Urban and Regional Planning, Türkiye
gizembayd@gmail.com

Keywords: Urban Heat Island, Nature-Based Solutions, Urban Resilience, Istanbul

Climate change has become one of the most important environmental problems affecting cities on a global scale. Temperature increases caused by climate change have started to be felt more intensely in cities. The urban heat island effect (UHI) is a phenomenon that occurs as a result of urbanization and causes higher average temperatures in cities than in rural areas (Oke, 1982; Howard, 1818). UHI was first described by Howard (1818), who recorded that cities were warmer than rural areas. Later, in modern climatology, the UHI effect was systematically explained by Oke (1982) and reached its current definition. UHI is becoming an increasing problem, especially due to increasing surface permeability, decreasing green areas and thermal properties of building materials (Voogt & Oke, 1997).

The urbanization process exacerbates the urban heat island effect, leading to increased energy consumption, more frequent extreme heat events and increased public health risks (IPCC, 2014). According to a study conducted in a densely built metropolis such as Istanbul in Türkiye, increasing building density and decreasing amount of green space complicate thermal comfort conditions and increase the severity of the UHI effect (Okumuş & Terzi, 2021).

Although solutions have been developed to mitigate the UHI impact, traditional engineering-based approaches, such as highly reflective materials or cooling coatings, cannot ensure ecosystem services and environmental sustainability in the long term (Gill et al., 2007; Santamouris, 2015). To overcome these limitations, the concept of Nature-Based Solutions (NBS) has come to the fore. NBS was first proposed by the World Bank in 2008 as nature-based solutions to environmental problems. It was then conceptualized by IUCN (2009) and defined as a multifunctional strategy to strengthen the climate adaptation and resilience of cities in the European Commission's 2015 documents (MacKinnon et al., 2008; IUCN, 2009; European Commission, 2015).

When evaluated in the context of urban planning, according to studies, NBS provide many benefits such as regulating the microclimate, increasing thermal comfort and reducing carbon emissions by making ecological contributions. In this context, green roofs, vertical gardens and permeable surfaces are prominent practices to reduce the impact of UHI (Eggermont et al., 2015; Benedict & McMahon, 2002). However, questions such as how effective these practices are in different cities, in different morphological structures, and under which microclimatic conditions they work best are still under investigation. In particular, there are gaps in the literature on how effective NBS strategies are in densely built urban textures (Depietri & McPhearson, 2017).

Aim

The main objective of this study is to examine the role of nature-based solutions in mitigating the impact of UHI in the light of existing studies in the literature and to determine the most effective solution alternatives by comparatively analysing NBS applications on different surfaces (ground, roof and vertical) in a densely built-up area of Istanbul. For this purpose, microclimate simulations are performed using Ladybug software in the selected area and the cooling potentials of NBS applications are evaluated and analysed based on parameters such as surface and air temperature.

The research aims to contribute to the development of climate change adaptation strategies for urban planners, local governments and other decision makers in metropolises such as Istanbul.

Material and Method

In this study, microclimate simulations were conducted in a densely built-up area of Istanbul to assess the cooling potential of nature-based solutions (NBS) on the urban heat island (UHI) effect. The study is structured with a quantitative approach that allows for comparative analysis of different NBS scenarios.

Study Area Selection

Yenigün Neighbourhood in Bağcılar district of Istanbul was selected as the study area. This area was selected for case study due to its high building density, insufficient urban green space ratio, a texture in which different urban functions are intertwined, and limited natural factors affecting the microclimate (e.g. marine influences).
Furthermore, in the study conducted by Okumuş and Terzi (2021), the region including Yenigün Neighbourhood was identified as one of the areas with the highest surface urban heat island effect (SUHI) in Istanbul. In this context, the fact that the area offers a sample of areas with pronounced UHI impacts creates a suitable space to test the potential of nature-based interventions.
The simulations are conducted over an urban area of approximately 250x250 meters, allowing for a detailed assessment of the impacts at the local level. This scale is considered appropriate for both comparability of intervention scenarios and modelling detail and corresponds to the 200–300-meter range recommended in Emmanuel & Krüger (2012) for micro-scale urban climate modelling (Emmanuel & Krüger, 2012).

Data Sets and Analysis

The simulation studies were carried out using the Ladybug Tools plugin running in the Rhino + Grasshopper environment. Ladybug is an open-source environmental design tool that enables environmental analysis based on climate data and geometry. In this study, Ladybug Tools was used to calculate radiation load on surfaces of study area and simulated scenarios. (Roudsari & Pak, 2013).

The simulation process includes the following stages:

- Climate Data Integration – Climate data in EPW format for İstanbul was imported to Grasshopper-Ladybug environment. Direct and diffuse radiation values were used for cumulative sky matrix based on Perez Sky Model (Perez et al., 1990).
- 3D Spatial Modelling and Urban Geometry –The study area was modelled in 3D using Rhino. Buildings, roads and open spaces were recreated and assigned different surface categories (roof, ground, facade) to allow scenario-specific simulations.
- Radiation Analysis – Using Cumulative Radiation Analysis in Ladybug, the annual incident solar radiation (kWh/m²) on each surface and each scenario was calculated.

Simulation Scenarios

After analysing the current situation of the site, a total of three scenarios were defined:

- Scenario 1 - Ground Planting: Covering open areas and roadsides with grass and trees.
- Scenario 2 - Green Roofs: Planting scenario for all flat roofs.
- Scenario 3 - Vertical Gardens: Vertical gardens were applied to the south and west facades, which are most exposed to solar radiation. This choice was based on the expectation that these facades experience high levels of heat gain during the day and that the greening intervention would have the highest impact on thermal comfort (Perini et al., 2011; Wong et al., 2010).

Analysing the microclimate regulating effects of NBS in urban areas through simulations has been suggested in numerous studies (Gill et al., 2007; Norton et al., 2015). Open-source simulation tools such as Ladybug allow for rapid and comparative testing of different scenarios, making it possible to generate concrete data for planning decisions.

Findings

In this study, the effects of three different nature-based solution scenarios applied in urban area context on microclimate were evaluated through radiation analysis. The analyses were carried out on the basis of annual cumulative solar radiation (kWh/m²) and the extent to which each scenario reduces the energy accumulation on the surfaces was comparatively analysed.

The current situation, while most of the surfaces receive high radiation, green interventions on the ground and facades significantly reduced the radiation value. The ground green application scenario, despite having the smallest application area, provided the highest radiation reduction per m² (250 kWh/ m²) and was the most efficient scenario. Vertical green surfaces are the interventions that provide the highest radiation reduction in total (approximately 318.500 kWh). The green roof scenario was applied to a larger area but had more limited effect per m².

Table 1. Quantitative Findings of Simulation Analysis.

Scenario	Surface Area (m²)	Radiation Reduction (kWh)	kWh/m² Reduction	Cooling Potential per m² (°C)
SC1 - Green Ground	22686.54	58.500	2.57	0.01
SC2 - Green Roof	650.0	162.500	250.0	0.94
SC3 - Vertical Garden	22844.97	318.500	13.94	0.05

The results show that the effect of nature-based solutions vary not only according to the size of the application area, but also according to the orientation, location and urban context of the surface.

Conclusion

In the study, the microscale cooling potential of nature-based solutions applied in a dense built urban area with simulation based scenarios. Within the scope of the study three different nature-based solution application scenarios were modelled and the effects of these applications on solar radiation accumulation on surfaces were calculated and analysed. Radiation analysis conducted by Ladybug Tools plug in allows each scenario to be compared on annual basis based on energy load (kWh/m²).

According to the results, each nature-based solution intervention scenario provides different advantages in the spatial context. Vertical green surfaces provided the highest reduction in total radiation load. This was related with the size of the green facade areas and their orientation to the South-west in the scenario. On the other hand, ground green area scenario achieved the most efficient application for radiation load reduction. Despite it has the smallest application area, the radiation reduction per m². Green roofs, have a strong potential for generalizability throughout the urban areas despite having a lower unit effect.

From methodological aspect, Ladybug Tools enables rapid scenario generation with its open-source structure, however software limitations and detailed data cause some restrictions. In addition, since radiation analysis does not provide direct thermal data, it should be considered that this study provides a preliminary assessment framework.

As the result, it has been observed that even small nature-based solution interventions have positive effects in densely built urban areas, and this observation supports NBS applications in different scales in urban areas.

References

Bass, B., Sailor, D., Simmering, D., & Martilli, A. (2003). The impact of green roofs on Toronto's urban heat island. Environmental Research Letters, 8(4), 045022.

Benedict, M. A., & McMahon, E. T. (2002). Green infrastructure: Smart conservation for the 21st century. Renewable Resources Journal, 20(3), 12–17.

Depietri, Y., & McPhearson, T. (2017). Integrating the grey, green, and blue in cities: Nature-based solutions for climate change adaptation and risk reduction. In Nature-based Solutions to Climate Change Adaptation in Urban Areas (pp. 91–109). Springer

Eggermont, H., Balian, E. V., Azevedo, J. M. N., Beumer, V., Brodin, T., Claudet, J., … & Le Roux, X. (2015). Nature-based solutions: New influence for environmental management and research in Europe. GAIA - Ecological Perspectives for Science and Society, 24(4), 243–248.

Emmanuel, R., & Krüger, E. (2012). Urban heat island and its impact on climate change resilience in a shrinking city: The case of Glasgow, UK. Building and Environment, 53, 137–149.

European Commission. (2015). Towards an EU Research and Innovation policy agenda for Nature-Based Solutions & Re-Naturing Cities. Directorate-General for Research and Innovation. https://op.europa.eu/en/publication-detail/-/publication/5dff0734-9a12-11e5-8781-01aa75ed71a1

Fujibe, F. (2009). Urban warming in Japanese cities and its relation to climate change monitoring. International Journal of Climatology, 29(12), 1811–1822.

Gill, S. E., Handley, J. F., Ennos, A. R., & Pauleit, S. (2007). Adapting cities for climate change: The role of the green infrastructure. Built Environment, 33(1), 115–133.

Howard, L. (1818). The Climate of London: Deduced from Meteorological Observations Made in the Metropolis and at Various Places Around It. Harvey and Darton.

IPCC. (2014). Climate Change 2014: Impacts, Adaptation, and Vulnerability. Part A: Global and Sectoral Aspects. Contribution of Working Group II to the Fifth Assessment Report of the Intergovernmental Panel on Climate Change. Cambridge University Press.

IUCN. (2009). No time to lose: Make full use of nature-based solutions in the post-2012 climate change regime. IUCN.

Okumus, D. E., & Terzi, F. (2021). Evaluating the role of urban fabric on surface urban heat island: The case of Istanbul. Sustainable Cities and Society, 73, 103128.

Oke, T. R. (1982). The energetic basis of the urban heat island. Quarterly Journal of the Royal Meteorological Society, 108(455), 1–24.

Perez, R., Ineichen, P., Seals, R., Michalsky, J., & Stewart, R. (1990). Modeling daylight availability and irradiance components from direct and global irradiance. Solar Energy, 271-289.

Santamouris, M. (2015). Analyzing the heat island magnitude and characteristics in one hundred Asian and Australian cities and regions. Science of the Total Environment, 512–513, 582–598.

GEOLOGICAL ENGINEERING

Rock Mechanics

Detachments Induced By Thermal Cycling At Grain Boundaries of Fine Grained Marble

Dilek Karapınar[a], Yılmaz Mahmutoğlu[a], Orhan Apaydın[b],

[a] İstanbul Technical University, Faculty of Mining, Geology Engineering, Türkiye
[b] İstanbul Technical University, Faculty of Mining, Geophysics Engineering, Türkiye
dilekkarapinar@itu.edu.tr

Keywords: Afyon Sugar Marble, Sugaring, Grain Boundary, Thermal Cycling, Image Processing.

Aim

Marble is the most widely used type of stone in the construction of architectural elements in the historical period. However, it is sensitive to atmospheric factors and has limited durability. Factors such as rain, snow, cycling temperature changes, wind and pollutants have negative effects on the structural strength and appearance of such building blocks. Temperature can affect the rate of degradation and the pattern of salt migration in the stone. High temperature causes an increase in the rate of chemical change, low temperature causes freeze-thaw problem, and sudden temperature change causes internal stress due to different expansion (Mahmutoğlu, 2017).

The thermal expansion coefficient of the calcite mineral that forms the marble shows significant anisotropy. Heat-induced elongation along the c-axis, shortening in the a-axis direction and expansion in the opposite direction due to cooling occurs from the crystal axes. Dolomite mineral expands thermally in different amounts in each direction and shows elongation and shortening behaviour depending on heating and cooling. Therefore, this mineral is more resistant to degradation than calcite (Ruedrich et al., 2013; Shushakova et al., 2013). Due to the anisotropy in the thermal expansion coefficients of both minerals, permanent stresses develop at the grain joints due to temperature change. Kessler (1919) pointed out the permanent change in the internal structure of the material due to repeated heat treatment. Battaglia et al. (1993) showed that in heat-treated marble, even low temperature fluctuations can lead to irreversible permanent deformations that may result in failure and weakening. Siegesmund et al., (1999, 2000, 2008), Zeisig et al., (2002), Koch and Siegesmund, (2004), Luque et al., (2011) found that repeated heat treatment leads to a size change of about 1 mm/m and cohesion along grain boundaries is lost.

Due to its mineral composition, the periodic change in atmospheric temperature is of great importance in the disease of marbles. Although there are many different causes, the general view is that thermal cyclical is the main source of the event. Due to the thermal effect, sugaring problems occur in marbles.

The candied of marble, which is usually seen in the exterior elements of ancient and modern buildings, is one such degradation event. This term is derived from the transformation of calcite grains into sugar-like powder as a result of the dispersion of marble grains (Carfagni, 1999; Sassoni & Franzoni, 2014). Darot & Reuschle´* (2000), Mahmutoğlu (1998,2006), Ferrero and Marini (2001), Siegesmund et al., (2000b), Zeisig et al., (2002), Bandini and Berry (2013), Ghobadi & Babazadeh (2015), Khanlari & Abdilor (2015). Depending on the number of heat treatment periods, it was determined that the deterioration and opening between the calcite grains increased, and the cohesion along the grain boundaries of the material was partially lost (Mahmutoğlu 2006).

For this reason, in this paper, the tissue damage caused by the increasing and growing grain boundaries between the calcite grains due to heat treatment in Afyon (Sugar) marble, which is also widely used in our country, has been revealed by imaging the changing grain borders. This study aims to contribute to the literature in defining the behavior of Afyon Marble, which is used as a monument and decorative material, against thermal effect.

Material and Method

Material (Afyon Sugar Marble)

Marble, which is called finely crystalline Afyon Sugar, which is operated in the Afyon region, which has homogeneous and isotropic properties, was selected as the experimental material. Generally, the smooth-shaped grains are straight and slightly curvature, and the rock has a homoblastic texture. In the sections examined under the microscope, it was determined that the grain size generally varied between 0.5-2 mm (Figure 1a). According to the results of XRD analyzes performed to reveal the chemical content of marbles; It contains 96% calcite, about 2% dolomite and trace amounts of quartz. TG-DTA analyzes (Figure 1b) were performed on the marble sample in order to determine the thermal and gravimetric changes that occur in the material with the increase in temperature. According to the results of the analysis, the critical temperature values of the sample were seen as 900-950ºC.

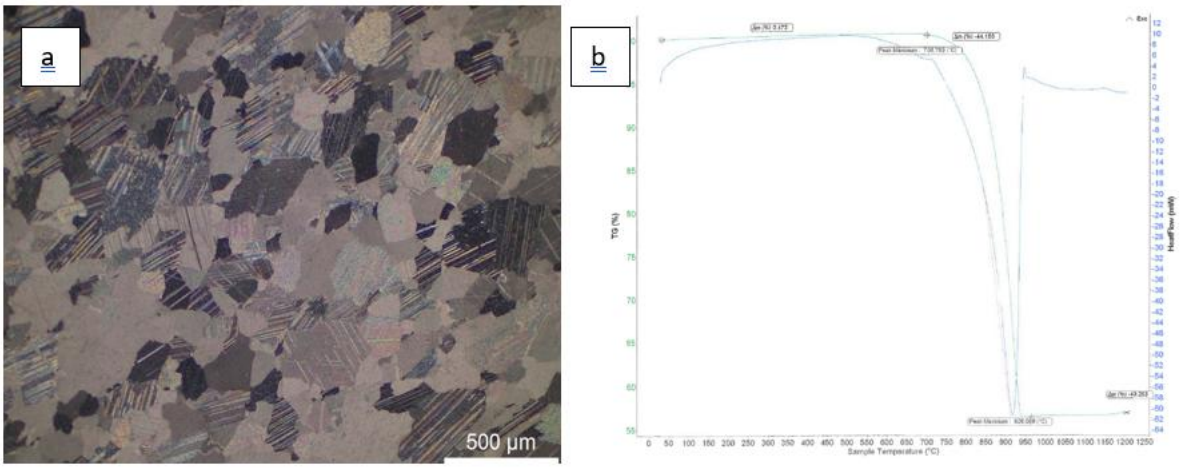

Figure 1. Optical microscope image of Afyon (Sugar) Marble (a), TG-DTA analysis (b).

Sample Preparation and Heat Cycling

The homogeneous and isotropic fine crystalline marble called Afyon Sugar, which is operated in Afyon region, was selected as the experimental material. Generally, the grains are straight and slightly curved and the rock has a homoblastic texture. It was determined that the grain size generally varied between 0.5-2 mm in the sections examined under microscope (Figure 1a). According to the results of XRD analyses performed to reveal the chemical content of the marbles; it contains 96% calcite, approximately 2% dolomite and trace amounts of quartz. TG-DTA analyses (Figure 1b) were performed on the marble sample in order to determine the thermal and gravimetric changes that occur in the material with increasing temperature. According to the results of the analysis, the critical temperature values of the sample were 900-950ºC. In other words, it is predicted that no endothermic reaction will occur as long as this material does not reach this temperature.

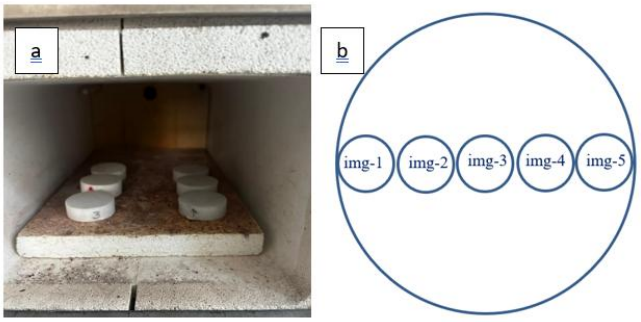

Figure 2. Marble samples subjected to heat treatment (a) and representative locations of photographic locations taken from sections (b).

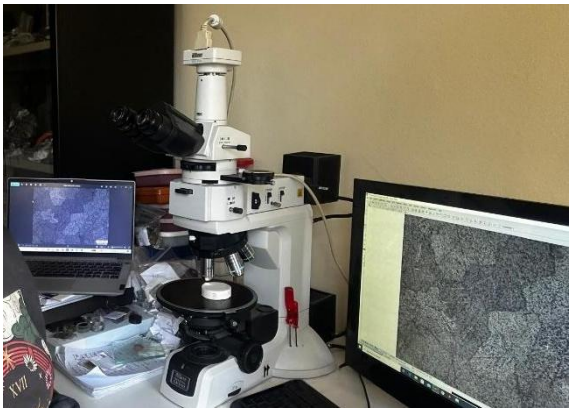

Figure 3. Photographing polished sections.

Processing of Images

The sample images were imaged and processed using the Matlab programme. The images were read in the programme in grayscale (0-255) and then a histogram of the pixel values of the image was drawn (Figure 5b). Grain boundaries appear dark (black). Pixel values below the threshold value (65) determined from the histogram were considered to correspond to this darkness. In addition to these dark colours, grain boundaries and discontinuities, it is seen that the heat interactions are negligible as a result of the follow-up of the sample from its original state. The regions below the determined threshold values were visualised with white colour (Figure 5c). Then the ratio of the area below this threshold value to the whole image was calculated (Figure 5d).

Findings

The photographed area in the A0 sample was re-imaged as the A4 sample after 4 times heat treatment. A certain area of both images was magnified and examined in detail (Figure 4a,b). In these regions, the images were processed (Figure 5) and it was observed that the grain boundaries of the same sample, which was subjected to heat treatment 4 times, grew and new borders were formed.

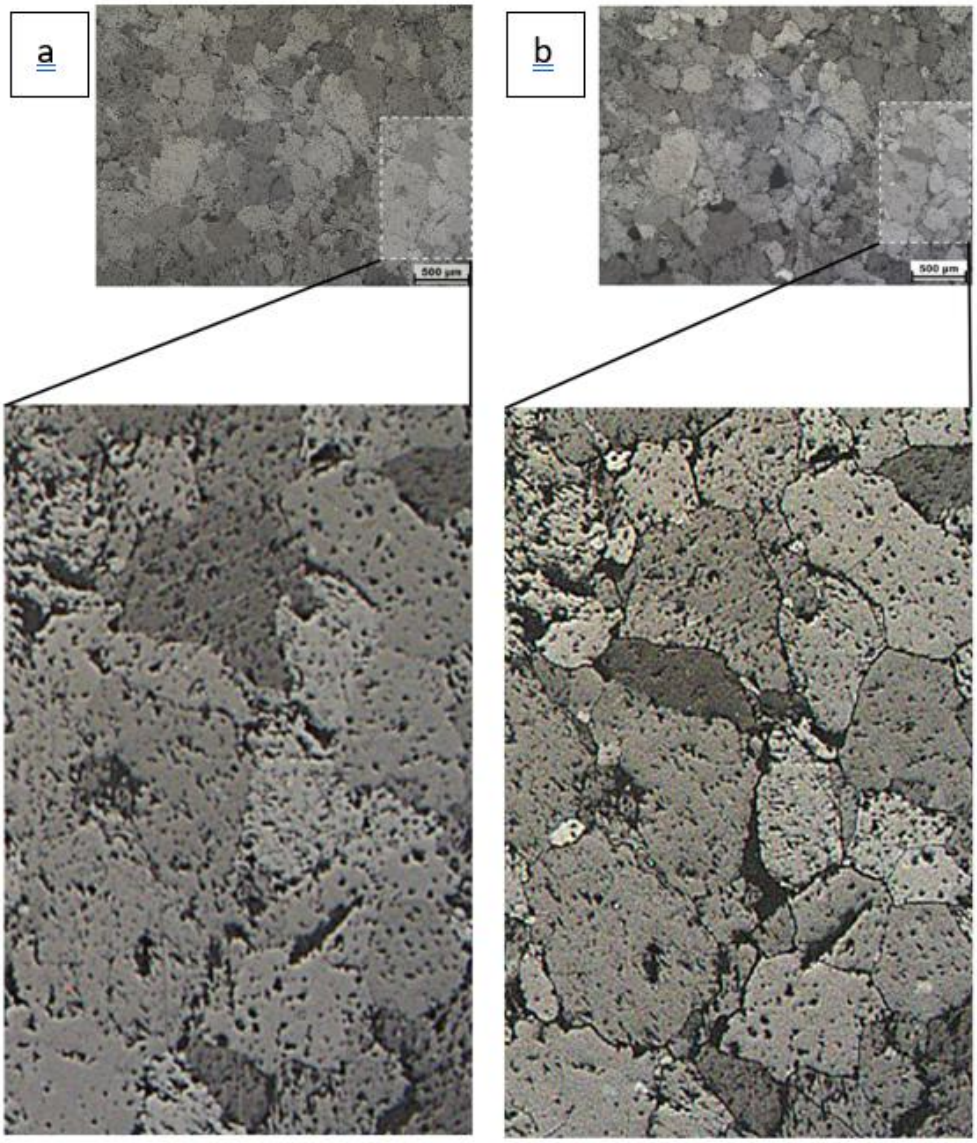

Figure 4. Detailed image of the A0 sample and its specific region (a), A4 sample and its detailed image of the specific region (b).

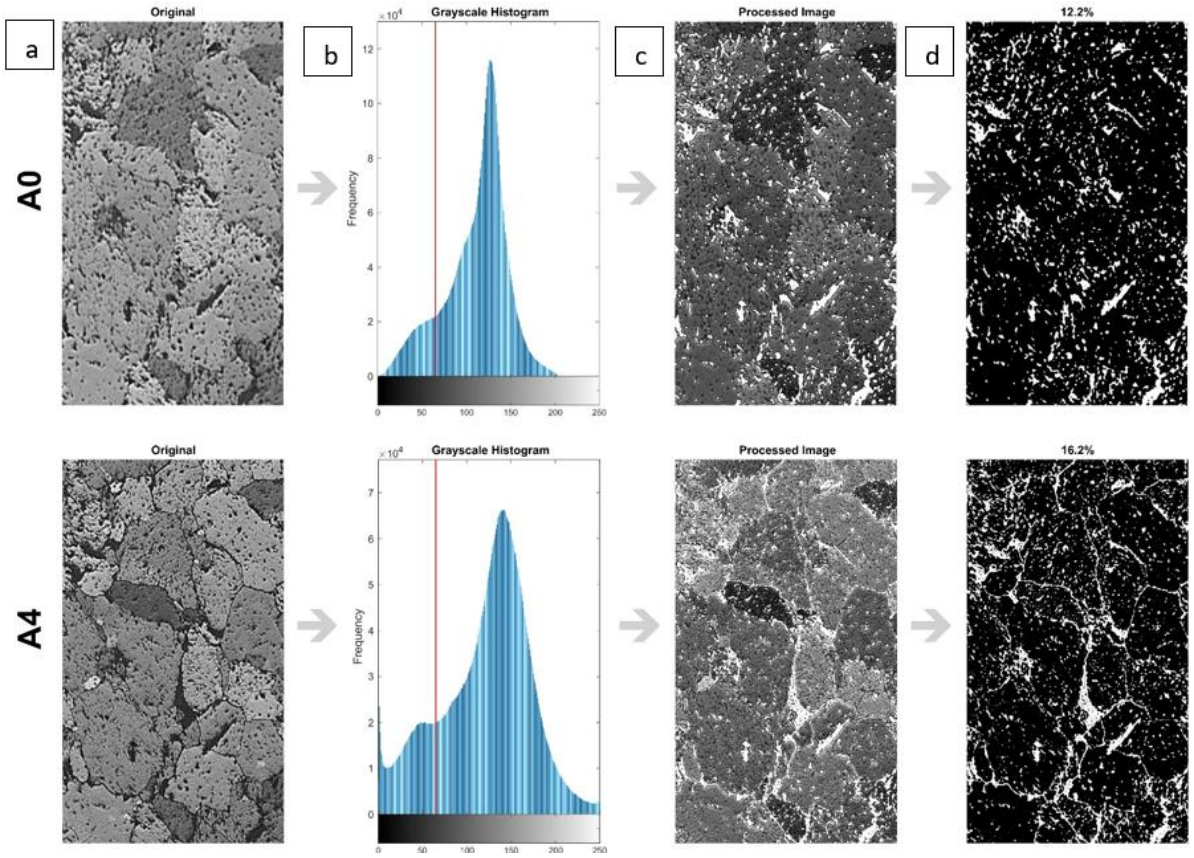

Figure 5. (a) Image of the original (A0) and heat-treated (A4) regions of the same sample, (b) grayscale histogram of the images, (c) representation of places below the threshold, (d) representation of varying grain boundaries.

Conclusion

The region determined in the original Afyon Marble, which was not heat treated, was photographed after heat treatment 4 times and the ratio of the black regions of the picture determined as the threshold value to the total area of the picture was calculated. This ratio was calculated as 12.2% in the A0 sample and 16.2% in the A4 sample. It was observed that the darkest black regions seen in the photographs are also seen in the natural state of some minerals along with the grain boundaries. In the calculation made by neglecting the effect of heat treatment on the black areas outside the grain boundaries, the relative areal increase in the grain boundaries caused by heat treatment in the examined region was calculated as 4%.

References

Bandini, A., & Berry, P., (2013). Influence of marble's texture on its mechanical behaviour. Rock Mech Rock Eng, 46, 785–799.

Battaglia, S., Franzini, M., & Mango, F. (1993). High-Sensitivity Apparatus for Measuring Linear Thermal Expansion: Preliminary Results on the Response of Marbles to Thermal Cycles (Vol. 16).

Carfagni, G. F. (1999). On the thermal degradation of marble. Int. J. Rock Mech. Min. Sci., 36, 119–126.

Darot, M., & Reuschle´*, T. (2000). Acoustic wave velocity and permeability evolution during pressure cycles on a thermally cracked granite. International Journal of Rock Mechanics & Mining Sciences, 37.

Ferrero, A. M., & Marini, P. (2001). Technical Note Experimental Studies on the Mechanical Behaviour of two Thermal Cracked Marbles. In Rock Mech. Rock Engng (Vol. 34, Issue 1). Springer-Verlag.

Ghobadi, MH., & Babazadeh, R. (2015). Experimental Studies on the Effects of Cyclic Freezing–Thawing,Salt Crystallization, and Thermal Shock on the Physical and Mechanical Characteristics of Selected Sandstones. Rock Mech. Rock Eng. , 48, 1001–1016.

Kessler, D. (1919). Physical and chemical tests of the commercial marbles of the United States.

Khanlari, G., & Abdilor, Y. (2015). Influence of wet–dry, freeze–thaw, and heat–cool cycles on the physical and mechanical properties of Upper Red sandstones in central Iran. Bull Eng Geol Environ., 74, 1287–1300.

Koch, A., & Siegesmund, S. (2004). The combined effect of moisture and temperature on the anomalous expansion behaviour of marble. Environmental Geology, 46(3–4), 350–363. https://doi.org/10.1007/s00254-004-1037-9

Luque, A., Ruiz-Agudo, E., Cultrone, G., Sebastián, E., & Siegesmund, S. (2011). Direct observation of microcrack development in marble caused by thermal weathering. Environmental Earth Sciences, 62(7), 1375–1386. https://doi.org/10.1007/s12665-010-0624-1

Mahmutoglu, Y. (1998). Mechanical Behaviour of Cyclically Heated Fine Grained Rock. Rock Mech. Rock Eng., 31(3), 169–179.

Mahmutoğlu, Y. (2006). The effects of strain rate and saturation on a micro-cracked marble. Engineering Geology, 82(3), 137–144. https://doi.org/10.1016/j.enggeo.2005.09.001

Mahmutoğlu, Y. (2017). Prediction of weathering by thermal degradation of a coarse-grained marble using ultrasonic pulse velocity. Environmental Earth Sciences, 76(12). https://doi.org/10.1007/s12665-017-6770-y.

Ruedrich, J., Knell, C., Enseleit, J., Rieffel, Y., & Siegesmund, S. (2013). Stability assessment of marble statuaries of the Schlossbrücke (Berlin, Germany) based on rock strength measurements and ultrasonic wave velocities. Environmental Earth Sciences, 69(4), 1451–1469. https://doi.org/10.1007/s12665-013-2246-x

Sassoni, E., & Franzoni, E. (2014). Sugaring marble in the Monumental Cemetery in Bologna (Italy): characterization of naturally and artificially weathered samples and first results of consolidation by hydroxyapatite. Applied Physics A: Materials Science and Processing, 117(4), 1893–1906. https://doi.org/10.1007/s00339-014-8629-3

Shushakova, V., Fuller, E. R., & Siegesmund, S. (2013). Microcracking in calcite and dolomite marble: Microstructural influences and effects on properties. Environmental Earth Sciences, 69(4), 1263–1279. https://doi.org/10.1007/s12665-012-1995-2

Siegesmund, S., Ullemeyer, K., Weiss, T., Tschegg, E. K., & Ullemeyer, Y. (2000a). Physical weathering of marbles caused by anisotropic thermal expansion. In Int J Earth Sci (Vol. 89). Springer-Verlag.

Siegesmund, S., Ullemeyer, K., Weiss, T., Tschegg, E. K., & Ullemeyer, Y. (2000b). Physical weathering of marbles caused by anisotropic thermal expansion. In Int J Earth Sci (Vol. 89). Springer-Verlag.

Siegesmund, S., Weiss, T., Vollbrecht, A., & Ullemeyer, K. (1999). Marble as a natural building stone: rock fabrics, physical and mechanical properties. Zeitschrift Der Deutschen Geologischen Gesellschaft, 150(2), 237–257. https://doi.org/10.1127/zdgg/150/1999/237

Zeisig, A., Siegesmund, S., & Weiss, T. (2002). Thermal expansion and its control on the durability of marbles. Geological Society Special Publication, 205, 65–80. https://doi.org/10.1144/GSL.SP.2002.205.01.06.

GEOMATICS ENGINEERING

Geodesy

Geographic Information Systems

Natural Hazards

Photogrammetry

Remote Sensing

On the Role of Earth Observations and Geodetic Data in Environmental and Climate Change

Solmaz Farnad[a*], Bihter Erol[a]

[a] Istanbul Technical University, Geomatics Engineering Department, Türkiye
farnads22@itu.edu.tr

Keywords : Climate Change Impact, Geodetic Data Integration, Groundwater Depletion Monitoring, Satellite Earth Observation, Sustainable Water Management.

Aim

1. Environmental Challenges and the Need for Monitoring

The Earth is facing numerous environmental challenges that are increasingly jeopardizing natural ecosystems and human welfare. Climate change, resource depletion, and rising human activity are intensifying these threats. One of the most urgent concerns is the depletion of groundwater resources, which are essential for agricultural production, industry, and human consumption. Groundwater is a critical resource in many parts of the world, particularly in regions with limited access to surface water, such as arid and semi-arid zones (Kala and Kumar, 2022).

In Türkiye, as in other countries, the depletion of groundwater is becoming a growing problem. Regions that rely heavily on groundwater for irrigation and drinking purposes are experiencing heightened water stress (Baykal et al., 2024), driven by both unsustainable water extraction and shifting climate patterns. This highlights the need for reliable and sustained monitoring of groundwater to inform resource management policies. However, widespread monitoring remains difficult due to the challenges of obtaining comprehensive in-situ data and the complexity of hydrological dynamics.

Satellite-based Earth observation systems are vital in addressing these challenges, enabling the tracking of environmental changes across large areas and over extended periods (Müller and Pail, 2022). These systems detect shifts in Earth's gravitational field, which correlate with changes in mass distribution, such as groundwater depletion or replenishment. As changing precipitation patterns and increased water scarcity worsen, these satellite datasets provide invaluable insights into groundwater dynamics, enabling early detection of resource loss and improved management strategies (Li et al., 2022).

2. Aim and Objectives of the Research

The goal of this research is to demonstrate how satellite-derived geodetic data, specifically from GRACE (Gravity Recovery and Climate Experiment) and GRACE-FO (GRACE Follow-On), can be used to monitor and analyze environmental changes, with a particular focus on groundwater depletion in Türkiye. Groundwater scarcity is a growing global issue, especially in areas where climate change and poor water management practices exacerbate water shortages. This study presents a novel approach by providing a detailed, region-specific assessment of groundwater fluctuations in Türkiye, contributing to global efforts to tackle this pressing issue. By analyzing GRACE and GRACE-FO satellite data from 2013 to 2025, this research will assess the effects of climate change on groundwater resources and provide valuable insights into trends in water availability.

The primary objective is to use GRACE and GRACE-FO data to track groundwater depletion and pinpoint areas in Türkiye that are experiencing increasing water scarcity. By integrating these satellite-based data with climate models, the research will help predict the future trajectory of groundwater resources, offering a new perspective on areas at risk of significant depletion and providing guidance for future water management strategies.

Additionally, this research will refine the application of GRACE and GRACE-FO data in areas where traditional ground-based monitoring methods are limited, contributing to the development of a global groundwater monitoring system that can be applied universally, advancing the field of environmental monitoring in innovative ways.

Material and Method

1. The Role of Earth Observations and Geodetic Data

Geodetic methods, particularly those relying on satellite observations, have transformed our capacity to track Earth's hydrological activities (Müller and Pail, 2022). The GRACE and GRACE-FO missions represent major advancements in this field, measuring subtle changes in Earth's gravitational pull caused by mass redistribution, such as the movement of water between land, oceans, and ice. These missions offer essential data on fluctuations in groundwater over time and space, providing precise estimates of groundwater availability and assessing the influence of climate change on this vital resource.

The GRACE mission, launched in 2002, revolutionized our understanding of water storage shifts, particularly in areas dependent on groundwater. GRACE-FO, launched in 2018, builds on this work by offering greater accuracy and precision in tracking these changes. The GRACE-FO mission uses cutting-edge technologies to monitor gravity variations, which enhances our ability to track groundwater resources and better understand the effects of climate change on water availability (Xiang et al., 2023).

The data from GRACE and GRACE-FO satellites is indispensable because it provides a global perspective on groundwater depletion, significantly extending monitoring beyond traditional ground-based methods. By integrating this data with local climate models, researchers can obtain more comprehensive insights into the ways climate change and alterations in land use influence groundwater resources. This integration allows for the analysis of critical parameters like precipitation patterns, temperature shifts, and evapotranspiration, helping to predict future water availability trends and enabling more informed water management decisions.

Moreover, GRACE and GRACE-FO are essential for studying the interactions between groundwater, surface water, and atmospheric factors. For instance, changes in groundwater storage can affect river systems, wetland environments, and agricultural output. Tracking these interactions provides insights into how climate change may alter regional water cycles and the overall availability of water resources (Li et al., 2024a).

2. International Collaboration and the GGOS

Given the global scope of environmental challenges such as groundwater depletion and climate change, international cooperation is indispensable for tackling these issues effectively. The Global Geodetic Observing System (GGOS) plays a pivotal role in fostering international collaboration in Earth observation (Plag and Pearlman, 2009). GGOS facilitates worldwide cooperation to collect and distribute geodetic data, ensuring that measurements of the Earth's physical properties, such as its shape, gravitational field, and rotational dynamics, are precise and consistent across different regions and time periods (Sehnal et al., 2024b).

By synthesizing data from various satellite missions, GGOS helps create global geodetic reference frames, which are vital for better analyzing and understanding Earth dynamic processes. These reference frames are used to monitor shifts in water storage, sea-level rise, land subsidence, and other phenomena affected by climate change. Observing Earth's hydrological systems and tracking changes water budgets come in front of the studies which require a unified geodetic infrastructure and data with global coverage. The fusion of geodetic data with climate models further refines predictions about future water availability and strengthens efforts to develop sustainable water management strategies.

The collaboration facilitated by GGOS is particularly critical for monitoring groundwater depletion, as it ensures that data gathered from different satellite missions and countries can be integrated into a unified framework. This enables researchers to track groundwater changes on a global scale, offering insights into areas where groundwater depletion is most severe, and helping policymakers to prioritize water management strategies accordingly (Sehnal et al., 2024a)

Findings

The findings from this research will significantly enhance our understanding of groundwater depletion in Türkiye and provide valuable insights for local water management strategies. By integrating GRACE and GRACE-FO satellite data with climate models, this study will improve our comprehension of how climate change influences groundwater resources, offering predictions that can guide future water management practices.

Conclusion

This research provides a comprehensive overview to the contribution of Earth observations and geodetic data to the studies on environmental and climate change, with a case study of groundwater budget analysis. The methodology developed in this research provides a structured approach for future studies in the case study area. It presents a systematic method for monitoring groundwater changes, which can be adapted to regions facing similar water scarcity challenges. This work will contribute to sustainable water management and climate change adaptation, offering a solid foundation for emerging researchers and future investigations on both local and global scales.

References

Baykal, T., Taylan, D., & Terzi, Ö. (2024). Determination of Groundwater Potential Zone Using AHP Based on GIS for Konya, Türkiye. Mühendislik Bilimleri ve Tasarım Dergisi, 12(4), 848-865. https://doi.org/10.21923/jesd.1495305.

Kala, A.K., & Kumar, M. (2022). Role of Geospatial Technologies in Natural Resource Management. In P. Kumar, R.K. Singh, M. Kumar, M. Rani, & P. Sharma (Eds.), Climate Impacts on Sustainable Natural Resource Management (First Edition). John Wiley & Sons Ltd.

Li, W., Bao, L., Yao, G., Wang, F., Guo, Q., Zhu, J., Zhu, J., Wang, Z., Bi, J., Zhu, C., Zhong, Y., & Lu, S. (2024). The analysis of groundwater storage variations from GRACE/GRACE-FO over the past 20 years, driven by influencing factors, and prediction in Shandong Province, China. Scientific Reports, 14, 5819. https://doi.org/10.1038/s41598-024-55588-3.

Li, W., Xie, X., Li, W., van der Meijde, M., Yan, H., Huang, Y., Li, X., & Wang, Q. (2022). Monitoring of Hydrological Resources in Surface Water Change by Satellite Altimetry. Remote Sens., 14, 5599. https://doi.org/10.3390/rs14215599.

Müller, J., & Pail, R. (2022). Geodesy 2030. Wißner-Verlag, 1-12. https://doi.org/10.12902/zfv-0392-2022.

Plag, H.P., & Pearlman, M. (Eds.). (2009). The Global Geodetic Observing System: Meeting the Requirements of a Global Society on a Changing Planet in 2020. Springer. https://doi.org/10.1007/978-3-642-02687-4_3.

Sehnal, M., Sánchez, L., Angermann, D., Craddock, A., Miyahara, B., & Steiner, L. (2024). Emphasizing the value of geodesy to science and society through IAG-GGOS. International Association of Geodesy Symposia. https://doi.org/10.1007/1345_2024_243.

Sehnal, M., Sánchez, L., Angermann, D., Rodríguez, J.C., & Lidberg, M. (2024). GGOS - The Global Geodetic Observing System of the International Association of Geodesy. EUREF Symposium 2024. https://doi.org/10.13140/RG.2.2.17879.69289.

Xiang, L., Wang, H., Steffen, H., Jiang, L., Shen, Q., Jia, L., Su, Z., Wang, W., Deng, F., Qiao, B., Cui, H., & Gao, P. (2023). Two Decades of Terrestrial Water Storage Changes in the Tibetan Plateau and Its Surroundings Revealed through GRACE/GRACE-FO. Remote Sens., 15, 3505. https://doi.org/10.3390/rs15143505.

GEOMATICS ENGINEERING

Geodesy

Geographic Information Systems

Natural Hazards

Photogrammetry

Remote Sensing

Spatial Problems And Effective Factors In Hospital Campus Structure

Özgür Elmas[a], Rahmi Nurhan Çelik[b]

[a] Istanbul Technical University, Graduate School, Geomatics Engineering Doctoral Program, Türkiye
[b] Istanbul Technical University, Faculty of Civil Engineering, Department of Geomatics Engineering, Türkiye
elmas17@itu.edu.tr

Keywords : Spatial Issues, Hospital Campuses, GIS.

Aim

One of the important application areas of Spatial Information Systems (SIS) is health-related research, planning and administrative processes using Geographical Information Systems (GIS) Technologies (Pandery ve Karnatak, 2025). GIS technologies significantly increase the quality and efficiency of health research by establishing the link between public health and geographic location (Nykiforuk ve Flaman, 2011). GIS applications provide the opportunity to make data contribution and analyses on many basic health issues such as regional development and spread of diseases, development of disease prevention and control approaches, analysis of disease risk factors and planning of health screening services (Biu vd., 2024). One of the most important application areas of GIS is health-related research, planning and administrative processes (Mitropoulos vd., 2006). Thus, the use of GIS enables managers to make informed decisions on issues such as facility location selection and optimizing resource allocation. With each passing day, the role of GIS applications in the strategic planning and management of healthcare facilities is increasing due to demands for more efficient and higher quality healthcare services (Neutens, 2015). GIS contributes to determining the level of accessibility to health services of different populations and creating solutions thanks to spatial data such as transportation times, transportation networks and geographical barriers (Khashoggi ve Murad, 2020).

In this study, the difficulties in reaching the hospital campus area and the health units within the campus, spatial inadequacies and spatial data quality were investigated specifically for three large hospitals with campus structures. The aim of this study is to determine approaches that will contribute to more efficient use of resources in state and private health institutions and to the most efficient and easy access of patients to hospital services, through the correct spatial analysis method.

Material and Method

While creating the sample, care was taken to ensure that the selected hospital campuses included all branches of medicine and differed in terms of establishment date and financial possibilities. In accordance with this purpose, a faculty of medicine affiliated to a state university with a campus structure in Istanbul (Istanbul Faculty of Medicine), a faculty of medicine affiliated to a foundation university (Koç University Faculty of Medicine) and a city hospital with a campus structure (Başakşehir Çam and Sakura City Hospital) were selected.

Interviews were conducted with people who worked in managerial positions (deputy chief physicians) in these hospital campuses, and the current status of the campuses and spatial problems were questioned. In addition, spatial data such as the establishment year of the campuses, settlement area, distance to main roads, earthquake effect, reconstruction process and student education were obtained from publicly available sources. In the light of the existing data, the spatial adequacy status of the campuses, ease of access to health units and inadequacies in spatial data infrastructure were discussed in light of the literature and solution suggestions were presented.

Findings

When the adequacy level of the spaces, ease of transportation and finding units and SIS were questioned regarding the Istanbul Faculty of Medicine (IFM), Koç University Faculty of Medicine (KUFM) and Başakşehir Çam and Sakura City Hospital (BÇSCH) campuses (Table 1).

It was stated that larger areas were needed in the IFM and KUFM campuses, while the areas in the BÇSCH campus were sufficient for now. When hospital administrators were asked whether patients and their relatives had difficulty finding the areas they were looking for on the campus, it was stated that they had difficulty for the IFM and KUFM campuses, while it was stated that there was a good directional sign system for the BÇSCH campus and there were colored directions on the roads. While it was stated that there was no SIS in which the spatial coordinates of the units were registered for the IFM and KUFM, it was stated that the SIS integrated with the Turkish national geographic information system for the BÇSCH was available and updated, and that a navigation system was established for employees and citizens where settlement coordinates could be seen, but it was not active. While a negative response was received to the question of whether spatial changes were recorded in SIS for the IFM campus, it was stated that spatial changes were recorded in SIS for the KUFM and BÇSCH campuses. It was stated that important spatial information such as emergency exits and fire extinguishing instructions for the IFM, KUFM and BÇSCH campuses are posted in visible places and recorded in SIS.

Table 1. Questions and answers regarding the spatial structuring and spatial information system (SIS)

Interview questions	Istanbul Faculty of Medicine Campus	Koç University Faculty of Medicine Campus	Başakşehir Çam and Sakura City Hospital Campus
Are the existing areas and spaces on the hospital campus sufficient? Is there a need for new areas?	There is a need for larger areas for clinics. There is a need for sports fields, green areas, sitting areas and parking areas.	It is not enough, new areas are needed.	Since hospitals are dynamic structures, new areas may be needed over time, but for now it is sufficient.
Are hospital staff and/or patients having difficulty finding the places they are looking for?	Yes, they are struggling. That's why we put consultants on the ground floor of many buildings.	In hospital corridors, we often encounter patients looking for a department.	There is a good signage system. There are also colored directions on the roads.
Is there a SIS in which spatial settlements are registered?	No, it does not exist.	No, it does not exist.	There is but it is not active
Are the units spatial coordinates available? Is it integrated with the Turkish national geographic information system? How often is SIS updated online?	No, it does not exist.	No, it does not exist.	It is registered and updated in the national information system.
Is there a SIS available to employees where location coordinates can be viewed?	No, it does not exist.	No, it does not exist.	There is a navigation system for employees and citizens, but it is not active.
How are spatial changes monitored? Are spatial changes recorded in SIS?	It is known where the sections were moved to, but the detailed layout is unknown.	Spatial changes are regularly recorded in their own systems and announced internally.	When changes are made, they are recorded in the system.

Is important spatial information, such as emergency exits and firefighting instructions, recorded in visible locations and in the SIS?	There is a system that works very well.	There is a record in the fire automation system, and there are also emergency escape sketches on the floors and walls of common areas.	Yes, it is mandatory according to our quality system.	of hospital

campuses.

Spatial data such as the establishment year, area (m²), distance to main roads and earthquake impact and reconstruction process obtained through literature review regarding the IFM, KUFM and BÇSCH campuses are given in Table 2.

Table 2. Spatial data for three hospital campuses.

Spatial data	Istanbul Faculty of Medicine Campus	Koç University Faculty of Medicine Campus	Başakşehir Çam and Sakura City Hospital Campus
Year of foundation	1944 and following years	2014	2020
Campus land area	Campus area:110.000 m²	Campus area:214.000 m²	Land area: 789.031 m²
Distance to main roads	- E5 (D100): 3-4 km - TEM (E80): 5-6 km - Metro 900 m - Tram line 200 m	- E5 (D100): 1-3 km - TEM (E80):7-9 km	-European Motorway: 4 Km -Istanbul Airport: 30 km -To the Anatolian Side:25 km - Metro line passes under the hospital.
Earthquake impact and reconstruction process	After the 1999 Gölcük Earthquake, some campus buildings suffered serious damage. For this reason, reconstruction was initiated as of the beginning of 2020.	Earthquake resistant structures were built using earthquake isolators and modern engineering technologies.	The buildings are constructed to be earthquake resistant.
Student education on hospital campus (2024)	- Faculty of Medicine (360 Students)	- Faculty of Medicine (41 Student) - Faculty of Nursing (41 Student)	No undergraduate education

Conclusion

The increasing number of patients observed every passing day, technological developments creating a need for new areas, and requirements such as parking, green areas and social facilities cause the existing campus areas to become insufficient over time. When choosing a location for hospital campuses, many factors such as short-term and long-term regional needs, financial opportunities, suitable land selection, and equal and accessible service provision gain importance. When the construction process of IFM is examined, it is seen that its establishment dates back to the Second World War (Url-2). In 1967, Cerrahpaşa Faculty of Medicine was separated as a separate faculty and the remaining part on the Capa campus continued its services under the name of IFM. The buildings of the Faculty of Dentistry, which continued its education on the Capa campus, were completely separated from the Capa campus in 2019 due to severe damage due to earthquakes. Since it was established on a limited land of 110 acres, the Çapa campus area is insufficient to meet today's needs (Table 2). Due to the old campus buildings and the negative effects of the earthquake, a reconstruction process has been initiated in IFM, which has negatively affected education, healthcare services, spatial services, access to units and SIS. On the other hand, the KUFM campus, which was completed in 2014, and the BÇSCH campus, which was completed in 2020, were established on larger areas (Url-1; Url-3). While it was stated that new areas were needed for the KUFM campus, it was emphasized that the existing area for the BÇSCH campus was sufficient for now, but since hospitals are dynamic structures, new areas may be needed over time (Tablo 1). Proximity to main roads is considered a positive variable for all three campus locations (Table 2).

GIS plays an active role in solving fundamental problems such as patient access and effective healthcare delivery by facilitating the planning of healthcare services (Shaw, 2017). Experience with three hospital campuses demonstrates the importance of GIS in selecting an optimum location with equal accessibility for patients that can meet healthcare expectations and educational needs.

Statement

This paper constitutes a part of the doctoral thesis titled Researching Spatial Data Quality and Attributes for Spatial Analysis and Testing on a Project (Mekansal Veri Kalitesi ve Niteliklerinin Araştırılması ve Bir Proje Üzerinde Test Edilmesi), which is currently underway at Istanbul Technical University, Graduate School, Geomatics Engineering Doctoral Program.

References

Biu, P.W., Nwasike, C.N., Nwaobia, N.K., Ezeigweneme, C.A., Gidiagba, J.O. (2024). GIS in healthcare facility planning and management: A review. World Journal of Advanced Research and Reviews 21(01), 12–19.

Khashoggi, B. F., Murad, A. (2020). Issues of Healthcare Planning and GIS: A Review. ISPRS International Journal of Geo-Information, 9(6), 352.

Mitropoulos, P., Mitropoulos, I., Giannikos, I., Sissouras, A. (2006). A biobjective model for the locational planning of hospitals and health centers. Health Care and Manage Sci, 9, 171-179.

Neutens, T. (2015). Accessibility, equity and health care: review and research directions for transport geographers. Journal of Transport Geography 43, 14-27.

Nykiforuk, C.I.J, Flaman, L.M. (2011). Geographic information systems (GIS) for Health Promotion and Public Health: a review. Health Promot Pract 12(1):63-73.

Pandery, K., Karnatak, H. (2025). Geographic information systems. R.S. Dwivedi (Ed.) *Advances in geospatial technologies for natural resource management* içinde (s. 41-63). CRC Pess.

Shaw, N.T, McGuire, S.K. (2017). Understanding the use of geographical information systems (GISs) in health informatics research: a review. J Innov Health Inform. 24(2):228–233.

Url-1 İstanbul İl Sağlık Müdürlüğü (t.y.). *Başakşehir Çam ve Sakura Şehir Hastanesi.* https://camsakurasehir.saglik.gov.tr/TR-449990/tarihcemiz.html, date retrieved 20.02.2025.

Url-2 Namal, F.A. (2012). *İstanbul Tıp Fakültesi kısa tarihçesi*. https://istanbultip.istanbul.edu.tr /tr/content/tarihce/istanbul-tip-fakultesi-kisa-tarihcesi%E2%80%8B, date retrieved 20.02.2025

Url-3 Vehbi Koç Vakfı Anslikopedisi (t.y.). *Koç Üniversitesi Sağlık Bilimleri Kampüsü,* https://ansiklopedi.vkv.org.tr/Kategoriler/Mekanlar/Saglik/Koc-Universitesi-Saglik-Bilimleri-Kampusu, date retrieved 23.02.2025

Social Vulnerability Analysis of the Cities Affected by the February 6 Turkey Earthquake

Hilal Akın[a], Himmet Karaman[a]

[a] Istanbul Technical University, Graduate Institute, Geomatics Engineering Program, Türkiye
[a] Istanbul Technical University, Faculty of Civil Engineering, Department of Geomatics Engineering, Türkiye
akinh22@itu.edu.tr

Keywords : Social Vulnerability, February 6 Earthquake, Spatial Statistic.

Aim

Since the first years of human existence on earth, earthquakes have been one of the most destructive disasters causing irreversible material and moral damages. Located on the Alpine- Himalayan tectonic belt and under the influence of active tectonic movements, Türkiye has faced many devastating earthquakes throughout its history. The second largest earthquake that happened in Turkey in the last 100 years was the 7.7 and 7.5 magnitude earthquake that occurred in Pazarcık district of Kahramanmaraş province on February 6, 2023. The aim of this study is to determine the level of vulnerability of local governments and the public to disasters through data such as demographic, socio-economic, cultural, and humanitarian attitudes, to conduct disaster preparedness studies with the analysis of the results obtained, and to conduct social vulnerability analysis, which is used to create more resilient societies to disasters, in 11 provinces affected by this earthquake. The study will not only determine the social vulnerability after the earthquake, but will also examine the solution methods applied in the subsequent processes and the material and moral damage repair works.

Material and Method

Through social vulnerability studies using Geographic Information Systems (GIS), a tool of geomatics, social vulnerability can be analysed, mapped and visualized, and different assessment methods can be proposed. In this study, the news prepared and published by Anadolu Agency and Cumhuriyet Newspaper from February 6, 2023, the date of the earthquake, until February 6, 2024, were first collected to obtain raw data, and 3824 news items were analyzed to study the long-term effects of the earthquake. The news content was then categorized into 24 sub-headings to see the socio-economic, demographic and other impacts on society. In the rest of the study, numerical data will be obtained using the Statistical Package for the Social Sciences (SPSS) program, which is used in many fields from health to engineering for analysis, visualization and evaluation. The extrapolation method, which allows comments and predictions to be made about the future using existing data, examines factors such as migration and urbanisation, housing and infrastructure, social support programmes, the impact of education and employment policies. However, it should be borne in mind that there may be calculation errors due to the uncertainty factor and insufficient data. In order to visualize the data, the data shared by the state was transferred to the ArcGIS program via Excel files. Then, the migration data was integrated by coordinating them onto the provincial administration border data shared by the General Directorate of Mapping of Türkiye. The map was colored according to the number of migrants and figure 2 was created.

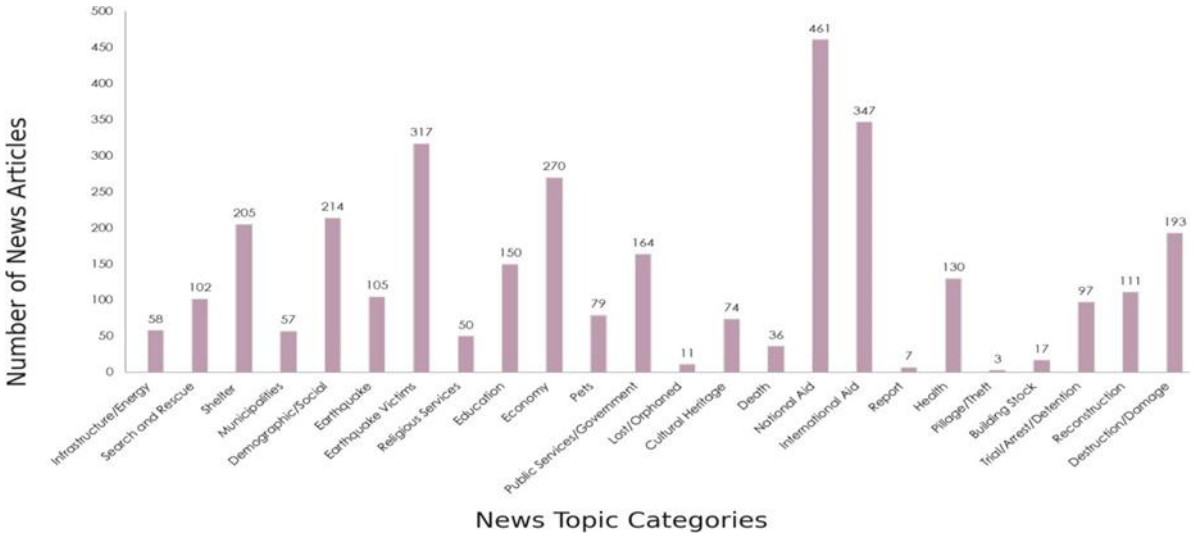

Figure 1. Distribution graph of earthquake-related news into 24 subcategories.

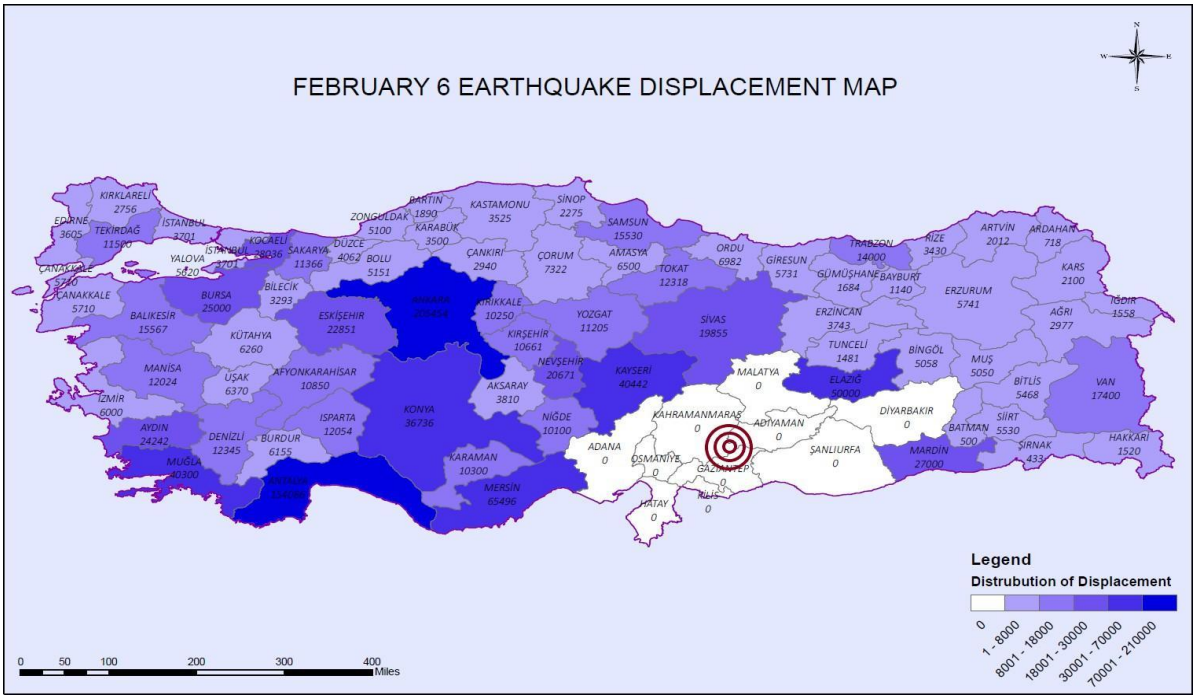

Figure 2. Map showing the migration of people displaced by the earthquake.

Findings

In the literature review, Armaş and Gavriş (2013) conducted a social vulnerability study of Bucharest, Romania, which has the highest earthquake risk in Europe. Factors such as elderly population density, income distribution, housing quality and living conditions were identified for the analysis. SoVI (Social Vulnerability Index) and SEVI (Spatial Multi-Criteria Social Vulnerability Index) were used as multi-criteria measurement methods. The results show that the most vulnerable regions are concentrated in the central and outer areas. As a policy recommendation for local governments, the importance of working on disadvantaged regions is emphasized.

In his study, Fekete (2019) started with a case study of social vulnerability in Germany and reviewed a total of 63 different scientific articles. In his study, he emphasised the importance of using common parameters for more reliable assessments, even if the results of social vulnerability analysis are close to reality and accurate. He concluded that the focus should not be on the results of the analysis, but rather on developing systems for understanding vulnerability analysis by administrations and the public, and for integrating it into everyday life.

On the basis of the information obtained, the study seeks to answer questions such as whether kinship relations have an impact on the spread of evacuations from the earthquake zone to the rest of the cities in the country, which districts are chosen for settlement, what are the reasons for moving, what is the rate of unemployment in the abandoned earthquake cities, whether there is a return, where the aid areas are concentrated, how long it takes for the aid to arrive, how many different institutions and organisations provide aid, and whether the migration areas are also aid areas.

For example after the news was separated according to cities, it was seen that the migration was not only from the earthquake zone to other cities of the country, but also from villages to cities within the city borders, from apartment buildings to state dormitories, among the cities in the earthquake zone for a certain period of time due to the teams and volunteers who came for aid.

Conclusion

Turkey is a country that has a high probability of facing many disasters due to its geological structure and geographical location. Although earthquake safety, precautions, strategic plans and public awareness activities have been accelerated as a result of major earthquakes, the February 6 earthquake with a magnitude of 7.7 and 7.5 centered in the Kahramanmaraş Pazarcık district has shown that the local government and the public still have a long way to go in terms of combating disasters. This study aimed to analyze the regions most affected by the February 6, 2023 earthquake in terms of social, physical, administrative components and economic factors, which are sub-classes of social vulnerability. For instance as a result of the statistical data obtained from the migration numbers, it was observed that there were almost equal numbers of incoming benevolent to those who left the region on the day of the earthquake. The remainder of the study will continue to show such results. The main findings obtained as a result of examining 3824 earthquake news items that constitute the study materials are that the people in the earthquake region are not aware of the extent of the devastating effects of disasters and that individuals in the construction sector have not worked with sufficient seriousness and responsibility and have only developed structures built on concrete and brick.

References

Armaş, I, Gavriş, A. (2013). Social vulnerability assessment using spatial multi-criteria analysis (SEVI model) and the Social Vulnerability Index (SoVI model) – a case study for Bucharest, Romania. Natural Hazards and Earth System Sciences, 1481-1499.

Fekete, A. (2019). Social Vulnerability (Re-)Assessment in Context to Natural Hazards: Review of the Usefulness of the Spatial Indicator Approach and Investigations of Validation Demands. Int.J.Disaster Risk Sciences, 220-232.

International Organization for Migration. (2023). 2023 Earthquakes Displacement Overview - Türkiye. Published 6 Mar 2023.

Sağıroğlu,Z., Ünsal, R., Özenci,F. (2023). Deprem Sonrası Göç ve İnsan Hareketlilikleri Durum Değerlendirme Raporu. AYBÜ-GPM Rapor Serisi-15 (Güncellenmiş 2.Baskı: 15 Nisan 2023). Ankara: Ankara Yıldırım Beyazıt Üniversitesi Göç Politikaları Uygulama ve Araştırma Merkezi (AYBÜ-GPM).

Url-1 https://www.aa.com.tr/tr/6-subat-depremlerinin-birinci-yili, date retrieved: 15.12.2024

Spatial Analysis and Optimization of E-Commerce Company's Parcel Collection Operations: The Case of Esenyurt, Istanbul

Fatma Reyyan Sarıkaya[a], Adalet Dervişoğlu[b]

[a] Istanbul Technical University, Geomatics Engineering Program, Türkiye

[b] Istanbul Technical University, Civil Engineering Faculty, Department of Geomatics Engineering, Türkiye

sarikaya22@itu.edu.tr

Keywords : Spatial Analysis, E-Commerce Logistics, Geographic Information Systems (GIS), Network Analysis, Multi-Criteria Decision Making (MCDM).

Aim

The rapid and continuous expansion of the e-commerce sector has significantly increased the complexity and sophistication of logistics operations. Thus, it is necessary to develop highly adaptable management strategies to meet both efficiency and changing consumer expectations.The e-commerce supply chain consists of several stages, including order processing, parcel collection, sorting at branch offices, and last-mile delivery (Figure 1). Among these, both parcel collection and last-mile delivery are critical processes that directly influence customer satisfaction and overall operational performance. While last-mile delivery has received considerable attention in academic and industry research, parcel collection — the first operational phase in the logistics chain — remains relatively underexplored despite its foundational importance.

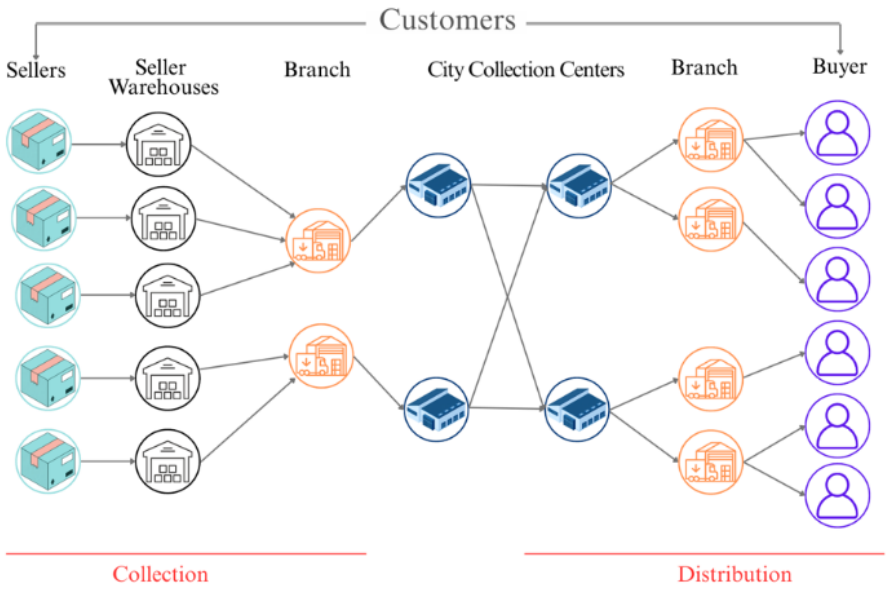

Figure 1. E-Commerce Logistics

Parcel collection operations in rapidly growing and densely populated metropolitan areas, such as Istanbul, face a range of challenges. These include heavy traffic congestion, limited road accessibility, growing shipment volumes, and restrictions on vehicle capacity and fleet availability. Logistics companies must transport parcels efficiently from a wide range of geographically dispersed collection points to their associated branch offices. This task becomes even more complex when companies aim to optimize route planning, manage fleet operations, and meet strict time constraints simultaneously.

This study specifically focuses on the spatial analysis of parcel collection operations in Esenyurt, a high-density urban district on the European side of Istanbul. Esenyurt is known for its significant residential population and fast-growing e-commerce activity, making it a critical area for urban logistics research. This research aims to assess the spatial distribution of collection points, evaluate the capacity and configuration of vehicle fleets, and examine the efficiency of parcel transportation from the field to branch-level facilities. By identifying both spatial and operational inefficiencies, the study intends to offer data-driven recommendations for improving logistics strategies in complex urban environments.

Material and Method

This study was based on logistics data from the day with the highest shipment volume to comprehensively evaluate the parcel collection system. The study area is Esenyurt, one of the most densely populated and logistically active districts on the European side of Istanbul. The analysis focuses on the peak period in November, specifically on 29 November 2024, which was identified as the busiest day in terms of shipment volume, with a total of 104,508 parcels processed. Figure 2 illustrates all parcel collection points along with the locations of the two branch offices.

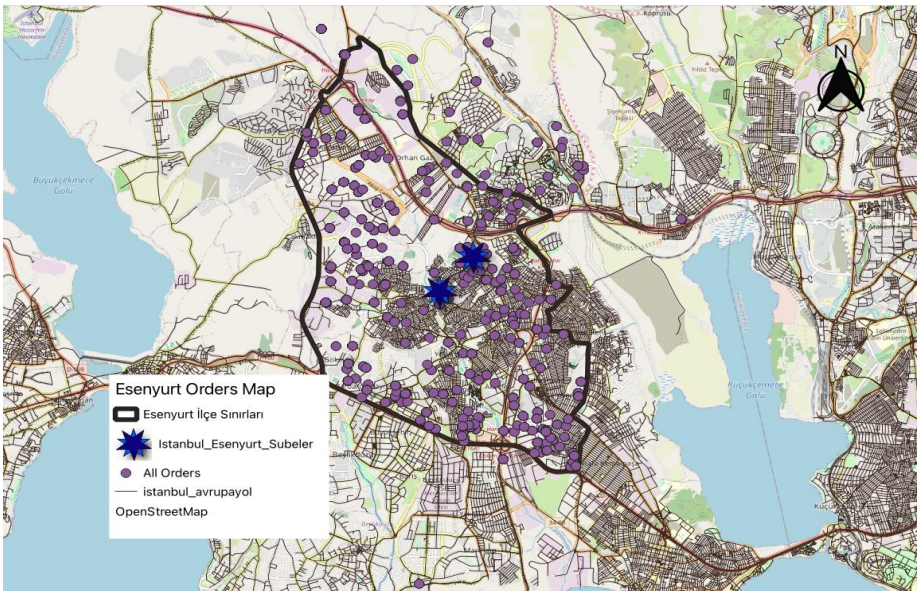

Figure 2. Esenyurt Orders Map.

This high volume was distributed between two main branches operating in the district: Esenyurt and Haramidere. The Esenyurt branch was allocated 9 vehicles, while the Haramidere branch was assigned 8 vehicles. Each vehicle had a capacity of 15,000 desi, defining a significant operational framework for daily parcel collection. As a result of field operations, 65,993 orders were successfully collected, whereas 38,515 orders remained uncollected, indicating that the system's available resources were insufficient to meet the full demand and that operational capacity limits were exceeded.

Analyzing operations on this peak day provided important insights into systemic bottlenecks, network capacity, and operational stress points within the existing infrastructure. The dataset includes detailed information such as the geographic coordinates of collection points, parcel dimensional weights (in desi), daily shipment volumes handled by each branch, and the time-dependent flow of orders throughout the day. All routing and accessibility analyses were conducted using road network data specific to the European side of Istanbul. Considering traffic density and spatial distribution is essential when evaluating operational data in large cities (Allen, Piecyk, & Piotrowska, 2018).

The methodological framework of the study is grounded in Geographic Information Systems (GIS) and network-based analysis techniques. GIS is a powerful tool for modeling, analyzing, and planning spatial relationships in urban logistics systems. In urban freight research, the use of such spatial tools is considered essential for addressing issues related to access

and infrastructure constraints (Dablanc, 2007). Accordingly, ArcGIS-based analyses were used to assess connectivity between collection points and branch facilities, travel times, and general accessibility.

To analyze the spatial distribution of parcel clusters, Kernel Density Estimation (KDE) was applied based on the desi values of parcels. This technique is commonly used to visualize shipment concentration patterns and understand delivery challenges within high-density areas (Lin, Chen, & Kawamura, 2016).

For route optimization, the Vehicle Routing Problem (VRP) was implemented, incorporating realistic constraints such as traffic intensity, vehicle capacity, service time per order, and driver break schedules. In the context of city logistics modeling, such optimization frameworks are key to improving route planning and resource efficiency (Anand, van Duin, Quak, & Tavasszy, 2015).

In addition, Multi-Criteria Decision-Making (MCDM) techniques were applied to evaluate various performance criteria simultaneously. These included vehicle load balance, route length, parcel volume, and time windows. MCDM provides a structured and comprehensive evaluation framework, particularly useful in transport planning where multiple objectives must be reconciled (Macharis & Bernardini, 2015).

In summary, the study integrates GIS, KDE, VRP, and MCDM approaches to build a multi-layered analytical framework. This enables the development of more efficient, flexible, and sustainable parcel collection strategies tailored to dense and complex urban settings like Esenyurt.

Findings

This study analyzed parcel collection processes in Esenyurt from both operational and spatial perspectives, revealing key issues affecting overall efficiency. One of the most prominent problems identified is the imbalance in vehicle capacity utilization. While some vehicles operate at full capacity during peak hours, others run with low occupancy rates, leading to route delays and increased fuel consumption. As illustrated in Figure 3, the desi-based kernel density heatmap visualizes the spatial distribution of parcel clusters and highlights the geographical factors contributing to this imbalance.

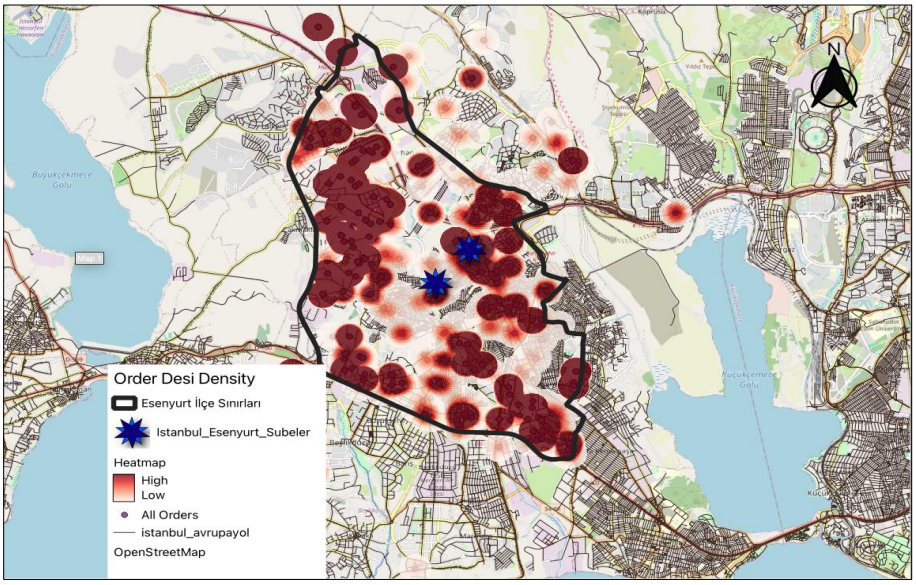

Figure 3. Kernel Density Heatmap Based on Parcel Volume (Desi).

A GIS-based Vehicle Routing Problem (VRP) analysis was conducted in the study, incorporating constraints such as average traffic intensity, vehicle capacity, and service duration. While the traditional method required 17 vehicles to complete daily collection operations, the optimized VRP solution successfully fulfilled the same task using only 7 vehicles. This corresponds to approximately a 59% reduction in vehicle usage, indicating that the system had been operating with significant excess capacity. However, it is important to note that this result is based on average traffic conditions during working hours, and actual performance may vary under real-world circumstances. The optimized routes for successfully collected orders are shown in Figure 4, and a summary of related statistics is presented in Table 1.

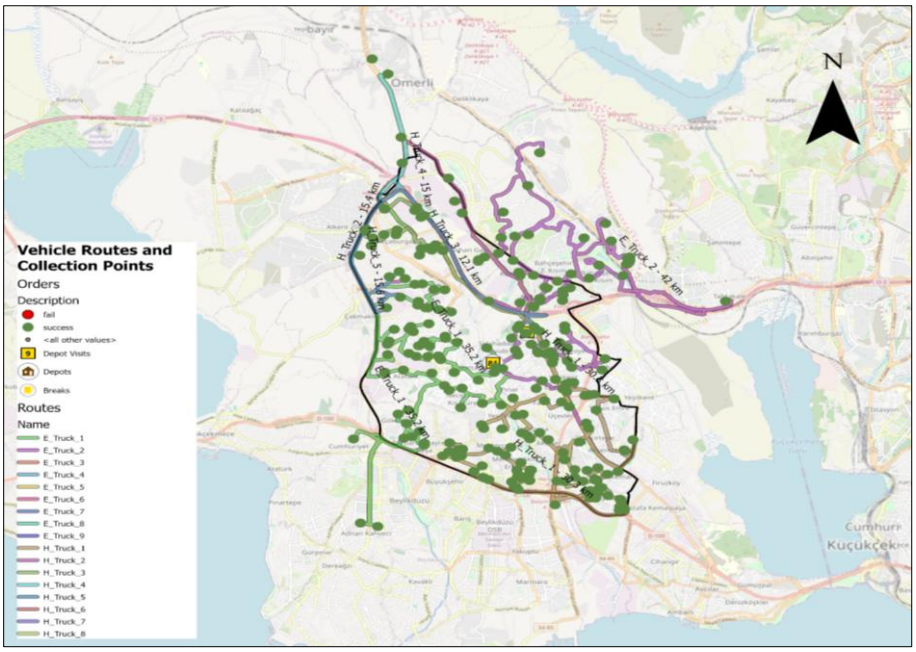

Figure 4. VRP Optimization Based on Successfully Collected Orders.

Table 1. Summary of Successfully Collected Orders.

Truck Name	Start Depot Name	End Depot Name	Capacity (desi)	Max Total Time (min)	Order Count	Total Time (min)	Travel Time (min)	Distance(km)
E_Truck_1	Esenyurt	Esenyurt	15000	600	70	144,1	251,2	35,18
E_Truck_2	Esenyurt	Esenyurt	15000	600	79	458,9	335,1	41,98
H_Truck_1	Haramidere	Haramidere	15000	600	96	194,8	171,1	30,32
H_Truck_2	Haramidere	Haramidere	15000	600	7	63,5	44,6	15,43
H_Truck_3	Haramidere	Haramidere	15000	600	23	93,7	79,8	12,08
H_Truck_4	Haramidere	Haramidere	15000	600	2	36,4	29,9	14,99
H_Truck_5	Haramidere	Haramidere	15000	600	4	68,1	52,2	15,64

Additionally, a full-demand scenario, which included all planned orders, was analyzed. The optimized routes for this scenario are presented in Figure 5, while route-based performance metrics are detailed in Table 2. This full-demand scenario offers critical insights into how the system would perform under maximum load conditions and emphasizes the need for additional resources during peak periods.

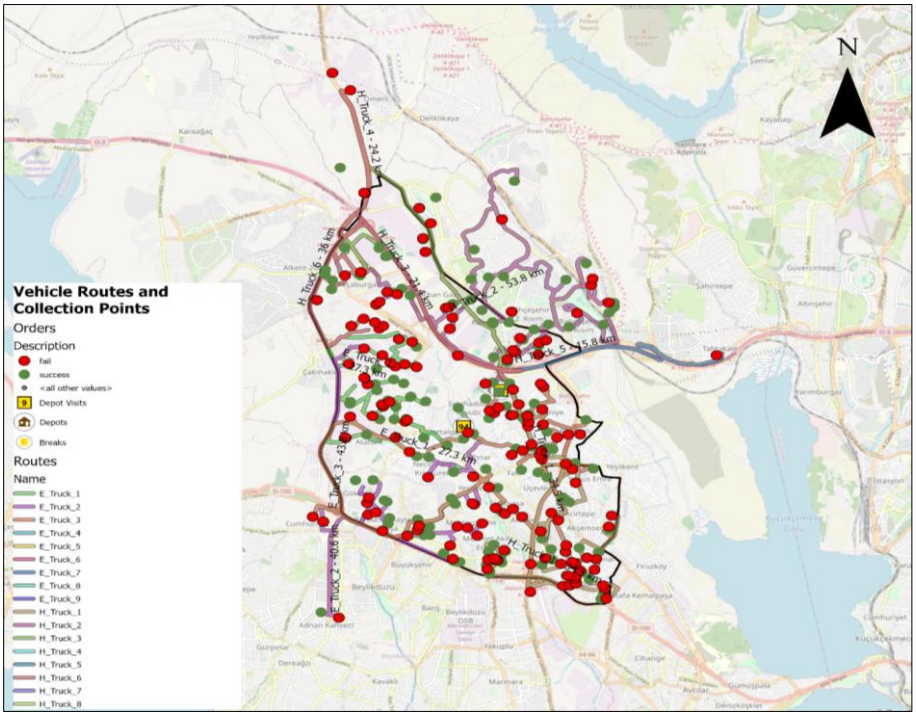

Figure 5. VRP Optimization Based on All Planned Orders.

Table 2. Summary of Routes from Full Demand VRP Scenario.

Truck Name	Start Depot Name	End Depot Name	Capacity (desi)	Max Total Time (min)	Order Count	Total Time (min)	Travel Time (min)	Distance (km)
E_Truck_1	Esenyurt	Esenyurt	15000	600	74	150,3	141,8	27,3
E_Truck_2	Esenyurt	Esenyurt	15000	600	57	116,3	138,6	40,5
E_Truck_3	Esenyurt	Esenyurt	15000	600	92	186,5	151,1	43,8
H_Truck_1	Haramidere	Haramidere	15000	600	99	199,9	119,2	34,4
H_Truck_2	Haramidere	Haramidere	15000	600	75	155,1	304,4	53,7
H_Truck_3	Haramidere	Haramidere	15000	600	18	96,9	56,3	21,3
H_Truck_4	Haramidere	Haramidere	15000	600	5	52,3	29,9	24,1
H_Truck_5	Haramidere	Haramidere	15000	600	2	56,4	28,1	15,8
H_Truck_6	Haramidere	Haramidere	15000	600	15	94,3	76,28	36,0

Seasonal fluctuations also impose considerable pressure on the collection system. Parcel volumes rise significantly during promotional campaigns or holiday seasons, causing already strained systems to become increasingly inefficient. Without a flexible and scalable strategy, delays, missed pickups, and customer dissatisfaction become inevitable in such periods.

All these findings clearly demonstrate the potential of GIS-based analysis and optimization techniques to enhance the efficiency of urban parcel collection processes while minimizing resource use.

Conclusion

This study presents a comprehensive spatial and operational analysis of parcel collection logistics in Esenyurt, Istanbul. Through the integration of GIS mapping, Multi-Criteria Decision-Making (MCDM) techniques, and Vehicle Routing Problem (VRP) solutions, the research identifies inefficiencies, constraints, and potential improvements within the urban logistics system. While traditional operational methods often result in inefficiencies due to high vehicle requirements and fragmented routing strategies, the optimization results obtained in this study represent a significant improvement.

By adopting a holistic approach to routing, the number of vehicles needed for daily operations was significantly reduced, leading to decreased field workload and lower logistical costs. Incorporating operational parameters—such as service time per order and scheduled driver breaks—ensured that the models remained grounded in real-world conditions. This not only

enhanced spatial efficiency but also supported more sustainable practices in terms of time management and workforce planning.

However, GIS-based VRP solutions (e.g., ArcGIS Network Analyst) can be time-consuming, particularly when working with large datasets. Therefore, in the later stages of the study, alternative optimization tools such as Google OR-Tools were employed. These tools offered improved computational speed, greater flexibility in scenario testing, and better scalability in solution generation.

Although this study's findings are specific to Esenyurt, the methodology provides a robust framework for optimizing logistics in other high-density urban areas. As e-commerce continues to expand globally, urban centers will face increasing pressure to streamline logistics while maintaining service quality. Future research could explore the integration of AI-powered demand forecasting, autonomous delivery systems, and IoT-enabled fleet monitoring to enhance urban logistics performance further.

In conclusion, spatial analysis and data-driven optimization techniques are powerful tools for modern urban logistics. This study demonstrates how geospatial data and multi-criteria evaluation can reveal hidden inefficiencies and guide smarter, more strategic decision-making in e-commerce parcel collection operations.

References

Allen, J., Piecyk, M., & Piotrowska, M. (2018). An analysis of the parcels market and parcel carriers' operations in the UK. University of Westminster. https://westminsterresearch.westminster.ac.uk/

Anand, N., van Duin, J. H. R., Quak, H., & Tavasszy, L. (2015). Relevance of city logistics modelling efforts: A review. European Transport/Trasporti Europei, 54(Paper No. 5), 1–16.

Dablanc, L. (2007). Goods transport in large European cities: Difficult to organize, difficult to modernize. Transportation Research Part A: Policy and Practice, 41(3), 280–285. https://doi.org/10.1016/j.tra.2006.05.005

Lin, J., Chen, Q., & Kawamura, K. (2016). Sustainability analysis of parcel delivery strategies: Courier dispatching and locker boxes. Transportation Research Part D: Transport and Environment, 47, 84–103. https://doi.org/10.1016/j.trd.2016.05.009

Macharis, C., & Bernardini, A. (2015). Reviewing the use of multi-criteria decision analysis for the evaluation of transport projects: Time for a multi-actor approach. Transport Policy, 37, 177–186. https://doi.org/10.1016/j.tranpol.2014.11.002

Transformation of Solid Waste Management in Baku: A GIS-Based MCDM Approach to Landfill Site Selection Beyond Balakhani

Kanan Alakbarlı[a], Dursun Zafer Seker[b]

[a] Istanbul Technical University, Graduate School, Geomatics Engineering Program, Türkiye
[b] Istanbul Technical University, Department of Geomatics Engineering, Türkiye
alakbarli17@itu.edu.tr

Keywords : Solid Waste Management, GIS, MCDM, AHP, Landfill Site Selection.

Aim

Baku, Azerbaijan's rapidly growing capital, faces mounting pressure on its solid-waste infrastructure. With a current population of 2.3 million—projected to nearly double in the metropolitan area—the city generates roughly 1.8 million tons of waste yearly (World Bank, 2018). Historically, inefficient waste disposal practices, exemplified by the pre-rehabilitation Balakhani landfill, have led to significant environmental degradation, including groundwater contamination and air pollution. Supported by international initiatives, such as the World Bank's Integrated Solid Waste Management Project, completed in 2016 and managed by Tamiz Shahar, Azerbaijan's waste authority, Balakhani was transformed into a sanitary landfill and industrial park, processing over 500,000 tons of waste annually through waste-to-energy incineration, recycling, and landfill gas capture (World Bank, 2021). Despite these advancements, urban sprawl has reduced the buffer zone between Balakhani and residential areas to less than 2 kilometers, raising concerns about odor, health risks, and capacity limits, projected to be exhausted within a decade given a 3% annual waste growth rate (Huseynova, 2023). This situation underscores the urgent need to identify alternative sanitary landfill sites to sustain and build upon SWM progress in the city.

This study aimed to evaluate the transformation of solid waste management in Baku, specifically focusing on the Balakhani case, and to develop a spatially optimized framework for selecting alternative landfill sites using Geographic Information Systems (GIS) and multi-criteria decision-making (MCDM) techniques. The primary objective is to propose viable landfill locations beyond Balakhani that minimize the environmental impact, ensure social acceptability, and maintain economic feasibility, thereby supporting Baku's long-term waste management strategy. Landfill site selection is a complex decision-making process that requires the integration of environmental, social, and economic factors. Traditional methods often lack spatial precision and stakeholder consensus, necessitating advanced tools such as Geographic Information Systems (GIS) combined with Multi-Criteria Decision-Making (MCDM) techniques such as the Analytic Hierarchy Process (AHP). This study aims to develop an optimized landfill site selection framework for Baku by leveraging GIS-MCDM and AHP to identify sustainable locations that minimize environmental impact and address urban growth pressures. Drawing on international case studies (Khan & Samadder, 2021; Nas et al., 2010; Younes et al., 2021) and local data (Tamiz Shahar, n.d.), this study evaluates the success and limitations of the Balakhani transformation and proposes a scalable model for Azerbaijan's waste management future. This study also seeks to contribute to the global SWM literature by demonstrating the application of GIS-based MCDM in a rapidly developing urban context.

Material and Method

The methodology integrates GIS technology with the Analytic Hierarchy Process (AHP), a widely used MCDM method, implemented using ArcGIS Pro software to assess potential landfill sites in Baku, which is depicted in Figure 1 step by step. Regarding criteria identification, specific criteria under different categories, such as environmental, social, and economic, were selected based on literature review and local context, considering the availability of the necessary dataset as well: distance from residential areas, proximity to transportation networks (roads), groundwater depth (to avoid contamination), slope, elevation, land use type, surface water proximity, fault line proximity, distance from sensitive areas such as protected areas and airstrips.These align with Azerbaijan's environmental regulations and international standards

(Islamic Development Bank, 2020). Spatial data were sourced from multiple platforms, including the Humanitarian Data Exchange for administrative boundaries, OpenStreetMap for environmental and infrastructure-related geospatial information, and print-based maps published in the atlas that were digitized afterward in a GIS environment. Waste statistics were derived from the World Bank (2021) and Tamiz Shahar (n.d.) and supplemented by field observations near Balakhani. Using ArcGIS Pro, the dataset was processed, and spatial layers were created for each criterion. The Boolean overlay excluded unsuitable areas (such as residential zones and water bodies), whereas the weighted overlay analysis ranked suitable sites. Based on the threshold values, the raster maps were reclassified on a 1-5 suitability scale (1 = least suitable, 5 = most suitable). AHP Implementation: AHP assigned weights to criteria, reflecting their relative importance and considering stakeholder priorities. Pairwise comparison matrices were constructed with input from waste management experts and local authorities, following a 1-9 scale and consistency ratios, ensuring reliability by validating the weighting process. Environmental factors received the highest weight by considering the groundwater depth and topographical factors, reflecting regulatory priorities and Balakhani's lessons on groundwater protection, followed by combined technical and socioeconomic factors. Weighted scores were integrated into GIS to produce a final suitability map using ArcGIS Pro's Weighted Overlay tool, combining the thematic layers into a final suitability map, validated against Balakhani's current location and projected waste volumes (1.8 million tons/year growing at 3%). The map classified the study area into five suitability zones: highly suitable, suitable, moderately suitable, less suitable, and unsuitable. This hybrid approach mirrors successful applications in diverse contexts, such as Konya, Turkey (Nas et al., 2010) and Srinagar, India (Khan & Samadder, 2021), adapted to Baku's unique urban and environmental profile. Considering the availability of data used for map generation regarding site selection analysis presented on the Table 1, limitations generally cover the lack of open-source data regarding the geological structure of country and complexity regarding for finding digitally available groundwater data. To overcome these difficulties, hard-copy or paper-based sources like atlas depicting the ecological situation of Azerbaijan, including groundwater depth was used. For this purpose, the digitization was applied by transforming the paper-based atlas to digital form in corresponding coordinate system via GIS tools for using groundwater factor in the analysis.

a

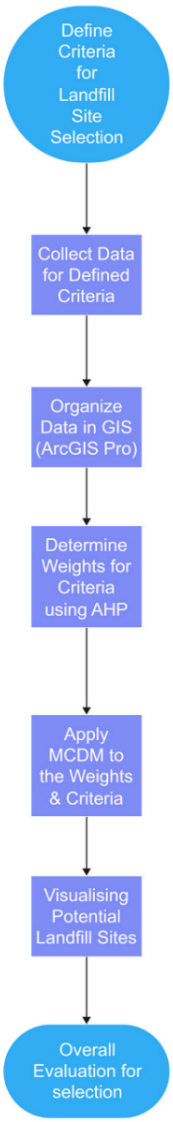

Figure 1. Overall Flowchart of Suitability Analysis.

Table 1. Factors and their relevant dataset sources.

Factors	Used Dataset
Elevation	USGS SRTM DEM 30m
Slope	USGS SRTM DEM 30m
Groundwater	Ecological Atlas of Azerbaijan (hard-copy)
Waterbodies	OpenStreetMap Geofabrik Service
Settlements	OpenStreetMap Geofabrik Service
Roads	OpenStreetMap Geofabrik Service
Protected areas	The World Database on Protected Areas (WDPA-UN)
LULC	Sentinel-2 10m
Faults (Seismic)	Global Earthquake Model Active Faults Database

Findings

As a result of the GIS-MCDM analysis, the suitability map depicted on the Figure 2 identified high-potential zones, with the most promising locations with the green color in peri-urban areas in the east and southwest of Baku, each exceeding 20 ha and meeting key criteria. These sites scored highly because of their distance from water bodies, flat terrain, and access to major roads, which reduced transportation costs. While the current sanitary landfill site,Balakhani, still locates on the suitable area according to generated suitability map, the other most suitable areas for new landfill sites offer greater isolation from populated areas and capacity for at least 25 years of waste disposal based on projected volumes. Balakhani's transformation reduced groundwater contamination risks by 60% post-2016 through liner systems and leachate management (World Bank, 2021); however, its proximity to urban expansion—now within 1.8 km of new housing—compromises long-term viability. With a capacity of 7 million cubic meters, it processes 500,000 tons annually but faces exhaustion by 2035 at current growth rates (Tamiz Shahar, n.d.). The proposed sites, with capacities exceeding 10 million cubic meters, could extend operational lifespans by 15-20 years by incorporating technologies such as landfill gas-to-energy, which currently recovers 10 MW at Balakhani (Islamic Development Bank, 2020). The framework's strengths lie in its spatial precision and adaptability, contrasting with Balakhani's ad-hoc siting in the 1980s. Limitations include data resolution specifically regarding the geological structure and lack of digitally available information about the location of groundwater throughout the country and exclusion of climate change impacts, such as rising precipitation affecting leachate volumes, warranting future research. Considering the CR (Consistency Ratio) value of applied AHP method in this study compared to the existing literature, the calculated value of 0.14 slightly exceeds generally accepted threshold value of 0.1, while value till to 0.15 is still considered as acceptable.

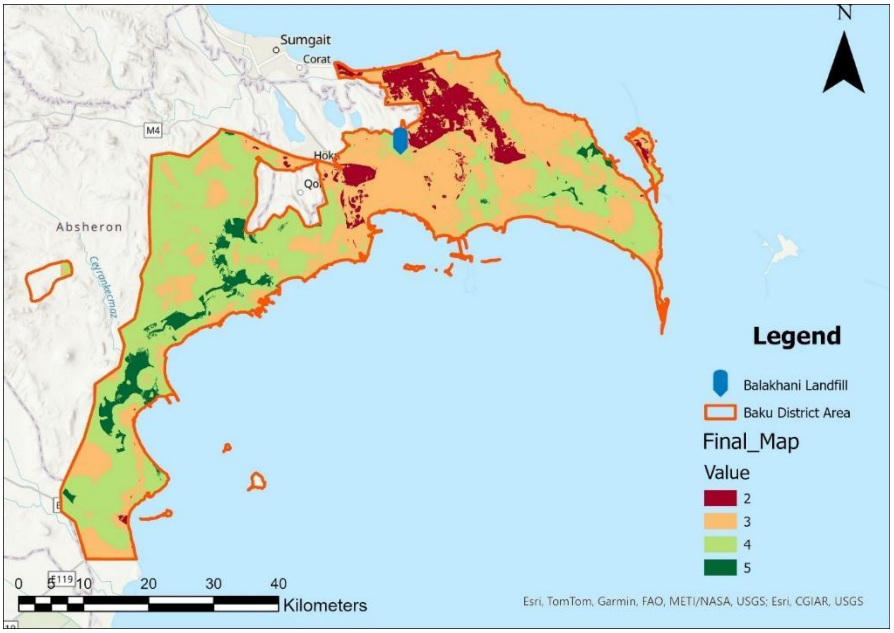

Figure 2. Generated Suitability Map for Landfill Site Selection in Baku.

Conclusion

While Balakhani's rehabilitation marks progress in Baku's waste management, the city must urgently identify new landfill sites to accommodate future waste volumes and prevent renewed environmental risks by integrating GIS with AHP while supporting Azerbaijan's sustainable waste management goals. The identified sites enhance environmental protection and operational efficiency, critical as Baku's waste generation nears 2 million tons annually. Limitations include potential data gaps (e.g., incomplete geological surveys) and the need for field validation, which could refine the suitability scores. Recommendations include conducting detailed environmental impact assessments (EIAs) for top-ranked sites, engaging local communities to ensure social acceptance, and exploring waste-to-energy integration to enhance sustainability. Future research could extend this methodology to other Azerbaijani cities or incorporate real-time waste-generation data for dynamic planning.

References

Huseynova, R. (2023). Policy brief: Solid waste management in Azerbaijan – Challenges and opportunities. Institute of Development and Diplomacy.

Khan, D., & Samadder, S. R. (2021). Landfill site selection using GIS based multi criteria evaluation technique: A case study of Srinagar city, India. Journal of Environmental Science and Engineering, 63(1), 12-25.

Nas, B., Cay, T., Iscan, F., & Berktay, A. (2010). Selection of MSW landfill sites for Konya, Turkey using GIS and multi-criteria evaluation. Environmental Monitoring and Assessment, 160(1-4), 491-500.

World Bank. (2018). What a waste 2.0: A global snapshot of solid waste management to 2050. World Bank Publications.

Younes, M. K., Baraoui, M., Al-Maghrabi, M. N., & Naja, K. (2021). AHP- and GIS-based site selection for a sanitary landfill: Case of Settat Province, Morocco. Waste Management & Research, 39(6), 789-801.

Url-1 https://www.isdb.org/sites/default/files/media/documents/2020-06/Success_Lflt_Azerbaijan_EN.pdf, date retrieved 01.04.2025.

Url-2 https://tamizshahar.az/en/projects/5, date retrieved 18.03.2025.

Url-3 https://ieg.worldbankgroup.org/sites/default/files/Data/reports/ppar_azerbaijanarp2.pdf, date retrieved 05.04.2025.

GEOMATICS ENGINEERING

Geodesy

Geographic Information Systems

Natural Hazards

Photogrammetry

Remote Sensing

Flood Risk Analysis with Geospatial Artificial Intelligence Techniques

Miraç Taha Derman[a], Muhammed Oğuzhan Mete[a]

[a] İstanbul Technical University, Geomatics Engineering Department, Geomatics Engineering Program, Türkiye
derman17@itu.edu.tr

Keywords : Flood, Hazard, Machine learning, Python, Vulnerability.

Aim

In recent years, extreme precipitation events, rapid build-up in urbanization, and irregular land use have significantly increased flood risk. In order to mitigate risks and increase urban resilience, there is a need for the integration of innovative approaches to classical disaster management methods. In this context, Geographic Information Systems (GIS) offer robust spatial analysis workflow and data processing for efficient decision-making capability. In addition, desktop GIS software has some limitations in processing large volumes of datasets. This study uses geospatial artificial intelligence (GeoAI) methods to develop a flood risk analysis model in an open-source Python environment. The proposed methodology is applied in the Marmara Region of Türkiye as a case study highlighting flood risk. The Marmara Region is one of the most critical regions in Türkiye in terms of economic and socio-cultural aspects. The region includes the provinces that connect the European and Asian continents. In addition to its geographical location, the abundance of development and job opportunities in the region has made it the country's most populous area. On the other hand, the Marmara Region is at high risk of disaster due to its climate diversity. Thus, it has become possible to build a high-resolution, automated, and repeatable analysis process with large data sets that were not feasible using traditional methods. In this regard, spatial data processing, modeling and analysis are carried out in an integrated manner through open-source libraries. The vulnerability of the Marmara Region in this context, with its potential to work in harmony with machine learning algorithms, positively affects flood management and offers an innovative perspective. In this context, the flood risk map of the Marmara Region is produced for eleven cities using open-source and governmental data gathered from official institutions to serve as an accessible guide for decision-makers.

This study aims to estimate the flood and inundation risk in the Marmara Region using Python-based multi-criteria analysis methods which is Analytic Hierarchy Process (AHP) and machine learning algorithms. It is aimed to obtain a holistic high-resolution flood and inundation risk map by combining hazard and vulnerability evaluations. While evaluating the criteria affecting flood and inundation in the Marmara Region, Hazard and Vulnerability parameters are taken as references from studies in the literature. With the Python-based methods used, the dependency on GIS tools is reduced and an automatable analysis process is presented.

A comprehensive flood risk estimation was carried out in the Marmara Region by creating maps using a machine learning-based method in the production of flood vulnerability maps and integrating these maps using the Python-based AHP method in the production of flood hazard maps. Hydrological data was integrated with spatial analysis. Historical disaster data and real-time meteorological parameters were associated using artificial intelligence algorithms. This comprehensive approach aims to develop strategies for the early detection of flood events that may occur in the Marmara Region by revealing how both Hazard and Vulnerability elements complement each other.

Material and Method

Within the scope of this study, hazard and vulnerability maps were produced to estimate the risk of flood and inundation disasters. The raw data used in the production of these maps were obtained from open-source and official institutions (Table 1). In this study, the authors' previously published studies (Demir & Keskin, 2022) and (Ghosh et al., 2022) were examined to determine the source data sets of flood and inundation analyses. Building, road, waterways, and water bodies data belonging to the study area were obtained from the Overturemaps web platform, which is an open-source data provider. In addition, Marmara Region study area polygon data was obtained from OpenStreetMap; ESRI open data within the scope

of land use; Digital Elevation Model (DEM) data with 25-meter resolution was obtained from USGS data portal; and population data was obtained from TUIK open-source data portal. The data obtained from official institutions were 40 years of daily precipitation data from the General Directorate of Meteorology (MGM); and flood and inundation inventory data from the General Directorate of State Hydraulic Works (DSİ) in the Marmara Region in the past 50 years. The study of Aydın and Birincioğlu (2022) was taken as a reference while creating the hazard map, especially on narrowing down map creation parameters. In this context, the criteria based on the Analytical Hierarchy Process (AHP) were applied with raster analyses in Python. Slope, aspect, elevation, flow direction, flow accumulation, waterways proximity, waterbodies proximity and precipitation analysis were performed. These data were divided into risk classes in parallel with the study of Aydın and Birincioğlu (2022) by processing the 30-meter resolution raster analyses performed in Python with libraries such as rasterio and geopandas. Each raster data obtained was weighted with AHP and the final hazard map was obtained. In this process, instead of GIS, a completely Python-based analysis process was carried out.

Table 1. Flood risk criteria and data sources.

Data Name	Data Source
Building	Overturemaps
Road	Overturemaps
LULC	ESRI
Work Area Polygon	OSM
Digital Elevation Model (DEM)	USGS
Waterways	Overturemaps
Waterbodies	Overturemaps
Precipitation	MGM
Population	TUIK
Flood Inventory	DSİ

While creating the vulnerability map, XGBoost and Random Forest (RF) models, which are machine learning models, were preferred based on the study of Koyuncu & Ekmekçioğlu (2024). In this context, elevation, aspect, plan curvature, profile curvature, drainage density, distance to drainage network, curve number, precipitation, Topographic Wetness Index (TWI), Topographic Roughness Index (TRI), Stream Power Index (SPI), population and land use classification analyses were performed using open-source Python libraries. Flood inventory data were processed and used with these analyses. Training and test data sets with 13 parameters and the flood inventory of the past 50 years; a raster stack was created in the data pre-processing steps. According to the obtained test set results, flooded and non-flooded regions were obtained on a point basis (with coordinates) as 1 and 0, respectively, due to the binary classification logic. Then, the flood susceptibility map was produced based on the Marmara Region borders by interpolating the 1 and 0 points with the Kriging method, which is one of the widely used methods in the literature (Koyuncu & Ekmekcioğlu, 2024). Class imbalance was eliminated by Random Under Sampling (RUS) and RUS was used for feature scaling. Thus, a flood vulnerability map was produced for the Marmara Region. Model performance was evaluated with F1-Score and AUROC metrics. Then, the results of XGBOOST and RandomForest (RF) machine learning models were compared.

Hazard and vulnerability maps were combined with libraries such as rasterio and geopandas used for raster calculation libraries in Python to create the final risk map. While small-scale and province-based studies are widely used for flood risk, this study used large-scale data to study the Marmara Region in a comprehensive manner. The big data was processed using open source python and machine learning algorithms.

Findings

It is not newly discovered that floods and inundations are one of the major natural disasters that frequently occur in nature and cause loss of life and property. Nevertheless, there are parameters that increase the risk of this disaster. Many factors, especially rainfall regime, river density and distance to these waterways, population density in the region, topographic structure of the land, water flow direction and accumulation affect the risk of floods and inundations. In this multi-parameter compound, determining flood and inundation risks in the region is essential for effective disaster management.

As a result of the analyses carried out in the Python environment, the areas with high flood risk in the Marmara Region are presented in the integration of the criteria determined for the hazard map. Proximity to waterways, high flow accumulation and precipitation, and low slope criteria stood out as determining factors in the increase in risk. The results obtained showed a risk distribution compatible with the flood inventory (Figure 1).

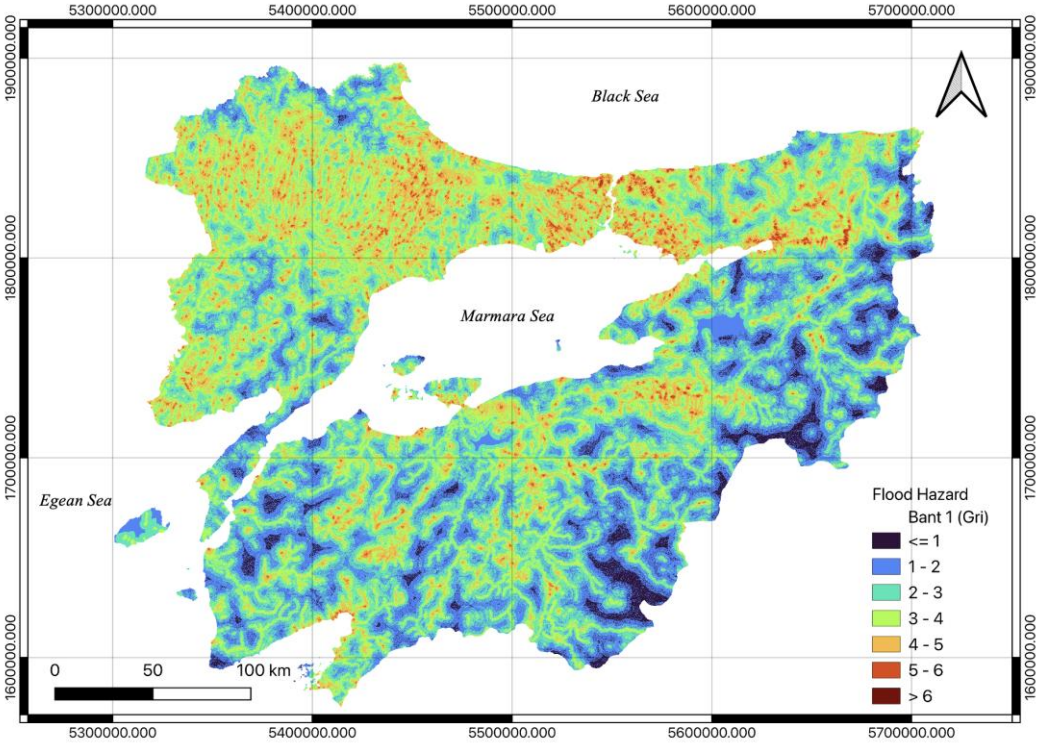

Figure 1. Marmara Region flood hazard map.

In the hazard map, it was observed that the northwestern and northern regions, where the density of rivers is high and the rainfall is high, are exposed to higher flood risk. This risk parameter is limited by the regions with high land slopes. According to the vulnerability results, the precipitation factor was found to be the most important variable in flood vulnerability mapping. This factor was respectively followed by the distance to the drainage network, the curve number and the Topographic Roughness Index (TRI). The results of XGBoost and RF methods were used to obtain the flood vulnerability map of the Marmara Region.

Conclusion

Floods and inundations, which are some of the natural disasters mostly affected by the realities of global warming and climate change happening today, cause many losses of life and property. When the human factor is added to the changing climate and weather conditions, floods are considered as a natural disaster that negatively affects human life. In order to prevent these disasters or reduce their effects, it is necessary to determine the region where the event may occur and to what extent it may be affected. In this study, the flood and inundation risk in the Marmara Region was evaluated through Python-based multi-criteria analysis methods (AHP) and machine learning algorithms. The final output of the study shows that hazard with Python-based analysis methods; vulnerability with machine learning algorithms; and flood risk maps created by the integration of these two maps provide high accuracy and efficiency in determining flood and inundation risks in the Marmara Region. Python-based analyses have offered significant advantages in terms of automating the dynamic process in flood risk assessment, repeatability and obtaining high-performance analysis output. In line with these advantages, a dynamic and continual framework for risk management has been proposed to regional and local governments.

In future studies, it is possible to include more parameters and criteria in model estimates on flood and inundation risk to expand the scope of the studies. Currently, the model and maps produced within the scope of this study provide a basis for being prepared for possible disasters in the future and are offered to be used by official institutions. With the potential regulation of the proposed model and maps, regional and local governments would be able to consider the disaster planning and therefore contribute to the reduction of losses and flood and inundation effects.

References

Aydin, M. C., & Sevgi Birincioğlu, E. (2022). Flood risk analysis using gis-based analytical hierarchy process: a case study of Bitlis Province. *Applied Water Science*, 12(6). https://doi.org/10.1007/s13201-022-01655-x

Demir, V., & Ülke Keskin, A. (2022). Taşkın Tehlike Haritalarının Oluşturulması (Samsun, Mert Irmağı Örneği). *Türkiye Coğrafi Bilgi Sistemleri Dergisi*, 4(1), 47-54. https://doi.org/10.56130/tucbis.1120501

Ghosh, A., Dey, P., & Ghosh, T. (2022). Integration of RS-GIS with Frequency Ratio, Fuzzy Logic, Logistic Regression and Decision Tree Models for Flood Susceptibility Prediction in Lower Gangetic Plain: A Study on Malda District of West Bengal, India. *Journal of the Indian Society of Remote Sensing*, 50(9), 1725–1745. https://doi.org/10.1007/s12524-022-01560-5

Koyuncu, Z., & Ekmekcioğlu, Ö. (2024). İstanbul İçin CBS Tabanlı Makine Öğrenmesi İle Sel Duyarlılık Haritasının Oluşturulması. *Doğal Afetler Ve Çevre Dergisi*, 10(1), 1-15. https://doi.org/10.21324/dacd.1254778

Seismic Hazard Assessment of Kahramanmaraş Region: Analysis of Earthquake Sources and Probabilistic Seismic Risk

Sajjad Alghezi[a], Abdullah Zülfikar[b]

[a] Istanbul Technical University, Graduate School, Geomatics Engineering Program, Türkiye
[b] Istanbul Technical University, Disaster Management Institute, Earthquake Engineering Program, Türkiye
alghezi22@itu.edu.tr

Keywords : Seismic Hazard, East Anatolian Fault Zone, Probabilistic Seismic Risk, Kahramanmaraş.

Aim

This study aims to assess the seismic hazard of the Kahramanmaraş region, located in southeastern Turkey, by applying a probabilistic seismic hazard analysis (PSHA) approach to both pre- and post-earthquake data spanning from 1980 to 2023. The research focuses on identifying and characterizing seismic sources within the region, i.e., the East Anatolian Fault Zone (EAFZ) Main Segment, its splays, and the influence of the Bitlis-Zagros Fold and Thrust Belt. By applying the frequency–magnitude distribution of earthquake ground motions from seismically recorded earthquakes and calculating Gutenberg-Richter parameters (a and b values), the study estimates exceedance probabilities for various magnitudes of earthquakes and calculates corresponding recurrence periods. The results provide critical data to quantify seismic hazard and support data to guide seismic design requirements, risk reduction, and urban resilience planning in one of Turkey's most seismically active regions.

Material and Method

This part accounts for the method used to evaluate the seismic hazard and risk in Kahramanmaraş. The study sought to evaluate earthquake data collected before and after the destructive February 6, 2023, earthquakes, including a magnitude Mw7.7 earthquake in Pazarcık and an aftershock Mw7.6 earthquake in Ekinozu as illustrated in the preliminary report by Garini and Gazetas (2023), the earthquakes spread through over 500 km of fault segments. The approach involves seismic source characterization, Gutenberg-Richter law-based frequency-magnitude distribution, and seismic risk estimation through probabilistic seismic hazard analysis (PSHA). Recent regional applications of probabilistic seismic hazard analysis in Turkey, such as those integrated into catastrophe modeling platforms (Akkar et al, 2022), have further demonstrated the critical role of PSHA in informing risk-based design and reinsurance frameworks.

The study area spans latitudes 36°00'N to 38°00'N and longitudes 35°00'E to 39°00'E (Figure 1). The study area encompasses the Kahramanmaraş region and its surroundings, located at the intersection of the Anatolian, Arabian, and African tectonic plates, a simplified tectonic map illustrating the fault systems is presented in Figure 2. The region is seismically active and primarily influenced by the East Anatolian Fault Zone (EAFZ), which accommodates the westward escape of the Anatolian Plate. Three key seismic source zones have been identified:

- Source Zone 1 – EAFZ Main Segment: A major left-lateral strike-slip fault that has generated multiple large earthquakes, including the Mw 7.7 event on 6 February 2023.
- Source Zone 2 – EAFZ Splays: Secondary fault branches off the main EAFZ, contributing to the distributed seismicity in the region.
- Source Zone 3 – Bitlis-Zagros Influence: A compressional regime linked to the Bitlis-Zagros Suture Zone, contributing thrust-related seismic activity.

Figure 1. Black box show the study area.

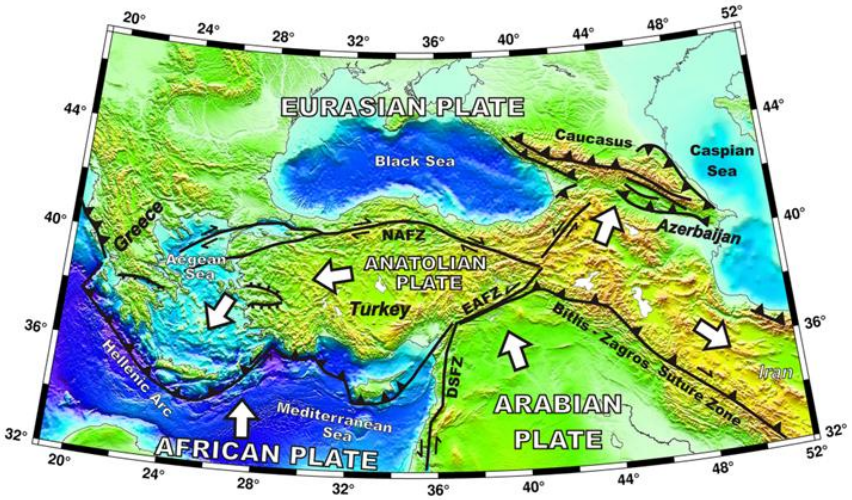

Figure 2. Simplified tectonic map of Turkey and its surroundings (Tan, O.2021).

Earthquake data were sourced from the Disaster and Emergency Management Presidency (AFAD) of Turkey. The dataset comprises: Pre-event period: January 1980 – 5 February 2023 and Post-event period: 6 February 2023 – December 2023. The dataset includes both earthquake event parameters (epicenter coordinates, magnitude, and depth) and associated ground motion recordings (Peak Ground Acceleration – PGA, and hypocentral distance). The total dataset consists of Pre-earthquake: 32 events, 1198 recordings and Post-earthquake: 44 events, 4034 recordings. This comprehensive dataset allowed us to analyze seismicity patterns both before and after the major 2023 earthquakes, figure 3 (Magnitude vs. Distance) showing data distribution.

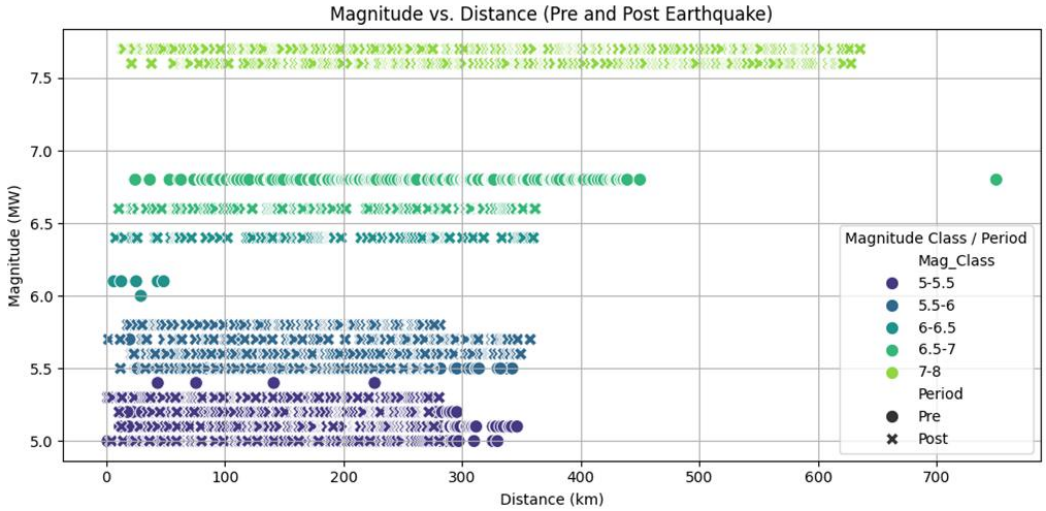

Figure 3. Magnitudes vs. Distance.

The frequency of earthquake events was computed in 0.5 magnitude unit bins ranging from Mw 5.0 to Mw 8.0. The cumulative frequency was also calculated to assess the recurrence characteristics. This distribution is summarized in Table 1.

Table 1. Magnitudes and cumulative frequency values at 0.5 unit intervals.

Magnitude	Frequency (N)	Cumulative Frequency (Ni)
5.0 - 5.4	51	72
5.5 - 5.9	14	21
6.0 - 6.4	3	7
6.5 - 6.9	2	4
7.0 - 7.4	0	2
7.5 - 8.0	2	2

The magnitude–frequency distribution was modeled using the Gutenberg–Richter law (Gutenberg & Richter, 1954).

$$\log 10N(M) = a - b\,M \qquad \textbf{(Equation1)}$$

where:

- $N(M)$: Cumulative number of earthquakes with magnitude M or greater,
- a: Measure of seismicity level in the region,
- b: Slope of the frequency-magnitude curve, indicative of the relative occurrence rates of small versus large earthquakes.

The least squares method (LSM) was employed to calculate the *a* and *b* values for the study area. This approach ensures robust parameter estimation by minimizing the residuals between observed and predicted values. The b-value was found to be approximately 0.63, suggesting a relatively higher frequency of smaller magnitude earthquakes, consistent with active strike-slip faulting. Figure 4 illustrates the magnitude-frequency relationship derived from the earthquake data.

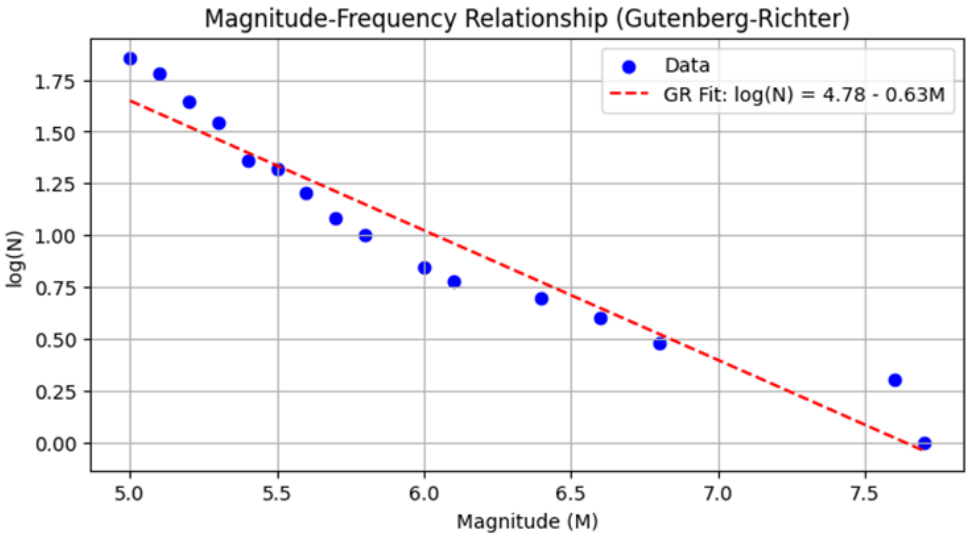

Figure 4. Magnitude-frequency relationship.

Using the combined event data over a 44-year period, the annual rate of occurrence $n(M)$ for earthquakes exceeding magnitude M was computed. The exceedance probability for a time interval T is modeled by the Poisson formulation (Baker, 2013).

$$P(M,T) = 1 - e - n(M) \cdot T \qquad \textbf{(Equation 2)}$$

where:

- $P(M,T)$: Probability of exceeding magnitude M in T years.
- $n(M)$: Annual rate of occurrence of earthquakes with magnitude $\geq M$.
- T: Time interval (years).

Recurrence periods Q (in years) are calculated as:

$$Q = 1 / n(M) \qquad \textbf{(3)}$$

Table 2 summarizes the probabilities of exceeding various magnitudes and their corresponding recurrence periods. Figures 5 and 6 visualize these results, providing insights into the temporal and spatial characteristics of seismic hazard in the region.

Table 2. Probabilities of exceeding magnitudes and recurrence periods over 10–100 year intervals.

M	10	20	30	40	50	60	70	80	90	100	Q(years)
5.00	100%	100%	100%	100%	100%	100%	100%	100%	100%	100%	0.58
5.23	100%	100%	100%	100%	100%	100%	100%	100%	100%	100%	1.26
5.45	99%	100%	100%	100%	100%	100%	100%	100%	100%	100%	2.1
5.68	95%	100%	100%	100%	100%	100%	100%	100%	100%	100%	3.67
5.90	88%	99%	100%	100%	100%	100%	100%	100%	100%	100%	6.29
6.13	74%	95%	100%	100%	100%	100%	100%	100%	100%	100%	8.8
6.35	60%	89%	98%	100%	100%	100%	100%	100%	100%	100%	11
6.58	45%	79%	95%	98%	100%	100%	100%	100%	100%	100%	14.67
6.80	32%	65%	85%	93%	98%	100%	100%	100%	100%	100%	22
7.00	20%	49%	72%	82%	91%	98%	99%	100%	100%	100%	44
7.25	13%	35%	55%	68%	80%	91%	95%	98%	99%	100%	66
7.47	8%	24%	40%	51%	64%	77%	86%	92%	95%	98%	88
7.70	5%	15%	26%	35%	47%	59%	70%	80%	86%	90%	110

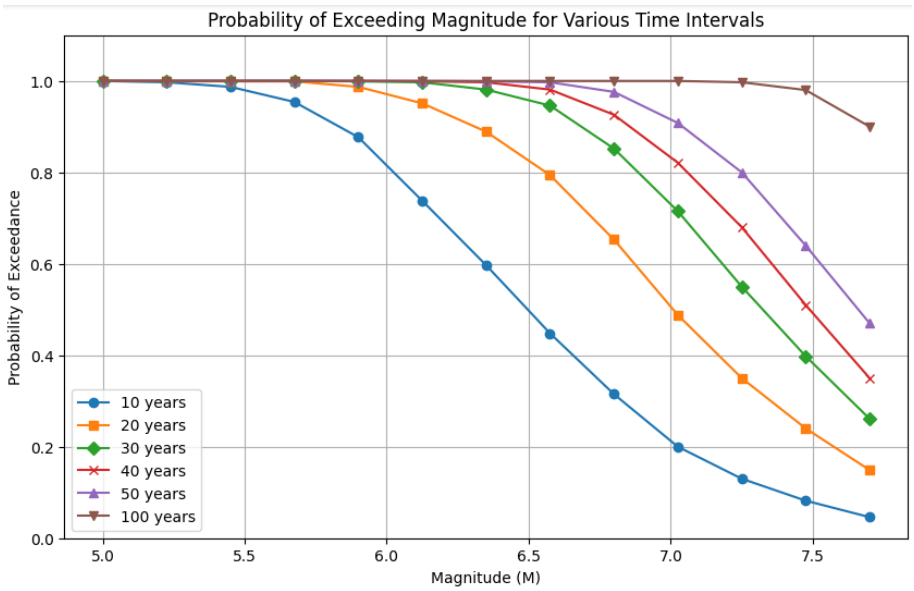

Figure 5. Probabilities of exceeding various magnitudes.

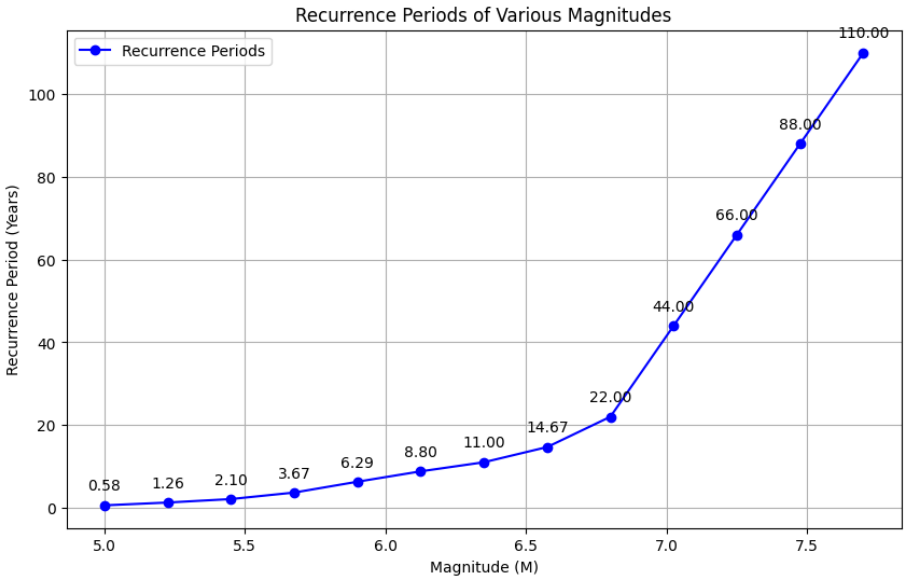

Figure 6. Recurrence periods of various magnitudes.

Findings

The seismic hazard assessment for the Kahramanmaraş region revealed critical insights into the tectonic activity and earthquake recurrence characteristics of this highly active zone. Analysis of the combined dataset from 1980 to 2023, which includes both pre- and post-earthquake data surrounding the Mw 7.7 and Mw 7.6 events of February 6, 2023, demonstrated the region's exposure to frequent moderate earthquakes and occasional large-magnitude events.

The magnitude–frequency distribution, as shown in Table 1, illustrates that the majority of events on record are within the range Mw 5.0–5.9, with significantly fewer events at magnitudes above Mw 6.5. While less common, the potential for damage for the larger events remains high due to the high population density and exposure of infrastructure in the region.

The Gutenberg–Richter relationship, fitted to the cumulative frequency data, yielded an a-value of 4.78 and a b-value of 0.63 (Figure 4). This b-value reflects a moderate slope, indicating a relatively high proportion of smaller to medium earthquakes, consistent with other seismically active strike-slip regions. The frequency–magnitude plot (Figure 4) confirms the reliability of this fit across the studied magnitude range.

The probabilistic risk analysis applied a Poisson model to estimate the probability of exceeding various magnitude thresholds over future time intervals. Results show that for a 100-year period, the probability of experiencing an earthquake of at least Mw 5.0 is effectively 100%, while the probability of a Mw 7.7 event is approximately 90% (Figure 5). The analysis also shows that events with Mw 6.5 have an estimated recurrence period of approximately 14.67 years, while Mw 7.7 earthquakes are expected approximately every 110 years (Figure 6 and Table 2).

These findings highlight a key duality in the seismic hazard profile of the region: frequent low-magnitude events pose persistent risks to non-engineered structures, while infrequent high-magnitude events can produce catastrophic damage across broad areas. In terms of structural safety, this means both frequent service-level ground shaking and rare design-level or collapse-level shaking must be considered in engineering practice. Given that the design life of most buildings is about 50 years, the exceedance probabilities associated with magnitudes above Mw 6.0 suggest a substantial seismic risk over the typical building lifespan.

From a geotechnical perspective, these results support the prioritization of seismic retrofitting in older or vulnerable structures, especially those located near known fault traces or on soft soils. Integration of local ground conditions into future hazard models would further improve accuracy.

Conclusion

This study provides a probabilistic seismic hazard assessment for the Kahramanmaraş region, utilizing earthquake data observed in a 44-year period including the major February 6, 2023, earthquakes. Seismic source zones, including the East Anatolian Fault Zone (main segment and splays) and the Bitlis-Zagros effect, were determined as the regional seismicity's major sources by the analysis.

Magnitude–frequency distribution follows Gutenberg–Richter relation with a b-value of 0.63, indicating moderate seismic regime dominated by small to medium earthquakes. However, probabilistic risk modeling also supports non-negligible probability of large-magnitude events (e.g., $Mw \geq 7.0$) on a 50 to 100-year return period. Notably, recurrence time for a Mw 7.7 event is around 110 years, while events with smaller magnitude like Mw 6.0–6.5 recur with a recurrence time of 10–15 years.

These results emphasize the importance of long-term planning for seismic resilience in the Kahramanmaraş region. Structural design criteria, urban planning initiatives, and emergency response measures must consider both the high frequency of small earthquakes and the low but significant hazard of large earthquakes. Site-specific soil properties, recent ground motion models, and building vulnerability analyses must be considered in future research to increase the validity and applicability of hazard estimates.

References

AFAD (Disaster and Emergency Management Presidency). (n.d.). Earthquake Data Bank. Retrieved from http://www.afad.gov.tr (Date of access: 2023/12/15)

Akkar, S., Kale, Ö., Atici, A., & Ulku, O. (2022). A brief note on the earthquake hazard module of Turk Reinsurance Inc.'s catastrophic event modeling platform for portfolio losses: Comparisons with OpenQuake. *Bulletin of Earthquake Engineering, 20*(11), 5835–5848.

Baker, J. W. (2013). Probabilistic seismic hazard analysis: White paper version 2.0. Stanford University. Retrieved from https://www.stanford.edu (Date of access: 2024/2/13)

Garini, E., & Gazetas, G. (2023). Preliminary report on the M7.8 and M7.5 earthquakes of February 6, 2023 in Turkey–Syria. https://doi.org/10.17605/OSF.IO/V4MSW

Gutenberg, B., & Richter, C. F. (1954). Seismicity of the Earth and Associated Phenomena (2nd ed.). Princeton University Press.

Tan, O. (2021). A homogeneous earthquake catalogue for Turkey. Natural Hazards and Earth System Sciences, 21, 2059–2073. https://doi.org/10.5194/nhess-21-2059-2021

GEOMATICS ENGINEERING

Geodesy

Geographic Information Systems

Natural Hazards

Photogrammetry

Remote Sensing

Generating a High-Definition Map (HD Map) via YOLO (You Only Look Once) Deep Learning-Based Object Detection Model

Yasin Memi[a], Hande Demirel[b]

[a] Istanbul Technical University, Graduate School, Department of Geomatics Engineering, Türkiye
[b] Istanbul Technical University, Faculty of Civil Engineering, Department of Geomatics Engineering, Türkiye
memi16@itu.edu.tr

Keywords : Object Detection; Panoramic Camera; LiDAR; Sensor Fusion.

Aim

Autonomous driving systems, High-Definition Maps and smart tracking technologies require advanced detection methods to increase environmental awareness and maximise object detection accuracy. Traditional object detection methods are usually based on a single sensor, but using only camera or only LIDAR (Laser Imaging Detection and Ranging) has several limitations. For example, cameras may be inadequate in low-light areas such as tunnels and underpasses, while LIDAR sensors cannot provide colour and texture information. This paper proposes a system that improves real-time object detection capability by combining 360° panoramic camera, LIDAR and GPS (Global Positioning System) data. The main objective of the study is to provide the highest detection and identification accuracy, reduce false positives, and determine the positions of objects in three dimensions with high precision with this sensor fusion approach.

Material and Method

The proposed system consists of three main components: 360° panoramic camera with Inertial Measurement Unit (IMU) integration, LIDAR sensor and GPS module. In addition, YOLO (You Only Look Once) deep learning-based object detection model and Python coding language are used. The 360° camera provides a complete view of the surroundings, avoiding blind spots in detection. The IMU used in conjunction with the camera measures the vehicle's rotation, acceleration and speed, enabling more precise image processing. The LIDAR sensor generates a high-precision 3D point cloud of the environment, providing distance and position information of objects. The GPS module is used to integrate the detected objects into the world coordinate system by georeferencing the point cloud created with 360° panoramic camera images and LIDAR sensor.

YOLO (You Only Look Once) deep learning-based object detection model performs real-time object detection by processing panoramic images. The YOLO model has high processing speed and accuracy with its single-pass detection architecture. OpenCV, PyTorch and NumPy libraries are used in the system developed using Python language. The sensor fusion module synchronises the data received from the camera and LIDAR to precisely determine the position of the objects.

Findings

The application was made with the data obtained by scanning the Ayazağa campus of Istanbul Technical University with the vehicle with the sensors used. Within the scope of the application, images taken at different points of the campus were evaluated in test scenarios. As a result of the experiments carried out on the roads, car parks and controlled test areas within the campus, it was observed that the number of photographs used in model training and the number of these photographs belonging to different locations significantly increased the detection accuracy. fter the false object detections in Image 1, more accurate results were obtained as in Image 2 as a result of the model developed by increasing the test images. Compared to the YOLO model where the camera is used alone, sensor fusion has increased the detection success. Object detection accuracy for vehicles, pedestrians, signposts and other objects has increased significantly. False positives were reduced due to LiDAR integration. In low light conditions such as tunnels, the camera-only YOLO model struggled to detect objects, while the system was able to produce more reliable results thanks to the LIDAR depth information.

Image 1

Image 2

Conclusion

This study presents an innovative 360° detection system that integrates panoramic imaging, LIDAR depth mapping and deep learning-based object detection. The results show that multi-sensor fusion improves object detection reliability and accuracy. Sensor fusion improves detection accuracy, reduces false detections and enables the system to operate more reliably in low light conditions. Thanks to the depth information provided by LIDAR, distance estimation has become more accurate, and the misclassification rate of detected objects has decreased with the labelling made with 360-degree panoramic camera images. However, there are some aspects of the system that need to be improved. First of all, it is of great importance to calibrate the camera and LIDAR accurately. Small calibration errors can lead to deviations in depth estimation. In future studies, it is suggested to investigate the effect of weather conditions on the detection performance, to increase the stability of the system by adding additional sensors such as radar, and to optimise the processing efficiency of the system by developing lighter, faster models.

References

Dai, Y., Kim, D., & Lee, K. (2024). An advanced approach to object detection and tracking in robotics and autonomous vehicles using YOLOv8 and LiDAR data fusion. *Electronics, 13*(12), 2250. https://doi.org/10.3390/electronics13122250

Murendeni, R., Mwanza, A., & Obagbuwa, I. C. (2025). Using a YOLO deep learning algorithm to improve the accuracy of 3D object detection by autonomous vehicles. *World Electric Vehicle Journal, 16*(1), 9. https://doi.org/10.3390/wevj16010009

Redmon, J., Divvala, S., Girshick, R., & Farhadi, A. (2016). You only look once: Unified, real-time object detection. *Proceedings of the IEEE Conference on Computer Vision and Pattern Recognition*, 779–788.

Vats, V., Nizam, M. B., & Davis, J. (2024). VaLID: Verification as late integration of detections for LiDAR-camera fusion. *arXiv preprint*, arXiv:2409.15529.

Yeong, D. J., Velasco-Hernandez, G., Barry, J., & Walsh, J. (2021). Sensor and sensor fusion technology in autonomous vehicles: A review. *Sensors, 21*(6), 2140. https://doi.org/10.3390/s21062140

GEOMATICS ENGINEERING

Geodesy

Geographic Information Systems

Natural Hazards

Photogrammetry

Remote Sensing

Investigation of Anthropogenic Effects in Protected Wetlands Using Remote Sensing and Geographic Information Systems: A Case Study of Manyas Bird Lake and Bird Paradise National Park

İlyas Bursa[a], Adalet Dervişoğlu[b]

[a] İstanbul Technical University, Graduate School, Geomatics Engineering Program, Türkiye
[b] İstanbul Technical University, Faculty of Civil Engineering, Department of Geomatics Engineering, Türkiye
bursa15@itu.edu.tr

Keywords : Ramsar Site, Manyas Lake, Remote Sensing, Anthropogenic Impact, Geographic Information Systems.

Aim

Water is fundamental to life's existence and sustainability. In terrestrial ecosystems, water bodies serve as critical habitats that support a wide range of organisms. Any negative alterations in these environments can directly and significantly impact biodiversity. In particular, the increasing influence of industrialization and human activities over time has posed substantial threats to these ecosystems, leading to potential disruptions in ecological balance and habitat integrity. Especially, the increased industrialization and human activities can threaten these regions from the past to the present. In fact, in the last half century, even in the Mediterranean ecosystems, whose surrounding lands have been cultivated for thousands of years, there has been a comprehensive and rapid change that has never been seen in history (Gülçin, 2021). Various national and international efforts are being made to protect freshwater resources, which also host many migratory bird species. There are 14 Ramsar Sites of international importance in Türkiye, and because of this Intergovernmental Convention, they must be protected. These areas are recognized for their essential values for humanity and are protected for conservation and sustainable use. One of these areas is the Manyas Bird Paradise and Lake Conservation Area, located within the borders of Balıkesir province. The region is vital for the 270 birds, 118 plants, and 23 fish species in Manyas Lake and the various reptile species it hosts (Url-1). The study aims to use remote sensing data and methods to determine changes in the water surface area of Manyas Lake, assess changes in land use/land cover (LU/LC) in the lake protection area, and analyze the changes using demographic and meteorological data.

Material and Method

Manyas Lake, also known as Lake Kuş (Bird Lake), is located in the Marmara Region of northwestern Türkiye, within the boundaries of Balıkesir Province. Covering an approximate surface area of 160 square kilometers, the lake lies at an elevation of around 18 meters above sea level. The lake has a width of 20 km in the east-west direction, 14 km in the north-south direction, an average depth of 3 m, and has constantly turbid and abundant nutrient (eutrophic) properties due to the colloidal clay it contains (Url-1). Due to its shallow waters, the lake is highly sensitive to seasonal and anthropogenic changes. The important streams feeding the lake are the Sığırcı Stream, coming from the north, and Manyas Stream and Kara Stream, reaching the lake from the south (Figure 1).

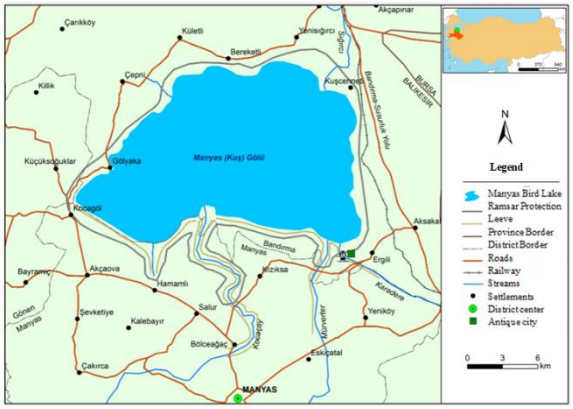

Figure 1: Manyas Lake and Surroundings (Url-2).

The important human settlements within the area are Kocagöl, Çepni, Kuşcenneti, Gölyaka, Bereketli, Yenisığırcı, Doğa, Ergili, Kızıksa, Akçakova and Salur neighborhoods.

Manyas Lake is internationally recognized for its ecological importance, particularly as a critical habitat for waterbirds. The Kuşcenneti (Bird Paradise) National Park, established in 1959, is situated on the northeastern shore of the lake and is designated as a Ramsar Site due to its significance for bird biodiversity. Over 270 bird species have been recorded in the area, including pelicans, herons, storks, and many migratory species.

The vector data used in the study (Buffer zone, Core protection zone, and Ecological impact limit) were obtained from the Ministry of Agriculture and Forestry (Figure 2). The buffer zone boundary is defined to reduce human pressure around the protected wetland. In the strictly/core protected area, human activity is completely prohibited. Ecological impact boundary refers to the spatial limit beyond which human activities, such as construction, agriculture, or resource extraction, are expected to have significant, measurable, or irreversible effects on an ecosystem's structure, function, or biodiversity.

Figure 2. Buffer zone boundary (red), Core protection zone (blue), Ecological impact boundary (yellow).

The population data of the settlements were obtained from the Turkish Statistical Institute (TUIK). Meteorological data were obtained from the General Directorate of Meteorology.

Sentinel-2 images were utilized both to monitor changes in the lake's water surface area and to assess alterations within the protected areas, owing to their accessibility as free remote sensing data sources, their adequate spatial resolution (10 m), and their high temporal resolution (5 days).

The most widely used Normalized Difference Water Index (NDWI) in the literature was used to determine the change in the lake surface area. This index enhances the presence of water while suppressing vegetation and soil features. NDWI is calculated using the near-infrared (NIR) and green bands of satellite imagery with the formula:

$$NDWI = (Green - NIR) / (Green + NIR)$$

High NDWI values indicate open water, low or negative values represent vegetation, soil, or built-up areas. It's commonly used in environmental monitoring, agriculture, and water resource management.

In addition, seasonal water surface area changes between 1985 and 2020 was determined by applying NDWI to spring and autumn Landsat satellite images. While Sentinel 2 images have been available since 2015, Landsat satellite images have been available since 1972, but their spatial resolution is lower than Sentinel 2's (30m).

A supervised random forest algorithm was used to determine land use/land cover (LU/LC) change in the area within the buffer zone boundaries, and images belonging to the years 2015, 2017, 2019, 2021, and 2023 were classified. The Random Forest algorithm is a supervised learning method widely used in machine learning. It is an ensemble-based algorithm that works with high accuracy in classification and regression problems. In the classification, four classes (water bodies, artificial area/bare soil, weak vegetation/shrubs and vegetation) were selected to determine the changes, and images from July and August were used.

Findings

Figure 3 shows the NDWI results applied within the protected area boundaries from the 2015-2023 Sentinel 2 images.

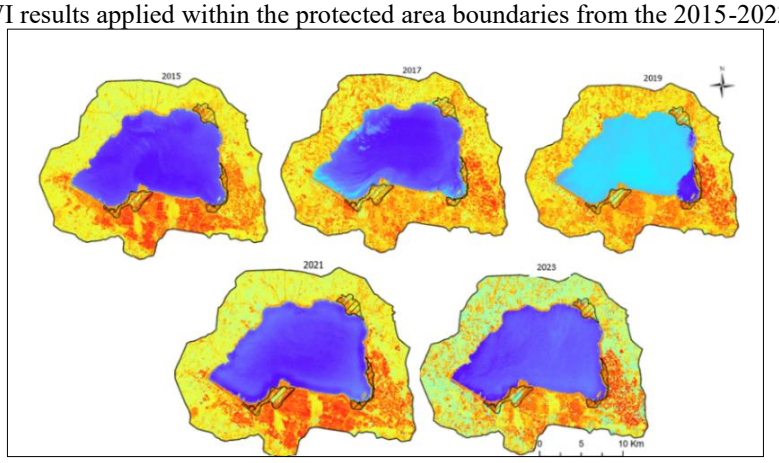

Figure 3: NDWI maps for years 2015, 2017, 2019, 2021, and 2023.

According to the NDWI results applied to five Sentinel 2 images from 2015 to 2023, the water surface area has fluctuated over the observed period. It was determined to be less than 150 km² in 2015. Later, it significantly increased by expanding to 155.9 km² in 2019. However, this trend reversed, and the area shrank to less than 150 km² in 2021. These changes in surface area can be attributed to annual rainfall fluctuations, which can significantly affect water levels in such ecosystems. This pattern highlights the dynamic nature of the water body and its sensitivity to climatic factors and the remarkable rainfall variability.

Figure 4a shows the water surface areas obtained according to the NDWI results applied to Landsat Satellite images in hectare units. The closest meteorological station to Manyas Lake is Bandırma station, and the data from this station were used to interpret these results (Figure 4b).

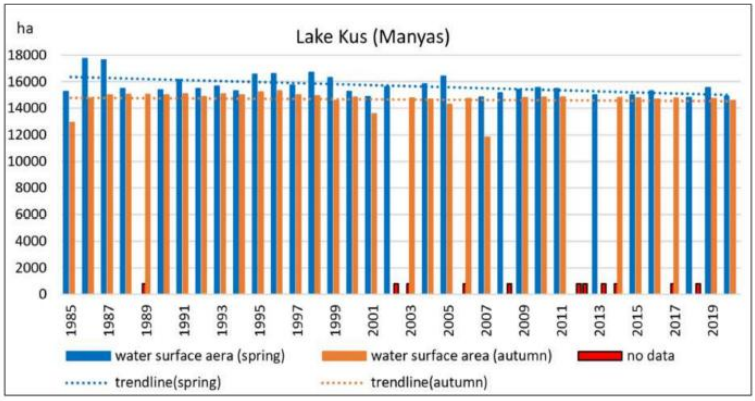

a)

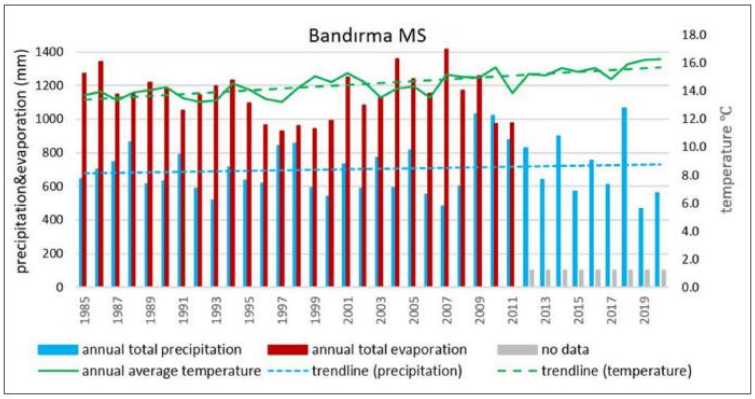

b)

Figure 4. a)1985-2020 Fall and spring water surface area changes and change trends (Dervisoglu, 2021).
b) Annual total precipitation, evaporation and average temperature, and their trendlines (Dervisoglu,2021).

When the graph showing the annual water surface areas in Figure 4 a is examined, it can be seen that there was a decrease in the spring, and the trend did not change much in the autumn months. When the meteorological data were examined an increase in the annual total precipitation trend and temperature was found. The average precipitation (35 years) was 704.16 mm and the average evaporation (27 years) was 1141.87 mm, indicating that evaporation was about 1.62 times more than precipitation. While the lake had a water surface area of 15,269.35 ha in 1985, it decreased to 14,919.41 ha with a 2.3% loss in 2020. The main reason for the high-water level difference in the spring and autumn months is the withdrawal of water from the lake for agricultural activities.

Random Forest image classification was applied to five Sentinel 2 images between 2015 and 2023 to assess potential land use/land cover (LU/LC) changes in the study area (Figure 5a). The analysis revealed fluctuations among different land cover classes over the years; however, these changes did not follow a unidirectional trend but exhibited oscillatory patterns. The graph in Figure 5b shows the results obtained from the classification made in the buffer area.

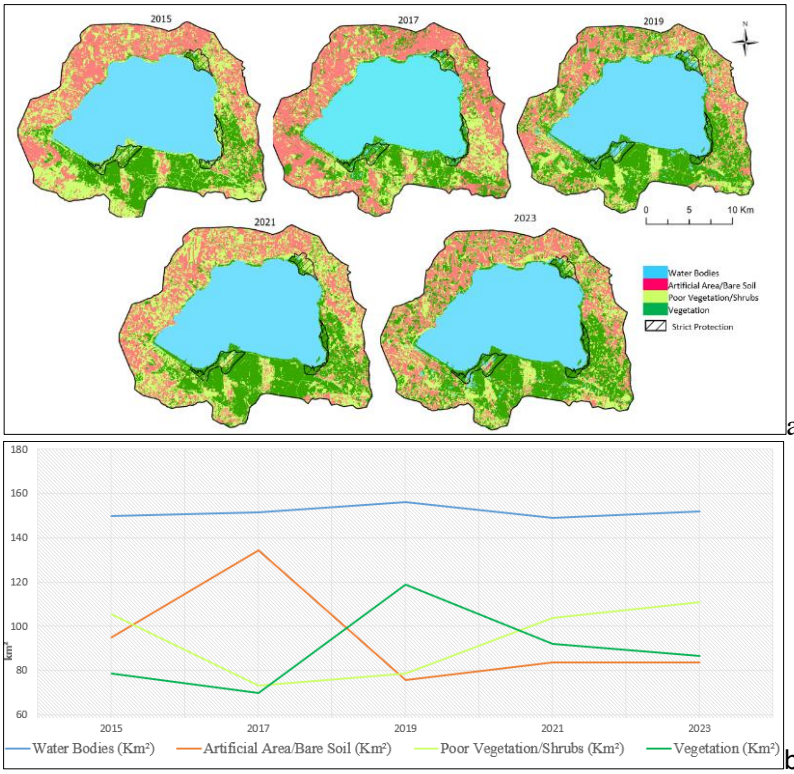

Figure 5: a) LU/LC Classification of the Lake protection area for years 2015, 2017, 2019, 2021, and 2023. b) LU/LC changes in buffer zone area (km²).

When Figure 5b is examined, although there are small fluctuations in the water surface area between 2015 and 2023, the general trend is stable (around 150 km²). Artificial Area/Bare Soil areas were around 100 km² in 2015, and peaked with a significant increase in 2017 (around 130 km²). A sudden decrease is observed in 2019, and its area decreased to approximately 80 km² as of 2023. This change can be interpreted as a decrease in artificial surfaces or re-covering bare lands with vegetation. The vegetation area, approximately 90 km² in 2015, peaked with a significant increase in 2019 (around 120 km²). It then showed a decreasing trend; it decreased to 80 km² levels again as of 2023. This situation may suggest a temporary improvement in vegetation and then deterioration, and harvesting agricultural areas may have been effective in the change.

The neighborhoods and towns around Manyas Lake are in close contact with the lake ecosystem and the surrounding natural life. When their populations were analyzed, it was determined that they tended to decrease. The population of the Manyas district showed a general decreasing trend between 2015 and 2024. The population, which was 20,154 in 2015, declined to 17,890 in 2024.

Conclusion

This study used Sentinel-2 and Landsat images and remote sensing techniques to analyze the LU/LC and water surface area changes in Manyas Lake. Although water surface areas occasionally show an increase or decrease, no significant change can be mentioned.

No specific one-directional change trend has been observed in the field. This can be explained by the fact that a large part of the land consists of agricultural areas and the study's short temporal range. The dominance of the vegetation class is noticeable in the strictly protected areas. Since the region consists mainly of agricultural land, the land cover constantly changes, making it difficult to reach a definitive conclusion about classification. Data spread over a more extended period and field exploration research will increase the accuracy. Agricultural activities around Manyas Lake have changed

significantly over the years. A considerable increase has been observed in paddy (rice) cultivation areas, especially south of the lake. This situation indicates the transition from traditional subsistence farming to commercial farming (Url-3).

In addition, when the lake waters recede in the summer months, vegetable farming is carried out in the emerging areas (Url-4). However, increased agricultural activities negatively affect the lake water quality and the lake ecosystem because of the fertilizers and pesticides used. For this reason, agricultural practices should be carried out with sustainable and environmentally friendly methods.

Various measures must be implemented in Ramsar protected areas to ensure sustainability and biodiversity conservation. In this context, the natural hydrological structure of wetlands should be preserved, and destructive activities such as drainage and landfilling must be avoided. Pollution, especially from agricultural and industrial sources, should be strictly controlled. Regular monitoring, scientific data collection, and public awareness are critical. Remote sensing images and methods are very effective tools for monitoring these areas regularly.

References

Dervisoglu, A. (2021). Analysis of the temporal changes of inland Ramsar sites in Turkey using Google Earth Engine. ISPRS International Journal of Geo-Information, 10(8), 521.

Gülçin, D. (2021). Examining the relationship between landscape diversity and carbon storage potential with remote sensing and GIS techniques. Journal of ADÜ Ziraat, 18(1), 89-96. doi: 10.25308/aduziraat.82226

Url-1 The Magical Beauty of Balıkesir: Bird Paradise. http://www.balikesir.gov.tr/kuscenneti, date retrieved 20.03.2025.

Url-2 Manyas Gölü. https://aktuelarkeoloji.com.tr/kategori/arkeoloji/manyas-golu, date retrieved 10.01.2025.

Url-3 https://gastroeko.com/2023/11/20/prof-dr-yilmaz-ari-manyas-golundeki-ekosistemin-bozulma-nedeni-sanayi-uretimine-oncelik-verilmesi-ve-cevresel-kaygilarin-geri-plana-itilmesiydi/, date retrieved 20.02.2025.

Url-4 https://dogadernegi.org/manyas-kus-golu/, date retrieved 20.02.2025.

Aircraft Contrails Detection with Deep Learning Methods on Remote Sensing Images

Çağatay Yıldırım[a], Hande Demirel[a]

[a] İstanbul Technical University, Graduate Institute, Geomatics Engineering Department, Geomatics Engineering Phd. Program, Türkiye
cagatay.yildirim@itu.edu.tr

Keywords : Contrail Detection, Satellite Imagery, Deep Learning, Infrared Bands, Environmental Monitoring.

Aim

Aircraft contrails contribute to climate change by affecting Earth's radiation balance. Detecting and analyzing contrails is crucial for understanding their environmental impact. In this study, a deep learning-based approach is developed to identify contrails using satellite imagery. Due to the limited temporal resolution of Sentinel-2, GOES-16 satellite data is utilized for more frequent observations.

By analyzing the top-performing models in the Google Open Contrails competition, it is observed that processed satellite images, such as Ash Color and IR False Color composites, provide better contrail detection accuracy. Various deep learning architectures, including EfficientNet V2, CoAtNet, and MaxVit, are evaluated, with MaxVit emerging as the most effective model due to its ability to capture both local and global features. Additionally, loss functions like Dice Loss, Focal Loss, and Lovasz-softmax improve segmentation accuracy.

The study identifies that bands 11, 14, and 15 (infrared bands) are most effective for contrail detection, while band 16 may provide further insights into high-altitude contrails. Large datasets are processed efficiently using the HDF5 format, and data augmentation techniques are applied to enhance model performance.

While this research focuses on 2D imagery, contrail altitude remains a critical factor for accurate detection. Future work can integrate altitude data to refine contrail identification. This study highlights the potential of deep learning for contrail detection, contributing to aviation regulations and sustainable air traffic management.

This study aims to develop and evaluate advanced deep learning models for detecting aviation-induced contrails using satellite imagery. The primary objective is to improve the accuracy and efficiency of contrail detection in order to support environmental monitoring and reduce aviation's impact on climate change. By comparing multiple state-of-the-art models, the research focuses on identifying the most effective approach for robust contrail identification under varying atmospheric conditions.

Material and Method

The dataset used in this study is sourced from GOES-16 satellite imagery, with a focus on infrared bands 11, 14, 15, and 16. These bands were selected to enhance contrail visibility through Ash Color and IR False Color composite generation. Data were stored in HDF5 format and augmented with flipping, rotation, and brightness adjustments.

Three deep learning architectures—EfficientNetV2, CoAtNet, and MaxViT—were selected for evaluation. Among them, MaxViT was identified as the most effective due to its ability to capture both local and global features. Training was performed with an 80–20 training-validation split using the Adam optimizer and learning rate scheduling. Focal Loss, Dice Loss, and Lovász-Softmax were applied to address class imbalance. Model performance was evaluated using metrics such as mIoU, precision, recall, and Dice coefficient.

Findings

The experimental results demonstrated that MaxViT outperformed other models with a high segmentation accuracy (mIoU ≈ 87%) and fast inference speed. Infrared bands significantly enhanced contrail visibility, particularly during nighttime observations. Composite imagery further aided manual and automated detection. The use of Focal Loss and Lovász-Softmax improved detection of thin and hard-to-identify contrails. Data augmentation contributed to better generalization across varied atmospheric conditions. The low inference latency of MaxViT supports potential real-time deployment in operational monitoring systems.

Conclusion

This research highlights the effectiveness of deep learning, particularly MaxViT, in identifying contrails from GOES-16 satellite data. The integration of infrared bands and optimized training strategies enhanced detection accuracy and model robustness. While current results are promising, limitations remain, including the lack of altitude data. Future work should focus on incorporating 3D spatial information and validating the model on datasets from other satellite platforms. The outcomes of this study support ongoing efforts in aviation climate impact assessment and real-time environmental monitoring systems.

References

Berman, M., Rannen Triki, A., & Blaschko, M. B. (2021). The Lovász-softmax loss: A tractable surrogate for the optimization of the intersection-over-union measure in neural networks. IEEE Transactions on Pattern Analysis and Machine Intelligence, 43(4), 1296–1308.

Bier, A., & Burkhardt, U. (2018). Variability in contrail ice nucleation and its dependence on soot number emissions. Atmospheric Chemistry and Physics, 18, 12557–12572.

Bier, A., Burkhardt, U., & Bock, L. (2017). Synoptic control of contrail cirrus life cycles and their modification due to reduced soot number emissions. Geophysical Research Letters, 44(8), 4138–4147.

Chen, X., et al. (2020). Symbolic discovery of optimization algorithms. Nature Machine Intelligence, 2, 165–172.

Dai, Z., et al. (2021). CoatNet: Marrying convolution and attention for all data sizes. Advances in Neural Information Processing Systems (NeurIPS).

Digby, R. A. R., et al. (2020). An observational constraint on aviation-induced cirrus from the COVID-19-induced flight disruption. Geophysical Research Letters, 47(24).

Gierens, K., Matthes, S., & Rohs, S. (2017). How well can persistent contrails be predicted? Atmospheric Chemistry and Physics, 17, 9935–9948.

Kärcher, B. (2002). Formation and radiative forcing of contrail cirrus. Geophysical Research Letters, 29(8), 1–4.

Kulik, L. (2021). Satellite-based detection of contrails using deep learning. Nature Communications, 12.

Lee, D. S., et al. (2021). The contribution of global aviation to anthropogenic climate forcing for 2000 to 2018. Atmospheric Environment, 244, 117894.

Lin, T.-Y., et al. (2020). Focal loss for dense object detection. IEEE Transactions on Pattern Analysis and Machine Intelligence, 42(2), 318–327.

Loshchilov, I., & Hutter, F. (2017). Decoupled weight decay regularization. arXiv preprint, arXiv:1711.05101.

Ng, J. Y.-H., et al. (2019). OpenContrails: Benchmarking contrail detection on GOES-16 ABI. Google Research. Retrieved May 20, 2025, from https://sites.research.google/contrails/

Sudre, C. H., et al. (2020). Generalised dice overlap as a deep learning loss function for highly unbalanced segmentations. IEEE Transactions on Medical Imaging, 39(11), 2999–3010.

Tan, M., & Le, Q. (2021). EfficientNetV2: Smaller models and faster training. Proceedings of the International Conference on Machine Learning (ICML).

Teoh, R., et al. (2022). Aviation contrail climate effects in the North Atlantic from 2016–2021. Atmospheric Chemistry and Physics, 22, 5737–5749.

Tu, Z., et al. (2022). MaxViT: Multi-axis vision transformer. Proceedings of the IEEE Conference on Computer Vision and Pattern Recognition (CVPR).
Yue-Hei Ng, J., et al. (2019). OpenContrails: Benchmarking contrail detection on GOES-16 ABI. Google Research. Retrieved May 20, 2025, from https://sites.research.google/contrails/

Enhancing Sentinel-1 SAR Geolocation Accuracy: The Impact of DEM on Orthorectification Performance

Sena Oğuzhanoğlu[a], Filiz Sunar[b]

[a] Istanbul Technical University, Graduate School, Geomatics Engineering Program, Turkey
[b] Istanbul Technical University, Faculty of Civil Engineering, Department of Geomatics Engineering, Turkey
oguzhanoglu17@itu.edu.tr, fsunar@itu.edu.tr

Keywords : DEM, Orthorectification, SAR Geolocation Accuracy, Sentinel-1.

Aim

Spaceborne Synthetic Aperture Radar (SAR) is a critical Earth Observation technology that monitors local and global environmental conditions. Unlike optical sensors, it operates day and night in all weather conditions. It actively transmits and receives microwave signals to generate images. Amplitude and phase components of SAR imagery enable applications such as surface deformation analysis and land cover classification. SAR imagery uses phase differences to accurately represent surface features, with side-looking geometry providing distinct range measurements based on signal travel time and Doppler effects (Gisinger, 2020). However, this side-looking geometry introduces geometric distortions - foreshortening, layover, and shadowing - that cause pixel shifts in range and azimuth directions (i.e., affect terrain representation) and require geometric corrections.

In addition, terrain elevation, orbit, and atmospheric errors affect the accuracy of SAR geolocation. Although technological advances by satellites such as TerraSAR-X and Sentinel-1 have significantly improved orbital accuracy, reducing elevation-related errors is still challenging (Li and Zeng, 2024). Early work in SAR remote sensing identified the need for precise orthorectification to reduce geometric distortions, improve the geolocation accuracy of SAR images, and provide reliable spatial analysis. Therefore, methods were developed that integrated Digital Elevation Models (DEMs) and precise orbital parameters.

The effectiveness of orthorectification depends on the resolution and accuracy of the DEM used, since errors in elevation data (dz) proportional to the angle of incidence (θ) can lead to position shifts (dx) (i.e., planimetric errors), as shown in Figure 1 (Shimada, 2010). Global DEMs, such as the Shuttle Radar Topography Mission (SRTM), and more recent high-resolution data sets, such as WorldDEM, significantly improve the geolocation accuracy. Higher resolution DEMs provide a more accurate terrain representation, especially in regions with complex topography, thereby improving SAR-based environmental monitoring and GIS applications. Evaluating the performance of different DEMs in SAR orthorectification is crucial to optimize geolocation accuracy and ensure the integrity of the derived spatial information.

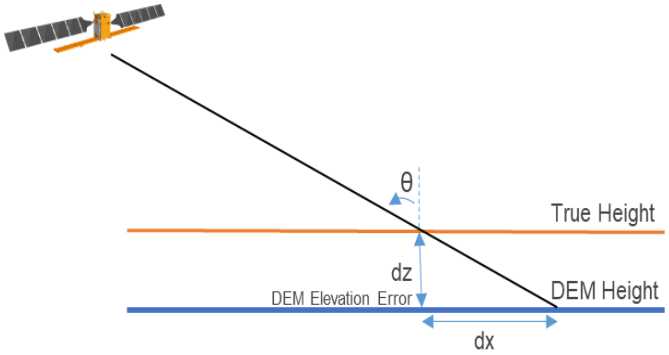

Figure 1. Effect of DEM errors on planimetric accuracy of the orthorectification.

For this purpose, this study assesses the impact of different DEMs on SAR geolocation accuracy using Sentinel-1 satellite images. Several DEMs, including SRTM 1 Arc-Second 30 m (DTED Level 2) and SRTM 3 Arc-Second 90 m (DTED Level 1), and a DEM generated from Sentinel-1 satellite imagery are used for orthorectification in the study area of Gölbaşı, Ankara. Their performance is evaluated using ground control points and quantified by metrics such as Root Mean Square Error (RMSE) and Circular Error at 90% Confidence Level (CE-90).

Material and Method

Gölbaşı, located in Ankara province, Turkey, was selected as the study area because of its relatively homogeneous land cover. The region consists mainly of open areas with minimal forest and shrub cover, which minimizes volume scattering effects in SAR imagery (Figure 2).

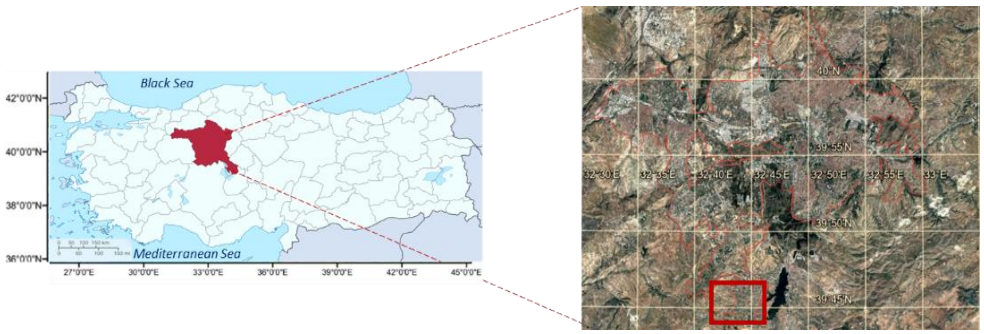

Figure 2. Satellite image of test areas in Ankara – Gölbaşı (red box) (©2020, Google Earth).

For the geolocation accuracy analysis, selected DEMs were applied to Sentinel-1 GRD (Ground Range Detected) satellite imagery in VV polarization. VV polarization was chosen because it provides higher backscatter contrast between different surface types, which improves feature discrimination, especially in open areas with minimal vegetation cover. Also, DEM generated from Sentinel-1 SLC (Single look Complex) satellite images. Sentinel-1 operates in C-band and the acquisition parameters of Sentinel-1 Interferometric Wide (IW) mode data used in this study are presented in Table 1.

Table 1. Sentinel-1 Interferometric Wide properties.

Characteristics	Value
Centre frequency	5.405 GHz (~5.55 cm)
Bandwidth	0-100 MHz
Polarization	Dual HH+HV, VV+VH Single HH, VV
Pulse Repetition Frequency	1 000 - 3 000 Hz
Sampling	10 bits
Swath	250 km
Incidence angle	29.1° - 46.0°
Sub-swaths	3
Maximum NESZ	-22 dB

The first step in this study is to generate a Digital Elevation Model (DEM) from Sentinel-1 SAR data using Interferometric Synthetic Aperture Radar (InSAR) techniques. This process uses Sentinel-1 Single Look Complex (SLC) images to derive

topographic information by exploiting phase differences between SAR acquisitions. The interferometric workflow includes co-registration of master and slave images to ensure precise alignment, followed by interferogram generation to capture phase variations associated with terrain elevation. Coherence estimation is performed to assess the quality of the interferometric fringes to ensure reliable phase unwrapping. Then, Goldstein phase filtering improves phase continuity, phase unwrapping is applied to resolve phase ambiguities and retrieve accurate elevation information. The unwrapped phase is then converted to elevation values using a phase-to-elevation transformation (Osmanoğlu et al., 2016) Finally, the generated DEM is validated against reference dataset before being used in the orthorectification process.

Once the interferometric DEM is generated, it is incorporated into the orthorectification process along with existing DEMs, including SRTM 30 m and SRTM 90 m. Orthorectification is performed using Sentinel-1 Ground Range Detected (GRD) products, applying Range Doppler Terrain Correction (RDTC) techniques within SNAP ESA's Sentinel-1 Toolbox. The RDTC method uses orbit state vectors, radar timing annotations and DEM inputs to correct for geometric distortions. This method allows Sentinel-1 SAR data to be projected into a uniform map coordinate system (UTM) (Bayanudin and Jatmiko, 2016). The orthorectification results obtained from different DEMs are then compared to evaluate the influence of the DEM on the geolocation accuracy.

To evaluate the accuracy of the orthorectified images, ground control points (GCPs) are used to measure the residual displacement between the reference and corrected SAR images. The assessment is performed using quantitative metrics, including Root Mean Square Error (RMSE) and Circular Error at the 90% Confidence Level (CE-90), according to the National Standard for Spatial Data Accuracy (NSSDA). The final accuracy assessment provides insight into the optimal DEM selection for Sentinel-1 SAR geolocation correction, ensuring accurate spatial alignment for further geospatial applications.

Findings

The geolocation accuracy evaluation showed that the resolution of the digital elevation model (DEM) directly affects the orthorectification quality of Sentinel-1 imagery. Among the DEMs evaluated, the SRTM 30-meter dataset significantly reduced position errors compared to the SRTM 90-meter dataset. The geolocation accuracy evaluation showed that the resolution of the digital elevation model (DEM) directly influences the orthorectification quality of Sentinel-1 imagery. The Sentinel-1-derived interferometric DEM demonstrated competitive accuracy but showed localized inconsistencies due to coherence limitations and phase unwrapping challenges.

Statistical validation using ground control points (GCPs) showed that higher resolution DEMs yielded lower RMSE and CE-90, underscoring the importance of fine-scale elevation data in SAR geolocation. The critical role of elevation accuracy in minimizing spatial misalignment was highlighted, particularly in complex terrain areas where coarser DEMs resulted in more pronounced discrepancies. Although interferometric DEMs are a suitable alternative, their reliability depends on phase coherence. These results emphasize the importance of selecting a DEM based on the application and terrain conditions.

Conclusion

These results highlight the importance of DEM selection in obtaining accurate SAR geolocation, as higher-resolution datasets significantly improve spatial accuracy. The comparison between DEMs showed that DEM resolution directly impacts orthorectification accuracy.

With increasing confidence in SAR-based geospatial applications, the selection of an optimal DEM is critical to ensure accurate terrain representation and minimize spatial inconsistencies. Future research should investigate multi-source data fusion and adaptive filtering techniques to further improve SAR geolocation accuracy, especially in high relief environments where terrain-induced distortions remain a challenge.

References

Bayanudin, A. A., & Jatmiko, R. H. (2016). Orthorectification of Sentinel-1 SAR (synthetic aperture radar) data in some parts of South-Eastern Sulawesi using Sentinel-1 toolbox. IOP Conference Series: Earth and Environmental Science, 47, 012007.

Gisinger, C. (2020). SAR imaging geodesy—Towards absolute coordinates with centimeter accuracy [PhD Thesis, Technische Universität München]. Technische Universität München.

Li, F., & Zeng, Q. (2024). High-resolution spaceborne SAR geolocation accuracy analysis and error correction. Remote Sensing, 16(22), Article 4222.

Osmanoğlu, B., Sunar, F., Wdowinski, S., & Cabral-Cano, E. (2016). Time series analysis of InSAR data: Methods and trends. ISPRS Journal of Photogrammetry and Remote Sensing, 115, 90–102.

Shimada, M. (2010). Ortho-rectification and slope correction of SAR data using DEM and its accuracy evaluation. IEEE Journal of Selected Topics in Applied Earth Observations and Remote Sensing, 3(4), 657–671.

Offshore Wind Turbine Site Selection in the Aegean Sea

Şule Feride Ardıç[a], Adalet Dervişoğlu[b]

[a] Istanbul Technical University, Geomatics Engineering Program, Türkiye
[b] Istanbul Technical University, Faculty of Civil Engineering, Department of Geomatics Engineering, Türkiye
ardic17@itu.edu.tr

Keywords : Offshore Wind Turbines, GIS, Site Selection, Remote Sensing, Aegean Sea.

Aim

With the increasing global energy demand, the need for renewable energy sources is also rising. The main reasons for the rise in energy demand are industrialization and population growth. The limited availability of fossil fuels, the environmental impact of carbon emissions, and the necessity to combat climate change have further accelerated the shift toward renewable energy sources. In this context, wind energy, as a sustainable and clean energy source, stands out as a significant alternative. In particular, offshore wind energy offers more stable and higher energy production capacity compared to onshore wind farms (Esteban Pérez et al., 2011). Consequently, offshore wind farms have gained a prominent place in the energy policies of many countries.

Offshore wind energy projects also offer economic opportunities. Large-scale projects with high installed capacity can enhance national energy independence by reducing energy imports in the long term. Additionally, these projects create local employment opportunities and can accelerate technological development.

Offshore wind farms (Grid-Connected Offshore Wind Farms) offer a significant solution for assessing wind potential in open seas. Offshore wind energy provides stable and high-capacity power output due to strong and consistent wind flows, making it a crucial element of modern energy strategies.

The primary objective of this study is to identify the most suitable locations for offshore wind energy farms in the Aegean Sea and comprehensively evaluate the region's wind energy potential. To achieve this, wind resources in the region have been analyzed on an hourly and annual basis, examining wind speeds, directions, and frequencies. Meteorological data obtained from weather stations, lighthouses, and buoys have been utilized to generate wind profiles and estimate wind speeds at turbine hub heights. Furthermore, a multi-criteria assessment has been conducted, considering factors such as the region's bathymetric structure, maritime traffic, environmental and ecological constraints, grid connection feasibility, and economic viability (Tercan et al., 2020; Tortumluoğlu & Doğan, 2021). Based on these findings, this study aims to provide a scientific foundation for the development of sustainable and efficient offshore wind energy potential in the Aegean Sea.

Türkiye's geographical advantage of being surrounded by seas on three sides enhances the feasibility of offshore wind energy projects. The Aegean Sea, with its high wind potential, stands out as an attractive region for such projects (Satir et al.,2018). To maximize this potential, several critical factors, including meteorological analyses, seabed depth studies, environmental considerations, and the suitability of energy transmission infrastructure, must be considered. Identifying potential suitable locations involves assessing regions with high and consistent wind flow. Additionally, site selection for offshore wind turbines aims to minimize their impact on marine ecosystems and other environmental factors.

Materials and Method

Detailed analyses are essential for optimal site selection and project planning. Remote sensing technology is recommended for examining wind potential in the Aegean Sea. In this study, hourly wind data from meteorological stations, lighthouses, and buoys operated by the Turkish State Meteorological Service, as well as remote sensing data obtained from ECMWF's Copernicus Marine Service, have been utilized to assess wind energy potential. ECMWF's Copernicus Marine Service (CMEMS) is a remote sensing data source provided by the European Centre for Medium-Range Weather Forecasts (ECMWF), which is used for monitoring various oceanographic and meteorological parameters. This service provides

crucial data on wind speed, sea surface temperature, wave height, and ocean currents. In this study, wind data obtained from CMEMS was utilized to conduct large-scale spatial analyses for assessing the wind energy potential in the Aegean Sea. This dataset plays a key role in identifying the most suitable locations for offshore wind turbines by determining near-surface wind speeds. The limited number of buoys and meteorological stations measuring wind data in Turkey's marine areas presents a challenge in accurately determining wind potential. Therefore, remote sensing data has been employed to enable large-scale and spatial analyses.

Meteorological stations typically conduct measurements at heights ranging from 5 to 20 meters. However, since wind turbines are generally installed at hub heights between 70 and 100 meters, specific methods are required to estimate wind speeds at these altitudes (Soukissian et al., 2017). In this study, the logarithmic wind profile law has been applied to adjust surface wind speed measurements obtained from meteorological stations and buoys to turbine hub heights. The wind data from the satellite were taken at a height of 10 meters, just like the data from the weather station. In order to extrapolate the wind speeds to 100 meters, which corresponds to the typical turbine hub height, the logarithmic wind profile was utilized.

Hourly wind data collected from stations, lighthouses, and buoys have been visualized as annual wind roses, and wind frequency analyses have been conducted. In addition, the Weibull probability distribution was applied to statistically characterize the wind speed regimes at each location. Remote sensing wind data has been analyzed using Geographic Information Systems (GIS) software. Spatial analyses were performed using GIS to assess wind energy potential.

Findings

The findings indicate that the western and northern parts of the Aegean Sea exhibit significant wind energy potential. Since water depth is a crucial factor in offshore wind turbine deployment, fixed-bottom wind turbines have been considered for shallow areas with depths below 50 meters, while floating platforms have been evaluated for deeper waters. This approach broadens the applicability of wind energy projects across a larger area.

Moreover, environmental constraints, such as maritime traffic, continental shelf boundaries, ecological sensitivities, and protected areas, have been considered as limiting factors. Based on GIS analyses and Weibull distribution modeling, specific locations off the coasts of Çeşme, Karaburun and Seferihisar have emerged as promising sites due to their high wind potential, suitable water depths, and proximity to energy transmission infrastructure. Figure 1 presents the annual mean wind speed distributions over the Aegean Sea for the years 2018 to 2023. The wind speed data were obtained from CMEMS satellite observations and extrapolated to 100 meters above sea level using the logarithmic wind profile law. Areas where wind speeds exceed the 7 m/s threshold—considered critical for offshore wind energy feasibility—are distinctly highlighted. These maps not only assist in identifying high-potential offshore wind zones but also enable the evaluation of interannual wind consistency. Notably, regions along the northwestern Aegean coast, particularly the Çeşme–Karaburun–Ayvalık corridor, exhibit persistent high wind speeds (>7 m/s) across all analyzed years.

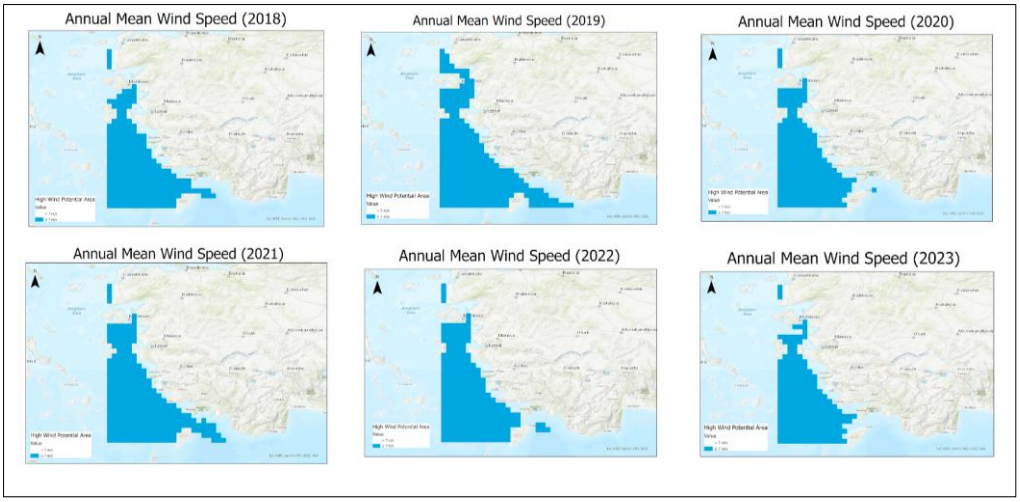

Figure 1. Annual Mean Wind Speed Maps (2018–2023) for the Aegean Sea.

Conclusion

This technology facilitates the collection of critical data regarding wind potential, marine conditions, and other environmental factors. This study provides a crucial scientific basis for identifying potential locations for offshore wind turbines in the Aegean Sea. Preliminary findings suggest that the region possesses substantial potential for wind energy production. However, in addition to technical feasibility, environmental and socio-economic factors must also be considered. The results obtained can guide energy policies and investment decisions. Future studies should incorporate more detailed meteorological modeling and environmental impact assessments to further refine the region's energy production potential.

In conclusion, specific locations in the Aegean Sea stand out as favorable sites for offshore wind turbine deployment due to their high wind potential, suitable water depths, and proximity to energy transmission infrastructure. The findings can serve as a roadmap for energy policies and investment strategies. Future research should focus on comprehensive meteorological modeling and environmental assessments to ensure the sustainable and efficient development of offshore wind energy in the Aegean Sea.

References

Esteban Pérez, M. D., Diez Gonzalez, J. J., López Gutiérrez, J. S., & Negro Valdecantos, V. (2011). Why offshore wind energy? *Renewable Energy, ISSN 0960-1481, 2011-02, Vol. 36, No. 2*.

Satir, M., Murphy, F., & McDonnell, K. (2018). Feasibility study of an offshore wind farm in the Aegean Sea, Turkey. *Renewable and Sustainable Energy Reviews*, *81*, 2552-2562.

Soukissian, T., Papadopoulos, A., Skrimizeas, P., Karathanasi, F., Axaopoulos, P., Avgoustoglou, E., ... & Katsafados, P. (2017). Assessment of offshore wind power potential in the Aegean and Ionian Seas based on high-resolution hindcast model results.

Tercan, E., Tapkın, S., Latinopoulos, D., Dereli, M. A., Tsiropoulos, A., & Ak, M. F. (2020). A GIS-based multi-criteria model for offshore wind energy power plants site selection in both sides of the Aegean Sea. *Environmental Monitoring and Assessment*, *192*, 1-20.

Tortumluoğlu, M. İ., & Doğan, M. (2021). Açık deniz rüzgar türbinleri için uygun yer seçim kriterlerinin irdelenmesi ve kuzey ege kıyılarına uygulanması. *Dokuz Eylül Üniversitesi Mühendislik Fakültesi Fen ve Mühendislik Dergisi*, *23*(67), 25-41.

Evaluating The Temporal Consistency Of Sar And Optical Vegetation Indices For Cotton Monitoring Using Sentinel-1 And Sentinel-2

Alp Eren Furkan Demirci[a], Ayşe Filiz Sunar[a]

[a]Istanbul Technical University, Faculty of Civil Engineering, Department of Geomatics Engineering, Turkey
demirci15@itu.edu.tr, fsunar@itu.edu.tr

Keywords : Radar and Optical Vegetation Indices, Synthetic Aperture Radar (SAR), Dual-Polarization Backscatter, Polarimetric Decomposition, SAR-Optical Data Fusion.

Aim

Agricultural monitoring plays a crucial role in ensuring food security, optimizing resource use, and mitigating the impacts of climate change. Cotton, as one of the most economically significant crops, requires continuous observation to assess growth conditions, detect stress factors, and support precision farming practices. In regions such as the Aegean Region of Turkey, where cotton production is a major agricultural activity, remote sensing technologies provide an effective means to track crop development over large areas with high temporal and spatial resolution.

Optical remote sensing has been widely used to monitor vegetation dynamics through indices such as the Normalized Difference Vegetation Index (NDVI) and Enhanced Vegetation Index (EVI), which offer insights into vegetation vigor, chlorophyll content, and biomass. However, cloud cover and signal saturation in dense canopies often limit their effectiveness. Synthetic Aperture Radar (SAR), with its all-weather, day-and-night imaging capabilities, provides a complementary solution. Radar-derived vegetation indices, such as the Radar Vegetation Index (RVI), leverage SAR's structural sensitivity, offering additional insights into crop conditions (Hu et al., 2024). Integrating SAR and optical vegetation indices has shown promise for improving agricultural monitoring by capturing both spectral and structural crop characteristics. In particular, dual-polarization SAR data (VV and VH) and polarimetric decomposition metrics—including entropy, anisotropy, and alpha angle—can enhance the assessment of crop structure, biomass, and phenological changes.

This study aims to analyze the temporal consistency between radar-derived vegetation indices from Sentinel-1 (S1) and optical vegetation indices from Sentinel-2 (S2) for monitoring cotton elds in the Aydın province, Aegean Region of Turkey. The analysis covers the entire cotton growing season (May to October 2024), focusing on 11 adjacent fields, to assess how dual-polarization SAR backscatter metrics and advanced polarimetric features correlate with optical vegetation indices. The spatial distribution of the study area and the selected cotton fields is illustrated in Figure 1.

Figure 1. Satellite image of the study area, obtained from Google Earth.

Material and Method

The study area includes 11 neighboring cotton fields spread across three different locations in the Aegean Region of Turkey, where cotton farming holds significant economic importance. Sentinel-1 and Sentinel-2 datasets covering the full growing season from May to October 2024 are used. This temporal scope ensures the capture of key phenological stages, including

early vegetative growth, flowering, boll formation, and senescence. The key technical specifications of Sentinel-1 and Sentinel-2 sensors utilized in this study are summarized in Table 1.

Table 1. Technical specifications of Sentinel satellites (URL-1).

Feature	Sentinel-1	Sentinel-2
Sensor Type	Synthetic Aperture Radar	Multispectral Optical Sensor
Frequency/Spectral Range	C-band (5.405 GHz)	Visible, NIR, Red Edge, SWIR (13 bands)
Polarization	Dual (VV+VH)	N/A
Spatial Resolution	~10 m (IW mode)	10 m (VNIR), 20 m (Red Edge, SWIR), 60 m (atmospheric)
Temporal Resolution	6–12 days (depends on region and orbit)	5 days (at equator with twin satellites)
Swath Width	~250 km (IW mode)	290 km
Cloud Sensitivity	Not affected by clouds or weather	Affected by clouds, atmospheric conditions
Primary Strengths	Structural, moisture content, biomass detection	Vegetation vigor, chlorophyll content, land cover mapping
Main Agricultural Use	Crop structure, water stress, biomass mapping	Phenology, canopy vigor, vegetation indices

Sentinel-1 preprocessing includes radiometric calibration, speckle filtering, noise removal, and terrain correction. Backscatter coefficients (σ^0) will be used to derive VV/VH ratios and the Radar Vegetation Index (RVI) (Hu et al., 2024). Where applicable, polarimetric parameters(entropy, anisotropy, alpha angle) will be extracted, which correlate with biomass and plant height (Harfenmeister et al., 2021).

For Sentinel-2, Level-2A surface reflectance data will be used to calculate vegetation indices, with cloud masking applied using the Scene Classification Layer (SCL). Time-series analysis will include correlation and regression modeling to assess radar-optical relationships. Processing will be conducted in Google Earth Engine (GEE) and Python for scalability and reproducibility.

The specific optical and SAR vegetation indices calculated in this study are summarized in Table 2, along with their mathematical formulations and primary applications in crop monitoring. These indices were selected based on their established relevance in capturing canopy vigor, biomass, moisture dynamics, and structural characteristics of cotton fields.

Table 2. Overview of Sentinel-1 and Sentinel-2 derived vegetation indices.

Index / Parameter	Formula / Definition	Source / Spectral-SAR Bands	Purpose / Applications
NDVI	(NIR - Red) / (NIR + Red)	S2 Bands 8 & 4	Vegetation greenness, biomass, LAI
NDRE	(NIR - RedEdge) / (NIR + RedEdge)	S2 Bands 8 & 5	Chlorophyll content, nitrogen stress
EVI	2.5 * (NIR - Red) / (NIR + 6*Red - 7.5*Blue + 1)	S2 Bands 8, 4, 2	High biomass, soil/atmosphere minimized
NDWI	(NIR - SWIR) / (NIR + SWIR)	S2 Bands 8 & 11	Vegetation water content
MSAVI	(2 * NIR + 1 - sqrt((2 * NIR + 1)^2 - 8*(NIR - Red))) / 2	S2 Bands 8 & 4	Soil influence minimized
GCI	(NIR / Green) - 1	S2 Bands 8 & 3	Chlorophyll estimation
ARVI	(NIR - (2*Red - Blue)) / (NIR + (2*Red - Blue))	S2 Bands 8, 4, 2	Atmospheric resistance
SAR_ratio	VH / VV	S1 VH & VV	Vegetation structure, moisture reduction
SSD	VH - VV	S1 VH & VV	Vegetation vs bare soil indicator
SND	(VH - VV) / (VH + VV)	S1 VH & VV	Scale-invariant vegetation index
SSRM_VH	(VH^2) / sqrt(VV)	S1 VH & VV	Enhances VH vegetation signal
SSRM_VV	(VV^2) / sqrt(VH)	S1 VH & VV	Highlights VV dominant scattering
Entropy(H)	Degree of randomness (0-1)	Sentinel-1 SLC	Vegetation structure complexity, growth stage

Alpha Angle (α)	Mean scattering angle (0° surface, 45° volume, 90° double-bounce)	Sentinel-1 SLC	Dominant scattering mechanism, canopy-water detection
Anisotropy (A)	Second vs third eigenvalue ratio	Sentinel-1 SLC	Secondary scattering mechanism, complex canopies
Coherence	Phase stability (0-1)	Sentinel-1 SLC	Growth monitoring, vegetation change detection

Findings

Figure 2 presents a visual comparison of the study area using two different remote sensing datasets: Sentinel-1 VV polarization and Sentinel-2 NDVI imagery. The Sentinel-1 VV polarization (left) highlights variations in surface roughness and structural properties, making it particularly useful for distinguishing land cover types and detecting changes. In contrast, the Sentinel-2 NDVI imagery (right) provides insights into vegetation health and distribution by emphasizing chlorophyll activity. The combined analysis of these datasets enhances the understanding of land cover characteristics and vegetation conditions. The correlation analysis between Sentinel-1 SAR and Sentinel-2 optical vegetation indices was conducted across 11 representative cotton fields to assess the consistency and complementarity of radar and optical signals. As summarized in Table 3, both positive and negative correlations were observed, reflecting the complex interaction between crop structure, moisture content, and spectral responses. The spatial patterns of correlation were consistent across the three fields, confirming the robustness of these relationships. These results highlight that while general linear relationships between SAR and optical datasets are moderate, specific index combinations demonstrate strong agreement, supporting their combined use for monitoring crop conditions.

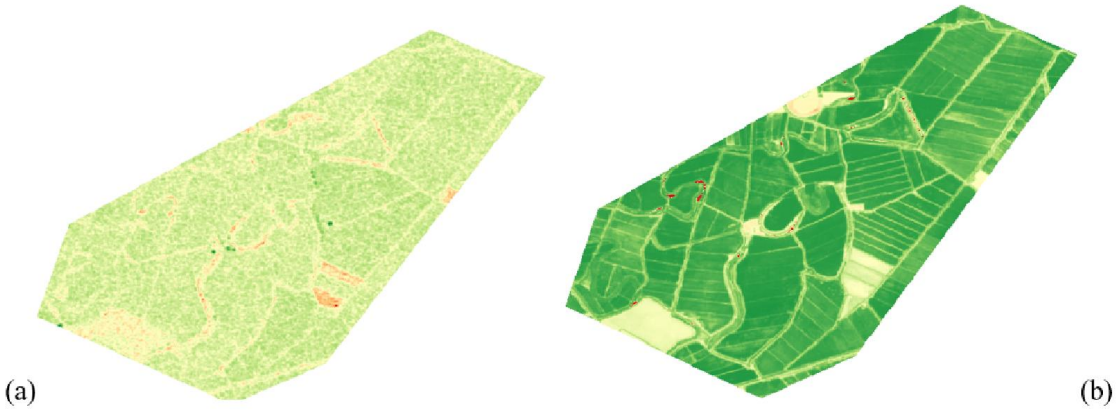

Figure 2. Visual comparison of two different satellite datasets. (a) Sentinel-1 VV polarized image. (b) Sentinel-2 NDVI image.

Table 3. Pearson correlation coefficients between Sentinel-1 and Sentinel-2 vegetation indices for three areas.

Field	Highest Positive Correlation (r) S1_Index - S2_Index	Highest Negative Correlation (r) S1_Index - S2_Index
Area-1	+0.67 VH–NDVI	-0.60 SSD-MSAVI
Area-2	+0.75 VV-MSAVI	-0.71 SSD-MSAVI
Area-3	+0.72 VH-MSAVI	-0.64 SSD-MSAVI

The strongest positive correlations were consistently found between Sentinel-1 VV mean backscatter and optical vegetation indices such as NDVI and MSAVI with coefficients exceeding +0.6. This indicates that the VV polarization backscatter is highly responsive to vegetation vigor and canopy density under specific growth conditions. On the other hand, significant negative correlations were identified between structural SAR indices, particularly SAR Simple Difference (SSD), and specific Sentinel-2 spectral bands sensitive to water content and biomass. The lowest correlation values reached -0.71, suggesting reduced radar returns in areas with dense and moist canopies.

Overall, the findings reinforce the potential of integrating SAR and optical vegetation indices to monitor cotton crop development, structure, and physiological status, offering a reliable approach for growth stage assessment and vigor analysis.

Conclusion

This study underlines the importance of integrating multi-sensor remote sensing for cotton monitoring in the Aegean Region. The temporal consistency between Sentinel-1 SAR and Sentinel-2 optical vegetation indices effectively captures cotton phenological dynamics, highlighting key growth stages where SAR metrics align with optical indicators. Notably, during boll formation and maturation, SAR-based parameters—especially polarimetric decomposition features—remain sensitive to structural and moisture variations, offering an advantage over optical indices that often saturate in dense canopies.

The findings emphasize the potential of SAR-derived entropy, anisotropy, and alpha angle as proxies for biophysical crop traits such as biomass and water content, providing critical insights for irrigation management and early stress detection. By complementing optical data, SAR extends agricultural monitoring beyond its well known all-weather capability, contributing to more robust and data-driven precision agriculture strategies for sustainable cotton production.

References

Barnes, E.M., Clarke, T.R., Richards, S.E., Colaizzi, P.D., Haberland, J., Kostrzewski, M., Waller, P., Choi, C., Riley, E., Thompson, T.L., (2000). Accuracy assessments of vegetation indices using ground-based measurements of leaf area index. Remote Sensing of Environment, 73(1), 87-93.

Cloude, S.R., Pottier, E., (1997). An entropy-based classification scheme for land applications of polarimetric SAR. IEEE Transactions on Geoscience and Remote Sensing, 35(1), 68-78.

Gao, B.C., (1996). NDWI—A normalized difference water index for remote sensing of vegetation liquid water from space. Remote Sensing of Environment, 58(3), 257-266.

Gitelson, A.A., Kaufman, Y.J., Stark, R., Rundquist, D., (2002). Novel algorithms for remote estimation of vegetation fraction. Remote Sensing of Environment, 80(1), 76-87.

Harfenmeister, K., Itzerott, S., Weltzien, C., Spengler, D., (2021). Agricultural monitoring using polarimetric decomposition parameters of Sentinel-1 data. Remote Sensing, 13(4), 575. https://doi.org/10.3390/rs13040575
Huete, A., Didan, K., Miura, T., Rodriguez, E.P., Gao, X., Ferreira, L.G., (2002). Overview of the radiometric and biophysical performance of the MODIS vegetation indices. Remote Sensing of Environment, 83(1-2), 195-213.
Kaufman, Y.J., Tanré, D., (1992). Atmospherically resistant vegetation index (ARVI) for EOS-MODIS. IEEE Transactions on Geoscience and Remote Sensing, 30(2), 261-270.
Nasirzadehdizaji, S., Mahdianpari, M., Salehi, B., (2020). Investigating SAR vegetation indices sensitivity to crop structure and biomass. Remote Sensing, 12(4), 723. https://doi.org/10.3390/rs12040723
Qi, J., Chehbouni, A., Huete, A.R., Kerr, Y.H., Sorooshian, S., (1994). A modified soil adjusted vegetation index. Remote Sensing of Environment, 48(2), 119-126.
Rouse, J.W., Haas, R.H., Schell, J.A., Deering, D.W., (1974). Monitoring vegetation systems in the Great Plains with ERTS. NASA Special Publication, 351, 309.
Veloso, A., Ceschia, E., Demarez, V., Baup, F., Marais Sicre, C., Dejoux, J.F., (2017). Understanding the temporal behavior of crop SAR backscatter and the implications for vegetation monitoring. Remote Sensing of Environment, 199, 324-334.
Wu, J., Chen, L., Zhang, Y., (2020). Improved vegetation structural parameter retrieval from SAR data using SSRM indices. Remote Sensing, 12(5), 820. https://doi.org/10.3390/rs12050820
Zhang, Y., Su, S., Hong, Y., Hong, Z., (2024). Radar vegetation indices for monitoring surface vegetation: Developments, challenges, and trends. Science of The Total Environment, 901, 173974. https://doi.org/10.1016/j.scitotenv.2024.173974
Url-1, Sentinel satellites, https://sentinels.copernicus.eu/web/sentinel/missions, date retrieved 21.03.2025.

HEAT FLUID

Fluid Mechanics

Generation of Proper Inflow Conditions with Hydrodynamic Stability Approach: A Case Study For An Axially-Rotating Pipe Flow

Taha Gunaydin[a], I. Bedii Ozdemir[a]

[a] İstanbul Technical University, Department of Mechanical Engineering, Fluids Group, Türkiye
gunaydin18@itu.edu.tr, bozdemir@itu.edu.tr

Keywords: Hydrodynamic Stability, Inflow Boundary Conditions, Turbulence, Unsteady Flow.

Aim

With the advancement of computers in the last few decades, computationally demanding time-dependent calculations such as Direct Numerical Simulation (DNS) and Large Eddy Simulation (LES) have become increasingly popular in many engineering flows. An inherent problem within these simulations is that they require realistic turbulent inflow conditions, which directly determine the downstream features of the flow (Klein et al., 2001). Various methods (Dhamankar et al., 2018) exist for generating inflow conditions such as transition inducing conditions, turbulence library methods, recycling-rescaling of perturbations, synthetic turbulence generation etc. An important trade-off exists between the computational effort and the accuracy of the final solutions in all of these methods. As, for example, the synthetic turbulence generation offers an easy implementation in time-dependent simulations without requiring excessive computational effort and time. The main disadvantage of this method is the need for a development region, which refers to the distance downstream of the inlet before turbulence becomes fully developed (Dhamankar et al., 2018). This is also called the adaptation region and depends highly on the characteristics of the inflow condition, and usually the aim is to decrease the size of this region as much as possible (Tabor & Baba-Ahmadi, 2010). The synthetic inflow can be constructed with respect to many constraints based on known turbulence properties, such as the turbulent spectra and Reynolds-stresses. However, methods that better represent experimental data are structurally more involved (Fathali et al., 2008) and are intrinsically more complex. A simpler method should require less computational effort.

This study aims to use hydrodynamic stability analysis to construct divergence-free space-time correlated turbulent inlet conditions for an axially rotating pipe flow with Re = 2500 and a swirl number of 0.5.

Material and Method

The method consists of using eigensolutions obtained from the hydrodynamic stability approach. The procedure of hydrodynamic stability analysis involves the decomposition of physical quantities, i.e. velocity and pressure, into their time-averaged and fluctuating parts. Then, the incompressible continuity and momentum equations in cylindrical coordinates (see Figure 1) are rewritten in terms of the decomposed quantities.

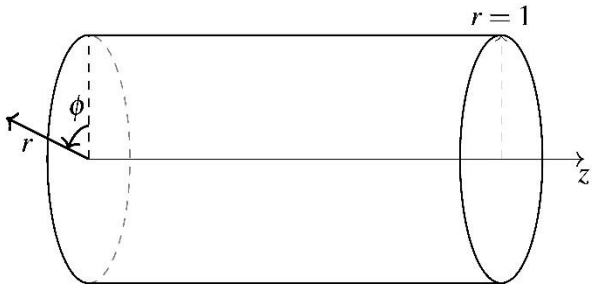

Figure 1. A sketch representing the problem domain with the cylindrical coordinates.

These equations are time averaged and subsequently subtracted from the original equations yielding the modal equations, consisting of the unknown fluctuating quantities. The yielded equations are linearized around the mean flow field obtained from previous experimental and computational studies (Facciolo, 2006) (Figure 2) to obtain a set of linear differential equations

$$\frac{\partial u_r'}{\partial r}+\frac{1}{r}u_r'+\frac{1}{r}\frac{\partial u_\phi'}{\partial \phi}+\frac{\partial u_z'}{\partial z}=0 \tag{1a}$$

$$\frac{\partial u_r'}{\partial t}+\frac{\overline{U_\phi}}{r}\frac{\partial u_r'}{\partial \phi}-2\underline{U_\phi}\frac{u_\phi'}{r}+\underline{U_z}\frac{\partial u_r'}{\partial z} = -\frac{1}{2}\frac{\partial p'}{\partial r}+\frac{1}{Re}\left[\frac{\partial^2 u_r'}{\partial r^2}+\frac{1}{r}\frac{\partial u_r'}{\partial r}+\frac{1}{r^2}\frac{\partial^2 u_r'}{\partial \phi^2}-\frac{2}{r^2}\frac{\partial u_\phi'}{\partial \phi}-\frac{u_r'}{r^2}+\frac{\partial^2 u_r'}{\partial z^2}\right] \tag{1b}$$

$$\frac{\partial u_\phi'}{\partial t}+u_r'\frac{\partial \overline{U_\phi}}{\partial r}+u_r'\frac{\overline{U_\phi}}{r}+\frac{\overline{U_\phi}}{r}\frac{\partial u_\phi'}{\partial \phi}+\underline{U_z}\frac{\partial u_\phi'}{\partial z} = -\frac{1}{2r}\frac{\partial p'}{\partial \phi}+\frac{1}{Re}\left[\frac{\partial^2 u_\phi'}{\partial r^2}+\frac{1}{r}\frac{\partial u_\phi'}{\partial r}+\frac{1}{r^2}\frac{\partial^2 u_\phi'}{\partial \phi^2}+\frac{2}{r^2}\frac{\partial u_r'}{\partial \phi}-\frac{u_\phi'}{r^2}+\frac{\partial^2 u_\phi'}{\partial z^2}\right] \tag{1c}$$

$$\frac{\partial u_z'}{\partial t}+u_r'\frac{\partial \overline{U_z}}{\partial r}+\frac{\overline{U_\phi}}{r}\frac{\partial u_z'}{\partial \phi}+\underline{U_z}\frac{\partial u_z'}{\partial z}=-\frac{1}{2}\frac{\partial p'}{\partial z}+\frac{1}{Re}\left[\frac{\partial^2 u_z'}{\partial r^2}+\frac{1}{r}\frac{\partial u_z'}{\partial r}+\frac{1}{r^2}\frac{\partial^2 u_z'}{\partial \phi^2}+\frac{\partial^2 u_z'}{\partial z^2}\right] \tag{1d}$$

In Equation 1, an overbar denotes time-averaged quantities and ( )' denotes time-fluctuating quantities, $u_j(j=r,\phi,z)$ denotes the non-dimensionalized velocity component j, p is non-dimensionalized pressure and Re is the radius-based Reynolds number.

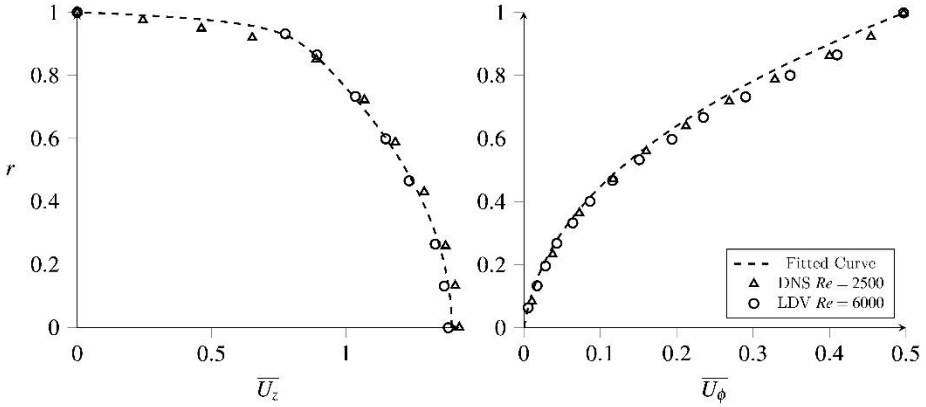

Figure 2. Mean velocity profiles obtained from previous experimental and computational studies and curves fitted to the data.

We then introduce normal-mode solutions for the fluctuating quantities such that

$$u_r' = \hat{u}_r(r)e^{i(k_z z+k_\phi \phi-\omega t)}+(*) \tag{2a}$$

$$u_\phi' = \hat{u}_\phi(r)e^{i(k_z z+k_\phi \phi-\omega t)}+(*) \tag{2b}$$

$$u_z' = \hat{u}_z(r)e^{i(k_z z+k_\phi \phi-\omega t)}+(*) \tag{2c}$$

$$p' = \hat{p}(r)e^{i(k_z z+k_\phi \phi-\omega t)}+(*) \tag{2d}$$

where a hat over a quantity denotes the eigenfunction associated with the corresponding fluctuating quantity, $(*)$ denotes the complex conjugate, i is the imaginary unit, k_z is the eigenvalue in the streamwise direction, k_ϕ is the wavenumber in the azimuthal direction and ω is the frequency associated with the corresponding eigenfunction. Inserting Equation (2) into Equation (1), we obtain an eigenvalue problem

$$\frac{d\hat{u}_r}{dr} = -\frac{\hat{u}_r}{r} - \frac{ik_\phi}{r}\hat{u}_\phi - ik_z\hat{u}_z \tag{3a}$$

$$\frac{d\hat{p}}{dr} = -2W\hat{u}_r + 4\frac{\underline{\underline{U_\phi}}}{r}\hat{u}_\phi + \frac{2}{Re}\left[\frac{d^2\hat{u}_r}{dr^2} + \frac{1}{r}\frac{d\hat{u}_r}{dr} - \frac{\hat{u}_r}{r^2} - \frac{k_\phi^2\hat{u}_r}{r^2} - k_z^2\hat{u}_r - \frac{2ik_\phi\hat{u}_\phi}{r^2}\right] \tag{3b}$$

$$\frac{d^2\hat{u}_\phi}{dr^2} = ReW\hat{u}_\phi + Re\left(\frac{d\underline{\underline{U_\phi}}}{dr} + \frac{\underline{\underline{U_\phi}}}{r}\right)\hat{u}_r + Re\frac{ik_\phi}{2r}\hat{p} - \left[\frac{1}{r}\frac{d\hat{u}_\phi}{dr} - \frac{\hat{u}_\phi}{r^2} - \frac{k_\phi^2\hat{u}_\phi}{r^2} - k_z^2\hat{u}_\phi + \frac{2ik_\phi\hat{u}_r}{r^2}\right] \tag{3c}$$

$$\frac{d^2\hat{u}_z}{dr^2} = ReW\hat{u}_z + Re\left(\frac{d\underline{U_z}}{dr}\right)\hat{u}_r + Re\frac{ik_z}{2}\hat{p} - \left[\frac{1}{r}\frac{d\hat{u}_z}{dr} - \frac{k_\phi^2\hat{u}_z}{r^2} - k_z^2\hat{u}_z\right] \tag{3d}$$

where $W = -i\omega + \frac{\underline{\underline{U_\phi}}}{r}ik_\phi + ik_z\underline{U_z}$. The eigenvalue problem as presented in Equation (3) is then converted into a boundary value problem with a normalization condition, which is an inner product of the eigenfunction $\hat{u}_z$ with its complex conjugate and with a kernel function G

$$\gamma = <\hat{u}_z, \hat{u}_z> \geq \int_0^1 \hat{u}_z G(r)\hat{u}_z^* dr = 1 \tag{4}$$

To solve the eigenvalue problem (3) with the normalization condition (4) the parallel-shooting method is employed. The parallel-shooting method involves the integration of equations from the boundaries up to a mid-point arbitrarily chosen (Keller, 2018). The boundary conditions are determined from the no-slip condition at the wall and the regularity of solutions at the center of the pipe (Meseguer & Trefethen, 2000). However, to integrate the equations, unknown conditions from both boundaries must be guessed. The equations are integrated and a discrepancy vector is obtained at the mid-point. Finally, the multivariable Newton-Raphson method is employed to update the guess values, and the discrepancy at the midpoint is eliminated iteratively (Vetterling & Press, 1992) with a relative tolerance of 1E-6.

Using the obtained Fourier modes, the instantaneous velocity fluctuations with the correct space-time correlations were calculated and added to the mean flow to obtain the inflow conditions.

Findings

The modal equations result in eigenfunctions, with associated eigenvalues and wavenumbers. It is found that all modes are decaying with downstream distance in the solution domain investigated here. This complies with previous findings of other hydrodynamic stability analyses (Lessen et al., 1968). For each frequency ω and azimuthal wavenumber k_ϕ, discrete modes exist and each eigenfunction within each mode has a unique spatial distribution in the radial direction. A dispersion relation, shown in Figure 3, displays part of the solution domain with the eigensolutions that have the least amount of spatial decay at non-dimensional frequency $\omega = 0.1$.

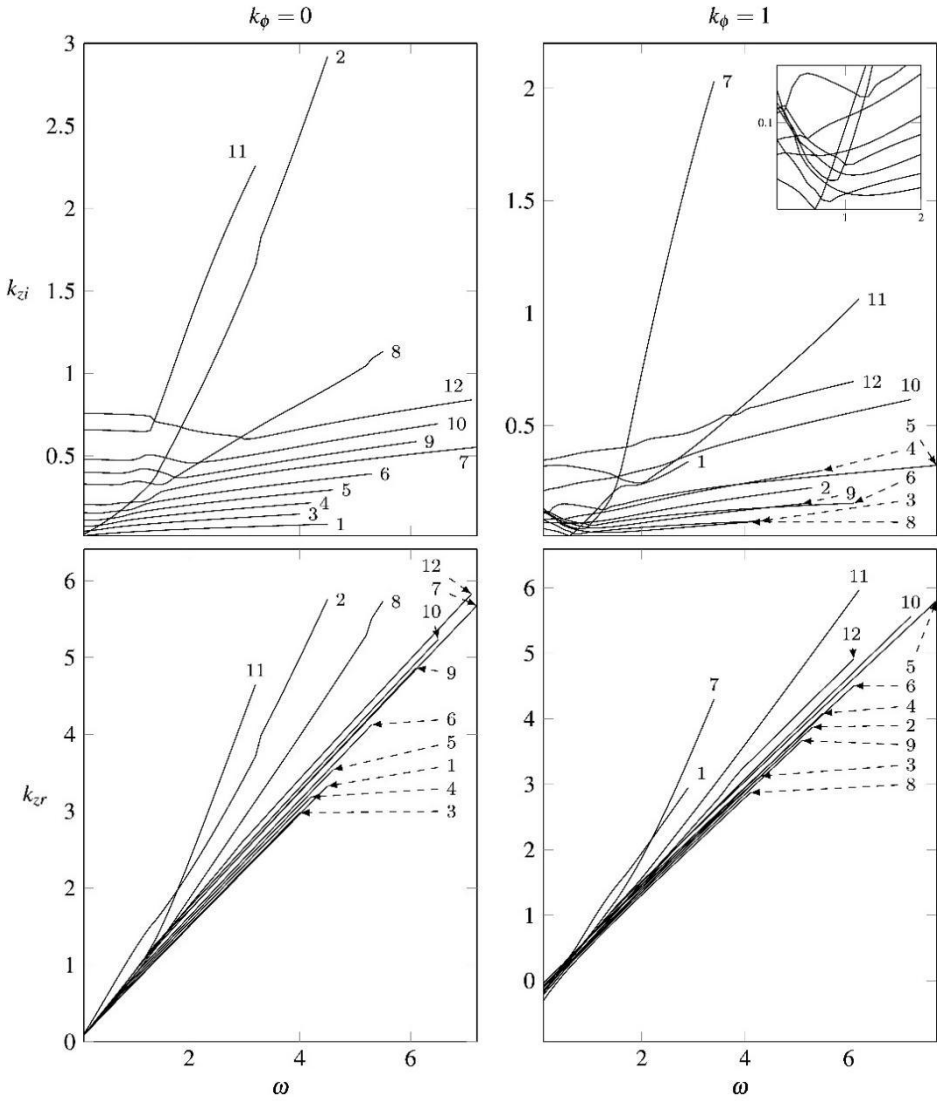

Figure 3. The dispersion relation showing the relation between the eigenvalues ω, wavenumbers k_ϕ and k_{zr}, as well as the decay rates k_{zi} of the eigensolutions.

It is found that for both axisymmetric ($k_\phi = 0$) and non-axisymmetric ($k_\phi = 1$) solutions, the decay rates k_{zi}, which are the imaginary parts of k_z for a given mode, are a function of the frequency. Local minima of k_{zi} exist for each mode, but a general increasing trend for the decay rates can be observed across all modes with increasing frequency. Moreover, a localization of the solutions is observed with increasing frequency. In Figure 4, the first 6 non-axisymmetric modes are shown. It can be seen that the localization is the shrinkage of the radial domain in which amplitudes are relatively large. The exact location around which the localization occurs (the radial point at which eigenfunctions have the maximum amplitude) depends on the mode number and is consistent for a given mode through all three components of the velocity perturbation field. The relative amplitudes of the three eigenfunctions change with frequency, however when the global contribution of kinetic energy is assessed, it is observed that the axial eigenfunctions have the largest contribution amongst the two others. On top of that, a positive correlation between the decay rate of a given mode and the position of eigenfunction maximum is seen. This implies that modes which have a higher concentration of kinetic energy near the wall region have higher decay rates. Also, these modes have relatively higher k_{zr} (real part of k_z), meaning that they have smaller phase velocities ω/k_{zr}. This clearly shows the effect of viscosity to both the decay rate and phase velocity of wave solutions.

Since viscosity has a large influence in the near-wall region due to shear, these results are relevant from a flow physics perspective.

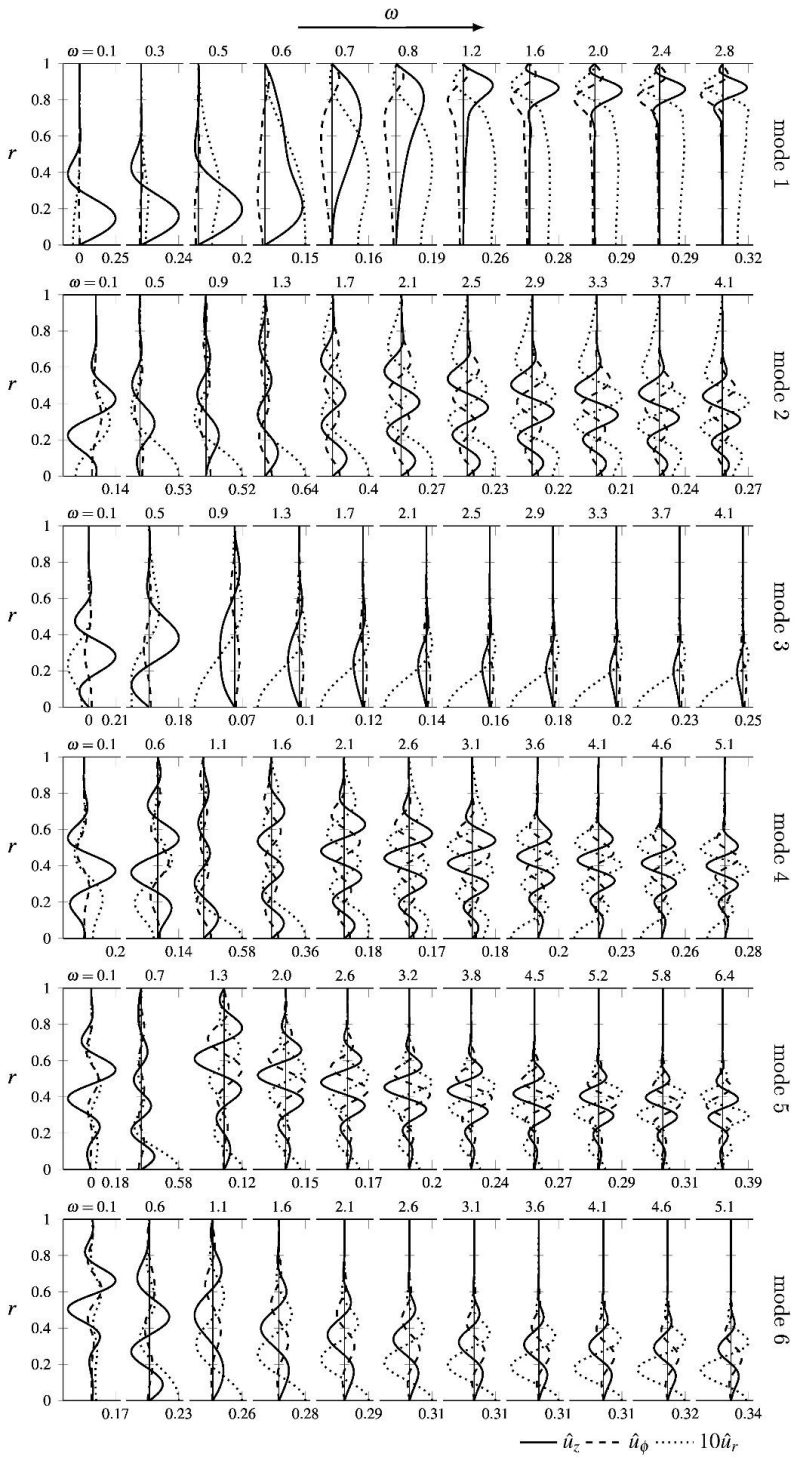

Figure 4. The first 6 non-axisymmetric ($k_\phi = 1$) modes containing the spatial distributions of $\hat{u}_z$ (axial eigenfunction, solid lines) $\hat{u}_\phi$ (azimuthal eigenfunction, dashed lines) and $\hat{u}_r$ (radial eigenfunction, dotted lines) for different frequencies ω.

For the generation of inflow conditions, 5 non-axisymmetric modes are selected, 3 of which show near-wall maxima. A total of 239 eigenfunctions sampled between dimensional frequency of 0.7 to 42 Hz are used to construct a time-dependent fluctuating velocity field. When compared with the findings of previous DNS studies (Facciolo, 2006), RMS values obtained from the perturbation field obtained with the modal analysis in this study capture the trend very well, as shown in Figure 5. The RMS values for the axial velocity field agree very well with the DNS results, whereas the azimuthal RMS values are over-predicted in the near-wall region. On the other hand, the RMS values for the radial velocity component are under-predicted over the entire domain.

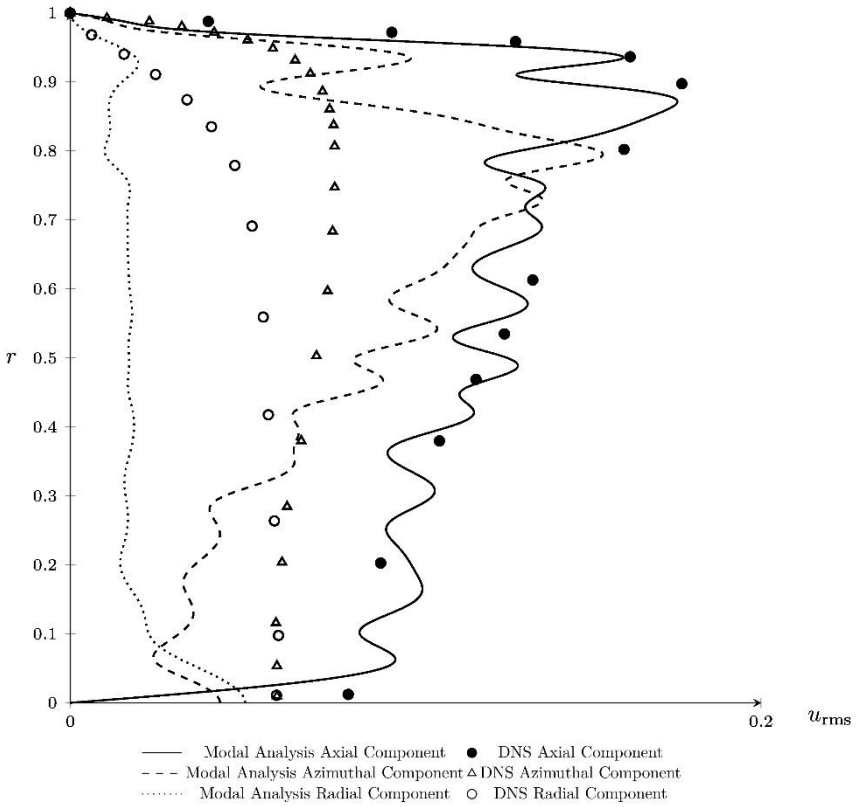

Figure 5. The RMS distributions of the fluctuating velocity field constructed with the selected eigensolutions and RMS distributions from DNS results.

Conclusion

In this study, the use of hydrodynamic stability theory for the generation of inflow conditions is assessed through the RMS distributions obtained from the fluctuating velocity field. It is found that when a specific subset of solutions are used, a fluctuating velocity field with RMS distributions close to DNS results are obtained. This clearly makes this method a good candidate to generate synthetic turbulence for time-dependent calculations such as LES and DNS. On top of that, the obtained modes present a deterministic perspective of understanding turbulence development, in that the presence of near-wall maxima show a strong correlation with the decay rate of eigenmodes and the inverse of phase velocities.

References

Dhamankar, N. S., Blaisdell, G. A., & Lyrintzis, A. S. (2018). Overview of turbulent inflow boundary conditions for large-eddy simulations. Aiaa Journal, 56(4), 1317-1334.
Facciolo, L. (2006). A study on axially rotating pipe and swirling jet flows (Doctoral dissertation, KTH).

Fathali, M., Klein, M., Broeckhoven, T., Lacor, C., & Baelmans, M. (2008). Generation of turbulent inflow and initial conditions based on multi-correlated random fields. International journal for numerical methods in fluids, 57(1), 93-117.
Keller, H. B. (2018). Numerical methods for two-point boundary-value problems. Courier Dover Publications.
Klein, M., Sadiki, A., & Janicka, J. (2001). Influence of the boundary conditions on the direct numerical simulation of a plane turbulent jet. In Second Symposium on Turbulence and Shear Flow Phenomena. Begel House Inc..
Lessen, M., Sadler, S. G., & Liu, T. Y. (1968). Stability of pipe Poiseuille flow. Physics of Fluids, 11(7), 1404-1409.
Meseguer, A., & Trefethen, L. (2000). A spectral Petrov-Galerkin formulation for pipe flow I: Linear stability and transient growth.
Tabor, G. R., & Baba-Ahmadi, M. H. (2010). Inlet conditions for large eddy simulation: A review. Computers & Fluids, 39(4), 553-567.
Vetterling, W. T., & Press, W. H. (1992). Numerical recipes: example book C. Cambridge University Press.

HISTORY OF SCIENCE AND TECHNOLOGY

History of Engineering

History of Mathematics

History of Physics

History of Sciences

The Transformation of Armored Vehicles as a Response to Amphibious Warfare: A Comparative Analysis of the Dieppe Raid and the Normandy Landings

Göktuğ Berk Çakı[a]

[a]Istanbul Technical University, Institute of Graduate Studies, Programme in History of Science and Technology, Türkiye
caki21@itu.edu.tr

Keywords: Amphibious Warfare, Armored Vehicles, Dieppe Raid, Normandy Landings, Military Innovation.

Aim

Amphibious operations have long posed a unique set of challenges to military planners, particularly due to their reliance on cross-domain coordination, unpredictable littoral geography, and heavily defended coastlines. The evolution of armored vehicles during the interwar and Second World War periods reflects a direct response to these complexities. This study aims to investigate how the transformation of armored vehicles was shaped by the practical demands of amphibious warfare and the doctrinal efforts to reclaim offensive initiative in static, defense-dominated theatres.

The core objective of the research is to explore the extent to which this transformation resulted from accumulated battlefield experiences rather than a linear progression of technological improvement. In doing so, the study challenges technologically deterministic perspectives by emphasizing the co-constitutive role of operational failure, engineering improvisation, and institutional learning in the redesign of armored units for seaborne assaults. Rather than treating tanks as isolated instruments of mechanized warfare, the study approaches them as parts of a broader military-technical ecosystem shaped by strategic imperatives and material constraints.

By focusing on the comparative analysis of two pivotal amphibious operations—the Dieppe Raid (1942) and the Normandy Landings (1944)—this research identifies how operational shortcomings in the former catalyzed significant doctrinal and technical innovation by the time of the latter. The study asserts that vehicles like the DD tanks, LVTs, and Hobart's "Funnies" were not simply new machines, but rather integrated battlefield solutions born of specific historical problems. Ultimately, this thesis contributes to a richer understanding of amphibious warfare by examining how armored technologies were transformed not solely by invention, but by necessity.

Material and Method

This research employs a comparative historical methodology rooted in the analysis of military doctrines, engineering developments, and battlefield reports. By focusing on two amphibious operations—Dieppe (1942) and Normandy (1944)—the study identifies the tactical, operational, and technological factors that shaped the performance and transformation of armored vehicles. Each case is analyzed using a multi-scalar framework that includes three layers of interpretation: tactical execution, logistical integration, and doctrinal adaptation.

Primary sources include official after-action reports, military engineering manuals, and doctrinal writings by figures such as Heinz Guderian and Charles de Gaulle. Secondary literature provides historiographical context, with key references drawn from works on armored warfare, amphibious strategy, and military innovation.

In addition to historical documents, the study integrates strategic theory, particularly Colin S. Gray's assertion that "technology changes the character, not the nature of war," to assess how changes in vehicle design addressed enduring challenges in amphibious combat. Technological case examples—such as the Duplex Drive tanks, Landing Vehicle Tracked (LVT), and Hobart's Funnies—are not studied in isolation but as responses to specific operational shortcomings. The analysis aims to reveal how armored vehicle innovation was driven less by abstract engineering potential and more by real battlefield imperatives encountered in coastal assault scenarios.

Findings

The comparative analysis of the Dieppe Raid and the Normandy Landings highlights a fundamental shift in how armored vehicles were conceptualized, modified, and employed in amphibious warfare. At Dieppe, the Allied forces, particularly Canadian armored units, attempted a direct landing of Churchill tanks without adequate preparation for coastal obstacles. The result was operational failure: most tanks were destroyed or immobilized upon landing, unable to support infantry, and ultimately contributing to the mission's collapse.

This failure revealed critical gaps not only in equipment but also in doctrine and planning. There was no joint coordination between infantry, armor, and engineers to overcome beach obstacles, nor was there a contingency for the tanks' mechanical limitations on shingle beaches. Moreover, the absence of specialized vehicles capable of clearing mines, bridging anti-tank ditches, or navigating underwater impediments underscored a larger structural unpreparedness for integrated coastal assault.

In contrast, the Normandy Landings showcased a drastically revised approach. British and American forces fielded a range of purpose-built armored vehicles, from Sherman DD swimming tanks to Crab flails and AVREs equipped for engineering tasks. These designs directly addressed the obstacles identified at Dieppe—mines, sea walls, bunkers, soft terrain—and provided immediate firepower and logistical mobility. The deployment of LVTs and DUKWs by American forces further ensured continuous support beyond the beaches.

The success at Normandy was not due solely to superior machines, but to the integration of vehicle innovation with joint operations doctrine. Armor was no longer an isolated asset but part of a synchronized assault system involving naval fire support, air superiority, and engineering foresight. The findings confirm that battlefield performance of armored vehicles improved when technology was embedded within a holistic operational design shaped by earlier failures.

Conclusion

This study demonstrates that the transformation of armored vehicles in amphibious warfare was not the result of linear technological advancement, but a direct response to operational failure and tactical necessity. The comparison between Dieppe and Normandy illustrates a clear trajectory of institutional learning, where the shortcomings of 1942 led to the development of integrated, purpose-built solutions by 1944.

Rather than relying solely on technological innovation, success at Normandy emerged from a systemic shift in doctrine, planning, and coordination. The introduction of specialized vehicles—such as DD tanks, LVTs, and engineering-modified armor—reflects how the Allies redefined their approach to coastal assault through interdisciplinary adaptation. Engineering, logistics, and battlefield experience came together to overcome the rigid defensive structures that had paralyzed earlier amphibious attempts.

Ultimately, this research reaffirms the argument that in military history, technological tools achieve impact only when they are embedded in broader strategic thinking. Armored vehicles became effective not just because of their capabilities, but because they were redesigned and deployed in harmony with evolving doctrines of joint warfare. The transformation was not inevitable; it was earned through trial, error, and adaptation under fire.

References

Guderian, H. (2019). *Achtung-Panzer! Dikkat! Tank!* (E. Uğur, Trans.). Kastaş Yayınları.

Gray, C. S. (2006). *Strategy and history: Essays on theory and practice*. Routledge.

Kennedy, P. (2013). *Engineers of victory: The problem solvers who turned the tide in the Second World War*. Random House.

Speller, I., & Tuck, C. (2001). *Amphibious warfare: The theory and practice of amphibious operations in the 20th century*. Brassey's.

Parker, G. (2006). *Askeri devrim: Batı'nın yükselişinde askeri yenilikler, 1500–1800* (T. Zorlu, Trans.). Küre Yayınları.

HISTORY OF SCIENCE AND TECHNOLOGY

History of Engineering

History of Mathematics

History of Physics

History of Sciences

Scientific Tendencies in Early Nineteenth-Century Britain: William Sturgeon and The Annals of Electricity, Magnetism and Chemistry

Tuğçe Esenduran[a]

[a] Istanbul Technical University, Department of Humanities and Social Sciences, History of Science and Technology, Turkey
esenduran@itu.edu.tr

Keywords: Electricity, Magnetism, Electromagnetism.

Aim

The recognition of electromagnetism as an independent phenomenon in the early nineteenth century represented a main advancement in the exploration of electricity and magnetism. However, despite substantial experimental progress, the fundamental relationship between electrical and magnetic forces remained poorly comprehended. To attain a more thorough understanding of the scientific challenges of the 19th century, it is crucial to examine the main concerns of the first half of 19th century, as these earlier intellectual developments provided the foundation for subsequent discoveries in electromagnetism.

This study is structured around the table of contents of the A*nnals of Electricity, Magnetism, and Chemistr*y, conducted by William Sturgeon between 1836 and 1843 in 10 volumes. Those Annals, attended by both the general public and academic audiences, served as a platform for both disseminating information and fostering awareness of the developments bridging philosophical inquiry and the practical applications of early electrical technologies in England. The primary aim of the annals is to facilitate the exchange of similar observations, discoveries, and inventions among experimentalists who are not affiliated with formal scientific communities.

The Annals of Electricity, Magnetism and Chemistry features translations of newly published experimental scientific works from Germany, France, Italy, and America, reflecting the interests and intellectual pursuits of its readership. Its work reflects a concerted effort to elucidate the theoretical foundations of electrical experimentation, particularly the fundamental physical laws governing the field. The experiments, researches, and publications were not only enriched scientific discourse but also played a crucial role in expanding public understanding of electricity and its importance.

Material and Method

The advancements of the early nineteenth century arise not only from the combinations of experiments and mechanical thoughts but also theoretical understanding of problems. As we collect materials from scientific journals where various facts first appeared from different countries, we begin to recognize the underlying principles behind them, rather than merely focusing on their practical development. This study seeks to enhance the understanding of first half of 19th-century scientific tendencies with investigations, experiments and instruments by examining the evolution of electrical experimentation with their principles.

The Annals of Electricity, Magnetism and Chemistry, edited by Sturgeon, served as a key periodical that focused on the study, documentation, and experimentation of electromagnetism. This publication attracted a diverse group of contributors, including experimental scientists, instrument makers, electricians, and businessmen, all of whom shared a profound interest in electrical phenomena, viewing electricity as a fundamental natural force. The periodical covered a wide range of topics, including galvanism, the measurement of electricity, electroshock effects from Voltaic pairs, and chemical reactions induced by metals. It also explored the practical applications of electric currents, such as their influence on soft iron and the construction of more powerful electromagnets. Further, it documented the evolution of electromagnetic technology, from the development of electromagnetic apparatuses to the creation of coil-machines and electromagnetic engines. The Annals also examined the impact of electricity on various natural phenomena, such as its effects on geological formations, crystals, and plants, as well as its role in atmospheric phenomena, particularly lightning. Through these contributions, the whole ten

volumes of Annals provided a comprehensive record of the advancements and experimental efforts related to electromagnetic science during this main period.

Findings

Many key investigations have found from the era, which provide a deeper understanding of the scientific tendencies during the emergence of electromagnetism. First of all, the measurement of the magnitude of the electric current obtained from Volta's piles was one of the significant endeavours of the period. In this context, the measurement had achieved by comparing the various effects produced by the current. The current intensity, determined through its physical, chemical, and physiological effects, can be derived from one another. In particular, the physical effect of the electric current on a magnetic needle can be measured with high accuracy. Experiments from the period also indicate that the electric current is capable of generating heat, and the amount of electricity produced by the piles can be determined through the quantity of heat generated. Additionally, the main concern to get a more economical and more powerful arrangement between the scientific enquirers. Whole arrangements were in an attempt to get a sustainable battery with maximum power and minimum cost of operation. (Morus, 2019)

Another significant subject of study within the field of electromagnetism was the 'Galvanometer' which is used to measure the galvanic force generated by a conducting wire and serves as the medium for an electric current flowing from the positive to the negative pole of a galvanic or voltaic battery, or to assess the strength of any electric current, regardless of its source of excitation. Its operation is based on electromagnetism, a phenomenon discovered by Oersted in 1820, and its readings are indicated by the deflection of a magnetic needle placed within the range of the electrodynamic influence. The first type of galvanometer, known as Prof. Schweigger's multiplier, was constructed following the discovery of electromagnetism. While this instrument was adequate for most purposes, it required certain modifications to be suitable for research that demanded extreme precision and sensitivity. Experimental researches have focused on constructing larger sized galvanometers or multipliers beyond that point, aiming to improve their sensitivity and accuracy for more precise measurements. The galvanometer holds a crucial position in electrodynamical research, serving as an essential instrument for detecting and measuring small electric currents and it has also become a popular subject of discussion among philosophers.

The electrochemical action of electricity became evident in the 1830s through the electrical actions exerted by simple metals on fluids. Most experiments seem exceptionally well-designed to guide our understanding towards the source of chemical action. The experimentalists had an effort to find most compelling demonstration of how a simple galvanic arrangement can activate the powerful energies involved in the chemical transformation of matter.

The second major phase of research emerged with the invention of the electromagnet, in response to the need for stronger magnetic forces and the impracticality of large batteries, Sturgeon developed the electromagnet as an educational tool, following Oersted's announcement of the phenomenon of electromagnetism. This breakthrough allowed for further studies on the relationship between electricity and magnetism, leading to advancements in the construction of electromagnets and the development of new applications, such as the creation of electromagnetic engines and more efficient electrical machinery. This innovation sparked a wave of intensive experimentation aimed at improving electromagnets, leading to rapid and remarkable advancements in their design and functionality. The development of the electromagnet made the realization of a practical electric motor possible. For several years thereafter, the electric motor was referred to as the 'electromagnetic engine'.

A magnetic electrical machine, characterized by its efficiency, affordability, and immediate usability, is essential for experimental research. These machines emerged as one of the most significant instruments in electrical experimentation. Given the cost and operational challenges associated with voltaic batteries, magnetic electrical machines were increasingly adopted as primary tools for experimental investigations during this period. As a result of these, researches in electrodynamics, both in theoretical and experimental contexts, gained considerable interest among experimental philosophers.

Following Jacobi's 1835 invention of the high-speed rotary electric motor and the publication of his paper "On the Application of Electromagnetism to the Moving of Machines", which was translated and published in Sturgeon's Annals, interest in the development of electric motors increased significantly. There was a growing demand for an affordable and accessible source of power to drive electric machinery, trains, and transportation systems. As a result, electricity became a subject of widespread public interest, extending beyond experimental philosophers to engage individuals across all levels of society. As we realize from the articles, the development of experimental and philosophical apparatuses with practical applications gained significant momentum. And William Sturgeon noted that the electromagnetic engine described in the first volume of the Annals was capable of providing motion to machinery. He mentioned that successfully demonstrated by propelling both a boat and a locomotive carriage.

Another different area of investigation is electrical theory of mineral veins which stands as a distinct and intriguing aspect of electrical research. The interactions of minerals with voltaic electricity have particularly captured the scientific community's attention. Following Robert Fox's work on the "Influence of Electrical Action on Clay", numerous discussions and studies have emerged, further advancing our understanding of this fascinating field. That exploration highlights the dynamic relationship between electrical forces and matter, contributing to the broader discourse on the nature of electrical phenomena.

Conclusion

In conclusion, *Annals of Electricity, Magnetism, and Chemistry*, edited by Sturgeon between 1836 and 1843, documents numerous experiments conducted by individuals with a keen interest in electromagnetic phenomena. It provides significant insight into the scientific tendencies of nineteenth century England. The investigations of this era, particularly those focused on electromagnetism, display a distinct evolution in both theoretical and experimental approaches. The volumes of Annals of Electricity, Magnetism and Chemistry demonstrating clearly about scientific tendencies during its time in terms of electricity and magnetism phenomena. It is a good combination of different type of researches who have the theoretical or practical point of view including philosophers, experimentalists, instrument makers, scientific enquirers.

In early nineteenth-century physical science, the conservation of energy was a key concept. The development of energy conversion processes began with Volta's invention of the battery in 1800, leading to discoveries showing how energy could transform between different forms—chemical, electrical, heat, light, motion, and magnetism. (Clagett, 1969) Through the Annals, we gain a clearer understanding of how early electrical technologies bridged the gap between philosophical inquiry and practical application, while contributing to the advancement of this branch of science. As a result, this period was a key turning point in scientific thought, leading to modern physics and shaping future technological advancements. After having had a deep understanding of studies in that decade, the next phase of this study will focus on the network analysis between William Sturgeon and others who had deep interest in electricity, as reflected in those Annals.

References

Clagett, M. (Ed.). (1969). Critical Problems in the History of Science. Univ of Wisconsin Press (pp. 321-340).
Morus, I. R. (2019). When physics became king. University of Chicago Press (pp.102-3).

HISTORY OF SCIENCE AND TECHNOLOGY

History of Engineering

History of Mathematics

History of Physics

History of Sciences

Brief History Of Artificial Intelligence Approaches

İlkem Ahu Şahin[a], Aytekin Çökelez [a]

[a] İstanbul Technical University, Graduate School, History Of Science And Technology, Türkiye
sahinil20@itu.edu.tr

Keywords : Emergence of Machine Learning, Expert Systems, Histories of Artificial Intelligence Approaches , Symbolic AI.

Aim

Artificial intelligence (hereafter AI) has been modeled and implemented according to the various approaches since the emergence and grounding of the field in the middle of the twentieth century. Applications of formal logic for problem solving versus attempts in modeling human cognitive systems competed and opened path for further research. The different paths for finding a solution for artificial intelligence problems already branched out following the Dartmouth Conference of 1956. Symbolic, knowledge based, and data-driven approaches evolved throughout the years of study and implementation. The aim of this paper is to explore the emergence of different approaches on artificial intelligence implementation and present a summary as part of the overall historical narrative of AI.

Material and Method

This paper contains a part of a wider research conducted for the first author's PhD thesis in the field of history of artificial intelligence. The understanding of emergence and evolution of different artificial intelligence approaches is a key element of the overall research. The study starts from the middle of the twentieth century when artificial intelligence was defined as a separate field.

Determining the Purpose: There exist various narratives about the emergence and evolution of different artificial intelligence approaches. The purpose of the study is to compile them and present in a high-level summary for corresponding audience.

Identification: The exploration of the topic was conducted by examining literature through academic journals, portals and thesis centers related to the topic. As a result, the research scope was determined as a key section of the overall study of the history of artificial intelligence.

Analysis: The emergence of algorithms and its definition during the early years of AI was investigated to understand the conceptual background. Different AI models defined following the Dartmouth Conference of 1956 and evolving throughout the years were analyzed.

Synthesis: A historical narrative of the artificial intelligence approaches was compiled as a continuously evolving area.

Findings

Alan Turing provided a description of the universal machine and a list of concrete finite steps for the "decision problem" in his article "Computable Numbers" in the first half of the twentieth century. Thereby, Turing defined an algorithm, a clear definition of the solution generation procedure (Turing, 1936).
The emergence of algorithm dates to much older times than Turing's universal machine. The first algorithm was known to be presented by Ebu Abdullah Muhammed İbn Musa el Hârizmî (780-850), of Uzbek origin, in his book Hisab el Cebir ve el Mukabala, using Arabic numerals. El Hârizmî systematically described the calculation procedures in this first book known to be written on algebra. While reaching Europe, the title of the book was translated as Algoritmi de Numero Indorum in Latin due to the difficulty of pronouncing his author's name. Eventually, the term "algorithm" was born (Hazar, 2022).

An algorithm can be described as "a self-contained sequence of instructions and actions to be performed by a computational machine" (Deng: 2018, p.172). Developments regarding artificial intelligence (hereafter AI) algorithms and programming languages have been shaped according to the different approaches to the field starting from the middle of the twentieth century. In 1956, Herbert A. Simon, Allen Newell and John Clifford Shaw developed The Logic Theory (hereafter LT) at the RAND Corporation as a virtual machine, as a prototype of a computer program. The program could prove theorems from the Principia Mathematica of Alfred N. Whitehead and Bertrand A. W. Russell (Vayre, 2021). The Logic Theory is acknowledged as the first artificial intelligence program (Url-1).

Simon and Newell (1956, p.1) described the LT as a complex information processing system to discover proofs of theorems in symbolic logic: "This system, in contrast to the systematic algorithms that are ordinarily employed in computation, relies heavily on heuristic methods similar to those that have been observed in human problem solving activity. The specification is written in a formal language, of the nature of a pseudo-code, that is suitable for coding for digital computers."

The Logic Theory was designed for solving complex mathematical problems mimicking human cognitive processes. LT's designers demonstrated problem solving capability of a computer by discovering solutions in a complex nonnumerical domain using heuristic search (Penn, 2020; Vayre, 2021). Newell and Shaw (1957) explained that the problem they sought for a solution contained sufficient information and alternatives, yet there was lack of known clean-cut way of where the path to the solution was not clear at the start and vague rules of thumb were employed. LT was designed as a heuristic program for such complex problem-solving situations.

Simon and Newell presented their program in the Dartmouth Summer Research Project conference of 1956. The conference is recognized as the event in the history where the phrase "artificial intelligence" was first recorded, and the conceptual foundations of the field were laid.

Most researchers attending the conference, including the organizers John McCarthy and Marvin L. Minsky, did not see any point in studying human cognitive processes at that time where they shared the view that AI researchers should focus on formal logic instead. John McCarthy and Marvin Minsky later developed different views. McCarthy held logic as the primary focus area, whereas Minsky followed anti-logic approach. McCarthy developed the list processing language LISP in 1958 and proposed "IF, THEN" advice taker program in 1959 and worked on circumscription that Vayre (2021) describes as "a computing process by which the obstacles potentially impeding the logic inference engines can be isolated or minimized, to allow for navigation within a knowledge-based system" (p. 34). In 1962, McCarthy left Massachusetts Institute of Technology (hereafter MIT) AI Laboratory for the Stanford University AI Laboratory and worked on knowledge-based systems (Vayre, 2021). Minsky on the other hand continued at the MIT AI Lab where he received sufficient investments including from the U.S. Defense Advanced Research Projects Agency (DARPA) to work on establishing anti-logic approach on artificial intelligence. All these attempts played an important role in the development of artificial intelligence study approaches and influenced other researcher's work (Vayre, 2021).

Artificial intelligence research and implementation technologies went through several phases since the emergence of the field. From the middle of the twentieth century, different approaches such as symbolic manipulation, expert-systems databases, and data-driven machine learning approaches were explored. The symbolic approach introduced a heuristic symbolic information processor modelling of the human reasoning whereas the expert systems studies attempted to formalize human knowledge as databases of 'if–then' rules (Ali et al., 2023). In the early years of AI, from the mid-1950s to the 1980s, the symbolic AI approach was prevalent, based on the assumption that human thinking system used symbols in representing objects and problems (Anantrasirichai and Bull, 2021). Starting from 1960, expert knowledge engineering was applied for application domains where symbolic logical rules were used for the design of programs. Expert systems as knowledge-based AI systems were however lacking learning ability. They were mainly able to take human expert like decisions based on logical reasoning usually implemented by the inference rule algorithms in the form of "if-then-else". This approached worked well in narrowly defined application domains, yet it was insufficient to address uncertainty. Expert systems are still in use where the application domain is sufficiently narrow such as in the case of chess playing programs (Deng, 2018).

The next wave of AI, the data-driven machine learning relied on statistical models and simple neural networks. Training data was used by the engine to learn or tune existing parameters to keep up with uncertainties or changing conditions (Ali

et al., 2023). With machine learning, learning programs replaced the programmer and automatically learned the necessary algorithms from the data. This was possible because a certain pattern exists in big data. In other words, the hidden model underlying the observed data was extracted (Alpaydın, 2022). Deep learning as an approach differentiates from simple machine learning by the underlying deep and layered model structure of neural networks and associated end to end learning algorithms (Deng, 2018). The neural network approaches that stem from the 1940s are implemented in the contemporary times based on large databases to learn from data by computing patterns and correlations and make future forecasts accordingly (Ali et al., 2023).

Developments in machine learning and successes in deep learning have pointed out that intelligence can be achieved applying simple algorithms patiently and constantly rather than the need for inventing complex formulas and hence artificial learning became a driving force in intelligence. All these developments were a cure for the frustration caused by the old logic-based programmed expert systems in the 1980s. In the mid-80s, artificial neural network research boomed. Not only computer science, but also various disciplines such as electrical engineering, physics, statistics, psychology, cognitive science, neuroscience and linguistics were interested in this field. The advances in very-large-scale integration (VLSI) technology that coincided with this period also showed promise for implementing artificial neural networks that would distribute computation to large numbers of parallel processing units, with the capacity to create parallel hardware containing thousands of processors. Originally designed for fast image processing and transfer in graphical interfaces, the parallel computing, and data transfer architecture of the Graphics Processing Unit (GPU) was also deemed suitable and developed for machine learning. Artificial learning systems have become stronger than preceding expert systems with their success in representing uncertainties in the real-world using probability theory and models based on learning from examples that do not require programming (Alpaydın, 2022).

Conclusion

Artificial intelligence has been implemented according to different approaches since the grounding of the field in the middle of the twentieth century. Defenders of formal logic versus human cognitive system models for defining solutions appeared throughout the different waves in the history. Symbolic, knowledge based, and data-driven approaches were adapted, and some, by having transformed, survived to the present day.

This extended abstract contains a part of the ongoing dissertation work of İlkem Ahu Şahin for the degree of PhD in the History of Science and Technology, İstanbul Technical University, Türkiye.

References

Ali, S. M., Dick, S., Dillon, S., Jones, M. L., Penn, J., Staley, R. (2023). Histories of artificial intelligence: a genealogy of power. BJHS Themes, 8(1), 1-18. doi:10.1017/bjt.2023.15.

Alpaydın, E. (2022). Yapay Öğrenme: Yeni Yapay Zekâ. (Book). Tellekt.

Anantrasirichai, N., and Bull, D. (2021). Artificial intelligence in the creative industries: a review. Artificial Intelligence Review , 55, 589–656. doi:10.1007/s10462-021-10039-7.

Deng, L. (2018). Artificial Intelligence in the Rising Wave of Deep Learning: The Historical Path and Future Outlook [Perspectives]. IEEE Signal Processing Magazine, 35(1), 180-177. doi: 10.1109/MSP.2017.2762725.

Hazar, Z. (2022). From Leibniz To Artificial Intelligence: A Logical And Epistemologıcal Study On Formal Languages (In Turkish with abstract in English). PhD Thesis, Akdeniz Üniversitesi, Sosyal Bilimler Enstitüsü, Felsefe Anabilim Dalı, Antalya.

Newell, A., & Simon, H. A. (1956). The logic theory machine--A complex information processing system, In IRE Transactions on Information Theory. 2(3), 61-79. doi: 10.1109/TIT.1956.1056797.

Newell, A., & Shaw, J. C. (1957). Programming The Logic Theory Machine. In Papers presented at the February 26-28, 1957, Western joint computer conference: Techniques for reliability (IRE-AIEE-ACM '57 (Western)). (pp. 230–240). New York, NY: Association for Computing Machinery.

Penn, J. N. (2020). Inventing Intelligence: On the History of Complex Information Processing and Artificial Intelligence in the United States in the Mid-Twentieth Century. PhD Thesis, University of Cambridge, History and Philosophy of Science.
Turing, A. M. (1936). On Computable Numbers, with an Application to the Entscheidungsproblem. Proceedings of the London Mathematical Society, 42(1), 230-265.
Url-1 www.historyofinformation.com, date retrieved 30.04.2024
Vayre, J.-S. (2021). Artificial intelligence: between science and the market. Some socio-historical elements to better understand a strange scientific experiment (1956-1990). Original article in French published in 2021 in Gérer & comprendre, 145, 55-69.

HYDRAULICS AND WATER RESOURCES ENGINEERING

Hydrology

Spatio-Temporal Analysis of Long-Term Rainfall Erosivity Trends and Climate Impacts on Erosion Potential

Ahmet Faruk İpek[a], Ercan Kahya[a]

[a] Istanbul Technical University, Civil Engineering Department, Hydraulics Division, Turkey
faruk.ipek@itu.edu.tr

Keywords: Erosion Risk Assessment, Modified Fournier Index, Modified Mann-Kendall Method, Küçük Menderes Water Basin.

Aim

Erosion, driven by natural processes and human activities, leads to soil loss and reduced fertility. Precipitation amount and distribution play a crucial role in erosion dynamics. This study examines the impact of precipitation on erosion potential in the Küçük Menderes River Basin using 50 years (1974–2023) of monthly precipitation data. Modified Fournier Index (MFI) and Modified Mann-Kendall (M-MK) trend analysis methods are applied to assess long-term seasonal and annual variations across temporal and spatial scales. Data from five meteorological stations across coastal and inland areas provide insights into how precipitation trends influence erosion risk under varying climatic and geographical conditions. The study explores the relationship between precipitation trends and MFI, highlighting the role of intense rainfall in erosion and risk variations during dry periods. By evaluating climate variables such as precipitation regime, intensity, and distribution, the study aims to determine climate-induced erosion risks.

Study Area and Data

The Küçük Menderes River Basin, covering approximately 345,701 hectares, is primarily located in İzmir (SYGM, 2019). This study utilizes a complete 50-year (1974–2023) precipitation dataset from the Turkish State Meteorological Service. Data from five meteorological stations İzmir, Salihli, Selçuk, Ödemiş and Sultanhisar were analyzed (Figure 1).

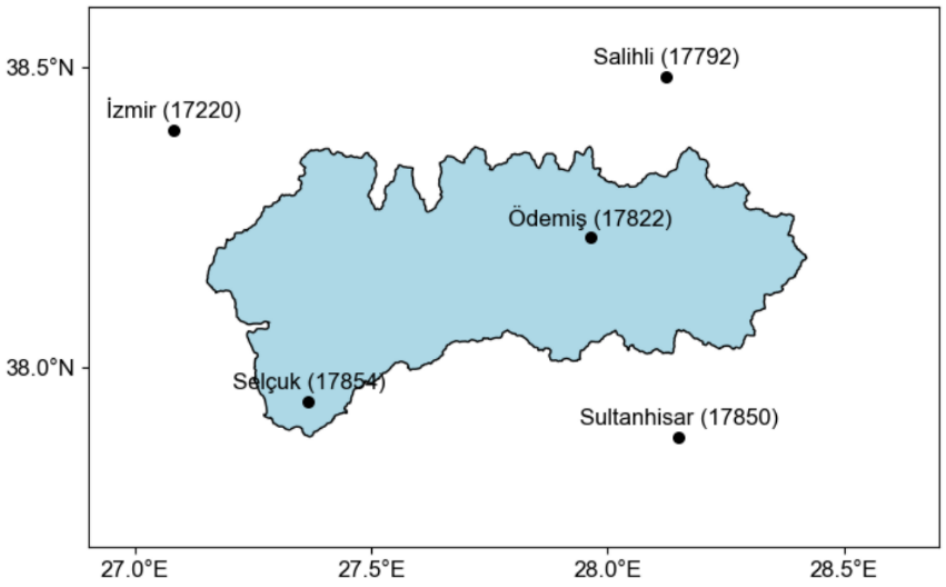

Figure 1: Meteorological observation stations.

Material and Method

Modified Fournier Index (MFI)

Introduced by Arnoldus (1977), the Modified Fournier Index (MFI) indirectly reflects precipitation's erosion potential. It is calculated as the ratio of each month's squared precipitation to the annual total and serves as a key parameter in erosion assessment.

$$MFI = (\sum (i=1 \text{ to } 12) P_i^2) / P_{total} \quad (1)$$

Here, P_i represents the montly precipitation (mm), P_{total} is the total annual precipitation (mm). With this approach, months with high precipitation are emphasized more, making the differences between dry and wet periods more distinct. Consequently, the estimation of precipitation-induced erosion risk becomes more accurate.

Modified Mann-Kendall (M-MK) Trend Test

The Modified Mann-Kendall (M-MK) test, developed by Hamed and Rao (1998), is an improved version of the Mann-Kendall test designed to detect trends in time series data while accounting for autocorrelation. In cases where data points are dependent on previous values, traditional Mann-Kendall results can be misleading. The M-MK test corrects for this by adjusting the variance before calculating significance. In this method, data points are arranged in chronological order, and each value is compared with subsequent values to compute the S statistic, which indicates whether the trend is increasing or decreasing. However, if the data exhibits autocorrelation, the variance of S is modified using a correction factor. After this adjustment, the Z statistic is computed to determine the significance of the trend. The test statistic is calculated as:

$$Z = S / \sqrt{V^*} \quad (2)$$

where S represents the trend direction, and V* is the adjusted variance that accounts for autocorrelation. If the absolute value of Z exceeds a critical threshold, the trend is considered statistically significant. A positive Z value suggests an increasing trend, while a negative Z value indicates a decreasing trend. If Z is close to zero, no significant trend is detected. By incorporating autocorrelation adjustments, the M-MK test provides a more reliable analysis for long-term datasets.

Findings

Precipitation amounts and MFI values show strong parallelism annually and monthly. In coastal stations (İzmir, Selçuk), MFI varies widely at high levels, while in continental Salihli, it remains lower and more stable. In transitional regions (Ödemiş, Sultanhisar), MFI is generally moderate (Figure 2). These findings suggest that erosion risk is higher in coastal areas due to more frequent extreme rainfall, whereas inland regions experience lower erosion potential due to more stable and limited precipitation patterns.

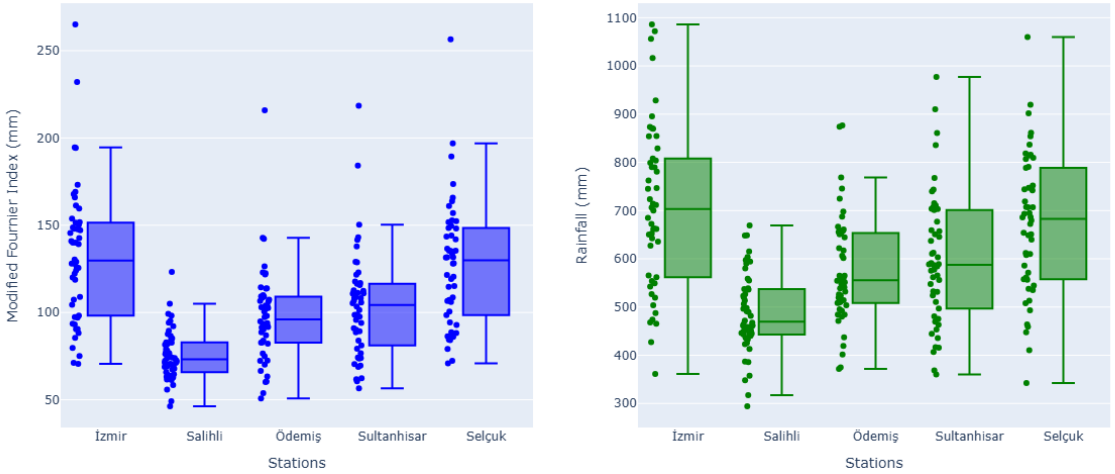

Figure 2: Boxplot representation of annual MFI and precipitation data by station.

On a monthly basis, MFI values rise to high levels in winter, with outliers exceeding 160 mm indicating increased erosion potential. In contrast, summer values drop to lower ranges, reflecting lower and less intense rainfall. High MFI values in İzmir and Selçuk highlight intense winter precipitation, while frequent winter outliers suggest occasional extreme rainfall events, further increasing erosion risk.

Additionally, an analysis of the 50-year dataset reveals significant declines in MFI values between 1991–1994 and in 2008, while sudden increases were observed in 1981 and 2001. Similarly, drought periods were identified in the Küçük Menderes Basin during 1992–1994, 2001, 2007, and 2008 (İpek & Kahya, 2022). This correlation indicates that declines in MFI align with drought conditions (Figure 3).

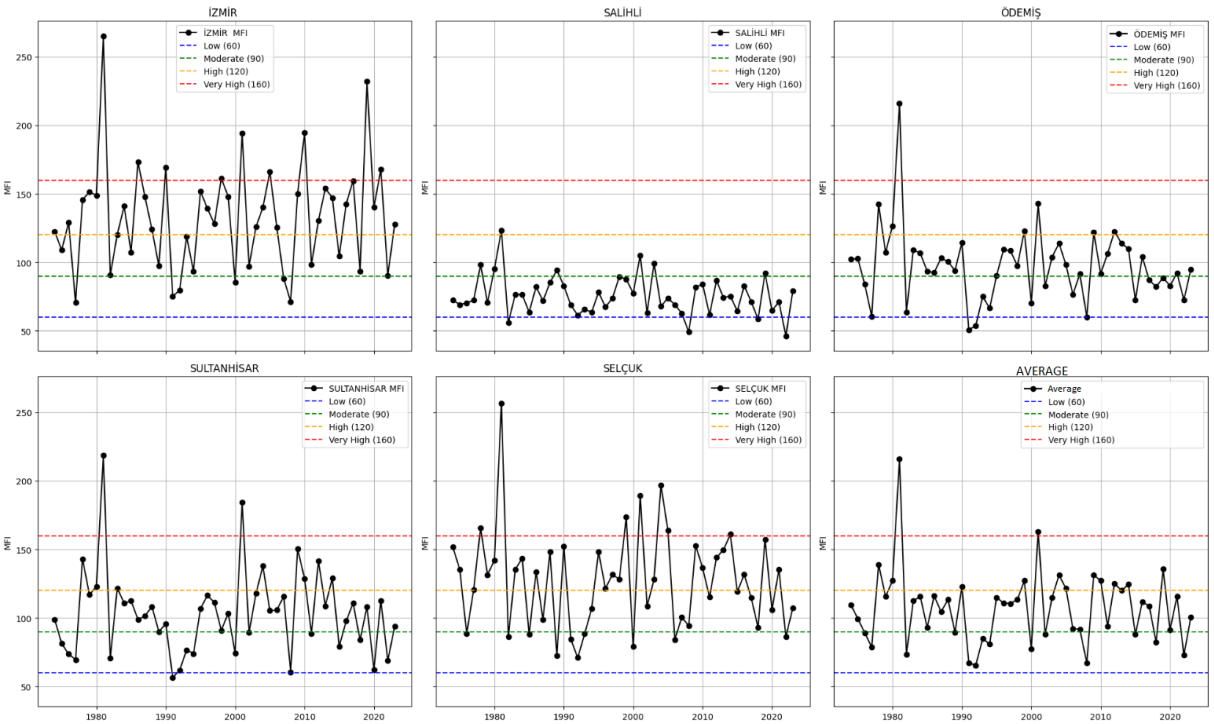

Figure 3: Modified Fournier Index (MFI) time series for individual stations and overall average.

According to Apaydın et al. (2006), high erosion potential is more frequent in maritime regions, while MFI remains stable at moderate levels inland. İzmir and Selçuk show increased erosion risk with 24 and 22 "very severe" cases and 9 and 7 "extremely severe" cases, respectively. In contrast, Salihli, with continental characteristics, is dominated by "moderate" cases (39), with almost no extreme events. Transitional regions Ödemiş and Sultanhisar have 26 and 24 "severe" cases, with 6 and 8 in the "very severe" category. These variations in MFI reflect differences in precipitation regimes from coast to inland areas (Table 1).

Table 1: The number of occurrences of erosion classes in Havza between the years 1974-2023.

Station	Low (0-60)	Moderate (61-90)	Severe (91-120)	Very Severe (121-160)	Extreme (>160)
İzmir	0	8	10	23	9
Salihli	4	39	6	1	0
Ödemiş	4	14	25	6	1
Sultanhisar	2	16	22	8	2
Selçuk	0	10	12	21	7

Precipitation and MFI (1974–2023) were analyzed using the M-MK method. Annual evaluations were conducted by eliminating seasonal influences. This was achieved by analyzing each month's data separately, preventing seasonal fluctuations from distorting overall trends. Trends were significant at $|Z| \geq 1.95$ ($p<0.05$). The results indicate that precipitation and MFI trends exhibited largely similar patterns across the basin. According to Figure 4, increasing trends are marked in blue, while decreasing trends are shown in red, with significant trends denoted by an asterisk. The parallel behavior of precipitation and MFI suggests that both variables are influenced by similar environmental and climatic processes. Though mostly not significant, notable changes appeared in specific periods and locations. In İzmir, June precipitation ($Z=2.36$) and MFI ($Z=2.39$) increased, suggesting higher summer erosion risk. Similarly, in Salihli, December precipitation ($Z=-2.14$) and MFI ($Z=-2.25$) declined, indicating irregular winter rainfall. Moreover, it was observed that increasing trends were more prevalent in summer months, while significant decreasing trends dominated in winter. This finding indicates a seasonal shift in the basin's precipitation regime, reflecting potential long-term changes in hydrological and climatic dynamics.

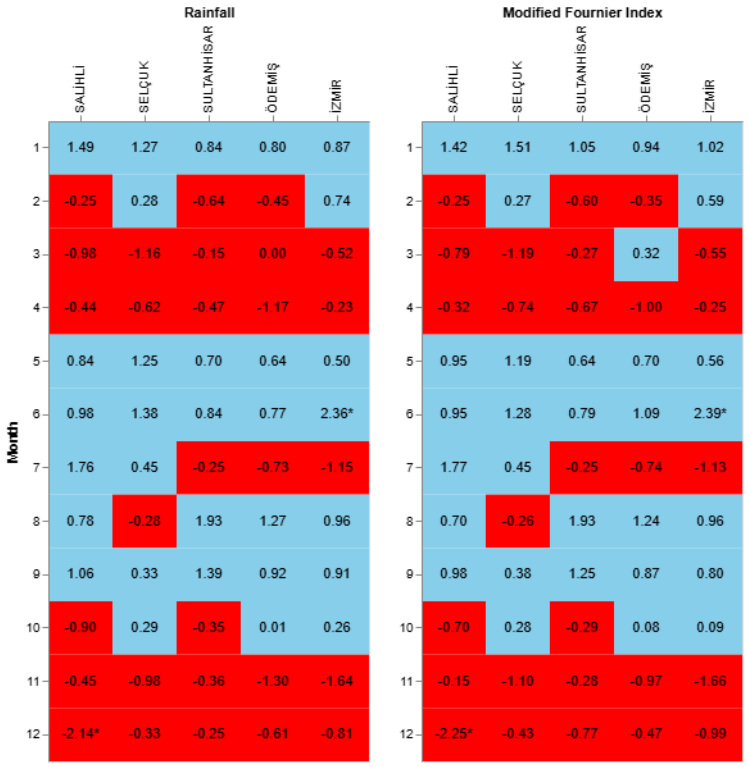

Figure 4: Comparison of monthly MFI and precipitation trends.

Trend maps used blue (increase), red (decrease), and solid arrows for significant trends Coastal areas showed rising trends, while inland regions declined due to microclimatic and topographic influences. Although most months exhibit similar trends across all stations, variations between stations were observed in certain periods. For instance, while increasing trends were detected in western stations during February, decreasing trends were observed in the eastern stations. This indicates that changes across the basin are not homogeneous and that local factors and microclimatic effects may play a significant role (Figure 5).

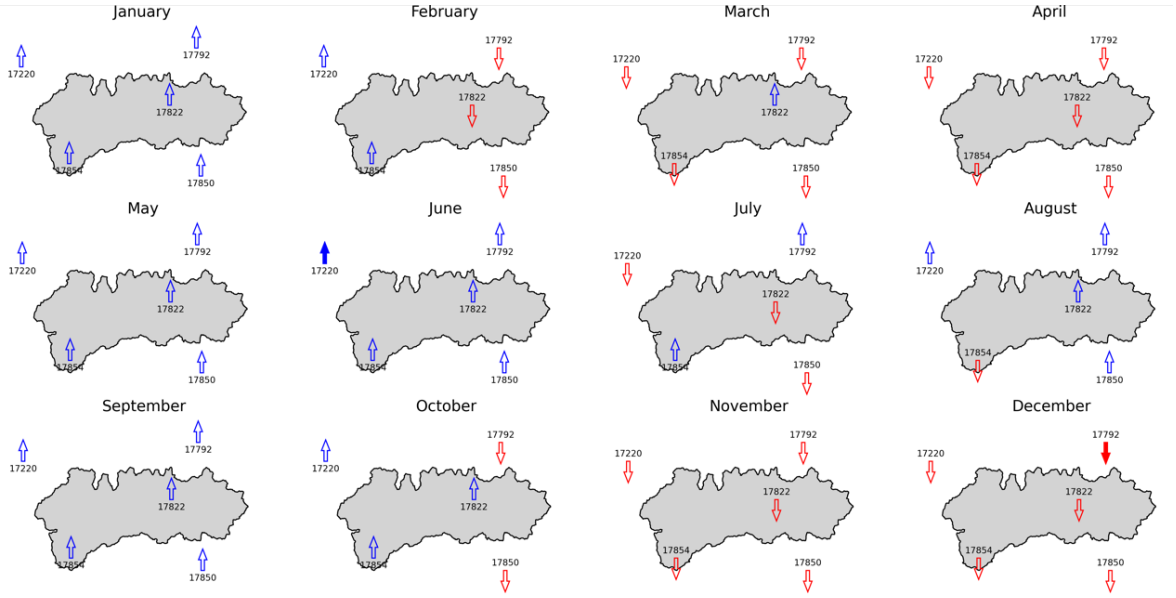

Figure 5: Monthly Modified Fournier Index trend maps.

According to the 50-year trend map, decreasing trends were observed at all stations except the İzmir station. However, these trends were not statistically significant at the 95% confidence level (Figure 6).

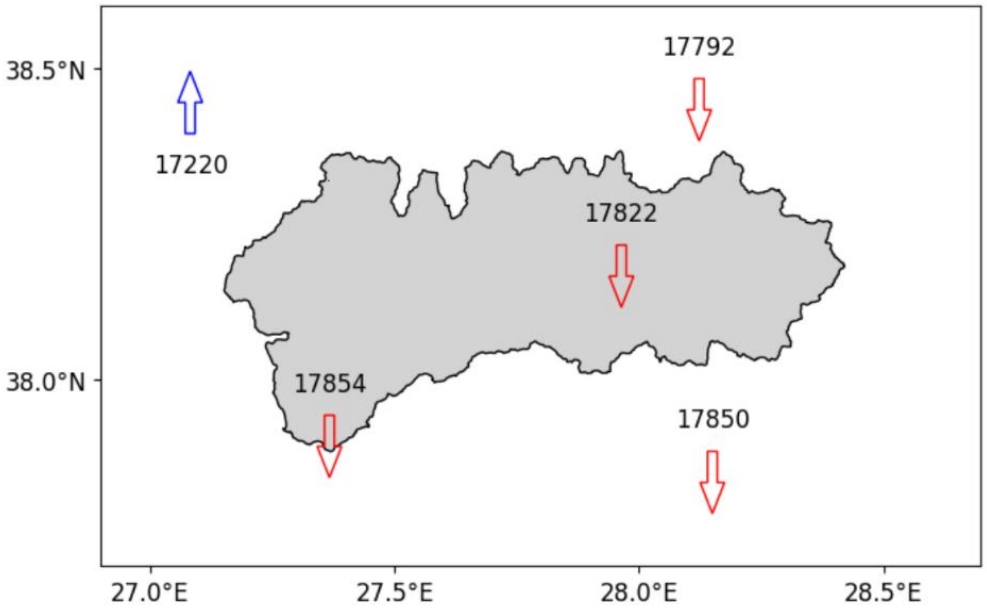

Figure 6: Yearly Modified Fournier Index trend maps.

Conclusion

In this study, the MFI and M-MK results obtained from 50 years (1974–2023) of precipitation data exhibited spatial and temporal variability. The high MFI values in coastal areas (İzmir, Selçuk) indicate a significant erosion risk due to intense rainfall, whereas in Salihli, which has a continental climate, MFI values remained at a "moderate" level, with limited

occurrences in extreme risk categories. Fluctuations observed in transitional regions (Ödemiş, Sultanhisar) highlight the influence of microclimatic and topographic factors.

On a monthly basis, MFI outliers exceeding 160 mm in winter months demonstrate the impact of short-term intense rainfall on erosion, while lower MFI levels during summer indicate a lower erosion risk. In the long term, the declines observed during drought periods in 1991–1994 and 2008, along with the sudden increases in 1981 and 2001, reveal significant fluctuations. While trend analyses did not show statistically significant trends in most stations, the positive trend in June precipitation in İzmir and the negative trend in December in Salihli suggest different scenarios for coastal and inland areas. The findings indicate that instead of a uniform pattern of change across the basin, period-specific and station-specific trends dominate, emphasizing the need to consider microclimatic, topographic, and climatic factors together.

References

Apaydin, H., Erpul, G., Bayramin, I., & Gabriels, D. (2006). Evaluation of indices for characterizing the distribution and concentration of precipitation: A case for the region of Southeastern Anatolia Project, Turkey. *Journal of Hydrology, 328*(3–4), 726–732. https://doi.org/10.1016/j.jhydrol.2006.01.019

Arnoldus, H.M.J., 1977. Methodology used to determine the maximum potential average annual soil loss due to sheet and rill erosion in Morocco. FAO Soils Bulletin 34, 39–51.

Hamed, K. H., & Rao, A. R. (1998). A modified Mann-Kendall trend test for autocorrelated data. *Journal of Hydrology, 204*(1–4), 182–196. https://doi.org/10.1016/S0022-1694(97)00125-X

İpek, A. F., & Kahya, E. (2022). Drought analysis of Küçük Menderes Water Basin. *International Graduate Research Symposium - IGRS'22*, 1–3 June 2022, Istanbul, Turkey.

S.Y.G.M. (2019). *Küçük Menderes Havzası taslak nihai nehir havza yönetim planı [Draft Final River Basin Management Plan for Küçük Menderes Basin].* Ministry of Agriculture and Forestry, Ankara, Turkey.

INDUSTRIAL DESIGN

Historical, Cultural and Social Context of Design

Product Design

Theory and Methodology in Industrial Design

Discovering The Choir Members' Practices: An Initial Understanding of The Intersection of Design, Music, and Community

Gürkay Aydoğmuş[a], Koray Gelmez[a]

[a] Istanbul Technical University/Graduate School, Department of Industrial Design, Industrial Design Program, Türkiye
aydogmus@itu.edu.tr

Keywords: Choir Communities, Research Through Design, User Experience.

Aim

Design, music, and community are three significant fields that transform and enhance human experience both individually and at the community level. Studies conducted at the intersection of these fields hold valuable potential to strengthen interactions between individuals and improve the experiences of communities. However, literature reviews reveal a lack of studies specifically focused on choir communities at the intersection of these three areas. In the field of music, studies examining user experiences from a design perspective are limited, highlighting a critical gap in the literature.

Babaç (2018), in an analysis of theses written between 2011 and 2018, emphasized the scarcity of studies addressing the behaviors and attitudes of choir members. Babaç (2018) noted that more rigorous research in choir management would expand the literature and suggest new pathways for the actions of choir management.

This study aims to address the aforementioned gap in the literature and conduct research to understand the user experiences of choir communities. Specifically, addressing the experiences and challenges faced by choir members offers an essential opportunity to develop user-centered design interventions. Furthermore, the other aim of the study is to develop design solutions that enhance the interactions among stakeholders within the choir ecosystem, making them more functional and effective. Stollak (1994) argued that the production of quality music requires a choir conductor to understand both the individual and collective needs and tendencies of the members. This approach provides significant insights for organizing and managing choir communities more effectively.

Material and Method

In the initial phase of the research, a literature review was conducted to examine academic studies situated at the intersection of design, music, and community. This review specifically focused on design studies aimed at understanding user experiences within music communities. However, the lack of studies dedicated to choir communities underscores the unique value and necessity of this research.

Following the literature review, an online survey was conducted with 74 members of various choirs in Türkiye. The purpose of this survey was to understand the communication dynamics within the choir ecosystem, identify issues within the community, and uncover detailed insights into the experiences of choir members. The survey included both multiple-choice and open-ended questions to evaluate participants' roles within the community, challenges in communication processes, and opinions on the organizational structure. Participants were asked a series of questions covering demographic information, time spent on choir activities, role distribution within the community, encountered challenges, use of technology, and future expectations. Participation in the survey was entirely voluntary, and respondents were invited through online platforms.

The research intends to utilize research through design approach, relying on the insights derived from the combination of designer and choir member roles. These methods enable the integration of the designer's identity with those of the musician and community member, facilitating a deep understanding. The research through design approach focuses on generating and communicating new knowledge and theories that emerge from a designer's own practices (Archer, 2004a; Hales, 1987). This process is both creatively and intellectually demanding, requiring the designer to take on the role of both an observer

and a participant within the user community. The primary goal of the study is to identify user needs and provide creative solutions by leveraging the combination of these multifaceted identities.

The "research through design" approach, increasingly used in the design field, will guide the next stages of this study. This approach positions the designer not only as a problem solver but also as an active participant in the design process. As Pedgley (2007) emphasizes in his work, the reflective practice and active participation of the designer are central to generating valuable insights and creating new knowledge. On this basis, the study aims to create both academic and practical value by delving into the experiences, observations and individual contributions of the designer, and to include this approach in future stages of the research to develop and test user-centered design interventions.

Findings

The data obtained from the survey were analyzed using thematic analysis, a qualitative method widely applied to identify recurring themes and patterns (Braun & Clarke, 2006). This approach provided in-depth insights into the experiences of choir members, highlighting both challenges and opportunities within their organizational and interpersonal dynamics.

Key issues identified included musical difficulties, time management, organizational inefficiencies, communication problems, and low motivation. Nonetheless, participants emphasized strong interpersonal cooperation and appreciated social activities that fostered cohesion.

Shared responsibility and inclusive decision-making were seen as important for sustaining the choir's functioning. While generally content, many members expressed a desire for growth—calling for more performance opportunities, a stronger internal structure, and balanced attention to musical and social development.

Technology emerged as a valuable tool, supporting communication, practice, and collaboration. These findings reveal areas where design-led interventions could enhance organizational effectiveness and strengthen the overall choral experience.

Conclusion

This study represents a unique effort to examine user experiences within choir communities from a design perspective, aiming to contribute both theoretically and practically. The literature review has highlighted a significant academic gap at the intersection of design, music, and community. Meanwhile, the survey findings clearly illustrate the prominent challenges in communication and organizational processes within choir communities, as well as the need for digital solutions to address these challenges.

By adapting research through design approach, the study enables the designer to assume an active role within the community. In future stages, it is planned to prototype user-centered design interventions, test them, and improve the processes through user feedback. This process is expected to enhance intra-community dynamics and improve the experiences of choir members.

In conclusion, this study aims not only to generate academic value but also to contribute to the transformation of choir communities into more effective, accessible, and user-focused structures. The research findings are expected to provide a new perspective on the relationship between design and music communities, offering meaningful contributions to both the literature and practical applications.

References

Archer, B. (1999). Personal facsimile via P. Roberts at Loughborough University.

Babaç, E. E., & Köse, H. S. (2018). Türkiye'de 2011-2018 Yılları Arasında Koro Alanında Yapılmış Olan Lisansüstü Tezlerin Bazı Parametreler Bakimindan İncelenmesi. *Online Journal of Music Sciences*, *3*(1), 32-55.

Braun, V., & Clarke, V. (2006). Using thematic analysis in psychology. *Qualitative Research in Psychology*, *3*, 77–101. doi:10.1191/1478088706qp063oa

Hales, C. (1987). *Analysis of the engineering design process in an industrial context*, PhD thesis, University of Cambridge, published by Gants Hill Publications.

Pedgley, O. (2007). Capturing and analysing own design activity. *Design studies*, *28*(5), 463-483.

Stollak, M. A., Stollak, G. E., Meyers, S., & Stollak, M. J. (1994). The Choir As Family, II. *Choral Journal*, *34*, 25-30.

Decoding Toxic Attachment Between Design Products and the Users: Understanding by using Metaphors

Bilge Ceren Ay[a], Ozge Celikoglu[a]

[a] Istanbul Technical University, Industrial Design Department, M.Sc. Industrial Design, Turkey
ayb15@itu.edu.tr

Keywords: Emotional Design, Industrial Design, Interaction Design, Metaphor, Product Attacment.

Aim

Users often form relationships with their products, though the reasons behind these attachments vary widely. These connections might be driven by emotional significance, daily utility, added functionality, or simple enjoyment. However, these relationships can sometimes lead to unexpected shifts in behavior, and in certain cases, these changes may not benefit the user in the long run. The main research aims to delve into the intricate, everyday relationships that users establish with their personal belongings, focusing particularly on behaviors that might be seen as problematic. By referring to these behaviors as "problematic," the study is interested in patterns such as "clinging" to objects, "hoarding" or accumulating items beyond practical need, experiencing a "fear of missing out" that drives unnecessary retention of possessions, and engaging in "non-purposeful use" where items are kept or used without a clear function. These behaviors reflect complex emotional and psychological interactions with owned products, shaped by personal and social factors.

Material and Method

This metaphor-based approach will enable the study to decode the links between user behavior and product design, revealing how behavioral states relate to the designed functions of products. Ultimately, the research has the potential to provide valuable insights for designers into how users interact with their products in ways that extend beyond the intended design, highlighting how objects influence behavior in complex, unintended ways.

To understand why the users feel attached to a product, it could be said that the product unfolds a special and personal meaning for the user (Mugge et al., 2008, p.427). For example, the attachment could be created by being an heirloom (Ahde-Deal, Paavilainen & Koskinen, 2017, p.2). In addition to this, users could create an ideal vision of themselves while using the product, therefore, the attachment could be built by the self-image (Govers & Mugge, 2004, p.4). Additionally, there are several opinions about product attachment in the means of "self-extension". Ball & Tasaki states that even though it's hard to confide it to themselves, people can tie their own self-worth to their belongings if the object is a part of self-schema (1992, p.158). The search of making sense to self as a cognitive element discussed more by Greenwald (1988), Erikson (1959) and more. It could be said that the attachment is initiated by the emotional responses to self image.

Letting go of their possessions is invariably more stressful for those that attach a more emotional value to their objects. Due to these difficulties in separation, consumers frequently store unused items at home in what may be called an interim stage, or "consumption limbo." Those who tend consistently to keep belongings, commonly labelled as packrats or keepers, usually seem to attach deeper emotional values to possessions. This can lead to hoarding tendencies, which are most prevalent for the people who derive emotional security from their possessions. When packrats finally decide to discard something, they usually experience feelings of guilt or sadness, whereas purgers, or those who easily discard their possessions, generally feel relieved. (Dommer & Winterich, 2021, p.44)

The linguistic traces could be seen in the keeper's sentences such as;
I haven't used it [Code – Passive Use; Theme – Use]. I'm afraid to [Code – Fear; Theme – Emotion], but again, I probably should [Code – Expected Behavior; Theme – Use]. (Kowalski & Yoon, 2022).

Even though acknowledging the reality of the usage situation, the user may not feel ready to face the disposal of the product. Individuals with hoarding problems like having complete control over their possessions and avoid others touching them, also they tend to have more resistance to empathize with other due to their need to control and configure their feelings first (David, Aluh & Blonner, 2021, p.1233) To understand this, metaphors can be seen as a linguistic and cognitive bridge to understand the connections, relations and actions. As systematically explained by Lakoff & Johnson (1980) there are several aspects of understanding the metaphorically defined concepts such as; ontological metaphors, personification, metonymy and more.

Lastly, toxic relationships can be exemplified as involvement of one partner who causes emotional and often physical harm to the other with his or her actions. In discussions of toxic relationships, the behaviors of the toxic partner are usually in focus. But equally important is the person who endures this behavior. (Solferino & Tessitore, 2021, p.7)

Findings

For fieldwork in this study, five semi-structured interviews have been held. They have been given a set of questions, which they can add more questions to answer and additional insights. This set of questions aims to explore the metaphorical and emotional dimensions of product-human relationships by having participants reflect on a significant object to them. Through facilitated interviewing, the study examines the object's past, creation, and symbolic meaning, including spatial and relational importance. The aim is to uncover underlying stories that may indicate patterns of toxic attachment or emotional attachment. In addition, participants are also requested to reflect about how these questions and findings might be translated into an interactive or physical research kit, which would help develop future design-oriented inquiry tools.

The question kit was provided to the participants via Whatsapp. They had 24 hours to give answers and make any additional suggestions. In addition, they may ask anything about the questions or the subject if there is any additional information needed in the answering process.

According to the findings, it could be said that the toxicity could be integrated with the quality of the metaphor. The participants have been given the words such as "assistant", "travel companion" and "express" to express their relationship with the chosen product. In the means of positivity, these words fell into a rather more positive spectrum.

Bag – *Travel Companion* – a friend, fellow, helper. / **positive**
spends a lot of time with a traveller. / **positive**

Mocha Pot – *Express* – fast, easy, high speed. / **positive**

Cellphone – *Assistant* – a thing ranks below / **negative**
helper / **positive**

Basketball – *Play* – enjoyment / **positive**
energy / **positive**

Notebooks – *Serendipity* – finding valuable things by chance / **positive**

In the mocha pot example, user gets angry after a friend of hers tries to disregard the product and harms it, because the tie between product and her have its roots by being functional and ease to use. Even the design of the mocha pot doesn't change in newly produced ones, therefore she sees a space and reason to feel attached to its irreplaceability. Additionally, establishing a connection between her boyfriend and her mocha pot makes it harder to reach the disposal phase. Also, as a metaphor, she aligns the mocha pot as a warmness in a cold morning.

In the notebook example, the user sees her notebooks as a time capsule which decodes her life phases during different times. In a similarly metonymic and metaphorical gesture, the time capsules will connect the future of the present with the past of that future. Such a frame is indicative not just of one particular perspective but indeed of an ontology of detachment through which the world and ourselves come to be presented as an object of contemplation and not an actor participating with each

other in an interactive world (Durrans, 2012, p.186.). Therefore, the time capsule metaphor holds a huge power in the user such as a physical way of reminder of losing their own past.

Notebook is a time capsule. – Time holds different versions of self. – The notebook holds different versions of me.

Lastly, two of the participants depicted that people around them see the product as a self-extension of the participants. Self is a strong thing to be connected to a product, therefore, disposal of self can be more and more damaging for the user.

Table 1. Metaphors and Attachment Types in Product Attachment.

Product	**Metaphor**	**Positive Attachment**	**Negative Attachment**
Bag	*Travel Companion*	Providing reassurance and comfort on journeys.	Struggle with replacing it, even when a new bag was needed.
Mocha Pot	*Express*	Affective link based on familiarity and function.	Apprehensive about adopting a different technique of coffee brewing despite potential advantages and worried about losing the product.
Cellphone	*Assistant*	Helper	Subordinate entity stress was the result when attempting to switch off.
Notebook	*Time Capsule*	Represented self-awareness and growth, confirming emotional connection with documentation of life experiences.	Discarding old notebooks as equivalent to losing a part of who they were, so they struggled to purge.

Conclusion

This study puts the multi-sided nature of attachment to product front and center, emphasizing its implications for consumer conduct. Healthy attachment can promote sustainability and genuine experiences of ownership, whereas toxic attachment can induce hoarding, psychological dependence, and emotional distress. Metaphoric use in user-product interaction has implications for designers who aim to create products consonant with users' psychology yet not promoting ill health in emotional dependence.

Future research should investigate intervention approaches that will reduce negative attachment behavior and enhance positive user experience. Methods such as the promotion of mindful use, frequent object evaluation, and product design with flexibility that supports emotional continuity but not material abundance can help reduce the negative consequences of attachment to products.

As limitations, conducting the study with only five participants for a sample made available limited data and constrained variation in the views collected using the process. For conducting subsequent studies, though, is to up the number of participants to no less than 15 to create room for expanded variability and depth in results. Furthermore, the current questionnaire should be revised so that it opens up better possibilities for probing emotional experiences and affections among the participants. Emphasizing the phrasing and framing of the questions can assist in bringing out multi-dimensional

responses, allowing respondents to articulate their feelings and relationships with products more strongly and from different directions.

References

Ahde-Deal, P., Paavilainen, H. & Koskinen, I. (2017) 'It's From My Grandma.' How Jewellery Becomes Singular, The Design Journal, 20:1, 29-43, DOI: 10.1080/14606925.2017.1252564

Belk, R. W. (1988). Possessions and the Extended Self. Journal of Consumer Research, 15(2), 139–168. http://www.jstor.org/stable/2489522

David, J., Aluh, D. O., Blonner, M., & Norberg, M. M. (2021). Excessive Object Attachment in Hoarding Disorder: Examining the Role of Interpersonal Functioning. Behavior Therapy, 52(5), 1226–1236. https://doi.org/10.1016/j.beth.2021.02.003

Dommer, S. L., & Winterich, K. P. (2021). Disposing of the self: the role of attachment in the disposition process. Current Opinion in Psychology, 39, 43–47. https://doi.org/10.1016/j.copsyc.2020.07.016

Govers, Pascalle C. M. and Ruth Mugge (2004). "'I Love My Jeep, Because It's Tough Like Me': The Effect of Product-Personality Congruence on Product Attachment," in Proceedings of the Fourth International Conference on Design and Emotion, ed. Aren Kurtgözü, Ankara, Turkey.

Kowalski, M.C., Yoon, J. (2022). I love it, I'll never use it: Exploring factors of product attachment and their effects on sustainable product usage behaviors. International Journal of Design, 16(3), 37-57. https://doi.org/10.57698/v16i3.03

Mugge, R., Schoormans, J., & Schifferstein, H. N. (2008b). PRODUCT ATTACHMENT: DESIGN STRATEGIES TO STIMULATE THE EMOTIONAL BONDING TO PRODUCTS. In Elsevier eBooks (pp. 425–440). https://doi.org/10.1016/b978-008045089-6.50020-4

Lakoff, G., & Johnson, M. (1980). Johnson Metaphors We Live by. Chicago: University of Chicago Press.

Solferino, N., & Tessitore, M. E. (2021). Human Networks and Toxic Relationships. Mathematics, 9(18), 2258. https://doi.org/10.3390/math9182258

INDUSTRIAL DESIGN

Historical, Cultural and Social Context of Design

Product Design

Theory and Methodology in Industrial Design

Testing the Aesthetic Responses to Small Household Appliances in The Context Of Incremental Innovation

Fatma Cizrelioğlu Karaer[a,b], H. Tengüz Ünsal[c]

[a] Marmara University, Faculty of Fine Arts, Industrial Design, Turkey
[b] Mimar Sinan Fine Arts University, Graduate School, Industrial Design, Turkey
[c] Mimar Sinan Fine Arts University, Faculty of Architecture, Industrial Design, Turkey
fatma.cizrelioglu@marmara.edu.tr

Keywords: Aesthetic Plesure, Incremental Innovation, Product Design.

Most of the products launched as a result of new product development processes consist of incremental design innovation by improving and visually differentiating existing products. Consumers can access hundreds of products with similar functions and usage features from any e-commerce site. The aesthetic pleasure of a product's appearance plays a significant role in consumer decision-making.

Aim

Through an empirical study, this research aims to analyze the aesthetic response to the appearance of small household appliances, which are similar in terms of technological features and usage characteristics. It aims to contribute to the design development processes of small household appliances by analyzing the relationships between aesthetic pleasure and the determinants of aesthetic pleasure. The results will be evaluated by comparing them with the findings of the literature.

Material and Method

The theoretical infrastructure of the research is based on Hekkert's unified model of aesthetics. Hekkert (2014) presents a general framework that can be used in research in the field of design aesthetics with his Unified Model of Aesthetics, which 'aims to explain our daily aesthetic preferences for artifacts.' Accordingly, the balance between two evolutionarily rooted and complementary pressures is at the center of aesthetic preferences. 'One of these pressures pushes us towards security and protection and leads us to favor choices that facilitate perceptual understanding, efficient processing, and group membership. The other pressure involves the desire to learn and achieve, leading to preferences for diversity, novelty, and uniqueness' (Hekkert, 2014, p. 291). These two opposing forces influence people's aesthetic choices at each of the perceptual, cognitive, and social levels of aesthetic judgment (Figure 1). At each level, aesthetic decisions are based on a trade-off between security and achievement needs, and people seek a balance between the two forces.

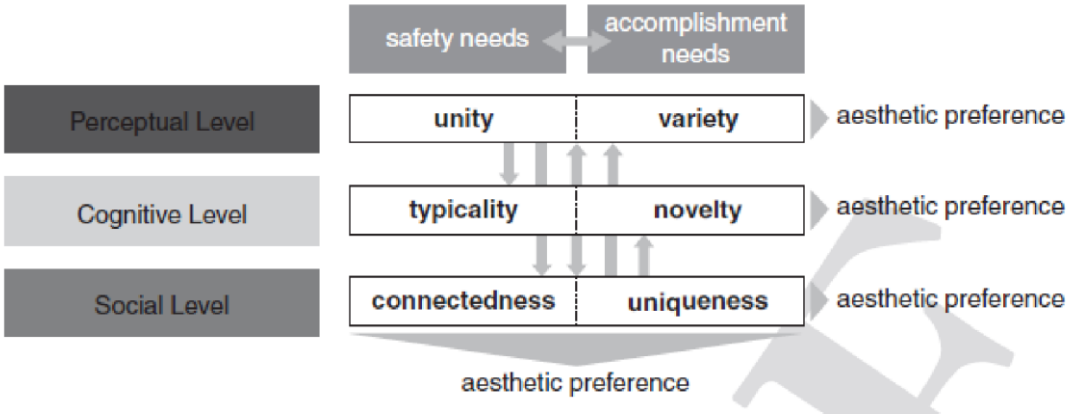

Figure 1. Aesthetic pleasure and its determinants (Hekkert, 2014).

The theory of perceptual aesthetics (Hekkert P., 2006) is based on the idea that people like anything that facilitates understanding. According to this idea, we enjoy things that support the efficient functioning of our sensory systems, including our brain. According to Gestalt psychologists, these things facilitate perceptual organization and help us to see relationships and differences so that we can regulate the flow of information more easily (Hekkert, 2014). We like some challenge in the form of variety to balance unity, even if it is only to enable us to perceive different entities; that is, at the perceptual level, we derive aesthetic pleasure from stimuli that fulfil our need for both unity and variety, creating a rich and complex aesthetic experience (Berghman & Hekkert, 2017, p. 137).

Perceptions of unity and variety enrich the aesthetic experience, but for these perceptions to become meaningful for subsequent actions, it is necessary to give them a context (Berghman & Hekkert, 2017). At the cognitive level, we try to categorize perceptual inputs by not defining them, and in doing so, we benefit from our past experiences (Berghman & Hekkert, 2017). Prioritising what is known, typicality, offers an evolutionary advantage as it enables us to make safer choices (Hekkert, 2014, p. 285). Biederman and Vessel (2006), examining the balance between typicality and novelty, found that novel stimuli are appreciated at higher levels; however, this is only the case when observers can recognize these stimuli (Berghman & Hekkert, 2017). This can be explained by Raymond Loewy's (1951) famous 'Most Advanced, Yet Acceptable (MAYA)' principle, which suggests that designs should be innovative yet familiar to be accepted by the audience. Hekkert, Snelders, and Van Wieringen (2003), in accordance with the MAYA principle, found that both novelty and typicality have independent and almost equally strong effects on aesthetic preferences.

In this study, the The Aesthetic Pleasure in Design (APiD) Scale (Blijlevens, et al., 2017) was a crucial tool used to assess aesthetic responses to products with incremental design innovation. This scale, with its ability to measure aesthetic pleasure and its determinants (novelty, variety, unity and typicality) as separate parameters, brought a level of scientific rigor and precision to the study. The scale, the validity and reliability of the Turkish form of which has been proven by previous studies (Ahat & Öztürk, 2018), was applied to the participants in Turkish. It is structured in a 5-point Likert-type format, and the response options are graded between 'Strongly Disagree' and 'Strongly Agree'.

The stimuli were selected from three product categories: Turkish coffee machine, Turkish tea maker and Electric Turkish Coffee Pot. These products have cooking characteristics specific to Turkish culture. The selection of the products to be used as stimuli in the research, an e-Marketplace was searched for each product category and the price range, colour option, material components were selected and filtered similarly (Figure 2). In order to prevent judgements that may occur due to brand image, brand names and signs on all images have been removed.

Figure 2. Product images used as stimuli.

In determining the participants, criteria such as being female due to familiarity with the product categories and, preventing gender-based evaluation differences, having purchased products from e-commerce sites because it is desired to have online purchasing experiences were used. Nine scales, three from each category, were applied to the participants (n:10). Pearson

correlation analyses were performed in Jamovi 2.6.17, an R-based open-source program, on a total of 90 data sets, 30 for each product category.

Findings

When all data were analyzed, the correlation coefficient for the relationship between **aesthetic pleasure and variety** was found to be 0.677 (Table 1). Electric tea makers are the category with the most decisive aesthetic pleasure-variety interaction (0.808). There is also a strong positive relationship between aesthetic pleasure and variety in Turkish coffee machines (0.711). For electric Turkish coffee pots, there is a moderate (0.535) relationship between aesthetic pleasure and variety. In line with these data, it can be said that the perception of variety obtained from the product's appearance is effective in revealing the aesthetic pleasure of the product. Consumers' positive inferences from the appearance of the product that the product consists of different parts and offers variety in terms of design elements are indicators that their aesthetic reactions will also be positive.

Table 1. Correlation matrix on aesthetic pleasure and its determinants.

		Variety	Unity	Novelty	Typicality
AESTHETIC PLEASURE	All data	0.677 ***	0.708 ***	0.710 ***	—
	Turkish coffee machine	0.711***	0.714***	0.656***	—
	Turkish tea maker machine	0.808***	0.700***	0.832***	—
	Electric turkish coffee pot	0.535**	0.729***	0.656***	0.393*

The correlation coefficients for the relationship between **aesthetic pleasure and unity** are very close for the whole data (0.708) and based on categories (0.729, 0.714, 0.700). There is a strong and positive relationship between aesthetic pleasure and unity (Table 2). As consumers' positive inferences about the harmony, order, and integrated appearance between the design elements of the products increased, their positive aesthetic reactions also increased.

Table 2. Correlation matrix for all data.

Correlation Martix						
		AESTHETIC PLEASURE	**NOVELTY**	**TYPICALITY**	**VARIETY**	**UNITY**
AESTHETIC PLEASURE	Pearson's r	—				
	df	—				
	p-value	—				
NOVELTY	Pearson's r	0.710***	—			
	df	88	—			
	p-value	<.001	—			
TYPICALITY	Pearson's r	0.089	-0.268*	—		
	df	88	88	—		
	p-value	0.402	0.011	—		
VARIETY	Pearson's r	0.677***	0.849***	-0.237*	—	
	df	88	88	88	—	
	p-value	<.001	<.001	0.025	—	
UNITY	Pearson's r	0.708***	0.570***	0.303**	0.544***	—
	df	88	88	88	88	—
	p-value	<.001	<.001	0.004	<.001	—

Note. *p <.05, ** p <,01, ***p <.001

The correlation coefficients for the relationship between aesthetic pleasure and unity are very close for the whole data (0.708) and based on categories (0.729, 0.714, 0.700). There is a strong and positive relationship between aesthetic pleasure and unity. As consumers' positive inferences about the harmony, order, and integrated appearance between the design elements of the products increased, their positive aesthetic reactions also increased.

When all the data are analysed, it is seen that there is no significant statistical relationship between **aesthetic pleasure and typicality**. When examined as categories, a moderate positive relationship is observed only for electric coffee pots (0.393). When all the data were analyzed together, the correlation coefficient of **aesthetic pleasure and novelty** was found to be 0.710. Accordingly, there is a positive and strong relationship between aesthetic pleasure and perceived novelty. The increase in the perceived novelty level of a design leads to an increase in the level of aesthetic pleasure obtained from the design. When analyzed by category, the highest relationship is observed in the electric tea maker category (0.832). The correlation coefficient is the same for Turkish coffee machines and electric tea makers (0.656). The significance level is

high in all three categories. It is seen that the correlation coefficients of the aesthetic pleasure-innovation relationship vary according to the categories. In the electric tea maker category, the tendency for aesthetic pleasure and innovation to positively affect each other is higher. In this case, it can be said that consumers perceive the product as newer as their positive aesthetic judgments increase while making evaluations for this product group.

The correlation coefficients for the relationship between **variety and unity** (Table 3) were 0.544 for all data, 0.443 for Turkish coffee machines, 0.694 for electric tea makers, and 0.586 for electric Turkish coffee pots. Although the significance value of the correlation for Turkish coffee machines was less than the others, a moderate and positive result was obtained for both the whole data and all categories. The findings show a directly proportional relationship between consumers' variety and unity evaluations in the evaluation of products with incremental design innovation.

Table 3. Correlation coefficients showing the relationship between variety and unity.

	Unity - Variety
All data	0.544 ***
Turkish coffee machine	0.443***
Turkish tea maker machine	0.694***
Electric turkish coffee pot	0.586**

Conclusion

Aesthetic pleasure and its determinants scale can be used as a suitable tool to test aesthetic responses to product appearance in order to choose among design alternatives in the new product development process.

According to the findings, the most critical factor affecting aesthetic pleasure in products with incremental design innovation is the perception of novelty. As the perceived novelty increases, the aesthetic pleasure received from the product's appearance also increases. Another significant result is the relationship between variety, unity, and aesthetic pleasure. According to the literature, variety, and unity evaluations are expected to be negative (Berghman & Hekkert, 2017, p. 137), but the findings show that there is a directly proportional relationship between consumers' perceptions of variety and unity in the evaluation of products with incremental design innovation. In this study, the results regarding the effect of variety and unity factors on the emergence of aesthetic pleasure are similar to the studies in the literature (Post, Nguyen, & Hekkert, 2017):

- In line with these data, it is seen that the perception of variety obtained from the product appearance is effective in the emergence of aesthetic pleasure about the product. Consumers' positive inferences from the appearance of the product that the product consists of different parts and offers variety in terms of design elements are indicators that their aesthetic reactions will also be positive.

- There is a strong and positive relationship between aesthetic pleasure and unity. As consumers' positive inferences about the harmony, order and integrated appearance between the design elements of the products increase, their positive aesthetic reactions also increase.

These findings offer various suggestions for design practice. When designing for product categories where distinctiveness factors are low, visual design factors such as symmetry, contrast, variety in elements, color differences, and gradations can be used to achieve an optimum balance between variety and unity to ensure positive aesthetic responses from consumers. At the same time, future research could examine consumer responses to controlled manipulations of these factors. In this study, the consumer group was held constant; future research could also investigate the aesthetic responses of different consumer groups.

References

Ahat, K., & Öztürk, S. (2018). Tasarımdan Alınan Estetik Haz Ölçeği'nin Türkçe Formunun Yapı Geçerliği ve Güvenirliği. *Journal of Social Research and Behavioral Sciences (SADAB), 4*(7), p. 83-105.

Berghman, M., & Hekkert, P. (2017). Towards a unified model of aesthetic pleasure in design. *New Ideas in Psychology, 47,* p. 136–144. doi:https://doi.org/10.1016/j.newideapsych.2017.03.004

Blijlevens, J., Thurgood, C., Hekkert, P., Chen, L., Leder, H., & Whitfield, T. (2017). The Aesthetic Pleasure in Design Scale: The development of a scale to measure aesthetic pleasure for designed artifacts. *Psychology of Aesthetics, Creativity, and the Arts, 11*(1), p. 86-98. doi:https://doi.org/10.1037/aca0000098

Hekkert, P. (2006). Design aesthetics: Principles of pleasure in design. *Psychology Science, 48*(2), p. 157–172.

Hekkert, P. (2014). Aesthetic responses to design: A battle of impulses. P. Tinio, & J. Smith içinde, *The Cambridge Handbook of the Psychology of Aesthetics and the Arts* (p. 277–299). Cambridge: Cambridge University Press.

Hekkert, P., Snelders, D., & Van Wieringen, P. (2003). 'Most advanced, yet acceptable': Typicality and novelty as joint predictors of aesthetic preference in industrial design. *British Journal of Psychology*(94), p. 111–124. doi:https://doi.org/10.1348/000712603762842147

Loewy, R. (1951). *Never leave well enough alone*. New York: Simon and Schuster.

Post, R., Nguyen, T., & Hekkert, P. (2017). Unity in Variety in website aesthetics: A systematic inquiry. *International Journal of Human Computer Studies*(103), p. 48–62. doi:https://doi.org/10.1016/j.ijhcs.2017.02.003

INDUSTRIAL DESIGN

Historical, Cultural and Social Context of Design

Product Design

Theory and Methodology in Industrial Design

User Narrative as Antenarrative: A Brief Overview

Fulden Ates[a,c], Ozge Merzali Celikoglu[b]

[a] Istanbul Technical University, Graduate School, Industrial Design, Turkey
[b] Istanbul Technical University, Faculty of Architecture, Industrial Design, Turkey
[c] Marmara University, Faculty of Fine Arts, Industrial Design, Turkey
ates20@itu.edu.tr

Keywords: Antenarrative, Narrative, User Narrative, User Research.

User narratives, which encompass the stories and experiences of users in their interactions with a product or service, represent a vital form of data in design research. Designers, consciously or unconsciously, have historically integrated narratives into their work (Shaw & Nickpour, 2022) and have internalized them (Trocchianesi, 2022). Every designed entity, including products, services, systems, and environments, inherently contains or conveys a narrative (Shaw & Nickpour, 2022). Such narratives allow designers to incorporate users' lived experiences into the design process, transforming these insights into design knowledge. Consequently, designers are expected to engage actively with these narratives and serve as narrative agents (Shaw & Nickpour, 2022). Nonetheless, despite the prevalent utilization of narratives in design, contemporary literature indicates that the narrative dimension of user research remains inadequately explored.

In user-centered design, narratives are frequently perceived as linear and complete, with designers treating user input as structured and finalized accounts. However, actual user narratives often present as fragmented, inconsistent, and open-ended. Such characteristics do not align well with traditional narrative theories, which typically emphasize coherence, causality, and cultural consistency.

By adopting a narrative-centric approach to user-centered design, this research seeks to illuminate the inspirational elements of user narratives that frequently remain implicit within the design process. When employed effectively, narratives can assist designers in uncovering and empathizing with diverse lived experiences, challenging dominant social or disciplinary narratives through a user-centered framework, and amplifying previously marginalized voices to achieve more desirable and relevant designs (Shaw & Nickpour, 2022; Tassinari et al., 2017). Unlike other user research methods, including user narratives in the design process mitigates the risk of stereotyping users, preserves objective details about users, and maintains the contextual integrity of the researched subjects.

Aim

This study aims to introduce a new perspective on user narrative by applying the concept of antenarrative to the design discipline. It revisits the structure of user narratives and proposes a fresh approach to inspire a more thorough exploration of narratives in user research, ultimately leading to more effective utilization.

Material and Method

This study employs a comprehensive conceptual literature review as its primary methodological approach. Rather than collecting empirical data, the research draws on theoretical and interpretive analysis of existing literature to thoroughly explore the applicability of antenarrative theory in the context of user research within the design.

The review emphasizes two central narrative frameworks: Jerome Bruner's (1991) theory of narrative as a culturally shaped and temporally ordered meaning-making process and David Boje's (2001) concept of antenarrative. With contrasting ontological assumptions, these frameworks provide a productive tension for evaluating how user narratives are understood and utilized in design processes. The study argues that antenarrative, focusing on fragmented and speculative storytelling, offers a more suitable lens for interpreting user narratives.

Findings

Jerome Bruner's narrative theory is frequently cited in discussions surrounding traditional narrative definitions. He argues that narratives play a vital role in helping individuals understand and communicate their experiences (Bruner, 1991). However, upon closer inspection, it becomes clear that user narratives—essential to the design process—differ considerably from Bruner's narrative definitions in several important ways.

When assessing narrative in design literature, it is evident that user narratives drawn from participants' experiences during research often come across as inconsistent and unstructured. For example, a user narratives may consist of disconnected events or various opinions rather than a seamless account of interactions with a specific product or situation. These narratives provide fragmented insights into users' lives, reflecting the diverse feedback from various individuals, lacking a coherent trajectory, and often displaying inconsistencies due to the array of inputs received.

Given these characteristics, it is apparent that user narratives stand apart from Bruner's traditional narrative framework and resonate more closely with Boje's (2001) idea of antenarrative. Boje (2001, p.1) describes antenarrative as chaotic and unstructured narrative forms that emerge before a conventional narrative takes shape. He defines it as "*the fragmented, non-linear, incoherent, collective, unplotted, and pre-narrative speculation, a bet.*" Antennarratives capture the early, unrefined stages of storytelling, providing accounts that lack formal structure but are rich in potential for exploration.

Unlike narratives, antenarratives are not bound by a specific format. They embrace diverse perspectives and focus on unfolding events, engaging with potential outcomes and contemplating future possibilities. While Bruner's narratives are typically organized and follow a clear chronological order, antenarratives introduce uncertainties regarding time and sequence. Bruner's narratives tend to center on past experiences and present situations, while antenarratives look ahead, considering multiple potential futures. This contrast between Bruner's structured narrative approach and Boje's dynamic antenarrative framework is not just a theoretical discourse but a rich and engaging one.

Although the idea of antenarrative is not new, it has yet to be fully embraced within design literature. Given that design processes naturally incorporate alternatives and speculation—key aspects of antenarratives—it is exciting to consider how integrating this concept could elevate design research further. By embracing the chaotic and unstructured nature of antenarratives, design research could become more open to diverse perspectives and potential outcomes, leading to more innovative and user-centered design solutions.

Conclusion

In the design process, antenarratives enable us to engage with stories that are still evolving—those incomplete, ambiguous, and sometimes conflicting experiences shared by users before they solidify into fixed narratives. This approach is crucial because it enables us to identify emerging patterns and hidden needs that conventional user research might overlook. By working directly with these narrative fragments, we can envision alternative futures and design more inclusive and innovative solutions that address the true complexity of user experiences. These solutions, designed with empathy and consideration, are more likely to meet the diverse needs of users. Importantly, this approach encourages designers to remain reflexive and continuously challenge their assumptions and biases.

In conclusion, viewing user narratives as antenarratives opens significant opportunities for user research in design. This study serves as a call to action, urging a broader investigation into the nature of narratives in user research. Such an exploration can facilitate their more impactful application, leading to a deeper understanding of user experiences and more effective design solutions.

References

Boje, D. (2001). *Narrative methods for organizational & communication research*. SAGE.
Bruner, J. (1991). The narrative construction of reality. *Critical Inquiry, 18*(1), 1-21.
Shaw, C., and Nickpour, F. (2022). Design as an agent of narratives: A conceptual framework and a first exploration in the context of inclusive paediatric mobility design. In *Proceedings of DRS2022*: Bilbao.
Tassinari, V., Piredda, F., and Bertolotti, E. (2017). Storytelling in Design for Social Innovation and Politics: A Reading Through the Lenses of Hannah Arendt, *The Design Journal, 20*(1), pp. 3486-3495.
Trocchianesi, R. (2022, May). Design Narrative. In *International Conference Design! OPEN: Objects, Processes, Experiences and Narratives* (pp. 603-610). Cham: Springer Nature Switzerland.

Prompt 'Design the Perfect Product': A Literature Review on AI Incorporation in Industrial Design Processes

Sude Kartalbaş[a], Aysun Ateş Akdeniz[b]

[a]İstanbul Technical University, Graduate School, Industrial Design Program, Turkey
[b]İstanbul Technical University, Faculty of Architecture, Department of Industrial Design, Turkey
kartalbas19@itu.edu.tr

Keywords: Industrial Design, Artificial Intelligence, Design Process.

Aim

Are we witnessing a revolution in design or just an algorithmic chaos? With the rapid development of Artificial Intelligence (AI), product design processes have been affected by it significantly. The definition of industrial design according to the World Design Organization is, the development of innovative products, services, systems, and experiences, industrial design is a strategic approach to problem-solving that fosters innovation, increases business success, and improves people's quality of life (2025). The increasing integration of AI into design presents both opportunities and challenges for designers with lots of new areas to expand. AI is developing faster than anything, keeping up with it has become crucial. The design discipline needs to devote attention to the challenges involved in integrating AI into systems, services, and products. Despite the impressive advancements in AI, there is a noticeable lack of discussion about this subject in the design community (Stoimenova & Price, 2020). This study aims to analyze the stages of the product design process where AI is utilized, examining its benefits and exploring its limitations. Emphasizing the gap which is understanding the balance between human creativity and AI-driven design, exploring how AI has been affecting and will be affecting the design process examining its implications for creativity, efficiency, and collaboration in design processes. The research starts with understanding how AI contributes to different stages of the design process in the industrial design sector, mostly including early ideation and visualization techniques. Escaping or unseeing AI is not an option anymore, choosing to learn how to manipulate and work with it can be beneficial. Like once craftsmen learn how to work with machinery, the designers will learn how to interact with AI as well.

The main goal of this paper is to do a systematic literature review on the current situation of AI in the industrial design sector and design processes providing insights. Data distribution of the reviewed articles foreshadows how AI can be incorporated into design processes differently and how it can potentially help to solve current pain points of the process efficiently—shedding light on the current situation and aiming to foresee the future. This not only educates researchers but also assists industrial designers in integrating AI safely and effectively into their processes.

Material and Method

The methodology used for this systematic review consists of using a research tool for finding the relevant literature, selecting suitable articles according to the filters, analyzing each source subsequently to the designated themes, and combining the relevant results, making room for future predictions accordingly. Enhancing the theoretical understanding of a particular problem should be the goal of a literature review, possibly by putting forth a new idea based on a variety of data (Baumeister, 2012). PRISMA Statement used for diagrams and checklists.

The tool used for finding and selecting eligible articles is EBSCOhost since it has a great variety of sources, using direct access through ITU. Also in addition, an AI-powered mapping system called LitMaps has been used to map out the literature and track how the topic has evolved showing how the papers are connected through references and citations. The collected articles are analyzed thematically by design context, design process, role of AI, methodology, AI tools, and future developments regarding AI in design workflows.

Research has been done using the definite statement which was (artificial intelligence or ai or a.i.*) AND (*design process or design method*) AND industrial design AND (*creative industries or creative industry or creative economy or creative sector*).* Only peer-reviewed and English journal articles dated between 2020-2025 are included. Applied Science & Technology Source Ultimate Publications used as the database filter. With all of the filters, initially, 26 articles remained. From these 26, a screening was done to find the associations between AI and Industrial design and the ones which are not directly related had been not selected. The final selection yields 10 articles to analyze in depth. The list of articles has been presented in Table 1.

Table 1. List of articles selected for in-depth analysis after applying the sampling and selection process.

Author(s)	Title	Journal	Year
Rapeepan Pitakaso, Thanatkij Srichok Surajet Khonjun et al.	Multi-Objective Sustainability Tourist Trip Design: An İnnovative ApproachFor Balancing Tourists' Preferences With Key Sustainability Considerations	Journal Of Cleaner Production	2024
Magdalena Ratalewska	Use Of Ict And Aı In Desıgn And Product Development By Sme's In The Creatıve Sector, Includıng Craft And Artısan Makers	Organızatıon And Management Series	2024
Eleonora Pantanoa, Francesca Serravalleb, Constantinos-Vasilios Priporasc,D	The Form Of Aı-Driven Luxury: How Generative Aı (Gaı) And Large Language Models (Llms) Are Transforming The Creative Process	Journal Of Marketıng Management	2024
Peng Lu A, Shih-Wen Hsiao B, Jian Tanga Fan Wu C	A Generative-Aı-Based Design Methodology For Car Frontal Forms Design	Advanced Engineering Informatics	2024
Tianxiong Wang, Liu Yang, Long Liu	Integrating Gra With İntuitionistic Fuzzy Vıkor Model To Explore Attractive Design Solution Of Wickerwork Cultural And Creative Products	Journal Of Engineering Design	2025
Jyh-Rong Chou	An İntegrative Review Exploring The Development Of Sustainable Product Design İn The Technological Context Of Industry 4.0	Advanced Engineering Informatics	2024
Bingkun Yuan A, Kai Wu A, Xinying Wu A,Chaoxiang Yang	Form Generative Approach For Front Face Design Of Electric Vehicle Under Female Aesthetic Preferences	Advanced Engineering Informatics	2024
Fabio Valoppi, Melissa Agustin, Felix Abik et al.	Insight On Current Advances İn Food Science And Technology For Feeding The World Population	Frontiers	2021
Guo Hui, Rose Dahlina Rusli, Asliza Bt Aris	Remodeling The Traditional Fashion Industry İn The Era Of Industry 4.0	International Journal Of Global Optimization And Its Application	2023
Zishun Guo, Meng Song, Xiaofen Fang, Cuiyun Lin et al.	Exploring Synergies Between Aıgc And Trız İn The Optimisation Of Road Cone Design Through İntegrated İnnovation Methods	Journal Of Engineering Design	2024

Findings

To detect the current integration, understanding and distilling the product design steps well is essential. Including not only the traditional design process but also new product development and sustainable product development phases will give a comprehensive understanding of the current situation. While some steps are mutual and familiar to AI more than others, only a few have innovative ways to use AI in design processes. AI is integrated into various phases of product design, including Idea Generation Steps, Prototyping and Simulation, Automation of Repetitive Tasks, and Presentation. The coding scheme used to analyse the articles are presented in Table 2.

Table 2. Coding scheme used to analyse the selected articles.

Categories	**General Question**	**Sub-Categories**
Context	Which Industrial Design Field?	Design sector Environment Creative Economy
Design Process	Which design step/steps consist AI?	Product Development Innovation Methods
Methodology	How the AI process was followed through the research?	Research strategy AI development Usage decisions
Tools	Which AI tools were used?	Generation Method Technology Controllability
Future Callings	Is there any foreshadowing for future usage of AI?	Implications of future Arguments Leading Concepts

The AI tools included in the studies are a mix of text to text, text to image, and image to image. These tools feed and rely on each other to navigate the designers in their process. With all of the papers analyzed, it can be said that AI is especially used for visualization in the design process. This included the basic conceptual designs for the end product. There are some utilization for other steps of the Traditional Design Process, yet To increase design efficiency and productivity, modern designers should become proficient in generative AI applications (Lu et al., 2024). Most of the papers focus on aesthetics and concepts rather than the current design problems such as Manufacturing Efficiency, Product Life Cycle or Sustainability. According to Verganti et al. with the development of AI more into the design practices, a counter act can be taken like a more effective and human-centered approach (2020).

Conclusion

It can be said that the design profession still mostly relies on humans and probably will stay like that for a while. Rather than being scared of it or seeing it as a threat, learning and exploring new ways to work with AI no matter what will be favorable. Despite its benefits, AI in design still has a lot to 'learn'. While AI technologies are essential for growing

creativity in industrial design and engineering, their influence is often seen as primarily supporting as their acceptance and effectiveness rely on the level of trust that is built between people and AI (Tsang & Lee, 2022).

Overall, this research provides a situational assessment of AI's role in product design processes and a foreshadowing for future usage scenarios. While this research is a great start to understanding the logic behind the current situation and evolution of AI in creative fields, further research is mandatory to explore this rapid progression and its long-term impacts on the industries in each region of the world. The impact of AI in design should be further investigated, in future studies and processes about sustainability and user-centered approaches.

This research only consists of some portion of the current studies and can be used as a guidance for the topic. There were only 26 related articles to the topic, due to it being relatively new and detailed. Also due to the nature of the development of AI, keeping up with the latest research and innovations is a must to make sure industrial designers have the ability to make use of the latest AI tools, adjust to changing design approaches, and handle new ethical and practical issues in the industry.

References

Baumeister, R. F. (2012). Writing a literature review. In Mitchell J. Prinstein (Ed.), *The Portable Mentor: Expert Guide to a Successful Career in Psychology* (ss. 119–132). Springer. https://doi.org/10.1007/978-1-4614-3994-3_8

Lu, P., Hsiao, S., Tang, J., & Wu, F. (2024). A generative-AI-based design methodology for car frontal forms design. *Advanced Engineering Informatics*, *62*, 102835. https://doi.org/10.1016/j.aei.2024.102835

Stoimenova, N., & Price, R. (2020). Exploring the Nuances of Designing (with/for) Artificial Intelligence. *Design Issues*, *36*(4), 45–55. https://doi.org/10.1162/desi_a_00613

Tsang, Y., & Lee, C. (2022). Artificial intelligence in industrial design: A semi-automated literature survey. *Engineering Applications of Artificial Intelligence*, *112*, 104884. https://doi.org/10.1016/j.engappai.2022.104884

Verganti, R., Vendraminelli, L., & Iansiti, M. (2020). Innovation and design in the age of artificial intelligence. *Journal of Product Innovation Management*, *37*(3), 212–227. https://doi.org/10.1111/jpim.12523

World Design Organization. (n.d.). *Definition of industrial design*. Retrieved March 21, 2025, from https://wdo.org/about/definition/

Exploring Emotions in Design Research: An Initial Mapping of Emotion-based Concepts

Gamze Uğurlukişi[a], Koray Gelmez[a]

[a] Istanbul Technical University, Graduate School, Department of Industrial Design, Industrial Design Master of Science Program, Türkiye

ugurlukisi18@itu.edu.tr

Keywords: Emotional, Bonding, Attachment, Longevity.

Aim

Emotional design is an approach that aims to evoke positive experiences in users, as introduced by Donald Norman in his book Emotional Design: Why We Love (or Hate) Everyday Things (2004). It is an effective method for designers who aim to trigger strong associations with emotions in the user. The importance of the emotional design approach is based on the bond between the user and the product, as a result of emotional interaction, which contributes to long-term success by increasing user satisfaction and loyalty (Yusa et al., 2023). The concept of emotional design, which has a wide range in the literature, provides a roadmap for examining the connections established by users, understanding user motivations, and integrating products into their daily routines more successfully.

Since design literature is a multidisciplinary and comprehensive field, it is a common fact that concepts often overlap across themes. Therefore, there is a need for studies that underline the fundamentals of emotional design.

This study aims to categorize the prominent studies that frame emotional concepts in design. The main purpose of the study is to understand the theoretical basis of the emotion-driven design concept and its versatile application forms and to provide an introductory-level map for researchers in this field.

This study does not propose a new emotional model, such as Norman's Three-Level Framework (2004) or Desmet's Product Emotion Model (2010). It contributes to the field by offering a broader thematic perspective, highlighting the conceptual relationships within emotional design literature. For example, while Yusa et al. (2023) conducted an application-oriented review and Ho & Siu (2012) focused on terminological distinctions, this study differs by providing an introductory-level mapping that synthesizes theoretical and strategic perspectives, rather than focusing on specific implementations or definitions.

Material and Method

This study identifies and organizes emotion-based concepts in design research. It presents an introductory-level map by categorizing base frameworks and common strategies.

The search process involved emotion-related keywords, such as "emotional bonding", "emotional attachment", "emotional interactions", and their relations to design. In order to identify prominent publications, keyword-based searches were conducted in academic databases such as Google Scholar and relevant design journals such as the International Journal of Design.

At the end of the search process, the selected studies were divided into two main categories: Theoretical framework and method/strategy. A conceptual map was created by separating these main categories into specific themes. This structure is intended to provide an overview for design researchers examining the emotional design literature.

Findings

An initial map was prepared (Fig. 1), which includes studies related to emotion. Category titles align with the study's aim to provide an overview of emotions in design research. The *theoretical framework* category includes studies that introduce frameworks and definitions. Under the *method/strategy* category, there are studies and approaches focused on examining or enhancing the emotional bond between users and products. Categories are divided into subthemes and color-coded to enhance readability.

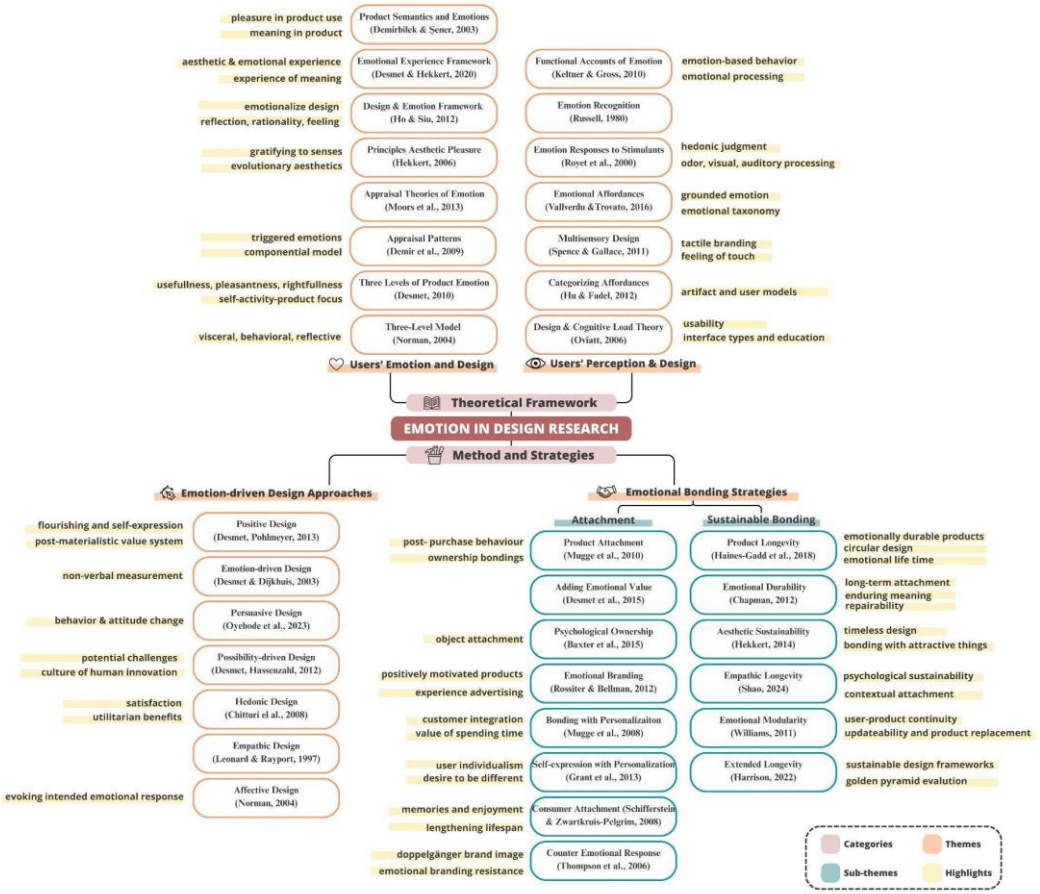

Figure 1: The Conceptual Map of Emotion in Design Research.

1. Theoretical Framework

The theoretical framework category includes studies based on core theories in emotion-based design research. It was divided into two themes:

(a) *Users' Emotion & Design,* which focuses on creating a theoretical framework to understand users' emotions; and

(b) *Users' Perception & Design,* which includes studies aimed at understanding the perceptual aspects of users and combining cognitive theories with the field of design.

a. Users' Emotion & Design

Among the studies that explore users' emotional responses, the Three-Level Model stands out (see Norman, 2004). Studies on appraisal theories are key in explaining emotion-focused evaluation processes (see Lazarus, 1991; Demir et al., 2009;

Moors et al., 2013). There are also important studies that propose a three-layered analysis structure for emotional experience (see Desmet, 2010; Desmet & Hekkert, 2020).

Ho and Siu (2012) introduce terminology and propose the *'emotionalize design'* from a new perspective. On the other hand, Hekkert outlined the principles of aesthetic pleasure in the study he published in 2006.

These studies have the potential to be a starting point for researchers, as they form the conceptual foundation for understanding the role of emotion in design.

b. Users' Perception & Design

In studies examining the users' perceptual engagement with design, affordance stands out as a key concept (see Hu & Fadel, 2012; Vallverdu & Trovato, 2016). These studies are prominent in understanding users' interpretation of actions embedded in products.

Additionally, the examination of tactile, visual, and auditory interactions appears as another important topic in this section. Studies investigating how emotional perception is formed by multisensory themes provide a foundation (see Royet et al., 2000; Spence & Gallace, 2011).

These studies emphasize that emotional reactions are shaped by direct sensory and perceptual engagement within the emotion theories in design. For researchers, the perceptual aspect of the emotional design concept and understanding how users interpret and react will provide additional information.

2. Methods & Strategy

The second main category includes methods and strategies that build an emotional connection between users and products. These studies propose ways to integrate emotion into design processes.

This category is divided into two themes:

(a) Emotion-based Design Approaches, which include methodologies that center emotions in the design process; and

(b) Emotion Bonding Strategies, which focus on strategies to create or strengthen the bond between the user and the products.

a. Emotion-based Design Approaches

Designing to evoke specific emotional responses is discussed within the scope of *affective design* (see Norman, 2004). Also, some concepts focus on emotional dimensions in specific contexts. For example, *positive design* emphasizes self-expression and flourishing for users; *persuasive design* aims to behavior change by influencing emotions; and *possibility-driven design* that accepts diverse emotions as a challenge (see Desmet & Pohlmeyer, 2013; Oyebode et al., 2023; Desmet & Hassenzahl, 2012).

In addition, it will be beneficial to examine the design for fun or hedonic purposes and how they differ from utilitarian benefits (see Chitturi et al., 2008; Desmet & Dijkhuis, 2003).

These studies can be guiding for researchers, as they represent approaches that share a common goal of integrating emotional depth into design processes.

b. Emotion Bonding Strategies

Personalization is a prominent strategy among many strategies aimed at building an emotional bond between user and product (see Mugge et al., 2008; Grant et al., 2013). Another study is *psychological ownership*, which highlights the importance of time and effort spent by the user (see Baxter et al., 2015).

Product attachment is another approach, which includes studies about emotional responses such as trust, satisfaction, and loyalty (see Schifferstein & Zwartkruis-Pelgrim, 2008; Mugge et. al, 2010).

Additionally, some studies aim to extend the psychological and physical lifespan of products, examine the role of user effort in sustaining bonds, and discuss repairability and dignified product aging. Within the scope of sustainability-oriented bonding, the concepts of product longevity, emotional durability, and aesthetic sustainability stand out (see Chapman, 2012; Haines-Gadd et al., 2018; Hekkert, 2014)

These studies focus on improving both the individual user experience and extending the product life through bonding while strengthening the emotional depth.

Conclusion

This study offers an introductory overview of emotion concepts in design research, organized in two main categories: theoretical framework and methods & strategies. The resulting map provides a structured understanding of diverse approaches for design researchers.

Rather than offering a detailed literature review, this paper outlines the prominent concepts and offers a conceptual foundation. This categorization supports future research about emotional design. As emotional design is a broad field, mapping studies like this help guide researchers.

References

Baxter, W. L., Aurisicchio, M., & Childs, P. R. N. (2015). A psychological ownership approach to designing object attachment. *Journal of Engineering Design*, *26*(4–6), 140–156. https://doi.org/10.1080/09544828.2015.1030371

Chapman, J. (2012). *Emotional durability: Design objects and experiences*. Routledge.

Chitturi, R., Raghunathan, R., & Mahajan, V. (2008). Delight by Design: The Role of Hedonic versus Utilitarian Benefits. *Journal of Marketing*, *72*(3), 48-63. https://doi.org/10.1509/JMKG.72.3.048

Demirbilek, O., & Sener, B. (2003). Product design, semantics and emotional response . *Ergonomics*, *46*(13–14), 1346–1360. https://doi.org/10.1080/0014013031000161087 4

Demir, E., Desmet, P. M. A., & Hekkert, P. (2009). Appraisal patterns of emotions in human-product interaction. *International Journal of Design, 3*(2), 41-51.

Desmet, P., Overbeeke, K., & Tax, S. (2001). Designing products with added emotional value: Development and application of an approach for research through design. *The Design Journal, 4*(1), 32–47. https://doi.org/10.2752/146069201789378496

Desmet, P. M. A., & Dijkhuis, E. (2003). A wheelchair can be fun: A case of emotion-driven design. In *Proceedings of the 2003 International Conference on Designing Pleasurable Products and Interfaces (DPPI '03)* (pp. 22–27). Association for Computing Machinery. https://doi.org/10.1145/782896.782903

Desmet, P. M. A., & Hassenzahl, M. (2012). Towards happiness: Possibility-driven design. In M. Zacarias & J. V. de Oliveira (Eds.), *Human-computer interaction: The agency perspective* (Vol. 396, pp. 3–27). Springer. https://doi.org/10.1007/978-3-642-25691-2_1

Desmet, P. M. A., & Hekkert, P. (2007). Framework of product experience. *International Journal of Design*, 1(1), 13–23.

Desmet, P. M. A. (2010, March). *Three levels of product emotion*. Paper presented at the International Conference on Kansei Engineering and Emotion Research (KEER 2010), Paris, France.

Grant, K. E., Straker, K., Muller, C., & Wrigley, C. (2013). The search for individualism: Self-expression through product personalisation. *The International Journal of Designed Objects, 6*(1), 17–30. https://doi.org/10.18848/2325-1379/CGP/v06i01/38694

Haines-Gadd, M., Chapman, J., Lloyd, P., Mason, J., & Aliakseyeu, D. (2018). Emotional durability design nine—A tool for product longevity. *Sustainability, 10*(6), 1948. https://doi.org/10.3390/su10061948

Harrison, K. (2022). *A design approach for extending product longevity: Combating the challenges faced by modern product obsolescence* (Master's thesis, Auburn University). Auburn University.

Hekkert, PPM. (2006). Design aesthetics: Principles of pleasure in design. *Psychology Science, 48*(2), 157- 172.

Hekkert, P. (2015). Aesthetic responses to design: A battle of impulses. In A. Berleant & T. Smith (Eds.), *The aesthetic mind: Philosophy and psychology* (pp. 277–297). Cambridge University Press. https://doi.org/10.1017/CBO9781139207058.015

Ho, A. G., & Siu, K. W. M. G. (2012). Emotion Design, Emotional Design, Emotionalize Design: A Review on Their Relationships from a New Perspective. *The Design Journal*, *15*(1), 9–32. https://doi.org/10.2752/175630612X13192035508462

Hu, J., & Fadel, G. M. (2012). Categorizing affordances for product design. In *Proceedings of the ASME 2012 International Design Engineering Technical Conferences and Computers and Information in Engineering Conference (IDETC/CIE)* (pp. 325–339). American Society of Mechanical Engineers. https://doi.org/10.1115/DETC2012-70933

Karahanoğlu, A. (2008). *A study of consumers' emotional responses towards brands and branded products* (Master's thesis, Middle East Technical University). Middle East Technical University.

Keltner, D., & Gross, J. J. (1999). Functional Accounts of Emotions. *Cognition and Emotion*, *13*(5), 467–480. https://doi.org/10.1080/026999399379140

Lazarus, R. S. (1991). *Emotion and adaptation*. Oxford University Press.

Leonard, D., & Rayport, J. F. (1997). Spark innovation through empathic design. *Harvard Business Review*, 75(6), 102–113.

Moors, A., Ellsworth, P. C., Scherer, K. R., & Frijda, N. H. (2013). Appraisal Theories of Emotion: State of the Art and Future Development. *Emotion Review*, *5*(2), 119-124. https://doi.org/10.1177/1754073912468165

Mugge, R., Schifferstein, H. N. J., & Schoormans, J. P. L. (2010). Product attachment and satisfaction: Understanding consumers' post-purchase behavior. *Journal of Consumer Marketing, 27*(3), 271–282. https://doi.org/10.1108/07363761011038347

Mugge, R., Schoormans, J. P. L., & Schifferstein, H. N. J. (2009). Emotional bonding with personalised products. *Journal of Engineering Design*, *20*(5), 467–476. https://doi.org/10.1080/09544820802698550

Norman, D. (2004). *Emotional design: Why we love (or hate) everyday things*. Basic books.

Oviatt, S. (2006). Human-centered design meets cognitive load theory: Designing interfaces that help people think. In *Proceedings of the 14th ACM International Conference on Multimedia (MM '06)* (pp. 871–880). Association for Computing Machinery. https://doi.org/10.1145/1180639.1180831

Oyebode, O., Steeves, D., & Orji, R. (2024). Persuasive strategies and emotional states: Towards designing personalized and emotion-adaptive persuasive systems. *User Modeling and User-Adapted Interaction, 34*(1), 1175–1225. https://doi.org/10.1007/s11257-023-09390-x

Rossiter, J. R., & Bellman, S. (2012). Emotional branding pays off: How brands meet share of requirements through bonding, companionship, and love. *Journal of Advertising Research, 52*(3), 291–296. https://doi.org/10.2501/JAR-52-3-291-296

Royet, J.-P., Zald, D. H., Versace, R., Costes, N., Lavenne, F., Koenig, O., & Gervais, R. (2000). Emotional responses to pleasant and unpleasant olfactory, visual, and auditory stimuli: A positron emission tomography study. *Journal of Neuroscience*, 20(20), 7752–7759. https://www.jneurosci.org/content/20/20/7752

Russell, J. A. (1994). Is there universal recognition of emotion from facial expression? A review of the cross-cultural studies. *Psychological Bulletin, 115*(1), 102–141. https://doi.org/10.1037/0033-2909.115.1.102

Schifferstein, H. N. J., & Zwartkruis-Pelgrim, E. P. H. (2008). Consumer-product attachment: Measurement and design implications. *International Journal of Design, 2*(3), 1-13.

Spence, C., & Gallace, A. (2011). Multisensory design: Reaching out to touch the consumer. *Psychology & Marketing*, 28(3), 267–308. https://doi.org/10.1002/mar.20392

Shao, H. (2024). *Design for emotional durability: Investigating the relationship between emotions and product longevity in industrial design* (Master's thesis, Auburn University). Auburn University.

Thompson, C. J., Rindfleisch, A., & Arsel, Z. (2006). Emotional Branding and the Strategic Value of the Doppelgänger Brand Image. *Journal of Marketing, 70*(1), 50–64.

Vallverdú J, Trovato G. Emotional affordances for human–robot interaction. *Adaptive Behavior*. 2016;24(5):320-334.

https://doi.org/10.1177/105971231666823

Williams, B. T. (2011). *Emotional modularity in product design* (Master's thesis, Auburn University). Auburn University.

Yusa, I. M. M., Ardhana, I. K., Putra, I. N. D., & Pujaastawa, I. B. G. (2023). Emotional design: A review of theoretical foundations, methodologies, and applications. *Journal of Aesthetics, Design, and Art Management*, 3(1), 1–14. https://doi.org/10.58982/jadam.v3i1.308

Understanding Creativity: A Survey-Based Investigation into the Psychology of Designers' Creativity during the Ideation Phase

Naz Feryal Cezayirli[a], Aysun Ateş Akdeniz[b]

[a] Istanbul Technical University/Graduate School Industrial Design Program, Türkiye
[b] Istanbul Technical University, Faculty of Architecture, Department of Industrial Design, Türkiye
cezayirli23@itu.edu.tr

Keywords: Cognitive Biases, Creativity Triggers, Design Intuition, Eureka Moments, Spontaneous Transfer.

Aim

Designers hold a unique place between creativity and reality. They have the ability to generate limitless ideas and bring them to the real world, by "changing existing situations into preferred ones" (Simon, 2019). This raises the question of how designers form these ideas? Can the habits and behaviors of these creative individuals guide one to the doors of creativity? With these questions in mind, this study aims to shed light on the cognitive and psychological processes industrial designers undergo during idea generation. By utilizing a survey aimed at designers, their habits and mental processes during the design ideation phase are explored. It should be noted that although the processes of individuals are highly subjective, the similarities are to be explored in order to find a repeating pattern that could be used to lead the way to creativity. There have been a number of studies studying design creativity and how it is related to design. One study compares university design students' and tutors' creativity. In this study it is revealed that there are clear differences between tutors and students in how they assess their creative potential, although both find it difficult to define it (Rodgers & Jones, 2017). Another study explores the idea generation phase among designers depending on experience. It is stated that designers utilize their knowledge of existing designs and how they transform these to suit new designs. (Sarkar & Chakrabarti, 2017). One study examines the creative processes through a psychoanalytic lens, exploring concepts of play, particularly word play, aesthetic and sensory experiences and repetition (Holm-Hadulla, 2003). In light of these findings, this study aims to utilize the findings utilize previous studies to explore and identify the creative tools in ideation phase further in order to shed light on cognitive and psychological processes among industrial designers.

Material and Method

This study utilizes an online survey method for data collection. 20 designers practicing in Turkey, aged 23 through 34 have participated in the survey. The survey questions for this study have been designed using Dr. Max A. Houck's Upside Down Triangle survey method, and is consisting of three main parts. The first part is demographics and consists of 9 open ended questions. This part is necessary to be able to view the data from a sociological perspective and is necessary during the contextual analysis phase. The second part of the survey includes 7 open ended questions on design behavior and design habits. These questions are asked in a way that urges the designer to raise awareness of their own processes. The third and last part of the survey includes 7 open ended questions which are more specific and challenging. They are aimed directly at specific cognitive processes using specific keywords that aim to pave the way for further research.
Once the participants start exploring their cognitive processes, the questions guide them to think about more unconscious processes like their cognitive biases, design intuition and Eureka moments. Finally the main question of this study is explored, which is how designers trigger creativity moments.

Findings

The answers for the survey have been analyzed using thematic analysis. The reason why thematic analysis has been chosen to analyze the data is because it offers rich yet complex qualitative analysis, as well as provides theoretical freedom (Braun & Clarke, 2006).

The results have been gathered under 5 sub categories according to the analysis results. The study initiates by exploring designers' habits and rituals during the beginning of the design ideation phase.
The first aspect that has been explored was how designers start their processes. Almost half of the participants expressed that they start their ideation process through research, while the rest utilize a diving in approach and starting with idea generation directly.
During their creative processes, it is revealed that all designers adapted their own ways to foster creativity. While some explore previous works for inspiration, others utilize workshops and DIY projects or visit exhibitions and museums. Not surprisingly, the ones who chose solitary activities also preferred to work alone during idea generation.
Strernberg and Lubart define six resources for creativity; intelligence, knowledge, thinking styles, personality, motivation, and environment (Sternberg et al., 1996). This supports the findings of the study that each designer adapts their own way of fostering creativity.
Another aspect this study explored is cognitive biases during the ideation phase. The designers who were aware of and could navigate their cognitive biases also seemed to trust their intuition. In a study about cognitive biases, it is suggested that these biases are "maps to the design of the mind" (Haselton, 2015). This suggests that designers who are aware of their cognitive processes are more in tune with their ideas, allowing them to navigate their creative processes more easily than those who aren't. Consequently, this awareness may contribute to a stronger trust in their intuition overall.
When asked if they explore seemingly unrelated topics to gain inspiration, 10 participants stated they don't while the other 10 stated they do. One way of doing this was stated as talking to friends from other fields as well as expanding their own knowledge through research. In research this is called "spontaneous" transfer, where knowledge and insights from one domain are applied to another, leading to novel ideas (Weisberg, 2006; Price & Driscoll, 1997).
Another aspect that is explored in the study is Eureka moments. In literature it is described as moments of spontaneous and inspired breakthrough insights (Steyn & Buys, 2011). Almost half of the participants reported never having these Eureka moments, however a quarter of the participants mentioned they have experienced it during seemingly unrelated moments. This suggests that there may be a correlation between these seemingly random ideation moments and the unconscious mental processes. It may suggest that the unconscious mind continues working on design problems in the background, bringing insights to the consciousness when the mind is at ease.
Finally the participants are asked how they trigger creative moments. Although almost half of the participants didn't believe this wasn't possible, the rest stated they have their own methods. Some prefer walking or listening to music in order to quiet their minds, the rest adapted a dive-in approach where they actively create through activities like writing and by simply doing. This correlates with research where immersive activities can foster creativity (Csikszentmihalyi, 1990).

Conclusion

This study is aimed at exploring the cognitive processes of designers during the ideation phase, revealing their creative habits and triggers of their innovative ideas. The results revealed a variety of approaches among the participants, demonstrating that there is no one-size-fits-all method for fostering creativity. The study also highlighted the importance of understanding cognitive biases, with those who are more aware of their biases often having a stronger trust in their design intuition.
Additionally, the study found that inspiration can come from engaging with unrelated fields and expanding knowledge through research, called "spontaneous transfer" in creative processes. Eureka moments, although not very frequent for many designers, also revealed important aspects of the creative process, suggesting that unconscious mental processes continue to contribute to idea generation even when designers aren't consciously focused on a problem.

In terms of triggering creativity, immersive activities such as walking, listening to music, or diving into a task were reported by the participants as effective methods during idea generation. These findings are supported with previous research suggesting that engaging the mind in different ways can lead to increased creativity.
The reliance on an online survey restricted the depth of information gathered, as it mostly captured what designers were consciously aware of in their processes. Additionally, the limited sample size of the survey prevents a broader generalization

of the results. To build upon these initial findings, future research will incorporate in-depth qualitative methods, such as one-on-one interviews and design workshops, to further explore the unconscious processes that influence creativity.

References

Braun, V., & Clarke, V. (2006). Using thematic analysis in psychology. Qualitative Research in Psychology, 3(2), 77–101. https://doi.org/10.1191/1478088706qp063oa

Csikszentmihalyi, M. (1990). Flow: The Psychology of Optimal Experience. Harper & Row.

Haselton, M. G., Nettle, D., & Andrews, P. W. (2015). The Evolution of Cognitive Bias. The Handbook of Evolutionary Psychology, 724–746. doi:10.1002/9780470939376.ch25

Holm-Hadulla, R. M. (2003). Psychoanalysis as a creative shaping process. The International Journal of Psychoanalysis, 84(5), 1203–1220. https://doi.org/10.1516/8rar-e635-mp73-nwq9

Price, E. A., & Driscoll, M. P. (1997). An inquiry into the spontaneous transfer of problem-solving skill. Contemporary Educational Psychology, 22(4), 472–494. https://doi.org/10.1006/ceps.1997.0948

Rodgers, P. A., & Jones, P. (2017). Comparing University design students' and tutors' perceptions of creativity. The Design Journal, 20(4), 435–457. https://doi.org/10.1080/14606925.2017.1323503

Sarkar, P., & Chakrabarti, A. (2017). A model for the process of idea generation. The Design Journal, 20(2), 239–257. https://doi.org/10.1080/14606925.2017.1272244

Simon, H. A. (2019). Sciences of Artificial. The Mit Press.

Sternberg, R. J., & Lubart, T. I. (1996). Investing in creativity. American Psychologist, 51(7), 677– 688. https://doi.org/10.1037/0003-066x.51.7.677

Steyn, J. L., & Buys, A. J. (2011). Creativity and 'Eureka' in science and engineering. South African Journal of Industrial Engineering, 22(2), 1-17. https://doi.org/10.7166/22-2-11

Weisberg, R. W. (2016). Creativity: Understanding innovation in problem solving, science, invention, and the Arts. Wiley.

INDUSTRIAL ENGINEERING

Decision Making

Engineering Management

Industrial Data Analytics

Knowledge Management

Manufacturing Management

Multi Criteria Decision Making For Selecting Best Banking Service Channel

Mustafa Akça[a], Yusuf İlker Topçu[a]

[a] Istanbul Technical University/Institute of Science, Industrial Engineering, Engineering Management Program, Turkey
akcam15@itu.edu.tr

Keywords: AHP, Banking, Decision Making.

Aim

The aim of this study is to find the most appropriate alternative among the possible banking service channels utilizing the Analytic Hierarchy Process (AHP) which is one of the most widely used multi-criteria decision-making method and revealing criteria importance for ranking options of banking service types. The alternatives which are state/private and digital/physical are choosen based on the literatüre and today's trend in banking.

Material and Method

In today's banking world, customer behaviors are analyzed to determine whether a banking model that prioritizes physical branches or a model that focuses on digital channels by providing services through internet and mobile banking is the most appropriate approach. In this study, , first the necessary criteria and related sub-criteria for the model will be determined by considering previous studies and expert opinions on this topic. Then, the Analytic Hierarchy Process (AHP) method will be used to reveal the importance of the criteria and the sub-criteria based on the experts' judgments. These criteria are listed as physical conditions, technical infrastructure, security and privacy. As a final step, the model will evaluate four alternatives service channels based on the branch-focused banking model and the digital-focused banking model. The objective data for the performance of alternatives with repsect to criteria will be obtained using the data of a private bank operating in Turkey. In the study, four alternatives will be evaluated . These alternatives are defined as follows: the state-supported digital-only banking model, the state-supported banking model providing both digital and physical services, the private capital-supported digital-only banking model, and the private capital-supported banking model offering both digital and physical services. the TOPSIS method will be utilized to recommend the most suitable banking modelThe findings obtained from this study are also expected to serve as a reference for decision-makers who are bank managers and finance executives in future studies on banking models.

Findings

Finance and banking expert preferences may differentiate based on criteria such as the region they work in, as well as their socioeconomic status of working region, education level, age, and gender. In this study, state hybrid models takes first place then private hybrid model, state digital model and private digital model follows in order. To achieve a more robust solution, increasing the number of survey participants and reaching out to individuals while considering these criteria can be applied in future studies.

Conclusion

The state-supported digital-only bank, the state-supported bank providing both physical and digital services, the private digital-only bank, and the private bank offering both physical and digital services will been evaluated using the AHP method. These four alternatives have then been ranked using the TOPSIS method. As a result, this ranking also provides insight into the foundations of banking services offered without physical branches, which are becoming increasingly widespread in the country. Also privacy and security criteria affects selection of the why the state hybrid model are takes first place.

References

Almaiah, M. A., Al-Rahmi, A. M., Alturise, F., Alrawad, M., Alkhalaf, S., Lutfi, A., Al-Rahmi, W. M., & Awad, A. B. (2022). Factors influencing the adoption of internet banking: An integration of ISSM and UTAUT with price value and perceived risk. *Frontiers in Psychology*, *13*. https://doi.org/10.3389/fpsyg.2022.919198

Başar, M. S., & Kul, S. (2020). Evaluation of Mobile Banking Apps in Terms of Usability with Analytical Hierarchy Process. *Bilgi Yönetimi*, *3*(1), 39–49. https://doi.org/10.33721/by.677976

Beshah, B., & Kitaw, D. (2013). AHP APPLICATION IN a FINANCIAL INSTITUTION. *International Journal of the Analytic Hierarchy Process*, *5*(1). https://doi.org/10.13033/ijahp.v5i1.135

Bozdoğan, T., Odabas, A., & Shegiwal, A. H. (2021). Analysis of financial performance of foreign banks having branches in Turkey by TOPSIS and ELECTRE methods. *Alanya Akademik Bakış*, *5*(2), 1049–1067. https://doi.org/10.29023/alanyaakademik.871031

Campbell, D., & Frei, F. (2009). Cost Structure, Customer Profitability, and Retention Implications of Self-Service Distribution Channels: Evidence from Customer Behavior in an Online Banking Channel. *Management Science*, *56*(1), 4–24. https://doi.org/10.1287/mnsc.1090.1066

Diener, F., & Špaček, M. (2021). Digital Transformation in Banking: A Managerial Perspective on Barriers to change. *Sustainability*, *13*(4), 2032. https://doi.org/10.3390/su13042032

Geng, D., Abhishek, V., & Li, B. (2015). When the bank comes to you: branch network and customer Multi-Channel banking behavior. *International Conference on Information Systems*. https://aisel.aisnet.org/icis2015/proceedings/eBizeGov/14

Hosseini, M., Abdolvand, N., & Harandi, S. R. (2022). Two-dimensional analysis of customer behavior in traditional and electronic banking. *Digital Business*, *2*(2), 100030. https://doi.org/10.1016/j.digbus.2022.100030

Hummel, D., Schacht, S., & Maedche, A. (2017b). Multi-Channel Choice in Retail Banking Services: Exploring the role of Service Characteristics. *WIRTSCHAFTSINFORMATIK*, 619. https://aisel.aisnet.org/cgi/viewcontent.cgi?article=1074&context=wi2017

Ic, Y. T., Celik, B., Kavak, S., & Baki, B. (2020). Development of a multi-criteria decision-making model for comparing the performance of Turkish commercial banks. *Journal of Advances in Management Research*, *18*(2), 250–272. https://doi.org/10.1108/jamr-05-2020-0083

Kumar, M., & Gupta, S. (2020). Security perception of e-banking users in India: an analytical hierarchy process. *Banks and Bank Systems*, *15*(1), 11–20. https://doi.org/10.21511/bbs.15(1).2020.02

Önder, E., Taş, N., & Hepşen, A. (2013). Performance evaluation of Turkish banks using fuzzy analytical hierarchy process and TOPSIS methods. *SSRN Electronic Journal*. https://avesis.istanbul.edu.tr/yayin/23b2a7b0-7b73-45a7-a121-3cb1a50b0bbf/performance-evaluation-of-turkish-banks-using-fuzzy-analytical-hierarchy-process-and-topsis-methods

Riyanto, A., Primiana, I., Yunizar, N., & Azis, Y. (2019). Digital Branch: Banking innovation in Indonesia to face 4.0 industry challenges. *IOP Conference Series Materials Science and Engineering*, *662*(7), 072002. https://doi.org/10.1088/1757-899x/662/7/072002

Shashi, B., & Yadav, S. R. (2009). AHP Application in Banking: Unfolding utility in a situation of Financial crisis. *ISAHP Proceedings*. https://doi.org/10.13033/isahp.y2009.008

Sonea, A., Guo, W., & Jarvis, S. (2019). EXPLORATORY SPATIAL ANALYSIS OF "ACCESS" TO PHYSICAL AND DIGITAL RETAIL BANKING CHANNELS IN THE UK [Dataset]. In *Zenodo (CERN European Organization for Nuclear Research)*. https://doi.org/10.5281/zenodo.3417102

Tekçam, R. (2015). Performance Assessment In Banking Sector Th rough Analitical Hierarchy Process: Th e Case Of Public Banks, Private Commercial Banks And Participation Banks. *DergiPark (Istanbul University)*. https://dergipark.org.tr/tr/pub/afes/issue/44777/556914

Tran, T. (2019). Applying AHP in evaluation of Vietnamese Commercial banks. *International Journal of Analysis and Applications*. https://doi.org/10.28924/2291-8639-17-2019-132

Vaidya, O. S., & Kumar, S. (2004). Analytic hierarchy process: An overview of applications. *European Journal of Operational Research*, *169*(1), 1–29. https://doi.org/10.1016/j.ejor.2004.04.028

Vazifedust, H., & Bani'Asadi, M. (2014). Prioritizing the client trust factors in electronic banking using analytic hierarchy process. *Management Science Letters*, *4*(4), 695–702. https://doi.org/10.5267/j.msl.2014.2.023
Yaghubi, N., & Seyedin, S. M. (2015). Ranking the technical dimensions of e-banking service quality evaluation models using Analytical Hierarchy Process. *Advances in Computer Science : An International Journal*, *4*(1), 37–43. http://www.acsij.org/documents/v4i1/ACSIJ-2014-4-1-625.pdf

A Comparative Analysis of Machine Learning and MCDM Sorting Methods in Electric Vehicle Selection

Mehmet Demir[a], Umut Asan[b]

[a] Istanbul Technical University, Management Faculty, Engineering Management, Turkey
[b] Istanbul Technical University, Management Faculty, Turkey
demir22@itu.edu.tr

Keywords: Electric Vehicles, Machine Learning, MCDM, TOPSIS-Sort-B, Decision Tree, Multinominal Logistic Regression, Sustainable Transportation.

Aim

The transition to sustainable transportation has gained significant attention due to growing environmental concerns, particularly greenhouse gas emissions caused by conventional internal combustion engine vehicles. Electric vehicles (EVs) have emerged as a promising solution to this problem; however, selecting the most suitable EV remains a complex decision-making problem due to multiple conflicting criteria, including cost, performance, battery technology and sustainability factors. The complexity of this decision necessitates robust classification methods that can accommodate both quantitative and qualitative factors. In this context, multi-criteria decision-making (MCDM) approaches provide structured and interpretable classification, whereas machine learning (ML) techniques offer data-driven solutions with high predictive performance.

The aim of this study is to make a comparison between MCDM-based sorting and ML-based classification methodologies in the context of EV selection. In sorting problems, a predefined set of categories must be established, and actions are assigned to these categories independently of other actions (Figueira et al., 2005). In this problem, the decision-maker (DM) attempts to partition the set of alternatives into several categories (Bouyssou et al., 2006) In the context of MCDM approaches, sorting methods have been shown to be favoured over ranking and choosing techniques due to facilitating the decision-making process for decision makers by reducing cognitive burden. In this study, sorting of EVs into preference-based classes has been shown to render the selection process more structured and manageble.

Material and Method

First, hierarchical clustering is employed to determine the optimal number of preference-based categories, followed by the application of TOPSIS-Sort-B for MCDM-based classification. Concurrently, machine learning (ML) classification methods, encompassing decision tree, multinomial logistic regression, naive bayes, linear discriminant analysis (LDA), support vector machine (SVM), and artificial neural networks (ANN), are implemented to categorize EVs based on their features. The classification outcomes of these methodologies are then compared to assess their reliability and accuracy in EV selection.

The present study utilises data obtained from ev-database.org, the largest publicly available EV database, containing detailed specifications of 439 electric vehicles currently on the market. The dataset comprises multiple attributes relevant to EV selection, organized into the following performance metrics: acceleration, top speed, range, battery architecture, battery warranty (both in years and kilometres), charging speed, fast charging speed, fuel equivalent, vehicle weight, seating capacity, turning circle, price, vehicle volume, total cargo volume, drive type, automatic charging support, pre-conditioning, V2L support, tow hitch availability, dedicated EV platform, and heat pump.

In order to ensure data quality and consistency, pre-processing steps were implemented. Missing values were handled using an imputation strategy based on the average values within each vehicle segment, thereby preserving segment-specific characteristics. Categorical variables were converted into numerical representations using one-hot encoding to facilitate

their integration into machine learning (ML) models. Additionally, min-max scaling was applied to numerical variables, normalizing their range between 0 and 1 to ensure comparability across features.

Prior to the implementation of the sorting algorithm, a preliminary clustering analysis was conducted to determine the optimal number of categories. To address the lack of labels in the dataset, hierarchical clustering was employed, utilising a range of linkage methods. The dendrogram suggested that three clusters represented the optimal grouping, corresponding to high, medium, and low preference classes. This data-driven clustering approach provided a robust foundation for the subsequent classification process.

Following the clustering phase, classification was conducted using two distinct methodologies. The first approach employed the TOPSIS-Sort-B method, an MCDM-based sorting technique, to classify EVs into high, medium, and low preference categories. This sorting process required predefined limit profiles, which were systematically determined using the lower and upper quartiles of each attribute to ensure a balanced distribution of categories. Additionally, criteria weights were established through the Analytic Hierarchy Process (AHP), where two domain experts assigned weights via pairwise comparisons. The results highlighted that price, range, fast charging speed, and battery warranty period were the most influential factors in EV selection, aligning with consumer preferences and market trends.

The second approach involved the use of machine learning (ML) classification, leveraging multiple algorithms to validate the categorisation derived from the MCDM sorting process. The dataset was split into a training set (90%) and a testing set (10% - nearly 40 instances) to evaluate the generalisation performance of each model. Model performance was assessed using standard classification metrics, including accuracy, precision, recall, and F1-score. The ML classification results were subsequently compared with the MCDM sorting outputs to examine their agreement and reliability.

Findings

Among the ML models tested, multinomial logistic regression exhibited the highest classification accuracy, achieving 98%, followed by ANN with 95%, decision tree with 90%, and SVM with 90%. The performance metrics for all models are summarized in Table 1. The results of this investigation demonstrated strong consistency between MCDM sorting and ML-based approaches.

Table 1. Performance Metrics**.**

Model	Accuracy	Precision	Recall	F1-Score
Decision Tree	0.90	0.90	0.90	0.90
Multinominal Logistic Regression	0.98	0.98	0.98	0.97
Naive Bayes	0.83	0.84	0.83	0.82
LDA	0.88	0.88	0.88	0.87
SVM	0.90	0.92	0.90	0.90
ANN	0.95	0.96	0.95	0.95

Conclusion

This research emphasises the merits of integrating MCDM sorting with ML-based classification to establish a dependable and interpretable decision-making framework for EV categorisation. The methodological approach adopted in this study offers significant insights for policymakers, industry experts, and consumers by enhancing decision support mechanisms in sustainable transportation. Future research could explore hybrid decision-making frameworks, incorporate additional EV attributes, or extend the dataset to enhance the classification robustness. The findings contribute to the broader goal of facilitating informed EV selection, ultimately supporting the transition toward sustainable mobility.

References

Figueira, J., Mousseau, V., & Roy, B. (2005). ELECTRE methods. In J. Figueira, S. Greco, & M. Ehrgott (Eds.), Multiple Criteria Decision Analysis: The State of the Art Surveys (pp. 133–162). New York: Springer Science+Business Media Inc.
Bouyssou, D., Marchant, T., Pirlot, M., Tsoukia`s, A., & Vincke, P. (2006). Evaluation and decision models with multiple criteria: Stepping stones for the analyst (Vol. 86). Springer Science & Business Media.

A Bayesian Network-Based Approach for Analyzing Railway Accidents

Derya Cephe[a], Umut Asan[a]

[a] Istanbul Technical University, Industrial Engineering, MSc in Industrial Engineering, Türkiye
deryacephe18@gmail.com, cephe22@itu.edu.tr

Keywords: Bayesian Network, Railway Safety, Accident Analysis, GeNIe.

With the increasing demand for transportation, railway systems have gained significant momentum due to their economic and environmental advantages. However, if necessary safety measures are not implemented, accidents may result in severe injuries and fatalities. The primary objective in such accidents is to prevent loss of life and serious injuries. Effective accident prevention strategies can significantly reduce, or even eliminate, these adverse consequences. However, in order to develop preventive measures, past accident data must first be systematically analyzed.

In recent years, the fatality rate associated with railway accidents has shown a declining trend globally. Between 2010 and 2021, the average number of significant accidents per million train-kilometers in European Union (EU) countries was recorded as 0.5 (European Union Agency for Railways [ERA], 2023), whereas in Turkey, this rate was approximately 2.48 for the same period (Turkish State Railways [TCDD], 2023). Analyzing the statistics of the Turkish State Railways, this rate, which was around 5 per million train-kilometers in the 2010s, decreased to 1.3 by 2021, showing remarkable improvement (TCDD, 2023). However, existing data indicate that Turkey still has significantly higher accident rates compared to European countries (Figure 1).

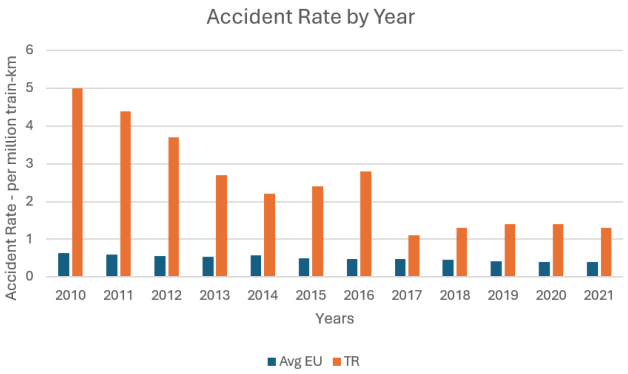

Figure 1. Accident Rates per Million Train-Km in European Countries and Turkey (2010-2021).

Aim

The primary objective of this study is to conduct an in-depth analysis of railway accidents in Turkey and propose preventive measures to avoid similar accidents in the future, providing guidance for the sector. In this context, Bayesian Network-based probabilistic prediction models were employed, expert opinions were utilized, and analyses were conducted using a model developed in the GeNIe software.

This study offers unique academic and industrial contributions, including: The development of a model that accounts for uncertainties, allowing for a more accurate representation of real-world conditions. It is the first study to analyze railway accidents in Turkey using the Bayesian Network approach. A hybrid Bayesian approach was adopted, integrating both data-driven analysis and expert knowledge. This methodology provides a novel contribution to international literature. International studies predominantly develop data-driven models based on existing accident data, with hybrid models used in cases of data scarcity. However, in this study, expert opinions were not only used to address data gaps but also to gain a deeper understanding of railway safety and develop a needs-based approach.

Material and Method

This study thoroughly examines railway accident data from the past seven years in Turkey. The methodology consists of three main stages: data collection and variable identification, statistical analyses and Bayesian Network modeling, and scenario development.

The data used in this study were obtained from TCDD's statistical yearbooks and face-to-face interviews with TCDD officials. The selection of variables was guided by international literature and safety-related accident variables defined in the ERA directives.

The categorical variables used in the study and their definitions are as follows:

- Technology Level: Represents the level of technology in the year of the accident.
- Season: Indicates the season in which the accident occurred.
- Railway Line: Denotes the name of the railway line where the accident occurred.
- Minor Injury: Indicates whether minor injuries occurred in the accident.
- Serious Injury: Indicates whether serious injuries occurred in the accident.
- Fatality: Indicates whether the accident resulted in fatalities.
- Cost Amount: Represents the financial cost incurred due to the accident.
- Accident Level : Defines the level of the accident in terms of safety impact.
- Accident Type: Describes the type of accident.
- Accident Cause: Identifies the primary cause of the accident.

To systematically analyze the relationships among these variables and assess their statistical significance, IBM SPSS software was utilized. The applied statistical methods include Crosstab Analysis, which was used to visualize associations between categorical variables, and the Chi-Square Test, which determined the presence of statistically significant relationships among categorical variables. The strength of these significant relationships was further assessed using Cramér's V and Phi coefficients.

In order to investigate railway accidents in greater depth, a Bayesian Network-based modeling approach was employed. The modeling process consisted of two key stages. In the qualitative stage, relationships between variables were identified based on statistical analysis results and expert evaluations. In the quantitative stage, Conditional Probability Distributions (CPDs) between variables were calculated, and the model underwent statistical validation (Asan, n.d.).

During the model development process, the data were initially organized in MS Office Excel and subsequently processed in the GeNIe Academic software to construct the Bayesian Network model (Figure 2). This model was designed to analyze accident patterns under various scenarios, offering decision-makers valuable insights to improve railway safety management.

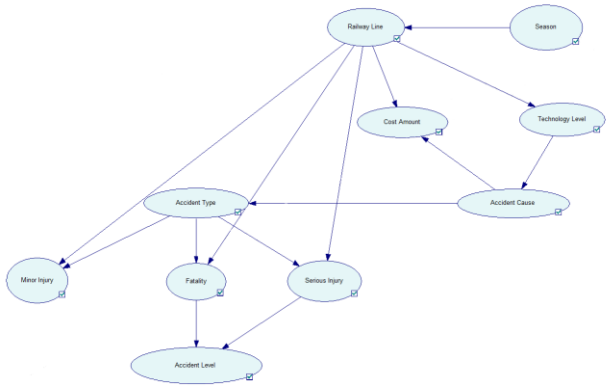

Figure 2. Bayesian Network Model Developed in GeNIe.

The analysis included four distinct scenarios. Scenario-0, the Current Situation, represents the existing accident conditions, serving as a baseline for comparison. Scenario-1, the Best-Case Scenario, simulates an ideal condition where accidents are minimized to a "minor" level, aligning with global safety strategies and best practices. Scenario-2, the Worst-Case Scenario, reflects the most adverse conditions, where accidents are categorized as "major," leading to increased fatality and severe injury rates. Scenario-3, the Line-Based Scenario, examines how different railway lines are impacted by geographical location, management structure, and environmental factors, providing a more granular perspective on accident risks. These scenarios are structured to guide decision-makers in strengthening railway safety management and preventing future accidents.

Findings

The statistical analyses and Bayesian Network model outputs reveal several critical insights into railway accident patterns. Seasonal variations have a notable impact on the occurrence and distribution of railway accidents, indicating a need for adaptive safety measures throughout the year. The causes, types, and financial costs of accidents exhibit significant variation depending on the railway line, suggesting that infrastructure, operational conditions, and environmental factors play a crucial role in accident dynamics. Furthermore, accident costs are influenced by multiple factors, including seasonal conditions, railway line characteristics, technological advancements, and the underlying cause of the accident. The level of technology implemented on a railway line not only affects the primary cause of accidents but also determines the financial burden associated with them. The findings also indicate that the cause of an accident is a strong determinant of the accident type, which, in turn, directly influences the severity of consequences, including fatalities, serious injuries, and minor injuries. Additionally, the number of fatalities is impacted not only by the type of accident but also by the specific railway line where the incident occurs, emphasizing the role of infrastructure and safety standards in different regions. Lastly, accident severity is primarily determined by the number of fatalities and serious injuries, highlighting the importance of preventive measures and rapid emergency response strategies in mitigating the most severe outcomes of railway accidents.
The results obtained from the scenario testing provide significant insights into the patterns and severity of railway accidents under different conditions. In Scenario-0 (Current Situation), the majority of accidents occur at a minor level, with relatively low fatality and serious injury rates. However, derailments and collisions remain critical risks, highlighting the need for further safety improvements. Human errors and equipment failures are identified as major contributing factors, and the current level of technology indicates room for enhancement in accident prevention measures.
In Scenario-1 (Best-Case Scenario), where accidents are minimized to a minor level, fatalities and serious injuries are entirely eliminated, aligning with the expectations of an optimized safety strategy. This scenario underscores the potential effectiveness of preventive measures in significantly reducing accident severity.
Conversely, Scenario-2 (Worst-Case Scenario) presents the most adverse conditions, where accidents are classified as major, leading to a substantial increase in fatality and serious injury rates. Pedestrian collisions and level crossing accidents emerge as dominant contributors, particularly in specific railway lines. The findings indicate that human errors remain the most influential factor in this scenario, further emphasizing the importance of human-centered safety interventions and infrastructural improvements.
Scenario-3 (Line-Based Scenario) reveals notable variations in accident severity and frequency across different railway lines. While serious accidents constitute only 3% of the overall dataset, this rate increases to 6% on Line-3 but decreases to 0% on Lines 4 and 8. A closer examination of fatality rates shows an upward trend on Lines 3 and 4, whereas Line 2 exhibits a complete elimination of fatalities. When analyzing the underlying causes of accidents, human errors occurring outside the system increase to 33% on Line-4, while equipment-related failures become more prevalent on Line-2. In terms of accident types, derailments and collisions remain the most frequently observed incidents, with certain railway lines exhibiting an increasing trend. These findings highlight the necessity of tailored safety measures that address the specific risks associated with different railway lines, ensuring a more effective accident prevention approach.

Conclusion

In conclusion, this study provides a comprehensive analysis aimed at reducing accident severity in Turkish railway systems, utilizing a Bayesian Network model to uncover key findings. The results indicate that accident severity is directly influenced by fatalities and serious injuries, while human factors have an indirect impact. As the first study to analyze railway accidents in Turkey using Bayesian Networks, it makes a significant contribution to the development of safety policies and the implementation of risk-based maintenance strategies to minimize accident severity.

Future research should focus on refining the dataset by incorporating signal level variables for railway lines and sections. This would allow decision-makers to develop line-specific recommendations to reduce the severity of potential accidents. Additionally, expert feedback suggests that further investigation is needed to explore the relationship between accident type and accident severity. Therefore, future studies should concentrate on specific railway lines, conduct comparisons with international and European safety standards, and evaluate compliance with global safety norms.

References

Asan, U. (n.d.). Managerial decision making: Bayesian networks [Course lecture notes]. Istanbul Technical University.

European Union Agency for Railways. (2023). Safety overview 2023. ERA. Retrieved from https://www.era.europa.eu

Turkish State Railways (TCDD). (2023). 2019-2023 annual statistics. Strategy Development Department, Statistics and Analysis Office.

INDUSTRIAL ENGINEERING

Decision Making

Engineering Management

Industrial Data Analytics

Knowledge Management

Manufacturing Management

Impact of Organizational Life Cycle on R&D Project Prioritization Criteria

Furkan Yasin Taksim[a], Erhan Bozdağ[a]

[a] Istanbul Technical University, Department of Industrial Engineering, Engineering Management M.Sc. Program, Turkey
taksim22@itu.edu.tr

Keywords: R&D Project Selection, Organizational Life Cycle, BWM, AHP.

Aim

Research and Development (R&D) is a fundamental driver of innovation, economic growth, and competitive advantage in a dynamic business environment. It provides organizations with a systematic process of exploring new knowledge, technologies, and methodologies to create new products, improve existing products, and enhance their operational processes. By encouraging creativity and scientific expertise, R&D serves various industries, from technology to manufacturing. The role of R&D is critical for enabling organizations to meet the needs of evolving markets, anticipate future trends, and sustain long-term growth. Management of the R&D process requires a strategic approach, balancing creativity with practicality and risk with potential reward. Organizations must allocate resources wisely, select appropriate projects, and establish mechanisms for knowledge transfer and intellectual property protection. Moreover, encouraging a culture of innovation, and interdisciplinary collaboration can increase the effectiveness of R&D efforts [1].

To create the culture of R&D with continuous improvement and sustainable growth, organizations should prioritize the right R&D projects. Therefore, there is a need for a selection strategy for organizations. For assessing these projects, the criteria set used in this selection process should be determined by strategic objectives, industry dynamics, and available resources. Since these variables are different in each of the life cycle stages, the weight and priority of these criteria can change depending on the phases of the lifecycle of the company [2]. Companies have different objectives, needs, and priorities in various lifecycle stages, like startup, growth, maturity, and decline. This difference highlights the necessity of addressing R&D project selection criteria by considering lifecycle stages. This study aims to explore the differentiation in R&D project selection criteria across the various stages of the organizational life cycle.

Material and Method

In this study, first, a literature review on R&D project selection and R&D itself is conducted. In the literature review, the study by Souza et al. is used as a base for the criteria set for R&D project selection [3]. In this study, there are 66 relevant studies from 1970 to 2020 analyzed and 263 criteria were retrieved from these studies. With the help of decision-makers, these criteria are grouped into 23 criteria. Since 23 criteria cover a large part of the criteria used in the literature, it is used as a base set in our study as well. Studies that are before 2020 but not on the article list covered by Souza et. al and studies after 2020 both in the world and in Türkiye are also examined in our study. Besides these articles, studies about R&D and Innovation are also examined to check whether any criteria are not on the criteria acquired from the literature review or not. The final set of criteria used in this study and reference of articles to these criteria are given in Table 1.

Table 1. Summary of criteria set and their references used in this study.

Criteria	References
Commercial and Market Risk (CMR)	[3], [4], [5], [7], [8]
Competitiveness and Partnership (COP)	[1], [3], [4], [5], [8]
Corporate Image (COI)	[3]
Environmental Impact (ENI)	[3], [4], [8]
Extendibility (EXT)	[3], [4], [5]
External Environment Income (EEI)	[3], [8]
Financial Benefit (FIB)	[1], [3], [6], [7], [8]
Financial Income (FII)	[1], [3], [4], [6], [8]
Impact in Human Development (IHD)	[3], [4]
Internal Environment Income (IEI)	[1], [3], [4], [8]
Market Potential and Attractiveness (MPA)	[1], [3], [4], [5], [6], [7], [8]
Material Resources (MAR)	[1], [3], [4], [8]
Non-Financial Benefit (NFB)	[3], [4]
Organizational Requirements (ORR)	[3], [4]
Quality Requirements (QTR)	[3], [4], [8]
Scope Risk (SCR)	[3], [8]
Social Impact (SOI)	[3], [4], [8]
Strategic Fitness (STF)	[1], [3], [6], [7], [8]
Technical Contribution and Innovativeness (TCI)	[3], [4], [5], [8]
Technical Issues and Constraints (TIC)	[3], [4], [7], [8]
Technical Risk (TER)	[3], [4], [8]
Timing Requirements (TIR)	[1], [3], [4], [7], [8]
Work Resources (WOR)	[1], [3], [4], [5], [8]

After the literature review and determination of criteria, definitions of organizational life cycle theory and its implementation in our study are structured. Literature reviews of organizational life cycle theory and organizational

characteristics by life cycle are examined. The list of characteristics is determined for each life cycle of organizations. In this study, 4 stages of the organizational life cycle are used: Birth, Growth, Mature, and Decline. Companies are defined by authors in each organizational life cycle to be used in surveys. Then, surveys are conducted for each organizations and participants are asked to fill out 2 of these surveys: One of them is Company A, one of them is either Company B, C or D. In this method, the aim is to have one answer for one company to check the consistency of decision-makers. And the other answer is used to check whether other organizational life cycle stages cause difference in R&D project selection criteria or not. There are 3 decision-makers in this study from industry and the experience of these decision-makers are 6-years, 6-years and 5-years.

After getting results from decision-makers, the Analytical Hierarchy Process (AHP) and Best-Worst Method (BWM) are used to calculate criteria. Since BWM has similar results with AHP with fewer comparisons for decision-makers [9], BWM is used to prioritize 8 main criteria sets and AHP is used to prioritize sub-criteria ranging from 2 to 4. In this way, the comparisons required in this study are reduced. Then, Spearman's Rank Correlation method is used to analyze relations between decision-makers and stages of the organizational life cycle.

Findings

To calculate global weights, criteria weights for the main criteria and sub-criterion are calculated and multiplied. The results of global criteria weights for each decision-maker and organization are given in Table 2. Based on this, the findings about criteria change are given below.

Table 2. Criteria weights acquired in this study.

Criteria	Company A			Company B	Company C	Company D
	DM1	DM2	DM3	DM1	DM2	DM3
EEI	0,11003	0,09893	0,02990	0,00674	0,00895	0,04366
IEI	0,02201	0,03298	0,01495	0,04045	0,06265	0,00873
MAR	0,06680	0,06595	0,06726	0,01049	0,02557	0,01123
WOR	0,26718	0,13191	0,13453	0,05243	0,15344	0,06737
FIB	0,08459	0,03409	0,04300	0,13384	0,09209	0,08930
MPA	0,03863	0,05411	0,07512	0,03999	0,02092	0,02217
NFB	0,00882	0,01074	0,01641	0,01493	0,00633	0,00642
CMR	0,03991	0,20091	0,05521	0,04495	0,04459	0,06941
SCR	0,00692	0,05315	0,02654	0,00533	0,00351	0,00610
TER	0,01919	0,08438	0,01914	0,01264	0,01157	0,01879
FII	0,07753	0,02758	0,03476	0,07415	0,04705	0,05075
ORR	0,00872	0,00795	0,01985	0,02881	0,10805	0,01721
QTR	0,01705	0,01257	0,01525	0,01627	0,01692	0,00748
TIR	0,02874	0,01785	0,01086	0,00661	0,00699	0,00315
EXT	0,00282	0,00924	0,01997	0,01599	0,00589	0,00923
TCI	0,00877	0,01679	0,03630	0,13486	0,01944	0,11746
TIC	0,02724	0,03050	0,01099	0,03792	0,06418	0,03049
COP	0,07022	0,03827	0,18148	0,18298	0,05408	0,07908
COI	0,00783	0,01327	0,05496	0,02305	0,01478	0,01891
STF	0,02098	0,02760	0,09987	0,07262	0,19790	0,28937
ENI	0,00496	0,00612	0,00659	0,00452	0,00231	0,00245

IHD	0,04446	0,00971	0,01045	0,01014	0,02517	0,00760
SOI	0,01660	0,01541	0,01659	0,03028	0,00762	0,02363

- Environmental Impact is the least important criterion in each stages of organizational life cycle.
- Organizational Requirements shifts most significantly through life cycle stages. It is 3rd important criterion in mature stages, where 20th in birth stage, 12th in growth stage and 14th in decline stage.
- Work Resources is the most important criterion in birth stage, 6th important criterion in growth stage and decline stage and 2nd important criterion in mature stage.
- Corporate Image is the most important criterion in growth stage, 3rd important criterion in birth stage, 7th important criterion in mature stage and 4th important criterion in decline stage.
- Strategic Fitness is the most important criterion in mature and decline stage, 8th important criterion in birth stage and 5th important criterion in growth stage.

It can be concluded that some of the criteria can change by the organizational life cycle of the organizations but in order to check whether there is a significant difference between these stages or not, Spearman's Rank Correlation method is used to analyze relations between decision-makers and different companies. The result of Spearman's Rank Correlation is given in Table 3.

Table 3. Spearman's Rank Correlation Coefficients.

Company A			**Company B**	**Company C**	**Company D**	**Coefficient**
DM1	**DM2**	**DM3**	**DM1**	**DM2**	**DM3**	
■	■					0,65
■		■				0,39
■			■			0,35
■				■		0,55
■					■	0,48
	■	■				0,57
	■		■			0,23
	■			■		0,30
	■				■	0,45
		■	■			0,59
		■		■		0,45
		■			■	0,71
			■	■		0,72
			■		■	0,83
				■	■	0,64

The coefficient of Spearman's Rank Correlation interprets the relation between two ranked variables. The coefficient value of 1 means perfect positive correlation, value of -1 means perfect negative correlation and value of 0 means there is no correlation [9]. Based on this, the findings of this study are given below.

- Coefficient values for Company A for each evaluation pairs are between 0 and 1. Therefore, it is concluded that there is a consensus among decision-makers.

- Coefficient values for Company A and Company C for each evaluation pairs are between 0 and 1. Therefore, there is a correlation between these companies and no significant difference in criteria weights in the birth and mature stages.
- Coefficient values for Company A and Company D for each evaluation pairs are between 0 and 1. Therefore, there is a correlation between these companies and no significant difference for criteria weights in birth and decline stages.
- The coefficient value for Company B and Company C for each evaluation pairs are between 0 and 1. Therefore, there is a correlation between these companies and no significant difference in criteria weights in growth and mature stages.
- The coefficient value for Company B and Company D for each evaluation pairs are between 0 and 1. Therefore, there is a correlation between these companies and no significant difference in criteria weights in the growth and decline stages.
- The coefficient value for Company C and Company D for each evaluation pairs are between 0 and 1. Therefore, there is a correlation between these companies and no significant difference in criteria weights in the mature and decline stages.

Conclusion

In this paper, the effect of organizational life cycle stages on R&D project selection criteria is studied. After deciding the criteria set, the survey that consists of both BWM and AHP is conducted. Referring to the findings, even though some criteria weights change by life cycle stages of the organization, it is concluded that there is no significant difference in criteria weights of R&D project selection for different stages. Therefore, it is important for R&D professionals to understand in what stage they are evaluating while they are prioritizing R&D projects. It will help them to make their decisions better. For future research, scholars can reach more decision-makers to check whether the result can change or not. It is also possible to research the effect of organizational life cycle stages on R&D project portfolio selection instead of R&D project selection since it brings different criteria to the problem.

References

Taherdoost, H. (2024). Innovation Through Research and Development. Signals and Communication Technology.
Mohapatra, S. (2012). *Business Process Reengineering: Automation Decision Points in Process Reengineering.* Springer.
Souza, D. G., Santos, E. A., Soma, N. Y., & Silva, C. E. (2021). MCDM-Based R&D Project Selection: A Systematic Literature Review. *Sustainability*.
Huang, C.-C., Chu, P.-Y., & Chiang, Y.-H. (2008). A fuzzy AHP application in government-sponsored R&D project selection. *Omega*, 1038-1052.
Ma, D., Chang, C.-C., & Hung, S.-W. (2013). The selection of technology for late-starters: A case study of the energy-smart photovoltaic industry. *Economic Modelling*, 10-20.
Şen, H. (2023). R&D Project Selection with Gray-WASPAS Method. *The European Journal of Research and Development*, 37-45.
Liao, Z. (2001). International R&D project evaluation by multinational corporations in the electronics and IT industry of Singapore. *R and D Management*, 299-307.
Garces, E., Daim, T., & Dabic, M. (2023). Evaluating R&D Projects in Regulated Utilities: The Case of Power Transmission Utilities. *IEEE Transactions on Engineering Management*, 533-553.
Şahin, M. (2021). A comprehensive analysis of weighting and multicriteria methods in the context of sustainable energy. *International Journal of Environmental Science and Technology*, 1591–1616.

Structuring Challenges for Textile Industry in Adopting the Digital Product Passport

Sena Nur Dursun[a], Seyda Serdarasan[a]

[a]Istanbul Technical University, Industrial Engineering Department, Türkiye
dursuns17@itu.edu.tr

Keywords : Digital Product Passport, ISM, MICMAC, Supply Chain Management, Textile Industry.

Aim

The textile and apparel industry is a significant contributor to environmental pollution, necessitating the integration of sustainability practices across its supply chain. The European Union's Digital Product Passport (DPP) initiative aims to revolutionize the textile industry by enhancing sustainability, transparency, and traceability throughout the product lifecycle, from raw materials to the end consumer. This study aims to identify and analyze the challenges hindering the adoption and implementation of DPP in textile industry and to determine the interrelationships and driving forces among these challenges using Interpretive Structural Modeling (ISM) and MICMAC analysis. Ultimately, this research seeks to provide strategic insights for stakeholders to facilitate a smoother transition towards DPP compliance and enhanced sustainability in textile industry.

Challenges in the Adoption of DPP in the Textile Industry

The adoption and implementation of DPP in the textile and apparel industry face several challenges, as identified through a review of the literature and insights from industry experts. These barriers hinder the effective integration of DPP and highlight the complexities associated with digital traceability in the textile industry. The key challenges include:

1. Technological and Data Management Challenges:
    - Complex data collection across the product lifecycle: Gathering and maintaining accurate data from raw material sourcing to end-of-life poses significant difficulties [1, 3]
    - High costs of sensor-based data collection: Implementing advanced tracking technologies such as RFID and blockchain requires substantial investment [1]
    - Issues related to data quality, security, and storage: Ensuring the integrity and protection of digital product information is a key concern. [1, 2]
    - Lack of secure data sharing infrastructure: Companies hesitate to share sensitive product data due to security risks and a lack of standardized frameworks [1]
    - Lack of standardized data formats and infrastructure: Inconsistent data management practices hinder interoperability across the supply chain. [1, 3]
    - Interoperability issues between systems: Incompatibility between different digital systems used by stakeholders disrupts seamless data exchange. [6]

2. Organizational and Logistical Challenges:
    - Reluctance to share information among partners: Competitive concerns and distrust among supply chain actors slow down data sharing. [1, 3]
    - Lack of expertise and specialized knowledge: Many stakeholders lack technical proficiency in DPP implementation [1, 2]
    - Need for standardization across the supply chain: Harmonizing processes and criteria for DPP compliance remains a challenge. [1, 3]
    - Difficulty in matching materials with eco inventories:Proper classification of materials based on

sustainability credentials is complex and resource-intensive [1]

3. Financial and Economic Barriers:
    - High costs of technology implementation (e.g., blockchain):
    - Investment in digital infrastructure is a significant barrier, especially for SMEs. [2, 3]
    - Insufficient financial resources: Many textile firms, particularly small and medium enterprises, struggle to allocate funds for DPP-related projects. [1, 2, 6]
    - High costs of certifications and verifications: Compliance with sustainability standards adds additional financial burdens. [2]

4. Regulatory and Legal Uncertainty:
    - Uncertainty around future regulations and compliance requirements: Businesses face difficulties in planning due to evolving regulatory landscapes. [1, 3]
    - Lack of clear legislative framework and guidance:
    - Unclear policies hinder the structured implementation of DPP [2, 3]
    - Confusion regarding DPP implementation steps and roles: Stakeholders lack clarity on how to effectively integrate DPP into their operations. [1]

5. Knowledge and Expertise Gaps:
    - Lack of expertise in DPP-related methodologies and eco-design: A shortage of trained personnel slows down the adoption process. [1, 2]
    - Insufficient training and specialized knowledge among stakeholders: Capacity-building initiatives are needed to support widespread implementation [2]

6. Consumer and Market-Related Issues:
    - Consumer reluctance to engage with product information: Limited awareness and interest among consumers reduce the demand for DPP-enabled products.[3]
    - Concerns about the utility and cost-effectiveness of DPP for consumers: The added value of DPP must be clearly communicated to end-users. [2, 3]
    - Lack of involvement from sales and marketing departments: A weak connection between sustainability initiatives and marketing strategies affects adoption rates. [2]

7. Other Barriers:
    - Resistance to change within organizations: Traditional business models and corporate inertia slow down the transition.[3]
    - Lack of a systematic approach to integrating environmental improvements: Fragmented sustainability initiatives hinder holistic implementation. [2]

Material and Method

This research will employ a mixed-methods approach, commencing with a comprehensive literature review to identify key challenges associated with DPP implementation in the textile industry, considering both academic studies and industry reports. This review will also analyze relevant EU regulations and global best practices in DPP implementation.
To explore the complex relationships among challenges identified from existing literature and expert opinions, data will be collected through a sectoral survey targeting various stakeholders in the textile industry, including manufacturers, suppliers, brands, consumers, associations, and regulatory bodies. The study will then apply Interpretive Structural Modeling (ISM) and MICMAC analysis to establish a hierarchical structure and assess the influence-dependence power of each challenge.

Interpretive Structural Modeling (ISM) was developed by Warfield in the 1970s as a method for structuring complex systems [7]. ISM applies graph theory iteratively to represent a complex system as a directed graph. It is a process that transforms poorly defined and ambiguous cognitive models into well-defined models that are useful for various analytical purposes and especially useful when dealing with ambiguous and qualitative issues, turning them into structured decision-making tools.[5]. In this study, ISM will be used to systematically analyze the challenges identified, establishing a hierarchical structure that illustrates their contextual relationships.

Following the ISM analysis, MICMAC (Matrice d'Impacts Croisés Multiplication Appliquée à un Classement / Cross Impact Matrix Multiplication Applied to Classification), one of the quantitative methods of cross-impact analysis, used to examine events and/or trends (variables) and their interrelationships [4], will be applied. MICMAC will classify the identified challenges based on their driving power and dependence, thereby identifying key driver variables and providing a deeper understanding of their structural interdependencies within the system. It complements ISM by offering quantitative insight into the system's dynamics, supporting more effective decision-making. Together, these methods provide a robust analytical foundation to support strategic planning for DPP implementation in the textile sector.

Findings

This study is expected to provide a structured analysis of the key challenges hindering the implementation of the Digital Product Passport (DPP) in the textile industry. By applying ISM and MICMAC methodologies, the research will identify critical barriers and their interdependencies, offering a strategic roadmap for effective DPP adoption. The expected findings will support stakeholders—particularly small and medium-sized enterprises (SMEs)—in developing targeted actions to overcome these obstacles. Ultimately, the study aims to contribute to enhanced supply chain transparency, improved sustainability practices, and better alignment with EU regulatory frameworks.

Conclusion

This research will offer a systematic analysis of the challenges hindering the adoption of DPP in the textile industry, utilizing ISM and MICMAC methodologies to map interdependencies and driving factors. The findings will assist industry stakeholders—ranging from manufacturers to policymakers—in formulating targeted strategies to mitigate barriers and facilitate a seamless transition towards DPP compliance.

By addressing these challenges, the study aims to support the textile industry's sustainability efforts, improve supply chain transparency, and enhance compliance with EU regulations. Special emphasis will be placed on how small and medium-sized enterprises (SMEs) can navigate these obstacles, ensuring an inclusive and equitable implementation process for all stakeholders involved in the textile supply chain.

Through these insights, this study contributes to advancing sustainable practices and digital traceability in the textile industry, reinforcing the importance of integrating technological innovations with regulatory frameworks to drive meaningful environmental and economic impact.

References

Abedi F, Saari UA, Hakola L (2024) Implementation and Adoption of Digital Product Passports: A Systematic Literature Review. In: Proceedings of the 30th ICE IEEE/ITMC Conference on Engineering, Technology, and Innovation: Digital Transformation on Engineering, Technology and Innovation, ICE 2024. Institute of Electrical and Electronics Engineers Inc.

Alfnes E, Romsdal A, Strandhagen JO, et al (2023) Advances in Production Management Systems. Production Management Systems for Responsible Manufacturing, Service, and Logistics Futures. Springer Nature Switzerland, Cham

Domskienė J, Gaidule E (2024) An overview of technological challenges in implementing the digital product passport in the textile and clothing industry. AUTEX Research Journal 24:. https://doi.org/10.1515/aut-2024-0002

Godet M (1994) From anticipation to action: A handbook of strategic prospective. UNESCO Publishing

Malone DW (1975) An introduction to the application of interpretive structural modeling. Proceedings of the

IEEE 63:397–404. https://doi.org/10.1109/PROC.1975.9765
Özbek A, Kiraz A, Erkan EF (2023) Analysing barriers of digitalization in apparel sector: a fuzzy DEMATEL approach. Journal of the Textile Institute. https://doi.org/10.1080/00405000.2023.2279197
Warfield JN (1974) Toward Interpretation of Complex Structural Models. IEEE Trans Syst Man Cybern SMC-4:405–417. https://doi.org/10.1109/TSMC.1974.4309336

Sector-Specific Supplier Evaluation Based on LARGS Dimensions

Gözde Çinkay [a], Şeyda Serdar Asan [a]

[a] İstanbul Technical University, Industrial Engineering, Türkiye
cinkay23@itu.edu.tr

Keywords: LARGS, Organizational Supplier Assessment (OSA), Supplier Selection, Supply Chain Management.

Aim

Supply Chain Management (SCM) encompasses the flow of materials, information, and financial resources across organizational boundaries. In today's dynamic and complex supply chain environments, supplier selection has become increasingly strategic. Supplier management significantly influences a company's overall performance and the sustainability of long-term partnerships. Contemporary companies are now evaluating suppliers not only on the basis of cost and quality but also on their resilience, environmental impact, and adaptability [1]. These evolving expectations necessitate comprehensive frameworks capable of addressing multidimensional requirements, especially in intricate sectors such as automotive manufacturing. This shift is reflected in the Lean, Agile, Resilient, Green, and Sustainable (LARGS) paradigms. Traditional supplier evaluation models typically emphasize cost, quality, and delivery performance, often neglecting critical aspects such as sustainability and resilience. This creates a misalignment between evaluation practices and the strategic competencies required to remain competitive in volatile and uncertain environments [2].
Considering the increasing complexity and interconnectivity of supply chains, particularly within the automotive industry, companies must develop and integrate competencies related to flexibility, resilience, and sustainability. The present study aims to investigate whether industry-specific supplier evaluation criteria align with the LARGS dimensions, utilizing Organizational Supplier Assessments (OSA) to provide empirical insights into supplier performance.

Material and Method

Literature Review

Lean:

Lean supply chain management, pioneered by Toyota, aims to reduce costs through waste elimination and enhance efficiency by creating value streams [3]. It requires effective cooperation and coordination among supply chain actors, with a focus on optimizing the flow of goods, information, and finances. Lean emphasizes operational and managerial efficiency, responding quickly and predictably to customer demands by minimizing time, inventory, and unnecessary expenditures [4].

Agile:

Agility in the supply chain refers to the capacity to respond rapidly to variable demand and to manage high-volume, diverse product portfolios in a cost-effective manner [3]. While lean emphasizes waste reduction, agile supply chains prioritize responsiveness, competence, flexibility/adaptability, and speed. Agile suppliers are capable of quickly adapting to changes in market conditions and customer requirements, thus enhancing the ability to manage uncertainty and gain a competitive edge.

Resilient:

A resilient supply chain is defined by its ability to withstand unexpected disruptions, maintain operational continuity, and control performance outcomes. It encompasses the capacity to mitigate disruption impacts, recover efficiently, and leverage new opportunities. Resilient suppliers are characterized by flexibility, cost efficiency, risk mitigation, and adherence to safety and environmental standards [4]. Strategies such as inventory buffering, production network diversification, nearshoring, multi-sourcing, and ecosystem partnerships can be employed to build supply chain resilience.

Green:

Emerging in the early 1990s, green supply chain management gained prominence alongside increasing environmental awareness. Its primary goal is to prevent pollution and enhance environmental performance throughout the supply chain. Green supply chains contribute to cost savings, innovation, corporate image enhancement, and social responsibility. Practices include recycling, remanufacturing, reduction, and refurbishment. Tools such as green procurement and environmental management systems promote cleaner production, reduced transportation emissions, and sustainable logistics practices [5].

Sustainable:

Sustainable supply chain management integrates economic, social, and environmental objectives to foster inter-organizational collaboration and support long-term development goals. It aims to reduce ecological footprints and costs while ensuring compliance with regulations and maintain competitiveness. This approach is increasingly recognized as a key pillar of industrial sustainability [6].

Challenges in automotive sector SC:

The automotive industry is exposed to a wide array of risks stemming from political, environmental, social, and technological factors. It is highly interconnected globally, technologically sophisticated, and subject to rapid changes in regulatory and market conditions. The LARGS framework aligns well with sectoral needs, offering capabilities for operational efficiency (Lean), quick responsiveness (Agile), risk mitigation (Resilient), environmental compliance (Green), and long-term viability (Sustainable). To maintain competitiveness, automotive manufacturers adhere to local regulations, comply with international quality standards, and develop alternative suppliers or materials. Suppliers are expected to adopt sustainable practices to fulfill environmental and social responsibilities and align with green and sustainability standards [12].

Although various supplier evaluation frameworks exist in the literature, few address all five LARGS dimensions comprehensively. Table 1 presents a summary of the relevant criteria identified in previous studies.

Table 1. Table 1. LARGS Dimensions According to the Literature.

LARGS Dimension	Key Evaluation Criteria	References
Lean	- Manufacturing process effectiveness	[3], [4], [7], [8]
	- Management effectiveness	
	- Supply redundancy / Inventory management	
Agile	- Supply chain robustness / Response speed	[3], [4], [8]
	- Customization / Product flexibility	
	- Collaboration	
Resilient	- Risk management	[3], [4], [9]
	- Supplier selection processes / Dual sourcing	
	- Production planning	
Green	- Eco-friendly processes	[3], [4], [10]
	- Carbon footprint reduction	
	- Waste management / Circular economy	
Sustainable	- Social sustainability	[3], [4], [11]
	- Environmental sustainability	
	- Regulatory compliance	

Methodology

This study assesses supplier selection criteria in the context of the LARGS framework by analyzing OSA data from an automotive manufacturer's supplier network. The methodology involves the following key steps:

1. Data Collection: Supplier evaluation criteria identified from the literature were mapped to the LARGS dimensions. These were then matched with the criteria used in the manufacturer's Organizational Supplier Assessment system.
2. Confirmatory Factor Analysis (CFA): CFA was employed to validate whether the supplier evaluation criteria reflect the LARGS dimensions as latent variables.
3. Scoring Suppliers: Supplier scores for each LARGS dimension were calculated using factor loadings derived from the CFA.
4. Evaluation Framework: The current supplier ranking was compared with the rankings obtained using the LARGS-based evaluation framework.

Findings

The process of matching OSA criteria with LARGS dimensions has been completed, and data from the supplier database are currently being analyzed. Preliminary analyses involve conducting Confirmatory Factor Analysis (CFA) to verify the alignment of evaluation criteria with LARGS constructs. An evaluation framework is being developed to assist decision-makers in interpreting the results and making informed supplier selections.

Conclusion

This study introduces a sector-specific supplier evaluation model grounded in the LARGS framework. The model enhances the accuracy of decision-making processes and enables supply chain managers to identify suppliers that are not only cost-efficient but also agile, resilient, environmentally responsible, and sustainable.

The proposed LARGS-based model is expected to surpass traditional evaluation approaches by offering a more holistic and future-oriented perspective. It provides strategic value in complex and rapidly evolving sectors such as automotive manufacturing.

Future research may focus on adapting the model to other industries or integrating it with decision-support tools to enhance its applicability and impact.

References

Sun, H., Zhang, B., & Ni, W. (2022). A hybrid model based on SEM and fuzzy TOPSIS for supplier selection. Mathematics, 10(19), 3505. https://doi.org/10.3390/math10193505

Purba, H. H., Aisyah, S., Hasibuan, S., & Jaqin, C. (2025). Literature review of lean, agile, resilient, green (LARG) in automotive manufacturing industry. BIO Web of Conferences, 58, 02002. https://doi.org/10.1051/bioconf/20225802002

Ghazvinian, A., Feng, B., Feng, J., Talebzadeh, H., & Dzikuć, M. (2024). Lean, agile, resilient, green, and sustainable (LARGS) supplier selection using multi-criteria structural equation modeling under fuzzy environments. Sustainability, 16(4), 1594. https://doi.org/10.3390/su16041594

Sonar, H., Gunasekaran, A., Agrawal, S., & Roy, M. (2022). Role of lean, agile, resilient, green, and sustainable paradigm in supplier selection. Cleaner Logistics and Supply Chain, 4, 100059. https://doi.org/10.1016/j.clscn.2022.100059

Baki, R. (2022). An integrated multi-criteria structural equation model for green supplier selection. International Journal of Precision Engineering and Manufacturing-Green Technology, 9, 1063–1078. https://doi.org/10.1007/s40684-021-00415-7

Alegoz, M., & Yapıcıoğlu, H. (2019). Supplier selection and order allocation decisions under quantity discount and fast service options. Sustainable Production and Consumption, 18, 1–12. https://doi.org/10.1016/j.spc.2019.01.001

Mohammed, A., Harris, I., Soroka, A., Naim, M., Ramjaun, T., & Yazdani, M. (2021). Gresilient supplier assessment and order allocation planning. Annals of Operations Research, 296(1–2), 335–362. https://doi.org/10.1007/s10479-020-03611-x

Salleh, N. H. M., Abd Rasidi, N. A. S., & Jeevan, J. (2020). Lean, agile, resilience, and green (LARG) paradigm in supply chain operations: A trial in a seaport system. Australian Journal of Maritime & Ocean Affairs, 12(4), 200–216

Sharma, V., Raut, R.D., Mangla, S.K., Narkhede, B.E., Luthra, S., Gokhale, R., (2020). A systematic literature review to integrate lean, agile, resilient, green and sustainable paradigms in the supply chain management. Business Strat. Environ. 1–22.

Ramakrishnan, K. R., & Chakraborty, S. (2020). A cloud TOPSIS model for green supplier selection. Facta Universitatis, Series: Mechanical Engineering, 18(3), 375–397.

Jain, N., & Singh, A. (2019). Sustainable supplier selection under must-be criteria through Fuzzy inference system. Journal of Cleaner Production, 248, 119275. https://doi.org/10.1016/j.jclepro.2019.119275

Sahu, A. K., Sharma, M., Raut, R. D., Sahu, A. K., Sahu, N. K., Antony, J., & Tortorella, G. L. (2023). Decision-making framework for supplier selection using an integrated MCDM approach in a lean-agile-resilient-green environment: Evidence from Indian automotive sector. The TQM Journal, 35(4), 964–1006. https://doi.org/10.1108/TQM-12-2021-0372

Customer Preferences For Mobile Operating Systems In Smartphones Using Conjoint Analysis

Cansu Aksu[a]

[a] Istanbul Technical University, Department of Industrial Engineering of the Graduate School, Engineering Management Master of Science Program, Türkiye
aksuc21@itu.edu.tr

Keywords: Customer Preference, Conjoint, Mobile OS.

Aim

Smartphones have become an integral part of modern life and have greatly affected customers' interactions with technology. In this context, the choice of operating systems (OS) of a smartphone is an important factor that reflects customers' expectations and needs from their devices. Customer preferences play a critical role in directing the development of OS and affecting market dynamics (Böhm et al., 2015). This research was conducted to understand customer preferences for mobile OS in smartphones and to determine which attributes shape these preferences using conjoint analysis.

Material and Method

Conjoint analysis is a multivariate technique used to determine end users' preferences and understand how they make decisions when faced with multiple trade-offs. It operates on the assumption that various factors influence the decision-making process simultaneously. There is a conjoint analysis research in the literature focusing on consumer perspectives regarding mobile service platforms (Nikou et al., 2014).

In this research, a conjoint analysis was conducted to understand customer preferences for mobile OS in smartphones. Conjoint analysis is applied via Sawtooth Software, in this research. Sawtooth Software is a widely used tool in academic and market research for conducting conjoint analysis (Sawtooth Software, 2025). The researcher inputs the determined attributes and their levels into the software, selects the appropriate conjoint analysis method, and designs a survey through the software. Subsequently, the conjoint analysis is conducted within the software using the responses collected from participants.

A literature review was conducted to identify the attributes, analyzing 41 academic articles. During the attributes selection process, articles related to customer preferences, satisfaction, and perspective in mobile operating systems were examined, along with comparative and general information on mobile OS. As a result, 86 attributes, categorized as software-related and hardware-related, were identified. In this research, to conduct the conjoint analysis, software-related attributes were selected.

From the 19 identified software-related attributes, it was necessary to reduce them to 7 due to the impracticality of implementing a survey with more than 7 attributes. To determine these 7 attributes, a survey using 7-point Likert scale was designed. The survey began with demographic questions, followed by a task where participants were asked: "When purchasing a smartphone, which features of the operating system are most important to you? Please rate the following features based on their importance to you." A total of 47 participants completed the survey, and the result of the top 7 most important attributes identified is shown in Table 1.

Table 1. Result of attributes selection survey.

Ranking	Factors	Importance		Frequency in the articles
		Mean	Standard Deviation	
1	Freeze/Crash	6.21	1.41	10
2	Security	6.17	1.45	21
3	Privacy	6.15	1.47	10
4	Reliability of Apps	6.04	1.41	25
5	User Experience	6.00	1.38	26
6	Quality of Apps	5.87	1.44	6
7	Multitasking	5.64	1.42	4

Regarding to Table 1, importance of selected attributes and the frequency of these attributes in the 41 articles were consistent with each other. It was found that 5 of the attributes determined through the survey matched those frequently mentioned in the literature. By integrating both survey results and academic literature, a more reliable and comprehensive analysis was conducted.

The research is conducted using the conjoint analysis methodology via Sawtooth Software. For the conjoint analysis, the Adaptive Choice-Based Conjoint (ACBC) method was used to be the most suitable approach based on factors such as sample size and the number of attributes (Orme, 2013). The identified 7 attributes and their levels were defined in the Sawtooth Software system and presented to 47 participants through various scenarios immediately after the demographic questions. The identified attributes and their levels are shown in Table 2.

Table 2. Attributes and levels determined for the research.

Attributes	Level 1	Level 2
Freeze/Crash	Rare	Sometimes
Security	Advanced security, comprehensive protection	Basic security
Privacy	Guaranteed high data confidentiality	The best possible data privacy
Reliability of Apps	Only verified, approved apps	More apps available for download from anywhere
User Experience	Simple, understandable, quick to learn	A little more complex, may take some time to learn
Quality of Apps	Fulfil the functions expected from the application, usually without error	Basically, it works properly, but sometimes small errors occur
Multitasking	Ability to use multiple applications almost flawlessly	Basic level of trouble-free use when running multiple applications

Findings

From conjoint analysis using Sawtooth Software, it was found that the Freeze/Crash is the most important attribute when preferring an operating system for smartphones, with an average importance of 22.01%. Then, with varying average importance given to Security, Reliability of Apps, User Experience, Quality of Apps, Privacy and finally Multitasking resulted as the other preferred attributes while choosing an operating system for smartphones, respectively. Result of conjoint analysis is shown in Table 3. When result of conjoint analysis and result of attributes selection survey are compared, it seems that attributes ranking of importance is different. This difference indicates the benefit of conjoint analysis.

Table 3. Result of conjoint analysis.

Attributes	Average Importance
Freeze/Crash	22.01%
Security	17.62%
Reliability of Apps	14.81%
User Experience	14.51%
Quality of Apps	11.97%
Privacy	9.64%
Multitasking	9.44%

When the average importance values are examined based on demographic responses, the most important operating system attribute in both age groups between 18-24 and 25-34 is Freeze/Crash. The least important attribute is the Quality of Apps at the age of 18-24, while it is Multitasking for 25-34.
In terms of undergraduate and graduate education, the most important attribute for both is Freeze/Crash. The least important attribute is Multitasking for undergraduate education, while it is Privacy for graduate education.
Based on the operating system used, Freeze/Crash is the most important attribute for both Android and iOS users. The least important attribute for Android users is Privacy, while it is Multitasking for iOS users.
In terms of the smartphone usage purpose, the most important attribute in both personal use and personal and business use is Freeze/Crash. While the Quality of Apps is the least important for personal use, Multitasking is the least important for personal and business use.
For gender, Freeze/Crash is the most important attribute for both men and women. Multitasking is the least important attribute for women, while Privacy is the least important attribute for men.

Conclusion

The aim of this research is to understand customer preferences for mobile operating system in smartphones and to determine which attributes shape these preferences using conjoint analysis. According to the findings obtained from conjoint analysis, it was observed that Freeze/Crash is the most important attribute when preferring an operating system in smartphones, with different average importance values according to all demographic segments. When examined in terms of the operating system attribute that is given the least importance in operating system preference in smartphones, differences are seen according to demographic segments, and it was observed that the Multitasking has the least importance. In addition, it can be said that the operating system attribute that operating system developers should pay the most attention to in smartphones is Freeze/Crash. The fact that the number of attributes is 7 and the number of levels for each attribute is limited to 2 in order to make the survey more understandable and easier to answer, and the small sample size may create a limit for this research. Therefore, the findings obtained from this research can be hypothesized and tested using a larger sample size in the future research.
I would like to sincerely thank Sawtooth Software for their valuable support.

References

Böhm, S., Adam, F., & Farrell, W. C. (2015). Impact of the mobile operating system on smartphone buying decisions: A conjoint-based empirical analysis. *In M. Younas et al. (Eds.), MobiWis 2015, LNCS 9228* (pp. 198–210). Springer International Publishing.
Nikou, S., Bouwman, H., & de Reuver, M. (2014). A consumer perspective on mobile service platforms: A conjoint analysis approach. *Communications of the Association for Information Systems, 34*(1), Article 82
Orme, B. K. (2013). Which conjoint method should I use? *Sawtooth Software.* Retrieved from https://content.sawtoothsoftware.com/assets/a2ef3ee0-7002-4a5c-ae61-0104587fa1f7
Sawtooth Software (2025). About us. *Sawtooth Software*. Retrieved from https://sawtoothsoftware.com/about-us

INDUSTRIAL ENGINEERING

Decision Making

Engineering Management

Industrial Data Analytics

Knowledge Management

Manufacturing Management

Predicting the Closing Time of Debt Files in Legal Stage Using Machine Learning and Deep Learning Methods

Şeyda İrem Bilgehan[a], Başar Öztayşi[a]

[a] Istanbul Technical University/Graduate School, Industrial Engineering, Türkiye
bilgehan@itu.edu.tr

Keywords: Deep Learning, Legal Debt Collection, Machine Learning.

Aim

Nowadays, in many sectors, ensuring regular income distribution and reducing financial risks have become important goals. Companies and banks face situations where they have difficulty receiving payment for the products, loans or services they provide. In situations of these kind, it may seriously affect their financial situations, cash flows and even the reputation of the business. Debt collection processes are carried out to collect the outstanding amount in case of unpaid invoices or loan payments. For a successful debt collection process, it is of great importance to analyze large-scale datasets coming to debt collection agencies from banks, telecommunication companies, energy and natural resource companies using data science methods (Onar et al., 2018). If outstanding debts are not paid within the specified time, their cases will proceed to the legal stage and will followed up by lawyers within the scope of legal debt collection (Altınok et al., 2021). In this study, it is aimed to make analyses for predicting closing time of debt files in legal proceedings based on the debtor' s and debt collection agency' s features using machine learning and deep learning algorithms. It is also aimed to help make operational decision, enhance financial management, improve cash flow and collection speed in the light of these predictions.

Material and Method

In this study, a dataset containing details of the debtor' s and debt collection agency' s features is used. The dataset consists of 20 base features, 13 of which are numerical, five are temporal, and two are string data types and with a total of 4,000 rows. Base features are total debt amount, follow-up type, enforcement type, geographic region, geographic region score, agencies speed score, communication quality score, creditor speed score, country general speed score, lien data quality, legal follow-up application date, finalization legal proceedings date, asset detection date, collection start date, collection completion date, follow-up completion time, asset detection time, collection start time, collection completion time and legal file closing time. In this study, the columns with temporal data type were initially converted to date format, while the columns with object data types were converted to categorical data type and then to numerical data type by using label encoder. Secondly, all rows containing missing values were removed from the dataset in order to ensure data completeness and avoid issues related to missing values. Subsequently, columns which are categorical data type were converted to numerical data type by using one-hot encoding method. With the aim of evaluating which categorical data transformation method yields more successful results, two distinct models were developed for each machine learning and deep learning technique, one applying the one-hot encoding method and the other applying the label encoding technique. Then, for the purpose of identifying the independent variables that enhance the predictive power and accuracy of the model, correlation analysis was conducted between the dependent variable and the independent variables. Additionally, correlation analysis was performed among the independent variables, and feature selection was performed based on these analyses. After data preparation and feature selection were completed, eleven machine learning and deep learning algorithms, including Linear Regression, Ridge Regression, Lasso Regression, Elastic Net Regression, Decision Tree Regression, Random Forest Regression, Gradient Boosting Regression, Support Vector Regression, K-Nearest Neighbour Regression, Artificial Neural Network Regression and Convolutional Neural Network Regression were applied to the dataset during the modelling process. Most of these machine learning and deep learning algorithms are frequently used in the literature and generally said to give high performance (Bashar et al., 2023; Kim et al., 2016). In this study, in addition to classical machine learning

and deep learning algorithms, four stacking algorithms were also applied to the dataset. In the first Stacking Regression model, K-Nearest Neighbour Regression and Logistic Regression were applied as base learners, followed by Logistic Regression as the meta model. In the second Stacking Regression model, Ridge Regression, Random Forest Regression, Gradient Boosting Regression, and Support Vector Regression models were applied as base learners, followed by Ridge Regression as the meta model. In the third Stacking Regression model, Linear Regression, Decision Tree Regression, Support Vector Regression, and Random Forest Regression models were applied as base learners, followed by Polynomial Regression as the meta model. In the fourth Stacking Regression model, Linear Regression, Decision Tree Regression, Support Vector Regression, and Random Forest Regression models were applied as base learners, followed by Linear Regression as the meta model. It was used three key metrics, such as Root Mean Squared Error, Mean Absolute Percentage Error, R-Squared and Adjusted R-Squared to evaluate the performance of the regression models.

Findings

The results indicated that the three top-performing models were the third Stacking Regression model, Linear Regression model and Ridge Regression model, respectively. Their R-Squared values were 0.85525, 0.85521 and 0.85518, respectively. These models were followed by Support Vector Regression model, the fourth Stacking Regression model and Elastic Net Regression within 0.85515, 0.85512 and 0.85498 R-Squared values, respectively. It was observed that the one-hot encoding transformation technique was used in five of them. Moreover, the second Stacking Regression model and Lasso Regression model exhibited high R-Squared values, both above 0.85. It was observed that deep learning algorithms did not perform efficiently due to the relatively small to medium size of the dataset.

Conclusion

In conclusion, 11 of 15 applied regression models has R-squared values between 0.80897 and 0.85525 and provided an efficient solution to predict legal follow-up file closing time. However, it was observed that deep learning algorithms could not provide a sufficient solution. In the continuation this study, improvement efforts will be undertaken to increase the number of rows and improve data quality in order to develop models that produce better results. We expect that stacking and deep learning algorithms will perform better with medium to large-sized datasets. Moreover, deep learning algorithms such as Long Short-Term Memomry and Gated Recurrent Unit will be applied and to enhance the overall performance and obtain better results.

References

Altınok, N., Farrokhizadeh, E., Tekin, A., Khameneh, S. G., Oztaysi, B., Onar, S. C., Kabak, O., Kasap, A., Sahin, A., & Ayaz, M. (2021). Predicting performans of legal debt collection agency. In International Conference on Intelligent and Fuzzy Systems (pp. 514-522). Springer, Cham.

Bashar, M. A., Nayak, R., Astin-Walmsley, K., & Health, K. (2023). Machine learning for predicting propensity-to-pay energy bills. Intelligent Systems with Applications, 17, 200176.

Kim, J. & Kang, P. (2016). Late payment prediction models for fair allocation of customer contact list to call center agents. Decision Support Systems, 85, 84-101.

Onar, S. C., Oztaysi, B., & Kahraman, C. (2018). A fuzzy rule based inference system for early debt collection. Technological and Economic Development of Economy, 24(5), 1845-1865.

INDUSTRIAL ENGINEERING

Decision Making

Engineering Management

Industrial Data Analytics

Knowledge Management

Manufacturing Management

Understanding University Reputation: A Stakeholder-Centered Model for Reputation

Orhan Dursun[a], Çiğdem Altın Gümüşsoy[a]

[a] Istanbul Technical University, Industrial Engineering PhD Program, Türkiye
dursunorh@itu.edu.tr

Keywords: University Reputation, Corporate Quality, Emotional Appeal, Measurement Model.

Aim

Reputation is a complex and evolving concept, with its interpretation varying across contexts and academic disciplines. Traditionally, reputation has been described as "beliefs or statements regarding the character of a person or entity" (Longman, 1978). According to Drucker (2004), reputation is primarily shaped by stakeholder perceptions, whereas Deephouse (2000) conceptualized it as an aggregate outcome of social interactions and information exchange. Recent studies have extended these ideas, with scholars like Albino et al. (2023) exploring how reputation is influenced by not only traditional factors like product quality and customer service but also organizations' environmental and social responsibility efforts. Moreover, an increasing body of literature, such as the work of Dutton & Heaphy (2023), points out that reputation is increasingly shaped by the evolving relationship between organizations and their stakeholders, especially in the digital age.

Stakeholders are individuals or groups that can affect or are affected by an organization's activities, goals, and policies (Freeman, 1983). Their perceptions and expectations are critical in shaping corporate reputation. The degree to which stakeholders influence an organization varies and each group emphasizes specific reputation attributes (Brown & Dacin, 1997). Measuring reputation is crucial for its management, as organizations cannot manage what they cannot measure (Drucker, 1954). Reputation management is especially critical in universities, where core services such as education and research are directly influenced by stakeholder perceptions. As organizations face increasing scrutiny from diverse stakeholder groups, reputation management will remain an essential part of strategic decision-making. Recent studies (Coombs & Holladay, 2020) argue that organizations must proactively manage their reputations by anticipating stakeholder expectations and responding swiftly to reputational crises. Therefore, in the current study, we aim to identify significant factors that affect the university's reputation. First, a literature review on reputation and university reputation was conducted, and then the interviews with different university stakeholders were done to reveal important concepts related to university reputation.

Material and Method

First, a literature review was conducted to explore significant factors of the university's reputation, and then semi-structured interviews were conducted with the stakeholders about the university's reputation perceptions. In the interviews phase, in-depth, face-to-face interviews were conducted with a total of 14 stakeholders. The sample included 2 academicians, 3 university students, 2 administrative staff members, 1 alumni association representative, 1 press representative, 1 municipal official, 1 tutoring center representative, 2 industry chamber representatives, and 1 civil society organization representative. The inclusion of diverse stakeholder groups in the sample aligns with the principle of encompassing both internal and external perspectives on university corporate reputation management. The interviews ranged from 1 to 2.5 hours. Audio recordings were taken and later transcribed. The primary objective was to identify the specific implications of reputation for universities and the national context.

Findings

Literature Review:

The literature review shows that traditional reputation models have examined dimensions with the perceived quality and prominence (Rindova et al., 2005), academic and external performance (Alessandri et al., 2006), and affective and cognitive reputation perceptions (Perez & Torres, 2017). Dumitriu (2018) explores educational service quality, while Foroudi et al. (2019) analyze the role of website features and online engagement.

More recent studies emphasize stakeholder engagement, transparency, and digital influence as central to reputation management (Albino, Smith, & Taylor, 2023; Berens, van Riel, & Heaphy, 2023; Dutton & Heaphy, 2023; Xu, Li, & Zhao, 2023; Zhao, Wang, & Liu, 2023). Berens et al. (2023) argue that greater transparency and accountability are essential in higher education, where feedback mechanisms from students, faculty, and external actors directly influence institutional perception. The role of digital platforms in reputation formation has become increasingly significant. Dutton and Heaphy (2023) emphasize that online communities and social media discourse are pivotal in shaping public perception, with digital engagement influencing university branding. Zhao et al. (2023) stress the importance of social media sentiment and online interactions, demonstrating how universities must actively monitor and respond to digital reputation trends. The concept of resilience in reputation management is also gaining attention. Xu, Li, and Zhao (2023) argue that institutions with strong reputations can better withstand crises and recover more effectively. This aligns with previous studies on corporate reputation, which emphasize trust and consistency as fundamental to long-term success.

While many studies focus on specific stakeholder groups—such as students (Sung & Yang, 2009; Polat, 2011; Sultan & Wong, 2019), alumni (Dumitriu, 2018), and faculty (Perez & Torres, 2017)—few adopt a comprehensive, multi-stakeholder perspective. The present study addresses this gap by proposing a University Reputation Model that integrates stakeholder trust, transparency, and digital engagement as key components of reputation management.

Interviews:

The results of the interview revealed the topics such as "the definition of reputation," "the definition of reputation in universities," "factors influencing reputation," "experiences associated with reputation," "international reputation perception," and "factors negatively affecting reputation." The key statements identified as critical during the interviews are listed below:

- Reputation is an abstract concept.
- Trust is perceived as the concept most closely related to reputation.
- Reputation is the cumulative result of sustained university efforts and serves as an indicator of either continuity or decline.
- A sense of belonging, like trust, is another critical concept.
- "Excellence" or the "aspiration for leadership" should also be considered essential in enhancing reputation.
- The quality of university output influences reputation.
- Faculty and staff quality is crucial to a university's reputation, with particular emphasis on respected faculty members.
- International visibility and collaborations contribute to reputation.
- Service quality, in terms of process quality, and producing highly competent graduates, in terms of output quality, impact reputation.
- Scientific competence is another key indicator of quality.
- Social responsibility projects and contributions to civil society are also considered elements of reputation.
- Personalized engagement with students is regarded as a significant indicator of university quality, with a specific mention of its impact on the reputation
- Strengthening university capabilities (ensuring quality) should come first, followed by improving communication and reputation. In other words, reputation cannot be enhanced without first meeting fundamental quality criteria.

- "Training students with practical skills" has been identified as a crucial factor in educational quality, serving as an indicator of service quality.
- Establishing international ties and collaborating with international partners is essential for universities.

Based on the literature, interview findings, and analysis, **reputation** can be defined as an abstract and multifaceted construct shaped by stakeholder perceptions and organizational quality. In universities, it reflects academic excellence, faculty competence, service quality, international recognition, and social responsibility. It serves as both an outcome and an indicator of sustained organizational success.

The key factors for evaluating universities can be categorized into six primary constructs. **Academic leadership** is defined by a university's prominence in the scientific field, its reputation for success, and international recognition (Alessandri et al., 2006; Karaköse, 2006). **Quality of services** encompasses the provision of high-quality education, the ability to produce qualified graduates, and the emphasis on practical training alongside theoretical instruction (Alessandri et al., 2006; Icil, 2008). **Emotional appeal** reflects students' and stakeholders' sense of belonging, trust, and positive perception of the institution (Alessandri et al., 2006; Alniacik et al., 2010). **Employee competence** highlights the expertise and professionalism of academic and administrative staff, ensuring high standards (Safir & Sumer, 2006). **Social responsibility** is the commitment of an organization to contribute to societal and environmental well-being in ways that also support its own sustainability and reputation (Fombrun & Foss, 2001). Finally, **student orientation** evaluates the university's commitment to delivering value to students and fostering a supportive academic environment (Sung & Yang, 2009). University reputation is shaped by academic leadership, service quality, emotional appeal, employee competence, and student orientation, each contributing to institutional credibility and stakeholder perception. Strong academic leadership and service quality enhance a university's global standing, while emotional appeal, competent staff, and student-centered approaches foster trust, engagement, and long-term sustainability.

Conclusion

This study examines the determinants of university reputation by the following factors: employee competence, academic leadership, student orientation, social responsibility, quality of services, and emotional appeal. Each factor and its relationship with the university's reputation are explained.

Given the increasing importance of corporate reputation in higher education, universities must continuously measure and manage their reputation by aligning their strategic priorities with stakeholder expectations. Future research could expand this analysis to include cross-cultural comparisons or longitudinal studies to track reputation changes.

References

Albino, J., Smith, R., & Taylor, P. (2023). *Corporate Reputation and Stakeholder Engagement: A Multi-Dimensional Approach*. Journal of Business Ethics, 167(4), 345-362.

Alessandri, S. W., Yang, S., & Kinsey, D. F. (2006). *An Integrative Approach to University Image: Reputation, Branding, and Identity Management*. International Journal of Educational Advancement, 6(3), 196-211.

Alniacik, U., Alniacik, E., & Erdogmus, N. (2010). Corporate Reputation: A Study on Developing University Reputation Models. *International Journal of Business and Management Studies, 2*(1), 45-58.

Berens, G., van Riel, C. B. M., & Heaphy, J. (2023). *Transparency and Accountability in Corporate Reputation Management*. Corporate Communications: An International Journal, 28(2), 156-174.

Brown, T. J., & Dacin, P. A. (1997). *The Company and the Product: Corporate Associations and Consumer Product Responses*. Journal of Marketing, 61(1), 68-84.

Coombs, W. T., & Holladay, S. J. (2020). *The Handbook of Crisis Communication* (2nd ed.). Wiley-Blackwell.

Deephouse, D. L. (2000). *Media Reputation as a Strategic Resource: An Integration of Mass Communication and Resource-Based Theories*. Journal of Management, 26(6), 1091-1112.

Drucker, P. (1954). *The Practice of Management*. Harper & Row.

Drucker, P. (2004). *Managing in the Next Society*. St. Martin's Press.

Dumitriu, D. (2018). Quality Function Deployment in Higher Education: Identifying Key Factors for Educational Service Quality. *Journal of Education Policy, 22*(1), 85-102.
Dursun, O., & Altin Gumussoy, Ç. (2021). *The effects of quality of services and emotional appeal on university reputation: stakeholders' view.* Quality assurance in education, 29 (2/3), 166 – 182.
Dutton, J. E., & Heaphy, E. D. (2023). *Stakeholder Engagement in the Digital Age: How Online Communities Shape Organizational Reputation*. Academy of Management Review, 48(2), 317-332.
Fombrun, C. J. (2007). *Corporate Reputation: Definition and Measurement*. Corporate Reputation Review, 10(1), 1-16.
Fombrun, C., & Foss, C. (2001). *Business ethics: Corporate responses to social and environmental responsibility.* Corporate Reputation Review, 4(3), 205–213.
Foroudi, P., Dinnie, K., Kitchen, P. J., Melewar, T. C., & Foroudi, M. M. (2019). Corporate Brand Identity and Corporate Brand Reputation in Higher Education Institutions. *Journal of Business Research, 116*, 653-669.
Freeman, R. E. (1983). Strategic Management: A Stakeholder Approach. *Advances in Strategic Management, 1*, 31-60.
Gümüşsoy Altın, Ç. (2009). *Elektronik-Açık Eksiltme Teknolojisinin Kullanımını Etkileyen Faktörlerin Genişletilmiş Teknoloji Kabul Modeli İle Açıklanması*, İstanbul Teknik Üniversitesi Fen Bilimleri Enstitüsü.
Icil, G. (2008). Higher Education Reputation Metrics and Measurement. *Education and Society, 16*(3), 200-218.
Karaköse, T. (2006). University Prestige and Public Perception: A Study on Academic Leadership. *Turkish Journal of Higher Education, 14*(2), 150-169.
Longman (1978). *Longman Dictionary of Contemporary English*. Pearson.
Perez, M., & Torres, D. (2017). University Image and Reputation: An Analysis of Affective and Cognitive Dimensions. *Higher Education Review, 49*(3), 215-230.
Polat, S. (2011). The Relationship Between Organizational Image and Student Academic Achievement. *Journal of Higher Education Studies, 18*(2), 94-110.
Rindova, V. P., Williamson, I. O., Petkova, A. P., & Sever, J. M. (2005). Being Good or Being Known: An Empirical Examination of the Dimensions, Antecedents, and Consequences of Organizational Reputation. *Academy of Management Journal, 48*(6), 1033-1049.
Safir, A., & Sumer, M. (2006). Faculty and Institutional Reputation: The Role of Academic and Administrative Staff. *Journal of Educational Administration, 19*(4), 205-220.
Sultan, P., & Wong, H. Y. (2019). Service Quality in Higher Education: A Review and Research Agenda. *International Journal of Quality and Service Sciences, 11*(1), 1-20.
Sung, M., & Yang, S. U. (2009). Student-University Relationship and Reputation. *Public Relations Review, 35*(2), 150-152.
Xu, J., Li, H., & Zhao, Y. (2023). Corporate Reputation and Resilience: The Role of Stakeholder Trust. *Strategic Management Journal, 44*(3), 456-472.
Zhao, X., Wang, Y., & Liu, Z. (2023). *Social Media Analytics and Corporate Reputation: The Influence of Online Sentiment on Brand Equity*. Journal of Interactive Marketing, 45(1), 134-152.

INDUSTRIAL ENGINEERING

Decision Making

Engineering Management

Industrial Data Analytics

Knowledge Management

Manufacturing Management

Analysing the Automotive Production: A Bibliometric Analysis on Lean-Green Management

Ayşe Melissa Ergün [a], Hür Bersam Sidal [a]

[a] Istanbul Technical University (ITU), The Department of Management Engineering, Master in Management Program, Turkiye
erguna17@itu.edu.tr

Keywords: Lean-Green Management, Lean, Green, Automotive, Bibliometric Analysis.

Aim

The lean management concept is a widely used and implemented production improvement solution especially in the automotive sector. Lean management, originating from the Toyota Production System, focuses on maximizing value for customers while minimizing waste through the continuous improvement of processes. These principles have historically enabled automotive companies to achieve higher efficiency levels with a reduction of costs and resource waste (Kiran, 2017). However, in recent years the need for an efficient production system became no longer sufficient for companies. The increasing importance of green production and environmental sustainability pushed companies to modify their manufacturing systems in a more environmentally conscious way (Schutzbach et al., 2022). As a result, the recent improvements in the automotive sector has surpassed the lean management directives and currently are in need of a more sustainable and green transformation. Especially after the wave started by the Paris Agreement and consequently the European Green Deal, the adoption of sustainable and environmentally conscious practices gained importance with the urgency of combating climate change and aiming to transition towards a greener and more sustainable industry. At this point a comprehensive approach like Lean-Green (LG) Management, which combines lean management and green applications, gained popularity in the sector. This approach integrates lean principles with environmental sustainability, emphasizing resource conservation, energy efficiency, and the reduction of carbon footprints (Tripathi et al., 2021). By embracing this dual strategy of Lean-Green Management, the automotive industry is not only aiming to enhance operational efficiency but also demonstrates its commitment to long-term sustainability and global ecological well-being. Overall, LG management is a subject open to improvement and further research. For this reason, this study seeks to identify the literature progress regarding LG management, by conducting bibliometric research in the automotive sector. It aims to identify the current standing of the literature and explore the future research directions for scholars.

Material and Method

The bibliometric analysis in this study has been conducted by limiting the available data by its publication year. The study is focused on publications after the year 2015 as it includes environmental sustainability, 2015 can be seen as a milestone for sustainability research with the help of the Paris Agreement (Bendig et al., 2023). Thus, it was decided that for LG management, analysing more current publications i.e. after 2015 will be more meaningful. The study is also concentrated on the automotive sector as the building blocks of lean management were set in the automotive sector. Additionally, the innovative and competitive nature of the automotive industry played a role in this selection as the sector motivates the companies to become more efficient and ecological (Kosasih et al., 2023). Using the Scopus database, the research was done within the titles, abstracts and keywords of the publications by focusing on the subject LG management and automotive with a limitation on the publication years. This database choice was done as Scopus is a reliable and up-to-date scientific database with a rigorous indexing criterion and detailed citation data availability, which are particularly important for a bibliometric analysis. The 1516 publications found through this research were then subjected to a screening process. At the end of this process 58 publications were selected to be included in this study. The selection criteria being the

availability for retrieval, the sectoral compatibility with the analysis and the content coherence. The gathered data is then uploaded to Biblioshiny software in order to create tables and illustrations from the selected publications.

Findings

This bibliometric analysis provides a comprehensive overview of the published research documents on lean and green management within the automotive sector. The analysed publications consist of 48 articles, 7 conference papers and 3 reviews with an international co-authorship of 33.66%. The findings highlight the increasing academic and industrial interest especially after 2021 in integrating lean principles with green practices to address contemporary environmental and operational challenges. The keyword analysis identified the keywords as sustainable development with 16 occurrences; manufacturing, sustainability, industrial research and lean production with 8 occurrences; supply chain management with 7 occurrences; agile manufacturing systems, manufacture, green economy, environmental management with 6 occurrences. As LG management was born by combining the more conventional approaches such as lean management with newly emerging sustainable approaches, the fact that sustainable development was highly researched is only a natural consequence. Moreover, the conducted analysis shows that researchers focus on collaborative frameworks which are combining productivity, efficiency and ecological responsibility. The bibliometric analyses also identified the core publications in the LG management field by using Bradford's law. This law is a bibliometric principle that describes the distribution of scientific literature on a specific subject. It suggests that journals can be divided into groups based on their productivity in publishing relevant articles. The core sources are the ones which publish a significantly large number of articles on the subject. The core sources defined by using Bradford's law for LG management include Sustainability (Switzerland), Production Planning and Control, Journal of Cleaner Production, Business Strategy and The Environment and IFIP Advances in Information and Communication Technology. These findings can navigate researchers towards these core sources to easily stay updated in a rapidly evolving field. Overall, the annual growth rate of the publications analysed is 32.5%. This high annual growth rate shows that in the academic community Lean-Green (LG) Management became a hot-topic in recent years.

Conclusion

The comprehensive approach of Lean-Green (LG) Management, which integrates lean management principles with green applications, has attracted attention of the automotive sector in recent years. This approach combines lean principles with environmental sustainability, prioritizing resource conservation, energy efficiency, and the reduction of carbon footprints. This study sheds a light on the progression of literature and maps the academic landscape of Lean-Green (LG) management studies by conducting a bibliometric analysis within the automotive sector. By identifying and highlighting the trends and the themes within this domain, the analysis identifies the core publications that have significantly contributed to the advancement of knowledge in LG management. In conclusion, the integration of lean management principles with environmentally sustainable practices has emerged as an important approach in the automotive industry, addressing both operational efficiency and ecological responsibility. By combining the waste reduction and productivity enhancing strategies of lean management with sustainable solutions aiming to minimise environmental impact, LG Management offers a comprehensive framework for optimizing manufacturing processes while decreasing resource consumption and pollution. This approach promotes economic performance by lowering costs and improving productivity and aligns with global sustainability goals by ensuring energy efficiency and lower carbon emissions. Despite its contributions, this research is not without its limitations. Overall, one notable limitation of this research is its reliance on a single database, which may constrain the comprehensiveness of the findings. To develop a wider understanding of the literature, future studies could integrate multiple databases other than Scopus. As Lean-Green (LG) Management can also be suitable for different sectors than the automotive industry, it is possible to include diverse disciplines and industries for future research. This broader scope would create a more integrated and impactful accumulation of knowledge in Lean-Green (LG) Management. As industries continue to face increasing environmental challenges and productivity goals, the evolution of LG Management should be ensured and researched as a framework for sustainable industrial practices.

References

Bendig, D., Kleine-Stegemann, L., & Gisa, K. (2023). The green manufacturing framework—A systematic literature review. In Cleaner Engineering and Technology (Vol. 13). Elsevier Ltd. https://doi.org/10.1016/j.clet.2023.100613

Kiran, D. R. (2017). Lean Management. In Total Quality Management (pp. 363–372). Elsevier. https://doi.org/10.1016/b978-0-12-811035-5.00025-8

Kosasih, W., Pujawan, I. N., Karningsih, P. D., & Shee, H. (2023). Integrated lean-green practices and supply chain sustainability framework. Cleaner and Responsible Consumption, 11. https://doi.org/10.1016/j.clrc.2023.100143

Schutzbach, M., Kiemel, S., & Miehe, R. (2022). Eco Lean Management - Recent Progress, Experiences and Perspectives. Procedia CIRP, 107, 350–356. https://doi.org/10.1016/j.procir.2022.04.057

Tripathi, V., Chattopadhyaya, S., Mukhopadhyay, A. K., Sharma, S., Singh, J., Pimenov, D. Y., & Giasin, K. (2021). An innovative agile model of smart lean–green approach for sustainability enhancement in industry 4.0. Journal of Open Innovation: Technology, Market, and Complexity, 7(4). https://doi.org/10.3390/joitmc7040215

Improvement Study In The Inner Door Production Area With Lean Production Approach

İsa Emre Gül[a], Seda Yanık [b]

[a] Istanbul Technical University, Graduate School, Industrial Engineering, Istanbul, Turkey
[b] Istanbul Technical University, Faculty of Management, Department of Industrial Engineering, Istanbul, Turkey
guli15@itu.edu.tr

Keywords: EAWS, Lean Production, MTM-UAS, Productivity.

Aim

Lean production is a philosophy of a manufacturing method that is frequently used worldwide. According to this method, any process that the customer would not be willing to pay for and that does not add value to the final product should be eliminated. Companies also adopt the lean production philosophy and use lean production methods to reduce their costs in order to maintain their commercial existence and preference. Bhuiyan and Baghel said that the aim of lean manufacturing is to produce the products with high quality in the most efficient way possible while providing less human effort, inventory, time for product development and space to respond to customer demands at a higher level (Bhuiyan & Baghel, 2005). Eliminating these wastes will contribute to the profitability of companies. In the study of Yamamoto, Mistead and Lloyd, in the philosophy of lean production, there are seven types of waste known as the seven wastes, which are transportation, waiting time, overproduction, defective production, inventory, motion, and overprocessing (Yamamoto et al., 2019).
The aim of this study is to contribute to the annual productivity target of the refrigerator factory by improving the flow in the inner door production area. The flow of this area will be examined, and processes identified as contrary to the lean manufacturing principles will be eliminated, thereby increasing the availability of employees during their cycle time and reducing the number of workers to achieve efficiency targets. With this study, in addition to improving efficiency, it is aimed to reduce the scrap rate in the production of inner doors by simplifying the flow. By reducing scrap rates, another form of waste will be eliminated.

Material and Method

The inner door material subject to the study is the plastic part, generally white in colour, located on the inner side of refrigerator doors, where the door shelves are assembled. These parts are shaped using a mold after undergoing a pre-heating process in the inner door production area. Fridge and freezer inner doors can be seen in the Figure 1.

Figure 1. Freezer and fridge inner doors.

The inner doors produced in the manufacturing area are then subjected to a process called door foaming on the assembly line. In this process, a substance called polyurethane is filled between the door sheet metal and the inner door to provide insulation for the door. To ensure that the protrusion called "nail" and "dike" on the inner door are completely filled with polyurethane and to allow the air trapped between the inner door and the door sheet to be expelled, a drilling process is applied. The drilling process can be observed in the Figure 2.

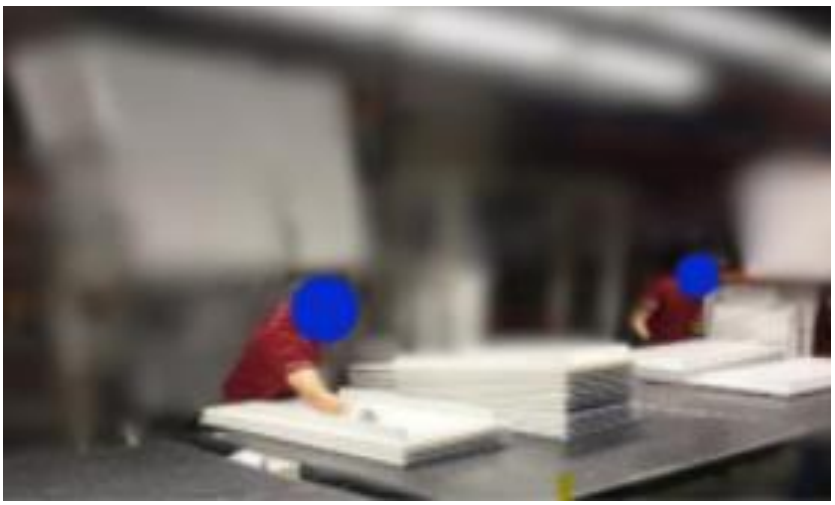

Figure 2. Drilling operation.

In order to examine the current flow in the inner door production area, two methods have been applied. First of all, a flowchart of the production area was drawn. The flowchart of the area has been prepared from the plastic roll loaded on the machine to its readiness for door foaming on the assembly line. Another flow determination method used was the Spaghetti diagram. The movements of employees in the production area were examined using a Spaghetti diagram over the layout plan. Thanks to these two diagrams, processes that could be considered waste in the inner door production area have been identified, and within the scope of the study, the improvement of these points has been planned. In the study, attention was paid to layout and operation sequences to plan for increased efficiency and reduced scrap.

A target work plan was created for the areas identified for improvement using flowcharts and spaghetti diagrams. Two methods called MTM-UAS and EAWS were used to determine the suitability of this work plan. A method time study was conducted to check whether the process times of the workers in the new work plan to be implemented are in accordance with the cycle time of the production machine. When we examined the method time techniques in the literature, it was determined that the most commonly used method in production is the MTM method. According to a study conducted by Çakmakçı and Karasu (2007), there are many MTM methods and before applying these methods, the method appropriate to the variables should be selected. MTM-UAS was selected as the MTM method suitable for the conditions specified in this article. Niu stated that almost a quarter of the workers in Europe suffer from back and muscle pains after a survey study (Niu, 2010). Thus, for the ergonomics study, methods that evaluate ergonomics in terms of posture and weights to assess the loads and risks on employees' bodies were examined. When we examined the articles in the literature, we found that industrial organizations generally use the EAWS method. According to Fischer et al. (2023), the EAWS method is a comprehensive ergonomic analysis and evaluation method used especially in the automotive industry to evaluate working postures and working conditions. Therefore, the EAWS Digital application, which employs the EAWS method, was used in this study.

Findings

As a result of this study, the number of employees in the inner door production area has been reduced with proper working conditions in terms of ergonomics. Ergonomic assessment results can be observed in Figure 3. Also, MTM-UAS studies can be observed in Table 1 for freezer operator and Table 2 for fridge operator. With the reduction in the number of employees, improvements have been achieved both in the company's employee costs and in productivity measurements. By reducing the number of workers in the area by 1 person per shift and 3 people daily, the company achieved a savings of 46,038 Euros in employee costs.

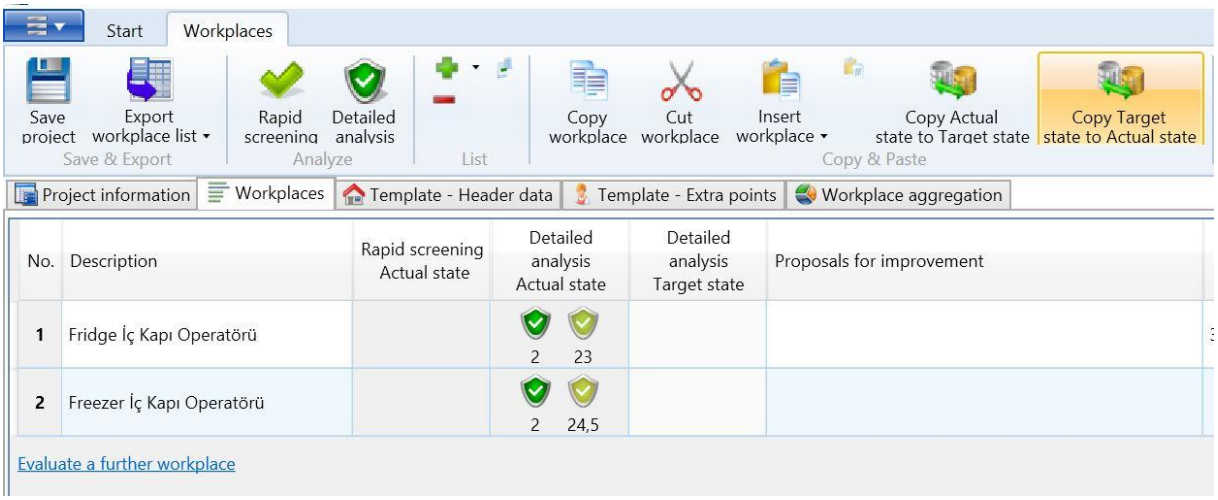

Figure 3. EAWS Results.

Table 1. Freezer operator MTM-UAS study.

Operations		MTM Results		
		Code	TMU	Freq
Op.1	Take the 6 stacked freezer inner doors from the machine and pull them in front of you.	AJ3	12.50	0.17
Op.2	Perform visual inspection of inner doors	VA	30.00	2.00
Op.3	Drill the first corner of the inner door with the drilling tool	HC3	85.00	1.00
		ZA1	5.00	1.00
Op.4	Drill the other 3 corners of the inner door with the drilling tool	PC3	135.00	3.00
		ZA1	15.00	3.00
Op.5	Put the drilled inner doors on the side statio	AH2	45.00	1.00
		ZA1	5.00	1.00
Op.6		AM1	15.83	0.17
		KA	16.67	0.67

	Take the 6 freezer inner doors whose drilling operation has been completed and put them into the cart	PA1	1.67	0.17
Op.7	Walk to get the fridge inner door	KA	33.33	1.33
Op.8	With the help of the drilling tool, drill the middle dike point of the fridge inner door 2 times	HB2	60.00	1.00
		ZA1	10.00	2.00
		PB2	60.00	2.00
Op.9	Take the 6 refrigerator inner doors, the drilling operation of which has been completed, and put them into the cart	AJ1	6.67	0.17
		KA	16.67	0.67
		PA1	1.67	0.17
	Total Time (TMU)		555.00	
	Total Time (s)		19.98	

Table 2. Freezer operator MTM-UAS study.

Operations		MTM Results (s)		
		Code	TMU	Freq
Op.1	Take the 6 stacked fridge inner doors from the machine and pull them in front of you	AM3	21.67	0.17
Op.2	Turn the direction of 6 inner doors	PA3	4.17	0.17
		ZA3	3.33	0.17
		AL3	19.17	0.17
		ZA3	3.33	0.17
Op.3	Perform visual inspection of inner doors	VA	60.00	4.00
Op.4	Drill the left and right lower corner of the seal of the inner doors using the drilling tool	HB3	150.00	2.00
		ZA1	10.00	2.00
Op.5	Drill the lower left and right dike end points of the inner doors with the drilling tool	PB2	60.00	2.00
		ZA1	10.00	2.00
Op.6	Drill the left and right bottle rack point of the inner doors using the drilling tool.	PB1	40.00	2.00
		ZA1	10.00	2.00
Op.7	Pull the top point of the inner door	AH2	45.00	1.00
Op.8	Put the drilled inner doors on the side station	AL2	105.00	1.00
		ZA1	5.00	1.00
	Total Time (TMU)		546.67	
	Total Time (s)		19.68	

On the other hand, since 3 out of the 23 people working in the field were reduced, the efficiency value of the inner door production area was improved to 15% in the efficiency measurements. Similarly, since 3 out of the 1432 employees working in the factory were reduced, an overall productivity improvement of 0.21% was achieved in the factory. As a result of simplifying the flow, which can be observed in Figure 4, and early detection of errors, a decrease from 7% to 4% in scrap rates was observed in the inner door production area, and a reduction in scrap costs was experienced. When calculating scrap costs, the recyclability of the plastic was taken into account, resulting in a gain of 30,772.45 Euros.

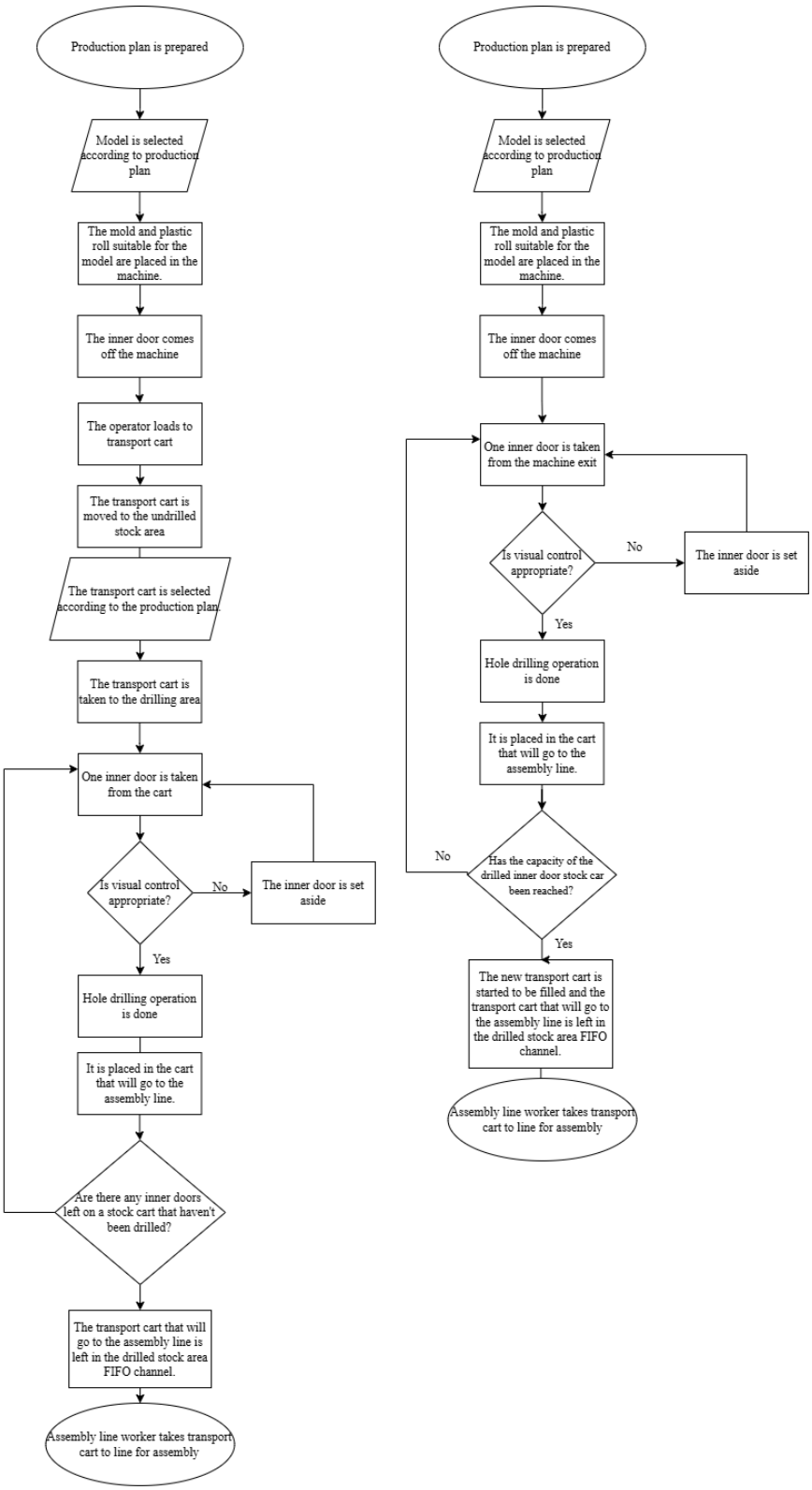

Figure 4. Flow in the production area.

Conclusion

To summarize the work done, the philosophy of lean production is an important approach for companies to increase their profits today. The adoption of this philosophy and the elimination of waste within this method are greatly aided by the use of flowcharts and spaghetti diagrams as two very useful visualization tools. The use of these tools not only allows for the easy identification of points where waste occurs but also makes the dimensions of improvements more comprehensible when compared to the diagrams and charts drawn in the new situation. Additionally, by valuing employees, it should be ensured that they can comfortably work within the cycle time through time studies, and it is necessary to eliminate the risk of future problems related to musculoskeletal health through ergonomic analysis. Eliminating these wastes can both increase workplace productivity and reduce scrap rates.

References

Bhuiyan, N., & Baghel, A. (2005). An overview of continuous improvement: from the past to the present. Management decision, 43(5), 761-771.

Cakmakci, M., & Karasu, M. K. (2007). Set-up time reduction process and integrated predetermined time system MTM-UAS: A study of application in a large size company of automobile industry. The International Journal of Advanced Manufacturing Technology, 33, 334-344.

Fischer, C., Rupprecht, P., & Schlund, S. (2023). Different approaches of conducting ergonomic assessment utilizing digital human models and motion capture in industrial site assembly. In Proceedings of the 6th International Conference on Intelligent Human Systems Integration (IHSI 2023) (pp. 348–358). AHFE International.

Niu S. (2010). Ergonomics and occupational safety and health: an ILO perspective. Applied ergonomics, 41(6), 744–753. https://doi.org/10.1016/j.apergo.2010.03.004

Yamamoto, K., Milstead, M., & LIoyd, R. (2019). A Review of the Development of Lean Manufacturing and Related Lean Practices: The Case of Toyota Production System and Managerial Thinking. International Management Review, 15(2), 21.

INFORMATICS

Computational Design Tools and Methods

A Decision Support Model Proposal For Urban Green Space Site Selection Problem Based on Multi-Criteria Decision Making

Erdal Kondakcı[a], Gülen Çağdaş[a]

[a] İstanbul Technical University, Graduate School, Architectural Design Computing Doctoral Programme, Türkiye
kondakci@itu.edu.tr, cagdas@itu.edu.tr

Keywords: Urban Green Spaces, Site Selection Problem, Multi-criteria Decision Making, Multi-objective Optimization.

Aim

As a result of the increasing urban population and densification around the world, the pressure on the existing urban green spaces is increasing and the service potential of green spaces is decreasing. In addition, due to the change of land use types from green space to other functions, it is seen that the quantity of green spaces decreases and remains insufficient. Attempting to provide ecosystem services with limited green infrastructure, which is threatened by density growth, has emerged as a major challenge (Haaland and Van den Bosch, 2015). Considering the ecological, climatic, social, economic and health benefits/services it provides, the loss of urban green spaces in the urban fabric is evaluated as a serious problem area. In addition to its benefits, green infrastructure is an important part of sustainable urban development due to its low cost, ease of transformation, renewal and development (Spatari et al., 2011). For this reason, many studies aiming to improve and increase urban green spaces' quality and quantity are carried out. In the urban studies literature, the determination of the most suitable places to be green spaces in the urban fabric is considered as a location allocation problem that includes many criteria and purposes. Since there are many factors affecting a suitable site selection, effective results can be obtained to support the decision-making processes by using GIS and computational methods. Even when urban green space site selection is considered as a multi-criteria decision-making (MCDM) problem including various discrete and continuous models, the methods, techniques, objectives and criteria used for planning a green system including new green spaces differ depending on the geography, context and scope.

Based on the mentioned context, the aim of the research is to address the problem of site selection for urban green spaces within the framework of a decision support model (DSM) based on multi-objective optimization (MOO). The aim of this model is to ensure that the location of new green spaces is selected in the most efficient way to increase the benefits provided by green spaces. For this purpose, the literature review on green space site selection is analyzed by PRISMA systematic analysis method and a DSM is proposed in line with the obtained site selection methods and criteria.

Material and Method

Research Design

The research is designed as three stages: 1) Problem statement and systematic literature review, 2) Determination of criteria and data collection, 3) Developing a DSM proposal (Figure 1).

Considering the aim of the research and related works, a systematic literature review methodology is adopted, which deals with the urban green space site selection problem by using computational methods. For this purpose, the main research questions are as follows: 1) What are the MCDM methods used in the site selection of urban green spaces? 2) What are the main objectives determined for the site selection of urban green spaces? 3) What criteria and constraints are used in the site selection of urban green spaces? 4) What spatial data and data models are used in the site selection of urban green spaces?

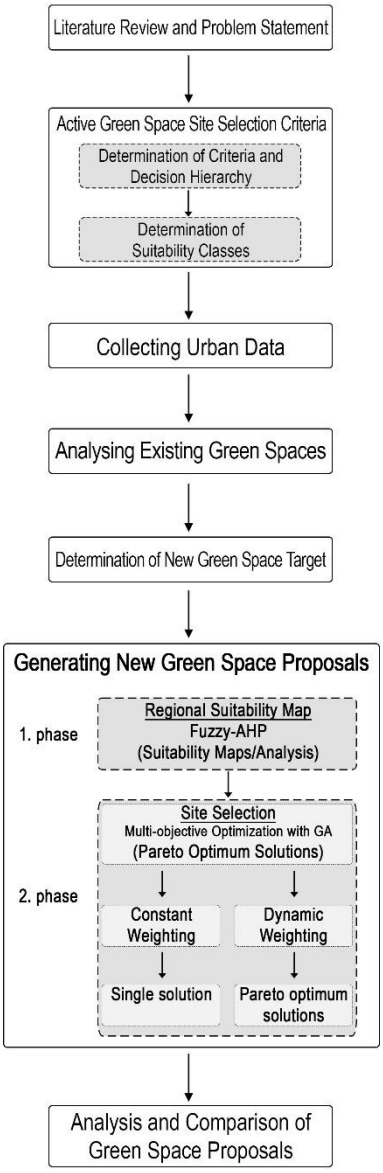

Figure 1. Research design and DSM flow chart.

Literature Review

Systematic literature review is made by following PRISMA protocol (Figure 2). Structured searches in selected major scientific databases (Scopus and Web of Science) is carried out and additional records will be added through cross-referencing and authors' knowledge on the domain. Outcomes of literature analysis are provided a methodological framework, to identify key features of urban green space site selection problem domain and to identify research gaps for guiding future research to be carried out in different geographies for developing sustainable and resilient cities.

Studies in this field are generally categorized into two groups. The first group treats green space site selection as an MCDM problem, where the most suitable zones are mapped regionally. Methods like AHP and Fuzzy-AHP, combined with GIS techniques, are typically used to generate suitability maps that highlight areas with the highest and lowest suitability values. In the second group, the site selection problem is addressed directly through MOO methods, resulting in point-by-point

selection maps. While MOO models typically aim to calculate 3-4 objectives, green space studies often involve more objectives, which can make it challenging for optimization models to produce functional and consistent results. Additionally, due to the large number of criteria in urban green space planning, not all criteria can be defined as objective functions, leading to some being excluded from the model. For example, Neema and Ohgai (2010, 2013), Neema et al. (2013), Yuan et al. (2011), and Zhang et al. (2017) defined different numbers of objectives, including factors such as population density, air quality, noise pollution, heat island effects, water quality, recreational value, and day-night temperature differences.

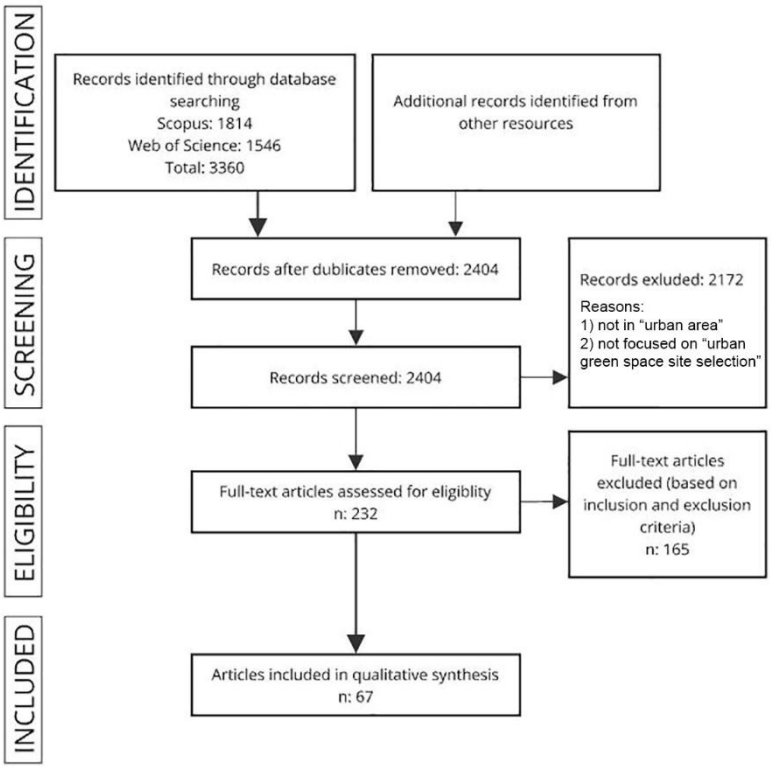

Figure 2. PRISMA protocol flow chart.

Determination of Criteria and Data Collection

The small number of objectives addressed in the multi-objective optimization approach, the exclusion of some basic criteria for green space planning, and the limited inclusion of expert knowledge make it necessary to discuss the effectiveness of the results. In particular, it is possible that a DSM that takes into account expert knowledge, global and local criteria instead of site selection models based solely on mathematical calculation may produce more effective results. For this purpose, firstly, the results obtained from the literature review are used to structure the decision hierarchy model which constitutes the basic data set of the decision support system including green space site selection criteria as two categories namely physical criteria and ecological criteria (Figure 3).

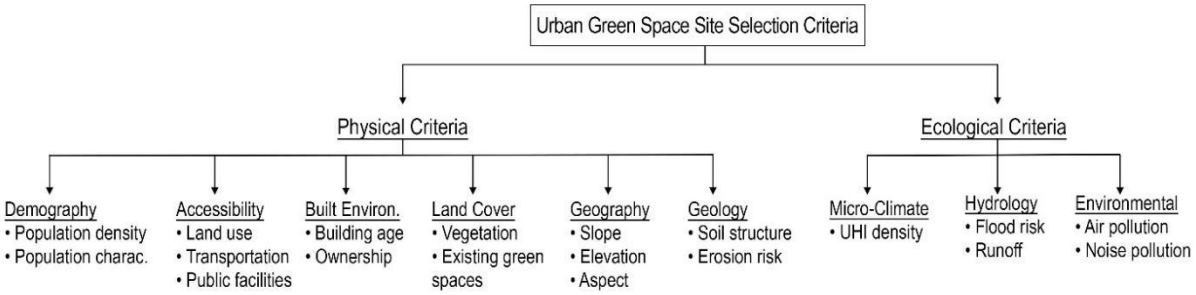

Figure 3. Decision hierarchy model.

Following procedures are adopted for the determination of the criteria and data collection to analyze existing urban green spaces:

1) Determination of the criteria to be used for site selection of active green areas: As a result of the systematic literature review, the factors to be considered in green space planning are determined. These are grouped hierarchically as main criteria and sub-criteria and a decision hierarchy model is created.
2) Determining the suitability classes of the criteria: As a result of the literature review, 5 different suitability classes (very high, high, medium, low, very low) are defined for some of the criteria, also, suitability classes based on fuzzy membership function are defined.
3) Collection and preparation of urban data to be used in the research: Open source maps (openstreetmap, Google Maps/Earth, etc.), city guide maps of municipalities, Landsat satellite images, geological maps, official sources related to the existing built environment and demographics, and maps used in related research are used for data collection. The collected data are organized and analyzed in GIS environment and processed with spatial analysis tools in different layers.
4) Analysis of existing green areas: At this stage, the existing green areas are analyzed in line with the accessibility criteria and service capacity to reveal the needs in the current situation. In order to examine the accessibility and service capacity, green areas are analyzed in the GIS environment by considering the ideal service distances related with population density.

Model Proposal

A review of the literature reveals that a holistic model of site selection, starting from the upper scale (regionally) and progressing towards exact site selection, is an innovative and unique approach to urban green space site selection. Based on this, a two-stage DSM is developed. In the first stage of the model, Fuzzy-AHP method is used to generate regional level suitability maps for site selection, and in the second stage, MOO method is used to propose exact locations for different types of green spaces (Figure 4). In this way, it is aimed to create a holistic DSM.

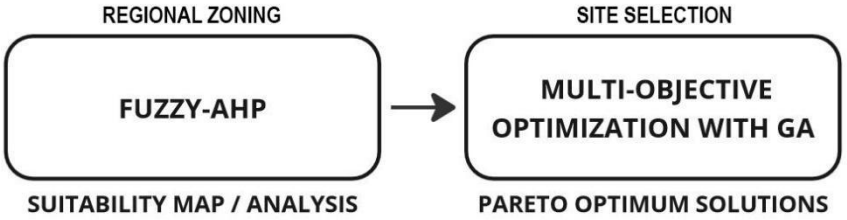

Figure 4. DSM diagram.

In order to identify the most suitable locations for active green spaces within the city, a DSM is developed that both takes into account the main factors affecting site selection and aims to increase the ecological, environmental and climatic benefits provided by green spaces while utilizing MCDM methods. A flowchart of the design of this model and the procedures

adopted to create the knowledge generation mechanism was given previously in Figure 1. Accordingly, the steps including computational methods and techniques followed to find optimum locations for new green spaces are summarized below:

1) Planning new green space target: At this stage, variables such as the number, type and total size of new active green areas are determined.
2) Generation of new green space proposals: In this stage, a two-stage DSM is used to generate green space proposals. In the first stage, Fuzzy-AHP method is used to generate suitability maps and in the second stage, multi-objective optimization method is used for exact location selection.
   2.1) Suitability map (Fuzzy-AHP): Two different suitability maps are obtained by weighting the main criteria and sub-criteria, which are divided into two groups as physical and ecological site selection criteria, with the Fuzzy-AHP method. Expert/author knowledge is used for weighting.
   2.2) Site selection optimization: In this stage, MOO is performed to pinpoint the locations of new green space proposals. Three objectives are identified: meeting physical criteria, meeting ecological criteria and increasing the average recreation value. The principle of minimizing the weighted total distance is applied. Two strategies are followed for weighting:
      a) Fixed weighting: Weighting is done for the three objectives to be optimized using expert/author knowledge. In line with the determined weights, a site selection proposal for active green areas is produced.
      b) Dynamic weighting: While a single solution is produced in fixed weighting, more than one solution is produced with different weight combinations in dynamic weighting. For this, multi-objective optimization methods based on evolutionary algorithms are used.

Conclusion

The proposed DSM systematically addresses the problem of urban green space site selection and provides analysis from the upper scale to the neighborhood scale. In this way, the ecological, environmental and climatic benefits provided by green spaces can be maximized and the results of different alternatives can be seen in advance. The model is also scalable in terms of the number of criteria and objectives. In addition, different types of green areas can be included in the model and the complex patterns they will create can be analyzed. Basically, a model that represents different layers of the city and provides decision support by analyzing the relationship between layers from a holistic perspective has been put forward. Site selection for new green spaces in densely built urban areas is challenging due to property rights. In countries like Turkey, where urban transformation against earthquakes is on the agenda, it would be beneficial to consider criteria such as ownership, building stock quality, and green space adequacy together when making new planning decisions in densely built-up areas. The multi-layered structure of the model is seen effective in developing new solutions in this context.

References

Haaland, C., & van den Bosch, C. K. (2015). Challenges and strategies for urban green-space planning in cities undergoing densification: A review. Urban Forestry & Urban Greening, 14(4), 760-771. https://doi.org/10.1016/j.ufug.2015.07.009

Spatari, S., Yu, Z., & Montalto, F. A. (2011). Life cycle implications of urban green infrastructure. Environmental Pollution, 159(8), 2174-2179. https://doi.org/10.1016/j.envpol.2011.01.015

Neema, M. N., Maniruzzaman, K. Md., & Ohgai, A. (2013). Urban Greening Using an Intelligent Multi-Objective Location Modelling with Real Barriers: Towards a Sustainable City Planning. Current Urban Studies, 01(04), 75-86. https://doi.org/10.4236/cus.2013.14008

Neema, M. N., & Ohgai, A. (2010). Multi-objective location modeling of urban parks and open spaces: Continuous optimization. Computers, Environment and Urban Systems, 34(5), 359-376. https://doi.org/10.1016/j.compenvurbsys.2010.03.001

Neema, M. N., & Ohgai, A. (2013). Multitype Green-Space Modeling for Urban Planning Using GA and GIS. Environment and Planning B: Planning and Design, 40(3), 447-473. https://doi.org/10.1068/b38003

Yuan, Z., Tiemao, S., & Chang, G. (2011). Multi-objective optimal location planning of urban parks. 2011 International Conference on Electronics, Communications and Control (ICECC), 918-921. https://doi.org/10.1109/ICECC.2011.6066364

Zhang, Y., Murray, A. T., & Turner, B. L. (2017). Optimizing green space locations to reduce daytime and nighttime urban heat island effects in Phoenix, Arizona. Landscape and Urban Planning, 165, 162-171. https://doi.org/10.1016/j.landurbplan.2017.04.009

Computational Memorability Model Based on Object Size

Fatma Seven[a], Sema Alaçam[a]

[a] Istanbul Technical University/Graduate School, Informatics, Architectural Design Computing, Turkey
sevenf22@itu.edu.tr

Keywords: Visual Perception, Computational Model, Architectural Design, Object Size.

Aim

People make sense of and sustain their lives with the help of the information they receive from the environment. Although perception is a very complex process, it occurs in a very short period of time. Perception is the process of interpreting the stimuli coming from the external world in the mind and gaining meaning. For this reason, this process is not only shaped by the senses. Factors such as cultural background, experiences and personality characteristics of individuals shape perception (Wade & Swanston, 2013). The type of perception that people use at the highest level is visual perception. The fact that the area in the brain for visual perception is larger than the sum of the areas related to the other four senses is also related to this situation. Humans perceive their environment dominantly through vision. Visual perception has an important role in the perception of architectural design. It enables strategic design decisions in areas such as education, museums and exhibition places, and retail environment designs (Shynu & Suseelan, 2023). Therefore, understanding the relationship between spatial elements and visual perception enables the shaping of people's perceptions in spaces (Yılmaz, 2004).
In a space with many objects, even if the light from the objects hits the eye, not all of them are remembered. Remembering, being aware of the objects in the environment is related to perception. Previous studies have shown that the objects that people remember and forget the most in a scene are similar (Dubey et al., 2015). Therefore, what is the common feature that makes objects memorable or forgettable? Studies conducted to answer this question have examined many factors affecting remembering. Dubey et al. tried to find an answer to this question by examining factors such as color, visual salience, object categories (Dubey et al., 2015). Celikkale et al. (2015) examined the effect of semantic features and visual attention on memorability. Basavaraju et al. (2019) examined the memorability of objects from the perspective of location and size factors. The aim of this study is to examine the relationship between object size and memorability. In this context, a computational model that evaluates visual perception based on memorability was designed. The main difference in this study is the scoring of a video's memorability and the use of more abstract representations of objects.

Material and Method

The methodology of the study consists of four steps. In the first step, the experimental environment was created, then a computational model was developed, data was collected from participants, and finally, the collected data was evaluated. Figure 1 shows the methodology of the study. For this study, a case study was conducted with forty-three participants.

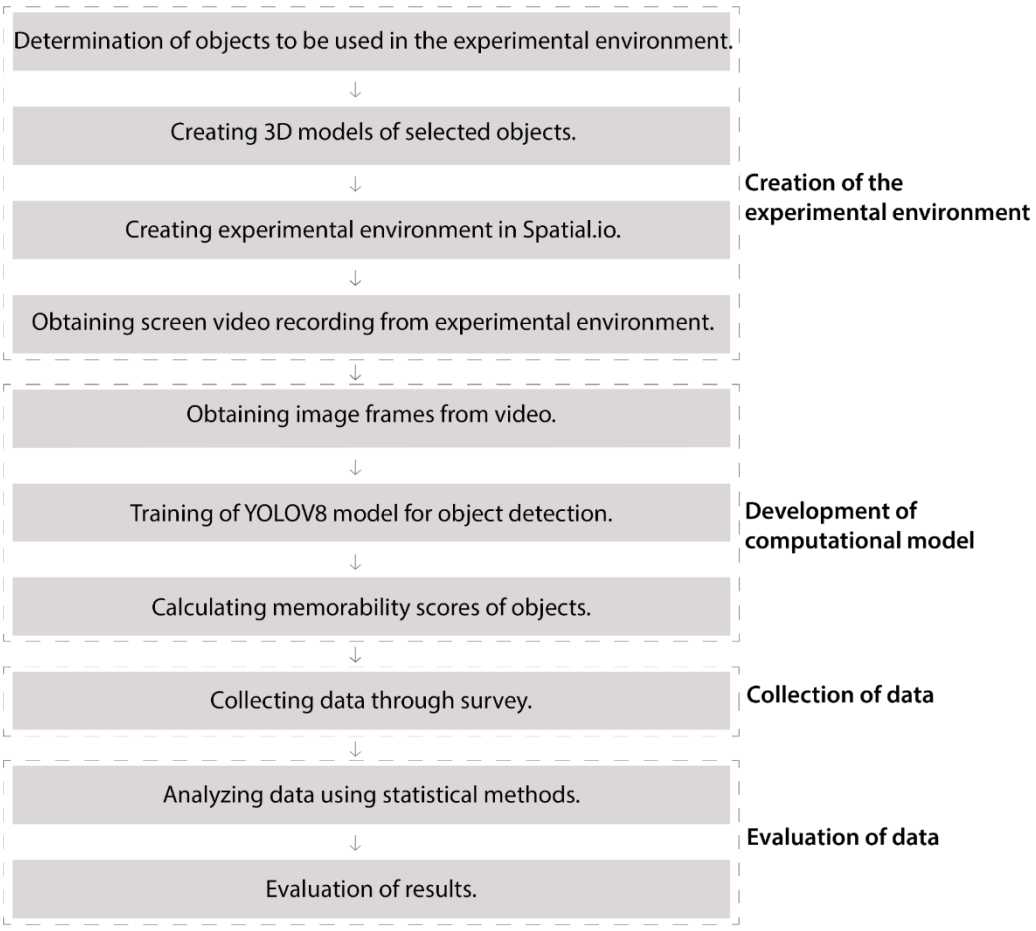

Figure 1. Methodology Diagram.

An experimental environment was prepared through the Spatial.io platform for the first part of the study. This experimental environment contains 9 selected objects of different sizes. These objects are the wardrobe, radio, oven, stool, drawer, suitcase, vending machine, briefcase and monitor that people see in daily life. Color, texture and material factors that could affect visual perception were kept same for all objects.

A virtual tour was conducted in the designed experimental environment. This tour lasted 20.5 seconds. During the tour, the screen was recorded to obtain a video that would later be shown to participants and used to compute the memorability score. Then, frames were extracted from this video. Two frames for each second were obtained through the VLC Media Player program. For the 20.5 second tour, 41 image frames of 1920x880 pixels were saved. Figure 2 shows a sample frame saved. Some of these frames were used to train the YOLOv8 model.

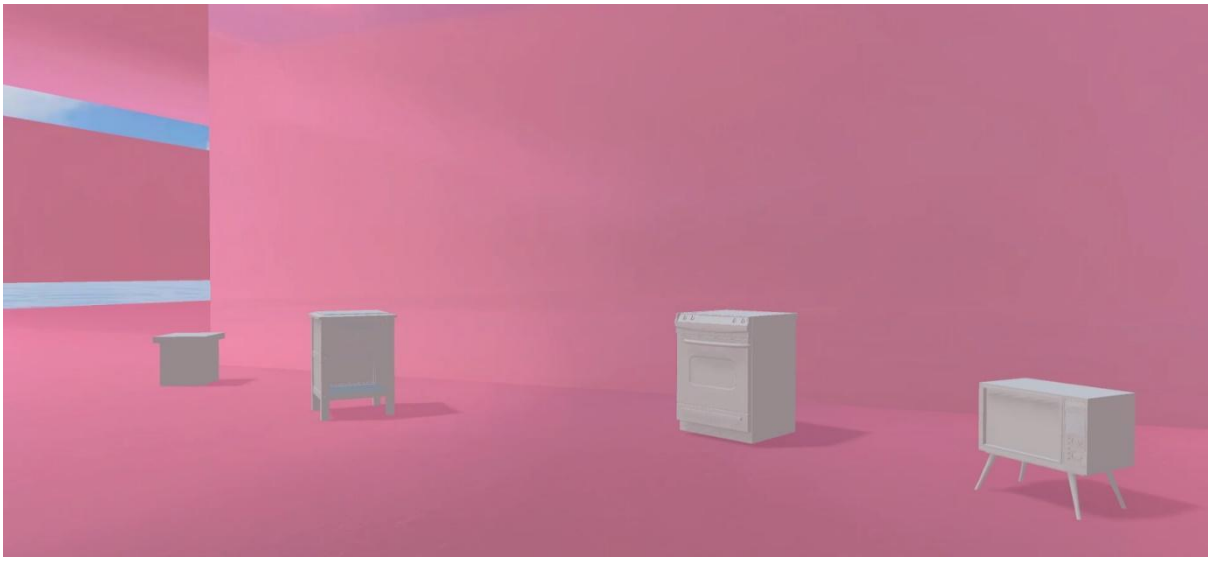

Figure 2. Sample frame from video of the experimental environment.

In the next step, object detection was performed on the image frames. The object detection model YOLOv8 was used for this process. A dataset was created for training via Roboflow using video frames. For the 21 selected frames, 9 classes were identified and object labeling was performed. At the end of the labeling process, the number of images in the dataset was increased to 51 by rotation. The dataset was divided into three parts: training, validation and testing. The dataset prepared in Roboflow was transferred to the Google Colab environment. After this step, the training process started. For the YOLOv8 model, the task was set to detect, mode to train and the number of epochs was set to 25. In this way, all objects in each frame were identified and their bounding box data was obtained.

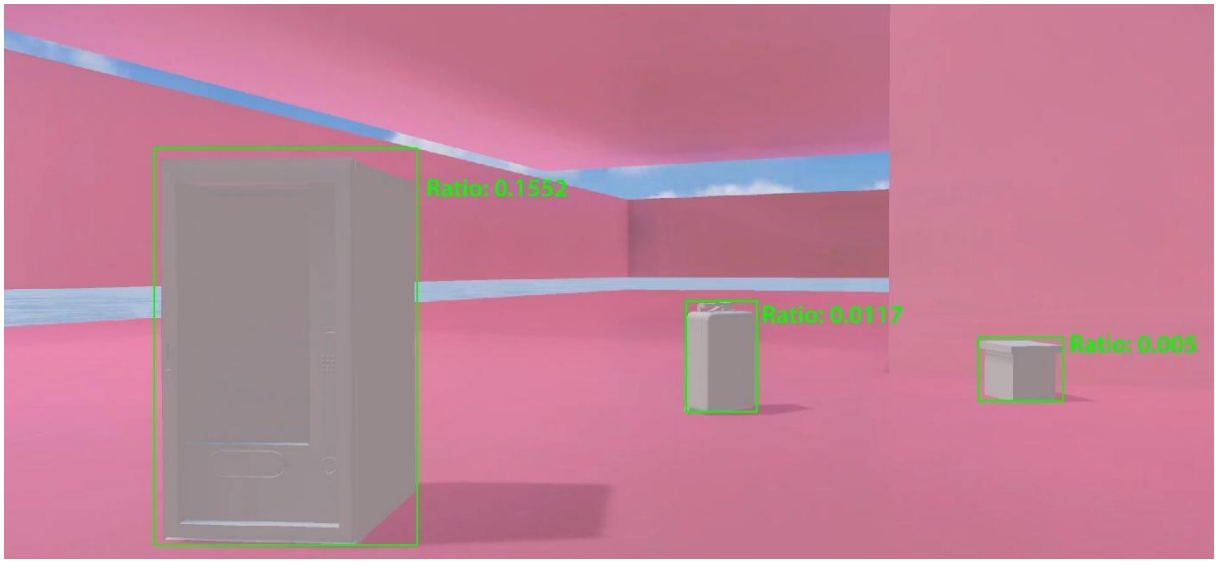

Figure 3. Example of a frame with calculated ratio values.

After this stage, the aim was to determine the area covered by each object in the image for each frame. For this purpose, the bounding box area of the relevant object was divided by the area of the entire image. Figure 3 shows a sample frame for which the ratios were calculated. This process was performed for every object in the image frame. In some images, the model used was incomplete or inaccurate in object detection. In these cases, the ratios of the objects were calculated

manually. The size ratio information for the objects was calculated for the 41 image frames. The calculated values were recorded in an Excel table. Table 1 shows the size ratio of each object for the first 5 image frames. The size ratios obtained for each object were summed up, taking all frames into account. The sum of the values was called the memorability score. Table 2 shows the memorability score calculated for each object.

Table 1. Size ratios for the first 5 frames.

FRAMES	Briefcase	Monitor	Vending	Suitcase	Stool	Drawer	Oven	Radio	Wardrobe
F1	0,0238	0	0,0122	0,0023	0,0014	0,0038	0,0043	0	0
F2	0,0239	0	0,0121	0,0024	0,0014	0,0038	0,0044	0	0
F3	0,029	0,0079	0,0125	0,0024	0,0015	0,0043	0,0042	0	0
F4	0,0384	0,0103	0,0142	0,0028	0,0016	0,0048	0,0013	0	0
F5	0,025	0,0129	0,0159	0,0031	0,0018	0,0054	0	0	0

Table 2. Memorability scores.

	Briefcase	Monitor	Vending	Suitcase	Stool	Drawer	Oven	Radio	Wardrobe
Memorability Scores	0,144	0,1197	0,9044	0,2841	0,1726	0,4531	0,6299	0,3401	0,9552

Participants were asked to watch the screen recording video and answer a survey twenty minutes later. In the survey, each object was shown, and participants were asked to rate how well they remembered them on a scale of 1 to 7. From the survey results, average memorability scores were obtained for each object based on participant data.

Findings

The participants' data and the data obtained from the developed model were compared. According to our model, the wardrobe and vending machine got the highest memorability scores, while the monitor and briefcase got the lowest scores. Figure 4 shows the memorability scores obtained from the model in graph format. According to the participants, the most memorable object was the wardrobe, while the least memorable object was the monitor. Figure 5 shows the average memorability scores obtained from participants. Furthermore, a correlation analysis was performed between the average scores obtained from the survey and the scores obtained from the model. The Pearson correlation coefficient was 0.69. This indicates that our model has a strong positive relationship with the data obtained from the participants.

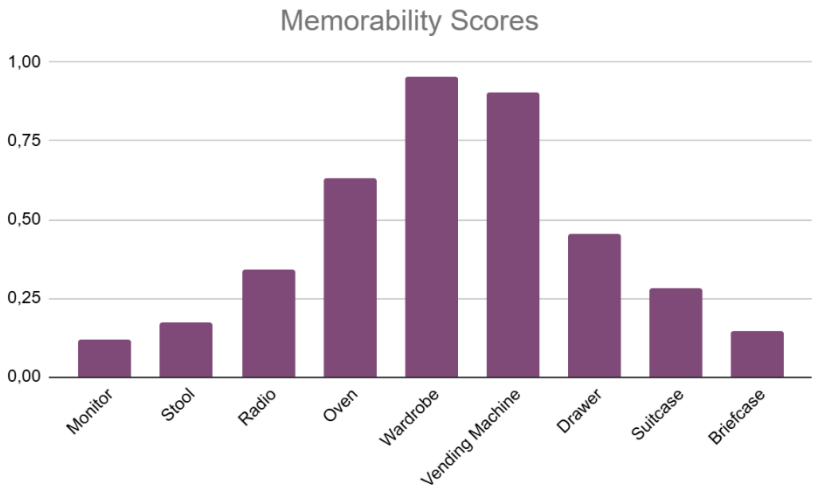

Figure 4. Memorability graph from model's data.

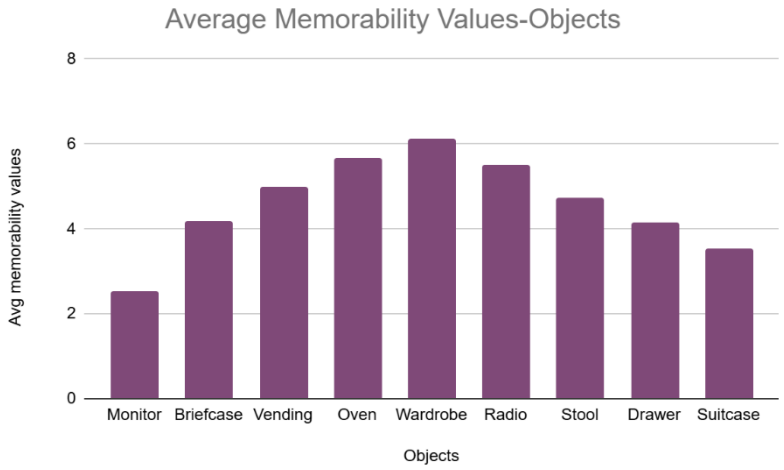

Figure 4. Memorability graph from participants' data.

Conclusion

This research contributes to the study of visual perception through a computational model and offers practical insights in areas such as architectural design, education and advertising. The study analyzes the effects of object size on visual perception and memorability and predicts the degree of memorability of objects of different sizes.

As a result of the surveys, it was determined that the size factor has a strong positive relationship with memorability. The number and variety of participants in the case study is one of the limitations of the study. In addition, due to the abstract representation of objects, object detection has not worked correctly and completely for every image frame. As a result of this abstraction, many factors affecting visual perception have not been included in the model. The study was conducted by analyzing video recordings rather than in real time. Future studies can be conducted with a higher number of participants from similar professions to reduce individual differences. Furthermore, real-time perception measurement can be performed. Future studies can offer new perspectives for further development of the model by examining the impact of factors such as location and semantic features.

Acknowledgement

This case study was conducted with the approval of the ITU Social and Human Sciences Scientific Research and Publication Ethics Committee. In the early stages of this study, the project titled "Modelling Visual Perception of Timevarying Scenes Using Likelihood" at Istanbul Technical University Scientific Research Projects Department made a significant contribution. We would also like to thank the participants.

References

Basavaraju, S., Gaj, S., & Sur, A. (2019). Object memorability prediction using deep learning: Location and size bias. *Journal of Visual Communication and Image Representation*, *59*, 117-127.

Celikkale, B., Erdem, A., & Erdem, E. (2015). Predicting memorability of images using attention-driven spatial pooling and image semantics. *Image and vision Computing*, *42*, 35-46.

Dubey, R., Peterson, J., Khosla, A., Yang, M. H., & Ghanem, B. (2015). What makes an object memorable?. In *Proceedings of the ieee international conference on computer vision* (pp. 1089-1097).

Shynu, R. V., & Suseelan, A. (2023). Human cognition and emotional response towards visual environmental features in an urban built context: a systematic review on perception-based studies. Architectural Science Review, 66(6), 468-478. https://doi.org/10.1080/00038628.2023.2232339

Wade, N., & Swanston, M. (2013). *Visual perception: An introduction*. Psychology Press.

Yılmaz, Ö. (2004). Mimari Mekanda Görsel Algı ve Manipülasyon İlişkilerinin İrdelenmesi. (154575) [Master's thesis, Yıldız Teknik Üniversitesi]. YÖK Tez. https://tez.yok.gov.tr/UlusalTezMerkezi/

INTERNATIONAL MASTER OF INTERIOR ARCHITECTURAL DESIGN

Interior Architecture

Technology in Interior Design

Use of Mycelium-Based Materials as an Interior Design Component: A Digital Fabrication Approach

Müge Özkan[a], Orkan Zeynel Güzelci[b]

[a] Istanbul Technical University, Graduate School, Istanbul, Türkiye
[b] Istanbul Technical University, Department of Interior Architecture, Istanbul, Türkiye
ozkanm22@itu.edu.tr, guzelci@itu.edu.tr

Keywords: Biodegradable Materials, Digital Fabrication, Interior Design, Mycelium-Based Materials, Sustainable Design.

This study explores the integration of digital fabrication technologies into the design and production of mycelium-based components. Initially, it introduces mycelium through a literature review, outlining its properties and how it is adopted in design-related disciplines. Subsequently, modular and customized suspended ceiling components are designed for a given space using a parametric design approach. Molds are produced via 3D printing to shape mycelium-based components, and the molding process is sequentially applied to plaster, silicone, and mycelium materials. This process is repeated at three different scales, ranging from smaller to larger. The material's overall form, level of detail, texture, and growth process are examined based on experimental results. This approach contributes to the integration of sustainable design, biomaterials, and innovative production techniques.

Introduction and Research Aim

In recent years, the construction industry has significantly impacted the ecosystem while remaining essential to modern society. With rapid production advancements, it has become a major consumer of natural resources (Balaras et al., 2005). Although sustainable materials are increasingly used, their long-term effects remain uncertain (Du Plessis, 2007). Achieving sustainability requires not only renewable materials but also environmentally compatible design approaches that enhance the quality of life. Designers, inspired by nature, integrate natural processes into digital design methods and explore new materials, including microorganisms (Elbasdi and Alaçam, 2016).
The primary goal of this study is to find an answer to the following question:

- How mycelium-based biomaterials, which aim to provide a solution to environmental problems, can be more effectively used within the discipline of interior design?

In the field of interior design, a suspended ceiling has been chosen as an interior design element where the potential of mycelium can be utilized. In this context, a suspended ceiling design has been developed that does not limit the nature and structural properties of the material. The molds required for the implementation of the design and the improvement of mycelium have been produced using 3D printing. This study focuses on optimizing the overall form of mycelium using molds produced at different scales and to evaluate the effects of substrate variables on the final product by observing them and comparing the findings with previous research results.

Materials and Methods

Mycelium is the vegetative, or root structure, of fungi and consists of hyphae, which are long, branching filamentous structures. It forms a dense network capable of connecting various substrates, creating strong and lightweight composites (Goidea et al., 2020). These mycelium-based materials can be cultivated using agricultural waste, making them a sustainable alternative to traditional construction materials. Due to their high potential, they have been the subject of various applications and academic research over the last two decades (Madusanka et al., 2024). However, despite the novelty of the material, a gap still exists between its use in architectural applications and large-scale commercial production. Most existing research and projects remain at the proof-of-concept stage, but their common goal is to raise societal awareness for the

transition to bio-based products (Ross et al., 2016). Therefore, developing designs and prototypes using mycelium is a valuable step toward achieving innovative solutions for a bio-based future.

The small size and volume limitations of current mycelium-based products pose challenges for the construction industry. Producing large, solid mycelium blocks is nearly impossible at this stage due to the organism's need for oxygen for optimal growth. Therefore, new production methods should be developed, taking into account the microorganism's natural aerobic characteristics and durability (Elsacker et al., 2021). Molding and 3D printing are commonly used to shape mycelium composites; however, traditional molding methods limit the organism's viability and restrict design capacity. As a result, digital fabrication techniques should be incorporated into the process (Mohseni, 2023). These methods not only overcome structural design limitations but also enable the creation of complex forms that are difficult to achieve with traditional techniques (Elsacker et al., 2021).

Experiments

Within the scope of this research, an experimental study was conducted that included the parametric design and material-based fabrication phases. The design was developed to align with the natural properties of mycelium, maximizing its potential. Several key criteria were considered: (i) creating a design that respects the unique characteristics of mycelium rather than forcing it into molds designed for traditional materials, and (ii) ensuring a modular structure that facilitates both production and implementation. To carry out the application experiment, the designed suspended ceiling molds were 3D printed in three different scales. Each mold was tested sequentially with plaster, silicone, and finally mycelium to explore how different production processes influence material properties. Plaster and silicone experiments were conducted to assess mold functionality, while mycelium experiments used wood chips and paper pulp as substrate components, providing essential nutrients for fungal growth. After each experiment, the molds were refined and re-produced to enhance material and design compatibility. The research was conducted in four stages, each involving systematic experimentation to refine the mold and optimize product development:

(i) Design Process: The previous efforts at producing mycelium-based suspended ceilings and treating mycelium as a direct substitute for traditional materials have been seen as a limitation to fully utilizing its potential. To address this problem, a custom-designed suspended ceiling form was developed using Rhinoceros 3D, ensuring alignment with the material's natural texture and properties. As shown in Figure 1 on the left, a three-layer mold was designed. Since the system follows a modular approach, a divider mold was used at the bottom. This divider ensures that each of the 42 individual modules can grow independently. The middle layer is the formwork component that shapes the mycelium, while the top layer serves as the mold's cover. This cover compresses the material to help it retain the intended form and creates a dark environment conducive to optimal mycelium growth. The image on the right presents the design's interior view.

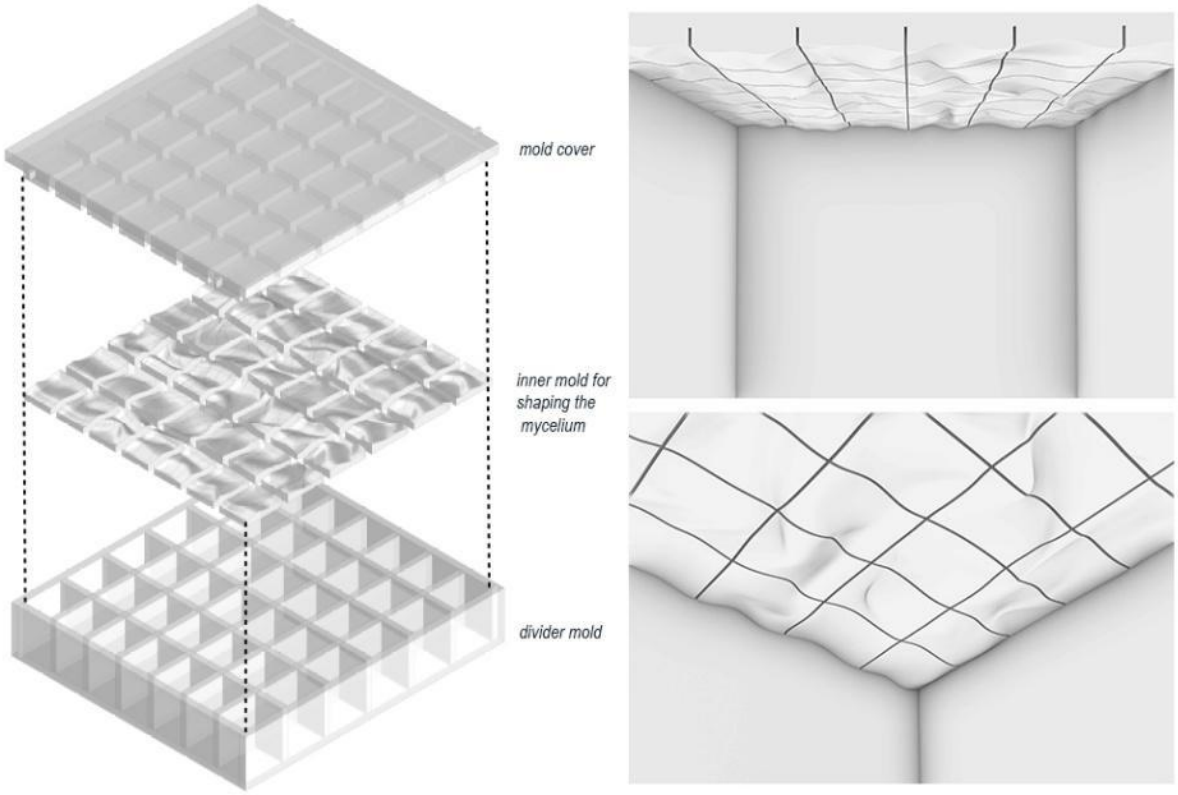

Figure 1. The design is modeled in Rhinoceros 3D. Left: Layers of the final mold; Right: Appearance of the ceiling from the interior space.

(ii) Mold Material: The designed suspended ceiling was divided into equal parts (curved surfaces) to facilitate integration into the space. The final design consists of 42 unique pieces, each with distinct forms. The mold was modeled and 3D-printed using to incorporate mycelium into the design effectively. To evaluate the final product, the molds were printed at three different scales (Figure 2). After each iteration, tests were conducted, and the mold design was optimized accordingly. The Figure 2 (right) shows a close-up view of the intermediate part of the final version of the mold. This component represents the middle layer of the three-part mold system and is the section responsible for shaping the mycelium.

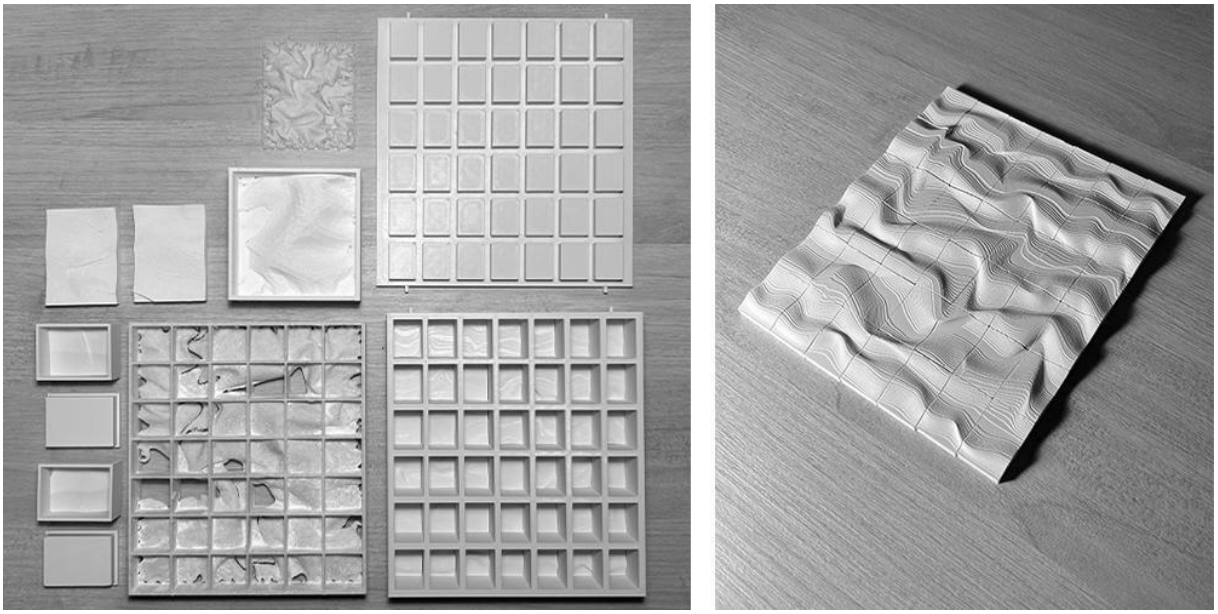

Figure 2. Left: 3D-printed molds visuals in various scales; Right: Final form that will shape the mycelium.

(iii) Material Application: Three different materials—plaster, silicone, and mycelium—were selected for the experiment. Plaster and silicone were either poured or placed into molds, while mycelium was placed and left to grow (Figure 3). The materials were tested at three different scales and left to either dry or grow, depending on their properties.

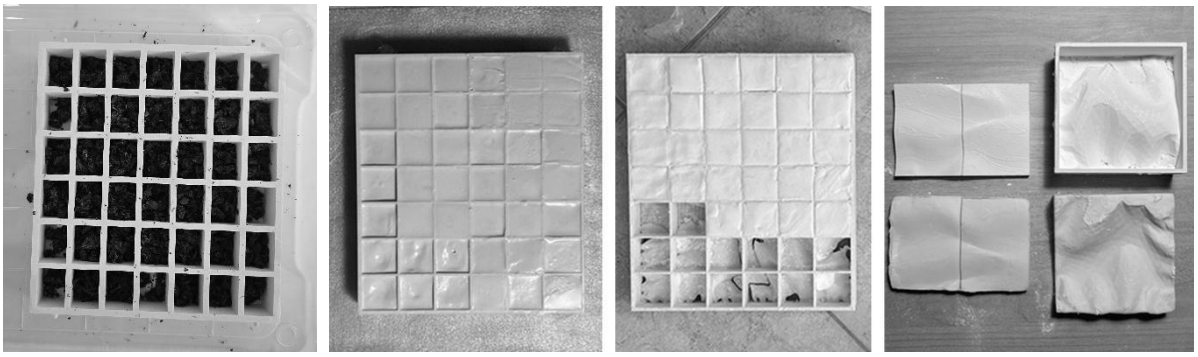

Figure 3. Molds are filled with various materials. From left to right: Mycelium, plaster, silicone, and silicone removed from the mold.

(iv) Evaluation of Results: The mycelium placed in the molds was observed for a growth period of 15 days (Figure 4). This phase of the study is ongoing; upon completion of the growth process, drying procedures will be conducted to obtain the final product. The resulting modules will be 3D scanned using Polycam, and their form accuracy and formation behavior will be assessed through physical comparisons in CloudCompare, thereby concluding the fourth phase.

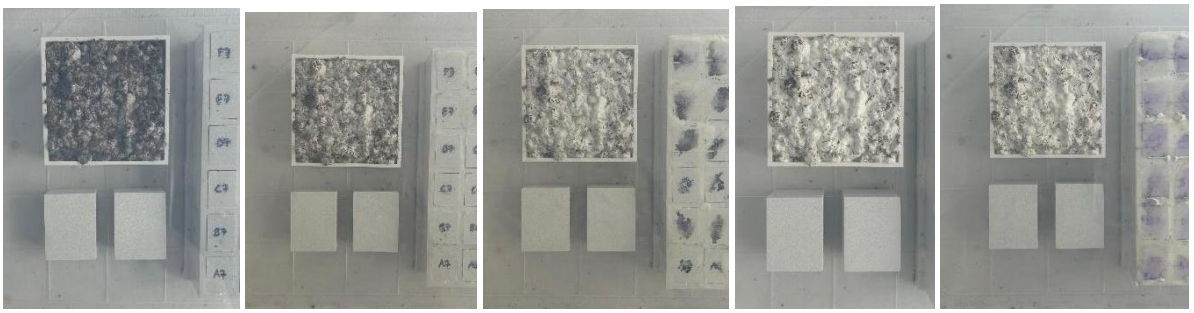

Figure 4. Progression of mycelium growth in the mold. From left to right: Days 4, 6, 7, 9, and 15.

Finding and Conclusion

Despite its promising potential, scaling up mycelium-based production presents challenges such as ensuring repeatability, optimizing growth conditions, managing the complexity of the sterilization process, and integrating these materials into existing construction applications. Ongoing research seeks to address these issues by exploring new fungal species and refining production processes. However, due to the interactive nature of microorganisms and their highly sensitive material properties, significant constraints may arise in the design process. Rather than perceiving these constraints as limitations, they can be seen as opportunities for developing functional architectural solutions.

The literature review revealed that mycelium-based suspended ceiling designs have often followed the same design and molding techniques used for traditional materials, treating them as direct substitutes. This approach is believed to hinder the material's full potential. To overcome this limitation, a material-specific design was developed that allows mycelium to retain its natural texture and growth pattern. As part of this study, molds were initially tested using plaster, followed by silicone. In the first mold, the plaster could not be removed, necessitating the use of silicone. While the silicone was successfully removed, it damaged the material. The same tests were repeated for the other two mold scales. Throughout these experiments, the molds were refined and optimized to enable the safe removal of mycelium without damage. To ensure a dark environment for mycelium to grow, a cover was designed to compress the material inside the mold, allowing it to take full shape. Since mycelium is a material that must be used within a short timeframe, preliminary preparations were made to minimize errors.

This study is derived from an ongoing master's thesis. At its current stage, the optimized forms of suspended ceiling components and their corresponding molds are being tested with mycelium material. In the future study, the acoustic performance of the designed and manufactured suspended ceiling components can be examined. The findings and outcomes of this study are expected to offer a new perspective for future research with mycelium-based materials.

References

Balaras, C. A., Droutsa, K., Dascalaki, E., & Kontoyiannidis, S. (2005). Heating energy consumption and resulting environmental impact of European apartment buildings. *Energy and Buildings, 37*(5), 429–442.

Du Plessis, C. (2007). A strategic framework for sustainable construction in developing countries. *Construction Management and Economics, 25*(1), 67–76.

Elbasdi, G. & Alaçam, S. (2016). An investigation on growth behaviour of mycelium in a fabric formwork. *Proceedings of the Parametricism Vs. Materialism: Evolution of Digital Technologies for Development (8th ASCAAD Conference)* (pp. 65–74).

Elsacker, E., Søndergaard, A., Van Wylick, A., Peeters, E., & De Laet, L. (2021). Growing living and multifunctional mycelium composites for large-scale formwork applications using robotic abrasive wire-cutting. *Construction and Building Materials, 283*, 122732.

Goidea, A., Floudas, D., & Andréen, D. (2020). Pulp Faction: 3D printed material assemblies through microbial biotransformation. *Fabricate 2020* (pp. 42–49). UCL Press.

Madusanka, C., Udayanga, D., Nilmini, R., Rajapaksha, S., Hewawasam, C., Manamgoda, D., & Vasco-Correa, J. (2024). A review of recent advances in fungal mycelium-based composites. *Discover Materials, 4*(1), 13.
Mohseni, A. (2023). MycoPrint: *Robotic 3D Printing of Mycelium-Based Composites*. [Master's thesis, The Pennsylvania State University]. https://etda.libraries.psu.edu/files/final_submissions/28017.
Ross, P. (2016). Your rotten future will be great. *In The Routledge Companion to Biology in Art and Architecture* (pp. 252–260). Routledge.

INTERNATIONAL MASTER OF INTERIOR ARCHITECTURAL DESIGN

Interior Architecture

Technology in Interior Design

A Strategy for Dataset Preparation in AI Model Training: The Case of Hotel Room Interiors

Yaren Cengiz [a], Orkan Zeynel Güzelci[b], Derya Güleç Özer[c], Koray Kıdış[d]

[a]Istanbul Technical University, Graduate School, International Master of Interior Architectural Design Program, Türkiye
[b]Istanbul Technical University, Department of Interior Architecture, Türkiye
[c] Istanbul Technical University, Department of Architecture, Türkiye
[d] Yeşim Kozanlı Architecture (YKA), Türkiye
cengizy23@itu.edu.tr

Keywords: Artificial Intelligence, Interior Design, Training, Text to Image, Dataset Preparation.

In recent years, the use of artificial intelligence in architecture and interior design has increased. Specifically, text-to-image models generate consistent results when trained with customized datasets. This study examines strategies for training an AI model and preparing a dataset to generate images reflecting the style of a design studio. Descriptive texts accompanying the images (renders) were prepared, and the model was trained and tested. Initial findings indicate that automated labeling methods are insufficient compared to expert annotations, spelling errors in English negatively affect the results, non-3D graphic-like elements hinder model training, and data diversity is crucial for both effective model training and outcomes.

Introduction and Research Aim

In recent years, the use of artificial intelligence in design disciplines such as architecture and interior design has been increasing. Current, studies emphasize that AI models generate more successful results when trained with customized datasets (Gan et al., 2023; Lee et al., 2024). However, the training process of AI models functions as a 'black box,' preventing direct user intervention and observation. This highlights the need for a comprehensive investigation into how this process works and to what extent different parameters influence model training.
In this context, the primary aim of this research is to train a text-to-image AI model that can generate hotel room interior images matched with the style of a design studio practicing in the field of interior design Yeşim Kozanlı Architecture (YKA) and to develop a strategy for generating descriptive captions for the images required for this training.

Material and Method

Text-to-image diffusion models utilize artificial intelligence techniques to take a text input and generate corresponding images based on that text. In this context, MidJourney, DALL-E, and Stable Diffusion are examples of widely used generative AI tools for text-to-image creation. Among these tools, Stable Diffusion 1.5 is open-source and provides free usage. Additionally, Stable Diffusion 1.5 allows the use of customized datasets as input folder. Users can generate images with Stable Diffusion 1.5 by running it locally on Windows-based computers through the Terminal window using various interfaces. In this study, the subscription-based version of eden.art, a cloud-based platform for model training and image generation, was used. In this context, renderings of a design studio Yeşim Kozanlı Architecture (YKA) constituted the study's material.

Experiments

In the scope of this study, the development and test of the AI model was carried out including: data collection, dataset preparation, model training, image generation with trained model, and observation of the outputs (Figure 1).

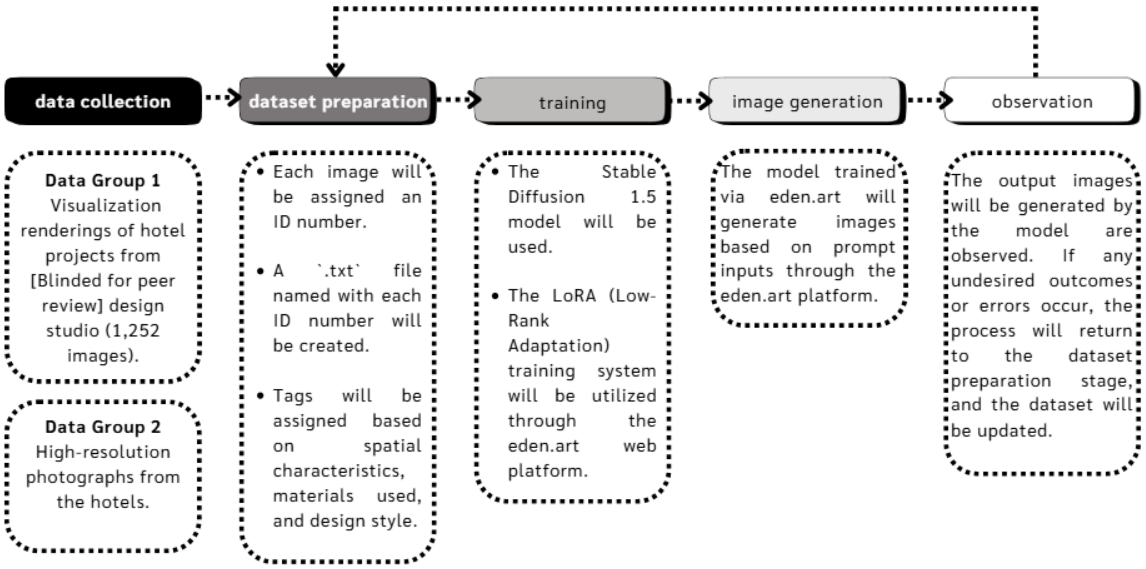

Figure 1. Training and testing phases of the AI model.

Data Collection: Accessing high-quality datasets from the web in fields such as interior design is a challenge. In this case, data can be obtained through collaboration with interior design offices. The collected data must be sufficient in quantity for effective model training (Gan et al., 2023) and should have diversity (Lee et al., 2024). In this context, to train AI in line with a specific style and enable it to generate images accordingly, 1252 renderings from nine hotel projects of a design studio Yeşim Kozanlı Architecture (YKA) were obtained.

Dataset Preparation: For training the AI model, the processes of data classification and generating descriptive text for the images were applied. In the data classification process, the collected data was divided into subsets to evaluate the model's performance. In this study, the renderings created for nine hotel projects by Yeşim Kozanlı Architecture (YKA) were first categorized by space types and then by perspectives/viewpoints.

In the captioning phase, the images used for training and their corresponding descriptive texts were named sequentially with the same filenames, such as 1.png and 1.txt, and collected in an input folder. While writing captions for interior renders, details of furniture, colors, materials, textures, lighting, composition, and other design elements were specified. In addition to architectural knowledge, captions were written in English with grammatically structured sentences, as noted by Lee et al. (2024), to ensure the AI model could effectively interpret them.

Model Training and Image Generation: Using the prepared dataset, seven different models were trained through eden.art platform. Among these models, five were trained exclusively with renderings taken from specific angles, one was trained with mixed images from different angles, and another was trained using captions generated by the wd-v1-4-vit-tagger-v2 auto-tagging tool.

Subsequently, each model was tested by running it with given prompts, and the outputs were observed by the authors (Figures 2 and 3). For example, when the results were found unsatisfactory due to discrepancies such as differences in requested viewpoints, incorrect placement and forms of interior elements, or material inconsistencies, or if evident errors were detected, the dataset preparation, training, and generation phases were repeated.

Caption: front view of mediterranean designed hotel room, double sized bed on the pine wood platform, rattan oval bedhead, three blue and sea themed drawings on the wall above bedhead, light greige fabric wallcovering on the half of the wall that behind the bedhead, two wood frame on the wall, light grey fabric sofa on the pine wood platform, blue and grey patterned pillows on the sofa and bed, foldable oval wood coffee table in front of the sofa, light brown wallpaper on the wall, black side door on the right, pendant rattan ventilator lamp above the sofa

Figure 2. Dataset creation example (the image belongs to the design studio).

Prompt: *right-perspective view of mediterranean hotel room, double sized bed, rattan oval bedhead, white sheets and pillows, natural elements, wardrobe with rattan doors, grey sofa, sunlight coming from the outside.*

Figure 3. Image Generation Example (Image generated by the trained AI model.)

Findings and Conclusion

The findings obtained from the experienced process and outputs are as follows:

- The automatic labeling method was found to be less successful compared to descriptive texts prepared by the experts.
- English expression errors led to incorrect image generations.
- When the number of interior design elements was not explicitly specified in the prompt, there was a risk of uncontrolled element additions.
- The required number of interior images and descriptive texts was determined to prevent overfitting during AI model training and testing.
- Non-architectural 2D graphical elements (text, poster, logo, etc.) in the training dataset were not effectively learned by the model.
- Interior design elements that were not fully visible in the training dataset were also generated incompletely during the testing phase.

The findings listed above regarding image selection and descriptive text writing for model training will be expanded with tests presented in the next step of the research. Additionally, these findings will be systematically detailed to develop a strategy for future model training.

References

Chen, J., Shao, Z., & Hu, B. (2023). Generating interior design from text: A new diffusion model-based method for efficient creative design. *Buildings, 13*(7), 1861.

Gan, R., Wu, X., Lu, J., Tian, Y., Zhang, D., Wu, Z., ... & Song, Y. (2023). idesigner: A high-resolution and complex-prompt following text-to-image diffusion model for interior design. *arXiv preprint arXiv:2312.04326*.

Lee, J. K., Jeong, H., Kim, Y., & Cha, S. H. (2024). Creating spatial visualizations using fine-tuned interior design style models informed by user preferences. *Advanced Engineering Informatics, 62* (2024), 102686.
Tong, H., Türel, A., Şenkal, H., Yagci Ergun, S. F., Güzelci, O. Z., & Alaçam, S. (2023). Can AI Function As A New Mode of Sketching: A Teaching Experiment with Freshman. *International Journal of Emerging Technologies in Learning (iJET)*, *18*(18), 234-248.
Yıldırım, B., & Demirarslan, S. (2021). A Cloud Computing Based Software in AI-Powered Interior Architecture Design And Presentation Tools: The Coohom Case. *The Journal of Social Sciences, 54*(54), 589-610.

LANDSCAPE ARCHITECTURE

Heritage and Identities

Innovative Technologies for Landscape Design and Management

Landscape Design

From Tradition to Globalization: The Conceptual Transformation of Korean Landscape in Global City Seoul

Mülkiye Kart[a], Ebru Erbaş Gürler[b]

[a] Istanbul Technical University, Graduate School, Landscape Architecture Program, Turkey
[b] Istanbul Technical University, Faculty of Architecture, Landscape Architecture Program, Turkey
kartm@itu.edu.tr

Keywords: Commodification, Globalization, Landscape Transformation, Seoul, Traditional Landscape.

The extended abstract should be between 1000 and 2000 words, including the reference section. The paper's title, author names, affilication and email address are not included in this word count. The following sections are required. If necessary, you may create sub-titles. Equations should be written in the text format, not as images. However, references to the equations within the text are required. If you use images and tables, please place them in the appropriate sections. A maximum of 5 tables and 5 images may be used. All images and tables not created by the author must include proper source citations. Please note that the organizers are not responsible for any copyright issues. Authors are solely responsible for obtaining permission to use copyrighted materials.

Introduction

Since ancient times, the relationship between landscapes and cities has evolved through a continuous dialogue in both the East and the West. The urban and landscape development of Seoul, however, has been shaped within the framework of the traditional Korean landscape philosophy, which emphasizes harmony with nature, particularly during the Joseon Dynasty (1392–1910). The selection of Seoul as the capital was guided by the principles of Pungsu-jiri (the Korean adaptation of Feng Shui), which dictated that the city be surrounded by four sacred mountains—Bukaksan, Naksan, Namsan, and Inwangsan. This positioning both provided geographical protection and ensured a spiritually and energetically balanced environment. Within this understanding, the free and harmonious flow of Qi was prioritized, and the balance of Yin and Yang was maintained, making Seoul not just an administrative center but also a city designed to embody ecological and cosmological harmony (Lee, 2008, pp. 389-390; Kim, 2003, p. 3).

However, throughout the 20th century, Seoul underwent radical transformations within the context of globalization. The destructive effects of Japanese colonial rule (1910–1945), the upheavals of World War II, and the deep trauma caused by the Korean War (1950–1953) not only reshaped the physical structure of the city but also profoundly altered its memory, the representation of its landscapes in the urban context, and its collective identity. These historical breaking points played a decisive role in shaping Seoul's future development policies, intensifying the tension between tradition and modernization (Kim, 2003; Hwang, 2003).

Seoul stands as a rare example among global cities. In the early 1950s, it was a war-ravaged, non-capitalist city. Yet, within just 35 years, it experienced rapid economic growth and successfully introduced itself as a dynamic metropolis on the world stage through the 1988 Summer Olympics. This extraordinarily swift transformation—and its ongoing evolution—offers critical insight into how landscapes, once infused with deep cultural and historical meaning, have been redefined as instruments of global marketing. It highlights how urban identity has been strategically commodified and turned into a consumable object within the capitalist dynamics of the global arena.

Aim

This study aims to examine how the conceptual framework of traditional Korean landscapes has evolved over time. Focusing on landscape transformation through the lens of commodification, it explores how traditional Korean landscapes have been reshaped by modernization, how urban identity has been marketed on a global scale, and how landscapes have been positioned within the discourse of the global city. Based on the findings of the extensive literature review, critical

breaking points that shape Seoul's landscape transformation from the Joseon Dynasty to the present have been identified, followed by an analysis of archival materials, such as historical photographs from the colonial period, alongside photographs taken on-site in Seoul. The interplay between traditional Korean landscapes and modern/global landscapes, along with representational strategies and identity transformation, is examined within an analytical framework.

Material and Method

Based on the findings of the extensive literature review, critical breaking points that shape Seoul's landscape transformation from the Joseon Dynasty to the present have been identified, followed by an analysis of archival materials, such as historical photographs from the colonial period, alongside photographs taken on-site in Seoul. The interplay between traditional Korean landscapes and modern/global landscapes, along with representational strategies and identity transformation, is examined within an analytical framework.

Findings

Based on the findings, the relationship between traditional Korean landscapes and globalization can be traced back to Seoul's initial encounters with Western urban planning practices. The Treaty of Ganghwa, signed with Japan in 1876, marked a significant turning point in Korea's opening to the outside world (Hwang, 2003, p. 370). However, early modernization efforts were interrupted by the Japanese occupation in 1910, during which urban space became a tool for colonial representation. Under Japanese rule, Seoul's spatial structure and landscapes were transformed to reflect imperial power (Kim, 2003; Hwang, 2003) and historically significant sites—such as palace gardens, which had been central to the traditional landscape—were repurposed into amusement parks and zoos (Kim, 2017) by stripping them of their original cultural significance. Likewise, natural landscape elements such as sacred mountains were adapted to fit the concept of "public parks," not as spaces for public use but as symbols of colonial hegemony (Hwang, 2003, p. 382).

In the post-World War II era, capitalist countries implemented various reforms to recover quickly and rebuild by aiming to prevent a return to the turbulent pre-war conditions (Harvey, 2003). However, Seoul's case diverges from this pattern. Although Korea gained independence from Japan in 1945, this independence did not immediately lead to stability and peace. The division of Korea into North and South—under Soviet and American influence, respectively—intensified regional tensions. In 1950, the outbreak of the Korean War devastated the nation, both politically and economically. Following the Korean War, the country's reconstruction was heavily supported by Western economic and political aid (Hüseyinoğlu, 2007, p. 141) Modernization efforts gained momentum in the 1960s, and by the 1970s, development of urban housing and infrastructure was seen as a solution to improving quality of life. By the 1980s, radical steps were taken to position Seoul as a global city. In preparation for the Olympics, the south side of the Han River was designated as the city's new business center, while reimagining the river and its surroundings as the city's key representative space (SMG, 2015, p. 10, 15; Hwang, 2003). Thus, the 1988 Olympics played a pivotal role in reinforcing Seoul's global image while marking a significant milestone in its transformation into one of the key showcase sites of global capitalism (Joo et. al, 2017).

The 1997 Asian financial crisis (IMF crisis) brought fundamental changes to Seoul's urban development strategies. In an effort to mitigate the economic downturn, a series of reforms were implemented by embracing neoliberal urban dynamics and introducing the strategic use of urban identity as a branding tool. From this critical turning point onward, urban transformation was both about physical restructuring and about aesthetic and managerial strategies (Joo, 2018). Mega projects, initiatives such as the "Design Seoul" campaign, and other city branding efforts were shaped by a growing emphasis on attracting global capital. Public space redevelopment, often justified through discourses on environmental sustainability and cultural heritage preservation, became an integral part of the city's branding process (Hwang, 2014; Paek, 2017; Križnik, 2011). Consequently, urban landscapes have increasingly become commodified and consumable image elements that respond to the demands of global investors and tourism.

Conclusion

In conclusion, Seoul's development underscores the intricate relationship between tradition and globalization. The city's landscapes, initially shaped by traditional Korean philosophies, have undergone substantial transformation due to historical events and processes of modernization. This study illustrates how these landscapes have evolved into global assets, thereby influencing the city's urban identity. It is imperative to preserve the cultural significance of these spaces while addressing the challenges posed by globalization, ensuring the retention of Seoul's distinct character within the contemporary urban context.

References

Harvey, D. (2003). *The condition of postmodernity: An enquiry into the origins of cultural change* (S. Savran, Trans.). Metis Yayınları. (Original work published 1989) **Url-1** http://ardayuceyilmaz.org/wp-content/uploads/2017/12/Postmodernliğin-durumu.pdf

Hwang, JT. (2014). 'Territorialized urban mega-projects beyond global convergence: The case of Dongdaemun Design Plaza & Park project, Seoul', *Cities*, 40, 82–89. **Url-2** https://doi.org/10.1016/j.cities.2014.03.007

Hwang, K. (2003). Seoul's Parks and Green Space in the 20th Century: From a City in Nature to Nature in the City. In Kwang-Joong Kim (Ed.), *Seoul, 20th Century: Growth and Change of the Last 100 Years* , 365–432 . Seoul : Seoul Development Institute **Url-3** https://www.seoulsolution.kr/sites/default/files/gettoknowus/Seoul%2020th%20Centruy%20growth%20%26%20change%20of%20the%20last%20100%20years.pdf

Hüseyinoğlu, A. (2007). Doğu Asya Ülkelerinin Sanayileşme Ve Kalkınma Deneyimleri: Güney Kore Örneği. *Stratejik Araştırmalar Dergisi,* 11, 140-143. **Url-4** https://tasam.org/Files/Icerik/File/dogu_asya_ulkelerinin_sanayilesme_ve_kalkinma_deneyimleri_guney_kore_ornegi_326d27ef-b019-42de-9955-679254ac4758.pdf

Joo, Y.-M. (2018). Megacity Seoul: Urbanization and the Development of Modern South Korea (1st ed.). Routledge. **URL-5** https://doi.org/10.4324/9781315278018

Joo, Y, Bae, Y & Kassens-Noor, E. (2017). Mega-events and mega-ambitions: South Korea's Rise and the Strategic Use of the Big Four Events, Palgrave Macmillan, London. **Url-6** https://doi.org./10.1057/978-1-137-53113-1

Kim, KJ . (2003). Introduction: Growth and Change of the 20th Century Seoul. In Kwang-Joong Kim (Ed.), *Seoul, 20th Century: Growth and Change of the Last 100 Years* , 1 - 20. Seoul : Seoul Development Institute. **Url-7** https://www.seoulsolution.kr/sites/default/files/gettoknowus/Seoul%2020th%20Centruy%20growth%20%26%20change%20of%20the%20last%20100%20years.pdf

Kim, S. -J. (2017). Post- Colonialism and the Restoration of Cultural Identity: A Study on Reconstruction of Changgyeong Palace, *The Review of Korean Studies,* 20, 54-80. **Url-8** https://accesson.kr/rks/assets/pdf/7833/journal-20-2-53.pdf

Križnik, B. (2011). Selling Global Seoul: Competitive Urban Policy and Symbolic Reconstruction of Cities. *Revija za sociologiju*. 41, 291-313. **Url-9** https://hrcak.srce.hr/75527

Lee, K. S. (2008). Bee-Bo Forest: Traditional landscape ecological forest in Korea. In S. K. Hong, N. Nakagoshi, B. Fu, & Y. Morimoto (Eds.), *Landscape ecological applications in man-influenced areas* (pp. 389-394). Springer. **Url-10** https://doi.org/10.1007/1-4020-5488-2_23

Paek, S. (2017). The Entangled Everyday: *Design Seoul* and the Disciplining of Commercial Signs, *Journal of Asian Architecture and Building Engineering*, 16 (1), 139-146. **Url-11** https://doi.org/10.3130/jaabe.16.139

Seoul Metropolitan Government (SMG). (2015). Seoul Solution for Urban Development 01. Seoul: Seoul Metropolitan Government. **Url-12** https://seoulsolution.kr/sites/default/files/gettoknowus/Seoul%20Solution%20for%20Urban%20Development_Part1.pdf

LANDSCAPE ARCHITECTURE

Heritage and Identities

Innovative Technologies for Landscape Design and Management

Landscape Design

The Use of Computer Vision in Observing Human Behavior in Landscape Architecture

Gizem Yağmur Gölbaşı[a], Melih Bozkurt[a]

[a] Istanbul Technical University, Department of Landscape Architecture, Turkey
golbasi16@itu.edu.tr

Keywords: Computer Vision (CV), Landscape Architecture, Observation, Human Behavior.

Aim

Artificial Intelligence (AI) is rapidly spreading across various disciplines, offering numerous opportunities. Computer Vision (CV) is a sub-branch of AI and is a system designed based on natural vision to extract meaningful information from digital images such as photos and videos (Marasinghe et al., 2023). The increasing integration of AI and CV technologies with various disciplines has created new possibilities for analyzing human behavior in urban areas. Landscape architecture, a field focused on the planning, design and management of outdoor spaces, benefits greatly from understanding how people interact with their environment, especially in public spaces (Ibrahim et al., 2020). While CV has great potential for visual data processing, its use in landscape architecture is not yet widespread. This study aims to explore the potential of CV in detecting and analyzing human interactions in public spaces through methods such as classification, segmentation and localization, object tracking, action recognition, and perception (Pai et al., 2024). This research aims to provide insights into how individuals navigate through landscapes, interact with urban elements and react to different environmental conditions. The findings from this study can help landscape architects to design more accessible, functional and user-centered public spaces by incorporating data-driven decision-making processes (Wilkins et al., 2022).

Material and Method

The proposed methodology includes four processes: collection of visual material, data labeling for the training dataset, CV model training and application of the trained model to the visual material.

Compilation of Visual Data: In the visual material compilation phase, visual data appropriate to the relevant topic are collected. Visuals can be obtained from online open sources, existing data sets or field studies. In this process, the aim is to create the most appropriate data set for model training by evaluating whether the data is suitable in terms of quality, resolution and diversity.

Data Labeling for the Training Dataset: In the data labeling phase for the training data set, the collected visual materials are labeled according to the determined spatial criteria. Since the existing training data sets cannot meet the needs of the research to be conducted within the scope of landscape architecture, it is a very important stage to create a training data set on the spatial data axis. This process may involve different approaches such as detection of people and objects in space, segmentation or classification. The labeling process can be performed manually (bounding box, polygon, mask, etc.) or using semi-automatic or automatic tools. An accurate and consistent labeling process is critical to the success of the model.

CV Model Training: In the CV model training phase, the model was trained on the labeled dataset using supervised learning techniques. In this process, the architecture of the model is selected first (for example, approaches such as CNN, YOLO, Mask R-CNN may be preferred). Then, data preprocessing steps (normalization, data augmentation, etc.) are applied to make the model learn more efficiently. During the training process, certain hyperparameters are used to analyze the model's performance metrics such as accuracy, error rate, etc., and the model with the best results is selected.

Applying the Trained Model to Visual Material: At the stage of applying the trained model to the visual material, the model is tested on new images, and its performance is evaluated. In this process, the objects or regions detected by the model are marked on the images and the prediction results are analyzed. The accuracy and error rates of the model are calculated to determine its success. In addition, the results are analyzed in detail using manual analysis and different performance metrics. In line with the data obtained, the model is improved and retrained when necessary to achieve more successful results.

Findings

The application of CV techniques in landscape architecture stands out as an important method for the analysis of human behavior and movement patterns. CV-based data collection and analysis methods minimize the margin of human error by providing objective and verifiable results. In this context, they provide significant advantages in terms of identifying problems related to the use of urban areas, effectively prioritizing the solution processes of existing problems and developing more efficient planning strategies.

These methods based on visual data analysis enable faster and more effective decision-making processes compared to traditional observation and assessment techniques. By enabling the processing of large-scale data sets, CV technology supports spatial planning decisions and helps us understand human behavior at the urban scale in detail.

Future research can extend these findings by integrating additional factors such as demographic differences, environmental conditions and long-term behavioral trends. By integrating technological innovations with landscape architecture, it will be possible to design smarter and adaptive urban spaces that are sensitive to user needs (Wilkins et al., 2022). In this direction, AI-supported analysis systems will contribute to more efficient, sustainable and human-oriented design of public spaces.

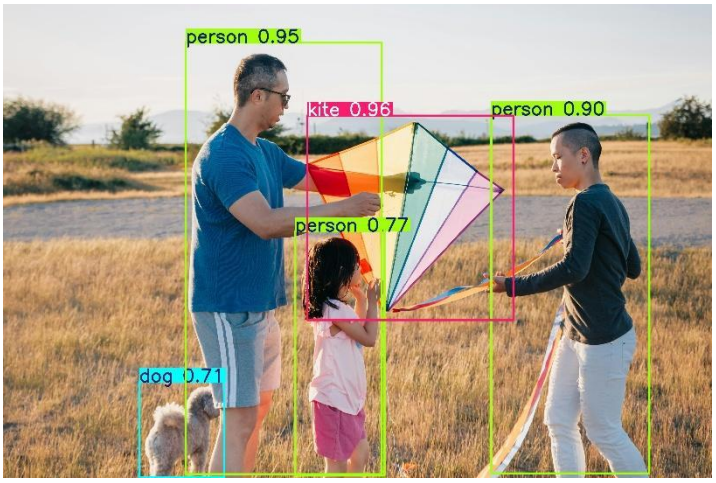

Figure 1. Human, animal and object detection with computer vision.

Conclusion

This research reveals that CV techniques are powerful and innovative tools for observing and analyzing human behavior in landscape architecture. By utilizing AI-assisted sensing and monitoring techniques, it is possible to obtain in-depth and meaningful data about space and user interactions (Väisänen et al., 2021).

Data-driven design decisions guide the creation of user-friendly and functional public spaces by enabling more systematic and objective assessments compared to traditional observation methodologies. CV-based analysis methods not only examine current spatial use, but also predict future trends, allowing urban design processes to become dynamic and adaptive.

As a result, the integration of CV and AI-supported analytics into landscape architecture enhances the analytical capabilities of the discipline, encouraging the development of more comprehensive, data-driven and innovative approaches in landscape architecture. In this way, it will be possible to design sustainable and user-centered urban spaces that better understand human-environment interaction. This study underscores the transformative role of CV in landscape architectural research, promoting a paradigm shift from intuition-based design to evidence-driven, adaptive planning strategies.

References

Ibrahim, M. R., Haworth, J., & Cheng, T. (2020). Understanding cities with machine eyes: A review of deep computer vision in urban analytics. *Cities*, 96, 102481. https://doi.org/10.1016/j.cities.2019.102481
Url-1 www.sciencedirect.com, date retrieved 25.02.2025.
Marasinghe, R., Yigitcanlar, T., Mayere, S., Washington, T., & Limb, M. (2024). Computer vision applications for urban planning: A systematic review of opportunities and constraints. *Sustainable Cities and Society*, 100, 105047. https://doi.org/10.1016/j.scs.2023.105047
Url-2 www.sciencedirect.com, date retrieved 25.02.2025.
Pai, N.-S., Hong, L.-S., Chen, P.-Y., Zhong, Z.-H., & Huang, W.-Z. (2024). Vision system with personnel recognition and tracking functions for use in a space with multiple persons. *Sensors and Materials*, 36(5), 1881. https://doi.org/10.18494/sam4527
Url-3 https://sensors.myu-group.co.jp/, date retrieved 24.03.2025. Väisänen, T., Heikinheimo, V., Hiippala, T., &
Väisänen, T., Heikinheimo, V., Hiippala, T., & Toivonen, T. (2021). Exploring human–nature interactions in national parks with social media photographs and computer vision. *Conservation Biology*, 35(2), 424–436. https://doi.org/10.1111/cobi.13704
Url-4 https://conbio.onlinelibrary.wiley.com, date retrieved 21.02.2025.
Wilkins, E. J., Van Berkel, D., Zhang, H., Dorning, M. A., Beck, S. M., & Smith, J. W. (2022). Promises and pitfalls of using computer vision to make inferences about landscape preferences: Evidence from an urban-proximate park system. *Landscape and Urban Planning*, 219, 104315. https://doi.org/10.1016/j.landurbplan.2021.104315
Url-5 www.sciencedirect.com, date retrieved 25.02.2025.

LANDSCAPE ARCHITECTURE

Heritage and Identities

Innovative Technologies for Landscape Design and Management

Landscape Design

Understanding Play: How Playground Exuipment Shapes Cognitive, Social, and Pyhsical Behaviors in Children Aged 3-12: A Case Study in Maltepe Orhangazi City Park

İçim Gündoğan Ata[a], Melih Bozkurt[a]

[a] Istanbul Technical University, Faculty of Architecture, Department of Landscape Architecture, Turkey
gundogan18@itu.edu.tr

Keywords: Behavior, Children, Play Equipment.

Aim

Play is an activity that children, as well as individuals of all ages, engage in during their own time and for their own purposes (Shackell et al., 2008). Play provides numerous benefits for children; therefore, they should be given ample opportunities to engage in it (Bredekamp & Copple, 1997). Outdoor play, in particular, offers a wide range of benefits for a child's development (Bilton, 2010). Children who play outside demonstrate better cognitive, emotional, social, physical, and intellectual development (Bilton, 2010).

The study aims to analyze how cognitive behaviors, social interactions, and activity levels are influenced by playground equipment and to evaluate the suitability of the play structures in Maltepe Orhangazi City Park for supporting child development. By examining this data, the study seeks to establish criteria that can inform the design of playground equipment to better support children's development.

Material and Method

Maltepe Orhangazi City Park was chosen as the case study area due to its high recreational value and significant foot traffic. The park attracts a diverse range of users from different socioeconomic and educational backgrounds (Korkut et al., 2021), ensuring a more objective study. Additionally, the park features a variety of playground equipment, allowing for the observation of children engaging with different play structures.

The park includes parkour equipment, fixed equipment such as swings and seesaws, climbing structures, and tower equipment, made from different materials. Overall, it contains five parkour structures, 29 fixed structures, eight climbing structures, and 14 tower structures. These play elements cater to different age groups. For the study, the 3–12 age group was selected, with 3–5 years representing preschool children and 5–12 years representing school-aged children (Banumathe et al., 2012; National Program for Playground Safety, 2010).

To observe physical activity, age, and gender, the SOPLAY (System for Observing Play and Leisure Activity in Youth) observation method was employed, with additional cognitive and social parameters derived from the literature. SOPLAY categorizes physical activity levels as sedentary, walking, and very active (McKenzie et al., 2000). Cognitive parameters included dramatic, constructive, and functional play behaviors (Piaget, 1932; Smilansky, 1968). Dramatic play, also known as symbolic play, occurs when children pretend to be someone else or use an object imaginatively (Piaget, 1932). Constructive play is goal-oriented, such as climbing to the top of a structure (Piaget, 1932; Smilansky, 1968). Functional play involves repetitive movements, such as swinging (Piaget, 1932; Smilansky, 1968). Social interactions were classified as solitary, parallel, and positive or negative interactions (Maxwell et al., 2008). Solitary play was noted when children played alone, whereas parallel play was recorded when children played near others but did not interact directly (Parten, 1932).

Once the parameters were determined, direct observation commenced. A total of 685 children were observed in Maltepe Orhangazi City Park, with each child observed for three minutes and recorded only once. Pearson chi-square tests were used to analyze the data (Can, 2023).

Findings

The analysis revealed that gender had no significant relationship with playground equipment preferences. The distribution of boys and girls across different equipment types, including climbing structures, towers, and static equipment, showed minimal variation. The data indicates that both boys and girls use all types of playground equipment in relatively similar proportions, with girls slightly favoring static and tower-type elements (56.0% and 51.1%, respectively) and boys showing a minor preference for climbing structures (51.9%). This finding suggests that playground designs should focus on inclusivity rather than gender-specific features.

Age, however, emerged as a crucial factor influencing playground equipment preferences. Younger children (ages 3–5) preferred static and tower-type equipment, while older children (ages 5–12) were more inclined toward physically demanding structures such as climbing and parkour elements.

Distinct relationships were observed between playground equipment and play behaviors. Static equipment primarily supported functional play, such as repetitive physical activities, while climbing and parkour elements encouraged constructive play. Tower structures, on the other hand, facilitated both constructive and dramatic play behaviors.

Social interactions varied across equipment types. Parallel play, where children engage in side-by-side activities, was most commonly observed on climbing, parkour, and tower equipment. Static equipment supported independent play and positive interactions, such as collaboration and sharing, but also showed instances of negative interactions.

Physical activity levels also varied significantly with equipment types. Static elements were associated with sedentary behavior, while towers encouraged moderate activity.

Conclusion

In conclusion, the study demonstrates that age, cognitive behaviors, social interactions, and physical activity levels are significantly influenced by playground equipment, while gender has no notable effect. These findings highlight the importance of diverse playground equipment in fostering various play behaviors and promoting child development by addressing different developmental needs.

To translate these insights into practice, playgrounds should be designed to be inclusive and age-appropriate, with gender-neutral equipment and distinct zones for younger (3–5) and older (6–12) children. A balanced mix of static, tower, and climbing elements should support different types of play—functional, constructive, dramatic, and social—encouraging both independent and group interactions. Layouts must promote movement through thoughtful spatial planning, while ensuring safety and accessibility for all users.

Additionally, the study provides valuable insights for urban planners and designers, emphasizing the necessity of balanced equipment arrangements that cater to different age groups and encourage holistic development. However, further research is needed to examine long-term impacts and explore variations across different cultural and socioeconomic contexts. This study offers a framework for designing inclusive and developmentally supportive playgrounds.

References

Banumathe, K. R., Ram, V. I., Pinto, A., & Jonathan, S. (2012). An observational study on sensory based outdoor play preferences in children aged between 3-12 years: A preliminary study. International Journal of Current Research and Review, 04(17), 20–28.

Bilton, H. (2010). Outdoor learning in the early years: Management and innovation. Routledge.

Bredekamp, S. and Copple, C. (Ed.) (1997). Developmentally Appropriate Practice in Early Childhood Programs Serving Children From Birth to Age 8, (Rev. Baskı). Washington, DC: National Association for the Education of Young Children.

Can, A. (2023). SPSS ile bilimsel araştırma sürecinde nicel veri analizi (11th ed.). Pegem Akademi.

Korkut, C., Gültekin, P., & Özdede, S. (2021). İstanbul Maltepe-Kartal kıyı şeridi örneğinde rekreasyonel kullanıcı memnuniyetinin belirlenmesi ve rekreasyon olanaklarının değerlendirilmesi. Düzce University Faculty of Forestry Journal of Forestry, 17(2). http://dergipark.gov.tr/journal/256/workflow/active

Maxwell, L. E., Mitchell, M. R., & Evans, G. W. (2008). Effects of Play Equipment and Loose Parts on Preschool Children's Outdoor Play Behavior: An Observational Study and Design Intervention. Children, Youth and Environments , 18(2), 36–63. https://doi.org/10.7721/chilyoutenvi.18.2.0036

McKenzie, T. L., Marshall, S. J., Sallis, J. F., & Conway, T. L. (2000). Leisure-time physical activity in school environments: An observational study using SOPLAY. Preventive Medicine, 30(1), 70–77. https://doi.org/10.1006/pmed.1999.0591

National Program for Playground Safety (NPPS). (2010). Handbook for public playground safety. Washington, DC: U.S. Consumer Product Safety Commission.

Parten, M. B. (1932). Social participation among preschool children. Journal of Abnormal and Social Psychology, 27, 243–269.

Piaget, J. (1932). The moral judgment of the child. New York: Free Press.

Shackell, A., Butler, N., Doyle, P., & Ball, D. (2008). Design for play: A guide to creating successful play spaces. Play England. http://www.playengland.org.uk

Smilansky, S. (1968). The effects of sociodramatic play on disadvantaged children: Preschool children. New York: John Wiley & Sons.

MANAGEMENT

Economics

Finance

Human Resource Management

Marketing

Organization

Production Management

Central Bank Digital Currencies (CBDCs): a countermeasure to Anti-Money Laundering (AML) challenges posed by cryptocurrencies?

Albina Gaisina[a], Matthias Finger[b]

[a] Istanbul Technical University, Graduate School, PhD in Economics Program, Türkiye
[b] Istanbul Technical University, Department of Economics, Türkiye
gaisina21@itu.edu.tr

Keywords: Central Bank Digital Currency (CBDC), Cryptocurrency, AML, CeFi, DeFi.

Aim

This study examines whether Central Bank Digital Currencies (CBDCs) are developed to address money laundering risks associated with cryptocurrencies. It focuses on piloted/launched CBDCs to assess this relationship empirically.
While existing research has analysed the rise of cryptocurrencies and the development of CBDCs independently, there is a gap in comprehensively analysing the relationship between these two. Specifically, there is limited exploration into how the money laundering aspect of cryptocurrencies in both CeFi and DeFi spaces influences central banks' decisions to develop CBDCs in such a way that, technology- and regulation-wise, they represent a potential response.
Consequently, our research aims to fill this gap by empirically analysing the impact of cryptocurrency-related money laundering on the effectiveness of AML measures in countries adopting CBDCs. Furthermore, the study aims to contribute to the topic theoretically by introducing a layered theoretical concept of privacy, compliance, and regulation by design in CBDCs which is linked with Kane's regulatory dialectic theory (Dupuis et al., 2022).

Material and Method

As for the theory behind the study, we utilise Kane's regulatory dialectic (1977, 1988) to explain why CBDCs emerged as a response to the challenges posed by cryptocurrencies. According to Kane's framework, as cryptocurrencies introduce new evasion tactics, regulatory bodies struggle to enforce effective AML measures. In response, CBDCs with built-in compliance, like KYC protocols and real-time monitoring, aim to address regulatory loopholes. Furthermore, we introduce a novel layered framework of CBDC design principles for AML enforcement, where: "privacy by design" uses tiered privacy mechanisms to balance user anonymity with traceability for high-risk transactions; "compliance by design" integrates privacy-enhancing technologies (PETs) to enforce AML rules while maintaining user privacy; and "regulation by design", where regulatory principles are embedded directly into the CBDC infrastructure, aligning with the "code is law" concept and RegTech to prevent money laundering proactively.
Overall, based on the comprehensive literature review, the following research hypotheses are formulated to build our empirical analysis. See Table 1:

Table 1. Summary of Hypotheses.

Hypothesis	Statement	Expected relationship
H1	The enhancement of financial inclusion through CBDCs improves AML effectiveness, as they can be a more trustworthy payment option.	Positive
H2	The reduction of the shadow economy via CBDC adoption enhances AML effectiveness due to higher transparency.	Positive
H3	Higher levels of crypto ownership in countries are negatively associated with AML effectiveness due to challenges in monitoring.	Negative
H4	The selection of CBDC technology providers is aligned with central banks' regulatory goals.	Positive
H5	The use of DLT in CBDCs is a key proxy for improving transparency and regulatory compliance.	Positive
H6	The type of CBDC (wholesale vs. retail) serves as a proxy for AML effectiveness.	Positive
H7	The CBDC structure (token vs. account-based) influences AML effectiveness, with account-based models preferred for better monitoring.	Positive
H8	CBDC adoption improves AML effectiveness but creates challenges in balancing privacy with regulatory compliance.	Positive
H9	Greater privacy in CBDCs negatively impacts AML effectiveness.	Negative
H10	CeFi activity is negatively associated with AML effectiveness.	Negative
H11	DeFi activity is negatively associated with AML effectiveness.	Negative
H12	Cryptocurrency regulation is positively associated with AML effectiveness.	Positive
H13	CBDCs with built-in AML compliance enhance AML effectiveness.	Positive
Source: Authors' compilation		

The research empirically tests the hypotheses using cross-sectional data from multiple jurisdictions that have launched or adopted CBDCs. Models were estimated as of December 2024 using Ordinary Least Squares (OLS) with heteroscedastic-robust standard errors on cross-sectional data in the main results.
The initial regression model is specified as follows:

$$\text{AML_Effectiveness}_i = \beta_0 + \beta_1 \text{CeFi}_i + \beta_2 \text{DeFi}_i + \text{CBDC}_i\theta + X_i\gamma + \epsilon_i \ldots . \text{Eqn1} \text{ (Equation 1)}$$

The dependent variable (AML effectiveness) is represented by the FATF AML index, the AML Basel score (inverted) and the AML organised crime index, obtained from the corresponding websites. For all AML proxies higher rankings correspond with countries with stronger AML frameworks.
Key independent indicators include cryptocurrency adoption in both the CeFi and DeFi spaces obtained from the Chainalysis report, as well as CBDC-related data focused on technological factors. Specifically, CBDC proxies were derived from the CBDC tracker and the Atlantic Council's CBDC tracker as follows: adoption status (launched/pilot), type

(retail/wholesale/both), structure (account/token), technology provider (local/international), technology platform (defined/not defined), and usage of DLT (DLT/no DLT).

The control variables include: cryptocurrency regulation (legal/partial ban/general ban); data privacy (presence or absence of data protection/privacy laws); shadow economy (in %); crypto ownership (in %); financial inclusion (account, % age 15+); internet penetration (in %); GDP per capita (ln). Control variables were sourced from publicly available macroeconomic databases.

Data availability and consistency across jurisdictions influenced the use of a cross-sectional approach. As of December 2024, only three countries have fully launched CBDCs, meaning that there are low within-country variations for panel analysis. Since the AML proxies and CBDC adoption vary substantially between countries but not necessarily within countries over short periods, a cross-sectional approach is sufficient for identifying differences at a given point in time. Additionally, key variables of the study (AML Effectiveness and CBDC proxies) are either slow-moving or remain constant over time, implying low within-country variations over time. By starting with these variables based on backward elimination, we are able to detect the effects of our main CBDC proxies when they are introduced.

Several robustness checks were conducted to validate our results. A Two-Stage Least Squares (2SLS) regression was used, treating CeFi and DeFi variables as endogenous and instrumented with crypto trading volume, trading volume per internet user, and crypto trade volume relative to average monthly wage. Additionally, GMM estimation was applied, and checks were done using a fully retail CBDC sub-sample, as well as an interaction term between crypto regulation and CBDC adoption status.

Findings

Table 2 below presents the results for the three models for each AML proxy separately.

Table 2. Regression results.

	FATF	Basel	Organised crime
Crypto regulation binary	0.1233.	0.5628.	0.5222
	(0.0639)	(0.2966)	(0.5445)
CBDC provider binary	-0.2974***	-0.4718	-0.9436
	(0.0664)	(0.4095)	(0.8849)
Crypto ownership binary	-0.2322***	-1.1390***	-1.2326*
	(0.0574)	(0.3010)	(0.5100)
CeFi	-0.5177***	0.6796	-1.9691*
	(0.1269)	(0.7690)	(0.8399)
Log (GDP per capita)	0.2257***	0.4752***	0.6768***
	(0.0201)	(0.1191)	(0.1764)
Constant	0.6666***	0.0166	-0.0943
	(0.1793)	(0.9807)	(1.5138)
Controls	No	No	No
Observations	36	35	36
R-squared	0.7184	0.5518	0.3629
Adj. Rsquared	0.6715	0.4746	0.2567
F	33.5912	11.6283	11.2691

Significance codes: 0 '***' 0.001 '**' 0.01 '*' 0.05 '.' 0.1 ' ' 1
Source: Authors' own work

The obtained coefficients demonstrate that only hypotheses H3, H4, H10 and H12 were empirically validated in this study. See the explanations below.

The results suggest that in countries with higher cryptocurrency ownership, AML effectiveness tends to be lower **(H3).** Similarly, Alnasaa et al. (2022) examined the relationship between cryptocurrency adoption, corruption, and financial controls. Their results indicate that higher levels of cryptocurrency adoption are associated with higher corruption and more restrictive capital controls. The authors conclude that to manage the risks associated with cryptocurrencies, it is needed to implement robust KYC.

Secondly, our results illustrate that higher CeFi trading has a negative relationship with AML effectiveness **(H10)**. Leuprecht et al. (2023) confirm the role of CeFi exchanges in facilitating money laundering, particularly in the placement and layering stages. Furthermore, the study by Carpentier-Desjardins et al. (2025) investigated 1,153 crime events in the crypto industry from 2017 to 2022. Their findings indicated that two-thirds of the financial losses were attributed to CeFi and one-third to DeFi. Hence, CeFi still remains a main channel for financial crime.

A key insight from our study is that CBDC technology providers play a significant role in shaping AML effectiveness **(H4).** In our findings, AML effectiveness is lower in countries with local CBDC providers, suggesting to use international providers for better AML. While we could not find explicit empirical support for this, DiGiammara et al. (2023) emphasised how central banks select tech providers to align with regulatory environments. For example, the Central Bank of the Bahamas chose NZIA Ltd. due to its multi-factor authentication and transaction monitoring, whereas the Eastern Caribbean CBDC adopted IBM Hyperledger Fabric for its secure and scalable blockchain.

Further, our results indicate that AML effectiveness is higher in jurisdictions allowing legal cryptocurrency use (compared to bans) **(H12)**. The paper by Griffith and Clancey-Shang (2023) showed that even if the 2021 Chinese crypto ban led to a price drop and increased volatility, it did not eliminate crypto activity but shifted cryptocurrency markets to less regulated environments, making further AML regulation even harder. These spillover effects after China's 2017 cryptocurrency regulatory changes were also observed in the empirical study by Borri and Shakhnov (2020). Shirakawa and Korwatanasakul (2019) investigated the relationship between institutional strength, financial openness, and regulatory approaches to cryptocurrency across 218 economies. They found that jurisdictions with stronger governance frameworks are more likely to adopt a less restrictive regulatory stance on cryptocurrency.

Finally, our results show that AML effectiveness is higher in countries with higher GDP per capita, indicating the countries' capacity to combat illicit activities. While we did not cover this in our literature review, the empirical result turned significant. In line with this, Šikman and Grujić (2021) find that higher GDP per capita is associated with greater AML effectiveness. In an analysis of 165 countries, Ofoeda et al. (2022) found that stronger AML frameworks are positively associated with higher GDP per capita, however up to a threshold, with developed countries generally enforcing more effective AML regulations. Interestingly, Matsui and Perez (2021) apply machine learning techniques to identify key drivers of CBDC adoption, finding that GDP per capita, alongside financial development and institutional quality, is one of the strongest predictors of CBDC adoption.

It should be noted that since the highest number of observations for most of the estimated models in our study was 36, there was insufficient statistical support for all the hypotheses of the affected variables.

Conclusion

This research focused on the potential impact of CBDCs on AML, inspired by the risks associated with cryptocurrencies. Our findings highlight how the nature of cryptocurrencies and the level of their regulation influence AML effectiveness. However, given the early stage of CBDC adoption, the lack of consistent, quantified data poses challenges for data

collection. Among CBDC indicators, the only statistically significant variable was the CBDC technology provider. Results suggest that international CBDC providers may better align with global AML laws.

Furthermore, the core idea of our research is that carefully designed CBDCs with built-in AML features have the potential to enhance AML effectiveness across jurisdictions, since they can be more trustworthy than cryptocurrencies if they balance privacy. According to our results, for cryptocurrencies the focus should be on strong AML regulatory frameworks rather than bans.

This study represents one of the first empirical attempts to assess the AML implications of CBDCs in light of the risks associated with cryptocurrencies. Given several limitations dictated by data availability, we recommend the following directions for future research. As more countries adopt CBDCs, larger datasets will become available. Moreover, future research could collect additional information about CBDC design, such as consensus mechanisms, tier systems, and the use of PETs. Additionally, a shock regression panel analysis could be applied by dividing datasets into pre- and post-CBDC periods.

References

Alnasaa, M., Gueorguiev, N., Honda, J., Imamoglu, E., Mauro, P., Primus, K., & Rozhkov, D. (2022). Crypto, corruption, and capital controls: Cross-country correlations. International Monetary Fund.

Borri, N., & Shakhnov, K. (2020). Regulation spillovers across cryptocurrency markets. Finance Research Letters, 36.

Carpentier-Desjardins, C., Paquet-Clouston, M., Kitzler, S., & Haslhofer, B. (2025). Mapping the DeFi crime landscape: An evidence-based picture. Journal of Cybersecurity, 11(1).

DiGiammara, C., Omarini, A., Kauffman, R. J., & Kwansoo, K. (2023). Evaluating effects of the payment ecosystem on CBDC adoption and design. Proceedings of the 56th Annual Hawaii International Conference on System Sciences.

Dupuis, D., Gleason, K., & Wang, Z. (2022). Money laundering in a CBDC world: A game of cats and mice. Journal of Financial Crime, 29(1), 171–184.

Griffith, T., & Clancey-Shang, D. (2023). Cryptocurrency regulation and market quality. Journal of International Financial Markets, Institutions and Money, 84, 101744.

Leuprecht, C., Jenkins, C., & Hamilton, R. (2023). Virtual money laundering: Policy implications of the proliferation in the illicit use of cryptocurrency. Journal of Financial Crime, 30(4), 1036–1054.

Matsui, T., & Perez, D. (2021). Data-driven analysis of central bank digital currency (CBDC) projects drivers. arXiv.

Ofoeda, I., Agbloyor, E., & Abor, J. Y. (2022). Financial sector development, anti-money laundering regulations, and economic growth. International Journal of Emerging Markets, 19(1), 191–210.

Shirakawa, R., J. B., & Korwatanasakul, U. (2019). Cryptocurrency regulations: Institutions and financial openness. ADBI Working Paper No. 978. Asian Development Bank Institute.

Šikman, M. M., & Grujić, M. (2021). Relationship of Anti-Money Laundering Index with GDP, financial market development, and Human Development Index. NBP: Journal of Criminalistics and Law, 26(1), 21–33.

MANAGEMENT

Economics

Finance

Human Resource Management

Marketing

Organization

Production Management

Investor Attention and Asymmetric Conditional Volatility: Evidence from GARCH-X and GJR-GARCH-X Models

Müge Özdemir[a], Oktay Taş[b]

[a] Istanbul Technical University, PhD Program in Management, Türkiye
[b] Istanbul Technical University, Department of Management Engineering, Türkiye,
ozdemir19@itu.edu.tr

Keywords: Investor Attention, Conditional Volatility, Behavioral Finance, Emerging Markets.

Aim

This study investigates the dynamic role of investor attention in shaping the conditional volatility of stock returns, with a particular focus on volatility asymmetries. We examine whether investor attention—quantified through the Abnormal Search Volume Index (ASVI) as proposed by Da et al. (2011)—contributes significantly to the persistence and responsiveness of market volatility, particularly in the context of emerging markets. Unlike conventional GARCH-type models (Bollerslev, 1986; Glosten et al., 1993), which rely solely on historical return dynamics, our approach incorporates a behavioral dimension by embedding ASVI into both GARCH-X and GJR-GARCH-X frameworks. We initially estimate standard GARCH and GJR-GARCH models separately for low-attention, high-attention, and long-short (high-minus-low) portfolios to assess attention-specific volatility profiles. In a second step, we extend this framework by embedding ASVI into conditional volatility models for risk-adjusted returns derived from CAPM (Sharpe, 1964), Fama-French three-factor (Fama & French, 1993), and Carhart four-factor (Carhart, 1997) models. This two-stage design enables a comprehensive assessment of attention-driven volatility both at the raw return and residual return level. By systematically integrating behavioral attention metrics into volatility modeling, this study contributes to the growing body of research in behavioral asset pricing and provides practical insights for risk forecasting, especially in attention-sensitive and information-inefficient markets such as Borsa Istanbul.

Material and Method

This study employs a weekly dataset comprising 364 stocks listed on the Borsa Istanbul All Shares Index (XUTUM), covering the period from October 2016 to October 2021. Stock-level financial variables—including weekly returns, market capitalization, book-to-market ratios, and momentum indicators—are obtained from the Reuters database. Investor attention is proxied using the Abnormal Search Volume Index (ASVI), which is calculated from Google Trends following the methodology of Da et al. (2011). To improve measurement accuracy, a keyword filtering strategy is implemented to exclude ticker symbols with dual meanings in Turkish (e.g., SISE, MAVI), ensuring that ASVI captures genuine financial attention. Each week, stocks are ranked by their ASVI values and categorized into three groups: the top 30% (high-attention portfolio), the bottom 30% (low-attention portfolio), and the middle 40% (excluded from the analysis). A dynamic long-short trading strategy is then constructed by taking long positions in high-attention stocks and short positions in low-attention stocks, with portfolios rebalanced weekly.
To assess abnormal returns of these attention-based portfolios, we estimate the following benchmark factor models:

$$R_{p,t} - R_{f,t} = \alpha_p + \beta_1\left(R_{m,t} - R_{f,t}\right) + \varepsilon_{p,t} \quad (1)$$

$$R_{p,t} - R_{f,t} = \alpha_p + \beta_1\left(R_{m,t} - R_{f,t}\right) + \beta_2 SMB_t + \beta_3 HML_t + \varepsilon_{p,t} \quad (2)$$

$$R_{p,t} - R_{f,t} = \alpha_p + \beta_1\left(R_{m,t} - R_{f,t}\right) + \beta_2 SMB_t + \beta_3 HML_t + \beta_4 WML_t + \varepsilon_{p,t} \quad (3)$$

In the second part of the analysis, we investigate how investor attention influences conditional volatility patterns. Initially, GARCH(1,1) and GJR-GARCH(1,1) models are applied to raw return series of the low-, high-, and long-short (high-low) portfolios to assess how attention correlates with volatility persistence and asymmetries. The models are further extended by incorporating lagged ASVI as an exogenous regressor:

$$\sigma_t^2 = w + \alpha\varepsilon_{t-1}^2 + \beta\sigma_{t-1}^2 + \lambda ASVI_{t-1} \quad (4)$$

$$\sigma_t^2 = w + \alpha\varepsilon_{t-1}^2 + \gamma\varepsilon_{t-1}^2 I_{t-1} + \beta\sigma_{t-1}^2 + \lambda ASVI_{t-1} \quad (5)$$

$$I_{t-1} = \{1 \quad if \quad \varepsilon_{t-1} < 0\ (negative\ shock)\ 0 \quad if \quad \varepsilon_{t-1} \geq 0\ (positive\ shock)\ \} \quad (6)$$

To isolate the behavioral component in volatility beyond factor exposures, we then model the conditional variance of the residuals from the CAPM, Fama-French, and Carhart regressions using GARCH-X and GJR-GARCH-X frameworks. This approach captures attention-induced risk that is orthogonal to traditional risk factors.

All volatility models are estimated via Quasi-Maximum Likelihood Estimation (QMLE), which provides robust estimates even under non-normal error distributions. Model performance is evaluated using Akaike Information Criterion (AIC) and Bayesian Information Criterion (BIC). Additionally, residual diagnostics including the Ljung-Box test (for autocorrelation), ARCH-LM test (for remaining ARCH effects), and Jarque-Bera test (for normality) are conducted to ensure model adequacy.

This two-stage modeling approach enables a comprehensive evaluation of how investor attention influences both return generation and time-varying risk, thereby highlighting the behavioral dynamics embedded in market volatility.

Findings

Table 1 demonstrates that investor attention, proxied by the Abnormal Search Volume Index (ASVI), significantly impacts portfolio-level return performance. Dynamic long-short portfolios—formed by taking long positions in high-attention stocks and short positions in low-attention stocks—exhibit statistically significant alpha values across all benchmark models. Equally weighted portfolios deliver the strongest results: under the CAPM model, weekly alpha reaches 210 basis points (t = 16.393), and under the Fama-French and Carhart models, alpha remains robust at approximately 190 basis points ($p < 0.01$). These outcomes underscore the predictive validity of attention-based signals and are in line with earlier findings by Da et al. (2011), Ying et al. (2015), and Tan and Taş (2019), especially within the context of small-cap stocks, where information frictions are more pronounced.

Table 1. Risk-adjusted performance of attention-based portfolios under the factor models.

	Equal weighted portfolio (attention based)					
	Alpha	Rm-Rf	SMB	HML	WML	R^2
(1) CAPM Model	0.021***	0.063				0.006
	(16.393)	(1.216)				
(2) Fama-French Three Factor	0.019***	0.108**	0.195***	-0.625***		0.296
	(12.441)	(2.440)	(2.781)	(-9.032)		
(3) Carhart Four Factor	0.019***	0.109**	0.187***	-0.559***	0.122**	0.455
	(12.732)	(2.490)	(2.688)	(-7.649)	(2.513)	

Note. ***, **, and * symbols represent the statistical significance of the results at the 1%, 5%, and 10% significance levels, respectively. t-statistics are provided in parentheses.

Turning to volatility dynamics, Tables 2 and 3 present the conditional variance estimates obtained from GARCH-X and GJR-GARCH-X models. The ASVI coefficient (λ) is consistently positive and statistically significant across all specifications, supporting the hypothesis that increased investor attention correlates with heightened return volatility. The GJR-GARCH-X model applied to high-low portfolios yields the strongest explanatory power, with $\lambda = 0.534^{***}$ and $R^2 = 0.894$, confirming the predictive relevance of ASVI in volatility modeling.

Table 2. Conditional volatility of the attention-based portfolio returns based on attention.

	GARCH-X			GJR-GARCH-X		
	low	high	High-low	low	high	High-low
c	3.182^{***}	1.784^{***}	0.485^{***}	5.185^{***}	5.787^{***}	2.689^{***}
	(3.565)	(2.753)	(3.416)	(3.661)	(2.673)	(2.756)
$\alpha\ (\varepsilon_{t-1}^2)$	0.301^{***}	0.452^{***}	0.221^{**}	0.159^{***}	0.161^{***}	0.075^{***}
	(6.302)	(2.853)	(2.521)	(3.428)	(4.349)	(5.228)
$\beta(\sigma_{t-1}^2)$	0.404^{***}	0.422^{***}	0.466^{***}	0.443^{***}	0.485^{**}	0.236^{***}
	(4.476)	(4.743)	(10.507)	(6.445)	(2.554)	(7.213)
$\gamma(I_{t-1})$				-0.135^{***}	0.203^{**}	0.316^{*}
				(-3.208)	(2.182)	(1.904)
$\lambda(ASVI_{t-1})$	0.041^{*}	0.224^{*}	0.345^{***}	0.156^{***}	0.393^{***}	0.534^{***}
	(1.721)	(1.942)	(5.475)	(3.226)	(2.651)	(4.052)
R^2	0.421	0.462	0.471	0.489	0.536	0.668

Note. ***, **, and * symbols represent the statistical significance of the results at the 1%, 5%, and 10% significance levels, respectively. t-statistics are provided in parentheses.

Table 3. Conditional volatility on the long-short portfolio returns based on attention.

	GARCH-X			GJR-GARCH-X		
	CAPM	3 factor	4 factor	CAPM	3 factor	4 factor
	High-low	High-low	High-low	High-low	High-low	High-low
c	3.124^{***}	3.859^{*}	3.582^{***}	2.274^{**}	2.852^{***}	2.718^{**}
	(3.356)	(3.367)	(3.363)	(2.467)	(2.864)	(2.346)
$\alpha\ (\varepsilon_{t-1}^2)$	0.313^{**}	0.299^{**}	0.254^{***}	0.095^{***}	0.085^{***}	0.074^{***}
	(2.436)	(2.463)	(2.768)	(5.463)	(5.447)	(5.474)
$\beta\ (\sigma_{t-1}^2)$	0.306^{***}	0.266*	0.106^{***}	0.233^{***}	0.229^{***}	0.124^{***}
	(5.768)	(6.463)	(8.436)	(7.478)	(7.965)	(7.351)
$\gamma\ (I_{t-1})$				0.316^{**}	0.294^{***}	0.223^{***}
				(2.457)	(3.367)	(2.854)
$\lambda\ (ASVI_{t-1})$	0.284^{***}	0.154^{***}	0.092^{***}	0.342^{***}	0.215^{***}	0.126^{***}
	(5.023)	(5.976)	(5.355)	(4.035)	(4.035)	(4.355)
R^2	0.728	0.743	0.753	0.808	0.817	0.894

Note. ***, **, and * symbols represent the statistical significance of the results at the 1%, 5%, and 10% significance levels, respectively. t-statistics are provided in parentheses.

Notably, the asymmetry parameter γ is significant in nearly all GJR-GARCH-X estimations, reinforcing the leverage effect (Black, 1976; Christie, 1982). These results suggest that negative return shocks, particularly in high-attention portfolios, generate disproportionately larger increases in volatility. This behavioral asymmetry aligns with findings from Barber and Odean (2008), who argue that investors overreact more strongly to adverse information. Collectively, these results indicate that attention not only influences returns but also plays a structural role in volatility persistence and asymmetry.

Conclusion

This study provides compelling empirical evidence that investor attention, proxied by the Abnormal Search Volume Index (ASVI), plays a pivotal role in shaping the conditional volatility of stock returns in an emerging market context. By integrating ASVI into GARCH-X and GJR-GARCH-X models, we demonstrate that attention not only amplifies volatility but also induces asymmetric and persistent effects—particularly in response to negative return shocks.

The findings show that attention-based long-short portfolios yield statistically significant alpha even after adjusting for standard risk factors using CAPM, Fama-French, and Carhart models. Moreover, ASVI consistently emerges as a significant explanatory variable across all volatility model specifications, enhancing both in-sample fit and out-of-sample forecasting power. Among the models tested, GJR-GARCH-X proves to be the most comprehensive framework, capturing volatility clustering, asymmetric responses, and attention-driven dynamics in a unified structure. Our results confirm that investor attention is not merely a reflection of market activity but an active force that shapes volatility patterns—particularly in high-attention and small-cap stocks. This behavioral volatility channel aligns with theoretical expectations from the leverage effect (Black, 1976; Christie, 1982) and information-based trading hypotheses such as the Mixture of Distributions Hypothesis (Clark, 1973) and Sequential Information Flow Hypothesis (Copeland, 1976).

In practical terms, incorporating attention-based signals into volatility modeling offers valuable improvements for asset pricing, portfolio risk management, and systemic risk monitoring. These implications are particularly relevant in emerging markets like Borsa Istanbul, where market inefficiencies and investor sentiment play an outsized role in shaping price dynamics (Özdemir & Taş, 2025).

Overall, this study contributes to the behavioral finance literature by formalizing the role of real-time attention measures in volatility forecasting. It underscores the importance of incorporating investor psychology into econometric models of risk, offering actionable insights for both academics and financial practitioners operating in increasingly sentiment-sensitive market environments.

References

Barber, B. M., & Odean, T. (2008). All that glitters: The effect of attention and news on the buying behavior of individual and institutional investors. *The review of financial studies*, *21*(2), 785-818.

Black, F. (1976). Studies of stock price volatility changes. In *Proceedings from the American statistical association, business and economic statistics section* (p. 177).

Bollerslev, T. (1986). Generalized autoregressive conditional heteroskedasticity. *Journal of econometrics*, *31*(3), 307-327.

Carhart, M. M. (1997). On persistence in mutual fund performance. Journal of Finance, 52(1), 57–82.

Clark, P. K. (1973). A subordinated stochastic process model with finite variance for speculative prices. Econometrica, 41(1), 135–155.

Copeland, T. E. (1976). A model of asset trading under the assumption of sequential information arrival. *The Journal of Finance*, *31*(4), 1149-1168.

Da, Z., Engelberg, J., & Gao, P. (2011). In search of attention. Journal of Finance, 66(5), 1461–1499.

Fama, E. F., & French, K. R. (1993). Common risk factors in the returns on stocks and bonds. Journal of Financial Economics, 33(1), 3–56.

Glosten, L. R., Jagannathan, R., & Runkle, D. E. (1993). On the relation between the expected value and the volatility of the nominal excess return on stocks. *The journal of finance*, *48*(5), 1779-1801.

Özdemir, M., & Taş, O. (2025). Investor attention and its impact on portfolio volatility and sectoral risk spillovers in Borsa Istanbul. *Borsa Istanbul Review*, *25*(1), 107-126.

Tan, R., & Taş, O. (2019). The role of attention in the Turkish stock market: Evidence from Google search volume. Emerging Markets Review, 39, 100638.

How Was Financial Performance Affected by ESG In The After- Covid Era? A Global Analysis

Sırma Şeker[a], Cumhur Ekinci[a]

[a] Istanbul Technical University, Department of Management Engineering/Faculty of Management, Türkiye

seker16@itu.edu.tr/ekincicu@itu.edu.tr

Keywords: Covid, Sustainability, Financial Performance.

Aim

Covid-19 emphasized ethical and social values that are important for our ecosystem. Therefore, companies have started to develop new strategies regarding their sustainability performance measured by ESG (Environmental, Social and Governance) scores. The level of companies' sustainability performance affects their profits in normal times (Velte, 2017; Chen et al., 2023). But what about times of crisis? Certain intangible assets, such as image or reputational capital, act as a shield in times of crisis (Aliyah, 2024). These capitals can be gained through ESG, especially during economic downturns (Liu et al., 2023). Supporting this view, some studies find ESG improves financial performance during (Cardillo et al., 2023; Liu et al., 2023) and after Covid period (Aksoy & Yılmaz, 2024). However, others find ESG decreases financial performance (Demers et al., 2020) or does not create a significant positive change on financial performance (Bodhanwala & Bodhanwala., 2023). There may be several reasons for these complex findings. Unlike some studies, this relationship needs to be analyzed over a longer period in order to see the effects of social image and reputation. With these benefits, the company can start to be positively evaluated by its stakeholders (Hwang et al., 2021). Most of the studies are limited to only during Covid period (Liu et al, 2023, Cardillo et al., 2023), not after Covid period. In addition, Covid may have different effects on different ESG pillars (E, S or G). Since the cause of the outbreak of the pandemic is indirectly linked to environmental damage, the value attributed to different ESG pillars may have differentiated, which can significantly effect financial performance. Based on these facts, with nearly 13,000 companies from 58 different stock exchanges, we analyze whether there is a difference in the impact of ESG (E, S or G) on long-term financial performance during and after Covid-19.[10]

Material and Method

Data

The dataset consists of sustainability performance scores such as ESG (Environmental, Social and Governance) scores and its subscores (E, S and G); financials such as sales revenue, total assets, total liabilities, market capitalization, net income; company informations such as country of headquarters, the date of establishment, board statistics such as number of board meetings and number of female and male board members. The data is retrieved from Thomson Reuters database.

Method

In order to examine whether ESG, E, S or G actually increases profits and to compare 2020 during crisis period with 2021 and 2022 post crisis period, we need to employ difference-in-difference (DID) analysis (Li et al, 2012). We converted basic framework of DID into the emprical specification is outlined by the following equations:

[10] This study was funded by TUBITAK (Project No 122K345).

$$ROA/TQ_{i,t}=\beta_0 + \beta_1 Tm_t + \beta_2 Td_i + \beta_3(Tm_t*Td_i) + \beta_4 LSize_{i,t} + \beta_5 SAss_{i,t} + \beta_6 Lev_{i,t} + \beta_7 LAge_{i,t} + \beta_8 LNbm_{i,t} + \beta_9 Bgd_{i,t} + \alpha_i + \delta_t + \epsilon_{it}$$

where ROA (Return on Assets) or TQ (Tobin's Q) as firm performance, Tm_t is a dummy variable equal to one after or before the crisis period and zero otherwise, Td_i is a dummy variable equal to one for the company above median ESG and zero otherwise. Tm_t*Td_i refers to the interaction effect (DID estimator) and equal to one if the company is in a crisis period with higher ESG than the median, ε_{it} is the error term representing unobservable factors. β_3 shows the difference in the change in performance of firms with high ESG, E, S, G score compared to firms with a lower score in 2021 or 2022 compared to 2020. β_4- β_9 shows the effect of control variables (LSize is the logarithm of total assets, SAss is the ratio of sales revenue to total assets, Lev is the ratio of total debt to total assets, LAge is the logarithm of firm age, LNbm is the logarithm of the number of board meetings, Bgd is the percentage of board gender diversity in 2021 or 2022).

Findings

Table 1 presents the descriptives of the variables. For each variable, there are mean, standard deviation, minimum, maximum and median values. For example, companies average ESG score is 47.25 during and after Covid period. Again, we see a gradual increase in ESG scores in Covid period. Based on the average ESG pillars, we conclude that E scores are lower than S and G scores (37.55<48.70 or 52.17). The strongest in each pillar is the G score (>50). So, stakeholders attributed more value to the governance score in pandemic.

Table 1: Descriptive Statistics Of ESG (E, S and G) Scores.

Variable	Value	Variable	Value	Variable	Value	Variable	Value
MeanEsg	47,25	**MeanE**	37,55	**MeanS**	48,7	**MeanG**	52,17
SdEsg	20,11	**SdE**	28,42	**SdS**	23,14	**SdG**	21,8
MinEsg	1,11	**MinE**	0,05	**MinS**	0,21	**MinG**	0,18
MaxEsg	95,52	**MaxE**	99,22	**MaxS**	98,6	**MaxG**	99,62
MedianEsg	46,68	**MedianE**	35,99	**MedianS**	48,16	**MedianG**	52,63

In addition to the descriptives, we applied Pearson correlation and multicollinearity tests. We conclude that there is no correlation problem between our independent variables. Moreover, we applied the Breusch-Pagan test and find that the data is heteroskedastic. Therefore, we used robust standard errors in the OLS-based DID analysis.

In table 2, there are the results of difference-in-difference analysis using OLS comparing Covid period 2020 with 2021 measuring ESG, E, S and G on financial performance. D (Timet*Treatedi) refers to the interaction effect and equal to one if the company is in a crisis period with higher ESG than the median. The coefficient is positive in all models (both ROA and TQ). Hence, in 2021, firms with high ESG (than the median) had better financial performance than firms with low ESG. Coefficients are low for ROA, but quite high for TQ.Therefore, we conclude that those who invested in ESG during 2020 gained higher profits in 2021. In table 3, for more longer period, we compare 2020 to 2022. All of the findings are the same for overall ESG. In table 2 and 3, the coefficients of control variables are not reported due to space limitations, but all of the variables are significant (except for board gender diversity in some models). According to our findings, the only difference between table 2 and table 3 is about ESG pillars. In table 2, we see that E, S and G are more profitable in terms of TQ, while E, G and S in terms of ROA, respectively. But in table 3, we see that E, G and S are more profitable in terms of TQ, while E, S and G in terms of ROA, respectively.

Table 2: DID Analysis Results For ESG, E, S and G Comparing Covid Period 2020 With 2021.

	20-21ESG		**20-21E**		**20-21S**		**20-21G**	
	Roa	**TQ**	**Roa**	**TQ**	**Roa**	**TQ**	**Roa**	**TQ**
C	0.038***	11.211***	0.041***	11.053***	0.036***	11.392***	0.032***	10.955***
	(0.008)	(0.427)	(0.008)	(0.435)	(0.008)	(0.421)	(0.007)	(0.406)
DEsg	0.006***	0.437***						
	(0.002)	(0.063)						
DE			0.008***	0.500***				
			(0.001)	(0.057)				
DS					0.005***	0.323***		
					(0.001)	(0.060)		
DG							0.004*	0.355***
							(0.002)	(0.066)
TmEsg	0.008***	-0.663***						
	(0.001)	(0.052)						
TmE			0.008***	-0.675***				
			(0.001)	(0.046)				
TmS					0.009***	-0.593***		
					(0.001)	(0.048)		
TmG							0.010***	-0.606***
							(0.001)	(0.050)
TdEsg	0.000	-0.181*						
	(0.001)	(0.074)						
TdE			-0.000	-0.294***				
			(0.001)	(0.072)				
TdS					0.001	0.019		
					(0.001)	(0.072)		
TdG							-0.000	-0.315***

							(0.001)	(0.070)
Obs.	14606	14652	14604	14650	14604	14650	14606	14652
AdjR²	0.1922	0.1590	0.1928	0.1595	0.1921	0.1593	0.1914	0.1590

Table 3: DID Analysis Results For ESG, E, S and G Comparing Covid period 2020 With 2022.

	20-22ESG		**20-22E**		**20-22S**		**20-22G**	
	Roa	**TQ**	**Roa**	**TQ**	**Roa**	**TQ**	**Roa**	**TQ**
C	0.041***	11.100***	0.043***	11.108***	0.039***	11.156***	0.035***	10.812***
	(0.008)	(0.411)	(0.008)	(0.422)	(0.007)	(0.406)	(0.007)	(0.393)
DEsg	0.007***	0.561***						
	(0.002)	(0.071)						
DE			0.009***	0.748***				
			(0.002)	(0.069)				
DS					0.006**	0.332***		
					(0.002)	(0.070)		
DG							0.004*	0.442***
							(0.002)	(0.075)
TmEsg	0.003*	-1.110***						
	(0.001)	(0.059)						
TmE			0.002	-1.202***				
			(0.001)	(0.057)				
TmS					0.004**	-0.969***		
					(0.001)	(0.056)		
TmG							0.005***	-1.026***
							(0.001)	(0.059)
TdEsg	0.001	-0.178*						
	(0.001)	(0.074)						
TdE			0.000	-0.282***				
			(0.001)	(0.071)				
TdS					0.001	0.016		

					(0.001)	(0.072)		
TdG							-0.000	-0.306***
							(0.001)	(0.070)
Obs.	12913	13016	12911	13014	12911	13014	12913	13016
AdjR^2.	0.1969	0.1685	0.1974	0.1708	0.1965	0.1675	0.1958	0.1677

Conclusion

The aim of our study is to examine whether ESG actually increases profits in a time of crisis like Covid-19. According to our findings, firms invested in ESG gained short-term profits in 2021 and 2022, but gained much more long-term profits in 2021 and 2022. So, we conclude that ESG kind of investments is valuable after crisis periods and positively evaluated by stakeholders with a more longer period of time. Therefore, even if there is a cost impact, the ability of financially strong companies to make investments such as ESG in times of crisis is not harmful for shareholders, rather becomes a profitable situation in the long run. Our findings are in line with legitimacy theory, which states that ESG provides important benefits such as legitimacy. But these benefits can be seen in a more longer period of time.

After Covid, we observe that especially S and G scores has a similar impact on financial performance. However, those who invested in E score during Covid acquired a significant market value after Covid. From our point of view, in Covid, stakeholders started to pay more attention to environmental issues and allocated more funds to green investments in post-Covid recovery policies (EU Green Deal, "Green Recovery" in the US). This became value enhancing. Therefore, we conclude that, the value judgements of stakeholders that identifies with crisis are important in these kind of situations.

Our findings are very important for managers and decision makers. Managers should engage in such investments in times of crisis to generate long-term profits. However, they should identify which issues (ESG sub-scores) are valued more by stakeholders in times of crisis. Our findings reveal that environmental issues (environmental resource consumption, carbon emissions and innovation) were more important during and after Covid period. Further studies may reveal which environmental subscores (environmental resource consumption, carbon emissions or innovation) were more profitable in Covid period.

References

Aksoy, M., & Yilmaz, M. K. (2024). Financial performance of emerging market companies during the COVID-19 pandemic: moderating role of sustainability performance. Journal of Global Responsibility.

Aliyah, S. N. (2024). Guardian of Image: Evaluating Corporate Reputation as a Shield Against COVID-19 Fallout on Firm Performance. Journal of Economics, Business, and Accountancy Ventura, 27(1).

Bodhanwala, S., & Bodhanwala, R. (2023). Environmental, social and governance performance: influence on market value in the COVID-19 crisis. Management Decision, 61(8), 2442-2466.

Cardillo, G., Bendinelli, E., & Torluccio, G. (2023). COVID-19, ESG investing, and the resilience of more sustainable stocks: Evidence from European firms. Business Strategy and the Environment, 32(1), 602-623.

Hwang, J., Kim, H., & Jung, D. (2021). The effect of ESG activities on financial performance during the COVID-19 pandemic—Evidence from Korea. Sustainability, 13(20), 11362.

Li, COVID., Graham, D. J., & Majumdar, A. (2012). The effects of congestion charging on road traffic casualties: A causal analysis using difference-in-difference estimation. Accident Analysis & Prevention, 49, 366-377.

Liu, L., Nemoto, N., & Lu, C. (2023). The Effect of ESG performance on the stock market during the COVID-19 Pandemic—Evidence from Japan. Economic Analysis and Policy, 79, 702-712.

Velte, P. (2017). Does ESG performance have an impact on financial performance? Evidence from Germany. Journal of global responsibility, 8(2), 169-178.

MANAGEMENT

Economics

Finance

Human Resource Management

Marketing

Organization

Production Management

Remote Work and Virtual Presenteeism: Insights from the Turkish Organizational Context

Deniz Mat Artun[a], Prof. Dr. Fatma Küsküa[a]

[a] Istanbul Technical University, Management Program, Turkey

matartun20@itu.edu.tr

Keywords: Remote Work, Virtual Presenteeism, Qualitative Analysis.

Aim

Following the COVID-19 pandemic, work environments has significantly changed worldwide, forcing organizations to adapt to remote work. Workplace dynamics have been majorly transformed since remote work has become an essential part of work settings. Remote work practices have also altered how employees engage with work while being sick or feeling unwell (Biron et al., 2021; Shimura et al., 2021). This study investigates how remote work affects virtual presenteeism, a relatively unexplored phenomenon in the presenteeism literature. Traditionally, presenteeism has been defined as "showing up for work when one is ill" (Johns, 2010). However, recent studies have expanded this definition and included being present physically but not functioning properly (Cooper, 1996; Cooper and Lu, 2016). As organizations adapt to remote work settings, virtual presenteeism has emerged as the act of continuing to work from home despite feeling unwell (Ruhle and Schmoll, 2021; Salvoni et al., 2024). Presenteeism has been addressed as one of the major factors that negatively affect productivity (Patel et al., 2023), cause severe health issues (Karanika et al., 2021), and result in employee absence (Bergström et al.,2009). Therefore, it is a critical topic to explore to improve the productivity of remote employees. By addressing this research gap, this study aims to provide insights into how remote work practices affect presenteeism.

While presenteeism has mainly been studied in traditional work settings, such as offices (Johns, 2010; Cooper & Lu, 2016), more in-depth research about how remote work settings affect this phenomenon is needed (Fiorini, 2024). Studying virtual presenteeism has become a crucial need since remote employees face challenges regarding a lack of visibility and supervisory pressures. Moreover, research on presenteeism has been dominated by North American and Scandinavian samples (Böckerman and Laukkanen, 2010; Johns, 2010). However, cultural differences and national values are significant factors that affect the presenteeism behavior of employees (Cooper & Lu, 2016; Ferreira et al., 2022). As a result, studies from the Turkish organizational context that investigate presenteeism and especially its new form under virtual work settings are essential.

Material and Method

This study utilizes a qualitative approach using open-ended survey responses from professionals in Türkiye to capture in-depth insights into remote work experiences. We combined qualitative content analysis with thematic analysis to capture both the structured and emergent dimensions of virtual presenteeism in remote work settings. While qualitative content analysis provided a systematic framework for classifying and organizing key concepts, thematic analysis enabled the identification of underlying patterns and meanings within participants' responses. Following an extensive literature review, a semi-structured questionnaire has been formulated to allow respondents to narrate their experiences without any restrictions.

This survey was distributed via LinkedIn. 439 respondents have answered the open-ended survey questions. Statements from 168 respondents, who work remotely at private institutions, have been selected to ensure the homogeneity of the sample and focus on the virtual presenteeism dynamics in corporate work settings.

In the survey, 14 demographic questions have been asked to gather data about the age, gender, educational level, sector, department, position, title, seniority, marital status, and number of children. The open-ended survey question about presenteeism has been formulated as:

When you work remotely, do you continue to work if you feel sick or unwell? Does this situation affect you and your job? How does your manager act towards taking sick leave? Could you give some examples?

While this study does not use traditional qualitative methods such as interviews or focus groups, the open-ended questions encouraged participants to share detailed insights in their own words. This approach helped us to reach a broader and more diverse sample while capturing rich, qualitative data. Thematic analysis can still be effective applied to the open-ended survey responses by analyzing them as qualitative textual data. We have identified themes through a systematic coding process, and developed themes that capture recurring patterns in the data (see Table 1). Through thematic analysis, we identified key patterns and find out the common themes related to virtual presenteeism (see Table 2). In order to improve the coding reliability, two researchers worked at different stages of coding. Additionally, researcher reflexivity has been practiced during the study as the researchers are familiar with the context of the research. While personal assumptions and interpretations have been critically examined in order to minimize bias, findings have been cross-checked to ensure the inclusion of diverse narratives, rather than emphasizing certain cases.

Table 1: Research Design.

<table>
<tr><th>Preparation for Research</th><th>Data Collection</th><th>Data Analysis</th><th>Distribution of Findings</th></tr>
<tr><td>Literature Review</td><td rowspan="4">Forming open- ended questions

Collecting responses</td><td rowspan="4">Analysis of Data

Interpretation of Results</td><td rowspan="4">Discussion of Findings</td></tr>
<tr><td>Qualitative Survey Design</td></tr>
<tr><td>Sample Selection</td></tr>
<tr><td>Obtaining informed and voluntary consent</td></tr>
<tr><td colspan="4">Researcher Reflexivity:

Experiences of the researchers / Researchers' familiarity with the context</td></tr>
</table>

Table 2: Examples of Conceptualization and Categorization of Presenteeism Statements.

Participant Quote	Conceptualization	Categorization	Theme
Even when I am too ill to go to work, I continue to work, though my performance tends to be compromised.	Working while sick/not feeling well	Working while sick	Presenteeism
I don't have the luxury of being sick. If I had taken sick leave, they would likely have continued to send me work, assuming I could manage it from bed.	Working while on sick leave		
	The perception that being sick is a luxury		
When we're at home, they don't want us to take sick leave. If we do, they say, "It's up to you, but your salary will be deducted."	The deduction of salary when taking sick leave	Perception of "working from home is equivalent of leave"	
My manager sees working from home as taking time off.	The perception of working from home as being equivalent to taking time off		
Even if you're feeling ill, you're still held accountable for the tasks that need to be completed that day, with the assumption that being at home means you should be able to handle them.	The attitude of "You're at home anyway."		
There is this mindset that you can't be sick when you're working from home.	One cannot be sick while working from home		
I've barely been able to take sick leave, even when I'm feeling unwell. There seems to be a perception that you can't be sick when you're working from home.	One cannot be sick while working from home		
My boss thinks that I do not work enough because I am married and I have a kid. So, I work more and try to prove that I am working. For this reason, I do not take sick leave when I am sick	Perceived bias due to marital or parental status		
Even when I wasn't feeling well, I continued working. They say I can share my condition and request time off, but when I did, I received responses like, "This is a really bad time, we're going through a busy period—would it be possible to take leave later?"	Sick leave not being considered a valid reason for time off	The supervisor's attitude towards sickness and sick leaves	Supervisor Behaviour
He says, "You can take the sick leave, but I am the one who approves the leave."			
As someone who has had COVID, I can truly say I felt like I was on the verge of death. With hospital tests, medical reports, and the sick leave prescribed by my doctor, I still receive no sympathy—no "get well soon" even when I mention it. Even when I was working in the office, no one paid	Lack of empathy or acknowledgement from supervisor		

attention, as if they didn't even notice when I was barely holding on.			
There is this perception that if I get worse, no one will believe me.	Fear of stigma and disbelief		

Findings

Our findings reveal that married female employees with children narrate higher instances of virtual presenteeism since they avoid taking sick leaves in order to prove their dedication to work. Supervisory pressure has been noted as one of the factors that lead to virtual presenteeism. Since remote work has made it challenging for employees to be visible, they perceive the need to continuously signal their commitment to work, which can lead to working while sick. Respondents also note that they feel guilty for attending to family responsibilities while working from home; therefore, they tend to work when they are sick or unwell in an effort to compensate. This finding is also valid for single remote employees.

Consequently, the dual demands of professional work and domestic responsibilities, along with the pressures from the workplace, create emotional and physical challenges for remote employees, often leading to virtual presenteeism. In our sample, married female employees with children have been the ones who have reported severe cases of virtual presenteeism.

Conclusion

This study highlights virtual presenteeism as a negative impact of remote work, since it can lead to burnout, reduced productivity, and health-related risks (Hemp, 2004). Since remote work has become an essential part of work settings (Toscano et al., 2024), organizations should implement new sick leave policies that are compatible with remote work settings to mitigate virtual presenteeism. The main limitation of this research is the generalizability of the results is also limited as the sample of this study is limited to employees who work at private corporations. Future research should further explore how virtual presenteeism differs across industries and what the long-term effects of virtual presenteeism would be.

References

Bergström, G., Bodin, L., Hagberg, J., Aronsson, G., & Josephson, M. (2009). Sickness presenteeism today, sickness absenteeism tomorrow? A prospective study on sickness presenteeism and future sickness absenteeism. J Occup Environ Med, 51(6).

Biron, C., Karanika-Murray, M., Ivers, H., Salvoni, S., & Fernet, C. (2021). Teleworking While Sick: A Three-Wave Study of Psychosocial Safety Climate. Psychological Demands, and Presenteeism. Front. Psychol, 12, 734245.

Böckerman, P., & Laukkanen, E. (2010). Predictors of sickness absence and presenteeism: Does the pattern differ by a respondent's health? J. Occup. Environ. Med, 52, 332–335.

Cooper, C. (1996). Hot under the collar. Times Higher Education, Supplement, June 21, 12–16.

Cooper, C. L., & Lu, L. (2016). Presenteeism as a global phenomenon: Unraveling the psychosocial

mechanisms from the perspective of social cognitive theory". Cross Cultural & Strategic Management, 23(2). **Ferreira, A. I., Mach, M., Martinez, L. F., & Miraglia, M.** (2022). Sickness presenteeism in the aftermath of COVID-19: Is presenteeism remote-work behavior the new (Ab) normal? Frontiers in Psychology, 12, 748053. **Fiorini, L. A.** (2024). Remote workers' reasons for changed levels of Absenteeism, Presenteeism and Working outside agreed hours during the COVID-19 pandemic. Sage Open, 14(1), 21582440241240636.

Hemp, P. (2004). Presenteeism: At work–but out of it. Harv Bus Rev, Oct;82(10):49-58, 155.

Johns, G. (2010). Presenteeism in the workplace: A review and research agenda. Journal of Organizational Behavior, 31(4), 519–542.

Karanika-Murray, M., Biron, C., Hervieux, V., Whysall, Z., & Chen, H. (2021). Managing presenteeism to optimise health and performance. In T. Wall, C. Cooper, & P. Brough (Eds.), The SAGE handbook of organizational wellbeing (p. 232 47). SAGE reference.

Mat-Artun, D., & Küskü, F. (2025). Exploring dual narratives of supervisory trust in remote supervisor–subordinate relationships. International Social Science Journal, 75(255), 81-96.

Patel, C., Biron, M., Cooper, S. C., & Budhwar, P. S. (2023). Sick and working: Current challenges and emerging directions for future presenteeism research. Journal of Organizational Behavior, 44(6), 839–852.

Ruhle, S. A., & Schmoll, R. (2021). COVID-19, Telecommuting, and (Virtual) Sickness Presenteeism: Working From Home While Ill During a Pandemic. Front. Psychol, 12, 734106.

Salvoni, S., Biron, C., Gilbert, M. H., Dextras-Gauthier, J., & Ivers, H. (2024). Managing virtual presenteeism during the COVID-19 pandemic: A multilevel study on managers' stress management

competencies to foster functional presenteeism. International Journal of Environmental Research and Public Health, 21(9), 1115.

Shimura, A., Yokoi, K., Ishibashi, Y., Akatsuka, Y., & Inoue, T. (2021). Remote Work Decreases

Psychological and Physical Stress Responses, but Full-Remote Work Increases Presenteeism. Front. Psychol, 12, 730969.

Toscano, F., González-Romá, V., & Zappalà, S. (2024). The Influence of Working from Home vs. Working at the Office on Job Performance in a Hybrid Work Arrangement: A Diary Study. J Bus Psychol.

MANAGEMENT

Economics

Finance

Human Resource Management

Marketing

Organization

Production Management

Navigating the Paradox of Connectivity and Isolation: Impacts on Digital Nomads' Psychological Well-Being

Mahin Farshbaf Maherian[a], Adnan Veysel Ertemel[a]

[a]Istanbul Technical University, Department of Management, Istanbul, Turkey

maherian@itu.edu.tr

Keywords: Digital Nomads, Isolation, Connectivity, Well-Being, Loneliness.

Aim

Digital nomads utilize technology to work remotely while traveling, enjoying freedom and flexibility, but at the cost of potential social isolation. As of 2023, their numbers have grown to millions [1]. This study examines the paradox of connectivity and isolation in the digital nomad lifestyle. While digital nomads rely on constant connectivity for work and relationships, the absence of stable in-person communities presents unique psychological challenges. [2]. There is a clear gap in the literature regarding how digital nomads balance constant connectivity with frequent periods of isolation. This study explores how they perceive and manage these dual demands and the impact of this balance on their psychological well-being [3]. This research examines the strategies employed by digital nomads to maintain social connections, cope with loneliness, and assesses their impact on mental health. It is hypothesized that nomads who effectively balance connectivity and solitude will report higher psychological well-being than those who struggle with this balance [4]. This study aims to illuminate the overlooked interplay between constant connectivity and the isolation inherent in the digital nomad lifestyle. It also examines whether effective connectivity management can act as a protective factor for mental health [5].

Materials and Methods

1. Research Design & Sample

A quantitative survey captured the social and psychological experiences of digital nomads. The study targeted N = 300 self-identified digital nomads, achieving 300 valid responses (100% of the target). Participants were recruited through online communities frequented by digital nomads, including Facebook groups, subreddits, and Nomad List [6]. To ensure a relevant sample, the inclusion criteria required respondents to self-identify as a digital nomad, work remotely as their primary income source, have maintained a location-independent lifestyle for at least six months, be 18 years or older, and be proficient in English [2]. Individuals new to digital nomadism, as well as those who are primarily remote workers, were excluded from the focus on experienced digital nomads. [7]. The final sample comprised a diverse cross-section of digital nomads, representing a range of ages, nationalities, and professions, with a predominant focus on the tech, creative, and freelance sectors, providing a robust basis for examining general patterns.

2. Data Collection

- Data were collected through a structured online questionnaire over a year, covering demographics, work/travel patterns, and standardized scales. Participants provided informed consent and could withdraw anytime; all responses were anonymized. The study utilized the following validated instruments:
- Lubben Social Network Scale (LSNS-6) [8]: A 6-item measure assessing social network size, frequency of contact, and perceived support. Higher scores indicate stronger social networks and lower isolation.
- Revised UCLA Loneliness Scale (R-UCLA) [9]: A 20-item scale measuring subjective loneliness and social isolation, with higher scores reflecting greater loneliness.

- Social Media Use Integration Scale (SMUIS) [10]: A 7-item scale evaluating social media's role in daily social routines and identity. Higher scores indicate greater digital connectivity and integration.
- Warwick-Edinburgh Mental Well-Being Scale (WEMWBS)[11]: A 14-item scale assessing mental well-being, including happiness, relaxation, and optimism. Higher scores denote better psychological well-being.

3. Data Analysis

Responses were analyzed using SPSS. Descriptive statistics characterized the sample and key variables. Internal consistency was assessed, with Cronbach's alpha values of 0.73 (R-UCLA), 0.65 (LSNS-6), 0.97 (SMUIS), and 0.95 (WEMWBS), indicating acceptable to excellent reliability. [9]; [8]; [12]; [11]).

Pearson correlation analyses explored relationships between connectivity, isolation, and well-being. Multiple regression tested the predictive effects of isolation (R-UCLA, LSNS-6) and connectivity (SMUIS) on well-being (WEMWBS), controlling for age, gender, and nomad duration [5].

To test whether digital connectivity buffers the impact of loneliness, a moderation analysis included an interaction term (R-UCLA × SMUIS) in the regression. Statistical significance was set at $p < 0.05$ (two-tailed), with results presented in tables and charts for clarity.

Findings

Digital nomads exhibited notable variability in social connectivity and well-being. Loneliness levels were moderate, with R-UCLA scores near the mid-point, indicating that while not extreme, loneliness remains a concern for many. Social network strength was also moderate, with most participants maintaining contact with 2–4 close friends or family members on a monthly basis, but lacking extensive local networks.

Table 1. R-UCLA Loneliness Scale - Item Statistics.

Item Code	R_UCLA - Item Statistics	
	Mean	Standard Deviation (Std)
R_UCLA_Q1	3.153	0.795
R_UCLA_Q2	2.217	0.795
R_UCLA_Q3	2.103	0.850
R_UCLA_Q4	3.017	0.848
R_UCLA_Q5	2.120	0.853
R_UCLA_Q6	2.197	0.970
R_UCLA_Q7	2.987	0.679
R_UCLA_Q8	2.693	1.044
R_UCLA_Q9	2.037	0.666
R_UCLA_Q10	1.587	0.619
R_UCLA_Q11	2.927	0.619

R_UCLA_Q12	2.010	0.682
R_UCLA_Q13	2.157	0.903
R_UCLA_Q14	2.113	0.694
R_UCLA_Q15	3.150	0.650
R_UCLA_Q16	1.923	0.647
R_UCLA_Q17	2.263	0.737
R_UCLA_Q18	2.003	0.692
R_UCLA_Q19	3.380	0.661
R_UCLA_Q20	2.080	0.846

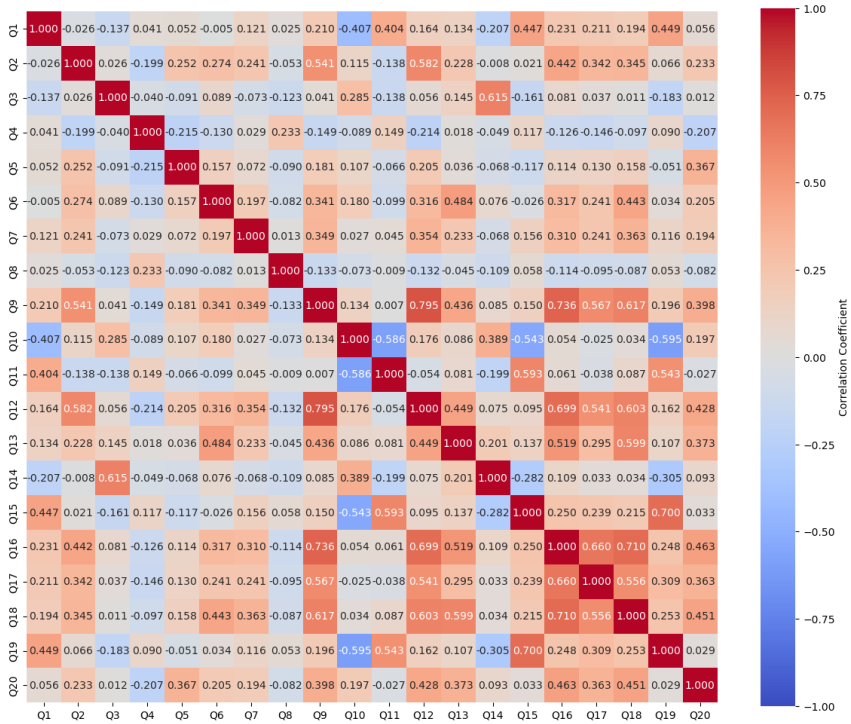

Figure 1. R-UCLA- Inter-Item Correlation Matrix.

Table 2. LSNS6- Lubben Social Network Scale - Item Statistics.

Item Code	LSNS6- Item Statistics	
	Mean	Standard Deviation (Std)
LSNS6_Q1	4.163	0.812
LSNS6_Q2	2.903	1.048
LSNS6_Q3	2.960	1.078
LSNS6_Q4	2.397	0.896
LSNS6_Q5	2.930	1.004
LSNS6_Q6	3.600	0.933

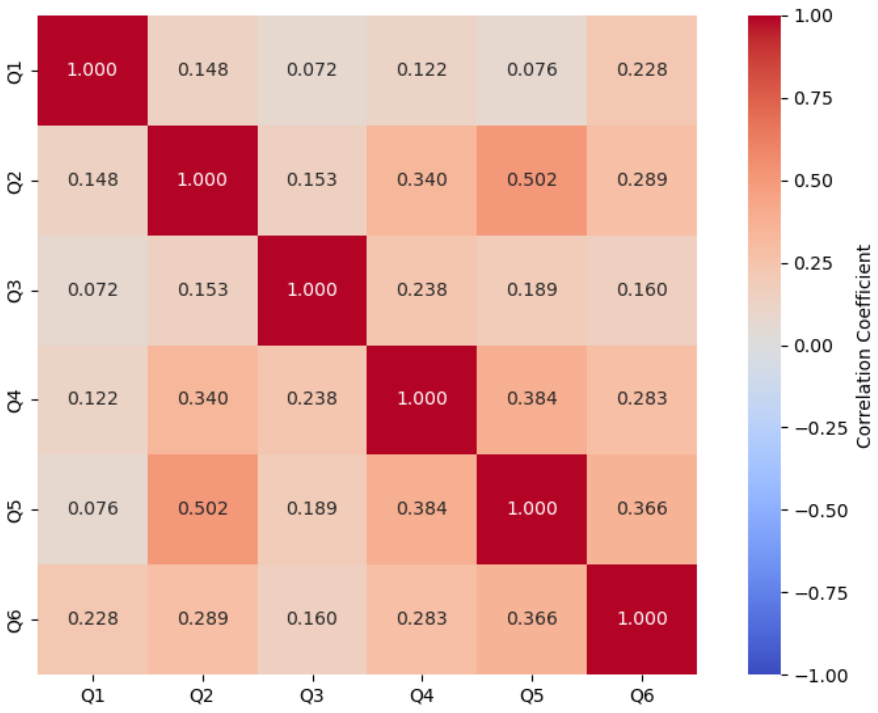

Figure 2. LSNS6- Inter-Item Correlation Matrix.

SMUIS were moderate to high. Most participants used social media daily for social and professional connections, though integration varied—some relied on it heavily, while others used it more sparingly. The average SMUIS score (around 2.0–2.3 on a 5-point scale) indicates a fair but not overwhelming reliance on digital connectivity.

Table 3. SMUIS- Social Media Use Integration Scale - Item Statistics.

Item Code	SMUIS - Item Statistics	
	Mean	**Standard Deviation (Std)**
SMUIS_Q1	1.947	0.840
SMUIS_Q2	2.143	0.852
SMUIS_Q3	1.980	0.858
SMUIS_Q4	2.007	0.985
SMUIS_Q5	2.360	0.987
SMUIS_Q6	1.823	0.841
SMUIS_Q7	2.387	1.043

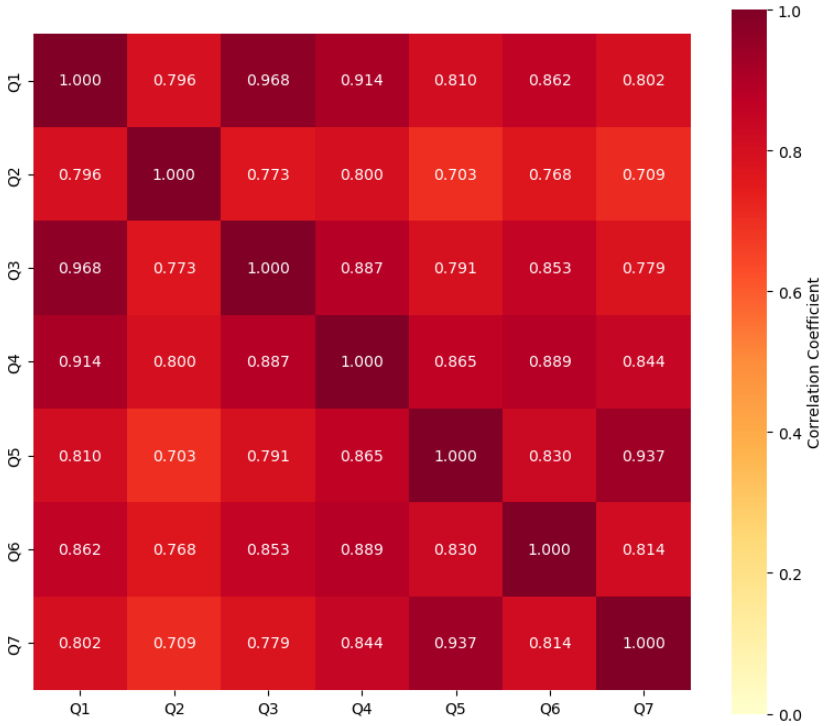

Figure 3. SMUIS- Inter-Item Correlation Matrix.

Mental well-being (WEMWBS) was generally positive, with average scores in the upper half of the scale (around 3.5–4 per item on a 1–5 scale), suggesting that most respondents felt content and mentally healthy despite occasional loneliness. Notably, even participants experiencing loneliness did not always report poor well-being, hinting at personal resilience or effective coping strategies.

Table 4. WEMWBS- Warwick-Edinburgh Mental Wellbeing Scale - Item Statistics.

Item Code	WEMWBS - Item Statistics	
	Mean	Standard Deviation (Std)
WEMWBS_Q1	3.557	0.858
WEMWBS_Q2	3.563	0.861
WEMWBS_Q3	3.167	0.796
WEMWBS_Q4	3.513	0.955
WEMWBS_Q5	3.440	0.814
WEMWBS_Q6	3.587	0.832
WEMWBS_Q7	3.483	0.941
WEMWBS_Q8	3.830	0.908
WEMWBS_Q9	3.420	1.226
WEMWBS_Q10	3.430	1.218
WEMWBS_Q11	4.410	0.886
WEMWBS_Q12	3.310	0.918
WEMWBS_Q13	3.983	0.927
WEMWBS_Q14	3.617	0.860

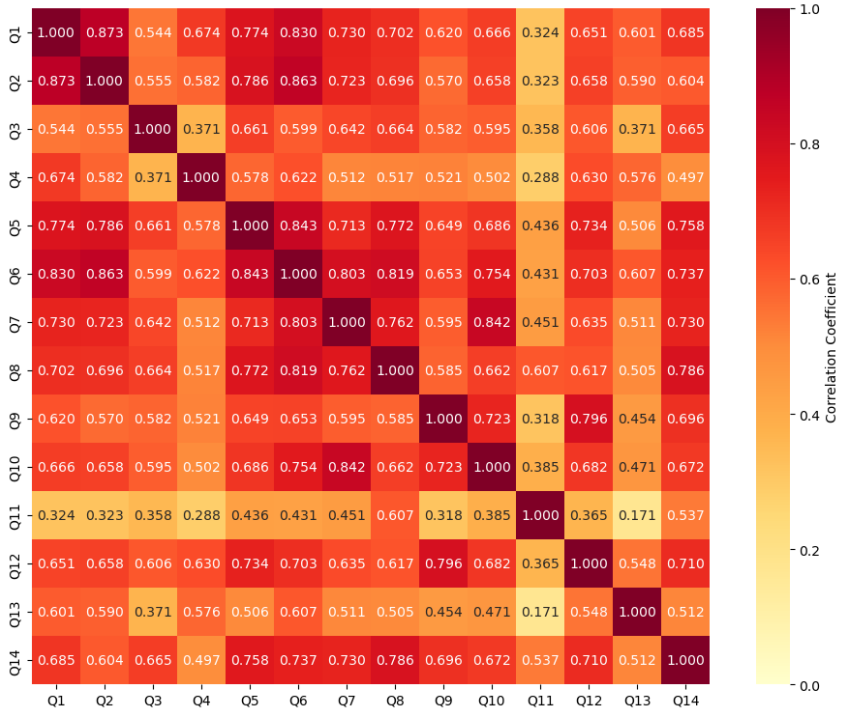

Figure 4. WEMWBS- Inter-Item Correlation Matrix.

All scales demonstrated reliability, with SMUIS (α = 0.97) and WEMWBS (α = 0.95) showing excellent internal consistency. R-UCLA (α = 0.73) and LSNS-6 (α = 0.65) had slightly lower values, likely due to the broader constructs they measure. LSNS-6's lower reliability may reflect the varied social connections of digital nomads, such as strong friendships but weaker family ties or vice versa.

Correlation Analysis: Table 5 presents Pearson correlation coefficients among loneliness (R-UCLA), social network size (LSNS-6), social media integration (SMUIS), and well-being (WEMWBS). Several relationships were statistically significant and aligned with expectations.

Table 5. Correlation Matrix of Key Study Variables (N = 300).

	(R-UCLA)	(LSNS-6)	(SMUIS)	(WEMWBS)
(R-UCLA)	1	-0.50**	-0.18*	-0.56**
(LSNS-6)	-0.50**	1	0.1	+0.45**
(SMUIS)	-0.18	0.1	1	0.12
(WEMWBS)	-0.56**	+0.45**	0.12	1

*p < 0.05, **p < 0.01 (two-tailed tests)

As shown in Table 5, loneliness was strongly negatively correlated with well-being ($r \approx -0.56$, $p < 0.01$), supporting Hypothesis 2. Social network strength (LSNS-6) was positively associated with well-being ($r \approx +0.45$, $p < 0.01$) and negatively related to loneliness ($r \approx -0.50$, $p < 0.01$), highlighting the importance of social connectedness for mental health.

Digital connectivity showed a more nuanced effect. Social media integration (SMUIS) had a slight negative correlation with loneliness ($r \approx -0.18$, $p < 0.05$), suggesting it may slightly reduce loneliness but not eliminate it. However, its correlation with well-being was insignificant ($r \approx +0.12$, p = n.s.), indicating that frequent social media use does not necessarily improve mental health. This suggests that the nature of online engagement—meaningful interactions versus passive browsing—matters more than the frequency of usage. While digital connectivity provided a slight buffer against loneliness, face-to-face connections remained more influential for well-being.

Regression and Moderation Analysis

Regression analysis confirmed that loneliness strongly predicts lower well-being ($p < 0.001$), while stronger social networks correlate with higher well-being ($p < 0.001$). Digital connectivity (SMUIS) showed a weak positive association with well-being but was not a strong standalone predictor.

Moderation analysis revealed that loneliness had a less severe impact on well-being for highly connected digital nomads compared to those with lower digital connectivity ($p < 0.05$). This suggests online engagement can buffer loneliness but not fully replace in-person connections.

Social support remains the strongest predictor of well-being, with digital connectivity providing only partial protection against isolation.

Conclusion

This study reveals that digital nomads navigate a delicate balance between connectivity and isolation, employing structured strategies that enable them to tolerate loneliness as a trade-off for autonomy, while cautioning against excessive and passive social media use, which can undermine their well-being. Although divorced participants showed lower social media engagement, resilience and purposeful digital interaction helped buffer the effects of isolation, partially supporting H1 and H3 and disproving H2's assumption that isolation invariably harms well-being. These findings underscore the importance of intentional digital engagement and highlight the potential benefits of coworking spaces and targeted coping strategies in promoting psychological well-being among digital nomads.

References

MBO Partners, The Digital Nomad Lifestyle: Opportunities and Challenges, MBO Partners Website (2024).

O. Hannonen, Emergent geographies of digital nomadism: conceptual framing, insights and implications for tourism, Tourism Geographies (2023). https://doi.org/10.1080/14616688.2023.2299845.

C. Miguel, C. Lutz, F. Majetić, R. Perez-Vega, M. Sánchez-Razo, It's not All Shiny and Glamorous: Loneliness and Fear of Missing Out among Digital Nomads, 2023. https://hdl.handle.net/10125/103196.

L.C. Hawkley, J.T. Cacioppo, Loneliness Matters: A Theoretical and Empirical Review of Consequences and Mechanisms, Annals of Behavioral Medicine 40 (2010) 218–227. https://doi.org/10.1007/s12160-010-9210-8.

P. Verduyn, O. Ybarra, M. Résibois, J. Jonides, E. Kross, Do Social Network Sites Enhance or Undermine Subjective Well-Being? A Critical Review, Soc Issues Policy Rev 11 (2017) 274–302. https://doi.org/10.1111/sipr.12033.

MBO partners', Authentic and Intentional State of Independence in America 2024, (2024).

C. Miguel, C. Lutz, F. Majetić, R. Perez-Vega, M. Sanchez-Razo, It's not All Shiny and Glamorous: Loneliness and Fear of Missing Out among Digital Nomads, in: 2023. https://doi.org/10.24251/HICSS.2023.564.

R. O'Sullivan, A. Burns, G. Leavey, I. Leroi, V. Burholt, J. Lubben, J. Holt-Lunstad, C. Victor, B. Lawlor, M. Vilar-Compte, C.M. Perissinotto, M.A. Tully, M.P. Sullivan, M. Rosato, J.M. Power, E. Tiilikainen, T.R. Prohaska, Impact of the covid-19 pandemic on loneliness and social isolation: A multi-country study, Int J Environ Res Public Health 18 (2021). https://doi.org/10.3390/ijerph18199982.

C.A. Bulger, R.A. Matthews, M.E. Hoffman, Work and personal life boundary management: Boundary strength, work/personal life balance, and the segmentation-integration continuum., J Occup Health Psychol 12 (2007) 365–375. https://doi.org/10.1037/1076-8998.12.4.365.

M.A. Jenkins-Guarnieri, S.L. Wright, B. Johnson, Development and validation of a social media use integration scale., Psychol Pop Media Cult 2 (2013) 38–50. https://doi.org/10.1037/a0030277.

R.S. Gajendran, D.A. Harrison, The Good, the Bad, and the Unknown About Telecommuting: Meta-Analysis of Psychological Mediators and Individual Consequences, Journal of Applied Psychology 92 (2007) 1524–1541. https://doi.org/10.1037/0021-9010.92.6.1524.

M.A. Jenkins-Guarnieri, S.L. Wright, B. Johnson, Development and validation of a social media use integration scale., Psychol Pop Media Cult 2 (2013) 38–50. https://doi.org/10.1037/a0030277.

MANAGEMENT

Economics

Finance

Human Resource Management

Marketing

Organization

Production Management

Organizing Through Code: A Bibliometric Review of Algorithms in Organizational Contexts

Hakan Sanrı[a]

[a] University of Glasgow, Adam Smith Business School, United Kingdom
2421355s@student.gla.ac.uk

Keywords: Algorithms, Bibliometric Analysis, Keyword Co-Occurrences, Organizations.

Aim

The integration of algorithms into organizational contexts has transformed the nature of doing business. Going beyond a mathematical computation, algorithms have become not only technological tools but also organizational actors. Algorithms, once being studied almost exclusively from technical perspective, have lately been popular among management researchers. Despite this growing body of literature, there remains a lack of comprehensive studies that unpack the evolutionary trajectory of the field, highlight the research trends – particularly from organizational perspective. Considering these gaps, I ask:

• How has the volume and thematic focus of academic publications on algorithms in organizational contexts evolved over time?
• Which countries, disciplines, and studies have contributed most significantly to this field?
• What are the major themes and trends in the research area?

This study aims to map the evolving landscape of research on algorithms used in organizational contexts. Specifically, I am interested in understanding the main characteristics of the field which grows rapidly. To achieve research objectives, I analysed 282 documents indexed in Scopus database by applying bibliometric analysis techniques. The results show that there has been a massive increase in publication output. Organizational and managerial implications of algorithms are gaining increasing attention within the academic community and more researchers are focusing on or building upon work in that field. The co-occurrence analysis of 168 keywords revealed six thematic clusters. While the number of publications on human-machine interaction and platform capitalism has shown a declining trend over time, interest in impact of algorithms on employee well-being has grown. Identifying thematic structure of the field and understanding how it evolves can offer valuable insights for managers to better align organizational strategies.

Material and Method

I conducted a bibliometric analysis to better understand how algorithm-related studies are organized within the field of organizational studies. To avoid the publications dealing with the technical or mathematical aspects of algorithms and better screen the studies focusing on organizational contexts, the following search string was carefully designed and used to retrieve data from the Scopus database:

TITLE-ABS-KEY ("artificial intelligence in organizations" OR "AI in business" OR "AI in organizations" OR "artificial intelligence in business" OR "algorithmic management" OR "algorithms in the workplace" OR "machine learning in organizations" OR "machine learning in business" OR "predictive analytics in business" OR "algorithmic technologies") AND TITLE-ABS-KEY ("organization*" OR "organizational change" OR "organizational structure" OR "organizational design" OR "organizational decision making" OR "workplace" OR "employee*" OR "digital work" OR "algorithmic work" OR "platform work" OR "gig economy") AND PUBYEAR > 2016 AND PUBYEAR < 2026 AND (LIMIT-TO (SRCTYPE , "j")) AND (LIMIT-TO (DOCTYPE , "ar")) AND (LIMIT-TO (LANGUAGE , "English"))

I limited the source type to journal, document type to article and language to English. The initial search targeting article titles, abstracts and keywords for the period from 2017 to April 2025 returned 291 documents. After a quick screening based on abstract content, 9 documents were excluded from the dataset and 282 records were retrieved for analysis. I used an open-source tool, the VOSviewer software, to visualize bibliometric network and identify the structure and evolution of the field (Van Eck & Waltman, 2010).

Findings

This section is organized as follows. First, I describe the characteristics of my dataset through descriptive bibliometric analysis. Second, I introduce the six clusters emerged from Co-Occurrence Analysis (Keyword Analysis) which reveals thematic structure of the field. I further discuss the research focuses of these clusters, explaining how these research patterns evolved over time.

Descriptive Bibliometric Analysis

There has been a massive increase in publication output in just seven years. From just 2 publications in 2017, the scholarly output grew by an average annual growth rate of approximately 72%, soared to 104 in 2024. Although the vast majority of the published documents come from the field of Social Sciences (almost 80%), studying algorithms in organizational contexts has increasingly received attention within Computer Science subject area as well (13.6%). The leading countries in knowledge production within this field are United States, United Kingdom and Germany. European Commission is the top funding institution for this domain, followed by The National Natural Science Foundation of China and Ministry of Science and Technology of the People's Republic of China. The results show that organizational and managerial implications of algorithms are gaining increasing attention within the academic community and more researchers are focusing on or building upon work in that area (see Figure 1). Table 1 shows the publications with the highest number of citations.

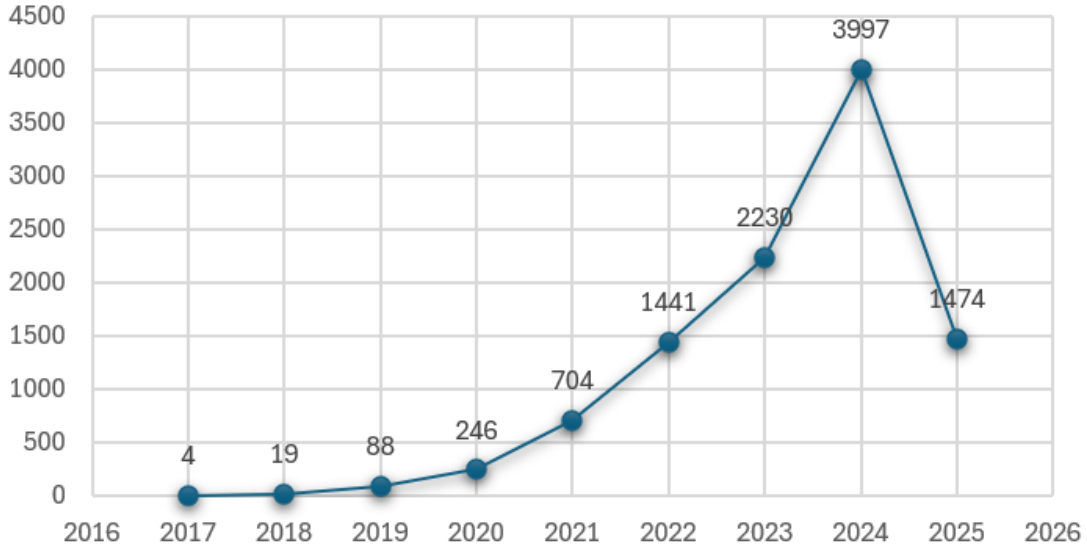

Figure 1. Number of citations.

Table 1. Most cited articles in the field.

Document Title	Author(s)	Publication Year	Journal Title	Total Citations
Good Gig, Bad Gig: Autonomy and Algorithmic Control in the Global Gig Economy	Wood, A.J., Graham, M., Lehdonvirta, V., Hjorth, I.	2019	Work, Employment and Society	1093
Algorithms at work: The new contested terrain of control	Kellogg, K.C., Valentine, M.A., Christin, A.	2020	Academy of Management Annals	1010
Artificial intelligence and management: The automation-augmentation paradox	Raisch, S., Krakowski, S.	2021	Academy of Management Review	808
Platform-Capital's 'App-etite' for Control: A Labour Process Analysis of Food-Delivery Work in Australia	Veen, A., Barratt, T., Goods, C.	2020	Work, Employment and Society	418
Artificial intelligence in business: State of the art and future research agenda	Loureiro, S.M.C., Guerreiro, J., Tussyadiah, I.	2021	Journal of Business Research	306

Co-Occurrence Analysis (Keyword Analysis)

Co-occurrence analysis is one of the widely used techniques to understand the thematic structure of the field. The co-occurrence analysis of 168 keywords revealed six thematic clusters in the domain of algorithms in organizational contexts (see Figure 2). The total link strength of 2310 across 1480 keyword links indicates a rich and well-connected thematic structure in the field.

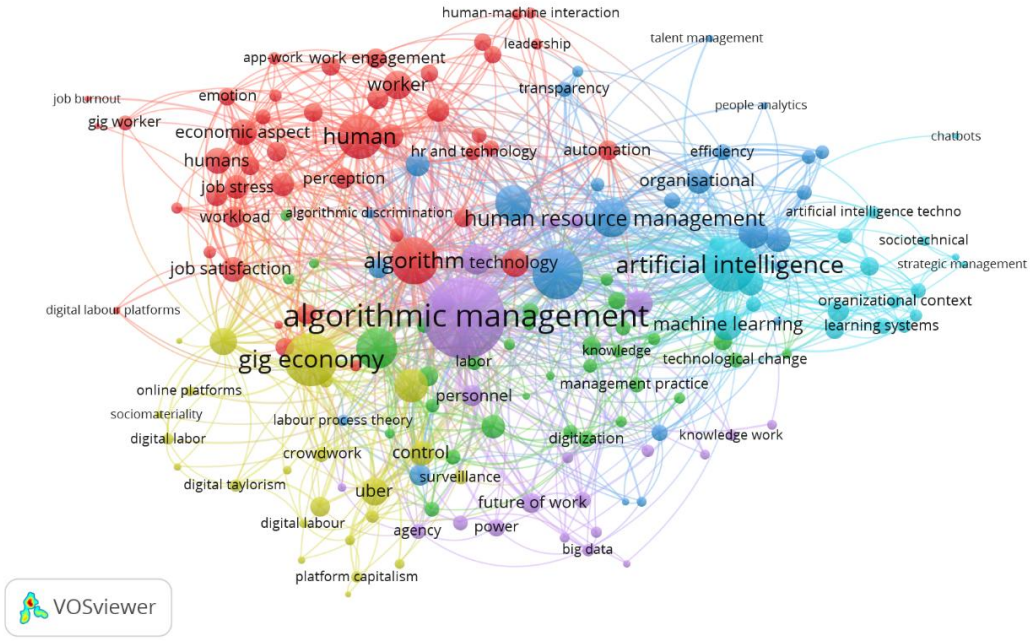

Figure 2. Keyword co-occurrence network map.

Cluster 1 (red cluster) has 46 items. This cluster focuses on how algorithms affect employee well-being. The studies in this cluster prioritize the human element at the algorithmic workplace. Cluster 2 (green cluster) has 32 items and discusses work practices, micro-level dynamics of algorithmic systems at work. Cluster 3 (blue cluster) has 26 items and captures research focused on integration of algorithmic innovations into HR practices. The studies in this cluster also concentrate on algorithmic governance. Cluster 4 (yellow cluster) has 23 items. This cluster explores the employment relationships in gig work. Cluster 5 (purple cluster) seems an emerging cluster with 22 items. This cluster focus on philosophical and future-oriented challenges of algorithmic technologies. The final cluster, Cluster 6 (turquoise cluster) is centered on how organizations integrate AI into their business operations considering their strategic management implications. After interpreting each cluster, I labelled them with a representing research theme (see Table 2).

Table 2. Thematic groups.

Cluster	Theme	Representative Keywords
Cluster 1	The impact of algorithmic technologies on workplace well-being	automation, emotion, gig worker, job burnout, job satisfaction, job stress, platform labour, workload
Cluster 2	Algorithms and changing nature of work	algorithmic control, digital transformation, flexibility, management practice, technology affordances
Cluster 3	Algorithmic human resource management	algorithmic discrimination, algorithmic fairness, management by algorithm, people analytics, performance, workers

Cluster 4	Platform work and digital labour	digital capitalism, digital labour, digital Taylorism, gig work, platform capitalism, platforms, resistance
Cluster 5	Philosophical and future-oriented challenges of algorithmic technologies	agency, AI, future of work, philosophical aspects, sociotechnical systems, technological unemployment
Cluster 6	AI adoption in organizations	adoption, artificial intelligence technologies, deep learning, learning systems, strategic management

Conclusion

This study does not attempt to provide a timeline of algorithms nor present the technical details behind the algorithmic technologies, but it hopes to contribute to our understanding of algorithms in organizational contexts and shed light on future research. To understand the research structure of the field, I conducted a co-occurrence analysis to the dataset including 282 documents. The data shows a massive increase in research output over the years, with a notable surge in the last few years. The deployment of algorithmic innovations and their significant effects on organizations can be considered the reason behind this jump and a turning point for research on algorithms. The findings suggest that the discussions within the field can be categorized into six distinct clusters. While the number of publications on human-machine interaction and platform capitalism has shown a declining trend over time, interest in impact of algorithms on employee well-being has grown. Identifying thematic structure of the field and understanding how it evolves can offer valuable insights for managers to better align organizational strategies.

References

Kellogg, K.C., Valentine, M.A., & Christin, A. (2020). Algorithms at work: The new contested terrain of control. Academy of Management Annals, 14(1), 366-410.

Loureiro, S.M.C., Guerreiro, J., & Tussyadiah, I. (2021). Artificial intelligence in business: State of the art and future research agenda. Journal of Business Research, 129, 911-926.

Raisch, S., & Krakowski, S. (2021). Artificial intelligence and management: The automation-augmentation paradox. Academy of Management Review, 46(1), 192-210.

Van Eck, N.J., & Waltman, L. (2010). Software survey: VOSviewer, a computer program for bibliometric mapping. Scientometrics, 84(2), 523-538.

Veen, A., Barratt, T., & Goods, C. (2020). Platform-Capital's 'App-etite' for Control: A Labour Process Analysis of Food-Delivery Work in Australia. Work, Employment and Society, 34(3), 388-406.

Wood, A.J., Graham, M., Lehdonvirta, & V., Hjorth, I. (2019). Good Gig, Bad Gig: Autonomy and Algorithmic Control in the Global Gig Economy. Work, Employment and Society, 33(1), 56-75.

MANAGEMENT

Economics

Finance

Human Resource Management

Marketing

Organization

Production Management

Supplier Performance Evaluation with Balanced Scorecard

Hanife Özcan[a], Hür Bersam Sidal[a]

[a]Istanbul Technical University, Department of Management, Management, Turkey

ozcanh15@itu.edu.tr

Keywords: Balanced Scorecard, Supplier Performance Evaluation, Supplier Selection, Digital Era İn Textile İndustry, Multi-Criteria Decision Making.

Aim

In today's competitive business world, supply chain management has become a critical factor for businesses to achieve sustainable growth and competitive advantage. In today's world, the textile sector stands out as a sector where the complexity of the supply chain, market conditions and customer expectations change rapidly and constantly, and digitalization in production processes has become important. For this reason, the sector attaches great importance to effective supplier management. The ability of businesses to demonstrate high performance in the sector in which they operate does not only depend on the performance of the business itself. The success of the suppliers with whom businesses work directly impacts their performance. Therefore, special attention should be given to supplier selection in order to gain a competitive advantage, succeed, and maintain sustainable success.

It has become inevitable for supplier selection processes to adapt to this transformation with the spread of Industry 4.0 technologies. By establishing strong relationships with their suppliers, businesses aim to increase their operational efficiency, reduce costs and make the most of the advantages offered by digitalization. In this context, supplier performance evaluation is an important process that supports businesses in achieving their strategic goals.

Material and Method

In this study, an evaluation model that includes the effects of digitalization in the textile sector has been created based on the Balanced Scorecard (BSC) method used for supplier performance evaluation. By translating long term business strategies into short term operational practices, the organization will be able to react and adapt to current and future changes and developments immediately with a balanced scorecard. Including these criteria in a structure allows management to measure performance more comprehensively and over the long term, rather than focusing on immediate goals. The study aims to evaluate supplier performance using the Balanced Scorecard method, which integrates multiple performance dimensions beyond financial metrics. This research provides a broader perspective such as financial, internal processes, customer, learning and development, enabling a comprehensive evaluation of suppliers in the textile sector.

Findings

In order to determine the criteria for the sector in question, a list of possible criteria specific to the textile sector was created with a focus on digitalization, using literature studies. First, the main criteria were determined, and similar studies in the literature were used as a basis for determining these criteria. Quality, price, delivery, service, technological competence and innovation capability were determined as six main criteria. Then, possible performance evaluation criteria were analyzed separately and included under the relevant main criteria, and thus grouped performance criteria were created, as seen in Table 1. The sub-criteria of the quality main criterion are product quality, error-free product quantity, quality standards, and smart and environmentally friendly production processes. Sub-criteria related to the main price criterion are; affordable/competitive price, discount rate, payment terms (term), and strategic partnerships by purchasing shares from suppliers with critical technologies. Delivery-related sub-criteria are on-time delivery, complete delivery, order delivery times and shortening supply chain cycle times. Another selection criterion, technological competence, includes the level of digitalization, automation and

rapid prototyping, machinery and equipment competence. Sub-criteria related to the main service criterion consist of rapid response to processes and flexibility, capacity adequacy, sustainability oriented approach and customer satisfaction levels, respectively. The last main selection criterion, innovation capability, includes the tendency of suppliers to be innovative, the ability to develop new products and personnel training. It was determined and finalized in line with the deep interviews conducted with experts who actively work in the purchasing and product of well-known companies in the textile sector. Then, it is categorized under BSC dimensions. In summary, performance evaluation criteria are indicators that enable the monitoring of the responsibilities expected from suppliers. Furthermore, Multi-Criteria Decision-Making (MCDM) methods have been utilized to analytically determine the importance levels of the identified criteria. This method allows the selection of the most suitable suppliers by determining the weights of the criteria. Determining the criteria weights shows businesses the most important selection criterion in the study and also provides information about the performance of their suppliers. When the business is viewed from this perspective, the balanced scorecard provides a detailed picture of the organization's performance and guides managers in performance management. The model developed in the study provides a comprehensive decision-making strategic management mechanism to improve the supplier selection processes of businesses in the textile sector.

Table 1: Balanced Scorecard and Perspectives.

FINANCIAL	
Main criterion	**Sub-criterion**
Price	Affordable/competitive price
	Discount rate
	Payment terms (term)
	Strategic partnerships by purchasing shares from suppliers with critical technologies
CUSTOMER	
Main criterion	**Sub-criterion**
Quality	Product quality,
	Error-free product quantity,
	Quality standards
	Smart and environmentally friendly production processes
Delivery	On-time delivery
	Complete delivery
	Order delivery times
	Shortening supply chain cycle times

INTERNAL BUSINESS	
Main criterion	**Sub-criterion**
Service	Rapid response to processes and flexibility
	Capacity adequacy
	Sustainability oriented approach
	Customer satisfaction levels
Technological Competence	Level of digitalization
	Automation and rapid prototyping
	Machinery and equipment competence
LEARNING AND GROWTH	
Main criterion	**Sub-criterion**
Innovation Capability	The tendency of suppliers to be innovative
	The ability to develop new products
	Personnel training

Conclusion

The results of the study show that the model developed to measure the impact of digitalization on the supplier selection process contributes to businesses' alignment with their digital transformation strategies. The integration of the Balanced Scorecard and Multi-Criteria Decision-Making methods offers a systematic, multi-dimensional, and digitalization-sensitive approach to supplier performance evaluation. By conducting an example Balanced Scorecard scoring specific to the textile sector, a ready-to-use supplier performance evaluation system has been provided to the industry. It is recommended that businesses that are selecting suppliers consider their supply chain as a whole and regularly evaluate supplier performance, clarify suppliers that are open to improvement in addition to those that will be discontinued, and provide them with the necessary support. According to the findings of the study, it is important for suppliers who currently stay away from Industry 4.0 technologies and do not invest in this area to be aware that they will have difficulties in being preferred in the face of rapidly developing technologies. This will guide them in creating their own strategic plans to reduce production costs, increase production efficiency, and transform supply chain processes. The study contributes to both the academic literature and industry practices by offering a scientific perspective on supply chain management and supplier selection processes in the textile sector from a digitalization standpoint.

References

Aljoulani, Y. Y. A., & Ebghaei, F. (2023). Dijitalleşmenin Tedarik Zinciri ve Tedarikçi Seçimi Yaklaşımlarına Etkileri: Analitik Hiyerarşi Prosesi Üzerine Bir Uygulama. *New Era International Journal of Interdisciplinary Social Researches*, *8*(19), 72-88.

Domínguez, E., Pérez, B., Rubio, Á. L., & Zapata, M. A. (2019). A taxonomy for key performance indicators management. *Computer Standards & Interfaces*, *64*, 24-40.

Dudic, Z., Dudic, B., Gregus, M., Novackova, D., & Djakovic, I. (2020). The innovativeness and usage of the balanced scorecard model in SMEs. *Sustainability*, *12*(8), 3221

Esmeray, M. (2023). CRITIC yöntemiyle tedarikçi performans kriterlerinin önceliklendirilmesi: Tekstil sektöründe bir uygulama. *Anadolu İktisat ve İşletme Dergisi*, *7*(1), 27-36.

Mondragon, A. E. C., Mastrocinque, E., Tsai, J. F., & Hogg, P. J. (2019). An AHP and fuzzy AHP multifactor decision making approach for technology and supplier selection in the high-functionality textile industry. *IEEE Transactions on Engineering Management*, *68*(4), 1112-1125.

Nebati, E. E. (2024). Tekstil Sektöründe Endüstri 4.0 Perspektifinde Dijital Teknoloji Uygulamalarının Değerlendirilmesi. *Cumhuriyet Üniversitesi İktisadi ve İdari Bilimler Dergisi.*

Samir, K., Khabbazi, M. R., Maffei, A., & Onori, M. A. (2018). Key performance indicators in cyber-physical production systems. *Procedia CIRP*, *72*, 498-502.

Türkmen, M., & Demirel, A. (2022). SWARA Ağırlıklı Bulanık COPRAS Yöntemi ile Tedarikçi Seçimi. *Alanya Akademik Bakış*, *6*(1), 1739-1756.

YARALI, C., & ERGUN, H. (2021). Balanced scorecard'ın kurum performansına etkisi. *Bucak İşletme Fakültesi Dergisi*, *4*(1), 101-122.

Yücel, Y. B. (2018). *Çok kriterli karar verme teknikleri ile tekstil sektöründe en uygun tedarikçi seçimi ve bir yazılım uygulaması* (Master's thesis, Bartın Üniversitesi, Sosyal Bilimler Enstitüsü).

Performance Evaluation Model Based on Balanced Scorecard for Industry 4.0 Applications in the Fast Moving Consumer Goods Sector (FMCG)

Ceren Dilbaz[a], Hür Bersam Sidal[a]

[a] Istanbul Technical University, Management Program, Türkiye
dilbaz@itu.edu.tr

Keywords: Balanced Scorecard, Fast-Moving Consumer Goods, Industry 4.0, Performance Evaluation.

Aim

Industry 4.0 technologies offer innovative solutions to optimize production, enhance resource efficiency, and respond quickly to customer demands.The opportunities offered by Industry 4.0, such as digitalization, automation, and data analytics, provide companies with more precise and accurate measurement tools to monitor and manage their performance [1]. Thus, proposing a model to evaluate the performance of Industry 4.0 applications is essential. The implementation of Industry 4.0 applications in the Fast-Moving Consumer Goods (FMCG) sector is essential for enhancing operational efficiency, improving supply chain transparency, and meeting the rapidly evolving consumer demands. Performance evaluation of these technologies, including IoT, big data analytics, and automation, is crucial to assess their impact on productivity, cost reduction, and sustainability, thereby enabling firms to adapt strategically in a highly competitive market [2]. This study proposes a model based on the Balanced Scorecard to help FMCG companies assess Industry 4.0 performance, improve efficiency, and gain a competitive edge.

Material and Method

This study employs the Balanced Scorecard (BSC) model as a foundation for measuring Industry 4.0 performance. BSC consists of four main dimensions: financial, customer, internal processes, and learning and growth [3].The sub-dimensions within these categories were determined through an extensive literature review. Following the completion of the model's design process, a comprehensive survey was conducted to determine the relative importance of the main and sub-dimensions.

Within the scope of this study, data were collected from managers working in various companies in the fast-moving consumer goods (FMCG) sector using a Likert scale-based questionnaire. The survey results were analyzed in detail using the Analytic Hierarchy Process (AHP), a multi-criteria decision-making method. Based on the importance weights derived through AHP, an Industry 4.0 performance evaluation was conducted for a selected company operating in the FMCG sector. To facilitate the company's self-assessment, a survey was administered to managers from different departments. The responses, collected using the Likert scale, were analyzed by evaluating the performance of each unit separately. As a result of this analysis, Industry 4.0 performance scores were calculated both at the unit level and overall, enabling comparisons between the main dimensions and across departments.

Findings

The results of the BSC analysis, conducted based on the AHP method, indicate that the financial dimension is the most critical factor in the evaluation of Industry 4.0 performance. An examination of the sub-criteria within the financial dimension reveals that company-wide total cost holds a weight of 24%, inventory management 12%, and profitability 10%. Within the customer dimension, customer satisfaction was found to have an importance weight of 12%, while customer reliability was assigned a weight of 7%. In the internal processes dimension, product quality accounted for 8%, whereas operational efficiency carried a weight of 2%. Within the learning and growth dimension, qualified workforce was determined to have an importance weight of 5%, while reducing employee turnover was assigned a weight of 1%. The importance weights related to the Balanced Scorecard are presented in Table 1. These findings suggest that financial indicators and customer-oriented criteria are prioritized in the

assessment, whereas factors such as process flexibility and employee engagement are comparatively less significant.

Table 1. Importance Weights of the BSC**.**

Main Criteria	Weight of Main Criteria	Sub-Criteria	Weight of Sub-Criteria	Overall Weight	Percentage %
Financial Dimension	0,49	Company-Wide Total Cost	0,49	0,24	24%
		Inventory Management	0,24	0,12	12%
		Profitability	0,20	0,10	10%
		Sales	0,12	0,06	6%
Customer Dimension	0,28	Customer Satisfaction	0,44	0,12	12%
		Customer Reliability	0,25	0,07	7%
		Response Speed to Customers	0,20	0,06	6%
		Market Share	0,11	0,03	3%
Internal Processes Dimension	0,16	Product Quality	0,48	0,08	8%
		Reduction of Defective Product Rate	0,29	0,05	5%
		Operational Efficiency	0,16	0,02	2%
		Flexibility in Production Processes	0,07	0,01	1%
Learning and Growth Dimension	0,08	Qualified Workforce	0,59	0,05	5%
		Employee Motivation	0,28	0,02	2%
		Reduction in Employee Turnover Rate	0,13	0,01	1%

In AHP analysis, the consistency ratio (CR) is calculated to assess the accuracy and reliability of the decision matrix. According to Saaty, CR should be less than 10%. First, the maximum eigenvalue (λ_max) is used to compute the consistency index (CI) using the Equation 1.

$$CI=(\lambda_{max}-n)/(n-1) \quad \text{(Equation 1)}$$

In the AHP method, λ_max is calculated by multiplying the pairwise comparison matrix with the weight vector, then dividing the resulting values by the corresponding weights and taking their average. It is used for consistency analysis.Then, the consistency ratio is determined using Equation 2, where RI (random index) values are obtained from standard tables.

$$CR=\frac{CI}{RI} \quad \text{(Equation 2)}$$

The values of the random index values for n-dimensional matrices are provided in Table 2. A CR of 10% or below indicates that the decision-making process is consistent and reliable. These calculations help identify and correct inconsistencies in the analysis [4]. As shown in Table 3, the consistency ratios of the sub-criteria under the financial dimension, customer dimension, internal processes dimension, and learning and growth dimension, along with the main criteria, were found to be below 10%. This confirms that all criteria are consistent.

Table 2. Random Index Values.

n	1	2	3	4	5	6	7	8	9	10
RI	0	0	0,58	0,90	1,12	1,24	1,32	1,41	1,45	1,49

Table 3. The λ_max Values, consistency indices, and Consistency Ratio Values of the Criteria.

	Main Criteria	Financial Dimension Sub-Criteria	Customer Dimension Sub-Criteria	Internal Processes Dimension Sub-Criteria	Learning and Growth Dimension Sub-Criteria
λ_max	4,28	4,18	4,15	4,28	3,12
Consistency Index	0,09	0,06	0,05	0,09	0,06
Consistency Ratio	0,10	0,07	0,06	0,10	0,10

In accordance with the importance weights determined using the AHP method, the impact of Industry 4.0 applications on performance was analyzed within the scope of an Industry 4.0 performance evaluation for a company operating in the FMCG sector, specifically focusing on the production, supply chain, and information technology departments. The corresponding impact scores are presented in Table 4.

Table 4. Performance Comparison of Industry 4.0 Applications Across Departments Based on the Balanced Scorecard Main Dimensions.

	Performance Evaluation Score Information Technology Department	Performance Evaluation Score Supply Chain Department	Performance Evaluation Score Production Department
Financial Dimension	1,8	1,89	1,87
Customer Dimension	1,1	1,1	1,3
Internal Processes Dimension	0,6	0,69	0,62
Learning and Growth Dimension	0,2	0,28	0,24
Total Score	3,7	3,96	4,03

In this context, the financial dimension evaluates the contribution of Industry 4.0 applications to the company's economic benefits. The Information Technology Department has shown the lowest performance with a score of 1.8. The Supply Chain Department, with a score of 1.89, holds the leading position, indicating that Industry 4.0 applications have optimized financial processes within the supply chain. The Production Department ranks second with a score of 1.87. The findings suggest that the Supply Chain Department gains the most benefit from Industry 4.0 applications in the financial dimension.

In the customer dimension, the impact of Industry 4.0 applications on customer satisfaction and expectations was evaluated. Both the Information Technology and Supply Chain departments performed equally with a score of 1.1. The Production Department achieved the highest performance in this dimension with a score of 1.3. This result indicates that the Production Department has more effectively integrated customer-focused Industry 4.0 applications.

In the internal processes dimension, the level of digitalization and efficiency of internal operations was considered. The Information Technology Department recorded the lowest performance with a score of 0.6. The Supply Chain Department achieved the highest performance with a score of 0.69, while the Production Department ranked second with a score of 0.62. The leadership of the Supply Chain Department demonstrates that Industry 4.0 applications are more effectively utilized in process management, while the Information Technology Department shows a need for improvement in the digitalization of processes.

In the learning and growth dimension, the impact of Industry 4.0 applications on knowledge sharing, employee development, and organizational learning was analyzed. The Information Technology Department scored the lowest with 0.2, while the Supply Chain Department achieved the highest performance with 0.28. The Production Department ranked second with a score of 0.24. Overall, low scores were observed across all departments in this dimension, indicating that Industry 4.0 applications have not been sufficiently integrated into learning and development processes.

Based on the analysis and calculations conducted for all departments, the company's overall Industry 4.0 performance score was determined to be 3.93 out of 5.

Conclusion

It has been demonstrated through existing research that traditional performance measurement criteria, which rely solely on financial indicators, are insufficient in today's competitive environment. In this context, this study, which specifically focuses on the fast-moving consumer goods sector, aims to comprehensively analyze the effects of Industry 4.0 applications in line with the sector's unique dynamics.

In this study, the Balanced Scorecard method, which includes both financial and non-financial elements, was adopted as a holistic performance evaluation model. The analyses conducted based on the importance weights determined by the AHP method reveal that the effects of Industry 4.0 applications on performance vary across departments, with the supply chain and production departments benefiting more from this transformation process. Notably, the optimization of financial processes stands out as one of the most tangible gains of digital transformation, while organizational learning and development processes have not fully benefited from this transformation.

To monitor the long-term impact of Industry 4.0 and maintain a sustainable competitive edge, companies should repeat the evaluation regularly (e.g., annually or semi-annually). Involving multiple departments in the process can offer a broader perspective, aiding strategic decisions. Prioritizing the learning and growth dimension is crucial for securing long-term competitiveness.

References

Jacob, K., Woschanka, M., & Nadine, O. (2024). Industry 4.0 Technologies and their Implications for Environmental Sustainability in the Manufacturing Industry. 5th International Conference on Industry 4.0 and Smart Manufacturing. Elsevier.

Javaid, M., Haleem, A., Singh, R. P., & Sinha, A. K. (2024). Digital economy to improve the culture of industry 4.0: A study on features, implementation and challenges. Green Technologies and Sustainibility, 2(2). doi:https://doi.org/10.1016/j.grets.2024.100083

Kaplan, R. S., & Norton, D. P. (1992). The Balanced Scorecard - Measures That Drive Performance.

Saaty, T. L. (2008). Decision making with the analytic hierarchy process. International Journal of Services Sciences, 83-98.

MANAGEMENT ENGINEERING

Finance

Marketing

Quantitative Methods

The Effect of ESG Ratings on Firm's Financial Performance in Borsa Istanbul

Alper Ataker[a], Oktay Taş[a]

[a] Istanbul Technical University, Management Engineering, Management Engineering (Dr), Turkey
ataker22@itu.edu.tr

Keywords: ESG (Environmental, Social, Governance) Scores, Financial Performance, Long-Term Stock Returns, Borsa Istanbul.

Aim

This research explores how Environmental, Social, and Governance (ESG) ratings affect the financial success of companies listed on Borsa Istanbul. The main goal is to figure out if firms with better ESG scores typically do better than the overall market, as shown by the BIST-100 index, over different time periods—like 1 month, 3 months, 6 months, and 1 year. The study also breaks down how much each part of ESG—the Environmental (E), Social (S), and Governance (G) aspects—contributes on its own, as well as how any ESG-related controversies might affect a company's performance. By looking at an emerging market like Turkey, the research aims to gather real-world evidence on the financial impact of ESG practices in a setting where rules and investor understanding of sustainability are still developing.

This research really hits the mark, especially with the world increasingly focusing on sustainable investing and demanding more openness in how companies are run. As everyone from investors to regulators puts more stock in sustainability, figuring out how environmental, social, and governance (ESG) factors impact a company's bottom line is becoming super important. This study adds to what we already know by shedding light on how ESG practices affect a company's performance in a developing market, where the way ESG is adopted might be quite different from what we see in more established economies.

Material and Method

This research uses Refinitiv's ESG ratings for companies listed on Borsa Istanbul in 2022 and 2023. It measures these firms' financial success by looking at their stock returns over various periods, using methods like Ordinary Least Squares (OLS) regression and panel data analysis. The main factors considered are the overall ESG score and its individual parts (Environmental, Social, and Governance), with the firms' stock returns, compared to the BIST-100 index, as the outcome of interest. The study also considers ESG controversy scores to see how they affect stock performance. It examines three main models: (1) the combined ESG score against financial performance, (2) the individual ESG parts against financial performance, and (3) the detailed sub-components of ESG against financial performance. This approach, driven by data, keeps the impact of company size and transparency to a minimum, offering a strong and reliable examination of how ESG scores connect to financial results.

Findings

The study's findings show that companies with better ESG scores tend to do better financially, beating out their competitors. It turns out that the Social (S) part of ESG has the biggest influence on how well a company does, followed by the Environmental (E) and then the Governance (G) parts. This implies that things like how a company treats its employees, its stance on human rights, and how responsibly it makes its products are really important for its financial success. On the flip side, when companies get caught up in ESG-related controversies, it hurts their stock prices, emphasizing how crucial it is for businesses to be open and ethical in how they operate.

Interestingly, while ESG factors significantly influence individual firm returns, no significant relationship is found between ESG scores and the performance of the BIST-100 index. This indicates that ESG effects are firm-specific rather than market-wide, meaning that companies with strong ESG practices may outperform their peers but do

not necessarily drive broader market trends. These findings align with global research, which has consistently shown that ESG integration can lead to improved financial performance, particularly in terms of risk management and long-term value creation.

Conclusion

The study concludes that ESG ratings play a crucial role in enhancing firm financial performance, particularly in emerging markets like Turkey. Firms with higher ESG scores tend to achieve better stock returns, with the Social component being the most influential driver of financial success. The findings support several theoretical frameworks, including Stakeholder Theory, Resource-Based View, Legitimacy Theory, and Signaling Theory, by demonstrating that ESG practices contribute to long-term value creation, risk mitigation, and investor confidence.
For investors, ESG scores can serve as reliable indicators of financial stability and long-term value creation. The study suggests that investors should consider firm-specific ESG practices rather than relying solely on overall market trends when making investment decisions. Companies with strong social performance, in particular, may offer better risk-adjusted returns, making social factors a key focus for sustainable investment strategies.
For firms, integrating ESG considerations into corporate strategies is essential for improving financial performance and managing reputational risks. The study highlights the importance of addressing ESG controversies, as they can have a significant negative impact on stock performance. Firms should also adopt sector-specific ESG strategies, as different industries respond uniquely to ESG drivers.
For policymakers, the study provides evidence to support the development of stronger ESG disclosure regulations and incentives for sustainable business practices. Regulatory bodies should consider implementing measures such as tax benefits, grants, or preferential access to capital markets to encourage ESG adoption. Additionally, promoting ESG-focused financial instruments, such as green bonds and sustainability-linked loans, could further support sustainable business practices in emerging markets.
Despite its contributions, the study acknowledges several limitations. The research relies on ESG scores from Refinitiv, which may not fully capture all aspects of a firm's sustainability efforts. Future studies could incorporate alternative ESG ratings and proprietary sustainability metrics to provide a more comprehensive analysis. The study's time horizon is also limited to 2022 and 2023, which restricts the ability to assess long-term financial impacts. Expanding the timeframe could provide deeper insights into ESG trends and performance over multiple economic cycles.
Furthermore, while the study identifies correlations between ESG scores and financial performance, it does not establish a definitive causal link. Future research could employ causal inference techniques, such as difference-in-differences (DiD) or instrumental variable (IV) approaches, to strengthen causal claims. Additionally, a more detailed industry-level analysis could provide more granular insights into how ESG factors influence firm performance across different sectors.
In conclusion, this research underscores the growing importance of ESG factors in financial performance, particularly in emerging markets like Borsa Istanbul. The findings provide meaningful insights for investors, corporate managers, and policymakers, encouraging the integration of ESG principles into investment strategies and corporate decision-making. Future research can build on these insights by incorporating longer-term data, alternative ESG rating methodologies, and more sophisticated econometric models to further refine our understanding of the ESG-financial performance nexus.

References

Amel-Zadeh, A., & Serafeim, G. (2018). Why and how investors use ESG information: Evidence from a global survey. Financial Analysts Journal, 74(3), 87–103.
Arslan, M., & Kılıç, E. (2023). Market reaction to ESG disclosures: Evidence from Borsa Istanbul. Journal of Financial Markets, 11(4), 567–589.
Barney, J. (1991). Firm resources and sustained competitive advantage. Journal of Management, 17(1), 99–120.
Bayram, E. (2024). The impact of ESG scores on stock performance: The case of Borsa Istanbul. Date retrieved 10.01.2025, from https://repository.bilkent.edu.tr/bitstreams/73a9da5d-b3cf-4852-a21f-7f24b2c38c2e/download

Boubaker, S., Cellier, A., Manita, R., & Saeed, A. (2022). Does it pay to be green in emerging markets? International evidence from ESG scores. Journal of Corporate Finance, 72, 102113.
Çelik, M., & Yıldırım, T. (2023). Sector-specific impact of ESG scores on firm performance: Evidence from Borsa Istanbul. Journal of Business Ethics, 18(2), 345–367.
Capital Markets Board of Turkey (CMB) (2022). Capital Markets Board of Turkey: Sustainability principles compliance framework. Date retrieved 05.01.2025, from https://www.cmb.gov.tr
Feng, G., Long, H., Wang, H., & Chang, C. (2022). Environmental, social, and governance, corporate social responsibility, and stock returns. Corporate Social Responsibility and Environmental Management, 29(5), 1884–1895.
Freeman, R. E. (1984). Strategic management: A stakeholder approach. Pitman Publishing.
Friede, G., Busch, T., & Bassen, A. (2015). ESG and financial performance: Aggregated evidence from more than 2000 empirical studies. Journal of Sustainable Finance & Investment, 5(4), 210–233.
Hart, S. L., & Dowell, G. (2020). Invigorating the resource-based view of the firm. Academy of Management Review, 45(1), 27–40.
Hill, C. W., Jones, G. R., & Schilling, M. A. (2021). Strategic management: An integrated approach. Cengage Learning.
Husted, B. W., de Jesus Salazar, J. L., & Montiel, I. (2016). A critical review of corporate social responsibility (CSR) in emerging markets. Journal of Business Research, 69(1), 155–163.
International Integrated Reporting Council (IIRC) (2021). Integrated reporting framework. Retrieved on January 12, 2025, from https://integratedreporting.org
Jensen, M. C., & Meckling, W. H. (1976). Theory of the firm: Managerial behavior, agency costs, and ownership structure. Journal of Financial Economics, 3(4), 305–360.
Kartal, M. T., Kılıç Depren, S., Pata, U. K., & Taşkın, D. (2024). Modeling the link between environmental, social, and governance disclosures and scores: The case of publicly traded companies in the Borsa Istanbul Sustainability Index. Financial Innovation, 10(1), 1–25.
Kaya, A., & Özdemir, B. (2024). ESG scores and financial performance: Evidence from BIST 100. Journal of Sustainable Finance & Investment, 15(1), 89–105.
Luo, X., & Bhattacharya, C. B. (2006). Corporate social responsibility, customer satisfaction, and market value. Journal of Marketing, 70(4), 1–18.
Saygili, E., Arslan, S., & Birkan, A. O. (2022). ESG practices and corporate financial performance: Evidence from Borsa Istanbul. Borsa Istanbul Review, 22(1), 139–150.
Wang, Y., & Li, X. (2024). The impact of ESG scores on firm performance in the Chinese stock market. Journal of Corporate Finance, 30(1), 112–130.
Whelan, T., Atz, U., & Casey, J. (2021). ESG and financial performance: The case for sustainability-focused investing. NYU Stern Center for Sustainable Business, 12(1), 3–24.

TEFAS's Effect on the Turkish Mutual Funds Landscape

Mehmet Sami Boz[a]

[a] Bogazici University, Economics, Turkey
sami.boz@bogazici.edu.tr

Keywords: Fund Competition , Mutual Funds , TEFAS.

Aim

This study rigorously examines the impact of the Turkey Electronic Fund Trading Platform (TEFAS) on the Turkish mutual fund market. Introduced in January 2015, TEFAS aimed to enhance market transparency, accessibility, and competition by allowing investors to access a wide array of mutual funds through a single platform. This research focuses on dissecting the multifaceted effects of TEFAS on competition dynamics, fee structures, and performance characteristics within the Turkish mutual fund landscape. Specifically, the research aims to:

1. **Assess the impact of TEFAS on competition within the Turkish mutual fund market:** This involves evaluating whether TEFAS has led to increased competitive pressures, as evidenced by changes in market concentration, fund entry/exit rates, and shifts in market share among different fund management companies.
2. **Determine whether TEFAS has influenced fee structures:** This includes analyzing whether TEFAS has resulted in a reduction in average fees, a convergence of fees across similar fund categories, and changes in the distribution of fee levels.
3. **Investigate the relationship between fees and performance:** This explores whether the introduction of TEFAS has altered the relationship between fund fees and performance, particularly in the context of existing literature suggesting that lower-performing funds often charge higher fees. The research seeks to determine whether TEFAS has mitigated this phenomenon by increasing investor awareness and price sensitivity.
4. **Analyze the role of regulatory interventions in shaping market dynamics:** This acknowledges that the effects of TEFAS are intertwined with other regulatory changes and interventions by the Capital Market Board of Turkey (SPK). The research aims to disentangle the specific impact of TEFAS from these concurrent regulatory influences.
5. **Provide insights into investor outcomes:** Ultimately, the study aims to understand how the changes brought about by TEFAS have affected investor welfare, including access to diverse investment options, cost efficiency, and overall portfolio performance.

Material and Method

This study employs a quantitative research design, utilizing a comprehensive dataset of Turkish mutual fund data spanning from January 2005 to June 2020. The data was meticulously sourced and cleaned to ensure accuracy and reliability. The dataset includes; daily fund prices, assets under management (AUM), fund fees (Expense Ratios), fund names and categories, company affiliations, and benchmarks.
The analysis period is primarily focused on January 2011 to January 2019 to create a balanced pre- and post-TEFAS implementation dataset. Funds with less than one year of total duration were excluded to ensure data quality. The final dataset for regression analysis comprises 465 funds.
The research is structured into three primary analytical components:

1. **Descriptive Analysis:**
    - **Fund Entry and Exit Trends:** Analyzing the number of new fund entrants and exits over time, particularly around the TEFAS introduction date, to assess its impact on market dynamism.

- **Market Share Evolution:** Tracking the market share of different fund categories and fund management companies to understand changes in competitive positioning.
- **Concentration Measures:** Calculating the Herfindahl-Hirschman Index (HHI) to assess market concentration and identify potential shifts in competitive intensity.

2. **Fee Versus Performance Analysis:**
   - **Performance Evaluation:** Calculating Jensen's alpha using the Capital Asset Pricing Model (CAPM) to evaluate fund performance relative to appropriate benchmarks for each category. The alpha is regressed upon the fee level of the fund.
   - **Regression Analysis:** Conducting regressions to examine the relationship between alpha and fund fees, controlling for other factors such as fund size and market share. Assessing the statistical significance of the relationship between fees and performance and comparing the pre- and post-TEFAS periods.
3. **Competition Analysis:**
   - **Panel Data Regressions:** Employing panel data regressions to assess the competitive effects of TEFAS on fee structures, using fund fees as the dependent variable and a treatment dummy for the post-TEFAS period.
   - **Control Variables:** Including control variables such as fund performance (alpha), company size (categorized using k-means clustering on AUM), and market share to account for other factors that may influence fee levels.
   - **Fixed Effects:** Incorporating fixed effects for years to control for time-invariant unobserved heterogeneity and isolate the impact of TEFAS.
   - **Robust Standard Errors:** Clustering standard errors at the fund level to address potential serial correlation within funds.
   - **Herfindahl-Hirschman Index (HHI):** Including HHI as a control variable in the regressions to account for the influence of market concentration on fee structures.

Findings

The analysis yielded several key findings:

1. **Increased Market Access and Competition:** The introduction of TEFAS was followed by a significant increase in the number of new mutual fund entrants, suggesting that the platform has lowered barriers to entry and promoted market dynamism.
2. **Categorization Changes:** Significant shifts were observed in the distribution of funds across categories, particularly in variable and equity funds, reflecting the impact of regulatory changes and evolving investor preferences.
3. **Market Share Dynamics:** The market share analysis revealed trends of increasing dominance in specific categories, such as equity funds, post-TEFAS implementation. However, smaller categories like commodity and eurobond funds remained relatively stable. The slight increase in market concentration, as measured by the Herfindahl-Hirschman Index (HHI) we found.
4. **Mixed Signals on Fee and Performance Relationships:** We get mixed signals about fee and performance links. Also, no significant result between fee and performance can be seen in pre and post-treatment periods. The equity fund category exhibited a positive and significant relationship between alpha and fees. Variable funds showed a predominantly negative relationship. Money market funds also showed positive relationships.
5. **Fee Convergence and Variance Reduction:** Introducing TEFAS has led to decreased general fees for funds in each category, with the most substantial declines observed in the money market and eurobond funds, suggesting increased competitive pressure. The regression analysis for variance in fee levels across different mutual fund categories yields insightful results regarding the competitive dynamics following the introduction of the TEFAS platform. Specifically that introducing TEFAS has led to a decrease in fee variance in equity, variable, money market, and bond funds. Increased fee variance in private sector bond,

commodity, and eurobond funds. Also we find that higher market concentration generally led to lower fee variance, indicating more standardized fee structures in concentrated markets.

6. **Heterogeneous Effects Across Categories:** The impact of TEFAS varied across different fund categories, with some categories experiencing more pronounced changes in fee structures and market concentration than others.

Table 1. Regression with Mean Fee as Dependent Variable.

	Equity	Variable	Money Market	Bond	Private Sector Bond	Commodity	Eurobond
Treatment	-0.009***	-0.009***	-0.019***	-0.009***	-0.008	-0.008***	-0.015***
Company Size	0.001	0.006	0.003	0.018***	-0.002	0.018	0.003
Market Share	0.039***	-0.083***	0.003	0.004	-0.001	-0.004	0.001
Alpha	1.200***	0.916***	-0.001	-2.050*	-0.947	-1.395***	-2.582

Notes:
*p<0.1; **p<0.05; ***p<0.01.
Fixed year effects are used. Standard errors were clustered at the fund level to ensure robustness.

Conclusion

This study concludes that the introduction of TEFAS has had a significant and multifaceted impact on the Turkish mutual fund market. The platform has facilitated market access, increased competition, and promoted fee convergence in major fund categories. While the evidence on fee and performance relationships remains mixed. The findings are not fully consistent with international literature, suggesting that there may be unique factors at play in the Turkish market. The varying effects across different fund categories underscore the importance of considering specific market segments in regulatory and competitive analyses. Overall, these results highlight the complexity of market dynamics and the importance of considering specific category characteristics in regulatory and competitive analyses.

Furthermore, while TEFAS appears to have achieved its aim of increasing competition and accessibility, the increase in market concentration warrants further monitoring to ensure a balanced and competitive market environment. Regulators should consider targeted interventions to promote competition in specific fund categories and address potential distortions in the fee-performance relationship. Further research could explore the long-term effects of TEFAS, the impact of specific regulatory interventions, and the dynamics of investor behavior in the Turkish mutual fund market.

References

Elton, E. J., Gruber, M. J., Brown, S. J., & Goetzmann, W. N. (2014). Modern Portfolio Theory and Investment Analysis (9th ed.). Wiley.

Erzurumlu, Y. Ö. (2001). Evaluation of Portfolio Performance of Mutual Funds (Order No. 28589115). Available from ProQuest Dissertations & Theses Global. https://www.proquest.com/dissertations-theses/evaluation-portfolio-performance-mutual-funds/docview/2569583918/se-2

Forgy, E. W. (1965). Cluster analysis of multivariate data: efficiency vs interpretability of classifications. Biometrics, 21(4), 768-769.

Gil-Bazo, J., & Ruiz-Verdú, P. (2008). When cheaper is better: Fee determination in the market for equity mutual funds. Journal of Economic Behavior & Organization, 67(3-4), 871-885.

Gil-Bazo, J., & Ruiz-Verdú, P. (2009). The relation between price and performance in the mutual fund industry. Journal of Finance, 64(5), 2153-2183.
Hlavac, M. (2022). *stargazer*: *Well-Formatted Regression and Summary Statistics Tables*. (version 5.2.3)[R package] https://CRAN.R-project.org/package=stargazer
Jensen, M. C., Black, F., & Scholes, M. S. (1972). The capital asset pricing model: Some empirical tests. In M. C. Jensen (Ed.), Studies in the Theory of Capital Markets (pp. 79-121). Praeger Publishers.
Reilly, F. K., & Brown, K. C. (2012). Investment Analysis and Portfolio Management (10th ed.). Cengage Learning.
Rhoades, S. A. (1993). The Herfindahl-Hirschman Index. Federal Reserve Bulletin, 79, 188.
Yatırım Fonlarına İlişkin Esaslar Tebliği (2013 Jul 9). Resmi Gazete (28702) https://www.resmigazete.gov.tr/eskiler/2013/07/20130709-14.htm
SPK. (2013 Dec 12). Yatırım Fonlarına İlişkin Rehber. Retrieved from https://mevzuat.spk.gov.tr/Rehber/Dosya/35
Takasbank. (2024, May 18). About Us. Retrieved from https://www.takasbank.com.tr/en/about-us/introduction/takasbank
TEFAS. (2024, May 18). About Us. Retrieved from https://fundturkey.com.tr/(S(5fhndy3aplafpqjjbcjt1go0))/Hakkinda.aspx
Wahal, S., & Wang, A. (2011). Competition among mutual funds. Journal of Financial Economics, 99(1), 40-59.

MANAGEMENT ENGINEERING

Finance

Marketing

Quantitative Methods

Adoption of Smart Small Home Appliances: An Analysis of Social and Behavioral Factors

Betül İmamoğlu[a], Huriye Şebnem Burnaz

[a] Istanbul Technical University/Departmant of Management, Management Engineering Program, Turkey
imamoglub19@itu.edu.tr

Keywords: Smart Home Appliances, Technology Adoption, Consumer Behavior.

Aim

This study aims to develop a conceptual model that explains how consumers in Turkey adopt and interact with smart small home appliances, especially those featuring mobile-based remote control functionalities. Unlike Western markets, where fully integrated smart home systems are more common, Turkish consumers often use isolated smart products—such as connected washing machines or robot vacuums—without broader platform adoption.
This behavioral pattern suggests that traditional technology adoption models focusing on economic or technical rationality may be insufficient to explain usage in this context. Therefore, this study emphasizes perceptual, behavioral, and contextual dimensions of adoption, aiming to create an integrated framework that includes both technological and personal drivers. The model is developed through a combination of literature review and expert insights, and is designed to be empirically tested in a forthcoming quantitative phase.

Material and Method

This research uses a two-step mixed methods design. The first step stands on a qualitative study to understand the topic in depth. The second step incorporates a survey-based quantitative study that will based on qualitative insights along with literature survey.

Phase 1 – Qualitative Study

Semi-structured interviews were conducted with three professionals from a multinational white goods and small appliance company operating in Turkey:

A Website Marketing Executive, A Website Marketing Specialist, A Brand Marketing Manager.

Phase 2 – Planned Quantitative Study

Based on the first phase, a survey has been created to measure the eight variables using a 7-point Likert scale. The survey will also collect demographic data and past usage behavior. The goal is to reach smart appliance users and potential adopters from different regions and age groups in Turkey.

Findings

The qualitative phase yielded valuable insights from three expert interviews (60–90 minutes each) with professionals in website marketing, digital strategy, and brand management. Their observations illuminated why many Turkish consumers fail to adopt smart appliance features—despite owning compatible devices. The findings point to a complex mix of perception gaps, habitual behavior, and communication barriers.

Eight major themes emerged from the data:
1. Limited Perceived Usefulness:

Users often misunderstand smart features. As the Website Marketing Executive stated:

"They assume if there's remote diagnostics, the machine is going to break. But 'start laundry from work' gets a positive response."
Usefulness must be framed within relatable, daily contexts (Davis, 1989; Li et al., 2023).

2. Habitual Use Resists Change:

"People go back to manual mode—they trust what they grew up with."
Even when aware, users often default to old routines (Li et al., 2021).

3. Low Ease of Use from Technical Barriers:

"If Wi-Fi drops, users don't know how to reconnect. Installers don't help."
Lack of support reduces usability (Basarir-Ozel et al., 2023).

4. Lack of Visibility and Social Proof:

"If influencers don't show the smart feature, no one does."
Low visibility weakens adoption (Moore & Benbasat, 1991; Ferreira et al., 2023).

5. Misunderstood Value:

"Less foam means not clean to them. So detergent-saving sounds bad."
Users apply outdated heuristics to judge performance (Schwartz, 1992; Li et al., 2023).

6. Segmented Innovativeness:

"Urban professionals are open. In smaller cities, people fear data sharing."
Adoption varies by region and lifestyle (Li et al., 2023; Li et al., 2021).

7. Lack of Trust:

"They ask, 'Who has access to my dishwasher?'"
Data security concerns create psychological resistance (Li et al., 2023).

8. Low Trialability:

"If they could try it in the store even once, it would help."
Hands-on experience reduces uncertainty (Moore & Benbasat, 1991).

Together, these findings show that ownership does not equal adoption. While consumers may purchase smart appliances, a wide array of behavioral, perceptual, and contextual barriers prevent them from using key features—especially remote-control capabilities. These barriers mirror the constructs outlined in the proposed model and will serve as the empirical basis for the quantitative phase.

Conclusion

This research introduces a model to help understand why Turkish consumers accept or resist using smart small home appliances. The model brings together ideas from well-known theories and adapts them based on real feedback from professionals in the field. So far, the findings are based only on interviews. The next step will

involve testing the model with a broader group of users through a national survey. Once this step is completed, we hope to provide clear insights into the factors that shape technology acceptance. Until then, the model and findings should be treated as exploratory. No policy or marketing recommendations are offered at this stage.

References

Basarir-Ozel, B., Nasir, V. A., & Turker, H. B. (2023). Determinants of smart home adoption and differences across technology readiness segments. Technological Forecasting and Social Change, 197, 122924. https://doi.org/10.1016/j.techfore.2023.122924

Davis, F. D. (1989). Perceived usefulness, perceived ease of use, and user acceptance of information technology. MIS Quarterly, 13(3), 319–340. https://doi.org/10.2307/249008

Ferreira, L., Oliveira, T., & Neves, C. (2023). Consumer's intention to use and recommend smart home technologies: The role of environmental awareness. Energy, 263, 125814. https://www.sciencedirect.com/science/article/pii/S0360544222027001

Li, L., Li, T., Cai, H., Zhang, J., & Wang, J. (2023). I will only know after using it: The repeat purchasers of smart home appliances and the privacy paradox problem. Computers & Security, 128, 103156. https://doi.org/10.1016/j.cose.2023.103156

Li, W., Yigitcanlar, T., Erol, I., & Liu, A. (2021). Motivations, barriers and risks of smart home adoption: From systematic literature review to conceptual framework. Energy Research & Social Science, 80, 102211. https://doi.org/10.1016/j.erss.2021.102211

Moore, G. C., & Benbasat, I. (1991). Development of an instrument to measure the perceptions of adopting an information technology innovation. Information Systems Research, 2(3), 192–222. https://doi.org/10.1287/isre.2.3.192

Schwartz, S. H. (1992). Universals in the content and structure of values. Advances in Experimental Social Psychology, 25, 1–65. https://doi.org/10.1016/S0065-2601(08)60281-6

Venkatesh, V., Thong, J. Y. L., & Xu, X. (2012). Consumer acceptance and use of information technology: Extending the unified theory of acceptance and use of technology. MIS Quarterly, 36(1), 157–178. https://doi.org/10.2307/41410412

Understanding Consumer Acceptance and Purchase Intentions in Unmanned Retail Stores

Gözde Erdoğan[a]

[a] Istanbul Technical University, Faculty of Management, Engineering Management Master of Science Program, Türkiye
gencg23@itu.edu.tr

Keywords: Consumer Acceptance, Shopping Intentions, Technology Paradoxes, Technology Readiness, Unmanned Stores.

Aim

This study aims to thoroughly explore consumer shopping intentions in unmanned retail stores. Unmanned stores provide an innovative shopping experience that operates without human intervention through the integration of automated systems, offering the potential to reduce labor costs in the retail sector. (Figure 1.). The objective of the research is to determine how technological innovations are accepted, alongside the perceived benefits and ease of use by users, and how these factors influence shopping behavior. Specifically, the relationship between the level of technological readiness and shopping intentions will be examined. Additionally, by investigating the effects of users' perceptions of enjoyment on shopping intentions, strategies aimed at increasing customer satisfaction in unmanned stores will be developed.

Figure 1. Unmanned Store.

Material and Method

The study began with a comprehensive literature review examining factors that influence consumer behavior in unmanned retail stores, drawing from academic publications across various disciplines. In this study, survey-based data collection methods reported in the literature were taken as the basis. Surveys were used as the primary data collection tool in the reviewed studies; however, no original survey was conducted within the scope of this research. According to the reviewed literature, the survey participants were individuals from diverse demographic backgrounds who had experience shopping in unmanned retail stores.

In the relevant literature, variables such as shopping intentions, perceived ease of use, perceived benefit, perceived enjoyment, and levels of technological readiness were commonly measured using 5-point and 7-point Likert scales. This study compiled and comparatively analyzed the findings from these sources.

The data obtained from the literature were interpreted to better understand the relationships between variables, particularly by referencing studies that employed structural equation modeling (SEM). Additionally, findings from studies that included hypothesis testing were examined to identify and interpret the relationships among the variables.

The Technology Acceptance Model (TAM), a widely recognized model, has been extensively employed in the literature. The Technology Acceptance Model (TAM) examines consumers' intentions to use technology, discussing perceived ease of use and perceived benefit to understand shopping intentions.
The main components in the survey can be defined as follows:

Perceived Ease of Use: The level of difficulty and obstacles users encounter during the shopping process in unmanned stores.

Perceived Benefit: The advantages of shopping in unmanned stores, such as time savings and shopping convenience.

Perceived Enjoyment: The pleasure and satisfaction experienced by customers while shopping in an unmanned store.

Shopping Intentions: Factors determining consumers' desire and motivation to shop in unmanned stores.
Technological Readiness: Consumers' abilities to adapt to new technologies and their perceptions towards these technologies, divided into four categories: (Figure 2.)

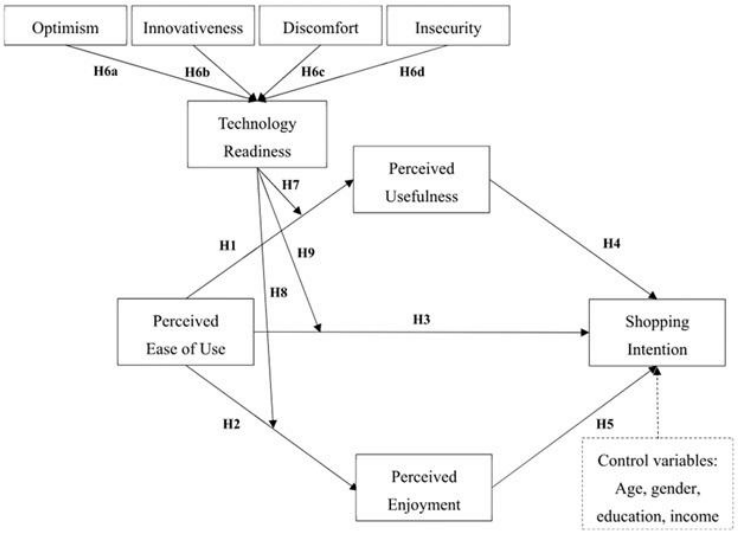

Figure 2. Factors that affect and are affected by technology readiness (Chang, Y-W. and Chen J. 2021).

- Optimism: Belief in the control, flexibility, and efficiency offered by technology.
- Innovativeness: Tendency to be a pioneer in technology.
- Discomfort: Negative feelings arising from a lack of control over technology.
- Insecurity: Distrust in technology and concerns about potential harm.

Paradoxes of Technology: A technology paradox occurs when the very innovations designed to enhance efficiency, control, or privacy simultaneously introduce challenges such as inefficiencies, chaos, or public exposure, leading to a conflicted user experience. (Figure 3.)

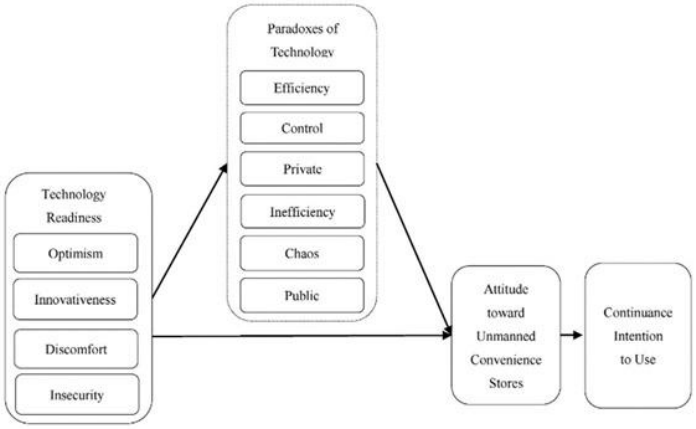

Figure 3. Factors that affect and are affected by paradoxes of technology (Park, H J. and Zhang Y. 2022).

Efficiency/Inefficiency Paradox: While technology can speed up the shopping process and save time, errors or limited human assistance may lead to inefficiencies. Users may feel frustrated due to negative experiences despite the benefits of efficiency.

Control/Chaos Paradox: Technologies like self-service checkouts offer users greater control during shopping. However, situations such as crowds and long waits can create chaos, leading to confusion even when users believe they are in control.

Private/Public Paradox: Technology can cater to users' private needs, yet some may develop negative attitudes towards it due to concerns over miscommunication and confusion during shopping. This paradox creates a conflict between the unique benefits of innovation and the overall user experience.

The analysis of collected data was conducted in detail to test hypotheses and derive conclusions. Structural equation modeling was used to determine the relationships between variables, examining the impact of the level of technological readiness and the dynamics between other components.

Findings

The research results show that perceived ease of use has a significantly positive effect on perceived benefit and perceived enjoyment. This indicates that the use of unmanned stores is an important factor in enhancing consumer experience. Additionally, technological readiness was found to positively influence the relationships between perceived ease of use and shopping intentions. These findings highlight the elements needed to make consumers' experiences in unmanned stores more positive. It was determined that perceived enjoyment increases consumers' desire to shop and plays an important role in shopping intentions.

Furthermore, it was identified that among control variables, only education level had a significant effect on shopping intentions, while other demographic factors were not influential. It was observed that individuals with higher education levels are more open to new technologies and interact more comfortably in unmanned stores. This demonstrates the important role of education level in the acceptance of technological innovations.

The study also highlighted the effects of technological readiness factors (optimism, innovativeness, discomfort, and insecurity). Optimism and innovativeness positively affected consumers' perceived benefit and ease of use. In contrast, negative factors such as discomfort and insecurity have the potential to diminish these positive relationships. Users with low technological readiness experience more anxiety in their interactions with unmanned stores, leading to a negative attitude toward technology use.

In this context, it was determined that the elements of technological readiness play a crucial role in influencing consumer behavior. Reducing concerns related to the acceptance of technological innovations can help consumers have a more positive shopping experience in unmanned stores. Specifically, fostering a positive perception of technology has the potential to strengthen consumers' shopping intentions.

Moreover, other factors affecting user experiences in unmanned stores should also be considered. For instance, factors such as store atmosphere, product variety, and customer service can directly impact consumer satisfaction

and shopping intentions. In this context, it is important for retailers to pay attention to these elements and develop strategies to enhance the shopping experience.

The Efficiency/Inefficiency Paradox highlights how technology can save time in shopping but also create issues like errors and limited human assistance, leading to frustration despite its efficiency. The Control/Chaos Paradox shows that while technologies like self-service checkouts give users more control, factors like crowds and long waits can cause chaos and confusion. Lastly, the Private/Public Paradox illustrates that while technology caters to private needs, concerns over miscommunication can lead to negative attitudes, creating a conflict between the benefits and the overall experience. Retailers need to address these tensions to improve acceptance and satisfaction in unmanned stores.

In conclusion, it was determined that consumers' perceived privacy protection, efficiency, and trust perceptions vary, with individuals open to high technology having a more positive experience. Conversely, those with low technological readiness had more negative experiences, adversely affecting the use of technology.

Table 1. Literature Review.

No	Journal Title	Year	Article Title	Authors	Abstract
1	Journal of Retailing and Consumer Services	2025	Consumer preferences for unmanned stores: A choice experiment study	Yasser Moustafa Shehawy, Syed Md Faisal Ali Khan, Nasser Ali M Khalufi, Riyaz Sheikh Abdullah	The study examines factors affecting shopping intentions in AI-powered automated stores, identifying positive effects of innovativeness and optimism and negative effects of insecurity. Perceived ease of use, benefit, enjoyment, personalization, and interaction are significant determinants of shopping intentions.
2	Journal of Retailing and Consumer Services	2025	Consumer preferences for unmanned stores: A choice experiment study	Youngwon Nam, Sihyun Lee, Hoyoung Lee,	The study examines consumer preferences for unmanned stores and reveals that both technological and store-related features influence consumer choices. It was found that as advanced technology levels increase, consumer preferences decrease, and payment technologies differ from other features.
3	Journal of Retailing and Consumer Services	2022	Technology readiness and technology paradox of unmanned convenience store users	Hyun Jung Park, Yining Zhang	Technological readiness does not directly affect the use of unmanned stores. Instead, it is affected through technology paradoxes. Users open to high technology experience greater paradoxical satisfaction, while those with lower technological readiness exhibit more negative attitudes, influencing the intention for continuous use of the technology.

4	Journal of Retailing and Consumer Services	2021	What motivates customers to shop in smart shops? The impacts of smart technology and technology readiness	Yu-Wei Chang, Jiahe Chen	The study examines the motivations influencing consumer shopping intentions in smart stores, particularly evaluating the role of technological readiness in this process. The results indicate that perceived ease of use affects shopping intentions and that technological readiness strengthens this effect.
5	Journal of Retailing and Consumer Services	2020	Shopping intention at AI-powered automated retail stores (AIPARS)	Rajasshrie Pillai, Brijesh Sivathanu, Yogesh K. Dwivedi	Using the Technology Acceptance Model, the study examined factors influencing the adoption of robot-assisted retail services and identified perceived benefit as a significant mediator in customer acceptance. Education and socio-cultural norms affect customers' attitudes toward and adoption of robots.

Conclusion

The research contributes to the literature by identifying key factors affecting consumer acceptance of unmanned stores. Notably, the positive effects of perceived ease of use and benefits on shopping intentions highlight the importance of adopting these technologies in the retail sector. For effective deployment of unmanned stores, consumer perceptions of security, privacy, and ease of use are crucial.

Retailers can accelerate the adoption of this new shopping experience by enhancing technology preparedness and developing strategies. Future research should delve deeper into cultural and demographic factors and contribute to the literature.

While technological innovations have the potential to enhance customer satisfaction and workforce efficiency, necessary measures for acceptance are discussed in the literature. The experience in unmanned stores can reshape socioeconomic structures and employment dynamics. Therefore, the societal impacts of these systems should be emphasized in the literature.

Moreover, the efficiency/inefficiency paradox arises as technology can significantly speed up the shopping process and save time; however, errors or limited human assistance may lead to inefficiencies. Users may feel frustrated due to negative experiences despite the efficiency benefits these innovations promise. Similarly, the control/chaos paradox is evident in technologies like self-service checkouts, which offer greater control to users during shopping. Nevertheless, situations such as crowded stores and long wait times can lead to chaos and confusion, ultimately detracting from the shopping experience even when users believe they are in control.

Furthermore, the private/public paradox is noteworthy in that technology can cater to users' private needs effectively, yet some may develop negative attitudes towards it due to concerns over miscommunication and confusion during the shopping process. This paradox creates a conflict between the unique benefits of innovation and the overall user experience, impacting consumers' willingness to embrace unmanned retail technologies.

In conclusion, by developing user-friendly applications and solutions that meet consumer needs, retailers can lay the foundation for a sustainable future in unmanned retail, contributing not only to the literature but also to the overall enhancement of consumer experiences. Addressing these paradoxes in future research will provide deeper insights into the complexities surrounding technology adoption in retail settings.

References

Chang, Y-W. and Chen J. (2021), What Motivates Customers to Shop in Smart Shops? The Impacts of Smart Technology and Technology Readiness, Journal of Retailing and Consumer Services, 58
Nam, Y., Lee, S., and Lee, H. (2025), Consumer Preferences for Unmanned Stores: A Choice Experiment Study, Journal of Retailing and Consumer Services, 82
Park, H J. and Zhang Y. (2022), Technology Readiness and Technology Paradox of Unmanned Convenience Store Users, Journal of Retailing and Consumer Services, 65
Pillai, R., Sivathanu B., and Dwivedi Y K. (2020), Shopping Intention at AI-Powered Automated Retail Stores (AIPARS), Journal of Retailing and Consumer Services, 57
Shehawy, Y M., Khan S F A, Khalufi N A. and Abdullah R S. (2025), Customer Adoption of Robot: Synergizing Customer Acceptance of Robot-Assisted Retail Technologies, Journal of Retailing and Consumer Services, 82

MARITIME STUDIES

Maritime Human Resources

Maritime Security

Importance of Safety Awareness and Safety Culture Onboard with Alternative Fuels

Aysel Camci[a], Firat Bolat[b]

[a] Istanbul Technical University, Graduate School, Maritime Studies, Türkiye
[b] Istanbul Technical University, Maritime Faculty, Maritime Transportation Management, Türkiye
camci23@itu.edu.tr

Keywords: Human Factor, Maritime, Maritime Safety, Safety Awareness.

Aim

Approximately 90% of global transportation is conducted via maritime routes, underscoring the sector's critical role in economic sustainability and international trade. However, maritime transportation faces several challenges threatening its long-term viability. While the industry is influenced by political, environmental, and technological factors, onboard safety remains a fundamental pillar for sustainable development (Pyć, 2020).

Although safety is essential in all industrial sectors (Kamis et al., 2020), maritime safety presents unique complexities compared to land-based industries. According to the International Maritime Organization (IMO), seafaring is among the most hazardous occupations globally (Maritime Safety, n.d.). Studies show that maritime operations share characteristics with other high-risk industries, especially in how safety culture affects behavior and safety outcomes (Andrei et al., 2020). Following historical tragedies such as the Titanic disaster, international frameworks like the Safety of Life at Sea (SOLAS) Convention were implemented to mitigate accidents (SOLAS, n.d.). Nevertheless, the evolving nature of the maritime sector requires continuous advancements in safety understanding and implementation.

Three core elements define onboard safety: the human factor, regulatory frameworks, and technological innovation (Baig et al., 2024). The concept of "safety culture" emerged after the Chernobyl disaster, introduced by the International Atomic Energy Agency (Berg, 2013). The National Institute for Occupational Safety and Health (NIOSH) defines it as the collective attitudes, perceptions, and experiences related to safety within an organization (Definition Examples of Safety Culture and Overlap With Safety Climate, n.d.). Among various components, "seafarers' awareness of safety culture" is crucial (Jung, 2021).

Human error is the primary contributor to maritime incidents. It accounts for around 80% of all accidents (Pyć, 2020; Sha, 2020; Jung, 2021), 85% of collisions (Sha, 2020), and a significant majority of tanker incidents and onboard fires (Berg, 2013). In South Korea alone, 338 maritime accidents were reported in 2019 (Jung, 2021). Furthermore, maritime transportation is reportedly 25 times riskier than aviation in terms of fatalities per 100 kilometers traveled (Berg, 2013).

Maritime safety culture relies on collaboration among seafarers, regulatory authorities, and ship management (Håvold, 2010). Measures like double-hull requirements and the International Safety Management (ISM) Code have aimed to enhance safety onboard (The International Safety Management (ISM) Code, n.d.). However, the central role of the human factor persists. From a legal and political perspective, instruments like the International Code of Safety for Ships Using Gases or Other Low-flashpoint Fuels (IGF Code) remain inadequate for covering many emerging alternative fuels.

From a managerial perspective, the adoption of ship-specific and adaptable safety strategies is essential for effective implementation (Baig et al., 2024; Berg, 2013; Teperi et al., 2018). However, human factors remain difficult to address comprehensively. Although the International Convention on Standards of Training, Certification and Watchkeeping for Seafarers (STCW) provides a regulatory framework (STCW, n.d.), concerns persist regarding its adequacy in addressing technological advancements and alternative fuel operations (Cicek et al., 2019). It is claimed that training alone is insufficient to instill a robust safety culture (Håvold, 2010), particularly as knowledge gaps and low competency levels continue to contribute to human error (Elsokary et al., 2025).

A recent study in Egypt illustrates regional disparities in safety knowledge, with port workers in Port Said outperforming those in Alexandria and other areas (Elsokary et al., 2025). Additionally, psychological and environmental stressors, including fatigue, multicultural crew dynamics, digitalization, and exposure to adverse physical conditions (e.g., noise, temperature, and humidity), complicate the establishment of an effective safety culture (Sha, 2020; Formela et al., 2019; Pyć, 2020). Insufficient awareness often leads to negligent behavior, which is a leading cause of collisions and accidents (Hsu et al., 2023; Baig et al., 2024).

Technological advancements have significantly reduced crew sizes over the past decades—from 40–50 crew members to approximately 20 on tankers (Håvold, 2010). While this change has enhanced operational efficiency, it has also intensified fatigue and stress levels. Critics argue that, despite the ISM Code's intentions, low manning levels and constant operational demands hinder effective adherence to safety protocols (Størkersen et al., 2016). Safety outcomes are closely linked to communication and risk management practices (Andrei et al., 2020), yet the current operational landscape often imposes excessive working hours and mental health burdens such as depression and anxiety (Håvold, 2010).

Compounding these issues is the maritime industry's transition to alternative fuels in response to stringent environmental targets. The IMO aims to reduce greenhouse gas (GHG) emissions by 50% by 2050 and CO_2 emissions by 70% by 2030, relative to 2008 levels (2023 IMO Strategy on Reduction of GHG Emissions From Ships, n.d.). Lloyd's Register identifies several alternative fuels with potential—ammonia, biofuels, electric, hydrogen, LNG, LPG, and methanol (Fuel for Thought - Alternative Marine Fuels | LR, n.d.). Among these, LNG is notable for its infrastructure readiness, yet its low flashpoint (-184°C) presents serious safety hazards (LNG Powers Unprecedented Year for Orders of Alternative-fuelled Vessels, 2025). Methanol and ammonia also pose risks due to their low flashpoints and corrosive or toxic properties (Zincir & Deniz, 2021).

While hydrogen and electric fuels show promise for short-distance shipping, their applicability for long voyages remains limited. The shift to gaseous fuels introduces new hazards, especially for non-tanker vessels traditionally less exposed to fuel-related risks. Despite improved safety technologies, human error—including procedural deviations and inadequate safety awareness—continues to undermine maritime safety (Nair, 2022).

Method & Findings

In this context, the present study assesses the readiness of the maritime industry's safety culture for alternative fuel adoption. A PESTEL analysis reveals that political and economic factors significantly influence safety culture development. For instance, crew reduction policies exacerbate fatigue and stress, undermining safety performance. Furthermore, training curricula have not adequately evolved to address the operational requirements of hazardous fuels. Although some familiarization programs and certifications exist—especially for LNG-fueled vessels—comprehensive safety culture education remains lacking even for conventional fuel systems.

Conclusion

In conclusion, the human factor is central to the sustainability of global maritime operations. Given that most maritime accidents stem from human error, enhancing safety awareness and culture among crew members is imperative. Although alternative fuels are being introduced to align with emission reduction goals, they introduce unique safety challenges. Economic considerations are important, but greater investment in safety training and education is essential to mitigate the additional risks associated with these new fuels.

References

Andrei, D., Grech, M. R., Griffin, M., & Neal, A. (2020). Assessing the determinants of safety culture in the maritime industry. *The International Journal of Maritime Engineering*, *162*(A4). https://doi.org/10.3940/rina.2020.a4.620

Baig, M. Z., Lagdami, K., & Mejia, M. Q., Jr. (2024). Enhancing maritime safety: A comprehensive review of challenges and opportunities in the domestic ferry sector. *Maritime Technology and Research*, *6*(3), 268911. https://doi.org/10.33175/mtr.2024.268911

Berg, H. P. (2013). Human Factors and Safety Culture in Maritime Safety (revised). *TransNav the International Journal on Marine Navigation and Safety of Sea Transportation*, *7*(3), 343–352. https://doi.org/10.12716/1001.07.03.04

Berg, N., Storgård, J., & Lappalainen, J. (2013). *The impact of ship crews on maritime safety*. Publications of the Centre for Maritime Studies, University of Turku A, 64, 1-48.

Cicek, K., Akyuz, E., & Celik, M. (2019). Future skills Requirements analysis in Maritime industry. *Procedia Computer Science*, *158*, 270–274. https://doi.org/10.1016/j.procs.2019.09.051

Definition Examples of Safety Culture and Overlap with Safety Climate. (n.d.). https://www.cdc.gov/niosh/learning/safetyculturehc/module-1/4.html

Elsokary, M. I. a. I., Elsamie, G. H. A., & Shehata, A. S. (2025). Enhancing maritime safety through tailored training programs: A pre and post assessment study. *Research Square (Research Square)*. https://doi.org/10.21203/rs.3.rs-6257165/v1

Formela, K., Neumann, T., & Weintrit, A. (2019). Overview of definitions of maritime safety, safety at sea, navigational safety and safety in general. *TransNav the International Journal on Marine Navigation and Safety of Sea Transportation*, *13*(2), 285–290. https://doi.org/10.12716/1001.13.02.03

Fuel for Thought - alternative marine fuels | LR. (n.d.). https://www.lr.org/en/knowledge/research/fuel-for-thought/

Håvold, J. I. (2010). Safety culture and safety management aboard tankers. *Reliability Engineering & System Safety*, *95*(5), 511–519. https://doi.org/10.1016/j.ress.2010.01.002

Hsu, S., Lee, M., & Chang, Y. (2023). Application of rough set theory and Bow-Tie analysis to Maritime safety Analysis Management: A case study of Taiwan ship collision incidents. *Applied Sciences*, *13*(7), 4239. https://doi.org/10.3390/app13074239

International Convention on Standards of Training, Certification and Watchkeeping for Seafarers (STCW). (n.d.). https://www.imo.org/en/ourwork/humanelement/pages/stcw-conv-link.aspx

Jung, M. (2021). Examining perceptual differences in maritime safety climate: A case study of Korean seafarers. *Journal of Marine Science and Engineering*, *9*(4), 381. https://doi.org/10.3390/jmse9040381

Kamis, A. S., Fuad, A. F. A., Saadon, M. S. I., & Fadzil, M. N. (2020). The Impact of Basic Training on Seafarers' Safety Knowledge, Attitude and Behaviour. *Journal of Sustainability Science and Management*, *15*(6), 137–158. https://doi.org/10.46754/jbsd.2020.08.012

LNG powers unprecedented year for orders of alternative-fuelled vessels. (2025, January 10). DNV. https://www.dnv.com/news/lng-powers-unprecedented-year-for-orders-of-alternative-fuelled-vesselss/

Maritime safety. (n.d.). https://www.imo.org/en/OurWork/Safety/Pages/default.aspx

The International Safety Management (ISM) Code. (n.d.). https://www.imo.org/en/ourwork/humanelement/pages/ISMCode.aspx

Nair, P. R. (2022). *A safety analysis on the potential risks onboard ships that would use ammonia as marine fuel* [MA Thesis, World Maritime University]. https://commons.wmu.se/cgi/viewcontent.cgi?article=3081&context=all_dissertations

Pyć, D. (2020). Maritime safety culture as a condition for sustainable shipping. *Zeszyty Naukowe Akademii Morskiej W Szczecinie*. https://doi.org/10.17402/400

SOLAS. (n.d.). https://www.imo.org/en/KnowledgeCentre/ConferencesMeetings/Pages/SOLAS.aspx

Sha, M. (2020). *A study of the human factors in maritime safety* [MA Thesis, World Maritime University]. https://commons.wmu.se/cgi/viewcontent.cgi?article=1272&context=msem_dissertations

Størkersen, K. V., Antonsen, S., & Kongsvik, T. (2016). One size fits all? Safety management regulation of ship accidents and personal injuries. *Journal of Risk Research*, *20*(9), 1154–1172. https://doi.org/10.1080/13669877.2016.1147487

Teperi, A., Lappalainen, J., Puro, V., & Perttula, P. (2018). Assessing artefacts of maritime safety culture—current state and prerequisites for improvement. *WMU Journal of Maritime Affairs*, *18*(1), 79–102. https://doi.org/10.1007/s13437-018-0160-5

Zincir, B., & Deniz, C. (2021). Methanol as a fuel for marine diesel engines. In Alcohol as an alternative fuel for internal combustion engines (pp. 45-85). Singapore: Springer Singapore.)
2023 IMO Strategy on Reduction of GHG Emissions from Ships. (n.d.). https://www.imo.org/en/OurWork/Environment/Pages/2023-IMO-Strategy-on-Reduction-of-GHG-Emissions-from-Ships.aspx

MATERIAL SCIENCE AND ENGINEERING

Ceramics, Glass, Refractory Materials

Materials Synthesis and Processing

Nanomaterials

Improvement of the Selenium Retention and Control of the Color Stability in Selenium Containing Glasses

Elif Fagıye Yaylacı[a,b], Merve Akdemir Kutluğ[b], Ahmet Caner Kayaalp[b], Reha Yavuz[a]

[a]Istanbul Technical University, Faculty of Chemical and Metallurgical Engineering, Department of Chemical Engineering, Türkiye
[b] Şişecam Science Technology and Design Center, Türkiye
yaylaci18@itu.edu.tr

Keywords: Manganese Dioxide, Oxidizing Agent, Selenium Retention, Sodium Nitrate.

Aim

Selenium is utilized as a coloring agent in glass products, in conjunction with other colorants, to produce pink, bronze, and grey-colored glasses. Besides, it is also used as a decolorizing agent during the production of clear glass batches. Selenium can be incorporated into the glass batch in various raw material forms. Selenium has different oxidation states within the glass structure, including 2-, 0, 4+, and 6+. The color of the glass changes depending on these different oxidation states of selenium. The Se^{2-}, Se^{4+} and Se^{6+} forms have a colorless effect on the glass, the Se0 form gives the glass a pink color and the Se_x^{2-} forms form a polyselenide called FeSe, which gives the glass red-brown color (Longobardo, 1994). The valence levels of selenium present in the glass and their effects on the coloration of soda-lime-silicate glasses are given in Table 1.

Table 1. The oxidation states of selenium and their impact on the coloration of soda-lime-silicate glasses (Jitwatcharakomol, 2005).

Different Oxidation States of Selenium	Effect on the color of the glass
Selenide (Se^{2-})	Colorless
Elemental Selenium (Se^{0})	Pink
Selenite (Se^{4+})	Colorless
Selenate (Se^{6+})	Colorless
Polyselenide (Se_x^{2-} (x > 1))	Red-Brown

Selenium exhibits two absorption peaks in the visible region, with a maximum at 500 nm and a flatter peak around 750 nm (Jitwatcharakomol, 2005). In contrast, iron selenide (FeSe) displays a broad absorption peak in the 400-500 nm range, starting around 400 nm and reaching a maximum at approximately 490 nm (Bamford, 1977). Spectral absorption graph of elemental selenium and iron selenide is shown in Figure 1.

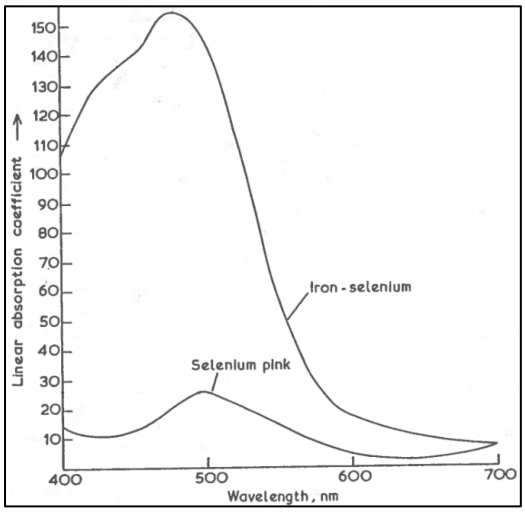

Figure 1. Spectral absorption graph of elemental selenium and iron selenide (Bamford, 1977).

Selenium has a melting point of 217°C and a boiling point of 685°C at standard atmospheric pressure (1 atm) (Jones & Boulos, 1996). The primary disadvantage of selenium is its low retention in bulk glass due to its high volatility. This issue makes it challenging to use selenium effectively in glass production. It is known that selenium, which cannot be retained in the glass batch, separates from the melt in the form of selenium dioxide (SeO_2). This separation prevents selenium from remaining within the glass, making it difficult to achieve the desired color and properties. Various studies and experimental research have shown that approximately 80% to 90% of selenium evaporates during the melting process (Jitwatcharakomol, 2005). The volatilization of selenium depends on various parameters such as the furnace atmosphere, the moisture content of the batch, the melting temperature, and the chemistry of the glass batch (e.g., the reduction state of the glass). One of the challenges associated with the high evaporation rate of selenium is the increased production costs. Due to the high cost of selenium and selenium-containing compounds, the high volatility of these materials leads to increased raw material costs. Additionally, the high volatility causes issues with color stability in products manufactured using selenium. Furthermore, it may pose environmental risks. The high volatilization of selenium-containing compounds in flue gases can make the atmosphere around glass melting furnaces toxic (Inoue & Tachibana, 1971). In order to address these issues, the aim of this study is to investigate the effects of different levels of oxidizing agents such as sodium nitrate and manganese dioxide on selenium retention and glass coloration.

Material and Method

After preparing 100 grams of glass batches, all materials were thoroughly mixed to obtain a homogeneous mixture. The mixture was then melted in ceramic crucibles at 1450°C for 3 hours. Upon completion of the melting process, the glass samples were annealed to reduce internal stress. After the annealing process, the cooled glass samples were cut, their surfaces were polished, and they were made ready for analysis. The chemical composition analysis of the obtained glass samples and the Se percentages were analyzed using an X-ray fluorescence (XRF) device. The Se percentages measured in the glass samples were used to calculate the selenium retention percentages. The color parameters were determined using a UV-Vis spectrophotometer with a tungsten lamp.
In experimental studies, sodium nitrate was added within the specified range per 100 g of glass to observe its effect on selenium retention. Subsequently, manganese dioxide was added within the same range to the 100 g glass batches without sodium nitrate to observe the effect of manganese dioxide.

Findings

In experiments conducted with glass batches containing different levels of sodium nitrate, it was observed that the selenium retention rate showed a maximum increase of 83.08% within the specified range compared to experiments without sodium nitrate. Additionally, as the amount of sodium nitrate added to the glass batches

increased, the reduction state of the glass gradually decreased, and the glass became more oxidizing. Figure 2 shows the selenium retention percentages in glasses with different levels of sodium nitrate.

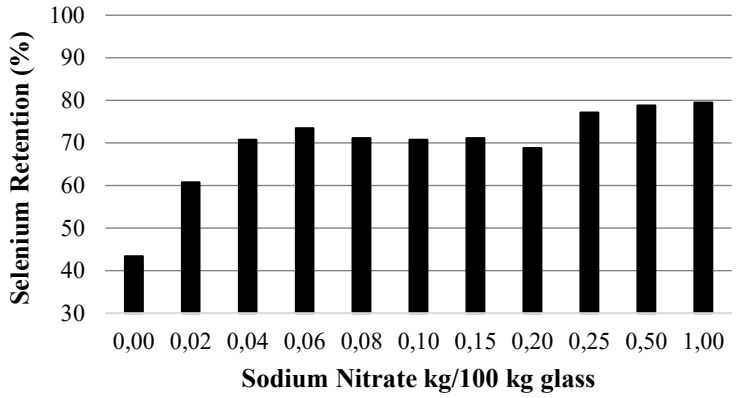

Figure 2. Selenium retention (%) in glasses with different levels of sodium nitrate.

In experiments conducted with glass batches containing different levels of manganese dioxide, it was observed that the selenium retention rate showed a maximum increase of 79.99% within the specified range compared to experiments without manganese dioxide. Similar to the series containing sodium nitrate, the reduction state of the glass decreased with increasing manganese dioxide.

Conclusion

This study investigated the effects of using different levels of sodium nitrate and manganese dioxide which are used as oxidizing agents, on selenium retention and glass coloration. Experimental studies conducted with varying amounts of sodium nitrate showed that as the amount of sodium nitrate added to the glass batch increased, a general trend of increased selenium retention was observed, although this was not a gradual increase.

However, it is known that sodium nitrate can lead to harmful nitrogen oxide emissions, causing environmental pollution. Therefore, different oxidizing agents that could enhance selenium retention and reduce harmful nitrogen oxide emissions as alternatives to sodium nitrate have been investigated. For this reason, the effect of a similar oxidizing agent, such as manganese dioxide, on selenium retention in glass was examined. In the experiments conducted, it was observed that when different amounts of manganese dioxide were added to the glass batches, selenium retention increased with the increasing amount of manganese dioxide. These results suggest that manganese dioxide could be an effective alternative for enhancing selenium retention.

In future studies, research can be conducted on other potential oxidizing agents, apart from sodium nitrate and manganese dioxide, that can enhance selenium retention in glass, ensure color stability, and reduce adverse environmental impacts. Additionally, the effects of parameters such as melting temperature on selenium retention can be examined. These studies should also include a detailed analysis of economic costs and methods for reducing the production costs of selenium-containing glass.

References

Bamford, C. R. (1977). *Colour generation and control in glass*. Elsevier Scientific Publishing Company.

Inoue, T., & Tachibana, M. (1971). *Preparation of glass containing selenium* (U.S. Patent No. US3628932A). United States Patent and Trademark Office. https://patents.google.com/patent/US3628932A/en

Jitwatcharakomol, T. (2005). *Optimization and control of selenium chemistry and color in flint glass melts* (Doctoral dissertation, Rheinisch-Westfälische Technische Hochschule Aachen). https://core.ac.uk/reader/36426580

Jones, J. V., & Boulos, E. N. (1996). *Neutral gray absorbing glass comprising manganese oxide for selenium retention during processing* (U.S. Patent No. US5521128A). United States Patent and Trademark Office. https://patents.google.com/patent/US5521128A/en

Longobardo, A. V. (1994). *Selenium encapsulation for producing colored glass* (European Patent No. EP0618177A1). European Patent Office. https://patents.google.com/patent/EP0618177A1/en

MATERIAL SCIENCE AND ENGINEERING

Ceramics, Glass, Refractory Materials

Materials Synthesis and Processing

Nanomaterials

A Study About Tin Nanoparticles and Production of Core-shell Structure

Ayşe Zuhal Karakaş[a], Ş. Samet Kaplan[a],M. Şeref Sönmez[a]

[a] Department of Metallurgical and Materials Engineering, Faculty of Chemistry and Metallurgy, ITU Ayazaga Campus, 34469, Maslak/Istanbul
karakasay19@itu.edu.tr

Keywords: Nanoparticle, Polyol Method, Core-Shell.

Aim

This study focuses on the synthesis of nano-sized reactive tin (Sn) particles via the polyol method and the investigation of Sn/CuO core-shell structures for potential applications in low-temperature reactive bonding and soldering. Diethylene glycol (DEG) served as the solvent, polyvinylpyrrolidone (PVP) as the stabilizing agent, and sodium borohydride ($NaBH_4$) as the reducing agent. Two distinct tin precursors, tin (II) 2-ethylhexanoate and tin (II) chloride ($SnCl_2$), were evaluated to determine their influence on nanoparticle formation. The synthesis involved dissolving PVP and $NaBH_4$ in DEG at room temperature, followed by precursor addition, controlled precipitation using acetone, and subsequent washing and drying processes. The impact of $NaBH_4$ concentration and precursor selection on particle morphology and crystallinity was systematically investigated. Structural and morphological characterizations were performed via X-ray diffraction (XRD) and scanning electron microscopy (SEM). The research of Sn/CuO core-shell structures aims to enhance reaction kinetics and interfacial adhesion, thereby improving process efficiency in metal-ceramic integration for advanced microelectronic applications. In the light of this information, aim of this study is to develop nano-sized reactive particles and investigate their potential applications for low-temperature reactive bonding and soldering. The primary goal is to synthesize tin (Sn) nanoparticles using the polyol method and subsequently fabricate Sn/CuO core-shell structures. These structures are expected to enhance reaction kinetics and improve process efficiency in metal-ceramic integration. The research also focuses on optimizing process parameters such as precursor selection, reaction time, temperature, and pH, as well as evaluating the characterization of the synthesized nanoparticles.

Introduction

The term nanoscale generally comprises of the size or dimensions between 1 to 100 nanometers meaning 10^{-9} meters. Nanomaterials however, are materials have governable significant dimensions which 100nm or under 100nm. There are some basic procedures to create nanomaterials and they can be list as; "condensation from a vapor phase, precipitation from solution, chemical vapor deposition, chemical reactions (particularly reduction or oxidation), processes used to generate colloidal phases, self-assembly using surfaces, mechanical attrition" [5,6]. Increasing interest in nanomaterials through the years, substantial researches have been realized about "pure metal nanoparticles". For example, silver, palladium, copper, gold, tin, platinum. Especially, tin has very important role in microelectronic applications because it is reckoned as soldering material frequently. Tin also known as interconnection material in the area of electronics [2]. While synthesizing these nanoparticles, there are various approaches yet, wet chemical paths preferred. Particularly, (modified) polyol process is used for this purpose. While using this process many of the parameters are modifiable such as solvent or precursor's type, molecular weight or type of capping agent and concentration of so many agents [3]. The name polyol comes essentially from poly-alcohol which are acknowledged as reducing agents. In this process polyols can be listed as DEG, EG, PEG, TEG and TTEG. It should also be noted that, if the power of polyol isn't enough for the reducing then, extra reducing agent can be used [4]. Core-shell nanostructures should also be mentioned within the scope of the study. The development of core-shell nanostructures has enabled the control of various properties for use in different fields. Core-shell nanoparticles originate from two or more materials. Core-shell particles can be used in various fields like optics, electronics, biomedical, catalysis and their properties can be different from main materials. For example, core materials' properties can be improved by shell materials. So, in general, particles which has different features than each other are brought together to achieve desired properties [1].

Material and Method

In the synthesis, diethylene glycol (DEG) was used as the solvent, while polyvinylpyrrolidone (PVP) acted as a stabilizing agent. Sodium borohydride ($NaBH_4$) was employed as a reducing agent, and two different tin precursors were examined: tin (II) 2-ethylhexanoate and tin (II) chloride ($SnCl_2$). The synthesis procedure involved dissolving PVP and $NaBH_4$ in DEG at room temperature, followed by the addition of the tin precursor. The solution was stirred via magnetic stirrer, precipitated with acetone, and washed with ethyl alcohol before being centrifuged. The final product was dried at oven before characterization. This process repeated with different amounts of $NaBH_4$ to examine the effect of reducing agent and different tin precursors. In Table 1, details of the experimental parameters are given. X-ray diffraction (XRD) and scanning electron microscopy (SEM) were used to analyze the crystalline phases and morphology of the nanoparticles.

Table 1. Experiment conditions.

Experiment No	NaBH4(g)	PVP(g)	DEG (ml)	Sn Precursor
1	2	1	240	2g $SnCl_2$
2	2.5	1	240	2g $SnCl_2$
3	2	1	200	2ml Sn(II)-2ethylhexanoate
4	2.5	1	200	2ml Sn(II)-2ethylhexanoate

Findings

XRD patterns of the samples produced by the polyol method, which details are given in the materials and methods section, are given in Figure 1. As can be seen from Figure 1, looking at the XRD patterns of experiment 1 and experiment 2, it is understood that Sn could not be obtained. XRD analysis showed that samples synthesized with $SnCl_2$ contained impurities, prompting further optimization of the reducing agent and precursor concentrations. However, in the XRD patterns representing experiment 3 and experiment 4, it is understood that Sn is produced. For the samples synthesized using Sn (II) 2-ethylhexanoate, XRD analysis demonstrated single-phase Sn formation, regardless of the $NaBH_4$ concentration. However, in samples with higher $NaBH_4$ concentrations, a background signal was observed, indicating the possible presence of amorphous content. SEM analysis revealed that the Sn nanoparticles did not exhibit a spherical morphology.

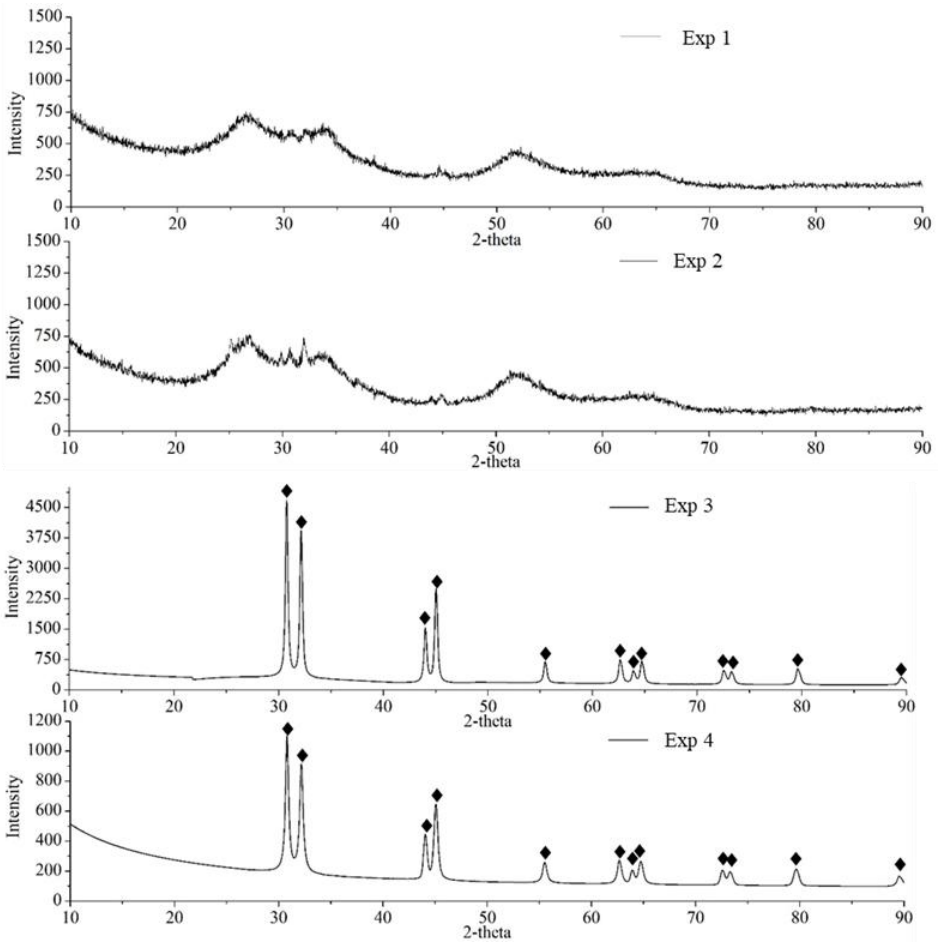

Figure 1. XRD pattern comparison of samples.

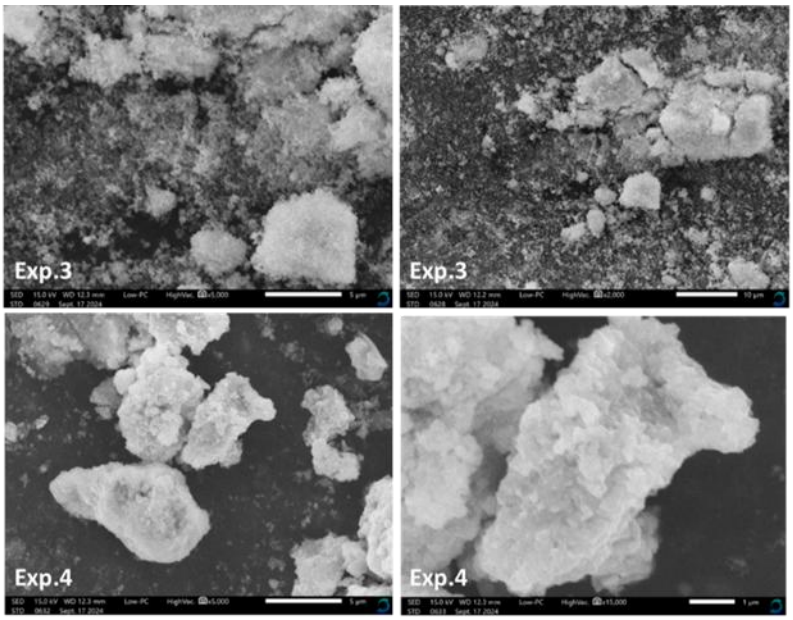

Figure 2. SEM image of experiment 3 and experiment 4.

Conclusion

The study denote that synthesized Sn nanoparticles using the polyol method, with Sn (II) 2-ethylhexanoate proving to be a more effective precursor than $SnCl_2$. It was observed that there was no significant relationship between changing the amount of $NaBH_4$ and particle formation. Future work will focus on refining reaction parameters and investigating additional characterization techniques to enhance the performance of reactive nanoparticle systems for low-temperature metal-ceramic integration

Declaration of AI Usage

This research incorporates artificial intelligence (AI) tools. The AI-generated content has been critically reviewed and validated by the authors to ensure accuracy, originality, and compliance with ethical research standards. The authors confirm that the primary intellectual and analytical contributions are their own, and AI was used solely as an auxiliary tool to enhance the research process.

Acknowledge

Authors would like to acknowledge that this study is financially supported by TUBITAK under the Project no 222N235.

References

Chaudhuri, R. G., & Paria, S. (2011). Core/shell nanoparticles: Classes, properties, synthesis mechanisms, characterization, and applications. *Chemical Reviews*, *112*(4), 2373–2433. doi:10.1021/cr100449n

CHEE, S.-S., & LEE, J.-H. (2012a). Synthesis of tin nanoparticles through modified polyol process and effects of centrifuging and drying on nanoparticles. *Transactions of Nonferrous Metals Society of China*, *22*, 707–711. doi:10.1016/s1003-6326(12)61791-9

Chee, S. S., & Lee, J. H. (2013). Effects of ph on tin nanoparticles prepared using a modified polyol synthesis. *Applied Mechanics and Materials*, *376*, 93–96. doi:10.4028/www.scientific.net/amm.376.93

Fiévet, F., Ammar-Merah, S., Brayner, R., Chau, F., Giraud, M., Mammeri, F., … Viau, G. (2018). The polyol process: A unique method for easy access to metal nanoparticles with tailored sizes, shapes and compositions. *Chemical Society Reviews*, *47*(14), 5187–5233. doi:10.1039/c7cs00777a

Pokropivny, V., Lohmus, R., Hussainova, I., Pokropivny, A., & Vlassov , S. (2007). *INTRODUCTION TO NANOMATERIALS AND NANOTECHNOLOGY*. Tartu, Estonia: Tartu University Press.

Ramesh, K. T. (2009). *Nanomaterials Mechanics and Mechanisms*. New York, USA: Springer.

MATHEMATICAL ENGINEERING

Applied Mathematics

Data Science and Machine Learning

Mathematical Modeling

Symmetry Analysis on Rosenau Type Equations

Tugce Sezer [a], Cihangir Özemir [a]

[a] Istanbul Technical University, Department of Mathematical Engineering, Turkey
sezert22@itu.edu.tr

Keywords: Lie Symmetries, Rosenau Equation, Symmetry Classification.

Aim

In the field of nonlinear wave theory, the study of shallow-water wave propagation has been a major area of research for several decades. Numerous mathematical models have been developed to analyze and demonstrate the intricate dynamics of such waves. Beginning with the foundational Korteweg–de Vries (KdV) equation, a range of models, including the regularized long wave (RLW), Rosenau, and Kawahara equations, have played critical roles in describing wave propagation and interactions.

The Rosenau equation (Rosenau, 1988) was introduced to describe wave phenomena involving both dispersion and nonlinearity, particularly in contexts such as wave-wave and wave-boundary interactions. By integrating concepts from the RLW equation to more effectively represent nonlinear dispersive waves in continuous media (e.g., fluids), the Rosenau-RLW equation (Pan & Zhang, 2012) was proposed, incorporating a viscous term. This model was later extended into the generalized Rosenau-RLW equation.

To address higher-order dispersive systems, such as shallow-water waves affected by surface tension, the Kawahara equation was formulated, introducing fifth-order dispersion. Its generalized form has since found application in diverse fields, including ion-acoustic waves in plasmas and nonlinear acoustics. In an effort to unify insights from both the Rosenau and Kawahara models, the Rosenau-Kawahara equation was introduced, and subsequently generalized into the Rosenau-Kawahara equation.

Despite these developments, there has been relatively limited research focused on the Lie symmetry analysis of equations within the Rosenau family. Collectively, these partial differential equations illustrate a trend toward increasing generality and adaptability, enabling the modeling of a broader range of nonlinear wave phenomena.

Lie group analysis has become a widely used method for studying both ordinary and partial differential equations, and its application extends to difference equations, integral equations, and fractional equations as well. Central to this approach are smooth, one parameter transformations that form a Lie group, which is an algebraic structure that is simultaneously a group and a smooth manifold. The tangent space at the identity element of this manifold forms a Lie algebra, whose basis consists of vector fields that generate the symmetry transformations leaving the differential equation unchanged. If an equation remains invariant under n such transformations, it is said to possess an n-dimensional Lie algebra. The process of identifying the Lie algebra associated with a differential equation is algorithmic and applicable to any such equation.

For an ordinary differential equation of order k, the existence of a symmetry generator allows its order to be reduced by one. If the ordinary differential equation admits a $(k-1)-$dimensional Lie algebra, it may be reducible to a first-order equation. Similarly, for a partial differential equation with m independent variables, a symmetry generator enables the reduction of one independent variable. If the PDE admits an $(m-1)$-dimensional Lie algebra, it can be transformed into an ODE of the same order.

Beyond these practical advantages, especially valuable for nonlinear differential equations, which often lack general solution methods, Lie group analysis also facilitates the classification of equation families containing arbitrary functions or coefficients. In this framework, entire families of equations are analyzed and grouped based on the Lie algebras they admit. In the present study, we apply this methodology to perform a Lie symmetry classification of a Rosenau-type equation featuring a general form of nonlinearity.
In this work, we perform the analysis on a Rosenau-type equation of the form:

$$u_t + \varepsilon u_x + \alpha u_{xxt} + \eta u_{xxx} + \beta u_{xxxxt} + \gamma u_{xxxxx} + (f(u))_x = 0$$

where $f(u)$ represents a general nonlinear function. The existence and stability of solitary wave solutions to this equation have been previously investigated in (Duran & Muslu, 2024). When $f(u) = u^n$, the equation is referred to as the generalized Rosenau-RLW-Kawahara equation. Numerous exact (Tasbozan, Celik, Kurt & Akinyemi, 2024) and numerical (Wang & Dai, 2018; Wang, Cheng, & Dai, 2022) solutions have been proposed for this power-law nonlinearity case.

Material and Method

This study primarily focuses on the symmetry analysis, reductions, and exact solutions of the aforementioned equation. Adopting a group-theoretical framework, we consider the Rosenau-type equation in the form:

$$u_t + \alpha u_{xxt} + \eta u_{xxx} + \beta u_{xxxxt} + \gamma u_{xxxxx} + (g(u))_x = 0$$

Here, the term u_x from the original equation is embedded within $\big(g(u)\big)_x$. The analysis is conducted under the assumptions that $(\beta, \gamma) \neq (0,0)$ and $g''(u) \neq 0$, to ensure the presence of nonlinearity.

Findings

The Lie group analysis yields a classification of Lie algebras corresponding to various forms of the nonlinearity $g(u)$. The classification includes polynomial, logarithmic and exponential nonlinearity types. For other functional forms of $g(u)$, the equation admits a trivial two-dimensional Abelian algebra $< \partial_t, \partial_x >$. Following the exploration of optimal systems for Lie algebras, the associated reductions of the PDE to ordinary differential equations are obtained.

Conclusion

In this study, we investigated a Rosenau-type equation involving a general nonlinearity f(u). While earlier research focused primarily on the quadratic case, numerous variants have since been developed and explored from various perspectives. Building on the literature summarized in the introduction, we analyzed this class of equations using Lie group-theoretical methods.
Our symmetry classification demonstrates that, within this family of equations, the maximum dimension of the Lie symmetry algebra is three. Furthermore, we carried out reductions of each specific class to ordinary differential equations using the corresponding optimal systems of one-dimensional subalgebras.
As future work, we aim to derive exact solutions for the partial differential equation with polynomial-type nonlinearities. Additionally, we plan to incorporate numerical solutions for selected ordinary differential equations obtained through the reduction process.
The results of this work and aforementioned forthcoming investigations will attract attention of researchers working on various fields, such as wave propagation, qualitative analysis of PDEs or numerical approaches. The work also has the potential of being a guide for application of the analysis carried out to the similar families of equations.

References

Duran, A. & Muslu, G. (2024). On solitary-wave solutions of Rosenau-type equations, Commun. Nonlinear Sci., 137, 108130.

Pan, X. & Zhang, L. (2012). On the convergence of a conservative numerical scheme for the usual Rosenau-RLW equation, Applied Mathematical Modelling, 36(8), 3371–3378.

Rosenau, P. (1988). Dynamics of dense discrete systems high order effects, Progress of Theoretical Physics, 79(5).

Tasbozan, O., Celik, E., Kurt, A. & Akinyemi, L. (2024). Investigation on the new exact solutions of generalized Rosenau-Kawahara-RLW equation with p-th order nonlinearity occurring in ocean engineering models, Appl. Math. J. Chinese Univ., 39(4), 642–653.

Wang, X., Cheng, H. & Dai, W. (2022). Conservative and fourth-order compact difference schemes for the generalized Rosenau–Kawahara–RLW equation, Engineering with Computers, 38, 1491–1514.

Wang, X. & Dai, W. (2018). A new implicit energy conservative difference scheme with fourth-order accuracy for the generalized Rosenau–Kawahara-RLW equation, Computational and Applied Mathematics, 37, 6560–6581.

Exploring Rayleigh Waves in Layered Media

Tugce Sezer[a], Semra Ahmetolan[a], Ayse Peker-Dobie[a], Ali Demirci[a]

[a] Istanbul Technical University, Department of Mathematical Engineering, Turkey
sezert22@itu.edu.tr

Keywords: Rayleigh Waves, Irregular Surfaces, Perturbation Methods.

Aim

The study of elastic waves in layered media with different elastic properties is an important research topic due to its applications in various engineering fields such as geophysics, seismology and metallurgy. For example, because the Earth's crust is considered a layered elastic medium that varies in stiffness and density with depth, both the free surface and the interfaces between layers may contain irregularities. These irregularities affect the reflected and refracted waves and directly affect wave propagation (Graff, 2012).

Elastic wave propagation is used in seismic research in earth sciences; In materials science, to understand the internal structure and mechanical properties of materials, to increase the durability of materials and to detect defects; In structural strength assessment, it is an important tool used to measure the durability and stability of structures. There are many studies on the propagation of elastic waves in layered media with irregular surfaces (Kuo & Nafe, 1962; Ben-Hador & Buchen, 1999; Vishwakarma & Xu, 2016; Zhang, Qin, Li & Kube, 2020; Ahmetolan, Peker-Dobie, Deliktas-Ozdemir & Caglayan, 2023). In general, analyzing the effect of irregularities on boundary surfaces on wave propagation presents mathematical difficulties. In addition, sometimes the geometry of the problem may require that the functions representing irregularities on the boundary surfaces be selected in a certain structure.

In this study, the problem of propagation of Rayleigh waves in a semi-infinite space with a layer of non-uniform thickness consisting of different homogeneous materials is examined.

Material and Method

It is assumed that the free surface is free of traction, and both displacement functions and stresses are continuous at the interface. The free and interface surfaces are treated as non-specialized functions that vary depending on the direction of propagation. The main aim of this work is to obtain the equations characterizing the propagation of such waves.

First, the formulation of the problem was made using the theory of elasticity: equations of motion and boundary conditions modeling wave propagation were obtained. Then, order problems were obtained by selecting an appropriate asymptotic perturbation method. The dispersion relation is expressed as a function of the wave's phase velocity, wave number, and wave propagation direction. In the following parts of the study, wave propagation is examined using real linear material properties and under the assumption that irregular boundary conditions exhibit periodic properties.

The spatial and material coordinates of a point in three-dimensional space are defined according to the same orthogonal coordinate system as (x_1, x_2, x_3) and (X_1, X_2, X_3), respectively. The equations of motion are

$$x_1 = X_1 + u_1^{(m)}(X_1, X_2, t), \qquad x_2 = X_2 + u_2^{(m)}(X_1, X_2, t), \qquad x_3 = X_3, \qquad m = 1, 2.$$

Here t is the time, $u_1^{(m)}$ and $u_2^{(m)}$ represent the displacements in the X_1 and X_2 directions, respectively. Here, $m = 1$ refers to the layer D_1 and $m = 2$ to the half space D_2. In the absence of body forces, the equations of motion take the following form:

$$T_{k1,k}^{(m)} = \rho_0^{(m)} \ddot{u}_1^{(m)}, \qquad T_{k2,k}^{(m)} = \rho_0^{(m)} \ddot{u}_2^{(m)} \ .$$

Here $T_{KI}^{(m)}$ represents the first Piola-Kirchhoff stress tensor and $\rho_0^{(m)}$ represents the initial density of the relevant medium.

It is assumed that the boundary of the layered half-space $X_2 = h + g_1(X_1)$ is traction free, that displacements and stresses are continuous at the interface $X_2 = g_2(X_1)$, and that displacements do not occur as $X_2 \to -\infty$. Boundary conditions are

$$N_K^{(1)} T_{KI}^{(1)} = 0 \quad on \quad X_2 = h + g_1(X_1)$$

$$u_1^{(1)} = u_1^{(2)}, \quad u_2^{(1)} = u_2^{(2)} \quad on \quad X_2 = g_2(X_1)$$

$$N_K^{(1)} T_{KI}^{(1)} = N_K^{(2)} T_{KI}^{(2)} \quad on \quad X_2 = g_2(X_1)$$

$$u_1^{(2)}, \quad u_2^{(2)} \to 0 \quad as \quad X_2 \to -\infty.$$

By substituting the explicit form of T_{Kl} into the equation of motions and the boundary conditions, while neglecting nonlinear terms, and then replacing u_1, u_2 and (X_1, X_2, X_3) with u, v and (X, Y, Z), respectively, linear equations of motion and boundary conditions are obtained.

Using an asymptotic perturbation method, an asymptotic solution is derived for the problem of linear Rayleigh waves with small but finite amplitude propagating in a layer with irregular free surfaces that vary slowly in the direction of propagation. The slow change in the boundary surfaces is represented by a small parameter $\epsilon > 0$, which measures the amplitude of the geometric change of the surfaces,

$$g_i = g_i(\epsilon X), \qquad i = 1, 2.$$

In order to distinguish between the slow and fast changing features of the waves, new variables

$$x_1 = \epsilon X\,, \quad t_1 = \epsilon t\,, \quad y = Y\,.$$

are defined. The phase variable $\theta = kX - \omega t$ is defined. Here k is the wave number and $\omega = c\,k$ is the angular velocity. The equations $\theta_{,\{Xt\}} = k_{,t} = (-\omega)_{,X} = \theta_{,\{tX\}}$ are satisfied and spatial inhomogeneity does not affect the frequency but causes a change on the wave number. In the case where the displacements are functions of $\{\theta, x_1, y, t_1\}$, the asymptotic extensions are

$$u^{(m)} = \sum_{n=1}^{\infty} \epsilon^n u_n^{(m)}(\theta, x_1, y, t_1) \qquad v^{(m)} = \sum_{n=1}^{\infty} \epsilon^n v_n^{(m)}(\theta, x_1, y, t_1).$$

Findings

The expansions are put into the equations of motion and boundary conditions and arranged according to the ϵ orders. Thus, hierarchical order problems are obtained. In this study, it is sufficient to examine the first two order problems.

The first problem has linear homogeneous equations and homogeneous boundary conditions, while the second order problem is a perturbation problem with linear non-homogeneous equations and non-homogeneous boundary conditions. By examining the first order problem, the changes of the solutions depending on the fast variables y, θ; by examining higher order problems, its dependence on slow variables will be determined. Under the assumption that $c_{1T} < c_{1L} < c < c_{2T} < c_{2L}$, the solutions for the first-order equations, including all modes, are obtained as follows:

$$u_1^{(1)} = \sum_{l=1}^{\infty} \left[A_1^{(l)} e^{-ik_{PL}y} + A_2^{(l)} e^{ik_{PL}y} + p_T A_3^{(l)} e^{-ik_{PT}y} - p_T A_4^{(l)} e^{ik_{PT}y}\right] e^{il\theta} + c.c.,$$

$$v_1^{(1)} = \sum_{l=1}^{\infty} \left[-p_L A_1^{(l)} e^{-ik_{PL}y} + p_L A_2^{(l)} e^{ik_{PL}y} + A_3^{(l)} e^{-ik_{PT}y} + A_4^{(l)} e^{ik_{PT}y}\right] e^{il\theta} + c.c.,$$

$$u_1^{(2)} = \sum_{l=1}^{\infty} \left[A_5^{(l)} e^{k_{Lv}y} + i\nu_T A_6^{(l)} e^{k_{LvT}y}\right] e^{il\theta} + c.c.,$$

$$v_1^{(2)} = \sum_{l=1}^{\infty} \left[-iA_5^{(l)} e^{k_{Lv}y} + A_6^{(l)} e^{k_{LvT}y}\right] e^{il\theta} + c.c.,$$

Here, $A_i^{(l)}$ are the first order amplitude functions with respect to $\{x_1, t_1\}$. In order to obtain the exact structures of the coefficient functions $A_i^{(l)}$ these solutions are substituted into the boundary conditions of the first-order problem.

$$W^l U_1^l = 0$$

system is obtained. Where W is the dispersion matrix and

$$U_1^l = \left[A_1^{(l)}\ A_2^{(l)}\ A_3^{(l)}\ A_4^{(l)}\ A_5^{(l)}\ A_6^{(l)}\right]^T.$$

Conclusion

Since we are working with linear Rayleigh waves in the plane, the harmonic resonance condition is not satisfied for the wave number of the fundamental wave.

$det\ det\ W^l = 0\ for\ l = 1$ and $det\ det\ W^l \neq 0\ for\ l \geq 2.$

Using $det\ det\ W^1 = 0$ the dispersion relation is obtained. Since the structure of the dispersion relation, which gives the change of free and interface surfaces, is very complex, it is not possible to calculate the phase velocity relations $c = c(k, X)$ of the waves analytically. Therefore, the graphs of the implicit functions $c = c(k, X)$ are obtained from the dispersion relation as a result of numerical calculations. In order to determine the exact variation of the coefficient functions A in the first-order solutions depending on the slow variables $\{x_1, t_1\}$, the analysis of the second-order, $O(\epsilon^2)$, problem will be continued. Numerical solutions of the dispersion relation are found using real material parameters. Thus, the effects of material parameters, wave number variation and irregularity of the boundary surfaces on wave propagation are being investigated.

References

Ahmetolan, S., Peker-Dobie, A., Deliktas-Ozdemir, E., & Caglayan, E. (2023). Propagation of Lamb waves in an elastic layer with irregular surfaces. Wave Motion, 119, 103136.

Ben-Hador, R., & Buchen, P. (1999). Love and Rayleigh waves in non-uniform media. Geophysical Journal International, 137(3), 521–534.

Graff, K. F. (2012). Wave motion in elastic solids. Courier Corporation.

Kuo, J. T., & Nafe, J. E. (1962). Period equation for Rayleigh waves in a layer overlying a half space with a sinusoidal interface. Bulletin of the Seismological Society of America, 52(4), 807–822.

Vishwakarma, S. K., & Xu, R. (2016). Rayleigh wave dispersion in an irregular sandy earth's crust over orthotropic mantle. Applied Mathematical Modelling, 40(13-14), 8647–8659.

Zhang, S., Qin, L., Li, X., & Kube, C. M. (2020). Propagation of Rayleigh waves on curved surfaces. Wave Motion, 94, 102517.

Understanding Predator- Prey Dynamics Through Equilibrium State Classification

Kerime Nur Kavadar[a], Ali Demirci[a]

[a] Istanbul Technical University, Faculty of Science and Letters, Department of Mathematical Engineering, Türkiye
kavadar20@itu.edu.tr

Keywords: Equilibrium Classification, Predator- Prey Stability, Nonlinear Population Dynamics.

Aim

This study aims to analyze the stability of the logistic predator-prey model based on the Lotka-Volterra equations. By incorporating logistic growth, the research provides a more realistic representation of predator-prey interactions, considering environmental limitations. The study also seeks to classify different equilibrium states based on initial conditions and dominance relationships, ultimately offering a structured framework for stability analysis. The Lotka-Volterra system is widely used in various scientific fields beyond ecological modeling. In economics, it has been applied to model competition between firms, representing how market share dynamics evolve over time (Strogatz, 2018). The model helps predict how dominant firms maintain their position and how smaller competitors enter or exit the market. The competitive interactions between businesses can be likened to predator-prey dynamics, where dominant firms (predators) consume market share while smaller firms (prey) struggle to survive. In epidemiology, the system helps describe disease spread and interactions between infected and susceptible populations (Tang & Zhang, 2005). The predator-prey framework is particularly useful in modeling the spread of infectious diseases where the infection (predator) propagates through the population of susceptible individuals (prey). This application is crucial for understanding the dynamics of epidemics and developing control strategies such as vaccination and quarantine measures. Engineering applications include network traffic flow and resource allocation in communication systems, where the predator-prey framework captures competition for bandwidth or processing power (Zhang, Koura, & Su, 2020). In such systems, users competing for limited resources can be analyzed using similar mathematical principles. This approach is used to optimize network protocols and improve efficiency in data transmission. Additionally, in social sciences, Lotka-Volterra models are employed to study opinion dynamics, migration patterns, and conflict resolution scenarios (Berryman, 1992). Political competition, for example, can be framed as a predator-prey interaction where dominant ideologies suppress emerging ones, while in migration studies, the interaction between local and incoming populations can be modeled in a similar way. These diverse applications highlight the model's versatility in capturing competitive and cooperative interactions across multiple domains.

Material and Method

The material and method section should be written in Times New Roman font, justified-alignment and in 10-point size. The study involves a comprehensive literature review on predator-prey models, focusing on the classical Lotka-Volterra equations and their logistic extensions. The logistic predator-prey model is examined theoretically by transforming it into a dimensionless form to simplify the analysis (Murray, 2002). The reason for using a dimensionless transformation is to reduce the number of parameters and make the model easier to analyze mathematically. Stability is evaluated through local linearization techniques, particularly using the Jacobian matrix and eigenvalue analysis. This method allows for determining whether small deviations from equilibrium states grow over time (indicating instability) or diminish (indicating stability). Different classifications are proposed based on initial population conditions and species dominance, enabling a structured understanding of the system's equilibrium behavior. The approach involves identifying equilibrium points and assessing their stability using qualitative and numerical methods (Nowak & May, 2000). The equilibrium states are classified based on whether species coexistence is possible or if competitive exclusion occurs. The system's response to different parameter

values is also analyzed to understand how changes in environmental or biological conditions affect stability. To validate the theoretical findings, computational simulations are planned using MATLAB, allowing visualization of distinct stability regions. These simulations will be used to compare theoretical predictions with numerical solutions, providing additional insight into how population dynamics evolve over time. Sensitivity analysis will be performed by varying key parameters, such as growth rates and competition coefficients, to observe their impact on stability (Guckenheimer & Holmes, 2013). Additionally, bifurcation analysis will be conducted to determine how qualitative changes in the system occur as parameters are varied, offering deeper insights into critical transition points.

Findings

The findings section should be written in Times New Roman font, justified-alignment and in 10-point size. The analysis reveals that the stability of the logistic predator-prey model depends on the nature of interspecies interactions and initial population distributions. In cases of weak competition, both species can coexist, leading to an equilibrium state (Nowak & May, 2000; May, 2019). However, strong competition results in the extinction of one species. Three main dynamic scenarios are identified:

- The initially dominant species maintains its dominance, leading to a stable equilibrium where one species thrives while the other remains at a lower population level.
- The initially dominant species remains dominant but declines in population due to competitive interactions, resulting in a fluctuating or semi-stable equilibrium.
- The initially dominant species loses its dominance at equilibrium, leading to a reversal in population hierarchy over time.

These findings contribute to a deeper understanding of population dynamics, particularly regarding long-term stability under varying ecological conditions. Additionally, the numerical classification of equilibrium states provides valuable insights into how species interactions influence stability, making the model applicable to broader real-world problems such as economic market competition, epidemiological control strategies, and resource management (Guckenheimer & Holmes, 2013). The findings indicate that specific parameter conditions determine whether the predator-prey system is stable or unstable. For instance, when competition coefficients are below a critical threshold, both species can coexist without one eliminating the other. However, when competition exceeds this threshold, exclusion occurs. These insights help in designing sustainable ecosystem management strategies, economic policies, and technological systems that rely on competitive interactions (Murray, 2002). Further, the results show that external perturbations, such as environmental changes or fluctuations in resource availability, can alter the stability conditions of the system. For example, in an ecological setting, climate change or habitat destruction could shift equilibrium points and push species towards extinction. In an economic context, policy changes or technological disruptions could influence firm survival and competition patterns. By understanding these stability conditions, policymakers and scientists can make informed decisions about intervention strategies in various domains.

Conclusion

The study highlights the significance of logistic growth in predator-prey models and provides a systematic classification of equilibrium behaviors. The results confirm that species interactions and initial conditions play a crucial role in determining system stability. The logistic component of the model introduces a more realistic limitation on population growth, making it more applicable to real-world systems where unlimited growth is not possible. Future research will involve the numerical validation of theoretical findings through computational simulations and the application of the model to real-world ecological data. This approach will enhance the applicability of the logistic predator-prey model in biological and environmental studies. Additionally, the framework developed in this study can be extended to include multi-species interactions, stochastic effects, and spatial heterogeneity, making it applicable to more complex ecological and socio-economic systems. Further investigations could also explore the implications of additional nonlinearities, such as Allee effects and time delays, which can significantly influence system stability. The inclusion of stochastic elements in the model would allow

for the analysis of random environmental fluctuations and their effects on population dynamics. These extensions would provide a more detailed understanding of predator-prey dynamics in natural and artificial environments. Moreover, interdisciplinary collaborations between mathematicians, ecologists, economists, and engineers can refine the model and expand its range of applications. By incorporating more complex interactions and refining parameter estimation techniques, future studies can enhance the predictive power and practical relevance of the logistic predator-prey model in various scientific and industrial applications.

References

Berryman, A. A. (1992). The origins and evolution of predator-prey theory. Ecology, 73(5), 1530–1535. https://doi.org/10.2307/1940005

Guckenheimer, J., & Holmes, P. (2013). Nonlinear oscillations, dynamical systems, and bifurcations of vector fields. Springer Science and Business Media.

May, R. M. (2019). Stability and complexity in model ecosystems. Princeton University Press.

Murray, J. D. (2002). Mathematical biology I: An introduction. Springer.

Nowak, M. A., & May, R. M. (2000). Virus dynamics: Mathematical principles of immunology and virology. Oxford University Press. https://doi.org/10.1093/oso/9780198504184.001.0001

Strogatz, S. H. (2018). Nonlinear dynamics and chaos: With applications to physics, biology, chemistry, and engineering. CRC Press.

Tang, Y., & Zhang, J. W. (2005). A competition model for two CPU vendors. Physica A: Statistical Mechanics and its Applications, 348, 465–480. https://doi.org/10.1016/j.physa.2004.09.018

Zhang, Y., Koura, Y. H., & Su, Y. (2020). Predator–prey approach in modeling users' data packets forwarding. The Journal of Supercomputing, 76(10), 8343–8356. https://doi.org/10.1007/s11227-020-03230-0.

Effects of Weak Heterogeneity on Nonlinear Love Wave Interactions

Berna Yavaş[a], Semra Ahmetolan[b], Ali Demirci[b]

[a]Istanbul Technical University Graduate School, Mathematical Engineering, Turkey
[b] Istanbul Technical University, Faculty of Science and Letters, Department of Mathematical Engineering, Turkey
yavas22@itu.edu.tr

Keywords: Nonlinear Elasticity, Weak Heterogeneity, Love Waves, Thin Layer Approximation.

Aim

Elastic waves in waveguides exhibit dispersion, meaning their phase velocities depend on the wave number. Given their crucial applications in geophysics, non-destructive testing, and signal processing, dispersive elastic waves have been widely studied. In particular, the propagation of shear horizontal (SH) waves in layered media with varying elastic properties has become a key research area in engineering fields like geophysics, seismology, and metallurgy. Studies have explored the effects of linear and nonlinear material behavior, as well as inhomogeneity, on wave propagation.

Early research focused on linear wave propagation in elastic media with depth-dependent heterogeneity. Avtar, derived the dispersion relation for Love waves in a double-layered heterogeneous medium, while Kowalczyk et al. analyzed SH wave propagation in a nonhomogeneous half-space, where the shear modulus and density vary as a power function of depth. Kumari et al. studied Love-type waves in a layered isotropic structure with two heterogeneous layers over a homogeneous half-space, deriving a dispersion equation.

Recent studies have examined nonlinear wave propagation. Demirkus investigated nonlinear SH waves in a hyperbolically heterogeneous hyperelastic layer over a rigid substratum, deriving a nonlinear Schrödinger (NLS) equation to describe their self-modulation and demonstrating bright solitary SH waves influenced by heterogeneity and nonlinearity. Deliktas-Ozdemir et al. used the multiple scales method to analyze nonlinear SH wave propagation in a double-layered elastic plate with heterogeneous isotropic hyperelastic materials. Ahmetolan et al. extended this analysis to SH waves in a weakly inhomogeneous half-space with a nonlinear thin layer, deriving an NLS equation to study the effects of heterogeneity and nonlinearity.

This study explores Love wave interactions in a nonlinear homogeneous thin layer overlying a nonlinear heterogeneous semi-infinite medium. Our research extends previous work by incorporating the nonlinear material properties of the layer into the boundary conditions of the semi-infinite heterogeneous medium. Additionally, we analyze how both the layer's nonlinear properties and the medium's heterogeneity influence wave propagation.

Material and Method

First, the boundary value problem characterizing the propagation of nonlinear Love waves in a semi-infinite medium covered by a finite-thickness layer was considered. It was assumed that there are no stresses on the free surface and that both the stresses and displacements are continuous at the interface. The material of the layer was assumed to be nonlinear, homogeneous, and isotropic, while the material of the semi-infinite medium was considered nonlinear, heterogeneous, and isotropic. Using the thin-layer approximation, the following equation of motion and the boundary condition on the free surface were derived:

$$h\rho_1 \frac{\partial^2 v}{\partial t^2} - h\mu_1 \frac{\partial^2 v}{\partial X^2} + \mu_2 \frac{\partial v}{\partial Y}\left(1 + \frac{\rho_2 n_2}{\mu_2} Q(v)\right) = h\rho_1 \eta_1 \frac{\partial}{\partial X}\left\{\frac{\partial v}{\partial X}\left(\left(\frac{\partial v}{\partial X}\right)^2 + \frac{\mu_2^2}{\mu_1^2}\left(\frac{\partial v}{\partial Y}\right)^2\right)\right\} \quad on \ Y = 0 \tag{1}$$

$$\rho_2 \frac{\partial^2 v}{\partial t^2} - \mu_2 \left(\frac{\partial^2 v}{\partial X^2} + \frac{\partial^2 v}{\partial Y^2}\right) - \left(\frac{d\mu_2}{dY}\frac{\partial v}{\partial Y}\right) = \rho_2 \eta_2 \left[\frac{\partial}{\partial X}\left(\frac{\partial v}{\partial X} Q(v)\right) + \frac{\partial}{\partial Y}\left(\frac{\partial v}{\partial Y} Q(v)\right)\right] + Q(v)\left(\frac{\partial(\rho_2 \eta_2)}{\partial Y}\frac{\partial v}{\partial Y}\right) \quad , Y < 0. \tag{2}$$

$$v \to 0 \quad as \quad Y \to -\infty \tag{3}$$

Here, μ_i represents the shear modulus, ρ_i the density, and η_i the nonlinear material parameter, where $i = 1$ corresponds to the layer and $i = 2$ to the semi-infinite medium. Q is the nonlinear derivative operator. Under the assumption that the material forming the semi-infinite medium has weak heterogeneity, the material parameters are taken as follows, where $\varepsilon > 0$ is a small parameter:

$$\mu_2(y) = \mu_{2_0}(1 - \varepsilon^2 e^{dy}),\ \rho_2(y) = \rho_{2_0}(1 + \varepsilon^2 e^{dy}),\ \eta_2(y) = \eta_{2_0}(1 + \varepsilon^2 e^{fy}) \quad d, f > 0. \tag{4}$$

Applying the multiple scales method, which is an asymptotic perturbation technique, the independent variables are defined as:

$$x_i = \varepsilon^i X, \quad t_i = \varepsilon^i t, \quad y = Y, \quad i = 0,1,2. \tag{5}$$

Here, $\varepsilon > 0$ also measures the weakness of nonlinearity. The variables x_0, t_0, y are the fast variables that describe the rapid variations in the problem, while x_1, x_2, t_1, t_2 are the slow variables that characterize the slow variations. Subsequently, the displacement function v is considered as a function of these new variables, and the following asymptotic series expansion in terms of ε is applied:

$$v = \sum_{n=1}^{\infty} \quad \varepsilon^n v_n(x_0, x_1, x_2, y, t_0, t_1, t_2). \tag{6}$$

The independent variables (5) and the asymptotic expansion (6) are applied to the equations of motion and the boundary conditions. By collecting terms with similar powers of ε, a hierarchy of problems is obtained, allowing the sequential determination of v_n. Since this study focuses on the problem of nonlinear wave interactions, it is sufficient to examine the first three orders of the problem.

Findings

By analyzing the first-order problem, the variations of the solutions with respect to the fast variables x_0 and y can be determined. Examining the higher-order problems will reveal the dependence of the solutions on the slow variables. Assuming the linear phase velocity satisfies $c_1 < c < c_2$, this study considers the interaction of co-directional Love waves. Therefore, the solution of the first-order problem, assuming that harmonic resonance conditions are not satisfied, is given as:

$$v_1 = \sum_{j=a,b} \quad A_{1j}(x_1, x_2, t_1, t_2) e^{p_j y} e^{i\phi_j} + c.c., \quad p_j = k_j\left(1 - c_j^2/c_2^2\right)^{1/2}, \quad \phi_j = \left(k_j x_0 - \omega_j t_0\right). \tag{7}$$

This wave solution satisfies the dispersion relation obtained from the boundary condition:

$$-h\omega_j^2 + c_1^2 h k_j^2 + c_1^2 \gamma_0 p_j = 0, \quad j = a, b \tag{8}$$

Note that this first-order solution and the solution of the linear problem are of the same form. The only difference is that in the linear problem A_{1j} is constant, but here it is a slowly varying complex function representing the nonlinear self-modulation of a wave train. Obviously, to complete the first-order solution of the nonlinear problem, A_{1j} has to be determined. This can be achieved by examining the higher-order perturbation problems. On the other hand, the weak heterogeneity of the half space occurs in higher-order perturbation problems.

From the compatibility condition in the second-order problem, it is found that A_{1j} remains constant in a frame of reference moving with the group velocity V_{gj} of the wave. The compatibility condition in the third-order problem yields a system of equations for $A_j = k_j A_{1j}$. When the group velocities of the co-directional waves are equal to each other, i.e., $V_{g_b} = V_{g_a}$, this system will lead to the following coupled nonlinear Schrödinger (CNLS) equations:

$$i\frac{\partial A_a}{\partial \tau} + \Gamma_a \frac{\partial^2 A_a}{\partial \xi^2} + \Delta_{aa}|A_a|^2 A_a + \Delta_{ba}|A_b|^2 A_a + \Lambda_a A_a = 0 \qquad i\frac{\partial A_b}{\partial \tau} + \Gamma_b \frac{\partial^2 A_b}{\partial \xi^2} + \Delta_{bb}|A_b|^2 A_b + \Delta_{ab}|A_a|^2 A_b + \Lambda_b A_b = 0 \tag{9}$$

Here, the coefficients Γ_a and Γ_b are the linear dispersion coefficients; Δ_{aa} and Δ_{bb} are the nonlinear coefficients which describe the self-modulation of the wave packets; Δ_{ab} and Δ_{ba} are the nonlinear coupling coefficients of the cross-modulation between two wave packets and Λ_a, Λ_b are known as external potential and show the effect of heterogeneity. Thus, once solutions for A_a and A_b are derived from (9) for given initial values of the form $A_a(\xi,0) = A_{a0}(\xi)$ and $A_b(\xi,0) = A_{b0}(\xi)$, then the first-order solution v_1 can be constructed by (7).

Conclusion

In this study, the propagation and interaction of nonlinear Love waves in a nonlinear homogeneous thin layer overlying a nonlinear heterogeneous semi-infinite medium was investigated. By applying the thin layer approximation, the boundary value problem was transformed into a free-surface boundary condition for the semi-infinite medium. However, despite this transformation, the derived boundary condition still retains the linear and nonlinear material properties of the layer. Subsequently, using the multiple scales method, the obtained equations were analyzed, leading to first-order and higher-order perturbation solutions.

The compatibility conditions derived from the second and third-order problems led to a system of coupled nonlinear Schrödinger (CNLS) equations, which govern the evolution of wave amplitudes. These equations describe the nonlinear interactions of co-directional Love waves, incorporating effects of dispersion, self-interaction and cross-interaction, and the effect of the heterogeneity of the half-space. Future work will focus on the numerical solutions of the derived CNLS equations.

References

Ahmetolan, S., Demirci, A., Peker-Dobie, A., & Ozdemir, N. (2024). SH waves in a weakly inhomogeneous half space with a nonlinear thin layer coating. *Zeitschrift für Angewandte Mathematik und Physik*, *75*(2), 68.
Avtar, P. (1967). Love waves in a two-layered crust overlying a vertically inhomogeneous half-space I. *Pure and Applied Geophysics*, *66*(1), 48–68.
Deliktas-Ozdemir, E., Ahmetolan, S., & Tuna, D. (2022). Existence of solitary SH waves in a heterogeneous elastic two-layered plate. *Zeitschrift für Angewandte Mathematik und Physik*, *73*(6), 220.
Demirkus, D. (2018). Non-linear bright solitary SH waves in a hyperbolically heterogeneous layer. *International Journal of Non-Linear Mechanics*, *102*, 53–61.
Kowalczyk, S., Matysiak, S., & Perkowski, D. M. (2016). On some problems of SH wave propagation in inhomogeneous elastic bodies. *Journal of Theoretical and Applied Mechanics*, *54*(4), 1125–1135.
Kumari, N., et al. (2016). Influence of heterogeneity on the propagation behavior of Love-type waves in a layered isotropic structure. *International Journal of Geomechanics*, *16*(2), 04015062.

MATHEMATICAL ENGINEERING

Applied Mathematics

Data Science and Machine Learning

Mathematical Modeling

A Case Study in Time Series Classification Using Machine Learning and Deep Learning

Barış Küçük[a], Atabey Kaygun[b]

[a] Istanbul Technical University, Graduate School, Mathematical Engineering Program, Türkiye
[b] Istanbul Technical University, Department of Mathematical Engineering, Türkiye
kucukb22@itu.edu.tr

Keywords: Time Series, EEG Classification, Machine Learning, Deep Learning, Neural Networks.

Aim

Electroencephalography (EEG) is widely used in neuroscience and medical diagnostics to analyze brain activity in clinical applications as it can help in the identification of neurological disorders and cognitive states. Classification of EEG signals plays a crucial role in the diagnosis of neurological conditions and the development of brain-computer interface (BCI) systems. The primary aim of this study is to develop and evaluate a classification pipeline based on time-frequency representations of EEG data, particularly spectrogram images, using both traditional machine learning deep learning models. This work also seeks to compare the performance of various approaches and discuss the practical implications of classification accuracy in medical applications.

Material and Method

Dataset Description

The dataset used in this study originates from a comprehensive research initiative aimed at identifying EEG-based biomarkers of genetic predisposition to alcoholism. It was compiled and made publicly available through the UCI Machine Learning Repository. EEG signals were recorded from 122 subjects, equally divided into two distinct groups: alcoholic and control. During the experiment, each participant was exposed to visual stimuli consisting of pictures selected from the standardized 1980 Snodgrass and Vanderwart picture set. These stimuli were presented in three conditions; a single stimulus (S1), two matching stimuli (S1 and S2 match), or two non-matching stimuli (S1 and S2 nonmatch). EEG recordings were collected from 64 scalp electrodes. The signals were sampled at 256 Hz over a duration of 1 second per trial, resulting in 256 data points per electrode per trial. Each subject completed 120 trials and data from each trial were stored in individual text files. These files include metadata such as subject ID (which also encodes subject group), trial type, and stimulus condition. The recorded signals were stored as four-column entries: trial number, electrode label(sensor position), timestamp (0–255) and voltage in microvolts (μV) [1].

Preprocessing

Preprocessing of the dataset required careful handling due to its size and structure. Subjects were grouped based on the prefix of their identifiers: those beginning with "co2a" or &"co3a" were labeled as alcoholic, while others were assigned to the control group. To efficiently combine trials for each subject, the Polars library was initially used for its memory efficiency and speed on large-scale tabular data. Following the merging stage, the more flexible Pandas library was preferred for further data manipulation.
Three additional columns were appended to each trial dataset to enhance the tabular structure: the subject name, group label ('a' for alcoholic 'c' for control) and the stimulus matching condition (S1-obj, S2-nomatch, or S2-match). This preprocessing was conducted separately for alcoholic and control groups to prevent memory overload. After combining all trials, the dataset reached approximately 179 million rows, necessitating optimized data management. To this end, the data was converted into the Parquet format which provided faster loading and minimized memory issues. Strategic memory handling, including kernel restarts and incremental processing was employed throughout the analysis.

After sorting each trial by timestamp, the data was reshaped using a pivot operation to format voltage values by trial and sensor. Sensor names were standardized to match the 10–20 Electrode Placement System, a widely accepted convention in EEG analysis. Three incompatible sensors labeled X, Y, and nd were excluded from further analysis to maintain EEG format integrity.

Modeling Approaches

The classification of EEG signals in this study followed a comprehensive modeling pipeline involving both traditional machine learning algorithms and advanced deep learning techniques. The process initially focused on tabular representations of the EEG data, where statistical and frequency-domain features were extracted from each of the 64 channels per trial. These features were used to train classical supervised models such as Logistic Regression, Support Vector Machines (SVM), as well as powerful ensemble methods including XGBoost, LightGBM, and AdaBoost [2].

Subsequently, deep learning approaches have been used to capture more complex spatial and temporal dynamics within EEG signals. In the first deep learning phase, 1D Convolutional Neural Networks (CNNs) were applied to tabular EEG data to extract local temporal patterns across channels. However, when the EEG signals were transformed into spectrogram images, 2D CNNs were used to exploit both spatial and frequency-based features in a visual format [3], [4]. By feeding EEG sequences into LSTM architectures, the models have been studied to effectively learn the dynamic signal transitions over time that are often crucial in brain activity interpretation [5]. In addition to CNN and LSTM models, other deep learning approaches were also examined to assess their potential contributions. For maximum accuracy and to avoid overfitting, the models were optimized through subject-based cross-validation, dropout and hyperparameter tuning. All applications were implemented in Python using libraries such as Scikit-learn, Tensorflow and Keras.

Findings

The comparative performance of the models revealed key insights into the suitability of various approaches for EEG-based classification. Among the classical machine learning algorithms, XGBoost achieved the highest accuracy on the tabular feature set, with a classification accuracy of 72.3%, outperforming LightGBM (69.1%) and AdaBoost (67.2%). The ensemble-based models demonstrated robustness to inter- subject variability and imbalanced class distributions.

However, 1D CNN significantly improved upon these results, achieving a classification accuracy of 78.3%. This highlights the strength of convolutional neural networks in handling EEG data, as they are better suited to learning spatial hierarchies and features directly from the raw data.

When transitioning to deep learning models, significant improvements were observed. The 2D CNN, trained on spectrogram images, achieved an impressive classification accuracy of 92.4%. This model benefitted from the rich time-frequency representations of EEG signals, allowing it to capture more detailed and complex features of the data compared to the classical machine learning models.

Additionally, the LSTM model applied to raw time-series EEG data achieved an accuracy of 94.9%, showcasing its ability to capture temporal dependencies that are not easily accessible to image-based models like the 2D CNN. These findings underscore that while traditional machine learning models can serve as a useful baseline, deep learning models, particularly CNN and LSTM-based architectures, offer substantial improvements in decoding cognitive states from EEG data.

Conclusion

This study presented a multi-stage pipeline for the classification of EEG signals associated with genetic predisposition to alcoholism, integrating both conventional machine learning and deep learning methods. The experimental results suggest that ensemble-based models like XGBoost can be used for structured tabular data, while deep learning models, particularly CNNs and LSTMs are highly effective in extracting meaningful patterns from raw signals and spectrogram representations.

The performance of 2D CNNs and LSTM models demonstrates the advantage of modeling both spatial-frequency and temporal dynamics of EEG signals. Furthermore, the hybrid architectures highlighted the complementarity of visual and sequential signal features with classification performance.
These outcomes indicate a strong potential for deep learning models in clinical EEG analysis, especially in early detection and diagnosis scenarios. Future work will focus on expanding the dataset, enhancing interpretability of deep models and exploring domain adaptation techniques for subject-invariant learning.

References

Begleiter, H. (1995). EEG Database [Dataset]. UCI Machine Learning Repository. https://doi.org/10.24432/C5TS3D.
Bentéjac, C., Csorgő, A., & Martínez-Muñoz, G. (2019). A Comparative Analysis of XGBoost. pp. 3-6. https://doi.org/10.48550/arXiv.1911.01914
Talaei Khoei, T., Ould Slimane, H. & Kaabouch, N. Deep learning: systematic review, models, challenges, and research directions. Neural Comput & Applic 35, 23103–23124 (2023). pp. 1-6. https://doi.org/10.1007/s00521-023-08957-4
Alzubaidi, L., Zhang, J., Humaidi, A.J. et al. Review of deep learning: concepts, CNN architectures, challenges, applications, future directions. J Big Data 8, 53 (2021). pp. 15-20. https://doi.org/10.1186/s40537-021-00444-8
Mienye, I. D., Swart, T. G., & Obaido, G. (2024). Recurrent Neural Networks: A Comprehensive Review of Architectures, Variants, and Applications. Information, 15(9), 517. pp. 4-9. https://doi.org/10.3390/info15090517.

MATHEMATICAL ENGINEERING

Applied Mathematics

Data Science and Machine Learning

Mathematical Modeling

Modeling Rare Metal Market Dynamics: A Nonlinear Approach withInvestment and Geopolitical Risk

Furkan Emre Işık[a], Ali Demirci[a]

[a] Istanbul Technical University/Faculty of Science and Letters, Departmant of Mathematics, Mathematical Engineering, Turkey
isikf17@itu.edu.tr

Keywords: Bifurcation, Dynamical Systems, Nonlinear System Modeling.

Aim

The rare earth element (REE) market is characterized by complex interactions among supply, demand, price fluctuations, and geopolitical risk. These elements are essential for various advanced technologies, including electric vehicles (EVs), renewable energy systems, and defense applications. Understanding the dynamics of this market requires a robust modeling framework that captures nonlinear relationships and feedback mechanisms. The REE market is subject to disruptions due to political interventions, trade restrictions, and investment cycles, making it highly volatile. This study aims to develop and analyze a nonlinear dynamical system representing the REE market, integrating key factors such as supply from different regions, demand driven by EV adoption, price evolution, and investment inmining operations. Traditional linear models often fail to capture the nonlinear dependencies present in commodity markets, particularly when investment decisions, supply constraints, and price adjustments occur dynamically. By formulating a system of nonlinear ordinary differential equations (ODEs), this study seeks to explore the fundamental structure of market stability, equilibrium states, and bifurcation behavior. A primary objective of this research is to investigate critical thresholds that drive market instability or structural shifts. By understanding how different parameters influence market stability, policymakers and industry leaders can anticipate potential crises andtake preventive measures. This study also contributes to the broader literature on nonlinear economic systems by demonstrating how nonlinear interactions between supply, demand, and investment lead to complex market behaviors. Ultimately, the findings may provide insights into the long-term sustainability of rare earth resource management and inform strategies for stabilizing the market amid external shocks.

Material and Method

A nonlinear system of ordinary differential equations (ODEs) is formulated to model the interactions between key market components. The model introduces nonlinear dependencies to reflect real-world behavior, where investment follows a power-law response to price, supply reacts to investment in a nonlinear fashion, and demand exhibits nonlinear sensitivity to price fluctuations. Unlike standard linear economic models, this framework explicitly incorporates dynamic feedback loops that characterize the rare earth market. To analyze system behavior, equilibrium points are determined by setting the rate of change of the system variables to zero and solving for steady-state solutions. The stability of these equilibria is then evaluated through Jacobian matrix eigenvalues, where negative real parts indicate stability and positivereal parts signal instability [6]. This approach allows us to identify conditions under which market stability is maintained or disrupted. Furthermore, bifurcation analysis is performed to explore how small parameter changes can induce qualitative shifts in market behavior. Specifically, bifurcations are examined concerning geopolitical risk, price elasticity of demand, and investment sensitivity to price fluctuations. The presence of bifurcations suggests the existence of tipping points, beyond which the market transitions from a stable to an unstable state [4]. By mapping these transitions, we can assess potential risk factors leading to extreme volatility in rare earth prices. Computational simulations are used to validate the theoretical findings, providing insight into how the market evolves over time under different scenarios. Sensitivity analysis is conducted to determine the influence of key parameters, allowing us to gauge their relative importance in driving

market dynamics. This methodological approach enables a comprehensive investigation of the nonlinear characteristics of the REE market, enhancing our ability to anticipate supply crises and price fluctuations.

Findings

The analysis reveals the existence of multiple equilibria in the system, dependent on parameter values such as investment responsiveness toprice and geopolitical risk. Linear stability analysis shows that under certain conditions, the system exhibits oscillatory behavior due to the interplay between supply fluctuations and investment cycles. Moreover, bifurcation analysis identifies critical thresholds where small changes in parameters induce abrupt shifts in market stability. Key findings include:

Investment-Price Feedback Loop: Nonlinear investment response to price amplifies market volatility, leading to self-sustained oscillations or market crashes [5].

Geopolitical Risk as a Bifurcation Parameter: Increasing geopolitical risk beyond a certain threshold shifts the market from astable equilibrium to an unstable regime, where supply shortages drive exponential price increases [3].

Nonlinear Demand Suppression: High prices induce nonlinear suppression in demand, which stabilizes the system under certain conditions but exacerbates volatility under others [2].

Multiple Attractors: The system exhibits multistability, meaning different initial conditions or parameter values can lead to vastly different market outcomes (e.g., stable supply vs. crisis states) [1].

These results underscore the importance of nonlinear interactions in rare earth market dynamics and highlight the potential for sudden, unpredictable shifts due to investment behavior and geopolitical disruptions. Policy implications include the necessity for strategic investment planning and international cooperation to mitigate market instability.

Conclusion

This study demonstrates that a nonlinear dynamical system approach provides valuable insights into the behavior of the rare earth market. By incorporating nonlinear feedback loops between supply, demand, price, and investment, the model captures key features of real-world market behavior that traditional linear models fail to address. The identification of bifurcation points and multiple equilibria highlights the market's susceptibility to sudden shifts, offering a theoretical framework for anticipating disruptions. The findings emphasize the need forproactive strategies to stabilize the REE market, particularly through policies that regulate investment cycles and mitigate geopolitical risks. Further research should integrate stochastic elements and empirical validation using real-world data to refine the model's predictive capability. Additionally, incorporating external policy interventions, technological advancements, or environmental constraints could provide a more comprehensive understanding of long-term market dynamics. Ultimately, this study contributes to the broader literature on nonlinear economic modeling and offers practical insights for policymakers and industry stakeholders navigating the complexities of the rare earth market.

References

Chian, A. C. (2007). Complex Systems approach to economic dynamics. Springer Science & Business Media.

Deng, S., Prodius, D., Nlebedim, I. C., Huang, A., Yih, Y., & Sutherland, J. W. (2021). A dynamic price model based on supply and demand with application to techno-economic assessments of rare earth element recovery technologies. Sustainable Production and Consumption, 27, 1718–1727. https://doi.org/10.1016/j.spc.2021.04.013

Gong, X., & Xu, J. (2022). Geopolitical risk and dynamic connectedness between commodity markets. Energy Economics, 110, 106028. https://doi.org/10.1016/j.eneco.2022.106028

Introduction to applied nonlinear dynamical systems and chaos. (2003). In Texts in applied mathematics. https://doi.org/10.1007/b97481

Kurkina, E. S. (2017). Mathematical models of investment cycles. Computational Mathematics and Modeling, 28(3), 377–399. https://doi.org/10.1007/s10598-017-9371-4

Strogatz, S. (2024). Nonlinear dynamics and chaos: With Applications to Physics, Biology, Chemistry, and Engineering.

MECHANICAL ENGINEERING

Additive Manufacturing

Automotive

Computational Fluid Dynamics

Computational Solid Mechanics

Fluid Mechanics

Industrial Data Analytics

Machine Design

Machine Dynamics, Vibration, and Acoustic

System Dynamics and Control

Evaluation of Mechanical Properties of SLM AlSi10Mg Alloy Produced with Different Production Parameters

Hasret Baş[a], Raşid Ahmed Yıldız[a]

[a] Istanbul Technical University/Science Engineering and Technology Institute,
Departmant of Mechanical Engineering, Materials and Manufacture Master of Science Program, Turkey
bash22@itu.edu.tr

Keywords: Laser Powder Bed Fusion, AlSi10Mg Alloy, Tensile Testing, Ved.

Aim

AlSi10Mg alloy, produced using LPBF technology, is frequently used today in aerospace and automotive, where high strength and lightness are preferred. According to the information from the literature, AlSi10Mg alloy with SLM had better or comparable mechanical properties than the cast AlSi10Mg alloy. In this study, the optimum parameter was selected by examining the mechanical properties of AlSi10Mg alloys produced with different parameters.

Additive Manufacturing (AM), often used for metals and known as 3D printing for polymers, has the potential to revolutionize product manufacturing through new materials and existing processes. [1] AM can also cut product development time and costs by forming process chains with other technologies, beyond just creating complex models. [2] Powder Bed Fusion (PBF) is one of seven AM methods, using a laser, heat, or electron beam to melt and fuse material into a 3D object. [3] Powder bed fusion uses laser or electron beams to melt and fuse metal or alloy powders, including methods like selective laser melting (SLM), selective laser sintering (SLS), direct metal laser sintering (DMLS), electron beam melting (EBM), and selective heat sintering (SHS). [4] For producing SLM AlSi10Mg parts, SLM is expected to be ideal for lightweight and thermal control components in aerospace and automotive, thanks to aluminum's low density and high thermal conductivity. [5,6] SLM AlSi10Mg parts are known for their high strength and low ductility. [6] SLM alloys also exhibit anisotropic mechanical properties. [6,8] In SLM-produced AlSi10Mg, mechanical properties are strongly influenced by the size and shape of eutectic Si in the microstructure. [5] Wei Li et al. [7] investigated the effect of artificial aging at different temperatures on the tensile strength and microstructure of the material. In the artificial aging processes carried out at 450, 500, 550 °C for 2 hours, a significant decrease is observed in both tensile and yield strengths of the specimens at 450 °C whist a large increase in ductility of can be observed. As temperatures increased to 500 and 550 °C, tensile and yield strengths continued to decrease, while ductility continued to increase. It has been suggested that this is due to the temperature-dependent changes in the variation in size of Si. K. Kempen et al. [8] compared the SLM-produced AlSi10Mg alloy with the conventionally cast AlSi10Mg alloy and indicated that the AlSi10Mg alloy produced by SLM exhibited higher mechanical properties than the cast AlSi10Mg alloy or were comparable. It was indicated that the reason for this is that SLM AlSi10Mg parts have a very fine microstructure and fine Si phase distribution. Alessia Teressa Silvestri et al. [9] tested and compared samples produced on different machines and in different building directions. They stated that ultimate tensile strength, yield strength, and modulus of elasticity showed different values depending on different machines, but the elongation at break was almost the same. It has been suggested that although the influence of the building direction and the equipment is evident in the diagrams, it is not possible to choose a clear production parameter in any case illustrated by the experimental work. Nevertheless, it has been stated that products with the best mechanical behaviour can be obtained and in all cases are better or comparable to samples produced with traditional technology. [8,9] In this study, laser power, scanning speed, scanning range and orientation parameters were investigated. It was investigated how the yield strength, tensile strength, elongation at break and modulus of elasticity changed with the change of these parameters.

Material and Method

Tensile tests of tensile test specimens produced using SLM Solutions powders and the Nikon SLM 500HL printer were performed in accordance with ASTM E8-09 standards. A Shimadzu Autograph machine was used as the tensile testing machine. Specimen elongation was determined using two CCD cameras (which were used as video extensometers). The test was conducted with the moving ram set at 5 mm/min, thus having an initial strain rate of 2.38×10-3 s-1. Tensile tests were performed on a total of 12 specimens, 4 specimens from the scan speed parameter and 3 samples from each of the other parameters.

The strength of Al alloys produced by additive manufacturing is notable; however, their mechanical behavior can deteriorate significantly due to process-related flaws, especially porosity, which is the most damaging. This issue arises from a non-optimized process, making the careful selection of building parameters essential to obtain a nearly fully dense final part. [10] Maverick Giovagnoli et al. [10] argued that while VED can provide a rough estimation for porosity, it is insufficient for predicting microstructure and mechanical properties, and therefore inadequate for determining the optimum processing parameters. Wayne E. King et al. [11] the occurrence of keyhole mode melting identified as a cause of porosity formation and a transition threshold for the keyhole mode determined. This keyhole transition threshold determined by a parameter called Normalized Enthalpy, which evaluates the laser power, scanning speed and beam diameter on a single scale. However, VED will be used in this study. Table 1 shows the calculated VED values according to the applied production parameters.

Table 1: Production parameters of the samples and volumetric energy density (VED) values calculated according to these parameters

Batch Name	Scan Speed (mm/s)	Hatch Spacing (µm)	Laser Power (W)	Build Direction (°)	Thickness of Layer (µm)	VED (J/mm^3)
SS 1000	**1000**	170	370	0	30	72,55
CG	**1200**	170	370	0	30	60,46
SS 1300	**1300**	170	370	0	30	55,81
SS 1400	**1400**	170	370	0	30	51,82
H 150	1200	**150**	370	0	30	68,52
H 130	1200	**130**	370	0	30	79,06
H 110	1200	**110**	370	0	30	93,43
P 350	1200	170	**350**	0	30	57,19
P 330	1200	170	**330**	0	30	53,92
P 310	1200	170	**310**	0	30	50,65
BD 35	1200	170	370	**35**	30	60,46
BD 45	1200	170	370	**45**	30	60,46
BD 90	1200	170	370	**90**	30	60,46

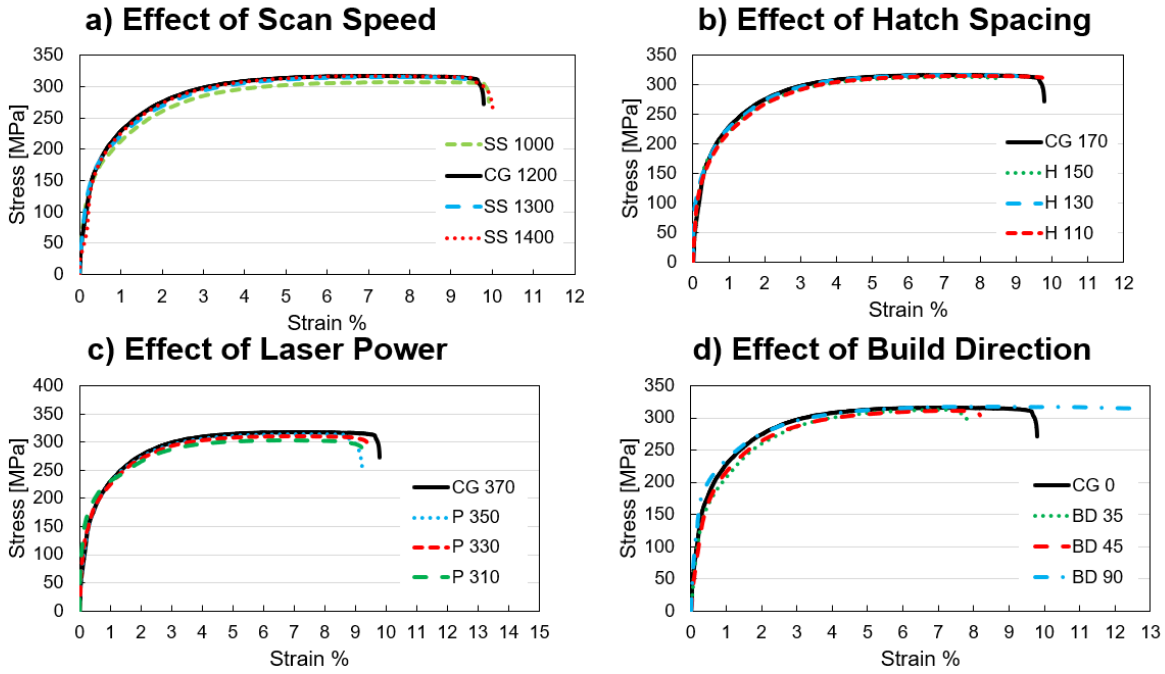

Fig 1: Effect of production parameters on mechanical behaviour.

Findings

In Fig 1(a), the effect of scanning speed on mechanical properties is investigated. As can be seen, when the scanning speed was low, the yield and tensile strengths were also relatively low compared to other scanning speeds. Because the highest VED value is reached when the scanning speed decreases and the increase in VED value increases the amount of energy given by the laser to the powder bed, causing the temperature to increase. As the temperature increases, the recoil pressure created by the molten metal vapor creates a narrow and deep melt pool called the keyhole. The keyhole is unstable and when it collapses, protective gases such as argon are trapped inside. This causes porosity and causes the yield and tensile strength to decrease. At lower VED values, the powders do not melt completely due to insufficient energy input and full bonding between layers cannot be achieved. This causes increased porosity and decreased strength. In Fig 1(b), the effect of hatch spacing was investigated. Here, it is seen that the CG specimen, which has the lowest VED value (60.46 J/mm^3) among the 4 samples, is better than the other specimens in terms of yield and tensile strength and ductility. Again, it is thought that keyhole formation causes porosity. In Fig 1(c), the effect of laser power was investigated. Here, the CG sample, which has a higher VED value (60.46 J/mm^3) than the other samples, has better mechanical properties as in other evaluations. The reason for this may be the formation of porosity due to insufficient melting at low VED value. In Fig 1(d), the effect of build direction was investigated. U. Patakham et al.
[12] stated that SLM AlSi10Mg exhibits isotropic properties when as-built and anisotropic properties after heat treatment. Shengzhao Yang et al. [13] stated that the horizontal specimen had the highest yield strength and highest elongation, the specimen with 45° orientation had the highest tensile strength, the lowest ductility was seen in the vertical specimen, and the highest ductility was seen in the vertical specimen. They attributed the low ductility and early fracture of 45° inclined samples to the high porosity rates in the contour areas. They state that the main effect in horizontal and vertical orientations arises from the alignment of the Al-Si eutectic phases. These data are consistent with our results. While the horizontally produced sample BD 90 has the highest yield and tensile strength and elongation, the samples with 35° and 45° orientation have lower yield and tensile strength. The CG sample produced perpendicularly shows mechanical properties at average values.

Conclusion

As a results, when we look at the graphics, it is seen that the BD 90 sample (produced horizontally to the table plane) has the best mechanical properties (flow strength, rupture strength, rupture prolongation). The higher breaking prolongation is important for the predictability of damage formation. However, there is no significant necking. Nevertheless, we can say that it has a higher ductility because the rupture is higher. Therefore, the best parameters are the production parameters of the BD 90 sample. However, these samples cover a lot of space on the table. And these samples can only be separated from the table by water jet and wire erosion. CG samples allow more parts production at one time and can be easily separated from the table. For BD 90 and CG samples with the same VED value (60,46 J/mm3), BD 90 sample parameters may be preferred if the ductility is very important compared to the usage area. In addition, CG sample parameters also have very good mechanical features and are preferable in terms of cost and ease of production.

References

Mower, T. M., & Long, M. J. (2016). Mechanical behavior of additive manufactured, powder-bed laser-fused materials. *Materials Science and Engineering: A*, *651*, 198-213.

Gibson, I., Rosen, D., Stucker, B., Khorasani, M., Rosen, D., Stucker, B., & Khorasani, M. (2021). *Additive manufacturing technologies* (Vol. 17, pp. 160-186). Cham, Switzerland: Springer.

Url 1 https://engineeringproductdesign.com/knowledge-base/powder-bed-fusion/, date retrieved 17.03.2025.

Takata, N., Kodaira, H., Sekizawa, K., Suzuki, A., & Kobashi, M. (2017). Change in microstructure of selectively laser melted AlSi10Mg alloy with heat treatments. *Materials Science and Engineering: A*, *704*, 218-228.

Praneeth, J., Venkatesh, S., & Krishna, L. S. (2023). Process parameters influence on mechanical properties of AlSi10Mg by SLM. *Materials Today: Proceedings*.

Patakham, U., Palasay, A., Wila, P., & Tongsri, R. J. M. S. (2021). MPB characteristics and Si morphologies on mechanical properties and fracture behavior of SLM AlSi10Mg. *Materials Science and Engineering: A*, *821*, 141602.

Li, W., Li, S., Liu, J., Zhang, A., Zhou, Y., Wei, Q., ... & Shi, Y. (2016). Effect of heat treatment on AlSi10Mg alloy fabricated by selective laser melting: Microstructure evolution, mechanical properties and fracture mechanism. *Materials Science and Engineering: A*, *663*, 116-125.

Kempen, K., Thijs, L., Van Humbeeck, J., & Kruth, J. P. (2012). Mechanical properties of AlSi10Mg produced by selective laser melting. *Physics Procedia*, *39*, 439-446.

Silvestri, A. T., Astarita, A., El Hassanin, A., Manzo, A., Iannuzzo, U., Iannuzzo, G., ... & Squillace, A. (2020). Assessment of the mechanical properties of AlSi10Mg parts produced through selective laser melting under different conditions. *Procedia Manufacturing*, *47*, 1058-1064.

Giovagnoli, M., Silvi, G., Merlin, M., & Di Giovanni, M. T. (2021). Optimisation of process parameters for an additively manufactured AlSi10Mg alloy: Limitations of the energy density-based approach on porosity and mechanical properties estimation. *Materials Science and Engineering: A*, *802*, 140613.

King, W. E., Barth, H. D., Castillo, V. M., Gallegos, G. F., Gibbs, J. W., Hahn, D. E., ... & Rubenchik, A. M. (2014). Observation of keyhole-mode laser melting in laser powder-bed fusion additive manufacturing. *Journal of Materials Processing Technology*, *214*(12), 2915-2925.

Patakham, U., Palasay, A., Wila, P., & Tongsri, R. J. M. S. (2021). MPB characteristics and Si morphologies on mechanical properties and fracture behavior of SLM AlSi10Mg. *Materials Science and Engineering: A*, *821*, 141602.

Yang, S., Zhang, Y., Juan, R., Li, Z., Wu, J., Akinwamide, S. O., ... & Lian, J. (2025). Effect of building orientation, thickness, and contouring on the microstructure and mechanical properties of AlSi10Mg via laser powder bed fusion. *Materials Science and Engineering: A*, *923*, 147685.

MECHANICAL ENGINEERING

Additive Manufacturing

Automotive

Computational Fluid Dynamics

Computational Solid Mechanics

Fluid Mechanics

Industrial Data Analytics

Machine Design

Machine Dynamics, Vibration, and Acoustic

System Dynamics and Control

Optimizing Urban Micro-Mobility: Ergonomic Design, Structural Integrity, and Dynamic Analysis of Electric Kick Scooter

Kadir Rıdvan Düzelli[a], Mehmet Oğuz Mutlu[b]

[a] Istanbul Technical University/Faculty of Mechanical Engineering, Department of Mechanical Engineering, Automotive, Türkiye
[b] Istanbul Technical University/Faculty of Mechanical Engineering, Department of Mechanical Engineering, Mechanical Engineering (Ph.D.), Türkiye
duzelli21@itu.edu.tr

Keywords: Electric Kick Scooter, Finite Element Analysis, Vehicle Dynamics, Safety, Ergonomics.

Aim

In recent years, the increasing urban population and growing traffic congestion in metropolitan areas have led to significant time loss due to prolonged vehicle idling. This inefficiency has prompted a shift toward compact, cost-effective, and environmentally friendly personal urban transportation alternatives such as bicycles, motorcycles, and scooters. Among these, electric kick scooters have gained considerable popularity due to their ease of use, portability, compact storage, and the elimination of parking requirements (Asperti et al.,2022a).

This academic study aims to investigate the dynamic behavior, ride safety, and ergonomic performance of an electric kick scooter through computational modeling and simulation. Key objectives include evaluating vehicle dynamics under various driving scenarios, analyzing rider comfort and safety, and optimizing the structural and functional aspects of the scooter.

The design of the electric kick scooter was initially developed using CAD software. Benchmarking analyses were conducted by examining the technical specifications of commercial scooter models, from which critical design parameters were derived. The propulsion system consists of a brushless DC (BLDC) hub motor mounted on the front wheel, while the battery pack is housed within the deck beneath the rider's feet. This battery compartment must be structurally robust to withstand external impacts and designed to prevent water ingress due to its proximity to the ground. Structural analyses using Finite Element Analysis (FEA) was applied to validate mechanical safety.

The electric kick scooter was designed without a suspension system; instead, damping is passively provided through tire pressure adjustments. This approach aims to absorb road-induced vibrations, particularly in the critical 1–8 Hz frequency band to which the human body is most sensitive. These vibrations significantly affect rider comfort and must be mitigated through optimized posture and minimal contact pressure.A comprehensive dynamic model of the electric kick scooter and the human body is essential to analyze the discomfort caused by vibrations and evaluate the overall riding experience. In order to analyze this situation correctly, it is aimed to benefit from mathematical modeling and vertical dynamic analysis of the rider and the electric kick scooter.

The study also considers vertical, longitudinal, and lateral vehicle dynamics. Simulations are conducted under various road conditions and loading scenarios to assess stability, maneuverability, and rider safety. The ultimate goal is to enhance ride quality, minimize injury risks,and contribute to the safe adoption of electric kick scooters as a sustainable urban mobility solution.

Material and Method

The design process of the electric kick scooter began with a comprehensive review of technical documentation provided by various existing brands through their official websites. However, due to the inaccessibility or incompleteness of certain dimensions and technical parameters, physical measurements were conducted on widely used shared mobility scooters in urban areas. These measurements were obtained using precision tools such as calipers, tape measures, and rulers, and were compiled into technical documentation to guide the design process. Based on the gathered measurements and technical data, the electric kick scooter model was created using CATIA V5, taking actual dimensions into account.

To analyze the structural durability and stress distribution of the scooter's battery compartment and the platform beneath the rider's feet, the FEA method was applied. The analyses included Von Mises stress evaluation,static displacement analysis, static strain assessment, and safety factor evaluation under maximum load-bearing conditions. Furthermore,potential impact forces to the underside compartment of the scooter were considered in the simulations. Along side static analysis, a fatigue analysis was conducted to evaluate the structural endurance of the deck. In the static analysis, virtual loads were assigned to regions susceptible to impact from the ground, particularly under the foot platform. Fig. 1 illustrates representative scenarios of the scooter encountering elevated surfaces or shallow pits. Such impacts are anticipated to cause structural deformation or damage to the battery compartment depending on the material properties and the severity of the impact.

The deck of the electric kick scooter, where the rider stands, is made of aluminum alloy 6063-T1. This material was selected due to its high strength-to-weight ratio—offering comparable durability to steel while being approximately one-third of its weight (Chandrasekhar & Deva Kumar, 2019). The parameters of the material properties of the aluminum alloy in Table 1 were used in FEA analysis.

Table 1. Properties of Aluminium Alloy 6063-T1.

Property	**Value**	**Units**
Elastic Modulus	69000	N/mm^2
Poisson's Ratio	0.33	N/A
Shear Modulus	25800	N/mm^2
Mass Density	2700	kg/m^3
Tensile Strength	150	N/mm^2
Yield Strengrh	90	N/mm^2

As the design does not include a suspension system, vibrations caused by surface irregularities are primarily absorbed and regulated through tire pressure. Therefore, various internal tire pressure levels were simulated using the FEA tool, and comparative analyses were conducted to determine the optimal tire pressure value.

Additionally, to evaluate the aerodynamic performance of the scooter design, Computational Fluid Dynamics (CFD) analyses were carried out. These simulations assessed the effects of airflow approaching the scooter from different directions, as shown in Fig. 2 . By referencing the drag coefficient, the accuracy and efficiency of the design were validated.

To investigate the dynamic interaction between the rider and the electric scooter, analyses were conducted for the vertical, longitudinal, and lateral dynamics of the vehicle. Initially, a schematic physical model representing both the rider and the scooter was developed, followed by the creation of a corresponding mathematical model. Fig. 3

illustrates the schematic representation of the dynamic system. For the vertical dynamics, generalized Lagrangian equations of motion were used as the basis for the mathematical formulation. The resulting differential equations were implemented and solved in MATLAB. Additionally, simulations of the scooter's longitudinal and lateral dynamics were performed in MATLAB, enabling virtual scenario-based modeling of its dynamic behavior.

In the final phase of the study, the electric motor and battery system of the scooter were modeled in MATLAB/Simulink. Within this framework, the mechanical and electrical components of the scooter were comprehensively defined, and system-level calculations were performed considering parameters such as motor torque, battery power, and overall system efficiency.

Findings

The load defined for the analysis was applied from the underside of the platform, since the battery is located beneath the deck platform of the electric kick scooter. The FEA included evaluations of Von Mises stress, static displacement, static strain, and the factor of safety under maximum load-bearing conditions. The results obtained from these analyses are presented in Table 2. As shown in the table, both the minimum and maximum values for each analysis type have been documented and observed to the material durability limited.

Table 2. FEA results obtained from the analysis of the force applied from below to the deck of the electric kick scooter.

Analysis Name	Method	Minimum Value	Maximum Value
Stress Analysis	Von Mises	4.283e-001 N/m^2 Node : 50,840	1.456e+007 N/m^2 Node : 75,762
Displacement	URES	0.000e-000 mm Node : 372	1.486e-002 mm Node : 31,974
Strain Analysis	ESTRN (Equivalent of strain)	3.710e-011 Node : 32,589	4.353e-004 Node : 34,306
Factor of Safety	FoS	6.180e+000	2.101e+008

The effect of crosswind loads on the lateral stability and power consumption of the electric kick scooter was investigated through aerodynamic analyses under varying wind conditions. Two primary loading scenarios were defined: forward motion under headwind (upwind) and lateral stability under crosswind conditions. For the power consumption case, the scooter was simulated traveling at a constant speed of 25 km/h against an average headwind of 15 km/h. In the lateral stability scenario, a 90-degree crosswind was applied while the scooter moved forward at the same speed, simulating a critical side-wind condition. The drag coefficients were calculated based on the projected areas perpendicular to the wind direction, with the longitudinal drag coefficient derived from the frontal area and the lateral drag coefficient from the side profile. CFD analysis was performed using the values in Table 3 to perform the flow analysis. (Acarer, Arslan, & Uyulan, 2021)

Table 3. Parameters according to wind direction (Acarer, Arslan, & Uyulan, 2021).

Parameters	Upwind Direction	Sidewind Direction
Wind Angle (degree)	0º	90º
Wind angle relative to the moving electric kick scooter(degree)	0º	50º
Aerodynamics Drag Coefficient(C_D)	0.79	0.80
Frontal Area (m^2)	0.53	0.60
Longitudinal C_D	0.79	0.60
Lateral C_D	N/A	0.74
Lateral Moment (N.m)	1	23

To represent the fundamental dynamics of the electric scooter with an onboard rider, a linear dynamic model was developed. The cooter frame was modeled as a rigid body, and its suspension was represented by equivalent elements providing vertical stiffness and damping.Tires were simplified based on their radial stiffness and damping properties. The rider was modeled as a double-series spring-damper system with vertical motion connected to the deck. The hand-arm system was modeled with greater complexity, using dual-series spring-damper systems to represent both vertical and longitudinal motions, linking the handlebar to the upper body of the rider. This comprehensive model is illustrated in Fig. 3 and offers a systematic framework for vertical dynamic analysis of e-scooters (Asperti et al.,2022b)

Fig. 4 compares the system's frequency and phase responses for the damped and undamped models. In the amplitude diagram (Figures 4.a and 4.b), the blue curve exhibits high-pass filter characteristics—attenuating low-frequency signals while allowing higher frequencies topass with less attenuation. Conversely, the red curve

behaves like a low-pass filter, transmitting low-frequency signals with less attenuation. In the phase diagram (4.c and 4.d), the blue curve shows a gradual transition from positive to negative phase, while thered curve transitions more abruptly. This indicates that damping effectively alters the system's frequency response and significantly influences its vibrational behavior.

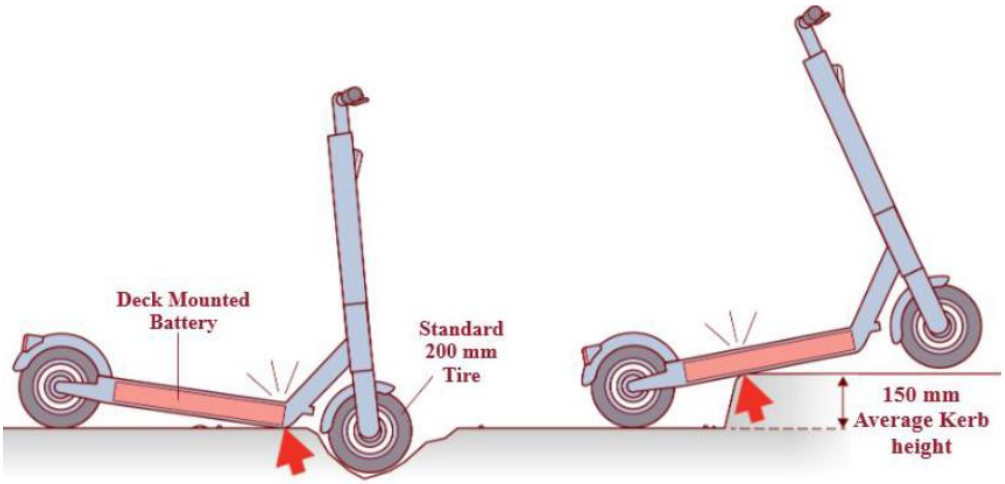

Figure 1. Some mechanical damage senarios on electric scooters.

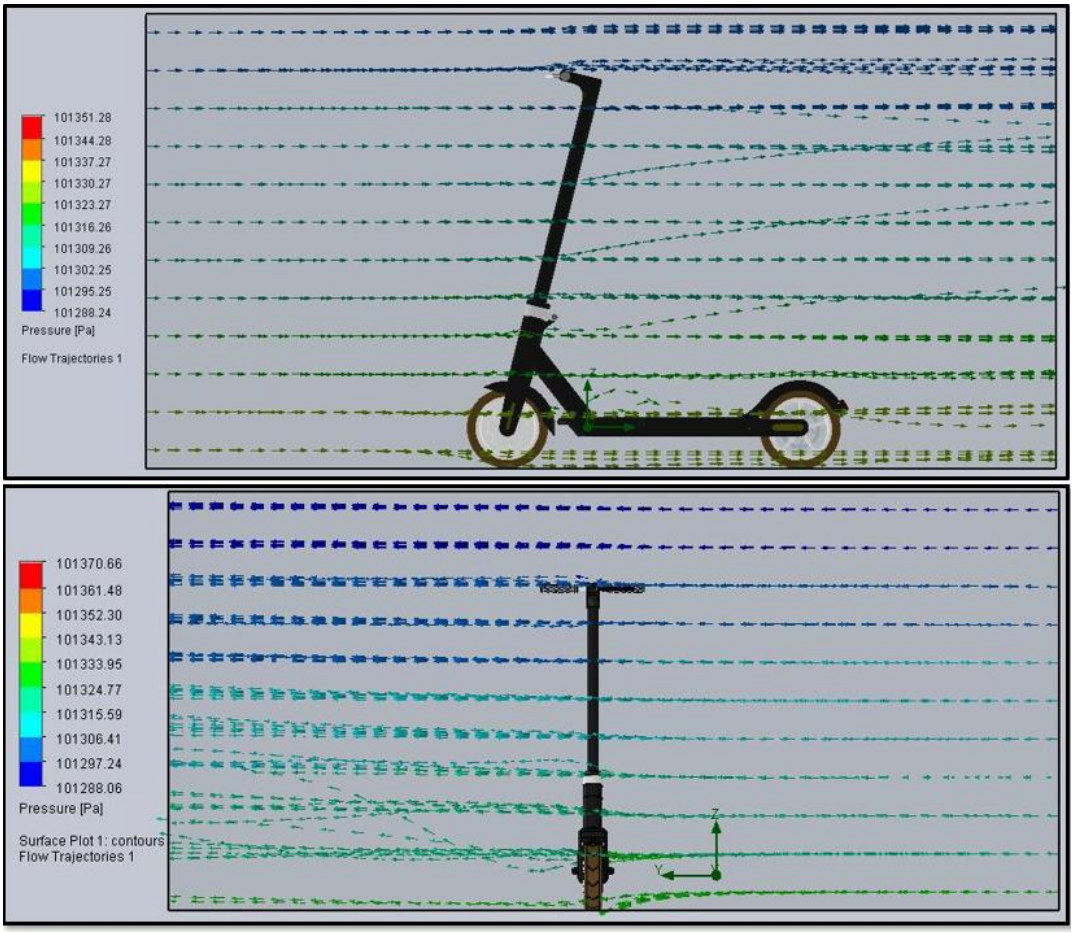

Figure 2. Flow analysis of electric scooter in different wind angle directions.

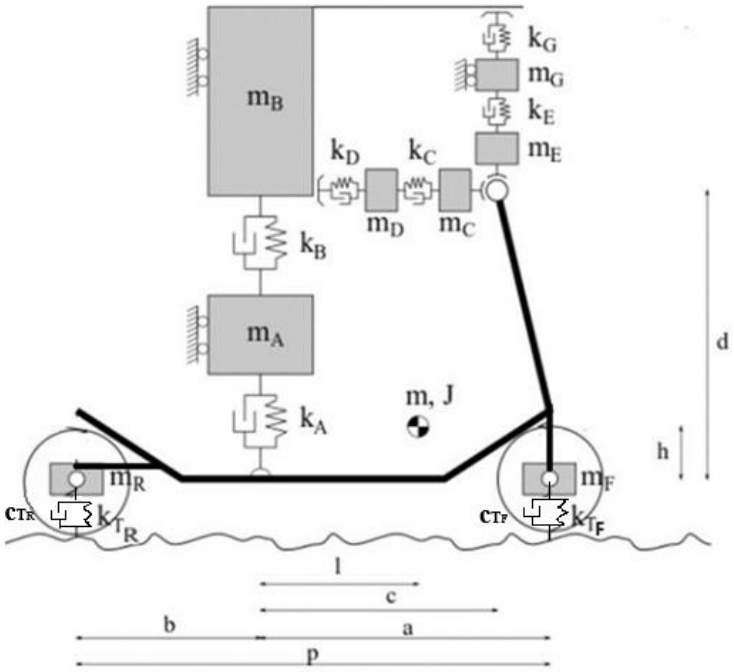

Figure 3. Biodynamic model for the rider and elektric kick scooter model without suspensions.

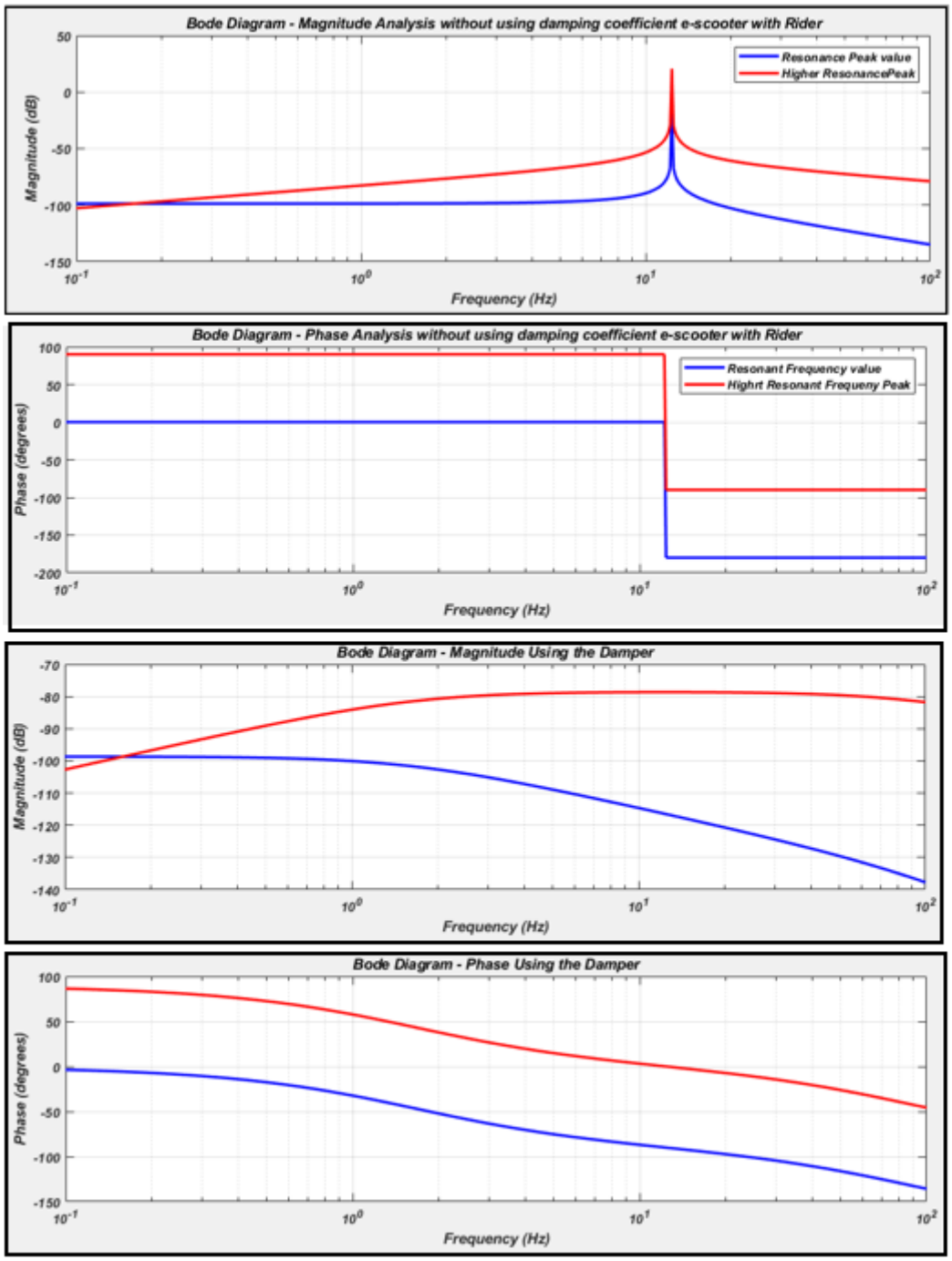

Figure 4. Frequency and phase response of the electric kick scooter system with and without damping (4.a & 4.b) illustrates the Bode magnitude and phase response of the e-scooter system without a damping component, and (4.c & 4.d) demonstrates the system's response with an implemented damping coefficient.

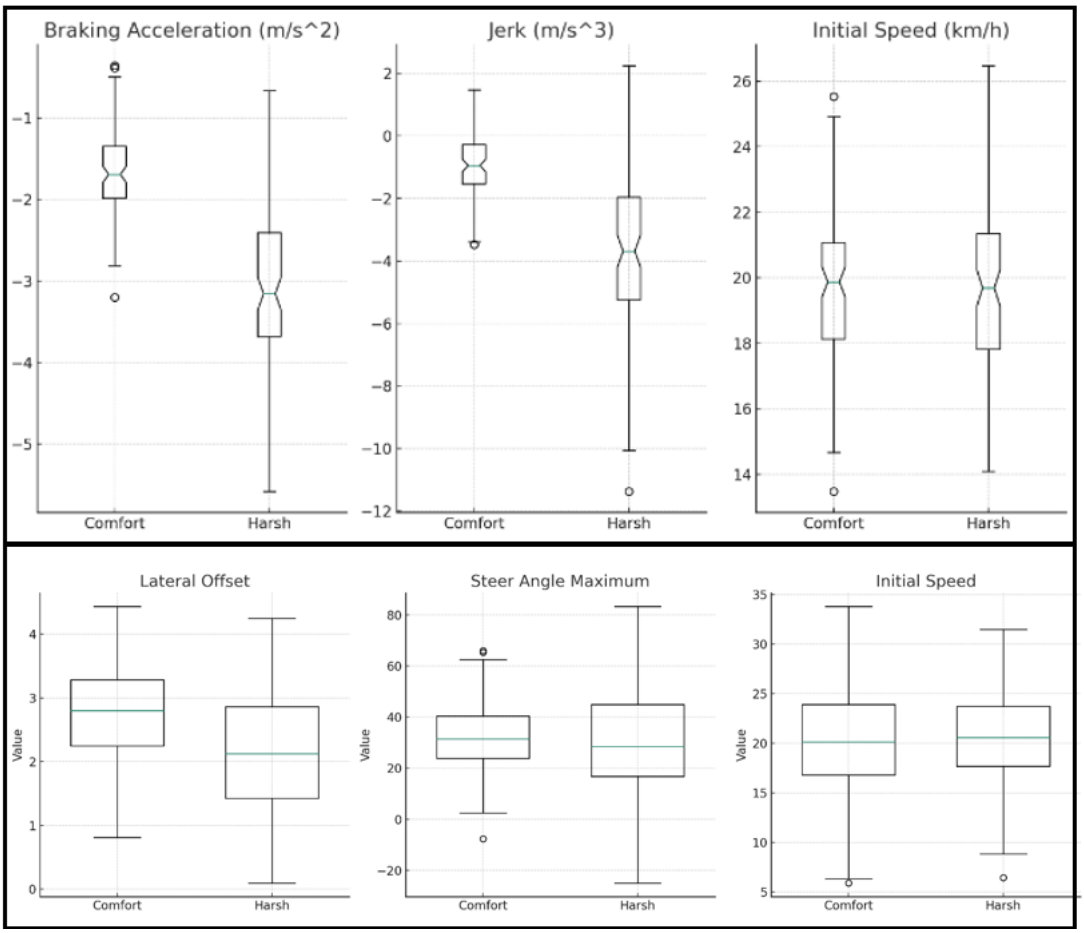

Figure 5. Comparison of braking and steering metrics under Comfort and Harsh riding conditions. (9.a) Braking acceleration, jerk, and initial speed distributions under comfort and harsh braking maneuvers, (9.b) Lateral offset, maximumsteering angle, and initial speed variations during evasive steering tasks in both riding conditions.

In the longitudinal and lateral dynamic analyses, rider performance and safety were evaluated under different maneuvering scenarios. Participants were asked to bring the scooter to a complete stop in front of a cardboard obstacle—either comfortably (relaxed braking) or abruptly (emergency braking). In two separate steering maneuvers, riders were instructed to turn either gently or forcefully before reaching the obstacle. Tasks were randomized across participants to eliminate ordering bias. Table 4 presents the comparison of braking performance under both comfort and harsh conditions. In comfortable braking, lower negative acceleration and jerk values were observed, whereas in harsh braking, both metrics increased significantly due to abrupt stopping. Initial braking speeds were comparable across both conditions.

Table 4. Comparative metrics of braking performance for the electric kick scooter during evasive maneuvers in Comfort and Harsh conditions.

Parameters	Standard Deviation	Comfort	Harsh
Acceleration (m/s^2)	M±SD	-1.70±0.60	-2.90±1.05
Jerk (m/s^3)	M±SD	-1.00±0.95	-3.20±2.70
Strain Analysis	M±SD	20.00±2.30	20.00±2.60

*M = Mean, SD = Standard Deviation

Table 5 compares lateral offset, maximum steering angle, and initial speed under both conditions. In the comfort scenario, riders maintained a greater lateral distance from the obstacle (≈2.7 m), suggesting more relaxed and safer maneuvering. In contrast, the harsh condition involved closer proximity to the obstacle and a wider distribution of steering angles, indicating more abrupt maneuvers. Additionally, the initial speed was higher in the harsh condition (≈21.5 km/h), implying that riders required quicker reaction times. These metrics are visually represented in the boxplots shown in Fig. 5, where both sets (5.a and 5.b) illustrate performance variations in braking and steering behaviors using median values and outlier data.

Table 5. Comparison of average lateral offset, maximum steering angle, and initial speeds for the electric kick scooter under Comfort and Harsh riding conditions.

Parameters	Standard Deviation	Comfort	Harsh
Lateral offset (m)	M±SD	2.75±0.80	2.10±1.00
Steer Angle Maximum	M±SD	32.60±14.50	33.70±22.00
Initial speed (km/h)	M±SD	20.00±5.15	21.50±5.00

*M = Mean, SD = Standard Deviation

Conclusion

In conclusion, this study presents a comprehensive investigation into the ergonomic design, structural integrity, and dynamic performance of an electric kick scooter, with the aim of enhancing rider safety, comfort, and vehicle efficiency under urban mobility conditions. FEA results showed that the deck-mounted battery compartment has sufficient structural strength, with a maximum Von Mises stress of 14.56 MPa and a safety factor above 2.1×10^8. Displacement and strain analyses revealed minimal deformation, ensuring platform stability during operation. The results obtained from the aerodynamic analyses performed in both upwind and crosswind scenarios highlight the

importance of taking wind-induced instability into account for safe vehicle design and control, especially when exposed to crosswind. Dynamic modeling and simulations of vertical, longitudinal, and lateral vehicle responses showed that system damping plays a crucial role in mitigating resonance effects within the 1–8 Hz sensitivity range of the human body. As illustrated in the Bode diagrams, damping effectively reduced both magnitude and phase responses, improving rider comfort. Additionally, performance evaluations in different riding conditions revealed that riders under "harsh" scenarios exhibited higher peak jerks (–3.20 ± 2.70 m/s³) and braking accelerations (–2.90 ± 1.05 m/s²) compared to "comfort" scenarios (–1.70 ± 0.60 m/s²). Steering analysis further indicated that riders in comfort conditions maintained a greater lateral clearance (2.75 ± 0.80 m) from obstacles, reflecting more stable maneuvering behavior. In conclusion, the integration of structural simulations, CFD analysis, and biodynamic modeling has provided a robust framework for evaluating the performance and safety of electric kick scooters.

References

Acarer, S., Arslan, E., & Uyulan, C. (2021). Aerodynamic investigation of an e-scooter & rider system through computational fluid dynamics approach. In 10th International Automotive Technologies Congress (OTEKON 2020) (pp. 1–10). https://doi.org/10.13140/RG.2.2.31017.11363.

Asperti, M., Vignati, M., & Braghin, F. (2022a). Modeling of the Vertical Dynamics of a Kick e-Scooter on Distributed Road Irregularity.

Asperti, M., Vignati, M., & Braghin, F. (2022b). Modelling of the vertical dynamics of an electric kick scooter. IEEE Transactions on Intelligent Transportation Systems, 23(7), 9266–9274. https://doi.org/10.1109/TITS.2021.3098438

Chandrasekhar, S., & Deva Kumar, M. L. S. (2019). Preparation & mechanical characterization of Aluminium 6063 metal matrix composite reinforced with graphite & silicon carbide. International Research Journal of Engineering and Technology (IRJET). Retrieved from https://www.irjet.net.

Electrification of Heavy Commercial Truck: Vehicle Modeling with Using MATLAB/Simulink, Energy Efficiency Analysis and Economic Comparison with Conventional Diesel Engine

Kadir Rıdvan Düzelli[a], Osman Taha Şen[a]

[a] Istanbul Technical University/Faculty of Mechanical Engineering, Department of Mechanical Engineering, Automotive, Türkiye
duzelli21@itu.edu.tr

Keywords: Electrification, Heavy Commercial Truck, Vehicle Modeling, Energy Efficiency, Economy.

Aim

In recent years, the environmental concerns associated with internal combustion engine (ICE) vehicles, particularly the emission of unburned hydrocarbons and harmful particulate matter from fossil fuel consumption, have significantly contributed to global pollution, climate change, and the intensification of the greenhouse effect. These adverse effects not only threaten human health but also pose a serious risk to environmental sustainability. As a solution, battery electric vehicles (BEVs) are increasingly considered a viable alternative to conventional vehicles due to their zero-emission capabilities and ability to utilize clean energy sources.

Globally, freight transportation is carried out through various modes, including road, maritime, and air transport. Among these, road transportation, facilitated by trucks and heavy commercial vehicles, plays a crucial role in maintaining supply chains and ensuring the continuity of global trade. The transition of heavy commercial vehicles to electrified systems is essential for promoting sustainable transportation with clean energy sources. In this context, the primary objective of this study is to replace the power transmission system of a diesel-powered heavy commercial vehicle with a fully battery-electric powertrain, thereby transforming the truck into a fully electric commercial vehicle. Furthermore, this study aims to conduct a comprehensive analysis of the electrified heavy commercial truck, focusing on key performance metrics such as powertrain efficiency, environmental impact, and energy/fuel economy. A comparative assessment will be performed against a similar heavy commercial vehicle equipped with an internal combustion diesel engine to evaluate these aspects under identical operating conditions. By systematically comparing electric and conventional powertrain systems, this research seeks to demonstrate the superior advantages of electrified commercial vehicles in terms of energy efficiency, sustainability, and overall performance.

Material and Method

During the electrification process, a detailed selection of an electric motor and battery cells was conducted to match the technical specifications of the conventional truck. The powertrain of the electric truck was modeled using two fundamental structures: the mechanical model and the electrical model (Giordano, 2018). Fig.1 presents the structural diagram of the electric vehicle model, visually summarizing its two key components and their interactions.

In the mechanical model, the vehicle's operating speed profile was first established, followed by the definition of key vehicle parameters to align with the selected heavy commercial truck configuration. The resistance forces acting on the truck, including rolling resistance, aerodynamic drag, and grade resistance, were formulated and integrated into the vehicle dynamics analysis. These parameters were utilized to compute the required traction force and power demand for various operating conditions. The final stage of mechanical modeling involved verifying the compatibility of the selected electric motor's technical parameters with the calculated mechanical properties. This process ensured an optimal balance of torque, power, and rotational speed, enabling the electric truck to achieve the desired acceleration and sustain efficient operation under full-load conditions. The results

obtained from the mechanical model represent the vehicle's performance and power demand. Based on these outcomes, the required electrical energy is determined and requested from the electrical model.

The electrical model was developed to ensure the compatibility of the battery pack and electric motor in delivering the required power output. Additionally, battery pack configuration—including series and parallel cell arrangements, physical structure planning, and electrical performance analysis—was conducted to establish an optimal propulsion system. Proper management of the electrification process is critical for enhancing the accuracy of dynamic analysis and modeling results, ensuring the development of a robust and efficient power transmission system.

The modelling and analysis of the electric commercial truck were conducted using MATLAB/Simulink software. In the MATLAB/Simulink environment, vehicle modelling could be performed using two fundamental approaches: forward approach method and backward approach method. In this study, the forward approach method in MATLAB/Simulink was employed to model the electric vehicle (Nakarmi, Ale, & Budhathoki, 2022). The 'Vehicle Dynamics Blockset' module available in MATLAB/Simulink provides pre-configured blocks for essential components such as the vehicle body, wheel dynamics, electric motor, battery system, Proportional-Integral (PI) controller, and drive cycle components (Kiyakli & Solmaz, 2018). By integrating these predefined components, the electric vehicle model was developed, and the parameters and results obtained from previous sections were systematically incorporated into the respective Simulink blocks. Fig. 2 illustrates the forward approach method-based vehicle model of the electrified heavy commercial truck, developed in MATLAB Simulink.

In this study, theoretical formulations were employed to assess the performance, efficiency, environmental impact, and energy/fuel economy of both the electrified heavy commercial truck and its conventional counterpart powered by an ICE. These formulations were systematically implemented in Microsoft Excel to enable an accurate comparative analysis. The electrified truck model incorporated technical parameters such as the MATLAB/Simulink analysis results, specifications of the electric motor and battery system, and resistance forces affecting the vehicle. These parameters were essential for accurately simulating the truck's real-world performance under different driving conditions. For the conventional diesel truck, engine data and experimental parameters from relevant studies were integrated into Microsoft Excel to conduct the necessary ICE calculations. This approach ensured a standardized and data-driven comparison between the electrified and conventional heavy commercial trucks. The findings derived from these calculations are presented and analyzed in the subsequent section.

Findings

The simulation process of the electric truck model in MATLAB/Simulink involved analyzing key performance indicators, including the total distance travelled (range), battery State of Charge (SoC), variations in current values, and the comparison between the reference speed and the actual vehicle speed (Nakarmi et al., 2022). These analyses were conducted to verify whether the electric motor could effectively draw sufficient energy from the battery to propel the vehicle efficiently.

By simulating the electrified commercial truck for 2000 seconds in MATLAB/Simulink using the Heavy Heavy-Duty Diesel Truck (HHDDT) driving cycle as a reference, the total distance travelled was determined to be 36.9 km. The vehicle's range, the comparison between the actual driving speed and the reference speed, and the SoC of the battery cells throughout the simulation were analyzed. The battery charge level was initially set to 90%, considering the energy consumption of the electric motor, road conditions, and system losses. After completing the predefined speed-time reference cycle, the battery's final charge level was recorded at approximately 84.5%. Additionally, the variations in current drawn from the battery over time were examined, where fluctuations in current values were observed during acceleration and deceleration periods, indicating the dynamic power demands of the vehicle.

The energy consumption and cost analysis of the electrified heavy commercial truck under both loaded and unloaded conditions were evaluated, and the results are summarized in Table 1 . Since load factor has a substantial impact on energy consumption, optimizing vehicle payload is crucial for energy efficiency. As the vehicle load

increases, the power demand from the electric motor rises, leading to a proportional increase in energy consumption per kilometer.

Operating costs for electric heavy commercial trucks depend on both unit electricity pricing and total energy consumption. In this study, calculations were performed using DC charging tariffs to determine both the per-kilometer energy cost and total cost analysis. Additionally, battery capacity and corresponding charging costs at different load conditions were assessed to estimate the charging station costs associated with the given battery capacity. All results presented in Table 1 were obtained through MATLAB/Simulink and Microsoft Excel under different loading conditions.

Table 1. Energy consumption and cost analysis of the electrified heavy commercial truck according to different load cases.

Load Condition	**Fully Loaded**	**Unloaded**
Total Energy Consumption (E_{total}) [kWh]	114,25	54,35
Total Power (P) [kW]	205,66	97,83
Electricity Unit Cost [$C_{electric}$] [TL/kWh]	12,99*	10,99**
Distance Covered in 2000 Seconds (d) [km]	36,9	36,9
Energy Consumption per Kilometer (E_{km}) [kWh/km]	3,1	1,47
Electricity Cost per Kilometer [TL/km]	40,22	16,18
Total Electricity Cost [TL]	1484,21	597,31
Battery Capacity [kWh]	374,7	374,7
Charging Station Cost [TL]	4867,22	4117,84

* DC charging tariff applies for power between 180-400 kW at a rate of 12.99 TL/kWh.

** DC charging tariff applies for power below 180 kW at a rate of 10.99 TL/kWh.

Fig. 3 presents the efficiency map of the electric motor simulated in MATLAB/Simulink under the HHDDT driving cycle. The map, developed using predefined motor speed and torque inputs, provides a visual representation of the motor's operational efficiency across different load conditions. The electric motor demonstrates a high efficiency of approximately 96% over a wide range of speeds and torque levels. Modelled as a 1-D look-up table, the map delivers real-time efficiency values based on torque and speed parameters.

The conventional heavy commercial truck utilized in this study is equipped with a 7.33-liter, 6-cylinder turbocharged diesel engine featuring an intercooler and Bosch Common Rail Injection system, capable of delivering 240 PS at 2400 rpm and 840 Nm of torque between 1200–1800 rpm (Hacıbekir, 2006). Fuel consumption and cost were evaluated at five distinct engine speeds using the same reference driving cycle and operating conditions applied to the electrified vehicle. Table 2 presents the comparative analysis of fuel consumption, total power output, and economic metrics. These results were used to assess the operational efficiency of the internal combustion engine relative to the electrified counterpart. Specific Fuel Consumption (SFC) values ranged from 199 to 214 g/kWh, with detailed evaluations conducted based on engine operating duration for accuracy.

The first graphic in Fig. 4 illustrates the relationship between SFC (g/kWh) and engine speed (RPM) under full-load conditions, providing insight into the efficiency trends of the diesel engine across various operating ranges. For the same HHDDT drive cycle, fuel consumption per kilometer was analyzed while maintaining the same driving range for accurate comparison (Pantoja Gallegos et al., 2022). Table 2 indicates that fuel consumption per kilometer decreases as engine speed increases, suggesting a more cost-efficient operation at higher motor speeds.

Table 2. Fuel consumption and economic results of the conventional diesel engine at different engine speeds and output power.

Fuel Consumption and Economics Analysis					
Engine Speed [rpm]	1200	1400	1800	2100	2400
Specific Fuel Consumption (SFC) [g/kWh]	209	201	199	205	214
Total Power [kW]	105,6	126,7	158,3	172,2	177,2
Diesel Unit Cost [TL/L]	46,62*	46,62*	46,62*	46,62*	46,62*
Distance Covered in 2000 Seconds (d) [km]	36,9	36,9	36,9	36,9	36,9
Fuel Consumption per Kilometer [L/km]	5,42	4,65	4,47	4,29	4,04

Fuel Cost per Kilometer [TL/km]	252,87	216,79	208,7	200,46	188,57
Total Fuel Cost [TL]	9331,10	7999,67	7701,22	7396,95	6954,08

* Fuel cost calculations are based on the diesel price recorded on 04/03/2025

When assessing the relationship between SFC and power output, results indicate that fuel consumption decreases up to a certain power level but increases again beyond this threshold. Second graphic in Fig. 4 demonstrates that power demand initially grows inversely with fuel consumption, but at higher power levels, fuel consumption becomes directly proportional.

Fig. 5 presents the torque vs. engine speed relationship of the diesel engine under full throttle conditions. At full throttle, the combustion chamber receives the maximum air-fuel mixture, which forces the engine to operate at maximum load. This figure provides insights into the correlation between engine torque and speed, as well as the impact of fuel consumption at full load conditions.

Heavy commercial electric trucks offer significant environmental advantages over conventional diesel trucks. With zero CO_2 emissions and lower noise levels, they contribute to reduced air and noise pollution. When powered by renewable energy sources, their carbon footprint can be nearly eliminated. Table 3 summarizes the clean energy and environmental sustainability comparison between both truck types

Table 3. Comparison of CO_2 emissions and noise pollution between heavy commercial electric truck and conventional diesel-powered counterpart.

Comparison Criteria	**Heavy Commercial Electric Truck**	**Conventional Diesel Truck**
CO_2 Emissions [g/km]	0	720-900
Noise Pollution [dB]	65	80-95

The findings of this study present a detailed comparison between the electrified heavy commercial truck and its conventional diesel-powered counterpart. The results were obtained through various computational analyses, employing separate tables and graphical representations to illustrate energy consumption and economic outcomes.

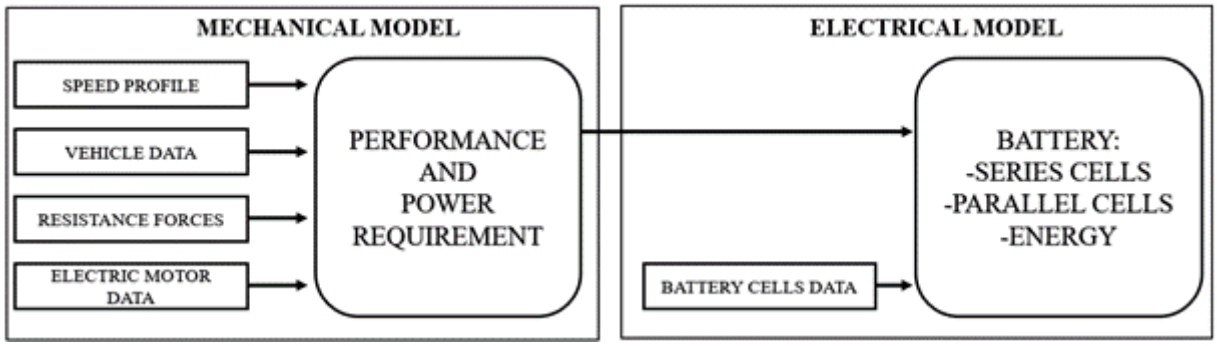

Figure 1. Battery electric vehicle model structure.

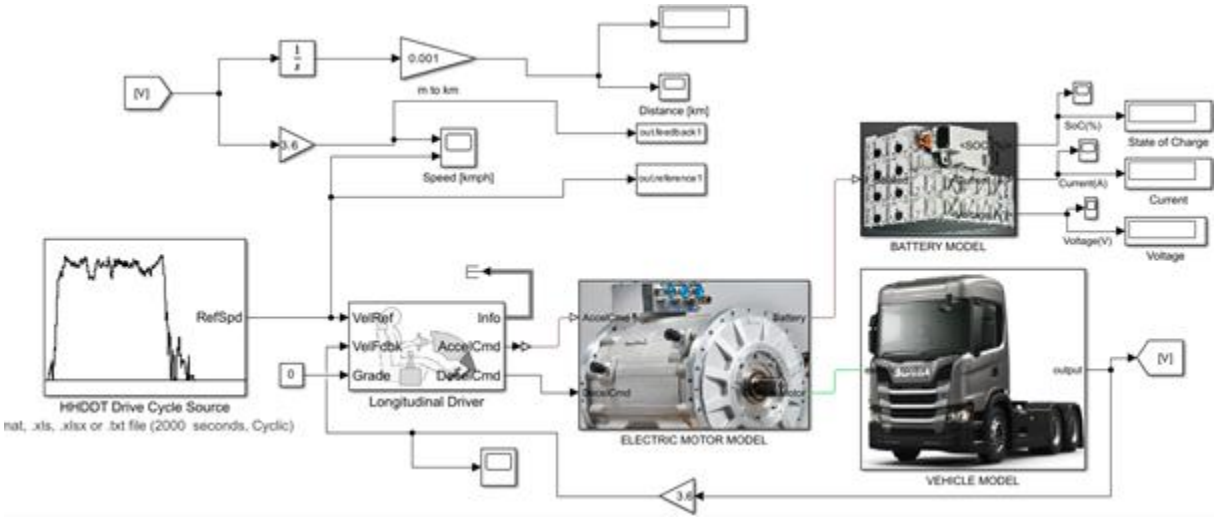

Figure 2. Modeling of the electrified heavy commercial truck with using MATLAB/Simulink.

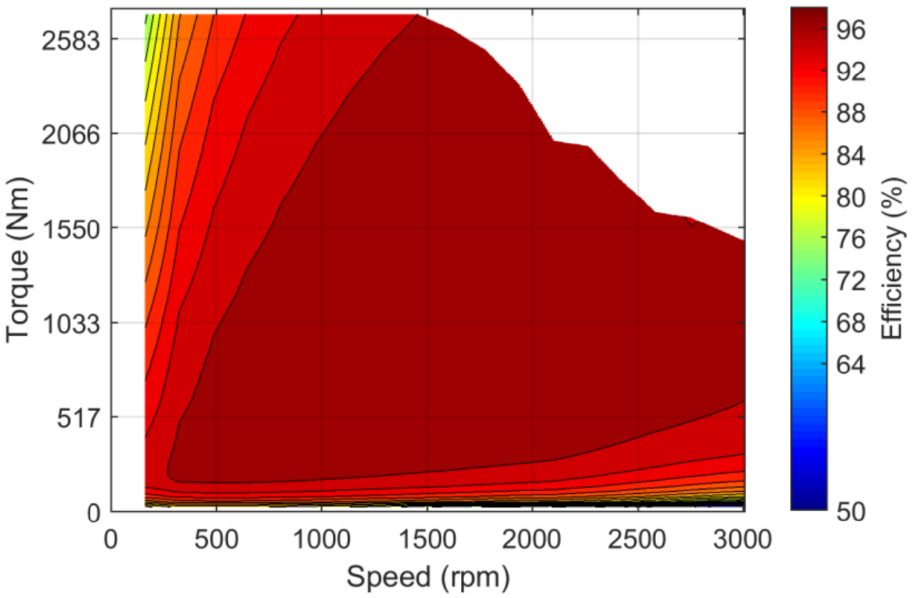

Figure 3. Operating efficiency map of the electric motor.

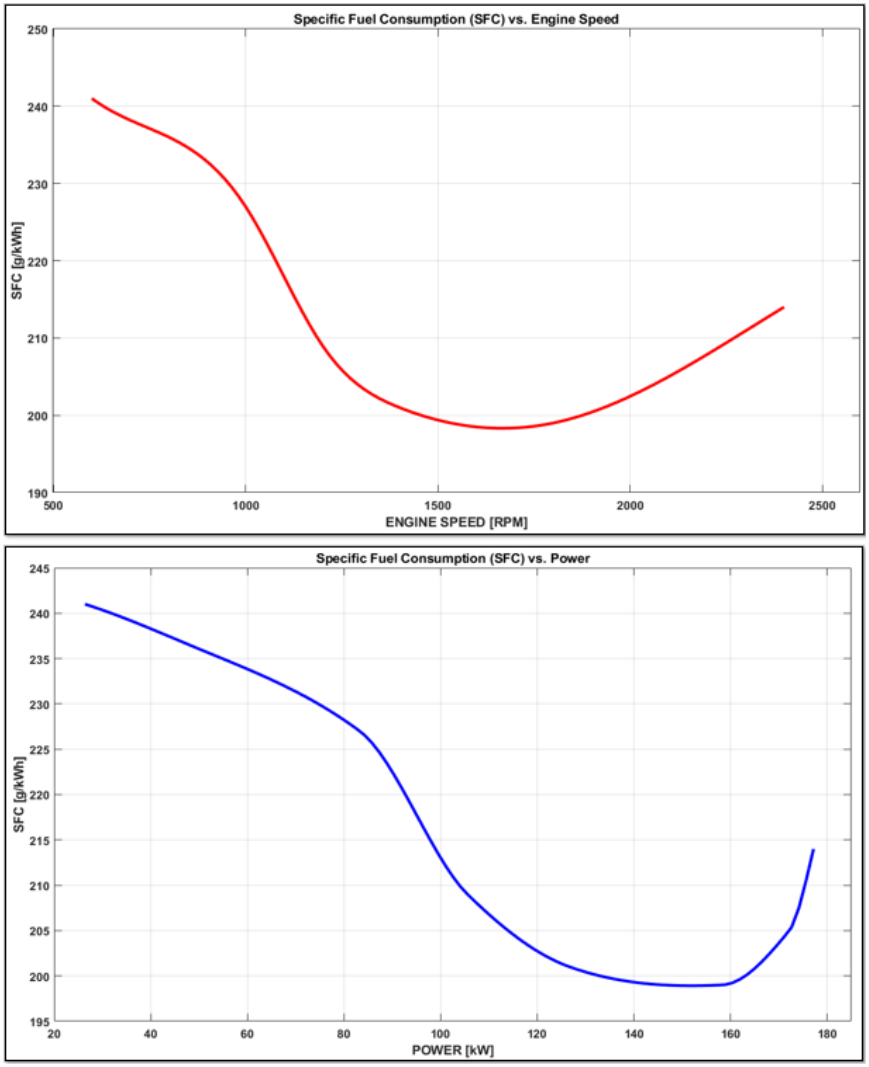

Figure 4. SFC curves of heavy commercial diesel truck based on engine speed and power.

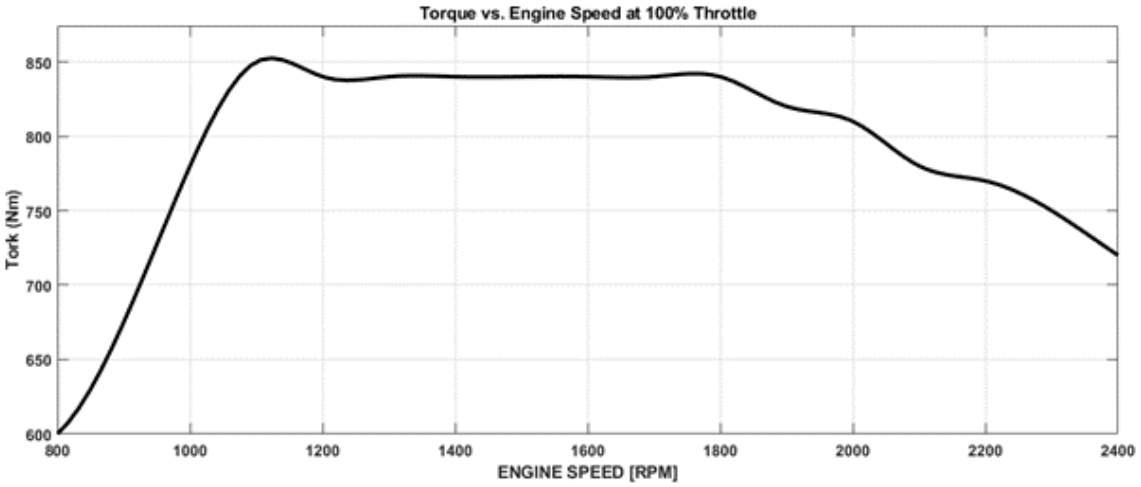

Figure 5. Torque vs. engine speed at full throttle for the diesel engine.

Conclusion

In this study, the electrification of a conventional diesel-powered heavy commercial truck was achieved by converting it into a battery-electric vehicle. Comparative analyses were conducted based on performance, efficiency, environmental impact, and economic feasibility using various calculations, simulations, and modeling processes. The results indicate that electric powertrain systems provide higher torque and power output, leading to superior vehicle performance. Additionally, the battery-electric truck demonstrated approximately 40% higher energy efficiency than its diesel counterpart due to reduced mechanical and combustion losses. In terms of environmental sustainability, it operates with 100% cleaner energy, eliminating carbon emissions, and reduces noise pollution by approximately 25%. Finally, economic analysis highlights that electric powertrains offer lower operational costs and enhanced energy efficiency, making them a more viable alternative to conventional diesel systems for heavy-duty transportation.

References

Giordano, F. (2018). Longitudinal dynamic modelling and simulation of a full electric vehicle (Master's thesis, Politecnico di Torino). https://webthesis.biblio.polito.it/

Hacıbekir, T. (2006). Adaptif seyir sistemlerinin yakıt tüketimine etkisinin incelenmesi (Yüksek lisans tezi). İstanbul Teknik Üniversitesi, Fen Bilimleri Enstitüsü.

Kiyakli, A. O., & Solmaz, H. (2018). Modeling of an electric vehicle with MATLAB/Simulink. International Journal of Automotive Science and Technology, 2(4), 9–15. https://doi.org/10.30939/ijastech..475477

Nakarmi, A. R., Ale, B., & Budhathoki, D. (2022). Modeling and performance analysis of a converted electric vehicle using forward approach method in MATLAB/Simulink and analyzing the experimental results. International Research Journal of Engineering and Technology (IRJET), 9(12), 347–354. https://www.irjet.net/archives/V9/i12/IRJET-V9I1260.pdf

Pantoja Gallegos, J. L., Dominguez Vergara, N., & Dominguez Perez, D. N. (2022). Calculation of the fuel consumption, fuel economy and carbon dioxide emissions of a heavy-duty vehicle. Journal of Physics: Conference Series, 2307(1), 012025. https://doi.org/10.1088/1742-6596/2307/1/012025

ANN-Based PID Tuning Mechanism For A Vehicle Control SystemConsidering Improved Path Following

Başar Zaman[a], Volkan Bekir Yangın[a], Özgen Akalın[a]

[a] Istanbul Technical University, Mechanical Engineering Department, Automotive, Türkiye
zaman22@itu.edu.tr

Keywords: ANN, Ziegler-Nichols, PID Control, Path Tracking.

Aim

There exist several control methods to improve vehicle path tracking performance [1,2] and PID control method is one of the most common strategies for an improved path tracking ability such as its usage for differential braking as a steering system back up [4]. However, conventional controller tuning methods could be very time consuming and have a lack of adaptability for varying road conditions. Therefore, artificial neural network (ANN) based tuning methods are leveraged where controller gains are adjusted in an online manner to achieve superior path tracking performance [3]. The objective of this study is to compare vehicle path tracking performance by using PID control strategy based on ANN tuning with the path tracking accuracy of the PID control strategy where the controller gains are tuned based on Ziegler-Nichols method. PID controller creates differential brake forces to follow the reference trajectory as a back-up for the steering system in case of failure. The effectiveness of differential brake forces generated via ANN over Ziegler Nichols based PID tuning method for improving trajectory tracking accuracy and vehicle stability is proved in this study. The proposed methodology is validated through a Simulink-ADAMS co-simulation, where a test vehicle performs a NATO Double Lane Change (DLC) maneuver using differential braking for steering redundancy.

Material and Method

This study employs a Simulink-ADAMS co-simulation framework to evaluate PID-based differential braking control in a NATO Double Lane Change (DLC) maneuver at a constant vehicle speed of 60 km/h. The representative scheme is given in Figure 1.

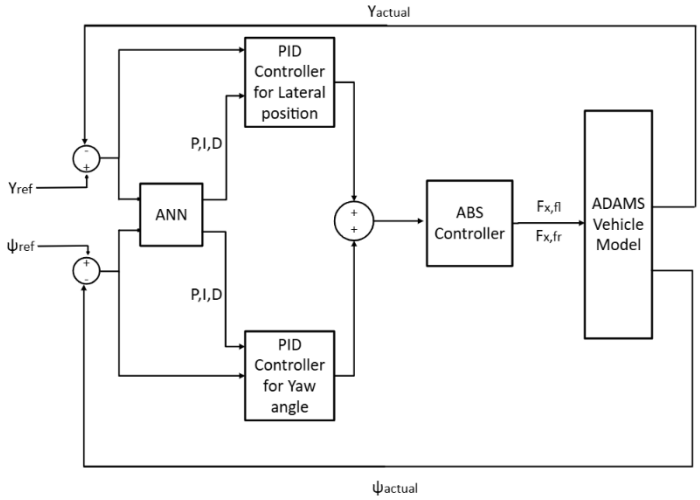

Figure 1. Controller Architecture.

The vehicle model used in this study represents the FED Alpha (Fuel Efficiency Demonstrator) vehicle. This model has been validated up to 64 kph, ensuring reliable simulation results within this speed range. The vehicle has a mass of 5482.67 kg and a wheelbase of 3.202 meters.

A dual PID control architecture used in the PID controller block. One of the PID controllers compensate for the lateral position error, another PID controller eliminates the yaw angle. Both PID controller blocks were tuned based on the offline Ziegler-Nichols method and ANN based online PID tuning and the results were compared to assess lateral position and yaw angle correlation with the reference lateral position and yaw angle values. The outputs from both PID controllers are combined to compute the necessary differential brake forces, enabling the vehicle to follow the reference trajectory while ensuring stability.

Two PID tuning methods are examined in this study. First, Ziegler-Nichols method is used for both PID controller block tunings in an offline manner. This approach involves determining the ultimate gain (K_u) and ultimate period (T_u) based on system response characteristics. PID gains are then computed using established empirical tuning formulas. However, with this method, P, I and D gains remain constant throughout the maneuver preventing adaptation for the changing path conditions. For the lateral position PID block, P, I and D gains were used as 0.07, 0.0467 and 0.0263. P, I, D gains for yaw angle controller block were 18,12 and 6.75. ANN based online PID tuning method is used for both lateral position and yaw angle PID contollers. ANN provides high adaptation to the changing path conditions and P,I,D gains are adjusted through the maneuver to minize the error between measured and reference lateral position and yaw angle values. The neural network is trained on a dataset consisting of lateral position, yaw angle outputs and corresponding optimal PID gains.

Findings

The results in Figure 2 show that the ANN-based PID tuning achieves closer adherence to the reference trajectory for both lateral position (Y) and yaw angle (ψ) than the Ziegler-Nichols method. While both controllers initially track the reference well, the Ziegler-Nichols approach exhibits higher oscillations in both lateral position and yaw angle, particularly after 5 seconds, indicating increased instability. In contrast, the ANN-based controller smooths the response, reducing overshoot and oscillations, leading to improved trajectory tracking and vehicle stability. These findings suggest that ANN-based tuning adapts more effectively to dynamic conditions, enhancing precision and robustness in path-following tasks. Also, another method to assess path tracking accuracy is to calculate Root Mean Square Error (RMSE) values for the lateral position and yaw angle. RMSE is a widely used metric for path tracking accuracy as it quantifies the average deviation between reference and actual trajectory. As RMSE becomes higher, this means higher deviation from the reference trajectory. When RMSE values for the lateral position-yaw angle for ANN and Ziegler-Nichols methods are compared; RMSE value is decreased by %2.62 in lateral position and %4.60 in yaw angle when ANN based online PID tuning is used. This result also indicates the superiority of ANN based PID tuning over Ziegler-Nichols PID tuning method.

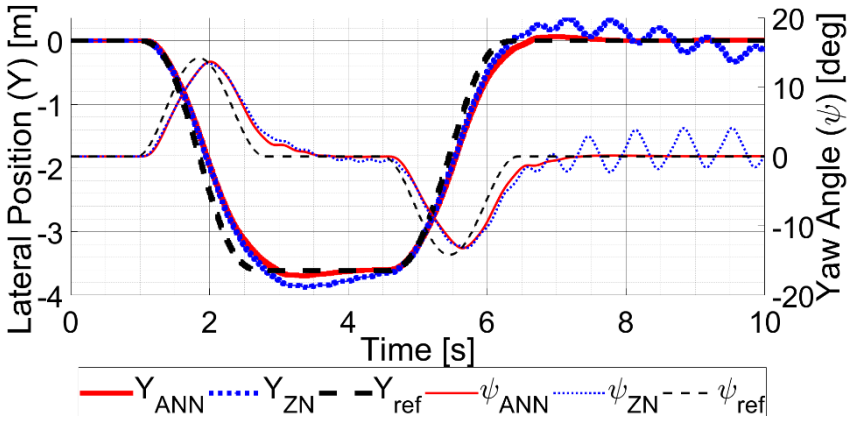

Figure 2. Path tracking performance results.

The comparison of differential brake force applications illustrated in Figure 3 between ANN-based tuning and Ziegler-Nichols (ZN) tuning highlights significant differences in control strategy and stability. The ANN-based approach applies smoother and more continuous braking forces, dynamically adjusting the left and right brake forces based on vehicle state, resulting in better modulation and reduced oscillations. In contrast, the ZN-based

method exhibits high-frequency oscillations and abrupt brake force changes, indicating a more aggressive and less stable braking pattern. The excessive fluctuations in the ZN approach may lead to unnecessary braking interventions, potentially reducing vehicle stability and comfort. These results suggest that ANN-based tuning provides better adaptability and smoother braking control, enhancing overall trajectory tracking and stability in differential braking-based steering applications.

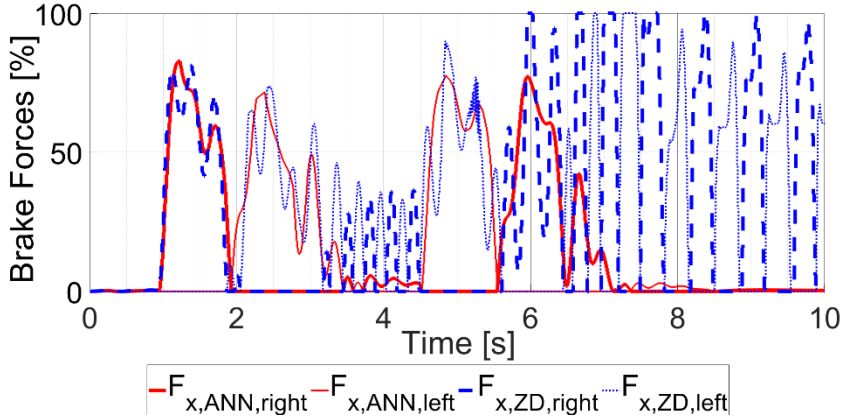

Figure 3. Brake forces generated via ANN or Ziegler-Nichols tuned PID controllers.

Conclusion

This study demonstrates that ANN-based PID tuning outperforms the Ziegler-Nichols (ZN) method in path tracking and braking control by providing smoother, more adaptive responses. The ZN-based method exhibits significant oscillations, particularly in yaw angle and lateral position tracking, due to fixed PID gains that fail to adapt to changing vehicle dynamics. The aggressive proportional control in ZN leads to overcorrections, while the absence of adaptive damping results in persistent oscillations, especially after trajectory changes. Additionally, in braking control, ZN-based tuning applies abrupt, high-frequency brake force variations, potentially reducing vehicle stability. In contrast, the ANN-based approach dynamically adjusts PID gains, leading to improved stability, reduced overshoot, and better trajectory adherence. These findings highlight the effectiveness of AI-driven control strategies in autonomous and safety-critical applications, where adaptive tuning enhances robustness, stability, and performance under varying conditions.

References

Ahmadian, N., Khosravi, A., & Sarhadi, P. (2022). Driver assistant yaw stability control via integration of AFS and DYC. *Vehicle System Dynamics, 60*(5), 1742–1762. https://doi.org/10.1080/00423114.2021.1879390

Botes, W., Botha, T. R., & Els, P. S. (2022). Real-time lateral stability and steering characteristic control using non-linear model predictive control. *Vehicle System Dynamics, 60*(5), 1063–1085. https://doi.org/10.1080/00423114.2022.2057334

Hu, C., Xie, L., Zhang, Z., & Xiong, H. (2024). A novel model predictive controller for the drifting vehicle to track a circular trajectory. *Vehicle System Dynamics*. https://doi.org/10.1080/00423114.2024.2347494

Qin, S. J., & Badgwell, T. A. (2003). A survey of industrial model predictive control technology. *Control Engineering Practice, 11*(7), 733–764. https://doi.org/10.1016/S0967-0661(02)00186-7

Siampis, E., Velenis, E., & Longo, S. (2015). Rear wheel torque vectoring model predictive control with velocity regulation for electric vehicles. *Vehicle System Dynamics, 53*(11), 1555–1579.

Tokay, D., Yangın, V. B., & Akalın, Ö. (2023). Viability of differential braking-based steering redundancy for an autonomous vehicle. In *Proceedings of the IAVSD 2023 Conference*.

Yangın, V. B., Akalın, Ö., & Yalçın, Y. (2024, April). High-speed trajectory following of a heavy-duty vehicle via adaptive nonlinear model predictive controller. *International Journal of Vehicle Performance, 10*(2). https://doi.org/10.1504

Yoshida, H., Shinohara, S., & Nagai, M. (2008). Lane change steering manoeuvre using model predictive control theory. *Vehicle System Dynamics, 46*(Supplement), 669–681. https://doi.org/10.1080/00423110801916012

Combustion Model Analysis on Validation Purpose of a Spark Ignition Engine

Akay Delihasan[a], Ahmet Yapmaz[a], Barış Doğru[a]

[a] Istanbul Technical University, Department of Mechanical Engineering, Automotive Division, Turkey
delihasan@itu.edu.tr

Keywords: Engine Combustion Model, Mass Fraction Burned, SI Engine.

Aim

The aim of this study is to build up one-dimensional (1-D) model for a spark ignition (SI) engine at a part load condition by using SI Wiebe combustion model. The most realistic results could be obtained by an experimental study, but it takes time and if a system capable of precise measurement established is expensive. The problem could be defined with universally valid expressions and equations with a theoretical study. However, analytical solutions often rely on simplifying assumptions, reducing accuracy. A mathematical model for any physical system should be developed and is needed to be solved using a numerical method which is faster and cheaper than other methods in most cases. It is referred to as verification when the mathematical model is numerically solved. But the developed mathematical model may not accurately represent the system, so this does not necessarily mean that the problem has been solved correctly. The key point is to develop the correct mathematical model for the physical system, solve it accurately, and compare it with experimental data to validate it, ensuring that the model aligns with the real-world behaviour. This is the validation process. The originality of this study lies in attempting to create a more accurate simulation of the previous modelling study based on experimental data, in other words a further investigation on former 1-D simulation model. A 1-D model has been used since it provides quick insights into overall engine performance and fuel consumption. It is significantly faster and cheaper with reduced computational cost than three-dimensional modelling [1].

Material and Method

Internal combustion engine (ICE) operated vehicles have been mostly used at part load conditions rather than at high load conditions where their overall efficiency levels reach the maximum. Therefore, it has much more importance to focus on part load efficiency improvement of ICEs. A throttle valve is used in intake line of a conventional SI engine in order to control the air quantity suctioned into the combustion chamber. Wide-open throttle (WOT) conditions match with full load operation conditions where maximum amount of air has been taken into the combustion chamber in order to generate nominal power output. Throttle valve has been opened less at part load conditions in comparison to WOT conditions since power requirement is less, resulting in an increase of pumping losses and a reduction in overall efficiency [2,3]. In experimental stage of this research, a four-cylinder SI engine has been operated with conventional gasoline fuel at steady state part load conditions including 1800 rpm engine speed and 3 bar brake mean effective pressure (BMEP) where throttle valve angle is 14°, corresponding to 15.5% opening area of WOT position. Test-bench experiments have been carried out at Istanbul Technical University Automotive Engine Laboratory. The test-bench engine is water cooled to control engine temperature and also fuel is injected into the intake port to control air-fuel ratio in stoichiometric one in a sensitive way. The SI research engine specifications are given in Table 1.

Table 1. SI research engine specifications.

Feature	Value
Stroke Volume	1820 cm^3
Bore x Stroke	85 x 80 mm
Compression Ratio	9:1
Intake Valve Opening	16˚CA bTDC
Intake Valve Closing	40˚CA aBDC
Exhaust Valve Opening	40˚CA bBDC
Exhaust Valve Closing	16˚CA aTDC

Mass fraction burned (MFB) could be considered as a ratio between released combustion energy of burned fuel and the total combustion energy at the end of combustion. Rassweiler and Withrow conducted a study which states in summary that pressure rise percentage aligned with the burned charge percentage by weight during combustion [4].

Idealized SI engine combustion assumes constant volume heat addition into the combustion chamber at TDC as well-known in Otto Cycle [5]. However, actual combustion processes occurring in SI engines need a time interval between spark plug activation and combustion termination. Heat release curve of SI engines resembles an S-shape profile and modelled with Wiebe combustion as shown in equation 1.

$$x_b = 1 - e^{-a\left(\frac{\theta-\theta_0}{\Delta\theta}\right)^{m+1}} \quad \text{(Equation 1) [1]}$$

"x_b" is the MFB, "θ" is the crank angle, "θ_0" is the start of combustion, "$\Delta\theta$" is the burning duration, "m" is shape factor, and "a" is efficiency factor. The combustion rate of the fuel-air mixture starts at a low-level right after the spark discharge, rises to its highest point roughly halfway through the combustion process, and then gradually declines to nearly zero by the end of combustion. As could be seen in Figure 1, the flame-development stage corresponding to MFB0-MFB10 interval is the crank-angle range from spark discharge to when a notable fraction of the cylinder mass has been burned. The rapid-burning stage characterized by MFB10-MFB90 interval is the crank-angle range in which the main portion of fuel is burned. The burning completion stage indicates the last part of combustion process [5,6].

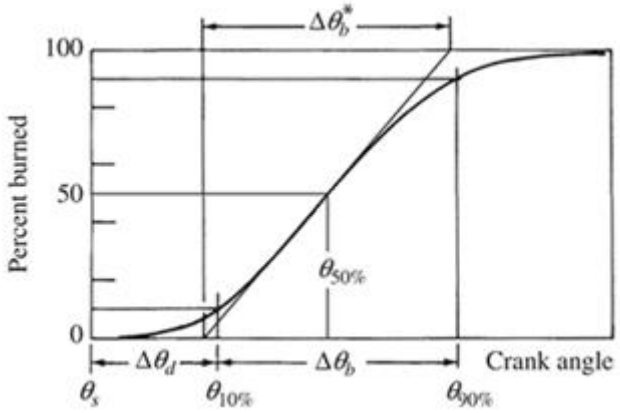

Figure 1. Combustion stages in SI engines on mass fraction burned vs. crank angle curve [6].

In order to fix the combustion curve in means of approximate MFB10 and MFB90 points via crankshaft angle, the 50% burn time is preferred rather than ignition time since it aligns closely with peak pressure as seen in Figure 2, making it a useful starting point [7]. In the experimental study, the peak firing pressure (PFP) value is considered

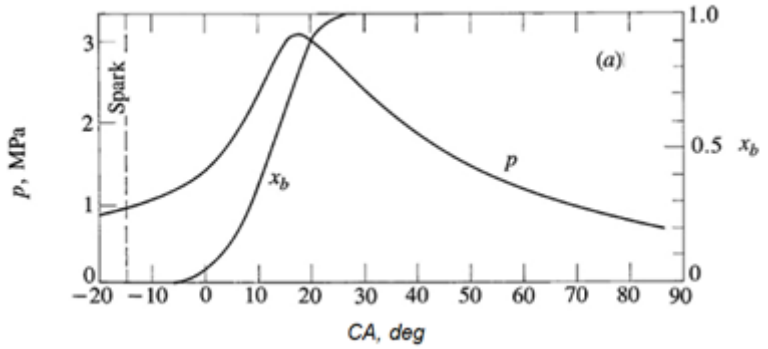

Figure 2. Cylinder pressure and mass fraction burned vs. crank angle curve of an SI engine [6].

close to the crank angle corresponding to the MFB50 point in the SI Wiebe combustion model. In the Wiebe function used in the combustion model, the parameter expressed as $\Delta\theta$, which defines the MFB0 to MFB100 range in terms of crank angle, is manipulated to ensure that the MFB50 point is close to the PFP.

Findings

Pressure vs. crank angle graph of experimental and simulation results conducted by Doğru et al. [8] is given in Figure 3.

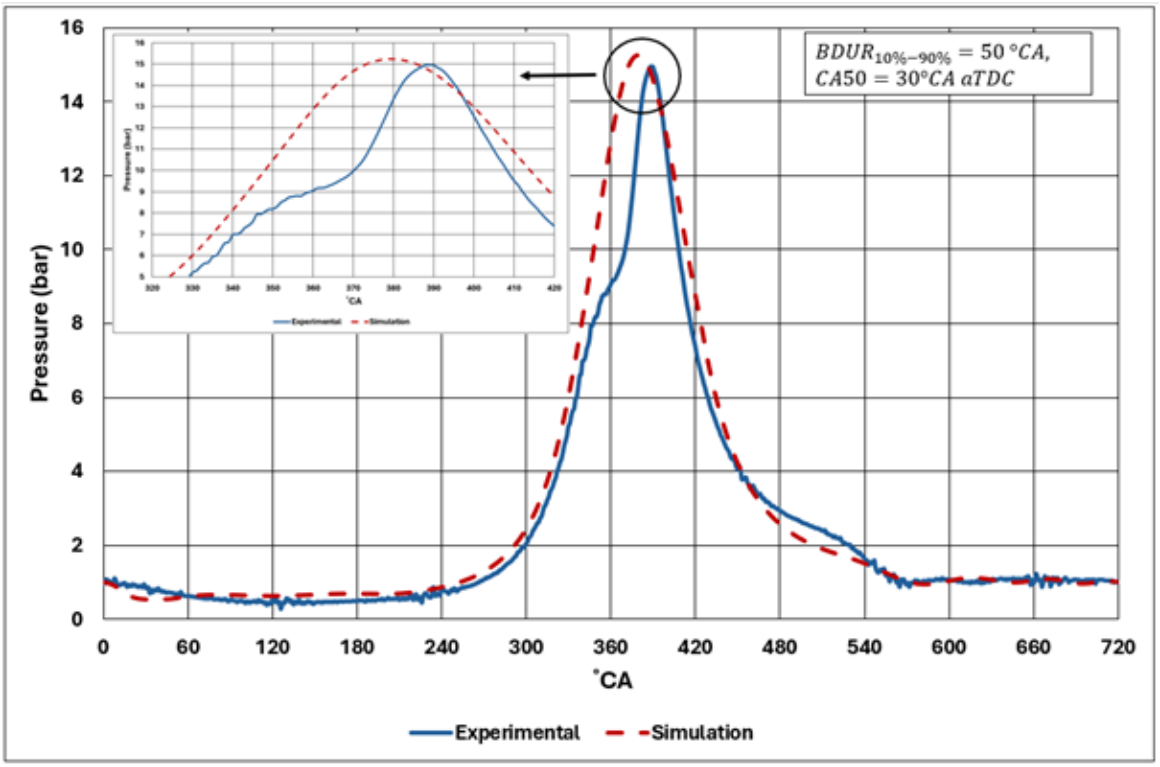

Figure 3. Pressure vs. crank angle curve of experimental and simulation study.

The crank angle at which the highest pressure obtained is closer to the TDC and PFP value is higher than that in the experimental ones although this difference could be accepted with a good accuracy since the percent errors are

below 2.5% as could be seen in Table 2. In former simulation study, burning duration between MFB10 and MFB90 was taken to be 50˚CA, and MFB50 crank angle was set to 30˚CA aTDC.

In 1-D engine modelling approach, the consistencies between the PFP, the timing of PFP, and the net indicated mean effective pressure ($IMEP_{NET}$) values signify a high degree of modelling accuracy and reliability. The results of former simulation study raised a research question of whether a more realistic simulation model could be developed for validation purpose. PFP value and the crank angle at which it is obtained are strongly dependent on the burning duration and the crank angle at which MFB50 value is reached. Numerous optimisation attempts have been carried out by adjusting the crank angle parameters associated with the combustion duration and MFB50 values. In this study, these two parameters have played a critical role on integrating a robust combustion model in order to match a better validation agreement against the experimental data in comparison to the former simulation model.

Pressure vs. crank angle graph of experimental and optimized simulation results is given in Figure 4. As a result, the peak pressure value and the corresponding crankshaft angle at which it occurs have been obtained in a better agreement against the experimental results. The accuracy of PFP magnitude and timing as crankshaft angle has been calculated are below 1% as seen in Table 2. The results demonstrate that a better combustion model approach has been developed compared to former simulation results. In the optimized simulation study, burning duration between MFB10 and MFB90 was taken to be 40˚CA, and MFB50 crank angle was set to 30˚CA aTDC.

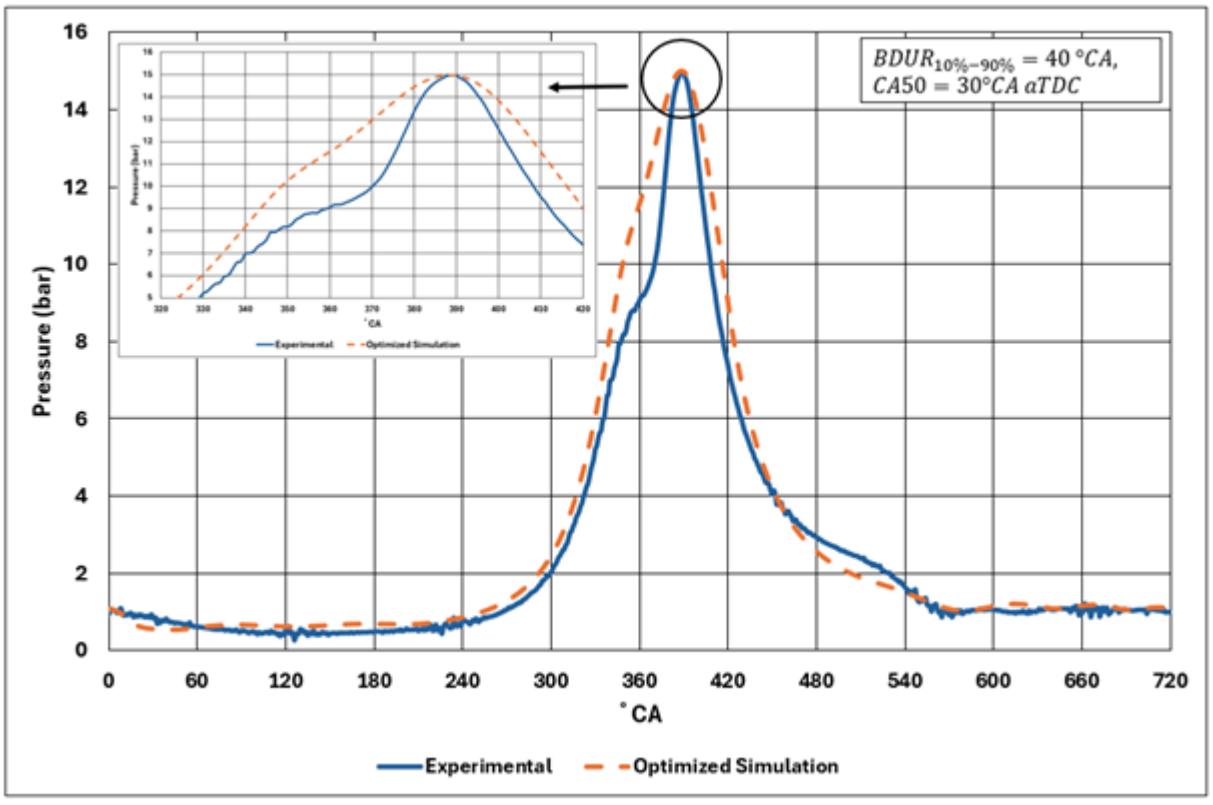

Figure 4. Pressure vs. crank angle curve of experimental and optimized simulation study.

The accuracy of $IMEP_{NET}$ finding decreases from 2% to 0.5%. The pressure levels at compression stroke after intake valve closing (IVC) point have been observed higher than that in experimental data for both simulations.

Table 2. Comparison of experimental, simulation and optimized simulation results.

@1800 rpm, 3 bar BMEP	$IMEP_{NET}$	P_{max}	θ_{Pmax}	BSFC
	(bar)	(bar)	(˚CA)	(g/kWh)
Experimental	3.75	14.96	389.0	477
Simulation	3.68	15.02	379.3	471
Error (%)	-1.87	0.40	-2.49	-1.26
Optimized Simulation	3.77	14.99	388.4	473
Error (%)	0.53	0.20	-0.15	-0.84

Conclusion

A 1-D model of a gasoline-fuelled engine was re-simulated. Validation was performed at one test point of 1800 rpm and 3 bar BMEP based on the Wiebe combustion framework. The optimized simulation results, achieved by adjusting the crankshaft angle values for combustion duration and MFB50, indicate a much better agreement against experimental data with respect to maximum cylinder pressure, PFP crank angle, and $IMEP_{NET}$ output. $IMEP_{NET}$, P_{max}, θ_{Pmax}, and BSFC were calculated with less than 1% error. It is more appropriate to use 40˚CA for MFB10-MFB90 burning duration rather than 50˚CA without adjusting MFB50 crank angle of 30˚CA. As a future study, the factors contributing to the pressure values being higher than those obtained experimentally during the compression phase should be examined and corresponding inconsistencies should be eliminated. Simulation studies are going to be extended for a matrix including different low load and engine speed ranges.İ

References

Onorati, A., & Montenegro, G. (2020). 1D and multi-D modeling techniques for IC engine simulation. SAE International.

Kutlar, O. A., Arslan, H., & Çalık, A. T. (2005). Methods to improve efficiency of four stroke, spark ignition engines at part load. Energy Conversion and Management, 46(20), 3202–3220.

Baykara, C., Kutlar, O. A., Doğru, B., & Arslan, H. (2017). Skip cycle method with a valve-control mechanism for spark ignition engines. Energy Conversion and Management, 146, 134–146**.**

Rassweiler, G. M., & Withrow, L. (1938). Motion pictures of engine flames correlated with pressure cards. SAE Transactions, 42.

Kirkpatrick, A. T. (2020). Internal combustion engines: Applied thermosciences (4th ed.). Wiley.

Heywood, J. B. (2018). Internal combustion engine fundamentals, Second Edition. McGraw-Hill.

Pour, R. S. (2017). One dimensional modelling of SI engines fuelled with gasoline-alcohol blends (Master Thesis). Marmara University, Department of Mechanical Engineering.

Doğru, K. K. J. R. D., & Lot, R. (2018). Valve timing optimisation of a spark ignition engine with skip cycle strategy. Energy Conversion and Management*, 173*, 95–112.

MECHANICAL ENGINEERING

Additive Manufacturing

Automotive

Computational Fluid Dynamics

Computational Solid Mechanics

Fluid Mechanics

Industrial Data Analytics

Machine Design

Machine Dynamics, Vibration, and Acoustic

System Dynamics and Control

Multi-Objective Aerodynamic Shape Optimization of Helicopter Nose

Yiğit Can Özdemir[a], Sertaç Çadırcı[a]

[a] Istanbul Technical University, Faculty of Mechanical Engineering, Department of Mechanical Engineering, Türkiye
ozdemiry22@itu.edu.tr

Keywords: Helicopter Nose, Aerodynamic Interaction, Download Drag, Parasite Drag, Aerodynamic Shape Optimization.

In this study, multi-objective aerodynamic shape optimization of helicopter nose is performed in order to enhance helicopter performance. As a result, 500 design points are obtained and the influence of each design parameter on the objectives is numerically shown. The study suggests that download drag is governed by certain geometric features of the helicopter nose. With shape optimization, approximately 14% and 1% enhancements are achieved in download drag and parasite drag, respectively.

Aim

Helicopters are rotorcraft that take off and land vertically, hover and fly forward, backward, and sideways. Performance criteria for helicopters are based on both hover and forward flight performances so helicopter airframe designs must be made considering efficient flight in these two different flight conditions.

During the design process of a helicopter, there is a strong phenomenon as an interaction between the main rotor and the airframe which emerges especially during hovering and at low forward flight speeds. Because of the downwash of the helicopter's main rotor, download drag occurs on the helicopter's body towards the ground. The download drag depends on the downwash velocity of the main rotor and the helicopter's airframe geometry. Download drag has an impact on many performance parameters such as helicopter's payload weight and efficiency of hovering [Bagai and Leishman, 1992] [Leishman and Bi, 1990] [Bramwell, 1966] [Renaud, 2008] [Venegoni, 1977]. Total drag in forward flight produced by a helicopter is the sum of the parasite drag, induced drag, and profile drag. Parasite drag is a type of aerodynamic drag caused by non-lifting parts of the helicopter. It includes the skin-friction drag and pressure drag associated with nose, fuselage, engine cowling, rotor hubs, landing gears and empennage. Parasite drag increases with the square of the airspeed so after a certain airspeed, parasite drag becomes the dominant source for total drag. Parasite drag has an impact on many performance parameters like helicopter's maximum attainable forward speed, range and fuel consumption [Venegoni, 1977] [Keys and Wiesner, 1975] [Leishman, 2006]. Helicopter nose geometry is part of an airframe which affects an aircraft's flight performance. It is the part that needs to be worked on due to the complex structure and limited design space, especially for a helicopter.

The design and optimization of aerodynamic components is challenging due to the large number of design variables; thus, different strategies have been developed to overcome these challenges. The different strategies include adjoint optimization methods, surrogate models, hybrid routines that combine lower- and higher-fidelity evaluations and feature-extraction approaches based on dimensionality reduction techniques [Tejero, 2023].

In this study, multi-point, multi-objective aerodynamic shape optimization of helicopter nose is performed in order to reduce the download drag and the parasite drag to enhance the performance of the helicopter.

Material and Method

CFD based aerodynamic shape optimization is performed by coupling Siemens NX, Star CCM+ and HEEDS. Parameters are determined to create different cross-sections in the three-dimensional domain. While determining the parameters, it is aimed to reduce computational cost and save time with a minimum number of parameters and to scan different geometries, to ensure that these geometries are aesthetically smooth and manufacturable at the same time.

A simple helicopter geometry is generated to be used in this study. Helicopter geometry, main rotor disk and the nose part to be optimized are illustrated in Figure 1.

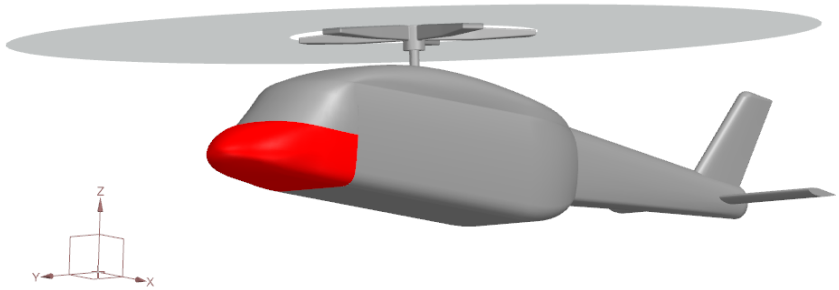

Figure 1. Geometry of the helicopter and main rotor disk.

Parametric design is performed with Siemens NX CAD software. Figure 2 shows the design parameters of interest in the study. The first parameters are x- and z-positions in the domain of Point 1 and Point 2. Their y-position is constant, and the z-position of Point 2 is always the same z-position of Point 1. Thus, there are three parameters arising from these two points. Another parameter is the angle between the ground and Line 1. It has a tangential relationship with the middle curve. By changing the angle of Line 1, the slope of the upper surface of the nose changes. The curve depth is another parameter affecting the curvature of Curve 1. Finally, a further parameter is the height of Line 2 from the ground. In total, there are six parameters to control the geometry of the helicopter's nose.

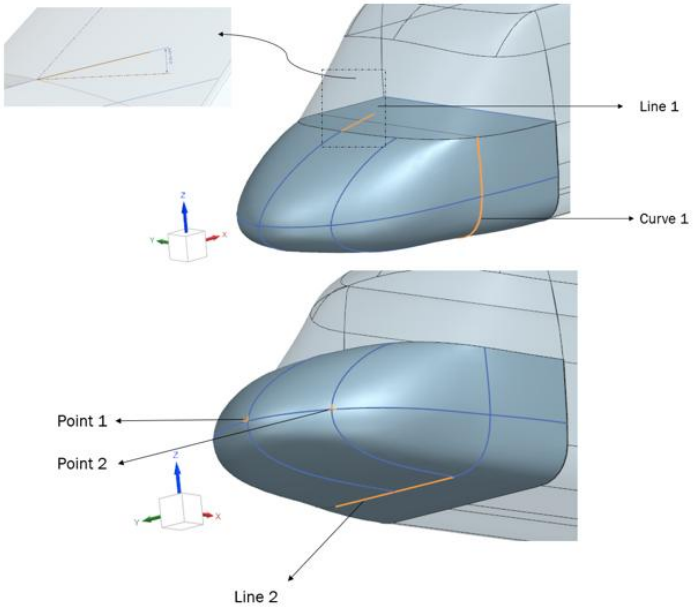

Figure 2. Design parameters of the helicopter nose.

Grid generation and CFD analyzes are performed using Star-CCM+, a commercial CFD software. To obtain reliable results from CFD analyzes, computational domain with high-quality mesh is significant. A mesh independence study is carried out to accurately calculate force- and moment- coefficients. Therefore, results are compared with T625 helicopter test results. As a result, high-density polyhedral mesh with approximately 9 million elements is selected to continue which is illustrated in Figure 3. The boundary layer zone consists of prism cells where wall functions are employed in the calculations.

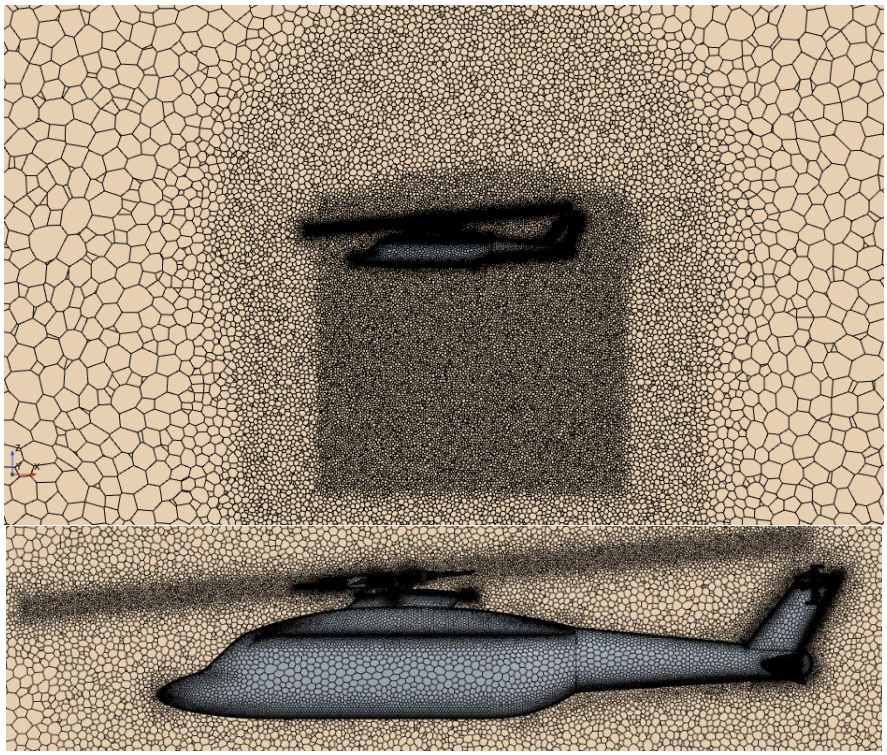

Figure 3. Mesh Structure.

Among RANS-based turbulence models, the SST k-ω turbulence model is preferred. The flow is assumed to be at steady-state and implicit density based coupled solver is used. In order to simulate main rotor flow, Virtual Disk Model of Star-CCM+ is employed. For optimizing the nose of the helicopter, HEEDS software's Multi-Objective SHERPA algorithm is applied. MO-SHERPA (Multi-Objective SHERPA) is a modified version of the algorithm SHERPA for multi-objective Pareto search. It uses a non-dominated sorting scheme to rank designs but shows differences from NSGA-II and NCGA algorithms [Chase, 2009]. The objectives are selected and evaluated according to different flight conditions which are hover flight and high-speed forward flight. Download drag must be minimized to enhance hover performance, parasite drag must be minimized to enhance forward flight performance and the minimum volume requirement of the nose must be satisfied.

Findings

The relations between different design objectives are obtained from HEEDS and suitable alternatives are evaluated in terms of hover flight performance, forward flight performance, nose volume, smoothness and manufacturability. As can be seen in Figure 4, parasite drag is not significantly affected by the nose geometry. It is observed that there is a tradeoff relation between download drag and volume of the helicopter nose. As the volume of the nose decreases, i.e. the projection area becomes smaller, download drag decreases, as can be seen in Figure 4.

The download drag is reduced from 3773 N to 3238 N. With this decrease, a 14% improvement is achieved for download drag. For parasite drag, there is no great improvement, but parasite drag is reduced from 2923 N to 2902 N which means nearly 1% improvement is achieved. The new design is selected to meet the 1.6 cubic meter volume requirement; thus, the volume is decreased from 1.8 cubic meter to 1.61 cubic meter.

Figure 5 shows that static pressure contours around the baseline and the optimized design during hover flight. There is a remarkable decrease in high-pressure and low-pressure regions above and below the front of the airframe. So, it causes download drag to reduce.

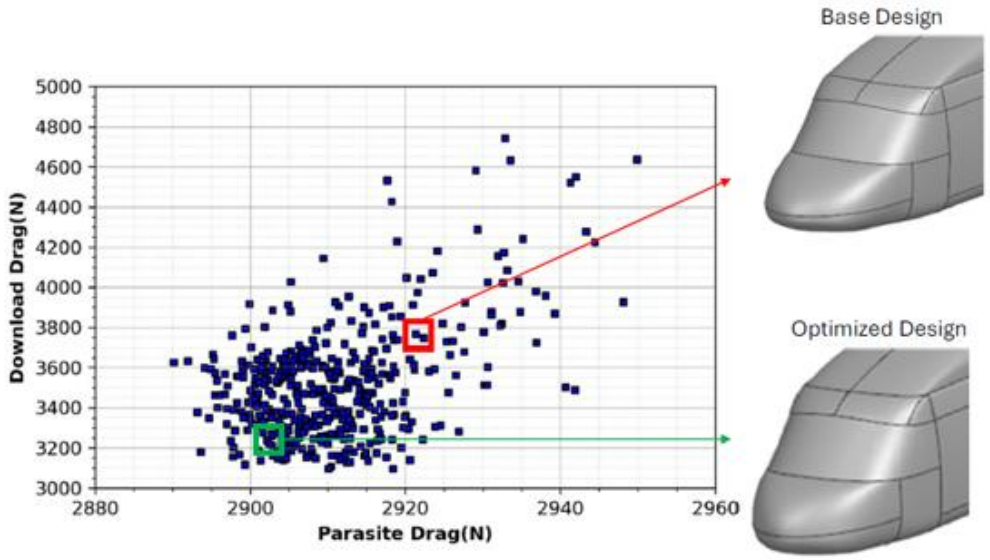

a) Baseline and optimized design in design space.

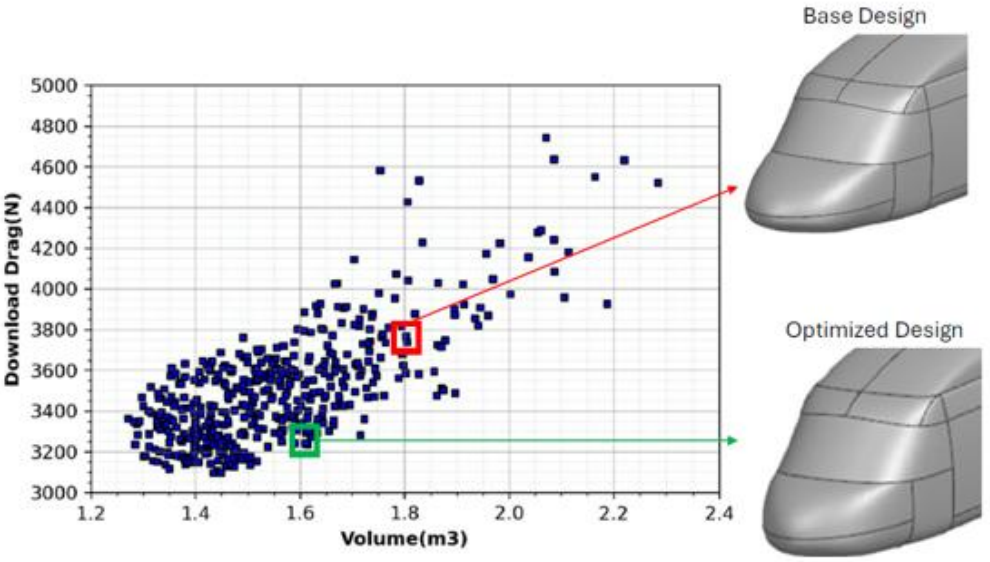

b) Baseline and optimized design in download drag versus volume plot.

Figure 4. Design space.

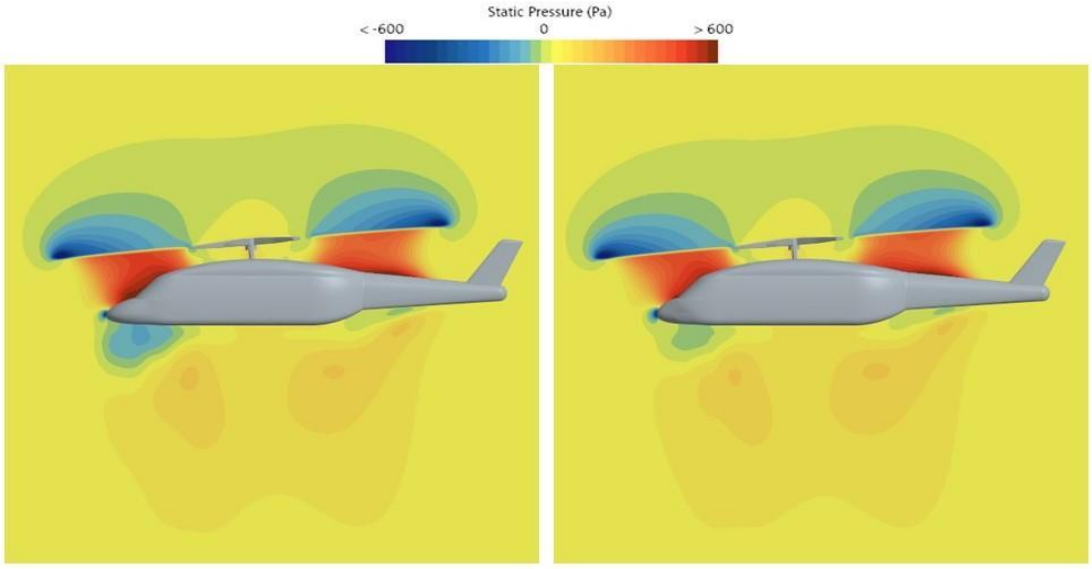

Figure 5. Static pressure contours during hover flight.

Conclusion

Hover and forward flights have a significant role in helicopter performance. It is aimed to reduce the download drag and parasite drag without compromising the stability on the pitch axis by optimizing the nose shape. Design parameters are selected to scan different geometries in a wide range. Virtual disk model is employed to consider the aerodynamic interaction between the main rotor and the airframe in a cost-effective way. One of the best performing alternatives selected from the optimization results are compared with the baseline nose design. It is observed that the nose geometry has a greater effect on the download drag than on the parasite drag. With proposed shape optimization, approximately 14% and 1% improvements are achieved in download drag and parasite drag, respectively.

References

Bagai, A., & Leishman, J. G. (1992). Experimental study of rotor wake/body interactions in hover. Journal of the American Helicopter Society, 37(4), 48-57.

Bramwell, A. R. S. (1966). A theory of the aerodynamic interference between a helicopter rotor blade and a fuselage and wing in hovering and forward flight. Journal of Sound and Vibration, 3(3), 355-383.

Chase, N., Rademacher, M., Goodman, E., Averill, R., & Sidhu, R. (2009). A benchmark study of multi-objective optimization methods. BMK-3021, Rev, 6, 1-24.

Keys, C. N., & Wiesner, R. (1975). Guidelines for reducing helicopter parasite drag. Journal of the American Helicopter Society, 20(1), 31-40.

Leishman, J. G. (2006). Principles of aerodynamics (2nd ed.). Cambridge University Press.

Leishman, J. G., & Bi, N. P. (1990). Aerodynamic interactions between a rotor and a fuselage in forward flight. Journal of the American Helicopter Society, 35(3), 22-31.

Renaud, T., O'Brien, D., Smith, M., & Potsdam, M. (2008). Evaluation of Isolated Fuselage and Rotor-Fuselage Interaction Using Computational Fluid Dynamics. Journal of the American Helicopter Society, 53(1), 3-17.

Tejero, F., MacManus, D. G., Sanchez-Moreno, F., & Sheaf, C. (2023). Neural network-based multi-point, multi-objective optimisation for transonic applications. Aerospace Science and Technology, 136, 108208.

Venegoni, M., Magni, E., & Baldassarrini, R. (1977). An industrial rationale for the aerodynamic design of the fuselage.

Analysis of Effects of Tip Clearance on Axial Pump Performance

Mehmet Deniz Pacaci[a], Levent Ali Kavurmacioglu [b]

[a] Istanbul Technical University Graduate School, Heat-Fluid, Turkey
[b] 2Istanbul Technical University, Mechanical Engineering Department, Turkey
pacaci@itu.edu.tr

Keywords: Tip Clearance, Axial Pumps, Hydraulic Efficiency, Tip Leakage Vortex.

Aim

Axial pumps are widely used in different industries such as marine, energy and different applications and require different installation and maintenance specifications. Tip clearance distance is the distance between blade and casing which is necessary for thermal expansion and safety; but it creates leakage flow and mechanical losses and it has a significant effect on hydraulic performance and cavitation formation of axial pumps. Tip leakage vortex can be optimized and made parametric using numerical methods. Several investigations have been conducted in this field to observe tip vortex evolution and its characteristics [1-2].
Tip vortex mainly triggered by pressure difference between pressure and suction sides of the blade. High pressure triggers flow separation and results in tip leakage from pressure side to suction side. This reverse flow forms tip leakage vortex on hydraulic machines. Tip leakage vortex can be observed experimentally and numerically. Thus, clearance distance can be optimized. Lin Z. et. al. suggests that while many axial pump CFD studies have focused on tip vortex flow characteristics for a certain tip clearance; Shen J. et. al. focused to observe effects of tip clearance distance on tip vortex flow.
Within the scope of this study, effects of different tip clearance distances have been investigated for an axial pump numerically.

Material and Method

An industrial axial pump blade has been selected for this study and numerical analysis have been conducted within the scope of this study. Parameters have been selected as follows: fluid is water. Total number of rotor blades of pump are four, 3D model is prepared as 90° rotational periodic.

Song X. Et. al. suggests 157 m^3/s flow rate.

Blade hub diameter is 100 mm and tip diameter is 240 mm. Two different tip clearances are analyzed. First distance is 2 mm; second distance is 4 mm. Shroud diameters are different per tip clearances; first shroud diameter is 244 mm; second shroud diameter is 248 mm.

Zhang H. suggests that angular velocity is 152 rad/s.

Average static pressure at outlet is assigned as 0 kPa.

In addition to general mass and momentum conservation equations, Reynolds-averaged Navier-Stokes (RANS) equations can provide a general and specific information for formation of tip leakage vortex [1].

For turbulence, shear stress transport is used.

Three different domains have been designed for this investigation: inlet, rotor and outlet. Rotor length has been selected as 180 mm; length of inlet and outlet domains has been selected as 180 mm and 900 mm, respectively. All domains have been designed 90 degree rotational periodic. This has been demonstrated in Fig. 1 Design configuration of flow domain.The material and method section should be written in Times New Roman font, justified-alignment and in 10-point size.

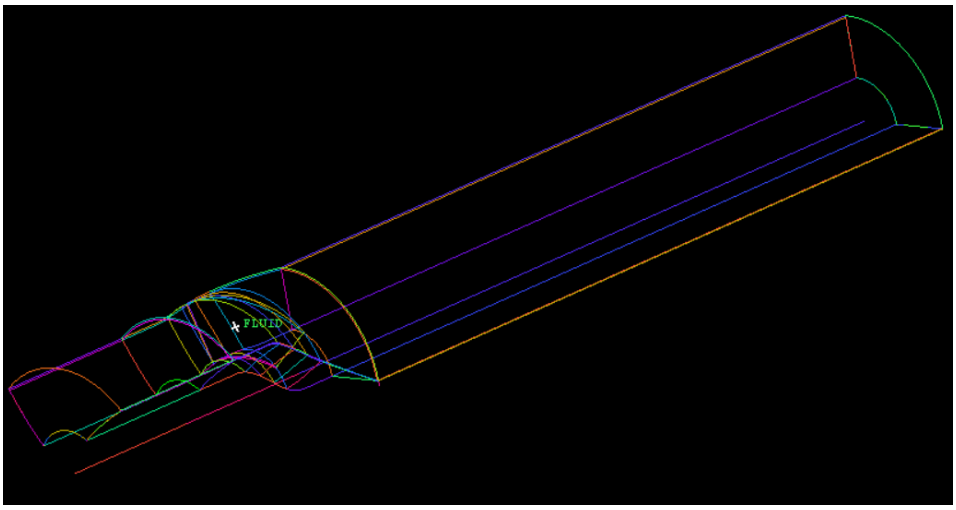

Figure 1 : Design configuration of flow domain.

In this study, numerical investigations have been conducted by using Ansys 2023 R1. Specifically, Icem CFD has been used for meshing; CFX-Pre, CFX Solver Manager and CFD Post have been used for analysis and post processing.

All geometry has been blocked and structured mesh has been used. It's been stated that to handle problems related with structured grid for complex geometries, block-structured CFD methods have been developed as Versteeg H.K. and Malalasekera W. suggest to cope with different difficulties related with structured grid.

Mesh has been generated for two different domains per tip clearances, 2 mm and 4 mm respectively. This is demonstrated in Fig. 2: Rotor mesh view sample (with 2 mm tip clearance).

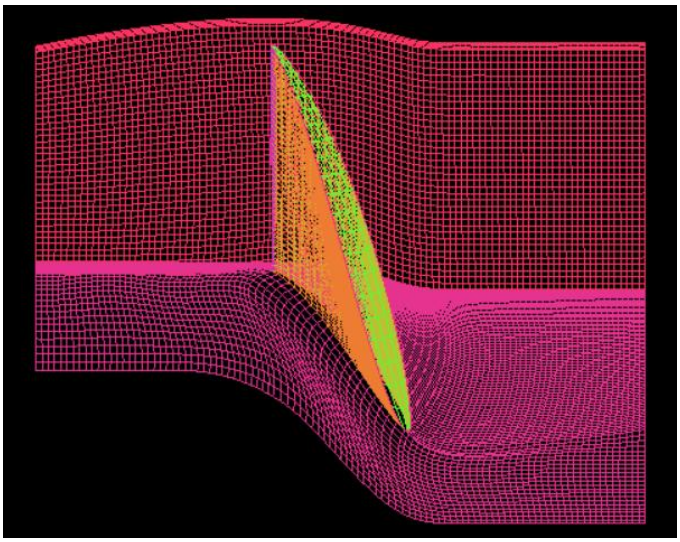

Figure 2 : Rotor mesh view sample (with 2 mm tip clearance).

During the mesh generation process, hexahedral elements were used in all regions to accurately resolve especially near wall regions. Multiple mesh topologies were generated and highest mesh quality was carefully monitored. Boundary layer grid has been designed for small y+ values. Due to stability and quality considerations, the highest-quality mesh was selected for the simulation; quality issues limited the use of alternative meshes. During the CFX analysis, the development of the normal moment on the blade surface was tracked, and the mesh was also observed based on its ability to capture consistency.

In first mesh setup, hexagonal elements have been used with total 976.089; in second mesh, total element number is 1.403.700.

The turbulence model SST has been selected.
In CFX Solver Manager, stability and convergency are observed per normalization of normal moment affecting on blade as well as different RMS values.

Findings

After completion of analysis of both cases, results have been compared to each other by graphics. Cross sections have been taken from leading edge, middle of blade and trailing edge sides. It's been observed that flow directions are quite different from each other. 2 mm tip clearance resulted in reverse flow on concave side nearby leading edge and major vortexes on both leading edge pressure side and trailing edge suction side. In 4 mm tip clearance case, higher velocity values have been calculated; again there are reverse flow but tip vortex has only been observed on trailing edge side. This has been demonstrated in Fig. 3.

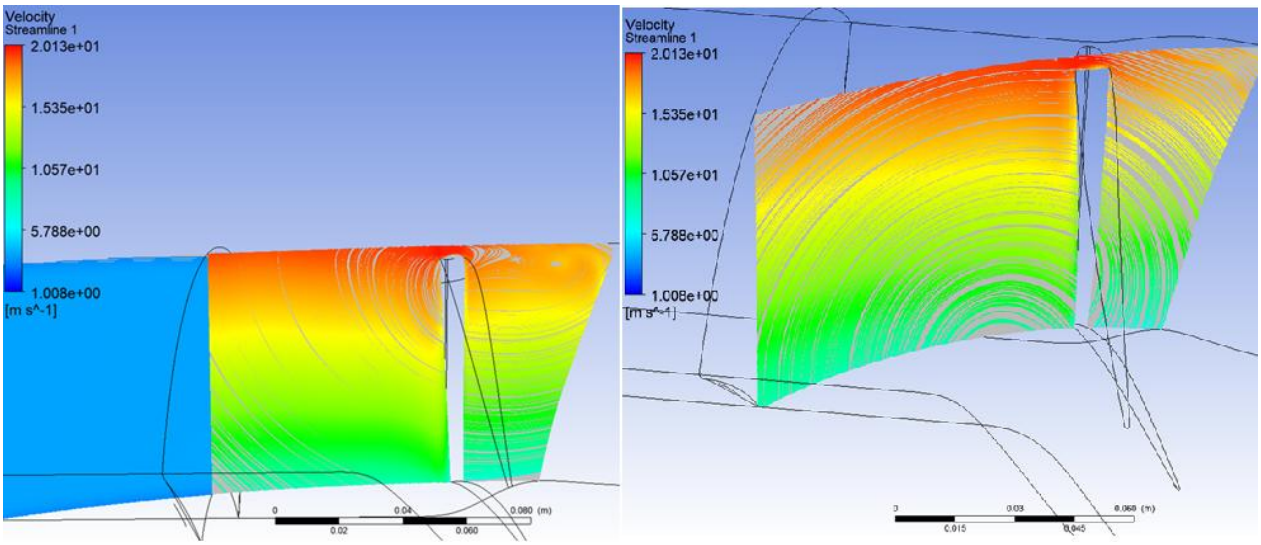

(a) (b)

Figure 3 : Streamlines on cross section view near leading edge (a) 2 mm tip clearance, (b) 4 mm tip clearance on right side).

Streamlines on cross section view near leading edge (2 mm tip clearance on left side; 4 mm tip clearance on right side), Fig.4 Streamlines on cross section view of middle of the blade (2 mm tip clearance on left side; 4 mm tip clearance on right side), and in Fig. 5 Streamline graphics on cross section view near trailing edge (2 mm tip clearance on left side; 4 mm tip clearance on right side)

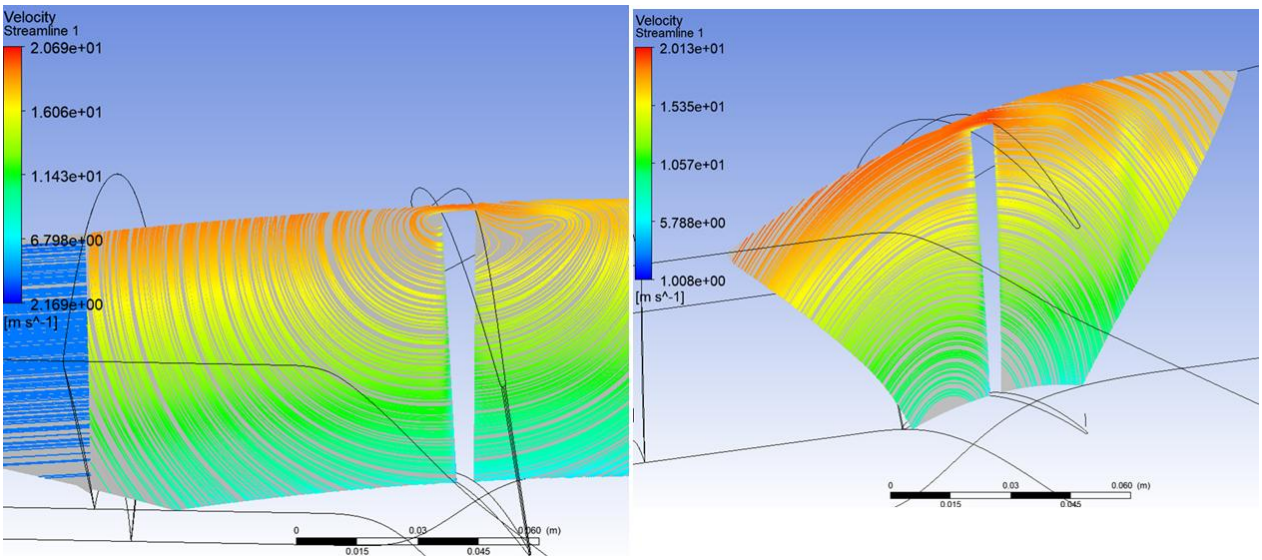

(a) (b)

Figure 4 : Streamlines on cross section view of middle of the blade, (a) 2 mm tip clearance, (b) 4 mm tip clearance on right side).

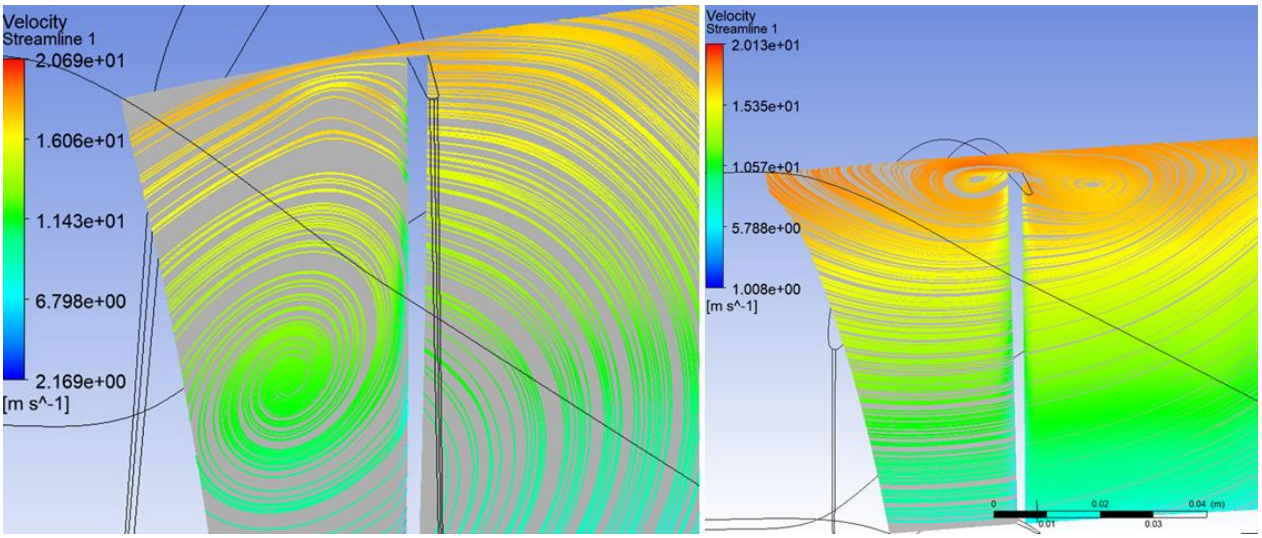

(a) (b)

Figure 5 : Streamline graphics on cross section view near trailing edge, (a) 2 mm tip clearance on left side, (b) 4 mm tip clearance on right side.

Results have been demonstrated in Table 1 Calculation results of both analysis. Torque, power, efficiency, total head, total pressure ratio have been reviewed for these tip clearance distances. In addition, pressure distribution in whole domain in streamwise direction has been reviewed and pressure coefficient (C_p) on blade surfaces has been checked for both cases; C_p distribution graph has been taken as sample in Fig. 6.

Table. 1 : Calculation results of both analysis.

Results	2 mm tip clearance distance	4 mm tip clearance distance
Torque (one blade row) ($kg.m^2/s^2$)	3.14	3.02
Power (all blades) ($kg.m^2/s^3$)	477.5	458.6
Efficiency	0.657	0.647
Total Head (m)	0.81	0.77
Total Pressure Ratio (Out/In)	10.7	13.7

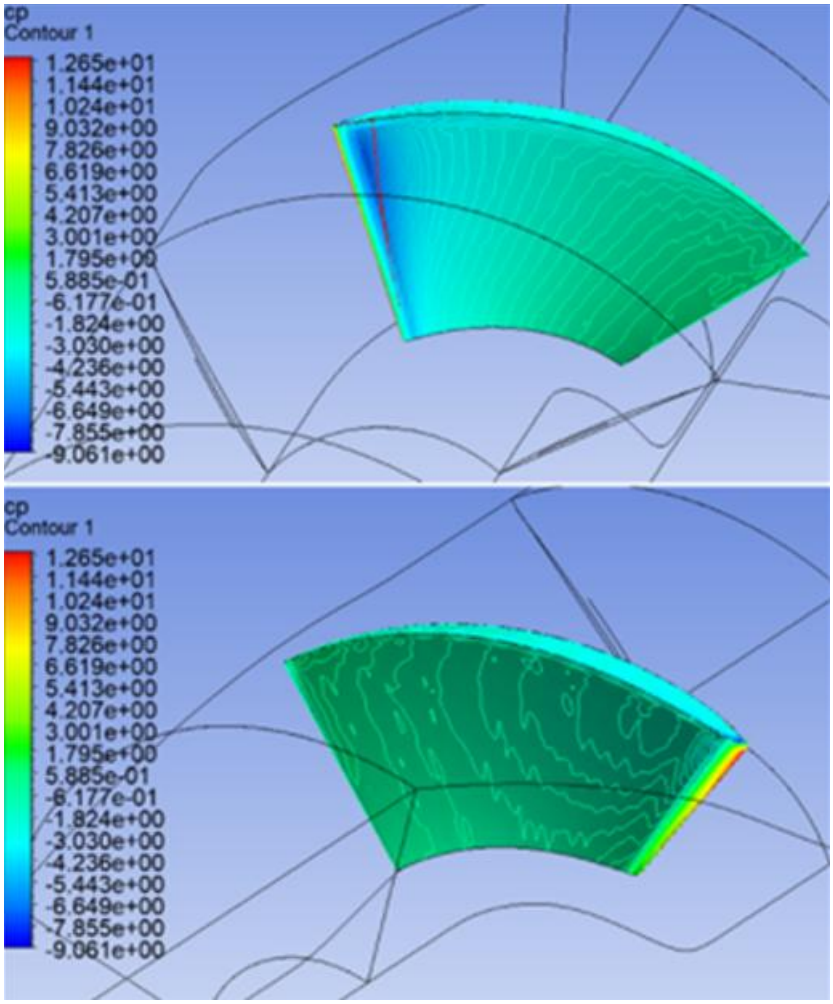

Figure 6 : Cp distribution on blade surfaces for 4 mm tip clearance.

Conclusion

It's been observed that low tip clearance results in higher head and efficiency. Higher tip clearance results in higher pressure difference, thus, higher noise is expected. Lower tip clearance is a better design solution than higher.
Tip leakage vortex core trajectory can be adjusted and changed by tip clearance. However, vortex position may still vary dramatically in different regions on blade. Tip clearance has significant effect on topology of flow separation, tip leakage vortex and other possible vortexes.

Finally, it may have also been concluded that tip clearance shall be adjusted according to other characteristics such as stack axis thickness, trailing edge thickness etc. on the outermost surface of the blade. Passive control methods such as winglet, squaler tip can be also applied to blade geometry.

References

Lin Z., Yang F., Guo J., Jian H., Sun S., Jin X. (2023). Leakage Flow Characteristics in Blade Tip of Shaft Tubular Pump.
Url-1 https://www.mdpi.com, date retrieved 04.2025.
Shen J., Xu F., Cheng L., Pan W., Ge Y., Li J., Zhang J. (2022). Simulation of Internal Flow Characteristics of an Axial Flow Pump with Variable Tip Clearance.
Url-2 https://www.mdpi.com, date retrieved 04.2025.
Song X., Cao P., Zhang J., Lv Z., Li G., Liu L. (2024). Dynamic Analysis of Tip Leakage Phenomena in Axial Flow Pumps Using a Square-Cavity Jet Model, Water, 16, 676.
Url-3 https://www.mdpi.com, date retrieved 04.2024.
Versteeg H.K., Malalasekera W. (2007). An Introduction to Computational Fluid Dynamics (Second Edition, p. 310). Pearson Prentice Hall.
Zhang H., Wang J., Zhang D., Shi W., Zang J. (2021). Numerical Analysis of the Effect of Cavitation on the Tip Leakage Vortex in an Axial-Flow Pump, Journal of Marine Science and Engineering, 9, 775.
Url-4 https://www.mdpi.com, date retrieved 04.2025.

Aerodynamic Performance Enhancement of a 27-Inch Apc Propeller Through Geometric Modifications

Mehmet Emin Arslan[a], Sertaç Çadırcı[a]

[a] Istanbul Technical University, Department of Mechanical Engineering, Türkiye
arslanme16@itu.edu.tr

Keywords: Airfoil Thickness, CFD simulation, Propeller design, Static Pitch, Twist Angle.

This study aims to improve the aerodynamic performance of a 27-inch APC propeller through modifying geometric design parameters, including static pitch, twist angle, and airfoil thickness distributions. Computational Fluid Dynamics (CFD) simulations at multiple operating conditions demonstrate that certain aggressive twist adjustments yield notable efficiency gains, while thickness changes can reduce aerodynamic performance at higher advance ratios. A validated CFD framework supports these findings, providing a balanced view of the trade-offs between propeller thrust, and propeller efficiency. The results offer valuable design guidance for propellers requiring optimal performance across a broad operational envelope.

Aerodynamic efficiency of a propeller is crucial for the performance of aerial vehicles. As these vehicles become more prevalent, propellers play a growing role in delivering efficient thrust. Early design choices significantly influence both efficiency and flight endurance (Chen et al., 2020), underscoring the importance of propeller optimization. Researchers have employed optimization algorithms combined with CFD or semi-empirical approaches to refine blade twist and chord for improved efficiency (Sedelnikov et al., 2024). In an earlier study, a fast vortex-lattice aerodynamic tool was integrated with a subsonic point-source noise model to optimize twist, chord, and sweep, thereby showing that adjusting the twist angle can simultaneously enhance efficiency and reduce noise (Miller & Sullivan, 1985). Meanwhile, a calculus-of-variations approach demonstrated that although the best twist distribution varies with operating conditions, a single twist angle configuration can still achieve near-optimal performance across different flight phases (Dorfling & Rokhsaz, 2014). Overall, these investigations highlight those well-considered geometric modifications can deliver gains in thrust generation and energy efficiency. However, there remains a gap in understanding how combined modifications of twist angle and airfoil thickness distribution may further improve propeller performance.

Aim

The aim of this study is to improve the aerodynamic performance of a 27-inch APC propeller by modifying its geometric parameters. Three main parameters are considered: static pitch, twist angle distribution and airfoil thickness distribution across the blade span. The goal is to increase overall efficiency across a range of operating conditions. A baseline design, referred to as the Standard 27×13 Propeller, was derived from the vendor's published geometry data of the 27×13E model (APC Propellers.). From this baseline geometry, several static pitch variants were created by adjusting the pitch values in the geometry data. In the twist and thickness distribution studies, four levels of modification were investigated.

Material and Method

The computational domain was sized relative to the propeller diameter D as shown in Figure 1. The appropriate domain size was determined regarding both the radial and axial extents. Once further enlargement showed no significant effect on thrust or torque, the domain boundaries were deemed adequate (Lopez Mejia et al., 2017). To save computational time and conduct cost-effective simulations, the Multiple Reference Frame (MRF) technique was chosen instead of a sliding mesh approach. In the MRF method, rotating and stationary zones are treated in a steady-state manner, reducing computational overhead (Gullberg & Sengupta, 2011). At the inlet of the computational domain, uniform velocity is employed. At the outlet of the computational domain pressure outlet

boundary condition is specified for incompressible flow assumptions. The symmetry boundary condition is defined in the farfield region of the domain (Kyaw & Jinming, 2021).

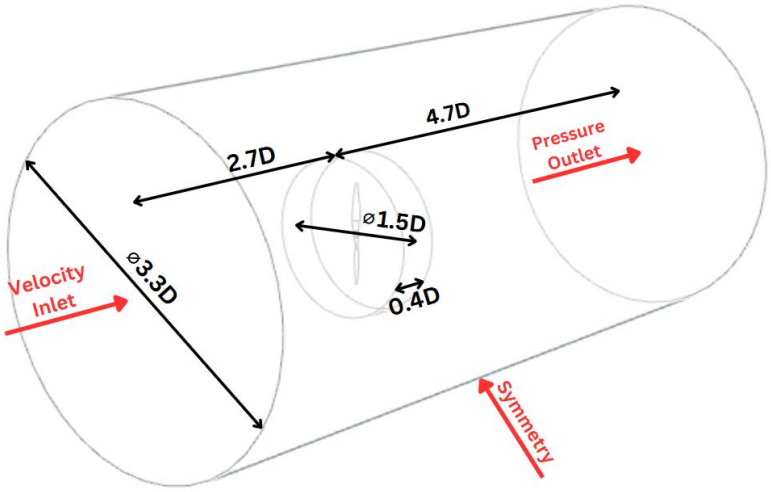

Figure 1. Computational domain setup and boundary conditions.

The mesh configuration, illustrated in Figure 2, features local refinements near the blade surfaces and in the wake region. A mesh independence analysis was performed by progressively refining the grid and monitoring variations in thrust and torque. Once additional refinement produced negligible changes in these parameters, it was concluded that the selected mesh resolution adequately captured all relevant flow physics. As a result, it was shown that a mesh consisting of 2.5 million elements was sufficient to approach the thrust value provided by the vendor with an approximate relative error of 5%. Among all tested turbulence models in the turbulence sensitivity analysis, realizable k-ε model with standard wall functions was shown to be the most favourable turbulence model in terms of computational savings and matching with the vendor's performance data.

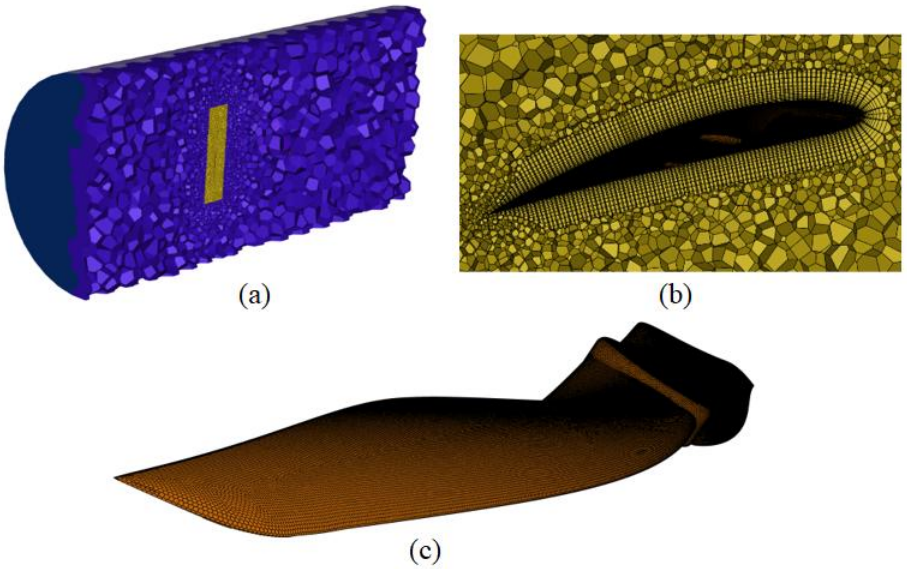

Figure 2. Illustration of mesh arrangements: (a) general mesh section, (b) close-up view of mesh layers around the airfoil, and (c) propeller surface mesh.

Various blade configurations have been derived from the baseline geometry and modifications have been conducted to parametrically investigate the effect of the blade geometry on the aerodynamic performance indicators. From the baseline geometry, static pitch variants (7, 10, 16, and 19 inches) were generated by adjusting

pitch values as shown in Figure 3.a. To determine the blade twist angle at any radial station, the local twist angle was calculated using the formula $\beta(r) = \left(\frac{P}{2\pi r}\right)$ (Giljarhus et al., 2022) where P denotes the pitch length. All simulations were conducted at a constant rotational speed of 3000 RPM, covering inlet velocities corresponding to advance ratios (J) ranging from approximately 0.1 to 0.6. The thrust and torque outputs were then represented by the thrust coefficient (C_T) and the power coefficient (C_P), respectively and then plotted as the efficiency versus advance ratio.

Using the verified setup, the effects of modifications in twist distribution and thickness distribution were investigated. For the studying the effect of the twist angle, four variants—A1, A2, B1, and B2—were derived from the Standard 27×13 Propeller. In the A-series, the twist angle was reduced at the root and gradually increased toward the tip, whereas in the B-series the twist angle was increased at the root and then decreased toward the tip. In both approaches, the twist at 75% of the blade span was held constant to preserve the propeller's nominal pitch reference point as shown in Figure 3.b.

For the thickness study, another four variants—again labelled as A1, A2, B1, and B2—altered the airfoil thickness distribution across the blade span using two strategies. In the Uniform Thickness approach (A-series), thickness was reduced at the root and slightly increased at the tip, while preserving the baseline thickness value at 75% of the blade span. In the Tapered Thickness approach (B-series), airfoil thickness was increased at the root and reduced at the tip, maintaining the same mid-span thickness as the baseline. The variations of the airfoil thickness along the blade span for both approaches is shown in Figure 3.c. All CFD simulations using the modified geometries were evaluated in terms of the efficiency, an estimated aerodynamic indicator was computed calculated as JC_T/C_P (Dantsker et al., 2022).

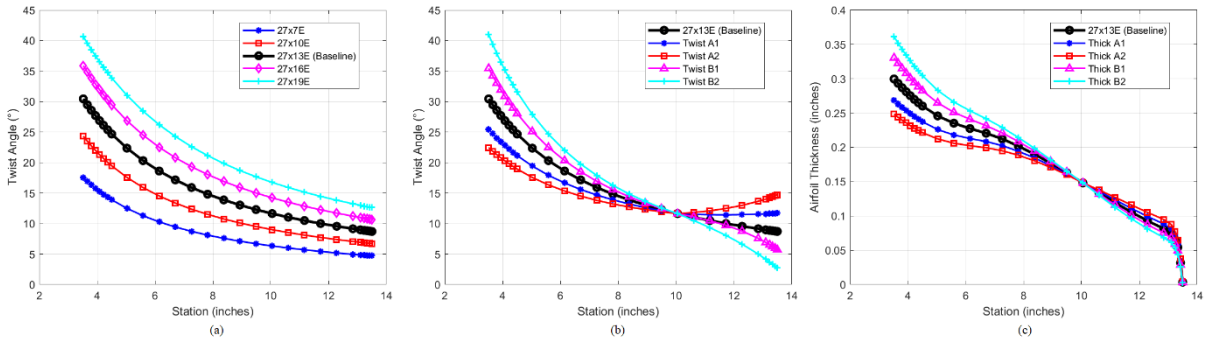

Figure 3. Distribution of propeller parameters along the blade span: (a) Static pitch variants, (b) Twist-modified variants, and (c) Thickness-modified variants.

Findings

The static pitch study identified the Standard 27×13 Propeller as offering the best compromise among variants (7, 10, 16, and 19 inches), balancing performance at different freestream speeds as shown in Figure 4.a. At low to moderate advance ratios, the 27×13 Propeller displayed relatively high efficiency alongside solid thrust output, which made it a logical choice for further shape optimization.

In the twist study, the propeller's baseline efficiency declined as the advance ratio J increased typical behavior for a fixed-pitch propeller. At low J values, the efficiency of all modified twist-angle variants was almost indistinguishable from the baseline. However, as J advanced into moderate and higher regimes, the performance differences became more evident. In particular, the aggressive twist variants (B1 and B2) sustained a noticeable increase in estimated efficiency compared to the baseline, especially at $J \approx 0.5$ as it can be seen in Figure 4.b. Even at $J \approx 0.6$, where overall efficiency typically drops, the B1 and B2 configurations maintained a higher efficiency compared to the baseline. In contrast, the mild twist variants (A1 and A2) provided only small efficiency gains at high advance ratios.

At low and moderate J values, all modified airfoil thickness-variants exhibited efficiency levels comparable to the baseline. However, at higher advance ratios, these modifications yielded a drop in the efficiency compared to the

baseline configuration. As Figure 4.c shows, at $J \approx 0.6$, the baseline geometry demonstrated an efficiency of roughly 0.50, whereas the thickness-modified variants dipped to approximately 0.42, indicating a slight performance penalty at higher speeds. This result suggests that any structural benefits gained from adjusting the blade thickness distribution may come at the cost of decreased aerodynamic efficiency at moderate to high advance ratio values.

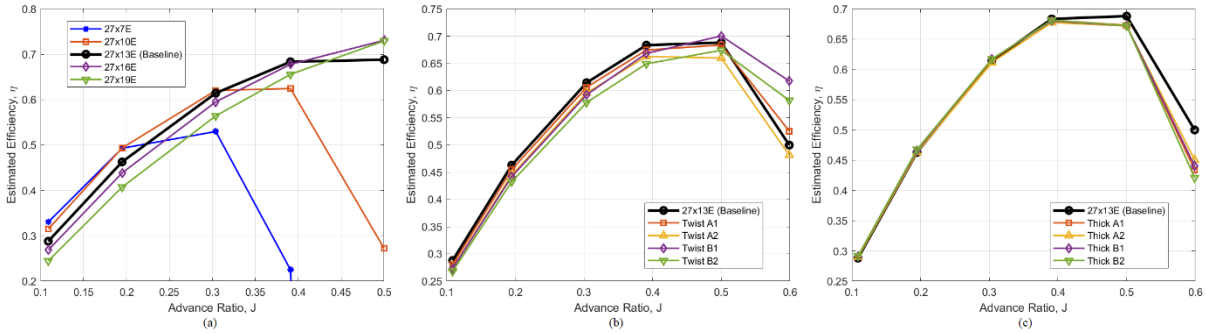

Figure 4. Efficiency comparison of (a) static pitch variants, (b) twist modified variants, and (c) thickness modified variants.

Conclusion

This study demonstrates that modifiying a 27-inch APC propeller's geometry can lead to substantial enhancements in aerodynamic efficiency. Among the static pitch variants, the 13-inch pitch was chosen for detailed exploration based on its balanced performance across varying speeds. The twist study shows that more aggressive modifications (B1 and B2) yield notably higher efficiency at increased advance ratios, making them especially advantageous for high-speed applications. By contrast, airfoil thickness modifications—whether uniform or tapered—cause a modest reduction in efficiency at higher advance ratio, even though they may offer structural or manufacturing benefits. Future research may incorporate structural and acoustic analyses to yield a fully optimized propeller design that meets all operational requirements.

References

APC Propellers. Downloads. (n.d.). Retrieved May 19, 2025, from https://www.apcprop.com/technical-information/file-downloads/

Chen, G., Ma, D., Jia, Y., Xia, X., & He, C. (2020). Comprehensive Optimization of the Unmanned Tilt-Wing Cargo Aircraft With Distributed Propulsors. *IEEE Access*, *8*, 137867–137883. https://doi.org/10.1109/ACCESS.2020.3012481

Dantsker, O. D., Caccamo, M., Deters, R. W., & Selig, M. (2022). Performance Testing of APC Electric Fixed-Blade UAV Propellers. In *AIAA AVIATION 2022 Forum*. American Institute of Aeronautics and Astronautics. https://doi.org/10.2514/6.2022-4020

Dorfling, J., & Rokhsaz, K. (2014). Constrained and Unconstrained Propeller Blade Optimization. In *Journal of Aircraft* (Vol. 52). https://doi.org/10.2514/6.2014-0563

Giljarhus, K. E. T., Porcarelli, A., & Apeland, J. (2022). Investigation of Rotor Efficiency with Varying Rotor Pitch Angle for a Coaxial Drone. *Drones*, *6*(4), Article 4. https://doi.org/10.3390/drones6040091

Gullberg, P., & Sengupta, R. (2011, April 12). *Axial Fan Performance Predictions in CFD, Comparison of MRF and Sliding Mesh with Experiments*. SAE 2011 World Congress & Exhibition. https://doi.org/10.4271/2011-01-0652

Kyaw, K., & Jinming, Y. (2021). Numerical Analysis of the Turbulent Flow around DTMB 4381 Marine Propeller. *Scientific Research Journal*, *9*, 19–22. https://doi.org/10.31364/SCIRJ/v9.i03.2021.P0321846

Lopez Mejia, O., Escobar, J., & Perez, A. (2017). *Computational Study of the Wake of a Quadcopter Propeller in Hover*. https://doi.org/10.2514/6.2017-3961

Miller, C. J., & Sullivan, J. P. (1985, January 1). *Noise constraints effecting optimal propeller designs*. Soc. of Automotive Engr. Gen. Aviation Aircraft Meeting and Exposition, Wichita, KS. https://ntrs.nasa.gov/citations/19850011613

Sedelnikov, A., Kurkin, E., Quijada-Pioquinto, J. G., Lukyanov, O., Nazarov, D., Chertykovtseva, V., Kurkina, E., & Hoang, V. H. (2024). Algorithm for Propeller Optimization Based on Differential Evolution. *Computation*, *12*(3), Article 3. https://doi.org/10.3390/computation12030052

Process Optimization of Polymer Melt Impregnation Systems by Extrusion Method

Mehmet Usta[a], Aliihsan Koca[a], Mustafa Doğu[b]

[a]Istanbul Technical University, Mechanical Engineering Department, Heat - Fluid Program, Turkey
[b]Mir Innovation And Technology Center, Turkey
ustam16@itu.edu.tr

Keywords: CFD, Composite, Extrusion, Impregnation, Polymer.

Aim

The primary objective of this study is to optimize the polymer melt impregnation process through a combination of experimental and numerical methods. Specifically, the research aims to: Investigate the effects of key extrusion parameters—including temperature, pressure, and screw speed—on impregnation efficiency. Validate experimental results with Computational Fluid Dynamics (CFD) simulations to gain insights into the flow dynamics and polymer-fiber interactions within the extruder. Determine the impregnation ratio of the composite using high-resolution microscopy images processed with ImageJ, thereby establishing a direct correlation between processing conditions and impregnation quality. Provide comprehensive guidelines for optimizing polymer-based composite production for enhanced industrial applications.

Materials and Methods

This study employs a variety of polymer matrices, including polypropylene (PP), polyethylene terephthalate (PET), and polyamide (PA), which are widely used in composite manufacturing due to their versatile properties. Polypropylene (PP) is a thermoplastic polymer known for its chemical resistance, low density, and cost-effectiveness, commonly used in automotive parts and packaging. Polyethylene terephthalate (PET) is recognized for its strength, dimensional stability, and moisture resistance, making it ideal for textiles, packaging, and engineering components. Polyamide (PA), or nylon, offers high mechanical strength, temperature resistance, and abrasion resistance, commonly used in automotive, aerospace, and electrical industries.

To enhance the mechanical properties, reinforcing fibers such as glass fibers and carbon fibers are incorporated into the composite material. Glass fibers provide significant improvements in tensile strength, impact resistance, and durability. They are cost-effective and widely used in various applications, from construction to automotive parts. Carbon fibers are included for their exceptional strength-to-weight ratio, high stiffness, and fatigue resistance. These fibers are ideal for high-performance, lightweight structures in industries such as aerospace and automotive. Carbon fibers also offer superior thermal conductivity, chemical resistance, and dimensional stability, further enhancing the properties of the composites.

The combination of these polymers and reinforcing fibers results in composite materials with a balanced mix of mechanical, thermal, and chemical properties, making them suitable for a range of demanding applications. The selection of these materials allows for optimizing composite performance for specific uses.

Figure 1. Experimental Setup.

In the continuous fiber-reinforced filament production line, the equipment is arranged in the following sequence: creel, spreading system, extruder, impregnation die, cooling system, and puller. In the process, carbon fibers are unwound from the creel system and passed through the spreading system. The spread fibers are then guided into the impregnation die, where they are combined with molten polymer. The process uses a Gülnar-brand single-screw extruder with a screw diameter of 16 mm, an L/D ratio of 30, and a production capacity ranging from 0.1 to 1 kg/hour. After being coated with polymer in the impregnation die, the fibers exit the die in cylindrical form and pass through an air-cooling system. The movement of the filaments along the production line is ensured by the puller unit.

The polymer melt impregnation process is performed using a single-screw extrusion system. In this system, the polymer melt and fibers are combined under controlled conditions. Various extrusion die profiles, heating zone configurations, and screw speed settings are investigated to assess their impact on impregnation efficiency. The study also examines the role of shear forces and residence time inherent to single-screw systems, as these factors critically affect fiber wetting and dispersion.

To quantitatively evaluate the impregnation quality, high-resolution optical microscope images were captured at magnifications of 2x, 3x, 5x, and 10x. In addition, Scanning Electron Microscope (SEM) images were obtained at higher magnifications of 144x, 800x, and 5000x to enable more detailed microstructural characterization. These images reveal the distribution and penetration of the polymer within the fiber bundles. All captured images were analyzed using the ImageJ software, which allowed for the calculation of the impregnation ratio—i.e., the percentage of the fiber surface that is effectively wetted by the polymer matrix. This combined optical and electron microscopic evaluation provides a comprehensive insight into the microstructural quality of the composite and facilitates a direct correlation between processing parameters and impregnation outcomes.

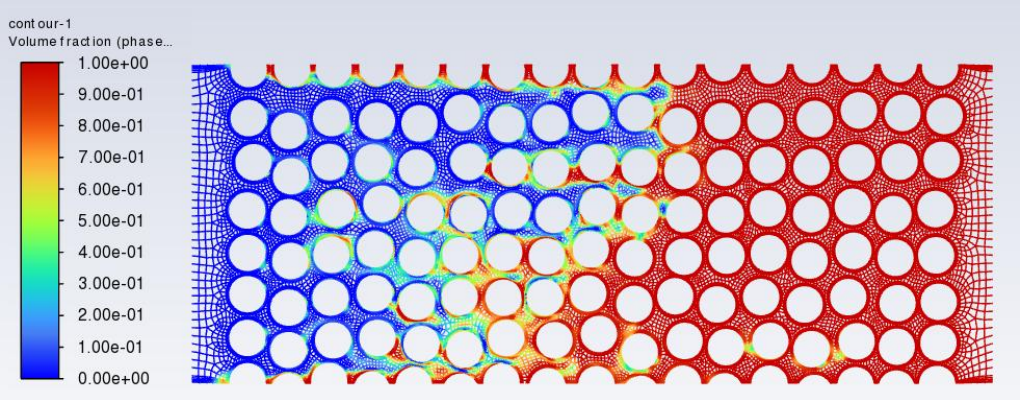

Figure 2. 2D CFRP Analys.

The figure shows the volume fraction contour of a 2D carbon fiber-reinforced polymer (CFRP) cross-section subjected to a pressure of 90 kPa for 10 seconds. The distribution of fiber content within the matrix is visualized, illustrating the impregnation efficiency under these process conditions.

CFD simulations were employed to model the complex interactions between the polymer melt and reinforcing fibers during the extrusion process. The simulations focused on predicting the flow dynamics, temperature distribution, and the effect of shear forces on fiber impregnation. As illustrated in Figure 2, a two-dimensional cross-sectional model of a die for PA6 (polyamide 6) was constructed to analyze the flow behavior of the polymer melt among circular fiber bundles. Under conditions of 90 kPa pressure and 220°C temperature, the polymer was simulated to flow between the fiber tows, aiming to achieve effective impregnation of the fiber bundle.

Figure 2 shows the volume fraction contours of the polymer phase within the fiber architecture. The color gradient—from blue (0% volume fraction) to red (100% volume fraction)—illustrates the progression of polymer penetration across the fiber domain. The blue region on the left indicates the inlet where the polymer begins to infiltrate, while the red region on the right shows areas where the polymer has fully impregnated the fiber bundle. This visual clearly demonstrates how polymer flow develops spatially and highlights regions of incomplete impregnation, which is crucial for evaluating processing effectiveness. These numerical results were then compared with experimental data—including the impregnation ratios determined from microscopy—to validate the process and identify the optimal processing conditions.

Findings

The CFD simulations provided valuable insights into the flow behavior within the extruder. The numerical models accurately predicted the distribution of the polymer around the fibers, confirming that an optimal range of extrusion parameters leads to improved impregnation efficiency. The analysis identified that maintaining an extrusion temperature in the range of 220–260°C, along with an appropriate combination of screw speed and pressure, maximizes fiber impregnation. These simulation results were in close agreement with the experimental observations, thereby confirming the reliability of the numerical model.

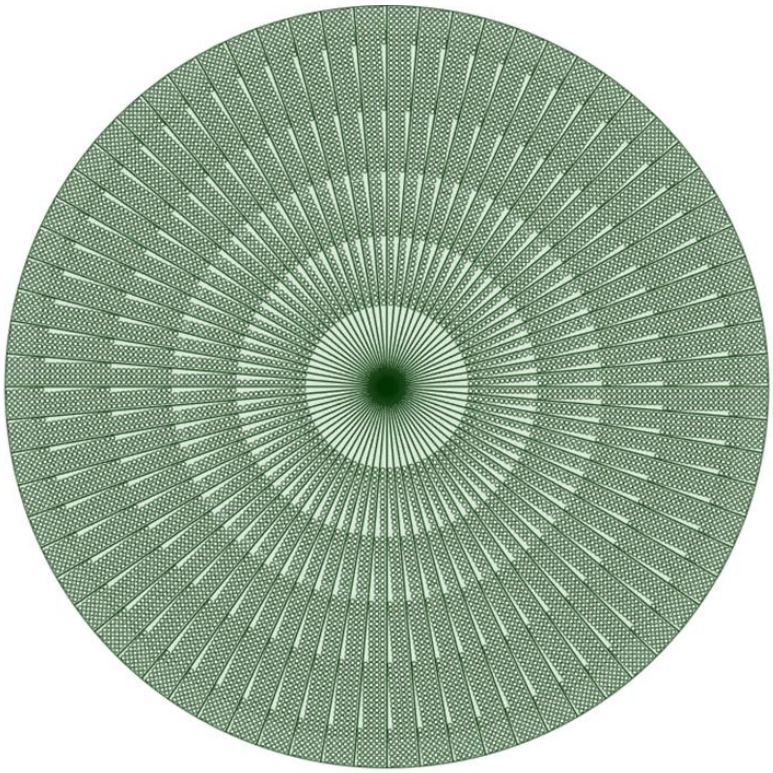

Figure 3. Fiber Bundle "Illustration of a fiber bundle containing 12,000 fibers, each with a diameter of 7 micrometers."

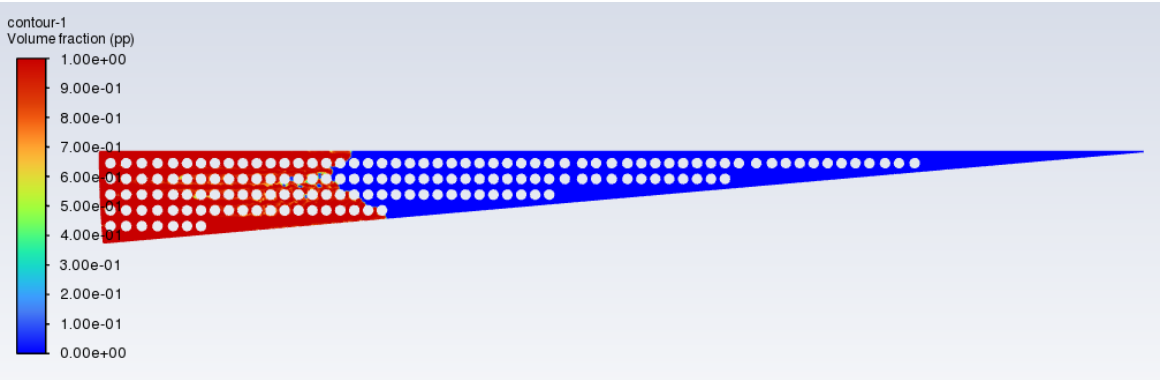

Figure 4. 5-degree circular fiber bundle ''5-degree circular fiber bundle and corresponding volume fraction contour."

The CFD simulations offered valuable insights into the flow behavior and impregnation dynamics within the extrusion die. Figure 3 illustrates a full fiber bundle consisting of 12,000 individual fibers, each with a diameter of 7 µm. This bundle was subjected to impregnation under conditions of 90 kPa pressure and 220°C temperature for 10 seconds. Due to the complexity and size of the model, the entire circular fiber bundle was divided into 72 equal sectors, each representing a 5-degree slice, to enable a more manageable simulation. As shown in Figure 4, a 5-degree segment of the circular bundle was modeled, where the polypropylene polymer enters from the arc boundary and advances between the fibers toward the center. The contour visualization of the volume fraction reveals how effectively the polymer permeates through the fiber matrix along the radial direction.

Additionally, earlier CFD results (as seen in the first image) highlight the interaction of polymer flow with the fibrous structure in a 2D planar section. The red-to-blue gradient in the volume fraction contour clearly indicates the progressive infiltration of the polymer, supporting the assessment of impregnation efficiency. The tapered

domain in the second image demonstrates how fiber spacing and orientation influence flow uniformity and impregnation performance under extrusion-driven conditions.

Overall, the simulations confirmed that an optimal range of processing parameters—particularly maintaining the extrusion temperature between 220°C and 260°C, combined with controlled pressure and screw speed—enhances the impregnation quality. These results closely align with experimental observations, validating the accuracy and reliability of the numerical model for predicting fiber–polymer interactions in industrial-scale manufacturing setups.

Table 1. Mesh Independence Analysis.

MESH INDEPENDENCE ANALYS			
	MESH1	MESH2	MESH3
EDGE SIZING(M)	0,0000003	0,0000002	0,0000004
ELEMENT SIZING(M)	0,0000005	0,0000004	0,0000006
METHOD	ALL TRIANGLE	ALL TRIANGLE	ALL TRIANGLE
NODES	66694	112510	44677
ELEMENTS	119519	204607	78782
VOLUME FRACTİON	0,42	0,42	0,40

Mesh independence analysis is a validation step performed in finite element (FEM) or computational fluid dynamics (CFD) simulations to ensure that the results are not dependent on the mesh density. In this analysis, the variation of the solution is examined as the number of elements (mesh quality) increases. If the results no longer change significantly beyond a certain mesh density, the solution is considered mesh-independent. However, if the results continue to vary, a finer mesh or a different meshing method may be required. In the graphical representation, the X-axis represents the mesh number, while the Y-axis shows the simulation result (e.g., volume fraction). As the mesh number increases and the results stabilize, it indicates that an appropriate mesh density has been achieved.

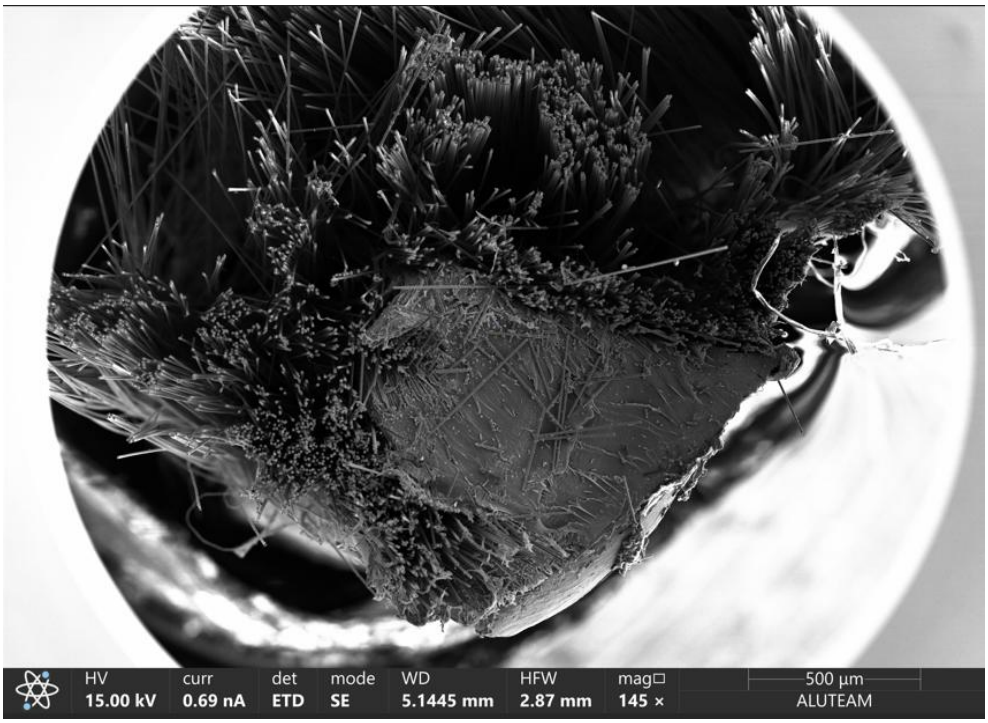

Figure 5. Section 1 fiber bundle SEM images 145X.

The high-resolution microscope images—captured at magnifications of 2x, 3x, 5x, and 10x and SEM images taken at 144x, 800x, and 5000x, were analyzed using ImageJ to quantitatively evaluate the impregnation quality of the composites. This multi-scale imaging approach enabled the visualization of polymer distribution and penetration into the fiber bundles with exceptional detail. The analysis revealed that samples processed under optimized conditions exhibited significantly higher impregnation ratios, reflecting more effective wetting of the fiber surfaces by the polymer matrix. These observations were further supported by the microstructural evidence from SEM, which highlighted improved polymer-fiber interface integrity. The enhanced impregnation quality directly correlates with the observed improvements in both mechanical and thermal properties, emphasizing the importance of precise process control in composite manufacturing.

Conclusion

Table 2. Impregnation Ratios and Fiber Counts for Three Different Cross-Sections.

Parameter	Unit	Section 1	Section 2	Section 3
High-Density Region	count / 10,000 μm²	100	60	120
Medium-Density Region	count / 10,000 μm²	87	40	100
Low-Density Region	count / 10,000 μm²	74	30	73
Average Fiber Count	count / 10,000 μm²	87.00	43.33	97.67
Total Area (via ImageJ)	μm²	1,432,955.67	2,912,031.39	1,325,414.93
Total Area (via Equivalent Radius R)	μm²	1,431,938.25	2,896,404.48	1,327,833.00
Calculated Total Fiber Count	count	12,467	12,619	12,945
Impregnated Area (via ImageJ)	μm²	340,216.34	1,187,561.72	691,207.54
Impregnation Ratio	-	0.24	0.41	0.52
Number of Impregnated Fibers	count	2,960	5,146	6,751

Table 3. Impregnation Rate and Number of Impregnated Fibers for General Average.

General Average	Value
Average Impregnation Rate	0.39
Average Number of Impregnated Fibers	4,952

This study successfully integrates experimental analysis and CFD simulations to optimize the polymer melt impregnation process in single-screw extrusion-based composite manufacturing. The findings demonstrate that precise control of processing parameters significantly enhances the mechanical and thermal properties of the final composite materials. In particular, the integration of high-resolution microscopy analysis to determine the impregnation ratio offers a robust method for evaluating and correlating the microstructural quality with processing conditions.

Additionally, experimental results obtained from three separate fiber bundle cross-sections, with 46 measurements in total (as shown in Figure 5, magnifications of 144x), revealed that the impregnation ratio, calculated using the ImageJ software as the ratio of the impregnated area to the total area, yielded an average experimental impregnation rate of 0.39. It was also observed that, out of 12,000 fibers, 4,952 were impregnated, as shown in Tables 2 and 3. Furthermore, the impregnation ratio calculated for the 5° fiber bundle in Figure 4, based on the same method using ImageJ, was found to be 0.42. This result, in combination with the experimental findings, indicates a strong correlation between the experimental and simulation-based impregnation rates (0.39-0.42), demonstrating the reliability of the simulations.

Future research should focus on extending these methods to more complex fiber architectures and alternative polymer matrices, potentially incorporating artificial intelligence for further process optimization. Overall, this study provides valuable insights that can drive the development of high-performance, efficient, and reliable composite manufacturing processes for industrial applications.

References

A. Tamayol, M. Bahrami (2010) "Parallel Flow Through Ordered Fibers: An Analytical Approach " Mechatronic Systems Engineering, School of Engineering Science, Simon Fraser University, BC, V3T0A3, Canada

Ali Tamayol and Majid Bahrami (2010) "Transverse Permeability Of Fibrous Porous Media " Proceedings of the 3rd International Conference on Porous Media and its Applications in Science and Engineering

B. R. Gebart (1992) "Permeability Of Unidirectional Reinforcements For Rtm " Journal of Composite Materials

C. Y. Wang (1996) "Stokes Flow Through An Array Of Rectangular Fibers " Int. J. Multiphase Flow Vol. 22, No. I, pp. 185-194,

Cahyo Budiyantoro, Heru S.B. Rochardjo and Gesang Nugroho (2020) "Effects Of Processing Variables Of Extrusion–Pultrusion Method On The Impregnation Quality Of Thermoplastic Composite Filaments" Polymers

Derek B. Ingham and Iaon Pop (1998) "Transport Phenomena In Porous Media "

Dipen Kumar Rajak , Durgesh D. Pagar , Pradeep L. Menezes and Emanoil Linul (2019) "Fiber-Reinforced Polymer Composites: Manufacturing, Properties, and Applications" Polymers

Fuji Wang, Gongshuo Wang, Hongquan Wang, Rao Fu, Yajing Lei, Jianing He (2023) "3d Printing Technology For Short-Continuous Carbon Fiber Synchronous Reinforced Thermoplastic Composites: A Comparison Between Towpreg Extrusion And In Situ Impregnation Processes" Chinese Journal of Mechanical Engineering: Additive Manufacturing Frontiers 2

James Garofalo , Daniel Walczyk (2021) "In Situ Impregnation Of Continuous Thermoplastic Composite Prepreg For Additive Manufacturing And Automated Fiber Placement " Composites Part A

Julia Studer, Clemens Dransfeld, Jon Jauregui Cano, Andre Keller, Marianne Wink, Kunal Masania, Bodo Fiedler (2019) "Effect Of Fabric Architecture, Compaction And Permeability On Through Thickness Thermoplastic Melt Impregnation" Composites Part A

P. Nygard and CG. Gustafson (2000) "Continuous Glass Fiber - Polypropylene Composites Made By Melt Impregnation'' Department of Machine Design and Materials Technology Norwegian University of Science and Technology Trondheim, Norway

P.J. Batesa, J. Kendall, D. Taylor, M. Cunninghamb (2002) "Pressure Build-Up During Melt Impregnation " Composites Science and Technology 62 379–384

R . Byron Bird, Charles F Curtiss, Robert C Armstrong, Ole Hasager (1987) "Dynamics of Polymeric Liquids"

R. Byron Bird, Warren E. Stewart, Edwin N. Lightfoot (2007) "Transport Phenomena Polymers "

R. J. Gaymans and E. Wevers (1997), Twente University of Technology, PO Box 277, 7500 AE Enschede, The Netherlands "Impregnation Of A Glass Fibre Roving With A Polypropylene Melt In A Pin Assisted Process "

R. Marissen , L. Th. van der Drift, J. Sterk (2000) "Technology For Rapid Impregnation Of Fibre Bundles With A Molten Thermoplastic Polymer " Composites Science and Technology 60

Ran Tian (2022) "Design And Evaluation Of A Continuous Fibre Reinforced Thermoplastic Prepreg Manufacturing Line " Ottawa-Carleton Institute For Mechanical And Aerospace Engineering University Of Ottawa

Sana Koubaa, Steven Le Corre and Christian Burtin (2013) "Thermoplastic Pultrusion Process: Modeling And Optimal Conditions For Fibers Impregnation" Journal of Reinforced Plasticsand Composites

Son Ich Ngo , Young-Il Lim, Moon-Heui Hahn , Jaeho Jung (2018) "Prediction Of Degree Of Impregnation In Thermoplastic Unidirectional Carbon Fiber Prepreg By Multi-Scale Computational Fluid Dynamics" Chemical Engineering Science 185 64–75

Willem Van De Steene, Jan Verstockt, Joris Degrieck, Kim Ragaert , Ludwig Cardon (2018)"An Evaluation Of Three Different Techniques For Melt Impregnation Of Glass Fiber Bundles With Polyamide 12" Polymer Engineering And Science

Yasuhiko Murata, Ryunosuke Machiya and Takuma Komori (2020) "Influence Of Processing Conditions On The Generation Of Surface Defects In A Heat-And-Cool Hybrid Injection Molding Technique For Carbon Fiber-Reinforced Thermoplastic Sheets And Development Of A Suitable Mold Heated By Far-Infrared Radiation" Polymers

Investigation of Thermal-Flow Performance in Close Circuit Cooling Towers

Efe Gürle[a], Tahsin Engin[a]

[a]Istanbul Technical University, Department of Mechanical Engineering, MSc in Heat - Fluid Program, Turkey
gurle17@itu.edu.tr

Keywords: Closed Circuit Cooling Tower, Computational Fluid Dynamics (CFD), Heat and Mass Transfer, Multiphase Analysis, Staggered Tube Arrangement.

Aim

In this study, a two-dimensional Computational Fluid Dynamics (CFD) model has been developed to understand the counterflow air-water interaction in a closed-loop cooling tower of the packaged type. During the modeling process, a multiphase flow method and the SST k-ω turbulence model were integrated. Additionally, the shear force term and water evaporation were incorporated to determine the circular distribution of the falling film flow and specific humidity fields.

This study analyzes thermal parameters such as flow behavior, specific humidity, water and air temperatures, air velocity, heat transfer coefficient, saturation temperature, and mass transfer rate in a staggered tube arrangement. Simulation results showed that mass transfer rate increased with higher air velocity, which indicates improved performance. Also revealed that the heat transfer coefficient on the spray side exhibits an exponential increase with rising air velocity. However, results indicates that the heat transfer between the water film and the outer tube surface is not adequately captured in the 2D model. A 3D design is necessary to reveal regions where the water does not always contact the tube surface.

The main aim of this study is to investigate a two-dimensional Computational Fluid Dynamics (CFD) model to better understand the counter-current air-water interaction and thermal behavior in a packaged-type closed-circuit cooling tower (CCCT). The objectives of the study include investigating the key parameters such as flow behavior, specific humidity, water and air temperature, air velocity, heat transfer coefficient, saturation temperature and evaporation rate. Additionally, the study integrates the Mixture multiphase method and SST k-ω turbulence model to simulate the air-water interface and counter-current flow across the staggered tube bundle using Fluent software. The CFD results are validated by comparing the heat transfer coefficient between the water film and the outer surface with experimental data. Ultimately, this research aims to provide a deeper understanding of the complex mechanisms governing heat and mass transfer in CCCTs and to contribute to the optimization of cooling tower design and operational parameters.

Material and Method

A two-dimensional CFD model was developed using the mixture multiphase method combined with the Shear Stress Transport (SST) k-ω turbulence model to simulate counter-current air-water interactions in a closed-circuit cooling tower. The computational domain was discretized using a fully structured quadrilateral mesh containing over 50,000 elements to ensure high-resolution accuracy in capturing flow and heat transfer behavior, as shown in Figure 1. Only the last row of coils was considered with water directed toward the center of the pipe to achieve a uniform film distribution and observe the evaporation dynamics.

Simulations were performed using ANSYS Fluent, incorporating additional physics such as water vapor diffusion and advection to capture humidification and heat-mass transfer more effectively. To enable evaporation below the saturation temperature, a UDF was written and integrated into the Evaporation - condensation Lee model responsible for mass transfer. An explicit formulation was used with a volume fraction cutoff value of 1e-6. Since the dispersed model tends to overpredict the evaporation rate compared to practical observations, the interface modeling was set to Sharp/Dispersed and the drag coefficient model that provided the best convergence was the Symmetric model.

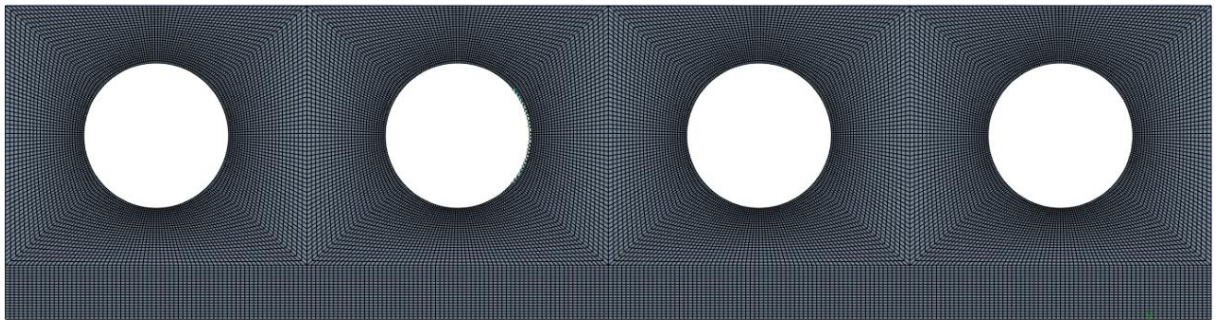

Figure 1. The mesh structure of computational domain generated by Ansys Fluent**.**

Surface tension force modeling was based on the Continuum Surface Force (CSF) approach, with wall adhesion set at 90°. The slip velocity was modeled using the Manninen et al. approach. For pressure-velocity coupling, the Coupled method was employed. Boundary conditions included varying air velocities of 0.01 m/s, 0.5 m/s, 1 m/s, 1.5 m/s, with a constant water inlet velocity of 1 m/s. The process air conditions and initial temperatures were set according to experimental measurements.

To support the numerical approach, an experimental study was conducted using a CCCT equipped with 10 rows of staggered serpentine tubes under real atmospheric conditions. During testing, inlet and outlet air temperatures were recorded to evaluate the cooling performance of the system. The heat transfer coefficient between the falling water film and the outer tube surface was determined using empirical correlations and resistance-based calculations. These experimentally obtained values were then used to validate the CFD model by comparing the numerical results with measured data, ensuring that the simulation accurately captured the air-water interaction and coupled heat-mass transfer processes within the cooling tower.

Findings

A mesh independence study was conducted with models between 50,000 to 100,000 elements, and the resulting outlet specific humidity showed variations within a ±10% error margin, confirming the reliability of the mesh, as shown in Figure 2.

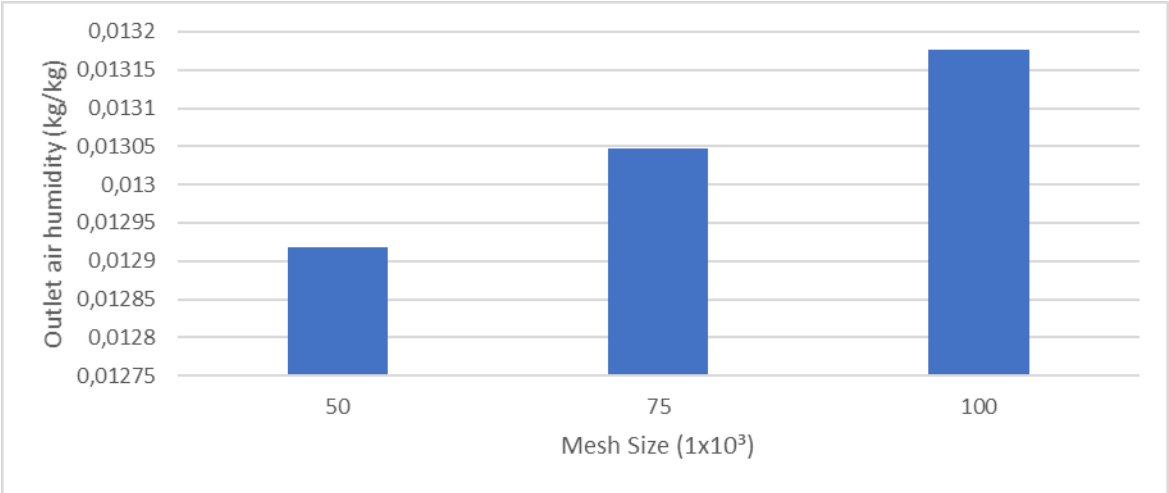

Figure 2. The mean value of outlet air humidifies under three quadrilateral mesh sizes.

The air velocity varied from 0 to 1.5 m/s in the widest section of the tower and increased in narrower sections due to contraction effects. As the air velocity increased, the water film began to thin at the bottom of the tube. Similarly, as the air velocity increases, the spray film heat transfer coefficient, outlet air specific humidity and mean mass transfer rate also increase. These trends are presented in Figure 3.

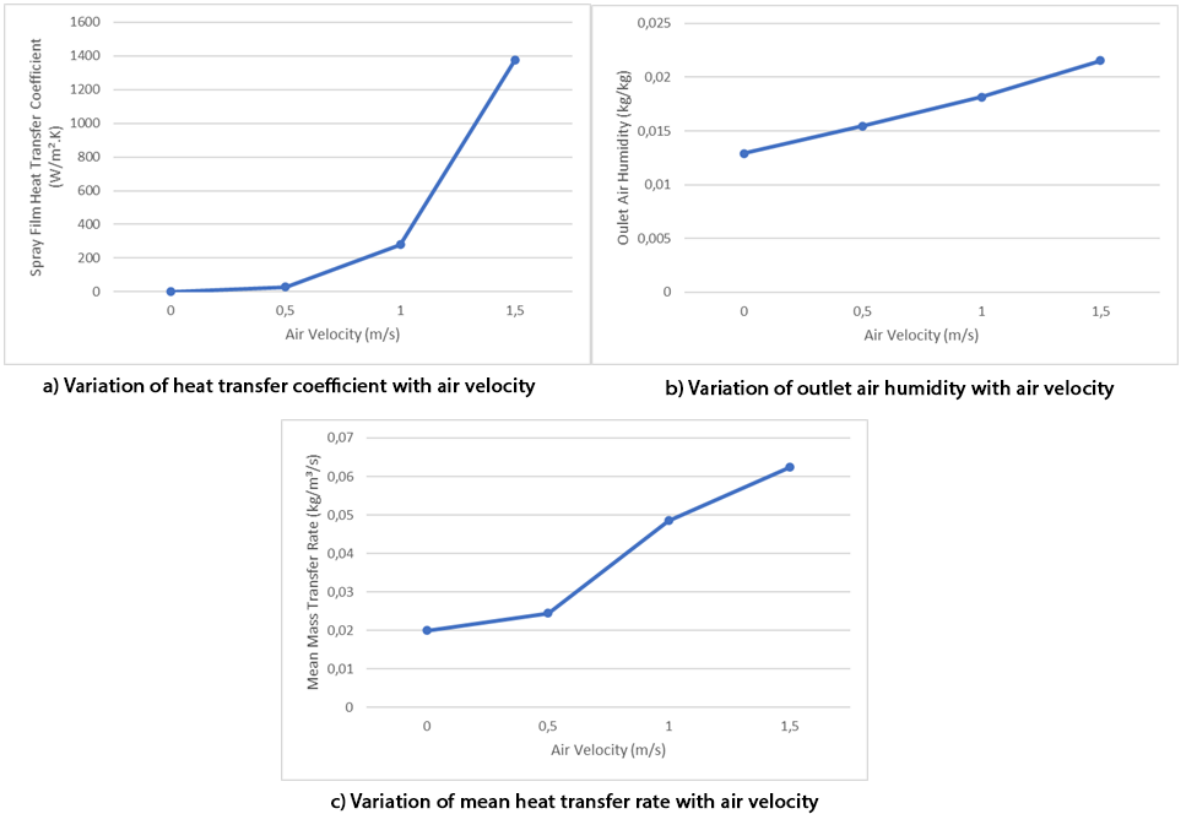

Figure 3. Variation of Different Parameters with Air Velocity: (a) Heat Transfer Coefficient, (b) Outlet Air Humidity, (c) Mean Heat Transfer Rate.

At an air velocity of 1.5 m/s, the specific humidity obtained from the simulation was 0.021 kg/kg, whereas the experimental value was 0.019 kg/kg, indicating that the simulation result is approximately 10% higher. The contours of temperature, specific humidity, and mass transfer rate with respect to air velocity are presented in Figure 4.

In terms of experimental data, the dry and wet bulb temperatures of inlet air were recorded as 29.02°C and 19.73°C, respectively. The process water entered the tower at 34.88°C and was cooled to 25.90°C at the outlet. Data were averaged over one hour under steady-state conditions to ensure accuracy. The range and approach values were calculated as 6.97°C and 6.17°C, respectively, as shown in Figure 5. Based on appropriate thermal resistance calculations, the spray heat transfer coefficient was determined to be 752.07 W/m²·K. The total evaporation loss observed in experiment was 0.8 m³/h. However, spray heat transfer coefficient was found to be around 1400 W/m²·K based on the simulation results.

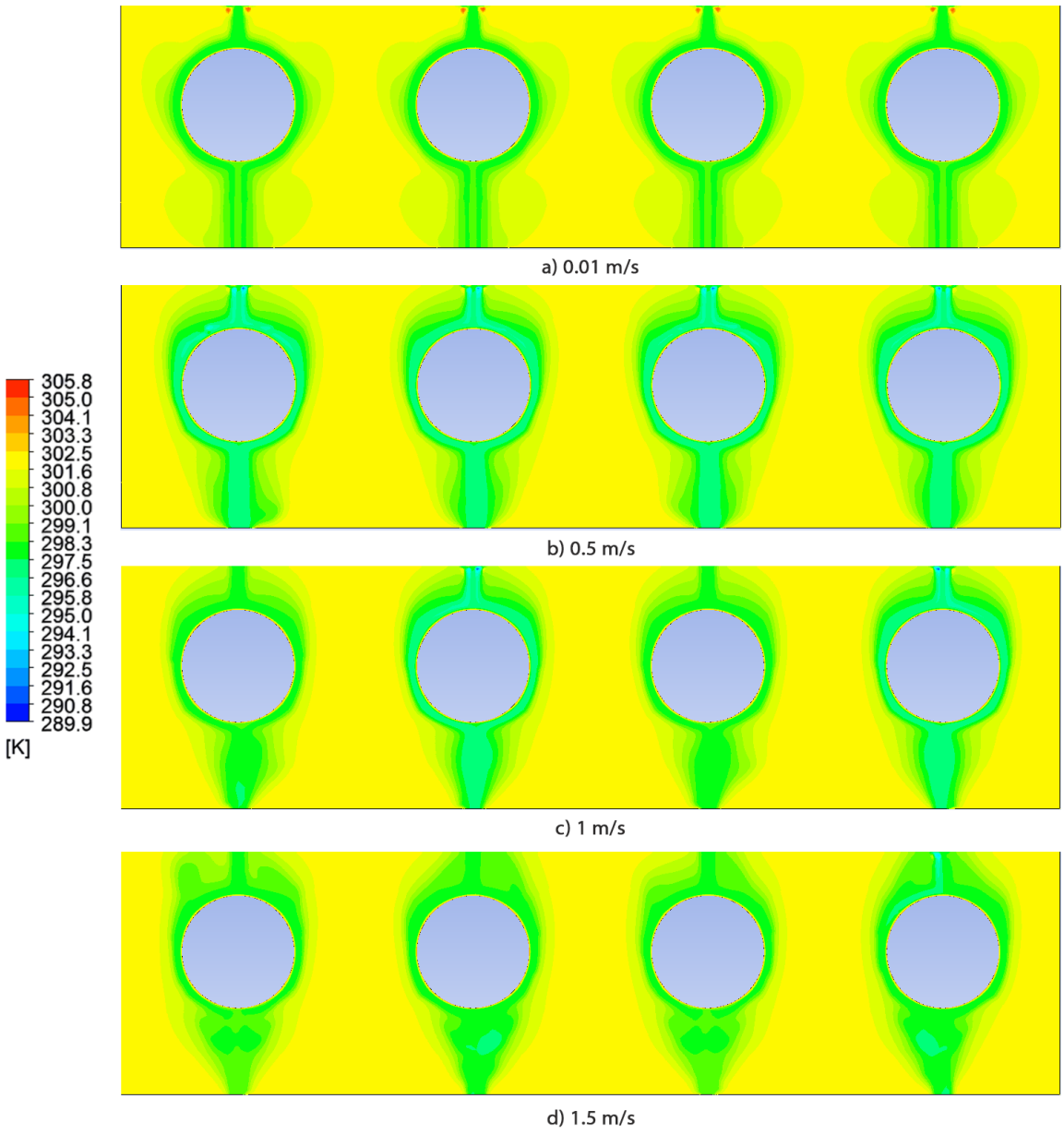

(1) Temperature contours around the serpentine tubes depending on the air velocity

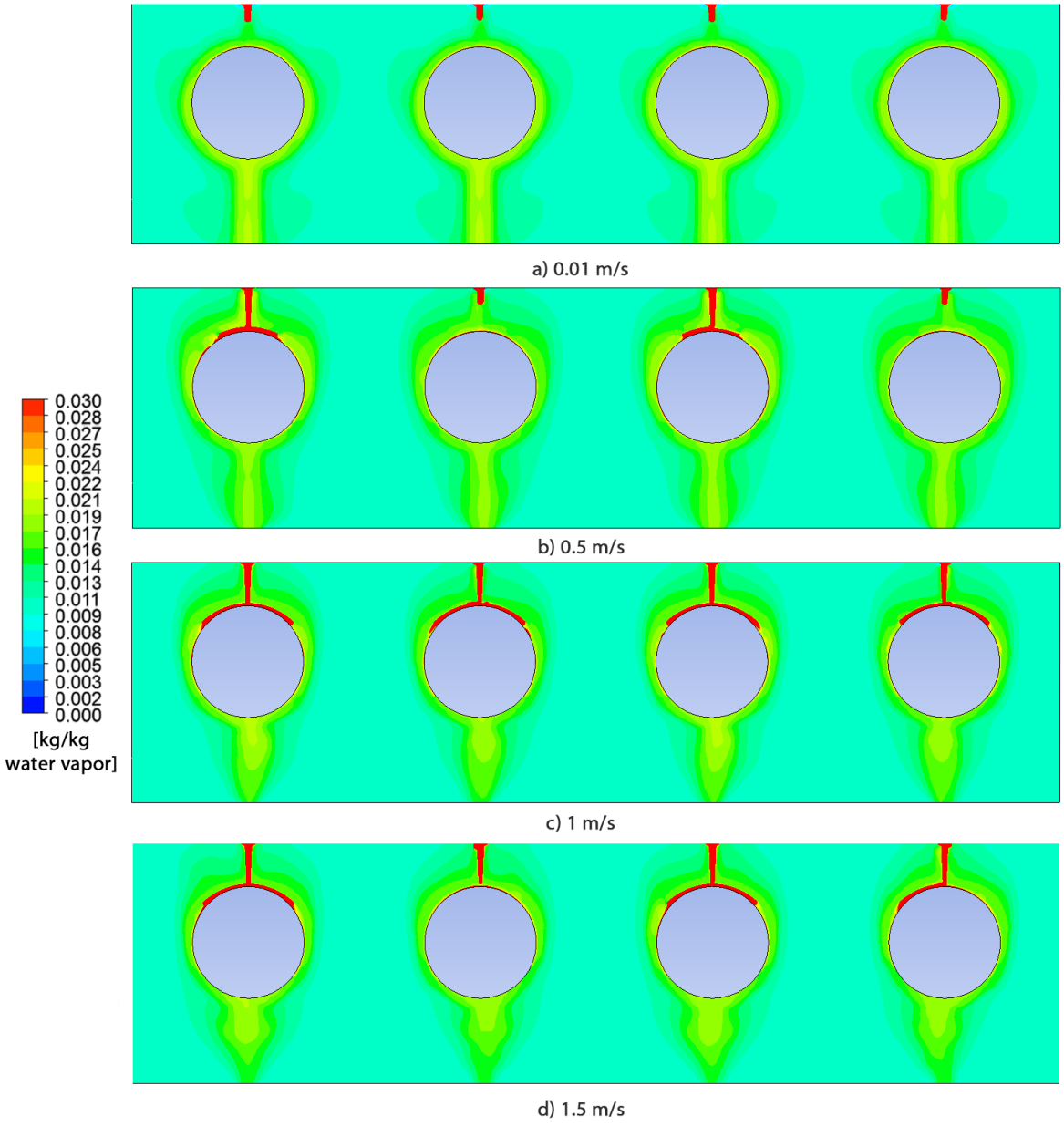

(2) Mass fraction of water vapor contours around the serpentine tubes depending on the air velocity

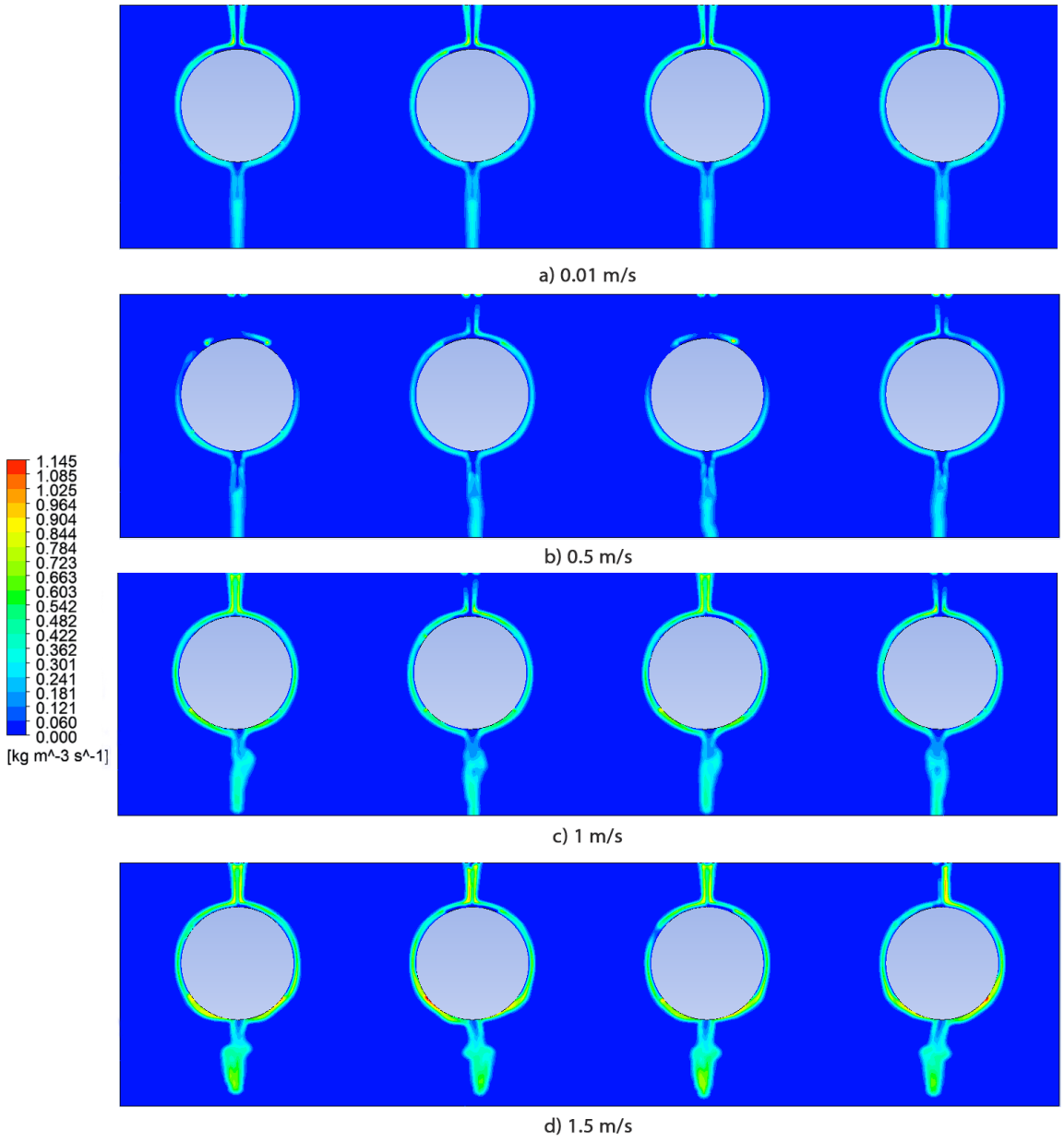

(3) Mass transfer rate contours around the serpentine tubes depending on the air velocity

Figure 4. Variation of different parameters around the serpentine tubes depending on the air velocity.

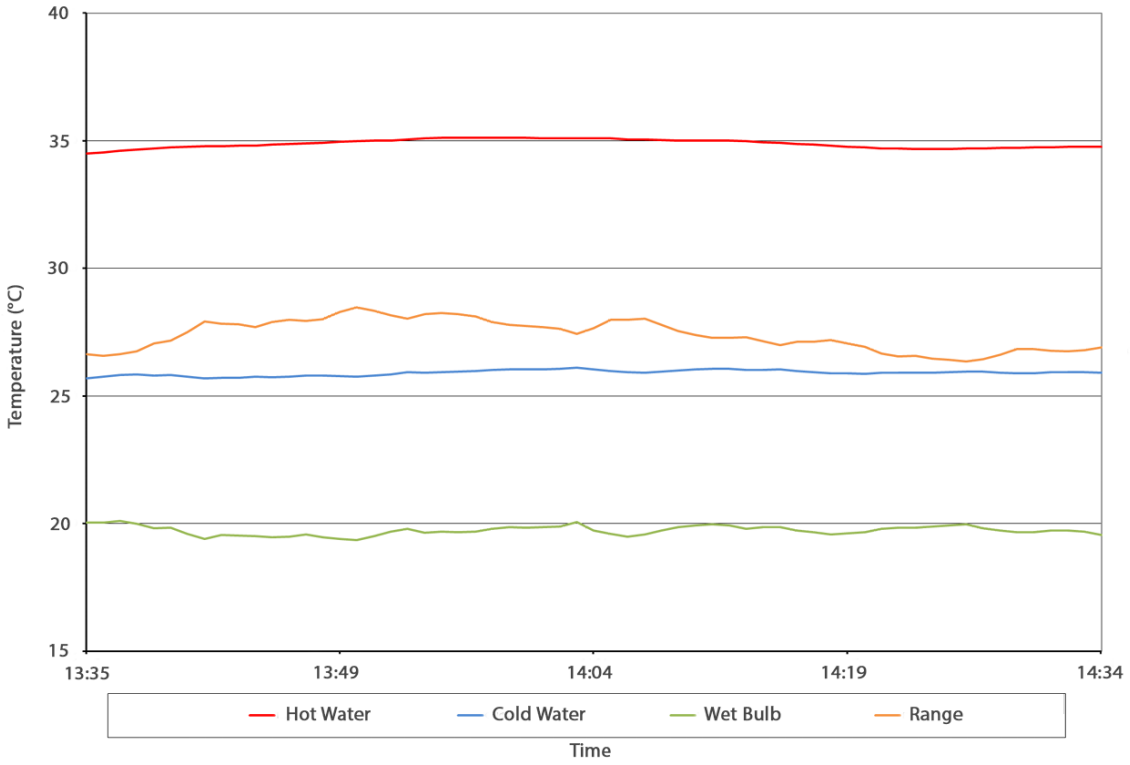

Figure 5. Variation of hot water, cold water, wet bulb temperature, and range over a 1-hour period in the cooling tower.

Conclusion

This study successfully developed a 2D CFD model employing the Mixture multiphase method and SST k-ω turbulence model to analyze counter-current air-water interaction in a closed-circuit cooling tower. Simulation results showed different agreement with experimental findings, with the heat transfer coefficient exhibiting an error margin of approximately +100%, which indicates that the heat transfer between the water film and the outer tube surface is not adequately captured in the 2D model. A 3D design is necessary to reveal regions where the water does not contact the tube surface. These non-wetted areas would reduce the local heat transfer coefficient, leading to a more realistic, non-uniform water film distribution, unlike the uniform assumption inherent in 2D simulations. Temperature contours of the spray water indicated progressive heating, and the simulated mass transfer rate increment aligned well with increasing air velocity. With dry and wet bulb inlet air temperatures recorded at 29.02°C and 19.73°C, and process water cooling from 34.88°C to 25.90°C, the system demonstrated a 6.97°C range and 6.17°C approach. Overall, this study provides valuable insights into heat and mass transfer mechanisms in CCCTs and offers practical guidance for understanding design and enhancing thermal performance in industrial cooling applications.

References

Xie, X., Liu, H., He, C., Zhang, B., Chen, Q., & Pan, M. (2019). Deciphering the heat and mass transfer behaviors of staggered tube bundles in a closed wet cooling tower using a 3-D VOF model. Applied Thermal Engineering, 161, 114202.
Url-1 https://doi.org/10.1016/j.applthermaleng.2019.114202
Xie, X., He, C., Xu, T., Zhang, B., Pan, M., & Chen, Q. (2017). Deciphering the thermal and hydraulic performances of closed wet cooling towers with plain, oval and longitudinal fin tubes. Applied Thermal Engineering, 120, 203–218.
Url-2 https://doi.org/10.1016/j.applthermaleng.2017.03.138

Qiu, Q., Jiang, W., Shen, S., Zhu, X., & Mu, X. (2015). Numerical investigation on characteristics of falling film in horizontal-tube falling film evaporator. Desalination and Water Treatment, 55(12), 3247–3252. **Url-3** https://doi.org/10.1080/19443994.2014.968907

Chen, J., Zhang, R., & Niu, R. (2015). Numerical simulation of horizontal tube bundle falling film flow pattern transformation. Renewable Energy, 73, 62–68.

Url-4 https://doi.org/10.1016/j.renene.2014.08.007

Wickert, D., & Prokop, G. (2021). Simulation of water evaporation under natural conditions—A state-of-the-art overview. Experimental and Computational Multiphase Flow, 3, 242–249.

Url-5 https://doi.org/10.1007/s42757-020-0071-5

Xie, X., He, C., Zhang, B., & Chen, Q. (2018). Heat transfer enhancement for the coil zone of closed wet cooling towers through field synergy analysis. In M. R. Eden, M. G. Ierapetritou, & G. P. Towler (Eds.), Computer Aided Chemical Engineering (Vol. 44, pp. 1927–1932). Elsevier.

Url-6 https://doi.org/10.1016/B978-0-444-64241-7.50316-5

Liu, H., Wu, Z., Zhang, B., Chen, Q., Pan, M., Ren, J., & He, C. (2023). A large-scale stochastic simulation-based thermodynamic optimization for the hybrid closed circuit cooling tower system with parallel computing. Energy, 283, 128434.

Url-7 https://doi.org/10.1016/j.energy.2023.128434

MECHANICAL ENGINEERING

Additive Manufacturing

Automotive

Computational Fluid Dynamics

Computational Solid Mechanics

Fluid Mechanics

Industrial Data Analytics

Machine Design

Machine Dynamics, Vibration, and Acoustic

System Dynamics and Control

A Novel Approach for Robust Identification and Characterization of Mechanical Shock Loads for Structural Durability Assessment

Doğukan Elibol[a], Mesut Kırca[a]

[a] Istanbul Technical University, Faculty of Mechanical Engineering, Solid Mechanics Programme, Türkiye
elibol16@itu.edu.tr

Keywords: Accelerated Structural Durability Tests , Acceleration Data Processing , Automotive Low Cycle Fatigue , Mechanical Shock Loads , Shock Load Extraction.

Aim

Advancements in mechanical engineering have improved structural durability by enabling lighter, stronger designs through innovations in computational analysis and fatigue prediction (Akbaba et al., 2022). Fatigue is classified into high-cycle fatigue (HCF) and low-cycle fatigue (LCF). HCF results from repeated small load cycles, while LCF occurs under higher stress amplitudes, leading to rapid failure (Chen et al., 2014; Jimenez, 2018).
Accurate load spectrum determination is critical, particularly for high-inertia automotive components like battery systems and fuel tanks, which experience mechanical shocks from sudden accelerations, potentially causing LCF failures (Prueter, 2021; Wang, 2023). Testing such components in electrodynamic shakers using real-world acceleration data is expensive and complex. Accelerated fatigue testing replicates long-term damage under controlled conditions, but precise load spectrum determination is essential to prevent overengineering or premature failures (Chen et al., 2014; Sisemore et al., 2017).
This study investigates the accelerated testing of vehicle structural components affected by impact-induced Road Load Data (RLD). Road conditions like potholes and speed bumps generate shock based loads, contributing to most of the total damage (Kubo, 2018). Examples of such roads are illustrated in Figure 1. Predicting these loads is essential for shaker tests. However, extracting them from RLD acceleration data is complex. Shock loads that are embedded within gaussian stationary signals, require isolation and transformation into simplified waveforms (half-sine, damped-sine) for efficient testing. This approach improves test acceleration, cost reduction, and practical implementation.

Figure 1. Shock induced roads.

Mechanical shock loads in the automotive industry exhibit both deterministic and stochastic characteristics depending on their source. Deterministic shocks occur under controlled conditions (Frajnković, 2018), while stochastic shocks occur from real-world irregularities (Manouchehry Nya, 2019; Billal, 2015; Zhou, 2023). These loads are transient, non-stationary and non-ergodic (Özga, 2023), which makes frequency-domain methods such as FFT, STFT, and PSD unsuitable (Abdullah, et al., 2009). Figure 2 shows randomly distributed shock profiles

from repeated measurements on the same vehicle, road, and maneuvers, showing the stochastic nature of mechanical shock loads.

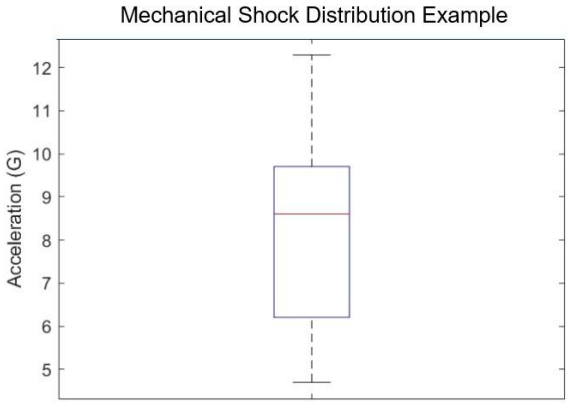

Figure 2. Mechanical shock distribution example.

Many studies fail to capture the stochastic, non-stationary nature of shock loads, particularly in vibration embedded signals (Rouillard, 2024). Time-domain methods typically apply a threshold, but they require case-specific adjustments and rather than transforming, they only crop the signal (Kırbaş, 2023). Statistical filtering techniques like moving crest factor, RMS, and kurtosis similarly lack sufficient simplification and require extensive tuning (Lepine, 2018). Shock Response Spectrum (SRS) is widely used but struggles with multiple shocks in a signal, lacks precise time and phase information, and can be overly conservative (Alexander, 2018). Rainflow based block load methods capture load distribution but not frequency and phase, making them suitable only for quasi-static conditions. (Halfpenny, 2006). Some advanced studies apply machine learning algorithms to detect mechanical shock loads (Gorges, 2019). While effective, these approaches add complexity, struggle with generalization, and increase computation time.

This study presents a data processing method for autonomously detecting mechanical shock loads in acceleration signals without separate tuning. It efficiently identifies LCF shock loads, determines impact timing, frequency, and waveforms, and supports multiple test conditions. Simplified signals enable easier implementation for electrodynamic shakers.

Material and Method

Structural products used in the automotive industry are mostly made of aluminum or steel materials (Trzepieciński, 2024). Validations were conducted on a steel specimen using finite element analysis for design verification. Table 1 presents its mechanical properties, and Figure 4 shows its visual representation. The specimen, subjected to inertial loads, was driven by RLD data with shock loads, and resulting stress values were analyzed. Transient dynamic analyses were performed in Abaqus and Ansys Mechanical. Original and processed RLD profiles were applied separately, and stress history was compared (Fig. 5). Fatigue analyses were conducted using nCode and Femfat. The proposed multi-step method was implemented using nCode and Matlab softwares.

Table 1. Specimen mechanical properties**.**

Material	Structural Steel
Thickness	4 mm
Weight	0.22 kg
Hanging Weight	5 kg
Bending Natural Frequency	42 Hz
Material Damping Ratio	2%

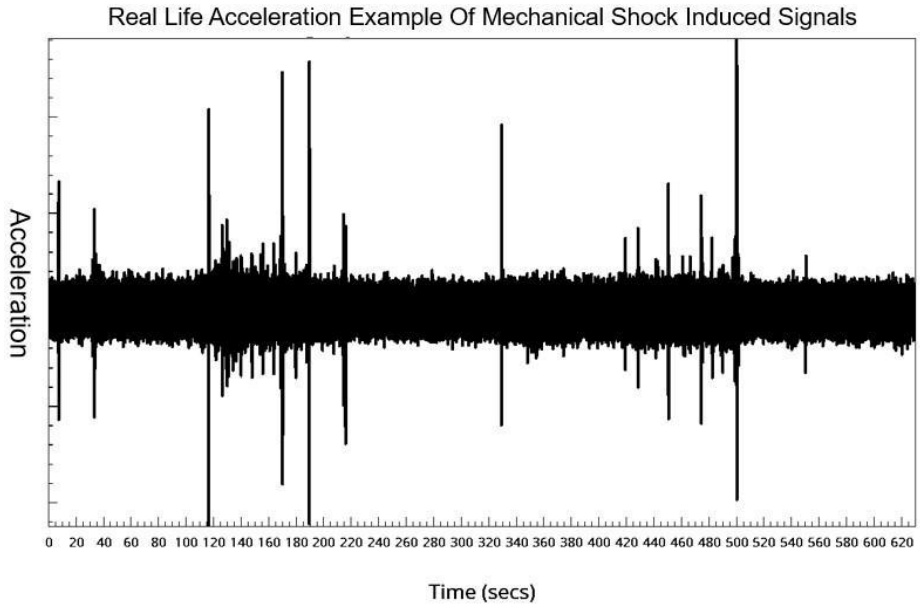

Figure 3. Acceleration measurement example.

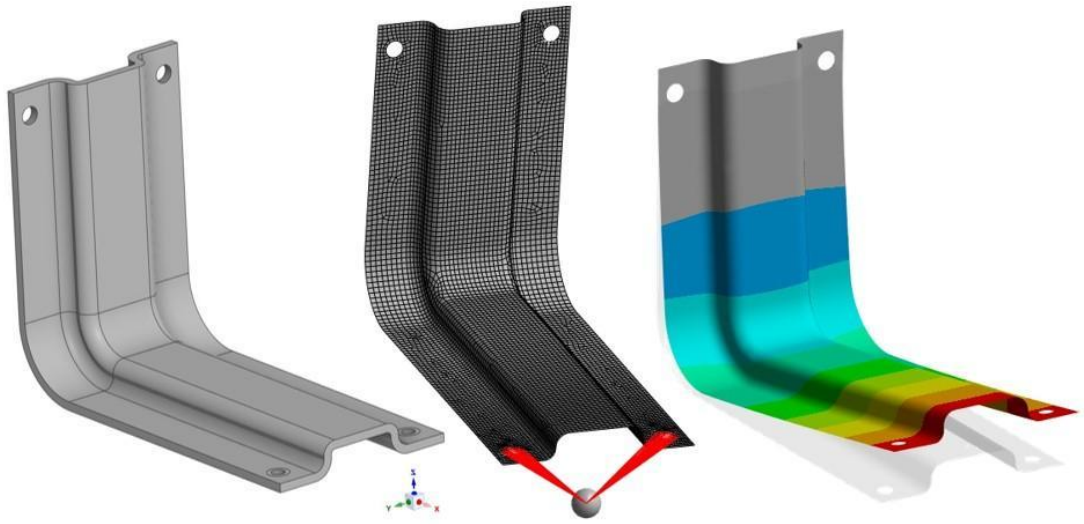

Figure 4. 3D & FE model of the specimen and the dominant mode shape.

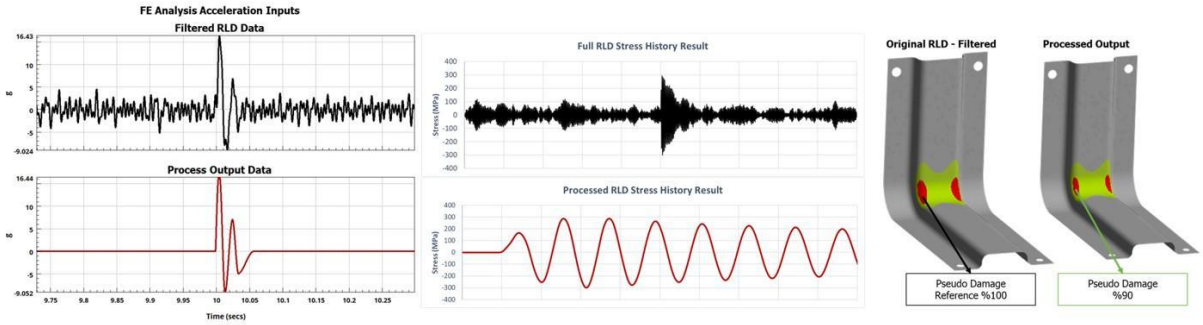

Figure 5. Stress history & fatigue damage comparison.

Used excitation loads are real acceleration data obtained from an actual automotive proving ground, including road profiles such as potholes and curb strikes (Fig.1). Additionally, synthetic road data, were generated. Synthetic road data was generated using a full-car dynamic model (Figure 6), a common approach in validation studies (Rouillard, 2024).

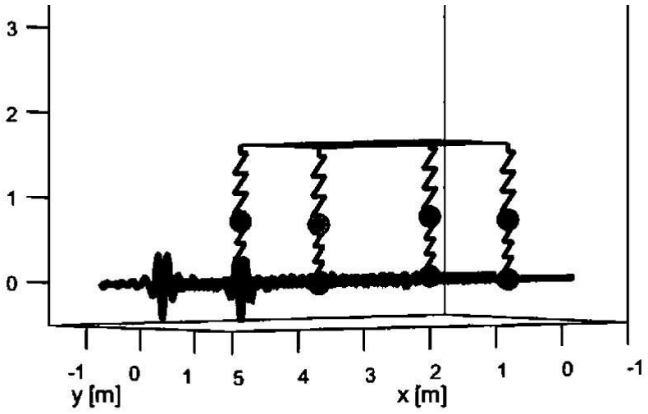

Figure 6. Full car model.

Figure 7 demonstrates the step-by-step process of the proposed method on a sample RLD. After collecting acceleration data, the first step is filtering and adjusting the sample rate to 2048 Hz for consistency. Filtering (2–250 Hz) removes noise, non-damaging loads, and unrealistic trends. The data is then segmented into 1-second transient windows and adjusted to oscillate around a zero mean (mean removal).

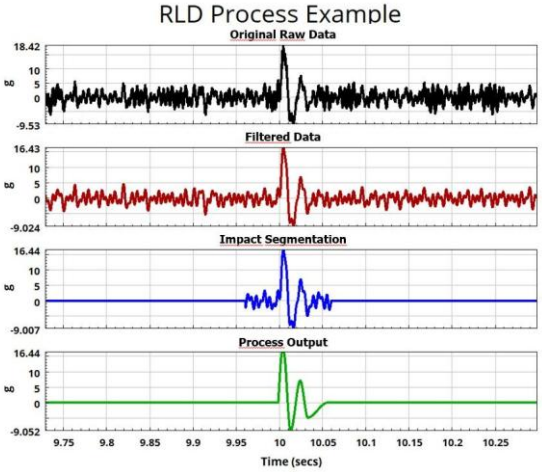

Figure 7. Proposed method's transformation example.

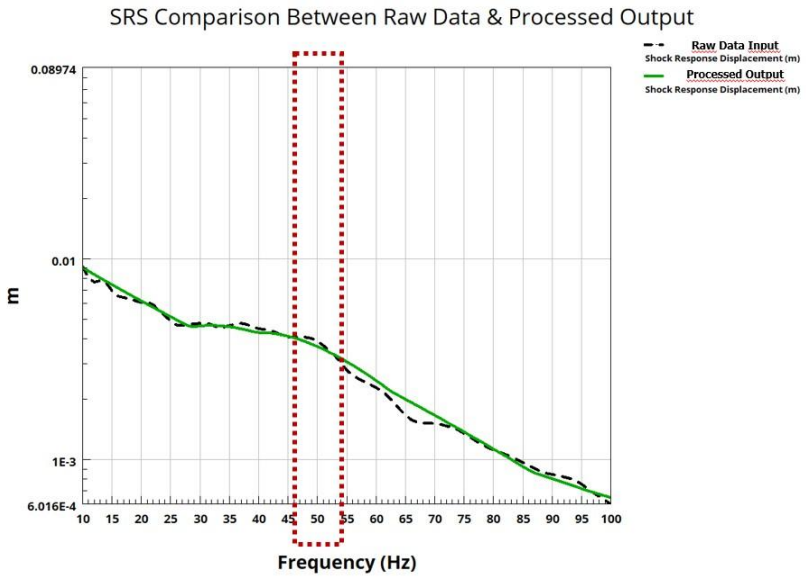

Figure 8. SRS comparison & validation.

The next step is the parametric identification of potential impact regions in the data. Repeated studies on both real and synthetic data have demonstrated that segments containing loads above 3.5 standard deviations correspond to impact events. All other windows are zeroed out, effectively isolating the segments where impacts are expected. Next, zero-crossing points of the first derivative are identified, retaining only these points to detect reversals. However, due to random loads at multiple frequencies, the data remains complex. To refine it, reversal points are further processed using statistical parameters in Table 2.

Table 2. Statistical parameters**.**

Ideal Sampling Rate	Min. 2048 Hz
Filtering Bandwidth	2-250 Hz
Mean Removal	Every 1024 Data Points
Impact Parameter	<3.5 Standard Deviation
Impact Period	Between 5-100 ms
Range Gate Factor	1.4
Width Factor	3
Allowable Width	Range/Width Factor
Allowable Range	Range/Range Factor
Waveform Factor	Peak/Valley Ratio

Reversal points closer than the minimum period are removed, reversal points farther apart than the maximum period are retained and points with a vector length shorter than the defined width parameter are eliminated, while longer ones are kept.

During this process, backward checks are conducted to ensure that no peaks or valleys are lost. If any are missing, the data is readjusted. As a result of these steps, impact regions within the zero-valued sections are successfully identified.
For datasets with multiple impacts, separate rainflow analyses are conducted for each segment. If transformed correctly, each window contains one impact, having only start, end, peak, and valley points. Finally, shock amplitudes are verified, discarding those below the predefined range (Table 2).

The rainflow analysis at this stage accurately provides amplitude and frequency values, while the ratio of data points determines its waveform. For further inspection or storage, the data is resampled to a 2048 Hz sampling rate using Makima interpolation.
Makima interpolation is an improved version of Akima spline interpolation, designed to prevent excessive oscillations and ensure smooth curve fitting. It is particularly effective for time-series data and irregular datasets, providing stability against sudden changes (Akima, 1970).
The proposed method does not require manual corrections or parameter adjustments at any stage. Unlike simple downsampling, which may lose exact amplitude information, this method preserves high-frequency variations, ensuring that no significant peak is overlooked. All parameters have been formulated based on the statistical properties of the data and fine-tuned through hundreds of trials to ensure accuracy.

Finding

The proposed method operates without needing additional tuning across real and synthetic road signals. A dataset of 100 synthetic RLDs was processed, and its accuracy is shown in Table 3.

Table 3. Proposed method's performance**.**

Impact Detection Accuracy	Amplitude Detection Accuracy	Frequency Detection Accuracy
93%	95%	85%

Finite element analyses have shown that the maximum stress amplitude responses of the original RLD and the simplified RLDs are highly comparable (Fig.5). In fatigue analyses, it was found that using the stress data obtained through the proposed transformation and the original RLD yielded highly similar damage results (Fig.5)
Based on these findings, the proposed method is found to be applicable in the load spectra generation. For further validation, a Shock Response Spectrum (SRS) analysis was conducted. In the expected damage frequency ranges, the new profile produced similar displacement responses to the original RLD (Fig. 8). However, unlike direct SRS-based shock profiles, this method captures real frequency, phase, and amplitude data while accounting for repeated varying loads, making it more accurate and less conservative.

Conclusion

Defining the load spectrum is key to avoiding conservatism or early failures in accelerated fatigue testing. This study extracts shock loads from RLD, creating simplified profiles to enhance vehicle fatigue assessments.
Mechanical shock loads in automotive applications are stochastic, transient, and non-stationary. Many RLD studies fail to capture these loads accurately, especially in vibration embedded signals. Frequency domain methods are inapplicable, some time-domain methods crop data without simplification, SRS struggles with overlapping shocks, and rainflow analysis alone ignores shock timing and frequency. AI/ML methods enhance detection but add complexity and high computational costs.
This study presents an autonomous method for extracting mechanical shocks from acceleration signals. It automates filtering, sampling, impact detection, segmentation, and simplification while preserving frequency and amplitude, requiring no manual tuning and closely matching the original RLD.

Finite element validations were conducted in Abaqus and Ansys Mechanical, while fatigue assessments employed nCode and Femfat softwares. Synthetic and actual measurement signals were tested. Comparison, including SRS validation, showed the method's accuracy, efficiency, and scalability, benefiting automotive fatigue assessment.

References

Akbaba, Ö., Yıldırım, B., & Canbaloğlu, G. (2022). Vibration-based fatigue analysis of a structure integrated on an air vehicle by using experimental and theoretical methods. Results in Engineering, 14, 100310. https://doi.org/10.1016/j.rineng.2022.100310

Chen, H., Chen, Y., & Yang, Z. (2014). Coupling damage and reliability model of low-cycle fatigue and high-energy impact based on the local stress–strain approach. Chinese Journal of Aeronautics, 27(4), 955–963. https://doi.org/10.1016/j.cja.2014.03.008

Jimenez, M. (2018). Accelerated fatigue test in mechanical components. In Contact and Fracture Mechanics. https://doi.org/10.5772/intechopen.72640

Wang, W. (2023). Mechanical research on reinforced concrete materials. Materials, 16(21), 6892. https://doi.org/10.3390/ma16216892

Prueter, P. E. (2021). Fatigue-life assessment. In ASM Handbook Volume 11A: Fatigue and Fracture. ASM International. https://doi.org/10.31399/asm.hb.v11A.a0006819

Sisemore, C., Babuska, V., & Booher, J. (2017). Energy based representation of 6-DOF shaker shock low-cycle fatigue tests. In Shock & Vibration, Aircraft/Aerospace, Energy Harvesting, Acoustics & Optics (Vol. 9). https://doi.org/10.1007/978-3-319-54735-0_13

Kubo, P. L., & Kamarianakis, D. J. (2018). Assessment of the vertical load applied to the pavement on pothole events by a commercial truck. International Journal of Heavy Vehicle Systems, 25(3/4), 223–234.

Frajnković, M. O., Kosobudzki, M., Jamroziak, K., & Rouillard, C. R. (2018). Structural integrity of in-wheel motors. SAE Technical Papers.

Manouchehry Nya, R. A., & Sadeghi, S. (2019). Reliability-based fatigue life of vehicle spring under random loading. International Journal of Structural Integrity, 10(2).

Billal, M. K., Gorges, C. Ö., Özdemir, R., & Kaya, M. (2015). Simulation of vehicle pothole test and techniques used. SAE Technical Papers. https://doi.org/10.4271/2015-01-0637

Zhou, S. Y., Zhang, H., Chen, Z., & Li, H. (2023). Load simulation of the impact road under durability and misuse conditions. SAE Technical Papers. https://doi.org/10.4271/2023-01-0775

Özga, A., & Sęk, M. (2023). Application of unsupervised learning algorithms for analysis of the vibrations of an oscillator forced by a random series of impulses. Vibrations in Physical Systems, 34(1).

Abdullah, S., Nizwan, C., & Nuawi, M. Z. M. (2009). A study of fatigue data editing using the short-time Fourier transform (STFT). American Journal of Applied Sciences, 6(4), 565–575. https://doi.org/10.3844/ajassp.2009.565.575

Rouillard, V., & Zhang, L. M. (2024). Road vehicle shock detection algorithm using the Hilbert envelope. Computer Methods in Applied Mechanics and Engineering. https://doi.org/10.1016/j.cma.2023.116637

Kırbaş, U. (2023). Effects of pothole type pavement distress on whole-body vibration. Road Materials and Pavement Design, 24(6), 1403–1424. https://doi.org/10.1080/14680629.2022.2072756

Lepine, J., & Vallée, R. (2018). Evaluation of shock detection algorithm for road vehicle vibration analysis. Vibration, 1(2), 220–238. https://doi.org/10.3390/vibration1020016

Alexander, J. E. (2018). A new method to synthesize an SRS compatible base acceleration with energy and temporal moments to improve MDOF system response (First part). In Proceedings of IMAC 36. SandV.

Halfpenny, A. (2006). Methods for accelerating dynamic durability tests. HBM nCode White Paper.

Gorges, C. Ö., & Lindner, R. (2019). Impact detection using a machine learning approach and experimental road roughness classification. Mechanical Systems and Signal Processing, 117, 738–756. https://doi.org/10.1016/j.ymssp.2018.07.043

Trzepieciński, T., & Nowak, S. M. (2024). Current trends in metallic materials for body panels and structural members used in the automotive industry. Materials, 17(3), 590. https://doi.org/10.3390/ma17030590

Akima, H. (1970). A new method of interpolation and smooth curve fitting. Journal of the ACM, 17(4), 589–602. https://doi.org/10.1145/321607.321609

Kosobudzki, M., & Jamroziak, K. (2018). Selected methods of accelerated durability tests of systems and subsystems of high mobility vehicles. IOP Conference Series: Materials Science and Engineering, 400(4), 042034. https://doi.org/10.1088/1757-899X/400/4/042034

White, D. R., & Fekete, J. F. (1992). Noise in measurements obtained by sampling. Measurement Science and Technology, 3(1), 1–7. https://doi.org/10.1088/0957-0233/3/1/001

Modeling Hydrogen-Induced Failure of AISI 4135 Steel by Finite Element Analysis

Dorukhan Güngör[a], Emin Sünbüloğlu[b]

[a] Istanbul Technical University, Graduate School, Mechanical Engineering, Turkey
[b] Istanbul Technical University, Faculty of Mechanical Engineering, Turkey
gungord@itu.edu.tr

Keywords: Finite Element Method, Hydrogen Embrittlement.

Aim

The rising trend in hydrogen technologies along with net-zero emission goals has accelerated research on the phenomenon of hydrogen embrittlement, which describes a condition where materials experience premature failures or a shift in mechanical behavior from ductile to brittle due to the presence of hydrogen in metallic materials. Due to its small atomic size, hydrogen diffuses into the interstitial lattice sites of metallic materials, as well as into intergranular sites such as dislocations and grain boundaries. Accumulation in these regions alters the mechanical behavior of metallic materials, making it more susceptible to brittle failure [1].
The stress distribution, exposed hydrogen environment, temperature, applied strain rate and microstructure of the material are all known to affect hydrogen embrittlement susceptibility. As expected, the probability of hydrogen-induced failure increases with increasing applied stress, hydrogen concentration and microstructural impurities [2,3]. Besides, the slow strain rate tests reported in the literature indicate that hydrogen-induced failure stress dramatically decreases at very low strain rates, without exception. Some of the reported test results indicate fractures occurring even within the elastic region due to high hydrogen concentration in the material [4,5]. There are a couple of hypotheses proposed for the hydrogen embrittlement mechanism over several decades:

- Hydrogen-Enhanced Decohesion Model (HEDE)
- Hydrogen-Enhanced Localized Plasticity (HELP)
- Absorption Induced Dislocation Emission (AIDE)
- Hydrogen-Enhanced Strain Induced Vacancy (HESIV)

HEDE is based on the weakening of interatomic bonds among iron atoms due to their interaction with hydrogen ions. It is accepted that the hydrogen-induced fracture starts with fracture initiation gap formation [2]. The HELP asserts that the hydrogen concentration in both interstitial sites and trap sites increases the dislocation activity. As a result, premature failure occurs due to a reduction in the stress required for dislocation movement [2,6]. The AIDE model proposes that the adsorbed hydrogen weakens the atomic bonds and leads the formation of dislocation centers, which then propagate under reduced stress due to the presence of hydrogen [2,6]. The latter hypothesis, HESIV, depends on enhanced internal vacancy formation and agglomeration due to mobile hydrogen within the material [7]. The consensus in the literature is that the interactive effect of these proposed mechanisms leads to the hydrogen-induced fracture in metallic materials [8].
There are numerous approaches available in the literature to model the hydrogen diffusion and failure limits of the materials. Phase-field approaches, finite element and finite difference methods are utilized to model hydrogen diffusion from the micro to the macro scale [1, 9-12]. By coupling hydrogen diffusion and mechanical models, both the effect of the stress-state on hydrogen concentration distribution and the effect of this distribution on fracture limit can be investigated. The cohesive zone modeling approach is widely preferred in the literature for this purpose [13-16]. Besides, some studies have implemented statistical approaches to evaluate failure probability [17, 18]. Moreover, both statistical and machine learning approaches, trained with experimental data, have also been developed to predict hydrogen-induced fracture [19, 20].

Although many approaches have been published in the literature, there is still a need for a solid approach that is suitable for utilization in industrial practice for predicting the failure limit and designing reliable engineering systems [21]. In this study, an experimental stress-dependent critical hydrogen concentration curve was integrated into a coupled hydrogen diffusion and mechanical finite element model to predict the failure limit of a specimen under various loading conditions. This approach aims to enable accurate material selection for engineering systems and to address the lack of a practical modeling framework in the existing literature. A 3D model framework is required to address industrial problems and to ensure practicality. However, a 2D model framework is needed to prove the proposed methodology and to validate 3D model framework. The method and preliminary results of the developed 2D model are briefly described in the following sections. A 3D model and the alteration of plastic deformation behavior due to the presence of hydrogen will be further investigated in future work.

Material and Method

A coupled thermal and mechanical finite element model framework was developed using the heat transfer analogy to calculate hydrogen mass transport [1, 10, 11]. Isotropic work hardening during plastic deformation was modeled using a power law, as shown in Equation 1 [22].

$$\sigma = \sigma_y(1 + \frac{E\varepsilon_p}{\sigma_y})^n \tag{1}$$

Here, n is the hardening coefficient, and ε_p is the plastic strain. The coupling term, gradient of hydrostatic stress, is calculated by means of the accordingly selected shape functions, global and isoparametric coordinate transformations and the coordinates of integration points [10, 23]. The model accounts for hydrogen concentration accumulated in interstitial lattice sites as well as traps such as grain boundaries, dislocations, and carbide interfaces. However, for the sake of simplicity, only dislocation sites were considered in the preliminary simulations. The variation of dislocation density with respect to plastic strain is evaluated using the relation proposed by Kumnick and Johnson [24]. The experimentally determined failure stress versus critical hydrogen concentration curve was implemented into the model, and failure was tracked based on the ratio between the actual stress and the critical stress derived from the current total hydrogen concentration, as shown in Equation 2.

$$R_f = \frac{\sigma_{actual}}{\sigma_{critical}} \tag{2}$$

Here, R_f is the indicator to track the failure in the model framework.
The experimental data for AISI 4135 steel, illustrated in Figure 1, were implemented into the UMAT and UMATHT subroutines to calculate the failure indicator ratio [25].

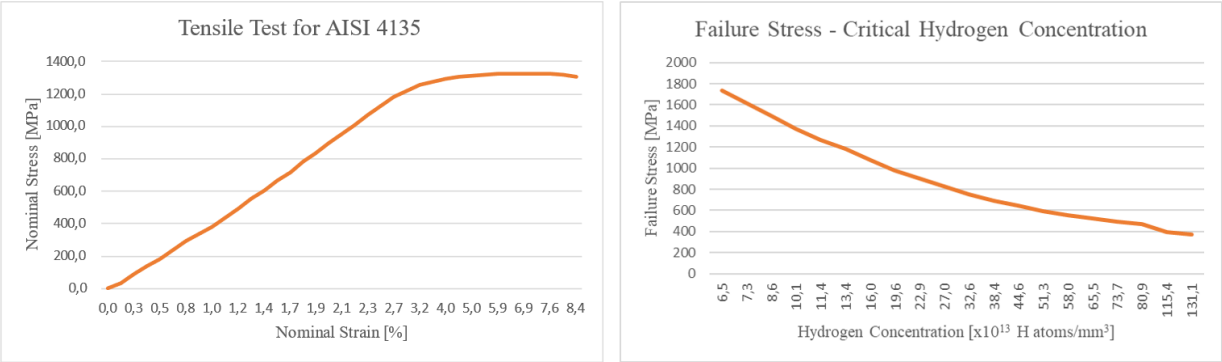

Figure 1. Experimental curves for AISI4135 steel [25].

The general model framework developed in Abaqus is given in Figure 2.

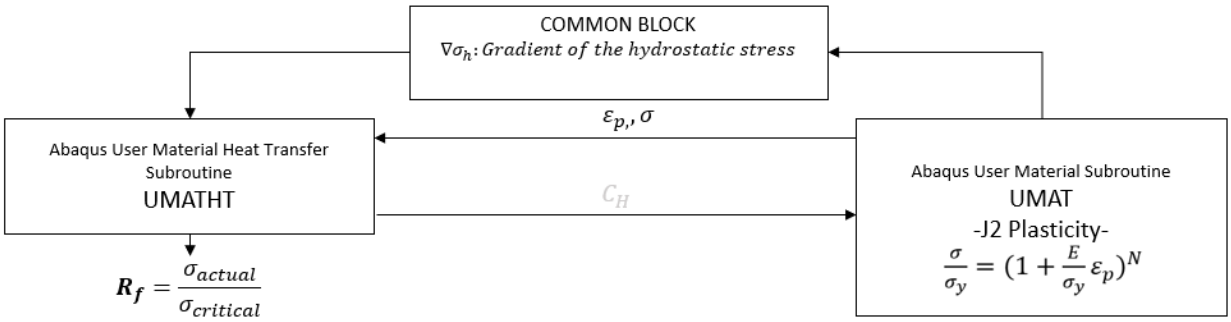

Figure 2. Model framework developed in Abaqus.

Findings

Most tensile tests in the literature are conducted using pre-charged and coated notched specimens. A coating is applied to the specimens to prevent hydrogen desorption and to maintain the hydrogen concentration at its initial level during the tests. Therefore, the simulation was done with a predefined hydrogen concentration ($2.6x10^{12}$ atoms/mm^3), assuming the specimen is insulated, and using a displacement rate of 4 μm/s. The parameter set used in the simulation are given in Table 1.

Table 1. Parameter set used in the simulation.

Parameter	Value
Initial concentration [atoms/mm^3]	2.6E+12
Diffusion coefficient (Surface film coef. = Conductivity) [mm^2/s]	2.01E-07
Dislocation density [sites/mm^3]	8.3E+13
Dislocation binding energy [Nmm/mol]	5.86E+07
Young's Modulus [MPa]	45000
Poisson Ratio	0.3
Initial Yield Strength [MPa]	1181
Work-Hardening Exponent	0.009

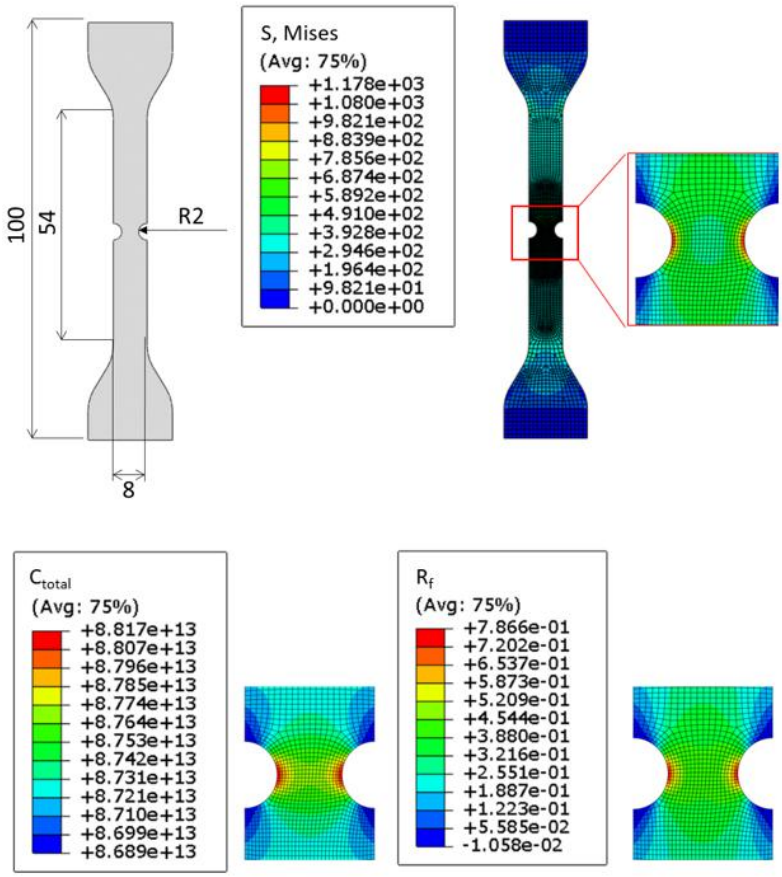

Figure 3. Simulation results.

Simulation results, Figure 3, show that even if the sample is insulated, hydrogen redistribution within the specimen is consistent with stress distribution, leading to increased local concentrations in these critical areas. This finding is significant in terms of its consistency with modeling studies available in the literature. In addition, the preliminary results indicate that the experimental dataset has been successfully integrated into the code. Immediately after the transition to the plastic region, the failure ratio R_f increases to around 0.8, which can be considered critical.

Conclusion

A 2D finite element model framework was developed in the Abaqus environment, and an experimental curve for AISI 4135 steel was integrated to assess the failure limit, aiming to fill the gap for a practical and accurate tool. The preliminary results are in good agreement with the findings available in the literature, and the developed model structure is sufficiently mature for further implementations and validation of 3D model framework which will be developed in future works as described in the introduction.

References

Zhang, Z., Peeters, J., Popovich, V., & Ayas, C. (2022). Combined effects of stress and temperature on hydrogen diffusion in non-hydride forming alloys applied in gas turbines. international journal of hydrogen energy, 47(71), 30687-30706.

Lynch, S. (2012). Hydrogen embrittlement phenomena and mechanisms. Corrosion reviews, 30(3-4), 105-123.

Cho, L., Bradley, P. E., Lauria, D. S., Connolly, M. J., Seo, E. J., Findley, K. O., ... & Slifka, A. J. (2021). Effects of hydrogen pressure and prior austenite grain size on the hydrogen embrittlement characteristics of a press-hardened martensitic steel. international journal of hydrogen energy, 46(47), 24425-24439.

Zhou, C., Ye, B., Song, Y., Cui, T., Xu, P., & Zhang, L. (2019). Effects of internal hydrogen and surface-absorbed hydrogen on the hydrogen embrittlement of X80 pipeline steel. International Journal of Hydrogen Energy, 44(40), 22547-22558.

Momotani, Y., Shibata, A., Terada, D., & Tsuji, N. (2017). Effect of strain rate on hydrogen embrittlement in low-carbon martensitic steel. International journal of hydrogen energy, 42(5), 3371-3379.

Brück, S., Schippl, V., Schwarz, M., Christ, H. J., Fritzen, C. P., & Weihe, S. (2018). Hydrogen embrittlement mechanism in fatigue behavior of austenitic and martensitic stainless steels. Metals, 8(5), 339.

[7] Nagumo, M. (2004). Hydrogen related failure of steels–a new aspect. Materials Science and Technology, 20(8), 940-950.

Djukic, M. B., Bakic, G. M., Zeravcic, V. S., Sedmak, A., & Rajicic, B. (2019). The synergistic action and interplay of hydrogen embrittlement mechanisms in steels and iron: Localized plasticity and decohesion. Engineering Fracture Mechanics, 216, 106528.

Hussein, A., Kim, B., Verbeken, K., & Depover, T. (2024). The Effect of Grain Boundary Misorientation on Hydrogen Flux Using a Phase-Field-Based Diffusion and Trapping Model. Advanced Engineering Materials, 26(22), 2401561.

Fernández-Sousa, R., Betegón, C., & Martínez-Pañeda, E. (2020). Analysis of the influence of microstructural traps on hydrogen assisted fatigue. Acta Materialia, 199, 253-263.

Barrera, O., Tarleton, E., Tang, H. W., & Cocks, A. C. F. (2016). Modelling the coupling between hydrogen diffusion and the mechanical behaviour of metals. Computational Materials Science, 122, 219-228.

Das, T., Chakrabarty, R., Song, J., & Yue, S. (2022). Understanding microstructural influences on hydrogen diffusion characteristics in martensitic steels using finite element analysis (FEA). International Journal of Hydrogen Energy, 47(2), 1343-1357.

Jemblie, L., Olden, V., & Akselsen, O. M. (2017). A coupled diffusion and cohesive zone modelling approach for numerically assessing hydrogen embrittlement of steel structures. International Journal of Hydrogen Energy, 42(16), 11980-11995.

Olden, V., Thaulow, C., Johnsen, R., & Østby, E. (2007). Cohesive zone modeling of hydrogen-induced stress cracking in 25% Cr duplex stainless steel. Scripta Materialia, 57(7), 615-618.

Raykar, N. R., Maiti, S. K., Raman, R. S., & Aryan, S. (2013). Study of hydrogen concentration dependent growth of external annular crack in round tensile specimen using cohesive zone model. Engineering Fracture Mechanics, 106, 49-66.

Jemblie, L., Olden, V., & Akselsen, O. M. (2017). A review of cohesive zone modelling as an approach for numerically assessing hydrogen embrittlement of steel structures. Philosophical Transactions of the Royal Society A: Mathematical, Physical and Engineering Sciences, 375(2098), 20160411.

Novak, P., Yuan, R., Somerday, B. P., Sofronis, P., & Ritchie, R. O. (2010). A statistical, physical-based, micro-mechanical model of hydrogen-induced intergranular fracture in steel. Journal of the Mechanics and Physics of Solids, 58(2), 206-226.

Nagao, A., Dadfarnia, M., Somerday, B. P., Sofronis, P., & Ritchie, R. O. (2018). Hydrogen-enhanced-plasticity mediated decohesion for hydrogen-induced intergranular and "quasi-cleavage" fracture of lath martensitic steels. Journal of the Mechanics and Physics of Solids, 112, 403-430.

Takagi, S., Terasaki, S., Tsuzaki, K., Inoue, T., & Minami, F. (2007, February). Application of local approach to hydrogen embrittlement fracture evaluation of high strength steels. In Materials science forum (Vol. 539, pp. 2155-2161). Trans Tech Publications Ltd.

Fangnon, E., Malitckii, E., Latypova, R., & Vilaça, P. (2023). Prediction of hydrogen concentration responsible for hydrogen-induced mechanical failure in martensitic high-strength steels. international journal of hydrogen energy, 48(14), 5718-5730.

Djukic, M. B., Bakic, G. M., Zeravcic, V. S., Sedmak, A., & Rajicic, B. (2016). Hydrogen embrittlement of industrial components: prediction, prevention, and models. Corrosion, 72(7), 943-961.

Martínez-Pañeda, E., Fuentes-Alonso, S., & Betegón, C. (2019). Gradient-enhanced statistical analysis of cleavage fracture. European Journal of Mechanics-A/Solids, 77, 103785.

Díaz, A., Alegre, J. M., & Cuesta, I. I. (2016). Coupled hydrogen diffusion simulation using a heat transfer analogy. International Journal of Mechanical Sciences, 115, 360-369.
Kumnick, A. J., & Johnson, H. H. (1980). Deep trapping states for hydrogen in deformed iron. Acta Metallurgica, 28(1), 33-39.
Wang, M., Akiyama, E., & Tsuzaki, K. (2005). Effect of hydrogen and stress concentration on the notch tensile strength of AISI 4135 steel. Materials Science and Engineering: A, 398(1-2), 37-46.

A Comparative Modal Analysis of Homogenized and Full-Scale FE Models of Sandwich Composite Structures with Re-entrant Auxetic Core

Özgür Değirmenci[a], Kadir Günaydin[b], Halit Süleyman Türkmen[c], Şafak Yılmaz[a]

[a] Istanbul Technical University, Faculty of Mechanical Engineering, Türkiye
[b] General Electric Aerospace, Türkiye Teknoloji Merkezi, Türkiye
[c] Istanbul Technical University, Faculty of Aeronautics and Astronautics, Türkiye
degirmencio@itu.edu.tr

Keywords: Homogenization, Re-entrant Auxetic, Lattice Structures, Modal FEM Analysis.

Aim

Additive manufacturing is increasingly utilized across various industries, including aerospace, automotive, robotics, and biomedical fields [2]. Lattice structures and auxetic materials are gaining considerable attention due to their exceptional mechanical properties, particularly their potential for superior energy absorption capacity [3]. Auxetic materials exhibit a counterintuitive behavior due to their negative Poisson's ratio; they contract orthogonally under compressive force, leading to densification of the material near the applied load. This unique property also causes them to expand transversely when stretched axially, offering significant advantages in various applications [1-3]. This interest has led to the development of lightweight materials and structures for high energy absorption, such as honeycomb configurations and auxetic materials featuring re-entrant or anti-tetra-chiral core geometries [3].

Recent advancements in additive manufacturing have increased the internal geometric complexity of new designs, thereby enhancing efficiency. However, directly modeling these intricate geometries numerically requires significant computational resources. Predicting the mechanical properties of these components through finite element modeling (FEM) instead of physical testing is essential for saving both cost and time [1]. Due to the extensive geometry preparation, meshing, and computational time required for lattice structures, various methods have been explored to accurately predict mechanical properties.

To address these challenges, the use of equivalent media with average or effective mechanical properties has become common practice to reduce computational time while maintaining accuracy in FEM analysis. One effective method for modeling complex geometries is the homogenization approach. Numerical homogenization evaluates effective material properties by utilizing energy equivalence between explicit (full-scale) shown in Figure 1. and implicit (simplified) geometries shown in Figure 2. This approach allows for the modeling and analysis of complex geometries through implicit unit cells with effective material properties, rather than explicit unit cells with isotropic material, simplifying numerical models and reducing meshing and solve time [1]. Homogenization integrates multi-scale functionality, allowing effective properties derived from microscale unit cells to be applied in subsequent analyses and components of complex geometries at larger scales progressively. The homogenization method requires the periodicity of minimum unit cells in all applicable directions. Specifically, periodic boundary conditions must be imposed on the structural boundaries.

This study proposes using the homogenization method for one of the most common types of lattice structures: re-entrant auxetic. Comparative modal analyses were performed for both explicit (full-scale) FE model with isotropic material and implicit (simplified) finite element (FE) model with homogenized material. The first ten mode shapes were extracted from both models and compared in terms of mode shapes and natural frequencies. The results demonstrated that homogenization can be successfully applied to sandwich composite structures with auxetic re-entrant core without significantly compromising accuracy [1]. The implicit (simplified) FE model predicted natural frequencies with a difference range of less than 5% compared to the explicit (full-scale) FE model across all mode shapes.

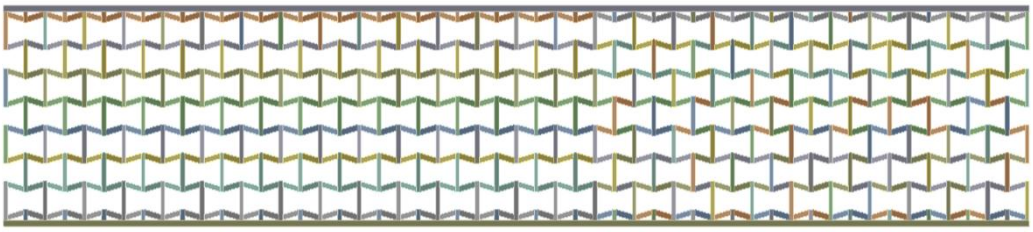

Figure 1. Explicit (Full-Scale) FE Model.

Figure 2. Implicit (Simplified) FE Model.

Material and Method

For this study, the re-entrant type of auxetic structure geometry (shown in Figure 3) was chosen for numerical simulation. This type of auxetic structure is characterized by a periodic arrangement of unit cells with negative angles, resulting in its negative Poisson's ratio behavior. Auxetic behavior involves transverse expansion under tension and contraction under compression. In the re-entrant type structure, this behavior is achieved through the bending or stretching of diagonal ribs under tensile loads [2].

Finite element model (FEM) for an auxetic re-entrant structure was developed using Ansys Workbench 2020 R2. To determine the equivalent material properties of the solid bodies, homogenized material properties were obtained using the Ansys Material Designer module. The unit cell, or the smallest representative volume element (RVE), corresponding to this structure is shown in Figure 3. An RVE can be defined as the smallest volume of a material that accurately represents the effective material properties [1].

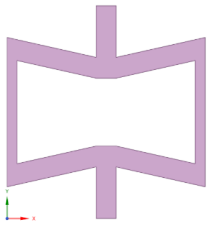

Figure 3. 1x1 Unit cell in X and Y directions.

Isotropic material properties, such as Young's modulus of elasticity and Poisson's ratio, for the explicit (full-scale) FE model were derived from tensile testing conducted during this study. Additionally, the material density was measured using the same tensile test coupons.

Modal analysis was conducted on both the explicit (full-scale) FE model and the homogenized (simplified) FE model. A free-free boundary condition was applied, allowing the lattice structure to move freely at its boundaries during the analysis. The primary advantage of using free boundaries is the elimination of the effects of boundary conditions [1]. The natural frequencies and corresponding mode shapes were obtained from the modal analysis. The first ten mode shapes were considered for comparison.

In Material Designer, anisotropic analyses were initially performed, revealing that the structure exhibited orthotropic symmetry behavior based on the resultant stiffness matrix. Consequently, orthotropic analyses were utilized in Material Designer [1].

Subsequently, sensitivity studies were conducted to better understand how the homogenized material properties change in various scenarios. The impact of extrude length in the Z direction was examined across five different cases, ranging from the original extrude length (100%) to 5% of the original length. Additionally, the effect of the number of unit cells stacked in the X and Y directions was analyzed across eight different cases, starting from a 1x1 unit cell configuration to an 8x8 unit cell configuration. Lastly, a mesh size convergence study was performed by conducting a series of simulations with eight different mesh sizes, and the results of the mesh convergence study are presented in Figure 4.

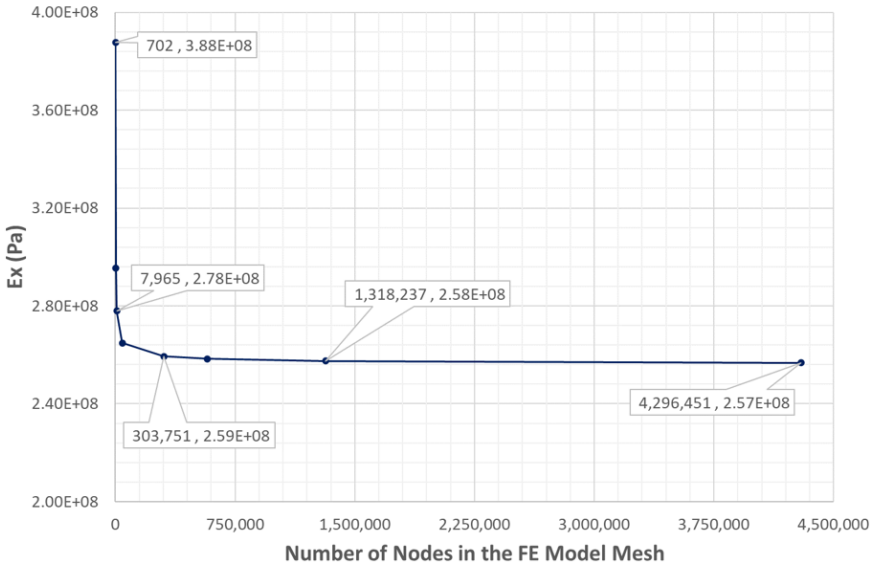

Figure 4. Meshconvergence study for the elasticity modulus in the X direction (E1, Ex).

Following the homogenization of the auxetic re-entrant structure, the stiffness matrix was obtained, along with Young's modulus of elasticity, shear modulus of elasticity, and Poisson's ratio in the X, Y, and Z directions [1].

When comparing the meshing of both the homogenized (simplified) FE model and the explicit (full-scale) FE model, there is a significant reduction in meshing time and the total number of elements and nodes, despite both models utilizing fine and structured hex meshing with SOLID185 elements throughout. The homogenized FE model consists of 337,125 nodes and 311,808 elements. In contrast, the explicit FE model contains 1,185,500 nodes and 897,600 elements. This reduction in nodes by approximately 3.5 times greatly decreases the time required for FE meshing and model preparation, ultimately leading to faster solve times. Therefore, during this study, the modal analysis solve time for the homogenized FE model was approximately 43 times shorter compared to the solve time for the explicit FE model.

Total deformation with respect to the first five mode shapes for both the explicit (full-scale) FE model and the homogenized (simplified) FE model are shown in Figure 5. The natural frequencies for the first ten mode shapes are provided in Table 1. It is evident from Table 1. that there is a very good correlation between the implicit and explicit models for the first ten mode shapes of the auxetic re-entrant lattice structure. Comparison of the natural frequencies based on the implicit and explicit models for the first ten mode shapes (Table 1) reveals that the maximum error is less than 5% in all cases. Additionally, it is observed that the implicit model resulted in lower natural frequencies in all cases [1].

Mode Shape Number	Explicit (Full-Scale) FE Model with Isotropic Material	Implicit (Simplified) FE Model with Homogenized Material	Difference%
1	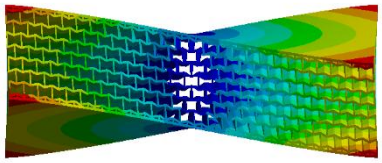 **Frequency = 342 Hz**	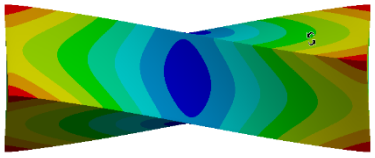 **Frequency = 335 Hz**	**-2.1%**
2	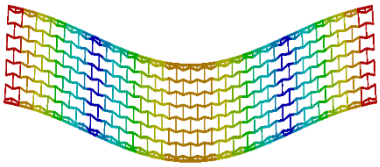 **Frequency = 425 Hz**	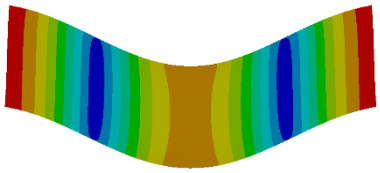 **Frequency = 414 Hz**	**-2.5%**
3	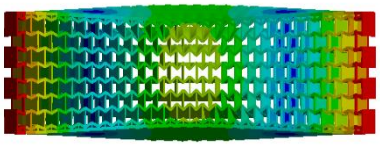 **Frequency = 624 Hz**	**Frequency = 606 Hz**	**-2.9%**
4	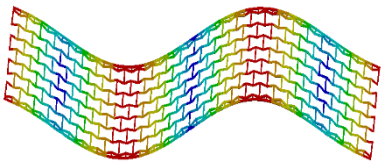 **Frequency = 666 Hz**	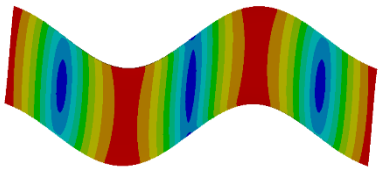 **Frequency = 651 Hz**	**-2.3%**
5	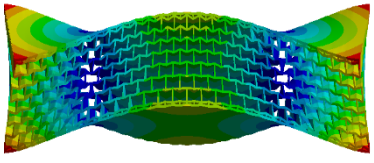 **Frequency = 855 Hz**	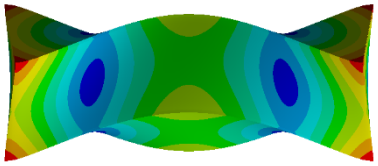 **Frequency = 831 Hz**	**-2.8%**

Figure 5. Total deformation of the first five mode shapes of the re-entrant explicit and implicit FE model results.

Table 1. Modal Response Results FEA Results, Natural Frequencises (Hz) For Re-entrant Structure.

Mode Shape Number	Explicit (Full-Scale) FE Model with Isotropic Material Natural Frequencies (Hz)	Implicit (Simplified) FE Model with Homogenized Material Natural Frequencies (Hz)	Difference %
1	342.6	335.4	-2.1%
2	425.1	414.3	-2.5%
3	624.8	606.4	-2.9%
4	666.4	651.3	-2.3%
5	855.1	831.1	-2.8%
6	965.8	934.0	-3.3%
7	1191.0	1149.8	-3.5%
8	1472.3	1441.5	-2.1%
9	1498.5	1456.3	-2.8%
10	1528.1	1462.1	-4.3%

Findings

This study examined the efficiency of applying a homogenization method to re-entrant auxetic structures. Through homogenization, orthotropic material properties were calculated. Modal analyses were conducted, extracting the first ten mode shapes from both explicit and implicit models. The results were compared in terms of mode shape, maximum deformation, and natural frequency. Figure 5. illustrates the total deformation for the first five mode shapes of the re-entrant auxetic explicit and implicit FE models, while the natural frequencies for the first ten mode shapes are provided in Table 1.

The main findings are as follows:

- There is a very good correlation between the ten mode shapes derived from the explicit and implicit models.
- The maximum natural frequency difference between the explicit and implicit models is 4.3%, with all other differences being less than 4%.

Conclusion

The key conclusions are as follows:

- Utilizing the homogenization method simplifies the numerical model and reduces its size. This leads to a significant reduction in FE modeling effort and computational solve time, making the homogenization method highly effective, time-efficient, and computationally efficient while maintaining acceptable accuracy.

- It identifies and addresses potential needs related to analytical methods for complex geometrical structures.

This study investigated the feasibility of applying a homogenization method to re-entrant auxetic core structures. Future research will focus on the experimental validation of the numerical results.

References

Gunaydin, K., Gülcan, O., Tamer, A. (2025). Application of Homogenization Method in Free Vibration of Multi-Material Auxetic Metamaterials. Vibration, 8(1), 8010002.

Jiang, D., Thissen, H., Hughes, T.C., Yang, K., Wilson, R., Murphy, A.B., Nguyen, V. (2024). Advances in additive manufacturing of auxetic structures for biomedical applications. Materials Today Communications, 40, 110045.

Zhou, J., Liu, H., Dear, J.P., Falzon, B.G., Kazancı, Z. (2023). Comparison of different quasi-static loading conditions of additively manufactured composite hexagonal and auxetic cellular structures. International Journal of Mechanical Sciences, 244, 108054.

Parametric Investigation of Mechanical Properties for Laser Powder Bed Fusion Processed Inco718 Auxetic Metamaterials

Kubilay Özgönül[a], Hacı Abdullah Taşdemir[a]

[a] Istanbul Technical University, Faculty of Mechanical Engineering, Mechanical Design Program, Turkey
ozgonul21@itu.edu.tr

Keywords: Auxetic re-entrant structure, Crush force efficiency, Energy absorption, Metamaterial, Parametric investigation.

Aim

Auxetic structures, widely recognized as a class of metamaterials, are known for exhibiting extraordinary mechanical properties that distinguish them from conventional materials. These structures possess a unique characteristic: a negative Poisson's ratio, which means that they expand in all directions when stretched, as opposed to most materials that contract perpendicular to the direction of applied force. Along with this, auxetic materials also demonstrate negative linear compressibility, meaning that they become stiffer when compressed, and negative thermal expansion coefficients, indicating that they contract when subjected to increases in temperature. These peculiar properties make auxetic structures highly advantageous in a wide array of industrial applications, where energy absorption, impact resistance, and durability are critical [1].

Among the various practical applications, auxetic structures have gained significant attention in industries such as automotive, construction and aerospace engineering, where their ability to absorb energy efficiently makes them ideal candidates for use in crash boxes, impact protection systems, and blast-resistant materials. For instance, in the automotive industry, auxetic materials can be incorporated into vehicle safety structures to enhance crashworthiness by improving their energy absorption capacity during collisions. Similarly, in the construction and defense sectors, auxetic metamaterials are increasingly being explored for blast-resistant applications due to their ability to withstand high-impact forces and mitigate damage during explosions. As a result, the development of auxetic materials has opened new opportunities for the design of advanced, high-performance structures that can withstand extreme conditions while minimizing damage [2,3].

The crushing behavior and energy absorption characteristics of various types of auxetic metamaterials have been extensively studied in the literature. Researchers have investigated how the auxetic behavior of these materials influences their mechanical properties, such as strength, stiffness, and energy dissipation, when subjected to external forces.

In the current study, the mechanical properties of re-entrant auxetic structures, which are fabricated using additive manufacturing techniques from Inconel 718 material, are thoroughly examined under axial compressive loads. The focus of this investigation is to understand how changes in the geometric parameters of the re-entrant unit cells affect the overall mechanical behavior of the structure. The re-entrant structure, which is a specific type of auxetic material, is particularly interesting due to its ability to maintain enhanced strength when subjected to in-plane compressive loads, which are often encountered in real-world applications.

Material and Method

Before proceeding with the analysis of geometric parameters, a validation study was carried out to ensure the accuracy of the finite element simulations. To validate the accuracy of the FEM analyses performed in this thesis geometry presented in the Figure 1, the boundary conditions in the FEM model were adjusted to align with the stress-strain curve obtained from the reference test study [4].

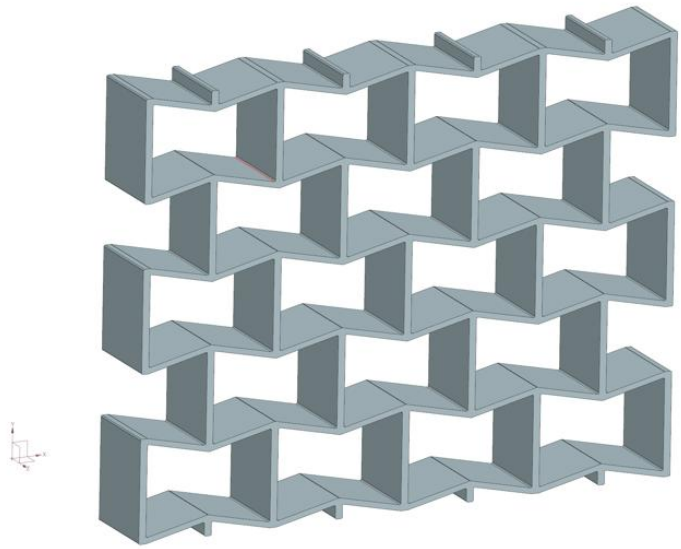

Figure 1. FEM model geometry.

In the reference study [4], the same test was conducted three times on the identical geometry, yielding consistent results which are illustrated in Figure 2. The FEM analysis in this work also produced similar results, thereby confirming the validity of the model which is presented in Figure 3.

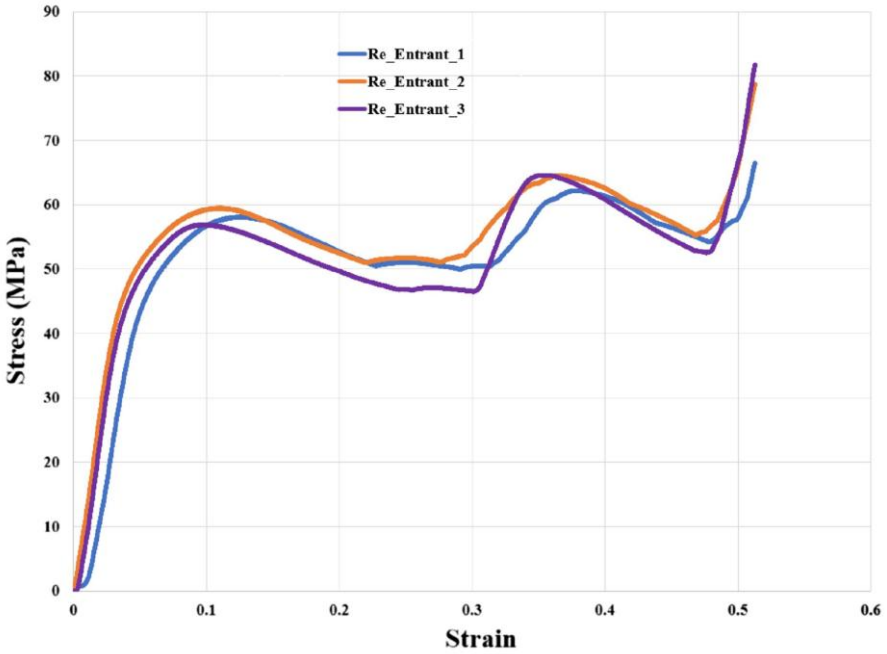

Figure 2. Reference test study stress vs strain results [4].

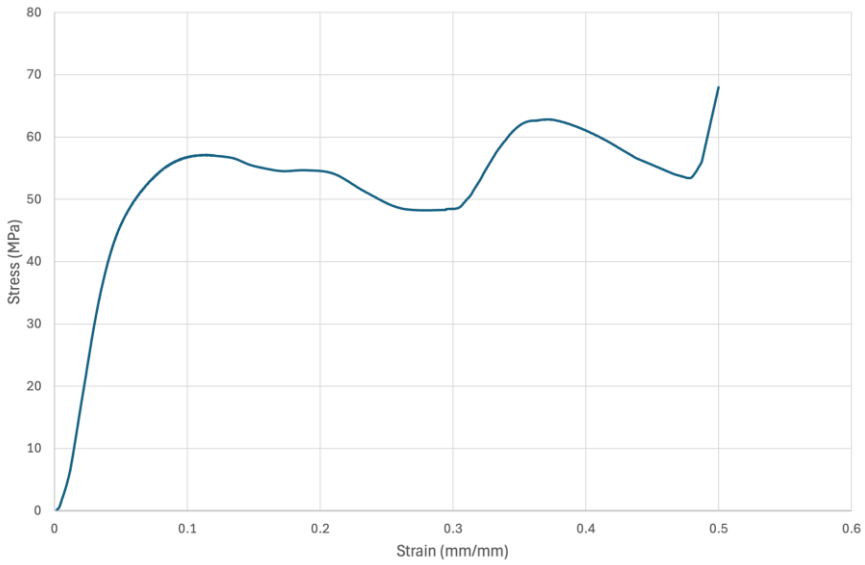

Figure 3. In this current thesis study stress vs strain results.

In the reference study [4], Quasi-static compression tests were carried out using an Instron 5985 universal testing machine (Instron Inc., Norwood, MA, USA) with a constant crosshead velocity of 0.5 mm/min. In these tests, the bottom crosshead was held stationary while the top crosshead moved towards the bottom. The specimens were compressed until the displacement of the top crosshead reached 40 mm.

For the FEM analyses validation study, the COMSOL Multiphysics finite element software program [5], was utilized to examine the influence of design parameter variations on the mechanical properties of the structure. The finite element model consisted of a bottom plate of the core structure, which was fully constrained in all directions. The top plate, however, underwent axial compressive displacement until a total displacement of 40 mm was reached with a constant crosshead velocity of 0.5 mm/min, while the other directions of the bottom plate remained fixed. The material employed in this analysis, INCO 718 powder whose chemical composition is shown in Table 1, has a density of 8190 kg/m³ and a Poisson's ratio of 0.294 [6].

Table 1. Chemical Composition of Inconel 718 [4].

Element	Ni	Cr	Nb	Mo	Ti	Mn	Si	Al	Fe
Wt %	53.00	18.50	5.00	3.00	0.66	3.00	0.35	0.35	Bal

The validation study compared the simulation results with those from previously published studies in the literature, ensuring that the boundary conditions, material properties, loading scenarios, and other parameters were defined correctly for further analysis. This validation provided a solid foundation for the subsequent investigation of the re-entrant structure's mechanical properties.

The study then focused on several critical mechanical properties of the re-entrant structures, including yield strength, energy absorption (EA), specific energy absorption (SEA), mean crush force (MCF), and crush force efficiency (CFE). These properties were assessed for eight different geometries of re-entrant structures, with various geometric parameters which are illustrated in Figure 4. The geometric parameters are wall cell lengths, heights, angles, and wall thicknesses being systematically varied. The goal was to determine how these factors influenced the material's overall behavior under axial compressive loading, particularly focusing on its ability to absorb energy and resist deformation.

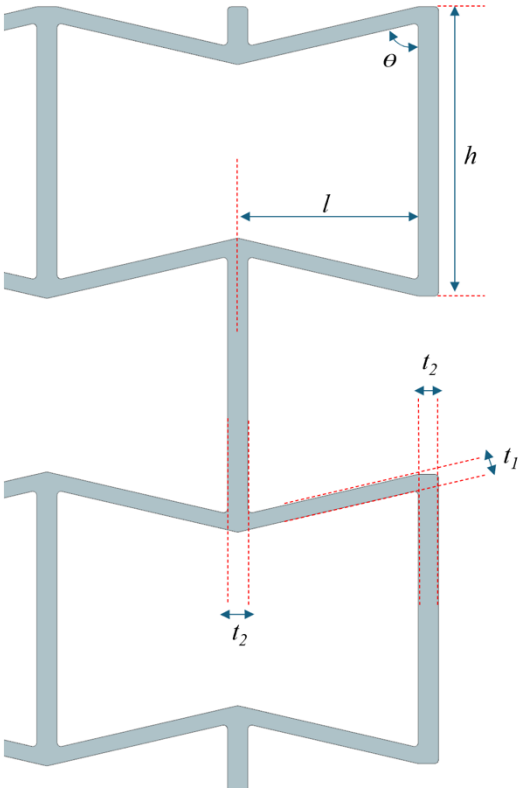

Figure 4. Geometric design parameters.

Finite element analysis results were used to evaluate and compare the absorbed energy at different strain levels, as well as the toughness of the re-entrant structures. The force-displacement curves obtained from these simulations were converted into stress-strain curves, which were then analyzed using curve fitting functions in MATLAB [7]. This allowed the researchers to determine absorbed energy and toughness values for each configuration, as well as provide insights into how the geometric parameters influenced the overall mechanical performance of the structures.

Findings

In this study, a comprehensive investigation was conducted to evaluate the mechanical behavior of re-entrant auxetic structures manufactured from Inconel 718 using additive manufacturing techniques. A validated finite element model was first established by aligning simulation results with experimental data from a reference study [4], ensuring the accuracy and reliability of the subsequent analyses. Following this validation, a detailed parametric study was carried out to assess the influence of key geometric parameters—including unit cell angle, length, height, and wall thickness—on critical mechanical properties such as energy absorption (EA), specific energy absorption (SEA), mean crush force (MCF), and crush force efficiency (CFE). Eight different geometries were systematically examined under axial compressive loading, providing insights into how design modifications affect the structural performance and energy absorption capabilities of auxetic materials. This work not only confirms the sensitivity of auxetic behavior to geometric tuning but also provides a framework for optimizing such structures in engineering applications requiring enhanced compressive performance.

The results demonstrated that increasing the wall thickness of the unit cells significantly enhanced all considered performance metrics. Thicker walls improved load-bearing capacity and facilitated greater energy dissipation, resulting in higher EA and SEA values, as well as increased MCF and more efficient force distribution as indicated by improved CFE. In contrast, an increase in the unit cell length led to reductions in structural stiffness and energy absorption capabilities, thereby diminishing all four mechanical indicators. Similarly, increasing the unit cell height contributed to reduced stability under compression and lowered the structure's energy absorption

performance. Additionally, enlarging the internal re-entrant angle weakened the auxetic effect, which in turn resulted in a decrease in EA, SEA, MCF, and CFE. These trends clearly illustrate the sensitivity of mechanical performance to geometric configurations, affirming that even small changes in design parameters can substantially impact the structural integrity and energy absorption behavior of auxetic materials.

Conclusion

In conclusion, this study provides valuable insights into the relationship between the geometric parameters and the mechanical properties of re-entrant auxetic structures. By altering key design factors such as wall length, height, thickness, and angle, it is possible to optimize the performance of these materials for specific engineering applications. These findings contribute to the ongoing development of auxetic metamaterials, which are expected to play an increasingly important role in industries that require high-energy absorption and exceptional mechanical performance, such as automotive, aerospace, construction and defense.

References

Lakes, R. (1993). Advances in negative Poisson's ratio materials. Advanced Materials, 5(4), 293–296.
Jacob, G., Fellers, J., & Simunovic, S. (2002). Energy absorption in polymer composites for automotive crashworthiness. Journal of Composites.
Ingrole, A., Hao, A., & Liang, R. (2016). Design and modeling of auxetic and hybrid honeycomb structures for in-plane property enhancement. Materials & Design.
Gülcan, O. (2024). Crashworthiness of laser powder bed fusion processed In718 auxetic metamaterials. Journal of the Brazilian Society of Mechanical Sciences and Engineering, 46, 414.
COMSOL. (2024). COMSOL Multiphysics® 6.2 [Computer software]. COMSOL AB.
Url-1 https://met3dp.com/inconel-718-powder-20240118/, date retrieved 26.02.2025
MATLAB (2017). R2017b, The MathWorks Inc.

Hybrid Optimization Method for I-Section Beams: A Comparative Study with Detailed FEM

Ahmet Aktaş[a], Hacı Abdullah Taşdemir[a]

[a]Istanbul Technical University Faculty of Mechanical Engineering, Department of Solid Mechanics, Türkiye
aktasahm16@itu.edu.tr

Keywords: FEA, I-beam, Optimization.

Aim

I-section beams have been fundamental components in structural engineering for over a century, frequently employed in ship interiors and decks, aircraft wings and fuselage structures, helicopter airframes and tail sections, as well as large structural frameworks, bridges, and building frames. These beams are commonly preferred over other cross sectional geometries due to their lighter weight and higher load carrying capacity. The main objective of this study is to develop an advanced optimization tool for I-section beams by merging established analytical and empirical methods from the literature with numerical approaches. This method integrates various failure modes (such as buckling, crippling, and stress-based failures) to ensure a minimum weight design that meets the required strength, based on user defined loads and geometric parameters (thickness, width, length). Initially, a load finite element model (LDFEM) model is constructed for the entire structure to rapidly estimate the loads acting on the beam of interest. These LDFEM derived loads are then used as input for the optimization process. The results obtained from this tool are compared with those from a detailed finite element model (DFEM) of the relevant structure, thereby allowing an assessment of the error margin in preliminary design. DFEM has a much finer mesh and includes smaller structural elements. It provides an accurate evaluation of the actual load distributions and stress patterns to assess the accuracy of the preliminary LDFEM based estimates. Through this integrated approach, the study aims to evaluate how accurately beam sizing can be performed prior to the use of high accuracy DFEM analyses. This will establish a practical and cost effective methodology suitable for preliminary design iterations.

Material and Method

The methodology of this study begins with the construction of a simplified LDFEM to determine the force distributions acting on an I-section beam. The loads obtained from this model are then input into a hybrid sizing method that integrates both analytical and empirical formulas to select a safe (Reserve Factor (RF) ≥ 1) and lightweight design from various geometric configurations. The optimal cross sectional dimensions identified by this method are then applied to a more accurate DFEM model and analysed under the same loading conditions. The DFEM stress results of the beam are compared with the applied stress values calculated using the LDFEM based loads which is showing how close the design of the simplified model is to reality and the extent of any associated error. This approach provides a quick, cost-effective solution at the initial design stage, while allowing the accuracy of the method to be verified against higher accuracy DFEM data.

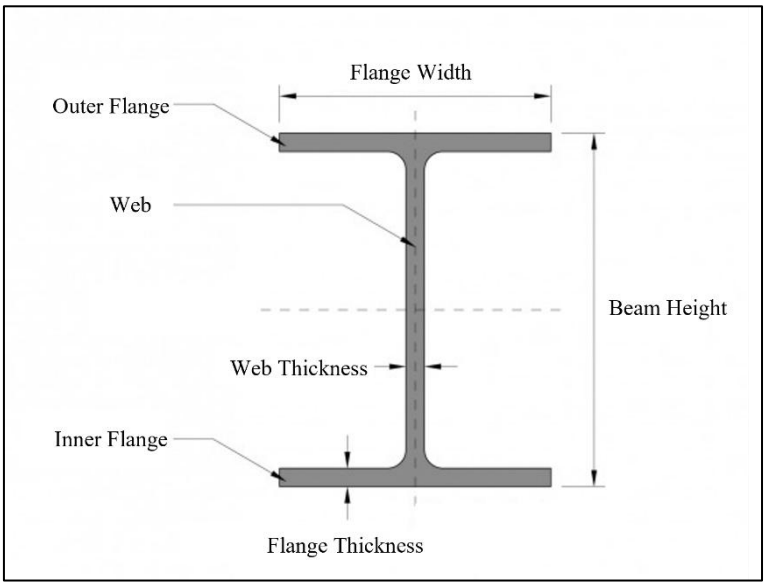

Figure 1. Illustration of an I-Section beam showing principal regions and dimensions.

Hybrid Sizing Method

The method performs optimization by separately evaluating the outer flange, inner flange, and web regions of an I-section beam. Potential failure modes in the inner and outer flanges include Johnson or Euler buckling, crippling and both compressive and tensile yielding. Under compressive loads, long-column behavior is assessed using Euler's buckling approach (Abbott, 2017), whereas short columns are analyzed with Johnson's method (Abbott, 2017). Crippling is calculated using an empirically derived formula (Flabel, 1997), taking into account material properties, flange width, flange thickness, and boundary conditions. In addition, the minimum and maximum stresses in the flange are compared against the material's compressive and tensile yield strengths, provide a strength evaluation in conjunction with the stability checks. For the web region, the method considers compressive and shear buckling failures (Gerard, 1957). The effect of the opening hole on the web on reducing the strength was taken into account by using the formula obtained by numerical methods (Wang, 2009). The approach assumes linear-elastic, isotropic material behaviour for all beam components, and web thickness, length, and height serve as key optimization parameters. From these analyses, the resulting RF is computed for each failure mode, and any design maintaining RF ≥ 1 across all modes is considered acceptable. Among these valid configurations, the tool identifies the lightest option as the optimum solution.

LDFEM

The LDFEM model is a numerical approach that uses relatively large mesh elements and omits certain detailed subcomponents. This strategy significantly reduces the modeling effort and preparation time, allowing for a rapid estimation of the load distributions acting on one or more beams. Because the LDFEM employs coarser elements and does not account for all structural details, the predicted loads may deviate from those obtained through more refined simulations. The extent of this deviation can be determined by constructing a DFEM model, which adopts finer mesh resolution and includes additional structural elements for greater accuracy. The loads derived from the LDFEM are subsequently utilized as inputs to the hybrid sizing method's analytical and empirical formulas, enabling an efficient preliminary evaluation of the beam design.

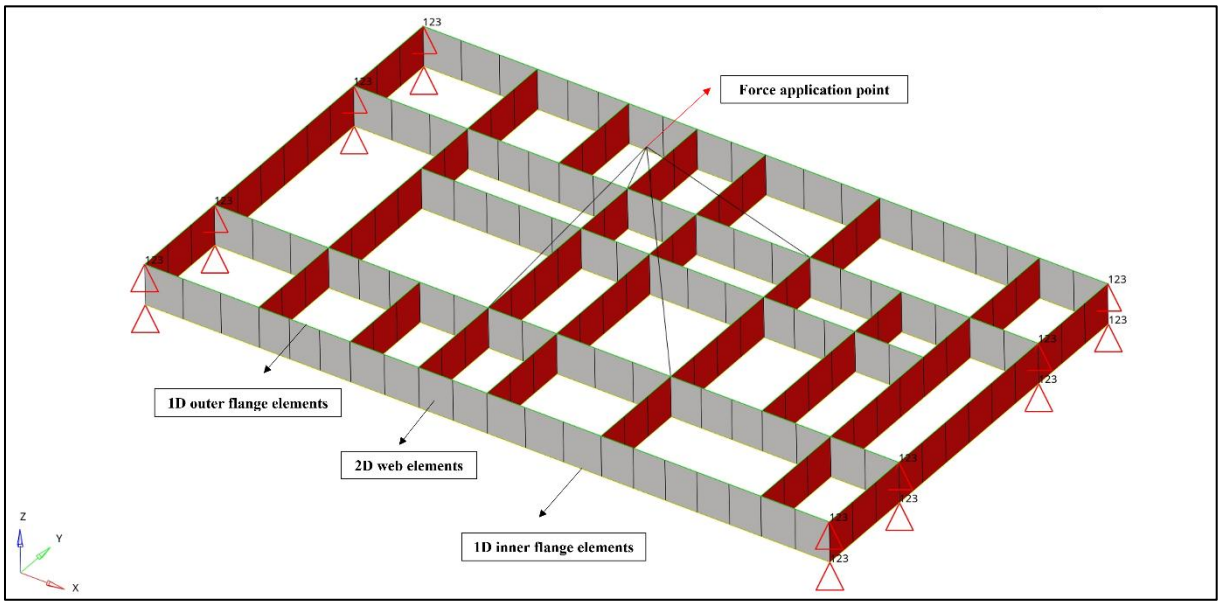

Figure 2. Illustration of the LDFEM.

DFEM

The DFEM model offers a far more comprehensive representation of the structure by including fasteners, angles, straps, and other small scale components that are omitted in the LDFEM. In contrast to the larger mesh elements used for the LDFEM, the DFEM may employ significantly finer discretization (for instance, a 5 mm element size), capturing localized stress concentrations and load paths with greater accuracy. In this study, a DFEM was developed to evaluate how closely the LDFEM reflects the true load flow through the structure, particularly under the same boundary conditions and applied forces. Constructing the DFEM is a more resource intensive and time consuming process due to its higher level of detail and denser mesh. Consequently, one of the goals of this work is to determine the extent of potential error introduced when using the LDFEM derived loads in the hybrid sizing method. By comparing the DFEM results with those from the LDFEM based analysis, it becomes possible to assess the balance between modeling simplicity and accuracy, thereby clarifying how reliable the preliminary load estimates from LDFEM can be in a detailed design context.

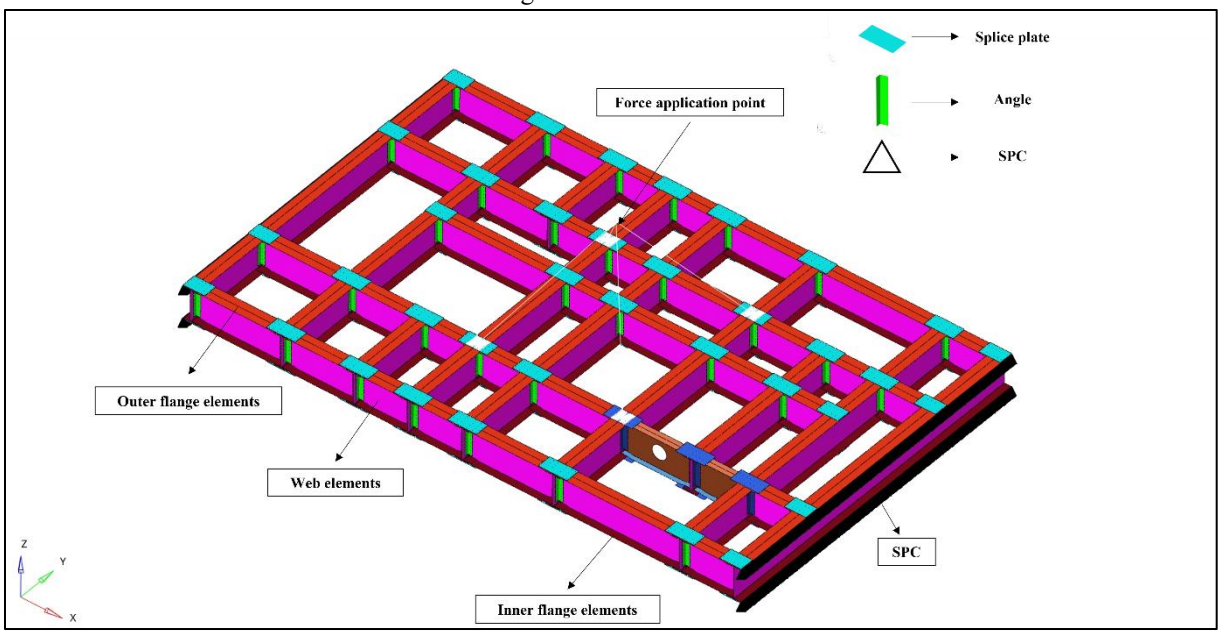

Figure 3. Illustration of the DFEM.

Findings

A hybrid optimization tool was used to determine the optimum dimensions of an I-section beam made from 2024 T42 Clad Aluminum. For the flange regions, the algorithm evaluated 19 thickness values, 21 widths and 61 lengths (24,339 total combinations), while the web section considered 19 thickness values and 11 widths (209 combinations). Initially, the outer flange was 2.5 mm thickness and 80 mm width, the inner flange was 3.0 mm thickness and 80 mm width, and the web thickness was 3.0 mm. After optimization, the outer flange was reduced to 0.8 mm thickness and 50 mm width, the inner flange to 1.0 mm thickness and 50 mm width, and the web to 2.0 mm thickness. This redesign reduced the overall beam weight from 1,536 g to 591 g, a 61% reduction. Under these conditions, the critical RF were 1.15 for tension yield in the outer flange, 1.05 for crippling in the inner flange and 1.34 for shear buckling in the web.

To validate the LDFEM approach, the DFEM model was constructed with approximately 462,000 elements, compared to the 574 element LDFEM. Under the same loading conditions, the DFEM predicted loads that differed on average by about 15% from the LDFEM based estimates. The outer flange and web showed slightly higher loads in the DFEM, while the inner flange showed a slight lower load. At local stress concentrations, such as flange-web intersections, the differences were more significant. But the overall error remained close to 15%. Given the significant computational savings, these results suggest that the hybrid sizing method is sufficiently accurate for preliminary sizing with DFEM serving as a reliable final check for critical regions and safety margins.

In addition, the hybrid approach provides a quick and reasonably accurate solution at the initial design stage, particularly for large or complex structures. After this initial stage of sizing, the optimized dimensions can be used in the DFEM for comprehensive verification. In cases where the structure has fewer detailed parts and more basic loading conditions, the hybrid method alone can provide reliable results without the need for DFEM.

Conclusion

This study has presented a hybrid optimization method for I-section beams, combining analytical and empirical formulas with the LDFEM to speed up the initial sizing process. By systematically evaluating a wide design space and maintaining a positive RF, the hybrid optimization method ensures that the beam design remains both lightweight and structurally safe. The method reduced the beam weight by 61% compared to a baseline configuration, while ensuring safety against multiple failure modes. A subsequent comparison with the DFEM showed that the average discrepancy in the load was approximately 15%, which is acceptable for early stage design decisions. Although certain localized regions, such as flange-web intersections, displayed higher differences, the overall accuracy of the hybrid approach was sufficient for guiding preliminary design in large or complex structures. From an engineering standpoint, the proposed methodology offers significant computational savings relative to creating a fully detailed model at every iteration. Designers can achieve rapid, near optimal configurations before turning to more detailed DFEM analyses. In simpler applications, where loads and structural details are less complex, the hybrid method may serve as an effective standalone solution. In more critical cases, a final DFEM check provides a detailed assessment of stress distributions and local stability. Future work could expand the hybrid approach by introducing additional failure modes and exploring alternative formulas or methods for failure calculations. The method could also address multiple or asymmetric cutouts in the web and investigate the inclusion of ribs on the web during the optimization process.These developments would further extend the suitability of the method for use in a wide range of engineering applications.

References

Abbott, R. (2017). *Analysis & design of composite & metallic flight vehicle structures*, 196-197.

Flabel, J. C. (1997). *Practical Stress Analysis for Design Engineers*, 354-425.

Gerard, G., & Becker, H. (1957). *HANDBOOK OF STRUCTURAL STABILITY. PART i. BUCKLING OF FLAT PLATES*. https://doi.org/10.2172/4343548

Wang, G., Sun, H., Peng, H., & Uemori, R. (2009). Buckling and ultimate strength of plates with openings. Ships and Offshore Structures, 4(1), 43–53. https://doi.org/10.1080/17445300802479437.

Structural Optimization of LPDC Aluminum Wishbone for Sheet Metal Design in Rear Suspension System for Electric C-SUV Vehicles

Alparslan Erdirençelebi[a]

[a]Istanbul Technical University, Mechanical Engineering Departmant, Solid Mechanics Program, Turkey
erdirencelebi17@itu.edu.tr

Keywords: Aluminium Wishbone Design, Automotive Suspension Technology, Design for Durability, Sheet Metal Wishbone Design, Strcutural Optimization.

Aim

Electric C-segment SUVs face pressure to reduce manufacturing costs while meeting performance targets. This study aims to replace a low-pressure die-cast (LPDC) aluminum rear suspension wishbone in a independent rear suspension with a cost-effective sheet metal design using S550 high-strength steel. The motivation is to leverage the lower material and production costs of stamped steel without sacrificing critical performance attributes. The wishbone must maintain wheel alignment and stability under load, enabling proper camber and toe characteristics during cornering and braking (Reimpell, Stoll, & Betzler, 2001). Aluminum control arms are lightweight, reducing unsprung mass and benefiting handling and ride quality (Reimpell et al., 2001). However, cast aluminum components entail high material and processing costs (Nagarjuna & Devaki Devi, 2012). In contrast, stamped steel arms are inexpensive and commonly used in cost-sensitive vehicle models (Nagarjuna & Devaki Devi, 2012). The objective is to achieve significant cost reduction by switching to an S550 steel sheet metal wishbone, while ensuring the new design meets or exceeds the original's performance constraints. Key performance criteria include: (1) Stiffness retention – the new arm must preserve suspension kinematics, keeping camber and toe change within acceptable limits under load; (2) Durability – it must endure proof and extreme loads without failure and offer adequate fatigue life; (3) Packaging – the geometry must fit within the existing suspension architecture and clear surrounding components. By focusing on structural optimization of the wishbone's design, the study targets a solution that balances weight, strength, and cost, thereby improving manufacturing feasibility for mass-production EVs without undermining vehicle dynamics or safety.

Material and Method

The design methodology integrates material selection, computational optimization, and rigorous simulation analysis. Material Selection: S550 steel was chosen for its high strength (yield strength on the order of 550 MPa) and good formability, allowing thinner gauges to be used to counteract its higher density relative to aluminum. Although steel is roughly three times heavier than aluminum per unit volume, its Young's modulus is also about three times higher (≈210 GPa vs. 70 GPa), which aids stiffness. The baseline LPDC wishbone is an aluminum alloy (e.g., AlSi7Mg) part whose geometry and performance served as a starting reference (Nagarjuna & Devaki Devi, 2012). Design & Optimization: A design space was defined based on the packaging envelope of the original arm. A topology optimization approach was employed to conceive an initial load-efficient shape for the sheet metal design, given the existing hard points and space constraints. This optimization prioritized material distribution for maximizing stiffness-to-weight ratio, yielding a conceptual geometry that could meet the load paths of the suspension. Using this as a guide, a detailed CAD model of a sheet metal wishbone was developed. The design consists of stamped steel sections seam-welded into a closed-cross-section control arm, providing bending and torsional rigidity comparable to the cast arm. Throughout the design process, manufacturing constraints were imposed (minimum bend radii, stamping draw depth limits, weld accessibility) to ensure the concept is production-feasible.
Finite Element Analysis (FEA): The candidate steel wishbone design was subjected to extensive FEA to evaluate structural performance. Stiffness Analysis: Quasi-static stiffness tests were simulated by applying representative

loads at knuckle connecting hardpoints and measuring the resulting deflection between the hardpoints. The compliance directly correlates with camber and toe changes. The optimized steel arm achieved equivalent stiffness to the aluminum arm, owing to the higher elastic modulus of steel and an optimized boxed geometry, thereby preserving wheel alignment characteristics under load. Strength and Durability: FEA was conducted for extreme load cases such as pothole strikes and curb impacts (proof loads). The steel design remained within the elastic range under these loads, with von Mises stresses below the yield threshold, indicating no plastic deformation or cracking. Fatigue life estimation was performed using an amplitude-based approach: load spectra from road load data or standards were applied to assess if the design would survive the required number of cycles. Since steel exhibits an endurance limit (a stress amplitude below which infinite life is possible), the design was iterated until all stress hotspots were reduced under this limit or had acceptable life. Weld regions were given special attention in fatigue analysis, using appropriate weld fatigue factors. Comparative Evaluation: After optimization and analysis, the steel wishbone's performance was benchmarked against the original aluminum component. Prior research (Fuchs & Salmon, 2011) demonstrated that a well-designed lightweight steel control arm can achieve equivalent structural performance to an aluminum arm at lower cost, a finding corroborated by our results. Similarly, multidisciplinary optimization studies (e.g., Heo, Kang, Lee, & Choi, 2013) guided the refinement of our design to meet all targets. The final design underwent a design for manufacturability review with tooling engineers to confirm that the sheet metal forming and welding processes are feasible at scale (Yu, Jia, & Huang, 2021). The outcome of this methodical approach is an optimized S550 steel wishbone design that satisfies the mechanical performance requirements while significantly reducing

Findings

The feasibility study confirms that the sheet metal S550 steel wishbone can successfully replace the LPDC aluminum wishbone without compromising suspension performance. In static stiffness analyses, the steel design demonstrated comparable camber and toe stiffness, meaning it maintains wheel alignment under cornering and braking loads essentially as well as the aluminum arm (Fuchs & Salmon, 2011). This ensures that vehicle handling dynamics and tire wear characteristics remain consistent. The higher elastic modulus of steel contributed to maintaining rigidity, even though the part's mass is higher (Reimpell et al., 2001). Durability results indicate that the optimized steel arm meets or exceeds the required fatigue life. The combination of a robust design and steel's favorable fatigue endurance properties (having an endurance limit) resulted in a component that can endure repetitive road loads over the vehicle's service life without crack initiation. In fact, steel control arms are known for their ability to withstand heavy loads and impacts; our design shows no signs of localized weakness under peak loads, and the stress distribution is smooth, minimizing potential fatigue hot spots. Packaging and weight: The new wishbone fits within the same geometric envelope as the original, with minor modifications in shape to accommodate the stamping process (such as flanges and ribs). All clearances to other suspension links, brake components, and the chassis are maintained. The weight of the steel arm is unavoidably higher than the aluminum arm; however, through careful optimization of thickness and shape, the weight increase was kept as low as feasible. The final design's mass is only marginally higher, a small trade-off for a substantial cost reduction. This added unsprung mass is considered acceptable for a C-SUV EV, especially given that battery weight often dominates and the slight increase has negligible impact on overall vehicle efficiency. Finally, the cost advantages are significant: the material cost per arm is lower due to steel's lower price per kilogram and the near-net-shape forming that minimizes waste. Production costs per piece drop thanks to faster cycle times in stamping (once tooling is in place) compared to casting and the elimination of extensive machining operations. While exact figures are proprietary, the automaker can expect a notable reduction in suspension system cost, contributing to a lower overall vehicle cost (Nagarjuna & Devaki Devi, 2012).

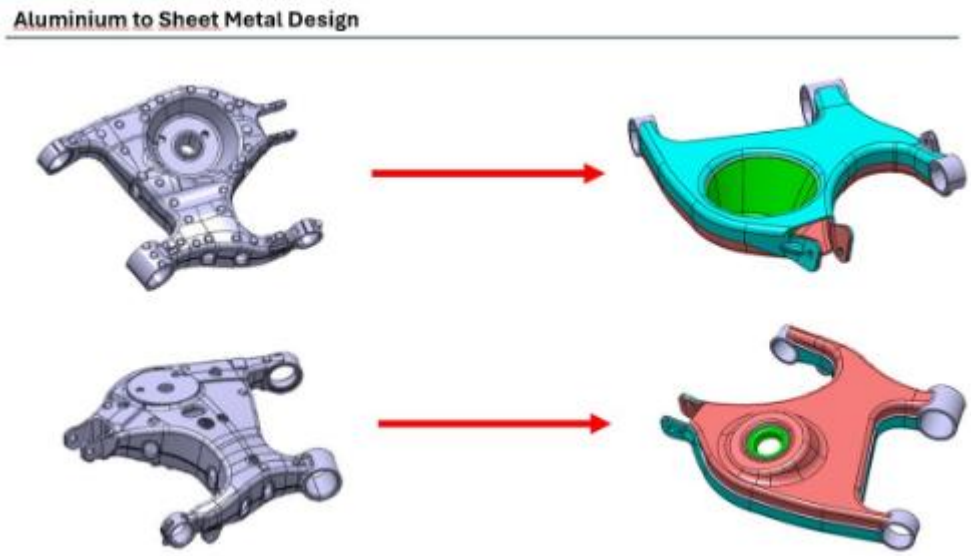

Figure 1. Aluminium to Sheet Metal Wishbone Design.

Conclusion

This work demonstrates a successful material and design substitution in an EV rear suspension component, yielding both economic and engineering benefits. The optimized S550 sheet metal wishbone achieves equivalent stiffness and durability performance to the original LPDC aluminum wishbone, validating that critical parameters such as camber compliance, toe stiffness, and fatigue life are preserved. The transition to a steel design offers a substantial cost reduction, aligning with the cost targets for mass-market electric SUVs without impairing vehicle dynamics or quality. Crucially, the redesign was accomplished with minimal impact on weight and no compromise to fit or function – a testament to the efficacy of structural optimization techniques in chassis component development. From a manufacturing standpoint, the new design leverages high-volume production methods (progressive stamping, automated welding) that promise reliable quality and cycle times, thus enhancing production efficiency (Yu et al., 2021). The implications of this work extend beyond the specific part: it showcases a systematic approach to re-engineering existing components for better cost-performance balance, which can be applied to other aluminum-to-steel conversions in the vehicle (Reimpell et al., 2001). Overall, replacing the aluminum rear wishbone with an optimized steel assembly is found to be practical and beneficial, delivering cost savings and maintaining performance. This contributes positively to the manufacturing feasibility and sustainability of the EV's design. The outcome supports the broader strategy of using the right material in the right place – employing aluminum where ultra-lightweight is paramount and using advanced high-strength steels where cost-effectiveness can be achieved without detriment to performance (Nagarjuna & Devaki Devi, 2012). As electric C-SUV platforms continue to mature, such optimization efforts will be key to balancing range, performance, safety, and cost. The success of this project encourages further exploration of material optimization in automotive suspensions, reinforcing that innovative design can unlock the potential of traditional materials in modern EV applications.

References

Fuchs, H., & Salmon, R. (2011). Lightweight MacPherson strut suspension front lower control arm design development (SAE Technical Paper No. 2011-01-0562). SAE International. https://doi.org/10.4271/2011-01-0562

Heo, S. J., Kang, D. O., Lee, J. H., & Choi, J. H. (2013). Shape optimization of lower control arm considering multi-disciplinary constraint condition by using progress meta-model method. International Journal of Automotive Technology, 14(3), 499–505. https://doi.org/10.1007/s12239-013-0068-0

Nagarjuna, P., & Devaki Devi, K. (2012). Design and optimization of sheet metal control arm for independent suspension system. International Journal of Engineering Research and Applications, 2(5), 535–539.

Reimpell, J., Stoll, H., & Betzler, J. W. (2001). The automotive chassis: Engineering principles (2nd ed.). SAE International.
Yu, Z., Jia, H., & Huang, X. (2021). Design of the lower control arm of an electric SUV front suspension based on multi-disciplinary optimization technology. Jordan Journal of Mechanical and Industrial Engineering, 15(1), 7–14.

Post-Buckling Behavior of Metallic Panels

Taha Çimen[a], Ata Muğan[a]

[a] Istanbul Technical University, Mechanical Engineering, Solid Mechanics Program, Turkiye
ciment17@itu.edu.tr

Keywords: Buckling, Post-Buckling, Post-Buckling Strength, Secondary Buckling Load.

Aim

The primary aim of this thesis is to investigate the effect of plastic strain on the critical buckling load of panels subjected to reloading. When plasticity occurs during the post-buckling stage of thin-walled structures, their stiffness is altered, which in turn influences their buckling resistance. However, the extent of this reduction and its implications on structural performance remain insufficiently explored.

Numerically, finite element simulations are performed in Abaqus to evaluate the impact of plastic strain accumulation on the critical buckling load. A total of 18 different models are created for numerical analysis, considering two different materials. The panel dimensions are varied with side lengths of 500 mm, 650 mm, and 750 mm, while the thickness is set to 2 mm, 3 mm, and 4 mm for each case.

By comparing the critical buckling loads of plastically deformed and undeformed panels, this research aims to quantify the reduction in buckling resistance due to prior plastic deformation. The findings will contribute to a deeper understanding of post-buckling behavior in engineering structures and provide guidelines for design improvements and failure prevention in load-bearing applications.

Material and Method

The finite element analyses were conducted via software ABAQUS to simulate panels under shear load. To create FE models, S4R elements, which are shell elements with reduced integration, were utilized. The used shell elements have 5 integration points. In ABAQUS, nodes of S4R elements have 6 DOF with three rotational and three translational. Also, the 30x30 mesh was selected as the minimum required mesh after the mesh convergence study.

In Figure 1, the used boundary condition that provides clamped edges and pure shear loading is given. It can be seen that the edges of the plates can move freely in both directions. In order to compare and validate the numerical findings with the data that is theoretically accessible, the clamped boundary condition was used.

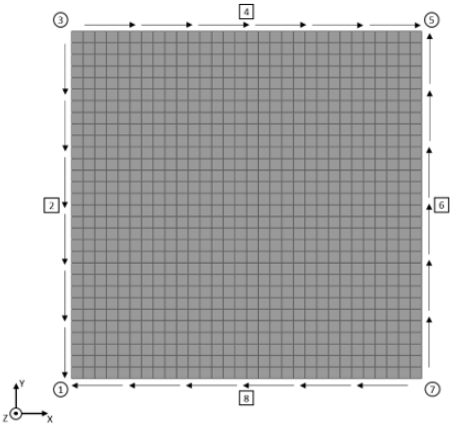

No	u_x	u_y	u_z	θ_x	θ_y	θ_z
1	■	■	■	■	■	■
2	□	□	■	□	■	□
3	□	□	■	■	■	■
4	□	□	■	■	□	□
5	□	□	■	■	■	■
6	□	□	■	□	■	□
7	□	□	■	■	■	■
8	□	□	■	■	□	□

□: Free ■: Fixed

Figure 1. Boundary Condition of FE Model.

The used panel material in this thesis is AL-5754 alloy and ST-37. The data used to define materials were taken from stress-strain graphs found in literature [1], [2].

The calculation of the critical buckling load of the panel that has plastic strain is conducted in five steps:

- The Linear Buckling Analysis (Eigenvalue Extraction)

First, the eigenvalues and eigenmodes of the panel were calculated using a linear buckling analysis step, which employs the Lanczos eigen solver. The boundary condition was applied as shown in Figure 1, and 1 N is applied as a shell edge load.

- The Nonlinear Post-Buckling Analysis (Static Riks Method)

After obtaining the eigenmodes, the panel was analysed using a Static Riks analysis step to determine its post-buckling capacity. Although the same boundary conditions as in the linear buckling analysis were applied, the magnitude of the shell edge load was determined based on the panel's eigenvalue. In this step, the first eigenmode of the panel, shown in Figure 2, is introduced as an initial imperfection using the *IMPERFECTION command. The imperfection magnitude is set to t/100, where 't' is the panel thickness.

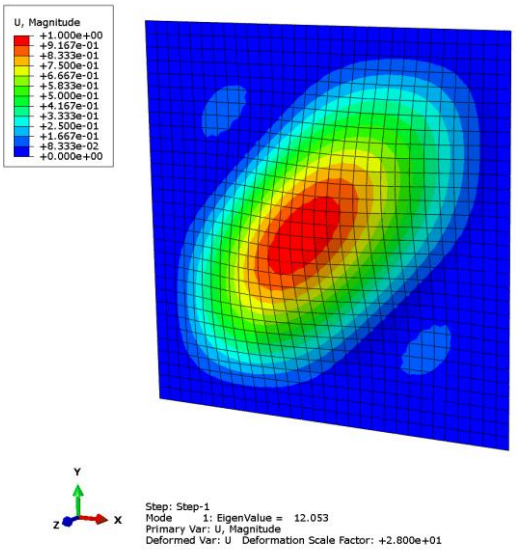

Figure 2. First Eigenmode of Panel.

The introduction of an initial imperfection is essential for this type of analysis, as it enables the structure's post-buckling behavior to be captured, allowing the ultimate load (V_u) to be determined. Without an imperfection, the model may not progress beyond the buckling bifurcation point, preventing an accurate post-buckling load-displacement response from being obtained.

- Defining Plastic Strain After Post-Buckling

To evaluate the secondary buckling load of the panel, the different levels of plastic strain such as 25%, 50%, 75%, and 100% developed in the post-buckling stage were separately transferred to new models using the *PREDEFINED FIELD function. This ensures that the residual plastic strains and deformations from the previous post-buckling analysis are correctly applied as the initial state in the new analysis.

- Strain Relaxation Step

Since both elastic and plastic strain are developed while reaching the ultimate load, an additional static step was introduced to allow the elastic stain to relax, leaving only the plastic strain in the model. This step was created using same boundary condition, but external load was not applied.

- Secondary Buckling Load Calculation

After completing the strain relaxation step, a linear buckling analysis was conducted again on the plastically deformed panel to determine its new critical buckling load.

Findings

In this study, the finite element (FE) analyses were conducted for eighteen different panel configurations made from AL-5754 alloy and ST-37, with varying dimensions and thicknesses. The panel sizes and thicknesses were chosen to ensure that plastic strain would occur under the ultimate (post-buckling) load, thereby allowing the evaluation of the effect of plastic strain on the linear buckling load.

- Linear Buckling Analysis

The linear buckling analysis was performed to calculate the critical buckling loads (V_{cr}) and associated mode shapes used to define initial geometric imperfections in the post-buckling analysis. The results and panel dimensions can be found in Table 1. It is revealed that the critical buckling load increases significantly with increasing panel thickness, due to the bending stiffness scales with the cube of thickness. Thus, even when in-plane dimensions remain constant, thicker panels exhibit greater resistance to buckling.

Table 1. The Critical Buckling Loads of Panels.

Materials	F_{CR}^{FEM} (N)	Materials	F_{CR}^{FEM} (N)
AL57-500x2	15117.5	ST37-500x2	45056.0
AL57-500x3	50980.0	ST37-500x3	151940.0
AL57-500x4	120695.0	ST37-500x4	359745.0
AL57-650x2	11631.75	ST37-650x2	34667.8
AL57-650x3	39238.55	ST37-650x3	116948.0
AL57-650x4	92943.5	ST37-650x4	277017.0
AL57-750x2	10082.25	ST37-750x2	30048.0
AL57-750x3	34014.0	ST37-750x3	101377.5
AL57-750x4	80587.5	ST37-750x4	240172.5

- Post-Buckling Analysis

For the investigation of structural performance beyond the critical point, nonlinear post-buckling analyses were conducted using Static Riks method. The post-buckling loads (F_u), corresponding shear plastic strains (ε) are given in Table 2.

Table 2. The Ultimate Buckling Loads of Panels.

Materials	F_U (N)	Materials	F_U (N)
AL57-500x2	34619.1	ST37-500x2	82452.5
AL57-500x3	75144.5	ST37-500x3	180808.6
AL57-500x4	132161.0	ST37-500x4	334562.9
AL57-650x2	35825.8	ST37-650x2	84589.4
AL57-650x3	76907.6	ST37-650x3	183608.4
AL57-650x4	133838.6	ST37-650x4	321339.7
AL57-750x2	36699.4	ST37-750x2	86237.7
AL57-750x3	77892.0	ST37-750x3	185520.8
AL57-750x4	134581.1	ST37-750x4	324232.9

The results show that there is a clear dependence between thickness and post-buckling load. It can be concluded from Table 2 that thinner panels and lower elastic modulus causes lower the ultimate buckling load, while the thicker panel and higher elastic modulus causes higher F_u values.

- Secondary Buckling Analysis

In this section, the secondary buckling behavior of the panels was investigated. This analysis was conducted using plastic strains in the post-buckling stage. To study the effect of plastic strain on the critical buckling load during reloading, four levels of plastic strain were applied: 25%, 50%, 75%, and 100% of the total plastic strain that occurs at the ultimate buckling load.

The secondary buckling loads and percentage of reduction of critical buckling load of AL-5754 alloy and ST37 panels for different plastic strain levels are presented in Figure 3, Figure 4 and Figure 5. The results show that the buckling resistance is reduced in occurrence of plastic strain for all panel configurations due to the critical buckling load decreases as the applied plastic strain increases.

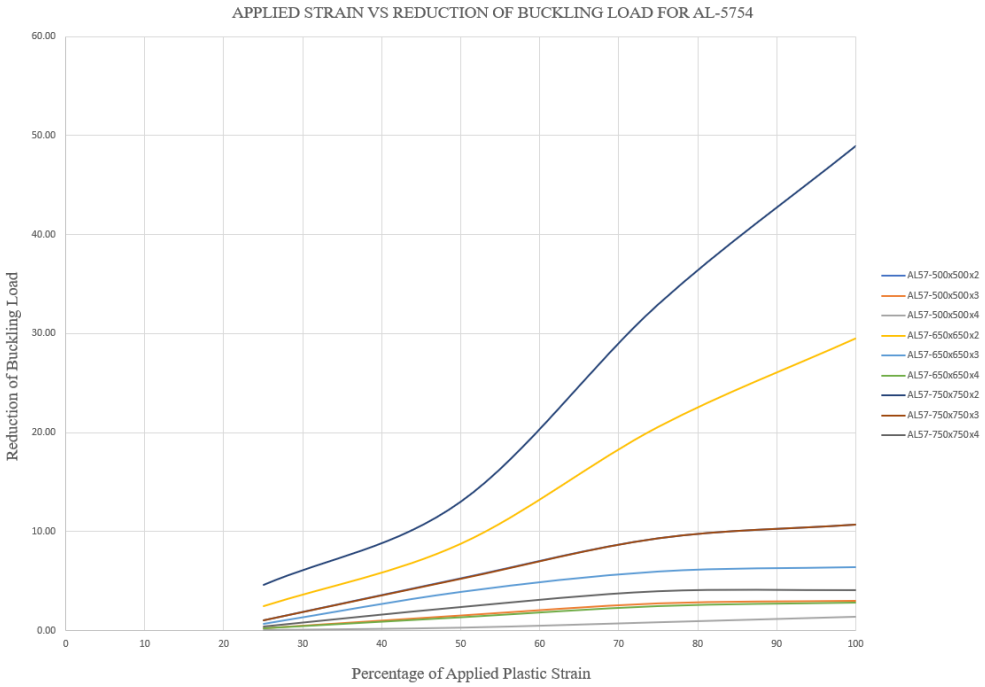

Figure 3. Applied Strain vs Reduction of Secondary Buckling Load for AL-5754.

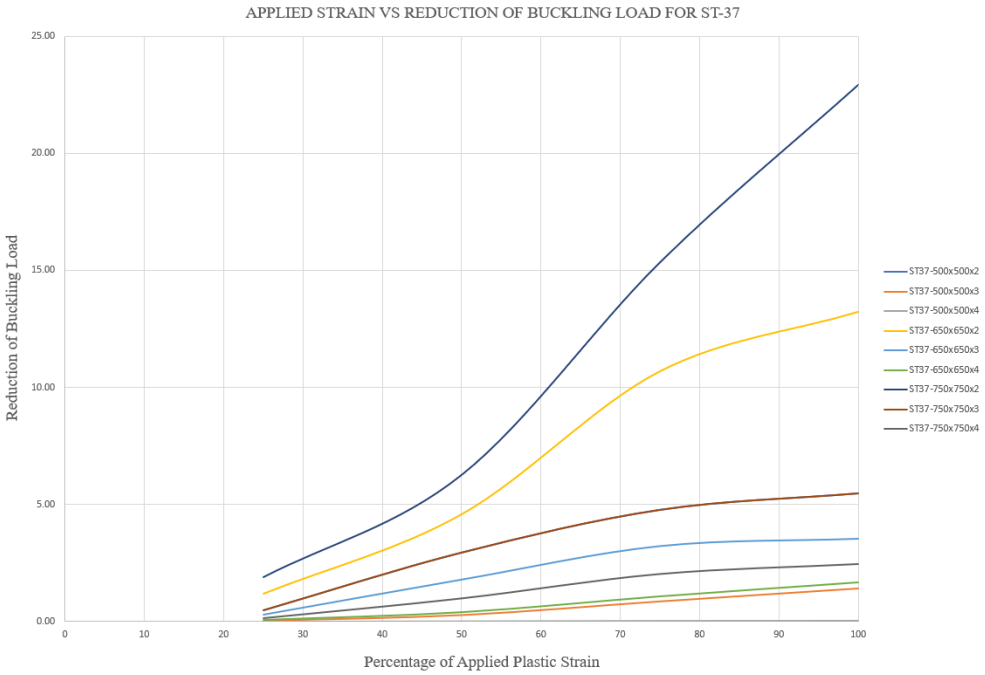

Figure 4. Applied Strain vs Reduction of Secondary Buckling Load for ST-37.

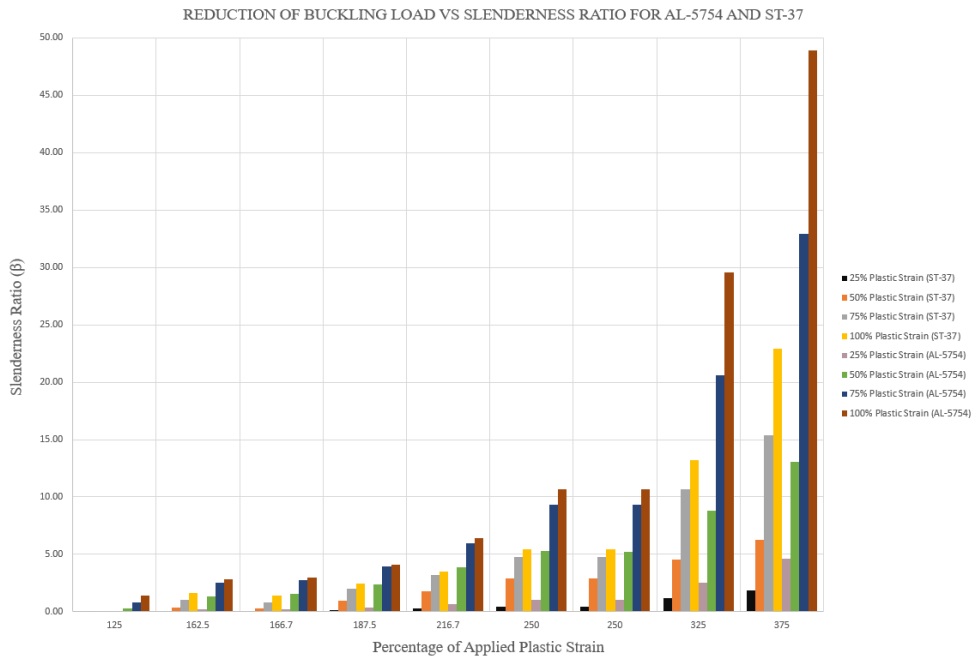

Figure 5. Slenderness Ratio (β) vs Applied Strain for AL-5754 and ST-37.

At low slenderness ratios, both AL-5754 and ST-37 show very small reductions in buckling load, even under 100% plastic strain. This indicates shorter and thicker panels are more resistant to plastic strain. However, as the slenderness ratio increases, the reduction becomes much higher especially for AL-5754.

Moreover, it can be seen from the figures that the reduction of buckling load is calculated the same for the 750X750X3 mm and 500X500X2 mm panel configurations. The common property of these panels is their slenderness ratio and post-buckling reserve, which directly affect the percentage reduction in buckling load.

While the reduction for ST-37-500×500×2 panel configuration increases gradually from 0.5% at 25% strain to 5.5% at 100%, the AL-5754 panel of the same size shows 1.03% at 25%, and 10.7% reduction is calculated when 100% plastic strain is applied, which means that the aluminium panels loses their stiffness than steel plates under the same conditions.

ST-37-500×500×3 panel shows only 1.4% reduction at 100% strain, while the reduction of secondary buckling load of AL-5754 reaches more than twice as much, which is 3.02%. In 500×500×4 panels, there is almost no reduction for the ST-37 panel, while AL-5754 still shows a larger reduction under 100% plastic strain. The calculated reductions are 0.008% and 1.4% for the AL-5754 and ST-37, respectively. These results clearly show that thicker steel panels are nearly unaffected, while aluminium still loses some strength.

The difference becomes even clearer as the slenderness ratio increases. The reductions of 650×650×2 panels are calculated as 13.2% and 29.5% at 100% strain for the ST-37 and AL-5754, respectively. These reductions are decreased with increasing thickness. However, the aluminium panels always show higher reduction compared to steel panel even in same slenderness ratio. For example, 3.5% and 6.4% values are calculated for 650×650×3, and 1.6% and 2.9% values are calculated for 650×650×4 panel configurations for ST-37 and AL-5754 materials, respectively.

The biggest difference is seen in 750×750×2 panels, where the ST-37 panel reduces by 22.9%, but AL-5754 drops sharply by 48.9%, showing that thin and large aluminium panels lose nearly half of their buckling strength under full plastic strain. In the 750×750×3 configuration, ST-37 shows 5.5%, while AL-5754 shows 10.7%. Even in 750×750×4 panels, ST-37 shows 2.4% and AL-5754 has 4.07%.

These values show that ST-37 steel is more resistant to buckling strength reduction after plastic strain, especially in thicker or shorter panels. In contrast, AL-5754 panels are more sensitive and can lose a significant part of their capacity, especially when thin and slender.

Conclusion

In this study, the effects of plastic strain on the critical buckling behavior of slender panels under in-plane shear loading were investigated. Both numerical analysis and experimental study were used to understand influence of plastic strain, developed in the post-buckling stage, on the critical buckling load during reloading.

The results showed that as plastic strain increases, the secondary buckling load decreases. This effect becomes more significant in panels with higher slenderness ratios and smaller thicknesses. In general, slender and thin panels are more sensitive to plastic strain, while thicker and shorter panels preserve most of their buckling strength.

When different materials were compared, ST-37 panels performed better than AL-5754 panels in terms of resistance to plastic strain. For example, at 100% plastic strain, the AL-5754 panel with a slenderness ratio of 375 showed up to 48.9% reduction, while the ST-37 panel of the same size showed only 33% reduction.

Among the materials, panels made from ST-37 show the least sensitivity to plastic stain especially for panels with 4 mm thickness, which maintain nearly their full buckling capacity with less than 2% reduction.

The findings confirm that both material selection and geometric properties (slenderness ratio and thickness) have a strong influence on secondary buckling load of panel and their post-buckling performance. For structural applications where panels may undergo plastic deformation and be reloaded, ST-37 is a more reliable material for designs requiring high stability and load-carrying capacity after buckling. especially in shorter and thicker forms. This makes ST37 a good choice for structures that may experience overloading or reloading conditions.

References

Zlatanovic, D. L., Balos, S., Bergmann, J. P., Köhler, T., Grätzel, M., Sidjanin, L., & Goel, S. (2020). An experimental study on lap joining of multiple sheets of aluminium alloy (AA 5754) using friction stir spot welding. *The International Journal of Advanced Manufacturing Technology*, *107*(7–8), 3093–3107. https://doi.org/10.1007/s00170-020-05214-z

Esmaeili, F., Rahmani, A., Barzegar, S., & Afkar, A. (2015). Prediction of fatigue life for multi-spot welded joints with different arrangements using different multiaxial fatigue criteria. *Materials & Design (1980-2015)*, *72*, 21–30. https://doi.org/10.1016/j.matdes.2015.02.008

MECHANICAL ENGINEERING

Additive Manufacturing

Automotive

Computational Fluid Dynamics

Computational Solid Mechanics

Fluid Mechanics

Industrial Data Analytics

Machine Design

Machine Dynamics, Vibration, and Acoustic

System Dynamics and Control

Weight and Volume Optimization of Two Stage Wolfrom Planetary Gear Mechanism

Kadir Kanat[a], Ali İmre Aydeniz[a], Cevat Erdem İmrak[a]

[a] Istanbul Technical University, Mechanical Design Program, Türkiye
kanat18@itu.edu.tr

Keywords: Fine Sizing, Gear System, Optimization, Particle Swarm Optimization, Wolfrom Planetary.

Aim

Wolfrom planetary mechanisms are gear systems used in all, especially in the aviation and energy industries. It is a compact power transmission system with five different gears. It also appears in the literature as systems without planet carriers (carrierless system). Its advantages include the possibility of concentric operation, high transmission ratio and durable systems. Due to having two different internal gear groups and the large number of gear groups, these are systems that operate with high cost and low efficiency. Due to the operation of 5 different gear groups (Figure 1.) and the use of coaxial planetary shafts, low tolerances and profile shifting operations in gears are frequently encountered situations in these mechanisms.

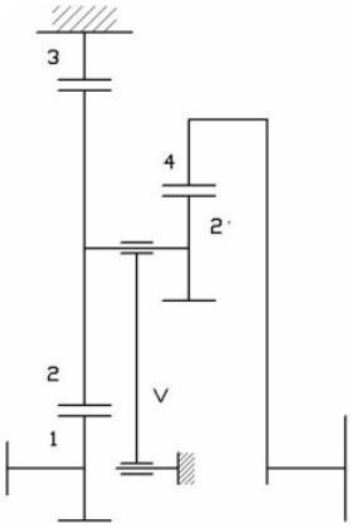

Figure 1. Wolfrom Planetary Mechanism System Design.

The aim of the study is to design a gearbox with minimum volume and weight that will provide the desired torque and speed requirements at the output of a Wolfrom planetary mechanism. The results of the used optimization method and gear commercial software (KissSoft) will be compared. In this system, also called the two stage planetary mechanism, in order to provide power transmission, the planetary gear groups must operate in different pitch circles. This situation also shows that the assembly conditions must be taken into consideration when designing. In addition, one of the design criteria is to use small gears in order to provide the minimum volume and weight that we aim for. For this, profile shifting must be done in order to obtain the minimum number of gears without experiencing undercutting situations. In particular, positive profile shifting was done due to the number of teeth falling below 17 in planetary gears. In this way, gear strength was tried to be provided with minimum gears. The parameters to be optimized are determined as the number of teeth, module, tooth thickness, pressure angle, material and material quality, and center distance.

Material and Method

In the first stage of the study, "Fine Sizing" optimization was performed for the center planet group via KissSoft software. The main purpose of "Fine Sizing" optimization is to give value ranges for certain variables in gear groups and to determine constants. With the determined values, all mountable macro geometry iterations that can occur in the gear group have emerged. With "Fine Sizing", both the internal gear mesh and the external gear mesh are optimized for planetary (Figure 2.). While performing planet modeling, variable values were determined as module in the range of 1.5-2.5, center distance between 45-55, tooth width in the range of 5-20, profile shift ratio between -0.6 and 1. As fixed values, pressure angle was determined as 20 degrees and profile shift ratio of internal gear was determined as 0. It was also considered that the study was an easy-to-produce mechanism rather than a simulation. The reason why the profile shift ratio of internal gear was taken as 0 is that the critical role in planet strength calculations is in the planet and sun gears and the profile shift ratio of internal gear has no connection with the profile shift ratio between planet and sun gear. In addition, the effects of the change in the number of planets on gear strength were observed.

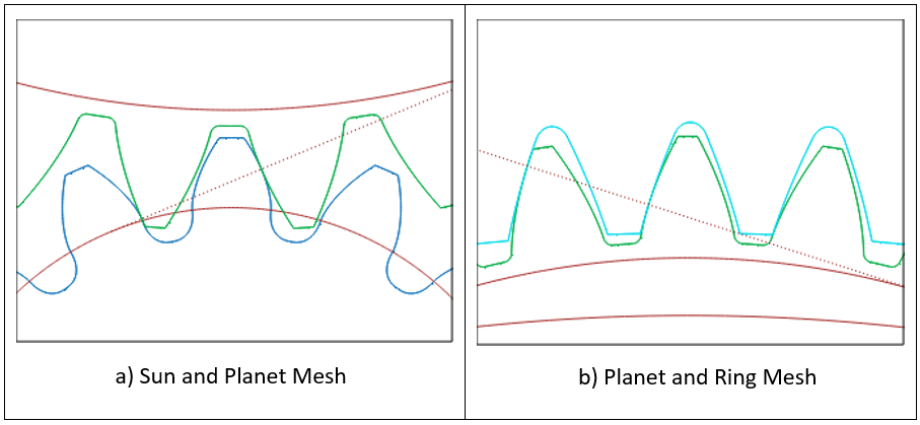

Figure 2. Wolfrom Planetary Mechanism Gear Profiles.

In the second stage of the study, "Particle Swarm Optimization" (PSO) method was used for volume optimization of two-stage Wolfrom type planetary gear system. Planetary gear systems are widely used in modern engineering applications with their high efficiency and compact structure features. Volume optimization is of great importance in terms of these systems taking up less space and reducing material costs. In the study, it was aimed to design the system in minimum volume by considering the geometric and mechanical design parameters of the gear stages. In the optimization process, it was aimed to obtain the most suitable gear dimensions within the framework of the determined constraints (such as strength, durability, and construction limitations). PSO optimization was coded. The inputs for the Wolfrom planetary gear mechanism were determined as the same data as in the "Fine Sizing" process. Gear strength control was performed according to gear bending and pitting. The module parameter was determined as a result of the hertzian pressure of the gear surface (pitting) and gear root bending. In addition, factors such as dynamic load factor, application factor and form factor (K_A, K_V etc.) were used when determining the module.

Findings

During the studies and literature review, it was seen that the most important issue while designing a two-stage wolfrom mechanism was planetary macro geometry design. The concentric operation of the planetary gears in two stages shows that the difference in the number of teeth between the internal gears should be equal to the difference in the number of teeth between the planets or a maximum of two. It was observed that gear pairs could operate with positive profile shifting in the case of a maximum difference. In addition, since it is a carrierless system design, it was concluded that crowning should be applied as micro geometry on gear surfaces due to the bending that will occur in the planetary gear shafts. Crowning aims to spread the Hertz pressure surface on gear surfaces to the middle of the tooth width. Also, a systematic approach was put forward to keep the gear ratio constant. As

seen in the gear ratio formula, there are five different gear tooth numbers. This formula should also be taken into consideration when making the optimization.
The internal gear and planet meshes in two stages were also checked according to the interference conditions. The optimization conditions were checked according to the minimum gear numbers. In places where there will be interference, it was determined as a suggestion to reduce the addendum coefficient of the internal gear. Reducing the addendum coefficient of the internal gear without reducing the contact ratio below 1 prevents interference, if any.

Conclusion

As a result, the PSO study and "Fine Sizing" results were evaluated. In the incoming results, while the volumes of the Wolfrom planetary mechanisms were close to each other, similar results were obtained in the number of gears. In the "Fine Sizing" results, the optimum result was obtained by the elimination method. While elimination was made, the minimum root safety and minimum flank safety factors were taken as 1.1 for each gear and the values below were eliminated (Figure 3.). In addition, the results where the undercut and contact ratio were below 1 were eliminated. Among the remaining results, the gear set that met the minimum volume and weight conditions and complied with the gear strength criteria was selected. The PSO algorithm has attracted attention by providing a faster solution compared to traditional methods. The weights of the gearboxes formed after approximately 200 different iterations in the created algorithm were compared (Figure 4.). This algorithm has operated an iterative process to find the optimum parameter combination under certain constraints in gear design. The results obtained have shown that while a significant reduction of 13.5% was achieved in the total volume of the gears, basic requirements such as strength and durability were met. It has also been observed that the optimization performed with the "KissSoft Fine Sizing" yielded similar results in terms of volume. During the optimization, the compliance of parameters such as the contact ratio with the limit values was checked and the design life was increased. As a result, this study has contributed to establishing a balance between lightness and durability in gear design. In particular, the optimization of parameters such as surface contact stress and contact ratio increased the performance of gear systems. In addition, the results obtained have revealed that the PSO algorithm is an effective method in gear optimization.

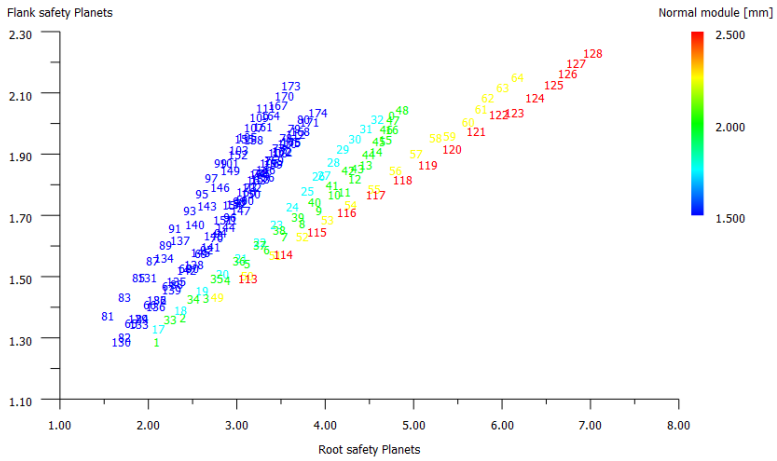

Figure 3. KissSoft Fine Sizing Planetary Safety Results.

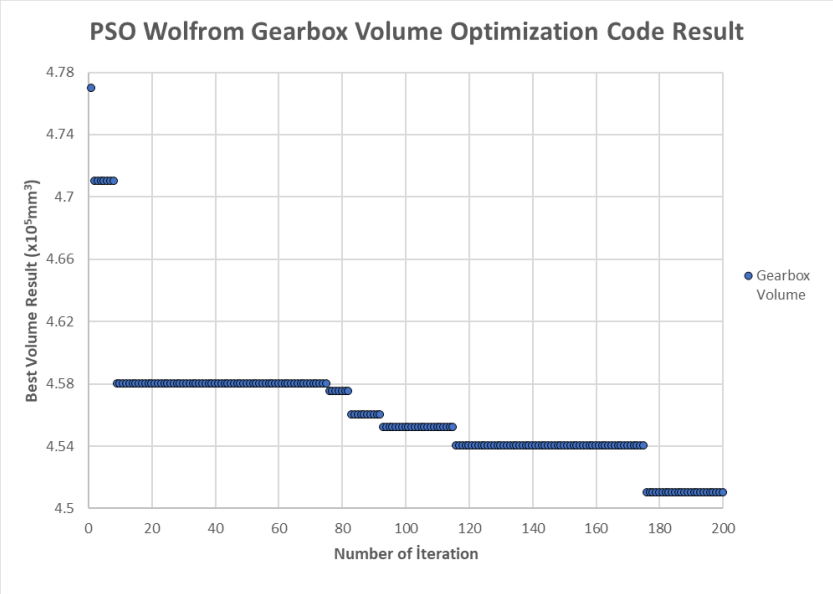

Figure 4. Particle Swarm Optimization Iteration Code Results.

References

ANSYS Inc. (2020). ANSYS User Manual. Canonsburg, PA: ANSYS Inc.

Anula Khare, Saroj Rangnekar. (2013). A review of particle swarm optimization and its applications in Solar Photovoltaic system.

Chandel, D. K., (2023). Design And Optimization Of Spur Gear For Optimal Weight With Particle Swarm Optimization Technique.

Cooley, C. G., Parker, R. G. (2014). A Review of Planetary and Epicyclic Gear Dynamics and Vibrations Research.

Crispel, S., López García, P., Saerens, E., Varadharajan, A., Verstraten, T., Vanderborght, B., & Lefeber, D. (2021). A novel Wolfrom-based gearbox for robotic actuators. IEEE/ASME Transactions on Mechatronics, 26(5), Article 3079471. https://doi.org/10.1109/TMECH.2021.3079471

Daoudi, K., & Boudi, E. M. (2018). Optimal volume design of planetary gear train using particle swarm optimization. 2018 4th International Conference on Optimization and Applications (ICOA). https://doi.org/10.1109/ICOA.2018.8370577

Durgut, İ. (2009). Alın Dişlilerin Bilgisayar Simülasyonu. Yüksek lisans tezi, İstanbul Üniversitesi, Makina Mühendisliği Anabilim Dalı.

Fetvacı, C. (2014). Evolvent Düz Dişlilerde Alttan Kesmenin Bilgisayar Simülasyonu. Mühendis ve Makina, cilt 55, sayı 656, s. 50-58.

Golenko, A., (2009). 3K Mechanical Paradox transmissions: The shaping of the meshing zone for better efficiency. Archives of Civil and Mechanical Engineering, Vol. 9, No. 2, pp. 39–46.

Hosna, A., Djeddou, F., Hamouda, A. (2023). A New Hybrid Particle Swarm Optimization and Jaya Algorithm for Optimal Weight Design of A Gear Train. SAE International Journal of Materials and Manufacturing-V132-5EJ

Khare, A., & Rangnekar, S. (2013). A review of particle swarm optimization and its applications in solar photovoltaic system. Applied Soft Computing, 13(5), 2997–3006. https://doi.org/10.1016/j.asoc.2012.11.033

Norton, R. L. (2020). Machine Design: An Integrated Approach. Pearson Education.

Miler, D., Žeželj, D., Lončar, A., Vučković, K. (2018). Multi-Objective Spur Gear Pair Optimization Focused On Volume And Efficiency. Mechanism and Machine Theory 125 (2018) 185–195. https://doi.org/10.1016/j.mechmachtheory.2018.03.012

Sedak, M.; Rosi´c, B., (2021) Multi-Objective Optimization of Planetary Gearbox with Adaptive Hybrid Particle Swarm Differential Evolution Algorithm. Appl. Sci. 2021, 11, 1107. https://doi.org/10.3390/ app11031107

Stefanović-Marinović, J. (2008).Multicriterion optimization of planetary power transmission gear pairs. (in Serbian), PhD Thesis.Niš: University of Niš, Faculty of Mechanical Engineering.
Theling, J., Brimmers, J., & Brecher, C. (2021). Reducing mass while improving the operational behavior: Form optimization of planetary gearbox housings. *Forsch Ingenieurwes, 85*(5), 543–551. https://doi.org/10.1007/s10010-021-00445-2
Türk Standardları Enstitüsü. (2021). TS ISO 6336-1:2017 - Dişliler - Dişli çarklarının mukavemeti - Bölüm 1: Temel kurallar. Türk Standardları Enstitüsü.
Rossman, A. M. (1934). Mechanical movement (U.S. Patent No. 1,970,251). United States Patent Office. https://patents.google.com/patent/US1970251A/
Wehrle, E., Concli, F., Cortese, L., Vidoni, L. (2017). Design Optimization Of Planetary Gear Trains Under Dynamic Constraints And Parameter Uncertainty. In *ECCOMAS Thematic Conference on Multibody Dynamics,* June 19-22, 2017, Prague, Czech Republic.
Yücenur, S. ve Temiz, V. (2003). Dişli Çarklar, 1. Bölüm: Düz Alın ve Konik Dişli Çark Mekanizmaları, Ders Notu.

Examining the Impact of Groove Profiles and Dimensional Parameters on Shear Pin Strength

Mehmet Ozan Yitim[a,b], Cevat Erdem İmrak[a], Adem Candaş[a]

[a]Faculty Mechanical Engineering, Istanbul Technical University, Istanbul, 34475, Türkiye
[b]GraduateSchool, Istanbul Technical University, Istanbul, 34475, Türkiye
yitim15@itu.edu.tr

Keywords: Shear Pin, Design Optimization, Stress Concentration, Correlation.

Aim

As mechanical design engineers, the whole design process needs to follow the right path for some main purposes such as cost, maintainability, manufacturability, accessibility, toughness/endurance, etc. Therefore, to maintain the balance between two key objectives such as strength and safety, it is necessary to deliberately leave certain weak points (such as shear pins) in the design, especially in structures working under uncertain and high loads. Shear pins can be considered as safety pins. This study focuses on the shear pin design process and the investigation of geometric optimization of the shear pins.

Shear pins are widely used in mechanical, aerospace, and structural engineering applications where controlled failure mechanisms are required. The failure of a shear pin occurs primarily due to shear stress exceeding the material's yield strength. However, the presence of grooves (Fig. 1a, 1b) and variations in diameter and thickness can alter stress distribution, influencing both the pin's load-bearing capacity and fatigue life.

Figure 1. a) Various types of shear pins, b) Parts of a shear pin.

Despite existing research on shear pin design, a systematic optimization framework incorporating geometric parameters remains underdeveloped. This study aims to fill this gap by employing Finite Element Analysis (FEA) to achieve the optimal geometric design result.

Material and Method

The study begins with an examination of the most prevalent shear pin geometries used in widely applied shear pin designs. The classical designs usually comprise straight cylindrical pins with single or multiple grooves to control failure points [1]. These designs lack uniform stress distribution leading to abrupt material fatigue and fracture. Therefore, this study employs Finite Element Analysis (FEA) and experimental testing to establish stress concentration factors for different groove configurations [2]. By varying parameters such as groove depth, width, and curvature, this research proposes a method to determine the optimal groove geometry for predictable and controlled failure at specified loads. The geometric parametric study examines various groove types, namely V-notch, U-notch, and rounded-notch grooves.

The primary shear mechanism examined in this study is the double shear pin mechanism (Fig. 2). Double-plane shear mechanisms are widely used in various applications, particularly in structures subjected to high loads from

torsional, transverse, or axial forces. For instance, transverse loads on beam members generate bending moments, while in certain safety applications, shear pins help distribute these moments and absorb excessive loads to minimize damage to critical structural components. The fundamental formula for single-plane shear capacity is given as follows,

$$\tau_{s.shear} = \frac{F}{A_{shear}} \quad (1)$$

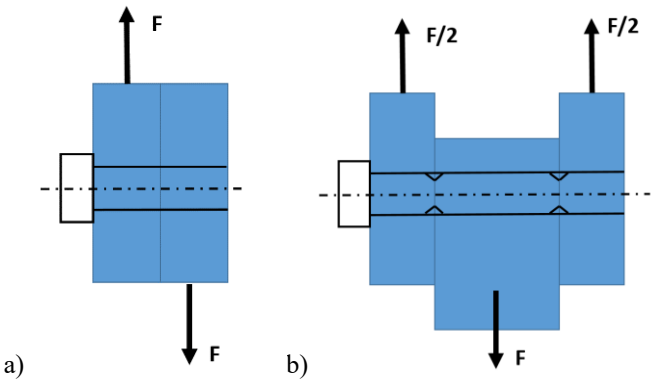

Figure 2. a) Single shear loads and b) Double shear loads acting on the pin.

The double shear mechanism is analyzed using both analytical methods and the Finite Element Method (FEM), as well as experimentally [3]. After all calculations and evaluations, a single correlated and verified model is obtained. Once verification is complete, all remaining design options are evaluated using FEA solutions. To differentiate groove designs, key parameters such as shear diameter, nominal diameter, width, and groove shape are considered for optimal design selection. For finite element analysis, the most suitable mesh parameters have been determined. Mesh convergence method was studied first for describing the most suitable FEA method. Quadratic Hex 3D elements (SOLID186) were chosen for bulk material on pin, because they are sufficient for our case with respect to displacement and stress calculation accuracy, as well as computation cost. To find the best mesh sizing, mesh convergence study was done, with details shown in Fig. 3 and Table 1. Example pin geometry and mesh study has been done, 1mm of element size will adequate for the application.

Table 1. Mesh convergence iterations.

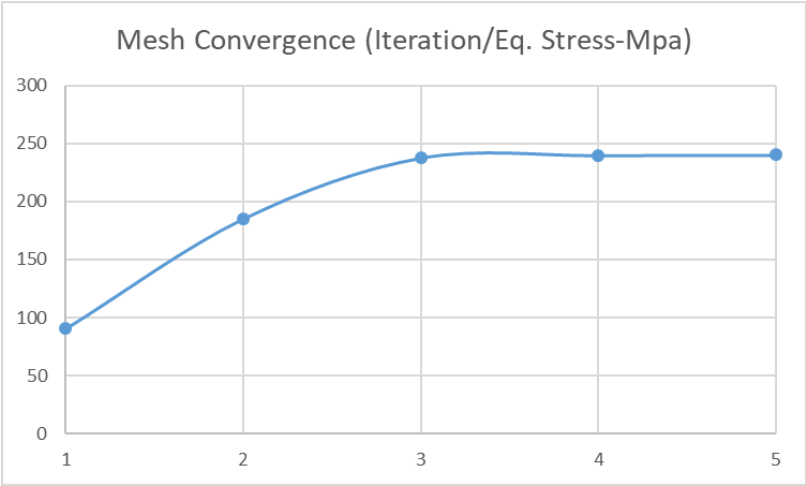

Table 2. Mesh convergence iteration element and node numbers.

	Element Size (mm)	Equivalent Stress 2 (MPa)	Change (%)	Nodes	Elements
1	4	90.3		933	458
2	2	185.3	68.9	5632	3240
3	1,2	237.9	24.9	31921	20683
4	1	239.6	0.71	58363	38596
5	0.8	240.1	0.001	91804	62900

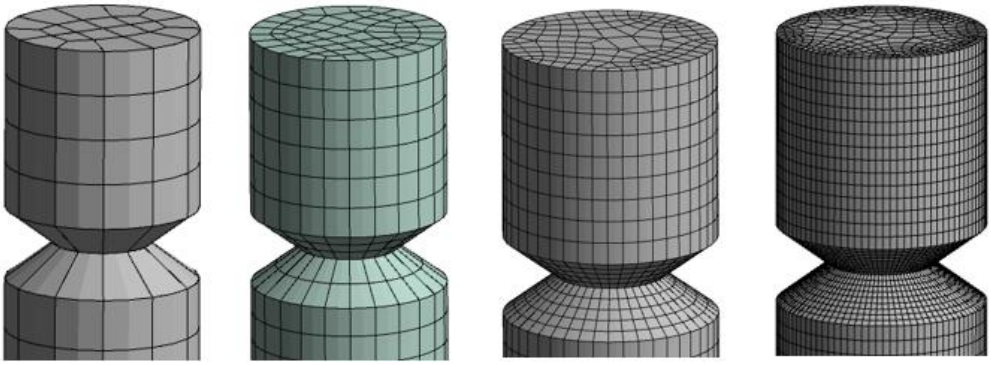

Figure 3. FEA mesh details.

Finite element models are obtained as load applied on the pin middle surface radially and distributed linearly, the both ends of the pin have been fixed for 6 degrees of freedom as deformable condition, and linear static analysis has been done on this pin only FE model as shown in Fig. 4. The stress results taken on max stress plane on the pin and maximum radial displacement values have been read from middle surface of the pin. The boundary conditions are presented in Fig. 5 [4].

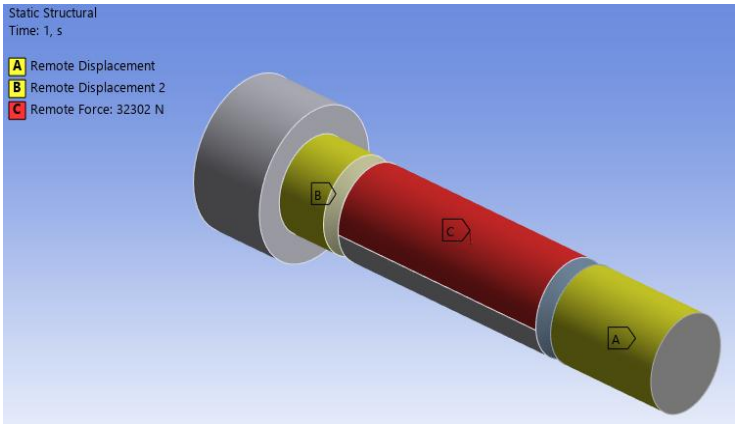

Figure 4. FEA boundary conditions for V shape groove pin.

Findings

The cross-sectional geometries of grooves in shear pins have a significant impact on strength. In this regard, the V-notch, U-notch, and rounded-notch profiles to be examined and compared in this study are shown in Fig. 6.
In addition, material spectral and mechanical shear tests have been done. Results are, the material of the sample pin specified as free cutting steel that the yield stress has been given below, also the 32kN of radial load considered as shear yield of the pin. The further analysis processes have been carried out by guide of this results.

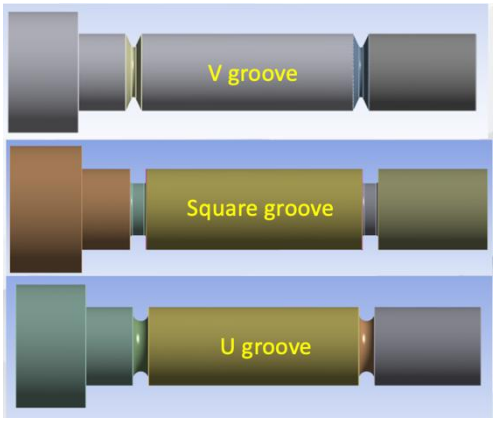

Figure 5. CAD models of different groove profiles.

The initial FEA analysis and design process have been done using the same procedure given in [5,6]. The model has been prepared with linear free cutting steel material (1.0727) and loaded by displacement from the very middle section of the pin. The pure shear condition has occurred and the material carries the load till it reaches the yield point (440 MPa).

After test-analysis corelation studies [6], the further analysis have been done fort he comparison between different shaped grooves. 3 main mechanical results are taken as the comparison criterias. Radial shear stiffness of the pin, maximum stress ocurred on shear plane and average stress ocurred on groove section. The result tables as shown below.

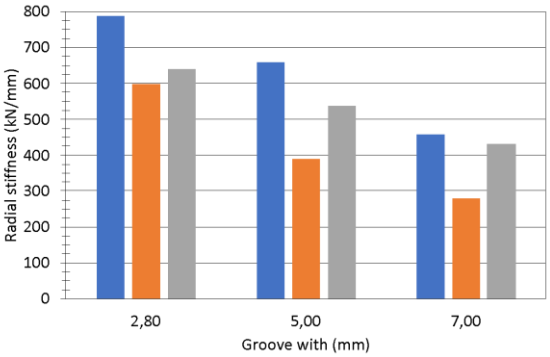

Table 3. Radial stiffness comparison.

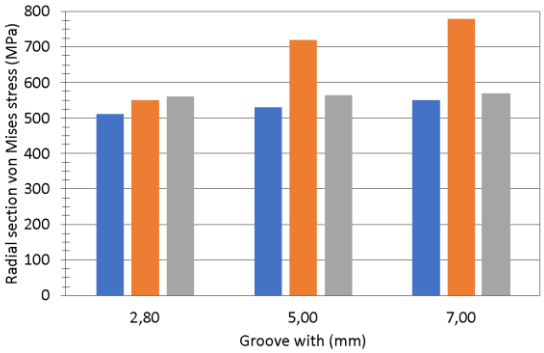

Table 4. Maximum stress ocurred on shear plane.

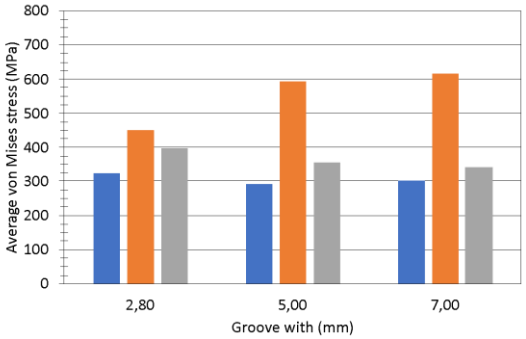

Table 5. Average stress on groove section.

Conclusion

By this study, at first, engineering routines was tried to cover from the beginning sequentally, design, analytical aproaches, FE analysis ann mechanical test for calidation. Correlation techniques used and physical & analytical studies overlapped.
At the and, material strength is highly dependent on shear pin groove geometrical properties,

Increasing the groove width effected the results as, changing the stress tensor from shear dominant to bending side, so that the pin's shank areas also started to carry bending loads, by most of the cases the stress levels got higher and overall radial stiffness of the pins got lower too, but for V and U grooves the average stress on groove area gots smaller an the reason of this can be expressed as above.
Also the groove profile type effected the both stiffness and stress levels directly as seen on the analysis, V groove got better results on most of the cases, this results cause thought as, the material stock in the groove profile is higher on V groove, so that the stiffness on groove got higher.

References

Russell Q. Bridge, T. Sukkar, I. G. Hayward, M. van Ommen, (2001) Behaviour and design of structural steel pins, Steel and Composite Structures, DOI:10.1296/SCS2001.01.01.06
R.J. Grant, J. Smart, P. Stanley, (1994) A parametric study of the elastic stress distribution in pin-loaded lugs, Journal of Strain Analysis 29 Page 299–307.
T. Peng and N. Guo, (2016) Experimental and numerical studies of shear pin fractures based, on linear and bilinear models, Mechanika, vol. 22, no. 4, Page 245–250
J. Vican, M. Farbak, (2020) Analysis of high-strength steel pin connection, Civil Environ. Eng. 16 (2) 276–281.
N. Sundarraj, B. Dattagurut and T. S. Ramamurthyz. (1995) Analysis of a double shear lap joint with interference fit pin. Computers & Structures Vol. 55 No. 2 Elsevier
Tianbo Peng , Ning Guo, (2016) An equivalent linear model for shear pin fractures and its experimental verification. DOI:10.21595/JVE.2016.16882

MECHANICAL ENGINEERING

Additive Manufacturing

Automotive

Computational Fluid Dynamics

Computational Solid Mechanics

Fluid Mechanics

Industrial Data Analytics

Machine Design

Machine Dynamics, Vibration, and Acoustic

System Dynamics and Control

Investigation and Optimization of the Effect of Different Profile Modifications on Gear Noise and Strength in the Gearbox with Single-Stage Spur Gear

Hakan Yardımcı[a], Ali Gökşenli[a], Ali İmre Aydeniz[a]

[a]Istanbul Technical University, Faculty of Mechanical Engineering, Department of Mechanical Engineering, Türkiye
yardimci22@itu.edu.tr

Keywords: Single Stage Spur Gearbox, Gear Modifications, Gear Noise, Müller Method.

Aim

Spur gears are widely used in power transmission applications due to their high torque carrying capacity and low energy losses. The most common use is gearbox. Gearboxes are intermediate equipment that provides torque-speed conversion between the motor and the machine in industrial applications. While it generally increases the motor torque according to the needs of the machine it will drive, it reduces the motor speed to the machine operating speed. Thus, it is a solution in applications requiring low speed and high torque where the direct motor cannot be used.

Today, due to the increase in competition conditions and the improvement of design and manufacturing conditions depending on the development of technology, the demand for gearboxes that can carry high torque per unit volume and have a minimum sound level is increasing day by day. Especially with the spread of electric vehicles, the sound level of gearboxes that provide torque-speed conversion between the electric motor and the wheel has become important in terms of driving comfort. In addition, gearboxes that are lighter in terms of energy efficiency and can carry high torque in smaller volumes have become inevitable for electric vehicles. Without changing the main gear parameters (macro geometry), torque carrying capacity can be significantly increased with micron-level modifications made to the profile and the noise level can be reduced thanks to the reduction of transmission error and homogeneous gear contact. Thus, it is possible to produce quieter gearboxes that can carry higher torque in the same volume.

Material and Method

In this study, a gearbox with single-stage spur gear will be examined (Figure 1). Deformations in the gear, shaft and bearings supporting the gear under load will be calculated using analytical methods using the FVA Workbench program. The pressure distribution on the gear surface will be analysed and the noise level will be found. According to the ISO6336:2019 (Calculation of load capacity of spur and helical gears) norm, KHβ (load distribution factor) and gear flank surface safety (SH) and gear tooth root safety (SF) will be calculated. Considering all the deformations and the pressure distribution on the gear surface, lead crowning and helix angle modifications will be applied in the gear width direction. After finding the optimum KHβ and lead crowning and helix angle modification values that provide homogeneous surface pressure distribution, sound optimization will be carried out.

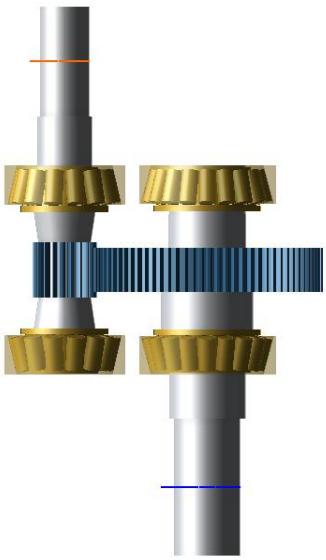

Figure 1. Single Stage Spur Gearbox Model.

According to the SIGG (Schwab, Ishikawa, Güntsch, Göpfert) approach, long and short tip relief modifications will be found in sound optimization. The SIGG approach is an analysis method developed to reduce transmission error (TE), improve load distribution and reduce vibration level in gear systems. This approach, which is especially used in precision and high-performance gear applications, focuses on optimizing the tip relief amount. According to the SIGG model, applying a controlled modification at the starting point and exit point of tooth contact improves the contact dynamics of the gear and provides a more stable operation. In this way, the noise and vibration levels in gear systems decrease significantly, while the load distribution becomes more homogeneous. The short and long tip relief modifications obtained thanks to this approach will be applied to the gears to reduce sudden pressure increases at the root and tip of the gear, thus achieving a more homogeneous transition and reducing the sound level.

The Müller method will be used in calculating the sound level (Equation 1). In gear systems, the tooth load level and excitation level are directly related to the forces generated at the point where the gears come into contact with each other. According to the study conducted by Müller (1991), these levels can be expressed as the weighted sum of the adjusted amplitudes of the engagement forces. In other words, when the gears rotate, forces of a certain magnitude occur when the teeth come into contact with each other. These forces change over time and cause vibrations at certain frequencies. While the tooth load level expresses the magnitude of these forces, the excitation level indicates the potential of these forces to create vibration and noise. The method described by Müller involves evaluating these forces with certain weighting coefficients instead of directly adding them. Thus, it becomes possible to more accurately estimate how much vibration and noise the gears will produce during operation. This approach is especially important in terms of vibration analysis and evaluating the acoustic performance of gear systems. Such models are used to design quieter and more efficient gear systems. In our study, the sound level produced by the unmodified gear will be determined with the Müller method and the sound level will be tried to be reduced by applying different tip relief modifications.

$$L_{Fz} = 10.lg\left[\frac{1}{(\omega_0.F_0)^2}\sum_{i=1}^{k}(i.\omega_z.F_i)^2\right] dB$$

Equation 1. The Tooth Excitation Level by Müller (**Müller, R.** (1991).

In this study, the gearbox with a 130mm axis distance was examined. The gear module was 2.5mm, the teeth number of pinion was 21, and the teeth number of wheel gear was 83. In the gearbox with a 3.95 gear ratio, the

pressure angle was 20° and the profile shift coefficient were 0.3391 and -0.3391, respectively. The pinion tip diameter was Ø59.2mm, its width was 44mm, the wheel gear tip diameter was Ø210.8mm, and its width was 40mm. Tapered roller bearings were used to be mounted without clearance on the input and output shafts. Heat-treated 21NiCrMo2 case-hardened steel with a surface hardness of 58-62HRC and a material quality of MQ was used as gear material. In the analysis to be performed under load, the gearbox input power was 55kW and the input speed was 1500rpm.

Findings

In the first stage, for unmodified gears, the load distribution factor was found to be KHβ: 1.13 according to Method B using the ISO6336:2019 norm. Accordingly, gear safety values were calculated as SH: 1.04 and SF: 1.54. These gear safety values provide the minimum safety values SH≥1.0 and SF≥1.4 required in the norm. With the help of FVA Workbench software, the effect of deformations occurring in all parts including gear, shaft and bearing on the pressure distribution on the gear surface during gear contact was examined. When the pressure distribution was examined, it was seen that a maximum of 1634MPa Hertzian pressure occurred on the gear surface (Figure 2). This value is above the allowable contact stress (σHlim) value of 1500MPa defined in the ISO6336-5 (Part 5: Strength and quality of materials) norm. σHlim is the maximum stress value that gears can withstand against repeated loading without surface fatigue damage such as pitting. In this case, according to the calculation made according to ISO6336 norm, the gears are safe, but according to the maximum stress value resulting from analytical calculation considering deformations, they are unsafe.

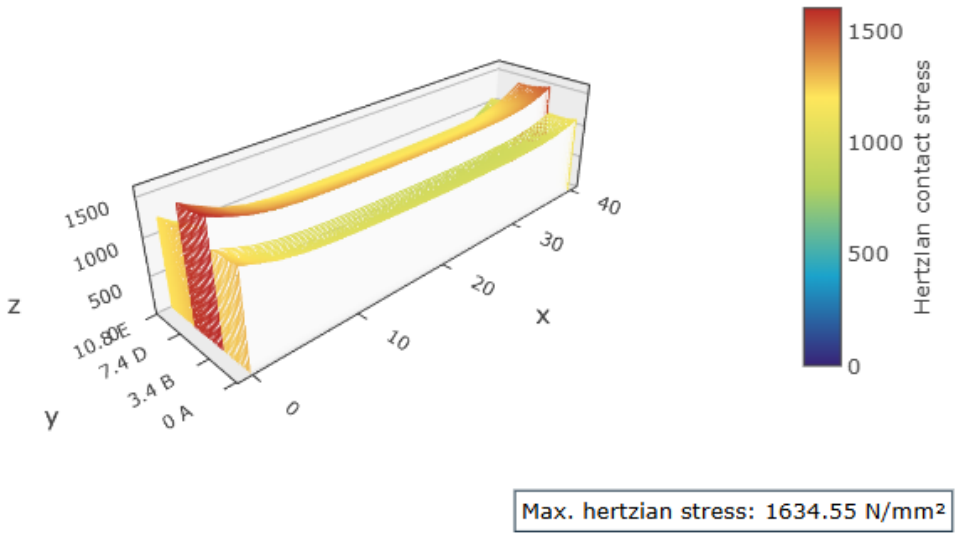

Figure 2. Hertzian Pressure Distribution on The Unmodified Tooth Surface.

In the second stage, lean crowning and helix angle modification were applied on the pinion tooth surface to reduce the maximum stress. As a result of the analyses made according to both rotation directions, +3µm helix angle modification was applied on the right surface of the tooth, -4µm helix angle modification was applied on the left surface of the tooth and +7µm lean crowning was applied on both tooth surfaces. After the optimization process, KHβ was improved to 1.03. In this way, gear safeties increased to SH: 1.09 and SF: 1.66 values. The pressure distribution on the tooth surface was became more homogeneous and the maximum pressure value was reduced from 1634MPa to 1406MPa (Figure 3). Thus, the maximum pressure value remained below the limit value of σHlim:1500MPa defined in the ISO6336-5 norm.

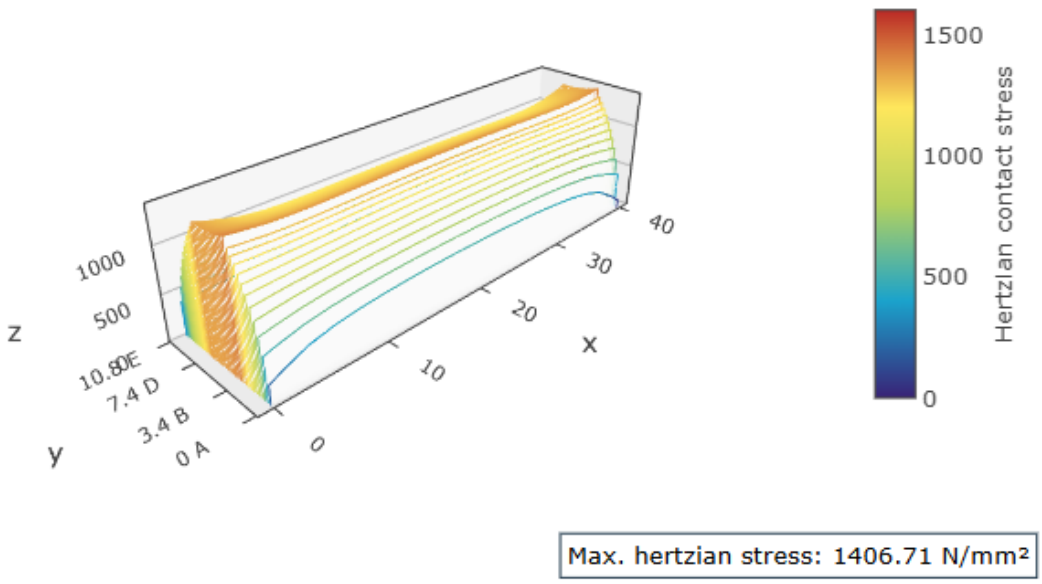

Figure 3. Hertzian Pressure Distribution on The Modified Tooth Surface.

In the third stage, the sound optimization was examined. The short and long tip relief values suggested by the SIGG method were applied to the tooth profile. In both short and long type, the amount of tip relief is C_αa:20µm. The starting point of the tip reliefs are Ø57.4 mm and Ø209.3 mm, respectively, in the short tip relief and the pinion and wheel gear. In the long tip relief, the starting point of the tip reliefs are Ø55.6 m and Ø207.7 mm, respectively, the pinion and wheel gear. In the calculations made after applying the tip relief modifications, the transmission error value decreased slightly from 11.32µm to 11.26µm when the short tip relief was applied and decreased significantly to 6.49µm when the long tip relief was applied. When the pressure distribution on the tooth surface was examined, a transition from low pressure to high pressure was achieved from the tooth root and tooth tip regions towards the tooth centre. The gear excitation levels before and after the tip relief were compared using the Müller method. While the gear excitation level was 42.50 dB in the unmodified gear, this value decreased slightly to 42.07 dB when short tip relief was applied and decreased significantly to 35.75 dB when long tip relief was applied.

Conclusion

In conclusion, gearbox with a single-stage spur gear was examined, and the effect of deformations in the gearbox components under load on gear contact was investigated. Various modifications were applied to improve the increase strength and reduce the noise level (Table 1). When the gear safeties were checked for the gear without modification, it was determined that the tooth root and flank safeties were sufficient according to the ISO6336 norm, but the maximum surface pressure formed on the tooth surface due to deformation was approximately 9% above the allowed value. In this case, it was seen that the ISO6336 norm alone was not sufficient in gear safety calculations and that deformation calculations made with the help of advanced software should also be taken into account. It was observed that gear modifications made at the micron level (lean crowning and helix angle modification) improved the gear safeties and reduced the maximum surface pressure value by 14% below the allowed limit value. Additionally, it was determined that lean crowning, helix angle modification and short tip relief modifications were insufficient in reducing the noise level, and that when long tip relief was applied, the noise level was significantly reduced by 16%. As a result, it has been determined that gear modification have a great effect on high torque, low noise level gearbox designs that will meet today's expectations.

Table 1. Output Parameters.

	ISO6336:2019 without modification	Lead Crowning + Helix angle modification	Lead Crowning + Helix angle modification + Short Tip Relief	Lead Crowning + Helix angle modification + Long Tip Relief
KHβ	1,13	1,03	1,03	1,03
SH	1,04	1,09	1,09	1,09
SF	1,54	1,66	1,66	1,66
Max. Pressure [Mpa]	1634	1406	1406	1406
Transmission Error [μm]	11,32	11,27	11,26	6,49
Excitation Level [dB]	42,50	42,48	42,07	35,75

References

Davoll, P. and Garlo, C. (2007). Transmission error and noise emission of spur gears.

International Standards ISO 6336-1. (2019). Calculation of load capacity of spur and helical gears - Part 1: Basic principles, introduction and general influence factors

International Standards ISO 6336-5. (2016). Calculation of load capacity of spur and helical gears - Part 5: Strength and quality of materials

International Standards ISO 21771. (2007). Gears - Cylindrical involute gears and gear pairs - Concepts and geometry

Kissling, U. (2008). Effects of profile corrections on peak-to-peak transmission error. In Proceedings of the International Conference on Gearing and Transmission Design.

Munro, R. G. and Houser D. (2002). Transmission Error Concepts

Munro, R. G., Morrish, L and Palmer D. (1999). Gear transmission error outside the normal path of contact due to corner and top contact

Müller, R. (1991). Schwingungs- und Geräuschanregung bei Stirnradgetrieben. TU München.

Palmer, D., & Fish, M. (2010). Evaluation of methods for calculating effects of tip relief on transmission error, noise and stress in loaded spur gears. In AGMA Technical Resources. American Gear Manufacturers Association.

SIGG, E. (1965). Recommended tip relief acc. to SIGG. In AGMA Paper 109.16, Profile and Longitudinal Corrections on Involute Gears. American Gear Manufacturers Association

Semi-Analytical Investigation of Nonlinear Tuned Mass Dampers Using the Multi-Term Harmonic Balance Method

Okan Çengel[a], Osman Taha Şen[a]

[a] Istanbul Technical University, Department of Mechanical Engineering, Machine Dynamics, Vibrations and Acoustics, Turkiye
okancengel98@gmail.com

Keywords: Nonlinear Tuned Mass Damper, Harmonic Balance Method, Passive Control Device.

Aim

A Tuned Mass Damper (TMD) is a passive control device widely used to mitigate vibrations in structures by targeting a specific excitation frequency. However, when the excitation frequency varies, especially near the primary system's natural frequency, a linear TMD may not effectively suppress vibrations. To address this limitation, incorporating nonlinear elements into the TMD's coupling path can broaden the frequency band over which it effectively reduces vibrations, thereby limiting the primary structure's vibration amplitude across a wider range of excitation frequencies (Den Hartog, 1985).

Applications of nonlinear TMDs include reducing structural responses to seismic vibrations (Sadek et al., 1997), mitigating wing loads in aerospace engineering (Kwok & Samali, 1995), and suppressing vibrations in cutting tools during turning operations (Lee et al., 2001). Moreover, nonlinear TMDs have been applied in various engineering fields. In civil engineering, they are used to control vibrations in structures subjected to unpredictable forces such as earthquakes and wind loads. For example, the installation of TMDs in skyscrapers and bridges has proven effective in mitigating vibrations and enhancing structural stability (Webster & Vaicaitis, 1992). These studies aim to optimize TMD parameters to enhance vibration reduction performance, acknowledging that real-world applications often involve inherent nonlinear characteristics due to large displacements or the use of limiting devices.

In summary, nonlinear TMDs offer a robust solution for vibration control across various applications by extending the effective frequency range and improving the resilience of primary structures against variable excitation forces. In this study, the nonlinear TMD problem will be solved using the semi-analytical multi-term harmonic balance method (MHBM). Results will be presented in the frequency domain to investigate the performance of the system while systematically varying the system's parameters. This approach will provide insights into how changes in parameters affect the effectiveness and robustness of the nonlinear TMD, ultimately guiding the optimization of design parameters for enhanced vibration control.

Material and Method

Sen and Singh (2018) investigated the mechanism of energy transfer between two subsystems interconnected by a nonlinear elastic element, where the external force excitation is applied solely to the mass component of the second oscillator. In contrast, the current study applies force excitations simultaneously to both mass components, with nonlinear couplings present both between the ground and the first mass, and between the two masses.

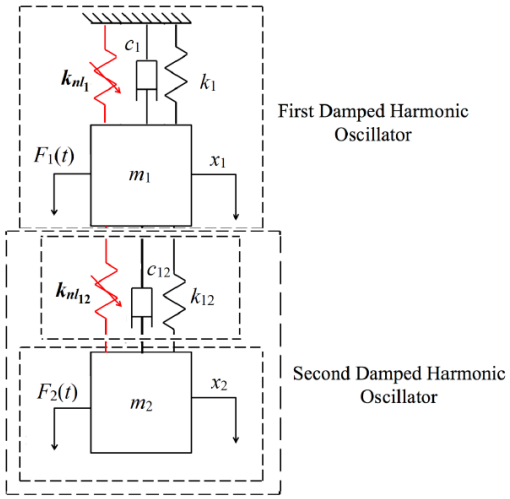

Figure 1. 2-DOF nonlinear vibration absorber system.

The nonlinear elastic elements are modeled by assuming cubic-type nonlinearities. The nonlinear equations governing the dynamic behavior of the system depicted in Figure 1 can be expressed as follows:

$$m_1\ddot{x}_1 + (c_1 + c_{12})\dot{x}_1 + (-c_{12})\dot{x}_2 + (k_1 + k_{12})x_1 + (-k_{12})x_2 + k_{nl_1}{x_1}^3 + k_{nl_{12}}(x_1 - x_2)^3 = {F_1}^S + {F_1}^D \sin\sin(wt + \varphi_1) \quad \#(1)$$

$$m_1\ddot{x}_2 + (-c_{12})\dot{x}_1 + c_{12}\dot{x}_2 + (-k_{12})x_1 + k_{12}x_2 + k_{nl_{12}}(x_2 - x_1)^3 = {F_2}^S + {F_2}^D \sin\sin(wt + \varphi_2) \quad \#(2)\#\ \#$$

To simplify these governing equations, the following dimensionless parameters are introduced:

$$\mu = \frac{m_2}{m_1} \quad \gamma = \frac{c_{12}}{c_1} \quad \lambda = \frac{k_{12}}{k_1} \quad w_n = \sqrt{\frac{k_1}{m_1}} \quad \xi = \frac{c_1}{2m_1 w_n} \quad \alpha_1 = \frac{k_{nl_1}{x_0}^2}{k_1} \quad \alpha_{12} = \frac{k_{nl_{12}}{x_0}^2}{k_1} \quad \tau = w_n t \quad X_1 = \frac{x_1}{x_0} \quad X_2 = \frac{x_2}{x_0} \quad x_0 = \frac{{F_1}^S}{k_1} \quad \#(3a-n)$$

$$\sigma = \frac{{F_2}^S}{{F_1}^S} \quad \varepsilon_1 = \frac{{F_1}^D}{{F_1}^S} \quad \varepsilon_2 = \frac{{F_2}^D}{{F_2}^S}$$

Thus, the dimensionless nonlinear governing equations become:

$$X_1'' + [2\xi(1+\gamma)]X_1' + (-2\xi\gamma)X_2' + (1+\lambda)X_1 - \lambda X_2 + \alpha_1 X_1^3 + \alpha_{12}(X_1 - X_2)^3 = 1 + \varepsilon_1 \sin\sin\left(\frac{w}{w_n}\tau + \varphi_1\right) \quad \#(4)$$

$$\mu X_2'' + (-2\xi\gamma)X_1' + (2\xi\gamma)X_2' - \lambda X_1 + \lambda X_2 + \alpha_{12}(X_2 - X_1)^3 = \sigma + \varepsilon_2 \sin\sin\left(\frac{w}{w_n}\tau + \varphi_2\right) \quad \#(5)$$

where, $X_i' = \frac{dX_i}{d\tau}$ ve $X_i'' = \frac{d^2X_i}{d\tau^2}$

The MHBM is employed to obtain the steady-state response of the nonlinear system subjected to harmonic excitation. For simplicity, the governing equations (Eqs. 4-5) are reformulated in the spatial domain by introducing a linear transformation of the independent variable, $\theta = \omega\tau$. Thus, derivatives with respect to τ are redefined in terms of θ, yielding the following nonlinear equations in the θ-domain:

$$\omega^2\frac{d^2X_1}{d\theta^2} + [2\xi(1+\gamma)]w\frac{dX_1}{d\theta} + [-2\xi\gamma]w\frac{dX_2}{d\theta} + (1+\lambda)X_1 - \lambda X_2 + \alpha_1 X_1^3 + \alpha_{12}(X_1 - X_2)^3 = 1 + \varepsilon_1 \sin\sin\left(\frac{\theta}{w_n} + \varphi_1\right) \quad \#(6)$$

$$\mu\omega^2\frac{d^2X_2}{d\theta^2} + (2\xi\gamma)w\frac{dX_2}{d\theta} + [-2\xi\gamma]w\frac{dX_1}{d\theta} - \lambda X_1 + \lambda X_2 + \alpha_{12}(X_2 - X_1)^3 = \sigma + \varepsilon_2 \sin\sin\left(\frac{\theta}{w_n} + \varphi_2\right) \quad \#(7)$$

The dimensionless dependent variables X_1 and X_2 are approximated by truncated Fourier series expansions, where N_h denotes the number of harmonics retained:

$$X_1(\theta) = a_{1,0} + \sum_{n=1}^{N_h} a_{1,2n-1}\, sin\, sin\,(n\theta) + a_{1,2n} cos(n\theta) \#(8a)$$

$$X_2(\theta) = a_{2,0} + \sum_{n=1}^{N_h} a_{2,2n-1}\, sin\, sin\,(n\theta) + a_{2,2n} cos(n\theta) \#(8b)$$

The assumed solutions (Eqs. (8a) and (8b)) are discretized as $X_1 = \Gamma a_1$ and $X_2 = \Gamma a_2$ where Γ is the discrete Fourier transform matrix, and a_1 and a_2 represent the unknown Fourier coefficient vectors for variables x_1 and x_2. The matrix Γ is defined as:

$$\Gamma = [1\ sin\, sin\,(\theta_0)\ \ cos\, cos\,(\theta_0)\ \cdots\ sin\, sin\,(N_H\theta_0)\ \ cos\, cos\,(N_H\theta_0)\ 1\ sin\, sin\,(\theta_1)\ \ cos\, cos\,(\theta_1)\ \ldots\ sin\, sin\,(N_H\theta_1)\ \ cos\, cos\,(N_H\theta_1)\ \vdots\vdots\vdots\ddots\vdots \\ \vdots\ 1\ sin\, sin\,(\theta_{N-1})\ \ cos\, cos\,(\theta_{N-1})\ \cdots\ sin\, sin\,(N_H\theta_{N-1})\ \ cos\, cos\,(N_H\theta_{N-1})\ ] \#(9)$$

where N is the number of discrete points.

Furthermore, the non-dimensional governing equations (Eqs. (6-7)) are written in discrete form as:

$$R_1 = w^2\Gamma D^2 a_1 + [2\xi w(1+\gamma)]\Gamma D a_1 + (-2\xi\gamma w)\Gamma D a_2 + (1+\lambda)\Gamma a_1 - \lambda\Gamma a_2 + \alpha_1(\Gamma a_1)^3 + \alpha_{12}(\Gamma a_1 - \Gamma a_2)^3 - \Gamma - \left(\frac{\theta}{w_n} + \varphi_1\right) \#(10)$$

$$R_2 = \mu w^2\Gamma D^2 a_2 + [2\xi w]\Gamma D a_2 + (-2\xi\gamma w)\Gamma D a_1 + \lambda\Gamma a_2 - \lambda\Gamma a_1 + \alpha_{12}(\Gamma a_2 - \Gamma a_2)^3 - \Gamma\sigma\left(\frac{\theta}{w_n} + \varphi_2\right) \#(11)$$

where D is the differential operator. The differential operator matrix is defined as:

$$D_{(2N+1)x(2N+1)} = [0\ 0\ 0\ \cdots\ 0\ 0\ 0\ 0\ -n_1\ \cdots\ 0\ 0\ 0\ +n_1\ 0\ \cdots\ 0\ 0\ \vdots\vdots\vdots\ddots\vdots\ 0\ 0\ 0\ \ldots\ 0\ -n_N\ 0\ 0\ 0\ \ldots\ +n_N\ 0\ ] \#(12)$$

Note that Eqs. (10) and (11) constitute a set of coupled nonlinear algebraic equations. Therefore, the unknown coefficient vectors a_1 and a_2 are determined by minimizing the residue functions:

$$R_1 = w^2 D^2 a_1 + [2\xi w(1+\gamma)] D a_1 + (-2\xi\gamma w) D a_2 + (1+\lambda) a_1 - \lambda a_2 + \alpha_1\Gamma^+(\Gamma a_1)^3 + \alpha_{12}\Gamma^+(\Gamma a_1 - \Gamma a_2)^3 - 1 - \left(\frac{\theta}{w_n} + \varphi_1\right) \#(13)$$

$$R_2 = \mu w^2 D^2 a_2 + [2\xi w] D a_2 + (-2\xi\gamma w) D a_1 + \lambda a_2 - \lambda a_1 + \alpha_{12}\Gamma^+(\Gamma a_2 - \Gamma a_2)^3 - \sigma\left(\frac{\theta}{w_n} + \varphi_2\right) \#(14)$$

Here, Γ^+ denotes the pseudo-inverse of the discrete Fourier transform matrix. The residue minimization is iteratively performed using the Newton-Rapson method, where $\eta = [\ a_1\ a_2\ w]^T$ and $R = [\ R_1\ R_2\ ]^T$ represent the vectors of unknowns and residues, respectively, and i indicates the iteration number:

$$\eta_{i+1} = \eta_i + J_i^{-1} R_i \#(15)$$

Note that the excitation frequency ω is also treated as an unknown in the Newton-Raphson procedure, allowing clearer analysis of the system's dynamics at turning points on the frequency response curve. Additionally, the Jacobian matrix J in Eq. (15) is defined as follows:

$$J = \left[\frac{\partial R_1}{\partial a_1}\ \frac{\partial R_1}{\partial a_2}\ \frac{\partial R_1}{\partial w}\ \frac{\partial R_2}{\partial a_1}\ \frac{\partial R_2}{\partial a_2}\ \frac{\partial R_2}{\partial w}\right] \#(16)$$

Using the residue minimization outlined in Eq. (15), Eqs. (13) and (14) are solved iteratively for chosen parameters values. The subsequent step involves systematically examining the performance of the nonlinear tuned mass damper (TMD) system by varying key system parameters. Specifically, the following scenarios will be analyzed:

Influence of Linear Stiffness (λ): The performance of the nonlinear TMD system will be evaluated by varying the linear stiffness parameter. The aim is to understand how changes in linear stiffness influence the overall dynamic response and effectiveness of vibration suppression.

Linear Primary System Coupled with a Nonlinear Secondary System: The primary system maintains linear characteristics, while the secondary system exhibits nonlinear behavior. Frequency response curves and system performance metrics for these cases will be presented.

Nonlinear Primary System with Varying Secondary System Nonlinearity: Here, both the primary and secondary systems exhibit nonlinear characteristics. The nonlinearity parameter for the primary system remains fixed, while the secondary system's nonlinearity is varied.

Findings

Influence of Linear Stiffness (λ):

Table 1. Relative linear stiffness effect on X_1 and X_2 displacements.

Case	N_h	N	μ	γ	λ	ξ	σ	α_1	α_{12}	ε_1	ε_2
1	80	200	0.05	0.2	0.05	0.005	$\frac{\mu}{\mu+1}$	0.01	0.01	0.1	0
2	80	200	0.1	0.2	0.1	0.005	$\frac{\mu}{\mu+1}$	0.01	0.01	0.1	0
3	80	200	0.2	0.2	0.2	0.005	$\frac{\mu}{\mu+1}$	0.01	0.01	0.1	0

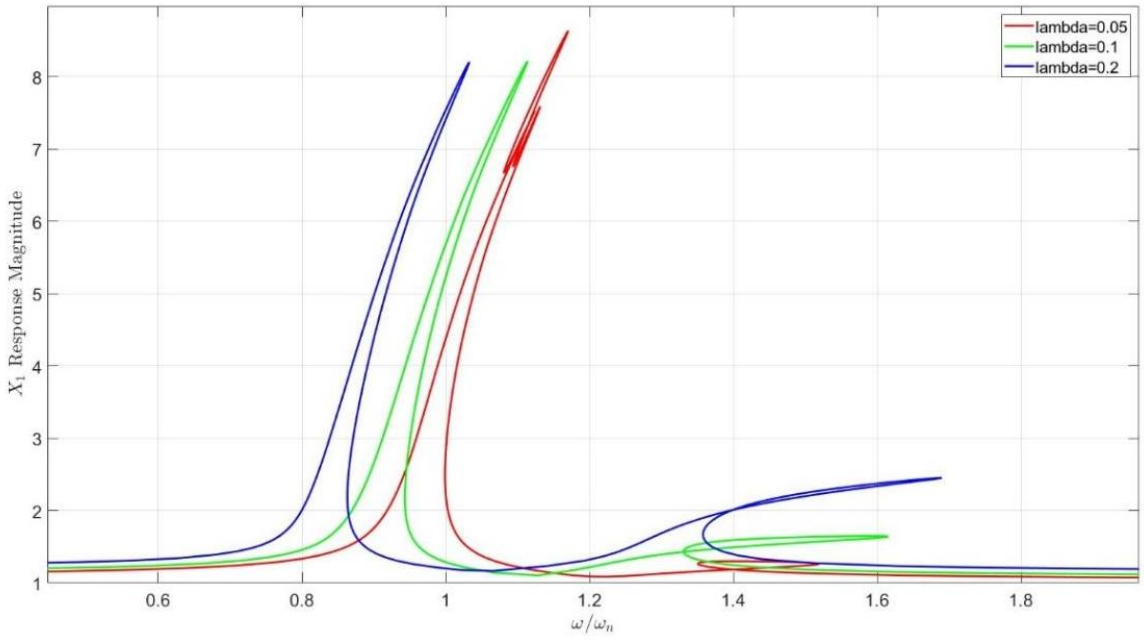

Figure 2. Frequency response curves showing the effect of linear stiffness(λ).

The results indicate that as the linear stiffness parameter(λ) decreases, the second natural frequency of the system shifts downward. However, the presence of hardening type nonlinearities ($\alpha_1 > 0$, $\alpha_{12} > 0$) restricts a significant leftward shift in the frequency response curves near the second natural frequency. This suggests that while adjusting λ influences the system's frequency characteristics, the nature of the nonlinear elements plays a crucial role in shaping the system's dynamic response. The frequency response analysis further reveals that at lower values of λ, the system experiences a more pronounced frequency shift, affecting vibration mitigation performance.

Linear Primary System Coupled with a Nonlinear Secondary System:

Table 2. System parameters for the linear primary system and nonlinear secondary system analysis.

Case	N_h	N	μ	γ	λ	ξ	σ	α_1	α_{12}	ε_1	ε_2
1	80	200	0.2	0.2	0.2	0.005	$\frac{\mu}{\mu+1}$	0	0	0.1	0
2	80	200	0.2	0.2	0.2	0.005	$\frac{\mu}{\mu+1}$	0	0.001	0.1	0
3	80	200	0.2	0.2	0.2	0.005	$\frac{\mu}{\mu+1}$	0	0.005	0.1	0

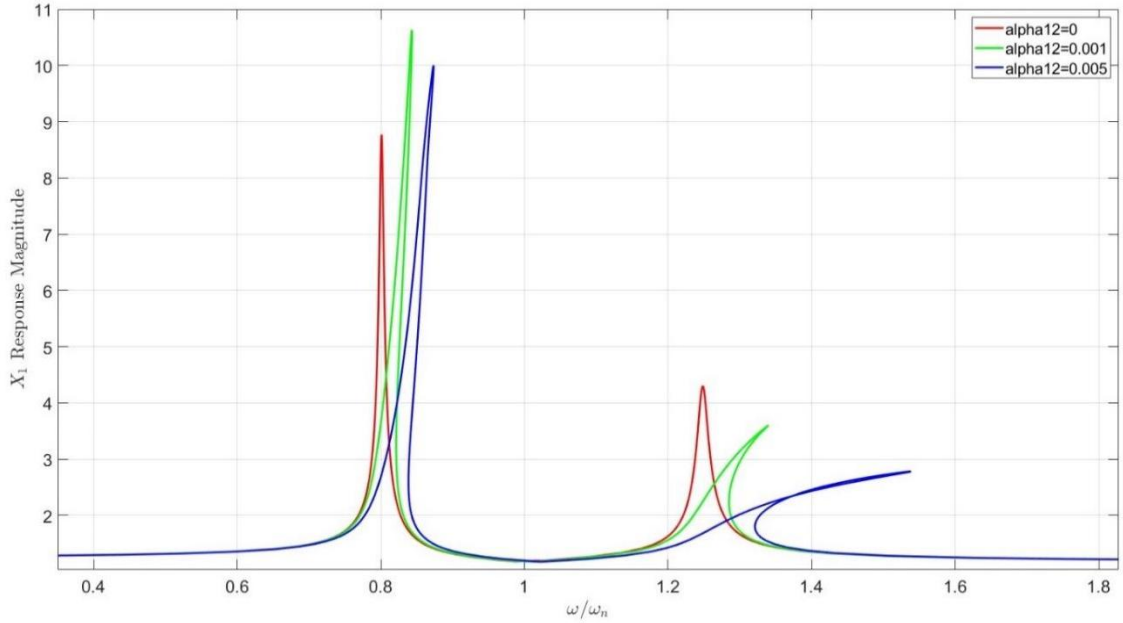

Figure 3. Frequency response curves for the linear primary and nonlinear secondary system.

When the primary system remains linear while the secondary system exhibits nonlinear characteristics, the frequency response curves indicate that increasing nonlinearity in the secondary system effectively reduces the vibration amplitudes of the primary system at specific excitation frequencies. This highlights the potential of nonlinear TMDs in improving vibration mitigation by redistributing energy within the system. The nonlinearity enhances damping behavior by introducing additional energy dissipation mechanisms, reducing the amplitude of forced vibrations.

Nonlinear Primary System with Varying Secondary System Nonlinearity:

Table 3. System parameters for the nonlinear primary system with variable secondary system nonlinearity.

Case	N_h	N	μ	γ	λ	ξ	σ	α_1	α_{12}	ε_1	ε_2
1	80	200	0.2	0.2	0.2	0.005	$\frac{\mu}{\mu+1}$	0.001	0	0.5	0
2	80	200	0.2	0.2	0.2	0.005	$\frac{\mu}{\mu+1}$	0.001	0.001	0.5	0
3	80	200	0.2	0.2	0.2	0.005	$\frac{\mu}{\mu+1}$	0.001	-0.001	0.5	0

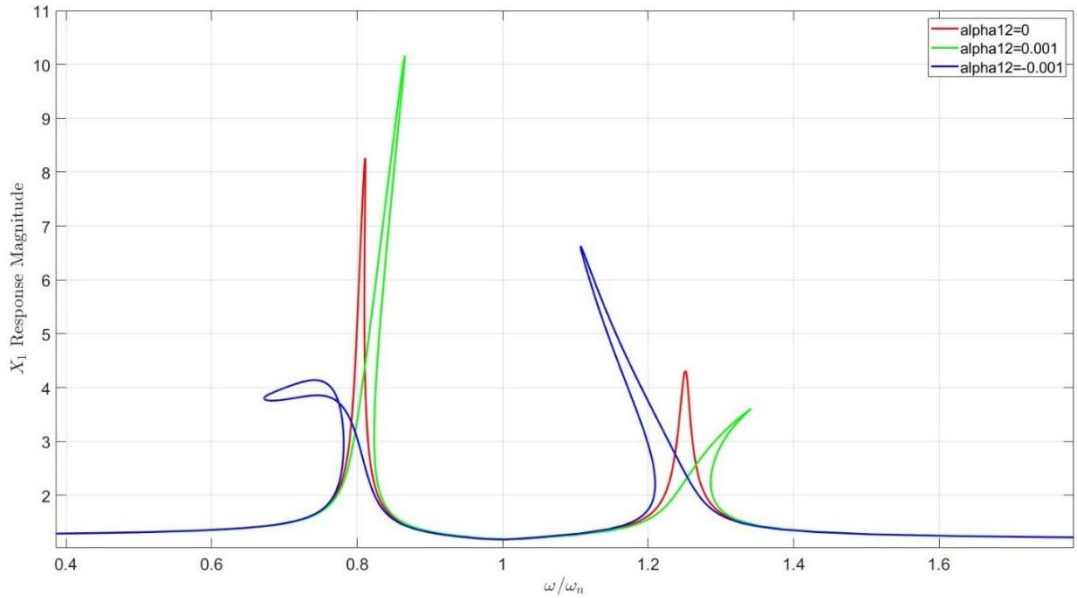

Figure 4. Frequency response curves for the nonlinear primary system with variable secondary system.

For cases where both the primary and secondary systems exhibit nonlinear behavior, different levels of nonlinearity in the secondary system lead to notable variations in the frequency response. The introduction of a softening-type nonlinearity ($\alpha_{12}<0$) results in saturation effects near both natural frequencies, particularly in the lower frequency range. This behavior suggests that appropriately tuning the nonlinearity of the secondary system can enhance the system's resilience to external excitations. The results demonstrate that strong nonlinear couplings influence frequency shift patterns and energy exchange mechanisms within the system.

Conclusion

This study presents a semi-analytical investigation of a nonlinear TMD system using the MHBM. By systematically varying key parameters, including linear stiffness and nonlinearity levels, the study explores their impact on vibration suppression effectiveness.

The results highlight that introducing nonlinearity in the secondary system extends the operational bandwidth of the TMD, improving its ability to mitigate vibrations across a wider frequency range. The findings also

demonstrate that a hardening-type nonlinearity prevents excessive shifts in response curves, while a softening-type nonlinearity introduces saturation effects that influence the overall system behavior. Moreover, when both the primary and secondary systems exhibit nonlinearities, complex frequency interactions emerge, emphasizing the importance of careful parameter selection in nonlinear TMD design.

Overall, the study provides valuable insights into the dynamics of nonlinear TMDs, offering a foundation for optimizing their design in various engineering applications, including civil structures, aerospace components, and machining systems.

Future work may focus on experimental validation and the exploration of additional nonlinearity types to further refine the theoretical understanding of nonlinear vibration control.

References

Den Hartog, J. P. (1985). Mechanical vibrations. Dover Publications.

Kwok, K. C. S., & Samali, B. (1995). Performance of tuned mass dampers under wind loads. Engineering Structures, 17(9), 655–667.

Lee, E. C., Nian, C. Y., & Tarng, Y. S. (2001). Design of a dynamic vibration absorber against vibrations in turning operations. Journal of Materials Processing Technology, 108(3), 278–285.

Sadek, F., Mohraz, B., Taylor, A. W., & Chung, R. M. (1997). A method of estimating the parameters of tuned mass dampers for seismic applications. Earthquake Engineering & Structural Dynamics, 26(6), 617–635.

Sen, O. T., & Singh, R. (2018). Energy exchange between two sub-systems coupled with a nonlinear elastic path. In INTER-NOISE and NOISE-CON Congress and Conference Proceedings (Vol. 257, No. 1, pp. 387–398). Institute of Noise Control Engineering.

Webster, A. C., & Vaicaitis, R. (1992). Application of tuned mass dampers to control vibrations of composite floor systems. AISC Engineering Journal, 29(3), 117–122.

Investigating the Use of Crash Dummies as Human Body Models for Whole-Body Vibration Evaluation

Safa Eren Pepeç[a], Özgen Akalın[b]

[a] Istanbul Technical University, Mechanical Engineering, Machine Dynamics, Vibration and Acoustics Programme, Turkey
[b] Istanbul Technical University, Mechanical Engineering, Automotive Engineering Programme, Turkey
pepec16@itu.edu.tr

Keywords: Whole-Body Vibration (WBV), Crash Dummies, Ride Comfort, Finite Element Analysis (FEA), Biomechanical Response.

Aim

Ride comfort has become a key parameter in modern vehicle design, directly influencing user, health, satisfaction and the competitiveness of vehicles in the market. Among the many factors affecting ride comfort, whole-body vibration (WBV) is of particular concern, as it impacts occupant health and perception during vehicle operation [1].

Traditional methods for assessing WBV exposure have largely relied on multibody dynamics (MBD) human body models [2] and direct human testing [3]. However, the ethical concerns surrounding the use of real human subjects and limits in vibration experiments have made it impractical to conduct large-scale or controlled studies. As a result, numerical methods involving MBD human body models have been widely adopted to simulate and analyze WBV effects. Despite their advantages, correlating these models with real-world conditions remains a challenge.

To overcome this limitation, crash dummies—whose biomechanical characteristics are designed to represent human responses—have emerged as a viable alternative for WBV studies. Notably, the finite element (FE) models of crash dummies, which are extensively validated for safety testing, can also be applied to comfort studies. These FE models enable the simulation of detailed vibration responses in various body regions, making crash dummies a valuable tool for WBV analysis [4].

Material and Method

Methodology

This study utilizes FE simulations (LS-Dyna) to assess the potential of using crash dummies, specifically 50th percentile male THOR dummy, for whole-body vibration (WBV) evaluations in vehicles. The methodology integrates dummy models seated on a passenger seat subjected to short-duration shock inputs in x, y and z directions. The vibration responses from key body regions (chest, head, and pelvis) are then analyzed and compared with natural frequency ranges from ISO 2631[5] and the literature.

CAE Model

The case is simulated on a generic passenger seat, with a shock input applied that simulates a vehicle passing over an obstacle as shown in Figure 1. The shock duration is approximately 1 second, and the data based on measurement from seat pad of a vehicle. The seat and the dummy models are based on finite element models for LS-Dyna.

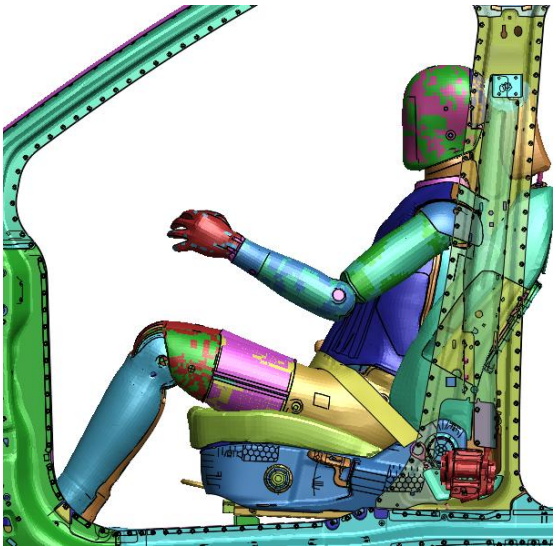

Figure 1. CAE Model Setup.

Dummy Model Characteristics

The dummy model is represented in detail using FE modeling techniques that capture the biomechanical properties of the human body. The THOR dummy model includes precise representations of key body regions, such as the chest, head, and pelvis etc. with corresponding material properties and damping characteristics. These models are validated against experimental crash test data to ensure their responses to crash pulses—such as force, acceleration, and deceleration—are accurate. Since crash dummy FE models are already validated through crash tests, their biomechanical response to impact forces is well-established, ensuring their reliability in simulating human-like responses in dynamic crash conditions. This validation supports their use in vibration studies, where their behavior under dynamic loads can be effectively extrapolated to WBV assessments.

Data Acquisition

The simulation involves applying the shock input to the dummy seated on a vehicle body. Vibration response data for critical body regions, including the chest, head, and pelvis, are recorded and processed. These responses are characterized by peak accelerations and frequency components, which are extracted from the recorded signals. The data is processed at a sampling rate of 1000 Hz to ensure high fidelity and accuracy in the vibration measurements.

Findings

The dynamic response assessment of the THOR dummy under whole-body vibration (WBV) conditions was conducted using a finite element (FE) model in LS-DYNA. The analysis revealed distinct resonance behaviors across different body regions. Figure 3 shows that in the Z-axis, significant resonance peaks were detected around 4–5 Hz, closely matching seated human body natural frequencies reported in previous studies [1]. Additionally, a peak was observed around 25 Hz in the head-Z axis, which aligns well with documented axial resonance frequencies of the human head [1]. In Figure 2, X-axis response showed peaks between 2-8 Hz, corresponding to seat-back oscillations, in agreement with findings from [4]. Since the THOR dummy was tested with an inclined backrest, the higher frequency response in the -X direction aligns with findings in the literature, suggesting that seatback inclination significantly influences WBV response and perceived discomfort. This indicates that the increased peaks in the -X direction at frequencies above 10 Hz are likely due to the altered dynamic response of the human body when the backrest is inclined, leading to a shift in resonance behavior. the equivalent comfort contours shift the maximum sensitivity to higher frequencies [1].

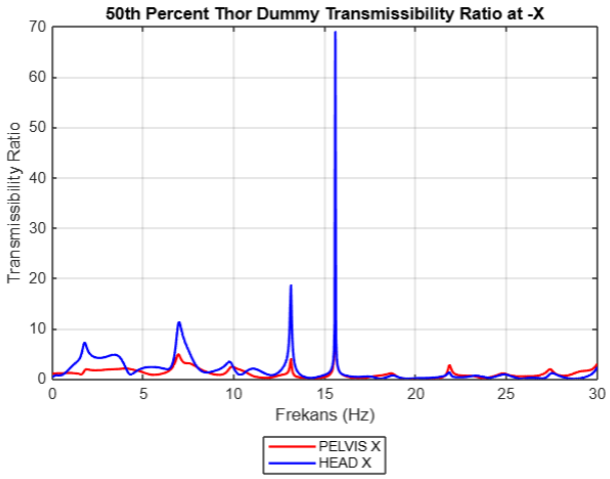

Figure 2. Transmissibility Ratio at -X Axis.

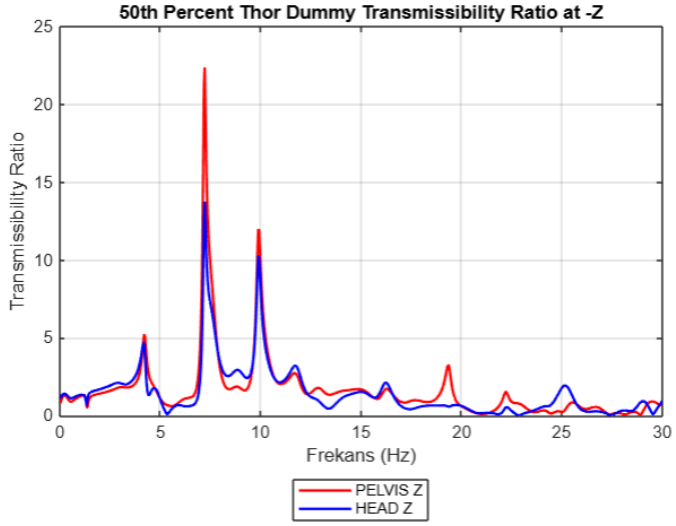

Figure 3. Transmissibility Ratio at -X Axis.

Conclusion

This study investigated the feasibility of using crash test dummies for whole-body vibration (WBV) assessments in vehicles. By subjecting a THOR dummy to shock-induced vibrations caused by a vehicle passing over an obstacle in LS-DYNA, dynamic response characteristics were analyzed and compared with known human body natural frequencies from the literature. The results demonstrated that the dummy exhibits distinct resonance peaks in frequency ranges consistent with human biomechanical responses, particularly in the pelvis and head regions. In the Z-axis, where vertical vibrations dominate, resonance peaks were observed around 4–5 Hz, aligning well with established WBV natural frequencies for the seated human body [1]. Similarly, X-axis responses exhibited resonant behavior in 2 Hz, corresponding to lateral human body vibrations in the -x direction, aligning with previous studies [5]. 8 Hz peak in -X direction may be occurred due to contribution of excitation in -Z axis resonant area. Also, strong peaks around 13–15 Hz. indicate the influence of the inclined seat position. Additionally, the head-Z axis response showed a peak around 23 Hz, which is consistent with the axial resonance frequency of the human head referred as 25Hz [1].

Overall, the findings suggest that advanced crash dummies can serve as viable surrogates for WBV analysis in vehicle environments. Their ability to replicate fundamental biomechanical responses indicates potential

applicability in ride comfort evaluations, seat design optimizations, and vibration exposure studies. Further refinement of dummy stiffness parameters and damping characteristics could enhance their fidelity for WBV-specific research, making them a valuable tool for automotive ergonomics and occupant comfort studies.

References

Deubel, C., Ernst, S., & Prokop, G. (2023). Objective evaluation methods of vehicle ride comfort—A literature review. Journal of Sound and Vibration, 548, 117515. https://doi.org/10.1016/j.jsv.2022.117515

Wu, J., Zhang, L., & Meng, D. (2023). Ride comfort analysis of seated occupants based on an integrated vehicle-human dynamic model. SAE Technical Paper 2023-01-0914. https://doi.org/10.4271/2023-01-0914

Rakheja, S., Dong, R. G., Patra, S., Boileau, P.-É., Marcotte, P., & Warren, C. (2010). Biodynamics of the human body under whole-body vibration: Synthesis of the reported data. International Journal of Industrial Ergonomics, 40(6), 710–732. https://doi.org/10.1016/j.ergon.2010.06.005

Kumbhar, P., Xu, P., & Yang, J. (2012). A literature survey of biodynamic models for whole body vibration and vehicle ride comfort. Proceedings of the ASME Design Engineering Technical Conference, 6, 671–687. https://doi.org/10.1115/DETC2012-71061

International Organization for Standardization. (1997). ISO 2631-1:1997 — Mechanical vibration and shock — Evaluation of human exposure to whole-body vibration — Part 1: General requirements. Geneva, Switzerland: ISO.

Comparison of Time and Frequency Domain Approaches for Fatigue Life Estimation Using the Finite Element Method

Ahmet Fatih Turhan[a], Osman Taha Şen[a]

[a] Istanbul Technical University, Faculty of Mechanical Engineering, Department of Mechanical Engineering, Türkiye
turhana21@itu.edu.tr

Keywords: Dirlik Method, Fatigue, Finite Element Analysis, Frequency-Domain, Time-Domain.

Aim

Fatigue, defined as the progressive and localized structural damage caused by repeated or fluctuating stresses, is one of the most critical failure modes in components subjected to cyclic or random dynamic loading. Over time, numerous fatigue life estimation methods have been developed typically classified into time-domain and frequency-domain approaches. Time-domain fatigue analysis applies the entire load history step by step, yielding explicit cycle-by-cycle stress or strain data for damage accumulation (Matsuishi & Endo, 1968). Conversely, frequency-domain approaches offer significant computational efficiency by relying on the power spectral density of the load, rather than simulating each time step (Dirlik, 1985).

Extensive research underscores both the strengths and potential limitations of these contrasting methodologies. The rainflow cycle counting algorithm, widely regarded as the standard in time-domain fatigue analysis, remains a cornerstone due to its precise capture of load reversals (Lee, Barkey & Kang, 2012). Conversely, Dirlik's method exhibits robust performance in numerous frequency-domain applications, though it can underestimate fatigue damage under certain conditions — especially when the loading features prominent periodic components, multiple resonance peaks, or significant non-Gaussian behavior (Quigley & Lee, 2012). Notably, Quigley and Lee (2012) observed that Dirlik's approach fell short by up to 30% for certain automotive components, while other researchers reported instances where it predicted more damage in broadband or narrowband scenarios (Benasciutti & Tovo, 2004). Likewise, Ragan & Manuel (2007) found notable discrepancies whenever the excitation departed from purely stationary or broadband assumptions, underscoring the influence of modal interactions and geometric factors on final fatigue life estimates. Furthermore, Demirkaya & Tüfekci (2020) carried out a study with a difference of up to approximately 58 times between time domain and frequency domain fatigue lives.

Despite their considerable advantages in computational efficiency, the accuracy of frequency-domain methods in predicting fatigue life remains uncertain. This study aims to evaluate the fatigue life predictions obtained from frequency-domain analyses by comparing them against time-domain fatigue analyses, which are considered the reference standard.

Material and Method

In this study, the core input data consisted of an acceleration–time signal and its frequency-domain equivalent as a power spectral density signal, both of which were synthetically generated rather than recorded from a physical test. A MATLAB script was used to produce white noise acceleration data, ensuring adequate coverage of the frequency range up to 2048 Hz. This same script then applied a Fast Fourier Transform to convert the acceleration–time signal into its corresponding power spectral density. Both datasets are shown in Figure 1. Consequently, the same loading was characterized in two ways — directly as a time history and as a PSD — for subsequent finite element analyses.

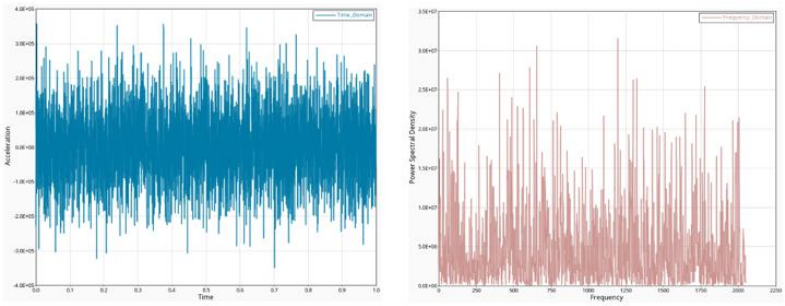

Figure 1. The acceleration-time data in the time domain and its corresponding Power Spectral Density (PSD) representation in the frequency domain.

All numerical simulations were carried out using OptiStruct, with identical finite element meshes, boundary conditions, and linear-elastic material models. The geometric dimensions of the models used are shown in Figure 2 and Figure 3. In the Notched Plate model, the linear material properties were defined as E = 70 GPa, Poisson's ratio = 0.3, and a density of 1.85×10^{-9} ton/mm³, while in the L-Plate model, E = 207 GPa, Poisson's ratio = 0.3, and a density of 7.88×10^{-9} ton/mm³ were used. While the number of elements of Notched Sample is 25,071, the number of elements of L-Plate is 15,991. Shell elements were preferred during the study due to the low computational cost. The only difference was whether the loading was applied transiently in the time domain or as a random vibration in the frequency domain, loading was applied in the z direction in both models. To evaluate and compare the responses before proceeding to fatigue life calculations, the Transient Dynamic statistics over time results were compared with the Random Vibration RMS over frequencies (3-sigma) outputs, examining both contour plots and numerical values to ensure consistency in overall stress distributions and magnitudes. Since there were no physical test data for correlation, the Transient Dynamic (time-domain) simulation served as the reference results throughout the study.

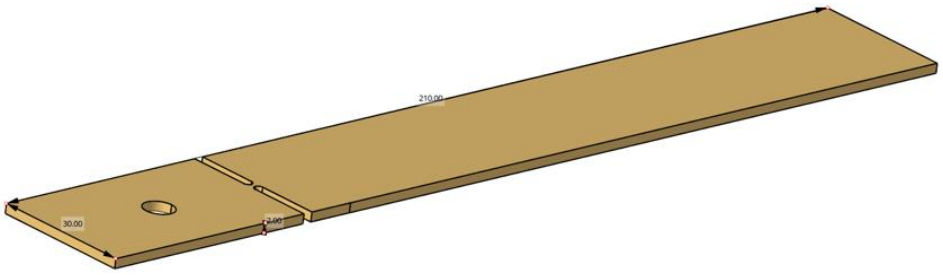

Figure 2. Geometric dimensions of the Notched Sample.

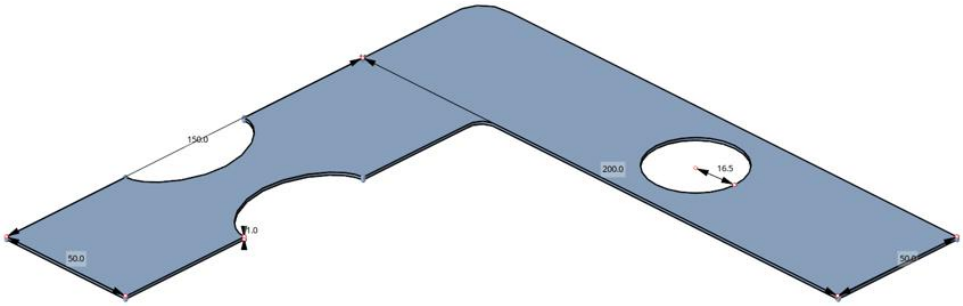

Figure 3. Geometric dimensions of the L-Plate.

Once the mechanical responses from each analysis were verified, fatigue life predictions were performed in Altair HyperLife using a conventional stress-based (S–N) approach that does not account for nonlinear or plastic deformations. Since direct correlation with a physical test was not targeted, the S-N curve to be used in fatigue analysis was obtained using the Estimate from UTS input method. In HyperLife software, the SN curve was created

by estimation method with UTS = 1000 MPa for L-Plate and UTS = 500 MPa for Notched Sample. In the frequency-domain route, the Dirlik method was used to convert the PSD-derived RMS stresses into an equivalent damage estimate, and average stress effects are neglected, as it is desirable not to affect the results under investigation. By combining these steps - synthetic load generation in MATLAB, separate transient and random vibration analyses in OptiStruct, and subsequent fatigue life assessment in HyperLife - the study aimed to compare fatigue analyses performed in the frequency domain with fatigue analyses performed in the time domain, which is considered as a reference.

Findings

Analyses were conducted on both the Notched Sample and the L-Plate using time-domain (Transient Dynamic) and frequency-domain (Random Vibration) methods, applying the same finite element meshes and boundary conditions to ensure comparability. In the Notched Sample, the time-domain Transient Dynamic analysis — using the acceleration–time input in OptiStruct — yielded a peak statistical stress of 600.110 MPa at element ID 5441. By contrast, the PSD-based random vibration simulation reported an RMS over frequencies (1-sigma) stress of 185.527 MPa at the same critical element. Notably, multiplying the 1-sigma result by three (3-sigma) brings the stress to approximately 556.580 MPa, which is in close agreement with the time-domain outcome of 600.110 MPa. An examination of the stress distributions presented in Figure 4 reveals that both methods produce identical contour patterns. In both analyses, the element with ID 5441 is identified as the most critical one. Fatigue life calculations for the Notched Sample employed a synthetic S–N curve derived via the "Estimate from UTS" method with UTS = 1000 MPa. In the time domain, the notched specimen achieved 21,177 cycles, whereas the Dirlik-based fatigue analysis in the frequency domain yielded 22,726 cycles — about a 7.315% increase over the Transient Dynamic result.

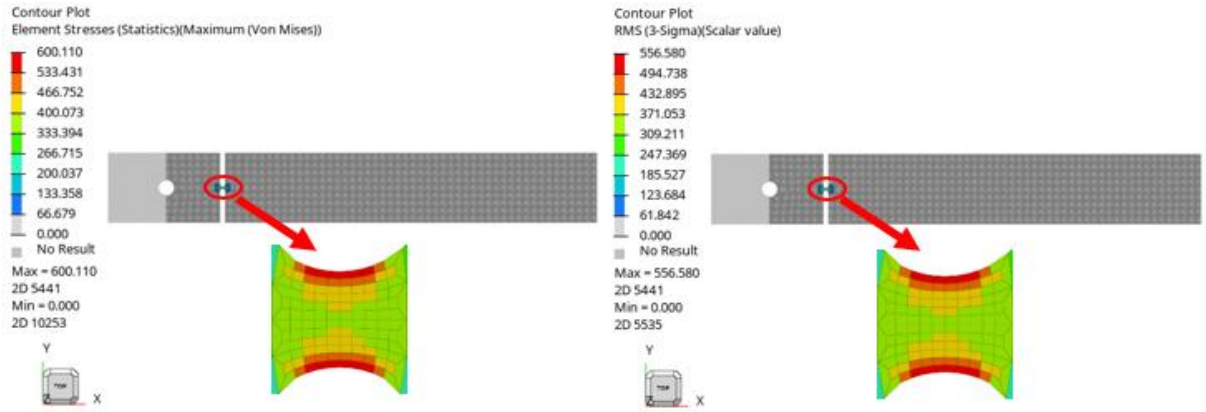

Figure 4. Time-domain (transient dynamic) and frequency-domain (random vibration) analysis results for the Notched Sample.

A similar pattern emerged for the L-Plate model. With the same acceleration–time signal in a Transient Dynamic simulation, the highest stress — 314.359 MPa — arose at element ID 26776. The corresponding Random Vibration analysis gave a 1-sigma RMS stress of 96.430 MPa, and its 3-sigma equivalent 289.289 MPa again closely matched the time-domain statistical peak of 314.359 MPa. Despite the minor differences in the stress distributions shown in Figure 5, both methods exhibit very similar contours and identify the element with ID 26776 as the most critical one. Fatigue predictions, using an S–N curve estimated with UTS = 500 MPa, resulted in 52,137 cycles for the Transient Dynamic case versus 55,477 cycles when the Dirlik method was employed on the PSD data exhibiting a 6.406% higher value.

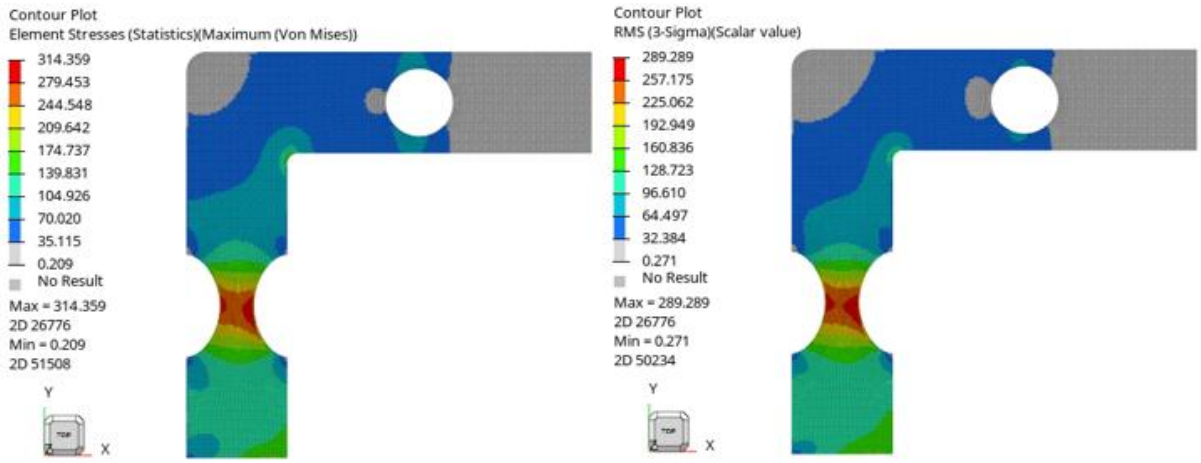

Figure 5. Time-domain (transient dynamic) and frequency-domain (random vibration) analysis results for the L-Plate.

According to results shown in Table 1, fatigue life predictions in the frequency domain tend to be slightly higher than fatigue life predictions in the time domain; this observation is consistent for both geometries. This highlights how spectral fatigue methods, especially the Dirlik approach, can slightly overestimate service life compared to direct cycle-by-cycle analysis and highlight the need to account for this slight life difference when choosing PSD-based fatigue predictions in future studies.

Table 1. Comparison of time-domain vs. frequency-domain results.

Model	Transient Dynamic Stress (MPa)	Random Vibration Stress (MPa)	Time-Domain Fatigue Life (cycles)	Frequency-Domain Fatigue Life (cycles)	Difference in Fatigue Life (%)
Notched Sample	600.110	556.580	21,177	22,726	+7.315%
L-Plate	314.359	289.289	52,137	55,477	+6.406%

Conclusion

In this study, fatigue life predictions from time domain (Transient Dynamics) and frequency domain (Random Vibration) simulations were compared under synthetic acceleration-time data and its frequency domain counterpart, PSD data loading using Notched Specimen and L-Plate geometries. Since direct physical test data was not available, the time domain Transient Dynamics results served as the reference against which the frequency domain (PSD-based) simulations were compared.

Fatigue life estimates generally aligned well across methods but revealed a consistent offset, with the Dirlik-based frequency-domain calculations yielding around 7% higher life for the Notched Sample and about 6% for the L-Plate. This difference highlights the known tendency of spectral fatigue methods to slightly overestimate service life compared to direct cycle-by-cycle counting. While this margin is relatively small, it remains a meaningful distinction for design and safety considerations. Quigley & Lee (2012) also reported that Dirlik's method fell short by up to 30% for certain automotive components, reinforcing the notion that modeling details and the nature of the load input can significantly impact the accuracy of frequency-domain predictions.

In a similar study in the literature Demirkaya and Tüfekci (2020), a difference of up to approximately 58 times in fatigue life results obtained from time and frequency domains was observed. However, in the present study, the deviation remained modest, below 10%, highlighting that frequency-domain methods can produce fatigue life predictions in close agreement with time-domain solutions if the input signals and modeling assumptions are well-defined.

The fatigue analyses in the study were conducted using the S-N method under uniaxial loading; however, the results may vary under multiaxial loading conditions and low-cycle fatigue applications. Moreover, although the effects of mean stress were neglected in this study, the difference between time-domain and frequency-domain fatigue life predictions may become more pronounced in studies where the mean stress effect is considered.
Overall, the findings underscore that PSD-based simulations reliably track the same damage trends as time-domain analyses but may slightly overestimate the number of cycles to failure. The results demonstrated that, in both geometries, the same element was identified as the critical location under random loading, indicating that neither domain approach missed the underlying stress hot spots. Considering the computational advantages of random vibration analyses, these methods can be highly valuable for early design iterations or broad parametric assessments. However, if accurate or conservative life predictions are paramount, supplementing PSD-based results adjusting with a suitable safety factor is recommended especially in scenarios where the final design decision hinges on the precise fatigue limit.

References

Matsuishi, M., & Endo, T. (1968). Fatigue of metals subject to varying stress. Presented to the Japan Society of Mechanical Engineers, Fukuoka, Japan.
Dirlik, T. (1985). Application of computers to fatigue analysis (Doctoral dissertation). University of Warwick, Coventry, UK.
Lee, Y.L., Barkey, M.E., & Kang, H. (2012). Metal fatigue analysis handbook: Practical problem-solving techniques for computer-aided engineering. Butterworth-Heinemann.
Quigley, J., & Lee, Y. (2012). Assessing Dirlik's fatigue damage estimation method for automotive applications. SAE International Journal of Passenger Cars – Mechanical Systems, 5(2), 911–920.
Tovo, R., & Benasciutti, D. (2006). Spectral methods for lifetime prediction under wide-band stationary random processes. International Journal of Fatigue, 28(1), 1–9.
Benasciutti, D., & Tovo, R. (2004). Rainflow cycle distribution and fatigue damage in Gaussian random loadings. Dipartimento di Ingegneria, Universita degli Studi di Ferrara, Technical Report No. 129.
Ragan, P., & Manuel, L. (2007). Comparing estimates of wind turbine fatigue loads using time-domain and spectral methods. Wind Engineering, 31(2), 83–99.
Demirkaya, Ö.F., & Tüfekci, K. (2020). Zaman ve frekans düzleminde yorulma ömrü hesaplama yöntemlerinin sonlu elemanlar yöntemi ile incelenmesi. Mühendislik Bilimleri ve Tasarım Dergisi, 8(2), 467–478.

Analytical Investigation of Modal Curvatures of Damaged Beams

Ozan Ürel[a], Uğurcan Eroğlu[a]

[a]Istanbul Technical University, Mechanical Engineering, Solid Mechanics, Turkey
ozanurel52@gmail.com

Keywords: Beam Theory, Closed-Form Solutions, Damage, Vibration.

Aim

Monitoring of dynamic parameters such as natural frequency, mode shapes and modal curvature is a frequently preferred method for structural damage detection since it provides information about the general condition of the structure. The effectiveness of structural health monitoring and damage detection applications based on the study of dynamic behavior has been demonstrated by various studies conducted in different fields [1]. In mechanical engineering, there are several studies on post-earthquake condition assessment of structural systems ranging from rotors and shafts to structural systems related to aircraft engineering, and in civil engineering for historical buildings, long-span bridges and high-rise structures [2-6].

Various parameters such as mathematical modeling of the structure and damage, quality of measurement data and data processing methods play an important role in accurate and reliable damage detection [7]. The study of modal characteristics that are least affected by measurement errors and uncertainties that may occur under different operating conditions plays an important role in improving the accuracy of structural health monitoring [8-10].

The practicality of measuring and analyzing natural frequencies has led to the use of this parameter in frequency calculations of damaged structural systems [11-16], as well as the prediction of damage by analyzing the changes in natural frequencies [17-23]. The fact that the natural frequency changes caused by damage can be affected by external factors negatively affects the reliability of the results obtained as a result of a damage estimation study to be carried out by measuring natural frequencies. The use of modal curvatures is a good option for the study, as they are less affected by the adverse effects of environmental conditions and have shown successful results in research on the investigation of various structural systems [24,25,26]. Nevertheless, in the case of damage over large areas, the fact that it affects structural properties in areas where damage is not present and the use of a dense sensor for high accuracy damage detection indicates that extensive research is needed to increase the applicability of modal curvatures [27-29].

Earlier studies based on the use of natural frequencies to match the data obtained in the process of structural damage detection with mathematical models used co-frequency curves [30-34]. The fact that obtaining a single solution in this method is only valid for the ideal case has led researchers to use optimization methods that include a multi-point search method. Examples of solution algorithms that include this method are genetic algorithms [7,35,36,37,38], differential evolution algorithm [39,40,41] or many similar algorithms and hybrid techniques [42-46]. It can be seen that these methods can produce a good solution under ideal conditions, but when various uncertainties begin to occur in the measurement conditions, the solution may be unacceptably inaccurate. Accordingly, it is possible to reach the desired parameter by using an appropriate algorithm by removing the noise that may occur during data collection and processing. "Beamforming algorithms" will be used in this study. Beamforming is a technique that uses the channel information at the transmitter to appropriately weight the transmitted signals and make them more compatible with the channel conditions. It is widely used in areas such as signal strength enhancement in wireless networking, radar systems and medical monitoring. It is a suitable method for estimating damage located far away from sensors. However, it has been preferred in damage detection studies in structural mechanics.

In this study, a solution method for the damage detection problem is presented by analyzing the modal curvature changes in beam-type structural elements. In the future, it is aimed to improve the study with Bartlett and Minimum Variance Distortionless Response (MVDR) techniques, which are beamforming algorithms. It is aimed to compare

the inferences made by using the modal curvatures of the bending vibrations of damaged beams with conventional methods and to reveal the advantages of the beamforming algorithms used in this investigation.

Material and Method

1-Dimensional Beam Model

In 3-dimensional Euclidean space ($\mathbb{R}3$), the geometry formed by planes with double axes of symmetry, always connected to a line of length L at its geometric centre, represents the bar to be investigated in this study. In this case, the line is called the axis of the bar and the plane perpendicular to this axis is called the cross-section of the bar. The Oxyz Cartesian coordinate set to be used to describe the position of any point on the bar is described in such a way that the z-axis is located along the bar axis and the xy-axes are located along the principal directions of the bar section. With the assumption of small displacement and deformation, the deformed state of the bar is described by the displacement of the points on the bar axis and small rotations of the bar section. For forces and force couples in the plane only, the deformed bar axis will remain in its plane and the sections with area A will rotate only about its axis. This deformation state is called 'simple bending'. Deformation of the bar when only vertical (along the y-axis) displacements are considered,

$$\gamma = \frac{dv}{dz} + \Omega\,, \qquad \chi = \frac{d\Omega}{dz} \quad \#(\,SEQ\ Denklem\ \backslash *\ ARABIC\ 1)$$

are described by the expressions. In the case where shear deformation is neglected and there is a linear relationship between bending moment (M) and curvature, assuming Hooke's material, the kinematic expressions take the following form,

$$\frac{dv}{dz} = -\Omega\,, \qquad \frac{d\Omega}{dz} = \frac{M}{EI} \quad \#(\,SEQ\ Denklem\ \backslash *\ ARABIC\ 2)$$

Here EI indicates the bending stiffness of the sections about the x-axis. Assuming that each bar piece will be in equilibrium in the deformed state, the relations between the cross-sectional effects and external loads are as follows,

$$\frac{dV}{dz} = -q\,, \qquad \frac{dM}{dz} = V \quad \#(\,SEQ\ Denklem\ \backslash *\ ARABIC\ 3)$$

Where V is the shear force in the sections and q is the distributed load in the y-axis direction. According to d'Alembert's Principle, which states that the structure will be in equilibrium under the effect of external loads and inertia forces at all times,

$$q = -\rho A\ddot{v} \quad \#(\,SEQ\ Denklem\ \backslash *\ ARABIC\ 4)$$

Here, ρ is the density of the bar. With the assumption that the motion is a harmonic motion with angular frequency and the following nondimensionalisations,

$$\underline{v} = \frac{v}{L}, \underline{z} = \frac{z}{L}, \underline{V} = \frac{VL^2}{EI}, \underline{M} = \frac{ML^3}{EI}, \omega^{-2} = \frac{\omega^2 L^4 \rho\, A}{EI} \quad \#(\,SEQ\ Denklem\ \backslash *\ ARABIC\ 5)$$

the equations of motion of the analysed bar can be formulated as follows,

$$\frac{dy}{d\underline{z}} = Ay, y = \{\underline{v}\ \underline{\Omega}\ \underline{V}\ \underline{M}\}^T, A = \begin{bmatrix} 0 & -1 & 0 & 0 \\ 0 & -\omega^{-2} & 0 & 0 \\ 0 & 1 & 0 & 0 \\ 0 & 0 & 1 & 0 \end{bmatrix}, \underline{z} \in [0,1] \quad \#(\,SEQ\ Denklem\ \backslash *\ ARABIC\ 6)$$

the solution of this set of equations is known in terms of the principal matrix (transfer matrix or matrix) and initial values as follows,

$$y(z) = Y(z, z_0)y(z_0), A_{ij}\ \epsilon^{\sim}, Y(z, z_0) = exp\ exp\ [(z - z_0)A] \quad \#(\ SEQ\ Denklem\ \backslash *\ ARABIC\ 7)$$

As also practised in the literature, accepting z0=0 will simplify the expressions of the principal matrix. In this case, the non-zero elements of the principal matrix are as follows,

$$Y_{11} = \frac{1}{2}\left[cos\ cos\left(\sqrt{\omega}z\right) + cosh\ cosh\left(\sqrt{\omega}z\right)\right]; Y_{12} = \frac{-1}{2\sqrt{\omega}}\left[sin\ sin\left(\sqrt{\omega}z\right) + sinh\ sinh\left(\sqrt{\omega}z\right)\right];\ Y_{13} = \frac{Y_{12}}{\omega^2};$$

$$Y_{14} = \frac{1}{2\omega}\left[cos\ cos\left(\sqrt{\omega}z\right) - cosh\ cosh\left(\sqrt{\omega}z\right)\right]; Y_{21} = \frac{\sqrt{\omega}}{2}\left[sin\ sin\left(\sqrt{\omega}z\right) - sinh\ sinh\left(\sqrt{\omega}z\right)\right]; Y_{22} = Y_{11}; \quad \#(\ SEQ\ Denklem\ \backslash *\ ARABIC\ 8)$$

$$Y_{23} = -Y_{14}; Y_{24} = -Y_{22}; Y_{31} = \omega^2 Y_{12}\ ; Y_{32} = \omega^2 Y_{23}\ ; Y_{33} = \omega^2 Y_{11};\ Y_{34} = \omega^2 Y_{23};$$
$$Y_{41} = \omega^2 Y_{14}\ ;\ Y_{42} = -\omega^2 Y_{13}\ ; Y_{43} = -Y_{23}; Y_{44} = Y_{11}$$

In order to find the 4 unknown initial values, a total of four boundary conditions are written, two for each end. The conditions used are as follows,

Cantilever; $\nu = 0, \Omega = 0$
Simply supported; $\nu = 0, M = 0$
Free end; $V = 0, M = 0$

Here; ν is translations, Ω is rotation, V is shear force and M is moment. This set of algebraic equations, homogeneous in terms of initial values, is the set of equations from which the characteristic equation for the solution of natural frequencies is obtained. For non-zero solutions of the initial values vector, the operator applied to it must be singular. Natural frequency values are obtained with this condition, which appears as an equation with infinite root and requires numerical solution. The set of algebraic equations for a bar with fixed supports at both ends, which will also be analysed in its damaged form, is expressed as follows,

$$H(\omega)y(0) = 0,$$

$$H(\omega) = \begin{bmatrix} 1 & 0 & 0 & 0 \\ 0 & \frac{cos\ cos\sqrt{\omega} + cosh\ cosh\sqrt{\omega}}{2} & \frac{\sqrt{\omega} - cosh\ cosh\sqrt{\omega})}{2} & 0 \\ -\frac{sin\ sin\sqrt{\omega} + sinh\ sinh\sqrt{\omega}}{2\sqrt{\omega}} & \frac{\sqrt{\omega} + sinh\ sinh\sqrt{\omega})}{2} & 0 & \frac{sin\ sin\sqrt{\omega} - sinh\ sinh\sqrt{\omega}}{2\omega^{\frac{1}{2}}} \\ \frac{sin\ sin\sqrt{\omega} + sinh\ sinh\sqrt{\omega}}{2\sqrt{\omega}} & 1 & \frac{cos\ cos\sqrt{\omega} - cosh\ cosh\sqrt{\omega}}{2\omega} & \frac{cos\ cos\sqrt{\omega} - cosh\ cosh\sqrt{\omega}}{2} \end{bmatrix} \quad \#(\ SEQ\ Denklem\ \backslash *\ ARABIC\ 9)$$

For a non-zero solution,

$$det\ det\ H(\omega) = 0,\ \ sin\ sin\sqrt{\omega}\ sinh\ sinh\sqrt{\omega} = 0 \quad \#(\ SEQ\ Denklem\ \backslash *\ ARABIC\ 10)$$

must be satisfied,

$$\omega = n^2\pi^2, n\ \epsilon\ Z^+ \quad \#(\ SEQ\ Denklem\ \backslash *\ ARABIC\ 11)$$

is obtained. The expression obtained is substituted into equation (9) and the initial values are obtained in a parameter dependent form. Based on dimensionless values,

$$\langle \nu, \nu \rangle = \int_0^1 \quad \nu^2 dz = 1 \quad \#(\ SEQ\ Denklem\ \backslash *\ ARABIC\ 12)$$

when the mass normalization defined as follows, the vector of initial values for these boundary conditions is obtained as follows,

$$y(0) = \sqrt{2}n\pi\ \{0\ \ 1\ \ -n^2\pi^2\ \ 0\}^T \quad \#(\ SEQ\ Denklem\ \backslash *\ ARABIC\ 13)$$

Damage Model for 1-Dimensional Structures

It is possible to model a potential damage as a reduction in bending stiffness in a certain part of the beam. In this case,

$$A = \begin{bmatrix} 0 & -1 & 0 & 0 & 0 & -\omega^2 & 0 & 0 & 0 & 0 & 0 & 1 & \frac{1}{1-\varepsilon\eta(z)} & 0 & 0 \end{bmatrix} \quad \#(SEQ\ Denklem\ \backslash *\ ARABIC\ 14)$$

To express the reduction in bending stiffness, Ciambella et al. [26] proposed a piecewise polynomial. A precise expression of this function can be written by relating the increase in strain energy around the crack tip to the variation along the axis of the bar and the increase in flexibility caused by this energy increase. In all cases it is known that this will be maximum at the crack location and will converge to zero as one moves away from the crack. The use of a piecewise function increases the computational effort as it implies that the solution will also be piecewise. Instead, a continuous function will be used in this study. If the properties that the function describing the decrease in bending stiffness must satisfy are described,

$$\eta(z) \epsilon\ [0,1], \forall z\ \epsilon\ [-\delta + z_c, \delta + z_c], \eta(z_c) = 1$$

$$\eta(z) = 0, \forall z\ \epsilon \notin [-\delta + z_c, \delta + z_c] \quad \#(SEQ\ Denklem\ \backslash *\ ARABIC\ 15)$$

Here zc is the centre of damage and δ is the area of damage. Here zc is the centre of damage and delta is the area of damage. In accordance with these descriptions, the normal distribution function can be used as,

$$\eta(z) = exp\left[\frac{-(z-z_c)^2}{\beta}\right] \quad \#(SEQ\ Denklem\ \backslash *\ ARABIC\ 16)$$

According to the parameter ε, which describes the magnitude of the damage and is assumed to be small, if the perturbation expansion is performed around ε=0, i.e. the undamaged state,

$$y = y_0 - \varepsilon y_1, \omega^2 = {\omega^2}_0 - \varepsilon {\omega^2}_1, A = A_0 - \varepsilon A_1$$

$$A_0 = \begin{bmatrix} 0 & -1 & 0 & 0 & 0 & -{\omega^2}_0 & 0 & 0 & 0 & 0 & 0 & 1 & \frac{1}{1-\varepsilon\eta(z)} & 0 & 0 \end{bmatrix}, A_1 = [0\ -1\ 0\ 0\ 0\ -{\omega^2}_1\ 0\ 0\ 0\ 0\ 0\ 1\ \ -\eta(z)\ 0\ 0\ ] \quad \#(SEQ\ Denklem\ \backslash *\ ARABIC\ 17)$$

The sub-index '0' describes the quantities derived for ε=0, while the index '1' the value of the derivative of the function with respect to the parameter at ε=0. When these expansions are placed in the differential equation set, the zeroth and first order equations and their solutions are as follows,

$$\frac{dy_0}{dz} = A_0 y_0, \frac{dy_1}{dz} = A_0 y_1 + A_1 y_0$$

$$y_0 = Y_0(z, z_0)\ y_0(z_0) \quad \#(SEQ\ Denklem\ \backslash *\ ARABIC\ 18)$$

$$y_1(z) = Y_0(z, z_0)\ y_1(z_0) + Y_0(z, z_0) \int_{z_0}^{z} \quad Y_0(z_0, \xi) A_1 y_0(\xi) d\xi\ ,$$

The solution of the zeroth order equation is the solution of the undamaged beam. The first order equations, on the other hand, contain inhomogeneities consisting of the zeroth order solution. This is always encountered in the perturbation method. The boundary conditions written to find the initial values of the zeroth order solution will give a set of homogeneous algebraic equations as follows,

$$H(\omega_0)\ y_0(z_0) = 0 \quad \#(SEQ\ Denklem\ \backslash *\ ARABIC\ 19)$$

The expression is similar to equation (9). For the first order, a non-homogeneous set of algebraic equations with the same (singular) operator is obtained.

$$H(\omega_0)\ y_1(z_0) = b(\omega_1) \quad \#(SEQ\ Denklem\ \backslash *\ ARABIC\ 20)$$

The non-homogeneous part of this set depends on the first order natural frequencies, i.e. the effect of damage on the natural frequency. Since the operator applied to the unknown vector is singular, the solution of this equation can only be found if the Fredholm compatibility condition is satisfied [49].

$$a^T b(\omega_1) = 0, a \in R^4, H^T(\omega_0) = 0 \quad \#(SEQ\ Denklem\ \backslash *\ ARABIC\ 21)$$

When the first order natural frequency obtained from this condition is used in Eq. (17), the natural frequencies of the damaged bar are obtained. In addition, if the unknown initial values from equation 20 are solved with this frequency change, the field functions describing the motion of the beam are obtained. This allows the modal curvatures described by the second derivative of the vertical displacement to be calculated under appropriate normalization. Since the first-order solution is linearly independent of the zeroth-order solution, this normalization is done by using the expression,

$$\langle v_0, v_1 \rangle = 0 \quad \#(SEQ\ Denklem\ \backslash *\ ARABIC\ 22)$$

This expression, also known as 'intermediate normalization' in perturbation technique, means that the projection of the modal strain energy of the zero-order solution onto the total solution is 1. This can be compared to the fact that the projection of two unit vectors whose directions are very close to each other can also be assumed to be equal to 1.

Findings

Simply Supported Damaged Beams

In this section, the case of damage to a simply supported bar, for which the zeroth order solution (undamaged case) is known, is analyzed. For this problem, the vector a described by Eq. (21) is found as follows,

$$a = a\,\{-(-1)^n\ n^2\pi^2\ -(-1)^n\ n^2\pi^2\ 1\}^T, n \in Z^+ \quad \#(SEQ\ Denklem\ \backslash *\ ARABIC\ 23)$$

From this, the first order frequency expression describing the decrease in natural frequency is obtained as follows,

$$\omega^2_1 = \frac{1}{4} n^{\frac{9}{2}}\sqrt{\beta}n^4 e^{-\pi n(\pi\beta n+2iz_c)}\{2\left(erf\left(\frac{1-z_c}{\sqrt{\beta}}\right)+erf\left(\frac{z_c}{\sqrt{\beta}}\right)\right)e^{-\pi n(\pi\beta n+2iz_c)}+erfc\left(\frac{z_c-i\pi\beta n}{\sqrt{\beta}}\right) \quad \# \ +erfc\left(\frac{i\pi\beta n-z_c+1}{\sqrt{\beta}}\right)$$
$$-e^{4i\pi n z_c}\left(erf\left(\frac{-i\pi\beta n-z_c+1}{\sqrt{\beta}}\right)+erf\left(\frac{z_c+i\pi\beta n}{\sqrt{\beta}}\right)\right)-2\}\ (24)$$

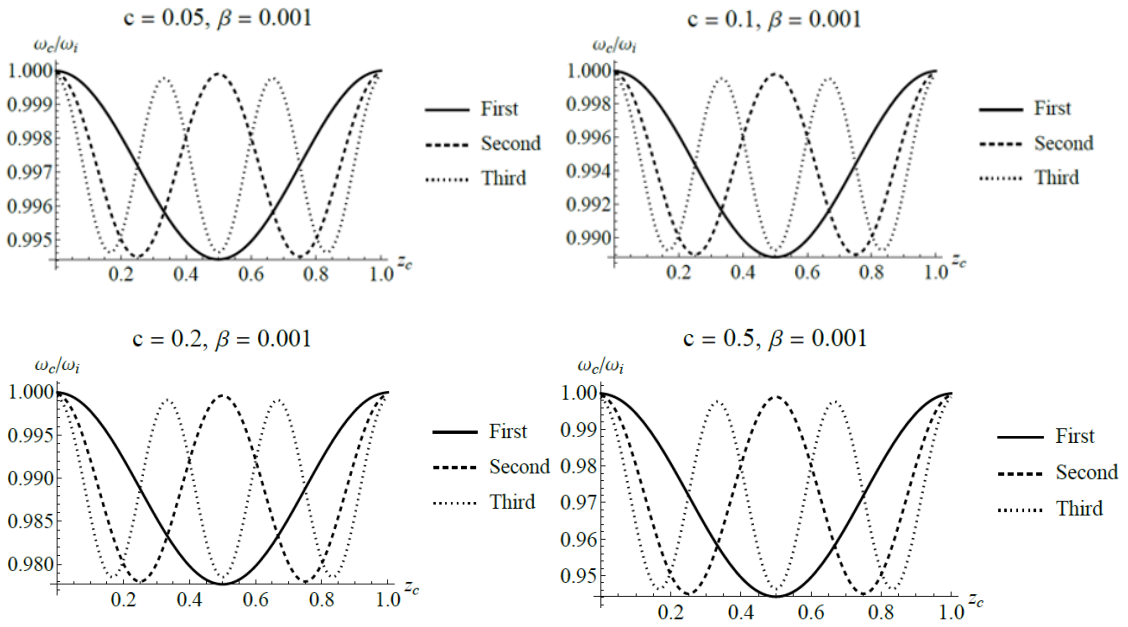

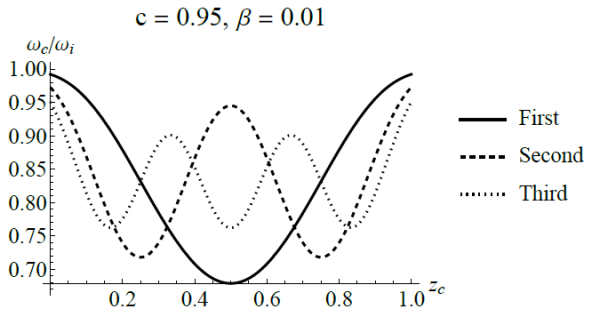

Figure 1. Effect of severity of the damage on the first 3 natural frequencies of a damaged bar with two end hinges.

The damage width parameter β = 0.001 was assumed constant and the effect of crack location on the first three natural frequencies was analyzed and the obtained frequency plots are shown in Figure-1. The comparison was made for five different damage magnitudes, c = 0.05, c = 0.1, c = 0.2, c = 0.5 and c = 0.95. In the graphs, the horizontal axis indicates the damage location (zc), while the vertical axis indicates the ratio of the damaged bar frequency to the undamaged bar frequency (ωc/ωi). According to the results, it can be seen that the shape of the curves expressing the natural frequencies in the first three modes does not change with increasing damage magnitude, but the natural frequency ratios decrease.

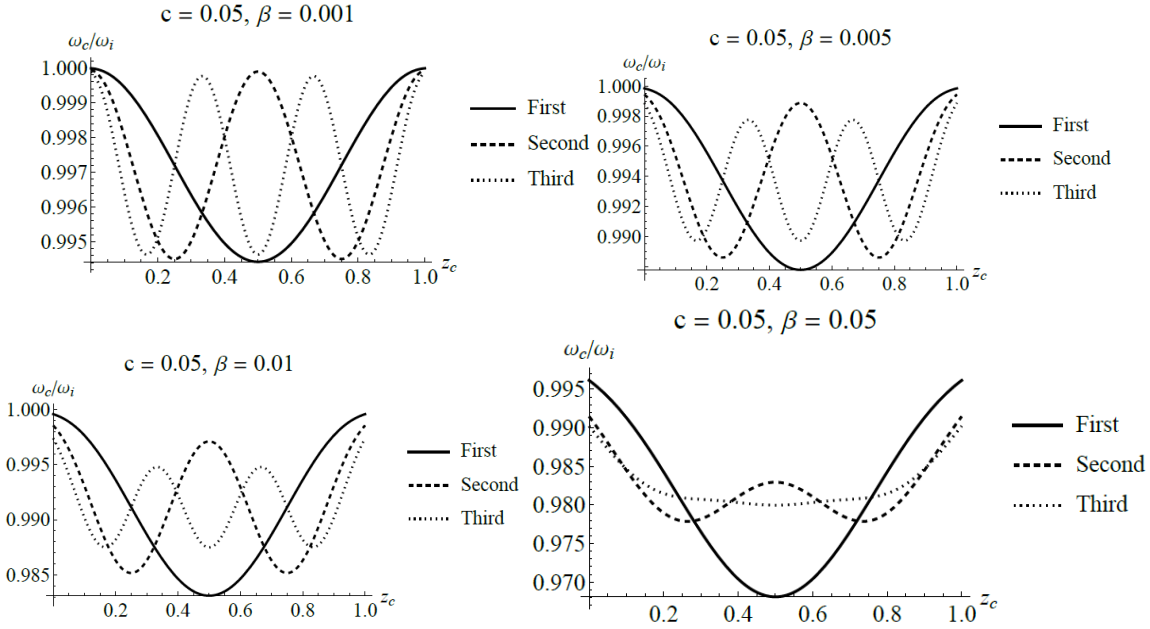

Figure 2. Effect of crack width on the first 3 natural frequencies of a damaged bar with two end hinges.

The damage magnitude parameter c = 0.05 was considered constant and the effect of crack width on the first three natural frequencies was analysed and the frequency graphs obtained are shown in Figure-2. It is observed that the natural frequency values decrease with the increase of the parameter expressing the damage width and the curves of the second and third modes tend to resemble the curve of the first mode and it can be said that the higher modes are more affected by this increase.

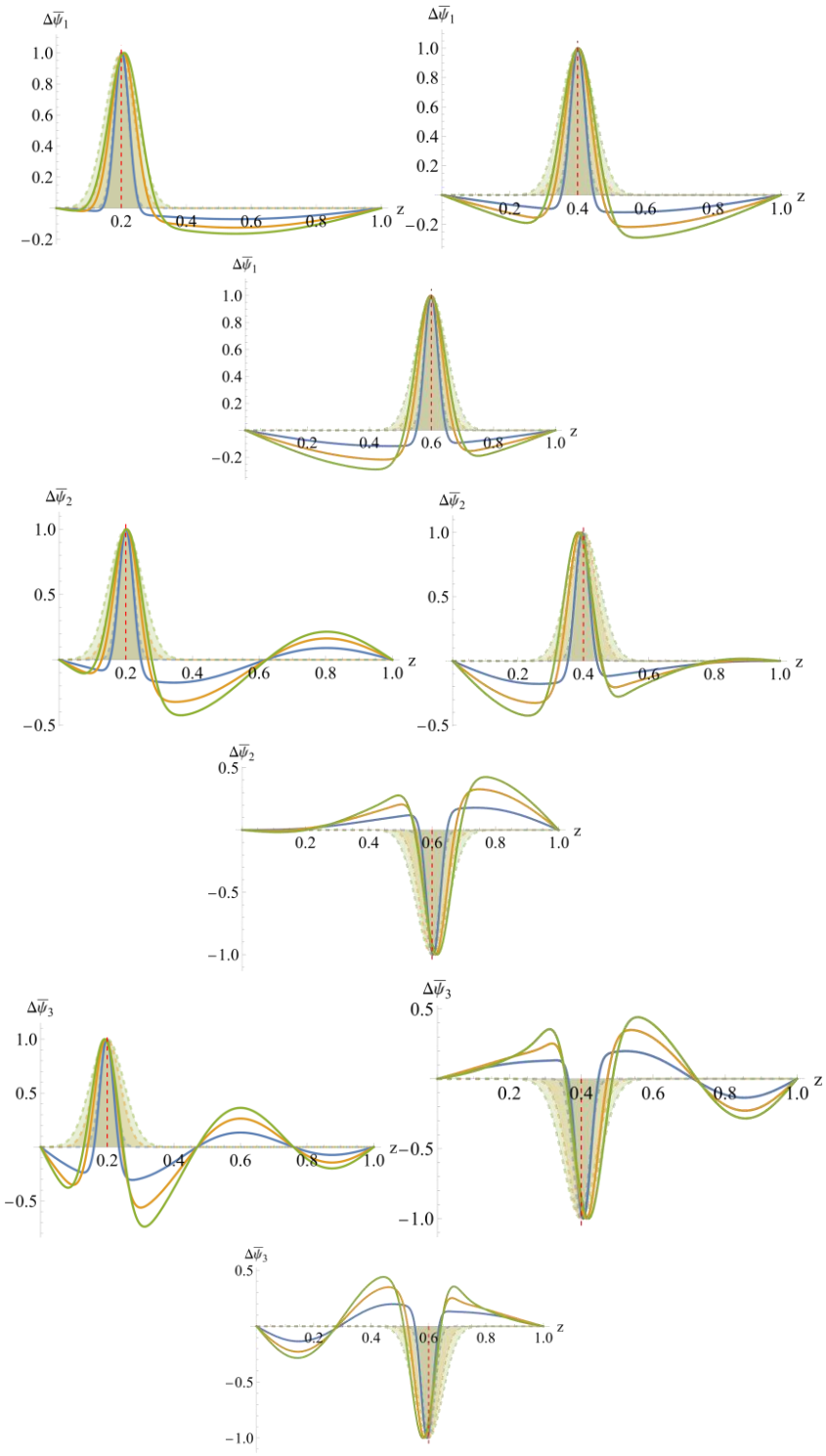

Figure 3. Modal curvature changes of the first three modes for 3 different damage locations and 3 different damage widths (blue, yellow, green: b = 0.001, 0.003, 0.005).

For three different damage locations (zc = 0.2, 0.4, 0.6) and three different damage widths (β = 0.001, 0.003, 0.005) the changes in the modal curvatures of the beam (ΔΨ) were plotted. It was observed that as the value of the parameter 'β', which represents the damage width, increases, the modal curvatures of the first three modes spread over a wider area in the relevant damage zone. In addition, the effect of the damage width on the mode shape can

be followed by plotting the function that characterises the decrease in flexural stiffness depending on the damage width parameter on the graph. Based on the graphs, it is seen that there is a peak in modal curvatures in the damage zone, but there are also extremum points outside the damage zone. If measurements are made at these points, it may be evaluated that the damage is around the extremum points. This increases the risk of error in determining the actual location of the damage. In addition, due to the symmetry of the investigated system, it can be said that the change in the mode shapes is the same in case of damage in symmetrical regions.

Conclusion

In the part of the study up to this stage, a solution to the problem of damage detection in beams was presented by analyzing modal curvature changes in beam type structural elements. According to the results obtained, it can be said that monitoring the changes in modal curvatures gives successful results in determining the damage parameters. The function $\eta(z)$ describing the damage and the proposed closed form solution are the unique parts of the study. In the future, it is aimed to improve the solution with Bartlett and MVDR techniques, which are beam forming algorithms. It is aimed to compare the inferences made by utilizing the modal curvatures of bending vibrations of damaged beams with conventional methods and to reveal the advantages of the beamforming algorithms used in this research.

References

C. R. Farrar, S. W. Doebling, Damage detection II: field applications to large structures. In: J. M. M. Silva and N. M. M. Maia (eds.), Modal analysis and testing, Nato Science Series, Kluwer Academic Publishers, Dordrecht, Netherlands, 1999.

A. D. Dimarogonas, Vibration of cracked structures: A state of the art review, Engineering Fracture Mechanics 55 (5) (1996) 831–857.

S. W. Doebling, C. R. Farrar, M. B. Prime, D. W. Shevitz, Damage identification and health monitoring of structural and mechanical systems from changes in their vibration characteristics: a literature review, Los Alamos National Loboratory report LA-13070-MS.

A**. Pau, F. Vestroni,** Vibration analysis and dynamic characterization of the colosseum, Structural Control and Health Monitoring 15 (8) (2008) 1105–1121.

Memisoglu Apaydin, N., Zulfikar, A. C., & Cetindemir, O. (2022). Structural health monitoring systems of long-span bridges in Turkey and lessons learned from experienced extreme events. Journal of Civil Structural Health Monitoring, 12(6), 1375-1412.

Kaynardağ, K., & Soyöz, S. (2014). 'Structural Health Monitoring Of A Tall Building. In Second European Conference On Earthquake Engineering And Seismology (pp. 25-29).

U. Eroglu, E. Tufekci, Exact solution based finite element formulation of cracked beams for crack detection, International Journal of Solids and Structures 96 (2016) 240–253

A. Deraemaeker, E. Reynders, G. De Roeck, J. Kullaa, Vibration based shm: comparison of the performance of modal features vs features extracted from spatial filters under changing environmental conditions, in: ISMA2006 International Conference on Noise and Vibration Engineering. p, 2006, pp. 849–864.

R. Hou, Y. Xia, Review on the new development of vibration-based damage identification for civil engineering structures: 2010–2019, Journal of Sound and Vibration 491 (2021) 115741.

Shokrani, Y., Dertimanis, V. K., Chatzi, E. N., & N. Savoia, M. (2018). On the use of mode shape curvatures for damage localization under varying environmental conditions. Structural Control and Health Monitoring, 25(4), e2132.

Gounaris, G. ve Dimarogonas, A. (1988). A finite element of a cracked prismatic beam for structural analysis, Computers and Structures, 28(3), 309–313.

Papadopulos, C.A. ve Dimarogonas, A.D. (1987). Coupling of bending and torsional vibration of a cracked Timoshenko shaft, Ingenieur-Archiv, 57, 496–505.

Papadopulos, C.A. ve Dimarogonas, A.D. (1992). Coupled vibration of cracked shafts, Journal of Vibration and Acoustics, 114, 461–167.

Loya, J., Rubio, L. ve Fernández-Sáez, J. (2006). Natural frequencies for bending vibrations of Timoshenko cracked beams, Journal of Sound and Vibration, 290(3-5), 640–653.
Viola, E., Nobile, L. ve Federici, L. (2002). Formulation of Cracked Beam Element for Structural Analysis, Journal of Engineering Mechanics, 128(2), 220–230.
Kisa, M. ve Arif Gurel, M. (2007). Free vibration analysis of uniform and stepped cracked beams with circular cross sections, International Journal of Engineering Science, 45(2-8), 364–380.
Cawley, P. ve Adams, R.D. (1979). The location of defects in structures from measurements of natural frequencies, Journal ofStrain Analysis, 14(2), 49–57.
Chinchalkar, S. (2001). Determination of Crack Location in Beams Using Natural Frequencies, Journal of Sound and Vibration, 247(3), 417 – 429.
Kim, J.T. ve Stubbs, N. (2003). Crack detection in beam-type structures using frequency data, Journal of Sound and Vibration, 259(1), 145–160.
Cerri, M.N. ve Ruta, G.C. (2004). Detection of localised damage in plane circular arches by frequency data, Journal of Sound and Vibration, 270, 39–59.
Pau, A., Greco, A. ve Vestroni, F. (2010). Numerical and experimental detection of concentrated damage in parabolic arch by measured frequency variations, Journal of Vibration and Control, 17(4), 605–614.
Benedetti, A., Pignagnoli, G. ve Tarozzi, M. (2018). Damage identification of cracked reinforced concrete beams through frequency shift, Materials and Structures, 51(6), 147.
Greco, A., D'Urso, D., Cannizzaro, F. ve Pluchino, A. (2018). Damage identification on spatial Timoshenko arches by means of genetic algorithms, Mechanical Systems and Signal Processing, 105, 51–67.
D. H. Nguyen, Q. B. Nguyen, T. Bui-Tien, G. De Roeck, M. AbdelWahab, Damage detection in girder bridges using modal curvatures gapped smoothing method and convolutional neural network: Application to bo nghi bridge, Theoretical and Applied Fracture Mechanics 109 (2020) 102728.
M. Dilena, A. Morassi, M. Perin, Dynamic identification of a reinforced concrete damaged bridge, Mechanical Systems and Signal Processing 25 (8) (2011) 2990–3009.
A. Pandey, M. Biswas, M. Samman, Damage detection from changes in curvature mode shapes, Journal of Sound and Vibration 145 (2) (1991) 321–332.
G. De Roeck, E. Reynders, D. Anastasopoulos, Assessment of small damage by direct modal strain measurements, Lecture Notes in Civil Engineering 5 (2018) 3–16.
J. Ciambella, F. Vestroni, The use of modal curvatures for damage localizationin beamtype structures, Journal of Sound and Vibration 340 (2015) 126–137.
J. Ciambella, A. Pau, F. Vestroni, Modal curvature-based damage localization in weakly damaged continuous beams, Mechanical Systems and Signal Processing 121 (2019) 171–182.
Chinchalkar, S. (2001). Determination of Crack Location in Beams Using NaturalFrequencies, Journal of Sound and Vibration, 247(3), 417 – 429.
Patil, D. ve Maiti, S. (2003). Detection of multiple cracks using frequency measurements, Engineering Fracture Mechanics, 70(12), 1553 – 1572.
Nandwana, B. ve Maiti, S. (1997). Detection of the location and size of a crack in stepped cantilevered beams based on measurements of natural frequencies, Journal of Sound and Vibration, 203(3), 435 – 446.
Liang, R. Y., Choy, F. K., & Hu, J. (1991). Detection of cracks in beam structures using measurements of natural frequencies. Journal of the Franklin Institute, 328(4), 505-518.
Owolabi, G. M., Swamidas, A. S. J., & Seshadri, R. (2003). Crack detection in beams using changes in frequencies and amplitudes of frequency response functions. Journal of sound and vibration, 265(1), 1-22.
Vakil-Baghmisheh, M.T., Peimani, M., Sadeghi, M.H. ve Ettefagh, M.M. (2008). Crack detection in beam-like structures using genetic algorithms, Applied Soft Computing, 8(2), 1150–1160.
Xiang, J., Zhong, Y., Chen, X. ve He, Z. (2008). Crack detection in a shaft by combination of wavelet-based elements and genetic algorithm, International Journal of Solids and Structures, 45(17), 4782 – 4795.

Mehrjoo, M., Khaji, N., & Ghafory-Ashtiany, M. (2013). Application of genetic algorithm in crack detection of beam-like structures using a new cracked Euler–Bernoulli beam element. Applied Soft Computing, 13(2), 867-880.
Yao, P., & Lu, M. (2023). Structural damage identification of high-order shear beams based on a genetic algorithm. Proceedings of the Institution of Civil Engineers-Smart Infrastructure and Construction, 177(2), 60-72.
Eroglu, U. ve Tufekci, E. (2017). Crack modeling and identifictaion in curved beams using differential evolution, International Journal of Mechanical Sciences, 131-132, 435–450.
Wang, N., Jiang, Y., Zhong, Y., & Shao, L. (2021). An adaptive damage detection method based on differential evolutionary algorithm for beam structures. Measurement, 178, 109227.
Seyedpoor, S. M., & Pahnabi, N. (2021). Structural damage identification using frequency domain responses and a differential evolution algorithm. Iranian Journal of Science and Technology, Transactions of Civil Engineering, 45(2), 1253-1264.
K. Saridakis, Chasalevris, A., Papadopoulos, C. ve Dentsoras, A. (2008). Applying neural networks, genetic algorithms and fuzzy logic for the identification of cracks in shafts by using coupled response measurements, Computers and Structures, 86(11), 1318 – 1338.
S. Moradi, Razi, P. ve Fatahi, L. (2011). On the application of bees algorithm to the problem of crack detection of beam-type structures, Computers and Structures, 89(23-24), 2169–2175.
M.V. Baghmisheh, Peimani, M., Sadeghi, M.H., Ettefagh, M.M. ve Tabrizi, A.F. (2012). A hybrid particle swarm–Nelder–Mead optimization method for crack detection in cantilever beams, Applied Soft Computing, 12(8), 2217 – 2226.
A. Khatir, Capozucca, R., Khatir, S., & Magagnini, E. (2022). Vibration-based crack prediction on a beam model using hybrid butterfly optimization algorithm with artificial neural network. Frontiers of Structural and Civil Engineering, 16(8), 976-989.
B. Firouzi, Abbasi, A., & Sendur, P. (2022). Improvement of the computational efficiency of metaheuristic algorithms for the crack detection of cantilever beams using hybrid methods. Engineering Optimization, 54(7), 1236-1257.

MECHANICAL ENGINEERING

Additive Manufacturing

Automotive

Computational Fluid Dynamics

Computational Solid Mechanics

Fluid Mechanics

Industrial Data Analytics

Machine Design

Machine Dynamics, Vibration, and Acoustic

System Dynamics and Control

Nonlinear System Identification of a 2-DOF Gimbal System

Batuhan Kalkan[a], Ayhan Kural[a]

[a] Istanbul Technical University, Mechanical Engineering Departmant, System Dynamics and Control Program, Turkey
kalkan22@itu.edu.tr, kuralayh@itu.edu.tr

Keywords: Gimbal Nonlinear Modelling, Identification, Friction.

Aim

Gimbal systems are used to keep the payloads they carry at a certain stabilization accuracy under the disturbing effects caused by the movement of the platforms they are placed on (Hilkert, 2008). These systems are especially preferred in military applications for the tasks of recognizing and tracking targets in the line of sight thanks to the electro-optic systems they carry as payloads. Control algorithms must be developed to meet the motion control and stabilization requirements in gimbal systems. In order for control algorithms to be applied successfully, dynamic models similar to the real system must be obtained. There are many parameters that need to be known in order to create a dynamic model of gimbal systems. Even if these parameters are determined from the design or datasheets, there may be major differences between the obtained model and the real system. For this reason, after the production of gimbal systems, system identification application is performed and dynamic models of the system are created. In this way, control algorithm development studies can be carried out in a computer environment without the need for a real system.
In this study, linear and nonlinear dynamic models of the azimuth axis of a 2-dof gimbal system were created in order to meet the motion control and stabilization requirements of the sight system in the gun turret of a land vehicle.

Material and Method

In this study, there is a DC motor, encoder and gyrocope on the azimuth axis of the gimbal system. Electrical energy is converted into mechanical energy by the current command applied to the DC motor and the system is moved. The current controller of the DC motor is controlled by a driver. The gyroscope gives the angular speed of the gimbal system relative to the ground. The angular speed coming from the gyroscope is used as a feedback signal in the speed control algorithm. Nonlinear friction and unbalance models are developed with the angular position coming from the encoder and the angular speed data produced from this angular position. Figure 1 shows a visual of the gimbal system used in a similar study (Lee et al., 2020).

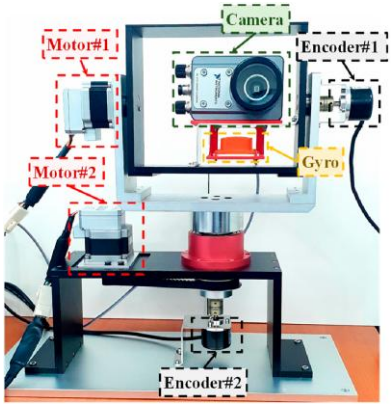

Figure 1. A sample of 2-dof gimbal system design (Lee et al., 2020).

The gimbal system is modeled as a single input and single output with current input and angular speed output. The block diagrams of the model are shown in Figure 2 below. The nonlinear dynamic model of the gimbal system consists of the motor model, inertia, friction model, unbalance model and gyroscope model (Özçelik et al., 2022). The current control loop is designed by the digital motor driver thanks to the PWM (Pulse Width Modulation) in the motor model. In the tests conducted with the current controller, it was seen that it works ~100% correctly (Tezgelen, 2020). The gimbal system designed for current input and angular speed output is shown by the following Equation 1 by the linear transfer function. W(s) represents the angular speed output, I(s) represents the current input, Kt represents the motor torque constant, J represents the inertia of the system and B represents the friction of the system.

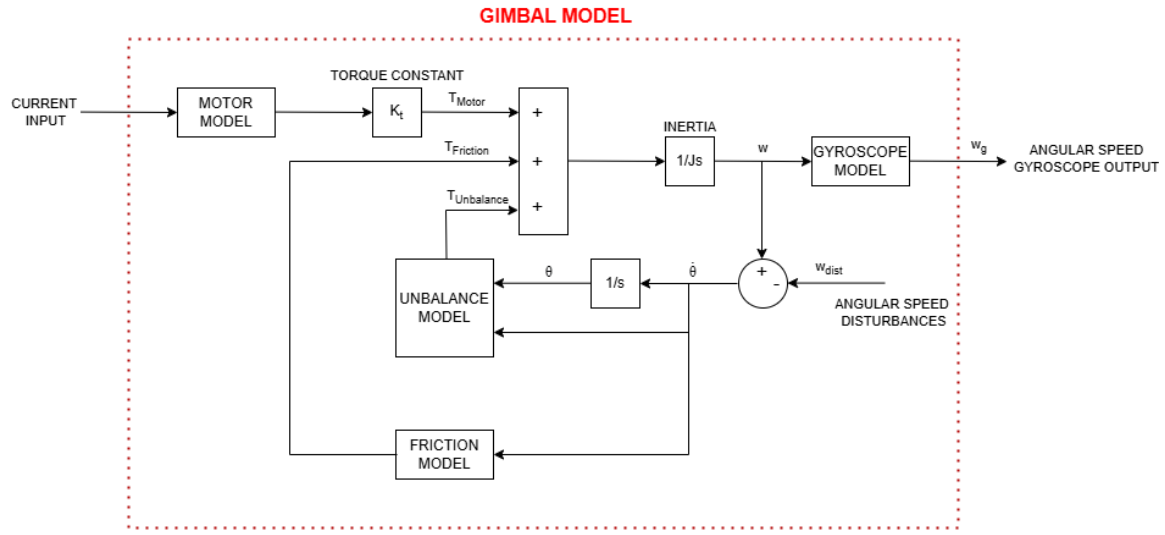

Figure 2. Block diagrams of gimbal system.

Equation 1 Transfer function of gimbal system

$$\frac{W(s)}{I(s)} = \frac{1}{\frac{Js}{K_t} + \frac{B}{K_t}}$$

FRF (Frequency Response Function) wave was applied to the gimbal system as current input and angular speed outputs were obtained from the gyroscope (Özdoğan, 2016; Olsson, 1998). The targeted bandwidth of the gimbal was determined as 8 [Hz] and for this reason, system identification was performed up to 25 [Hz]. In order to create the FRF signal, a sine sweep signal was created from 1 [Hz] to 25 [Hz] with 0.25 [Hz] increments and each frequency value was repeated 16 times in order to reveal the dynamics of the system (Çetinyol, 2023; Eroğlu, 2023). The FRF signal design is shown in figure 3 below. The FRF signal created at 2.4 [A], 3 [A], 3.6 [A], 4.2 [A] and 4.8 [A] current amplitudes was applied to the system.Transfer functions were obtained using the System Identification Toolbox in Matlab. Real Data is the angular speed data obtained from the gyroscope after the current commands applied to the real system. Estimation Data is the angular speed data obtained by applying the current commands applied to the real system separately to the transfer function obtained as a result of system identification. The formula in Equation 2 below was used to calculate RMS Accuracy.

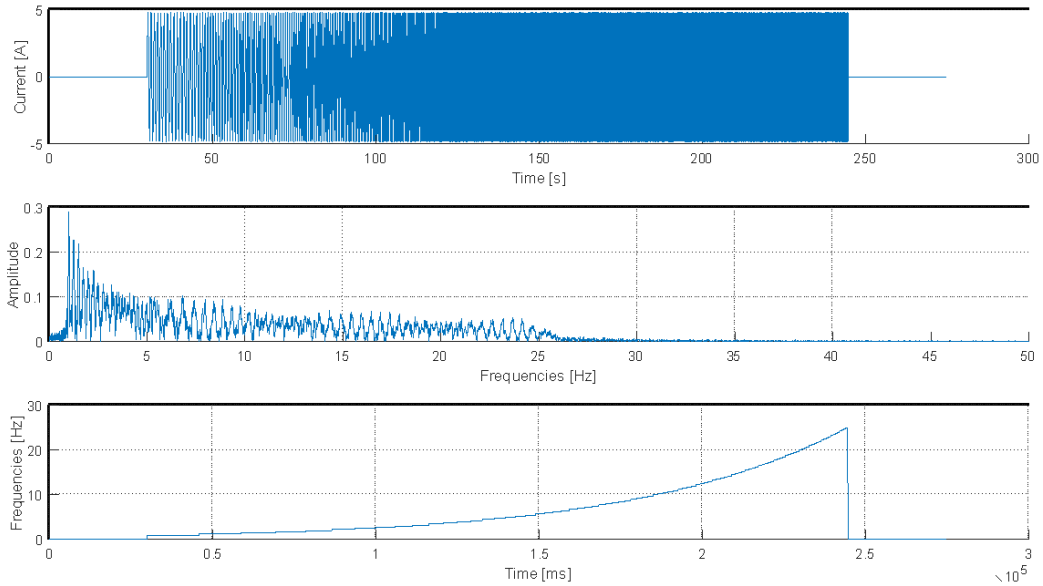

Figure 3. Sine sweep signal design.

Equation 2 RMS Accuracy

$$RMS\ Accuracy = \left(1 - \frac{rms(RealData - EstimationData}{rms(RealData)}\right) * 100$$

Table 1 below shows the RMS Accuracy, J/Kt and B/Kt values calculated as a result of the system identification applications. It was observed that the test result with an amplitude of 4.8 [A] had the highest system identification success and the J/Kt value was accepted as the inertia of the system and the B/Kt value was accepted as the friction of the system to be used in the linear system model.

Table 1. Results of System Identification.

Test No	Amplitude [A]	RMS Accuracy Linear System Identification	J/Kt	B/Kt
1	2.4	79.1433	0.0186	0.1552
2	3	82.3678	0.0187	0.1259
3	3.6	85.1759	0.0183	0.0917
4	4	86.6240	0.0183	0.0751
5	4.8	88.3800	0.0182	0.0649

Since the friction in gimbal systems can vary depending on the direction and speed of the movement, nonlinear models were created. As a result of literature research, it was observed that the modeling success of gimbal dynamic models increased with the addition of the Lugre friction model (Olsson, 1998; Sincar, 2015; Mashayekhi et al., 2022). The Lugre friction model parameters consisting of pre-slip and sliding phases were calculated with tests performed on the Azimuth axis (Sisu, 2023; Yang et al., 2016).

Unbalance is divided into two as static and dynamic unbalance. Since the axis of the flank does not shift to one side in any way when it is released, static unbalance is zero. Dynamic unbalance can vary depending on the angular position and angular speed. The unbalance effect was examined by rotating the axis of the flank at different speeds. After the curve fitting studies, it was seen that the change in the unbalance current depending on the angular position in the axis of the flank was too low to be considered significant. The unbalance model was created by creating the unbalance current polynomial depending on the angular speed (Poyrazoğlu, 2017; Çetinyol, 2023).
Figure 4 below shows a gyroscope model. Since the bandwidth of the gyroscope used was very high, a lowpass filter was not used (Tezgelen, 2020). Angular speed data from the gyroscope was recorded without giving any command to the gimbal system. The gyroscope noise was calculated by taking the standard deviation of this angular speed. The gyroscope delay was determined in the optimization studies of the dynamic model of the system designed in Matlab/Simulink (Baskın et al., 2017).

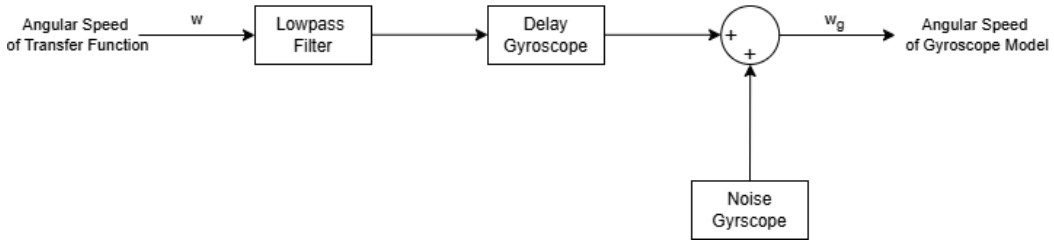

Figure 4. Gyroscope modelling representative.

The dynamic model in this study was implemented in MATLAB/Simulink using a fixed-step discrete solver (with no continuous states) at a sampling frequency of 1000 [Hz].

Findings

In Matlab/Simulink, sine sweep current waves with different amplitudes used for system identification were applied as input to both linear and nonlinear dynamic models of the gimbal system's azimuth axis, and the angular speed values in the gyroscope model were obtained (EstimationData). After the sine sweep current waves with different amplitudes applied to the real system were applied, the angular speed values read from the gyroscope were compared (RealData). According to Table 2 below, it is seen that the success of the linear system model decreases by half at different amplitudes, while the success of the nonlinear gimbal model is high at different amplitudes.In Figure 5 below, the similarity between the response of the real system and the response of the simulation model to the sine sweep signal with a current amplitude of 4.8 [A] is calculated to be approximately 95%.

Table 2. Comparison of Linear and Nonlinear Modelling.

Test No	Amplitude [A]	RMS Accuracy Linear Modelling	RMS Accuracy Nonlinear Modelling
1	2.4	46.3199	85.6004
2	3	61.2113	87.4529
3	3.6	78.5073	92.6000
4	4	85.3936	94.2643
5	4.8	88.3749	95.0356

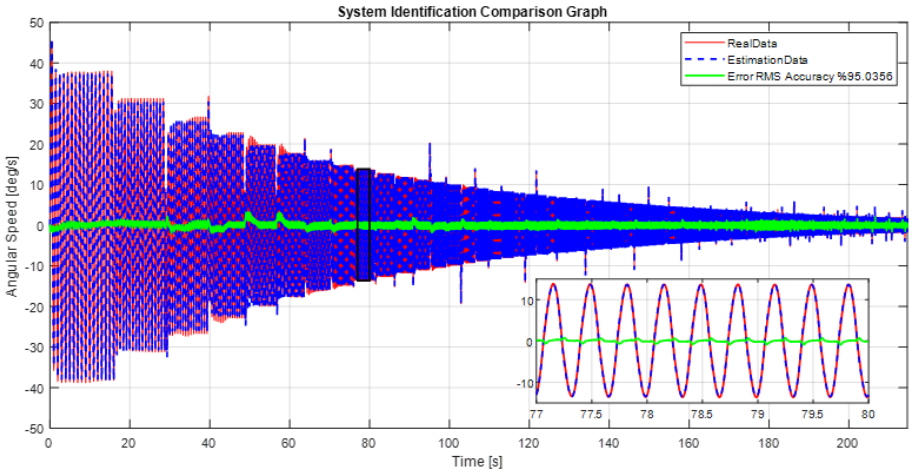

Figure 5. Comparison of Real and Simulation systems.

Conclusion

As a result of this study, linear and nonlinear gimbal system dynamic models were created in Matlab/Simulink. Current commands consisting of sine sweep waves with different amplitudes were applied to these simulation models and angular speed data were obtained. The same tests were performed on the real system and angular speed data were obtained from the gyroscope. It was observed that linear modeling could be applied quickly, but modeling success was low. It was observed that nonlinear modeling could take time because nonlinear parts needed to be created with controlled tests, but modeling success was high. In future studies, control algorithms can be developed in a simulation environment without real system.

References

Baskin, M., & Leblebicioğlu, M. K. (2017). Robust control for line-of-sight stabilization of a two-axis gimbal system. Turkish Journal of Electrical Engineering and Computer Sciences, 25(5), 3839-3853.

Çetinyol, E. (2023). Performance of fractional order controllers for two axis gimbal system (Master's thesis, Istanbul Technical University). YÖK Ulusal Tez Merkezi, (895445).

Eroğlu, H. (2023). Comparative analysis of PI, LQR, and gain scheduled super twisting sliding mode controllers for gimbal system (Master's thesis, Istanbul Technical University). YÖK Ulusal Tez Merkezi, (894549).

Hilkert, J. M. (2008). Inertially stabilized platform technology concepts and principles. IEEE control systems magazine, 28(1), 26-46.

Lee, D. H., Tran, D. Q., Kim, Y. B., & Chakir, S. (2020). A robust double active control system design for disturbance suppression of a two-axis gimbal system. Electronics, 9(10), 1638.

Mashayekhi, A., Behbahani, S., Nahvi, A., Keshmiri, M., & Shakeri, M. (2022). Analytical describing function of LuGre friction model. International Journal of Intelligent Robotics and Applications, 6(3), 437-448.

Olsson, H., Åström, K. J., De Wit, C. C., Gäfvert, M., & Lischinsky, P. (1998). Friction models and friction compensation. Eur. J. Control, 4(3), 176-195.

Özçelik, M., Kürkçü, B., & Bayraktaroğlu, Z. Y. (2022, November). Modelling and simulation of 2 dof gimbal system with experimental system identification. In 2022 10th International Conference on Systems and Control (ICSC) (pp. 508-515). IEEE.

Özdoğan, G., & Leblebicioğlu, K. (2016). Frequency response function measurement and parametric SISO system modelling of a gyro-stabilized infrared electro optic gimbal system. Transactions of the Institute of Measurement and Control, 38(5), 512-528.

Poyrazoğlu, E. (2017). Detailed modeling and control of a 2-dof gimbal system (Master's thesis, Middle East Technical University, Turkey). YÖK Ulusal Tez Merkezi, (463566).

Sincar, E., Balkan, T., & Platin, B. E. (2015, July). Compensation of friction effects in gyro-stabilized motion platforms. In 2015 American Control Conference (ACC) (pp. 3242-3248). IEEE.
Sisu, S., Poyrazoğlu, E., & Kalkan, M. (2023). LuGre sürtünme giderme yönteminin ataletsel stabilize elektro-optik sistemlerde kontrol performansına etkisi [Effect of LuGre friction compensation method on control performance for inertial stabilized electro-optical systems]. TOK 2023, Türkiye.
Tezgelen, O. (2020). İki Eksen Gimbal Sistemleri için Gürbüz Kontrol Yöntemlerinin Karşılaştırılması (Master's thesis, TOBB ETÜ Fen Bilimleri Enstitüsü). YÖK Ulusal Tez Merkezi, (641187).
Yang, H., Zhao, Y., Li, M., & Zhou, Y. J. (2016). Study on the friction torque test and identification algorithm for gimbal axis of an inertial stabilized platform. Proceedings of the Institution of Mechanical Engineers, Part G: Journal of Aerospace Engineering, 230(10), 1990-1999.

Trajectory Analysis of a Medium-Range Ballistic Missile Threat via Design and Simulation

Doruk Ünal[a], İlker Murat Koç[a], Ukte Aksen[b]

[a] Istanbul Technical University, Department of Mechanical Engineering, System Dynamics and Control Program, Turkey
[b] Aselsan Inc., Avionics & Guidance Systems, Turkey
unaldo23@itu.edu.tr

Keywords: Ballistic Missile , Flight Path Prediction , Range Estimation , Trajectory Analysis.

Aim

The primary objective of this study is to analyze the trajectory and acceleration characteristics of a medium-range ballistic missile through detailed design and simulation. By accurately modeling the missile's dynamic behavior during each phase of flight, the study aims to generate comprehensive trajectory data. This information is essential for the development of ballistic missile-specific tracking algorithms and the precise prediction of impact points, contributing to the enhancement of missile defense systems and overall strategic planning.

Material and Method

This research employs a two-stage propulsion system consisting of three major phases: an initial thrust stage, a sustained thrust stage, and a free-flight (coasting) stage. The missile adheres to conventional aerodynamic design principles, featuring an axially symmetric cylindrical body with a conical nose and swept-shaped fins, ensuring optimized aerodynamic performance. The missile's total initial mass is 22,000 kg, with a tapered fin structure at both the tail and intermediate stages to enhance stabilization during flight and reduce aerodynamic disturbances. The geometric configuration and stage separation sequence of the missile are illustrated in Figure 1.

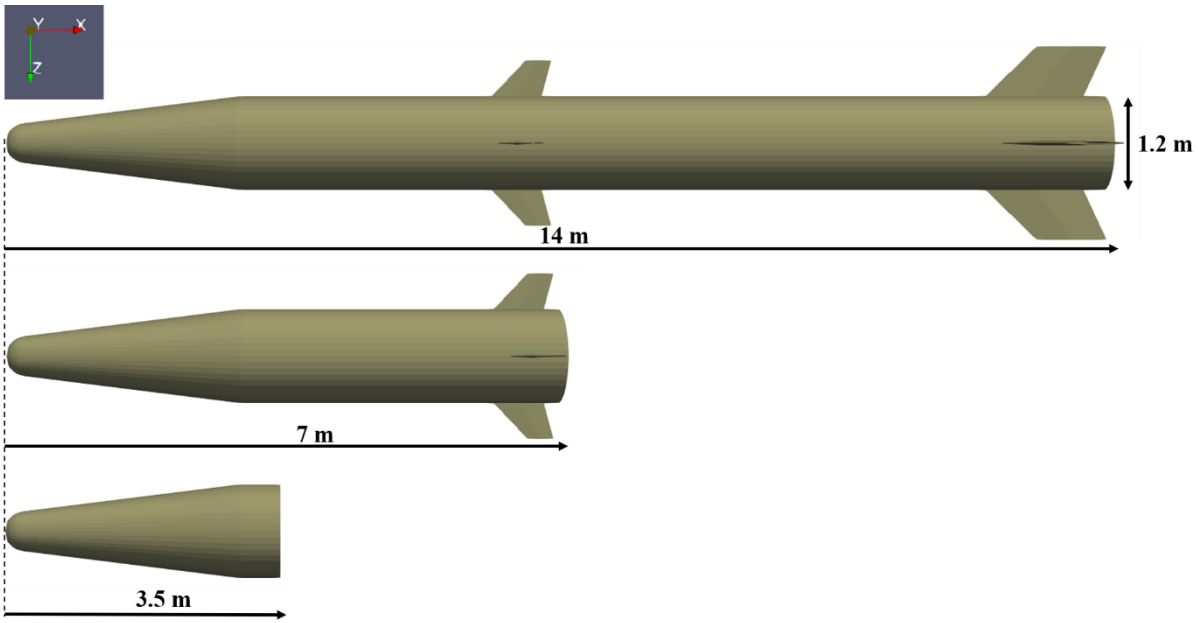

Figure 1. Representation of the three-stage ballistic missile model.

The missile's trajectory is simulated using a six degrees of freedom (6-DOF) model implemented in the MATLAB/Simulink programming environment [3,1]. The aerodynamic coefficients required for the flight simulation are derived from DATCOM software, providing a linearized representation of aerodynamic forces and

moments as functions of Mach number, angle of attack, and sideslip angle. To effectively utilize the aerodynamic coefficients, atmospheric modeling is incorporated to account for variations in air density, temperature, speed of sound, and pressure, which directly impact aerodynamic effects. A standard atmospheric model is implemented to ensure realistic aerodynamic effect estimations as the missile traverses different altitude layers and experiences changing environmental conditions [2].

In addition to aerodynamic modeling, the study incorporates comprehensive force models that account for all significant forces influencing the missile's flight dynamics. The forces considered in this study encompass:

- **Thrust Acceleration:** The missile undergoes a staged solid-propellant propulsion system where thrust is applied during the first and second stages [4]. The initial thrust stage is designed for rapid altitude gain, while the sustained thrust stage extends the missile's range before transitioning into the coasting phase. This ensures optimal fuel efficiency while maximizing range.
- **Gravitational Acceleration:** The simulation includes Earth's gravitational effects, modeled based on the WGS-84 gravitational model to ensure precise force representation throughout the flight envelope [3]. The gravitational pull remains a dominant force, particularly influencing the trajectory during the later stages as the missile ascends to higher altitudes and begins its descent phase.
- **Coriolis Acceleration:** Due to the rotation of the Earth, the missile experiences Coriolis acceleration, which introduces a slight deviation in its trajectory, particularly in the lateral direction at extended ranges [2]. This force becomes more pronounced as the missile reaches higher altitudes and velocities.

Trajectory outputs are expressed in Earth-Centered Earth-Fixed (ECEF) and Latitude-Longitude-Altitude (LLA) coordinate systems, allowing precise analysis and validation of missile behavior. The acceleration effects are extracted for each flight phase to assess their impact on trajectory characteristics and overall missile performance, providing crucial insights into the missile's motion in various operational scenarios.

Findings

The simulation results provide detailed insights into the acceleration effects across different missile stages, as depicted in Figure 2. The findings demonstrate significant variations in acceleration, highlighting the dominant physical forces at each stage of the missile's trajectory.

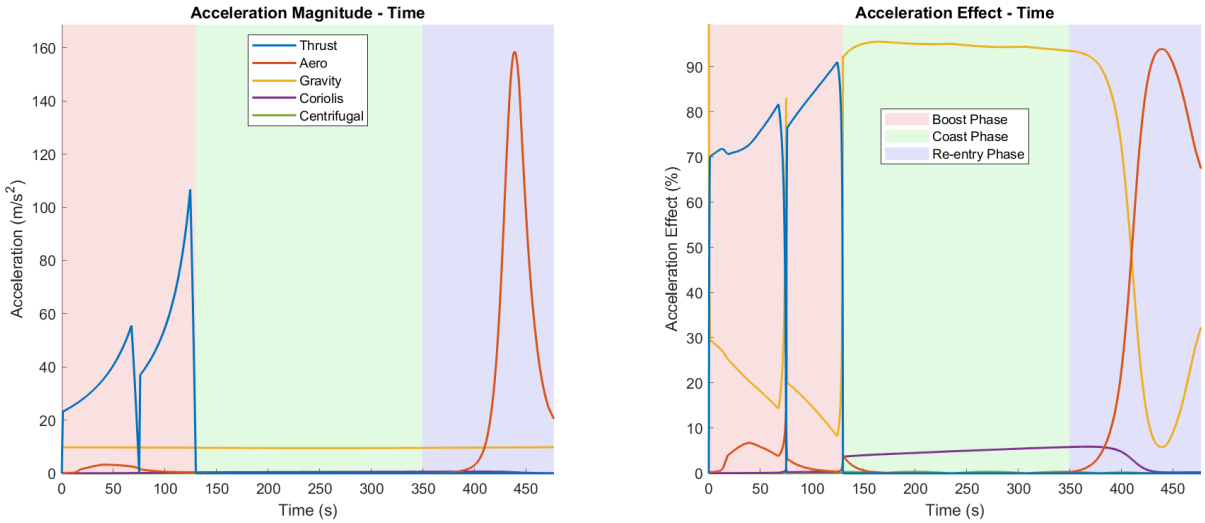

Figure 2. Acceleration effects on the missile at different flight phases.

1. **Initial Thrust Stage:** The first-stage propulsion system generates a rapid increase in acceleration, reaching peak values within the first few seconds after launch. This high acceleration phase is critical for clearing the launch area and overcoming the denser atmospheric layers. The thrust force results in a sharp

increase in net acceleration as the missile consumes fuel. Atmospheric drag is also significant in this phase due to the denser lower atmosphere, contributing to initial velocity fluctuations.

2. **Sustained Thrust Stage:** The second stage is optimized for maintaining energy efficiency while counteracting gravitational deceleration. This stage exhibits a lower thrust force than the initial stage, but as fuel consumption continues, the acceleration effect increases rapidly due to the decreasing total mass of the missile. Atmospheric drag effects diminish at higher altitudes, resulting in improved energy retention.
3. **Coasting (Free-Flight) Phase:** Once the propulsion phases are completed, the missile enters its coasting phase, where no additional thrust is applied. During this stage, gravitational pull predominantly influences acceleration, leading to a gradual reduction in velocity and altitude. Coriolis acceleration exerts a minor influence, particularly on the lateral deviation of the trajectory, affecting the final impact location. This phase is crucial for trajectory estimation, as the missile's motion follows a near-ballistic path. After the start of this phase, the simulations can be conducted primarily by considering gravitational and Coriolis forces until the reentry phase, simplifying computational efforts while maintaining accuracy.
4. **Reentry Phase:** As the missile reenters the denser atmospheric layers, it decelerates significantly due to aerodynamic drag. The acceleration values sharply decrease, highlighting the decline in missile speed and kinetic energy dissipation. During this phase, drag effects dominate, significantly influencing the missile's final descent trajectory and impact parameters. For accurate simulation of this phase, ballistic coefficient estimation or a priori information is crucial to model drag effects accurately. The rapid deceleration observed in this phase is critical in determining impact characteristics and final velocity prior to ground impact. Understanding the drag variations allows for more accurate impact prediction models and enhances the development of defensive countermeasures.

The detailed acceleration data provides a comprehensive understanding of the missile's dynamic behavior, forming a crucial foundation for developing tracking algorithms and trajectory estimation models. The findings reinforce the importance of detailed force modeling and accurate aerodynamic representation in missile trajectory simulations.

Conclusion

This study successfully develops a detailed simulation model of a medium-range ballistic missile, focusing on acceleration effects throughout the flight. The findings highlight the varying contributions of thrust, gravity, Coriolis acceleration, and aerodynamic drag across different flight stages, offering valuable insights into the missile's dynamic response. This study's trajectory and acceleration data are instrumental in refining ballistic missile tracking methodologies, improving impact point prediction accuracy, and enhancing defensive strategies.

Future research can build upon these results to enhance advanced filtering techniques, such as adaptive Kalman filtering and interacting multiple model (IMM) approaches, for real-time trajectory estimation. Additionally, integrating machine learning-based parameter estimation techniques could improve prediction accuracy in missile defense applications. Exploring additional high-fidelity computational fluid dynamics (CFD) simulations could refine drag estimates, improving overall system performance and strategic analysis.

References

Etkin, B. (2005). *Dynamics of atmospheric flight* (pp. 121–189). Courier Corporation.
NOAA, NASA, & USAF. (1976). *U .S . Standart Atmosphere, 1976*. National Oceanic and Atmospheric Administration (NOAA), Aeronautics and Space Administration (NASA), and United States Air Force (USAF).
Stevens, B. L., Lewis, F. L., & Johnson, E. N. (2015). *Aircraft control and simulation: Dynamics, controls design, and autonomous systems* (pp. 1–141). John Wiley & Sons.
Sutton, G. P., & Biblarz, O. (2011). *Rocket propulsion elements (*pp. 1–44). John Wiley & Sons.

MECHATRONICS ENGINEERING

Autonomous Vehicles

Control Systems

Robotics

Vehicle Design

WaveDrive: A Pipeline for Gesture Recognition Using Hands Coordinates

Abdülkerim Sipahi[a], Erdinç Altuğ[a]

[a] Istanbul Technical University, Mechatronics Engineering, Autonomous Vehicles, Türkiye
sipahi22@itu.edu.tr

Keywords: Autonomous Vehicles, Gesture Height, Gesture Recognition, Operator Detection, Pipeline.

Aim

The main aim of this paper is to develop an AI-based medium (WaveDrive) which evaluates the visual feed from a camera to enhance human communication and interaction with autonomous vehicles. The introduced pipeline addresses the problems of specific human operators' detection and precise interpretation of their hand gestures into actionable commands, such as Stop, Go Straight, Go Left, or Go Right. The main motivation behind this work was to improve safety and efficiency during short-term (but continuous) interactions between humans and self-driving vehicles / robots. Dynamic environments which include busy construction sites, smart warehouses, and industrial areas are all scenarios which could be considered when developing solutions in this field of study.
This study addresses a branch of explicit communication between operators and autonomous vehicles. Due to the challenges of getting hold of voice commands in high ambient noise environments, the paper focuses on providing a solution which interprets direct waved gesture messages. This bridges different gaps by providing well-defined communication channels and makes the system more reliable and certain in command generation under complex situations and diverse environmental conditions.

Material and Method

The WaveDrive pipeline is structured into four distinct yet interconnected sequential components: (1) Operator detection, (2) Gesture orientation recognition, (3) Gesture position prediction, and (4) Command generation.
The first 3 AI components required a time-extensive data collection and labelling process which was carefully conducted at Istanbul Technical University's Gümüşsuyu campus parking lot under specific conditions to ensure consistent and controlled lighting conditions. The place selection also focused on introducing different environmental factors to the gathered images in order to add variation and avoid any overfitting while testing the vision models. The photo gathering setup involved positioning volunteers at distances of 3.3 and 4.4 meters from the camera ensuring the inclusion of both fully and partially visible human subjects to simulate realistic operational cases. Volunteers performed a predefined set of gestures wearing reflective vests in two distinct colors (orange and yellow), and images were additionally diversified by including scenarios where participants wore gloves, thereby enhancing the generalizability of the data.
The Faster-RCNN [1] algorithm was implemented on WaveDrive for the operator detection stage training across various dataset combinations to identify operators under various conditions. Faster R-CNN is particularly noted for its two-stage detection process, involving region proposal and refinement, enabling robust operator detection even against complex or cluttered backgrounds.
Later in the pipeline, the large-size YOLOv10 [2] model was installed to recognize robustly the orientation (palm or dorsal sides) of the waived gestures. The selection of this model was particularly due to its well-known capability in detecting small and detailed objects efficiently. It was optimized through training on multiple dataset configurations accounting for variations such as vest colors and glove usage. Both the operator detection and gesture orientation recognition models were trained on visual data which was separated with an 80 percent portion for training versus 20 percent for testing.
The gesture position prediction component employed two duplicate Adaptive Neuro-Fuzzy Inference System [3] (ANFIS) acting in parallel (using threading in Python). ANFIS combines the learning capabilities of neural networks with fuzzy logic's interpretive strength. It decreases the uncertainty making the communication medium more reliable in the interpretation phase. Basically, the pipeline here preprocesses the hand coordinates predicted by the YOLO model to calculate the **magnitude** (Equation 1) and **orientation** (Equation 2) of the vector generated

from the origin of the operator bounding box. Both of those values are fed into ANFIS to predict the positioning of the gestures regarding their sides (left or right hands) and height (high, medium, or low) - 6 combinations. Unlike the earlier models, this component was trained on CSV data which was divided in 70 percent for training and 30 percent for testing.

$$|V| = \sqrt{(x_c^2 + y_c^2)} \quad \text{(Equation 1)}$$

$$\theta = (\frac{y_c}{x_c}) \quad \text{(Equation 2)}$$

Command generation was performed by combining the results from the gesture orientation recognition and position prediction stages. Detected gesture orientations (palm or dorsal) and positions (side and height) were translated into predefined commands (Stop, Go Straight, Go Left, Go Right) using a lookup table that matches specific gesture combinations to their corresponding actions. The predefined lookup table was designed to be flexible with different cultures that might interpret the same gestures with different meanings or need to extend the defined commands.

Findings

The study showed significant improvements in all parts of the WaveDrive pipeline. The Faster R-CNN model had excellent accuracy (mean Average Precision of 0.9091) as in Table 1, reliably detecting operators even in tough environments. The YOLOv10 model also performed very well, achieving a mean Average Precision of 0.99454, clearly distinguishing between back and front (palm and dorsal) hand orientations. Training leveraging dataset collections that included all image variations (different vest colors and gloves usage) generated models with better performance.

Table 1. Faster R-CNN Training Results.

Dataset	mAP (mean Average Precision)	RPN Classification Loss	RPN Localization Loss	Faster R-CNN Classification Loss	Faster R-CNN Localization Loss
Y	0.9091	0.002	0.0034	0.0237	0.0069
O	**1**	0.0018	0.0032	0.0249	0.0068
O + Y	0.9091	**0.0013**	**0.0023**	**0.0205**	**0.0054**

RPN is the Region Proposal Network

Table 2. Performance Summary of YOLOv10 on all subsets of the created dataset.

Dataset	Precision	F1 Score	mAP@50	Val Loss Box	Val Loss Classification	Train Loss Box	Train Loss Classification
Y	0.99955	0.997	0.995	0.528	0.270	0.593	0.333
OW	0.985	0.986	0.993	0.459	0.252	0.503	0.285
YWO	0.994	0.997	0.995	0.391	0.220	0.453	0.294
OWO	0.982	0.981	0.993	0.416	0.279	0.497	0.361

OW + YW	0.996	0.993	0.994	0.484	0.235	0.523	0.274
OWO + YWO	0.994	0.994	0.995	0.341	0.199	0.413	0.254
ALL	0.998	0.997	0.995	0.403	0.208	0.463	0.240

mAP@50 is the mean Average Precision at Intersection of Union greater than or equal to 50%.

The ANFIS model achieved an accuracy of 92.43% for gesture position prediction, demonstrating strong performance overall. However, it faced challenges in accurately distinguishing between left and right hands at medium-height elevations, highlighting areas needing further improvement. Figure 1 clearly demonstrates the performance of the model on the test data. (Equation 3 – Equation 8) clearly show the tuned membership functions.

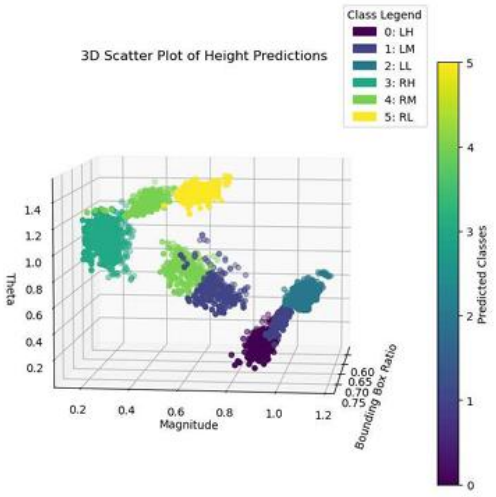

Figure 1. ANFIS Performance Visualization.

$$\mu_{Low}(|V|) = \frac{1}{1 + \left|\frac{|V| - 0.0827}{0.1362}\right|^{2(2.0184)}} \quad \text{(Equation 3)}$$

$$\mu_{Medium}(|V|) = \frac{1}{1 + \left|\frac{|V| - 0.7595}{0.0960}\right|^{2(1.8740)}} \quad \text{(Equation 4)}$$

$$\mu_{High}(|V|) = \frac{1}{1 + \left|\frac{|V| - 1.0543}{0.0436}\right|^{2(2.2869)}} \quad \text{(Equation 5)}$$

$$\mu_{Low}(\theta) = \frac{1}{1 + \left|\frac{\theta - 0.0352}{0.1362}\right|^{2(1.7634)}} \quad \text{(Equation 6)}$$

$$\mu_{Medium}(\theta) = \frac{1}{1 + \left|\frac{\theta - 0.6949}{0.0732}\right|^{2(1.5228)}} \quad \text{(Equation 7)}$$

$$\mu_{High}(\theta) = \frac{1}{1 + \left|\frac{\theta - 1.4723}{0.0633}\right|^{2(2.1177)}} \qquad \text{(Equation 8)}$$

Testing the integration (Figure 2) both outdoors (Figure 3) and indoors (Figure 4.) under different lighting conditions confirmed the effectiveness of WaveDrive pipeline, with outdoor tests showing better overall performance due to more favorable lighting conditions and to specifically collecting the images before at external environments. Gestures were better recognized at closer distances, while there was slight variability at longer distances due to less stable bounding box predictions. Additionally, wearing gloves improved recognition performance, providing clearer visual distinctions and better accuracy overall.

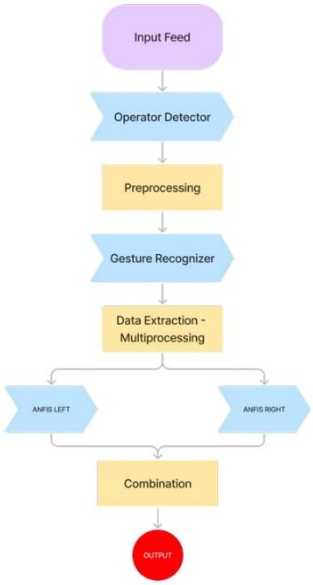

Figure 2. WaveDrive Flowchart .

Figure 3. Outdoor Standalone Testing.

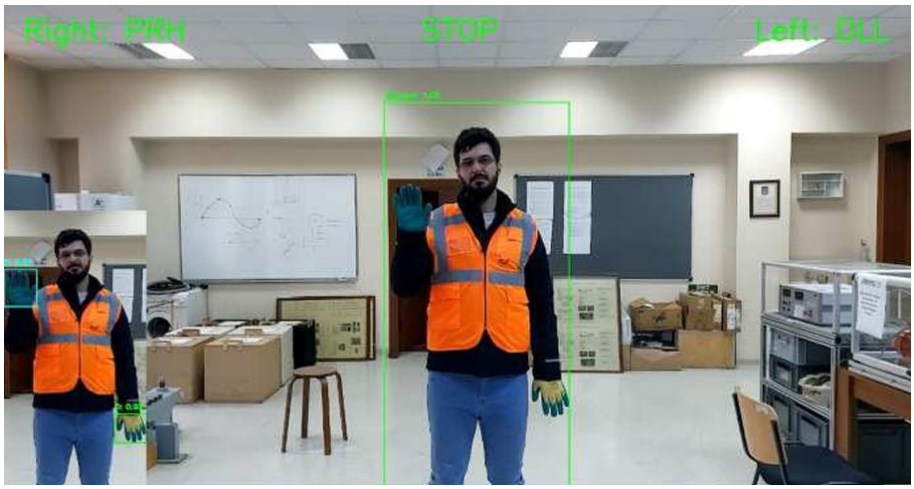

Figure 4. Indoor Standalone Testing.

Conclusion

The WaveDrive pipeline constitutes a significant advancement in autonomous vehicle communication through gesture-based systems. The pipeline is able to deal with real-world nuances in gesture recognition by integrating robust computer vision and deep learning technologies. This paper conclusively demonstrates the pipeline's capability to accurately recognize operators consistently, identify gesture orientation correctly, and predict gesture location accurately.

The robustness of WaveDrive in various test conditions is indicative of its usability and reliability in real-world application and is a giant leap towards universal application of gesture-based communication systems. However, the system's small deficiencies at longer ranges suggest future scope for improvement. Future research can focus on improving the flexibility of the system for more complex, dynamic, and uncontrolled environments, enhancing real-time computation performance, and further improving optimized hardware solutions to increase the usability of WaveDrive in a broad spectrum of industrial and safety-critical applications. It can also focus on studying dynamic gestures instead of static postures of operators.

Lastly, this study provides a tangible foundation for propelling explicit gesture-based interactions towards safer and more effective human-vehicle interaction, potentially transforming operational practice across different industry sectors.

References

Ren, S., He, K., Girshick, R., & Sun, J. (2017). *Faster R-CNN: Towards real-time object detection with region proposal networks.* IEEE Transactions on Pattern Analysis and Machine Intelligence, 39(6), 1137–1149. https://arxiv.org/abs/1506.01497

Wang, A., Chen, H., Liu, L., Chen, K., Lin, Z., Han, J., & Ding, G. (2024). *YOLOv10: Real-time end-to-end object detection*. arXiv. https://arxiv.org/abs/2405.14458

Jang, J.-S. R. (1993). *ANFIS: Adaptive-network-based fuzzy inference system.* IEEE Transactions on Systems, Man, and Cybernetics, 23(3), 665–685. https://doi.org/10.1109/21.256541

MECHATRONICS ENGINEERING

Autonomous Vehicles

Control Systems

Robotics

Vehicle Design

A Study on the Performance of GNN, PDA, and JPDA in a ROS-Based Tracking Framework

Nurettin Özçelik[a], Volkan Sezer[b]

[a] Istanbul Technical University, Graduate School, Mechatronics Engineering Program, Smart and Autonomous System Laboratory (SASlab), Türkiye
[b] Istanbul Technical University, Faculty of Electrical and Electronics Engineering, Department of Robotics and Autonomous Systems Engineering, Smart and Autonomous System Laboratory (SASlab), Türkiye
ozcelikn22@itu.edu.tr

Keywords: Data Association, Kalman Filter, Mobile Robot, Multi-Target Tracking.

Aim

Robots in dynamic areas must detect and track moving and static objects like people, enabling tasks like guidance or patrol. Multi-target tracking involves estimating number of objects and maintaining a distinct track for each, typically including an ID and state such as position and velocity. A multi-target tracking system follows a repeated cycle (Blackman & Popoli, 1999) that processes sensor measurements and updates object tracks over time, as illustrated in Figure 1. It starts by converting raw data from sensors into usable observations such as bounding boxes. After that, data association module matches these observations to existing tracks, with gating used to remove unlikely matches. Track creation and deletion are handled by a track management component, while a prediction step estimates future positions for next round of associations.

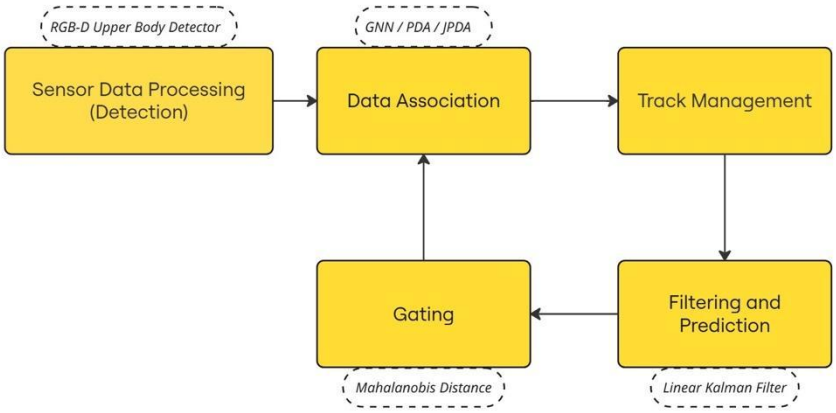

Figure 1. Block diagram illustrating the general structure of a conventional multi-target tracking system, along with its specific implementation details in this study.

During data association, various ambiguities may occur. As shown in Figure 2, measurements Z_4 and Z_5 fall within the gating regions of both targets T_1 and T_2, leading to assignment uncertainty. Target T_1 contains multiple measurements within its gate, creating ambiguity in selection. T_3 has an empty gate, raising possibility of occlusion or leaving scene. Meanwhile, Z_1 falls outside all gates and may indicate clutter or a new target. To address these challenges, a variety of data association strategies can be employed—from simple approaches like Global Nearest Neighbor (GNN) (Konstantinova et al., 2003) which selects the closest matching observation, to more advanced probabilistic methods such as Probabilistic Data Association (PDA) (Bar-Shalom et al., 2009) and Joint Probabilistic Data Association (JPDA) (Bar-Shalom et al., 1991), which perform soft assignment by distributing the influence of each measurement across multiple potential tracks based on their likelihood.

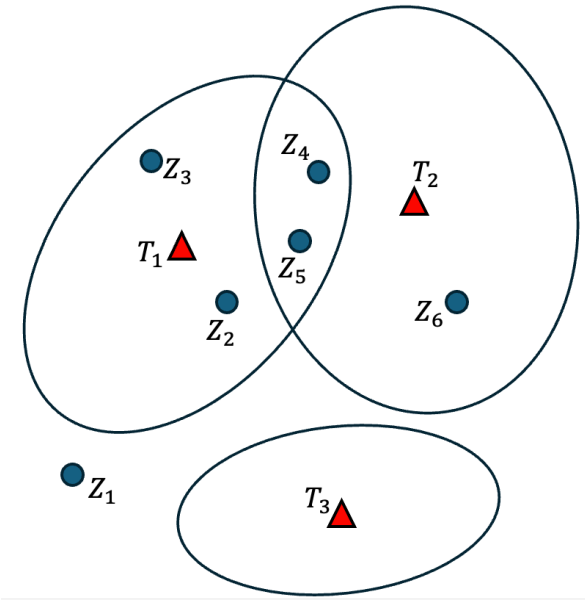

Figure 2. Illustration of typical data association ambiguities in multi-target tracking.

The relevance of comparing GNN, PDA, and JPDA has also been emphasized in prior work on multi-vehicle tracking (Buluttekin et al., 2017), where the authors evaluate these algorithms using a two-vehicle scenario and demonstrate the robustness of JPDA in cluttered environments. Our study aims to implement and compare these three algorithms in a simulation environment built with ROS and Gazebo, where sensor inputs, robot motion, and human movement can be modeled. By evaluating their performance under controlled yet practical scenarios, the goal is to better understand the characteristics and limitations of each approach in the context of mobile robots performing tasks such as person following.

Material and Method

The decision of which measurement should be used in the correction step in Kalman filter is handled by the data association algorithm. The first method considered in this study is GNN, which constructs a cost matrix where each entry represents Mahalanobis distance between a predicted track state and a measurement within its gating region. In the implementation, a large constant value (e.g., 999) is assigned as the cost for the measurement that falls outside the gate. A globally optimal assignment between tracks and measurements is computed using linear assignment algorithms such as Hungarian, Auction, or JVC (Crouse, 2016), which is used in this implementation. The global optimality of the result is ensured by the constraint that each measurement can be assigned to at most one track, and each track to at most one measurement.

PDA algorithm, originally developed for single-target tracking, computes the posterior probability that each measurement within the gate is the true measurement of the target, along with the probability that none of them is correct. These probabilities are then used as weights for the corresponding innovations in the Kalman filter update. As a result, all gated measurements contribute to the correction step, proportionally to their likelihood. PDA operates under a key assumption: there exists only one true target in the cluttered scene, and all other measurements are considered to be false alarms.

JPDA is designed to handle multiple targets simultaneously. It constructs a validation matrix, where each element is set to 1 if the corresponding measurement falls within the gating region of a given track. Based on this matrix, all valid joint association hypotheses are generated. Feasible associations are those that satisfy the one-to-one assignment constraint used in GNN. The probability of each joint hypothesis is then computed based on the likelihoods of individual associations. Finally, marginal association probabilities—such as the probability of assigning measurement Z_1 to track T_2—are obtained by summing the probabilities of all joint hypotheses that include that specific assignment. The innovation weighting step follows the same procedure as in PDA. As a consequence, JPDA accounts for the possibility that a shared measurement may originate from another target,

rather than treating it as clutter. For both PDA and JPDA implementations, the probability of detection $P_D = 0.8$, the probability that the true measurement lies within the gating region $P_G = 0.95$, and the spatial clutter density $\lambda = 0.05$ were used to compute association probabilities.

For comparison purposes, all data association algorithms were implemented as Python scripts in ROS, sharing a common structure for track initialization, deletion logic, and filtering. The SPENCER framework (Linder et al., 2016) serves as the baseline, providing message definitions, detection module (upper-body detector), RViz visualization plugins, and an OSPA metric (Ristic et al., 2011) calculator for performance evaluation. The experiments are conducted in the Gazebo simulation environment using an Ackermann-type mobile robot similar to the MIT Racecar. The robot model, described in URDF and derived from a SolidWorks design based on real-world dimensions, is equipped with a 2D LiDAR and a stereo camera. For human models, Gazebo actor plugin, which allows for scripted movement, is used. Ground truth positions of them is available through Gazebo. The simulation environment is based on the "Hospital World" provided by AWS RoboMaker, as shown in Figure 3.

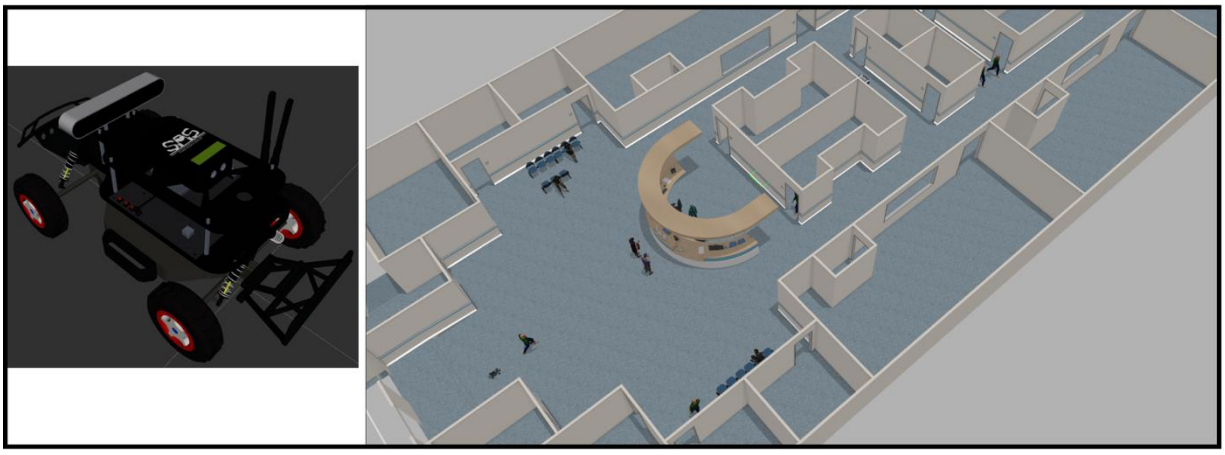

Figure 3. Left: Mobile robot used in the study. Right: Gazebo world for scenario.

A nearly constant velocity motion model was used to predict the state of each track. The state vector is defined as $x = [x, y, v_x, v_y]^T$ representing the 2D position and velocity of a tracked object. The state transition matrix F used in this model is defined in Equation (1) while the process noise is modeled as zero-mean Gaussian noise with covariance Q, given in Equation (2). Δt denotes the time interval between two consecutive tracking cycles. The measurement model observes only the 2D position, and the measurement noise covariance R is a diagonal matrix with all entries set to 0.05. For all three data association algorithms, the process noise level was set to $q_L = 0.1$.

$$F = [1\ 0\ \Delta t\ 0\ 0\ 1\ 0\ \Delta t\ 0\ 0\ 1\ 0\ 0\ 0\ 0\ 1\ ] \quad (1)$$

$$Q = \left[\frac{\Delta t^3}{3}\ 0\ \frac{\Delta t^2}{2}\ 0\ 0\ \frac{\Delta t^3}{3}\ 0\ \frac{\Delta t^2}{2}\ \frac{\Delta t^2}{2}\ 0\ \Delta t\ 0\ 0\ \frac{\Delta t^2}{2}\ 0\ \Delta t\right] q_L \quad (2)$$

After each data association step, every unmatched measurement is used to initiate a tentative track. If a tentative track is updated with a measurement in 10 separate steps, it is promoted to a confirmed track. Conversely, if it remains unmatched for 20 consecutive steps, it is deleted. A similar timeout rule is applied to confirmed tracks, but with a longer threshold of 40 steps. When probability that none of the measurements are correct is greater than %95 for a track, the track is flagged as missed in JPDA implementation.

Findings

The test scenario, as illustrated in Figure 4, was designed to evaluate the performance of data association algorithms under realistic and challenging tracking conditions. In this setup, the robot is manually driven to follow a single target person. Other people occasionally enter the scene, causing temporary occlusions of the tracked person. In some cases, two people walk side by side in close proximity, increasing the likelihood of measurement

ambiguity. Furthermore, new individuals enter and exit the environment over time, resulting in dynamic variations in the number of targets.

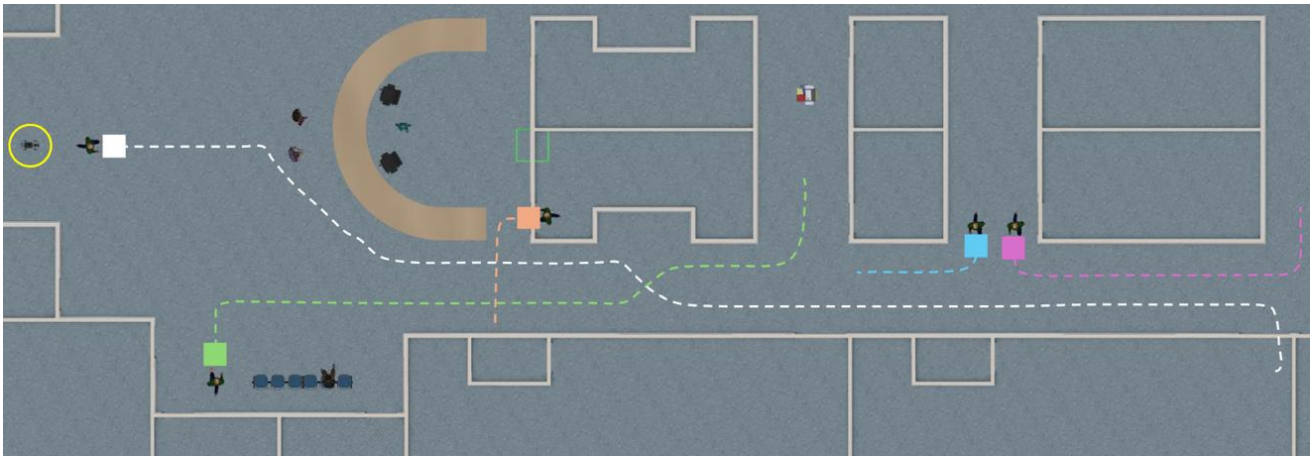

Figure 4. Path of each moving person in the scenario. Squares are starting points and yellow circle contains mobile robot.

The human actors in the simulation mostly moved at a constant speed of approximately 0.75 m/s. To ensure a fair comparison across different data association algorithms, the scenario was executed once and recorded as a ROS bag file. During evaluation, this bag file was replayed for each algorithm, allowing all methods to operate under identical sensor inputs and environmental conditions and the tracking output displayed in Rviz, as demonstrated in Figure 5. The system operated at 10 Hz.

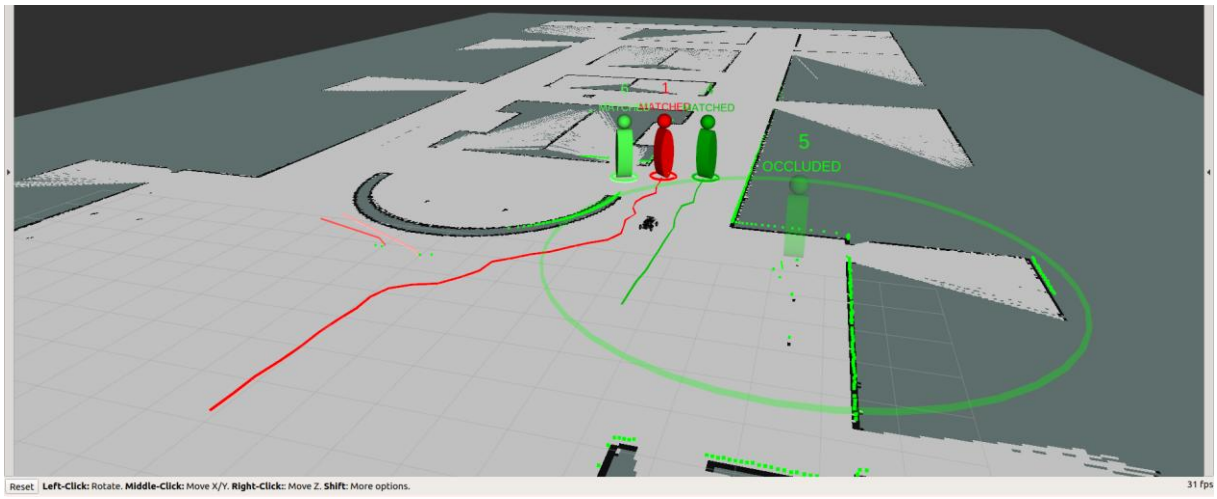

Figure 5. Visualization of tracking results in Rviz.

For performance evaluation, the Optimal Sub-Pattern Assignment (OSPA) metric was used. OSPA is well-suited for multi-target tracking tasks, as it jointly captures three types of errors: localization error, cardinality error, and labeling error. Localization error measures the spatial distance between correctly matched estimated and ground-truth targets. Cardinality error penalizes the mismatch in the number of estimated versus true targets, reflecting missed or false tracks. Labeling error, on the other hand, accounts for identity switches—cases where the associations between tracks and targets are inconsistent over time. For each time step, OSPA is calculated for each method with parameters $p = 1$ (order), $c = 0.5$ (cut-off distance), and $a = 10$ (cardinality penalty). All results represent the mean of OSPA scores computed over the full tracking sequence. Lower values indicate better performance in terms of tracking accuracy and identity consistency.

As summarized in Table 1, GNN and JPDA yielded similarly low OSPA distances, while PDA performed significantly worse with an OSPA of 0.907. The high cardinality and localization errors observed in PDA stem from its inherent assumption of single-target tracking as outlined in Material and Method section. PDA also exhibited wrong measurement-track association during the last part of the scenario. When two individuals walked in close proximity, the track's estimated position shifted to the middle of them, and once they separated, the tracker began updating its state using measurements from the wrong person—once again, a direct consequence of the single-target assumption. In contrast, both GNN and JPDA maintained multiple tracks and consistently achieved reliable measurement-to-track associations throughout the scenario. Although JPDA is theoretically better equipped to handle ambiguous cases—such as the persistent interference caused by closely spaced targets—no substantial advantage was observed over GNN in this scenario. This can be attributed to the relatively clean nature of the scenario: even when targets approached each other, they rarely shared a common measurement within their validation gates. One contributing factor may be due to the absence of externally added clutter and the fact that human actors moved at nearly constant velocities, closely aligning with the assumptions of the motion model. The similarity in performance suggests that under controlled conditions with limited measurement ambiguity, even simple methods like GNN can perform comparably to more complex probabilistic approaches such as JPDA.

Table 1. OSPA metric results for three data association algorithms.

Algorithm/Metric	GNN	PDA	JPDA
OSPA Distance	0.284	0.907	0.291
Localization Error	0.153	0.450	0.159
Cardinalization Error	0.131	0.499	0.132
Labeling Error	0.0	0.008	0.0

Conclusion

This study presents the implementation and evaluation of three data association algorithms—GNN, PDA, and JPDA—within a ROS-based tracking system, tested in a Gazebo simulation environment. The complete tracking pipeline was developed in Python, including track initialization, deletion logic, Kalman filtering, and association strategies. A realistic test scenario was designed where the robot followed a human while interacting with other moving individuals. The results highlight the importance of algorithm selection based on scenario complexity, showing that even simple methods like GNN can perform comparably to more complex approaches under structured conditions.

Future work may involve testing the system under more challenging conditions by introducing manually generated clutter without significantly increasing false positives. Additionally, defining an association confidence metric could enable dynamic switching between algorithms like GNN, JPDA, or suboptimal nearest neighbor within a hybrid framework.

Reference

Bar-Shalom, Y., Daum, F., & Huang, J. (2009). *The probabilistic data association filter.* IEEE Control Systems, 29(6), 82–100.

Bar-Shalom, Y., & Fortmann, T. E. (1991). *Tracking and Data Association.* Volume 179. Elsevier Science Publishing.

Blackman, S., & Popoli, R. (1999). *Design and analysis of modern tracking systems.* Norwood, MA: Artech House.

Buluttekin, H., Aksu, E., & Bhanuprakash, A. (2017). *Comparative study of data association approaches for multiple vehicle tracking.* In 2017 21st International Conference on System Theory, Control and Computing (ICSTCC) (pp. 278–284).

Crouse, D. F. (2016). *On implementing 2D rectangular assignment algorithms.* IEEE Transactions on Aerospace and Electronic Systems, 52(4), 1679–1696.

Konstantinova, P., Udvarev, A. and Semerdjiev, T. (2003). *A Study of a Target Tracking Algorithm Using Global Nearest Neighbor Approach.* International Conference on Computer Systems and Technologies - CompSysTech'2003

Linder, T., Breuers, S., Leibe, B., & Arras, K. O. (2016). *On multi-modal people tracking from mobile platforms in very crowded and dynamic environments.* IEEE International Conference on Robotics and Automation (ICRA) 2016

Ristic, B., Ba-Ngu Vo, Clark, D., & Ba-Tuong Vo. (2011). *A metric for performance evaluation of multi-target tracking algorithms.* IEEE Transactions on Signal Processing, 59(7), 3452–3457.

MECHATRONICS ENGINEERING

Autonomous Vehicles

Control Systems

Robotics

Vehicle Design

Steer-by-Wire System Modeling and Control Using Optimal PID Controller

Seyitcan Şahin[a], Erhan Yumuk[b]

[a] Istanbul Technical University, Electrics-Electronics, Control and Automation Department, Mechatronics Engineering, Türkiye
[b] Istanbul Technical University, Electrics-Electronics, Control and Automation Department, Controls Engineering, Türkiye
sahins22@itu.edu.tr, yumuk@itu.edu.tr

Keywords: Genetic Algorithm, PID Controller, Steer-by-Wire.

Aim

Steer-by-wire (SbW) systems is an important change in vehicle steering technology by replacing the mechanical linkage between the steering wheel and the wheels with a fully electronic system including sensors, actuators, and control units. This transformation not only allows for advanced vehicle design flexibility, weight reduction and lower center of gravity, but also allows new possibilities in vehicle safety, automation, and adaptive control. The first objective of this study is to model a steer-by-wire system using MATLAB/Simulink and to design an optimal PID controller to regulate steering performance based on a time-domain performance metric. With this, the mechanical link between the steering wheel and wheel response is entirely removed, and control is performed electronically.

A secondary objective of the research is to assess the robustness of the proposed control system under varying levels of steering torque and vehicle speed. By investigating these operating conditions, the study provides insights into the resilience and adaptability of the SbW system and find areas where additional improvements might be needed.

Material and Method

The modeling process starts with a detailed breakdown of the main components of a steer-by-wire system, all of them were identified and showed in a Simulink-based environment. The key hardware elements include the steering actuator, torque and angle sensors, an electronic control unit (ECU), and a force feedback motor that simulates the road feel to the driver . These components are interconnected via high-speed communication protocols such as CAN or FlexRay and function together to transform driver input into appropriate wheel movements.

The developed steer-by-wire model, which is given in Figure 1, simulates the transformation of the driver's torque input into actual wheel movement through a sequence of physical and control-based components. The input torque signal is first converted into angular acceleration using the system's moment of inertia and damping coefficient. This acceleration is then integrated to obtain angular velocity, and subsequently integrated again to yield the steering wheel angle. This calculated angle is fed into MATLAB's built-in steering block, which models the vehicle's dynamic response and outputs the corresponding target wheel angle. This target angle is then used as a reference input for the controller. The output of the controller determines the required rotation of the motor in order to achieve the desired wheel deflection. This motor command passes through a coefficient that represents the rack-and-pinion conversion ratio, indicating how many degrees the motor must rotate. The resulting command is fed into the DC motor model, and after passing through the same mechanical coefficient again, the resulting actual wheel angle is obtained and compared against the reference for feedback control.

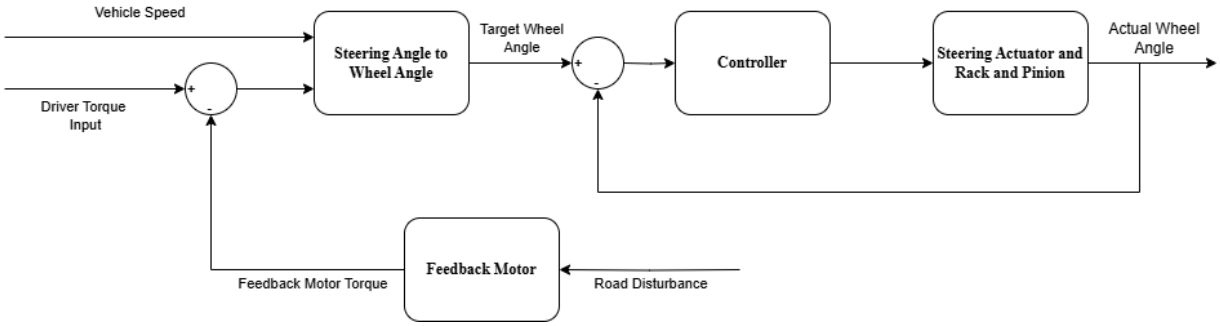

Figure 1. Block Diagram of the Designed Steer-by-Wire System Architecture.

A disturbance signal is used to simulate external effects such as road irregularity, potholes and cracks. Then the disturbance signal is fed to the feedback motor, where the wheel angle error is converted into the amount of torque required to simulate the same degree to the steering wheel. After that, the torque value is summed with the driver's torque input, the final net torque is fed to the system.

The force feedback motor is modeled using parameters such as motor inertia, damping coefficient, torque constant, and gear ratio, adapted from literature (Marouf et al., 2012). The system dynamics for the motor are captured using a second-order differential equation that represents its electromechanical behavior. The steering actuator is modeled similarly, converting electrical control signals into mechanical angular displacement (Mohamed et al., 2014).

For the control system design, PID controller was designed due to its well-known effectiveness in time-domain tracking and ease of implementation. The transfer function is given in Equation 1:

$$C(s) = K_p + \frac{K_i}{s} + K_d s \quad (1)$$

where Kp, Ki and Kd denote the proportional, integral and derivative gains, respectively. To prevent high-frequency noise amplification from the derivative term, a first-order low-pass filter is applied after differentiation. This filtering is implemented in Simulink using a transfer function block. The PID controller parameters is tuned using a Genetic Algorithm (GA) to optimize control system performance.

The cost function for optimization is based on the Integral of Time-weighted Absolute Error (ITAE), which penalizes prolonged errors more severely and improves system response smoothness by reducing oscillations. This is given in Equation 2,

$$ITAE = \int \quad t|e(t)|dt \quad (2)$$

where e(t) is the error signal and t is the simulation duration. ITAE increases the penalty for errors that persist over time.

One of the key advantages of using a GA for PID tuning is its ability to avoid local minima and effectively explore a wide solution space, which is particularly beneficial when optimizing nonlinear or complex systems (Xu et al., 2019; Załeski & Szczepanik, 2024).

The GA-based optimization is implemented within Simulink using MATLAB's Global Optimization Toolbox. The population size, mutation rate, crossover fraction, and generation limits are selected based on a trade-off between optimization time and solution accuracy, flow chart is given in Figure 2. This GA setup follows a real-coded, elitist configuration with stochastic uniform selection and intermediate crossover, in accordance with standard practices in control optimization (Dastanpour et al., 2014).

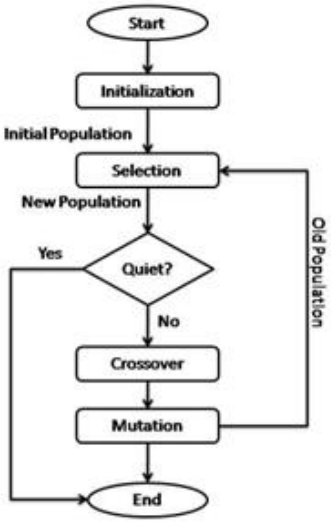

Figure 2. Genetic Algorithm Flow Chart (Dastanpour et al., 2014).

After the optimal PID gains for 50 kph vehicle speed and maximum of 10 Nm driver torque input are obtained, they are tested under a variety of input scenarios, including step and ramp steering inputs, varying speed profiles, and torque disturbances.

Findings

The complete SbW model in Simulink was successfully implemented with actuator behavior and vehicle steering response. Initial results from the PID controller tuned with GA showed acceptable performance under nominal conditions. Figure 3 shows the control system response using the GA-tuned PID controller. The GA-tuned PID controller achieved fast settling times, minimized overshoot, and minimal ITAE metric. Specifically, under constant-speed conditions, the controller maintained accurate tracking of the desired steering angle, even in the presence of moderate external torque disturbances. However, the optimal PID controller struggled to maintain stability when high external torque disturbances or rapid input changes were introduced. Overshoot and oscillations were particularly noticeable during abrupt steering maneuvers or low-speed parking conditions where steering sensitivity is higher.

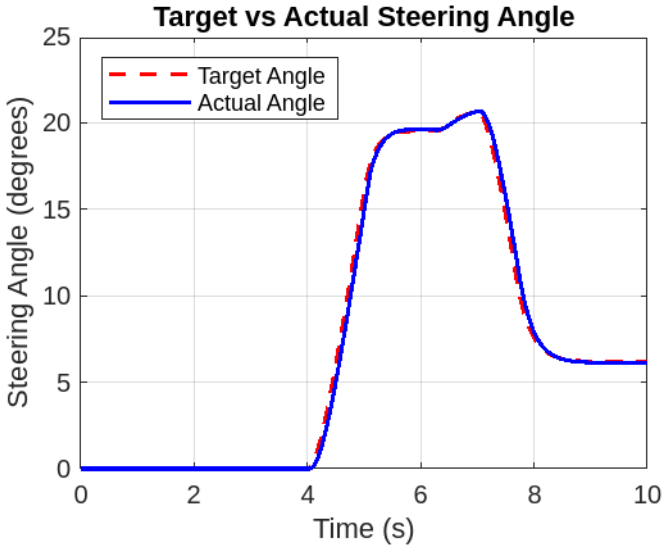

Figure 3. The responses of target and actual wheel angles using GA Tuned PID.

A series of robustness tests were conducted to evaluate how the control system performs when subjected to varying vehicle speeds and applied torques. The simulations demonstrated that speed changes had minimal impact on the system's performance, indicating a very effective way of robustness with respect to vehicle velocity. However, when the applied steering torque was significantly altered (such as during emergency maneuvers or aggressive cornering) the system's response began to degrade. This was realised through increased settling times and higher overshoot in the steering angle output. This control system response is illustrated in Figure 4.

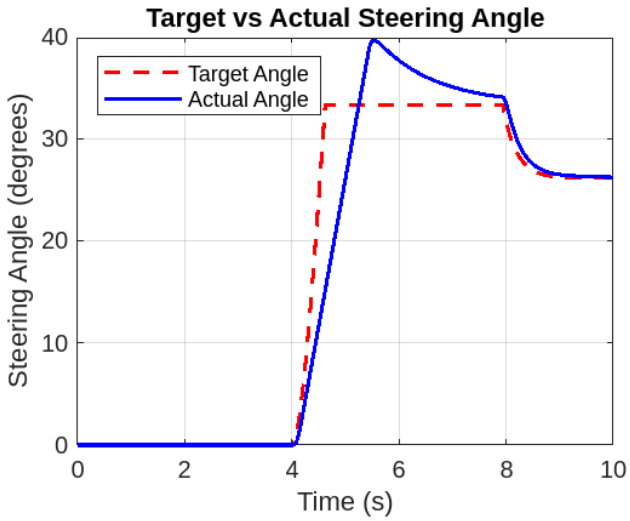

Figure 4. System Response Under High Torque Input.

Conclusion

This study successfully shows the development and control of a steer-by-wire system in a MATLAB/Simulink environment using a GA-tuned PID controller. The simulation results confirm that GA-based tuning offers good performance under nominal torque input, particularly in terms of minimizing error metrics and improving time-domain response.

The results also show an important limitation: while speed variations have negligible effect on control performance, torque inputs are still a problem for fixed-gain PID controllers. This finding suggests that implementing adaptive control strategies (such as gain scheduling based on torque magnitude or adaptive models) could significantly enhance system robustness.

These observations align with previous findings in the literature, which suggest that PID controllers, while effective in linear and nominal cases, may require adaptive or nonlinear control enhancements to perform well under highly dynamic or uncertain operating conditions (Tumari et al., 2017; Sun et al., 2016). The limitations of fixed-gain PID control in the presence of rapidly changing torque inputs highlight the need for future work in the area of adaptive gain scheduling or model-predictive control techniques.

Future work will explore the integration of vehicle-speed-dependent steering ratios to enhance low-speed maneuverability and high-speed stability.

References

Coudon, J., Canudas-de-Wit, C., & Claeys, X. (2006). *A new reference model for steer-by-wire applications with embedded vehicle dynamics.* Proceedings of the 2006 American Control Conference.

Dastanpour, A., Ibrahim, S., & Mashinchi, M. R. (2014). *Used genetic algorithm for support artificial neural network in intrusion detection system.* Data, March 2014.

Irmer, M., Degen, R., Nüßgen, A., Thomas, K., Henrichfreise, H., & Ruschitzka, M. (2016). *Development and analysis of a detail model for steer-by-wire systems.* IEEE Transactions on Industrial Electronics, 63(4), 2251–2260.

Lei-yan, Y., Ping-li, Y., & Feng, L. (2009). *Research on dynamics modeling and genetic algorithm optimization of automobile steer-by-wire system.* 2009 Second International Conference on Information and Computing Science, IEEE.

Marouf, A., Djemaï, M., Sentouh, C., & Pudlo, P. (2012). *A new control strategy of an electric-power-assisted steering system.* IEEE Transactions on Vehicular Technology, 61(8), 3857–3867.

Mohamed, E. S., & Albatlan, S. A. (2014). *Modeling and experimental design approach for integration of conventional power steering and a steer-by-wire system based on active steering angle control.* International Journal of Mechanical Engineering and Applications, 2(6), 104–112.

Sun, Z., Zheng, J., & M., Z. (2016). *Robust control of a vehicle steer-by-wire system using adaptive sliding mode.* IEEE Transactions on Industrial Electronics, 63(4), 2251–2260.

Tumari, M. Z. M., Saealal, M. S., Abd Rashid, W. N., Saat, S., & Mohd Nasir, M. A. (2017). *The vehicle steer-by-wire control system by implementing PID controller.* Faculty of Engineering Technology, Universiti Teknikal Malaysia Melaka.

Xu, F., Liu, X., Chen, W., Zhou, C., & Cao, B. (2019). *Fractional order PID control for steer-by-wire system of emergency rescue vehicle based on genetic algorithm.* Central South University Press and Springer-Verlag.

Załeski, A., & Szczepanik, M. (2024). *Parametric optimization of linear ball bearing with four-point connection in steer-by-wire steering column by means of genetic algorithm.* Applied Sciences, 14(8046).

METALLURGY AND MATERIALS ENGINEERING

Composite and Polymer Materials

Corrosion and Wear

Energy Materials

Extractive Metallurgy

Mechanical Metallurgy

Metals and Alloys

Surface Treatment and Coatings

Characterization of Talc and Reduced Graphene Oxide Reinforced Polypropylene Composites: Thermal, Mechanical and Structural Properties

İrem Düzenli[a,b], Yeliz Köse[c], Cemile Gürer[a], Yavuz Emre Yağcı[b], Fatma Seniha Güner[a,d]

[a] Istanbul Technical University, Faculty of Chemical-Metallurgical Engineering, Department of Chemical Engineering,Turkey
[b] Farplas Otomotiv A. S., Taysad Organize Sanayi Bolgesi, Turkey
[c] Bilecik Şeyh Edebali University, Faculty of Engineering, Department of Metallurgy and Materials Engineering, Turkey
[d] Sabancı University, Nanotechnology Research and Application Center (SUNUM), Turkey
duzenli17@itu.edu.tr

Keywords: Polymer Composites, Polypropylyne, Reduced Graphene Oxide, Talc.

Aim

Due to their low density, low cost, ease of processing, and good chemical resistance, polymers are widely used in engineering applications (Kovacs & Suplicz, 2013). The demand for synthetic polymers in the automotive and aviation sectors has increased in recent years. Polyethylene, polypropylyne (PP), polycarbonat and polyamide are commonly used for inner, exterior and other functional parts for these areas (Lapcik et al., 2008). Among these polymers, polypropylene (PP) stands out due to its excellent moldability, mechanical properties, low cost and high recyclability making it widely used . Talc is generally used as reinforcement filler for PP because of its low cost and suitable flaky particle morphology (Kinoshita et al., 2023). Its content has magnesium silicat and its general chemical formula is $Mg_3Si_4O_{10}(OH)_2$ (Castillo et al., 2013). In recent years researchers focus on reinforced polymers with nano materials instead of commonly used fillers like talc. These materials are generally carbon-based materials. Carbon nanotups, carbon nanofibers, graphene and graphene-based materials such as graphene oxide (GO) and reduced GO (rGO) can be given as examples of carbon-based nano fillers. Graphene and graphene-based materials are gaining attention due to superior mechanical, thermal and electrical properties (Ghasemi et al., 2016). This study aims to investigate the effect of using talc and graphene-based additives in a hybrid form on the properties of PP.

Material and Method

In this study, PP (SABIC PP 595A, SABIC, Saudi Arabia) has chosen for main matrix, talc (RoseTalc RT-G 15, Gülmer, Turkey) and rGO (Aerofen, Turkey) have chosen for filler. Firstly, the material containing 10 wt. % rGO was prepared by Aerofen using a twin-screw extruder with stage temperatures of 50-140-145-150-160-180 °C. Then, the material containing 20 wt. % Talc was prepared by Farplas using a twin-screw extruder with stage temperatures of 50-185-190-200-205-210-220-225-225-230 °C. The prepared mixtures were then blended at 200 °C and 100 rpm using a 35 g capacity melt mixer to produce the PP/Talc18/rGO1 and PP/Talc16/rGO2 materials. The weight percentages of the components in the PP composites are provided in Table 1.

Table 1. The weight percentage composition of the materials.

Material	PP (%)	rGO (%)	Talc (%)
PP	100	0	0
PP/Talc20	80	0	20
PP/rGO10	90	10	0
PP/Talc18/rGO1	81	1	18
PP/Talc16/rGO2	82	2	16

To characterize the prepared composites and investigate their properties differential scanning calorimetry (DSC), thermal gravimetric analysis (TGA), Fourier transform infrared spectroscopy (FTIR), tensile and impact tests were performed. DSC test was carried out with Perkin Elmer DSC 4000 in a nitrogen atmosphere at a heating rate of 10°C/min, in the temperature range of 25-200 °C. TGA was conducted with Perkin Elmer TGA 4000 at a heating rate of 10°C/min from ambient temperature up to 550 °C in a nitrogen atmosphere to examine the thermal stability and degradation. FTIR was used to analyze the functional groups of the materials with Perkin Elmer Spectrum Two in the wavelength range of 650-4000 cm^{-1}. Tensile strength and elongation values were determined by the tensile test according to ISO 527. Impact testing was performed with a notched Charpy analysis according to ISO 178. Mechanical test specimens, including dog-bone (for tensile analysis) and flat bars (for impact analysis), were prepared using hot pressing at 200°C.

Findings

As a result of the DSC analysis, the melting points for PP, PP/Talc20, PP/rGO10, PP/Talc18/rGO1 and PP/Talc16/rGO2 were found to be 167.4, 167, 166.24, 165.3 and 165.61°C, respectively. It has been observed that no significant change in the melting temperature (T_m) occurred, as the crystal form of PP remained unchanged and Tm is solely dependent on its crystal structure (Patra et al., 2022). According to the TGA results shown, PP shows degradation in a single step (Bajsić et al., 2012). It can be said that the addition of talc and rGO separately increases the degradation onset temperature. In the mixtures containing both fillers, this value shows an increase compared to the neat PP. When examining the FTIR analysis, unlike the groups present in the neat PP matrix, the PP/Talc20, PP/Talc18/rGO1 and PP/Talc16/rGO2 mixtures show a Si-O-Si bond at ~1014 cm^{-1} and an OH deformation at ~670 cm^{-1} (Linares et al., 2019). The mechanical properties of the composites were investigated using the prepared dog-bone and flat bar specimens. Looking at these analyses the results showed that, following the tensile analysis, the tensile strength of the PP/Talc16/rGO2 mixture was found to be higher than the others. The tensile strength of PP/Talc16/rGO2 showed a 10.96% increase compared to neat PP. This higher value can be attributed to the synergistic effect of talc and rGO in the mixture (Mehrjerdi et al., 2013). Looking at the Charpy Notched Impact test results, it is observed that the impact resistance decreases with the addition of talc. The platelet-like structure of talc and its ability to increase crystallinity contribute to an increase in rigidity, which consequently leads to a reduction in impact resistance (Ammar et al., 2017). In addition rGO exhibits an increase in impact resistance due to its interfacial compatibility and hierarchical structural formation capability but its impact may vary depending on the content percentage (Xie et al., 2021).

Conclusion

This study investigate the effects of hybrid additives (talc and rGO) on the properties of PP. According to the DSC analysis, no significant change in the melting points was observed. The TGA analysis showed that the addition of these hybrid additives resulted in an increase in the initial degradation temperatures of the composites, suggesting

improved thermal stability. Based on the tensile test results, the PP/Talc16/rGO2 mixture exhibited the highest tensile strength, showing a 10.96% increase compared to neat PP. It was also observed that the impact resistance decreased with the addition of fillers.

References

Ammar, O., Bouaziz, Y., Haddar, N. & Mnif, N. (2017). Talc as reinforcing filler in polypropylene compounds: Effect on morphology and mechanical properties. Polymer Science, 03(02).

Bajsić, E. G., Rek, V., & Pavić, B. O. (2012). The influence of talc content on the thermal and mechanical properties of thermoplastic polyurethane/polypropylene blends. Journal of Elastomers & Plastics, 45(6), 501–522.

Castillo, L. A., Barbosa, S. E., & Capiati, N. J. (2013). Influence of talc morphology on the mechanical properties of talc filled polypropylene. Journal of Polymer Research, 20(5).

Ghasemi, F. A., Ghasemi, I., Menbari, S., Ayaz, M., & Ashori, A. (2016). Optimization of mechanical properties of polypropylene/talc/graphene composites using response surface methodology. Polymer Testing, 53, 283–292.

Kinoshita, T., Yamamoto, T., Luo, C., Ide, K., Aoki, K., & Uetsuji, Y. (2023). Mechanical characterization and design of hybrid reinforced polypropylene composites with talc fillers and cellulose fibers. Composites Part B Engineering, 266, 110971.

Kovacs, J., & Suplicz, A. (2013). Thermally conductive polymer compounds for injection moulding: The synergetic effect of hexagonal boron-nitride and talc. Journal of Reinforced Plastics and Composites, 32(16), 1234–1240.

Lapcik, L., Jindrova, P., Lapcikova, B., Tamblyn, R., Greenwood, R., & Rowson, N. (2008). Effect of the talc filler content on the mechanical properties of polypropylene composites. Journal of Applied Polymer Science, 110(5), 2742–2747.

Linares, P. B., Castillo, L. A., & Barbosa, S. E. (2019). Pro-Degradant effect of TALC nanoparticles on polypropylene films. Journal of Polymers and the Environment, 27(8), 1666–1676.

Mehrjerdi, A. K., Adl-Zarrabi, B., Cho, S., & Skrifvars, M. (2013). Mechanical and thermo-physical properties of high-density polyethylene modified with talc. Journal of Applied Polymer Science, 129(4), 2128–2138.

Patra, S. C., Swain, S., Senapati, P., Sahu, H., Murmu, R., & Sutar, H. (2022). Polypropylene and Graphene Nanocomposites: Effects of Selected 2D-Nanofiller's Plate Sizes on Fundamental Physicochemical Properties. Inventions, 8(1), 8.

Xie, K., Wang, W., Li, Y., Xu, M., Zhang, Y., & Gao, W. (2021). Study on Structure-Performance Relationship of RGO Enhanced Polypropylene Composites with Improved Atomic Oxygen Resistance. SSRN Electronic Journal.

Thermal and Mechanical Properties of Reduced Graphene Oxide Reinforced Polypropylene Composites

Cemile Gürer[a], Yeliz Köse[b], İrem Düzenli[a], Fatma Seniha Güner[a,c]

[a] Istanbul Technical University, Faculty of Chemical and Metallurgical Engineering, Department of Chemical Engineering, Türkiye
[b] Bilecik Şeyh Edebali University , Faculty of Engineering, Department of Metallurgy and Materials Engineering, Türkiye
[c] Sabancı University, Nanotechnology Research and Application Center (SUNUM), Türkiye
gurerc19@itu.edu.tr

Keywords: Mechanical Properties , Nanocomposites , Polypropylene , Reduced Graphene Oxide , Thermal Stability.

Aim

Polymer composites are widely used in various industries such as aerospace, automotive, and defense due to their high specific modulus and specific strength properties. These materials offer advantages such as reduced fuel consumption owing to their low density and can be easily processed into complex geometries using conventional manufacturing methods (Du & Cheng, 2012; Hsissou et al., 2021). Graphene oxide (GO) plays a crucial role as a filler material in nanocomposites due to its high surface-to-volume ratio, excellent dispersibility in both aqueous and organic solvents, and extensive reactive surface functional groups, which facilitate strong interactions with polymer matrices. These properties prevent aggregation, improve processability, and strengthen interactions between fillers and polymers (Compton & Nguyen, 2010). Furthermore, the superior mechanical properties of GO, such as its high Young's modulus and tensile strength, contribute to the enhancement of mechanical performance in polymer composites (Abdullah & Ansari, 2015). GO contains oxygen functional groups such as hydroxyl, epoxy, and carboxyl, which readily interact with polymer matrices (Phiri et al., 2017). These functional groups enhance the compatibility of GO and reduced graphene oxide (rGO) with polymer matrices, broadening their application in nanocomposite production. rGO has a structure similar to GO and can be produced via chemical or thermal reduction processes. Despite the reduction process, some functional groups remain on the surface (Phiri et al., 2018). When used as a reinforcement in polymer matrices, rGO improves mechanical properties such as Young's modulus, tensile strength, and toughness compared to pure polymers (Jang et al., 2014). This study aims to investigate the mechanical and thermal properties of polypropylene (PP) composites containing different concentrations of rGO.

Material and Method

Masterbatch containing 10 wt.% rGO was diluted with pure PP to prepare composites with 1, 3, and 5 wt.% rGO using a twin-screw extruder. Since polymer nanocomposites are widely used in high-temperature environments, investigating their thermal stability is crucial (Zhang et al., 2021). The thermal stability of polymer composites depends on two main factors; the composition of the constituent polymers and the interphase bonding and morphology within the polymer composites (Mat-Shayuti et al., n.d.). Graphene based nanomaterials have been shown to neutralize macroradicals formed during thermal degradation (George et al., 2018). Therefore, these nanomaterials are frequently used as reinforcements in polymers requiring high thermal and flame resistance. In this study for thermogravimetric analysis (TGA), each sample was heated from room temperature to 550°C under a pure nitrogen atmosphere at a heating rate of 10°C/min to prevent oxidation and other reactions. Differential scanning calorimetry (DSC) analyses were conducted for each sample under a nitrogen atmosphere with a heating/cooling rate of 10°C/min. The samples were first heated from 25°C to 200°C, then cooled back to 25°C, followed by heating from 25°C to 300°C. The melting temperatures (T), crystallization temperatures (T), and melting enthalpies (ΔH) were determined from the thermograms. Dog-bone-shaped specimens were prepared

using an injection molding machine, and tensile tests were conducted under ambient conditions at a crosshead speed of 5 mm/min. Five samples were tested, and the average results were recorded. For the flexural test, specimens with dimensions of 80 mm × 10 mm × 4 mm were prepared via injection molding. The three-point bending test was conducted using a Zwick Roell testing machine (1 N load cell) with a support span of 64 mm, in accordance with DIN ISO 178. Five samples were tested, and the average results were recorded.

Findings

The total weight loss was measured as 99.6% for the 1 wt.% composite, 97.8% for the 3 wt.% composite, and 95.8% for the 5 wt.% composite. The temperature corresponding to 50% weight loss (T) was defined, and the thermal stability of neat PP significantly improved with the inclusion of rGO. The T values increased with higher rGO content, recorded as 459.3°C for 1 wt.% PP/rGO, 460.7°C for 3 wt.% PP/rGO, and 463.3°C for 5 wt.% PP/rGO. The incorporation of rGO into the PP matrix increased the crystallization and melting temperatures of neat PP. This suggests that rGO exhibits a strong heterogeneous nucleation effect and promotes PP crystallization during cooling (Chen et al., 2018). The analysis confirmed an increase in melting and crystallization temperatures with increasing rGO content. The modulus and strength of composites generally increase with filler content, whereas elongation at break decreases. This is primarily because rigid filler materials reinforce the polymer matrix by restricting polymer chain mobility and enhancing load-bearing capacity (Ren et al., 2018). The results demonstrated that increasing the rGO content led to improvements in tensile strength and yield strength. Specifically, increasing the rGO content from 1 to 5 wt.% resulted in a 6.9% increase in tensile strength and a substantial 403.9% increase in yield strength, while elongation at break decreased by approximately 82.85%. The findings indicated that increasing the rGO content enhanced the flexural modulus. Increasing the rGO content from 1 to 5 wt.% resulted in a 20.8% increase in flexural modulus, a 7.5% increase in flexural strength, and a 6.91% decrease in f lexural elongation.

Conclusion

This study highlights the significant enhancement of both thermal and mechanical properties in PP composites reinforced with rGO. TGA results showed that the addition of rGO improved the thermal stability of the PP matrix, as evidenced by the higher T values and reduced overall weight loss with increasing rGO content. This indicates that rGO effectively strengthens the polymer's resistance to thermal degradation, making the composites more suitable for high-temperature applications. DSC further confirmed the positive impact of rGO on the crystallization and melting temperatures of PP, suggesting that rGO promotes heterogeneous nucleation, enhancing the crystallization process during cooling. This property is particularly beneficial for applications requiring precise control of the material's thermal properties. Mechanical testing revealed substantial improvements in both tensile and flexural properties with increasing rGO content. Specifically, a significant increase in tensile strength, yield strength, and flexural modulus was observed, making the composites more robust under load. Although elongation at break and flexural elongation decreased with higher rGO concentrations, these trade-offs are acceptable for applications where higher strength and rigidity are prioritized, such as in automotive and aerospace components. Overall, PP/rGO composites exhibit exceptional potential for use in industries requiring materials with both high thermal stability and superior mechanical performance. The incorporation of rGO not only enhances the performance of PP in these critical areas but also opens the door to further innovations in the development of advanced materials for high-demand applications.

References

Abdullah, S. I., & Ansari, M. N. M. (2015). Mechanical properties of graphene oxide (GO)/epoxy composites. *HBRC Journal*, *11*(2), 151–156.

Chen, Y., Yin, Q., Zhang, X., Xue, X., & Jia, H. (2018). The crystallization behaviors and rheological properties of polypropylene/graphene nanocomposites: The role of surface structure of reduced graphene oxide. *Thermochimica Acta*, *661*, 124–136.

Compton, O. C., & Nguyen, S. T. (2010). Graphene oxide, highly reduced graphene oxide, and graphene: Versatile building blocks for carbon-based materials. In *Small* (Vol. 6, Issue 6, pp. 711–723).

Du, J., & Cheng, H. M. (2012). The fabrication, properties, and uses of graphene/polymer composites. In *Macromolecular Chemistry and Physics* (Vol. 213, Issues 10–11, pp. 1060–1077).

George, G., Simon, S. M., Prakashan, V., Sajna, M., Faisal, M., Wilson, R., Chandran, A., Biju, P. R., Joseph, C., & Unnikrishnan, N. V. (2018). Green and facile approach to prepare polypropylene/: In situ reduced graphene oxide nanocomposites with excellent electromagnetic interference shielding properties. *RSC Advances*, *8*(53), 30412–30428.

Hsissou, R., Seghiri, R., Benzekri, Z., Hilali, M., Rafik, M., & Elharfi, A. (2021). Polymer composite materials: A comprehensive review. In *Composite Structures* (Vol. 262). Elsevier Ltd.

Jang, H. K., Kim, H. I., Dodge, T., Sun, P., Zhu, H., Nam, J. Do, & Suhr, J. (2014). Interfacial shear strength of reduced graphene oxide polymer composites. *Carbon*, *77*, 390–397.

Mat-Shayuti, M. S., Abdullah, M. Z., & Megat-Yusoff, P. S. M. (n.d.). *THERMAL properties and morphology of Polypropylene/Polycarbonate/Polypropylene-Graft-Maleic anhydride blends*. https://doi.org/10.1051/03001

Phiri, J., Gane, P., & Maloney, T. C. (2017). General overview of graphene: Production, properties and application in polymer composites. In *Materials Science and Engineering: B* (Vol. 215, pp. 9–28). Elsevier Ltd.

Phiri, J., Johansson, L. S., Gane, P., & Maloney, T. (2018). A comparative study of mechanical, thermal and electrical properties of graphene-, graphene oxide- and reduced graphene oxide-doped microfibrillated cellulose nanocomposites. *Composites Part B: Engineering*, *147*, 104–113.

Ren, Y., Zhang, Y., Fang, H., Ding, T., Li, J., & Bai, S. L. (2018). Simultaneous enhancement on thermal and mechanical properties of polypropylene composites filled with graphite platelets and graphene sheets. *Composites Part A: Applied Science and Manufacturing*, *112*, 57–63.

Zhang, W., Zhang, J., Ding, Y., He, Q., Lu, K., & Chen, H. (2021). Pyrolysis kinetics and reaction mechanism of expandable polystyrene by multiple kinetics methods. *Journal of Cleaner Production*, *285*.

METALLURGY AND MATERIALS ENGINEERING

Composite and Polymer Materials

Corrosion and Wear

Energy Materials

Extractive Metallurgy

Mechanical Metallurgy

Metals and Alloys

Surface Treatment and Coatings

Fabrication of Al Matrix MMC Cold Spray Coatings on AZ31 Magnesium Alloy

Efecan Madazlı[a], Erdem Balcı[a], Sezgin Cengiz[b], Hüseyin Çimenoğlu[a]
[a] Istanbul Technical University, Department of Metallurgical and Materials Engineering, Materials Science and Engineering, Turkey
[b] Gebze Technical University, Defence Technologies Institute, Turkey
madazli17@itu.edu.tr

Keywords: AZ31, Lightweight, Cold Spray, Wear Resistance.

Aim

Magnesium alloys are widely used in the automotive and aerospace industries due to their superior strength-to-weight ratio. Among the magnesium alloys, the Mg-Al-Zn alloy system (AZ series) offers increased mechanical properties by the precipitation hardening mechanism. AZ series alloys are used in automotive as wheels, seat rests, oil pans, cylinder head covers, and various frames in the chassis, and they are used in aerospace as brackets. [1] The alloy can be anodised to increase the corrosion and wear resistance; however, the resulting oxide is porous. Hence, the increase in the number of mentioned properties is limited.

Among the various surface modification methods, cold spray is a cost-efficient thermal spraying method where the particles do not reach their melting temperature. The method allows pure metal, alloy, and metal matrix composite (MMC) to be deposited on the substrate without disrupting the microstructure, which is achieved by conventional heat treatment or precipitation hardening treatments. Cold spray is also an attractive method in additive manufacturing and cost-efficient dimensional restoration of parts. Parts can also be cold sprayed and machined to their final dimension as a restoration procedure.[2] The cold spray method offers fast, cost-efficient and effective solutions to the maintenance of operating parts.

Among the studied cold spraying MMC coating blends, the aluminium matrix offers the optimum properties for embedding hard, wear-resistant particles. When compared with ceramic-based MMC coatings, intermetallic compound (IMC) based MMC coatings offer better interfacial bonding and less susceptibility for brittle phase formation. Al_2Zr is a hard, corrosion-resisting IMC found in the Al-Zr binary phase diagram. The compound has a density of 4.42 g/cm^3, a hardness of approximately 900 HV, a melting point of 1660 °C and is the compound with the highest melting point in the binary system. Owing to these properties, the Al_2Zr IMC provide higher hardness and operating temperature to the cold spray MMC coatings, along with increased metallurgical bonding and stable phase structure. [3] To the knowledge of the authors, Al/Al_2Zr composite coatings via the cold spray method are the first of their kind in the literature. This study aims to fabricate a cheap, wear-resistant and lightweight coating on the AZ31 alloy.

Materials and Methods

In this study, the AZ31 plates were obtained and cut to 15 mm specimen sizes. The specimens are grit blasted to ensure the adhesion of the coating layer to the substrate. The Al_2Zr IMC is obtained as cast buttons, produced via the vacuum arc melting method at 610 mbar pressure Argon atmosphere and 500 A. The obtained IMC buttons were crushed manually and ground in a high-energy ball mill at 300 RPM with zirconia spheres for 4 hours. The coating powders were mixed in a %40 Al_2Zr - %60 Al ratio. The blending and further grounding were performed in a mechanical alloying device at 10 Hz for 3 min with zirconia spheres to ensure complete and thorough blending. The grit-blasted specimens were mounted on the cold spray chuck, and particles were deposited at the surface with air pressurized to 6 bars with a 10 mm specimen standoff distance. The deposition process consisted of 4 passes.
Structural characterisation is achieved via X-ray diffraction (XRD) and scanning electron microscope (SEM) imaging. Both methods were conducted on unprocessed and cold spray processed AZ31 specimens. The XRD analysis is performed with $Cu_{K\alpha}$ radiation between the angles of 20º - 80º. Reciprocating ball on flat wear test was

performed for mechanical testing. The wear tests were performed at 3N load, 50 m sliding distance, 10 mm/s sliding speed and 5 mm wear track length. In order to evaluate the wear loss, surface profilometry is performed on both of the worn samples. The study aims to evaluate and compare the wear resistance of the unprocessed and cold spray processed specimens.

Findings

The XRD spectrum of the cold spray-processed AZ31 alloy is presented in Figure 1. The characteristic peaks belonging to aluminium are detected in the spectrum and are compared with the peaks in the literature.[4] Peaks of Al_2Zr are compared with the literature and found to be consistent with the works.[5, 6]

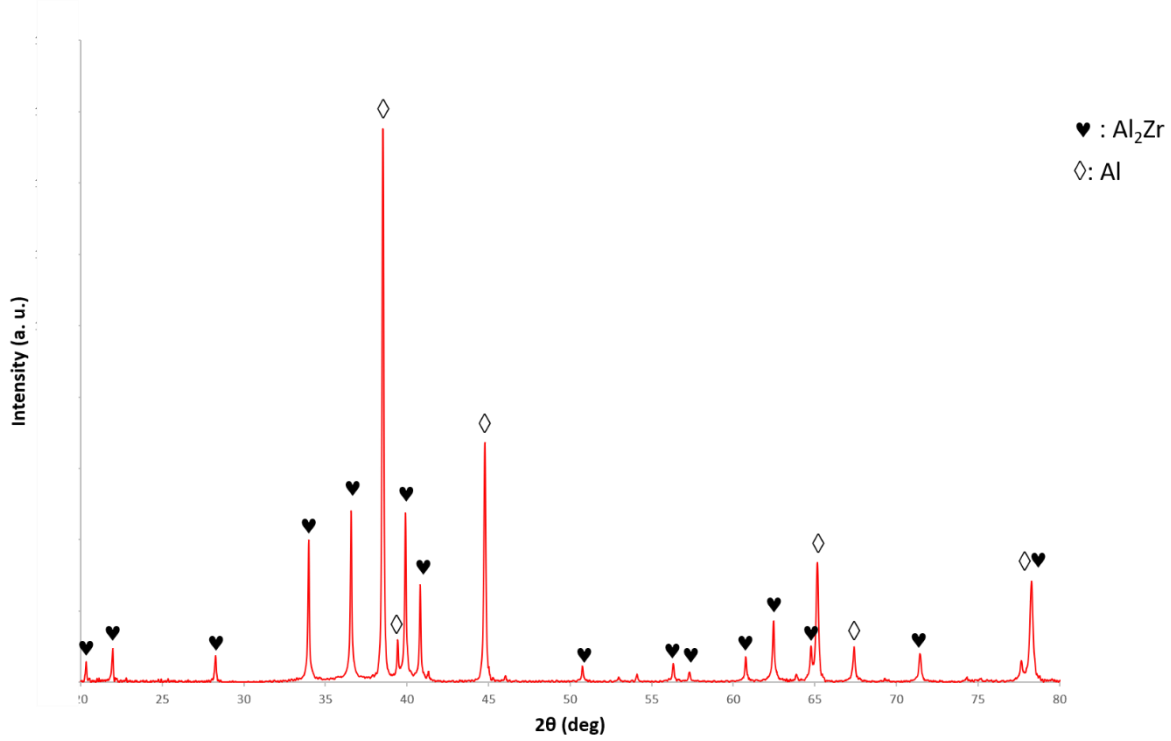

Figure 1. XRD spectrum of Al/Al_2Zr coated specimen.

The cross-sectional backscattered electron SEM images of the cold spray-processed AZ31 alloy are presented in Figure 2. The white particles indicate IMC, whereas the grey background indicates the aluminium matrix. The cold spray coating thickness is measured to be 438 µm on average. Roughly 100 µm thickness could be achieved per pass. The particles of Al_2Zr are found to be distributed evenly in the aluminium matrix. However, the particle dimensions indicate the grounding process to be inadequate due to the high hardness of the IMC, resulting in an uneven size distribution throughout the matrix. The aluminium matrix supports the Al_2Zr IMC without extreme strain hardening, and no cracking in the matrix is detected. The bonding of cold spray coating to the substrate AZ31 is achieved successfully, and no porosity or interfacial cracks between the substrate are detected.

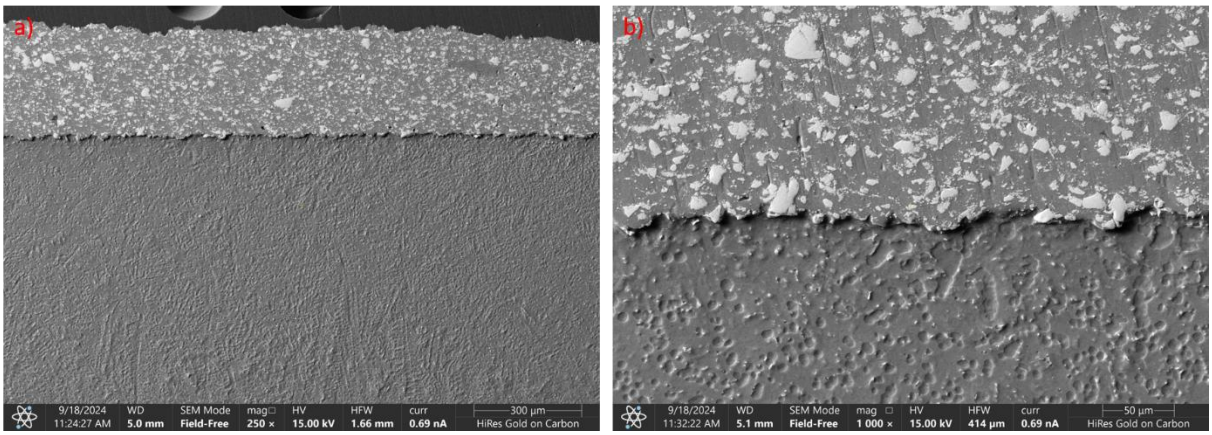

Figure 2. SEM images of the Al/Al_2Zr coated AZ31 specimen, a) cross section and b) interface.

The results of the wear tests performed are presented in Figure 3. The wear track depth and width of the unprocessed AZ31 alloy were found to be greater than that of the cold spray processed AZ31 (denoted CS%40), resulting in higher wear resistance. The volume loss of unprocessed AZ31 is calculated as 3.3 x 10^{-3} mm^3 N^{-1} m^{-1}, whereas the volume loss of cold spray processed AZ31 is 0.9 x 10^{-3} mm^3 N^{-1} m^{-1} supporting the higher wear resistance result observed in the wear track profiles. The wear track of cold spray processed AZ31 showed no delamination of coating or dislocation of the IMC particles, further supporting the strong bonding between the aluminium matrix and the IMC. The unprocessed AZ31 wear track showed plastic deformation-dominated wear mode. The counterface of both cold spray processed and unprocessed AZ31 revealed material transfer, indicating the wear mode is adhesive.

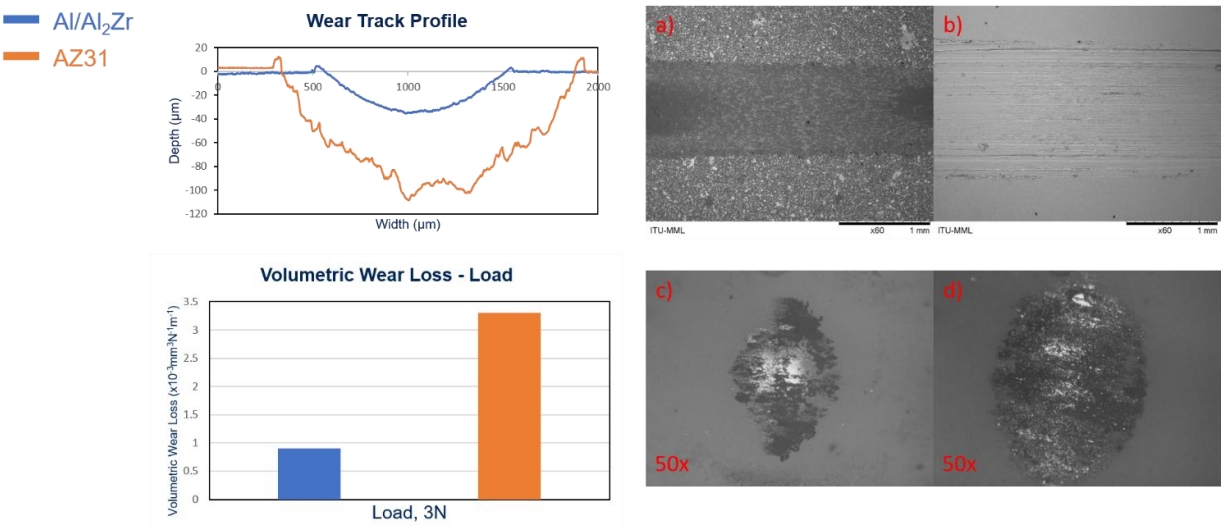

Figure 3. Wear track profile and the volumetric wear loss graphs for cold spray processed and unprocessed AZ31. a) Wear track of cold spray processed AZ31, b) wear track of the unprocessed AZ31, c) optical microscope image of counterface in image a, at x50 magnification and d) optical microscope image of counterface in image b, at x50 magnification.

Conclusion

The wear resistance of the AZ31 alloy is increased by approximately 4 times with the cold spray process. The resulting coating is found to be dense and defect-free within itself and at the coating/substrate interface. The IMC and the matrix are found to be firmly bonded. The coating showed no delamination or dislocation of hard particles. The study aims to further increase the wear resistance by subsequent micro-arc oxidation of the Al/Al_2Zr cold

spray coating after deposition and improve the size distribution by further milling and optimising the grounding operations.

References

Liu, B., Yang, J., Zhang, X., Yang, Q., Zhang, J., & Li, X. (2023). Development and application of magnesium alloy parts for automotive OEMs: A review. *Journal of Magnesium and Alloys*, *11*(1), 15-47.

Raoelison, R. N., Verdy, C., & Liao, H. (2017). Cold gas dynamic spray additive manufacturing today: Deposit possibilities, technological solutions and viable applications. *Materials & Design*, *133*, 266-287.

Xie, X., Yin, S., Raoelison, R. N., Chen, C., Verdy, C., Li, W., ... & Liao, H. (2021). Al matrix composites fabricated by solid-state cold spray deposition: A critical review. *Journal of Materials Science & Technology*, *86*, 20-55.

Ayieko, C. O., Musembi, R. J., Ogacho, A. A., Aduda, B. O., Muthoka, B. M., & Jain, P. K. (2015). Controlled texturing of aluminum sheet for solar energy applications.

Hu, Z., Xu, Y., Chen, Y., Schützendübe, P., Wang, J., Huang, Y., ... & Wang, Z. (2019). Anomalous formation of micrometer-thick amorphous oxide surficial layers during high-temperature oxidation of ZrAl2. *Journal of Materials Science & Technology*, *35*(7), 1479-1484.

Xu, Y., Jeurgens, L. P., Huang, Y., Li, C., Liu, Y., & Wang, Z. (2020). Effect of structural order on oxidation kinetics and oxide phase evolution of Al–Zr alloys. *Corrosion Science*, *165*, 108407.

METALLURGY AND MATERIALS ENGINEERING

Composite and Polymer Materials

Corrosion and Wear

Energy Materials

Extractive Metallurgy

Mechanical Metallurgy

Metals and Alloys

Surface Treatment and Coatings

Investigation of Reduction of Chromite Ore with Hydrogen

Ayse Deniz[a,b*], Cagdas Ekin Zohra[a], Selcuk Kan[a], Ceren Imer[b], Gokhan Basman[c], Yavuzhan Kaya[b], Onuralp Yücel[a]

[a]Istanbul Technical University, Faculty of Chemistry-Metallurgy, Department of Metallurgical and Materials Engineering, Türkiye
[b]Corex Holding BV, YILDIRIM Tower, Türkiye
[c]ETI Krom Inc, Türkiye
deniza16@itu.edu.tr

Keywords: Ferrochrome, Chromite Reduction, Hydrogen, Carbon Emissions..

Aim

Ferrochrome (FeCr) is an essential material in metallurgical industries, particularly in the production of stainless steel, which ensures corrosion resistance and durability. Approximately 80% of global FeCr production supports the stainless-steel sector, with high-carbon ferrochrome (HC FeCr) being the dominant form (International Chromium Development Association, n.d.). However, the traditional carbothermic reduction method used for FeCr production, reliant on coke and operating at temperatures exceeding 1600°C in submerged arc furnaces (SAFs), results in substantial energy consumption and carbon emissions (Basson & Daavittila, 2013). On average, producing one ton of HC FeCr emits 4.7–6.1 tons of CO_2-equivalent greenhouse gases, presenting a critical environmental challenge (Wei et al., 2023). The energy required to produce HC FeCr varies between 40 and 59 GJ per metric ton, contingent upon the mode of supply. Of all the steps, smelting uses the greatest energy, making up between 64% and 98% of the total. Smelting arc furnaces depend on electricity, which has a major influence on the FeCr alloy's impact on the environment (Wei et al., 2023).

This study investigates the reduction behavior of chromite ore using hydrogen (H_2) as an alternative reductant to achieve a more environmentally friendly and sustainable FeCr production process than carbothermic methods. The primary objective is to reduce carbon emissions by minimizing the reliance on traditional carbon (C)-based reductants and optimizing gas-based reduction processes. Studies have shown that reduction temperature, duration, and gas composition are decisive factors in the metallurgical conversion rate and mechanical strength of chromite pellets. For example, Wu et al. (2024) showed that lowering the temperature by 3 hours at 1100 °C in an atmosphere with 10% methane (CH_4) and 90% H_2 resulted in a total metallization rate of 36.3%, with rates of 69.3% for iron (Fe) and 10.3% for Chrome (Cr).

The study aims to identify the optimal reduction conditions by analyzing the development of metallic phases and chromium carbide compounds, while also examining the influence of H_2 and CH_4 on process sustainability. This study seeks to advance low-emission metallurgical methods aligned with future decarbonization objectives by the systematic analysis of temperature, gas composition, and reaction time.

Materials and Methods

Chromite ore samples (42-44 Al_{min} grade – Turkish Ore) were conducted for reduction experiments in a horizontal tube furnace (Lenton, T_{max}=1800°C) under certain atmospheres. Chemical composition of the chromite ore is given in Table 1.

Table 1. Chemical composition of Chromite Ore (wt. %).

Material	Cr_2O_3	Al_2O_3	CaO	SiO_2	MgO	Fe_2O_3	TiO_2	S	P_4O_{10}	C	NiO
Turkish Ore	44.58	7.93	0.32	10.92	21.77	13.29	0.08	0.00272	0.001	0.112	0.18

The reduction of chromite ore using H_2 and CH_4 gases was investigated. The experimental setup includes an alumina-based ceramic combustion boat containing 10 g of chromite ore positioned in the middle region of a Lenton tube furnace. Reducing gas (H_2) was fed into the system via stainless steel tubes with controlled flow rates. Gas flow rates were maintained at 0.21 l/min, dependent upon the individual experiment.

The furnace was not evacuated before the experiment. Instead, a continuous flow of high-purity argon (Ar) gas was used to create and maintain an inert atmosphere during the heating and cooling phases. During heating and cooling processes, the system is fed inert gas to prevent any oxidative interaction in the reaction environment. The reduction parameters, such as temperature (between 1300°C and 1500°C) and dwell time (up to 4 hours), were investigated. Table 2 gives detailed data on the experiments on the reduction of chromite ore with H_2 gases.

Table 2. Experiments on the reduction of chromite ore with H_2.

Experiment No	Temperature (ºC)	Reduction Gas (L/min)	Dwell time (min)	Mass Change (g)	Experimental Mass Loss (%)
1	1300	0.21 l/min H_2	120	-0.67	6.67
2	1400	0.21 l/min H_2	120	-0.81	7.90
3	1500	0.21 l/min H_2	120	-1.00	9.48
4	1500	0.21 l/min H_2	180	-1.25	12.02
5	1500	0.21 l/min H_2	240	-1.83	17.35

5 experiments were conducted to investigate the H_2 reduction of chromite ore. The mass loss presented in the Table 2 represents the percentage change in mass observed as a result of the reduction experiment. The samples used in the experiment are approximately 10.56 grams (g). The theoretical mass loss during the reduction of a chromite ore sample using H_2 is approximately 1.91 g for 10.56 g of sample. The total theoretical mass loss due to the reduction of chromium oxide (Cr_2O_3) and iron oxide (Fe_2O_3) phases in the sample was found to be 18.07% based on stoichiometric calculations.

At the end of the experiment, products were weighed to calculate mass loss and then analyzed by Panalytical X'Pert Pro X-ray diffraction (XRD), utilizing Cu-Kα radiation with a scanning rate of 10°/min to find patterns within the 10-90° range, employing a step size of 0.02 at ITU to identify the phases generated during reduction.

Findings

XRD graphs were analyzed to examine which phases of the products were formed in the first place. The results of the experiments were compared with Low-Carbon Ferro Chrome (LC FeCr), as C is not expected in the content of the sample. LC FeCr contains 0.05% C and a minimum of 65% Cr.

To investigate the influence of temperature, experiments 1, 2, and 3 were carried out with identical dwell times and gas flow rates. The XRD results of the reduction of chromite ore at 1300, 1400, and 1500 ℃ with a gas flow rate of 0.21 L/min for 2 hours are shown in Figure 1.

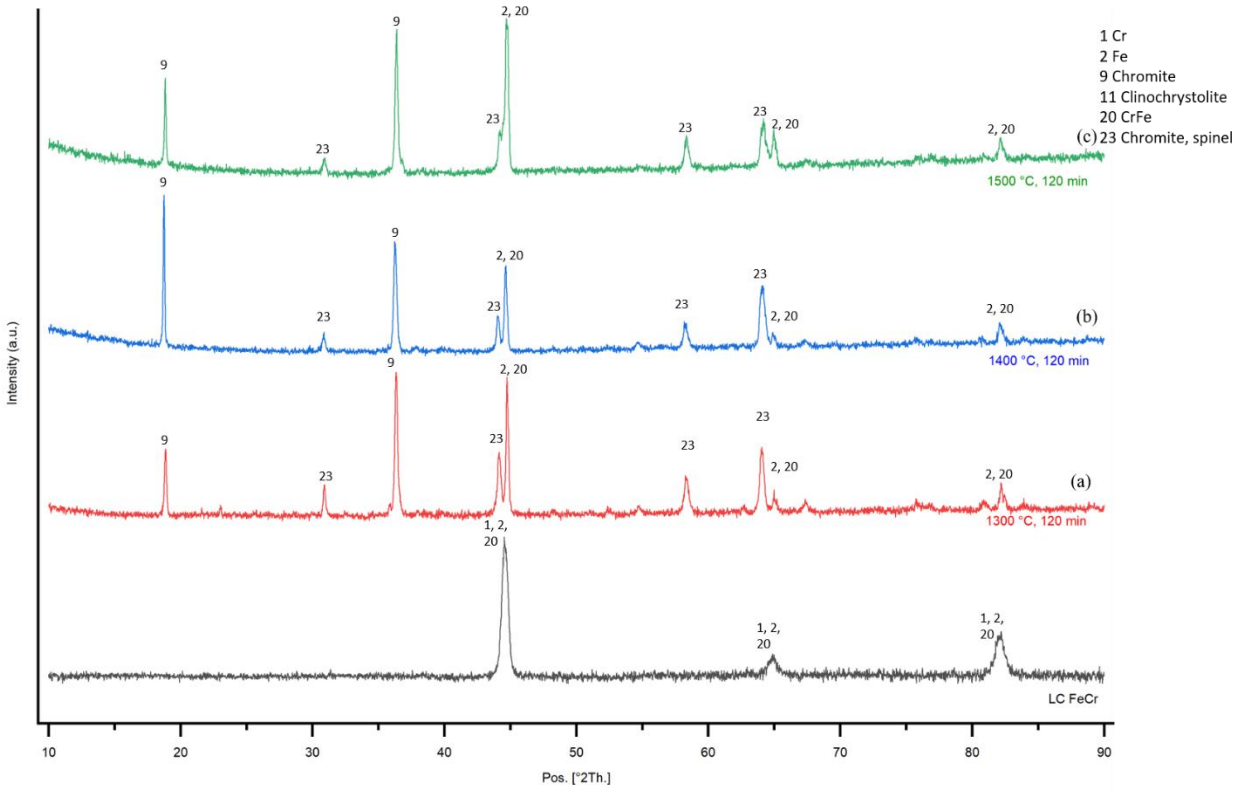

Figure 1. The XRD results of the reduction of chromite ore at 1300, 1400, and 1500 °C with a gas flow rate of 0.21 l/min for 2 hours.

When the XRD results were examined (Figure 1), metal peaks were found at the same degrees as LC FeCr. α-Fe (BCC) peak was detected in the XRD graphs of all 3 experiments. The phase identification of α-Fe (BCC) was confirmed by comparison with the ICDD PDF card No. 01-089-7194. The diffraction peaks corresponding to the spinel chromite phase (particularly those labeled as 9 and 23) are still observable in all samples, but a gradual decrease in their intensity is observed as temperature increases. This may indicate partial decomposition of the spinel structure; however, the extent of the transformation cannot be definitively determined based solely on peak intensity. Additionally, the presence and marked intensification of peaks assigned to Cr, Fe, and CrFe phases (peaks 1, 2, and 20) at high temperatures may indicate an increase in metallic phase formation; however, this interpretation remains qualitative without further phase quantification. Although reflections associated with metallic phases become more pronounced at 1400 °C and 1500 °C, the persistence of chromite peaks suggests that complete reduction may not have occurred under the conditions studied. Additionally, the experimental patterns do not fully align with that of the LC FeCr reference, which could point to an incomplete transformation, or possibly the presence of other residual phases not fully resolved by XRD alone.

The Fe phase observed in XRD analysis indicates that Fe_2O_3 is reduced by H_2 to metallic Fe. This finding coincides with the studies in the literature that Fe_2O_3 can be reduced in a H_2 atmosphere (Rukini et al., 2022).

At 1500 °C, experiments 3, 4, and 5 were analyzed together to investigate the effect of dwell time. In the experimental study, an experimental mass loss of approximately 9.48%, 12.02%, and 17.35% was observed during the reduction of the ore, respectively. Of these values, only experiment 5 is close to the theoretical mass loss (18.09%) and can be explained by the removal from the system as H_2O formed during reduction.

Conclusion

When the studies are examined, it is thought that the increase in temperature and time will lead to an increase in metal formation. More analyses are needed to analyze the results in detail, to determine the amount of metal and to identify the phases formed, and more experiments are needed for hydrogen reduction of chromite ore.

The reduction of chromite ore with H_2 revealed that Fe_2O_3 was effectively reduced to metallic Fe, whereas Cr_2O_3 reduction was limited due to thermodynamic constraints. Higher temperatures and prolonged durations enhanced mass loss and phase transformation, indicating the role of thermal energy in breaking down spinel structures. Mixed gas or stepwise reduction approaches may further improve efficiency and support sustainable metallurgical practices.

References

Basson, J., & Daavittila, J. (2013). High carbon ferrochrome technology. In *Elsevier eBooks* (pp. 317–363).
Rukini, A., Rhamdhani, M. A., Brooks, G. A., & Van Den Bulck, A. (2022). Metals production and metal oxides reduction using hydrogen: A review. *Journal of Sustainable Metallurgy, 8*(1), 1–24.
Wei, W., Samuelsson, P. B., Jönsson, P. G., & Yang, W. (2023). Energy consumption and greenhouse gas emissions of high-carbon ferrochrome production. *JOM, 75*, 1206–1220.
What is ferrochrome (FeCr) and what is it used for. (n.d.). *ICDA – International Chromium Development Association*. Retrieved May 22, 2025, from https://www.icdacr.com/about-chrome/ferrochrome/
Wu, S., Feng, X., Zhang, Y., Ma, L., & Li, Y. (2024). Methane–hydrogen-based pre-reduction chromite: Reduction behavior and pellet compressive strength. *JOM, 76*, 4858–4872.

Production and Characterization of Lanthanum Hexaboride Powder

Deniz Nalci[a], Mehtap Arslan-Kaba[a], Guldem Kartal Sireli[a], M. Kursat Kazmanli[a]

[a]Istanbul Technical University, Faculty of Chemical and Metallurgical Engineering, Department of Metallurgical and Materials Engineering, Türkiye
nalcid@itu.edu.tr

Keywords: Lanthanum Hexaboride, Molten Salt Electrolysis, Thermionic Emitter.

Aim

Rare-earth hexaborides exhibit exceptional thermal, electrical, magnetic and physical properties. Among them, lanthanum hexaboride (LaB_6) is a critical material for advanced technological applications due to its remarkable characteristics, including a high melting point and low work function (2.6 eV) [1]. Thanks to their unique properties, hexaborides are used in important applications, including electron emission and thermoelectric devices, thin film coatings, photon detectors, and superconducting materials [2]. The production of LaB_6 has traditionally been conducted using metallothermic reduction, chemical vapor deposition (CVD) and molten salt electrolysis methods. In the metallothermic method, boron compounds are reduced with metals that have a high affinity for oxygen, typically magnesium [2]. However, this process leads to the formation of unwanted by-products and results in low purity, making it unsuitable for especially semiconductor applications. The CVD method, on the other hand, involves the reduction of boron halides with hydrogen gas, producing high-purity LaB_6 [3]. Despite this advantage, it has several drawbacks, including the use of toxic and corrosive gases, the requirement for expensive equipment, and low production efficiency. With traditional molten salt electrolysis, high purity production is possible in ultra short times. Since the environment is very corrosive in fluoride and chloride electrolyte production, the system must be adjusted very well [4]. In addition, halides pose a serious threat to health and the environment.

In this study, high-purity LaB_6 powder was synthesized using a novel and environmentally friendly molten salt electrolysis method incorporating oxide-based salts. Additionally, the structural characterization of the produced LaB_6 powder was conducted. The use of borax as an electrolyte in molten salt electrolysis enables green production by achieving high purity and high capacities in a remarkably short time.

Materials and Methods

Grade 2 titanium (Ti) was chosen as a cathode material with dimensions of 2.5 cm × 6 cm × 1 mm. The chemical composition of the cathode material is presented in Table 1. To remove contaminants such as oil and dirt, the surface was first ground with 800 and 1000-grit sandpaper, followed by ultrasonic cleaning in an acetone bath.

Table 1. Chemical composition of the grade 2 titanium used.

Element	C	N	O	H	Fe	Ti
wt%	≤ 0.080	≤ 0.030	≤ 0.25	≤ 0.015	≤ 0.30	≥ 98.9

The parameters examined in the production of LaB_6 powder were determined based on previous studies of the research group [5]. Accordingly, the process was conducted at 900°C with a current density of 200 mA/cm^2 for 1 hour. The electrolyte composition used in the experiment was 93 wt% $Na_2B_4O_7$, 5% La_2O_3, and 2% CaF_2. These experimental parameters are shown in Table 2.

Table 2. Experimental parameters examined in LaB_6 production.

	Cathode Material	Temperature	Current Density	Electrolyte Composition wt%	Time
Experiment	Ti	900 ºC	200 mA/cm2	93% Na2B4O7+ 5% La2O3+ 2% CaF2	60 min

The electrolysis was conducted within a medium-frequency induction furnace. The titanium substrate was used as a cathode, a graphite crucible containing electrolyte was utilized as an anode. The electrolyte composition included lanthanum oxide (La_2O_3) and borax ($Na_2B_4O_7$), with a small addition of calcium fluoride (CaF_2) at 2 wt% as an activator [6]. After the electrolysis completed, the cathode was withdrawn, and the remnant electrolyte was eliminated by rinsing them in boiling water. The deposited powder was then scraped off and thoroughly washed with hot water. To remove impurities, an HCl washing process was carried out. The powder was then filtered and dried. The produced powder was structurally characterized by X-ray diffractometry (XRD), scanning electron microscopy (SEM) and raman spectroscopy.

Findings

The XRD results of the powder collected on the cathode surface in the experiment are presented in Figure 1. According to the XRD analysis, LaB_6 structure was obtained under these experimental parameters. In addition to the LaB_6 main phase, $LaBO_3$ formation was observed before HCl cleaning. All of the $LaBO_3$ phases were removed after the cleaning process with HCl.

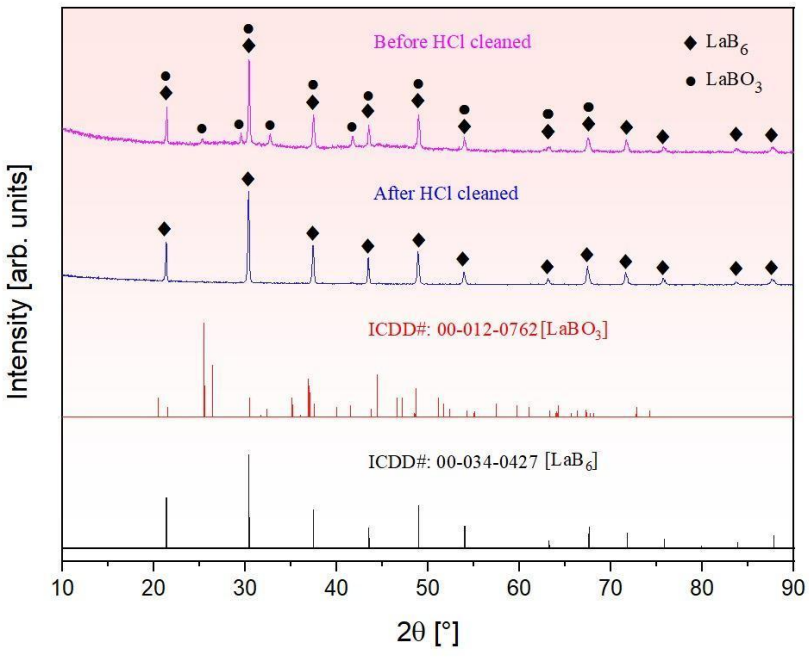

Figure 1. XRD pattern of LaB_6 powder synthesized from a composition of 93 wt% $Na_2B_4O_7$, 5% La_2O_3, and 2% CaF_2, before and after HCl cleaning [Ti cathode, 900 °C, 200 mA/cm²].

The SEM analysis conducted to investigate the morphology of the synthesized powder is shown in Figure 2. The SEM results revealed that the characteristic cubic morphology was observed. The crystals exhibit homogeneous and uniform distribution. When the SEM results are evaluated together with the XRD analysis, no phases other than LaB_6 were detected.

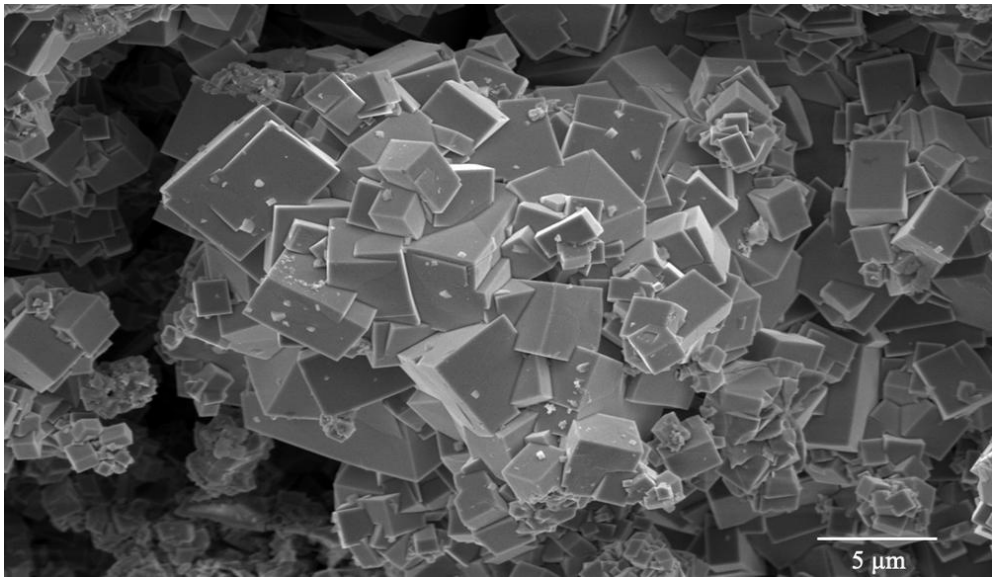

Figure 2. SEM image of LaB_6 powder obtained from a compositon of 93 wt% $Na_2B_4O_7$, 5% La_2O_3, and 2% CaF_2, after HCl cleaning [Ti cathode, 900 °C, 200 mA/cm²].

LaB_6 shares a structural similarity with CsCl in terms of its unit cell, which is a simple cubic crystal structure [7]. In this configuration, lanthanum ions are positioned at the center, while boron octahedra are located at the corners of the crystal [8]. Raman-active modes are mainly influenced by octahedral boron cluster [9]. Three Raman-active modes of this octahedral structure are the A_{1g} and E_g stretching modes, as well as the T_{2g} bending mode [10]. According to the literature, these three vibrational modes are observed within the frequency range of 600–1400 cm^{-1} [11]. Raman spectroscopy was conducted on the LaB_6 powder. In Figure 3, the Raman spectroscopy results before and after HCl cleaning are presented. The Raman peaks of the powder cleaned with HCl are observed at 770 cm^{-1}, 1118 cm^{-1}, and 1263 cm^{-1}, corresponding to the T_{2g}, E_g, and A_{1g} active raman modes, respectively [12]. The acid cleaning process did not have a significant effect on the raman peaks.

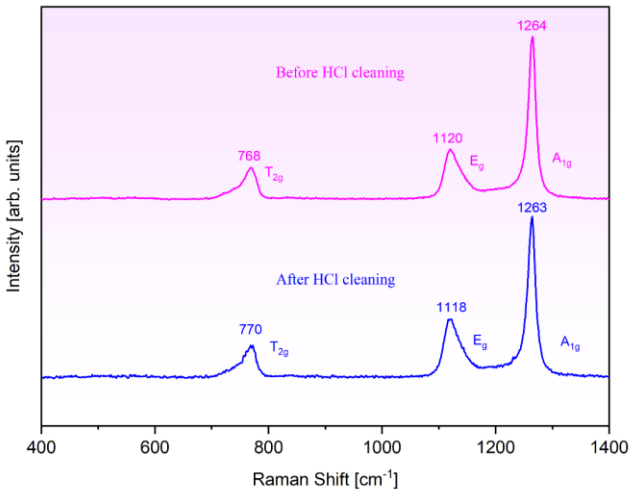

Figure 3: Raman spectra of LaB_6 powder synthesized from a composition of 93 wt% $Na_2B_4O_7$, 5 wt% La_2O_3, and 2 wt% CaF_2, before and after HCl cleaning [Ti cathode, 900 °C, 200 mA/cm^2]

Conclusion

In this research, it has been shown that it is possible to produce high purity LaB_6 powder using borax electrolyte by molten salt electrolysis method. XRD and SEM analysis results showed that these experimental parameters

were effective in the production of high purity LaB_6 powder. The characteristic T_{2g}, E_g and A_{1g} modes of LaB_6 powder produced in raman spectroscopy were obtained. In addition, considering the advantages of the low cost of the production system and raw material source, the use of environmentally friendly electrolyte and the ability to obtain high amounts of product in short periods of time have been demonstrated. This study aims to utilise the boron resources of our country to produce high value-added advanced technology products.

References

Şimşek, T., Chattopadhyay, A. K., Barış, M., & Bilen, M. (2019). Low temperature synthesis and characterization of pure lanthanum hexaboride nanocrystals. Journal of Solid State Chemistry, 276, 238–243.

Cahill, J. T., & Graeve, O. A. (2019). Hexaborides: A review of structure, synthesis, and processing. Journal of Materials Research and Technology, 8(6), 6321–6335.

Kher, S. S., & Spencer, J. T. (1998). Chemical vapor deposition of metal borides: 7. The relatively low temperature formation of crystalline lanthanum hexaboride thin films from boron hydride cluster compounds by chemical vapor deposition. Journal of Physics and Chemistry of Solids, 59(8), 1343–1351.

Kamaludeen, M., Selvaraj, I., Visuvasam, A., & Jayavel, R. (1998). LaB_6 crystals from fused salt electrolysis. Journal of Materials Chemistry, 8(10), 2205–2207.

Heper, K. K. (2024). Production of cerium hexaboride by molten salt electrolysis (Unpublished master's thesis). Istanbul Technical University, Graduate School of Science and Engineering.

Ozguvenc, E. E. (2024). Production of vanadium borides by molten salt electrolysis. SSRN.

Bai, L., Ma, N., & Liu, F. (2009). Structure and chemical bond characteristics of LaB_6. Physica B: Condensed Matter, 404(22), 4086–4089.

Korsukova, M. M., & Gurin, V. N. (1987). Physicochemical problems in the preparation of defect-free monocrystals of lanthanum hexaboride. Russian Chemical Reviews, 56(1).

Mattox, T. M., Chockkalingam, S., Roh, I., & Urban, J. J. (2016). Evolution of vibrational properties in lanthanum hexaboride nanocrystals. The Journal of Physical Chemistry C, 120(10), 5188–5195.

Groome, C., Roh, I., Mattox, T. M., & Urban, J. J. (2017). Effects of size and structural defects on the vibrational properties of lanthanum hexaboride nanocrystals. ACS Omega, 2(5), 2248–2254.

Ponosov, Y. S. (2022). Raman-active phonons in thin film hexaborides. In D. S. Inosov (Ed.), Rare-Earth Borides (pp. 443-479). Jenny Stanford Publishing.

Lee, S., Lee, W., Lee, S. H., & Moon, K. (2019). Raman spectroscopic evidence of impurity-induced structural distortion in SmB_6. Journal of Raman Spectroscopy, 50(11), 1661–1671.

METALLURGY AND MATERIALS ENGINEERING

Composite and Polymer Materials

Corrosion and Wear

Energy Materials

Extractive Metallurgy

Mechanical Metallurgy

Metals and Alloys

Surface Treatment and Coatings

Effects of Stress Relief Annealing Time on Mechanical Properties and Operating Cost in Lamellar Graphite Cast Iron Engine Blocks

Furkan Üstün[a,b], Ali Kalyon[c]

[a] Yalova University, Natural and Applied Sciences, Turkey
[b] Döktaş Inc., Department of Production, Turkey
[c] Yalova University, Faculty of Engineering, Department of Mechanical Engineering, Turkey
furkan.ustun@doktas.com

Keywords: Lamellar Graphite Cast Iron, Stress Relief Annealing, Mechanical Properties, Residual Stress, Engine Block.

Aim

The aim of this study is to investigate the effects of increasing the stress-relief heat treatment time on the mechanical properties and operational costs of motor blocks produced from lamellar graphite gray cast iron EN GJL-250 material. The lamellar graphite gray cast iron material used in the production of motor blocks offers advantages such as lower production costs, durability, and thermal conductivity, making it suitable for a wide range of applications, from automotive engines to truck, boat, tractor, and other industrial vehicle engine blocks [Arran A.,Elliott R.]. Motor blocks must meet mechanical durability, fatigue resistance, and high thermal conductivity requirements, especially under harsh operating conditions.Therefore, the design and material properties of the motor block play a crucial role in ensuring efficient engine operation. During the casting process, cooling variations that occur after the production of the engines induce stresses on the motor block, and it is not possible to prevent this situation under mass production conditions.[Baş B., Şen N.B]. The optimal solution for businesses in this regard is post-production stress-relief heat treatment processes. This study aims to demonstrate how increasing the stress-relief heat treatment time affects the mechanical properties and residual stresses of the motor block.[Yenici B.S.,Çoşar B.] Additionally, this study aims to evaluate the cost-effectiveness of stress-relief heat treatments from the perspective of businesses and determine the optimal (graph) stress-relief heat treatment time.

Material and Method

The motor blocks used in this study are made of lamellar graphite gray cast iron EN GJL-250 material. The motor block production took place at the Döktaş Orhangazi factory. The raw materials used in the production include gray cast iron, automotive scrap, and recycled runners. The chemical composition of the engine block is shown in table 1.

Table 1. Chemical composition of the engine block (EN GJL 250).

Chemical Composition											
C	Si	S	Mo	Cr	Cu	Sn	Mn	Ti	Mg	P	Ni
3.100	2.137	0.77	0.022	0.268	0.663	0.073	0.857	0.020	0.001	0.026	0.024

The cleaning and grinding processes of the produced motor blocks were carried out in the fettling department of Döktaş. Figure 1 shows the pattern and filter placement in the molding line during the production of the motor blocks. After casting, the blocks are left in the cooling tunnel for 3 hours and then allowed to cool in the atmospheric environment. During this process, internal stresses caused by uneven cooling are generated in the blocks. Therefore, after grinding and cleaning, the blocks underwent stress-relief heat treatment.

Figure 1. Core and filter placement before molding of engine blocks.

For the heat treatment, the motor blocks were subjected to stress-relief annealing in a System Teknik branded natural gas heated 6-burner trolley-type furnace. During the heat treatment, the stress-relief times and cooling rates of the blocks were considered as variable parameters. These variables were adjusted on the stress-relief heat treatment curve by setting holding times and cooling durations. The 10-hour and 15-hour stress-relief heat treatment curves are shown in Figures 2 and 3. In the 10-hour heat treatment curve, the temperature reaches 600°C within 2 hours and is held at 600°C for 2 hours. Then, the blocks are cooled in the furnace at 75°C per hour until they reach 150°C, after which the furnace doors are opened. In the 15-hour heat treatment curve, the temperature also reaches 600°C within 2 hours, and the blocks are held at 600°C for 3 hours. Then, the cooling continues at a rate of 40°C per hour until the blocks reach 300°C. After 150°C, the cooling rate is 75°C per hour, and the furnace doors are opened.

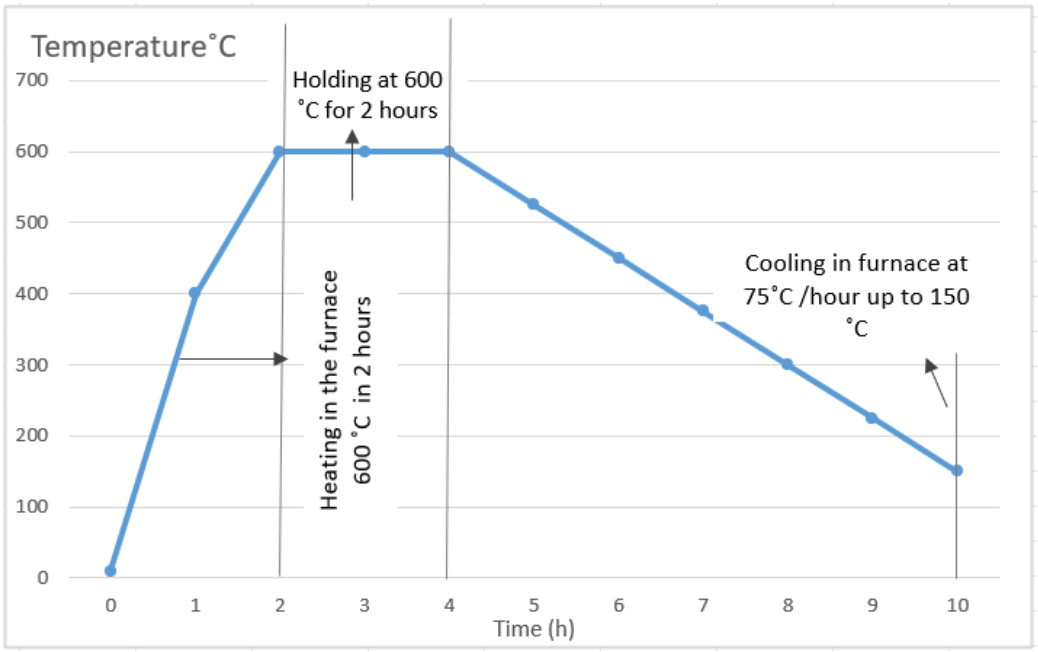

Figure 2. 10 hours stress relief chart.

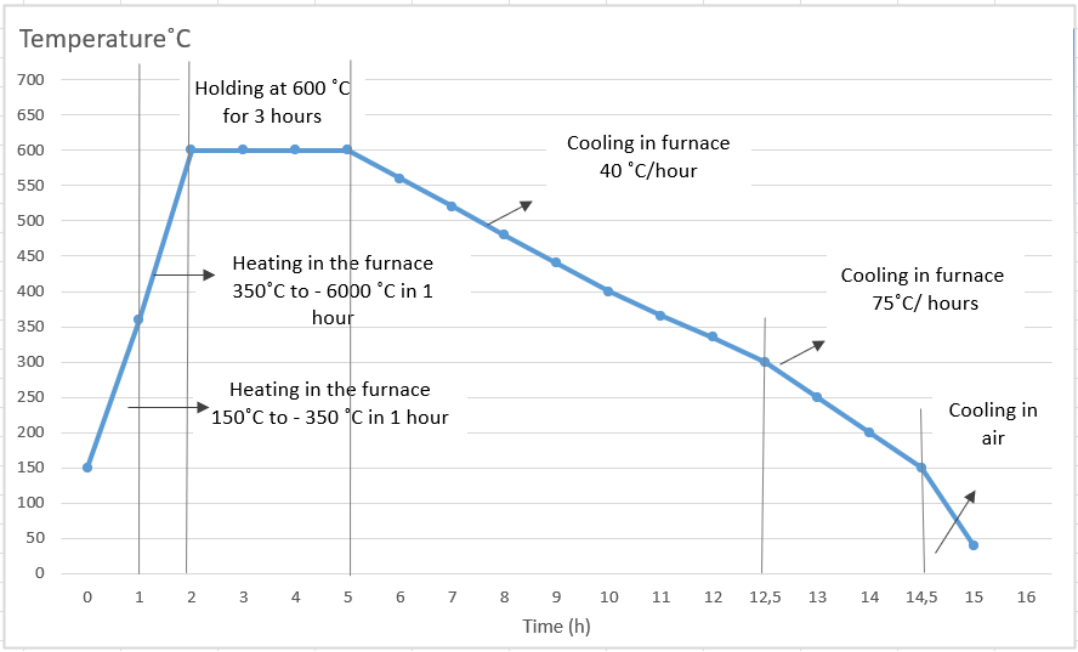

Figure 3. 15 hours stress relief chart.

Equipment Used

- **Dimensional Measurement:** Dimensional measurements of the motor blocks were performed using a Coord 3 CMM device.
- **Tensile Test:** Tensile tests were carried out using a Shimadzu brand device with a 250 kN capacity and an extensometer. The tests were conducted according to customer technical specifications.
- **Hardness Measurement:** Hardness measurements were taken using a Reicherter brand device with a 10 mm diameter probe and a 3-ton capacity. The hardness measurements were conducted on the head and crankcase surfaces in accordance with ASTM E10-96 standards.

- **Chemical Analysis:** Chemical analyses were performed using an ARL 4460 optical emission spectrometer. Sampling was done using a ladle sampling tool from the molten metal before casting.
- **Microstructure Analysis:** Microstructure analysis was carried out using a Nikon optical microscope. The analyses were conducted according to the instructions specified in the customer's technical specifications.
- **Residual Stress Measurement:** Residual stress measurements were performed using an IMC Chronosflex data collection system and 19 analog channels.The stress measurements were carried out with devices capable of data collection at a speed of 100 Hz.

Sample Preparation and Testing

Samples from the motor blocks were taken from areas suitable for tensile testing according to customer technical specifications and then machined to conform to DIN 50125 standards using a lathe. A visual of the sample is shown in Figure 4. Hardness measurements were made on samples taken from the head and crankcase surfaces according to ASTM E10-96 standards. For microstructure analysis, the samples were prepared according to the instructions specified in the customer's technical specifications. The chemical composition of the motor block was determined using the ARL 4460 optical emission spectrometer.

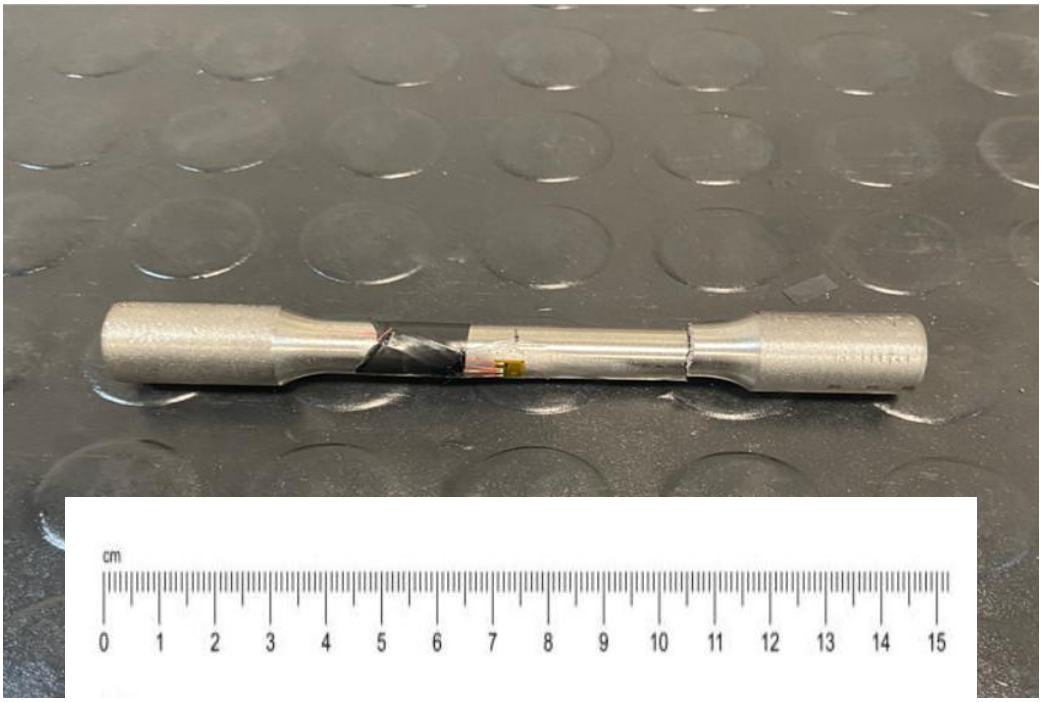

Figure 4. Tensile test sample prepared according to DIN 50125 Standarts.

Experimental Parameters

In this study, the variable parameters included the holding time and cooling durations in the stress-relief heat treatment curve. Two different stress-relief heat treatment recipes of 10 hours and 15 hours were applied to the motor blocks, and mechanical properties were tested and analyzed after these heat treatments.

Findings

This study examined the effects of stress-relief heat treatment times on the mechanical properties of EN GJL-250 lamellar graphite gray cast iron motor blocks. The results obtained after the 10-hour and 15-hour stress-relief heat treatments are presented in detail in Table 2.

Table 2.Results of mechanical tests after 10-hour and 15-hour stress relief heat treatment.

Heat Treatment Duration	After 10-Hour Stress-Relief Heat Treatment	After 15-Hour Stress-Relief Heat Treatment
Residual Stress [MPa] SG 5.2	-75.97	-40.47
Residual Stress [MPa] SG 5.3	-65.10	-25.00
Residual Stress [MPa] SG 5.5	-108.14	-20.38
Residual Stress [MPa] SG 10.	-4.97	-2.98
Tensile Strength [N/mm²]	248	246
Average Hardness [Brinell]	210	208
Dimensional Measurement [mm]	480	480.1

Residual Stresses: According to the results shown in Table 2, the residual stresses measured after the 10-hour stress-relief process were -75.97 MPa, -65.10 MPa, -108.14 MPa, and -4.97 MPa in the SG 5.2, SG 5.3, SG 5.5, and SG 10 regions, respectively. However, after the 15-hour stress-relief process, a significant reduction was observed in these values. The residual stresses measured after the 15-hour process were -40.47 MPa, -25.00 MPa, -20.38 MPa, and -2.98 MPa, indicating a reduction of 50% to 80% in the residual stresses.The cutting depth and residual strain measurement visual is shown in Figure 5.

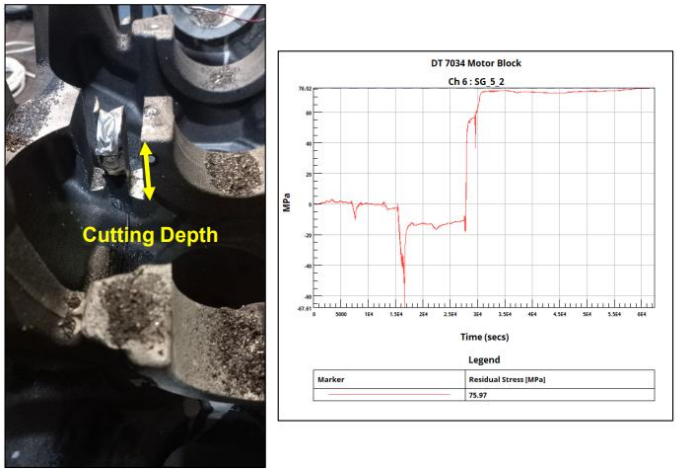

Figure 5. Residual strain measurement and depth of cut image.

Tensile Strength and Hardness: No significant change was observed between the tensile tests and hardness measurements after both heat treatment durations. After the 10-hour stress-relief process, the tensile strength was 248 N/mm², and the average hardness was 210 Brinell. After the 15-hour process, the tensile strength was 246 N/mm², and the average hardness was 208 Brinell. The difference between these values is quite small and negligible. This suggests that the hardness values did not decrease significantly, which is crucial for maintaining the motor block's high performance under harsh working conditions.

Dimensional Measurements: The effect of heat treatment time on dimensional measurements was also examined. After the 10-hour stress-relief process, the dimensional measurement was 480 mm, while after the 15-hour process, the measurement was 480.1 mm. This result indicates that no significant dimensional change occurred in the motor block after either heat treatment duration, and the motor block remained within the desired tolerance limits.

Microstructure Analysis: Microstructure analysis was performed after both heat treatment durations. Microscopic examination revealed the presence of similar A-type graphite structures in both cases. Additionally,

the matrix structure was found to be 99% pearlitic in both samples. This indicates that no significant change occurred in the microstructure of the motor blocks after both the 10-hour and 15-hour stress-relief processes.10 hours and 15 hours annealed unetched microstructure images are shown in Figure 6 and 7.

Figure 6. 10 hours annealed unetched microstructure image 100 X Magnification.

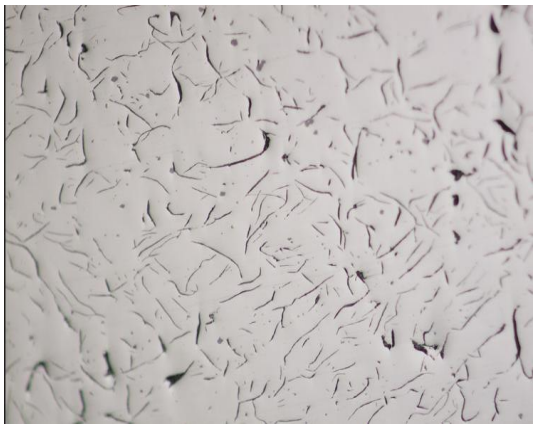

Figure 7. 15 hours annealed unetched microstructure image 100 X Magnification.

Cost Analysis: The additional costs of extending the heat treatment time for businesses are calculated and presented in Table 3. The analysis highlights that extending the stress-relief heat treatment time will increase costs for natural gas, electricity consumption, and labor. If one annealing cycle is performed daily, with 280 cycles annually, the use of the 15-hour recipe would result in an additional annual cost of 26.273 €. The impact on the unit part cost is 0.4%. This increase is considered insignificant when considering the high performance and durability required for the motor blocks over their service life.

Table 3. Effect of 15 hours stress relieving heat treatment on difference cost calculation and unit part cost calculation compared to 10 hours stress relieving treatment.(The calculation is based on 28 000 pieces per year.)

Cost Item	Annual Cost (€)
Annual Natural Gas Cost Difference	€ 16 949
Annual Labor Cost Difference	€ 8 400
Annual Electricity Cost Difference	€ 924
Total Annual Cost Difference	€ 26 273
Impact on Unit Part Cost	0.4 %

Conclusion

In this study, motor blocks produced by sand casting using EN GJL-250 material were annealed with two different stress-relief heat treatment recipes, and their mechanical properties were examined. No significant change was observed in hardness, tensile strength, and dimensional measurements. The microstructures of both cases showed similar A-type graphites, and the matrix was found to be 99% pearlitic. The most significant variability was observed in the residual stress measurements. By increasing the stress-relief annealing time and lowering the cooling temperature, the residual stresses in the motor blocks were reduced by 50% to 80%, remaining within the tolerance limits specified in the customer's technical specifications. These results are important for ensuring high performance when the motor is subjected to dynamic and static stresses during its service life. This study confirmed the optimal stress-relief heat treatment graph required to minimize internal stresses in lamellar graphite gray cast iron motor blocks produced by sand casting. The additional cost associated with increased heat treatment time is considered negligible when considering the motor's lifetime, performance, and potential quality issues.

References

Aran, A. (1991). *Casting technology seminar notes*. TMMOB Chamber of Mechanical Engineers, Istanbul Branch.

ASM International. (n.d.). *ASM Handbook, Volume 4: Heat Treating*.

Baş, B. (2022). *Production and examination of the properties of GG25-based cast iron engine blocks* (Master's thesis).

Çoşar, B., & Aygüzer, Y. (n.d.). *Textbook of casting branch of metallurgical technology and professional technology*.

Elliott, R. (1988). *Cast iron technology*. Butterworth & Co. Ltd.

Foundry Academy TÜDOKSAD. (n.d.). *Dökme demir türlerine genel bir bakış*. https://dokumhane.net/kutuphane/dokme-demir-turlerine-genel-bir-bakis/

Şen, N. B. (2018). *Investigation of the mechanical, metallurgical, and economic effects of metallurgical silicon carbide and ferro silicon additives on the material in the production of lamellar graphite cast irons* (Master's thesis).

Yenici, B. S. (Yıl). *Heat treatment of gray and ductile cast irons* (Master's thesis).

METALLURGY AND MATERIALS ENGINEERING

Composite and Polymer Materials

Corrosion and Wear

Energy Materials

Extractive Metallurgy

Mechanical Metallurgy

Metals and Alloys

Surface Treatment and Coatings

Precious Metal (Au, Pd, Pt, Rh) Recovery Using Torrefied Biomass Species Such As Forest, Marine And Agricultural Biomass

Cansu Kargı[a], Mahmut Ercan Açma[a], Hanzade Haykırı Açma[b], Nil Özbek[b], Serdar Yaman[b]

[a]Istanbul Technical University, Metallurgical &Materials Engineering Department,Chemical & Metallurgical Engineering Faculty, 34469, Maslak, Istanbul, Turkey
[b]Istanbul Technical University, Chemical Engineering Department, Chemical & Metallurgical Engineering Faculty, 34469, Maslak, Istanbul, Turkey
kargic@itu.edu.tr

Keywords: Biomass, Adsorption, Metal-Alloy, Precious Metal Removal.

Aim

The recovery of precious metals using biomass is of great environmental and economic importance. While traditional mining methods cause environmental pollution due to high energy consumption and toxic chemicals, the use of biomass enables the recovery of heavy metals and valuable elements through biological processes without harming nature.[1] Precious metals such as gold, platinum and palladium found in electronic waste (e-waste), mining waste and industrial waste can be recovered using biomass.

While traditional methods require large amounts of energy and chemicals, biomass-based methods are inexpensive and more energy efficient. Metal ion recovery can be achieved by utilising the metal adsorption capacity of natural organisms. Therefore, the recovery of precious metals from biomass has great potential in terms of both environmental sustainability and economic value creation.(Wang, S., & Chen, C. (2006)

In this study, the recovery behaviour of precious metals from refinery solutions using different biomasses was investigated.

The recovery of precious metals from industrial and electronic waste streams has gained increasing attention due to the scarcity and high economic value of these elements. Biomass-derived sorbents offer a sustainable and cost-effective alternative for the selective adsorption of precious metals from aqueous solutions. (Veglio, F., & Beolchini, F. (1997).)

This study aims to explore the potential of torrefied biomass materials in the recovery of gold (Au), platinum (Pt), palladium (Pd), and rhodium (Rh) from solution, with a focus on optimizing torrefaction conditions and adsorption parameters..

Material and Method

Biomass has started to be used not only as a fuel and energy source, but also as an alternative material in various fields of use, due to its features such as having great potential, being renewable and sustainable, and being carbon-neutral. The torrefaction process applied in this context is carried out by heating the biomass to a temperature range of 200-300°C in an airless environment. As a result of this process, some changes occur in the biomass structure. While hemicellulosics are degraded, other macromolecules such as cellulose and lignin are hardly affected. In addition, the biomass changes from hydrophilic to hydrophobic due to the removal of oxygen-containing functional groups. The surface area of the biomass expands somewhat and its sorptive capacity improves. In this study, the recovery of precious metals (gold, platinum, palladium, rhodium) from solution was tested by using various biomass materials including forest biomass, marine biomass and agricultural wastes that had undergone torrefaction. Namely, corn waste as agricultural biomass, rhododendron as forest biomass, algae samples were used as marine biomass. In this context, some of the parameters that need to be controlled during both biomass sample preparation and metal retention were examined. Of which, the torrefaction temperature and the exposure time at the final torrefaction temperature accounted for the parameters relevant during the preparation stage of

biomass samples. Besides, the parameters that investigated during the metal retention included temperature, stirring speed. In this way, adsorption capacities of torrefied biomass samples toward Au, Pt, Pd, Rh were determined. Effects of the mentioned parameters on the metal recovery from solution were discussed and the optimum conditions were specified. Statistical analysis was also employed to understand the effectiveness of the individual parameters on sorption capacities. Concentration of these metals were examined by ICP technique. To enhance the sorption capacity of biomass, torrefaction was applied to different biomass sources, including forest biomass (rhododendron), marine biomass (algae), and agricultural waste (corn waste). The torrefaction process involved heating biomass in an oxygen-free tube furnace at temperatures between 200 and 300°C. This treatment altered the physicochemical properties of the biomass by increasing its hydrophobicity and modifying its surface structure, making it more suitable for metal adsorption.

For instance, Sharma et al. (2013) demonstrated that up to 85% of gold (Au) ions could be recovered using Spirulina platensis microalgae Likewise, modified corn stalks have been reported to selectively adsorb palladium (Pd) ions with high efficiency (Zhang, L., Wang, Y., & Zhao, J. (2019). In another study, torrefied biomass derived from forest residues showed promising results for the recovery of rhodium (Rh) ions, attributed to its increased surface porosity and carbon content(Lee, K., Oh, M., & Park, J. (2021).)

Key experimental parameters were assessed at two stages: biomass preparation and metal adsorption. During biomass preparation, torrefaction temperature and exposure time were varied to determine their influence on sorption efficiency. In the metal adsorption stage, factors such as temperature and stirring speed were optimized to enhance the recovery rates of the target metals.

The adsorption efficiencies of the torrefied biomass samples were evaluated using Inductively Coupled Plasma (ICP) spectroscopy, which measured the concentration of metals before and after adsorption. Additionally, statistical analyses were conducted to identify the significance of each parameter on metal recovery.

Biomass samples used in this study; Rhododendron, maize stalks as agricultural waste biomass sample and seaweed sample as marine biomass sample were selected.

The selected samples were kept under laboratory conditions for one week and then kept in an oven at 60 °C . After these processes, the samples were ground in a ring mill and the entire ground sample was sieved so that the grain size was less than 250 microns. To determine the thermal behaviour of the samples, thermal analyses were carried out in a nitrogen atmosphere and the torrefaction temperatures were determined from the DTG curves obtained.

The torrefaction of each sample was carried out in a horizontal tube reactor under N_2 atmosphere at specified temperatures. Solutions containing 10 ppm Au, Pt, Pd and Rh were prepared. 0.1 gram of torrefied sample was mixed with the solution by stirring in the mixer for 18 hours and then filtered. The obtained liquid portion was subjected to ICP analysis to determine the adsorption efficiency of Au, Pt, Pd and Rh on the torrefied biomasses (Figure 1). The ICP experiments were repeated twice to ensure the repeatability of the results.

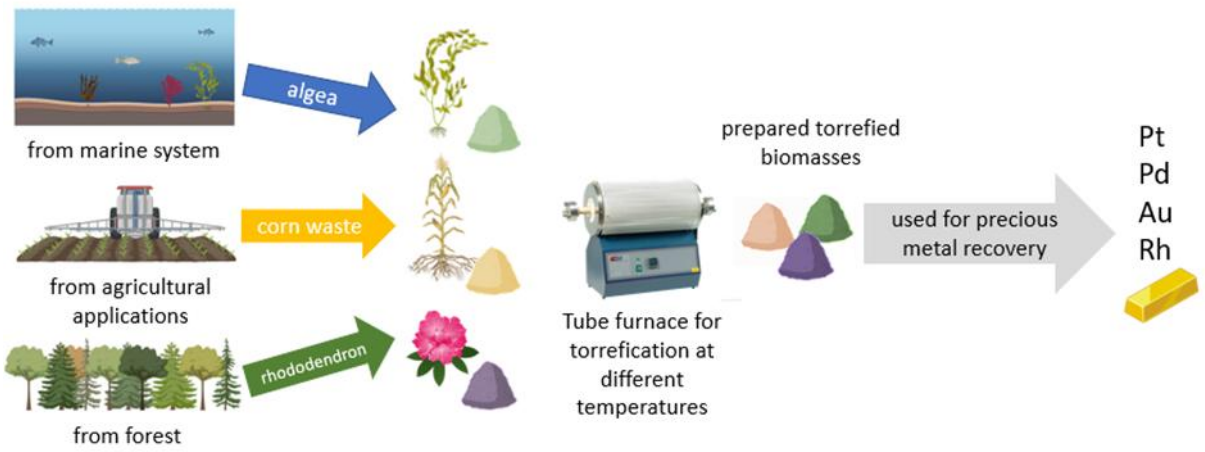

Figure 1. Graphical summary for this work.

Findings

From the samples with high yields, ICP experiments were carried out by producing semi-coke again under the specified conditions for control purposes.

The findings provide valuable insights into optimizing biomass-based sorbents for precious metal recovery and contribute to the development of environmentally friendly and economically viable methods for extracting valuable metals from solution. Future research should focus on scaling up the process and assessing the recyclability of torrefied biomass sorbents for long-term industrial applications.

The results demonstrated that torrefied biomass materials exhibited strong sorption capabilities for precious metal recovery. Nearly 99% of Au was recovered by all torrefied biomass samples, with corn waste torrefied at 200°C performing similarly to those torrefied at higher temperatures. For Pt recovery, approximately 90% was successfully removed using corn waste-based sorbents torrefied at 200°C. In the case of Pd, algae-based sorbents torrefied at 550°C showed the highest efficiency, achieving 100% adsorption. Similarly, the highest Rh recovery was observed with algae-based sorbents torrefied at 550°C. These findings suggest that torrefaction conditions and biomass type play a crucial role in optimizing metal adsorption efficiency.

Conclusion

This study highlights the significant potential of torrefied biomass as an efficient and sustainable sorbent for precious metal recovery. Torrefaction enhances the sorption properties of biomass by modifying its surface structure and hydrophobicity. Among the tested biomass sources, algae torrefied at 550°C demonstrated the highest recovery rates for Pd and Rh, while corn waste torrefied at 200°C effectively recovered Au and Pt, offering a low-energy alternative for metal recovery applications

References

Wang, S., & Chen, C. (2006). *Biosorption of heavy metals by Saccharomyces cerevisiae: A review.* Biotechnology Advances, 24(5), 427–451.
Veglio, F., & Beolchini, F. (1997). *Removal of metals by biosorption: A review.* Hydrometallurgy, 44(3), 301-316.
Sharma, A., Gupta, V. K., & Rani, B. S. (2013). *Biosorption of gold by Spirulina platensis biomass.* Bioresource Technology, 148, 63–67.
Zhang, L., Wang, Y., & Zhao, J. (2019). *Recovery of palladium from wastewater using modified corn stalk.* Environmental Science and Pollution Research, 26(7), 6781–6790.
Lee, K., Oh, M., & Park, J. (2021). *Torrefied biomass as adsorbent for rhodium recovery from acidic solution.* Journal of Hazardous Materials, 412, 125226.

Effect of Heat Treatment on Inconel 718 Superalloy Produced by Cold Spray Additive Manufacturing

Serra Bayram[a], Erdem Balcı[a], Aptullah Karakaş[b], Murat Baydoğan[a]

[a]Istanbul Technical University, Faculty of Chemical and Metallurgical Engineering, Department of Metallurgy and Materials Engineering, Türkiye
[b]Repkon Makine ve Kalıp Sanayi ve Ticaret Anonim Şirketi, Türkiye
bayrams17@itu.edu.tr

Keywords: Inconel 718, Cold Spray Additive Manufacturing, Heat Treatment.

Aim

Inconel 718 is an nickel-based superalloy with a wide range of applications in the gas turbine engines and aerospace industry, due to its ability to withstand temperatures up to 650 °C (Thomas et al., 2006). Conventionally, the production of the alloy has been accomplished through casting, forging and rolling. However, alternative methods have also been employed in recent years. The most current of these alternative methods is the cold spray method (Garfias et al., 2025). Initially employed in surface coating technology, the cold spray method has evolved to play a pivotal role in additive manufacturing, facilitating the production of Inconel 718 alloy. The method involves the successive application of layers through spray deposition, resulting in the formation of new layers as the process progresses. This process is conducted at supersonic speeds and low temperatures, ensuring preservation of the initial microstructure of the base material. The deposition process is thus repeated until desired form of the final part is achieved. It should be noted that no melting or sintering stage is incorporated. In alternative additive manufacturing methods, the material is melted and deposited in layers, and is exposed to elevated temperatures. This results in residual stresses being induced in the material. Furthermore, these alternative additive manufacturing methods are not compatible with heat-sensitive materials (Yin et al., 2018). Inconel 718 alloy, produced by conventional casting and forging methods, exhibits superior mechanical properties in comparison to material produced exclusively by cold spray additive manufacturing. The application of secondary processes, such as hot isostatic pressing and heat treatment, serves to enhance these lower mechanical properties. The cold spray process is applied layer by layer without melting, thus enabling the creation of a microstructure with high porosity due to its inherent nature. It has been demonstrated that the reduction of porosity in base materials characterized by high porosity values can be achieved through the application of specific heat treatments (Assadi et al., 2011). These heat treatments are also implemented with the objective of enhancing corrosion resistance. The precipitation hardening mechanism is responsible for the formation of phases such as γ' ($Ni_3(Al,Ti)$) and γ'' (Ni_3Nb), resulting in enhanced strength.

Material and Method

Inconel 718 sample, utilized as the substrate in the study, was produced by cold spray additive manufacturing method. The sample produced by the cold spray process was subsequently subjected to a heat treatment process at 1200 °C for 2 h. Hardness and Archimedes density measurements were conducted prior to and following the heat treatment process. Samples were prepared from the cross sections prior to and following the application of heat treatment. Porosity measurements were performed on the polished microstructure by using point counting method. Subsequently, the samples were subjected to etching with a waterless Kalling solution comprising 2 grams of $CuCl_2$, 40 ml of HCl, and 60 ml of ethanol. Subsequent analyses were performed on the etched samples, employing both an optical microscope and a scanning electron microscope (SEM). Electron microscopy analyses were performed using energy dispersive x-ray spectroscopy (EDS) and mapping methods.

Findings

When the microstructure of Inconel 718 sample was examined, a layer-by-layer formation was observed in the microstructure. This observation is attributed to the nature of the cold spray additive manufacturing production method. Porosity measurements made on the microstructure after the heat treatment showed a decrease in porosity fractions compared to before the heat treatment. The porosity fraction in the sample produced only with cold spray additive manufacturing is 1.25%, and in the sample with the heat treatment process is 0.07%. This indicates the effectiveness of the heat treatment at 1200 °C in minimizing the porosity level. As illustrated in Figure 1, the cross-sectional optical microscope images of etched samples are presented, both prior to and following the application of the heat treatment.

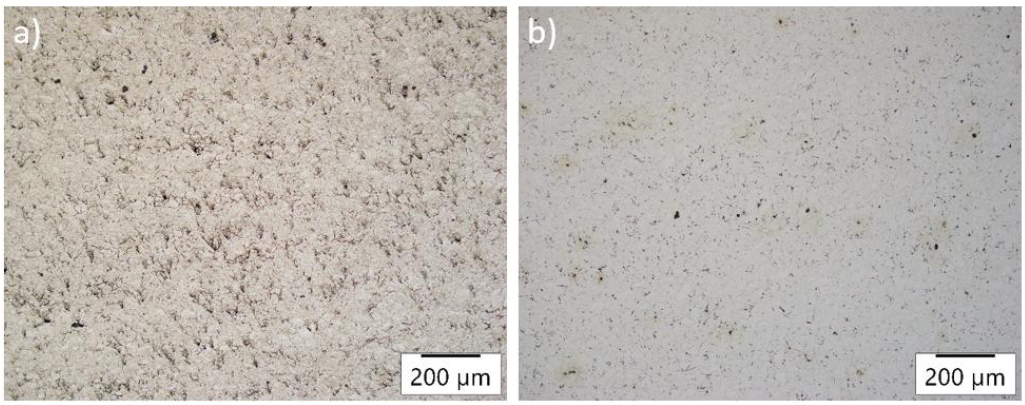

Figure 1. Cross-sectional optical microscope images of the etched samples a) before and b) after the heat treatment.

As illustrated in Figure 2, the images obtained from the SEM analyses prior to and following the heat treatment process are displayed. The microstructure of the samples revealed the presence of both grain formation and the formation of annealing twins. The presence of titanium nitride (TiN) phases was determined both prior to and following the process of the heat treatment.

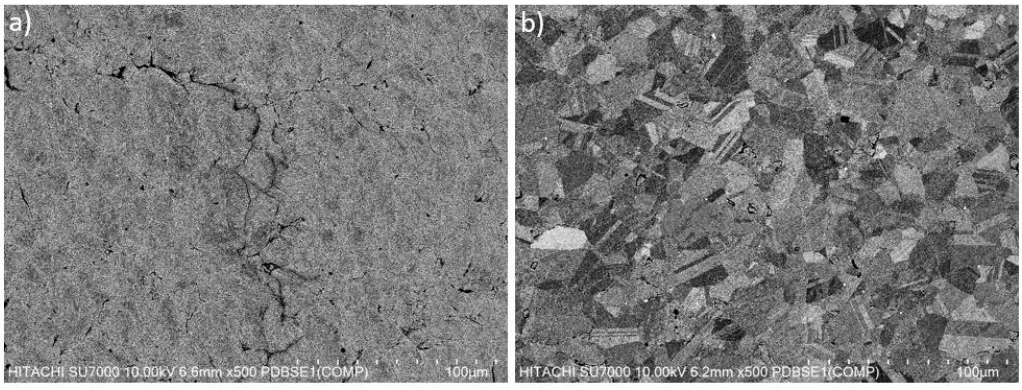

Figure 2. a) Before b) after the heat treatment SEM analysis images of Inconel 718 alloy produced by cold spray additive manufacturing.

Furthermore, the SEM mapping analysis of the region of the grain boundaries in Figure 3 determined the presence of Nb and Mo-rich phases precipitated along the grain boundaries.

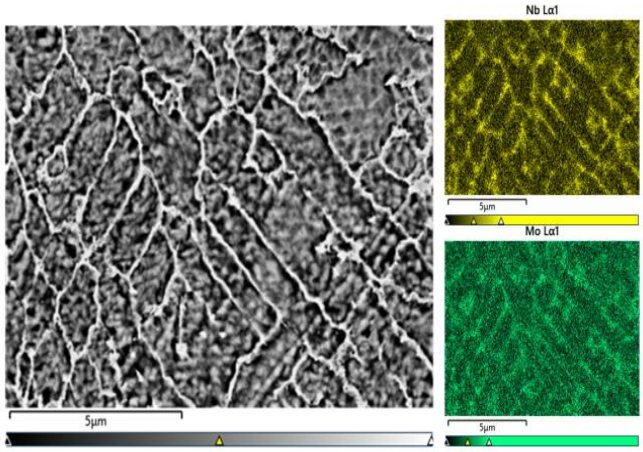

Figure 3. SEM Mapping analysis of Inconel 718 alloy produced by cold spray additive manufacturing after the heat treatment process.

Conclusion

A SEM examination was conducted prior to the application of heat treatment, which revealed a highly porous and hollow microstructure. Intergranular segregation was observed between layers. The heat treatment process led to a decrease in the porosity, thereby enhancing the microstructural properties of the base material. In comparison to the material that underwent no heat treatment and possessed higher porosity values, the material could demonstrate enhanced oxidation resistance. Annealing twins, as observed in the microstructure subsequent to the heat treatment, have a potential to enhance strength and improve creep strength. This can be attributed to the partial prevention of dislocation movement. The presence of Nb and Mo-rich phases at the grain boundaries was observed to be more prevalent than the Laves phases detected in the Inconel 718 microstructure. The precipitation of Laves phases in a controlled manner has been shown to impede grain boundary sliding and augment the high-temperature strength to a certain extent. However, these phases are known as hard and brittle intermetallic compounds, which have a detrimental effect on ductility and toughness of the material when their percentage in the microstructure and grain boundaries is excessive. Laves phases can be minimized by an ageing processes following a homogenization heat treatment. The ageing processes ensure that the Nb element precipitates as γ" (Ni_3Nb) and mechanically increases the strength of the material.

References

Assadi, H., Schmidt, T., Richter, H., Kliemann, J. O., Binder, K., Gärtner, F., Klassen, T., Kreye, H. (2011). On parameter selection in cold spraying. Journal of thermal spray technology (Vol. 20, pp.1161-1176).

Garfias, A., Kindermann, P., Vaz, R. F., Albaladejo-Fuentes, V., Sánchez, J., Ünsal, I., Schlick, G., Cano, I. G. (2025). Repair of Inconel 718 parts by Cold Spray Additive Manufacturing: The effect of substrate preheating on thick coatings properties. Journal of Alloys and Compounds (Vol. 1010).

Thomas, A., El-Wahabi, M., Cabrera, J. M., & Prado, J. M. (2006). High temperature deformation of Inconel 718. Journal of Materials Processing Technology (Vol.177, pp.469-472).

Yin, S., Cavaliere, P., Aldwell, B., Jenkins, R., Liao, H., Li, W., & Lupoi, R. (2018). Cold spray additive manufacturing and repair: Fundamentals and applications. Additive manufacturing (Vol. 21, pp.628-650).

Effect of Niobium Addition on the Microstructural Features of Titanium Alloys for Dental Implants

Sena Burcu Hayirci[a], Faiz Muhaffel[a], Hüseyin Cimenoglu[a]

[a]Istanbul Technical University, Department of Metallurgical and Materials Engineering, Türkiye
hayirci16@itu.edu.tr

Keywords: Powder Metallurgy, Titanium, Titanium-Niobium Alloy.

Aim

Recent progress in the field of dental implants has significantly enhanced their feasibility for longer lifespan, through the development of materials that offer improved corrosion and wear resistance, biocompatibility and reduced toxicity. Metals and their alloys are particularly favored in biomedical applications due to their relatively low modulus, good fatigue strength, corrosion resistant and good biocompatibility. Despite their many advantages, titanium and its alloys cannot meet all the requirements. One of the primary limitations is their inherently low surface hardness and high friction coefficient, which leads to severe adhesive wear (Li et al., 2014; Korneva et al., 2022).

Titanium, which has allotropic transformation like Fe, Co, Zr, is in the α-Ti phase with hexagonal closed packed (HCP) structure at room temperature, while it transforms into the β-Ti phase with body centered cubic (BCC) structure above 883°C. According to the lattice structure at room temperature, Ti alloys can be classified as α, α+β and β type when alloying element are added. The alloying elements of titanium are classified as neutral, α-stabilizers and β-stabilizers according to their effects on the transus temperature. Neutral elements (Sn, Zr) have little effect on the transus temperature, while α-stabilizers (Al, O, N, C) shift the α phase field to higher temperatures and β-stabilizers (Mo, V, Ta, Nb) shift the β phase field to lower temperatures (Kaur and Singh, 2019; Peters et al., 2003).

Ti-6Al-4V, one of the most commonly used titanium alloys has prompted the search for alternative compositions due to concerns over the potential toxicity of aluminum and vanadium, as well as its relatively high elastic modulus. Compared to other β-phase stabilizers such as Ta, Zr, Nb offers superior biocompatibility (Ibrahim et al., 2022; Han et al., 2015).

Titanium and its alloys have a protective, inert oxide layer on the surface at room temperature. Increasing the thickness of this oxide layer, which contributes to the surface properties of the material, results in an increase in chemical, physical and mechanical properties. Methods such as anodization, micro-arc oxidation and thermal oxidation can be used for controlled oxide layer applications. The increase in corrosion and wear resistance and hardness in the coating obtained as a result of micro arc oxidation and the low cost and equally effective method of thermal oxidation bring these two methods to the forefront in thick oxide layer formation methods (Velten et al.,2002; Wilks et al., 2009).

This study aims to investigate the effect of varying Nb content (x = 0, 23, 45 wt.%) on the microstructure of the sintered Ti-xNb. The objective is to developed materials with improved hardness and wear resistance while ralso evaluating the role of Nb in modifying the alloy's microstructural characteristics and mechanical performance.

Material and Method

In this study, the spherical Ti and Nb powders (Alfa Aesar, 99% purity, ≤45μm) were weighted for different ratios Ti-xNb (x = 0, 23, 45 Nb wt.%), and samples were produced by powder metallurgy. The mixtures were mixed in a turbula mixer for 1 hour for a homogeneous distribution. The powder mixtures were pressed in a 13 mm mould under a pressure of 370 MPa with a uniaxial press (MSETMMP 0710). The green bodies were sintered in a tube furnace (ProthermPTF17/75/300) under argon gas for about 1 hour at 1400°C.

Archimedes' densities were measured. The phase composition of sintered samples was investigated by X-ray diffractometer (XRD, X'Pert PRO PANalytical). The analysis conditions were Cu-Kα radiation at 35 kV and 40 mA with the range of 20°- 80° at 0.02° step size. Sample surfaces and cross-sections were examined with light optical microscopy (OM, Nikon Eclipse L150) and Scanning electron microscopy (SEM, Hitachi TM-1000) for higher magnifications. Mechanical characteristics of the specimens were evaluated with Vickers hardness (TUKON 1102) and wear test (Tribotech Oscillating Tribotester). For Vickers hardness assessment, 100 g load was applied. The reciprocating wear test were carried out x1.5 simulated body fluid (SBF) environment at 37°C. The counter face was chosen as 6 mm diameter alumina ball and ball's amplitude and sliding speed were 2mm, 6mm/s under 1N for a total sliding distance of 50m. After the wear tests, wear tracks formed on the samples were examined by using EDS equipped SEM (SEM, Hitachi TM-1000) and 2-D surface profilometer (Veeco Dectac 6 M). Also, the contact surface of the counter face balls was examined by OM.

Findings

Archimedes' densities are measured for Ti, Ti-23Nb and Ti-45Nb. Archimedes' and theoretical densities and % porosity can be seen in Table 1. Because niobium has a higher density than titanium, theoretical and Archimedes' densities are increased by Nb addition, as shown in Table 1. Porosity calculation based on theoretical and Archimedes' density measurements indicates porosity increasing with Nb addition due to the slow diffusion rate of niobium compare to titanium.

Table 1. Archimedes' density, relative density and porosity values of the sintered samples.

	Ti	Ti-23Nb	Ti-45Nb
Theoretical density (g/cm^3)	4.51	5.32	6.08
Archimedes' Density (g/cm^3)	4.24 ± 0.05	4.72 ± 0.11	4.85 ± 0.20
Porosity (%)	5.98	11.23	20.23

XRD phase analysis shows only α-Ti peaks for Ti. XRD pattern of Ti-23Nb indicates both α-Ti and β-Ti peaks. After %45 weight Nb addition β-Ti phase stabilized in the microstructure. The phase ratios calculated by the Rietveld method for Ti 23Nb were 41.2 wt% α-Ti and 58.8 wt% β-Ti. This value corresponds to 59.3 vol% β-Ti.

SEM images of Ti-xNb (x= 0, 23, 45 Nb wt%) were given in Figure 1. SEM images confirmed porosity increase as the result of Nb addition. By using ImageJ software based on different SEM images of Ti-23Nb β-Ti calculated 59.18 ± 1.3 % vol. Moreover, while α-Ti seen in Ti, β-Ti was seen in Ti-45Nb and β-Ti coexisted with α-Ti in Ti-23Nb.

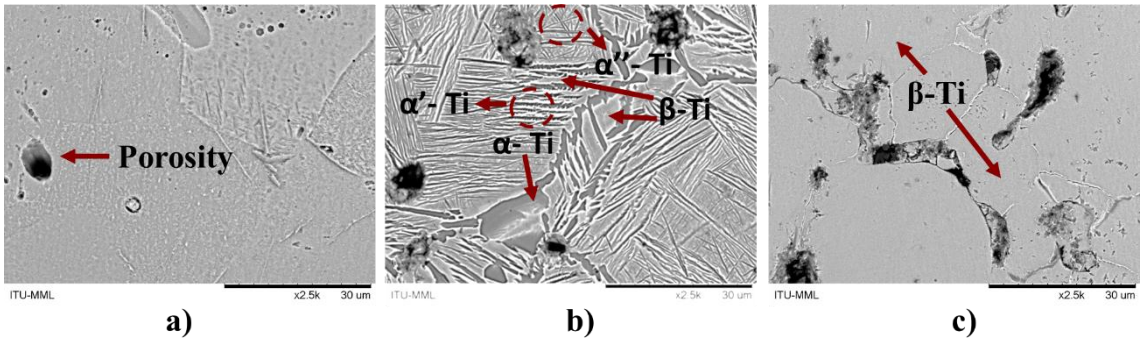

Figure 1. SEM micrographs of a) Ti, b) Ti-23Nb and c) Ti-45Nb samples.

Vickers' Hardness of the samples are measured as 315, 357 and 205 HV0.1 for Ti, Ti-23Nb and Ti-45Nb, respectively. It is suggested that the α"-Ti increased the hardness for Ti-23Nb. Because of β -Ti is more ductile compare to Ti, the lowest hardness was measured in Ti-45Nb, as 205 HV0.1.

The tribological performance of Ti, Ti-23Nb and Ti-45Nb alloys has been conducted in 1.5× SBF solution. The results showed a clear correlation between increasing Nb content and deteriorating wear resistance in Ti. In particular, the volumetric wear loss values increased from about 2.1×10^{-3} mm³ for Ti to 9.4×10^{-2} mm³ for Ti-45Nb, indicating a more than 40-times increase in material loss with 45 wt% Nb. The average coefficient of friction increased from ~0.3 (Ti) to ~0.4 (Ti-23Nb) and reached ~0.65 (Ti-45Nb); Ti-45Nb also exhibited more irregular and unstable friction behavior.

Optical and SEM analyses revealed a progression in wear mechanisms from mild adhesive wear in Ti to severe adhesive and abrasive wear in Nb-containing alloys, with Ti-45Nb showing the largest and most damaging wear scars, wide grooves and material delamination.

Conclusion

In this study, Ti-xNb (x = 0, 23, 45 Nb wt%) sintered at 1400°C was characterized from the view of the Nb addition effects on the microstructure, and the main findings are as follows:

• An increase in porosity was observed with the addition of Nb, and this increment was confirmed by SEM images. The higher porosity leads to a reduction in the modulus of elasticity. Nb addition reduces the elastic modulus in Ti (~110 GPa), and the elastic modulus approaches the elastic modulus of bone tissue (10-30 GPa).
• XRD results confirm that the β phase is stabilized by the addition of Nb, which is a β stabilizer.
• Nb addition slightly increase the hardness of Ti-23Nb and further addition of Nb led to a higher fraction of β-Ti in the microstructure and a reduction in hardness. While the hardness of the Ti was ~315 HV 0.1, the hardnesses of Ti-23Nb and Ti-45Nb alloys measured as ~357 HV0.1 and ~ 221 HV0.1, respectively.
• Ti-xNb alloys exhibited adhesive wear as the dominant mechanism, with the intensity of this wear increasing proportionally to the niobium content in the alloy.

Consequently, while increased Nb content adversely affects the wear resistance and frictional behavior of Ti alloys in their untreated state, surface modifications such as thermal oxidation and micro-arc oxidation can effectively overcome these limitations and enable the use of β-Ti alloys in applications where both mechanical compatibility and wear resistance are critical.

Acknowledgement

The authors would like to express their acknowledgements to Batuhan Sorusbay and H. Ozkan Gulsoy for the production of Ti-Nb alloys. Also, authors would like to thank Res. Ass. Mertcan Kaba for support.

References

Ibrahim, M. K., Kaba, M., Muhaffel, F., Ağaoğulları, D., & Cimenoglu, H. (2022). Thermal oxidation of a porous Ti23Nb alloy for wear related biomedical applications: Effect of oxidation duration. *Surface and Coatings Technology*, 439, 128429.

Kaur, M., & Singh, K. (2019). Review on titanium and titanium based alloys as biomaterials for orthopaedic applications. *Materials Science and Engineering: C*, *102*, 844-862.

Korneva, A., Straumal, B., Gornakova, A., Kilmametov, A., Gondek, Ł., Lityńska-Dobrzyńska, L., ... & Zięba, P. (2022). Formation and thermal stability of the ω-phase in Ti–Nb and Ti–Mo alloys subjected to HPT. *Materials*, *15*(12), 4136.

Li, Y., Yang, C., Zhao, H., Qu, S., Li, X., & Li, Y. (2014). New developments of Ti-based alloys for biomedical applications. *Materials*, *7*(3), 1709-1800.

Peters, M., Hemptenmacher, J., Kumpfert, J., & Leyens, C. (2003). Structure and properties of titanium and titanium alloys. Titanium and titanium alloys: fundamentals and applications, 1-36.

Velten, D., Biehl, V., Aubertin, F., Valeske, B., Possart, W., & Breme, J. (2002). Preparation of TiO2 layers on cp-Ti and Ti6Al4V by thermal and anodic oxidation and by sol-gel coating techniques and their characterization. *Journal of Biomedical Materials Research: An Official Journal of The Society for Biomaterials and The Japanese Society for Biomaterials*, 59(1), 18-28.

Wilks, R. G., Santos Jr, E., Kurmaev, E. Z., Yablonskikh, M. V., Moewes, A., Kuromoto, N. K., & Soares, G. A. (2009). Characterization of oxide layers formed on electrochemically treated Ti by using soft X-ray absorption measurements. *Journal of Electron Spectroscopy and Related Phenomena*, 169(1), 46-50.

Recycling-Driven Variations in Mechanical Properties and Weldability of 6XXX Series Aluminium Alloys for Electric Vehicle Structural Parts

Zeynep Tutku Özen[a], Necip Ünlü[a]

[a]Istanbul Technical University, Metallurgical and Materials Engineering, Türkiye
ozenz@itu.edu.tr

Keywords: 6xxx Alloy, Aluminium, Mechanical Properties, Recycling, Welding.

Aim

Aluminium alloys especially 6xxx series, are widely preferred in structural parts of electric vehicles (EV) due to their high specific strength, corrosion resistance and recyclability. The European Commission (EC) has determined Critical Raw Materials (CRM) which means Europe is depended to other continents for their supply and yet CRMs have emerged to be recycled. Bauxite which is the primary ore of aluminium, magnesium (Mg) and silicon (Si) which are the main alloying elements of 6xxx aluminium alloys are stated in the CRM list of EC. To balance CRMs usage in EVs, 2 solutions can be adapted. The first one is to limit usage of CRMs (6111 alloy development), and the second one is to recycle what has already existed. In this work, both approaches have been studied and compared with the performances of the alloys produced without recycling.

Material and Method

In this study, 6063 and 6082 alloys are selected for EV structural part production. They have been produced using both primary feedstock and post-consumer scraps. Post consumer scraps in this study have been separated from waste first by eddy-current separator and then with Multi Pick system which enables separation of aluminium alloys with respect to their main alloying elements using Laser Induced Beam Spectrometer (LIBS) technology. As an alternative for these alloys, 6111 alloys have been developed. Figure 1 shows industrial production steps of the extrusion profiles of EVs structural parts.

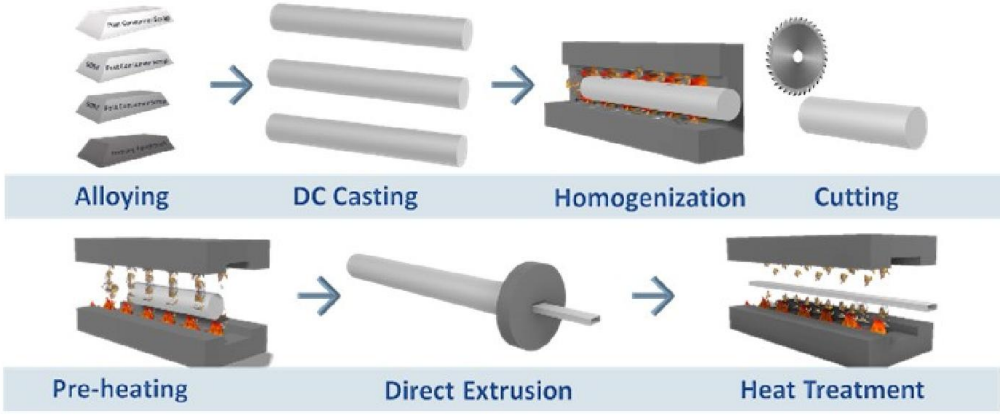

Figure 1. Process flow-chart for 6xxx aluminium alloy production.

Production route started using post-consumer scraps, primary aluminium and alloying elements. Table 1 demonstrates used feedstock for each alloy production.

Table 1. Feedstock Content.

	6063-C	6082-C	6063-R	6082-R	6111
Post-Consumer Scrap	0	0	16%	34%	0
6063 PC Scrap	0	0	54%	12%	0
6082 PC Scrap	0	0	0	44%	0
Primary Feedstock	100%	100%	30%	10%	100%

Determined feedstocks have been melted in a prototype casting furnace with 500 kg capacity and then direct chill (DC) cast into billets. Billets have been homogenised in Hertwich Batch Type Furnace. 6111 billets have been heated up to 540 °C in 7 hours and kept in this temperature for another 7 hours. 6082 billets are heated up to 555 °C in 6 hours and kept for another 6 hours. 6063 billets are heated to 570 °C in 6 hours and kept for another 6 hours. Homogenised billets are cut into length (850-1050 mm) that can be fed into 29 MN extrusion press. Pre-heating is applied to cut billets. 6111 extrusion is applied in 490°C induction heat with 4,5 mm/s speed having 538°C exit temperature 6082alloys extrusion is applied in 490°C induction heat with 5,1 mm/s speed having 533°C exit temperature. 6063 alloys Extrusion is applied in500°C induction heat with 7,5 mm/s speed having 556°C exit temperature. After the Extrusion procedure, T5 heat treatment has been applied. Profile samples are prepared for investigation using Struers Secotom-15 cutting equipment. After that they have mounted to the bakelite. Struers Tegramin-30 grinding equipment is used to complete sample preparation. Samples are chemically analyzed using Thermo fischer Optical Emission Spectrometer. ZwickRoell Z050 Tensile Testing Equipment is used for anisotropy, bake paint and plate bending tests. Anisotropy tests are carried out with respect to EN ISO 6892-1:2020 in room temperature. Bake paint tests are applied to the specimens with respect to EN ISO 6892-1:2020 standard after exposing 180°C for 20 minutes. Plate bending tests were conducted according to the VDA 238-100 standard. Following this standard, bending test specimens were prepared with dimensions of 30x60mm. Roller spacings used in the test were adjusted to be twice the sample thickness, and bending tests were performed using the specified punch as outlined in the standard. In the test procedure, a preload of 30N was applied, with a test speed set at 20 mm/min. The drop-in force was defined as 60N, meaning that the test was halted when there was a deviation of this magnitude in the applied force. Finally, Tungsten Inert Gas (TIG) welding is applied to profiles joining. Welding speeds of 8 – 8,5 and 9 m/min have been applied to the samples. Welding zones are investigated via Optical microscope of Zeiss Axio Imager and hardness test is applied. Figure 2 demonstrates the used equipments and the experimental loop of the study.

Figure 2. Schematic representation of the experimental setup, including the equipment used and the experimental loop.

Findings

The Table 2 demonstrates the results of the OES analysis where "C" stands for conventional production using no scrap and "R" stands for alloys produced with recycling content. All alloys are validated with respect to EN 573-3 standard.

Table 2. Chemical Compositions of the Alloys measured by OES.

	Si	Fe	Cu	Mn	Mg	Cr	Ni	Zn	Pb	Ti
6063-C	0,559	0,219	0,03	0,041	0,561	0,012	0,01	0,031	0,004	0,02
6082-C	0,849	0,235	0,075	0,545	0,861	0,02	N/A	0,04	N/A	0,02
6063-R	0,648	0,265	0,075	0,103	0,502	0,015	0,01	0,063	0,0047	0,021
6082-R	0,869	0,227	0,071	0,535	0,879	0,05	N/A	0,045	N/A	0,038
6111	0,672	0,156	0,872	0,246	0,681	0,002	N/A	0,008	N/A	0,041

Anisotropy analysis results have been shown in Table 3. According to the results, the yield strengths of 6063 alloys decrease from parallel to perpendicular direction. While the yield strength of the 6082 alloys increases from the direction of 0° to 90° while it shows lowest value at 45°.

Table 3. Anisotropy results obtained from tensile test.

	Angle	Rp0,2 [MPa]	Rm[MPa]	A (%)
6063-C	0	218	247	12,2
6082-C	0	264	296	13,7
6063-R	0	244	270	13,16
6082-R	0	267	293	15,3
6111	0	306	326	10
6063-C	45	210	239	5,2
6082-C	45	261	288	8,2
6063-R	45	238	257	5,95
6082-R	45	264	287	9,1
6111	45	302	325	5,3
6063-C	90	238	271	6,1
6082-C	90	268	302	8,5
6063-R	90	281	321	8,9
6082-R	90	276	300	9,2
6111	90	303	324	7,6

Tensile strength of the alloys showed similar behavior with yield strengths. When the testing direction is diagonal and perpendicular to the extrusion direction, tensile strengths of the 6063 alloys are 4-5% lower than the 0°. This behavior is primarily due to the alignment of grains and precipitates along the direction of extrusion. Highest tensile strength values are achieved with testing in 0° angle for 6063 alloys. 6082alloys highest strength seen at 90° angle. The tensile strength of these alloys has decreased from 0° to 45°. The unexpected result of 6082 alloy can be explained by its high alloying rates and Cu elements have created Al_2Cu precipitates which caused directional strengthening. Comparison of the yield strengths, tensile strengths and elongation behaviors of the recycled and conventional alloys carried out. Less CRM used alloy shower highest strength properties while recycled alloys have higher than the conventional ones. The reason behind this may be explained by the chemical composition. Higher Si content yields in more Al-Si particles formation and precipitation of them increases the strength.

Table 4 demonstrates the bake paint test results. According to bake paint results it can be noticed that yield and tensile strength of both 6063 and 6082 alloys have been increased. However, the elongations of both alloys have slightly decreased.

Table 4. Bake Paint Test Results.

	Rp0,2 [MPa]	Rm[MPa]	A (%)
6063-C	258	274	12,2
6063-R	233	278	11,7
6082-R	279	306	15
6111	306	330	11

This process promotes the formation of fine, coherent precipitates (e.g., Mg_2Si in 6063 and Al_2Cu in 6082), which impede dislocation motion and enhance strength. The more significant increase in 6082 alloy can be attributed to its higher alloying content, which provides a greater potential for precipitation strengthening. The decrease in elongation after the bake-paint test is a typical consequence of increased precipitation density. While the precipitates improve strength, they also reduce the material's ability to deform plastically, leading to lower elongation. According to these results it can be discussed that the thermal treatment applied before tensile test section of bake paint test has increased the strength of the alloys. As characteristics of aluminium alloys, one can notice that these alloys have converged to the peak age aging condition. Recycling content has caused increased strength but decreased elongation because of increased precipitation hardening mechanisms in the microstructure. Table 5 shows the plate bending results. It can be noticed that all the alloys have passed the target value. Comparisons were made by considering a minimum bending angle of 90° for the 6082 and 6111 alloys, and a minimum of 120°C for the 6063 alloy. The obtained results exhibit satisfactory performance compared with mechanical properties.

Table 5. Plate Bending Test Results.

	α	Target	Thickness	Result
6063-C	88°	120°	4,3	124°
6063-R	124°	120°	3,8	124°
6082-R	65°	90°	3,7	92°
6111	67°	90°	4,3	95°

Figure 3 demonstrates microstructures of the welding zones. It can be seen that penetration of the welding area is more qualified in recycling content alloys. The micrographic analyses showed a good quality of the weld, in terms of throat and depth of penetration, and comply with the required standards. The presence of porosity appears to be marked but still does not affect the weld's resistant section. The hardness measured showed consistent values throughout all the welding samples. The Heat Affected Zone (HAZ) showed values in the range of 73-75 HB, while the weld itself is 63-65 HB.

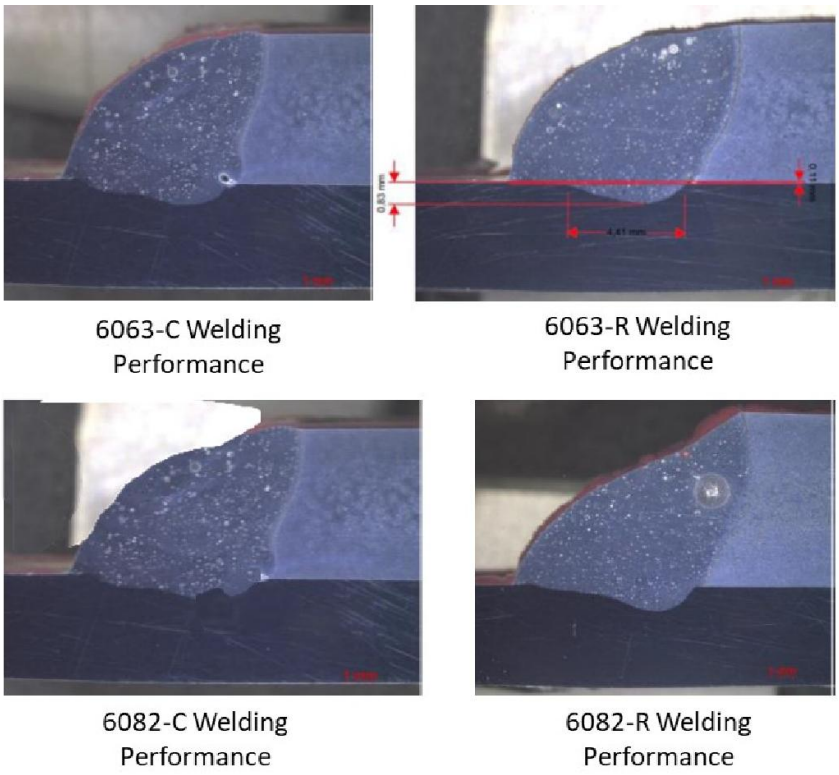

Figure 3. Weld Zone Investigation via Optical Microscope.

Conclusion

The In this study, comprehensive mechanical characterization of three distinct alloys (6063, 6082, and 6111) produced via DC casting method was conducted. Their chemical compositions were determined through the OES method. Subsequently, the billets were extruded and transformed into final shapes. After extrusion, profiles were subjected to quenching and subsequent artificial aging to attain the T5 temper condition. Tensile and bending tests were conducted in accordance with EN standards to assess the performance of the profiles. Additionally, bake paint test was conducted to comprehend the thermal stability of the profiles. Considering the directional alignment of grains during the extrusion process, investigations into their anisotropic behavior were also conducted. Evaluation of all results reveals that the mechanical performance of the material is in good accordance with European standards. To sum up, the mechanical properties, elongation percentage, bending values, thermal stability, and microstructure performance obtained after productions using recycled materials within the study are comparable and similar to standard productions.

References

Automobile standards, VDA 238–100, (2017). Test Specification: Plate Bending Test for Metallic Materials

Billy, R. G., Muller, D. B. (2023). Aluminium use in passenger cars poses systemic challenges for recycling and GHG emissions. Resources, Conservation and Recycling, 190, 106827.

Bonatti, R. S., Rodrigues, J. F., Peixoto, L. C., Baldo, R. F., Bortolozo, A. D., & Osório, W. R. (2023). Anisotropic tensile and compressive strengths of al-4WT.%Cu alloy powder: Part 2- effect of dendritic arm spacings. Metals, 13(7), 1282.

European Norm, International Organization for Standardization. (2020). Metallic materials - Tensile testing (EN-ISO 6892-1: 2020)

Ozen, Z.T. et al.; (2024). Enhancing Recycling Efficiency and Critical Raw Material Substitution in 6xxx Alloys; Production with Respect to Their Extrusion Feasibility and Mechanical Properties. In: Wagstaff, S. (EDS) Light Metals 2024. TMS 2024. The Minerals, Metals, Materials Series. Springer, Cham.

Turkish Standards, European Norm [TS-EN]. (2024). Aluminium and aluminium alloys - Chemical composition and form of wrought products - Part 3: Chemical composition and form of products (TS-EN 573-3).

METALLURGY AND MATERIALS ENGINEERING

Composite and Polymer Materials

Corrosion and Wear

Energy Materials

Extractive Metallurgy

Mechanical Metallurgy

Metals and Alloys

Surface Treatment and Coatings

Effect of Pack Aluminizing on Hydrogen Charging Behavior of Ti6Al4V Alloy Fabricated by Selective Laser Melting

Belgin Ataman[a], Burak Bayram[a], Erdem Balcı[a], Murat Baydoğan[a]

[a] Istanbul Technical University, Faculty of Chemical and Metallurgical Engineering, Department of Metallurgy and Materials Engineering, Türkiye
ataman17@itu.edu.tr

Keywords: Additive Manufacturing, Pack Aluminizing, Ti6Al4V Alloy, Hydrogen Charging.

Aim

The primary objective of this study is to comprehensively investigate the surface properties of Ti6Al4V alloy fabricated through Selective Laser Melting (SLM) after exposure to hydrogen charging and applying aluminizing. The study aims to analyze the microstructural changes and potential embrittlement effects induced by hydrogen absorption in the SLM-manufactured Ti6Al4V alloy, which is widely used in aerospace, biomedical, and industrial applications due to its superior mechanical strength and corrosion resistance. Furthermore, this research explores the impact of pack aluminization on the hydrogen charging behavior of the alloy. By combining optical microscope and hardness testing, this research provides a characterization of the microstructural modifications induced by hydrogen exposure and pack aluminization treatment.

Material and Method

Ti6Al4V alloy is the most commonly used commercial titanium alloy. Due to the addition of elements such as aluminium and vanadium, it possesses high strength and ductility, good corrosion resistance, and low modulus of elasticity, making it suitable for a wide range of industrial applications, especially in the biomedical, aerospace, and automotive sectors. In recent years, additive manufacturing (3D printing) has gained prominence for producing complex titanium alloy parts with minimal material waste. Additive manufacturing is a manufacturing technology where parts are produced by layering materials based on a 3D model using computer-aided CAD software and then joining these layers. Currently, three different additive manufacturing methods are in use: selective laser melting (SLM), laser metal deposition, and electron beam melting (EBM). SLM uses a high-powered laser to melt and fuse metallic powders, layer by layer, to form a 3D object. This process is particularly well-suited for titanium alloys as it offers controlling the microstructure, which directly affects the mechanical properties of the part.

Aluminizing is a process in which aluminum is deposited onto the surface of the titanium alloy in a high-temperature vacuum or gaseous environment. As a result of this process, intermetallic phases form between titanium and aluminum, significantly increasing the surface hardness and oxidation resistance of the alloy. Additionally, the aluminizing process can improve the performance of titanium alloys in high-temperature applications by enhancing their oxidation and wear resistance.

A serious problem that compromises the structural integrity of many alloys used in engineering applications is hydrogen embrittlement (HE). It refers to the deterioration of mechanical properties such as ductility, toughness, and load-bearing capacity due to the ingress and interaction of hydrogen with the metal's microstructure. Titanium alloys are extensively utilized in aerospace, biomedical, and marine applications due to their excellent strength-to-weight ratio and corrosion resistance. However, the presence of hydrogen, either during manufacturing or in service, poses significant challenges, making an in-depth understanding of HE mechanisms essential. Hydrogen charge is a process used to study issues such as hydrogen embrittlement in titanium alloys. When hydrogen diffuses into the Ti6Al4V alloy, it can induce microstructural changes that negatively affect the mechanical properties. The hydrogen charging process is essential for investigating these effects and understanding the interactions between hydrogen and the alloy.

In this study, the surface properties of Ti6Al4V alloy fabricated by the SLM method after aluminizing and hydrogen charge were investigated. For this purpose, the pack aluminizing method was employed. In this method, $AlCl_3$ powder was used as the activator, Al_2O_3 powder as the filler material, and aluminium powder as the aluminium source. After mixing these powder components, they were placed into a steel crucible, and then the Ti6Al4V alloy to be coated was immersed into the powder mixture. The pack aluminizing process was performed at 700 °C for 4 h. After the coating process was completed, the samples were cooled in the furnace to the room temperature. For comparison, as built with aluminizing and as built without aluminizing samples were subjected to the hydrogen charge process. Hydrogen charging was conducted in an electrochemical cell, where the electrolyte consists of glycerin and H_3PO_4 with a ratio of 2:1. In the cell, the cathode is a platinum sheet, and the anode is the material to be charged. Cross sectional microstructures of the samples were made by using optical microscopy. Microhardness of the samples was measured by Vickers microhardness method.

Findings

Figure 1 shows average surface and cross-section hardness values for the as built, as built charged, and as built aluminizing charged samples. The average hardness values for cross section of the as built sample was measured as 395 HV0.3. As built charged sample was measured 433 HV0.3, as built aluminized charged sample was measured 401 HV0.3. Based on these results, the cross-sectional hardness of the sample did not change significantly after the coating process. However, in the absence of coating, the cross-sectional hardness increased. The hardness of the hydride layer in as built charged sample was measured 366 HV0.3.

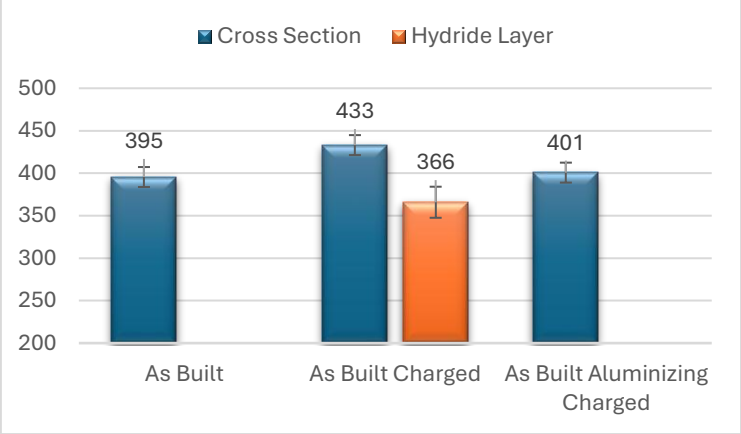

Figure 1. Vickers hardness measurements.

Figure 2 shows etched cross sectional images for as built, as built charged and as built aluminizing charged samples. According to these images, a dark layer was observed on the charged surface. It is an indication of hydrides formation in the surface region after the hydrogen charging process. On the other hand, the surface of the aluminized sample does not have a color change, possible due to enhanced resistance to hydrogen charging.

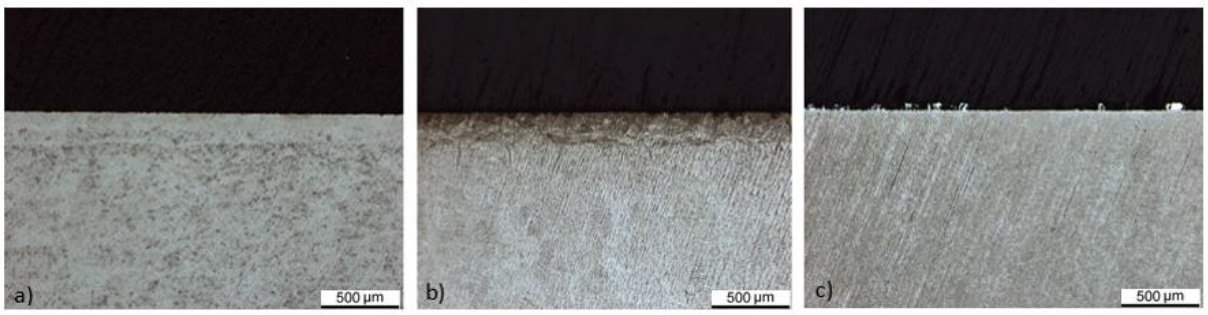

Figure 2. Cross sectional optical microscope images a) as built b) as built charged, c) as built aluminizing charged.

Conclusion

The aluminizing process involves the formation of aluminides on the surface, which enhances oxidation and wear resistance. This process also modifies the microstructure and composition of the surface. The presence of aluminium has been demonstrated to influence the diffusion and accumulation of hydrogen within the material (Zhao et al., 2007). The aluminium based coating may act as a barrier, limiting hydrogen penetration into the alloy, thereby reducing its hardening effect (Zeng et al., 2023).

The lower hardness values observed in the aluminized samples can be attributed to the aluminized layer restricting hydrogen absorption, thereby mitigating the hardening effect typically induced by hydrogen charging (Christ et al., 2000). Furthermore, phase transformations or microstructural changes occurring during the aluminizing process may contribute to the reduction in hardness. In conclusion, these results indicate that the aluminizing process, followed by hydrogen charging, leads to a noticeable reduction in hardness (Gao et al., 2024). The as built charged sample has higher hardness values than as built and aluminizing charged samples.

In summary, the aluminized coating was degraded after the charging process; however, it prevented the formation of a hydride layer. While there was no significant change in the hardness of the coated sample, an increase was observed in the cross-sectional hardness of the uncoated sample.

References

Christ, H. J., Decker, M., & Zeitler, S. (2000). Hydrogen diffusion coefficients in the titanium alloys IMI 834, Ti 10-2-3, Ti 21 S, and alloy C. *Metallurgical and Materials Transactions A*, *31*, 1507-1517.

Gao, K., Zhang, Y., Yi, J., Dong, F., & Chen, P. (2024). Overview of surface modification techniques for titanium alloys in modern material science: a comprehensive analysis. *Coatings*, *14*(1), 148.

Zhao, J. W., Ding, H., Zhao, W. J., Tian, X. F., Xiao, H. W., & Hou, H. L. (2007, October). Influences of Hydrogenation on Microstructure and Microhardness of Ti6Al4V Alloy. In *Materials Science Forum* (Vol. 561, pp. 295-298). Trans Tech Publications Ltd.

Zeng, S., & Li, F. (2023). Research status of aluminum base coating on titanium alloy. *Coatings*, *13*(9), 1525.

A Comparative Study of Ni-SiC and Micro-Arc Oxidation Coatings Produced on the Al-Si Casting Alloy

Özkan Karaman[a], Faiz Muhaffel[a]

[a] Istanbul Technical University, Department of Metallurgical & Materials Engineering, Istanbul, Türkiye
karamano17@itu.edu.tr

Keywords: Al-Si Casting Alloy, Micro-Arc Oxidation, Ni-SiC Composite Coating.

Aim

Aluminium and its alloys are widely used in automotive and aerospace industries thanks to their superior properties, such as high specific strength, excellent formability, and corrosion resistance. Moreover, they have attracted many industries owing to electrical conductivity, low thermal expansion coefficient and high thermal conductivity, which are other important properties. Among the aluminium alloys, Al-Si casting alloys are one of the most favoured alloys owing to good castability, suitability of many casting methods and having a wide strength range in addition to outstanding properties of aluminium alloys. However, application areas of Al-Si castings are limited due to their low wear resistance and low hardness. The surface properties of Al-Si casting are insufficient, especially in rotating and reciprocating sliding conditions. In order to overcome these disadvantages, various types of surface modification methods have been improved, such as conventional anodizing, hard anodizing, thermal spray coating, physical vapour deposition (PVD), chemical vapour deposition (CVD), cold spraying, nickel ceramic composite coating and micro-arc oxidation (MAO).

Ni-SiC composite coating is one of the most common electroplating coatings that enhance the tribological behaviour of Al-Si casting. The size of the coating may vary depending on applications but is commonly between 70-200 µm, and the hardness of the coating is usually between 500-600 HV. In Ni-SiC coating, Ni holds and supports SiC particles as a matrix by plating to bore surfaces. SiC particles are the reinforcement phase and provide the desired tribological properties of coating with approximately 2500 HV hardness. The size of the particles is 1-10 µm, and it forms 20% of the coating. Nikasil, the commercial name of Ni/SiC coating, has been used for several years by many automotive firms. In addition to the standard application of this coating, the presence of sulphur in the fuels can react with the nickel coating, causing corrosion and premature failure. Nikasil coating can be used when the sulphur level is low and the quality of fuel is high, as in sports car applications, but alternative coating needs have arisen.

Micro arc oxidation coating (MAO), also known as plasma electrolytic oxidation (PEO), is another electrochemical process to obtain the desired surface properties of aluminium alloys. MAO coating offers remarkable wear and corrosion resistance by forming a complex ceramic layer on the substrate. The complex layer mainly consists of aluminium oxides (α-Al2O3, γ-Al_2O_3) and mullite ($3Al_2O_3{\cdot}2SiO_2$) phases, and this layer acts as a protective layer between the base metal and corrosion environment. The oxide layer has a porous structure, which is favourable for retaining lubricant. Moreover, its oxidized layer provides superior adhesion properties compared to deposition coatings. In addition, micro arc oxidation is a enviromental friendly coating due to using non-toxic electroltyres during the process. Besides all these advantages, MAO coating is not as common as Nikasil coating on Al-Si casting on an industrial scale.

The purpose of this study is to develop an MAO process as an alternative to the Nikasil coating, which is widely used industrially on Al-Si casting alloys. There are some studies to investigate both coating separately. However there are no specific comprehensive work to compare both coatings directly. In this way, SEM and XRD analyses were conducted on MAO coatings fabricated from Al-Si casting. Further, it aims to develop an alternative coating for commercial application and examine the application of MAO to Al-Si castings.

Material and Method

Samples with the dimension of 10 mm x 10 mm x 4 mm (L x W x T) cut from the Al-Si casting alloy tensile test bar were used as the substrate for MAO coating. Prior to the MAO process, the samples were grounded by using SiC abrasive papers up to a size of P2500. Then, it was washed with ethanol and distilled water and dried at room temperature.

In this study, the MAO equipment used included a 30 kW bipolar pulsed DC power supply unit, a stainless steel electrolyte container, an air pump for mixing the electrolyte and an external cooling system. The stainless steel container served as a cathode, and samples were connected to the electrochemical cell as an anode. The electrolyte consisted of sodium aluminate, sodium hydroxide and sodium phosphate. The positive and negative voltages were selected as 450 and 100 V, respectively. The process duration was 4 min.

The samples were cut to a size of 10 mm x 10 mm x 10 mm (L x W x T) dimensions from Al-Si casting alloy, which has commercial Nikasil coating. Then, it was washed with ethanol and distilled water and dried at room temperature. The structures of both samples were characterized by using a scanning electron microscope (SEM, Hitachi TM-1000). In order to identify phases, energy dispersive X-ray spectrometer (EDX) analysis was performed on the coatings. A qualitative phase analysis of the coatings was conducted by using X-ray diffraction (XRD, X'Pert PRO PANalytical).

Findings

Surface SEM micrographs of MAO coatings fabricated on an Al-Si casting substrate are shown in Figure 1 at 500x, 1000x, 2500x and 5000x magnification. The surface of the coated samples is composed of typical morphology, including micro-pores and micro-cracks. The different sizes of pores are uniformly distributed along the surface, arising from the discharge channels which are formed during the coating process. Moreover, micro-cracks are observed on the surface. These cracks are common in MAO coatings and result from a high thermal gradient between molten oxide and cold electrolytes during the process.

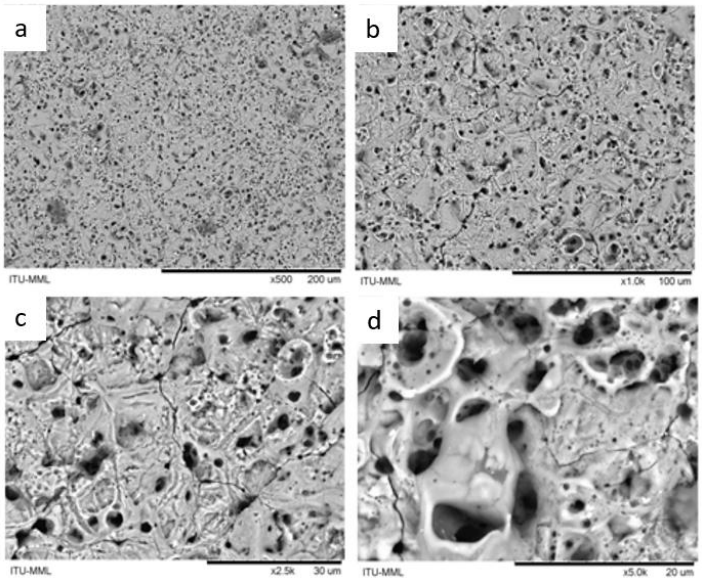

Figure 1. Surface SEM micrographs at (a) 500x, (b) 1000x, (c) 2500x, (d) 5000x magnifications.

The XRD spectra of MAO coating are shown in Figure 2. The coating was mainly composed of Al_2O_3. Aluminium and silicon peaks, which came from underlying substrates, were also observed, caused by the penetration of X-rays with the substrate material.

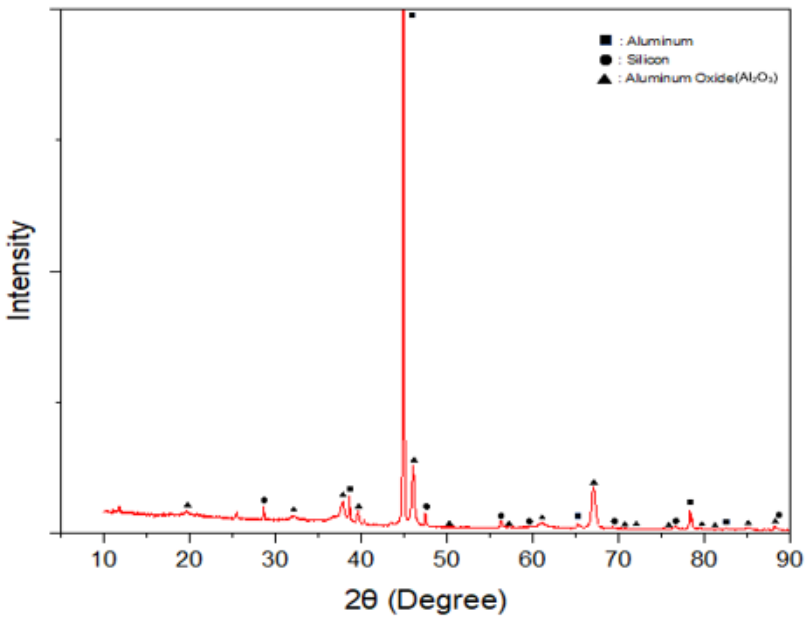

Figure 2. XRD spectrum of the MAO sample.

Conclusion

In the present study, MAO coating was successfully formed on an Al-Si casting substrate in an alkaline electrolyte. SEM analysis was conducted on the coating. It revealed that the surface of the coating had a conventional morphology, including micro-pores and micro-cracks throughout the surface, causing discharge channels during the process. Furthermore, XRD analysis was performed, and the phase of the coating was characterized. The coating layer was composed of aluminium oxide (Al_2O_3) as a main phase, and aluminium and silicon were detected from the base metal.

References

Davis, J. R. (2007). Properties and selection: Nonferrous Alloys and special-purpose materials. Metals Park, OH: ASM International.

Vargel, C. (2020). The advantages of aluminium. In Corrosion of Aluminium (pp. 9–16). Elsevier.

Kumar, R., and Dhiman, S. (2013). A study of sliding wear behaviors of Al-7075 alloy and Al-7075 hybrid composite by response surface methodology analysis. Materials and Design, 50, 351–359.

Dong, H. (2010). Surface Engineering of light alloys: Aluminium, magnesium and titanium alloys. Boca Raton, FL: CRC

Javidani, M. and Larouche, D. (2014). Application of cast al–si alloys in internal combustion engine components, *International Materials Reviews*, 59(3), pp. 132–158.

Mistry, K., Priest, M. and Shrestha, S. (2009) 'The potential of plasma electrolytic oxidized eutectic aluminium-silicon alloy as a cylinder wall surface for lightweight engine blocks', *Proceedings of the Institution of Mechanical Engineers, Part J: Journal of Engineering Tribology*, 224(2), pp. 221–229.

Jiang, B.L. and Wang, Y.M. (2010) 'Plasma electrolytic oxidation treatment of aluminium and titanium alloys', *Surface Engineering of Light Alloys*, pp. 110–154.

Enhancing CMAS and Hot Corrosion Resistance of YSZ Thermal Barrier Coatings via Aluminium Cold Spray

Ahmed Emin Tok[a], Muhammed Karabaş[b], Faiz Muhaffel[a]

[a] Istanbul Technical University, Department of Metallurgical & Materials Engineering, Istanbul, Türkiye
[b] Department of Aeronautics and Astronautics, Kırklareli University, Kırklareli, Türkiye
toka17@itu.edu.tr, mkarabas@klu.edu.tr, muhaffel@itu.edu.tr

Keywords: CMAS, Cold Spray, Corrosion, Gas Turbine, Thermal Barrier Coating.

In this study, an aluminium coating was applied using the cold spray method to enhance the CMAS and hot corrosion properties of YSZ (yttria-stabilized zirconia) thermal barrier coating (TBC) systems on a stainless steel substrate. Following the aluminium deposition, the coated aluminium will undergo thermal oxidation to form a new oxide layer. This newly formed layer is expected to play a crucial role in mitigating the detrimental effects of CMAS and hot corrosion. The investigation will focus on analysing the CMAS and hot corrosion behaviour of the system with the aluminium oxide layer in order to understand its impact on the durability and performance of the coating under high-temperature conditions. Ultimately, the goal is to improve the resistance of the material to these damage mechanisms, thereby extending the lifespan and reliability of thermal barrier coatings in industrial applications.

Aim

Thermal barrier coatings (TBC) have been widely used in the gas turbine industry for over 30 years. TBCs consist of at least three component layers. The first layer is the bond coat applied to the base material. During operation, an intermediate layer called thermally grown oxide (TGO) forms. The final layer is the ceramic top coat, which enables an increase in the operating temperature. The selected ceramic material has very low thermal conductivity, allowing for a temperature drop of up to 200 K throughout the coating [1]. Two commonly used methods for the production of thermal barrier coatings are thermal spray and EB-PVD methods. While many other methods exist, they have not yet become accepted industrial methods. Each process produces very different and distinct microstructures, each with its specific advantages and disadvantages [2]. When examining various industries, one of the most commonly used thermal barrier coatings is the yttria-stabilized zirconia (YSZ) structure. Pure zirconia (ZrO_2) has distinct characteristics, such as a high melting point (2680 ºC) and low thermal conductivity (1.6 W/mK). However, the phase transformation of zirconia between room temperature and higher operating temperatures presents a significant challenge. At room temperature, zirconia exists in a monoclinic phase, but at temperatures above 1170 ºC, it transitions to a tetragonal phase. This transformation exhibits martensitic characteristics and results in a volume increase of approximately 3-5%. This volume expansion can lead to internal stresses within the material, causing crack formation.

To prevent volume expansion, zirconia must be stabilized with the appropriate elements, most commonly using yttria (Y_2O_3). The Y_2O_3 ratio varies depending on the application and operating conditions. For example, stabilized zirconia containing 6-8% Y_2O_3 is used in high-temperature applications, such as turbine engines [3, 4]. Thermal barrier coatings (TBCs) may be subjected to three primary damage mechanisms: CMAS, hot corrosion, and thermal shock [5, 6, 7]. Protection against these damage mechanisms can provide significant benefits in terms of lifespan and efficiency. Research on aluminium coatings is ongoing. For example, Rami and colleagues observed that coatings containing aluminium oxide provide better insulation [8]. In this study, the goal is to improve the hot corrosion and CMAS behaviour of the coating using an industrial method like aluminium cold spray.

Material and Method

Initially, samples with YSZ coatings were applied to stainless steel substrates in the form of disks using thermal spray. Then, aluminium spraying was carried out using cold spray with various parameters. These parameters were determined as the spray nozzle traverse speed, powder feed rate, and spray nozzle distance. For one sample, spraying was performed at a 10 mm distance with a feed rate of 1 unit at speeds of 30 cm/min and 40 cm/min. The coating formation was then examined using optical microscopy. Afterwards, another sample was sprayed at a 10 mm distance with the same speeds (30 cm/min and 40 cm/min) but with a powder feed rate of 2 units. All process parameters used in the present study are listed in Table 1. The optical microscopy images of the coatings are present in the study. SEM and EDS analyses, along with X-ray diffraction (XRD) tests, are planned for the characterisation of the coatings. SEM and optical microscopy are planned to analyze the microstructures and alumina transformations. Subsequently, a formal investigation into CMAS and hot corrosion behaviour will be conducted.

Table 1. Experimental parameters of the cold spray process used in the present study.

Experiment No.	Powder Feed (level)	Pacing (cm/min)	Powder Size (mesh)	Spraying Distance (mm)	Pressure(bar)	Result
1	1	30	325	10	6	Discontinuous and inadequate formation
2	1	40	325	10	6	Discontinuous and inadequate formation
3	2	40	325	10	6	Discontinuous formation
4	2	30	325	10	6	Successful formation

Findings

Upon examining the surface morphologies through SEM and optical microscopy, it was observed that more distinct coating formations occurred with the parameters involving a traverse speed of 30 cm/min. Furthermore, when the powder feed rate was increased from 1 unit to 2 units, a more continuous coating was also observed. Cross-sectional analysis of the samples revealed that a traverse speed of 30 cm/min, combined with a 2-unit powder feed rate, resulted in the formation of a more continuous and thicker coating, as can be seen in Figure 1. In the process of alumina formation, thermal oxidation is planned to be applied to the coating exhibiting optimal characteristics. It is anticipated that the most continuous and homogeneous coating, after thermal oxidation, will yield the best results in terms of CMAS and hot corrosion behaviour.

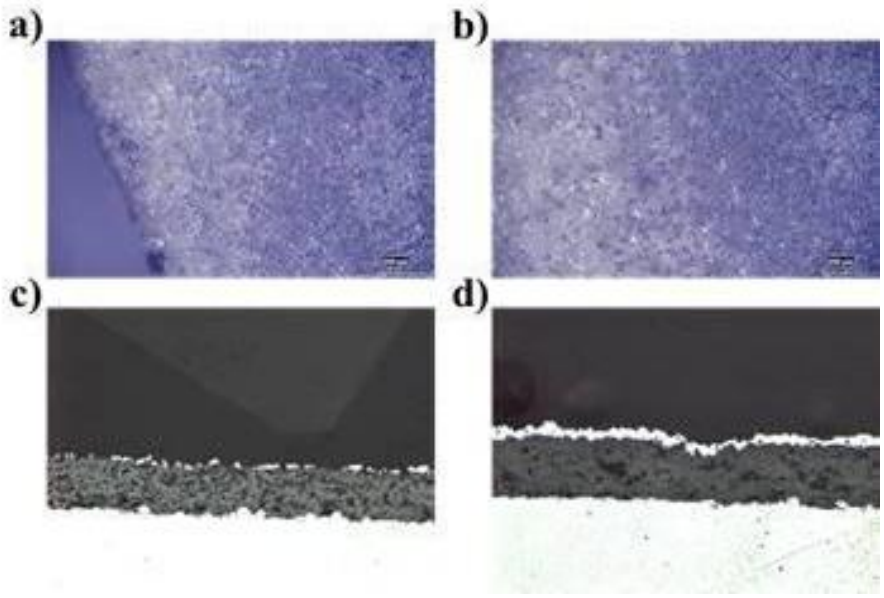

Figure 1. Optical microscopy images of a) Experiment no. 1, b) Experiment no. 2, c) Experiment no. 3, d) Experiment no. 4.

Conclusions

According to the results of this study, several conclusions can be drawn:

- Cold spray aluminium coatings on ceramic systems are improved by lowering traverse speeds and increasing powder feed rates.
- The use of homogenous and continuous coatings facilitates the achievement of impermeability and helps to preserve the structure.
- Sacrificial aluminium provides a more effective means of protecting the structure from corrosion.

Acknowledgement

The authors are grateful for the financial support from Istanbul Technical University Scientific Research Projects (ITU-BAP, Project Number: 46645).

References

Design of thermal barrier coatings. (2014). [Phd. Thesis]. University West.

Dokur, M. M. (2014). Çok Katmanlı CYSZ / Al2O3 ve CYSZ / Al2O3+YSZ Termal Bariyer Kaplamaların Üretimi ve Isıl-Mekanik Özelliklerinin Belirlenmesi. (Phd. Thesis). Istanbul Technical University.

Gupta, M. (2014). Design of Thermal Barrier Coatings A modelling approach. University West.

Gao, L., Guo, H., Wei, L., Li, C. ve Xu H. (2015) Microstructure, Thermal Conductivity and Themal Cycling Behavior of Thermal Barrier Coatings Prepared by Plasma Spray Physical Vapor Deposition Surface and Coatings Technology 276

Moskal, G., Swadzba, L., Hetmanczyk, M., Witala, B., Mendala, B., Mendala J. ve Sosnowy, P. (2012) Characterization of Microstructure and Thermal Properties of Gd2Zr2O7-type Thermal Barrier Coating Journal of the European Ceramic Society 32

Ramesh, M., Marimuthu, K., Karuppuswamy, P., & Rajeshkumar, L. (2021). Microstructure and properties of YSZ-Al2O3 functional ceramic thermal barrier coatings for military applications. Boletín De La Sociedad Española De Cerámica Y Vidrio, 61(6), 641–652.

R. Miller, "Thermal barrier coatings for aircraft engines: history and directions," Journal of Thermal Spray Technology, vol. 6, no. 1, pp. 35–42, Mar. 1997.

Yilbas, B. S., Al-Zaharnah, I., & Sahin, A. (2014). Flexural Testing of Weld Site and HVOF Coating Characteristics. In Materials Forming, Machining and Tribology. Springer Berlin Heidelberg.

A Comparative Study Of Anodized Coating And Micro-Arc Oxidation Coatings Produced On The Al-Si Casting Alloy

Furkan Tezer[a,b], Faiz Muhaffel[b]

[a]Torun Metal, Kalite Mühendisi, Kocaeli,Türkiye
[b] Istanbul Technical University, Department of Metallurgical & Materials Engineering, Istanbul, Türkiye
tezer19@itu.edu.tr

Keywords: Peo, Aluminum, Coating, Corrosion, Mao.

Aim

Aluminum alloys are the most widely used materials that provide weight advantage, especially in the automotive, aviation, military, marine and railway industries, thanks to their very ambitious mechanical properties such as high strength/weight ratio, flexibility in static and dynamic loading working environment and good formability [1]. Aluminum is often combined with other elements to produce various commercial alloys. An example of this is Al-Si alloys. This alloy constitutes more than 80% of the cast aluminum alloys in the world [2]. Al-Si-Cu alloys are the dominant casting alloys preferred in high pressure die casting due to their excellent castability. In order to fully meet the needs of the sector, the Al-Si-Cu alloy must also provide electrical insulation and advanced surface mechanical properties such as hardness, wear and corrosion resistance [3]. EN AB 46000, the most common die casting alloy in Europe, is one of the most important representatives of the Al-Si-Cu alloy group [4].

When comparing all casting techniques for aluminum alloys, the high-pressure die casting method carries the flag as a forming technology that is very close to the final shape commonly used for light metals such as Al, Mg and Zn alloys. It is one of the most well-known and efficient methods for mass-produced aluminum parts. HPDC has the ability to produce aluminum parts with intricate and thin-walled parts, high measurement accuracy and low surface roughness.[5]

The insufficiently high surface hardness and low wear resistance of aluminum alloys are enhanced by different surface modification methods, including conventional anodization, conversion coatings, physical vapor deposition (PVD),chemical vapor deposition (CVD),thermal spraying and micro arc oxidation (MAO). When these methods are considered, the MAO process, also known as plasma electrolytic oxidation (PEO), is an innovative and environmentally friendly method, which is electrochemical surface oxidation in an alkaline electrolyte and under higher voltage or current density conditions compared to conventional anodic oxidation. Immediately after this process, a thin, hard wear and corrosion resistant oxide layer can be formed on the surface of various metals such as Al, Ti, Mg, Zr and their alloys. [6]

In this context, there are countless studies in the literature reporting significant increases in wear and corrosion resistance as a result of coating the surfaces of aluminum and its alloys with an alumina layer using the MAO process. [7]

Plasma electrolytic oxidation (PEO), also known as microarc oxidation (MAO), is an electrochemical plasma-assisted technology preferred for the development of ceramic coatings that improve multiple properties on the surface of different valve metals. PEO combines electrochemical oxidation processes with plasma discharges to sinter the treated metal surface. The properties of PEO coatings are closely related to the type of alloy being treated, the chemical composition of the electrolyte used and the electrical parameters implemented during the process. The prominent properties of PEO coatings include high wear resistance strong corrosion protection high hardness and excellent adhesion to metallic substrates.The surface condition of PEO coatings also provides a suitable ground for the adhesion of other overcoatings such as sol-gel layers and can act as a reservoir for liquid or solid lubricants, creating self-lubricating properties. [1] Despite all its advantages, MAO coating is not currently as common as anodizing coating on Al-Si alloys.

The aim of this study is to apply an MAO process as an alternative to the anodizing coating used industrially on Al-Si casting alloys and to compare its mechanical, corrosion and tribological properties.

Materials and Method

Samples with dimensions of 15x15x4 mm were cut from en ac 46000 aluminum ingot and then drilled with a tip with a diameter of 1.9 mm from one edge for micro arc oxidation. Then, the samples were grinded with 180-320 400-600 800 1200 2500 sandpapers respectively. It was applied to both surfaces. Right after, Samples were washed with ethanol and distilled water and dried at room temperature. Then the samples were subjected to MAO test. Afterwards, SEM and XRD were performed on the samples resulting from the MAO test.

As experimental equipment: 30 kW bipolar pulsed DC power supply unit, stainless steel electrolyte container, an air pump for mixing the electrolyte and an external cooling system were used. The stainless-steel container acted as cathode and the samples were connected to the electrochemical cell as anode.

Findings

Figure 1 shows the surface SEM photographs of MAO coatings produced on Al-Si casting substrate at 500x, 1000x, 2500x and 5000x scale magnifications. Micropores and microcracks are seen on the surface of the samples and this shows that we encounter a typical morphology. Different pore sizes are evenly distributed throughout the surface resulting from discharge channels formed during the coating process. In addition, microcracks are observed on the surface. These cracks are a common occurrence in MAO coatings and the reason is the high thermal gradient between the molten oxide and cold electrolytes

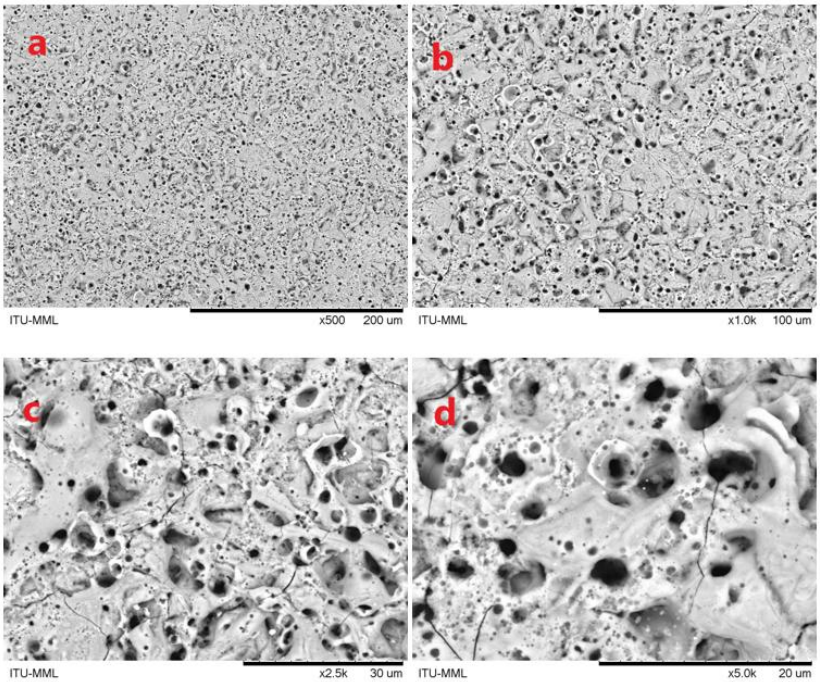

Figure 1. Surface SEM micrographs at (a) 500x, (b) 1000x, (c) 2500x and (d) 5000x magnifications.

Conclusion

In this study, MAO coating was successfully implemented on Al-Si casting substrate in an alkaline electrolyte. SEM analysis was performed on the coating. It realised that the surface of the coating had a conventional morphology with micropores and microcracks along the surface, causing discharge channels during implemention of the MAO. In addition, XRD analysis was done. Aluminum and silicon were detected from the base metal. Anodized coating will be performed and the study will be continued.

References

Alberto, F., & Giulio, T. (2014). The effects of microstructure heterogeneities and casting defects on the mechanical properties of high-pressure die-cast AlSi9Cu3(Fe) alloys. Metallurgical and Materials Transactions A, 45A, 5486.

Alves, S. A., Bayón, R., Fernández-López, P., Gutiérrez-Berasategui, E., & San-José, J. T. (2024). Plasma electrolytic oxidation (PEO) as a promising technology for the development of high-performance coatings on cast Al-Si alloys: A review. Coatings, 14, 217.

Baydoğan, M., Faiz, M., & Yürektürk, Y. (2015). Characterization of micro arc oxidized 6082 aluminum alloy in an electrolyte containing carbon nanotubes. Surface and Coatings Technology, 269, 83–90.

Baydoğan, M., Çimenoglu, H., Faiz, M., Kayalı, E. S., Meydanoglu, O., & Tazegül, O. (2014). Wear and corrosion characteristics of novel alumina coatings produced by micro arc oxidation on AZ91D magnesium alloy. Surface and Coatings Technology, 258, 168–173.

Çimenoglu, H., Gökçe, Ö., Koca, M., Mohammadzadeh, S., Muhaffel, F., & Paksoy, H. P. (2017). Formation of a corrosion-resistant alumina coating on a 6061 aluminum alloy using a combination of micro-arc oxidation and sealing treatments. Materials and Technology, 51(1), 117–121.

Giulia, S., & Giulio, T. (2024). Effect of surface roughness and eutectic segregation on anodising of Al-Si-Cu alloys. Materials Science and Technology, 40(17), 1245–1254.

Liu, Y., & Xiong, S. (2024). Research progress on thermal conductivity of high-pressure die-cast aluminum alloys. Metals, 14, 370.

METEOROLOGICAL ENGINEERING

Atmosphere, Meteorology

Aviation Meteorology

Renewable Energy

Heatwave Analysis Approach

Anıl Eken[a], Sevinç Asilhan[a]

[a] Istanbul Technical University/Department of Climate Science and Meteorological Engineering, Faculty of Aeronautics and Astronautics, Türkiye
eken22@itu.edu.tr

Keywords : Heatwave Analysis, Heatwave Characterization, Heatwave Coefficient, Heatwave Unit.

Aim

This paper aims to offer a new perspective on the analysis of heatwaves. The heatwave is one of the most natural weather hazards. According to the UN, a study found that from 2000 to 2019, approximately 489,000 heat-related deaths occurred each year, including more than 70,000 who died during the 2003 heatwave in Europe (Zhao, 2021). Heatwave analysis, risk identification, and measurements against heatwaves are weak and unsuccessful; therefore, new perspectives are required in the analysis because human losses are highly due to heatwave, especially in urban area or city centres. For example, a study from South Korea found that a total of 590,639 deaths was observed during the study period; of these, 493,911 were in urban areas, and the remaining deaths were in rural areas (Kang & Park, 2020). Because of all those reasons, the cities in a country must be considered in the heatwave analysis, so the climatological city-specific heatwave coefficient identification were aimed to form as a new perspective, leading to the heatwave prediction and heatwave risk identification in the cities of the countries; it must be identified in each city for public health associated with heatwaves, which can be achieved by using only the longest climatological temperature data for the city. Those climatological temperatures of the cities are aimed to integrated into a coefficient to show the heatwave coefficient (HWC) of the cities, which represents the climatological-city specific coefficient and climatological heatwave risks of those cities.

Developing a city-specific heatwave analysis approach were aimed in this research, which were significant to forecast, mitigate, and eliminate the hazards and risks of heatwaves. Cities on the Mediterranean, Aegean, and Adriatic coasts suffer from forest fires associated with heatwaves, and people lost their lives and forests every summer. Also, EU states blame people for attempts to commit arson in forests, especially the people from non-EU countries, including immigrant or refugees, even meteorologists and environmentalists (France24, 2023). A research express that wildfires are political events (Karyotakis, 2024). If wildfires are politic events and the politics do not bring a solution to the problems of wildfires and heatwaves through a science and systematic mathematical methodology developed depending on objective data, those events cannot be described as politics, which can be defined as unacceptable behaviours such as blame and slander. Heatwave management policies serve nature, the environment, and people to save lives (BBC, 2018), ecology, life for humanity, eliminate diseases and forest fires before, during, and after heatwaves, and to increase the quality of life, humans, and the environment; not such as politics. Because of all those reasons, heatwave. Unit (HWU) and HWC have been aimed and developed to predict the onset, development, and severity of the heatwave. Heatwaves, along with climate change, have an increasing impact on human health, which is important to diagnose and take precautions before the passage of heatwave. For this reason, suggestions were aimed at about indices such as humidex and heat index. Through this heatwave methodology, it was proposed to determine the presence and absence of heatwave during a forest fire, which may contribute to the identification of burning attempts or other reasons behind events. At least the heatwave was aimed to distinguished, which measures the power of the heatwave via HWU, depending on HWC.

Below 25 ^{0}C, forest fires are not expected, so the months that have a climatological temperature above 25 ^{0}C were expected to be forest fire and heatwave risk months; therefore, climatological temperatures above 25 ^{0}C of the months were aimed to group for the determination of HWC in Figure 1. However, each month's heatwave analysis below 25 ^{0}C temperatures can also be implemented; the result can be associated with the warming or heatwave; so, heatwave can also be determined in cold months. Drought and heatwaves are extreme events that are closely related to climate with heatwave conditions, which can intensify drought conditions and vice versa (Mishra &

Mukherjee, 2020). Therefore, the high HWC not only shows heatwave risk or heat-related illness risky cities, but also potential drought risky via HWU and dry heatwave types and climate risky places because HWC as a climatological heatwave coefficient reflects the climatological risks or problems on cities due to warming. Especially summer months were categorized in this research, which are associated with heatwaves and forest fires, although heatwaves can occur in every climatic month.

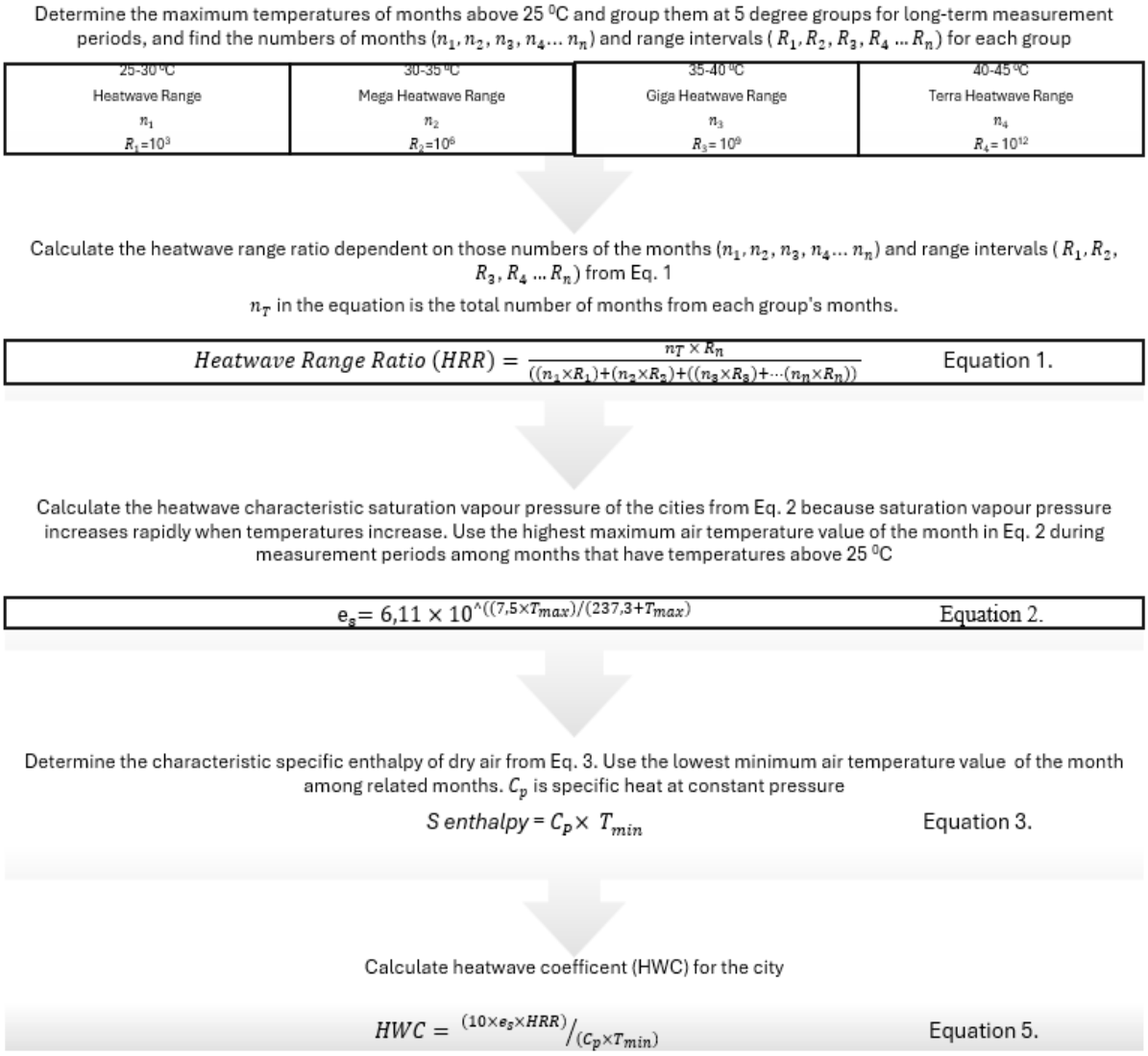

Figure 1. Climatological city-specific heatwave coefficient (HWC) determination process.

Climate change is increasing the frequency and intensity of heatwaves, raising concerns about their detrimental effects on air quality; however, a role for heatwave-human-environment interaction in air pollution exacerbation has not been established (Wang, 2024). The impacts of heatwaves on air quality can substantially very depending on the characteristics of heatwaves (Jin, 2023). Heatwaves are also related to air pollution; therefore, measurement of heatwaves via HWU and the characterization of heatwave types become significant, especially the comparison of heatwave types or fluctuations of pollutant concentrations during high HWU values. The exact mechanisms connecting heatwave to extreme rainfall process is not well understood yet, a there could be found on convective development due to heat over the surface, the identification of the heatwave or convection via HWU and heatwave types, especially the moist heatwave types that lead to convective precipitation and can also be significant to forecast the summer extreme precipitation after heatwave, and were aimed to be used in the future warming or

cooling of climate for cities. Briefly, new heatwave analysis and heatwave type identification methodologies were developed to achieve those aims.

Material and Method

The saturation vapor pressure, which is a function of air temperature, provides a basis for determining other thermodynamic properties of moist air (Huang, 2018). Specific enthalpy is a thermodynamic property that is the sum of specific enthalpy and the product of pressure and specific volume (Jamil, 2023). In the calculation of HWC, the heatwave range ratio (HRR), characteristic saturation vapor pressure, and characteristic specific enthalpy were used, which are a result of the longest climatological temperature data of the cities and defined as climatological city-specific heatwave coefficient. In characteristic saturation pressure calculation, the city's climatological minimum temperature was used because characteristic saturation vapor pressure and enthalpy are climatological temperature limits of heat in cities for the longest available measurement periods. HRR was obtained through grouping the months climatologically in the city for a 5 0C temperature interval and a 103-fold range ratio for each 5 0C interval. The calculation of HWC can be seen in Figure 1.

The HWU unit calculation can be seen in Figure 2, while the characterization of heatwave type can be seen in Figure 3. HWU depends on the hourly temperature and hourly relative humidity of the day, which was evaluated in 12-hour averages as nighttime (18-06) between 6 pm and 6 am and daytime (06-18) between 6 am and 6 pm hours in a day for both variables (temperature and relative humidity), which was compared with HWC to determine

The warming or heatwave in the city. RH18-06/RH06-18 in Figure 2 also becomes an important identification of moist heatwaves from dry heatwaves, which can be seen in Figure 4.

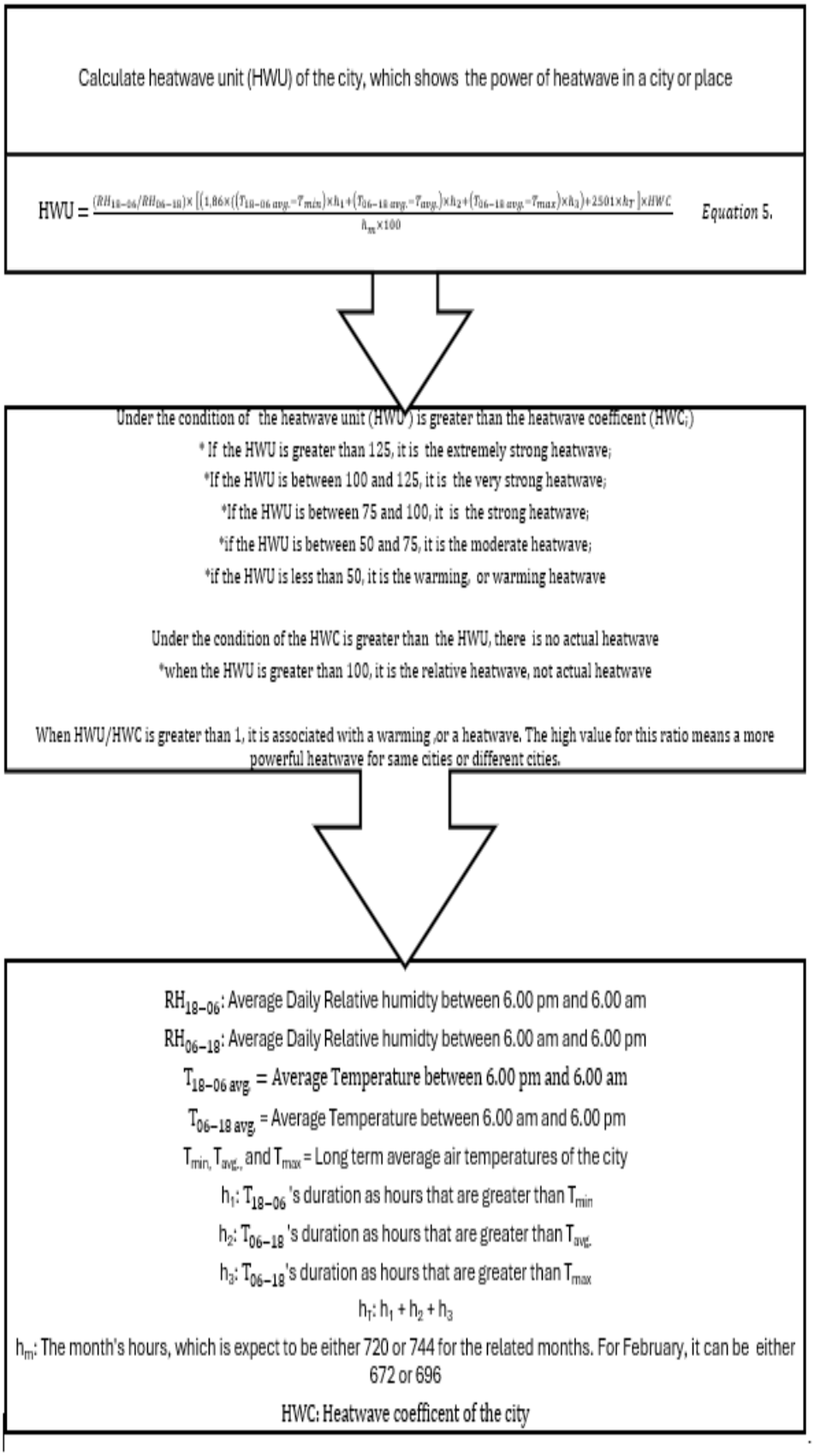

Figure 2. HWU determination process.

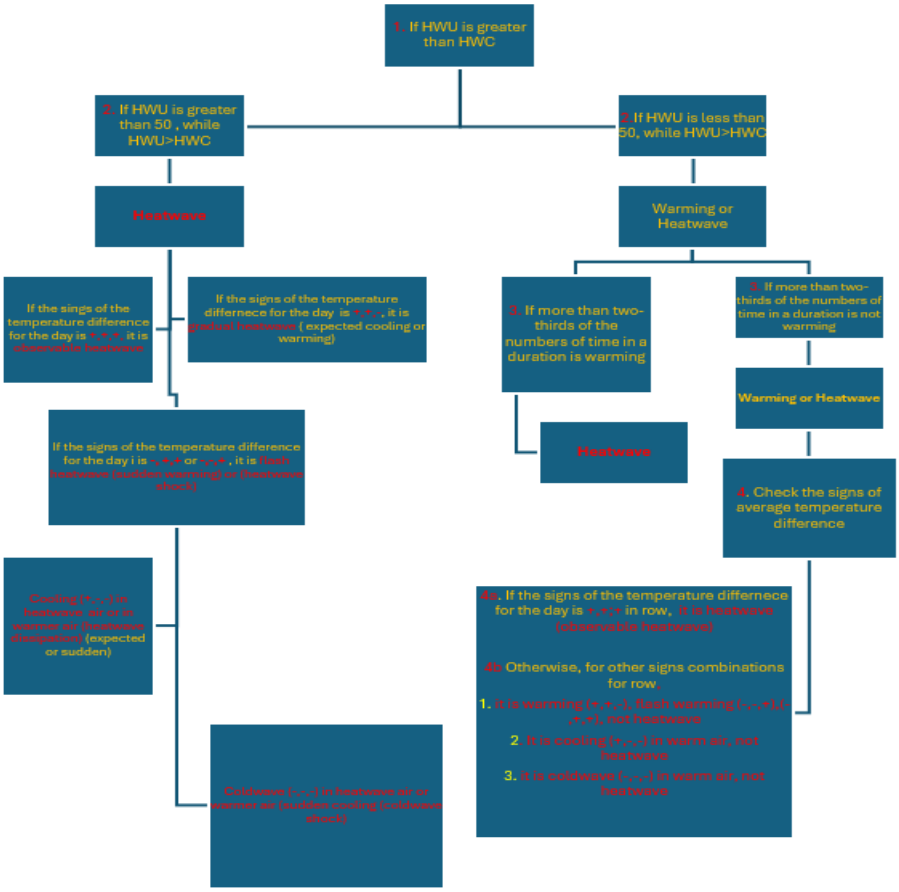

Figure 3. Characterization of heatwave types depending on HWU and average temperature.

R_N: Nighttime RH values between 6 pm and 6 am (RH_{18-06}), R_D: Daytime RH values between 6am and 6 pm (RH_{06-18}), and R_{HR}: Heatwave ratio ($R_{HR}=R_N/R_D = RH_{18-06}/RH_{06-18}$)

Figure 4. Characterization of heatwave types depending on RH.

Environment Canada uses humidex ratings to inform the public when conditions of heat and humidity are potentially uncomfortable (CCOHS, 2025). The humidex was introduced into Canada in 1965, which is calculated with a series of complex formulae using a combination of temperature and humidity level (The Canadian Encyclopedia, 2025). Rothfusz (1990) showed an equation for estimating heat index (HI), which consists of a series of multiple regression analysis of air temperature and relative humidity, based on the assumption described in the very first version developed by (STEADMAN, 1979). The heatwave analysis approach was also compared to Canada Humidex and Rothfusz's heat index (HI) close to the Kula district (38.25 N and 28.25 E) of Manisa city in Türkiye, vertically for June 2024 for each day to compare those three methods.

Findings

The climatological city-specific HWC determination process was implemented in each Turkish city in this study and HWCs were determined for each one. High HWC cities were observed in Southeastern Anatolian cities, which are prone to deaths due to extreme heat, heatwave, drought, and warming compared to other regions, relatively.

HWU and HWC were vertically implemented in Manisa city for June 2024. All days of the month for 1000 mb and 950 mb levels were heatwaves, which were observable and moist heatwave types. 28 days for 900 mb were heatwaves, while 2 days' HWU values were below HWC that were not heatwave. For 850 mb level, only 4 days' HWU values were above HWC, and at the 800 mb level, all days' HWU values in the month were less than HWC, which was associated with complete cooling; so, heatwave was active from the surface down to 900 mb in the location.

The HWU/HWC method and humidex of Canada were consistent and reasonable for vertical analysis, but HI were inconsistent and contradictory. The convective development and its precipitation were not observed in the location, although chronic heatwave was determined.

Conclusion

Heatwave and heatwave type analysis were introduced and implemented, which measures the heatwave in cities and determine the presence or absence of heatwave during forest fires. Chronic heatwave was determined in the location. Under the low HWU, arson attempts can be behind the forest fires, not heatwave. Low HWC cities and moist heatwave types can lead to convective precipitation after heatwaves, compared to high HWC cities and moist heatwave types, because exceeding the high HWC cities' value is not easy for convective development. The method measures and identifies heatwave during forest fires, convective precipitation development, and air pollution, which may also be used in industrial facilities' smokestacks to observe heat contribution of the facilities to the atmosphere via measuring hourly RH and temperature value in the inside of chimney to calculate HWU and compare it with HWC. The facilities may be taxed dependent on this extreme HWU value contribution into atmosphere.

Reference

BBC. (2018, July 24). Retrieved from Greece wildfires: Dozens dead in Attica region: https://www.bbc.com/news/world-europe-44932366. Accessed 20 December 2024

CCOHS. (2025). Retrieved from https://www.ccohs.ca/oshanswers/phys_agents/humidex.html. Accessed 5 May 2023

France24. (2023, August 25). Retrieved from Greek wildfires spur anti-migrant sentiment: https://www.france24.com/en/live-news/20230825-greek-wildfires-spur-anti-migrant-sentiment. Accessed 20 December 2024

Huang, J. (2018, June 1). A Simple Accurate Formula for Calculating Saturation Vapor Pressure of Water and Ice. Journal of Applied Meteorology and Climatology, 1265-1272. doi:10.1175/JAMC-D-17-0334.1

Jamil, F. (2023, June 5). Concise summary of existing correlations with thermophysical properties of seawater with applications: A recent review. Applied Thermal Engineering, 227. doi:10.1016/j.applthermaleng.2023.120404

Jin, H.-G. (2023, August 1). Do heat waves worsen air quality? A 21-year observational study in Seoul, South Korea. Science of The Total Environment , 884.

Kang, C., & Park, C. (2020, August 7). Heatwave-Related Mortality Risk and the Risk-Based Definition of Heat Wave in South Korea: A Nationwide Time-Series Study for 2011–2017. International Journal of Environmental Research and Public Health. doi:10.3390/ijerph17165720

Karyotakis, M.-A. (2024, December). The political ecology of wildfire: Media and the politics of blame in the Evros wildfires in Greece. Trees, Forests, and People. doi:10.1016/j.tfp.2024.100682

Mishra, A. K., & Mukherjee, S. (2020, December 8). Increase in Compound Drought and Heatwaves in a Warming World. Geophysical Research Letters. doi:10.1029/2020GL090617

Rothfusz, L. P. (1990). Retrieved from https://www.weather.gov/media/ffc/ta_htindx.PDF. Accessed 10 December 2024

STEADMAN, R. (1979, July 1). The Assessment of Sultriness. Part I: a temperature-humidity index based on human physiology and clothing science. Journal of Applied, 18(7), 861-873. doi:10.1175/1520-0450(1979)018<0861:TAOSPI>2.0.CO;2

The Canadian Encyclopedia. (2025). Retrieved from https://www.thecanadianencyclopedia.ca/en/article/humidity-and-humidex. Accessed 15 December 2024

Wang, T. (2024). Heatwave exacerbates air pollution in China through intertwined climate-energy-environment interactions. Science Bulletin, 2765-2775. doi:10.1016/j.scib.2024.05.018

Zhao, Q. (2021, July). Global, regional, and national burden of mortality associated with non-optimal ambient temperatures from 2000 to 2019: a three-stage modelling study. THE LANCET-Planetary Health, 5(7), 415-425. doi: 10.1016/S2542-5196(21)00081-4

METEOROLOGICAL ENGINEERING

Atmosphere, Meteorology

Aviation Meteorology

Renewable Energy

Repowering at Türkiye's Leading Power Plant: An Analysis of Energy Production Increase

İpeknur Hazar[a,b], Mehmet Özkan Başar[b], Elçin Tan[a]

[a] Istanbul Technical University, Faculty of Aeronautics and Astronautics, Department of Climate Science and Meteorological Engineering, Türkiye
[b] Entek Elektrik Üretim A.Ş., Head Office, Strategy and Business Development Directore, Türkiye
hazar18@itu.edu.tr

Keywords : Wind Energy, Repowering, Wind Turbine.

Aim

Renewable energy is indispensable in combating climate change due to its unlimited nature, eco-friendly characteristics, and technological efficiency gains. Solar, hydroelectric, geothermal, and especially wind energy offer effective alternatives to fossil fuels, with wind energy providing notable advantages through low operating costs and high capacity.

In response to rising energy demand and environmental concerns, Türkiye has prioritized renewable energy investments (Ministry of Environment, Urbanization, and Climate Change & Presidency of Strategy and Budget of the Republic of Türkiye, 2023). The country's long-term climate strategy should maximize wind energy efficiency while modernizing existing plants and strengthening technological infrastructure. This strategy aims to optimize production capacity through enhanced plant potential and innovative technologies, contributing to sustainable development both locally and internationally.

Repowering refers to modernizing outdated wind farms by replacing old turbines with modern technology to boost performance. It offers benefits such as increased capacity factor, reduced operating costs, and lower environmental impacts. Key advantages include higher specific energy production from increased hub heights, superior performance of new multi-megawatt turbines, improved wind resource assessment, better utilization of prime windy sites, fewer turbines leading to reduced visual impact and avian mortality, minimized use of undeveloped land, improved grid integration, lower capital and maintenance costs, and job creation (Serri, Lembo, Airoldi, Gelli, & Beccarello, 2018).

The primary objective of this study is to quantitatively determine the change in the production capacity factor when a repowering application is implemented in one of Türkiye's oldest wind farms. In this study, the performance of the existing plant will be analyzed in detail, and a model will be developed to assess the expected increase in efficiency and the effects on the capacity factor following repowering. In doing so, the study systematically examines both the advantages and potential challenges associated with the repowering process, thereby demonstrating the contribution of plant modernization to the broader renewable energy strategy.

Material and Method

Various data sources and computational approaches were integrated in the materials and methods section to evaluate the plant's production performance. Initially, production data for the 2018–2024 period were obtained from the Transparency Portal of Energy Exchange Istanbul (EXIST), known in Turkish as Enerji Piyasaları İşletme A.Ş. (EPİAŞ), and used as a reference during the simulation process (Url-1, accessed February 5, 2025). Information on the plant's land area and turbine locations was sourced from the Turkish Energy Market Regulatory Authority (EPDK) and transferred to the WindPRO software, while turbine-type data were obtained from the Turkish Wind Energy Association (TÜREB) Statistical Report (Türkiye Rüzgar Enerjisi Birliği, n.d.; Url-2, accessed March 4, 2025; Url-3, accessed February 12, 2025). The existing installation comprises three E40 turbines (0.5 MW, 65 m hub height) and four E82 turbines (2.3 MW, 78.3 m hub height). Additionally, the EMD-WRF Europe+ MesoScale (EMD-WRF) dataset was downloaded (Url-4, accessed February 3, 2025). A 0.03°×0.03°

resolution version of the EMD-WRF data for 2018–2024 was calibrated against the EPİAŞ data and then extended to cover the period from 2005 to 2024 for production calculations.

The PARK module of WindPRO was applied to the production calculations. Initially, a 10% technical and suitability loss was imposed on the EMD-WRF data to reflect realistic operational conditions. A scaling factor was then applied to accurately reproduce the production values for the 2018–2024 period, ensuring that the simulation results aligned with the EPİAŞ data. A graphical comparison of the production curves from EPİAŞ and WindPRO for 2018–2024 revealed very similar oscillations, confirming the validity of the methodology.

To further assess the plant's performance, the analysis was extended to a 20-year period (2005–2024). This long-term simulation provided a solid basis for evaluating both the historical performance of the plant and the potential production increase following repowering. In addition to assessing the existing plant, the production performance of new turbine models was analyzed under similar computational conditions. This evaluation ensured that the integration of new turbines did not exceed the plant's production license limits, as grid capacity restrictions were maintained. Consequently, this approach allowed for a comprehensive comparative assessment of the advantages and disadvantages of the repowering application.

Findings

Before presenting the results, it is important to note that the EMD-WRF dataset was scaled by 89.4% to match actual generation data from EXIST. This calibration ensured that the simulation results accurately represented real operational performance. The applied scaling factor is site-specific and depends on both the model setup and the local meteorological conditions.

Initial simulations for the 2018–2024 period indicated that the existing plant's annual production was 32.1 GWh. Within the scope of the repowering evaluation, eight different turbine models were examined. Among these, the best result was achieved by integrating the new Goldwind182 turbine, with a capacity of 7.5 MW and a hub height of 110 meters. With this turbine, the annual production increased to 47.5 GWh, representing an approximate 48% increase.

In addition, the Vestas V162 turbine model with a capacity of 6.2 MW and a hub height of 119 meters yielded an annual production of 44.6 GWh, corresponding to a 39% increase compared to the current setup. These results demonstrate the potential of repowering to significantly boost energy output, depending on turbine specifications and site compatibility.

Conclusion

In conclusion, the repowering application demonstrates significant potential for enhancing the production performance of the existing plant. Considering the constraints imposed by the production license capacity and grid capacity limits, the integration of the Goldwind182 turbine—which resulted in a 48% increase in production—demonstrates the effectiveness of the repowering strategy. Similarly, the Vestas V162 turbine also provided considerable improvement, with a 39% increase in energy output. These results confirm that even under existing licensing and grid constraints, upgrading turbines can yield notable gains in production and efficiency. Moreover, the long-term analysis covering 2005–2024 supports the contribution of this strategy to sustainable energy production. It is also critical to note that the regulatory framework for repowering is essential; legal regulations substantially increase the feasibility of such modernization projects and provide vital support in accelerating the transformation process within the energy sector.

References

Ministry of Environment, Urbanization, and Climate Change & Presidency of Strategy and Budget of the Republic of Türkiye. (2023). *Türkiye's 2053 long-term climate strategy* (report). Foreword (p. 2).

Serri, L., Lembo, E., Airoldi, D., Gelli, C., & Beccarello, M. (2018). Wind energy plants repowering potential in Italy: Technical-economic assessment. *Renewable Energy, 115*, 382–390. https://doi.org/10.1016/j.renene.2017.08.031

Türkiye Rüzgar Enerjisi Birliği. (2025). *Türkiye Rüzgar Enerjisi İstatistik Raporu – Temmuz 2024*. https://tureb.com.tr//yayinlar/turkiye-ruzgar-enerjisi-istatistik-raporlari/5 (accessed February 12, 2025)
Url-1 https://seffaflik.epias.com.tr/electricity/electricity-generation/ex-post-generation/real-time-generation (accessed February 5, 2025)
Url-2 https://lisans.epdk.gov.tr/epvys-web/faces/pages/lisans/elektrikUretim/elektrikUretimOzetSorgula.xhtml (accessed March 4, 2025)
Url-3 https://www.wind-pro.com (accessed February 12, 2025)
Url-4 https://www.emd-wrf.eu (accessed February 3, 2025)

MINING ENGINEERING

Excavation Mechanics

Machine Learning-Based Prediction of Thrust Force in Tunnel Boring Machines

Hadi Alizadeh[a], Ömür Acaroğlu Ergün[a]

[a] Istanbul Technical University, Mining Engineering Department, Mining Engineering, Türkiye
alizadeh23@itu.edu.tr

Keywords: Tunnel Boring Machine, Machine Learning, Thrust Force Prediction, Rock Mechanics, Performance Estimation.

Aim

Accurate prediction of thrust (normal force) in Tunnel Boring Machines (TBMs) is critical for optimizing excavation efficiency, cutterhead design, and operational cost management. O. Acaroglu et al (2008) developed a fuzzy logic model to predict the specific energy (SE) requirements for Tunnel Boring Machines (TBMs), with a focus on Constant Cross-Section (CCS) disc cutters.Satar Mahdevari et al (2014) developed a support vector regression (SVR) model to predict the penetration rate (PR) of Tunnel Boring Machines (TBMs) in hard rock tunneling, using the Queens Water Tunnel project in New York as a case study. A. Salimi, J. Rostami, C. Moormann, and A. Delisio (2016) explore the application of nonlinear regression and artificial intelligence (AI) algorithms to predict the performance of Tunnel Boring Machines (TBMs) in hard rock conditions. Ebrahim Ghorbani and Saffet Yagiz (2024) developed a machine learning approach using gradient boosting algorithms to predict the penetration rate (PR) of Tunnel Boring Machines (TBMs) in varied rock conditions. Arsalan Mahmoodzadeh et al. (2021) applied machine learning models to forecast the lifespan of Tunnel Boring Machine (TBM) disc cutters. Yin Bo, Quansheng Liu, Xing Huang, and Yucong Pan (2022) developed a real-time rock mass classification model for hard-rock tunneling, using CatBoost integrated with Sequential Model-Based Optimization (SMBO). Andreas Benardos (2008) from the National Technical University of Athens explores the use of artificial intelligence (AI) methods, particularly artificial neural networks (ANNs), for predicting Tunnel Boring Machine (TBM) performance in underground development. Yang Liu, Shuaiwen Huang, Di Wang, Guoli Zhu, and Dailin Zhang (2022) developed a kernel support vector machine (KSVM) model to predict the need for disc cutter replacements in Tunnel Boring Machines (TBMs). Saffet Yagiz and Halil Karahan (2015) used various optimization techniques including Differential Evolution (DE), Hybrid Harmony Search (HS-BFGS) and Grey Wolf Optimizer (GWO) for estimating TBM penetration rate. Ling, J., Sun, C., Wang, Q., & Zhang, H. (2024). Analysis of Rock Breaking Load Characteristics and Efficiency Optimization of Roller Cutters under Multi-Factor Coupling.

While traditional methods like fuzzy logic (Acaroglu et al., 2008) have been applied to predict specific energy (SE), this study focuses on advancing thrust prediction using machine learning (ML). Leveraging the same dataset from the Colorado School of Mines' Earth Mechanics Institute, this work employs a Random Forest Regressor to model thrust (NF) based on rock properties, cutter geometry, and cutting parameters. The primary objective is to demonstrate the superiority of ML over conventional methods in capturing complex, non-linear relationships to achieve high predictive accuracy.

The objective of this study is to develop a machine learning model, specifically a Random Forest Regressor, to accurately predict thrust force (normal force) in TBM operations based on rock and cutter parameters.

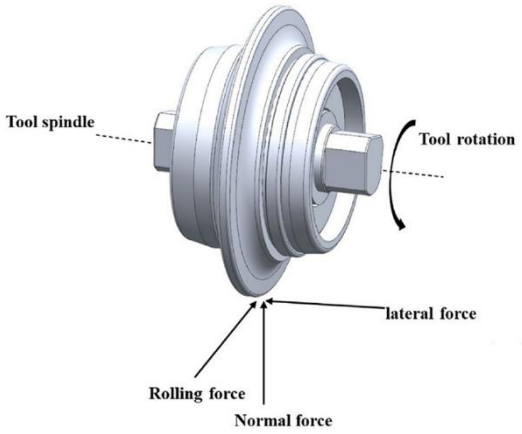

Figure 1. Cutting forces acting on a disc (Ling, J., Sun, C., Wang, Q., & Zhang, H. (2024)).

Material and Method

The dataset used in this study originates from a previously published research article and comprises six input parameters: uniaxial compressive strength (UCS), Brazilian tensile strength (BTS), disc diameter (DD), tip width (DTW), cutter spacing (S), and penetration (p). These inputs are used to predict thrust (NF), a key mechanical output critical for TBM performance. The dataset, originally utilized for fuzzy logic-based SE prediction, was preprocessed to address outliers and normalized to ensure balanced model training.

The Random Forest Regressor, an ensemble learning algorithm, was selected for its ability to handle high-dimensional, non-linear data through bootstrap aggregation and feature randomness. The model was trained on 80% of the data, with 20% reserved for testing. Hyperparameter tuning (e.g., tree depth, number of estimators) was conducted via grid search to optimize performance. Model efficacy was evaluated using R-squared (R^2) and mean squared error (MSE).

Figure 2, The residual plot shows the difference between actual and predicted values for both the training and test sets. In the training set, most residuals are clustered around zero, indicating a good fit, though some dispersion increases with higher predicted values, suggesting possible heteroscedasticity. A few outliers exist, such as residuals below -10,000, but they don't significantly impact the model. In the test set, residuals are also centered around zero, showing that the model generalizes reasonably well; however, there is greater variance at higher predicted values, including some extreme errors below -15,000, which may point to slight overfitting. Despite this, the residuals display no clear trend or pattern, supporting that the Random Forest model's assumptions hold. Overall, the model performs well, with mostly random residuals close to zero. Enhancing performance further may involve hyperparameter tuning, feature transformation, or analyzing outliers.

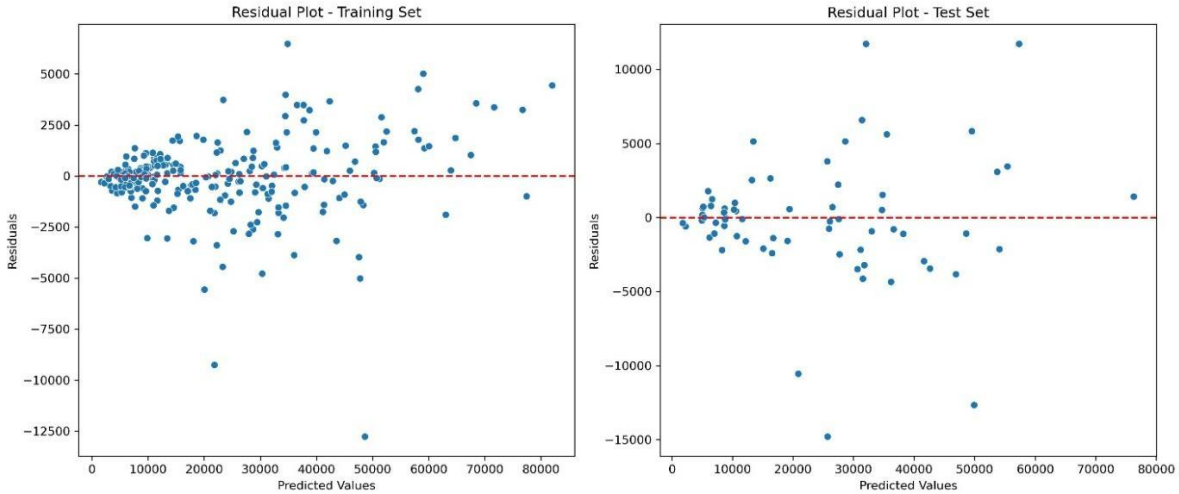

Figure 2. Residual Plot for the Random Forest Regressor model predicting Normal Force (NF).

Figure 3, the lift chart, The model curve rising above the baseline indicates that the model is effective at prioritizing high actual values, such as high Normal Force. The red dashed 45° line represents random guessing, serving as a benchmark. A steeper lift in the early percentiles of the curve suggests that the model is particularly good at identifying and capturing the highest values early on, which reflects strong predictive performance.

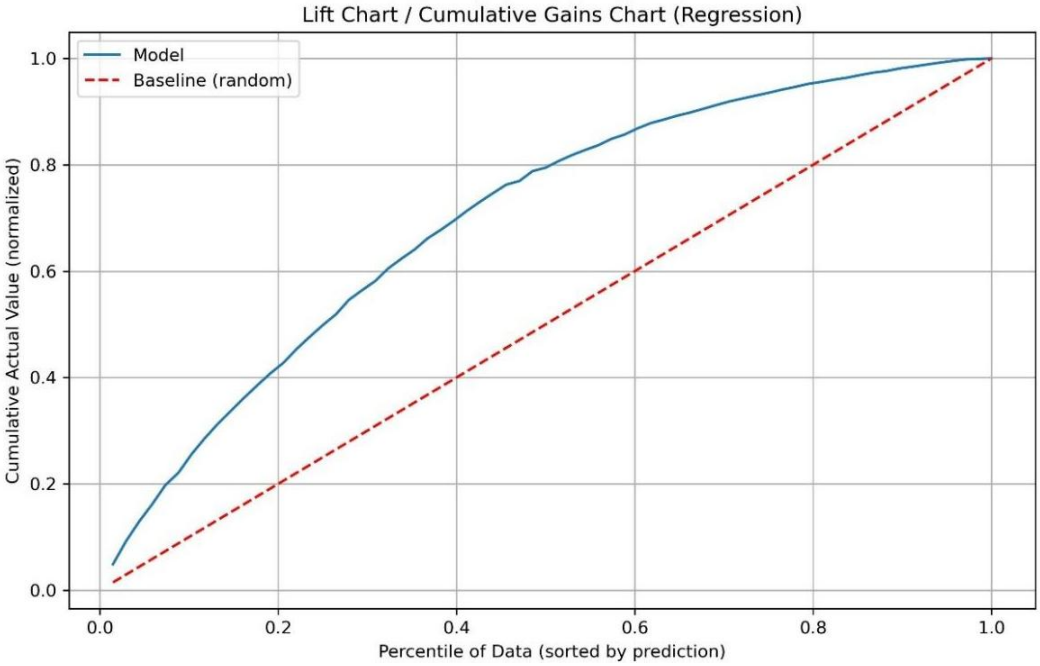

Figure 3. Lift chart.

Findings

The machine learning model was evaluated based on performance metrics such as R^2 (coefficient of determination), Mean Squared Error (MSE), and Mean Absolute Error (MAE). Among the models tested, the Random Forest Regressor achieved the highest accuracy with an R^2 value of 0.94 on the test dataset, indicating excellent predictive capability.

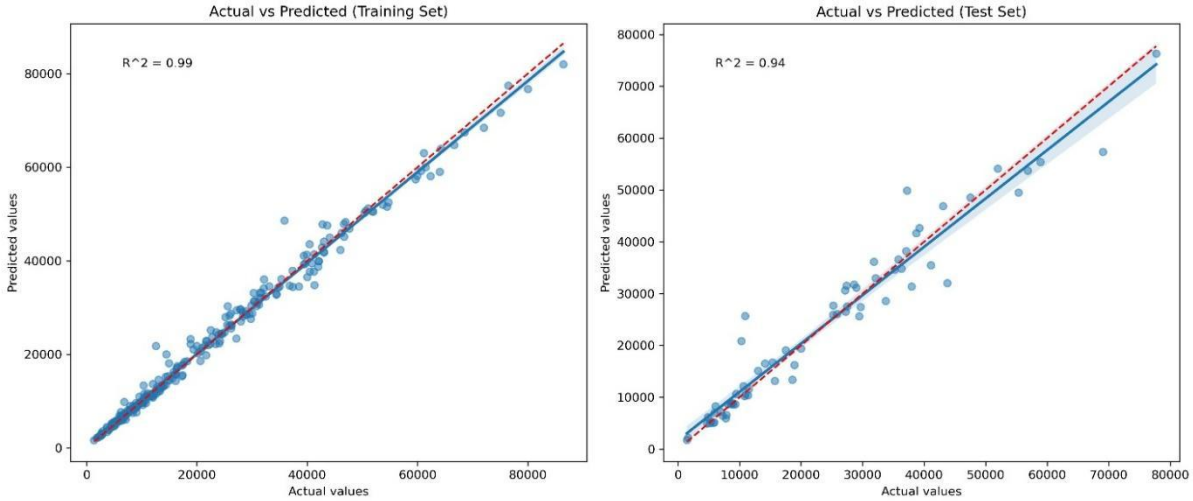

Figure 4. Random Forest regression model.

The results confirm that the machine learning-based approach significantly improves the accuracy of thrust force prediction compared to traditional methods. Figure 4 presents the predicted vs. actual thrust force values, demonstrating a strong correlation between the model's predictions and the experimental results.

Additionally, feature importance analysis revealed that penetration depth (p) and UCS are the most influential parameters in determining the thrust force, aligning with theoretical expectations in rock cutting mechanics.

Conclusion

This study demonstrates the effectiveness of machine learning models, particularly the Random Forest Regressor, in accurately predicting the Thrust Force (Normal Force) in TBM operations. The high R^2 values obtained indicate that ML models outperform traditional empirical approaches, offering improved precision and reliability.
The application of ML-based predictions in TBM operations can assist engineers in making data-driven decisions, optimizing machine performance, reducing wear on cutting tools, and ultimately enhancing the efficiency of tunnel excavation projects. Future research may explore deep learning techniques and hybrid modeling approaches to further refine the predictive capability of TBM performance estimation models.

References

Acaroglu O, Ozdemir L, Asbury B. A fuzzy logic model to predict specific energy requirement for TBM performance prediction. Tunnelling Underground Space Technol 2008;23:600–8. http://dx.doi.org/10.1016/j.tust.2007.11.003.

Breiman, L. (2001). Random forests. Machine Learning, 45(1), 5-32.

Rostami, J., & Ozdemir, L. (1993). A new model for performance prediction of hard rock TBM. Proceedings of the Rapid Excavation and Tunnelling Conference, 793-809.

Yagiz S. Utilizing rock mass properties for predicting TBM performance in hard rock condition. Tunn Undergr Space Technol. 2008;23:326–339. https://doi.org/10.1016/j.tust.2007.04.011

Saffet Yagiz, Halil Karahan, (2015). Application of various optimization techniques and comparison of their performances for predicting TBM penetration rate in rock mass. https://doi.org/10.1016/j.ijrmms.2011.02.013

Benardos AG, Kaliampakos DC. Modeling TBM performance with artificial neural networks. Tunnelling Underground Space Technol 2004;19:597–605. http://dx.doi.org/10.1016/j.tust.2004.02.128 .

Ebrahim Ghorbani, Saffet Yagiz Estimating the penetration rate of tunnel boring machines via gradient boosting algorithms. https://doi.org/10.1016/j.engappai.2024.108985

Satar Mahdevari et al (2014), A support vector regression model for predicting tunnel boring machine penetration rates. https://doi.org/10.1016/j.ijrmms.2014.09.012

Ling, J., Sun, C., Wang, Q., & Zhang, H. (2024). Analysis of Rock Breaking Load Characteristics and Efficiency Optimization of Roller Cutters under Multi-Factor Coupling. KSCE Journal of Civil Engineering. https://doi.org/10.1007/s12205-024-1864-z

MOLECULAR BIOLOGY - GENETICS AND BIOTECHNOLOGY

Bioimaging

Drug and Vaccine Development

Metabolic and Evolutionary Engineering

Metagenomics and Protein Engineering

Microbial Biotechnology and Genetics

Nanobiotechnology

Recombinant Production of Two Novel Ferredoxin-NADP$^+$ Reductases from Pseudomonas mandelii KGI_MA19

Kaan Dizer[a], Hande Mumcu[a,b], Aycan Kayrav[a,b], Elif Mehveş Özer[a,b], Nevin Gül Karagüler[a,b]

[a]Istanbul Technical University, Graduate School, Molecular Biology - Genetics and Biotechnology Program, Türkiye
[b]Istanbul Technical University, Faculty of Science and Letters, Department of Molecular Biology and Genetics, Türkiye
dizer24@itu.edu.tr

Keywords: Ferredoxin-NADP$^+$ Reductase, Oxidoreductases, Recombinant Protein Production, Expression Optimization.

Aim

Ferredoxin-NADP$^+$ reductases (FNR, EC 1.18.1.2) are a family of monomeric enzymes containing noncovalently bound flavin adenine dinucleotide (FAD) cofactor as their prosthetic group. The first case of isolated FNR was reported in 1956 using pea chloroplasts (Avron and Jagendorf, 1956). Thereafter, it was shown that the catalytic function of the chloroplast reductase was to facilitate the electron transfer between the reduced iron-sulfur protein ferredoxin (Fd) and NADP$^+$ (Equation 1.), generating NADPH required for CO_2 assimilation in cyanobacteria and plants (Shin and Arnon, 1965).

$$2Fd_{red} + NADP^+ + H^+ \leftrightarrow 2Fd_{ox} + NADPH \qquad (1)$$

This reaction requires the transfer of electrons from the one-electron donor Fd to the two-electron acceptor NADP$^+$. FNR facilitates this process by linking one-electron and two-electron carriers, a function determined by the biochemical characteristics of its FAD prosthetic group. Flavins (Fl), including FAD, can exist in three redox states: oxidized, semiquinone (one-electron reduced radical), and hydroquinone (fully reduced form) (Dudley et al., 1964). The FNR catalytic cycle (Figure 1.) begins with the sequential reduction of FAD to its semiquinone form ($FADH^{\cdot}$), followed by its further reduction to hydroquinone form ($FADH^-$) (Corrado et al., 1996). The final reaction steps likely involve hydride transfer from $FADH^-$ to NADP$^+$, leading to the release of NADPH (Carrillo and Ceccarelli, 2003; Karplus and Faber, 2004; Medina and Gomez-Moreno, 2004). Additionally, this reaction can also occur in the reverse direction with FNR using NADPH to reduce Fd, which is particularly relevant in nonphotosynthetic plant tissues (Onda et al., 2000; Aliverti et al., 2001) and cyanobacterial heterocysts (Weber-Main et al., 1998) where specific isoforms possess redox potentials favoring this reverse electron flow.

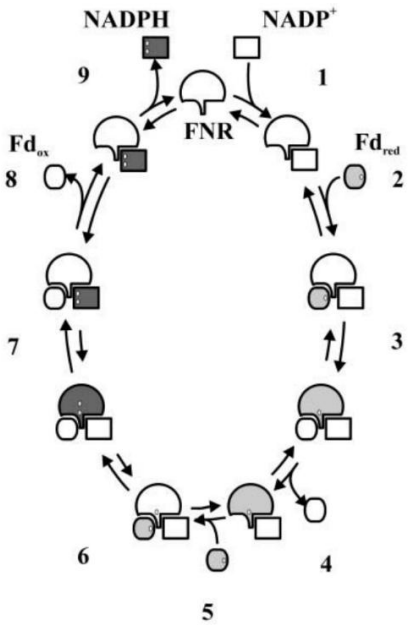

Figure 1. The catalytic cycle of ferredoxin-$NADP^+$ reductase (Carrillo and Ceccarelli, 2003).

After the chloroplast reductase was isolated, novel FNRs were discovered in various organisms, including phototrophic and heterotrophic bacteria, mitochondria of animals and yeast, and the apicoplasts of intracellular parasites (Jungermann et al., 1974; Chen and Yoch, 1989; Hanukoglu and Gutfinger, 1989; Bianchi et al., 1995; Razquin et al., 1996; Lacour and Dumas, 1996; Vollmer et al., 2001). Research on several species has shown that FNR functions as an electronic switch at the key branching points of different electron transfer pathways. In heterotrophic organisms and tissues, the reaction primarily drives Fd reduction, providing mobile low-potential electrons for various metabolic processes, including nitrogen and hydrogen fixation, steroid hydroxylation, anaerobic pyruvate assimilation, fatty acid desaturation, and the synthesis of amino acids and dNTPs (Carrillo, 1998).

FNR exhibits strong NADP(H) oxidoreductase activity and low affinity for NAD(H). The site where the reduced FAD donates its electrons can accommodate a wide range of oxidants in an irreversible manner. This led the original discoverers of FNR to describe the enzyme as a "thylakoid-bound NADPH diaphorase" (Avron and Jagendorf, 1956). Some of the oxidants of FNR include NAD^+, ferricyanide, substituted phenols, nitro derivatives, viologens, quinones, and cytochromes (Carrillo and Vallejos, 1987). While the diaphorase activity is generally not physiologically significant, it has greatly contributed to the understanding of the function and catalytic mechanism of FNRs and can adopt practical applications in the pharmaceutical industry and bioremediation in the near future (Shah and Spain, 1996; Kranendonk et al., 1997).

In this study, cloning, heterologous expression, and purification of two novel ferredoxin-$NADP^+$ reductases, namely Fpr1 and Fpr2, from previously characterized Pseudomonas mandelii KGI_MA19 and the optimization of conditions affecting recombinant protein production were aimed. In further studies, these FNRs will be compared with often-used ferredoxin reductases in terms of their electron transfer capabilities and coupled with different ferredoxins to reconstitute the catalytic activities of cytochrome P450s, a protein family of high industrial significance.

Material and Method

The genomic DNA of Pseudomonas mandelii KGI_MA19 was isolated and used as a template for PCR reactions to amplify the fpr1 and fpr2 genes with attached restriction sites. The PCR products were digested using NdeI and HindIII restriction enzymes. The digested products were ligated into the pET-28a(+) expression vector, which had been cut with the same enzymes, using T4 DNA ligase. Chemically competent E. coli BL21 (DE3) cells were transformed with the constructed plasmids and incubated overnight at 37°C on lysogeny broth (LB) agar plates

containing 40 µg/mL kanamycin. The next day, a few single colonies were picked from each plate, and the presence of fpr genes was analyzed by colony PCR. LB liquid cultures were prepared for each selected positive colony and incubated overnight at 37°C with shaking at 200 rpm. The cells were harvested by centrifugation, and the constructed plasmids were isolated. To further confirm the presence of the fpr1 and fpr2 genes in the isolated plasmids, a diagnostic digest was performed using HindIII on both the isolated plasmids and the empty pET-28a(+) vector.

The expression of FNR proteins was performed using E. coli C43 (DE3) cells as expression hosts. The chemically competent E. coli C43 (DE3) cells were transformed with the constructed expression plasmids and cultured overnight in LB at 37°C and 200 rpm. These precultures were then used to inoculate the main cultures of terrific broth (TB). The main cultures were grown at 37°C with gentle shaking until OD_{600} reached 0.8. When OD_{600} reached 0.8, the cultures were induced by adding isopropyl β-D-1-thiogalactopyranoside (IPTG), and incubation continued at 25°C for 16 hours. The E. coli cells were harvested by centrifugation, and the cell pellets were stored at −20°C until further use. The cell pellets were resuspended in 20 mM sodium phosphate buffer (pH 8.0) containing 0.5 M NaCl and disrupted by sonication. After centrifugation, the His-tagged proteins in the cell lysates were purified by immobilized metal ion affinity chromatography (IMAC) using Ni^{2+}-charged HisTrap affinity columns according to the manufacturer's instructions. Fractions containing the purified proteins were collected, concentrated using Amicon Ultra centrifugal filters, and stored at −20°C.

Findings

After the PCR reactions of the fpr1 and fpr2 genes, products with respective sizes of 793 bp and 791 bp were obtained (Figure 1.). Many single colonies were observed on LB agar plates after transformation (Figure 2.).

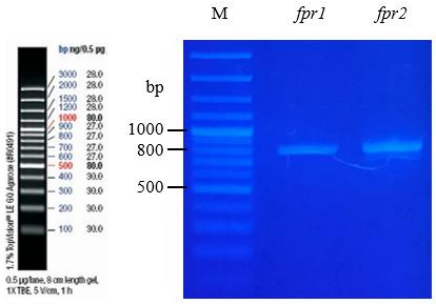

Figure 2. PCR products of fpr1 and fpr2 genes.

All three selected colonies tested positive for the fpr1 gene, and two out of four colonies were confirmed to have the fpr2 gene by colony PCR (Figure 3.). Two positive colonies from each plate were selected for plasmid isolation. After the diagnostic digest, all constructed plasmids were confirmed to contain the genes of interest since there was a significant size difference between the constructed plasmids (≈6200 bp) and the empty pET-28a(+) vector (5369 bp) (Figure 4.).

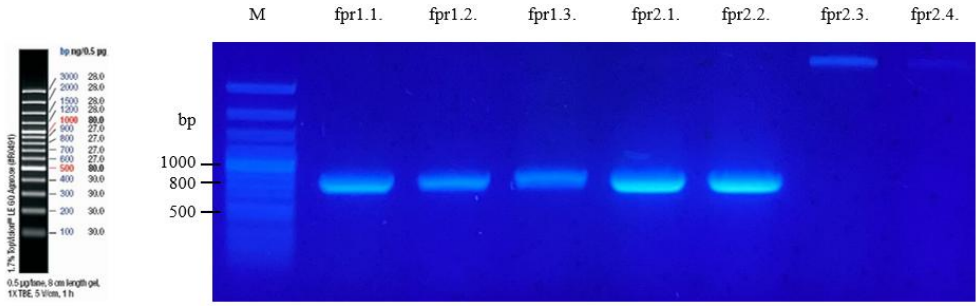

Figure 3. Colony PCR results.

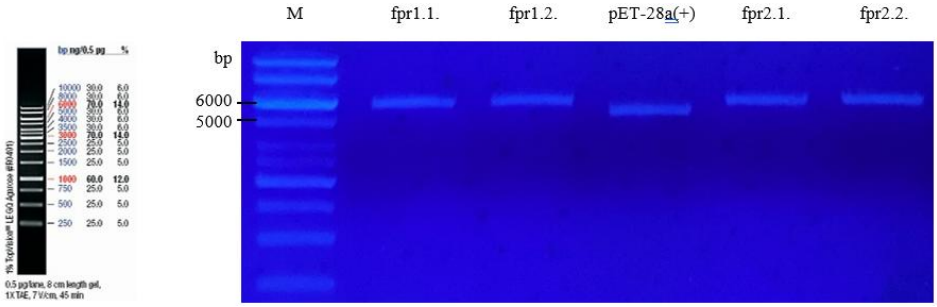

Figure 4. Diagnostic digestion results of constructed plasmids.

Following the purification of Fpr1, the purified protein showed a band at approximately 25 kDa, significantly lower than the expected size of 31.9 kDa (Figure 5.). The E1, E2, and E3 fractions were selected for buffer exchange and concentration. However, under the same conditions, the purification of the Fpr2 protein resulted in significant impurity. Therefore, optimization of the Fpr2 purification process is still ongoing. In future experiments, the induction time will be reduced to obtain the protein with relatively higher purity.

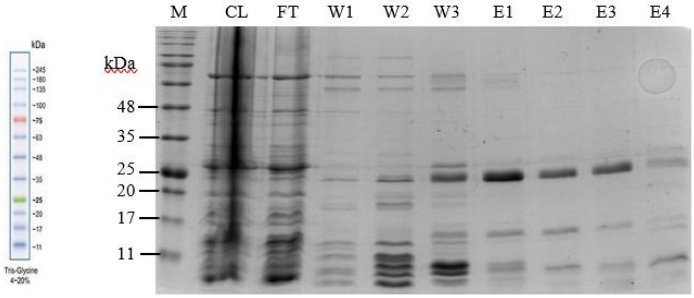

Figure 5. SDS-PAGE analysis of purified Fpr1. Abbreviations: M, marker; CL, clear lysate; FT, flow-through; W, wash; E, elution.

Both purified proteins exhibited a yellowish appearance, a direct consequence of the FAD prosthetic group, which displays a yellow color when fully oxidized.

Conclusion

In this study, Fpr1 and Fpr2 ferredoxin-$NADP^+$ reductases from the previously characterized Pseudomonas mandelii KGI_MA19 were heterologously expressed in the E. coli expression system and purified to a level sufficient for further studies in which the catalytic activities of these FNRs will be required. As a continuation of this study, the electron transfer capabilities of these FNRs will be tested and compared to commonly used ferredoxin reductases, such as adrenodoxin reductase (AdR) and putidaredoxin reductase (PdR). Additionally, Fpr1 and Fpr2 will be coupled with ferredoxins from Pseudomonas mandelii KGI_MA19, as well as several other Fds, for a cytochrome c reduction assay to determine the most efficient redox pair that can be used for in vitro activity reconstitution of cytochrome P450s.

References

Aliverti, A., Faber, R., Finnerty, C. M., Ferioli, C., Pandini, V., Negri, A., Karplus, P. A., and Zanetti, G. (2001). Biochemical and crystallographic characterization of ferredoxin−$NADP^+$ reductase from nonphotosynthetic tissues. Biochemistry 40, 14501–14508.

Avron, M. & Jagendorf, A.T. (1956). A TPNH diaphorase from chloroplasts. Arch. Biochem. Biophys. 65, 475–490.

Bianchi, V., Haggard-Ljungquist, E., Pontis, E. & Reichard, P. (1995). Interruption of the ferredoxin (flavodoxin) $NADP^+$ oxidoreductase gene of Escherichia coli does not affect anaerobic growth but increases sensitivity to paraquat. J. Bacteriol., 177, 4528–4531.

Carrillo, N. & Vallejos, R.H. (1987). Ferredoxin-NADP$^+$ reductase. In The Light Reactions. Topics in Photosynthesis (Barber, J., ed.), Vol. 8, pp. 527–560. Amsterdam, the Netherlands: Elsevier.

Carrillo, N. (1998). Partition of ferredoxin-NADP$^+$ oxidoreductase between photosynthesis and antioxidant metabolism. In Photosynthesis: Mechanisms and Effects (Garab, G., ed.), Vol. 3, pp. 1511–1516. Kluwer, Dordrecht, the Netherlands.

Carrillo, N., & Ceccarelli, E. A. (2003). Open questions in ferredoxin-NADP$^+$ reductase catalytic mechanism. European journal of biochemistry, 270(9), 1900–1915.

Chen, Y.P. & Yoch, D.C. (1989). Isolation, characterization and biological activity of ferredoxin-NAD+ reductase from the methane oxidizer Methylosinus trichosporium OB3b. J. Bacteriol., 171, 5012–5016.

Corrado, M. E., Aliverti, A., Zanetti, G., and Mayhew, S. G. (1996). Analysis of the oxidation-reduction potentials of recombinant ferredoxin-NADP$^+$ reductase from spinach chloroplasts. Eur. J. Biochem. 239, 662–667.

Dudley, K.H., Ehrenb erg, A., Hemmerich, P. & Müller, F. (1964). Spektren und Strukturen der am Flavin-Redoxsystem beteiligten Partikeln. Helv. Chim. Acta 47, 1354–1383.

Hanukoglu, I. & Gutfinger, T. (1989). cDNA sequence of adrenodoxin reductase. Identification of NADP$^+$-binding sites in oxidoreductases. Eur. J. Biochem. 180, 479–484.

Jungermann, K., Kirchniawy, H., Katz, N. & Thauer, R.K. (1974). NADH, a physiological electron donor in clostridial nitrogen fixation. FEMS Microbiol. Lett. 43, 203–206.

Karplus, P. A., and Faber, H. R. (2004). Structural aspects of plant ferredoxin:NADP$^+$ oxidoreductases. Photosynth. Res. 81, 303–315.

Kranendonk, M., Commandeur, J.N., Laires, A., Rueff, J. & Vermeulen, N.P. (1997). Characterization of enzyme activities and cofactors involved in bioactivation and bioinactivation of chemical carcinogens in the tester strains Escherichia coli K12 MX100 and Salmonella typhimurium LT2 MA100. Mutagenesis 12, 245– 254.

Lacour, T. & Dumas, B. (1996). A gene encoding a yeast equivalent to mammalian NADPH-adrenodoxin oxidoreductases. Gene 174, 289–292.

Medina, M., and Gomez-Moreno, C. (2004). Interaction of ferredoxin–NADP$^+$ reductase with its substrates: optimal interaction for efficient electron transfer. Photosynth. Res. 79, 113–131.

Onda, Y., Matsumura, T., Kimata-Ariga, Y., Sakakibara, H., Sugiyama, T., and Hase, T. (2000). Differential interaction of maize root ferredoxin:NADP(+) oxidoreductase with photosynthetic and non-photosynthetic ferredoxin isoproteins. Plant Physiol. 123, 1037–1045.

Razquin, P., Fillat, M.F., Schmitz, S., Stricker, O., Böhme, H., Go´mez-Moreno, C. & Peleato, M.L. (1996). Expression of ferredoxin-NADP$^+$ reductase in heterocysts from Anabaena sp. Biochem. J. 316, 157–160.

Shah, M.M. & Spain, J.C. (1996). Elimination of nitrite from the explosive 2,4,6-trinitrophenylmethylnitramine (tetryl) catalyzed by ferredoxin NADP$^+$ oxidoreductase from spinach. Biochim. Biophys. Res. Commun. 220, 563–568.

Shin, M. & Arnon, D.I. (1965). Enzymic mechanisms of pyridine nucleotide reduction in chloroplasts. J. Biol. Chem. 240, 1405– 1411.

Vollmer, M., Thomsen, N., Wiek, S. & Seeber, F. (2001). Apicomplexan parasites possess distinct nuclear-encoded, but apicoplast-localized, plant-type ferredoxin-NADP$^+$ reductase and ferredoxin. J. Biol. Chem. 276, 5483–5490.

Weber-Main, A. M., Hurley, J. K., Cheng, H., Xia, B., Chae, Y. K., Markley, J. L., Martinez-Julvez, M., Gomez-Moreno, C., Stankovich, M. T., and Tollin, G. (1998). An electrochemical, kinetic, and spectroscopic characterization of [2Fe-2S] vegetative and heterocyst ferredoxins from Anabaena 7120 with mutations in the cluster binding loop. Arch. Biochem. Biophys. 355, 181–188.

Site-Directed Mutagenesis on Inactive CYP102A178 from Hydrothermal Hot Spring Hisaralan-Balıkesir

Elif Mehveş Özer[a,b], Başak Birdal[a,b], Kaan Dizer[a,b], Hande Mumcu[a,b,c], Nevin Gül Karagüler[a,b,c]

[a]Istanbul Technical University, Graduate School, Molecular Biology - Genetics and Biotechnology Program, Türkiye
[b]Istanbul Technical University, Dr. Orhan Öcalgiray Molecular Biology, Biotechnology and Genetics Research Center (ITU-MOBGAM), Türkiye
[c]Istanbul Technical University, Faculty of Science and Letters, Department of Molecular Biology and Genetics, Türkiye
ozere16@itu.edu.tr

Keywords: Hydrothermal Hot Spring, Self-sufficient P450, Site-Directed Mutagenesis.

Aim

Cytochrome P450s that use heme as a prosthetic group are monooxygenase enzyme systems that play essential roles in xenobiotic and drug metabolism, steroid and natural bioproduct synthesis (McDonnell, A. M., and Dang, C. H., (2013)). The active site of the enzyme contains cysteine residues that are bound to heme, which has a highly conserved motif among organisms. Even though some P450s require external redox partners, some cytochromes found as natural fusion proteins, called self-sufficient P450s, have their redox partners on the same polypeptide chain (Li, Z., et. al., (2020). CYP102A178 is a self-sufficient P450 that was recently obtained from the Hisaralan hydrothermal region of Balıkesir in Türkiye, and it has been defined with metagenomic approaches and bioinformatic applications by the Protein Engineering and Metagenomics group at Istanbul Technical University. The fact that CYP102A178 is obtained from Hisaralan, a thermophilic region, makes the enzyme's characterization more vital since it is an extremozyme and potentially can be active in high temperatures. The sequencing and multiple-sequence alignment results have shown that CYP102A178 has a tyrosine residue at the 440th position. This residue, which has a highly conserved heme-bound cysteine among other species, could potentially be responsible for inactive P450. This project aims to change the tyrosine residue with PCR-based site-directed mutagenesis to cysteine. Since the mutation is found at the active site, particularly at the heme-bound conserved location, it is thought to be playing an important role in the activity and functionality of the protein.
Within the scope of this project, the Y440C mutation of CYP102A178 were constructed. The biochemical characterizations will be carried out following the purification of the reverse mutated "potentially active" CYP102A178 (Y440C), and inactive CYP102A178 collected from Hisaralan. The findings of this project will provide evidence of the role and importance of heme-bound cysteine in the functionality and activity of the protein by reverse mutation.

Material and Method

1. Recombinant Expression and Purification

The plasmid of inactive CYP102A178 collected from Hisaralan was transformed to E. coli C43 chemically competent cells. The cells were centrifuged at 13000xg for 5 mins, and the supernatant was removed. Then, the resuspended cells were spread to kanamycin positive LB agar and incubated at 37 °C for 18 hours.
After 18-hour incubation, a selected positive colony was inoculated to 10 ml LB containing 10 µl (1:1000) kanamycin and incubated at 37 °C, 200 rpm for 18 hours.
10 ml of incubated pre-culture was transferred to 1-liter of TB and autoinducing media, which contains 0.6% glycerol, 0.05% glucose and 0.2% lactose, and the appropriate amount of kanamycin (1:1000), 5-ALA (5-Aminolevulinic acid), thiamine, riboflavin and trace element supplements was added further separately for finding the optimal medium for the expression condition. The culture was incubated at 20 °C and 25 °C for 12 to 24 hours

at 200 rpm, for selecting the appropriate induction conditions as well. The cells were harvested at 4000 rpm, at 4 ºC. The cells were sonicated (20 s on/20 s off for 3 mins) then, centrifuged. The supernatant was collected as clear lysate, which contains the protein of interest. For finding the optimal conditions for induction, expression studies are still being performed.

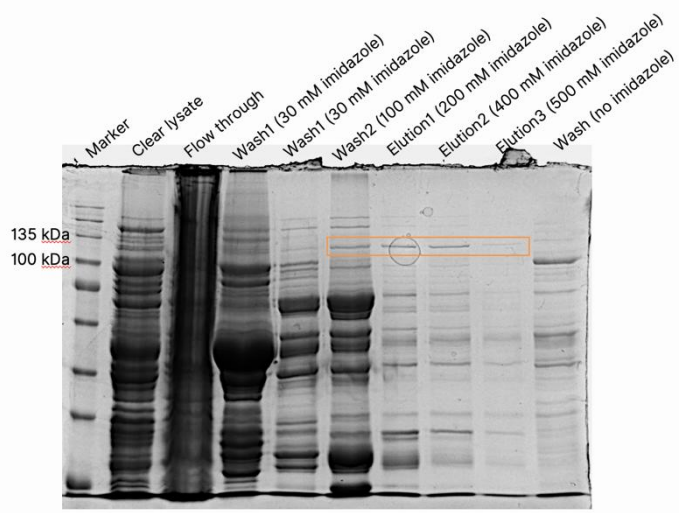

Figure 1. SDS-PAGE image for purified inactive CYP102A178 is shown. Molecular weight of CYP102A178 is 119 kDa and the protein is marked with orange square.

Immobilized Metal Affinity Chromatography (IMAC) purification of inactive CYP102A178 was carried out by cytiva HisTrap column. Purified protein was verified with SDS-PAGE, as can be seen in Figure 1, above. For the removal of residual imidazole and concentration of protein, 50 kDa cut-off Amicons was used.

2. PCR-based site-directed mutagenesis

A single substitution mutation was introduced into the CYP102A178 gene at position 440 with site-directed mutagenesis by usage of overlap extension PCR. The following gene-specific mutagenic primers was used for changing the tyrosine into cysteine amino acid residue.

Forward mutagenic primer: TGAGCGCGCCTGTATCGGCAT (5'->3')

Reverse mutagenic primer: ATGCCGATACAGGCGCGCTCA (5'->3')

For overlap extension PCR, another set of primers, which are plasmid-specific, were used and their sequences are shown below.

BamR (plasmid-specific) reverse primer: GCTAGTTATTGCTCAGCGG (5'->3')

T7 (plasmid-specific) forward primer: TAATACGACTCACTATAGGG (5'->3')

For overlap extension PCR, 2 fragments were obtained by independent PCRs. Forward mutagenic and BamR reverse primers were used to amplify the first fragment, while reverse mutagenic and T7 forward primers were used to amplify the second fragment. Both fragments are shown in Figure 2 below. PCR conditions for the nested PCRs are given in Tables 1 and 2.

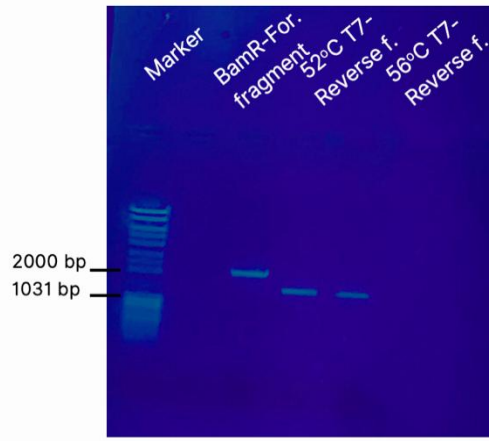

Figure 2. 0.7% Agarose gel image showing the BamR-forward mutagenic primer-fragment in the third lane, having 2.1 kb molecular weight, gradient PCR results for T7-reverse mutagenic primer fragment is shown at 4 and 5th lanes, having 1.4 kb molecular weight.

Table 1. PCR conditions for BamR-forward mutagenic primer fragment.

	Temperature (°C)	Time
In. Denaturation (x1 cycle)	98	30 sec
Denaturation (x30 cycle)	98	10 sec
Annealing (x30 cycle)	61	30 sec
Extension (x30 cycle)	72	1 min 3 sec
Final Extension (x1 cycle)	72	10 min

Table 2. PCR conditions for T7-Reverse mutagenic primer fragment.

	Temperature (°C)	Time
In. Denaturation (x1 cycle)	98	30 sec
Denaturation (x30 cycle)	98	10 sec
Annealing (x30 cycle)	56	30 sec
Extension (x30 cycle)	72	42 sec
Final Extension (x1 cycle)	72	10 min

After obtaining 2 fragments separately, an overlap PCR without any primers were set for annealing 2 fragments. Agarose gel result for the overlap PCR can be seen in Figure 3; gel extraction was performed for purifying the overlapped product from other non-annealed fragments.

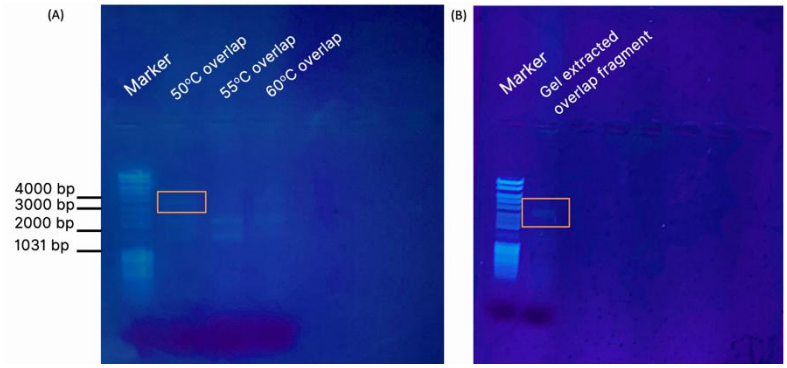

Figure 3. Gradient and primer-less overlap PCR was used for annealing 2 fragments (A), Overlapped fragments are marked with orange square, having 3.4 kb molecular weight. Overlapped fragment was gel extracted (B).

However, PCR amplification of overlapped product wasn't achieved yet, PCR optimization studies for amplification of the overlapped product is still being made. After successful amplification, the PCR product will be cloned to TOPO plasmid and will be blunt-end cloned to E. coli TOP10 cells. Expression, purification and characterization studies for potentially active CYP102A178 will be made further.

3. Spectral scanning and CO-binding assay

2 types of spectral scanning of purified active and inactive CYP102A178 will be performed. Purified enzymes will be reduced by 15 mg/ml Na-dithionate by a few minutes of incubation, their spectral scanning will be performed at 350-700 nm UV-VIS. The reduced samples will be saturated by CO to >90% level, and the same spectral scanning will be performed. Before and after saturation values will be used for drawing CO spectral graphic. As an alternative, characteristic Soret maxima of CYP102A178 will be determined for the water-bound state. Spectral scanning will be performed between 350-700 nm and the values obtained from the scanning will be used for low spin state characteristic Soret. With spectral scanning, characteristic Soret band of inactive CYP102A178 was determined as 408 nm, the characteristic Soret peak due to heme group of the enzyme can be seen in Figure 4, below.

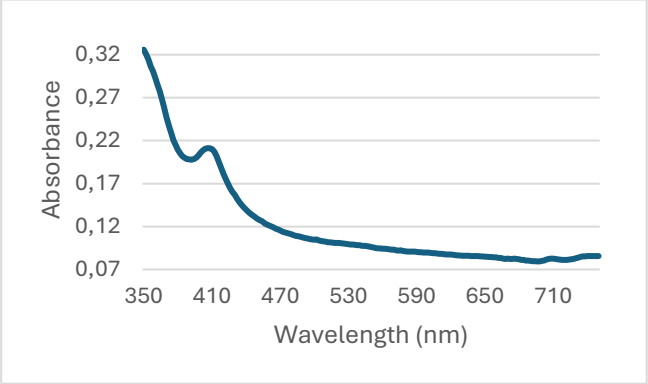

Figure 4. Spectral scanning of inactive CYP102A178 is shown for 350-700 nm, Soret maxima peak can be seen at 408 nm.

CO-binding assay will be performed both for active and inactive enzymes to determine their activity, a shift from 450 to 420 nm will be indicating the inactive or misfolded protein.

Findings

Recombinant expression, purification and biochemical characterization studies for inactive CYP102A178 was performed. Even though expression optimization studies were conducted for the inactive enzyme, only limited expression was achieved, there was no overexpression. The tyrosine residue, which could be responsible for inactive form of the enzyme could be a potential explanation for limited recombinant expression. Characteristic Soret maxima was determined with spectral scanning at 408 nm for the inactive enzyme. Overlap extension PCR with 2 sets of primers was used for Y440C mutation, but amplification of the final overlapped product couldn't achieve yet, PCR optimization studies are still being held. After successful PCR, cloning and Sanger sequencing, following expression, purification and characterization with CO-binding assay will be performed further for comparing inactive and potentially active CYP102A178.

Conclusion

Gene specific forward and reverse mutagenic primers with plasmid specific primers (BamR and T7) and PCR conditions for desired (Y440C) mutation at pET28(a)+CYP102A178 construct were designed and determined. Autoinducing medium containing necessary supplements, with induction at 25 °C were selected as the optimal conditions for recombinant expression of inactive CYP102A178 collected from Hisaralan but optimization studies are still being made. Spectral scanning, which will be held at later stages of the project, will compare the mutated and inactive CYP102A178. With the characterization step that is performed with CO-binding assay, functionality of the inactive and active CYP102A178 will be determined.

References

Li, Z., Jiang, Y., Guengerich, F. P., Ma, L., Li, S., & Zhang, W. (2020). Engineering cytochrome P450 enzyme systems for biomedical and biotechnological applications. Journal of Biological Chemistry, 295(3), 833-849.
McDonnell, A. M., & Dang, C. H. (2013). Basic review of the cytochrome p450 system. Journal of the advanced practitioner in oncology, 4(4), 263.

MUSIC

Ethnomusicology

Music Business and Management

Music Performance

Music Theory

Sonic Arts

Sound Engineering and Design

Sonified Memory of the 2020 Aegean Sea Earthquake

Doruk Başoğlu[a]

[a] Istanbul Technical University, Music, Ethnomusicology, Turkey
basoglu22@itu.edu.tr

Keywords: Autoethnography, Data Sonification, Multimedia.

Introduction

What is that event we feel as an earthquake, or try to make sense of by checking with one another: "Was that an earthquake?" or "Did you feel it?" I usually check the stillness of the water in a jug or look for swinging ceiling lamps. Besides the usual minor earthquakes, I have only experienced one major earthquake in my life—a destructive one where houses collapsed and people lost their lives. Even in the middle of such a strong tremor, I could still ask myself, "Is this an earthquake?" because I didn't fully understand what was happening. It was only when my uncle rushed in that the situation crystallized—the place transformed into the earthquake itself. That's when we transitioned into "drop, cover, and hold on." Looking back, I realize that, aside from the drills we practiced in elementary school, that was the first time I ever truly performed "drop, cover, and hold on." I believe that paralysis seems entirely plausible in such an unexpected event. But if we fully recognized what was happening, would that also be the moment when we understood what needed to be done?

According to Kandilli Observatory and Earthquake Research Institute Press Release (2020), on October 30, 2020, a very strong earthquake with an instrumental magnitude of 6.9 occurred in the Aegean Sea, between the north of Samos Island and off the coast of Doğanbey-Izmir, at 14:51 local time (Figure 1). It was felt over a wide area, particularly in İzmir and its districts, as well as throughout the Aegean and Marmara regions. Unfortunately, 119 people lost their lives and 1053 people got injured in Izmir, and Samos. I experienced the event at home with my mom, aunt, uncle, and two young cousins. It was the biggest seismic tremor I have ever felt in my life. The following week was quite traumatic for me. I could do nothing but follow the news, waiting to hear whether more people would be pulled from the wreckage of collapsed buildings. Although I was mostly traumatized by it, I was also fascinated by that powerful seismic vibration I experienced at home. I thought about how I can reflect on that rare physical sensation. That experience, together with the sad memory of the 2023 Kahramanmaraş Earthquakes led me to research tectonic experiences through sound, vibration, and body. With Sonified Memory of the 2020 Aegean Sea Earthquake, I explore what I recognized in the moment of the earthquake and what I realized afterward, through my engagement with scientific data and the artistic production process.

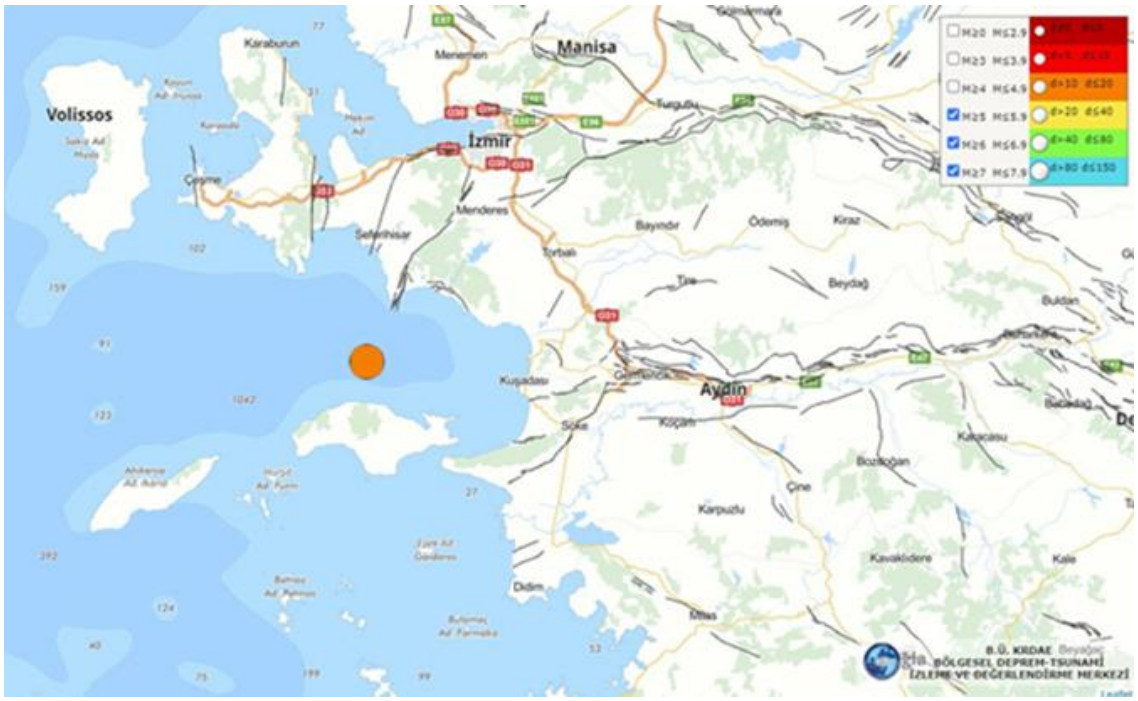

Figure 1. 2020 Aegean Sea Earthquake map (Kandilli Observatory and Earthquake Research Institute, 2020).

Seismic Data Sonification

Earthquake sonification has been a common method since the 1960s for processing earthquake data (Michael, 2019). The sonification process involves speeding up seismic waveform data and shifting the pitch, as seismic waves must be accelerated to reach the human hearing range, since earthquakes produce vibrations mostly below 10 Hz, which humans are not capable of hearing (Hirai et al., 2012). However, in case the more the data is sped up, the more once can grasp the vibratory texture of the event as whole, meaning the contribution of lower frequencies to the whole group of vibrations. On the contrary, the more the data is sped up, the shorter the sonification occurs. Reducing the duration in the event may somehow make it harder for us to process it by hearing, by making the earthquake sound for just a very little moment in space-time.

Aim

This study explores the ways in which tectonic vibrations are felt, remembered, and sensed by human bodies, examining the intersection of seismic phenomena, memory, affect and sensations. It seeks to create an artistic form of seismic waveform data sonification to recreate my memory of the earthquake, reflecting not only the temporal aspect of the event but also its emotional and physical impact. The aim is to understand how the tectonic vibrations manifested in the shaking I felt at home five years ago, how much earlier my cat in İzmir could have sensed the earthquake—particularly the earlier arrival of vertically propagating primary waves from the epicenter—and how the sonification and my artistic choices to reproduce the earthquake via Virtual ANS software correlate politically and ethically with the shaking I experienced. By bridging the gap between scientific data and personal narrative, this work seeks to develop an alternative way of understanding the spatio-temporal, sensory, and emotional dimensions of the earthquake experience, connecting objective seismic data with subjective human perception.

Material and Method

Located 5 kilometers away from where I physically vibrated with the earthquake, the Balçova (BLCB) seismology station recorded seismic vibrations originating from the northeast of Samos Island, 58 kilometers away from the epicenter. The seismogram recording of the BLCB seismology station was collected from the Kandilli Observatory Regional Earthquake and Tsunami Research Institute database. Using the ObsPy seismology software and the Virtual ANS spectral synthesizer, the frequency spectrogram of the seismic waveform data (Figure 2) from this

earthquake was sonified. While moving back and forth between image and sound, I carefully adjusted the settings on the Virtual ANS software, observing the sonic outcomes and their alignment with my memory of the event. The reproduction tempo is set as 60 beats per minute for every beat to take 1 second. The playback rate is changed to 5 pixels per beat. Since the horizontal axis of the seismic spectrogram image contains 616 pixels, it takes 123 seconds to reproduce the whole image, as the original duration of the event recorded by BLCB seismology station between 11.51 to 11.53, 2 minutes. The multimedia interface of Virtual ANS, while sounding the earthquake's frequency spectrogram, was combined with the chronological order of events in my recalled experience. By inscribing my episodic memory of the temporal order of events that occurred at home during the earthquake, a 2-minute-long audiovisual material (Figure 3) was created to reproduce the shaking with the 2020 Aegean Sea Earthquake at home.

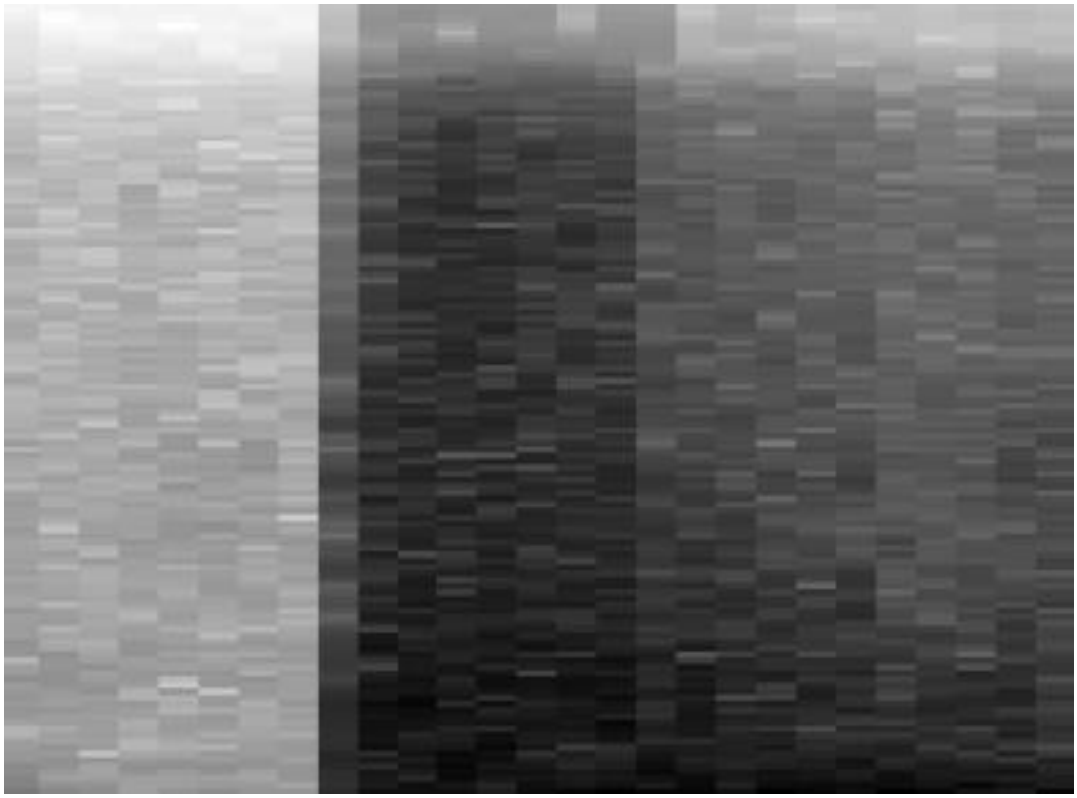

Figure 2. BLCB seismogram recording's frequency spectogram image, October 30 2020, from 11.51 to 11.53.

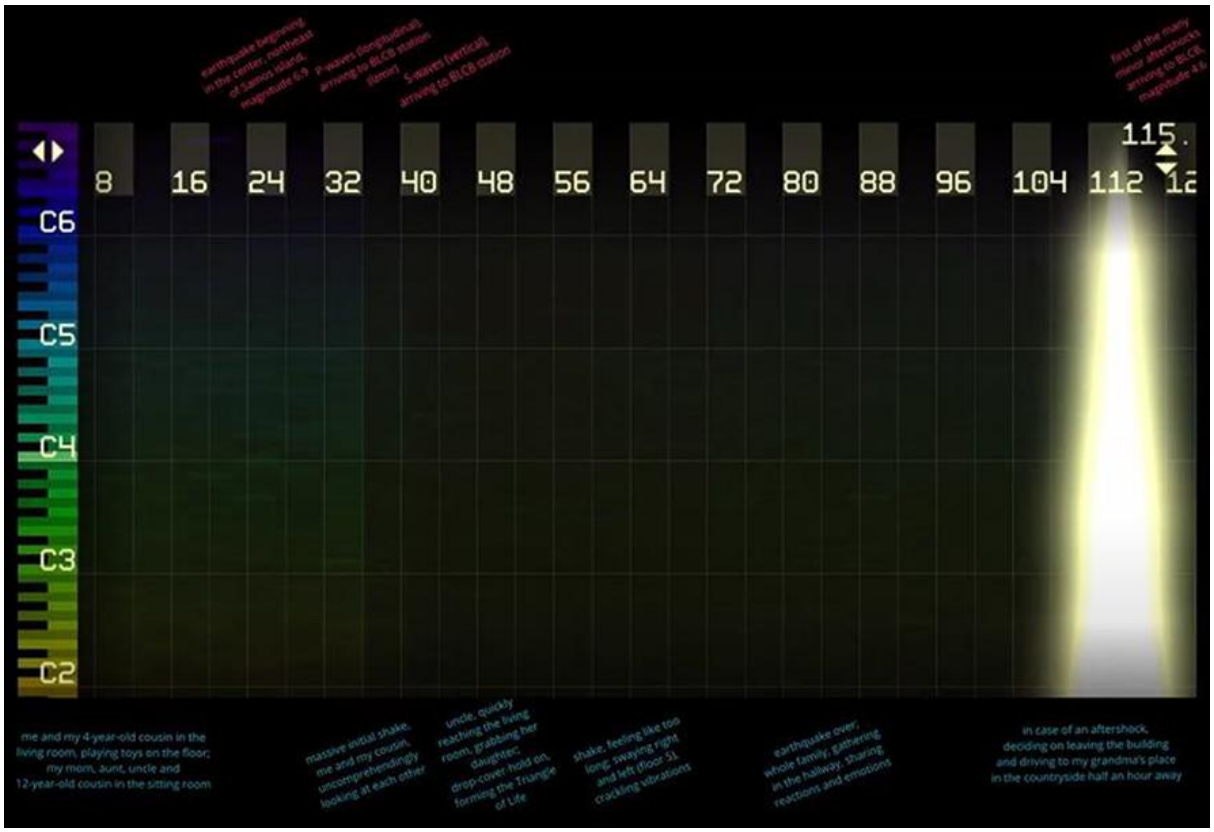

Figure 3. Seismic frequency spectrogram image sonification on Virtual ANS playback interface, along with my earthquake experience depicted over the timeline. "me and my 4-year-old cousin in the living room, playing toys on the floor; my mom, aunt, uncle and 12-year-old cousin in the sitting room - massive initial shake, me and my cousin uncomprehendingly looking at each other - uncle, quickly reaching to the living room, grabbing her daughter; drop-cover-hold on, forming the Triangle of life - shake, feeling like too long; swaying right and left at floor 5, crackling vibrations - earthquake over; whole family, gathering in the hallway, sharing reactions and emotions - in case of an aftershock, deciding on leaving the building and driving to my grandma's place in the countryside half an hour away".

Findings

The ultimate sound is like a broadband noise that is not particularly creepy and, if its source is not specified, could resemble the base-level sound of any constant process. When the earthquake event takes place, what is heard as changing is not much beyond the overall intensity; no particular group of sounds stands out to indicate that something specific happened. Instead, it sounds like an intensification of the existing noise. However, on the spectrogram and from the sonification, we can still see and hear that the earthquake emerges with a sudden saturation at the bottom of the spectrum. While the time-compressed earthquake data sonifications do not fully capture the dynamic range of the phenomena, Virtual ANS allows one to perceive the shifts in frequency and loudness of the seismic vibrations from an auditory perspective. While listening to the temporal and timbral qualities of the Sonified Memory of the 2020 Aegean Sea Earthquake, I was able to reconstruct the sequence of events in the house—how one act followed another, and another act followed that. This approach not only embodied the intensity of the orderly events from my memory but also allowed me to explore the intersection of scientific data and personal narrative. Such an artistic auto-ethnography helped me revisit the earthquake experience, and placed me into a personal transformation process. I was able to narrate my densely lived experience in an alternative way, creating new meaning and understanding from the chaos I had endured.

Conclusion

The sonification of the 2020 Aegean Sea Earthquake's frequency spectrogram evolved into a process of both remembering and reconstructing, as I narrated my experience by inscribing my voice and text onto the sonification interface during the audiovisual playback created by Virtual ANS software. Moreover, shifting between the data from different seismographs, including those beyond the BLCB seismology station, that recorded the earthquake, as well as navigating between sound, image, and coding, enriched my conceptualization of earthquakes beyond a human-centered perception range. This multidimensional exploration not only deepened my understanding of the intricate relationship between body, sound, vibration, movement, and time but also revealed how seismic phenomena can be experienced and interpreted through multiple sensory and artistic lenses. By engaging with the earthquake data in this way, I was able to uncover new layers of meaning, connecting the scientific and the personal, the objective and the subjective. What one could learn from such a process of remembering, at best, would be a kind of mental preparedness for a similar experience in the future—which, I guess, I eventually realized during the 2025 Istanbul Earthquake. I recognized that we were experiencing real tectonic seismicity. I quickly reached out to the washing machine—just as I had previously decided—and dropped, covered, and held on without losing any time. Like my uncle did for me five years ago, I shouted to my flatmate to recognize the shaking, take his position, and wait. The attack and decay of the vibration, as well as the building's oscillatory profile, felt familiar to me; I observed the vibrational time of the quake in relation to my previous tectonic experience. When I realized that I didn't feel the same shock during the 2025 Istanbul earthquake, I understood how reassuring body memory can be in the moment of a disaster. In conclusion, this process of reinterpreting the earthquake through sound and memory has opened up a space for healing and reflection, allowing me to reframe my relationship with the event as a form of future preparedness.

Lastly, the relationship of sound with other forms of graphic or digital representations is fascinating in terms of their indexicality to each other. Though neither intended to be heard nor graphically viewed, seismic waveform data constantly document the frequency of the ground's wiggle under the lands, oceans, volcanoes, mines… Prior to this sonification process, I had no idea how my physical experience of tectonic vibrations through the solid would sound to my auditory organs, as sound waves. I never knew that one day I could seismically play that tactile sensation underneath my feet, inside the building, in the Triangle of Life five years ago. I also didn't know that I could listen to the physical movement, speed and texture of this solid earth matter, captured by a transduction instrument in Izmir, built by Kandilli seismologists 20 years ago. In conclusion, this artistic and auto-ethnographic approach to seismic data highlighted the potential of sonification as a transformative tool for bridging scientific data, personal memory, and emotional resonance.

References

Kandilli Observatory and Earthquake Research Institute. (2020). 30 Ekim 2020 Ege Denizi depremi [Press release]. http://www.koeri.boun.edu.tr/sismo/2/30-ekim-2020-mw6-9-ege-denizi-izmir-depremi/, date retrieved 01.06.2024

Hirai, T., Kurata, K., Fukuwa, N., & Mori, M. (2012). Synthesis of earthquake sound using seismic motion record and its application to audiovisual earthquake experience system. Proceedings of the 15th World Conference on Earthquake Engineering. Retrieved from https://www.iitk.ac.in/nicee/wcee/article/WCEE2012_0380.pdf, date retrieved 20.05.2025

Michael, A. J. (2019). Earthquake sounds. Encyclopedia of solid earth geophysics, 1-5.

MUSIC

Ethnomusicology

Music Business and Management

Music Performance

Music Theory

Sonic Arts

Sound Engineering and Design

Music Memes and the Relationship Between Music Marketing and Humor in Turkey: The Past, Present, and Future

Alp Timuçin Bulut [a], Can Karadoğan [b]

[a] Istanbul Technical University, Graduate School, Music Master's Program, at İTÜ/MİAM (Dr. Erol Üçer Center for Advanced Studies in Music), Türkiye
[b] Istanbul Technical University, İTÜ TMDK (Turkish Music State Conservatory) Music Technology Department & İTÜ MİAM (Dr. Erol Üçer Center for Advanced Studies in Music), Türkiye
buluta22@itu.edu.tr, karadoganc@itu.edu.tr

Keywords: Music, Humor, Meme Culture, Digital Activism.

Aim

The significant role of music and humor in creating and enhancing experiences, as well as fostering connections and building enduring memories, cannot be overstated. In recent times, digital platforms have transformed the ways in which we discover and disseminate music, with memes and viral trends becoming increasingly popular. Historically, Turkey has employed satire and folklore in its marketing strategies, but the current landscape is dominated by digital culture, as social media and memes have taken over from traditional approaches. Currently, music memes function as not only a source of amusement but also serve as a tool for making social commentary, thereby shaping individuals' perceptions of music and cultural identity. This study aims to examine the historical and contemporary impact of humorous music content on Turkish audiences, with a focus on determining whether music memes create a lasting cultural and emotional impact or merely generate transient impressions. For example, research on digital culture reveals that memes have created a new language of communication among individuals while diminishing the influence of traditional media tools (Shifman, 2014). The communicative power of memes has been observed throughout history, not only in the field of music but also in politics and economics, where they have created significant impacts. As an example, The GameStop incident, when examined within the framework of subculture and social identity, demonstrates the impact of digital platforms on financial markets (Tanrıverdi & Pehlivan, 2023). In another resarch about politics shows It has been noted that caps are sometimes used as ideological and political tools, while at other times they function as a means of communication with both supporters and opposing views (Kahya, 2018).

Material and Method

This study employs a qualitative methodology, incorporating content analysis and case studies of digital music marketing campaigns and music memes in Turkey. Archival research examines how humor and music have historically been used to evoke emotions and foster cultural bonds. Additionally, digital ethnography will be used to analyze viral music memes, digitally marketed music videos, and audience reactions on social media platforms to assess levels of engagement and perception. This study will also examine historical music-related cartoons used in Turkish media, analyzing their role in shaping public opinion and cultural discourse. Furthermore, articles published in music magazines will be reviewed to understand how humor and music have been discussed over time. Interviews with musicians, cultural experts, and digital content producers will provide further insights into the psychological and social effects of humorous music content. Turkish case studies will be evaluated alongside international examples to provide a comparative perspective on the role of humor in music marketing and audience interaction.

Findings

The emerging findings reveal that both music and humor exert a significant influence over cultural narratives and personal opinions. Turkish music marketing has successfully merged past and present elements to generate a sense of nostalgia and community, an approach that has been further enhanced by digital platforms like memes and viral campaigns. Memes offer easily accessible and engaging content, which can provoke emotional responses rapidly. However, there is also a risk that they might trivialize rich cultural traditions, which could lead to superficial and transient impressions. Music is a strong way to people impress their ideas.Furthermore, In a study examining the impact of music on social identities, it was emphasized that music serves as an important social tool for individuals to express themselves and as a domain where social identities are reflected (Sağır & Öztürk, 2015). Music memes have been successful in driving digital activism, enabling individuals to engage in serious social and political discussions using humor and satire. Research suggests that when integrated effectively, music and humor can strengthen social bonds, bolster collective memory, and encourage deeper cultural engagement. Humor and music coming together online show how people engage with content in various ways based on culture. Personal taste and understanding of digital tools also play a role. A key finding is the change in audience engagement from just consuming music to actively participating in it. Online platforms let people remix and share music memes. This creates a culture where humor is a vital communication tool.

Unlike traditional music marketing controlled solely by industry experts, digital meme culture enables users to craft narratives and influence trends. They can form online communities based on shared jokes and music tastes. Challenges remain regarding the sustainability of music memes in maintaining audience engagement. Humor can make content go viral but may not maintain long-term interest in an artist or music trend. Music companies and musicians using memes for promotion need to balance authenticity with marketing. Audiences often reject humor that feels too commercial or fake. Music memes can break through language and cultural barriers. Humor is often tied to culture, but themes like satire and irony resonate universally. This allows music memes to reach a wide audience globally, expanding the influence of Turkish music beyond national borders. The rapid spread of memes enables musicians to quickly adapt to trends, keeping their content relevant in the ever-changing digital landscape. The monopolistic structure of traditional music marketing is being replaced by a dynamic structure where users can create trends and shape content. Music memes are at the center of this structure and have become an important tool in marketing strategies. However, humor that feels overly commercialized and artificial is generally perceived negatively by the audience.

The authenticity of humor stands out as a determining factor in the acceptance of content. Therefore, music producers and marketing experts should turn to strategies that include sincere and culturally meaningful humorous elements.The marketing dimension of the study shows how music memes are positioned as strategic communication tools rather than cultural narratives. The power of viral content to trigger emotional interaction is particularly valuable in terms of creating brand equity, strengthening the artist's image and connecting with the target audience.Through music memes, artists are remembered and talked about not only for their songs but also for the meme culture of which those songs are a part. This creates a kind of cultural "co-branding" effect and becomes an element that supports permanence in music marketing.Moreover, humor's ability to incorporate both universal and local elements makes it easier for Turkish music to cross borders and reach international audiences. The cross-cultural transitivity of forms of expression such as satire, irony, and parody makes it possible for memes to function in the global digital market.

Conclusion

The impact of humor on music should not be underestimated, as it has the potential to significantly enhance our enjoyment and appreciation of songs. Studies have demonstrated that humor can facilitate memory retention, thereby suggesting that amusing elements in music could contribute to an increased likelihood of recalling specific songs and the artists associated with them. Humor plays a critical role in engaging people and informing their musical tastes, all while reinforcing cultural values and beliefs. With this in mind, future academic inquiries would be well-served to explore the lasting cultural ramifications of music memes and their potential to exert influence beyond their initial surge in popularity. The impact of these memes on the transformation of music-listening habits and their utilization in online activism remain largely unexplored. Additionally, research that delves into the

influence of music memes on humor trends across various generations is both timely and essential. By comparing Turkish music meme trends with those observed on a global scale, a more comprehensive understanding of the interplay between humor and music-related content can be achieved. As Turkish music continues to mature and adapt within the digital realm, it is of the utmost importance to investigate the role of humor in shaping audience receptions and behaviors. This line of inquiry significantly enriches our understanding of the intricate relationship between humor, music, and digital culture and emphasizes the continually evolving nature of music engagement in the modern era. On the other hand, internet memes have been noted to play an active role in internet-based communication as a digital cultural object.(Yılmaz,2017)

Furthermore, humor and music play a crucial role in the formation of collective identity and community building. Through shared jokes, nostalgic references, and viral trends, online audiences develop a sense of belonging that transcends geographical boundaries. Whether through satire, irony, or parody, humorous music content fosters a dynamic space where individuals engage with one another, reinforcing cultural ties and collective memory. Music memes act as a digital storytelling mechanism, allowing communities to express themselves, critique societal norms, and celebrate musical heritage. This interplay between humor and music not only enhances entertainment but also serves as a powerful social tool that strengthens community bonds and collective experiences. Which is another form of humor memes, as a digital cultural object, play an active role in internet-mediated communication.(Yılmaz, 2017).

From a marketing perspective, music memes offer a lower-cost, more intimate and faster response strategy than traditional advertising methods. However, the viability of such content depends not only on its viral potential, but also on its authenticity and social sensitivity. Commercially motivated, fake or forced humor is easily detected by the audience and is often met with a negative reaction. It is therefore important for artists and music marketing teams to develop creative strategies to ensure that content 'naturally goes viral'.

The international impact of music memes is also noteworthy. Despite cultural differences, some forms of humor (e.g. visual jokes, gestures, absurd expressions) can find universal appeal. In this respect, music memes can be considered as a tool with the potential to bring Turkish music to international audiences. Especially for diaspora communities and digital migrants, this content functions as both a reminder of identity and a means of social bonding.

References

Kahya, Y. (2018). Bir iletişim aracı olarak mizah: Sosyal medyada spor temalı 'caps' kültürü. Avrasya Uluslararası Araştırmalar Dergisi, 6(15), 1020-1030. https://doi.org/10.33692/avrasyad.510079

Sağır, A., & Öztürk, B. (2015). Sosyolojik bağlamda müzik ve kimlik: Karabük Üniversitesi örneği. Uşak Üniversitesi Sosyal Bilimler Dergisi, 8(2), 121-154. https://doi.org/10.12780/uusbd.48205

Shifman, L. (2014). Memes in digital culture. MIT Press.

Tanrıverdi, Y., & Muratoğlu Pehlivan, B. (2024). Gamestop olayı: Alt kültür ve sosyal kimlik çerçevesinde bir inceleme. İstanbul Ticaret Üniversitesi Sosyal Bilimler Dergisi, 23(51), 2281-2318. https://doi.org/10.46928/iticusbe.1558931

Yilmaz, Ç. (2017). İnternet-ortamlı mem çalışmaları: Uluslararası alanyazına bir bakış ve Türkiye'deki olanaklar (Internet-mediated meme studies: A detailed review of international literature and potentialities in Turkey). 8(15), September.

MUSIC

Ethnomusicology

Music Business and Management

Music Performance

Music Theory

Sonic Arts

Sound Engineering and Design

Challenging Conventions: Clara Wieck's Op. 20 and the Gendered Landscape of 19th-Century Music

İrem Hayrioğlu[a]

[a] Istanbul Technical University/Social Sciences Institute, Music, Music Performance, Turkiye
iremhayrioglu@gmail.com

Keywords: Clara Wieck, Gender and Composition, Romanticism, Variations Op. 20, Women in Music.

Aim

In spite of the fact that Clara Wieck is the most widely recognized female composer of the present day, her compositional capabilities have not been sufficiently investigated. Academic studies predominantly focus on her role as a pianist or teacher, often neglecting her identity as a composer. This analysis aims to examine how Schumann developed her artistic individuality despite societal constraints, how her style evolved over time, and how Op. 20 serves as both a deeply personal confession and a declaration of artistic independence. By addressing these questions, this study highlights Clara Wieck's contributions beyond her roles as a pianist and Robert Schumann's spouse, emphasizing her rightful place as a composer who demanded recognition.

In 1853, Clara composed Variations on a Theme by Robert Schumann, Op. 20 in honor of Robert's 43rd birthday, using a theme from Bunte Blätter, Op. 99. This work represents one of Clara's last piano compositions and serves as a critical point in her stylistic development. To understand her compositional identity, her career can be divided into three distinct periods: the early years (1830s–1840s), the mature period (1850s), and the late period (1860s and beyond). This study will provide an in-depth examination of these periods with a particular focus on Op. 20.

Material and Method

This study focuses on Clara Wieck's Variations on a Theme by Robert Schumann, Op. 20, because it represents a critical turning point in her stylistic development, bridging her earlier virtuosic writing with a more introspective, harmonically complex language. While previous studies (e.g., Buer, 2000; Reich, 2001) have analyzed the autobiographical and technical aspects of this work, they often treat it within broader surveys of her life rather than as a site of artistic declaration. Through a detailed musicological analysis of Op. 20—focusing on its harmonic, rhythmic, motivic, and formal innovations—this study aims to highlight aspects of her compositional voice that have been underexplored.

A feminist theoretical lens is also applied to reevaluate how gendered expectations influenced both the reception of her work and her self-perception as a composer. Primary sources such as concert programs, personal correspondence, and historical critiques are used to situate Op. 20 within the broader cultural and personal context of mid-19th-century Europe. In doing so, this analysis offers new insights into how Wieck's compositional language matured independently of her better-documented roles as a pianist and muse, challenging earlier narratives that inadvertently subordinate her identity as a composer.

Findings

Clara Wieck's formative years (1830s–1840s) were profoundly affected by her father, Friedrich Wieck, who significantly influenced her pianistic and creative growth. During this period, she created compositions that conformed to the virtuoso standards of the era, highlighting dexterity and technical excellence. Soirées Musicales, Op. 6 (1836) is a quintessential composition from this era, characterized by swift figurations and ornamental embellishments akin to those of Chopin and Liszt. Likewise, her Piano Concerto in A Minor, Op. 7 (1833–1835) exemplifies her initial emphasis on magnificence and virtuosity over substantial theme evolution.

In the mature period (1850s), Clara's composing approach progressed towards enhanced harmonic depth, structural intricacy, and emotional closeness. Op. 20 exemplifies this transition by elaborating on Robert Schumann's theme with harmonic sophistication and emotional profundity. Despite societal limitations that frequently obscured her

individuality as a composer, Op. 20 underscores her artistic independence within the Romantic tradition. Moreover, numerous historical documents indicate Robert Schumann's intrigue with the interplay of tone, color, and character, especially his preference for the key of F-sharp minor, which he linked to a nebulous and sad essence. This key, widely featured in Bunte Blätter, also plays a crucial role in Clara's Op. 20, enhancing their musical conversation.

Insights acquired during the performance preparation indicate that the structure of the variations is intentionally designed to oscillate between instability and resolve, both harmonically and emotionally. Specifically, Variation III's rhythmic fluidity and tonal ambiguity, along with Variation VI's progressively introspective and fractured texture, underscore Clara's ability to subvert the listener's expectations in favor of reflection. These selections indicate a deliberate manipulation of musical time and narrative—a characteristic frequently overlooked in current analytical work.

Moreover, it is significant because prior research has seldom recognized Op. 20 as Clara Schumann's ultimate completed solo piano work. This study, grounded in analytical inquiry and performative involvement, posits that the variations collectively function as a retrospective self-portrait, with each representing a distinct phase in her artistic and emotional evolution. The practice and memorization of the work revealed that the cycle not only elaborates on a certain theme but also defines a profoundly personal narrative loop.

An in-depth analysis of each variant, both analytically and in terms of performance practice, uncovers a comprehensive framework that reflects Clara's developing identity. The initial variation presents a Romanticized interpretation of Robert's subject, characterized by intricate elaboration and harmonic richness. The expressive intimacy indicates the influence of Mendelssohn and a hint of salon-style elegance—an emblem of Clara's nascent musical identity. Variation II, more delicate and uncertain, expresses emotional weakness, potentially reflecting the sensation of youthful doubt. The third version intensifies the emotional complexity: harmonically rich and rhythmically constricted, it suggests psychological turmoil—possibly illness, depression, or grief. Breath and phrasing emerge as essential instruments for the artist in expressing its intrinsic significance.

Variation IV exhibits a notable disparity through its virtuoso brightness and swift articulation. Clara demonstrates her pianistic prowess through rapid staccato passages and dynamic energy. Variation V, characterized by its intense octave writing and vigorous dynamics, conveys a profound sense of turmoil—nearly a musical dissent. This may reference Clara's unhappiness with societal constraints or possibly Robert's Florestan persona. The abrupt transition in Variation VI to a rigid canon structure signifies a reversion to discipline and contemplation, potentially evoking her formative studies with her father. This variation's sense of control and internal tension might be seen as a sound metaphor for obedience and initial creative training.

The seventh variation cohesively unites the expressive elements of the cycle, culminating in a serene yet potent finish. It is abundant in thematic references and structural unity, offering both formal resolution and emotional validation. It appears to be Clara's ultimate artistic declaration—simultaneously a farewell and a subtle affirmation of identity. Consequently, Op. 20 can be interpreted as more than only a birthday present for Robert Schumann; it serves as a comprehensive and introspective work, cognizant of its own conclusion.

In the late period (1860s and thereafter), subsequent to Robert Schumann's demise in 1856, Clara's compositional productivity diminished markedly. She predominantly forsook writing to prioritize her career as a performer and instructor, shaped by personal sorrow and societal constraints that dissuaded women from engaging in composition as a permanent vocation.

During the 19th century, female composers were anticipated to create salon music—enjoyable, small-scale compositions that adhered to gendered norms of musical artistry. Although variation form was esteemed by male composers such as Brahms, Beethoven, and Mendelssohn, Clara Wieck's involvement in the genre contests the notion that women's compositions were merely decorative. Her employment of contrapuntal textures, harmonic intricacy, and motivic evolution positions her with prominent composers of her era, challenging the marginalization of female composers in the annals of music history.

Furthermore, Op. 20 holds considerable importance for Clara's career as a performer. During a period when she was financially sustaining her family through concert appearances, this work was produced not for monetary profit but for sheer artistic gratification. Unlike Soirées Musicales, which satisfied audience demand for spectacular virtuosity, Op. 20 is a contemplative composition that emphasizes musical profundity over technical exhibition.

This distinction highlights the desire for female artists to exhibit technical excellence to attain reputation. In contrast to male composers, who were not obligated to demonstrate their virtuosity in their works, female composers were compelled to validate their merit as performers. Clara Wieck's capacity to reconcile these expectations while maintaining a dedication to musical profundity is apparent in Op. 20.

Conclusion

Though history often portrays Clara Wieck as being overshadowed by Robert Schumann, the reality is that she was the one financially supporting their family, raising their children, and premiering her husband's works—all while maintaining her own artistic career. While the men around her admired her resilience, her personal writings reveal persistent self-doubt. In her letters, she repeatedly expressed the belief that, as a woman, her artistic potential was inherently limited, thereby underestimating her own accomplishments. Variations on a Theme by Robert Schumann, Op. 20 exemplifies her fully developed compositional voice, yet her self-imposed doubts reflect the broader gendered constraints of her era. Despite these challenges, she sought the recognition that had been denied to her in life. It remains compelling to consider how her compositional voice might have evolved had she been afforded the same artistic freedoms as her male contemporaries.

References

Buer, K. (n.d.). Extra-compositional References and Private Meaning in Clara Schumann's Variations on A Theme of Robert Schumann, Op. 20 [University of Northern Colorado]. Rocky Mountain Society for Music Theory, United States of America. https://arts.unco.edu/music/rocky-mountain-society-music-theory/2020conferencebuer.pdf

Davies, J., & Grimes, N. (2023). Clara Schumann: Changing Identities and Legacies. Nineteenth-Century Music Review, 21(1), 3–11. https://doi.org/10.1017/s1479409823000034

De Almeida Monteiro Da Silva, E. M. (2008). Clara Schumann: compositora x mulher de compositor. https://doi.org/10.11606/d.27.2008.tde-05072009-234006

De Lara, A. (1945). Clara Schumann's teaching. Music and Letters, 26(3), 143. https://doi.org/10.1093/ml/26.3.143

Detels, C., & McClary, S. (1992). Feminine endings: music, gender, and sexuality. Journal of Aesthetics and Art Criticism, 50(4), 338. https://doi.org/10.2307/431414

Goertzen, V. W. (2014). Arrangements by Clara Schumann. Notes, 70(3), 522–525. https://doi.org/10.1353/not.2014.0019

Green, L. (2023). Gender, musical meaning and education. In Routledge eBooks (pp. 123–131). https://doi.org/10.4324/9781003419495-13

Higgins, P. (1993). Women in Music, Feminist Criticism, and Guerrilla Musicology: Reflections on recent polemics. 19th-Century Music, 17(2), 174–192. https://doi.org/10.2307/746332

HOWE, B. J. (2010). On stage and in class: women artists in Mid-19th-Century wheeling. Appalachian Journal, 37, 184–209. https:///Users/iremhayrioglu/Desktop/Gender and Music/HOWE-StageClassWomen-2010.pdf

Nakagawa, E. (2020). Like Minds in Variations: Clara Schumann's Variations on a Theme by Robert Schumann, Op. 20. Mahidol Music Journal, 3.

Reich, N. B. (2001). The Artist and the Woman. Cornell University Press.

Reich, N. B., & Burton, A. (1984). Clara Schumann: Old Sources, New Readings. The Musical Quarterly, LXX(3), 332–354. https://doi.org/10.1093/mq/lxx.3.332

Schumann, R. (1993). The marriage diaries of Robert & Clara Schumann. https://openlibrary.org/books/OL1421211M/The_marriage_diaries_of_Robert_Clara_Schumann

Steblin, R. (2013). The gender stereotyping of musical instruments in the Western tradition. Canadian University Music Review, 16(1), 128–144. https://doi.org/10.7202/1014420ar

Tosi, A., & Rosslyn, W. (2012). Women in Nineteenth-Century Russia: Lives and culture. In Open Book Publishers. https://doi.org/10.11647/obp.0018

Messiaen as Liturgist: A Contextual Reading of the Vingt Regards sur l'Enfant-Jésus

Robert McDonald[a]

[a] Istanbul Technical University, Center for Advanced Studies in Music (MIAM), Türkiye
robbiemacplayspiano@gmail.com

Keywords: Catholicism, Liturgy, Messiaen, Vingt Regards sur l'Enfant-Jésus.

Aim

Olivier Messiaen's paraliturgical religious music has benefited from thorough scholarship on its theological, ornithological, theoretical, and prismatic properties. His compositional output and the above inspiring forces have been strangely divorced by many academicians from his longest lifetime appointment, the organist at Église de la Sainte-Trinité in Paris. That he played countless Masses and other liturgical services for Catholic worship for more than 60 years may indicate a coded yet necessary index through which to hear and "practice" large-scale works like Vingt Regards sur l'Enfant-Jésus, which at two hours is itself a ritual beyond mere cognitive engagement, and still renders an opacity to modern audiences due to its layers of religious symbolism. Without the context of liturgy, the work fails to merely conform to the usual desirable models, be they a highly programmatic concert piece, an academic monument rife with subtext for analysis, or a historical testament of a piece written under Nazi occupation and just a few years following Messiaen's own imprisonment at Stalag VIII-A during the height of the Second World War. Certainly these each contain a part of the story, but a liturgical framework suggests a holistic viewing of Messiaen and his work from the compositional chair and the organ bench, and necessarily points to a connection between the two stations of a lengthy career. Central to my research was an attempt to experience a performance of the Vingt Regards in a new manner, with the worshipful posture that the composer maintained throughout his accomplished life.

Material and Method

My first task was to study liturgy in its ecclesiastical contexts, and compare Catholic models with my own Protestant heritage. As I surveyed the literature on Messiaen, a noticeable trend toward his liturgical inspirations emerged, and the relationship of his concert music and the liturgy, without having been formally explored by published scholars. My research therefore extended through a significant portion of what has been written on Messiaen over the past several decades, and also into the liturgy itself, so as to provide a clear definition of its use inside the Church and into other parts of life. Since Vingt Regards and other comparable works are not written for the liturgy itself, but rather further liturgical praxis into concert and secular settings, the theological discussions of liturgical and anthropological scholars like James K.A. Smith and others yielded immense benefit toward a more cross-disciplinary study. I created a simple matrix of the movements of the Vingt Regards and several elements from a liturgical service, including sermons, hymns, prayers, blessings, sacraments, and processions, and considered how this enhanced an understanding of Messiaen's religious music. Following this research, interviews with Catholic musicians fluent in liturgical patterns was highly valuable; in May 2025 I was fortunate to meet Thomas Lacôte, the current organist at la Trinité, observe a Sunday Mass from the organ loft, and share a brief discussion following the service. Finally, as a performer of most of the movements of Vingt Regards, I am keenly interested in the ongoing task of finding performance settings that bring this music and an audience into closer proximity, and drawing out liturgical actions that normalize the music rather than create further alienation and misunderstanding.

Findings

"Liturgy" itself is not outside of Messiaen's lexicon when considering the titles or movement titles to his compositions: the opening movement of Quatuor pour la fin du temps is marked "Liturgie de cristal", and the

suggestive Trois Petites Liturgies de la Présence Divine for mixed ensemble are concert works described by Robert Scholl as "paraliturgical" in their liminal stations (Scholl, 2024). These have value in being inclusive to those outside of the faith, while retaining liturgical properties. From the discussions of Smith and others, I considered five critical components inherent in the liturgy: the use of sacrament, repetition, narrative, embodiment, and pedagogy. All components conform to a viewing of Messiaen's music. Sacraments like the Eucharist are a mystical centerpoint to liturgical services, and similarly Messiaen reserves a hallowedness when penning movements XI. Première communion de la Vierge or XV. Le baiser de l'Enfant-Jésus, both about communion with the Christ Child. The liturgy is highly recurrent so as to guide the heart to a healthier modus operandi; Messiaen often gets lost in his own writing through lengthy restatements of entire passages, potentially in an effort to shut out the horrors of a ravaged Europe in 1944. Narrative is a driving force in liturgical services, communicating the gospel through a series of planned elements, as Messiaen skillfully sets the stage (movements I–III.), introduces central characters (IV., VIII.), foreshadows what is to come (VI. and VII.), builds the suspense (XIII. and XIV.), creates a climactic event (XV.), and promises an end to the story (XIX. and XX.). Catholic services go beyond theoretical engagement to somatic corporate actions, through kneeling, singing, eating and drinking, and receiving blessings with outstretched hands. A corollary embodiment is more coded in Vingt Regards, but potential can be found in experimenting with mixed media, extra sensorial prompts, and other somatic exercises like those found in Pauline Oliveros's Sonic Meditations. Finally, the liturgy is inherently didactic as parishioners gradually grow in their catecheses, learning the heart of God through the practices of the Church. Messiaen similarly exhibited the care of a teacher throughout his career, giving no shortage of programmatic materials in order to instruct musicians and listeners. The performer of Vingt Regards then serves as a kind of priest tasked with handling the source material and contextualizing it for the enrichment, education, and enjoyment of their audience.

Conclusion

Considering the liturgical components of Messiaen's religious music generally, and Vingt Regards in particular, distinguishes it from surrounding music with alternative aims. The intent of Messiaen's paraliturgical offerings go beyond historic or academic models, they further aid the faithful in search of beauty and truth. The role of the Church is to shepherd parishioners through the regular use of the liturgy, or the sum of the aesthetic, moralistic, and teleological parts; similarly Messiaen aims to woo his church into an upward gaze of wonder through music that is sacramental, repetitive, storied, somatic, and pedagogical. By synthesizing Messiaen's roles as liturgist and composer, the music of the Vingt Regards comes into sharper focus as music of worship.

References

Brown, D. (2007). God and Grace of Body: Sacrament in Ordinary. Oxford University Press.
Burger, C. (2009). Olivier Messiaen's Vingt Regards sur l'enfant-Jésus: Analytical, Religious, and Literary Considerations [DMA Dissertation, The University of Texas at Austin]. https://tinyurl.com/mskjebfe
Burton, R. (2016). Olivier Messiaen: Texts, Contexts, and Intertexts (1937-1948) (R. Nichols, Ed.). Oxford University Press.
Bruhn, S. (2007). Messiaen's Contemplations of Covenant and Incarnation: Musical Symbols of Faith in the Two Great Piano Cycles of the 1940s. Pendragon Press.
Dingle, C., & Fallon, R. (Eds.). (2013). Messiaen Perspectives 1. Sources and Influences. Ashgate Publishing.
Dingle, C., & Simeone, N. (Eds.). (2007). Olivier Messiaen: Music, Art and Literature. Ashgate Publishing.
Greeley, A. (2000). The Catholic Imagination. University of California Press.
Hill, P. (Ed.). (2008). The Messiaen Companion. Faber and Faber.
Johnson, R. (2008). Messiaen (C. Rae, Ed.). Omnibus Press.
Maas, S. (2009). The Reinvention of Religious Music: Olivier Messiaen's Breakthrough Toward the Beyond. Fordham University Press.
Messiaen, O. (1944). Technique de mon langage musical (J. Satterfield, Trans.). Leduc.
Nichols, A. (1999). Celestial Banquet: Messiaen's Sacred Music in Context. The Downside Review, 117(408), 173-190. https://doi.org/10.1177/001258069911740802
Oliveros, P. (1974). Sonic Meditations. Smith Publications.

Ratzinger, J. (1981). The Feast of Faith: Approaches to the Theology of the Liturgy (G. Harrison, Trans.) (Rev ed.). Ignatius Press.
Samuel, C. (1986). Olivier Messiaen: Music and Color, Conversations with Claude Samuel (E. Glasow, Trans.). Amadeus Press.
Scholl, R. (Ed.). (2024). Messiaen in Context. Cambridge University Press.
Scholl, R. (2024). Olivier Messiaen: A Critical Biography. Reaktion Books.
Shenton, A. (Ed.). (2010). Messiaen the Theologian. Ashgate Publishing.
Smith, J. (2009). Desiring the Kingdom: Worship, Worldview, and Cultural Formation (Cultural Liturgies, Volume 1). Baker Academic.

The Relentless Clash of Dissonant Harmonies and Lyric Melodic Lines… An Extensive Look into the Sound of Sergei Prokofiev

Selçuk Ener[a]

[a] Istanbul Technical University, Music, Music Performance, Türkiye
ener22@itu.edu.tr

Keywords: Industrial Revolution, Machine Music, Prokofiev.

Aim

This paper will be focusing on the sound of one of the most prolific composers of the early 20th century, Sergei Prokofiev. Prokofiev's music, while consisting of sharp dissonances and motor driven, tight rhythmic patterns, also involves subtle sarcastic or humorous motives and lyric themes. These components of his music, constantly clashing and battling each other, are creating a striking, dazzling sound which is extremely unique. I believe that the changing paradigms of day to day life that came with the Industrial Revolution in the 19th century as well as the political turmoil that led to October Revolution in 1917 and the two world wars that followed have huge effects and contributions to Prokofiev's sound. The main objective of this paper is to analyze the contributions of industrial revolution and the political, social environment in Russia on Prokofiev's sound through looking into his music and having a chronological look into his life starting from his childhood and education, his abroad years in Paris and his later years in Soviet Russia.

Material and Method

To understand the effects of new industrialized lifestyle and the political environment of the composer's early years on the development of his unique sound, I will be using two approaches. The first approach will be a historical one, focusing first on the effects of industrialization on classical music in general (examples from 1920s which are called machine music) and then on Prokofiev's childhood, his musical education, influences and how he was effected by the trending compositional practices of his early years. The second approach will be analyzing the composer's music through case studies such as his 3rd piano sonata and his second symphony. These compositions, both written through 1910s and 1920s, contains evident links to Prokofiev's influences from industrialization, politics and war. I will be identifying and showing the sections of his music that are influenced by the industrializing world through highlighting sections in score.

The first step to understand the elements creating the sound of Prokofiev is to do extensive readings on the life and the compositions of the composer. Many musicologists and musicians have written articles and books on various topics, some examples including but not limited to Stephen Press's book on Prokofiev's operas, pianist Boris Berman's book on his piano sonatas or Harlow Robinson's extensive biography, throughout the years, and these resources are the first step to the research on the composer. As the research continues, the music, which is the main element of our research will be studied. The 1917 3rd piano sonata and the 1925 2nd symphony are excellent case studies and are selected to be examined, analyzed and studied in detail in order to understand the harmonies, rhythms, melodies and motifs, their roots or in general the main components that are creating the unique sound of the composer. Especially the moderato section gives us a great example of the lyric melodic lines supported with chromatic figures on the left hand which creates many dissonant harmonies clashing with the lyric nature of this section. Another very good source to understand the output of Prokofiev is his letters, journals and interviews as well as the comments of his close circle on the composer such as his wife, sons, teachers, students or contemporary musicians. Some very good research material are, Simon Morrison's book on Lina Prokofiev, or Anthony Phillips's anthology on the composer's diaries. These material are our primary resources in order to understand his struggles, ambitions, influences all contributing to our understanding of the elements creating his style of composition and sound.

Findings

After the research was completed, it is evident that Sergei Prokofiev, among many other composers of the early 20th century, was deeply influenced by the new sounds that were brought into life by the industrial revolution (the factories, railroads, steam engines and machines). His compositional techniques were also influenced by his upbringing in the politically chaotic Russian Empire in his early years as well as the dark and somber atmosphere that the two world wars created. These influences are quite apparent in our case studies that are his 3rd piano sonata (filled with mechanic rhythmic patterns influenced by engines and machines) and his 2nd symphony which was described as "a piece of iron and steel" by the composer himself referring to the changing day to day sounds of the early 20th century. His later sonatas number 7, 8 and 9 (which are also known as war sonatas) are also great examples of how much the composer's sound was effected and influenced by the second world war.

Conclusion

In conclusion, this paper is focusing on the unique sound of one of the most prolific composer of the early 20th century, Sergei Prokofiev. My main objective is to show and prove that the composer's rhythmically mechanical, relentless, and extremely dissonant but at the same time also quite lyrical sound was hugely influenced by the industrialized world and the political events of the early 20th century.

References

Bartig, K. (2014). Composing for the Red Screen: Prokofiev and Soviet film. Oxford University Press.
Bartig, K. (2017). Sergei Prokofiev's Alexander Nevsky. Oxford University Press.
Berman, B. (2023). Prokofiev's Piano Sonatas: A guide for the listener and the performer. Yale University Press.
de Castro, P. (2022, August 30). Machines, films, and operas: A (mostly) Soviet perspective – intersections. Érudit. https://www.erudit.org/en/journals/is/2019-v39-n2-is07232/1091837ar/
Fairclough, P. (2019, March 15). The Russian Revolution and music: Twentieth-Century music. Cambridge Core. https://www.cambridge.org/core/journals/twentieth-century-music/article/abs/russian-revolution-and-music/72626E7F0D97DEAECCF269A748DE875C
Jaffé, D. (2008). Sergey Prokofiev. Phaidon.
Lumbroso, A. (2017, December 21). Russian revolution in music: 1917 and the aftermath. Izba Arts. https://www.russianartandculture.com/russian-revolution-music-1917/
Minturn, N. (1997). The music of Sergei Prokofiev. Yale Univ. Press.
Morrison, S. A. (2008). Sergey Prokofiev and his World. Princeton University Press.
Morrison, S. A. (2009). The People's Artist: Prokofiev's soviet years. Oxford University Press.
Morrison, S. A. (2013). Lina and Serge the love and wars of Lina Prokofiev. Houghton Mifflin Harcourt.
Nebolsin, E. (2017, August 27). Masterclass Eldar Nebolsin / prokofiev sonata 3. YouTube. https://www.youtube.com/watch?v=drBenty9ryU&t=1860s
Nihan, U. E. (1970, January 1). İkinci Dünya Savaşı'nın Sovyet Klasik müziği'ne etkileri. Konservatoryum. https://iupress.istanbul.edu.tr/tr/journal/cons/article/ikinci-dunya-savasinin-sovyet-klasik-muzigine-etkileri
Press, S. (2016). Prokofiev's ballets for Diaghilev. Taylor and Francis.
PROKOFIEV, S. (2022). Sergey Prokofiev diaries 1924-1933: Prodigal son. FABER AND FABER.
Prokofiev, S., & Shlifshteĭn, S. I. (1959). Autobiography, articles, Reminiscenses. Foreign Languages Publishing House.
Robinson, H. (1987). Sergei Prokofiev: A biography. Viking.
Rothe, F. (1942). Russian music - JSTOR. https://www.jstor.org/stable/4332310
Sagall, S. (2017, December 11). A wave of creativity: Music and the Russian Revolution. Culture Matters. https://www.culturematters.org.uk/index.php/culture/education/item/2689-music-and-the-russian-revolution
Savkina, N. (2023). Natalia P. Savkina - nv.mosconsv.ru. https://nv.mosconsv.ru/sites/default/files/pdf/2023_2_N_Savkina_EN_.pdf
Tompkins, D. G. (2020, March 12). Prokofiev, Soviet influence, and the music world in Stalinist Central Europe. OUP Academic. https://academic.oup.com/book/41056/chapter-abstract/349407497?redirectedFrom=fulltext&login=true

MUSIC

Ethnomusicology

Music Business and Management

Music Performance

Music Theory

Sonic Arts

Sound Engineering and Design

Effects of Performance Space on Free Improvisation Practices

Aslıhan Adlin[a]

[a]Istanbul Technical University, Graduate School, Musicology and Music Theory Program, Türkiye
adlina@itu.edu.tr

Keywords: Space, Free Improvisation, Performance Space, Place, Experience.

Aim

Music-space interaction is most apparently related to acoustics, however, the experience of space as atmosphere, especially in free improvisation practices, does not seem to have gained enough prominence to be the focus of a research topic. The experimental and unpredictable nature of free improvisation makes the space in which it is experienced versatile and variable. Rather than approaching space solely as an acoustic phenomenon, considering it as an element socially constructed by musicians and listeners and actively involved in the music is important to grasp the role of space in free improvisation. In addition, space and music create an atmosphere for those present at that moment, namely the musician and the listener. Examining this dynamic and changing space, which is constructed socially by its performers and audience, might have methodological challenges. Thus, this study aims to review the methodologies used in the relevant literature, providing examples for future studies that examine the relationship between space and free improvisation practices in the context of musicians' experience of space as an atmosphere. It demonstrates three case studies and discusses different approaches to performance space involved in free improvisation practices.

Material and Method

The methodology of this study is a field research conducted in a studio recording as a pilot study to find out what aspects of space can be approached and examined, as well as a literature review. The research has been conducted on the axis of space, free improvisation, and the music-space relationship. To understand the meaning of the space concept from a phenomenological perspective, approaches from different disciplines in social sciences were examined. Additionally, studies were reviewed on music-space interaction to apprehend the contexts in which the concepts of music and space come together. Later, the research was focused on free improvisation, and studies that addressed this genre concerning the notion of space were investigated. Three studies were found on this approach, and the methodologies of these three case studies have been discussed. After examining the methods used in these studies, a studio recording was made as a participant observer, and interviews were conducted with other musicians about the spatial experience in the studio.

Findings

Most studies on free improvisation have focused on creativity and the interaction between performer and audience (Ford, 1995; Andean, 2023; Wilson & MacDonald, 2016; Canonne, 2018; Hatipoğlu, 2022). Few studies taking spatial interaction in its center have been found in the written literature of this genre. Here, three cases relating space and free improvisation from different perspectives will be examined through their methodologies.

The first case is a study by Pauline Oliveros (2007) in which she explains three different performances by the Deep Listening Band and compares acoustic features of three different places through the listening experience of musicians and the audience. These places are a cistern with 45 seconds of reverberation time, Biblioteca National in Buenos Aires, Argentina, and the chapel of Pomfret School in Connecticut. This study shows that changing acoustical characteristics in different places has an impact on musicians' listening perception, and Oliveros states that these characteristics for musicians are musical parameters like as melody, rhythm, harmony, or timbre. Additionally, Oliveros, here, points out that listening practices in different acoustical environments change accordingly, and changing places provide changing experiences for listening (Oliveros, 2007, pp. 68-69).

Chris Atton's mention to performance space in free improvisation is the second case of this study. Atton investigates (2012) free improvisation genre culture and the transformation of the performance space by analyzing

live performances in Leeds, England, from a micro-sociological perspective on cultural interactions between performers and audience, and socioeconomics. He provides analyses of four free improvisation performances placed in Termite Club between 1985-1999 and demonstrates performers' approach to space with their claiming it as a musical territory. In these examples, musicians choose to play the performance space either playfully or in a physically threatening way, giving that, Atton discusses the unpredictability of live experiences that create an unstable music culture (Atton, 2012, p. 439).

The third case is David Leahy's study (2021) regarding his "Musicians in Space (MiS)" project. Leahy here uses a phenomenology-based heuristic methodology and conducts two-staged research including a series of performances in several British cities and participant interviews following these performances. With this study, Leahy aims to give insight into developing a comprehensive and non-hierarchical method for music-making by providing the opportunity for free improvisers to shape their spatial location during the performances (Leahy, 2021, pp. 335-336). The study shows that the flexibility in moving in the space fosters immersive listening and provides a deep connection for both musicians and the audience.

The three case studies show that space might be involved and discussed in free improvisation studies from different perspectives. Except for acoustical measurements, socially constructed space and its phenomenological experience are evaluated by mostly qualitative methods such as listening practices, theoretical discussions, and interviews.

Following this literature review, a pilot study was conducted in PERA Studio at the Bahçeşehir University, Conservatory, and musicians were asked to evaluate their experience of space. These evaluations have raised new questions about how to approach the recording studio spatially. The psychology of recording in the studio has a distinctive aspect from the performance experience in other spaces. In this context, discussions are ongoing to compare the experience in the studio with the spatial experience in different areas.

Conclusion

Focusing on studies related to performance space and its impact on free improvisation practices, this study aimed to provide a perspective of the methodologies used in the pertinent literature to gain insight into space investigations. The three case studies by Oliveros, Atton, and Leahy examined in this study show that there is no commonly accepted methodology to conduct such research on the impacts of space on free improvisation yet, they commonly rely on the phenomenological perspective. So, this study drew attention to the limitations of methodologies used in the field and opened qualitative and quantitative approaches for discussion. In addition, the pilot study conducted in this research shows that each spatial experience raises new questions but also provides an in-depth understanding of the space itself. The hope is that this study will shed light on the creation of new methods in future studies. By finding a peculiar methodology, a further study might involve a set of experiments in different places through a versatile analysis and exploration of performance space.

References

Andean, J. (2023). "Group Performance Paradigms in Free Improvisation". Organised Sound. 27(2), pp. 106–116.

Atton, C. (2012). "Genre and the cultural politics of territory: The live experience of free improvisation". European Journal of Cultural Studies. 15(4), pp. 427–441.

Canonne, C. (2018). "Rehearsing Free Improvisation? An Ethnographic Study of Free Improvisers at Work". Society for Music Theory. 24(4).

Ford, Charles C. (1995). "Free collective improvisation in higher education". British Journal of Music Education. 12, pp. 103-112.

Hatipoğlu, Zeynep A. (2022). A Practice-based Research on Musical Improvisation: Collaborative Improvisation as a Play. PhD Thesis. Istanbul Technical University.

Leahy, D. (2021). "Musicians in Place and Space: The Impact of a Spatialized Model of Improvised Music Performance". Musical Spaces - Place, Performance, and Power, (1st ed). New York: Jenny Stanford Publishing.

Oliveros, P. (2007). "Improvising With Spaces". 13th International Conference on Auditory Display, Montréal, Canada.

Wilson, G. B., & MacDonald, R. A. R. (2016). "Musical choices during group free improvisation: A qualitative psychological investigation". Psychology of Music, 44(5), pp.1029-1043.

Cyclic Unity and Romantic Expression in Robert Schumann's Fantasiestücke, Op. 12: A Schenkerian Perspective

Doğucan Temizel[a]

[a] Istanbul Technical University, Department of Music, Music Programme, Türkiye
temizeld@itu.edu.tr

Keywords: Cyclic, Robert Schumann, Schenkerian Analysis, Tonality.

Aim

From the Renaissance through the early Romantic periods, the cyclic principle evolved as a compositional tool in Western classical music. In this tradition, Robert Schumann's Fantasiestücke, Op. 12 (1837), represents how cyclic organization can create a musical narrative in a multi-movement work. The research aims to examine the underlying melodic and harmonic relationships of Schumann's Fantasiestücke. Using the Schenkerian perspective I will demonstrate how it reveals the fundamental structural coherence of the cycle despite the diversity of the character pieces within the overarching formal design. Some music scholars, such as Arthur Komar (1971), Patrick Mccreless (1986), David Neumeyer (1982), and Peter Kaminsky (1989), debate whether Schenkerian analysis applies to the music of the Romantic era. This study suggests that Schenker's concept of Ursatz (Fundamental structure) and Composing-out (Auskomponierung) is still valid for the Romantic repertoire since it can illustrate fundamental structures even in fragmented music with tonal ambiguity.

Material and Method

The stylistic aspects of Fantasiestücke, Op. 12 balance resonant sonorities with dynamic piano texture while utilizing a blurred harmonic language that undermines conventional tonal hierarchies. Moreover, Schumann's original title, 'Phantasien,' in which Brown (2001) indicates that there is an allusion made to E.T.A. Hoffmann's 'Fantasiestücke in Callots Manier' (1814–15), positions the piece in a broader nineteenth-century fantasia tradition. This literary association, therefore, shows his intent in relating individual movements in an organized whole, following on in a process evident in earlier cycles such as Papillons, Op. 2 (1829–31), Carnaval, Op. 9 (1834–35), and Davidsbündlertänze, Op. 6 (1837).
For the methodology, I used the analytical perspective based on Schenker's Free Composition (1935). I created the representations of structural relationships through the reductive Schenkerian graphs, which are Schenker's core theories being used as a basis for teaching purposes, on which Forte and Gilbert (1982), Beach (2012), and Cadwallader, Gagné, and Samarotto (2020) expanded. The first phase includes examining the foreground (Vordergrund) and middle-ground (Mittelgrund) structures of the work exhibiting how techniques of extension and recurring motifs sustain continuity within certain sections and how they contribute to the development of the narrative. It also shows how the detailed graphs can represent the implementation of fairly disguised harmonic progressions through sections, and of the prolongation of substituted tonic harmony across these eight character pieces. The second phase begins with a discussion of how these basic elements all work together to form a single organic unity within the overall structure.

Findings

The analytical results reveal that each piece's fundamental line consists mainly of descending Urlinie, 3^, 2^, 1^. In particular, in Warum?, the prolonged structural motion concludes at the 3^ on the final chord without resolution, whereas in Grillen, the introduction of the first Urlinie pattern 5^, 4^, 3^, 2^, 1', indicates a pivotal large-scale transition. The tonal axis extends in the substituted tonic D♭ (♭VII) between Des Abends and In der Nacht, then leads to C major (V) in Fabel, and arrives at F major (I) in Traumes Wirren. Ultimately, at the finale, Ende vom Lied accommodates the F major tonality by consolidating these elements, particularly at the coda, an abrupt modulation to the D♭major before the closure that reinforces the work's tonal coherence. The Schenkerian graphs

show how these harmonic progressions modify conventional formal structures on the local and large-scale levels. In addition, recurring intervallic gestures, such as descending and ascending stepwise motions and leaps of the 6th interval, further unify the cycle. This primary motive occurs either at the beginning or in the transitions between the character pieces.

Conclusion

In conclusion, my interpretive study shows that Schumann's Fantasiestücke Op. 12 encompasses a formal integrity through the revelation of 'F' as a pitch element and tonality that underpins the cycle's Ursatz as an organic structure. In addition, the musical dialogue between 'Eusebius and Florestan' represented in succession throughout the entire piece includes harmonically innovative techniques, such as remote-key relations, destabilizing modulations, and tonal ambiguity. For this regard, an adapted Schenkerian analysis explicitly connects narrative and theoretical perspectives so that these insights may help performers and music scholars. Besides, it contributes to a deeper comprehension of Schumann's compositional techniques in cyclic works, enriching the nineteenth-century music analysis.

References

Agawu, V. K. (1989). Schenkerian Notation in Theory and Practice. Music Analysis, 8(3), 275–301.
Url-1 https://doi.org/10.2307/854291, date retrieved 30.12.2024.
Ayotte, B. (2004). Heinrich Schenker: A Research and Information Guide. New York: Routledge.
Beach, D. (2012). Advanced Schenkerian Analysis. New York: Routledge.
Brown, M. J.E. (2001). Fantasiestück. Grove Music Online.
Url-2 https://0-doi-org.divit.library.itu.edu.tr/10.1093/gmo/9781561592630.article.09294, date retrieved 05.04.2024.
Brown, M. (2005). Explaining Tonality: Schenkerian Theory and Beyond. Rochester, NY: University of Rochester Press.
Burton, A. (1988). Robert Schumann and Clara Wieck: A Creative Partnership. Music & Letters, 69(2), 211–228.
Url-3 http://www.jstor.org/stable/855217, date retrieved 03.01.2024.
Cadwallader, A. C., & Gagné, D. & Samarotto, F. (2020). Analysis of Tonal Music. New York: Oxford University Press.
Chernaik, J. (2011). Schumann's Doppelgängers: Florestan and Eusebius revisited. The Musical Times, 152(1917), 45–55.
Url-4 http://www.jstor.org/stable/41440730, date retrieved 14.04.2024.
Cubero, D. (2022). Blurred Harmonies in Robert Schumann and Johannes Brahms. Intégral 35, 1–25.
Url-5 https://www.esm.rochester.edu/integral/35-2022/cubero/, date retrieved 18.03.2024.
Damschroder, D. (2018a). Tonal Analysis: A Schenkerian Perspective. New York: W. W. Norton.
Damschroder, D. (2018b). Harmony in Mendelssohn and Schumann. Cambridge: Cambridge University Press.
Daverio, J. (1993). Nineteenth-century Music and the German Romantic Ideology. New York: MacMillan Publishing Company.
Daverio, J. (1997). Robert Schumann, Herald of a "New Poetic Age." New York: Oxford University Press.
Dill, H. J., & Schumann, R. (1989). Romantic Irony in the Works of Robert Schumann. The Musical Quarterly, 73(2), 172–195.
Url-6 http://www.jstor.org/stable/742065, date retrieved 20.11.2024.
Domínguez, I.M.C. (2014). Robert Schumann y el Fragmento Romántico: Fantasiestücke Op.12. (Master thesis). Politécnico do Porto, ESMAE.
Url-7 http://hdl.handle.net/10400.22/8835, date retrieved 19.10.2024.
Forte, A., & Gilbert, S.E. (1982). Introduction to Schenkerian Analysis. New York: W.W. Norton & Company, Inc.
Geck, M. (2013). Robert Schumann, The Life and Work of A Romantic Composer. Chicago: University of Chicago Press.

Kaminsky, P. (1989). Principles of Formal Structure in Schumann's Early Piano Cycles. Music Theory Spectrum, 11(2), 207–225.
Url-8 https://www.jstor.org/stable/745936, date retrieved 06.04.2024.
Macdonald, H. (2001). Cyclic form. Grove Music Online.
Url-9 https://0-doi-org.divit.library.itu.edu.tr/10.1093/gmo/9781561592630.article.07001, date retrieved 10.01.2024.
Perrey, B. (2007). The Cambridge Companion to Schumann. Cambridge: Cambridge University Press.
Rosen, C. (1998). The Romantic Generation. Harvard University Press.
Snarrenberg, R. (2001). Schenker, Heinrich. Grove Music Online.
Url-10 https://0-doi-org.divit.library.itu.edu.tr/10.1093/gmo/9781561592630.article.24804, date retrieved 20.10.2023.
Schenker, H. (1979). Free Composition (Der freie Satz) (E. Oster, Trans.). New York: Longman Inc. (Original work published 1935).
Tekin, H. S. J. (2010). Robert Schumann's Miniature Piano Pieces and Literary Ideas. (Doctoral dissertation). Istanbul Technical University, Institute of Social Sciences.
Url-11 http://hdl.handle.net/11527/12471, date retrieved 06.01.2024.

MUSIC

Ethnomusicology

Music Business and Management

Music Performance

Music Theory

Sonic Arts

Sound Engineering and Design

Exploring Dance Floor Tactility: Sonic Ethnography and Artistic Inquiry through Audio Paper

Gazele Aydın[a]

[a] İstanbul Technical University, MIAM, Sonic Arts, Turkey
ayding22@itu.edu.tr

Keywords: Artistic Research, Dance Floor, Sonic Ethnography, Tactility.

Aim

This paper will introduce a section from my thesis that explores dancefloor tactility through sonic ethnography and artistic research. The focus will be on the methodologies and theoretical framework that guide my research, as well as the necessity of an audio paper as an outcome. While I will include excerpts from the audio paper, the presentation itself will follow a conventional format; it will outline how my research process and methodology leads to the creation of an audio paper and the creative audio is needed to comprehend dance floor tactility. By demonstrating how sound can function as both a research method and a form of knowledge production, I aim to highlight that the addition of an audio paper is an important method for sonic ethnography and artistic research practice. In this research sonic ethnography and artistic research methodology has been employed as methods to enhance the understanding of dance floor tactility. By editing a collection of field recordings and manipulating sounds according to context and meaning, and by using these field recording collages in feedback interviews in a cyclical form to deepen the analysis, this research aims at a reflective listening and creation process. This study allows participants in a reflective listening process; through feedback interviews, the research not only gathers interpretations of sonic tactility but also allows the sonic material to evolve based on feedback. This cyclical approach aligns with artistic research principles and also sonic ethnography, where the creation and contextual analysis of sound are integral.

Material and Method

Sonic ethnography, as outlined by Gershon (2019), emphasizes the relational and processual nature of sound, revealing the complex interactions between humans and their sonic environments. For many studies sound has been central to ethnographic practices, but the sonic often remained neglected to a second-class positionality in ethnographic research. But sound is an important, integral part of ethnographic processes; most forms of ethnography rely on rendering ideas, interactions, and images as texts; they often maintain Western visually oriented conceptualizations of sense-making. But when examining a field, such as the dance floor, which is inside a rich sonic environment, doing ethnography in sound is crucial. Peterson and Brennan (2021) further highlights this importance of sonic ethnography as a collaborative and immersive practice, prioritizing the acoustemological aspect of sound as a way of knowing. They mention that sonic ethnography understands sound as processual and relational; and it requires collaborative practices that bring together different perspectives towards listening. Furthermore Littlejohn (2021) underscores the importance of field recordings and editing in sonic ethnography, emphasizing how field recordings and their manipulation offer partial truths and insights into the lived experience of a site. Collecting field recordings and editing them according to a context offers new and different understandings of experiences, meanings and relations between experience and meanings, different from textual ethnography.

Sonic ethnography, as a methodology, allows immersive engagement with sound, collecting experiences through listening and field recording. However, rather than treating these recordings as fixed data, this research engages with them artistically with the audio paper; editing and manipulating them to reveal new layers of meaning. This artistic approach aligns with artistic research principles, where creative processes become a method of inquiry.In this context, the editing on sonic ethnography works also have an artistic tendency. As a musician and researcher I have both insider and outsider roles in my field. This duality gives me space to experiment on both my roles as

musician and researcher. Because artistic research is a practice based, open ended, self critical, context aware research that embodies participatory act, self reflective text and creation making I believe it is an important ally for sonic ethnography, doing ethnography in sound while creating sound, getting feedback and writing on it can bring inclusive outcomes.

In this research Garcia's concept of sonic tactility provides a theoretical foundation for understanding how sound can be felt beyond the auditory sense, engaging the body through beats, flesh and grain. According to Garcia, because the dance floor employs electronic dance music, it has tactile qualities. This research explores dance floor tactility through experimenting on features of sonic tactility presented by Garcia in terms of tactility through vibrations, tactility through association and tactility through sonic texture itself. To explore these sonic qualities, field recordings were gathered from actual dance floors, while additional materials were sourced from online spaces, including radios, albums and DJ sets that are actively followed by local dance floor participants. This combination of real-world and virtual soundscapes provided a different approach to understanding how sound manifests tactility in the context of electronic dance music.

Findings

This research demonstrates how sound can be experienced not just as an auditory phenomenon but as a bodily, tactile encounter. By analyzing field recordings from both real and virtual dancefloor environments, this study examines how sound acts upon the body through vibrations, associations, and textures. As a result, the final audio work reflects a layered exploration of dancefloor tactility. The manipulation of these field recordings, whether through editing or contextualization, has demonstrated how different sounds can evoke various associations, textures, and emotional responses. This process aligns with Littlejohn's (2021) view that field recordings, when edited, provide insights into the lived experience and can reveal partial truths about a sonic environment. The integration of participant feedback further deepens the analysis, making it possible to capture multiple perspectives and meanings attached to these sonic experiences. The use of an artistic approach in sonic ethnography, particularly through the creation of an audio paper, has also emphasized the performative nature of research, allowing sound to evolve as an integral part of the inquiry itself.

Conclusion

Several different audio works have been done and by reflecting on those audio works this research extends ethnographic representation beyond traditional written formats, embracing the sonic as a mode of knowing and knowledge production. The final audio paper, shaped through fieldwork, artistic intervention, and participant feedback, ultimately reflects a multi-layered exploration of dancefloor tactility, approaching sound not only as an object of study but as a methodological and epistemological framework in itself.

References

García-Mispireta, L. M. (2023). Together, somehow: Music, affect, and intimacy on the dancefloor. Duke University Press.

Gershon, W. S. (2019, August 28). Sonic ethnography in theory and practice. Oxford Research Encyclopedia of Education. https://doi.org/10.1093/acrefore/9780190264093.013.850

Hannula, M., Vadén, T., & Suoranta, J. (2014). Artistic research methodology: Narrative, power and the public (Vol. 15). Peter Lang.

Littlejohn, A. (2021). Sonic ethnography. In S. Pink & S. Leder Mackley (Eds.), Audiovisual and digital ethnography (pp. 26–41). Routledge. https://doi.org/10.4324/9781003132417

Peterson, M. L., & Brennan, V. L. (2021). A sonic ethnography: Listening to and with climate change. Resonance: The Journal of Sound and Culture, 1(4), 371–375. https://doi.org/10.1525/res.2020.1.4.371.

MUSIC

Ethnomusicology

Music Business and Management

Music Performance

Music Theory

Sonic Arts

Sound Engineering and Design

Spatial Auditory Masking in 3D Audio: Challenges, Experimentation and Implications for Immersive Sound

Emre Tenker[a], Taylan Özdemir[a]

[a] Istanbul Technical University, Centre for Advanced Studies in Music, Music, Türkiye
tenker@itu.edu.tr

Keywords: Spatial Auditory Masking Phenomenon, Aural Perception, Masking Threshold, Dolby Atmos, Audio Coding, 3D Audio.

Aim

Auditory perception is continuously evolving with advancements in 3D audio technologies, expanding traditional monaural and stereophonic formats into more immersive spatial sound environments that heighten the sense of realism. These innovations have been significantly impacting industries such as music production, gaming, virtual and augmented reality (VR/AR), cinema sound and assistive hearing technologies. Unlike conventional two-dimensional audio, 3D audio systems allow for precise spatial positioning of sound sources, resulting in a heightened sense of realism and listener immersion. However, as the auditory space is filled with more sound sources, the perception of individual auditory elements becomes more complex due to auditory masking effects, in which one sound obscures the perception of another. While spectral and temporal masking are well-documented in psychoacoustics, the role of spatial auditory masking in immersive sound environments remains an active area of research.

Spatial auditory masking refers to the phenomenon in which a sound becomes less audible due to the presence of another sound, depending on their relative spatial positions [4]. The human auditory system relies on binaural cues, such as interaural time differences (ITD), interaural level differences (ILD), and head-related transfer functions (HRTF), to localize and separate sounds in a three-dimensional environment. These mechanisms contribute to spatial release from masking (SRM), which occurs when sounds are easier to detect due to their spatial separation. Understanding spatial auditory masking is crucial for optimizing sound clarity and intelligibility in modern immersive audio formats. This study aims to investigate the impact of spatial positioning on auditory masking thresholds in a controlled Dolby Atmos environment, examining how different spatial arrangements of the masker and the maskee influence detection. The findings will provide insights into psychoacoustics and spatial audio applications, with implications for audio mixing and immersive sound design. The aim section should be written in Times New Roman font, justified-alignment and in 10-point size.

Material and Method

This study includes a literature review of how locations of auditory objects affect the auditory masking thresholds and subjective listening tests which are conducted in a calibrated Dolby Atmos studio, ensuring accurate spatial reproduction of sound sources. The foundation of the literature review is primarily based on Blauert's "Spatial Hearing: The Psychophysics of Human Sound Localization" [1], while the experimental design is inspired by the work of Nishiguchi and his collaborators [6][7], as presented in their articles published by the Audio Engineering Society.

The experiment includes a masker and a maskee presented from various spatial positions. The masker is a narrowband pink noise centered at 400 Hz, with a bandwidth limited to 350–450 Hz using a band-pass filter, while the maskee is a pure 400 Hz sine tone [2]. To ensure that the pink noise masker does not exceed the target frequency range, a band-pass filter is applied using REQ 2 Waves EQ, with the high-pass filter set at 350 Hz and the low-pass filter at 450 Hz. This ensures that the masker energy remains within the same frequency band as the maskee. During the experiment, participants are seated at the sweet spot and presented with masker and maskee signals from different spatial locations to determine how their relative positioning influences detectability. The masker

plays continuously, while the maskee is introduced in discrete 2 dB SPL steps until the participant perceives it. Upon detection, the participant presses a key and the masking threshold is recorded.

The experiment consists of five sessions that are divided into nine groups. Session 0 serves as an introductory phase and includes Group 0, which performs Test 0 to familiarize participants with the task. Session A follows, comprising Group 1 and Group 2, which collectively cover Tests 1 to 14. Group 1 observes conditions where the masker remains directly in front of the listener, while the maskee travels to various locations along the horizontal plane. Group 2 is similar to Group 1, but in this case, the maskee travels along the horizontal plane with maximum elevation, allowing the investigation of vertical localization effects on spatial masking.

Session B includes Group 3 and Group 4, covering Tests 15 to 28. These groups replicate the conditions of Group 1 and Group 2 respectively, but instead of the center speaker, the masker in front of the listener is a phantom signal produced by the left and right speakers, providing insight into masking effects created by phantom auditory sources.

Throughout Session C, Group 5 examines symmetrical median plane combinations, while Group 6 focuses on symmetrical frontal plane combinations. Both Group 5 and Group 6 investigate masking thresholds across minimum and maximum elevations for the same spatial configurations.

Session D includes Group 7 and Group 8, which were designed to examine spatial auditory masking across diagonal sound source placements across the frontal and median planes.

All sessions take place after different durations of silent breaks to mitigate auditory fatigue [5]. This structure allows for a systematic assessment of spatial masking thresholds while balancing the participant's cognitive load and minimizing the effects of fatigue over the course of 49 total tests.

The experiment involved a diverse group of voluntary participants with varying levels of expertise in sound and music-related fields. Participants were categorized into distinct groups based on their academic and professional backgrounds, including sound engineers with completed doctoral degrees (Experts), ongoing PhD candidates in sound engineering (Future Experts), master's students in related disciplines (Prospects), and individuals from adjacent fields such as ethnomusicology, performance, and music theory. Additional groups included participants with no formal background in music or sound studies to provide a comparative basis for perceptual thresholds. All participants confirmed having normal hearing and relevant demographic and experiential data—such as age, years of critical listening experience, and areas of musical engagement—were collected to support further analysis.

Findings

Previous studies on spatial auditory masking have revealed several key findings that provide a valuable framework for understanding the relationship between sound source positioning and masking thresholds. Research indicates that spatial separation between the masker and maskee generally lowers masking thresholds, with the least masking observed between left and right opposed sources, showing a reduction of up to 5 dB compared to coincident sources [3]. However, symmetrical positioning of the maskee relative to the frontal plane does not consistently reduce masking, challenging initial expectations. Additionally, phantom masker signals produced by virtual sources exhibit similar masking thresholds to those of real sound sources, suggesting that spatial auditory masking occurs consistently with both physical and virtually localized sound images. Masking thresholds reported across these studies typically range between -35 dB and -26 dB probe-to-masker ratios [3], with increased masking observed at certain elevations and cases of selective masking reduction linked to interaural phase difference phenomena. In addition to examining horizontal and frontal plane interactions, our study incorporates height channels to explore how vertical spatial positioning influences masking thresholds. This expanded spatial dimension allows for a more comprehensive investigation into the effects of sound source elevation on auditory masking, contributing to a broader understanding of spatial perception in immersive environments. As spatial audio technologies continue to evolve, these findings offer critical insights into optimizing sound clarity and reducing masking interference in immersive environments.

Our initial results indicate that spatial masking decreases as both azimuth and elevation between the masker and maskee increase. This suggests that greater spatial separation across multiple dimensions enhances the listener's ability to detect the target signal. The findings support the role of three-dimensional spatial unmasking in complex auditory scenes.

Conclusion

This study provides new insights into how spatial positioning affects auditory masking thresholds, contributing to a better understanding of sound perception in immersive environments. The findings have direct applications in Dolby Atmos mixing and sound design, as they demonstrate how strategic spatial placement of audio elements can reduce masking effects, ensuring better clarity and depth in 3D audio environments. Additionally, these results contribute to VR/AR audio development, where ensuring critical auditory cues remain perceptible is essential for creating a realistic and interactive user experience. The study also offers implications for hearing aid and cochlear implant development, where understanding spatial release from masking can improve speech intelligibility in noisy conditions.

As 3D audio technologies continue to evolve, understanding spatial auditory masking will be crucial in shaping the next generation of immersive sound experiences. Further research could expand on these findings by investigating how different frequency ranges, room acoustics and dynamic sound movements influence masking thresholds, ultimately leading to refinements in spatial audio engineering and psychoacoustic modeling.

References

Blauert, J. (1997). Spatial hearing: The psychophysics of human sound localization (Rev. ed.). MIT Press.
British Standards Institution. (2001). Electroacoustics—Audiological equipment: Part 1: Pure-tone audiometers (BS EN 60645-1:2001; IEC 60645-1:2001). British Standards Institution.
Dick, S., Sweidan, R., & Herre, J. (2019). Investigation of Masking Thresholds for Spatially Distributed Sound Sources. In the 147th Audio Engineering Society International Convention 2019. New York, NY, US: Audio Engineering Society.
Howard, D., & Angus, J. (2017). Acoustics and psychoacoustics (5th ed.). Routledge.
International Telecommunication Union. (2015). Methods for the subjective assessment of small impairments in audio systems (Recommendation ITU-R BS.1116-3). International Telecommunication Union.
Nishiguchi, T., Ueno, H., Iwamiya, S., & Sato, T. (2019). Spatial auditory masking for three-dimensional audio coding. Audio Engineering Society Convention 147.
Nishiguchi, T., Ueno, H., Iwamiya, S., & Sato, T. (2020). Spatial auditory masking caused by phantom sound images. Audio Engineering Society Convention 149.

Methodology on Participatory Media Analysis: Insights from the Audio Modding Scene on Nexus Mods

Başar Ünder[a], Taylan Özdemir[b]

[a] Istanbul Technical University Graduate School, Music PhD Program, Türkiye
[b] Istanbul Technical University, Turkish Music State Conservatory, Music Technology Department, Türkiye
under@itu.edu.tr

Keywords : Game Audio, Game Modding, Participatory Media, Sound Design, User-Generated Content.

Aim

This study explores participatory sound design in video game modding communities, focusing on The Elder Scrolls V: Skyrim Special Edition (Skyrim SE). In particular, it investigates how players modify game audio and how these practices reflect user expectations and preferences. Situating this inquiry within Henry Jenkins' (2006) concept of participatory culture—defined by low barriers to entry, community support, and meaningful contribution—the research highlights how modders and users co-create the auditory experience of a game.
The aim is twofold: (1) to identify which categories of sound are most frequently modified and endorsed, and (2) to develop a scalable methodology for analyzing participatory trends in game audio modding using real-world data from Nexus Mods.

Material and Method

This study adopts a platform-based content analysis methodology to investigate how the Skyrim SE audio modding community shapes game sound through participatory practices. Data was collected from Nexus Mods, focusing on the twenty most-endorsed audio mods, a sample that represents community-preferred and widely-used content. Each mod entry includes two key text fields:
- Tags (user-defined metadata)
- Text (free-text description by the mod author)

To analyze mod content, we developed a categorization system informed by domain knowledge and established taxonomies such as the Universal Category System (UCS). The categories used were:
- Enhancements – fidelity upgrades, remasters, overhauls
- Music – background music or soundtrack additions
- Combat Sounds – weapon, spell, or impact sound effects
- Ambient – environmental or spatialized sounds (e.g., wind, rain, dungeons)
- Voice (Shouts & Player Sounds) – vocalizations such as dragon shouts and grunts
- Utility for Modders – sound scripting tools or frameworks
- Mod Patches – compatibility layers between audio mods or updates

Classification was carried out in two stages:
1. Automated Tag Matching: Each mod's tags were matched against predefined keyword lists to infer categories.
2. Manual Review: Mods with ambiguous or missing tags were reviewed through close reading of their descriptions to ensure accurate classification.

Once each mod was assigned to a single audio category, we constructed two numeric vectors:
- A Creator Focus Vector (number of mods per category)
- A User Preference Vector (total endorsements per category)

We applied the cosine similarity formula to measure the alignment between creator focus and user approval:

$$\text{cosine similarity} = (A \cdot B) / (\|A\| \times \|B\|)$$

Where:

- A = mod count per category
- B = endorsements per category

This model was adapted from Dey et al. (2016), who used a similar framework to quantify alignment in broader modding ecosystems. While their focus spanned multiple games, our adaptation zeroes in on audio-specific modding to provide domain-level insight into participatory resonance.
Although the dataset includes only 20 mods, this sample represents a targeted examination of the most impactful audio contributions within the community. The methodology is scalable to larger datasets and adaptable across modding platforms.

Findings

The analysis yielded a cosine similarity score of ≈0.98, indicating a remarkably high degree of alignment between creator output and user appreciation. This suggests that in the Skyrim audio modding scene, modders are highly attuned to player expectations. The most common categories were 'Enhancements' and 'Ambient', which together comprised over half of the selected mods. For example, 'Audio Overhaul for Skyrim SE'—a comprehensive remaster of ambient and combat sounds—garnered tens of thousands of endorsements, signaling strong communal approval. Similarly, the 'Sounds of Skyrim' series focused on expanding environmental immersion and was frequently cited in user reviews as a must-have mod for new players. These examples reinforce the idea that community consensus prioritizes realism and environmental depth in sound design. On the other hand, less represented categories like 'Utility for Modders' and 'Mod Patches' had fewer mods and lower cumulative endorsements, suggesting more niche appeal or backstage usage. The methodology's ability to surface these distinctions offers a replicable framework for analyzing participatory design focus within modding ecosystems.

Conclusion

High alignment between modder output and user endorsement reflects a healthy participatory ecosystem. In this context, modders act not only as creative individuals but also as responsive contributors to a shared aesthetic vision. The results affirm the notion that participatory media is not only about access to creation tools but about active listening, cultural negotiation, and shared meaning-making. In the case of audio modding, modders appear to internalize user preferences and produce content that directly addresses community desires for immersion, realism, and sonic quality.

Moreover, the methodology presented here bridges computational and cultural analysis. By offering a means to quantify aesthetic alignment, it invites further applications across modding communities and media types. Future work may involve cross-game comparisons, longitudinal tracking of mod trends, or deeper ethnographic study of modder-player dialogue. Ultimately, this study contributes to growing scholarship that recognizes fan production not as peripheral, but as central to media experience.

References

Banks, J. (2013). Co-creating Videogames. Bloomsbury Academic.
Bethesda Game Studios. (2016). The Elder Scrolls V: Skyrim Special Edition [Video game]. Bethesda Softworks.
Collins, K. (2008). Game Sound: An Introduction to the History, Theory, and Practice of Video Game Music and Sound Design. MIT Press.
Collins, K. (2013). Playing with Sound: A Theory of Interacting with Sound and Music in Video Games. MIT Press.
Dey, T., Kim, J., Ng, P. H., Mankoff, J., & Zheng, Y. (2016). Playing by the Crowd: Understanding Player Modding Behavior in Video Games. CHI PLAY 2016, 129–142. https://doi.org/10.1145/2967934.2968090
Elder Scrolls Mods Wiki contributors. (n.d.). Sounds of Skyrim. In Elder Scrolls Mods Wiki. Retrieved March 6, 2025, from https://tes-mods.fandom.com/wiki/Sounds_of_Skyrim
Jenkins, H. (2006). Convergence Culture: Where Old and New Media Collide. NYU Press.
Jørgensen, K. (2014). Sound in a Participatory Culture: A Review of Playing with Sound (Collins, 2013). Game Studies, 14(1). http://gamestudies.org/1401

Nexus Mods. (2023). Audio Overhaul for Skyrim SE [Mod]. Retrieved March 6, 2025, from https://www.nexusmods.com/skyrimspecialedition/mods/12466

Postigo, H. (2007). Of Mods and Modders: Chasing Down the Value of Fan-Based Digital Game Modifications. Games and Culture, 2(4), 300–313. https://doi.org/10.1177/1555412007307

Sotamaa, O. (2003). Computer Game Modding, Intermediality and Participatory Culture.

Wikipedia contributors. (n.d.). Skyrim modding. In Wikipedia. Retrieved March 6, 2025, from https://en.wikipedia.org/wiki/Skyrim_modding

Transformation of Digital Audio from Metaverse to Web3

Günsel Işık Gruson[a], Taylan Özdemir[a]

[a]Istanbul Technical University, Music Department, Music PhD Program, Turkey
gunyilmaz@itu.edu.tr

Keywords: Metaverse, Web3, NFT.

The digital audio transmission format was envisioned as part of the digital transformation in the 1990s with Dolby Digital's 5.1 capable AC3 codec. After the 2000s, stereo analog broadcasting was gradually abandoned and replaced by digital broadcasting. Today, digital audio streaming is part of new markets that includes VR concerts taking place at video game events in metaverses[11]: In fact, the concept of the metaverse (a virtual universe visited by VR glasses) was first introduced as an idea in Neal Stephenson's 1992 novel Snow Crash and was first implemented as a gathering event, such as live concerts, in 2003 with 'Second Life'. Research projects such as 'Empty Room', which has been ongoing since 2013 on composing in VR and sound spatialization, have demonstrated the potential of musical practices in digital universes and since 2017, millions of Play Station users have introduced to VR concerts utilizing Unreal Engine.[12] Sharing the features of the metaverse that offers an immersive, interactive, 3D experiences and togetherness of the social community in a game concept, new digital economy instrument 'Web3' (e.g., blockchain-based games, eSports) offers 'virtual trades' such as earning, buying and selling digital assets with 'decentralized' real-time payments through 'cryptocurrency wallet' which eliminates the commission that goes to the third parties. Meanwhile, a unique blockchain -achieved through code algorithms that create a string data protocol- is essential for 'non-fungible tokens' (NFTs) as digital legal proof of creator ownership, as well as for the security of cryptocurrencies (Bitcoin, Ethereum, Phantom, Polygon, etc.). Thus, in theory, the new digital economy model opens a window into the future of the distribution, reception and copyright for artists, composers, designers and content creators; it contains the possibility of transforming the digital music markets and related industries together.

Aim

While digital audio technology is evolving, how is the transition taking place between the metaverse and the digital economy instrument, Web3? How can Web3 and NFTs be applied to music? This brief research aims to introduce the connection and integration of music in the new digital economy order.

Material and Method

In the preliminary study, the inadequacy of secondary data in Web3, the existence of conceptual gaps and the uncertainty regarding the possible connection of digitized audio with NFTs in the context of musical practice were observed. Therefore, beside technopolitical publications and the latest standard instructions on sound distribution, primary data on related subjects such as international conferences, interviews with experts and online pages with technology content have been carefully evaluated.

Findings

1) Promising to support the rights of individual artists and internet entrepreneurs in the new digital economy order, Web3 and NFT still may seem like 'utopian futuristic ideas' however their potential and use for music has been already implemented as will be seen in the following examples: 1) Taylor Swift who promotes herself, owns her

[11] Whereas a headset is required in VR, where users can move in a virtual space, it is not required in the Metaverse, which consists of various universes in an interconnected network.

[12] Some of the early VR concerts that are given by using Epic Games' Unreal Engine (3D computer graphic game engine) are Sony's Chainsmokers' Paris concert in 2017; Marshmello's live, motion captured VR concert in Fortnite, in 2019; Travis Scott's VR concert with pre-recorded five songs from *Astroworld* album (2018) in 2020; VR concerts of Muse, Justin Bieber and Finland metal band Nightwish in 2021.

own copyrights and 'uses the fan-artist (fan-token) system' contributes to the small investor model in the context of decentralization. 2) Referring to the fact that 'artists' cannot earn income from YouTube video views, Snoop Dogg - who known as a property owner in Web3- acclaims that he can buy NFTs to remix (and 'control') their albums. 3) Kings of Leon who released their 2021 album as an NFT on the 'Yellowheart platform' and offered new delivery strategies -such as a new album or concert tickets to their listeners as promotions- have shown that new e-marketing strategies can be successful. 2) In return, to be one of the artists in Web3, it is important to be surrounded by a community that can invite one to e-marketing platforms, therefore, understanding these new concepts seems crucial: For instance, in the field of music marketing, some of the Web3 communities in NFT platforms can be listed as Friends With Benefits, SongCamp, Royal, Zora. In addition, some of the music NFT marketplaces are 'catalog' (songs can be streamed and marketed while adding to open music library), 'sound.xyz:' (artists can stream their tracks, a mixed album can be sold and listening parties can be organized) and 'Async Music' (recorded tracks can be sold separately). However, 'Mint Songs' is one of the rare platforms that does not require an invite for an artist to take part in the NFT world. 3) Hypothetically, it is predicted that with Web3, independent content producers will be freed from the dominance of large platforms, shared management will become indispensable and monopolization will decrease. Accordingly, it is promised that NFT owners will have control over digital creations and that intermediaries will be eliminated however when owning a NFT and becoming a member of a blockchain, high commission is charged from users and paradoxically, this 'hegemonial' and closed structure brings gatekeepers to mind.

Conclusion

1) In this research, valid examples of digital audio and music use in Web3 (which does not have a classical banking system but instead has a decentralized structure and offers a consistent digital economic system) have been briefly presented. While new e-markets are being developed for universes of the digital age where hyperreality will be shaped, it is seen that metaverse platforms will be used more actively for social events such as music festivals or artist-fan meetings of the future. 2) Since the access model offered by the music platforms to the artists is not a profitable mechanism, a promising system of NFT can replace or be an alternative to the traditional 'label' application where the music can be accepted and valued as digital asset. Furthermore, through NFT, digitized versions of artworks such as recorded takes from archives, can be valued, bought, sold or remixed in audiovisual industry; enhanced with Next Gen technologies (e.g., AR/VR, holograms, AI) for sonification purposes or incorporated into industrial design products. 3) The possibilities provided by VR technology are appreciated by the fact that the shared moment is remotely accessible to a large number of people; therefore, VR events (that can include all types of VR meetings and VR concerts) will be more developed with 3D real time technology and the new production methods. 4) Although the dominance of AI technology over the future is widely emphasized, economists, creators and designers of Metaverses may also gain more importance.

References

ITU-R BS.2076-3: Audio Definition Model (02/2025)
Olivieri, F et al. (Nov. 2019) EBU Technology & Innovation Technical Review: Scene-Based Audio and Higher Order Ambisonics: A technology overview and application to Next-Generation Audio, VR and 360° Video. San Diego, California, USA: Qualcomm Technologies Inc.
Url-1 https://blog.fr.playstation.com/2022/11/02/playstation-vr2-sortira-en-fevrier-au-prix-de-e599-99/ date retrieved 20.03.2024
Url-2 https://medium.com/echo3d/the-best-vr-events-and-concerts-planned-for-2021-c1f28b3040d2 date retrieved 11.03.2024
Url-3 www.danishsoundcluster.dk/adm-nga-delivery/ date retrieved 08.02.2022
Url-4 www.forbes.com/sites/legalentertainment/2021/02/09/the-future-of-live-events-ar-vr-and-advertising/?sh=5bf2b2042b65 date retrieved 16.04.2024
Url-5 www.lense.fr/intel-technology-to-drive-8k-forward/ date retrieved 20.04.2024
Url-6 www.musicbusinessworldwide.com/artists/travis-scott/ date retrieved 21.05.2024

Url-7 www.musicbusinessworldwide.com/sony-acquires-250m-stake-in-epic-games-maker-of-fortnite/ date retrieved 16.04.2024
Url-8 www.nftnow.com/guides/complete-guide-to-the-nft-music-ecosystem/ date retrieved 11.03.2023
Url-9 www.t24.com.tr/yazarlar/fusun-sarp-nebil/taylor-swift-in-muthis-bilet-satislarinin-arka-planinda-ne-var,37518 date retrieved 22.04.2024
Url-10 www.variety.com/2021/digital/news/sony-immersive-reality-concert-madison-beer-ces-1234882988/ date retrieved 09.03.2023

MUSICOLOGY AND MUSIC THEORY

Ethnomusicology

Historical Musicology

Music Theory

Popular Music

Ecomusicological Methods in Soundscape Research: Analyzing Sounds on the Water in Haliç

Semin Tunalı[a]

[a] Istanbul Technical University, Graduate School, Musicology and Music Theory, Turkey
sener16@itu.edu.tr

Keywords: Ecomusicology, Soundscape, Golden Horn, Rowing, Ethnomusicology.

Aim

This research aims to explore ecomusicological methods used to study soundscapes and apply them in the analysis of the specific acoustic environment of Haliç (Golden Horn). Haliç is a historically and geographically significant waterway in Istanbul and has an attractive biodiversity. These features make this area ecologically important and worth examining. The intention of this study is to determine the sounds of the environment in the field and to understand how these sounds contribute to spatial awareness. In that aspect, the study will try to explain the human and non-human interactions/intra-actions, particularly in the context of rowing, where auditory cues play a crucial role in navigation and synchronization.

Ecomusicology, as an interdisciplinary field combining ethnomusicology, sound studies, and ecological research, provides various methodological approaches to understanding the relationship between sound, environment, and human and non-human interactions. Established research methods in ecomusicology include methods such as field recordings, comparative analysis, soundwalks, sound mapping etc. This research will show us how these approaches can be adapted to this specific soundscape.

Ultimately, this study aims to assess the effectiveness of ecomusicological methods in studying urban aquatic soundscapes, providing insights into both the sonic environment of Haliç and the broader applicability of these methods to similar ecological and cultural contexts.

This research is the starting point of a study to be done for the author's PhD dissertation, and it is inspired from the author's personal experiences in rowing, where sound serves as a vital guide for synchronization, navigation, and engagement with the environment.

Material and Method

For this research the author has adopted a qualitative methodology, combining fieldwork, observation, sound recordings, and interviews to analyze the soundscape of Haliç. Since the research is based on real-life experience and evidence, the collected data is empirical. The details of the used methods are as below:

Field Recordings and data-collection: The author did several field recordings between October 2024 and January 2025. The recordings were not taken regularly. They consist of recordings taken at random days and random hours. The author used a Tascam DR40X recorder to record environmental sounds, capturing sounds within the reach of the device when it was located on the rowing boat, over the water. In addition, she used her mobile phone to capture videos and sounds.

Observation: The author documented her personal experience and auditory (as well as visual) observations during rowing sessions. She observed how sound affected her movement, her decisions on the water, and her environmental perception. The observation helped her to reveal the relationship of the human and non-human beings in the field.

Interviews: A short questionnaire was prepared, and the fellow rowers were asked about their experience during their own rowing sessions. She collected information regarding their perception of the sounds and their environments, their awareness and interaction with their environment. She tried to find out common points between her own perception and the perception of the participants.

Sound Analysis: Sounds were classified into three main categories:

- Anthropogenic (Human-made) Sounds – Boat engines, ferry announcements, road traffic, construction noise, human voices.

- Biophonic (animal) Sounds – Bird calls, aquatic life sounds.
- Geophonic Sounds – Water movement, wind, rain.

Literature Review and Approaches: While evaluating the data, the author mainly benefited from Schaffer's approach to the sound and noise pollution, and his concept of soundscape; Oliveros' deep listening concept; Ingold's view about sound and immersive experience. Other studies about soundscape were taken as example as well. Main foci of these studies were the soundscapes of certain neighborhoods and cultural meaning of the sounds; noises on the water, underwater noises and their impacts on the environment.

Findings

We infer from the analysis of field recordings, observations, interviews several key findings regarding the soundscape of Haliç:

1. Dominance of Anthropogenic Sounds:
   - The soundscape is largely influenced and formed by human activity, with the most dominant sounds originating from boat engines, road traffic, tram announcements, and people's voices on the shore.
   - These sounds create an auditory masking effect, reducing the ability to hear natural sounds or biophonic sounds clearly.
2. Role of Sonic Elements in Navigation and Awareness:
   - Rowers rely on natural sounds as well as other rowers' and engine noises to orient themselves.
   - Avian species, including cormorants, seagulls, ducks, and herons, are key contributors to the sonic environment apart from anthropogenic noises.
   - Some birds, such as ducks and geese, react to human presence and activities, particularly when anticipating food. Their vocalizations and movements change in response to environmental stimuli, including interactions with humans on the shoreline. Observations also suggest that waterfowl communicate with each other through sound, especially when responding to shared stimuli like food availability.
3. Sonic Synchronization in Rowing:
   - Sound plays a crucial role in rowing synchronization, as rowers depend on the rhythmic sounds of their oars and sliding seats to maintain coordinated movement.
   - When rowing in the dark or in conditions with limited visibility, rowers rely primarily on auditory cues to navigate.
4. Sound as an Immersive Experience:
   - Participants are aware of their environmental sounds although their perception depends on several factors. They described their rowing experience as deeply immersive, shaped by a continuous engagement with environmental sounds.
   - The presence or absence of specific sounds (such as bird calls, water ripples, or engine noise) influences rowers' emotional and physical states.
   - Certain sounds, particularly biophonic and geophonic sounds (e.g., water movement, birds), were reported to have a calming and meditative effect. Mechanical noise incite rowers to move away from noisy parts on the water because they cannot find the piece they are looking for and cannot get all the benefits they are supposed to obtain with their training.
5. Sound Pollution and Its Ecological Implications:

Human-induced noise pollution affects the natural soundscape, probably disrupts animal communication and alters the acoustic environment. Urban noise pollution affects Haliç and human-induced voices blend in with the biophonic voices in Haliç. Further investigation is necessary to measure the dimension of this disturbance and how the human and non-human elements react to this pollution.

Conclusion

The soundscape of Haliç is a rich and dynamic environment shaped by the interactions of human and non-human actors. This environment deserves a deeper analysis because of its value, its significance as location and its

biodiversity. This study reveals that we can conduct an ecomusicological analysis on this habitat following the methods used in similar ecomusicological studies.

So far, this study has revealed the complex interplay between human and non-human sound sources in that urban aquatic environment. The findings suggest that sound is a fundamental element in ecological relationships, and it shapes both human experiences and non-human behaviors. By listening to the voices of both humans and non-humans, we can develop a deeper appreciation for the sonic complexity of our environment and the ecological narratives embedded within them.

The research also underlines the importance of the environmental awareness. We can reach this awareness through active listening and participatory soundscape documentation.

Future research will consider expanding soundscape studies to include long-term sound monitoring projects by conducting a more serious field research with a specific program, including regular sound recordings taken on definite times. The content of interviews may be extended with more participants. The classification of existing sounds in the soundscape, the definition of human and non-human factors, of their interactions and intra-actions and determination of participants' experiences already brings out the state of environmental awareness. Henceforth, through interdisciplinary collaboration, expanded studies and immersive listening practices, we can work towards a more sustainable and sonically attuned urban environment. Raising awareness of sonic environments through ecomusicological research can contribute to broader ecological consciousness and sustainable urban planning strategies.

References

Allen, A. (2013). Ecomusicology: Ecoliterature and Musicology as an Interdisciplinary Approach. Journal of Musicology, 30(3), 345-365.

Feld, S. (2012). Sound and Sentiment, Birds, Weeping, Poetics, and Song in Kaluli Expression (3rd ed.). Duke University Press.

Guyette, M. Q., & Post, J. C. (2015). Ecomusicology, Ethnomusicology, and Soundscape Ecology. Scientific and Musical Responses to Sound Study. In Current Directions in Ecomusicology: Music, Culture, Nature.

Ingold, T. (2007). Earth, Sky, Wind, and Weather. Journal of the Royal Anthropological Institute, 13, 19-38.

Kytö, M. (2019). Ecocriticism and the Anthropocene in the Water Soundscape Composition Contest. In Howell, T. (Ed.), The Nature of Nordic Music (1st ed.). Routledge.

Oliveros, P. (2005). Deep Listening: A Composer's Sound Practice. iUniverse.

Pedelty, M., Dirksen, R., Hatfield, T., Pang, Y., & Roy, E. (2020). Field to Media: Applied Ecomusicology in the Anthropocene. Popular Music, 39(1), 22-42.

Schafer, R. M. (1993). The Soundscape: Our Sonic Environment and the Tuning of the World. Destiny Books.

Titon, J. T. (2020). Within Ethnomusicology, Where Is Ecomusicology? Etnomüzikoloji Dergisi, 3(2).

Yelmi, P. (2016). Protecting Contemporary Cultural Soundscapes as Intangible Cultural Heritage: Sounds of Istanbul. International Journal of Heritage Studies, 22(4), 302–311.

MUSICOLOGY AND MUSIC THEORY

Ethnomusicology

Historical Musicology

Music Theory

Popular Music

Analysis Of Some Makams From The Arabic Music Conference 1932

Mohamed Mostafa Ahmed Mohamed[a]

[a] Istanbul Technical University, Social Sciences Institute, Musicology and Music Theory Department, PhD Program, Türkiye

ahmed@itu.edu.tr

Keywords: 1932 Conference, Committee of Makams-Rhythm and Composition, Makams, Notations, 1932 Conference Book.

The 1932 conference featured seven committees, notably the Committee of Makams, Rhythm and Composition, which was vital in exploring scales and rhythms in Arabic and oriental music. This committee concentrated on the makams, examining notations, musical symbols, names, and forms presented in the research. Their decisions and findings were documented in the 1932 conference book, underlining the significance of thorough analysis in preserving the legacy of discussions that shaped the understanding of Arabic music during this pivotal time.

Introduction

The twentieth century marked a significant transformation in Arabic music, fostering remarkable advancements. A key contributor to this development was the 1932 Arabic Music Conference, which played an essential role in Egypt's scientific, artistic, and musical progress during this era. Despite its importance, the conference proceedings have gone mainly unexamined in Egyptian libraries for nearly a century, receiving limited scholarly attention.

The Cairo conference organized its research and findings into seven sections across various committees. Each member chose a committee that aligned with their expertise and interests. During their initial meetings, each committee elected a chairman and a secretary. The committees were categorized as: a) Committee of Recording, b) Committee of Music History, c) Committee of Makams, Rhythms and Compositions, d) Committee of Instruments, e) Committee of Scale, f) Committee of General Matters, g) Committee of Music Education.

Among the seven committees established during the conference, the Committee of Makams, Rhythm, and Composition played a vital role in developing a systematic approach to Arabic music. Its primary objective was to explore and codify the critical musical elements of makams and rhythms, creating a coherent framework for standardizing these components across various regions, including Egypt, Syria, and Iraq (Katz, 2015). Notable European scholars such as Baron d'Erlanger and Sachs significantly influenced the committee's efforts, often employing Western methodologies for analyzing and classifying Arabic music (Thomas, 2007). Consequently, the conference not only reflected the cultural ambitions of the Arab world but also underscored the geopolitical dynamics of the era as Arab nations endeavored to assert their cultural independence in the face of colonial pressures (Llano, 2023).

Aim

This study focuses on the makam analyses presented in the 1932 conference book and aims to compare selected makams with their counterparts in contemporary Arabic music. It will explore differences across various aspects, including tones, symbols, and methodologies for presenting the makams. A comparison will be drawn between the makams documented in the early twentieth-century conference book and those taught in the twenty-first century at the Higher Institute of Arabic Music.

The primary objective is to bridge the gap between the past and the present by analyzing the selected makams from the minutes recorded by the Committee of Makams, Rhythm, and Composition in the official conference book. By examining these primary sources, the analysis will assess how early twentieth-century formulations relate to makam theory and practice as taught today, particularly at the Higher Institute of Arabic Music. This exploration

aims to highlight the evolution and continuity of makam practice within the context of contemporary music education.

Materials And Methods

This study evaluates the theoretical models presented in the official 1932 conference publication to explore the historical development of Arabic makams. It involves a comparative analysis of Egyptian makams as documented in the 1932 source, alongside corresponding concepts in modern Arabic and Turkish music traditions.

The methodology includes a review of both primary and secondary sources in Arabic, English, and French. Key texts, articles, and books were consulted to provide historical and analytical context. Selected makams were further examined through musical analysis, focusing on structure and pedagogy.

Findings

The study of Turkish music provides insights that align with the methodologies employed during the 1932 conference for notating Egyptian makams. The Rast note corresponds to G within the Turkish music makam framework. Certain makam families, such as Ajem, which relates to the Beyati family in Turkish music, exhibit similar structures in the conference book; however, in contemporary Arabic music, Ajem makam often aligns with the Western major scale (Arabic, 1933; Hashad, 2015).

Conclusion

The 1932 conference aimed to unify Arabic music and firmly establish its identity, drawing inspiration from Egypt's cultural renaissance in the early nineteenth century. It successfully harmonized the terminology for makams and rhythms across Arab countries, ultimately standardizing both lyrical and instrumental forms of Arabic music. Remarkably, participants agreed on the unification of musical terminology, including note names, with minimal disagreements. The conference book has since become an essential reference, marking a pivotal shift from the scarcity of scientific resources on Arabic music in Egypt.

The analysis employs various methodologies, and the makam explanations presented at the 1932 conference encompass a range of octaves, providing a broader perspective on the makams. Moreover, the incorporation of makams in pedagogical contexts is evident in the scores included in the conference book, reflecting contemporary teaching methodologies found in Turkish music. Notably, some discrepancies exist in the symbols representing the makams between the 1932 conference and modern Arabic music, which do not entirely correspond with those used in Turkish music.

Upon reviewing the makams from the Institute of Oriental Music and those curated by Baron d'Erlanger, it becomes clear that Baron offers a more extensive selection that closely aligns with Turkish music traditions, organizing makams according to their respective degrees. In contrast, the 1932 Institute's approach to makams minimized redundancy by refraining from presenting them under different names (Arabic, 1933).

References

Arabic, M. (1933). Kitab Moatemar El-Musika El-Arabya, Book of Arabic Music Conference, Cairo: Copyright Supreme Council of Culture.

Hashad, M. (2015). Maqam, the formal curriculum book for the makams at the Higher Institute of Arabic Music. Dar Merit, Cairo p. 18-32.

Katz, J. I. (2015). Henry George Farmer and the First International Congress of Arab Music (Cairo, 1932), Copyright by Koninklijke Brill NV, Leiden, The Netherlands.

Llano, S. (2023). Empire, diplomacy, and the racial imagination: Spain at the Cairo Congress of Arab Music (1932), The Journal of North African Studies, 28:3, 589–634.

Thomas, A. Elise (2007). "Intervention and Reform of Arab Music in 1932 and Beyond", Conference on Music in the World of Islam, Assilah.

Music as Refuge From Reality: Schopenhauerian Aesthetics Revisited

Selim Güre[a]

[a] Istanbul Technical University, Turkish Music State Conservatory, Musicology, Türkiye
gurese17@itu.edu.tr

Keywords: German Idealism, Musical Aesthetics, Musical Perception, Philosophical Pessimism, Psychology of Aesthetics.

Aim

Taking my departure from the third section of The World as Will and Representation, Schopenhauer's magnum opus, I posit that the merit of aesthetic contemplation is not to be sought in its revelatory potential, but its capability to distract the audience from what is called in the pessimistic literature "the brotherhood of suffering between everything alive" (Zapffe & Tangenes, 2004). Within this framework, aesthetic contemplation serves as a momentary refuge from reality. I use the word 'refuge' instead of 'escape' precisely because 'refuge' implies 'a place to escape with the intention of returning to one's place of origin,' whereas a given act of escape need not necessarily carry an intention of return. To this end, I draw upon various empirical findings concerning 'flow states' and 'function of music' research (Harmat et al., 2021; Schäfer et al., 2013). I conclude by arguing that music, while not necessarily being a pathway to 'the kernel of being' as Schopenhauer postulated, may nonetheless serve as a momentary refuge from the bleak reality often depicted in his writings (Jacquette, 2007).

Material and Method

I employ a bidisciplinary approach incorporating the Schopenhauerian worldview, and a close reading thereof, with contemporary psychological research on aesthetic experience. The philosophical lens, rooted in Schopenhauer's understanding of human existence and suffering, offers a foundation for investigating the psychological benefits of engaging with art. The methodological focus is on combining these philosophical insights with modern empirical studies on human emotional responses to art and the cognitive processes underlying aesthetic appreciation.

The principal material for this investigation is the philosopher's seminal work, The World as Will and Representation, particularly the third section, in which he lays out the nature of aesthetic contemplation (Vandenabeele, 2008). Schopenhauer articulates that aesthetic engagement, through art, enables an individual to momentarily transcend the will — the fundamental driving force of all human striving — and achieve a state of pure, selfless perception (Shapshay, 2023). This moment of detachment from the relentless cycle of desire, suffering, and striving reveals to the individual an opportunity to experience the world not as a manifestation of will, but as an objective reality (Alperson, 1981). This critical concept forms the basis of the theoretical inquiry presented in this study.

Secondary materials consist of a plethora of articles published on Schopenhauer's aesthetic teleology and related subjects. These include interpretations of his theories on the nature of aesthetic experience, critiques of his pessimism, and recent debates regarding the significance of his views on music as a unique and elevated form of art (Leikert, 2021; Venetianer, 1873; Wicks, 2020). Moreover, I incorporate findings from psychological studies concerning 'flow states,' where individuals become fully immersed and engaged in an activity to the extent that they experience an altered state of consciousness, characterized by deep focus, joy, and a sense of timelessness (Tan & Sin, 2021). By juxtaposing Schopenhauer's arguably dated apprehension with contemporary approaches, I aim to illuminate how aesthetic contemplation, especially through music, can serve as a symbolic refuge.

Findings

The study provides several insights into the nature of aesthetic contemplation and its psychological benefits. First, Schopenhauer's notion of transcendence through art resonates with modern psychological findings on 'flow' and the cognitive immersion induced by activities pertaining to music (Johanis, 2024). Empirical studies show that

music, as one of the most powerful forms of aesthetic engagement, can elicit a flow state where listeners experience a temporary escape from the demands and stresses of daily life (Harmat et al., 2021). The phenomenon of 'flow' is often accompanied by a sense of timelessness, complete absorption in the experience, and a loss of self-consciousness — all features that align with Schopenhauer's idea of aesthetic contemplation.

The extent to which music, in particular, serves as an emotional and psychological refuge is notable (Leikert, 2021). Numerous research on the matter indicate that music has a profound ability to regulate emotions, reduce stress, and even mitigate symptoms of anxiety and depression (Dhippayom et al., 2022; Hartmann et al., 2023; Xu et al., 2024). These effects are particularly pronounced when the individual listens to music in a deeply engaged, contemplative manner, allowing the mind to detach from the anxieties of existence (Dalton, 2024). Schopenhauer's claim that art provides a refuge from the otherwise ceaseless suffering of life is supported by studies showing that aesthetic experiences can function as a psychological sanctuary, providing relief from emotional turmoil and offering temporary respite from not only existential but also day-to-day concerns (Cormack, 2022; Ridder & Jacobsen, 2024).

Moreover, the relationship between Schopenhauer's philosophical assertions and contemporary neuroscience provides valuable insights into the effects of music on the brain. Neuroimaging studies reveal that listening to music activates regions associated with focus and reward, thereby providing grounds for flow states and further suggesting that music can function as a mental 'refuge' (Vuust et al., 2022). These findings suggest that music offers not only emotional relief but also a means of cognitive disengagement, where listeners may momentarily disconnect from their immediate surroundings and inner conflicts. This aligns with Schopenhauer's understanding of aesthetic contemplation as an interruption of the will's grip on the individual.

The empirical data concerning 'musical imagery' — the ability to mentally hear music without actual sound — supports the idea that aesthetic engagement in music can create an internal space for reflection and transcendence (Floridou et al., 2022). As per Schopenhauer, the contemplation of music allows an individual to move beyond the confines of individual desires and experience the world as an objective and harmonious whole. This transcendence, while not necessarily revealing the deepest metaphysical truths, provides an opportunity for the listener to experience a sense of unity with the world, albeit only temporarily. However, there ought to be limitations in Schopenhauer's theory of music as a path to metaphysical insight. Schopenhauer believed that music, as the most direct expression of the will, could reveal the essential nature of existence. Contemporary research, while acknowledging music's emotional and cognitive benefits, suggests that the effect of music on the listener is more transient and subjective, rather than revelatory in the metaphysical sense that Schopenhauer envisioned. In essence, music serves more as a momentary refuge than as a profound means of accessing the "kernel of being."

Conclusion

In conclusion, this study affirms the relevance of Schopenhauer's ideas in contemporary discussions on aesthetic experience while also highlighting the ways in which modern psychological research has expanded and refined our understanding of the psychological effects of indulgence in art. Aesthetic contemplation, especially through music, indeed offers a metaphorical refuge from the suffering intrinsic to the human condition, providing listeners with temporary relief from the relentless cycle of desire and vicissitude. While music may not lead to the metaphysical revelations Schopenhauer posited, it may serve as an emotional sanctuary, a momentary respite from the life force (der Wille zum Leben). By incorporating Schopenhauer's philosophy with recent empirical findings, this study demonstrates that music can offer more than mere pleasure or entertainment: it provides a space for reflection, emotional regulation, and, perhaps most importantly, a brief seclusion from the harsh realities of day-to-day existence. Through this lens, music emerges not as a path to ultimate truth, as Schopenhauer would rather have us believe, but as a vital tool for inner reflection — a momentary refuge in an otherwise turbulent world.

References

Alperson, P. (1981). Schopenhauer and musical revelation. The Journal of Aesthetics and Art Criticism, 40(2), 155–166.

Cormack, M. (2022). Escapism Through Music: K-Pop and Emotional Support. YA Hotline, 116.

Dalton, D. M. (2024). Pessimistic aesthetics and the re-valuation of guilty pleasures: On the moral and metaphysical significance of escapism. Journal of Aesthetics & Culture, 16(1), 2341722.

Dhippayom, T., Saensook, T., Promkhatja, N., Teaktong, T., Chaiyakunapruk, N., & Devine, B. (2022). Comparative effects of music interventions on depression in older adults: A systematic review and network meta-analysis. EClinicalMedicine, 50.

Floridou, G. A., Peerdeman, K. J., & Schaefer, R. S. (2022). Individual differences in mental imagery in different modalities and levels of intentionality. Memory & Cognition, 50(1), 29–44.

Harmat, L., De Manzano, Ö., & Ullén, F. (2021). Flow in Music and Arts. In C. Peifer & S. Engeser (Eds.), Advances in Flow Research (pp. 377–391). Springer International Publishing.

Hartmann, M., Mavrolampados, A., Toiviainen, P., Saarikallio, S., Foubert, K., Brabant, O., Snape, N., Ala-Ruona, E., Gold, C., & Erkkilä, J. (2023). Musical interaction in music therapy for depression treatment. Psychology of Music, 51(1), 33–50.

Jacquette, D. (2007). Schopenhauer's Proof that Thing-in-ltself is Will. Kantian Review, 12(2), 76–108.

Johanis, T. C. (2024). Investigations of Flow State Experience, Perception, and Expression in Music Performance [PhD Thesis, University of Toronto (Canada)].

Leikert, S. (2021). Wo sind wir, wenn wir Musik hören?: Musik und psychoanalytische Subjekttheorie. Forum der Psychoanalyse, 37(3), 267–280.

Ridder, H. M. O., & Jacobsen, S. L. (2024). Facing the music or music for escapism. Dansk Musikterapi, 21(Special Issue), 5–9.

Schäfer, T., Sedlmeier, P., Städtler, C., & Huron, D. (2013). The psychological functions of music listening. Frontiers in Psychology, 4, 511.

Shapshay, S. (2023). The Moral Weight of Art in Schopenhauer. In The Schopenhauerian Mind (pp. 198–210). Routledge.

Tan, L., & Sin, H. X. (2021). Flow research in music contexts: A systematic literature review. Musicae Scientiae, 25(4), 399–428.

Vandenabeele, B. (2008). Schopenhauer on Aesthetic Understanding and the Values of Art. European Journal of Philosophy, 16(2).

Venetianer, M. (1873). Schopenhauer als Scholastiker: Eine Kritik der Schopenhauer'schen Philosophie mit Rücksicht auf die gesammte Kantische Neoscholastik. C. Duncker's Verlag (C. Heymons).

Vuust, P., Heggli, O. A., Friston, K. J., & Kringelbach, M. L. (2022). Music in the brain. Nature Reviews Neuroscience, 23(5), 287–305.

Wicks, R. L. (2020). Classical Beauty and the Expression of Personal Character in Schopenhauer's Aesthetics. In The Oxford Handbook of Schopenhauer (pp. 209–224). Oxford University Press Wicks New York.

Xu, H., Li, A., & Apuke, O. D. (2024). The impact of group music therapy in ameliorating the depression among patients with dementia in care homes: A randomized control trial. Geriatric Nursing, 56, 304–311.

Zapffe, P., & Tangenes, G. (2004). The last messiah. PHILOSOPHY NOW-IPSWICH-, 35–39.

MUSICOLOGY AND MUSIC THEORY

Ethnomusicology

Historical Musicology

Music Theory

Popular Music

Folk Music and Classical Composition: A New Framework in Scottish Music Based on Bartok's Three Folk Music Categorizations

Senay Yılmaz[a]

[a] Istanbul Technical University, Music, Music Theory, Türkiye

senayyilmaz1@gmail.com

Keywords: Scots Melodies, Bartok's Folk Categories, Folk-classical interaction, Arrangements, Modality.

Aim

Introduction

Scottish folk music, like all folk traditions, has played a crucial role in shaping national identity, serving as both a cultural artefact and an artistic influence. In classical music, folk traditions have often been preserved through arrangements and adaptations, yet the interaction between folk and classical idioms is more complex than mere quotation. This research seeks to investigate how Scottish folk music has influenced classical composition, focusing on the implicit transmission of folk elements rather than dşrect melodic quotation.

The primary framework for this study is Bela Bartok's tripartite classification of folk music's influence on classical composition, as explained in The Influence of Peasant Music on Modern Music. While Bartok's theory has been widely applied in the context of Eastern European music, it has not yet been systematically used to examine Scottish music before. By employing this model, this research has categorised Scottish-influenced classical compositions into three distinct types and, more importantly, established a refined third category that challenges conventional understandings of folk-inspired music.

The key contribution of this research was to demonstrate that folk music could permeate classical compositions without direct quotation - a process often overlooked in previous studies. Rather than viewing folk influence as mere borrowing, this study explored how Scottish folk idioms including rhythmic patterns, modal structures, and textural features, subtly manifested within classical works and how these elements were embodied in classical compositions.

Literature Review

The relationship between folk and classical music has been extensively studied in various contexts. Early research on Scottish folk music's integration into classical works focused on arrangements and adaptations of traditional melodies. Prominent examples include Beethoven's and Haydn's Scottish Song Arrangements and Mendelssohn's Scottish Symphony, all of which incorporate direct references to folk tunes. However, these works fall into Bartók's first two categories and do not fully account for more nuanced forms of folk music integration.

Existing studies have examined composers influenced by Scottish folk music and identified explicit quotations of folk melodies, yet there has been little systematic analysis of works that embody folk characteristics without quoting specific tunes. This gap in the literature is where this study intervenes.

Additionally, Bartók's theoretical framework has been applied primarily to Hungarian, Romanian, and Slovak folk music, leaving Scottish folk music largely unexamined. This research contributes a new perspective to folk-classical interactions by extending Bartók's model to a Scottish musical context and refining his third category as it applies to compositions that exhibit Scottish qualities without directly borrowing folk material. A significant number of examples were found during the analysis of selected pieces for the third category. By addressing this gap, the study broadens the application of Bartók's framework and offers a deeper understanding of how Scottish folk traditions subtly permeate classical compositions. This approach provides a foundation for future research on implicit folk influences and encourages a reevaluation of how cultural identity is expressed in classical music.

Material and Method

Bartok's Three Categories and Their Application to Scottish Music

This study applied Béla Bartók's categorization of folk music's influence on classical composition to Scottish music, dividing compositions into three distinct types.

The first category, "Directly Arranged Folk Melodies", consisted of compositions that incorporated unaltered folk tunes with minimal modification, often presented with harmonic accompaniment. Examples of this approach included Beethoven's 25 Scottish Songs and Haydn's arrangements for George Thomson's Scottish collections, both of which retained the original folk melodies while adapting them for a classical framework.

The second category, "Folk-Inspired Compositions", encompassed works that did not directly use traditional folk melodies but were clearly modeled after folk styles. These compositions captured the essence of folk music through melodic contour, rhythmic structure, and form. A key example was Bruch's Scottish Fantasy, which evoked Scottish musical characteristics despite employing newly composed themes rather than existing folk tunes.

The third category, "Subconscious Folk Influence", comprised compositions that contained no direct folk quotations yet retained defining elements of Scottish folk music. These works incorporated Scottish modal language, ornamentation, phrasing, rhythmic stress, and instrumentation, creating a distinctly Scottish sound world without referencing specific melodies. Hamish MacCunn's The Land of the Mountain and the Flood served as an example of this category, as it conveyed a strong Scottish character without explicitly borrowing folk material.

This study primarily focused on Category 3, analyzing compositions that fell outside the conventional definitions of folk-inspired music but still exhibited the unmistakable sonic fingerprint of Scottish folk traditions.

Analytical Approach

The approach is designed to capture the essence of Scottish folk influence by analyzing key musical parameters such as modal and harmonic structures, rhythmic and melodic patterns, orchestration, and form. By focusing on these components, the study seeks to determine how composers internalized and transformed folk idioms within a classical framework. The goal is to identify the distinct sonic fingerprints that mark a composition as rooted in Scottish folk tradition, even if these connections are not overtly stated.

The following analytical criteria were applied to examine the selected compositions in Category 3:

Modal and Harmonic Analysis

This research identified the frequent use of Dorian, Mixolydian, and pentatonic scales, characteristic of Scottish folk music. These modes shape the distinct tonal color of Scottish melodies, often evoking simplicity and timelessness. The Dorian mode, with its minor quality and raised sixth, and the Mixolydian mode, marked by its lowered seventh, were particularly prominent in the analyzed compositions.

The study also explored drone effects and pedal points, reminiscent of the sustained harmonies typical of bagpipe music. These elements contribute to harmonic stability and often anchor melodies, reinforcing the traditional Scottish soundscape.

Attention was also given to intervallic relationships within melodies. Open intervals, such as fourths and fifths—common in Scottish folk traditions and emphasized in bagpipe music—were frequently observed. These intervals enhance the distinctive melodic contour and tonal texture across various instruments. Their subtle presence suggests a deeper, subconscious influence of Scottish folk traditions, even when direct quotations of folk melodies are absent.

Rhythmic and Melodic Structure

The analysis focused on recognising rhythmic patterns characteristic of Scottish folk traditions, such as the distinctive "Scottish snap," which consists of a short, accented note followed by a longer one. This rhythm

contributes to the energetic and dynamic quality of Scottish dance music. Strathspey accents, known for their strong, syncopated stress patterns, and jig rhythms, characterised by lively, compound meter patterns, were also frequently observed.

In terms of melody, the study examined phrasing for contour patterns reflective of oral tradition transmission, including the use of repetitive motifs, stepwise motion, and ornamental figures. These features help maintain the folk character of the music, even when not directly quoting traditional tunes.

Orchestration and Form

The study examined instrumentation choices that reflected folk performance practices, particularly the emulation of fiddle techniques in string writing, such as ornamentation, double stops, and drone-like open strings.

In terms of form, it observed structures resembling folk dance forms like reels and jigs, characterised by repetitive rhythmic figures and symmetrical phrasing. These elements contributed to creating a subtle yet distinct folk character within the classical compositions. By applying these criteria, this research constructed a new framework for understanding implicit folk influence in classical composition.

Category 3 and Selected Composers

This study identified several composers and works as candidates for Category 3, focusing on compositions that embody Scottish folk characteristics without directly quoting traditional melodies. Examples include Hamish MacCunn's The Land of the Mountain and the Flood, which evokes a strong Scottish atmosphere through its use of modal harmonies and rhythmic patterns reminiscent of folk traditions. James MacMillan's Tryst incorporates rhythmic and textural elements inspired by Scottish folk music, particularly through its dynamic phrasing and ornamentation. James Oswald's Airs for the Seasons subtly integrates modal structures and phrasing that reflect folk practices, while Erik Chisholm's Sonatine Ecossaise demonstrates folk-inspired rhythms and melodic contours without direct quotation.

Selected works by David Johnson, Francis George Scott, and John McEwen also displayed characteristics aligned with Category 3. These compositions revealed folk influence through modal language, rhythmic motifs, and instrumentation choices that echoed traditional Scottish sounds.

A detailed analysis of these works confirmed that they embody Bartók's third category, demonstrating how Scottish folk idioms can subtly shape classical compositions in terms of form, texture, and style—without explicit references to traditional melodies. This highlights the depth of subconscious folk influence present in Scottish classical music.

Findings

Research Significance & Goals

This research offers a new theoretical perspective on the adaptation of Scottish music within classical composition. It challenges the conventional assumption that folk influence relies on direct melodic quotation, instead emphasizing how cultural idioms can subtly shape compositional style. It explores how Scottish musical characteristics—such as modal structures, rhythmic patterns, and textural elements—manifest within classical works without direct reference to folk melodies. It also examines the compositional techniques that facilitate the internalization and reinterpretation of folk elements, revealing how these influences become embedded within the musical language of classical composers. By applying and refining Bartók's model, this research expands the classification of folk-influenced classical works, particularly regarding compositions that reflect folk characteristics through subconscious or indirect means.

Ultimately, this study broadens the understanding of folk music's role in classical composition, offering new insights into how cross-genre interaction shapes musical identity and cultural expression.

Conclusion

By applying Bartók's framework in an innovative way, this study redefines the boundaries between folk and classical music within the Scottish context. Category 1 consists of direct arrangements of folk songs by classical composers, preserving the original melodies with minimal modification. Category 2 includes compositions that feature direct quotations or identifiable patterns from folk songs, incorporating them into classical forms while maintaining a recognizable folk character.

Category 3, however, represents a previously under-explored dimension of folk-classical synthesis. It focuses on compositions where folk influence is present through subtle, implicit elements—such as modal language, rhythmic structures, and textural choices—without the use of direct quotations. This category highlights how folk traditions can shape the stylistic and aesthetic aspects of classical music in less overt but equally significant ways.

This research establishes a foundational model for future studies on how folk traditions are assimilated into classical compositions beyond direct quotation. By demonstrating how folk music can influence classical language on a subconscious level, it bridges ethnomusicology and music analysis. Ultimately, this study contributes to a broader understanding of Scottish musical identity and encourages a more nuanced approach to examining cross-genre musical interactions.

References

Baker, J. P. (1927). Sir Alexander Mackenzie: And his work at the Royal Academy of Music, London. The Musical Quarterly, 13(1), 14–28. Oxford University Press.

Clements, J. (2013). The creation of "ancient" Scottish music history, 1720–1838 (Doctoral dissertation). University of Glasgow.

Cowgill, R. (2007). Music in the British provinces: 1690–1914. Ashgate.

Elliott, K. (1957–1958). Scottish song, 1500–1700. Proceedings of the Royal Musical Association, 84, 1–12. Taylor & Francis, Ltd. on behalf of the Royal Musical Association.

Gelbart, M. (2013). Once more to Mendelssohn's Scotland: The laws of music, the double tonic, and the sublimation of modality. 19th Century Music, 37(1), 3–36. https://doi.org/10.1525/ncm.2013.37.1.3.

Graham, G. F. (1848). The songs of Scotland: Adapted to their appropriate melodies, arranged with pianoforte accompaniments (Vol. 1). Wood & Co. [Archive] https://archive.org/details/songsofscotland00grah/page/n3/mode/2up.

Johnson, D. (1971). An eighteenth-century Scottish music library. R.M.A. Research Chronicle, 9, 90–95.

McKerrell, S. (2016). Focus: Scottish traditional music. Routledge.

Ross, D. F. (2009). Scottish traditional music. Edinburgh University Press.

Sachs, J. (1970). Hummel and George Thomson of Edinburgh. The Musical Quarterly, 56(2), 270–287. https://doi.org/10.1093/mq/LVI.2.270.

Spearman, M., Stell, G., & Lynch, M. (1988). The Scottish medieval town. John Donald.

Thomson, G. (Ed.). (1822). A select collection of original Scottish airs for the voice (Vols. 1–4, New ed.). Preston. Retrieved from https://archive.org/details/songsofscotland00grah/page/n3/mode/2up.

Harmony in Brouwer's Late Period: Use of Extended Tonality in the First Movement of Del Pensador

Tamer Celik[a], Recep Gül[a]

[a]Istanbul Technical University/Graduate School, Conservatory, Music Theory and Composition, Turkey
celikt17@itu.edu.tr

Keywords: Leo Brouwer, Extended Tonality, Neo-Riemann Theory, Music Theory, Guitar Music.

Aim

Leo Brouwer is arguably one of the most influential guitar composers of the 20th century. His musical style is very diverse and encompasses different compositional aesthetics. His musical oeuvre is generally categorized into three distinct periods. Nevertheless, in his interview with Paul Reed Century (Century, 1985), Brouwer himself adds a fourth one, which indicates the period after 1984. Even though there are numerous studies regarding his first three periods, analysis for the fourth is scarce. This study aims to show the ways in which Brouwer utilizes techniques of extended tonality, thus gaining a better understanding of his last musical period. Extended tonality, developing from classical major-minor tonality, is a system with a set of rules that include relaxed functional constraints, the freedom to combine chords in sentences, and the ambiguity of the key (Rohrmeier & C. Moss, 2021). Combining modal scales with tonal ones and the use of non-functional progressions, this tonal palette draws the unique world Brouwer's music manifests itself.

Materials and Methods

Previous research on the harmonic syntax of Brouwer focused on his earlier three periods. A pedagogical perspective has been employed in order to analyze Brouwer's tonal (Pastilla, Penaranda, 2009), whereas set-theoretical approaches have been utilized for his non-tonal/avant-garde works (Century, 1991). A study on La Espiral Eterna (1971), a piece from Brouwer's avant-garde period, has revealed the existence of three note clusters predominantly used in the piece (Century, 1985). El Decameron Negro (1981) has been analyzed by Demir (2023) focusing on it rhythmic and formal structure. Brouwer's sarabandes have been studied in the thesis of Fülöp (2021), in which tonality and harmonic chord progressions were examined. An analysis of Canticum, a work written in 1968, from his second period revealed that the three-note cluster approach has been freemployed (Suzuki, 1981). La Espiral Eterna has been analyzed by Gülfırat in the thesis "Symmetrical and Cyclical Relationships in La Espiral Eterna." In this study, Gülfırat (2023) revealed that symmetric x, y, and z cells of Bela Bartok were utilized (Treitler, 1959). Although a set-theoretical approach could be the most of post-tonal works of Brouwer, observed that it poses several limitations in describing Recuperacion de La Memoria, such as analyzing chord progressions, cadential points, and resolutions. For example, a set-theoretical method can examine certain intersections of this piece, but may not precisely, whereas extended tonality reveals the hidden tonal structure of this piece. Moreover, Schenkerian approach determines whether a piece is constructed with tonal or not. Our analysis contributes to the study of twentieth-century music, not only in the use of functional tonality or set theory for atonality but also by employing the concept of extended tonality for the composition of neo-tonal music.

To our knowledge, no previous studies investigated Brouwer's fourth-period works. This study aims to assess the part of Del Pensador's first movement, utilizing extended tonality as a central concept, investigating Brouwer's style in his late period. Extended tonality can reveal hierarchical relationships in pieces that do not readily seem tonal in the foreground level. Nevertheless, it has the power to uncover hidden tonal relations as well as the use of neo-tonal constructions. Rohrmeier et al. (2021) proposed a formal model for extended tonality that stemmed from Neo-Riemannian and Tonfeld theories. Neo-Riemann theory analyses triadic chord progressions via parsimonious voice-leading transformation, utilizing a geometric map called Tonnetz. Tonfeld theory complements Neo-Riemannian theory's triadic approach and extends it to hexatonic, octatonic, and fifth-related collections. It is not based on voice leading; instead, individual tones are regarded as elements of a particular tone (pitch) field (Polth, 2018). We claim that the extended tonality concepts can reveal the usage of hidden tonality in the first movement of the Sonata del Pensador.

Findings

Our analysis showed that tonal and modal collections organize the first movement of Del Pensador. The interplay between multiple closely-related scales has been extensively used. It can further be observer that the organizations via collections and their related chords mostly entail diatonic and modal ones throughout the piece.

As a general overview, the first movement of Del Pensador, in particular, has been evaluated by indicating the specific characteristics of all formal sections. The form of the piece is as follows: A- B- C- A'- D- B'-E- A- B-Coda, the measures of A: 1-8, B: 9-25, C: 26-42, A': 43-50, D: 50-58, B': 59-71, E: 72-95, A: 96-103, B: 104-120, and Coda: 121-123. We observed that this segmentation delineates the differentiation of tonal and modal collections clearly. For instance, in measures 1-2 and 5-6 (A section), as seen in Figure 1, a stack of fifths is used, whereas in measures 9-16 (B section), as seen in Figure 2, D-9 chord sonority and octatonic 2-3 A collection are used.

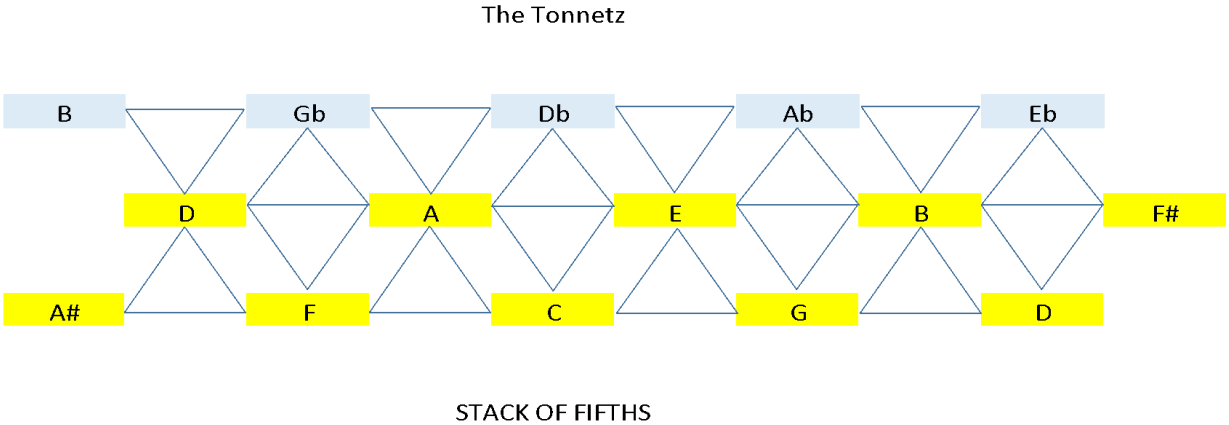

Figure 1: Notes shaded in yellow represent the chord sonorities in measures 1-2 and 5-6 within the axis of D.

As shown in Figure 2, Brouwer expands the musical narrative by employing both diatonic and octatonic collections. D-9 sonority, in measures 9-16 (B section), establishes a theme and subsequently extends the tonality through the octatonic 2-3 A collection.[13] While D-9 sonority comprises a fifth-related collection, represented as a rightward fifth-step progression on the Tonnetz[14], the octatonic collection, consisting of D, Eb, F, F#, G#, A, B, and C, appears diagonally upward to the left on the Tonnetz, as demonstrated in Figure 3. D functions as the tonic.

[13] The naming convention of the octatonic is the same as in Francoli (2008).

[14] Tonnetz is a conceptual lattice diagram representing tonal space, first described by Leonard Euler in 1739.

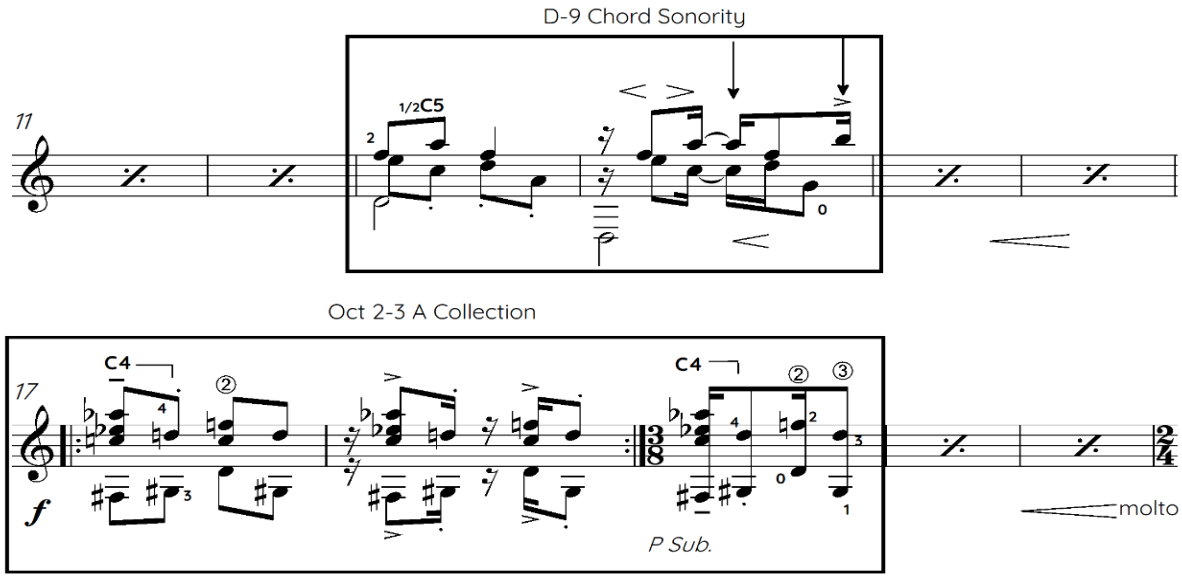

Figure 2: Two collections are merged to form the B section.

The Tonnetz

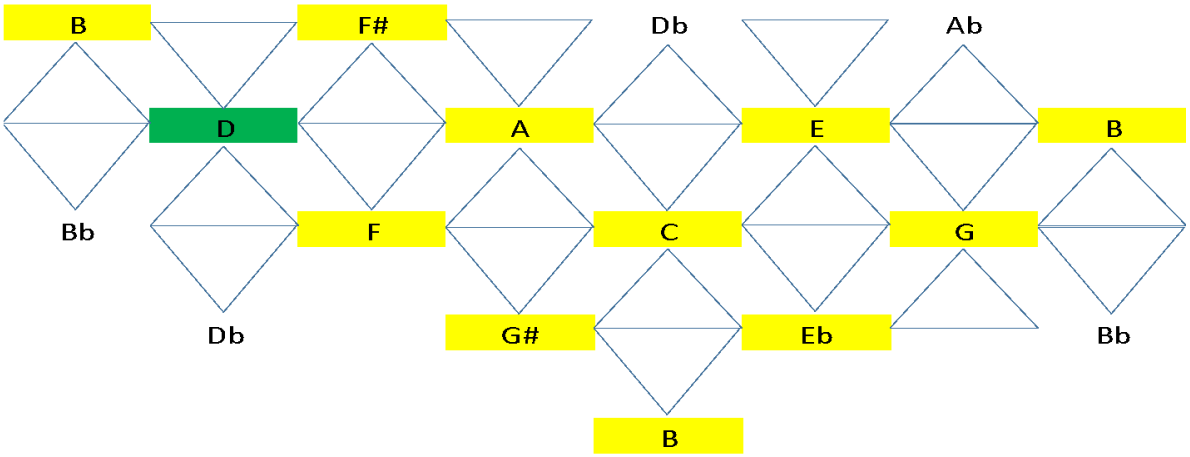

Figure 3: Fifth-related and Octatonic collections' Map.

In the E section, Brouwer employs E Lydian scale to establish a theme, which is enriched with B harmonic major, B major, E major, E major Phrygian (Figure 4a), and ultimately E acoustic collections (Figure 4b). These collections serve to guide the passage back to the beginning, as illustrated in Figure 4a-b.

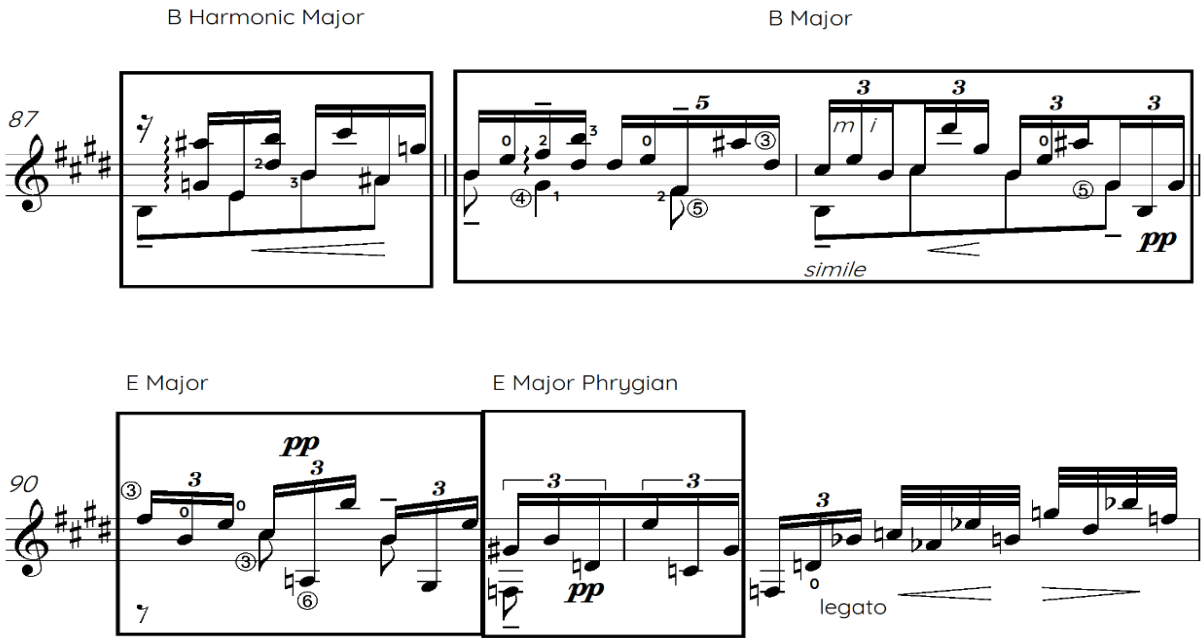

Figure 4a: Diatonic collections.

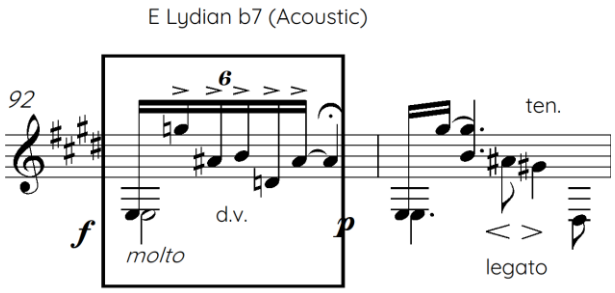

Figure 4b: Diatonic collection, E Acoustic Scale.

We also explored this passage (E) within the framework of Schenkerian approach, in order to explore hidden layers of tonality, as illustrated in Figure 5. At first glance, B leaps into its octave in measure 77, with A# functioning as a neighbor note. The melodic line begins on B in measure 78 and descends into G. Although A# is absent, an imaginary continuum can be presumed. Bass line prolongs the overall harmonic structure using only two degrees: II and iii. In measures 78-79, the passage exhibits increased motion, including arpeggiation, fifth leaps, and neighbor tones.

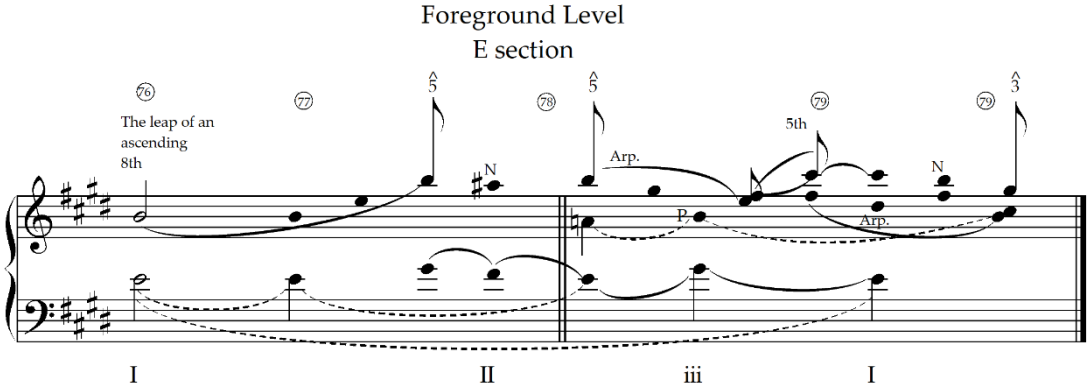

Figure 5: Schenkerian approach to E section, harmonic progression is I-II-iii-I while the melodic line degree is 5ˆ-4ˆ-3ˆ.

An incomplete neighbor motion from A# to B emerges in the upper octave before returning, in measures 86-88, creating a sense of superposition. A# serves as a leading tone in the E Lydian Mode. The composer consistently employs this tone, incorporating fifth and fourth leaps to frame the section, as shown in Figure 6.

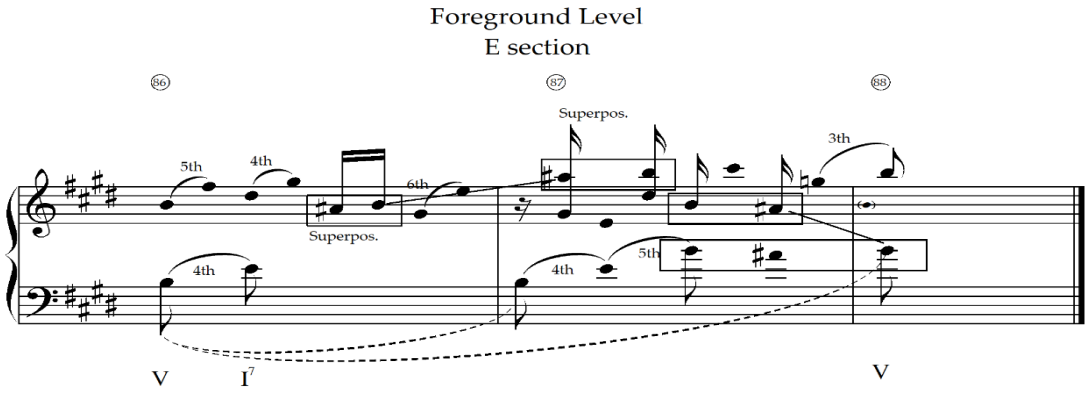

Figure 6: Superposition of the A#-B motive represented at Foreground Level.

In Figure 7, the entire E section is analyzed at the middleground level. G# prolongs the melodic line towards B in measure 88, and subsequently initiates the linear progression, sustaining the prolongation until the cadence point. Harmonically, E supports the entire passage through an extended I-II-V-I cadential progression. Notably, E suggests underlying functional tonality, which remains concealed throughout the whole segment.

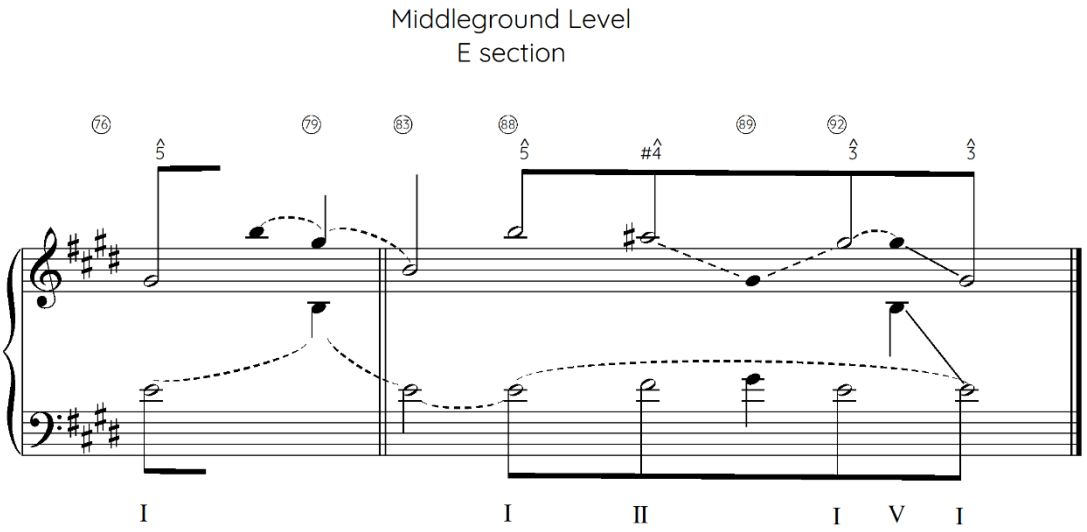

Figure 7: The E harmonic progression of the entire E segment follows I-II-I-V-I while the melodic line progresses through the degree 5ˆ-#4ˆ-3ˆ.

Upon examining the pitch distribution of the entire E section, it is evident that the melodic line prominently features the scale degree 5ˆ-#4ˆ-3ˆ (E-G#-B-A#), as illustrated in Figure 8. The embedded use of E Lydian scale in combination with E major functions as the key generator of the concept of extended tonality in this section. The same progression is repeated at the level of middle-ground, as seen in Figure 7. All these examples demonstrate that in addition to octatonic scale, Brouwer employed an intricated series of diatonic collections in order to extend functional tonality.

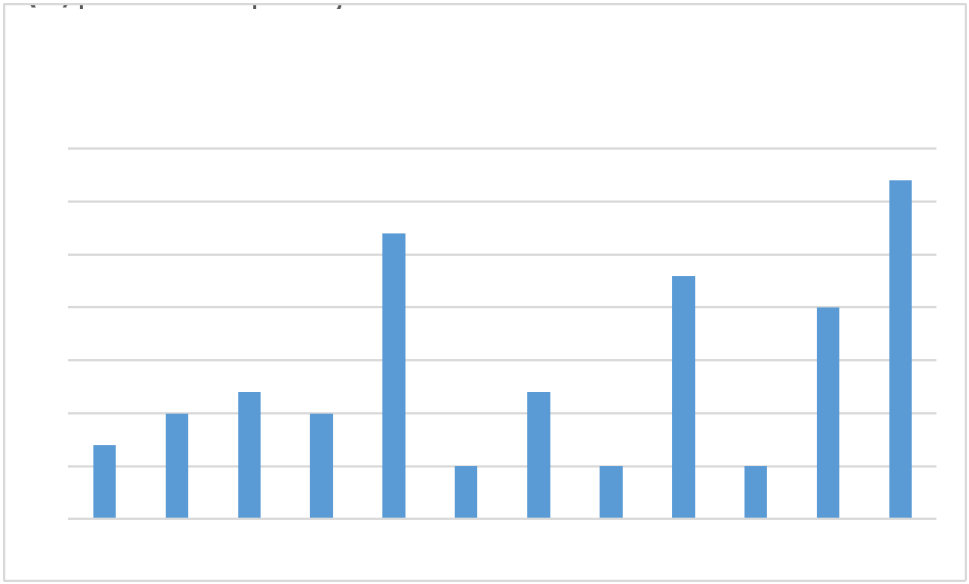

Figure 8: The pitch distribution of the E section highlights the prominence of E, G#, B, and A#.

Conclusion

In summary, this study aimed to investigate Brouwer's final period of guitar music. The theoretical framework of the Recuperacion de la Memoria has been to understand the ways in which pitch collections and their interrelationships were organized. We discovered that the entire section consisted of chord sonorities, octatonic 2-3 A, and fifth-related collections in the key of D, accompanied by connecting passages. Moreover, E section of the movement, which has been evaluated more throughly at both the foreground and middleground via Schenkerian approach, revealed that the roles of collections are also embedded behind the complexity of the foreground. The Schenkerian analysis indicated that the use of functional tonality was concealed throughout the entire section. Overall, our work highlighted the harmonic and melodic implications of the scales in question, as well as their structural similarities and interconnections.

The study showed how the concepts of the extended tonality could offer insights into the structure of Brouwer's fourth period. However, a more comprehensive analysis is necessary in order to understand the inner workings of these schemes. While Schenkerian analysis remains a valuable tool for exploring contemporary music, the coexistence of tonality, atonality, and increasing complexity in modern compositions presents analytical challenges. A singular may not be sufficient to fully interpret such music; therefore, a synthesis of multiple frameworks is essential.

By the twentieth century, musical movements such as tonal, atonal, and twelve-tone music emerged in the classical guitar repertoire, with Leo Brouwer's works exemplifying these trends. This study aimed to explore the application of the extended tonality framework, providing a foundation for future research in this area. Beyond its academic contributions, this article may also serve as a valuable resource for composers in structuring their works.

References

Berke Demir, H. (2023). Leo Brouwer 'ın El Decameron Negro Başlıklı Yapıtının Formal, Müzikal ve Yorumsal İncelenmesi (Master Thesis). Mimar Sinan Fine Art University.

Century, P. R. (1985). Idiom and Intellect: Stylistic Synthesis in The Solo Guitar Music of Leo Brouwer. University of California Santa Barbara.

Francoli, M. A. (2008). Understanding Post-Tonal Music. McGraw-Hill Companies.

Fülöp, K. (2021). The Sarabande in Leo Brouwer's Work for the Classical Guitar (Master Thesis). Escola Superior de Musica Eartes Do Espedaculo.

Gülfırat, D. (2023). Leo Brouwer'ın Müziğinde Avangard: "La Espiral Eterna" adlı Eserde Simetrik ve Çembersel İlişkiler (Doctorate in art). Yasar University.

Polth, M. (2018). The Individual Tone and Musical Context in Albert Simon's Tonfeldtheorie. Society for Music Theory, 24(4). https://mtosmt.org/issues/mto.18.24.4/mto.18.24.4.polth.html
Rohrmeier, M., & C. Moss, F. (2021). A Formal Model of Extended Tonal Harmony. Proceedings of the 22nd International Society for Music Information Retrieval Conference, 10.

Analysis of Vertical Structures in the Context of Set Theory in Ivan Wyschnegradsky's 24 Preludes in Quarter Tone System for Two Pianos, Op. 22

Selçuk Canberk Dağtekin[a]

[a] Istanbul Technical University/Graduate School, Music, Türkiye
canberkdagtekin@yahoo.com

Keywords: Ivan Wyschnegradsky, Microtonality, Quarter-Tone System, Set Theory.

Aim

The aim of this thesis proposal is to adapt set theory to the 24-TET quarter-tone system and to analyze the vertical structures selected from Ivan Wyschnegradsky's 24 Preludes for Two Pianos in Quarter-Tone System, Op. 22 in the context of set theory.

Material and Method

In this study, set theory, its use in music analysis and how set theory is adapted to the quarter-tone system are mentioned. The vertical structures selected from Ivan Wyschnegradsky's 24 Preludes for Two Pianos in Quarter Tone System, Op. 22 were analyzed in the context of set theory adapted to the quarter tone system.

Findings

In this case, it can be said that 22,88% of the prime forms of the analyzed vertical structures according to the quarter-tone system set theory are the same as the others, 38,98% are included by the others and 38,14% have some pitches in common with the others. Based on this, it can be stated that Ivan Wyschnegradsky uses vertical structures that are structurally and timbally like each other. Although the composer produced works in quarter-tones or other microtonal aesthetics, which were considered far ahead of his time, he followed a similar aesthetic approach to the composers of the period before him. Apart from his understanding of microtonal timbre, Ivan Wyschnegradsky's works are similar to those of his predecessors or composers of his period in many respects.

Prelude Number	First Vertical Structure	Second Vertical Structure	Third Vertical Structure	Fourth Vertical Structure	Fifth Vertical Structure
1	(0 1 3 7 11 13)	(0 4 6 8 12 19 21)	(0 2 4 13 15)		
2	(0 1 7 13)	(0 1 6 7 13)	(0 1 2 3 9 16 17)	(0 1 2 3 5 7)	(0 1 7 12 17)
3	(0 2 9 13)	(0 7 14)	(0 1 5 12 17)	(0 2 9 15)	(0 2 3 9 15)
4	(0 2 8)	(0 3 10)	(0 7 14)	(0 4 11)	(0 1 3)
5	(0 1 7 14)	(0 2 6 7 11)	(0 6 8 15)	(0 1 6 7 14)	(0 2 7 8 15)
6	(0 1 2 8 13 14)	(0 2 8 14)	(0 1 3 6 7 12 13 18 19)	(0 1 5 6 11 13 18)	(0 2 4 14)
7	(0 4 11 17)	(0 1 4 11 17)	(0 1 8 13)	(0 5 12 17)	(0 1 2 7 8 13 15 18)
8	(0 2 7 13 18)	(0 2 6 8 12 14 18 20)	(0 1 6 7 10 13 18 19)	(0 1 2 10 13)	(0 1 2 3 8 13 14 15 17)
9	(0 5 12 17)	(0 2 7 13 18)	(0 2 5 10 17)	(0 2 4 5 11 17)	(0 2 6 8 11 13 15 19)
10	(0 1 3)	(0 6 13)	(0 5 10 15)	(0 7 14)	(0 3 11)
11	(0 2 6 8 13 18)	(0 1 5 7 13 18)	(0 2 6 8 11 13 17 19)	(0 2 4 6 8 12 14 18 20)	(0 1 2 3 6 7 8 10 12 13 17 18 19 20)
12	(0 4 6 12 17)	(0 4 5 6 12 17)	(0 1 2 6 7 8 12 13 14 18 19)	(0 6 12)	(0 4 6 8 12 18)
13	(0 1 8 13)	(0 2 7 12)	(0 2 4 6 9 11 15 17 20)	(0 2 5 7 9 11 15 18 20)	(0 6 13)
14	(0 6 11 17)	(0 1 3)	(0 5 10)	(0 1 11)	(0 1 11)
15	(0 2 5 6 7 9 12 18)	(0 1 2 6 9 12)	(0 3 4 8 9 16)	(0 1 5 6 8 13 18 19)	(0 1 2 3 6 8 13 18)
16	(0 2 5 8 15)	(0 2 5 9 12 18)	(0 2 7 9 13 18)	(0 7 11 18)	(0 1 8 9 10 16)
17	(0 2 7 13 18)	(0 1 7 11 13 18)	(0 1 7 11 13 18)	(0 2 4 7 13 18)	(0 1 3 5 7 13 16 18)
18	(0 2 9 16)	(0 5 12)	(0 1 4)	(0 2 7 10 11 17)	(0 1 2 7 9 14 17 18)
19	(0 1 2 8 13)	(0 1 2 7 12)	(0 1 5 7 10 12 14 17 20)	(0 4 5 6 10 11 12 17)	(0 5 10 17)
20	(0 2 10)	(0 5 13)	(0 5 13)	(0 1 9)	(0 1 6)
21	(0 2 7 8 15)	(0 2 7 9 16)	(0 1 5 7 13 16)	(0 1 7 9 12)	(0 1 3 8 9 10 16 17)
22	(0 5 12)	(0 3 8 11)	(0 4 7 11)	(0 1 2)	(0 1 2 3 5 9 11 13 18)
23	(0 2 4 6 11)	(0 2 4 6 9 15)	(0 2 4 6 11)	(0 1 3 6 9 12 14 16 19)	(0 2 4 5 11 16)
24	(0 5 6 11 17)	(0 1 7 12 18)	(0 1 2 3 4 11 12 17)	(0 1 2 3 4 9 10 17)	(0 2 5 7 9 11 14)

Figure 1. The prime forms of the selected vertical structures from Ivan Wyschnegradsky's 24 Preludes in Quarter Tone System for Two Pianos according to the quarter-tone system set theory (Dağtekin, 2024).

Prelude Number	First Vertical Structure	Second Vertical Structure	Third Vertical Structure	Fourth Vertical Structure	Fifth Vertical Structure
1	(0 1 3 7 11 13) 5	(0 4 6 8 12 19 21) 5	(0 2 4 13 15) 4		
2	(0 1 7 13) C	(0 1 6 7 13) C	(0 1 2 3 9 16 17) 5	(0 1 2 3 5 7) 5	(0 1 7 12 17) C
3	(0 2 9 13) C	(0 7 14) S3	(0 1 5 12 17) C	(0 2 9 15) C	(0 2 3 9 15) 4
4	(0 2 8) C	(0 3 10) C	(0 7 14) S3	(0 4 11) C	(0 1 3) S3
5	(0 1 7 14) C	(0 2 6 7 11) 4	(0 6 8 15) C	(0 1 6 7 14) C	(0 2 7 8 15) S2
6	(0 1 2 8 13 14) C	(0 2 8 14) C	(0 1 3 6 7 12 13 18 19) 8	(0 1 5 6 11 13 18) 6	(0 2 4 14) C
7	(0 4 11 17) C	(0 1 4 11 17) C	(0 1 8 13) S2	(0 5 12 17) S2	(0 1 2 7 8 13 15 18) 7
8	(0 2 7 13 18) S3	(0 2 6 8 12 14 18 20) C	(0 1 6 7 10 13 18 19) C	(0 1 2 10 13) C	(0 1 2 3 8 13 14 15 17) 7
9	(0 5 12 17) S2	(0 2 7 13 18) S3	(0 2 5 10 17) 4	(0 2 4 5 11 17) 5	(0 2 6 8 11 13 15 19) 7
10	(0 1 3) S3	(0 6 13) S2	(0 5 10 15) 3	(0 7 14) S3	(0 3 11) C
11	(0 2 6 8 13 18) C	(0 1 5 7 13 18) C	(0 2 6 8 11 13 17 19) 7	(0 2 4 6 8 12 14 18 20) 8	(0 1 2 3 6 7 8 10 12 13 17 18 19 20) 10
12	(0 4 6 12 17) C	(0 4 5 6 12 17) C	(0 1 2 6 7 8 12 13 14 18 19) 10	(0 6 12) C	(0 4 6 8 12 18) C
13	(0 1 8 13) S2	(0 2 7 12) C	(0 2 4 6 9 11 15 17 20) 6	(0 2 5 7 9 11 15 18 20) 6	(0 6 13) S2
14	(0 6 11 17) C	(0 1 3) S3	(0 5 10) C	(0 1 11) S2	(0 1 11) S2
15	(0 2 5 6 7 9 12 18) 6	(0 1 2 6 9 12) 5	(0 3 4 8 9 16) 5	(0 1 5 6 8 13 18 19) 7	(0 1 2 3 6 8 13 18) C
16	(0 2 5 8 15) 4	(0 2 5 9 12 18) C	(0 2 7 9 13 18) 5	(0 7 11 18) C	(0 1 8 9 10 16) C
17	(0 2 7 13 18) S3	(0 1 7 11 13 18) S2	(0 1 7 11 13 18) S2	(0 2 4 7 13 18) 5	(0 1 3 5 7 13 16 18) 6
18	(0 2 9 16) C	(0 5 12) S2	(0 1 4) C	(0 2 7 10 11 17) 5	(0 1 2 7 9 14 17 18) 6
19	(0 1 2 8 13) C	(0 1 2 7 12) C	(0 1 5 7 10 12 14 17 20) 7	(0 4 5 6 10 11 12 17) 5	(0 5 10 17) C
20	(0 2 10) C	(0 5 13) S2	(0 5 13) S2	(0 1 9) C	(0 1 6) C
21	(0 2 7 8 15) S2	(0 2 7 9 16) 4	(0 1 5 7 13 16) C	(0 1 7 9 12) 4	(0 1 3 8 9 10 16 17) 6
22	(0 5 12) S2	(0 3 8 11) 3	(0 4 7 11) 3	(0 1 2) C	(0 1 2 3 5 9 11 13 18) 6
23	(0 2 4 6 11) S2	(0 2 4 6 9 15) C	(0 2 4 6 11) S2	(0 1 3 6 9 12 14 16 19) 6	(0 2 4 5 11 16) 5
24	(0 5 6 11 17) 4	(0 1 7 12 18) C	(0 1 2 3 4 11 12 17) 6	(0 1 2 3 4 9 10 17) 6	(0 2 5 7 9 11 14) 5

Figure 2. Similarity chart of the prime forms of the selected vertical structures from 24 Preludes in Quarter Tone System for Two Pianos by Ivan Wyschnegradsky according to the quarter-tone system set theory (Dağtekin, 2024).

The comparison of interval class vectors according to the quarter-tone system set theory in the vertical structures analyzed in this study is important for understanding which intervals Ivan Wyschnegradsky used and how often. The evaluation of these findings is also important for understanding the frequency of the composer's use of 12-TET and 24-TET intervals and interval classes in the piece.

Prelude Number	First Vertical Structure	Second Vertical Structure	Third Vertical Structure	Fourth Vertical Structure	Fifth Vertical Structure
1	[121202110221]	[031312223031]	[030100002040]		
2	[100002100011]	[200013200011]	[421001343210]	[342221100000]	[100021210111]
3	[010100101020]	[000000200100]	[100120210012]	[010001102010]	[111002102011]
4	[010001010000]	[001000100100]	[000000200100]	[000100100010]	[111000000000]
5	[100001200110]	[110221101010]	[010001112000]	[200012210110]	[110011221010]
6	[310012110132]	[010002010101]	[412148412144]	[210143310132]	[020100000201]
7	[000101200020]	[101101210120]	[100010110011]	[000020200002]	[321034431241]
8	[010022110030]	[030306030303]	[302136312133]	[211000011121]	[542122323453]
9	[000020200002]	[010022110030]	[011020211101]	[121112202021]	[041333323060]
10	[111000000000]	[000001100010]	[000030001200]	[000000200100]	[001000010010]
11	[020123120121]	[110123210031]	[041234323060]	[060608060604]	[975691011768 85]
12	[010112110021]	[210122210022]	[730371073037 5]	[000002000001]	[020304020202]
13	[100010110011]	[010020100101]	[052434326160]	[052434326160]	[000001100010]
14	[000012100020]	[111000000000]	[000020000100]	[100000000110]	[100000000110]
15	[233234312122]	[212112111111]	[201221131011]	[311154320242]	[332143321222]
16	[012011111110]	[012112212111]	[020122212030]	[000101200020]	[310001243100]
17	[010022110030]	[110113300131]	[110113300131]	[021122111130]	[142223223151]
18	[010000211100]	[000010100001]	[101100000000]	[111111312210]	[142223223151]
19	[210011110021]	[210021100111]	[133352523432]	[420245410132]	[000020200101]
20	[010000010100]	[000010010010]	[000010010010]	[100000011000]	[100011000000]
21	[110011221010]	[020010312100]	[111112122021]	[111011111011]	[421012564210]
22	[000010100001]	[002010020010]	[001200200010]	[210000000000]	[352323344241]
23	[030211101010]	[031212103020]	[030211101010]	[135144243351]	[121121111121]
24	[100023100021]	[100013200021]	[532111233331]	[532112443210]	[042231303111]

Figure 3. Interval class vectors of selected vertical structures from 24 Preludes in Quarter Tone System for Two Pianos by Ivan Wyschnegradsky according to the quarter-tone system set theory (Dağtekin, 2024).

Prelude Number	Usage Frequency of Interval Classes											
	IC 1	IC 2	IC 3	IC 4	IC 5	IC 6	IC 7	IC 8	IC 9	IC 10	IC 11	IC 12
1	1	8	2	6	1	4	3	3	5	2	9	2
2	11	6	3	2	5	8	9	5	3	3	4	3
3	2	3	1	2	2	3	7	1	5	1	5	3
4	1	2	2	1	0	1	4	1	0	2	1	0
5	5	3	0	2	4	6	8	4	4	2	4	0
6	9	6	2	3	9	15	8	4	2	6	10	10
7	5	2	2	2	6	6	11	5	1	3	9	4
8	10	9	5	5	7	16	7	8	6	9	13	10
9	1	8	3	4	10	7	10	4	6	1	11	4
10	1	1	2	0	3	1	3	1	1	3	2	0
11	10	20	6	16	16	28	17	18	9	15	19	11
12	9	7	0	8	10	20	10	7	0	5	11	11
13	1	11	4	8	9	9	9	5	12	3	14	2
14	3	1	1	0	3	2	1	0	0	3	4	0
15	12	8	9	7	15	14	11	9	5	6	10	8
16	3	5	4	3	4	7	9	7	8	3	7	1
17	3	9	3	5	8	13	10	4	4	4	17	3
18	3	6	4	4	4	4	8	4	6	4	6	2
19	9	7	3	5	14	9	13	4	3	7	9	7
20	2	1	0	0	3	1	0	4	1	1	2	0
21	7	7	3	1	5	6	12	12	10	3	5	2
22	5	6	5	5	4	3	6	6	4	2	6	2
23	2	14	7	8	9	9	6	5	9	4	11	2
24	12	10	6	4	8	10	12	7	9	6	9	4
Total	**127**	**160**	**77**	**101**	**159**	**202**	**194**	**128**	**113**	**98**	**198**	**91**

Figure 4. The usage frequency of interval classes according to the preludes of the selected vertical structures from Ivan Wyschnegradsky's 24 Preludes in Quarter Tone System for Two Pianos and the sum of the frequency of interval classes of the vertical structures analyzed in the piece (Dağtekin, 2024).

Ranking of the Total Usage Frequency of the Interval Classes	Total Usage Frequency of the Interval Classes	Types of Interval Classes	Intervals Covered by Interval Classes
1	202	Interval class 6	Minor third Major sixth
2	198	Interval class 11	Major fourth Minor fifth
3	194	Interval class 7	Neutral third Neutral sixth
4	160	Interval class 2	Minor second Major seventh
5	159	Interval class 5	Supermajor second Subminor third Supermajor sixth Subminor seventh
6	128	Interval class 8	Major third Minor sixth
7	127	Interval class 1	Subminor second Supermajor seventh
8	113	Interval class 9	Supermajor third Minor fourth Major fifth Subminor sixth
9	101	Interval class 4	Major second Minor seventh
10	98	Interval class 10	Perfect fourth Perfect fifth
11	91	Interval class 12	Augmented fourth Diminished fifth
12	77	Interval class 3	Neutral second Neutral seventh

Figure 5. Ranking of the total usage frequency of the interval classes in the selected vertical structures from 24 Preludes in Quarter Tone System for Two Pianos by Ivan Wyschnegradsky and the intervals included by the interval classes (Dağtekin, 2024).

Looking at the total values of the intervals in the vertical structures analyzed in the piece, it can be said that the intervals in the 12-TET chromatic system are used 780 times, while the intervals in the 24-TET quarter-tone system are used 868 times. Accordingly, the intervals in the 24-TET quarter-tone system are used 88 times more than the intervals in the 12-TET chromatic system in the vertical structures analyzed in the work. Accordingly, it can be stated that Ivan Wyschnegradsky uses 24-TET quarter-tone system intervals more frequently in the vertical structures in the work, although he also includes the intervals in the 12-TET system.

In this context, it can be said that Ivan Wyschnegradsky wanted to create a piece that contains vertical structures built with the interval classes of the quarter-tone system rather than the interval classes of the tampered system in most of the structures he used. Comparing the interval constructions according to the quarter-tone system set theory in the vertical structures analyzed in this study is important for understanding Ivan Wyschnegradsky's aesthetic

perception. For this reason, the following tables show the interval constructions of the selected vertical structures from the work.

It can be said that 6 of the vertical structures analyzed are vertical structures constructed in quarter-tones with series pitches, 33 of them are constructed in quarter-tones with third intervals, 18 of them are constructed in quarter-tones with fourth intervals and 20 of them are vertical structures constructed with mixed intervals. According to the table, it can be said that 2 of the vertical structures analyzed are the vertical structure defined by Ivan Wyschnegradsky, 28 are tone clusters wider than one octave and 11 are tone clusters. Accordingly, the vertical structures in quarter-tones with third intervals were used the most among the analyzed structures, and the vertical structures defined by Ivan Wyschnegradsky were used the least.

From this point of view, although it is understood that Ivan Wyschnegradsky composed the work analyzed in this study with mathematical methods and constructed the structures in its content, it can be said that the composer equally utilized symmetry and asymmetry to position, name and make sense of the structures he created in this system.

By summing up the percentage expressions of the similarity of the prime forms of the vertical structures according to the quarter-tone system set theory and dividing by the number of vertical structures analyzed, it was found that the average similarity rate of the prime forms of the selected vertical structures for this thesis according to the quarter-tone system set theory was 91.87%.

Prelude Number	First Vertical Structure	Second Vertical Structure	Third Vertical Structure	Fourth Vertical Structure	Fifth Vertical Structure
1	%83	%71	%80		
2	%100	%100	%71	%83	%100
3	%100	%100	%100	%100	%80
4	%100	%100	%100	%100	%100
5	%100	%80	%100	%100	%100
6	%100	%100	%89	%86	%100
7	%100	%100	%100	%100	%88
8	%100	%100	%100	%100	%78
9	%100	%100	%80	%83	%88
10	%100	%100	%75	%100	%100
11	%100	%100	%88	%89	%71
12	%100	%100	%91	%100	%100
13	%100	%100	%67	%67	%100
14	%100	%100	%100	%100	%100
15	%75	%83	%83	%88	%100
16	%80	%100	%83	%100	%100
17	%100	%100	%100	%83	%75
18	%100	%100	%100	%83	%75
19	%100	%100	%78	%63	%100
20	%100	%100	%100	%100	%100
21	%100	%80	%100	%80	%75
22	%100	%75	%75	%100	%67
23	%100	%100	%100	%67	%83
24	%80	%100	%75	%75	%71

Figure 6. Percentage expressions of the similarities of the prime forms of the selected vertical structures from 24 Preludes in Quarter Tone System for Two Pianos by Ivan Wyschnegradsky according to the quarter-tone system set theory (Dağtekin, 2024).

Prelude Number	Average Similarity Ratio	Prelude Number	Average Similarity Ratio	Prelude Number	Average Similarity Ratio
1	%78	9	%90,2	17	%91,6
2	%90,8	10	%95	18	%91,6
3	%96	11	%89,6	19	%88,2
4	%100	12	%98,2	20	%100
5	%96	13	%86,8	21	%87
6	%95	14	%100	22	%83,4
7	%97,6	15	%85,8	23	%90
8	%95,6	16	%92,6	24	%80,2

Figure 7. Percentage expressions of the averages of the similarity ratios of the prime forms of the selected vertical structures from Ivan Wyschnegradsky's 24 Preludes in Quarter Tone System for Two Pianos according to the quarter-tone system set theory according to the preludes (Dağtekin, 2024).

As a result of the analysis of the vertical structures in the work according to the quarter-tone system set theory, it can be said that they are generally similar. In this context, it can be stated that although Ivan Wyschnegradsky proceeds from his own aesthetic perception and maintains his point of view throughout the work, he remains under the influence of the Eurocentric music he has been involved in since his student days, and remains faithful to his previous compositional understanding, except for the structures he created with the quarter-tones timbre.

Conclusion

In Ivan Wyschnegradsky's works, most of which are microtonal, it is seen that he is in search of a new timbre and system. Set theory, which is also a mathematical analysis method, was preferred to make sense of the structures and aesthetic approach used in 24 Preludes in Quarter Tone System for Two Pianos and other microtonal works, perhaps the most important of the works created by the composer using highly mathematical methods in this search. Seeking the scope of this study, the simplified forms of the vertical structures in the work written using the accidentals in quarter-tones were reached through set theory.

The importance of the quarter-tones, which is the main system used by the composer in many of his works, emerges here. It is thought that this system will provide the composer with a widening and expansion of the composer's pitch choice and creative palette from the point of view of the Eurocentric buffer system. This situation can also explain the logic of Ivan Wyschnegradsky's writing many of his works in quarter-tones, having a quarter tone piano like composers who lived in different periods and produced works in different genres such as L. van Beethoven, P. I. Tchaikovsky, L. Boulanger, B. Evans, and constructing his works by playing on this piano like other composers.

As perhaps the most important of the conclusions reached in this study, it can be stated that Ivan Wyschnegradsky's works, most of which are written using microtonal materials, constitute an understanding that can be considered as a continuation of the concept of "Emancipation of Dissonance", which was put forward by A. Schoenberg with his atonal approach, and which was likened to the liberation of society and humanity by composers such as C. Ives, D. Ellington and L. Harrison. It is thought that the analysis of the vertical structures in this work will also be instructive in terms of the timbral enrichment of works in genres that include these pitches or that have been written or will be written in other systems. In this context, it can be thought that the structures in the piece written in quarter-tones, which we are trying to analyze, can also be used in the context of liberating / deepening the consonance in works created through different systems. At the same time, this study is expected to inspire not only composers and theoreticians but also improvising musicians in terms of the application of mathematical microtonality and set theory systems and gaining new perspectives.

This study has been shaped by the findings and conclusions obtained in the light of the analysis made with the quarter-tone system set theory, which was created by adapting the set theory to the quarter-tones. It is thought that other microtonal works can be analyzed with a similar approach. It is expected that this study will be a guide for future studies in the context of making sense of the structures and systems used by Ivan Wyschnegradsky and other composers in their microtonal works and will be useful for people who will compose or improvise in microtonal systems.

Ivan Wyschnegradsky, who can be considered as one of the most important composers who made many contributions to microtonal systems and works, created his works with systems and tools that he created entirely on his own, without using folk music or the elements put forward by movements such as spectralism with different tools. The results of the analysis of 24 Preludes in Quarter Tone System for Two Pianos, which stands in a different place in terms of its use of the diatonic chromatic system, are thought to be important in terms of making sense of different musical perspectives, especially the concept of microtonality, both at that time and in the future. It is expected that this study will open new horizons for musicians, composers, theorists and improvisers who want to go beyond the first sixteen improvisers, who are after the meaning, systematization and analysis of different timbres that will be created by the pitches and their combination, and contribute to the search for original ideas and ways of many curious music people who contribute to music by producing new methods and concepts, such as Ivan Wyschnegradsky and other composers who produced microtonal works and systems in the twentieth century.

The concepts of set theory, octave division, diatonic chromaticism, diatonic chromaticism, microtonality and similar systems, which are useful tools offered to composers by mathematics, which is often used as an important tool in the creation of music, can be used to analyze the music of composers such as Ivan Wyschnegradsky, who produced works that simultaneously contain tradition and future understanding of different systems, While guiding the search for the paths of improvisers who shape time through structures and pitches, and contributing to the production of musical structures and works to be created by musical people like Ivan Wyschnegradsky who shape their own musical materials and boundaries, it is thought that will liberate us in terms of timbre, philosophy and aesthetics with the new horizons it opens in the process of maintaining the tradition and shaping the future, and will accompany our wanderings in different musical worlds where our curiosity will always be renewed.

References

Dağtekin, S. C. (2024). *İvan Vişnegradskiy'in iki piyano için çeyrek ses sisteminde 24 Prelüt, Op. 22 eserindeki dikey yapıların set teorisi bağlamında analizi* (Master's thesis, Ankara Music and Fine Arts University, Institute of Music and Fine Arts).

Jedrzejewski, F. (2000). *Ivan Wyschnegradsky et la Musique Microtonale.* Université Paris I.

Roig-Francolí, M. A. (2021). *Understanding Post-Tonal Music.* Routledge.

Stefanija, L., & Stanevičiūtė, R. (2020). *Microtonal Music in Central and Eastern Europe.* Birografiko Bori.

Straus, J. N. (2016). *Introduction to Post-Tonal Theory.* WW Norton & Company.

Wyschnegradsky, I. (2017). *Manual of Quarter-Tone Harmony.* Underwolf Editions.

Exploring Perde-Çeşni Transformations in Tanburi Cemil Bey's Nikriz Makam

Burak Kesgin[a]

[a] Istanbul Technical University/Graduate School, Department of Musicology and Music Theory, Music Theory and Composition Programme, Türkiye
kesgin15@itu.edu.tr

Keywords: Analysis, MakamNetz, Nikriz Makam, Perde-Çeşni Transformation, Tanburi Cemil Bey.

Aim

This study aims to analyze four instrumental works composed by Tanburi Cemil Bey, one of the prominent performers of the late Ottoman period, in the *Nikriz makam*, consisting of two *Longa* and two *Zeybek* forms. The objective is to classify the *Perde/Çeşni* transformation principles that Cemil Bey consciously or unconsciously employed while composing these works. Cemil Bey's mastery in performing *taksim*, the improvisatory form of Turkish Music, and his pioneering role in this field are widely recognized and acknowledged by many music researchers. In addition to being a highly influential performer, he composed a total of thirty-four works, including thirteen vocal and twenty-one instrumental compositions. This study will examine the structural elements underlying the variety of *makam* modulations that Cemil Bey introduced within the framework of *Nikriz Makam* while composing his works. Furthermore, the research will analyze the formal structures and *seyir* characteristics of these four pieces to determine the balance between the traditional structure of the *Makam* and Cemil Bey's unique contributions.

Material and Method

The materials examined in this study consist of four works composed by Cemil Bey in *Nikriz makam*: *Nikriz Longa*, *Nikriz Longa 2*, *Nikriz Zeybek*, and *Nikriz Zeybek 2*. The works have been classified and labeled uniquely for this study as "1" and "2" versions. *Nikriz Zeybek 1* is composed in *Aksak usûl* and consists of nineteen measures. *Nikriz Zeybek 2* is also in *Aksak usûl* and comprises eighteen measures. *Nikriz Longa 1* is composed in *Nim Sofyan usûl* with a total of twenty-four measures, structured as two *hane* and a *teslim*. Lastly, *Nikriz Longa 2* is also in *Nim Sofyan usûl* and contains thirty-four measures. While the scores of these works are available in the TRT notation archive, they have been re-notated via MuseScore software for this study due to the necessity of specific annotations. Additionally, certain discrepancies identified between the performance and the archived scores were corrected during this process. The formal structures, *makam seyir* characteristics, and *çeşni* modulations of each piece were analyzed according to the *Perde/Çeşni*transformation model. The transformation points and overlaps were meticulously marked on the scores, providing insights into their musical functions and contexts.

The analytical model is based on the *Perde/Çeşni* transformation model developed by Prof. Dr. Ozan Baysal (Baysal et al. 2024). The model investigates and explains the relationships between two *makam* or *çeşni* structures by focusing on pitch sets, intervallic structures, and pivot *perde*. This analysis model, which is based on Kleonides' concept of modulation, emphasizes the necessity of shared pivots or transformation chains to explain harmonic relationships in modal structures. Accordingly, Cemil Bey's works in *Nikriz makam* have been analyzed through three main transformation types defined within the model: Intraconnected (*Girift) Relationship Transference (Kaydırım),* and *Fixed-Axis Transformations*.

Fixed-Axis transformations occur between different *Perde/Çeşni* structures while maintaining the main or secondary pivot *perde* as constant and are indicated with the abbreviation "P-to-P", "S-to-S" or "S-to-P" in the notations. *transferenrd* typically result from shifting an existing *Perde/Çeşni* structure upwards by perfect fourth or fifth intervals. Finally, *Girift Relationships* are based on the overlap of at least three consecutive *perde* between two *Perde/Çeşni* sets, enabling more fluid and ambiguous modulations. All these transformations are explicitly marked on the scores throughout the analysis.

In our research, we have also used MakamNetz, a web application that aims to model *makam* and *çeşni* structures and their mutual relationships in Turkish Makam Music in the form of a network or map.MakamNetz provides not

just a list of *makam* and *çeşni* but also a map that visualizes the intuitive yet often unsystematically articulated structural relationships between them by considering the transition pathways and connections. However, our analyses revealed that not all connections within the network hold equal significance in practice. For instance, some pathways, although equidistant in the network, are employed at varying frequencies in performance practices. By addressing such structural imbalances, MakamNetz can enable a more accurate modeling of modulations and diversities between *makam*. The *Perde/Çeşni* transformation analyses in this study were conducted entirely through the MakamNetz application (Gül et al., 2024).

Findings

As a result of the analyses, it was found that Cemil Bey utilized *makam* modulations flexibly across all four works. In *Nikriz Longa 1*, besides following the classical *Nikriz makam seyri*, structures outside the conventional descriptions were also employed. Particularly in the development section, *Neva* and *Gerdaniye perde* functioned as secondary pivots, facilitating smoother modulations between *çeşni*.

In *Nikriz Zeybek 1*, the introduction almost fully adheres to the *Rast makam* structure. Some sources even label this piece as *Rast Zeybek*. The *girift* relationships between *Rast/Rast* and *Segâh/Segâh* impart a distinctive character to the piece's *makam* structure. In addition, frequent *S-to-P* transformations towards the final sections provided a strong return to *Nikriz makam*.

In *Nikriz Zeybek 2*, the *S-to-P* transformation principle was consistently applied from the beginning to the end, resulting in a sense of melodic uniformity. Cemil Bey emphasized the main melodic theme across the entire piece. The structure displays the superimposition of *Rast/Nikriz* and *Neva/Buselik çeşni*. Cemil Bey concentrated on two main melodic ideas, shaping the composition around them.

Similarly, *Nikriz Longa 2* primarily employed *S-to-P* transformations. Although this piece displays greater *çeşni* variety, its transformation logic resembles that of *Nikriz Zeybek 2*. At times, this composition also ventures beyond the traditional *makam* framework.

Conclusion

In conclusion, this study enhances the visibility of the transformation principles Cemil Bey employed while structuring his compositions in *Nikriz makam*, supported by visual analyses. Moreover, while identifying these transformations, the research highlights the composer's expertise. Cemil Bey, while adhering to the conventional characteristics of *Nikriz makam*, simultaneously integrates both the stylistic elements of his era and his distinctive musical persona. The study also confirms his skillful and functional use of other *Makam* structures such as *Rast*, *Segâh*, and *Müstear* within his compositions. Overall, this research offers an in-depth analysis both in terms of the under-explored *Nikriz makam* and the compositional features of Cemil Bey's period, once again revealing the *Makam* richness of his works.

References

Baysal, O., Gül, R., Şeftali, Y. C., Sindar, G., Yalçın, Z., & Çolakoğlu Sarı, G. (2024, July 4). Introducing MakamNetz: A virtual guide to Turkish makam universe. *21st Sound and Music Computing Conference*, Porto, Portugal, 361–366.

Gül, R., Baysal, O., Buruk, Y., & Şeftali, Y. C. (2024). Exploring Perde-space: 3-D Tonnetz visualization for makam music. *Proceedings of the 21st Sound and Music Computing Conference*, Porto, Portugal, 220–233.

MUSICOLOGY AND MUSIC THEORY

Ethnomusicology

Historical Musicology

Music Theory

Popular Music

The Issue of "Originality" in Arabesk Music: Analysis of Musical Borrowings, Similarities, and Production Practices from Arab music

Yiğit Sarıgül[a]

[a] Istanbul Technical University, Department of Musicology and Music Theory, Turkey
sariguly15@itu.edu.tr

Keywords: Arabesk Music, Originality, Musical Quotation, Arab Music, Copyright.

Aim

The primary aim of this study is to critically examine the issue of "originality" in the context of arabesque music that emerged in Turkey during the 1960s and 1970s, by analyzing the nature of its melodic relations with Arab music through musicological methods. The frequently voiced claim in public discourse that "arabesque music is a copy of Arab music" often relies on reductionist perspectives that lack concrete musicological evidence. This study seeks to identify specific examples that may be considered direct quotations or instances of plagiarism through technical musical analyses; however, it emphasizes that these examples do not represent the entirety of the genre. Arabesque music is not confined solely to Arab musical traditions; rather, it is a multi-layered form that interacts with various musical lineages, including Turkish folk music, Classical Turkish music, and Western music. In this regard, the study not only addresses musical similarities, but also explores the historical, cultural, and industrial contexts in which these melodic transfers took place.

Although Ottoman influence in Egypt weakened by the late 19th century, musical forms such as peşrev and semai and instruments like the tanbur and qanun had already spread across the Arab world. Scholars note that Arab music had been influenced by Turkish and Persian traditions via the Ottoman Empire since the 15th century (Touma, 2003), and despite Egypt's modernization, Ottoman traces persisted (Danielson, 1997; Racy, 1977). This continuity is evident in Umm Kulthum's vocal aesthetics, which emphasize lyrical expression, in contrast to Turkish songs where melodic structures dominate (Danielson, 1997, pp. 111, 161). Additionally, figures like Zekâi Dede, who taught and performed in Egypt, and artists such as Refik Fersan and Münir Nurettin Selçuk, who gave concerts there, reflect sustained musical exchange, making it historically inaccurate to view Arab and Turkish music traditions as disconnected (Rona, 1960, p. 243; Bardakçı, 1995, p. 7; Özcan, 1995, p. 413; Özalp, 2000, p. 224).

Therefore, the question of "originality" in arabesque music cannot be reduced to the mere technical identification of melodic similarities. During the 1960s and 1970s, the institutionalization of composition in Turkey was still in its infancy, and the systematic production of original works had not yet been established. Within this context, turning to melodic material from the Arab world became both an aesthetic and practical choice for local producers. In particular, melodies derived from Egyptian and Syrian sources were often regarded as ordinary components of musical circulation and production during this period (Stokes, 2020, p. 139).

As such, the early examples of arabesque music were shaped less by a pursuit of originality and more by the reworking of existing melodic structures through local lyrics and arrangements. This mode of production reflects not only musical similarities but also the aesthetic norms, industrial conditions, and institutional shortcomings of that era.

Material and Method

This study examines three significant works from the early period of arabesque music: "Gündüzüm Seninle" (1965) by Suat Sayın, "Ağlatan Yıllar" (1972) by Orhan Akdeniz, and "Kullarına Kul Yaratmış" (1979) by Mustafa Sayan. Each of these pieces is analyzed comparatively alongside corresponding works from the Arab repertoire: Mohamed Abdel Wahab's "Bafakkar Fih" (1957), Riyad Al-Sunbati's "Leily Nehary La Ya Habeeby" (1963), and Abdel Wahab's "Fi Youm We Leilah" (1978), respectively.

The methodology of the study is based on transcription-based comparative analysis of melodic structures. Transcriptions of pieces from both traditions were prepared using the same tonal center, and metric structures and tempi were considered in carrying out measure-by-measure comparisons. The analyses focus exclusively on the

introductory sections and metrical instrumental passages of the songs; repeated segments and vocal performances were deliberately excluded.

Additionally, disc and MESAM archives were consulted to obtain recording information, release dates, and production data. Where available, interviews with composers and relevant secondary sources were also incorporated into the study. The goal of this methodological approach is to reveal how melodic borrowings were structurally integrated and to assess the aesthetic considerations that shaped these practices within the production context of the period.

Findings

Released in 1965 under the Grafson label and performed by Ziya Taşkent, Gündüzüm Seninle stands out as an early example of arabesque music composed by Suat Sayın. The melodic similarities it shares with Mohamed Abdel Wahab's 1957 composition Bafakkar Felli Nassini cannot be sufficiently explained as mere "inspiration." In particular, the core melody of the aranağme (instrumental interlude) section is directly adopted as the main theme in Gündüzüm Seninle, with its structural integrity largely preserved. The chorus is also built on a repetition of this theme, indicating that the entire piece is constructed around a single melodic nucleus. This suggests that rather than being a reinterpreted form, the work is based on a direct melodic transfer.

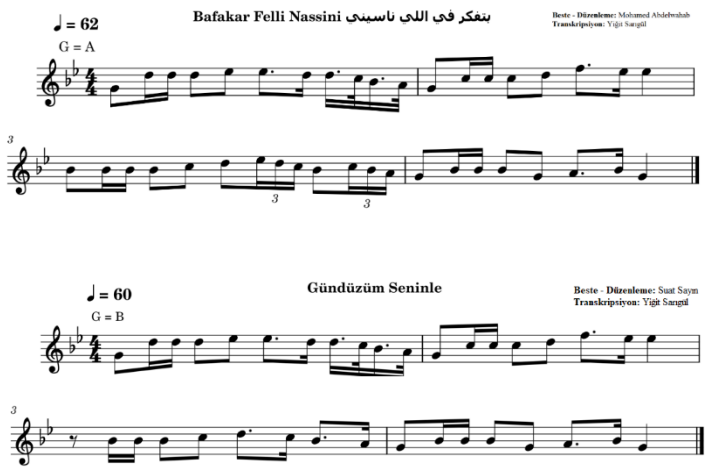

Figure 1. Transcriptions of the songs Gündüzüm Seninle and Bafakar Felli Nassini.

Both compositions are written in 2/4 meter and have very similar tempo markings (approximately 60–62 bpm). This rhythmic parallelism reinforces the notion that the general formal structure of the Turkish piece is largely derived from the Arab original. Aside from a triplet figure at the end of the third measure and in the fourth, no significant rhythmic differences are observed. This minor variation may be considered a matter of performance interpretation, but it does not constitute a meaningful distinction in terms of originality.

In terms of instrumentation, Suat Sayın's arrangement includes Turkish instruments -clarinet, qanun, and a string section- aiming to evoke a local expressive atmosphere. However, these localization efforts do not obscure the fact that the melodic foundation of the piece was directly borrowed.

Orhan Akdeniz emerged as a prominent figure in the development of arabesque music during the 1970s, playing an active role as a musician, arranger, and producer. His influence is particularly evident in the early recordings of artists such as Müslüm Gürses, Esengül, and Mine Koşan, making him a defining contributor to the musical output of the period. Released in 1972 on his own record label, the song Ağlatan Yıllar appears on the surface to be an original Turkish composition; however, a detailed analysis reveals a strong melodic connection to Leily Nehary La Ya Habeeby, a piece composed for Umm Kulthum. The introductory (muqaddima) section of the Arabic song forms the melodic backbone of Ağlatan Yıllar, in which only the lyrics are translated into Turkish and the arrangement is simplified.
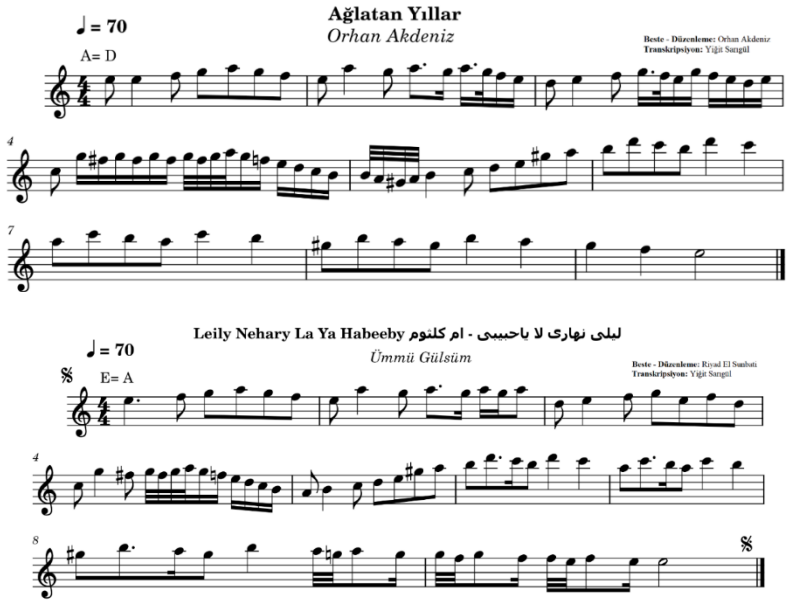
Figure 2. Transcriptions of the songs Ağlatan Yıllar and Leily Nehary La Ya Habeeby.

In the transcription-based comparative analysis, it was observed that both compositions are performed at approximately 70 bpm and in an 8/8 meter. Despite differences in tonal centers, they share a similar frequency range. The melodic contours, intervallic usage, and repetition patterns within the first eight measures of the introduction align almost identically. The orchestration also exhibits notable parallels; however, Akdeniz intensifies the dramatic effect through the inclusion of local instruments such as the electro bağlama, and employs the qanun and strings to create a two-voice harmonic texture. Compared to Sunbati's original arrangement, Akdeniz's version is more condensed and intense, although the melodic core remains unaltered.

This example does not merely represent melodic inspiration; rather, it points to a mode of production in which a direct borrowing is structurally reconfigured and released into the market. Nevertheless, Akdeniz's technical contributions to the arrangement may be interpreted as an effort to reshape the melodic material within his own aesthetic framework. Still, it is evident that such efforts cannot obscure the underlying issue of melodic originality. Ağlatan Yıllar exemplifies how melodic borrowing in the early period of arabesque music arose not only from the absence of copyright enforcement, but also from an unestablished compositional tradition.

Since the 1960s, Mustafa Sayan has been a significant figure in the early development of arabesque music, serving both as a composer and arranger (Şener, 2022). His travels to Egypt and the repertoire he performed there demonstrate that his musical orientation was directly influenced by the Arab world. In particular, the orchestral aesthetic he established through the use of string instruments strongly parallels Egyptian orchestral traditions. In this context, his composition Kullarına Kul Yaratmış is built upon a melodic structure taken from the third muqaddima section of Fi Youm We Leilah, a piece composed by Abdelwahab and performed by Warda.
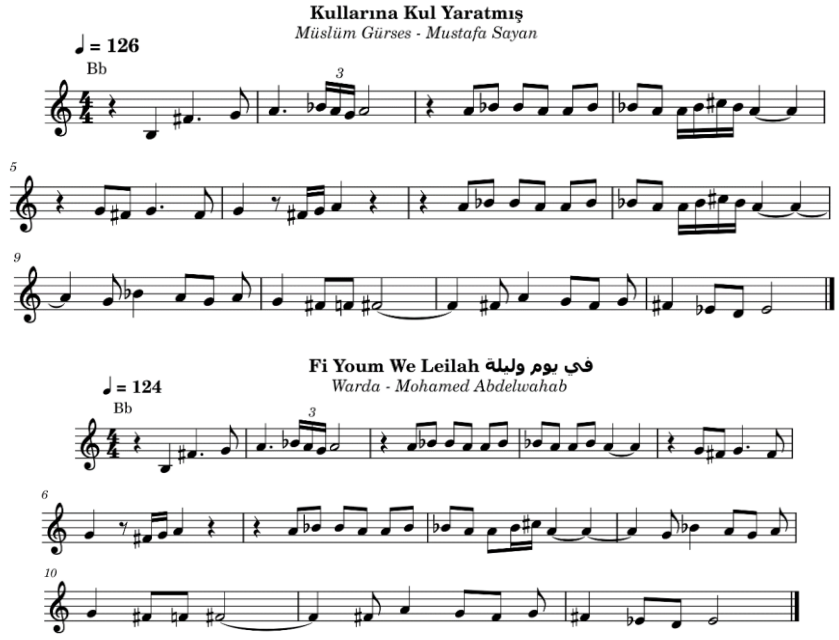
Figure 3. Transcriptions of the songs Kullarına Kul Yaratmış and Fi Youm We Leilah.

According to transcription-based analysis, both pieces are in the key of B♭, with E♭ as the finalis. Their metronomic tempos are also very close (124–126 bpm), which suggests that the melodic structure was not merely inspired by, but rather directly transferred from the original. The muqaddima section of Abdelwahab's composition, which begins at 22:53, is used as the main theme from the opening of Sayan's piece and is further expanded throughout the composition. Although some short phrases were reordered, the principal melody and structural outline remain unchanged.

Sayan's arrangement features a string ensemble reflecting Egyptian orchestral performance practices, along with instruments such as ney, qanun, and double bass. This instrumentation reveals that the influence from Egyptian music is not only melodic but also formal. The melodic similarities identified in the piece thus appear to be the product of a systematic transfer practice rather than mere aesthetic affinity. Within this framework, Kullarına Kul Yaratmış exemplifies how, due to the absence of copyright regulation and an established tradition of original composition, arabesque music of the period frequently drew directly from external sources. At the same time, the piece reflects a creative reconfiguration approach characteristic of the era's music production. However, from a musicological standpoint, the direct transfer of the core melody may fall within the bounds of plagiarism.

Conclusion

Through the comparative analysis of three early arabesque compositions, this study demonstrates that the use of melodic material from the Arab music repertoire -particularly from composers like Mohamed Abdelwahab and Riyad Al-Sunbati -was not merely the result of individual artistic decisions, but a structural component of the production practices in Turkey during the 1960s and 1970s. These borrowings often extend beyond inspiration, showing striking similarities in pitch, rhythm, and melodic contour. While these parallels may be interpreted as plagiarism from a strictly musicological perspective, they should also be understood within the broader context of the period's underdeveloped compositional institutions, lack of copyright enforcement, and the music industry's demand for emotionally resonant, familiar material.

In this light, the reworking of Egyptian melodies with Turkish lyrics and instrumental textures was not always an act of creative transformation but often a direct transfer with minimal alteration. Although arabesque music eventually evolved into a more localized and stylistically distinct form, its early stages were marked by a dependence on external sources. This reveals that the relationship between Arab and Turkish music was neither wholly imitative nor entirely original, but complex, layered, and historically contingent. Therefore, these examples

should be seen not simply as technical duplications, but as practices shaped by the cultural economy, aesthetic values, and industrial conditions of their time.

References

Avcı, M. (2019). Arabeskin oynak/değişken anlam dünyası ve jeneolojisi: Arabeskin bilinmeyen tarihi. *X. Uluslararası Hisarlı Ahmet Sempozyumu & 10th International Hisarlı Ahmet Symposium*, 251–256.

Bardakçı, M. (1995). Refik Fersan ve hatıraları. Pan Yayıncılık.

Danielson, V. (1997). The voice of Egypt: Umm Kulthum, Arabic song, and Egyptian society in the twentieth century. University of Chicago Press.

Güngör, N. (1993). Arabesk: Sosyokültürel açıdan arabesk müzik. Bilgi Yayınevi.

Küçükkaplan, U. (2012). The cultural background and socio-musical analysis of Arabesque music in Turkey since the 1930s. *Master's thesis*, Mimar Sinan Fine Arts University.

Özbek, M. (1991). Popüler kültür ve Orhan Gencebay arabeski. İletişim Yayınları.

Özcan, N. (1995). Refik Fersan. *İslam Ansiklopedisi, 12*, 412–413.

Özalp, N. (2000). Türk musikisi tarihi. Milli Eğitim Bakanlığı Yayınları.

Özyıldırım, M. (2013). Arap ve Türk musikisinin XX. yüzyıl birlikteliği. Bağlam Yayınları.

Racy, A. J. (1977). Musical change and commercial recording in Egypt, 1904–1932. *Doctoral dissertation*, University of Illinois at Urbana-Champaign.

Reigle, R. F., Şener, S., & Oğul, B. (2022). Re-evaluating the roots of arabesk music: Grup Metronom. *Musicologist, 6*(2), 169–209.

Rona, M. (1960). 50 yıllık Türk musikisi. Türkiye Yayınevi.

Şener, S. (2022). Play it all!: String ensembles in the Turkish music industry. *Doctoral dissertation*, Istanbul Technical University.

Stokes, M. (2020). Türkiye'de arabesk olayı. İletişim Yayınları.

Touma, H. H. (2003). The music of the Arabs (L. Schwartz, Trans.). Amadeus Press.

It's Corn!: From Everyday Life's 'Sound' to Viral Musical Meme

Cevher Sarıgül[a]

[a] Istanbul Technical University, Department of Musicology and Music Theory, Turkey
sarigulcevher@gmail.com

Keywords: TikTok, Music Meme, Users, Digital Culture.

Aim

This study aims to explore how everyday sounds evolve into viral musical memes within the participatory culture of the digital age, with a specific focus on the short-form video platform TikTok. These viral transformations are not merely products of spontaneous creativity but are shaped by algorithmic flows, platform affordances, and user engagement. Musical memes, as a distinctive category of multimodal content, reflect not only user participation but also the logic of viral circulation that underpins digital media ecologies.

Taking *It's Corn!* as a central case study, this research investigates how a sound fragment from everyday life, specifically a child's spontaneous expression of joy, was remixed into a musical meme and disseminated globally. This process reflects a transition from a soundscape, rooted in the textures of ordinary lived experience, to a mediascape. In this context, sound becomes a unit of exchange, performance, and commodification within digital platforms. The study examines how such transformations construct viral culture and also engages with issues such as authorship of creative acts in digital spaces, personal expression, and commodification. Particular attention is given to questions of consent and ethical representation, especially when individuals featured in viral content, like children, may not fully comprehend or control their participation in such processes.

Material and Method

This research adopts a qualitative case study approach, focusing on *It's Corn!* as a representative example of a musical meme that emerged from a spontaneous moment in everyday life. Throughout the research process, netnography was employed as the primary method, supported by content analysis and case study techniques. The study involved the observation of how musical memes are produced, circulated, and reconfigured within TikTok's participatory environment. User engagement, comment sections, and the creative reuse of original sounds were tracked, while a multimodal analysis considered the integration of audio, visuals, and platform-specific features such as "Duet" and "Stitch." These technical affordances were essential in understanding how users interact with sound and how these interactions contribute to memetic transformations.

To provide a broader cultural context, additional viral musical memes such as *Bing Bong*, *Harlem Shake*, and *Savage Love* were briefly referenced. These cases illustrate how everyday utterances or spontaneous audio fragments evolve into digital cultural artifacts through user participation and remix culture. The analysis is grounded in a theoretical framework informed by memetic theory, participatory media studies, sound studies, and musicology. Rather than aiming for statistical generalization, the study adopts an interpretive approach to understand how digital sound objects acquire memetic status, circulate across digital platforms, and reflect broader aesthetic, cultural, and industrial patterns in music and media ecosystems.

Findings

The viral spread of *It's Corn!* on TikTok illustrates how a casual street interview evolved into a musical meme and eventually into a globally circulated cultural product. Originating from a child named Tariq expressing his excitement about corn, the video was musically remixed by the Gregory Brothers, a TikTok-based music creator duo. It then gained traction through TikTok's features such as "Use This Sound," triggering widespread user engagement.

This transformation can be meaningfully examined through Murray Schafer's concept of the soundscape. Schafer (1994) defines soundscapes as the acoustic environments created by the totality of sounds in a given space. These sonic environments are not passive backdrops but active cultural terrains that shape and reflect human behavior and social contexts. In this sense, *It's Corn!* exemplifies how a simple expression from a child, originally part of a

routine and unspectacular moment, was reinterpreted as a culturally resonant sound event and quickly disseminated through TikTok's sound-driven infrastructure.

This memetic evolution also aligns with Arjun Appadurai's concept of the mediascape, which refers to the flow of media content across borders that reshapes cultural perception and global narratives (Appadurai, 1996). Mediascapes are not merely channels of information but mechanisms through which cultural meanings are continuously constructed and distributed. In the case of *It's Corn!* the sound transcended its original physical and social context and entered a digital mediascape where it became subject to algorithmic amplification, remix culture, and performative reinterpretation by users. This shift from a local, lived experience to a digitally constructed cultural phenomenon illustrates how everyday sound can be reconstituted as a unit of digital capital and collective creativity.

The centrality of sound on TikTok further supports what Abidin and Kaye (2021) have described as an "auditory turn." This marks a platform-wide transition from visual primacy to sonic engagement. It is particularly evident in how users reimagined the expressive potential of *It's Corn!* through thousands of participatory videos, remixes, duets, and lip-syncs. These examples showcase the meme's affective and humorous qualities in diverse contexts.

While this study primarily focuses on how a sound fragment from everyday life is transformed into a musical meme through user creativity, platform affordances, and algorithmic curation, it is important to acknowledge that such content can also be interpreted through other cultural lenses. For instance, the phrase "I can tell you all about it," voiced by the child, may unintentionally evoke deeper resonances when viewed in relation to African American history, where corn has been symbolically tied to land, survival, and identity. Although the meme's viral spread is not analyzed here through that historical frame, the possibility of ironic echoes, especially considering the racialized history of labor and agriculture in the United States, opens up further lines of inquiry beyond the scope of this research.

This transformation also invites critical ethical considerations. The child at the center of the original video becomes part of a larger media spectacle, often without sustained consent or control. One of the most pressing concerns involves the issue of consent, particularly in the case of minors. Tariq, the child whose joyful remarks sparked the meme, may not have fully understood the scale and implications of his sudden digital fame. This raises important questions about the ethics of using a child's likeness in viral content, especially when the consequences and reach of that exposure are not made clear to them or their guardians. Moreover, the social dynamics of virality contribute to a power imbalance. While remixers and secondary content creators often gain visibility, audience engagement, and even monetization opportunities, the original subjects, especially those without agency such as children, tend to be marginalized or rendered secondary. Their creative input or presence may be celebrated in form but overlooked in recognition and reward. These ethical tensions are further shaped by the design and incentives of digital platforms themselves. TikTok, like many short-form video platforms, facilitates rapid content creation, remixing, and dissemination. Although these features promote creativity and participatory culture, they frequently neglect to address creator rights, consent protocols, and long-term accountability. In the context of memes like *It's Corn!* this becomes particularly visible. While derivative content thrives and circulates widely, the originators of the viral moment,those who appear in or contribute to the foundational media; are often excluded from formal credit or financial gain.

This reveals a paradox in which viral fame on such platforms brings immense visibility but little recognition, increased cultural impact but limited control. For vulnerable individuals such as children, this gap between participation and protection underscores the urgent need for clearer ethical frameworks in platform governance and digital content circulation.

Conclusion

This study examined how everyday sounds are transformed into musical memes on platforms like TikTok, focusing on their cultural, aesthetic, and ethical dimensions. Through the case of *It's Corn!* it revealed how a spontaneous moment of speech can be remixed, circulated, and collectively reshaped into a global cultural product via the platform's algorithmic structure and user creativity. This transformation shows that digital sound objects are no longer just sonic experiences but are embedded within participatory, interactive, and manipulative practices. Musical memes are not merely humorous content; they are deeply entangled with platform economies, creative

production, and user visibility. They raise critical questions about who is considered a "creator," how visibility is distributed, and who benefits from digital cultural production. These dynamics map new forms of inequality within participatory culture, especially when vulnerable subjects, such as children, are at the center of viral content and where ethical boundaries become blurred.

The reproducibility and brevity of musical memes created by users can be seen as signaling a fault line or a pipeline that extends into the music industry. Circulating within TikTok's flow, these short, repeatable formats offer not only new modes of engagement but also inspiration for creative strategies and content ideas that may inform music production itself. As a result, we may be witnessing the TikTokification of the music industry. This reflects a gradual adaptation to the platform's aesthetic logic. Users' creative interventions encourage new musical forms optimized for virality (such as short songs), and yet this creativity is often folded into the logic of platform capitalism, leaving users with limited recognition or compensation.

Ultimately, this study suggests that musical memes transform sound into more than something to be heard. They become something to play with, remix, and circulate. This signals a shift in both musical aesthetics and digital economies, proposing an expanded space of inquiry between musicology and media studies in the context of contemporary digital culture.

References

Abidin, C., & Kaye, D. B. V. (2021). Audio memes, earworms, and templatability: The "aural turn" of memes on TikTok. In L. W. Green & M. J. Leach (Eds.), *Critical Meme Reader: Global Mutations of the Viral Image* (pp. 58–68). Institute of Network Cultures.

Appadurai, A. (1996). *Modernity at Large: Cultural Dimensions of Globalization* (Vol. 1). University of Minnesota Press.

Bezemer, J., & Kress, G. (2015). *Multimodality, Learning and Communication: A Social Semiotic Frame.* Routledge. https://doi.org/10.4324/9781315687537.

Blackmore, S. (1999). *The Meme Machine.* Oxford: Oxford University Press.

Buchel, B. (2012). *Internet memes as means of communication* Masaryk University, Faculty of Social Studies.

Dawkins, R. (2006). *The Selfish Gene: 30th Anniversary Edition, with a New Introduction by the Author* (30th Anniversary edition). Oxford University Press.

Kaye, B. (2022). Please Duet This: Collaborative Music Making in Lockdown on TikTok. *Networking Knowledge: Journal of the MeCCSA Postgraduate Network*, 15(1), 59–77.

Kim, J. (2012). The institutionalization of YouTube: From user-generated content to professionally generated content. *Media, Culture & Society*, 34(1), 53–67. https://doi.org/10.1177/0163443711427199.

Schafer, R. M. (1994). *The Soundscape: Our Sonic Environment and the Tuning of the World.* Destiny Books.

Schafer, V., & Pailler, F. (2024). *Online Virality: Spread and Influence.* Walter de Gruyter GmbH & Co KG.

Shifman, L. (2013). *Memes in Digital Culture.* MIT Press.

Url-1 The CEO of Corn #cornboy [Video]. *YouTube.* https://www.youtube.com/watch?v=1VbZE6YhjKk date retrieved 22.05.2025

Url-2 It's Corn hashtag. [Video]. *TikTok*.
https://www.tiktok.com/search/video?q=its%20corn&t=1733750774217 date retrieved 22.05.2025

Url-2 Bing Bong Song hashtag. [Video]. *TikTok*.
https://www.tiktok.com/search?q=bing%20bong%20song&t=1733756033426 date retrieved 22.05.2025

NANOSCIENCE AND NANOENGINEERING

Nanoparticles

Nanotechnology for Energy Systems

Polymer and Nano Composites

Radiation Attenuation of MWCNT and Magnetic Nanoparticle Reinforced PMMA Comparative Analysis of Coefficient

Deniz Hande Aydın[a], Nilgun Baydogan[a]

[a] Istanbul Technical University, Energy Institute, Turkey

Keywords: PMMA , MWCNT , Radiation shielding, Gamma Transmission, Neutrons.

Poly(methyl methacrylate) (PMMA) is a thermoplastic material used in various industrial applications due to its lightweight and durable structure. Multi-walled carbon nanotubes (MWCNT) and magnetic nanoparticles are widely used to improve the mechanical, electrical and radiation attenuation properties of composite materials. It is important to comparatively investigate the ionizing radiation attenuation performance of polymer composites reinforced with MWCNT and cobalt-containing magnetic nanoparticles.
In the experiments, measurements were carried out by gamma transmission method using Co-60 and Cs-137 sources. By analyzing the linear attenuation coefficient (μ) and half-value thickness (HVL), the effects of magnetic reinforcement particles and nanoparticle (MWCNT) additives containing cobalt on the radiation absorption capacity of polymer samples were evaluated. By examining the radiation permeability properties of the polymer composite structure, HVL values were determined and comparatively, the gamma radiation absorption capacity was investigated. This study includes results for the development of lightweight and effective radiation shielding materials.

Aim

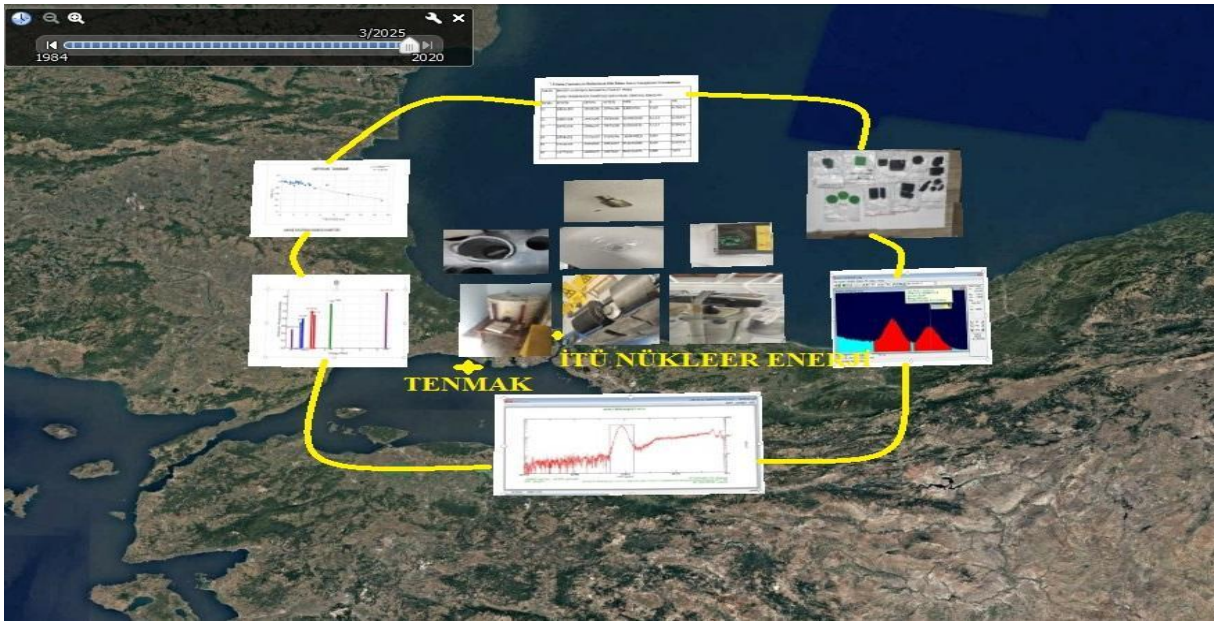

Figure 1.Graphical representation of the study.

Poly(methyl methacrylate) (PMMA) is a thermoplastic material widely used in various industrial applications due to its lightweight and durable structure. Multi-walled carbon nanotubes (MWCNTs) and magnetic nanoparticles are widely used to improve the mechanical, electrical and radiation shielding properties of composite materials. A comparative study of the ionizing radiation attenuation performance of polymer composites reinforced with MWCNTs and cobalt-containing magnetic nanoparticles is of great importance. In the experiments, gamma, beta and neutron transmission measurements were carried out using Co-60, Cs-137, Sr-90, Am-241 sources. The linear attenuation coefficient (μ) and half-value layer (HVL) were analyzed to evaluate the effects of cobalt-containing magnetic reinforcement particles and MWCNT additives on the radiation absorption capacity of polymer samples.

The gamma, beta and neutron radiation shielding properties of polymer composite structures were evaluated by determining the HVL values and comparing their radiation absorption capacities. This work provides insights into the development of lightweight and effective radiation shielding materials.

Method

In the experiments, gamma transmission method was applied using Co-60 and Cs-137 sources to determine the gamma radiation attenuation performances. Gamma transmission, which was carried out in ITU Energy Institute Radiation Detection and Measurement Laboratory, was performed using NaI Scintillation detector. Scintillation detectors are systems that detect ionizing radiation by converting it into visible light. NaI(Tl) crystal produces light (scintillation) when interacting with gamma rays.Gamma ray interaction : Gamma rays lose energy by interacting with the NaI(Tl) crystal through the photoelectric effect, Compton scattering, or pair production mechanisms. Light production : This loss of energy results in the production of visible light photons within the NaI(Tl) crystal. Photomultiplier tube (PMT) is activated : The light emitted by the crystal is detected by a photomultiplier tube (PMT). The PMT generates a signal by converting the light photons into electrons. Electronic signal processing : The signal from the PMT is amplified, converted into digital data, and analyzed. Collimator working mechanism; Collimator selects the rays coming from a certain angle or direction and allows them to reach the detector. Collimators used in scintillation detectors are usually made of lead and are used for the following purposes: Directing the rays : Blocking the rays coming from different angles and allowing only those coming from a certain direction to pass. Reducing background noise increases the sensitivity of the measurements by blocking gamma rays coming from unwanted directions.

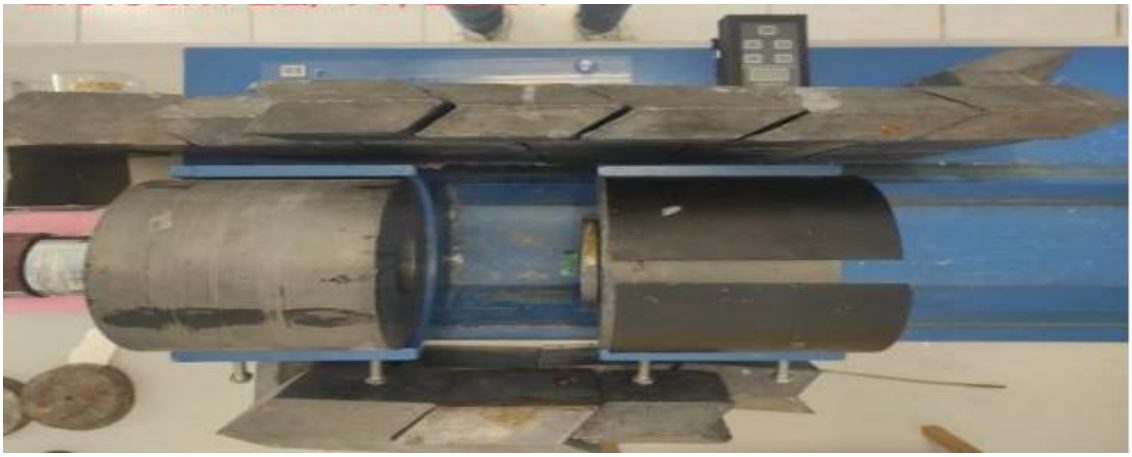

Figure 2. Gamma spectroscopy with NaI scintillation device.

Beta measuring device: The beta filter in front of the detector is in the closed position .Since beta particles cannot pass through the filter, only gamma rays are measured. The measurement obtained showed the background gamma radiation (gamma dose rate) . The detector's beta filter was in the open position , Beta particles can also reach the detector and are included in the measurement. In this case, the measurement obtained gives the sum of (Beta + Gamma). To find the beta number, pure beta is found by subtracting the gammas from the total count. Then, a graph is created showing the count amount depending on the thickness.

Figure 3. Beta spectroscopy and survey meter.

It is based on the principle that gamma rays interact with atoms of matter as they pass through the material. As a result of these interactions, gamma rays lose some or all of their energy. The gamma radioisotope source and detector are placed on both sides of the material on the same axis and the radiation intensity coming from the source and passing through the material is measured. The count values obtained using different thickness values of the material are compared to the count value obtained without using the material, and relative count values are obtained for each thickness value of the material. Thickness-relative count graphs are drawn for each material, gamma attenuation curves of the material are created, compared with each other and evaluated in line with the purpose. The gamma radiation attenuation capacity of the materials was analyzed by measuring the linear attenuation coefficient (μ) and half-value thickness (HVL). Radiation measurements were performed using a NaI(Tl) sodium iodide scintillation detector. This detector detected gamma photons with high sensitivity, allowing accurate determination of radiation attenuation coefficients.

Figure 4. Neutron measuring device.

Howitzer and Neutron hand detector Neutron measurement; The measurement is repeated 3 times using the Howitzer neutron detector , AM241 as the material and source.Since the source being worked on is active, a protective container and rope services are used inside the welding howitzer to minimize radiation exposure and similar measurements are obtained by maintaining the distance between the source materials. It is supported by protective methods such as paraffin, wooden barriers and cadmium to minimize scattering. 3 measurements were made and the material observes by keeping the experiment time the same.

Findings

During the experiment, firstly the radiation of the laboratory environment was measured. Then, the measurement was made while the source was present, then the measurements were made while the source and the material were together, and the i and ı values of the samples with increased thickness were obtained.

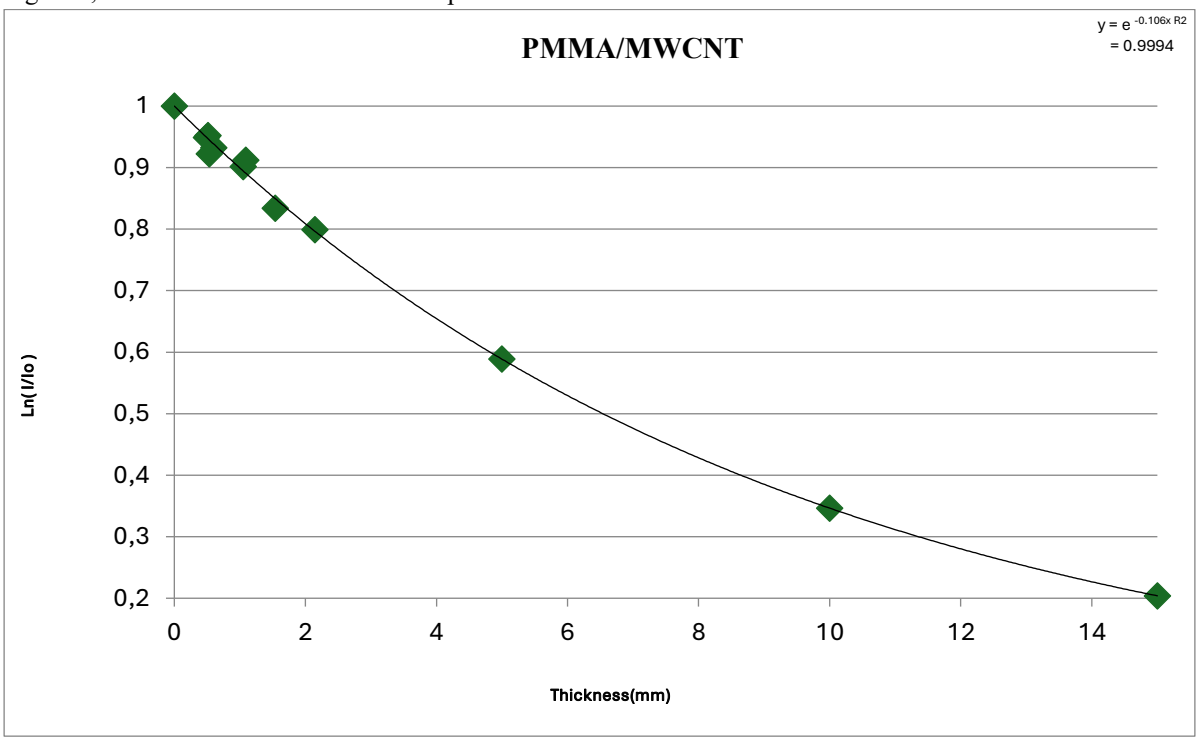

Figure 5. Gamma transmission relationship between the linear attenuation coefficient and the thickness of materials containing and nanoparticle doped PMMA/Mwcnt.

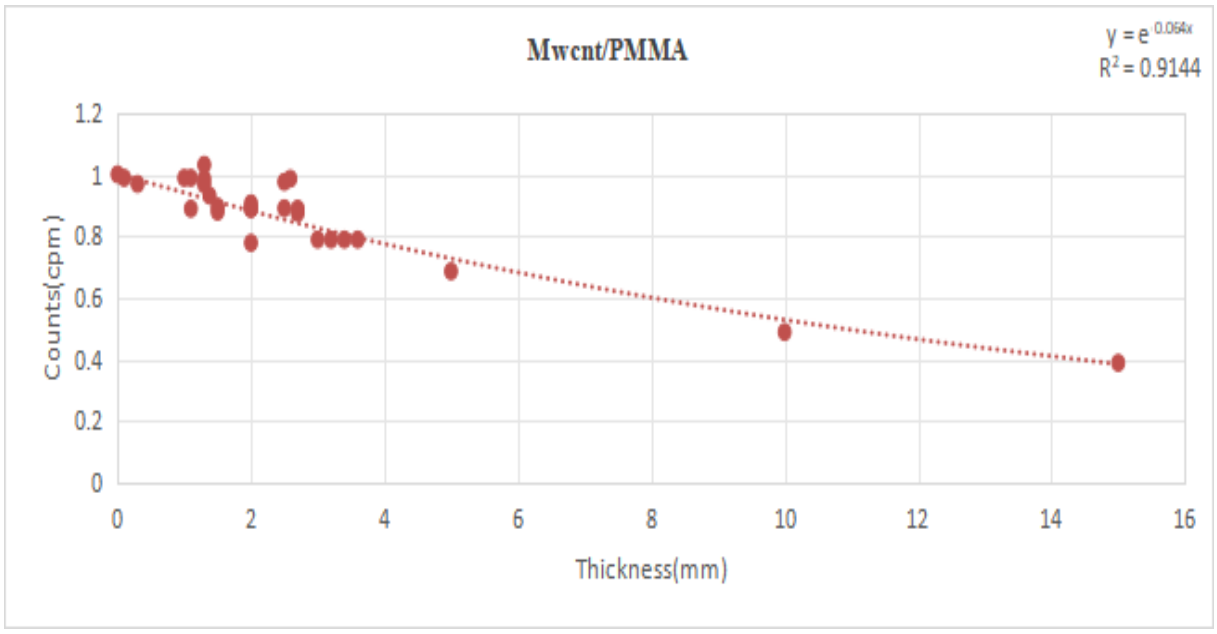

Figure 6. Beta counting graph of nanoparticle doped PMMA/Mwcnt.

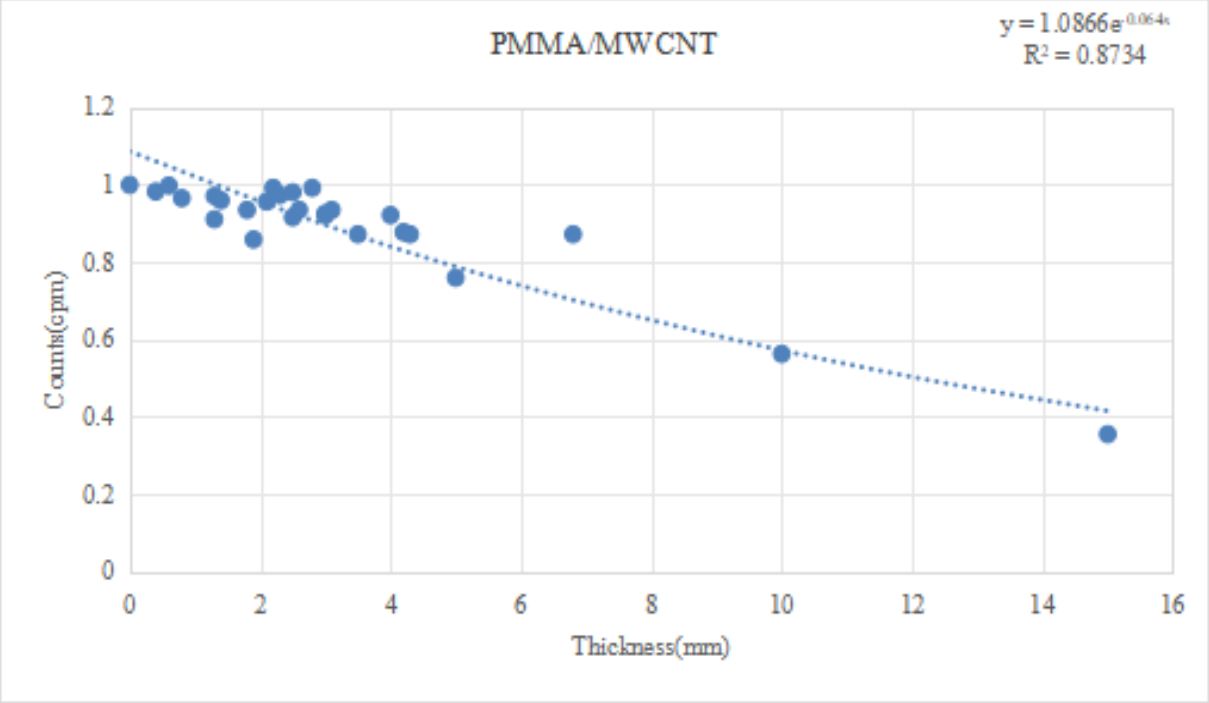

Figure 7. Neutron counting graph of nanoparticle doped PMMA/Mwcnt.

The rpe and attenuation coefficient values were found in accordance with the values obtained. As a result of the values found, the variance parts and the percentage distributions of the thickness permeabilities were calculated. According to the channel range selected in the Maestro program and the energy of the source, the highest discrimination was obtained with the material pairs

Table 1. Thickness dependent beta comparison percentile values.

Isotope	Decay Type	Main Energy Levels (MeV)
Cesium-137 (Cs-137)	Beta (-) and Gamma	0.662 MeV (Gamma)
Cobalt-60 (Co-60)	Beta (-) and Gamma	1.17 MeV, 1.33 MeV (Gamma)
Strontium-90 (Sr-90)	Beta (-)	0.546 MeV (Beta), 2.28 MeV (Yttrium-90 decay)
Americium-241 (Am-241)	Alpha and Gamma	5.486 MeV (Alpha), 0.059 MeV (Gamma)

Relative percentage error (rpe), linear attenuation coefficient (μ) percentages and Ln(ı/ıo) used to analyze the radiation absorption or permeability of the material. Peak heights gave a more discrimination result compared to the energy ranges of the peaks. If special results are selected and compared to increase discrimination in each method, discrimination increases.
This allows us to distinguish the differences between our samples, even if they are small. MWCNT and magnetic nanoparticle doped PMMA composites increase the radiation attenuation performance by gamma transmission technique . It proves that MWCNT doped composites supported with magnetic nanoparticles are more effective in absorbing gamma radiation compared to samples containing only MWCNT.

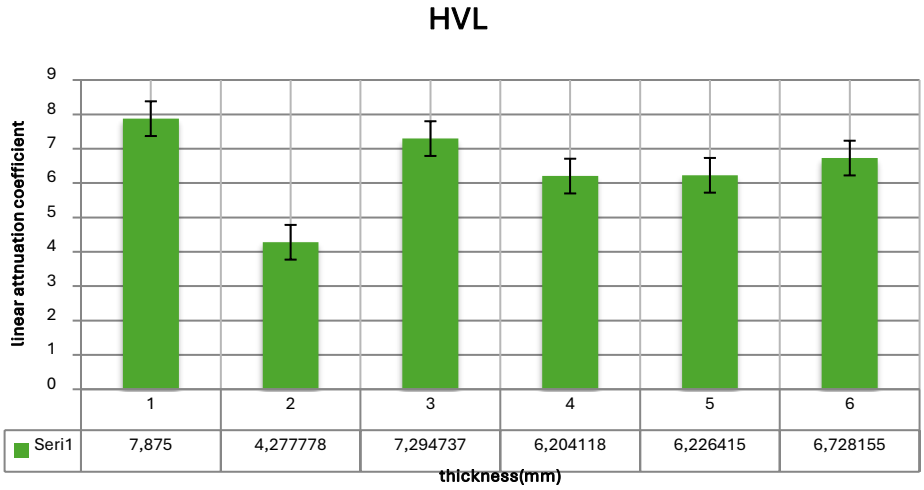

Figure 8. Linear attenuation coefficient ratio of half-value layer numbers and nanoparticle source PMMA/MWCNT containing materials.

It has also been observed that Co- 60 absorbs high energy gamma photons better, while Cs137 has a significant effect on the absorption of medium energy gamma rays.In the study, the coefficients of MWCNT and magnetic nanoparticle reinforced PMMA composites against gamma, beta and neutron radiation are clearly evident in detail. In the experiments:For gamma radiation, the coefficients of the distribution of Cesium-137 and Cobalt-60 sources were calculated. When the materials were distributed homogeneously and spread out, a significant improvement was observed.In the experiments conducted with Strontium-90 source for beta radiation, it was observed that PMMA-based materials absorb beta radiation at a high rate. Comparison of HVL (Half Value Thickness) values showed that the coupling capacity was increased with higher MWCNT content.In terms of neutron radiation, MWCNT reinforced PMMA samples were examined and it was determined that the neutron absorption capacity increased due to the high neutron capture cross section of MWCNT reinforced PMMA.

Table 2. Comparison of my thesis with literature studies and findings.

Study	Material Used	Metot	Techniques	Radiation Type	Findings	Conclusions	Error Sources	Literature
Al-Sarray et al. (2021)	PMMA Reinforced with Nanoparticles	Monte Carlo Simulation	Spectrometric Analysis	Gamma, Neutron	The effect of nanoparticle distribution on attenuation coefficient was	It was determined that nanoparticle distribution is effective	Simulation error margin, lack of experimental validation	Al-Sarray, 2021 [10]

					calculated			
Acerbi et al. (2024)	PMMA Reinforced with Gadolinium Oxide Nanoparticles	Experimental	Neutron Shielding	Neutron	The attenuation coefficient increased due to gadolinium's neutron capture cross-section	PMMA was made suitable for neutron shielding in nuclear applications	Sample homogeneity, spectrometer measurement sensitivity	Acerbi, 2024 [11]
Tang et al. (2024)	Radiation Shielding Concrete (RSC)	Experimental & Simulation	Radiation Absorption Tests	Gamma	The radiation attenuation performance of additives in concrete was tested	Shielding efficiency was demonstrated through macro and microstructure analyses	Variations in concrete mixture, measurement duration	Tang, 2024 [12]
A. M. Onaizi et al. (2024)	Radiation Shielding Concrete (RSC)	Experimental & Review	Gamma and Neutron Absorption Tests	Gamma, Neutron	The effects of radiation on concrete were examined, and attenuation properties of concrete materials were tested	Shielding performance was enhanced by adding heavy aggregates and nanoparticles to concrete	Variability in concrete composition, measurement errors in laboratory conditions	Radiation Shielding Concrete Article,2024 [13]

M. Pandey et al. (2025	MXene/Polymer Nanocomposites	Experimental & Simulation	EMI Shielding Tests	Electromagnetic Waves	EMI shielding efficiency was increased	EMI protection and high charge storage capacity were improved	Variability in nanocomposite synthesis process	Pandey, 2025[14]
D. H. Aydın, N. Baydoğan (2025)	MWCNT and Magnetic Nanoparticle Reinforced PMMA	Experimental & Theoretical	Gamma, Beta, and Neutron Transmission Techniques	Gamma, Beta, Neutron	Radiation attenuation coefficients were measured, and nanoparticle homogeneity was examined	PMMA-based composites showed improved radiation shielding ability, proving their suitability for aerospace and energy applications	Measurement device sensitivity, sample preparation errors, environmental factors	D. H. Aydın, N. Baydoğan, 2025[15]

Conclusion

MWCNT and magnetic nanoparticle doped PMMA composites can be considered as lightweight and effective radiation shielding materials.

Such materials offer potential applications in nuclear power plants, medical imaging devices and aerospace applications. They can also have a wide range of applications such as space technologies, defense industry and industrial radiation shields. In the aviation and space industry, MWCNT and magnetic nanoparticle reinforced polymer composites may have various advantages in terms of electromagnetic environment repellency.

References

Acerbi, L., et al. (2024). Neutron shielding properties of PMMA reinforced with gadolinium oxide nanoparticles: An experimental study.

Al-Sarray, M., et al. (2021). PMMA reinforced with nanoparticles: Monte Carlo simulation for spectrometric analysis of gamma and neutron attenuation.

Aydın, D. H., & Baydoğan, N. (2025). Gamma, beta, and neutron transmission in MWCNT and magnetic nanoparticle reinforced PMMA composites.

Calvo-de la Rosa, J., García-Santiago, A., Hernàndez, J.M., Vazquez-Aige, M., Lopez-Villegas, J.M., & Tejada, J. (2024). Barium hexaferrite based nanocomposites as Random Magnets for microwave absorption . ArXiv. https://arxiv.org/abs/2402.14324

Calvo-de la Rosa, J., Vazquez-Aige, M., Pérez, P., Medina, L., Marín, P., Lopez- Villegas, J. M., & Tejada, J. (2024). Broadband radar absorption in high-filling factor magnetic composites . ArXiv. https://arxiv.org/abs/2407.05818

Calvo de la Rosa, J., Bou Comas, A., Hernandez, J. M., Marin, P., Lopez-Villegas, J. M., Tejada, J., &

Chen, M., Li, X., Zhou, Z., & Wu, Y. (2024). High-temperature and radiation-resistant carbon nanotube composites for thermal shielding in space applications. Composites Science and Technology, 236, 109841. https://doi.org/10.1016/j.compscitech.2024.109841

Chudnovsky, E. M. (2023). New approach to designing functional materials for stealth technology: Radar experiment with bilayer absorbers and optimization of the reflection loss .
ArXiv. https://arxiv.org/abs/2307.14784

H., Park, SY, Kim, H. J., & Choi, W. K. (2024). Electromagnetic thrust and shielding performance of plasma propulsion systems integrated with nanocomposites. Acta Astronautica, 209, 50-63.
https://doi.org/10.1016/j.actaastro.2024.03.007

Onaizi, A. M., et al. (2024). The effects of radiation on concrete: A review of gamma and neutron absorption properties.

Pandey, M., et al. (2025). MXene/polymer nanocomposites for enhanced EMI shielding: Experimental and simulation insights.

Senturk, B., & Yilmaz A. , G. (2024). Investigation of Radar Absorbing Composite Materials Using Carbon Nanotubes with Different Particle Sizes and Weight Fractions . Journal of Erciyes University Institute of Science. https://dergipark.org.tr/tr/pub/erciyesfen/issue/89386/1400990

Song, W., Zhao, Y., Liu, Y., Zhang, X., Wang, L., & Zhang, H. (2024). Graphene- based composites for multifunctional electromagnetic shielding and thermal management in aerospace applications. Carbon, 215, 118245. https://doi.org/10.1016/j.carbon.2024.118245

Tang, X., et al. (2024). Radiation absorption tests on radiation shielding concrete: Experimental and simulation approaches.

U.S. Department of Energy. (n.d.). *Radioactivity explained: How unstable nuclei release energy through decay.* Retrieved from https://www.energy.gov

Wang, L., Xu, Y., Gao, J., & Tang, Z. (2025). Lightweight and high-strength polymer- based electromagnetic shielding composites for aerospace applications. Progress in Aerospace Sciences, 153, 100910. https://doi.org/10.1016/j.paerosci.2025.100910

Zhang, X., Sun, P., Chen, C., Wang, L., & Liu, Y. (2025). Magnetic nanoparticle- enhanced radar absorbing materials for stealth technology: A review. Materials Today, 55, 35-52.
https://doi.org/10.1016/j.mattod.2025.01.0127. Lee, J.

NANOSCIENCE AND NANOENGINEERING

Nanoparticles

Nanotechnology for Energy Systems

Polymer and Nano Composites

Thermo-responsive PNIPAAM Based Hydrogels with Bio-inspired Additives for Biomedical Applications

Rabia Yılmaz[a,b], Özgür Yılmaz[b,c], Sevgi Gülyüz[b], Birgül Benli[a,d]

[a] Istanbul Technical University, Graduate School, Nanoscience and Nanoengineering Program, Turkey
[b] Tübitak Marmara Research Center, Turkey
[c] Istanbul University, Department of Pharmaceutical Chemistry, Pharmacy Program, Turkey
[d] Istanbul Technical University, Mines Program, Mineral Processing Engineering Department, Turkey
yilmazr22@itu.edu.tr

Keywords: Collagen , Hydrogel , PNIPAAm Polymer.

Aim

Hydrogels, recognized as soft and moisture-rich materials with a three-dimensional network structure capable of holding a substantial amount of water, have found extensive applications in areas such as controlled drug delivery carriers, tissue engineering scaffolds, and biosensors. Their widespread use is attributed to their distinctive characteristics, including biocompatibility, biodegradability, water retention, and adhesive properties. It is well established that stimulus-responsive polymer hydrogels serve as adaptable drug delivery platforms, enabling drug release to be regulated by various external factors. Among them, thermoresponsive hydrogels have gained significant attention due to their ease of temperature control and applicability in both in vitro and in vivo environments. Poly(N-isopropylacrylamide) (PNIPAAM), one of the most extensively studied thermoresponsive synthetic polymers, is particularly valuable in the development of materials for biomedical applications. PNIPAAM exhibits a phase transition around its lower critical solution temperature (LCST), which is approximately 32°C. Above this threshold, the polymer undergoes a rapid transformation from a hydrophilic to a hydrophobic state, resulting in the expulsion of water. Due to this unique characteristic, PNIPAAM hydrogels have been widely utilized in diverse fields, including drug release, self-healing materials, and tissue engineering. Recently, increasing research has focused on the synthesis of copolymers incorporating PNIPAAM with biodegradable components to construct polymeric networks with enhanced properties. Collagen hydrogels are three-dimensional network structures composed of collagen protein and have high water retention capacity. These hydrogels have a wide range of uses in biomedical applications such as tissue engineering and drug delivery systems due to their biocompatibility and biodegradability. Collagen hydrogels provide a suitable microenvironment for cell adhesion, growth and differentiation with their structures that mimic the natural extracellular matrix (ECM). However, the mechanical strength of natural collagen hydrogels is generally low. Therefore, methods such as chemical cross-linking or modification with synthetic polymers are used to improve their mechanical properties. Another important area of use of collagen hydrogels in medical applications is to support wound healing. Thanks to their high water content and biocompatibility, these hydrogels can accelerate the healing process by providing a moist healing environment when used as a wound dressing. Clays are natural inorganic additives widely used to improve both structural and functional properties in hydrogel systems. These substances, especially clay minerals with layered silicate structures such as montmorillonite, bentonite and kaolin, are integrated into hydrogel matrices and improve important properties of these structures such as mechanical, thermal and swelling behaviors. Clay particles in the hydrogel create physical cross-links between polymer chains, making the network structure more robust and stable. This is of great importance in terms of achieving the desired mechanical strength, especially in biomedical applications. In addition, the presence of clays in the hydrogel directly affects the swelling behavior. For example, the addition of clays such as montmorillonite limits the water absorption capacity of the hydrogel, providing a more controlled and slow swelling process. This feature is particularly advantageous in drug delivery systems. In controlled release applications, it is desired to release the drug slowly over a certain period of time, and the clay additive plays a regulatory role in this process. In our study, we synthesized an injectable hydrogel by combining pnipam and collagen. We also aimed to add additives such as

clay to provide mechanical support for use in tissue engineering, rapid drug screening systems, and drug delivery, etc.

Material and Method

2.1 Material

Collagen(Type 1), N-isopropylacrylamide(NIPAAM), Azobisisobutyronitrile(AIBN), Methanol (99% purity), *1-Ethyl-3-(3-dimethylaminopropyl)carbodiimide* (EDC), N-Hydroxysuccinimide (NHS), Acetone (99% purity), Mercaptoundecanoic acid (MUA), diethylether.

2.2 Method

Synthesis of PNIPAAM

PNIPAAM was synthesized by radical polymerization. AIBN was used as radical initiator and MUA was used as functionalizer. NIPAAM, AIBN and MUA was dissolved in methanol. Then, vacuum and nitrogen were applied to remove the air from the volumetric flask containing the mixture. Finally, it was mixed with a magnetic stirrer in an oil bath at 70 degrees for 24 hours. The next day the mixture was evaporated at 50-60 degrees. Acetone is used to dissolve the formed PNIPAAM polymer. After dissolving it with acetone, it was precipitated by adding it dropwise to cold diethylether. The precipitated polymer was decanted and left in a vacuum oven overnight to dry completely. The fully cured polymer is ready to be used for hydrogel formation.

Synthesis of Pnipaam-Collagen Hydrogel

MES solution was prepared to dissolve collagen and PNIPAAM polymer. The pH of the solution was adjusted to 5. Then, collagen was dissolved in MES solution. At the same time, PNIPAAM was dissolved in a separate beaker of mes solution. EDC and NHS were used as activator. They were also dissolved separately in MES solution. Once all were completely dissolved, they were combined and left on a magnetic stirrer overnight at room temperature. The mixture was placed on a dialysis membrane to remove impurities. The membrane was kept in distilled water at 4 degrees for 4 days. Then, the mixture was precipitated in distilled water adjusted to 50 degrees and after waiting for a while, gel formation was observed.

Findings

The temperature-sensitive PNIPAAM polymer was successfully synthesized. Then, it was mixed with the required amount of type 1 collagen under appropriate conditions for hydrogel formation. PNIPAAM-collagen hydrogel was formed. It was observed that the formed hydrogel was in liquid form at 25 degrees and in solid form at 37 degrees. The necessary characterization studies for the synthesized PNIPAAM polymer and PNIPAAM-collagen hydrogel are continuing. Additionally, research continues on clay, which will be used to provide mechanical support.

Conclusion

As a result of this study, a thermosensitive PNIPAAM-collagen hydrogel was successfully synthesized, exhibiting desirable physical and chemical properties at physiologically relevant temperatures. The hydrogel responded effectively to temperature changes, particularly around body temperature, making it a promising candidate for biomedical applications where thermoresponsiveness is critical. Characterization analyses, including morphological, rheological, and swelling behavior assessments, revealed that while the synthesized hydrogel meets fundamental performance criteria, its mechanical strength can be further improved. To enhance these mechanical properties without compromising the biocompatibility or natural structure of the collagen network, incorporation of suitable additives has been proposed. Among these, naturally occurring nanoclays, such as montmorillonite or bentonite, are particularly promising due to their layered structure, high surface area, and ability to interact with polymer chains to reinforce the hydrogel matrix. By integrating such reinforcing agents, it is anticipated that the hydrogel will gain enhanced durability and structural integrity, thereby expanding its potential applications. In this context, the developed PNIPAAM-collagen hydrogel is envisioned for use in advanced biomedical fields such as tissue engineering, wound healing, and controlled drug delivery systems, where both

biocompatibility and functional performance are crucial. Future studies will focus on optimizing the formulation by testing various additive concentrations and evaluating their effects on long-term stability, degradation behavior, and in vivo performance.

References

Ana, I. D. (2024). Collagen hydrogel in drug delivery and tissue engineering. In S. Jana (Ed.), *Biomaterial-based hydrogels* (Chapter 8). Springer.
Url-1 https://doi.org/10.1007/978-981-99-8826-6_8 date retrieved 02.05.2025.
Ding, C. , Zhang M. , Zheng, J. , Yang, Q. , & Feng, R. (2019). Thermal and pH duaresponsive hydrogels based on semi-interpenetrating network of poly(N-isopropylacrylamide) and collagen nanofibrils. *Polymer International*.
Url-2 https://doi.org/10.1002/pi.5852 date retrieved 01.05.2025.
Lai, J.-Y. , & Hsieh, A.-C. (2012). A gelatin-g-poly(N-isopropylacrylamide) biodegradable in situ gelling delivery system for the intracameral administration of pilocarpine. *Biomaterials*, *33*(7), 2372–2387.
Url-3 https://doi.org/10.1016/j.biomaterials.2011.11.085 date retrieved 29.04.2025.
Sever, E. , & Pulat, M. (2023). MMT katkılı IPN tipi hidrojellerin sentez ve karakterizasyonu. *Gazi Üniversitesi Fen Fakültesi Dergisi*, *4*(2), 80–92.
Url-4 https://dergipark.org.tr/tr/pub/guffd date retrieved 01.05.2025.

PETROLEUM AND NATURAL GAS ENGINEERING

Geothermal Engineering

Natural Gas Engineering

Reservoir Engineering

Utilization of Carbon Dioxide Gas (CO_2) for Gas Lift Systems In Geothermal Wells

Force Lugembe Ndege [a], Ömer Inanç Türeyen [a]

[a] Istanbul Technical University, Petroleum and Natural Gas Engineering, Petroleum and Natural Gas Engineering, Turkey
ndege21@itu.edu.tr

Keywords: Flash Point Pressure, Gas Lift Systems, Geothermal Energy, Solubility of Carbon Dioxide Gas in Water, Well Head Pressure.

Aim

Geothermal wells experience a decline in pressure between the bottomhole pressure and the wellhead pressure (during both static and dynamic conditions) due to friction, gravity, and kinetic energy loss encountered during fluid flow from the reservoir to the surface. In some cases this decline could be large, leading to reduced production rates. High wellhead pressures are necessary for maintaining high production rates and keeping the geothermal power plants operational. To address the pressure loss during fluid flow in geothermal wells, artificial lift techniques are employed, such as line shaft pumps and electrical submersible pumps (ESPs), which are widely used in Türkiye and globally.

This study investigates the feasibility and potential benefits of using carbon dioxide (CO2) gas lift systems in geothermal wells as an innovative artificial lift technique. The utilization of CO2 gas for gas lift in geothermal wells, though not widely researched and adopted, presents a promising approach to enhancing the productivity and efficiency of geothermal energy extraction. By integrating CO2 gas lift systems, operators can improve flow rates, increase overall system efficiency, and reduce operational costs.

The study involves several stages, including the analysis of the thermodynamic behavior and solubility of CO2 in water at various pressures and temperatures encountered during geothermal fluid flow. Using Duan's solubility data, the solubility of CO2 in water was predicted with high accuracy through linear interpolation coding techniques, covering pressures up to 2000 bar and temperatures of 533K. Additionally, geothermal pressure profiles, partial pressures of steam and CO2, and flash point pressures were simulated by coding and validated, to understand the effects of varying CO2 mass fractions. It was discovered that increasing CO2 mass fractions reduced pressure losses, leading to higher wellhead pressures.

This study's findings indicate that CO2 has a profound effect on the wellhead pressure. Therefore, CO2 gas lift systems may serve as a viable alternative to conventional artificial lift techniques. By addressing challenges such as declining productivity and operational inefficiencies, the integration of CO2 gas lift systems contributes to improved energy production and lower operational costs. This research provides a comprehensive understanding of the effects of CO2 on the production performance for geothermal wells.

Material and Method

To be able to link the wellhead pressure to the bottomhole pressure in wells containing geothermal water with CO_2, the solubility of CO_2 with pressure and temperature must be known. For this study, the solubility of CO_2 in water is modelled with the model provided by the following Duan and Sun,(2003). A python code that determines the CO_2 solubility in water at any temperature and pressure up to 533.15K and 2000bar with high accuracy has been developed. The results of CO_2 solubility in water values were compared with the existing Duan's concentration of CO2 in water as indicated in Duan's 2003 to check the validity of the coding. The results were also compared with the experimental data obtained from Wiebbe and Gaddy ((1935); (1940)) in the same temperature and pressure range. Figure 1 gives the behaviour of solubility with temperatures for various pressures.

$$ln m_{CO_2} = ln y_{CO_2} \varphi_{CO_2} P - {\mu^{I(0)}}_{CO_2}/RT - 2\,\lambda_{CO_2-Na}(m_{Na}+m_K+2m_{Ca}+2m_{Mg}) - \zeta_{CO_2-Na-Cl}\, m_{Cl}(\quad m_{Na} + m_K + m_{Ca} + m_{Mg}) + 0.07 m_{SO_4}$$

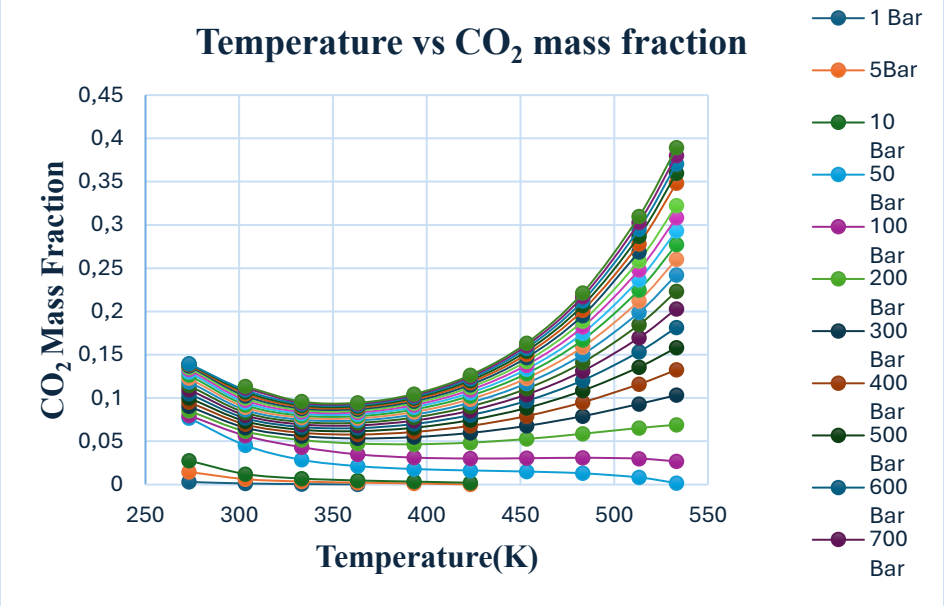

Figure 1: The plot of Temperature vs code calculated CO2 mass fraction data.

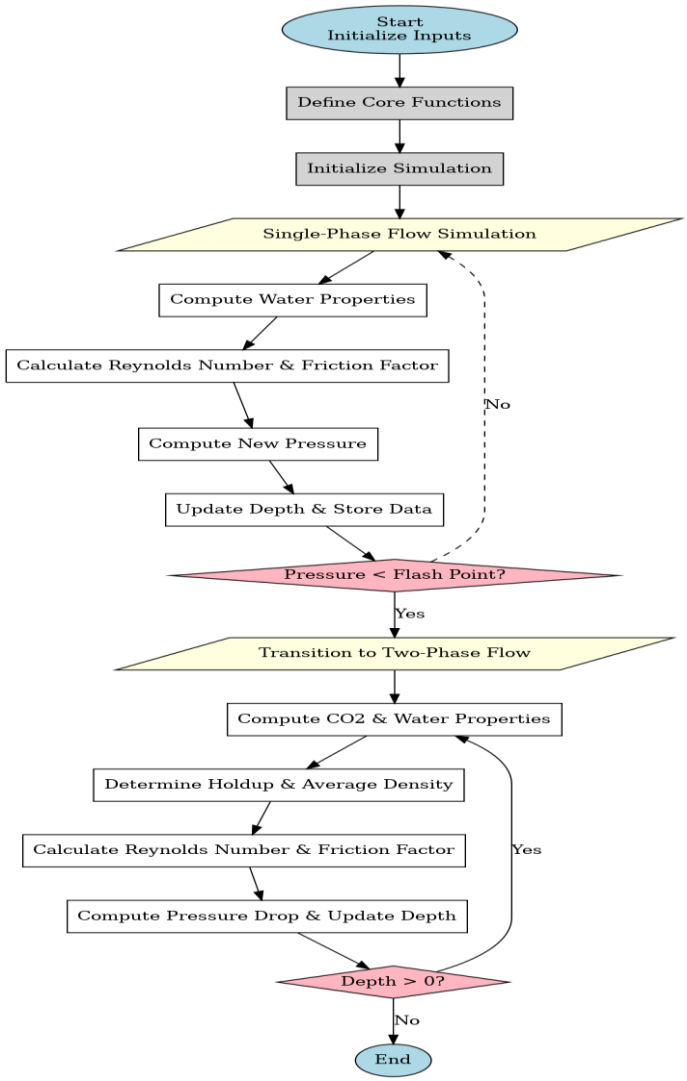

Figure 2: Flowchart for computing the wellbore pressure profile.

Findings

Numerical Modelling Methodology for Geothermal Well Pressure Profile

In this study, a computational model was developed to analyze the pressure profile along a geothermal wellbore, accounting for different pressure losses, including frictional, gravitational, and kinetic energy losses. The model is implemented as a stepwise numerical algorithm, computing wellhead pressure at various CO_2 mass fractions. The core structure of the model follows a systematic approach, integrating thermodynamic property calculations and iterative pressure drop computations.

Flowchart for Geothermal Well Pressure Profile Code Structure

A python code was written in the Visual code studio to simulate the flow in geothermal wells containing CO2. The flow chart of the code is given in Figure 1 outlines the key computational stages, including input initialization, function definitions, single-phase and two-phase flow simulations, and finalizing the computation.

Development of The Well Pressure Profile Model

During production, a typical pressure profile is given in Figure-3. As it is clear, at the lower sections of the well, there is single phase flow. At a certain depth, flashing occurs, and the two-phase region begins. The two-phase region consists of gas and water flow. In geothermal wells that produce water with CO2, the gas phase will be composed of both CO2 and steam. The flashing point occurs in the region where the deviation from the straight line begins. Furthermore, the slope of the pressure profile changes significantly because of the formation of the two phases. Figure 5 below serves as a visualization model, to help with visualization of the necessary parameters. The model developed in this study is capable of generating the pressure profile for wells that produce water with dissolved CO2.

To ensure the reliability and accuracy of the developed geothermal well pressure profile code, a validation process was carried out using real field data from two geothermal wells: AF-21 from Afyon (Cinar et al., 2006) and OB-16 from Germencik (Tureyen et al., 2014). These wells were chosen due to the availability of well-documented pressure profiles, making them ideal for testing the performance of the numerical model.

Figure 4 gives the results of the comparison of the model developed in this study to the AF-21 well. As it is clear, the model developed in this study provides a good match to the actual field data. Figure 5 gives the match to the OB-16 well pressure profile. Again, a fairly good match is obtained.

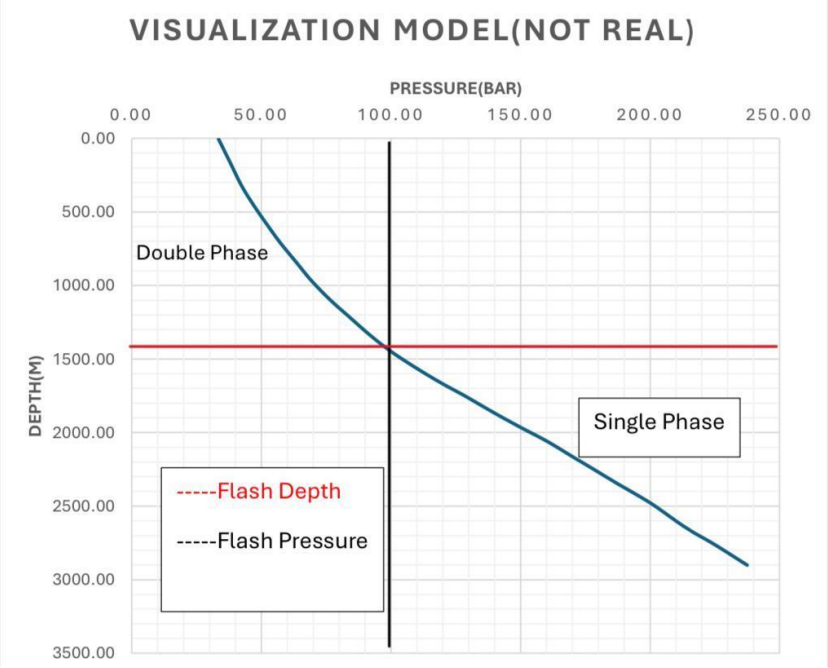

Figure 3: visualization model.

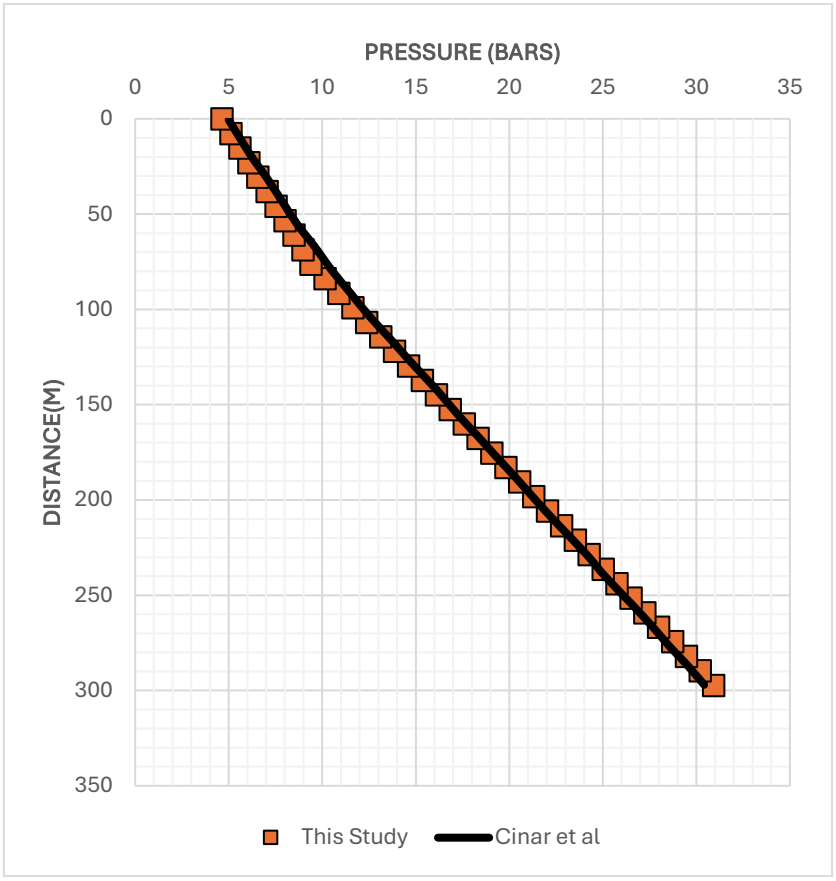

Figure 5: The pressure profile of the AF- 21 well and the model, where the mass fraction of the dissolve CO2 is at 0.9%.

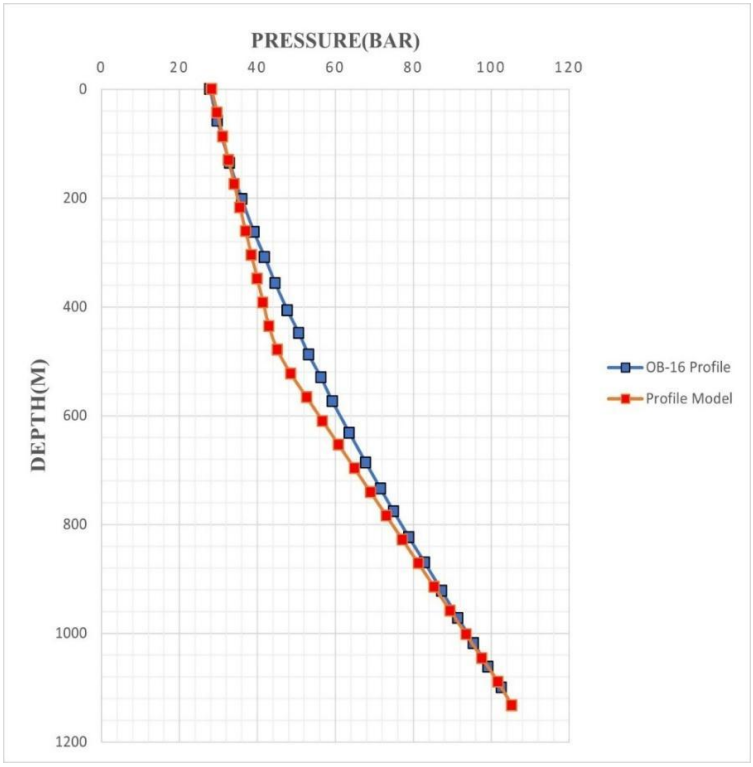

Figure 5: The pressure profile of the OB- 16 well and the model, where the mass fraction of the dissolved CO2 is at 2.1%.

Conclusion

A CO_2 solubility code was developed based on Duan's 2003 equation of state. The results obtained from the model demonstrated high accuracy when compared with experimental and modeling data, maintaining an error margin within 0.04% in the temperature range of 273 to 533 K and pressures up to 2000 bar. The model effectively predicts CO_2 solubility in water under geothermal conditions, making it a reliable tool for designing CO_2-based gas lift systems. The model can also be used to predict the flash point pressure and CO_2 mass fraction retained in liquid phase during the double phase flow in geothermal wells.

Furthermore, a geothermal well pressure profile code was designed to simulate the pressure behavior of geothermal wells under different CO_2 mass fractions. This numerical model accounted for pressure losses due to friction, gravity, and kinetic energy effects along the wellbore. The simulation results indicated that increasing CO_2 mass fractions effectively reduced pressure losses and contributed to higher wellhead pressures, thereby enhancing well productivity. The stepwise computational approach incorporated thermodynamic property calculations, phase transition modeling, and iterative pressure drop calculations to accurately represent real-world well conditions.

The findings of this study suggest that CO_2 gas lift systems could serve as an efficient and cost-effective alternative to conventional artificial lift methods in geothermal wells. By improving flow rates and increasing energy production efficiency, the integration of CO_2 gas lift can lead to significant operational advantages, including lower maintenance costs and reduced energy consumption.

In conclusion, this research successfully validates the potential of CO_2 gas lift systems for geothermal wells through both theoretical modeling and numerical simulations. The developed solubility model and well pressure profile code offer valuable computational tools for optimizing gas lift design in geothermal energy production. Future work should focus on experimental validation, field-scale implementation, and further exploration of CO_2 phase behavior under varying geothermal conditions. By advancing the understanding and application of CO_2 gas lift, this study paves the way for the adoption of innovative and sustainable solutions in geothermal energy production.

References

Duan, Z., & Sun, R. (2003). An improved model calculating CO 2 solubility in pure water and aqueous NaCl solutions from 273 to 533 K and from 0 to 2000 bar. www.elsevier.com/locate/chemgeo.

Gaddy, C. A., & Wiebe, G. (1935).) Zelvinskii. In J. Chem. Ind. (U. S. S. R.) (Vol. 57, Issue 2). https://pubs.acs.org/sharingguidelines.

Wiebe, R., & Gaddy, V. L. (1940). Solubility of Carbon Dioxide in Water The Solubility of Carbon Dioxide in Water at Various Temperatures from 12 to 40° and at Pressures to 500 Atmospheres. Critical Phenomena*. https://pubs.acs.org/sharingguidelines.

PETROLEUM AND NATURAL GAS ENGINEERING

Geothermal Engineering

Natural Gas Engineering

Reservoir Engineering

Natural Gas Hydrate Modelling

Devrim Başar Han[a] , Murat Çınar[a]

[a] Istanbul Technical University, Petroleum and Natural Gas Engineering, Master Program, Türkiye
han22@itu.edu.tr

Keywords: Gas Hydrates, Hydrate Formation, Hydrate Mitigation, Natural Gas Distribution, Natural Gas Pipelines.

Aim

Gas hydrates are clathrate inclusion compounds in which water molecules form hydrogen-bonded cages in a lattice structure stabilized by encapsulating a small guest molecule such as methane or ethane [1]. A gas hydrate is an ice-like solid that can exist at temperatures up to 25˚C in systems with moderate pressure at 7 MPa. Water in natural gas may condense and alter the physical state to an unwanted two-phase flow [2]. The pipelines used in the production of oil and gas can experience serious safety and flow assurance problems because of plugging by solid deposits of gas hydrates, waxes, asphaltenes, and scale [3]. These conditions are commonly encountered in oil and gas offshore process facilities [4]. In this study we focus on the hydrate formation conditions that could be encountered in natural gas urban distribution systems. Based on data from a gas distribution company, the effects of various conditions on gas hydrate formation were investigated.

Within the conditions of a natural gas system, besides pressure and temperature, it is concluded that the primary factor influencing hydrate formation is the water content for such systems. According to average composition we plotted the average gas composition at various water contents and observed the behavior. Hydrate formation estimations are based on complex thermodynamic relations. In this work we provide a simple relation that would estimate hydrate formation temperature at a given pressure and water content for a typical natural gas composition encountered in urban distribution lines, on the fact that the composition in natural gas distribution lines is relatively constant. The relation proposed is compared with the generalized thermodynamic relations. The results are consistent. The equation works for a pressure range of 100-1 bar within engineering accuracy.

Material and Method

Using the data provided, aqueous phase calculations were performed, and the necessary conversions were made based on NIST Webbook [5] data. The base water content calculated as 2.09x10-5 $\frac{mol\ H_2O}{mol\ Gas}$, indicating that one mole of natural gas is flowing by 2.09×10^{-5} moles of water. The hydrate forming curve behavior of the different gas composition was analyzed at different water ratios to develop a more detailed model. The gas compositions for each month over a period of four years are given, the samples with the maximum and minimum methane content were evaluated, and presented in Table 1 and Table 2, respectively. The sample with the maximum methane content named as "Max gas composition" and the sample with the minimum methane content named as "Min gas composition". Max and min gas compositions at different water mole fractions and hydrate formation curves are presented in Figure 1.

This study was conducted for specific water ranges. The cases for different water fractions are defined as follows:
Case 1: 6.96×10^{-4} mol water
Case 2: 1.04×10^{-3} mol water
Case 3: 2.09×10^{-3} mol water
Case 4: 4.19×10^{-3} mol water
Case 5: 6.27×10^{-3} mol water

Table 1. The gas composition sample with the lowest methane content. Named as min gas composition.

Methane	Ethane	Propane	n-butane	I-butane	n-pentane	I-pentane	Hexane	Nitrogen	CO2
93.1820	3.6987	1.1252	0.2292	0.1936	0.0414	0.0539	0.0147	1.1345	0.3268

Table 2. The gas composition sample with the highest methane content. Named as max gas composition.

Methane	Ethane	Propane	n-butane	I-butane	n-pentane	I-pentane	Hexane	Nitrogen	CO2
95.8254	2.3966	0.7072	0.1022	0.1032	0.0131	0.0185	0.0102	0.6448	0.1786

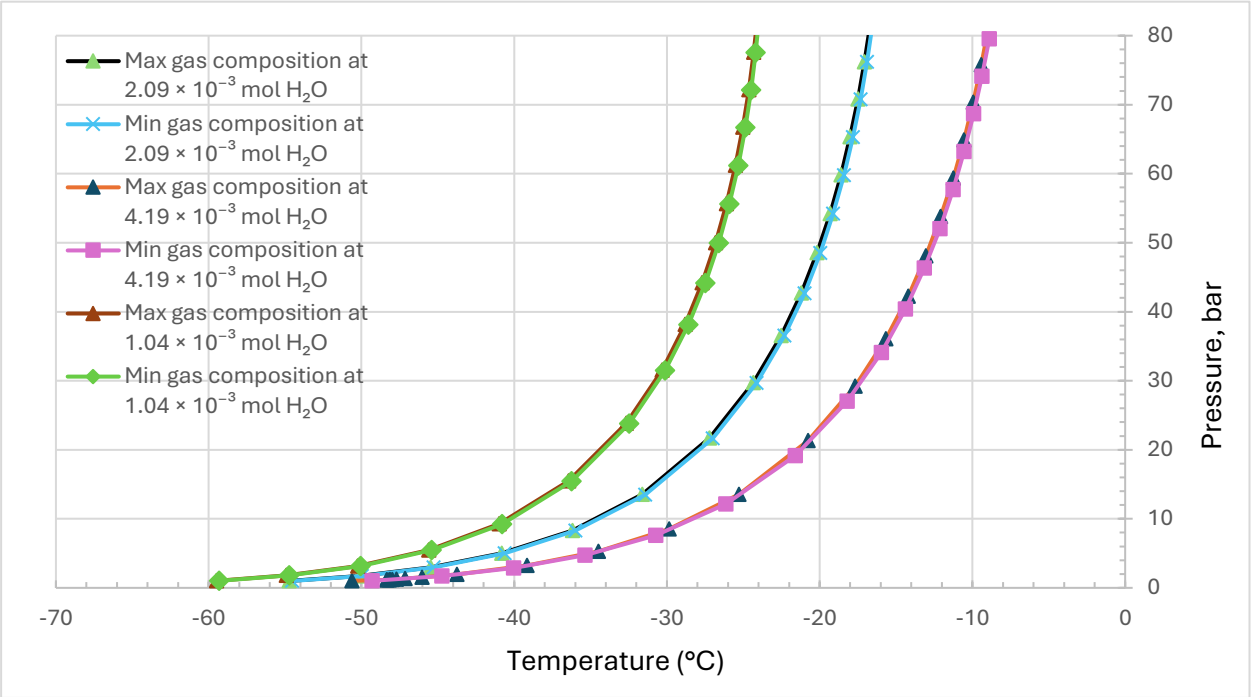

Figure 1. Effect of max and min gas compositions on hydrate formation process for case 2, case 3 and case 4.

When an average gas composition was generated and the hydrate formation curves were plotted, a similar behavior to the curves in Figure 1 was observed. The hydrate formation curves of the average gas composition are plotted.

Table 3. Average gas composition.

Methane	Ethane	Propane	n-butane	I-butane	n-pentane	I-pentane	Hexane	Nitrogen	CO2
94.5077	3.7169	0.7667	0.1220	0.1158	0.01426	0.02013	0.01616	0.5804	0.14033

Since the hydrate formation curves of the average gas composition and the hydrate formation curves of the max and min gas compositions exhibit the same behavior, all hydrate forming curve for average gas composition, max gas composition and min gas composition shown in Figure 2. Thus, subsequent calculations and analyses will be conducted based on the average gas composition.

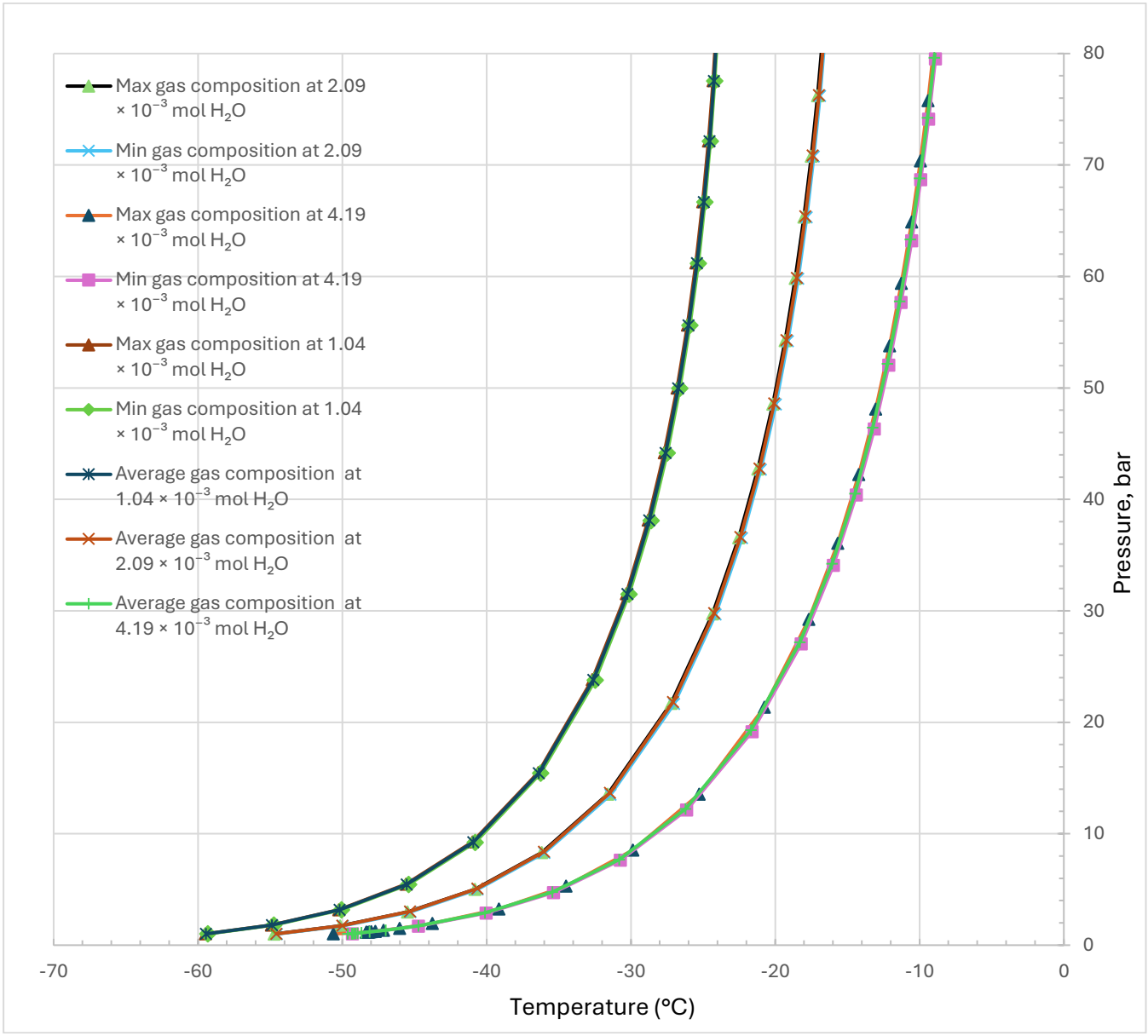

Figure 2. Comparison of max gas composition, min gas composition and average gas composition on hydrate forming curves for case 2, case 3 and case 4.

Average gas composition approach facilitates a more precise assessment of the effect of water content on hydrate formation. According to hydrate forming behavior of average gas composition at each water contents, curve parameters are determined. These curves were fitted on logarithmic trend lines so the equations were logarithmic. The curves given in Figure 3. Equations and R^2 values given in Table 1.

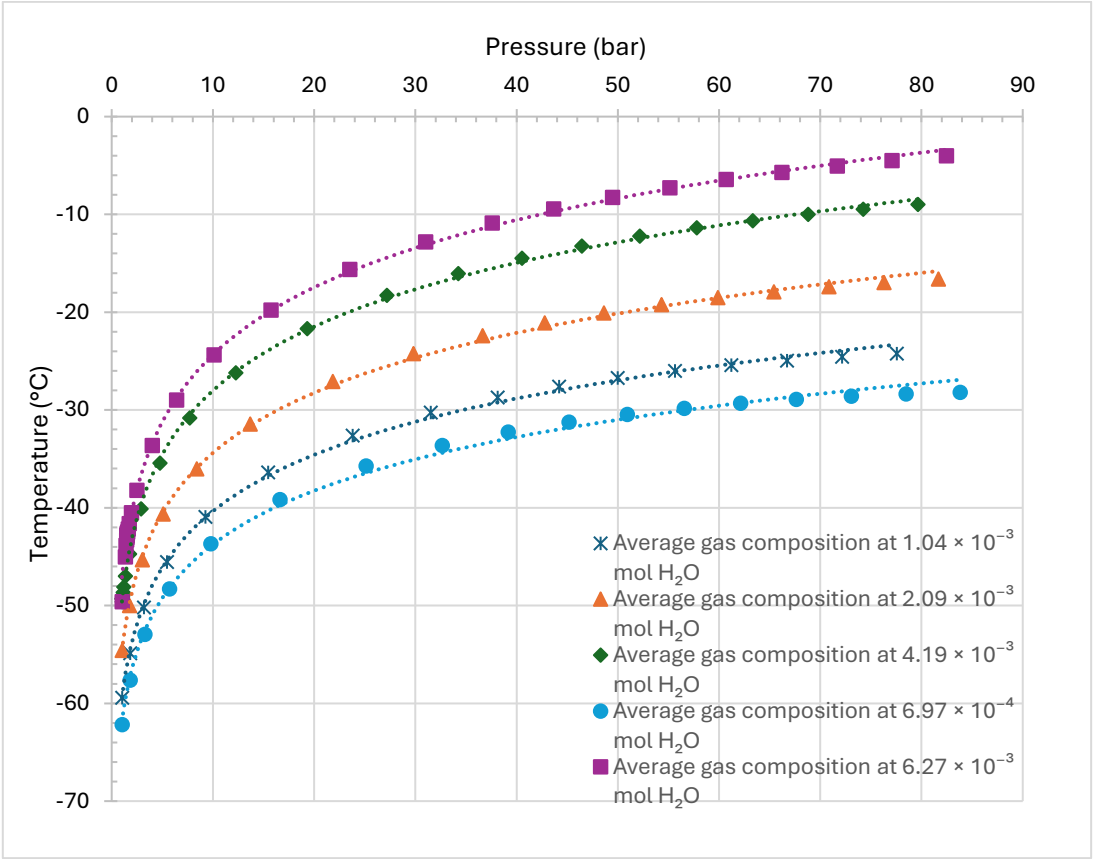

Figure 3. Hydrate forming curves of average gas composition for each case.

General equation for hydrate forming curves;

$y = a\ ln\ ln\ (x\ ) - b$ …… (1.1)

Since the general equation is $y = a\ ln\ ln\ (x\ ) - b$, the behavior of the parameters needs to be analyzed. To understand how the coefficients of equations in Table 1 behave, the parameter values were recorded as shown in Table 2.

Table 4. Equations and R^2 values of hydrate formation curves for the average gas composition at each case.

Water Content, mol	Equation	R^2 Value
6.97×10^{-4} mol H_2O	y = 7.9219ln(x) - 61.9947	0.9971
1.04×10^{-3} mol H_2O	y = 8.3144ln(x) - 59.4947	0.9986
2.09×10^{-3} mol H_2O	y = 8.8530ln(x) - 54.7768	0.999
4.19×10^{-3} mol H_2O	y = 9.4247ln(x) - 49.7153	0.9997
6.27×10^{-3} mol H_2O	y = 9.9374ln(x) - 47.2376	0.9988

Table 5. Parameters of the equations with the average gas composition for each case.

	Coefficients	
Water contents, mol	***a***	***b***
0.000697	7.9219	61.9947
0.00104	8.3144	59.4947
0.00209	8.8530	54.7768
0.00419	9.4247	49.7153
0.00627	9.9374	47.2376

To generalize the behavior of the coefficients, the graph of water content versus coefficients was plotted, which shows that both the "a" and "b" parameters follow logarithmic trendlines. Since the general equation for hydrate forming curve for average gas composition (equation 1.1) given as $y = a\ ln\ ln\ (x\ ) - b$ the equation for the "a" parameter will be substituted into the general equation in place of "a". In this equation, the x-axis represents water content; therefore, "x" corresponds to the water content."
Similarly, the equation of "b" parameters will be put instead of "*b"* in equation 1, again the "x" variable represents water content.

According to the behavior of parameter "a", the equation of parameter "a" is obtained as:

$y = 0.8844\ ln\ ln\ (x\ ) + 14.347$ …… (1.2)

Similarly, according to the behavior of parameter "b", the equation for parameter "b" is derived as follows:

$y = -6.814\ ln\ ln\ (x\ ) + 12.603$ …… (1.3)

If equations 1.2 and 1.3 are substituted into the equation 1.1 in place of the corresponding terms, then equation 1.1 becomes:

$(x) + 14.347)P\ - (x) + 12.603)$ …… (1.4)

Where "y" represents temperature, "x" denotes water content, and "P" stands for pressure. Using this equation, the temperature can be determined when the pressure and water content are known.
Similarly, the equation can be rearranged to express pressure as follows:

$P = e^{\frac{(x)\ +12.603))}{(0.8844 ln ln\ (x)\ +14.347)x}}$ …… (1.5)

Findings

These equations for pressure and temperature were derived based on the average gas composition in each case. To develop the model, the water content was varied in small increments, and the calculated pressure-temperature values were compared between calculated pressure - temperature and received or automatically calculated values with CSMGem [6] computer programming which uses complex thermodynamic relation (CPA infochem model). Since the results include a large number of graphs, only two representative cases are presented: the case 5 in Figure 4 and the case 1 in Figure 5.
As can be observed from Figures 4 and 5, the program outputs and the experimental results are in strong agreement. This suggests that Equation 1.4 provides reliable and accurate results.

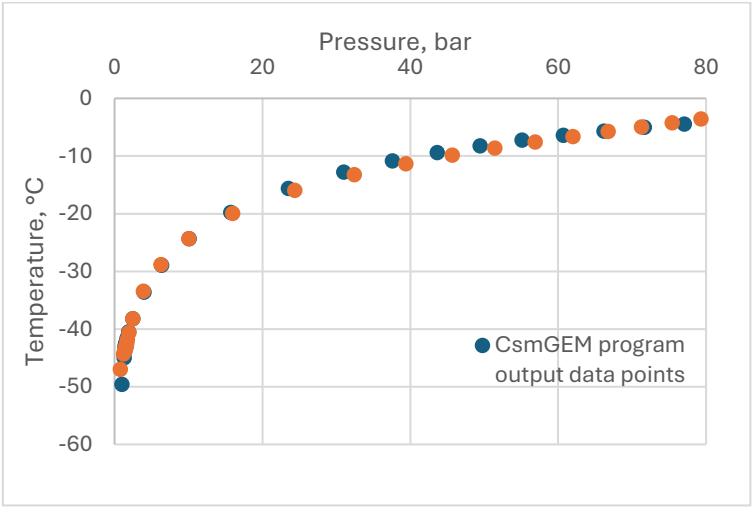

Figure 4. Comparison of simulation data and calculated data from derived equation (1.4). Comparison for case 5.

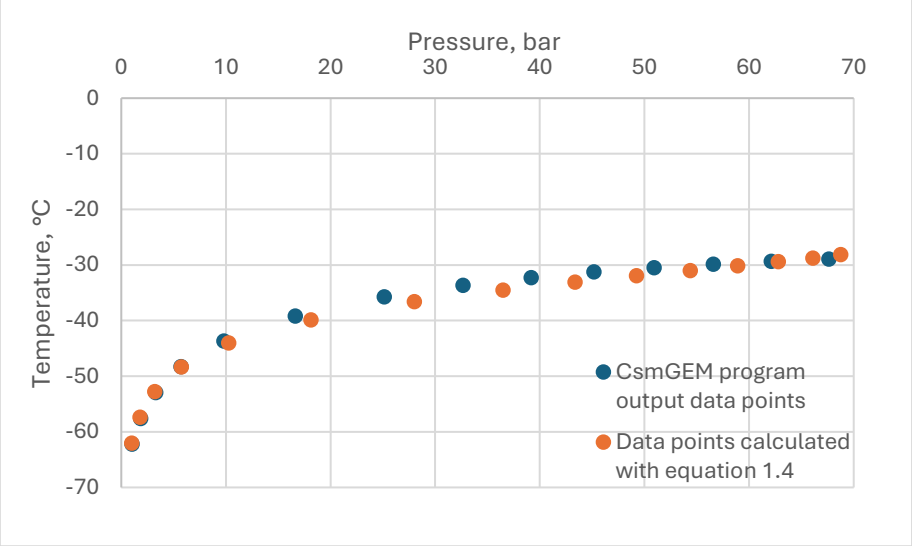

Figure 5. Comparison of simulation data and calculated data from derived equation (1.4) for case 1.

The results show better consistency with the program output at higher water contents. When it comes to low water ratios at low temperature the outcomes are consistent because of the hydrate forming process occurring naturally, but as the temperature gets high, the process is affected by another parameter. If the water content is high, the gas hydrate forming process merges at low temperature and increases in parallel with program output data.

Conclusion

This study, analyzed the formation of gas hydrates in urban natural gas flow lines, and a generalized equation was derived to predict temperature and pressure conditions for hydrate formation. The results showed that water content plays a crucial role in the formation process, with higher water percentages leading to more consistent hydrate formation patterns at lower temperatures. The developed logarithmic model effectively correlates water content with temperature and pressure parameters, and the derived equations were validated using EOS(equation of state) models. The comparison between proposed equation and EOS results demonstrated a high level of agreement, particularly at higher water contents. Additionally, the model was further verified through machine learning predictions (random forest model), achieving a remarkable accuracy of 99.4%. These findings provide a valuable tool for optimizing heating strategies in natural gas pipelines, mitigating hydrate-related flow assurance issues. Future work may focus on refining the model by incorporating additional influencing factors such as gas composition variations and external environmental conditions to enhance its predictive capabilities.

References

Boxall, J., Hughes, T., & May, E. (2011, July 17–21). *Direct electrical heating of liquid-filled hydrate blockages*. In *Proceedings of the 7th International Conference on Gas Hydrates (ICGH 2011)* (Vol. 3, pp. 2189–2195). Edinburgh, Scotland.

Colorado School of Mines. (2007). *CSMGem Version 2.1* [Computer software]. Colorado.

Nathan, D., & Theo, M. (Eds.). (2008). *Determination of water content of natural gases: State of the art; Natural gas research progress*. Nova Science Publishers, Inc.

NIST Chemistry WebBook. (n.d.). *NIST WebBook*. Retrieved March 15, 2025, from https://webbook.nist.gov/chemistry/fluid/

Sloan, E. D., & Koh, C. A. (2008). *Clathrate hydrates of natural gases* (3rd ed.). Taylor and Francis Group LLC: CRC Press.

Van Rossum, G., & Drake, F. L. (2009). *Python 3.12.2 reference manual*. CreateSpace.

Zerpa, L. E., Salager, J., Koh, C. A., Sloan, E. D., & Sum, A. K. (2011). Surface chemistry and gas hydrates in flow assurance. *Industrial & Engineering Chemistry Research, 50*(1), 188–197. https://doi.org/10.1021/ie100873k.

PETROLEUM AND NATURAL GAS ENGINEERING

Geothermal Engineering

Natural Gas Engineering

Reservoir Engineering

Comparison of Thermophysical Gas Properties

Nariman Valiyev[a], Ömer İnanç Türeyen[a]

[a] Istanbul Technical University, Mines Faculty, Petroleum and Natural gas Engineering, Turkey

valiyev17@itu.edu.tr

Keywords: Compressibility Factor, Density, Viscosity, Critical Properties, Reservoir Volume.

Aim

Underground storage of natural gas has been an important topic over the decades. The underground storage of hydrogen on the other hand is attracting considerable attention. Finally, the sequestration of carbon dioxide has been an important topic over the two decades. These three gases have been the center point of research for many researchers. In all applications the physical properties of these gases must be computed. Many of the gas's physical properties are essential for safe, effective, and cost-effective underground storage. These characteristics have an impact on overall safety, operational effectiveness, and storage location selection. Understanding how these gases behave under different reservoir conditions has become increasingly important due to rising energy demands and the need for carbon capture and storage (CCS) technology to reduce greenhouse gas emissions (Guo & Ghalambor, 2005). Because of its potential for use in renewable energy applications, hydrogen is becoming a prominent contender for energy storage in the future. Its storage characteristics, however, are very different from those of traditional natural gas. Likewise, sequestration of carbon dioxide is essential for lowering atmospheric emissions, necessitating a thorough examination of its storage behaviour (Li et al., 2023).

Thus, this study compares the physical characteristics of three commonly used gases and examines how they behave at various pressures and temperatures. The viability and effectiveness of storing these gases underground will be better understood thanks to this comparative study, which is essential for improving storage plans and guaranteeing the security and integrity of storage reservoirs.

Material and Method

The main thermophysical gas properties applied for the comparison of the mentioned gases are:

- compressibility factor (also known as z-factor)
- pressure over compressibility factor (p/z)
- density
- viscosity
- gas compressibility
- gas formation volume factor
- reservoir volume

For the calculation of these parameters the critical properties of the gases and reference reservoir pressure and temperature range are needed. The pressure and temperature range applied for the calculation of the gas properties are for typical reservoir conditions. The critical properties of hydrogen (H_2), carbon dioxide (CO_2), and methane (CH_4) are tabulated in table 1.

Table 1. The critical properties of gases.

Gas name	Critical pressure (bar)	Critical temperature (K)
Hydrogen	13	33.2
Carbon dioxide	73.8	304.2
Methane	46.4	190.6

With the help of critical properties and equations applied from the handbook, the main thermophysical properties are calculated and compared (Craft et al., 1991). The key gas parameter for the calculation of all properties is compressibility factor. By obtaining z-factor other properties can be computed. The gas deviation factor (z) is calculated using the "Dranchuk and Abou Kassem" method. The density, compressibility, formation volume factor and reservoir volume are given by Equations 1, 2, 3 and 4 respectively:

$$\rho = \frac{pM}{zRT} \quad \textbf{1}$$

$$c = \frac{1}{\rho}\left(\frac{\partial \rho}{\partial p}\right)_T = \frac{1}{p} - \frac{1}{z}\left(\frac{\partial z}{\partial p}\right) \quad \textbf{2}$$

$$B = \frac{p_{sc}}{T_{sc}}\frac{zT}{p} \quad \textbf{3}$$

$$V = \frac{p_{sc}}{T_{sc}}\frac{zT}{p}G \quad \textbf{4}$$

Here ρ (kg/m^3) is the density, p (bar) is pressure, M (kg/kg.mole) is the molecular weight, z is the gas deviation factor, R is the Universal gas constant, 8.314×10^{-2} bar.m^3/(K.kgmole), T is temperature (K), G (sm^3) is the volume of gas at standard conditions, and V (m^3) is the volume of gas at reservoir conditions (Craft et al., 1991). For calculating viscosity, the Coolprop software has been used (Yang et al., 2017).

Findings

From the results obtained for all gas properties, all three gases behave differently from each other at same pressure and temperature. The main reason why these gases act differently from each other is that their molecular and critical properties are very distinct. Figure-1 gives the results of the comparison of the gas deviation factors. From the results of the gas deviation factor (z-factor) hydrogen gas has shown to have the higher gas deviation factors for each pressure and temperature. This is followed by methane and carbon dioxide. This is primarily due to the fact that hydrogen has the lowest molar mass, critical pressure and critical temperature compared to other gases. The comparison of density is given in Figure-3. When comparing gases with density values, carbon dioxide has the highest density, because this gas has higher molecular weight and lowest gas deviation factor. In fact, there is a significant difference between the density of carbon dioxide and the other two gases at high pressures. Figure-4 gives the comparison of viscosity with pressure for different temperatures. Once again, we see that carbon dioxide has a much higher viscosity when compared with other gases. The compressibility behavior of carbon dioxide, methane and hydrogen are given in Figure-5. As expected, methane and hydrogen display a typical behavior of compressibility, where the compressibility decreases with pressure. The change of compressibility with temperature for methane and hydrogen is very small. The compressibility behavior of carbon dioxide, on the other

hand, is somewhat counterintuitive. Especially at low temperatures, with increasing pressure, compressibility initially decreases, then increases, and finally decreases afterwards. This behavior of decreasing, increasing and then decreasing again becomes less dominant at higher temperatures. This behavior can be explained via the density behavior. Let's consider the compressibility of carbon dioxide at 313.15 K (40 °C). Between pressures of 56 bar and 85 bar, the compressibility of carbon dioxide displays an increasing behavior. This corresponds to the region where there is a rapid increase in density (as can be seen in Figure 3). Once the rapid increase of density diminishes the compressibility starts to decline. When we compare the compressibility of carbon dioxide, methane and hydrogen, for a specific temperature, at lower pressures, the compressibility of carbon dioxide is higher than that of methane and hydrogen. At higher pressures, the compressibility of carbon dioxide becomes less than that of methane and hydrogen.

Figures 6 and 7 give the comparison of the formation volume factor and the reservoir volumes of the gases respectively. The reservoir volumes have been compared for the case where the volume of the gases at standard conditions have been taken the same. The formation volume factor and reservoir volume have shown similar results, where methane and hydrogen showed higher values at each temperature and pressure compared to carbon dioxide. The reason is that the carbon dioxide has higher compressibility.

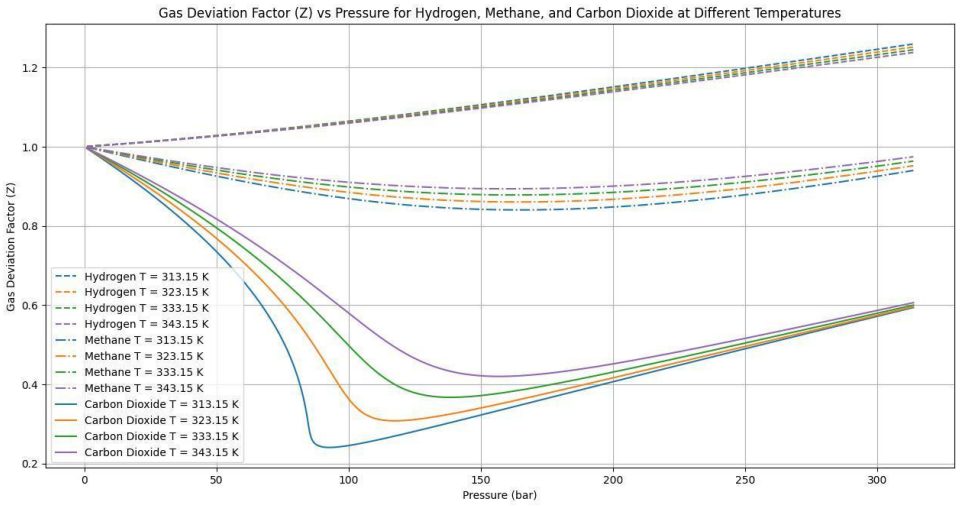

Figure 1. Compressibility factor (Z) vs Pressure for Hydrogen, Methane, and Carbon Dioxide.

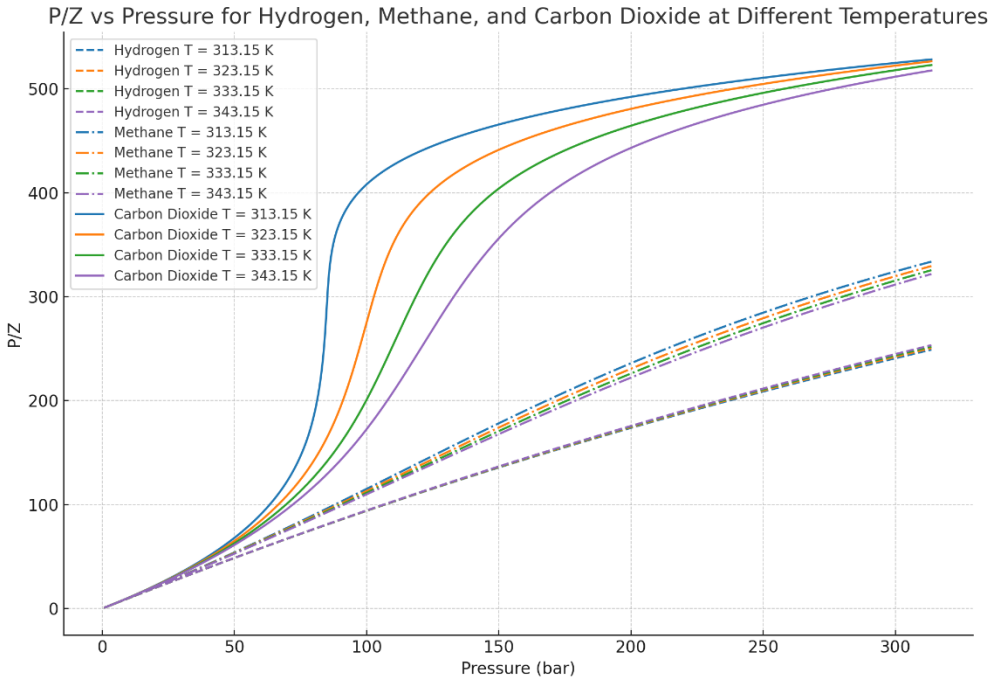

Figure 2. P/Z vs Pressure for Hydrogen, Methane, and Carbon Dioxide.

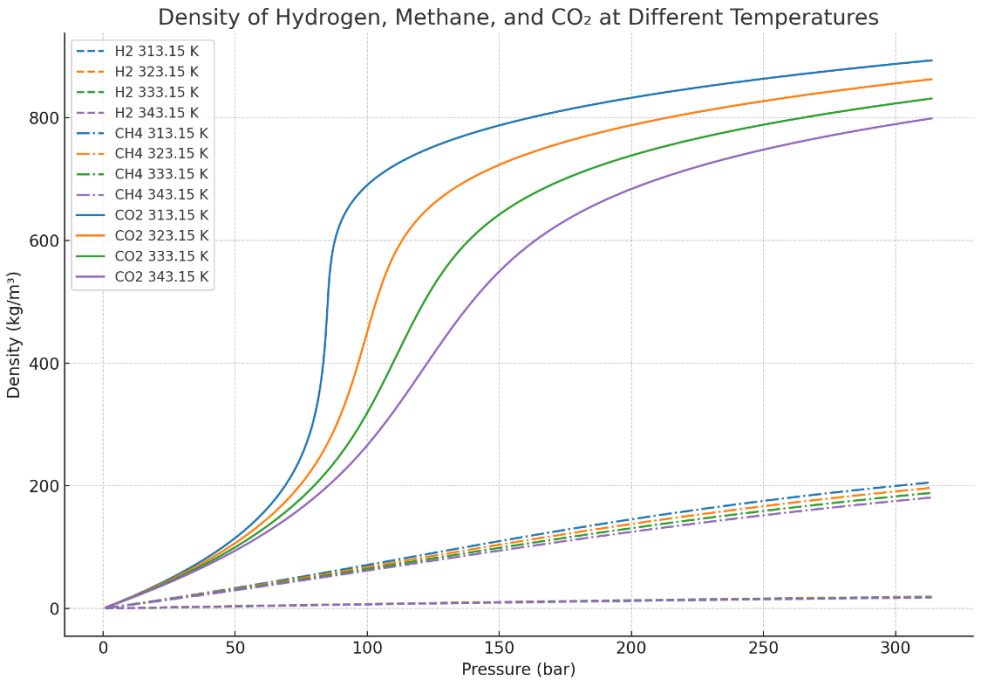

Figure 3. Density vs Pressure for Hydrogen, Methane, and Carbon Dioxide.

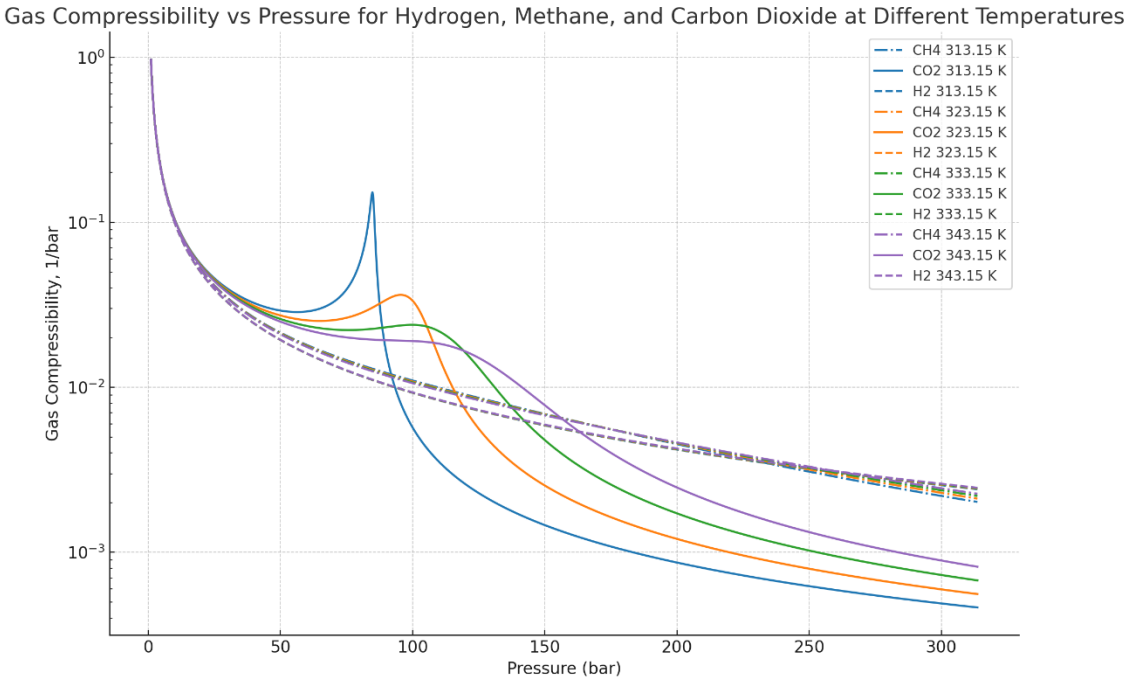

Figure 4. Gas Compressibility vs Pressure for Hydrogen, Methane, and Carbon Dioxide.

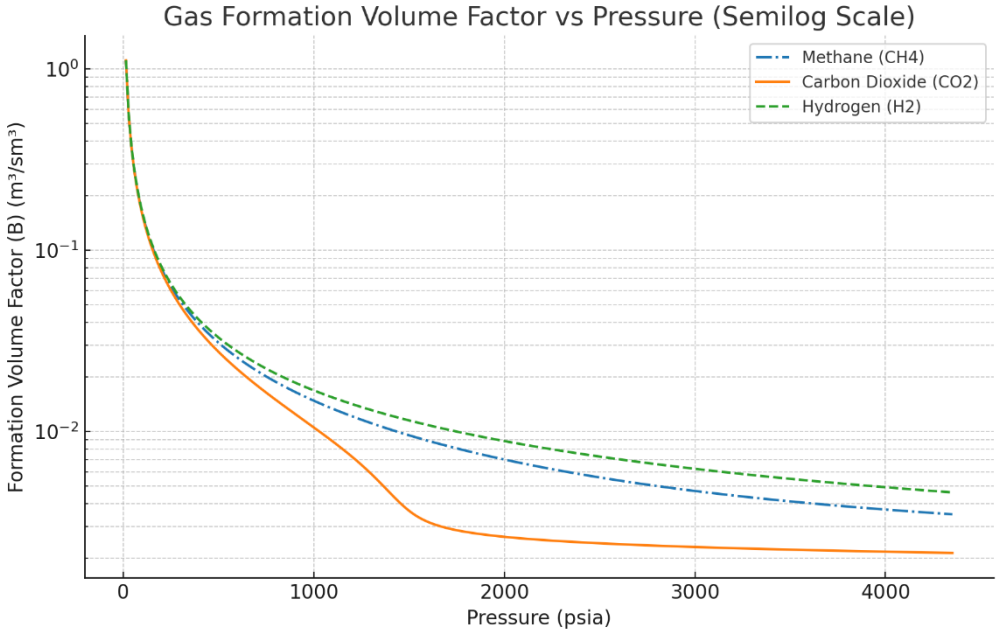

Figure 5. Gas Formation Volume Factor vs Pressure for Hydrogen, Methane, and Carbon Dioxide.

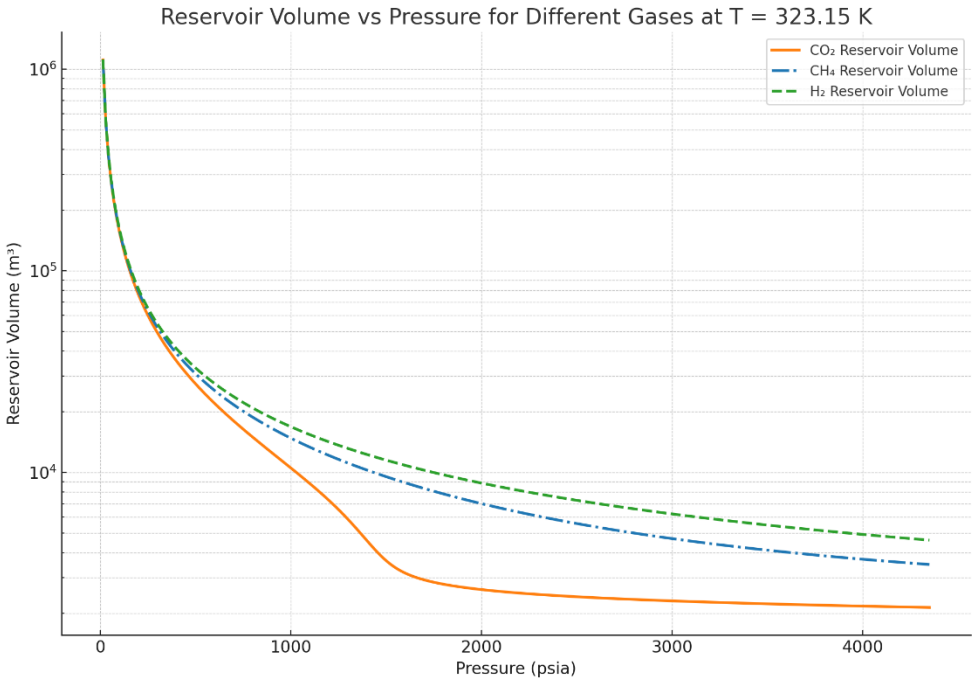

Figure 6. Reservoir Volume vs Pressure for Hydrogen, Methane, and Carbon Dioxide.

Conclusion

To conclude, in this study the comparison of three gases was calculated and analyzed under reservoir conditions. From the results obtained, it was found that all three gases showed distinct behavior due to their variations in critical properties and molecular weights. The results indicate that carbon dioxide has a much different behavior when compared with methane and hydrogen. Especially the compressibility behavior of carbon dioxide is quite counterintuitive.

The results of this investigation shed important light on how these gasses behave when stored in subterranean formations. When planning and running subterranean gas storage facilities, these variations in physical behaviour must be carefully considered. Optimizing injection and withdrawal procedures, reducing energy losses, and guaranteeing storage site stability are all made possible by an understanding of the basic gas properties under reservoir conditions. This study also emphasizes how crucial it is to choose the right storage conditions depending on the characteristics of the gas to avoid unanticipated reservoir reactions that could compromise operational effectiveness and safety.

Overall, the comparison of carbon dioxide, hydrogen, and methane under reservoir conditions offers vital data for applications involving subterranean storage, enhancing energy security and advancing more environmentally friendly energy sources.

References

Craft, B. C., Hawkins, M. F., & Terry, R. E. (1991). Applied Petroleum Reservoir Engineering Second Edition Revised by.

Guo, Boyun., & Ghalambor, Ali. (2005). *Natural gas engineering handbook*. Gulf Pub. Co.

Li, F., Ma, W., & Zhang, X. (2023). Database of thermophysical properties of H2/CO2/CO/CH4/H2O mixtures. International *Journal of Hydrogen Energy, 48*(44), 16923–16935. https://doi.org/10.1016/j.ijhydene.2023.01.066

Yang, X., Zhang, S., & Zhu, W. (2017). A new model for the accurate calculation of natural gas viscosity. *Natural Gas Industry B, 4*(2), 100–105. https://doi.org/10.1016/j.ngib.2017.07.011.

A Machine Learning Approach to Forecast Production Performance of Hydraulically Fractured Horizontal Wells in Tight Oil Sandstone Reservoirs

Ferhat Yurttagül[a], Burak Kulga[a]

[a] Istanbul Technical University, Petroleum and Natural Gas Engineering, Reservoir Engineering, Turkey
yurttagul16@itu.edu.tr

Keywords: Artificial Neural Network (ANN), Hydraulic Fracturing, Tight Oil Sandstone Reservoirs, Production Forecasting, Numerical Reservoir Simulation.

Aim

This study targets tight oil sandstone reservoirs with hydraulically fractured horizontal wells, where permeability can be as low as 0.001 mD (Boak & Kleinberg, 2020) and porosity can be around 4% (Yao, et al., 2013), causing some difficulties in production. Hydraulic fracturing and horizontal well technologies complement each other and are generally employed together to increase hydrocarbon production in tight formations. However, the efficiency rate of these approaches varies depending on the reservoir characteristics and it needs to be investigated in detail. The main objective of this study is to develop an artificial neural network (ANN) model that can predict the production performance of a hydraulically fractured horizontal well in a tight oil sands reservoir with near-accuracy and rapidity. In developing our final machine learning (ML) tool, a large-scale simulation dataset needs to be created using a commercial software program and necessary information such as oil production rate, total production time, and cumulative production data needs to be obtained. This will enable the construction and training of a well-designed ANN model. Since traditional numerical simulation methods are labor-intensive, time-consuming, involve extensive numerical calculations, and are prone to convergence problems, this study provides a solution to reduce computation time to a fraction of a second by using a well-developed ML tool. The final ML tool is considered to be a practical and rapid decision support tool that helps reservoir engineers predict the production performance of hydraulically fractured horizontal wells in tight oil sandstone reservoirs with an error rate of less than 8%.

Material and Method

Reservoir data (porosity, permeability, number of fractures, etc.) to be used in commercial simulation software (CMG, 2015) were found from the literature and minimum-maximum limits were determined for random assignment in MATLAB. First, the parameters of 5000 different scenarios were randomly generated in MATLAB within specified ranges. An example 5-fractured reservoir drawing, along with fracture and well location layout, is shown in Figure 1. In the next step, simulation files were created in a suitable format for simulator with these parameters. Then, 5000 simulations were run and production data were extracted. Some data is needed to be cleaned due to convergence errors of the commercial simulator; thus, the number of available datasets is reduced to 3369. As a result of the code written to collect the data and organize it for the ANN model, input and output data were compiled. Input data are the parameters collected to be used in the simulation and are listed in Table 1. The data were generated based on literature. For instance; fracture length (400-1200 ft) is based on (Ostojic, Rezaee, & Bahrami, 2012), permeability (0.001-0.1 mD) is based on (Boak & Kleinberg, 2020), oil saturation (60-85%) and porosity (4-16%) are based on (Yao, et al., 2013). Output data (15) was created by dividing the time from the end of production at a fixed production rate until the minimum production rate was reached into twelve equal parts. The first and last of the time data and all of the rate data (13) were taken. A large number of randomly generated parameters, combined with many extreme conditions, led to high error rates in some data sets. These data sets were identified and cleaned, and the final data set number was reduced to 3369. Finally, the ANN model was trained and tested using MATLAB, and performance analyses were performed. The structure of the model is a neural network consisting of three hidden layers in the form of 40-35-30. The schematic view of the model is shown in Figure 2, and the symbolic representation of the outputs is shown on a sample production-time chart in Figure 3.

While creating the model, the data was divided into three as training (70%), validation (15%) and test (15%). Early stopping and dropout methods were applied to prevent overfitting during the training phase. The accuracy of the model was measured by examining the mean percentage errors and compared with traditional simulation methods.

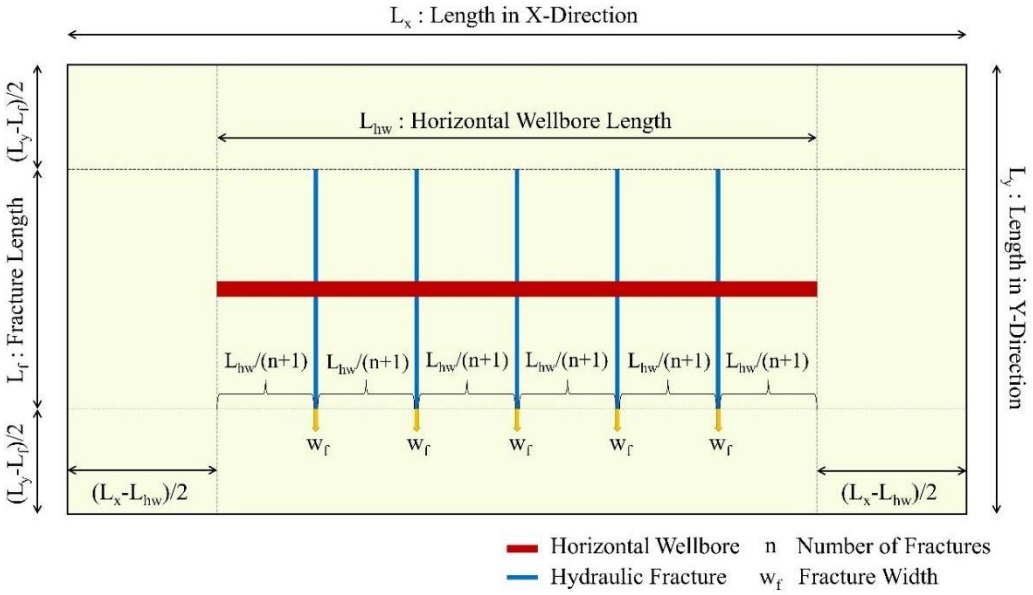

Figure 1. Top view of a sample numerical reservoir model with 5 transverse hydraulic fractures.

Table 1. Ranges of input parameters used in generating training data.

Parameters	Minimum Value	Maximum Value	Unit
Number of Fractures	5	30	-
Horizontal Wellbore Length	1000	5000	ft
Length of Fracture	400	1200	ft
Thickness	100	350	ft
Permeability	0.001	0.1	mD
Porosity	4	16	%
Initial Temperature	150	250	°F
Initial Pressure	3500	7500	psi
Width of Fracture	0.04	0.1	inch
Permeability of Fracture	2000	15000	mD
Specific Gravity of Gas	0.65	0.9	-
API	40	50	-
Solution Gas/Oil Ratio	200	2000	scf/STB
Flowrate Specified	400	1200	STB/D
Minimum Oil Rate	50	100	STB/D
Oil Saturation	60	85	%
Water Saturation	15	30	%
Residual Oil Saturation	0.15	0.35	-
Corey Exponents	1	3	-

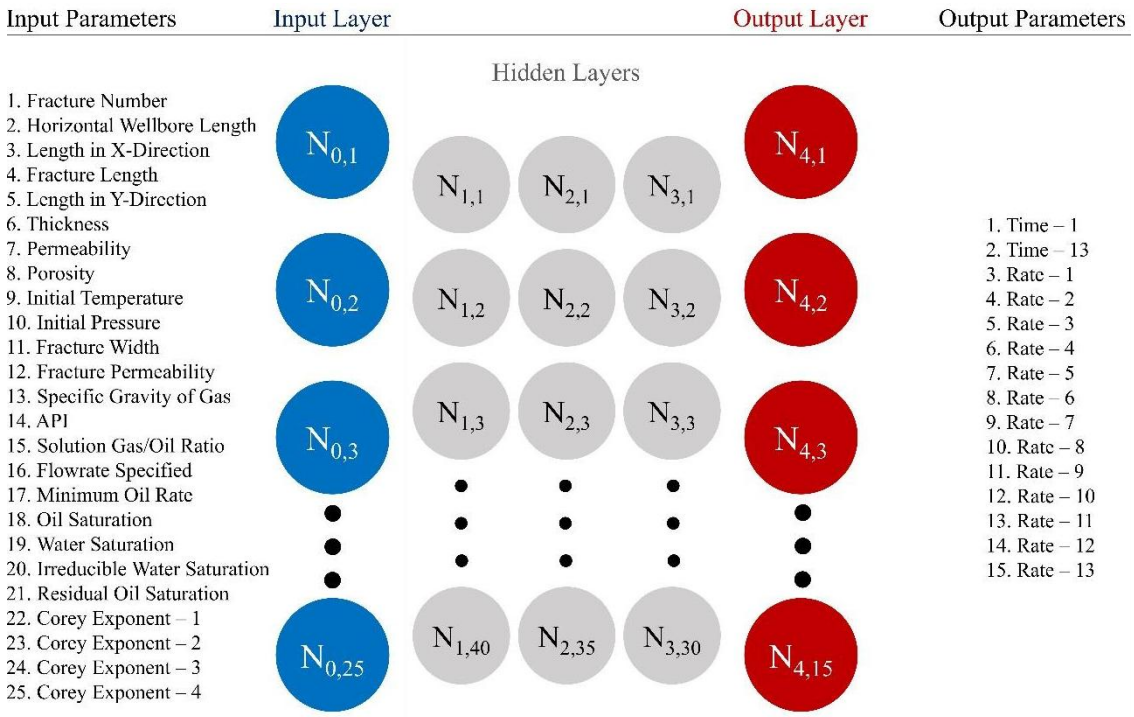

Figure 2. Schematic view of the ANN model.

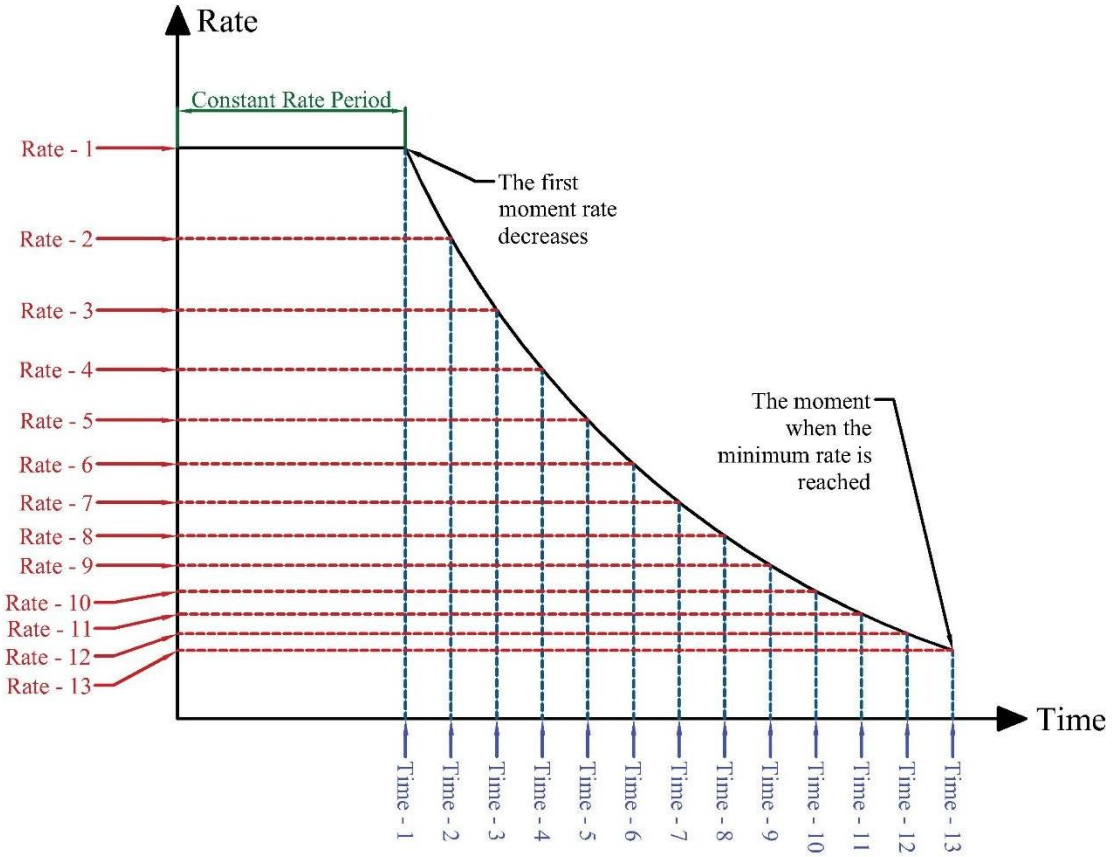

Figure 3. Display of outputs on a sample production graph.

Findings

The results obtained from the training and testing phases showed that the model was able to successfully predict production performances under different reservoir conditions. The average error rate was below 8%, which proved the high accuracy of the model. The model was particularly successful in predicting oil production rates (average error 4-5%). Moreover, error rates down to 1% towards the minimum rate levels (Figure 3) balance Time - 1 and Time - 13 errors which has the most error percentage (~%20). The average error percentages are shown in Figure 4. As can be seen, there is a higher error rate in the first- and last-time data compared to the others. This is due to the combination of some randomly generated extreme parameters. However, the success of estimating the rate data compensate the error rate of time data, and provide overall average error is 8%. The production graph of an example scenario was plotted with both ANN and simulation and compared (Figure 5). This method significantly reduced the production performance analysis time compared to traditional simulation methods and provided consistent predictions under different reservoir conditions. This model has become a useful tool for reservoir engineers in fracture design and production planning.

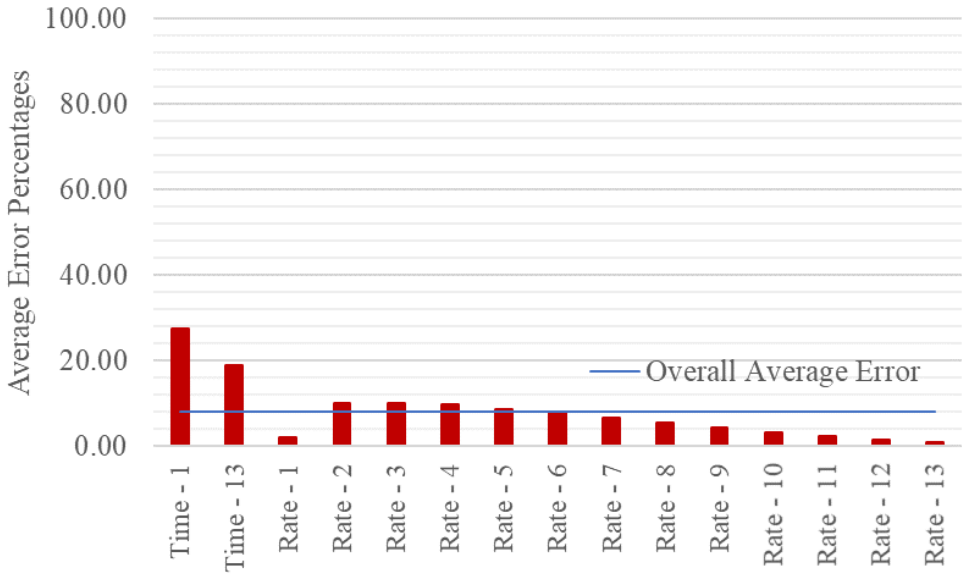

Figure 4. Average error percentages for time and rate prediction.

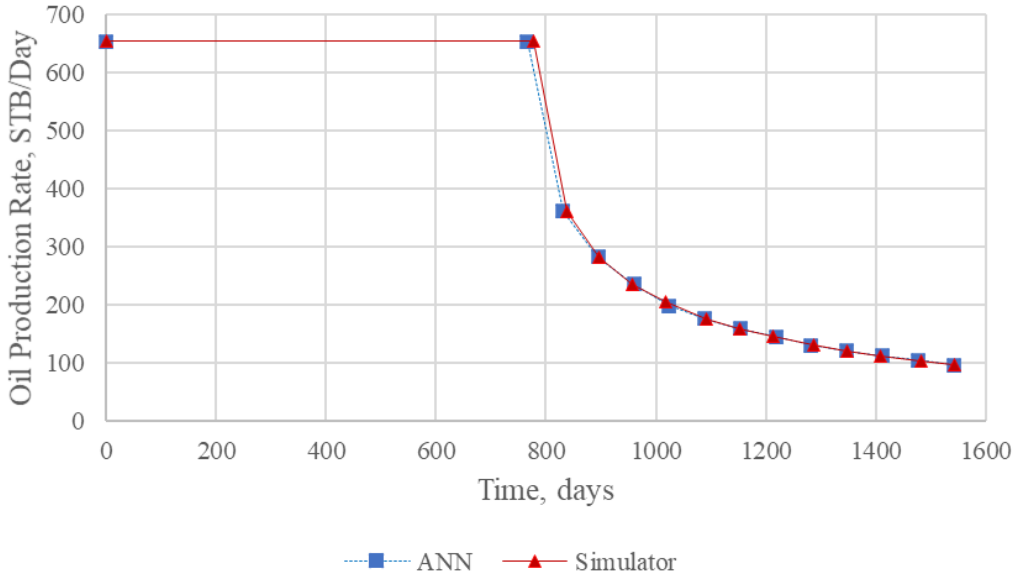

Figure 5. Comparison of production data of a sample scenario from ANN and simulator.

This example is a scenario consisting of random parameters created for ANN model. The input data of this scenario is listed in Table 2, and the error percentages of the outputs according to the simulation data are listed in Table 3. The overall average error for time data of this highly successful scenario is 1.11%, and the overall average error for rate data is 0.503%.

Table 2. Input parameters of the sample scenario.

Parameters	Value	Unit	Parameters	Value	Unit
Number of Fractures	26	-	API	46	-
Horizontal Wellbore Length	1675.52	ft	Solution Gas/Oil Ratio	1627.18	scf/STB
Length in X-Direction	2453.96	ft	Flowrate Specified	654	STB/D
Length of Fracture	628.63	ft	Minimum Oil Rate	95.69	STB/D
Length in Y-Direction	970.53	ft	Oil Saturation	71	%
Thickness	263.38	ft	Water Saturation	29	%
Permeability	0.08	mD	Irreducible Water Saturation	0.08	-
Porosity	9.99	%	Residual Oil Saturation	0.29	-
Initial Temperature	171.35	°F	Corey Exponents - 1	1.55	-
Initial Pressure	4235.46	psi	Corey Exponents - 2	1.41	-
Width of Fracture	0.08	inch	Corey Exponents - 3	1.83	-
Permeability of Fracture	3833.53	mD	Corey Exponents - 4	1.29	-
Specific Gravity of Gas	0.81	-			

Table 3. Error percentages of sample scenario data compared to the simulator.

Error Percentages				
Time - 1	**Time - 13**	**Rate - 1**	**Rate - 2**	**Rate - 3**
1.477	0.741	0.421	1.117	0.923
Rate - 4	**Rate - 5**	**Rate - 6**	**Rate - 7**	**Rate - 8**
0.882	0.895	0.673	0.554	0.329
Rate - 9	**Rate - 10**	**Rate - 11**	**Rate - 12**	**Rate - 13**
0.357	0.246	0.103	0.042	0.002
Overall Time Error: 1.11% - Overall Rate Error: 0.503%				

Conclusion

This research was focused on building an ANN model that can approximate the productivity of horizontally fractured tight oil sandstone reservoirs. Using commercial software, a set of simulations was developed for specific input constraints such as porosity, permeability, fracture characteristics, and reservoir condition. In turn, oil output parameters incorporated the oil production rate, total production time, and cumulative oil production volume. The ANN model was trained and validated using 3369 cleaned datasets and achieved an average rate of error below 8% on all datasets. It was evident that the model was able to rapidly and accurately estimate production performance which decreased computational cost when juxtaposed with brute force numerical simulations. The ANN's ability to increase the efficiency of decision-making for reservoir engineers in production forecasting and fracture optimization makes this approach compelling.

References

Boak, J., & Kleinberg, R. (2020). Shale Gas, Tight Oil, Shale Oil and Hydraulic Fracturing. *Future Energy*, 67-95.

CMG. (2015). *CMG IMEX Reservoir Simulation Software, version 2015.* Calgary, Alberta: Computer Modeling Group Ltd.

Ostojic, J., Rezaee, R., & Bahrami, H. (2012). Production performance of hydraulic fractures in tight gas sands, a numerical simulation approach. *Journal of Petroleum Science and Engineering*, 75-81.

Yao, J., Deng, X., Zhao, Y., Han, T., Chu, M., & Pang, J. (2013). Characteristics of tight oil in Triassic yanchang formation, Ordos Basin. *Petroleum Exploration and Development*, 161-169.

PHYSICS ENGINEERING

Condensed Matter Physics

High Energy and Particle Physics

Mathematical Physics

Optics and Photonics

Dynamo Process in Proto-Neutron Stars

İrem Bakır[a], Kazım Yavuz Ekşi[a]

[a] Istanbul Technical University, Physics Engineering Department, Physics Engineering Program, Türkiye
bakirir@itu.edu.tr

Keywords: Dynamo, Magnetic Fields, Magnetohydrodynamics (MHD), Stars: Magnetars, Stars: Neutron.

Aim

The primary aim of this study is to address the seemingly contradictory trends in the formation of magnetars. Magnetars, a subset of young neutron stars, possess extremely strong magnetic fields. The conventional models explaining the origin of such intense magnetic fields often require very specific and extreme conditions. These conditions appear incompatible with the observed birth rates of magnetars, which are comparable to the rates of core-collapse supernovae. To reconcile this discrepancy, we propose that both pulsars and magnetars undergo a dynamo process during the proto-neutron star (PNS) stage. Central compact objects (CCOs) are presented as the exception, not participating in the dynamo process.

Material and Method

To explore this hypothesis, we employ a shear-driven dynamo model for the generation of magnetic fields in PNSs. This model is an adaptation of a one-dimensional dynamo model initially proposed by Wickramasinghe et al. (2014) for magnetic field generation in white dwarf mergers. The original model is extended to incorporate the unique parameters and evolutionary characteristics of PNSs, specifically addressing the effects of the changing radius and gravitational mass of the PNS. The dynamo model describes how kinetic energy from the motion of a conductive fluid can be converted into magnetic energy. In the context of a PNS, this involves the interaction of differential rotation (where different parts of the star rotate at different speeds) and convection (the rising and falling of hot and cold material). The model is rooted in the principles of magnetohydrodynamics (MHD), which governs the dynamics of electrically conducting fluids in the presence of magnetic fields. The fundamental equation used is the magnetic induction equation. We apply the mean-field dynamo model, where large-scale magnetic fields are generated by small-scale turbulent flow. This approach simplifies the complex MHD equations by separating the fields into mean and fluctuating components. The evolution of the toroidal (B_φ) and poloidal (B_p) magnetic field components are described using reduced dynamical equations, derived from the mean-field dynamo equations. These equations account for the generation and diffusion of the magnetic fields, as well as the effects of the shrinking radius of the PNS. The model also incorporates criteria for the stability of the magnetic fields. These criteria, based on the ratio of magnetic energy to gravitational potential energy, determine whether the fields will decay due to instabilities. The model considers the transport of angular momentum within the PNS, which affects the shear rate that drives the dynamo process. This includes the effects of viscous processes, magnetorotational instability (MRI), and convection. The model incorporates the changing radius and gravitational mass of the PNS as it evolves, using exponential decay functions based on data from Camelio et al. (2017). The evolution of the spin angular velocity is also considered, primarily focusing on the effects of the changing moment of inertia. The model equations are solved numerically using the Runge-Kutta method. The initial parameters are set to be representative of a PNS, and the implications of varying these parameters are studied.

Findings

The numerical simulations reveal several key dependencies and evolutionary paths for PNSs. Depending on the initial rotational period at the onset of its development, a PNS can transform into a magnetar, a low-B magnetar, or a normal pulsar. The dynamo process amplifies the initial magnetic fields inherited from the progenitor star. The toroidal field grows until it reaches a saturation value, while the poloidal field also increases and approaches its saturation value. The shear rate, which drives the dynamo process, reaches a maximum value during the contraction phase of the PNS and then gradually declines due to the increasing internal viscosity. The saturation values of the magnetic fields are sensitive to several parameters:

Higher initial shear rates lead to significantly enhanced saturation values of the magnetic fields.
The saturation value of the poloidal field exhibits a positive correlation with α, while the saturation value of the toroidal field increases less steeply with α.
As the buoyancy factor increases, the poloidal field experiences an increment; however, for a > 0.5, the rate of this increase becomes slower. The toroidal field increases with the buoyancy factor for a < 1.7, whereas for a > 1.7, it decreases with a.
Both fields exhibit an increasing trend with the initial mass of the PNS, but the enhancement in the saturated toroidal field strength is comparatively less pronounced than that observed in the saturated poloidal field strength.
When the PNS undergoes a dynamo mechanism with a larger initial radius, the magnetic fields reach higher intensities at the point of saturation.
The saturated fields show only a minimal dependence on Bp,0, and Bφ,0 has nearly no influence on them. In short, the initial values of the poloidal and toroidal fields are not important in setting the final values of the fields in the dynamo process.
A PNS transitions into a magnetar following the dynamo process with a rotational period of P ∼ 2−3 ms and magnetic field components up to Bp ∼ 1014 G, Bφ ∼ 1016 G. It is also observed that it has the potential to ultimately become a high-magnetic field pulsar, exhibiting a strong toroidal magnetic field ∼ 1015 G.
The saturation values of the fields increase as the average density grows, up to a certain value. However, after exceeding this threshold, the fields begin to show an inverse relationship and decrease as the average density increases.
The dynamo process is terminated smoothly by increasing the viscosity after 45 seconds, representing the cooling and crust formation of the PNS.
Central compact objects (CCOs) are suggested not to participate in the dynamo process, as their magnetic fields can be explained by flux conservation alone. Their slower initial periods (P0 ≃ 100 milliseconds) are unlikely to trigger dynamo action.

Conclusion

The study concludes that the α − Ω dynamo process during the PNS phase can explain the observed variety of neutron stars, including magnetars, low-B magnetars, normal pulsars, and high-field pulsars. The initial conditions of convective flow and rotation rate, as well as internal structural parameters, play a crucial role in determining the final magnetic field strengths. PNSs with very rapid rotation rates are more likely to become magnetars, while those with more moderate spin rates can evolve into high-magnetic field pulsars or normal pulsars. The model suggests that normal pulsars with Bp ≳ 1011 G might also exhibit Bφ ∼ 1015 G, which is supported by the existence of low-magnetic field magnetars and magnetar behavior observed from some rotationally-powered pulsars. We propose that all neutron stars may have small-scale fields, but the dynamo action organizes these fields into dipole and toroidal fields. The relatively strong small-scale fields of CCOs could be attributed to the fact that they have not undergone a dynamo process

References

Camelio, G., Lovato, A., Gualtieri, L., Benhar, O., Pons, J. A., & Ferrari, V. (2017). Evolution of a proto-neutron star with a nuclear many-body equation of state: Neutrino luminosity and gravitational wave frequencies. Physical Review. D/Physical Review. D., 96(4). https://doi.org/10.1103/physrevd.96.043015.
Guilet, J., Reboul-Salze, A., Raynaud, R., Bugli, M., & Gallet, B. (2022). MRI-driven dynamo at very high magnetic Prandtl numbers. Monthly Notices of the Royal Astronomical Society, 516(3), 4346–4353. https://doi.org/10.1093/mnras/stac2499.
Moffatt, H. K. (1978). Magnetic field generation in electrically conducting fluids. In Cambridge University Press eBooks. http://ci.nii.ac.jp/ncid/BA10562419.
Thompson, C., & Duncan, R. C. (1993). Neutron star dynamos and the origins of pulsar magnetism. The Astrophysical Journal, 408, 194. https://doi.org/10.1086/172580.
Wickramasinghe, D. T., Tout, C. A., & Ferrario, L. (2013). The most magnetic stars. Monthly Notices of the Royal Astronomical Society, 437(1), 675–681. https://doi.org/10.1093/mnras/stt1910.

Constraints on New Physics with Light Mediators and Generalized Neutrino Interactions via Coherent Elastic Neutrino Nucleus Scattering

Sevgi Karadağ[a,b], Muhammed Deniz[c], Henry Tsz-King Wong[b]

[a] Istanbul Technical University, Faculty of Science and Letters, Physics Engineering Program (PhD), Turkiye
[b] Academia Sinica, Institute of Physics, Taiwan
[c] Dokuz Eylul University, Department of Physics, Turkiye
karadags@itu.edu.tr

Keywords: Neutrino Physics, Beyond Standard Model, Non-Standard Interactions.

Aim

Neutrino interactions with matter have long been considered promising avenues for uncovering new physics phenomena. Coherent Elastic Neutrino-Nucleus Scattering (CEνNS), described by Eq. (1), serves as a crucial channel for testing the Standard Model (SM) of electroweak theory at low energies and opens up numerous opportunities to expand our understanding of physics. It also provides a unique probe for exploring physics beyond the SM (BSM). Particularly, probing non-standard interactions (NSI) with neutrino-nucleus scattering has been a subject of intense interest in recent years.

$$\nu_\alpha\left(\underline{\nu}_\alpha\right) + A(Z,N) \rightarrow \nu_\alpha\left(\underline{\nu}_\alpha\right) + A(Z,N) \ , \tag{1}$$

These studies have investigated various NSI scenarios, such as those based on simplified models focusing on light mediators, model-independent approaches effective in the high mediator mass regime, and exotic neutral current interactions, along with experimental observables and implications for neutrino flavor physics and astrophysical processes.

This work aims to provide comprehensive NSI analysis for accelerator-based (COHERENT) and reactor-based (TEXONO) CEνNS experiments and to present constraints on the relevant parameters using recent TEXONO pPC-Ge (2024), TEXONO nPC-Ge (2016), and COHERENT CsI and LAr data for comparison. All possible Lorentz-invariant interaction types—vector (V), axialvector (A), scalar (S), pseudoscalar (P), and tensor (T)—are investigated within both simplified model and model-independent approaches, offering a broad and systematic exploration of new physics scenarios.

Material and Method

CEνNS, which involves neutral-current (NC) interactions between neutrinos and quarks within an atomic nucleus, is a tree-level process described within the SM. In this process, neutrinos interact coherently with a nucleus through neutral boson exchange at low energies, as illustrated in Figure 1.

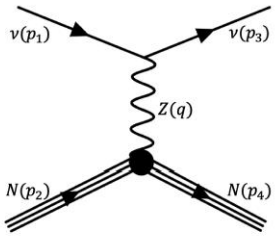

Figure 1: A tree-level Feynman-diagram of CEνNS process.

The process gives the largest cross-section compared to other neutrino interactions so far. The cross-section is enhanced by the square of the neutron number, as demonstrated in Equations (2), (3), and (4), making heavy nuclei ideal targets. Specifically, Eq. (2) defines the cross-section,

$$\left[\frac{d\sigma}{dT_N}\right]_{SM} = \frac{G_F^2 m_N}{4\pi}\left(Q_{SM_V}^2 K_V + Q_{SM_A}^2 K_A\right) \quad (2)$$

Eq. (3) describes the kinematic terms,

$$K_V = 1 - \frac{m_N T_N}{2E_\nu^2} - \frac{T_N}{E_\nu} + \frac{T_N^2}{2E_\nu^2} \quad , \quad K_A = 1 + \frac{m_N T_N}{2E_\nu^2} - \frac{T_N}{E_\nu} + \frac{T_N^2}{2E_\nu^2} \quad (3)$$

and Eq. (4) describes the vector and axialvector components of the SM weak charge,

$$Q_{SM_V} = [Z(1 - 4\theta_W) - N]\, F_V(q^2) \quad , \quad Q_{SM_A}^2 = \frac{8\pi}{2J+1}\left(\Delta_u^p - \Delta_d^p\right)^2 S_{11}^T(q^2), \quad (4)$$

where, θ_W is the Weinberg angle, J is the total angular momentum of the nucleus, $F_V(q^2)$ is the nuclear form factor, and $S_{11}^T(q^2)$ represents the spin structure functions.

Detecting such process is challenging due to the nuclear recoil energy being confined to the low keV range. This challenging objective was finally accomplished with the advancement of accelerator neutrino technology in 2017 by the COHERENT Collaboration, a few decades after its initial formulation. Since the first detection of CEνNS, numerous efforts, including those by the TEXONO Collaboration, have been made to detect the process and improve our understanding of this phenomenon.

To explore potential deviations from the Standard Model (SM), we consider new physics scenarios within the framework of simplified models involving light mediators (V, A, S, P, and T). The corresponding differential cross-sections for these new mediators are given as,

$$\begin{aligned}
\left[\frac{d\sigma}{dT_N}\right]_V &= \frac{G_F^2 m_N}{4\pi}\left(\frac{2Q_V^2}{\left(m_V^2+2m_N T_N\right)^2} + \frac{2\sqrt{2}\, Q_V Q_{SM_V}}{m_V^2+2m_N T_N}\right)|F_V(q^2)|^2\, K_V\,, \\
\left[\frac{d\sigma}{dT_N}\right]_A &= \frac{G_F^2 m_N}{4\pi}\left(\frac{2Q_A^2}{\left(m_A^2+2m_N T_N\right)^2}\right) S_{00}^T(q^2)\, K_A\,, \\
\left[\frac{d\sigma}{dT_N}\right]_S &= \frac{G_F^2 m_N}{4\pi}\frac{Q_S^2}{\left(m_S^2+2m_N T_N\right)^2}\, |F_S(q^2)|^2\, K_S\,, \\
\left[\frac{d\sigma}{dT_N}\right]_P &= \frac{G_F^2 m_N}{4\pi}\frac{Q_P^2}{\left(m_P^2+2m_N T_N\right)^2}\, |F_P(q^2)|^2\, K_P\,, \\
\left[\frac{d\sigma}{dT_N}\right]_T &= \frac{G_F^2 m_N}{4\pi}\frac{Q_T^2}{\left(m_T^2+2m_N T_N\right)^2}\left[8S_{00}^T(q^2)\, K_V + 16S_{00}^L(q^2)\left(1 - \frac{T_N}{E_\nu}\right)\right],
\end{aligned} \quad (5)$$

where $K_S = \frac{m_N T_N}{E_\nu^2} + \frac{T_N^2}{2E_\nu}$ and $K_P = \frac{T_N^2}{2E_\nu^2}$. The nuclear form factors $|F_X(q^2)|^2$ associated with each interaction type are modeled using the ***Helm form factor*** approach. The axialvector and tensor cases correspond to spin-dependent interactions, and their nuclear structure captured by ***spin structure functions,*** $S_{00}^T(q^2)$ and $S_{00}^L(q^2)$, which correspond to transverse and longitudinal spin responses,respectively. In Eq. (5), new charges are defined as $Q_X = g_{X\nu} g_{XN}/G_F$, where $g_{X\nu}$ and g_{XN} denote the couplings of new mediators to neutrino and nucleus, respectively. Here, $X = V, A, S, P, and\ T$ indicates the interaction type.

To investigate NSI in a model-independent framework, the new couplings defined in the simplified model can be converted to epsilon parameter space, usually denoted as $\varepsilon_{\alpha\beta}^{qX}$, using the relation

$$\varepsilon_{\alpha\beta}^{qX} \simeq \frac{g_{X\nu} g_{XN}}{\sqrt{2} G_F m_X^2} \quad . \quad (6)$$

This relation allows the differential cross-sections for light mediator models, given in Eq. (5), to be reformulated in terms of model-independent NSI parameters.

Our analysis uses data from both COHERENT and TEXONO experiments. The COHERENT experiment at the Spallation Neutron Source (SNS) detects neutrinos from stopped-pion decays, utilizing CsI(Na) and liquid argon (LAr) detectors. These experiments operate at higher neutrino energies and larger momentum transfer (q^2) regime

and allow interactions with multiple neutrino flavors (ν_μ, $\underline{\nu}_\mu$, ν_e). On the other hand, the TEXONO Collaboration is conducting an intensive research program on low-energy neutrino physics (< 10 MeV) at the Kuo-Sheng Nuclear Power Plant in Taiwan. In 2016, the collaboration conducted an experiment using a high-purity n-type point-contact germanium (nPC-Ge) detector cooled by liquid nitrogen with a threshold energy of 300 eV. In 2024, they upgraded experiment facilities with an advanced p-type point-contact germanium (pPC-Ge) detector, which has an improved threshold energy of 200 eV. TEXONO experiment detects low-energy electron antineutrinos ($\underline{\nu}_e$), reducing flux uncertainties associated with the presence of multiple neutrino flavors in accelerator-based experiments.

In this work, we employ a minimum$-\chi^2$ approach to derive NSI constraints from event rate predictions, considering both simplified model and model-independent frameworks. For all five interaction types (V, A, S, P, and T), we explore mass-coupling ($M_X - g_X$) parameter space in the simplified model, while in the model-independent case, we investigate the corresponding flavor-conserving (FC) and flavor-violating (FV) $\varepsilon_{\alpha\beta}^{qX}$ −parameter spaces for vector-type interaction.

Findings

Our results present the first NSI analysis of the TEXONO experiment and highlight the complementary nature of reactor and accelerator neutrino experiments in probing NSI. COHERENT experiments generally provide stronger bounds due to their higher neutrino energy range and multiple neutrino flavors, especially for FV NSI (as shown in Figure 2), while TEXONO experiment with pPC-Ge (2024) data offers competitive constraints for FC scenarios (as seen in Figure 3), and light mediator models (as seen in Figure 4) thanks to its sensitivity to low-energy neutrinos and reduced flux uncertainties.

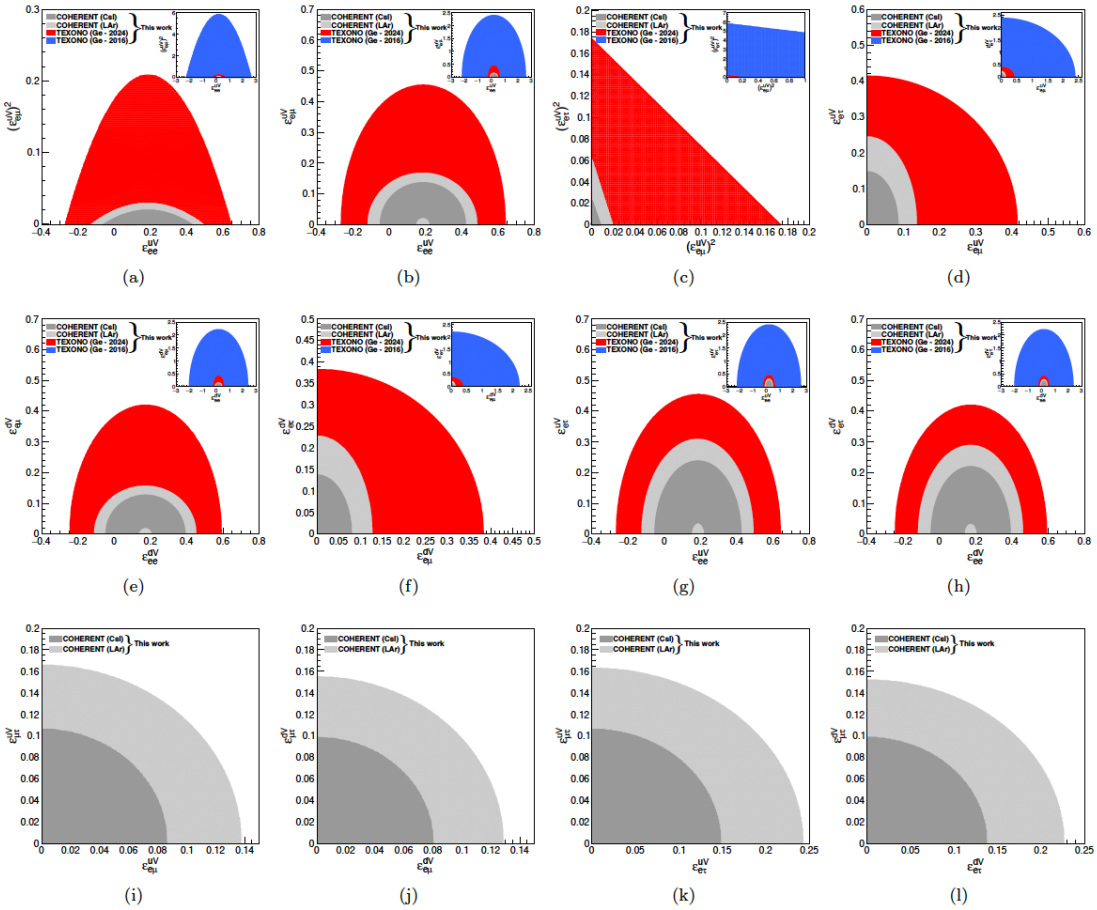

Figure 2: The 90% CL allowed region in the following parameter spaces for vector-type NSI in the FV case: $\varepsilon_{ee}^{uV} - \left(\varepsilon_{e\mu}^{uV}\right)^2$, $\varepsilon_{ee}^{uV} - \varepsilon_{e\mu}^{uV}$, $\left(\varepsilon_{e\mu}^{uV}\right)^2 - (\varepsilon_{e\tau}^{uV})^2$, $\varepsilon_{e\mu}^{uV} - \varepsilon_{e\tau}^{uV}$, $\varepsilon_{ee}^{dV} - \varepsilon_{e\mu}^{dV}$, $\varepsilon_{e\mu}^{dV} - \varepsilon_{e\tau}^{dV}$, $\varepsilon_{ee}^{uV} - \varepsilon_{e\tau}^{uV}$, $\varepsilon_{ee}^{dV} - \varepsilon_{e\tau}^{dV}$, $\varepsilon_{e\mu}^{uV} - \varepsilon_{\mu\tau}^{uV}$, $\varepsilon_{e\mu}^{dV} - \varepsilon_{\mu\tau}^{dV}$, $\varepsilon_{e\tau}^{uV} - \varepsilon_{\mu\tau}^{uV}$, and $\varepsilon_{e\tau}^{dV} - \varepsilon_{\mu\tau}^{dV}$.

TEXONO pPC-Ge (2024) data shows significant improvements over the previous TEXONO nPC-Ge (2016) data, as shown in Figures 2a-h, 3a, and 4a-e. In Figures 2i-l and 3b-d, bounds are only provided for the COHERENT experiment, which benefits from a multiple-flavor neutrino flux. In contrast, no limits can be provided for TEXONO in these scenarios due to its single-type neutrino flavor.

For light mediators in simplified model, the enhanced sensitivity of TEXONO pPC-Ge strengthens constraints in the low-momentum transfer region, and yields results competitive with those of other reactor neutrino experiments, as seen in Figures 4a and 4c. This is crucial for detecting potential new light bosons, which could mediate novel interactions beyond the SM. The new constraints from TEXONO pPC-Ge are comparable to those from COHERENT in most cases and even surpass them in scalar case in Figure 4c.

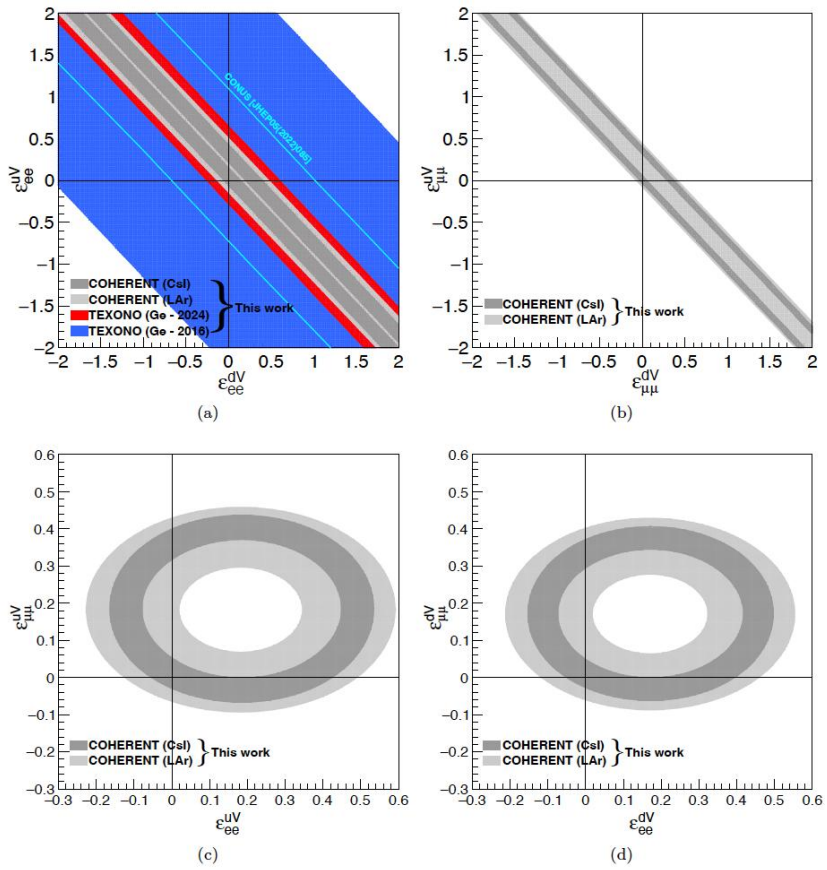

Figure 3: The 90% CL allowed region in the $\varepsilon_{ee}^{dV} - \varepsilon_{ee}^{uV}$, $\varepsilon_{\mu\mu}^{dV} - \varepsilon_{\mu\mu}^{uV}$, $\varepsilon_{ee}^{uV} - \varepsilon_{\mu\mu}^{uV}$, and $\varepsilon_{ee}^{dV} - \varepsilon_{\mu\mu}^{dV}$ parameter spaces for vector-type NSI in the FC case.

Among the five interaction types, the pseudoscalar case (Figure 4d) yields the weakest constraints due to its cross-section being heavily suppressed by nuclear recoil energy. Furthermore, axialvector and tensor interactions (Figures 4b and 4e) are also less constrained, as they are spin-dependent interactions and have contributions only from unpaired nucleons in the nucleus. In contrast vector and scalar type interactions (Figures 4a and 4c) are the most tightly constrained, with cross-sections scaling with the square of neutron number.

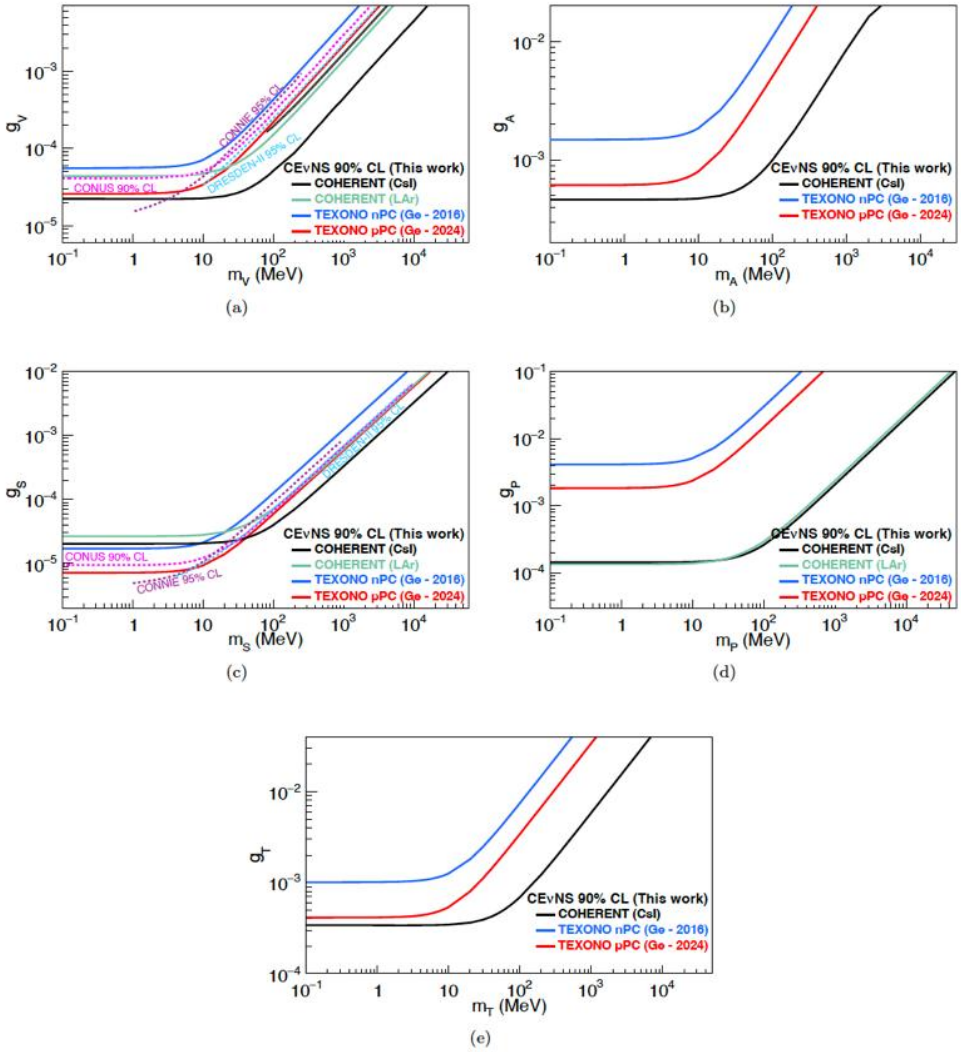

Figure 4: Bounds at 90% CL are presented for (a) vector, (b) axialvector, (c) scalar, (d) pseudoscalar, and (e) tensor mediator masses and couplings, derived from the TEXONO nPC-Ge and pPC-Ge, and COHERENT CsI(Na) and LAr experiments.

These findings confirm that both experimental approaches contribute uniquely to probing different NSI parameter spaces, reinforcing the need for complementary experimental strategies.

Conclusion

CEvNS has progressed from a theoretical concept to a measurable phenomenon, and its observation has opened a broad research program exploring neutrino properties, dark matter detection, nuclear structure, astrophysics, and physics beyond the Standard Model (BSM). In this context, our work provide valuable insights into the interplay between different NSI interaction types and experimental conditions. These findings highlight the critical role of future CEνNS experiments in refining NSI constraints and advancing our understanding of neutrino interactions. Advancements in detector technology, lower energy thresholds, and increased event statistics will further improve sensitivity to NSI effects. Future experiments with enhanced capabilities, including next-generation neutrino detectors and dark matter experiments, will provide additional opportunities to test BSM physics. As part of a global effort, TEXONO is emerging as a competitive player in the CEvNS landscape, with strong potential to lead future constraints, especially in the reactor neutrino sector. Our study contributes to these efforts by establishing a robust framework for NSI analysis using both simplified model and model-independent approaches.

References

Ackermann, N., et al. (2025). First observation of reactor antineutrinos by coherent scattering. *arXiv preprint*, arXiv:2501.05206. https://arxiv.org/abs/2501.05206.

Akimov, D., et al. (COHERENT Collaboration). (2017). Observation of coherent elastic neutrino-nucleus scattering. *Science, 357*(6356), 1123–1126. https://doi.org/10.1126/science.aao0990.

Akimov, D., et al. (COHERENT Collaboration). (2022). Measurement of the coherent elastic neutrino-nucleus scattering cross section on CsI by COHERENT. *Physical Review Letters, 129*(8), 081801. https://doi.org/10.1103/PhysRevLett.129.081801.

Freedman, D. Z. (1974). Coherent neutrino nucleus scattering as a probe of the weak neutral current. *Physical Review D, 9*(5), 1389. https://doi.org/10.1103/PhysRevD.9.1389.

Freedman, D. Z., Schramm, D. N., & Tubbs, D. L. (1977). The weak neutral current and its effects in stellar collapse. *Annual Review of Nuclear and Particle Science, 27*, 167–207. https://doi.org/10.1146/annurev.ns.27.120177.001123.

Helm, R. H. (1956). Inelastic and elastic scattering of 187-MeV electrons from selected even-even nuclei. *Physical Review, 104*(5), 1466–1475. https://doi.org/10.1103/PhysRev.104.1466.

Hoferichter, M., Menéndez, J., & Schwenk, A. (2020). Coherent elastic neutrino-nucleus scattering: EFT analysis and nuclear responses. *Physical Review D, 102*(7), 074018. https://doi.org/10.1103/PhysRevD.102.074018.

Karadag, S., et al. (TEXONO Collaboration). (2025). Constraints on new physics with light mediators and generalized neutrino interactions via coherent elastic neutrino nucleus scattering. *arXiv preprint*, arXiv:2502.20007. https://arxiv.org/abs/2502.20007.

Karmakar, S., et al. (TEXONO Collaboration). (2025). New limits on coherent neutrino-nucleus elastic scattering cross section at the Kuo-Sheng reactor neutrino laboratory. *Physical Review Letters*, 134(12),121802. https://doi.org/10.1103/PhysRevLett.134.121802.

Wong, H. T., et al. (2006). Research program towards observation of neutrino-nucleus coherent scattering. *Journal of Physics: Conference Series, 39*, 266. https://doi.org/10.1088/1742-6596/39/1/064.

PHYSICS ENGINEERING

Condensed Matter Physics

High Energy and Particle Physics

Mathematical Physics

Optics and Photonics

Investigation of Structural and Optoelectronic Properties of metal/ZnS Junction under Density Functional Theory (DFT)

Haris Kulosmanovic[a], Murat Çalışkan[b]

[a] Yildiz Technical University, Graduate School of Science and Engineering, Physics MSc Program, Türkiye
[b] Yildiz Technical University, Department of Physics, Türkiye
haris.kulosmanovic@std.yildiz.edu.tr

Keywords: Density Functional Theory (DFT), Metal/ZnS Junction, Schottky Diodes, Optimization.

The combination of metal and semiconductor (metal/semiconductor junction) is one of the fundamental methods for creating active electronic components known as Schottky diodes. These diodes are renowned for their fast-switching speed and significantly lower forward voltage drop compared to conventional silicon diodes. Although it was developed quite early, even in the very beginnings of semiconductor technology, not enough material can be found in the available literature that explains what exactly happens during the formation of this junction at the quantum level. In order to better understand how the charges within the materials used in this work behave, we approached the investigation of individual properties of the materials and heterostructures composed of them under Density Functional Theory.

Aim

The aim of this thesis is to attempt to fill the gap that exists in the literature and theoretically explain the quantum nature of semiconductor devices formed using zinc sulfide. Also in this connection, certain physical properties of materials, metals and semiconductors, such as lattice constant, band structure, work function, etc., have been individually investigated. Finally, after all the research has been done, which will provide a better insight into the physical and optical properties of the combination of these materials, the possibility of using them in devices and for what purposes they could be useful will be discussed.

Material and Method

The materials studied in this work include metals (gold, silver, copper), while zinc sulfide (ZnS) served as the semiconductor.

Gold

Gold is a dense, soft, and malleable metal with a distinctive yellow luster, making it highly prized for both decorative and industrial applications. It has excellent conductivity of electricity and heat, and is highly resistant to corrosion and oxidation, contributing to its durability and widespread use in electronics and jewelry.

Silver

Silver is a lustrous, ductile, and highly conductive metal, known for having the highest electrical and thermal conductivity of any element. It is also relatively soft and malleable, with a brilliant white metallic appearance, making it valuable for use in jewelry, electronics, and as a reflective coating.

Copper (Cu)

Copper is a reddish-brown metal known for its excellent electrical and thermal conductivity, second only to silver among pure metals. It is highly malleable, ductile, and resistant to corrosion, making it widely used in electrical wiring, plumbing, and industrial applications.

Zinc sulfide (ZnS)

Zinc sulfide (ZnS) is a crystalline solid known for its wide bandgap, making it a valuable semiconductor material in optoelectronics. It exhibits luminescent properties and can appear in two primary crystal structures, zincblende and wurtzite, contributing to its use in applications like LEDs, infrared optics, and glow-in-the-dark materials.

Method

In this ongoing study, all calculations will be conducted using Density Functional Theory (DFT) with the GGA-PBE functional. The initial phase will involve optimizing the materials by determining the lattice constants, k-points grid, and cutoff energy (ENCUT) to ensure convergence and accuracy. Subsequently, a supercell will be constructed to model the metal/semiconductor junction. To analyze the electronic properties of the junction, planar average potential, charge density difference, and Bader charge analysis will be performed. Additionally, band structure calculations will be carried out for all materials to investigate their electronic behavior. These comprehensive calculations are expected to provide detailed insights into the structural and electronic properties of the materials and the metal/semiconductor interface.

Findings

Before starting any calculation, it is important to optimize the materials. Optimizations are done by performing the same calculation for different values of the same quantity for which we want to find the optimum. The goal of optimization is to find the ideal parameters for carrying out all further calculations and thus reduce their computational cost. The first optimization that needs to be done is the cutoff energy optimization. Cutoff energy, often denoted as ENCUT, is the maximum kinetic energy of the plane waves used in DFT calculations, determining the accuracy of the basis set for representing electronic wave functions (Fiolhais et al., 2003).

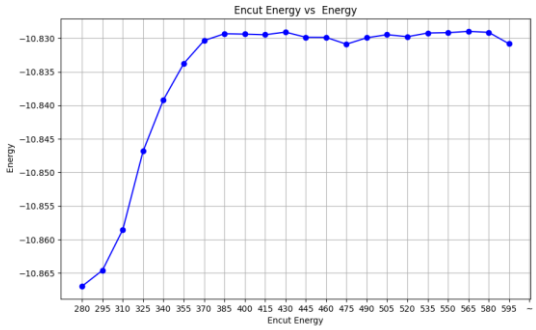

Figure 1. ENCUT optimization for silver.

As can be seen from the Figure 1, the cutoff energy values begin to converge after 400 eV, therefore we can freely use this cutoff energy value for further calculations. A similar thing was done for k-points optimization. In this optimization we determine the optimal grid of k-points in the Brillouin zone for numerical calculations, ensuring accurate sampling of electronic states while balancing computational efficiency (Lee, 2016).

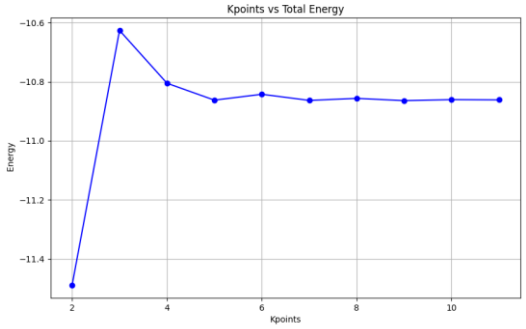

Figure 2. K-POINTS optimization for silver.

As shown in Figure 2, the total energy values begin to converge near a k-points value of 4. Finally, the crystal lattice optimization was performed and the lattice constant for which the crystal has minimal energy was found. The results obtained are quite similar to the results obtained in the experimental study of these crystals.

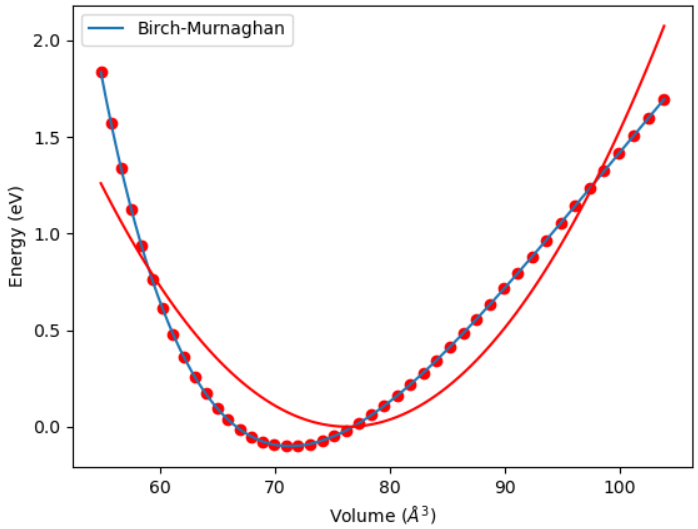

Figure 3. Lattice constant optimization for silver.

For example, the lattice constant of silver obtained in this work is 4.14 Å, which is in close agreement with the experimental value of 4.079 Å (Davey, 1925). Birch-Murnaghan equation of state fit was applied to the obtained data. The Birch-Murnaghan equation of state is widely used to fit the energy-volume relationship of materials, providing an accurate determination of the equilibrium lattice constant, bulk modulus, and its pressure derivative. This method is particularly effective for studying the structural properties of solids under compression or expansion, making it a standard tool in computational materials science (Birch, 1947).

$$P(V) = \frac{3B_0}{2}\left[\left(\frac{V_0}{V}\right)^{\frac{7}{3}} - \left(\frac{V_0}{V}\right)^{\frac{5}{3}}\right]\left\{1 + \frac{3}{4}(B_0' - 4)\left[\left(\frac{V_0}{V}\right)^{\frac{2}{3}} - 1\right]\right\}$$

Equation 1. Birch-Murnaghan equation of state.

Birch-Murnaghan equation of state is given in equation 1. Where:

- $P(V)$: Pressure as a function of volume
- V_0: Equilibrium volume (volume at zero pressure)
- B_0: Bulk modulus at zero pressure
- B'_0: Pressure derivative of the bulk modulus at zero pressure

The parameters from the Birch-Murnaghan equation of state for the silver crystal were found to be:

- $P(V)$ = -10.813086 GPa
- V_0 = 90.870389 Å^3
- B_0 = 5.771012 GPa
- B'_0 = 71.303748

After all elements were optimized, the formation of supercells was started, on which the behavior of the Schottky junction would be studied. First, by checking the mismatch ratios, it was determined that it was most favorable to work with the (111) plane in the case of each material. When the supercells (Au/ZnS, Ag/ZnS and Cu/ZnS) were formed, the ideal distances between the materials were found in a similar way as was done in the optimization of the material properties at the beginning. That is, the same calculation was performed for different values of the distance and the one with the lowest energy was found. It was also determined that the energy graph of the distance between the materials follows the Buckingham potential function (Fang et al., 2022). The optimal value for the Ag/ZnS junction is 3.246 Å. After this, Planar Average Potential, Charge density difference and Bader charge analysis calculations will be performed and after that the exact nature of these junctions will be determined.

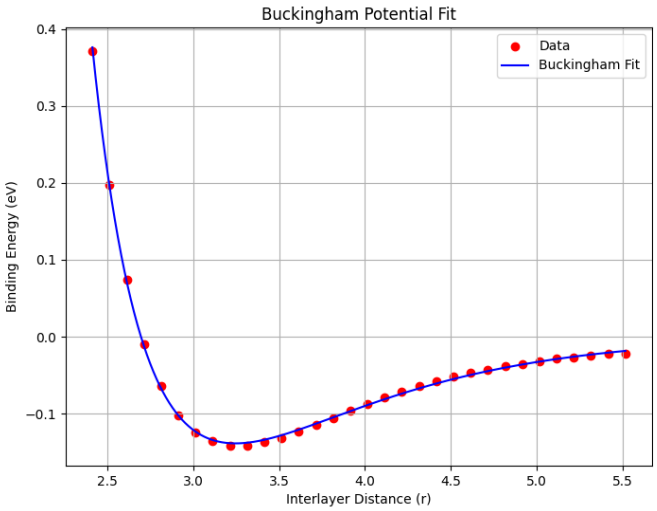

Figure 4. Optimal distance between Ag and ZnS slabs.

Conclusion

In this study, the structural and optoelectronic properties of metal/ZnS junctions were investigated using Density Functional Theory (DFT) with the GGA-PBE functional. The optimization of material properties, including lattice constants, k-points, and cutoff energy, provided a solid foundation for further calculations. The results showed close agreement with experimental values, particularly in the case of lattice constants, where the calculated value of 4.14 Å for silver closely matched the experimental value of 4.079 Å. The application of the Birch-Murnaghan equation of state further validated the accuracy of the structural optimizations. The formation of supercells for the metal/ZnS junctions, particularly focusing on the (111) plane, revealed that interlayer distances vs binding energy graph followed the Buckingham potential function. For instance, the optimal distance for the Ag/ZnS junction was determined to be 3.246 Å. These findings provide valuable insights into the electronic and structural properties of metal/ZnS interfaces, which are crucial for the development of efficient Schottky diodes and other optoelectronic devices. Future work will involve detailed analyses of planar average potential, charge density difference, and Bader charge to further elucidate the nature of these junctions. The results obtained in this study not only enhance our understanding of the quantum-level interactions in metal/semiconductor junctions but also pave the way for the design and optimization of advanced electronic and optoelectronic devices.

Acknowledgement

This paper has been written based on the preliminary studies of my ongoing master's thesis under the supervision of Doç. Dr. Murat Çalışkan in the Graduate School of Science and Engineering Master's Program at Yildiz Technical University.

References

Birch, F. (1947). Finite elastic strain of cubic crystals. *Phys. Rev., 71*, 809–824.
Davey, W. P. (1925). Precision measurements of the lattice constants of twelve common metals. *Phys. Rev., 25*, 753–761.
Fang, Q., Li, M., Zhao, X., Yuan, L., Wang, B., Xia, C., and Ma, F. (2022). van der waals graphene/mos 2 heterostructures: tuning the electronic properties and schottky barrier by applying a biaxial strain. *Materials Advances, 3*(1), 624–631.
Fiolhais, C., Nogueira, F., and Marques, M. (2003). A Primer in Density Functional Theory, volume 620.
Lee, J. G. (2016). Computational materials science: an introduction. CRC press.

PHYSICS ENGINEERING

Condensed Matter Physics

High Energy and Particle Physics

Mathematical Physics

Optics and Photonics

Imaging Ellipsometry for Material Characterization and Defect Analysis

Furkan Yıldız[a], Esra Zayim[b], Muharrem Aşar[c]

[a] Istanbul Technical University, Optics and Photonics, Türkiye
[b] Tubitak National Metrology Institute, Optics and Photonics, Türkiye
yildizf22@itu.edu.tr

Keywords: Classical Spectroscopic Ellipsometry, CUDA, Defect Analysis, Imaging Ellipsometry, Power Electronics.

Aim

This study focuses specifically on the detection and assessment of material imperfections, as well as on the quantification of the corresponding optical constants by utilizing imaging ellipsometry—a very modern and advanced analytical tool. Traditional methods in spectroscopic ellipsometry are faced with numerous complications in characterizing the freestanding behavior of materials in certain applications, such as in defect evaluation. As illustrated in Figure 1, the major hindrance is the relatively large beam spot size, which restricts the achievable spatial resolution, combined with model-dependent analyses that tend to oversimplify the complex nature of materials by disregarding local heterogeneities. As such, the aim of this study is the creation of a high-resolution Imaging Ellipsometer capable of substantially overcoming the limitations of traditional methods. While traditional methods continue to exhibit significant success in areas such as power electronics, semiconductor manufacturing, and advanced material sciences, this research aims to offer more sensitive and versatile equipment for material analysis. The aim section should be written in Times New Roman font, justified-alignment and in 10-point size.

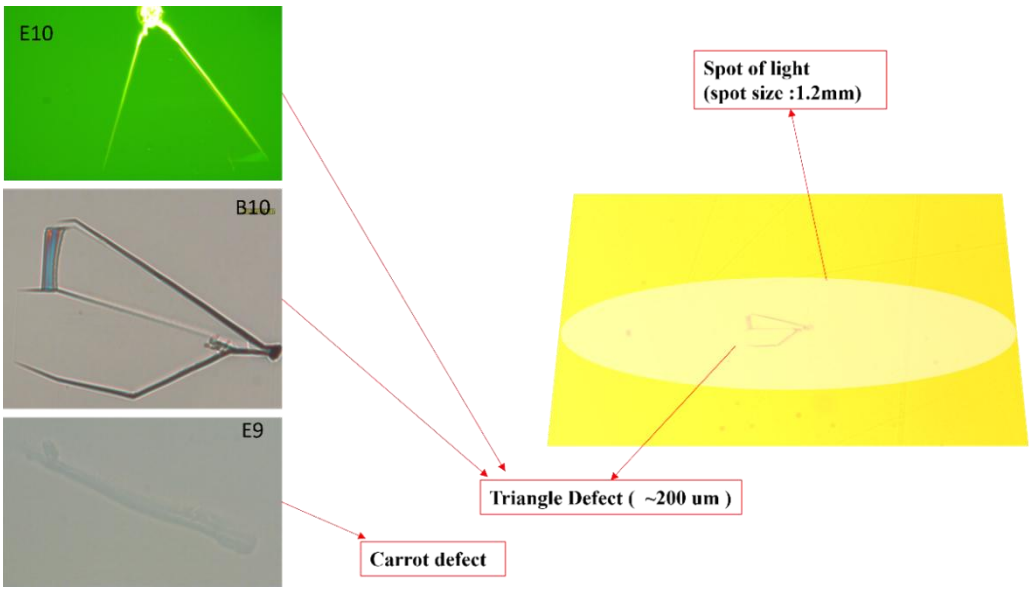

Figure 1. llustrate of the Defect size/shapes.

The impetus for such developments largely lies with the growing need for precision within material analysis that enables the evolution of nanotechnology and complex devices for different industries. Surface irregularities, structural defects, and subsurface inconsistencies largely impact the efficiency and reliability of materials that are utilized within complex technological systems. Even though conventional ellipsometry is well known for the ability of measurement of different optical properties such as refractive index and material thickness, it falls short of the precision needed for detection of these characteristics at the nanolevel. The Imaging Ellipsometer overcomes the shortcoming by combining the precision of imaging with state of the art algorithms and thereby optimizing the conventional procedures within the environments of academia and industry [1].

Material and Method

The Imaging Ellipsometry device, as shown in Figure 2, significantly differentiates itself from traditional systems by combining hundreds of complex components with highly complex computer techniques for the purpose of carrying out its goals. The core of the device lies with the tunable laser source that emits at fixed wavelength but with the capability of functioning at multiple discrete wavelengths of 633 nm, 612 nm, 604 nm, 594 nm, and 543 nm. The ability of the device to be tunable imbues it with the ability of analyzing materials under different conditions of optics and making it highly flexible and enabling complete wavelength-dependent material characterizations. The optics include the components of the motorized compensator and the analyzer that allow for precise control of the state of the transmitted light that it crucially needed for ellipsometry measurements. The device includes the complement of a highly numerical aperture of 0.75 Nikon Plan Fluorite objective that enables excellent transmitted light collecting capability and resolving of minute details on the surface of materials.

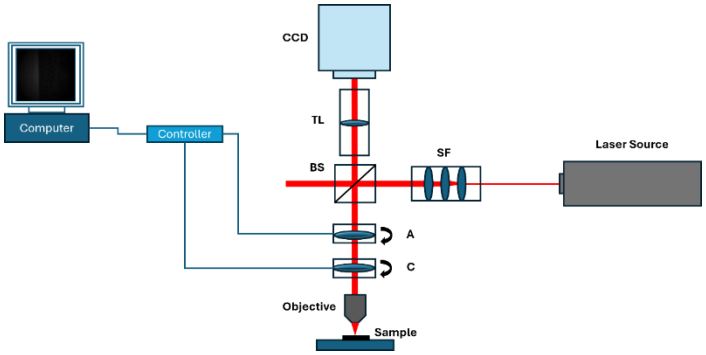

Figure 2. Schematic of a Imaging-ellipsometry optical configuration with rotary compensator and analyzer.

A beam splitter is used to precisely direct the light in the system, and a Retiga-R6 CCD camera successfully captures resulting optical information with high fidelity. The choice of the Retiga-R6 is important because of its sensitivity and pixel density, allowing the system to handle large datasets generated by imaging ellipsometry. Unlike traditional ellipsometry, which would measure a single point or a small area, this system analyzes information from over 5 million pixels, matching the high-resolution images it produces. This large increase in data volume required a new way of processing, leading to the development of CUDA-based software written in C++. By leveraging the parallel processing potential of GPU-based CUDA cores, the software skillfully manages the corresponding computational complexity, performing real-time optical signal analyses and reconstructing detailed maps of material properties.

A distinguishing feature of this Imaging Ellipsometer is the use of the unique single-arm geometric design over the more widespread dual-arm geometries of conventional systems. The dual-arm design splits the incident and reflection pathways of the light apart while the single-arm design converges these pathways into a more compact and efficient framework. Even with the introduction of difficulties by increased computational requirements, the use of a GPU counteracts these by making it easy for it to rapidly process lengthy data sets while making the feasible performance of operations within it more of a reality. The combination of these innovations at the hardware and the software levels produces a device that increases the resolution while it maintains efficiency of operation making it appropriate for industrial quality assurance processes and for the laboratory environments.

Findings

The findings of this study confirm the capability of the newly invented Imaging Ellipsometer system for overcoming the deficiencies of conventional spectroscopic ellipsometry. A thorough experimental study involving gallium nitride (GaN), silicon carbide (SiC), and several alternative substrates utilized for the purpose of power electronics and optoelectronic devices was conducted. The materials were chosen for study due to the prominence of their technological importance and the difficulties of characterizing the materials due mainly to the presence of the kind of defects that can compromise device performance. The Imaging Ellipsometer proved the ability of the equipment to find and study such types of defects with unmatched precision by identifying such characteristics of

the material such as the presence of microcracks, inclusions, and roughness of the surface that are often ignored or underassessed by conventional techniques.

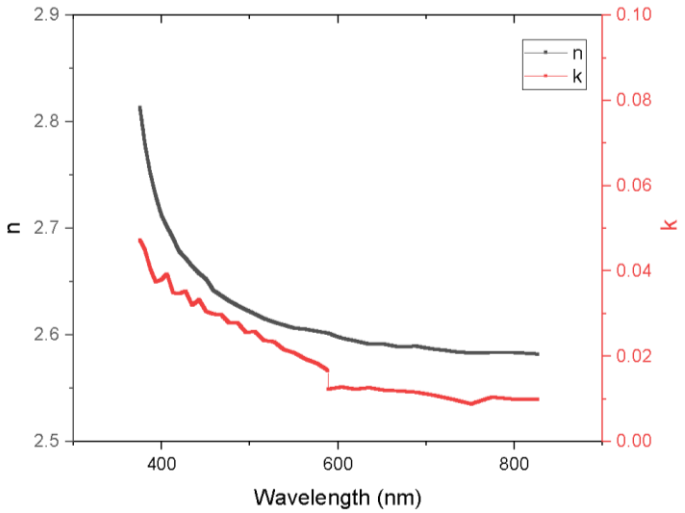

Figure 3. Optical constants of GaN:C determined from the fit.

Concurrently with the analysis of the defects, as shown in Figure 3, the system showed a remarkable capability to determine the optical constants of the material, namely the refractive index and the extinction coefficient. The measured values were compared with those obtained from standard spectroscopic ellipsometry, showing improved accuracy and spatial resolution. For example, in the case of GaN samples, the Imaging Ellipsometer produced highly detailed mappings of the optical properties that corresponded with the known positions of the defects, thus providing information on how these defects affect light interactions at the nanometer scale. Similarly, in the case of SiC samples, the system detected changes in the optical constants over the sample surface, leading to a wider understanding of material quality and homogeneity. The enhanced resolution of the Imaging Ellipsometer can be attributed to the high numerical aperture objective and pixel-level precision provided by the CCD camera; however, the latter's exceptional accuracy is mainly attributed to the powerful computational platform that supports the system. The software, which employs CUDA for parallel processing of millions of data points, ensures that fine details in material properties are retained—an element that is not present in conventional ellipsometry techniques. This ability is of particular importance for the analysis of thin films and multilayer structures, where even slight imperfections can have a dramatic impact on performance. As such, the results validate the hypothesis that the Imaging Ellipsometer outperforms previous models, placing the device at the leading edge of research in materials science and industrial applications.

Conclusion

This study presents the new Imaging Ellipsometer system that highly improves the functionality of ellipsometry equipment [3]. With the combination of high-resolution imaging with complex computer algorithms, the resultant system overcomes the limitation of conventional spectroscopic ellipsometry with the ability of thorough defect analysis and the measurement of the optical constants. The combination of the use of the tunable laser source, optics with the capability of high numerical apertures, and processing using GPUs represents the complete solution for increasing the sensitivity and the practicality of ellipsometry measurements further. Experimental results show that the improvement enables accurate material characterizations of GaN and SiC materials that give researchers and engineers more insight into material quality and performance.

The implications of this development extend beyond the laboratory, with potential applications in industries such as semiconductor manufacturing, renewable energy, and advanced electronics. In power electronics, for example, the ability to detect and mitigate defects in wide-bandgap materials like SiC and GaN could lead to more efficient and reliable devices, supporting the transition to sustainable energy systems. Similarly, in material science, the Imaging Ellipsometer offers a versatile platform for exploring new substrates and thin-film technologies, accelerating the pace of discovery and innovation [2].

This investigation adds substantially to the science of ellipsometry and represents a valuable asset for the wide spectrum of scientists wishing to extend the frontiers of material science, industry professionals aiming at enhancing the quality and efficiency of products, and researchers exploring new frontiers of materials science and nanosciences. The combination of enhanced resolution, precision, and computing efficiency within this context represents the core basis for subsequent material characterizations that are necessary for the development of more meaningful and accurate developments of science and technology.

References

Fujiwara, H., & Collins, R. W. (Eds.). (2018). *Spectroscopic ellipsometry for photovoltaics* (Vol. 1). Cham: Springer.

Grundmann, J., Bodermann, B., Ermilova, E., Weise, M., Hertwig, A., Klapetek, P., ... & Pereira, S. F. (2024). Optical and tactile measurements on SiC sample defects. *Journal of Sensors and Sensor Systems*, *13*(1), 109-121.

Liu, S., Du, W., Chen, X., Jiang, H., & Zhang, C. (2015). Mueller matrix imaging ellipsometry for nanostructure metrology. *Optics express*, *23*(13), 17316-17329.

POLITICAL STUDIES

Political and Social Thought

Political Philosophy

State Construction of the "Othering" Mechanisms Leading to Stigmatization and Discrimination

Ela Gülboy

Istanbul Technical University, Graduate School, Political Studies, Turkey
gulboy23@itu.edu.tr

Keywords: Othering, Stigmatization, Coloniality.

Aim

In this presentation I will discuss how modern states construct the categories of the "other" to achieve domination and control in power relations, also how these othering practices may both symbolically and relationally lead to the stigmatization and then discimination of ethnic, racial, cultural, and ideological groups. Furthermore, I will also talk about how similar stigmatization processes take place in the inter-state relations. I will aim at drawing attention to how these othering processes can be internalized by the stigmatized groups bearing the fact that state stigmatization can be avoided and othering processes may be balanced with this fundamental awareness.

Material and Method

My method is the critical examination of othering as a process which leads to stigmatization and discrimination at national and international levels. It includes examining and discussing the major existing theories on othering, and analyzes different approaches developed by social thinkers such as Edward Said, Erving Goffman, Bruce G. Link and Jo C. Phelan, Ayşe Zarakol, Pierre Bourdieu and Michel Foucault.

Findings

Othering initially correlates to an ontological question. Human beings treat everything and everyone around themselves as the other even from the time they start the first speak, and be able to say "I." The realization and separation of self from the other, advances over time by socially and politically constructed complex mechanisms of otherization. Othering processes create binary relations. It emphasizes difference. In that sense, it dictates what or who is normal and who is not, by defining the condition and boundaries of a belonging. It defines the categories of "us" versus "them" or "I" versus "You."

The othering is a process enforced by dominant groups through a specific use of discourse; symbols, culture, social norms, and laws. These power groups or dominant nations set the norms of normality, the factors that decide who will be deemed valuable or expandable. Political construction of the "other" is an effective tool which enables states to activate a criterion that causes humanity to be divided into two asymmetrical and unequal groups; one, whose identity is valued, versus whose identity is devalued. The latter group is susceptible to discrimination whereas the former group embodies the society's or nation's norms and determines the boundaries of normativity by marking the difference of the "other".

While othering emphasizes difference, the concept of stigmatization -initially introduced by Erving Goffman- emphasizes the other's inferiority in various sorts. Being stigmatized can cause a reaction of resistance to the power groups and to its everyday restraints but it may also result in the internalization or ingraining of this alleged inferiority. One of the consequences of internalizing a stigma is that it causes the individual or the group to look at oneself from the value system of the advantageous groups as explored by Edward Said, in his works on post colonial era. This effect can also manifest itself as self-stigmatization, a by-product of the states continuous othering practices.

As Link and Phelan explore, both othering and stigmatization are socially constructed. Groups and communities are subjected to othering processes formed under these comparative judgments. In a positive reading, awareness of othering may serve the purpose of plurality and progress in a society under the varying advantages and dynamics of such different groups, however this presentation will concentrate on the negativity and deterioriating effects of

political othering when it becomes severely disruptive under political dominance, economic ambitions, and power relations.

Within a nation state, othering practices include labeling of particular groups because of ethnic, cultural, ideological differences, gender identities, religious/sectarian belongings among others. Constant othering practices result in stigmatization which in turn negatively affects the status of the stigmatized, causing inequality within a nation. In order to understand the symbolic power of the state over its citizens, Pierre Bourdieu examines the role of the state in the formation of particular cognitive structures, which in turn affects the perception of social reality. The state has the capacity to impose certain principles which can create the conditions of constructing the other. Bourdieu explains how the state produces ideologies to justify its position, how it continually constructs and reconstructs the state thinking and the mode of public thinking that corresponds with the stat's particular interest. His analysis shows how symbols, practices, and cultural forms reinforce social hierarchies and legitimize state power and perpetuate symbolic capital.

Michel Foucault's works furthermore emphasize how power, language, and knowledge serve the state's authority by manipulating meaning and reality. We experience the consent building capacity of the state, not only through security forces and courts but also through cultural hegemony. The othering mechanisms which are constructed by the state become embodied in institutions, its bureaucracy and furthermore in the everyday life. The state is the creator of the categories and hierarchies that dispenses the symbolic values and this allows individuals and groups to become stigmatized and devalorized. State's construction and degrading of the "other" leads to downward mobility of the "other" towards the periphery because of immigration, inequality in labor, and social cultural rights policies, unequal allocation of resources to other communities, even the gentrification projects within cities. Discriminated groups are heavily repressed for their votes in the hope of better financial standards. The fractured and hierarchized "other" is excluded from decision making processes and is hindered by having full access to resources and opportunities. Hence the state function to distribute material and non-material resources with a balancing intent is violated by the exclusion of the "other." This exclusion creates an institutionalized stigma affecting the institutions and bureaucracy of the government. These separatist and discriminative policies decompose the unity of nations. These can be based upon several attributes such as identity, economic conditions, religion, ideology. Furthermore, consistent exposure to othering leads to social and psychological problems, such as alienation from the society and to be perceived as a threat and a burden. Simultaneously othering paves the way for the successful "Divide and Rule" politics for the ruling parties and autocratic leaders. Stigmatized groups also serve as scapegoats for governments especially during economic recessions and high inflation periods. Creating an internal enemy or the "other" simplifies the accountability and offers an alibi.

The dischotomy established betwen a Eurocentric North American superiority of whiteness versus the inferiority of the rest of the world, Global South or Non-West has been one of the most prominent forms of othering. In this International level, dominant states impose their own categories. The othering and the eventual stigmatization is usually justified by attributing an inferiority to another nation's economic or political development or cultural values.

From the pre-state era to colonial period othering have been practiced by the ruling groups. Categories such as barbarians, savages, non-believers or people of color, the discourse of superiority versus inferiority or civilized West and uncivilized Non-West strengthened this dichotomy in a course of time. During the European colonizations between 16th to 20th century, the stigmatization of certain nations or groups helped the colonizing countries to easily exert power, extract natural resources and turn the stigmatized groups into free or cheap labor. Edward Said investigated these sharp epistemological bifurcations of the Orient and the Occident in the postcolonial times which enabled the ongoing asymmetrical power relations today. Said names the Orient as "imaginative geography" which is a constructed place devised for political apprehension. The process of othering sustains Western hegemony and coloniality. In this regard, Ayse Zarakol who analyzes the global hierarchies of otherization draws attention to how the externally imposed categories of difference or backwardness operates as a process of stigmatization. Economically, industrially, and culturally advanced nations progressively became the parties to decide on these norms and categorizations. These categorizations of "developing" and "underdeveloped"

countries, or the "core" versus "periphery;" these ongoing bifurcations affect also the state representatives in their international dealings. They shape the state leaders' understanding of their own nation's place in international relations. These ingrained stigmas, biasses and factionalized prejudices construct the "us against them" understanding upon engineered fears and insecurities. This allows the legitimation of violence and the right to intervene in the acts possessions and the culture of the "other." The epitome of 9/11 attack created another phase in global security. The threat of the other is further reduced to a mere risk factor, thereby allowing for oppressive and sometimes illegal measures without concrete evidence, to wage wars, to occupy territories, claim resources, and perpetuate systemic oppression.

Conclusion

This discussion of the literature on the othering practices and political divisions are aimed at forming a conceptual basis for further studies to increase consciousness against the stigmatization processes. These deeply rooted stigmatizations circumvent effective resistance to the political and social construction and reconstruction of othering, engineered by the states. The crucial factor for stigmatization is that the labelled individual or group is usually permanently marked with this stigma. In the end, there will always be othering but the negativity loaded on stigma might be overcome by recognizing the differences through laws and social practices which ensure equal rights. For this purpose, works related to theoretical and sociological problems of present political systems, comprehensive studies on political consequences of othering processes, the analysis of real life examples, the effective resistance methods and practices carry the utmost importance to initiate a reform for balanced political systems and relations.

References

Bourdieu, Pierre. (1984). Distinction: A Social Critique of the Judgement of Taste. London, Routledge. (pp 141, 170).
Bourdieu, Pierre. (2014). On the State: Lectures and the College de France. Cambridge: Polity Press.
Foucault, M. (1981). The Order of Discourse. Young, R. Uniting the Text. A Post-Structuralist Reader, Routledge
Foucault, Michel (1995). Discipline and Punish: The Birth of the Prison, Vintage Books.
Said Edward W (1985). Orientalism Reconsidered. Cultural Critique, No. 1 (pp 2-5).
Said, Edward W (1979) Orientalism, Vintage Books NY, (pp 56-57, 150, 2).
Goffman, E. (1963). Stigma: Notes on the management of spoiled identity. Englewood Cliffs, NJ: Prentice-Hall.
Link, B. G., & Phelan, J. C. (2001). Conceptualizing stigma. *Annual Review of Sociology, 27,* (pp 363–385).
Zarakol, Ayşe. (2011). After Defeat: How East Learned to Live with the West, Cambridge University Press. (pp 4-7, 104).

POLITICAL STUDIES

Political and Social Thought

Political Philosophy

An Evaluation of Socrates, Plato and Aristotle Regarding Their Conceptualizations of Political Legitimacy

Giray Çavdar[a]

[a]Istanbul Technical University, Department of Sociology, Political Studies Masters Program, Turkey
cavdar22@itu.edu.tr

Keywords: Aristotle, Plato, Political Legitimacy, Socrates.

Aim

The aim of this paper is to analyze the thoughts of three crucial Ancient political thinkers, Socrates, Plato, and Aristotle on political legitimacy of a given authority in a society.

This will contribute to the discussions of political legitimacy which are especially crucial if one were to make evaluations of the populist regimes that are in the rise in the recent years. Although these thinkers may not provide a full road-map for evaluation of political legitimacy in the modern era, they can still help with putting forward some principles which are utilized by more contemporary thinkers. Their thoughts are important because they lay down the foundation for the discussions that could come later.

Material and Method

The main methodology that will be utilized in this paper is content analysis. Socrates' Crito and Euthyphro, Plato's Republic, and Aristotle's Nicomechean Ethics and Politics will be utilized to underline their ideas on political legitimacy. This will be followed by a comparative analysis of these different thinkers and their conceptions of political legitimacy. Each different thinker's contribution will be summarized in a sentence, and different criticisms will be put forward in the same way. It will also underline how these different thinkers could contribute to one another for putting forward a more complete definition of political legitimacy.

These thinkers are picked because they constitute the foundation of political philosophy in their discussions with all three thinkers reflecting a perspective on understanding political legitimacy with Socrates focusing on individual obligations, Plato focusing on collective legitimization and Aristotle dealing with the moral implications of political legitimacy. They are not the whole of ancient philosophy, but it could be argued that they are the most crucial part of it.

Findings

One of the main arguments Socrates puts forward, as could be seen in Crito, is that a legitimate authority obligates individuals from a moral perspective. Socrates puts this forward as an essential condition for political legitimacy, meaning that a political authority cannot be considered legitimate without having the capacity to imply moral obligations (Plato,*Crito*, 50a–51c). This definition is limited in the sense that although it provides a condition for the existence of political legitimacy, it does not expand on the requirements that need to be fulfilled on the part of the state, meaning this can't be the whole of political legitimacy. It only states a quality of legitimacy, not what needs to be done to attain it. This means that this principle is only useful for defining the responsibilities of a state that is already legitimate and not what an authority can do to attain legitimacy (*Crito*, 50b–51b)

Plato brings a solution to this short-coming by suggesting that a legitimate government promotes the common good and cohesion among the different parts of the populace. Compared to the earlier definition put forward by Socrates, this definition is more expansive on the grounds that it proposes a common good as a condition that must be fulfilled on the part of the state for it to be legitimate. If a state does not fulfill the obligation of promoting common good, it is no longer legitimate and can not entail moral obligations, as put forth by Socrates (Plato, *Republic*, 427d–434c).

However, this definition also has its limitations since Plato's characterization of legitimacy is not based on individuals but rather on the community as a collective good. This is problematic because it allows the instrumentalization of individuals for the sake of what is considered to be the common good, which could be considered a violation of moral laws.

This emphasis on collective understanding of political legitimacy also paves the way for an understanding of political legitimacy akin to "might makes right" which is more of a descriptive statement rather than a philosophical one (Plato, *Republic*, 420b, 473c–474a).

Aristotle's conception of political legitimacy proposes an alternative to this collective reading of the issue of political legitimacy which completely disregards the well-being of the individual. Aristotle suggests in Nicomachean Ethics that eudaimonia is something central to people's fulfillment in life and that this is only achievable if and only if people live according to virtues that are in accordance with their lives which necessitates the existence of individual eudaimonia within a collective body concerned with the common goods. Aristotle even goes far enough to define humans as "Political Animals" whose self-realization relies in the participation regarding the issues of political body (Aristotle, *Nicomachean Ethics*, 1097a15–20; *Politics*, 1253a1–20).

Therefore, Aristotle argues that political authority is legitimate so far as it promotes the virtues of individuals within a society which is in accordance with the collective identity. Although Aristotle still puts the good of the collective body before the that of individual, he also incorporates individual good as something that is positively affected by the good of the collective, striking a balance between the two. However, this definition is also problematic on the grounds that it does not quite explain how such an authority, even if it is legitimate, could have the legitimacy to apply its power on individuals under its domain. Aristotle's definition of political authority is problematic in the sense that it necessitates an original reason regarding why people would be obligated by a specific authority at the first place therefore creating a different problem when it comes to the evaluation of political legitimacy (Aristotle, *Nicomachean Ethics*, 1098a)

As a combination of these three different thinkers, it could be concluded that an authority is legitimate so far as it promotes the common and individual good of the individuals and this results in this authority's commands entailing moral obligation.

This definition, however, also has its short-comings. One of these, as mentioned with Aristotle, it requires an original position from which political legitimacy could be derived but none of the thinkers mentioned here have no mention of such a thing. Moreover, although in this definition virtues are put forward as a fact that connects the individual to the collective body, this definition is lacking regarding where the individual will matters. Another problem that is faced in this text is also defining what common good is since Plato's definition relies on highly hierarchical picture of what society should be like which accepts injustices such as slavery as normal institutions. For a more complete definition of political legitimacy, these problems are needed to be addressed.

Although outside the scope of this text, these short-comings could be addressed through future thinkers such as Hobbes, who puts forward state of nature as an original point through which political legitimacy could be judged, and John Locke who argues that consent is essential in understanding how a political authority is legitimate. Plato's definition of political legitimacy could be grounded better if one were to utilize Rousseau and his definition of "General Will" to define what common good is without reinforcing hierarchical structures as normal as put forward by Plato.

Conclusion

In this abstract, multiple attitudes to political legitimacy belonging to the Ancient Greek philosophers were mentioned. At first Socrates' definition of political legitimacy was explained with him suggesting that political legitimacy is something that entails moral obligation on the part of those that are subject to political authority.

Later, Plato was evaluated, and it was suggested that he defined political legitimacy as tied to the authority promoting the common good and protecting cohesion within society. This was criticized on the grounds that it failed to take into consideration the importance of individuals when evaluating what is the common good.

This was followed by Aristotle and his theory of political legitimacy based on individual virtue was put forward where his suggestion of political legitimacy was that a political authority was legitimate so far as it promoted the individual virtues of people within a society.

Combining all these thinkers, it was suggested that political authority was legitimate so far as it promoted common and individual good and, therefore, entailed political obligation on the part of those who are governed.

At the end of the findings section, this definition was criticized on the grounds that although it put forward a definition of political legitimacy, it was not sufficient in itself since it did not explain why one would happen to be obligated by a political authority in the first place and it was also suggested that this problem could be solved by referencing Thomas Hobbes' state of nature regarding original political obligation. Moreover, it was also suggested that one could reference Locke to clarify how individuals could come into play regarding the issue of political legitimacy and Rousseau regarding how to conceptualize common good as a concept independent of existing conservative power structures. However, these three thinkers are outside the scope of this paper and therefore were not analyzed under the scope of this text.

References

Aristotle. (2009). *Politics* (E. Barker, Trans.; R. F. Stalley, Rev.). Oxford University Press. (Original work published ca. 350 B.C.E.)
Aristotle. (2009). *Nicomachean ethics* (D. Ross, Trans.; L. Brown, Ed.). Oxford University Press. (Original work published ca. 350 B.C.E.)
Plato. (2008). *Defence of Socrates; Euthyphro; Crito* (D. Gallop, Trans.). Oxford University Press.
Plato. (2008). *Republic* (R. Waterfield, Trans. & Ed.). Oxford University Press. (Original work published ca. 380 B.C.E.)

POLYMER SCIENCE AND TECHNOLOGY

Porous Materials

Material Science

Synthesis and Characterization of Sulfonated Polysulfone for Proton Exchange Membrane Fuel Cells

Turan Can Özmen [a,c], Nesrin Köken [b], Vahid Vatanpour [c], Nilgün Kızılcan [b], Mehmet Emin Paşaoğlu [c,d], Börte Köse-Mutlu [c,d], İsmail Koyuncu [c,d]

[a]Istanbul Technical University, Graduate School of Science Engineering and Technology, Department of Polymer Science and Technology, Turkey
[b]Istanbul Technical University, Faculty of Science, Department of Chemistry, Turkey
[c]National Research Center on Membrane Technologies, Istanbul Technical University, Turkey
[d]Environmental Engineering Department, Istanbul Technical University, Turkey

Keywords: Proton Exchange Membrane, Proton Exchange Membrane Fuel Cells, Proton Conductivity, Sulfonated Polysulfone, Evaporation-Induced Phase Separation, Electrospinning.

Aim

Fuel cells operate by converting chemical energy into electrical energy through an electrochemical reaction, typically involving hydrogen and oxygen. One of the most promising types of fuel cells is the Polymer Electrolyte Membrane Fuel Cell (PEMFC), also referred to as the Proton Exchange Membrane Fuel Cell. This fuel cell type utilizes a polymeric membrane as an electrolyte, positioned between the anode and cathode, to facilitate the selective conduction of protons while acting as an electronic insulator. Hydrogen gas is supplied to the anode, where it undergoes oxidation, generating protons and electrons. The protons migrate through the membrane to the cathode, where they combine with oxygen to form water. This reaction not only produces electrical energy but also results in water vapor as a by-product, making PEMFCs an environmentally sustainable power generation technology.

Despite its advantages, the commercialization of PEMFCs remains hindered by the high cost of key materials, particularly the polymer electrolyte membrane (PEM). Currently, Nafion, a perfluoro sulfonic acid-based polymer, is the industry standard for PEMs due to its high proton conductivity, chemical stability, and mechanical robustness. However, its prohibitive cost and performance limitations at elevated temperatures necessitate the development of alternative polymeric materials with comparable or superior properties. In this study, we focus on the fabrication and characterization of sulfonated polysulfone (SPSU) composite membranes as a cost-effective and efficient alternative for PEMFC applications. A proton conductivity of 615.46 mS/cm, which is quite high compared to literature values, was obtained from the membrane produced with Aquivion. In contrast, conductivity values of 1.3 mS/cm and 1.08 mS/cm were recorded for sulfonated polysulfone (SPSU) and PES polymers mixed in different ratios.

In this study, the target was to synthesize polysulfones and their sulfonated versions, and then to prepared membranes by them. We have also developed a sulfonated polysulphone for membrane technology such as fuel cells. All polysulfones which are characterized by Fourier transform infrared (FTIR), nuclear magnetic resonance (NMR), differential scanning calorimetry (DSC) and gel permeation chromatography (GPC). We had two kind of NMR analysis for these polysulfones as ^{1}H NMR and ^{13}C NMR to characterize polysulfone backbone. Polysulfones glass transition (Tg) are determined by differantial scanning calorimetry (DSC). Characteristics of membranes were investigated by measuring the contact angle, pore sizes, and using scanning electron microscopy (SEM) images.

Material and Method

Reagent-grade chemicals with the highest purity were used in this study. Sulfuric acid (Merck MW = 98.08 g/mol, 99.999%), Dichloromethane (MW = 84.93 g/mol, ≥99.5%), Chlorosulfonic acid (MW = 116.52 g/mol, 99%).

Polysulfone (PS, Mw 30,000) was previously synthesized and directly used at Resin Pol. Lab. L108 ITU. Polysulfone were used for the synthesis and membrane preparation, were purchased and dried at 100 ºC under vacuum before use.

Synthesize of the sulfonated polysulfone (SPSU)

To enhance the proton conductivity of polysulfone, sulfonation was performed using two different methods. The degree of sulfonation (DS) is a critical parameter influencing the membrane's ionic conductivity, mechanical strength, and water uptake capacity.

• Method 1

In the first sulfonation method, polysulfone (PSU) was dissolved in sulfuric acid (H_2SO_4) with 96% purity. The solution was allowed to react for five hours, followed by a drying process. Subsequently, 0.5 mL of chlorosulfonic acid ($ClSO_3H$) was added to 50 g of dried PSU and subjected to continuous stirring for 48 hours, as illustrated in Figure 1. Upon completion of the reaction, the sulfonated polymer was precipitated by carefully pouring the solution onto ice to dissipate excess heat and prevent unwanted side reactions. The resulting solidified polymer underwent multiple washings with deionized water to neutralize residual acid, ensuring complete removal of reaction by products [1].

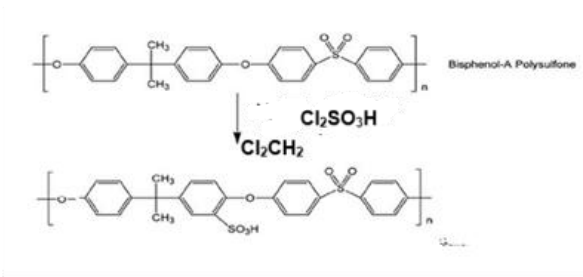

Figure. 1. Formation reaction of SPSU (Method 1).

• Method 2

The second sulfonation method employed chlorosulfonic acid in dichloromethane (DCM) as the sulfonating agent, as illustrated in Figure 2. Finally, the SPES underwent several washes in an ice-water bath and subsequently subjected to extensive washing to eliminate excess reagents followed by a 24 h drying period in a vacuum oven set at 60 ◦C [2].

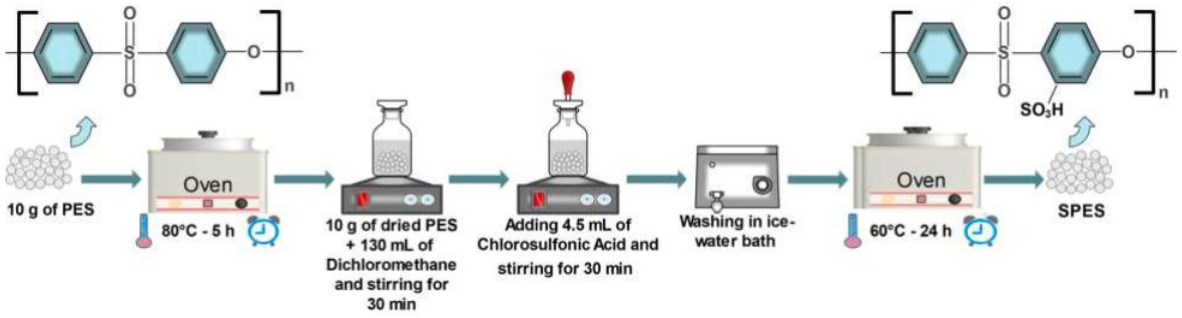

Figure 2. Sulfonation reaction process of polysulfone (Method 2) [3].

Determination of Sulfonation Degree

The sulfonation degree (DS) was quantified through a titration-based analytical approach. In this method, 0.1 g of sulfonated polymer was dissolved in 10 mL of dimethylformamide (DMF). The proton concentration was determined by titrating the solution with 0.1 M NaOH, using phenolphthalein as an indicator. The DS was found to be 16% for the first method and 35.2% for the second method, demonstrating that the latter method resulted in

a higher degree of sulfonation. The following equation was used to calculate DS. Where M is the NaOH concentration (M), V is the volume of NaOH added at the equivalence point (mL), and W is the SPSU weight (g).

$$PSU' DS\% = (0.442M \times V \times 100)/(W - 0.08 \times V)$$

Membrane Fabrication Techniques

The sulfonated polymers were processed into thin membranes using three distinct fabrication techniques:

1. Electrospinning
2. Doctor Blade Coating
3. Evaporation-Induced Phase Separation (EIPS)

Electrospinning

Electrospinning is a widely used technique for fabricating porous membranes, offering high surface area and tunable morphology. It has applications in fuel cells, lithium-ion battery separators, sensor materials, and biomedical engineering. The electrospinning apparatus used in this study consisted of a high-voltage power supply, a polymer solution feeding system, and a rotating collector drum.

The sulfonated polymer solution was loaded into a syringe and subjected to a high electric field, which overcame the surface tension and ejected fine polymer jets toward the collector. As the solvent evaporated during flight, dry nanofibers accumulated, forming a nonwoven electrospun membrane. The process duration was approximately seven hours, with real-time monitoring to prevent nozzle clogging. Any interruptions due to clogging were promptly addressed to ensure uniform membrane formation.

Doctor Blade Coating

Doctor blade coating, also known as blade coating, is a common method for producing thin polymer films. In this technique, the sulfonated polymer solution was evenly spread over a glass substrate using a reciprocating blade with a precisely controlled gap. Following uniform deposition, the coated substrate was immersed in deionized water to induce phase separation, leading to the formation of a solid membrane.

Evaporation-Induced Phase Separation (EIPS)

EIPS is a membrane fabrication technique that relies on controlled solvent evaporation to achieve phase separation. The polymer solution, containing a volatile solvent and a less volatile nonsolvent, was cast onto a flat substrate and placed in a temperature-controlled environment for 24 hours. As solvent evaporation progressed, polymer demixing occurred, resulting in the formation of a porous membrane structure. The drying process was carefully managed to prevent defects such as partial accumulation or surface irregularities.

Characterization of Membranes

To evaluate the suitability of the fabricated membranes for PEMFC applications, various characterization techniques were employed, including:

FT-IR spectra were measured using Bruker Alpha FTIR spectrophotometer (ATR sampling accessory), directly from the sample.

All ^{1}H-NMR, and ^{13}C-NMR data were obtained from a Varian spectrometer (AC 500 MHz) at room temperature. DMSO-d_6 was used as solvent. Chemical shifts (in ppm) were reported downfield from Si $(CH_3)_4$.

Morphology of products was examined by scanning electron microscope, ESEM XL30 ESEM-FEG Philips and the samples for the SEM measurement are prepared by gold coating. SEM imaging was conducted to examine the morphological characteristics of the membranes, particularly pore distribution, fiber alignment (for electrospun samples), and overall surface uniformity.

Findings

The ATR-FTIR spectra from the unsulfonated PSUmembrane (M1) was given in Figure 2. The main difference in the spectrum was the presence of two absorbances at about 1029 cm^{-1} and 1072 cm^{-1} in the SPES, which could be related to the symmetrical S-O stretch of the sulf onated groups(Figure 3).

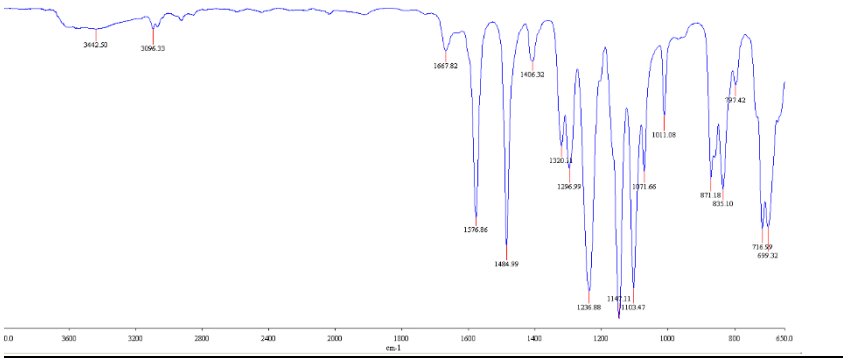

Figure 2. FTIR spectrum of PSU-M1.

The intensity of this peak in SPES spectra was increased towards the unsulfonated PSU[4]. The peak of 629 cm^{-1} is related to the S-O bending vibration and 830 cm^{-1} is related to the S-O-C stretching vibration of sulfonated groups. FT-IR analysis was performed to confirm the presence of sulfonate groups in the polymer backbone. Characteristic absorption peaks were observed in the range of 1030 cm^{-1} to 1098 cm^{-1}, corresponding to symmetric and asymmetric vibrations of sulfonate functional groups. The intensity of these peaks increased with sulfonation degree, corroborating findings from the literature.

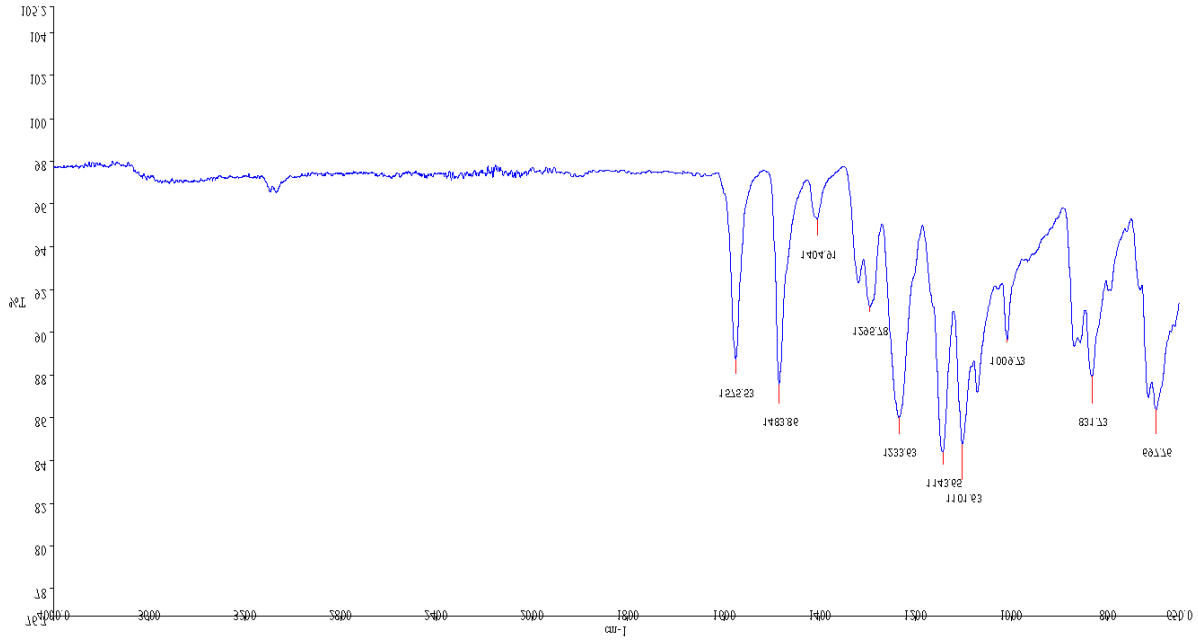

Figure 3. FTIR spectrum of SPSU (%35.2 DS).

•Membrane Performance Testing:

The fabricated membranes were subjected to contact angle measurements to assess hydrophilicity, gas permeation tests to evaluate selectivity, and proton conductivity measurements to determine ionic transport properties.

Conclusion

This study successfully synthesized and characterized sulfonated polysulfone membranes using two different sulfonation methods and three distinct membrane fabrication techniques. The results demonstrated that the degree of sulfonation significantly influences membrane properties, with higher sulfonation leading to enhanced proton conductivity. The findings of this study contribute to the ongoing development of cost-effective, high-performance PEMs, facilitating the broader adoption of fuel cell technology for sustainable energy applications. Future work will focus on optimizing fabrication conditions to further enhance membrane efficiency and durability.

Acknowledgments

The authors would like to thank the Scientific and Technical Research Council of Turkey (TUBITAK) 1004 Program (İTÜ Project No: 22AG018).

References

Lu, D.; Zou, H.; Guan, R.; Dai, H.; Lu, L. (2005). Sulfonation of polyethersulfone by chlor-osulfonic acid. Polym Bull , 54:21e8.

Divya, K.; Sri Abirami Saraswathi, MS. Rana D., Alwarappan, S.; Nagendran, A. (2018) Custom- made sulfonated poly (ether sulfone) nanocomposite proton exchange membranes using exfoliated molybdenum disulfide nanosheets for DMFC applications. Polymer 147, 48–55.

Shirvan, B.; Rahimi, M.; Zinadini, S. (2023). High electricity generation and wastewater treatment enhancement using a microbial fuel cell equipped with conductive and anti-biofouling CuGNSs/SPES proton exchange membrane, Energy Conversion and Management 294, 117559.

Zinadini, S.; Zinatizadeh, A.; Rahimi, M., Vatanpour, V.; & Rahimi, Z. (2017). High power generation and COD removal in a microbial fuel cell operated by a novel sulfonated PES / PES blend proton exchange membrane. Energy 125, 427–438. https://doi.org/10.1016/j.energy.2017.02.146

RAILWAY SYSTEMS ENGINEERING

Railway Systems Engineering

Signaling Systems in Railways

Traction Systems in Railways

Fiber Bragg Grating Sensor: Princibles, Applications, and Emerging Trends

Serhat Boynukalın[a], Kemal Atakan Kırca[b]

[a]Istanbul Technical University, Graduate Education Institute, Department of Railway Systems Engineering, Türkiye
[b]Istanbul Technical University, Faculty of Electrical and Electronics, Department of Electronics and Communication Engineering, Türkiye
boynukalin@itu.edu.tr

Keywords: Fiber Bragg Gratings (FBG), Fiber Optic Sensors, Railway Safety, Optical Sensing, Structural Health Monitoring.

Aim

Fiber Bragg Grating (FBG) sensors operate based on the principle of light reflection at specific wavelengths, determined by periodic variations in the refractive index within the fiber core. These reflected wavelengths, known as Bragg wavelengths, shift in response to external stimuli such as temperature and strain, making FBG sensors exceptionally well-suited for detecting changes in physical and environmental conditions with high sensitivity and resolution.

This study aims to analyze how thermal and mechanical influences affect the performance of FBG sensors, particularly focusing on temperature-induced expansion and strain-related elasticity. By quantifying the Bragg wavelength shift through analytical models and simulation tools, the research seeks to offer a deeper understanding of the FBG sensing mechanism under real-world conditions. This knowledge is crucial for optimizing sensor performance in critical monitoring applications.

In parallel, the study investigates the practical use of FBG sensors across various engineering fields, such as railway safety, aviation, structural health monitoring, and border security. Application scenarios include the use of FBG-equipped clearance trains for detecting rail track deformations, aircraft wing deformation tracking during flight conditions, and real-time vibration monitoring for perimeter security. The research incorporates both laboratory simulations and field tests to assess sensor reliability, robustness, and response time in each of these domains.

Moreover, the study evaluates different grating structures—uniform, chirped, and apodized—based on their wavelength reflection behavior and susceptibility to interference. It also explores the integration of digital modulation and coding techniques (e.g., PN-coding) to enhance signal clarity, extend sensing range, and support multiplexed measurements. Ultimately, the research highlights the transformative potential of FBG sensors in developing smart, proactive, and sustainable monitoring systems capable of improving safety and operational efficiency in diverse industrial contexts.

Material and Method

This study employed a multi-stage methodology to evaluate the performance of Fiber Bragg Grating (FBG) sensors in environmental sensing applications. The approach involved theoretical modeling, simulation using specialized software, and practical validation through prototype testing in real-world scenarios.

Initially, the optical behavior of FBG sensors was modeled based on Bragg's law, which defines the relationship between the grating period, refractive index, and reflected wavelength. The impact of external factors such as temperature and strain on the Bragg wavelength was quantified using standard equations incorporating thermal expansion and photoelastic coefficients (Karaman & Ünverdi, n.d.).

Simulation experiments were conducted using OptiSystem software to optimize the optical link design and modulation schemes. The system setup included a laser source, Mach-Zehnder and Direct Modulators, and photodetectors. Performance was evaluated under varying environmental parameters and signal conditions, with

particular focus on signal stability, wavelength shift accuracy, and the influence of coding techniques such as pseudorandom noise (PN) codes (Boynukalın et al., 2023).

For practical assessment, a prototype "clearance train" equipped with FBG sensors was deployed on railway tracks. The sensors continuously recorded strain and temperature data while in motion, allowing for real-time identification of track irregularities. Data was collected, processed, and interpreted to validate the sensors' reliability and responsiveness.

Furthermore, different FBG configurations were analyzed to determine their suitability for diverse application requirements. Performance metrics such as sensitivity, response time, multiplexing capacity, and resistance to electromagnetic interference were evaluated.

Overall, the combined use of analytical modeling, simulation tools, and field testing ensured a comprehensive assessment of FBG sensor effectiveness in industrial monitoring contexts.

Findings

The research demonstrated that Fiber Bragg Grating (FBG) sensors offer high sensitivity and reliability in monitoring physical parameters across a wide range of applications. Key findings from simulation studies and prototype testing are as follows:

Railway Infrastructure Monitoring:

FBG sensors installed along railway tracks successfully detected minute variations in strain and temperature, signaling potential infrastructure degradation or deformation. The use of advanced modulation schemes, particularly the Dual-Drive Mach-Zehnder Modulator, significantly improved signal resolution and accuracy in identifying local defects or stress concentrations. The clearance train application verified the practicality of using mobile FBG sensor platforms for real-time railway diagnostics (Boynukalın et al., 2023).

Aircraft Wing Structural Health Monitoring:

The application of FBG sensors in aircraft wings enabled continuous, real-time tracking of structural deformation and temperature fluctuations during simulated flight conditions. Sensor data effectively indicated load distributions and stress accumulation, which are critical for early fatigue detection (Ma and Chen, 2019). When combined with structural health monitoring software and inverse finite element methods, FBG data enabled the creation of accurate digital twins, improving predictive maintenance and operational safety (Kefal, 2020).

Security and Border Intrusion Detection:

FBG cables embedded underground or along perimeters reliably detected vibrations and movement associated with unauthorized intrusion. These systems exhibited strong resistance to electromagnetic interference and provided low false alarm rates. The technology demonstrated significant potential in enhancing security for borders and critical infrastructure (Fermann, 2016).

Building Structural Health Monitoring

FBG sensors embedded in structural elements such as columns and beams accurately captured micro-strain and displacement caused by environmental and operational loads. Real-time alerts enabled preventive maintenance strategies in bridges, towers, and high-rise buildings, reducing inspection costs and ensuring safety (Webb, 2007).

Seismic Monitoring and Early Warning Systems:

The sensors proved capable of detecting low-amplitude seismic waves, which precede major earthquake events. Their deployment near fault zones enabled early warnings by monitoring stress build-up and micro-displacements. The precision and responsiveness of FBG sensors offer a promising tool for earthquake risk mitigation (Laudati et al., 2008).

In all tested scenarios, FBG sensors demonstrated excellent performance in harsh environments, high accuracy in measurement, and strong adaptability through multiplexed deployment. These findings underscore the value of FBG technology as a versatile and robust solution for advanced sensing applications.

Conclusion

The findings of this study confirm that Fiber Bragg Grating (FBG) sensors are highly effective tools for monitoring environmental and structural parameters such as strain, temperature, and vibration. Their immunity to electromagnetic interference, compact size, and capability to operate under harsh conditions make them a superior alternative to conventional electronic sensors in many critical applications.

FBG sensors demonstrated notable performance in railway infrastructure monitoring, aircraft wing stress analysis, seismic activity detection, and security systems. Their precision in capturing real-time physical changes allows for early detection of anomalies, thereby enhancing safety, enabling predictive maintenance, and reducing operational costs (Boynukalın et al., 2023).

The use of advanced coding schemes and multiplexing configurations further improved measurement accuracy and extended the applicability of FBG sensors over long distances. Despite certain limitations, such as sensitivity to extreme temperatures and higher initial costs, ongoing advancements in sensor design and signal processing continue to expand their utility and efficiency.

In conclusion, FBG-based optical sensing technology represents a transformative advancement in modern monitoring systems. Its adaptability and precision offer significant potential to reshape safety, diagnostics, and maintenance practices across transportation, aerospace, civil infrastructure, and security domains.

References

Boynukalın, S., Paker, S., & Atieh, A. (2023). Investigation of hybrid remote fiber optic sensing solutions for railway applications. Photonics, 10(864). https://doi.org/10.3390/photonics10080864

Fermann, M. E. (2016). Optical fiber sensors for security applications. Journal of Lightwave Technology, 34(4), 1123–1134. https://doi.org/10.1109/JLT.2015.2499381

Karaman, L., & Ünverdi, N. Ö. (n.d.). Fiber Bragg ızgara tabanlı optik sensörün analizi. Retrieved from http://www.mohid.com, date retrieved 29.06.2006.

Kefal, A. (2020). Lamine kompozit ve sandviç plakaların şekil ve gerilme algılaması için yeni bir dört-düğüm noktalı ters-plaka elemanı. Gazi Üniversitesi Mühendislik Mimarlık Fakültesi Dergisi, 35(4), 1767–1782. https://doi.org/10.17341/gazimmfd.557477

Laudati, A., Mennella, F., Giordano, M., D'Altrui, G., Calisti, C., & Cusano, A. (2008). A fiber-optic Bragg grating seismic sensor. IEEE Photonics Technology Letters, 19, 1991–1993. https://doi.org/10.1109/LPT.2007.909628

Ma, Z., & Chen, X. (2019). Fiber Bragg gratings sensors for aircraft wing shape measurement: Recent applications and technical analysis. Sensors, 19(1), 55. https://doi.org/10.3390/s19010055

Webb, D. J. (2007). Fiber Bragg grating sensors in structural health monitoring. Key Engineering Materials, 293, 3–10. https://doi.org/10.4028/www.scientific.net/KEM.293-294.3

RAILWAY SYSTEMS ENGINEERING

Railway Systems Engineering

Signaling Systems in Railways

Traction Systems in Railways

Energy Efficiency Optimization through Metro Scheduling: Mixed-Integer Linear Programming (MILP) and Genetic Algorithm Approaches

Mustafa Karaipek[a], Abdurrahman Yılmaz[b]

[a]Istanbul Technical University, Mechatronics Engineering Master of Science Program, Türkiye
[b] Istanbul Technical University, Department of Control and Automation Engineering, Türkiye
karaipek@itu.edu.tr

Keywords: Energy Efficiency Optimization, Genetic Algorithm, Mixed-Integer Linear Programming (MILP), Railway, Time Table.

Aim

The use of urban rail systems is steadily increasing, bridging a significant gap in transportation and serving the public. According to the "Distribution of Public Transport Journeys by Main Transportation Modes" report published in June 2022, the share of rail systems in public transport in Istanbul is 26% and continues to rise[1]. The expansion of rail systems in urban areas has reduced road traffic, especially in densely populated cities, thereby decreasing urban carbon emissions and contributing positively to the environment. The goal is to expand the rail network to reduce individual car use and make it a cost-effective transportation method. To achieve this, efficiency must be increased and energy consumption reduced. Numerous studies have been conducted to improve energy efficiency in existing rail systems. These have focused on different parameters, such as energy recovery through regenerative braking[2], simultaneous optimization of train schedules and maintenance planning to increase infrastructure capacity usage[3], shared corridors for freight and passenger trains[4], and the use of deep reinforcement learning (DRL) for rescheduling high-speed trains under disruptions[5]. These approaches underline the multidisciplinary nature of the challenge, requiring integration of operations research, artificial intelligence, and civil engineering techniques to effectively address energy efficiency in complex rail systems.
In this study, metro schedules have been optimized to improve energy efficiency in urban rail systems. The goal was to optimize train services based on passenger demand, reduce unnecessary services, and lower overall energy consumption. The core strategy was to reschedule frequencies based on station-level passenger density, increase dwell times during off-peak hours or at low-demand stations, and transport the same passenger volume with fewer trips. While doing so, certain constraints were considered: meeting minimum service levels for passenger demand, not exceeding specific waiting times, and maintaining minimum frequencies during certain times of the day. Passenger travel time was also taken into account to ensure satisfaction, ensuring that waiting times at stations did not exceed acceptable limits. Simulation studies using data from the Gayrettepe–Istanbul Airport metro line showed that energy savings could be achieved through this approach.

Material and Method

Both deterministic and heuristic methods were used and compared. Mixed Integer Linear Programming (MILP), a deterministic optimization method, and Genetic Algorithm (GA), a heuristic method, were applied. MILP is highly effective for solving optimization problems involving both continuous and integer variables, and it was used to determine the optimal timing and frequency of metro services. While theoretically providing a global optimum, MILP can be inefficient for large-scale problems, hence GA was also tested for performance comparison. Genetic Algorithms are inspired by natural evolutionary processes and are capable of effectively searching large solution spaces. They can generate numerous alternative solutions and evolve them using genetic operators to reach near-optimal results, offering advantages for transportation systems with large datasets. The objective function was defined mathematically with the aim of minimizing total energy consumption. Variables such as service timing, dwell times, and number of trips were mathematically modeled. Passenger satisfaction was also considered when defining constraints. Simulations were conducted using both methods to compare performance.In defining the constraints of the optimization model, not only operational rules (e.g., minimum headways) but also

passenger behavior patterns were considered. For example, the model penalized excessive waiting times that could potentially cause station overcrowding or lower passenger satisfaction.

Findings

Simulation studies were conducted on the Gayrettepe–Istanbul Airport metro line, and the model's real-world performance was assessed. Analyses using actual passenger density data showed that demand-based scheduling significantly reduced energy consumption without compromising passenger capacity. Trains maintained frequency during peak hours but operated more flexibly during off-peak times, avoiding unnecessary energy use. While GA delivered faster results, it had slightly lower performance in terms of energy savings compared to MILP. However, GA was deemed more suitable for large-scale systems requiring fast solutions.

The results demonstrate that dynamic control of rail systems can significantly enhance energy efficiency. Adapting schedules quickly for special days or nights increases flexibility and enables greater energy savings. Despite energy savings, there was no notable decline in service quality. The proposed schedule adhered to constraints such as minimum frequency and maximum waiting times. Simulation results showed no meaningful increase in passenger wait times, and optimized intervals helped balance passenger density.Moreover, results showed that adjusting dwell times slightly at low-density stations helped smooth out bottlenecks without creating backlogs. This situation also contributed to more stable energy draw from the electrical grid, which is beneficial for energy distribution management. Without reducing passenger satisfaction, it was observed that the current passenger demand could be met with 98 train trips instead of 110 in the existing operation, as a result of the optimization study.

Conclusion

This study shows that demand-based scheduling in urban rail systems can significantly enhance energy efficiency. Replacing fixed schedules with dynamic plans that adapt to real-time demand reduces energy consumption and improves overall system efficiency.In large metropolises like Istanbul, operating metro lines more efficiently yields major environmental and economic benefits. The developed model can also be adapted to other urban rail systems. Smart, demand-based scheduling in rail systems not only reduces operational costs but also supports environmental sustainability. Simulation results revealed proportional reductions in carbon emissions alongside energy savings. Future work can explore additional parameters and constraints to further enhance energy efficiency, such as incorporating regenerative braking or optimizing train driving dynamics.Furthermore, incorporating real-time passenger feedback mechanisms and integrating the model into central traffic control systems could enhance adaptability. An 11% reduction in the number of train trips was achieved, and energy savings were obtained while carrying the same passenger demand.

References

İstanbul Büyükşehir Belediyesi. (2022). İstanbul ulaşım ve hareketlilik raporu, Haziran 2022. https://cdnuym.ibb.gov.tr/cdn/uym/NewReports/Istanbul_Ulasim_ve_Hareketlilik_Raporu_Haziran_2022.pdf

Pan, Z., Chen, M., Lu, S., Tian, Z., & Liu, Y. (2020). Integrated timetable optimization for minimum total energy consumption of an AC railway system. IEEE Transactions on Vehicular Technology, 69(4), 3641–3653. https://doi.org/10.1109/TVT.2020.2975603

Zhang, C., Gao, Y., Yang, L., Gao, Z., & Qi, J. (2020). Joint optimization of train scheduling and maintenance planning in a railway network: A heuristic algorithm using Lagrangian relaxation. Transportation Research Part B: Methodological, 134, 64–92. https://doi.org/10.1016/j.trb.2020.02.008

Yıldırım, M. S., Karaşahin, M., & Gökküş, Ü. (2021). Scheduling of the shuttle freight train services for dry ports using multimethod simulation–optimization approach. International Journal of Civil Engineering, 19(1), 67–83. https://doi.org/10.1007/s40999-020-00553-0

Ning, L., Li, Y., Zhou, M., Song, H., & Dong, H. (2019, October). A deep reinforcement learning approach to high-speed train timetable rescheduling under disturbances. 2019 IEEE Intelligent Transportation Systems Conference (ITSC), Auckland, New Zealand, 3469–3474. https://doi.org/10.1109/ITSC.2019.8917383

A Safety-Critical Railway Interlocking Architecture Based on SCADE and HIMA PLCs with Python-Driven Simulation and Control

Serhat Boynukalın[a], Feride Berra Köseoğlu[b], Erdem Kısaç[b]

[a] Istanbul Technical University, Graduate Education Institute, Department of Railway Systems Engineering, Türkiye
[b] Istanbul Technical University, Faculty of Electrical and Electronics, Department of Control and Automation Engineering, Türkiye
boynukalin@itu.edu.tr

Keywords: Hima Plc, Modbus Tcp, Railway Interlocking, Scade Display, Safety-Critical Systems.

Aim

This study will design a cost-effective, scalable, fail-safe railway interlocking system that adheres to international safety standards using the SCADE (Safety Critical Application Development Environment) platform. Communication between the simulation interface and a HIMA PLC is established via the Modbus protocol, enabling real-time control of field components such as railway switches. To ensure system reliability and safety, the project emphasizes compliance with standards like EN 50128, EN 50129, and EN 50716.
Integrating certified tools and protocols becomes vital considering the catastrophic consequences of operational failures in railway systems, such as the Chatsworth and Graniteville accidents (Hartong, Goel, & Wijesekera, 2011). With their redundant architecture and SafeEthernet protocol, HIMA PLCs provide the backbone of secure communication and continuous operation in safety-critical environments (HIMA, n.d.-b), (HIMA, n.d.-c).
In addition to enhancing operational safety, the project contributes to sustainable transport goals by promoting railway usage, which offers significantly lower carbon emissions compared to other modes of transportation (Küresel Amaçlar, 2020; Bollen, 2022).

Materials and Method

This project aimed to implement a fail-safe system for railway signaling by complying with safety standards and using SCADE and HIMA PLCs through Modbus TCP integration. For this purpose, an interlocking interface was intended to be designed using a model-based approach, and communication was established with PLCs via the Modbus TCP protocol. These main components are detailed below.

Graphical Interface—HMI: The goal was to design a user-friendly interface via SCADE Display. The user could see the routes and request routes clearly, read and control the status of all switches, track circuits, and signal lights, and facilitate error detection in case of any fault, and allow for intervention.
The proposed system integrates a graphical user interface developed in SCADE Display with a HIMA PLC via the Modbus TCP/IP protocol. The primary objective is to enable real-time communication between the control system and field equipment such as railway switches and signal lights (Ansys, 2021).
The development process began with designing an intuitive interface that visualizes track availability and enables route selection (Ansys, 2021).

PLC: HIMA PLCs read the data coming from the interface, process it, and transfer the data received from field devices back to the interface. Additionally, they make decisions within the framework of safety standards and play a role in making the project fail-safe.
The HIMA PLC logic was developed using the SILworX platform to meet redundancy and safety requirements. Within this architecture, each bit exchanged through Modbus represents a command or feedback signal critical to the interlocking logic. The PLC processes commands received from the interface and returns corresponding status feedback, forming a closed-loop control cycle (Ansys, 2021).

Modbus TCP: This protocol ensures communication between the interface and the PLC by operating using input and output bit lists. These lists carry out command exchange and transmit status information to the user.
The Modbus protocol, chosen for its open-source nature and widespread industrial adoption, facilitates data exchange between the interface and the PLC (Simply Modbus, n.d.).
Although Modbus lacks inherent security features such as encryption or authentication, the system architecture ensures it is used in a closed and isolated network, minimizing vulnerability (Marrone, 2024).

The interlocking interface developed in this project was designed to enable real-time data monitoring, control of field devices, and communication with them. The HMI was designed with SCADE Display. At this stage, SCADE Display provided ease through its model-based design environment and generated code compliant with safety standards (Ansys, 2021).
However, during the project's compilation phase, additional code was written for Modbus TCP integration, and all code files were compiled manually.
Python and C programming were employed to implement the communication layer—initial development efforts involved using SCADE's Python API to access and manipulate interface variables. However, due to limitations, an alternative approach using C was adopted. By directly modifying the auto-generated header files, real-time variable control and interface responsiveness were achieved (Ansys, 2021).
In addition to C-based implementation, Python was also integrated into the system to extend its functionality. Using the SCADE Python API, dynamic variable control mechanisms were developed, enabling more flexible interaction with the interface and improving development efficiency (Ansys, 2021).
The process starts by receiving user commands via the interface prepared using SCADE Display, and then transmitting these commands to the PLC via Modbus TCP. The commands reaching the PLC are applied to the field devices within the critical safety limits provided by HIMA. The user can see the results of their commands and the status of the field equipment via the interface.
During the design process, the aim was to obtain a system suitable for a fail-safe structure. HIMA PLCs with SIL 3–4 levels were used as controllers. Modbus Slave Simulator was used, and tests were conducted in these simulation environments.
Communication reliability was ensured through iterative testing using Modbus slave simulators, and synchronization between the interface and PLC was validated through integration testing (Ansys, 2021).
The software used in the project was designed according to fail-safe principles, stopping all movements and switching field equipment to safe positions in case of errors.
All components were developed and tested according to RAMS principles (Reliability, Availability, Maintainability, and Safety), as defined by EN 50126. The methodology emphasizes fail-safe operation and scalability, ensuring the system is suitable for real-world railway applications (CENELEC, 2017).

Findings

During the testing process, it was verified whether the signal data received from the field was correctly represented in the graphical user interface. In this regard, variables controlling the visibility of a signal lamp were defined in the SCADE Display environment, and the relevant variables were mapped to specific Modbus register addresses in the C language code. By externally manipulating these registers via the Modbus Slave Simulator, different values were assigned, and it was observed that these changes were reflected instantly and accurately on the SCADE Display interface. This method confirmed that the system correctly processed the data exchanges transmitted over Modbus TCP/IP and reliably presented them on the user interface.
The implemented interlocking system successfully demonstrated reliable and fail-safe communication between the graphical user interface and the HIMA PLC using the Modbus TCP/IP protocol. All critical bits associated with turnout commands and signal indications were exchanged accurately, and their real-time reflections were confirmed through the SCADE Display interface. The interface responded dynamically to the status of the field components, enabling clear visualization of track conditions and signal states.
Thus, the system's real-time monitoring and control capability was successfully verified. During the design process, software and hardware selections followed the industry standards and fail-safe requirements specified in the project, meeting all expected criteria in terms of safety, flexibility, and integrity.
SCADE Display, certified for SIL 3–4 applications, facilitated a structured development process with integrated safety analysis and certified code generation (Ansys, 2021). The designed interface contributed to compliance with safety integrity requirements as defined in railway standards such as EN 50129:2020 for functional safety of electronic systems, and EN 50716:2023 for software development processes (CENELEC, 2023). During the testing phase, it was confirmed that changes to variables in the PLC logic were correctly and safely reflected on the graphical display and vice versa. This confirmed the robustness of the two-way communication system.
As a result, the developed system overcomes the limitations of existing traditional solutions and offers a reliable solution compatible with modern industrial automation needs.
HIMA PLCs proved highly reliable under simulation, maintaining continuous operation even in failure scenarios. Their built-in redundancy features ensured that safety logic could still be processed in the event of component faults, meeting the project's functional safety goals (HIMA, n.d.-b). Moreover, communication through SafeEthernet, developed to meet SIL 3–4 requirements, added an extra layer of security to data transfer operations (HIMA, n.d.-c).

The key findings obtained within this study's scope show that using modular architecture and open-source communication protocols in industrial automation systems significantly increases system flexibility and reliability. The data communication provided using the Modbus protocol enabled uninterrupted and reliable data flow between different components; changes on the interface could be observed consistently and in real time. The system's ability to respond quickly in tests conducted via the slave simulator confirmed the robustness of the communication structure. It revealed that the integrity between the user interface and field data could be maintained.

Furthermore, using scalable and open-source technologies like Modbus and commercial off-the-shelf PLC components, the project offers a cost-effective solution for broader deployment in large-scale transportation infrastructure.

Regarding sustainability, the project aligns with the goals of reducing environmental impact by promoting railway transportation. Compared to road or air transport, rail systems are significantly more energy-efficient and produce fewer emissions (Bollen, 2022; Selipa, 2024; Küfeoğlu, 2024).

The designed system also contributes to social sustainability by supporting the development of accessible and safe public transport networks. Aligning with the United Nations' 2030 Agenda for Sustainable Development, the system addresses the need for safe, inclusive, low-emission transport solutions, especially for vulnerable populations (Küresel Amaçlar, 2020).

Conclusion

As a result, the developed system overcomes the limitations of existing traditional solutions and offers a reliable solution suitable for modern industrial automation needs.

This study demonstrates the feasibility of designing a fail-safe, scalable, cost-effective railway interlocking system that complies with internationally accepted safety standards. Integrating SCADE Display with HIMA PLCs using the Modbus protocol successfully achieved a secure and reliable communication loop between the user interface and field elements.

The results reveal that the method can be easily adapted to different systems and yield successful outcomes in various application areas.

The graphical interface allowed real-time monitoring and control of track availability, switch states, and signal indications while operating within a safety-certified environment.

Based on simulation outputs, the developed graphical interface meets current standards and has established a foundation to accommodate future expansion and scaling needs.

Open communication protocols and commercial off-the-shelf hardware contributed to the system's economic viability and scalability for larger rail infrastructure projects.

During the design process, software and hardware selections followed the industry standards and fail-safe requirements specified in the project, meeting all expected criteria in terms of safety, flexibility, and integrity.

The adoption of standardized and certified tools, such as SCADE Display (compliant with EN 50716), the SILworX platform, and the SafeEthernet protocol, ensured that the system achieved high safety integrity while minimizing development and certification costs (HIMA, n.d.-a), (HIMA, n.d.-b), (HIMA, n.d.-c), (Ansys, 2021).

The method proposed within the scope of this study has proven its success theoretically and practically through the tests and integration processes conducted.

The system's architecture and behavior were also evaluated concerning EN 50129:2020, which outlines the requirements for the functional safety of safety-related electronic systems in railway applications. Compliance with this standard reinforces the system's robustness for deployment in real-world signalling environments (CENELEC, 2018).

The designed system's compatibility with existing structures demonstrates that the method can be effectively used in real-world applications.

From an environmental standpoint, the project aligns with the European Green Deal and global sustainability targets by promoting railway transport as a low-emission, energy-efficient mode of travel (European Commission, 2021). Furthermore, the system's contribution to public safety and infrastructure reliability positions it as a strong candidate for future deployment in innovative and sustainable cities.

In summary, the project validates the potential of combining model-based design, functional safety standards, and industrial communication protocols to create modern, safe, and efficient railway control systems. It meets the technical requirements of fail-safe operation and real-time performance and supports broader economic, environmental, and social sustainability goals.

References

Ansys. (2021). Ansys SCADE Suite Datasheet. Retrieved from https://www.ansys.com/content/dam/product/embedded-software/ansys-scade-suite/ansys-scad e-suite-2021-r2-datasheet.pdf, date retrieved 13.02.2025.

Bollen, J. (2022, February 22). World Environment Day: five positive impacts of the railway. Network Rail. Retrieved from https://www.networkrail.co.uk/stories/world-environment-day-five-positive-impacts-of-the-railway/, date retrieved 13.02.2025.

CENELEC. (2017). EN 50126-1: Railway Applications – The Specification and Demonstration of Reliability, Availability, Maintainability and Safety (RAMS) – Part 1: Generic RAMS Process. Retrieved from https://standards.globalspec.com/std/10262901/en-50126-1, date retrieved 01.03.2025.

CENELEC. (2018). EN 50129: Railway Applications – Communication, Signalling and Processing Systems – Safety Related Electronic Systems for Signalling. Retrieved from https://standards.globalspec.com/std/13113133/en-50129, date retrieved 02.03.2025.

CENELEC. (2023). EN 50716: Railway Applications – Requirements for Software Development. Retrieved from https://standards.iteh.ai/catalog/standards/clc/32d1d924-9bfd-477e-adf4-de6e3358be77/en-50716-2023, date retrieved 13.02.2025.

European Commission. (2021). The European Green Deal. Retrieved from https://commission.europa.eu/strategy-and-policy/priorities-2019-2024/european-green-deal_e n, date retrieved 05.03.2025.

Hartong, M., Goel, R., & Wijesekera, D. (2011). Positive Train Control (PTC) failure modes. Journal of King Saud University – Science, 23(3), 311–321. https://doi.org/10.1016/j.jksus.2010.12.003 date retrieved 18.03.2025.

HIMA. (n.d.-a). Rail. Retrieved from https://www.hima.com/rail date retrieved 10.03.2025.

HIMA. (n.d.-b). HIMA Official Website. Retrieved from https://www.hima.com/, date retrieved 08.03.2025.

HIMA. (n.d.-c). SafeEthernet. Retrieved from https://www.hima.com/en/products-services/safeethernet, date retrieved 10.03.2025.

Küfeoğlu, S. (2024). Transportation sector emissions. In Sustainable Development Goals Series (pp. 493–554). https://doi.org/10.1007/978-3-031-70322-5_10, date retrieved 10.03.2025.

Küresel Amaçlar. (2020). Sürdürülebilir Şehirler ve Topluluklar. Retrieved from https://www.kureselamaclar.org/amaclar/surdurulebilir-sehirler-ve-topluluklar/, date retrieved 10.03.2025.

Marrone, S. (2024). Formal security assessment of Modbus protocol. Retrieved from https://www.academia.edu/108392430/Formal_security_assessment_of_Modbus_protocol, date retrieved 18.03.2025.

Selipa, E. (2024, September 19). Making rail transport more sustainable, comfortable and quieter. **Europe's Rail.** Retrieved from https://rail-research.europa.eu/latest-news/making-rail-transport-more-sustainable-comfortable -and-quieter/, date retrieved 18.03.2025.

Simply Modbus. (n.d.). About Modbus. Retrieved from https://www.simplymodbus.ca/FAQ.htm#Modbus, date retrieved 18.03.2025.

REAL ESTATE DEVELOPMENT

Real Estate Development

An Event-Driven Architecture in Real Estate Development

Özlem Sertbaş[a], Hakan Yaman[b]

[a] Istanbul Technical University, Graduate Program in Real Estate Development, Turkey
[b] Istanbul Technical University, Faculty of Architecture, Department of Architecture, Turkey
sertbas23@itu.edu.tr

Keywords: EDA, Project Management, RED.

Aim

Real estate development (RED) is a long-term process that covers everything from the initial idea of a project to its final operation. It starts with an idea and is subsequently evaluated through feasibility studies to determine its financial viability, compliance with regulations, and market demand. Then, it moves to the pre-construction phase, which includes the tender process, selecting contractors, finalizing the project, and setting the budget. Then the construction phase and continues through the sale or leasing of the property. Finally, it includes managing and maintaining the building once it's up and running. Basically, RED is a continuous cycle that integrates financial, technical, and operational considerations to create usable and valuable spaces. RED projects are dynamic and typically involve long durations. RED projects also require coordination among multiple parties who may have both common and conflicting goals, making time management a critical factor for success (Eppinger et al., 2013). External factors, including the involvement of stakeholders, can significantly impact the planning and development process. These factors may result in unexpected additional expenses and delays, making it essential to have a comprehensive understanding of the process in order to accurately estimate total costs (Atkin & Borgbrant, 2010). RED has traditionally relied on the experience and intuition of developers and investors. This approach, based on experiences and instinct, involves leveraging past experiences to make informed decisions about future projects (Ruddock, 2008; Turner, 2017). Although traditional approaches used in these processes are generally based on experience and market conditions, emerging technologies have the potential to revolutionize this field. Implementing RED processes through an automated system has the potential to lower error rates, address the shortcomings of conventional approaches, and establish a scientific framework. Considering these aspects, one of the newly adopted methodologies, Event-Driven Architecture (EDA), could serve the development of this system.

Material and Method

This study introduces the result of a literature review and the potential of EDA methods to explore their application in RED processes. Literature review is carried out to understand how EDA has been used in previous studies and to identify its potential in the context of RED. This analysis will establish a basis for understanding the integration of EDA into these processes and the advantages it may offer.

Event-Driven Architecture (EDA) is a software architectural pattern that facilitates communication between distributed systems through the production, detection, consumption, and reaction to events. It enables systems to be adaptable, flexible, and robust, ultimately achieving agility in managing business processes (Sookoo et al., 2016; Vargas et al., 2008). Asynchronous Communication, loose coupling, real-time, scalability and flexibility offered by EDA can meet the needs of RED processes and provide the infrastructure for an agile approach to real estate processes.

Conducting a key search using the terms ("event-driven architecture" OR "event-driven" OR "EDA" OR "reactive architecture") AND ("real estate" OR "property" OR "realty" OR "land development") AND ("development" OR "construction" OR "project management" OR "urban planning") AND ("integration" OR "system" OR "platform" OR "application") AND ("data" OR "information" OR "analytics" OR "insight") reveals findings from a literature review and analysis of existing studies on Scopus. However, none of the papers reviewed specifically address the use of EDA within the realm of RED. For this reason, the literature review focuses on how EDA has been applied in other sectors and if EDA is feasible for RE. To achieve this, a second search was conducted using the keywords ("event-driven" OR "event-based" OR "event-oriented" OR "asynchronous") AND ("system" OR "architecture" OR "framework" OR "model") AND ("application" OR "use" OR "implementation" OR "deployment") AND

("sector" OR "industry" OR "field" OR "domain") AND ("healthcare" OR "finance" OR "transportation" OR "manufacturing" OR "retail" OR "telecommunications" OR "education"). The results of this extensive investigation offer valuable insights into the successful application of EDA in various fields.
This study revealed valuable insights into the successful implementation of EDA in various sectors. The results from both studies may guide the creation of an EDA framework for real-time data processing in RED. However, the practical application of this framework is beyond the focus of this paper.

Findings

The literature review and analysis reveal that none of the papers explicitly address the use of EDA in RED. However, there are notable research works that could offer valuable insights into the potential application of EDA within this field. Adaptability and Flexibility, Proactive Event-Driven Computing, Modularity and Loose Coupling are general principles and benefits of EDA. EDA empowers organizations to be versatile, responsive, and resilient in their management of business processes, ultimately leading to enhanced agility (Sookoo et al., 2016). The flexibility and scalability of EDA can support the dynamic nature of real estate projects, which often involve multiple stakeholders and changing requirements. Proactive event-driven computing can build upon EDA by anticipating and addressing potential negative events or capitalizing on future opportunities through the use of automated decision-making technologies (Engel & Etzion, 2011). Proactive event-driven computing could help in predicting and mitigating risks in real estate projects, such as delays or cost overruns. EDA exhibits similarities with service-oriented architecture (SOA), including modularity and loose coupling. Additionally, it is capable of processing events asynchronously, which enhances its responsiveness to real-time changes (Jieming & Yu, 2009). EDA could be used to integrate real-time data from various sources (e.g. market trends, construction progress, environmental conditions) to make informed decisions. Several industries utilize EDA systems. In the telecommunications industry, event-driven systems play a crucial role in managing and optimizing communication networks. They facilitate efficient data transmission and effectively handle substantial amounts of real-time events (Sachs et al., 2013). Also, in transportation, these systems are crucial for traffic management, enabling real-time monitoring and decision-making based on continuous data from sensors (Dunkel et al., 2008, 2011). EDA helps in managing congestion and improving the efficiency of transportation networks. In supply chain management sector, Event-driven systems enhance the responsiveness and flexibility of supply chains by processing events related to inventory levels, shipment tracking, and demand fluctuations (Chandy et al., 2007; Sachs et al., 2013). In the context of Industry 4.0, event-driven systems are used for real-time data integration and decision-making on the shop floor, improving production efficiency and flexibility (Ferrer et al., 2015; Roset et al., 2005; Rossit et al., 2019; Umer et al., 2018) for the manufactoring sector. In financial sector, event-driven systems are employed in trading platforms to exploit arbitrage opportunities, manage risks, and ensure compliance with regulatory requirements (Chandy et al., 2007; Chung-Sheng Li, 2005; Selby, 2005). Also, in public health sector, Event-driven systems support disease surveillance by processing real-time health data to detect and respond to outbreaks promptly (Chung-Sheng Li, 2005). Likewise, they are used for real-time congestion management and other critical operations in power grids, ensuring stability and efficiency in power control centers (Kumar et al., 2011). EDA facilitates the integration and communication of IoT devices across various environments, such as mobile, edge, fog, and cloud, enhancing the scalability and responsiveness of IoT applications (Berjón et al., 2022). These systems also support large-scale data dissemination and autonomic computing, improving the management and operational efficiency of enterprises (Pietzuch et al., 2007). Event-driven systems are used in the oil and gas industry as well to monitor and optimize production processes in real-time (Chung-Sheng Li, 2005).

Conclusion

RED is a complex, long-term process, then using a real-time monitoring system could help manage risks more effectively. By continuously tracking key milestones, resource use, compliance with regulations, and budget performance, this system would allow teams to spot potential issues early and to react before delays become costly. EDA is a system that reacts instantly to changes or events could improve RED processes by enabling faster data analysis and smarter decisions. With EDA, stakeholders could get clearer, up-to-date information, offering a better project management.

Conventional decision-making in RED typically depends on experience and intuition; however, an EDA-based system provides a more adaptable, data-driven option. Integrating real-time data with predictive analytics can establish a more flexible framework for risk management and decision-making. However, more research is needed to see if such systems are practical for the industry and whether EDA can work alongside or even replace older methods in some cases. While EDA shows promise for RED, its real-world effectiveness and how well it can scale up for large projects still need more profound study.

References

Atkin, B., & Borgbrant, J. (Eds.). (2010). *Performance improvement in construction management*. Spon Press. https://doi.org/10.4324/9780203876084

Berjón, R., Mateos, M., Beato, M. E., & Fermoso García, A. (2022). An Event Mesh for Event Driven IoT Applications. *International Journal of Interactive Multimedia and Artificial Intelligence*, *7*(6), 54. https://doi.org/10.9781/ijimai.2022.09.003

Chandy, K. M., Charpentier, Michel., & Capponi, A. (2007). Towards a theory of events. *Proceedings of the 2007 Inaugural International Conference on Distributed Event-Based Systems*, 180–187. https://doi.org/10.1145/1266894.1266929

Chung-Sheng Li. (2005). Real-time event driven architecture for activity monitoring and early warning. *Conference, Emerging Information Technology 2005.*, 182–185. https://doi.org/10.1109/EITC.2005.1544382

Dunkel, J., Fernandez, A., Ortiz, R., & Ossowski, S. (2008). Event-Driven Architecture for Decision Support in Traffic Management Systems. *2008 11th International IEEE Conference on Intelligent Transportation Systems*, 7–13. https://doi.org/10.1109/ITSC.2008.4732715

Dunkel, J., Fernández, A., Ortiz, R., & Ossowski, S. (2011). Event-driven architecture for decision support in traffic management systems. *Expert Systems with Applications*, *38*(6), 6530–6539. https://doi.org/10.1016/j.eswa.2010.11.087

Engel, Y., & Etzion, O. (2011). Towards proactive event-driven computing. *Proceedings of the 5th ACM International Conference on Distributed Event-Based System*, 125–136. https://doi.org/10.1145/2002259.2002279

Eppinger, S. D., Bonelli, S., & Gonzalez, A. M. (2013). Managing Iterations in the Modular Real Estate Development Process. In *Reducing Risk in Innovation* (pp. 37–44). Elsevier. https://doi.org/10.3139/9783446437937.005

Ferrer, B. R., Iarovyi, S., Lobov, A., & Lastra, J. L. M. (2015). Towards processing and reasoning streams of events in knowledge-driven manufacturing execution systems. *2015 IEEE 13th International Conference on Industrial Informatics (INDIN)*, 1075–1080. https://doi.org/10.1109/INDIN.2015.7281884

Jieming, W., & Yu, D. (2009). A Study on RFID Book Information Management System with an EDA/SOA. *2009 Second International Symposium on Electronic Commerce and Security*, 451–455. https://doi.org/10.1109/ISECS.2009.157

Kumar, Y. P., Khaparde, S. A., Joshi, R. K., & Pentayya, P. (2011). Real-time congestion representation using event driven architecture. In *17th Power Systems Computation Conference, PSCC 2011*. Power Systems Computation Conference (PSCC). https://www.scopus.com/inward/record.uri?eid=2-s2.0-84943774243&partnerID=40&md5=c42464792fa6b10df20e84c219459458

Pietzuch, P., Muhl, G., & Fiege, L. (2007). Distributed Event-Based Systems: An Emerging Community. *IEEE Distributed Systems Online*, *8*(2), 2–2. https://doi.org/10.1109/MDSO.2007.8

Roset, B. J. P., Nijmeijer, H., Van Eekelen, J. A. W. M., Lefeber, E., & Rooda, J. E. (2005). Event driven manufacturing systems as time domain control systems. *Proceedings of the 44th IEEE Conference on Decision and Control*, 446–451. https://doi.org/10.1109/CDC.2005.1582196

Rossit, D. A., Tohmé, F., & Frutos, M. (2019). A data-driven scheduling approach to smart manufacturing. *Journal of Industrial Information Integration*, *15*, 69–79. https://doi.org/10.1016/j.jii.2019.04.003

Ruddock, L. (Ed.). (2008). Market interdependencies between real estate, investment, development and construction: The Dutch experience. In *Economics for the Modern Built Environment* (0 ed., pp. 249–268). Routledge. https://doi.org/10.4324/9780203938577-20

Sachs, K., Kounev, S., & Buchmann, A. (2013). Performance modeling and analysis of message-oriented event-driven systems. *Software & Systems Modeling*, *12*(4), 705–729. https://doi.org/10.1007/s10270-012-0228-1

Selby, R. (2005, August 30). Event-Driven Software Architectures for Large-Scale Systems. *Space 2005*. Space 2005, Long Beach, California. https://doi.org/10.2514/6.2005-6657

Sookoo, K., Van Belle, J.-P., & Seymour, L. (2016). Implementing an Event-Driven Enterprise Information Systems Architecture: Adoption Factors in the Example of a Micro Lending Case Study. In A. M. Tjoa, L. D. Xu, **M. Raffai, & N. M. Novak** (Eds.), *Research and Practical Issues of Enterprise Information Systems* (Vol. 268, pp. 293–308). Springer International Publishing. https://doi.org/10.1007/978-3-319-49944-4_22

Turner, V. K. (2017). Obstacles to developing sustainable cities: The real estate rigidity trap. *Ecology and Society*, *22*(2), art1. https://doi.org/10.5751/ES-09166-220201

Umer, M., Mahesh, B., Hanson, L., Khabbazi, M. R., & Onori, M. (2018). Smart Power Tools: An Industrial Event-Driven Architecture Implementation. *Procedia CIRP*, *72*, 1357–1361. https://doi.org/10.1016/j.procir.2018.03.058

Vargas, L., Bacon, J., & Moody, K. (2008). Event-Driven Database Information Sharing. In A. Gray, K. Jeffery, & J. Shao (Eds.), *Sharing Data, Information and Knowledge* (Vol. 5071, pp. 113–125). Springer Berlin Heidelberg. https://doi.org/10.1007/978-3-540-70504-8_11

SCIENCE, TECHNOLOGY AND SOCIETY

Communication of Science and Technology

Social and Ethical Dimensions of AI

Social Dimensions of Science and Technology

A Bibliometric Analysis of Metaverse Technologies in Healthcare Services

Seckin Damar[a], Gulsah Hancerliogullari Koksalmis[a,b]

[a] Istanbul Technical University, Department of Industrial Engineering, Faculty of Management, Istanbul, Turkey
[b] University of Central Florida, Department of Industrial Engineering and Management Systems, Orlando, USA
damar17@itu.edu.tr

Keywords: Metaverse, Healthcare Services, Bibliometric Analysis, Web of Science.

Aim

The aim of this study is to provide a comprehensive bibliometric analysis of the healthcare metaverse, an interdisciplinary domain that integrates immersive technologies, such as Virtual Reality (VR), Augmented Reality (AR), Mixed Reality (MR), and Extended Reality (XR), with medical services and education. These technologies have transformed how healthcare is delivered, particularly following the COVID-19 pandemic, by enabling new modalities for clinical training, remote therapy, surgical simulation, and mental health interventions. The acceleration of digital health platforms has exposed the need for scalable, flexible, and accessible healthcare models, which immersive technologies increasingly support. Broadly defined, the metaverse refers to a shared digital space created through the convergence of physical and virtual environments. In healthcare, this digital transformation extends beyond entertainment to create interactive environments for diagnostics, education, and collaboration, challenging traditional care models and introducing new ethical and operational concerns. The growing reliance on simulation-based environments, wearable biosensors, and telepresence technologies has reinforced the healthcare metaverse's potential to fill gaps in medical infrastructure and health equity, particularly in remote or underserved areas. This research is framed within the Science, Technology, and Society (STS) perspective, which examines how innovations co-evolve with institutional structures, societal norms, and ethical frameworks. Applying this lens to the healthcare metaverse reveals critical issues of equity, access, and the changing dynamics between professionals and patients in digital contexts. In doing so, the study not only assesses the technological diffusion of the metaverse but also explores its socio-political embeddedness within healthcare systems. Despite growing academic attention, the field remains conceptually fragmented and methodologically underexplored. This study addresses that gap by applying bibliometric techniques to map the intellectual landscape, identify leading contributors, and analyze structural patterns of the literature. By uncovering thematic clusters and deviations from classical bibliometric laws, the study offers both a diagnostic overview of the field and a foundation for future STS-informed research into the sociotechnical dynamics of healthcare innovation.

Material and Method

This study employed a bibliometric approach using 3,721 publications retrieved from the Web of Science Core Collection spanning from 1994 to 2022. The dataset was generated using targeted search queries incorporating terms such as "metaverse", "virtual reality in health", "augmented reality in health", and related phrases. The analysis was conducted using VOSviewer for mapping co-authorship, keyword co-occurrence, and bibliographic coupling networks. Microsoft Excel was used for descriptive statistics and application of bibliometric laws, including Lotka's Law (author productivity), Bradford's Law (journal dispersion), and Zipf's Law (keyword distribution). Publications were categorized by country, institution, author, document type, research area, and language. These bibliometric laws are widely used to examine the structural characteristics and maturity of research fields, making them especially suitable for analyzing a fast-evolving and interdisciplinary domain like the healthcare metaverse. From an STS perspective, bibliometric methods also offer valuable insight into the institutionalization of emerging fields, the power structures embedded in knowledge production, and the epistemic communities driving innovation.

Findings

The results show that while the USA, England, and Italy lead in terms of publication volume and impact, international collaboration is strong among European, Asian, and North American countries. This pattern indicates that despite geopolitical boundaries, global interest in healthcare transformation through immersive technology is growing. Influential institutions include Università Cattolica del Sacro Cuore and Istituto Auxologico Italiano, and prominent authors include G. Riva and C. Botella. Keyword co-occurrence revealed 12 thematic clusters, such as stroke rehabilitation, simulation, mental health, pain management, wearable technologies, and VR-based education. For instance, "virtual reality" appeared in more than 35% of the documents, indicating its dominant role in this literature. Unexpectedly, the field did not conform to traditional bibliometric laws: the keyword distribution did not align with Zipf's Law, authorship frequency deviated from Lotka's Law, and journal dispersion diverged from Bradford's Law. This divergence suggests that the field is still in a dynamic, exploratory phase characterized by disciplinary overlap and rapid conceptual expansion. The co-authorship networks demonstrated low author-level collaboration despite strong institutional and national links. This may reflect barriers in interdisciplinary communication or the nascency of shared academic platforms. The bibliographic coupling analysis revealed emerging research streams across clinical and educational domains, with varying degrees of technological integration. The rise in annual publication and citation trends after 2007 reflects the growing academic and practical interest in immersive technologies for healthcare service delivery and the subsequent expansion of related scholarly communities.

Table 1. Most influential authors according to total link strength (TLS) and citation.

	According to TLS			According to citation		
Rank	Author	Documents	TLS	Author	Documents	Cites
1	G. Riva	65	2056	G. Riva	65	1768
2	P. Langhorne	35	1044	P. Langhorne	2	1585
3	J. Bernhardt	39	951	J. Bernhardt	1	1226
4	G. Kwakkel	30	776	G. Kwakkel	1	1226
5	Z. Bao	20	711	Z. Bao	1	952
6	J. W. Chung	23	692	J. W. Chung	1	952
7	A. Ehrlich	1	545	A. Ehrlich	1	952
8	V. R. Feig	1	545	V. R. Feig	1	952
9	A. M. Foudeh	1	545	A. M. Foudeh	1	952
10	A. Gasperini	1	545	A. Gasperini	1	952

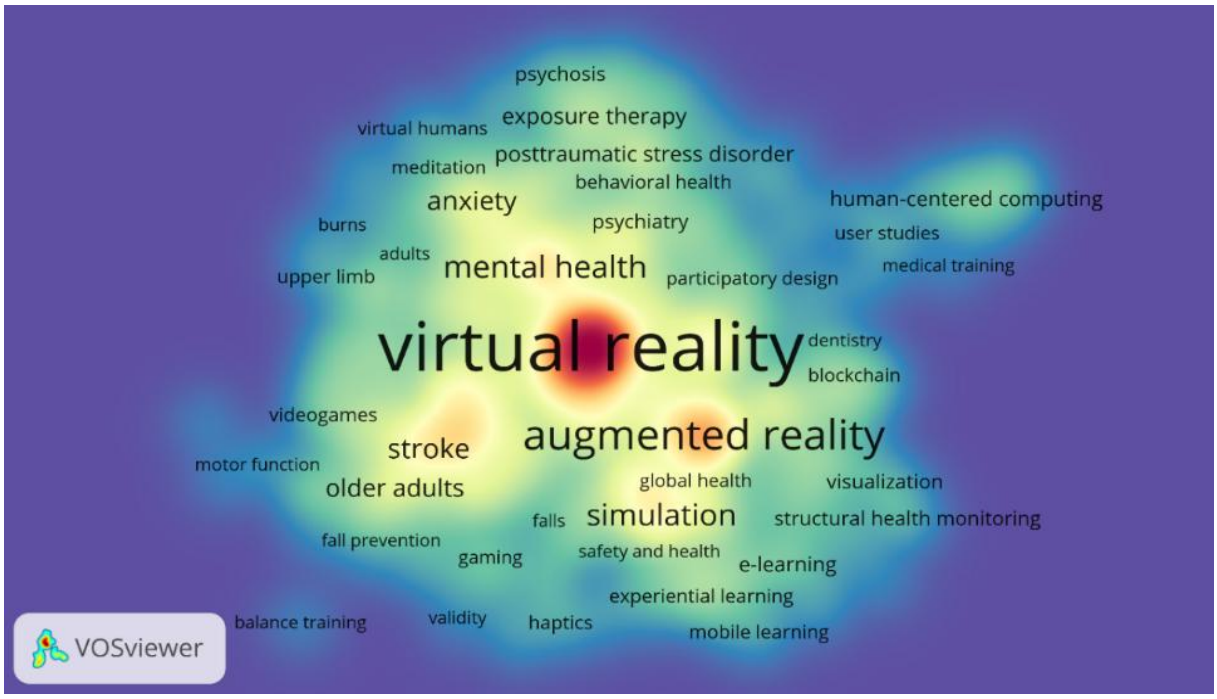

Figure 1. Co-occurrence analysis of author-keywords.

Conclusion

This study is the first comprehensive bibliometric examination of the healthcare metaverse, integrating classical bibliometric laws and network analysis. The results highlight the fragmentation and emergent nature of the field, emphasizing its relevance for interdisciplinary research and science policy. Theoretically, this study contributes to STS by elucidating the mechanisms through which technological innovations shape and are shaped by the healthcare domain. It underscores the importance of institutional actors and epistemic networks in the co-production of healthcare knowledge. Practically, the findings serve as a strategic guide for researchers, policymakers, and technology developers to navigate and contribute to this evolving field. These results may inform funding priorities, collaborative agendas, and curriculum development for medical educators seeking to integrate extended reality into training programs. As digital transformation accelerates in healthcare, understanding the knowledge structures behind metaverse applications becomes essential, particularly for designing inclusive telemedicine services and simulation-based medical education programs that address real-world challenges.

References

Ahmad, M., & Batcha, M. S. (2020). Examining the scientific productivity of authors in dyslexia research: a study using Lotka's law. Library Philosophy and Practice (e-Journal), 4(5), 4198.

Belk, R. W., Belanche, D., & Flavián, C. (2023). Key concepts in artificial intelligence and technologies 4.0 in services. Service Business, 17(1), 1-9.

Damar, M. (2021). Metaverse Shape of Your Life for Future: A bibliometric snapshot. Journal of Metaverse, 1(1), 1-8.

Koo, H. (2021). Training in lung cancer surgery through the metaverse, including extended reality, in the smart operating room of Seoul National University Bundang Hospital, Korea. Journal of Educational Evaluation for Health Professions, 18.

Musamih, A., Yaqoob, I., Salah, K., Jayaraman, R., Al-Hammadi, Y., Omar, M., & Ellahham, S. (2022). Metaverse in healthcare: Applications, challenges, and future directions. IEEE Consumer Electronics Magazine (Early Access), 1-13.

Petrigna, L., & Musumeci, G. (2022). The metaverse: A new challenge for the healthcare system: A scoping review. Journal of functional morphology kinesiology, 7(3), 63.

Rajeswari, S., Dhanasekar, N., & Sathya, S. (2021). Scientometric analysis based on dimension of research productivity of faculty in VIT University from Web of Science. Library Philosophy and Practice, 1-20.

Riva, G., Baños, R. M., Botella, C., Mantovani, F., & Gaggioli, A. (2016). Transforming experience: the potential of augmented reality and virtual reality for enhancing personal and clinical change. Frontiers in psychiatry, 7, 164.

SCIENCE, TECHNOLOGY AND SOCIETY

Communication of Science and Technology

Social and Ethical Dimensions of AI

Social Dimensions of Science and Technology

Unintended Consequences of Generative AI in Product Ideation: A Product Management Perspective

Tuğçe Gültekin Atlı[a] , Deniz Tunçalp[b]

[a] Istanbul Technical University, Department of Management Engineering, Master's Degree Program, Türkiye
[b] Istanbul Technical University, Department of Management Engineering, Faculty of Management, Türkiye
atli22@itu.edu.tr

Keywords: Decision-Making Bias, Generative AI, Innovation Management, New Product Development (NPD), Product Ideation.

Aim

The adoption of Generative Artificial Intelligence (GenAI) in product ideation has significantly transformed the new product development (NPD) process, enabling faster brainstorming, enhanced market insights, and automation-driven creativity. Unlike traditional AI systems focused primarily on analysis and classification, GenAI creates original content across multiple formats, demonstrating capabilities for divergent thinking and creative recombination particularly valuable for product innovation. In product ideation contexts, these technologies excel at generating numerous alternative concepts, creating connections between disparate domains, and developing detailed user personas based on market data.

While AI-driven ideation tools such as ChatGPT, Midjourney, Gemini, and Copilot have facilitated idea generation, they have also introduced several unintended consequences that impact creativity, originality, and decision-making. Emerging research suggests that while GenAI might increase individual productivity, it could potentially reduce the diversity of ideas across organizations through mechanisms such as training data bias and standardization of outputs.

This study explores how GenAI is reshaping product ideation in the B2B and B2C sectors, focusing on the unintended risks and challenges associated with AI-generated ideas. The research examines how product managers perceive and navigate these risks, particularly creativity fixation, decision-making bias, innovation standardization, and ethical concerns. By critically analyzing these emerging patterns, the study aims to contribute to the discourse on responsible AI adoption in product management while advancing the Science, Technology and Society (STS) literature by exploring the complex socio-technical interactions between human creativity and artificial intelligence systems in organizational settings.

Material and Method

This study employs a qualitative exploratory approach using semi-structured interviews with experienced product managers from B2B and B2C domains. Eight product managers with at least two years of experience in new product development and direct experience implementing GenAI within their ideation workflows were selected for the study. Participants were from the same sector but possessed expertise and experience in different domains, with representation across both B2B and B2C contexts to ensure comprehensive coverage of product management perspectives.

Data collection involved in-depth interviews conducted through video conferencing, with session durations ranging from 40 to 60 minutes. Each interview was recorded with participant consent and professionally transcribed. Prior to the main study, a pilot interview was conducted to refine the interview protocol and ensure question clarity and relevance. Based on this pilot, adjustments were made to terminology, question sequencing, and prompt specificity.

The research protocol followed a three-step framework: (1) exploring general understanding of GenAI and its integration into workflows, (2) in-depth exploration of experiences with GenAI in new product ideation, and (3) examination of unintended consequences and future perspectives. The interview guide consisted of 14 questions distributed across these three sections, with additional follow-up prompts developed to ensure consistent exploration of key themes. Projective techniques were incorporated into the protocol to help participants articulate

tacit knowledge and implicit assumptions, including asking them to compare ideation processes before and after GenAI adoption using metaphorical descriptions.

Data analysis employed the Gioia methodology, a rigorous qualitative approach involving a systematic three-stage analytical process: (1) coding raw data using "informant-centric" terms, (2) identifying deeper patterns and relationships to develop second-order themes, and (3) distilling these themes into aggregate theoretical dimensions. First, all interview recordings were professionally transcribed verbatim, with transcripts verified for accuracy against the original recordings. Field notes taken during interviews were integrated with transcripts to capture contextual information and non-verbal cues. Initial coding involved an open, line-by-line examination of the data to identify first-order concepts using participant-centric terms. These second-order themes were further consolidated into four aggregate theoretical dimensions: (1) GenAI's role in product ideation processes, (2) creativity fixation and cognitive dependency, (3) standardization of innovation outputs, and (4) decision-making biases and ethical concerns.

Throughout the analytical process, the research team engaged in constant comparison techniques to ensure consistency and validity in the interpretation of data. A comparative dimension was also included to examine how unintended consequences manifested differently across B2B and B2C product management contexts.

Findings

The findings highlight that while GenAI significantly enhances efficiency in product ideation, it also introduces challenges that require critical evaluation. The most significant unintended consequences identified include creativity fixation, homogenization of innovation, decision-making bias, and ethical concerns related to intellectual property and data security.

Product managers reported deep integration of GenAI tools into their daily workflows, with ChatGPT emerging as the universally preferred tool. These tools were primarily positioned as personal assistants rather than replacements for product managers. While participants consistently acknowledged efficiency benefits, their assessments varied—some reported nearly tenfold increases in efficiency for documentation tasks, while others suggested quality improvements might be offset by increased time investment in task completion.

A prevalent concern across interviews was AI's potential to constrain rather than enhance creative thinking. Seven of eight participants expressed that their creativity was being negatively affected through regular AI use. As one participant revealed, "I initially thought it helped my creative process, but now I find myself going straight to AI without thinking first, which has reduced my creativity." This indicates how tools adopted for efficiency can reshape cognitive habits in unanticipated ways. Some participants reported developing dependency patterns, with one admitting, "I've become somewhat dependent on it. I feel the need to consult it even when I know the answer, thinking it might suggest something better."

All participants unanimously observed that GenAI tends to produce standardized, predictable outputs rather than truly innovative ideas. As one participant noted, it typically presents "things that have been known in the market for a long time, compiled and collected." Another characterized AI's outputs as "outdated thoughts" that fail to capture current trends. This standardization in AI-generated content represents a significant concern for product managers whose competitive advantage depends on differentiated thinking.

Decision-making biases emerged as another critical concern. Participants described challenges in verifying AI-generated information, with one explaining, "I try to get references when AI answers, so I can actually cross-check," but often encountered difficulties because "AI often can't provide proper citations." This verification challenge created situations where, as the same participant admitted, "Sometimes I have to use it as a source even when I can't verify the information."

Ethical and intellectual property concerns were also significant. Data security emerged as a primary concern, with participants developing informal safeguards against potential information leakage. One participant revealed an unwritten organizational rule: "We have an unwritten rule not to mention our company name to AI tools." Intellectual property considerations revealed divergent viewpoints, with some participants concerned that "ideas produced by AI belong to the AI itself" and "the same idea could be given to different people, including competitors," while others offered more relaxed assessments, comparing AI-generated ideas to open-source innovation models.

Conclusion

This study illuminates the dual impact of Generative AI in product ideation processes. While GenAI provides significant efficiency gains, especially in documentation and content creation, the findings reveal a complex landscape of unintended consequences that product managers must navigate. GenAI-induced creativity fixation emerged as a particularly concerning phenomenon, with most participants reporting diminished independent thinking over time. As one participant noted, "I initially thought it helped my creative process, but now I find myself going straight to AI without thinking first," illustrating how cognitive patterns can be subtly reshaped by AI tools.

The standardization of innovation represents another significant challenge, as participants unanimously reported that GenAI produces predictable, often outdated outputs that lack truly disruptive potential. Product managers described AI-generated ideas as presenting "things that have been known in the market for a long time," raising concerns about industry-wide homogenization of product concepts if these tools become universally adopted without critical intervention.

Decision-making biases were exacerbated by verification challenges, as participants struggled to authenticate AI-generated information while sometimes feeling compelled to use it even when unverified. This creates potential propagation of misinformation through organizational decision chains. Furthermore, with no formal governance frameworks in place, product managers have developed informal practices to protect proprietary information, such as unwritten rules against mentioning company names to AI tools.

The implications for product management suggest an evolving hybrid approach. Participants demonstrated strategic task allocation, using AI primarily for structured documentation and communication tasks while maintaining human primacy for creative direction and strategic decisions. This selective application helps mitigate risks while capturing efficiency benefits. Product managers also developed adaptive strategies over time, such as thinking independently before consulting AI "to avoid bias," and creating matrix frameworks to provide structure for AI-assisted tasks.

From a theoretical perspective, this research challenges simplistic notions of AI as either purely augmentative or substitutive. The findings reveal a complex interplay where initial productivity gains can gradually shift toward dependency patterns and creative constraint if not carefully managed. The study contributes to STS literature by documenting how technological systems reshape cognitive habits and decision-making processes in professional contexts.

Practical implications include the need for organizations to develop formal governance frameworks for AI-assisted ideation, establish protocols for critical evaluation of AI-generated concepts, and implement training that helps product teams maintain creative autonomy while leveraging AI capabilities. As GenAI tools continue to evolve, finding the optimal balance between computational efficiency and human creativity remains crucial for organizations seeking sustainable innovation advantage.

References

Anderson, B. R., Shah, J. H., & Kreminski, M. (2023). Homogenization Effects of Large Language Models on Human Creative Ideation. **Url-1** http://dx.doi.org/10.1145/3635636.3656204, date retrieved 30.05.2025.

Boden, M. A. (1998). Creativity and artificial intelligence. Artificial Intelligence, 103(1-2), 347-356. **Url-2** https://doi.org/10.1016/S0004-3702(98)00055-1, date retrieved 30.05.2025.

Braun, V., & Clarke, V. (2006). Using thematic analysis in psychology. Qualitative Research in Psychology, 3(2), 77-101. **Url-3** https://doi.org/10.1191/1478088706qp063oa, date retrieved 30.05.2024.

Brown, T. (2009). Change by design: How design thinking creates new alternatives for business and society. Collins Business. **Url-4** https://www.harpercollins.com/products/change-by-design-tim-brown, date retrieved 30.05.2024.

Davenport, T. H., & Ronanki, R. (2018). Artificial intelligence for the real world. Harvard Business Review, 96(1), 108-116. **Url-5** https://hbr.org/2018/01/artificial-intelligence-for-the-real-world, date retrieved 30.05.2024.

Frank, T., Piller, F. T., & Marion, T. J. (2024). Generative AI, Innovation, and Trust. The Journal of Applied Behavioral Science.
Url-6 http://dx.doi.org/10.1177/00218863241285033, date retrieved 30.05.2024.
Gioia, D. A., Corley, K. G., & Hamilton, A. L. (2013). Seeking qualitative rigor in inductive research: Notes on the Gioia methodology. Organizational Research Methods, 16(1), 15-31.
Url-7 https://doi.org/10.1177/1094428112452151, date retrieved 30.05.2024.
Hsu, G. T., & Bechky, B. A. (2023). Exploring the Digital Undertow: How generative AI impacts social categorizations in creative work.
Url-8 https://journals.sagepub.com/doi/10.1177/26317877241275118, date retrieved 30.05.2024.
McKinsey. (2024). The state of AI in 2024: Gen AI adoption spikes and starts to generate value. McKinsey & Company.
Url-9 https://www.mckinsey.com/capabilities/quantumblack/our-insights/the-state-of-ai-2024, date retrieved 30.05.2024
Mosier, K. L., & Skitka, L. J. (2018). Human decision makers and automated decision aids: Made for each other? In Automation and human performance (pp. 201-220).
Url-10 https://doi.org/10.1201/9781315137957, date retrieved 30.05.2024.
Runco, M. A. (2014). Creativity: Theories and themes: Research, development, and practice. Academic Press.
Url-11 https://doi.org/10.1016/C2012-0-06920-7, date retrieved 30.05.2024.
Schuller, A., Janssen, D., Blumenröther, J., Probst, T. M., Schmidt, M., & Kumar, C. (2023). Generating personas using LLMs and assessing their viability.
Url-12 http://dx.doi.org/10.1145/3613905.3650860, date retrieved 30.05.2024.
Ulrich, K. T., & Eppinger, S. D. (2019). Product design and development. McGraw-Hill.
Url-13 https://www.mheducation.com/highered/product/product-design-development-ulrich-eppinger/M9781260043655.html, date retrieved 30.05.2024.
Veale, M., & Binns, R. (2017). Fairer machine learning in the real world: Mitigating discrimination without collecting sensitive data. Big Data & Society, 4(2).
Url-14 https://doi.org/10.1177/2053951717743530, date retrieved 30.05.2024.

SCIENCE, TECHNOLOGY AND SOCIETY

Communication of Science and Technology

Social and Ethical Dimensions of AI

Social Dimensions of Science and Technology

The Impact of Music Platforms on Music Production and Taste Profiles in Türkiye: The Case of Spotify

Mert Sarıkaya[a], Ebru Belgin Yetişkin Doğrusöz[b]

[a] Istanbul Technical University, Graduate School, Sociology, Science, and Technology Studies, Türkiye
[b] Istanbul Technical University, Faculty of Science and Letters, Department of Sociology, Türkiye
sarikayam21@itu.edu.tr

Keywords: Platform Capitalism, Algorithmic Governance, Music Industry, Digital Streaming, Actor-Network Theory.

Aim

Departing from the Science, Technology and Society (STS) studies, this research explores the music industry's transformation in the era of platform capitalism with a focus on Spotify. This study specifically examines how global platform dynamics manifest in Türkiye's unique cultural and economic context, creating localized impacts on artists, production practices, and consumption patterns. The study analyzes the mediating function performed by the digital streaming platform Spotify and how it shapes the music industry via its technical infrastructure and business practices. It examines the ways in which Spotify has changed power dynamics, production methods and consumption habits. This transformation represents significant shifts in how music is produced, distributed and commodified. Rather than attempting to cover all aspects of this transformation comprehensively, this research strategically focuses on algorithmic governance and the resulting platform dependencies that have emerged in Istanbul's music ecosystem.The study aims to explore the complex relationships between human and non-human elements in the socio-technical system revolved around Spotify, including artists, listeners, producers, algorithms, and technological infrastructures. Actor-Network Theory (ANT) is particularly valuable for this research as it enables the analysis of how agency is distributed across networks rather than residing solely in human actors or technological systems. This theoretical approach uniquely positions us to understand how algorithmic systems and human actors co-produce the contemporary music ecosystem through what we identify as forms of "hybrid agency." Thus, the objective of the research is to explore how these platform dynamics are translated in a local context.

Material and Method

The research uses a mixed-method approach combining primary and secondary data collection methods. Primary data was gathered through semi-structured interviews with 12 music industry professionals in Türkiye between March-April 2025, following ethical approval from Istanbul Technical University. Participants included independent and signed musicians, sound engineers, managers, producers, music journalists, digital marketing professionals, and record label employees, providing a representative cross-section of Türkiye's music ecosystem. The interviews lasted approximately 45 minutes each and focused on understanding participants' direct experiences with Spotify, particularly regarding algorithmic bias, pressure to create algorithmically successful content, financial dependency, and practices that reinforces platform dependency. In the quantitative phase, secondary data collection was based on analysis of personal Spotify account data, including taste profiles and streaming history metrics. Descriptive statistical analysis was applied to visualize and interpret these data sets, revealing how platforms classify and commodify user preferences. Secondarydata collection method involves a systematic review of the literature on the effects of platform capitalism in the music industry, the digital music economy, and algorithmic governance of Spotify. The theoretical framework draws primarily on ANT to analyze the interaction of various actors and systems to demonstrate how they shape musical practices and experiences. This framework positions Spotify not as a neutral intermediary but as an active mediator that reconfigures power dynamics.

Findings

The research findings reveal four key dimensions of the impact of platform capitalism in the music ecosystem in Türkiye. First, Spotify's recommendation algorithms have created new forms of "hybrid agency". This creates a situation where musical preferences become entangled with machine learning. This concept helps explain how human intention and technological systems co-produce musical experiences that would not exist through either human or algorithmic action alone. These algorithms generate what might be called "taste profiles", which are digital fingerprints of listeners' musical preferences that become increasingly detailed with each interaction. While these profiles facilitate personalized experiences, they simultaneously create "filter bubbles" that limit genuine musical discovery and serendipity. These algorithmic enclosures represent a significant shift from previous modes of music discovery that relied more heavily on social recommendations, music criticism, and radio programming.
Second, platform dynamics have transformed production practices where artists increasingly design their music to perform well within algorithmic systems. This includes changing the duration and shortening songs, and placing hooks at the beginning to prevent skipping. Our interviews with Turkish music professionals revealed that the question "How will this sound on Spotify?" has become more important than artistic decisions. This is a shift where choices made are increasingly influenced by algorithmic impositions rather than artistic considerations.
Third, the thesis also reveals the effects of platform dependency. While Spotify present itself as democratic space where any artist can distribute their work, this research reveals a more complex reality. The platform's claims of democratization conflict with the empirical evidence that shows increasing concentration of streaming revenue among a small percentage of top artists. In the Turkish context, this is further complicated by the privileged position of distributors with local offices who have direct relationships with Spotify's editorial team, creating new gatekeeping mechanisms that disadvantage truly independent artists. Algorithmic systems mostly benefit already popular artists, making it increasingly difficult for independent musicians to gain visibility without significant marketing budgets or placement on editorial playlists in Spotify. This dependency extends to data-centricity, as artists increasingly make creative and marketing decisions based on metrics provided through tools like Spotify for Artists.
Fourth, the research illuminates the changing financial landscape of music. The pay-per-stream model mostly benefits highly streamed artists with large catalogs, and record labels. Independent artists now must increasingly invest in advertisements on social media platforms and continuously create for the standards of algorithms. In Türkiye, these economic dynamics are intensified by lower subscription fees which makes it almost impossible for artists to sustain themselves economically through streaming revenues alone.

Conclusion

This research explores how platform capitalism transforms the music ecosystem in Türkiye by creating new power dynamics, and dependencies for artists. This study's contribution lies in its exploration of how global platform dynamics are localized within Türkiye's specific cultural and economic context, revealing both universal and localized patterns of platform capitalism. The research contributes to our understanding of how technology reshapes cultural production through subtle but pervasive mechanisms of algorithmic governance and digital mediation. Digital platforms enable broader access to music, but they also introduce new forms of control and dependency through platform capitalism. The supposedly straightforward act of streaming a song now involves complex networks of data centers, content delivery networks, and algorithmic systems that track, analyze, and monetize every interaction. Finallythe research reveals a paradox: the very features that appear to democratize music distribution actually create new gatekeepers and barriers. Rather than viewing this transformation in simplistic terms of democratization or exploitation, our ANT approach reveals a more nuanced reality where agency is distributed across human and non-human actors, creating new socio-technical arrangements that both enable and constrain artistic expression. Algorithmic curation systems replace traditional expert-based selection methods while creating new forms of inequality and dependency. Artists must now consider not only the creative aspects of music-making but also the technical and data-driven aspects.This reconfiguration of the music industry requires new theoretical approaches and policy interventions to address emergent power imbalances. This research has significant implications for exploring contemporary music production under platform capitalism. By continuing to examine the socio-technical networks that constitute the contemporarymusic ecosystem, we can

better understand how to create more equitable conditions for listeners, musicians, musical production and consumption in the age of platform capitalism.

References

Aguiar, L., & Waldfogel, J. (2018). Platforms, Promotion, and Product Discovery: Evidence from Spotify Playlists (Working Paper No. 24713). National Bureau of Economic Research. https://doi.org/10.3386/w24713

Anderson, A., Maystre, L., Anderson, I., Mehrotra, R., & Lalmas, M. (2020). Algorithmic Effects on the Diversity of Consumption on Spotify. Proceedings of The Web Conference 2020, 2155–2165. https://doi.org/10.1145/3366423.3380281

Annabell, T., & Rasmussen, N. V. (2024). Spotify (Un)wrapped: How ordinary users critically reflect on Spotify's datafication of the self within creative workshops. Journal of Gender Studies, 1–17. https://doi.org/10.1080/09589236.2024.2433674

Berger, R. (2015). Now I see it, now I don't: Researcher's position and reflexivity in qualitative research. Qualitative Research, 15(2), 219–234. https://doi.org/10.1177/1468794112468475

Bowker, G. C., & Star, S. L. (2008). Sorting things out: Classification and its consequences (1. paperback ed., 8. print). MIT Press.

Callon, M. (1984). Some elements of a sociology of translation: Domestication of the scallops and the fishermen of St Brieuc Bay. The Sociological Review, 32(S1), 196–233. https://doi.org/10.1111/j.1467-954X.1984.tb00113.x

Callon, M. (2004). The role of hybrid communities and socio-technical arrangements in the participatory design. Journal of the Center for Information Studies, 5(3), 3–10.

Cheney-Lippold, J. (2011). A New Algorithmic Identity: Soft Biopolitics and the Modulation of Control. Theory, Culture & Society, 28(6), 164–181. https://doi.org/10.1177/0263276411424420

Cormen, T. H., Leiserson, C. E., Rivest, R. L., & Stein, C. (2009). Introduction to algorithms (3rd ed.). MIT Press.

Couldry, N., & Mejias, U. A. (2019). Data Colonialism: Rethinking Big Data's Relation to the Contemporary Subject. Television & New Media, 20(4), 336–349. https://doi.org/10.1177/1527476418796632

Creswell, J. W., & Creswell, J. D. (2018). Research Design: Qualitative, Quantitative, and Mixed Methods Approaches (5th ed.). SAGE Publications.

Debruyne, F. (2021). Tracing the music actor-network: Losing the meaning of musical experience? The limits of a routinization of science and technology studies applied to techniques and knowledges of music. In B. Zimmermann & T. Pinch (Eds.), Rethinking music through science and technology studies (pp. 247-268). Routledge.

Dijck, J. van, & Poell, T. (2013). Understanding Social Media Logic. Media and Communication, 1(1), 2–14. https://doi.org/10.17645/mac.v1i1.70

Dredge, S. (2024, March 4). James Blake: "The brainwashing worked and now people think music is free." Music Ally. http://musically.com/2024/03/04/james-blake-the-brainwashing-worked-and-now-people-think-music-is-free/

Eriksson, M., Fleischer, R., Johansson, A., Snickars, P., & Vonderau, P. (2019). Spotify Teardown: Inside the Black Box of Streaming Music. The MIT Press. https://doi.org/10.7551/mitpress/10932.001.0001

European Commission. Directorate General for Competition. (2019). Competition policy for the digital era. Publications Office. https://data.europa.eu/doi/10.2763/407537

Galletta, A. (2013). Mastering the semi-structured interview and beyond: From research design to analysis and publication (pp. xiii, 245). New York University Press. https://doi.org/10.18574/nyu/9780814732939.001.0001

Galloway, A. R. (2006). Protocol: How control exists after decentralization (1st MIT Press paperback ed). MIT Press.

Galloway, A. R., & Thacker, E. (2007). The exploit: A theory of networks. University of Minnesota Press.

Gawer, A., & Cusumano, M. (2015). Business Platforms. International Encyclopedia of the Social & Behavioral Sciences.(2nd ed., Vol. 2, pp. 37-42). https://doi.org/10.1016/B978-0-08-097086-8.73012-1

Gillespie, T. (2010). The politics of 'platforms.' New Media & Society, 12(3), 347–364. https://doi.org/10.1177/1461444809342738
Gillespie, T. (2014). The Relevance of Algorithms. In T. Gillespie, P. J. Boczkowski, & K. A. Foot (Eds.), Media Technologies (pp. 167–194). The MIT Press. https://doi.org/10.7551/mitpress/9780262525374.003.0009
Gillespie, T. (2018). Custodians of the internet: Platforms, content moderation, and the hidden decisions that shape social media. Yale University Press. https://doi.org/10.12987/9780300235029
Harkins, P. (2015). Following the Instruments, Designers, and Users: The Case of the Fairlight CMI. Journal on the Art of Record Production, 9,1-18.
Hennion, A. (1993). The passion for music: A sociology of mediation (M. Rigaud & P. Collier, Trans.; First issued in paperback). Routledge, Taylor & Francis Group.
Kasap, O., & Yalcintas, A. (2021). Commodification 2.0: How Does Spotify Provide Its Services for Free? Review of Radical Political Economics, 53(1), 157–172. https://doi.org/10.1177/0486613420924163
Kenney, M., & Zysman, J. (2016). The Rise of the Platform Economy. Issues in Science and Technology, 32(3), 61–69.
Langley, P., & Leyshon, A. (2017). Platform capitalism: The intermediation and capitalization of digital economic circulation. Finance and Society, 3(1),11-31. https://doi.org/10.2218/finsoc.v3i1.1936
Latour, B. (1992). Where Are the Missing Masses? The Sociology of a Few Mundane Artifacts. In W. E. Bijker & J. Law (Eds.), Shaping technology/building society: Studies in sociotechnical change (pp. 225–258). MIT Press.
Latour, B. (1993). We have never been modern. Harvard University Press.
Latour, B. (1996). On actor-network theory: A few clarifications. Soziale Welt, 47(4), 369-381.
Law, J. (1992). Notes on the theory of the actor-network: Ordering, strategy, and heterogeneity. Systems Practice, 5(4), 379–393. https://doi.org/10.1007/BF01059830
Magaudda, P. (2014). The Broken Boundaries between Science and Technology Studies and Cultural Sociology: Introduction to an Interview with Trevor Pinch. Cultural Sociology, 8(1), 63–76. https://doi.org/10.1177/1749975513484604
Magaudda, P. (2021). Smartphones, streaming platforms, and the infrastructuring of digital music practices. In T. Tofalvy & E. Barna (Eds.), Popular music, technology, and the changing media ecosystem (pp. 241–255). Palgrave Macmillan. https://doi.org/10.4324/9780429268830-17
Michael, M. (Ed.). (2000). Reconnecting culture, technology and nature: From society to heterogeneity. Routledge.
Mooney, J., & Pinch, T. (2021). Mooney, J., & Pinch, T. (2021). Sonic Imaginaries: How Hugh Davies and David Van Koevering Performed Electronic Music's Future. In B. Zimmermann & T. Pinch (Eds.), Rethinking music through science and technology studies (pp. 141-161). Routledge.
Nieborg, D. B., & Poell, T. (2018). The platformization of cultural production: Theorizing the contingent cultural commodity. New Media & Society, 20(11), 4275–4292. https://doi.org/10.1177/1461444818769694
Pelly, L. (2025). Mood Machine: The Rise of Spotify and the Costs of the Perfect Playlist (1st ed). Atria Books.
Pinch, T., & Bijsterveld, K. (2004). Sound Studies: New Technologies and Music. Social Studies of Science, 34(5), 635–648. https://doi.org/10.1177/0306312704047615
Plantin, J.-C., Lagoze, C., Edwards, P., & Sandvig, C. (2016). Infrastructure studies meet platform studies in the age of Google and Facebook. New Media & Society, 20. https://doi.org/10.1177/1461444816661553
Schedl, M., Zamani, H., Chen, C.-W., Deldjoo, Y., & Elahi, M. (2018). Current Challenges and Visions in Music Recommender Systems Research. International Journal of Multimedia Information Retrieval, 7(2),95-116. https://doi.org/10.1007/s13735-018-0154-2
Seaver, N. (2019). Knowing Algorithms. J. Vertesi & D. Ribes (Eds.), Digital STS: A field guide for science & technology studies (pp. 412–422). Princeton University Press. https://doi.org/10.1515/9780691190600-028
Seaver, N. (2022). Computing taste: Algorithms and the makers of music recommendation. University of Chicago Press.
Shitole, S., Bere, S. S., & Hanchate, D. B. (2024). Music Recommendation System on Spotify Using Deep Learning. International Research Journal of Engineering and Technology, 8(11), 1278-1284.
Srnicek, N. (2016). Platform Capitalism. Polity Press.

Star, S. L., & Ruhleder, K. (1996). Steps Toward an Ecology of Infrastructure: Design and Access for Large Information Spaces. Information Systems Research, 7(1), 111–134. https://doi.org/10.1287/isre.7.1.111
Sterne, J. (2015). The MP3 as a cultural artifact. Communication & Langages, 184(2), 41–60.
Tofalvy, T., & Koltai, J. (2021). "Splendid Isolation": The reproduction of music industry inequalities in Spotify's recommendation system. New Media & Society, 25(8), 1984-2003. https://doi.org/10.1177/14614448211022161
Tomasi, F., Cauteruccio, J., Kanoria, S., Ciosek, K., Rinaldi, M., & Dai, Z. (2023). Automatic Music Playlist Generation via Simulation-based Reinforcement Learning. Proceedings of the 29th ACM SIGKDD Conference on Knowledge Discovery and Data Mining, 4948–4957. https://doi.org/10.1145/3580305.3599777
van Dijck, J., Poell, T., & de Waal, M. (2018). The Platform Society. Oxford University Press.
Van Dijk, J. A. G. M. (2019). The Digital Divide. Polity Press.
Zimmermann, B. (2021). Similarity and difference in sound studies (and elsewhere). In B. Zimmermann & T. Pinch (Eds.), Rethinking music through science and technology studies (pp. 19-43). Routledge.

SHIPBUILDING AND OCEAN ENGINEERING

Hydrodynamics of Marine and Offshore Structures

Marine Environmental Impact and Pollution Control

The Penglai 19-3 Incidents: Failures, Response, and Regulatory Lessons

Gulled Makaran[a], Ceren Bilgin Gu¨ney[a]

[a]Istanbul Technical University, Shipbuilding and Ocean Engineering, Offshore Engineering Program, Turkiye

makaran22@itu.edu.tr

Keywords: Bohai Bay Oil Spill, Offshore Maintenance, Sustainability, Somalia Offshore.

Abbreviations

CG: Chinese Government

COPC: ConocoPhillips China Inc.

EIA: Environmental Impact Assessment

IOGP: International Association of Oil & Gas Producers

IMO: International Maritime Organization

MEPL: Marine Environmental Protection Law

NGO: Non-Governmental Organizations

O&M: Operations and Maintenance

PRC: People's Republic of China

SOA: State Oceanic Administration

Aim

The study presented in these extended abstract aims to lay the groundwork for an ongoing master's thesis on sustainable operations and maintenance practices in offshore oil and gas activities, with a focus on developing a framework tailored to the future of Somalia's offshore sector. It examines the Penglai 19-3 incidents—the primary catalysts of China's largest offshore oil spill in Bohai Bay in 2011—with a particular focus on the accidents at Platforms B and C. The objective is to conduct a case study analysis of these events to identify operational and regulatory shortcomings, evaluate response strategies, and assess environmental impacts. By detailing the failures—including inadequate maintenance and inspection practices, deficiencies in risk assessment and management, delayed reporting, and weak regulatory oversight—the study seeks to extract critical lessons from these incidents. These insights are intended to inform and support the development of more robust and sustainable operations and maintenance (O&M) frameworks for the offshore oil and gas industry.

Materials and Methods

The methodology adopted in this study combines a comprehensive literature review and case analysis to investigate offshore oil spill and prevention response, focusing on the Bohai Bay 2011 Oil Spill Incident. A systematic literature review was conducted to gather insights into the causes, impacts, and mitigation strategies for oil spills. Sources included peer-reviewed journals, governmental reports, and industry publications. Key focus areas included oil spill environmental impacts and reasons to draw parallels and derive lessons applicable to the Bohai Bay 2011 Oil Spill Incident. The Bohai Bay 2011 Oil Spill Incident was chosen as the primary case study due to its significance as one of the largest offshore spills in China's history. Data were collected from governmental reports, environmental studies, and independent assessments to provide a detailed account of the

incident, including the causes, response measures, and environmental consequences. Key aspects of the case study included examining operational practices, regulatory gaps, and the response strategies implemented during the spill.

Findings

Based on the author's review and independent assessment of the Penglai 19-3 incident, several operational, maintenance, and risk management weaknesses were identified. These findings, summarized below, highlight critical factors contributing to the 2011 Bohai Bay oil spill and inform risk mitigation strategies for emerging offshore fields such as those in Somalia.

The 2011 Bohai Bay Oil Spill, recognized as China's largest offshore oil spill (Yang et al., 2017), occurred as a series of oil spill incidents at the Penglai 19-3 and Suizhong 361 oil fields in the Bohai Sea. This study focuses particularly on the incidents at Platforms B and C of the Penglai 19-3 oilfield, which were the main triggers of the 2011 Bohai Bay Oil Spill and does not cover the Suizhong 361 spill in detail. The Bohai Sea is a semi-enclosed continental shelf sea in the northern region of China. It is surrounded by land on three sides and connected to the Yellow Sea through the narrow Bohai Strait (Figure 1), The first spill at Penglai 19-3 was caused by a leak in a subsurface reservoir during water injection operations, resulting in the release of oil from a natural geological fault on June 4th. The second spill occurred on Platform C on June 17 when operators encountered unexpected high pressure while drilling a water injection well, leading to a loss of well control and the subsequent release of a large volume of oil (Wang et al., 2020a).

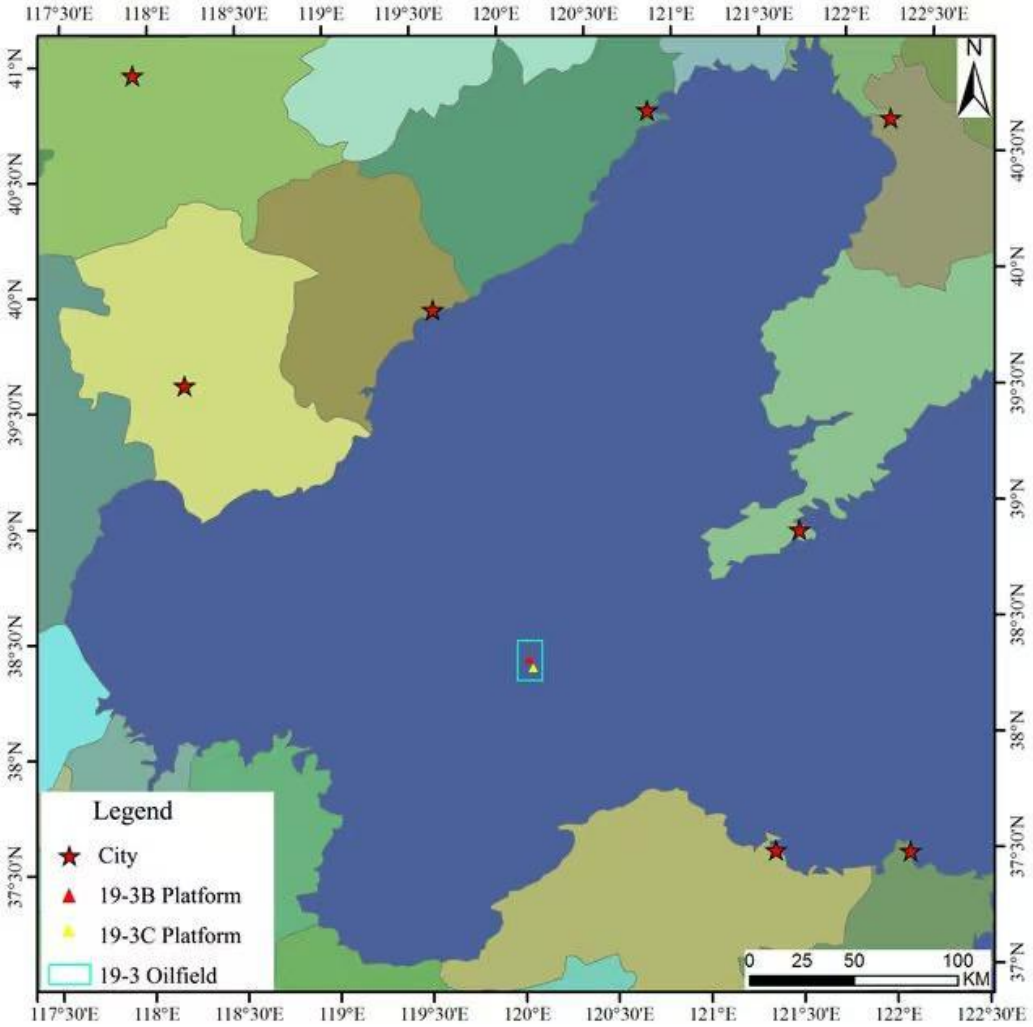

Figure 1: Location of the Bohai Sea with Penglai 19-3 oil field platforms B and C (marked by red and yellow triangles, respectively, at approximately 120°E, 38.5°N) (Yan et al., 2015).

The primary issue was poor integration between subsurface geological knowledge and operational practices, especially regarding fault compartmentalization and pressure monitoring. The field's structural complexity and compartmentalized reservoir system were not fully considered during water injection operations, increasing the risk of localized overpressure.

The oil platform was operated by ConocoPhillips China Inc. (COPC), which reported the release of 723 barrels of oil and 2620 barrels of mineral oil-based drilling muds into the sea over several days [2]. However, the spill turned out to be much larger, as shown in Table 1. Over the following months, oil continued leaking from the seafloor at a steady rate. By early July 2011, an oil slick covering 840 square kilometers had formed around the spill site (Chenglin Liu, 2014). The Chinese government eventually estimated that more than 60,000 barrels of oil and drilling mud had spilled into the Bohai Sea (Yang et al., 2017). The spill directly threatened the marine ecosystems and economies of three provinces: Shandong, Hebei, and Liaoning (Pan et al., 2015).

Table 1: Timeline and Impact of the 2011 Penglai 19-3 Oilfield Oil Spill Incident (Wang et al., 2020a)(Yang et al., 2017)(China.org.cn, 2011)(Zhang, Y. Z., 2013).

Date	Event Summary	Volume Estimate	Polluted Area	Notes
June 4, 2011	Leaking oil detected near Platform B	Not reported	Not specified	Initial detection, no immediate response reported
June 17	Second spill reported near Platform C	Not reported	Not specified	COPC delays reporting to State Oceanic Administration (SOA)
July 5	SOA briefing; NGOs demand apology	723 barrels oil, 2,620 barrels mud (COPC)	Not specified	COPC accused of concealing spill for ~1 month
July 13	SOA criticizes ineffective containment	Not updated	4,240 km²	Production halt ordered; response deemed inadequate
July 14	COPC updates estimate	1,500 barrels (COPC)	Not specified	Revised estimate still underreported
Aug 12	Company admits larger spill volume	>3,200 barrels (COPC)	Not specified	Concedes insufficient leak checks
Aug 23	SOA reports extensive pollution	Not specified	5,500 km²	870 km² severely contaminated; aligns with Zhao's >5,500 km²
Aug 31	COPC claims leaks sealed	>60,000 barrels (CG)	5,500 km²	CG estimate: cleanup deadline met
Sept 7	State Council warns of environmental issues	Zhao: tons range	>5,500 km²	Long-term ecological risks noted

The initial response efforts were criticized for their delayed and inadequate nature, with reports of the spill being downplayed or concealed by the operating company (Lustgarten, A., 2008). Eventually, the spilled oil was contained using various techniques such as skimming, dispersants, and sorbent materials (Wang et al., 2020b). The spill had significant impacts on the marine environment and local fisheries in the Bohai Sea region, as shown in Figure 2.

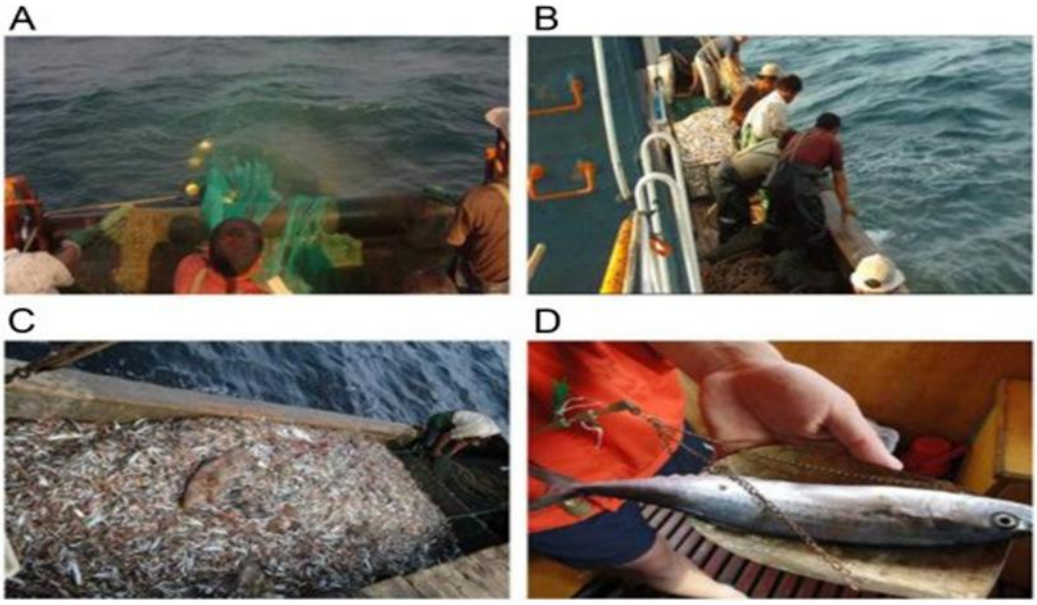

Figure 2: Illustration of the field investigations conducted: A) deploying the trawling net into the sea; B) retrieving the trawling net from the sea; C) unloading the catch onto the deck of the vessel; D) measuring the biological metrics of the primary catch (Pan et al., 2015).

One of the significant contributors to the Bohai Bay 2011 Oil Spill Incident was inadequate maintenance and inspection practices (Wang et al., 2020b). Offshore drilling operations require robust infrastructure monitoring to detect vulnerabilities in equipment and seabed stability (Guo et al., 2019). In this case, the high-pressure water injection led to cracks in the seabed, a failure that could have been prevented through regular inspections and predictive maintenance protocols (Wang et al., 2020b). The lack of advanced technologies to monitor underwater infrastructure in real time exacerbated the problem, delaying the detection of cracks and leaks (Jiang, 2022). Additionally, the absence of systematic equipment audits and insufficient training of maintenance personnel revealed serious flaws in operational readiness (Ettayib & Kara, 2025). The spill also exposed significant gaps in risk assessment and management practices (Wang et al., 2020b). Effective offshore operations depend on comprehensive risk analysis to anticipate potential hazards (S LI & Zhang, 2013). In this case, the high-pressure water injection system's operational limits were not adequately evaluated, leading to conditions that the infrastructure could not withstand (Zou & Wang, 2017). Furthermore, contingency planning was either absent or insufficient, as evidenced by the delayed response to the spill (xu & Zhao, 2014). Without a robust risk management strategy, the operators failed to prioritize early warning systems or establish rapid response mechanisms, allowing the spill to escalate (ZHOU, 2014). Regulatory oversight also played a role; weak enforcement of safety protocols and limited industry accountability prevented proactive risk mitigation efforts (Li, 2013). The challenges of addressing the spill were compounded by delayed reporting and a lack of strong regulatory frameworks (Liu et al., 2012). Operators did not report the incident promptly to Chinese authorities, which delayed emergency containment efforts (Chen, 2012). This delay indicated a failure in communication channels between the oil company and regulators, a critical component of effective risk management (Zhang & xu, 2014). At the time, although China had Environmental Protection Laws and Regulations in China as shown in Table 2, its offshore drilling regulations lacked detailed safety standards and enforcement mechanisms, leaving companies without clear accountability for operational risks (Yu & ZHOU, 2014).

Table 2: Major Environmental Protection Laws and Regulations in China (Government of China, n.d.-a),(Government of China, n.d.-b)].

Regulation	Description
The Environmental Protection Law of the PRC (September 1979)	Covers all environmental protection issues.
The Marine Environmental Protection Law of PRC (August 1982)	Aims to protect the marine environment and resources, prevent pollution damage, maintain ecological balance,safeguard hu- man health, and promote the development of marine programs.
Regulations of the PRC concerning environmental protection in offshore oil exploration and exploitation (December 1983)	Prevents pollution damage to the marine environment by off- shore oil exploration and exploitation.
Regulations of the PRC concerning the dumping of wastes at sea (March 1985)	Strictly controls the dumping of wastes at sea to prevent pollution damage to the marine environment.
Management guidelines on environmental protection at construction projects of the PRC (March 1986)	Strengthens the management of the environmental impact as- sessment of construction projects.

China implemented regulatory reforms following the Penglai 19-3 oil spill, as outlined in Table 3. These reforms included strengthened environmental regulations, enhanced oil spill response and preparedness, improved offshore safety regulations, more stringent monitoring and inspection protocols, strengthened penalties for non-compliance, international cooperation, development of an offshore oil spill response network, and promotion of cleaner energy exploration. Implementation occurred through legislative updates and administrative directives starting in 2012, such as revising environmental protection laws, mandating contingency plans and real-time monitoring systems, and aligning with IMO/IOGP standards by 2014. Enforcement is managed by the State Oceanic Administration (SOA) and other agencies via increased inspections, third-party audits, fines, and public disclosure requirements.

Table 3: Offshore Regulatory Reforms Following the Penglai 19-3 Spill (Zhang, Y. Z., 2013),(Ettayib & Kara, 2025), (Yu & ZHOU, 2014), (State Oceanic Administration, n.d.), (Ministry of Natural Resources, n.d.).

Category	Reform	Year	Notes
Strengthened Environmental Regulations	Revision of Environmental Protection Laws	2013	Mandated EIAs and spill contingency plans following Penglai spill
Strengthened Environmental Regulations	Enhanced Pollution Control and Liability	2016	MEPL updated for ecological damage compensation and coastal protection
Enhanced Oil Spill Response	Mandatory Emergency Drills and Plans	2012	Improved spill preparedness post-Penglai
Improved Offshore Safety	New Drilling Standards and Safety Audits	2012	Addressed well control failures

Monitoring/Inspections	Frequent Checks and Real-Time Data	2013	Strengthened oversight after spill
Penalties	Tougher Fines and License Revocation Risks	2013	Increased accountability
Institutional Reform	Ministry of Natural Resources Established	2018	Centralized marine oversight, replacing SOA for better coordination
International Cooperation	Alignment with IMO/IOGP Standards	2014	Adopted global best practices
Spill Response Network	National Spill Response Plan Development	2015	Unified response framework
Cleaner Energy	Sustainability Reports Mandated	2015	Promoted greener operations

Author's Contribution

This study proposes a novel synthesis of the Penglai 19-3 failures by organizing them into three categories. First, geohazard assessment and fault identification, which allowed oil leaks through natural faults during injection. The second was weak maintenance and monitoring, which made it difficult to detect leaks and cracks early. The third was poor communication with government regulators, which delayed the emergency response. This way of organizing the problems makes it easier to understand how one failure led to another. It also helps suggest simple actions like better hazard training, real-time pressure checks, and faster reporting to avoid the same problems in future offshore operations.

Conclusion

The Penglai 19-3 incidents critically underscore the need for a comprehensive and proactive approach to offshore oil spill prevention and response. This case revealed significant deficiencies in operational practices, including inadequate maintenance and gaps in risk assessment, along with shortcomings in monitoring, communication, and regulatory enforcement. These findings highlight the urgency of implementing robust safety measures and aligning offshore operations with international standards.

Building on this analysis, the study lays a foundation for identifying critical components of sustainable operations and maintenance (O&M) practices, particularly in regions with developing offshore capacities. The institutional and technical gaps observed in the Penglai case serve as a reference point for formulating context-aware policy recommendations, especially within the scope of the ongoing master's thesis on Somalia's offshore sector.

Preventive strategies—such as regular infrastructure maintenance, real-time environmental monitoring, and stronger regulatory oversight—are essential for minimizing the risk of future spills. These insights contribute to the development of practical guidelines that support both environmental protection and operational reliability in emerging offshore contexts.

References

Chen, J. (2012). Emergency containment delays in the Bohai Bay 2011 oil spill. Energy and Environment Research, 7(3), 101–110.

Chenglin Liu. (2014). Escaping Liability Via Forum Non Conveniens: ConocoPhillips's Oil Spill in China. 2014, 17(2), 137.

China.org.cn. (2011, October 21). Timeline of Bohai Bay oil spill. China.Org.Cn. http://www.china.org.cn/environment/2011-10/21/content_23689286.htm

Ettayib, M., & Kara, B. (2025). Offshore Oil and Gas Platforms, Environmental Regulation, and Marine Pollution In China: Asymmetry Analyses. SSRN. https://doi.org/10.2139/ssrn.5085260
Government of China. (n.d.-a). Marine Environmental Protection Law of the PRC (1982). State Council of the PRC. https://english.www.gov.cn/archive/pressbriefing/2014/08/23/content281474983042445.htm
Government of China. (n.d.-b). Regulations concerning environmental protection in offshore oil exploration and exploitation (1983). Ministry of Ecology and Environment. https://english.mee.gov.cn/Resources/laws/regulations/MarineEnvironment/200710/t20071022111648.shtm
Guo, W., Zhang, S., & Wu, G. (2019). Quantitative oil spill risk from offshore fields in the Bohai Sea, China. Science of The Total Environment, 688, 494–504. https://doi.org/10.1016/j.scitotenv.2019.06.226
Jiang, M. (2022). Compensation and prevention of damage resulting from offshore drilling in China [maastricht university]. https://doi.org/10.26481/dis.20221123mj
Li, P. (2013). Regulatory weaknesses in offshore oil drilling in China. Ocean Policy Studies, 36(4), 77–84.
Liu, H. M., Liu, G. W., & Ma, L. Z. (2012). The Problem of Dealing the Culture Difference in Cooperation with Oversea Oil Company from Penglai 19-3 Oil Spill Accident. Advanced Materials Research, 518–523, 3096–3101. https://doi.org/10.4028/www.scientific.net/AMR.518-523.3096
Lustgarten, A. (2008). Buried secrets: Is natural gas drilling endangering US water supplies. ProPublica. https://www.propublica.org/article/buried-secrets-gas-drilling-and-water-pollution-1111
Ministry of Natural Resources. (n.d.). Notice on the establishment of the Ministry of Natural Resources and its marine management functions. MNR.Gov.Cn. http://www.mnr.gov.cn
Pan, G., Qiu, S., Liu, X., & Hu, X. (2015). Estimating the economic damages from the Penglai 19-3 oil spill to the Yantai fisheries in the Bohai Sea of northeast China. Marine Policy, 62, 18–24. https://doi.org/10.1016/j.marpol.2015.08.007
S LI, & Zhang, X. (2013). Offshore operational limits: Lessons from Bohai Bay. Journal of Offshore Mechanics, 62(3), 45–56.
State Oceanic Administration. (n.d.). Report on the environmental impact of the Bohai Bay 2011 oil spill incident. SOA.Gov.Cn. http://www.soa.gov.cn
Wang, Y., Lee, K., Liu, D., Guo, J., Han, Q., Liu, X., & Zhang, J. (2020a). Environmental impact and recovery of the Bohai Sea following the 2011 oil spill. Environmental Pollution, 263, 114343. https://doi.org/10.1016/j.envpol.2020.114343
xu, J., & Zhao, M. (2014). Early warning and rapid response mechanisms in offshore drilling. Environmental Management Review, 72(4), 67–76.
Yan, J., Wang, L., Chen, L., Zhao, L., & Huang, B. (2015). A Dynamic Remote Sensing Data-Driven Approach for Oil Spill Simulation in the Sea. Remote Sensing, 7(6), 7105–7125. https://doi.org/10.3390/rs70607105
Yang, Y., Li, Y., Liu, G., Pan, Q., & Wang, Z. (2017). A hindcast of the Bohai Bay oil spill during June to August 2011. Acta Oceanologica Sinica, 36(11), 21–26. https://doi.org/10.1007/s13131-017-1135-7
Yu, F., & ZHOU, K. (2014). Aligning offshore drilling regulations with international standards. Journal of Maritime Law, 49(1), 23–34.
Zhang, T., & xu, Q. (2014). Risk communication gaps in offshore drilling operations. Environmental Safety Journal, 58(2), 45–55.
Zhang, Y. Z. (2013). ConocoPhillips Oil Spill and Eco-Disasters in the Bohai Bay. In Chinese Research Perspectives on the Environment (Vol. 1, pp. 67–81). Brill.
ZHOU, P. (2014). Regulatory oversight and accountability in offshore drilling. Ocean Policy Studies, 48, 112–120.
Zou, K., & Wang, J. (2017). China's Practice in Marine Environmental Contingency Planning. In A. Telesetsky, W. Gullett, & S. Lee (Eds.), Marine Pollution Contingency Planning (pp. 62–82). Brill | Nijhoff. https://doi.org/10.1163/9789004355507_005

SOIL MECHANICS AND GEOTECHNICAL ENGINEERING

Environmental Geotechnics

Foundation Engineering

Geotechnical Earthquake Engineering

Geotechnics

Evaluation of Geotechnical Characteristics of Recycled Concrete Aggregate-EAF Slag Mixtures

Seyedsina Norouzian[a], Bilal Korkmaz[a], Aslı Yalçın Dayıoğlu[a]

[a]Istanbul Technical University, Department of Civil Engineering, Soil Mechanics and Geotechnical Engineering, Türkiye
norouzian22@itu.edu.tr

Keywords: Electric Arc Furnace (EAF) Slag, Geotechnical Properties, Recycled Concrete Aggregate (RCA), Waste Utilization.

Aim

The construction industry needs to adopt new sustainable practices because of the reduction of natural resources. Additionally, to decrease the environmental challenges posed by waste generation, some new materials should be utilized in various functions. Recycled concrete aggregate (RCA) and electric arc furnace (EAF) slag are two industrial products with considerable potential for reuse in different applications in construction practices. Nonetheless, their utilization is limited due to the insufficient data for their engineering properties and their long-term performance. The other issue that has significant importance is the swelling potential that it should be ensured. This study aims to specify this gap by performing a comprehensive characterization of RCA and EAF slag, evaluating their properties as alternatives to conventional construction materials.

As the result of the tests is shown below, the data for RCA aligns with the typical range of conventional granular materials. (Das, 2015). Additionally, EAF slag in case of complication performance and density outperforms natural aggregate. As expected, the mixture exhibits intermediate properties. The primary goal of this study is to reach the physical, mechanical, and geotechnical properties of RCA, EAF, and the mixture of them at different ratios by weight. The findings of this research are expected to provide sufficient data and considerable insights into the workability of using RCA and EAF slag in construction applications and promoting the reuse of waste material. Additionally, the swelling potential of EAF slag should be decreased to be utilized in a long-term period. By indicating the determined properties of the materials, this research can reach the purposes of sustainable engineering, such as waste management, environmental protection, and natural resource conservation. Additionally, the test results will be able to present functional data for the applications that can be utilized in the construction industry.

As a result, this study aims to connect waste management and civil engineering. Moreover the findings of the study will help to develop guidelines for the use of these materials in various applications and contribute to a more sustainable construction system.

Material and Method

Materials

The materials that have been under investigation in this research are:
1-Recycled Concrete Aggregate (RCA) is sourced from demolished concrete structures. The materials are removed from impurities such as wood, metal, and plastic.
2-Electric Arc Furnace (EAF) Slag is obtained from steel manufacturing facilities. EAF slag has been collected, cooled, and processed to extract metallic residues. The slag was crushed and sieved according to standard procedures to reach the needed specifications for this study.

The mixed forms of RCA and EAF slag were prepared to evaluate the combined performance of these materials.

Figure1. EAF slag and RCA.

Methods

A comprehensive series of laboratory tests was conducted to evaluate the different properties of the materials, such as index and engineering properties. The methods used are described in detail below:
A sieve analysis was done to determine the particle size distribution of the mentioned materials. They were passed through the standard series of sieves ranging from 75 mm to 75 µm, and then the percentage of material retained on each sieve was calculated. This test was performed according to ASTM C136/C136M-14.
The specific gravity of materials is determined by using a pycnometer. The specific gravity is measured according to the volume of displaced water. The process was done based on ASTM C127-15.

To evaluate the compaction properties, the standard Proctor test was done at different moisture contents. By utilizing standard molds and a hammer that should be dropped from a specific height, the properties were assessed. The dry density and optimum moisture content of the materials and the mixture of them were determined. This test is critical for understanding the compaction behavior of the material and the maximum reachable dry unit weight, which influences their performance in the applications. The test was done based on ASTM D698.

To evaluate the bearing capacity and strength of RCA and EAF slag and their mixtures, the CBR test was performed. The test was done under both dry and water-soaked conditions:

Dry CBR: The samples were prepared with optimum moisture content and were tested without soaking.

Water-Soaked CBR: Samples were submerged in water for at least 96 hours in order to create a simulation of long-term exposure to moisture; after that, the CBR test was performed.

The strength data were obtained from both conditions and were compared to standard crushed stone aggregates. The test is relevant to assess the performance of materials in road subgrades and base layers. The test was performed according to ASTM D1883-16.
To assess the volumetric stability of materials, conducting this test is needed. Compacted soil samples are saturated with water, and the change in sample height is measured during a specified time duration. This test has significant importance in order to evaluate the material performance during a long-term time interval. Materials with low

swelling potential are more sustainable for geotechnical applications. The procedure is done based on the ASTM D4546-14.

By using a direct shear apparatus, the shear strength parameters of materials are assessed. Samples are subjected to varying normal stresses, and the shear stresses are recorded to determine the internal friction angle and cohesion. These parameters are so crucial for assessments of materials performance in case of slope stability and embarkment applications. The test is done according to ASTM D3080/D3080M-11.

All tests were performed according to international standards. Mostly including ASTM to ensure the reliability of the results. Additionally, during all the procedures, samples were prepared, tested, and data were recorded by careful attention to reduce the errors and minimize probable mistakes and guarantee the accuracy of findings. The series of data that were collected from the standard laboratory tests have been analyzed to compare the properties of the materials with conventional construction materials properties.

Findings

The experimental data from the sieve analysis, specific gravity, compaction, and California Bearing Ratio (CBR) tests provide a series of data that can show different properties of RCA, EAF slag, and the mixture (50% EAF + 50% RCA). Below is a comprehensible analysis of the results and findings.

RCA: The grain size distribution of this material shows that the gravel percentage (G) of it is 31.1%, the sand percentage (S) is 67.6%, and the percentage of fine grains (M and C) are 1.3%. Its uniformity coefficient (Cu) is 10.57, and the coefficient of gradation (Cc) is 0.772. According to the Unified Soil Classification system (USCS), RCA was classified as SP (poorly graded sand), and according to AASHTO classification, RCA is a granular material used in road subgrades that was classified under the A-1-a category.

EAF slag: The grain size distribution of EAF slag shows that 62.2% is gravel (G), 37% is sand (S), and 0.80% is fine grains (M and C). EAF slag is coarse grained, and the uniformity coefficient (Cu) is 8.64, and the coefficient of gradation (Cc) is 1.17. According to the Unified Soil Classification system (USCS), RCA was classified as GW (well-graded gravel), and according to AASHTO classification, EAF shows excellence of stability for various applications and was classified under the A-1-a category.

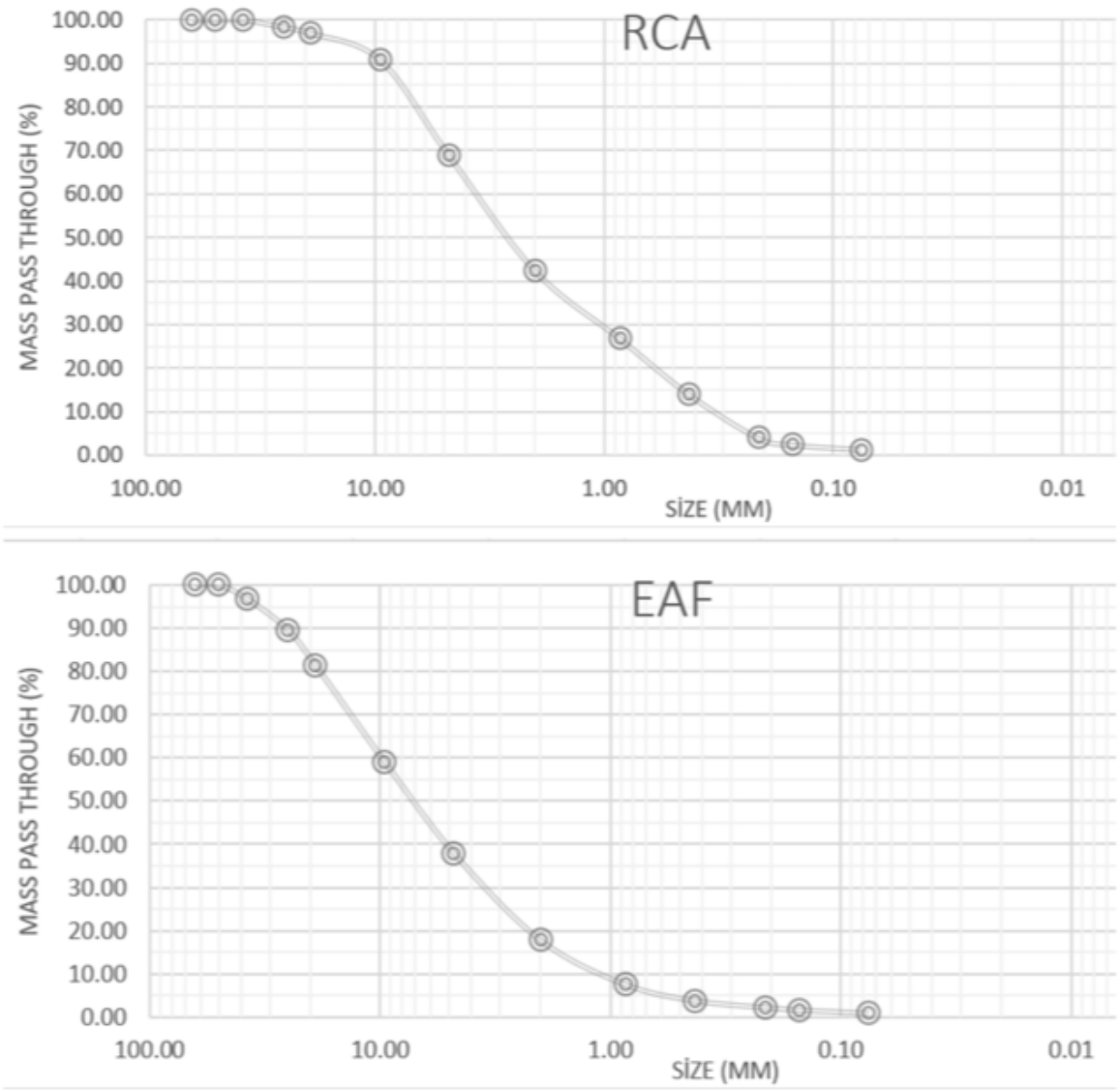

Figure2. Grain size distribution curve (EAF and RCA).

The specific gravity of RCA (2.59) is a little bit lower than the conventional natural sand soil aggregates (2.6-2.8), which is related to the existence of adhered mortar in RCA (Oikonomou, 2005).
On the other hand, EAF slag indicates a superior specific gravity (3.74) because of its metallic content. This high specific gravity increases its sustainability for road base layers and the other high-density applications.
The compaction test result indicates that, the data for RCA aligns with the typical range of conventional granular materials. (Das, 2015). Additionally, EAF slag in case of complication performance and density outperforms natural aggregate. As expected, the mixture exhibits intermediate properties.

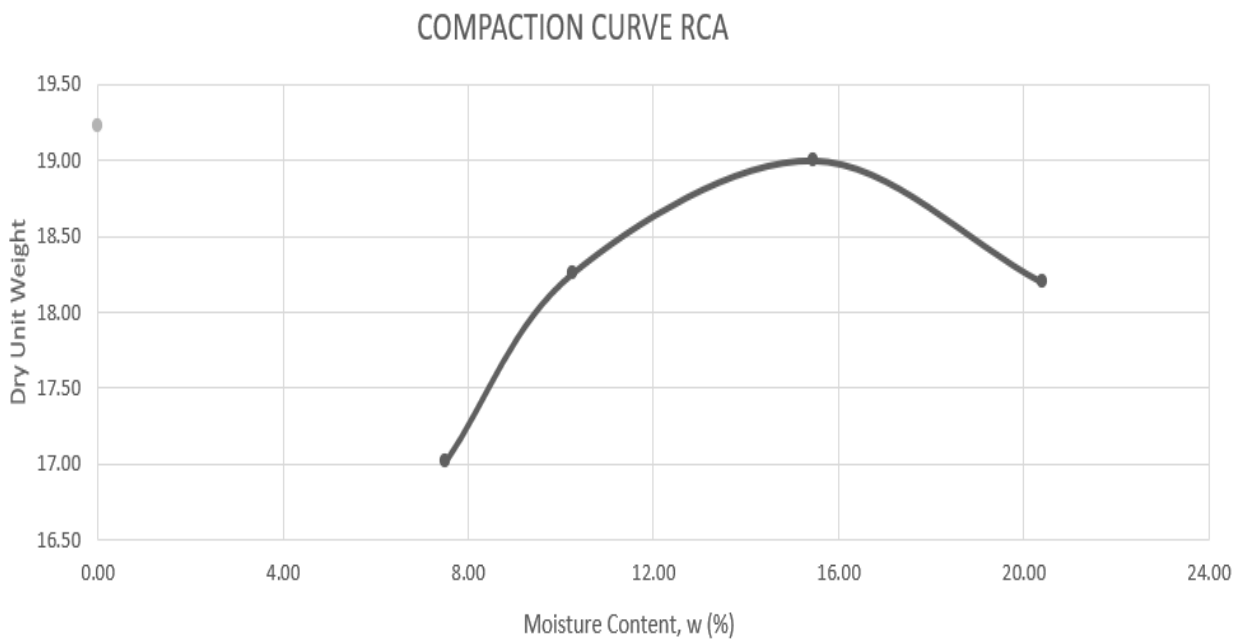

Figure3. Compaction curves of materials (RCA).

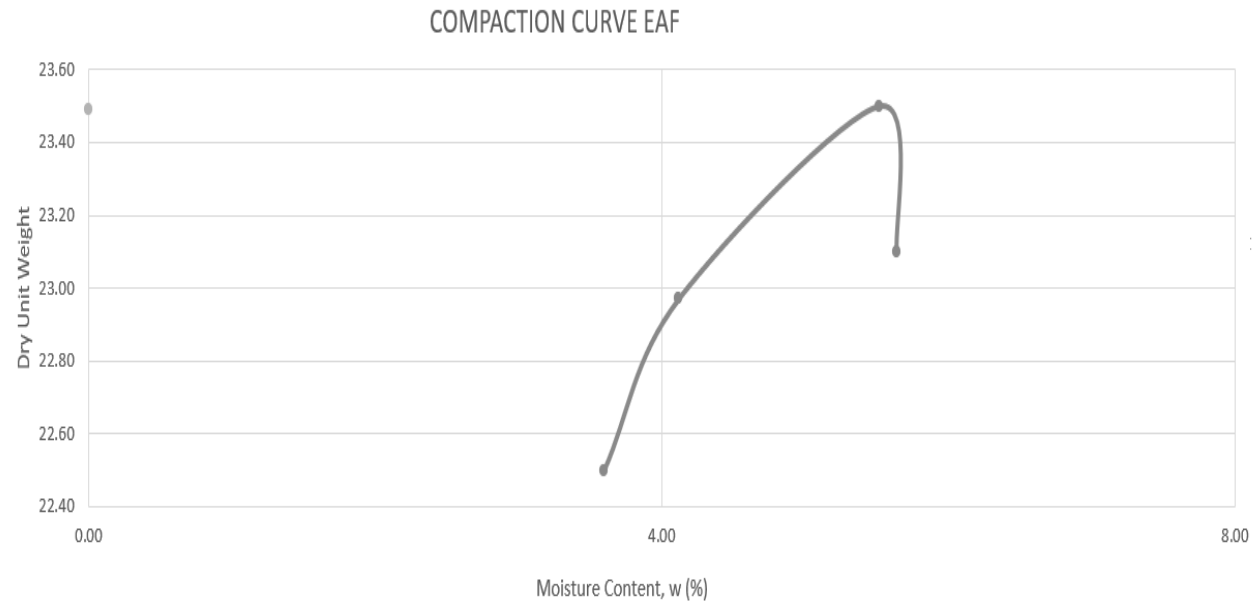

Figure4. Compaction curves of materials (EAF).

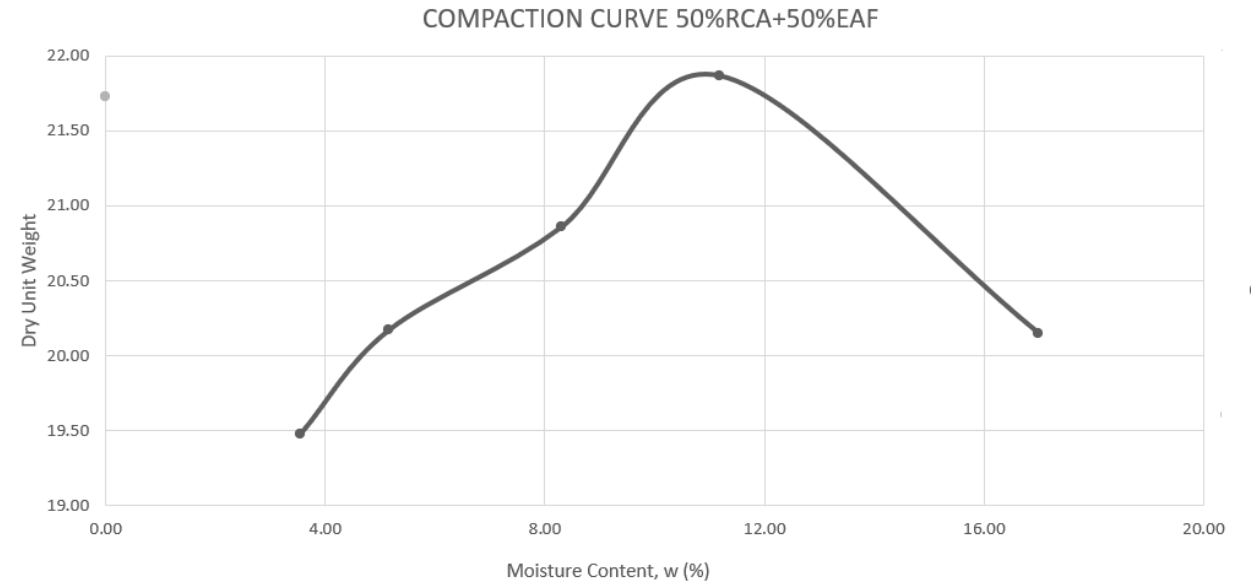

Figure5. Compaction curves of materials (50%RCA+50%EAF).

4. California Bearing Ratio (CBR)

The result, as shown below, indicates that EAF has a CBR value higher than conventional materials. As well, the mixture of the materials shows higher load-bearing capacity. The swelling percentage of RCA is almost 0%, and this property for EAF is 3.44% in the soaked CBR test result.

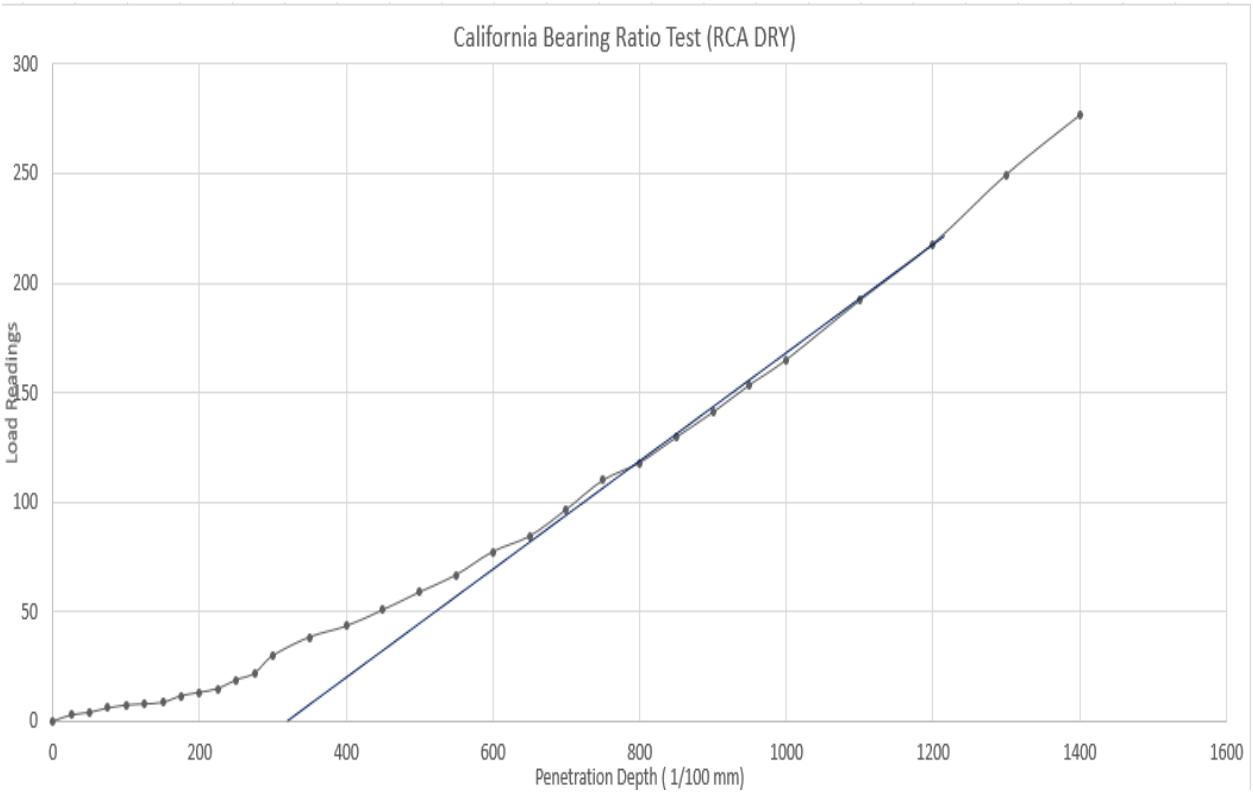

Figure6. CBR test result for RCA(Dry).

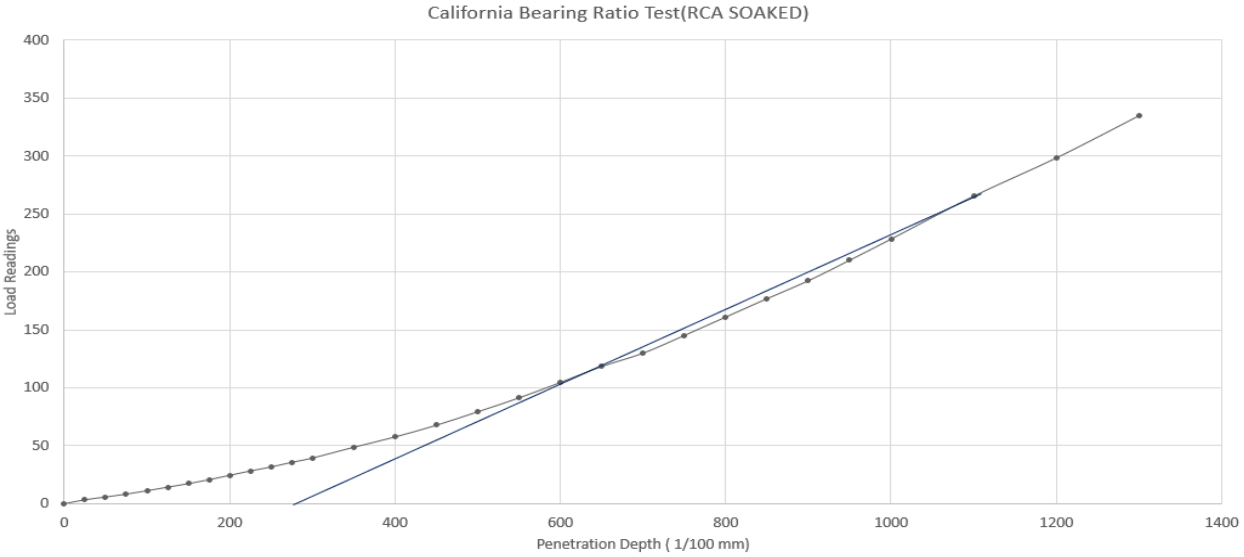

Figure7. CBR test result for RCA(Soaked).

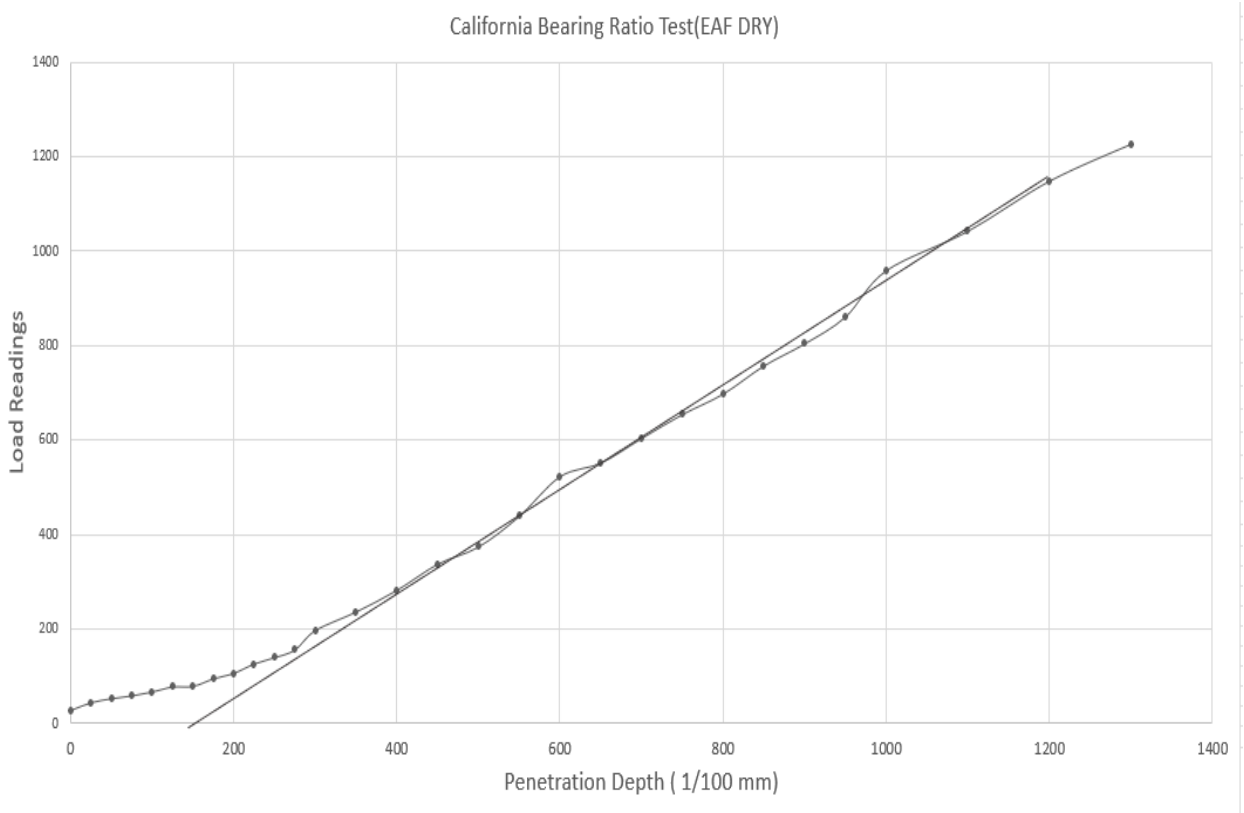

Figure8. CBR test result for EAF(Dry).

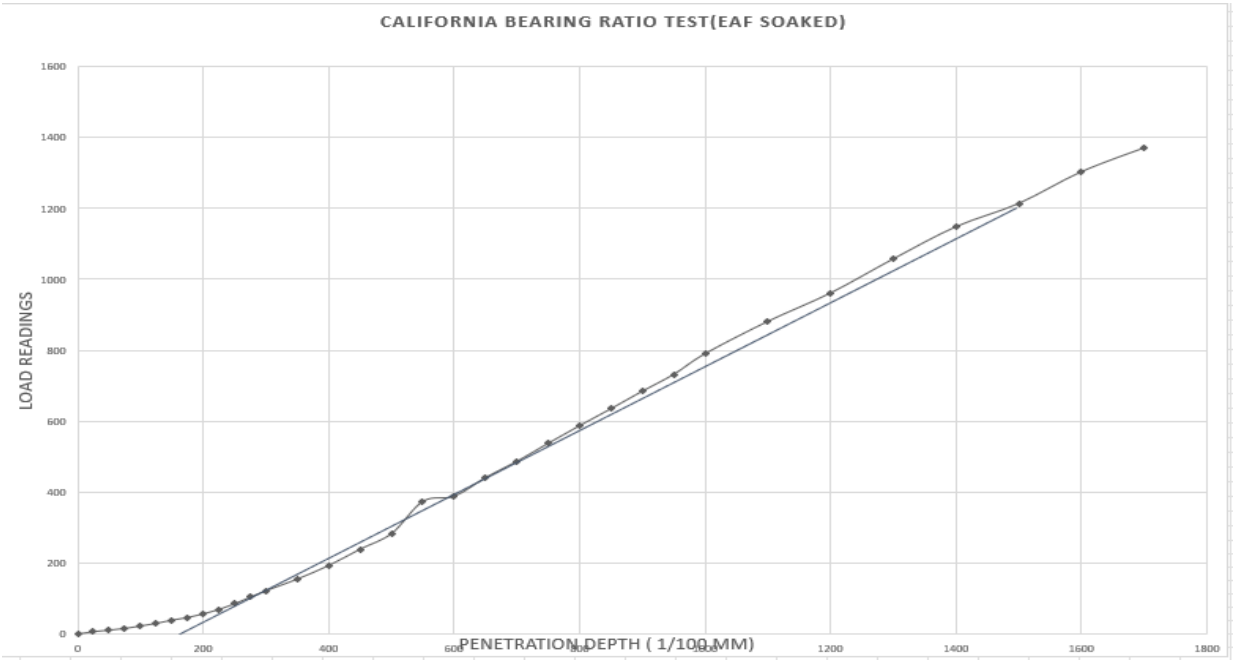

Figure9. CBR test result for EAF(Soaked).

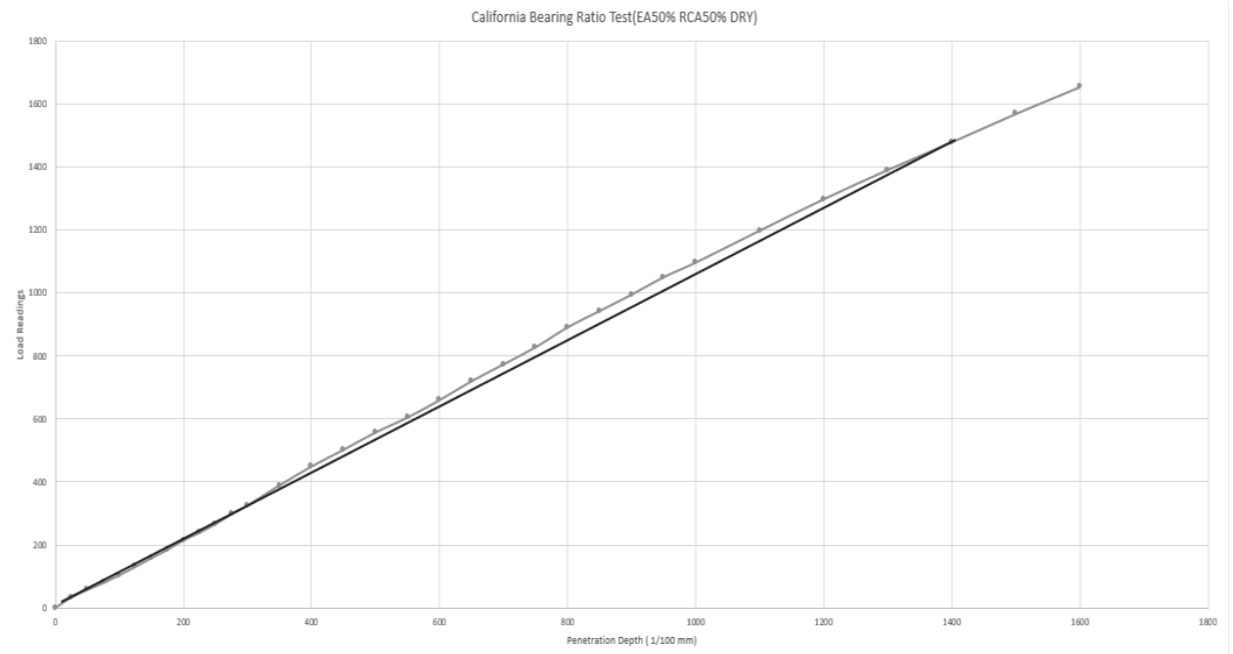

Figure10. CBR test result for the mixture (50% RCA+50% EAF).

Conclusion

The utilization of RCA and EAF slag is suitable and aligns with global needs to provide sustainable construction material and methods by decreasing the use of natural materials and managing and reducing waste generation. (Oikonomou, 2005; Pasetto & Baldo, 2012). These materials also has environmental and economic benefits. such as reducing the utilization of conventional materials and natural aggregates, using waste materials for construction applications, and reducing the cost of projects by using recycled materials.

EAF slag provides high strength, density, and stability. Its CBR value and high specific gravity of EAF slag show its significant performance compared to natural aggregates (Pasetto & Baldo, 2012; Arulrajah et al., 2013).
RCA indicates suitability for low-traffic applications as a supplementary material, especially when it is mixed with EAF slag. Additionally, as shown before, its grain distribution and compaction features align with granular materials.
Furthermore, the mixed material of EAF and RCA shows sustainability, cost-effectiveness with superior performance, and significant properties such as CBR value that is higher than conventional materials and the materials themselves.
Additionally, accelerated swelling tests and direct shear tests are currently being performed to assess more properties of these materials and provide more comprehensible data for more conditions and ensure better their sustainability and performance.

References

American Association of State Highway and Transportation Officials (2012). Classification of soils and soil-aggregate mixtures for highway construction purposes (AASHTO M145).
Arulrajah, A., Piratheepan, J., Disfani, M. M., & Bo, M. W. (2013). Geotechnical and geoenvironmental properties of recycled construction and demolition materials in pavement subbase applications. Journal of Materials in Civil Engineering, 25(8), 1077-1088. ASTM International. (2011). ASTM C136/C136M-14: Standard test method for sieve analysis of fine and coarse aggregates.
ASTM International. (2015). ASTM C127-15: Standard test method for relative density (specific gravity) and absorption of coarse aggregate.
ASTM International. (2017). ASTM D2487-17: Standard practice for classification of soils for engineering purposes (Unified Soil Classification System).
ASTM International. (2016). ASTM D698-16: Standard test methods for laboratory compaction characteristics of soil using standard effort.
ASTM International. (2016). ASTM D1883-16**:** Standard test method for California bearing ratio (CBR) of laboratory-compacted soils.
ASTM International. (2014). ASTM D4546-14: Standard test methods for one-dimensional swell or collapse of soils.
ASTM International. (2011). ASTM D3080/D3080M-11: Standard test method for direct shear test of soils under consolidated drained conditions.
Chester, R. (2002). Materials Selection and Engineering. In A.A. Baker, L.R.F. Rose, R. Jones (Eds.), Advances in the Bonded Composite Repair of Metallic Aircraft Structure (2nd ed., Vol. 1, pp.19-40). New York: Wiley.
Das, B. M. (2015). Principles of geotechnical engineering (8th ed.). Cengage Learning.
Oikonomou, N. D. (2005). Recycled concrete aggregates. Cement and Concrete Composites, 27(2), 315–318.
Pasetto, M., & Baldo, N. (2012). Experimental evaluation of the high-performance base course and road base asphalt concrete with electric arc furnace steel slag. Construction and Building Materials, 34, 291–297.
Url-1 www.mohid.com, date retrieved 29.06.2006.

SOIL MECHANICS AND GEOTECHNICAL ENGINEERING

Environmental Geotechnics

Foundation Engineering

Geotechnical Earthquake Engineering

Geotechnics

Dynamic Site Response Analyses For A Site With A Deep Cut

Yusuf Şahin[a], Gürkan Özden[b]

[a] Istanbul Technical University, Graduate School, Soil Mechanics and Geotechnical Engineering, Türkiye
[b] Istanbul Technical University, Civil Engineering Faculty, Soil Mechanics and Geotechnical Engineering, Türkiye
sahinyus17@itu.edu.tr

Keywords: Design Spectra, Dynamic Soil Response, Finite Element, Retaining System

Aim

In earthquake engineering, the seismic performance of structures is not solely dependent on the structural system but is also directly influenced by the dynamic properties of the underlying soil. In this context, site response analyses are among the fundamental engineering procedures used to understand how ground motion is altered as it propagates through soil layers and to estimate the resulting surface motion. These analyses have been mandated for certain soil classifications under the Turkish Building Earthquake Code (TBDY) since its enforcement in 2018. Local site conditions can significantly affect both the amplitude and frequency content of ground motions arriving at the surface. Neglecting these effects, especially in soft, thick, or heterogeneous soil profiles, may result in considerable deficiencies in structural design.

Among various site response analysis methods, one-dimensional (1D) site response analysis is the most commonly employed. This method is suitable for soil profiles that can be idealized as horizontally layered and laterally continuous, assuming seismic waves propagate only in the vertical direction. In such stratified media, reflections and refractions at layer boundaries with different dynamic properties alter the wave propagation characteristics, ultimately modifying surface ground motion. 1D analyses allow the computation of spectral characteristics and amplification factors based on these wave propagation mechanisms.

The use of 1D site response analyses in engineering practice dates back to the 1960s. The equivalent linear analysis method proposed by Seed and Idriss (1970) assumes that soil behaviour under small strains can be represented using linear elastic formulations. In this approach, the dynamic response of soils is characterized by the shear modulus (G) and damping ratio (ξ), which are iteratively updated during cyclic loading.

However, it has been observed that this approach is inadequate in capturing the behaviour under large strain, high-amplitude motions. This led to the development of nonlinear soil models. Reduction curves introduced by Vucetic & Dobry (1991) and Ishibashi & Zhang (1993) offered alternatives applicable to various soil types. The degradation relationships between shear modulus and damping ratio with shear strain, developed by Darendeli (2001), enabled more realistic modelling of soil behaviour by including factors such as plasticity index, effective stress, and number of loading cycles.

One of the key outputs of 1D site response analysis is the design response spectrum and associated spectral quantities. These include spectral acceleration (Sa), spectral velocity (Sv), and spectral displacement (Sd), which represent the maximum responses of single-degree-of-freedom (SDOF) systems with unit mass subjected to ground motion. Among these, Sa is particularly emphasized in structural design against horizontal seismic loads. Keeping the natural period of a structure as far as possible from the dominant periods of the soil profile is crucial for controlling structural behaviour.

The calculation of these spectral quantities is generally based on the damped free vibration response of a system. According to Kramer (2024), spectral acceleration represents the peak absolute acceleration response of a unit-mass SDOF system in dynamic analysis. The mathematical framework for obtaining spectral quantities from ground motion recordings dates back several decades. The Turkish Building Earthquake Code (TBDY 2018) defines design spectra based on spectral acceleration and velocity components for different soil classes and seismic hazard levels. These spectra are directly used in engineering design and in evaluating the results of site response analyses.

Turkey lies on active tectonic zones with significant seismic potential. As a result, most of its densely populated cities are located in earthquake-prone areas. Given the aging building stock, unplanned urbanization, and irregular migration, urban transformation projects have accelerated in recent years. During this transformation process, the use of deep excavation support systems and deep foundation elements has become common in high-rise and basement-intensive projects.

However, the influence of such systems on the dynamic behaviour of soils has not been sufficiently investigated. Site response analyses typically focus only on the natural soil profile, while the impact of engineering structures like retaining systems and foundation elements on soil-structure interaction is often overlooked. In reality, even if a soil profile appears suitable for 1D analysis, the stiffness of structural components in a retaining system or their geometric configuration can render the analysis inherently two- or even three-dimensional. Example configurations of such structural arrangements within a plot are presented in Figure 1. For this reason, the integration of foundation and shoring systems into two- or three-dimensional site response analyses is essential to accurately capture the realistic behaviour of the ground.

Figure 1. A building plot that may not be included in the scope of one-dimensional ground response analysis.

Furthermore, the elastic design spectra defined in TBDY 2018 are limited to five generic soil classes, from ZA to ZE. This classification is insufficient to capture the diversity of local soil behaviours and the impact of engineering applications. It also fails to account for the influence of foundation and retaining systems constructed within a given profile on the site response spectrum. As a result, potential spectral mismatches or amplifications may be underestimated in design. Therefore, site response analyses should be supported by more detailed modelling and multi-dimensional approaches to enhance reliability.

Material and Method

As part of this study, two-dimensional finite element analyses were conducted in the time domain. In this context, nonlinear soil behaviour was taken into account, and both one-dimensional and two-dimensional site response analyses were performed under free-field boundary conditions. Additionally, in the two-dimensional models, retaining systems representing structural effects were also modelled, and their influence on the dynamic behaviour of the soil was evaluated.

During the modelling process, lateral displacements of the retaining system components within the excavation zone (excluding the socket region) were constrained in order to limit uncontrolled horizontal deformations that may occur during excavation. This approach aimed to minimize the influence of excavation stages on the analysis. The boundary conditions were defined to realistically simulate wave propagation. Free-field boundaries were applied along the lateral edges to prevent artificial reflections of seismic waves from the model limits. At the bottom boundary, a compliant base was implemented to allow input motion transmission while preventing wave reflections.

The geometry of the numerical model is shown in Figure 2, and the parameters associated with the soil profile are presented in Table 1. The model illustrated in the figure represents a typical soil profile and a two-dimensional retaining system cross-section, representative of conditions in the İzmir city center. For improved numerical stability, velocity-time input records were preferred.

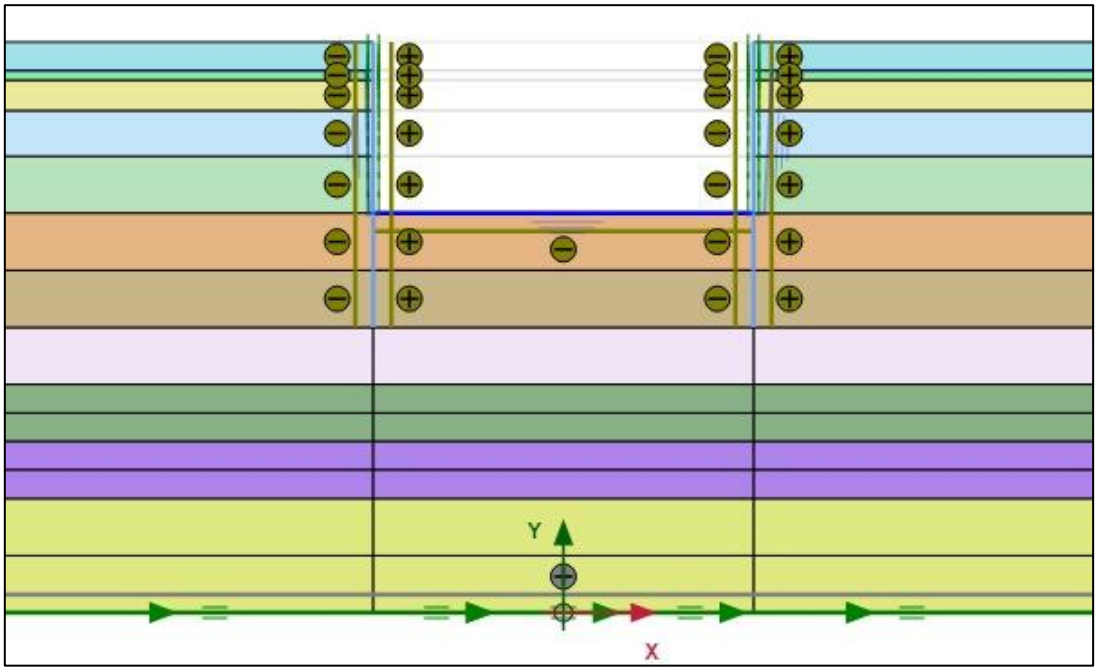

Figure 2 Geometry of finite element model.

Table 1. Characteristics of soil layers.

SOIL LAYERS	h (m)	γ_n (kN/m^3)	φ' (°)	V_s (m/s)	s_u (kPa)	E_{50} (MPa)	$\gamma_{0.7}$ (%)	G_0 (MPa)
FILL-1	1.5	18	30	160		8.0	0.0085	46.1
FILL-2	0.5	18	30	180		8.0	0.0118	58.3
VERY SOFT CLAY-1	1.6	16	-	110	10	5.3	0.0290	19.4
VERY SOFT CLAY-2	2.4	16		122	15	4.9	0.0330	23.8
VERY SOFT CLAY-3	3.0	17		142	20	6.5	0.0720	34.3
SOFT CLAY-1	3.0	18		157	25	7.7	0.0850	44.4
SOFT CLAY-2	3.0	18		172	30	8.5	0.0850	53.3
MEDIUM STIFF CLAY-1	3.0	18		187	35	9.2	0.0900	62.9
MEDIUM STIFF CLAY-2	3.0	20		207	50	11.0	0.0950	85.7
MEDIUM STIFF CLAY-3	3.0	20		235	54	11.1	0.1060	110.5
MEDIUM DENSE TO VERY DENSE SAND	6.0	20	34	275		36.2	0.0550	151.3

Findings

As a preliminary phase of this ongoing research, three representative ground motion records from the DeepSoil database which widely adopted in conventional 1D analyses, were carefully selected and implemented in the numerical simulations. Selected earthquake motion properties are given in Table 2.

Table 2. Properties of selected earthquakes.

Earthquake Motion	a_{max} (g)	V_{max} (m/s)	T_0	Effective Duration (s)
Kocaeli	0.151	0.14	0.164	11
Loma Gilroy	0.357	0.28	0.399	5
Mammoth Lake	0.378	0.138	0.164	11

Table 3 presents the maximum PSA values for each ground motion record under three modelling conditions: one-dimensional (1D), two-dimensional (2D), and two-dimensional (2D) with retaining structures .

Table 3. Maximum spectral acceleration values.

Earthquake Record	PSA_{max} (g)		
	1D	2D Free Field	2D Diaphragm Wall
Kocaeli	0.47	0.52	1
Mammoth Lake	0.82	1.3	1.44
Loma Gilroy	1.06	1.1	1.4

The results obtained from this study clearly demonstrate that excavation support elements such as diaphragm walls have a significant effect on the seismic motion computed at the foundation level. In particular, in the short-period range, the inclusion of such systems in the model led to noticeable increases in spectral acceleration values. For example, during the Kocaeli earthquake, the peak spectral acceleration (PSA) under free-field conditions was approximately 0.52 g, whereas it increased to as high as 1.0 g in the model that included the retaining system. Spectral acceleration curves for foundation level for every chosen seismic record can be seen in Figure 6. Similar trends were observed in the Mammoth Lake and Loma Gilroy ground motion records. This increase suggests that the retaining system alters the horizontal constraints imposed on the soil. In order to see the differences clearly between analyses methods, in Figure 7, spectral accelerations are given in much tighter period interval.

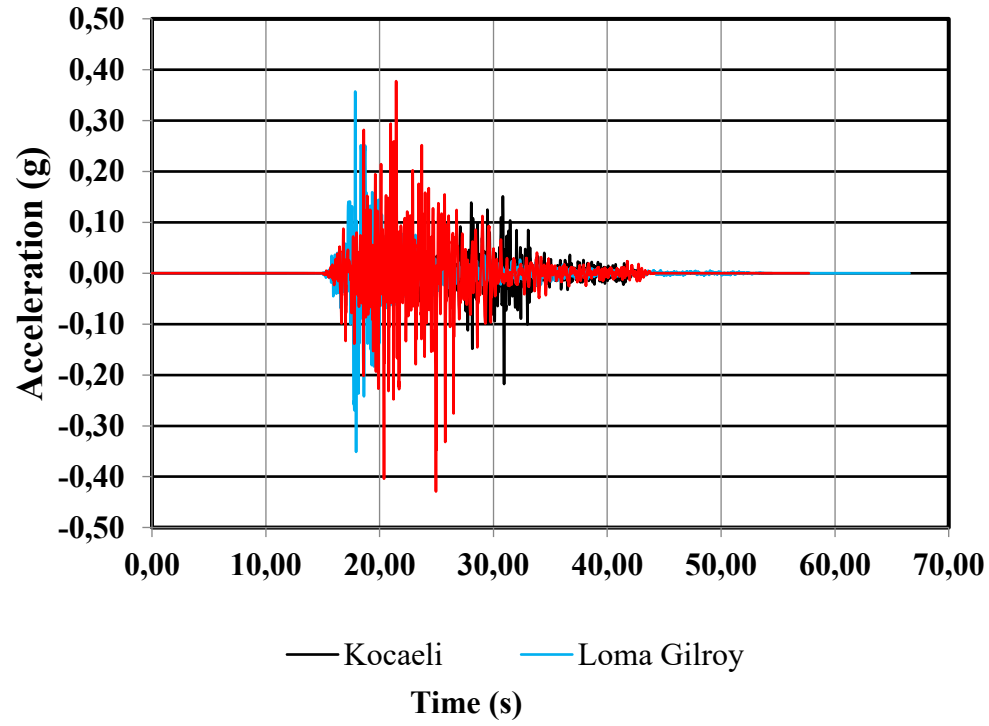

Figure 3. Acceleration-time curves of 3 earthquake records used in the analysis.

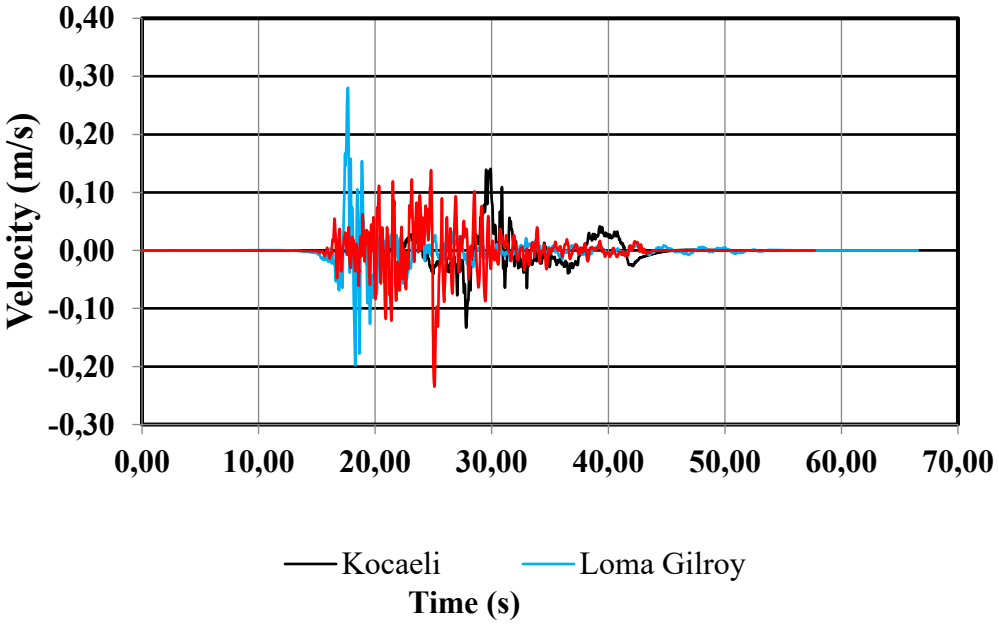

Figure 4. Velocity-time curves of 3 earthquake records used in the analysis.

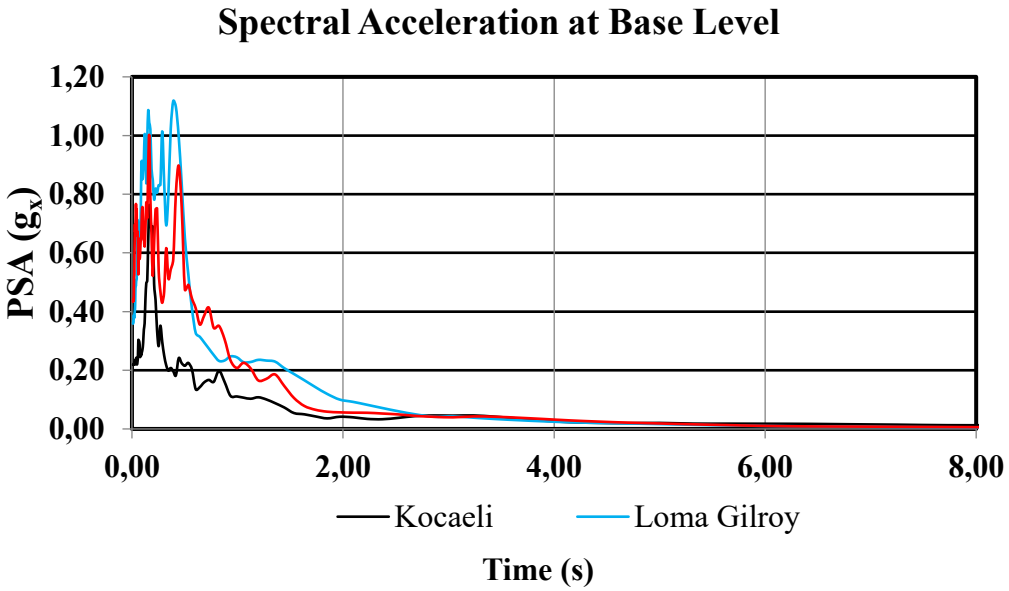

Figure 5. Acceleartion spectra of the selected earthquake record at base level of the model.

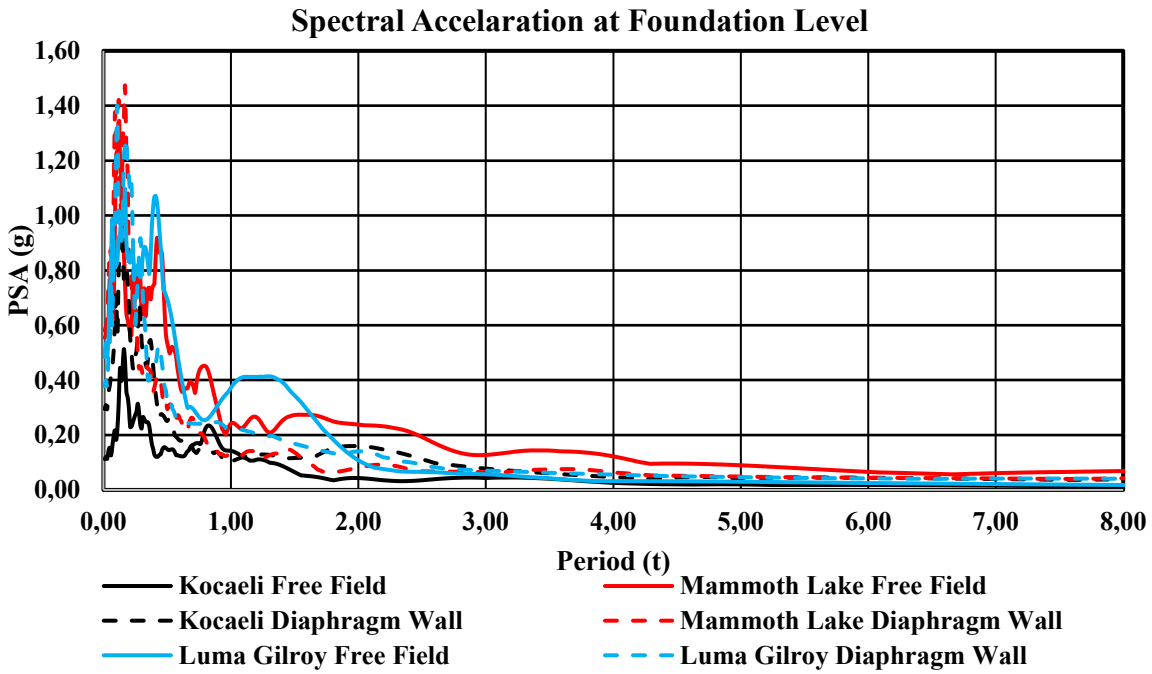

Figure 6. Spectral acceleration at the bottom of foundation (t = 0-8 s).

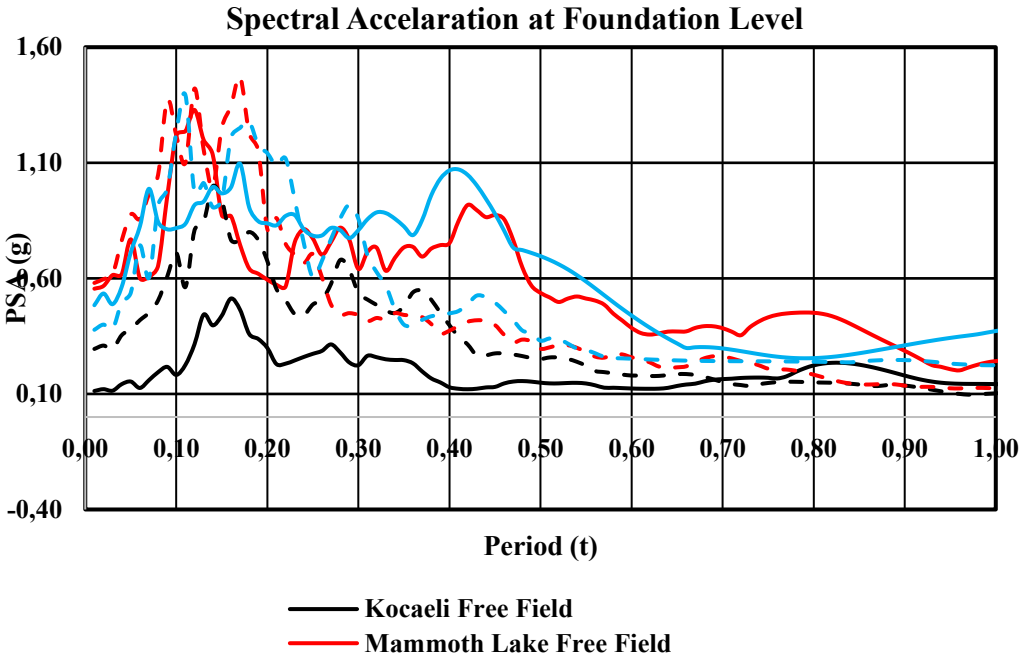

Figure 7. Spectral acceleration at the bottom of foundation (t = 0-1 s).

Conclusion

The findings indicate that idealized spectra based only on generalized soil classifications may be insufficient for cases where buildings with basements surrounded by rigid retaining systems such as diaphgram walls, and that multidimensional analyses incorporating soil-structure interaction yield more realistic results, with noticeably increased spectral acceleration values in the short-period range. Yet, the necessity of three-dimensional analyses becomes more apparent in buildings with extensive base areas, particularly in regions where geological formations vary significantly.

References

Seed, H. B., & Idriss, I. M. (1970). Soil moduli and damping factors for dynamic response analyses (Report No. EERC 70-10). Earthquake Engineering Research Center, University of California, Berkeley.

Vucetic, M., & Dobry, R. (1991). Effect of soil plasticity on cyclic response. Journal of Geotechnical Engineering, 117(1), 89–107.

Ishibashi, I., & Zhang, X. (1993). Unified dynamic shear moduli and damping ratios of sand and clay. Soils and Foundations, 33(1), 182–191.

Darendeli, M. B. (2001). Development of a new family of normalized modulus reduction and material damping curves (Doctoral dissertation). The University of Texas at Austin.

Kramer, S. L. (2024). Geotechnical Earthquake Engineering (2nd ed.). Pearson Education.

Republic of Turkey, Ministry of Environment and Urbanization. (2018). Turkish Building Earthquake Code (TBDY 2018). Official Gazette, March 18, 2018, No. 30364.

Plaxis. (2024). PLAXIS 2D Reference Manual (Version 2024.1). Bentley Systems. Retrieved from https://www.bentley.com

SOIL MECHANICS AND GEOTECHNICAL ENGINEERING

Environmental Geotechnics

Foundation Engineering

Geotechnical Earthquake Engineering

Geotechnics

Modelling Lateral Spreading in a Sandy Soils

Hamed Feizollahzadeh Ardabili[a], Ayfer Erken[a]

[a]Istanbul Technical University, Civil Engineering Department, Geotechnical Engineering Program, Turkiye
feizollahzadeha@itu.edu.tr

Keywords: Liquefaction, Lateral Spreading, Sand, Opensees, PM4Sand.

Aim

The definition of liquefaction is the during earthquake under undrained conditions, effective shear resistance of saturated sandy soil would decrease radically, causing excess pore water pressure to be generated. This conditions also make effective stress to decline and make the granular soils to liquefy and behave like a viscous fluid. Additionally, loosening sand effective shear resistance results in the transformation of stress from sand particles to porewater pressure, (Toloza Barría P, 2018).

This condition causes the loss of strength and stiffness that contributes to the ground settlement. The impact of liquefaction can be observed in the nature of the movement of ground surface motion. One of the Liquefaction phenomena is lateral displacement. Gentle slopes underlain by loose sands which are prone to liquefaction-induced lateral spreading must have a shallow water table as well as slopes between 0.3 to 5%, (Idriss and Boulanger, 2008).

The scope of this study is to properly built a soil model which can simulate as well as capture a sandy soil behavior. To do this, it is paramount that the set-up of soil, constitutive soil parameters and boundary condition should be chosen as appropriate as possible. There are not many available examples to understand the Opensees platform and how to model a soil. Therefore, many attempts should be made for evaluating and understanding this platform properly. One of this research's goal is to calibrate as well as validate the PM4Sand constitutive model parameters.

Material and Method

In this study Opensees platform was utilized. Opensees is a finite element software which allows its user to simulate and analyze the seismic response of structural and geotechnical systems. Soil's dimensions are 20-meter width and 4-meter depth in the middle of the soil as a constitutive model PM4Sand was used. The reasons for utilizing PM4sand is that this model can capture post-liquefaction reconsolidation. The experimental data is driven from a coordinated program which is called LEAP, Liquefaction Experiments and Analysis Projects. It provides researches with a reliable source of data for calibration as well as validation of their numerical modeling for analysis of liquefaction phenomenon. In this program, sandy layer in the centrifuges test was setup up with 5° slope to evaluate the lateral spreading phenomenon as a result of liquefaction. Furthermore, for calibrating soil parameters, strain-controlled cyclic simple shear test was modelled and verified by different experiments for different relative densities. The first step of modelling is to in PM4Sand as suggested by, (Chen et al. 2019), is to find the best fit for cyclic stress ratio versus number of cycles. Then finding the best fit for shear stress and shear strain is the next goal. The boundary condition was selected as free-Field condition which are two columns at sides of soil model. The soil columns width is much bigger than main soil's elements. Additionally, the columns thickness was selected 1000 meter, so that, the boundary effect would be eliminated and the result in the middle of the soil model would not be affected.

Findings

In this study, the result of Cambridge university experiment was selected for validation of soil model. There are two different model were simulated and analyzed. The results of this study show that OpenSeespy platform using PM4Sand constitutive model can perfectly capture the soil behavior during liquefaction. The paramount soil parameters were found and their effects are pointed out. In Table 1, the list of important parameters for the first model with the big-column side boundary is listed.

Table 1. First soil model Calibrated PM4Sand parameters and their values.

Primary parameters	D_r	Relative density	40%	Modified
	G_0	Shear Modulus coefficient	390.0	Calibrated
	h_{po}	Contraction rate parameter	0.42	Calibrated
	$\rho_{saturated}$	Mass density of the material	1.99	(Wang et al. 2019)
Secondary parameters	e_{max}	Maximum void ratio	0.7389	(Chen et al. 2019)
	e_{min}	Minimum void ratio	0.4915	(Chen et al. 2019)
	ϕ_{cv}	Critical state effective friction angle	35.6	(Chen et al. 2019)

Although in Boulanger and Ziotopoulou (2015) have a formula for calculating G0 in this thesis it was decreased to capture the lateral displacement results.
It will be observed in the results of the simulation; the model can capture the behavior of the experiment during the consolidation phase. In this study, the excessive pore water pressure, acceleration, and lateral displacement of the model were compared with a centrifuge experiment done by Cambridge University. The simulated model in this study is perfectly aligned with the experimental study.

The first step is the calibration of the soil parameter in the PM4Sand constitutive model. As it is evident from Figure 1, the soil parameter is calibration, and the next step is to compare the acceleration at different layers.

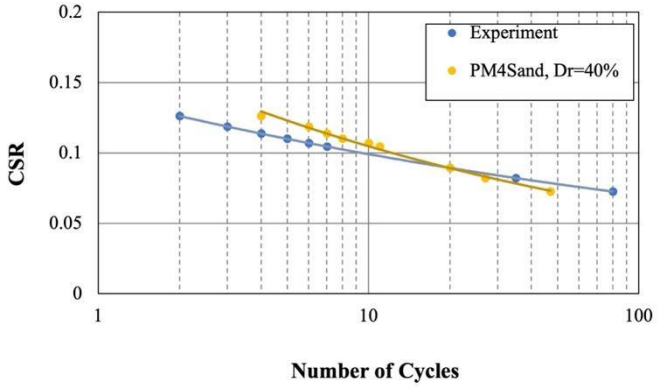

Figure 1. CSR Vs. number of cycles for the first and the second model, (Ana Maria Parra Bastidas, 2016).

The next step is to calibrate shear strain and shear stress of experimental data and simulation data. The experimental data for sand with 40 percent relative density that were utilized is from (Ana Maria Parra Bastidas, 2016). In Figure 2 the shear stress and shear strain of simulated and experiment data is compared and the results show that the simulation data is aligned with experiment.

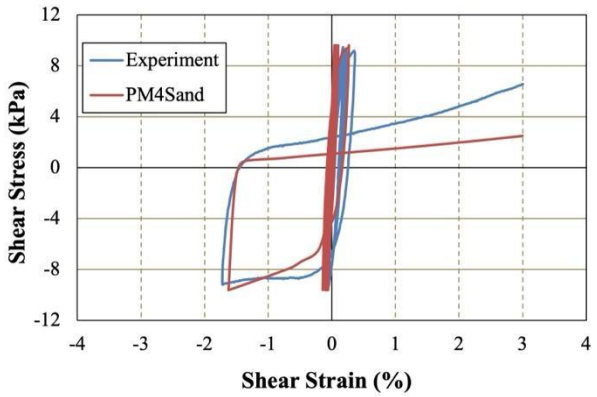

Figure 2. Shear stress vs. Shear strain of sand with Dr=40%, the cyclic stress is 95 kPa, (Ana Maria Parra Bastidas, 2016).

For next step of calibration, the Figure 3 represents another soil behaviour. In the plot the shear strain versus pore water pressure of the sandy soil with 40 percent relative density is shown. As it is evident, the behaviour of the experiment and simulation are almost the same.

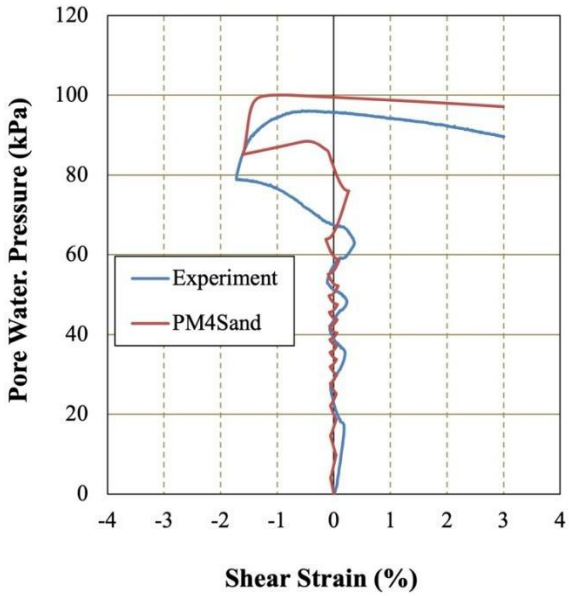

Figure 3. Pore water pressure vs. Shear strain of sand with Dr=40%, the cyclic stress is 95 kPa, (Ana Maria Parra Bastidas, 2016).

After calibrating the model's parameter, the next step is to validate the soil to evaluate whether model's setup and boundary conditions the producing prudent output. Therefore, next step is to build the model with free field boundary and validate it with centrifuge model results. The centrifuge model is Cambridge university experiment CU2 LEAP-2017 joined experiment. The first step and the most important output to make comparison is the acceleration of the input motion versus the output. In Figure 4. represents the acceleration at 1.5-meter below the surface of experiment and simulation results soil model. As it is obvious from Figure the model can capture the behavior of soil.

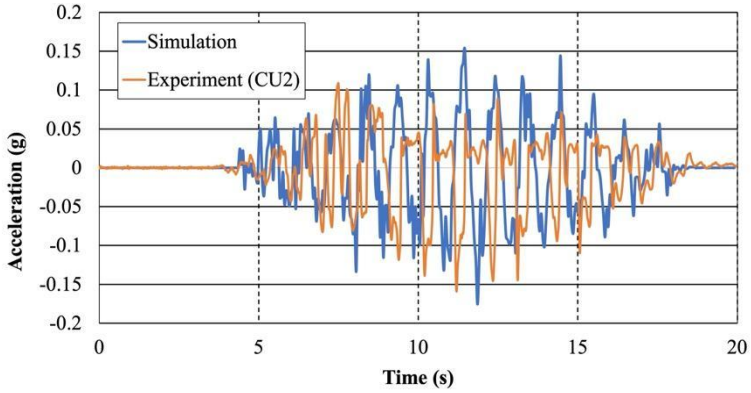

Figure 4. Acceleration Vs. Time at 1.5-meter below the surface, (Manzari, M. T, 2020).

The Figure 5. represents the acceleration versus time at surface of the soil. This figure is provided so that it will provide more about the validation of the soil simulation. As it can be seen from the Figure 5 simulated models aligned with the experiment data.

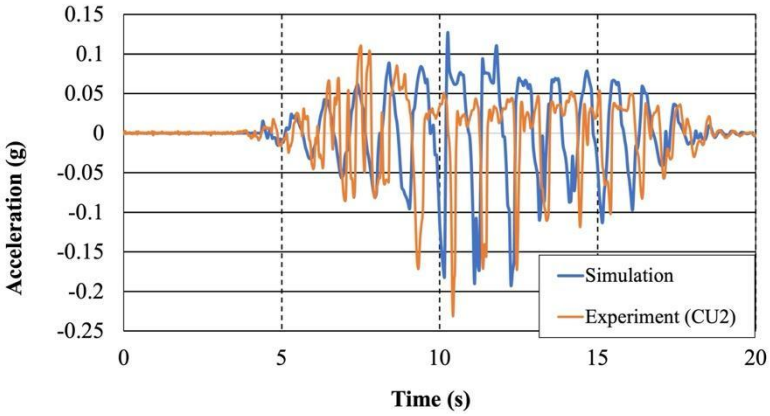

Figure 5. Acceleration Vs. Time at the surface, (Manzari, M. T, 2020).

After evaluating acceleration, the next step is evaluating pore water pressure at different depth. In Figure 6 it can be observed that at 3.5-meter below the surface model captured the maximum excessive porewater pressure and consolidation after the shake. Pore water pressure should be evaluated in different depths, therefore, in Figure 7, excess pore water pressure was evaluated at 3.5-meter below the surface. As it can be observed in both depths model can follow the experiment data. The excess pore water pressure the peak and after the shaking is over can be consolidated as same as the experiment.

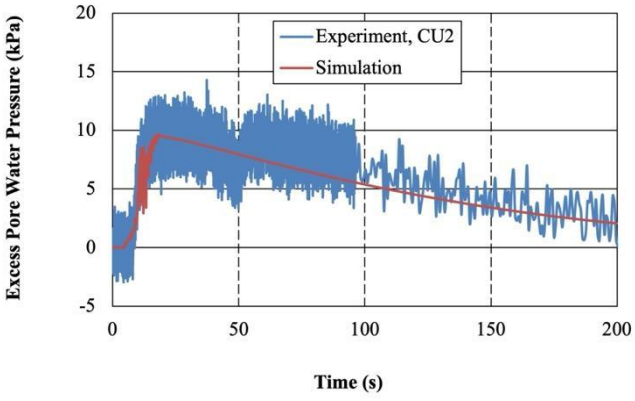

Figure 6. Excess Pore Water Pressure Vs. Time at 1-meter below the surface, (Manzari, M. T, 2020).

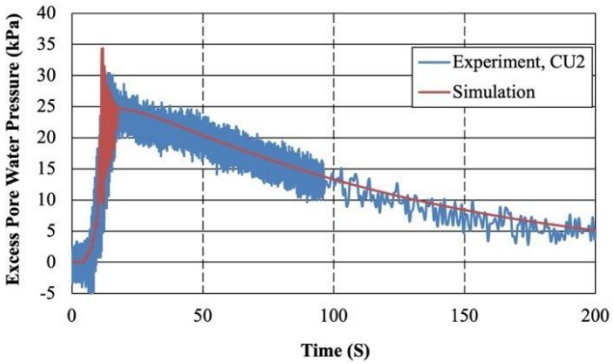

Figure 7. Excess Pore Water Pressure Vs. Time at 1-meter below the surface, (Manzari, M. T, 2020).

The next and the last step is the lateral displacement of the model at the surface. Figure 8 shows the lateral displacement at the surface. The results of the model are perfectly aligned with the experimental data. As it is evident from the Figure, model captured the behavior of soil. The lateral displacement of the model is as same as experimental data. This research's goal is to assess the lateral displacement during dynamic loading. As it can be seen from the plot the model is perfectly aligned with experimental data.

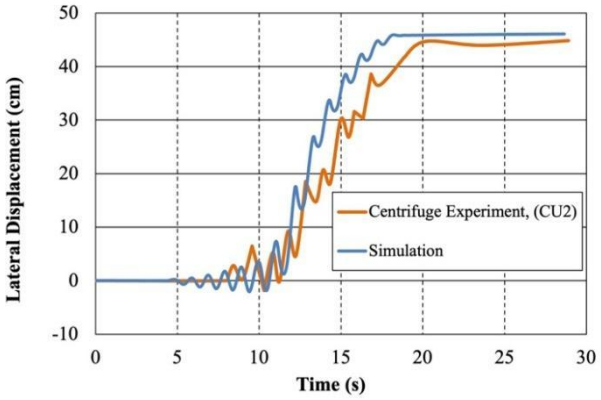

Figure 8. Lateral Spreading Vs. Time at the surface.

Figure 9 represents vertical displacement during dynamic loading. Maximum vertical displacement is 5 cm. Due to the fact that in the experiment there was not any output for vertical displacement the output of simulation solely were share.

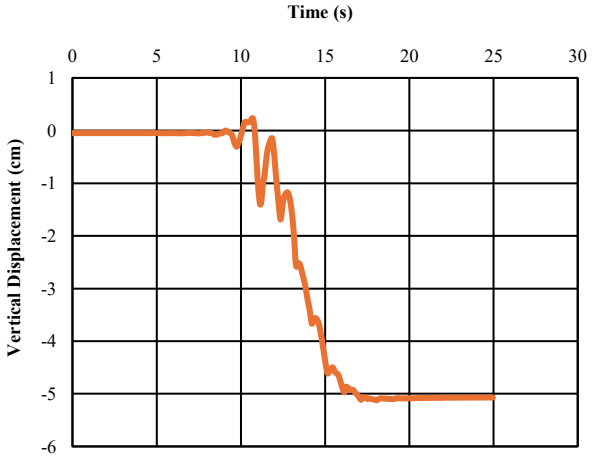

Figure 9. Vertical Displacement Vs. Time at the surface.

Conclusion

To sum-up model is calibrated. The calibration of the model was the first step. After calibration, validation of the model had to be done. In validation phase consists of three steps that should have been done. The first step was to assess the acceleration at different depths. The next step was to evaluate excess pore water pressure in different depths. At last, the lateral displacement of the soil at the surface was evaluated. Calibration as well as validation of the model was done, and compared with high accuracy. It can be observed that the model's setup and boundary, and soil parameters are calibrated and validated.

References

Bastidas, A. M. P. (2016). Ottawa F-65 Sand Characterization. Ph.D. thesis, University of California, Davis.

Boulanger RW, Ziotopoulou K. (2015). PM4Sand (Version 3), A sand plasticity model for earthquake engineering applications. Report No. UCD/CGM-15/01, Center for Geotechnical Modelling, University of California, Davis, CA, p 112.

Castiglia M,Fierro T, Magistris F, (2020), Pipeline Performances under Earthquake-Induced Soil Liquefaction: State of the Art on Real Observations, Model Tests, and Numerical Simulations.

Chen, L., Ghofrani, A., & Arduino, P. (2019). Prediction of LEAP-UCD-2017 centrifuge test results using two advanced plasticity sand models. In B. Kutter et al. (Eds.), Model tests and numerical simulations of liquefaction and lateral spreading: LEAP-UCD-2017. New York: Springer.

Chen, L., (2020). Implementation, verification, validation, and application of two constitutive models for earthquake engineering applications. University of Washington. Ph.D. thesis.

Hamada, M. (2014). Soil liquefaction and countermeasures. Engineering for earthquake disaster mitigation. Springer, Japan, pp 125–152.

Idriss, I. M. & Boulanger, R. W. (2008). Soil liquefaction during earthquakes, MNO-12. Oakland, CA, USA: Earthquake Engineering Institute.

Kramer, S.L. (1996). Geotechnical earthquake engineering. prentice Hall, Newjersey.

McGann, C. & Arduino, McGann, C. & Arduino, P,
https://opensees.berkeley.edu/wiki/index.php?title=Dynamic_2D_Effective_Stress_Analysis_of_Slope.

Manzari, M. T., El Ghoraiby, M., Zeghal, M., Kutter, B. L., Arduino, P., Barrero, A. R., Bilotta, E., Chen, L., Chen, R., and Chiaradonna, A. (2020). LEAP-2017: Comparison of the Type-B numerical simulations with centrifuge test results. Model tests and numerical simulations of liquefaction and lateral spreading, Springer, 187–218.

Montgomery J, Ziotopoulou K. (2020). Numerical simulations of selected LEAP centrifuge experiments with PM4Sand in FLAC. In: Model tests and numerical simulations of liquefaction and lateral spreading. Springer; p. 481–97, https://doi.org/10.1007/978-3-030-22818-7_24.

Toloza Barría P, (2018) Liquefaction modelling using the PM4S and soil constitutive model in PLAXIS 2D. M.Sc. Dissertation, Delft University of Technology.

Wang, R., Chen, R., & Zhang, J.-M. (2019). LEAP-UCD-2017 simulations at Tsinghua University. In B. Kutter et al. (Eds.), Model tests and numerical simulations of liquefaction and lateral spreading: LEAP-UCD-2017. New York: Springer.

STRUCTURAL ENGINEERING

Bridges

Finite Element Methods

Reinforced Concrete Structures

Seismic Performance

Steel Structures

Structural Damages

Investigation of the Effects of Vibration Dampers Positioned on Hanger Cables of an Existing Suspension Bridge

Muhammed Emin Demir[a], Kadir Ozakgul[b]

[a] Istanbul Technical University, Graduate School, Structural Engineering Master of Science, Türkiye
[b] Istanbul Technical University, Department of Civil Engineering, Civil Engineering, Türkiye
demirmuh18@itu.edu.tr

Keywords: Suspension Bridge, Hanger Cable, Vibration, Stockbridge Damper.

Aim

The objective of this scientific work was to investigate the effects of Stockbridge dampers positioned on the hanger cables, which are one of the main structural elements of an existing suspension bridge. These Stockbridge dampers have been positioned on the hanger cables because of their vibration reducing nature and they are suitable to have an effect on many structural expositions (Larsen et al., 2021). Within the framework of structural engineering, it is crucial to determine the structural behaviour and effects of the dampers in a correct manner, so that optimisation and development of new approaches would be possible. The main objective of this study is to investigate the structural behaviour of the hanger cables with Stockbridge vibration dampers installed. The evaluation of efficiency of the Stockbridge dampers and their effectiveness under different conditions were aimed. In this study, positive consequences of installing dampers in terms of vibration were focused. This study utilises the site measurements for the comparisons to understand the differences between with or without dampers installed on hanger cables. This scientific work aims to make contribution to modern suspension bridge design procedures within the scope of the structural engineering with results obtained with the site experiments, processing, and computations.

Material and Method

In a suspension bridge, hanger cables are critical structural elements that transfer the loads of the deck and the superstructure to the main cable. Since suspension cables also carry the dynamic loads of the suspension bridge, provide a connection between the structural elements of the suspension bridge and are open to many dynamic external factors such as wind, they are subject to vibrations (Chen et al., 2018). Considering the applications in different bridges in terms of structural engineering, applications of placing vibration dampers on suspension bridges by optimising them with different designs in order to take precautions against vibrations have been made in suspension bridges. The effectiveness of the vibration dampers on suspension bridges of different designs and different specifications was tested after commissioning in the field and their positive contribution to the suspension bridge dynamics was observed (Inoue et al., 2017). In order to dampen the vibrations in the hanger cables and keep them under control, Stockbridge vibration dampers were installed in the hanger cables.
Stockbridge dampers, the mass dampers positioned on the hanger cables of an existing suspension bridge, were experimented with on-site experiments. Ambient vibration records were obtained using a three-dimensional accelerometer placed on the hanger cable. Forced vibrations of the hanger cables were also recorded with a three-dimensional accelerometer placed on the hanger cable while applying force directly to the hanger cable. These field vibration records were taken for different situations. In order to take the unlike situations into consideration, different hangers with unique lengths and conditions were measured. Some of the longest cables on the bridge were recorded before and after the installation of the damper. To determine the difference due to the damper, the vibrations were measured with and without the damper for both free and forced vibration situations. A flowchart of the method illustrating the data analysis procedure is shown in Figure 1.

Figure 1. Data Analysis Procedure Flowchart.

The experimental on-site vibration measurement records were analysed using MATLAB software (The MathWorks Inc., 2024). Fast Fourier Transform was used to convert the time domain data to the frequency domain; therefore, to calculate the modes of the vibrations. Dominant frequencies of the hanger cables and Fourier Amplitude Spectra were calculated. As seen in Figure 2 and Figure 3, forced vibration acceleration measurement of a hanger cable analysed and Fourier Amplitude Spectra at after forced vibration condition conducted for both situations hanger cable equipped with damper (see Figure 2) and without damper (see Figure 3).

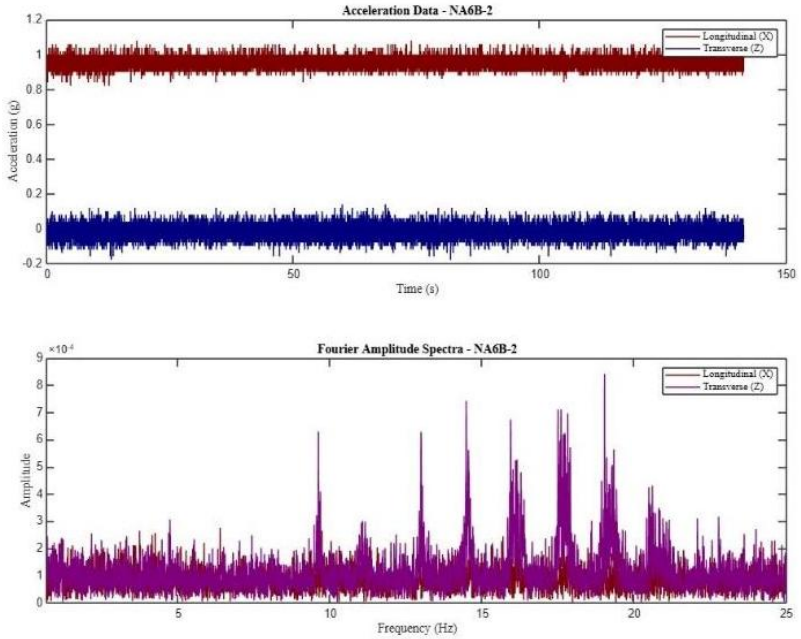

Figure 2. With Damper Acceleration Data and Fourier Amplitude Spectra (The MathWorks Inc., 2024).

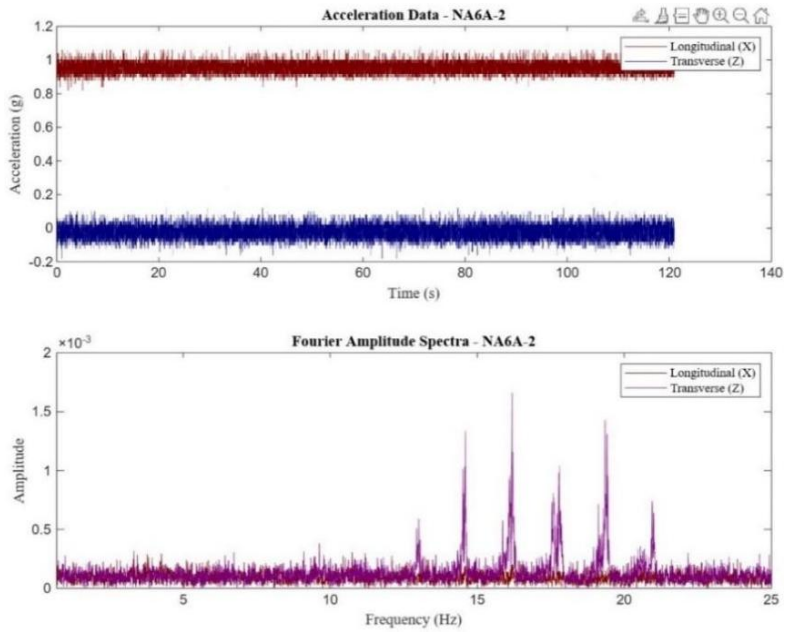

Figure 3. Without Damper Acceleration Data and Fourier Amplitude Spectra (The MathWorks Inc., 2024).

As seen in Figure 2 and Figure 3, the amplitudes of vibrations after forced vibration are reduced at the hanger cable equipped with damper condition.

Comparisons were also made between the vibrations of the hanger cables before and after the installation of the damper. Modal analyses were also performed on the processed field measurement data. Modal damping ratios obtained and changes in natural frequencies identified. For the effective damping ratios under the influence of Stockbridge dampers, the amplitude of the vibrations after the forced vibration experiment measurements would be utilised.

Findings

After the analysis of the vibration data, dynamic behaviour of hanger cables characterised. In the forced vibration cases the FFT and PSD analyses verified that the Stockbridge vibration dampers have a crucial role in reducing the amplitude of vibration and dominant frequency peaks. Modal analyses showed outputs revealing that Stockbridge dampers effectively redistribute the vibrational energy and improve damping of the hanger cable comparatively to the situation of uninstalled dampers. The vibration records with amplitude declines after forced excitation were used for the estimation the effective damping ratios, to make quantitative measure of the enhancement at dynamic performance in terms of vibration for the hanger cables provided by the Stockbridge dampers.

A comparison was made between the processed site experiment results of long hanger cables with vibration dampers and shorter hanger cables without vibration dampers. The study proven that long cables of the existing suspension bridge equipped with Stockbridge vibration dampers are having significant reductions in vibration amplitude and damping performance of long hanger cables is improved by the vibration dampers. Damping ratios of the damper equipped hanger cables have positively increased compared to the hanger cables without dampers.

Conclusion

For conclusion, this experimental research validates the efficiency of the Stockbridge vibration dampers installed on the hanger cables of an existing suspension bridge by providing analyses of the vibration records at different initial conditions. It could be stated that, after evaluating with the application of advanced signal processing techniques to the vibration records measured on site both ambient and forced vibration situations, the hanger cables equipped with Stockbridge vibration dampers have a positive impact on dynamic behaviour by means of reducing the vibration and lowers the vibration energy transferred to the suspension bridge structure. Modal analysis performed confirms that the Stockbridge vibration dampers contribute to the enhanced damping ratios.

Overall, the results of this research authenticate the effectiveness of Stockbridge vibration dampers in terms of improving the dynamic performance of suspension bridge hanger cables, and also highlight the importance of integrating comprehensive vibration analysis methods through the application and optimisation of hanger cable vibration dampers for the suspension bridge design.

Potential challenges of the proposed methodology at the measuring stage could be where using the proper equipment and work time selection is important because of the variable intensity of usage of the suspension bridge. When developing new approaches for other bridges, used methodology needs to be modified by utilising the parameters of the structure such as boundary conditions, vibration damper characteristics and modal analysis of the bridge.

The possible limitations could be considered as understanding and analysing the effects of the vortex induced vibrations on the hanger cables of the suspension bridges which needs complex analysis with laboratory and site measurements.

References

Chen, W., Gao, D., Li, H., & Hu, H. (2018). Wake-flow-induced vibrations of vertical hangers behind the tower of a long-span suspension bridge. *Engineering Structures*, *169*, 188–200. https://doi.org/10.1016/j.engstruct.2018.05.049

Inoue, M., Takai, Y., Uzun, M. K., & Kawakami, T. (2017). IZMIT Bay Suspension Bridge – Wind Induced Vibrations. IABSE Reports, 109, 374–380. https://doi.org/10.2749/vancouver.2017.0374

Larsen, A., Andersen, K. G., & Jamal, A. (2021). Wind Induced Hanger Vibrations – the Hålogaland Suspension Bridge. *Structural Engineering International*, *32*(1), 62–70. https://doi.org/10.1080/10168664.2021.1930332.

The MathWorks Inc. (2024). MATLAB version: R2024b, Natick, Massachusetts: The MathWorks Inc.

STRUCTURAL ENGINEERING

Bridges

Finite Element Methods

Reinforced Concrete Structures

Seismic Performance

Steel Structures

Structural Damages

Artificial Intelligence Based Surrogate Models for Stiffened Plate Buckling Analysis

Hasan Kıyık[a], Metin Orhan Kaya[b]

[a] Istanbul Technical University/Faculty of Aeronautics and Astronautics, Department of Aeronautical and Astronautical Engineering, Graduate School, Türkiye
[b] Istanbul Technical University, Faculty of Aeronautics and Astronautics, Department of Aeronautical Engineering, Türkiye
kiyik16@itu.edu.tr

Keywords: Artificial Intelligence, Surrogate Modelling, Optimization, Stiffened Plate, Finite Element Analysis.

Aim

In structural engineering applications, accurately predicting the buckling behavior of stiffened plates is crucial yet computationally demanding, especially when employing traditional finite element (FE) solvers directly within iterative design optimization frameworks [1]. This study presents a novel approach that employs artificial intelligence (AI) based surrogate models [2] to efficiently evaluate critical buckling load factors and corresponding mass values of stiffened plates. Initially, a comprehensive dataset was generated using finite element analyses conducted via ANSYS software [3], encompassing diverse configurations of stiffened plates characterized by variations in stiffener height, stiffener thickness, and base plate thickness. Subsequently, the resulting dataset was systematically divided into training and test sets, facilitating the development and rigorous evaluation of several AI-driven regression models. The surrogate models developed in this work exhibit strong predictive capabilities, significantly reducing computational overhead compared to direct FE simulations. By rapidly approximating complex FE responses, the proposed methodology enables swift exploration of design spaces, markedly accelerating structural optimization processes. Ultimately, this research underscores the practicality and efficiency of AI-based surrogate modeling as a robust alternative to conventional finite element methods, particularly for iterative optimization tasks in the analysis and design of stiffened structural plates.

Material and Method

In this study, stiffened plate models [4] were designed and analyzed using ANSYS [3], a commercial finite element solver, to generate the necessary dataset for training and testing artificial intelligence based surrogate models. Various stiffened plate configurations were systematically modeled by varying geometric parameters such as stiffener height, stiffener thickness, and base plate thickness, and their corresponding critical buckling load factors and mass values were computed. The resulting dataset was partitioned into distinct training and testing subsets to rigorously evaluate model performance.

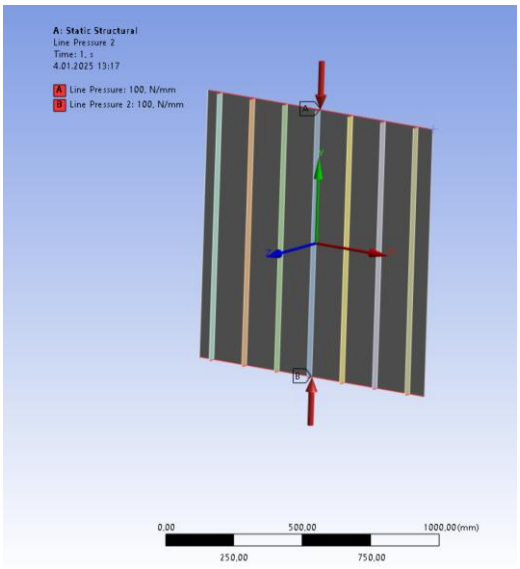

Figure 1. Loading Conditions of the Eigenvalue Buckling Analysis.

Table 1. Randomly Selected Samples from the Training Data Set.

Input			Output	
Plate Thickness [mm]	Stiffener Thickness [mm]	Stiffener Height [mm]	Load Factor	Mass [Kg]
2.5	20	30	5.372	18.56
3.5	2	45	2.87	11.44
4	4	45	5.10	14.57

For surrogate modeling, several state-of-the-art AI algorithms were implemented and evaluated in the MATLAB environment, including Artificial Neural Networks (ANN) [5-6], Support Vector Regression Machines (SVRM) [7-8], Ensemble Learning methods [9-10], and Gaussian Process (GP) [11-12] regression models. To ensure an unbiased and thorough comparison of model performance, hyperparameters for each AI model were optimized through a systematic grid search method [13]. This approach allowed for a fair assessment of predictive accuracy and generalization capabilities across different surrogate modeling techniques, thus facilitating the identification of the most effective model for accurately predicting stiffened plate buckling behavior.

For the studied stiffened plate buckling analysis, 245 number of samples are generated using ANSYS finite element solver with linear sampling method (5x7x7). The samples were generated as follow; Plate Thickness [mm]: 2-4, Stiffener Thickness [mm]: 2-20, Stiffener Height [mm]: 20-50. These generated samples will be used to train the AI models to predict the Load Factor, and Mass [Kg] characteristics by creating a mapping between inputs (Plate Thickness [mm], Stiffener Thickness [mm], Stiffener Height [mm]) and outputs (Load Factor,Mass [Kg]) of the train data samples. In order to check the generalization capabilities of the AI models and prevent models from overfitting, an additional 50 samples generated using Latin-Hyper-Cube sampling method will be used for benchmark purposes.

Findings

a) Surrogate Modelling

The following error metrics are used to benchmark the prediction performance of each AI-based surrogate model. Each model's hyperparameters are determined via grid search optimization with the validation method of K-fold (K=5) [14]. The performance results givenin Table 2 belong to each model's test samples response using Mean absolute Error (MAE, such as equation 1) and Relative Mean Error (RME, such as equation 2).

T: Targeted value, P: Predicted Value by AI model, n: total number of samples.

$$MAE = \frac{1}{n}\sum_{i=1}^{n} |T_i - P_i| \quad (1)$$

$$RME = \frac{100}{n}\sum_{i=1}^{n} \frac{|T_i - P_i|}{|T_i|} \quad (2)$$

Table 2. Regression Performance of Load Factor for Each Surrogate Model for Test Samples. All Not Mentioned HP (Hyperparameter) are Taken as Default Values in MATLAB 2023B.

Model	Optimal HP	MAE	RME [%]
Artificial Neural Networks-ANN	# hidden-layers: 3; # Neurons: 54-45-10; Activation function: sigmoid;	0.07	1.7
Support Vector Regression Machine-SVRM	Kernel Function: Polynomial; Polynomial order 2;Epsilon 0.0032; Box constraint 0.001	0.64	14.1
Ensemble Learning	Method LSBoost; # Learning Cycle 239; Learning Rate 0.105; Max # splits 171	0.42	9.6
Gaussian Process-GP	Kernel Function: ard matern 52; Sigma 0.000713; Basis Function Constant	0.1	2.2

Table 3. Regression Performance of Mass for Each Surrogate Model for Test Samples. All Not Mentioned HP are Taken as Default Values in MATLAB 2023B.

Model	Optimal HP	MAE	RME [%]
Artificial Neural Networks-ANN	# hidden-layers: 2; # Neurons: 7-151; Activation function: tanh;	0.02	0.04
Support Vector Regression Machine-SVRM	Kernel Function: Polynomial; Polynomial order 2;Epsilon 0.005945; Box constraint 575.96	0.04	0.3
Ensemble Learning	Method LSBoost; # Learning Cycle 491; Learning Rate 0.0961; Min Leaf Size 1; Max # splits 4	0.63	4.3
Gaussian Process-GP	Kernel Function: squaredexponential; Sigma 0.0001898; Basis Function none; Kernel scale 975.2	0.01	0.02

As it can be seen from the results given in Tables 2-3, ANN model is found to be the best model for prediction of Load Factor, while GP model is found to be the optimal surrogate model for prediction of Mass characteristic. In the next subsection, both of these models will be deployed to assist in an optimization process.

b) Surrogate Model Assisted Optimization

In this section, the obtained ANN and GP models will be used to assist optimization of the studied stiffened plate buckling analysis. Here it is aimed to obtain the maximum load factor of a design with a targeted mass value. The cost function (such as equation 3) that will guide the optimizer algorithm is defined as cost function. Although the selection of the optimization algorithm is an important matter for computational efficiency of the whole process, with the usage of surrogate model for creating response of cost function for candidate solution requires far more less computational budget (both memory and computation time <1 ms) compared to the traditional approach of directly using finite element solvers such as ANSYS (computational time for each evaluation >1 minutes).

$$Cost_i(PT_i, ST_i, SH_i) = Min\left[|M_T - M(PT_i, ST_i, SH_i)| + \frac{1}{LF(PT_i, ST_i, SH_i)}\right] \quad (3)$$

MT: is the targeted Mass value, $Cost_i(PT_i, ST_i, SH_i)$: is the cost value of the ith candidate solution, $M(PT_i, ST_i, SH_i)$: is the response of surrogate model for the predicted value of Mass for the ith input, $LF(PT_i, ST_i, SH_i)$: is the response of the surrogate model for predicted value of Load Factor for the ith input.

Herein three different optimization algorithms (Random Search [15], PSO [16], GA [17]) are deployed for finding the optimal values of for a targeted Mass value of 11.44 kg with maximized Load Factor. For a fair benchmark between algorithms, the function evaluation of each method is limited to 2000. This corresponds to the following Hyper parameters for each algorithm; PSO (particle swarm optimization) & GA (genetic algorithm): 40 iterations with 50 populations, and max evaluation of 2000 for random search. The obtained optimal values of design variables, the corresponding Load factor, and Mass values are presented in Table 4 alongside the finite element result of the same design configuration from ANSYS.

Table 4. Optimal Design Variables Obtianed from Optimization Algorithms for $M_T = 11.44$, with Maximum Function Evaluation of 2000. The Obtained Surrogate Model Results are Compared with ANSYS Results.

Algorithm	Input			Surrogate/ANSYS	
	Plate Thickness [mm]	Stiffener Thickness [mm]	Stiffener Height [mm]	Mass [Kg]	Load Factor
Random Search	2.45	5.35	44.63	11.42 / 11.42	3.85 / 3.79
Genetic Algorithm	2.63	4.82	44.46	11.41 / 11.44	4.05 / 4.23
Particle Swarm	2.73	4.45	44.98	11.41 / 11.44	4.12 / 4.32
MOGA+ANSYS	2.95	3.52	47.71	11.445	3.97
	2.95	3.52	47.528	11.44	3.94
	2.96	3.52	47.35	11.45	3.94

As it can be observed from Table 4, the proposed surrogate model assisted optimization approach can achieve better simulation results compared to ANSYS optimization tool results. Here it should also be considered that, if we neglected the initialization cost of generating AI models (training and test samples), the whole optimization process is took less than a minutes for all the mentioned optimization algorithms, while a single function evaluation for MOGA (Multi-Objective Genetic Algorithm) + ANSYS is likely to take more than 2 minutes. Thus, for different optimization targets, the proposed approach can obtain more than 10 of optimized designs in the same duration for a case where the designer can only achieve a single optimization design using MOGA+ANSYS approach.

Conclusion

Total of 295 number of data samples (245 Training + 50 Test) for a stiffened plate is generated. Using these data samples a series of AI surrogate models are created and their performances are benchmarked. For prediction of Load Factor characterics Artificial Neural Network found to be the optimal AI approach where, for Mass value prediction Gaussian Regression process is found to be the better solution. The selected optimal surrogate models of Load Factor (ANN) and Mass (GP) are integrated to optimization algorithms to accelerate the whole optimization process. As a result a computationally efficient optimization approach is achieved where not only managed to find better performance metric compared to the traditional approach of directly using ANSYS and built-in optimizers, but also can obtain these results in a fraction of computational time compared to the benchmark approach. The obtained results are validated for different types of optimization algorithms (PSO, GA, RS) with simulated results from the ANSYS.

References

Zhang, S., & Mikulich, M. (2021). Parametric CAD modelling of aircraft wings for FEA vibration analysis. Journal of Applied Mathematicsand Physics, 9(5), 889-900.

Ma, W., Nie, K., & Wang, S. (2024, November). Dynamic optimization design of thin plate structure based on surrogate model. In Journalof Physics: Conference Series (Vol. 2882, No. 1, p. 012020). IOP Publishing.

Zakuan, M. A. M. B. M., Aabid, A., & Khan, S. A. (2019). Modelling and structural analysis of three-dimensional wing. International Journalof Engineering and Advanced Technology, 9(1), 6820-6828.

Quinn, D., Murphy, A., McEwan, W., & Lemaitre, F. (2009). Stiffened panel stability behaviour and performance gains with plate prismaticsub-stiffening. Thin-Walled Structures, 47(12), 1457-1468.

Rusia, S., & Pathak, K. K. (2016). Application of artificial neural network for analysis of triangular plate with hole considering differentgeometrical and loading parameters. Open Journal of Civil Engineering, 6(1), 31-41.
Singh, D., Rai, S., & Gupta, A. (2024). Vibration analysis of sandwich functionally graded material plate with cut-outs using artificialneural network technique. Thin-Walled Structures, 202, 112072.
Monares, J. A. R., & Juárez, R. F. (2024). Regression Models for Estimating the Stress Concentration Factor of Rectangular Plates. InArtificial Intelligence in Prescriptive Analytics: Innovations in Decision Analysis, Intelligent Optimization, and Data-Driven Decisions (pp.429-450). Cham: Springer Nature Switzerland.
Li, L., Liu, D., Ren, S., Zhou, H. G., & Zhou, J. (2021). Prediction of welding deformation and residual stress of a thin plate by improvedsupport vector regression. Scanning, 2021(1), 8892128.
Daş, O., & Daş, D. B. (2022). Free vibration analysis of isotropic plates using regressive ensemble learning. Avrupa Bilim ve TeknolojiDergisi, (38), 428-434.
Haggag, M., Elruby, A. Y., Ismail, M. K., AbdelAleem, B. H., & El-Dakhakhni, W. (2024). Failure mode and capacity prediction for bolted T-stub connections using ensemble learning. Journal of Constructional Steel Research, 212, 108288.
Ming, W., Zhang, G., Li, H., Guo, J., Zhang, Z., Huang, Y., & Chen, Z. (2014). A hybrid process model for EDM based on finite-elementmethod and Gaussian process regression. The International Journal of Advanced Manufacturing Technology, 74, 1197-1211.
Guo, M., & Hesthaven, J. S. (2018). Reduced order modeling for nonlinear structural analysis using Gaussian process regression.Computer methods in applied mechanics and engineering, 341, 807-826.
Pontes, F. J., Amorim, G. F., Balestrassi, P. P., Paiva, A. P., & Ferreira, J. R. (2016). Design of experiments and focused grid search forneural network parameter optimization. Neurocomputing, 186, 22-34.
Zhang, L., Hu, J., Meng, X., & Jin, P. (2022). An efficient optimization method for periodic lattice cellular structure design based on the K-fold SVR model. Engineering with Computers, 1-15.
Andradóttir, S. (2006). An overview of simulation optimization via random search. Handbooks in operations research and managementscience, 13, 617-631.
Mthembu, L., Marwala, T., Friswell, M. I., & Adhikari, S. (2011, April). Finite element model selection using Particle Swarm Optimization.In Dynamics of Civil Structures, Volume 4: Proceedings of the 28th IMAC, A Conference on Structural Dynamics, 2010 (pp. 41-52). New York,NY: Springer New York.

Finite Element Analysis of Symmetrical Laminated Sandwich Plates with Stress Singularities Using Gradient Elasticity Theory

Aziz Mert Yavuz[a,b], Ülkü Hülya Çalık Karaköse[a]

[a]Istanbul Technical University, Faculty of Civil Engineering, Department of Civil Engineering, Türkiye
[b] Istanbul Medeniyet University, Faculty of Engineering and Natural Sciences, Department of Civil Engineering, Türkiye
yavuzaz@itu.edu.tr

Keywords: Sandwich Plate, Gradient Elasticity, Removal of Singularities, Internal Length Scale Parameter.

Aim

Classical continuum theories which are widely used in the macro-scale analyses of laminated sandwich plates are not capable of describing the deformation phenomena accurately at the micron and nano-scale observations since microstructural effects are not accounted for. Stress and strain singularities occur under point loads, at sharp crack tips and re-entrant corners of those systems when classical elasticity is used. To eliminate the singularities, gradient elasticity can be used as an alternative to classical elasticity. In gradient elasticity, micro-structural effects are considered by using additional constitutive parameters namely internal length scale parameters which are included into the higher-order gradient terms.
The aim of this study is to remove the stress singularities occurring under point loads and at sharp crack tips of symmetrical laminated sandwich plates using gradient elasticity theory and perform stress and relative error analyses. For that purpose, a MATLAB code is developed.

Material and Method

The formulation of the sandwich plate is based on the first order shear deformation theory. Undeformed and deformed states of a plate edge section under the assumptions of this theory are shown in Figure 1.

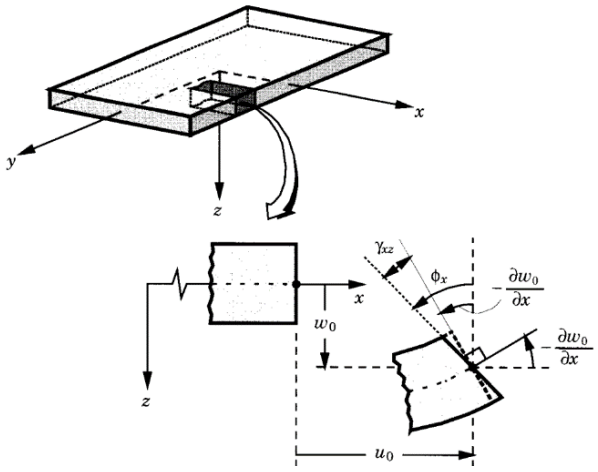

Figure 1. Undeformed and deformed states of a plate edge section (Reddy, 2004).

Displacement field according to this theory is given in Equation 1.

$$u(x,y,z) = u_0(x,y) + z\emptyset_x(x,y)$$

$$v(x,y,z) = v_0(x,y) + z\emptyset_y(x,y) \quad (1)$$

$$w(x,y,z) = w_0(x,y)$$

Cross-section of a laminated symmetrical sandwich plate is shown in Figure 2.

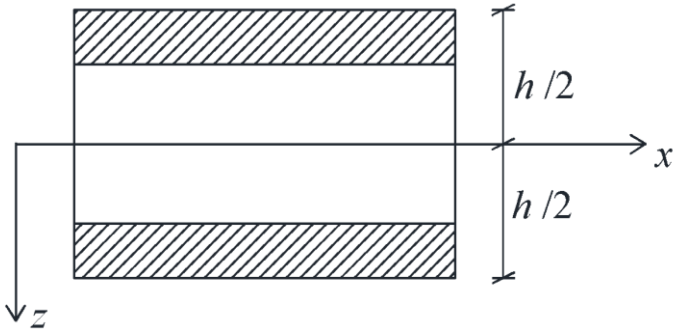

Figure 2. Laminated symmetrical sandwich plate cross-section.

The governing equations of gradient elasticity are fourth-order partial differential equations (p.d.e.) so that at least C^1 continuous shape functions are required. One of the gradient elasticity theories which is derived by Aifantis and co-workers (Ru-Aifantis gradient elasticity theory) is preferred in this study due to its straightforward finite element implementation, (Ru and Aifantis, 1993; Aifantis, 1992). The mathematical structure of Ru-Aifantis theory allows fourth-order p.d.e. to be solved as a decoupled sequence of two sets of second-order p.d.e. Thus, C^0 continuous (linear) shape functions suffice for the spatial discretization and only one internal length scale parameter is sufficient for satisfactory results, (Askes, 2011; Askes and Aifantis, 2011; Askes et al., 2008; Tenek and Aifantis, 2002; Çalık-Karaköse and Askes, 2015; Çalık-Karaköse, 2023; Bagni and Askes, 2015). The linear elastic constitutive relations are enriched with the Laplacian of the strain as shown in Equation 2,

$$\sigma_{IJ} = C_{IJKL}\left(\varepsilon_{KL} - L^2\varepsilon_{KL,MM}\right) \tag{2}$$

where σ, C and ε are the stress, constitutive and strain tensors, respectively and l represents the internal length scale parameter. The equilibrium equations in fourth order are defined as shown in Equation 3,

$$C_{ijkl}\left(u_{k,jl} - l^2 u_{k,jlmm}\right) + b_i = 0 \tag{3}$$

where u_k is the displacement vector and b_i are the body forces.

As shown in Equation 4, the first analysis step of Ru-Aifantis theory, classical elasticity solution is performed where displacements are obtained.

$$C_{ijkl}u^c_{k,jl} + b_i = 0 \tag{4}$$

In the second step, the obtained u^c_k classical elasticity displacements are used as input values to find the gradient-enriched stresses, as shown in Equation 5.

$$\sigma^g_{ij} - l^2\sigma^g_{ij,mm} = C_{ijkl}u^c_{k,l} \tag{5}$$

The finite element used in the implementation is a rectangular element having five degrees of freedom per node (three translations and two rotations) which can be used for sandwich plate models subjected to in-plane forces as well as out-of-plane forces, Figure 3. Since its formulation is based on the first order shear deformation theory, it can also be used for moderately thick and thick laminated sandwich plates where shear deformation effects are of importance. Linear shape functions are used for all degrees of freedom for simplicity.

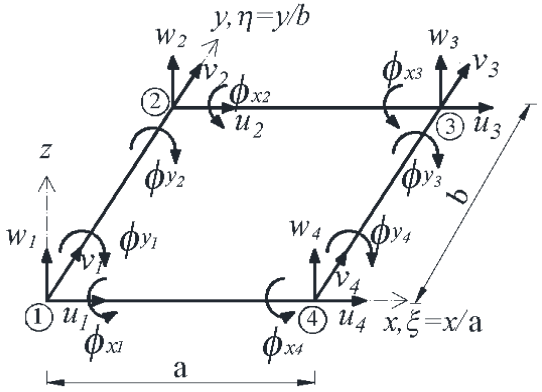

Figure 3. Laminated sandwich plate finite element.

The set of equations obtained from the finite element discretization is given in Equation 6.

$$[K_{uu}\ 0\ -K_{u\sigma}^{T}\ K_{\sigma\sigma}]\left[\underline{u^c}\ \underline{\sigma^g}\right] = \left[\underline{f}\ \underline{0}\right] \tag{6}$$

Here, K_{uu} is the first and $K_{u\sigma}\ and\ K_{\sigma\sigma}$ are the second solution step element stiffness matrices. The first set of equations gives the unknown nodal displacements $\underline{u^c}$. The gradient enriched stresses $\underline{\sigma^g}$ are obtained using the second set of equations where the nodal displacements are used as input data.

Findings

Two numerical examples are carried out to show the efficiency of the presented approach in eliminating the stress singularities occurring under point forces and at sharp crack tips. The first example is a clamped square plate subjected to a central point load and the second example is an axially loaded sandwich plate with sharp cracks (Mode I fracture problem), Figure 4.

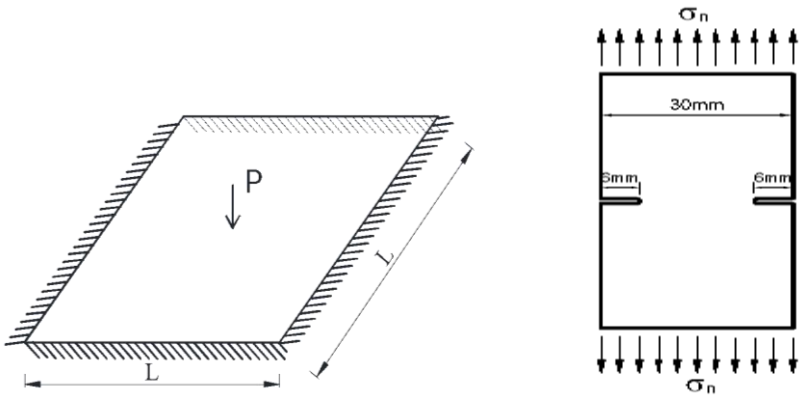

Figure 4. Clamped sandwich plate under central point load and Mode I fracture problem.

Both examples have the same cross-sectional properties, the face sheet thickness is 0.01m and core thickness is 0.08 m. Elastic moduli of the face sheets and the core are E_1=200 GPa and E_2=8 GPa, respectively. In Figure 5, σ_X stress components at the top surface of the clamped plate which is discretized using a 32x32 mesh are plotted for the classical elasticity and gradient elasticity solutions. It is observed that singularity occurring under the point load is removed with the usage of gradient elasticity.

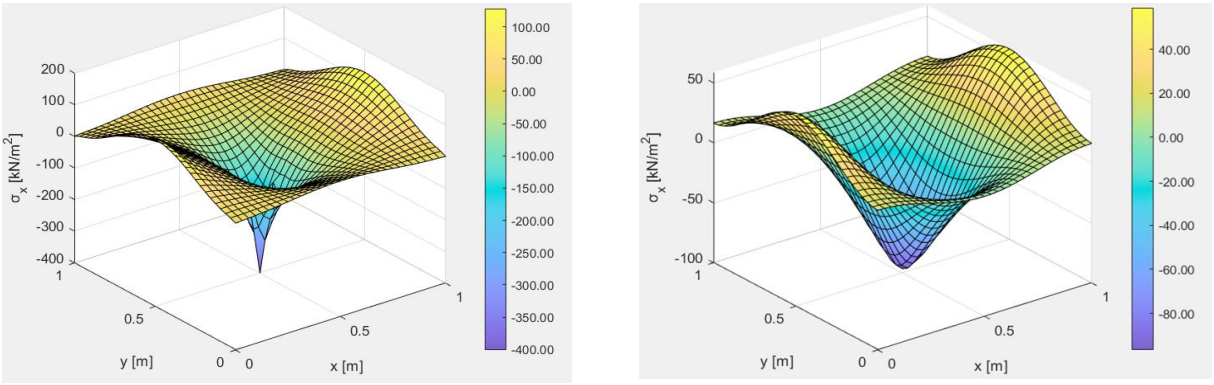

Figure 5. Clamped plate under central point load - Surface plots of σ_x stresses (left - classical elasticity solution), (right - gradient elasticity solution (l=0.125m)).

The σ_x stresses under the point load and at the top points of the face sheet and the core are given in Table 1. It is seen that in classical elasticity solution, the stress values diverge with mesh refinement for both laminates. The stresses converge to finite values with the usage of gradient elasticity indicating the removal of singularities.

Table 1. Classical elasticity and gradient enriched σ_x stresses under the point load.

mesh	σ_x (Classical)		σ_x (Gradient enriched) ℓ=0.125 m		σ_x (Gradient enriched) ℓ=0.25 m	
	Face	Core	Face	Core	Face	Core
(4x4)	-91.457	-2.927	-43.271	-1.385	-17.367	-0.556
(8x8)	-204.896	-6.557	-76.953	-2.463	-31.103	-0.995
(16x16)	-310.533	-9.937	-91.970	-2.943	-37.022	-1.185
(32x32)	-400.993	-12.832	-96.619	-3.092	-38.819	-1.242
(64x64)	-484.093	-15.491	-97.888	-3.132	-39.302	-1.258

In addition, convergence studies are carried out to show the effectiveness of the finite element implementations. For that purpose, relative error analyses in L2 norm are performed using Equation 7.

$$\|e\|_2 = \frac{\|\sigma_e - \sigma_c\|}{\|\sigma_e\|} \qquad (7)$$

Here, σ_e and σ_c are the exact and calculated stresses, respectively where the exact stresses are the stress values of the finest mesh (64x64) solution treated as the reference mesh solution.

In Figure 6, the relative stress errors in L2 norm are plotted against the number of degrees of freedom in bi-logarithmic scale for classical elasticity and gradient elasticity solutions. Relative errors decrease with increasing number of degrees of freedom. The slopes of the obtained straight lines which give the convergence rates of the numerical solution to the exact solution show that gradient elasticity solution has considerably higher convergence rate compared to the classical elasticity solution.

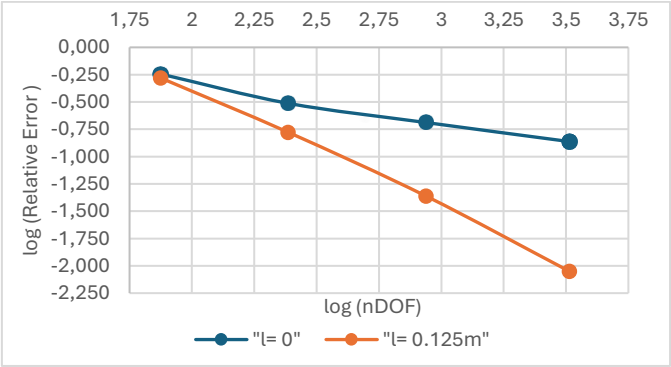

Figure 6. L2 Norm of relative stress errors for classical elasticity and gradient elasticity solutions.

In Figure 7, σ_X stress components of the Mode I fracture problem are plotted for the classical elasticity and gradient elasticity solutions. Note that due to symmetry, one fourth of the plate is used in the calculations assigning appropriate boundary conditions and it is discretized using a 32x32 mesh. Singularity occurs at the sharp crack tip with the usage of classical elasticity and it is removed when gradient elasticity is used as seen in Figure 7.

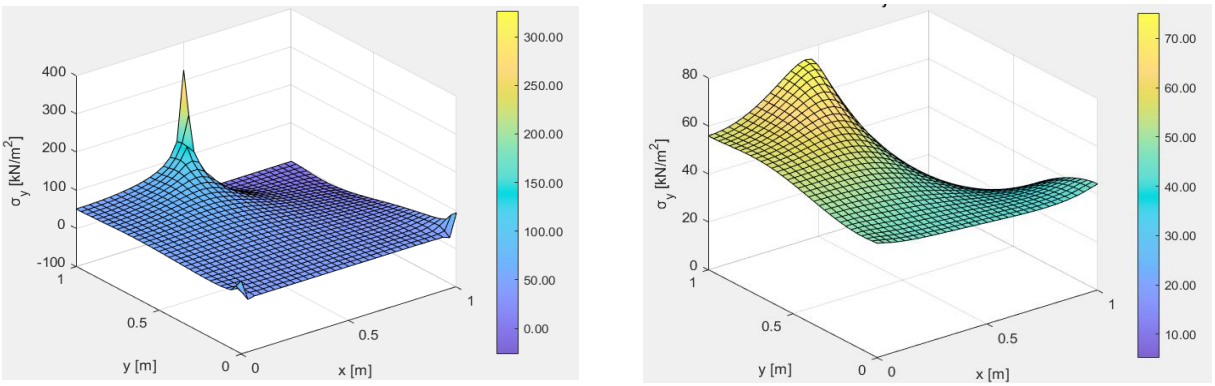

Figure 7. Mode I fracture problem - Surface plots of σ_x stresses (left - classical elasticity solution), (right - gradient elasticity solution (l=0.125m)).

In Table 2, σ_y axial stresses at the crack tip are given for the face sheet and the core. As in the first example, it is observed that the stresses increase in classical elasticity solution with mesh refinement for both laminates and they converge to finite values with the usage of gradient elasticity.

Table 2. Classical elasticity and gradient enriched σ_y stresses at sharp crack tip.

mesh	σ_y (Classical)		σ_y (Gradient enriched) ℓ=0.125 m		σ_y (Gradient enriched) ℓ=0.25 m	
	Face	Core	Face	Core	Face	Core
(4x4)	110.022	4.401	70.399	2.816	53.777	2.151
(8x8)	160.008	6.400	71.948	2.878	53.912	2.157
(16x16)	229.422	9.177	71.208	2.848	53.556	2.142
(32x32)	326.607	13.064	70.191	2.808	53.198	2.128
(64x64)	463.373	18.535	69.425	2.777	52.949	2.118

Figure 8 shows the relative stress errors in the L2 norm plotted against the number of degrees of freedom in a bi-logarithmic scale for both classical and gradient elasticity solutions with increasing internal length scale parameters. It is observed that relative errors decrease with increasing the number of degrees of freedom as well as the length scale parameter. Classical elasticity solution has lower convergence rate compared to gradient elasticity solution and the convergence rates do not change for increasing length scale parameters indicating that the smallest parameter l=0.125m is sufficient for satisfactory results.

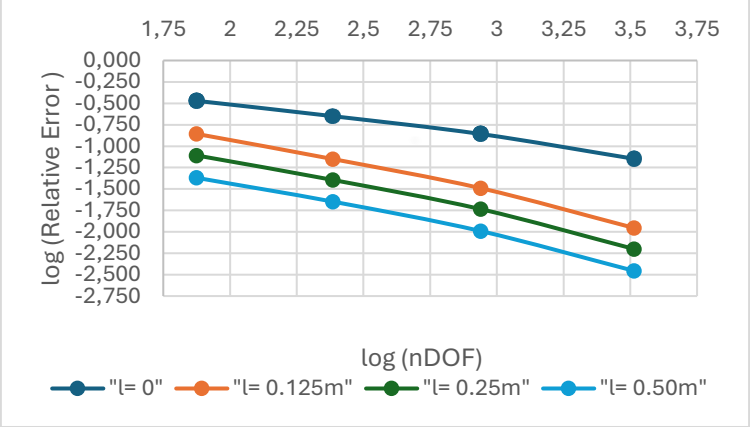

Figure 8. L2 Norm of relative stress errors for classical elasticity and gradient elasticity solutions.

Conclusion

It is demonstrated through numerical examples that stress singularities occurring under concentrated forces and at sharp crack tips are removed and smooth distributions are obtained with the usage of gradient elasticity theory. Due to the small elastic modulus of the core material, the stress values at the face sheets are considerably larger than the core values. It is observed from the classical elasticity solutions that the stress singularities occurring under the point load and at the sharp crack tip become more apparent with mesh refinement. Stress values get closer for all meshes with gradient elasticity. The relative stress errors decrease considerably with mesh refinement for both classical elasticity and gradient elasticity solutions. Convergence rates of gradient elasticity solutions are higher than the rates of classical elasticity solutions.

References

Aifantis, E.C. (1992). "On the role of gradients in the localization of deformation and fracture", International Journal of Engineering Science, 30, 1279-1299.

Askes, H. (2011). "Gradient elasticity theories and finite element implementations for static fracture", First IJFatigue and FFEMS Joint Workshop, Forni di Sopra (UD), Italy, March 7-9.

Askes, H., Aifantis, E.C. (2011). "Gradient elasticity in statics and dynamics: An overview of formulations, length scale identification procedure, finite element implementations and new results", International Journal of Solids and Structures, 48, 1962-1990.

Askes, H., Morata, I., Aifantis, E.C. (2008). "Finite element analysis with staggered gradient elasticity", Comput. Struct., 86, 1266-1279.

Bagni, C., Askes, H. (2015). "Unified finite element methodology for gradient elasticity", Comput. Struct., 160, 100-110.

Çalık-Karaköse, Ü. H. (2023). "Finite element implementation of gradient elasticity theory on thin and thick plates", Acta Mech. 234, 511-531.

Çalık-Karaköse, Ü.H., Askes, H. (2015). "A recovery-type a posteriori error estimator for gradient elasticity", Computers and Structures, 154, 204-209.

Reddy J.N. (2004). "Mechanics of laminated composite plates and shells. Theory and analysis", 2nd edition, CRC Press.

Ru, C.Q. and Aifantis, E.C. (1993). "A simple approach to solve boundary-value problems in gradient elasticity", Acta Mechanica, 101, 59-68.

Tenek L.T., Aifantis E.C. (2002). "A two-dimensional finite element implementation of a special form of gradient elasticity", Computer Modeling in Engineering & Sciences, 3, 731-741.

Effect of Strut Shape and Relative Density on the Homogenized Material Properties and Anisotropy of Octet-Truss Unit Cell

Soheil Gholibeygi[a], Hale Ergün[b], Bahar Ayhan[b]

[a] Istanbul Technical University, Civil Engineering Department, Structural Eng. PhD Prog., Türkiye
[b] Istanbul Technical University, Civil Engineering Department, Mechanics Division, Türkiye
gholibeygi19@itu.edu.tr

Keywords: Homogenization, Octet-truss, Anisotropy, Tapered Strut, Finite Element Method.

Aim

Cellular materials and lattice structures have drawn significant attention due to their exceptional mechanical properties. Truss-based lattice structures, in particular, offer advantages such as high specific strength, superior stiffness-to-weight ratio, excellent energy absorption capacity and lightweight characteristics. These properties make them highly applicable in various industries, including aerospace, defense, biomedical engineering, automotive design, and sports equipment manufacturing. Additionally, their structural behavior can be fine-tuned by adjusting factors such as topology, strut shape, cell size, and base material (Morrish et al., 2017; Qi et al., 2019).

Lattice structures generally exhibit two distinct mechanical responses: stretching-dominated and bending-dominated behavior. Those governed by stretching mechanisms tend to have a high stiffness-to-weight ratio, whereas bending-dominated structures excel in energy absorption (Habib et al., 2018).

The octet-truss lattice, a statically determinate space-filling Platonic solid, is known for its stretching-dominated meso-structural behavior. Among various lattice geometries, the octet-truss was selected due to its near-isotropic elastic response, making it a suitable choice for applications requiring uniform mechanical performance.

At the microscopic level, the basic unit cell of a lattice structure, often called the Representative Volume Element (RVE), exhibits a heterogeneous nature. However, when viewed at the macroscopic scale, it can be represented as a homogeneous anisotropic continuum. To simplify the analysis and design of lattice structures, a homogenization approach is commonly used. This method replaces the intricate geometry of the RVE with an equivalent homogeneous material at the macroscopic level, whose mechanical properties are effective material parameters. Although the base material of the lattice is isotropic, the overall mechanical response after homogenization can become fully anisotropic. This is due to the fact that the effective elastic properties are influenced by the RVE's geometry at the microscale, including its orientation (De Pasquale et al., 2018).

In this study, three different strut shapes were considered. Those are cylindrical, tapered, and dumbbell-shaped. This research explores how these different strut shapes affect the homogenized properties of an orthotropic octet-truss unit cell, all of which exhibit cubic symmetry. Additionally, the relative density is varied from 0.05 to 0.4 in increments of 0.05 to assess its influence. The study also examines the anisotropic behavior of the samples. The homogenization method is based on reaction force calculations to determine the effective material properties by using finite element software (ABAQUS, 2022).

Material and Method

The homogenization approach for RVE involves applying uniform strain conditions at the microscale, as can be seen in Figure 1, to determine the effective elastic properties. Additionally, periodic boundary conditions (PBCs) are necessary to simulate the deformation of the surrounding material, ensuring that the external surfaces of the deformed RVE remain periodic. These PBCs are implemented using EasyPBC which was developed to automate the identification and generation of necessary boundary node sets, constraint equations, displacement boundary conditions, and post-processing calculations for determining effective elastic properties (Omairey et al., 2019). It was written in the Python language utilizing ABAQUS commands. This plug-in facilitates the application of PBCs by generating node sets for each side, edge, and corner of the RVE. During this process, constraint equations are

established to link each node with its corresponding counterpart on the opposite side, ensuring periodicity in deformation. The code generates these constraint equation sets based on the required homogenized properties, adjusting applied displacements at specific reference points through boundary conditions.

$$\begin{aligned}[E_1(v_{23}v_{32}-1)/D\ -E_1(v_{21}+v_{23}v_{31})/D\ -E_1(v_{31}+v_{21}v_{32})/D\ 0\ 0\ 0\ -E_2(v_{12}\\ +v_{13}v_{32})/D\ E_2(v_{13}v_{31}-1)/D\ -E_2(v_{12}v_{31}+v_{32})/D\ 0\ 0\ 0\ -E_3(v_{13}\\ +v_{12}v_{23})/D\ -E_3(v_{13}v_{21}+v_{23})/D\ E_3(v_{12}v_{21}\\ -1)/D\ 0\ 0\ 0\ 0\ 0\ 0\ G_{23}\ 0\ 0\ 0\ 0\ 0\ 0\ G_{13}\ 0\ 0\ 0\ 0\ 0\ 0\ G_{12}\ ]\end{aligned} \tag{1}$$

$$D = v_{12}(v_{21}+v_{23}v_{31}) + v_{23}v_{32} + v_{13}(v_{31}+v_{21}v_{32}) - 1$$

$$\underline{\rho}_{co} = 6\pi\sqrt{2}\left(\frac{R}{L_{strut}}\right)^2 - \frac{32}{2-\sqrt{2}}\left(\frac{R}{L_{strut}}\right)^3 \tag{2}$$

$$\underline{\rho}_{to} = 24\pi\sqrt{2}\left(\frac{R}{L_{strut}}\right)^3 + \frac{2\pi\sqrt{2}}{5}\frac{h}{L_{strut}}\left(\frac{R}{L_{strut}}\right)^2(3+4\alpha+8\alpha^2) - \frac{16}{\sqrt{2}-1}\left(\frac{R}{L_{strut}}\right)^3 \tag{3}$$

$$\underline{\rho}_{do} = 3\pi\sqrt{2}\left(\frac{R}{L_{strut}}\right)^2 - \frac{8}{\sqrt{2}-1}\left(\frac{R}{L_{strut}}\right)^3 - 6\pi\sqrt{2}\,(1-\alpha^2)\frac{h}{L_{strut}}\left(\frac{R}{L_{strut}}\right)^2 \tag{4}$$

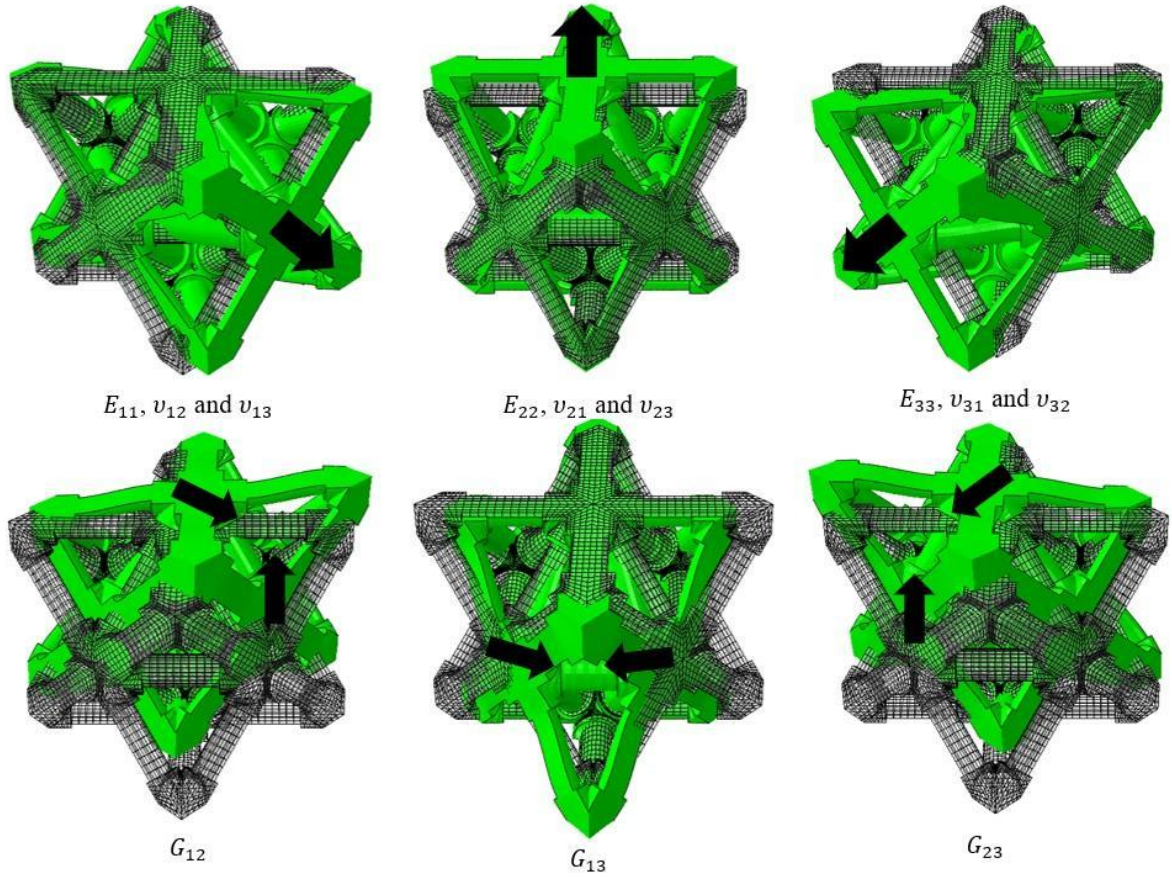

Figure 1. Required displacement type boundary condition to estimate the effective elastic properties of an RVE.

Reaction force data must be specifically requested for the reference point where displacement is applied on a given surface, depending on the required elastic modulus. To determine the corresponding stress value, this reaction force is divided by the area of the affected surface, and the resulting stress is then used to calculate Young's modulus by dividing it by the applied strain. Additionally, the output data from the same job used to compute Young's modulus is also utilized to estimate Poisson's ratios in the two transverse directions. This is done by calculating the transverse strain and dividing it by the applied axial strain. Also, Shear moduli are determined by calculating the ratio of shear stress to shear strain in the corresponding directions.
This plug-in computes all homogenized elastic moduli, shear moduli, and Poisson's ratios. Using Equation 1, a stiffness matrix is generated for each unit cell. Subsequently, ELATE, an open-source online tool for analyzing and visualizing elastic tensors, is utilized to examine the anisotropy and spatial variation of Young's modulus, shear modulus, and Poisson's ratio of the unit cells (Gaillac et al., 2016).

Cylindrical, tapered and dumbbell-shaped struts were used in this study as shown in Figure 2. They have been used to simulate Octet-Truss unit cells in order to investigate the effect of strut geometry on the mechanical properties and the anisotropy of this lattice material. All unit cells have the same cell side length of $L_{uc} = 6\,mm$ resulted with the same strut length of $L_{strut} = \frac{L_{uc}}{\sqrt{2}} = 3\sqrt{2}\,mm$. The length and the radius of the struts are denoted by L_{strut} and R, respectively. For tapered and dumbbell-shape configurations, the strut ends are of cylindrical shape over a length of strut diameter $2R$. Here, $h = L_{strut} - 4R$ is the middle part of the strut where the modification is conducted for the tapered and the dumbbell-shaped struts. In tapered one, between these two end regions, the strut radius changes gradually in a parabolic manner reaching its extreme value of αR at the strut center. However, in the dumbbell-shaped struts, between the two end regions, the strut radius changes abruptly to the value of αR. The strut shape is therefore defined through the factor α, with $\alpha < 1$ describing notched configurations and $\alpha = 1$ describing a perfectly cylindrical configuration (Tancogne-Dejean et al., 2016). The results for the values of this factor $\alpha = 0.5, 0.6, 0.7, 0.8, 0.9, 1.0$ are presented in this study.

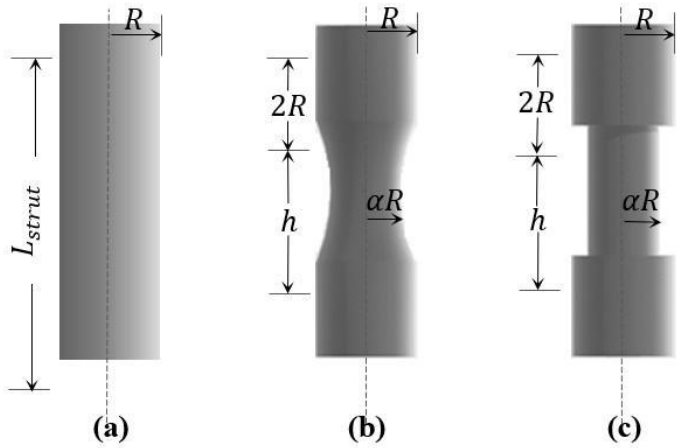

Figure 2. Geometry of **(a)** cylindrical, **(b)** tapered and **(c)** dumbbell-shaped struts.

The relative density of a lattice material $\underline{\rho}$ is defined as the ratio of the macroscopic density of the cellular material and the density of the bulk material. Relative density of octet-truss unit cell $\underline{\rho}_{co}$ is already given with Equation 2 for cylindrical struts (Tancogne-Dejean et al., 2016). The analytical expression of the relative density for tapered $\underline{\rho}_{to}$ and dumbbell-shaped $\underline{\rho}_{do}$ octet-truss are derived and presented in Equation 3 and Equation 4, respectively. In order to make a comparison between the unit cells with different shaped struts, the relative density is kept constant and the required radius values of the struts are calculated by using Equations 2, 3 and 4. The results for the relative density values of $\underline{\rho} = 0.05, 0.1, 0.15, 0.2, 0.25, 0.3, 0.35, 0.4$ are presented in this study.

Hexagonal linear element type C3D8R, that is available in ABAQUS library, is used with mesh seed size of $0.2\,mm$ in all models. The number of elements in a unit cell was approximately between 17408 and 65664, depending on their relative density value. Mesh of the cylindrical, tapered and dumbbell-shape octet truss unit

cells for the same relative density of $\underline{\rho}_{co} = \underline{\rho}_{to} = \underline{\rho}_{do} = 0.2$ are shown in Figure 3. Tapered factor α for tapered and dumbbell shaped struts in this figure are both $\alpha = 0.5$.

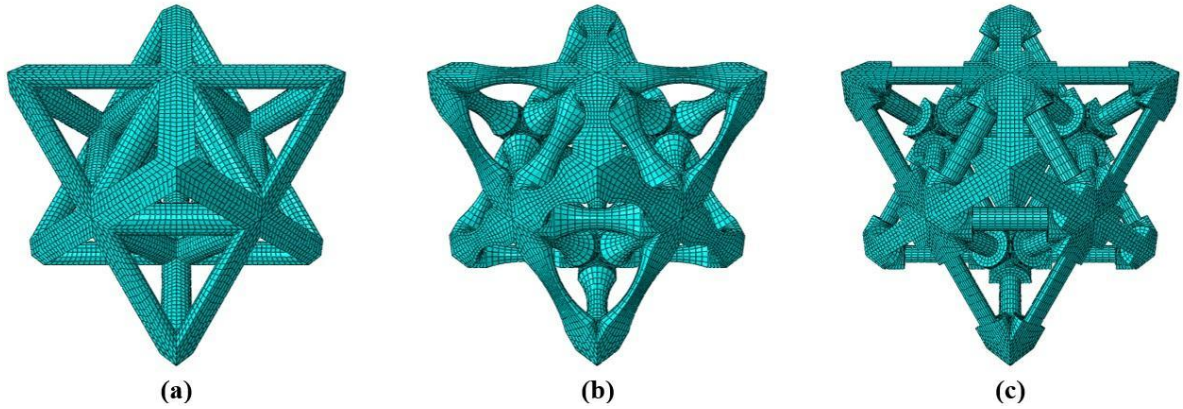

Figure 3. Mesh of octet truss unit cells for constant relative density $\underline{\rho}_{co} = \underline{\rho}_{to} = \underline{\rho}_{do} = 0.2$ with **(a)** cylindrical ($\alpha = 1$), **(b)** tapered ($\alpha = 0.5$) and **(c)** dumbbell-shaped struts($\alpha = 0.5$).

In this study, Nylon-12 is the bulk material with which octet truss lattice unit cell is additively manufactured. This isotropic linear elastic material is used in all simulations that has elastic modulus of $E = 969.52\ MPa$ and Poisson's ratio of $\upsilon = 0.33$.

Findings

The homogenized values of E_{11}^{c} and G_{12}^{c} for cylindrical octet-truss unit cell for different values of relative density are tabulated in Table 1. Also, effective material properties of tapered unit cells (E_{11}^{T}, G_{12}^{T}) and dumbbell-shaped unit cells (E_{11}^{D} and G_{12}^{D}) along with their variations relative to the cylindrical octet-truss are tabulated in Table 2. Data in this table is also plotted in Figure 4. Generally speaking, as relative density increases, the influence of strut shape becomes more pronounced. The values with which maximum improvements has obtained for each relative density are printed in bold font in Table 2. These maximum data are marked with red circles in Figure 4 . For example, it can be seen that the maximum improvement of 13.01% in Elastic modulus is obtained for relative density of $\bar{\rho} = 0.4$ by modeling the octet-truss with tapered struts for $\alpha = 0.7$. Also, in the same model, the maximum enhancement of 8.61% in shear modulus G_{12} is obtained for $\alpha = 0.8$ in comparison to the cylindrical one. The shaded cells in Table 2 and the shaded regions in Figure 4 highlight the cases when there is degradation in modulus values. In this figure, data for $\alpha = 1$ represent the homogenized modulus of cylindrical octet-truss unit cells. These values are plotted with dashed horizontal lines for each curve in order to compare with the other modified strut configurations.

Table 1. Homogenized E_{11}^{c} and G_{12}^{c} values of octet-truss with cylindrical struts for different $\underline{\rho}$ relative density values.

$\underline{\rho}$	E_{11}^{c} **(MPa)**	G_{12}^{c} **(MPa)**
0.05	6.399	4.610
0.10	14.342	10.042
0.15	24.172	16.433
0.20	35.740	23.605
0.25	49.364	31.673
0.30	65.581	40.709

0.35	85.530	51.422
0.40	108.204	63.085

Table 2. Homogenized E_{11}^T, G_{12}^T, E_{11}^D and G_{12}^D values of tapered and dumbbell-shaped octet-trusses.

		Tapered				**Dumbbell-shaped**			
$\underline{\rho}$	α	E_{11}^T (MPa)	$(\frac{E_{11}^T-E_{11}^c}{E_{11}^c})\%$	G_{12}^T (MPa)	$(\frac{G_{12}^T-G_{12}^c}{G_{12}^c})\%$	E_{11}^D (MPa)	$(\frac{E_{11}^D-E_{11}^c}{E_{11}^c})\%$	G_{12}^D (MPa)	$(\frac{G_{12}^D-G_{12}^c}{G_{12}^c})\%$
0.05	0.5	5.596	−12.6	4.028	−12.62	5.138	−19.7	3.759	−18.47
	0.6	6.097	−4.72	4.386	−4.86	5.867	−8.32	4.272	−7.34
	0.7	6.366	−0.53	4.576	−0.73	6.275	−1.94	4.552	−1.25
	0.8	**6.476**	**1.20**	**4.656**	**1.00**	6.437	0.59	4.652	0.91
	0.9	6.468	1.07	4.651	0.89	6.466	**1.05**	4.656	**0.99**
0.10	0.5	13.130	−8.45	9.091	−9.47	11.291	−21.27	8.042	−19.91
	0.6	14.279	−0.44	9.893	−1.48	12.915	−9.95	9.142	−8.96
	0.7	14.612	1.89	10.185	1.42	14.158	−1.28	9.966	−0.75
	0.8	14.743	**2.80**	10.295	**2.52**	14.698	**2.48**	10.310	**2.67**
	0.9	14.600	1.80	10.219	1.76	14.619	1.93	10.239	1.97
0.15	0.5	22.622	−6.41	15.046	−8.44	18.156	−24.89	12.566	−23.53
	0.6	24.528	1.47	16.353	−0.49	21.650	−10.43	14.855	−9.60
	0.7	25.337	4.82	16.967	3.25	23.585	−2.43	16.075	−2.18
	0.8	25.404	**5.10**	17.094	**4.02**	24.726	2.29	16.793	2.19
	0.9	24.936	3.16	16.860	2.60	24.853	**2.82**	16.861	**2.60**
0.20	0.5	34.321	−3.97	21.887	−7.28	26.596	−25.59	17.798	−24.60
	0.6	37.208	4.11	23.792	0.79	32.039	−10.35	21.150	−10.40
	0.7	38.261	**7.05**	24.716	4.71	34.824	−2.56	22.929	−2.86
	0.8	38.117	6.65	24.802	**5.07**	36.842	3.08	24.185	2.46
	0.9	37.108	3.83	24.319	3.03	36.979	**3.47**	24.294	**2.92**
0.25	0.5	49.070	−0.60	30.084	−5.02	36.325	−26.41	23.431	−26.02
	0.6	53.124	7.62	32.740	3.37	44.162	−10.54	28.086	−11.32

	0.7	54.593	**10.59**	33.906	**7.05**	49.741	0.76	31.458	−0.68
	0.8	53.564	8.51	33.590	6.05	51.716	**4.77**	32.749	3.40
	0.9	51.671	4.67	32.822	3.63	51.552	4.43	32.789	**3.53**
0.30	0.5	65.764	0.28	38.825	−4.63	48.007	−26.80	29.833	−26.72
	0.6	71.511	9.04	42.512	4.43	58.819	−10.31	36.00	−11.57
	0.7	73.514	**12.10**	44.084	**8.29**	66.496	1.40	40.475	−0.57
	0.8	72.682	10.83	44.050	8.21	69.312	5.69	42.335	4.00
	0.9	69.915	6.61	42.859	5.28	69.666	**6.23**	42.700	**4.89**
0.35	0.5	86.195	0.78	49.136	−4.45	62.007	−27.5	37.033	−27.98
	0.6	93.724	9.58	53.714	4.46	77.017	−9.9	45.261	−11.98
	0.7	95.833	**12.05**	55.427	7.79	86.851	1.54	50.837	−1.14
	0.8	94.854	10.90	55.583	**8.09**	90.424	5.72	53.150	3.36
	0.9	90.808	6.17	53.915	4.85	90.611	**5.94**	53.700	**4.43**
0.40	0.5	108.392	0.17	59.852	−5.13	78.375	−27.57	45.074	−28.55
	0.6	118.278	9.31	65.632	4.04	97.554	−9.84	55.209	−12.49
	0.7	122.283	**13.01**	68.428	8.47	110.667	2.28	62.392	−1.10
	0.8	121.066	11.89	68.515	**8.61**	115.445	6.69	65.538	3.89
	0.9	115.199	6.47	66.098	4.78	115.89	**7.10**	66.471	**5.37**

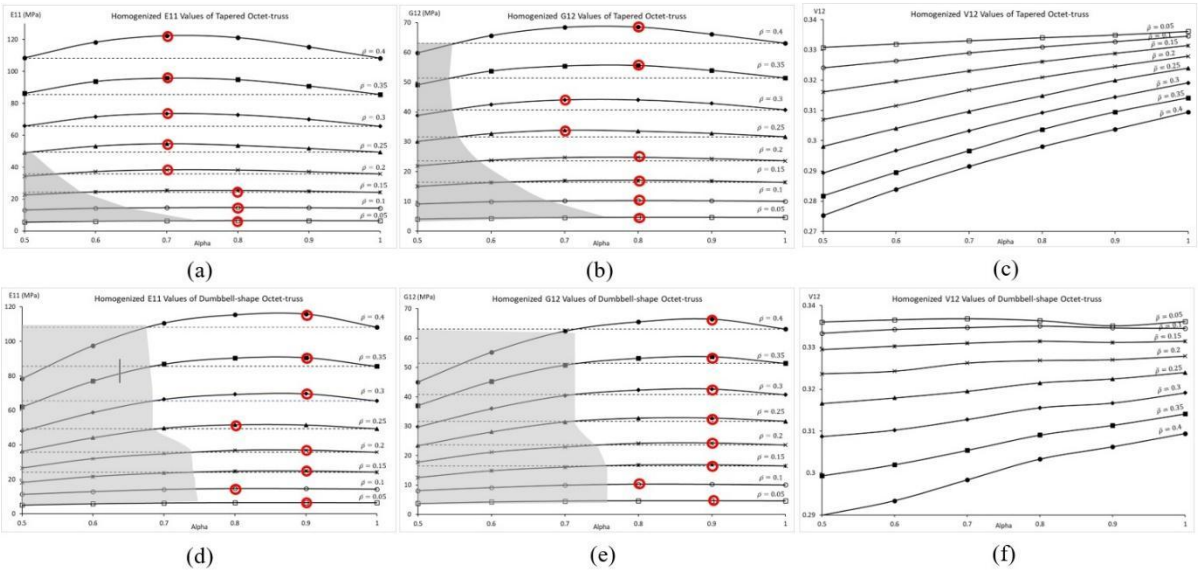

Figure 4. Homogenized value **(a)** E_{11}, **(b)** G_{12} and **(c)** υ_{12} of tapered, **(d)** E_{11}, **(e)** G_{12} and **(f)** υ_{12} of dumbbell-shaped octet-truss unit cell.

Figure 4 indicates that at low relative densities of $\bar{\rho} < 0.15$, the differences in Young's modulus and shear modulus among octet-truss unit cells with various strut shapes are negligible. However, for higher relative densities ($\bar{\rho} \geq 0.15$), tapered octet-truss unit cells exhibit the highest elastic and shear modulus at $0.7 \leq \alpha \leq 0.8$ interval, whereas in dumbbell-shaped unit cells, the highest values occur within the range of $0.8 \leq \alpha \leq 0.9$. Additionally, as α increases, the homogenized Poisson's ratio also increases. Overall, tapered struts are preferable over cylindrical and dumbbell-shaped ones for achieving improved effective material properties.

According to Figure 5, by increasing relative density $\bar{\rho}$, homogenized value of E_{11} and G_{12} increase for all models. Black line represents the cylindrical octet-truss.

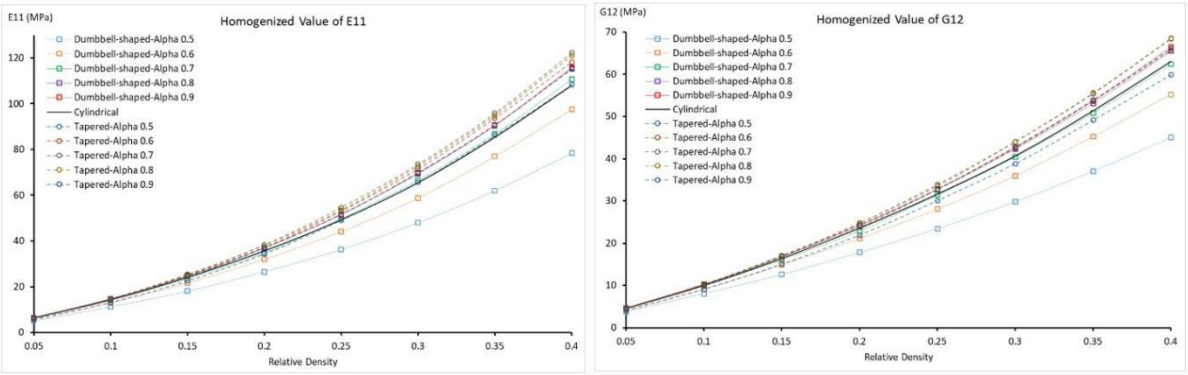

Figure 5. Homogenized value **(a)** E_{11} and **(b)** G_{12} of octet-truss unit cell.

Anisotropy is defined as the ratio of the maximum to the minimum values of the related material properties (Gaillac et al., 2016). To analyze the impact of strut shape on the anisotropy of Young's modulus, shear modulus and Poisson's ratio, stiffness matrices of three model, each with a relative density of 0.4 and tapering factor of $\alpha = 0.7$ for tapered and dumbbell-shaped unit cells, were computed and imported into the ELATE online tool (Gaillac et al., 2016). The results are presented in Table 3. This allowed for the calculation of minimum, maximum, and anisotropy values, as well as the extraction of spatial dependencies. The results indicate that the tapered octet-truss exhibits the highest minimum and maximum values for E and G. Furthermore, modeling the struts with tapered and dumbbell shapes reduces anisotropy, bringing its value closer to one which suggests that the structure becomes more isotropic.

Table 3. Minimum, maximum values of E, G, υ and anisotropy of tapered, dumbbell-shaped and cylindrical octet-truss for $\underline{\rho}$ =0.4 and $\alpha = 0.7$.

Strut shape	E	G	υ
Cylindrical	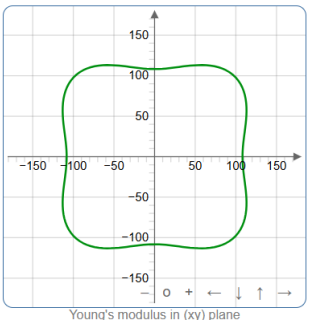 Young's modulus in (xy) plane	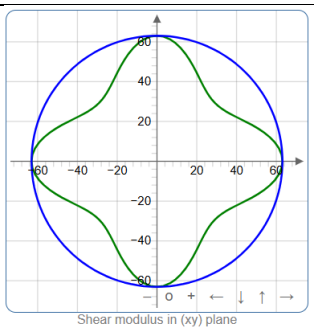 Shear modulus in (xy) plane	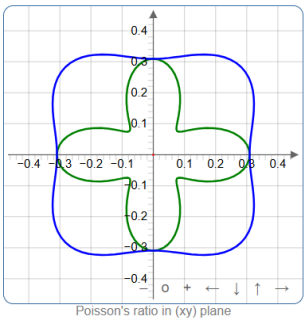 Poisson's ratio in (xy) plane
	$E_{min} = 108.2\ MPa$	$G_{min} = 41.322\ MPa$	$\upsilon_{min} = 0.10791$

	$E_{max} = 154.83MPa$ $Anisotropy = 1.431$	$G_{max} = 63.085\ MPa$ $Anisotropy = 1.527$	$\upsilon_{max} = 0.39962$ $Anisotropy = 3.7034$
Tapered	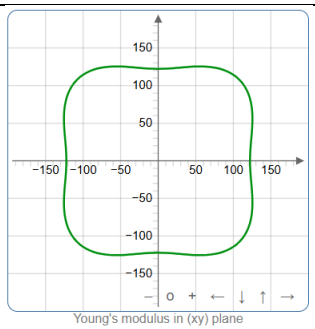 $E_{min} = 122.28\ MPa$ $E_{max} = 166.44\ MPa$ $Anisotropy = 1.361$	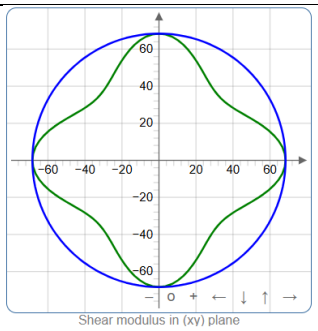 $G_{min} = 47.342\ MPa$ $G_{max} = 68.426\ MPa$ $Anisotropy = 1.445$	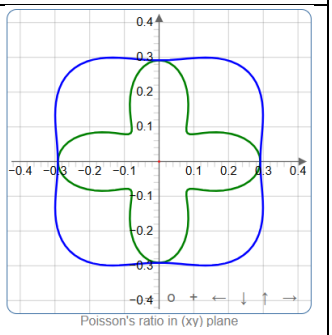 $\upsilon_{min} = 0.11549$ $\upsilon_{max} = 0.3639$ $Anisotropy = 3.1509$
Dumbbell	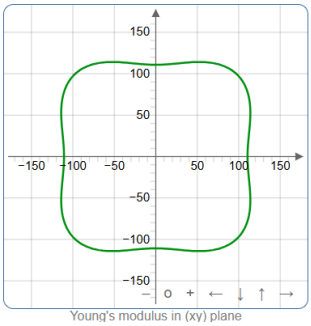 $E_{min} = 110.67\ MPa$ $E_{max} = 152.50\ MPa$ $Anisotropy = 1.378$	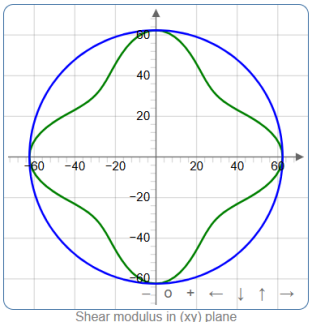 $G_{min} = 42.617\ MPa$ $G_{max} = 62.392\ MPa$ $Anisotropy = 1.464$	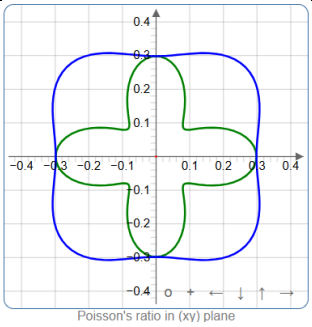 $\upsilon_{min} = 0.11662$ $\upsilon_{max} = 0.37565$ $Anisotropy = 3.2211$

Conclusion

At low relative densities ($\bar{\rho} < 0.15$), the differences in Young's modulus and shear modulus among octet-truss unit cells with various strut shapes are negligible.

For higher relative densities ($\bar{\rho} \geq 0.15$), tapered octet-truss unit cells with $0.7 \leq \alpha \leq 0.8$ exhibit the highest elasticity and shear modulus, whereas in dumbbell-shaped unit cells, the highest values occur within the range of $0.8 \leq \alpha \leq 0.9$.

As α increases, the homogenized Poisson's ratio also increases.

Tapered struts with $0.7 \leq \alpha \leq 0.8$ are preferable over cylindrical and dumbbell-shaped ones for achieving improved effective material properties.

Tapered octet-truss exhibits the highest minimum and maximum values for E and G. Modeling the struts with tapered and dumbbell shapes reduces anisotropy, bringing its value closer to one.

References

Abaqus/CAE (2022), Simulia. http://www.3ds.com/products/simulia/portfolio/abaqus.

De Pasquale, G., Montemurro, M., Catapano, A., Bertolino, G., & Revelli, L. (2018). Cellular structures from additive processes: Design, homogenization and experimental validation. Procedia Structural Integrity, 8, 75–82. https://doi.org/10.1016/j.prostr.2017.12.009

Gaillac, R., Pullumbi, P., & Coudert, F. X. (2016). ELATE: An open-source online application for analysis and visualization of elastic tensors. Journal of Physics Condensed Matter, 28(27). https://doi.org/10.1088/0953-8984/28/27/275201

Habib, F. N., Iovenitti, P., Masood, S. H., & Nikzad, M. (2018). Fabrication of polymeric lattice structures for optimum energy absorption using Multi Jet Fusion technology. Materials and Design, 155, 86–98. https://doi.org/10.1016/j.matdes.2018.05.059

Morrish, S. J. N., Pedersen, M., Wong, K. F. W., Todd, I., & Goodall, R. (2017). Size effects in compression in Electron Beam Melted Ti6Al4V diamond structure lattices. Materials Letters, 190, 138–142. https://doi.org/10.1016/j.matlet.2016.12.130

Omairey, S. L., Dunning, P. D., & Sriramula, S. (2019). Development of an ABAQUS plugin tool for periodic RVE homogenisation. Engineering with Computers, 35(2), 567–577. https://doi.org/10.1007/s00366-018-0616-4

Qi, D., Yu, H., Liu, M., Huang, H., Xu, S., Xia, Y., Qian, G., & Wu, W. (2019). Mechanical behaviors of SLM additive manufactured octet-truss and truncated-octahedron lattice structures with uniform and taper beams. International Journal of Mechanical Sciences, 163. https://doi.org/10.1016/j.ijmecsci.2019.105091

Tancogne-Dejean, T., Spierings, A. B., & Mohr, D. (2016). Additively-manufactured metallic micro-lattice materials for high specific energy absorption under static and dynamic loading. Acta Materialia, 116, 14–28. https://doi.org/10.1016/j.actamat.2016.05.054

STRUCTURAL ENGINEERING

Bridges

Finite Element Methods

Reinforced Concrete Structures

Seismic Performance

Steel Structures

Structural Damages

Using parametric design software to optimize hyperbolic paraboloid reinforced concrete shells in an example model

Izel Ece Yilmaz[a], Kutlu Darilmaz[b]

[a] Istanbul Technical University, Departmant of Civil Engineering, Structural Engineering Program, Turkiye
[b] Istanbul Technical University, Departmant of Civil Engineering, Turkiye
yilmaziz@itu.edu.tr

Keywords: Hyperbolic Paraboloid, Parametric 3D Modelling, Reinforced Concrete Shell Structure, Spatial Structure.

Aim

The hyperbolic paraboloid (hypar) is a doubly curved, anticlastic, ruled surface that looks architecturally complex to construct but structurally has a relatively simple shape formed by the combination of straight lines. This unique geometry became popular in architectural design during the mid-20th century. Its doubly curved surface provides exceptional structural rigidity, allowing architects to span large distances using surprisingly thin materials. Surface structures in architecture and engineering are components whose thickness is significantly less than their other dimensions, such as plates and shells. These structures are already efficient by design, but incorporating specific structural patterns (variations in thickness or openings) can further enhance their material efficiency while also creating visually interesting architectural spaces (Rivera et al., 2020). Due to this dimensional advantage, they are more likely to be used for specific design and structural engineering problems. In light of its high rigidity, the hyperbolic paraboloid resists uniform loads through tension, compression, or shear forces within its plane. This structural behavior enables it to remain remarkably thin while covering large spans by reducing out-of-plane bending. (Sprague, 2013) In this research paper, it is aimed to find the optimum characteristic features on an example model in architectural and structural terms by establishing various parameters from the design stage of the hyperbolic paraboloid shape. Hyperbolic paraboloids are among the most fascinating warped surfaces in construction. Though they have a double curvature, their shape is defined by two intersecting sets of straight lines, making it possible to use straight timber formwork and eliminating the need for costly curved molds (Sprague, 2013). Within this study, the reinforced concrete shell structures designed by Heinz Isler, Félix Candela, Pier Luigi Nervi, Eduardo Torroja, Bernard Lafaille, Fernand Aimond, Anton Tedesko, Sergio Musmeci and other renowned architects and engineers were thoroughly examined. Before Candela's groundbreaking free-edge shell designs, most shell structures incorporated edge ribs for stability. While hypar shells generate strong forces normal to their edges, their slender cross-sections -enabled by their double curvature- offer little resistance in that direction (Burger & Billington, 2006). Candela spent a considerable portion of his career experimenting with these types of structures. The experiences led to the construction of numerous free-edge vaults in different shapes, including triangles, squares, pentagons, hexagons, and octagons. The most famous of these is the shell roof of Los Manantiales in Xochimilco, Mexico which is one of Candela's finest works, often seen as a groundbreaking design that remains difficult to surpass (Tomás & Martí, 2010). The sample model in this study was created by taking inspiration from Felix Candela's famous buildings, Los Manantiales in Xochimilco and the Bacardi Rum Factory in Mexico.

Material and Method

The example model, composed of two intersecting curved-edged reinforced concrete hypar shells, was created using four parameters; support span, edge height, center height and edge overhang. The aim was to determine the most suitable and economical form for construction by generating design alternatives through varying these parameters. A parametric model of a hyperbolic paraboloid shell, inspired by Felix Candela's designs, was created using Rhinoceros 3D with the Grasshopper plug-in. Structural analysis was then performed using Structural Analysis and Design (SAP2000) commercial software by Computers and Structures Inc. In this study, the following stages were generally followed for parametric modeling and analysis: (1) defining the parameters that

will form the 3D model; (2) generating variable models according to the parameters; (3) creating a mesh structure for these models; (4) performing analyses in the static analysis program; (5) comparing the obtained results.

Findings

This study demonstrates that the 3D representation of shell structures using parametric analysis software enables designers to effectively explore various configurations, evaluate their structural behavior, and improve both form and structural performance at the conceptual design stage. In the design process of the sample shell structure, Felix Candela's structures were mostly taken into account. Visionaries in lightweight structures, such as Frei Otto and Félix Candela, developed a remarkable range of designs by integrating form and analysis, often utilizing techniques like form-finding (Goldbach & Lázaro, 2024). In order to push the design limits of these structures, various models were produced according to the parameters as mentioned earlier (support span, edge height, center height and edge overhang) and comparisons were made between them. The thickness of the designed shell structure was also kept as a parameter; however, the shell does not have a variable thickness, unlike Candela's structures, where the thickness is kept constant in the models. Within these models, a new hyperbolic paraboloid based reinforced shell models are presented to the literature. A group of obtained hypar shell models are given in Figure 1. Support span, edge height, center height and edge overhang values for the listed shapes in Fig.1 respectively: (a) 20,15,10,5; (b) 20,20,10,5; (c) 20,15,10,10; (d) 20,20,10,10; (e) 20,20,15,5; (f) 20,20,15,10.

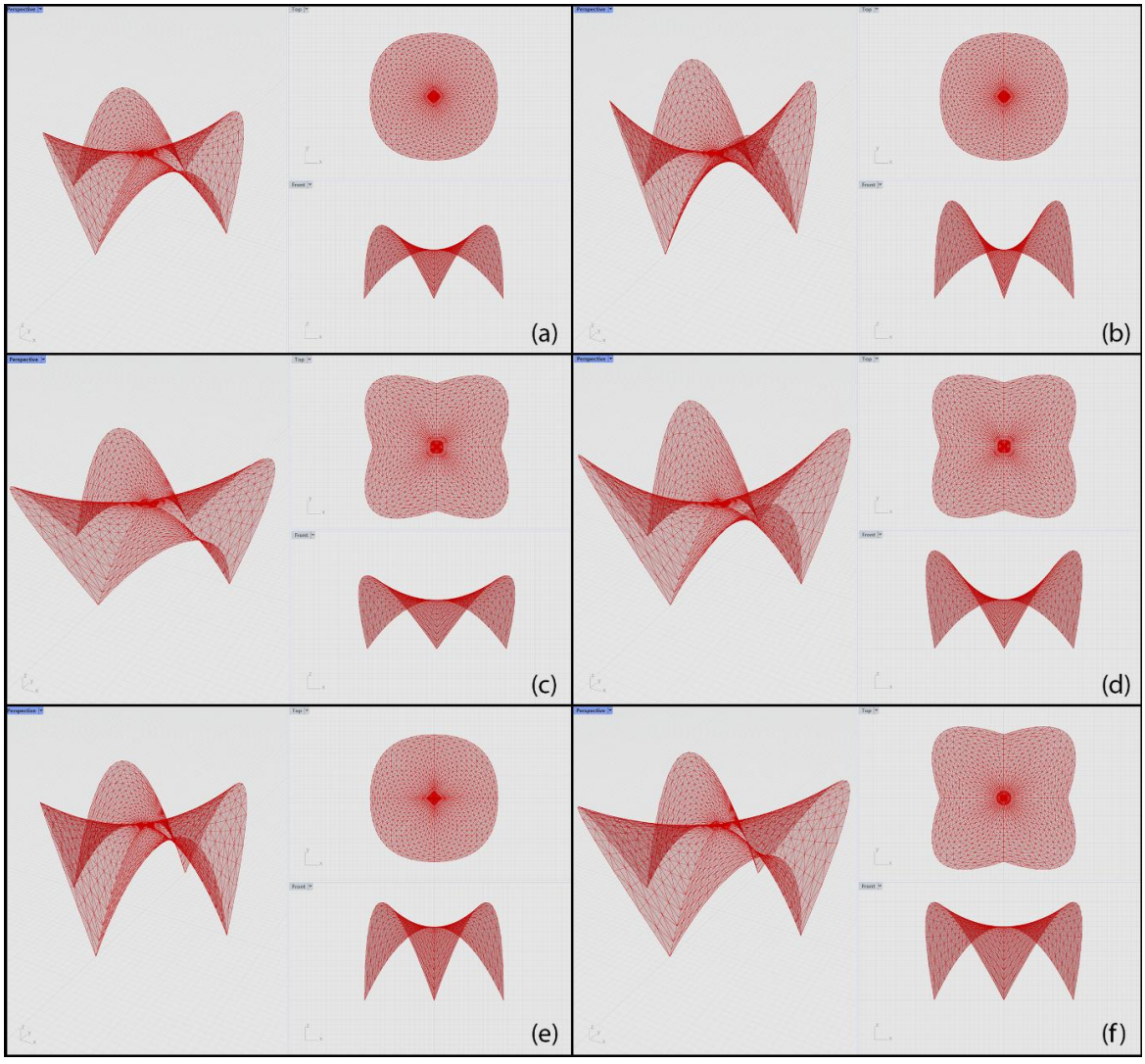

Figure 1. Support span, edge height, center height and edge overhang values for the listed shapes are respectively: (a) 20,15,10,5; (b) 20,20,10,5; (c) 20,15,10,10; (d) 20,20,10,10; (e) 20,20,15,5; (f) 20,20,15,10.

Conclusion

One challenge with hyperbolic paraboloid roofs is that they require extremely precise assembly during construction, which means workers need to have a high level of skill. This is especially true for thin concrete shell structures, as they have to be cast on-site with highly accurate formwork. On top of that, workers must carefully manage the concrete's thickness and ensure the surface stays smooth at every stage. (Wang et al., 2023) One of the biggest reasons for the move away from producing these hyperbolic paraboloid shell structures today is the increasing use of different methods to span large openings in structures and the difficulties mentioned. However, even minor enhancements to the form of these structures can lead to substantial improvements in their mechanical behavior. Various objective functions, including strain energy, overall weight, and tensile stress distribution on both shell surfaces, can be used to optimize their performance (Tomás & Martí, 2008). This study highlights the crucial role of 3D modeling and structural analysis in the design of shell structures. By utilizing parametric analysis software, designers can efficiently explore different configurations, assess their structural behavior, and refine both form and performance early in the design process, ensuring a more informed and optimized construction approach. Even though optimization can be achieved in terms of design, the development of construction techniques and construction methods for these shell structures can be developed as a future work suggestion.

References

Burger, N., & Billington, D. P. (2006). Felix Candela, Elegance and Endurance: An Examination of the Xochimilco Shell. *Journal of the International Association for Shell and Spatial Structures*, *47*(3).

Goldbach, A.-K., & Lázaro, C. (2024). CAD-integrated parametric design and analysis of lightweight shell structures. *Structures*, *64*, 106566. https://doi.org/10.1016/j.istruc.2024.106566

Rivera, D. A., Danhaive, R. A., & Mueller, C. T. (2020). Adaptive Framework for Structural Pattern Optimization. *Journal of the International Association for Shell and Spatial Structures*, *61*(4), 296-306. https://doi.org/10.20898/j.iass.2020.012

Sprague, T. S. (2013). "Beauty, Versatility, Practicality": The Rise of Hyperbolic Paraboloids in post-war **America** (1950-1962). *Construction History*, *Vol. 28*(No. 1).

Tomás, A., & Martí, P. (2008). *Shape and Size Optimisation of Concrete Shells Respecting the Original Design Form*. 172. https://doi.org/10.4203/ccp.88.172

Tomás, A., & Martí, P. (2010). Optimality of Candela's Concrete Shells: A Study of His Posthumous Design. *Journal of the International Association for Shell and Spatial Structures*, *51*(1).

Wang, Q., LI, Y., & WANG, Z. (2023). Application of Hyperbolic Paraboloid in Architectural Design. *Tehnicki Vjesnik - Technical Gazette*, *30*(5). https://doi.org/10.17559/TV-20230306000407

A Preliminary Comparison of Turkish Seismic Design Code and the Draft Seismic Design Communiqué based on the Outputs of Structural Analyses of Mid-Rise RC Buildings

Halit Emre Uygun[a], Caglar Goksu Akkaya[b], Alper Ilki[c]

[a] Istanbul Technical University, Structural Engineering Program, Türkiye
[b] Istanbul Technical University, Disaster Management Institute, Türkiye
[c] Istanbul Technical University, Department of Civil Engineering, Türkiye
uygun22@itu.edu.tr

Keywords: Base Shear, Natural Vibration Period, Reinforced Concrete, Relative Displacement, Seismic Design.

Aim

In February 2023, a sequence of consecutive earthquakes struck Türkiye on the same day, a Mw 7.7 earthquake with an epicenter in Pazarcık/Kahramanmaraş and a Mw 7.6 earthquake with an epicenter in Elbistan/Kahramanmaraş. These seismic events, followed by numerous aftershocks, affected 11 provinces and more than 14 million people, resulting in over 53,000 casualties, 100,000 injuries, extensive damage to more than 90,000 reinforced concrete (RC) structures, and an economic loss exceeding US$100 billion (Narlitepe et al., 2024). Investigations identified critical structural deficiencies, including poor material quality, construction defects failing to meet ductile design requirements, and design errors in several regions. In response to the severe impact and lessons learned from these earthquakes, new regulations (communiqué) were developed, which is still a draft, to introduce additional enhanced seismic design provisions to the existing seismic design code of Türkiye, Türkiye Building Earthquake Code (TBEC, 2018). In the scope of this study, two different RC buildings were designed based on the same real architectural plan. First, the structural system of Building 1 was designed according to TBEC (2018) under a 475-year return period earthquake ground motion (DD-2). Then, the structural system of Building 1 was modified in accordance with the additional seismic design requirements of the Draft Communiqué (2025), while maintaining the same architectural plan, and named as Building 2. This study presents a comparative structural analysis of these buildings, providing insights into the impact of the proposed regulatory amendments on seismic resilience.

Material and Method

The Draft Communiqué (2025) introduces additional seismic design provisions aimed at mitigating potential construction defects by imposing obligatory use of shear walls, stricter displacement and vertical stress limits, and limitations on column dimensions and irregularities of the structural system. For buildings classified with a building height class smaller than 6 (buildings higher than 10.5m for seismic design classes 1 and 2, and 17.5 m for seismic design classes 3 and 4), the minimum cross-sectional areas of RC shear walls (Aw) and columns (Ac) must be determined based on the number of storeys (N), building plan area (A), and short-period design spectral acceleration (Sᴅs) using Equations 1. and 2. These calculated minimum cross-sectional areas shall be satisfied independently in both principal directions.

$$A_w \geq min\ (0.002N, 0.02) S_{DS} A \quad \#(\ SEQ\ Denklem\ \backslash *\ ARABIC\ 1)$$

$$A_w + A_c \geq max(0.009, min\ (0.003N, 0.03)) S_{DS} A \quad \#(2)$$

For considering the relative storey drifts as per TBEC (2018), the approximate effective relative storey drift value for the 72-year return period earthquake ground motion (DD-3) is derived from the effective relative storey drift determined through the analysis, which is conducted under the DD-2 earthquake ground motion. The calculated drift for the DD-3 earthquake ground motion must remain within the allowable limit, which is determined based on the infill wall connection type (flexible or brittle) and the structural system type (RC or steel). Instead, the draft

communiqué introduces a stricter 1% storey drift limit for DD-2 earthquake ground motion. To ensure a regular structural system and efficient load transfer during an earthquake, the communiqué mandates that at least 50% of the beam-column axes in each direction must be arranged continuously from one end to the other of the building in plan. Furthermore, the cross-sectional aspect ratios of columns are restricted to a maximum of 1.5. Another new restriction is the allowable axial load ratio for columns and shear walls. Under TBEC (2018), the axial load limit for columns is set at 40% of axial load capacity of the columns (without consideration of reinforcement), whereas the draft communiqué reduces it to 35%. Similarly, for RC shear walls, the allowable axial load ratio is lowered from 35% in TBEC (2018) to 25% in the Draft Communiqué (2025).

Yalova, a city with a high seismic risk, was selected as the design location for the buildings. To represent the general soil conditions of the region, ZD soil class was used in the analysis. Based on data from the Earthquake Hazard Map of Türkiye, the short-period design spectral acceleration (S_{DS}) was determined as 1.446 for DD-2 earthquake ground motion level (AFAD, 2018). Each building was designed as a six-storey structure (total floor area of 582 m²) with a floor height of 3 m. The materials used in the buildings are C30/37 class concrete and B420C class reinforcing steel. To ensure an accurate representation of structural behavior under seismic loads, a software, which utilizes finite element analysis, was used for the structural design of the buildings (ETABS v19). In the modelling process, columns and beams were modelled as frame elements. RC shear walls and slabs were modelled as shell elements of maximum dimensions of 50 cm. While RC shear wall elements were manually partitioned, slab elements were automatically meshed, ensuring a precise structural representation. During the dynamic analyses, as per TBEC (2018), the effective section stiffness of cracked RC structural members was considered. The eigenvalue method was utilized to determine the modal characteristics of the structure, such as mode shapes and natural vibration period. In addition to that, the mode superposition method, which accounts for each vibration mode, was employed to calculate the base shear force of the buildings.

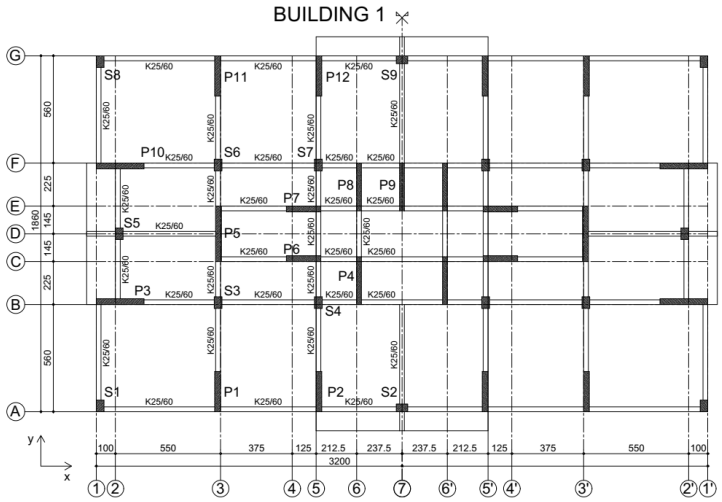

Column Sizes (cm)						RC Shear Wall Sizes (cm)					
Element No	Building 1	Building 2	Element No	Building 1	Building 2	Element No	Building 1	Building 2	Element No	Building 1	Building 2
S1	40/60	50/75	S8	40/60	50/75	P1	30/210	30/350	P8	25/250	25/250
S2	60/40	75/50	S9	60/40	75/50	P2	30/210	30/350	P9	25/250	25/250
S3	40/60	-	-	-	-	P3	250/30	650/30	P10	250/30	650/30
S4	40/60	50/75	-	-	-	P4	25/250	25/250	P11	30/210	30/350
S5	40/60	50/75	-	-	-	P5	30/290	35/390	P12	30/210	30/350
S6	40/60	-	-	-	-	P6	180/30	150/25	P13	-	475/30
S7	40/60	50/75	-	-	-	P7	180/30	150/25	P14	-	475/30

Figure 1. Plan and Element Sizes of Buildings 1 and 2.

Building floor plans, which has a symmetry in y direction are shown in Figure 1. As per Building 1, the effective relative storey drift, which was close to the limit value (calculated as 0.0173 for DD-2 earthquake ground motion), played a crucial role in determining the dimensions of the structural elements. Since the relative storey drift at the 5th and 6th floors remains below the calculated limit, the RC shear walls P1, P2, P11, and P12 in y direction were shortened by 30 cm, while P3 and P10 in x direction were shortened by 40 cm compared to those on the lower stories. The total area of the columns of Building 1 was 3.84 m² while that of RC shear walls were 5.16 m² and 9.91 m² in x and y directions, respectively. As per Building 2, the minimum required cross-sectional areas of RC shear walls and total vertical structural members, as determined by Equations 1. and 2., were calculated as 10.1 m² and 15.15 m², respectively. To meet the minimum RC shear wall area requirement in x direction, columns S3 and S6 were removed in the structural plan of Building 1, and the lengths of RC shear walls, namely P3 and P10, were extended, resulting in a total of 12.15 m² RC shear wall area and 16.64 m² total vertical structural element area in this direction. In y direction, the relative storey drift limit (0.01 drift ratio) was the key factor in determining the required RC shear wall area. The structural design included a total of 14.26 m² of RC shear walls and 18.76 m²

of vertical structural member cross-sectional areas. To enhance structural stiffness and control storey drift, 30/80 cm beams were used along two axes, and 35/70 cm beams were arranged along two axes in y direction.

Findings

In Building 2, the total cross-sectional areas of RC shear walls increased by 136% and 44% in the x and y directions, respectively, while the total cross-sectional areas of vertical structural members (RC shear walls and columns) increased by 85% and 36% in the x and y directions, respectively, compared to Building 1.

Figure 2a. presents the effective relative storey drifts for the DD-3 earthquake ground motion in both x and y directions for the respective buildings, along with the calculated limit value, which is 0.8% for brittle infill wall connection type specified by the TBEC (2018). Notably, at the 4th storey, where relative storey drifts reached their maximum values, the effective relative storey drifts in Building 2 were reduced by 58% in x direction and 33% in y direction with respect to Building 1 due to larger dimensions of structural members, as mentioned by the Draft Communiqué (2025). Figure 2b. presents the effective relative storey drifts for the DD-2 earthquake ground motion in both x and y directions for the respective buildings, along with the %1 limit value (for brittle infill wall connection type) specified by the Draft Communiqué (2025). The effective relative storey drifts at the 4th storey in Building 2 were reduced by 64% in x direction and 41% in y direction with respect to Building 1. It should be noted that there is no torsional irregularity in these buildings.

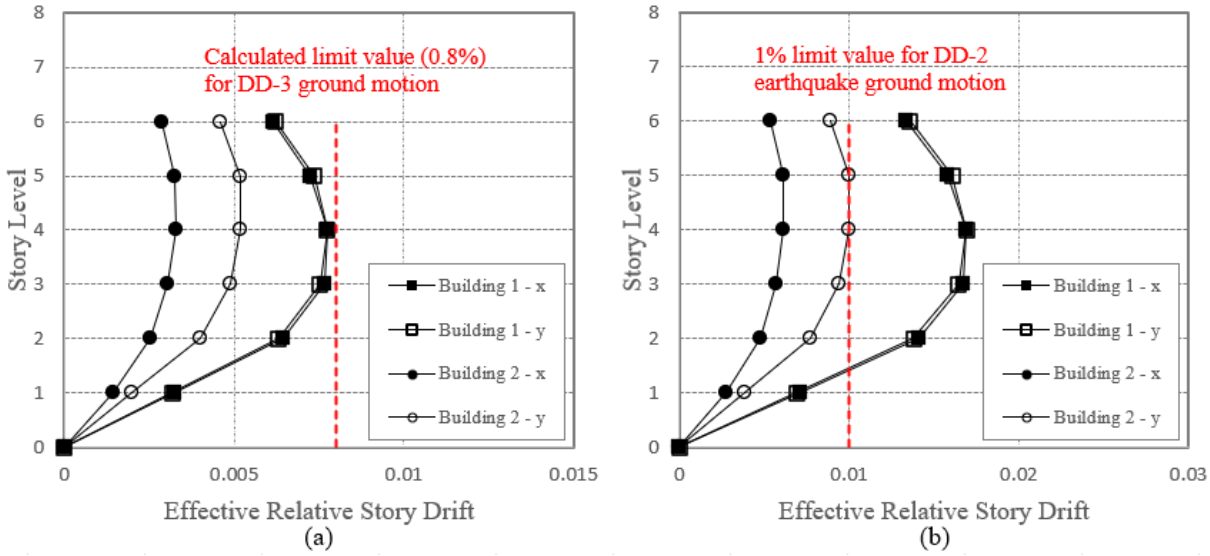

Figure 2. (a) Effective relative storey drift of the buildings for DD-3 earthquake ground motion and %0.8 limit value for TBEC (2018), **(b)** Effective relative storey drift of the buildings for DD-2 earthquake ground motion and %1 limit value for Draft Communique (2025).

Table 1. presents the vibration periods and base shear forces of the buildings along x and y directions. The decrease in the vibration periods by 61% in x direction and 30% in y direction for Building 2 is also mainly due to increased stiffness of the structural system in Building 2. For Building 2, the shortening of periods in both directions led to a significant increase in base shear force (by 111% in x direction and 33% in y direction).

Table 1. Natural vibration period and base shear force values of the buildings.

	Period (s)		Base shear force (kN)	
Buildings	*x* direction	*y* direction	*x* direction	*y* direction
Building 1	0.87	0.639	5046	6809
Building 2	0.34	0.449	10643	9066

Conclusion

The Kahramanmaraş-centred earthquakes that occurred in Türkiye in February 2023 caused destruction and casualties in a wide region covering 11 provinces. Following these earthquakes, work began on the Draft Communiqué (2025) that introduced additional seismic design requirements to the existing TBEC (2018) regulation. As part of this study, the additional requirements proposed by the Draft Communiqué (2025) were examined, and the structural systems of two buildings were designed using the architectural plan of an actual building, one based only on TBEC (2018) (Building 1) and the other incorporating both TBEC (2018) and the Draft Communiqué (2025) (Building 2). The structural analysis results of the buildings are presented comparatively below:

- The effective relative storey drifts of Building 2 are lower than those of Building 1, and its natural vibration period are shorter compared to Building 1 due to the increase in system stiffness resulting from the larger member sizes.
- In Building 1, the effective relative story drifts under the DD-2 earthquake ground motion exceed the 1% limit specified in the Draft Communiqué (2025).
- In Building 2, the 1% effective relative story drift limit (for brittle infill wall connection type) is observed to be a governing factor in the dimensioning of vertical structural members in the y direction. In case a flexible joint infill wall connection type had been selected during the design process, this limit would have increased to 1.5%, and the minimum vertical structural element area specified in the Draft Communiqué (2025) would have been sufficient for this structure.
- In Building 2, the lower relative story drifts compared to Building 1 lead to a reduction in residual deformations after the earthquake.
- The significant increase in base shear force in Building 2 compared to Building 1 in both directions is due to the shortening of the natural vibration periods.

References

Computer and Structures Inc. (2019*).* ETABS 2019: Integrated structural analysis and design software (Version 19). Berkeley, CA, USA.

Disaster and Emergency Management Presidency (AFAD) of Ministry of Interior Affairs of Türkiye. (2018). Türkiye Earthquake Hazard Maps. https://tdth.afad.gov.tr

Draft Communiqué. (2025). Ministry of Environment, Urbanization and Climate Change.

Narlitepe, F., Goksu, C., & Ilki, A. (2024). Comparison of ratio of spectral response to design accelerations with the observed seismic behavior of RC buildings during February 2023 Türkiye earthquakes. Proceedings of the WCEE 2024, Milan, Italy, 30 June-5 July 2024.

Türkiye Building Earthquake Code (TBEC) 2018. (2018). Official Gazette, Issue: 30364.

Effect of Heat Aging on the Axial Behaviour of PET FRP Confined Low-Strength Concrete

Mirsaeid Razavi[a], Birdal Koçak[a], Medine İspir Arslan[b], Korhan Deniz Dalgıç[c], Alper İlki[b]

[a] İstanbul Technical University, Graduate School, Department of Civil Eng., MSc Structural Eng. Program, Türkiye
[b] Istanbul Technical University, Faculty of Civil Engineering , Department of Civil Eng., Türkiye
[c] İzmir Institute Of Technology, Civil Engineering Departmant, Structural Engineering, Türkiye
razavi22@itu.edu.tr

Keywords: Heat Aging, Concrete Confinement, PET FRP.

Aim

Fiber-reinforced polymer (FRP) confinement is a widely accepted method for strengthening reinforced concrete structural members. By externally wrapping concrete elements with FRP, lateral deformation under compressive loading is effectively restricted, leading to significant improvements in compressive strength and ductility (Ilki et al., 2004). Over recent years, Polyethylene Terephthalate (PET) fiber reinforced polymers, derived mainly from recycled plastics, has attracted increasing attention as an eco-friendly and economically competitive alternative to traditional carbon and glass FRP materials (Bai et al., 2019). Researches have indicated that PET FRP confined concrete exhibits comparable improvement in compressive strength and a high improvement in ductility compared to conventional FRP materials, highlighting its potential for wider structural applications (Dai et al., 2012; Lam & Teng, 2003).

However, the durability of PET FRP confined concrete under prolonged exposure to elevated temperatures has not been thoroughly investigated. High-temperature conditions can present challenges related to the degradation of the polymer matrix and deterioration of the adhesive bond between FRP wraps and concrete substrates, potentially resulting in loss of confinement efficiency and structural stability (Benzerara et al., 2023). Understanding the effects of high-temperature on PET FRP confined concrete is crucial, particularly for structures located in hot climates or environments susceptible to thermal stresses.

To address this critical knowledge gap, the current study investigates the effects of sustained dry heating at 50°C for 6 weeks on the compressive behavior of PET-FRP-confined low-strength concrete specimens. The experimental program includes 12 low-strength concrete specimens wrapped with PET FRP, equally divided into two groups. One group was kept under normal laboratory conditions, while the other group was subjected to a continuous temperature of 50°C. Normal laboratory conditions involved ambient indoor settings with a temperature of approximately 20 ± 2°C and relative humidity ranging between 50% and 65%. Specimens were stored in a well-ventilated environment, free from direct sunlight, wind, or any form of artificial heating or cooling that could induce unintentional thermal effects.Following the thermal exposure period, axial compression tests were conducted on both groups to evaluate and compare the impact of elevated temperatures on compressive strength and overall confinement effectiveness. The findings of this research will provide novel insights into the thermal resilience of PET FRP and its suitability for structural applications under elevated temperature conditions.

Material and Method

The main test variables of the experimental study were the number of confinement layer of PET FRP (0, 2 and 3) and difference between curing conditions (laboratory and dry temperature cabinet).

A test program with 12 concrete specimens was planned. The specimens were standard cylindrical samples with a diameter of 150 mm and a height of 300 mm. These concrete specimens were produced using ready-mixed low strength concrete. The 28-day average compressive strength of the concrete used was determined to be approximately 9.02 MPa. Six of the twelve specimens were produced to be exposed to laboratory conditions, and the other six to dry heat.

Recycled PET sheets bonded to the concrete surface with epoxy resin were used as confining material. The PET sheet manufacturer reports that the density of PET sheets is 600 gr/m^2 and that PET FRP has a tensile strength of 950 MPa, a tensile strain capacity of 11.6%, and the first and second moduli of elasticity of 12 and 9.4 GPa. In order to experimentally determine the mechanical properties of PET FRP, five coupon specimens were prepared and tested in accordance with ASTM D3039M-17. The obtained properties are presented in Table 1. The values in parentheses show the relevant coefficient of variation. The wet lay-up method was used to apply the FRP sheet to the outer surface of the specimen. Initially, the surface of the specimen was cleaned. Then, a layer of epoxy resin was applied to the surface, and a continuous fiber sheet was impregnated with epoxy and bonded to the concrete surface, with fibers-oriented hoop-wise. Following the wrapping, an additional epoxy layer was applied to enhance resin impregnation. It should be noted that an overlap length of approximately 230 mm was adopted to eliminate the risk of slipping. After then, the upper and lower parts of the specimens (30 mm high) were confined with additional carbon FRP to avoid premature failure of the specimens around loading place. Lastly, the top and bottom surfaces of the specimens were capped with high strength repair mortar (4-5 mm thick) to provide a uniform distribution of the compression stresses. The confined specimens were left in the laboratory for curing.

Table 1. The mechanical properties of PET FRP obtained from the coupon tests.

Tensile strength (MPa)	Modulus of elasticity (GPa)-First	Modulus of elasticity (GPa)-Second	Tensile strain capacity (%)
493 (3.3%)	15.2 (7.7%)	5.5 (4.5%)	7.17 (5.2%)

Test program is presented in Table 2. Each specimen is denoted with symbols: "UN" indicates unconfined specimen. Confined specimens use a numerical prefix to represent the number of FRP layers, followed by "P" for PET (e.g., 1P for one layer of PET FRP). For the specimens exposed to heat aging, a "DH" is added to the end of the name. For instance, 3P-DH refers to the specimen with three layers of PET sheet subjected to dry heat at the cabin (Table 2).

Table 2. Test matrix.

Specimen	Condition	Total number of FRP layers	Total number of identical specimens
UN	Laboratory	0 (unconfined)	2
2P		2	2
3P		3	2
UN-DH	Heat aging	0 (unconfined)	2
2P-DH		2	2
3P-DH		3	2

An Instron closed-loop testing machine, with the capacity of 5000 kN, was used for conducting displacement-controlled monotonic uniaxial compression tests on all specimens. The displacement-controlled test of each specimen was conducted at a constant rate of 0.6 mm/min until the failure of the specimen. Axial deformations along the entire height of the specimen were measured using four TML CDP50 type linear variable displacement transducers (LVDT) with 50 mm capacity, fixed at each corner between the lower and upper steel loading plates. Additionally, four LVDTs with the same capacity, set at mid-height (with a gauge length of 150 mm) were used to measure the mid-height deformations. The measurements were recorded using a TML TDS-303 data logger and switch box and all obtained data were transferred to the computer for storage and processing. The setup and instrumentation of the tests are shown in Figure 1.

Figure 1. Test setup.

Findings

In order to understand the effect of test variables on the test results, the average stress-strain relationships are plotted and given in Figure 2 and the values of key points are presented in Table 3.

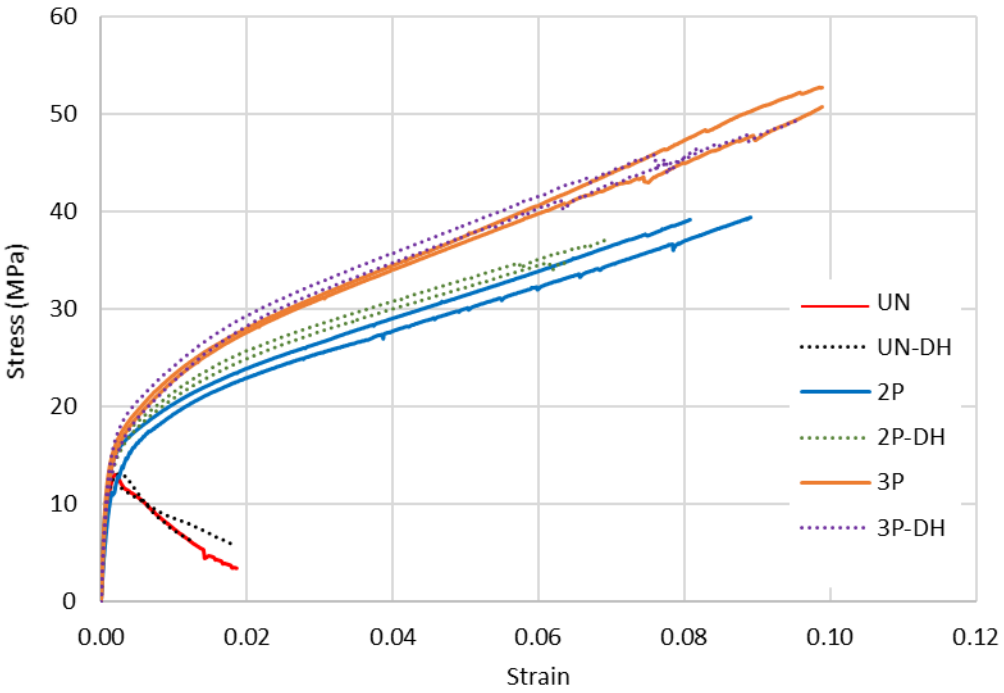

Figure 2. Stress-strain relationships.

Table 3. Test results.

Specimen	$f_{cc}(MPa)$	$\varepsilon_{cc}(\%)$	(f_{cc}/f_{co})	$\varepsilon_{cc}/\varepsilon_{co}$
UN	13.6 (f_{co})	0.00260 (ε_{co})	-	-
2P	39.3	0.07445	2.88	30.09
3P	51.1	0.09925	3.75	44.11
UN-DH	12.5	0.00252	-	-
2P-DH	36.3	0.06673	2.88	26.47
3P-DH	47.7	0.08876	3.82	35.23

The ratio of the axial strength of the specimen under the heat aging condition to the axial strength of the specimen under laboratory conditions is calculated as 0.91 for unconfined specimens, 0.92 for 2P specimens and 0.93 for 3P specimens. It is observed that there is a strength loss of around 6.6 to 8.7% due to heat aging. The ratio of the axial strain at peak stress of the specimen under the heat aging condition to the axial strain of the specimen under laboratory conditions is calculated as 0.97 for unconfined specimens, 0.90 for 2P specimens and 0.89 for 3P specimens. It is understood that there is a strain capacity loss of around 3.1% for the unconfined specimens and 10.5% for the PET FRP confined specimens due to heat aging. These ratios show that the effect of dried heat applied at 50°C for 6 weeks may be evaluated as negligible.

Conclusion

This experimental study examined the effects of sustained heat aging at 50°C for six weeks on low-strength concrete specimens confined with PET FRP. The results showed a moderate reduction in strain capacity (approximately 10.5%) under elevated temperature conditions, while the peak compressive strength was only slightly affected. Although this reduction may appear negligible at first, it raises important concerns regarding the long-term stability and reliability of PET FRP confinement systems at high temperatures. Since FRP strengthening systems are intended to maintain the long-term effectiveness of reinforced concrete members, it is imperative to investigate the potential for progressive degradation in strain capacity following extended or repeated thermal exposure. Therefore, further studies are required to examine the axial behavior of PET FRP-confined specimens under higher temperature levels and longer exposure durations to fully assess their long-term structural performance.

References

ASTM. (2017). Standard test method for tensile properties of polymer matrix composite materials. ASTM D3039M-17, West Coshohoken, PA. https://doi.org/10.1520/D3039_D3039M-17.

Bai, Y. L., Yan, Z. W., Ozbakkaloglu, T., Dai, J. G., Jia, J. F., & Jia, J. B. (2019). Dynamic behavior of PET FRP and its preliminary application in impact strengthening of concrete columns. *Applied Sciences (Switzerland)*, *9*(23). https://doi.org/10.3390/app9234987

Benzerara, M., Biskri, Y., Saidani, M., Slimani, F., & Belouettar, R. (2023). High-Temperature Behavior of Polyethylene-Terephthalate-Fiber-Reinforced Sand Concrete: Experimental Investigation. *Fibers*, *11*(5). https://doi.org/10.3390/fib11050046

Dai, J. G., Lam, L., & Ueda, T. (2012). Seismic retrofit of square RC columns with polyethylene terephthalate (PET) fibre reinforced polymer composites. *Construction and Building Materials*, *27*(1), 206–217. https://doi.org/10.1016/j.conbuildmat.2011.07.058

Ilki, A., Kumbasar, N., & Koc, V. (2004). Low strength concrete members externally confined with FRP sheets. *Structural Engineering and Mechanics*, *18*(2), 167–194. https://doi.org/10.12989/sem.2004.18.2.167

Lam, L., & Teng, J. G. (2003). Design-oriented stress-strain model for FRP-confined concrete. *Construction and Building Materials*, *17*(6–7), 471–489. https://doi.org/10.1016/S0950-0618(03)00045-X

STRUCTURAL ENGINEERING

Bridges

Finite Element Methods

Reinforced Concrete Structures

Seismic Performance

Steel Structures

Structural Damages

Seismic Performance Evaluation and Comparison of Different Structural Systems Using Nonlinear Time History Analysis

Volkan İvgen[a], Konuralp Girgin[a]

[a] Istanbul Technical University, Department of Civil Engineering, Structural Engineering , Türkiye
ivgen16@itu.edu.tr

Keywords: Etabs, Nonlinear Time-History Analysis, Seismic Evaluation, Seismic Performance, Tscb 2018.

Aim

The seismic performance of buildings is critical for ensuring their resilience in earthquake-prone regions. This study focuses on evaluating the seismic performance of various structural systems by employing the nonlinear time-history method. The objective is to compare the seismic performance and evaluation of different structural systems at both the element and system levels, providing insights into how structural choices can impact the seismic performance of a building. More specifically, the study investigates the effects of slab systems under seismic event on the deformation of structural members, energy dissipation of building, and relative displacement of floors. Three structural systems commonly used in seismic regions were selected for this study: a beam-slab system, a flat slab system, and a flat slab system with perimeter beams

Material and Method

The study assumes a hypothetical building located in the Mahmutbey, Istanbul, a region with high seismicity. The building in the study consists of one basement and eight above-ground floors, nine floors in total. The basement is designated for car parking area and the upper floors designed to function as a hotel. Each floor has a height of 3.5 meters, including the basement, resulting in a total building height of 24.5 meters above ground level. The building has an orthogonal structural system with five spans in the X-direction and three spans in the Y-direction, each eight meters long. The total building dimensions are 40 and 24 meters in the X- and Y-directions, respectively. C35 concrete grade and B420C reinforcement steel are used. Building is designed by considering design earthquake level whose probability of exceedance in 50 years is 10% in accordance with the Turkish Seismic Code for Buildings (TSCB) 2018 [1]. The design spectral accelerations for the region obtained from Turkish earthquake hazard map [2]. The values for S_{ds} and S_{d1} are 1.112 and 0.389, respectively. ETABS [3] software is adopted for the design and nonlinear time-history analysis. Dead and live loads are determined in accordance with TS 498 [4]. The lateral load resisting system is identical in all three structural types, with the same dimensions, layouts, and configurations. Three different column sizes are utilized in the design: 80x40 cm, 40x80 cm, and 80x80 cm. Two U-shaped core shear walls with a thickness of 30 cm are located at the center. The basement is surrounded by 30 cm thick rigid shear walls. The thickness of the slab varies according to the structural system: 20 cm for the beam-slab system, and 27 cm for both the flat slab system and the flat slab system with perimeter beams. The constructive requirements for structural members specified in TS 500 [5] are satisfied. Additionally, these structural members are designed in accordance with the TSCB 2018 [1].

Modeling the behavior of the structural components is essential for performing the nonlinear analysis. Accordingly, confined and unconfined concrete models, along with reinforcement steel models, are employed in compliance with the specifications of TSCB 2018 [7]. The concrete material properties are defined according to TSCB 2018 [1], which is adopted Mander model [6]. Distributed plasticity model is used for the columns and shear walls, meanwhile lumped plasticity model is used for the beams. Therefore, Fiber P-M_2-M_3 and Fiber P-M_3 are defined for the columns and shear walls, respectively. M3 hinges are defined for the beams subjected to flexure only. The shear walls are modeled with confined boundary zones and an unconfined web. The beams are modeled by using stiffness modification factor obtained from moment-curvature relationships. Slabs and basement walls are modeled elastically by using the corresponding stiffness modification factor for flexural and shear, as per TSCB 2018 [1].

The nonlinear time-history analysis was performed using 11 pairs of earthquake records, in accordance with TSCB 2018 [1]. The records are selected based on fault type, seismicity, and the soil class of the region. Consequently,

the selected records have magnitudes ranging from 6.6 to 7.5 and shear wave velocities (Vs30) between 360 and 760 m/s, with strike-slip fault type. The records are obtained from the PEER NGA West 2 database [7]. The selected records are scaled to the **M**aximum **C**onsidered **E**arthquake (MCE) using a simple scaling method, ensuring that the mean spectrum remains above the 1.3 times of target (MCE) spectrum in the range of $0.2T_p$ to $1.5T_p$. The acceleration time history records of the selected ground motions are applied to the model in both X and Y horizontal directions. Initially, the X- and Y-components of the ground motion are applied to the corresponding directions of the building. The analysis is then repeated with the components rotated 90 degrees to assess the building's seismic response.

For the performance evaluation, deformation limits corresponding to three damage levels—Immediate Occupancy (IO), Life Safety (LS), and Collapse Prevention (CP)—are determined based on the TSCB 2018 [1]. These limits are further adjusted according to the shear force ratios in reinforced concrete elements. The mean deformations for each element are obtained through the nonlinear time-history analysis. Average deformations are compared with the predefined thresholds to evaluate the performance of each structural system under the MCE. This comparative analysis provides an in-depth understanding of the building's response to seismic forces and allowed for an evaluation of the structural systems' ability to resist seismic effects. The results show that all buildings, except for flat slab system, have satisfied the controlled damage performance target.

Findings

The results from the nonlinear dynamic analysis reveal differences in seismic performances of the three structural systems. The beam-slab system exhibits the best performance, with the smallest deformations and the most uniform energy dissipation. This system has higher stiffness resulting in improved lateral resistance and reduced interstory drifts. On the other hand, the flat slab system demonstrates the weakest performance, with larger deformations, lower stiffness and higher interstory drifts. Energy dissipation in the flat slab system is more irregular, resulting in less efficient force distribution and greater risk of local failure. The performance of the flat slab system improves when beams are configured at the perimeter of the slab. The system surrounded by the beams demonstrates reduced interstory drifts. The perimeter beams contribute to distribute the seismic forces more uniformly, which improves its ability to resist lateral forces and enhancing its seismic performance.

Conclusion

Based on the findings, beam-slab systems are highly recommended for earthquake-resistant designs, especially in seismic regions. However, for buildings where flat slab systems are required due to functional or architectural reasons, configuration of perimeter beams significantly improves seismic performance. Overall, this study highlights the importance of selecting appropriate structural systems to optimize seismic resilience and provides valuable insights into improving the seismic performance of buildings in earthquake-prone areas.

References

Ministry of Interior, Disaster and Emergency Management Presidency. (2018). *Turkish Seismic Code for Buildings 2018 (TSCB 2018).* Ankara, Turkey

Ministry of Interior, Disaster and Emergency Management Presidency (2019). *Turkish earthquake hazard map*. Retrieved October 10, 2024, from https://tdth.afad.gov.tr/

Computers & Structures, Inc. (2020). *ETABS (Version 19.1.0) [Computer software].* Berkeley, CA: Computers & Structures, Inc.

Turkish Standards Institution. (1997). *TS 498: Design loads for buildings.* Ankara, Turkey.

Turkish Standards Institution. (2000). *TS 500: Requirements for design and construction of reinforced concrete structures.* Ankara, Turkey

Mander, J.B., Priestley, J.N., & Park, R. (1988). Theoretical stress-strain model for confined concrete. *Journal of Structural Engineering*, *114(8),* 1804-1826.

Pacific Earthquake Engineering Research (PEER) Center (2013). *Next Generation Attenuation-West 2*. Retrieved December 05, 2024, from http://ngawest2.berkeley.edu/Disaster

STRUCTURAL ENGINEERING

Bridges

Finite Element Methods

Reinforced Concrete Structures

Seismic Performance

Steel Structures

Structural Damages

Seismic Performance of Gravity Frames with Flush End-Plate Beam-to-Column Connections

Alper Demir[a], Cüneyt Vatansever[a]

[a] Istanbul Technical University, Civil Engineering Department, Structural Engineering Program, Türkiye
alper.demir@itu.edu.tr

Keywords: Nonlinear Analysis, Steel Connections

Aim

This study aims to investigate the nonlinear behavior of flush end-plate beam-to-column connections and evaluate the influence of different steel frame configurations on the seismic performance of a four-story steel building featuring a special moment-resisting frame as its primary seismic force-resisting system. Specifically, three gravity frame configurations integrated with the four-story steel building are examined: (1) a reference frame employing conventional pinned beam-to-column connections, (2) a frame incorporating two-bolted flush end-plate beam-to-column connections (FEP-2B), and (3) a frame with four-bolted flush end-plate beam-to-column connections (FEP-4B). The investigation assesses the impact of these configurations on the lateral stiffness and strength of the special moment-resisting frame. Initially, finite element analyses under cyclic loading are performed to capture the detailed nonlinear behavior of the connections. Subsequently, the derived moment–rotation curves are integrated into a structural model to conduct pushover analyses, thereby providing insights into the role of flush end-plate connections in enhancing the seismic performance of steel structures supported by gravity frames.

Material and Method

Both connections, shown in Fig.1, were designed as semi-rigid and partial-strength connections, with the primary objective of achieving plasticity through the yielding of the end plate. This design approach aims to enhance energy dissipation capacity and ductile behavior while also improving both strength and stiffness. Additionally, this approach is intended to reduce the risk of brittle failure by promoting plastic deformation within the end plate, rather than permitting tensile failure of the bolt, which could result in a sudden fracture. Consequently, a thin end-plate design strategy was consistently employed throughout the design process.

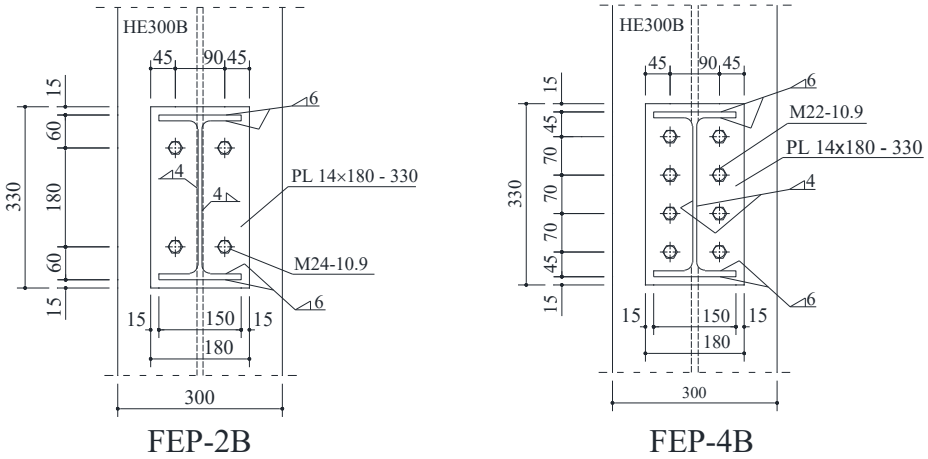

Figure 1. Flush end-plate configurations.

To investigate the influence of flush end-plate connections on frame behavior, a comprehensive finite element analysis was initially performed on two types of flush end-plate beam-to-column connections to obtain the moment-rotation curves of the connections. The finite element model was developed using ABAQUS software, incorporating material nonlinearity, geometric nonlinearity, and the cyclic nature of the applied loading. The modeling approach was validated against experimental data obtained from similar end-plate connection systems.
For the flush end-plate connections, a detailed contact model was implemented to accurately simulate the interactions among the bolts, end plates, and column surfaces. Friction coefficient was taken as 0.3 while penalty formulation and hard contact was utilized for tangential and normal behavior between interacting surfaces. All

components were discretized using C3D8R eight-node solid elements. The end-plate thickness was set at 14 mm for both the two-bolted and four-bolted configurations. While the beam and column sections and the material properties remained consistent across the models, variations were introduced in the bolt dimensions, bolt pretension loads, and spacings to investigate their effects on connection performance.

The steel material used in the analysis was modeled using a tri-linear engineering stress-strain model suggested by Baei et al. (2012) for 10.9 grade bolts and S275 steel. True stress-strain values were obtained using the material model explained by Kauffman et. al. (2001) to implement the material's post-yield behavior into the finite element analysis. The hardening rule followed the combined hardening model to include both isotropic and kinematic hardening, which is important for cyclic loading conditions. Elastic modulus and Poisson's ratio were taken as 200 GPa and 0.3, respectively.

The connections were subjected to cyclic loading in accordance with AISC 341-16, thereby simulating the nonlinear behavior typically observed during seismic events. Incremental displacements were applied at the free end of the beam, while the frame boundary conditions were modeled with fixed supports at both the base and the top of the column to replicate rigid connections. Additionally, the beam was constrained to prevent movement perpendicular to the loading direction. The loading protocol followed a displacement-controlled method, with load increments applied until a rotation of at least 0.6 radians was achieved.

Drawing upon the finite element analysis outcomes, a two-dimensional frame model representing a four-story structure was systematically derived from the three-dimensional building model depicted in Fig. 2 and 3. This model was subsequently employed to conduct a comprehensive pushover analysis. The structural elements were the same as the building designed by Karasu (2018). Three distinct frame configurations were considered for the structural analysis: a control frame featuring pinned connections for the gravity frames; a frame employing flush end-plate connections with a two-bolt configuration; and a frame utilizing flush end-plate connections with a four-bolt configuration. This approach was facilitated by an equivalent frame assumption, explained by Lignos et. al. (2000), where the moment-resisting frame is integrated alongside an equivalent one-bay gravity frame connected with rigid links, as shown in Fig. 3.

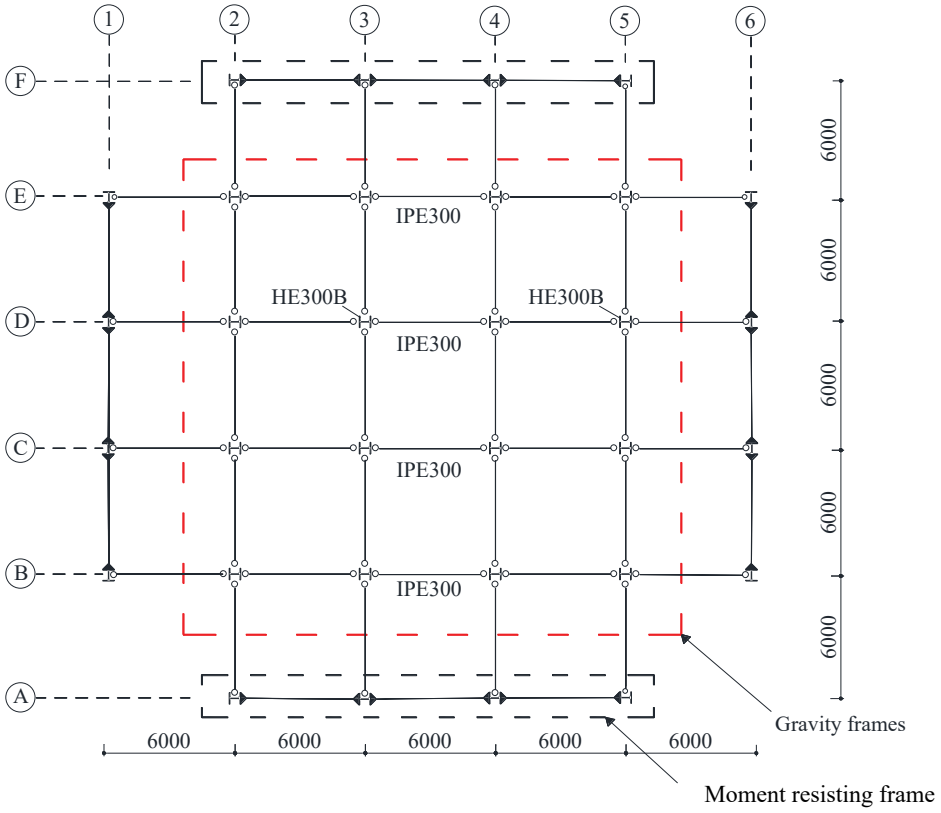

Figure 2. Plan view of the structural system

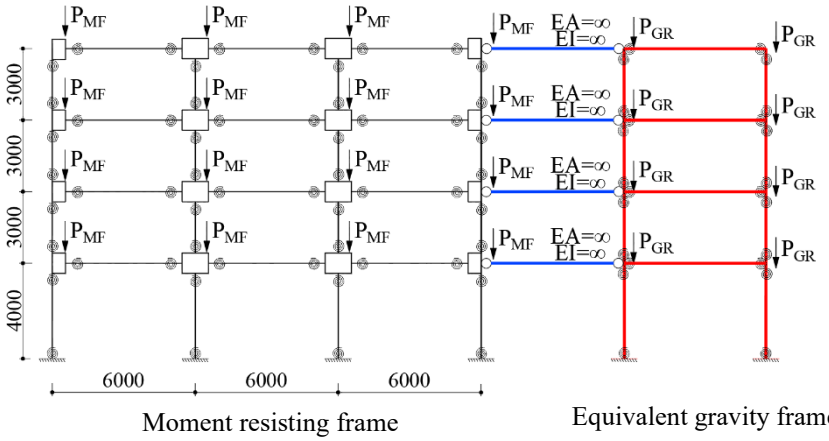

Figure 3. Equivalent frame model of the structure.

Nonlinear static pushover analysis was executed using OpenSEES structural analysis software. In this framework, the model was discretized using elastic beam–column elements, with the plastic hinge behavior represented by spring elements calibrated from the finite element analysis results. Concentrated plasticity approach was utilized for the spring elements using zero length elements. Uniaxial hysteretic material models were employed to characterize the moment–rotation behavior of the connections within the OpenSEES framework. Fig. 4 provides a graphical representation of the moment–rotation curves corresponding to these connections.

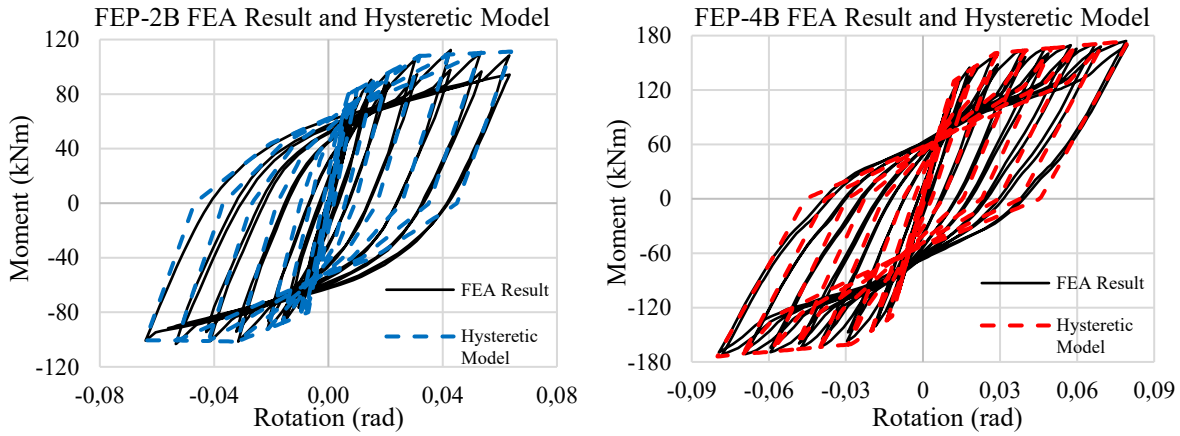

Figure 4. Moment-rotation curves obtained from FEA and hysteretic models.

The pushover response for each configuration was obtained as shown in Fig. 5 by incrementally applying lateral loads until a predefined target displacement was achieved.

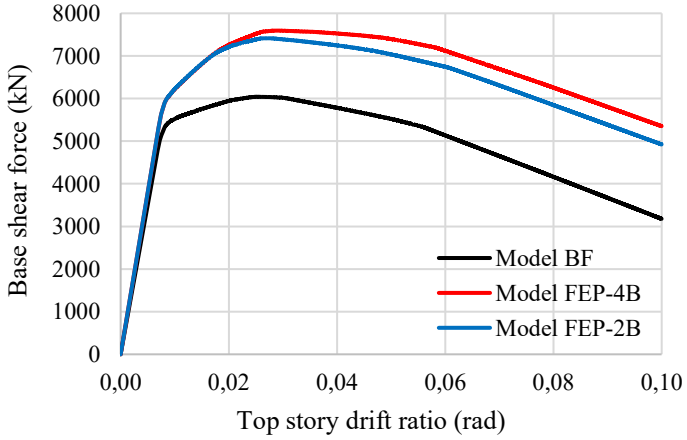

Figure 5. Pushover results .

Findings

The results from the finite element modeling and subsequent structural analyses reveal the following observation:

Finite element analyses of the connections: Both two-bolted and four-bolted connections displayed considerable strength and stiffness to be classified as semi-rigid and partial strength connections. It was observed that both connection configurations exhibited a high degree of ductility; however, the two-bolted configuration facilitated a more uniform yielding of the end plate.

Damage and Failure Mode: The failure mode indicated that the frame with the two-bolted connection showed localized yielding at the beam-to-column connections before significant displacement occurred. On the other hand, the four-bolted configuration delayed failure and showed higher initial stiffness.

Performance of the connections: Both flush end-plate connections exhibited significantly enhanced stiffness and energy dissipation compared to conventional pinned frames. Specifically, the two-bolted configuration demonstrated greater stiffness during the backloading phase, during which the end-plate underwent complete plasticization. In contrast, the four-bolted connection provided superior strength and stiffness, albeit with localized stress concentrations near the outer bolts.

Strength Comparison: When the pushover curves for the three frames were compared, the results showed a significant improvement in base shear strength for both flush end-plate configurations compared to the reference frame. Frame with two-bolted flush end-plate connections showed an 22% increase while the frame with four-bolted flush end-plate connections used demonstrated a 25% increase in base shear strength compared to the pinned model. This indicates that incorporating flush end-plate connections, especially the four-bolted configuration, may significantly improve the frame's lateral load resistance compared to using pinned connections for the gravity frames. Furthermore, both connection configurations exhibit an enhancement in post-yield stiffness.

Energy Dissipation: It can be concluded that the increased strength and stiffness achieved with the flush end-plate connections resulted in improved energy dissipation compared to the pinned control frame. These connections can be considered dissipative connections due to high ductility and strength achieved.

Conclusion

The findings of this study indicate that flush end-plate beam-to-column connections incorporated within gravity frames substantially enhance the structural performance of steel systems. Both the two-bolted and four-bolted flush end-plate configurations improved lateral load resistance and overall frame stiffness relative to the baseline configuration. Notably, the four-bolted configuration provided the most significant increase in strength, exhibited superior stiffness retention, and delayed the onset of failure, thereby emerging as a more effective strategy for enhancing seismic performance.

References

ABAQUS (2020). Dassault Systemes Simulia Corp., Abaqus/CAE User's Guide, Providence, RI, USA

Baei, M., Ghassemieh M., & Goudarzi, A. (2012). Numerical modelling of end-plate moment connection subjected to bending and axial forces. *The Journal of Mathematics and Computer Science,* 4 (3), pp. 463 – 472.

Ibarra, L.F., Medina, R.A., and Krawinkler, H. (2005). Hysteretic models that incorporate strength and stiffness deterioration, *Earthquake Engineering Structural Dynamics*, *34* (12), 1489-1511.

Karasu (2018). *The Study of The Behavior of Header End-Plate Beam-to-column Connections Under Cyclic Loads and The Investigation of Their Contributions to Structural Behavior Under Seismic Effects* (PhD Thesis). Istanbul Technical University, Graduate School, Istanbul.

Kaufmann, E. J., Metrovich, B., Pense, A.W. (2001). Characterization of Cyclic Inelastic Strain Behavior on Properties of A572 Gr. 50 and A913 Gr.50 Rolled Sections (ATLSS Report No. 01-13). Bethlehem, USA: Lehigh University.

Lignos, D. G., Krawinkler, H. (2011). Deterioration Modeling of Steel Components in Support of Collapse Prediction of Steel Moment Frames under Earthquake Loading, *Journal of Structural Engineering, 137* (11), 1291-1302.

OpenSEES (2021). *OpenSEES Documentation*. University of California, Berkeley. https://opensees.berkeley.edu.

TCDCSS (2016). Turkish code for design and construction of steel structures, Ministry of Environment and Urbanisation, Ankara, Turkiye.

TSCB (2018). *Turkish Seismic Code for Buildings, Specifications for Design of Buildings under Earthquake Action*, Disaster and Emergency Management Presidency, Ankara

Effect of Initial Imperfections in Short Link Beams on Frame Behavior

Bünyamin Mutlu[a], Cüneyt Vatansever[b]

[a] Istanbul Technical University/Disaster Management Institute, Earthquake Engineering Program, Turkey
[b] Istanbul Technical University/Civil Engineering Faculty, Turkey
mutlub23@itu.edu.tr

Keywords : Steel Multi-Tiered Eccentrically Braced Frames, Nonlinear Pushover Analysis, Reversed Cyclic Analysis, Link Beam Buckling, Column Buckling.

Aim

Multi-tier eccentrically braced frames (MT-EBFs) provide both seismic resilience and architectural comfort due to their favored structural arrangement. In these systems, short link beams act as critical energy dissipating elements by undergoing remarkable inelastic deformation during seismic events [3]. However, in multi-tier configuration, the lack of lateral support at intermediate levels presents a particular challenge, as intermediate link beams become weaker against buckling out-of-plane. While all elements, except link beams, are designed to remain elastic, such buckling can produce unexpected nonlinear behavior in the other frame components, leading to reduction in the system's energy dissipation capacity. This study investigates the application of initial imperfections to link beams as a potential solution to maximize their energy absorption capacity in MT-EBFs while preventing out-of plane buckling in link beams.

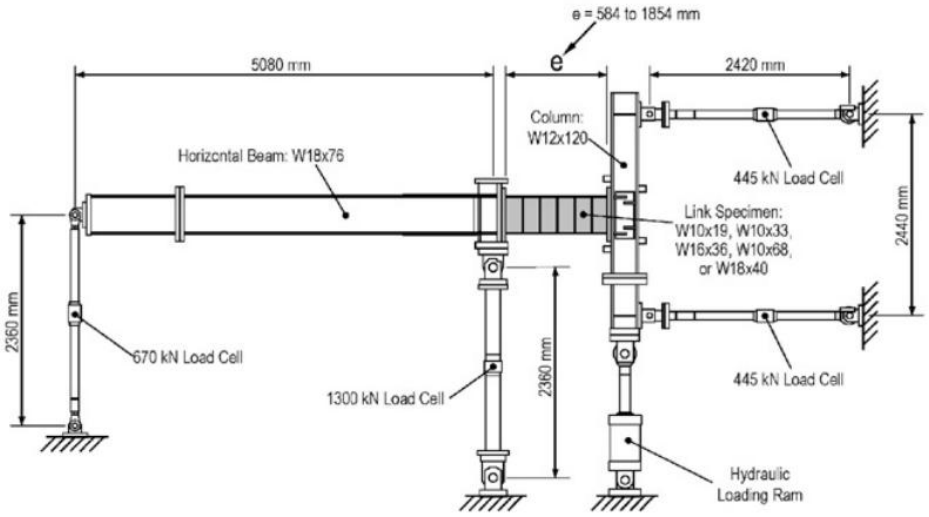

Figure 1: Okazaki and Engelhardt (2007) test setup.

Material and Method

The Open System for Earthquake Engineering Simulation (OpenSEES) [4] finite element analysis software is used for nonlinear pushover analysis. A nonlinear shear model is implemented to accurately capture the shear response of the link beam. The material properties are defined with an elastic modulus, E of 200 GPa and a yield strength, Fy of 345 MPa. Following the approach introduced by Ramadan and Ghobarah (1995) [5] and later refined and developed by Richards and Uang (2006) [6], the shear behavior is modeled using multiple springs located at both ends of the link beam. For columns, outer beams and braces the nonlinearBeamColumn command is used and 5 Gauss integration points are assigned for each element [7]. To represent the moment behavior of the link beam as well as the shear behavior, forceBeamColumn command is implemented. Steel sections are modeled using 10 fibers along the flange width and web depth and 2 fibers along the web thickness and flange thickness.

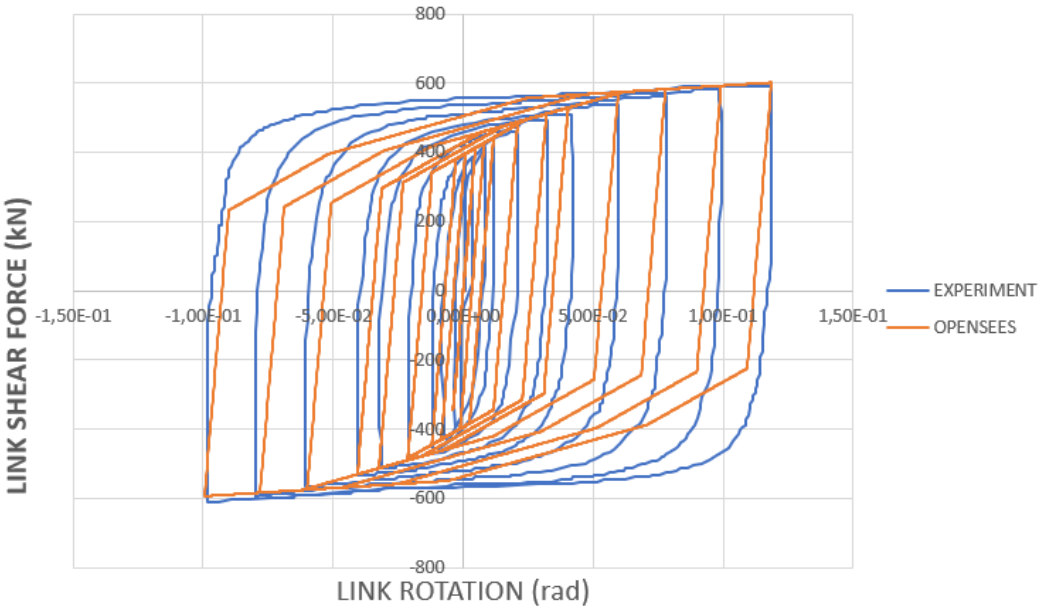

Figure 2: Verification of the link beam model against Okazaki and Engelhardt (2007) experimental data.

The numerical model is validated against experimental results from Okazaki and Engelhardt (2007) , with a comparison between the calibrated model and the test setup presented in Figure 1 and Figure 2. To simulate the combined response of the shear springs, translational springs were arranged in parallel. Nonlinear spring elements were integrated between externally and internally defined nodes, where all degrees of freedom were restrained except for the vertical displacement relative to the link beam axis. Each spring was assigned an ElasticPP material model, and their combined shear response was achieved using the ElasticPP Parallel command.

During the calibration of the numerical frame model, initial geometric imperfections were applied to properly simulate the buckling behavior of columns, outer beams, and braces. For columns, out-of-plane imperfections were defined as 0.001 times the total frame height, while in-plane imperfections were set to 0.001 times the tier height. Brace members received out-of-plane imperfections equal to 0.001 times their individual lengths. For outer beams, the out-of-plane imperfection magnitude was determined as 0.001 times the unbraced length where the unbraced length differs by level: at the roof level it is measured from the beam-column connection to the beam-brace connection, whereas at intermediate levels it corresponds to the full bay length. Boundary conditions and overall representation of frame model is given in Figure 3.

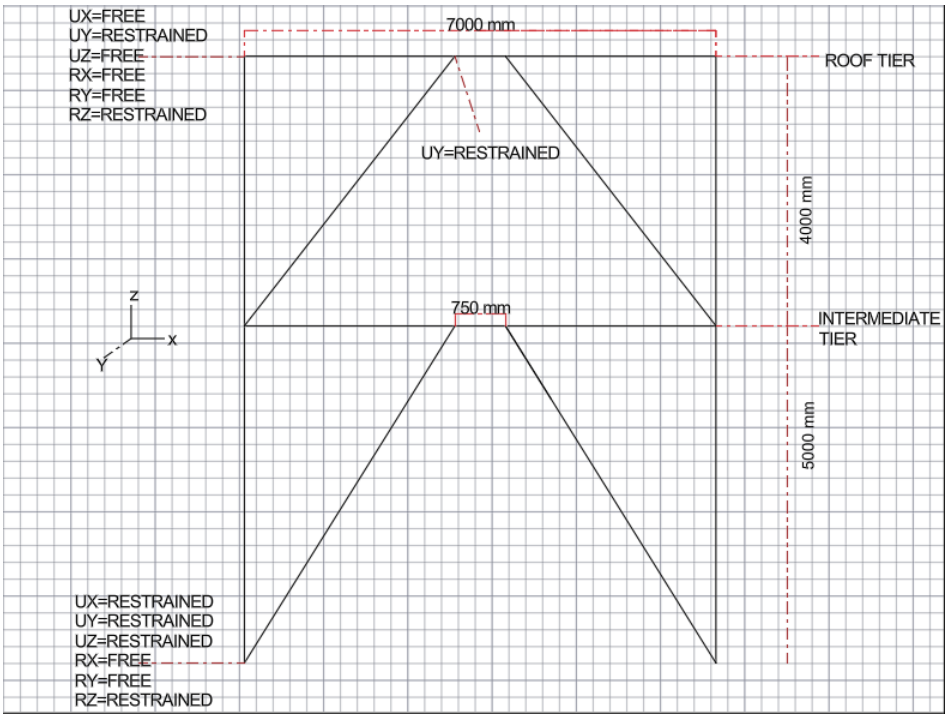

Figure 3: Overall frame information.

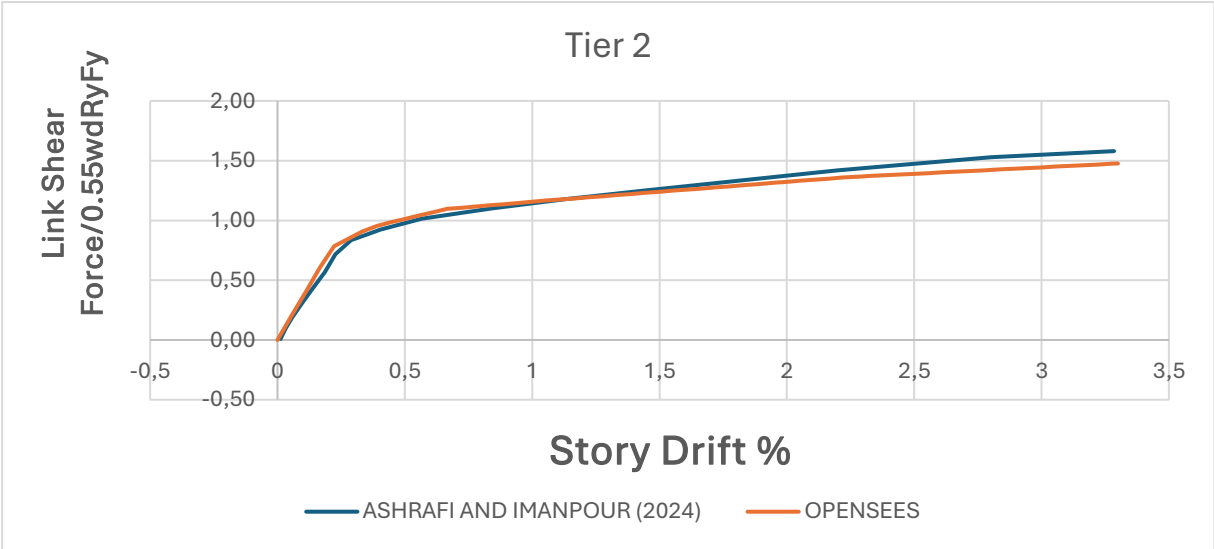

Figure 4: Frame level verification.

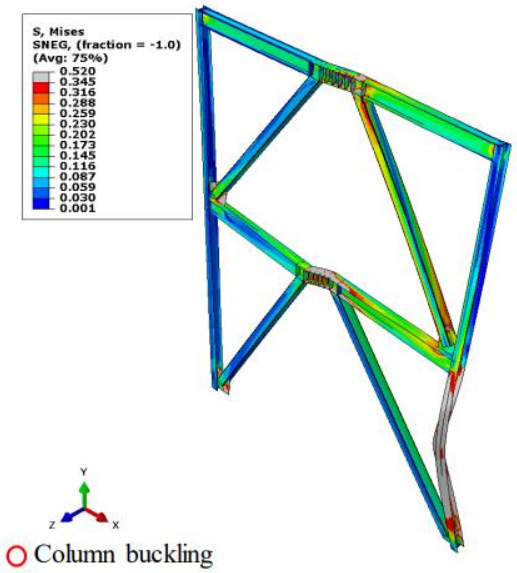

Figure 5: Column buckling in standart frame Ashrafi and Imanpour (2024)..

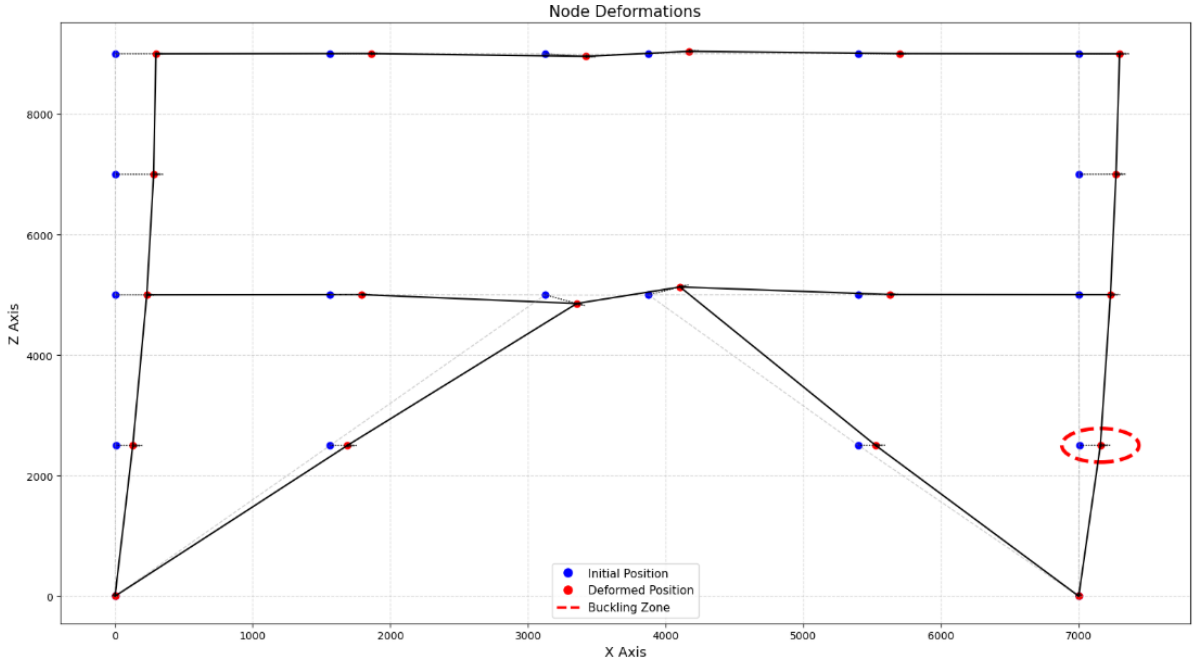

Figure 6: OpenSEES model column buckling.

Findings

In order to verify frame level behavior, two-story MT-EBF is calibrated from the reference paper data Ashrafi and Imanpour (2024) presented in Figure 4. Pushover analysis is conducted to the MT-EBF in two different frames called standart and improved. In the standard frame configuration of Ashrafi and Imanpour (2024) with W200×42 columns, W310×74 beams, and HSS203×7.9 braces column buckling occurred prior to the out-of plane buckling of the link beam (Figure 5). The nonlinear pushover analysis performed in OpenSEES software demonstrated buckling behavior in the subject column, as illustrated in Figure 6. Using W310×74 columns and W250×73 beams eliminated column buckling, confirming that optimized section design promotes structural stability. This study aims to examine how initial deviations in the link beam's alignment affect performance of the frame. This study will assess the permissible out-of-straightness at the link beam's ends, limited to a maximum of L/1000 L/500 and

L/200, with L being the combined length of the tier beam and link beam. The top view of frame with initial irregularity is illustrated in Figure 7.

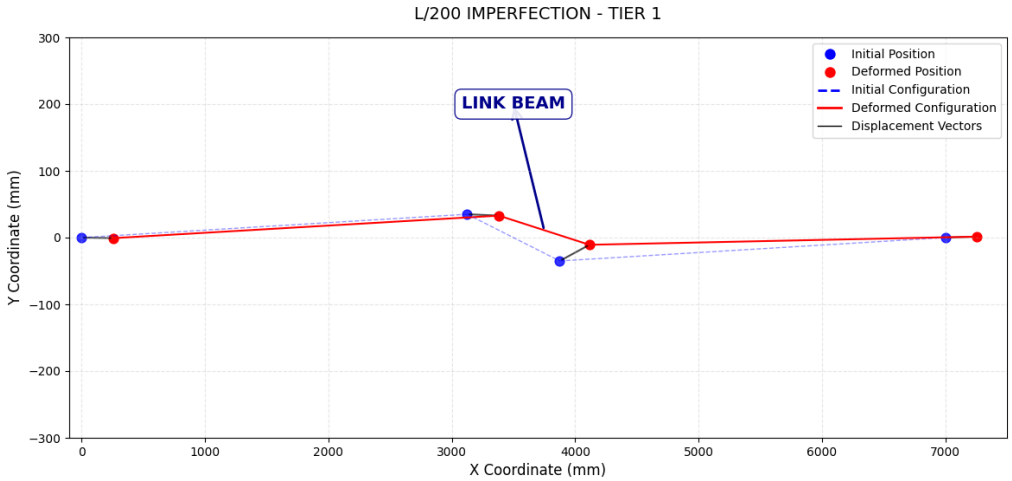

Figure 7: Top view of first tier with L/200 imperfection.

The research by Ashrafi and Imanpour (2024) demonstrated that optimized section configurations yield improved performance in both pushover and nonlinear response history analyses (NLHAs). Building on this work, the current study aspires to conduct comprehensive verifications at both element and frame levels. As the effect of link beam axis irregularities in MT-EBFs remains unexplored in existing literature, this study aims to present the first investigation of this critical aspect. The primary objective is to evaluate the seismic response of MT-EBF systems including both link beam behavior and overall frame performance when subjected to nonlinear pushover loading with introduced initial imperfections in the link beam axis.

From the pushover analysis, it is seen that while large shear force demands occurred in the first tier both in standard and improved configurations, roof link beam demands were relatively small. This phenomenon is also perceived when initial irregularity is applied.

By implementing a rotational spring in the weak axis of the link beam, capturing the nonlinear moment behavior is aimed. Results showed that the link beam is deformed in both shear and moment axes. When initial out-of straightness is increased, moment in the weak axis is also increased (Figure 8) , while shear force demand is reduced (Figure 9).

In short link beams, it can be stated that implementing initial imperfections to the link beam axis changes the yielding mechanism from only shear yielding to combined shear and weak axis flexural yielding in the link beam.

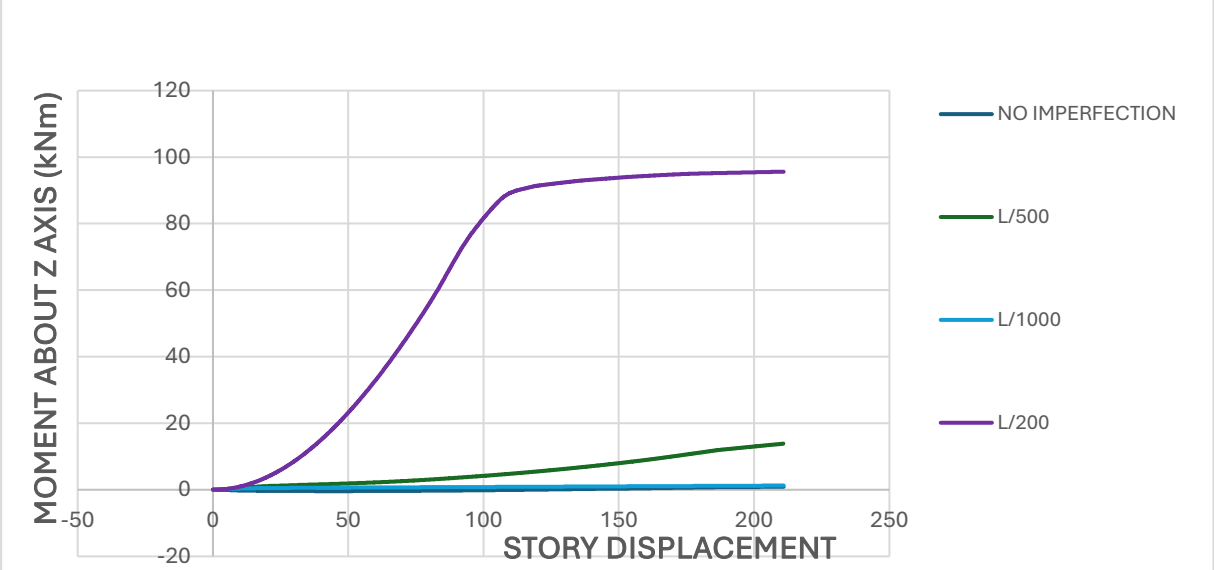

Figure 8 : Moment in weak axis/story displacement in link beam in tier 1.

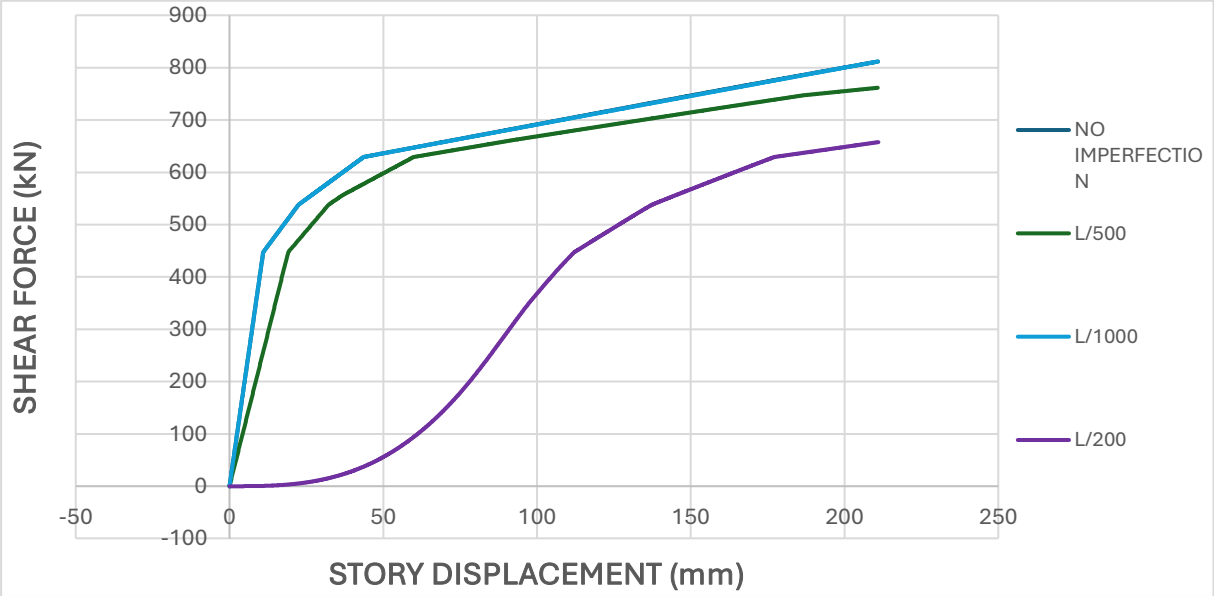

Figure 9: Shear force/story displacement in link beam in tier 1.

Conclusion

The effect of initial imperfections in short link beams on frame behavior was examined. Four different imperfeciton values including no imperfection with two different two-tiered EBF frames which were subjected to nonlinear pushover analysis.

Although the method of initial imperfection is examined only for a two-tiered eccentrically braced frame with nonlinear pushover analysis, it should be further investigated with various analysis procedures as well as in multi-tiered frame geometries.

References

Okazaki, T., & Engelhardt, M. D. (2007). Cyclic loading behavior of EBF links constructed of ASTM A992 steel. Journal of Constructional Steel Research, 63, 751–765. Doi: 10.1016/j.jcsr.2006.08.004

Ashrafi, A., & Imanpour, A. (2024). Analysis and design methods for improved stability of two-tiered steel eccentrically braced frames with continuous I-shaped links. Journal of Structural Engineering, 150(9). https://doi.org/10.1061/JSENDH.STENG-12940

M. Bruneau and A. M. Gilbert, Ductile Design of Steel Structures, 2nd ed. New York, NY, USA: McGraw-Hill, 2018.

OpenSEES. Open System for Earthquake Engineering Simulation (Version 3.5.0) [Computer software]. Pacific Earthquake Engineering Research Center, University of California, Berkeley. https://opensees.berkeley.edu.

Ramadan, T., & Ghobarah, A. (1995). Analytical model for shear-link behavior. Journal of Structural Engineering, 121(11), 1574-1580. Doi:10.1061/(ASCE)0733-9445(1995)121:11(1574)

Richards, P. W., & Uang, C.-M. (2006). Testing protocol for short links in eccentrically braced frames. Journal of Structural Engineering, 132(8), 1183–1191.https://doi.org/10.1061/(ASCE)0733-9445(2006)132:8(1183)

Mazzoni, S., McKenna, F., Scott, M. H., & Fenves, G. L. (2006). OpenSees Command Language Manual. Pacific Earthquake Engineering Research Center (PEER), University of California, Berkeley.

Blast-Resistant Steel Modular Structures Design with the Comparison of Dynamic Analysis Methods: SDOF and MDOF Systems

Nur Döğer[a], Barlas Özden Çağlayan[b]

[a] Istanbul Technical University, Faculty of Civil Engineering, Structural Engineering Program, Türkiye
[b] Istanbul Technical University, Faculty of Civil Engineering, Türkiye
doger16@itu.edu.tr

Keywords: SDOF and MDOF Systems, Blast-Resistant Steel Modular Structures, Finite Element Analysis, Blast Load, Numerical Integration.

Aim

Research on blast-resistant structure design has intensified due to the increase in industrial facilities and the growing demand driven by defense industry policies in various countries. Using blast-resistant modular structures (BRMS) is a sustainable and safe approach to prevent potential loss of life and economic damage to business owners from explosions. The modular nature of these structures minimizes negative impacts associated with on-site construction activities and increases their popularity due to their portability.

In this study, since there is no dedicated section for blast-resistant structural design in the current regulations and specifications in Turkiye, internationally recognized guidelines such ASCE Design of Blast Resistant Buildings in Petrochemical Facilities and UFC 3-340-02 have been taken as a reference for calculations. To accurately characterize an explosion, it is essential to examine its effects and the types of explosives involved. The effects of shock and pressure wave loads generated by explosions, as well as the variation of pressure values over time, have been analyzed. Depending on the explosion type, parameters such as pressure, impulse, duration, velocity, and wavelength have been calculated using established methodologies. The influence of factors such as distance from the blast source, angle of incidence, and reflection characteristics has been explained in detail. Furthermore, material behavior under blast loads has been investigated by evaluating parameters such as strength increase factors, dynamic increase factors, and deformation limits, including ductility ratio and rotation capacity.

This study aims to demonstrate the step-by-step element dimensioning calculations of a modular blast-resistant structure. In this context, the applicability of the single-degree-of-freedom (SDOF) analysis method is compared with finite element analysis (FEM) to examine how all structural elements behave under both approaches.

Material and Method

The most widely used basic analytical models in blast design applications are single-degree-of-freedom (SDOF) systems because of their simplicity. The SDOF method offers significant advantages in the preliminary design stage, as it is easily applicable and does not require complex modeling techniques.

SDOF models simplify the analysis of a structure's actual Multi-Degree-of-Freedom (MDOF) behavior by considering a single-mode shape. The calculations are based on the dominant deformation mode of structural members. In the design of structural components, the SDOF method generally yields more conservative results compared to the MDOF approach. However, this method does not account for dynamic vibrations or simultaneous interactions between structural elements.

The mathematical equation for the dynamic equilibrium of a damped, linear elastic SDOF system, can be written as follows:

$$M\,a + C\,v + K\,y = F\,(t)$$

Equation 1

M: mass, a: acceleration, C: viscous damping constant, v: velocity, K: stiffness, y: displacement, F: external blast force, t: time

In blast-resistant design, damping is usually neglected because the structure reaches maximum response in a very short duration, making the effect of damping on maximum displacement negligible. Therefore Equation (1) can be simplified as:

$$M\,a + K\,y = F\,(t)$$

Equation 2

As a case study, a blast-resistant modular structure (BRMS) is designed with dimensions of 13.2 m in length, 4 m in width, and 3.5 m in height. The structure is subjected to a surface burst explosion of 500 kg at a standoff distance of 30 m from the front wall. The scaled distance (Z) of the building is calculated as 3.78 $\frac{m}{kg^{\frac{1}{3}}}$. As this value exceeds 1.2 $\frac{m}{kg^{\frac{1}{3}}}$, the structural are classified as being subjected to far-range blast loading. The structural frame members of the building were designed using seismically qualified compact hollow structural sections (HSS) to ensure that their full plastic bending capacity could be reached before any local instability occurred. The roof purlins were selected as I-sections, while the roof deck and wall panels were constructed using crimped panels with a trapezoidal cross-section, providing significantly higher ductility capacity. S235 steel grade were used in the design of roof purlins, roof deck, wall siding and S355 structural steel grade was used for main beams, wall girts and columns. Steel grades were specified according to the EN 10025 standard.

Findings

SDOF equivalent analysis approach enables structural members to balance the kinetic energy generated by the explosion with their deformation abilities, allowing them to effectively dissipate the energy. The "Simplified Blast Load Function" approach is used to make the effects of blast waves on structures more comprehensible and easier to calculate. The simplified triangular impulse model is utilized to determine blast loads by primarily considering key parameters such as reflected pressure, dynamic wind pressure, and shock wave velocity. Additionally, parameters including front wall load, roof load, and clearing time were calculated to dimension blast-resistant structural elements.

There are alternative methods for nonlinear Single Degree of Freedom (SDOF) systems which are numerical integration, also known as the time history method, graphical and closed-form solutions. In this study, the Newmark numerical integration method, utilizing the linear acceleration approach and a bilinear resistance-deflection relationship, was applied. A MATLAB code was developed for numerical integration, and each structural member was individually analyzed based on the applied blast load. The motion of a structure under blast loading was calculated step by step. At each time step, displacements were determined, followed by the updating of velocity and acceleration values using the outcomes from the preceding and current steps. This approach ensures the continuity of dynamic analysis, allowing the structural response to be observed over time. MDOF system method will be analyzed using advanced finite element analysis software and structural member responses will be compared with the SDOF system method outputs.

Conclusion

After determining the blast loads, the steel structural elements were designed using single-degree-of-freedom (SDOF) analysis through numerical integration method. This process followed the guideline of ASCE Design of Blast Resistant Buildings in Petrochemical Facilities, considering the time-dependent effects of dynamic loads which are shown in Figure (1) according to front and roof loading calculations.

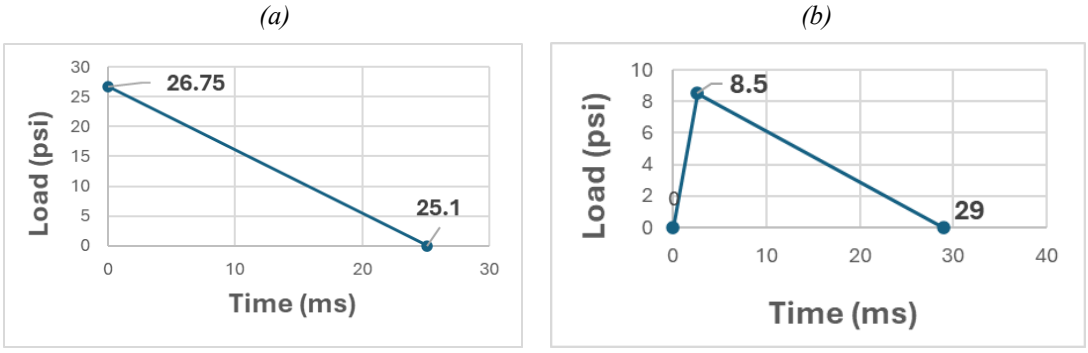

Figure 1. Pressure-time relation in front(a) and roof(b) blast loading graphs.

SDOF modeling using the numerical method was employed to calculate the maximum displacement and force demands on structural elements. After several iteration steps to determine roof deck size, the variation of time-dependent displacements and resistances of metal roof deck are shown in Figure (2) under dynamic roof blast loading impact. The maximum displacement occurs near the time when the blast load reaches its peak point. As the load decreases, the structural element attempts to return to its original position. However, due to plastic deformation and decreasing displacement and resistance amplitudes, the energy dissipation capacity gradually diminishes.

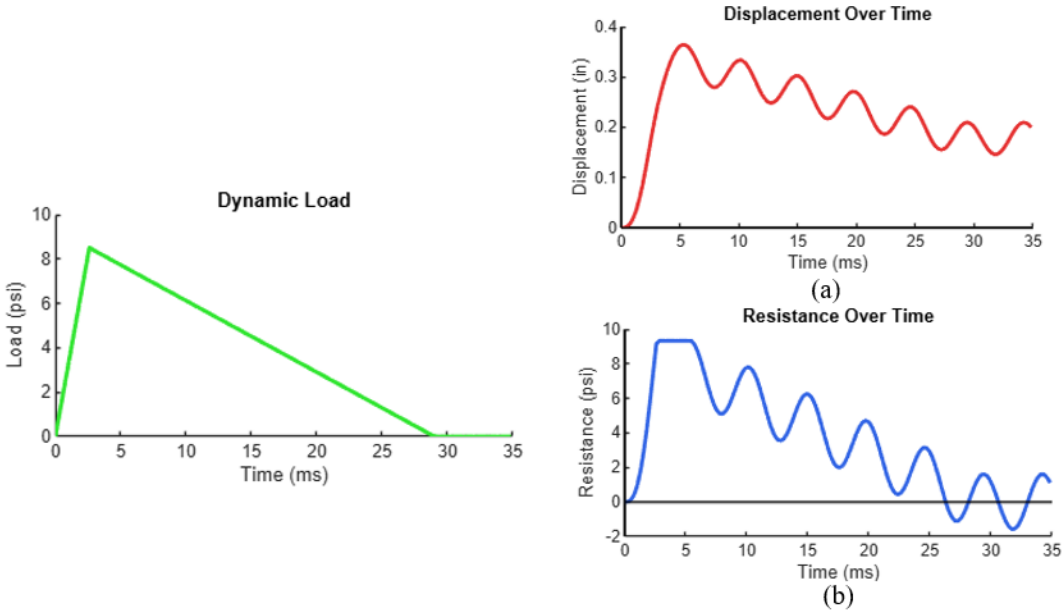

Figure 2. Displacement(a) and resistance(b) graphs of roof deck obtained from numerical integration.

Structural members were permitted to undergo plastic deformation, provided they remained within allowable limits for ductility ratio, rotation capacity, and frame sidesway at medium damage levels.

While the simplified numerical SDOF model provides conservative results suitable for preliminary design stages due to its efficiency, the MDOF model is preferred for more detailed, cost-effective designs, as it can capture complex interactions between structural elements.

References

American Society of Civil Engineers (ASCE). (2010). Design of blast-resistant buildings in petrochemical facilities (2nd ed.). Reston, VA: ASCE.
https://doi.org/10.1061/9780784410882

Biggs, J. M. (1964). Introduction to structural dynamics. New York, NY: McGraw-Hill Inc.

Summers, P. (2008). Design of modular blast-resistant steel-frame buildings in petrochemical facilities. Proceedings of the Structures Congress 2008, Vancouver, Canada.

https://doi.org/10.1061/41016(314)177
Williams, R. G., Wilson, W. A., & Dookeeram, R. (2016). Analysis of the response of a one-storey one-bay steel frame to blast. Journal of Structures, 2016, 8571542. https://doi.org/10.1155/2016/8571542
Erkmen, B., & Balcı, B. (2019). Evaluation of rigid body sliding analysis for modular steel structures subjected to blast loading. Eskişehir Technical University Journal of Science and Technology A - Applied Sciences and Engineering, 20(4), 413-426.
https://doi.org/10.18038/estubtda.500973
Department of Defense (DoD). (2008). Structures to resist the effects of accidental explosions. Washington, DC, UFC 3-340-02.
https://www.wbdg.org/ffc/dod/unified-facilities-criteria-ufc/ufc-3-340-02

STRUCTURAL ENGINEERING

Bridges

Finite Element Methods

Reinforced Concrete Structures

Seismic Performance

Steel Structures

Structural Damages

Vibration Fatigue-Based Optimization of Open Hole Design in Stiffened Panels

Görkem Aşcı[a]

[a] Istanbul Technical University, Solid Mechanics, Türkiye
asci23@itu.edu.tr

Keywords: Open-Holed Plate Design, Stiffened Panels, Stress Concentration, Structural Damage, Vibration Fatigue.

Aim

Open holes are indispensable features in engineering structures, particularly in fields like aerospace, automotive, and mechanical engineering. These geometric discontinuities are often intentionally introduced for purposes such as weight reduction, access, assembly, and mounting functionalities. While such modifications are vital for achieving high-performance, lightweight structures, they inherently introduce stress concentration zones that significantly affect mechanical behavior. These zones, being susceptible to localized high stress, become critical points for crack initiation and propagation, especially under fatigue loading.

The primary objective of this study is to comprehensively analyze how variations in hole size and location affect the structural performance of flat and rectangular metal plates. We aim to provide insights into the static, dynamic, and fatigue behavior of open-holed components through both analytical and numerical approaches. Special attention is given to vibration-induced fatigue, an area often overlooked in traditional fatigue analysis, despite its relevance in operational environments characterized by random, multi-directional excitation such as in aircraft, helicopters, and ground vehicles.

The research investigates the response of plates with systematically varied hole diameters and eccentricities. The behavior is characterized through modal analysis, frequency response functions (FRFs), and fatigue life assessments under Power Spectral Density (PSD) inputs. The resulting data are used to develop a set of decision-making guidelines for engineers designing open-holed structures subjected to complex loading. Ultimately, this study addresses a gap between classical stress analysis and the needs of modern fatigue design, especially where dynamic loading governs the life expectancy of structural components.

Material and Method

1. Finite Element Modeling

Ten models were created using HyperMesh 2021 to investigate two major parameters: hole size and hole location. The plates used in the simulation measured 100 mm × 100 mm with a thickness of 3 mm, representing a simplified yet realistic cross-section of aerospace-grade panels. Material properties were chosen in accordance with MMPDS data for aluminum alloys widely used in aircraft structures: young's modulus of 72 GPa, Poisson's ratio of 0.33, and density of 2700 kg/m^3.
The hole sizes varied from 0 mm (Model 1 - control) to 5 mm, 10 mm, 15 mm, and 20 mm (Models 2–5) (Figure 1), while the remaining models (6–10) (Figure 2) maintained a 20 mm hole but varied its horizontal position from 4 mm to 16 mm offset from the center. These configurations were chosen to study the superposition effect of hole presence and eccentricity on stress concentration and fatigue (Table 1).

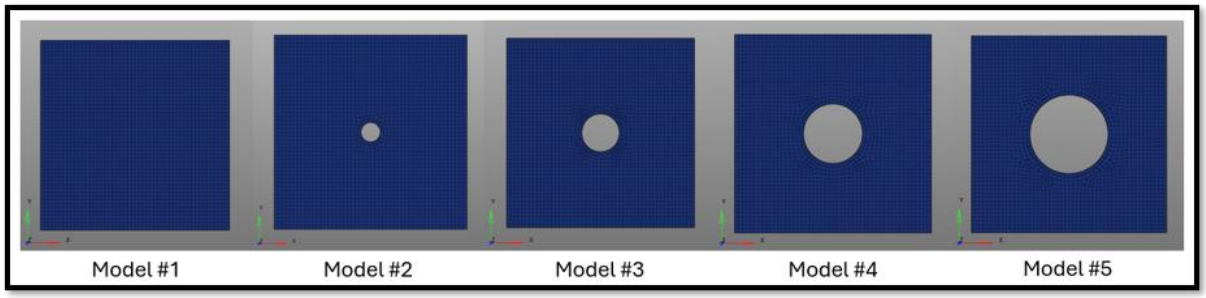

Figure 1. Comparison of First 5 Models (Increase of Hole Size).

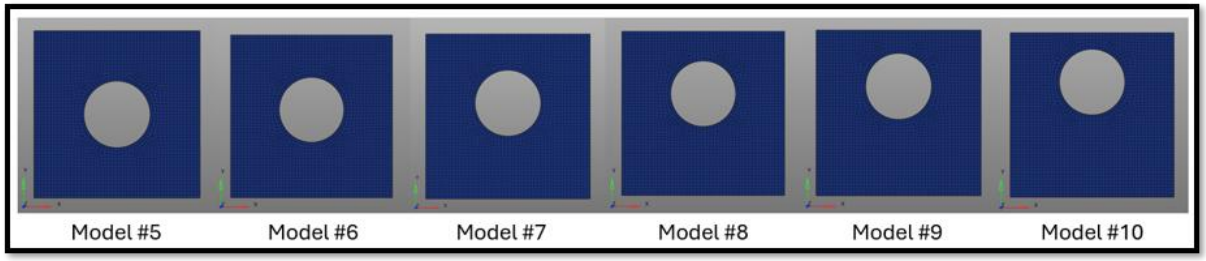

Figure 2. Comparison of Last 6 Models (Shifting of Hole).

Table 1. Explanation of 10 models to be used throughout the analyses.

Model #	Property
1	An aluminum plate without hole
2	An aluminum plate with 5mm hole at center
3	An aluminum plate with 10mm hole at center
4	An aluminum plate with 15mm hole at center
5	An aluminum plate with 20mm hole at center
6	An aluminum plate with 20mm hole at 4mm to center
7	An aluminum plate with 20mm hole at 8mm to center
8	An aluminum plate with 20mm hole at 12mm to center
9	An aluminum plate with 20mm hole at 16mm to center
10	An aluminum plate with 20mm hole at 20mm to center

2. Boundary Conditions and Load Case Selection

The study began by evaluating three different boundary conditions using modal analysis: free-free, simply supported, and clamped boundaries. Natural frequencies and mode shapes were analyzed across all conditions. The simply supported configuration was selected for detailed analysis due to its moderate stiffness response and its compatibility with theoretical validation models based on classical plate theory. The configuration is used with load-free selection.

3. Modal Analysis and Analytical Validation

MSC Nastran 2019 was used to extract the first ten natural frequencies and their corresponding mode shapes. To ensure the credibility of simulation results, MATLAB 2022 was used to calculate analytical solutions for the simply

supported plate case. These were compared with the MSC Nastran results, yielding an error range below 3% across all 10 modes, affirming the accuracy of the simulation workflow.

Findings

1. Modal Frequency Trends

The first ten natural frequencies for each model demonstrated an inverse relationship between stiffness and both hole size and eccentricity. As expected, larger holes reduced the stiffness of the plate, resulting in decreased natural frequencies. For instance, Model 1 (solid plate) had a first mode frequency of 46.39 Hz, whereas Model 5 (20 mm hole) had a slightly increased frequency due to mass reduction effects being dominant over stiffness loss.
Models 6 through 10, which varied the hole position while keeping the diameter constant, exhibited less predictable patterns. Initially, small offsets resulted in reduced frequencies, but as the hole moved closer to the edge, the mass redistribution altered the modal stiffness differently, in some cases increasing the natural frequency.
Models are required to be increased using parametric modeling techniques in future studies.

2. Frequency Response and Vibration Fatigue Framework

The Frequency Response Function (FRF) analysis was conducted by exciting the plate models with harmonic loads ranging from 1 Hz to 1000 Hz. Each model was subjected to 3-directional loads with an amplitude of 9810 N. The FRF outputs identified resonance frequencies and their associated amplification factors, which were crucial for fatigue evaluation.
A key aspect of vibration fatigue analysis is the integration of FRF data with Power Spectral Density (PSD) inputs, which define the energy distribution of excitation across frequencies. For this, standard aircraft vibration data from MIL-STD-810H was utilized.
Then, Root Mean Square (RMS) stress values were derived and used as input to the fatigue module in nCode 2019. Rainflow Counting and Miner's Rule were applied for damage accumulation.

3. Fatigue Life Trends

The fatigue lives for each model demonstrated that not only the presence of a hole but its size and location critically affect life expectancy. For example, Model 2 with a 5 mm central hole showed the highest damage (D = 3.009), translating to a very short fatigue life of 0.33 cycles. Interestingly, Model 5 with a 20 mm hole showed a damage value of only 0.0824, which is significantly lower due to the modal response being less aligned with the PSD peak frequencies.
In location studies, Model 6 (4 mm offset) had a damage value of 0.308, while Model 10 (16 mm offset) reached 1.497, indicating an almost 5x increase in damage. This trend shows that holes near edges can cause local resonance phenomena, increasing stress amplitudes drastically. The data supports a safe offset limit of 8 mm for maintaining fatigue integrity (Figure 3).

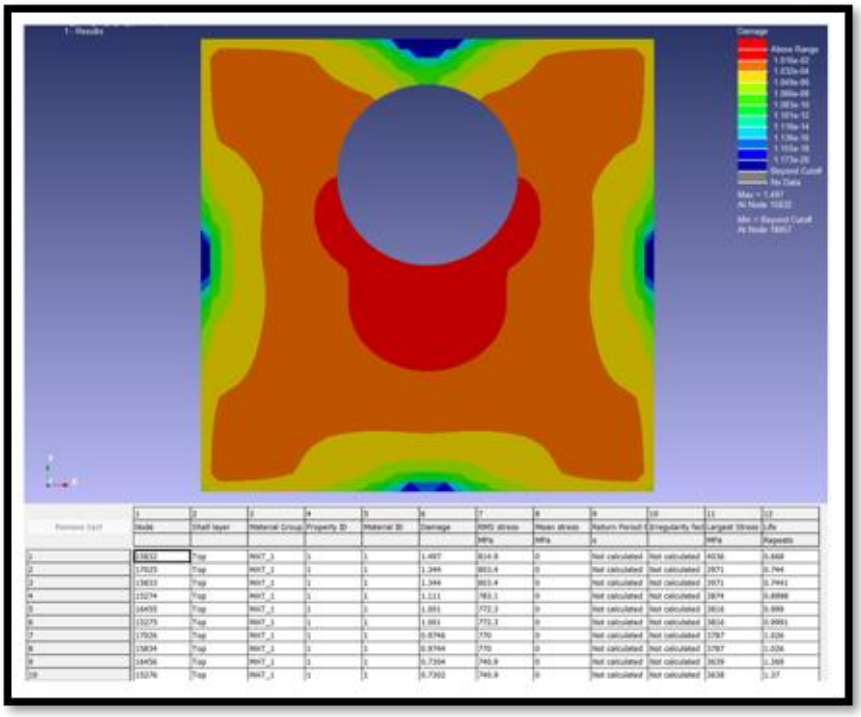

Figure 3. Outputs of Model 10.

Conclusion

This study confirms that the geometric configuration of holes in structural plates plays a vital role in their dynamic and fatigue behavior. Key findings are summarized as follows:

- Small holes can dramatically amplify local stress concentrations and cause disproportionately high fatigue damage (Figure 4).
- Increased hole size does not always correlate with increased damage due to competing effects of stiffness loss and mass redistribution.
- Off-center holes cause higher fatigue risk, especially when positioned close to plate boundaries due to modal distortion (Figure 5).
- Frequency content of excitation must be considered; resonance amplification can mislead fatigue life predictions if modal behavior is not integrated into the analysis.

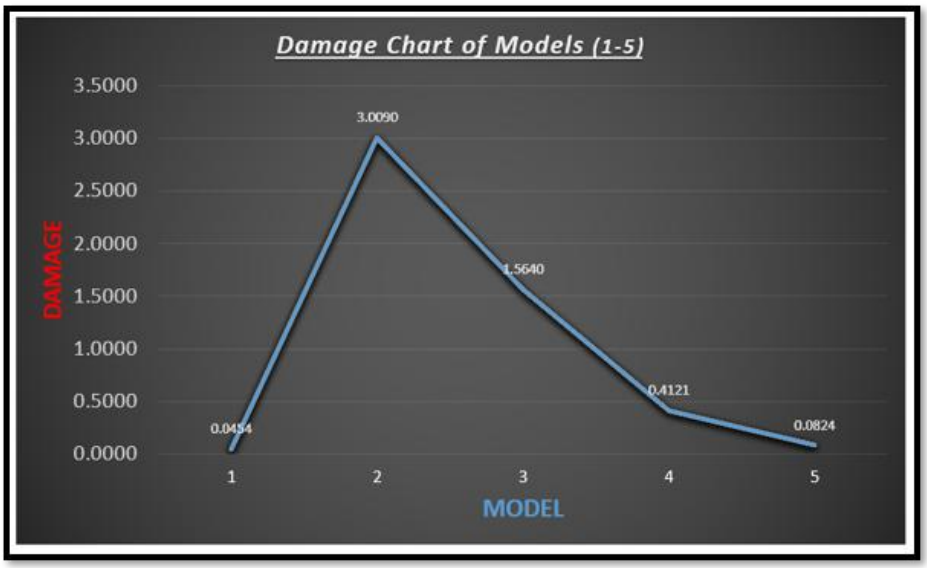

Figure 4. Damage Chart of Models (1-5).

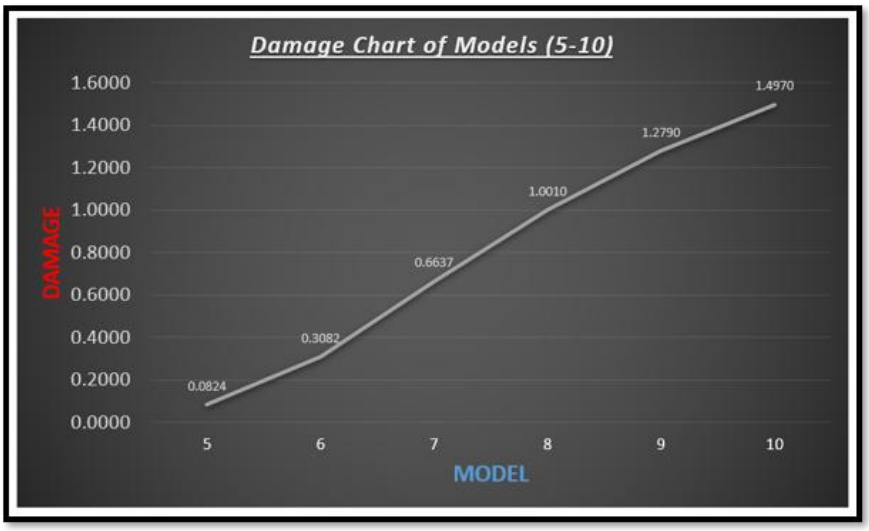

Figure 5. Damage Chart of Models (5-10).

The combined use of theoretical models, FEM simulation, and experimental standard-based PSD data has proven effective in comprehensively assessing the structural behavior under vibration fatigue. These findings are particularly relevant for engineers designing lightweight structures in vibration-prone environments such as aerospace and automotive platforms. The methodology presented in this study provides a reliable and validated workflow that balances computational efficiency with physical accuracy.

References

HBM Prenscia. (2019). nCode GlyphWorks user's manual: Rainflow counting and Miner's rule for fatigue damage analysis. https://www.hbmprenscia.com, date retrieved 13.05.2025.

International Organization for Standardization. (1995). Mechanical vibration—Road surface profiles—Reporting of measured data (ISO 8608:1995). https://www.iso.org, date retrieved 13.05.2025.

International Organization for Standardization. (1997). Mechanical vibration and shock—Evaluation of human exposure to whole-body vibration—Part 1: General requirements (ISO 2631-1:1997). https://www.iso.org, date retrieved 13.05.2025.

Lalanne, C. (2009). Mechanical vibration and shock analysis: Fatigue damage (Vol. 4). Wiley.

Lutes, L. D., & Sarkani, S. (2004). Stochastic analysis of structural and mechanical systems. Springer.

MSC Software Corporation. (2019). MSC Nastran 2019 user's guide: SOL 111 - Modal frequency response and random response analysis. MSC Software.

Paz, M., & Leigh, W. (2004). Structural dynamics: Theory and applications. Springer.

Peterson, R. E. (1974). Stress concentration factors (2nd ed.). Wiley.

Roberts, G. W., & Ewins, D. J. (2001). Vibration fatigue analysis based on frequency domain methods. Journal of Sound and Vibration, 243(3), 403–420.

Smith, S. W., & Clarke, T. A. (1998). The use of frequency response functions for fatigue life prediction. Proceedings of the Institution of Mechanical Engineers, Part C: Journal of Mechanical Engineering Science, 212(4), 263–275.

Thomson, W. T., & Dahleh, M. D. (1998). Theory of vibration with applications (5th ed.). Prentice Hall.

United States Department of Defense. (2019). Environmental engineering considerations and laboratory tests (MIL-STD-810H). Defense Logistics Agency. https://quicksearch.dla.mil, date retrieved 13.05.2025.

SUSTAINABILITY

Biodiversity

Climate Change Mitigation

Life Cycle Assessment

Reinforced Concrete Structures

Smart and Sustainable Cities

Sustainable Development Goals

Water and Waste Management

Assessing Decarbonization Strategies and Decoupling Trends of Türkiye's Private Sector Companies

Aslı Ceydanur Akbaba[a], Kadriye Elif Maçin[b], Börte Köse Mutlu[c]

[a] İstanbul Technical University, Sustainability Master of Science Program, Türkiye
[b,c] İstanbul Technical University, Civil Engineering Faculty, Department of Environmental Engineering, Türkiye
akbabaa23@itu.edu.tr, macin@itu.edu.tr, kosebo@itu.edu.tr

Keywords: Decoupling, Emission Reduction, Net Zero Targets, Decarbonization.

Aim

As businesses worldwide move toward low-carbon economies, the commitment of corporations to reduce greenhouse gas emissions has become increasingly significant in combating climate change. This study focuses on companies in Turkiye's BIST100 index (KAP, n.d.), specifically those in the Metal Products, Machinery, Electrical Devices, and Transportation sectors, to evaluate whether they can meet their emission reduction goals for 2030 and 2050. The research compares companies' publicly announced net-zero targets to their actual emission reduction trends, uncovering insights into how effective their decarbonization strategies are. Additionally, the study employs the Decoupling Index (DI) to determine whether economic growth is associated with increasing emissions or if companies are successfully reducing emissions while continuing to expand.

Material and Method

The research started with a review of 100 companies listed on the BIST100 index. The focus was on companies that publicly disclosed their sustainability or integrated reports, which included data on Scope 1, Scope 2, and relevant Scope 3 greenhouse gas emissions. The analysis was restricted to companies that have stated net-zero or emission reduction commitments for 2030 and 2050. From the initial pool of 100 companies, 46 met these criteria, demonstrating a commitment to accurate emission reporting and climate actions.

To ensure comparability, the research focused on companies within the Fabricated Metal Products, Machinery, Electrical Equipment, and Transportation Vehicles sectors, as these industries play a crucial role in Turkiye's industrial landscape and contribute significantly to national emissions. Using these criteria, seven companies were selected for an in-depth analysis, referred to as Firm 1 through Firm 7.

The study extracted each selected company's total emissions for 2023, along with their stated reduction targets for both 2030 and 2050. The research calculated the Expected Average Annual Reduction Rate (EAR) for 2030 and 2050 based on each firm's baseline emissions and their target reductions. Simultaneously, the Actual Average Annual Reduction Rate (AAR) was determined using emissions data from 2023 to gauge each company's progress toward its targets. Companies whose actual reduction rates exceeded their expected rates were deemed to be on track to fulfill their commitments; those falling short were identified as being at risk of not achieving their goals.

Furthermore, the Decoupling Index was used to explore the relationship between emissions trends and economic growth. To project Turkiye's per capita GDP for 2030 and 2050, a linear regression model was employed based on historical GDP data. The companies were classified into three categories regarding decoupling: absolute decoupling (indicating a decrease in emissions while GDP continues to grow), relative decoupling (indicating that emissions are increasing but at a slower rate than GDP), or no decoupling (where emissions are growing faster than GDP). This classification provided insights into which firms are genuinely pursuing sustainability and which ones need additional efforts to accomplish their targets (Karakaya, Bostan, & Özçağ, 2019).

Findings

The findings revealed that all seven firms reported their Scope 1, Scope 2, and Scope 3 emissions in line with the Greenhouse Gas (GHG) Protocol guidelines (Greenhouse Gas Protocol, n.d.). However, an examination of their progress in decarbonization indicated that companies in the Metal Products, Machinery, Electrical Devices, and

Transportation sectors are currently unlikely to meet their 2030 and 2050 emission reduction targets based on present trends. Many of these firms exhibited slower than required reduction trajectories, raising doubts about the feasibility of their proclaimed commitments.

Further examination of the sustainability reports highlighted companies' approaches to emission reduction. It became clear that many firms adopted intensity-based reduction targets, which focus on reducing emissions per unit of output rather than absolute reductions in total emissions. While this method improves efficiency allowing for growth alongside reduced emissions, it does not necessarily lead to significant overall decreases in emissions. Moreover, it was noted that companies had a common strategy for Scope 2 emissions reduction, primarily emphasizing the increased use of renewable energy for electricity consumption. Despite identifying renewables as a critical driver in cutting Scope 2 emissions, significant challenges remain in effectively tackling Scope 3 emissions.

For Scope 1 emissions, the companies implemented diverse energy efficiency initiatives, including optimizing compressed air systems, improving HVAC system efficiency, upgrading lighting systems, enhancing thermal insulation, utilizing heat recovery technologies, transitioning to energy-efficient motors, and adhering to LEED certification standards for manufacturing facilities. These strategies aim to cut direct emissions stemming from operations while boosting overall energy performance.

The Decoupling Index analysis provided deeper insights into the relationship between emissions trends and economic growth. By 2023, some companies successfully achieved absolute decoupling, meaning their emissions had decreased while their economic growth persisted. Others displayed relative decoupling, with emissions still rising but at a slower pace than the growth of GDP. In contrast, several firms showed no decoupling at all, indicating that their emissions were increasing more rapidly than economic growth, thereby signaling a need for more robust decarbonization measures.

The research also observed that many firms had recently enhanced their Scope 3 emissions reporting, leading to an artificial spike in total reported emissions. While increased reporting transparency can be beneficial, it complicates the measurement of progress over time and highlights the importance of accurately capturing Scope 3 emissions, which usually represent the largest component of a company's total emissions.

At the same time, comparing Expected and Actual Reduction Rates revealed that some companies might be capable of achieving their targets for 2030; however, they will likely face difficulties in meeting their 2050 commitments as the required rate of reduction escalates significantly after 2030. Notably, two companies in the white goods sector and one in transportation were found to be off-track for both their 2030 and 2050 targets. Companies showcasing a robust commitment to emission reductions tended to incorporate a range of strategies, including efficiency improvements, electrification initiatives, and substantial investments in renewable energy sources.

Conclusion

This study uncovers a critical gap between the declared decarbonization targets of companies and their actual progress in reducing emissions. While many firms have made strides in reducing Scope 2 emissions through enhanced renewable energy use, the overall trends in emissions suggest that existing strategies may not be enough to meet their 2030 and 2050 objectives. The analysis using the Decoupling Index highlighted varying success rates in dissociating emissions growth from economic expansion while certain companies achieved absolute decoupling, others still face challenges.

The findings further indicate that a number of firms continue to rely on intensity-based reduction strategies that, although beneficial, do not guarantee substantial decreases in total emissions. Furthermore, companies that broadened their Scope 3 reporting often faced an upward spike in their reported emissions, complicating the perceived progress toward targets. Moving forward, companies must adopt robust emission reduction strategies, improve their management of Scope 3 emissions, and outline realistic pathways for transition to align with broader climate goals.

References

Karakaya, E., Bostan, A., & Özçağ, M. (2019). Decomposition and decoupling analysis of energy-related carbon emissions in Turkey. Environmental Science and Pollution Research, 26(32), 32080–32091
Url-1 KAP. (n.d.). Endeksler https://www.kap.org.tr/en/Endeksler
Url-2 Greenhouse Gas Protocol. (n.d.). GHG protocol revised.
from https://ghgprotocol.org/sites/default/files/standards/ghg-protocol-revised.pdf

The Relationship between Sustainable Finance and The Carbon Border Adjustment Mechanism (CBAM): A Policy Impact Assessment and Hypothetical Case Study of A Cement Plant

Inci Nur Cetin[a]

[a] Istanbul Technical University, Environmental Sciences, Engineering and Management Program, Türkiye
cetin22@itu.edu.tr

Keywords: Carbon Border Adjustment Mechanism (CBAM), Cement Industry, Sustainable Finance.

Aim

The research aims to conduct a comprehensive Policy Impact Assessment (PIA) of the Carbon Border Adjustment Mechanism (CBAM) on a cement plant in a third-party country, evaluating both environmental and financial impacts within the framework of sustainable finance. The European Union's (EU) CBAM is designed to reduce carbon leakage by imposing a carbon price on imported goods, with the cement sector being one of the six most critical carbon-intensive industries. This study will examine the impact of CBAM policies on the Environmental, Social, and Governance (ESG) standards of the cement plant. By integrating a sustainable finance perspective, the research aims to identify both the direct and indirect effects of CBAM on the economic management and operations of the cement sector within regulatory frameworks.

Material and Method

This study employs a hypothetical case study design to assess the environmental and financial impacts of the EU's CBAM on a cement plant operating in a third- party country. Using both quantitative and qualitative methods, the research integrates scenario simulations, financial modelling, and policy mapping. Key performance indicators include environmental (CO_2 emissions, emission intensity), economic (production and compliance costs, profitability), technological (green technology adoption), and regulatory (HS Codes, compliance standards) metrics. Hypothetical scenarios model varying CBAM enforcement levels, assessing their effects on production, costs, and emission strategies. Financial analysis includes cost-benefit and sensitivity evaluations, while environmental assessment tracks emission reductions and green technology efficiency. Policy mapping examines EU and Turkish regulations, highlighting regulatory drivers and sustainability finance implications. The study also explores how ESG standards influence investment and corporate strategies. An integrated framework combining statistical analysis, policy review, and scenario modelling ensures a comprehensive assessment. While relying on secondary data and simulations, the study provides preliminary insights into CBAM's impacts, acknowledging limitations in market dynamics and policy enforcement that future empirical research should address.

Findings

Preliminary findings suggest that climate change impacts are driving the adoption of sustainable strategies across various sectors, including finance and industry. The need to address these effects concretely has led policymakers to emphasize economic outcomes. The CBAM and the Emissions Trading System (ETS) play a key role in guiding production facilities toward both environmental sustainability and economic competitiveness.

The hypothetical cement plant may need to reassess its emissions management strategies due to CBAM implementation, potentially leading to a shift toward cleaner technologies and a re-evaluation of supply chain dynamics. Compliance is expected to result in higher operating costs, but it may also enhance competitiveness through sustainable practices. Additionally, experts suggest that aligning with CBAM could promote a circular economy within the cement industry, encouraging investment in renewable energy sources and innovation in cleaner technologies.

In their analysis of the effects of new carbon management strategies on the cement sector, Sloan et al. (2023) provide insights into how these frameworks can improve adherence to carbon border adjustments. CBAM is

gaining importance in developing countries to reduce carbon dioxide emissions and to adapt to European practices. Sharma & Srivastava (2023) propose strategies on how these mechanisms can be used to optimize transition pathways in the energy sector. In Europe, CBAM is used to avoid carbon taxes and to maintain external competitiveness. Lau et al. (2021) examine the role of carbon capture technologies (CCS) technologies in Europe's carbon transition and explain the importance of implementing this mechanism in the cement sector. Rumayor et al. (2021) evaluates the potential of carbon recycling in the cement sector and provides examples of how such a mechanism can be implemented in international trade.

Conclusion

This study highlights the importance of a comprehensive Policy Impact Assessment in understanding the effects of CBAM on the cement sector. By analysing a hypothetical cement plant, it identifies key areas where environmental engineering can play a crucial role in mitigating climate impacts and promoting sustainable outcomes. In addition to offering insights for future policymakers, the findings can help cement producers enhance their strategic planning as they transition to more environmentally friendly operational models. For the cement industry to become more sustainable, decarbonization is a vital requirement, in order to reduce greenhouse gas emissions from the production of cement, multiple environmentally friendly methods are being researched. The effect of low-carbon techniques in reducing greenhouse gas emissions from cement production in developing countries is highlighted by Cheng et al. (2023). By integrating alternative fuels with carbon dioxide capture and storage (CCS) technology, Fennell et al. (2021) highlight the necessity of minimizing greenhouse gas emissions in the cement production process. Furthermore, in cement sector, Environmental, Social and Governance (ESG) goals are becoming more and more significant. In order to achieve the cement industry's zero emission goals, Jiang et al., 2024 highlight the importance of social and environmental aspects. The significance of green technologies in the industry and their possible role in power transitions are also examined by Muhsen et al. (2023), who offer a viewpoint in favor of the incorporation of ESG standards in cement plants.

Ultimately, this research contributes to the broader discussion on engineering solutions, climate policy, and sustainable finance in the context of industrial emissions management.

References

Cheng, D., Reiner, D. M., Yang, F., Cui, C., Meng, J., Shan, Y., ... & Guan, D. (2023). Projecting future carbon emissions from cement production in developing countries. Nature Communications, 14(1), 8213.

Fennell, P. S., Davis, S. J., & Mohammed, A. (2021). Decarbonizing cement production. Joule, 5(6), 1305-1311.

Jiang, K., Yu, H., Sun, Z., Lei, Z., Li, K., & Wang, L. (2024). Zero-emission cement plants with advanced amine-based CO2 capture. Environmental Science & Technology, 58(16), 6978-6987.

Lau, H. C., Ramakrishna, S., Zhang, K., & Radhamani, A. V. (2021). The role of carbon capture and storage in the energy transition. Energy & Fuels, 35(9), 7364-7386.

Muhsen, H., Al-Mahmodi, M., Tarawneh, R., Alkhraibat, A., & Al-Halhouli, A. A. (2023). The potential of green hydrogen and power-to-X utilization in Jordanian Industries: opportunities and future prospects. Energies, 17(1), 213.

Rumayor, M., Fernández-González, J., Domínguez-Ramos, A., & Irabien, A. (2021). Deep decarbonization of the cement sector: a prospective environmental assessment of CO2 recycling to methanol. ACS Sustainable Chemistry & Engineering, 10(1), 267-278.

Sharma, A. K., & Srivastava, M. K. (2023). A grey-DEMATEL approach to prioritize challenges for decarbonization of energy sector. Data Science and Intelligent Computing Techniques, SCRS, 307-316**.**

Sloan, B., Makuch, Z., Oraee-Mirzamani, N., & Oraee-Mirzamani, B. (2023). European Regulatory Approaches to Preventing Carbon Leakage: Rolling Back Johnson's EU 'Diplomacy' for a Brighter Environmental Future. European Energy and Environmental Law Review, 32(4).

SUSTAINABILITY

Biodiversity

Climate Change Mitigation

Life Cycle Assessment

Reinforced Concrete Structures

Smart and Sustainable Cities

Sustainable Development Goals

Water and Waste Management

The Intersection Infrastructure of LCA-BIM Inegration: Applicability in Turkey and Europe

Tuğba Ayvaz[a]

[a] Istanbul Technical University, Graduate School, Department of Architecture, Project and Construction Management, Turkey
ayvazt16@itu.edu.tr

Keywords: Life Cycle Assessment, Building Information Modeling, Carbon Emissions, Sustainability.

Aim

The construction industry faces increasing pressure to reduce carbon emissions throughout the building lifecycle, from material production to the end of its service life. Integrating Life Cycle Assessment (LCA) with Building Information Modeling (BIM) presents a promising strategy to embed environmental performance assessment into the design and operation of buildings. This paper aims to improve the feasibility of LCA-BIM integration by developing a "cross-infrastructure" that links BIM models with carbon emission data. Specifically, the focus is on directly embedding material-level carbon information (e.g., greenhouse gas emission factors) into BIM objects, proposing a dynamic framework in which each building component carries its own "carbon identity." The goal is to enable real-time calculation of both embedded and operational carbon footprints of a building within the BIM environment. The research offers solutions to data incompatibility and integration challenges in LCA-BIM, exploring the applicability of LCA-BIM integration in Turkey and Europe. By associating digital building models with dynamic carbon databases, it proposes a new BIM-based data infrastructure that could enhance decision-making for low-carbon design. As a result, the research focuses on sustainability-driven design throughout the building lifecycle in early-stage project decision-making processes, aligning with global carbon reduction goals while considering the feasibility of regional applications.

Material and Method

In the research, carbon emission statistics were obtained from the Turkish Statistical Institute (TUIK) and the European Union's Eurostat official database. A dataset on greenhouse gas emissions for EU member countries from 2010 to 2024 was created and analyzed. The data for Turkey was analyzed through TUIK. Emission factors for building materials were obtained from LCA databases such as Ecoinvent (a comprehensive life cycle inventory database), the Social Hotspot Database (SHDB), and EPDs. Additionally, industry tools such as One Click LCA and published Environmental Product Declarations were consulted to validate material-level carbon values. A systematic meta-analysis of the literature was conducted, with a notable observation that most of the literature was published within the last five years. Revit, a BIM tool, was used to develop a building model representing a typical project. Within Revit, a custom parameter schema was applied to assign a unique "Carbon Identity" to each material and component. Autodesk Dynamo, a visual programming tool, was used to script the connection between Revit and Excel-based data tables containing emission factors. One Click LCA (a commercial BIM-LCA plugin) was used as a trial for comparison, highlighting the differences between our identity-based method and the existing plugin workflows. The key methodological innovation is the direct embedding of carbon data into BIM objects through unique identities. A material library was created, and an external mapping file "XYZ123" was linked to a CO_2 emission factor (e.g., kg CO_2 per kg of material). During BIM modeling, as elements were added or quantities changed, a live calculation routine was proposed, allowing for immediate access to a tangible carbon output for the design. By embedding data at the material level, it was suggested that carbon information travel alongside the BIM model. The method was applied step by step: (1) define the identity schema and populate the LCA dataset, (2) add identity parameters to Revit families, (3) develop Dynamo scripts for real-time connection, and (4) test the system on a case study building model. In summary, it involved gathering reliable data sources, critically reviewing existing research, and proposing a prototype system within Revit that demonstrates a new approach to integrating LCA into BIM via embedded carbon identities.

Findings

A comparative analysis of CO_2 trends reveals divergent patterns between Europe and Turkey. Over the past decade, per capita emissions in countries like Germany and Italy declined steadily—from 10.9 to 8.1 tons in Germany, and 7.6 to 5.3 tons in Italy (Climate Transparency, 2024). In contrast, Turkey's total greenhouse gas emissions surged by 134% (TUIK, 2023). While Europe must further enhance LCA–BIM integration to maintain progress, Turkey faces an urgent need to adopt it to curb rising emissions. Although construction sector emissions have declined in Europe, Germany and the Netherlands still exceed Turkey in per capita values, with Germany leading in total construction-based CO_2 between 2010 and 2024 (World Bank).

Operational carbon—especially from HVAC systems—dominates a building's life cycle footprint, often comprising up to 93% of total GWP (Cheng et al., 2020). Yet, many BIM–LCA studies focus only on embodied carbon, neglecting operational impacts (Ortiz et al., 2009). Current tools typically extract material quantities for embodied calculations but omit energy use. Integrating operational simulations requires exporting BIM models to energy tools (e.g., Insight, DesignBuilder), a step often skipped due to its complexity (Cheng et al., 2020). Cheng et al.'s manual method using gbXML highlights the crucial role of operational carbon.

Neglecting operational emissions can yield misleading results—buildings with sustainable materials but poor energy performance may still have high footprints. Our proposed method addresses this by embedding operational data within BIM via Carbon IDs and Insight integration, thus closing a major gap in current practice.

Meta-analysis also identified key barriers: lack of material libraries supporting integration, reliance on manual data transfer, dataset mismatches, and absence of dynamic updating. These limitations slow down workflows and increase error potential (Chen et al., 2024). Repeated manual adjustments for every design revision remain a major obstacle to seamless BIM–LCA integration.

Uniqueness and Practical Value of the Proposed ID-Tag Method:

The proposed Carbon ID tagging system offers a unique solution for the BIM-LCA intersection infrastructure. By assigning each material/component in the BIM model a unique carbon identifier, the dynamic definition of the emission factor for each object is achieved without user intervention. This methodology was validated in a prototype building model: as materials in the BIM design were changed, the embodied carbon totals were instantly updated, confirming a live connection between design choices and LCA results. The system facilitates sustainable decision-making processes by integrating unit carbon emissions per material into the BIM environment, which project decision-makers are already familiar with. This approach is an extension of the automated data exchange proposal defined by Chen et al. (2024). Chen et al. (2024) found that automating data exchange "reduces errors in manual calculations and data collection" while improving efficiency.

If material suppliers and LCA database providers collaborate on standardizing Carbon Identities (similar to barcodes or product identifiers), BIM software could universally incorporate carbon data, providing consistent carbon emission rates across projects and regions. The meta-analysis identified the lack of such standardization as a major gap in current research. The identification of product identities in the digital environment could be facilitated through government policies. This would promote an integrated design philosophy where the carbon footprint in the BIM model becomes as instantaneous a metric as cost or structural load. Such immediacy is crucial for real-world adoption because, if seamlessly integrated into feedback workflows, design teams are more likely to consider carbon criteria. In this way, a digital copy of the building is created from early design to operation and demolition

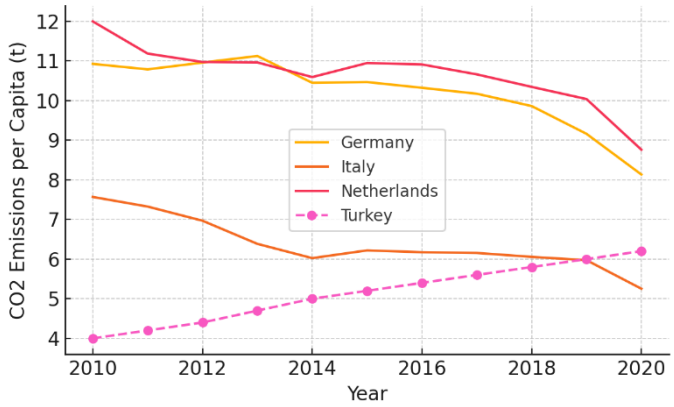

Figure 1. Per capita CO_2 emissions (building sector-based) in European countries vs. Turkey, 2010–2020.

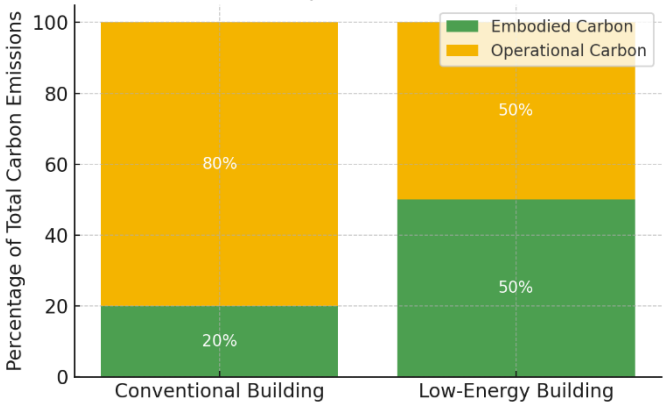

Figure 2. Illustration of embodied vs. operational carbon share in a building's life cycle.

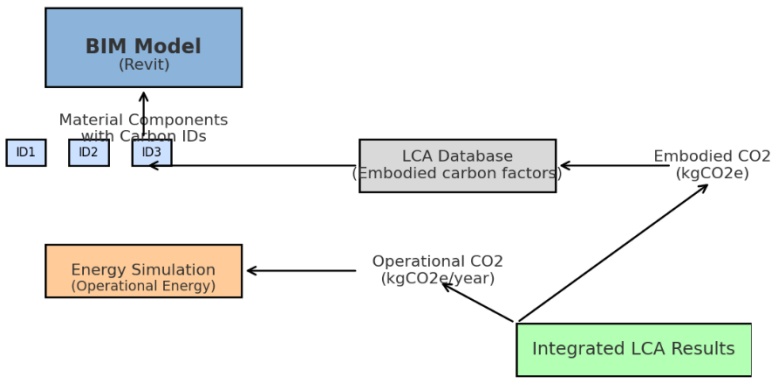

Figure 3. System architecture for the proposed BIM–LCA integration using embedded Carbon IDs.

Conclusion

This study explored the intersection of LCA and BIM, proposed a new integration framework, and assessed its applicability in Turkey and Europe. The key findings can be summarized as follows:

1. While European countries have progressively reduced construction-related carbon emissions (both embedded and operational), emissions in Turkey are rising, emphasizing the urgent need for improved carbon management in Turkey's construction sector.

2. Despite operational carbon emissions accounting for the largest share of a building's life cycle emissions, many existing BIM-LCA applications focus solely on embodied carbon. This gap in the literature indicates that neglecting the operational phase may lead to suboptimal decisions. Therefore, a robust BIM-LCA integration (including the proposed system) must incorporate energy simulation data to capture operational impacts.
3. The shift toward BIM-LCA integration has been hindered by labor-intensive manual data entry, unreliable or limited-scope plugins, and fragmented data sources, which negatively affect LCA adoption in BIM workflows. These challenges, well-documented in numerous studies, provided insights into the development of our material identity tagging strategy.
4. The proposed Revit-based Carbon Identity system was applied and tested, demonstrating clear advantages in overcoming the fundamental barriers to BIM-LCA integration. By embedding carbon emission factors at the material level within the BIM model, the system provided real-time data synchronization when designers made modifications to the model.

The steps of the system were applied sequentially: mapping LCA database entries to BIM material definitions, assigning a Carbon Identity to each material, and calculating values on a project-specific basis via Dynamo scripts. To include operational carbon, Insight was used. The total carbon output was verified against a traditional LCA conducted in parallel to ensure that the results of the ID method were within an acceptable margin of error. The consistency accuracy was found to be less than 5%.

This study highlights the importance of integrating both embodied and operational carbon into BIM models for better sustainability decision-making and shows how the proposed method can effectively address the challenges in current BIM-LCA workflows.

From a broader perspective, the proposed system offers an adaptable and scalable path toward true digital twin integration for sustainability. Essentially, every building component in the digital model carries metadata about its environmental impact, laying the foundation for a future where complete "carbon digital twins" of buildings can be maintained. In such a future scenario, a building's digital twin would continuously monitor both embedded carbon (as materials are changed or added) and operational carbon (via sensors and building management systems), providing real-time information about the building's performance relative to climate goals.

Our study is a step in this direction, enabling design-phase analysis. The research presented here paves the way for such advancements, demonstrating that LCA-BIM integration can be both technically feasible and highly practical. This brings the industry one step closer to truly sustainable building life cycles.

References

Akbarieh, A., Jayasinghe, L. B., Waldmann, D., & Teferle, F. N. (2020). BIM-based end-of-lifecycle decision making and digital deconstruction: Literature review. Sustainability, 12(7), 2670. DOI: 10.3390/su12072670

Chen, Z., Chen, L., Zhou, X., Huang, L., & Sandanayake, M. (2024). Recent technological advancements in BIM and LCA integration for sustainable construction: A review. Sustainability, 16(3), 1340. DOI: 10.3390/su16031340

Cheng, B., Li, J., Tam, V. W. Y., Yang, M., & Chen, D. (2020). A BIM-LCA approach for estimating the greenhouse gas emissions of large-scale public buildings: A case study. Sustainability, 12(2), 685. DOI: 10.3390/su12020685

Climate Transparency. (2022). Turkey – Climate Transparency Report 2022. Climate Transparency Initiative.

Url-1 https://www.climate-transparency.org/wp-content/uploads/2022/10/CT2022-Turkey-Web.pdf, date retrieved 24.03.2025.

Eurostat. (2025). EU GHG emissions from the production and consumption (footprint) perspectives (FIGARO application) [Data set: cli_gge_foot]. Retrieved from Eurostat Database.

Url-2 https://ec.europa.eu/eurostat/databrowser/view/cli_gge_foot/default/table, date retrieved 24.03.2025.

Figueiredo, K., Pierott, R., Hammad, A. W., & Haddad, A. (2021). Sustainable material choice for construction projects: A Life Cycle Sustainability Assessment framework based on BIM and Fuzzy-AHP. Building and Environment, 196, 107805.

Guignone, G., Calmon, J. L., Vieira, D., & Bravo, A. (2023). BIM and LCA integration methodologies: A critical analysis and proposed guidelines. Journal of Building Engineering, 73, 106780. DOI: 10.1016/j.jobe.2023.106780

Ortiz, O., Castells, F., & Sonnemann, G. (2009). Sustainability in the construction industry: A review of recent developments based on LCA. Construction and Building Materials, 23(1), 28–39. DOI: 10.1016/j.conbuildmat.2007.11.012

Zong, C., Margesin, M., Staudt, J., Deghim, F., & Lang, W. (2022). Decision-making under uncertainty in the early phase of building façade design based on multi-objective stochastic optimization. Building and Environment, 226, 109729.

SUSTAINABILITY

Biodiversity

Climate Change Mitigation

Life Cycle Assessment

Reinforced Concrete Structures

Smart and Sustainable Cities

Sustainable Development Goals

Water and Waste Management

Effects Of Using Waste Glass Powder And Rice Husk Ash As A Partial Replacement With Cement In Mortar Productions

Mohamad Alaa Shurbaji [a], Özgür Ekincioğlu [a]

[a] Istanbul Technical University, Civil Engineering Department, Construction Engineering Program, Türkiye
shurbaji21@itu.edu.tr

Keywords: Waste Glass Powder (WGP), Rice Husk Ash (RHA), Supplementary Cementitious Materials (SCMs), Sustainable Construction, Waste Management.

Aim

The excessive use of Ordinary Portland Cement (OPC) in construction significantly contributes to energy consumption and environmental pollution due to carbon emissions. This study aims to enhance the environmental sustainability of cement-based materials by investigating the performance of mortars that incorporate rice husk ash (RHA) and waste glass powder (WGP) as supplementary cementitious materials (SCMs) to partially replace OPC. The main objective is to determine how RHA and WGP affect important mechanical characteristics including compressive and flexural strength, both separately and in combination. The study aims to find the best replacement values that improve mechanical performance and enhance sustainability by systemically changing the proportions of RHA and WGP in mortar compositions. The study also examines the synergistic advantages of combining RHA with WGP, showing how each improves microstructural properties, workability, and durability. The specific objectives include determining the optimal mix ratio of WGP and RHA in mortar and identifying the optimum percentage replacement of cement with the combined WGP-RHA mixture based on mechanical properties, workability, and durability assessments. Furthermore, the study aims to understand the pozzolanic reaction mechanism through microstructural and chemical analyses. The findings will provide valuable insights into the feasibility of utilizing these materials in construction applications, contributing to more sustainable building practices and effective waste management solutions.

Material and Method

CEN Reference sand

The sand used in this study according to EN 196-1:2016 The sand is prepared according to the same specifications and particle sizes as in the standard. The sand was prepared to meet all the requirements listed in EN 196-1:2016, including those related to particle size distribution, shape, and mineral composition. To achieve a uniform distribution and reduce variability in mortar workability and strength development, the particle sizes were carefully controlled through sieving and grading procedures.

Cement

The physical characteristics of the Portland cement, which was classified as CEM I 42.5N under the TS EN 197-1 standard, were measured to ensure adherence to the experimental structure of the study. Measured density of cement was 3.12 g/cm³.

Waste glass powder (WGP)

The waste glass powder (WGP) used in this study had an average particle size of less than 100 µm after sieving, which was provided by the company with an average particle size of 100 µm. This glass's homogeneity and purity can be due to its E-glass fiber origin. According to literature, a particle size of less than 100 µm effectively mitigates ASR expansion and enhancing the durability.

Rice husk ash (RHA)

Rice Husk Ash (RHA) is a valuable supplementary cementitious material in construction, known for its high pozzolanic properties. It consists of amorphous silica (SiO2), which can react with calcium hydroxide to form hydrated calcium silicate, enhancing the strength and durability of concrete. RHA has a high surface area due to its nanoscale particles.

Superplasticizer

Superplasticizer or a high-range water-reducing admixture with a brand name of Sika-4087 was incorporated into the mixtures to achieve the targeted slump value for ease of workability, placement, and consolidation in all concrete and mortar mixes. The used superplasticizer has a density of 1,07 g/cm3.

Method

The study aimed to identify the optimal ratio of waste glass powder (WGP) to rice husk ash (RHA) as supplementary cementitious materials (SCMs) for replacing 25% of ordinary Portland cement (OPC) by weight. Mortar samples were prepared with varying WGP:RHA ratios (0:25, 6.25:18.75, 12.5:12.5, 18.75:6.25, and 25:0) to assess their mechanical performance. A control mix containing 0% SCMs was included for baseline comparison. Following **EN 196-1:2016** standards, the mechanical properties—specifically flexural and compressive strength were evaluated at 7 and 28 days of curing to determine the influence of each combination on structural performance. Concurrently, the pozzolanic activity indices (PAI) of WGP and RHA were assessed in accordance with **EN 450-1:2013** guidelines. This involved evaluating the compressive strength of blended cement pastes containing 25% WGP or RHA against pure OPC paste, ensuring compliance with the standard's requirement of a minimum PAI of 75% at 28 days.

The chemical composition of OPC, RHA, and CCA was determined using X-ray fluorescence (XRF) analysis. For instance, RHA's high amorphous silica content (>80% SiO_2) and WGP's alkali-silica reactivity mitigation properties were confirmed through XRF.

Findings

The results of the seven-day mechanical test showed that mortars containing both rice husk ash (RHA) and waste glass powder (WGP) performed reliable results as control samples. All tested mix ratios, specifically 0R:25G (0% RHA, 25% WGP), 6.25R:18.75G (6.25% RHA, 18.75% WGP), 12.5R:12.5G (12.5% RHA, 12.5% WGP), 18.75R:6.25G (18.75% RHA, 6.25% WGP), and 25R:0G (25% RHA, 0% WGP), had noticeably high flexural and compressive strength values. These findings indicate that WGP and RHA, either separately or in combination, improved the mortar's structural integrity even when used to partially replace cement.

The pozzolanic activity index (PAI) for both RHA and WGP exceeded the minimum threshold of 75% as stipulated by **EN 450-1:2013**, validating their efficacy as supplementary cementitious materials (SCMs). For instance, RHA and WGP achieved a PAI of above 75%.

Conclusion

This study confirms that both waste glass powder (WGP) and rice husk ash (RHA) can be effectively utilized as partial substitutes for Ordinary Portland Cement (OPC) in mortar production. The findings align with the criteria outlined in the **EN 450-1:2013** standard, indicating that these materials meet the requirements for supplementary cementitious materials (SCMs).

This research highlights the broader potential of incorporating agricultural and industrial waste materials to promote more sustainable and environmentally conscious construction practices. The construction industry, a significant waste producer, can benefit from adopting circular economic principles by using materials like WGP and RHA, reducing landfill waste and lowering the demand for virgin materials.

This strategy encourages resource conservation and waste reduction, which are essential for reducing the negative effects of construction on the environment. The construction industry may decrease its carbon footprint and help create a more sustainable future through using these creative and sustainable waste management techniques.

References

Doe, J. (2022). The impact of waste materials on concrete strength. Journal of Materials Science, 57(10), 1234–1245.
Doe, J., Smith, A., & Johnson, K. (2022). Sustainable construction practices. Journal of Environmental Engineering, 148(4), 04022001.
Smith, J. (2020). Sustainable building materials. New York, NY: Routledge.
Johnson, K., & Thompson, R. (2019). Green construction techniques. London, UK: Sage Publications.
Doe, J. (2022). Using waste glass in concrete. In Proceedings of the International Conference on Sustainable Materials (pp. 123–135). New York, NY: ACM.
Smith, J. (2022). The use of waste materials in concrete (master's thesis). University of Technology.
ASTM C618. (Year). Standard specification for coal fly ash and raw or calcined natural pozzolan for use in concrete. American Society for Testing and Materials.
EN 196-1. (2016). Methods of testing cement – Part 1: Determination of strength. European Committee for Standardization.
EN 450-1. (2013). Fly ash for concrete – Part 1: Definition, specifications, and conformity criteria. European Committee for Standardization.

SUSTAINABILITY

Biodiversity

Climate Change Mitigation

Life Cycle Assessment

Reinforced Concrete Structures

Smart and Sustainable Cities

Sustainable Development Goals

Water and Waste Management

Investigation of Green Buildings Towards Net Zero Carbon Cities: Example in ITU Ayazağa Campus

Merve Maçin[a], İsmail Toröz[a]

[a] Istanbul Technical University, Department of Environmental Engineering, Environmental Sciences Engineering and Management Program, Turkey
macin16@itu.edu.tr

Keywords: Zero-Carbon Building, Carbon Emissions, Net-Zero Carbon, Green Building Certificate, LEED.

Aim

Anthropogenic activities resulted in an increase in pre-industrial global surface temperature and led to both long-term and short-term variations in climate. Increasing greenhouse gas emissions as a result of increased global industrialization and urbanization have triggered this climate change, creating one of the biggest global problems of today. Carbon dioxide is the most abundant greenhouse gas and has the most detrimental effect on the environment (Chen et al. 2023). The goal of carbon neutrality is to reduce or eliminate greenhouse gas through carbon capture, storage, and conversion within a specific period of time, resulting in 'zero emission' of greenhouse gas emissions (Oxford Net Zero, 2022).

The development of technology and modern lifestyle is causing urbanization to increase day by day. In 2050, cities will be home to 68% of the world's population. Cities occupy just 3 percent of the Earth's land but account for 60-80% of energy consumption and at least 70 % of carbon emissions (United Nations, 2018).

The European building stock consumes approximately 40% of primary energy and it is emissions responsible for 36% of the European Union (EU) greenhouse. A significant reduction of building energy demand is a requisite to meet Europe's greenhouse gas emissions reduction targets (JRC Science for Policy Report, 2016). The building sector plays a key role in the long-term strategy on the reduction of greenhouse gas emissions for the European Union as well as to achieve other objectives of the European Green Deal (European Commission, 2023). Buildings that are designed to reduce environmental impacts by using strategies for reducing energy and natural resource use are defined as sustainable, green or zero energy buildings. The LEED system is the most popular green building rating system in the world. Because LEED is a certification system based on sustainability and discusses the topics of energy and buildings, climate and site, building envelope and building systems in detail, it includes the steps led to achieve zero energy buildings.

Governments and local authorities create their own strategy for reaching net zero goal. To solve complex systems like greenhouse gas mitigation, future pathways should be carefully planned. The fact that data collection is a difficult and time-consuming process causes many researchers to use general data from common databases such as eco-invent instead of site-specific data. Databases are updated irregularly and often years later. Therefore, the use of general database information generally reduces the suitability and representation of the study (Hauschild M.Z., 2018). Therefore, in order to obtain the most accurate data, it is necessary to increase the amount of "primary data" by narrowing the field of study to pilot region as in this thesis study. This study investigates whether the current green building certification systems, specifically LEED, provide a sufficient framework of indicators to effectively meet the net zero carbon target.

Material and Method

Istanbul Technical University Department of Information Technologies Building was selected as a case study because of the data availability. This project, designed in 2017 and completed in 2020, with an area of 8500 m². The building received the prestigious LEED Platinum Certification, the top recognition for green buildings. It incorporates sustainable design principles, including orientation, harmony with the landscape, use of natural light, efficient water usage, material optimization, as well as renewable energy and energy efficiency aiming to decrease carbon footprint.

LEED evaluates buildings in 9 main categories. These are integrative processes, location and transport, sustainable sites, water efficiency, energy and atmosphere, material and resource, indoor environmental quality, innovation, and regional priority.

The carbon footprint of the building while operating was calculated to better understand the relationship between LEED and net zero. The GHG Protocol was followed in the preparation of this greenhouse gas inventory. Scope 1; covers direct greenhouse gas emissions generated on site. Scope 2; includes net indirect emissions from energy imports and exports. Scope 3; includes other indirect greenhouse gas emissions, such as product transport by third parties, outsourcing of core activities and off-site waste disposal/ management activities, water consumption and procurement related emissions.

Findings

The Department of Information Technologies Building released 1503 tCO_2eq greenhouse gases in 2020. But it is found that it was increased to 1928 tCO_2eq in 2021. Scope 2 is the highest contributor to the greenhouse gas emissions of the building with 1112 tCO_2eq due to electricity consumption of servers in the Information Technologies Building. The total emission value of 0.23 tCO_2eq/m^2 in 2021 is noteworthy when compared to previous studies. Güereca et al. (2013) found 0.060 tCO_2eq/m^2 emissions for building in a university in Mexico. According to Ozawa-Meida et al. (2013) and Bailey and LaPoint (2016), there was a wide range of results between 0.350 tCO_2eq/m^2 and 0.150 tCO_2eq/m^2.

Although this study provides a detailed evaluation, it's necessary to recognize some limitations that could affect the accuracy of the values reported. Findings can be affected by data availability. Comparing and interpreting results can be hindered by the fact that LEED parameters do not exactly match carbon footprint emissions.

Conclusion

The implementation of green building certification systems is more expensive and takes longer than conventional systems. However, net-zero carbon emissions targeted credits of green building systems can be beneficial for the environment, society, and economy, and this can lead to sustainable development. Although this study was restricted to one building, university campus green building and carbon footprint studies are valuable benchmarks for future improvements and comparative assessments.

References

Bailey, G., & LaPoint, T. (2016). Comparing greenhouse gas emissions across Texas universities. Sustainability, 8, 1–24.

Chen, L., Huang, L., Hua, J., Chen, Z., Wei, L., Osman, A. I., Fawzy, S., Rooney, D. W., Dong, L., & Yap, P.-S. (2023). Green construction for low-carbon cities: A review. Environmental Chemistry Letters, 21(3), 1627–1657.

European Commission. (2023). Annex 2: Report on renovation of the national stock of residential and non-residential buildings and on nearly zero-energy buildings. Science for Policy Report.

Güereca, L. P., Torres, N., & Noyola, A. (2013). Carbon footprint as a basis for a cleaner research institute in Mexico. Journal of Cleaner Production, 47, 396–403.

Hauschild, M. Z., Olsen, S. I., & Rosenbaum, R. K. (Eds.). (2018). Life cycle assessment: Theory and practice (1st ed.). Springer International Publishing.

Joint Research Centre (JRC). (2016). Synthesis report on the assessment of Member States' building renovation strategies. European Commission, Science for Policy Report.

Oxford Net Zero. (2022). What is net zero. Oxford Net Zero Initiative.

Ozawa-Meida, L., Brockway, P., Letten, K., Davies, J., & Fleming, P. (2013). Measuring carbon performance in a UK university through a consumption-based carbon footprint: De Montfort University case study. Journal of Cleaner Production, 56, 185–198.

An Inclusive Digital Accessibility Policy for Individuals with Disabilities

Oylum Bülbül[a], Hatice Ayataç[b]

[a] Istanbul Technical University/Graduate School, Urban Design Program, Türkiye
[b] Istanbul Technical University /Faculty of Architecture, Urban and Regional Planning Department, Türkiye
bulbuloyl@itu.edu.tr

Keywords: Inclusivity in Digital Content, Web Accessibility, Accessible Web, Inclusive Web, Design for Accessibility.

Aim

Cities are a network of physical infrastructures, natural spaces, and individuals. Today, the use of urban living spaces is built around digital data. As data-based access between individuals, institutions and urban services becomes stronger, access to urban quality similarly increases.

Digital access means access to education, healthcare, financial services, civil participation, and many other areas. Beyond being an optional service, it can be considered a social human right.

Digital technology is unevenly distributed across countries, genders, ethnicities and socio-economic strata worldwide. It is expected that digital access in everyday life should be inclusive and widely available to people from all socioeconomic structures.

The global crises and natural disasters we have experienced in recent years have brought the concept of digital inclusion to the forefront as a pressing need worldwide. It is considered a fundamental human right for people with disabilities and individuals under social protection to be in contact with their relatives and to receive public services like other individuals.

According to the study of Campoverde-Molina, Luján-Mora, S. & Valverde, L. (2021), the accessibility of university websites worldwide was addressed in the form of a comprehensive and systematic literature review. This review covering the years 2002-2019 was conducted and university websites published in 42 international articles that are pioneers in the field of accessibility were selected. The results of this study were obtained through an analysis and synthesis of evaluations of 9,140 universities in 67 countries. Of the 188 university web sites, 79 were found to be accessible in 2002. The results indicated that higher education websites become progressively inaccessible as complexity increases in 2005.

Findings from research conducted in recent years on the access of disabled students in higher education institutions in Türkiye to digital platforms are noteworthy in bringing the issue of digital accessibility to the agenda. The reviewed study provides an assessment of the accessibility, usability, quality performance and readability aspects of all Turkish public and private university websites. The majority of them did not meet the WCAG 2.0 accessibility criteria. In this study, out of 110 public university websites and 69 private university websites, only 10 public and 4 private university websites achieved basic level compliance (Akgül, Y., (2021).

All these results show that usability, quality performance and readability are low and emphasize that Turkish universities need to allocate more resources to make their websites more accessible, inclusive, usable and high-quality performance for all users.

In recent years, the findings of research on the access of students with disabilities in higher education institutions in Türkiye to digital platforms are noteworthy in bringing the issue of digital accessibility to the agenda.

At this point, the question of "Why is digital accessibility important and how can it be achieved?" comes to the fore.

The goal of "Making cities and human settlements inclusive, safe, resilient and sustainable" within the scope of Article 11 "Sustainable Cities and Communities" of the United Nations Sustainable Development Goals, to which our country is a party, is also a basis for this study (UNESCO National Commission for Türkiye, 2025). In this

direction, the "National Sustainable Development Coordination Board" was established on 19.02.2022 by the Strategy and Budget Presidency of Türkiye and the dissemination of inclusion and accessibility at the national level through all public structures was institutionalized (Türkiye Strategy and Budget Presidency, 2025).

In addition to the target of "By 2030, improve inclusive and sustainable urbanization and capacities for participatory, integrated and sustainable urban planning and management in all countries" (Target 11.3), it is seen that our country supports inclusive digital access by participating in the "Digital inclusion traveler" platform created within the United Nations (Türkiye Strategy and Budget Directorate, 2025).

In this context, the following questions become a priority:

- With what methods and elements can digital web content be handled inclusively and accessible?
- What are the elements that can be developed to ensure that digital access is widespread in an inclusive manner and can be used as equally as possible by people from all segments of society?

The research focuses on examining how inclusive and accessible digital content is presented in various examples based on the smart city concept, aiming to analyze and compare recommendations developed on this subject through international and national examples. This guide will try to reveal how accessible digital web content should be for all users, primarily individuals with disabilities, by examining university websites. The study, which is aimed to be developed in this context, will primarily serve as a digital application guide for university websites.

The infrastructure to be proposed will provide clues about how websites should be designed for users with disabilities, as well as the institutional infrastructure that provides inclusive digital accessibility in this regard (Bulbul, O., 2025).

Material and Method

Starting with the basic research questions, the study first examined the conceptual framework of inclusive and accessible digital content. Comparative analyses are planned based on international and national examples. University websites were compared in terms of technical aspects within the framework of accessibility guidelines (W3C). As a result of the comparison, the institutional structures of the two universities that stand out with the optimum most inclusive, and accessible features were examined in detail, and the guide proposed in the conclusion was based on this data. The study to be developed will primarily serve as a user experience-oriented digital application guide for university websites.

Findings

The basic elements which keep accessibility on the agenda and require the development of different design themes, are defined as "web content accessibility guidelines" (Firth, A., 2020).

Web content accessibility guidelines have a common purpose not only for people with disabilities but also for all users and all designers who produce tools for these users. When a web page is accessible, it can be said that accessibility is possible for everyone who uses it. The "Accessibility Guidelines" mentioned in the introduction (TÜBİTAK BİLGEM, 2025), produced for public websites, which were formalized in our country's legislation in 2022 (Türkiye Strategy and Budget Directorate, 2025), formed the basis of the accessibility and inclusion guidelines evaluated in this study.

This study focuses on website users with disabilities. These users may not be able to see, hear, move, or process some information easily or at all. They may have difficulty reading or understanding the text. They may not be able to use a keyboard or mouse effectively. They may have a text-only screen, a small screen, or a slow and unhealthy internet connection. They may not be fluent in or understand the language in which the document is written. They may be in a situation where their hands, eyes or ears are busy. They may have an older version of a browser, a completely different browser, a voice browser, or a different operating system (Firth, A., 2020). Accessible and inclusive web design is expected to meet the needs that arise from such problems.

Design guidelines examine typical scenarios that can create problems for users with specific disabilities and provide solutions for accessible design. Through design guidelines, content developers can create pages that

transform conveniently. Conversion pages remain accessible despite any of these limitations, including physical, sensory, and cognitive disabilities, limitations, and technological barriers. Here are some elements of web design guidelines;

- Adding Appropriate Alternative Text to Images
- Correct Selection of Headings
- Accessible Subfiles
- File Extensions that Preserve the Appearance
- Using World Wide Web Association Standards and Customized Bookmarks
- Adding Labels to Form Fields
- Grouping Form Fields
- Marking Tables
- Defining Text Language
- Controlling Color Contrast
- Avoiding Small Fonts
- Spaces
- Focusing Tools
- Correct Use of Text Data

A Digital Accessibility Policy was created based on the examples evaluated with accessibility guidelines. It has been defined which units will constitute the institutional infrastructure that ensures that these guidelines are user-oriented and inclusive within universities (Figure 1. Digital Accessibility Organizational Structure; Bulbul, O.,2025).

Figure 1. Digital Accessibility Organizational Structure (Bulbul, O., 2025).

In the evaluation that emerged as a result of the analysis;

- Establishment of an implementation team that identifies areas of responsibility and supervises the work to be carried out in line with the needs,
- The need for coordination between the implementation team and platform partners,
- Continuous development of the implementation tools by the Digital Accessibility Committee and the implementation team,
- The need for regular updates to reflect new technological and structural developments and feedback from within the university,

- Promoting equal access for all users and the widespread use of digital content created to improve the online media experience were found to be the key elements of the solution for access to digital accessibility (Figure 2. Digital Accessibility Policy; Bulbul, O.,2025).

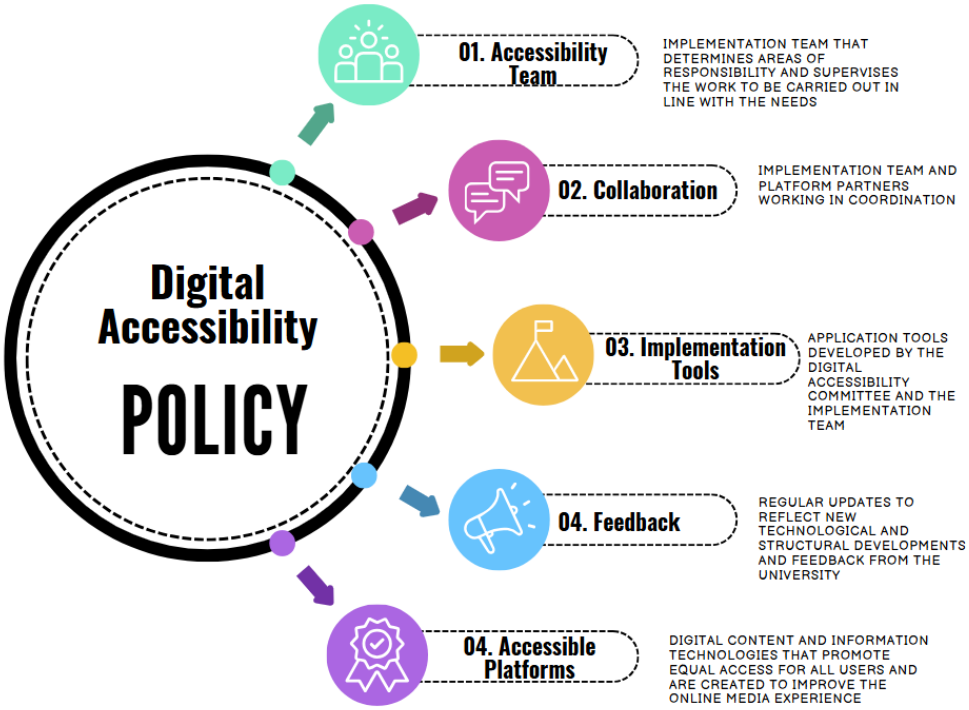

Figure 2. Digital Accessibility Policy (Bulbul, O., 2025).

There are many studies, showing that some aesthetic features (Mbipom, G., Harper, S.,2011) and visual design elements (Regan, B., 2004) that improve user experience directly interact with accessibility (Inal, Y., Guribye, F., Rajanen, D., Rajanen, M., & Rost, M. (2020).

Moreover, researches show that user experience is significantly related to perceived digital accessibility qualities (Aizpurua, A., Harper, S. & Vigo, M.,2016). It is seen that methodologies related to the user-centered digital web design approach affect accessibility (Yesilada, Y., Brajnik, G., Vigo, M., Harper, S., 2015).

Conclusion

The digital accessibility policy is established to promote equal access to digital content and information technologies for all users, with a priority on those with disabilities, and to improve the user experience of information technologies and digital/online media. This policy means that a disabled individual has the opportunity to access the same information, interact with the same people and benefit from the same services as a non-disabled individual in an equal manner and with the same ease of use.

It has been determined through the examples examined that the accessibility policy to be determined and operationalized in universities is not only a set of rules consisting of design guidelines but also inclusive and accessible when it is supported by a human, that is, a user-oriented institutional structure. This study provides clues on the elements of an accessible and inclusive institutional structure.

References

Aizpurua, A., Harper, S., Vigo, M. (2016). Exploring the relationship between web accessibility and user experience. International Journal of Human Computer Studies, (pp. 91,13-23).
Url-1 https://doi.org/10.1016/j.ijhcs.2016.03.008, date retrieved 23.05.2025
Akgül, Y., (2021). Accessibility, usability, quality performance, and readability evaluation of university websites of Turkey, (pp. 157-170).
Url-2 https://doi.org/10.1007/s10209-020-00715-w , date retrieved 23.05.2025
Bulbul, O., (2025). MS Thesis, Türkiye, Istanbul Technical University, Institute of Science, Urban Design Program, "A User Experience-Oriented Guide to Inclusive and Accessible Digital Content".
Campoverde-Molina, M., Luján-Mora, S. & Valverde, L., (2021). Accessibility of university websites worldwide: a systematic literature review, (pp. 133–168).
Url-3 https://doi.org/10.1007/s10209-021-00825-z , date retrieved 23.05.2025
Firth, A., (2020); Practical Web Inclusion and Accessibility, APress, London, (pp. 978-1-4842-5452-3).
Url-4 https://link.springer.com/book/10.1007/978-1-4842-5452-3, date retrieved 22.02.2025
Inal, Y., Guribye, F., Rajanen, D., Rajanen, M., & Rost, M. (2020). Perspectives and Practices of Digital Accessibility: A Survey of User Experience Professionals in Nordic Countries. Nordic Conference on Human-Computer Interaction.
Url-5 https://doi.org/10.1145/3419249.3420119, date retrieved 23.05.2025
Mbipom, G., Harper, S. (2011). The interplay between web aesthetics and accessibility. In Proceedings of the 13th International ACM SIGACCESS Conference on Computers and Accessibility (pp. 147-154).
Url-6 https://dl.acm.org/doi/10.1145/2049536.2049564, date retrieved 23.05.2025
Regan, B. (2004). Accessibility and design: A failure of the imagination. In Proceedings of the 2004 International Cross-Disciplinary Workshop on Web Accessibility (W4A) (pp. 29-37).
Url-7 https://doi.org/10.1145/990657.990663, date retrieved 23.05.2025
TÜBİTAK BİLGEM, The Public Internet Sites Guide (KAMİS) Project
Url-8 https://bilgem.tubitak.gov.tr/yte/kamis/, date retrieved 22.02.2025
Türkiye Strategy and Budget Directorate
Url-9 http://www.surdurulebilirkalkinma.gov.tr/amaclari/sehirleri-ve-yerlesim-yerlerini-kapsayici-guvenli-dayanikli-ve-surdurulebilir-hale-getirmek/ date retrieved 22.02.2025
Türkiye Strategy and Budget Presidency, Presidential Circular
Url-10 http://www.surdurulebilirkalkinma.gov.tr/2022-12-sayili-cumhurbaskanligi-genelgesiyle-ulusal-surdurulebilir-kalkinma-koordinasyon-kurulu-kurulmustur/, date retrieved 22.02.2025
UNESCO National Commission for Turkey Specialized Committee on Sustainable Development 2030 Goals
Url-11 https://www.unesco.org.tr/Pages/108/219/S%C3%BCrd%C3%BCr%C3%BClebilir-Kalk%C4%B1nma-2030-Hedefleri-%C4%B0htisas-Komitesi date retrieved 22.02.2025
W3C - World Wide Web Consortium, Web Standards
Url-12 https://www.w3.org/standards/, date retrieved 22.02.2025
W3C-Web Accessibility Initiative-WAI
Url-13 WCAG 2 Overview | Web Accessibility Initiative (WAI) | W3C date retrieved 22.02.2025
Yesilada, Y., Brajnik, G., Vigo, M., Harper, S. (2015). Exploring perceptions of web accessibility: a survey approach. Behaviour & Information Technology, 34(2), (pp. 119-134).
Url-14 https://doi.org/10.1080/0144929X.2013.848238, date retrieved 23.05.2025

SUSTAINABILITY

Biodiversity

Climate Change Mitigation

Life Cycle Assessment

Reinforced Concrete Structures

Smart and Sustainable Cities

Sustainable Development Goals

Water and Waste Management

Enhanced Efficiency of PLA-Based Membranes via Optimizing Coagulation Bath Temperature

Rana Memarzadeh[a], Vahid Vatanpour[b], Mohhamadreza Nofar[a]

[a] Istanbul Technical University, Polymer Science and Technology Program, Türkiye
[b] Istanbul Technical University, Environmental Engineering Program, Türkiye
orumieh23@itu.edu

Keywords: Polylactide (PLA), Membrane Production, Coagulation Bath Temperature, Phase Inversion, Permeability, Porosity.

Porous membrane technology has garnered significant attention in the fields of separation because of its extraordinary contributions to green chemistry and sustainable development. The porous membranes fabricated from polylactic acid (PLA) possess numerous advantages, including high permeability, biodegradability, and excellent biocompatibility. As a result, they exhibit promising prospects for various applications, such as water purification. Therefore, studies on the fabrication of PLA- based membranes, have begun to attract much attention in world science.

Permeability, dye rejection, and mechanical properties characterized the selected membranes. The results indicate that increased coagulation bath temperatures provide higher pore size and porosity with enhanced permeability but reduced mechanical strength. Lower temperatures provided more closed structures with reduced permeability. These results provide a deep insight into process-structure-property relationships in the production of PLA membranes, which are valuable guidelines for optimizing membrane performance in different applications.

Aim

Water purification is a critical global challenge, driving the need for advanced membrane technologies that are efficient, sustainable, and environmentally friendly. Conventional membranes, typically made from petroleum-derived, non-degradable synthetic polymers like polyether sulfone (PES) and polysulfone (PSf), offer robust performance but suffer from poor biocompatibility and significant environmental drawbacks due to disposal issues(L. Zhu et al., 2015) . In response, there is growing interest in developing membranes from biobased and biodegradable materials. Poly (lactic acid) (PLA) has emerged as a promising candidate for membrane fabrication, owing to its stable crystallization for porosity formation, excellent mechanical strength, thermal resistance, and renewable, biodegradable nature(Gao et al., 2014, 2015; Xiong et al., 2016; L. J. Zhu et al., 2015) . Additionally, cellulose nanocrystals (CNCs) have garnered attention as membrane modification materials for water treatment due to their abundant, sustainable, and biodegradable properties, coupled with high strength, large surface area, and functional chemical groups that enhance porosity, hydrophilicity, permeability, tensile strength, and antifouling performance(Bai et al., 2022). To further enhance membrane functionality techniques such as blending, surface coating or grafting, and interfacial polymerization are used Mixed matrix membranes (MMMs) incorporate nanomaterials into polymer matrices through blending or coating, followed by phase inversion, to create ultrafiltration membranes with superior physicochemical properties, including increased hydrophilicity, electronegativity, and mechanical strength, as well as enhanced permeability and foulant rejection(L. Zhu et al., 2015) . This work explores the potential of PLA-based membranes, NC modifications, and MMM fabrication as sustainable solutions for advancing water purification technologies.

This research attempts to estimate improving the sustainability of membrane manufacturing to produce biocompatible membranes by replacing synthetic polymers with bio-based polymers by using organic nanomaterials and employing environmentally friendly membrane fabrication methods like phase inversion casting while minimizing waste generation and energy consumption. The phase inversion process is a common membrane preparation method that is extremely sensitive to the coagulation bath conditions, and temperature is one of the key parameters in controlling the morphology and performance of membranes(Pabby et al., 2023) . This

study investigates how coagulation bath temperature affects the structure and functionality of PLA-based membranes. The technique of non-solvent induced phase separation (NIPS) fabricated membranes at various coagulation bath temperatures.

Material and Method

3.1 Materials

Polylactic acid (Ingeo 4060D) from Nature Works LLC (Plymouth, MN, USA), Spray-dried Crystalline nanocelluloses CNCs were provided by celluForce (Montreal,Canada), Dimethyl sulfoxide (DMSO), Polyvinylpyrrolidone (PVP, Mn = 4000), reactive red 120 (RR120, Mw = 1136.3 g/mol), reactive black 5 (RB5, Mw = 991.8 g/mol), and bovine serum albumin (BSA) were gained from Sigma-Aldrich.

3.2 Preparation of Membrane

Mixed matrix membranes were prepared by using Phase inversion methods containing First, PVP (1.0 wt%) was mixed with DMSO as a solvent and stirred for 30 min. Then different amounts of CNC (0.5, 1.0, and 2.0 wt%) were added to the above solution after the sonication of mixed solutions for dispersing the nanomaterials, after that, 18 wt% of PLA was dissolved in the prepared suspension and the obtained polymeric solution was stirred for 24 h. The degassing process was carried out by putting the polymeric solution in a heating oven for 3 h at 70 ℃ to remove any air bubbles from the solutions. The fabrication of membranes was done by pouring the degassed solution over the clean glasses with a thickness of 150 µm using an applicator and immersing it into a water bath at determined temperatures (10 °C,15 °C,20°C) to accomplish the phase inversion process. Eventually, the prepared membranes were kept distilled.

3.3 Characterization of the fabricated membranes

A dead-end filtration setup with four identical cells conjoined to a 20L reservoir was implemented for all filtration proficiency experiments. The performance of the membranes was assessed by an effective surface area of 19.63 cm^2. Before running the filtration tests, all the membranes were pre-compacted by passing the distilled water under the pressure of 0.2 MPa for 20 min. Then, the filtration of pure water was done for 60 min at an operating pressure of 0.1 MPa, and the first pure water flux (Jw_1) was obtained. In addition, the filtration of different organic solutions, including BSA protein (500 mg/L), RB5 dye (150 mg/L), and RR120 dye (150 mg/L) were carried out at the same pressure of 0.2 MPa. The permeated flux (J) of membranes was determined by using Eq. (1) (Gao et al., 2014):

$$J = \frac{V}{A \times t} \quad (1)$$

Here, A, V, and t are the effective area of membrane (m^2), the permeated solution volume (L), and the time of permeation (h), respectively., The BSA solution with the initial concentration of 500 mg/L was filtered for 60 min immediately after pure water filtration for evaluation of the antifouling property of the membranes, and its flux was recorded (J_p). In the following protein solution filtering, the fouled membranes were rinsed with pure water and immersed in distilled water for 20 min for the removal of the cake layer. Afterward, the membranes were placed in cells, and the second water flux (Jw_2) was recorded for 60 min at the same operational condition. Finally, FRR was calculated by using Jw_1 and Jw_2 based on Eq (2).

$$FRR(\%) = \left(\frac{Jw_2}{Jw_1}\right) \times 100 \quad (2)$$

The rejections of RB5 and RR120 were measured by Eq. (3):

$$R(\%) = \left(1 - \left(\frac{C_P}{C_f}\right)\right) \times 100 \quad (3)$$

Where the concentration of pollutant molecules in feed and permeate solutions are defined by C_p and C_f, respectively.

Findings

The wetting properties of membranes were evaluated by measuring the water contact angle as shown in Table 1. Membrane PLA-neat possessed high contact angles (top-surface with 77.981 ± 0.07°), which related to the intrinsic hydrophobic nature of PLA(Kian et al., 2022) . However, the addition CNCs to the membranes resulted in reduced contact angles indicating improved hydrophilicity on the surface of the membrane. These changes aligned well with the increase of pure water and Dye fluxes that penetrated through the membranes. Also, the permeability was observed to increase significantly for the 1.0 wt% CNC/20 C° membranes, which is likely due to the presence of macro void structures. Therefore, both surface wettability and pore structure were critical factors in permeability(Xiong et al., 2017).

Table 1. Contact angle, overall porosity, and tensile strength of the CNC/PLA nanoom posite membranes.

Membrane	Contact angle (°)	Overall Porosity (%)	Tensile Strength (Mpa)
1.0 wt% /10 ° C	67.01±0.17	62.20±0.86	32.98
1.0 wt% /15 ° C	67.09±0.05	67.11±1.6	27.05
1.0 wt% /20 ° C	67.01±0.35	68.05±2.9	25.1

The mechanical strength of membranes is an important characterization aspect since it is crucial in industrial applications as well as module configuration [10]. In this context, the temperature of the coagulation bath influences the rate of solvent-non solvent exchange and the solidification of the polymer solution. As reported in Table 1, the most significant enhancement is related to 0.1wt% CNC/10 °C the membrane with 32.98 MPa in comparison with 22.3 MPa of the bare membrane(Kian et al., 2021). This improvement can be attributed that lower temperatures can slow the process, allowing for more controlled mass transfer and potentially enhancing mechanical properties by reducing defects.

Membrane was evaluated for rejection of dye (Fig1.C). 0.1wt% CNC/10 °C revealed the highest removal for RB5 with 85.46% and RR120 with 96.62%. This was probably the small pore size. The highest permeate filtration through the membrane for 0.1wt% CNC/20 °C as compared to the others. Water flux penetration dramatically increased from 482.6 to 5952 L/m$^{2.}$.

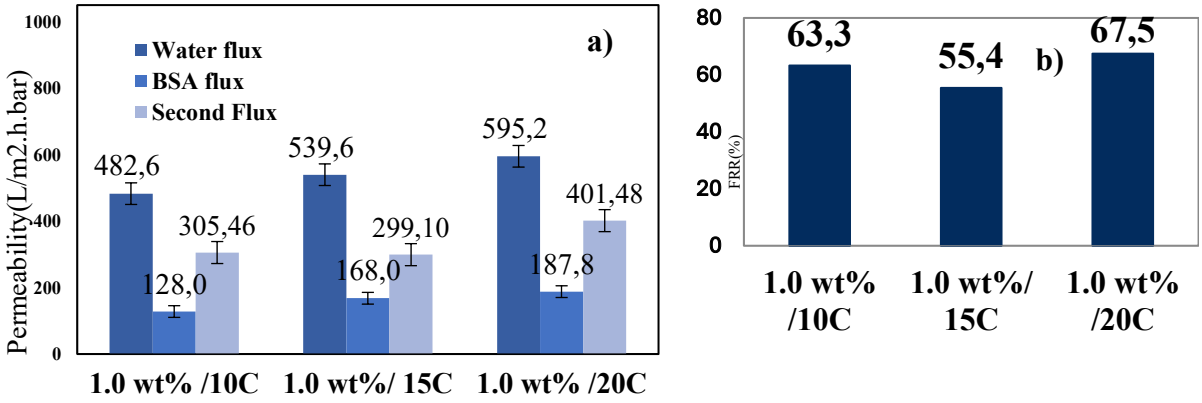

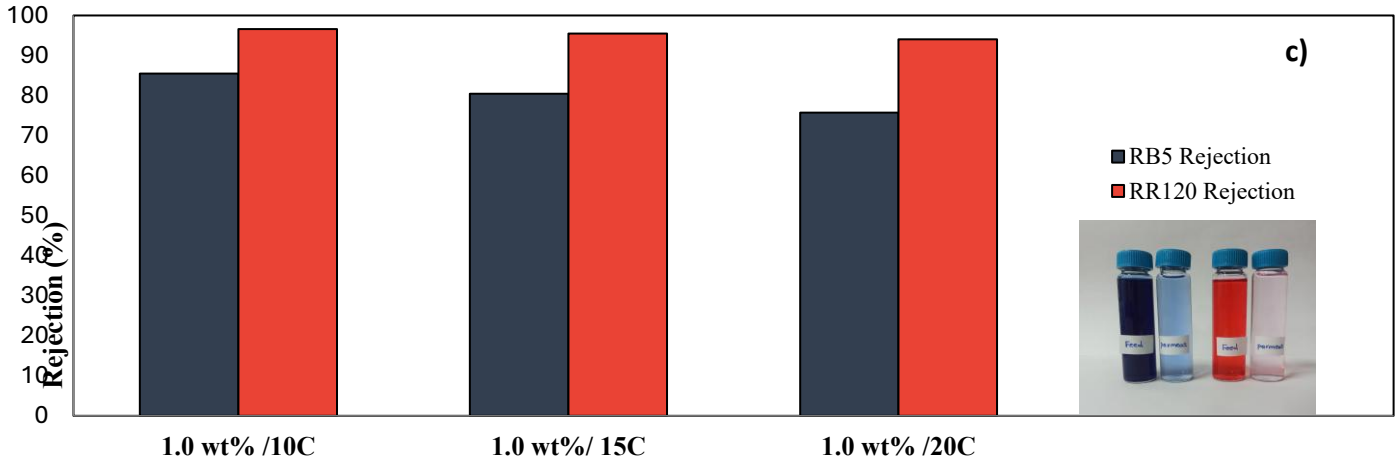

Figure 1. a) Pure water and BSA solution permeability of CNC nanocomposite membranes (average of at least four replications), b) Flux Recovery Ratio of the membranes C) Dye separation results of CNC nanocomposite membranes.

Conclusion

In this investigation, we prepared and characterized nanocellulose-enhanced PLA membranes, confirming their effectiveness systematically for water filtration application. The surface wettability was significantly improved for 0.1wt% CNC/20 °C membranes due to the presence of nanocellulose, which enhance hydrophilicity by introducing hydroxyl group on the membrane surface. In addition, 0.1 wt% CNC/10 °C membrane showed improvement in mechanical properties in terms of tensile strength, indicating their ability to withstand high pressure during water filtration. This was further evidenced by the filtration performance evaluation, which showed the 0.1wt% CNC/20 C° membranes presented the highest average water permeability of 595.2 L/m2h under the applied pressure 0.1MPa. As a result, these membranes are considered successful membranes that would be used for water filtration applications in the future.

References

Bai, L., Ding, A., Li, G., & Liang, H. (2022). Application of cellulose nanocrystals in water treatment membranes: A review. Chemosphere, 308, 136426. doi: 10.1016/J.CHEMOSPHERE.2022.136426

Gao, A., Liu, F., Shi, H., & Xue, L. (2015). Controllable transition from finger-like pores to inter-connected pores of PLLA membranes. Journal of Membrane Science, 478, 96–104. doi: 10.1016/J.MEMSCI.2015.01.004

Gao, A., Liu, F., & Xue, L. (2014). Preparation and evaluation of heparin-immobilized poly (lactic acid) (PLA) membrane for hemodialysis. Journal of Membrane Science, 452, 390–399. doi: 10.1016/J.MEMSCI.2013.10.016

Kian, L. K., Fouad, H., Jawaid, M., & Karim, Z. (2022). Crystalline nanocellulose based sustainable nanoscopic composite membrane production: removal of metal ions from water. Cellulose, 29(7), 3803–3816. doi: 10.1007/S10570-022-04494-W/METRICS

Kian, L. K., Jawaid, M., Alamery, S., & Vaseashta, A. (2021). Fabrication and Characterization of Novel Poly(d-Lactic Acid) Nanocomposite Membrane for Water Filtration Purpose. Nanomaterials 2021, Vol. 11, Page 255, 11(2), 255. doi: 10.3390/NANO11020255

Pabby, A. K., Wickramasinghe, S. R., & Sastre, A. M. (2023). Handbook of Membrane Separations: Chemical, Pharmaceutical, Food, and Biotechnological Applications, Third Edition. Handbook of Membrane Separations: Chemical, Pharmaceutical, Food, and Biotechnological Applications, Third Edition, 1–572. doi: 10.1201/9781003285656/HANDBOOK-MEMBRANE-SEPARATIONS-ANIL-PABBY-ANA-MARIA-SASTRE-RANIL-WICKRAMASINGHE/ACCESSIBILITY-INFORMATION

Xiong, Z., Liu, F., Gao, A., Lin, H., Yu, X., Wang, Y., & Wang, Y. (2016). Investigation of the heat resistance, wettability and hemocompatibility of a polylactide membrane via surface crosslinking induced crystallization. RSC Advances, 6(25), 20492–20499. doi: 10.1039/C5RA27030H

Xiong, Z., Zhong, Y., Lin, H., Liu, F., Li, T., & Li, J. (2017). PDLA/PLLA ultrafiltration membrane with excellent permeability, rejection and fouling resistance via stereocomplexation. Journal of Membrane Science, 533, 103–111. doi: 10.1016/J.MEMSCI.2017.03.028

Zhu, L. J., Liu, F., Yu, X. M., Gao, A. L., & Xue, L. X. (2015). Surface zwitterionization of hemocompatible poly(lactic acid) membranes for hemodiafiltration. Journal of Membrane Science, 475, 469–479. doi: 10.1016/J.MEMSCI.2014.11.004

Zhu, L., Liu, F., Yu, X., & Xue, L. (2015). Poly(Lactic Acid) Hemodialysis Membranes with Poly(Lactic Acid)-block-Poly(2-Hydroxyethyl Methacrylate) Copolymer As Additive: Preparation, Characterization, and Performance. ACS Applied Materials and Interfaces, 7(32), 17748–17755. doi: 10.1021/ACSAMI.5B03951/ASSET/IMAGES/MEDIUM/AM-2015-03951Q_0008.GIF

SUSTAINABILITY

Biodiversity

Climate Change Mitigation

Life Cycle Assessment

Reinforced Concrete Structures

Smart and Sustainable Cities

Sustainable Development Goals

Water and Waste Management

Evaluating the Water Footprint of Textile Products: A Comparative Study of Wool and Cotton in Türkiye

Gizem Aydın[a], Börte Köse Mutlu[a]

[a]Istanbul Technical University, Department of Environmental Engineering, Environmental Sciences, Engineering and Management Programme, Türkiye
aydingi17@itu.edu.tr

Keywords: Water Footprint, Cotton Production, Wool Production, Textile Industry, Water Consumption.

Aim

Textile fibers are divided into two groups as natural fibers and chemical fibers, and natural fibers are classified as plant fibers, animal fibers and mineral fibers, forming the group obtained completely from nature. Cotton, which is a cellulose-based seed fiber, is a plant fiber, and fibers obtained from sheepskin (wool) are protein-based animal fibers [1]. The aim of this study is to calculate and evaluate the blue, green and grey water footprints of cotton production and wool production in Türkiye and to compare the water footprints of textile products with wool and cotton raw materials.

Introduction

The increasing global demand for freshwater, driven by population growth and industrial expansion, has intensified concerns over water scarcity and pollution. The concept of the water footprint, introduced by Hoekstra and Hung [2] and later refined by Chapagain and Hoekstra [3], offers a framework for assessing the freshwater required to produce goods and services [4]. The textile industry is one of the largest consumers of freshwater resources, with raw material production and industrial processing contributing significantly to global water consumption and pollution. Among textile fibers, cotton and wool stand out due to their widespread use and distinct environmental footprints [5]. Cotton, a cellulose-based seed fiber, demands extensive irrigation, resulting in a high blue water footprint. Conversely, wool, derived from sheep, has a considerable grey water footprint due to animal waste runoff and industrial processing. This study evaluates and compares the water footprints of cotton and wool production in Türkiye, highlighting their respective environmental impacts and the need for sustainable water management practices in the textile sector.

Material and Method

In this study, the concepts of water footprint and the calculation method are discussed within the framework defined by Hoekstra et al. [6]. Blue water footprint refers to the consumption of surface and groundwater resources during the production process of a product. This consumption occurs through evaporation of water, its transfer to another water source or its inclusion in the composition of the product. Green water footprint refers to the use of rainwater that does not turn into surface runoff. Grey water footprint is related to pollution and is defined as the amount of fresh water required to dilute a certain pollutant load. [6-7]

Data were collected from industry reports and agricultural statistics for Türkiye, supported by previous research. The analysis covers the entire production cycle, from raw material extraction to the initial stages of processing raw fibres into textiles, as these stages generate the highest water consumption and pollution levels. Cotton production data, including production volumes and land use, were obtained from the Turkish Ministry of Agriculture and Forestry. Wool production data, including sheep population and wool yields, were sourced from the Turkish Statistical Institute (TUIK) [8-9]. For pollutant limits, the Water Pollution Control Regulation approved on 31.12.2004 was taken as basis.

Agricultural and industrial processes were considered for the calculation of the cotton textile water footprint. Water use from precipitation was assessed to determine the contribution of cotton to the green water footprint in the agricultural process, irrigation water use was assessed to determine the contribution of cotton to the blue water

footprint, and chemical inputs from fertilisers used in cotton production were assessed to determine the contribution of cotton to the grey water footprint. In the industrial processing of cotton, bleaching, dyeing, printing and finishing processes were considered. The blue water footprint of the industrial process and the wastewater characterization of these processes were evaluated based on water consumption in these processes, and the grey water footprint was evaluated.

The water footprint of wool production was estimated according to the water consumption that must be met according to the feeding needs of the sheep, maintenance and drinking water, and the water demand spent in the industrial process of wool. The water footprint of wool production was estimated according to the water consumption that must be met according to the feeding needs of sheep, maintenance and drinking water, and the water demand spent in the industrial process of wool. The green water footprint due to grazing in the feeding needs of sheep, and the green, blue and grey water footprint required by the use of concentrated feed were taken into account. In addition, the drinking water required for sheep, maintenance, and cleaning purposes were considered within the scope of the blue water footprint. Within the scope of grey water footprint, the water footprint resulting from nutrition in sheep farming and the water footprint resulting from wastewater during the industrial process were discussed.

Findings

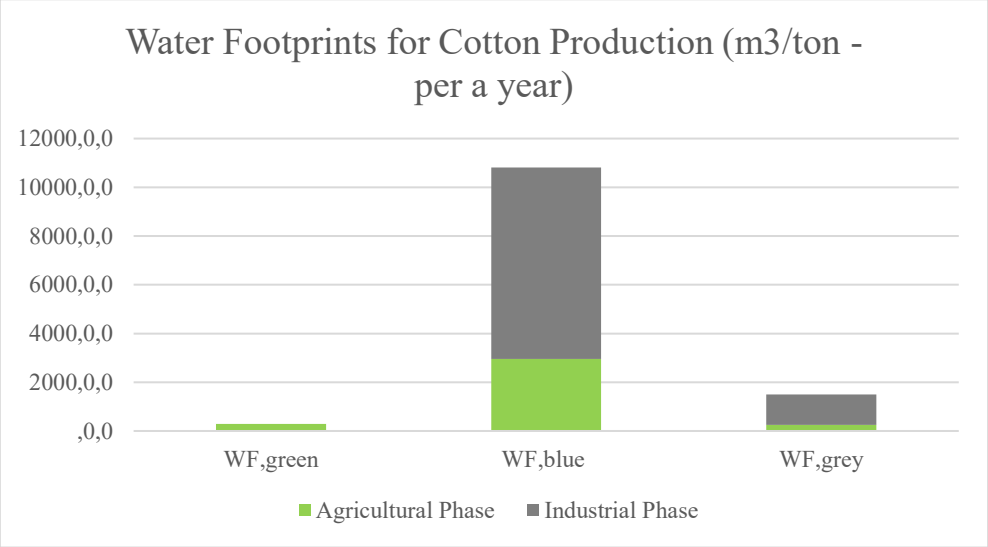

Figure 1. Water Footprints for Cotton Production.

The agricultural phase contributes to all types of water footprints, but stands out particularly in the blue water component, showing the critical impact of irrigation on cotton farming. Water-intensive processes during industrial processing (e.g. dyeing, printing, finishing), account for the largest share of total water use in the blue water footprint. The relatively low green water footprint suggests that cotton cultivation in the context studied relies more on artificial irrigation than on rainwater. The grey water footprint, although smaller in magnitude, is mainly due to the discharge of chemically contaminated wastewater from textile processes (e.g. bleaching and dyeing).

Figure 2. Water Footprints for Wool Production.

Green water footprint is the most dominant component in wool production, reaching nearly 29,000 m³/ton per year, and originates entirely from the animal husbandry phase. This reflects the substantial contribution of rain-fed grazing and feed crop cultivation to green water use. Blue water footprint remains relatively low (below 4,000 m³/ton), with minimal contribution from the industrial phase. The grey water footprint is caused by the fertilizer used in livestock grazing and the wastewater coming from processes in industrial stages.

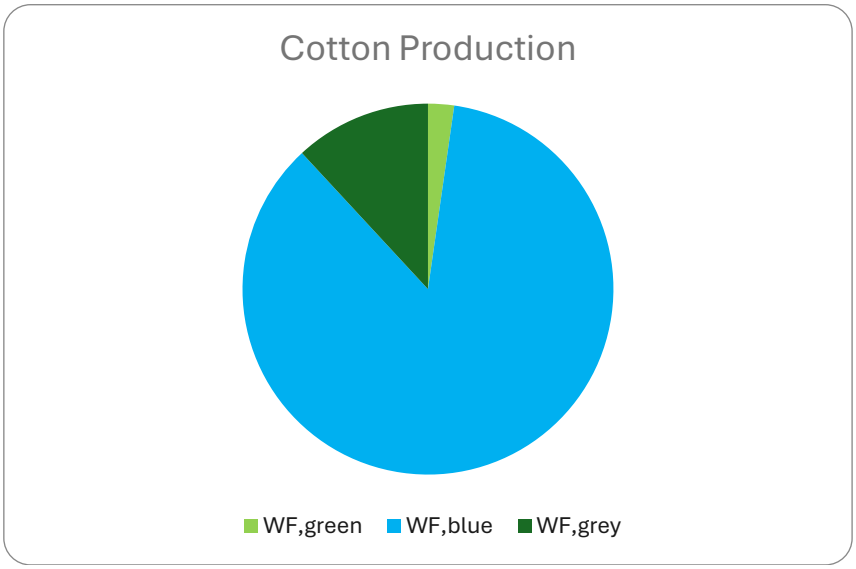

Figure 3. Distribution of Water Footprint Components: Green, Blue, and Grey Water in Cotton Production.

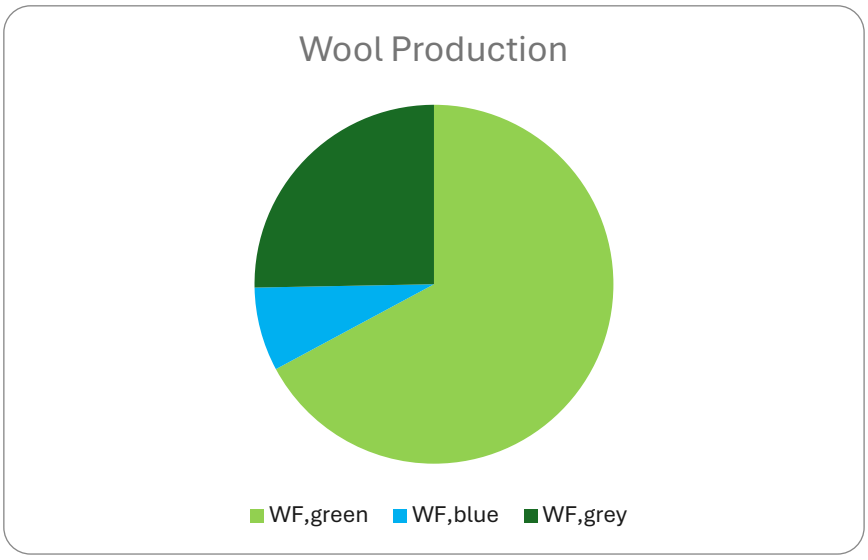

Figure 4. Distribution of Water Footprint Components: Green, Blue, and Grey Water in Wool Production.

The total water footprint of a cotton T-shirt is approximately 3 cubic meters, while that of a wool T-shirt is considerably higher, at around 11 cubic meters.

Conclusion

The study reveals that while cotton production places high pressure on freshwater resources (blue water footprint) due to irrigation, wool production makes a significant difference due to its high grey water footprint from wastewater discharge and animal waste stream. To reduce the water footprint of textile production, it is of utmost importance to implement sustainable irrigation in cotton farming and improve wastewater treatment in wool processing. These results highlight the critical role of raw material selection and process optimization in achieving water sustainability in the textile sector.

References

Okur, N. (2006). Bambu lifi ve iplik özelliklerinin diğer lif ve ipliklerin performans özellikleri ile karşılaştırmalı olarak incelenmesi.

Hoekstra, A.Y. and Hung, P.Q. (2002) 'Virtual water trade: A quantification of virtual water flows between nations in relation to international crop trade', Value of Water Research Report Series No. 11, UNESCO-IHE, Delft, the Netherlands.

Chapagain, A.K. and Hoekstra, A.Y. (2004) 'Water footprints of nations', Value of Water Research Report Series No. 16, UNESCO-IHE, Delft, the Netherlands.

Chapagain, A. K., Hoekstra, A. Y., Savenije, H. H., & Gautam, R. (2006). The water footprint of cotton consumption: An assessment of the impact of worldwide consumption of cotton products on the water resources in the cotton producing countries. Ecological economics, 60(1), 186-203.

Mikucioniene, D., Mínguez-García, D., Repon, M. R., Milašius, R., Priniotakis, G., Chronis, I., ... & Díaz-García, P. (2024). Understanding and addressing the water footprint in the textile sector: A review. AUTEX Research Journal, 24(1), 20240004.

Hoekstra AY, Chapagain AK, Aldaya MM, Mekonnen MM. 2011. The water footprint assessment manual: Setting the global standard. London: Earthscan. p. 203

Mekonnen, M., & Hoekstra, A. Y. (2010). The green, blue and grey water footprint of farm animals and animal products.

Turkish Ministry of Agriculture and Forestry, Durum Tahmin Raporu, PAMUK, (2024). Url-1 https://arastirma.tarimorman.gov.tr/tepge/Belgeler/PDF%20Tar%C4%B1m%20%C3%9Cr%C3%BCnleri%20Piyasalar%C4%B1/2024Temmuz%20Tar%C4%B1m%20%C3%9Cr%C3%BCnleri%20Raporu/Pamuk%20Tar%C

4%B1m%20%C3%9Cr%C3%BCnleri%20Piyasalar%C4%B1%20Raporu%20Temmuz-2024-v4.pdf data retrieved 01.02.2025
Turkish Statistical Institute, (2024). Url-2 https://data.tuik.gov.tr/Kategori/GetKategori?p=tarim-111 data retrieved 01.02.2025
Su Kirliliği Kontrolü Yönetmeliği, (2004). Url-3 https://www.mevzuat.gov.tr/mevzuat?MevzuatNo=7221&MevzuatTur=7&MevzuatTertip=5, date retrieved 01.02.2025

TEXTILE ENGINEERING

Smart and Functional Textiles

Sustainability in Textile and Fashion Industries

Textile Clothing and Fashion Design

Statistical Analysis of Short Fiber Content and Tenacity Using Exponential Regression

Çağdaş Aslan[a], Selin Hanife Eryürük[b], Michael Will[c]

[a] Istanbul Technical University, Institute of Graduate Education, Textile Engineering Department, Textile Engineering, Ph.D. Program, Türkiye
[b] Istanbul Technical University, Textile Engineering Department, Textile Engineering, Türkiye
[c] Rieter AG, Textile Technology Department, Switzerland
aslancagd@itu.edu.tr

Keywords: Recycled Cotton Fibers, Recycled Ring Yarn, SFC (Short Fiber Content), Yarn Tenacity.

Aim

The increasing consumer demand for sustainable and recycled textiles has led to a rise in the use of recycled cotton fibers. Among recycling methods, mechanical recycling is one of the most effective and widely used for cotton textile materials. Mechanically recycled cotton fibers are utilized in various applications, ranging from fiber-to-fiber recycling for high-quality yarns to downcycling into insulation, filling, or non-woven textiles (Abagnato et al., 2024). From an economic perspective, fiber-to-fiber recycling is the most viable option for spinners, even though the fibers are shortened during processing. The fiber-to-fiber recycling process directly impacts fiber-to-yarn spinning technologies, influencing the choice of spinning methods based on fiber length, quality, and efficiency. For decades, the rotor yarn production process has been widely used in the recycled yarn spinning industry due to its efficiency and adaptability. Nevertheless, ring spinning remains the leading technology in yarn production, known for its superior yarn quality and versatility across various applications. Consequently, utilizing mechanically recycled cotton (rCO) in ring spinning technology is essential for the market. However, integrating mechanically recycled cotton (rCO) into the ring spinning process presents unique challenges. Mechanically recycled cotton fibers often have lower quality compared to virgin cotton fibers, in terms of higher neps, impurity (contaminants) and ratio of short fiber content due to its own natural structure and processing additional tearing processes.

A critical parameter in this context is the short fiber content (SFC) of recycled cotton fibers. A high SFC adversely affects drafting performance, increases yarn irregularities and imperfections, and leads to a higher rate of yarn breaks, reducing machine efficiency and overall production output (Thibodeaux et al., 2008). Majumdar discovered through the research that as the proportion of short fibers in cotton increases, there is a substantial rise in yarn unevenness. This unevenness occurs because of drafting waves forming between the front and back rollers during the spinning process (Majumdar, 2011). Another major concern is the decrease in yarn tensile strength, which can cause several production quality defects in the downstream processes as well.

This study investigates the correlation between yarn tenacity and varying recycled fiber content, which inherently leads to different SFC levels. Understanding this relationship will provide insights into optimizing fiber selection and processing parameters to improve yarn quality.

Material and Method

Post-industrial waste (PIW) recycled cotton fibers were used in this study. The mechanically recycled cotton fibers consisted of black fabric scraps and produced through the mechanically recycling tearing method. To investigate this correlation six combed ring spinning yarns were produced with different blend ratio of recycled cotton fibers.

The recycled and virgin cotton fibers were blended using Rieter UNIblend A81 ensuring precise mixing and blending. Rieter Mixing Bale Opener B3/4 for cotton and Rieter Mixing Bale Opener MBO B36 for recycled cotton fibers were used. The trial plan included different blending ratios for the combed yarns; Yarn Reference (100% CO), Yarn 72 (75% CO – 25% rCO), Yarn 55 L-M-H (50% CO – 50% rCO), and Yarn 27 (25% CO – 75% rCO). For the 50% CO – 50% rCO samples, three comber settings were applied to assess the impact of noil level:

L (low noil), M (medium noil) and H (high noil). The top comb penetration, the detaching distance, and the distance between nipper and circular comb were selected as parameters to see the impact of the comber setting on combed recycled yarn trials. The detailed experimental plan and combing parameters are presented in the Table 1. The fiber properties of the finisher draw frame slivers were analyzed using Uster AFIS, as this is the final stage of slivers' doubling and blending in the spinning process. To evaluate yarn tensile strength, combed recycled ring yarns were tested using Uster Tensojet 5 (measuring tensile strength in cN/tex).

Table 1. Experimental plan.

	Y10M	Y72M	Y55L	Y55M	Y55H	Y27M
Process	Combed	Combed	Combed	Combed	Combed	Combed
CO %	100	75	50	50	50	25
rCO %	0	25	50	50	50	75
Blends	CO	CO/rCO	CO/rCO	CO/rCO	CO/rCO	CO/rCO
Comber settings	M	M	L	M	H	M
Noil %	14.3	19.4	24.4	25.9	31.4	33.8
Nips/min	600	600	600	600	600	600
Top comb penetration	0.5	0.5	-	0.5	0.5	0.5
Nipper-circular comb	0.3	0.3	0.5	0.3	0.3	0.3
Detaching distance	7.0	7.0	6.5	7.0	8.0	7.0
Ne	30	30	30	30	30	30

Findings

To assess how blending ratio and noil level influence yarn strength, six combed ring yarn samples were analyzed. The recycling ratio was increased incrementally from 0% to 75%. A fully recycled yarn sample (100% rCO) could not be produced and tested due to insufficient fiber cohesion in the slivers. The main objective of this study is to focus and do deep research on impact of short fiber content of mechanically recycled cottons in recycled ring yarn spinning technology.

In this study, exponential regression analysis was used to investigate the relationship between short fiber content (SFC(n) %) of slivers and tenacity (cN/tex) in combed recycled ring yarns. An exponential model was chosen because fiber strength typically decreases exponentially as SFC(n) increases. The resulting model showed a strong correlation, with an R^2 value of 0.9861, indicating that 98.61% of the variability in SFC(n) is explained by tenacity. As shown in Figure 1, yarn tenacity decreases as the proportion of recycled cotton increases.

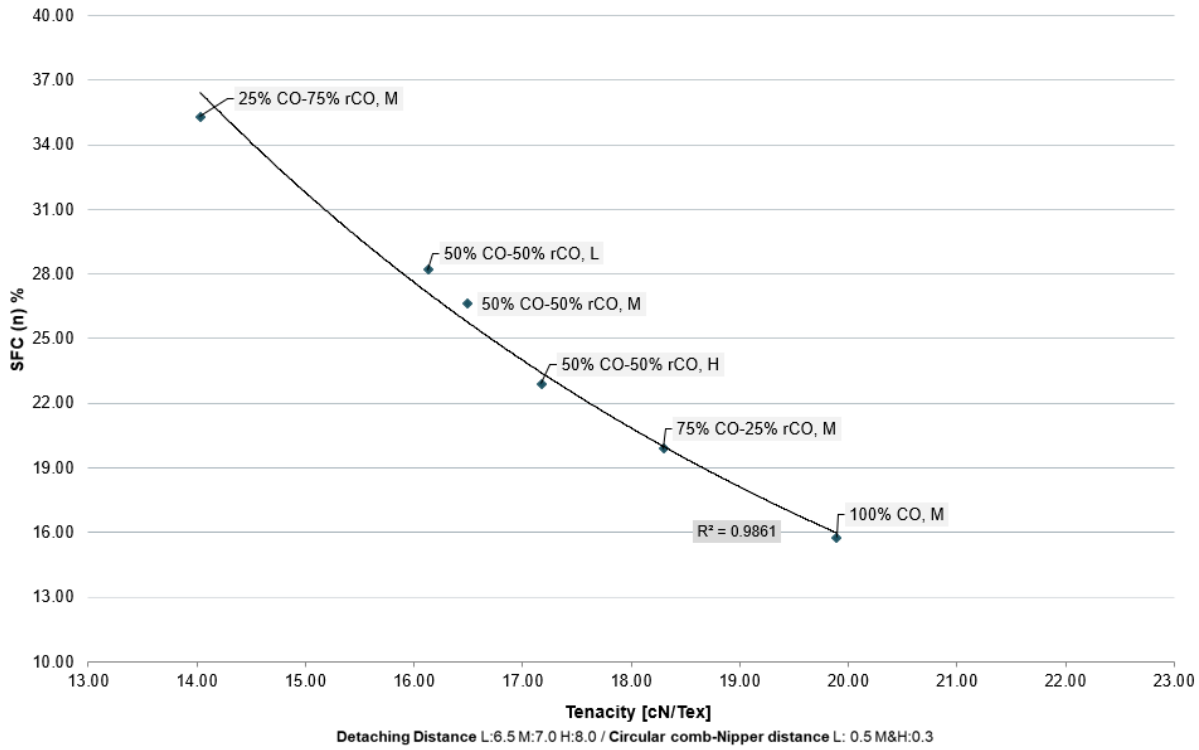

Figure 1. Relation between tenacity of ring yarn and SFC (n) of finisher draw frame slivers.

To further validate the relationship, Pearson correlation analysis was considered, but due to the non-linear trend, exponential regression provided a better fit. This approach allows for a more accurate prediction of fiber properties based on blend composition. Higher SFC was associated with increased yarn unevenness and imperfections, negatively impacting elongation and tenacity. The findings suggest that controlling short fiber content in recycled cotton blends is crucial for maintaining yarn performance and minimizing quality defects.

Conclusion

This study highlights the significant impact of short fiber content of mechanically recycled cotton on the tensile strength of combed recycled ring yarns. By optimizing fiber processing and blending techniques, the mechanical performance of recycled yarns can be improved, promoting more sustainable textile production. Further research is ongoing to explore the role of spinning parameters, the implementation of new techniques, and advanced fiber preparation methods in minimizing the negative effects of short fiber content of mechanically recycled cotton.

References

Abagnato, S., Rigamonti, L., and Grosso, M. (2024). Life Cycle Assessment Applications to Reuse, Recycling and Circular Practices for Textiles: A Review. Waste Management, 182, pp.74–90.

Majumdar, A. (2011). Adaptive Neuro-fuzzy Systems in Yarn Modelling. Soft Computing in Textile Engineering. Cambridge: Woodhead Publishing, pp.159–177.

Thibodeaux, D., Senter, H., Knowlton, J.L., McAlister, D., and Cui, X. (2008). The Impact of Short Fiber Content on the Quality of Cotton Ring-spun Yarn. The Journal of Cotton Science, 12, pp.368–377.

TEXTILE ENGINEERING

Smart and Functional Textiles

Sustainability in Textile and Fashion Industries

Textile Clothing and Fashion Design

Real Time Production Management in Garment Manufacturing Using IoT-Based Process Monitoring Devices (PMDs)

Bülent Koç[a], Selin Hanife Eryürük[a]

[a] Istanbul Technical University, Faculty of Textile Technologies and Design, Textile Engineering Department, Türkiye
kocbul18@itu.edu.tr

Keywords: Garment Manufacturing, Digitalization, Process Monitoring Devices (PMDs), Real-time Production Management, Operational Efficiency.

Aim

The ready-made garment (RMG) industry is becoming increasingly competitive due to its dynamic structure, rapidly changing customer demands, and global market integration (Noor et al., 2021). Traditional production management approaches, which rely on manual data tracking, periodic observations, and managerial interventions, are no longer sufficient in today's highly digitalized manufacturing environment. Managing production with outdated and inefficient methods hampers competitiveness and long-term sustainability, leading to sub-optimal resource utilization, high error rates, and a misalignment between operator skills and assigned tasks.

To overcome the limitations of traditional monitoring methods, Process Monitoring Devices (PMDs) provide a data-driven solution, facilitating real-time monitoring and optimization of manufacturing processes (Bonada et al.,2020; Giusti et al., 2018). Unlike conventional tools, PMDs leverage IoT technology and edge computing to rapidly process and interpret raw data, transforming it into actionable insights. These systems autonomously collect key production metrics, including output summaries, downtime analysis, and quality performance, mitigating inefficiencies associated with manual data tracking. Additionally, Application Programming Interface (API) integration enables seamless interaction with Enterprise Resource Planning (ERP), Manufacturing Execution System (MES), and other digital platforms, optimizing inventory management, equipment utilization, production planning, and overall operational efficiency (Guo et al., 2013; Garg, 2028).

Material and Method

This study focuses on the implementation of Process Monitoring Devices (PMDs) in sewing production to enable real-time monitoring, analysis, and data-driven production management. The primary objective is to evaluate the impact of PMD integration on performance, availability, quality improvement, and the control of production costs and other key inputs. Within this framework, the ITEX PMD (Figure 1), developed by ITM Tech Soft, has been selected as the sample application. The device, integrated into sewing machines, utilizes real-time data acquisition through current and optical sensors to analyze operator performance, machine efficiency, and downtime. This system facilitates continuous production monitoring, enabling precise decision-making for process optimization and operational efficiency in garment manufacturing.

Figure 1. ITEX PMD Iot-Based Process Monitoring Device.

Introduction to the PMD Device and Function Keys:

The PMD features a user-friendly interface with function keys designed for operator use. These keys allow operators to perform basic tasks such as assigning themselves to a machine, starting, and ending tasks. Additionally, the device's screen provides operators with real-time information (e.g., completed work count, cycle time, etc.). The PMD device uses RFID cards to match operators with machines, enabling real-time tracking of which operator is working on which machine and operation.

Installation of the PMD Device on Sewing Machines and Data Generation:

The PMD can be easily mounted on sewing machines using Power I/O devices and PMD Port mechanisms. This installation process is compatible with semi-automatic, automatic, and non-automatic machines. The PMD device collects data through current sensors and optical sensors. In thread-cutting machines, the current sensor detects changes in the thread-cutting motor's current to determine work counts. In non-thread-cutting machines, work counts and operation times are measured using current changes in the machine motor and optical sensors.

Figure 2 illustrates the connection diagram between the sewing machine, Power I/O device, and PMD device. This system is designed to ensure seamless data flow and enhance the traceability of production processes. PMD devices provide flexibility by being compatible with various machine types and models, minimizing the need for frequent hardware upgrades and offering a sustainable, adaptable production infrastructure. As a result, monitoring and control processes on the sewing line can be optimized without any loss of efficiency.

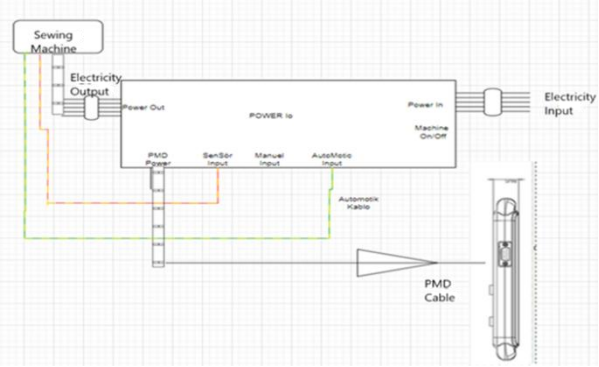

Figure 2. Connection Diagram between Sewing Machine, Power I/O ans ITEX PMD.

Data Storage and Transmission Mechanism:

As shown in the figure 3, ITEX PMDs and other data sources connect to the local server via wireless access points. Power over Ethernet (PoE) adapters provide power during data transmission to network equipment, supporting the efficient operation of the infrastructure. The local server collects, stores, and analyzes all production data, ensuring secure data processing and storage within the enterprise, reducing external dependencies.

The relational database created on the local server organizes data from PMD devices and ERP systems, making it available for line balancing and advanced analysis. As depicted, data flow is secured through a firewall, preventing unauthorized access during data transfer to the server. Data distribution via switches provides access to different departments, ensuring integrated data flow across the enterprise.

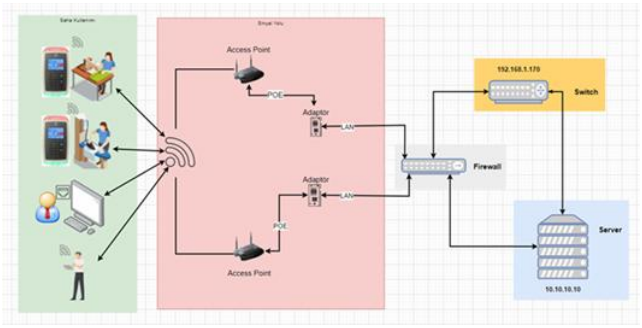

Figure 3. Integration of ITEX PMD with Central Database.

Figure 4 illustrates the seamless integration of ITEX PMDs, ITEX Soft, and the Web-Based Line Balancing Module, showcasing how real-time data translates into optimized workflows.

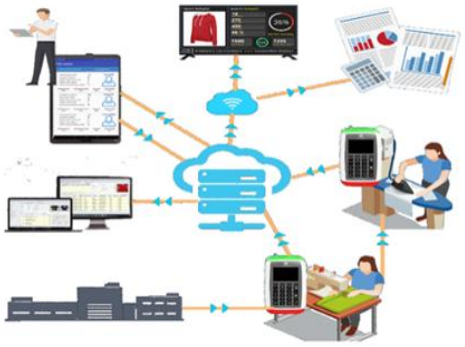

Figure 4. ITEX PMD Data Integration Eco System.

The ITEX ecosystem represents a transformative leap in garment manufacturing, combining real-time monitoring, predictive analytics, and dynamic workload balancing with lean manufacturing principles. By leveraging this synergy, the system achieves enhanced productivity, reduced waste, and sustainable operational excellence.

Operator and Machine Performance Monitoring:

The PMD monitors downtime due to operator- and factory-related delays, including breaks or operational changes, as well as operational interruptions such as machine failures or material shortages. Operators handling multiple tasks can transition between machines by removing their RFID card from one machine and scanning it on another. This system ensures that each operator's assigned tasks, completed work counts, cycle times, and performance levels are continuously tracked in real time and historically. Real-time production management dashboards, as illustrated in Figure 5, offer live data on various production metrics, helping shop floor managers make data-driven decisions quickly.

Figure 5. Examle of Real-time Production Management Dashbords.

Production Efficiency and Quality Analysis:

The Process Monitoring Device (PMD) system generates comprehensive reports that evaluate sewing line availability, performance, and efficiency. These reports offer detailed insights into the causes of downtime, including factory-level factors, and provide a robust analysis of operational efficiency across lines (Marariu et al., 2020). Table 1 presents the sewing line availability, performance, and efficiency metrics recorded over the past six months in a garment manufacturing facility.

Table 1. Example of Sewing Line Report.

Factory	Production Output Efficiency	Productivity	Performance	Availability	Production Quantity	Factory Lost Time	Factory Lost Time %	Employee Lost Time	Employee Lost Time%
ABC Apparel	56%	47%	66%	71.39%	165695	873239	19.01%	385659	8.39%
Line	Production Output Efficiency	Productivity	Performance	Availability	Production Quantity	Factory Lost Time	Factory Lost Time %	Employee Lost Time	Employee Lost Time%
Line 01	45%	39%	69%	56.19%	4817	36641	27.26%	16744	12.46%
Line 02	55%	55%	78%	70.36%	9328	108169	22.01%	35279	7.18%
Line 03	52%	41%	66%	61.74%	14048	67947	20.91%	45811	14.10%
Line 04	54%	52%	69%	74.56%	15710	69973	19.85%	17992	5.10%
Line 05	57%	53%	72%	73.14%	16310	55932	17.42%	28547	8.89%
Line 06	54%	43%	69%	62.15%	9425	73358	22.27%	32202	9.78%
Line 07	46%	46%	60%	76.73%	7991	62272	15.00%	24343	5.87%
Line 08	47%	38%	63%	59.60%	1826	36289	23.62%	27539	17.93%
Line 09	76%	50%	67%	73.99%	29632	66440	17.65%	33262	8.83%
Line 10	65%	50%	66%	75.92%	16149	83386	16.25%	37209	7.25%
Line 11	57%	53%	75%	71.21%	4995	23663	19.22%	10841	8.81%
Line 12	48%	36%	48%	73.41%	11899	73078	19.24%	26739	7.04%
Line 13	64%	49%	66%	75.00%	9524	56108	16.67%	25918	7.70%
Line 14	54%	49%	65%	75.39%	14041	59983	17.51%	23233	6.78%

In addition to efficiency monitoring, the PMD system also tracks repair and defect incidents for each production line. These are categorized using root cause analysis into machine-related problems, operator errors, stains, print and embroidery issues, or fabric-related defects. This classification enables the identification of recurring quality issues and supports the reduction of repair and rework rates while improving first-pass yield. As a result, the data derived from these analyses contributes significantly to enhancing Overall Equipment Effectiveness (OEE) (Xu et al., 2020). Table 2 summarizes the repair, rework, and defect counts observed over the same period, along with their classified causes.

Table 2. Repair, Rework and Defect Analysis of Sewing Lines.

Line	Sewing Repair	Iron Fault	Jute	Stain	Print	Hand Repair	Colour Difference	Cover Stitch Repair	Overlock Repair	Lock Stitch Repair	Total Repair	2nd Quality
Line 01	0	8	39	438	8	164	9	555	868	3147	5236	31
Line 02	13	0	157	959	2	148	279	723	642	2900	5823	100
Line 03	0	6	1024	3151	69	348	53	1830	670	1626	8777	122
Line 04	0	0	114	2148	1	150	17	1230	2526	1748	7934	77
Line 05	0	4	1436	4144	2	2112	48	543	679	1637	10605	51
Line 06	0	3	1266	1339	4	376	83	579	280	1303	5233	87
Line 07	0	36	287	1088	0	65	7	343	347	1481	3654	57
Line 08	0	3	453	1078	0	744	16	740	692	1426	5152	82
Line 09	0	0	436	1095	17	311	56	391	267	1017	3590	146
Line 10	0	0	1002	561	2	735	167	170	188	901	3726	29
Line 11	0	1	394	871	5	674	8	286	258	1468	3965	66
Line 12	0	17	821	1511	43	1014	108	924	776	3264	8478	82
Line 13	4	8	294	1193	59	733	123	630	574	3098	6716	107
Line 14	0	7	1041	1741	3	2016	88	807	1427	2991	10121	47
Total	**17**	**93**	**8.764**	**21.317**	**215**	**9.590**	**1.062**	**9.751**	**10.194**	**28.007**	**89.010**	**1.084**

Findings

ITEX PMD plays a key role in tracking machine malfunctions and downtime in garment production. The system monitors machine performance in real time, identifying disruptions and downtime causes, such as mechanical breakdowns or system errors, and logs the duration of these issues. It also tracks response times and resolution durations, helping minimize delays. By categorizing defects by their root causes, the system supports targeted interventions that improve efficiency and first-pass yield rates.

Table 3 shows machine malfunctions and associated downtime in minutes, while Figure 6 visually presents the causes and durations of these issues, offering insights into areas for improvement.

Table 3. Machine Malfunction and Downtime Analysis.

Group Type	Number of Faults	Fault Detection Time (minutes)	Fault Intervention Time (minutes)	Fault Completion Time (minutes)	Total Fault Downtime (minutes)	Average Downtime per Fault (minutes)	Maximum Intervention Time (minutes)
Needle Breakage	27	167	93	555	921	2	16
Needle Malfunction	860	327	193	1697	2432	2	19
Thread Breakage	58	575	122	483	1427	20	15
Technical Failure	373	2137	550	1200	4923	13	40
Stitch Skipping	91	502	189	428	1280	14	30
Pedal Malfunction	27	128	32	61	257	9	10
Feed Dog Adjustment	19	59	49	70	193	10	36
Needle Fracture	77	33	9	122	186	2	2
Machine Adjustment	293	1795	399	871	3694	12	32

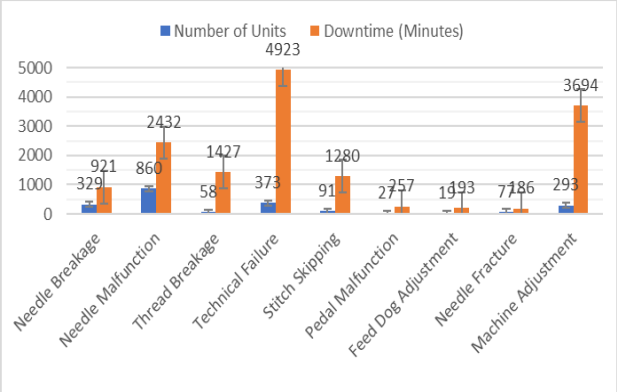

Figure 6. Distribution of Machine Malfunction Causes and Breakdown Durations.

With the ITEX PMD system, real-time traceability of sewing lines is achieved, allowing both the overall facility and individual sewing lines to be monitored for availability, performance, and sewing line efficiency. Reports generated by the system provide valuable insights into machine malfunctions, including causes, response times, resolution times, and total downtime, offering a comprehensive view of maintenance management. This data-driven approach enables better decision-making, contributing to the optimization of operational efficiency. The integration of digital lean management principles ensures that production processes are not only more transparent but also more effective, ultimately enhancing the operational performance of garment manufacturing facilities (Shahin et al., 2020).

In addition to real-time production tracking, the integration of PMD systems provides a significant contribution to digital line balancing processes. By continuously collecting performance data such as cycle times, work counts, and operator-machine interactions, PMDs enable dynamic line balancing decisions to be made in alignment with actual shop-floor conditions. These data-driven insights can be integrated with AI-powered balancing tools to automatically identify line bottlenecks, reallocate tasks based on operator skill profiles, and propose optimal operator replacements in cases of absenteeism. Moreover, by monitoring low-efficiency points in advance, the system supports proactive training planning and capacity forecasting. In this context, PMD devices serve not only as real-time monitoring tools but also as strategic enablers of agile and adaptive production planning, improving

productivity, responsiveness, and resource utilization on the sewing floor. This alignment between IoT-based monitoring and intelligent planning platforms strengthens the overall digital transformation framework in garment manufacturing.

Conclusion

Shop Floor Control devices, such as ITEX PMD, have the potential to transform factory operations, boosting overall efficiency by up to 10-30%, and significantly reducing the time burden on management and work-study officers (Koç and Eryürük, 2024). One of its standout features is its ability to maintain seamless production flow even in challenging scenarios, such as operator absenteeism. By automatically recommending replacement operators, PMD ensures that production remains on track without compromising efficiency, saving valuable time and resources for manufacturing plants (Martinez et al., 2020).

Moreover, the data-driven analytics provided by PMD facilitate the early detection of bottlenecks and enable timely interventions, effectively reducing downtime and improving line balance. This proactive approach can result in output gains of up to 30%, depending on the production context. Figure 7 illustrates the primary benefits of PMDs in the production environment.

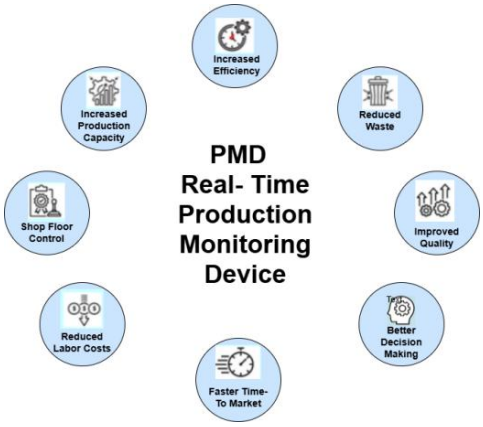

Figure 7. PMD Real-Time Production Monitoring Benefits.

In conclusion, the integration of PMD technologies represents a pivotal advancement in the digital transformation of the apparel industry. These systems contribute to enhanced operational efficiency, cost reduction, and improved sustainability by enabling data-driven decision-making. As global competition and sustainability expectations intensify, real-time monitoring tools such as ITEX PMD equip garment manufacturers with the agility and insight required to remain resilient and future-ready (Koç, 2023).

References

Bonada, F., Echeverria, L., Domingo, X., & Anzaldi, G. (2020). AI for improving the overall equipment efficiency in manufacturing industry. IntechOpen. https://doi.org/10.5772/intechopen.89967.

Garg, C. P. (2018). Implementation of lean tools in apparel industry to improve productivity and quality. CTFTTE, 4(1). https://doi.org/10.19080/ctftte.2018.04.555628.

Giusti, F., Bevilacqua, M., Tedeschi, S., & Emmanouilidis, C. (2018). Data analytics and production efficiency evaluation on a flexible manufacturing cell. 2018 IEEE International Instrumentation and Measurement Technology Conference (I2MTC). https://doi.org/10.1109/i2mtc.2018.8409677.

Guo, Z. X., Wong, W. K., & Guo, C. (2013). A cloud-based intelligent decision-making system for order tracking and allocation in apparel manufacturing. International Journal of Production Research, 52(4), 1100–1115. https://doi.org/10.1080/00207543.2013.838650**.**

Koç, B. (2025). Dikim işletmesinde yalın üretim ve sürdürülebilir yalın dijital model tasarımı [Unpublished doctoral dissertation]. Istanbul Technical University, Faculty of Textile Engineering.

Koç, B., & Eryürük, S. H. (2024). The role of process monitoring devices and digital line balancing in achieving operational excellence in garment manufacturing. Journal of Textile Engineering & Fashion Technology, 10(5), 180–186. https://doi.org/10.15406/jteft.2024.10.00386.

Martinez-Condor, B., Mamani-Motta, F., Macassi-Jáuregui, I., & et al. (2020). Lean production model aligned with organizational culture to reduce order fulfillment issues in micro- and small-sized textile businesses in Peru. IOP Conference Series: Materials Science and Engineering, 796(1), 012016–012016.

Morariu, C., Morariu, O., Răileanu, S., & Borangiu, T. (2020). Machine learning for predictive scheduling and resource allocation in large scale manufacturing systems. Computers in Industry, 120, 103244. https://doi.org/10.1016/j.compind.2020.103244.

Noor, A., Saeed, M. A., Ullah, T., Uddin, Z., & Khan, R. M. W. U. (2021). A review of artificial intelligence applications in apparel industry. Journal of Textile Institute, 113(3), 505–514. https://doi.org/10.1080/00405000.2021.1880088.

Shahin, M., Chen, F. F., Bouzary, H., & et al. (2020). Integration of lean practices and industry 4.0 technologies: Smart manufacturing for next-generation enterprises. International Journal of Advanced Manufacturing Technology, 107, 2927–2936.

Xu, K., Li, Y., Liu, C., Liu, X., Hao, X., Gao, J., & Maropoulos, P. (2020). Advanced data collection and analysis in data-driven manufacturing processes. China Machine Press, 33(1). https://doi.org/10.1186/s10033-020-00459-x.

TRADITIONAL DANCES

Dance, Traditional Dances in Terms of its Role in İnterdisciplinary İnteraction in Performance Areas

The Reinterpreting Choreographic Art Through Traditional Dances in Turkey: The Shaman Dance '7EDI' Project

Gulce Su Gumus[a], Eyüp Uzunkaya[a]

[a] Istanbul Technical University, Performing Arts Dept., Traditional Dances, Turkey
gumusg21@itu.edu.tr

Keywords: 7edi Project, Choreography, Cultural Heritage, Shaman Dance Theatre, Traditional Dances.

Aim

Traditional dances are significant forms of expression that embody the cultural heritage of societies. The processes of modernization and globalization have transformed the stage representations of these dances, incorporating modern choreography techniques and adding new dimensions to their performance. However, there is a limited number of studies in the literature examining how traditional dances in Turkey are reinterpreted through the art of choreography. The primary aim of this study is to address this gap by analyzing how traditional dances are reconstructed on stage through choreography.

Accordingly, this study focuses on the "7EDİ" project staged by Shaman Dance Theater. While investigating the fusion of traditional and contemporary dance within the project, it also explores how traditional dances are reinterpreted in the present day. The "7EDİ" performance is thematically structured around Turkey's seven regions and the seven hills of Istanbul, drawing inspiration from folk dances and music to create a contemporary narrative. By bringing together various cultural elements on stage, the performance functions as a cultural compilation, highlighting the ways in which staged works serve as curated representations of traditional heritage.

The central research question of this study examines the techniques employed by the art of choreography in adapting traditional dances for the stage and the role of this process in both preserving and reproducing Turkey's cultural dance heritage. Additionally, the study investigates whether staged performances function solely as artistic expressions or also serve as cultural compilations. Ultimately, this research aims to reveal the role of choreography in the preservation and sustainability of cultural heritage.

Material and Method

This study adopts qualitative research methods, utilizing both literature review and fieldwork-based data collection techniques. To understand how traditional dances in Turkey are integrated into contemporary performing arts, academic sources, books, and articles in the fields of dance and choreography were first examined. Research focusing on the fusion of folk dances with modern choreography provided the foundation for a broader evaluation of the artistic vision of the *"7EDİ"* project. This theoretical framework established the conceptual basis of the study.

In the applied section of the research, in-depth interviews were conducted with the creative team of Shaman Dance Theater. One- to- one interviews were held with the project's choreographers, executive team, and coordinators. Through these discussions, comprehensive insights were gained into the creative process of *"7EDİ"*, staging decisions, choreographic methods, and the ways in which traditional dance motifs were adapted to a contemporary stage language.

Additionally, visual analyses of the *"7EDİ"* performance were carried out. These analyses, based on performance recordings, examined the movement language of the dance, stage design, use of music, and narrative structure. By assessing concrete examples, this approach provided an opportunity to evaluate how traditional dance elements were integrated and transformed through contemporary choreography.

Through this combination of methods, the study adopts both a theoretical and practical analytical approach. The choreographic structure of the *"7EDİ"* project is examined from both an internal perspective (through interviews with artists and the creative team) and an external perspective (through visual analyses and literature review), ensuring a comprehensive evaluation.

Furthermore, the fact that the project's choreographers are Turkish artists highlights the influence of local artistic

perspectives on the choreographic process. This aspect contributes not only to the preservation of cultural heritage but also to the development of a distinctive form of expression in contemporary dance production. Ultimately, this study offers a significant perspective on how dance as an art form is represented in both national and international contexts within Turkey.

Findings

The findings of this study reveal how the *"7EDİ"* project establishes a relationship between traditional dances and contemporary choreography. The interviews conducted and analyses performed within the scope of the research provide detailed insights into the project's choreographic methods, staging approach, and musical structure. In this context, it has been observed that *"7EDİ"* creates a unique synthesis between traditional and modern elements.

The study identifies that folk dances from Turkey's seven regions have been restructured using modern choreography techniques. According to the choreographers, regional dance motifs have been preserved; however, during the staging process, these figures were stylized and integrated into a contemporary expressive language. Similarly, the musical structure consists entirely of original compositions, with each section's music specifically composed from scratch by Oğuzhan Balcı. The characteristic structures of local music were reinterpreted using modern orchestration techniques; rather than directly replicating folk melodies, they were reconstructed. These approaches demonstrate that the work harmonizes traditional and modern elements in an original manner, functioning as a cultural compilation both choreographically and musically.

Additionally, it was found that the choreographic process allowed dancers individual expressive space, enabling movements to be reshaped through their interpretations. This finding indicates that choreography extends beyond a purely technical arrangement; rather, it is an evolving creative process enriched by the dancers' artistic contributions. Overall, the *"7EDİ"* project successfully integrates traditional and modern dance elements, demonstrating that staged performances can function both as cultural compilations and as effective tools for transmitting cultural memory through the medium of performance.

Conclusion

This study has examined how the *"7EDİ"* project integrates traditional Turkish dances with contemporary choreography and whether the staged performances function as cultural compilations. The analyses conducted and the interviews with the project team reveal that *"7EDİ"* presents a unique and cohesive synthesis in terms of choreography, music, and stage design.

One of the most significant findings of this study is that traditional dances in contemporary performing arts should not be viewed merely as representations of the past but as dynamic and adaptable art forms. The choreographers reinterpreted dance motifs from various regions using modern staging techniques, allowing dancers to contribute their individual expressive interpretations. This approach ensured that the choreographic process was not a static structure but rather an interactive and creative formation. It also demonstrates that choreography extends beyond an aesthetic discipline to serve as a cultural and artistic medium of expression.

Additionally, choreography undergoes a historical evolution, and interviews with past and present artists provide a bridge between tradition and contemporary artistic practice. This perspective enables an examination of how choreography in Turkey has adapted to historical and societal transformations. The *"7EDİ"* project can thus be seen as a contemporary reflection of this historical continuity.

From a musical perspective, the project was composed entirely of original pieces, deliberately avoiding the direct use of traditional folk melodies. Composer Oğuzhan Balcı reinterpreted the musical characteristics of different regions of Turkey through modern orchestration techniques, establishing a strong network of interaction between music and dance. As a result, the *"7EDİ"* project is not only a choreographic endeavor but also a cultural reproduction process from a musical standpoint.

Another key finding is that staged performances can serve as cultural compilations. *"7EDİ"* brings together traditional dance and musical elements from various regions of Turkey and reinterprets them within a contemporary artistic context. This process highlights that choreography is not merely a tool for aesthetic expression but also plays an active role in preserving, transforming, and transmitting cultural heritage to future

generations. Media coverage supports this view, describing *"7EDİ"* as an innovative performance that brings Istanbul's historical and cultural identity to the stage. Critics and artistic communities have emphasized that the project successfully bridges tradition and modernity and possesses the qualities necessary for international festival participation.

In conclusion, this study has demonstrated how traditional dances can be adapted to modern performing arts through choreography and has provided significant contributions to the sustainability of cultural heritage. Projects like *"7EDİ"* serve as models for preserving, developing, and representing cultural heritage through artistic expression, while also holding the potential to inspire similar projects in the future.

References

Balcı, O. (2025, March 13). (G. S. Gümüş, Interviewer) İstanbul.

Bilgen, G. (2017). Liminalite kavramı ve koreografik dönüşüm: Laban hareket analizi efor prensipleri üzerinden değerlendirme. Mimar Sinan Güzel Sanatlar Üniversitesi, Güzel Sanatlar Enstitüsü.

Borak , S. (2025, March 6). (G. S. Gümüş, Interviewer) Istanbul.

Çankaya, Y. (2025, March 19). (G. S. Gümüş, Interviewer) Istanbul.

Demirbağ Turan, A. (2024, November 27). (G. S. Gümüş, Interviewer) Istanbul.

Hanna, J. L. (1979). Movements toward understanding humans through the anthropological study of dance [and comments and reply]. Current anthropology(20), 313-339. doi:https://doi.org/10.1086/202269

Kandemir, H. (2025). (G. S. Gümüş, Interviewer) Istanbul.

Kuraner, K. (2025, March 11). (G. S. Gümüş, Interviewer) Istanbul.

Muradova, T. (2021). Azerbaycan Halk Oyunlarının Koreografik Kompozisyonda Uygulanması. *Pearson Journal*, 218-226. doi:https://doi.org/10.46872/pj.258

Özpınar, E. (2025, March 6). (G. S. Gümüş, Interviewer) Istanbul.

Sevinç, C. (2024, March 18). (G. S. Gümüş, Interviewer) Istanbul.

Sürel, S. (2025, March 19). (G. S. Gümüş, Interviewer) Istanbul.

Tezcür , Ç. (2025, April 10). (G. S. Gümüş, Interviewer) Istanbul.

Tokmak, M. (2016). Sözlü tarih ve derinlemesine görüşme. *Ardahan Üniversitesi İktisadi ve İdari Bilimler Fakültesi Dergisi*(2), 83-89.

Türkoğlu, İ. (2025, April 28). Istanbul.

Uygun, M. (2025, April 18). (G. S. Gümüş, Interviewer) İstanbul.

YILMAZ, K. C. (2023). Türk Halk Dansları Ve Koreografi Sanatı Üzerine Yorumlayıcı Bir Yaklaşım. *Avrasya Sanat ve Medeniyet Dergisi*, 52-58. doi:https://doi.org/10.17740/eas.art.2023-V16-06

URBAN AND REGIONAL PLANNING

Climate Change and Planning

Smart Cities, Digitalization, and Data Science

Sustainability, Ecology, and Energy in Planning

Transportation Planning and Urban Infrastructure

Climate Change Adaptation in Urban Heritage Sites: The Case Of Istanbul Historic Peninsula

Tuğçe Türk[a], Turgay Kerem Koramaz[b]

[a] Istanbul Technical University, Graduate School, Urban Planning Graduate Program, Türkiye
[b] Istanbul Technical University Faculty of Architecture, Department of Urban and Regional Planning, Türkiye
turkt16@itu.edu.tr

Keywords: Climate Resilient Heritage, Climate-Friendly Heritage Conservation, Conservation Planning in Istanbul Urban Heritage Sites, Heritage Planning, Vulnerability Index.

Aim

The adverse impacts of global warming, which are happening faster than predicted, are beyond scientific discussion. Cities, where more than half of the world's population lives and where approximately 70% of the carbon footprint is created, are also the areas where the effects of climate change are felt the most and will be affected the most, considering that approximately 9.7 billion people will be sheltering by 2050 (UN, 2009). Since the 20th century, with the impact of accelerated urbanization, the implementation of adaptation policies to mitigate the current and future impacts of climate change and the development of prevention policies that reduce carbon emissions in all urban sectors to keep global warming under control have become the main problems and goals of urban governments, which has triggered interest in urban climate research that underpins current planning approaches. On the other hand, it is observed that urban climate risk is not sufficiently addressed in the planning processes of historic city centers, which are more vulnerable to the effects of climate change compared to modern cities and struggle with many more planning problems. Although many studies have been conducted to examine the issues raised in the planning of urban climate and urban heritage areas, respectively, studies aiming to increase the climate resilience of historic cities through conservation planning tools are not prominent enough (Baillie & Bayne, 2019; Kaushal et al., 2015; Riedinger-Whitmore, 2016; Vitkova et al., 2017; Wichansky et al., 2008). However, establishing a link between combating climate change and protecting historic cities is an issue that should be emphasized in the planning literature. Because the planning and management of historic cities are based on the complex interaction between climatic, social, economic, and cultural layers (Romero-Lankao et al., 2018), the climate-friendly historic city model contributes to the climate-sensitive design and sustainable urban development strategies through the use of traditional knowledge and techniques in the climate adaptation process. On the other hand, since the planning of cultural heritage areas that need to be protected requires an integrated and multidisciplinary approach that includes urban climate information, conducting climate impacts and vulnerability assessments in these areas strengthens the sustainability of conservation planning.

In this context, this study examines the strategies applied for climate-compatible planning of historic cities within the framework of conservation planning discipline. Because the information obtained in extensive research on climate-compatible planning of modern urban areas may not be sensitive enough to urban heritage areas (Bigio, 2014). When the literature is examined, it is seen that urban climate research is focused on environmental and ecological sciences, and studies on climate-oriented planning of historical urban areas are insufficient. In this respect, in order to protect cultural heritage sites and increase urban climate resilience, it is necessary to identify the main challenges faced, examine how vulnerable these areas are, and utilize the knowledge of heritage for climate-compatible planning. This study aims to raise academic awareness about the importance of incorporating traditional urban design practices into climate management by examining urban climate issues in conservation planning for cultural heritage sites. This focus aligns with the historic urban landscape (HUL) approach to managing and protecting urban landscapes proposed by UNESCO in 2011, which was developed to help historic cities cope with emerging climate challenges and inspire future urban development. The study hypothesizes that districts with urban heritage sites in Istanbul are more vulnerable to the climate crisis than other districts. In this context, when a climate change vulnerability index is created for the districts of Istanbul, it is investigated where

the most vulnerable cultural heritage sites are, the capacity of planning approaches in Istanbul's cultural heritage sites to accommodate other ecological attitudes such as adaptation to climate change, and how Istanbul's cultural heritage sites can be adapted to the climate crisis.
The main objective of the study is to assess the vulnerability of Istanbul's urban heritage sites to climate change and develop conservation planning tools to mitigate these impacts. The research establishes a quantitative framework based on district-level vulnerability indicators.

Material and Method

The study uses both qualitative and quantitative methods. Air quality and temperature measurements, carbon emission data, historical climate events and disasters (frequency of fires and floods), planning data (population, population development trends, building density, permeable surface ratio, water-energy-waste consumption, large land use data), protected area boundaries, Geographic Information Systems (GIS) and climate performance measurement models, as well as field surveys, questionnaires, and focus group discussions are used.
The study's methodology can be summarized in five stages (See Figure 1 Methodology Flowchart).

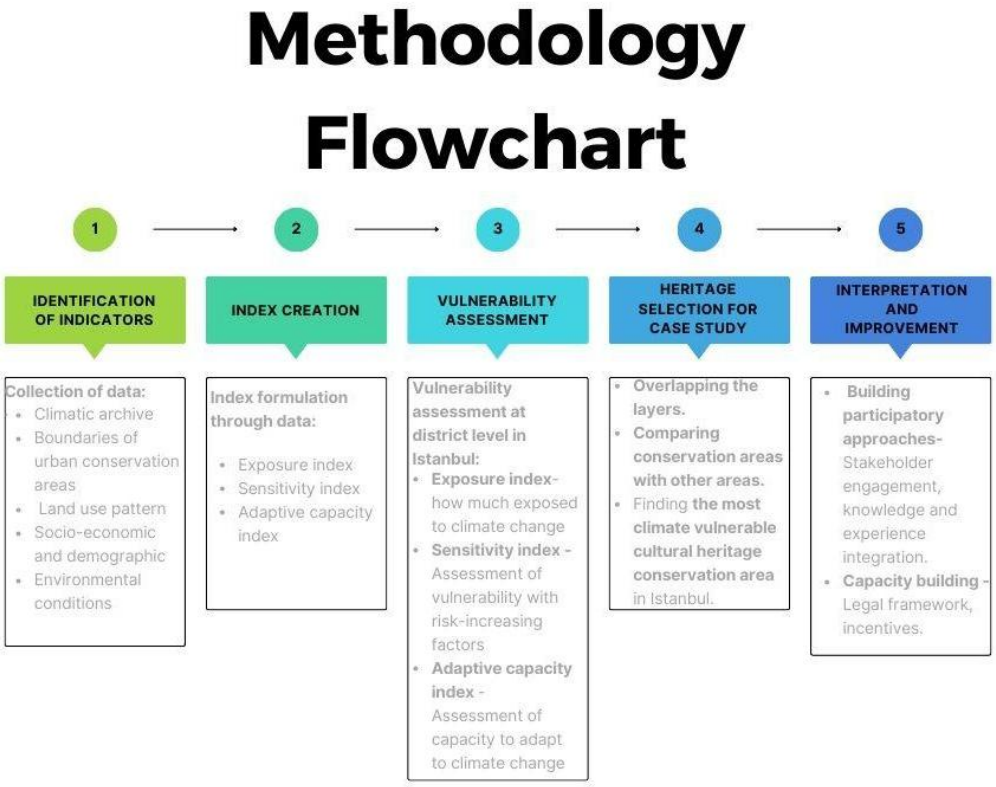

Figure 1: Methodology Flowchart **(**Flowchart summarizes 5 stages of methodology).

In the first stage, data collection is carried out at the level of neighborhoods and districts of Istanbul in order to determine the indicators. With the 20-year climate archive data obtained from the General Directorate of Meteorology, data on temperature and precipitation regime at the locations of the Observation Stations are analyzed. In order to analyze the relationship between climate data and land use data, land use data of Istanbul at the neighborhood level and the boundaries of registered natural and cultural protected areas are obtained from the relevant administrations and listed at the neighborhood level in order to reach the presence of natural and cultural protected areas, building-land density ratios, population density and the number of newly licensed projects. Various socio-economic data such as age distribution, child and elderly dependency ratios, and per capita household income at the neighborhood level from the General Directorate of Population and Citizenship, as well as the Istanbul Metropolitan Municipality's Data-Based Management Model research, which helps to analyze social awareness and usage habits regarding the environment, and the open data portal published as a result of socio-

demographic surveys of Istanbul residents are used. Finally, environmental data such as the amount of active and passive green space and the size of green space per capita at the neighborhood level are obtained from the relevant administrations, and data are collected at the neighborhood level.

In the second stage, indicator data is constructed by collecting exposure, sensitivity, and adaptive capacity indices.

In the third stage, a district-based vulnerability index is developed using a set of indicators consisting of socio-ecological, physical, and governance parameters, and spatial distribution is analyzed. This index integrates multidimensional factors such as exposure to climate risks (e.g., temperature increase, extreme precipitation, sea level rise), physical vulnerability of heritage sites, and adaptive capacity. Exposure analysis on how much the impacts of climate change are felt in order to make a comparison between protected areas and other areas, sensitivity analysis where risk multipliers such as historic building stock and vulnerable population groups are identified, and finally, adaptive capacity analysis, which can be defined as institutional and demographic strengths in combating climate change, are carried out.

In the fourth stage, based on the index results, the most vulnerable cultural heritage sites in Istanbul are identified, and the mechanisms of climate-induced degradation (chemical-physical erosion, moisture deformation) are examined in detail.

Finally, at the interpretation and improvement stage, climate adaptation strategies (passive cooling systems, increasing material resilience, risk mapping) are produced in a pilot cultural heritage site and integrated with policy recommendations.

Findings

Site selection for the case study on climate-sensitive planning in cultural heritage sites is made within the scope of the "climate vulnerability index" study prepared for Istanbul districts. This index study identifies cultural heritage areas in Istanbul that are most exposed and vulnerable to climate change.
The main finding of the study is that the districts of Istanbul with dense urban heritage areas are more vulnerable to the climate crisis than other districts. The other findings of the study will be presented as the most vulnerable urban heritage areas when a climate change vulnerability index is created for the districts of Istanbul, the capacity of planning approaches in Istanbul's urban heritage areas to accommodate other ecological attitudes such as adaptation to climate change, and the adaptation strategies of Istanbul's heritage areas to the climate crisis.

Conclusion

In conclusion, combating climate change and protecting urban heritage are two important issues that cannot be considered separately. Climate-smart urban planning in historic areas requires a multidisciplinary approach that integrates the protection of cultural heritage and the mitigation of risks posed by climate change. In this context, green infrastructure and planting strategies offer solutions compatible with traditional architecture to mitigate the heat island effect and optimize stormwater management without degrading the historic fabric (Fatorić & Biesbroek, 2020). At the same time, community participation supports socio-cultural sustainability by incorporating the traditional knowledge of local actors into planning processes (Labadi, 2017). Geographic information systems (GIS)-based risk mapping and adaptive planning models enable dynamic management of historic sites according to climate scenarios (Sesana et al., 2021). These strategies offer a holistic framework that places climate adaptation at the center of urban heritage management while balancing physical resilience with the preservation of cultural identity.
This study assesses the vulnerability of urban heritage sites in Istanbul to climate change through the demographic profile and key characteristics of the built environment, and develops strategies for their conservation and climate-adaptive planning. New tools and policies for climate-compatible planning in protected areas support capacity development for climate adaptation. The vulnerability index and conservation planning tools developed in the study directly contribute to the climate adaptation strategies of local governments.

References

Baillie, B. R., & Bayne, K. M. (2019). The historical use of fire as a land management tool in New Zealand and the challenges for its continued use. *Landscape Ecology, 34*, 2229–2244.

Bigio, A. G. (2014). Historic cities and climate change. In *Reconnecting the City: The Historic Urban Landscape Approach and the Future of Urban Heritage* (pp. 113–128).

Fatorić, S., & Biesbroek, R. (2020). Adapting cultural heritage to climate change impacts in the Netherlands: Barriers, interdependencies, and strategies for overcoming them. *Climatic Change, 162*(2), 301–320.

Labadi, S. (2018). Historical, theoretical and international considerations on culture, heritage and (sustainable) development. In *World Heritage and Sustainable Development* (pp. 37–49). Routledge.

Riedinger-Whitmore, M. A. (2016). Using palaeoecological and palaeoenvironmental records to guide restoration, conservation and adaptive management of Ramsar freshwater wetlands: Lessons from the Everglades, USA. *Marine and Freshwater Research, 67*(6), 707–720.

Romero-Lankao, P., Bulkeley, H., Pelling, M., Burch, S., Gordon, D. J., Gupta, J., ... & Munshi, D. (2018). Urban transformative potential in a changing climate. *Nature Climate Change, 8*(9), 754–756.

Sesana, E., Gagnon, A. S., Ciantelli, C., Cassar, J., & Hughes, J. J. (2021). Climate change impacts on cultural heritage: A literature review. *Wiley Interdisciplinary Reviews: Climate Change, 12*(4), e710.

Stewart, I. D. (2011). A systematic review and scientific critique of methodology in modern urban heat island literature. *International Journal of Climatology, 31*(2), 200–217.

Oke, T. R., Mills, G., Christen, A., & Voogt, J. A. (2017). *Urban climates*. Cambridge University Press.

United Nations. (2009). *Our growing population*. https://www.un.org/en/global-issues/population

Vítková, M., Müllerová, J., Sádlo, J., Pergl, J., & Pyšek, P. (2017). Black locust (*Robinia pseudoacacia*) beloved and despised: A story of an invasive tree in Central Europe. *Forest Ecology and Management, 384*, 287–302.

Wichansky, P. S., Steyaert, L. T., Walko, R. L., & Weaver, C. P. (2008). Evaluating the effects of historical land cover change on summertime weather and climate in New Jersey: Land cover and surface energy budget changes. *Journal of Geophysical Research: Atmospheres, 113*(D10).

URBAN AND REGIONAL PLANNING

Climate Change and Planning

Smart Cities, Digitalization, and Data Science

Sustainability, Ecology, and Energy in Planning

Transportation Planning and Urban Infrastructure

City Information Modeling: Identifying Knowledge Gaps and Research Priorities

Abdalrahman T. Y. Alashi[a], Özhan Ertekin[a]

[a] Istanbul Technical University/Graduate School, Department of Urban and Regional Planning, Doctor of Philosophy Program, Türkiye
alashi17@itu.edu.tr

Keywords: 3D City Modeling, City Information Modeling, PRISMA, Systematic Literature Review.

Aim

In recent years, City Information Modeling (CIM) has emerged as a powerful tool due to its potential in urban applications, gaining significant interest in both research and practical fields. This attention can be attributed to the effectiveness of Building Information Modeling (BIM) at a building scale. Recent research has delved into various aspects of CIM, ranging from the development of conceptual frameworks and testing integration frameworks for diverse data sources to the introduction of conceptual data models, literature reviews, commentary analysis, and more.

The scope of this research is twofold. Firstly, it aims to address this gap by conducting a systematic review using the Urban Planner PRISMA research process. By employing this methodology, the study seeks to shed light on the existing research gaps regarding CIM as an urban tool. Secondly, the research attempts to identify and evaluate the most efficient conceptual frameworks for data integration and processing within the realm of CIM. Additionally, the study aims to identify and highlight the most relevant and impactful literature reviews according to their mentioned scope.

Accordingly, this study aims to address that gap by conducting a comprehensive systematic literature review. The primary goals are to:

1. Highlight existing research gaps related to the urban-scale implementation of CIM.
2. Evaluate the most efficient conceptual frameworks for data integration and processing within CIM.
3. Identify the most relevant and impactful literature reviews in the field and analyze their scope.

Material and Method

Systematic literature reviews are commonly employed across different study areas by researchers to analyze literature with specific objectives and defined methodologies, ultimately yielding well-defined research outcomes. Page et al. (2021) have developed an updated version of the PRISMA statement, a systematic review guideline intended to enhance research outcomes across diverse fields. Given that the PRISMA statement may not fully meet the needs of urban planning studies, Abusaada and Elshater (2022) devised a PRISMA-based research BSMS review process customized for application by urban planners and urban designers, addressing the specific requirements of these fields.

For access to pertinent studies, researchers primarily rely on scholarly repositories like Scopus (Elsevier) and Web of Science (WoS). These yield a vast range of scholarly writings — from academic papers to book chapters — along with advanced bibliometric data like keywords, abstracts, and citation counts. This makes monitoring the frequency of important words more convenient, watching trends, ascertaining gaps in knowledge, and finding new research directions.

Findings

The review revealed several key insights:

- While interest in CIM has grown, practical applications remain limited due to the lack of standardized software, fragmented data systems, and unclear workflows.
- Existing literature heavily leans toward conceptual development, with relatively fewer studies offering empirical or software-based implementations.
- Data integration across various urban layers (e.g., infrastructure, environmental data, and social indicators) is still underdeveloped in most CIM applications.
- The most impactful literature reviews emphasized the interoperability between BIM, GIS, and CIM, yet offered varying conclusions regarding the feasibility of implementation.
- The adapted PRISMA-based method proved effective in highlighting thematic gaps, especially regarding the standardization of CIM practices, tool development, and scalability of frameworks.

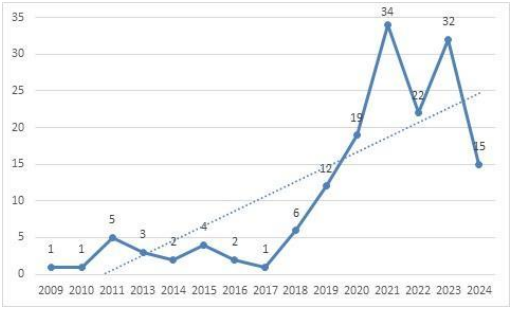

Figure 1. The document count for the 159 documents (SCOPUS).

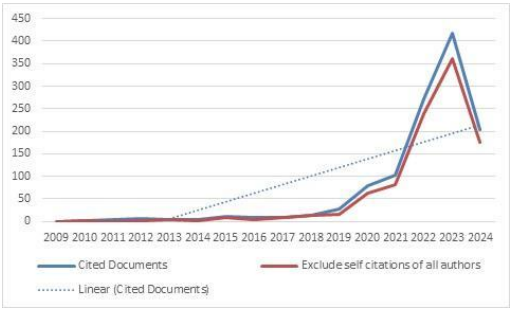

Figure 2. The citation count for the 159 documents, Self-citations included and excluded (SCOPUS).

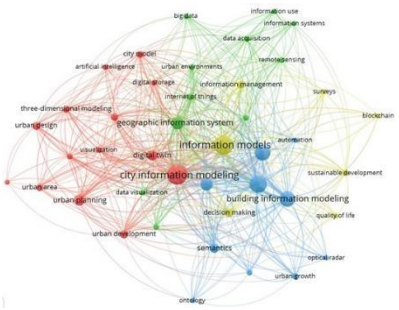

Figure 3. Analysis of the 159 documents retrieved from Scopus focusing on their keywords using VOSviewer (By Author).

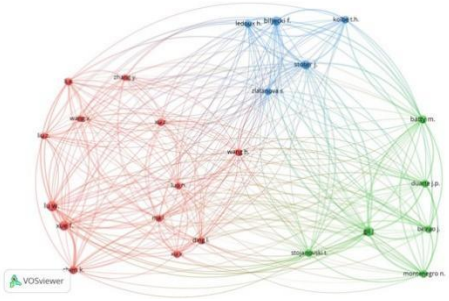

Figure 4. Network analysis based on co-citations of authors using VOSviewer (By Author).

Conclusion

While there is ample literature discussing CIM, there remains a considerable gap between conceptual understanding and practical implementation. This disparity is primarily attributed to the scarcity of CIM software solutions, the complexity of integrating diverse databases into the model, and the absence of clear guidelines regarding the most efficient workflows. This study demonstrates the critical need for a cohesive and actionable approach to implementing City Information Modeling at an urban scale. Through a systematic literature review using a PRISMA-based methodology tailored for urban planning, the research reveals a persistent gap between conceptualization and practical deployment. Key areas requiring further exploration include:

- The development of interoperable CIM tools.
- Standardization of data integration workflows.
- Emphasis on multi-scalar, real-world applications that bridge theory with practice.

Future research should focus on closing these gaps through cross-disciplinary collaboration, urban-scale UAV projects, and the creation of adaptable CIM platforms capable of handling complex urban datasets.

References

Abusaada, H., & Elshater, A. (2022). Notes on developing research review in urban planning and urban design based on PRISMA statement. *Social Sciences, 11*(9), 391.
Batty, M. (2007). Model cities. *Town Planning Review, 78*(2), 125–151.
Batty, M. (2009). Urban modeling. In *International Encyclopedia of Human Geography*. Elsevier.
Bilgilioglu, B. B., Ozturk, O., Sariturk, B., & Seker, D. Z. (2019). Object based classification of unmanned aerial vehicle (UAV) imagery for forest fires monitoring. *Fresenius Environmental Bulletin, 28*(3), 1011–1019.
Biljecki, F., Zhao, J., Stoter, J. E., & Ledoux, H. (2013). Revisiting the concept level of detail in 3D city modelling. In *8th 3DGeoInfo Conference & WG II/2 Workshop* (pp. 1–10). *ISPRS Archives, II-2/W1*.
Custers, B. (2016). Drones here, there and everywhere: Introduction and overview. In *The Future of Drone Use* (pp. 3–20). TMC Asser Press.
Fahlstrom, P., & Gleason, T. (2012). *Introduction to UAV systems*. John Wiley & Sons.
Kolbe, T. H. (2009). Representing and exchanging 3D city models with CityGML. In *3D Geo-Information Sciences* (pp. 15–31). Springer.
Lafarge, F., & Mallet, C. (2012). Creating large-scale city models from 3D-point clouds: A robust approach with hybrid representation. *International Journal of Computer Vision, 99*(1), 69–85.
Nan, L., & Wonka, P. (2017). PolyFit: Polygonal surface reconstruction from point clouds. In *Proceedings of the IEEE International Conference on Computer Vision* (pp. 2353–2361).
Oesau, S., Lafarge, F., & Alliez, P. (2016). Planar shape detection and regularization in tandem. *Computer Graphics Forum, 35*(1), 203–215.
Page, M. J., McKenzie, J. E., Bossuyt, P. M., Boutron, I., Hoffmann, T. C., Mulrow, C. D., ... & Moher, D. (2021). The PRISMA 2020 statement: An updated guideline for reporting systematic reviews. *BMJ, 372*, n71.
Sauerbier, M., & Eisenbeiss, H. (2010). UAVs for the documentation of archaeological excavations. *International Archives of Photogrammetry, Remote Sensing and Spatial Information Sciences, 38*(Part 5), 526–531.

Shi, X., Zhu, Y., Duan, J., Shao, R., & Wang, J. (2015). Assessment of pedestrian wind environment in urban planning design. *Landscape and Urban Planning, 140*, 17–28.
Stöcker, C., Bennett, R., Nex, F., Gerke, M., & Zevenbergen, J. (2017). Review of the current state of UAV regulations. *Remote Sensing, 9*(5), 459.

Deprivation Analysis In Turkey And Its Provinces: A Study Based On English Index Of Deprivation And Turkish Statistical Institute

Abdalrahman T. Y. Alashi[a], Özhan Ertekin[a]

[a] Istanbul Technical University/Graduate School, Department of Urban and Regional Planning, Doctor of Philosophy Program, Türkiye
alashi17@itu.edu.tr

Keywords: Deprivation Index, Deprivation Index of Turkey, Index of Multiple Deprivation, Regional Disparities, Spatial Inequality.

Aim

This study aims to construct a multidimensional deprivation index for Turkey and its provinces using domain-based indicators inspired by the English Indices of Deprivation (IoD). The objective is to reveal relative spatial inequalities and patterns of deprivation across the 81 provinces of Turkey using 2023 TURKSTAT data. The analysis seeks to support evidence-based planning, identify high-need areas, and inform equitable policy development.

Material and Method

The Composite Deprivation Index (CDI) was developed using seven domains: Income, Employment, Education, Health, Crime and Social Distress, Housing, and Living Environment. All domains were constructed based on 2023 provincial-level data from the Turkish Statistical Institute (TURKSTAT). Indicators within each domain were normalized using min-max scaling to allow comparability, and domains were weighted according to the English Indices of Deprivation 2019 model. The assigned weights were as follows:

- Income: 22.5%
- Employment: 22.5%
- Education: 13.5%
- Health: 13.5%
- Crime and Social Distress: 9.3%
- Housing: 9.3%
- Living Environment: 9.3%

Each domain score represents the normalized average of its selected indicators. All data processing and index calculations were conducted in Excel and SPSS. Spatial visualizations were developed using ArcGIS Pro software. Provinces were then ranked from the most deprived (rank 1) to the least deprived (rank 81).

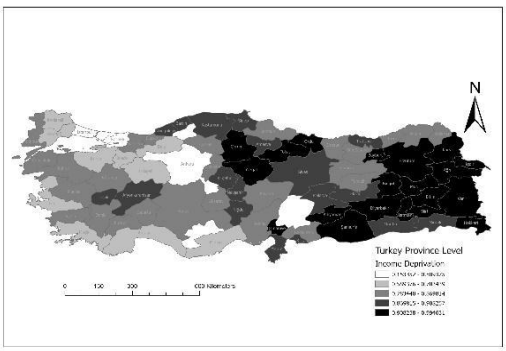

Figure 1. Income deprivation domain map 2023 (By Author).

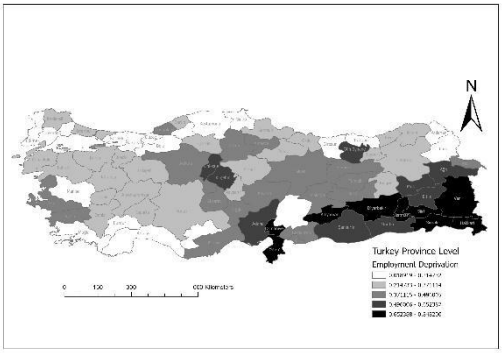

Figure 2. Employment deprivation domain map 2023 (By Author).

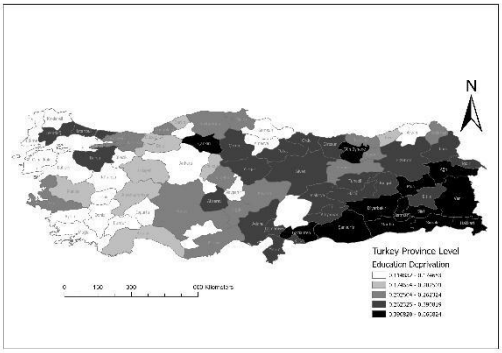

Figure 3. Education deprivation domain map 2023 (By Author).

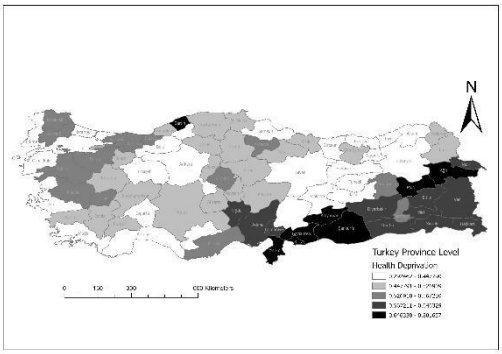

Figure 4. Health deprivation domain map 2023 (By Author).

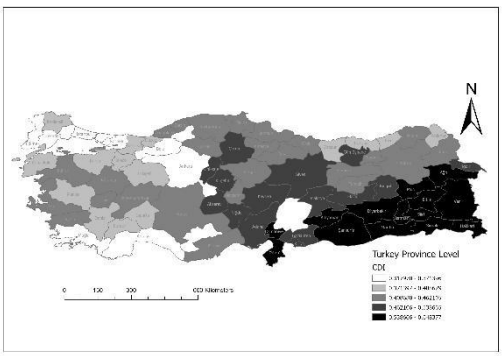

Figure 5. Overall Turkey Index of Multiple Deprivation 2023 (By Author).

Findings

The domain-level results show significant spatial disparities across Turkey. A strong east–west divide is visible across most domains, particularly in income, employment, education, and health deprivation. Provinces such as Şanlıurfa, Ağrı, Şırnak, Mardin, and Iğdır consistently appeared among the most deprived, while İstanbul, Ankara, Kocaeli, Tekirdağ, and Eskişehir were identified as the least deprived.

Income and Employment: Eastern provinces reported the highest levels of income and employment deprivation. Ağrı, Hakkari, Şırnak, and Muş were consistently ranked among the most deprived in both domains. In contrast, İstanbul, Tekirdağ, and Kocaeli achieved the lowest deprivation scores due to their strong economies and low unemployment rates.

Education and Health: The education domain revealed underperformance in literacy rates and school completion in provinces such as Şırnak, Bitlis, and Ağrı. Health deprivation was also severe in the southeastern provinces due to limited access to medical infrastructure and personnel. Western and central regions, such as Ankara and Eskişehir, performed best in both domains.

Crime and Social Distress: Deprivation related to crime and social distress was highest in large metropolitan areas like İstanbul, Ankara, and İzmir. The high incidence of recorded crimes, convictions, and suicides contributed to elevated scores in these urban provinces. Meanwhile, eastern and rural provinces showed lower recorded levels of social distress.

Housing and Living Environment: Housing deprivation was observed in both underdeveloped and rapidly urbanizing provinces, including Şırnak, Mardin, and Gaziantep. The living environment domain showed that provinces like Ardahan, Iğdır, and Ağrı faced severe infrastructural and environmental challenges, including a lack of access to piped water, electricity, and modern housing.

Composite Deprivation Index Results: The overall CDI scores reflected the cumulative impact of domain-based deprivation. Şanlıurfa, Ağrı, Şırnak, Mardin, and Iğdır emerged as the top five most deprived provinces, indicating persistent socio-economic and infrastructural challenges. In contrast, İstanbul, Ankara, Kocaeli, Tekirdağ, and Eskişehir ranked as the five least deprived provinces

Conclusion

The deprivation index developed in this study demonstrates that spatial deprivation in Turkey is not evenly distributed but rather concentrated in structurally disadvantaged provinces, particularly in the east and southeast. The findings emphasize the importance of multidimensional assessment and the role of spatial analysis in regional planning. Since the CDI is a comparative measure, even small changes in the deprivation scores of a few provinces can affect the overall ranking. This study contributes an adaptable deprivation index using only open, official statistical sources. It may serve as a planning tool for identifying priority areas, allocating resources, and promoting balanced regional development.

References

Atkinson, J., Salmond, C., & Crampton, P. (2014). The New Zealand Index of Deprivation 2013. University of Otago, Wellington.
Çağlar, A. (2020). İllerin yaşam kalitesi: Türkiye İstatistik Kurumu verileriyle veri zarflama analizine dayalı bir endeks. Eskişehir Osmangazi Üniversitesi İktisadi ve İdari Bilimler Dergisi, 15(3), 875–902. https://doi.org/10.17153/oguiibf.506704
Department for Communities and Local Government. (2019). The English Indices of Deprivation 2019. London.
McLennan, D., Barnes, H., Noble, M., Davies, J., Garratt, E., & Dibben, C. (2011). English indices of deprivation 2010: Technical report.
Payne, R. A., & Abel, G. A. (2012). UK indices of multiple deprivation—a way to make comparisons across constituent countries easier. Health Statistics Quarterly, 53(22), 2015–2016.
Smith, T., Noble, M., Noble, S., Wright, G., McLennan, D., & Plunkett, E. (2015). The English

Indices of Deprivation 2015. Department for Communities and Local Government.
The Office of the Chief Statistician (Scotland). (2009). Scottish Index of Multiple Deprivation 2009 Technical Report. The Scottish Government, Edinburgh.
TURKSTAT. (2021). Convicts discharged from prison by province where the crime was committed and type of crime at SR level 3. Ankara, Turkey.
TURKSTAT. (2021). Convicts received from prison by province where the crime was committed and type of crime at SR level 3. Ankara, Turkey.
TURKSTAT. (2024). Attained education level by provinces (Population 15 years of age and over). Ankara, Turkey.
TURKSTAT. (2024). Attained education level by provinces (Population 6 years of age and over). Ankara, Turkey.
TURKSTAT. (2024). Crude death rate by provinces. Ankara, Turkey.
TURKSTAT. (2024). Deaths by province and sex. Ankara, Turkey.
TURKSTAT. (2024). Gender parity index by province, level of education and school life expectancy. Ankara, Turkey.
TURKSTAT. (2024). Gross domestic product per capita by provinces. Ankara, Turkey.
TURKSTAT. (2024). House sales by provinces. Ankara, Turkey.
TURKSTAT. (2024). House sales to foreigners by provinces. Ankara, Turkey.
TURKSTAT. (2024). Infant mortality rate by provinces. Ankara, Turkey.
TURKSTAT. (2024). Life expectancy at birth by provinces and sex. Ankara, Turkey.
TURKSTAT. (2024). Mean years of schooling by provinces. Ankara, Turkey.
TURKSTAT. (2024). Population and annual average population growth rate by provinces. Ankara, Turkey.
TURKSTAT. (2024). Suicides by province and sex. Ankara, Turkey.
TURKSTAT. (2024). Total fertility rate by provinces. Ankara, Turkey.
TURKSTAT. (2025). Age dependency ratio by provinces. Ankara, Turkey.
TURKSTAT. (2025). Agricultural land and forest area by provinces. Ankara, Turkey.
TURKSTAT. (2025). Agricultural land by provinces. Ankara, Turkey.
TURKSTAT. (2025). Average size of households by provinces. Ankara, Turkey.
TURKSTAT. (2025). Daily wages of seasonal agricultural workers and the monthly wages of permanent agricultural workers by province. Ankara, Turkey.
TURKSTAT. (2025). Employment rate by province. Ankara, Turkey.
TURKSTAT. (2025). Labour force participation rate by province. Ankara, Turkey.
TURKSTAT. (2025). Median age by provinces and sex. Ankara, Turkey.
TURKSTAT. (2025). New distribution of health care professionals by provinces. Ankara, Turkey.
TURKSTAT. (2025). New distribution of number of hospital beds by provinces. Ankara, Turkey.
TURKSTAT. (2025). New distribution of number of hospitals by provinces. Ankara, Turkey.
TURKSTAT. (2025). New exports by province. Ankara, Turkey.
TURKSTAT. (2025). New imports by province. Ankara, Turkey.
TURKSTAT. (2025). Population migrated between provinces by province of residence and place of birth. Ankara, Turkey.
TURKSTAT. (2025). Unemployment rate by province. Ankara, Turkey.

URBAN AND REGIONAL PLANNING

Climate Change and Planning

Smart Cities, Digitalization, and Data Science

Sustainability, Ecology, and Energy in Planning

Transportation Planning and Urban Infrastructure

Rethinking Heritage-Tourism Relations: Critical Perspectives and Sustainable Futures for Cultural Sites

Büşra Yalçın[a], Turgay Kerem Koramaz[a]

[a] Istanbul Technical University, Urban and Regional Planning, Urban and Regional Planning, İstanbul
yalcinbus15@itu.edu.tr

Keywords: Heritage Conservation, Heritage Tourism, Responsible Tourism, Sustainable Tourism.

Aim

Traditionally, the concept of heritage has often been associated with a single cultural period or a specific political narrative, and its presentation, promotion, and economic utilization have been shaped accordingly (Hernandez et al., 2016). However, increasing global tourism mobility and its impacts on heritage sites have questioned the adequacy of traditional perspectives (Szromek et al., 2021; Aylan and Aylan, 2020). This study aims to examine the relationship between heritage and tourism from an interdisciplinary perspective, especially the way heritage is defined, the impacts of tourism on these areas, and sustainability-based solution approaches.

Material and Method

The main source data for this study is based on a comprehensive literature review conducted in the Web of Science (WOS) database using the keywords *"heritage," "tourism,"* and *"sustainability"*. During the search, the following categories were used as a basis: *"urban studies," "architectural studies," "regional urban planning," "area studies," "social studies,"* and *"cultural studies"*. The publications were filtered to include only those from recent years. The 66 articles obtained through the search were analyzed using content analysis methods. The titles, abstracts, and keywords of the studies were subjected to a preliminary evaluation and were evaluated according to three main groups: (1) perspectives on the concept of heritage, (2) problems identified in the relationship between heritage and tourism, and (3) solution-oriented sustainability strategies. Similar examples were evaluated together under each theme, and common trends and conceptual intersections were identified in studies from different geographical regions. Both theoretical approaches and empirical studies containing field data were taken into consideration; in this regard, publications with a critical perspective were prioritized for inclusion in the study. Additionally, the geographical distribution of publications, trends in their increase over the years, and the levels of interdisciplinary approaches were analyzed comparatively.

Findings

First, the publication information of the 66 articles reached was analyzed, and it was observed that the topic showed an increasing trend over the years. It was determined that 10 new articles were added to the literature between 2016 and 2019, 29 between 2020 and 2023, 20 in 2024, and 7 in the first months of 2025. This increase indicates that the subject has received growing international attention and has begun to be addressed with sensitivity. When examining the geographical distribution of the literature, it is observed that most studies are concentrated in countries such as China, Italy, and Spain, with a significant increase in academic interest, particularly in China, due to its intensive applications to UNESCO since 1985. The fact that only four studies from Turkey could be included in the review highlights the gap in the national literature (Çatalbaş et al., 2022; İsmailoğlu & Sipahi, 2021; Umar et al., 2022; Varolgüneş & Canan, 2018)

Perspectives to the concept of heritage in the studies

The study first examines approaches to the concept of heritage. The classification of cultural, natural, and mixed heritage defined by UNESCO has brought with it not only the prestige of being a world heritage site but also the effects of increasing tourist pressure (UNESCO, 1972). In cities such as Venice, Dubrovnik, and Barcelona, increased tourism activity following heritage status has led to the deterioration of the social fabric, rising housing

prices, and the loss of cultural authenticity (Bobic & Akhavan, 2022; Mihalic et al., 2021). In addition to these issues, the potential of unlisted heritage sites is also significant. The literature reveals that these insufficiently recognized areas offer great opportunities to preserve local identity, develop alternative types of tourism, and sustain cultural diversity (Imon, 2017; Zhang, 2021). For example, Ye's (2021) study on the St. Lazarus Neighborhood in Macau examines how an unlisted area was reintroduced to tourism and how the local community's living practices were transformed from a socio-political perspective. Similarly, Tang et al. (2025) examined traditional rural tourism villages in China and demonstrated how spatial planning elements such as settlement patterns, structures, street layouts, and architectural details significantly influence tourists' willingness to revisit. The findings support the idea that the design and experiential quality of heritage environments directly influence visitor satisfaction and participation, and offer concrete strategies for the development of sustainable rural heritage tourism.

Problems identified in the relationship between heritage and tourism

Secondly, critical approaches to tourism emerge as a key area of discussion in this study. In particular, excessive tourism in heritage areas leads to consequences such as exceeding carrying capacity, exclusion of local people from their neighborhoods, and erosion of cultural identity (Phi, 2020).
Along with excessive tourism, authenticity, social memory, and spatial belonging are rapidly being replaced by commercialized and reproduced superficial experiences. The theoretical framework developed by MacCannell (1976) through the concept of authenticity discusses this transformation with reference to the depth within the social structure. Zukin (2009) emphasizes that heritage is instrumentalized not only in aesthetic but also in economic and cultural branding processes. In a similar context, Wise (2016) highlights the importance of the triple bottom line approach in the renewal of urban tourism, noting that while economic and environmental sustainability are often prioritized, social sustainability, which includes elements such as community pride, local entrepreneurship, education, and volunteerism, is increasingly gaining attention. The study underscores the need to integrate these dimensions for a more holistic and context-sensitive understanding of urban tourism planning and renewal (Wise, 2016). In addition to these findings, Kang et al. (2025) investigated how emotional solidarity, particularly the feeling of welcome, affects tourist satisfaction and loyalty in heritage cities. In their studies focused on South Korea, they also revealed that nostalgia acts as a moderating factor that strengthens the relationship between tourists' emotional attachment and destination loyalty. By conceptualizing this within the framework of productive nostalgia, they offer a unique perspective on how emotional experiences can be integrated into sustainable heritage tourism strategies. Empirical studies conducted by Rasoolimanesh and Jaafar (2017), Orgaz-Agüera et al. (2020) emphasize that the sustainability of heritage tourism is significantly influenced by community participation, local perceptions, and equitable benefit sharing. These studies demonstrate that involving local stakeholders in tourism decision-making processes is one of the fundamental principles of sustainable tourism. Additionally, they underscore the importance of balancing heritage conservation, socio-economic development, and conflict mediation through inclusive governance models.

Solution-oriented sustainability strategies

The final section focuses on sustainable and responsible tourism practices as a solution approach. The concept of sustainable development, which was included in the 1987 Brundtland Report, Our Common Future, has been echoed in tourism practices over time and has become an international standard through the UNWTO's sustainable tourism guidelines (WCED, 1987; World Tourism Organization, 2019). Sustainable tourism aims to protect heritage sites through an approach that balances environmental, socio-cultural, and economic dimensions (Salazar, 2016). A notable example of this multi-dimensional approach is presented by Sarkar and colleagues (2025), who used CBS-based geo-spatial analysis to assess the ecotourism potential of the "Seven Sister States" in Northeast India. In their study, they classified regions based on their environmental and cultural capacities and provided applicable recommendations for developing sustainable tourism while preserving ecological and cultural integrity, including infrastructure development, community participation, and strategic marketing. However, the expansion of the concept's content and its lack of concrete application in practice led to the emergence of the concept of

responsibility as one of the sub-components of sustainability. This increasingly prominent approach has evolved into a separate conceptual framework in the literature under the name "responsible tourism."

Conclusion

The results of the study reveal that heritage sites must be protected not only physically, but also in terms of their cultural uniqueness, social continuity, and relationships with local communities. The prestige and promotional value provided by UNESCO status can become a new pressure mechanism for sites if it is not addressed in conjunction with sustainability and local sensitivity. On the other hand, making non-listed areas more visible, supporting alternative forms of tourism, and actively involving local actors in the process can help establish a healthier and more sustainable balance between heritage and tourism. Within this framework, the study aims to offer a holistic perspective that addresses the relationship between heritage and tourism not only from an economic perspective but also from cultural, social, and ethical dimensions.

References

Aylan, F. K., & Aylan, S. (2020). Aşırı turizm kavramının farklı boyutlarıyla incelenmesi: Instagram'da paylaşılan fotoğraf ve yorumların içerik analizi. *Journal of Tourism & Gastronomy Studies, 8*(1), 584–607.

Bobic, S., & Akhavan, M. (2022). Tourism gentrification in Mediterranean heritage cities: The necessity for multidisciplinary planning. *Cities, 124*, 103616.

Çatalbaş, F., & Eçemiş Kılıç, S. (2022). Thinking over a participatory model for planning and conservation of cultural heritage in "the port city of Izmir" in the perspective of Historical Urban Landscape (HUL) approach. *Megaron, 17*(3), 526–541.

Hernandez, J. M., Suarez-Vega, R., & Santana-Jimenez, Y. (2016). The inter-relationship between rural and mass tourism: The case of Catalonia, Spain. *Tourism Management, 54*, 43–57.

Imon, S. S. (2017). Cultural heritage management under tourism pressure. *Worldwide Hospitality and Tourism Themes, 9*(3), 335–348.

İsmailoğlu, S., & Sipahi, S. (2021). Social sustainability of cultural heritage: Erzurum Great Mosque (Atabey Mosque). *Open House International, 46*(4), 578–594.

Kang, S., Kim, W. G., & Lee, S. (2025). Using nostalgia to increase tourists' destination loyalty in heritage cities: From imagined to productive nostalgia. *International Journal of Urban Sciences*, 1–26.

MacCannell, D. (2013). *The tourist: A new theory of the leisure class*. University of California Press.

Mihalic, T., Mohamadi, S., Abbasi, A., & Dávid, L. D. (2021). Mapping a sustainable and responsible tourism paradigm: A bibliometric and citation network analysis. *Sustainability, 13*(2), 1–22. https://doi.org/10.3390/su13020853

Orgaz-Agüera, F., Castellanos-Verdugo, M., Acosta Guzman, J. A., Cobena, M., Oviedo-García, M. D., & Phi, G. T. (2020). Framing overtourism: A critical news media analysis. *Current Issues in Tourism, 23*(17), 2093–2097.

Rasoolimanesh, S. M., Jaafar, M., Ahmad, A. G., & Barghi, R. (2017). Community participation in World Heritage Site conservation and tourism development. *Tourism Management, 58*, 142–153.

Salazar, N. B. (2016). The local-to-global dynamics of world heritage interpretation. In *World Heritage, Tourism and Identity* (pp. 121–130). Routledge.

Sarkar, A., Mondal, M., Das, S., & Gayen, S. K. (2025). Revealing ecotourism potentiality in northeast seven sister states, India: A geospatial analysis using multifaceted GIS-based approach. *Asia-Pacific Journal of Regional Science*, 1–41.

Szromek, A. R., Kruczek, Z., & Walas, B. (2023). Stakeholders' attitudes towards tools for sustainable tourism in historical cities. *Tourism Recreation Research, 48*(3), 419–431.

Tang, H., Liu, X., Li, J., & Wang, H. (2025). Research on design intervention in spatial planning of traditional rural tourism: Based on the perspective of tourists' willingness to visit again. *Journal of Asian Architecture and Building Engineering*, 1–21.

Umar, N., Yüceer, H., & Aydın, R. (2022). Assessing community awareness for participatory conservation of cultural heritage: The case of Tepebağ Tumulus and its surroundings in Adana, Turkey. *Open House International, 48*(1), 38–54.
UNESCO. (1972). *Convention concerning the protection of the world cultural and natural heritage*. https://whc.unesco.org/en/conventiontext/
Varolgüneş, F. K., & Canan, F. (2018). A slow city movement: The case of Halfeti in Turkey.
WCED. (1987). *Our common future*. World Commission on Environment and Development.
Wise, N. (2016). Outlining triple bottom line contexts in urban tourism regeneration. *Cities, 53*, 30–34.
World Tourism Organization. (2019). *UNWTO guidelines for institutional strengthening of destination management organizations (DMOs): Preparing DMOs for new challenges*.
Ye, X. (2021). Making post-colonial place identity: The regeneration of the St Lazarus neighbourhood, Macau. *Open House International, 46*(1), 114–129.
Zhang, X. (2021). Impact of rural tourism on residents' well-being in traditional ancient villages: A case of North Guangxi. *Heritage Science, 9*(1), 1–9. https://doi.org/10.1186/s40494-021-00616-y
Zukin, S. (2009). *Naked city: The death and life of authentic urban places*. Oxford University Press.

URBAN AND REGIONAL PLANNING

Climate Change and Planning

Smart Cities, Digitalization, and Data Science

Sustainability, Ecology, and Energy in Planning

Transportation Planning and Urban Infrastructure

Determination of Saturation Flow Rate Right-Turn Adjustment Factor for Large Radii in Istanbul

Ozan Emekter[a], Kemal Selçuk Öğüt[a]

[a] Istanbul Technical University, Department of Civil Engineering, Civil Engineering, Turkey
emekter18@itu.edu.tr

Keywords: Right-Turn Adjustment Factor, Saturation Flow Rate, Signalized Intersections.

Aim

Signalized intersections are the most crucial chokepoints in urban traffic regarding safety and travel time. Conflicting traffic flows, including pedestrians, need to wait and give way to each other to avoid hazardous conditions and accidents. These points, then, naturally represent a significant impact on travel time experienced by all traffic users. Therefore, it is of utmost importance to design them properly and to avoid wasting time; timing the red and green traffic signals is an important part of this design. "Saturation flow rate" is a parameter used commonly in the process of signal timing, which is why it is important to determine its correct value. It describes the maximum hourly traffic volume that can pass through a certain section of road given unrestricted flow conditions. While it can be measured directly at an existing intersection, there are correspondingly similar ways of mathematically estimating this value in case fieldwork is not to be conducted or for planned new intersections.

The mathematical estimation method assumes an ideal base value for the saturation flow rate and adjusts this base value for various geometrical and operational factors of the intersection. As these factors are affected by drivers' perceptions, quite a few studies have been conducted all over the world to determine their mathematical models. This paper focuses on the right-turn adjustment factor for mixed lanes where both through and right-turning flows are present. Developing an accurate mathematical model for this adjustment factor will permit the correct determination of signal times that minimize delays. This study involves field measurements for three intersection approaches with similar characteristics and turning radii in Istanbul to develop a mathematical model that can be used as the right-turn adjustment factor for large right-turning radii in an urban setting.

This study aims to put forward a mathematical model to determine the saturation flow rate right-turn adjustment factor for large turning radii, namely 20 meters or higher. The saturation flow rate, SFR, is the key variable of traffic signalization in calculating the flow ratio, which is used to determine the cycle time and green times of each phase. Three approaches from existing intersections in the city of Istanbul have been selected for fieldwork, as seen in Figure 1, which are the East approach of the intersection between Okul St. and M. Ali Birand St. in Beykoz (Intersection 1), the South approach of the intersection between Büyükdere St. and Darüşşafaka St. in Sarıyer (Intersection 2), and the West approach of the intersection between Mareşal Fevzi Çakmak St. and Yavuz Selim Köprüsü St. in Eyüpsultan (Intersection 3). Their turning radii are 23, 20, and 20 meters, respectively. The only difference between them is that they have one, two, and three traffic lanes in the measured approaches. The study similarly aims to find whether the number of lanes affects the significance of the rate of right turns.

As SFR is affected by several factors, such as lane width, grade, vehicle composition, parking, and so on, these intersections have been selected with care so that all these factors, except the right-turn factor, are equal to their default values, which is one.

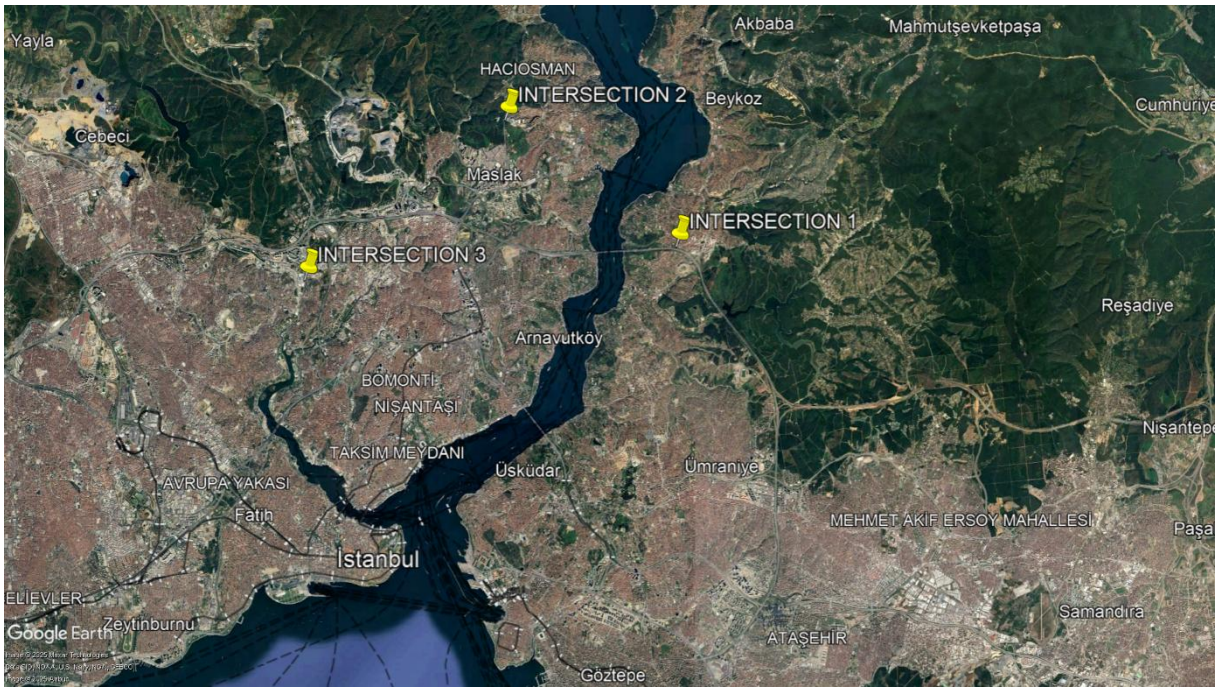

Figure 1. Intersections selected for fieldwork.

Material and Method

SFR is defined as the "equivalent hourly rate at which previously queued vehicles can traverse an intersection approach, assuming the green signal is available at all times and no lost times are experienced" (TRB, 2022). In other words, it is the maximum number of vehicles that a lane or lane group in an intersection approach can accommodate, given no restrictions and a constant supply of vehicles traveling at the highest flow rate possible. The first way to determine the SFR is to measure the headway at which vehicles discharge from a red-light queue and divide an hour by it, as seen in Equation 1.

$$s = \frac{3600}{h_s} \#(1)$$

$$where, s: saturation\ flow\ rate\ (veh/h) h_s: saturation\ headway\ (sec/veh)$$

The second way is multiplying its default value (base saturation flow rate, s_0) by adjustment factors as seen in Equation 2 when fieldwork is not performed (TRB, 2022, Chapter 19).

$$s = s_0 \times \prod_{i=1}^{13} f_i \#(2)$$

These adjustment factors are for lane width, heavy vehicles, and grade, existence of a parking lane and parking activity, the blocking effect of local buses, area type, lane utilization, right-turning vehicles, left-turning vehicles, pedestrian activity, bicycle activity, work zone presence, downstream lane blockage, and sustained spillback. As mentioned, the intersections selected for fieldwork in this study do not exhibit any of these factors other than right-turning vehicles, whose adjustment factor, f_{RT}, is to be determined. Therefore, the resulting relation is as shown in Equation 3.

$$s = s_0 \times f_{RT} \#(3)$$

Previous research into the right-turn adjustment factor includes Ibrahim et al. (2007), who presented Equation 4 as a result of their study for traffic conditions in Malaysia (p. 76).

$$f_{RT} = \frac{1}{1 + 0.54\sqrt{\frac{P_{RT}}{r}}} \#(4)$$

$$where, f_{RT}: right - turn\ adjustment\ factor P_{RT}: rate\ of\ right - turns r: turning\ radius\ (m)$$

Savitha et al. (2017) developed the model seen in Equation 5 for the turning radius in their study conducted in Bangalore, India.

$$f_{RT} = 1 + 4 \times \frac{r}{1000} \#(5)$$

$$where, r: turning\ radius\ (m)$$

This study, by contrast, does not utilize the turning radius in its proposed model and rather seeks to eliminate its influence by studying three turning movements with similar and large radii. Therefore, the model seen in Equation 6 is a better fit (TRB, 2022, Chapter 31).

$$f_{RT} = \frac{1}{1 + 0.18P_{RT}} \#(6)$$

Çalışkanelli and Tanyel (2017) developed Equation 7 for the city of İzmir in Turkey.

$$f_{RT} = \frac{1}{1 + 0.40P_{RT}} \#(7)$$

The proposed model in this study is shown in Equation 8, where α, β, and γ are parameters.

$$f_{RT} = \frac{1}{\alpha + \beta \times {P_{RT}}^{\gamma}} \#(8)$$

Equations 9 – 11 show how the parameters α and β were determined.

$$s = \frac{s_0}{\alpha + \beta \times {P_{RT}}^{\gamma}} \#(9)$$

$$\frac{1}{s} = \frac{\alpha}{s_0} + \frac{\beta \times {P_{RT}}^{\gamma}}{s_0} \rightarrow \frac{\alpha}{s_0} = A, \qquad \frac{\beta}{s_0} = B \#(10)$$

$$\frac{1}{s} = A + B \times {P_{RT}}^{\gamma} \#(11)$$

A regression analysis was conducted to calculate A and B, which then revealed α and β. The γ value is determined by assigning values that minimize the Sum of Squared Errors of the regression model. The base SFR, s_0, was determined to be about 1890 pcu/h in Istanbul (Dündar, 2018), which is used in this paper.

The SFR needs to be calculated based on the saturation headway, which is exhibited after the first few vehicles in a queue due to the time it takes them to react to the signal change and accelerate (Urbanik et al., 2015, Chapter 5). The first few vehicles do not have sufficient time or space to accelerate to the design speed by the time they reach the stop line, which increases their headways beyond the saturation headway. In order to accurately determine the SFR, the first few vehicles need to be disregarded in each cycle. This decision is made by using a one-way ANOVA test. The test is first conducted with all vehicles in the queue. Then, the first vehicles are excluded from the data set, and the test is repeated. The elimination of the first vehicles lasts till all vehicles have stable headways.

The headway measurements were taken for at least 30 cycles at each intersection. Afterward, the aforementioned regression analysis was performed to determine the parameters in the proposed model that show the relation between the rate of right turns and SFR.

Findings

The vehicle positions in the queue and their headways can be seen in Figure 2 for Intersection 1. The dashed line shows the saturation headway.

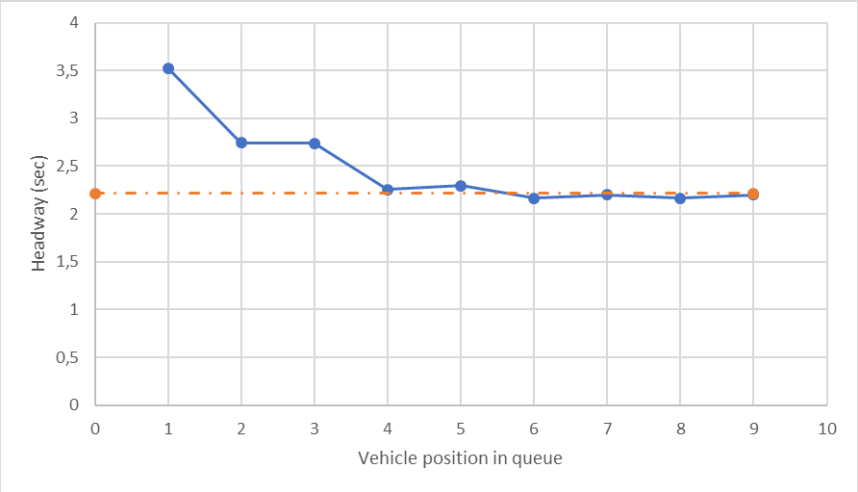

Figure 2. Through-only average headways for Intersection I.

A one-way ANOVA test concluded that the first three vehicles should be discarded as their means deviate too much from the rest due to the effects of reaction time and acceleration discussed earlier. After the third vehicle, the headways are stable. The vehicles between the fourth and last vehicle in the queue were considered in this study for calculations hereafter.

Accordingly, the saturation headway (h_s) for each measured cycle with right turns was calculated as the average headway without considering the first three vehicles. SFR (s) was then calculated for each cycle as per Equation 1.

The right-turn ratio (P_{RT}) in each cycle was calculated as the number of right-turning vehicles divided by the total number of vehicles, again, without considering the first three vehicles.

The initial regression model was conducted for $\gamma=1$, where 1/s is the dependent variable and P_{RT} is the independent variable. Then, by changing the γ value from 0.1 to 2.0 at intervals of 0.01, the regression models were calibrated. The model with the lowest Sum of Squared Errors was achieved when $\gamma=0.84$.

The scatter diagram of the regression analysis can be seen in Figure 3 for $P_{RT}^{0.84}$ and 1/s for all intersections.

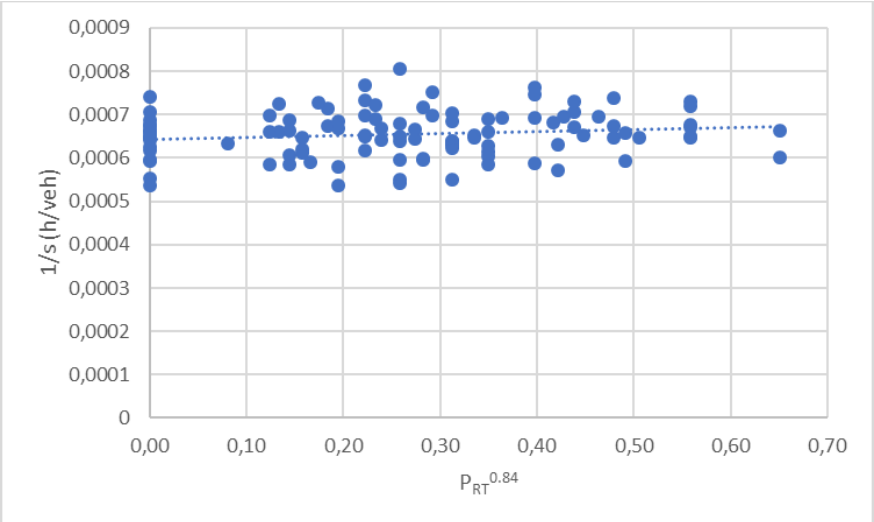

Figure 3. Scatter diagram of regression analysis.

The proposed right-turn adjustment factor was then determined as seen in the Equations. 12 – 15.

$$\frac{1}{s} = 0.000643536 + 4.502 \times 10^{-5} \times {P_{RT}}^{0.84} \#(12)$$

$$\alpha = A \times s_0 = 0.000643536 \times 1890 = 1.216 \#(13)$$

$$\beta = B \times s_0 = 4.502 \times 10^{-5} \times 1890 = 0.085 \#(14)$$

$$f_{RT} = \frac{1}{1.216 + 0.085{P_{RT}}^{0.84}} \#(15)$$

It should be noted that this model was derived from data for turning radii of 20 to 23 meters and is intended to be used for this interval.

The resulting model for SFR concerning right-turns is shown in Equation 16 and Figure 4.

$$s = \frac{1{,}890}{1.216 + 0.085{P_{RT}}^{0.84}} \#(16)$$

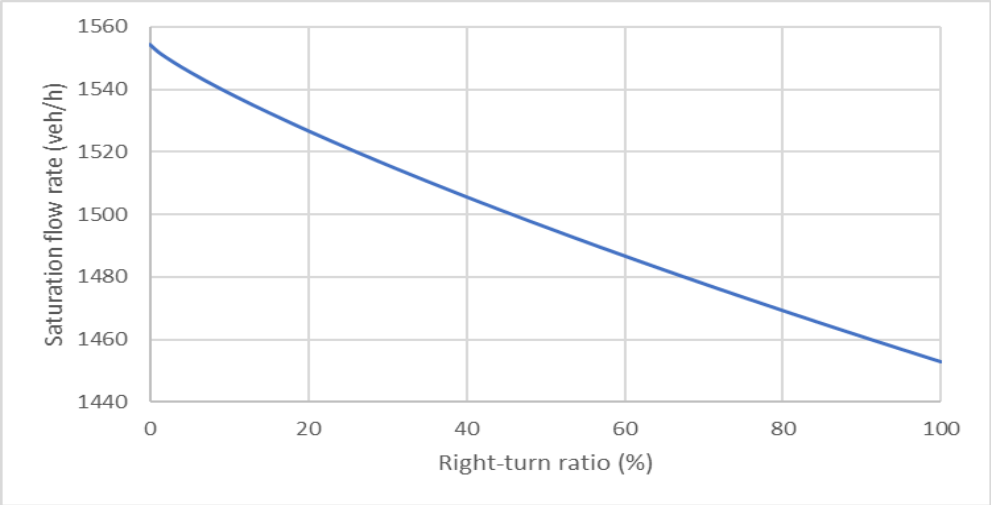

Figure 4. The change of SFR with respect to the right-turn ratio.

Conclusion

As the number of right-turning vehicles affects the SFR and this effect is represented by the right-turn adjustment factor, in this study, this effect with a turning radius of 20 meters or larger was studied, and an empirical model for this has been derived.

Initially, it can be observed that the rate of right-turns has less than a substantial effect on the saturation flow rate when the turning radius is large, but it is nevertheless there. In other words, the component involving this rate in the right-turn adjustment factor model has turned out to be small, yet significant.

As the results were quite similar across the three studied intersections, it has been concluded that the number of lanes does not have a significant influence on the right-turn adjustment factor when the turning radius is 20 meters or larger.

Crucially, the rightmost lane being mixed was found to affect the SFR as the measurements consistently yielded values less than s_0 even with no right-turns. This effect may be studied further.

Further research should focus on the effect of turning radii smaller than 20 m. Smaller radii should, in theory, result in increased hindrance caused by turning movements, and potentially the number of lanes playing a significant role.

References

Çalışkanelli, S., & Tanyel, S. (2017). *Sinyalize kavşaklarda doygun akım değerinin irdelenmesi*. Teknik Dergi. https://doi.org/10.18400/tekderg.346592

Dündar, S. (2018). *İstanbul'daki ışıklı kavşaklarda doygun akım değerini etkileyen geometrik değişkenlerin incelenmesi* (Publication No. 538219) [Doctoral dissertation, Istanbul Technical University]. National Thesis Center of the Council of Higher Education of Turkey. https://tez.yok.gov.tr/UlusalTezMerkezi/TezGoster?key=as2oTjW5jfr9IKSvmCdJYvyYFlUw778Mll-y86t1KAV6fphtThlkl-0aSIK3Edfa

Ibrahim, W. H. W., Hossain, Q. S., & Leong, L. (2007). Estimation of right-turn adjustment factor at signalized intersections for Malaysian traffic conditions: Considering turning radius and proportion of turning vehicles. *Advances in Transportation Studies, 12*. https://trid.trb.org/view/839243

Savitha, B. G., Murthy, R. S., Jagadeesh, H. S., Sathish, H. S., & Sundararajan, T. (2017). Study on geometric factors influencing saturation flow rate at signalized intersections under heterogeneous traffic conditions. *Journal of Transportation Technologies, 7*(1), 83–94. https://doi.org/10.4236/jtts.2017.71006

Transportation Research Board (TRB). (2022). *Highway capacity manual* (7th ed.). The National Academies Press. https://doi.org/10.17226/26432

Urbanik, T., Tanaka, A., Lozner, B., Lindstrom, E., Lee, K., Quayle, S., Beaird, S., Tsoi, S., Ryus, P., Gettman, D., Sunkari, S., Balke, K., & Bullock, D. (2015). *Signal timing manual* (2nd ed.). Transportation Research Board. https://doi.org/10.17226/22097

Towards Walkable and Green University Campuses: Observational Assessment of ITU Maslak Campus for Advancing the Sustainable Development Goals

Amira Moursy[a], Hatice Ayataç[a]

[a] Istanbul Technical University, City and Regional Planning Department, Türkiye.
ammar19@itu.edu.tr

Keywords: Composite Indicators, Green Campus, ITU Maslak Campus, Sustainable Development Goals, Walkability.

Aim

As global environmental and social challenges escalate, the role of university campuses in modeling sustainable development has become increasingly significant. University campuses serve as educational environments and living laboratories where sustainable development goals (SDGs) can be implemented and tested. In this context, promoting walkable and green campuses contributes directly to multiple SDGs, including SDG 3 (Good Health and Well-being), SDG 11 (Sustainable Cities and Communities), and SDG 13 (Climate Action). When integrated with green infrastructure and sustainable waste management, walkability can help reduce carbon footprints, encourage healthier lifestyles, and foster inclusive and vibrant academic communities (United Nations, 2015).

This study, conducted on Istanbul Technical University (ITU) Maslak Campus, forms part of a broader PhD project that examines the spatial, environmental, and experiential factors contributing to campus walkability. The key innovation in this research is the development and application of a multi-dimensional evaluation method for assessing the walkability of the campus. The assessment is structured around a hybrid set of 14 composite indicators, synthesized from existing walkability indexes and the UI Green Metric World University Ranking (UI Green Metric, 2023).

These indicators are grouped into three thematic categories: safe and secure green walking, convenience and attractiveness, and waste and pollution. The aim is to evaluate how these integrated indicators can guide progress toward more sustainable, livable, and inclusive campus environments, in alignment with the SDGs (Speck, 2013).

This extended abstract presents the observation-based phase of the study. While the research will ultimately include survey-based assessments of user perception, survey data collection is pending ethics committee approval. As such, this paper focuses on field observations conducted by the researcher using the composite indicators to evaluate pedestrian routes across the ITU Maslak Campus.

In this sense, the main objective of this study is to evaluate the walkability of ITU Maslak Campus through a detailed observational study guided by a composite indicator framework that integrates walkability indices and green campus sustainability criteria. Specific objectives include:

- Developing an indicator-based tool to assess campus walkability in alignment with SDGs.
- Applying this tool across multiple routes within the campus using structured observations.
- Identifying spatial patterns, strengths, and deficiencies in pedestrian infrastructure.
- Supporting strategic campus planning for sustainable mobility and enhanced quality of life.

The findings are intended to provide actionable recommendations for campus planning, aimed at fostering a more livable, equitable, and sustainable campus environment.

Material and Method

The methodology is based on a mixed-methods approach, integrating observational analysis with future participatory research involving students. Currently, the study focuses on the observation phase due to pending approval from the university's ethics committee for survey implementation.

The observational study involves walking through multiple selected routes across the ITU Maslak Campus, systematically applying the 14 composite indicators. These indicators are designed to assess both the physical infrastructure and subjective qualities of the walking experience.

1. Study Area and Route Selection

ITU Maslak Campus is one of Turkey's leading technical university campuses, located in Istanbul's urban core and serving thousands of students, faculty, and staff. The campus is characterized by diverse land uses, topographical variation, and a mixture of historical and modern buildings. The study area includes both primary and secondary pedestrian routes, selected to capture a range of conditions (e.g., flat vs. sloped areas, shaded vs. unshaded routes, proximity to services, and green spaces).
Twelve representative pedestrian routes were selected, capturing a range of spatial contexts such as:

- Central pedestrian spine.
- Dormitory access corridors.
- Sloped paths in green areas.
- Mixed pedestrian-vehicular routes.
- Peripheral academic building connectors.

2. Development of Composite Indicators

According to the walkability research literature (Southworth, 2005; Forsyth, 2015), the Green Metric University Ranking dimensions related to transportation, land use, and environment (UI Green Metric, 2023), and the analytical study of merging their criteria, a list of 14 composite measuring indicators is formulated. These indicators achieve common green and walkability goals, designed to assess the physical infrastructure and subjective qualities of the walking experience, and consist of a list of 7 goals within 3 major sectors specifically for campuses as follows (Table 1):

Table 1. Composite indicators list for walkable green campus (Source: the researcher).

Sectors	Goals	Indicators
1. Safe and secure green walking	1.1. Promote crossing safety	Indicator 1.1.1. Availability of crossings along streets.
		Indicator 1.1.2. Intersections with curb cut ramp
	1.2. Promote sidewalks and walking paths quality	Indicator 1.2.1. Sidewalk condition.
		Indicator 1.2.2. Sidewalks' coverage (building Awning, tree, arcade, etc.).
		Indicator 1.2.3. Sidewalk width
	1.3. Promote traffic security and behavior	Indicator 1.3.1. The proportion of well-lit streets.
		Indicator 1.3.2. Safe driving speeds.
2. Convenience and attractiveness	2.1. Promote pedestrians' amenities quality	Indicator 2.1.1. Permanent and temporary obstructions on streets.
		Indicator 2.1.2. Maintenance of building facade materials.
	2.2. Provide live streets	Indicator 2.2.1. The existence of accessible parks, open spaces, and recreation areas
3. Waste and pollution	3.1. Promote Air Quality	Indicator 3.1.1 Number of trees per linear kilometer.
		Indicator 3.1.2. The ratio of automobile streets to pedestrian streets.
	3.2. Promote cleanliness	Indicator 3.2.1. Drainage system to prevent puddles.
		Indicator 3.2.2. Sidewalk cleanliness.

Each of these indicators is evaluated using a combination of quantitative and qualitative field notes according to measuring levels (Table 2). These observations are carried out across varied routes during multiple site visits under varied conditions (morning/evening, weekday/weekend) to capture temporal variation. For each indicator, specific descriptive criteria were developed to minimize subjectivity and guide consistent scoring.

Table 2. Constructing criteria for measuring indicator levels (Source: the researcher).

Sectors	Goals	Indicators	Level 1	Level 2	Level 3	Level 4	Level5
1.Safe and secure green walking	1. Promote crossing safety	Indicator 1.1. Availability of crossings along streets.	with sufficient crossings	non-sufficient crossings			
		Indicator 1.2. Intersections with curb cut ramp.	with curb cut ramps	one-sided curb cut ramps	non-curb cut ramps		
	2. Promote sidewalks and walking paths quality	Indicator 2.1. Sidewalk condition.	excellent	good	fair	poor	
		Indicator 2.2. Sidewalks' coverage,	contains cover	no cover			
		Indicator 2.3. Sidewalk width	w>3	1.2<w<1.8	0.9<w<1.2	w<09	
	3. Prom	Indicator 3.1. The proportion of well-lit streets.	well-lit street	poor-lit street	not lit street		

	ote traffic security and behavior	Indicator 3.2. Safe driving speeds.	safe	not safe			
2.Convenience and attractiveness	4. Promote pedestrians' amenities quality	Indicator 4.1. Permanent and temporary obstructions on streets.	0-1 obstacles	2-3 obstacles	4-5 obstacles	>5 obstacles	
		Indicator 4.2. Maintenance of building facades materials.	excellent	good	fair	poor	
	5. Provide alive streets	Indicator 5.1. Existence of accessible parks, open spaces, and recreation areas.	exist	do not exist			
3. Was	6. Pr	Indicator 6.1. Number of trees per linear kilometers.	n>50	30<n<50	15<n<30	5<n<15	n<5

te and pollution	o mote Air Quality	Indicator 6.2. The ratio of automobile streets to pedestrian streets.	auto-street	pedestrian street			
	7. Promote cleanliness	Indicator 7.1. Drainage system to prevent puddles.	excellent	good	fair	poor	
		Indicator 7.2. Sidewalk cleanliness.	no litter	small amount of litter	some amount of litter	large amount of litter	

3. Observation Process

Field observations were conducted using the selected indicators for each route. Photos, sketches, and notes supported the data collection. Additional walks were conducted during different times of the day to capture variations in lighting, usage, and comfort conditions. The observational study was informed by subjective impressions related to spatial comfort, safety, and accessibility, thereby bridging quantitative and qualitative approaches.

4. Data Gathering

This stage has been conducted through contention and continuous visits to the study area to record the detailed and audit data into freehand sketched maps (Figure 1), and hand-written table sheets as a guideline sheet (Figure 2). It have been provided some materials to aid the process of data gathering as follows:

- Map outlining the case study area and mobile camera.
- Data collection table form for the selected indicators with their levels.
- A piece of 1-meter length string (to estimate sidewalk widths).
- Clipboard, white A4 sheets and pencils.

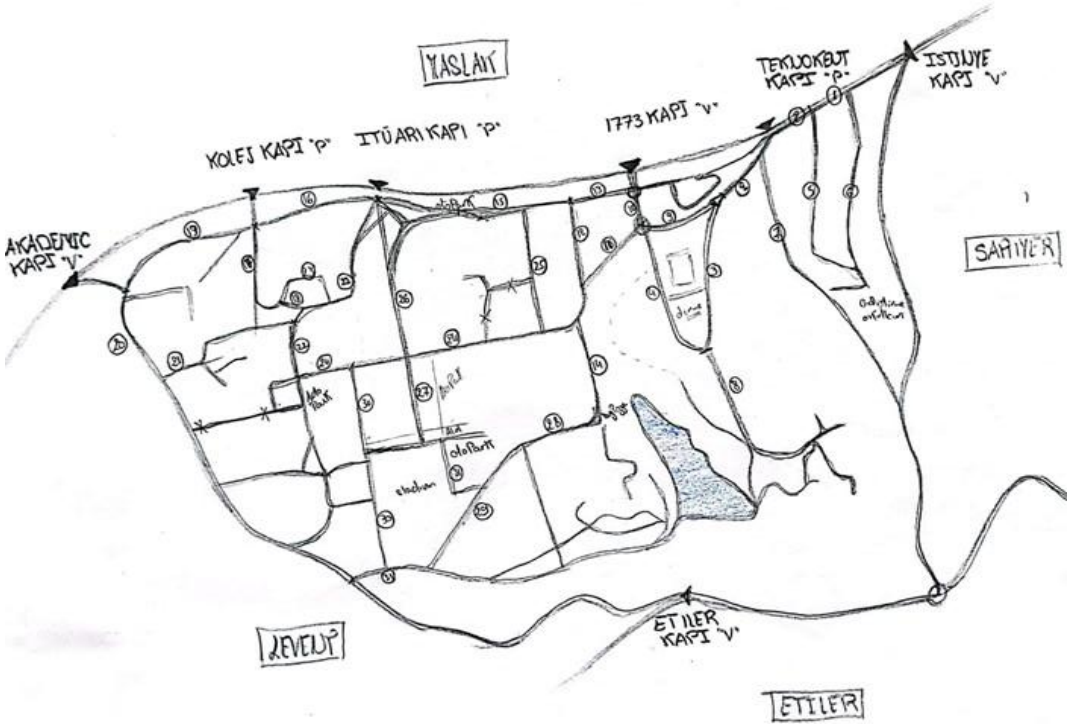

Figure 1. Freehand sketched map for data gathering (Source: the researcher).

Findings

Preliminary findings from the observation-based analysis suggest a mixed landscape of walkability on the ITU Maslak Campus. While the campus features numerous strengths like shaded walkways, pedestrian corridors, and green spaces, some challenges persist, particularly in terms of continuity, accessibility, and environmental quality.

- Strengths:
  - Abundance of green spaces and shaded walking paths in certain areas.
  - Proximity of key destinations within a walkable radius.
  - Strong potential for improvement through minor interventions.
- Challenges:
  - Inconsistent pedestrian infrastructure (e.g., sudden changes in sidewalk materials).
  - Insufficient seating, lighting, and wayfinding in some zones.
  - Barriers created by topography and vehicle-priority road design in central areas.

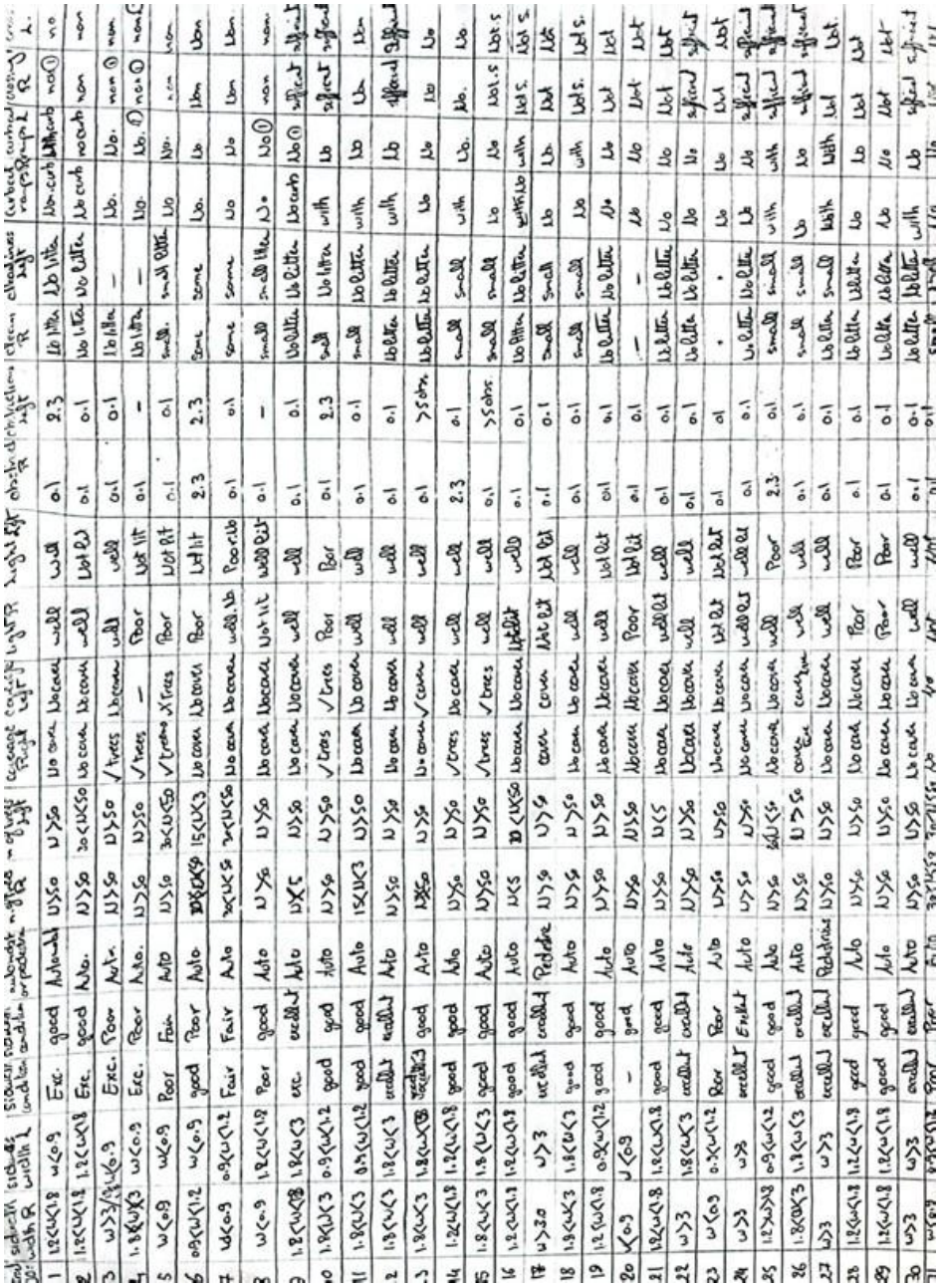

Figure 2. Data gathering manual sheet (Source: the researcher) .

In the category of Safe and Secure Green Walking, well-lit main corridors and large pedestrian plazas performed well. However, secondary paths and connectors between buildings were sometimes poorly lit or adjacent to vehicular traffic, reducing perceived safety, especially at night. Some routes, despite being lush and green, lacked protective buffers from nearby roads or had uneven pavement.

In terms of Convenience and Attractiveness, the central spine of the campus connecting major faculties and administrative buildings showed high walkability scores. This area included consistent walkway paving, visual interest, and gathering spaces with benches and shaded areas. However, peripheral areas such as dormitory access routes and hillside walkways were often disconnected, lacked signage, and presented steep or inaccessible gradients for some users.

Under the Waste and Pollution category, many walkways near academic buildings were clean and adequately equipped with waste bins. However, areas closer to vehicle parking lots, loading zones, and construction areas

were noisier, more polluted, and suffered from littering. These disparities indicate the need for targeted interventions in specific zones.

Conclusion

This extended abstract presents the results of an observational assessment of walkability on the ITU Maslak Campus using a composite indicator framework that merges walkability and green campus criteria. The analysis revealed a mixed walkability profile across the campus:

- Core pedestrian routes (e.g., the central spine) exhibited strong performance in terms of sidewalk quality, shade, and accessibility to key destinations.
- Peripheral and sloped areas, such as dormitory access routes and hillside paths, faced challenges related to lighting, walk surface uniformity, and wayfinding.
- While green space coverage and tree density contributed positively to perceived air quality, areas adjacent to roads and parking lots were more polluted and noisier.

These findings suggest that while the ITU Maslak Campus has a strong foundation for walkability, targeted improvements, such as better signage, enhanced lighting, and more continuous pedestrian infrastructure, are needed to create a more inclusive and sustainable walking environment.
The next phase of the study will incorporate user perspectives through surveys and daily walk diaries, which will deepen our understanding of how spatial features influence campus life, well-being, and sustainability. By integrating observational and participatory data, this research aims to inform both ITU's future mobility planning and broader green campus strategies aligned with the Sustainable Development Goals.

References

Ewing, R., & Handy, S. (2009). Measuring the unmeasurable: Urban design qualities related to walkability. *Journal of Urban Design, 14*(1), 65–84. https://doi.org/10.1080/13574800802451155
Finney, C. (2020). Participatory mapping and the emotional geographies of urban mobility. *Emotion, Space and Society, 34*, 100638. https://doi.org/10.1016/j.emospa.2019.100638
Forsyth, A. (2015). What is a walkable place? The walkability debate in urban design. *Urban Design International, 20*(4), 274–292. https://doi.org/10.1057/udi.2015.22
Forsyth, A., & Krizek, K. (2010). Promoting walking and bicycling: Assessing the evidence to assist planners. *Built Environment, 36*(4), 429–446. https://doi.org/10.2148/benv.36.4.429
Litman, T. (2021). *Evaluating transportation land use impacts: Considering the impacts, benefits and costs of different land use development patterns*. Victoria Transport Policy Institute. https://www.vtpi.org/landuse.pdf
Southworth, M. (2005). Designing the walkable city. *Journal of Urban Planning and Development, 131*(4), 246–257. https://doi.org/10.1061/(ASCE)0733-9488(2005)131:4(246)
Speck, J. (2013). *Walkable city: How downtown can save America, one step at a time*. Farrar, Straus and Giroux.
UI GreenMetric. (2023). *UI Green Metric World University Rankings Criteria*. https://greenmetric.ui.ac.id (Retrieved 18.02.2025)
United Nations. (2015). *Transforming our world: The 2030 Agenda for Sustainable Development*. https://sdgs.un.org/2030agenda (Retrieved 18.02.2025)
World Health Organization (WHO). (2020). *Health and sustainable development: Goals and strategies*. https://www.who.int (Retrieved 20.02.2025)

URBAN DESIGN

Design and Evaluation of Public Spaces

Urban Conservation

Urban Image and Identity

Urban Resilience

The Transformative Effect of Digital Art Installations on Public Spaces: The Case of Border Tuner

Gülay Didir[a], İsmail Eren Kürkçüoğlu[b]

[a] Istanbul Technical University, Graduate School, Urban Design Master Program, Türkiye
[b] Istanbul Technical University, Faculty of Architecture, Department of Urban Design, Türkiye
didir22@itu.edu.tr, ekurkcuoglu@itu.edu.tr

Keywords: Digital Art, Public Space, Spatial Transformation, Interactive İnstallation, Border Dynamics.

Aim

This study aims to explain clearly how digital art can change public spaces in three ways: the way the place looks and works, the way people feel and think while they are there, and the way the event is remembered later on. First, key ideas such as *space, place, public space,* and *digital art* are reviewed to set a solid base. Next, five well-known digital-art projects from different countries are compared to see which tools and methods are used most often and how the public reacts. After that, the research focuses on Rafael Lozano-Hemmer's *Border Tuner* and asks three main questions: (1) How did the light-and-sound system change the border zone between the two sides of the border while it was active? (2) How did the interactive parts help people on both sides talk to each other? (3) How did people continue to talk about the project after it was gone? By answering these questions, the study hopes to give artists, city planners, and decision-makers practical advice on choosing the right place, technology, and audience approach when they use digital art in cities.

Material and Method

The methodology begins with a theoretical exploration of the notions of space, place, public space, and digital art, tracing their historical development and mutual relations in the literature. This conceptual groundwork is followed by a comparative review of five digital-art interventions from around the world. The insights gleaned from these global examples then frame the case study of Rafael Lozano-Hemmer's *Border Tuner*. All spatial and perceptual findings are finally cross-referenced with the initial theoretical discussion and international precedents to evaluate the transformative capacity of digital art in public space.

Findings

Maps drawn before, during, and after the show show that *Border Tuner* changed how people used the border space for a short time: crowds gathered around the microphone towers, new meeting spots formed under the crossing light beams, and night-time activity in the area grew beyond its usual limits. A look at five other big digital artworks around the world confirms that temporary gear—projectors, sensors, and small stages—can quickly turn a quiet square or façade into a lively landmark without any permanent building work. Comments from about 1,200 social-media posts and interviews use strong words such as "together," "hope," and "moving," and a simple sentiment check shows that almost three-quarters of the reactions were positive. This boost in mood is strongest when visitors can control the light or sound themselves, so they feel like co-creators instead of passive viewers. Even after the equipment was removed, local news and community forums kept referring to the piece when discussing border issues, showing that the memory of a digital artwork can last much longer than the event itself and can fuel ongoing public debate.

Conclusion

The findings confirm that even time-bounded digital installations can leave a measurable imprint on the city. On a physical level, large-scale projections, multi-channel sound and responsive sensors can transform an otherwise unremarkable façade or plaza into a temporary landmark, drawing dense evening crowds and recalibrating pedestrian flows. This spatial re-programming, though short-lived, demonstrates that digital media provide urban

designers with a nimble toolset for testing alternative uses of public space without permanent construction. Equally important is the perceptual shift triggered by interactivity: when visitors modulate light, voice or data in real time, strangers are prompted to converse, exchange stories and view both the city and one another from a refreshed perspective. Such encounters nurture empathy across social or geopolitical divides—an effect clearly observed in *Border Tuner's* cross-border dialogues. Finally, the project's legacy endures beyond its dismantling; the shared memory of a luminous, participatory event can reinforce place identity and spark new debates over who public space is meant to serve. Taken together, these physical, perceptual and mnemonic impacts show that digitally mediated art is not merely a spectacle but a catalyst for civic reflection. Future studies should therefore track how long these layered impacts persist, compare results across cultural contexts and explore policies that encourage municipalities to host—and learn from—similar interventions.

To build on these insights, researchers could adopt longitudinal ethnographic approaches—returning to installation sites months or even years later to document whether initial behavioural changes become embedded in everyday routines. Mixed-method evaluations, combining pedestrian counts, GPS mobility traces and follow-up interviews, would shed light on the durability of spatial and social re-configurations. Moreover, comparative work across cities of varying size, governance style and technological capacity can reveal which institutional conditions best support inclusive digital art practices. At the policy level, cultural agencies might establish micro-grant schemes that pair artists with urban planners, ensuring that temporary interventions are aligned with broader regeneration or placemaking goals rather than remaining one-off spectacles. Ethical guidelines will also be essential: while sensors and data streams enrich interactivity, they raise privacy concerns that must be addressed through transparent data stewardship and community consent. Finally, sustainability should not be overlooked. Future projects could experiment with low-energy LED systems, solar-powered rigs and modular hardware that can be reused at multiple sites, thereby reducing the environmental footprint of large-scale digital artworks. By integrating such evaluative, institutional and ecological considerations, cities can move beyond the "wow" factor and harness digital art as a pragmatic, sustainable and socially responsive instrument for shaping public space.

References

Descartes, R. (1644). *Principles of Philosophy*.
Leibniz, G.W. (1714). *Monadology*.
Heidegger, M. (1971). *Building, Dwelling, Thinking*.
Norberg-Schulz, C. (1971). *Genius Loci: Towards a Phenomenology of Architecture*.
Relph, E. (1976). *Place and Placelessness*.
Tuan, Y.-F. (1977). *Space and Place: The Perspective of Experience*.
Certeau, M. (1984). *The Practice of Everyday Life*.
Lofland, L. H. (1998). *The Public Realm*.
Lynch, K. (1960). *The Image of the City*.
Lefebvre, H. (1991). *The Production of Space*.
Habermas, J. (1962). *The Structural Transformation of the Public Sphere*.
Jana, R., & Grosenick, U. (2006). *New media art*. Taschen.
Kim, S. (n.d.). *Technical notes on Rafael Lozano-Hemmer's "Border Tuner."* Retrieved May 12, 2025, Url-1 https://example.org/border-tuner-tech
Kwon, M. (2004). *One place after another: Site-specific art and locational identity*. MIT Press.
Lozano-Hemmer, R. (n.d.). *Border Tuner / Sintonizador Fronterizo*. Retrieved May 12, 2025, from https://www.lozano-hemmer.com/border_tuner.php
Paul, C. (2016). *Digital art* (3rd ed.). Thames & Hudson.
Saleh, N., Hasan, R., & Al-Hagla, K. (2022). Digital art installations and their impact on urban public spaces. *International Journal of Arts & Technology, 15*(2), 123-140.
Yao, Y., & Liu, Q. (2024). Interactive digital art in public squares: Effects on social ties and place identity. *Journal of Urban Cultural Studies, 11*(1), 45-59.

The Impacts of Building-Street Interaction on Behavior: A case Study on Privacy in Kadıköy

İrem İncetuzcu[a], Gülden Demet Oruç Ertekin[b]

[a] Istanbul Technical University, Graduate School, Interdisciplinary Urban Design (MSc), Türkiye
[b] Istanbul Technical University, Faculty of Architecture, Department of Urban and Regional Planning, Türkiye
incetuzcu22@itu.edu.tr

Keywords: Street & Building Types, Behavior, Privacy, Territoriality, Defensible Space.

The interaction between individuals and urban space has long been a central concern in environmental psychology and urban design. Scholars such as Bechtel and Churchman (2002), Lang (1987), and Göregenli (2005) have emphasized the role of spatial variables in shaping human behavior, particularly through the dynamic negotiation between private and public domains. Within the Turkish context, a study by Barlas (2014) have further explored how the physical environment influences everyday practices and collective urban life. This research builds on these interdisciplinary foundations, with a specific focus on privacy as a mediator of spatial behavior. It draws on Jan Gehl's (1971; 2013) work on human-scale urbanism and street life, as well as Oscar Newman's (1972) Defensible Space Theory, to analyze how morphological interfaces between buildings and streets influence behavior.

Rather than viewing privacy solely as a static boundary, this study conceptualizes it as a layered and context-dependent construct that shapes spatial use, visibility, and public engagement. By adopting this framework, the research contributes to a broader understanding of how built environments structure human activities and perceptions in urban space. Focusing on three morphologically distinct streets in Kadıköy, Istanbul, this study explores how variations in street and building typologies contribute to different behavioral outcomes, particularly in terms of spatial accessibility, visibility, and use. The research is situated within a broader inquiry into how urban form shapes lived experience and seeks to contribute to the ongoing discourse on human-centered urban design.

Aim

This study aims to investigate how variations in building-street interactions influence spatial behavior in urban settings, with a particular focus on privacy as a mediating factor. By analyzing three morphologically distinct streets in Kadıköy, Istanbul, the research seeks to:

- Understand how architectural features such as visibility, access, and enclosure shape human engagement with public space;
- Examine how different degrees of privacy affect the diversity, intensity, and duration of behavioral patterns;
- Map behavioral dynamics in relation to street morphology using spatial analysis and observational techniques;
- Contribute to urban design and environmental psychology by framing privacy not merely as a limiting condition, but as a formative element of public life.

Material and Method

The study was conducted in three selected streets in Kadıköy, Istanbul, chosen based on their distinct building-street interactions and varying levels of privacy. These streets feature a mix of residential and commercial uses, influencing how privacy is manifested and experienced in public spaces.

A multi-method approach was employed, combining spatial analysis, on-site observation, and behavioral mapping to examine how urban morphology affects human interactions. On-site observations were carried out to systematically record spatial behaviors of individuals on these streets, while behavioral mapping techniques were used to analyze how different street morphologies shape user interactions. To further assess the impact of privacy, the study incorporated urban design frameworks, specifically Oscar Newman's Defensible Space Theory and Jan Gehl's studies on urban life, to evaluate how spatial boundaries influence public engagement. Additionally, cross-sectional street drawings were analyzed to determine how visibility and access affect privacy and human behavior in urban settings.

To identify key areas of interaction, the study mapped the most lively points where people spent significant time, correlating spatial behavior with privacy dynamics. Special attention was given to thresholds, stairs, and ground-floor windows, which were recognized as critical elements shaping the interaction between buildings and streets. By integrating these qualitative and spatial methods, the research provides a comprehensive understanding of how privacy influences street behavior and contributes to urban design and environmental psychology.

Findings

The findings of the study underscore the significant influence of privacy on shaping behavioral patterns in urban streets. The observations revealed that the spatial morphology of buildings, particularly the degree of visual access, the presence of thresholds, and the configuration of street-facing elements, directly affects how individuals interact with public space. Three key behavioral dimensions were observed: duration of presence, diversity of activity, and type of user interaction (residents vs. regulars).

Zuhal Street displayed the highest degree of architectural surveillance due to its wide cross-section and elevated visual exposure from residential buildings (Figure 1). Despite the presence of some regular users, most individuals engaged only in transitory actions such as walking or pausing briefly. The front gardens and set-back entrances appeared to discourage long-term presence, signaling stronger privacy boundaries. This resulted in spatial behavior that was more cautious, quiet, and brief in nature.

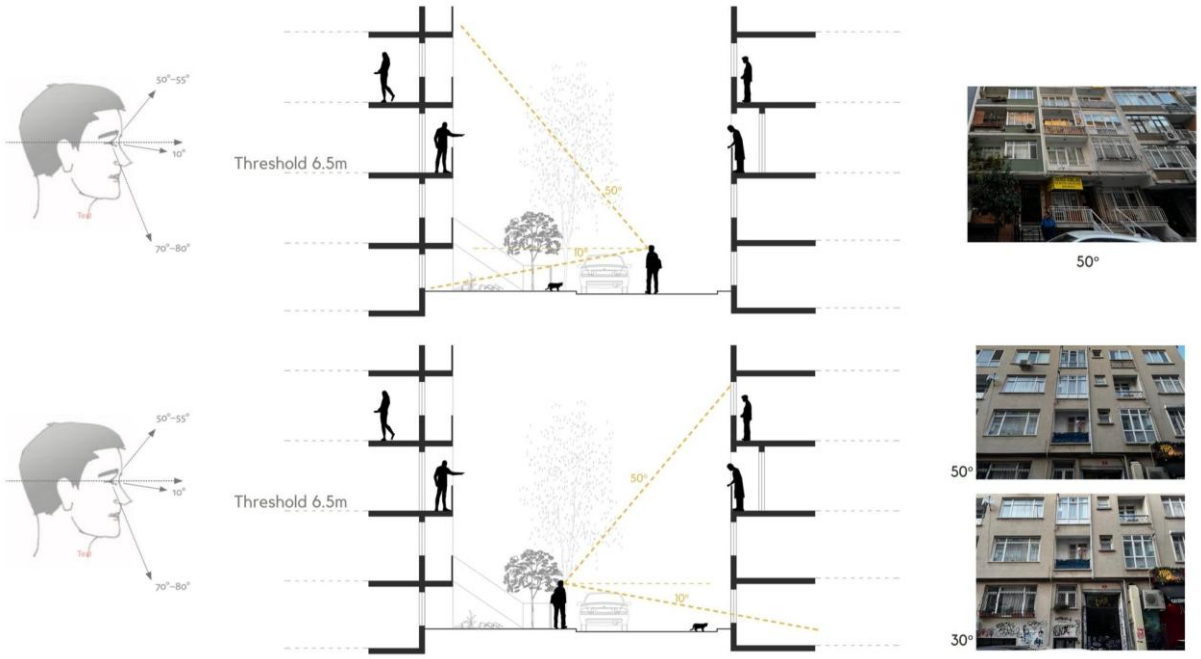

Figure 1. Section and the View of Left & Right Side from Zuhal Street.

Hacı Şükrü Street, with a moderate privacy profile, exhibited a more complex behavioral pattern. The most prominent point of engagement was the church wall, a non-residential structure that offered a visually open but socially protected edge. This created a semi-autonomous zone where people could sit, rest, or socialize without feeling surveilled (Figure 2). Residents were rarely visible in this space, whereas regulars used it as a gathering point. The spatial enclosure offered by the wall, combined with the lack of residential windows, contributed to more sustained informal use.

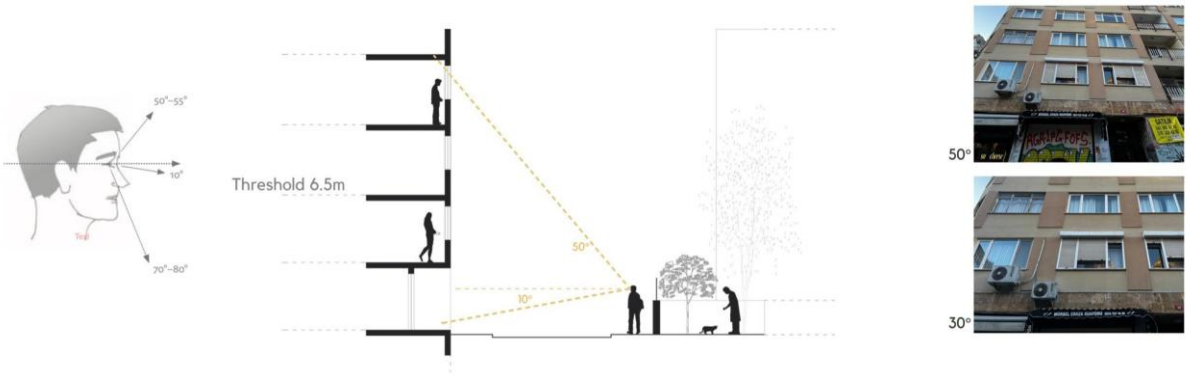

Figure 2. Section and the View of Left Side from Hacı Şükrü Street.

Kadife Street was the most socially active street, featuring minimal privacy enforcement and a dense mix of commercial and residential uses (Figure 3). The narrowness of the street limited visual control from buildings, and spatial elements such as wide doorsteps, low windows, and small thresholds were appropriated by users for a variety of informal activities—chatting, sitting, playing music, or simply lingering. The behavior here was diverse, interactive, and prolonged, highlighting the role of reduced spatial surveillance in enabling rich social dynamics.

Overall, the study confirms that as privacy thresholds increase, the publicness of the street diminishes, not just in terms of presence, but also in terms of behavioral spontaneity and social expressiveness. Conversely, when privacy boundaries are softened or blurred, streets accommodate a wider range of uses and users, fostering more vibrant public life.

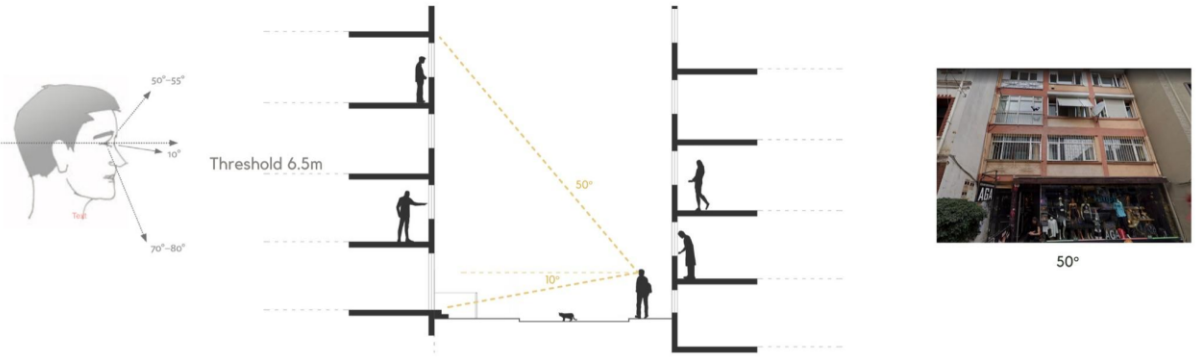

Figure 3. Section and the View of Left Side from Kadife Street.

Conclusion

The research demonstrates that the interaction between buildings and streets directly impacts urban behavior, particularly through the lens of privacy. The findings affirm that privacy can override public accessibility, influencing both the duration and nature of street interactions.

By mapping privacy levels and behavioral patterns, the study highlights the importance of urban design elements such as front gardens, staircases, door thresholds, and windows in shaping privacy dynamics. The results indicate

that wider streets intensify privacy effects, limiting public behavior, while narrower streets encourage social interactions.

This study contributes to urban design, environmental psychology, and public space planning by providing insights into how privacy should be strategically integrated into urban environments. Future research could expand these findings by examining the influence of cultural contexts and technological interventions in urban space management.

References

Barlas, A. M. (2014). Urban ceremonies urban streets. METU Faculty of Architecture.
Bechtel, R. B., & Churchman, A. (2002). Handbook of environmental psychology. John Wiley & Sons.
Gehl, J. (1971). Life between buildings: Using public space. Danish Architectural Press.
Gehl, J. (2013). How to study public life. Island Press.
Göregenli, M. (2005). Çevre psikolojisi. İzmir: Ege Üniversitesi Yayınları.
Lang, J. (1987). Creating architectural theory: The role of behavioral sciences in environmental design. New York: Van Nostrand Reinhold.
Newman, O. (1972). Defensible space: Crime prevention through urban design. Macmillan.
Westin, A. F. (1967). Privacy and freedom. Atheneum.

URBAN DESIGN

Design and Evaluation of Public Spaces

Urban Conservation

Urban Image and Identity

Urban Resilience

A Study Of Meaning In Ruins: Ancient Cities As Open-Air Museums

Bahar Çalışkan[a], Mehmet Emin Şalgamcıoğlu[b]

[a] İstanbul Technical University, Departmant of Architecture, Urban Design Master Program, Turkey
[b] İstanbul Technical University, Departmant of Architecture, Turkey
caliskanb23@itu.edu.tr

Keywords: Musealisation, Spatial Layout, Informal Education, Ancient City, UNESCO World Heritage List.

Aim

Ancient cities are the ruins of urban organizations that carry permanent settlement traces of the social, economic, and cultural activities of past civilizations to the present day. Today, the ruins that exist as a storyteller of the past have become an open-air museum. The architectural or urban design, religious, social, and cultural innovations that they witnessed or pioneered in history are the features that distinguish these city organizations from any other ruins, and how they present these features to audiences today is important. The aim of the study understand how ruin areas become meaningful perceptual space as an exhibition area and how ruin areas can narrate their heritage value to visitor with their exhibition route configuration and other information elements.

Material and Method

The material and method section should be written in Times New Roman font, justified alignment and in 10-point size. The study covers five ancient city settlements, Aphrodisias, Ephesus, Pergamon, Troy, and Xanthos, which are included in the UNESCO World Heritage List (WHL) and ancient Helenistic and Roman cities in Turkiye. Methodology applies in five stages. In the first stage, justified graphs were prepared to understand the organization of the exhibition paths. The j-graph gives a picture of the depth for all spaces in the structure, and it also shows ring properties of the spatial layout. Drawing on these ancient cities organization divides into two types, the first one is the ring type, where the entrance and exit of the exhibition on the same place, and the second type is the linear one, where the entrance and exit of the exhibition are located in different places. In the second stage, the UNESCO WHL selection criteria, representation like original structures, text, model, diagram, and other representations, and exhibition techniques are determined on site. In the third stage, human movement data was analyzed, according to visiting pattern and visiting sequences, and these data were combined with UNESCO criterias and determined the engagement of visitors with these values. In the fourth stage, space syntax analysis was created with the syntax2D program. Mean depth, integration-n, connectivity, and integibility analyses prepared from the syntax2D program. In the fifth stage, human movement data, spatial data, and syntactic data are analyzed together to understand which features guide and affect human movement in the ruin areas.

Findings

The Troy ancient city exhibition path has a ring-type exhibitioı road and the route is fully defined with wooden platforms. According to movement observation, people follow this road and integrate with UNESCO WHL criterias at the site. In the convex space 6, connectivity and integration data is higher than the average of the exhibition path, Also, this place is a high-speed area because of that some visitors skip visiting the northeast bastion of Troy, and this location is also an important feature of the site according to UNESCO. The Pergamon ancient city exhibition has a linear type of exhibition path, and the route is semi-defined with wooden material. but visitors use the exhibition road like a ring. According to movement observations and syntax data, visitors integrate just half of the UNESCO WHL criterias on the exhibition path. Convex space 2 Sanctuary of Athena, convex space 10 the sanctuary of Trajan, convex space 21 stage of theater and convexs space 30 gymnasium of the Demeter connectivity and integration datas higher than the average of the whole exhibition paths and these points works as returning points because of that visitors skipping half of the features of the sites UNESCO WHL critearia locations. The Ephesus ancient city exhibition path has a linear type exhibition road and is defined by original ancient roads and wooden covers. According to movement observation, people follow this road and integrate with UNESCO

WHL criterias at the site. In convex space 14 and convex space 29 start of the Curetes Streets connection and integration value are higher than the average value of the exhibition path, and a few visitors do not complete the road and return to these points. The Aphrodisias ancient city exhibition path has a ring-type exhibition road and is defined with stone stone-covered path and in some parts with a wooden platform. According to movement observation, people follow this road and fully integrate with UNESCO WHL criterias. In a convex space, 2 connectivity and integration data are higher than the average exhibition path, people do not skip any exhibited element in this area. In a convex space, 12 connectivity and integration value is higher than the average values, and some visitors skip visiting the sculptor's workshops and the council house. Xanthos exhibition road is a linear and non-defined, fully flexible exhibition path. UNESCO WHL criteria (ii) is not exhibited in the area, people can integrate criteria (iii) in the area, and it's shown in three parts, and some visitors skip the 17th mausoleum part.

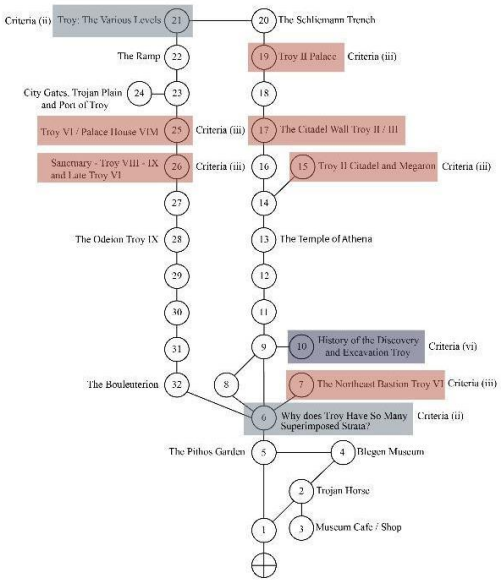

Figure 1. Troy J-Graph and Unesco Criterias.

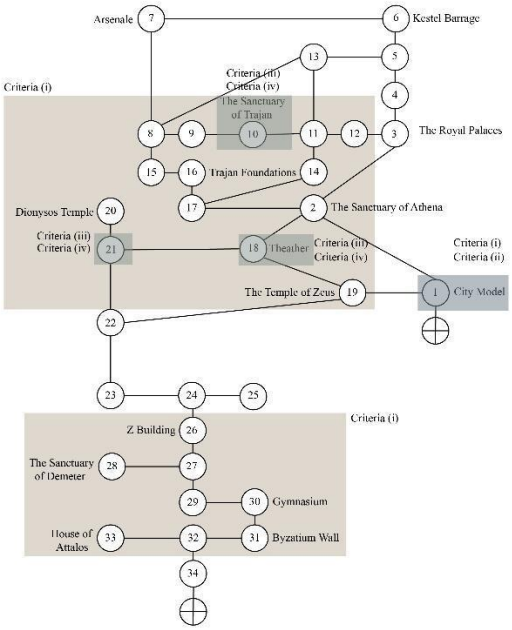

Figure 1. Pergamon J-Graph and Unesco Criterias.

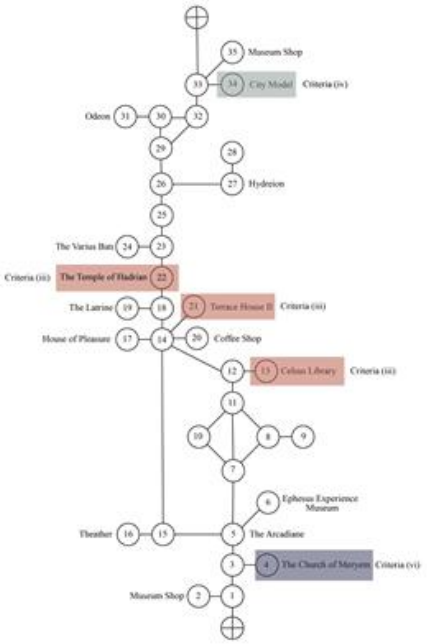

Figure 1. Ephesus J-Graph and UNESCO Criteria.

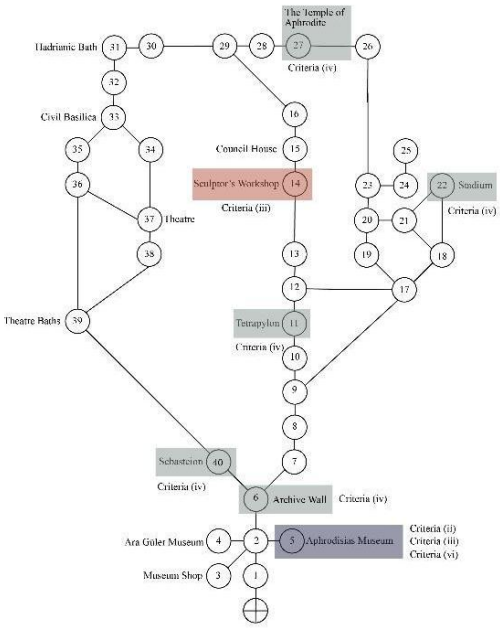

Figure 1. Aphrodisias J-Graph and Unesco Criterias.

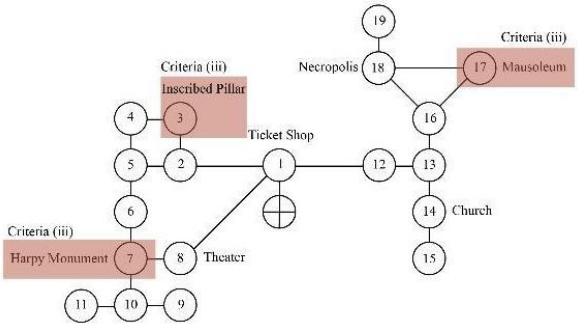

Figure 1. Xanthos J-Graph and UNESCO Criteria.

Conclusion

The evidence presented leads to the conclusion that when open-air ancient city exhibition paths have more than one space that has higher integration and connectivity value, in these places people move more flexibly, and these points can work as a returning Point and its cause that some visitors do not integrate with whole value of the city. As a secondary point, information boards placed which work with exhibited elements like ruins, architectural models, etc., and anastilosised and restored architectural elements work as stop points where people engage them, but people generally do not engage with information boards that do not work with any ruin or other representative object. All thing considered, anastilosited, restored architectural elements and their information board; also defined exhibition paths affect people's wayfinding and movement activities in ancient city areas.

References

Aykaç, P. (2019). Musealisation as a strategy for the reconstruction of an idealised Ottoman past: Istanbul's Sultanahmet district as a 'museum-quarter'. International Journal of Heritage Studies, 25(2), 160-177.
Bai, N. (2023). Sensing the Cultural Significance with AI for Social Inclusion: A Computational Spatiotemporal Network-based Framework of Heritage Knowledge Documentation using User-Generated Content.
Bataille, G. (1986). Erotism: Death and sensuality. City Lights Books.
Davis, P. (2011). Ecomuseums: a sense of place. A&C Black.
Desvallées, A., Mairesse, F., & Cummins, A. (2010). Key concepts of museology.
Eco, U. (1986). Function and sign: semiotics of architecture. In The city and the sign: An introduction to urban semiotics (pp. 55-86). Columbia University Press.
Frascari, M., & Goffi, F. (2017). Marco Frascari's Dream House: A Theory of Imagination. Routledge.
Gibson, J. J. (2014). The ecological approach to visual perception. Psychology Press.
Hershberger, R. G. (1970). Architecture and meaning. Journal of Aesthetic Education, 4(4), 37-55.
Hillier, B. (2007). Space is the machine: a configurational theory of architecture. Space Syntax.
Hillier, B., Hanson, J. (1984). The Social Logic of Space. Cambridge University Press, Cambridge.
Hillier, B., & Penn, A. (1991). Visible colleges: Structure and randomness in the place of discovery. Science in Context, 4, 23-49.
Kaplan, S., Bardwell, L. V., & Slakter, D. B. (1993). The museum is a restorative environment. Environment and Behavior, 25(6), 725-742.
Lefebvre, H. (1991). The production of space (D. Nicholson-Smith, Trans.). Blackwell.
Lynch, K. (1964). The image of the city. MIT Press.
Mumford, L. (1961). The city in history: Its origins, its transformations, and its prospects. Houghton Mifflin Harcourt.
Nelle, A. B. (2009). Museality in the urban context: An investigation of museality and musealisation processes in three Spanish-colonial World Heritage Towns. Urban Design International, 14(3), 152-171.
Okuyucu, E & Çoban, G. (2021). Analysis of the refunctioned Millet Hamam through ... The Turkish Online Journal of Design, Art and Communication, 11(1), 268–281. **Url-1** https://doi.org/10.7456/11101100/015
Peponis, J., & Wineman, J. (2002). The spatial structure of the environment and behavior. In R. Bechtel & A. Churchman (Eds.), Handbook of environmental psychology (pp. 271-291). New York: John Wiley.
Peponis, J., Zimring, C., & Choi, Y. K. (1990). Finding the building in wayfinding. Environment and Behavior, 22, 555-590.
Serrato, M., & Wineman, J. (1999). Spatial and communication patterns in research
Piacente, M. (Ed.). (2022). Manual of museum exhibitions. Rowman & Littlefield.
Psarra, S. (2009). Architecture and narrative: The formation of space and cultural meaning. Routledge.
Rapoport, A. (1990). The meaning of the built environment: A nonverbal communication approach. University of Arizona Press.
Relph, E. (1976). Place and placelessness. London: Pion.
Stokols, D. (Ed.). (2013). Perspectives on environment and behavior: theory, research, and applications. Springer Science & Business Media.
Tschumi, B. (1996). Architecture and disjunction. MIT Press.
Tversky, B. (2003). Structures of mental spaces: How people think about space. Environment and behavior, 35(1), 66-80.
UNESCO (2024). Operational guidelines for the implementation of the World Heritage Convention. Retrieved from: https://whc.unesco.org/en/guidelines/ date retrieved 21.03.2025
UNESCO. (n.d.). Xanthos-Letoon. UNESCO World Heritage Centre. **Url-1** https://whc.unesco.org/en/list/484 date retrieved 21.03.2025
UNESCO. (n.d.). Archaeological Site of Troy. UNESCO World Heritage Centre.
Url-1 https://whc.unesco.org/en/list/849 date retrieved 21.03.2025
UNESCO. (n.d.). Pergamon and its Multi-Layered Cultural Landscape. UNESCO World Heritage Centre.
Url-1 https://whc.unesco.org/en/list/1457 date retrieved 21.03.2025

UNESCO. (n.d.). Ephesus. UNESCO World Heritage Centre. **Url-1** https://whc.unesco.org/en/list/1018 date retrieved 21.03.2025

UNESCO. (n.d.). Aphrodisias. UNESCO World Heritage Centre.**Url-1** https://whc.unesco.org/en/list/1519 date retrieved 21.03.2025

Wineman, J. D., & Peponis, J. (2010). Constructing spatial meaning: Spatial affordances in museum design. Environment and Behavior, 42(1), 86-109.

URBAN DESIGN

Design and Evaluation of Public Spaces

Urban Conservation

Urban Image and Identity

Urban Resilience

The Impact of Space on Sound Perception: The Relationship Between Sound and Context

Kübra Türk[a], Meltem Erdem Kaya[b]

[a] Istanbul Technical University, Graduate School, Urban Design Program, Türkiye
[b] Istanbul Technical University, Faculty of Architecture, Landscape Architecture Program, Türkiye
turkk16@itu.edu.tr

Keywords: Soundscape, Contextual Perception, Auditory Cognition, Sonic Identity.

In the human sensory system, vision has always been regarded as the dominant mode of perception. This dominance also persists in spatial perception, where studies conducted by designers, urban planners, and architects are predominantly shaped by a visual-centric approach. However, spatial experience cannot be confined to visual input alone; space is fully perceived and experienced through the interaction of multiple senses. Alongside sight, senses such as hearing, touch, smell, and movement are fundamental components that influence an individual's spatial awareness. In particular, hearing offers powerful cues about the identity and character of a space. Despite sound being an element that defines space and shapes its atmosphere, it is often neglected in spatial design processes and is generally limited to acoustic control or noise management (Porteous, 1990). Nevertheless, the perceptual and semantic dimensions of sound make it a far more comprehensive subject of investigation.

One of the pioneering studies examining the role of sound in spatial perception is the World Soundscape Project (WSP), established in the 1970s at Simon Fraser University by Murray Schafer and his team. Under Schafer's leadership, this research group introduced the concept of the soundscape to the academic literature and brought an interdisciplinary perspective to the interaction between sound and environment. According to Schafer, a soundscape encompasses all the sounds perceived by individuals or communities within a specific environment (Fiebig, 2023). Schafer (1994) did not regard sounds solely as physical phenomena; instead, he classified them from acoustic, psychoacoustic, semantic, and aesthetic perspectives, revealing the multilayered structure of sound. He particularly focused on sound's ability to acquire different meanings depending on the context in which it is heard, thereby highlighting the dynamic relationship between sound and context. Schafer emphasized that two sounds with similar acoustic characteristics could evoke distinct perceptual and aesthetic responses depending on their context and argued that sounds might lose their identity when removed from their context. Indeed, the auditory system often fails to perceive the physical variations in sounds when they are listened to out of context, leading to alternative interpretations (Schafer, 1994).

Based on Schafer's exploration of the relationship between sound and context, this research investigates how sound perception can be manipulated depending on its context. Accordingly, the study analyzes how sounds are perceived under different contexts using urban sound recordings and a sound installation by Zimoun, who is known for creating kinetic sound sculptures with industrial materials (Öner, 2022). Similar to Zimoun's works, the research focuses on how sounds generated with familiar materials in everyday life can transform their identity when divorced from their original context. This relationship between sound and context reveals that spatial perception is not shaped solely by vision and that auditory input significantly influences the mental representation of space.

Aim

This study aims to emphasize the significance of sound and examine the determining role of context in sound perception. Specifically, it investigates how sounds that carry meaning and identity undergo perceptual changes when detached from their original context and presented in different environments. The study addresses the reciprocal interaction between sound and context and its effect on how individuals define, interpret, and mentally represent sounds.

Material and Method

This research was structured within a qualitative framework and is based on a survey conducted by digitally playing sound recordings to participants. The study involved 20 participants with diverse demographic backgrounds, including differences in age and occupation. During the research process, a total of 5 sound recordings, each carrying distinct semantic features, were utilized. These sound samples were categorized into two main groups: the first group consisted of industrial and mechanical sounds used in Zimoun's installations, while the second group comprised everyday urban sounds recorded in public spaces. This diversity aimed to analyze perceptual shifts in the participants' interpretations of sounds in relation to context.

The survey was conducted via an online platform, and participants were instructed to listen to the sounds in a quiet setting using headphones. This requirement was emphasized throughout the research to ensure consistency in listening conditions. To avoid guiding participants' perceptions, open-ended, straightforward, and non-leading questions were prepared.

For each sound recording, participants were asked two core questions: "What sound do you think you are hearing?" and "Where do you think you might have heard this sound? Please describe this environment with five words." Through these questions, the study aimed to gather data on how sounds were identified and to determine the assumed spatial contexts of these sounds. The collected responses were later processed and interpreted through word cloud analyses and qualitative evaluations.

Findings

The findings of this research clearly demonstrate the relationship between sound and context and its impact on sound perception. Participants' responses revealed that sounds tend to lose their identity when listened to out of context, resulting in misinterpretation or alternative identification of the sounds. In samples taken from Zimoun's sound installations, the majority of participants associated these sounds with different auditory environments, matching them with industrial settings such as factories, workshops, or construction sites. However, these sounds were actually produced by Zimoun using everyday objects and mechanical systems within an artistic context. This indicates that when sounds are removed from their context, they acquire new layers of meaning and that perceptions regarding the origin of sounds are shaped by listeners' spatial experiences and personal memories.

In urban sound samples, this perceptual deviation was also present but to a lesser extent. Most participants were able to identify the sounds as related to a coastal area, but there was still a noticeable dispersion in perception, with alternative interpretations present.

The research findings support Schafer's argument that sounds tend to lose their identity when removed from context. The participants' responses show that sound is perceived not merely based on its physical attributes but also through individual experiences, spatial memory, and contextual knowledge. These results reveal that sound functions not only as an acoustic datum but also as a tool for spatial and cultural interpretation, with sensory perception being closely tied to context.

Conclusion

This study explored the relationship between sound and context, revealing how sounds change identity on a perceptual level and how they can transform spatial contexts. The findings confirmed the initial hypothesis, showing that sounds tend to be perceived differently when detached from their original context. Notably, the fact that participants often misidentified or associated Zimoun's artistic sound installations and urban sound samples with incorrect spatial contexts demonstrates that sounds lose meaning when separated from their "place." This supports Schafer's assertion regarding the decisive role of context in perception.

Another significant finding of the study is that some sounds not only lose their identity but also possess the potential to manipulate and alter the listener's perception of the surrounding environment. This highlights that, in fields such as architecture and spatial design, sound should be regarded not merely as an auditory element but as a powerful design component capable of transforming spatial perception and memory.

In the future, the creation of a comprehensive research platform that classifies sounds capable of manipulating their context and brings such sounds together could contribute to a deeper exploration of the sound-space relationship.

References

Fiebig, A. (2023). Soundscape: A construct of human perception. In Schulte-Fortkamp, B., Fiebig, A., Hawkins, A., Popper, A. N., Sisneros, J. A., & Fay, R. R. (Eds.), Soundscapes: Humans and their acoustic environment (pp. 23-48). Springer. https://doi.org/10.1007/978-3-031-22779-0_2

Öner, A. (2022). The phenomenon of sound and hearing in spatial experience: The case of Zimoun (Master's thesis, Anadolu University, Eskişehir).

Porteous, J. D. (1990). Landscapes of the mind: Worlds of sense and metaphor. University of Toronto Press.

Schafer, R. M. (1994 ©1977). The Soundscape: Our Sonic Environment and the Tuning of the World. Rochester-Vermont: Destiny Books. *(Font Type: Times New Roman, Font Size: 10)*

URBAN DESIGN

Design and Evaluation of Public Spaces

Urban Conservation

Urban Image and Identity

Urban Resilience

Pedestrianization as a Tool to Create Resilient Cities Through Open Space Networks

Ilgın Yılmaz[a], Meltem Erdem Kaya[b]

[a] İstanbul Technical University, Graduate School, Urban Design, Türkiye
[b] İstanbul Technical University, Faculty of Architecture, Department of Landscape Architecture, Türkiye
yilmazil22@itu.edu.tr

Keywords: Pedestrianization, Urban Resilience, Open Spaces, Open Space Network.

Aim

Urban resilience is increasingly important for densely populated areas facing challenges such as fragmented urban form, ecological degradation, and social inequality. In high-density districts with limited intervention, failure to build resilience often leads to further decline in quality of life. This study explores how open space networks strengthened by pedestrianization can enhance resilience by promoting ecological continuity, social interaction, and spatial cohesion. Focusing on Bayrampaşa's Yenidoğan neighborhood, it examines the potential of pedestrian-oriented design to reconnect urban spaces and support adaptive environments.

Material and Method

This study is based on an in-depth literature review, urban morphology analysis, and field observation. The theoretical framework explores urban resilience, open space, and pedestrianization concepts focusing especially on the evolution of pedestrian-oriented design, walkability, and strategy typologies. These themes were examined both individually and in relation to each other, supported by key urban planning models that illustrate their spatial and social implications.

The case study focuses on Bayrampaşa, a densely built district in Istanbul characterized by mixed land uses, insufficient open space, and limited pedestrian infrastructure. Within this context, Yenidoğan neighborhood was selected for detailed analysis. Using 1/5000 land use data, street observations, and morphological mapping, urban patterns were analysed. Specific zones with varying physical characteristics were examined, and pedestrianization strategies were proposed based on observed spatial challenges.

Findings

As cities are transformed by environmental, social, and economic changes, the ways we plan and intervene in urban environments should also evolve. Urban resilience is defined as a city's capacity to withstand disruptions while continuing to function effectively (Mehmood, 2015). While sustainability focuses on maintaining balance, resilience emphasizes adaptability and flexibility. As urban populations exceed 50% of the global total (UNDRR, 2017), the increasing pressures of growth and spatial demand make resilience more critical.

Since the early 20th century, the adoption of automobiles has transformed the structure of cities. The freedom to travel long distances led to the rise of suburbs and reshaped urban planning priorities.

Table 1. Important Planning Ideas that Influenced by Automobile.

Planning Idea	Implications in urban morphology
Linear Urban Development (Arturo "Sorio y Mata)	● Aim: To preserve the relationship between nature and the city. ● Linear cities then became car oriented as the use of cars increase (Filippov, 2017).
Garden City (Ebenezer Howard)	● Aim: Decentralizing the overcrowded industrial city by creating self-contained settlements (Howard, 1902; Hall, 2002) ● Suburban development caused wide roads, parking lots and single-use zoning. It unintentionally encouraged automobile dependency and spatial fragmentation (Banister, 2005).
Neighborhood Unit (Clarence Perry)	● Aim: Organizing the city around walkable, self-contained communities (Perry, 1929). ● Resulted in an overemphasis on road hierarchy and urban segregation, which unintentionally increased automobile dependency (Southworth & Owens, 1993).
Satellite City (Raymond Unwin)	● Aim: To create smaller, self-contained urban areas located outside the big metropolitan centers (Unwin, 1909). ● Mid to late 20th century, dominance of the automobile has increased. The spatial segregation links central urban cores caused automobile dependency (Hall, 2002).
Broadacre City (Frank Lloyd Wright)	● Low density living areas caused spreading out homes and jobs. ● It was criticized for its effects on nature because of the urban sprawl impacts (Watson, 2018). ● It also increased the dependency on automobile and negatively impact the walkability in urban areas.
Radiant City/Villa Radieuse (Le Corbusier)	● Aim: Vertically organized urban structure defined by high-rise residential towers, large green open spaces, strict zoning and efficient infrastructure (Le Corbusier, 1935). Seperating pedestrian and vehicle traffic, placing the automobile at the center of urban mobility. ● Zoning and automobile infrastructure caused the rise of car dependency. Wide highways crossing urban centers, single-function districts, has led to the gradual disappearance of mixed-use, walkable environments (Jacobs, 1962).
Radburn (Clarence Perry, Henry Wright, Clarence Stein)	● Aim: Creating cul-de-sacs and traffic-free superblocks, seperating pedestrian movement and vehicle traffic, locating public areas were on pedestrian networks and in open spaces (Sharifi, 2016). ● Car was still needed for daily activities because superblocks often segregate these different activities (Southworth, M., & Ben-Joseph, E., 2003).

Table 2. Different Pedestrianization Strategy Classifications.

Source	Pedestrianization Strategies
European Commision (2024)	● Full Pedestrianization ● Phased Pedestrianization ● Multi-modal Prioritization (like Transit Oriented Development) ● Tactical Pedestrianization ● Traffic Calming
Project for Public Spaces (2019)	● Seasonal/Event Based Pedestrianization ● Traffic Calming ● Transit Oriented Development ● Parklets ● Tactical/Pop-up Pedestrianization ● Shared Streets ● Full Pedestrianization
Istanbul Historic Peninsula Context (EMBARQ Turkey, 2014)	● Seasonal/Event Based Pedestrianization ● Traffic Calming ● Transit Oriented Development ● Parklets ● Tactical/Pop-up Pedestrianization ● Shared Streets ● Full Pedestrianization
Hass-Klau (2015)	● Seasonal/Event Based Pedestrianization ● Traffic Calming ● Transit Oriented Development ● Parklets ● Tactical/Pop-up Pedestrianization ● Shared Streets ● Full Pedestrianization

Open space networks become essential infrastructure for climate adaptation and disaster resilience. Both people and ecosystems benefit from compact and connected cities where pedestrian pathways and green spaces blend together. Such environments enable flexible movement during disruptions, improve quality of life and enable cities to develop with change, not just survive it. According to these, Bayrampaşa Yenidoğan neighborhood was analysed because of its unique urban characteristics.

Figure 1. Land Use, Open Space and Solid&Void Analysis of Bayrampaşa (Produced by author from ArcGIS data of the 1/5000 plan).

Examining the data, there is no enough open spaces except than small, fragmented or useless green areas. The district divided by 2 highways in the east-west direction. It is characterized by old building inventory, very dense urban population, very dense urban development, industrial areas are intertwined with living areas, lack of open space, traffic congestion, limited pedestrian facilities and earthquake risk.

After analysing Bayrampaşa, Yenidoğan neighborhood was analysed in details. The neighborhood, where Bayrampaşa Municipality building is located, includes many different uses and daily visits are high, except for residents. The complex structuring in Bayrampaşa also shows itself here. Business centers, many of which house small producers, are part of daily life here. Residential areas are mostly in the form of long blocks, with low permeability. Streets are narrow and the distances between buildings are very limited.

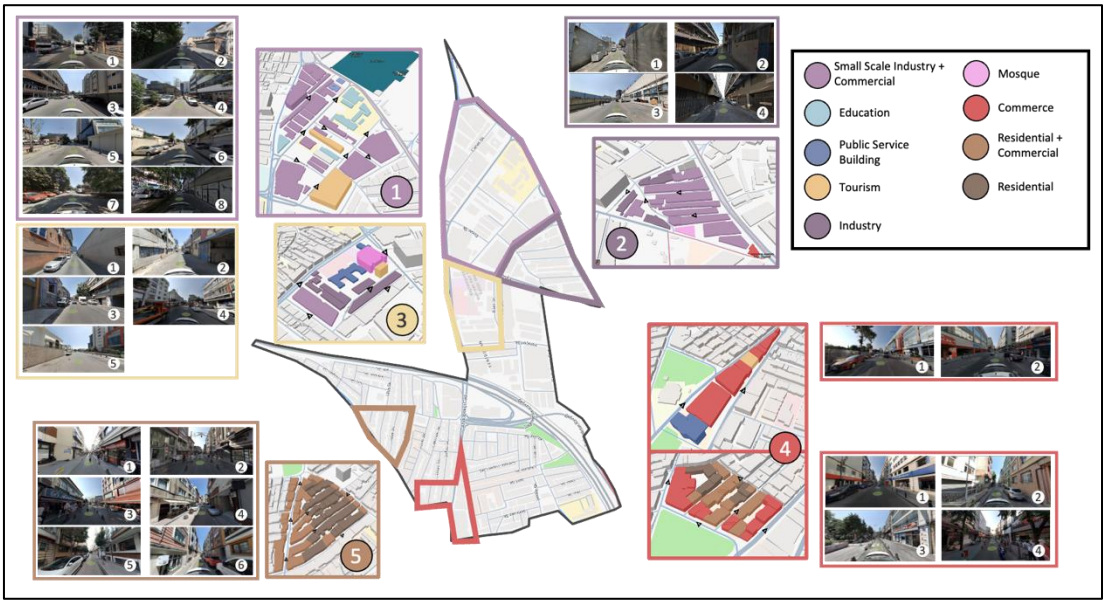

Figure 2. Land Use, Open Space and Solid&Void Analysis of Bayrampaşa (Produced by author from ArcGIS data of the 1/5000 plan).

Functions of the buildings in specific areas were identified with site observation and mapping. The problems in these areas also defined. The analysis of five sub-areas in Yenidoğan reveals pedestrian challenges. In the first and second areas, dominated by small-scale industry and commerce, sidewalks are either missing or blocked by vehicles, and green areas are nearly absent. Pedestrian access is unsafe due to high walls, and heavy traffic. The third area contains mixed uses but lacks a stable pedestrian infrastructure which goes beyond the main street where sidewalks are still partially inaccessible. The fourth zone is mainly residential, with some pedestrian improvements in the commercial areas. However, sidewalk invasions and lack of open spaces continue, and long, continuous

blocks limit walkability. The fifth area, which includes the municipality building and continues along a major transit corridor, shows potential due to a large vacant open space. However, this area remains underused and disconnected from the surrounding pedestrian network. According to these analysis, different pedestrianization strategies were matched with the area.

Table 3. Pedestrianization Strategies and Area Matching.

	Area				
Strategy	1	2	3	4	5
Full Pedestrianization				x	
Phased pedestrianization				x	
Multi-modal pedestrianization/TOD	x			x	
Tactical/Pop-up/Seasonal/Event based pedestrianization	x		x	x	
Traffic Calming	x			x	x
Parklets	x	x		x	x
Shared Streets			x	x	
Timed/Time Restricted pedestrianization	x	x		x	x
Green axes/Ecological Corridors					

Conclusion

This study concludes that pedestrianization is more than a mobility intervention, it is a necessary spatial strategy for building resilient urban environments. In areas like Yenidoğan, where density and fragmentation come together, pedestrianization can restructure the urban fabric by improving spatial continuity, social cohesion and ecological infrastructure. When open spaces are connected by well-designed pedestrian networks, they provide adaptive urban ecosystems that can absorb change, support biodiversity and improve public well-being.

Integrating open space networks with pedestrian routes is a step towards reimagining how urban infrastructure supports people and ecosystems. Pedestrianization offers a participatory and progressive way of urban regeneration. This approach reflects the values of sustainability, inclusiveness and long-term adaptability. The Bayrampaşa case demonstrates that even in highly dense urban environments, meaningful change is possible with location-specific design interventions and strategic reconfiguration of the open space system. Future studies should continue to explore the interaction of social equity, environmental health and spatial justice in pedestrianization initiatives, especially in rapidly urbanizing global cities to enhance urban resilience through open space systems.

References

Banister, D. (2005). Unsustainable transport: City transport in the new century. Routledge.

Carr, S., Francis, M., Rivlin, L. G., & Stone, A. M. (1992). Public Space. Cambridge University Press.

EMBARQ Turkey. (2014). Pedestrianization Project of Istanbul Historic Peninsula: Current Situation Assessment. Istanbul: EMBARQ Turkey.

European Commission. (2004). Reclaiming city streets for people: Chaos or quality of life? Directorate-General for the Environment Office for Official Publications of the European Communities. ISBN 92-894-3478-3. https://ec.europa.eu/environment/pubs/pdf/streets_people.pdf , date retrieved 01.04.2025

Filippov, V. (2017). Live history of the linear city. Innovative Project, 2(4), 6-34. https://doi.org/10.17673/ip.2017.2.04.1, date retrieved 12.05.2025

Gehl, J. (2010). Cities for People. Island Press.

Hall, P. (2002). Cities of tomorrow: An intellectual history of urban planning and design in the twentieth century (3rd ed.). Blackwell Publishing.
Hass-Klau, C. (2015). The pedestrian and the city. Routledge.
Jacobs, J. (1992). The death and life of great American cities. Vintage Books. (Original work published 1961)
Gregg, K. (2023). Victor Gruen versus Jan Gehl – and the contemporary model of pedestrianization, Journal of Urban Design, 28:5, 471-488. DOI:10.1080/13574809.2022.2147491
Le Corbusier. (1935). The Radiant City: Elements of a doctrine of urbanism to be used as the basis of our machine-age civilization. Orion Press.
Mehmood, A. (2015). Of resilient places: planning for urban resilience. European Planning Studies, 24(2), 407–419. https://doi.org/10.1080/09654313.2015.1082980
Newman, P., & Kenworthy, J. (1999). Sustainability and Cities: Overcoming Automobile Dependence. Washington, DC: Island Press.
Perry, C. A. (1929). The neighborhood unit. In Regional Survey of New York and Its Environs, Vol. VII. Neighborhood and Community Planning. New York: Regional Plan of New York and Its Environs.
Project for Public Spaces. (2019). Navigating Main Streets as Places. https://www.pps.org/product/navigating-main-streets-as-places-a-people-first-transportation-toolkit , date retrieved 03.05.2025
Sharifi, A. (2016). From Garden City to Eco-urbanism: The quest for sustainable neighborhood development. Sustainable Cities and Society, 20, 1–16. https://doi.org/10.1016/j.scs.2015.09.002, date retrieved 15.04.2025
Southworth, M., & Ben-Joseph, E. (2003). Streets and the shaping of towns and cities. Island Press.
Southworth, M., & Owens, P. M. (1993). The evolving metropolis: Studies of community, neighborhood, and street form at the urban edge. Journal of the American Planning Association, 59(3), 271–287. https://doi.org/10.1080/01944369308975890 , date retrieved 05.05.2025
UNDRR (United Nations Office for Disaster Risk Reduction). (2017). Words into Action Guidelines: National Disaster Risk Assessment
Unwin, R. (1909). Town planning in practice: An introduction to the art of designing cities and suburbs. London: T. Fisher Unwin. https://ia801306.us.archive.org/13/items/townplanninginpr00unwi/townplanninginpr00unwi.pdf , date retrieved 27.04.2025
Watson, J. (2018). The suburbanity of frank lloyd wright's broadacre city. Journal of Urban History, 45(5), 1006-1029. https://doi.org/10.1177/0096144218797923

POSTER PRESENTATIONS

AERONAUTICAL AND ASTRONAUTICAL ENGINEERING

Aircraft Design, Flight Dynamics And Performance

Control Systems: Adaptive, Intelligent, Digital, Optimal, Pneumatic-Hydraulic

Mechanical Vibrations And Structural Dynamics

Rotary Wing Aircraft

Spacecraft Control, Design And Performance

Theoretical, Computational And Experimental Aerodynamics And Fluid Dynamics

Theoretical, Computational And Experimental Structural Analysis And Design

Effect of Twist Distribution on Rotor Performance and Twist Applications for Rotor Blades

Tacettin Sancak[a], Özge Özdemir[b]

[a] Istanbul Technical University, Department of Aeronautical Engineering, Rotary Wing Aircraft, Türkiye
[b] Istanbul Technical University, Department of Aeronautical Engineering, Theoretical, Computational and Experimental Structural Analysis and Design, Türkiye
sancakt17@itu.edu.tr

Keywords: Twist Ratio, Helicopter Theory, Performance.

Aim

The scope of thesis study is to investigate the effect of twist ratio in hover and forward flight conditions via helicopter theory. After the outcome of the helicopter theory, the type of twist distributions have been examined such as ideal, linear and quadratic. Various flight conditions, flight speeds and twist ratios were reflected in performance equations and resulting graphs were obtained via MATLAB.

In order to satisfy the rotorcraft's needs, structural stresses, fuel consumption, and overall flight performance are all influenced by the aerodynamic efficiency of the helicopter rotor. One of the numerous design components that regulate rotor behaviour is the twist ratio, which is the variation in pitch angle along the rotor blade. The ability to passively or actively adjust the twist ratio allows for improved flying qualities in a variety of operating regimes. The goal of the thesis is to comprehend how twist affects performance characteristics in order to lower the power required for rotorcrafts to hover and fly forward. Moreover, the subsequent aim is to discover how the active twist ratio concepts are implemented.

Morphing structures are flexible and adaptive structural systems that can change their geometry, shape in order to meet the requirements for flight conditions of the rotorcraft. Morphing systems are made to dynamically optimise performance, lower drag, increase lift, or obtain stability while in flight, in contrast to traditional rigid components [1]. In order to accomplish smooth, continuous, or discrete deformations without the use of conventional mechanical joints or hinges, these structures usually combine smart materials (such as shape memory alloys, piezoelectric actuators, or compliant mechanisms) with sophisticated control systems. The active twist rotor (ATR) concept is a promising morphing rotor technology that enhances aerodynamic efficiency, reduces noise, and suppresses vibration by controlling the torsional deformation of rotor blades in real time [1]. Active twist rotors, in contrast to conventional passive or mechanically driven designs, use smart materials incorporated in or bonded to the blade structure, particularly shape memory alloys (SMAs) and piezoelectric actuators, to achieve distributed, adaptive twist control across the blade's span. In this paper, the main goal is to investigate the power consumption reduction by using this active twist rotor (ATR).

Material and Method

In order to calculate the effect of twist of the blade, the helicopter theory discipline must be studied. One of the most basic aerodynamic models for examining helicopter rotors, particularly in hover and vertical flight, is Momentum Theory, often referred to the Actuator Disc Theory. It views the rotor as an idealised, continually thin disc that accelerates the wind downward to produce thrust by giving it a pressure difference. It basically depends on conservation of mass, momentum and energy through the rotor-disk section shown if Figure 1.

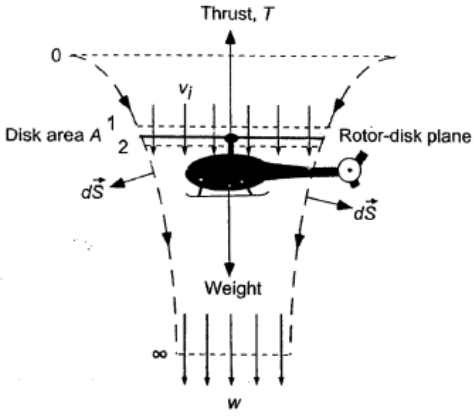

Figure 1. Flow representation for momentum theory in hover condition [2].

Conservation of mass between stations 2 and station ∞ could be written as in the Equation 1.

$$\dot{m} = \iint_{\infty} \rho \vec{w} \cdot d\vec{S} = \iint_{2} \rho \vec{v_i} \cdot d\vec{S}$$

$$\dot{m} = \rho w A_{\infty} = \rho v_i A \tag{1}$$

In the equation $\dot{m}$ is mass flux, ρ is air density, w is far wake velocity, v_i is induced velocity and and $d\vec{S}$ stands for area. Second approach for momentum theory is the application of conservation of momentum as in Equation 2.

$$F = T = \iint_{\infty} \rho(\vec{w}\, d\vec{S}) \cdot \vec{w} - \iint_{0} \rho(\vec{V}\, d\vec{S}) \cdot \vec{V}_{\hookrightarrow Equals\ to\ zero\ (\vec{V}=0)})$$

$$T = \dot{m} \cdot w \tag{2}$$

In this formula the F represents the force and will be equal to thrust generated by the rotorcraft which can be seen with the notation as T in the equation. Final principle for completing the theory is the conservation of energy [2]. Before considering this principle, work-energy relation must be introduced as in Equation 3, U is the energy and W is the work done through station 1 to 2 respectively.

$$U_1 + W_{1\to 2} = U_2 \tag{3}$$

After the definition of power in Equation 4, formula can be written for the conservation of energy in Equation 5.

$$Power = \frac{Work\ done}{time} = \frac{Force \times Distance}{time} = Force \times Velocity \tag{4}$$

$$(P_{ind})_{ideal} = T \cdot v_i = \iint_{\infty} \frac{1}{2} \rho(\vec{w}\, d\vec{S}) \cdot \overrightarrow{w^2}_{\hookrightarrow Equals\ to\ \frac{1}{2}\dot{m}} - \iint_{0} \frac{1}{2} \rho(\vec{V}\, d\vec{S}) \cdot \overrightarrow{V^2}_{\hookrightarrow Equals\ to\ zero\ (\vec{V}=0)}$$

$$(P_{ind})_{ideal} = T \cdot v_i = \frac{1}{2} \dot{m}\, w^2 \tag{5}$$

Afterwards, a nondimensionless paratemeter power coefficient can be determined respectively. Power coefficient is a critical parameter for comparing different rotorcrafts in the name of power efficiency. In hover there are two power coefficient definitions such as induced power coefficient C_{P_i} and the profile power coefficient C_{P_0} their formulas can be seen in Equation 6.

$$C_P = C_{P_i} + C_{P_0} = \frac{\kappa C_T^{3/2}}{\sqrt{2}} + \frac{\sigma C_{d_0}}{8} \tag{6}$$

In this formula, C_T is the thrust coefficient, σ is the correction factor from ideal to nonideal conditions, σ is the rotor solidity and the formula can be seen in Equation 7, C_{d_0} is the constant drag coefficient.

$$\sigma = \frac{N_b R c}{\pi R^2} = \frac{N_b c}{\pi R} \tag{7}$$

In rotor solidity formula the N_b is the number of blades and c is chord length of the airfoil and the R is the radius of the disk area. Induced power is the required power to provide an adequate thrust, profile power is to drag related power loss from the rotor blades.

In order to improve on momentum theory, Blade Element Theory (BET) examines the forces acting on each rotor blade's small differential sections, or elements. Lift and drag are locally calculated using the relative airflow, and

each blade is segmented along its span [2]. Figure 2 represents the top view for the blade, U_R is the radial component, U_T is the tangential component, U is the resultant velocity and Ω is the angular velocity.

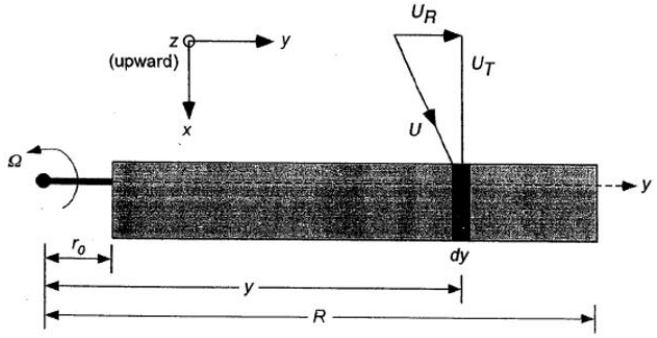

Figure 2. Top view of the rotor blade [2].

Figure 3 shows the blade element where U_P is perpendicular component, θ is the pitch angle, ϕ is the induced angle and α is the effective angle of attack.

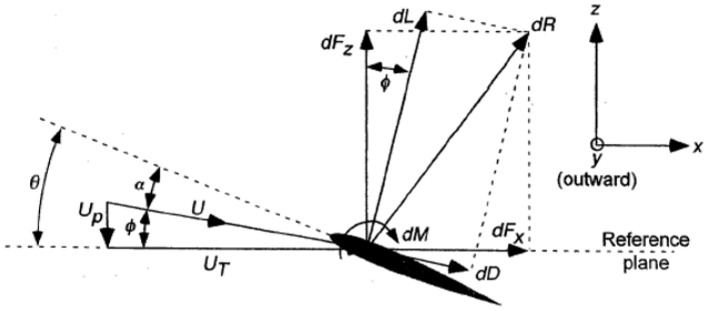

Figure 3. Side view of the rotor blade [2].

Final theory to obtain the performance results of a rotorcraft is the blade element momentum theory (BEMT) which is the combination of both momentum and blade element theory. In addition to accounting for the induced velocity resulting from momentum theory, it models the rotor by breaking the blades into small spanwise parts and computing the aerodynamic forces acting on each. In this section pitch angle will be a function of r nondimensional radial position. By using the BEMT, inflow ratio λ can be determined as in the Equation 8.

$$\lambda(r) = \lambda_i(r) = \frac{\sigma C_{l_\alpha}}{16}\left(\sqrt{1 + \frac{32}{\sigma C_{l_\alpha}}\theta r} - 1\right) \tag{8}$$

The inflow ratio is basically a dimensionless parameter for axial velocity component as it can be defined as the ratio of induced velocity to the rotor tip speed. By using inflow ratio and the pitch angle distribution as a function, thrust coefficient can be calculated as in the Equation 9.

$$C_T = \frac{1}{2}\sigma C_{l_\alpha}\int_0^1 (\theta r^2 - \lambda r)\, dr \tag{9}$$

Since the thrust coefficient is obtained, power coefficient can be found which indicates the power consumption.

Findings

Another challenge is to make inflow ratio more homogeneous distribution along the blade. Application of negative twist along the blade can make this possible, twist function is defined in Equation 10 as ideally twisted blade.

$$\theta(r) = \frac{\theta_{tip}}{r} \tag{10}$$

Rotorcraft can be untwisted, linearly twisted, quadratically twisted or ideally twisted. By the type of twist, corresponding twist formula will change. A linearly twisted function example can be seen in Equation 11.

$$\theta(r) = \theta_0 + r \cdot \theta_{tw} \tag{11}$$

By changing the twist rate θ_{tw}, the representative inflow ratio can be seen in Figure 4.

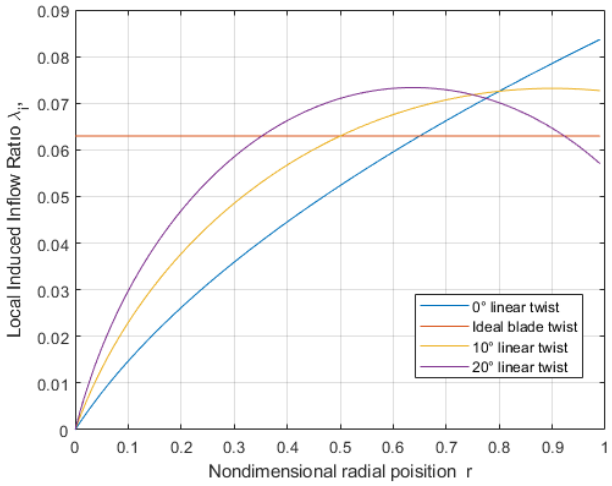

Figure 4. Inflow ratio distributions with various twist distributions.

Afterwards, thrust coefficient can be calculated in hover condition, subsequently the power coefficient can be found. For these calculations UH-60-A Sikorsky rotorcraft has been selected [3]. Required parameters from main rotor for computation the power coefficients are listed in Table 1.

Table 1. Sikorsky UH60A Characteristic Parameters [3].

Main Rotor Parameters	
Rotor Radius	8.1788 m
Rotor Speed	27.0 rad/s
Blade Chord Length	0.5273 m
Blade Twist Type	Nonlinear
Blade Airfoil	SC 1095 / SC 1094R8
Number of Blades	4
Blade Mass per Unit Length	13.92 kg/m

By using MATLAB, representative power coefficients are calculated for linearly twisted rotorcraft for various amount of linear twist angles as 0°, -4°, -8°, -12°, -16°. It can be clearly seen the negatively twisted blades consume less power for hovering as in shown in Figure 5.

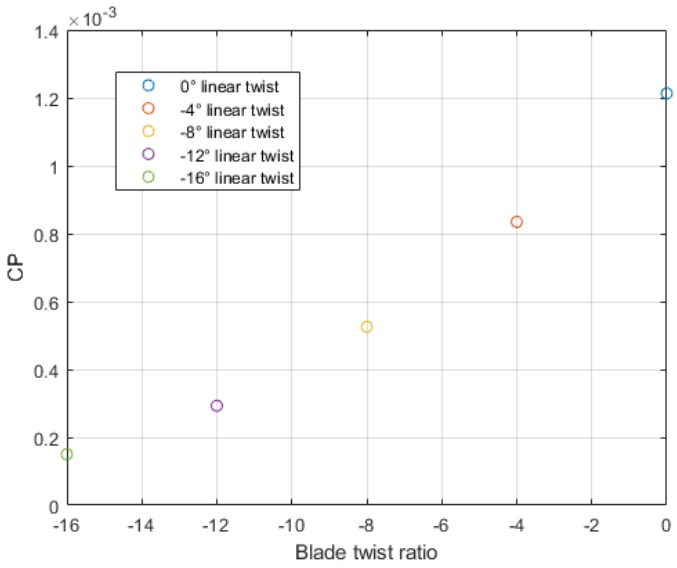

Figure 5. Power coefficient for various twist distributions for Hover.

Since the effect of twist distribution is determined, the method of active twist rotor must be decided. Active Fiber Composite (AFC) and Macro Fiber Composite structures can the examples for morphing the rotor blades. AFC structures as shown in Figure 6, includes embedded electrodes to have a high in-plane deflection and they are used in considerable high actuation cases [4].

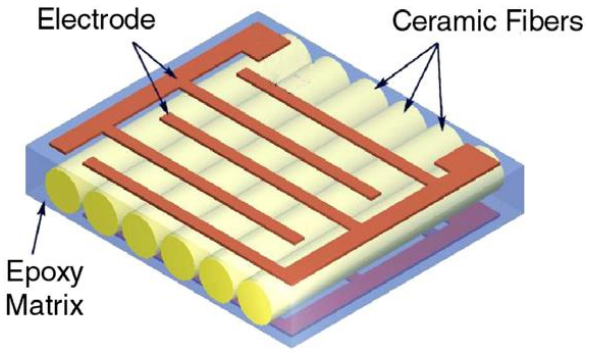

Figure 6. AFC (Active Fiber Composite) [5].

MFC structures are stacked as multi-layers and includes kapton, epoxy and piezoelectric PZT layers which can be seen in Figure 7.

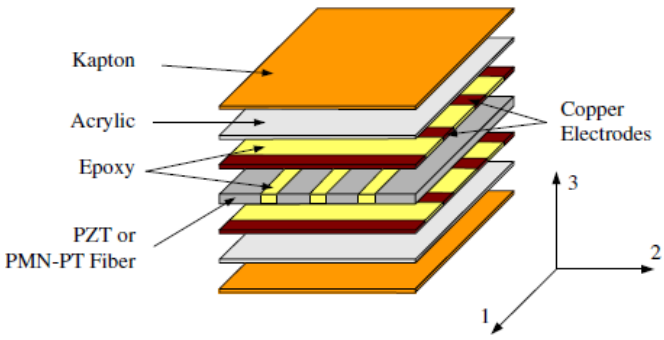

Figure 7. Layer structure of MFC [5].

The actuation performance and flexibility of a MFC piezoelectric fiber composite AMFC actuator are significantly better than those of a monolithic piezoceramic actuator. In ATR applications, MFC patches are usually oriented

along the longitudinal axis and bonded or integrated within the rotor blade's composite skin. The anisotropic composite structure of the blade interacts with the produced strain of the MFCs during activation, producing a torsional moment that modifies the blade's local pitch angle. Without the use of mechanical links or moving parts, system may generate dispersed twist profiles along the blade span by accurately adjusting the input voltage in response to flight conditions or closed-loop control signals. An example of MFC structure is shown in Figure 8 [6].

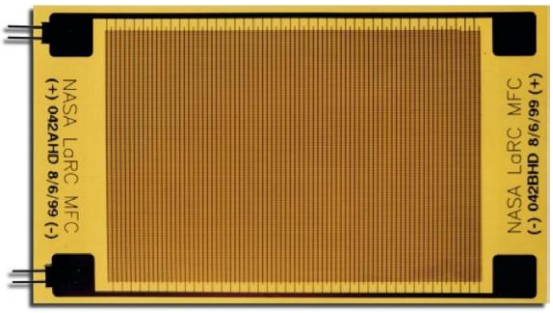

Figure 8. MFC Macro Fiber Composite [5].

A number of variables, including actuator location, blade stiffness distribution, material coupling effects, and control bandwidth, affect how successful MFC-based active twist systems are. Additionally, MFCs are a potential and versatile alternative for evolving rotor technologies due to their low weight, great durability, and compatibility with composite materials [7].

Conclusion

Rotorcraft performance is directly related to its power coefficient. In this research, the fund**a**mentals of helicopter theory have been understood. Afterwards, thrust coefficient is calculated in hover condition, subsequently the power coefficient can be found. It was critical to have homogenous inflow ratio distribution along the spanwise direction of the rotor in order to reduce the power consumption. With the scope of helicopter theory, various twist cases were compared to analyze the **e**ffect of twist. In the following stage, the methods of active twist rotor structures have been introduced and these methods compared and understood.

References

Schultz, M., & Hyer, M. (2004c). A Morphing Concept Based on Unsymmetric Composite Laminates and Piezoceramic MFC Actuators. 45th AIAA/ASME/AHS/ASC Structures, Structural Dynamics and Materials Conf. (Palm Springs, CA) AIAA-2004-1806.
Url-1 https://doi.org/10.2514/6.2004-1806.
Leishman, J. G. (2002). Principles of Helicopter Aerodynamics. Cambridge University Press.
Yeo, H., Romander, E. A., & Norman, T. R. (2011). Investigation of rotor performance and loads of a UH-60A individual blade control system. Journal of the American Helicopter Society, 56(4), 1–18.
Url-2 https://doi.org/10.4050/jahs.56.042006
Lonoce, M. (2016). Helicopter Blade twist optimization in forward flight.
Park, J., & Kim, J. (2005). Analytical development of single crystal Macro Fiber Composite actuators for active twist rotor blades. Smart Materials and Structures, 14(4), 745–753.
Url-3 https://doi.org/10.1088/0964-1726/14/4/033
Bent, A. A. (1997). Active fiber composites for structural actuation.
Wilkie, W. K., Inman, D. J., Lloyd, J. M., & High, J. W. (2006). Anisotropic Laminar piezocomposite actuator incorporating machined PMN–PT single-crystal fibers. Journal of Intelligent Material Systems and Structures, 17(1), 15–28.
Url-4 https://doi.org/10.1177/1045389x06055891

Span-Morphing Rotorcrafts: Performance Analysis and Mechanism Selection

Öykü Etçi[a], Özge Özdemir[a]

[a] Istanbul Technical University, Department of Aeronautical and Astronautical Engineering, Rotary Wing Aircraft, Türkiye
etci17@itu.edu.tr

Keywords: Variable Span Morphing, Rotorcraft Performance, Flight Efficiency.

Aim

The concept of morphing in the aerospace industry began with changing the shape of the wings in order to enhance the aircraft's performance, efficiency, and adaptability to different flight conditions. In rotorcraft applications, morphing structures can be used to modify blade geometry, including span length, chord length, twist distribution, and adaptive airfoil, to optimize the rotorcraft's aerodynamic performance [2].

During hover operation, power consumption is maximum in a rotorcraft as it requires continuous thrust equal to its weight without the assistance of aerodynamic lift. Since it also happens to be the flight condition where a rotorcraft spends most of its time, they are specifically designed to maximize performance in this flight regime [1].

A larger rotor area corresponds to a larger swept area, which generally results in better hover efficiency. In the hover condition, the efficiency is increased by enhancing thrust while reducing the required power. Therefore, increasing the rotor area by adjusting the span length is preferable, provided that the blade tip speed, V_{tip}, does not exceed the operational Mach number. However, in forward flight conditions, increased rotor diameter leads to higher profile drag, which can potentially reduce cruise performance. Thus, adjusting the rotor diameter based on the flight condition can significantly enhance the rotorcraft's efficiency.

The aim of this thesis is to enhance the efficiency of a rotorcraft during hover, climb, and forward flight conditions by dynamically adjusting the rotor diameter using mechanisms suitable for the related rotorcraft.

Material and Method

For analysis presented in this study, MATLAB was utilized as the primary computational tool. Three different mathematical approach were employed during performance analysis of rotorcrafts. Momentum Theory, Blade Element Theory (BET), and Blade Element Momentum Theory (BEMT).

Hover and axial climb regimes are relatively easy to model with Momentum Theory, which treats the rotor as an infinitely thin disc and assumes a constant velocity along the axis of rotation. This method provides an initial approximation of rotor thrust and power based on the conservation of fluid mass, momentum, and energy for more advanced analyses of rotor aerodynamics. The ideal power required to hover is given in Eq. (1) [1].

In momentum theory, nondimensionalizing velocities by blade tip speed (V_{tip}), Eq. (2), is essential to reduce the complexity of the mathematical equations and make the results more universally applicable. These nondimensional parameters include induced inflow ratio (λ_h), thrust coefficient, rotor power coefficient, and ideal power coefficient given in Eq. (3), Eq. (4), Eq. (5), Eq. (6) respectively.

Due to nonideal effects such as viscosity, Momentum Theory tends to underpredict the actual power required. However, since it is proportional to the required power calculated by the Momentum Theory, an induced power correction factor (κ) is introduced. This factor is calculated through various rotor measurements and flight tests [1]. For the hovering regime, the power coefficient is divided into two parameters. Induced ($C_{p,i}$), and profile ($C_{p,0}$) power coefficients are given in Eq. (7) Where σ is rotor solidity Eq. (8) and c_{d_0} is constant drag coefficient.

Forward flight condition requires a different approach than the hovering regime due to the aerodynamic complexity. The induced velocity for forward flight can be calculated using Eq. (9) which often requires numerical approaches like fixed-point iteration or the Newton-Raphson iteration method. The Newton-Raphson method for

calculating the inflow ratio is given in Eq. (10), where the initial inflow ratio is typically taken as the hover inflow ratio, $\lambda_0 = \lambda_h$. Since the rotorcraft is moving through the air, parasitic power must be accounted for to overcome skin friction and form drag. These drag components contribute to the required total power in forward flight along with induced power and profile power as given in Eq. (11) [1].

To further refine momentum theory, Blade Element Theory applies conventional airfoil theory to the rotating blades. In BET, rotor blades are considered rigid, despite their flexibility, as the dominant force generated by the rotation of the blades, centrifugal force, maintains the blades rigidity. BET analyzes the aerodynamic performance of the rotating blades by dividing them into small segments along the span and determining the overall behavior of the blade by summing the contributions of these individual sections [5].

Blade Element Momentum Theory becomes important as it combines both Momentum Theory and Blade Element Theory to provide a more accurate representation of aerodynamic effects by defining the effects of taper and twist on parameters such as thrust coefficient C_T, induced power coefficient C_{P_i}, and inflow ratio λ.

Findings

To evaluate rotorcraft performance, a disk loading versus power loading graph is important as it illustrates the trade-off between maximum hovering efficiency and high-speed forward flight, Figure 1. For a single-rotor aircraft in hover, disk loading is the ratio of thrust to rotor area Eq. (12), where rotor thrust equals the rotorcraft's weight, and power loading is defined as the ratio of thrust to the power required to hover. It is also inversely proportional to the induced velocity (Eq. (13)).

Conventional helicopters typically operate in the low disk loading, high power loading region, prioritizing hover efficiency with large rotors. In contrast, high-speed rotorcraft, such as tiltrotors and compound helicopters, feature higher disk loading, which enhances cruise performance at the cost of hover efficiency.

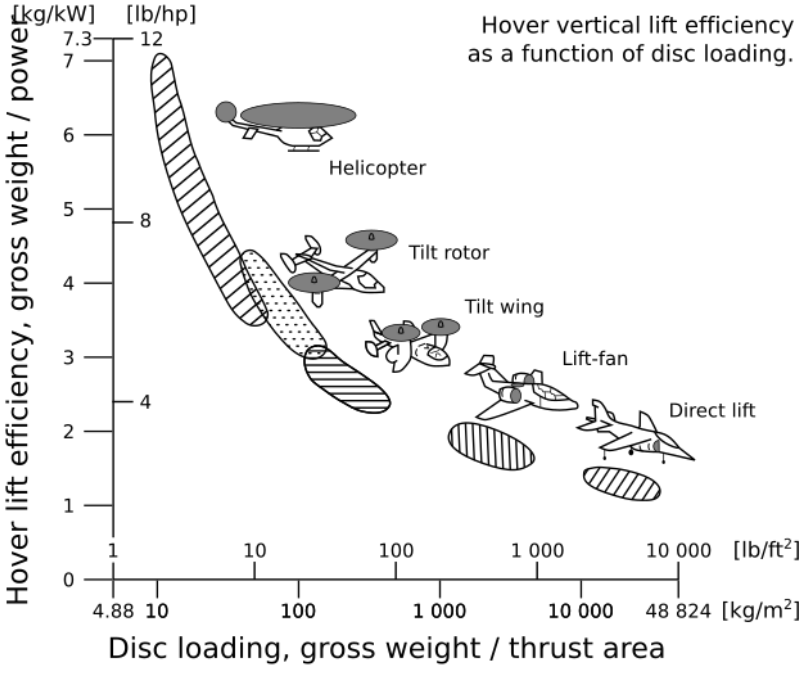

Figure 1. Hover vertical lift efficiency as a function of disc loading [4].

For several single-rotor UAVs given in Table 1, a disk loading versus power loading graph is plotted in Figure 2 to compare their efficiencies in hover. The equations below demonstrate that modifying the rotor area directly affects the performance, highlighting the trade-offs between hover efficiency and forward flight characteristics of the rotorcraft.

Table 1. UAV specifications.

UAV Name	Weight (kg)	Main Rotor Diameter (mm)
Blade 600X	4	1342
The Galaxy	8	1980
Vapor 55	24.9	2291
Alpha 800	14	1800
Tanan 300	300	5000
VSR 700	450	7200
Camcopter S-100	110	3400
A160 Hummingbird	2948	11900
NEO 300-S	75	3000
Vigilant	40	1830
MQ-8B Fire Scout	940.3	8400

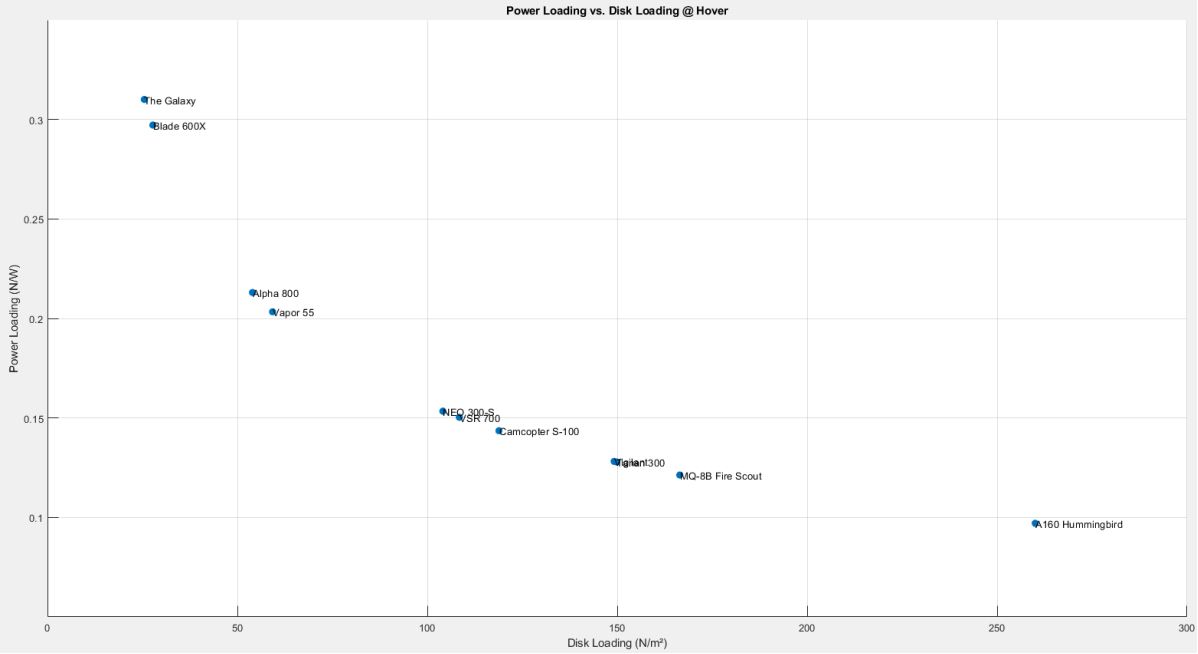

Figure 2. DL - PL for several UAVs.

Span morphing in rotorcrafts can be achieved through various mechanisms, each changing the blade construction in different ways. These mechanisms include telescoping blades, folding blades, and flexible blades which can be either passive or active depending on the system [3]. Active systems such as those using hydraulic or pneumatic actuators or smart materials require an external power source, allowing the user to precisely control the movement. On the other hand, a passive morphing system relies on forces acting on the structure, such as aerodynamic or structural forces, without needing any external power input, making them more energy-efficient but less controllable.

Active morphing includes systems like folding sections actuated by motors or hinges, shape memory alloy materials actuated by heat or an electrical input, hydraulic or pneumatic systems actuated by electric motors. For passive morphing systems, centrifugal force actuated telescoping blades by using a spring or a tensioned cable can be given as example.

Conclusion

By adjusting the span length dynamically, span morphing rotorcrafts have a unique advantage on optimizing the performance across different flight regimes achieving a balance between hover and forward flight efficiency. This can enhance mission flexibility, and improve overall operational efficiency while reducing the power consumption of a rotorcraft.

Depending on their size, performance, and mission requirements, different rotorcraft types use different morphing mechanisms. Smart materials such as piezoelectric actuators or shape memory alloys are often used in lightweight rotorcraft to provide precise control while minimizing the weight. There are also centrifugal force-actuated systems where rotor blades extend or retract based on rotor speed, making them simple and energy-efficient. Hydraulic and pneumatic actuators are frequently used in medium to large helicopters like military or commercial rotorcraft to precisely control the shape of the rotor blade, allowing them to adjust to changing flight conditions.

Equations

$$P = \sqrt{\frac{T^3}{2\rho A}} \#(1)$$

$$V_{tip} = \Omega R \#(2)$$

$$\lambda_h = \frac{1}{\Omega R}\sqrt{\frac{T}{2\rho A}} = \sqrt{\frac{C_T}{2}} \#(3)$$

$$C_T = \frac{T}{\rho A {V_{tip}}^2} \#(4)$$

$$C_P = \frac{{C_T}^{3/2}}{\sqrt{2}} \#(5)$$

$$C_Q = \frac{Q}{\rho A {V_{tip}}^2 R} \#(6)$$

$$C_p = C_{p,i} + C_{p,0} = \frac{K {C_W}^{\frac{3}{2}}}{\sqrt{2}} + \sigma\frac{c_{d_0}}{8} \#(7)$$

$$\sigma = \frac{N_b c}{\Pi R} \#(8)$$

$$\lambda = \mu\, tan(\alpha) + \frac{C_T}{2\sqrt{\mu^2 + \lambda^2}} \#(9)$$

$$\lambda_{n+1} = \lambda_n - \left[\frac{f(\lambda)}{f'(\lambda)}\right]_n \#(10)\#\#\#$$

$$C_p = C_{p,i} + C_{p,0} + C_{p,p} = \frac{KC_T{}^2}{2\sqrt{\mu^2+\lambda^2}} + \sigma\frac{c_{d_0}}{8}(1+K\mu^2) + \frac{1}{2}\frac{f}{A}\mu^3 \#(11)\ C_p = C_{p,i} + C_{p,0}$$

$$= \frac{KC_W{}^{\frac{3}{2}}}{\sqrt{2}} + \sigma\frac{c_{d_0}}{8}\ \#(\quad)\ C_p = C_{p,i} + C_{p,0} = \frac{KC_W{}^{\frac{3}{2}}}{\sqrt{2}} + \sigma\frac{c_{d_0}}{8}\ \#(\quad)$$

$$DL = \frac{T}{A}\ \#(12)$$

$$PL = \frac{T}{P} = \frac{1}{v_i} = \sqrt{\frac{T}{2\rho A}}\ \#(13)$$

References

Leishman, J. G. (2006). *Principles of Helicopter Aerodynamics* (2nd ed.). Cambridge University Press.
Li, D., Zhao, S., Da Ronch, A., Xiang, J., Drofelnik, J., Li, Y., Zhang, L., Wu, Y., Kintscher, M., Monner, H. P., Rudenko, A., Guo, S., Yin, W., Kirn, J., Storm, S., & De Breuker, R. (2018). A review of modelling and analysis of morphing wings. *Progress in Aerospace Sciences*, *100*, 46–62.
Url-1 https://doi.org/10.1016/j.paerosci.2018.06.002
Linden, A. W. (1972). *Variable Diameter Rotor Study*. Defense Technical Information Center.
Maisel, M. D., Giulianetti, D. J., & Dugan, D. C. (2000). *The History of the XV-15 Tilt Rotor Research Aircraft: From concept to Flight*. National Aeronautics and Space Administration, Office of Policy and Plans, NASA History Division: United States Government Printing Office.
SEDDON. (1990). *Basic Helicopter Aerodynamics* 67-3. Reston, VA: American Institute of Aeronautics & Astronautics.

AERONAUTICAL AND ASTRONAUTICAL ENGINEERING

Aircraft Design, Flight Dynamics And Performance

Control Systems: Adaptive, Intelligent, Digital, Optimal, Pneumatic-Hydraulic

Mechanical Vibrations And Structural Dynamics

Rotary Wing Aircraft

Spacecraft Control, Design And Performance

Theoretical, Computational And Experimental Aerodynamics And Fluid Dynamics

Theoretical, Computational And Experimental Structural Analysis And Design

Optimization Of Aluminum Plate Under Impact Loading

Ezgi Bakir[a], Vedat Ziya Dogan[b], Oğuzcan Inal[b], Zahit Mecitoğlu[b]

[a] Istanbul Technical University/Department of Aeronautical Engineering, Department, Theoretical, Computational And Experimental Structural Analysis And Design, Türkiye
[b]Istanbul Technical University, Aeronautical And Astronautical Engineering, Türkiye
bakirez16@itu.edu.tr

Keywords: Optimization, Impact, Metamodel, Multiobjective, LS-Dyna.

Aim

This study aims to optimize the thickness of an AL7050 aluminum alloy plate subjected to an impact load, with the goal of minimizing both the maximum stress and mass of the plate. The define of the problem is metamodel based multiobjective function optimization which is used for more than one objective function and can not find mathematical express of problem. The optimization process is based on FEM data obtained from LS-Dyna, which is used for impact analysis. Then surragated model is obtained using kringing method and than genetic algortihm is used as optimization method. The matemodels significantly reduces the computational cost of the optimization process by approximating the system's behavior, enabling more efficient exploration of the design space.

Material and Method

The material considered in this study is AL7050 plate, a high-strength aluminum alloys are widely used in aerospace and structural applications due to its exceptional strength-to-weight ratio, ease of processing and accesibility. Mechanical properties of aluminum plate are given in Table 1.

Table 1. Material Properties of AL 7050 plate [3].

Properties	Properties Value
Density	2.70 g/cm^3
Modulus of Elasticity	72 GPa
Yield Strength	455 MPa

The aluminum alloy plate dimensions are 100 mm by 100 mm, with the thickness being the key design variable to be optimized. To demonstrate out of plane impact loading finite element analysis (FEA) is performed using LS-Dyna which is used for especially explicit or implicit impact analysis. The plate is modeled with 2D quad elements, because a lot of analysis are runned to create design variable space, therefore, the analysis run time is important. The boundary conditions to represent fixed edges, 3 DOF (x, y and z) constrain is applied to all edges. The impact object is modeled as a spherical rigid ball which is modelled as 3D, hexa elements, impact the center of the plate with 10 m/s which is shown in Figure 1.

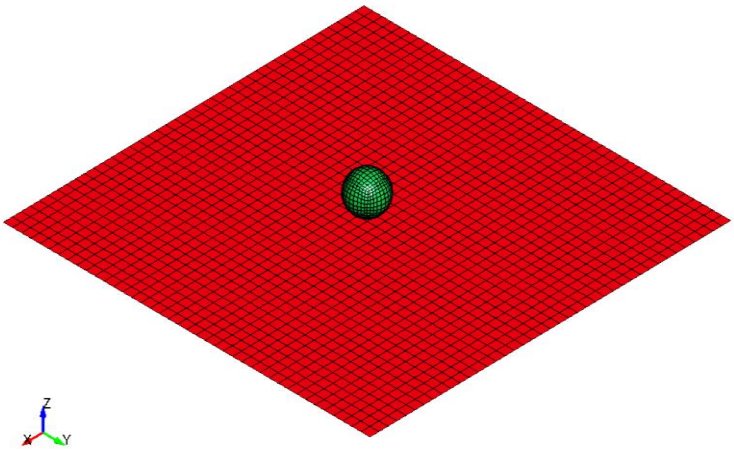

Figure 1. AL 7050 plate under out of plane impact loading FEM demonstration.

To optimize the problem, the objective function is used, which is mostly the mathematical expression. The mathematical expression of out of plane impact loading analysis is very complicated. Therefore, the surragated model is used. Kriging is a widely used surrogate modeling technique in computational engineering that is a mathematical interpolation technique associated with mining engineer Krige. Jack P.C. Kleijnen (2017) said that, Krige solved the problem of combining results (outputs, responses) obtained from a limited number of locations in gold mining. Later, this method was further developed by the French mathematician Matheron, who created the field of geostatistics or spatial statistics. The foundation of this approach is the stationary Gaussian process (GP), which means the GP has a constant average, expected value, a constant variance, and covariances that only depend on the distances between "points" in a 3D space, length, width and height. This process defines a multivariate normal or Gaussian distribution [1]. The Kriging model is trained using a set of simulation results obtained from LS-Dyna, where different plate thickness values and the corresponding impact responses are used as input-output data pairs. The kringing models and simulation data of thickness to stress and mass are given in Figure 2 and Figure 3 which are created by MATLAB, the optimized values are shown with a star mark.

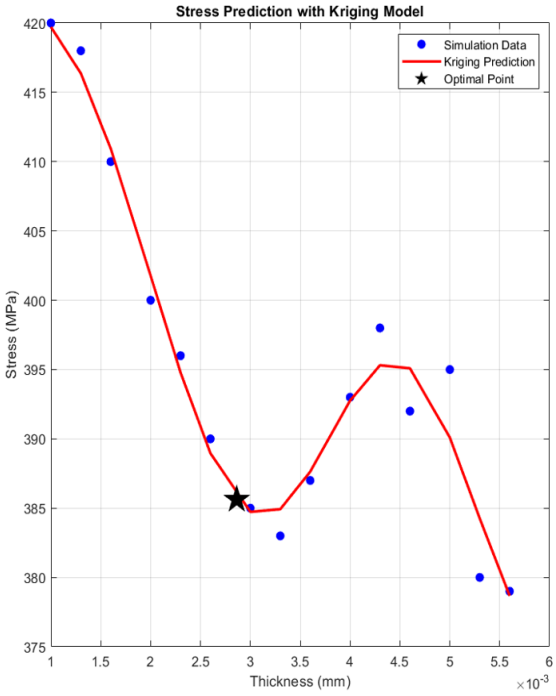

Figure 2. Graph of Thicknes -Stress in Matlab.

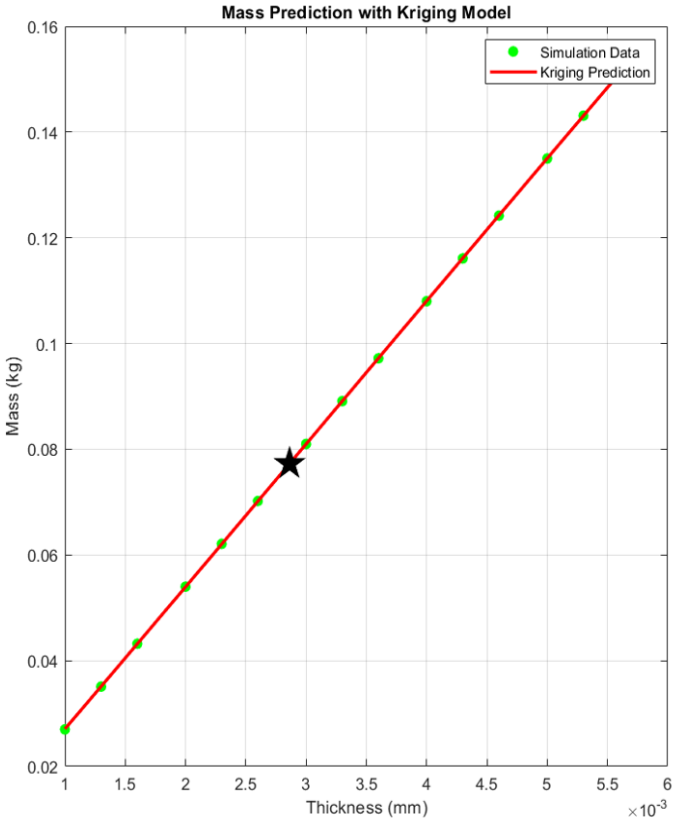

Figure 3. Graph of Thicknes -Mass in Matlab.

In addition, there is more than one objective function, stress and mass. The purpose of optimization is minimize stress and minimize mass, for that reason the problem becomes multiobjective optimization problem. To combine these objective function the weighted function is used which is shown in Figure 4.

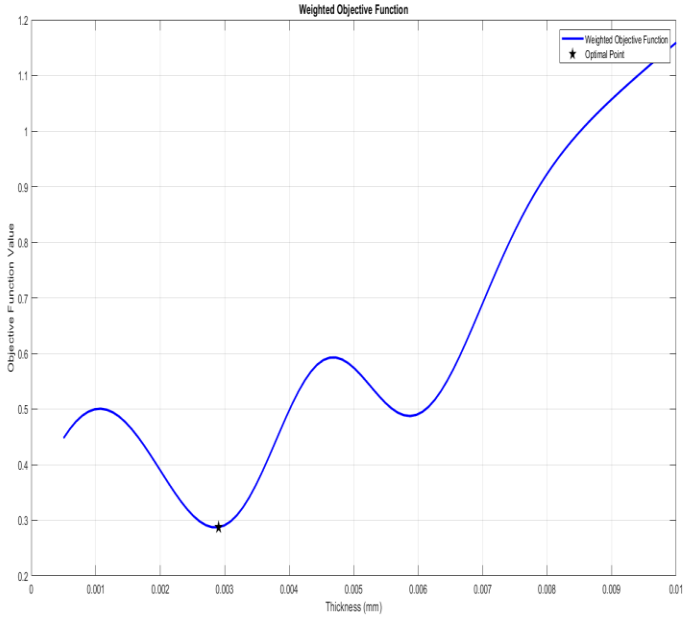

Figure 4. The weighted function to thickness graph of combination of two objective functions.

The optimization algorithm utilized is based on the genetic alghoritm (GA) method, which is well-suited for solving optimization problems. Saraswat and Sharma (2013) stated that MATLAB can be used to implement a genetic algorithm for solving optimization problems. It takes advantage of the power of genetic algorithms to quickly find good solutions in real time. The experimental results show that GATool can improve the fitness value by providing a set of nearly optimal solutions quickly. When looking at the effect of different genetic algorthmn parameters, it was found that increasing the population size can improve the system's performance. The crossover rate, however, does not have a big impact on the solution quality. [2]

Findings

The optimization study of the AL 7050 plate under out-of-plane impact loading consists of four main steps. First step is to obtain simulation data from LS-Dyna. The challenge of this part is identifying the maximum stress elements and the corresponding time. The maximum stress occurs at different times but the time step is kept constant for each analysis. Although, the maximum stress can occur between time intervals, it is observed that the maximum stress is reached when the impactor ball contacts the plate. The solution is to set the distance between the impactor ball and the aluminum plate to zero. An example of simulation data is shown in Figure 5.

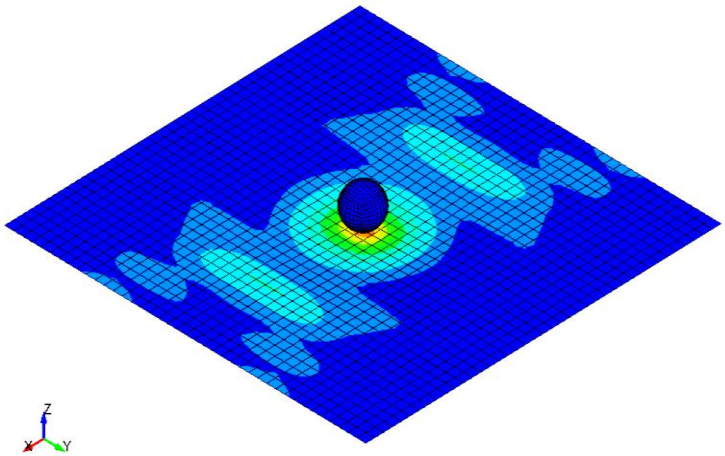

Figure 5. Von Mises Stress Distribution of Al7050 Plate Under Impact Load in LS-Dyna software.

The metamodel creation is the second part of the problem. The Kriging-based metamodel is used for this purpose and it provides accurate approximations of the maximum stress and mass for various plate thickness values. The mass to thickness kringing model is linear regression but the stress to thickness kringing model is polynomial function. This method also can used for obtained approximation results without any analysis. As a conclusion, the kringing model is provided to save time and to obtain objective functions.

After creation of the two objective functions, combination of these functions is the third step of this project. Also, the importances of objective functions are provided a solution for more complex optimization problems. For example, for this problem the weight of objective functions are given as equal, but if stress objective function weight is given more, the optimized thickness is found as thicker. To be conclude, Weighted function is usefull and easy applied method even if complex object functions.

The last step is genetic algothm optimization method. Genetic algorithm provide optimization for wide design of space results. The optimization process identifies an optimal thickness that balances structural performance in terms of stress with material efficiency. The optimal thickness minimizes both the maximum stress and mass, while ensuring that the plate remains within acceptable limits.

Conclusion

In conclusion, this study successfully optimized the thickness of an AL 7050 aluminum alloy plate under out of plane impact loading by minimizing both maximum stress and mass. A metamodel-based multiobjective optimization approach was employed, utilizing Kriging surrogate modeling to approximate the complex

relationships between plate thickness, stress, and mass, significantly reducing computational costs. The optimization process, driven by a weighted combination of stress and mass objectives, was efficiently executed using a genetic algorithm (GA), providing an optimal solution that balances structural performance and material efficiency. This approach demonstrates the effectiveness of advanced optimization techniques in achieving optimal designs while saving time and resources, particularly in aerospace and structural applications.

References

Kleijnen, J. P. C. (2007). Kriging metamodeling in simulation: A review. European Journal of Operational Research, 192(3), 707-716.
Url-1 https://doi.org/10.1016/j.ejor.2007.10.013
Saraswat, M., & Sharma, A. K. (2013). Genetic algorithm for optimization using MATLAB. International Journal of Advanced Research in Computer Science, 4(3), 155–159. Available at
Url-2 http://www.ijarcs.info.
Smiths Metal Centres. (2023). 7050 Aluminium Technical Datasheet.
Url-3 https://www.smithmetal.com/pdf/aluminium/7xxx/7050.pdf

Optimum Rudder Torque Tube Design for a Light Training Aircraft

Berkay Temizkan[a], Zahit Mecitoğlu[a]

[a] İstanbul Technical University, Aeronautical and Astronautical Engineering, Computational and Experimental Structural Analysis And Design Program, Turkey
temizkan16@itu.edu.tr

Keywords: Design, Light Training Aircraft, Optimization, Rudder Torque Tube.

Aim

The design and reliability of control systems in aviation are critically important, particularly for basic training aircraft in the light-category used in pilot training. Flight control systems are categorized into primary and secondary systems. The rudder control mechanism, a component of the primary flight control system, commands the aircraft's rightward yaw when the pilot presses the associated pedal (Federal Aviation Administration, 2023, p. 6-2). This study aims to determine the optimum design for the rudder torque tube, which is one of the main components of the rudder control system for a light training aircraft.

For this purpose, a preliminary design for the rudder control system was first developed by examining existing light training aircraft in the literature. Loads were determined in accordance with CS-23 Certification Specifications for Normal, Utility, Aerobatic, and Commuter Category Aeroplanes (European Aviation Safety Agency, 2010). An analytical model was created for the torque tube using beam theory and verified via the finite element method (FEM) model. An appropriate optimization method was selected for the optimization of the structure. After determining the appropriate constraints and objective function for the determined method, the structure was optimized, results were evaluated, and tube geometry was finalized. Fastener, gear and bearing were selected for the design. A detailed 3D CAD model was developed, and FEM analysis confirmed the safety of the final design.

Material and Method

A literature review was conducted to design an optimum rudder torque tube for a light training aircraft. Through this review, various aircraft within the light training aircraft category were examined. By obtaining the external geometric specifications of these aircraft, parameters such as average fuselage length, pedal position, distance between pedals, and fuselage width were determined. An analytical model was created to calculate the rudder control system loads using these parameters. The maximum load scenarios that the pilot can apply were obtained with requirements in the CS-23 Certification Specifications for Normal, Utility, Aerobatic, and Commuter Category Aeroplanes document. The resulting forces and moments acting on the torque tube were then determined. The rudder torque tube was analytically modeled in the frame of beam theory employing analytical formulas in Mechanics of Materials Book and Machinery's Handbook (Hibbeler, 2011; Oberg et al., 2016). The analytic model was coded in a computational environment using the MATLAB 2019b (The MathWotks Inc., 2019). The code first calculates the reaction forces and moments using static equilibrium equations. Then, the shear force and bending moment diagrams are obtained along the length of the rudder torque tube. In this methodology, shear force and bending moments are obtained in each section, which are used to compute the maximum von Mises stress.

In order to verify calculations in the code written using the MATLAB R2019b, finite element models were developed using the Hypermesh 2017 (Altair Engineering, 2018). Separate finite element model (FEM) models were created in order to model torque tube utilizing 1D CBAR, 2D SHELL and 3D TETRA elements. After applying appropriate boundary conditions and loads for each model, the finite element analysis was conducted using MSC NASTRAN 2019.0 (MSC Patran/Nastran, 2019). The results were evaluated to verify MATLAB generated calculations.

Various algorithms for the optimization of the rudder torque tube were examined and the genetic algorithm was determined as the most suitable approach. The boundary conditions and objective function for optimization were determined with the code created on MATLAB. The optimization was performed using MATLAB's Global Optimization toolbox. As a result of the optimization, values such as section thickness, outer diameter size, inner

diameter size, were obtained. Additionally, fastener, gear, and bearing selection were performed using analytical formulas. The loads acting on each fastener were calculated using analytical formulas. The diameter and type of the fasteners were determined using the formulations in the Airframe Structural Design book (Niu, 1999). For gear selection, calculations in the "Relatively Large Depth Beams" section in the Roark's stress and strain book were used (Roark et al., 2002). For bearing selection, the manufacturer documents of the bearings were examined. Suitable bearing was selected evaluating axial and lateral load capacities.
A detailed design model, which met specified design features, was created using the CATIA V5 6R2018 (Dassault Systemes, 2018). The STEP file of the detailed design model was exported from the CATIA program and imported to the Hypermesh. Then, the solution networks that will reflect this geometry were created using three-dimensional tetrahedral elements.

Findings

This study has several findings related to optimum design of the rudder torque tube for a light training aircraft.
One of the most important finding is the minimum wall thicknesses obtained in the torque tube as a result of optimization. The maximum force a pilot can apply to the pedal was determined by relevant articles in the CS-23 document. The maximum load that the pilot can apply to the rudder pedal under the limit condition is 890 N according to CS.23.397. For aircraft exceeding a design weight of 2268 kg, this load must be multiplied by 1.18. Additionally, CS.23.395 states that each flight control system and its supporting structure must withstand 125% of the calculated hinge moment. Therefore, the maximum applied force was determined as 1312.75 N. Furthermore, the fitting factor of 1.15 in CS.23.625 was included when calculating the final strength. The force moment values created by this load in the torque tube were calculated with static equilibrium equations. The schematic representation of the model used for these calculations is presented in Figure 1.

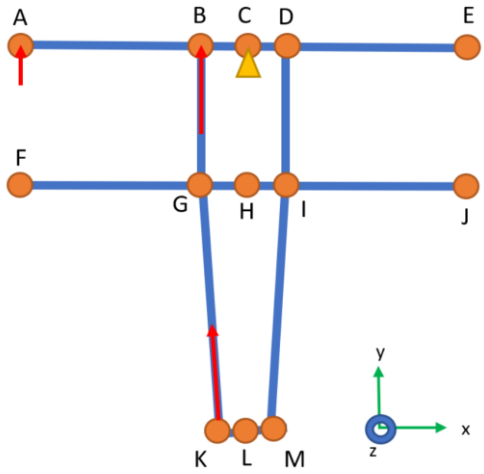

Figure 1. The schematic representation of rudder control system.

In this diagram, the pedal force applied at point A is transferred via cables at points B, G and K and through the torque tube bell-crank at point L. The forces and moments at this point were obtained in Table 1.

Table 1. Force and moments at point L.

Axis	Force [N]	Moment [N.mm]
X	6.67	23.48
Y	4071.79	1618.44
Z	186.81	366460.57

These obtained forces and moments were applied to the beam model representing the torque tube in figure 2. The forces were distributed along the bell-crank - torque tube connection. The boundary condition at the location where a spherical bearing was placed allowed for free rotation, whereas a fixed support was applied at the connection point between the torque tube and the rib.

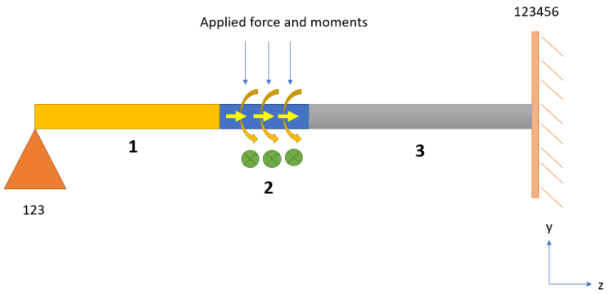

Figure 2. Beam model.

The calculations were made via MATLAB and the optimization was performed using the genetic algorithm with the Global Optimization toolbox of MATLAB. The objective function was defined as minimizing the volume of the torque tube while satisfying the constraints resulting from the forces and moments outlined in Table 1. As a result of the optimization, the optimum inner and outer radius values were determined for 3 different regions shown in Figure 2. As a result of the multiple iterations, the refined parameters for the optimization were determined. The best value and penalty values obtained at each generation in the optimization were plotted in the graph in Figure 3. The minimum inner and outer radius values for the torque tube are shown in Table 2.

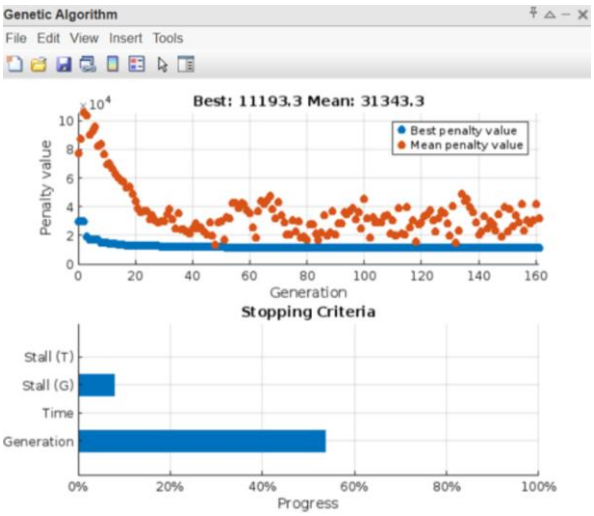

Figure 3. Genetic optimization results.

Table 2. The minimum inner and outer radius values for the torque tube.

Region	Inner Radius [mm]	Outer Radius [mm]
1	7	8
2	13.5	15.0
3	15.7	16.9

Conclusion

This study successfully developed an optimized design of the rudder torque tube for a light training aircraft. The maximum forces and moments acting on the torque tube were obtained in accordance with the CS-23 Certification Specifications. The torque tube was analytically modeled, and force and moment distributions across its length were computed. An optimization study was conducted using a genetic algorithm to determine the optimal inner and outer radius values in different regions of the tube, resulting in a preliminary design. Finally, a detailed design was developed by selecting appropriate fastener, gear and bearing. The structural integrity of the optimized design was validated through finite element analysis.

References

Altair Engineering. (2018). HyperMesh (Version 2018). Altair Engineering.
Dassault Systemes. (2018). CATIA V5R28, Computer-Aided Three-Dimensional Interactive Application, Software Package, Ver. 5.28, Dassault Systemes.
European Aviation Safety Agency. (2012). Certification specifications for normal, utility, aerobatic, and commuter category aeroplanes CS-23 (Amendment 3., pp. 1-C-8–1-D-3).
Federal Aviation Administration. (2023). Aviation maintenance technician handbook – Airframe: Volume 1 (FAA-H-8083-25C). U.S. Department of Transportation.
Hibbeler, R. C. (2011). Mechanics of materials (8th ed., pp. 405–642). Pearson Education India.
MSC Patran/Nastran. (2019). MacNeal-Schwendler Corporation, Software Package, Ver. California, 1963.
Niu, M.C. (1999). Airframe Structural Design, (2nd ed., pp. 101,112 368, 367-369). Hong Kong Conmilit Press Ltd., California.
Oberg, E., Jones ,F.D. , Horton H.L. , Ryffel H.H. (2016) . Machinery's Handbook (30th ed., pp 248 – 272) Industrial Press Inc.
Roark, R. J., Young, W. C., Budynas, R. G., & Sadegh, A. M. (2002). Roark's formulas for stress and strain. (7th ed., pp. 166–169). McGraw-Hill.
The MathWorks Inc. (2019). MATLAB Ver. R2019b, Natick, Massachusetts: The MathWorks Inc.

Structural Design and Analysis of Engine Mount Structure for Propeller Training Aircraft

Alper Aslan[a], Kaan Yıldız[b]

[a] Istanbul Technical University/Department of Aeronautical Engineering, Department, Theoretical, Computational And Experimental Structural Analysis And Design, Türkiye
[b] Istanbul Technical University/Aviation Institute, Theoretical, Computational And Experimental Structural Analysis And Design, Türkiye
aslana16@itu.edu.tr

Keywords: Engine Mount, Propeller Aircraft, Sizing, Static Analysis.

Aim

This project involves the determination and calculation of the load conditions for the engine mount structure of a propeller training aircraft. Furthermore, the identification of the engine mount members with the most appropriate thickness was achieved through both Hypermesh modeling and the MATLAB interface. The load conditions play a decisive role in the engine mount structure's concept and thickness. In order to perform the structural design and static analyses, it is essential to calculate the load conditions of the structure. The load conditions have been calculated using the aviation certifications outlined in CS-23 (European Aviation Safety Agency, 2012).

The engine mount structure consists of the structural elements that establish the connection between the engine and the fuselage of the aircraft. These components are subjected to significant loading conditions due to the forces exerted by the engine. Consequently, engine mount members must exhibit high resistance to both stress and buckling induced by these loading conditions.

This project is to calculate the engine loading conditions of a nose-propeller training aircraft and to design the most suitable and reliable engine mount structure that can withstand the calculated loading conditions. Therefore, a toolbox has been developed to calculate the engine mount structure thicknesses. Within the toolbox, a graphical output is provided for each 1D member. The figures display the reserve factor values as a result of a small increase in thickness. The person performing the calculation is given the opportunity to select the member thicknesses, thereby allowing for the inclusion of engineering judgment in the process.

With this toolbox, the sizing of one-dimensional elements can be easily performed. Additionally, an interface has been created to allow for the calculation of reserve factors. The reserve factor can be calculated for engine mount members with the desired thicknesses. As a result, the time required for the sizing of 1D structures such as the engine mount has been significantly reduced.

Material and Method

In this study, a comprehensive set of tools and methodologies was employed to design and optimize the engine mount structure for the nose propeller training aircraft. The primary design and analysis were conducted using Hypermesh, which facilitated the finite element modeling of the engine mount and surrounding structural components, including the frame, longeron, keel beam, and floor. These components were interconnected using connector modeling to simulate their interactions accurately. To model the engine mount members, 1D beam elements were utilized, and a mesh size of 10 millimeters was selected for precision in the analysis. Static analysis of the engine mount structure was performed using the MSC Nastran solver, providing critical data for stress distribution and load conditions across the structure. The force and moment pairs for each element from the analysis results were imported into Excel.

To determine the optimal thickness for the engine mount members, a custom MATLAB code was developed, incorporating safety factors derived from Von Mises stress, linear buckling, and local buckling criteria. The MATLAB program also considered the welding factor, accounting for reductions in material properties due to welding processes. Additionally, a graphical interface was designed to allow users to visualize and select the most appropriate radii for the engine mount members, enhancing the usability of the tool. The following equations were

employed for these calculations, σ_{11} is the normal stress in Equation 1, and σ_{12} is the shear stress in Equation 2. By using these two formula, Von Mises stress can be calculate as Equation 3 (Bruhn, 1973).

$$\sigma_{11} = \sigma_{axial} \pm \sigma_{bending} \quad \#(SEQ\ Equation \setminus *\ ARABIC\ 1)$$

$$\sigma_{12} = \sigma_{shear} \pm \sigma_{torsional} \quad \#(SEQ\ Equation \setminus *\ ARABIC\ 2)$$

$$\sigma_{vm} = \sqrt{\sigma_{11}^2 + 3\sigma_{12}^2} \quad \#(SEQ\ Equation \setminus *\ ARABIC\ 3)$$

$RF_{Von\ Mises}$ represents the reserve factor according to the Von Mises criteria, and it can be determined using Equation 4 where σ_{vm} is the Von Mises stress occurs on the beam elements. F_{tu} is the tension allowable for the selected material. There are four solutions for the Von Mises stress calculation due to the signs of bending and torsional stresses. The maximum Von Mises stress solution was selected for the calculations.

$$RF_{Von\ Mises} = \frac{F_{tu}}{\sigma_{vm}} \quad \#(SEQ\ Equation \setminus *\ ARABIC\ 4)$$

Equation 5 is used to determine the critical linear buckling axial loads, which must be compression forces. By comparing these with the axial loads on the engine mount members, the buckling reserve factor is calculated using this method. In Equation 5, E is the Young Modulus of selected material (Niu M. C., 1991). I is the moment of inertia. L is the length of the engine mount member. RF_{LiB} represents the reserve factor according to the linear buckling, and it can be determined using Equation 6, where P_{axial} is the axial load.

$$P_{cr} = \frac{\pi^2 EI}{L^2} \quad \#(SEQ\ Equation \setminus *\ ARABIC\ 5)$$

$$RF_{Linear\ Buckling} = \frac{P_{cr}}{P_{Axial}} \quad \#(SEQ\ Equation \setminus *\ ARABIC\ 6)$$

The local buckling equations are shown in Equation 7 to 10 (Yıldız K., 2018). For local buckling to occur, σ_{11} must be a compression load. σ_{cr} represents the critical stress for wall buckling, and it can be determined using Equation 7. γ is the correlation coefficient in Equation 8, where r_o and r_i are the outer and inner radii, respectively. RF_{LoB} is the reserve factor of local buckling as shown in Equation 10, where σ_{11} is the normal stress.

$$\sigma_{cr} = \frac{E}{\sqrt{3(1-\nu^2)}} \frac{r_o - r_i}{r_o} \quad \#(SEQ\ Equation \setminus *\ ARABIC\ 7)$$

$$\gamma = 1 - 0.901\left(1 - e^{-\phi}\right) \quad \#(SEQ\ Equation \setminus *\ ARABIC\ 8)$$

$$\phi = \frac{1}{16}\sqrt{\frac{r_o}{r_o - r_i}} \quad \#(SEQ\ Equation \setminus *\ ARABIC\ 9)$$

$$RF_{Local\ Buckling} = \frac{\sigma_{cr}}{\sigma_{11}} \quad \#(SEQ\ Equation \setminus *\ ARABIC\ 10)$$

The engine mount members need to be welded together to ensure their connections. Due to welding, a decrease in the material's allowable properties may occur; thus, the reduction factor, which called as welding factor, was used for the calculations. Welding factor was added as 1.2 to the toolbox and MATLAB code (Bruhn, 1973).

Findings

- **Engine Mount Load Case Calculations**

Initially, similar aircraft within the scope of training aircraft were examined. The Super-Tucano training aircraft was selected as a comparable model for this project due to its recognition for its design and mission capabilities. The engine used in the Super-Tucano and the compatible propeller types were researched to calculate the engine loads. For the nose propeller training aircraft, the design and analysis of which will be conducted within the scope of this project, the PT6A-67AF engine has been chosen. This engine, offering higher performance compared to others in the same series as the Super-Tucano, is still in production and features a high Thrust-to-Weight ratio. After investigating the propeller types compatible with the PT6A-67 engine series, it was determined that the Socata TBM700 propeller was suitable for both this engine and the type of aircraft on which the work will be carried out.

Based on the selected engine and propeller types, four load conditions were calculated to satisfy aviation certification requirements, following the guidelines in CS23 (European Aviation Safety Agency, 2012). In this phase, the calculations were based on the study by Olejnik et al., which focused on the design optimization of a very light aircraft engine mount, accounting for external flight loads (Olejnik et al., 2016). The parameters of the engine and propeller required for thrust and torque calculations were obtained from the PT6A-67AF and TBM700 documents (Pratt and Whitney Canada Corp., 2022; Hartzell Propeller., n.d.). The engine mount load cases were calculated, as shown in Table 1, using data from the engine and propeller documents.

Table 1. Engine Mount Load Cases - Limit.

Engine Mount Limit Load cases							
Subcase No.	**Load case Type**	**Nx [N]**	**Ny [N]**	**Nz [N]**	**Mx [Nmm]**	**My[Nmm]**	**Mz [Nmm]**
1	Pull Up	-4410.00	0	-13587.83	6778979.26	0	0
2	Pull Up	-4410.00	0	-18117.11	6389602.86	0	0
3	Pull Over	-4410.00	0	9058.554	6389602.86	0	0
4	Spin	0	-4015.96	0	0	0	0

- **Concept Analysis**

In the following stage, the coordinates for the connections of the engine mount structure were calculated based on the dimensions of the propeller engine. Five connection points were defined for the connection between the engine and the mount structure. Furthermore, four connection points were identified between the engine mount and the aircraft's front fuselage structure. Once the connection concept was finalized, the dimensions of the Super-Tucano aircraft were validated, and the positions of the frame and longeron stations were calculated. Subsequently, the master geometry design of the front fuselage was completed. At this stage, the coordinates for the connection points between the mount structure and the fuselage structure were fully determined.

The engine mount structure was designed based on five different concepts within the defined coordinates. Four previously calculated load conditions were applied to the structure at the propeller location using the Hypermesh program. The forces and moments for each beam element were obtained from the Hypermesh. The preliminary cross-sectional type and radii of the engine mount members were determined. The most suitable design concept was selected based on the Von Mises stress criterion. The selected engine mount concept design is shown in Figure 1.

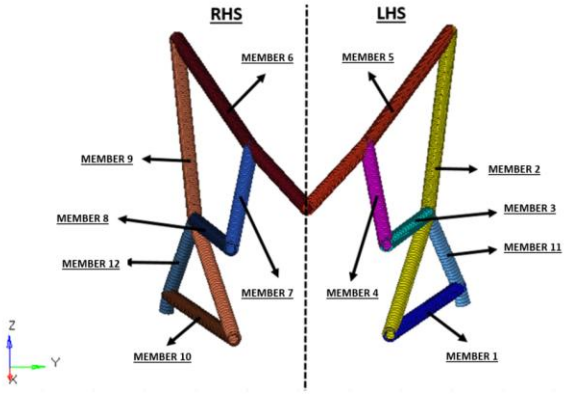

Figure 1. Engine Mount Concept.

- **Material**

The selection of materials for the engine mount members is critical, as these elements are subjected to vibration, temperature variations, and high levels of stress. Therefore, selecting a material capable of effectively withstanding these conditions is essential. A variety of materials were evaluated using MMPDS-23, and, among these, 4340 steel was selected due to its mechanical strength, insensitivity to temperature variations, excellent resistance to vibration-induced crack formation and propagation, and high tensile strength (Battelle Memorial Institute, 2013). Simultaneously, to proceed with the design of the front fuselage structure, AL7050 T7451 material, widely used in aviation, was selected for the front fuselage components.

Table 2. AL7050-T7451 Mechanical Properties.

AL7050 T7451 Mechanical Properties			
Thickness (in)	0.250-1.500	1.501-2.000	2.001-3.000
Basis	B-basis	B-basis	B-basis
F_{tu} [MPa]	524.00	524.00	517.10
F_{ty} [MPa]	461.94	455.05	455.05
F_{cy} [MPa]	441.26	441.26	441.26
F_{su} [MPa]	303.37	310.26	310.26
F_{bru} (e/D=1.5) [MPa]	758.42	772.21	765.31
F_{bru} (e/D=2.0) [MPa]	999.73	1006.63	992.84
F_{bry} (e/D=1.5) [MPa]	613.63	634.31	641.21
F_{bry} (e/D=2.0) [MPa]	717.05	737.73	751.52
E [MPa]	71015		
ν	0.33		

AISI 4340/AMS6414	
Thickness (in)	≤3.5
Basis	S Basis
F_{tu} [MPa]	1378.00
F_{ty} [MPa]	1212.64
F_{cy} [MPa]	1247.09
F_{su} [MPa]	826.80
F_{bru} (e/D=1.5) [MPa]	1874.08
F_{bru} (e/D=2.0) [MPa]	2445.95
F_{bry} (e/D=1.5) [MPa]	1756.95
F_{bry} (e/D=2.0) [MPa]	1929.20
E [MPa]	199810
ν	0.32

- **Calculation and Results**

Using the software, the user can select the most suitable radii for the engine mount structure members from the graphical interface. Figure 2 shows an example of the graphical representation that allows for the selection of the radius for engine mount member 1.

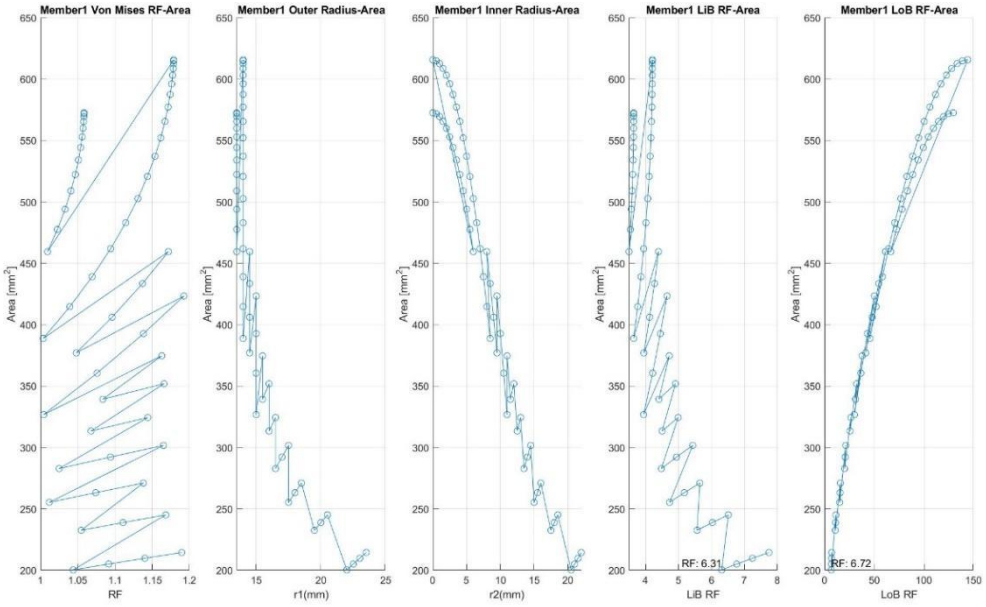

Figure 2. Output of software to select the suitable radii for Member 1.

A software toolbox has been developed that provides all relevant information about the engine mount members. The user can check the lowest reserve factor for each member. Additionally, the beam element number with the lowest reserve factor in each member, as well as the load condition number and weight parameters, can also be checked.

The engine mount members, for which the thicknesses were determined, were imported into the front fuselage finite element model previously prepared in the Hypermesh program, and another static analysis was performed. Comparisons were made between the results obtained from the engine mount members in this static analysis and the model previously created with only the engine mount members, and it was observed that differences in the boundary conditions used significantly affected the stresses on the engine mount members. Therefore, the force and moment pairs for the beam elements, exported from the Hypermesh program, were imported into Excel, and new thicknesses were calculated using MATLAB code. In this way, the most suitable thickness for the engine mount elements was determined.

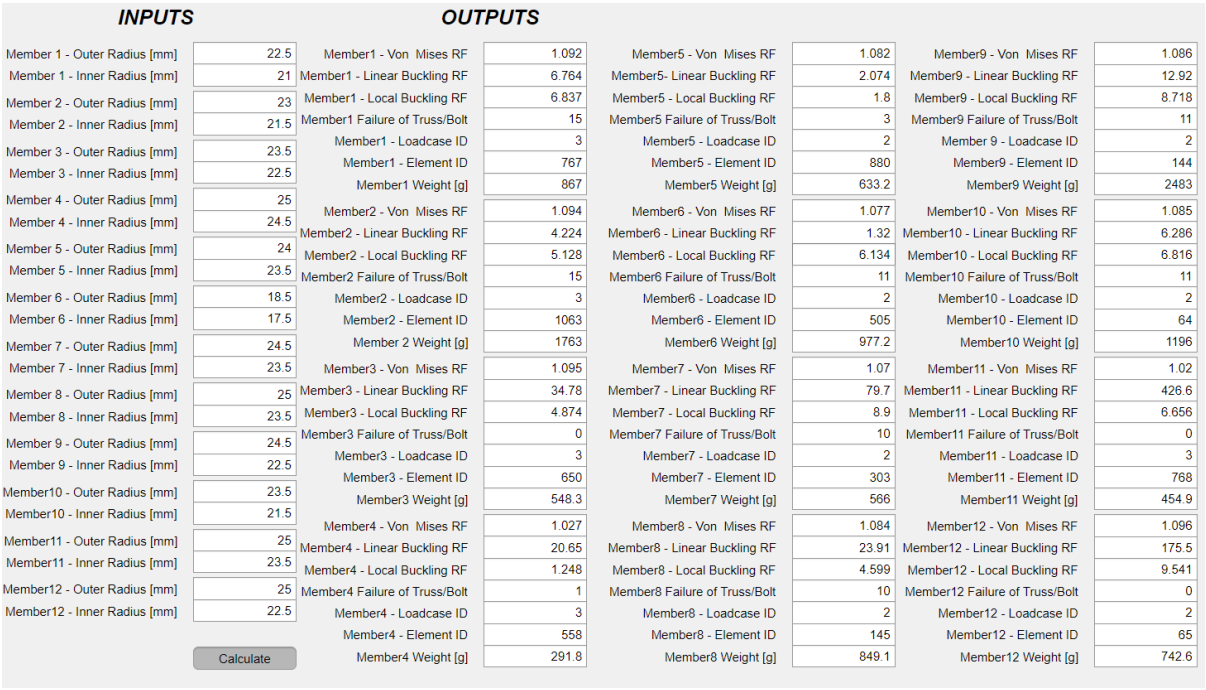

INPUTS		OUTPUTS							
Member 1 - Outer Radius [mm]	22.5	Member1 - Von Mises RF	1.092	Member5 - Von Mises RF	1.082	Member9 - Von Mises RF	1.086		
Member 1 - Inner Radius [mm]	21	Member1 - Linear Buckling RF	6.764	Member5- Linear Buckling RF	2.074	Member9 - Linear Buckling RF	12.92		
Member 2 - Outer Radius [mm]	23	Member1 - Local Buckling RF	6.837	Member5 - Local Buckling RF	1.8	Member9 - Local Buckling RF	8.718		
Member 2 - Inner Radius [mm]	21.5	Member1 Failure of Truss/Bolt	15	Member5 Failure of Truss/Bolt	3	Member9 Failure of Truss/Bolt	11		
Member 3 - Outer Radius [mm]	23.5	Member1 - Loadcase ID	3	Member5 - Loadcase ID	2	Member 9 - Loadcase ID	2		
Member 3 - Inner Radius [mm]	22.5	Member1 - Element ID	767	Member5 - Element ID	880	Member9 - Element ID	144		
Member 4 - Outer Radius [mm]	25	Member1 Weight [g]	867	Member5 Weight [g]	633.2	Member9 Weight [g]	2483		
Member 4 - Inner Radius [mm]	24.5	Member2 - Von Mises RF	1.094	Member6 - Von Mises RF	1.077	Member10 - Von Mises RF	1.085		
Member 5 - Outer Radius [mm]	24	Member2 - Linear Buckling RF	4.224	Member6 - Linear Buckling RF	1.32	Member10 - Linear Buckling RF	6.286		
Member 5 - Inner Radius [mm]	23.5	Member2 - Local Buckling RF	5.128	Member6 - Local Buckling RF	6.134	Member10 - Local Buckling RF	6.816		
Member 6 - Outer Radius [mm]	18.5	Member2 Failure of Truss/Bolt	15	Member6 Failure of Truss/Bolt	11	Member10 Failure of Truss/Bolt	11		
Member 6 - Inner Radius [mm]	17.5	Member2 - Loadcase ID	3	Member6 - Loadcase ID	2	Member10 - Loadcase ID	2		
Member 7 - Outer Radius [mm]	24.5	Member2 - Element ID	1063	Member6 - Element ID	505	Member10 - Element ID	64		
Member 7 - Inner Radius [mm]	23.5	Member 2 Weight [g]	1763	Member6 Weight [g]	977.2	Member10 Weight [g]	1196		
Member 8 - Outer Radius [mm]	25	Member3 - Von Mises RF	1.095	Member7 - Von Mises RF	1.07	Member11 - Von Mises RF	1.02		
Member 8 - Inner Radius [mm]	23.5	Member3 - Linear Buckling RF	34.78	Member7 - Linear Buckling RF	79.7	Member11 - Linear Buckling RF	426.6		
Member 9 - Outer Radius [mm]	24.5	Member3 - Local Buckling RF	4.874	Member7 - Local Buckling RF	8.9	Member11 - Local Buckling RF	6.656		
Member 9 - Inner Radius [mm]	22.5	Member3 Failure of Truss/Bolt	0	Member7 Failure of Truss/Bolt	10	Member11 Failure of Truss/Bolt	0		
Member10 - Outer Radius [mm]	23.5	Member3 - Loadcase ID	3	Member7 - Loadcase ID	2	Member11 - Loadcase ID	3		
Member10 - Inner Radius [mm]	21.5	Member3 - Element ID	650	Member7 - Element ID	303	Member11 - Element ID	768		
Member11 - Outer Radius [mm]	25	Member3 Weight [g]	548.3	Member7 Weight [g]	566	Member11 Weight [g]	454.9		
Member11 - Inner Radius [mm]	23.5	Member4 - Von Mises RF	1.027	Member8 - Von Mises RF	1.084	Member12 - Von Mises RF	1.096		
Member12 - Outer Radius [mm]	25	Member4 - Linear Buckling RF	20.65	Member8 - Linear Buckling RF	23.91	Member12 - Linear Buckling RF	175.5		
Member12 - Inner Radius [mm]	22.5	Member4 - Local Buckling RF	1.248	Member8 - Local Buckling RF	4.599	Member12 - Local Buckling RF	9.541		
		Member4 Failure of Truss/Bolt	1	Member8 Failure of Truss/Bolt	10	Member12 Failure of Truss/Bolt	0		
		Member4 - Loadcase ID	3	Member8 - Loadcase ID	2	Member12 - Loadcase ID	2		
		Member4 - Element ID	558	Member8 - Element ID	145	Member12 - Element ID	65		
	Calculate	Member4 Weight [g]	291.8	Member8 Weight [g]	849.1	Member12 Weight [g]	742.6		

Figure 3. Outputs of MATLAB Interface Design.

Conclusion

As a result of this study, the process, from engine selection to determining the thicknesses of the members for the engine mount structure of a nose propeller training aircraft, was developed. Throughout this process, software tools and an interface were developed to facilitate the design of engine mount members with the optimal thickness.

References

Battelle Memorial Institute. (2013). Metallic materials properties development and standardization (MMPDS-08).

Bruhn, E. F. (1973). Analysis and design of flight vehicle structures (Supplement). Tri-State Offset Company.

European Aviation Safety Agency. (2012). CS-23: Certification specifications for normal, utility, aerobatic, and commuter category airplanes (Amendment 3).

Hartzell Propeller. (n.d.). TBM 700A, B, C1, C2, and N (TBM 850). Retrieved March 8, 2025, from

Niu, M. C.-Y. (1991). Practical design information and data on aircraft structures. Conmilit Press.

Olejnik, A., Kłosowski, P., & Kowal, M. (2016). Design optimization of a very light aircraft engine mount with consideration of extremal flight loads. Archive of Mechanical Engineering, 63(4), 531–547.

Pratt & Whitney Canada Corp. (2022). Type-certificate data sheet No. EASA.IM.E.008 Issue 06 for PT6A-67 Series engines. Pratt & Whitney Canada Corp.

Yıldız, K. (2018). Cable actuated tensegrity structures for deployable space booms with enhanced stiffness

APPLIED INFORMATICS

Computational Electromagnetics

Data Analysis

Medical Image Analysis

Comparing Fractional Calculus And LSTM For Greenhouse Gas Emission Forecasting: Insights For Policy And Strategy

Gizem Göktaş Balkır[a], Nisa Özge Önal Tuğrul[a]

[a] Istanbul Technical University/Informatics Institute, Applied Informatics, Information and Communications Engineering, Istanbul, Türkiye
goktasg17@itu.edu.tr

Keywords: Climate Change, Fractional Calculus, Greenhouse Gas Forecasting, LSTM, Time Series Modeling.

Aim

Climate change has evolved into one of the most urgent environmental issues of our time, especially since the Industrial Revolution. The rise in global temperatures, sea level increases, more frequent extreme weather events, and the loss of biodiversity all pose significant threats to the sustainability of both societies and economies (Üstün, 2023). The World Economic Forum's Global Risks Report 2025 emphasizes the growing importance of environmental risks, highlighting climate change as a long-term threat to global economic stability and social cohesion (World Economic Forum, 2025).

Greenhouse gas (GHG) emissions, which are the leading cause of global warming due to their heat-trapping properties, originate primarily from energy production but also from agriculture, industry, and waste management. In response to this challenge, governments worldwide are developing policies aimed at reducing emissions to mitigate the impact of climate change and secure a more livable, stable future.

The Paris Agreement, adopted at COP21 (21st Conference of Parties) in 2015 and entered into force in 2016, aims to limit global warming to well below 2°C above pre-industrial levels, ideally keeping it to 1.5°C (United Nations, 2015). Türkiye ratified the agreement in 2021 and initially submitted an Intended Nationally Determined Contribution (INDC) to reduce its emissions by 21% by 2030 (Republic of Türkiye, 2022). Recognizing that this target may fall short amid rising energy demand, industrialization, and urbanization, Türkiye revised its pledge in 2023, increasing its reduction target to 41% and identifying 2038 as the peak year for national emissions (Republic of Türkiye, 2023). The updated plan includes strategies across key sectors—energy, industry, transportation, agriculture, and waste—and aims for net zero emissions by 2053.

These ambitions require reliable forecasting and modeling methods to assess progress, anticipate trends, and guide long-term planning efforts. In this context, accurate and comparative emission modeling has become an essential component of climate governance and scientific decision-making.

The aim of this study is to explore advanced modeling techniques to estimate and forecast GHG emissions in Türkiye. It compares two approaches: the Deep Assessment Methodology (DAM), based on fractional calculus, and the Long Short-Term Memory (LSTM) model, a deep learning method well-known for time series forecasting. By evaluating the performance of both models up to 2030, the study not only assesses forecast accuracy but also considers the practical applicability of fractional calculus to environmental modeling. Additionally, the study examines the impact of the COVID-19 pandemic on emissions, particularly the slowdown in industry and transportation.

Material and Method

The analysis uses national GHG emissions data published by the Turkish Statistical Institute (TÜİK), covering the years 1990 to 2022. The LSTM model was implemented in Python, using TensorFlow and Keras for training, while the DAM model was developed in MATLAB with customized algorithms using the Caputo fractional derivative (Önal Tuğrul et al., 2024). Model parameters were optimized to ensure best performance, and both models were evaluated using the Mean Absolute Percentage Error (MAPE), a widely used metric for assessing forecast accuracy.

The dual-model framework offers comparative insight into the strengths and limitations of machine learning and fractional calculus in emissions forecasting. This hybrid perspective provides a strong basis for understanding how these methods may complement each other in future integrated modeling strategies.

Findings

The main results are presented in Table 1. Model Fitting (1990–2022) and Table 2. Model Prediction Values (2023–2030). These tables include historical emissions data, model outputs for the same period, and projections for 2023–2030. Both DAM and LSTM predictions are presented separately to enable comparison.

Table 1. Model Fitting Values(1990-2022).

Year	GHG Values	LSTM Fitting GHG Values	DAM Fitting GHG Values
1990	228.00	228.00	228.00
1991	235.40	235.40	235.40
1992	241.81	241.81	241.81
1993	249.14	249.14	249.14
1994	242.77	242.77	242.77
1995	256.49	257.51	256.49
1996	275.85	263.15	275.85
1997	286.74	270.07	286.74
1998	288.14	278.43	288.14
1999	285.63	295.19	285.63
2000	306.39	308.87	305.96
2001	287.55	317.06	282.91
2002	292.47	319.84	295.91
2003	312.14	322.38	312.31
2004	321.69	329.66	328.44
2005	344.78	328.75	344.14
2006	365.23	345.56	359.58
2007	399.03	369.66	374.84
2008	394.92	386.88	389.94
2009	401.32	406.15	404.82
2010	405.27	422.38	419.43
2011	434.77	434.87	433.69
2012	455.16	439.53	447.57

2013	447.31	451.62	461.01
2014	466.38	465.16	473.99
2015	480.07	482.65	486.48
2016	504.09	493.85	498.46
2017	531.11	503.04	509.93
2018	528.08	523.92	520.90
2019	515.58	543.38	531.35
2020	530.18	559.95	541.30
2021	571.99	569.21	550.75
2022	558.27	573.18	559.73

Table 2. Model Prediction Values(2023-2030).

Year	**LSTM Prediction Values**	**DAM Prediction Values**
2023	581.60	563.96
2024	602.76	599.43
2025	626.23	622.12
2026	637.82	641.95
2027	665.59	659.12
2028	693.33	677.68
2029	723.21	681.32
2030	755.17	718.03

Figure 1. Model Values and Predicted GHG Emissions visualizes these results, contrasting actual emissions with model outputs.

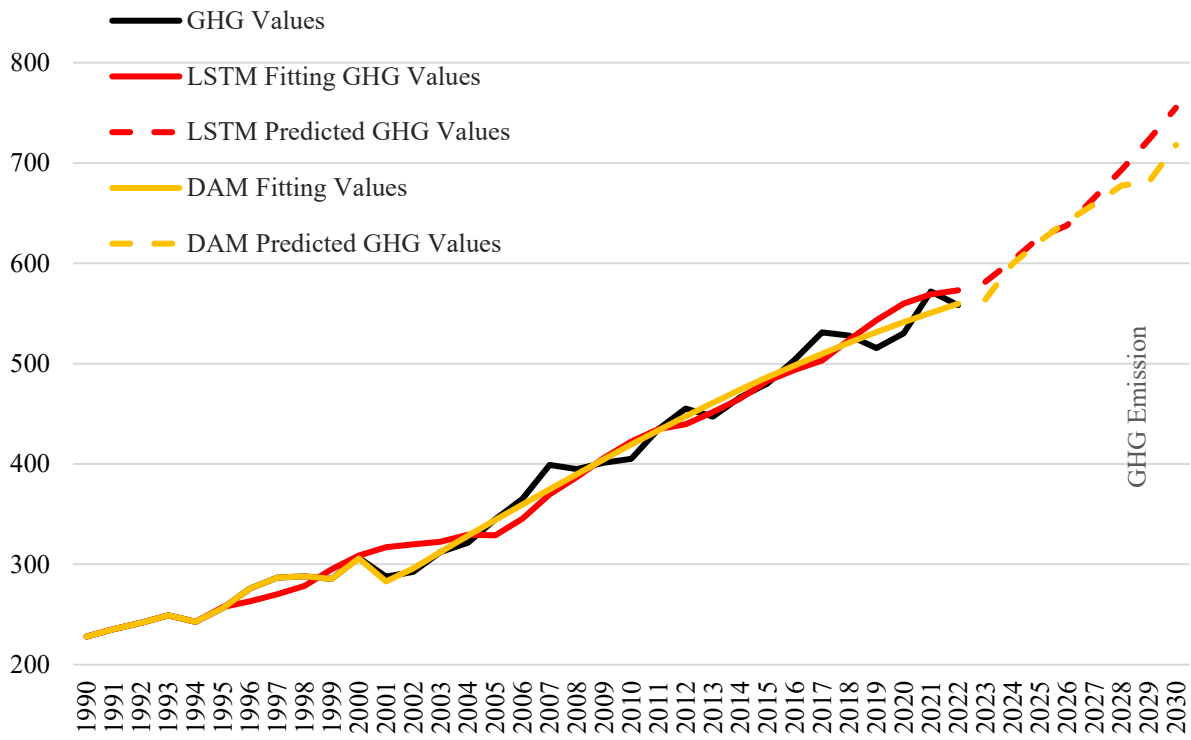

Figure 1. Model Values and Predicted GHG Emissions.

DAM achieved higher accuracy, outperforming LSTM with a MAPE of 1.8%, compared to 3.8% for LSTM. While LSTM is known for its strength in handling large datasets, DAM performed remarkably well even with limited data, benefiting from its transparent and interpretable structure. For 2030, DAM predicted emissions of 718.02 Mt CO_2e, while LSTM forecasted 755.2 Mt CO_2e.

The year 2030 was chosen as a benchmark because Türkiye has officially pledged to reduce its emissions to 695 Mt CO_2e by then under the Paris Agreement. Both models' forecasts exceed this target, highlighting the need for enhanced policy measures to meet climate commitments.

Energy production remains the dominant emissions source in Türkiye, contributing 71.8% of total GHG emissions—primarily due to coal-based electricity generation (Ministry of Energy and Natural Resources, 2024). This emphasizes the urgency of transitioning to renewable energy, enhancing efficiency, and investing in low-carbon technologies.

The study also analyzes the impact of the COVID-19 pandemic. Table 3. Model Fitting (1990–2018 – Pre-COVID) and Table 4. Model Prediction Values (2019–2030) show forecasts based on data excluding the pandemic years. This method allows an isolated evaluation of the pandemic's impact.

Table 3. Model Fitting Values(1990-2018-Pre COVID).

Year	GHG Values	LSTM Fitting GHG Values	DAM Fitting GHG Values
1990	228.00	228.00	228.00
1991	235.40	235.40	235.40
1992	241.81	241.81	241.81
1993	249.14	249.14	249.14
1994	242.77	242.77	242.77

1995	256.49	269.10	256.49
1996	275.85	274.54	275.85
1997	286.74	280.46	286.74
1998	288.14	287.63	288.14
1999	285.63	295.38	285.63
2000	306.39	307.39	305.96
2001	287.55	318.11	282.91
2002	292.47	323.21	295.91
2003	312.14	325.11	312.31
2004	321.69	328.26	328.44
2005	344.78	334.68	344.14
2006	365.23	338.02	359.58
2007	399.03	353.20	374.84
2008	394.92	374.65	389.94
2009	401.32	395.58	404.82
2010	405.27	418.49	419.43
2011	434.77	436.97	433.69
2012	455.16	452.91	447.57
2013	447.31	461.68	461.01
2014	466.38	475.97	473.99
2015	480.07	492.70	486.48
2016	504.09	512.92	498.46
2017	531.11	527.61	509.93
2018	528.08	541.37	520.90

Table 4. Model Prediction Values (2019-2030).

Year	**LSTM Prediction Values**	**DAM Prediction Values**
2019	549.03	551.38
2020	565.00	566.76
2021	588.86	590.95
2022	615.32	607.50

2023	640.84	620.65
2024	664.56	649.94
2025	692.89	664.83
2026	721.22	692.86
2027	749.61	711.20
2028	777.27	734.04
2029	804.54	760.77
2030	832.01	780.47

Figure 2. Visualization of COVID-Adjusted Model Values and Predicted GHG Emissions compares model outcomes based on pre-pandemic data. In this scenario, DAM predicted 780.46 Mt CO_2e, and LSTM forecasted 876.89 Mt CO_2e for 2030. However, when models include pandemic years, both project significantly lower emissions, illustrating the temporary reductions caused by COVID-19 restrictions.

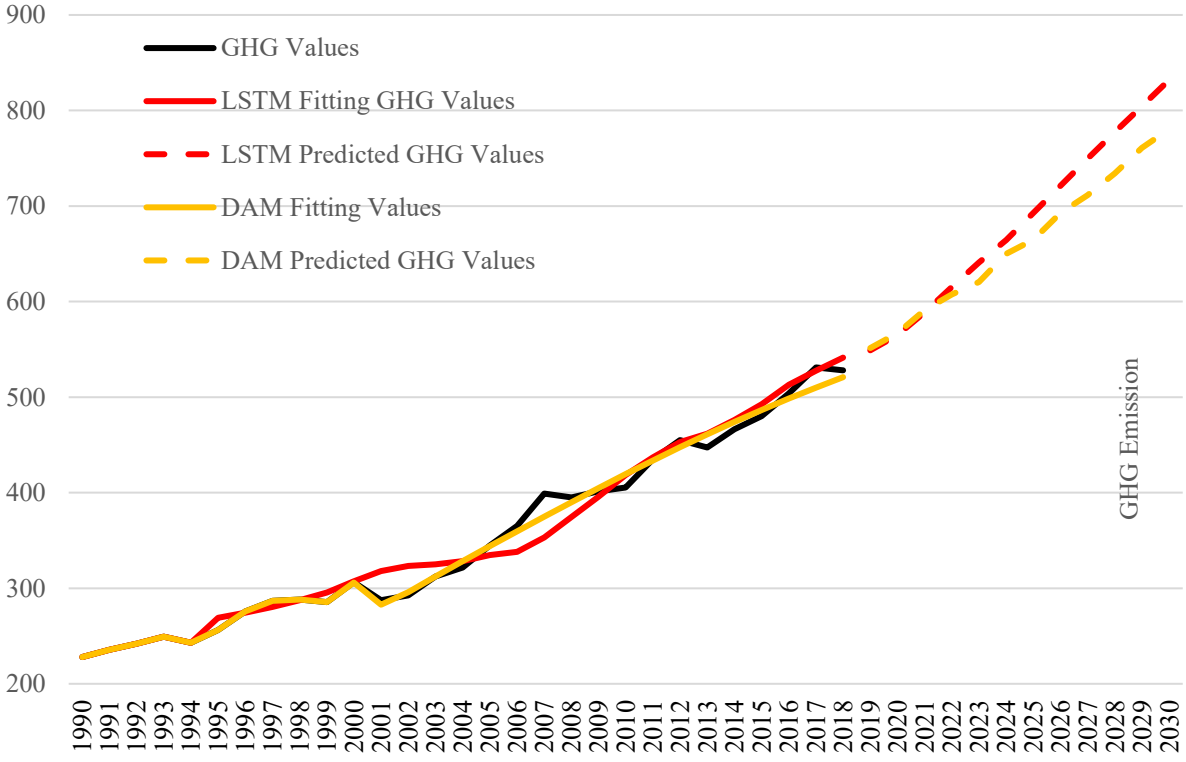

Figure 2. Visualization of COVID Adjusted Model Values and Predicted GHG Emissions.

These results confirm that model predictions are highly sensitive to training data and highlight the importance of including historical anomalies in long-term emission projections.

Similarly, a study conducted in Samsun Province found a 17.3 Gg CO_2e reduction in emissions from heating and transport during lockdown (Aykaç Özen, 2022). These insights underline the value of sustained structural change, rather than reliance on short-term disruptions.

Conclusion

This study demonstrates that the DAM model, with its fractional calculus-based structure, is a highly accurate and policy-relevant tool for modeling greenhouse gas (GHG) emissions. Compared to the LSTM model, DAM delivered more reliable forecasts and better captured long-term dependencies in emission trends.

The findings also suggest that reaching Türkiye's 2030 GHG target of 695 Mt may be challenging under current policy trajectories. This highlights the importance of strengthening mitigation efforts and considering additional measures. Moreover, the study examines the effects of reduced industrial and transportation activity during the COVID-19 period. When pandemic-related effects are excluded, it becomes clear that emissions would have been significantly higher. This underscores the fact that strong and targeted climate actions can lead to meaningful and measurable reductions in GHG emissions.

In conclusion, while current policies alone may not be sufficient, timely and science-based strategies can help close the gap. Beyond forecasting, the DAM model offers a novel analytical perspective for guiding future climate strategies.

References

Ayaz, İ. (2024). Forecasting CO_2 emissions with machine learning methods: Türkiye example and future trends. Malatya Turgut Özal University Journal of Engineering and Natural Sciences, 5(2), 82–87.**Url-1** https://doi.org/10.46572/naturengs.1595329, date retrieved 23.02.2025.

Aykaç Özen, N. (2022). COVID-19 kısıtlamalarının sera gazı emisyonlarına etkisi: Samsun örneği. Niğde Ömer Halisdemir Üniversitesi Mühendislik Bilimleri Dergisi, 11(1), 39–47. **Url-2** https://doi.org/10.28948/ngumuh.1005439, date retrieved 23.02.2025.

Enerji ve Tabii Kaynaklar Bakanlığı. (2024). Türkiye ulusal sera gazı envanteri (1990–2022). **Url-3** https://enerji.gov.tr/, date retrieved 15.12.2024.

Intergovernmental Panel on Climate Change (IPCC). (2021). Climate change 2021: The physical science basis.

Önal Tuğrul, N. Ö., Karaçuha, K., Ergün, E., Tabatadze, V., & Karaçuha, E. (2024). A novel modeling and prediction approach using Caputo derivative: An economical review via multi-deep assessment methodology. AIMS Mathematics, 9(9), 23512–23543. **Url-4** https://doi.org/10.3934/math.20241143, date retrieved 23.02.2025.

Republic of Türkiye. (2022). Intended Nationally Determined Contribution (INDC). United Nations Framework Convention on Climate Change (UNFCCC). **Url-5** https://unfccc.int/sites/default/files/NDC/2022-06/The_INDC_of_TURKEY_v.15.19.30.pdf, date retrieved 23.02.2025.

Republic of Türkiye. (2023). Türkiye Updated First Nationally Determined Contribution (NDC). United Nations Framework Convention on Climate Change (UNFCCC). **Url-6** https://unfccc.int/sites/default/files/NDC/2023-04/T%C3%9CRK%C4%B0YE_UPDATED%201st%20NDC_EN.pdf, date retrieved 23.02.2025.

Üstün, A. (2023). Türkiye'nin yeni ulusal katkı beyanı: Atalet mi atılım mı? *Kent Araştırmaları Dergisi*, 15(41), 437–463. **Url-7** https://dergipark.org.tr/tr/pub/kent/issue/74982/1172434, date retrieved 23.02.2025.

World Economic Forum. (2025). *Global risks report 2025*. **Url-8** https://www.weforum.org/reports/global-risks-report-2025, date retrieved 23.02.2025.

ARCHITECTURE

Architectural History

Architecture Design Theory

Building Construction Technologies

Building Materials and Technologies

Built Environment Design and Technologies

Conservation and Restoration

Environmental Control and Building Technology

Project and Construction Management

Sustainable Design

Civil Architecture in Pieter Coecke van Aelst's Depictions from His Journey to Istanbul

Emre Can Yılmaz[a]

[a]İstanbul Technical University, Graduate School, Architectural History, Türkiye

yilmazemre@itu.edu.tr

Keywords: 16th century Istanbul, Civil Architecture, Pieter Coecke van Aelst, Turkish House.

Aim

This abstract has been prepared using data obtained from studies conducted as part of the doctoral dissertation titled *"A Perspective on the Civil Architecture of the Period through the Ayasofya Foundations Tahrir Register,"* which is carried out within the Architectural History program at ITU and examines 16th-century Istanbul's civil architecture from multiple aspects.

The doctoral dissertation aims to explore the origins of a highly picturesque form of civil architecture: the Istanbul-based Turkish House. The research primarily focuses on 15th- and 16th-century Istanbul to identify the characteristics of what may be considered as a proto-Turkish House model.

Two main source types serve as the foundation for this investigation: visual and textual traces. The dissertation is based on a particularly valuable register, the Ayasofya Vakıfları Tahrir Defteri, which provides detailed architectural insights. Additionally, numerous visual documents from the period have been examined, among which the drawings of Pieter Coecke van Aelst stand out. Although well-known among researchers, their remarkable potential for documenting civil architecture has been somewhat overlooked. This study seeks to highlight that potential.

Material and Method

The woodblock print engravings of Aelst, titled "Ces moeurs & fachons de faire de Turcz avecq' les Regions y appartenantes" (The Morals and Customs of the Turks and Their Territories) [1], were posthumously published in Antwerp in 1553 by his wife. Created during his visit to Istanbul in 1533, these engravings have long been recognized as a widely referenced source among researchers, with numerous studies dedicated to them.

However, the specific examination of civil architectural elements within these depictions has the potential to shed new light on previous research concerning the subject. Therefore, it is crucial to first explain the significance of this engraving series as a visual source within its chronological context, assess its degree of consistency as a documentary record, and focus on the author himself as a key figure in its production. For this reason, Aelst is studied as a polymath whose activities spanned painting, linguistics, and beyond.

Aelst (1502–1550) was a highly versatile artist. While his depictions of Istanbul may have been disproportionately highlighted by Turkish researchers, he was, more broadly, one of the leading figures of early 16th-century Flemish art. A noteworthy aspect of Aelst, particularly relevant for architectural historians, is that, in addition to being a painter and a designer of tapestries and woodblock prints, he was also an architect proficient in multiple languages. As a manifestation of this, he translated architectural treatises by Vitruvius and his contemporary Serlio into Dutch. [2] His translations of Serlio, in particular, were published almost simultaneously with the original editions. In fact, even the later English translations of these works were based on Aelst's publications. These books also included numerous woodblock illustrations that Aelst reinterpreted, contributing significantly to the dissemination of Renaissance architectural ideas in Northern Europe and the revival of classical proportions and styles.

When examining Aelst from this perspective, it is essential to recognize that he was not merely a scribe in a diplomatic delegation, a cleric, a diplomat, or a sailor producing sketches out of casual observation. Instead, he was a highly trained professional with a solid architectural and artistic background. For researchers studying Istanbul and the Ottoman Empire, his works present a unique visual documentation opportunity. Until Melchior Lorck's depictions in 1559, no other 16th-century Western source provided visual records of such documentary value. It is widely accepted that Aelst traveled to Istanbul as part of the Habsburg diplomatic delegation led by Cornelis de Schepper. The most prominent reason for his visit appears to be his plan to sell tapestries in Istanbul. In this sense, beyond his artistic identity, his role also had a commercial aspect. [3] Given Aelst's commercial position, it is likely that his role provided him with an opportunity to make more objective observations before creating his depictions.

Findings

Pieter Coecke van Aelst's seven-scene engraving series can be analyzed under various headings in terms of its documentary value, historical accuracy, and realism.

First, it is important to note that realistic perspective was not a primary concern in urban depictions produced during the century of its creation and in the following centuries. However, Aelst's drawings exhibit a certain consistency in perspective and a deliberate effort toward mimesis. While it would be an overstatement to claim that the scenes adhere to a photographic level of perspective accuracy, it is evident that the author approached them with an editorial intent, shaping the composition according to what he wished to highlight. The original sketches, which later served as the basis for woodblock prints published posthumously, were likely created with the intention of being developed into tapestries.

This compositional approach explains why the drawings feature numerous dynamic figures engaged in various actions, lending them an extraordinary sense of movement and liveliness. Nevertheless, the proportional scaling of figures based on their vantage points, as well as the perspective precision in the placement of background landscapes, settlements, and buildings, contribute to the documentary quality of the work.

Another key aspect of evaluation is the historical accuracy of the figures' attire, tools, and weaponry. When cross-referenced with contemporary sources, such as Western-produced Ottoman costume albums, these details demonstrate remarkable consistency. The weapons, shields, and even the intricate details of sword hilts and guards align with the period's stylistic characteristics. Furthermore, an extensive array of objects, from musical instruments and horse harnesses to tableware, spoons, and water flasks, provides valuable insights into material culture. Such attention to detail makes it possible to detect any potential historical anachronisms, yet no significant inconsistencies emerge. The series also incorporates behavioral themes, depicting religious rituals, communal dining practices (such as eating from a shared dish on the floor), funeral ceremonies, celebratory events, and the Friday procession. All these rich details suggest that the author conducted serious, on-site observations and documented them with remarkable objectivity. Supporting the interpretation of these scenes, the British Museum's surviving copies of the engravings contain short explanatory texts. Additionally, the series features two decorative plates—one at the beginning and one at the end—providing contextual information. While the final plate includes the publication date, the opening plate bears the series title and a statement affirming that Aelst personally sketched these scenes "true to nature" in Turkiye in 1533 in preparation for print. This evidence indicates that Aelst's field sketches were not merely adapted into woodblock prints after his death; rather, he himself composed the final woodblock print designs. This direct authorship further enhances the documentary credibility of the final work.

Not all seven pieces in the "Ces moeurs & fachons de faire de Turcz avecq' les Regions y appartenantes" series contain explicit location information. However, it is evident that Aelst depicted places he encountered on his journey to Istanbul. The first engraving is explicitly labeled as Slavonia, while the fourth piece has been identified as Plovdiv (Philippopolis) based on geographical markers. The final two engravings, however, are unmistakably from Istanbul.

In the sixth scene (Figure 1), the view is from the Kasımpaşa hills, looking towards Cibali. The ease with which the neighborhoods depicted in the scene can be identified is a result of the consistent urban perspective. Several public architectural landmarks, such as the Galata Tower, Fatih Mosque, Yavuz Selim Mosque, Zeyrek, Eski İmaret, and the Haliç Walls, are depicted with realistic proportions, aligning well with their actual placements. In fact, this depiction represents an extremely exciting example of urban realism for a time as early as 1533, offering an unprecedented level of perspective accuracy. There is, in fact, no earlier drawing of this quality with such an urban realistic perspective.

Figure 1. 6th Scene from "Ces moeurs & fachons de faire de Turcz avecq' les Regions y appartenantes".

The layering progresses from the Golden Horn to Suriçi. Just behind the crowd in transition, due to the perspective, there is a building group that is depicted with remarkable detail and size, as it appears to be in the foreground. This building group, except for the areas obscured by the people in the foreground, can actually be considered a perfectly depicted example of a 16th-century Istanbul residence (Figure 2).

Figure 2. Detail from the 6th Scene, 16th century Istanbul Residence.

This residence consists of courtyard walls, a courtyard gate, several single-story masses, and a unit with a lower floor containing a "*sofa"*, an upper floor, and a smaller upper unit above that. If observed carefully, even the building materials can be discerned. Based on the figures standing by the door, watching the outdoor entertainment, it can be inferred that this residence likely belonged to a Muslim family.

Although this residence may not closely resemble the picturesque "Turkish House" often depicted, it actually describes a composition that can be easily traced in the foundation deeds (vakfiye) of the period. For instance, the walls surrounding the house evoke the concept of "muhavvata", which frequently appears in the period's vakfiyes. In these documents, the term was used to refer to the courtyard, though the word "courtyard" itself is rarely mentioned. Etymologically, muhavvata means an enclosed or walled area. In fact, on the left side of the aforementioned residence, there seems to be an enclosed plot. Such areas are also marked as "menzils" (property plots) in vakfiyes. For example, in the Ayasofya Vakfiyeleri Tahrir Defteri [4], under a record for the Molla Hüsrev Mosque District, it states: "formerly a horse mill, now a walled plot of land" (p.147b).

The structure resembling a "cihannüma" on the upper floor of the residence is strongly likely to be a "gurfe". It is apparent that the building material is wood, which is consistent with records found in the foundation deeds. For instance, in the Ayasofya Vakfiyeleri Tahrir Defteri, there is a record from the Sultan Bayezid Mosque District that states: "beyt-i süfli (lower house) and a small gurfe made of wood above it" (p.226b). In fact, there are numerous records in the period's vakfiyes that indicate the use of wooden panels as building materials (for example, AVTD p.206a: "made from wooden planks" – "masnu' min el elvah").

Conclusion

As a result, after much discussion on the documentary nature of the depictions, one might ask: why is there not a single pictorial "Turkish House" with eaves, overhangs, projecting upper floors, numerous windows, bay windows, and top windows among the civil architectural examples depicted by Aelst on Ottoman soil, despite his work's emphasis on realism? In fact, the absence of such a housing type in the drawings is, in itself, a form of evidence. The residential settlement at the center of one of the most famous scenes from his well-known work, though not

prominently highlighted due to its nature, likely depicts a 16th-century "Turkish House" in a clear and unambiguous manner. Its consistency with other contemporary visual and written sources, as well as its historical coherence within the broader context of the artwork, strongly suggests that it represents a typical 16th-century "Turkish House", in contrast to the ambiguous depictions often found in other records. Thus, these depictions make a significant contribution to understanding the position of the "Turkish House" in the early 16th century's architectural evolution.

References

Fenari Zade Muhyiddin Mehmed Şah b. Alaiddin Ali. (926 H.). Defter-i evkaf-ı Cami-i Şerif-i Ayasofya. İBB Atatürk Kitaplığı. Retrieved from http://katalog.ibb.gov.tr/yordam/?dil=0&p=1&q=ayasofya+muallim+cevdet&alan=tum_txt&demirbas=MC_Yz_O.000064

Serlio, S., & van Aelst, P. C. (1550). Reigles generales d'Architecture, sur les cincq manieres d'edifices, ascauoir, Thuscane, Dorique, Ionique, Corinthe, & Composite, auec les exemples des antiquites, lesquelz la pluspart concordent a la doctrine de Vitruue. Reueu & corrige, auec additions du mesme Aucteur oultre les precedentes impressions. Retrieved from https://books.google.com.tr/books?id=U8RaAAAAcAAJ

Url-1 https://www.britishmuseum.org/collection/object/P_E-6-1-7, date retrieved 24.03.2025

Wunder, A. (2003). Western travelers, eastern antiquities, and the image of the Turk in early modern Europe. Journal of Early Modern History, 7(1-2), 89-119.

ARCHITECTURE

Architectural History

Architecture Design Theory

Building Construction Technologies

Building Materials and Technologies

Built Environment Design and Technologies

Conservation and Restoration

Environmental Control and Building Technology

Project and Construction Management

Sustainable Design

Fiction And Reality In Architectural Representation: Spatial Readings In Graphic Novels

Cigdem Akifoglu[a], Pelin Dursun Cebi[a]

[a] Istanbul Technical University/Graduate School, Department of Architecture, Architectural Design Program, Türkiye
akifoglu22@itu.edu.tr

Keywords: Architectural Representation, Fiction, Graphic Novel, Reality, User-Space Relationship.

Aim

According to Umberto Eco (1994), fiction and reality interact reciprocally; while fiction can be inspired by reality, reality can be reshaped by fiction. Similarly, Paul Ricoeur (1979) explored the blurred boundaries between fiction and reality, arguing that fiction is not merely a mirror reflecting reality but also a lens through which new possibilities and meanings can be imagined. How, then, can Eco and Ricoeur's fiction and reality dialectic be reflected in architectural representation?

The dialogue between fiction and reality exhibits a dialectical structure in architecture as well. Depending on the circumstances, these two concepts mutually influence and transform one another. For instance, throughout the design process, the data and constraints of the physical context play a significant role in shaping fictional narratives of space. Conversely, fiction, through the possibilities and scenarios it presents, enables the reinterpretation and transformation of real spaces. In this context, the focus of this study is on how the dialogue between fiction and real space is represented in architectural design.

Pérez-Gómez (2007) states that traditional architectural representations operate within a geometrized and homogeneous framework, relying on unquestioned sets of descriptive projections. Similarly, As and Schodek (2008) describe architectural representations as mechanical productions based on geometric algorithms, presenting a clear and definite reality. At this point, it can be stated that real space in architectural representation is conveyed through representational tools such as plans, sections, models, and three-dimensional renderings, utilizing a reductive language governed by specific rules. In this regard, As and Schodek (2008) note that architectural representations tend to reduce users' ability to perceive and experience space to a secondary place within the design process. This research examines the transmission of reality in architectural representation through the depiction of tangible and measurable spatial features that assert a definitive reality. Accordingly, it will be discussed how architectural representation frames space through specific rules and limited tools, thereby reducing reality and prioritizing only the tangible features of the space. Therefore, architectural representation will be examined from a critical perspective that mostly excludes user experience.

Kahvecioğlu (2008) states that the concept of space in architecture cannot be limited to objective definitions such as physical shell, frame, boundary, or surface; rather, space is a phenomenon built upon human life and experience and can be explained through different concepts of reality. This statement emphasizes that space should not be regarded merely as an object represented by tangible and measurable features but rather as part of a dynamic process that gains meaning through user experience. The genuine meaning and livability of space are formed by the user's involvement and experience. The user and space relationship is shaped by possibilities restructured in the individual's mind and ongoing experiences. Hence, this relationship is not a fixed and completed process but rather a dynamic structure in continuous transformation. Within this scope, the adequacy of conveying a space with architectural representation methods, the main goal of which is to represent concrete reality, is an issue worth considering.

Material and Method

This research examines that the discussions developed by Paul Ricoeur and Umberto Eco on fiction and reader experience provide an important theoretical framework for approaching the dynamic relationship between the user and space from a perspective that goes beyond the boundaries of concrete reality and for examining the role of

fiction in architectural representation. According to Paul Ricoeur (1979), fiction opens up a new world in front of us by shaking our perception of reality. In these worlds, the individual creates a unique space of existence under their assumptions and preferences. As Umberto Eco (1994) states that reading fictional narratives is playing a game in which we learn to give meaning to the boundless events that have happened, are happening, and will happen in the real world. Fiction introduces the individual to the unknown aspects of the real world. It enables the individual to encounter new possibilities, surpassing the limited experiences of the real world. Fictional narratives allow the individual to create a unique journey based on their personal preferences. Each choice opens up the possibility of new experiences and discoveries.

Fiction encourages the active participation of the individual in the process by providing opportunities for varied temporal and spatial experiences. This study initiates a discussion about the role and tools of fiction in architectural representation, questioning the efficacy of architectural representation that imposes a specific reading format within a limited and rule-bound framework, and investigating alternative methods of representation for conveying the fictional aspect in architectural representation. In this context, graphic novels, which make the dynamic relationship between fiction and real space visible and thus involve the reader in the spatial narrative, are considered an alternative tool for representing architectural space. To analyze how the representational potentials and formal characteristics of graphic novels are employed in the representation of architectural space, a deconstruction method has been applied to selected graphic novels (Figure 1.).

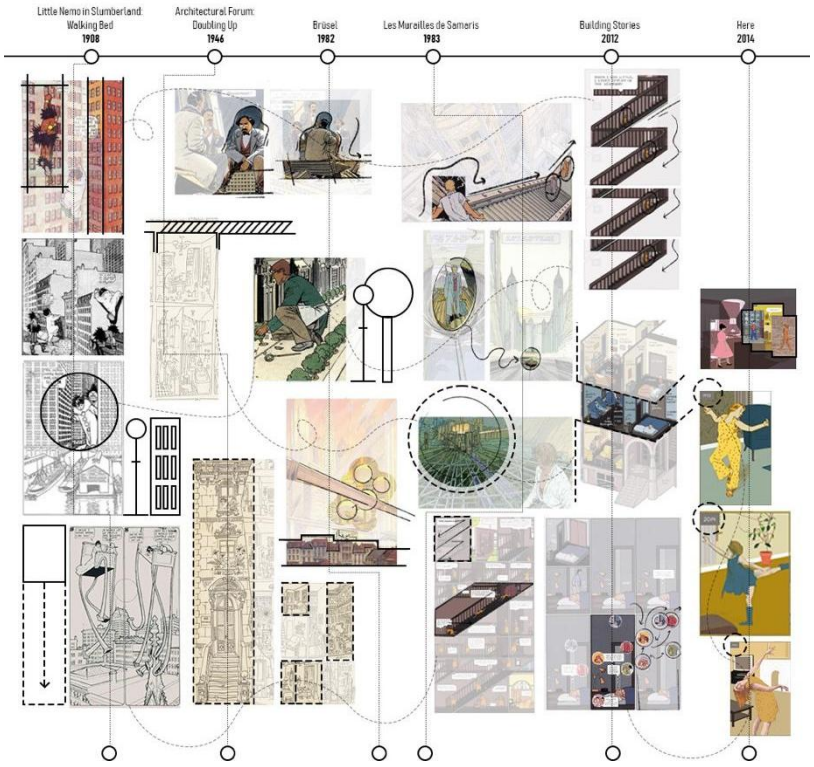

Figure 1. Deconstruction of selected graphic novels (Akifoglu, 2025).

Findings

Graphic novels are well-structured visual narratives that convey information, evoke sensory responses, and involve the reader into the narrative. Unlike architectural representation methods, in graphic novels, space is not presented within a limited framework; rather, it possesses a dynamic character shaped by the reader's involvement. Instead of representing space as a direct, concrete reality, graphic novels make alternative scenarios and possibilities related to space visible, encouraging the reader to reconsider space. Rather than positioning the reader as a mere observer, graphic novels place them as individuals actively participating in the narrative and constructing their

own spatial experience. Through graphic novels, fiction becomes visible, allowing the reader to engage with the space.

This research suggests the representational potentials of graphic novels as an alternative representation tool. In this regard, works such as Winsor McCay's *Little Nemo in Slumberland: Walking Bed,* Saul Steinberg's *Architectural Forum: Doubling Up,* Benoit Peeters and François Schuiten's *Brüsel* and *Les Murailles de Samaris,* Chris Ware's *Building Stories* and Richard Mcquire's *Here* have been selected as examples that highlight the visibility of fictional narratives in space by considering space not merely as a simple background but as an integral part of the narrative. The selected examples are analyzed through a deconstruction method, exploring how the boundaries of concrete reality are transcended by specific representation strategies, how fictional narratives containing alternative temporal and spatial scenarios become visible in spatial representation through these strategies, and how the reader becomes involved in space throughout this process.

Based on this framework, a cross-reading of selected graphic novels has been conducted based on the representation strategies identified through deconstruction method. This analysis enabled a comparative evaluation of how these strategies construct space within the interplay between fiction and reality across different narrative structures. For instance, the strategies employed to represent the temporal dimension of space in the graphic novel *Here* exhibit similarities to the representational techniques used in *Building Stories*. In both works, the temporal dimension of space is made visible through the representational potentials and formal characteristics of the graphic novels, incorporating time segments into the depiction of space. Rather than offering the reader a linear spatio-temporal structure, as typically encountered in real space, both graphic novels construct spatial narratives that encourage the reader to assemble their own interpretive framework. Within this non-linear spatio-temporal context, *Building Stories* centers on life unfolding within an apartment building, whereas *Here* explores the domestic structure of home life across multiple temporal layers (Figure 2.). In both cases, the shared representation strategies render the temporal scenarios of space visible and, significantly, shift narrative control to the reader, who actively participates in constructing the spatial narrative.

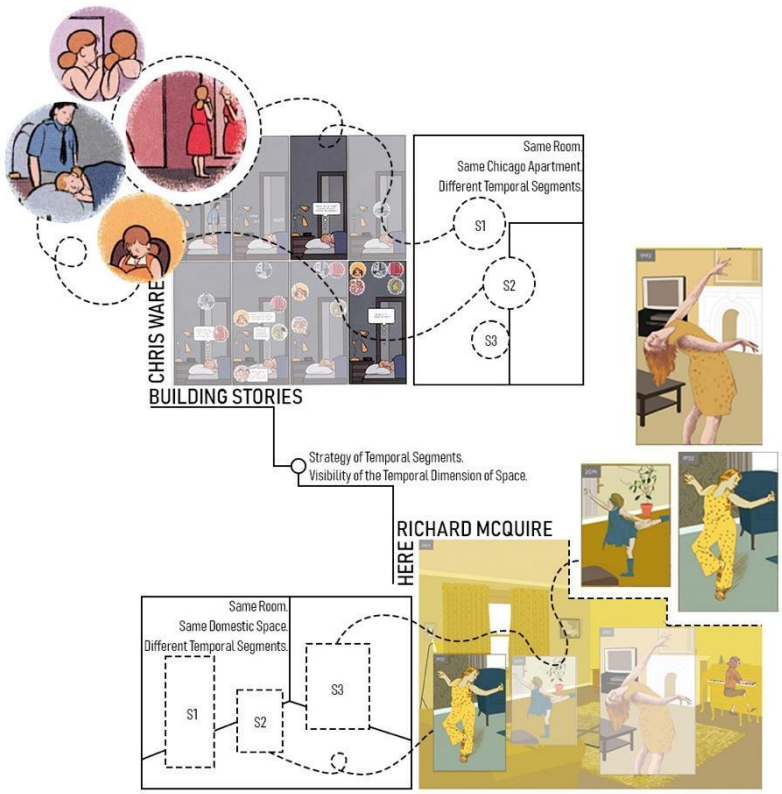

Figure 2. Visibility of temporal dimension of space (Akifoglu, 2025).

Conclusion

This research challenges the fixed and completed user-space relationship presented by traditional architectural representations, proposing graphic novels as an alternative representation tool that makes the fiction visible in spatial representation and emphasizes the dynamic relationship between the user and space. The findings reveal that graphic novels, through their representational strategies, distort and reconfigure reality, constructing multi-layered and dynamic spatial narratives on a spatio-temporal plane. These narratives make the dialectical relationship between fiction and reality visible, and most significantly, they highlight the reader (the user) as the primary agent who interprets, navigates, and reconstructs meaning within the spatial narrative.

As a result, the research offers a new perspective on real space, challenging the limits of traditional architectural representations and providing a conceptual foundation for architects seeking to explore the dynamic relationship between user and space through imaginative thinking. In this regard, by emphasizing the need for architects to have alternative tools for thinking, creating, and representing, the study argues that graphic novels and their representation strategies play a critical and mind-opening role in the representation of space, enabling the construction of user-centered spatial narratives within a spatio-temporal and interpretive framework.

References

As, I. & Schodek, D. (2008). *Dynamic Digital Representations in Architecture: Visions in Motion.* Taylor & Francis.

Eco, U. (1994). *Six walks in the fictional woods* (K. Atakay, Trans.). Can Publishing. (Original work published 1994; translation published 1995).

Kahvecioğlu, H. (2008). Mekanın üreticisi veya tüketicisi olarak zaman. *Zaman-mekan*, 142-149.

Perez-Gomez, A. (2007). Questions of representation: The poetic origin of architecture. In M. Frascari, J. Hale, **& B. Starkey** (Eds.), *From models to drawings: Imagination and representation in architecture* (pp. 11-22). Routledge.

Ricoeur, P. (1979). The function of fiction in shaping reality. *Man And World*, *12*(2), 123–141.

Deconstruction of Clothing: Clothing as a Spatial and Embodied Medium

Zeynep Özlem Dündar[a], Pelin Dursun Çebi[b]

[a] Istanbul Technical University, Graduate School, Architectural Design Program, Türkiye
[b] Istanbul Technical University, Faculty of Architecture, Department of Architecture, Türkiye
dundar23@itu.edu.tr

Keywords: Body and Space Relationship, Clothed Body, Affordance.

Aim

From a normative perspective, the ideal body is determined within the context of architectural design and static spatial configuration is constructed in accordance with the predefined norms on how the ideal form integrates into the space. Yet, the body is not sole and ideal; it is constantly open to manipulation and transformation in its relationship with bodies, its surroundings, or non-human actors. The existence of a disembodied space is as meaningless as the creation of a stable spatiality by the dynamic and changing body. These manipulations can physically shape the body through attachments that form a second skin, or perceptually through actions resulting from the affordances of the attachments. In the network of relationships the body establishes with space, the actors mediating this manipulation can be considered as a whole, consisting of both humans and non-human objects. According to Huyse (2024), some of the strategies that manipulate the body are abating, attaching, bonding, broadening, caging, campering, covering, deforming, dramatizing, elongating, encasing, enfolding, enveloping, exaggerating, excepting, expanding, fragmenting, freeing, gapping, hiding, insulating, isolating, masking, mocking, shaping, swelling, uncovering, wrapping etc. The aim of the research is to explore the transformative effects on the relationship between the body and space by thoroughly examining non-human actors that manipulate the body. Transformative effects contain both the transformation of the body, space and the perception. In this context, the effects of non-human actors, which may initially seem ineffective, can be more clearly revealed in the body-space experience, and perception.

The research begins with considering clothing which is an actor in the body-space dialectic, as a design object. It attempts to interpret the perception created by clothing on the body within a semantic framework. There is a connection between human-centered thinking and object-centered thinking. The design of every object is shaped towards a purpose. As mentioned by Gibson (2015), "The different objects of the environment have different affordances for manipulation" (p. 120). Objects are designed with all their potential possibilities -with their affordance; however, apart from the designer's intention, implicit potentialities can be discovered in different ecologies and users. As noted by Gibson (2015), "The affordances of the environment are what it offers the animal, what it provides or furnishes, either good or ill" (p. 119). Clothing is suitable for manipulating the body's potential for action as a second skin. According to what Spurrett and Brancazio said, "When we wear certain clothing, it enables us to change our appearance or abilities, shaping our capacities as agents, either supporting or constraining our possibilities for action" (Spurrett and Brancazio, 2024, p. 1901). When it comes to clothing, a design that is proper with the body is brought to mind as a result of socially acquired judgments, and efficiency is essential in this design. Questioning the design principles, usage areas, and affordances of objects like garments, which are associated with the body but considered ordinary, can enable the creative destruction of the judgments attributed to them. Here, the phrase "creative destruction" refers to deconstructing clothing in order to explore its interaction with the body, thereby revealing its role in the body-space relation.

Material and Method

As noted by Spurrett and Brancazio (2024), "That the human body is typically clothed in ways that transform its capabilities seems important for thinking about human embodiment and cognition" (p. 1990). In the research, clothing is considered as an actor who transforms the body and space with a focus on experience. Schlemmer (1961), "The transformation of the human body, its metamorphosis, is made possible by the costume, the disguise" (p. 25). Clothing is considered as a tool to reinterpret the body and, consequently, to rethink spaces. The space

defined by the body in conjunction with clothing; as well as the body's perception, actions, and interactions through wearable technologies, can be manipulated. As a result, the organization and experience of space can be diversified. The theoretical framework of the research is discussed through Latour's Actor-Network Theory (ANT), exploring the manipulative power of clothing in the body-space relationship. As noted by Latour (2005), "It was at this point that non-humans -microbes, scallop, rocks and ships, presented themselves to social theory in a new way" (p. 10). The body is open to manipulation, and thus, space becomes a system that constantly forms and deforms with the body. Moreover, ANT does not represent a finite system and allows for the consideration of both human and non-human objects within the same system. The way the theory allows for the simultaneous consideration of human and non-human entities also shapes the methodology of the research.

Findings

In the continuation of the research, selected works of artists who have conducted experimental studies in clothing design are examined in terms of bodily, spatial, and social dimensions. As noted by Loschek (2009), "The three-dimensionality of clothing suggests a comparison to architecture, which is evident in deconstructivism" (p. 190). Martin Margiela is known for his innovative designs that demonstrate how deconstruction functions in fashion. By critically approaching traditional design concepts, he adds new meanings to garments. In doing so, he deconstructs the body, emphasizing its parts rather than presenting it as a whole. He reverses the inner and outer surfaces of garments, stitches parts in contrasting ways, or designs incomplete garments to evoke a sense of incompleteness, making the gaps visible. In a similar approach, Rei Kawakubo deforms the garment by breaking it into pieces in her "*Body Meets Dress, 1997*" collection. She offers a critique of the traditional aesthetic norms imposed on the body. In this context, the garment becomes a transitional object, serving as a tool that spans from the traditional to the innovative, and from the individual to the space. In the works of Donna Sgro, the impact of various factors, ranging from the material of the garment to its design, on both the body and the space, is traced and examined. In Sgro's "*Fractured Garment"* design, the garment responds to the moving body due to the soft and flexible fabric it is made from. The garment shapes itself according to the body's movements, expanding with the possibilities inherent in the fabric. This invites a reconsideration of the relationship between the body and its surroundings.

Fig. 1. Rei Kawakubo, *Body Meets Dress, 1997* (Url-1).

Fig. 2. Donna Sgro, *Fractured Garment* (Url-2).

A similar situation can be observed in Jana Sterbak's "*Remote Control II, 1989"* design. Sterbak discusses dualities such as body – machine, male – female, and freedom – captivity through her design. The design incorporates a mechanical system that enables the skirt to expand, contract, or transform into various shapes. In this way, the body redraws its boundaries each time through external control. The physical qualities that the skirt presents to the

body and its surroundings hold new potential for action for the wearer. The body, by breaking down its sensory-coded perception, re-discovers and re-creates the space. By lifting the body off the ground, it deprives it of its conscious movement. In this context, both human and non-human actors create a dynamic power politics on the body. Although the connections between humans and non-human objects may break and repeatedly re-form, spatial creation continues to sustain its existence within the system in different forms. The space now becomes an ongoing ambiguity, constantly deteriorating and re-forming, never disappearing, for the body integrated with the skirt. In her works, Sgro represents garments as transformative structures. In the "*Architectonic Exhibition* 2014", garments are approached as an architectural form, with new forms of design and structure emerging through different types of materials and structural design. As mentioned by Hodge (2006), " Vocabulary derived from architecture has been applied to garments ("architectonic,""constructed," "sculptural," etc.)" (p. 11). As an architectural form, the garment blurs the boundaries of the body, creating spatiality between the body and the garment.

Fig.3. Jana Sterbak, *Remote Control II,* 1989 (Url-3). **Fig.4.** Donna Sgro, *Architectonic Exhibition*, 2014 (Url-4).

A similar situation can be observed in the works of Lucy Orta. In her "*Refuge Wear, 1992-98"* designs, the garment transforms into a temporary shelter and architecture on the body, functioning as an architectural form.

Fig. 5: Lucy Orta, *Refuge Wear*, 1992-98 (Url-5).

Conclusion

As a result, the social, political, perceptual, experiential, and spatial effects of clothing are examined through the flexibility provided by Actor-Network Theory. In addition to the social effects of clothing as an actor on the body, the reflection of its limitation or expansion of the body's actions on architectural space is questioned. While exploring how clothing can manipulate the body both physically and perceptually, the study also traces how, beyond merely being a covering for the body, clothing becomes an active component in the creation of space through various designer approaches and changing environmental dynamics such as material and technology. In this direction, the research criticizes the static understanding of the body and space, while problematizing non-human actors in the body-space relationship through the lens of clothing, thereby opening new perspectives in design processes.

References

Gibson, J. J. (2015). *The Ecological Approach to Visual Perception* (Classic ed.). Psychology Press Taylor & Francis Group. (Original work published 1986).

Huyse, M. (2024). Extending the Body. *Marthe Huyse*. https://marthehuyse.com/#footer, data retrieved 07.04.2025.

Hodge, B., Mears, P,, & Sidlauskas, S. (2006). *Skin + Bones: Parallel Practices in Fashion and Architecture*. Thames & Hudson.

Latour, B. (2005). *Reassembling the Social: An Introduction to Actor-Network-Theory.* Oxford University Press

Loschek, I. (2009). *When clothes become fashion: Design and innovation systems* (English edition). Berg. DOI: 10.5040/9781847883681

Schlemmer O., Moholy-Nagy, L., & Monar, F. (1961). *The Theater of the Bauhaus*. In W. Gropius (Ed.), Wesleyan University Press.

Spurrett, D., Brancazio, N. (2024). *Fashioning Affordances: A Critical Approach to Clothing as an Affordance Transforming Technology*. Philosophical Psychology, 37(7), 1899-1923. DOI: 10.1080/09515089.2023.2263478

Url-1 < https://www.vogue.com/fashion-shows/spring-1997-ready-to-wear/comme-des-garcons, data retrieved 07.04.2025.

Url-2 < https://donnasgro.com/Fractured-Garment, data retrieved 07.04.2025.

Url-3 < https://www.macba.cat/en/obra/r0180-remote-control-ii/, data retrieved 07.04.2025.

Url-4 < https://donnasgro.com/ARCHITECTONIC, data retrieved 07.04.2025.

Url-5 < https://www.studio-orta.com/en/artwork/86/refuge-wear-intervention-london-east-end-1998, data retrieved 07.04.2025.

The Interpretation of the Metaverse through Rhizome Philosophy

Beril Deren Simsek[a], Meltem Aksoy[a]

[a] Istanbul Technical University/Graduate School, Department of Architecture, Architectural Design Program, Türkiye
simsekb22@itu.edu.tr

Keywords: Metaverse, Multispace, Rhizomatic Connections, Rhizome Philosophy, Virtual Space.

Aim

In this study, a discussion is carried out on the metaverse, where there are simultaneous interactions between virtual space and real space. Regardless of time and location, the metaverse allows for a variety of experiences by allowing transitions between different spaces. In this paper, these intertwined spaces are referred to as multispace. It can be stated that the complex and multi-layered structure of the multispace within the metaverse shares similarities with Deleuze and Guattari's rhizome philosophy. In the light of these similarities, it is aimed to read multispaces spatially and conceptually through rhizomatic connections. In the context of the characteristics of rhizome philosophy, which expresses non-hierarchical and infinite proliferation, can the metaverse form a rhizome?

Material and Method

The rhizome philosophy, described by Deleuze and Guattari in their book "A Thousand Plateaus" (1980), represents a way of thinking that contrasts with the tree metaphor, which stands for a fixed and hierarchical framework. It expresses a decentralized form of organization that is network-like, where multiple connections are established. Each connection is connected to any other point while constantly creating a new one. This approach offers a flexible and dynamic structure without being tied to a fixed root (Deleuze & Guattari, 1980/2023). Rhizome, which does not show a linear growth model, reproduces through underground trunks formed by additional shoots upwards, downwards or laterally, as in the botanical meaning. It has no beginning, end or specific direction of spread. (Adkins, 2015).

Deleuze and Guattari have detailed how rhizomatic connections are formed and multiplied with six principles: "connectivity", "heterogeneity", "multiplicity", "asignifying rupture", "cartography" and "decalcomania". In this study, it is argued that the metaverse can be associated with the rhizome in that it does not have a certain boundary indicating where the connections will end, creates a decentralized communication network instead of a single authority and has a multi-layered structure. Within the framework of the rhizome philosophy, it has been discussed where multispaces are similar to the principles of the rhizome and a narrative has been created in this direction.

When looking at various metaverse platforms, it is seen that exhibition space and showroom designs are mostly prominent in the use of metaverse. Therefore, in the last stage of the study, the virtual gallery project called "NFTism" designed by Zaha Hadid Architects in the metaverse was selected as a case study and analysis was made over multispaces.

The metaverse transforms today's online experiences into interconnected and immersive virtual spaces where one can interact with others regardless of location (Levine, 2022). It can be said that the disappearance of physical and environmental boundaries in traditional architectural practice in these areas has created differences in spatial experiences. According to the definitions of Mantegna and Rinesi, while in "augmented reality (AR)" technology, a variety of spatial perceptions can be achieved by adding a new digital layer to the real world, with "virtual reality (VR)" technology, users can have a realistic experience. "Mixed reality (MR)", which is at the intersection of AR and VR applications, is defined as hybrid environments where real and virtual spaces can react to each other at the same time (Mantegna & Rinesi, 2023). The metaverse brings all these technologies together and enables transitions between spaces. These different technologies are gathered under the title of "extended reality (XR)" and form the interaction area of the metaverse (Image-1).

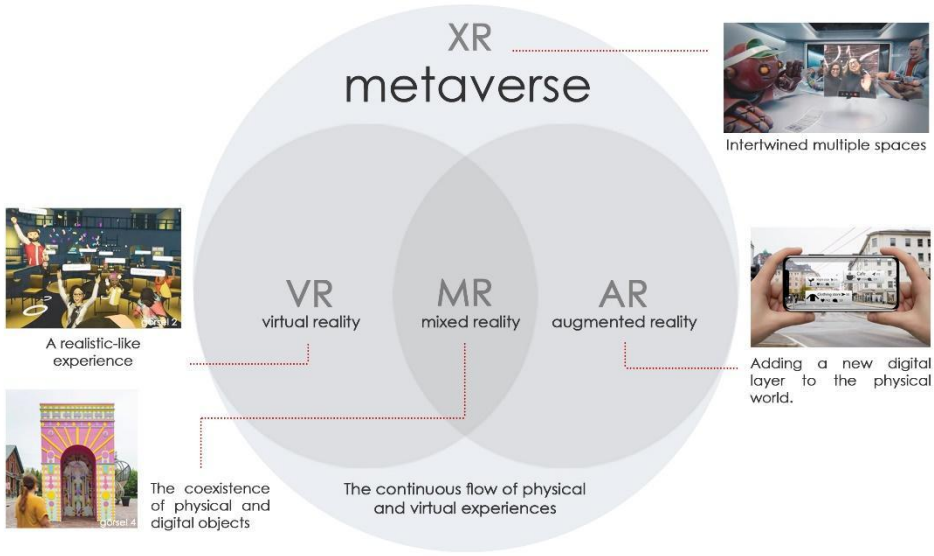

Image 1. The Scope of extended reality (Simsek, 2024).

XR technologies allow architects to redesign and experience spatial environments by transcending traditional boundaries. In this way, virtual spaces can be perceived at various scales and with different sensory organs. For instance, by incorporating XR technologies into a project designed for a real space, the space gains dimension and richness. Thus, instead of passive viewing, a transition is made to a multispace where users can explore the works from different scales. According to Hopkins (2023), multispace emerges at the intersection of the real and the virtual and it does not indicate a singular space. In this multispace, where the boundaries are constantly changing, the individual has the situation of being both alone and together at the same time. Therefore, it points to an open and pluralistic structure actively nourished by various experiences, identities and cultures.

Findings

Rhizome, unlike tree roots, refers to any point being connected to any other point. Connections are not fixed and specific, they are constantly reshaped. In this network of relationships, a heterogeneous structure is formed by the coming together of various interaction areas. At this point, the "connectivity" and "heterogeneity" principles of the rhizome philosophy can be associated with the metaverse. According to Ponde's definition, the metaverse is based on the concepts of interoperability and interconnectedness (Ponde, 2022). When switching between different spaces, the system can work interconnected, both within itself and with new additions, in harmony and interaction, as in the rhizome. In addition, the concept of accessibility in the metaverse can be interpreted with these principles of the rhizome. Depending on the level of integration of XR technologies into multispaces, there are differences in the spatial experience. For example, switching to a virtual space with VR tools can be perceived as more realistic than connecting to that space via a phone or computer. Dynamic, unstaid virtual spaces can be created with real-time updates. Similarly, the rhizome philosophy defines a constantly renewed, developing and dynamic organizational structure.

In the "multiplicity" principle of the rhizome philosophy, the rhizome multiplies connections, transforms them and creates innovations. Deleuze and Guattari have explained this principle with the concept of "lines of flight". Lines of flight encourage the formation of a different connection and create multiplicity. In other words, it can be said that these are effective in bringing different contexts together creatively. Similarly, the transitions between multispaces and the new intersections that emerge also show a rhizomatic growth. It can be thought that a system open to continuous expansion, without a specific beginning or end, is formed by the design and collective coming together of virtual spaces.

Moreover, new identities and bodies are formed through rhizomatic connections (Ballatyne, 2012). When virtually included in a space, areas and objects can be explored in three-dimensional and real-time experiences through

virtual bodies known as avatars, and multispace can be freely navigated. For instance, by pressing a direction button designed near the object, it can be instantly transformed to a different space and these spaces can be observed from different angles. This situation can be associated with the "lines of flight" in the rhizome philosophy. Thanks to new connections, a constant state of flow occurs between real and virtual spaces or within completely virtual spaces. This allows the perception of time and space to change.

According to the principle of "cartography", a rhizome acts like a map, as opposed to a template, it does not have a single entry point, and it has multiple entries. The map builds new connections. It can be disassembled, reversed, changed, reconnected and adapted to any kind of modification (Deleuze & Guattari, 1980/2023). From the perspective of the principle of "cartography", virtual spaces, unlike real spaces, can be designed by expanding the boundaries. When the physical boundaries brought by factors such as gravity, climatic conditions and materials are eliminated, multispaces can exhibit a rhizomatic structure; they can disperse, recombine and produce different variations by diversifying user experiences. For example, when evaluated in the context of an exhibition space, it may be possible to reconsider the artwork from different angles, switch to a new flow of information or open a different layer in the space through a QR code. In this way, while spatial features are enriched, it bears traces of the multidimensional structure of the rhizome.

Today, the concept of art has found a new medium in the metaverse through multispaces. This environment, which enables the active participation of the audience, adds flexibility to the ways in which works of art are exhibited. Traditional forms of representation have gained an interactive dimension with the innovations brought by digitalization. In the exhibition techniques of architecture, painting, design, music and performance arts, an experiential environment that transcends the boundaries of physical spaces is created thanks to the opportunities offered by the metaverse. Considering this, Zaha Hadid Architects' "NFTism" project offers a dynamic and multi-layered space design where various NFT (Non-Fungible Token) artworks are exhibited (Image-2). There is no fixed direction or specific roadmap while visiting the works in this multispace, and this allows visitors to have various experiences. Beyond being an exhibition space, the "NFTism" project highlights the flexible, multi-layered and network-like structure of architecture. This feature can be an example of how the basic principles of the rhizome philosophy can be transformed into a spatial experience. One of the important parts of the exhibition space, the "Z-Car One" vehicle designed by Zaha Hadid Architects, is an object that moves within the virtual exhibition space and whose parts can be examined separately (Image-3). Therefore, the representational power is increased and the transfer of information is taken to a different dimension, and an interaction area is created by establishing new connections between the artist and the visitor. NFT works placed on different surfaces and volumes create a more impressive environment by bringing together sound and image. In addition, the fact that visitors interact with each other in this multi-layered space also emphasizes the social power of the space.

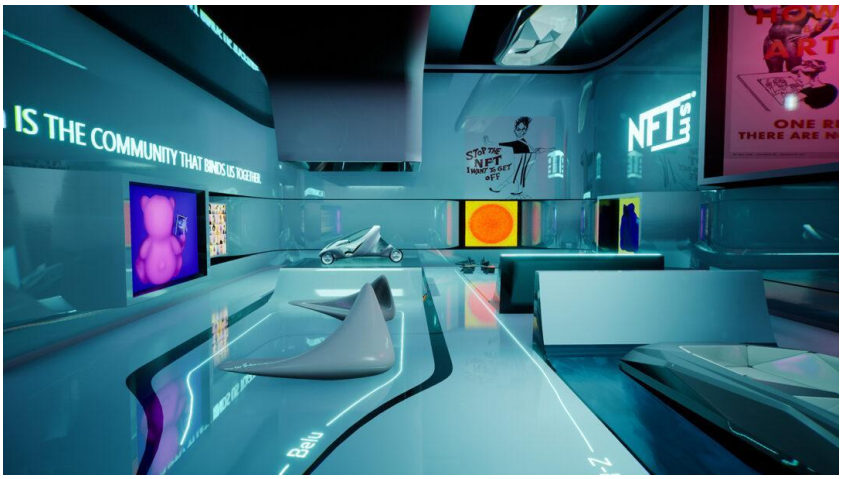

Image 2. "NFTism" at Art Basel Miami Beach, Zaha Hadid Architects, 2021.

Image 3. "NFTism" at Art Basel Miami Beach, Zaha Hadid Architects, 2021.

Conclusion

The dynamic and interconnected structure of the multispaces that make up the metaverse has significant parallels with Deleuze and Guattari's rhizome philosophy. In this study, the metaverse is examined through the principles of the rhizome. Multispaces that go beyond physical boundaries and constantly expand, reshape, and transform with user interactions make a network-like structure possible. Due to the nature of the rhizome, these connections have an unlimited growth potential and allow different relationships to emerge with the addition of new "lines of flight". Especially thanks to the opportunities provided by XR technologies, users can freely navigate, interact, and reshape the space itself in multispaces. From this perspective, it can be said that the metaverse forms a rhizome with its non-hierarchical, decentralized, and constantly changing structure. In the future, with the development of metaverse technologies, it is likely that virtual space experiences will diversify further and rhizomatic connections will become more apparent.

References

Adkins, B. (2015). Deleuze and Guattari's A Thousand Plateaus: A Critical Introduction and Guide. Edinburg University Press Ltd.

Ballantyne, A. (2023/2012). Mimarlar İçin Düşünürler: Mimarlar İçin Deleuze ve Guattari. (R. Öğdül, Trans.) Istanbul: YEM Yayınları.

Deleuze, G. & Guattari, F. (1980/2023). Bin Yayla: Kapitalizm ve Şizofreni (B. Abdioğlu, Trans.) Otonom Yayıncılık.

Hopkins, O. (ed.). (2023). Multispace: Architecture at the Dawn of the Metaverse. AD Architectural Design. Vol.93. John Wiley & Sons.

Levine, M. (2022). Episode 2: This is the metaverse [MOOC lecture]. In Meta, What is the metaverse?. Coursera.https://www.coursera.org/learn/what-is-the-metaverse.

Mantegna, M. & Rinesi, M. (2023). The Anti-Metaverse: Multispace and the Intersections of Reality. In Hopkins, O. (ed.). Multispace: Architecture at the Dawn of the Metaverse. AD Architectural Design. Vol.93. John Wiley & Sons.

Ponde, N. (2022). Episode 6: Interoperability in the Metaverse [MOOC lecture]. In Meta, What is the metaverse?. Coursera.https://www.coursera.org/learn/what-is-the-metaverse.

Url-1 https://www.zaha-hadid.com/design/nftism-at-art-basel-miami-beach/, date retrieved 23.03.2025.

Url-2 https://www.coursera.org/learn/what-is-the-metaverse, date retrieved 28.05.2024.

Url-3 https://moderninnova.com/2018/12/10/augmented-reality-artirilmis-gerceklik-nedir/, date retrieved 28.05.2024.

Evaluation of Social Performance in Public Squares Through Social Media Images : A Case Study of Taksim Square and Beyazıt Square

Muhammed Eker[a], Mehmet Emin Şalgamcığlu[a]

[a] Istanbul Technical University, Departmant of Architecture, Architectural Design Program, Türkiye
ekerm22@itu.edu.tr

Keywords: Social Performance, Space Syntax, Socio-Spatial Image, Isovist.

Aim

With the proliferation of social media, digital images have become an important source for reflecting the social construction of the city and everyday behaviour. Images, which are a partial product of the individual's perception of the city, contain important potential information to reveal the impact of the built environment on social constructs and social behaviour.

Research Question : **Can social media images that contain information about the social construction and behaviour of the city be used to evaluate the social performance of the urban area?**

The answer to this question has been investigated through two distinct urban squares in Istanbul (Taksim Square, Beyazıt Square), reflecting the community's different behavioural practices through their lifestyles and social structures. Various qualitative research and evaluation methods have been employed to assess the social content of images. Quantitative evaluation method has been employed for the syntactic assessment of images through the concept of isovist.(Benedikt, 1979) The syntactic evaluation of images utilized metrics such as Digital Space Interaction (DSI) and Digital Space Visibility (DSV) (Maldonado-Gil & Psarra, 2022).The DSI and DSV data generated from social media images were compared with the configurational Visibility Graph Analysis parameters of the space. The research aims to present a comprehensive assessment of the place by integrating observation, spatial syntax, digital data, with the goal of visualizing the socio-performance of the space.

This paper utilizes analysis methods developed by Psarra to examine Instagram images through the isovist tool developed by Benedikt. The research is developed within the context of Beyazıt Square and Taksim Square, which are believed to reflect distinct characters in terms of their social pattern, behavioral practices and are considered to possess contrasting features. Beyazıt and Taksim Squares, including their surrounding contexts, landmarks, functional diversity, and social patterns, exhibit distinct social performance character.

The aim of the study is to conduct research in order to comparatively evaluate the perceived social performances of Beyazıt Square and Taksim Square in Istanbul, which are thought to be distinct from each other. The analysis employs Digital Space Intelligibility tools (Maldonado-Gil & Psarra, 2022) to evaluate the social and spatial characteristics of these environments, both in Instagram photographs and real space. Isovists, developed by Michael Benedikt and utilized in various studies treat each Instagram photo of a space as an isovist. When collectively examined, all Instagram photos of the same space offer a comprehensive representation of the spatial characteristics, activities, and behavioral patterns occurring in that space.

Material and Method

The research utilized Instagram photographs as the prominent representation platform of visual media.The images shared publicly on the Instagram platform in the locations identified for the research, namely Taksim and Beyazıt, between November 2023 and January 2024, were scanned. One hundred images that met the specified criteria were selected for evaluation. The origin and vision field of the selected photos were manually geolocated in QGIS.

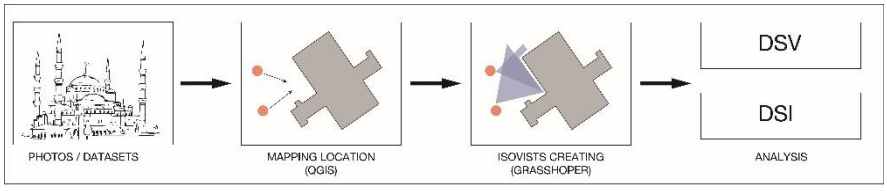

Figure 1. Method Diagram.

After completing the mapping process, the resulting dataset was exported to Grasshopper. Subsequently, a custom algorithm script was utilized within this program to compute two novel spatial measures: Digital Space Interaction (DSI) and Digital Space Visibility (DSV). Digital Space Interaction (DSI) assesses the spatial location attributes of the images. Digital Space Visibility (DSV) evaluates the connectivity characteristics of the depicted space.
To visualize and assess the distribution of the in the researched squares the Shannon-Weaver Diversity Index's entropy formula (Yoshimura vd., 2022) employed.
In order to compare this approach to Visibility Graph Analysis (VGA) (Turner, et al., 2001) measures, it was used DepthmapX software (Varoudis, 2015) to analyse each public space, calculating the values of integration and connectivity. For this study, a 150 m radius model from both public spaces was drawn, considering all spaces that are visible (eye-level). Consequently, it was quantified the measure of intelligibility (Hillier, 1996)for both cases.
The last part of the research measures the social indicators of a place through an observational study of the same places featured in the dataset, i.e. the Instagram photographs used in the analysis. Two categories were selected to measure the social indicators of a place, both of which are based on the framework developed by the Jan Gehl (Gehl & Svarre, 2013) : sociability and uses & activities

Figure 2. Instagram Photos.

Findings

Social Indicator Findings

The social performance of both squares has been calculated, taking into account the specified indicators. In Beyazıt Square, 35% of the photos depict scenes without any individuals. Social activities represent the most prevalent content, accounting for 32% of the images. Furthermore, 89% of the photos were taken during the daytime, with limited night time usage observed. The most common activity captured in photos is posing, constituting 28%, followed by political and activist gatherings as the second most prevalent activity at 28%. (Figure 3)
In Taksim Square, 30% of the photos depict scenes with 1-5 people. Landmark elements dominate the content of 32% of the photos. Posed activities are featured in 55% of the images. Additionally, 12% of the photos reflect the square's involvement in recent New Year's Eve events as a special activity. The observation of night time use in 35% of the photos indicates that the square hosts diverse activities throughout different times of the day (Figure 3).

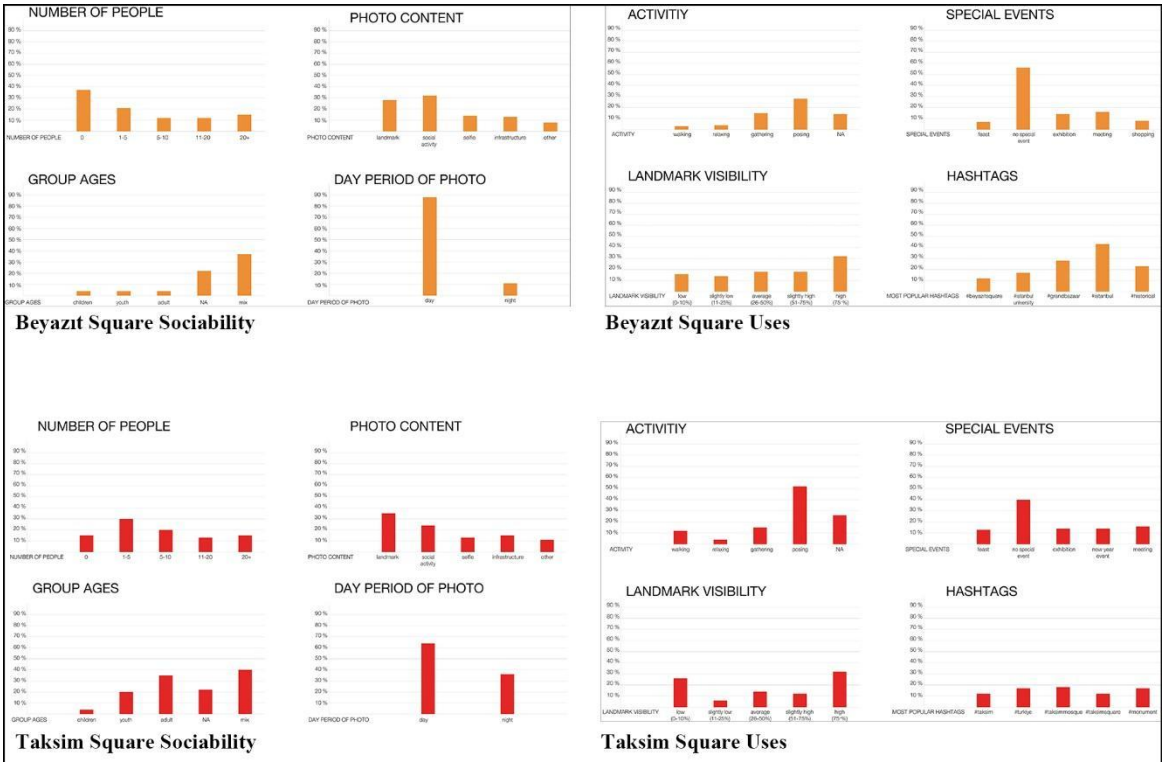

Figure 3. Sociability & Uses Analysis.

Physical Visual Syntactic Findings

The Visibility Graph Analysis and Axial Maps methods were employed for the physical visual syntactic analysis of the two spaces. Evaluations were conducted by calculating visual integration, connectivity, and intelligibility values. The DepthmapX (Varouidis, 2012) software was utilized to generate the analyses, and calculations were performed based on the obtained data.
In Beyazıt Square, the highest integration value is observed in the area around Beyazıt Mosque, Kapalıçarşı (Grand Bazaar), and the intersection of Ordu Avenue. Due to the three main landmark elements, Islamic Arts Museum, Beyazıt Mosque, and Istanbul University Entrance Structure, which disrupt the overall visual composition of the square, a heterogeneous and low integration value is observed throughout the square.(Figure 4)
In Taksim Square, the highest integration value is observed in the connection between Tarlabaşı Boulevard and Taksim Mosque. The area between the Republic Monument, Gezi Park, and Atatürk Cultural Center exhibits a homogeneous and lower integration distribution. In the area connecting Atatürk Cultural Center and İnönü Avenue, higher values are observed compared to the homogeneous integration in the square. (Figure 4)

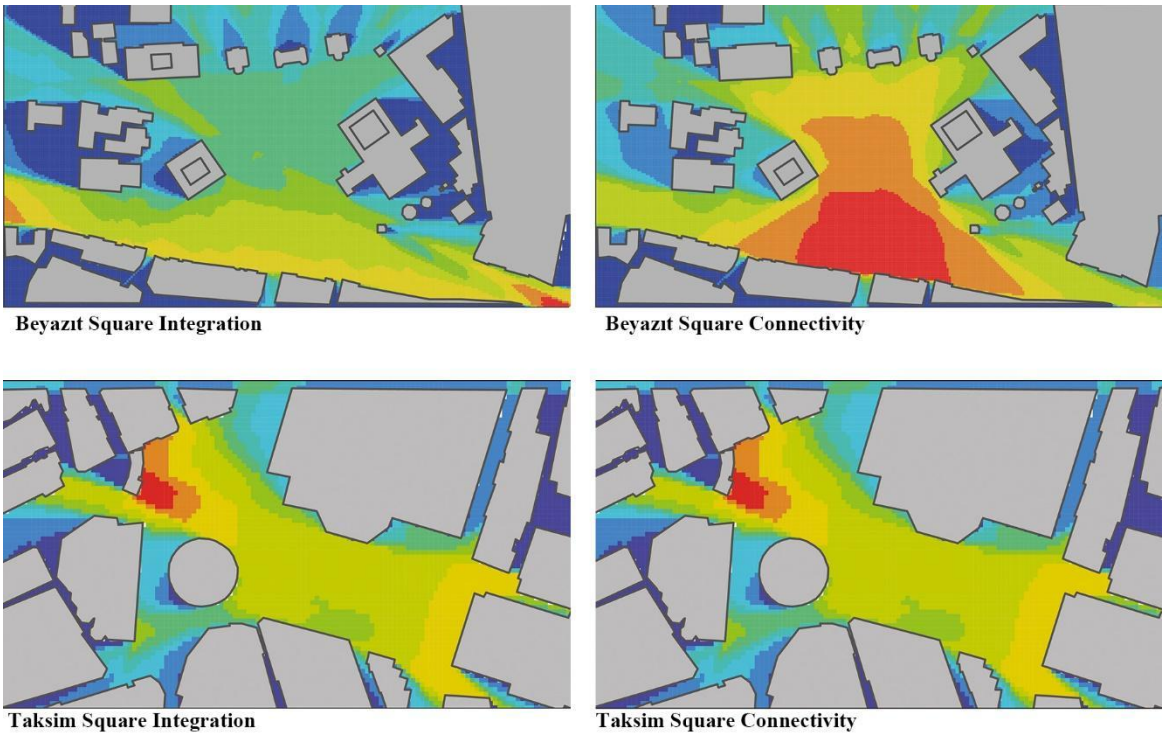

Figure 4. Physical Visual Syntactic Findings.

For both squares, R2 visual intelligibility values were calculated. In Taksim Square, the intelligibility value according to R2 is 0.696, indicating both a high integration value and ease of orientation, landmark visibility, and navigation. In Beyazıt Square, the intelligibility value according to R2 is 0.593, and although visually strong integration is observed, it is noted that orientation, landmark visibility, and navigation are not as easy as in Taksim.

Table 1. Physical Visual Intelligibility.

	Beyazıt Square	Taksim Square
Physical Visual Intelligibility	6.96	5.93

Digital Visual Syntactic Findings

As a result of the evaluations of Digital Space Interaction (DSI) derived from the Shannon-Weaver entropy formula, analyses reveal the formation of hotspots in Beyazıt Square, specifically in front of the Museum of Islamic Calligraphy Arts and between the Beyazıt Mosque and the Entrance Structure of Istanbul University.
In Taksim Square, a singular and homogeneous hotspot area has been identified, concentrated around the Monument of Republic. DSI index value of 9.02 in Taksim Square confirms a more homogeneous and centralized distribution around the Republic Monument.(Figure 5) In Beyazıt Square, a DSI value of 6.93 confirms a more concentrated distribution at two different points, with an overall more scattered and heterogeneous distribution throughout the square.(Table 2)
When the analyses of the Digital Space Visibility Index are evaluated, high values are observed in the area between the Entrance Structure of Istanbul University and Beyazıt Mosque in Beyazıt Square; this area indicates a location where social activities and events predominantly occur. In Taksim Square, high values are observed around the Republic Monument due to landmarks focusing on Taksim Mosque and the Monument of Republic.(Figure 5) In DSV assessments, Taksim exhibits a more homogeneous and centralized distribution in its visual field with a value of 8.92 compared to Beyazıt. However, it does not show as strong a homogeneous distribution as the DSI value; there is a more heterogeneous texture in the digital visuals of the space. In Beyazıt Square, it is observed that the collision of isovists concentrated in two different focal points demonstrates a more homogeneous distribution character compared to DSI with 7.02 value.(Table 2)

Table 2. DSI and DSV Index .

	Beyazıt Square	Taksim Square
Digital Space Integration (DSI)	6.93	9.02
Digital Space Visibility (DSV)	7.04	8.92

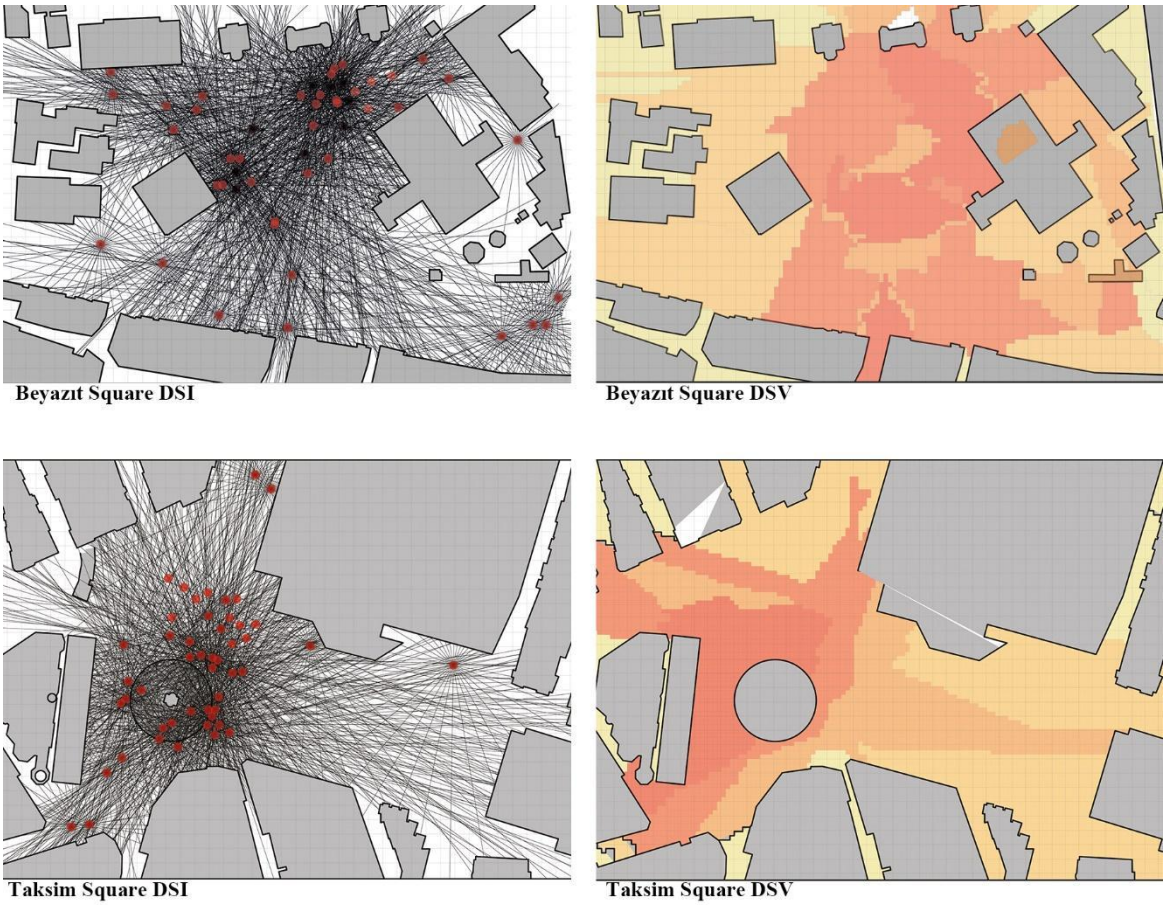

Figure 5. Digital Syntactic Findings.

Conclusion

The correlation between traditional space syntax methods and the visibility generated through digital images in the city has been tested. The statistical correlations were examined between the measure of physical space integration (VGA) and the digital measures of the Diversity Index of DSI and DSV.

The assessments revealed a high correlation (0.620) between VGA and DSV for Taksim Square, whereas a weak correlation (0.389) was observed for Beyazıt Square. Additionally, when examining the social indicator values for Taksim Square, it is evident that dimensions such as activity, nighttime usage, social usage density, and user diversity show higher correlation compared to Beyazıt Square.

This study aims to uncover the potentials and limitations inherent in each space. It is premised on the idea that visual data extracted from Instagram can serve as a valuable tool in deciphering the appeal spaces have for individuals, shedding light on their real-life usage and digital behavioral patterns. By examining how physical spaces are portrayed in digital media alongside spatial analysis of the physical environment, it provides insights into the notion of place. Here, 'place' is defined by individuals' preferences for specific environments, documented and communicated through photographs. Such analyses serve as valuable complements to traditional observational techniques and configuration analyses.However, the selected images represent a narrow sample and demographic,

shared through a single social media platform, meeting specific criteria within only a three-month period. While providing a significant assessment of the space's social performance, the sample has been limited.
The findings give rise to reflections on the role of digital media and their integration into spatial behaviors within urban and architectural environments. It is important to note that this research does not claim the faithful representation of real physical experiences of public spaces in digital photos. However, it does provide valuable information regarding social usage patterns.

References

Benedikt, M. L. (1979). To take hold of space: Isovists and isovist fields. Environment and Planning B: Planning and Design, 6(1), 47-65.

Gehl, J., & Svarre, B. (2013). How to study public life. Island Press.

Hillier, B. (1996). Space is the machine: A configurational theory of architecture. Cambridge University Press.

Hillier, B., & Hanson, J. (1984). The social logic of space. Cambridge University Press.

Maldonado-Gil, G., & Psarra, S. (2022). Constructing Sociospatial Maps From Instagram Images. 13th Space Syntax Symposium, Western Norway University of Applied Science.

Turner, A., Doxa, M., O'Sullivan, D., & Penn, A. (2001). From Isovists to Visibility Graphs: A Methodology for the Analysis of Architectural Space. Environment and Planning B: Planning and Design, 28(1), 103-121.

Van Nes, A., & Yamu, C. (2021). Introduction to Space Syntax in Urban Studies. Springer International Publishing.

Yoshimura, Y., Kumakoshi, Y., Milardo, S., Santi, P., Arias, J. M., Koizumi, H., & Ratti, C. (2022). Revisiting Jane Jacobs: Quantifying urban diversity. Environment and Planning B: Urban Analytics and City Science, 49(4), 1228-1244.

Url 1- Varouidis, T. (2012). DepthmapX [Software]. https://www.spacesyntax.online/software-and manuals/depthmap/, date retrieved 29.11.2023

Architectural Representation in the New Media Era and Lateness

Hasan Aydın[a,b], Ozan Önder Özener[a]

[a] İstanbul Technical University, Graduate School, Architectural Design Program, Turkiye
[b] Yıldız Technical University, Department of Architecture, Architectural Design Program, Turkiye
aydinhas18@itu.edu.tr

Keywords: Architectural Representation, Artistic Practices, Design Tools, Digital Design Media, Lateness.

Aim

Architectural representation has served as a bridge between ideas and reality through its various tools throughout history. Since the 16th century, evolving representational techniques — such as axonometric projection— have been among the factors influencing architectural discourse. However, the design tools that emerged in the last quarter of the 20th century and into the 21st century have led to a profound transformation in architectural representation. Computer aided design (CAD), building information modeling (BIM) and 3D modeling softwares are among the prominent examples of these tools. Vroman and Cannaerts (2022) argue that technological advancements have enabled a form of human-computer hybridization, allowing for translation and integration between analog and digital drawing practices. For instance, the proliferation of new tectonics in the 1990s parallels the simultaneous development of spline technology (Carpo, M. (ed.), 2013). Within the axis of this transformation, the transmission of architectural ideas has become increasingly complex, multilayered, and blurred. How is lateness, a concept that resists clarity, positioned in architectural representations that are the visual projection of these transfers?

The concept of 'lateness,' borrowed from Theodor Adorno's discussion of the late style, offers a critical lens for analyzing representations undergoing radical transformation. Adorno originally examined this concept in the context of music, identifying it in the fragmented and dissonant compositions of Beethoven's late works. In Peter Eisenman's interpretation, lateness signifies an architecture that resists stability, subverts conventional meaning-making methods, and engages in self-referential critique within the form-history framework. Lateness has no ties to any particular style, nor does lateness operate as a style in itself. It manifests itself as an interruption to linear time…(Eisenman, P. Iturbe, E. 2020). Eisenman approaches lateness as an aesthetic condition embedded with contradiction, resisting both unity and clarity in the architectural works he analyzes. At this point, the limitation of lateness to completed buildings becomes a subject that calls for critical scrutiny. Could lateness be inherent in contemporary architectural representations? In the age of new media, can architectural representations be read as a form of lateness, one that resists linear/deterministic closure and challenges established architectural narratives? The paper explores how hybrid drawings and collages embody the unresolved nature of lateness. As a methodological lens, it focuses on hybrid representations and bricolages. Hybrid representations facilitate novel design trajectories by synthesizing the controlled, constraint-driven logic of digital tools with the creative indeterminacy and freedom inherent in analog techniques. Instead of striving for pseudo-photo-realism, this new cult of the drawing explores and exploits its artificiality, making us as viewers aware that we are looking at space as a fictional form of representation (Jacob, 2017). Bricolages are created by bringing together fragments -such as images and materials- taken from different contexts in an eclectic and sometimes coincidental way. In this context, the representations in question are evaluated by considering their capacity to resist clarity, incorporate anachronistic elements, and engage in a fragmented visual logic.

Eisenman argues that the notion of lateness he brings into architectural practice is not a bridge between past and future, but rather something formally and temporally ambiguous. According to Bell (2021), lateness is the experience of forms tangentially dislocated from the social forces (sources) that limited them. Building on this, when translated into architectural representation, lateness can be observed in the disruption of traditional visual order, the displacement of temporal fragments, and the emergence of blurred spatial readings. Such instances of lateness may be found in hybrid representations and bricolages that combine techniques from different historical periods. As discussed above, these representations resist singular interpretations and challenge linear narratives.

Material and Method

Several architectural firms have employed unconventional representation strategies in competitions, contributing to more compelling narratives, with some even achieving recognition or awards. This conceptual potential of representation has also been emphasized by Scheer (2014), who argues that the manipulation of formal rules within a representation can generate new knowledge about phenomena. Strategies such as anachronism, fragmentation, and superimposition align closely with the notion of lateness. These strategies can be defined, respectively, as the use of concepts and objects outside their temporal context, the subdivision of visual elements into separate elements, and the emergence of distinct components within a single system. Moreover, successful representational strategies may become widespread among architects. In this context, award-winning projects offer a valuable area of inquiry for understanding the influence of representations associated with lateness in architectural competitions and practice.

The research focuses on the digital collages, conceptual representations, and experimental visual works produced by Openact Architecture and Le Erreria Office of Architecture, both of which have received recognition in housing and urban planning competitions. Axonometric projections, bricolages, and hybrid drawings are examined in detail.

This study employs a typological reading method to analyze selected architectural representations. In this approach, the observed representational techniques are categorized based on the extent to which they reflect the criteria associated with lateness. The analysis goes beyond the projected building and explores how representation becomes an act of critical resistance. This case study investigates the criteria of fragmentation, ambiguity, and incongruity within architectural representations produced in the context of competition culture.The presence of disrupted forms, layered spatial readings, and non-continuous geometries indicate the emergence of fragmentation. Ambiguity, as inherent to representation, offers wide possibilities for creative expression (Scheer, 2014). It can be observed in the superimposition of conflicting visual elements that resist singular interpretation. Finally, dissonance can be found in non-hierarchical compositions, temporal disjunctions, and unresolved tectonic relationships.

Many architectural design offices employ anachronistic and fragmented representational strategies to challenge conventional notions of space and time. These methods are particularly evident in the following examples:

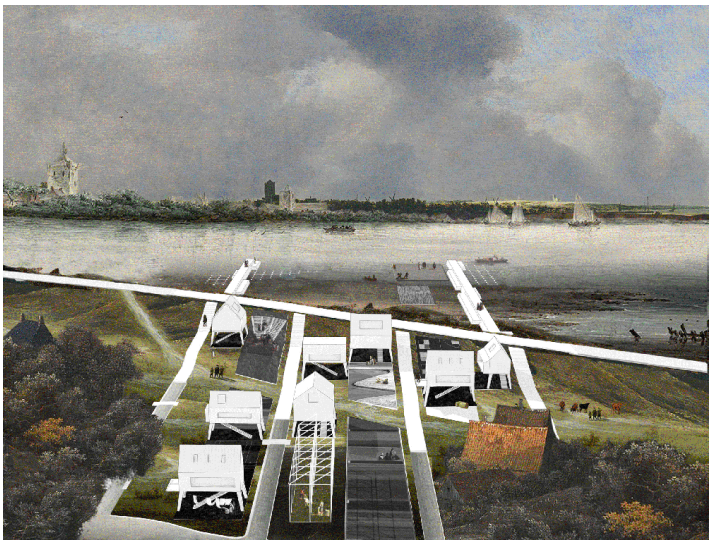

Image 1. Runner-up of EUROPAN13 - Streefkerk, Netherlands. Openact Architecture, 2015.

Architectural collages challenge conventional composition by bringing together historical references, speculative elements, and digital distortions. As seen in Image 1, the collage from Openact Architecture's second place proposal resists singular narrative through the superimposition of analog and digital elements while also expressing

ambiguity and disjunction. The colorless architectonics are seamlessly embedded into Streefkerk's landscape painting, creating a visual synthesis that further amplifies the composition's timeless and complex properties.

Image 2. Winner of EUROPAN15 - Vestre Toten, Norway. La Errería Office of Architecture, 2019.

As iconic as they are, axonometric projections resist perspectival dominance and allow for multiple, non-hierarchical readings of space. In contemporary practice, the resurgence of exploded and layered axonometric drawings signals a shift toward representations that embrace ambiguity and disjunction. As shown in Image 2, the award-winning Spanish architecture office La Errería generates disjunction by combining axonometric projection with the traditional plan. Moreover, the drawing incorporates multiple axonometric viewpoints within a single representation, whose arrangement conveys a sense of contingency.

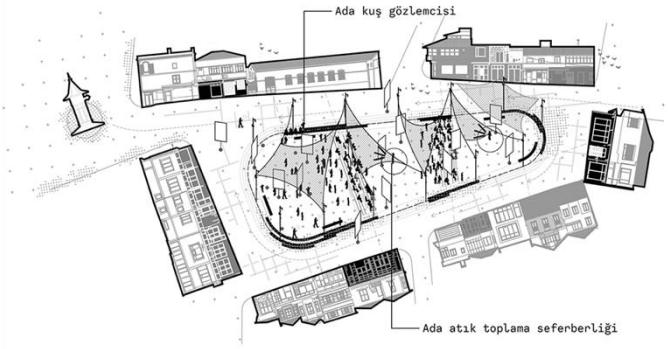

Image 3. Winner of Two-Phased Urban Design Competition - Istanbul, Turkiye. Openact Architecture, 2021.

In the example shown in Image 3, Openact Architecture creates a complex representation by combining axonometric drawing with façade views. The surrounding buildings are fragmented and detached from their perspectival depth. Incorporating multiple representational techniques, the drawing exhibits both fragmentation and disjunction.

Findings

It has been observed that architectural representations examined in the selected examples exhibit different aspects of lateness: fragmentation, anachronism, ambiguity, and contingency. The objects present in these representations must be reinterpreted in relation to their temporal and spatial positions. In all three cases, lateness is observed both through visual elements and through the use of alternative projection techniques. Based on these case studies, the research reveals that resistance to clarity in architectural representation has continuous dialogue with architectural practice.

This study reveals that lateness is not only a condition of built architecture but also an inherent characteristic of contemporary architectural representation. These findings demonstrate that hybrid representations offer a critical alternative to traditional architectural narrative. The use of elements that conflict in terms of time, scale and place makes these drawings more open to interpretation and distances them from linear narrative logic. Blurred spatial representations that reference the late style enables an architectural discourse that is deliberately left unresolved. Furthermore, with the increased emphasis on narrative in architectural competitions, representation surpasses its conventional functions and becomes a critical medium.

Conclusion

Lateness positions the representation it inhabits not merely as a tool for resolution, but as a site of resistance.This positioning offers a critical perspective on the trajectory of architectural representation in the age of new media. In doing so, it contributes to the ongoing discourse on the role of digital and hybrid representational techniques in architecture. This pictorial tale can be read as a theoretical guide to confront the architectural presentations of the last decade.

As architectural representation continues to evolve in the digital era, the embrace of lateness in hybrid drawings and collages suggests a paradigm shift toward representations that resist closure, challenge traditional spatial logic, and engage in ongoing critique. The use of layered, fragmented, and ambiguous imagery reflects a broader tendency in architectural discourse to question the clarity of form and meaning. This study argues that lateness is not only a theoretical construct but also an active representational approach that shapes contemporary architectural practice. Moving forward, architectural competitions and design methodologies will likely continue to prioritize representations that embody uncertainty, contradiction, and unresolved spatial conditions.

References

Adorno, T. (2002) Late style in Beethoven. In *T. Adorno, Essays on music* (S. Gillespie, Trans., pp. 564–568). University of California Press.

Bell, M. (2021,February 18) Lateness. *CAA Reviews*. https://doi.org/10.3202/caa.reviews.2021.13

Carpo, M. (Ed.) (2013). *The Digital Turn in Architecture 1992-2012.* (pp.8-14) Wiley. https://www.doi.org/10.1002/9781118795811

Cook, P. (2008). *Drawing: The Motive Force of Architecture.* (2nd ed., p. 132) Wiley.

Eisenman, P., & Iturbe, E. (2020). *Lateness*. (p. 20) Princeton University Press. https://doi.org/10.2307/j.ctvrs8zsh

Jacob, S. (2017, March 21). Architecture enters the age of post-digital drawing. *Metropolis*. https://metropolismag.com/projects/architecture-enters-age-post-digital-drawing/

Scheer, D. R. (2014). *The Death of Drawing* (1st ed., pp. 23-42) Taylor and Francis. Retrieved from https://www.perlego.com/book/1548345/the-death-of-drawing-architecture-in-the-age-of-simulation-pdf

Vroman, L., & Cannaerts, C. (2022). Other Perspectives: Extending the Architectural Representation. *Research in Arts and Education* 2022(2), 12–24. https://doi.org/10.54916/rae.122983

Url-1 https://www.europan-europe.eu/en/exchanges/Sewn-Heart , date retrieved 23.03.2025

Url-2 https://divisare.com/projects/306538-openact-architecture-protodike-e13-runner-up#lg=1&slide=0 , date retrieved 10.03.2025

Url-3 https://openact.eu/STATION-BUYUKADA , date retrieved 10.03.2025

The Mask as an Instrument of Spatial Construction

Naz Üstündağ[a], Pelin Dursun Çebi[b]

[a] Istanbul Technical University, Graduate School, Architectural Design Program, Türkiye
[b] Istanbul Technical University, Faculty of Architecture, Department of Architecture, Türkiye
ustundag22@itu.edu.tr

Keywords: Bauhaus Theatre, Body, Costume, Mask, Spatial Perception.

Aim

Grounded in the idea that bodily experience is essential to spatial understanding, this study approaches the mask as a bodily supplement. Beyond being a mere object, the mask can be seen as an interface that defines the boundaries of the body, transforms identity, and redefines the body's relationship to space. While it delineates the limits of both the space and the body that wears it, it also creates an experiential space that enables the audience to transcend these boundaries. The meaning that emerges is shaped not only by the movement of the body but also by the performer's role on stage, the function of the mask within the performance context, and the perspective of the audience. This study explores the mask as an experiential tool that shapes both the performer's body and influences the audience's relationship to space on stage.

Material and Method

In order to examine these dynamics, this research focuses on the Bauhaus Theatre, a significant example of modern theatre, and the works of Oskar Schlemmer. These works are approached with the perspective that they shaped an innovative and experimental research domain of their time, replacing traditional narrative structures with more abstract and dynamic forms of expression. In this regard, performance recordings and relevant written sources are utilized to map how the mask transforms bodily and spatial perception. Through this approach, the study investigates how the mask redefines spatial experience for both the performer and the audience, and how it generates multilayered narrative fields beyond physical structures.

Findings

While the mask may initially appear as a passive object on stage, once integrated with the body, it surpasses this passivity and becomes an active element. In its passive state, the mask exists merely as a shape or form; however, upon its integration with the performer's body, it acquires a dynamic structure, transforming into a force that drives the narrative on stage. According to Vartolioğlu (2022), the mask imposes instructions on the performer, who complies without hesitation. Although this authority may appear to restrict the performer, it actually fosters bodily exploration and facilitates the emergence of new forms of expression. The mask limits gestures and facial expressions, allowing the body to express itself solely through movement, thus transforming the body into the primary means of expression. This process, according to Meyerhold, develops bodily control and enhances movement sensitivity (Karaboğa, 2014). Furthermore, the mask plays a crucial role in transforming the performer's identity and presence on stage. As İspirli (2021) states, the integration of the mask with the performer's body leads to an identity transformation, detaching the performer from everyday movements and elevating them to an alternative plane. Therefore, rather than its mere existence, it is important to consider the purpose for which the mask is made, how it functions on stage, and the effects it produces.

The transformative power of the mask induces a continuous shift in the relationship between the performer and the mask. Güçbilmez (2014) states that the mask's dynamic structure, with its openness to change and transformation, constantly reshapes the relationship the performer establishes with it. This prevents the audience from forming a fixed perception of the mask, thereby transforming not only its physical manifestation on stage but also the audience's experience of space. The mask redefines the boundaries of the stage by creating a distance between itself and the audience that observes it. By concealing the underlying reality, it constructs a new domain of meaning within the audience's mind, shifting their role from a passive observer to an active interpreter. Thus, the interaction between the mask and the body alters the stage space from a fixed to a dynamic state.

The mask's influence on transforming spatial perception arises from its capacity to transcend its physical boundaries, thereby inducing change on both symbolic and imaginary levels. On the symbolic plane, the mask's visible surface evokes multilayered meanings for the audience. On the imaginary plane, its concealed side constructs an alternative reality in the audience's mind. This duality shifts the audience from a passive observer to an active participant in the meaning-making process. Lacan (1973) states that there is a gaze behind the mask and defines the audience's process of meaning-making in the gap of desire between the subject of representation and the observing gaze. The underlying ambiguity creates a desired gap for the audience, which is interpreted by the subject with each encounter. In this context, the mask functions not only as an element that transforms the wearer's body but also as a tool that directs the audience's gaze, alters their perception, and consequently reshapes the space itself. The surface of the mask is shaped by the audience's gaze, while its unseen side—the void behind it—acts as a gap or object of desire, invoking an image in the audience's mind that requires completion. The atmosphere created by the mask, combined with bodily movement, constructs a continuously evolving, multi-layered narrative on stage that unfolds for the audience in a dynamic process.

In the context of the Bauhaus, the transformative role of the mask becomes particularly evident in Schlemmer's designs, which seek to transcend the restrictive limitations imposed by organic bodies through stage costumes often associated with masks, exploring the potential of mechanical bodies capable of unrestricted movement within space. The synthesis of space and body, mediated through masks and costumes, redefines the body's relationship with movement. Schlemmer's designs aim to liberate the body, thereby facilitating freedom of movement (Schlemmer, 1961). They alter the performer's perception of space, disrupt habitual routines by restricting everyday movements on stage, and lead the audience to perceive the performers' bodies as both concealed and distorted (Figures 1, 2, 3). The concealed and distorted bodies, shaped by circularities, curvatures, diagonals, and lines, generate new spatial boundaries with each movement. Through the mask, each boundary dynamically activates the stage space, illustrating that architectural environments can be perceived as fluid, transformable, and open to interpretation, rather than as fixed structures. Thus, the mask, functioning both as a physical object and a symbolic agent, becomes central to the transformation of both body and space.

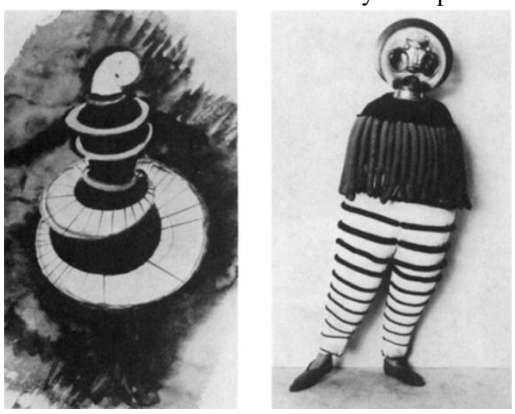

Figure 1. Triadic Ballet. (Schlemmer, 1961, p. 34).

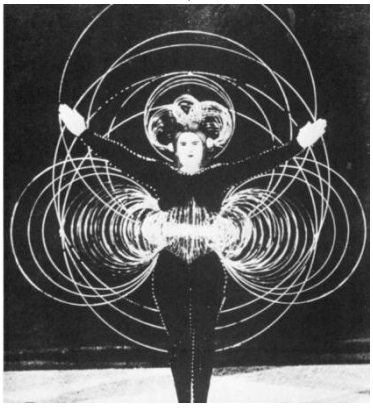

Figure 2. Triadic Ballet. (Schlemmer, 1961, p. 36).

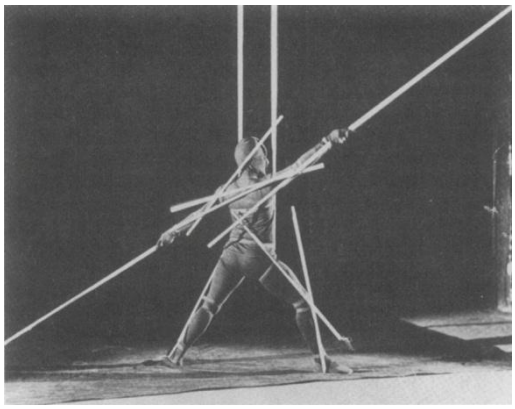

Figure 3. Pole Dance. (Lahusen, 1986, p. 75).

Conclusion

This study demonstrates that the mask, far from being a static theatrical prop, operates as a dynamic mediator between body and space. By transforming the performer's bodily expression and altering the audience's spatial perception, the mask emerges as a critical agent in constructing a fluid and mutable stage environment. The Bauhaus Theatre and Schlemmer's experimental designs exemplify how masks and costumes can extend bodily boundaries, restructure spatial relationships, and generate immersive, multilayered performative experiences. As both a physical object and symbolic interface, the mask challenges fixed notions of identity and spatiality, inviting continual reinterpretation. Ultimately, this research reveals that the mask is not merely worn but enacted—an instrument that shapes, disrupts, and redefines the architecture of performance space itself.

References

Cestel, T. (2022). Sanat ve mimarlıkta maskeleme stratejileri ile ötesinin varlığı. *METU Journal of the Faculty of Architecture/Mimarlık Fakültesi Dergisi*, 39(2), 159-180. https://doi.org/10.4305/METU.JFA.2022.2.3

Elliott, B., & Conneller, C. (2020). Masks in context: Representation, emergence, motility and self. *World Archaeology*, 52(5), 655-666. https://doi.org/10.1080/00438243.2020.1996770

Güçbilmez, B. (2014). Mask ve ilişkisellik, ses maskı ya da oyuncu maskı olarak kukla. In O. *Arıcı & K. Karaboğa (Eds.), Maske Kitabı* (pp. 40-45). Habitus Kitap.

Karaboğa, K., & Arıcı, O. (Eds.). (2014). *Maske Kitabı*. Habitus Kitap.

Lacan, J. (2013). *Psikanalizin Dört Temel Kavramı* (N. Erdem, Çev, Trans.). Metis Yayınları. (Original work published 1973)

Lahusen, S. (1986). Oskar Schlemmer: Mechanical Ballets? *Dance Research: The Journal of the Society for Dance Research*, 4(2), 65–77. https://doi.org/10.2307/1290727

Nikolić, S. (2014). The Bauhaus theater—Oskar Schlemmers design-in-motion concept. *SAJ-Serbian Architectural Journal*, 6(1), 43-62. https://doi.org/10.5937/SAJ1401043N

Schlemmer, O. (1961). *The theater of the Bauhaus* (A. Wensinger, Trans.; W. Gropius, Ed.). Wesleyan University Press. (Original work published 1925) [PDF] Retrieved from https://monoskop.org/images/a/a7/Gropius_Walter_ed_The_Theater_of_the_Bauhaus.pdf

Vartolioğlu, O. (2022). Çağdaş tiyatroda maskenin yeniden keşfi: Artaud'dan Lecoq'a. *ODÜ Sosyal Bilimler Araştırmaları Dergisi*, 12(2), 1551-1564. https://doi.org/10.48146/odusobiad.1114977

ARCHITECTURE

Architectural History

Architecture Design Theory

Building Construction Technologies

Building Materials and Technologies

Built Environment Design and Technologies

Conservation and Restoration

Environmental Control and Building Technology

Project and Construction Management

Sustainable Design

Tracing a Cultural Heritage from the Ottoman Era to the Present: A Study on the Conservation of Kepenekçi Sinan Mosque

Emrullah Ekinci[a], Yegân Kâhya Sayar[a]

[a] Istanbul Technical University, Restoration Program, Türkiye
ekincie22@itu.edu.tr

Keywords: 16th-century Classical Ottoman Architecture, Conservation, Historic Peninsula of Istanbul, Kepenekçi Sinan Mosque, Restoration.

Aim

Reflecting the layered legacy of Roman, Byzantine, and Ottoman civilizations, the Historic Peninsula has served as a significant cultural center throughout history (Kuban, 2010). Following the conquest of Istanbul, numerous buildings were constructed in the area. Among these, neighborhood mosques emerged as some of the most distinctive elements of the Ottoman urban fabric. These small-scale mosques functioned not only as places of worship but also as focal points of social life. Kepenekçi Sinan Mosque, situated at the intersection of historic streets leading to the Marmara Sea and embedded within the traditional neighborhood layout, is located at the junction of the Byzantine Mese Street and the Ottoman Uzunçarşı and Tahtakale routes (Eyice, 2021). The mosque is integrated into an urban circulation network that has remained uninterrupted from past to present. Mosques on the Historic Peninsula are generally constructed from stone and brick. Their roofs typically consist of domes or wooden coverings. According to Öz (1997), wooden roofs were commonly used in smaller, local mosques, while larger mosques featured brick domes. These architectural characteristics have enabled neighborhood mosques to serve as visual landmarks within the cityscape and have played a key role in shaping the distinctive urban fabric of the Historic Peninsula. In recognition of its rich cultural and historical heritage, the Historic Peninsula was declared an 'Urban and Historical Conservation Area' under the protection of the decision issued by the Istanbul Cultural and Natural Heritage Conservation Board No. I, dated July 12, 1995 and numbered 6848 (Archive of the Istanbul Number IV, the Regional Commitee for the Conservation of Cultural Assets) Reflecting the architectural character of 16th-century classical Ottoman design and serving as a significant example, Kepenekçi Sinan Mosque is today a valuable component of the cultural heritage that needs to be protected. This building was registered by the decision of the High Council of Real Estate Antiquities and Monuments (dated April 9, 1977, and numbered 9776) and was designated as a Group I conservation asset by the decision of the Istanbul Regional Board for the Protection of Cultural and Natural Assets in Renewal Areas (dated April 16, 2009, and numbered 713).

However, like many other historical buildings, Kepenekçi Sinan Mosque has been subjected to various interventions over the centuries and has partially lost its original architectural integrity. Particularly during the 20th century, unqualified repairs and reinforced concrete additions significantly damaged the building's original fabric and architectural coherence. This situation not only hinders a proper understanding of the building's historical and cultural significance but also poses a threat to its physical preservation. The aim of this study is to systematically document the current condition of Kepenekçi Sinan Mosque and to propose a restoration strategy in accordance with contemporary conservation principles.

Material and Method

The study employed historical research, detailed architectural documentation, and comparative analysis. The research was conducted in three main phases. In the first phase, the existing condition of the mosque was comprehensively documented using a combination of traditional and advanced measurement techniques (Figure 5). In this documentation process, the plans, sections, elevations, material usage, and damage assessment of the building were prepared in detail. In the second phase, archival documents, historical maps foundation records, and historical photographswere analyzed to understand the building's historical development (Figures 1, 2, 3 and 4).

Figure 1. Extract from the Pervititich map showing the Kepenekçi Sinan Mosque and its vicinity in the urban fabric of early 20th-century Istanbul.

Figure 2. The elevation of the mosque and its minaret as documented in a 1940s photograph (Istanbul Archaeological Museums Directorate).

Figure 3. The elevation of the mosque and its minaret as documented in a 1950s photograph. (Istanbul Regional Board No. IV for the Conservation of Cultural Assets**).**

Figure 4. Southwest facade of the mosque (Ekinci, 2025).

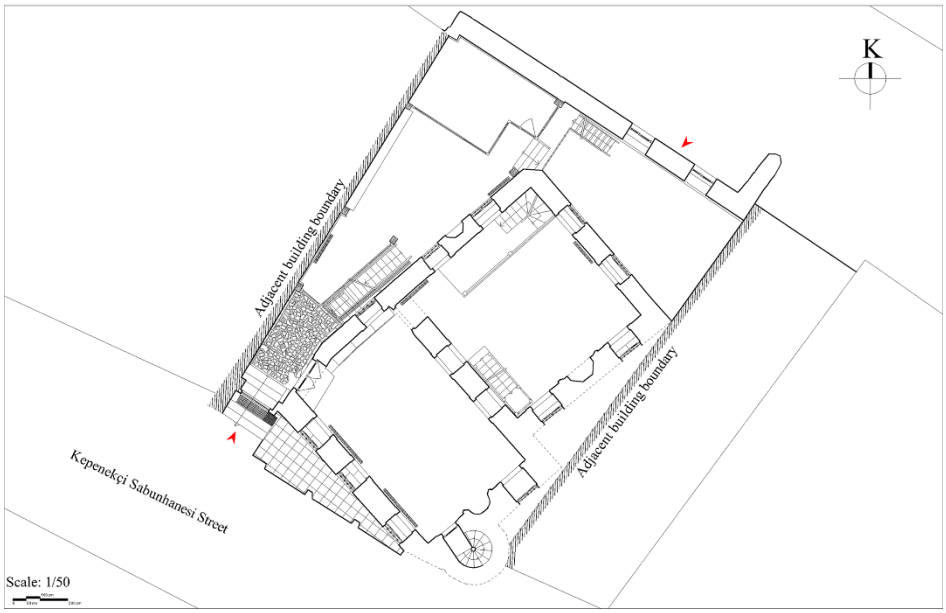

Figure 5. Ground floor plan based on the measured survey of the Kepenekçi Sinan Mosque (Ekinci, 2025).

The data obtained from these historical sources serve as reliable primary information for understanding the building's original state (Kâhya Sayar and Kahraman, 2017). In the third phase, a comparative analysis method was applied. To understand the original features and the characteristics of different periods of the building—which has undergone significant alterations to its original fabric due to restoration works carried out in the mid-20th century—a comparative study was conducted with other classical-period structures possessing similar characteristics within the Historic Peninsula.

Findings

When the construction material and techniques of Kepenekçi Sinan Mosque were analyzed, it was determined that the primary building material is limestone, and the walls were constructed using this material. While the base of the minaret was built with masonry stone, bricks were used in the shaft and were supported with stone bands at regular intervals, whereas the muqarnas section rising from the balcony was entirely constructed with bricks. The mosque has a rectangular plan, featuring two mihrabs and various arch types. A flat arch is used at the entrance, while pointed arches are employed in the window openings and in certain parts of the basement level (Figure 6). In the lower row of windows, a flat lintel system is observed on the interior, whereas both pointed arches and flat lintels are present on the exterior. The upper covering consists of a wooden framework system and is formed as a

hipped roof, covered with Marseille-type tiles.Within the scope of the documentation studies, the deterioration patterns and user interventions that have occurred in the building over time were analyzed in detail and categorized. This categorization includes damages such as element loss, material degradation, surface erosion, joint loss, surface pollution, vegetation growth, as well as user-induced repairs and interventions. Surface loss on the molding at the lower part of the minaret base on the south façade, as well as joint loss on the stone surfaces, was observed. On the northwest and northeast façades, layers of paint were found to partially cover the stone surfaces, and over time, color variations have appeared due to the removal of this paint using inappropriate cleaning methods. On the minaret, widespread soiling and brick loss were documented on the shaft, missing elements were observed on the balustrade, and moss growth was identified on the lower molding of the balustrade. In contrast, the muqarnas molding exhibited less surface contamination compared to the shaft. The most critical issue concerning the building is the interventions it underwent, particularly during the 20th century. While early photographs from the first half of the 20th century depict the building in good condition, reinforced concrete additions were introduced during restoration works in the 1960s, including the insertion of beams and columns along the northwest wall. On the northeast façade, the original masonry wall has recently been subjected to unauthorized alterations involving steel reinforcements. These interventions have significantly disrupted the building's original fabric, adversely affected its architectural integrity, and hindered the ability to accurately interpret the structure of the other façades from the exterior.

Conclusion

As a result of the analytical documentation and historical research conducted on Kepenekçi Sinan Mosque—which has undergone various interventions over time and experienced a significant loss of architectural integrity, particularly due to alterations made in the 20th century—it has been determined that the building has experienced both physical and structural changes, and its original fabric has been substantially compromised. In particular, reinforced concrete and steel additions have adversely affected the architectural integrity of the mosque, hindering the perception of its historical character and compromising its architectural identity.
In light of these findings, a comprehensive restoration proposal was developed, addressing the mosque's structural components, including the roof system, minaret, spatial organization, and stone masonry. The removal of inappropriate reinforced concrete interventions should be evaluated from a structural perspective, taking into account the load impact they exert on the building. If found appropriate in terms of structural safety based on technical calculations, their removal is recommended. The original materials should be restored in accordance with their historical characteristics, and surface cleaning, reintegration, and localized repairs should be carried out using traditional techniques.
This restoration approach aims to reestablish the architectural identity of Kepenekçi Sinan Mosque and highlight its historical significance within the urban fabric. The study presents a conservation framework that may serve as a reference not only for Kepenekçi Sinan Mosque but also for other Ottoman-era neighborhood mosques. The proposed restoration will extend the lifespan of this significant example of Ottoman architectural heritage and ensure its transmission to future generations with its original values preserved.

References

Akın, N. (2011). 19. yüzyılın ikinci yarısında Galata ve Pera [Galata and Pera in the second half of the 19th century]. İstanbul: Literatür Yayınları.
Dağdelen, İ. (Ed.). (2006). Alman mavileri: 1913–1914 I. Dünya Savaşı öncesi İstanbul haritaları [German blue maps: Maps of Istanbul before World War I, 1913–1914] (Archive Series: 6). İstanbul: İstanbul Büyükşehir Belediyesi Kültür A.Ş.
Dağdelen, İ. (Ed.). (2007). Charles Edouard Goad'ın İstanbul sigorta haritaları [Charles Edouard Goad's fire insurance maps of Istanbul]. İstanbul: İstanbul Büyükşehir Belediyesi Kütüphane ve Müzeler Müdürlüğü.
Eyice, S. (2021). Bizans devrinde Boğaziçi [The Bosphorus during the Byzantine era] (2nd ed.). İstanbul: Yeditepe Yayınevi.
Istanbul Archaeological Museums Directorate. (1946). Inventory sheet of Kepenekçi Sinan Mosque (No. 550, 6 December 1946).

Istanbul Regional Board No. IV for the Conservation of Cultural Assets. (1995). Decision dated 12 July 1995 and numbered 6848. Ministry of Culture and Tourism.
Kahraman, G., & Kahya Sayar, Y. (2017). The Ottoman archival documents about 1894 earthquake records of Fenari İsa Mosque. Restorasyon Konservasyon Çalışmaları [Restoration and Conservation Studies], (20), 11–23.
Kuban, D. (2010). İstanbul: Bir kent tarihi, Byzantion, Konstantinopolis, İstanbul [Istanbul: An urban history of Byzantion, Constantinople, Istanbul]. İstanbul: Türkiye İş Bankası Kültür Yayınları.
Öz, T. (2015). İstanbul camileri [Mosques of Istanbul] (Vols. 1–2, 4th ed.). Ankara: Türk Tarih Kurumu.
Pervititch, J. (n.d.). Sigorta haritalarında İstanbul / Istanbul in the insurance maps of Jacques Pervititch. İstanbul: Tarih Vakfı & AXA OYAK.

Documentation and Conservation Proposalofa 19th Century Ottoman Heritage: Kececizade Fuat Pasha Mosque

Filiz Avcı[1], Umut Almaç[2]

[1]Istanbul Technical University, Restoration Graduate Program, Türkiye
[2]Istanbul Technical University, Faculty of Architecture, Department of Architecture, Türkiye
avcif22@itu.edu.tr

Keywords: Architectural Conservation, Kececizade Fuat Pasha Mosque, Orientalism, Ottoman Architecture, Restoration.

Aim

This study aims to identify the conservation issues of Keçecizade Fuat Paşa Mosque, a notable example of Ottoman architecture built under Orientalist influences in the 19th century, through architectural documentation studies and to develop conservation recommendations to ensure the building's preservation for future generations. Within the scope of the study, the development of the building in the historical context was investigated and analysed comparatively with similar period buildings. Plan features, architectural features, and ornamental elements were discussed in detail. To ensure the sustainability of the building through the restoration project, necessary cleaning, consolidation, renovation, and intervention proposals for its use have been developed.

Material and Method

Archival research, photogrammetry, laser scanning and detailed measurement techniques were applied to document the building. The current condition of the building was expressed in scaled drawings (plan, section, facade, detail, etc.) prepared with the dataobtained during the architectural documentation process. Material analyses were conducted by determining the use of traditional building materials, such as stone, wood, plaster, and metal, in the building. The observed deterioration and damage have been classified and indicated on the scaled drawings.

With the help of archival research and on-site observations, the repairs the building has undergone in the past were evaluated, and the practices that damaged its integrity were identified. Research on the original condition of the mosque was conducted in accordance with the General Directorate of Foundations Archive, Ottoman archive documents, old maps and photographs, as well as other written and visual sources from the period,and comparisons with period buildings.

The restoration proposals for the building have been developed within the framework of international conservation principles (the Venice Charter, ICOMOS Principles and Regulations, and UNESCO Cultural Heritage Conservation Principles, etc.) as well as local legislation. Priority has been given to preserving the original materials and construction techniques.

Findings

The Kececizade Fuat Pasha Mosque was built within a complex that includes a mosque, mausoleum, graveyard area, entail, and ablution areas (Drawing 1: Site plan). There is different information about the construction date of the mosque in various sources. Semavi Eyice, in his article "Notes from Historical Graves," published in the Journal of the Institute of History, drew inferences about the mosque's construction date based on various publications and engravings. As a result of these inferences, it is assumed that the mosque was built after Fuat Pasha's death in 1869.

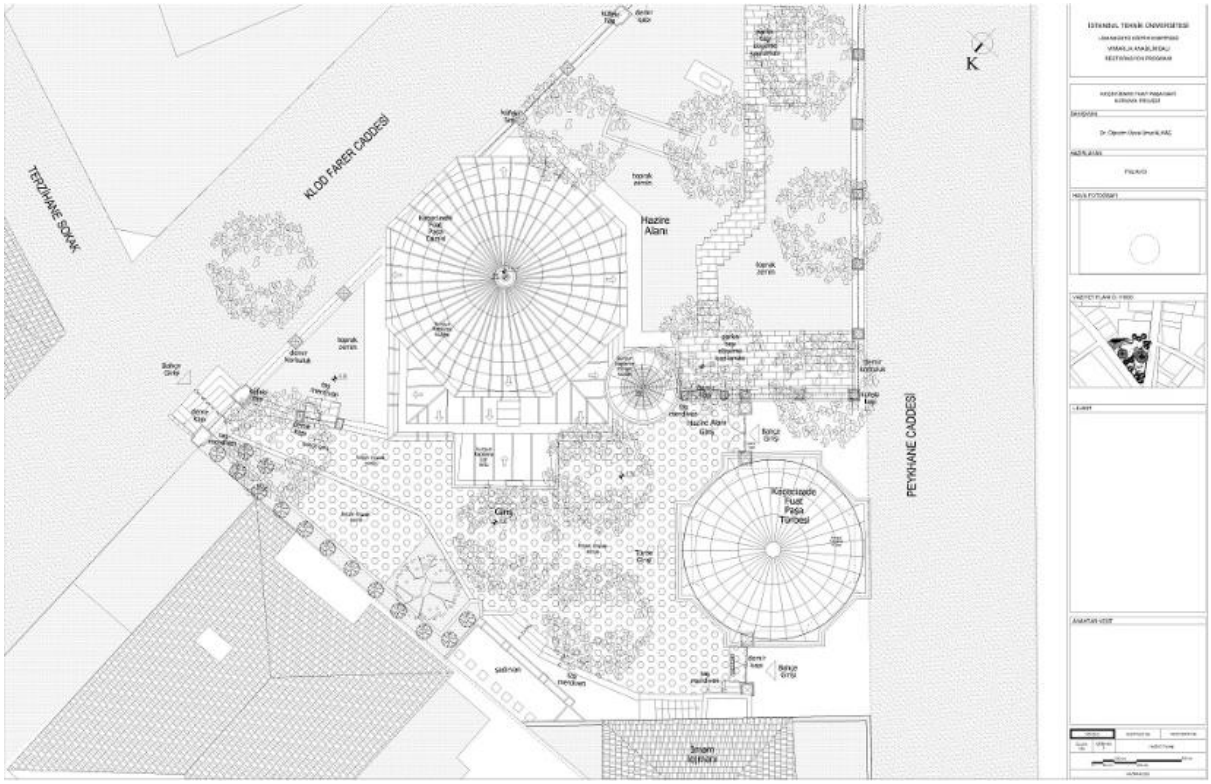

Drawing 1 : Site plan (Avcı, 2024).

The mosque was built in an orientalist style. The primary feature that enables the mosque to be treated in this style is the use of arched doors and windows with horseshoe arches. The tripartite arrangement with the addition of round windows is reminiscent of some Mamluk facades in Egypt. The capital soft the columns in the center of the double windows bear the motif of lotus leaves with outwardly curved tips, which is found in the lower parts of the floral decorated Moorish capitals. The interior is dominated by decorations in yellow, red, and blue colors, as recommended and applied to various European buildings of the same quality, in accordance with the fashion of Orientalism with a Maghreb component (Saner, 1998, p. 92).

Built with masonry construction technique, the building features an octagonal plan and is topped with a single dome. The dome is covered with lead sheets, devoid of windows or openings, and a copper finial (alem) is positioned on top (Figure 1).The minaret sits on a cut stone base with a plan scheme close to square and is built entirely of limestone(Figure 2).

Figure 1: Photo showing the mosque (Avcı, 2024).

Figure 2: Southwest facade photo (Avcı, 2024).

The minbar, mihrab, and pulpit are the architectural elements that have survived to the present day, preserving their originality. While the minbar draws attention with its intense use of geometric elements and floral motifs, it is decorated with fine marble artistry(Figure 3). The mihrab is arranged as a niche in the southeastern wall of the building and is construct edentirely of marble. The pulpit has an octagonal plan scheme and is designed in a more straight forward style. The building receives natural light through four horseshoe arched windows. The windows are positioned in a rectangular niche framed by moldings (Figure 4). The main walls and dome in the interior space are adorned with rich compositions featuring yellow, red, and blue tones (Figure 5). In the center of the dome, a decorative ornamental element made of plaster features relief floral ornamentation. The types of deterioration detected in the mosque include repairs made using inadequate materials, dirt on stone surfaces resulting from air pollution, improper additions to the building, and biological formations caused by moisture. The prevalence of cement-based pointings on the exterior facades of the building and the minaret shaft was

observed, and it was determined that this intervention caused deterioration on the stone surfaces. Due to air pollution, dark layers of dirt have accumulated on the stone surfaces of the building, resulting in significant discoloration, particularly at the base of the minaret. Various biological formations are observed in the pedestal section of the building due to the increased humidity. Corrosion was evident on the lead coatings on the central dome and minaret cone, and detachments were detected at the joints of the lead plates. The presence of different-coloured lead plates near the dome skirt indicates previous repair interventions in these areas. Similar deterioration was observed on the minaret cone.

Figure 3: Pulpit photo (Avcı, 2024).

Figure 4: Northeastern side photo (Avcı, 2024).

Figure 5: Dome decoration photo (Avcı, 2024).

The decorations on the interior facades of the building are generally in good condition; however, plaster and paint losses can be observed in limited areas. Traces of earlier period decoration were visible in some places where plaster detachment was present. In addition, historic photographs of the building uncovered during research carried out in the Archive of the Council revealed the presence of marble imitation plaster and various decorative patterns on the walls. Detailed research, including non-destructive testing (NDT) methods, is recommended in these areas to understand the extent and condition of any possible original architectural and decorative elements.

Critical or evident structural issues were not detected; however, documentation using accurate laser scanning tools revealed that the minaret deviated from the vertical by approximately 14 cm in the east ward direction. According to archival documents, the shaft on the balcony and the balustrades of the minaret were repaired in

1970 under the supervision of the Pious Foundation Directorate. Dirt on the surfaces, cracks and material losses were observed on the minaret's balcony railings due to environmental factors, precipitation and atmospheric conditions. These critical areas should be handled meticulously during the restoration process. To evaluate the structural condition of the mosque, the characteristics of the building's foundations should be determined through inspection pits opened during the restoration process. Additionally, the ground properties on which the building is located should be assessed using ground surveys.

Conclusion

Kececizade Fuat Pasha Mosque is one of the most important historical buildings of 19th-century Ottoman architecture, characterised by its interior and exterior ornaments, plan scheme, and construction materials. The building, which has maintained its original function to this day, has undergone various interventions and inadequate repairs at different times.

Within the scope of this study, it was determined that the mosque's function should be continued by preserving its authenticity, historic and aesthetic values. Conservation proposals aimto eliminate or prevent the damages caused by unqualified repairs, careless use and the physical conditions in which it is located. Accordingly, in light of contemporary conservation approaches and principles, the original materials should be conserved with minimum intervention as possible.

This research has documented the current condition of the building on a scientific basis and developed comprehensive conservation recommendations within the frame work of restoration theory, thereby ensuring the building's sustainability. The proposed interventions aim to preserve the original architectural character of the building while adapting it for the future, in accordance with current conservation principles. At the same time, the analyses and proposed restoration approach aim to establish a precedent for the conservation of similar historic buildings.

References

Çelik,Z.(1992).*Displaying the Orient: Architecture of Islam at nineteenth-century world's fairs*. University of California Press.

Eyice,S.(1973-1974).Notesfrom Historical Graves IV: KeçecizadeFuad Pasha's Grave.
IstanbulUniversity, Faculty of Literature, Journal of the Institute of History, 78 (pp. 304-313).

Kuban, D. (2007). *Ottoman architecture* (p. 605). YEM Publications.

Said,E.W. (1978).*Orientalism*. Pantheon Books.

Saner, T.(1998). Orientalismin19thcenturyIstanbularchitecture.In *PeraTurizmveTicaret A.Ş. Publication* (pp. 91-96). PeraTurizmveTicaret A.Ş.

Yavuz, Y. (2000). Orientalist approaches in late Ottoman and contemporary Turkish architecture. In Proceedings of the International Fourth Turkish Culture Congress *(November 4-7, 1997)* (Vol. 2, pp. 311-319). A.K.M Publications.

ARCHITECTURE

Architectural History

Architecture Design Theory

Building Construction Technologies

Building Materials and Technologies

Built Environment Design and Technologies

Conservation and Restoration

Environmental Control and Building Technology

Project and Construction Management

Sustainable Design

The Role of System Sections in Architectural Competitions: From Conceptual Design to Construction

Fulya Kılıç[a], Fatih Yazıcıoğlu[b]

[a] Istanbul Technical University, Graduate School, Environmental Control and Construction Technologies Program
[b] Istanbul Technical University, Faculty of Architecture, Department of Architecture
kilicf23@itu.edu.tr

Keywords: Detail, System Section, Architectural Competitions, Detail Sustainability.

Aim

Architectural competitions serve as a significant tool for fostering critical thinking and advancing innovative production processes in the fields of architecture and urban design. (Chupin, 2011) In these competitions, architects typically present their projects using three-dimensional visualizations and two-dimensional drawings. Although three-dimensional visuals dominate competition presentation boards, jury members also meticulously evaluate two-dimensional drawings. Given that the selected project has the potential for construction, competition briefs often require 1/50 and 1/20 scale system section details to support the project's feasibility.

This study examines the significance of system sections in architectural competitions in Türkiye and investigates their impact on the transition from conceptual design to construction. The primary objective is to evaluate the influence of system sections on jury evaluations, project constructability, and the transition from competition to construction. Additionally, the study explores how different architectural competition regulations shape the role of system details and how they affect the likelihood of winning projects being constructed.

Material and Method

This study adopts a mixed-method research approach incorporating literature review, case analysis, and future interviews with professional architects. The research examines 292 architectural competitions conducted in Türkiye, analyzing the presence and role of system section details. Among these, 92 competitions included system detail drawings, which were evaluated in detail. Competitions were categorized based on whether system sections were explicitly required, and the relationship between the inclusion of these details and project construction rates was examined. Furthermore, 45 system sections from 15 selected competitions underwent a two-stage evaluation process:

Visual Analysis: Assessment of drawing techniques, material representation, dimensioning, and technical scope. This phase evaluates the quality of technical drawings and their ability to communicate material and structural information effectively.

Performance Analysis: Examination of the impact of system details on the performance of building elements. This phase assesses the extent to which proposed system sections align with practical construction requirements and effectively convey buildability information to both jury members and future contractors.

In architectural design, the integration of building elements can be evaluated under three main categories: physical, visual, and performative. This tripartite classification enables a comprehensive assessment of system details, not only in terms of their technical functionality but also regarding spatial efficiency, aesthetic coherence, and multifunctional performance. For instance, a shear wall simultaneously serves as a load-bearing structure and partitioning shell, embodying all three forms of integration. Although not all designs exhibit these three types equally, analyzing system details through this framework allows for a more holistic understanding of their architectural significance and their role within competition projects. (Bachman, 2003; Yazıcıoğlu, 2007) Therefore, the performance analysis has been examined under seven subheadings:

1. Foundation-Floor on Ground- Ground Integration
2. Foundation-Floor on Ground-Wall Integration
3. Beam-Column-Floor-Exterior Wall Integration

4. Beam-Column-Floor-Interior Wall Integration
5. Beam-Column-Floor-Roof Integration
6. Roof-Exterior Wall-Column Integration
7. Roof-Interior Wall-Column Integration

Findings

The detail sustainability refers to the extent to which system details specified during the competition phase are maintained in the construction process in terms of long-term functionality, aesthetic integrity, and structural integration. The findings reveal that design-phase details can be altered during construction due to factors such as material availability, technical constraints, and budget considerations. Furthermore, the client's expectations and engagement are critical to the overall success of the project.

Architectural competition regulations in Türkiye are established by the Union of Chambers of Turkish Engineers and Architects (TMMOB), which defines competition types, specifications, jury responsibilities, required documents, and prize allocations in the 2003 Competition Regulation (TMMOB Mimarlar Odası, 2003). In contrast, international regulations, such as those from the Australian Institute of Architects and the Royal Institute of British Architects, often include additional requirements, such as material specifications, average budget estimations, and system detail drawings (Australian Institute of Architects, 2016; RIBA, 2019). In Türkiye, however, system details, material specifications, and budget information are not mandatory in all competitions, which contributes to lower construction rates.

An analysis of 292 architectural competitions in Türkiye revealed that the inclusion of system details in competition briefs began in 2010. Among the 168 system detail drawings obtained from the 92 analyzed competitions, only 23 belonged to competitions where system details were not explicitly required. The collected data indicate that only 45% of analyzed competitions progressed to the construction phase, while the remaining 55% were not built.

In this context, system sections obtained from competitions were analyzed in detail, comparing system sections from the competition phase with those in application projects. Due to the limited preparation time in architectural competitions and the conceptual nature of most projects, system details are often developed at a conceptual level or presented with varying degrees of detail and information. A total of 45 system details from 15 competitions were analyzed. The findings indicate that among the examined competitions, 10 had participants with high evaluation scores ranking at the top, while 5 competitions featured participants ranking lower. These results suggest that the clarity of system details in terms of drawing technique and their contribution to jury evaluations of project feasibility and cost perception positively influenced jury decision-making. Among the evaluation criteria, drawing technique emerged as the strongest area, whereas dimensioning information was found to be insufficiently emphasized. In terms of performance analysis, the integration of "Beam-Floor-Interior Wall-Column" was the most frequently overlooked system detail. Architects predominantly used system details to convey façade information, leading to the most common examples being "Beam-Floor-Exterior Wall-Column" integrations.

In the later stages of the research, the indirect impact of system details on jury evaluations will be examined in greater depth through professional interviews and analysis results. Additionally, the influence of limited preparation time on the depth and quality of system details will be investigated, aiming to gain a more comprehensive understanding of the representativeness and practical significance of system details across different project types.

The findings suggest that architectural competitions prioritize conceptual design over technical resolutions. However, the presence of system sections plays a crucial role in the transition of projects to the construction phase. Given the recent inclusion of system sections in Turkish competition requirements, policy changes should be considered to integrate technical drawings into the competition framework further.

Conclusion

This study highlights the critical role of system sections in architectural competitions, emphasizing their impact on jury evaluations and project construction rates. While system sections often remain at a conceptual level during competitions, their systematic integration can enhance project feasibility and constructability. The purpose of this study is to contribute to the literature on the significance of system details in architectural competitions, to investigate the influence of precise design on outcomes, and to give light on practical constructions and future research. In conclusion, the study demonstrates that addressing system details in architectural competitions within a holistic and systematic approach can enhance the constructability of projects and contribute to making jury evaluation processes more objective.

References

Australian Institute of Architects. (2016). *Model conditions for an architectural competition*.
Bachman, L.R. (2003). *Integrated Buildings*. Hoboken, N.J.: John Wiley & Sons.
Chupin, J.-P. (2011). Judgment by design: Towards a model for studying and improving the competition process in architecture and urban design. *Scandinavian Journal of Management*, 27 (2), 173–184. https://doi.org/10.1016/j.scaman.2010.12.004
Royal Institute of British Architects. (2019). *Concept design for new Ambassador's Residence: Preliminary briefing paper.*
TMMOB Mimarlar Odası. (2003). *Yarışmalar yönetmeliği*.
Yazıcıoğlu, F. (2007). *Mimarlık ofislerinde uygulamaya yönelik ayrıntıda tasarım süreci* (Yüksek lisans tezi). İstanbul Teknik Üniversitesi.

ART HISTORY

Art and Technology

Art History

Modern and Contemporary Art

Valorizing Cultural Heritage through Art and Movement: Spatial and Bodily Experience in a Promenade Performance

İpek Çakmak[a], Zeynep Kuban Tokgöz[b]

[a] Istanbul Technical University, Graduate School, Art History Master's Program, Türkiye
[b] Istanbul Technical University, Faculty of Architecture, Department of Architecture, Türkiye
cakmaki15@itu.edu.tr, kuban@itu.edu.tr

Keywords: Bodily Experience, Cultural Heritage, Performative Art, Spatial Experience, Valorization.

Aim

The re-signification of cultural heritage structures within collective memory and their perpetuation through intergenerational experiences can be achieved not only through physical preservation but also via artistic and performative interventions. In the process of 'valorization' of historical buildings and spaces, it is argued that inviting individuals to these sites through cultural and artistic events allows the collective judgment to determine the value of the place (Lorusso et al., 2016). When performative arts are chosen as a means of valorization, art is summoned into the historical structure through the artist and their body. Unlike other forms of art, in performative arts, the artist does not bring a completed artwork into the space; rather, they are physically present, creating their art in real-time and in a live manner. In this case, the audience experiencing the art in the space is referred to as 'spectators' rather than 'visitors'. The repetitive production process of performance art gains significance through the simultaneous presence of both the artist's and the spectator's bodies within the same space. As a subcategory of performative arts, promenade performances allow spectators to become part of the performative narrative, moving within the space and following the artist from one point to another. In this context, the spectators' perception of the artist's body, as well as their spatial experience in promenade performances, becomes an essential aspect of the performative encounter.

This study focuses on the spectators' experience in historical sites where performative arts are used as a tool for valorization. How can performative arts shape spectators' spatial perception? Can the artist's spatial experience influence that of the spectators? In this regard, *Dignità Autonome di Prostituzione (D.A.d.P.)* a show by Luciano Melchionna has been selected as a case study. It is a show format created in 2007 by Luciano Melchionna and Betta Cianchini, and it has been staged at Sant'Elmo Castle in Naples, Italy since 2022. This study aims to conduct a theoretical discussion on the perception of space and the body, as well as critically examine the movement and dramaturgical structure of the chosen performance.

Material and Method

This study uses a qualitative research approach to examine how performative arts shape the spatial experience of spectators in the valorization of historical sites. The movement dramaturgy and spatial relations of the selected case study, *Dignità Autonome di Prostituzione*, are analyzed through the bodily presence of spectators and their observations. The research employs cognitive and phenomenological approaches alongside participant observation to explore the relationship between space, body, and performance.

According to Çelebi (2020), value fundamentally requires a judgment formed in consciousness, which is directly linked to experience. In the valorization of historical buildings and sites, prioritizing artistic and experiential approaches aligns with Çelebi's proposed relationship between value, judgment, and experience. The spectators' spatial experience directly influences their perception of the space and, consequently, their judgment of its value. While performative arts provide an immersive and multi-sensory experience, this study specifically focuses on spectators' spatial and bodily perception.

The perception of space and body is examined in two aspects. The first concerns the spatial relations perceived directly through the spectators' own bodies. In this regard, the research investigates the consequences of the spectators' forced movement within the performance's dramaturgical structure, as opposed to the movement patterns of an ordinary visitor in the castle. The distinctive architecture of Sant'Elmo Castle, combined with the

expansive spatial movement design of the *D.A.d.P.* performance, aligns with Mark Johnson's (2005) image schemas of center-periphery, container, verticality, and source-path-goal. Johnson grounds these image schemas in fundamental sensory-motor experiences and links spatial perception to bodily cognition.

The second dimension of spatial and bodily perception focuses on the artist's body, which assumes the most active role within the space. However, this analysis is conducted from the spectators' perspective. In this context, the study questions how the artist's bodily experience becomes part of the spectators' experience, drawing upon mirror neuron theories. Sinigaglia and Rizzolatti (2019) conducted experiments following the discovery of mirror neurons, concluding that observing actions such as grasping, holding, or clutching in another body triggers similar motor responses in the observer's neurons. When applied to the spectator-artist relationship in performative arts, this framework suggests that the artist's embodied interactions with space, objects, and their own body may trigger analogous motor responses in spectators. From a cognitive perspective, observed actions are expected to contribute to the spectators' spatial experience and the judgments they form about it.

This study is conducted within the context of a single performance and a specific site. Therefore, the findings are not intended to be generalized; rather, the research aims to provide a conceptual discussion on the impact of performances in historical sites on spectator experience. While individual interviews were conducted with participants, the study primarily focuses on observational data and theoretical analysis.

Findings

Performative art practises in historical spaces transforms the way audiences experience the space. Additionally, in the selected performance example, the fact that the audience's movement is an integral part of the narrative makes this experience mandatory while also diversifying and reinforcing it.

The theater-based performance *Dignità Autonome di Prostituzione* employs an expansive spatial design where it is staged. In its editions at Naples' Sant'Elmo Castle, the performance primarily occupied the uppermost level of the castle, while various other indoor and outdoor areas were also integrated into the production. The performance begins with the audience moving up from the entrance of the castle to the top level, while performers initiate their acts on that ramp. This initial movement of the audience exemplifies the verticality and source-path-goal image schemas, as they both ascend and move toward a specific destination. By the time the sun sets, the audience is seated in the main performance area, where they begin to enjoy the music and dance performances. The actors, positioned at different elevations surrounding the audience, first perform dance choreographies and then recite their lines. (Figure 1.) This initial spatial arrangement, where the audience is encircled by performers at different heights, corresponds to the center-periphery image schema. Following this introduction and an explanation of the narrative, around thirty different performers are sequentially introduced. This leads to the part where the audience selects an actor whose solo performance they wish to watch. The actors, gathering an audience of twenty to fifty people around them, then lead them to predetermined spaces for their performances. (Figure 2.) These spaces can sometimes be offices, meeting rooms, or storage areas within the castle, or enclosed spaces such as chapels, cells, and dungeons, while they include also some open-air areas at different elevations of the castle. After selecting a performer in the main area, the audience moves toward the solo performance location and returns to the main space at the end, corresponding again to the source-path-goal image schema. Upon reaching the destination, if the space is an enclosed room, storage area, dungeon, or church (Figure 3.), this is perceived through a container image schema, climbing the stairs to different levels follows the image schema of verticality. Each audience member typically has time to watch three solo performances in one evening, or at most four if they manage their time well. This means that throughout the night, each spectator repeatedly engages with multiple source-path-goal schemas while also participating in various spatial interactions that activate the verticality and container image schemas.

Figure 1. Opening coreography around the main space, Author, 2024.

Figure 2. Actress is walking to her solo performing space with a group of audiences, Anna Abet, 2022.

Figure 3. A group of audience members is about to enter a room from the castle's outdoor space, Author, 2024.

In the movements of the performers, who are the main focus for the audience, we observe interactions with space, objects, and other bodies. The performer's body does not move alone; it responds to space and others. These interactions can influence the audience's experience and contribute to spatial memory, which can be discussed through mirror neuron theories. As the audience's spatial experience is shaped by movement, observing other bodies also affects their perception. Especially movements that may activate motor responses in the observer's brain are seen in the performers, who remain central throughout the performance. In this study, movements such as grasping, holding, and gripping—observed in the artist's body—are categorized into space-body, object-body, and body-body interactions. In space-body interactions, the performers engage with elements beyond the audience's immediate and potential spatial experience, incorporating the ramps, elevations, structures, and railings of the castle into their choreography and performance. During these moments, bodily actions such as grasping, holding, and gripping activate the mirror neurons of audience members in the observer position, according to Sinigaglia and Rizzolatti's (2019) mirror neuron experiments. (Figure 4.)

Figure 4. Hands grasping the added structure (foreground) and the castle's parapet (background), Anna Abet, 2022.

Regarding object-body interactions, the primary object forming the core of the performance's structure is the 'dollarini', small, colorful, printed representations of dollar banknote. Before every monologue performance starts, audience members need to "pay" the actors with these symbolic dollars for their art. (Figure 5.) After reaching an agreement on the price with the audience group, the actors collect the symbolic money from them. In this scenario, while the audience directly engages in an object-body interaction, they simultaneously observe the grasping and holding movements occurring both in the artist and in other audience members.

Figure 5. An audience member paying to the actress for her performance, with 'dollarini', The screen capture is taken from Rai News' video report titled "Dignità Autonome di Prostituzione: un inno alla vita" (Rai News, 2024).

The interaction between performers and the audience is not only established through dialogues or objects; physical contact also emerges as a form of body-to-body interaction. In such situations, the audience members touched by

the performers experience the contact directly, while other spectators in the same room observe both their fellow audience members and the actors engaging with them. Besides individual interactions during monologue performances, performers also re-engage with the audience in the main area at the end of the evening. Accompanied by music, they invite audience members to dance, linking arms with them in collective movements and concluding the event with shared bodily engagement.

Conclusion

In this study, by discussing the body-space experience related to spatial perception and the experience gained through observation within a theoretical framework. The performative structure of a promenade performance staged in a historical building has been analyzed from spatial and bodily perspectives; the findings have been grouped and exemplified. It is indicated that the movement structure of the performance, which also involves the audience, deepens their interaction with the space. At the same time, instead of performing on a designed or confined stage, the artist presents the performance in various areas of a medieval castle. This process, influenced by the unique architecture of the space, enhances the audience's spatial perception through both bodily and visual sensory experiences. This, at a conscious level, is directly reflected in the judgment mechanism that attributes value.

Performances not only highlight the physical dimensions of the space but also contribute to the audience's attribution of new meanings to the space through sensory and cognitive processes. The absence of a boundary between the artist and the audience, and even the physical contact established, allows the audience to perceive the space not merely as a spectator but as a direct participant in the experience. In this regard, performative art should be considered an effective tool among various art forms in the process of valorizing historical spaces.

In conclusion, performative arts staged in historical spaces enrich the sensory dimensions of the space, ensuring a strong place in the audience's memory and transforming the quality of their connection with the site. In the valorization process, the diversity of spatial experience, the multi-layered structure of the performance, and the integration of the movement design with the unique architecture of the space stand out as crucial elements that can contribute to the sustainable valorization of heritage sites.

References

Çelebi, E. (2020). An Original Analysis Attempt on the Concept of Value. İnönü Üniversitesi Kültür ve Sanat Dergisi, 2, 183–188. https://doi.org/10.22252/İjca.833770

Johnson, M. (2005). The philosophical significance of image schemas. In B. Hampe & J. E. Grady (Eds.), From Perception to Meaning (pp. 15–34). Walter De Gruyter. https://doi.org/10.1515/9783110197532.1.15

Lorusso, S., Cogo, G. M., & Natali, A. (2016). CONSERVATION SCIENCE IN CULTURAL HERITAGE. Conservation Science in Cultural Heritage, 16, 59–73. https://doi.org/https://doi.org/10.6092/issn.1973-9494/7165

Rai News. (2024, July). "Dignità Autonome di Prostituzione": *un inno alla vita* [Video]. *Rai News Campania.* https://www.rainews.it/tgr/campania/video/2024/07/dignita-autonome-di-prostituzione-castel-sant-elmo-212603c4-e3b1-4629-a6fc-fac250bdfb6d.html

Sinigaglia, C., & Rizzolatti, G. (2019). Beyindeki Aynalar. İstanbul: Alfa.

CHEMICAL ENGINEERING

Hydrogen Technologies, Fuels Cells, Energy Storage Materials

Modelling and Computational Systems

Nanotechnology, Surface Coatings and Films

Preparation and Characterization of Polysulfone Membranes for Proton Exchange Membrane Fuel Cells

Batuhan Sadıksöz[a], Nesrin Köken[b], Börte Köse-Mutlu[c], Vahid Vatanpour[c], Nilgün Kızılcan[b], Mehmet Emin Paşaoğlu[c], İsmail Koyuncu[c]

[a]Istanbul Technical University, Polymer Science and Technology Program, Turkey
[b]Istanbul Technical University, Department of Chemistry, Turkey
[c]Istanbul Technical University, Environmental Engineering Department, Turkey
sadiksoz23@itu.edu.tr

Keywords: Aquivion, Proton Conductivity, Proton Exchange Membrane, Sulfonated Polysulfone

Aim

Proton Exchange Membrane Fuel Cells (PEMFC) are crucial for renewable energy, offering high efficiency and low emissions. Proton exchange membranes (PEMs) enable proton transport while blocking electrons and gases, ensuring controlled reactions and electrical insulation (Sharaf & Orhan, 2014). Their high chemical durability and low electrical resistance improve fuel cell longevity and reliability. Perfluorosulfonic acid (PFSA) membranes, such as Nafion and Aquivion, are commonly used but face challenges due to high costs and performance decline at elevated temperatures. Developing cost-effective membranes with higher conductivity and broader operational temperature ranges is a key research focus. For PEMFC applications, membranes must prevent gas permeability while maintaining proton conductivity (Tellez-Cruz et al., 2021).

In this study, proton exchange membranes were produced using the solution casting method. Sulfonated polysulfone (SPSU), sulfonated polyethersulfone (SPES), and Aquivion® PW79S were used as polymers, while graphene oxide (GO) was incorporated as an additive. The effects of different material combinations on proton conductivity were evaluated to develop alternatives to Nafion.

Material and Method

Polysulfone (PSU, Udel® P-1700) was provided by Solvay, while another PSU with a molecular weight of 30.000 was synthesized in the ITU chemistry lab (D102). Polyethersulfone (PES, Ultrason® E6020P) was supplied by BASF. Aquivion® PW79S, N,N-dimethylacetamide (DMAc), N,N-dimethylformamide (DMF), 1-methyl-2-pyrrolidone (NMP), methanol, trimethylsilyl chlorosulfonate (TMSCS), chlorosulfonic acid, and toluene were all obtained from Sigma-Aldrich. Acetone, dichloromethane (DCM), bisphenol A (BPA), and sodium hydroxide (NaOH) were purchased from Merck. Additionally, Graphene Oxide (UGOX™) was bought from United Nano Tech Innovations Pvt Ltd. All chemicals were used as received without further purification.

PSU was synthesized by first mixing DMAc and toluene, followed by the addition of bis(p-chlorophenyl sulfone), BPA, and potassium carbonate. The reaction mixture was stirred and heated at 150°C for 4 hours. After completion, the mixture was cooled to room temperature and filtered. The polymer was then precipitated using a methanol-water solution, washed with methanol, and finally dried in a vacuum oven at 60°C for 12 hours.

Two different sulfonation methods were used, and in Sulfonation Method-1 (SM-1), the synthesized PSU and commercial PES were sulfonated separately using chlorosulfonic acid and dichloromethane. Initially, the polymers were dried at 80°C, then dispersed in DCM and stirred. Chlorosulfonic acid was gradually added, and the reaction proceeded under stirring. The resulting SPES and SPSU were washed in an ice-water bath and dried in a vacuum oven at 60°C (Shirvani et al., 2023).

In Sulfonation Method-2 (SM-2), commercial PSU was dissolved in DCM at 35°C under stirring. After achieving a homogeneous solution, TMSCS diluted in DCM was added dropwise, and the reaction was allowed to proceed. The sulfonated PSU was then precipitated using alcohol, filtered, washed, and dried. The required amount of TMSCS was determined by calculating the moles of repeating units in the polysulfone sample and applying a targeted sulfonation ratio, considering the molecular weight of TMSCS to obtain the corresponding mass.

The sulfonation degree (DS) of the polymers was determined using a titration method widely referenced in the literature (Devrim et al., 2009; Guan et al., 2005; Zhao et al., 2018). For 16% DS SPES and 35.2% DS SPSU from the first method (SM-1), and 30% DS SPSU from the second method (SM-2), the polymers were dissolved in DMF solvent, and the released H^+ ions were quantified by titration with 0.1 M NaOH using phenolphthalein as an indicator.

The repeating unit's molecular weight was 232 g/mol for SPES (coefficient: 0.232) and 442 g/mol for SPSU (coefficient: 0.442), with DS calculated using the following formulas.

For PES:

$$DS\% = \frac{(0.232 \times M \times V)}{(W - 0.08 \times V)} \times 100 \qquad (1)$$

For PSU:

$$DS\% = \frac{(0.442 \times M \times V)}{(W - 0.08 \times V)} \times 100 \qquad (2)$$

where M represents the NaOH concentration (M), V is the volume of NaOH added at the equivalence point (mL), and W is the weight of SPES (g).

The final calculations confirmed that the sulfonation degrees were 16% for SPES (sulfonated using SM-1), 35.2% for SPSU (sulfonated using SM-1), and 30% for SPSU (sulfonated using SM-2).

Membrane preparation involved stirring polymer solutions with different concentrations in dimethylacetamide (DMAc), N-methyl-2-pyrrolidone (NMP), or isopropyl alcohol (IPA) for 24 hours using a magnetic stirrer. The prepared solutions were then poured into glass petri dishes and placed in an oven at 70°C for 24 hours. After complete evaporation of the solvent, membranes were obtained for proton conductivity analysis.

The membrane conductivity test was performed using a cell where the membrane was placed in direct contact with platinum electrodes, and a voltage difference of 0-100 mV was applied across the two central electrodes.

$$H_2 \rightarrow H^+ + 2e^- \qquad (3)$$

Reaction (3) takes place, where the generated protons (H^+) pass through the membrane and are converted back into hydrogen on the other platinum electrode. During this process, the resulting current is measured from the outer electrodes.

$$\sigma = \frac{L}{R * A} = \frac{L}{R * W * T} \qquad (4)$$

where σ is the conductivity (mS/cm), L is the distance between the voltage-applied probes (0.425 cm), W is the width (cm), T is the membrane thickness (cm), and R is the resistance (Ohm-Ω).

The resistance (R) is determined from the slope (dV/dI) of the voltage (V) versus current (I) graph. Subsequently, the conductivity is calculated using the formula (4) mentioned above.

During the measurement, hydrogen gas (100% relative humidity - RH) was supplied while maintaining the cell temperature at 80°C. In the presence of conductivity, the current is expected to vary linearly with voltage. The resistance (R) value obtained from the slope of the dV/dI graph is then used to calculate the conductivity (σ).

Findings

The membrane produced with Aquivion achieved a proton conductivity of 615.46 mS/cm, which is higher than the general values in the literature. In contrast, for the PEMs prepared by mixing SPSU and PES polymers sulfonated using SM-2, conductivity values of 1.3 mS/cm and 1.08 mS/cm were recorded, respectively. On the other hand, no conductivity was obtained from the SPSU PEMs sulfonated using SM-1.

Conclusion

Based on the studies mentioned above, conductivity was obtained from the membranes produced using Sulfonation Method-2. However, the membranes derived from sulfonated polymers exhibited lower conductivity compared to the general literature, and the addition of Graphene Oxide did not affect their conductivity. In contrast, the membrane produced with Aquivion ionomer showed higher conductivity compared to the literature. In the continuation of our studies, new proton exchange membranes were developed by combining Aquivion ionomer, SPSUs obtained via both methods, GO, and Fe_3O_4@SiO_2@NH_2-SO_3H. Proton conductivity analyses will be conducted.

Acknowledgments

The authors would like to thank the Scientific and Technical Research Council of Turkey (TUBITAK) 1004 Istanbul Technical University(ITU Project No: 22AG018), and also ITU Research Foundation with ITU-BAP Project No: TYL-2024-45894

References

Devrim, Y., Erkan, S., Baç, N., & Eroğlu, I. (2009). Preparation and characterization of sulfonated polysulfone/titanium dioxide composite membranes for proton exchange membrane fuel cells. International Journal of Hydrogen Energy, 34(8), 3467–3475. https://doi.org/10.1016/j.ijhydene.2009.02.019

Guan, R., Zou, H., Lu, D., Gong, C., & Liu, Y. (2005). Polyethersulfone sulfonated by chlorosulfonic acid and its membrane characteristics. European Polymer Journal, 41(7), 1554–1560. https://doi.org/10.1016/j.eurpolymj.2005.01.018

Sharaf, O. Z., & Orhan, M. F. (2014). An overview of fuel cell technology: Fundamentals and applications. Renewable and Sustainable Energy Reviews, 32, 810–853. https://doi.org/10.1016/j.rser.2014.01.012

Shirvani, B., Rahimi, M., & Zinadini, S. (2023). High electricity generation and wastewater treatment enhancement using a microbial fuel cell equipped with conductive and anti-biofouling CuGNSs/SPES proton exchange membrane. Energy Conversion and Management, 294, 117559. https://doi.org/10.1016/j.enconman.2023.117559

Tellez-Cruz, M. M., Escorihuela, J., Solorza-Feria, O., & Compañ, V. (2021). Proton Exchange Membrane Fuel Cells (PEMFCs): Advances and Challenges. Polymers, 13(18), 3064. https://doi.org/10.3390/polym13183064

Zhao, J., Guo, L., & Wang, J. (2018). Synthesis of cation exchange membranes based on sulfonated polyether sulfone with different sulfonation degrees. Journal of Membrane Science, 563, 957–968. https://doi.org/10.1016/j.memsci.2018.05.023

CHEMICAL ENGINEERING

Hydrogen Technologies, Fuels Cells, Energy Storage Materials

Modelling and Computational Systems

Nanotechnology, Surface Coatings and Films

Computational Simulation of Corn Wet Milling for Starch Production: Revisiting a Conventional Biotechnological Process

Evrim Ceylan[a,b], H. Enis Karahan[a,c], Hale Gürbüz[a],

[a] Istanbul Technical University, Department of Chemical Engineering, Türkiye
[b] Sigma Process Technologies, Istanbul, Türkiye
[c] Istanbul Technical University, Synthetic Fuels & Chemicals Technology Center (ITU-SENTEK), Türkiye
ceylane22@itu.edu.tr

Keywords : Process Simulation, ASPEN Plus, Biomass, Corn Starch, Biocomponent.

Aim

The growing emphasis on environmental awareness and tightening regulations have led the chemical industry to move towards "Sustainable Business Models," favoring fossil resource minimization and waste prevention practices. Increased adoption and utilization of renewable resources lies at the core of this transition (Karuppiah et al., 2023). Conventional biotechnological processes (in short, bioprocesses), such as corn wet milling (CWM), offer an ideal platform for testing the utility of modern tools and approaches, such as synthetic biology, machine learning, and process integration/intensification (Amado et al., 2017; Byanju et al., 2023; Shih, 2018; Wang et al., 2017) . Along these lines, as being already profitable and highly widespread, we argue that CWM is arguably one of the most strategic targets for speeding up this transition. Nevertheless, we inevitably need to establish a solid basis for analyzing the potential of implementing these new developments as industrial processes, which is hard to realize without taking advantage of computational simulation platforms such as SuperPro Designer and Aspen Plus, to name a few (Cecílio et al., 2023; Cortes-Peña et al., 2020; Ramirez et al., 2008; Wooley & Putsche, 1996). Aspen Plus is undoubtedly the leading process simulation software as it covers a comprehensive set of theoretical models that enable accurate analyses (Al-Malah, n.d.). Also, recent progress made in ASPEN Plus, such as Biocomponent definition or enhanced thermodynamic modeling, improves its suitability for bioprocesses. Plus, CWM is an utterly complex process impacted by several factors, such as grain moisture content, SO2 concentration in steep water, temperature, and pH. On top, CWM involves multiphase unit operations, including not only liquid but also a solid phase, necessitating the use of a comprehensive platform for performing reliable simulations. Thus, we decided to test the capabilities of Aspen Plus in simulating CWM, synthesizing the open literature information on CWM with the expertise of Sigma Process Technologies. By doing so, here, we aim to adequately transfer our accumulated knowledge to Aspen Plus environment as faithfully as possible to pave the road for future process integration and intensification efforts.

Material and Method

We opted for Aspen Plus primarily due to the availability of an extensive database and reference studies for simulating conversion reactions involving lignocellulosic biomass (Cecílio et al., 2023) and the recent introduction of a physical property database for biocomponents (Wooley & Putsche, 1996). The CWM process, which is based on the separation of corn kernels into fractions, serves as a strong reference point in the integration of different processes (Figure 1). As a starting point, we focus on obtaining starch as the main product and gluten, germ, fiber, and corn steep liquor as by-products from corn grain by wet milling process.

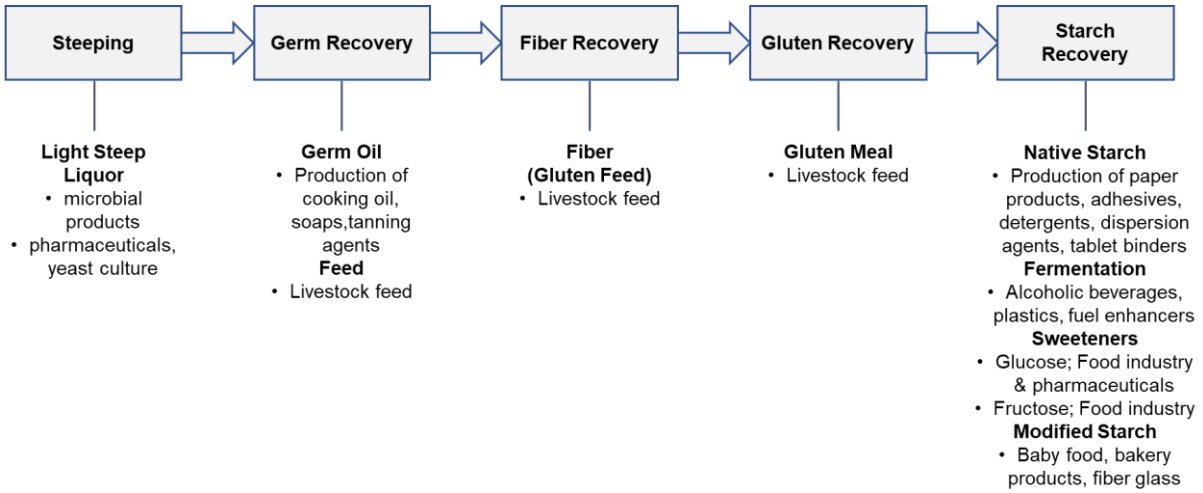

Figure 1. Schematic diagram of CWM-based products with usage areas of end-products (Amado et al., 2017; Rausch & Eckhoff, 2015; Serna-Saldivar, 2019).

Since it is a bioprocess involving multiphase unit operations, simulation studies are necessary to facilitate improvements within the process and to enable the integration of different processes into wet milling. We have specifically employed Aspen Plus V14 equipped with Properties and Simulation modules. The modeling of the wet milling process is based on the know-how of Sigma Process Technologies and several studies available in open literature. The process typically involves steeping, germ recovery, fiber recovery, gluten recovery, and starch washing steps, respectively (Eckhoff & Watson, 2009; Rausch & Eckhoff, 2015). Steeping, the step that includes the conversion of soluble monosaccharides in the structure of corn into lactic acid and the dispersion of the protein matrix by sulfur dioxide added to the system with steep water, is the most critical step that determines the efficiency of the process(Hull et al., 1996). The step that aims to soften the corn and obtain the components without damaging them in other steps is followed by the steps of milling and obtaining germ, fiber, gluten, and starch. The germ is collected from the overflow of the hydrocyclones based on the density differences. Subsequently, fiber recovery is achieved through a pressure screen that exploits differences in particle size. Finally, the separation of gluten and starch is performed using centrifuges that take advantage of density differences, and then the process is continued with washing, dewatering, and drying steps for all products (Rausch & Eckhoff, 2015). The process flow diagrams of the CWM process are represented as Corn cleaning and steeping steps (Figure 2), Germ recovery step (Figure 3), Fiber recovery step (Figure 4), Gluten recovery step (Figure 5), and Starch recovery step (Figure 6), respectively. Several basic properties required for simulating the CWM process, particularly those concerning solids handling, such as particle size distribution (PSD), density, and moisture content, have been collected from the literature (Serna-Saldivar, 2019).

S-101	V-101	P-101	V-102	P-102	V-105	P-103	E-101	V-103 + S-102 + V-104 + S-104	C-101	S-104
Corn Screen	Corn Hydraulic Transfer Tank	Sluice Water Pump	Corn Hydraulic Transfer Tank	Corn Feed Pump	Bisulfite Solution Tank	Bisulfite Pump	Bisulfite Sol.Heater	Steeping Tank	Sluice Water&Corn Collector	1st Grind Screen

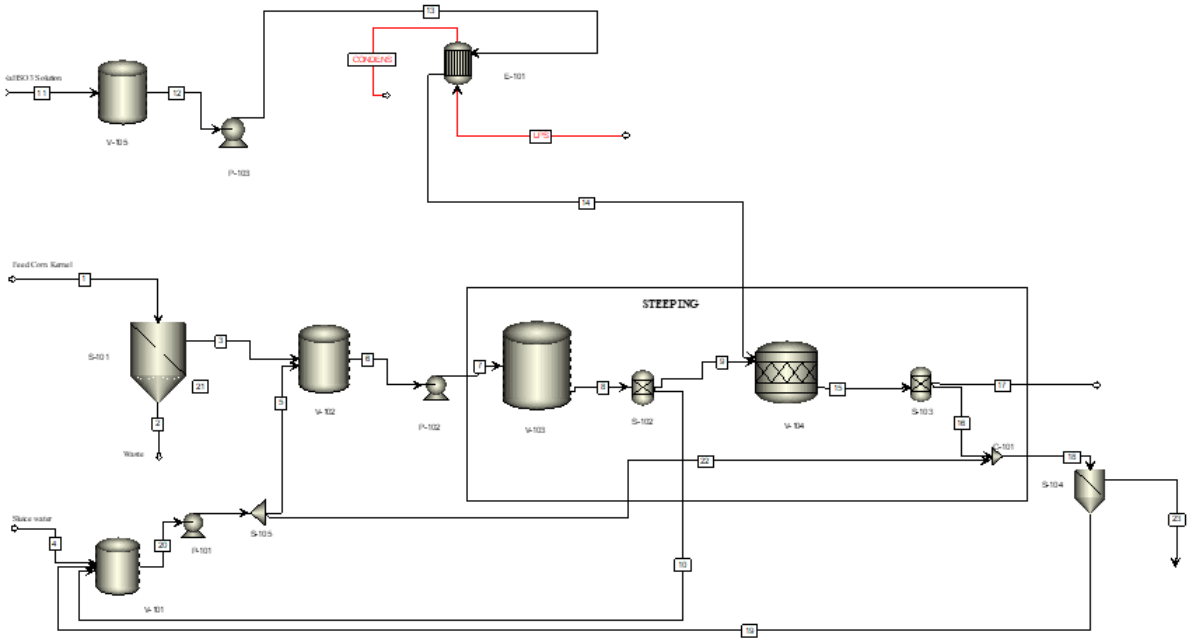

Figure 2. Corn cleaning and steeping steps of the process.

M-101	V-106	S-106	P-104	H-101	C-102	S-107	M-102	V-107
1st Grinding Mill	1st Grind Tank	1st Group Hydrocyclone (HyCyc) Separator	1st Grind Tank Pump	1st Group HyCyc	HyCyc Collector	2nd Grind Screen	2nd Grind Mill	2nd Grind Tank

V-107	P-105	S-108	H-102	C-103	W-101	P-106	D-101
2nd Grind Tank	2nd Grind Tank Pump	2nd Group HyCyc Separator	2nd Group HyCyc	Germ Collector	Germ Washer	Germ Dewatering Press	Germ Dryer

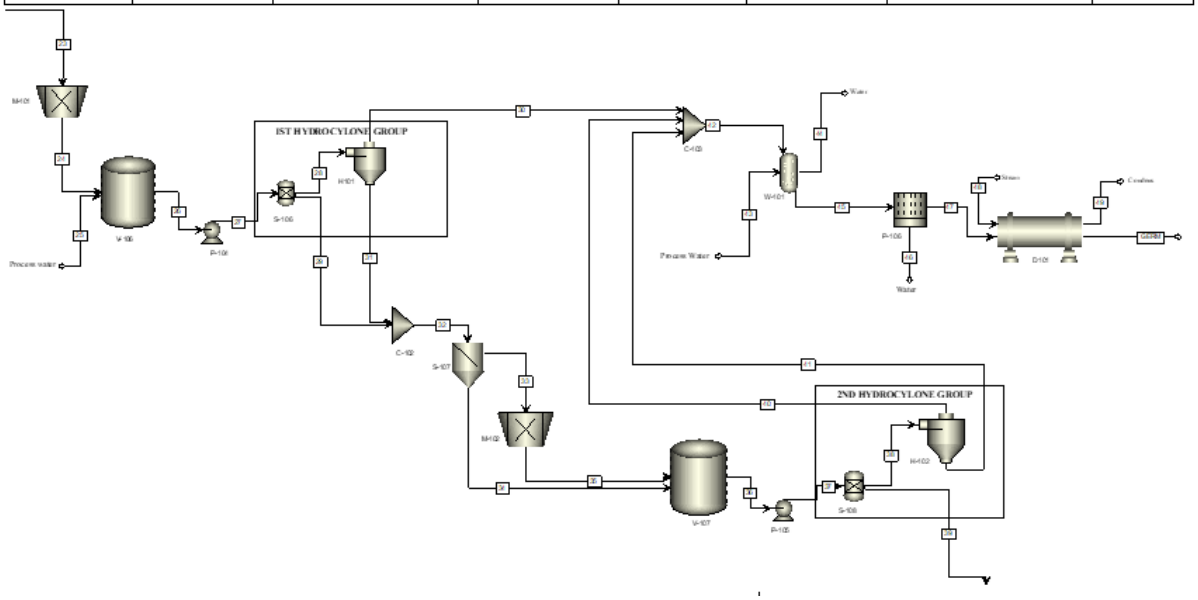

Figure 3. Germ recovery step.

M-103	S-109	V-108	P-107	W-102	S-110	P-108	D-102
Impact Mill	Fiber Separation Screen	3rd Grind Tank	3rd Grind Tank Pump	Fiber Washer	Fiber Wash Screen	Fiber Dewatering Press	Fiber Dryer

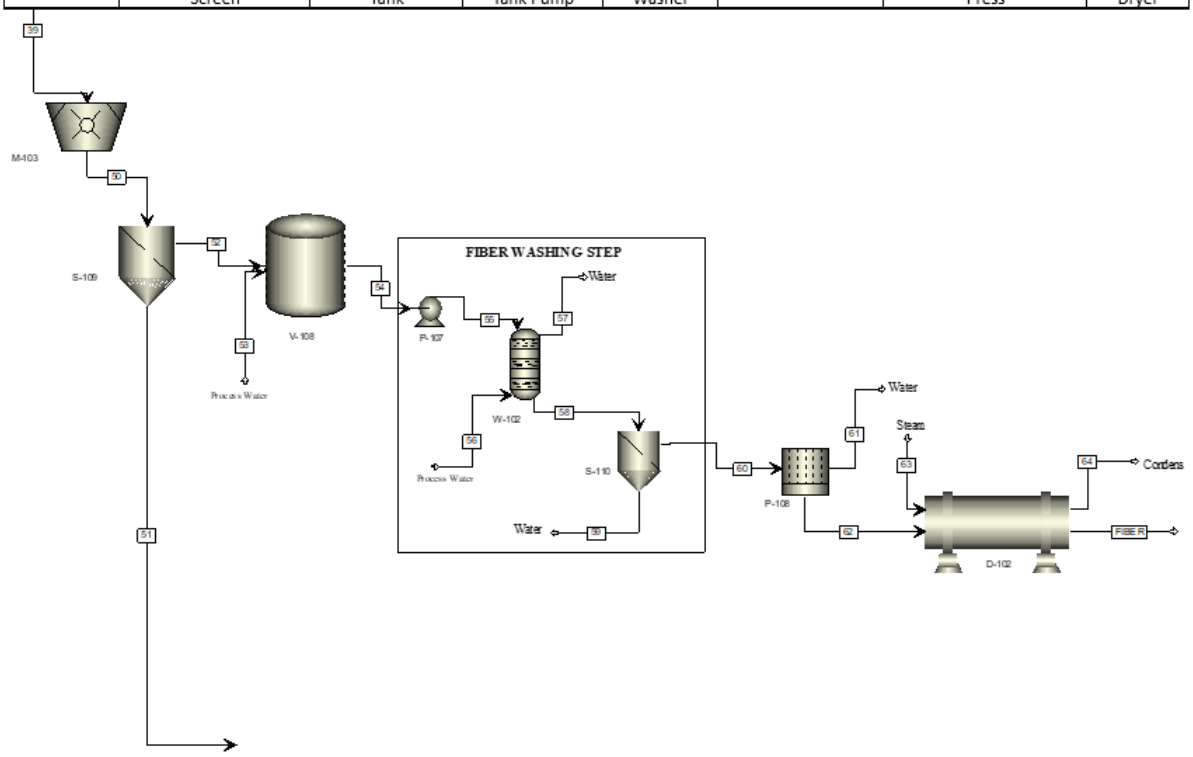

Figure 4. Fiber recovery step.

S-111	C-104	C-105	V-109	P-109	E-102	F-101	D-103
Centrifuge Separator	Primary Centrifuge	Gluten Thickener Centrifuge	Heavy Gluten Tank	Heavy Gluten Tank Pump	Gluten Heat Exchanger	Gluten Rotary Vacuum Filter	Gluten Dryer

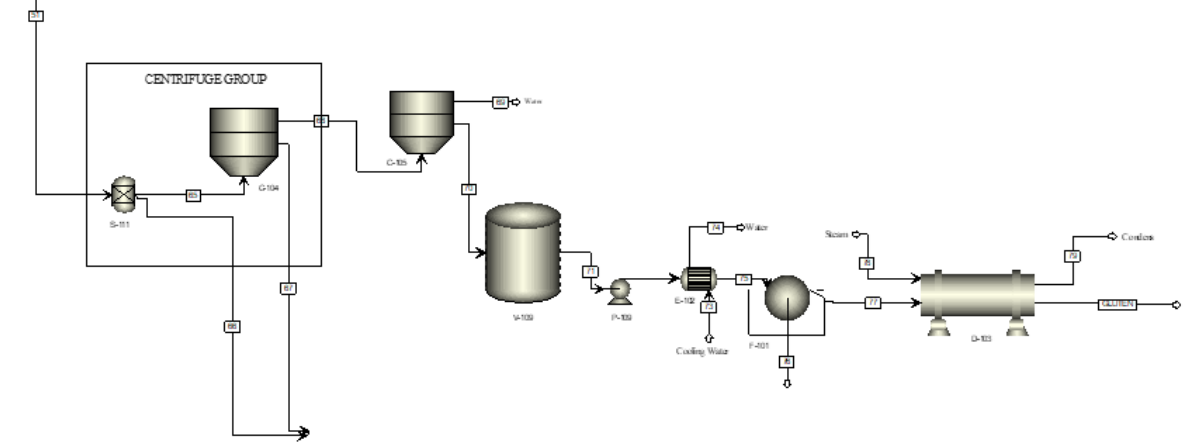

Figure 5. Gluten recovery step.

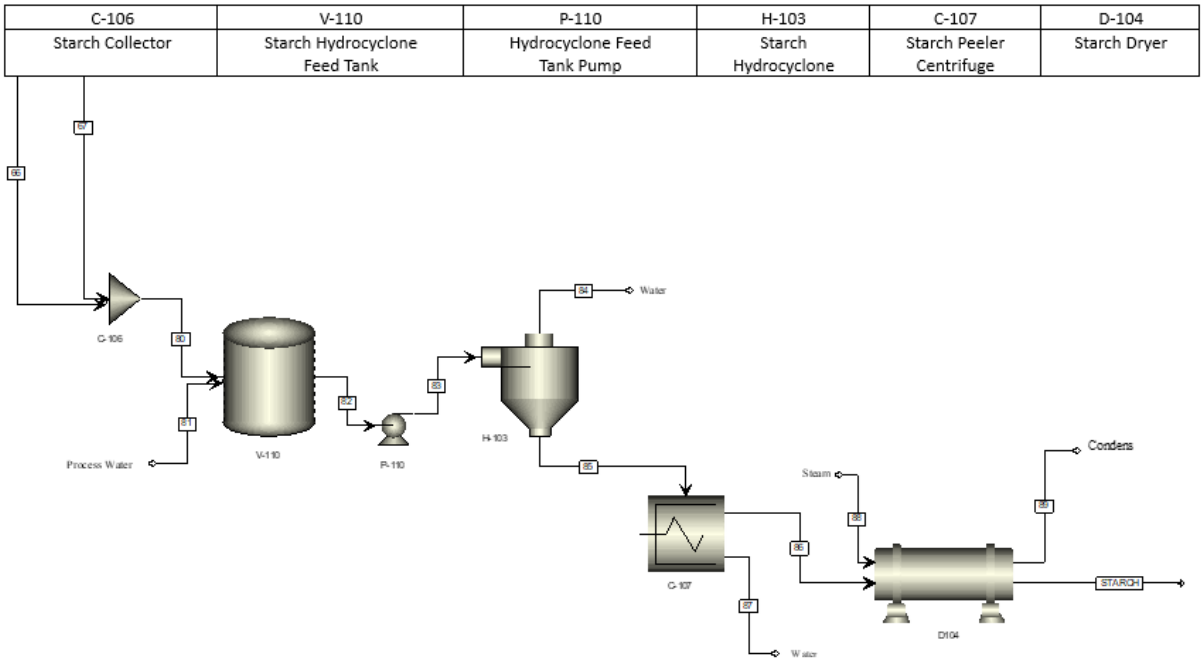

Figure 6. Starch recovery step.

One of the key challenges of simulating CWM process is that none of the corn components (e.g., germ, fiber, gluten, and starch) are included in the Aspen database by default. As the hemicellulosic fractions and protein structures have already completed their polymerization reactions, defining these components as a polymer is not a suitable approach. It is rather fair to register those as their monomers in the simulation environment (Serna-Saldivar, 2019). It is, on the other hand, common practice to consider starch and lignin as nonconventional solids due to their extremely long chain lengths and the challenges associated with defining their chemical formulas (Serna-Saldivar, 2019).

One of the critical steps that impact the overall efficiency of CWM is the steeping phase. During this phase, six tanks operate in a semi-continuous manner, allowing for continuous input and output to the general steeping system. In contrast, the batch scenario pertains only to the specifics of individual tanks. Consequently, only the general steeping system has been modeled in Aspen Plus, including the transportation of corn using sluice water and the reaction step of corn with mill water. Identifying the conversion of glucose to lactic acid in the reaction step (Hull et al., 1996) is deemed important due to the function of lactic acid in softening the corn kernels and enhancing the diffusion rate of sulfur dioxide (SO2) into the endosperm, dissolving endosperm proteins, and weakening the cell walls (Eckhoff & Watson, 2009; Rausch & Eckhoff, 2015). Notably, since the protein content of the kernel is classified within the amino acids, the identification of the dissolving endosperm proteins step is eliminated.

Findings

Corn kernels, the primary raw material input for the process, have a complex and heterogeneous structure that makes it impossible to characterize the feed stream in Aspen Plus as a straightforward conventional solid. When proximate and ultimate analysis results of those are known, different biomass materials can be classified as nonconventional solids in Aspen Plus. As no ultimate analysis data was not available in the literature for corn grains, we estimated the corn kernel composition by backcalculating from the composition of end products in CWM (basically starch, germ, gluten, fiber, and water-soluble compounds). The yields of the main products and byproducts obtained as a result of CWM are compared with the values reported in the literature. As seen in Table 1, our simulation results are close to literature values. It is important to remember that during this comparison, the yield will vary depending on the corn type and features such as moisture content value, which reinforces that our approach proved to be a good starting point.

Table 1. The comparison of main and side product yields compared to literature (Eckhoff & Watson, 2009).

	Reported Yield (Eckhoff & Watson, 2009)	Our Simulation Yield
Germ	6.78 ± 0.13	6.35
Fiber	13.37 ± 0.42	14.89
Gluten	10.91 ± 0.21	4.85
Starch	65.29 ± 0.16	73.91

Another challenge in that study is the inability to achieve effective separation in equipment, where separation is carried out according to density differences such as hydrocyclones or centrifuges. The light product, oil rich germ, should be separated from high dense products using a hydrocyclone model in Aspen Plus, by taking into account density differences (Eckhoff & Watson, 2009). However, in Aspen Plus, hydrocyclones are operated by focusing on particle size distribution without directly considering the density differences. During the wet milling simulation phase, the particle size distribution was established for the combined streams of CI Solid and NC Solid. However, it was not possible to delineate particle size characteristics based on individual components such as germ, gluten, and fiber. To operate the hydrocyclones effectively, a separator is placed before the hydrocyclone block to achieve the separation of light and heavy fractions, allowing the light stream to be fed into the hydrocyclone (Dickey et al., 1997). The separator and hydrocyclone block are evaluated as a system and with this assumption, germ recovery efficiency from the first hydro cyclone group is enhanced to 54.523% from 0.668%.

Conclusion

We argue that there is huge potential in revisiting the design aspects of conventional bioprocesses to implement modern biotechnological approaches down the line. As a start, here we focused on simulating CWM process, as it will probably maintain its pivotal role in starch industry in the future. However, we found out that the limited availability of open literature on this subject presents a substantial challenge. However, despite those limitations, our initial progress proved that Aspen Plus offers sample opportunities for simulating CWM, enabling further research and development.

Unlike the vast majority of existing studies that use starch as its monomer (glucose), we attempted to adopt a different approach: introducing starch as a nonconventional component. When starch was defined with the glucose monomer in the Aspen Plus, as in other references, it gave errors due to the lack of some thermophysical properties such as vapor pressure, heat capacity, density and enthalpy, and this required correct definitions in Aspen for these missing properties. On the other hand, the nonconventional definition neglects phase and chemical equilibrium calculations and is based on density and enthalpy modeling. Since starch, which we defined as NC in Aspen Plus, does not undergo any physical separation or chemical reaction during the CWM, our NC approach is sufficient for a study in the early-stage analysis.

This study reveals that Aspen needs further development in the biocomponent area and solid module. The assumptions made were aimed at filling these gaps in the program, and improvements will be made in these assumptions to enhance the reliability of Aspen Plus simulations.

References

Al-Malah, K. I. (n.d.). Aspen plus: chemical engineering applications.

Amado, I. R., Vázquez, J. A., Pastrana, L., & Teixeira, J. A. (2017). Microbial production of hyaluronic acid from agro-industrial by-products: Molasses and corn steep liquor. Biochemical Engineering Journal, 117, 181–187.

Byanju, B., Sen, S., Mansell, T., & Lamsal, B. P. (2023). Evaluation of corn steep liquor as fermentation media for recombinant Lactococcus lactis producing antifreeze proteins. Journal of the Science of Food and Agriculture, 103(5), 2512–2521.

Cecílio, D. M., Gonçalves, J. R. M., Correia, M. J. N., & Mateus, M. M. (2023). Aspen Plus® Modeling and Simulation of an Industrial Biomass Direct Liquefaction Process. Fuels, 4(2), 221–242.

Cortes-Peña, Y., Kumar, D., Singh, V., & Guest, J. S. (2020). BioSTEAM: A Fast and Flexible Platform for the Design, Simulation, and Techno-Economic Analysis of Biorefineries under Uncertainty. ACS Sustainable Chemistry and Engineering, 8(8), 3302–3310.

Dickey, L. C., Dallmer, M. F., Radewonuk, E. R., Parris, N., Kurantz, M., & Craig, J. C. (1997). Hydrocyclone Separation of Dry-Milled Corn. Cereal Chemistry, 74, 676-680.

Eckhoff, S. R., & Watson, S. A. (2009). Corn and Sorghum Starches: Production. In Starch (pp. 373–439). Elsevier.

Hull, S. R., Yang, B. Y., Venzke, D., Kulhavy, K., & Montgomery, R. (1996). Composition of corn steep water during steeping. Journal of Agricultural and Food Chemistry, 44(7), 1857–1863.

Karuppiah, K., Sankaranarayanan, B., & Ali, S. M. (2023). A systematic review of sustainable business models: Opportunities, challenges, and future research directions. Decision Analytics Journal, 8, 100272.

Ramirez, E. C., Johnston, D. B., McAloon, A. J., Yee, W., & Singh, V. (2008). Engineering process and cost model for a conventional corn wet milling facility. Industrial Crops and Products, 27(1), 91–97.

Rausch, K. D., & Eckhoff, S. R. (2015). Maize: Wet Milling. In Encyclopedia of Food Grains: Second Edition (Vols. 3–4, pp. 467–481). Elsevier.

Serna-Saldivar, S. O. (2019). Corn: Chemistry and Technology.

Shih, P. M. (2018). Towards a sustainable bio-based economy: Redirecting primary metabolism to new products with plant synthetic biology. Plant Science, 273, 84–91.

Wang, H., Mustaffar, A., Phan, A. N., Zivkovic, V., Reay, D., Law, R., & Boodhoo, K. (2017). A review of process intensification applied to solids handling. In Chemical Engineering and Processing - Process Intensification (Vol. 118, pp. 78–107). Elsevier B.V.

Wooley, R. J., & Putsche, V. (1996). Development of an ASPEN PLUS Physical Property Database for Biofuels Components.

CHEMICAL ENGINEERING

Hydrogen Technologies, Fuels Cells, Energy Storage Materials

Modelling and Computational Systems

Nanotechnology, Surface Coatings and Films

Fabrication and Characterization of Plant Extract-Added Bilayered Nanofiber Wound Dressing

Sinem Turhan[a], Ahsen Ünal Aslan[a], Ayşe Arifoğlu[a], Dilara Nur Dikmetaş[b], Hatice Funda Karbancıoğlu Güler[b], Melek Mümine Erol Taygun[a]

[a] Istanbul Technical University, Chemical Engineering Program, Turkey
[b] Istanbul Technical University, Food Engineering Program, Turkey
turhansi23@itu.edu.tr

Keywords: Electrospinning, Nanofiber Wound Dressing, Bilayered Nanocomposite, Medicinal Plant Extract, Sustainability.

Aim

The skin is the largest organ, protecting the body from the environment. In the case of trauma, surgery, burns, or chronic diseases, the skin's barrier is disrupted, and the skin's normal function is impaired. This can lead to more severe health problems in overall health. Therefore, it is quite important to cover and protect the wound to provide the proper environment for wound healing. Many traditional and innovative wound dressings are available to support wound healing stages (hemostasis, inflammation, proliferation, and remodeling). Even though traditional wound dressings such as gauze or bandages are cost-effective, their functions are insufficient to promote the healing of complex wounds. To provide a better environment to meet the needs of the wound area, innovative wound dressings, including hydrogels, nanoparticles, micelles, microspheres, sponges, scaffolds, films, and nanofibers, have been standing out [1]. Nanofibers having a diameter in the nanometer range are polymeric materials containing many superior properties like a high surface-to-volume ratio leading to a large surface area, high porosity, good mass transport ability, light-weight, and excellent mechanical properties. Among the fabrication methods of nanofibers, electrospinning is considered one of the most practical ways due to its simple equipment requirements, cost-effectiveness, and the ability to obtain continuous nanofibers with outstanding features [2, 3].

To meet the particular application area, synthetic and natural polymers can be combined in the fabrication of polymeric nanofibers. Even though natural polymers are a great candidate for tissue engineering by having superior biocompatibility and decreased immunogenicity in contrast to synthetic polymers, synthetic polymers have superior mechanical properties such as strength, viscoelasticity, and a higher rate of degradation. Therefore, combining synthetic and natural polymers to prepare nanofibers can be an effective way in terms of obtaining good biological characteristics, adjustable mechanical strength, and better performance. To eliminate the possibility of wound infection which can lead retardation of wound healing and bring about severe health problems, functionalized nanofibers with antibacterial agents such as antibiotics, metal nanoparticles, plant extracts, and antimicrobial peptides have been preparing by the researchers [1].

Especially medicinal plants are quite rich in terms of diverse bioactive compounds such as volatile oils, alkaloids, flavonoids, phenolic alcohols, quinones, saponins, and glycosides showing great antibacterial activity. Medicinal plants have been standing out for their effectiveness and fewer side effects compared to most other synthetic modern drugs [4]. Therefore, there are various studies on electrospun plant extract-loaded nanofiber wound dressing with antibacterial activity for promoting wound healing [1].

The plant species Cedrus deodara, planned to be used as a wound dressing plant extract, is a member of the Pinaceae family, conifers, and includes many of the commonly known conifers of commercial importance, such as cedar, fir, hemlock, larch, pine, and spruce. It is found throughout most of the Northern Hemisphere and generally in temperate climates, but occurs in species ranging from arctic to tropical [5]. Cedrus deodara, commonly known as deodar, is a species of western Himalayan cypress tree belonging to the Pinaceae family. It grows locally in eastern Afghanistan, northern Pakistan, northwestern India, southwestern Tibet, and western Nepal [6]. It is abundant in coniferous forests [7]. Commonly known as Himalayan cedar, C. deodara is widely used in Chinese beverages and herbal medicines for its nutritional and medicinal properties. C. deodara pine needles are considered as nutritious food source rich in protein, vitamins, and minerals [8]. Different parts of the

plant have been traditionally used to treat various diseases such as arthritis, asthma, stomach upsets, inflammation, microbial infections, neurological and skin disorders. The leaf and resin paste of the plant are used topically for wound healing [6].

In summary, this study aims to obtain plant extract (PE) added bilayered nanofiber wound dressings by using the electrospinning technique to utilize the mentioned therapeutic effects of the cedar wood extract. The cedar wood extract obtained from the plant waste was used in the polymer blend containing synthetic and natural polymers to promote wound healing by utilizing its antioxidant, antibacterial, and anti-inflammatory properties. Therefore, this study is also contribute to sustainability in terms of recycling woody waste and reintroducing it to the consumption chain.

Material and Method

Polycaprolactone (PCL), gelatin (Ge), cedar wood extract (0.5–5% w/w, from plant waste), acetic acid (AA), formic acid (FA), and deionized water were used as materials in this study. Among different types of electrospinning techniques, the blending electrospinning technique was chosen to form a nanofiber bilayer structure since it is the simplest and most effective method. Polymer blends with varying PCL: Ge ratios (30:70 to 70:30) were prepared by using AA: FA (1:1 v/v) as the solvent mixture and polymer blend electrospun into bilayered nanofiber nanocomposites. This process involved the blending of natural and synthetic polymers, which were prepared as a uniform solution and then electrospun through a single nozzle. In this study, polycaprolactone was used as a synthetic polymer due to its biodegradability, high processability, durability, and high solubility at room temperature conditions; gelatin was used as a natural polymer due to its high hydrophobicity, high biodegradability, and biocompatibility. The electrospinning process involved blending PCL and gelatin in various volume ratios, ranging from 30:70 to 70:30, to create a uniform solution. Cedarwood extract, obtained from plant waste, was incorporated into the polymer blend to enhance the healing properties of the wound dressing. The cedar wood extract concentration ranged from 0.5% to 5% by weight. In this bilayered structure, one of the nanofiber layers was made from PCL as a reinforcement layer, and the other layer was prepared from a blend polymer including PCL and gelatin. The combination of PCL and gelatin aimed to enhance the hydrophilicity of synthetic polymers, thereby promoting cell adhesion and growth. The effects of varying polymer blend concentrations and cedar wood extract concentrations were investigated on the samples. The morphological assessments (such as fiber diameter and uniformity) and chemical structure were investigated by Scanning Electron Microscopy (SEM) and Fourier transform infrared (FTIR), respectively to determine the properties of the obtained wound dressings.

Findings

The blend of the polymers in different ratios were electrospun into nanofibers under the relevant process conditions (i.e., solution concentration, applied voltage, tip-to-collector distance, flow rate, etc.). Figure 1 shows the chemical structure of the samples.

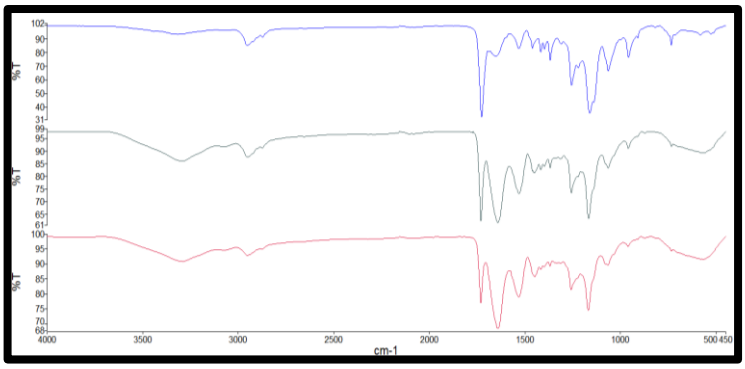

Figure 1. FTIR spectra of samples A (Pure PCL), B (PCL-Ge blend), and C (PCL-Ge with 5% extract). The top, middle, and bottom curves correspond to samples A, B, and C, respectively.

According to the FTIR spectra of the electrospun membranes, the gelatin characteristic peaks amide I (1650 cm^{-1}) and amide II (1540 cm^{-1}) were observed in (b) and (c), indicating that gelatin was successfully incorporated into these samples. The asymmetric CH_2 stretching (2943cm^{-1}) and symmetric CH_2 stretching (2866 cm^{-1}) appeared in all samples, representing the characteristic peaks of PCL. Strong peak at 1725 cm−1 belongs to the C=O double bond, peaks at 1293 and 1240 cm^{-1} are belong to the C–O, C–C stretching. The FITR results showed that PCL/gelatin hybrid nanofibers were successfully fabricated [8,9].

The morphological structure of the samples can be seen from Figure 2. According to the SEM images, it was seen that obtaineed GE:PCL samples without the plant extract showed nanofiber structures. However, 70:30 Ge:PCL sample indicated better nanofiber structure with homogeneous and bead-free based on both SEM observations and through the electrospinning process. Therefore, it was decided to add the plant extract into 70:30 Ge:PCL sample. The nanofiber mats maintained almost its homogeneous, bead-free structure after the inclusion of the plant extract. Furthermore, it was also detected that higher concentrations of plant extracts lead to thicker fibers due to increased viscosity. The electrospun Ge:PCL:PE nanofiber mats have fiber sizes in the range of 120-155 nm (Table 1), which closely mimic the collagen fibrils (50-500 nm) that compose typical human extracellular matrix, making them ideal for wound dressing material [10,11]. The visual inspection of the obtained samples by hand (Figure 3) indicated that the samples had enough hardness and dense structure for possible wound dressing applications.

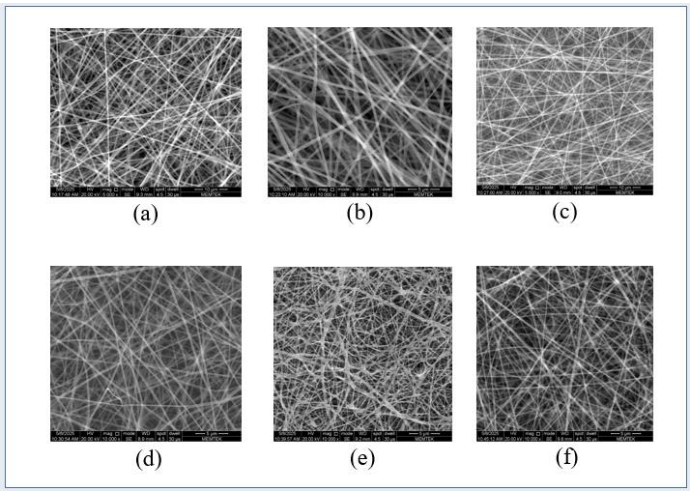

Figure 2. SEM images of the nanocomposite samples. (a) 70:30 Ge: PCL with 0.5 % extract, (b) 70:30 Ge: PCL with 2.5 % extract, (c) 70:30 Ge: PCL with 5% extract, (d) 70:30 Ge: PCL with % 0 extract, (e) 50:50 Ge: PCL with % 0 extract, (f) 60:40 Ge: PCL % 0 extract.

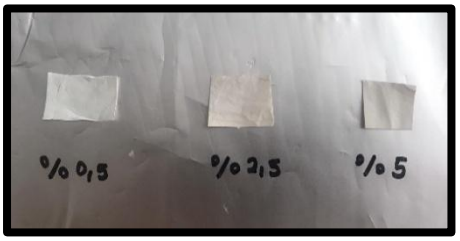

Figure 3. Nanocomposite samples containing %0.5 , %2.5, %5 extract respectively

Table 1. Average fiber diameter of samples in nanometers

Sample	**Average Fiber Diameter (nm)**
70:30 Ge: PCL (% 0.5 extract)	149.594 ± 31.845
70:30 Ge: PCL (% 2.5 extract)	120.798 ± 28.485
70:30 Ge: PCL (% 5 extract)	154.798 ± 30.137
70:30 Ge: PCL (% 0 extract)	116.814 ± 22.688
60:40 Ge: PCL (% 0 extract)	107.203 ± 27.264
50:50 Ge: PCL (% 0 extract)	139.777 ± 24.292

Conclusion

This study provided a substantial insight into the bilayered nanocomposites, including synthetic and natural polymers, and highlights their potential as a wound healing material. This study resulted in the fabrication of a sustainable and effective bilayered nanofiber wound dressing with cedar wood extract for advanced wound healing. The combination of both synthetic and natural polymers, taking advantage of the properties of medicinal plant extracts, provides the wound dressing with antibacterial, antioxidant, and anti-inflammatory properties. The electrospinning technique was used to fabricate nanofibers, offering a simple, cost-effective, and efficient method to obtain these wound dressings. The morphological analysis of the electrospun nanofiber structures revealed a homogeneous and bead-free fiber formation, which is a critical indicator of successful electrospinning. Notably, this uniform morphology was maintained even after the incorporation of cedar wood extract, indicating that the addition of the extract did not compromise the structural integrity of the fibers. Furthermore, the measured fiber diameters were found to be within the optimal range for wound dressing applications, offering a balance between porosity and mechanical strength that can support cell attachment and proliferation. These findings suggest that the developed nanofiber bilayer composites not only possess the desirable physical characteristics for wound healing but also maintain their structural consistency upon bioactive agent incorporation, highlighting their potential as effective and stable wound dressing materials.

References

Ahmadi Bonakdar, M.; Rodrigue, D. Electrospinning: Processes, Structures, and Materials. *Macromol* 2024, *4*, 58-103. https://doi.org/10.3390/macromol4010004

Akturk, A., Erol, M., Goller, G., & Küçükbayrak, S. (2021). Optimization and characterization of poly(Ɛ-caprolactone) nanofiber mats doped with bioactive glass and copper metal nanoparticles. *Chemical Papers, 75*(7), 1–15 https://doi.org/10.1007/s11696-021-01777-7

Al-Abduljabbar, A., & Farooq, I. (2022). Electrospun Polymer Nanofibers: Processing, Properties, and Applications. *Polymers*, *15*(1), 65. https://doi.org/10.3390/polym15010065

Chen, K., Hu, H., Zeng, Y., Pan, H., Wang, S., Zhang, Y., Shi, L., Tan, G., Pan, W., & Liu, H. (2022). Recent advances in electrospun nanofibers for wound dressing. *European Polymer Journal, 178*, 111490. https://doi.org/10.1016/j.eurpolymj.2022.111490

Hossain, M. S., Sharfaraz, A., Dutta, A., Ahsan, A., Masud, M. A., Ahmed, I. A., Goh, B. H., Urbi, Z., Sarker, Ke, R., Wang, Y., Sun, T., Yue, W., & Zhang, H. (2017). Electrospun PCL/gelatin composite nanofiber structures for effective guided bone regeneration membranes. *Materials Science and Engineering: C, 78*, 324–332. https://doi.org/10.1016/j.msec.2017.04.084

Lv, H., Zhao, M., Li, Y., Li, K., Chen, S., Zhao, W., Wu, S., & Han, Y. (2022). Electrospun chitosan–polyvinyl alcohol nanofiber dressings loaded with bioactive ursolic acid promoting diabetic wound healing. *Nanomaterials, 12*(17), 2933. https://doi.org/10.3390/nano12172933

M. M. R., & Ming, L. C. (2021). A review of ethnobotany, phytochemistry, antimicrobial pharmacology and toxicology of Nigella sativa L. *Biomedicine & pharmacotherapy = Biomedecine & pharmacotherapie*, *143*, 112182. https://doi.org/10.1016/j.biopha.2021.112182

Pathak, H., Pathania, S., Metha, S., & Sharma, R. (2023). Cedrus deodara (Roxb.): A review on the recent update on its pharmacological and phytochemical profile. *RPS Pharmacy and Pharmacology Reports, 2*(3), rqad026. https://doi.org/10.1093/rpsppr/rqad026

Rastegari, A., Manayi, A., Akbarzadeh, T., Hojjatifard, R., Samadi, N., Khanavi, M., Niknam, S., & Saeedi, M. (2023). *Cedrus deodara: In Vivo* Investigation of Burn Wound Healing Properties. *Evidence-based complementary and alternative medicine: eCAM*, *2023*, 5596964. https://doi.org/10.1155/2023/5596964

Tumen, I., Akkol, E. K., Süntar, I., & Keleş, H. (2011). Wound repair and anti-inflammatory potential of essential oils from cones of Pinaceae: preclinical experimental research in animal models. *Journal of ethnopharmacology*, *137*(3), 1215–1220. https://doi.org/10.1016/j.jep.2011.07.046

Yadav, S., Mishra, A., Kumar, S., Negi, A., Asha, & Maurya, V. (2021). Herbal wound healing agents. In *Preparation of Phytopharmaceuticals for the Management of Disorders: The Development of Nutraceuticals and Traditional Medicine* (pp. 169-184). Elsevier. https://doi.org/10.1016/B978-0-12-820284-5.00007-1

CHEMISTRY

Analytical Chemistry

Biochemistry

Drug Design & Drug Delivery (Computational and Experimental)

Energy Materials (Synthesis, Characterizations, Applications)

Inorganic Chemistry

Nanochemistry

Organic Chemistry

Physical Chemistry

Nanotechnology, Surface Coatings and Films

Polymer Chemistry

Method Development and Validation for Simultaneous Determination of Six Nitrosamines in Different Pharmaceutical Dosage Forms by GC-MS/MS Equipped with Headspace

Hayriye Icin[a,b], Hasan Tunel[b], Hakan Akbiyik[b], Gonul Kayar[b], Nevin Oztekin[a]

[a] Istanbul Technical University, Faculty of Science, Chemistry Department, Istanbul, Türkiye
[b] Abdi Ibrahim Pharmaceuticals R&D Center, Istanbul, Türkiye
icin20@itu.edu.tr

Keywords : Analytical Method, GC-MS/MS Headspace, N-nitrosamines, Pharmaceutical Dosage Forms.

Aim

Drug substances, which are used in drug products, are obtained via organic synthesis including reaction mechanisms. Reactive chemicals, reagents, solvents, catalysts and other excipients are used in the synthesis of drug substances. Due to degradation reactions during or after chemical synthesis result of using these ingredients, impurities can occur in all drug substances and related drug products. Qualification and quantification of these impurities has great importance to provide safety and efficacy of the drug products. The Threshold of Toxicological Concern (TTC) has been developed to identify a common exposure concentration for any chemical that does not have any information about its carcinogenicity or other toxic effects. However, some structural groups have been determined to have a theoretically significant carcinogenic risk potential even at intakes below the TTC (ICH M7, 2023). N-nitrosamines, members of "cohort of concern", are also classified as probable human carcinogens by the International Agency for Research on Cancer (IARC) (Wu et al, 2015). These compounds can originate from sources such as environmental water, food, textiles, tobacco, pesticides, plastics, cosmetics or veterinary drugs and human medicines. The presence of nitrosamines in drug substances and drug products may be caused by solvents, starting materials, processing water, excipients and degradation of substances or cross-contamination in multi-purpose facilities (Witkowska, Giebułtowicz, Dabrowska and Stolarczyk, 2022). The aim of this study is development and validation, an analytical method which can be used for determination of N-nitrosamines (NDMA, NDEA, NEIPA, NDIPA, NMPA, NDBA) in different pharmaceutical dosage forms without any matrix effect.

Material and Method

In this study, three pharmaceutical dosage forms used as suspension, emulsion and film coated tablet. The analytical method was developed by GC-MS/MS instrument equipped with Headspace module. An Agilent VF-WAXMS column is a high-performance polyethylene glycol column designed for GC/MS applications especially where trace analyses are required was used during analysis, which has 30 m length, 0.25 mm diameter and 1µm pore size. Helium was used as carrier gas. Water, Methanol and Sodium Carbonate were used as diluent and reagent during analysis.

For MSMS method parameters, dMRM (dynamic Multiple Reaction Monitoring) mode was selected to scan a wide range of m/z for providing detection of N-nitrosamines with the same chromatographic conditions.

Nitrosamine standards were supplied in solid form, including NDMA, NDEA, NEIPA, NDIPA, NMPA and NDBA. Individual stock standard solutions were prepared in Methanol in 250 µg/mL concentration from each nitrosamine standard. Internal standards (isotope-labelled nitrosamines) were supplied as liquid form in Methanol in 1000 ppm concentration, including NDMA-D6, NDEA-D10, NDIPA-D14, NMPA-D5 and NDBA-D18. Stock internal standard solution was prepared diluting from internal standards in 500 ng/mL concentration and diluted internal standard solution was prepared by diluting from stock internal standard solution in 50 ng/mL concentration with water. Final solution concentrations were adjusted as 1.92 ng/mL for NDMA, 0.53 ng/mL for NDEA, 8.0 ng/mL for NEIPA, 30.0 ng/mL for NDIPA, 2.0 ng/mL for NMPA, 0.53 ng/mL for NDBA and 2.0 ng/mL for each internal standard.

Three different pharmaceutical dosage forms were used for the analytical method development and validation studies. Product A is a suspension, Product B is an emulsion and Product C is a film coated tablet form. Placebos

were used for each pharmaceutical dosage form which were formulated without active ingredients. Sample solutions were prepared in 0.08 mg/mL concentration for Product A, 0.002 mg/mL concentration for Product B and 3.2 mg/mL concentration for Product C and, placebo solutions were prepared same as products. Internal standard solution was added into all solutions in 2.0 ng/mL concentration for each internal standard. Nitrosamines spiked sample solutions were prepared by adding stock standard mixture solution into the product solutions including internal standards. Blank solution, placebo solutions for each pharmaceutical product, standard solutions, sample solutions and nitrosamines spiked sample solutions were injected respectively.

In order to determine optimized method parameters, design of experiment (DoE) was applied by Minitab program. Scope of experimental design, oven temperature, vial equilibration time and vial pressure parameters were selected as factors. Full factorial design was applied, and peak areas and RSD values of nitrosamines were compared individually and cross-relatedly.

Method validation was performed with the parameters of specificity, limit of detection and limit of quantification, linearity and range, system precision, repeatability, intermediate precision, accuracy and recovery, robustness as changes in chromatographic method parameters and solution stability.

Findings

Nitrosamines were not detected in blank, placebo and sample solutions for Product A, B and C for batch analysis. Therefore, nitrosamines spiked sample solutions were used during method validation study for all parameters.

In the specificity study, it was seen that there was no interfering peak in blank and placebo solutions which had same m/z value with nitrosamine and internal standard peaks in standard, sample and nitrosamines spiked sample solutions. For LOD and LOQ determination, six consecutive injections were applied, concentrations were calculated via s/n, and RSD% (relative standard deviation) obtained less than 15.0% for six nitrosamines. According to obtained linearity results, the method was found linear in the concentration range of LOQ-150% level with a correlation coefficient more than 0.99 for all nitrosamines. System precision, repeatability and intermediate precision were evaluated according to RSD% values with the limit as not more than 15.0%. Accuracy results were found between 70.0-130.0% at LOQ, 100% and 150% levels. For robustness parameter, nitrosamine results obtained from changes in method parameters were compared to repeatability results and absolute differences were calculated and it was shown that analytical method is robust against to changes. And solution stability was shown for six nitrosamines during 68 hours for standard, placebo, sample and nitrosamine spiked sample solutions for three tested pharmaceutical finished products.

Conclusion

GC-MS/MS equipped with Headspace (HS) module provides significant advantages in terms of efficient analytical method for determination of nitrosamines because of avoiding matrix effect for various dosage forms of pharmaceutical drug products. Suitable HS parameters make it possible to analyze six nitrosamines simultaneously in drug products even for trace levels.

This study aimed to obtain effective results in less time by adapting more dosage forms to the same analytical method, with common linearity and LOD & LOQ parameters and applied successfully according to the results obtained from all validation parameters for six nitrosamines.

References

ICH M7: Assessment and Control of DNA Reactive (Mutagenic) Impurities in Pharmaceuticals to Limit Potential Carcinogenic Risk, https://database.ich.org/sites/default/files/ICH_M7%28R2%29_Guideline_Step4_2023_0216_0.pdf, data retrieved 17.05.2025.

Witkowska, A. B., Giebułtowicz, J., Dabrowska, M., Stolarczyk, E. U. (2022). International Journal of Molecular Sciences. Development of a Sensitive Screening Method for Simultaneous Determination of Nine Genotoxic Nitrosamines in Active Pharmaceutical Ingredients by GC-MS (Vol. 23, p.12125).

Wu, Q., Shi, H., Ma, Y., Adams, C., Jiang, H., Wang, J., Eichholz, T., Timmons, T. (2015). Separation and Purification Technology. Removal of N-nitrosamine precursors in drinking water system using adsorption methods (Vol. 156, pp.972–979).

CHEMISTRY

Analytical Chemistry

Biochemistry

Drug Design & Drug Delivery (Computational and Experimental)

Energy Materials (Synthesis, Characterizations, Applications)

Inorganic Chemistry

Nanochemistry

Organic Chemistry

Physical Chemistry

Nanotechnology, Surface Coatings and Films

Polymer Chemistry

Preparation of Peptide-GelMA Composite Hydrogel-Based Wound Dressing with 3D Printer and Its Physical Characterization

Dilay Yıldız[a], Ahmet Oğuzhan Paksoy[a], Ali Alparslan Çelik[b], Esra Pilavcı[b], Oğuzhan Gündüz[b], Onur Alptürk[a]

[a] Istanbul Technical University, Faculty of Science and Letters, Department of Chemistry, Türkiye
[b] Marmara University, Faculty of Technology, Department of Metallurgical and Materials Engineering, Türkiye
yildizd23@itu.edu.tr

Keywords: 3D Bioprinting, DLP, GelMA, Peptide-Based Hydrogels, Wound Dressings.

Wound healing requires a wound dressing that protects the wound bed to support skin regeneration and accelerate healing (Obagi et al., 2019). Wound dressing is a sterile compress acting as a barrier to protect the injured epidermal tissues from the outside and promote healing (Fahimirad & Ajalloueian, 2019). These dressings ideally should keep the wound moist to support wound healing, provide oxygen permeability, be biocompatible with the skin and be antibacterial to prevent infection (Liang et al., 2022).

Traditional wound dressings, such as gauzes, plasters, and bandages, remain widely used today due to their affordability and easy accessibility. However, they come with several drawbacks, including inadequate adhesion, insufficient absorption of wound exudate, and the need for frequent changes, which can cause discomfort and pain. More importantly, they often fail to provide adequate wound drainage (Brumberg et al., 2021). Therefore, there is a growing need for novel wound dressings.

Hydrogels are the current choice for the development of modern wound dressings. They can be described as intricate three-dimensional structures composed of hydrophilic polymer chains, exhibiting a quick swelling response upon contact with water. More than 90% of the hydrogel framework consists of water, forming a partially solid material that enables it to maintain a moist environment at the wound surface and facilitate tissue repair. Hydrogels possess numerous properties that make them ideal for wound dressings, including firm adhesion, shape adaptability, and mechanical protection, ensuring sufficient wound coverage. Additionally, hydrogel-based dressings are highly tuneable, allowing the incorporation of antibacterial and antimicrobial agents, cells, biomolecules, and growth factors (Gounden & Singh, 2024).

Some other polymers such as chitosan, alginate, and cellulose are frequently integrated in hydrogels. However, these materials suffer from certain setbacks. As such, they require covalent cross-linking agents for gelation, which can damage biocompatibility and biodegradability. Some of them have very low mechanical strength, lower porous structure, poor cell adhesion, deficient oxygen vapour permeability, poor stability and very poor water solubility. They are also not prone to controlled variability due to their complex and variable composition. These limitations can hinder the effectiveness of those polymers in hydrogel applications (Elango et al., 2023).

To overcome this problem, the most suitable biopolymer to be preferred as the main component of hydrogels is peptides. By changing peptide sequences, concentration and external stimuli, the stiffness, flexibility and durability of the hydrogel can be tuned (Clarke et al., 2018). Compared to conventional polymeric hydrogels, peptide hydrogels have several advantages, such as controllable structure and assembly, stimuli responsivity, biocompatibility, biodegradability, ease of modification, and specific biological activity (Liu et al., 2019; Sedighi et al., 2023) Peptide hydrogels can be combined with antimicrobial agents to reduce the risk of infection and support the healing process. Additionally, hydrogels with antimicrobial properties can be synthesized by incorporating antimicrobial peptides (Zhu et al., 2024).

Aim

The use of peptide hydrogels as a base material for wound dressings is a relatively recent development in the literature. Leveraging the advantages of peptides, our goal is to design a highly biocompatible GelMA-based composite hydrogel with antimicrobial properties and to fabricate it using Digital Light Processing (DLP) 3D printing. DLP was selected for its high resolution, rapid printing capabilities, and ability to produce intricate

structures with fine details while maintaining a biocompatible and cell-friendly environment. To enable photocrosslinking essential for DLP printing, improve mechanical strength, and enhance stability, gelatin methacryloyl (GelMA) was incorporated into the hydrogel formulation.

Material and Method

In this hydrogel, Ac-Ile-Val-Phe-Lys-NH_2 (IVFK) peptide, originally reported by Alshehri et al. (2021) was of choice because of its self-assembly ability in solution and high hydrogelation property. This peptide was synthesized by solid phase peptide synthesis (SPPS) method on Rink Amide resin. Initially, 150 mg Rink Amide resin was added to the column, swollen in DMF and then washed. The Fmoc protecting group was removed using 20% (v/v) piperidine/DMF. Subsequently, each amino acid (Lysine, Phenylalanine, Valine, Isoleucine) was dissolved in DMF, activated with HBTU, and basified with DIPEA. The amino acids were sequentially coupled to the resin. After each step, the resin was capped with acetic anhydride, pyridine, and DMF to block unreacted sites. Once the final amino acid was attached, the Fmoc group was removed, and the resin was washed with DMF and DCM, then dried under vacuum. The peptide was cleaved from the resin by using TFA (95%), TIPS (2.5%), and H_2O (2.5%) mixture. The crude product was collected, and residual solvents were removed under reduced pressure. The synthesized peptide was purified using reverse-phase preparative High-Performance Liquid Chromatography (HPLC) to achieve high purity. Following purification, the peptide was characterized using Mass Spectrometry (MS) to confirm its molecular weight.

Then GelMA, which has the acrylate-tipped structure required for printing on a DLP 3D printer and increases the mechanical strength of the hydrogel when combined with the peptide, was synthesized through the reaction of gelatin with methacrylic anhydride (MAA) under carefully regulated alkaline conditions, which allowed for an accurate degree of functionalization. The reaction was conducted at a constant temperature with continuous stirring to promote homogeneous modification. Then, extensive dialysis against deionized water was performed to eliminate unreacted MAA and byproducts. The resulting purified GelMA was then lyophilized, yielding a stable hydrogel precursor that is photo-cross-linkable and possesses improved mechanical strength with adjustable viscoelastic characteristics.

The bioink was formulated by initially dissolving the IVFK peptide in ultrapure water. Then, a few drops of 0.5 M NaOH solution were added, and the mixture was titrated with 0.1 M HCl solution until the pH reached ~7.4. The total volume was then adjusted to 1 mL using 0.1 M PBS. Separately, 200 mg of GelMA was dissolved in 2 mL of PBS, with stirring conducted at 60°C and 100 rpm, while the beaker was entirely covered with aluminium foil. Once the GelMA was fully dissolved, the previously prepared peptide solution was incorporated. Finally, 10 mg of LAP (photoinitiator) was added to improve the printability and stability of the hydrogel after the temperature was reduced to 40°C. The mixture was then stirred at 40°C and 100 rpm, thereby completing the preparation of the hydrogel.

The prepared hydrogel was transferred into the vat of the 3D DLP printer (Phrozen Sonic Mighty 14K Revo), and a design file in .ctb format was selected. Multiple printing trials were conducted under 405 nm UV light to optimize

the exposure time. Once the optimal exposure time was determined, ensuring the ideal hydrogel structure, printing was repeated using this parameter (Figure 1).

The printed hydrogel was then stored at 4°C. The printing parameters were carefully optimized to ensure compatibility with DLP technology, which provides precision in 3D printing. Finally, the printed hydrogels were

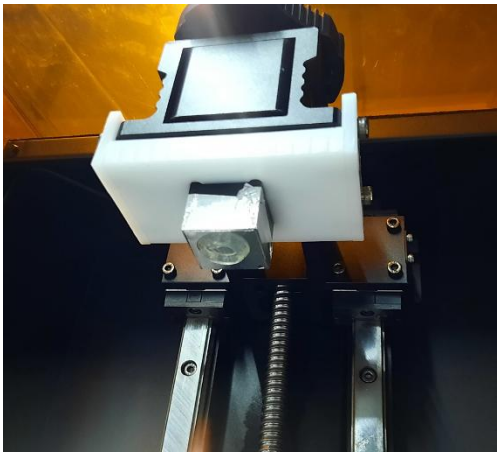

characterized using Fourier Transform Infrared Spectroscopy (FTIR) and Scanning Electron Microscopy (SEM).

Findings

The IVFK peptide was successfully purified using reverse-phase preparative HPLC. The purified peptide was then analyzed by LC-MS, confirming that its molecular weight matched the expected value (Figure 2). This result verifies the success of both the peptide synthesis and purification processes.

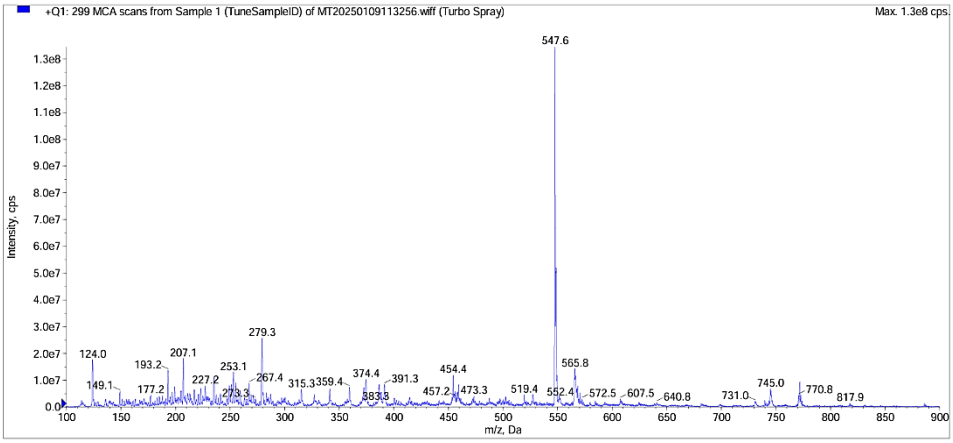

Figure 2. LC-MS spectrum of IVFK peptide.

The successful synthesis of GelMA enabled the formation of a hydrogel suitable for bioprinting, exhibiting structural integrity and maintaining its intended geometry after printing. The incorporation of the peptide/GelMA composition in the bioink contributed to the hydrogel's structural stability. The 3D-printed hydrogel demonstrated

stability and precise shape fidelity, indicating the appropriateness of the selected bioprinting parameters (Figure 3).

Figure 3. The printed peptide/GelMA composite hydrogel.

FTIR spectra of the IVFK/GelMA composite hydrogel, as shown in Figure 4, exhibited a broad absorption band at 3334 cm^{-1}, corresponding to the O–H and N–H stretching vibrations, indicative of hydrogen bonding interactions in the solid state. The strong peak at 1631 cm^{-1} is attributed to the amide I (C=O stretching), while the bands at 1546 cm^{-1} and 1463 cm^{-1} correspond to amide II and C–H bending vibrations, respectively. Notably, the amide I peak at 1631 cm^{-1} suggests β-sheet formation, a characteristic secondary structure of self-assembling peptides, which plays a crucial role in hydrogel stability. Additionally, the peak at 1245 cm^{-1} corresponds to C–N stretching and N–H bending (amide III), consistent with the presence of GelMA. These findings confirm the successful formation of a structurally integrated hydrogel.

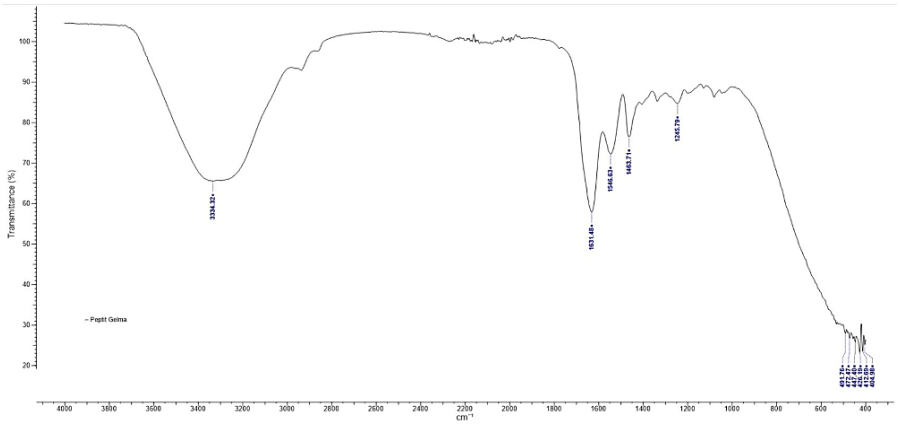

Figure 4. FTIR spectrum of the hydrogel.

SEM image, as seen in Figure 5, reveal a smooth, uniform and well-integrated hydrogel structure with preserved interlayer integrity and a compact surface, indicating successful polymerization under optimal crosslinking and curing conditions. Also, the porosity of wound dressing is relatively low, indicating dense, highly crosslinked structures. This well-defined morphology, minimal surface defects, and absence of phase separations confirm the homogeneous distribution of the polymer network and the structural stability of the hydrogel.

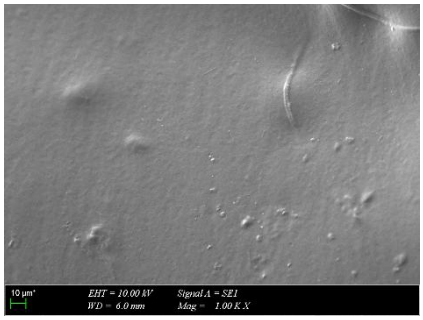

Figure 5. SEM image of the hydrogel.

Conclusion

The hydrogel was successfully printed using DLP 3D printing technology, allowing precise control over its structure and mechanical characteristics. The printed hydrogel exhibited an interconnected porous structure, likely stabilized by the combination of peptide self-assembly and cross-linking interactions.

In conclusion, preliminary results indicate that the development of peptide-based hydrogels in combination with GelMA presents significant advantages in biomaterial design by providing enhanced mechanical stability and tunable degradation rates. The integration of DLP 3D printing technology enables the fabrication of customized structures with precision and reproducibility, while also maintaining biocompability. The ability to fine-tune porosity, alongside the antimicrobial potential of peptide/GelMA hydrogels, underscores their promise as innovative modern wound dressing materials.

In the later stages of the study, the optimized methodology will be applied to another peptide with antimicrobial properties to expand its potential biomedical applications further.

References

Alshehri, S., Susapto, H. H., & Charlotte. (2021). Scaffolds from self-assembling tetrapeptides support 3D spreading, osteogenic differentiation, and angiogenesis of mesenchymal stem cells. Biomacromolecules, 22(5), 2094–2106.

Brumberg, V., Astrelina, T., Malivanova, T., & Samoilov, A. (2021). Modern wound dressings: Hydrogel dressings. Biomedicines, 9(9), 1235.

Clarke, D. E., Parmenter, C. D. J., & Scherman, O. A. (2018). Tunable pentapeptide self-assembled β-sheet hydrogels. Angewandte Chemie International Edition, 57(26), 7709–7713.

Elango, J., Zamora-Ledezma, C., & Maté-Sánchez de Val, J. E. (2023). Natural vs synthetic polymers: How do they communicate with cells for skin regeneration—A review. Journal of Composites Science, 7(9), 385.

Fahimirad, S., & Ajalloueian, F. (2019). Naturally-derived electrospun wound dressings for target delivery of bio-active agents. International Journal of Pharmaceutics, 566, 307–328.

Liang, Y., Liang, Y., Zhang, H., & Guo, B. (2022). Antibacterial biomaterials for skin wound dressing. Asian Journal of Pharmaceutical Sciences, 17(3), 353–384.

Liu, C., Zhang, Q., Zhu, S., Liu, H., & Chen, J. (2019). Preparation and applications of peptide-based injectable hydrogels. RSC Advances, 9(48), 28299–28311.

Obagi, Z., Damiani, G., Grada, A., & Falanga, V. (2019). Principles of wound dressings: A review. Surgical Technology International, 35, 50–57.

Sedighi, M., Shrestha, N., Mahmoudi, Z., Khademi, Z., Ghasempour, A., Dehghan, H., Talebi, S. F., Toolabi, M., Préat, V., Chen, B., Guo, X., & Shahbazi, M.-A. (2023). Multifunctional self-assembled peptide hydrogels for biomedical applications. Polymers, 15(5), 1160–1160.

Varshan Gounden, & Singh, M. (2024). Hydrogels and wound healing: Current and future prospects. Gels, 10(1), 43–43.

Zhu, J., Cheng, H., Zhang, Z., Chen, K., Zhang, Q., Zhang, C., Gao, W., & Zheng, Y. (2024). Antibacterial hydrogels for wound dressing applications: Current status, progress, challenges, and trends. Gels, 10(8), 495–495.

Preparation of 3D-Printed Peptide-Based Hydrogel Wound Dressing with GHK-Cu for Chronic Wound Treatment

Ahmet Oğuzhan Paksoy[a], Dilay Yıldız[a], Ali Alparslan Çelik[b], Ayşe Ceren Çalıkoğlu Koyuncu[b], Oğuzhan Gündüz[b], Onur Alptürk[a]

[a]Istanbul Technical University, Faculty of Science and Letters, Department of Chemistry, Türkiye
[b]Marmara University, Faculty of Technology, Metallurgical and Materials Engineering Department, Türkiye
paksoya17@itu.edu.tr

Keywords: 3D Bioprinting, Peptide-Based Bioinks, Chronic Wound Healing, Peptide-Based Hydrogel Wound Dressings, GHK-Cu.

Wound healing is a complex and dynamic process requiring an optimal tissue regeneration environment. An ideal wound dressing should maintain moisture, allow gas exchange, promote angiogenesis, prevent infections, and be biocompatible (Dhivya et al., 2015). Traditional wound dressings, such as gauze and foams, primarily serve as passive barriers, whereas modern wound dressings, including hydrogels, hydrocolloids, and bioactive dressings, actively contribute to the healing process. Hydrogels, in particular, provide a moist environment, support tissue regeneration, and enable controlled drug delivery. Functionalizing hydrogels with bioactive molecules, such as peptides, further enhances their therapeutic potential in wound healing (Koehler et al., 2018).

In recent years, peptides, including self-assembling and bioactive sequences, offer several advantages over conventional biopolymers and they are widely used in wound dressings. Their well-defined molecular structures allow precise tuning of their biochemical properties, while their ability to interact with cellular receptors makes them highly effective in modulating wound healing pathways. Self-assembling peptides can form nanofibrous hydrogels that provide structural support for cell attachment and migration (Alshehri et al., 2021). Compared to larger biopolymers, peptides offer superior control over degradation rates, reduced immunogenicity, and enhanced bioactivity at lower concentrations (Dong & Guo, 2021).

The major challenge in wound care is the limited effectiveness of conventional dressings in treating chronic wounds. Chronic wounds impose a significant burden on healthcare systems due to their prolonged healing process, high susceptibility to infections, and limited treatment options. In addition to providing a protective barrier, wound dressings are essential for maintaining an optimal environment that supports tissue regeneration. Among various wound dressing materials, hydrogels have emerged as promising candidates due to their high water content, excellent biocompatibility, and ability to mimic the extracellular matrix (ECM), thereby supporting cellular adhesion, proliferation, and differentiation (Liang et al., 2021).

A promising approach to addressing this challenge is the development of peptide-based wound dressings, incorporating bioactive peptides like GHK (Gly-His-Lys). GHK is a bioactive tripeptide with strong regenerative properties, making it an ideal candidate for wound healing applications (Pickart, 2008). It has been shown to enhance cell proliferation, stimulate angiogenesis, and regulate inflammation, all of which contribute to efficient tissue regeneration. Additionally, GHK plays a crucial role in ECM remodelling by promoting collagen synthesis and fibroblast activation. Studies have demonstrated that GHK also exhibits antioxidant properties, reducing oxidative stress and improving cellular resilience in damaged tissues (Lee et al., 2023). Furthermore, the copper-complexed form of GHK, known as GHK-Cu, has been identified as a potent wound-healing agent with enhanced biological activity. GHK-Cu plays a critical role in tissue repair by stimulating the production of collagen, elastin, and glycosaminoglycans while also upregulating genes associated with skin regeneration. Additionally, GHK-Cu enhances angiogenesis through vascular endothelial growth factor (VEGF) activation and contributes to reducing inflammation by modulating cytokine activity, thereby improving fibroblast proliferation and promoting collagen remodelling (Pickart & Margolina, 2018). These properties make GHK-Cu an attractive candidate for integration into bioactive wound dressings for the effective treatment of chronic wounds.

To fully harness the therapeutic potential of peptide-functionalized hydrogels, advanced fabrication techniques such as digital light processing (DLP) bioprinting are required to achieve precise structural control and optimize their biological performance. DLP is a high-precision 3D printing technique that offers significant advantages for fabricating wound dressings. Unlike conventional hydrogel preparation methods, DLP enables the rapid and accurate fabrication of complex structures with fine resolution and tunable mechanical properties (Zhou et al., 2024). One of the major advantages of DLP over other 3D printing techniques is its ability to create highly customized wound dressings with intricate geometries, ensuring precise fitting for irregular wound surfaces (Hu et al., 2024). Also, one of the advantages of this technique over its traditional counterparts is the ability to integrate multiple functional materials such as bioactive peptides into a single construct (Joshi et al., 2023).

Aim

In this study, we aim to prepare a wound dressing from peptide-GelMA composite hydrogel for the treatment of chronic wounds. For this, the peptide IVFK was chosen as it spontaneously self-assembles to a stable hydrogel in the aqueous milieu. The wound dressing made of IVFK peptide and GelMA was printed using a DLP 3D printer. Subsequently, GHK-Cu peptide was encapsulated into PLA microparticles and electrosprayed onto the printed hydrogel wound dressing. The chronic wound healing potential of the fabricated GHK-Cu encapsulated wound dressing was evaluated through biological assessments.

Material and Method

The IVFK peptide was synthesized according to the Fmoc-based solid-phase peptide synthesis (SPPS) technique with Rink Amide resin. The peptide was then purified via reverse-phase preparative high-performance liquid chromatography (HPLC) and characterized through mass spectrometry (MS).
GelMA was prepared by reacting gelatin with methacrylic anhydride (MAA) under controlled alkaline conditions, ensuring a precise degree of functionalization. The reaction was maintained at a constant temperature with continuous stirring to facilitate homogeneous modification, followed by extensive dialysis against deionized water to remove unreacted MAA and byproducts. The purified GelMA was then lyophilized to obtain a stable, photo-cross-linkable hydrogel precursor with enhanced mechanical integrity and tunable viscoelastic properties. When GelMA and the synthesised IVFK peptide were combined, a targeted hydrogel formulation was obtained. Then, this was loaded into a 3D printer (Phrozen 14K REVO) for DLP printing, resulting in the fabrication of peptide-based wound dressings (Figure 1).

Figure 1. 3D printing process of the peptide-based hydrogel wound dressing.

The encapsulation process of GHK-Cu into the fabricated hydrogel wound dressings was performed using an electrospraying technique (Figure 2), based on the methodology described by Taşcı et al. (2021). First, a polyvinyl alcohol (PVA) solution was prepared in 20 mL of dichloromethane (DCM) following the parameters optimized in the referenced study. Separately, a GHK-Cu solution was prepared by dissolving the peptide in ethanol before mixing it into the PVA solution. The resulting mixture was drawn into a 10 mL syringe and loaded into the

electrospraying pump (IPS-12, Inovenso). The electrospraying was performed at an applied voltage of 18 kV, a nozzle-to-substrate distance of 15 cm, and a flow rate of 20 µL/min. A previously fabricated 3D-printed GelMA-IVFK composite hydrogel wound dressing was positioned beneath the nozzle to facilitate uniform deposition. The electrospraying process was carried out for 30 minutes to ensure effective encapsulation of GHK-Cu onto the hydrogel surface (Figure 3). The results were evaluated through an optical microscope. (Olympus - Colorview) In addition to this approach, an alternative encapsulation method was also employed. Using the same electrospraying parameters, GHK-Cu was first dissolved in ethanol and then mixed into a PLA solution prepared in DCM. This mixture was electrosprayed directly onto an empty petri dish to generate microcapsules. Following the electrospraying process, the microcapsules were collected and dissolved in PBS. The resulting suspension was then incorporated into the bioink formulation alongside the GelMA-IVFK hydrogel during the 3D printing process. This method aimed to enhance the integration of encapsulated GHK-Cu within the hydrogel matrix, ensuring more effective and sustained release of the peptide within the wound dressing.

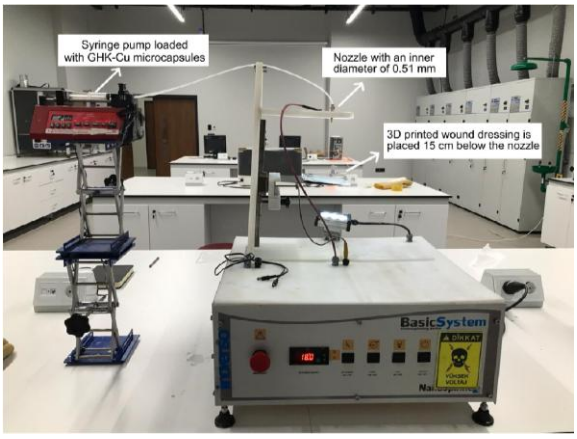

Figure 2. Electrospraying setup.

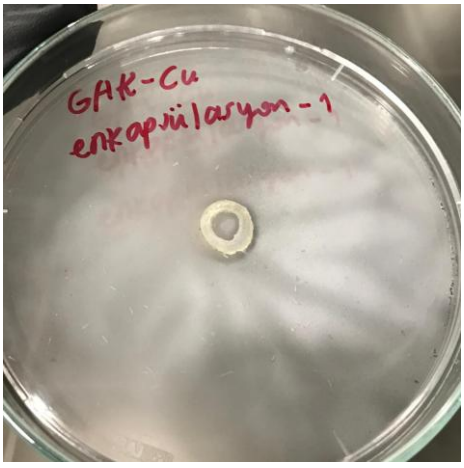

Figure 3. Encapsulated GHK-Cu onto the peptide-based hydrogel wound dressing.

The cytocompatibility of the produced GHK-Cu encapsulated GelMA-IVFK composite hydrogel wound dressings was evaluated using human dermal fibroblasts (HDF). Cell viability and attachment were assessed through MTT assays and fluorescence microscopy. The scaffolds were seeded with HDFs and incubated under standard culture conditions. Following incubation, MTT assays were performed to quantify cell metabolic activity, while fluorescence microscopy was used to visualize cell adhesion, morphology and proliferation on the hydrogel surface.

Findings

The IVFK peptide was efficiently synthesized and purified using reverse-phase preparative HPLC, with its identity confirmed by LC-MS characterization (Figure 4). GelMA was successfully synthesized and when combined with the peptide in solution, it formed a hydrogel with optimal viscosity for DLP-based 3D printing. This hydrogel was then effectively printed to fabricate hydrogel-based wound dressings, demonstrating its suitability for advanced wound healing applications (Figure 5).

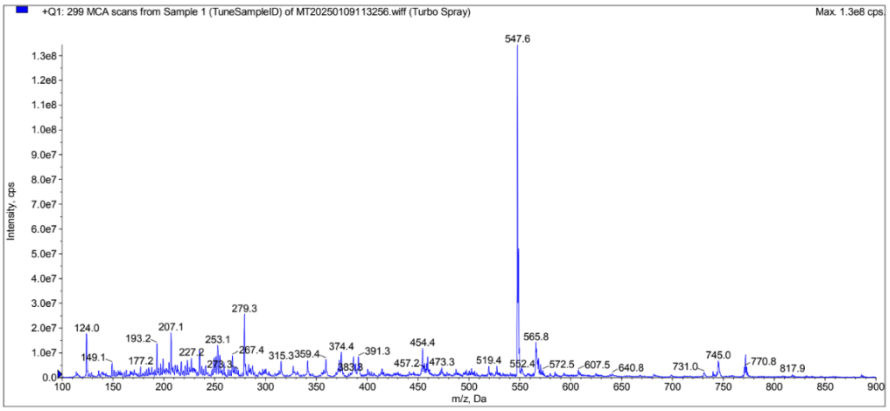

Figure 4. Mass spectrum of the synthesised IVFK peptide.

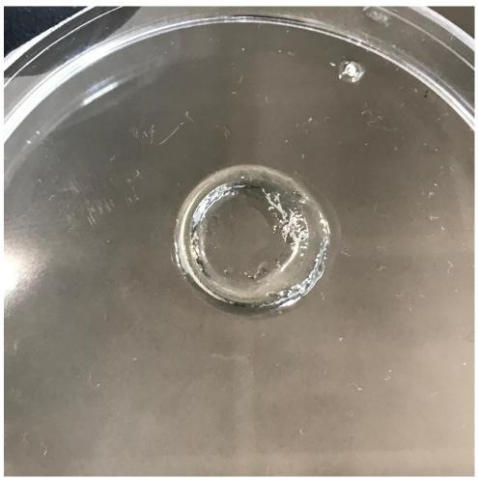

Figure 5. 3D printed peptide-based hydrogel wound dressing.

The encapsulation of GHK-Cu via electrospraying yielded successful results and the optimization of the process further enhanced the integration of encapsulated GHK-Cu into the produced wound dressing. Optical microscopy analyses confirmed uniform deposition without significant aggregation. Cytocompatibility studies demonstrated strong fibroblast attachment and proliferation, while MTT assays verified high cell viability. Additionally, fluorescence microscopy revealed that the cells maintained their normal morphology. These findings confirm the synthesis, fabrication, and functionalization of peptide-based wound dressing, highlighting their strong potential for chronic wound healing applications.

Conclusion

In light of the findings, this study successfully developed and characterized a novel peptide-functionalized hydrogel wound dressing from GelMA and IVFK, fabricated via DLP bioprinting. The incorporation of GHK-Cu through electrospraying enhanced the bioactivity of the hydrogel, making it a promising candidate for chronic wound healing applications. The efficient synthesis of the peptides, along with the fabrication of the hydrogel wound dressings, demonstrated excellent cytocompatibility, with favorable cell attachment and proliferation. Overall, the results highlight the potential of this peptide-functionalized hydrogel system in accelerating wound

healing, offering a customizable and bioactive solution for tissue regeneration. Further studies will focus on encapsulating other biologically active molecules into this 3D-printed hydrogel wound dressing.

References

Alshehri, S., Susapto, H. H., & Hauser, C. A. E. (2021). Scaffolds from self-assembling tetrapeptides support 3D spreading, osteogenic differentiation, and angiogenesis of mesenchymal stem cells. Biomacromolecules, 22(5), 2094–2106. https://doi.org/10.1021/acs.biomac.1c00205

Dhivya, S., Padma, V. V., & Santhini, E. (2015). Wound dressings - a review. BioMedicine, 5(4), 22. https://doi.org/10.7603/s40681-015-0022-9

Dong, R., & Guo, B. (2021). Smart wound dressings for wound healing. Nano Today, 41, 101290. https://doi.org/10.1016/j.nantod.2021.101290

Hu, Y., Tang, H., Xu, N., Kang, X., Wu, W., Shen, C., Lin, J., Bao, Y., Jiang, X., & Luo, Z. (2024). Adhesive, flexible, and fast degradable 3D-printed wound dressings with a simple composition. Advanced Healthcare Materials, 13(3), e2302063. https://doi.org/10.1002/adhm.202302063

Joshi, A., Kaur, T., Joshi, A., Gugulothu, S. B., Choudhury, S., & Singh, N. (2023). Light-mediated 3D printing of micro-pyramid-decorated tailorable wound dressings with endogenous growth factor sequestration for improved wound healing. ACS Applied Materials & Interfaces, 15(1), 327–337. https://doi.org/10.1021/acsami.2c16418

Koehler, J., Brandl, F. P., & Goepferich, A. M. (2018). Hydrogel wound dressings for bioactive treatment of acute and chronic wounds. European Polymer Journal, 100, 1–11. https://doi.org/10.1016/j.eurpolymj.2017.12.046

Lee, S., Lee, S. M., Lee, S. H., Choi, W. K., Park, S. J., Kim, D. Y., Oh, S. W., Oh, J., Cho, J. Y., Lee, J., Chien, P. N., Nam, S. Y., Heo, C. Y., Lee, Y. S., Kwak, E. A., & Chung, W. J. (2023). In situ photo-crosslinkable hyaluronic acid-based hydrogel embedded with GHK peptide nanofibers for bioactive wound healing. Acta Biomaterialia, 172, 159–174. https://doi.org/10.1016/j.actbio.2023.10.011

Liang, Y., He, J., & Guo, B. (2021). Functional hydrogels as wound dressing to enhance wound healing. ACS Nano, 15(8), 12687–12722. https://doi.org/10.1021/acsnano.1c04206

Pickart, L. (2008). The human tri-peptide GHK and tissue remodeling. Journal of Biomaterials Science, Polymer Edition, 19(8), 969–988. https://doi.org/10.1163/156856208784909435

Pickart, L., & Margolina, A. (2018). Regenerative and protective actions of the GHK-Cu peptide in the light of the new gene data. International Journal of Molecular Sciences, 19(7), 1987. https://doi.org/10.3390/ijms19071987

Taşcı, M. E., Dede, B., Tabak, E., Gur, A., Sulutaş, R. B., Cesur, S., İlhan, E., Lin, C.-C., Paik, P., Ficai, D., & et al. (2021). Production, optimization, and characterization of polylactic acid microparticles using electrospray with porous structure. Applied Sciences, 11(11), 5090. https://doi.org/10.3390/app11115090

Zhou, X., Yu, X., You, T., Zhao, B., Dong, L., Huang, C., Zhou, X., Xing, M., Qian, W., & Luo, G. (2024). 3D printing-based hydrogel dressings for wound healing. Advanced Science, 11(47), e2404580. https://doi.org/10.1002/advs.202404580

CHEMISTRY

Analytical Chemistry

Biochemistry

Drug Design & Drug Delivery (Computational and Experimental)

Energy Materials (Synthesis, Characterizations, Applications)

Inorganic Chemistry

Nanochemistry

Organic Chemistry

Physical Chemistry

Nanotechnology, Surface Coatings and Films

Polymer Chemistry

Synthesis and Characterization of Liposomal Formulations of Biguanide Derivative Active Pharmaceutical Ingredient

Sevgi Demiröz[a], Kader Poturcu[b]

[a]Süleyman Demirel University, Department of Chemistry, Graduate School of Natural and Applied Sciences, Türkiye
[b] Suleyman Demirel University, Department of Chemistry, Faculty of Engineering and Natural Science, Türkiye
kaderpoturcu@sdu.edu.tr

Keywords: Liposome, Biguanide Derivative API, Thin Film Hydration Method, Drug Delivery System, CTEM.

Aim

Liposomes are spherical structures that serve as drug-delivery vehicles. They consist of one or more lipid bilayers that encase an aqueous core, allowing for the encapsulation of various therapeutic agents, which are hydrophilic and hydrophobic (Liu et al., 2022). Liposomes demonstrate remarkable properties, including the ability to protect encapsulated drugs from physiological degradation (Bautzová et al., 2012), prolong the drugs' half-life, and regulate the release of drug molecules (Wang et al., 2009). Their excellent biocompatibility and safety profiles further enhance their appeal (Liu et al., 2022).
In this study, we synthesized a liposomal drug delivery system containing a biguanide derivative active pharmaceutical ingredient (API) using the thin-film hydration method under reduced pressure. The importance of the study is related to the that the cholesterol is widely used component during liposome synthesis. In this study, we aimed to use cholesterol-like compounds instead of cholesterol to synthesize liposomal formulation and investigate morphological structures of materials with High Contrast Transmission Electron Microscopy (CTEM). Additionally, the EE% and DL% values based on the calibration graph of the standard solution of the API, which exhibited a correlation coefficient (R^2) of 0.999, were calculated. The EE% values for F1, F2 and F3 were as follows: %98.15, %99.49 and %74.52. The % DL values in the same order for formulations were %1.85, %0.507 and %25.5, respectively.

Material and Method

1-Materials

The chemicals were acquired from the specified chemical companies as follows: L-alpha lecithin (Merck, Darmstadt, Germany), cholesterol-like component (Abcr, Karlsruhe, Germany), Methanol (Isolab, Germany), Trichloromethane (Isolab, Germany), biguanide derivative API (Merck, Darmstadt, Germany), buffer solution (Wisent, Canada).

2-Thin-film hydration method

Liposomal drug delivery systems were synthesized with the thin-film hydration method under reduced pressure with minor modifications to the literature (Thabet et al., 2022). Cholesterol-like structure: lecithin mixtures were dissolved in trichloromethane: methanol (3:1, v/v) organic solvent mixtures at three different ratios. After solution preparation, the mixture was evaporated at two hours and then the evaporation continued under reduced pressure with a vacuum pump (DRVAC300, Taiwan) to remove the all traces of the solvent and thin films were prepared (Torres-Flores et al., 2020). The thin- film was hydrated with buffer solution (pH 7.4) which contains dissolved biguanide derivative API and stirred 150 rpm for an hour at 40˚C. The drug loaded liposomal suspension was stored at 4˚C for further analyses.

3-Entrapment Efficiency

Drug-loaded liposomal formulations were ultracentrifuged at 14.000 rpm for 40 min to calculate percentage of Entrapment Efficiency (EE%) and Drug leakage (%DL). The supernatant was removed, and 1 ml buffer solution

was added to the Eppendorf tube that contains the pelleted part of the liposomal formulations and centrifuged again. The centrifugation steps were repeated three times. The supernatant taken at every step proceeded in UV-Vis spectrophotometer at the fixed wavelength of 233 nm to determine un-entrapped drug molecule in liposomal formulation using the following EE% and DL% equations (Kesharwani et al., 2021).

$$EE\% = \frac{amount\ of\ API\ added\ in\ liposome - amount\ of\ unentrapped\ API}{amount\ of\ API\ added\ in\ liposome} \times 100 \text{ (Eq.1.)}$$

$$DL\% = \frac{amount\ of\ API\ added\ in\ liposome - amount\ of\ unentrapped\ API}{total\ amount\ of\ liposomal\ formulation\ (drug+excepients)} \times 100 \text{ (Eq.2.) (Waghule et al., 2021)}$$

4-Characterization analysis

High Contrast Transmission Electron Microscopy (CTEM, FEI, Tecnai G2 Spirit Biotwin) containing LaB6 electron gun with an accelerating voltage of 20–120 kV was conducted on GEM loaded liposomes for imaging F1, F2 and F3 formulations. Ethanol diluted nanoparticles were dropped on carbon coated copper grids and let air-dried before imaging.

Findings

The selected biguanide derivative API has issues with gastrointestinal tolerance, a short half-life, and low bioavailability. To address these challenges, we synthesized liposomal drug delivery systems for this API using a cholesterol-like compound instead of cholesterol as a component of the liposome structure, as shown in Figure 1. To achieve this, three different drug-loaded liposomal formulations were synthesized.

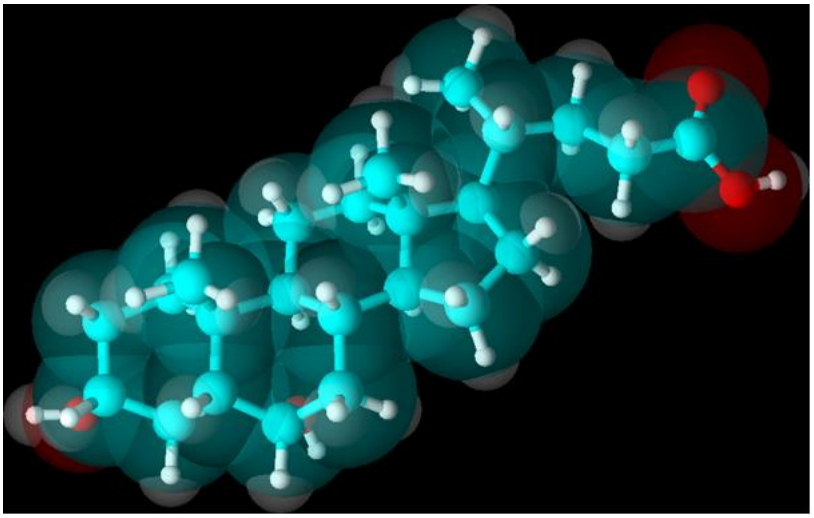

Figure 1. The three-dimensional optimized chemical structure of the cholesterol-like compound (HDCA) used in the synthesis of liposomes.

The physicochemical properties of the selected API were calculated using the ACD/Labs PhysChem Suite. At the studied pH, which simulates the physiological pH of the human body, the API has a net charge of +1 (see Figure 2 and Table 1). The -COOH functional group present in the cholesterol-like compound labeled as PS2 in the figure has a net charge of -1 at the analyzed pH, as illustrated in (Figure 2).

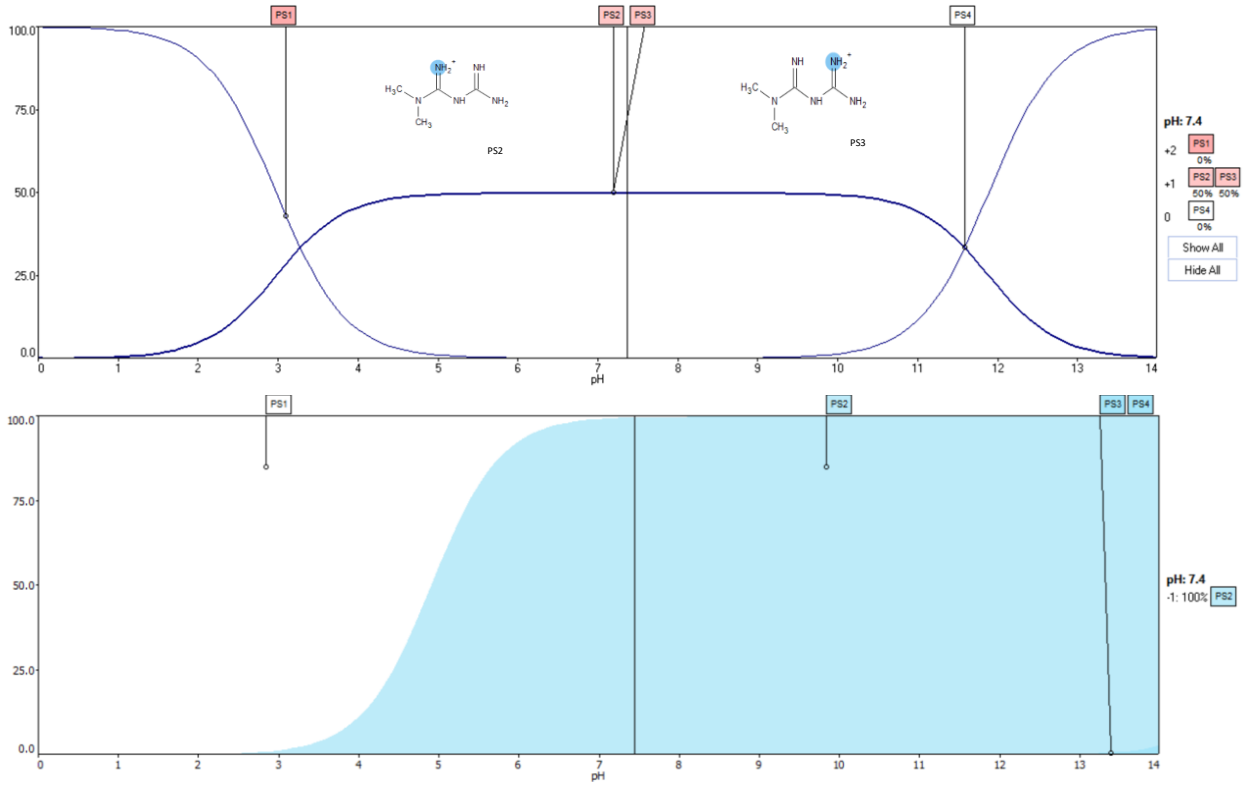

Figure 2. Protonation states (PS) vs pH graph of the biguanide derivative API (above) and the cholesterol-like compound (below) at the analyzed pH (pH 7.4).

Table 1. Net charge vs. pH of the biguanide derivative API.

Net charge/pH	1.7	2.0	3.0	4.0	4.6	5.0	6.0	6.5	7.0	7.4	8.0	9.0	10	11
q=0	0.00	0.00	0.00	0.00	0.00	0.00	0.00	0.00	0.00	0.00	0.00	0.00	0.01	0.11
q=+1	0.05	0.10	0.51	0.91	0.98	0.99	1.00	1.00	1.00	1.00	1.00	1.00	0.99	0.89
q=+2	0.95	0.90	0.49	0.09	0.02	0.01	0.00	0.00	0.00	0.00	0.00	0.00	0.00	0.00

The calibration graph for a standard solution of a biguanide API displays seven different concentrations (Figure 3).

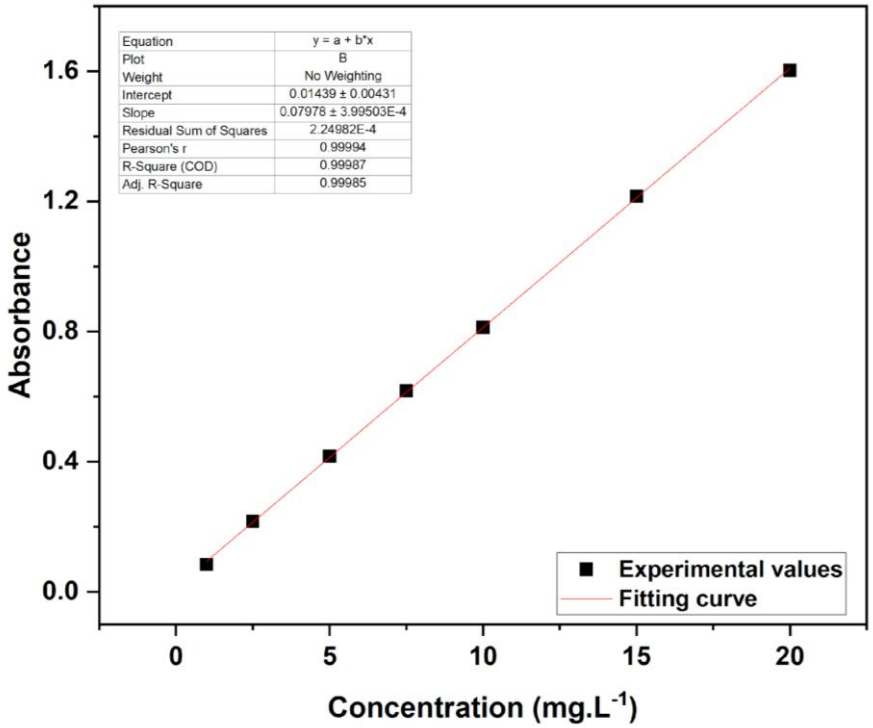

Figure 3. The calibration graph of standard solution of biguanide derivative API.

The regression equation is $y = 0.07978x\ (\pm 3.995 \times 10^{-4}) + 0.01439(\pm 0.00431)$ having a R^2 value of 0.9999 (Figure 3). This linear regression equation was used to calculate the EE% and DL% values of liposomal drug formulations.

EE% and DL% values

The ultracentrifugation process aims to determine the lowest absorbance value that indicates the absence of un-entrapped drug molecules in the supernatant. UV-Vis results for each centrifugation step are presented in Figure 4. Each step involves different dilution ratios, which must fall within the linear range of the calibration graph. To quantify the amount of entrapped drug molecules in the liposomal formulations, the pelleted structure remaining after the removal of the supernatant in the Eppendorf tube is lysed with isopropanol. This mixture is then centrifuged again, and the measurements are conducted using a UV-Vis spectrophotometer with the appropriate dilutions.

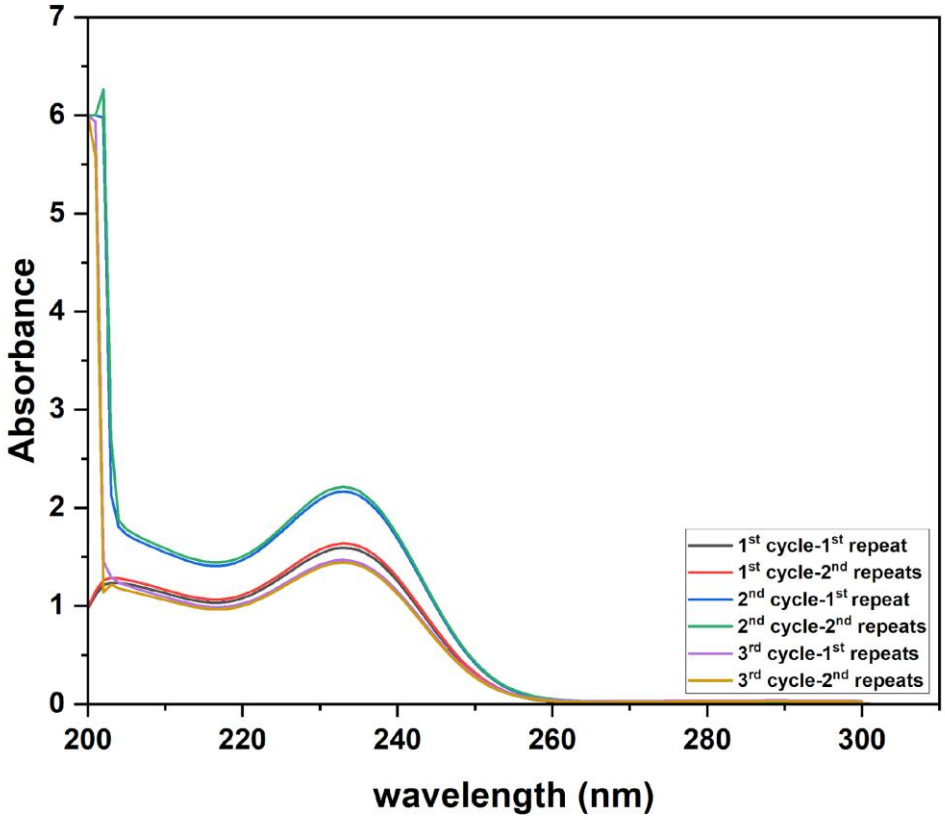

Figure 4. UV-Vis spectrum of drug-loaded formulations obtained after each centrifugation step.

The EE% values for three different drug-loaded liposomal formulations, designated F1, F2, and F3, were 98.2%, 99.5%, and 74.5%, respectively, calculated according to Equation 3. The DL% values for these formulations were 1.85%, 0.507%, and 25.5%, respectively. The highest EE% with the lowest DL% values were obtained with F2 formulations of the synthesized liposomal formulations.

CTEM analysis was performed to observe the morphology of MET loaded liposomes and confirm the particle size distribution results. High Contrast Transmission Electron Microscopy images of MET loaded liposomes prepared by ultrasonication for F2 formulations were given in the Figure 5. The liposomes generally exhibit spherical shape which agreed with the study of Dag and Oztop (2017). The particle size were between 500 nm to 100 nm were given in the Figure 5. The morphology of liposomes containing MET was partially bound to large or small drops (Gibis et al., 2012). Small liposomes tend to merge to decrease their curvature.

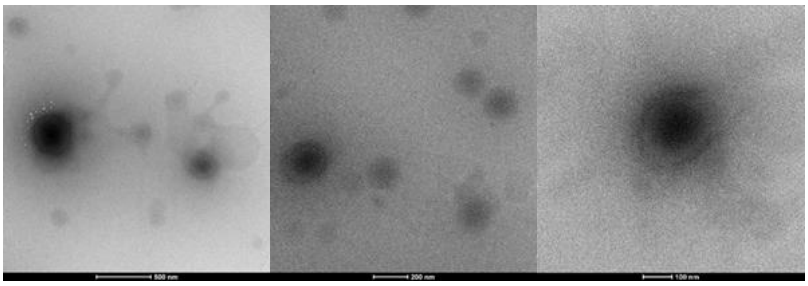

Figure 5. Morphology and size of F2 formulations ((A) 500 nm (B) 200nm (C) 100 nm) visualized by High Contrast Transmission Electron Microscopy (CTEM).

Conclusion

The thin-film hydration method is a widely used technique for preparing liposomal formulations. In these drug delivery systems, cholesterol is a widely used component, often combined with different phosphatidylcholine derivatives substances. The difference of this study is to increase of the short half-life and the oral bioavailability of the biguanide derivative API, metformin, using cholesterol-like structure instead of cholesterol for the synthesis of the liposomal drug delivery systems. Three different cholesterol-like structure-to-drug ratios were employed during liposome synthesis, while keeping the amount of the drug molecule constant. The plotted calibration graph of the API has a R^2 value of 0.9999. Using linear regression of this calibration graph, we calculated the amounts of un-trapped and entrapped drugs and subsequently determined the entrapment efficiency (EE%) and drug leakage percentages (DL%) for the synthesized formulations. The EE% values for formulations F1, F2, and F3 were as follows: 98.15%, 99.49%, and 74.52%, respectively. The corresponding drug leakage values were 1.85%, 0.507%, and 25.5%. The Metformin loaded liposomes generally exhibit spherical shape which is confirmed by CTEM analyses.

References

Bautzová, **T., Rabišková, M., Béduneau, A., Pellequer, Y., & Lamprecht, A.** (2012). Bioadhesive pellets increase local 5-aminosalicylic acid concentration in experimental colitis. *European Journal of Pharmaceutics and Biopharmaceutics*, *81*(2), 379–385. https://doi.org/10.1016/j.ejpb.2012.02.011

Kesharwani, P., Md, S., Alhakamy, N. A., Hosny, K. M., & Haque, A. (2021). QbD Enabled Azacitidine Loaded Liposomal Nanoformulation and Its In Vitro Evaluation. *Polymers*, *13*(2), 250. https://doi.org/10.3390/polym13020250

Liu, P., Chen, G., & Zhang, J. (2022). A Review of Liposomes as a Drug Delivery System: Current Status of Approved Products, Regulatory Environments, and Future Perspectives. *Molecules*, *27*(4), 1372. https://doi.org/10.3390/molecules27041372

Thabet, Y., Elsabahy, M., & Eissa, N. G. (2022). Methods for preparation of niosomes: A focus on thin-film hydration method. *Methods*, *199*, 9–15. https://doi.org/10.1016/j.ymeth.2021.05.004

Torres-Flores, G., Gonzalez-Horta, A., Vega-Cantu, Y. I., Rodriguez, C., & Rodriguez-Garcia, A. (2020). Preparation and Characterization of Liposomal Everolimus by Thin-Film Hydration Technique. *Advances in Polymer Technology*, *2020*(1), 1–9. https://doi.org/10.1155/2020/5462949

Waghule, T., Rapalli, V. K., Singhvi, G., Gorantla, S., Khosa, A., Dubey, S. K., & Saha, R. N. (2021). Design of temozolomide-loaded proliposomes and lipid crystal nanoparticles with industrial feasible approaches: comparative assessment of drug loading, entrapment efficiency, and stability at plasma pH. *Journal of Liposome Research*, *31*(2), 158–168. https://doi.org/10.1080/08982104.2020.1748648

Wang, N., Wang, T., Li, T., & Deng, Y. (2009). Modulation of the physicochemical state of interior agents to prepare controlled release liposomes. *Colloids and Surfaces B: Biointerfaces*, *69*(2), 232–238. https://doi.org/10.1016/j.colsurfb.2008.11.033

CHEMISTRY

Analytical Chemistry

Biochemistry

Drug Design & Drug Delivery (Computational and Experimental)

Energy Materials (Synthesis, Characterizations, Applications)

Inorganic Chemistry

Nanochemistry

Organic Chemistry

Physical Chemistry

Nanotechnology, Surface Coatings and Films

Polymer Chemistry

Immobilization of Cobalt Wastes in Ceramics for The Long-Term Storage in Deep Radioactive Waste Repository

Esra Varbil[a], Sema Akyil Erenturk[a]

[a] Istanbul Technical University, Energy Institute, Türkiye
varbil@itu.edu.tr

Keywords: Cobalt Waste, Feldspar, Immobilization, Chemical Durability, Leaching Rate.

Aim

High-level radioactive waste can be immobilized in glass, ceramics, glass-ceramics and glass composite materials and stored in geological final waste storage areas (Bernardo et.al., 2003). Vitrification is one of the first methods developed for the immobilization of high-level radioactive waste (Boccaccini et.al., 2004; Shelby, 2005; Lee et., al., 2006). Although waste can be reduced to smaller volumes with the vitrification method and products with high chemical and mechanical strength can be obtained, the waste intake capacity in the glass matrix is limited to 20-35% (wt). In ceramics, glass-ceramics and glass composite materials developed later, the waste intake capacity can increase to 50-70% (wt) and at the same time, high-strength materials can be obtained (Yanikomer and Erenturk, 2025; Jakkula and Deshpande, 2013). The aim of this study is to prepare ceramics with high chemical and mechanical strength, high waste absorption capacity and as low processing temperature as possible. In ceramics prepared with suitable composition, immobilization of ^{60}Co, one of the important fission products, was carried out. Then, the suitability of the main matrix and matrix compositions containing waste for long-term storage conditions underground was examined with detailed tests. The leaching of cobalt ions from ceramic products containing waste was found in terms of average dissolution rates (g cm^{-2} min) of the elements forming each ceramic composition based on unit mass losses after waiting in the oven at 90 ^oC for 7 days. Structural analysis of ceramics was performed by FTIR and XRD. The obtained results showed that the ceramic structure was a suitable matrix for the immobilization of ^{60}Co.

Material and Method

Feldspar was used as a ceramic raw material. Cobalt, a radioactive fission product, was immobilized in feldspar. Cobalt was added to the main matrix in certain proportions and the mixture was mixed homogeneously in an agate mortar and then pressed in a 33 mm mold with a 40-ton press. The mixture, which turned into pellets, was placed on a graphite block and turned into ceramics by applying heat treatment with controlled heat increases between 900 ^oC and 1200 ^oC in a high-temperature furnace. The product obtained was left to cool in the furnace until it reached room temperature.

The weights of the ceramics that were ready for the chemical resistance test were determined first. Then, the samples were subjected to the chemical resistance test by hanging them on a thin thread in 50 mL of bidistilled water in polyethylene containers and waiting in an oven at 90^oC for 1 week. The weights of the samples were weighed at certain time intervals and the pH value of the water was measured. Then, the time-dependent unit mass losses were calculated by considering the mass losses and surface areas of the samples. Based on the unit mass losses, the average dissolution rates of each ceramic composition were calculated in terms of (g cm^{-2} min) (Buelt et al., 1987; Komatsu et al., 1990; Bengisu et al., 2006).

Based on unit mass losses, the average dissolution rates of the elements forming each ceramic composition were found in terms of (g cm^{-2} min). The volume of the samples was measured using the Archimedes principle and their specific gravities were calculated from the sample weight and volume. The leaching rates of the elements found in the structure of the obtained glasses from the glass structure were calculated.

Structural investigation of all ceramic compositions examined was carried out by X-ray diffraction (XRD) and Fourier Transform Infrared Spectroscopy (FTIR) analyses.

Findings

Ceramic compositions have been used for years. Prepared ceramics have the desired properties for immobilization of radioactive waste. Feldspar was used as ceramic raw material. The results obtained showed that crystalline phases formed in feldspar main matrix ceramic structures play an important role in the immobilization of cobalt. In addition, it was observed that cobalt was immobilized in the feldspar matrix.
As a result of chemical durability tests, the average dissolution rate of cobalt-containing waste ceramics is very low and did not differ significantly depending on the waste rate.

Conclusion

Considering all the results, it was determined that ceramic structures prepared using feldspar, which is the preferred barrier material in radioactive waste management, can also be used in the immobilization of nuclear waste. Some changes to be made in the composition of such materials can increase their chemical and physical durability.
Different new compositions are still being studied for nuclear and radioactive waste immobilization. Especially ceramics are promising for waste immobilization. Within the scope of this study, the immobilization of cobalt, one of the important fission products, in ceramic matrices, one of the newly developed solidification materials in nuclear waste management, was investigated.

References

Bengisu, M., Brow, R.K., Yilmaz, E., Mogus-Milankovic, A., Reis, S.T. (2006). Aluminoborate and Aluminoborosilicate Glasses with High Chemical Durability and the Effect of P2O5 Additions on the Properties, Journal of Non-Crystalline Solids, 352, 3668–3676.

Bernardo, E., Varrasso, M., Cadamuro, F., Hreglich, S., 2006. Vitrification of Wastes and Preparation of Chemically Stable Sintered Glass-Ceramic Products, Journal of Non-Crystalline Solids, 352, 4017–4023.

Boccaccini, A.R., Bernardo, E., Blain, L., Boccaccini, D.N., 2004. Borosilicate and Lead Silicate Glass Matrix Composites Containing Pyrochlore Phases for Nuclear Waste Encapsulation, Journal of Nuclear Materials, 327, 148–158.

Buelt, J.L., Timmerman C.L., Oma K.H., FitzPatrick V.F., Carter J.G., (1987). In Situ Vitrification of Transuranic Waste: An Updated Systems Evaluation and Applications Assessment. PNL-4800 Suppl. 1, Pacific Northwest Laboratory, Richland, Washington, March.

Jakkula, S., Deshpande, V., 2013. Effect of MgO Addition on the Properties of PbO–TiO2–B2O3 Glass and Glass–Ceramics, Ceramics International, 39, S15–S18.

Komatsu, F., Takusagawa, A., Wada, R., Asahina, J.K., (1990). Application of Microwave Treatment Technology for Radioactive Wastes, Waste Management, 10, 211-215.

Lee, W.E., Ojovan, M.I., Stennett, M.C., Hyatt, N.C., 2006. Immobilisation of Radioactive Waste in Glasses, Glass Composite Materials and Ceramics, Advances in Applied Ceramics, 105(1).

Shelby, J.E., 2005, Introduction to Glass Science and Technology, Royal Society of Chemistry, Cambridge.

Yanikomer N., Akyil Erenturk S., (2025) Immobilization of simulated cesium wastes in ceramic matrices derived from some natural minerals, Nuclear Engineering and Technology 57 (2025) 103358.

CHEMISTRY

Analytical Chemistry

Biochemistry

Drug Design & Drug Delivery (Computational and Experimental)

Energy Materials (Synthesis, Characterizations, Applications)

Inorganic Chemistry

Nanochemistry

Organic Chemistry

Physical Chemistry

Nanotechnology, Surface Coatings and Films

Polymer Chemistry

Stimuli-Responsive Polymers Based on Calix[4]pyrrole and Pillar[5]arene Molecular Recognition

Deniz Memis[a], Necla Bektas[a], Abdullah Aydogan[a]

[a] Istanbul Technical University, Department of Chemistry, Türkiye
memisd@itu.edu.tr

Keywords: Calix[4]Pyrrole , Host−Guest Interaction , Pillar[5]Arene , Supramolecular Polymers.

Aim

Supramolecular polymers (SPs) are polymeric systems characterized by the ability of monomeric units to be connected through non-covalent reversible interactions (Wei et al., 2015). The behavior and conformation of these polymers are directly influenced by these interactions. SPs, which are synthesized by combining monomers with interaction motifs, hold significant importance in the production of materials with hybrid properties. The dynamic bonds between the monomers of SPs enable them to possess the properties of conventional polymers, as well as those of smart materials such as self-healing and responsiveness to external stimuli (Yan et al., 2013). The responsiveness of these materials is provided by means of dynamic bonds based on various intermolecular reversible interactions, such as π−π stacking, hydrophobic interactions, metal−ligand coordination, hydrogen bonding, anion recognition, and host−guest interactions (Li et al., 2012). The pyrroles units of calix[4]pyrroles provide a hydrogen-bonding array capable of binding anions selectively in organic media (Gale et al., 1996). By virtue of this, calix[4]pyrroles have become widely utilized in various applications, including supramolecular polymers (Bektas & Aydogan, 2023). Pillar[5]arenes are suitable hosts for electron-deficient molecules such as pyridinium and imidazolium cationic species and neutral molecules such as dibromoalkanes, alkanediamines, and alkylnitriles in the construction of supramolecular polymers (Li et al., 2019). The primary objective of this study is to synthesize alternating supramolecular polymers responsive to external stimuli from alkylnitrile functionalized calix[4]pyrrole and pillar[5]arenes bearing carboxylate units.

Material and Method

We report the synthesis and characterization of an alkylnitrile-functionalized calix[4]pyrrole (CPN) and two distinct pillar[5]arenes tethered with carboxylate units (P1 and P2). These compatible supramolecular monomers were subsequently utilized to synthesize two different supramolecular assemblies (designated as CPN + P1 and CPN + P2) based on orthogonal neutral nitrile and carboxylate ion recognition motifs in chloroform (Figure 1). The characterization of SAPs was conducted through a combination of ^{1}H NMR and two-dimensional diffusion-ordered ^{1}H NMR (DOSY) techniques, along with viscosity measurements. Furthermore, the linker chain length differences between pillar[5]arene cores and carboxylate units of P1 and P2 were investigated in relation to the SAP formation performance. Additionally, we conducted studies on the stimuli-responsive properties of SAPs against temperature, pH, and competing guest species.

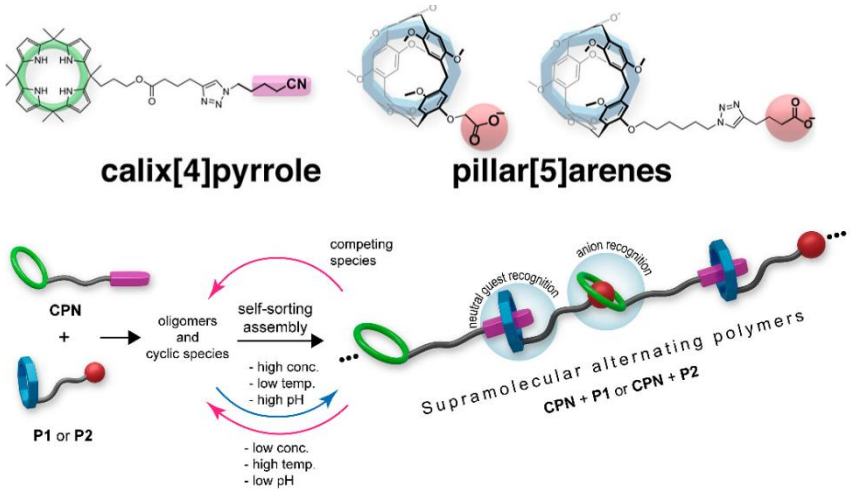

Figure 1. Cartoon representations depicting the supramolecular polymerization.

Findings

CPN + P1 and CPN + P2 SAP systems comprise calix[4]pyrrole and pillar[5]arene macrocycles capable of binding carboxylate units and forming inclusion complexes with alkylnitrile units, respectively. These noncovalent interactions are inherently dynamic due to hydrogen bonding and host-guest interactions, which can be modulated by external stimuli. Consequently, we subjected CPN + P1 and CPN + P2 to various stimuli, including temperature, acid-base, and competing species. SAPs of the aforementioned systems exhibited reversible disassembly and reassembly upon application of one of the aforementioned stimuli sources.

We commenced by investigating the temperature dependence of SAPs in chloroform through inverted vial tests. Notably, SAPs of CPN + P1 (434 mM) and CPN + P2 (387 mM) exhibited self-standing high-molecular-weight polymers at 25 °C (Figure 2). However, they were observed to transition to less-viscous states when the temperature of the supramolecular polymers was elevated to 50 °C. These findings demonstrated the thermoresponsive properties of CPN + P1 and CPN + P2.

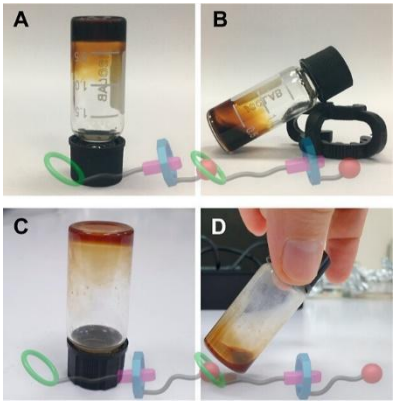

Figure 2. Responses of SAPs to temperature changes. Inverted vial tests of equimolar (A,B) CPN + P1, (C,D) CPN + P2 at (A,C) 25 °C and (B,D) 50 °C.

The pH-responsive behavior of supramolecular polymers was investigated using a sequential acid-base treatment method. The calix[4]pyrrole and alkylnitrile ^{1}H NMR resonance signals of CPN + P1 and CPN + P2 were monitored. The underlying principle of these experiments is the protonation and deprotonation of carboxylate units in P1 and P2 components, which disrupt their complexation with the calix[4]pyrrole units of CPN. Consequently, the sizes of SAPs could be controlled by pH changes. To achieve this objective, $CDCl_3$ solutions of SAPs (14 mM) were sequentially treated with equimolar methanesulfonic acid (MSA) and tetramethyl guanidine (TMG). When CPN + P1 or CPN + P2 was treated with MSA, the pyrrole NH resonance signals of SAPs exhibited upfield shifts,

indicating the destruction of calix[4]pyrrole-carboxylate complexation. Upon the introduction of TMG, the original chemical shifts of pyrrole NHs were restored, suggesting the reconstruction of calix[4]pyrrole-carboxylate interactions. The pH-responsive behavior of SAPs was further confirmed by DOSY experiments. After treatment with MSA, the increased D values were attributed to the destruction of supramolecular polymers and their subsequent reconstruction after treatment with TMG.

The responses of CPN + P1 and CPN + P2 against competing guest species were also investigated using ^{1}H NMR and DOSY experiments under the same conditions as those applied for pH-responsiveness. Tetrabutylammonium fluoride (TBAF) and 5-bromovaleronitrile (BVN) were selected as competing guests due to their frequent use in calix[4]pyrrole- and pillar[5]arene based supramolecular polymer systems (Ünlü & Aydogan, 2022). The calix[4]pyrrole core of CPN exhibits a stronger affinity for fluoride anion compared to carboxylate. Therefore, the addition of equimolar TBAF to SAP solutions disrupted the linear chains of CPN + P1 and CPN + P2. This was corroborated by the ^{1}H NMR spectra. pyrrole NH resonance signals, which exhibited a shift to >12 ppm. Additionally, the complete complexation of calix[4]pyrrole units was deduced from the sharper and completely upfield shifted pyrrole CH peaks around 5.6 ppm. The pillar[5]arene cores of P1 and P2 were also targeted using BVN as a competing guest. The responses of CPN + P1 and CPN + P2 were investigated. When equimolar BVN was added to the $CDCl_3$ solutions of supramolecular polymers, significant changes in the pillar[5]arene and calix[4]pyrrole-related peaks were observed. These results enabled us to propose that alternating linear supramolecular polymers of CPN + P1 and CPN + P2 were transformed into smaller aggregates in solution upon interactions with BVN. Support for this hypothesis was provided by additional DOSY experiments, revealing D values of 5.11×10^{-10} and 4.06×10^{-10} m^2 s^{-1} for CPN + P1 and CPN + P2, respectively, after treatment with BVN in $CDCl_3$. These values correspond to 1.68 and 2.00 times increases in D values and support the aforementioned results obtained from ^{1}H NMR experiments.

Conclusion

In conclusion, we have successfully designed, synthesized, and fully characterized complementary calix[4]pyrrole (CPN) and pillar[5]arene (P1 and P2) supramolecular monomers. These monomers are tethered with carboxylate and alkylnitrile functional groups and utilized to obtain SAPs (CPN + P1 and CPN + P2) in chloroform via. concurrent anion recognition and host-guest interactions. The formation and characterization of SAPs were monitored using a combination of techniques, including viscosity measurements and DOSY analyses. Additionally, the thermo-, pH-responsive properties of the SAPs of CPN + P1 and CPN + P2 and the influence of anionic and neutral competing species were elucidated through a series of viscosity, ^{1}H-, and DOSY-NMR experiments. To the best of our knowledge, this study presents the first instance of SAPs based on the simultaneous utilization of calix[4]pyrrole and pillar[5]arene molecular recognition, followed by their application in the formation of stimuli responsive systems. The ease of monomer synthesis, coupled with the facile preparation of the materials, is anticipated to pave the way for the production of advanced, multicomponent synthetic self-assembled systems.

The authors gratefully acknowledge financial support from the Scientific and Technological Research Council of Türkiye (TUBITAK, 221Z098). D.M. thanks TUBITAK and the Council of Higher Education of Türkiye (YOK) for their 2211A and 100/2000 PhD scholarships.

References

Bektas, N., & Aydogan, A. (2023). A poly-pseudorotaxane constructed by threading pillar[5]arene onto an ion-pair recognition-based calix[4]pyrrole supramolecular polymer [10.1039/D2OB02268K]. *Organic & Biomolecular Chemistry*, *21*(9), 1862-1867. https://doi.org/10.1039/D2OB02268K

Gale, P. A., Sessler, J. L., Král, V., & Lynch, V. (1996). Calix[4]pyrroles: Old Yet New Anion-Binding Agents. *Journal of the American Chemical Society*, *118*(21), 5140-5141. https://doi.org/10.1021/ja960307r

Li, H., Yang, Y., Xu, F., Liang, T., Wen, H., & Tian, W. (2019). Pillararene-based supramolecular polymers [10.1039/C8CC08085B]. *Chemical Communications*, *55*(3), 271-285. https://doi.org/10.1039/C8CC08085B

Li, S.-L., Xiao, T., Lin, C., & Wang, L. (2012). Advanced supramolecular polymers constructed by orthogonal self-assembly [10.1039/C2CS35099H]. *Chemical Society Reviews*, *41*(18), 5950-5968. https://doi.org/10.1039/C2CS35099H

Ünlü, F. Y., & Aydogan, A. (2022). Multiresponsive, Self-Healing, and Hierarchical Materials Constructed from Anion Recognition-Based Supramolecular Polymer Networks. *ACS Applied Polymer Materials*, *4*(7), 4774-4783. https://doi.org/10.1021/acsapm.2c00379

Wei, P., Yan, X., & Huang, F. (2015). Supramolecular polymers constructed by orthogonal self-assembly based on host–guest and metal–ligand interactions [10.1039/C4CS00327F]. *Chemical Society Reviews*, *44*(3), 815-832. https://doi.org/10.1039/C4CS00327F

Yan, X., Xu, D., Chen, J., Zhang, M., Hu, B., Yu, Y., & Huang, F. (2013). A self-healing supramolecular polymer gel with stimuli-responsiveness constructed by crown ether based molecular recognition [10.1039/C3PY00283G]. *Polymer Chemistry*, *4*(11), 3312-3322. https://doi.org/10.1039/C3PY00283G

CHEMISTRY

Analytical Chemistry

Biochemistry

Drug Design & Drug Delivery (Computational and Experimental)

Energy Materials (Synthesis, Characterizations, Applications)

Inorganic Chemistry

Nanochemistry

Organic Chemistry

Physical Chemistry

Nanotechnology, Surface Coatings and Films

Polymer Chemistry

Determination of Solubility of p-aminobenzoic Acid (PABA) Derivative Active Pharmaceutical Ingredient in Non-Aqueous Binary Mixture

Elif Sağlam[a], Kader Poturcu[a], Elaheh Rahimpour[b], Abolghasem Jouyban[b]

[a]Suleyman Demirel University, Department of Chemistry, Faculty of Engineering and Natural Science, Türkiye.
[b]Tabriz University of Medical Sciences, Pharmaceutical Analysis Research Center and Faculty of Pharmacy, Iran.
kaderpoturcu@sdu.edu.tr

Keywords: Solubility, P-Amino Benzoic Acid Derivative API, XRD.

Aim

The solubility of drugs and drug candidates is a critical physicochemical parameter in pharmaceutical analysis. Approximately 40% of marketed compounds are poorly soluble, and around 90% of drug candidates have soluble properties (Jouyban-Gharamaleki et al., 2020; Martínez et al., 2017). Various solubility enhancement techniques have been reported in the literature, including micronization, solid dispersion, the use of surfactants, co-solvency, pH adjustment, and more (Savjani et al., 2012).

In the present study, the solubility behavior of a p-aminobenzoic acid derivative active pharmaceutical ingredient was investigated in a propylene glycol+2-propanol non-aqueous binary mixture using the co-solvency method at 310.15K. The experimental solubility values were determined using at least three experiments conducted with diluted solutions. The minimum solubility was found to be 9.10 (± 0.44)$\times 10^{-3}$ mol.L^{-1} in neat 2-propanol, while the maximum solubility was 2.34 (± 0.06)$\times 10^{-1}$ mol.L^{-1} in neat propylene glycol at the studied temperature. Additionally, density measurements were determined in this binary mixture for saturated systems. Characterization tests of the saturated drug solutions were performed using X-ray diffraction (XRPD) analysis across 2theta values from 10°C to 90°C. According to the XRPD results, the crystallinity of the drug molecule remained unchanged, indicating no polymorphic transformation occurred during the dissolution process in the studied binary mixtures.

This study aims to determine the solubility values of p-aminobenzoic acid derivatives' active pharmaceutical ingredient (API) in propylene glycol+2-propanol non-aqueous binary mixtures using the co-solvency method. The density values of saturated API were also determined experimentally. The characterization tests were performed using XRPD analysis. Until now, no solubility data on selected non-aqueous binary mixtures has been available for this API in the literature.

This study was supported by TUBITAK 2209-A University Students Research Projects Support Program with the Project number of 1919B012320617, 2023/2nd term.

Materials and Method

Table 1 lists the chemicals used during experiments. The supplier provided the purities of the chemicals shown in the Table, and they were used without any purification.

Table 1. The list of chemicals used in this study.

Chemicals	Purity*	Supplier
p-amino benzoic acid derivative API (Procaine HCl)	0.99% (mass fraction)	Sigma Aldrich, China
Propylene glycol	≥99.5%	Carlo Erba, Germany
2-Propanol	≥99.5%	Supelco, Darmstadt, Germany

Absolute ethanol	≥0.999%	Supelco, Darmstadt, Germany
HPLC grade water	Conductivity: 0.55 µS/cm	Milli-Q water, Millipore

Solubility Analysis

A standard shake-flask method (Martínez et al., 2017) was employed to analyze the solubility of p-aminobenzoic acid derivative active pharmaceutical ingredient (API) in binary mixtures of propylene glycol (PG) and 2-propanol at 310.15 K. Excess amounts of the API were added to volumetric flasks containing 10 g of neat solvents or various solvent mixtures with different mass ratios (w_1=0.1–0.9). The flasks were then tightly sealed and placed on an orbital shaker (Heidolph, Germany) within an incubator system (MhmtGhsm Company, Dublin, Ireland). The drug solutions were shaken for 72 hours at the specified temperature.

After shaking, the saturated mixtures were centrifuged and diluted with a mixture of ethanol and water (30:70% v/v). Spectrophotometric measurements were conducted using a UV–Vis spectrophotometer (UV 1800 Perkin Elmer Inc., USA) at a fixed wavelength of 299 nm. A calibration curve was constructed using stock solutions of p-aminobenzoic acid derivative API within a concentration range of 2.5 $mg.L^{-1}$ to 25 $mg.L^{-1}$. This involved diluting the drug solutions from the stock solutions to create the calibration curve. The resulting calibration curve showed an R^2 value of 0.9996 within the studied concentration range.

The density values of the saturated API mixtures were determined using a 5 mL pycnometer, with an uncertainty of 0.001 g/cm^3. The solubility data and density values reported are averages of at least three replicate measurements.

X-ray Powder Diffraction (XRPD) Analysis

The characterization tests of p-aminobenzoic acid derivative API equilibrated in the saturated solutions were performed by XRD analyses (Rigaku Ultima IV, Tokyo, Japan) from 10° to 90°. The voltage and current applied were 40 kV and 15 mA, respectively using CuKa radiation. The scan speed was 5.00°.min^{-1} with a step width of 0.02°. All samples were dried in an oven at 100 °C before XRD analysis. XRD analyses were performed at the R&D Training and Measurement Center, X-Ray Diffraction Laboratory (METU, Türkiye).

Findings

The p-aminobenzoic acid derivative compounds that contain both amino and carboxyl groups at their structure are the commonly used building blocks in pharmaceuticals (Haroon et al., 2023). The p-aminobenzoic acid is a non-toxic compound, easily absorbed in the intestine, and they have broad biological activities (Al-Rubaie et al., 2021; Haroon et al., 2023). More than 184 drugs in the database of commercial drugs are p-aminobenzoic acid derivative synthetic compounds which have local anesthetic, anti-tuberculosis, anti-convulsant, and antineoplastic effects in therapeutic applications (Tang et al., 2020).

In the present study, the p-aminobenzoic acid -based local anesthetic drug (Figure 1) was selected for solubility analyses in PG+2-propanol non-aqueous binary mixtures. The density values of saturated API were determined experimentally. The raw API and saturated API characterization tests in non-aqueous binary mixtures were conducted using XRPD analyses.

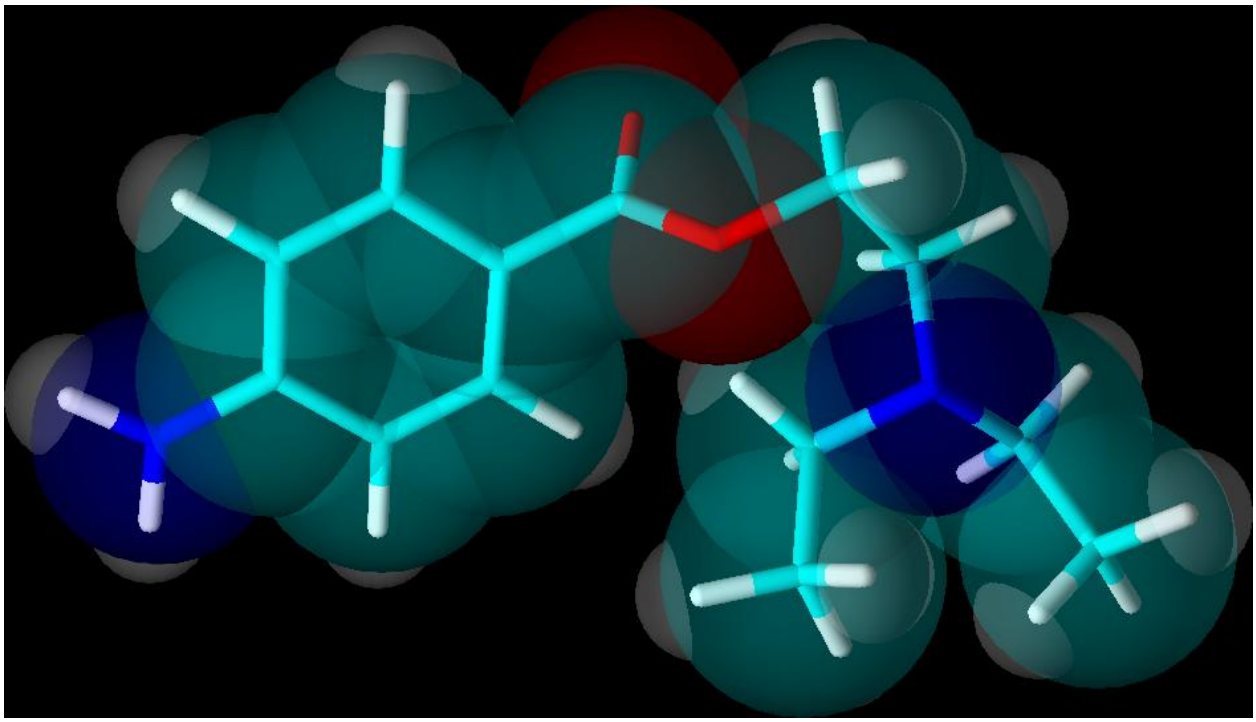

Figure 1. The 3D-optimized chemical structure of the p-aminobenzoic acid derivative API.

A standard stock drug solution was prepared and appropriately diluted to plot the calibration curve. The R^2 value obtained was 0.9996 within the studied concentration range, which included seven points on the calibration graph, as shown in Figure 2.

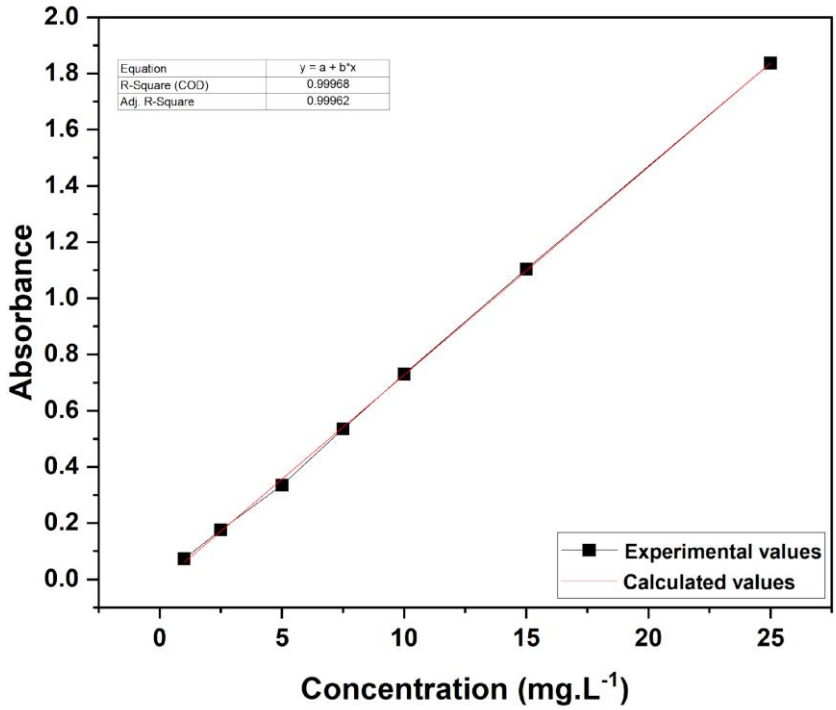

Figure 2. The calibration graph of the p-aminobenzoic acid derivative API.

The absorbance value of the saturated drug solutions at different mass fractions of PG in the PG+2-propanol non-aqueous binary mixtures were measured with UV-Vis spectrophotometer. Each mass fraction was prepared with

different dilution ratios and given in Figure 3. The UV-Vis maximum of saturated drug solutions was obtained at 299 nm as shown in spectrum.

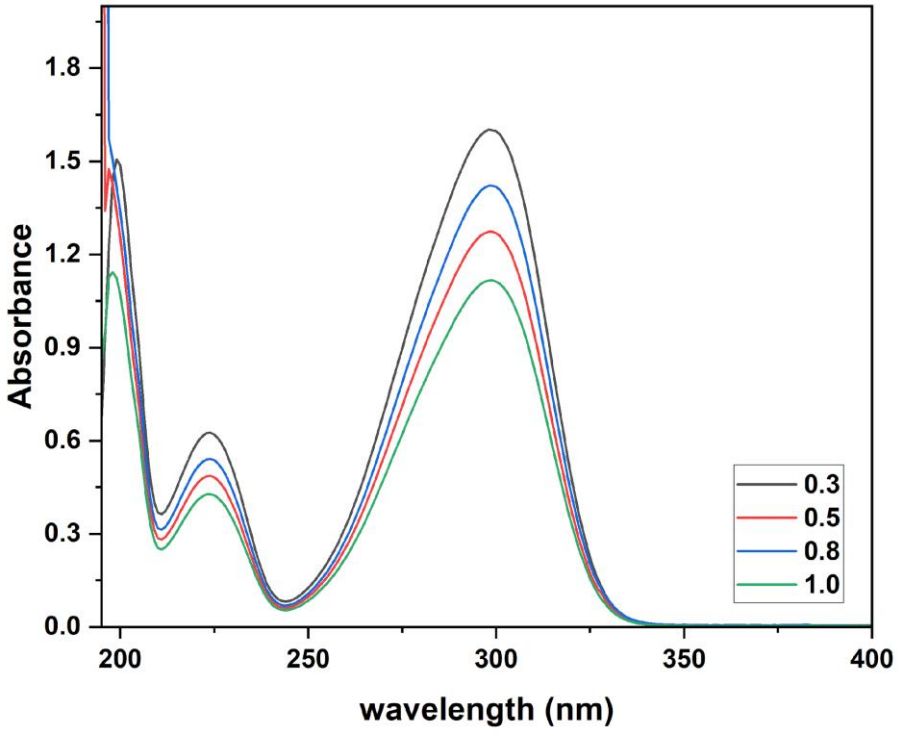

Figure 3. UV-Vis spectrum of saturated drug solutions in the PG+2-propanol non-aqueous binary mixtures.

The results of experimentally determined solubility values of p-aminobenzoic acid derivative API in molarity scale are given in Table 2.

Table 2. Experimental molar solubility (C_M/mol/L) values as the mean of three experiments for p-aminobenzoic acid derivative API in the PG+2-propanol non-aqueous binary mixtures at 310.15K.

w_1	C_M(mol/L)
0.0	$9.10(\pm0.44)\times10^{-3}$
0.1	$1.33(\pm0.09)\times10^{-2}$
0.2	$2.77(\pm0.12)\times10^{-2}$
0.3	$4.61(\pm0.24)\times10^{-2}$
0.4	$6.87(\pm0.29)\times10^{-2}$
0.5	$8.88(\pm0.31)\times10^{-2}$
0.6	$1.11(\pm0.05)\times10^{-1}$
0.7	$1.39(\pm0.02)\times10^{-1}$
0.8	$1.78(\pm0.05)\times10^{-1}$
0.9	$2.04(\pm0.15)\times10^{-1}$
1.0	$2.34(\pm0.06)\times10^{-1}$

*Standard deviation of results is given in parentheses.

Moreover, the density values for the saturated drug solutions at 310.15 K are also measured and given in Table 3.

Table 3. Measured density ($g.cm^{-3}$) of p-amino benzoic acid derivative API saturated solutions in the PG+2-propanol binary mixtures at 310.15K.

w_1	PG + 2-propanol
0.0	$0.746(\pm 3.59\times10^{-3})$
0.1	$0.760(\pm 1.01\times10^{-2})$
0.2	$0.784(\pm 3.61\times10^{-3})$
0.3	$0.806(\pm 5.37\times10^{-3})$
0.4	$0.824(\pm 3.96\times10^{-3})$
0.5	$0.853(\pm 2.83\times10^{-4})$
0.6	$0.869\ (\pm 3.96\times10^{-3})$
0.7	$0.891\ (\pm 1.70\times10^{-3})$
0.8	$0.915\ (\pm 1.10\times10^{-2})$
0.9	$0.946(\pm 1.27\times10^{-3})$
1.0	$0.971(\pm 3.12\times10^{-2})$

*Standard deviation of results is given in parentheses.

XRPD Analysis

The characterization tests of the p-aminobenzoic acid derivative API equilibrated in saturated solutions were conducted using XRPD analyses, as detailed in the literature by Foroughi et al. (Foroughi et al., 2023). The XRD patterns for both the raw and equilibrated p-aminobenzoic acid derivative API in PG and 2-propanol non-aqueous binary mixtures are presented in Figures 4 and 5. The XRPD analysis indicated that the characteristic peaks for the raw drug material and the residuals from the PG and 2-propanol binary solvent mixtures were similar. These results suggest that the crystallinity of the API remained unchanged, with no evidence of polymorphic transformation occurring during the dissolution process in the investigated binary mixture system.

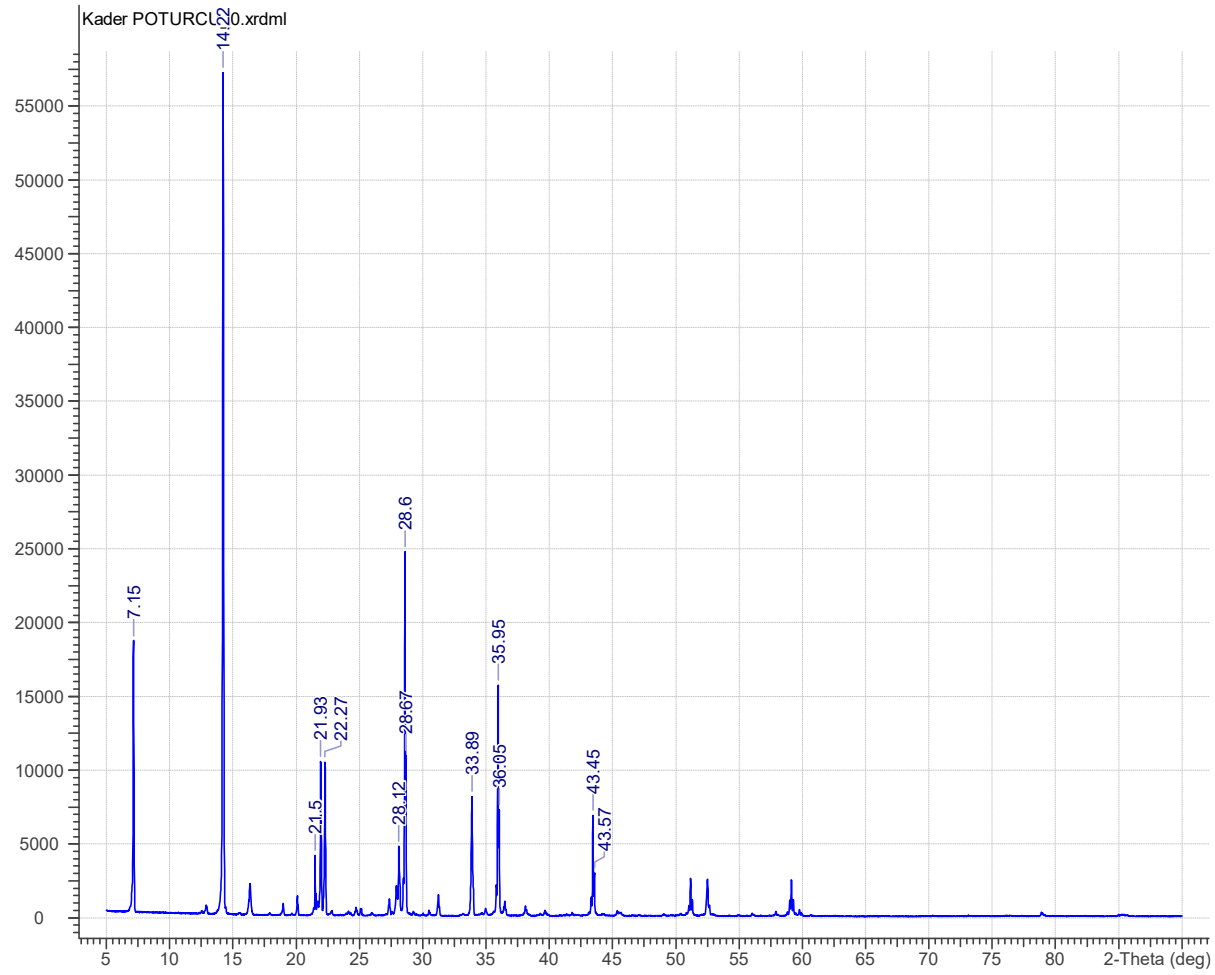

No.	Position	Intensity	FWHH	Asymmetry
1	7.1472	18787.0000	0.0797	0.0684
2	14.2244	57257.0000	0.0832	0.2503
3	21.4986	4216.0000	0.0300	0.1631
4	21.9319	10587.0000	-	-
5	22.2733	10541.0000	0.0912	0.5848
6	28.1162	4845.0000	-	-
7	28.6020	24793.0000	0.0754	-0.2563
8	28.6677	10999.0000	-	-
9	33.8935	8207.0000	0.1185	-0.3736
10	35.9550	15758.0000	0.0709	-0.8655
11	36.0469	7319.0000	-	-
12	43.4523	6936.0000	0.0669	-0.0318
13	43.5705	3031.0000	0.0802	-0.7264

Figure 4. XRPD pattern of p-aminobenzoic acid derivative raw drug.

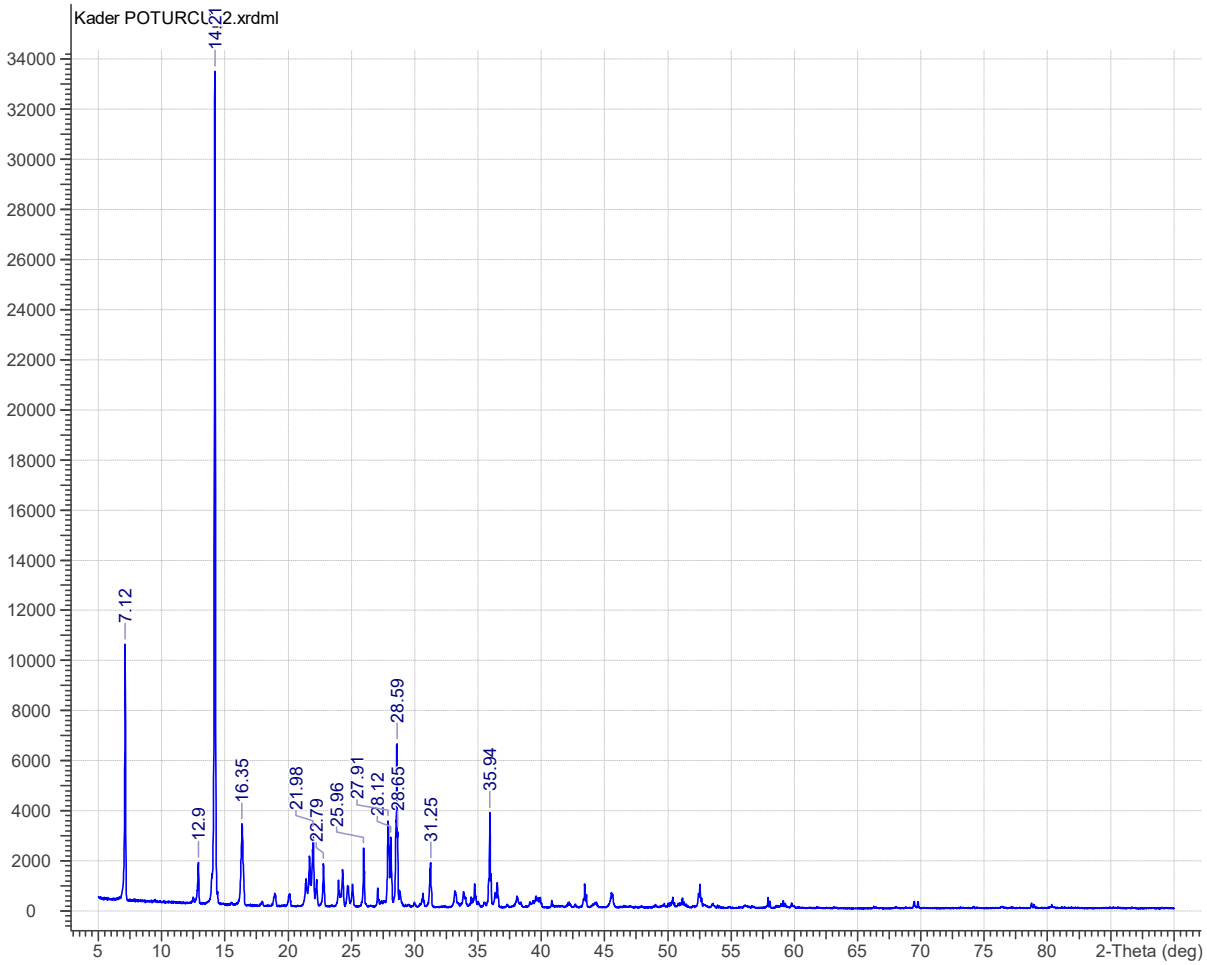

No.	Position	Intensity	FWHH	Asymmetry
1	7.1210	10639.0000	0.0803	-0.1425
2	12.8983	1936.0000	0.1018	-0.1186
3	14.2113	33513.0000	0.0869	-0.2028
4	16.3515	3480.0000	0.2175	0.2146
5	21.9844	3181.0000	-	-
6	22.7853	1885.0000	0.1136	0.6485
7	25.9629	2507.0000	0.1095	0.9484
8	27.9061	3591.0000	0.1573	0.5721
9	28.1162	2945.0000	0.1257	0.1043
10	28.5889	6671.0000	-	-
11	28.6546	3151.0000	-	-
12	31.2543	1923.0000	0.1331	-0.8739
13	35.9418	3932.0000	0.0652	-0.5961

Figure 5. XRPD pattern of equilibrated p-aminobenzoic acid derivative in PG+2-propanol non-aqueous binary mixtures.

Conclusion

The solubility analysis of the selected p-amino benzoic acid derivative API was conducted for the first time in non-aqueous binary mixtures at a temperature of 310.15 K. The minimum solubility value was found to be 9.10 (±0.44)×10^{-3} mol/L in neat 2-propanol, while the maximum solubility value was 2.34 (±0.06)×10^{-1} mol/L in neat PG at the studied temperature. XRPD characterization tests of both the raw API and the saturated API in PG+2-propanol binary mixtures showed that the crystallinity of the API remained unchanged. There was no polymorphic transformation occurring during the dissolution process in the PG + 2-propanol non-aqueous binary mixtures. Additionally, the density of the saturated drug solution was determined experimentally.

References

Al-Rubaie, A. Z., Al-Jadaan, S. A. S., Abd Al-Wahed, A. T., & Raadah, I. A. (2021). Synthesis, characterization and biological studies of some new organometallic compounds containing mercury, selenium and tellurium based on p-aminobenzoic acid. *Journal of Physics: Conference Series*, *2063*(1), 012003. https://doi.org/10.1088/1742-6596/2063/1/012003

Foroughi, H., Rahimpour, E., Kouhkan, M., Fathi Azarbayjani, A., & Jouyban, A. (2023). Solubility enhancement of atorvastatin calcium and ethanol-mediated transition with some surfactants. *Physics and Chemistry of Liquids*, *61*(4), 285–290. https://doi.org/10.1080/00319104.2023.2210252

Haroon, F., Farwa, U., Arif, M., Raza, M. A., Sandhu, Z. A., El Oirdi, M., Farhan, M., & Alhasawi, M. A. I. (2023). Novel Para-Aminobenzoic Acid Analogs and Their Potential Therapeutic Applications. *Biomedicines*, *11*(10), 2686. https://doi.org/10.3390/biomedicines11102686

Jouyban-Gharamaleki, V., Rahimpour, E., Hemmati, S., Martinez, F., & Jouyban, A. (2020). Mesalazine solubility in propylene glycol and water mixtures at various temperatures using a laser monitoring technique. *Journal of Molecular Liquids*, *299*, 112136. https://doi.org/10.1016/j.molliq.2019.112136

Martínez, F., Jouyban, A., & Acree Jr, W. E. (2017). Pharmaceuticals Solubility is Still Nowadays Widely Studied Everywhere. *Pharmaceutical Sciences*, *23*(1), 1–2. https://doi.org/10.15171/PS.2017.01

Savjani, K. T., Gajjar, A. K., & Savjani, J. K. (2012). Drug Solubility: Importance and Enhancement Techniques. *ISRN Pharmaceutics*, *2012*, 1–10. https://doi.org/10.5402/2012/195727

Tang, X.-M., Hu, W., Fan, L., Wang, H., Tang, M.-H., & Yang, D.-C. (2020). Synthesis and Evaluation of Novel Peptidomimetics Bearing p -aminobenzoic Acid Moiety As Potential Antidiabetic Agents. *Future Medicinal Chemistry*, *12*(11), 991–1013. https://doi.org/10.4155/fmc-2018-0372

CHEMISTRY

Analytical Chemistry

Biochemistry

Drug Design & Drug Delivery (Computational and Experimental)

Energy Materials (Synthesis, Characterizations, Applications)

Inorganic Chemistry

Nanochemistry

Organic Chemistry

Physical Chemistry

Nanotechnology, Surface Coatings and Films

Polymer Chemistry

MUF Resin with Low Formaldehyde Emissions for Wood-Based Panel Industry

Neslihan Karaca[a,b], Nesrin Köken[a], Başak Bengü[b]

[a] Istanbul Technical University/ Faculty of Science, Department of Chemistry, Türkiye
[b] Kastamonu Entegre Ağaç San. ve Tic. A.Ş., Department of R&D, Türkiye
karaca19@itu.edu.tr

Keywords: Melamine Urea Formaldehyde, Wood Adhesive, Particleboard, Low Formaldehyde Emission.

Aim

The wood-based panel industry extensively utilizes resins such as urea formaldehyde (UF), melamine formaldehyde (MF), phenol formaldehyde(PF) and melamine urea formaldehyde (MUF) due to their excellent adhesive properties and cost-effectiveness. However, these resins are well-known sources of formaldehyde emissions, which pose significant environmental and health concerns. This study aims to investigate the modification of MUF resin with silane compounds to reduce formaldehyde emissions from wood-based panels without compromising their mechanical and thermal properties. Specifically, the study focuses on evaluating the effects of silane incorporation at varying concentrations on the properties rheological and termal of MUF resin. Besides performance of particleboards produced with these modified resins.

Material and Method

In this study, control MUF resin was synthesized using melamine, urea, and formaldehyde chemicals, following established industrial procedures. Silane modification was performed by adding bis(trimethoxysilylpropyl)amine (BTMSPA) at three different weight ratios: 1%, 3%, and 5%. The modified and unmodified resins were then used to manufacture three-layer particleboards with a thickness of 8 mm. The pressing process was conducted at 200 °C for 4 minutes to ensure proper curing and bonding.
Physicochemical characterization of the resins included density measurements and rheological analyses. Viscosity and gelation time were determined using a rheometer under controlled temperature conditions. Thermal properties were assessed by differential scanning calorimetry (DSC) and thermogravimetric analysis (TGA). Mechanical properties of the particleboards were evaluated through internal bond strength (IB), modulus of elasticity (MOE), and modulus of rupture (MOR) tests, following relevant standards.
Formaldehyde emissions from the particleboards were quantified using the perforator method in compliance with TS EN 120 standard. In this method, samples were heated in toluene to release formaldehyde, which was then absorbed in distilled water and measured by photometric analysis(Popović et al., 2020).

Findings

The incorporation of silane compounds at 1%, 3%, and 5% ratios into Melamine Urea Formaldehyde (MUF) resin resulted in measurable changes in resin characteristics. Among these changes, rheological behavior was particularly influenced by the presence of silane, providing insight into the interactions between the silane compounds and the resin matrix. The rheological analysis of MUF resins modified with bis(trimethoxysilylpropyl)amine (BTMSPA) revealed a clear trend of increasing viscosity as the silane content increased from 1% to 5%. This increase in viscosity suggests that silane molecules interact with the resin matrix, possibly through the formation of siloxane bonds or hydrogen bonding with urea and melamine functional groups. Such interactions reduce the mobility of polymer chains, leading to a more viscous resin system. This behavior is consistent with previous studies that report silane compounds acting as coupling agents, enhancing cross-link density and molecular entanglement in thermosetting resins (Lee et al., 2022; Kumar et al., 2023). The higher viscosity may also influence the resin's flow during pressing, potentially affecting the impregnation of wood particles and ultimately the panel's mechanical properties.

Gelation time measurements showed a progressive extension with increasing silane content. This indicates that silane modification slows down the curing kinetics of MUF resin. The delay in gelation may be attributed to the steric hindrance introduced by silane groups or the alteration of reactive sites available for cross-linking. DSC thermograms supported this interpretation by exhibiting shifts in the exothermic curing peaks toward higher temperatures and broader peak profiles as silane concentration increased. These changes reflect a modified polymerization pathway, possibly involving the formation of siloxane networks that compete or cooperate with traditional formaldehyde-based cross-links. Such modification of curing behavior can be advantageous by providing a more controlled curing process, reducing internal stresses and defects in the final particleboard (Zhang et al., 2021).

Thermogravimetric analysis (TGA) demonstrated that the thermal stability of MUF resins was maintained after silane incorporation. The mass loss profiles exhibited typical multi-step degradation patterns corresponding to the decomposition of organic resin components. Importantly, no significant reduction in the onset decomposition temperature was observed, indicating that silane modification does not compromise the thermal resistance of the resin. This is critical for industrial applications, where particleboards are exposed to elevated temperatures during both pressing and service life. Furthermore, differential scanning calorimetry (DSC) results confirmed that the incorporation of silane did not negatively impact the curing kinetics of the resin, supporting the suitability of this modification for practical processing conditions.

Mechanical testing of particleboards bonded with silane-modified MUF resins revealed that internal bond strength (IB), modulus of elasticity (MOE), and modulus of rupture (MOR) values were comparable to those of boards produced with unmodified resin. This indicates that the structural integrity of the panels was preserved despite the chemical modification. The preservation of mechanical properties is essential to ensure that environmental benefits from reduced formaldehyde emissions do not come at the cost of product performance. The slight increase in viscosity and extended curing time did not negatively impact resin penetration or bonding quality. Similar findings have been reported in recent literature, where silane-modified adhesives maintained or improved mechanical properties in wood composites (Kumar et al., 2023).

The most significant outcome of this study is the reduction in formaldehyde emissions from particleboards bonded with silane-modified MUF resins. Formaldehyde release decreased progressively with increasing silane content, with even 1% silane addition producing measurable emission reductions. This effect is likely due to the chemical interaction between silane groups and free formaldehyde molecules, possibly through the formation of stable bonds that immobilize formaldehyde within the resin matrix. Additionally, silane-induced changes in curing kinetics and cross-link density may reduce the availability of free formaldehyde by promoting more complete polymerization. The perforator method results align with growing research emphasizing the role of resin modification in mitigating indoor air pollution and health risks associated with formaldehyde exposure (Zhang et al., 2021).

Conclusion

In conclusion, modification of Melamine Urea Formaldehyde (MUF) resin with silane compounds offers a very promising strategy to effectively reduce formaldehyde emissions from wood-based particleboards while preserving critical resin and panel properties. The study showed that silane addition increased resin viscosity and extended gelation time, indicating modified curing dynamics that remained compatible with industrial processing requirements. Thermal analyses confirmed that these modified resins maintained their thermal stability and ensured their suitability for high-temperature pressing used in particleboard production. Formaldehyde emission measurements show further reductions in emissions with increasing silane addition amounts. Considering the classification of formaldehyde as a human carcinogen and its role as a major indoor air pollutant, reducing its emissions is essential for consumer safety and regulatory compliance. This silane modification approach not only addresses these environmental and health concerns, but also aligns with global trends toward sustainable materials and green chemistry in the wood panel industry, providing a scalable and effective solution to meet increasingly stringent environmental standards and improve indoor air quality.

Acknowledgments

The authors would like to thank the Scientific and Technical Research Council of Turkey (TUBITAK) 2244 Industrial PhD Program-Istanbul Technical University-Kastamonu Entegre Ağaç San. ve Tic. A.Ş., with Project No: 118C107 and also Istanbul Technical University Research Foundation with ITU-BAP Project No: TDK-2023-44646.

References

Kumar, R., Singh, D., & Sharma, A. (2023). Rheological and thermal characterization of silane-modified urea-formaldehyde resins for particleboard applications. Polymer Testing, 115, 107837. https://doi.org/10.1016/j.polymertesting.2023.107837

Popović M, Điporovic MM, Gavrilović GI. (2020). New standards and regulations on formaldehyde emission from wood-based composite panels, Zastita Materijala, 61(2):152-160. doi:10.5937/zasmat2002152P

Zhang, Y., Wang, H., & Li, J. (2021). Advances in formaldehyde emission reduction from wood-based panels: A review of resin modification strategies. Journal of Cleaner Production, 280, 124456. https://doi.org/10.1016/j.jclepro.2020.124456

COMPUTATIONAL SCIENCE AND ENGINEERING

Computational Biology

Computational Fluid Dynamics

Identification of Inhibitors Targeting Two-component Regulatory System in Acinetobacter baumannii Called AdeRS

Fatih Kemaloğlu[a], Sefer Baday[b]

[a] Computational Science and Engineering Department, Informatics Institute Istanbul Technical University, Türkiye
[b] Applied Informatics Department, Informatics Institute Istanbul Technical University, Türkiye
kemalogluf23@itu.edu.tr

Keywords: Acinetobacter Baumannii, adeRS, Docking, Drug Target, Efflux Pump.

Aim

The objective of study is to identify novel inhibitors targeted to the two-component regulatory system in Acinetobacter baumannii called adeRS that regulate gene expression of adeABC efflux pump. AdeS is a transmembrane histidine kinase that senses signal and transmits to the adeR response regulator that initiates the transcription of adeABC efflux pump (Figure 1) (Wimalasekara, White, & Kumar, 2025). The adeABC plays a critical role in reducing antibiotic susceptibility to multiple type of drugs including aminoglycoside, β-lactam, tetracycline, fluoroquinolone, chloramphenicol, trimethoprim and tigecycline (Ciftci & Asik, 2011). Thus, our study targets the adeABC regulators to inhibit antibiotic resistance in A. baumannii. To achieve this, molecular docking and molecular dynamics (MD) simulations were performed to screen and evaluate potential inhibitors.

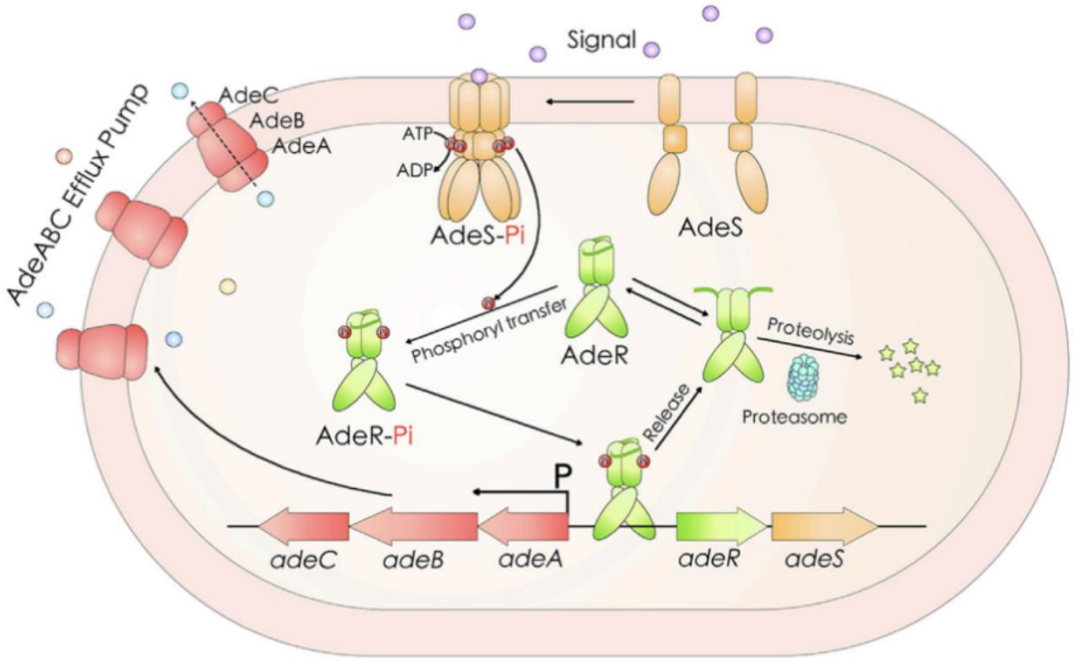

Figure 1. Schematic representation of the regulation of AdeABC gene expression. A signal from the environment causes autophosphorylation of the AdeS histidine kinase, and then AdeR becomes phosphorylated. Phosphorylated AdeR binds to a specific DNA sequence between the adeA and adeR promoter regions and initiates gene transcription (Ouyang et al., 2021).

Material and Method

To address this objective, ATP-binding domain of adeS (residue 204-357) and DNA binding domain of adeR (residue 139-247) were selected as receptor through in-silico studies. Both structure of adeS and adeR were solved (7CCH.PDB and 5X5L.PDB, respectively); however, some of the regions are missing (residue 298, 299, 307-319 in adeS and residue 159,199, 240-247 in adeR) (Wen et al., 2017, Ouyang et al., 2021). Therefore, we used

AlphaFold3 web server to model kinase domain of adeS (residue 139-357) with ATP and DNA-binding domain of adeR (residue 139-247) with HOLO state. Before virtual screening, we performed 1μs MD simulations of adeS to check its dynamics and stability with ATP and of adeR itself to obtain its APO state. There are studies in the literature showing that adeR mutations increase the expression of adeABC. The position of the mutations reported in these studies within the adeR protein have been examined. Among the reported mutations, only L192R and E291A are in the DNA-binding region targeted in this project (Yoon, Courvalin, & Grillot-Courvalin, 2013, Lari, Ardebili, & Hashemi, 2018). Therefore, these two mutations will be included in the molecular screening calculations. To understand whether there are structural changes in adeR due to these two mutations, 1 μs simulations were performed for each mutation. All systems were prepared in CHARMM-GUI web server (Jo, Kim, Iyer, & Im, 2008). Their atom parameters were generated with CHARMM36m force-field (Huang et al., 2016). All systems were run with NAMD3.0 simulation package (Phillips et al., 2020). Then, we clustered the trajectories from each system to obtain dominant structure to be used in molecular docking simulation. For virtaul screening, we applied a high-throughput screening of 3.3 million molecules retrieved from the ZINC20 database using GNINA, which is a deep learning-enhanced version of AutoDock VINA, where binding poses are generated similarly to AutoDock VINA, but scored using a CNN-based deep learning framework (McNutt et al., 2021). Molecules that are ranked in top-10K for GNINA pose score results were selected and redocked with GlideXP (Friesner et al., 2006). The top 200 molecules were clustered using the 'fingerprint clustering' method with the RDKit module, and a single representative molecule was selected for each cluster. In the final step, their ADME properties were assessed using QikProp. Among the ADME properties, molecules having higher bioavailability were selected and their dynamics in the binding site were tested performing 100ns MD simulation with Desmond. In the final stage, binding affinities were evaluated with thermal_mmgbsa.py on the last 20ns trajectories of the MD simulations.

Findings

In the first stage of our study, the structures of AdeS and AdeR were refined using molecular dynamics (MD) simulations. Each system was initiated with three different initial velocities. To analyze the simulation results, root mean squared deviation (RMSD) analysis was performed. Additionally, the RMSD of the ATP molecule was also calculated. In ATP-bound AdeS simulations, the ATP molecule remained stable in all systems. The RMSD value of the protein stabilized after deviating approximately 3.5 Å from the initial state (Figure 2). In wild-type and mutant AdeR simulations, the RMSD value stabilized after deviating around 1.5 Å from the initial position (Figure 3). In the clustering analysis, frames from AdeS simulations were divided into 100 clusters, while frames from AdeR simulations were grouped into 10 clusters. The conformation of AdeR in aqueous solution was compared with its DNA-bound conformation. In the AdeR crystal study, both the DNA-bound and unbound forms of the AdeR protein were resolved and structurally aligned. When we aligned the most dominant cluster we obtained for AdeR with the initial structure, we observed similar results to the conformationally changing regions suggested by the reference (Figure 4A-B). Normally, clustering calculations were planned to be done for 10 clusters. However, since the loop structure in the ATP binding region is very flexible, 10 clusters did not provide sufficient resolution. Therefore, clustering was performed for 100 clusters. To determine the protein structure to be used in docking calculations, not only the most dominant cluster was considered, but also the structure with the best potential for molecule binding was selected. For this, the representative structures of each cluster were docked with a randomly selected set of 5000 small molecules using the AutoDock Vina docking program. Based on the docking results, the structure that showed the highest average binding affinity and represented the cluster with the most frames was selected for docking calculations with 3.7 million molecules. As a result of these processes, 97 molecules in the AdeS ligand set and 84 molecules in the AdeR ligand set were tested using molecular dynamics simulations to evaluate their stability in the binding site. The binding affinities of molecules that remained stable in the binding site throughout the simulation were calculated. Finally, the 20 molecules with the highest binding affinities for AdeS and AdeR were suggested for experimental testing.

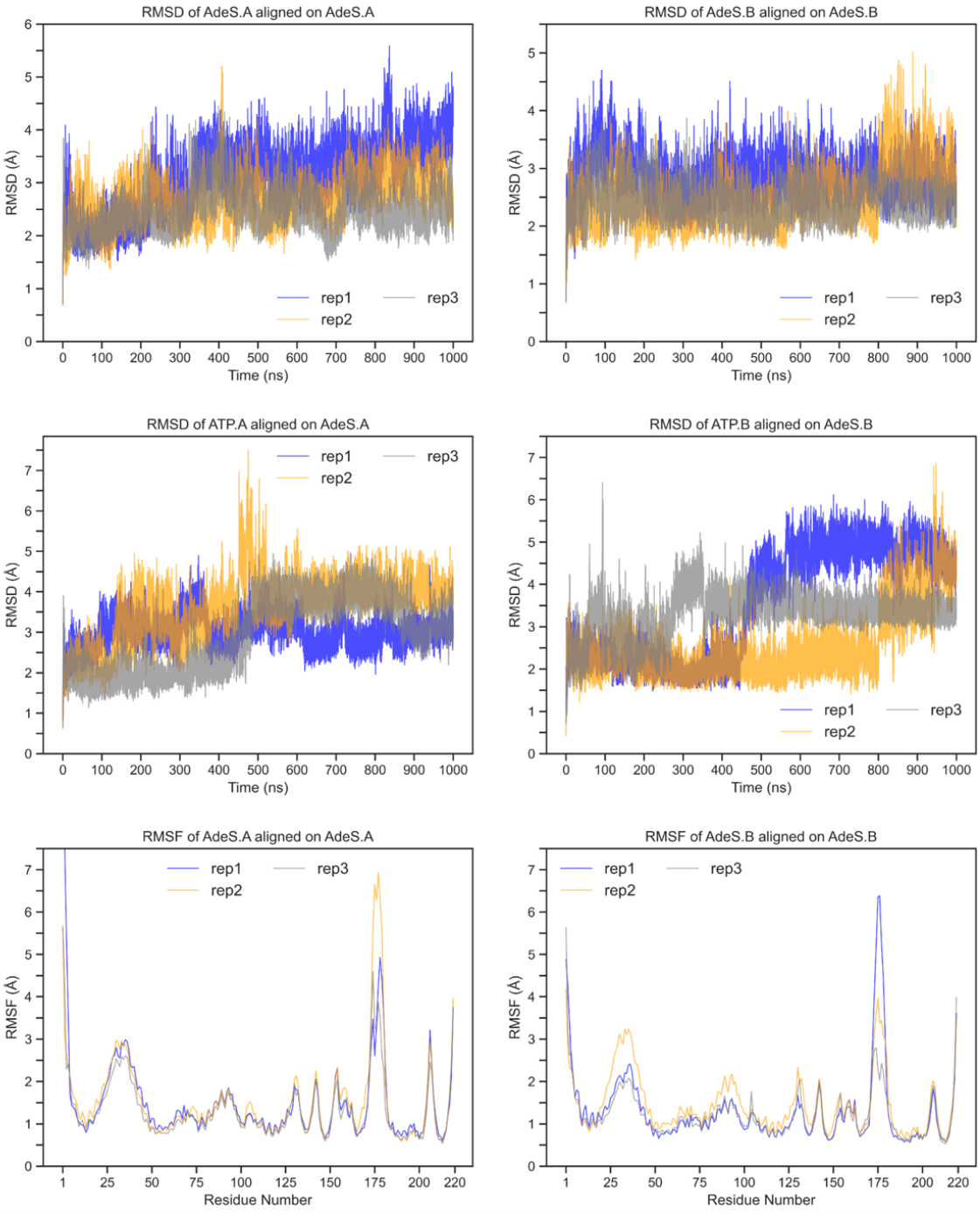

Figure 2. Frame Analysis of ATP-Bound AdeS Histidine Kinase.

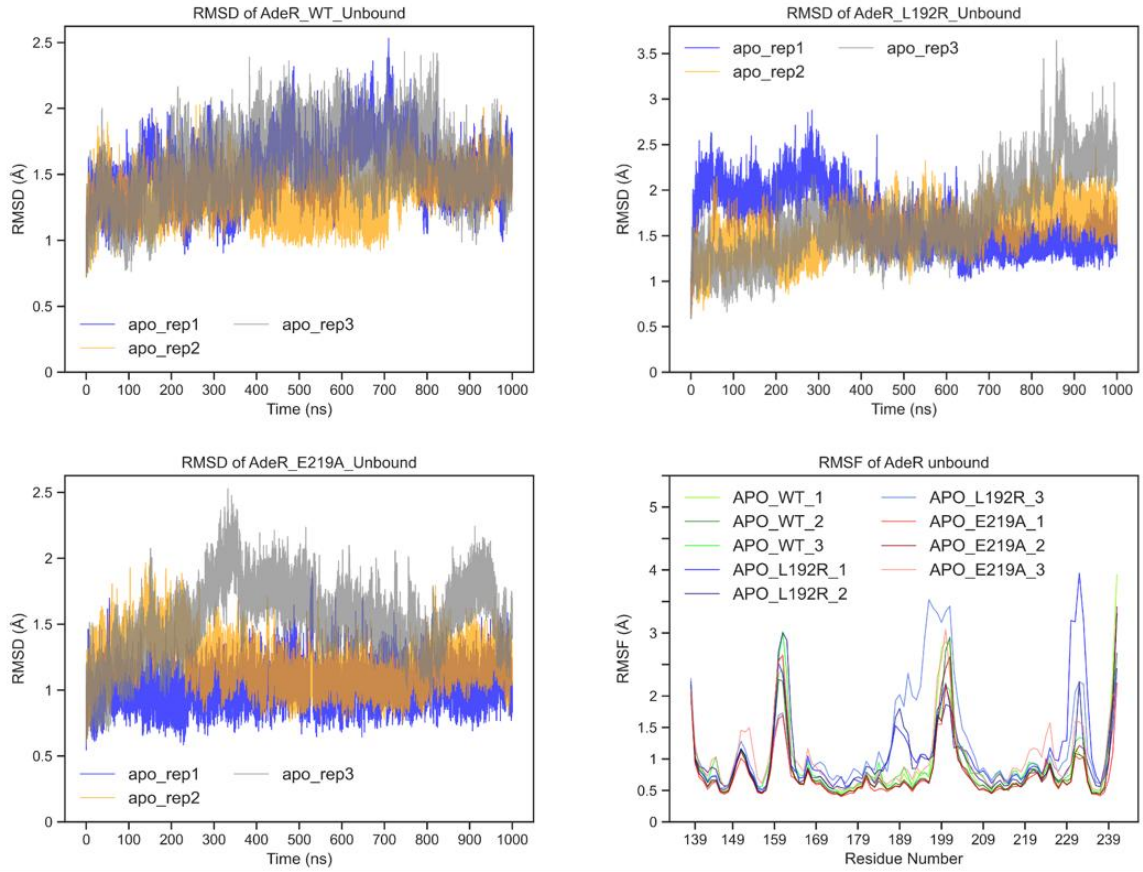

Figure 3. Frame Analysis of ATP-Bound AdeR Response Regulator.

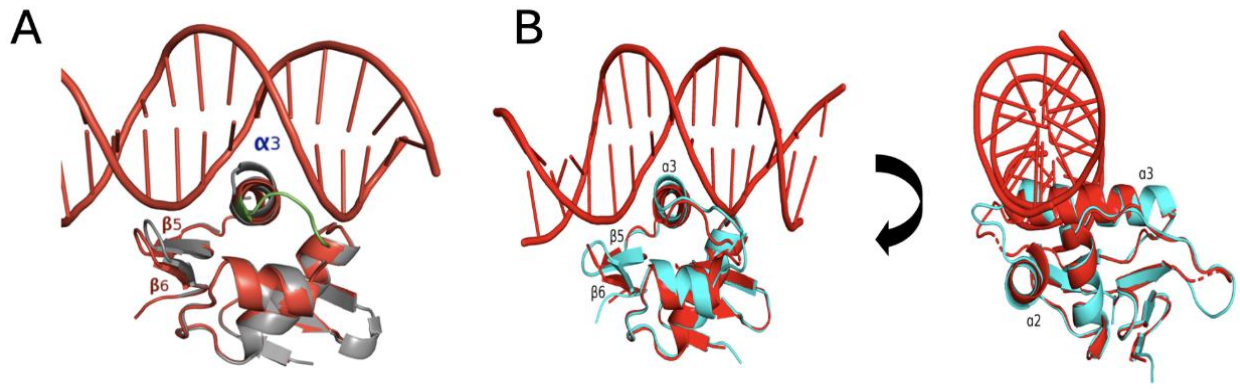

Figure 4. A) Structural Alignment of DNA-Bound and Unbound Forms of AdeR DBD Protein Red: DNA-bound structure, Grey: DNA-unbound structure (Wen et al., 2017). B) Structural Alignment of DNA-Bound AdeR DBD Crystal Structure (Red) with the First Cluster Representative Structure (Cyan).

Conclusion

Two-component regulatory systems play a crucial role in bacterial resistance to antibiotics (Scoffone et al., 2025). In this study, we identified potential molecules that can inhibit the AdeRS two-component proteins, which regulate the expression of the adeABC efflux pump, using in-silico methods. The approach aims to inhibit adeABC expression, allowing existing antibiotics to be used more effectively. As a result of our study, we identified potential

inhibitors against both proteins. As a future direction, our collaborators will conduct experimental testing on the suggested molecules.

References

Wimalasekara, R. L., White, D., & Kumar, A. (2025). Targeting *Acinetobacter baumannii* resistance-nodulation-division efflux pump transcriptional regulators to combat antimicrobial resistance. *NPJ Antimicrobials and Resistance, 3*(1), Article 4. https://doi.org/10.1038/s44259-024-00074-z

Ciftci, I. H., & Asik, G. (2011). Antibiotic resistance mechanisms of *Acinetobacter baumannii*. *ANKEM Dergisi, 25*(3), 196–207. https://doi.org/10.5222/ankem.2011.196

Wen, Y., Zhang, H., Li, J., Chen, Y., Wang, Y., Li, H., & Yang, C.-G. (2017). Mechanistic insight into how multidrug resistant *Acinetobacter baumannii* response regulator AdeR recognizes an intercistronic region. *Nucleic Acids Research, 45*(16), 9773–9787. https://doi.org/10.1093/nar/gkx624

Ouyang, Z., Zhou, H., Wang, Y., Ma, Y., He, X., & He, C. (2021). Proteolysis and multimerization regulate signaling along the two-component regulatory system AdeRS. *iScience, 24*(5), 102476. https://doi.org/10.1016/j.isci.2021.102476

Yoon, E. J., Courvalin, P., & Grillot-Courvalin, C. (2013). RND-type efflux pumps in multidrug-resistant clinical isolates of *Acinetobacter baumannii*: Major role for AdeABC overexpression and *adeRS* mutations. *Antimicrobial Agents and Chemotherapy, 57*(7), 2989–2995. https://doi.org/10.1128/AAC.02556-12

Lari, A. R., Ardebili, A., & Hashemi, A. (2018). *adeR-adeS* mutations & overexpression of the AdeABC efflux system in ciprofloxacin-resistant *Acinetobacter baumannii* clinical isolates. *Indian Journal of Medical Research, 147*(April), 413–421. https://doi.org/10.4103/ijmr.IJMR_644_16

Jo, S., Kim, T., Iyer, V. G., & Im, W. (2008). CHARMM-GUI: A web-based graphical user interface for CHARMM. *Journal of Computational Chemistry, 29*(11), 1859–1865. https://doi.org/10.1002/jcc.20945

Huang, J., Rauscher, S., Nawrocki, G., Ran, T., Feig, M., de Groot, B. L., Grubmüller, H., & MacKerell, A. D., Jr. (2016). CHARMM36m: An improved force field for folded and intrinsically disordered proteins. *Nature Methods, 14*(1), 71–73. https://doi.org/10.1038/nmeth.4067

Phillips, J. C., Hardy, D. J., Maia, J. D. C., Stone, J. E., Ribeiro, J. V., Bernardi, R. C., Buch, R., Fiorin, G., Hénin, J., Jiang, W., McGreevy, R., Melo, M. C. R., Radak, B. K., Skeel, R. D., Singharoy, A., Wang, Y., Roux, B., Aksimentiev, A., Luthey-Schulten, Z., ... Schulten, K. (2020). Scalable molecular dynamics on CPU and GPU architectures with NAMD. *The Journal of Chemical Physics, 153*(4), 044130. https://doi.org/10.1063/5.0014475

McNutt, A. T., Francoeur, P. G., Aggarwal, R., Masuda, T., Meli, R., Ragoza, M., Sunseri, J., & Koes, D. R. (2021). GNINA 1.0: Molecular docking with deep learning. *Journal of Cheminformatics, 13*(1), 43. https://doi.org/10.1186/s13321-021-00522-2

Friesner, R. A., Banks, J. L., Murphy, R. B., Halgren, T. A., Klicic, J. J., Mainz, D. T., Repasky, M. P., Knoll, E. H., Shelley, M., Perry, J. K., Shaw, D. E., Francis, P., & Shenkin, P. S. (2006). Extra precision glide: Docking and scoring incorporating a model of hydrophobic enclosure for protein-ligand complexes. *Journal of Medicinal Chemistry, 49*(21), 6177–6196. https://doi.org/10.1021/jm051256o

Scoffone, V. C., Trespidi, G., Barbieri, G., Arshad, A., Israyilova, A., & Buroni, S. (2025). The evolution of antimicrobial resistance in *Acinetobacter baumannii* and new strategies to fight it. *Antibiotics, 14*(1), Article 85. https://doi.org/10.3390/antibiotics14010085

Molecular Dynamics Simulations of CHK2 Kinase Domain Mutants

Ebru Tuncay[a], Clara Xazal Buran[a], Gizem Dinler Doganay[a], Levent Doganay[b], Mert Gur[c]

[a]Istanbul Technical University, Molecular Biology-Genetics and Biotechnology Program, Turkiye
[b] Umraniye Training and Research Hospital, Department of Medical Genetics, Division of Cancer Genetics, Turkiye
[c]University of Pittsburgh, Department of Computational and Systems Biology, USA
tuncay22@itu.edu.tr

Keywords : CHK2, DNA Repair, Molecular Dynamics Simulations, Mutations, Tumor-Suppressing Gene.

Aim

Cancer remains a significant global cause of mortality, highlighting the importance of understanding the complex molecular mechanisms that drive its development. The Checkpoint kinase 2 (CHEK2) gene is a critical target in cancer prevention, as it plays a pivotal role in maintaining genomic stability by regulating DNA repair processes and cell cycle checkpoints. Although mutations in CHK2 protein have been linked to a variety of cancers, many details of its catalytic cycle are still unclear and require further investigation. Understanding the molecular details of CHK2's function and dysregulation could lead to novel targeted therapeutic interventions and enhanced cancer management strategies.

As a key tumor-suppressing gene, CHEK2 encodes the vital serine/threonine kinase protein CHK2, essential for cell cycle checkpoint control and DNA repair pathways. Its role is crucial in preserving genomic stability and protecting against DNA damage. Key structural components of CHK2 include the N-terminal SQ/TQ cluster domain (SCD), a central forkhead-associated (FHA) domain, and the C-terminal serine/threonine kinase domain (KD). The SCD contains phosphorylation sites important for CHK2's substrate recognition. The FHA domain enables CHK2 to sense and respond to DNA damage signals, while the KD is responsible for phosphorylating target proteins (Ung, 2018).

Mutations in CHK2 have been linked to various cancers, such as breast cancer, underscoring its significant role across multiple cancer types. Such mutations or losses can impair CHK2's normal function, diminishing the cell's capacity to respond effectively to DNA damage, which can lead to uncontrolled cell growth and cancer development (Zhou, 2000). Understanding how CHK2 dysfunction contributes to cancer is important for developing targeted therapies and strategies to fight tumorigenesis.

This study investigates a set of CHEK2 gene variants in the KD to assess their potential mutational impact on CHK2 protein structure and dynamics through all-atom molecular dynamics simulations. Five mutations, namely G306A (Boonen, 2022), E351D (Richards, 2015), S356L (Lim, 2023), D409V (Branco, 2018), and V415I (White, 2022), were selected for in silico analysis. The primary aim was to determine how these mutations influence CHK2 dynamics and structural integrity, as disruptions in CHK2 function could impair DNA repair and cell cycle control, ultimately increasing breast cancer susceptibility. By investigating these mutations, this work seeks to deepen our understanding of CHK2's role in tumor suppression and provide insights into potential targeted therapies for individuals carrying CHEK2 mutations.

Material and Method

To obtain active wild type (WT) CHK2, starting structural model was constructed by combining structural information derived from the crystal structures with PDB IDs 3I6U (Cai Z. C., 2009) and 2CN5 (Oliver, 2006). Residues S379, T383, T387, and T389 within the CHK2 activation loop were phosphorylated. Additionally, the ADP molecule, two Mg^{2+} ions, and crystal water molecules derived from the 2CN5 structure were included in the system. Mutant structures containing G306A, E351D, S356L, D409V, and V415I were prepared using the Mutator plugin in VMD. All structures were subsequently solvated in a TIP3P water box, applying padding dimensions of 28 Å along the x-axis, 20 Å along the y-axis, and 28 Å along the z-axis. Systems were neutralized, and ion concentrations were adjusted to 210 mM KCl and 20 mM NaCl. All system preparation steps were performed using VMD (Humphrey W, 1996).

To evaluate the structural dynamics of CHK2 and the effects of the selected mutations, MD simulations were performed using NAMD 3.0 (Phillips JC, 2020)and the CHARMM36 all-atom force fields (Best, 2012). Two femtosecond time step was employed, and the SHAKE algorithm was applied to constrain bonds involving hydrogen atoms. Long-range electrostatic interactions were treated using the Particle Mesh Ewald (PME) method. All simulations were conducted under NPT ensemble conditions, with temperature and pressure held constant using a Langevin Nosé-Hoover approach.

Prior to production runs, systems were minimized and equilibrated in multiple steps. Initially, harmonic restraints were applied to the C_α, ADP, and Mg^{2+} atoms, allowing only water molecules to move freely. Following an initial unconstrained minimization, the heavy atoms of the protein, ADP, and Mg^{2+} were fixed, and the water molecules were equilibrated for 2 ns. Subsequent equilibration involved gradually releasing harmonic restraints on the C_α, ADP, and Mg^{2+} atoms. A final equilibration with no restraints was carried out before initiating production runs of 300 ns for each system.

To assess protein structural deformations throughout MD simulations, Root Mean Square Deviation (RMSD) (Phillips J. C., 2005) analysis was performed. RMSD quantitatively measures the average displacement of atoms between the structure at a given simulation time point and a reference structure. The starting structural model was used as reference structure. It is calculated as:

$$\mathrm{RMSD}(t) = \sqrt{\frac{1}{N}\sum_{i=1}^{N} \left(r_i(t) - r_i(0)\right)^2}$$

where N is the total number of atoms, $\mathbf{r}_i(t)$ is the position of atom i at time t, and $\mathbf{r}_i^{ref}$ is the position of atom i in the reference structure.

The flexibility of individual residues was probed via Root Mean Square Fluctuation (RMSF) (Karplus, 2002) analysis. RMSF provides a measure of residue-wise flexibility by quantifying fluctuations of atomic positions around their average positions throughout the simulation. It is calculated using the following formula:

$$\mathrm{RMSF} = \sqrt{\frac{1}{T}\sum_{t=1}^{T} \left\| r_i(t) - \langle r_i \rangle \right\|^2}$$

where T is the total number of trajectory frames, $\mathbf{r}_i(t)$ represents the position of residue i at time t, and $\langle \mathbf{r}_i \rangle$ is the average position of residue i across the entire trajectory.

In RMSD and RMSF calculations, only the coordinates of alpha carbon (C_α) atoms were used.

Findings

For each mutant, two 300 ns long MD simulation runs were carried out. Each simulation trajectory was independently analyzed for RMSD and RMSF values. RMSD analysis indicated that three mutants, G306A, D409V, and V415I, exhibited higher RMSD values relative to the WT, as shown in Figure 1. In these trajectories, the mutants remained above the WT RMSD curve, suggesting increased conformational mobility and structural instability.

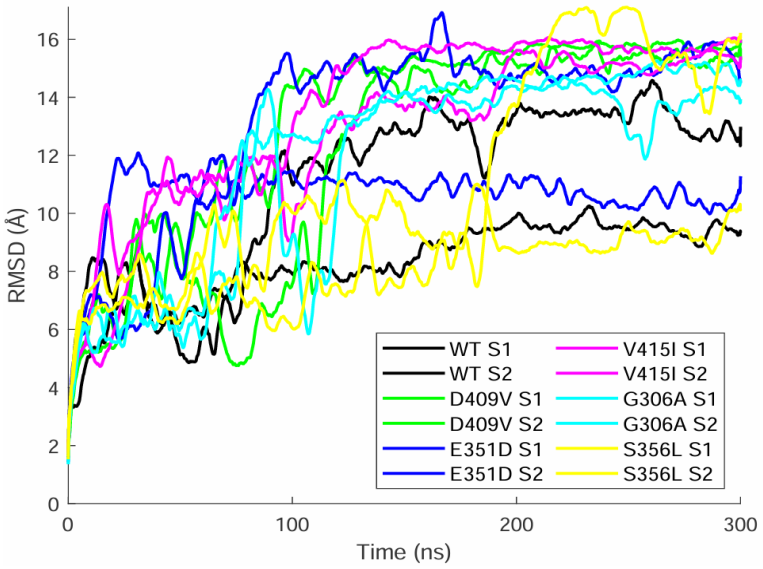

Figure 1. RMSD Comparison of Wild-Type and Mutant CHK2 Proteins.

In the 205-270 amino acid range, all mutations exhibit lower RMSF values compared to the WT (Figure 2). This region includes the Gly-rich region (residues 227–232), which is considered structurally significant. Additionally, in the 370-405 amino acid range, our analysis shows that the RMSF values of all mutations are noticeably higher than those of the WT. This region contains the A-loop (residues 368–394), which plays a crucial role in the protein's. Visual representations generated with VMD were added to the figure to highlight these critical regions.

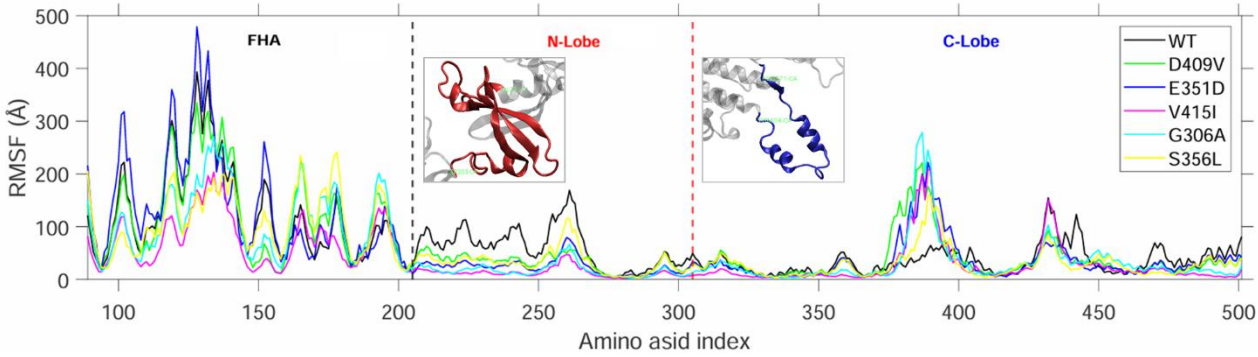

Figure 2. RMSF Values for Mutants and Wild Type by Amino Acid Index.

Conclusion

In summary, MD simulations of CHK2 revealed noteworthy structural and dynamic alterations resulting from five specific mutations within the kinase domain. RMSD analysis demonstrated that mutations G306A, D409V, and V415I induce notable conformational changes, potentially leading to structural deviations compared to the WT protein. These structural changes could compromise the stability required for CHK2's tumor suppressor functions. In addition to those structural changes shown by RMSD analysis, RMSF analysis further showed that these mutations affect protein dynamics, highlighting distinct fluctuations in the residues 205–270 and residues 370–405, both critical areas for CHK2's catalytic activity and regulatory role.

Collectively, these findings predict that the studied mutations could impact both the structural integrity and dynamic behavior of CHK2, potentially impairing its ability to regulate cell cycle checkpoints and respond effectively to DNA damage. Consequently, these mutations may increase susceptibility to cancer. This study

provides valuable insights into the functional consequences of CHEK2 variants and lays groundwork for future research into targeted therapies aimed at restoring CHK2's tumor-suppressive activities in affected individuals.

References

Best, R. B. (2012). Optimization of the Additive CHARMM All-Atom Protein Force Field Targeting Improved Sampling of the Backbone ϕ, ψ and Side-Chain χ1 and χ2 Dihedral Angles. Journal of Chemical Theory and Computation, 8(9), 3257-3273.

Boonen, R. A.-J. (2022). Functional analysis identifies damaging CHEK2 missense variants associated with increased cancer risk. Cancer Research, 82(4), 615-631.

Branco, P. R.-K. (2018). Uncovering association networks through an eQTL analysis involving human miRNAs and lincRNAs. . Scientific Reports, 8(1), 15050.

Cai, Z. C. (2009). Structure and activation mechanism of the CHK2 DNA damage checkpoint kinase. Molecular cell, 35(6), 818–829. https://doi.org/10.1016/j.molcel.2009.09.007.

Humphrey W, D. A. (1996). VMD: visual molecular dynamics. J Mol Graph, 33-8, 27-8. doi: 10.1016/0263-7855(96)00018-5. PMID: 8744570.

Karplus, M. &. (2002). Molecular dynamics simulations of biomolecules. Nature Structural Biology, 9(9), 646-652.

Kim, S. O. (2020). CHARMM-GUI Free Energy Calculator for Absolute and Relative Ligand Solvation and Binding Free Energy Simulations . J Chem Theory Comput, 16(11), 7207-7218.

Lim, B. W. (2023). Somatic inactivation of breast cancer predisposition genes in tumors associated with pathogenic germline variants. JNCI: Journal of the National Cancer 115(2), 181-189.

Oliver, A. W. (2006). Trans-activation of the DNA-damage signalling protein kinase Chk2 by T-loop exchange. . The EMBO journal, 25(13), 3179–3190 https://doi.org/10.1038/sj.emboj.7601209.

Phillips JC, H. D.-S. (2020). Scalable molecular dynamics on CPU and GPU architectures with NAMD. The Journal of chemical physics, 153(4), 044130. https://doi.org/10.1063/5.0014475.

Phillips, J. C. (2005). Scalable molecular dynamics with NAMD. J Comput Chem, 26(16), 1781-1802.

Richards, S. A.-F. (2015). Standards and guidelines for the interpretation of sequence variants: a joint consensus recommendation of the American College of Medical Genetics and Genomics and the Association for Molecular Pathology. . Genetics in medicine : official journal of the American College of Medical Genetics 17(5), 405–424. https://doi.org/10.1038/gim.2015.30.

Taylor, S. S. (2011). Protein kinases: evolution of dynamic regulatory proteins. Trends in biochemical sciences 36, 65-77.

Taylor, W. R. (2009). The checkpoint kinase Chk2 in cancer. . Cell Cycle, 8(5), 680-686.

Tibbetts, R. S. (2000). Functional interactions between the ATM protein and the CHK2 protein in the DNA damage response. . Nature, 404(6779), 570-574.

Ung, P. M. (2018). Redefining the Protein Kinase Conformational Space with Machine Learning. . Cell Chem Biol 25, 916-924.e912.

White, J. A. (2022). Whole-exome sequencing of Nigerian prostate tumors from the prostate cancer transatlantic consortium (CaPTC) reveals DNA repair genes associated with african ancestry. Cancer research communications, 2(9) , 1005-1016.

Zhou, B. B. (2000). The DNA damage response: putting checkpoints in perspective. Nature, 408(6811), 433–439.

COMPUTER ENGINEERING

Artificial Intelligence

Computer Networks

Cyber Security

Embedded Systems

Internet of Things

Neural Networks

Software Engineering

Effect of Topology on Energy Consumption in Low Power Wireless Sensor Networks

Namık Ceylan[a], Sıddıka Berna Örs Yalçın[b]

[a] Istanbul Technical University, Graduate Scholl, Electrical and Communication Engineering Program
[b] Istanbul Technical University Faculty of Electrical and Electronics Department of Electrical and Communication Engineering
ceylan23@itu.edu.tr, siddika.ors@itu.edu.tr

Keywords: Energy Saving, RPL, Topology, Wireless Sensor Networks, Cooja.

Aim

Wireless Sensor Networks (WSN) have been a very fast-growing practice. WSNs installed in difficult-to-access locations feature many sensors. Sensors in WSNs are expected to be able to set up their network, route packets, maintain network continuity, and self-repair the network against a change. The RPL protocol has been developed to perform these operations under the constraints of limited memory and processing power, a lossy wireless environment, most importantly, a limited energy supply. The battery life of the sensors determines the life of the network. The ability to save battery regardless of the source is a significant and critical issue in wireless sensor networks. What effect does topology formation have on energy consumption; we investigated this with Contiki Cooja Simulation. We studied energy consumption over different topics.

Material and Method

Wireless sensor networks are one of the most important structures of IoT systems. With the RPL protocol, sensors reach the main sensor directly or through neighboring sensors, automatically forming a network.A working group has been established by the IETF organization on the connection and transport of wireless sensor networks to the Internet. The goal of this working group, called 6LoWPAN, was to make low-power personal wireless area networks compatible with the IPv6 architecture. The 6LoWPAN structure is built on the 802.15.4 protocol previously standardized by the IEEE.With the features brought to the standard and stack structure, IEEE 802.15.4 compatible wireless sensor structures can communicate with the internet. IEEE 802.15.4 When verifying physical and data link layers, which are the first and second layers in the OSI architecture, the 6LoWPAN adaptation layer also acts as an interface between these two layers and the network layer. Wireless sensor nodes are by their very nature unlikely to work with existing routing protocols. For this reason, the IETF has adopted the IPv6 Routing Protocol for Low-Power and Lossy Networks (RPL) standards for low-power and lossy networks with another working group called ROLL (Routing over Low Power and Lossy Links) developed for IoT systems.
The main function of the RPL protocol is to enable the routing of data traffic between wireless sensors and the Internet cloud. In doing so, it also considers the features of wireless sensors such as low power consumption and loss. In RPL architecture, Objective Function (OF) methodology determines how RPL nodes translate one or more metrics into ranks, and how to optimize and select routes in a network. In the literature, there are objective functions considering several metrics like OF_0 with hop count, Minimum Rank with Hysteresis Objective Function (MRHOF) with Expected Number of Transmission (ETX) (known, OF_1).
The most critical issue in Wireless Sensor Networks is energy restriction. The battery life of the sensors determines the life of the network. It seems impossible to interfere with the many sensors installed in difficult geographies. Therefore, applications that will reduce energy consumption independently of the battery become important. The first step in networking is topology formation. In our study, we considered topology to examine its effect on energy consumption. For each sensor, the average power and energy consumption of the CPU, LMP, Rx, and Tx operating modes were calculated separately. Both single-hopping and multi-hopping topologies of the sensors trying to reach the main sensor were evaluated. The random and circular topologies were examined under the same conditions

and their average power and energy consumption were obtained by the Cooja Simulation, which we ran on Contiki-3.0, which we ran on.

Findings

In the figures, the main sensor (UDP-sink) is depicted in dark green, while the surrounding sensors (UDP-senders) are shown in yellow. The same number of sensors were arranged to form two distinct network topologies, and their energy consumption was analyzed during topology formation.
Each figure illustrates the spatial distribution of the main sensor and the other sensors. Additionally, the coverage area for each sensor is indicated in green. Accompanying tables present the average power consumption and calculated energy usage for each numbered sensor.
The average power and operational time values were derived from simulations conducted in Cooja, using Contiki OS version 3.0. Energy consumption was calculated by multiplying the average power by the corresponding active time. To ensure consistency across comparisons, sensor numbering remained identical between the two topologies, and each simulation ran for a duration of 20 minutes. The simulation parameters are summarized in Table 1.

Table 1. Contiki and Cooja configuration.

Simulation Parameter	**Value**
Operating System	Contiki-3.0
Radio Medium	Unit Disk Graph Medium
Sensör Menzili	100 m
MAC Layer	ContikiMAC
Network Protocol	RPL
Objektive Function	MRHOF
Sensor Type	Tmote Sky
Simulation Time	20 Minute

Circular Topology and Random Topology

A total of sixteen sensors (UDP-senders) were successfully deployed around a central main sensor (UDP-sink) without clustering too closely to one another. These sixteen sensors were arranged in two distinct configurations: one with a circular layout and the other with a random distribution within the coverage area of the main sensor. These two resulting topologies are illustrated in Figure 1 and Figure 2, respectively.

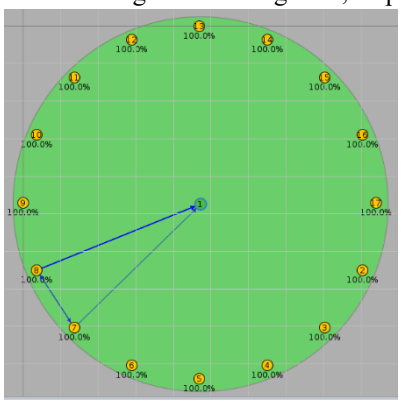

Figure 1. Circular Topology.

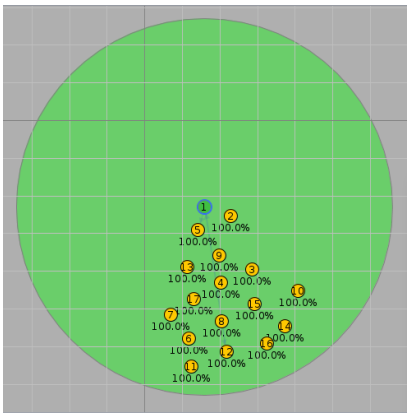

Figure 2. Random Topology.

The average power consumption in the CPU, LPM (low-power mode), Rx (receive), and Tx (transmit) modes, along with the time spent in each mode, was obtained from the Cooja simulation. Energy consumption was calculated individually for each operating mode, and the total energy consumption per sensor was determined by summing these values. This approach allowed for the total energy expenditure of each topology to be quantified. As presented in Table 2 and Table 3, the total energy consumed in the random topology was 2832.07 mJ, whereas the circular topology consumed 2603.28 mJ.

Table 2. Random topology power-energy consumption.

Sensor	CPU Power	LMP Power	Rx Power	Tx Power	Power	Energy
2	0.462	0.150	0.506	0.062	1.179	177.27
3	0.455	0.150	0.504	0.061	1.171	176.80
4	0.469	0.149	0.539	0.081	1.238	186.45
5	0.473	0.149	0.535	0.060	1.217	185.16
6	0.460	0.150	0.517	0.061	1.188	184.07
7	0.454	0.150	0.498	0.053	1.155	178.28
8	0.469	0.149	0.541	0.058	1.217	178.09
9	0.477	0.149	0.529	0.071	1.226	167.35
10	0.463	0.149	0.530	0.076	1.218	169.55
11	0.451	0.150	0.513	0.055	1.168	162.87
12	0.467	0.149	0.490	0.070	1.176	181.71
13	0.483	0.149	0.512	0.063	1.207	180.25
14	0.458	0.150	0.514	0.055	1.177	170.91
15	0.469	0.149	0.579	0.073	1.269	170.48
16	0.478	0.149	0.527	0.055	1.208	179.81
17	0.459	0.150	0.504	0.053	1.167	183.03
				Total	**19.18**	**2832.07**

Since sensors constantly communicate to establish and maintain the network, as well as to detect changes, sensors positioned very close to each other experience increased communication, which leads to higher energy consumption.

Circular Wide Topology and Random Wide Topology

In the initial circular and random topologies examined, the network was established without requiring multi-hop communication between sensors within the main sensor's range. In this study, the coverage area was expanded, and the network was designed to require four or more communication hops. The corresponding topologies are shown in Figures 3 and 4. As in the previous section, energy consumption was calculated for these configurations. As shown in Tables 4 and 5, the energy consumption for the random wide-area topology was 4101.35 mJ, whereas the circular wide-area topology consumed 3911.24 mJ.

Table 3. Circular Topology Power-Energy Consumption.

Sensor	CPU Power	LMP Power	Rx Power	Tx Power	Power	Energy
2	0.363	0.152	0.430	0.045	0.991	164.22
3	0.370	0.152	0.449	0.097	1.069	154.43
4	0.371	0.152	0.455	0.093	1.071	160.21
5	0.361	0.153	0.438	0.063	1.016	142.72
6	0.363	0.153	0.428	0.044	0.988	159.82
7	0.361	0.153	0.429	0.049	0.991	173.48
8	0.365	0.152	0.442	0.073	1.033	167.83
9	0.367	0.152	0.440	0.078	1.037	157.53
10	0.365	0.152	0.437	0.057	1.012	170.29
11	0.365	0.152	0.436	0.057	1.011	165.74
12	0.364	0.152	0.435	0.060	1.011	171.70
13	0.380	0.152	0.443	0.102	1.077	159.01
14	0.369	0.152	0.446	0.066	1.034	154.34
15	0.361	0.153	0.431	0.048	0.993	161.78
16	0.368	0.152	0.438	0.080	1.038	164.31
17	0.367	0.152	0.440	0.057	1.016	175.87
				Total	**16.39**	**2603.28**

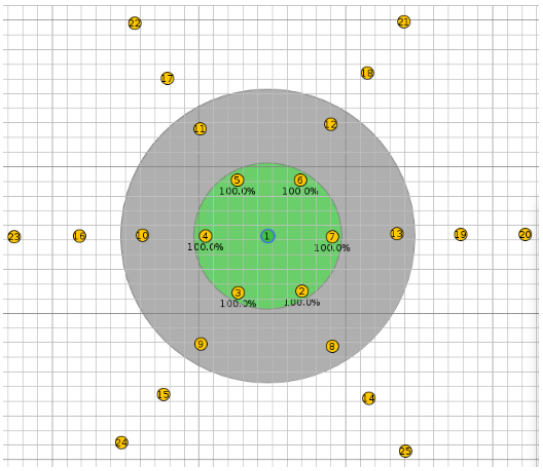

Figure 3. Circular Wide Topology.

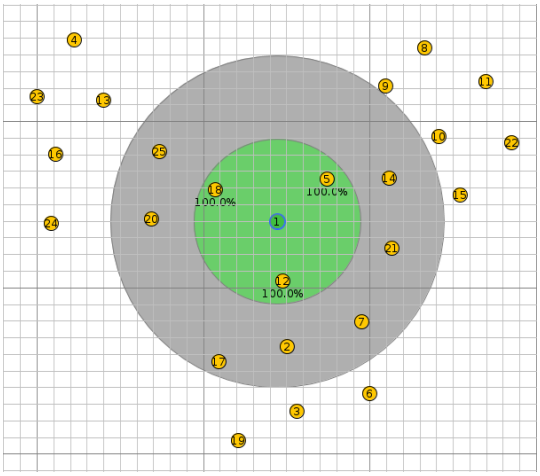

Figure 4. Random Wide Topology.

Energy consumption has increased due to unnecessary communication of the sensors in the group with each other and unnecessary jumping to reach the main sensor.

Table 4. Random wide topology power-energy consumption.

Sensor	CPU Power	LMP Power	Rx Power	Tx Power	Power	Energy
2	0.491	0.149	0.806	0.808	2.254	177.880
3	0.394	0.152	0.600	0.244	1.389	170.708
4	0.359	0.153	0.474	0.126	1.111	164.389
5	0.420	0.151	0.666	0.328	1.565	181.840
6	0.378	0.152	0.494	0.219	1.242	148.399
7	0.434	0.150	0.659	0.519	1.762	186.239
8	0.383	0.152	0.504	0.282	1.322	148.066
9	0.398	0.151	0.568	0.364	1.482	182.580
10	0.433	0.150	0.723	0.476	1.783	186.506
11	0.378	0.152	0.539	0.190	1.259	167.222
12	0.412	0.151	0.629	0.331	1.523	176.020
13	0.412	0.151	0.623	0.336	1.522	173.673
14	0.558	0.147	0.982	1.234	2.920	238.720
15	0.393	0.152	0.638	0.282	1.465	165.887
16	0.389	0.152	0.535	0.249	1.326	155.822
17	0.371	0.152	0.547	0.212	1.283	159.613
18	0.408	0.151	0.599	0.231	1.389	157.439
19	0.369	0.152	0.489	0.189	1.198	163.129
20	0.360	0.153	0.470	0.128	1.111	143.642
21	0.380	0.152	0.574	0.217	1.324	154.067
22	0.387	0.152	0.564	0.262	1.365	162.673
23	0.365	0.152	0.489	0.111	1.118	170.929
24	0.361	0.153	0.454	0.141	1.109	164.061
25	0.461	0.150	0.720	0.672	2.003	201.842
				Total	**35.82**	**4101.35**

Table 5. Circular wide topology power-energy consumption.

Sensor	CPU Power	LMP Power	Rx Power	Tx Power	Power	Energy
2	0.376	0.152	0.484	0.069	1.081	169.314
3	0.385	0.152	0.506	0.146	1.188	174.843
4	0.381	0.152	0.497	0.112	1.141	167.996
5	0.379	0.152	0.489	0.079	1.099	151.367
6	0.388	0.152	0.514	0.145	1.198	162.722
7	0.387	0.152	0.517	0.129	1.184	161.569
8	0.397	0.151	0.534	0.290	1.372	177.791
9	0.393	0.152	0.539	0.307	1.390	170.179
10	0.395	0.152	0.536	0.303	1.385	162.821
11	0.392	0.152	0.535	0.289	1.368	161.254
12	0.378	0.152	0.507	0.208	1.245	166.321
13	0.412	0.151	0.585	0.466	1.615	166.617
14	0.378	0.152	0.500	0.221	1.251	160.591
15	0.382	0.152	0.508	0.238	1.280	163.568
16	0.380	0.152	0.517	0.208	1.257	146.444
17	0.394	0.152	0.543	0.319	1.408	175.235
18	0.386	0.152	0.521	0.264	1.322	168.796
19	0.372	0.152	0.504	0.152	1.180	156.502
20	0.359	0.153	0.447	0.135	1.094	148.443
21	0.356	0.153	0.451	0.124	1.084	158.148
22	0.360	0.153	0.462	0.151	1.126	161.917
23	0.358	0.153	0.438	0.116	1.064	152.020
24	0.364	0.152	0.472	0.162	1.151	161.357
25	0.356	0.153	0.440	0.124	1.073	165.428
				Total	**29.56**	**3911.24**

Conclusion

Randomly sequenced sensors tend to increase energy consumption. In contrast, organizing sensors at relatively uniform, non-overlapping distances without placing them too close can reduce energy usage during network setup. This principle holds for both single-hop and multi-hop networks. Overall, circular topologies generally yield more favorable results in terms of energy efficiency. Carefully planning the deployment area and selecting the most suitable topology based on these findings can lead to significant energy savings. Future work could involve testing these configurations in real-world environments, as well as conducting a similar analysis for sensors equipped with additional security features.

References

Gupta, A., Gulati, T., & Bindal, A. K. (2022, April). WSN based IoT applications: A Review. In 2022 10th International Conference on Emerging Trends in Engineering and Technology-Signal and Information Processing (ICETET-SIP-22) (pp. 1-6). IEEE.

Guo, C., & Zhao, D. (2021, June). Joint Charging, Routing, and Power Allocations in Rechargeable Wireless Sensor Networks. In 2021 International Wireless Communications and Mobile Computing (IWCMC) (pp. 1436-1441). IEEE.

URL-1 GitHub, https://github.com/contiki-os/contiki/wiki/An-Introduction-to-Cooja, date retrieved 05.03.2025.

URL-2 GitHub, https://github.com/contiki-os/contiki/blob/master/examples/ipv6/rpl-collect/, date retrieved 05.03.2025.
URL-3 IETF, https://datatracker.ietf.org/doc/html/rfc6550, date retrieved 07.03.2025.
URL-4 IETF, https://datatracker.ietf.org/wg/6lowpan/charter/, date retrieved 05.03.2025.
URL-5 IETF, The Internet Engineering Task Force IETF, https://www.ietf.org/, date retrieved 05.03.2025.
URL-6 IETF, ROLL Charter of the ROLL working group. IETF, Description of Working Group, https://datatracker.ietf.org/wg/roll/about/, date retrieved 05.03.2025.
URL-7 ITU, https://polen.itu.edu.tr:8443/server/api/core/bitstreams/7952797c-9964-4490-b068-d899146a0d48/content, date retrieved 05.03.2025.
Mishra, S., Singh, P., Arora, D., & Agrawal, K. K. (2017, December). Analyzing and evaluating the performance of 6L0WPAN and RPL using CONTIKI. In 2017 International Conference on Intelligent Sustainable Systems (ICISS) (pp. 1100-1105). IEEE.

COMPUTER ENGINEERING

Artificial Intelligence

Computer Networks

Cyber Security

Embedded Systems

Internet of Things

Neural Networks

Software Engineering

Performance Comparison of PECNET as Financial Time Series Feature Extraction with Respect to TimeGPT, TSMixer, and Prophet

Muhammed Enes Bas[a] , Burak Berk Ustundag[a]

[a]Istanbul Technical University, Faculty of Computer and Informatics Engineering,

Department of Computer Engineering, Türkiye

basm22@itu.edu.tr

Keywords: Predictive Error Compensation, Overfitting, Stock Price Forecasting, Time Series.

Aim

Finance is one these industries that through the improvement of predictive abilities machine learning has impacted many industries. An important financial application, stock price forecasting, is still challenging because market data is dynamic, unpredictable, and non-linear. The Predictive Error Compensation Neural Network (PECNET) is feature extraction and fusion model for deep learning applications. PECNET combines iterative error compensation with wavelet-based feature extraction to deal with these kinds of issues. Considering stock market example, in non-linear and time-varying systems, no matter how good the method is, performance goes towards a convergence (Wolpert & Macready, 1997). That means it cannot exceed a certain level. The data used in train does not represent the model in its current state (Gama et al., 2014). Either the number of data according to time or the number of parameters needs to be increased (John, 2010). However, this time, for both cases, the number of parameters to be calculated, the total weight internal hyperparameter number leads to overfitting (Goodfellow et al., 2010). To use data without causing overfitting, PECNET works as a feature extractor for time series in different windows and as a fusion in increasing the number of different variables.

TSMixer, TimeGPT and Prophet models are among the prominent methods in financial time series forecasting. TimeGPT is effective in modelling long-term dependencies inspired by the transformer architecture and offers successful results in predicting volatile financial markets (Garza et al., 2023). On the other hand, TSMixer captures complex patterns with its multi-layer perceptron-based architecture, it is reported to achieve high accuracy rates in financial data sets (Ekambaram et al., 2023). Prophet maintains its resilience to irregularities in data sets thanks to its flexible modular, additive regression model structure developed by Facebook. It can explicitly model seasonal components and holiday effects (Taylor & Letham, 2018). Each of these models provides significant advantages in understanding the dynamic properties of financial time series thanks to their different methodological approaches. Comparative performance analysis reveals that model selection varies depending on the application context. In the study, their comparative performance is evaluated.

Material and Method

In this study we used stock market dataset for four major technology companies, Apple (AAPL), Microsoft (MSFT), Facebook (META), and Google (GOOGL). Each dataset consists of four different features. These are daily closing prices, trading volume, index values and price-to-earning (P/E) ratios. Three of these features obtained from Yahoo Finance (Yahoo, 2025) are closing price, volume, and index values. The fourth feature, price-to-earnings ratio is obtained from MacroTrends.net (Macrotrends, 2025). The dataset consists of approximately 8 years of data from January 2017 to December 2024.

Adding previous prediction errors as extra inputs or using recurrency in neural networks (NNs) is a traditional way of reducing prediction errors (Bao et al., 2017) (Montgomery et al., 2015). This increases training's weights size and needs to utilize extra training dataset for not being overfitted (Ustundag and Kulaglic, 2020). PECNET architecture includes this structure in an efficient way, and it gives better results when even the simplest ANN is used inside its structure. ANNs generally underperform when compared to LSTM in capturing temporal dependencies (Macit & Ustundag, 2023). But using ANN with PECNET approach substantially improves forecasting accuracy. It is evidenced by its significantly lower RMSE in drought forecasting experiment compared to LSTM (Ustundag and Kulaglic, 2020). It is also possible to apply PECNET to more advanced models instead of a standard ANN (Ustundag and Kulaglic, 2020).

The PECNET model architecture consists of multiple neural networks connected in a hierarchical manner to refine predictions iteratively. The first NN is our main predictor, which is named as primary network. It uses the closing price to make predictions for the next day. Based on this prediction, in our second neural network, we predict the closing price error of the next day. In this way, the second NN corrects the error of the first NN by removing the misleading of the first NN's predictions. PECNET can contain additional neural networks if information from other features is needed to be fused together. All predictions which are generated by the primary network and other subsequent networks lastly through compensated through an additional error compensation network. In Figure 1, the PECNET model's architecture is displayed.

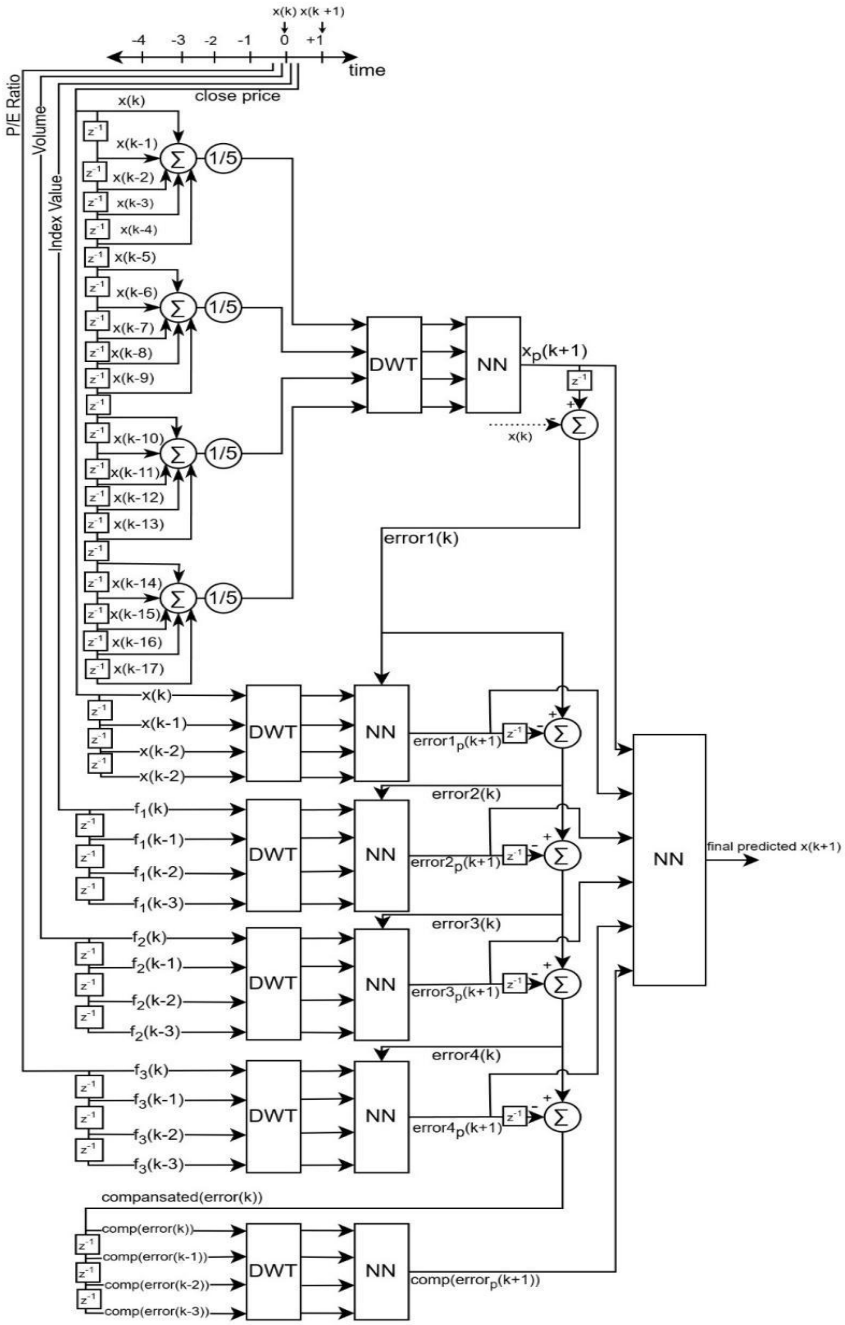

Figure 1. PECNET Model's Architecture.

In order to achieve the optimal feature extraction performance, each individual input variable undergoes their own preprocessing techniques that would consist of wavelet decomposition, successive windowing, and moving average smoothing. It also uses multiple error compensation at different stages, and features formed by fusing a number of stock indicators. The error compensation process also improves generalization since it systematically eliminates residual errors from previous predictions. This way minimizes the accumulation of noise and reduces overfitting.

Findings

The findings of several companies' closing price estimates were examined and, four separate models TimeGPT, TSMixer, Prophet, and PECNET were implemented using various input datasets. We used three distinct data sets. The first batch of data consists of the closing stock prices of four days in a row. The second batch of data consists of the closing stock prices of eight days in a row. The third dataset consists of four subsequent days and four weekly data. The models' outputs are the closing price for the following day.

In this experiment TimeGPT was overfitted, which remains a significant drawback, especially when trained on complex, high-dimensional financial data. TSMixer, in contrast, did not exhibit overfitting and demonstrated more generalization ability. Prophet was the closest model to PECNET in terms of evaluation metrics, but it demonstrated lower accuracy, with higher RMSE and MAE values. Through various techniques such as wavelet-based feature extraction, multi-stage error correction, and dropout regularization, PECNET successfully bridges the gap between statistical and deep learning models using neural network-based iterative compensation, multivariate financial indicators, discrete wavelet transform, and a supportive feature network. This ensures high prediction accuracy while addressing the modelling constraints and computational limitations of existing approaches. As seen in Table 1, PECNET achieves the lowest RMSE and an R^2 score of 0.96 demonstrating its superior generalization capabilities. When compared to TimeGPT, Prophet, and TSMixer, PECNET performs better.

Table 1. Test results for Microsoft Stock.

Model	Window Size	RMSE	MAE	R2
TimeGPT (19)	4 days	24.83	21.32	0.23
	8 days	28.66	23.12	0.20
	4 daily + 4 weekly	22.91	21.23	0.18
TSMixer (20)	4 days	7.53	6.26	0.91
	8 days	7.54	6.33	0.91
	4 daily + 4 weekly	6.94	5.57	0.93
Prophet (18)	4 days	5.10	3.95	0.93
	8 days	5.39	4.19	0.92
	4 daily + 4 weekly	5.15	4.02	0.94
PECNET	4 days	4.10	2.87	0.96
	8 days	4.90	4.08	0.93
	4 daily + 4 weekly	2.81	2.01	0.96

Conclusion

PECNET showed better results than the compared models. The findings showed that while TimeGPT encounter significant overfitting issues, TSMixer and Prophet did not overfit and exhibit stable prediction performance. TimeGPT's prediction accuracy is reduced when applied to unseen data. This is highlighting its inability to generalize effectively. Although Prophet and TSMixer avoiding overfitting, their prediction performances are worse than PECNET, which shows higher RMSE and MAE values.

PECNET superior performance can be attributed its ability to capture both short-term price volatility and long-term market trends, with it is Discrete Wavelet Transform (DWT) and hierarchical feature extraction mechanisms. It combines multiple time windows, exogenous financial indicators, and error correction layers to produce more precise and reliable forecasts than common models, which only use sequential time series inputs. These results indicate that the potential of PECNET as a powerful alternative to existing stock price prediction models, especially in high volatility and non-linearity environments. The findings shows that PECNET provides better prediction performance compared to state-of-the-art models with achieving lower RMSE and MAE values and higher R^2 scores. Finally, in light of these findings, we can say that PECNET is more successful than the leading models in the financial world.

References

Bao, W., Yue, J., & Rao, Y. (2017). A deep learning framework for financial time series using stacked autoencoders and long-short term memory. *PloS one*, *12*(7), e0180944.

Ekambaram, V., Jati, A., Nguyen, N., Sinthong, P., & Kalagnanam, J. (2023, August). Tsmixer: Lightweight mlp-mixer model for multivariate time series forecasting. In *Proceedings of the 29th ACM SIGKDD Conference on Knowledge Discovery and Data Mining* (pp. 459-469).

Gama, J., Žliobaitė, I., Bifet, A., Pechenizkiy, M., & Bouchachia, A. (2014). A survey on concept drift adaptation. *ACM computing surveys (CSUR)*, *46*(4), 1-37.

Garza, A., Challu, C., & Mergenthaler-Canseco, M. (2023). TimeGPT-1. *arXiv preprint arXiv:2310.03589*.

Goodfellow, I., Bengio, Y., Courville, A., & Bengio, Y. (2016). *Deep learning* (Vol. 1, No. 2). Cambridge: MIT press.

John Lu, Z. Q. (2010). The elements of statistical learning: data mining, inference, and prediction.

Macit, S., & Üstundag, B. B. (2023, December). Performance improvement in time series prediction through pecnet framework. In 2023 International Conference on Machine Learning and Applications (ICMLA) (pp. 1601-1605). IEEE.

Montgomery, D. C., Jennings, C. L., & Kulahci, M. (2015). *Introduction to time series analysis and forecasting*. John Wiley & Sons.

Taylor, S. J., & Letham, B. (2018). Forecasting at scale. *The American Statistician*, *72*(1), 37-45.

URL-1 https://finance.yahoo.com/, date retrieved 17.01.2025.

URL-2 https://www.macrotrends.net/, date retrieved 19.01.2025.

Ustundag, B. B., & Kulaglic, A. (2020). High-performance time series prediction with predictive error compensated wavelet neural networks. *IEEE Access*, *8*, 210532-210541.

Wolpert, D. H., & Macready, W. G. (1997). No free lunch theorems for optimization. *IEEE transactions on evolutionary computation*, *1*(1), 67-82.

COMPUTER ENGINEERING

Artificial Intelligence

Computer Networks

Cyber Security

Embedded Systems

Internet of Things

Neural Networks

Software Engineering

A Gamified Hybrid Application for Sports Club Fans: Development and Implementation

Ozan Ust[a], Robbert Oomens[b], Esma Güneş Kaya[a]

[a] Triodor R&D Center, Software Engineering, Türkiye
[b] Azerion, Sports, Netherlands
o.ust@azerion.com

Keywords: Digital Platform, Fan Engagement, Gamification, Monetization, Sports Clubs.

Aim

The aim of this study is to develop a digital platform that allows sports clubs to create a digital ecosystem that can be specifically tailored to the needs of their communities. This platform, which will strengthen the bond between sports clubs and their fans, gathers various functionalities in a single center. With a wide range of interaction features such as ticketing, news, live match center, and sports merchandise store, clubs can connect with their fans in a more personal and interactive way. With the developed platform, sports clubs can establish a closer relationship with their fans, increase their revenues through in-app purchases and improve the fan experience by using available historical data. With the digital platform that resulted from this project, an end-to-end integrated fan engagement tool and revenue model is offered to sports clubs.

Material and Method

Sports is a field that appeals to large audiences by becoming an indispensable part of daily life. The sports industry consists of components such as professional sports clubs, media, sponsorship and advertising, fan spending, etc. This industry is undergoing a significant transformation due to technological innovations and changing consumer behavior [1]. Sports clubs are increasingly emphasizing the use of digital platforms to increase their revenues and ensure their financial sustainability. By means through digitalization such as social media interaction, online product sales, digital subscription services, and blockchain-based assets, clubs are building stronger relationships with their fans, building loyalty and increasing revenue [2]. In the context of sports, fan engagement has been defined as a customer engagement behavior that focuses on the extra role behavior of the fan. [3]. The Consumers Online Brand Related Activities (COBRA) framework categorizes fan activities as consumption, contribution and creation [4]. When we look at the literature, there are studies investigating the ways in which sports clubs can increase their fan engagement levels [5].

With this innovative platform we have developed for sports clubs, we offer a wide range of services to fans, bringing together in one place functions such as playing games, purchasing tickets, and accessing sports content. In addition, it is designed with an integrated digital ad inventory and ad sales algorithm to maximize sponsorship and advertising revenues, which are a main source of income for clubs.

Findings

Studies were carried out in order to create different income channels for sports clubs and to increase the overall monetization rate from application users. To this end, the user experience of the platform was improved, ad slots were added for better monetization, and content and gamification layer operations were carried out. The Unity engine was used to develop a hybrid application framework with gamification features for the platform. For the ad slots operation, external structures for targeted ads were integrated using the supply chain of the company's main platform, the integrated digital ecosystem. To add monetization to the app, an in-house advertising SDK was integrated to the frontend and the Awin API was integrated to the backend. In order to integrate the advertising SDK, the necessary changes have been implemented to accommodate all ad format slots.

A gamification layer was designed to keep users coming back more often and thus increase engagement and time spent in the app. A mini-games feature has also been developed within the app that encourages competition and

rewards, providing additional interactive experiences to increase the users' time spent in the app. A new flow has been added to the app, which includes a number of different situations the mini-games can be found in. During the addition, separate scenarios were created for each situation to ensure clear communication to the user. Since not every mini-game can be included in every application, we separated them from the main application, designing them as features for the different applications we have. A communication layer was developed within the application to enable sports fans and sports clubs to communicate. Before, the only forms of communication available were sending push notifications or writing news articles. Communication/marketing pop-ups were added as a second communication layer. The ability to include a call to action here, either as a deep link or a direct URL, was added to further engage users.

A social layer was developed to increase interaction between users. The first version allows users to choose a background for the mini profile and change their avatar in a different menu structure than they are used to. These features are designed to work in conjunction with the gamification layer components, which will also be displayed in the mini-profile. Users can show their commitment to the club they support and the use of the app through this mini-profile, which can be viewed by others on the leaderboards. Since the gamification layer and social layer features were developed simultaneously, solutions were developed to some of the technical obstacles encountered in order to preserve the data structure.

The flow has been changed to allow users to link their existing ticketing accounts to their accounts in our app. By doing so, fans can now view their tickets or season passes within the app and also scan the QR code to enter the stadium. Following a request from existing clubs and subsequently the Football Association (FA), an Identity Based Access control for ticketing has been integrated within the app. This means that a user has to identify themselves with a driver's license, passport or ID card. This process uses NFC scanning of the chips inside these to link a user's profile to their identity. Additionally, a Consent Management Platform, a system that enables users to give and manage their explicit consent to the collection and processing of their personal data, was created for the app.

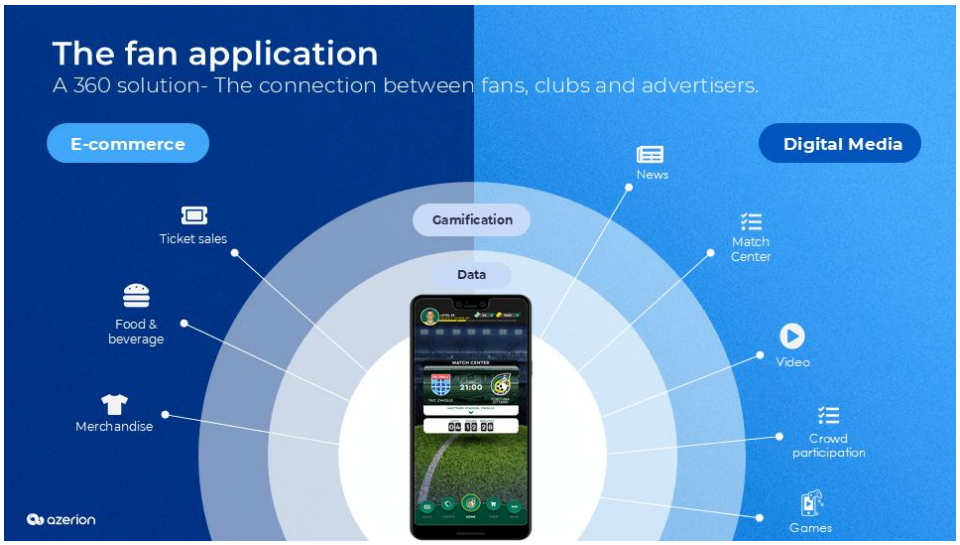

Figure 1. The fan application.

Conclusion

Digital transformation strategies for professional sports clubs support their long-term success by strengthening their economic structure. This platform eliminates the need for clubs to work with multiple service providers in different areas such as software development, content production and advertising technologies, and enables the management of processes in an integrated structure. Therefore, the innovative and competitive aspect of this project is that it brings together fans, sponsors, advertisers and content producers in a sports club's ecosystem on a single digital infrastructure, optimizing their interactions.

References

Richelieu, A. (2020). From sport to 'sportainment': The art of creating an added-value brand experience for fans, Journal of Brand Strategy

Venkitachalam, K., Schwartz B. and Soderman S., (2024). Marketisation, ownership and digitalisation strategies in the sport industry – generic insights and future research, Journal of Strategy and Management, 17 (3)

Yoshida, M., Gordon, B., Nakazawa, M., and Biscaia, R., (2014). Conceptualization and measurement of fan engagement: empirical evidence from a professional sport context, J. Sport Manag. 28 (4), 399–417

Vale, L., Fernandes, T., (2018). Social media and sports: driving fan engagement with football clubs on Facebook. J. Strat. Market. 26 (1), 37–55

Annamalai B., Yoshida M., Varshney S., Pathak A. A, and Venugopal P., (2021). Social media content strategy for sport clubs to drive fan engagement, Journal of Retailing and Consumer Services, 62, 102648

COMPUTER SCIENCE

Data Analysis

Data Science

Image Processing

Comparative Analysis of Large Language Models for Natural Language to SQL and Visualization Code Generation

Baykal Mehmet Uçar[a], Sefer Baday[a,b]

[a] Istanbul Technical University, Computational Science and Engineering, Informatics Institute, Türkiye
[b] Istanbul Technical University, Applied Informatics Department, Informatics Institute, Türkiye
ucarba22@itu.edu.tr

Keywords: Data Visualization, Large Language Models, Natural Language to SQL, Semantic Kernel, Text-to-Code.

Aim

The aim of this study is to develop and evaluate a pipeline leveraging Large Language Models (LLMs) to convert natural language queries into SQL statements and Python visualization scripts. The research compares performance metrics across several advanced LLMs, including OpenAI GPT-4o, Anthropic Claude 3.5 Sonnet, Meta Llama 3.1 70B, Google Gemini 1.5 Flash, and DeepSeek Chat.

This work is motivated by the goal of improving data accessibility and democratization within organizations. Non-technical users often face challenges when trying to retrieve data from databases, as this typically requires SQL knowledge or assistance from technical staff. By enabling natural language interactions with databases, the pipeline increases efficiency, reduces costs, and empowers more timely, data-driven decision-making (Kim et al., 2020; Qin et al., 2022).

The primary rationale for selecting these models is their recency and relevance at the time the experiments were initiated. Each model represents the latest or one of the latest iterations from its respective organization, thereby ensuring that the comparison reflects the cutting-edge capabilities available in the field. Furthermore, all selected models offer accessible inference APIs, making them suitable for integration into a standardized evaluation pipeline without the need for specialized hardware or fine-tuning efforts, which supports reproducibility and practical applicability.

Beyond their availability and release timing, the models were chosen to represent a diverse set of development philosophies and architectural innovations. OpenAI, Anthropic, Meta, Google, and DeepSeek have distinct approaches to model training, instruction tuning, and optimization, offering a broad view of current trends in LLM development. Additionally, the selection includes both closed-weight (e.g., OpenAI, Anthropic, Google) and open-weight (e.g., Meta, DeepSeek) models, which allows analysis not only of model performance but also of practical considerations such as deployment flexibility and cost implications (OpenAI, 2025; Anthropic, 2024; Google AI, 2025; Meta AI, 2024; DeepSeek, 2024).

The proposed system addresses three main domain problems:

- Data Accessibility: Providing a natural language interface to databases enhances accessibility for non-technical users, supporting data democratization efforts (Kaoshik et al., 2021).
- AI Democratization: Allowing users to leverage AI capabilities without requiring technical expertise contributes to broader AI adoption and usability within organizations.
- LLM-Agnostic Architecture: Another goal was to design the framework in a flexible way, allowing for the rapid addition of new models, so that the system can easily keep up with the fast-paced developments in generative AI and LLM technologies.

Material and Method

We utilized Microsoft's Semantic Kernel SDK to abstract interactions with various LLMs. Semantic Kernel is an open-source development kit that enables developers to integrate AI services, such as OpenAI and Azure OpenAI, with conventional programming languages like C# and Python, facilitating the creation of AI applications that combine the strengths of both paradigms (Microsoft, 2025). By leveraging Semantic Kernel, we efficiently

orchestrated complex AI tasks, including prompt chaining, recursive reasoning, and summarization, thereby enhancing the functionality and responsiveness of our system (Figure 1).

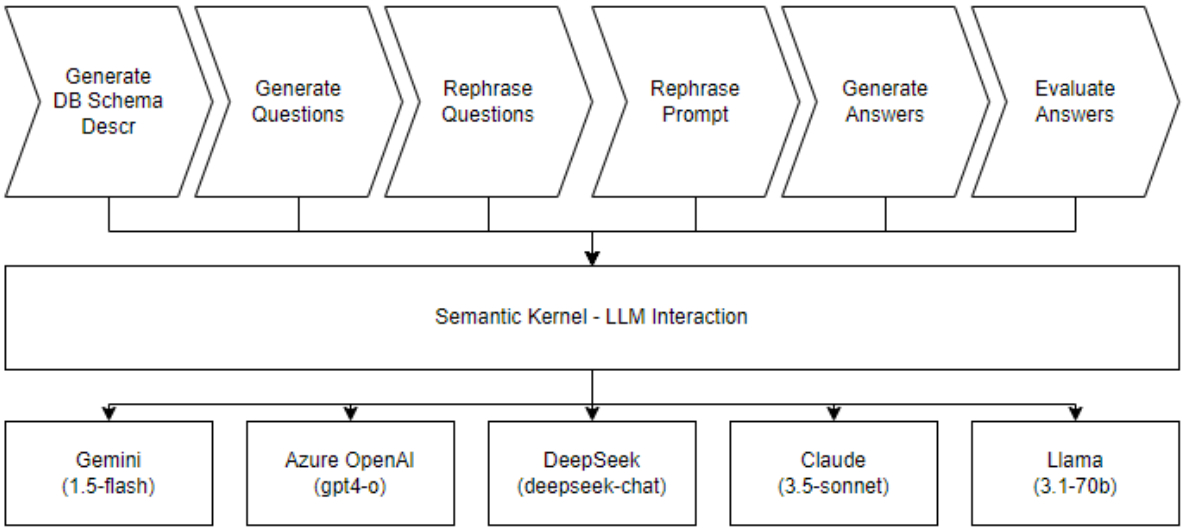

Figure 1. LLM-Based Pipeline Architecture for Natural Language to SQL and Visualization.

If a model (e.g., DeepSeek) is not supported by Semantic Kernel, developers can quickly integrate it by implementing interfaces like ChatCompletionClientBase or BaseModel, enabling compatibility with new APIs (Lagerkrans-Pandey and LaHaye, 2025).

The pipeline includes:

- Database Schema Description: Generated via LLMs with manual refinements.
- User Query Generation: LLM-generated queries categorized by complexity (simple, moderate, complex, very complex).
- User Query Handling: LLMs generate executable SQL and Python code based on user inputs and schema descriptions.
- Performance Evaluation:
    - Human Evaluation: Each query and code was manually scored based on the following rubric:
        - 100: Fully correct and executable
        - 75: Minor fixable issues (e.g., wrong column name)
        - 50: Structural issues requiring major edits
        - 25: Incorrect but partially relevant
        - 0: Irrelevant or completely incorrect
    - LLM-Based Evaluation: After identifying the most accurate model through human scoring, this model was used as an LLM-based evaluator. It reviewed the generated SQL and Python code for the remaining models and assigned scores accordingly, ensuring scalable and consistent benchmarking.

PromptToQueryResult is an asynchronous Python function designed to transform a user-provided natural language prompt into executable SQL and Python code through interaction with LLMs using the Semantic Kernel framework. The function enables query execution, result retrieval, and visualization generation in an end-to-end automated pipeline.

The pipeline consists of the following major steps:

- Kernel Initialization: The Semantic Kernel is initialized based on the selected LLM service, model name, and mode (e.g., chat).
- Prompt Handling: If no user prompt is provided, the user is interactively queried. Optionally, the prompt can be reformulated for clarity using the rephrase_prompt function, which invokes a dedicated rephraser plugin.

- Code Generation: The (rephrased) prompt and a predefined data schema are passed to an LLM through the execute_llm_prompt function. The model responds with structured text containing SQL and Python code enclosed within specific tags.
- Code Parsing: The generated result string is processed by parse_sql and parse_python_code functions to extract the respective code segments.
- SQL Execution: The extracted SQL query is executed against a configured database using the execute_sql function, which internally leverages the run_sql_query utility. If the execution fails, an automatic error correction mechanism is triggered through execute_fixed_query, which iteratively refines the SQL using the LLM.
- Python Code Execution: If Python visualization code is available, it is executed via the execute_python_code function within a controlled environment. Any execution errors invoke the execute_fixed_python_code function to attempt automatic code fixing through the LLM, with up to three retries.
- Output Handling: Upon successful query execution and visualization, outputs such as the DataFrame and generated plots are saved to specified directories. SQL queries, Python scripts, and user prompts are also optionally persisted to disk for traceability.

The core functionality of PromptToQueryResult is supported by several auxiliary asynchronous and synchronous functions:

- execute_llm_prompt: Sends structured requests to the LLM for code generation, SQL fixing, or Python code fixing, depending on the invoked plugin and function.
- rephrase_prompt: Rewrites the user prompt to enhance its clarity and precision using an LLM-powered rephraser.
- execute_sql: Executes SQL queries and returns results as pandas DataFrames.
- execute_python_code: Executes Python code snippets for visualization or post-processing tasks.
- execute_fixed_query: Attempts to automatically fix faulty SQL queries iteratively using LLM feedback.
- execute_fixed_python_code: Attempts to automatically fix faulty Python code iteratively using LLM feedback.
- parse_sql, parse_python_code: Parse and extract SQL and Python code from structured LLM responses.

The design implements robust error handling:

- SQL and Python code execution errors trigger automated retries with LLM-assisted correction.
- Each fixing function (execute_fixed_query, execute_fixed_python_code) performs up to three iterations before giving up and notifying the user.

Findings

The evaluation results show consistent yet distinct performance patterns across the tested models, based on both human-annotated and LLM-based scoring.

Human Evaluation: Among the initial models evaluated manually:

- Claude 3.5 Sonnet achieved the highest performance, with an average score of 99.36% (SQL: 99.26%, Python: 98.96%), demonstrating near-perfect accuracy and readability in both code types.
- GPT-4o followed with an average of 86.95%, performing slightly stronger in SQL than in Python visualization.
- Gemini 1.5 Flash scored 80.77% overall, with a relatively balanced performance across both outputs.
- These scores were manually assigned using a 5-level rubric, and reflect both correctness and required post-editing effort.

LLM-Based Evaluation: To scale the evaluation, the best-performing model (Claude 3.5) was also used as an LLM evaluator, scoring the generated SQL and Python code from all five models:

- Claude 3.5 Sonnet again led with an average score of 88.13%, supporting its consistency.
- GPT-4o and Gemini 1.5 Flash saw reduced overall scores (74.38% and 71.88%, respectively), especially in Python code quality.

- LLaMA 3.1 70B and DeepSeek Chat were included in the LLM-based phase and showed mixed results. While their SQL scores were competitive, Python outputs were generally weaker (e.g., DeepSeek's 35.00% in Python).
- These findings reveal that while multiple LLMs can handle SQL generation with reasonable success, generating correct and readable Python visualization code remains more challenging.

Tables 1 and 2 present detailed scores for both evaluation strategies.

Table 1. Human Evaluation Scores.

Model	Avg Score	SQL Score	Python Score
gpt-4o	86.95%	87.50%	79.27%
claude 3.5	99.36%	99.26%	98.96%
flash 1.5	80.77%	86.76%	81.82%

Table 2. LLM-Based Evaluation Scores.

Model	Avg Score	SQL Score	Python Score
gpt-4o	74,38%	97.50%	51.25%
claude 3.5	88.13%	98.75%	77.50%
flash 1.5	71.88%	80.00%	63.75%
deepseek-chat	66,25%	97,50%	35.00%
llama 3.1-70b	80.00%	92.50%	67.50%

Conclusion

Distinct strengths across LLMs were identified, with Claude 3.5 Sonnet consistently demonstrating superior performance in both human and LLM-based evaluations. These findings align with recent academic benchmarks, reinforcing Claude's strength in structured code generation tasks such as SQL and Python visualization.

While GPT-4o and Gemini Flash showed solid SQL generation capabilities, they were less consistent in producing high-quality Python visualizations. Models like LLaMA 3.1 70B and DeepSeek Chat exhibited promising SQL outputs but struggled with full visualization pipelines.

These results highlight the potential value of hybrid approaches, combining the complementary strengths of different models to improve robustness and accuracy. Future work will explore such model orchestration strategies to enhance overall pipeline effectiveness across diverse query types (Wang et al., 2024; Lieber et al., 2024).

References

Anthropic. (2024, June). *Introducing Claude 3.5 Sonnet*. https://www.anthropic.com/news/claude-3-5-sonnet (Accessed: April 6, 2025)

DeepSeek. (2024). *DeepSeek API documentation*. https://api-docs.deepseek.com/ (Accessed: April 6, 2025)

Google AI. (2025, March). *Gemini models — Gemini API*. https://ai.google.dev/gemini-api/docs/models (Accessed: April 6, 2025)

Kaoshik, R., Bhalotia, M., & Kanade, A. (2021). ACL-SQL: Generating SQL queries from natural language. In *CODS COMAD 2021: 8th ACM IKDD CODS and 26th COMAD* (pp. 240–244). Association for Computing Machinery. https://doi.org/10.1145/3430984.3431046

Kim, H., Xu, Y., Mao, Y., & Zhang, Y. (2020). Natural language to SQL: Where are we today? *Proceedings of the VLDB Endowment, 13*(10), 1737–1750. https://doi.org/10.14778/3401960.3401970

Lagerkrans-Pandey, S., & LaHaye, G. (n.d.). *Using Semantic Kernel with dependency injection*. https://devblogs.microsoft.com/semantic-kernel/using-semantic-kernel-with-dependency-injection/ (Accessed: April 6, 2025)

Lieber, O., Chiang, W., & Raffel, C. (2024). Jamba: A hybrid transformer-mamba language model. *arXiv preprint arXiv:2403.19887*. https://arxiv.org/abs/2403.19887

Meta AI. (2024, August). *Introducing Llama 3.1: Our most capable models to date*. https://ai.meta.com/blog/meta-llama-3-1/ (Accessed: April 6, 2025)

Microsoft. (n.d.). *Introduction to Semantic Kernel*. https://learn.microsoft.com/en-us/semantic-kernel/overview/ (Accessed: April 6, 2025)

OpenAI. (2025). *GPT-4o overview*. https://platform.openai.com/docs/models/gpt-4o (Accessed: April 6, 2025)

Qin, B., Liu, S., Ren, Y., & Ren, X. (2022). A survey on text-to-SQL parsing: Concepts, methods, and future directions. *arXiv preprint arXiv:2208.13629*. https://arxiv.org/abs/2208.13629

Wang, J., Li, S., & Ren, X. (2024). The Mamba in the Llama: Distilling and accelerating hybrid models. *arXiv preprint arXiv:2408.15237*. https://arxiv.org/abs/2408.15237

CONSTRUCTION MANAGEMENT

Construction Project Management

IT in Construction

Risk Management in Construction

Sustainability in Construction

Developing An Ontology For Artificial Intelligence Assisted Quality Control Systems In Mega Projects

Hasan Efekan Bilen[a], Onur Behzat Tokdemir[a]

[a] Istanbul Technical University, Civil Engineering Department, Construction Management Program, Türkiye
bilen23@itu.edu.tr

Keywords: Ontology, Artificial Intelligence, Quality Control.

Aim

Developing an ontology to improve AI-assisted quality control in mega construction projects, ensuring the meaning of data and the effective use of AI algorithms.

Introduction

The construction industry with its mega construction projects have come to require complex and large-scale operations. Such projects consist of a large number of stakeholders, materials, processes, and data. This complexity underlines the significance of an efficient and effective quality control system. The traditional quality control systems usually follow a reactive approach, intervening only after a defect has occurred (Priemus et al., 2013). Not only can this lead to cost increases and time losses, it can also pose safety risks. Artificial Intelligence (AI) has become more common use in construction processes to better detect errors and manage risks (Zhang et al., 2025). Recent years have shown that the technological advancements in AI has the potential to transform the quality control processes in the construction industry (Hire et al., 2022). In this regard, studies on quality control in large-scale projects highlight the significance of proactive approaches in the success of quality control systems (Aziz et al., 2019). Weighing in such various aspects as mentioned, AI-assisted quality control systems can increase productivity, decrease costs, and improve safety in construction projects. However, the effective and efficient use of AI in the construction industry is dependent on how meaningful and structured the relevant data is (Ayhan & Tokdemir, 2019). This is where ontologies come into play. An ontology is a knowledge model which explains the concepts of a particular subject or a field of study, describing the properties of the concepts and outlining the relationship between the concepts (Felicetti & Franco Niccolucci, 2024). Developing an ontology for the construction industry can help AI algorithms comprehend the data and facilitate assistance with effective decision support by defining key concepts such as risk, error, material, and the relationship among these concepts (e.g. risks leading to errors; materials being used in processes). This thesis focuses on developing an ontology for AI-assisted quality control systems in mega construction projects. Combining expert knowledge on construction industry and AI technologies, the ontology proves to help improve the quality control processes and ensure effective decision support. Within this scope, current quality control methods in the construction industry as well as AI applications have been analyzed. Following this, the methods and tools for developing the ontology have been determined. The resulting ontology has been in turn evaluated by experts and integrated with AI systems. Consequently, this study aims to contribute to more effective, efficient, and sustainable construction projects by presenting the potential use of AI in the construction industry.

Material and Method

This thesis study aims to develop an ontology for AI-assisted quality control in mega construction projects. In line with this aim listed below are the methodological steps which the study has followed:

A. Definition of Scope and Field

The preliminary step of the study is to identify the key concepts, processes, stakeholders, and data sources in large scale construction projects; experts of the construction industry have been consulted, a thorough literature review has been conducted, and current quality control systems have been analyzed. Consequently, the scope and the

focus of the study have been clearly identified. The scope can be further narrowed down by identifying critical areas in the mega construction projects such as material management, process monitoring, risk management, compliance assessment where AI applications are better suited for use to reduce the complex, intensely data-driven nature of such projects.

B. Establishing the Conceptual Model

Having identified the key concepts of quality control and their relationships with one another in mega construction projects in the preliminary step of the study, a conceptual model has been established (Figure 1). The model demonstrates the hierarchical and relational structure of the key concepts, laying the groundwork upon which the ontology is based.

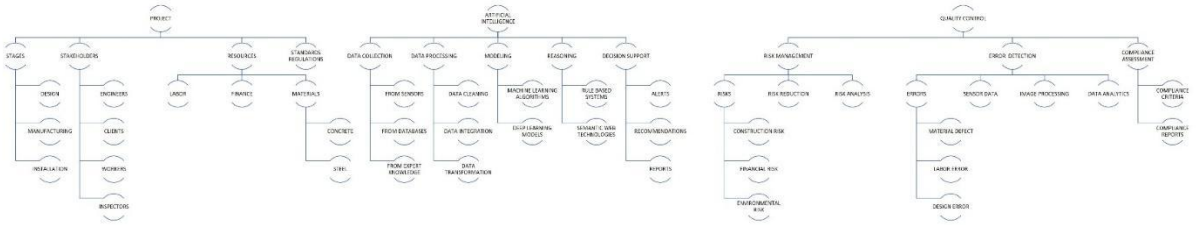

Figure 1. Conceptual model.

C. Developing the Ontology

Protégé is a comprehensive ontology editing software which produces ontological models in the OWL format (Musen, 2015). The ontology has been developed in Protégé with the conceptual model as the base. During the development, the hierarchical relationships between the concepts (e.g. quality control being a sub-category of project management; concrete and steel as sub-classes of material), their properties (e.g. material name, quality), constraints to regulate the relationships have been introduced. The form of expression for the ontology is the Web Ontology Language (OWL). Figure 2 below demonstrates the ontological model in OWL format, expressing the relationships between the concepts.

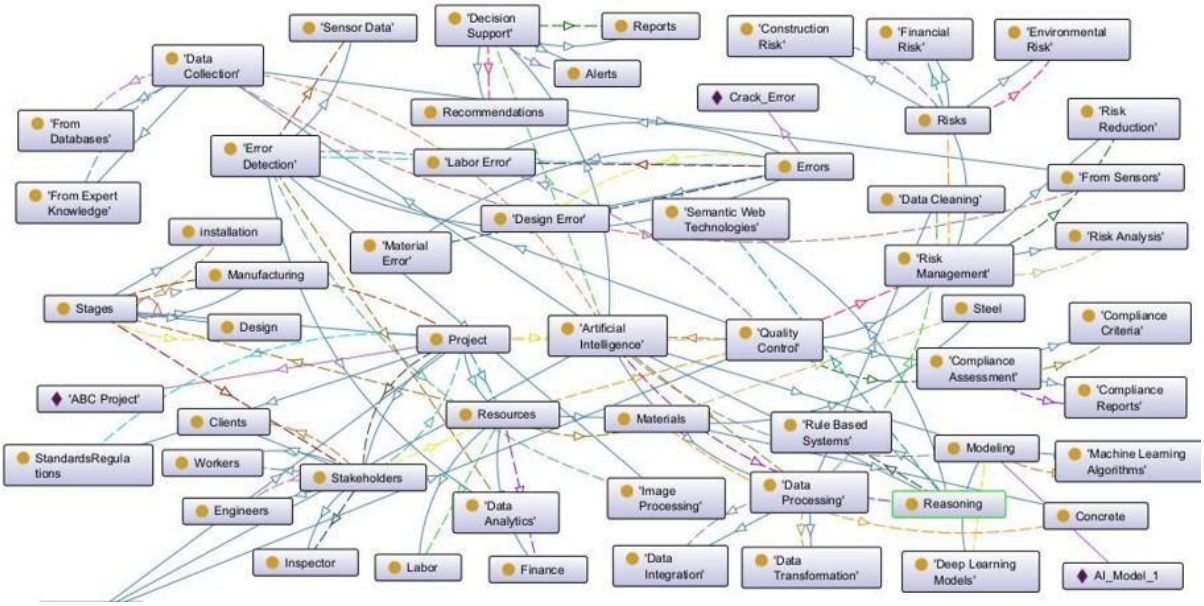

Figure 2. Ontological model.

D. Evaluation of the Ontology

The ontology thus far developed has been evaluated and tested by experts of the construction industry for reliability, accuracy and usability in the industry. The criteria used in the evaluation and testing of the ontology include how compatible the concepts and their relationships it details are with the real-world situations; how detailed and comprehensive it is; how suitable it is for AI use. The feedback received from the experts has been used to improve and update the ontology.

E. AI Integration

The main purpose of AI integration is making use of the developed ontology to assist with decision support in quality control processes. The integration step of the study determines how the ontology feeds information into AI systems and how the AI systems make use of the ontology (e.g. "Reasoning" on the ontology to derive conclusions). Furthermore, machine learning algorithms such as classification, clustering, prediction can be used in the integration of AI with the ontology.

Findings

Developed through Protégé, the ontology produces an extensive body of knowledge to provide AI algorithms with assistance during quality control processes. The main three constituents for the ontology have been determined as Project, Quality Control, and AI, modelling in detail their relationships with each other. The main findings obtained are as follows:

A. Constructing a Hierarchical and Relational Ontology

The ontology developed in Protégé is structured to demonstrate a hierarchical and relational structure: "Project"> "Resources" > "Material> "Concrete" (Figure 3). For instance, the "Project" class has "Design", "Manufacturing", "Installation" as subclasses; the "Stakeholder" class is sectioned by the subclasses of "Engineers", "Workers", "Clients", and "Inspectors". This hierarchical and relational structure clearly demonstrates the stakeholders and the processes in which they are involved in quality control processes.

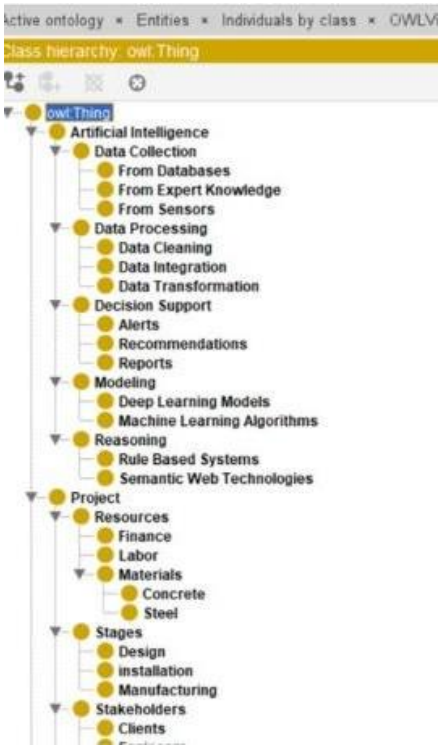

Figure 3. Class hierarchy.

B. Comprehensive Conceptual Model for Quality Control Processes

Developed in Protégé, the ontology has been designed to provide in detail the processes of quality control, e.g. Compliance Assessment, Risk Management, Error Detection. For instance, the subclasses of "Material Defect", "Labor Error" and "Design Error" are categorized and nested under the main class of "Error Detection". Risk Management class attributes "hasRiskType" (Figure 4) property to identify and define basic risks such as "Construction Risk", "Financial Risk", "Environmental Risk". The classifications as detailed help AI algorithms focus on certain types of risks when running analyses, helping reduce ambiguity in often complex and detailed construction projects (Salem et al., 2020).

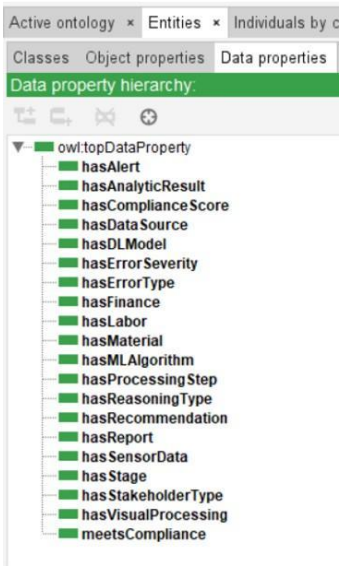

Figure 4. Data property hierarchy.

C. The Ontology Integrated with AI

The ontology contains data properties such as "hasSensorData" (Figure 4) which help to transfer information obtained from the database and sensors to AI algorithms in a meaningful way. The property "hasSensorData" is created to integrate sensory inputs into quality control processes. This property enables AI-assisted analyses of real-time sensory input. For instance, a sensor data stream to measure material quality such as concrete, generating automated alerts when below specified thresholds.

D. Testing Ontological Reliability using Reasoner

The ontology has been tested against its reliability in hierarchical structure, property attribution, and relationality using the Reasoner tool in Protégé. In accordance with the results of the testing, invalid concepts and relationships have been detected and removed. In one instance, it has been detected that a material was not only classified as an error type but also as a process type. This misclassification has been sorted out using the Reasoner tool in Protégé. Additionally, logical inconsistencies among certain concepts have been resolved by analyzing the relationship between risk levels and error types. Reasoner helped resolve conflicting properties where an error is classified as both "High" and "Low", ensuring logical consistency and coherency among classifications and properties.

E. Creating a Database for AI-assisted Decision Support Mechanisms

The ontology constitutes a database which helps AI-assisted decision-making mechanisms develop further. Properties such as "hasAlert", "hasRecommendation" and "hasReport" (Figure 4) help maintain data accuracy and reliability by enabling AI systems to make ontological inferences decision making processes (Horridge & Bechhofer, 2011). The AI systems for instance can create automated alerts for high-risk projects and offer suggestions on risk reduction. Properties such as "hasStandard" are created to help assure compliance with

standards and regulations (Figure 4), ensuring whether the quality control processes adhere to the industry standards and relevant regulatory requirements.

Conclusion

This study is aimed at developing an ontology to improve AI-assisted quality control in mega construction projects. The ontology has been designed to better comprehend the quality control processes in construction projects, structure the relevant data, and facilitate AI algorithms to work more efficiently and effectively. During the development of the ontology, the key concepts of quality control processes and their relations with each other have been determined through relevant literature review and consulting industry experts, rendering an ontological model in the Protégé software. The main three constituents for the ontology have been determined as Project, Quality Control, and AI. Project encompasses the stages, stakeholders, resources, standards, and regulations providing a structured body of subclasses. Quality Control introduces a systematic approach by defining risk detection, data analysis, compliance assessment and risk management. AI, on the other hand, facilitates artificial intelligence integration into quality control processes through data collection, data modelling, and focusing on decision support mechanisms. The hierarchical structure provided by the ontology facilitates the clarification of data from AI algorithms and enables better decision support in quality control processes in mega construction projects. Additionally, the ontology can be integrated with AI systems to help decision-making mechanisms in critical quality control processes such as optimized selection of material and compliance assessment. The contribution of this study is to assist with the decision support systems and mechanisms in AI-assisted quality control systems in the construction industry by providing an extensive and structured body of knowledge. It is suggested for the future that the ontology should be extended and tested in real-time in industrial projects. In this regard, the ontology can be populated with more data to be more comprehensive, efficient, and effective in the construction industry.

References

Ayhan, B. U., & Tokdemir, O. B. (2019). Safety assessment in megaprojects using artificial intelligence. Safety Science, 118, 273–287. https://doi.org/10.1016/j.ssci.2019.05.027

Aziz, H., Qvenild, R., & Falk, K. (2019). A Practical Study on How Proactive Quality Approach Can Improve System Development Process to Ensure System-Effectiveness and -Performance. INCOSE International Symposium, 29(1), 500–526. https://doi.org/10.1002/j.2334-5837.2019.00616.x

Felicetti, A., & Franco Niccolucci. (2024). Artificial Intelligence and Ontologies for the Management of Heritage Digital Twins Data. Data, 10(1), 1–1. https://doi.org/10.3390/data10010001

Hire, S. 1, Ranjan, A. 1, Ruikar, K. 2, Sandbhor, S. 1 1 C. E. D., & Civil Engineering, L. U. (2022). AI-driven safety checks for ladders used on construction sites. ProQuest, 092040. https://doi.org/10.1088/1755-1315/1101/9/092040

Horridge, M., & Bechhofer, S. (2011). The OWL API: A Java API for OWL ontologies. Semantic Web, 2(1), 11–21. https://doi.org/10.3233/sw-2011-0025

Musen, M. A. (2015). The protégé project. AI Matters, 1(4), 4–12. https://doi.org/10.1145/2757001.2757003

Priemus, H., Bosch-Rekveldt, M., & Giezen, M. (n.d.). Dealing with the complexity, uncertainties and risk of megaprojects: redundancy, resilience and adaptivity. International Handbook on Mega-Projects, 83–110. https://doi.org/10.4337/9781781002308.00011

Salem, A., Simpeh, E., & Fapohunda, J. (2020). CONSTRUCTION STAKEHOLDERS' PERSPECTIVE ON EXTERNAL RELATED RISK FACTORS INFLUENCING CONSTRUCTION PROJECT PERFORMANCE. Journal of Construction Project Management and Innovation, 10(1), 70–85. https://doi.org/10.36615/jcpmi.v10i1.192

Zhang, Y., Chow, C. L., & Lau, D. (2025). Artificial intelligence-enhanced non-destructive defect detection for civil infrastructure. Automation in Construction, 171, 105996–105996. https://doi.org/10.1016/j.autcon.2025.105996

Usage of Large Language Models in the Construction Industry: A Literature Review and Evaluation

Şirin Şevval Uçak[a], Onur Behzat Tokdemir[a]

[a] Istanbul Technical University, Civil Engineering Departmant, Construction Management Program, Türkiye
ucak18@itu.edu.tr

Keywords: Large Language Models (LLMs), Construction Industry Applications, Automation and Efficiency in Construction.

Aim

The purpose of this study is to explore the contributions of large language models (LLMs) in various areas of the construction industry and highlight the advantages, challenges, and limitations associated with their use. Specific examples will be provided regarding how these technologies benefit fields such as project management, contract management, document management, and occupational health and safety. Additionally, the limitations encountered during these processes and potential challenges related to the technology will be discussed.

Material and Method

This study investigates the use of LLMs in the construction industry through a comprehensive literature review. Relevant academic sources were identified using keywords such as "large language models" and "construction industry." The objectives, methodologies, and findings of these studies were examined to determine the key application areas of LLMs, which include project management, contract management, document management, and occupational health and safety. The analysis highlights the benefits, challenges, and limitations associated with LLM adoption in these domains, aiming to offer a well-rounded evaluation of their effectiveness within the construction sector.

Findings

A. Project Management and Planning

Large Language Models (LLMs) offer notable advantages in the planning and management of construction projects. Prieto et al. (2023) investigated the use of ChatGPT in scheduling and resource allocation tasks, reporting high levels of accuracy, efficiency, clarity, and consistency. The study found that ChatGPT can streamline project management by automating time-intensive preparatory tasks, thereby accelerating overall workflow.
Similarly, research by He C. et al. (2024) reported that a GPT-based model was used to categorize meeting discussions into meaningful topics, followed by the training of a BERT-based model for constraint classification. The study found that the proposed model improved constraint classification accuracy by 8.8% compared to traditional methods.
LLMs support project managers not only in schedule development but also in the early identification of potential constraints, offering proactive solutions. This capability contributes to more efficient and timely project execution. By enhancing critical planning tasks such as time and resource optimization, LLMs enable more accurate outcomes. These applications improve key performance factors such as on-time delivery and budget control, thereby enhancing overall project efficiency.

B. Contract Management and Automated Contract Analysis

Contract management is a critical aspect of the construction industry, and the adoption of LLM-based technologies in this domain is expanding rapidly. Moon et al. (2022) developed a BERT-based classification model to associate clauses in construction specifications with contract-related risk categories. The model achieved an accuracy of 88.9% and an F1 score of 93.4%, with particularly strong performance in the safety category, underscoring the potential of LLMs in risk identification.
To enhance the analysis of lengthy contracts, Gao et al. (2024) introduced a text segmentation method that combines content summarization and intelligent question-answering, allowing users to quickly access relevant provisions. Their model demonstrated 93.3% user satisfaction when tested on the FIDIC Red Book.
He Y. et al. (2024) used LLMs to automatically identify risks in construction contracts. To address the long processing times and inconsistent results of traditional risk detection methods, contract clauses were vectorized,

indexed in a database, and evaluated using the Retrieval-Augmented Generation method. This approach achieved 76.7% accuracy compared to traditional expert evaluations.
Kim et al. (2025) developed an NLP-based framework for automated detection of risk statements in contracts using BERT and spaCy's dependency parser. Their model achieved 95.5% sentence parsing accuracy and 91.3% accuracy in identifying risk-related sentences.
Overall, LLMs enhance contract management by automating the extraction of key clauses and identifying critical terms, risks, and contradictions. This significantly reduces review time and error rates, supporting more accurate and efficient decision-making in construction projects.

C. Document Management and Information Extraction

LLMs have greatly improved access to project-related information by enabling rapid and accurate analysis of large and complex document sets, thereby enhancing overall productivity. Wang et al. (2022) developed a question-answering system for extracting information from Building Information Modeling data, allowing users to query BIM models in natural language. The system achieved 81.9% accuracy but struggled with complex sentence structures.
Kim et al. (2024) proposed a framework using pre-trained BERT models for multilingual construction documents, particularly FIDIC contracts, demonstrating improved retrieval speed and cost efficiency.
Similarly, Wei et al. (2024) evaluated embedding models for classifying documents related to construction delay disputes. Their findings showed that embedding techniques, especially with the K-Nearest Neighbors algorithm, effectively captured semantic similarities, supporting informed decision-making.
Park et al. (2024) further emphasized the use of domain-specific terminology dictionaries and Word2Vec representations to improve semantic understanding in construction documents, contributing to more precise and context-aware document analysis.
These studies highlight the significant potential of LLMs to transform information retrieval and document management in the construction industry.

D. Worker Health and Safety

LLMs play a vital role in enhancing construction safety by identifying risks, analyzing accidents, and supporting the implementation of preventive measures. Xu et al. (2023) developed a BERT-BiLSTM-CRF model to improve safety management in coal mine construction, which achieved high accuracy in automating safety information extraction and named entity recognition.
Ahmadi et al. (2024) analyzed construction accident reports using advanced LLMs. The study accurately classified the fundamental characteristics of accidents, contributing significantly to the improvement of safety measures.
Lee et al. (2024) employed the Retrieval-Augmented Generation model to optimize information access in construction safety management, enabling faster retrieval and more timely implementation of safety protocols.
These advancements demonstrate the growing potential of LLMs to support proactive and data-driven safety practices in the construction industry.

E. Project-Based Applications

LLMs are effectively applied not only in general construction fields but also in more specific projects, demonstrating their versatility.
Chen and Zhang (2024) explored the effects of LLM-based agents in bridge operation and maintenance processes. The findings revealed that LLMs can enhance data stability during bridge monitoring and improve the accuracy of fault diagnosis.
Yang et al. (2024) developed a methodology to increase information extraction accuracy in digital twin water conservation projects using LLMs. This methodology provided a significant improvement over traditional model.
Yi et al. (2024) utilized LLMs for data storage and rapid access in drilling operations. While the system enhanced operational efficiency, some concerns regarding its accuracy were raised.
Jang and Lee (2023) investigated the integration of BIM with LLMs and demonstrated that this integration improves the design process. LLMs play a significant role in collaborative design processes.

Table 1. Advantages of Using LLMs in the Construction Industry.

Advantage	Description
Automation and Increased Efficiency	LLMs automate time-consuming processes such as the analysis of construction specifications, review of contract clauses, and risk management, thus increasing efficiency (Moon et al., 2022; Prieto et al., 2023). These models, which are highly successful in extracting meaning from text-based data, text generation, and learning relationships within text, can provide significant benefits in processes such as document categorization, content analysis, information extraction, and risk assessment (Lee et al., 2024).
Risk Management and Safety Analysis	LLMs contribute to improving safety measures by analyzing construction accident reports (Ahmadi et al., 2024). Additionally, in interpreting construction safety regulations and compliance processes, LLMs assist in understanding complex legal texts (Tran et al., 2024).
Information Access and Management	LLMs facilitate access to information in systems such as BIM, allowing construction professionals to quickly and accurately access project data (Wang et al., 2022).
Decision Support Systems	LLMs assist in complex decision-making processes such as automatically identifying and analyzing constraints in construction planning meetings (He, C., et al., 2024). LLM-based agents provide high efficiency in tasks like real-time data analysis and automatic reporting (Chen and Zhang, 2024).
Cost and Time Savings	LLMs reduce manual workloads, leading to cost and time savings in construction projects (Pu et al., 2024; Kim et al., 2024).

Table 2. Disadvantages of Using LLMs in the Construction Industry.

Disadvantage	Description
Model Accuracy and Reliability	The application of language models like ChatGPT in construction engineering underscores the importance of expert oversight due to potential risks such as bias, incomplete information, and erroneous content generation (Aluga, 2023). Context loss in lengthy, complex documents may also lead to misinterpretations or failures in recalling prior content (Li et al., 2023). For instance, Wang et al. (2022) found that NLP-based QA systems often struggle with complex sentence structures. Furthermore, LLMs may produce hallucinations—contradictions, factual inaccuracies, or incoherent outputs—stemming from unreliable training data, ambiguous prompts, or logical gaps (Huang et al., 2024; Perković et al., 2024). Such issues pose notable challenges in technical domains like construction.
Scalability and Integration Challenges	Integrating LLMs with existing construction management systems can involve technical and operational challenges. Especially in large-scale projects, the performance and scalability of these models may be questioned (Fuchs et al., 2023).
Data Privacy and Security Concerns	LLMs require large amounts of data, raising concerns regarding the privacy and security of this data. The misapplication of model outputs, along with data privacy and user security issues, are important matters that need to be addressed and resolved (Linegar et al., 2023; Liang et al., 2023). In construction projects, the handling of sensitive data can increase the risk of data leaks or misuse.

Limitations of Training Data	Although LLMs are trained as general language models, they require domain-specific data to perform adequately in technical fields like construction. A lack of such data can limit the performance of these models. For example, Kim et al. (2024) mentioned that the lack of domain-specific data negatively affected model performance during the information extraction process from multilingual construction documents.
Limitations in Complex Tasks	LLMs may show limited performance, particularly in complex and multidisciplinary tasks (Yang et al., 2024). Additionally, the explainability and transparency of LLM-generated results can be a significant issue, especially in decision support systems.
Cost and Resource Requirements	Training and fine-tuning LLMs require substantial computational power and storage capacity, which can limit the widespread use of these models in terms of resource intensity (Aathilakshmi et al., 2024). This can be especially costly for small and medium-sized construction firms.

Conclusion

This study explored the potential applications of LLMs in the construction industry. The findings indicate that LLMs offer considerable benefits across various domains, including project management, contract analysis, document handling, occupational safety, and technical operations such as bridge monitoring and digital twin projects. In project management, LLMs enhance efficiency in scheduling, constraint detection, and resource planning. In contract and document management, they streamline information extraction and risk identification, improving accuracy and reducing time. They also contribute to safety management by analyzing accident data and supporting preventive measures. Integration with BIM further enhances access to project data and strengthens decision-support systems.

Despite these advantages —such as automation, improved efficiency, and better risk and safety management— LLMs face limitations in handling complex linguistic structures and performing domain-specific analyses. Addressing these challenges requires domain adaptation and targeted training.

In conclusion, LLMs hold significant transformative potential for the construction sector, and their continued development will improve their alignment with industry-specific needs, expanding their impact across the field.

References

Aathilakshmi, S., Sivapriya, G., & Manikandan, T. (2024). LLM fine-tuning: Instruction and parameter-efficient fine-tuning (PEFT). In Generative AI and LLMs: Natural Language Processing and Generative Adversarial Networks (pp. 117-134).

Ahmadi, E., Muley, S., & Wang, C. (2024). Automatic construction accident report analysis using large language models (LLMs). Journal of Intelligent Construction, 3(1), 9180039.

Aluga, M. (2023). Application of CHATGPT in civil engineering East African Journal of Engineering, 6(1), 104-112.

Chen, X., & Zhang, L. (2024). Revolutionizing bridge operation and maintenance with LLM-based agents: An overview of applications and insights. arXiv.

Gao, Y., Gan, Y., Chen, Y., & Chen, Y. (2024). Application of large language models to intelligently analyze long construction contract texts. Construction Management and Economics, 43(3), 226-242.

Fuchs, S., Witbrock, M., Dimyadi, J., & Amor, R. (2024). Using Large Language Models for the Interpretation of Building Regulations.

He, C., Yu, B., Liu, M., Guo, L., Li, T., & Huang, J. (2024). Utilizing Large Language Models to Illustrate Constraints for Construction Planning. Buildings, 14(8), 2511.

He, Y., Tang, Y., & Chen, T. (2024). A study on large language model-based approach for construction contract risk detection. ICBDDM 2024, August 16–18, 2024, Shanghai, China. ACM.

Huang, L., Yu, W., Ma, W., Zhong, W., Feng, Z., Wang, H., Chen, Q., Peng, W., Feng, X., Qin, B., & Liu, T. (2024). A survey on hallucination in large language models: Principles, taxonomy, challenges, and open questions. arXiv.

Jang, S., & Lee, G. (2023). Interactive design by integrating a large pre-trained language model and building information modeling. arXiv.

Kim, J., Chung, S., & Chi, S. (2024). Cross-lingual information retrieval from multilingual construction documents using pretrained language models. Journal of Construction Engineering and Management,

Kim, J., Kwon, B., Lee, J., & Mun, D. (2025). Inherent risks identification in a contract document through automated rule generation. Automation in Construction.
Lee, J., Ahn, S., Kim, D., & Kim, D. (2024). Performance comparison of retrieval-augmented generation and fine-tuned large language models for construction safety management knowledge retrieval. Automation in Construction, 164, 105217.
Li, Y., Miao, N., Ma, L., Shuang, F., & Huang, X. (2023). Transformer for object detection: Review and benchmark. Engineering Applications of Artificial Intelligence, 126(Part C), 107021.
Liang, Z., Fang, Z., Huang, H., Wang, Z., Hong, Y., Liu, K., & Shang, P. (2023). Engineering exploration and research on large language models. Proceedings of the 5th International Conference on Internet of Things, Automation and Artificial Intelligence (IoTAAI 2023), 174-179.
Linegar, M., Kocielnik, R., & Alvarez, R. M. (2023). Large language models and political science. Frontiers in Political Science, 5, 1257092.
Moon, S., Chi, S., & Im, S. (2022). Automated detection of contractual risk clauses from construction specifications using bidirectional encoder representations from transformers (BERT). Automation in Construction, 138, 104465.
Park, Y., Moon, S., Kim, J., & Chi, S. (2024). Application of Domain-specific Thesaurus to Construction Documents based on Flow Margin of Semantic Similarity. International Conference on Construction Engineering and Project Management, 375–382.
Perković, G., Drobnjak, A., & Botički, I. (2024). Hallucinations in LLMs: Understanding and addressing challenges. In Proceedings of the 47th MIPRO ICT and Electronics Convention (MIPRO 2024) (pp. 1-6). IEEE.
Prieto, S. A., Mengiste, E. T., & García de Soto, B. (2023). Investigating the use of ChatGPT for the scheduling of construction projects. arXiv.
Pu, H., Yang, X., Li, J., & Guo, R. (2024). AutoRepo: A general framework for multimodal LLM-based automated construction reporting. Expert Systems With Applications, 233, 121123.
Tran, S. V.-T., Yang, J., Hussain, R., Khan, N., Kimito, E. C., Pedro, A., Sotani, M., Lee, U.-K., & Park, C. (2024). Leveraging large language models for enhanced construction safety regulation extraction. Journal of Information Technology in Construction (ITcon), 29, 1026-1038.
Wang, N., Issa, R. R. A., & Anumba, C. J. (2022). NLP-based query-answering system for information extraction from building information models. Journal of Computing in Civil Engineering, 36(6), 04022062.
Wei, F., Neary, R., Qin, H., Mao, Q., & Zhang, J. (2024). Empirical Evaluation of Embedding Models in the Context of Text Classification in Document Review in Construction Delay Disputes. 2024 IEEE International Conference on Big Data (BigData).
Xu, N., Liang, Y., Guo, C., Meng, B., Zhou, X., Hu, Y., & Zhang, B. (2023). Entity recognition in the field of coal mine construction safety based on a pre-training language model. Engineering, Construction and Architectural Management.
Yang, Y., Ye, F., Xu, D., Zhang, X., & Xu, J. (2024). LLM-Based Digital Twin Water Conservancy Knowledge Graph Construction. 2024 IEEE 36th International Conference on Tools with Artificial Intelligence (ICTAI), 979-8-3315-2723-5/24/$31.00.
Yi, M., Ceglinski, K., Ashok, P., Behounek, M., White, S., Peroyea, T., & Thetford, T. (2024). Applications of Large Language Models in Well Construction Planning and Real-Time Operation.

CONSTRUCTION MANAGEMENT

Construction Project Management

IT in Construction

Risk Management in Construction

Sustainability in Construction

Artificial Intelligence-Supported Risk Management and Visualization Techniques in the Construction Industry

Osman Berk Oğul[a], Onur Behzat Tokdemir[a]
Istanbul Technical University, Civil Engineering Departmant, Construction Management Program, Türkiye
ogul18@itu.edu.tr

Keywords: Artificial Intelligence, Construction Risk Management, Risk Visualization, Risk Assessment.

Aim

This study aims to classify and identify the various types of hazards that arise during building projects by analyzing the full spectrum of risks—technical, financial, legal, environmental, and human-related—and understanding their specific characteristics within the construction context. It also explores the use of artificial intelligence (AI) technologies, such as computer vision, natural language processing, deep learning, and machine learning, in enhancing risk management processes, particularly in data collection, risk assessment, and decision-making automation. Furthermore, the research critically evaluates existing literature to assess the effectiveness, maturity, benefits, and limitations of AI-based methods in real-world construction risk scenarios. Additionally, the study investigates risk visualization techniques, including Monte Carlo Simulation, Bayesian Networks, Fuzzy Logic, Risk Matrix, Bow-Tie Diagrams, and BIM-based visualizations, focusing on how these tools facilitate risk communication and aid stakeholders in interpreting complex data. Finally, by synthesizing the reviewed literature, the research identifies current gaps and proposes directions for future studies, particularly in integrating AI with visual analytics and practical project workflows.

Material and Method

This study employs a systematic literature review methodology to synthesize and analyze the current body of knowledge related to the integration of Artificial Intelligence in construction risk management. Scopus was chosen as the primary database due to its comprehensive coverage of peer-reviewed literature across engineering, technology, and applied sciences. The review followed a multi-stage protocol:
Keyword Development: Key terms such as "Artificial Intelligence," "Risk," "Construction Management," "Machine Learning," and "Building Site" were used in various combinations.
Inclusion Criteria: Only peer-reviewed journal articles and conference papers published between 2010 and 2024, in English, and with a clear focus on AI applications in construction risk management, were considered.
Screening Process: Abstracts and full texts were screened for relevance, quality, and methodological soundness. Duplicates and irrelevant studies were excluded.
Data from these studies were categorized based on AI technique, application domain (e.g., cost, schedule, safety), and type of visualization method used. In addition, keyword co-occurrence and cluster analysis were performed using VOSviewer software to identify dominant research themes and interconnections between subtopics.

Findings

A. Risk Types in the Construction Sector

Construction risks are typically categorized into several groups, including financial, technical, environmental, legal, contractual and administrative, occupational health and safety, and political risks. The dynamic and multi-layered nature of construction projects necessitates predictive approaches to risk management. For example, poor site conditions, delays in procurement, or miscommunication between subcontractors can lead to cascading risk effects throughout the project lifecycle (Sharma & Swain, 2011).

B. AI Applications in Risk Management

Design Optimization: AI-empowered Building Information Modeling (BIM) systems help detect clashes and identify potential hazards during early design stages (Gandhi, 2023).

Project Scheduling and Cost Estimation: Artificial Neural Networks (ANNs), support vector machines, and ensemble learning models are used to improve forecasting of budgets and timelines (Abioye et al., 2021).
Safety Monitoring: Real-time computer vision-based systems using drone imagery and wearable sensors detect safety violations and track worker behavior (Waqar et al., 2023).
Disaster Risk Simulation: Deep learning and digital twins simulate complex disaster scenarios (Kamari & Ham, 2022).
Quality Control: Image recognition and defect classification algorithms identify structural anomalies (Rafsanjani & Nabizadeh, 2023).

C. Risk Visualization Techniques

Risk visualization is not merely a supplementary tool but an essential component in translating technical risk assessments into intuitive, actionable formats for stakeholders at every level. The reviewed studies highlight the following techniques:
Monte Carlo Simulation (MCS): This technique generates thousands of possible outcomes based on probabilistic inputs, offering decision-makers a comprehensive understanding of the potential variation in cost, time, and resource-related risks. MCS is particularly useful for assessing financial uncertainties and scheduling deviations in large-scale projects where deterministic models fall short (Platon & Constantinescu, 2014).
Bayesian Networks: These probabilistic graphical models represent variables and their conditional dependencies via directed acyclic graphs. They allow dynamic risk updates as new evidence becomes available, making them ideal for risk analysis in project environments where uncertainty evolves over time (Charniak, 1991). They also facilitate scenario analysis by modeling the impact of one risk event on others.
Fuzzy Logic: This approach is beneficial in situations where inputs are vague, qualitative, or linguistic, such as expert judgments on project feasibility or safety. Fuzzy logic models interpret imprecise data and help create robust early-warning systems for hazard prediction (Dernoncourt, 2011).
Risk Matrices: These are commonly used tools to visually represent and prioritize risks based on their likelihood and impact. When integrated into digital dashboards, they can serve as real-time risk trackers across multiple project stages (Vicente, 2024).
Bow-Tie Diagrams: Bow-tie models map the relationship between causes, risk events, and consequences while identifying both preventive and mitigative controls. Their visual clarity makes them ideal for communicating high-level strategic risks to non-technical stakeholders (Turner et al., 2017).
BIM-Integrated Visualization: Building Information Modeling (BIM) platforms offer 3D and 4D simulations that help visualize physical construction elements along with associated risks. These visualizations allow the overlay of time-dependent data such as weather predictions or supply chain disruptions, thus enhancing proactive decision-making (Zhang et al., 2013; Zou et al., 2016).

D. Research Gaps and Future Directions

Despite the promise AI and visualization technologies hold, several areas remain underexplored or inadequately implemented:
Standardization and Data Interoperability: AI model training and scalability are hampered by disparate construction platforms' inconsistent data formats and structures. To increase consistency, shared data environments and standardized ontologies are required.
Explainability and Ethical AI Use: The majority of deep learning models used in the building industry are opaque systems that provide no insight into how they make decisions. Explainable AI (XAI) techniques must be used immediately to foster confidence, particularly in applications that are vital to public safety.
Cross-disciplinary Collaboration: It's still difficult to bridge the divide between legal professionals, construction engineers, project managers, and AI developers. In order to guarantee that AI technologies are not only technically sound but also operationally feasible and consistent with the law, collaborative frameworks are crucial.

Field Validation and Longitudinal Studies: A lot of AI models and visualization techniques are only tested in simulated settings. For evaluations of user acceptability, cost-effectiveness, and durability in actual construction projects, long-term empirical research is necessary.

Conclusion

This study has examined the role of Artificial Intelligence (AI) in enhancing risk management practices in construction projects and how visualization techniques can support these advancements. Recent literature indicates that AI applications are particularly effective in areas such as design optimization, cost and schedule forecasting, safety monitoring, disaster simulation, and quality control.

In addition, visualization techniques like Monte Carlo simulation, Bayesian networks, fuzzy logic, risk matrices, and BIM-based tools are essential for converting complicated risk data into understandable representations and enhancing decision-making during the course of a project.

However, the study also identifies several key limitations. The lack of standardized data formats, limited explainability of AI models, and the predominance of simulations over real-world applications restrict the broader adoption of these technologies. Furthermore, insufficient interdisciplinary collaboration poses challenges to the practical implementation of AI-based systems in construction workflows.

In conclusion, for AI-supported risk management approaches to be more effective and sustainable in the construction industry, efforts should focus on standardizing data structures, advancing explainable AI methods, and increasing field-based empirical studies.

References

Abioye, S. O., Oyedele, L. O., Akanbi, L., Ajayi, A., Delgado, J. M. D., Bilal, M., ... & Ahmed, A. (2021). Artificial intelligence in the construction industry: A review of present status, opportunities and future challenges. Journal of Building Engineering, 44, 103299.

Dernoncourt, F. (2011). Fuzzy logic and decision-making. *Fuzzy Systems and AI*.

Gandhi, T. (2023). What are the applications of AI in Civil Engineering Industry. https://www.linkedin.com/pulse/what-applications-ai-civil-engineering-industry-trupti-gandhi-nrbhf/ adresses citationed.

E. Charniak. Bayesian networks without tears, AI Mag. 12 (1991) 50–63.

Kamari, M., & Ham, Y. (2022). AI-based risk assessment for construction site disaster preparedness through deep learning-based digital twinning. Automation in Construction, 134, 104091.

Platon, V., and Constantinescu, A. (2014) „Monte Carlo Method in risk analysis for investment projects", ProcediaEconomics and Finance, Vol 15, pp 393-400.

Rafsanjani, H. N., & Nabizadeh, A. H. (2023). Towards human-centered artificial intelligence (AI) in architecture, engineering, and construction (AEC) industry. Computers in Human Behavior Reports, 100319.

Sharma, S. K., & Swain, N. (2011). Risk management in construction projects. Asia Pacific Business Review, 7(3), 107-120.

Turner, C., Hamilton, W. I., & Ramsden, M. (2017). Bowtie diagrams: A user-friendly risk communication tool. Proceedings of the Institution of Mechanical 89 Engineers, Part F: Journal of Rail and Rapid Transit, 231(10), 1088–1097. https://doi.org/10.1177/0954409716675006

Vicente, V. (2024). Risk Assessment Matrix: Overview and Guide. AuditBoard: https://www.auditboard.com/blog/what-is-a-risk-assessment-matrix/ adresses citationed

Waqar, A., Qureshi, A. H., Almujibah, H. R., Tanjung, L. E., & Utami, C. (2023). Evaluation of success factors of utilizing AI in digital transformation of health and safety management systems in modern construction projects. Ain Shams engineering journal, 14(11), 102551.

Zhang, S.J., Teizer, J., Lee, J.K., Eastman, C.M., Venugopal, M. Building information modeling (BIM) and safety: automatic safety checkingof construction models and schedules. Autom. Constr. 29, 183–195 (2013)

Zou, Y., Kiviniemi, A., Jones, S.W. Developing a tailored RBS linking to BIM for risk management of bridge projects. Eng. Constr. Archit.Manage. 23(6), 727–750 (2016).

CONTROL AND AUTOMATION ENGINEERING

Advances in Automatic Control Engineering

Applications of Control Engineering

Comparison Of Anti-Windup Methods for Fractional Order PI Controllers

Muhammed Ali Elaydın[a], Erhan Yumuk[a], Müjde Güzelkaya[a]

[a] Istanbul Technical University, Dept. of Control and Automation Engineering, Control and Automation Engineering Program, Türkiye
elaydin17@itu.edu.tr

Keywords: Fractional Order Controllers, Anti-Windup Methods, Integral Windup Mitigation.

Aim

Fractional-order control (FOC) is a specialized area in control theory that uses fractional-order integrators and derivatives to design control systems. Unlike traditional integer-order PID (IOPID) controllers, which have three parameters, fractional-order PID (FOPID) controllers include five parameters: proportional, integral, and derivative gains (K_p, K_i, K_d), as well as fractional orders of integration (α) and differentiation (μ). This provides greater flexibility and adaptability in controller design (Yumuk et. al.,2019).
However, like traditional PID controllers, FOPID controllers can experience integral windup, where the control signal saturates due to prolonged error accumulation, leading to overshoot and instability (Rahman et. al., 2018). Some methods proposed for integer order PID (IOPID) controllers, such as back calculation, conditional integration, and automatic reset configuration, can be adapted and used for anti-windup in fractional order PID (FOPID) controllers. In addition, some anti-windup methods have been specifically proposed for FOPID controllers. Examples of these include the fractional integrator reset method.
In this study, five anti-windup methods, i.e., conditional integration (clamping), back-calculation, automatic reset configuration (ARC), application of the ARC to fractional filtered PI configuration, and integrator order reset, are employed to design the Fractional Order PI Controller (FOPI). These five methods are compared on different order systems with different time delays to evaluate their effectiveness in preventing integral windup and improving system performance.

Material and Method

Integral windup is a common issue in control systems, occurring when the control signal exceeds the system's input range, leading to saturation and degraded performance. To address this problem, various anti-windup methods have been developed or adopted for fractional-order PID (FOPID) controllers. These methods aim to limit the integrator's effect during saturation, ensuring stability and improving system response. In this study, anti-windup methods were compared using the same fractional order PI (FOPI) controller for all methods. Figure 1 shows the block diagram of the control system and the FOPI controller.

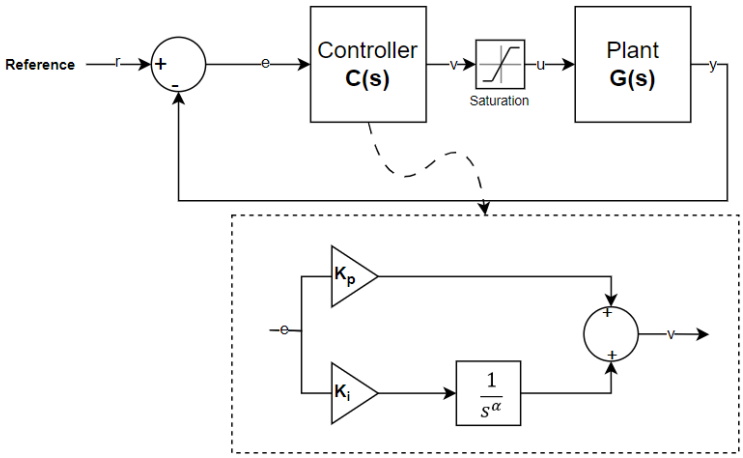

Figure 1: Control System and FOPI Controller Block Diagram.

In this section, the five anti-windup methods explained in detail below are used for designing FOPI:

(i) Conditional integration (clamping) method, disables the integral action when the control signal is saturated. Specifically, the integral coefficient (K_i) is set to zero during saturation, preventing further error accumulation. Once the control signal returns to the allowable range, the integral action is reactivated using the predefined integral coefficient. While simple, this method may result in slower recovery from saturation (Murad et. al., 2020). Figure 2 represents a block diagram of the conditional integration (clamping) method.

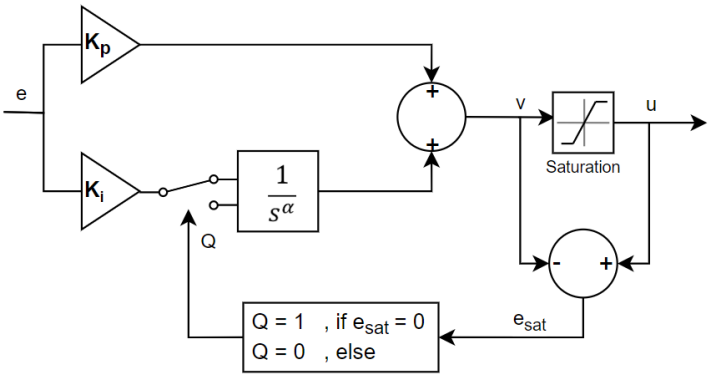

Figure 2: Conditional Integration Method.

(ii) The Back Calculation Method calculates the difference between the control signal before and after the saturation block. This difference is multiplied by a predefined anti-windup gain (k_{aw}) and fed back to the integrator. The feedback signal adjusts the integrator's output, preventing excessive error accumulation during saturation. For the classical back-calculation method, in FOPID controllers, k_{aw} is typically a fixed value (Ardjal et. al.,2022). Figure 3 illustrates the block diagram of the back calculation method.

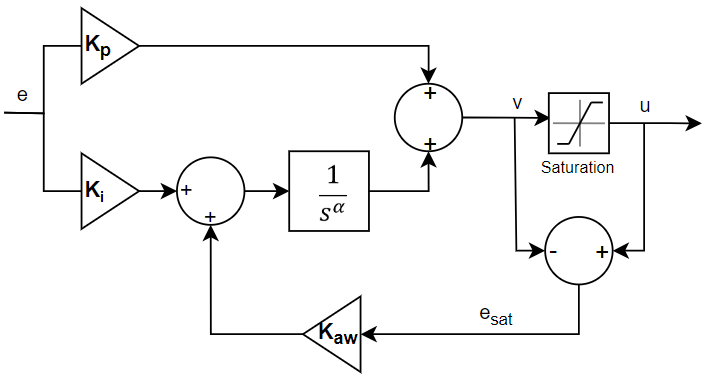

Figure 3: Back Calculation Method.

(iii) The automatic reset configuration (ARC) method modifies the control loop by placing the integrator terms in the feedback path rather than the forward path. Furthermore, an additional saturation block is placed in the forward path of the control loop. This method is expected to be effective in anti-windup because the FOPI controller predicts where the control signal will saturate in advance and generates a control signal that can adapt to saturation within itself. This configuration indirectly limits the integrator's output during saturation, reducing the risk of windup and improving system stability (Padula et. al., 2012). Figure 4 describes the block diagram of the automatic reset configuration method.

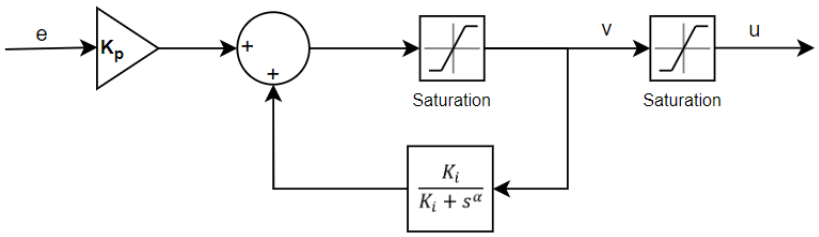

Figure 4: Automatic Reset Configuration (ARC) Method.

(iv) Application of the ARC to fractional filtered PI configuration builds upon the traditional approach of the automatic reset configuration method by maintaining the integrator terms in the feedback path and the saturation block in the forward path. However, this enhanced version introduces a fractional filter at the beginning of the controller. This fractional filter consists of two terms. The first one (α) is the integrator order of the FOPI controller. The second term is (λ) one of the requirement parameters in the controller design method. The fractional filter adds an additional layer of dynamic adjustment to the control loop, allowing for more precise tuning of the system's response. By incorporating this filter, the method further mitigates the effects of windup during saturation, enhances the controller's adaptability to varying system conditions, and provides better overall stability and performance (Meena et. al., 2024). Figure 5 pictures the block diagram of the automatic reset configuration method.

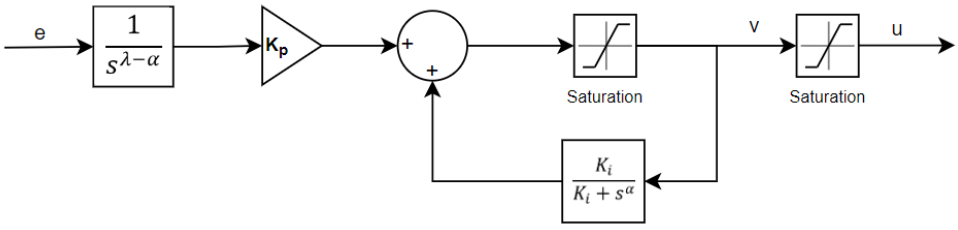

Figure 5: Application of the ARC to fractional filtered PI configuration.

(v) The fractional integrator order reset method is a unique approach for FOPID/FOPI controllers. This method leverages the flexibility of fractional-order controllers by dynamically adjusting the fractional integrator order (α) during saturation. When saturation is detected, the integrator order is reset to zero. This causes to reduction in the integrator's influence during saturation. Once the control signal returns to the allowable range, the integrator order is restored to its original design value. This method takes advantage of the additional degree of freedom provided by fractional-order controllers (Malezsa&Sierociuk, 2018). Figure 6 classifies the block diagram of the fractional integrator order reset method.

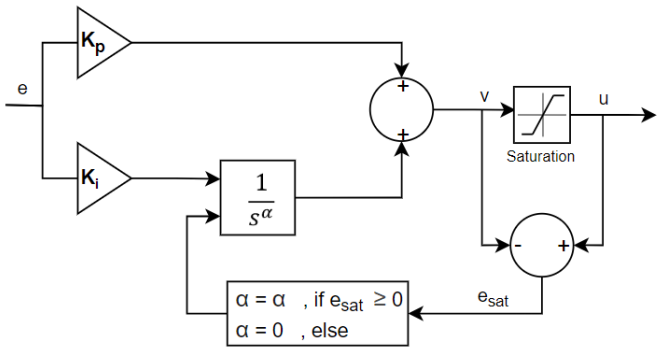

Figure 6: Fractional Integrator Reset Method.

These five methods were tested on different order systems with different time delays to evaluate their effectiveness in preventing integral windup and improving system performance. The fractional-order PI (PI^{α}) controller parameters (for some methods, just K_p and K_i; because of the configuration of the method) were kept constant across all tests to isolate the effects of the anti-windup methods.

Findings

The above-mentioned methods were tested on different order systems with different time delays for both step response and reference tracking. The methods were compared using first-order systems, second-order systems, and first-order plus time delay (FOPTD) systems. To generalize the study, different saturation limits and controller parameters were used during the comparisons.

As an example of the examined systems, a second-order system without time delay was considered for inclusion in the abstract. Saturation fundamentally affects two aspects of system behavior: it can cause overshoot and make the system respond more slowly. In the case study, the saturation limit was chosen with a particular focus on analyzing how much the system's response slows down. The G(s) system, whose transfer function is given in Equation 1, can be provided, where the saturation limit is ± 2.0.

$$G(s) = \frac{1}{s^2 + 3s + 2} \tag{1}$$

The controller parameters were specifically selected to analyze the benchmark system. Since the focus was on evaluating the speed of response, a set of parameters was chosen to ensure that the system would not exhibit overshoot, allowing for a fair comparison of response times. The parameters shown in Equation 2 are the fractional-order PI controller parameters, which are kept constant for all methods.

$$PI^{\alpha}:\ K_p = 1;\ K_i = 1;\ \alpha = 1.2 \tag{2}$$

For the example system, the comparison of reference tracking results for the examined anti-windup methods is shown in Figure 7.

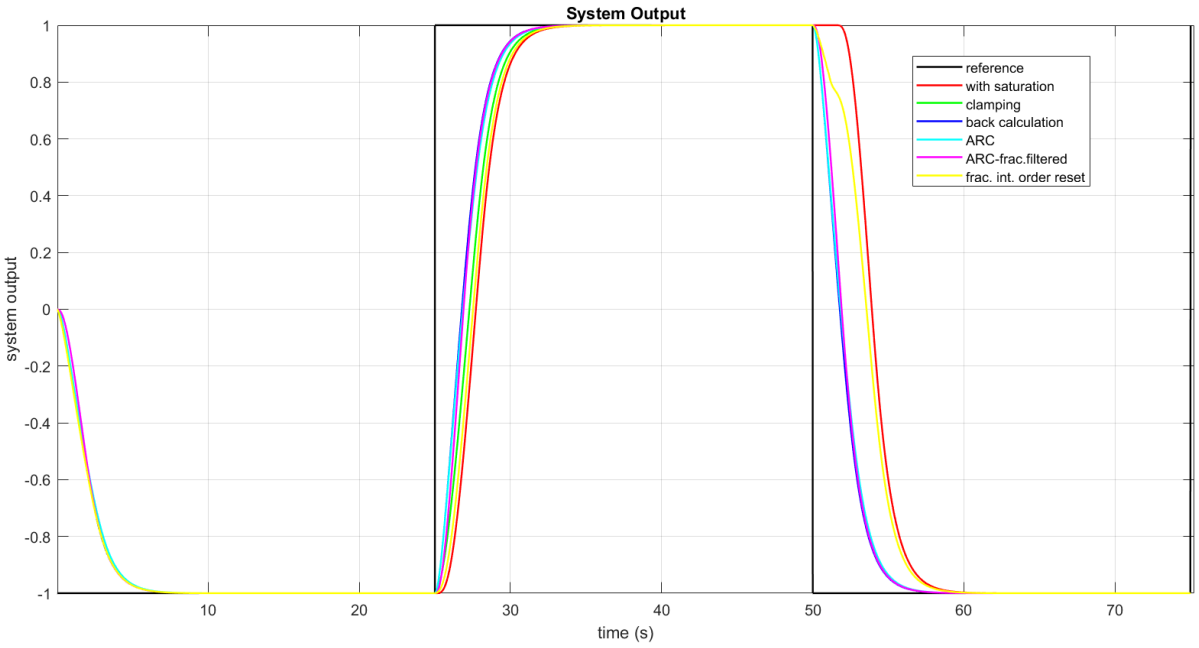

Figure 7: Reference Tracking Results for the Example System.

The system parameters and controller parameters were kept constant for all methods to ensure that only the effects of the anti-windup methods were compared. To allow for more comprehensive comparisons, simulations were repeated with different saturation limits. Although some classical methods produced similar results, the application of the ARC to fractional filtered PI configuration, which includes a fractional-order filter, was found to be one of

the most successful in reference tracking. Considering the phase with a reference of 1 applied at the 25th second in the system, the initial value is -1, and the reference value is 1. Under saturation, the system response reaches from -0.8 to 0.8 in 2.5 seconds. While the other methods rise within approximately 2.4 seconds, the ARC method achieves this in 2.2 seconds, and the fractional filtered ARC structure rises in 2.0 seconds. The analyses are being continued for different system models, different dead-time configurations, and different saturation limits.

Conclusion

Although fractional-order PID (FOPID) controllers are a relatively recent development in control theory, they require the same level of attention to issues like integral windup as traditional PID controllers. Various methods have been proposed to address integral windup in FOPID controllers, including adaptations of classical anti-windup methods and novel approaches that dynamically adjust the fractional integrator order. In this study, five anti-windup methods, i.e., conditional integration, automatic reset configuration, back-calculation, the application of the ARC to fractional filtered PI configuration, and integrator order reset, are employed to design Fractional Order PID Controllers (FOPID). The methods were tested on different order systems with different time delays by analyzing reference tracking and step responses.

The results indicate that while some classical methods provide reasonably good outcomes, others yield worse results in comparison. On the other hand, the results of methods specifically designed for fractional-order systems can vary under different systems and conditions. Nevertheless, it can be observed that the method applied using a fractional filter in the example system performs better than many of the classical methods.
In future studies, the effects of different system models, different dead-time configurations, and different saturation limits on the methods examined in this study will continue to be analyzed. The conditions under which the methods are relatively stronger or weaker will be investigated.

References

Adib Murad, M. A., Tzounas, G., & Milano, F. (2020). Modeling and simulation of fractional order PI control limiters for power systems. *IFAC-PapersOnLine, 53*(2), 13107–13112. Elsevier BV. https://doi.org/10.1016/j.ifacol.2020.12.2273

Ardjal, A., Bettayeb, M., & Mansouri, R. (2022). Improved model-free fractional-order intelligent proportional–integral fractional-order sliding mode control with anti-windup compensator. *Transactions of the Institute of Measurement and Control, 44*(16), 3092–3106. https://doi.org/10.1177/01423312221099302

Malesza, W., & Sierociuk, D. (2018). Fractional variable order anti-windup control strategy. *Archives of Electrical Engineering, 67*(3), 529–540. https://doi.org/10.24425/124258

Meena, R., Chakraborty, S., Pal, V. C., & Lala, H. (2024). Experimentally validated fractional-order PI with anti-windup for fractional-order plus time delay processes. *International Journal of Dynamics and Control, 12*(12), 4232–4243. https://doi.org/10.1007/s40435-024-01483-8

Padula, F., Visioli, A., & Pagnoni, M. (2012). On the anti-windup schemes for fractional-order PID controllers. In *Proceedings of the 2012 IEEE 17th International Conference on Emerging Technologies & Factory Automation (ETFA)*. IEEE. https://doi.org/10.1109/ETFA.2012.6489758

Rahman, F. R., Rohman, A. S., Munawar, I., & Sereyvatha, S. S. (2018). Speed control system of BLDC motor using PI anti-windup controller on an autonomous vehicle prototype (AVP). In *2018 International Conference on Sustainable Engineering and Technology (ICSET)*. IEEE. https://doi.org/10.1109/ICSENGT.2018.8606398

Yumuk, E., Güzelkaya, M., & Eksin, İ. (2019). Analytical fractional PID controller design based on Bode's ideal transfer function plus time delay. *ISA Transactions, 91*, 196–206. https://doi.org/10.1016/j.isatra.2019.01.034

CONTROL AND AUTOMATION ENGINEERING

Advances in Automatic Control Engineering

Applications of Control Engineering

DESIGN AND CONTROL OF A 120-TON CAPACITY TRANSPORTATION SYSTEM FOR INDUSTRIAL APPLICATIONS

Korel Dikmen[a], Lale T.Ergene[a]

Istanbul Technical University, Electrical Engineering, Turkey
dikmenk@itu.edu.tr

Keywords: Transportation System, Crane, PLC, HMI, Controller, Induction Motor

The main goal is to ensure the efficiency, safety, and automation of heavy load transportation systems used in large-scale manufacturing facilities, ports, mining sites, and steel plants.
Building automation systems are inevitable in every building in order to make life easier, decrease workload, and create safer and higher quality environments (Aydoğan, Özgün, & Karaaahmetoğlu, 2009; Özen & Şimşek, 2019). Today's automation technology generally makes use of computer-enhanced automation. PLC Systems are the most commonly preferred systems (Malik, Choudhry, Mehmood, & Hanif, 2010). With the developments in technology, various equipment and procedures are found to be in use in this field. With the increase in competition and consumer expectations worldwide, the need for smarter, faster, and more powerful technologies has been on the rise. Conventional industrial tasks were mainly controlled manually, which induced the risk of errors and proved to be more time-consuming and expensive. Automation resolves these issues by incorporating a variety of systems (process, machinery, software) that work together to achieve flexibility, better quality of products, and shorter production times in a cost-efficient manner. Automation reduces the probability of an error occurrence and provides energy and resource conservation. Therefore, the recent trend in industries is the shift towards faster and reliable automated systems over inefficient manual operations. Industrial automation has been the target of many studies that aim at increasing the performance level of the processes along with reducing their complexity (Nadgauda & Muthukumaraswamy, 2019; Waangping, 2023). Among the various automation techniques, PLC has been replacing the traditional relay controls due to its reliability, stability, flexibility, and ease of programming (Alzubaydy & Aziz, 2017). Asynchronous motors are widely used in industry due to their simple, economical, and robust structure, maintenance-free, and superior operating conditions. Various control techniques are used for the control of commonly used asynchronous motors (Çetinkaya & Kuşçu, 2018; Meshram et al., 2020; Terzioğlu et al., 2019). In this study, a transportation system is designed, programmed to control, and implemented in order to monitor and control the parameters of an automation system, which is a part of a harbor project.

Aim

This study focuses on the design and implementation of a 120-ton capacity transportation system for heavy load transportation in industrial applications and its control using PLC (Programmable Logic Controller).
PLC-Based control and automation to ensure the automatic and safe operation of the system, a PLC-based control mechanism has been developed. The PLC performs the following functions:

- Processing data from load sensors to prevent overloading,
- Providing precise speed and directional control for safe transportation,
- Integrating with the HMI system for real-time monitoring and fault monitoring,
- Implementing automatic stop and warning systems in emergency scenarios.

The transportation system consists of a high-strength steel structure, a hydraulic lifting mechanism, and motor systems with precise motion control. The movement and load balancing operations of the system are managed by using a PLC. The main goal is to ensure the efficiency, safety, and automation of heavy load transportation systems used in large-scale manufacturing facilities, ports, mining sites, and steel plants.

Material and Method

The system is designed based on the requirements, which specify the intended purpose and usage of the crane. Based on these requests, functional definitions and boundaries are determined for operations. The functional definitions include the crane's operating procedures, operational restrictions, and key safety considerations. The crane has four different operational modes required by the factory. To ensure the proper execution of these operational functions, software features are required, and their purposes are explained.

The system includes fourteen squirrel-cage induction motors. One lifting and two travel motors for 80-ton and one lifting and two travel motors for 40-ton and eight motors for the bridge are chosen and allocated for the complete system.

Two operation scenarios are designed. The first operation involves lifting and lowering a maximum load of 120 tons in synchronization using the 80-ton and 40-ton lifting groups. After lifting and lowering, the load is transported synchronously using both lifting groups or repositioned using the bridge group. The second operation consists of two steps. First step, the 40-ton lifting group remains stationary while the 80-ton lifting group lowers part of the sheet metal. During this process, the entire weight of the sheet metal rests on the 40-ton lifting group. Second step, the 80-ton lifting group moves. Once the movement is completed, the 80-ton lifting group lifts the lowered section of the sheet metal again, effectively flipping the front and back sides of the sheet. After the sheet orientation is changed, it is transported synchronously using both lifting groups or repositioned using the bridge group. The functional features of the transportation system are determined due to the application requirements. The design procedure includes functional descriptions that cover system operation procedures, operational restrictions, and key safety considerations.

Schneider TM241CEC24T PLC as a CPU, and Schneider HMIGTO3510 touchscreen was used in this system. The real-time monitoring and fault monitoring pages are designed on an HMI screen for this transportation system.

In lifting motor selection, a downward force occurs (or is generated). If we calculate this force correctly, we can determine the required mechanical power with the utmost accuracy. This downward force is, in turn, determined by the weights of the system.

In the calculation of the travel (or driving) motor power, load values, along with friction and wind values, are also taken into account. Differently from the lifting motor power calculation, moment values are calculated, and the travel (or driving) motor power is determined according to these moment values.

Induction motor drivers operate by rectifying the incoming AC voltage to a DC voltage, which is then supplied to an internal DC bus. Subsequently, this DC voltage is converted back (or inverted) to AC voltage at the desired frequency and voltage level. Using drivers in this system is primarily because the high power ratings of the motors prevent direct online starting. Furthermore, the customer's requirement for precise motor speed control also necessitated the use of drivers.

The lifting motor gearbox ratios, rotation speeds, and drum diameters of the lifting groups differ; a hook synchronization program is designed to ensure synchronized lifting and lowering operations. The detail of the designed hook synchronization layout is shown in Figure 1. This designed module captures the position information of the hooks, ensuring that the lifting or lowering operation ends at the same position where it started, thus maintaining the positional difference between the two hooks. By preserving the position difference between the two hooks during movement, the risk of load tipping is eliminated. To use this program, incremental encoders are installed on the lifting motors of both lifting groups. The positions of the hooks are determined by the encoders mounted on the rear of the motors.

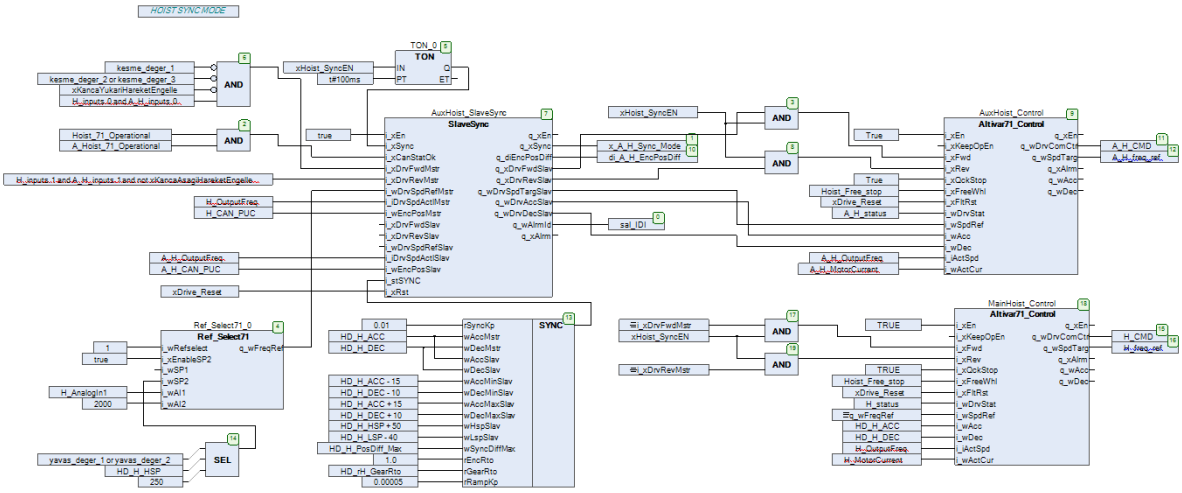

Figure 1. Hook synchronization program.

The travel synchronization program is designed to ensure synchronized load transportation using both lifting groups. The detail of the designed travel synchronization program is shown in Figure 2. Due to these differences, the linear speeds of the travel motors of the lifting groups are calculated to be different. The linear speeds can be equalized using the predefined gearbox ratios through the drive system. However, since the acceleration rates of the drives also vary, misalignments can occur during movement, leading to unbalanced load transportation. Therefore, the designed algorithm should also adjust the acceleration rates to ensure synchronized load transportation.

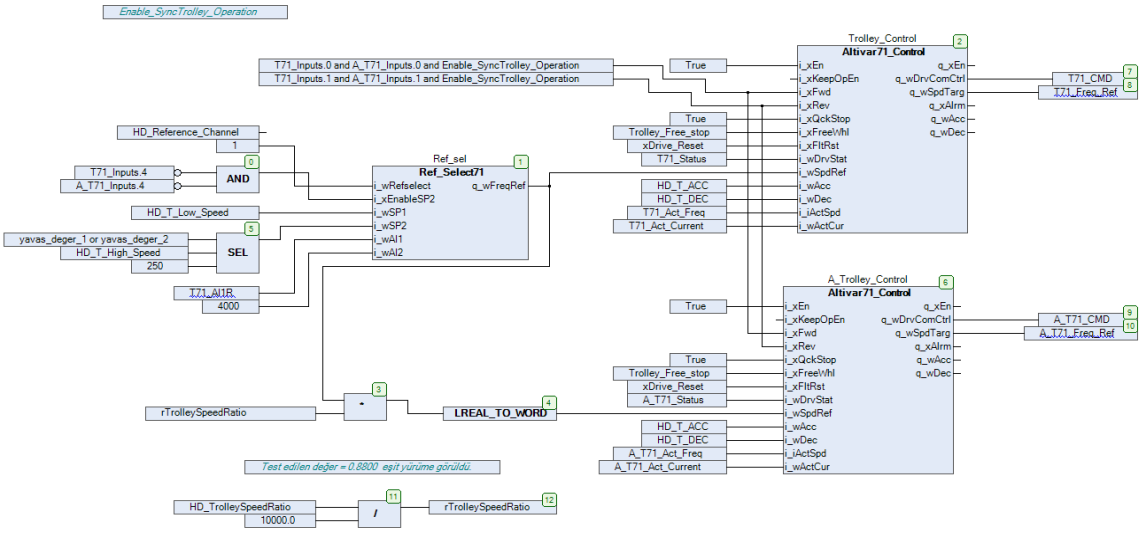

Figure 2. Travel synchronization program.

Overload protection for the lifting groups is ensured by pin-type load cells. To process the information received from the pin-type load cells, a load cell amplifier is used. The information obtained from the pin-type load cells is processed in the load cell amplifier after making the necessary adjustments and is then provided as an analog output signal. The analog signals from the load cell amplifier are directly transmitted to the PLC. These analog signals are evaluated within the PLC software, allowing modifications and restrictions in crane movements based on operational conditions. To enable these functions, one Schneider TM3TI4 analog input module was used in the system design. The loadcell scaling program is designed for overload protection, and detail of this program is shown in Figure 3.

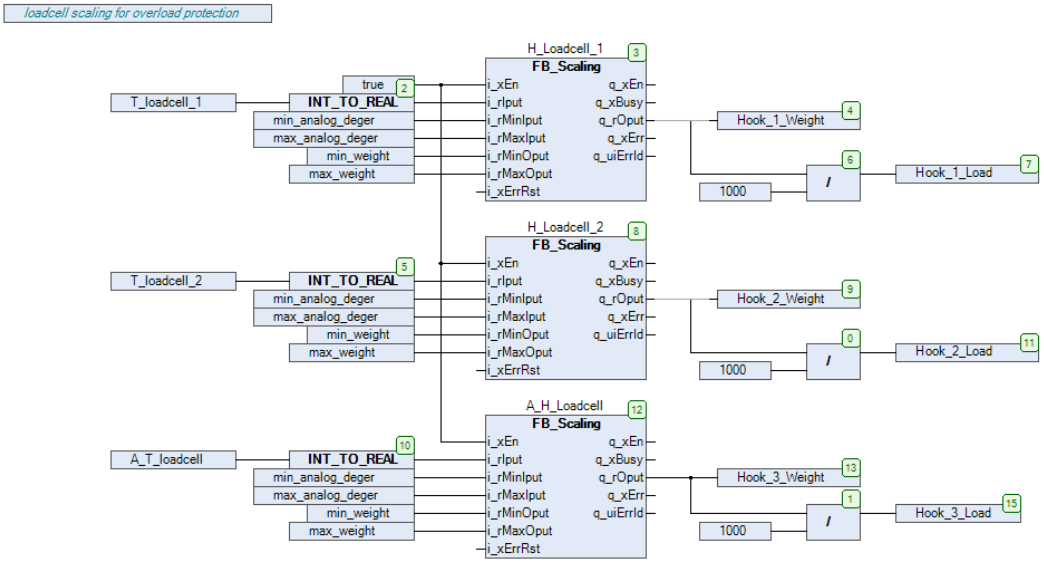

Figure 3. Loadcell scaling program.

Findings

The study covers the design and implementation of a PLC-based automation system for a 120-ton capacity transportation system. The performance of the system was evaluated based on key operational metrics and compared with traditional manual operation methods.

Key Observations:

- Synchronized Lifting Accuracy: The designed hook synchronization algorithm maintained a positional deviation within ±5 mm between the 80-ton and 40-ton lifting groups during lifting and lowering cycles, ensuring stable load handling.
- Load Transport Synchronization: The travel synchronization algorithm successfully equalized the linear speeds of different lifting groups, reducing misalignment occurrences by over 90% compared to manual control.
- Fault Monitoring & Safety: The PLC-based overload protection mechanism, integrating pin-type load cells and analog input modules, accurately detected simulated overloading conditions in 100% of test scenarios, triggering appropriate system responses.
- Operational Efficiency: Compared to conventional relay-based or contactor-based systems, the PLC-controlled automation system achieved a 20% reduction in load handling time and improved process repeatability, reducing operator-dependent variability.
- System Monitoring: The integration of HMI enabled real-time visualization of motor parameters (current, speed, torque) and temperature levels, enhancing diagnostics and reducing average fault detection time by an estimated 40%.

Overall, the system demonstrates measurable improvements in safety, reliability, and operational performance over traditional methods lacking automated synchronization and real-time monitoring.

Conclusion

In conclusion, the implementation of a PLC-controlled automation system in a 120-ton capacity transportation system has proven highly effective in improving operational efficiency, safety, and fault monitoring.

Performance evaluation using predefined metrics such as synchronization accuracy, overload detection reliability, and operational cycle time has shown that the system performs with high precision and consistency. For example, synchronized lifting was achieved within ±5 mm deviation, and overload protection was successfully triggered under all test conditions.

When compared to traditional systems based on manual control or simple contactor logic (without PLC, HMI, or drive systems), the proposed system offers significant advantages, including:

- Reduced operation time by 20%,
- Improved load handling stability,
- Enhanced fault monitoring and system visibility,
- Lower risk of operator-induced errors.

For future developments, the integration of a SCADA system is recommended to allow for remote monitoring, historical data logging, and advanced analytics, further enhancing system optimization. This study highlights that even in large-scale industrial applications, cost-efficient automation based on PLC and HMI technologies can substantially improve the precision and safety of transportation systems.

References

Alzubaydy, A. I. J., & Aziz, A. B. (2017). Automatic control of electrical overhead smart trolley crane AEOSTC based programmable logic controller (PLC). *American Journal of Engineering Research (AJER), 6*(12), 54–62.
Aydoğan, T., Özgün, M. E., & Karaaahmetoğlu, S. (2009). Siemens SIMATIC S7-200 CPU 224 model PLC kontrollü asansör. *SDU International Technologic Science, 1*(1), 1–9.
Çetinkaya, Ö., & Kuşçu, H. (2018). Asynchronous motor control using control panel. *IOSR Journal of Electrical and Electronics Engineering (IOSR-JEEE), 13*(3), 46–55.
Malik, A. H., Choudhry, M. A., Mehmood, T., & Hanif, A. (2010). A generic procedure for troubleshooting of PLC based control systems. *In 11th International Conference on Control, Automation, Robotics and Vision* (pp. 732–737). Singapore.
Meshram, A. D., Godbole, B. A., Jaminkar, T. P., Lohambare, T. G., Kande, M. A., & Keswani, R. A. (2020). PLC based control for induction motor. *International Journal of Advanced Research in Computer and Communication Engineering, 9*(4), 96–99.
Nadgauda, N., & Muthukumaraswamy, S. A. (2019). Design and development of industrial automated system using PLC-SCADA. *In IEEE 10th GCC Conference & Exhibition* (pp. 1–6).
Özen, F., & Şimşek, M. A. (2019). Realization of a building automation system using PLC and SCADA. *International Journal of Engineering and Innovative Research, 1*(1), 28–34.
Terzioğlu, H., Ağaçayak, A. C., Yalçın, G., & Neşeli, S. (2019). Design of monitoring of induction motor operating parameters with SCADA. *European Journal of Science and Technology (Special Issue)*, 418–427.
Waangping, D. (2023). *Electrical engineering, automation & control systems, theory and practical applications (EEACS)*. 979-8-3503-5853-7/23.

DATA ENGINEERING AND BUSINESS ANALYTICS

Big Data Analytics for Decision-Making

Predictive Analytics and Machine Learning in Business

Sentiment Analysis and Opinion Mining

Value-Based Strategy Development for AI Adoption in IT: A Means-End Chain Approach

Ayşe Nisa Akgün[a], Umut Asan[b]

[a] İstanbul Technical University, Departmant of Big Data and Business Analytics, Türkiye
[b] İstanbul Technical University, Departmant of Industrial Engineering, Türkiye
akguna16@itu.edu.tr

Keywords: Artificial Intelligence, Means-end Chain, Strategy, Value.

Aim

The Industry 4.0 process refers to a period in which radical changes are experienced in many sectors, along with the rapid development of technology and the spread of digitalization. In this process, innovative technologies such as AI, big data, the Internet of Things (IoT), and cyber-physical systems are integrated into business processes, enhancing efficiency, accelerating processes, and increasing flexibility. While Industry 4.0 symbolizes a new era that allows businesses to optimize their production and management processes, AI stands out as one of the technologies that stand out in this process. (Sarnıç and Acar, 2024)

AI has many different uses today. For instance, the use of AI applications in the field of HR management has increased by 300% in the last five years (Makers Consulting, n.d.). In the legal industry, AI can enhance efficiency and lower costs by automating repetitive tasks and streamlining workflows (Ultralytics, n.d.). In the e-commerce sector, AI can be used for chatbots, assistants, recommendations tools, visual and voice search, and customer relationship management (Fedorko, Kral and Bacik, 2022).

One of the most important areas of use is the IT sector. SAP Lean IX's AI survey of 226 global IT professionals in 2024 asked questions about the adoption of AI in the IT sector. 80% of survey participants said they currently use generative AI. 78% of participants said gen-AI enables them to finish their jobs faster, and 47% said it improves the quality of their work (SAP & LeanIX, 2024).

Although AI offers numerous advantages, the literature acknowledges that it also has certain drawbacks. This study explores the benefits and challenges of the growing use of AI in the IT sector and identifies core values that shape professionals' perceptions, adoption behaviors, and ethical considerations, based on individuals' responses. By integrating these core values with perceived benefits, potential drawbacks, and various sociodemographic characteristics, customized AI implementation strategies have been developed for different IT professionals.

In the literature review, several articles were identified that explored the underlying values associated with the use of Al. However, only a limited number of these studies employed Means-End Chain (MEC) analysis to uncover these values. Furthermore, no existing studies were found that directly investigate the motivations of employees in the IT sector concerning Al through MEC analysis. This gap in the literature highlights the unique contribution of our study, as it aims to address this underexplored area by employing MEC analysis to uncover the value-driven motivations of IT professionals in relation to Al technologies.

Material and Method

This study employs the MEC Theory, a value-based cognitive approach that helps us better understand individual behavior and decision-making. MEC establishes a connection between extremely abstract and intangible personal and emotional qualities (the ends) and the material characteristics of a product (the means) (Olson and Reynolds, 2001).

MEC Theory explains the underlying reason why certain outcomes are considered important by linking them to individuals' core values. To reveal these hierarchical value structures, a qualitative method known as laddering—developed by Gutman and Reynolds—is employed through in-depth interviews and analysis. The resulting ladders, which consist of interconnected attributes, consequences, and values, illustrate how individuals cognitively

associate an offering with their personal motivations. This structured linkage provides a clearer and more actionable understanding of people's perception and decision-making (Reynolds and Gutman, 1988).
The three hierarchical levels within this approach can be described as follows (Gutman, 1982):

- **Means:** The tangible features of the offering (product or service).
- **Consequences:** The functional or psychological effects that these features generate for the user.
- **End Values:** The individual's ultimate goals or personal values (e.g., happiness, success).

In this study, one-on-one in-depth interviews were conducted with 30 participants by applying the soft laddering method. The process began with demographic questions, followed by questions about the advantages and disadvantages of AI use. The interview, structured as a series of "why" questions, continued iteratively until each participant's underlying personal values were identified through their responses.
According to the soft laddering method, physical and online in-depth interviews lasting an average of 45 minutes were conducted. First, the following socio demographic questions were asked: Age, Gender, Seniority, Education Level. Then, starting with warm-up questions about AI, the following three questions were asked:

- Do you use AI in your daily workflow?
- How often do you use AI?
- For what purposes do you use AI the most?

Then, in the section about advantages, the following question was asked to find the attribute:

- What advantages might increasing or starting to use AI in your current workflows bring you?

Following the participant's response, the following question was asked to further explore the perceived advantages until a terminal value was reached:

- Why is this important to you?

Once the value was identified, the discussion shifted to the disadvantage section. The following question was then asked to identify the Attribute:

- What disadvantages might increasing or starting to use AI in your current workflows bring you?

After the participant responded to this question, additional questions were posed to explore the associated costs until a terminal value was reached.

- Why is this important to you?

While some participants were asked the question 'why is it important?' three times, some participants were asked up to six times.
In the light of the information provided by each participant in the interview, two separate matrices and hierarchical value maps (HVM) were prepared for the advantages and disadvantages that AI will create in the IT world. These maps contain attribute-consequence-value paths. Multiple correspondence analysis (MCA) was used to visualize the MEC components and demographic data from the interviews. Thus, the results are shown in a two-dimensional map. Based on the MCA analysis, an AI-implementation strategy was developed for the company.

Findings

All of the participants use AI in their daily workflows. While the vast majority use it for information retrieval, they do not place full confidence in the accuracy of the information AI provides.
While existing literature highlights key values underlying AI use, such as autonomy (Malouin, 2021), socialization (Rietz, 2021), self-actualization (Bankins & Formosa, 2023), and enjoyment (Rzepka, 2019), this study reveals that participants frequently emphasized additional values, including success, happiness, and dignity.
In some of the interviewees, the values obtained from the advantages map were the same as the values obtained from the disadvantages map. However, for most individuals, the value obtained as a result of advantage and disadvantage was different. For instance, while 'happiness' was found as a value in one interviewees advantages map, 'freedom' was found as a value in her disadvantages map.
Most participants emphasized productivity, time saving, and the opportunity for people to focus on more value-added work thanks to AI, as benefits and attributes. This output is consistent with the productivity increase (McKinsey & Company, 2020) argument that is frequently encountered in the literature under the advantages of using AI.

At almost every experience level, participants believe that they will have more diverse job opportunities as the use of AI increases.

Findings such as unemployment concerns (Rawashdeh, 2023) or remuneration changes (Ernst et al., 2019) due to AI, which are included as costs in the literature, were not frequently included in the study. In the interviews about disadvantages, it was frequently encountered that the quality of the work and people's creativity would decrease due to the intensive use of AI, as costs and attributes.

The results indicate that seniority within the sector, along with age, emerged as significant variables. At more junior levels, values such as staying in touch and freedom are more frequently repeated. As we approach the junior level, financial freedom concerns come to the fore as a cost.

As experience in the IT sector increases, core values such as self-actualization and dignity are more frequently repeated. More senior participants frequently stated that AI's hallucinations could cause problems in accessing accurate information, and therefore they had concerns about the scalability and sustainability of projects carried out with AI as costs.

Conclusion

In light of the findings provided above, it has been concluded that a single AI implementation strategy cannot be created within a company, and even if an umbrella strategy is created, sub-strategy clusters that appeal to the different values of employees with different socio-demographic features should be created.

A strategy proposal was presented for the senior and executive level with the theme of self-actualization and increasing their prestige in the sector in which they have been operating for many years. This strategy will not only strengthen the reputation of individuals, but will also strengthen the reputation of the company. Employees will increase their reputation and visibility by leading innovative AI projects. In this way, companies will be able to ensure that seniors and executives work willingly to become leaders in AI.

For employees close to the Gen-Z age group (junior and mid-level), a strategy has been developed to include them in projects that will result in them working more autonomously after using AI, emphasizing that the use of AI will make them more independent. Designing AI systems in a company that gives them control will motivate them to work. Giving them freedom to use AI tools and allowing them to choose the tools they will use will reinforce their sense of freedom. In order for them to progress successfully in their careers, they must be supported with technical training and be able to clearly see career opportunities within the organization.

Thus, two AI strategies produced for institutions will ultimately accelerate the institution's AI implementation. This structure separates strategies both horizontally (technical) and vertically (psychological/motivational), taking into account value-based differences within the institution. Thus, AI becomes not only a technological but also a human-centered and value-compatible transformation tool.

References

Bankins, S., & Formosa, P. (2023). *The ethical implications of artificial intelligence (AI) for meaningful work*. *Journal of Business Ethics*, 189, 1–21. https://doi.org/10.1007/s10551-023-05339-7

Ernst et al. (2019). The economics of artificial intelligence: Implications for the future of work. *IZA Journal of Labor Policy, 9*(4).

Fedorko, R., Kráľ, Š., & Bačík, R. (2022). *Artificial intelligence in e-commerce: A literature review*. In M. N. Al-Emran, A. A. Shaalan, & K. Abushark (Eds.), *Proceedings of CIS 2022: Communications in Intelligent Systems*). Springer. https://doi.org/10.1007/978-981-16-9113-3_50

Gutman, Jonathan. "A Means-End Chain Model Based on Consumer Categorization Processes."Journal of Marketing 46, 2 (1982):60—72.

Malouin, M. (2021). *The importance of learning in the age of artificial intelligence: The evolution of the role of the auditor* (Doctoral dissertation, Hungarian University of Agriculture and Life Sciences). MATE Repository.

McKinsey & Company. (2020). *İşimizin geleceği: Dijital Çağda Türkiye'nin Yetenek Dönüşümü*

Olson, J. C., and Reynolds, T. J. (Eds.) (2001). Understanding consumer decision making: the MeansEnd approach to marketing and advertising strategy. New Jersey: Routledge.

Rawashdeh, A. (2023). The consequences of artificial intelligence: An investigation into the impact of AI on job displacement in accounting. Journal of Science and Technology Policy Management. https://doi.org/10.1108/JSTPM-02-2023-0030

Reynolds, T. J., & Gutman, J. (1988). *Laddering theory, method, analysis, and interpretation*. In R. W. Pitts & A. G. Woodside (Eds.), *Personal values and consumer psychology* (pp. 155–176). Lexington Books.

Rzepka, C. (2019, August). *Examining the use of voice assistants: A value-focused thinking approach*. In Proceedings of the Twenty-Fifth Americas Conference on Information Systems (AMCIS 2019), Cancún, Mexico.

SAP & LeanIX. (2024). *AI survey results 2024: How organizations adopt and manage AI in IT*. LeanIX. Retrieved from https://www.leanix.net/en/ty/sap-leanix-ai-survey-results-2024

Sarnıç, A. ve Acar, S. (2024). Dördüncü endüstri devrinde işletmelerde yapay zekâ uygulamaları örnekleri üzerine nitel bir araştırma, İşletme, 5(2), 155-181.

DISASTER AND EMERGENCY MANAGEMENT

Debris Management

Post-Disaster Debris Recycling: Mobile Recycling Units and On-Site Separation

Esra İmer [a], Abdullah Can Zülfikar [a], Didem Saloğlu Dertli [a]

[a] Istanbul Technical University, Disaster Management Institute, Disaster Management Programme, Türkiye
imere24@itu.edu.tr

Keywords: Debris Management, Mobile Recycling Units (MRUs), On-Site Separation.

Aim

Post-disaster debris management is not merely a waste disposal process but a complex procedure encompassing environmental, economic, and social dimensions. The destruction caused by disasters generates a substantial amount of construction and demolition (C&D) waste **(Figure 1)**. Inefficient management of this debris can lead to resource depletion, environmental pollution, and economic losses. Traditional disposal methods are not sustainable in the long run. In this context, mobile recycling units (MRUs) and on-site separation methods enable the rapid and efficient recycling of debris. This study aims to examine the effectiveness of mobile recycling units (MRUs) and on-site separation methods in post-disaster debris management, assess their economic and environmental contributions, and discuss their applicability in disaster-affected areas. Specifically, the research investigates the impact of MRUs on debris disposal costs, logistical advantages, and recycling rates.

Figure 1: February 6 earthquakes in Kahramanmaraş, Türkiye (*TÜRKONFED, 2023).*

Material and Method

This study includes a systematic review of previous research on post-disaster debris management and, based on these studies, develops a conceptual project focusing on identifying the areas with the highest debris accumulation and designing a temporary storage and recycling site model for recycling and other disposal alternatives. As part of the literature review, academic articles, government reports, and data from international organizations have been analyzed regarding construction and demolition (C&D) waste management**,** disaster waste recycling processes, and the use of mobile recycling systems**.** Additionally, the effectiveness of mobile recycling facilities and on-site

separation systems has been evaluated through an assessment of recycling methods implemented in disaster-affected areas and academic research reports.

Findings

1. The Importance of On-Site Separation of Debris

Construction and demolition (C&D) waste accounts for 30% of the total waste generated worldwide (EPA, 2019). In addition to the types and composition of debris, the sheer volume, often exceeding several times the daily solid waste generated under normal conditions, can quickly overwhelm traditional disposal systems ***(Table 1).***

Table 1. Waste Quantities Generated Due to Disasters (Brown et al., 2011).

Year	Event	Amount of waste
2010	Haiti Earthquake	23-60 million tons
2009	İtaly-L'Aguila Earthquake	1.5-3 million tons
2008	China-Sichuan Earthquake	20 million tons
2005	ABD-Hurricane	76 million m3
2004	ABD/Florida, Frances, and Jeanne Hurricane	3 million m3
2004	Indian Ocean Tsunami	10 million m3
2004	ABD-Charley Hurricane	2 million m3
1999	Turkiye-Marmara Earthquake	13 million tons
1995	Japan-Kobe, Big Hanshin Awaji Earthquake	15 million tons

Debris disposal accounts for more than 27% of the total disaster costs (Fetter & Rakes, 2012). On-site recycling through mobile units reduces the burden on waste disposal sites and contributes to the economy by lowering costs. Global disasters and related losses have been recorded since the 1980s with the advancement of technology ***(Figure 2).*** These records have shown that economic losses have increased over time. In light of these data, traditional debris management systems are becoming inadequate for the growing number of disasters and the debris they generate.

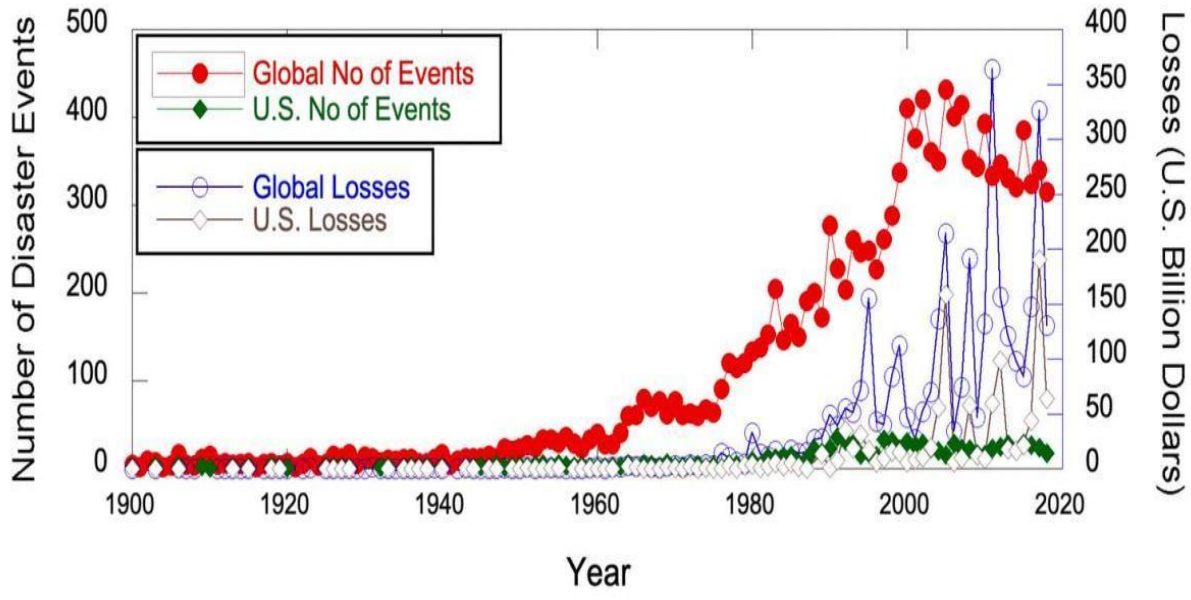

Figure 2. Global Disasters and Associated Losses After 1980, Emergency Events Database (EM-DAT) Data (Derrible, Choi, and Yeşiller, 2019).

2. Waste Types and Waste Disposal Options

The nature of debris or waste may vary depending on the type of disaster, but disaster debris is typically a mixture of one or more of the following categories (Table 2). Each of these waste categories presents unique challenges for disposal, even under normal conditions, and their disaster-related combinations often create new complex categories with increased challenges for separation, cleaning, and disposal.

- **Concrete and Mortar:** Constitutes the majority of demolished buildings.
- **Metals:** Includes recyclable materials such as steel and aluminum. Additionally, recycling steel consumes 75% less energy than producing new steel
- **Wood and Organic Materials:** Primarily sourced from rural buildings and furniture.
- **Plastic and Glass:** Obtained from interior furnishings and windows.
- **Hazardous Waste:** Includes materials such as asbestos, lead, paint, and chemicals that require special handling.

Table 2. Uses of Waste Generated from Disasters (Öztürk, 2017).

Waste material	Areas of Use
Metals	Steel, non-ferrous metals
Tiles	Clay production
Bricks	Clay production
Walls	Lime
Construction Timber	Lumber
Wood Waste	Compost, Energy production.
Green Waste	Compost, Energy production.
Electric Tools and Cable	Aluminum, copper
Plumbing Equipment and Copper Pipes	Brass, bronze

3. Debris Recycling Processes

The removal of debris from disaster zones is a difficult and costly process. Several methods exist for the proper management of disaster waste. The composition of disaster waste is similar to construction and demolition waste. Therefore, regular construction and demolition waste management methods can serve as a guide for disaster waste management. The most common way to manage construction waste is to collect all the waste from the site and transport it to landfills for final disposal; this method is the traditional approach to disaster waste. Another method involves transporting the collected waste to a recycling facility and sorting reusable and recyclable components either before or after transportation. However, this creates high costs due to the need for transporting the waste twice. One of the most environmentally friendly methods is sorting all materials at a temporary site according to their characteristics. This way, the disposal of untreated hazardous waste in landfills can be minimized (Onan, 2005). This method offers significant savings in logistics and time.

3.1. Mobile Recycling Units and On-Site Recycling

There are big differences between daily waste management and waste that occurs during a disaster. The large volume of disaster-related debris significantly strains existing storage capacities. The method focused on in this project is a study that enhances on-site separation through the previously mentioned temporary site sorting method. The study aims to identify the areas with the highest concentration of debris after a disaster and works on a model for temporary storage and recycling areas, considering recycling and other disposal alternatives ***(Figure 3).*** Mobile recycling units are modular systems equipped with portable equipment capable of processing various types of

debris and waste on-site ***(Figure 4).*** Compared to traditional fixed recycling facilities, they reduce logistical costs and offer the potential for rapid intervention.

Recycling Network

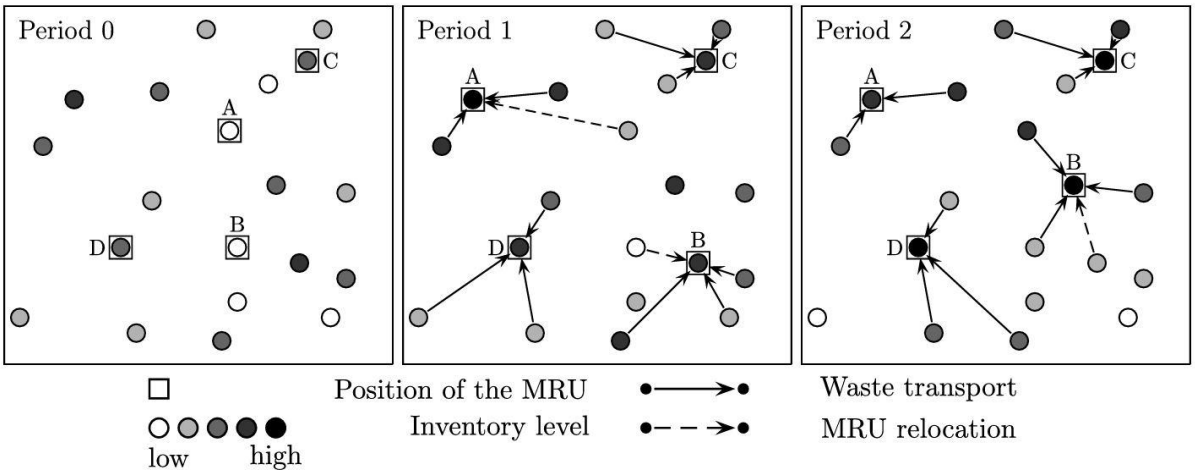

Figure 3. Graphical example of a recycling network (Alarcon-Gerbier and Buscher, 2024).

A network of 20 nodes is considered, where four MRUs can be relocated at the beginning of each period. A certain amount of waste is collected and stored at each node, graphically represented by different shades of gray for the nodes. Since storage capacity is limited, waste must be transported to another node or recycled on-site. As shown in Figure 3, the current inventory level and location of MRUs at each node are known. Based on this information and taking into account the amount of waste collected in subsequent periods, new locations of MRUs are defined to minimize total transportation costs. In this example, MRU B moves eastward at the beginning of period 1 due to the higher inventory level at that node. The same MRU moves north at the beginning of term 2. Some amount of waste still needs to be transported between nodes. If the MRU remains in its original position, the total distance traveled and therefore the total transportation costs are greater. It is important to emphasize that it is not necessary to transport waste from all nodes, as each node has some, albeit limited, storage capacity (Alarcon-Gerbier and Buscher, 2024).

4. Mobile Recycling Facility and On-Site Separation Concept Project

Within the scope of this study, a conceptual temporary social housing project was developed in the war-torn city of Marawi in the Philippines, using mobile recycling facilities and on-site segregation methods, with a focus on the reuse of debris. The project was designed theoretically to emphasize the reuse of rubble, the implementation of mobile recycling units, and on-site material separation. It originated from the question: *"Can a new city be built from the remnants of the old one?"* As an initial step, the method outlined in Figure 3 was applied at an urban scale. Following a rapid post-conflict site assessment, the most severely damaged areas of the city were mapped, and key nodal points were identified. A network was then established by installing mobile recycling systems at these nodes ***(Figure 4).*** A conceptual temporary social housing project was developed in the area with the highest concentration of debris, utilizing on-site recycling methods. Except for the primary structural framework, all other building components were designed using recycled debris materials ***(Figure 5).*** Following the mapping process, temporary mobile recycling facilities were installed at the designated nodes—i.e., the areas with the highest debris concentration—and the segregation and recycling process commenced ***(Figure 4).*** Debris sorted on the ground was lifted via a crane system for further processing and then stored in other units after being recycled.

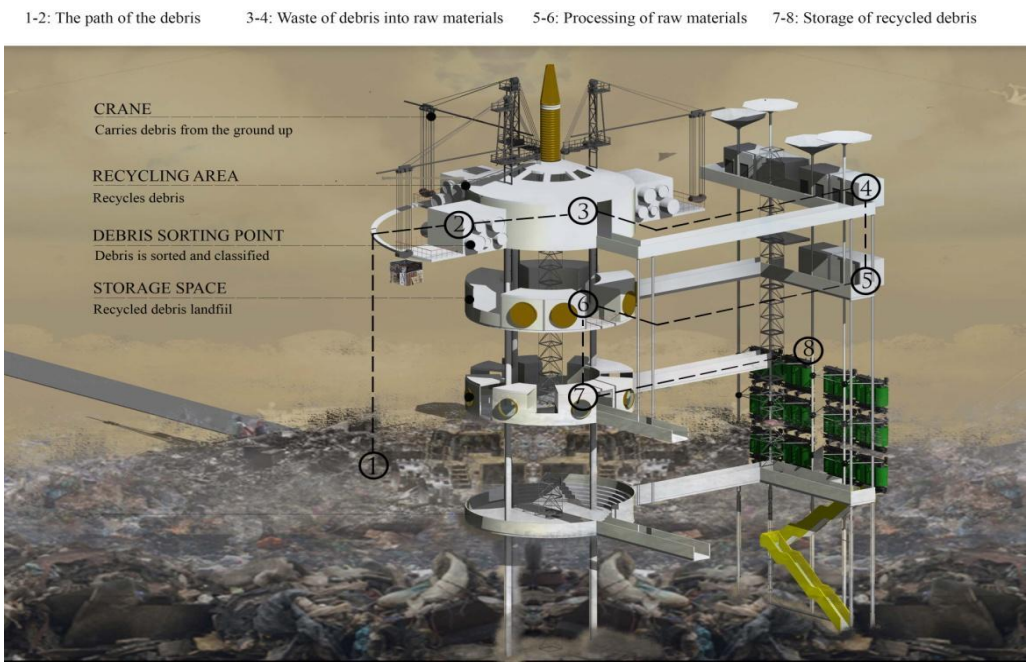

Figure 4. Concept Design of the Mobile Recycling Unit (MRU).

While the project's load-bearing structure was built using new materials, other structural elements (walls, windows, doors, flooring, etc.) were designed using recycled materials ***(Figure 5).*** After the project is completed, the removal of the mobile recycling facility from the site is planned.

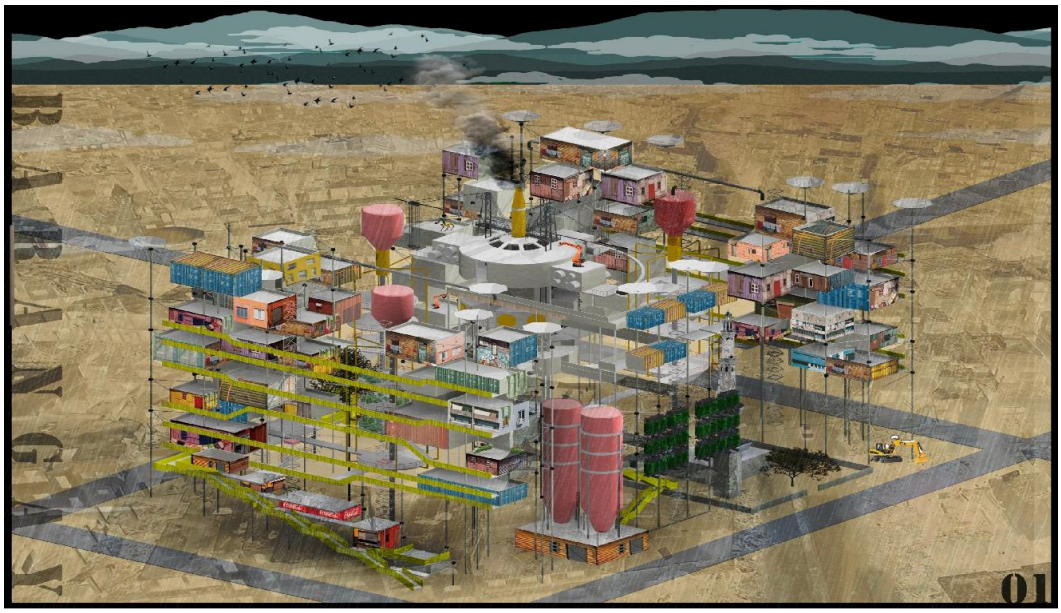

Figure 5. Concept Design of Social Housing Built Using Recycled Debris.

Conclusion

Disasters will continue to have devastating effects on both people and the environment in the future, just as they have in the past. While the loss of human lives is the most significant consequence of a disaster, the destruction of buildings and infrastructure also represents a major loss for both the economy and the ecosystem. The collapse of buildings and infrastructure during disasters generates large amounts of debris, such as concrete, bricks, and timber, adding an additional burden to communities. The disposal options for disaster-related waste and the

methods applied for its management play a crucial role in protecting both environmental and public health. As part of disaster management, the objectives of disaster waste management include minimizing risks to human life and health, reducing environmental hazards, and providing benefits to affected communities (Güler, 2018). In the post-disaster debris management process, mobile recycling units (MRUs) and on-site separation methods offer an environmentally and economically efficient alternative. Compared to traditional disposal methods, MRU systems consume less energy, facilitate the separation of recyclable materials within the debris, and reduce waste transportation costs. The widespread adoption of these methods will enhance the sustainability of waste management in disaster-affected areas.

References

Alarcon-Gerbier, E., & Buscher, U. (2024). The dynamic facility location problem with mobile production units: A waste recycling application. *Computers and Operations Research, 166*, 106609. https://doi.org/10.1016/j.cor.2024.106609

Brown, C., Milke, M., & Koon, B. (2011). Disaster waste management: A review article. *Waste Management & Research, 29*(12), 1073–1089. https://doi.org/10.1177/0734242X11421914

Derrible, S., Choi, J., & Yeşiller, N. (2019). Post-disaster cleanup is expensive, time-consuming, and wasteful. *FAMU-FSU College of Engineering*. https://eng.famu.fsu.edu/news/post-disaster-cleanup-conversation [Accessed July 12, 2019]

Fetter, B., & Rakes, T. (2012). Recycling disaster waste: Feasibility, method, and effectiveness. *Waste Management & Research, 30*(12), 1231–1242. https://doi.org/10.1177/0734242X12456332

Güler, Ü. A. (2018). Waste management in sustainable disaster management. *Journal of Natural Disaster Environment, 4*(2), 236–246. https://doi.org/10.21324/dacd.412380

Onan, K. (2005). *Report on construction and demolition waste management*. Türkiye Environmental Foundation Publications.

Öztürk, M. (2017). *Waste management mechanism in disasters*. TÜÇEV. http://tucev.org/dosyalar/files/afetlerde-atik-yonetimi.pdf [Accessed July 12, 2018]

U.S. Environmental Protection Agency. (2019). *Advancing sustainable materials management: 2017 fact sheet*. https://www.epa.gov/sites/production/files/2019-11/documents/2017_fact_sheet.pdf [Accessed July 12, 2020]

TÜRKONFED. (2023, February 14). Visual on the economic impacts of the earthquake [Figure]. *İklim Haber*. https://www.iklimhaber.org/turkonfed-depremin-maliyeti-84-milyar-dolari-asabilir/ [Accessed February 20, 2025]

ECOLOGY AND EVOLUTION

Anthropocene

Anthropogenic Impacts

Ecological Restoration Potential of Istanbul: Opportunities, Challenges and Risks

Saliha Akkayüz[a]

[a] Istanbul Technical University, Eurasia Institute of Earth Sciences, Earth System Science Program, Türkiye
kayas16@itu.edu.tr

Keywords: Urban Ecological Restoration, Biodiversity, Istanbul.

Aim

Urban green spaces are among the most important daily contact points with nature for urban residents, and growing evidence highlights their substantial benefits for health and recreation (Dearborn & Kark, 2010; Clarkson & Kirby, 2016). These spaces have also been shown to help prevent the negative effects associated with what is known as "nature deficit disorder" (Hartig & Kahn, 2016).). Moreover, studies indicate that people tend to prefer urban green spaces rich in species and natural diversity over species-poor lawns or standardized vegetation (Sikorski, 2018; Fischer, 2020).

Urban ecosystems have often undergone significant alterations and ecological degradation due to various factors, including green spaces designed with monocultures, low species diversity, and non-native species; soils that have been compacted and modified by human activities; heavy human use; construction activities; and habitat fragmentation that disrupts seed dispersal (McCleery, 2014). These ecological deficiencies significantly limit the capacity of urban areas to support biodiversity and weaken several key ecosystem functions and services that directly depend on biological diversity (Bullock, 2011; Lin, 2015; Lindemann & Matthies, 2018).

Various initiatives, such as the United Nations Decade on Ecosystem Restoration 2021–2030, underline the urgent need to improve urban ecosystems to better conserve biodiversity and make more effective use of the potential benefits provided by ecosystem services. In addition, several studies emphasize the need to reconsider the design and management of urban green spaces to help cities adapt to climate change (Mathey, 2011; Maimaitiyiming, 2014, Liu, 2017).

The often irreversible changes in urban ecosystems show that traditional ecological restoration approaches, which rely on historical reference systems, are only partially applicable to urban areas (Kollmann, 2019). In many cases, factors such as land scarcity, high costs, and permanent environmental alterations make it impossible to fully restore historical reference conditions in cities. Therefore, it is recommended to use urban reference systems — sites that experience similar conditions and constraints as restoration areas, but successfully sustain the desired species composition and ecosystem functions (Klaus, 2019).

This study investigates the ecological restoration potential of Istanbul, one of the most densely populated metropolises in the world. Despite experiencing intense urbanization pressure, Istanbul supports 2,512 plant taxa, exceeding the plant diversity of many European countries such as the United Kingdom and the Netherlands, which highlights the ecological value and significance of the city (Kabakçı, 2016; Akkemik, 2017; Özhatay, 2010; Avcı, 2014). The study aims to develop restoration strategies for improving degraded urban ecosystems, tailored to Istanbul's unique ecological characteristics and rich biodiversity. In this context, the potential increase in species richness and abundance following ecological restoration is also evaluated, with the aim of revealing the contribution of urban ecological restoration to biodiversity conservation.

Material and Method

Using Google Earth Engine (GEE), a 10-meter resolution NDVI map of Istanbul was produced (Figure 1). This map was combined with a spatial dataset obtained from the Istanbul Metropolitan Municipality (IMM), which classifies green spaces under IMM's responsibility according to their functions and types, along with their area measurements. Based on their characteristics, these green spaces defined by IMM were categorized into five

distinct Urban Reference System (URS) classes: severely degraded novel ecosystems, novel ecosystems, hybrid ecosystems (severely degraded historical ecosystems), degraded historical ecosystems, and historical ecosystems. Undefined areas were classified using an object-based spatial analysis approach. To assign areas outside IMM's responsibility to the appropriate URS categories, the NDVI raster data was reclassified using a threshold value of 0.2 to detect green spaces not previously categorized under any URS class. These areas were then converted from raster to polygons. Each resulting green space polygon was assigned values for area size (m²), shape metrics (perimeter-to-area ratio), and average NDVI.

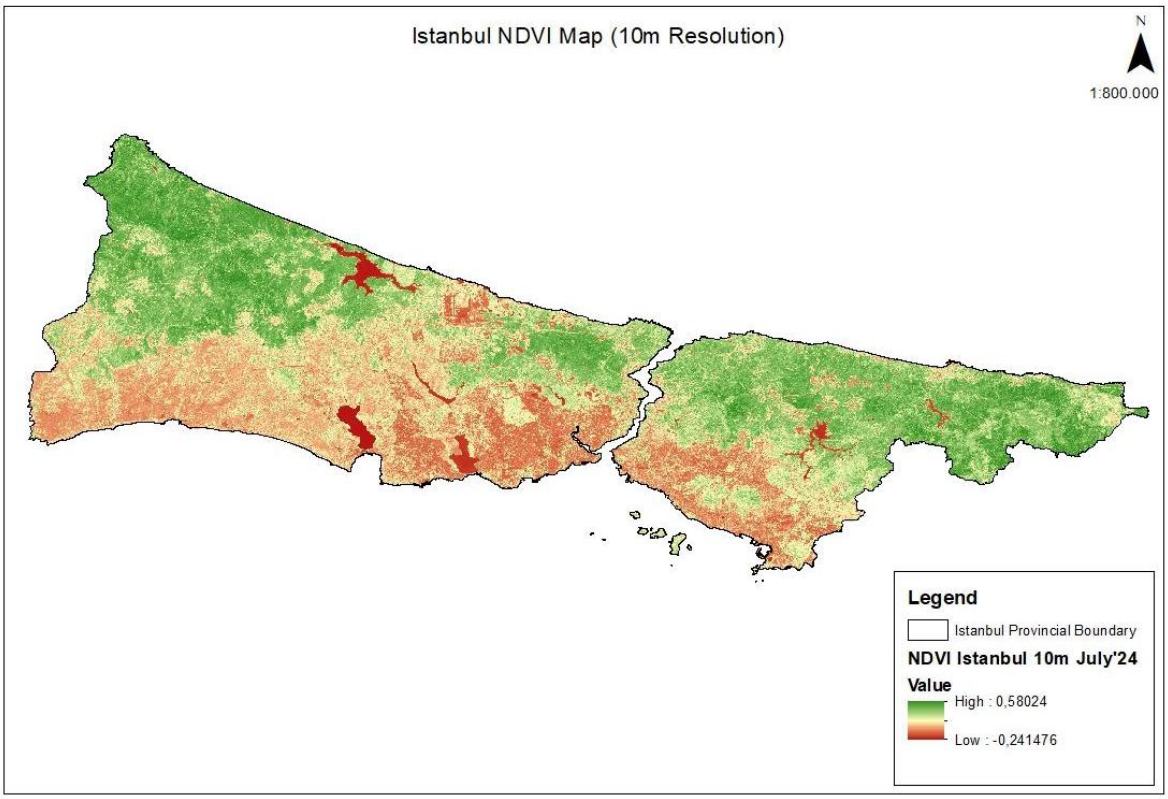

Figure 1. Istanbul NDVI Map (10 m Resolution).

The average NDVI value for each green space polygon was calculated using the "Zonal Statistics as Table" tool, and these values were used alongside area size and shape metrics in the classification rules. A decision tree approach was adopted to assign undefined areas to URS categories. Areas larger than 20,000 m² with NDVI values above 0.5 and shape ratios close to 1 were classified as historical ecosystems; areas with NDVI values between 0.4 and 0.5 and medium size were identified as degraded historical ecosystems. Small, homogeneous areas under 1,000 m² with low NDVI values were assigned to the novel ecosystem category.

The newly generated polygons resulting from this classification were then merged with the IMM-managed areas already categorized under URS, resulting in a comprehensive URS map covering the entire city of Istanbul. As a final outcome, a shapefile dataset was created that includes green space polygons assigned to one of the five URS classes mentioned above, encompassing the entire urban area.

Biodiversity data for Istanbul obtained from the Global Biodiversity Information Facility (GBIF) (GBIF.org (27 February 2025)) were overlaid on this map to analyze species richness and abundance across different ecosystem types.

For novel ecosystems where a return to historical, pre-disturbance conditions is not possible, habitat enhancement strategies aimed at improving ecosystem functions and/or biodiversity were proposed based on recommendations from the literature. Similarly, for severely degraded hybrid ecosystems and degraded historical ecosystems, restoration strategies recommended in the literature were identified (Smith & Fellowes, 2014).

To estimate biodiversity gains, the potential increase in species richness and abundance was calculated under the assumption that severely degraded novel ecosystems could be restored to the level of novel ecosystems. Likewise, the potential biodiversity contributions of transforming hybrid ecosystems into degraded historical ecosystems, and degraded historical ecosystems into historical ecosystems, were assessed.

Findings

The analyses demonstrated that green spaces in Istanbul can be categorized into URS classes based on both NDVI values and functional use classifications. Integrating NDVI data derived from remote sensing with spatial classifications provided by the Istanbul Metropolitan Municipality (IMM) enabled the identification of areas with the highest restoration potential.

Of the approximately 54.8 km² of green space managed by IMM, 42.17% (around 23.1 km²) consists of active green spaces where citizens can engage in recreational activities. The remaining 57.83% (approximately 31.68 km²) comprises passive green spaces, such as roadside slopes and medians, which are not publicly accessible. This indicates that passive green spaces, as they are not primarily designed for recreational use, offer broader opportunities for ecological restoration interventions. While restoration efforts in active green spaces must be balanced with recreational needs, passive areas allow for more flexible ecological interventions.

In active green spaces, ornamental areas designed with shrubs, roses, and flower beds—where direct human contact with vegetation is limited—offer an additional opportunity to enhance biodiversity through the inclusion of various native species. Moreover, creating more natural environments within these areas enhances the psychological benefits people derive from contact with nature (Standish, 2013).

Spatial overlays using GBIF data revealed that novel ecosystems have lower biodiversity compared to historical or hybrid ecosystems. This finding suggests that restoring degraded novel ecosystems could significantly contribute to biodiversity gains.

In hybrid ecosystems, which contain both historical and novel components, interventions such as reducing management intensity and reintroducing native species were found to enhance biodiversity. Proper restoration of these ecosystems could also help establish ecological connections between fragmented historical ecosystems (Anderson & Minor 2020).

The biodiversity analyses based on NDVI-based classifications and municipal maps underline the importance of applying differentiated restoration strategies tailored to each URS category.

Conclusion

Ecological restoration strategies developed specifically for Istanbul's urban context have shown potential to increase species richness and abundance. Through NDVI-based landscape classifications and spatial biodiversity data, ecosystem types with the greatest need for restoration can be identified and prioritized.

Restoration efforts that enhance connectivity, improve habitat quality, and integrate native species are expected to contribute to increased biodiversity both in degraded historical ecosystems and in newly emerging urban ecosystems. The findings demonstrate that even in cases where full historical restoration is not feasible, meaningful improvements in ecosystem functions and biodiversity levels can still be achieved.

In conclusion, ecological restoration efforts in Istanbul's urban green spaces present a significant opportunity not only for enhancing urban biodiversity, but also for strengthening ecosystem resilience and improving the quality of life for city residents.

References

Akkemik, Ü. (2017). İstanbul'un Doğal Bitkileri. Çekül Yayınları, ss. 1152.

Anderson, E. C., & Minor, E. S. (2020). Management effects on plant community and functional assemblages in Chicago's vacant lots. Applied Vegetation Science, 23(2), 266–276.

AVCI, M. (2014). Türkiye'nin Bitki Çeşitliliği ve Coğrafi Açıdan Değerlendirilmesi. In Ü. Akkemik (Ed.), Türkiye'nin Doğal-Egzotik Ağaç ve Çalıları (Vol. 1, pp. 28–53).

GBIF.org (27 February 2025). GBIF Occurrence Download. https://doi.org/10.15468/dl.je8x5c

Bullock, J. M., Aronson, J., Newton, A. C., Pywell, R. F., & Rey-Benayas, J. M. (2011). Restoration of ecosystem services and biodiversity: conflicts and opportunities. Trends in Ecology & Evolution, 26(10), 541–549.

Clarkson, B. D., & Kirby, C. L. (2016). Ecological restoration in urban environments in New Zealand.

Dearborn, D. C., & Kark, S. (2010). Motivations for conserving urban biodiversity. Conservation Biology, 24(2), 432–440.

Fischer, L. K., Neuenkamp, L., Lampinen, J., Tuomi, M., Alday, J. G., Bucharova, A., ... & Klaus, V. H. (2020). Public attitudes toward biodiversity-friendly greenspace management in Europe. Conservation Letters, 13(4), e12718.

Hartig, T., & Kahn Jr, P. H. (2016). Living in cities, naturally. Science, 352(6288), 938–940.

Huang, X., Wang, H., Shan, L., & Xiao, F. (2021). Constructing and optimizing urban ecological network in the context of rapid urbanization for improving landscape connectivity. Ecological Indicators, 132, 108319.

Kabakçı, T. N. (2016). İstanbul'un Bitki Çeşitliliği ve Odun Dışı Orman Ürünleri Açısından Değerlendirilmesi. İÜ Orman Fakültesi Orman Botaniği Bitirme Ödevi.

Klaus, V. H., & Kiehl, K. (2021). A conceptual framework for urban ecological restoration and rehabilitation. Basic and Applied Ecology, 52, 82–94.

Kollmann, J., Kirmer, A., Tischew, S., Hölzel, N., Kiehl, K., & Kollmann, J. (2019). Neuartige Ökosysteme und invasive Neobiota. Renaturierungsökologie, 435–447.

Lin, B. B., Philpott, S. M., & Jha, S. (2015). The future of urban agriculture and biodiversity-ecosystem services: Challenges and next steps. Basic and Applied Ecology, 16(3), 189–201.

Lindemann-Matthies, P., & Matthies, D. (2018). The influence of plant species richness on stress recovery of humans. Web Ecology, 18(2), 121–128.

Liu, H., Jia, Y., & Niu, C. (2017). "Sponge city" concept helps solve China's urban water problems. Environmental Earth Sciences, 76, 1–5.

Maimaitiyiming, M., Ghulam, A., Tiyip, T., Pla, F., Latorre-Carmona, P., Halik, Ü., ... & Caetano, M. (2014). Effects of green space spatial pattern on land surface temperature: Implications for sustainable urban planning and climate change adaptation. ISPRS Journal of Photogrammetry and Remote Sensing, 89, 59–66.

Marzluff, J. M., & Ewing, K. (2008). Restoration of fragmented landscapes for the conservation of birds: a general framework and specific recommendations for urbanizing landscapes. Urban ecology: An international perspective on the interaction between humans and nature, 739-755.

Mathey, J., Rößler, S., Lehmann, I., & Bräuer, A. (2011). Urban green spaces: Potentials and constraints for urban adaptation to climate change. In Resilient Cities: Cities and Adaptation to Climate Change – Proceedings of the Global Forum 2010 (pp. 479–485). Springer Netherlands.

McCleery, R. A., Moorman, C. E., & Peterson, M. N. (2014). Urban wildlife conservation. New York: Springer.

Özhatay, N., Erdem, A. Ö., & Özhatay, E. (2010). Şile'nin doğal bitkileri: "Işık Üniversitesi kampüs ve çevresinin florası". Işık Üniversitesi.

Platt, R. H. (2004). Regreening the metropolis: pathways to more ecological cities: Keynote Address. Annals of the New York Academy of Sciences, 1023(1), 49–61.

Sikorski, P., Wińska-Krysiak, M., Chormański, J., Krauze, K., Kubacka, K., & Sikorska, D. (2018). Low-maintenance green tram tracks as a socially acceptable solution to greening a city. Urban Forestry & Urban Greening, 35, 148–164.

Smith, L. S., & Fellowes, M. D. (2014). The grass-free lawn: Management and species choice for optimum ground cover and plant diversity. Urban Forestry & Urban Greening, 13(3), 433–442.

Standish, R. J., Hobbs, R. J., & Miller, J. R. (2013). Improving city life: options for ecological restoration in urban landscapes and how these might influence interactions between people and nature. Landscape Ecology, 28, 1213–1221.

ELECTRICAL ENGINEERING

Electric Power & Energy Systems

Electrical Machines

Electrical Vehicles

Power Electronics

Smart Grids

Load Frequency Control of Two Area Hybrid Power System Using a Neural Network-based Gradient Descent Method

Fatih Demircan[a], Ayşen Demirören[b]

[a]Istanbul Technical University, Graduate School, Electrical Engineering Program, Turkey
[b]Istanbul Technical University, Faculty of Electrical and Electronics Engineering, Department of Electrical Engineering, Turkey
demircanf22@itu.edu.tr

Keywords: Artificial Neural Network, Gradient Descent, Load Frequency Control, Meta-heuristic Optimization, Renewable Energy Systems.

Aim

With the growing awareness of resource scarcity and the need for sustainable practices, efficiency and sustainability have become critical priorities. As a result, renewable energy sources are increasingly being integrated into power systems, whether in isolated networks or interconnected systems. However, this transition introduces additional complexity and presents significant challenges in maintaining the stability and reliability of modern power systems. One of the main reasons for this complexity is the intermittent nature of renewable energy sources. For instance, solar energy can only be harnessed during daylight hours. Additionally, factors such as cloud cover or the unpredictable nature of wind can lead to sudden variations in power generation. These fluctuations may result in load-generation mismatches and subsequent frequency deviations. In addressing these imbalances, load frequency control (LFC) plays a crucial role. When modeling the system, incorporating nonlinear components of the system, such as the governor dead-band (GDB) and generation rate constraint (GRC), can produce simulation results that more accurately reflect real-world conditions by accounting for physical constraints. Metaheuristic methods are widely employed to determine the global optimum values of controller gains in multi-area power systems because it is very useful in producing solutions for complex systems. For gradient calculation, area-1, area-2 and wind turbine generator which have controllers in the system are modeled with artificial neural network. In this study, an artificial neural network based adaptive controller is designed for a two-area power system integrated with renewable energy systems and it is aimed that the controllers optimized with meta-heuristic algorithms will achieve better reductions in frequency deviations.

Material and Method

Tuning of the commonly used proportional integral derivative (PID) controller is generally preferred for LFC applications. For this purpose, mathematical models are employed to obtain reliable estimates (Kundur, 2022). The small-signal model of the two-area interconnected hybrid power system is shown in Figure 1. In this model, each area incorporates a conventional power plant; in addition, area-1 is integrated with a wind turbine generator (WTG), and area-2 is integrated with a photovoltaic system (PV) system. The power deviation equations provide a fundamental representation of the power balance within each area. As derived from the block diagram, the power deviation equations are presented in Equation 1. The rated power of turbines is 250 MW at nominal frequency of 50 Hz.

$$\Delta P_{total1} = \Delta P_{gc1} + \Delta P_{gw} - \Delta P_{L1} - \Delta P_{tieline} \#(1a)\ \Delta P_{total2} = \Delta P_{gc2} + \Delta P_{gpw} - \Delta P_{L2} - \Delta P_{tieline} \#(1b)$$

The mathematical model of the wind turbine output power is derived from (Mahto, 2017). To regulate the output power of the WTG, a pitch controller is employed, which adjusts the pitch angle of the turbine blades according to wind speed. This is intended to provide an advantage for LFC. The WTG system in this study consists of 20 wind turbines, generating 5% of the Area-1 power at full capacity. The transfer functions of the WTG part of the power system, including the pitch controller, hydraulic pitch actuator, data fit pitch response, blade characteristic, wind generator system and fluid coupling are shown in Figure 1.

The PV system integrated into the power system is focused on Maximum Power Point (MPP) tracking. The PV system is influenced by irradiation levels and temperature. In this study, the temperature is kept constant at 25°C. At full capacity, it generates 5% of the total Area-2 power as output. A detailed description of the PV system is provided in (Masikana, 2024).

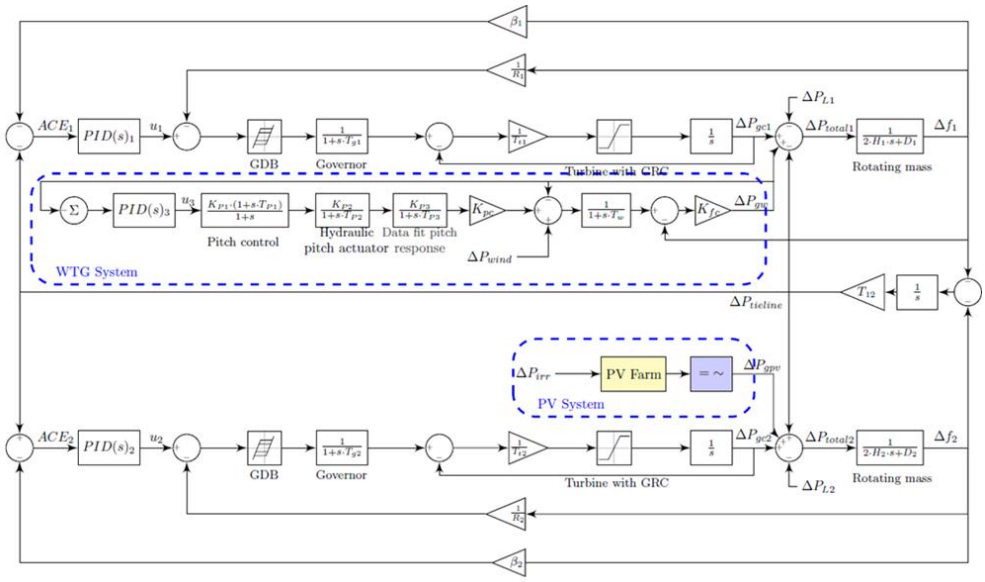

Figure 1. Hybrid two-area power system model for LFC.

As shown in Figure 1, there are three PID controllers in the system. The transfer function of the controller is expressed in Equation 2. where subscripts 1 and 2 represent the controller gains of Area-1 and Area-2, in that order, and subscript 3 represents the controller gain of the PID controller of the WTG. The output of the controller is given in Equation 3.

$$G_{PID1,2,3}(s) = K_{p1,2,3}.\left(1 + \frac{K_{i1,2,3}}{s} + K_{d1,2,3}.\frac{s}{100.s+1}\right) \#(2)$$

$$u_{1,2,3}(s) = G_{PID1,2,3}(s) \times ACE_{1,2,3}(s) \#(3)$$

Firefly algorithm assumes that variables have light intensities, similar to fireflies. The closer a solution is to the optimum, the brighter its light is, and the brighter fireflies attract the less bright ones. Additionally, a small random perturbation is added to this attraction. The closer the distance between them, the stronger the attraction force. Ultimately, the variables that yield the closest value to the desired result are assigned to the controller gains (Heris, 2015). In this study, the population size is selected as 40, and the maximum number of iterations is set to 50. The PID gains for Area-1 and Area-2 are searched within the range of (-1, 15). The gains of the WTG controller are searched within the range of (5, 15). The obtained values are presented in Table 1.

Table 1. Optimal PID gains obtained using FA and GA.

Algorithm	PID	K_p	K_i	K_d
FA	Area-1	1.7909	0.0286	4.1773
GA	Area-1	0.2945	0.1438	12.2079
FA	Area-2	0.4579	0.5274	4.9189
GA	Area-2	0.6035	0.4631	6.0448

FA	WTG	14.8947	9.0423	15
GA	WTG	8.9389	10.5382	10.6384

The dynamic control of a system with nonlinear and dynamic inputs, such as hybrid power systems, enhances control quality. In this study, the focus is on the gradient descent method for auto-tuning the PID parameters. The goal is to determine the variation law of the parameter vector ξ to be added to the system. The PID controller, with parameter vector ξ, needs to be automatically tuned to minimize the deviation function in Equation 4 (Nguyen, 2019). In this study, a separate gradient descent model is applied for each of the three controllers, and the values of e are denoted as ACE1, ACE2, and ACE3, respectively. By using the derivative results and signs of dJ/dξ < 0, dJ/dξ > 0 and dJ/dξ = 0, the minimum value of J is reached using the approach in Equation 5.

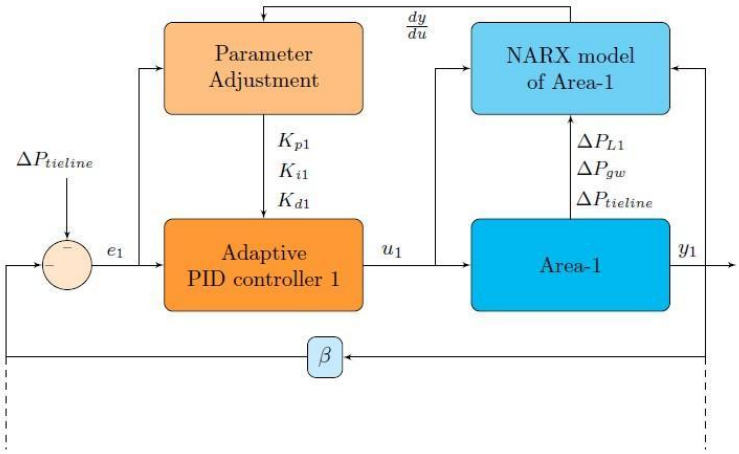

Figure 2. Adaptive PID controller scheme of Area-1.

$$J = \frac{1}{2}.e^2 \#(4)$$

$$\frac{d\xi}{dt} = -\alpha.\frac{dJ}{d\xi} \#(5)$$

The schematic of the power system model with the adaptive PID controller for Area-1 is shown in Figure 3. The schematic consists of four components: Area-1, NARX model, parameter adjustment, and adaptive PID controller. Here, the Area-1 component represents the model of the first area of our basic two-area hybrid power system. The NARX model component represents the trained artificial neural network (ANN) model for the first area. The parameter adjustment block calculates the parameter vector to be added to the controller gains using data received from the ANN and other parts of the system, and then transmits it to the adaptive PID controller.

In this study, the NARX model was chosen for the ANN application to model a time-series nonlinear system. The neural networks generated using the narxnet function in MATLAB have 14 neurons in the hidden layer for Area-1 and Area-2, with an input delay of 30 time-steps, while the WTG model has 10 neurons in its hidden layer with an input delay of 20 time-steps. The activation function used is tanh, and the training function employed is the Levenberg-Marquardt backpropagation. As a result of the input delay, the inputs are represented in the form of (x(t−1), x(t−2), ...x(t−30), y(t−1), y(t−2), ...y(t−30)). The inputs of the ANN models representing Area-1 and Area-2 are u1,2, ΔPL1,2, ΔPgw or ΔPgpv, and ΔPtieline while the output is Δf1,2. The inputs of the WTG ANN model are ΔPwind, Δf1, and u3 while the output is ΔPgw.

Equation 6 shows the mathematical expression of the ANN model. X is the input matrix of the ANN. To obtain the parameter vector of the adaptive PID controller, the chain rule is applied to reach the dJ/dξ (Nguyen, 2019, Taşören, 2020). In Equation 7, dJ/dξ is the derivative of J with respect to the PID parameters, dJ/de is the derivative of J

with respect to the error, and de/dy is clearly shown in Figure 1 and Figure 2, dy/du ≈ dy/dXu is obtained from Equation 6, and du/dξ is derived from Equation 3. As a result, the equality of the PID parameter vector is given in Equation 8.

$$y = W_{out}^{T}.tanh\ tanh\ (W_{in}^{T}.X + b_{in})\ + b_{out} \#(6)$$

$$\frac{dJ}{d\xi} = \frac{dJ}{de}.\frac{de}{dy}.\frac{dy}{du}.\frac{du}{d\xi} \#(7)$$

$$\xi(n) = \xi(n-1) - \alpha.\frac{dJ}{d\xi}(n) \#(8)$$

Findings

In this study, the performances of GA-PID, FA-PID, and a neural network-based adaptive PID controller trained on values obtained from FA have been compared using PID coefficients derived from a single scenario. The study was modeled and simulated in the MATLAB/Simulink environment. In the scenario in this study, the input variables are shown in Figure 3. Under these conditions, the performance of the adaptive PID controller is compared with that of the non-adaptive controllers. Figure 4 presents the responses of Δf1, Δf2, ΔPtie and ΔPgw, respectively. As observed in the graphs, the adaptive PID has demonstrated significant improvements in frequency deviations starting from the 80th second. During the 80–120 second interval, the frequency deviations obtained with the other two controllers exceed 0.02 Hz, with a settling time of up to thirty seconds. In contrast, the adaptive PID limits the deviation to 0.05 Hz and achieves stability within fifteen seconds. A similar behavior is observed from the 130th second onward. This effect is also reflected in the ΔPtie response; however, no noticeable performance improvement is observed in ΔPgw. Furthermore, when examining the performance indices of the three controllers in Table 2, it is observed that the adaptive PID outperforms the other controllers significantly in terms of IAE, ISE, and ITAE results. Finally, Figure 5 presents the real-time variation of the controller coefficients.

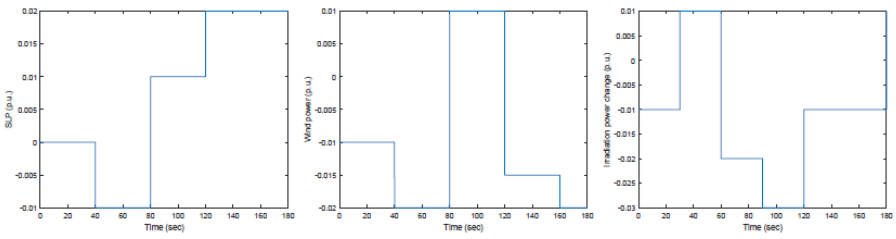

(a) (b) (c)

Figure 3. Power system input variations (a) ΔP_{L1} (b)ΔP_{wind} (c) $\Delta P_{irr.}$

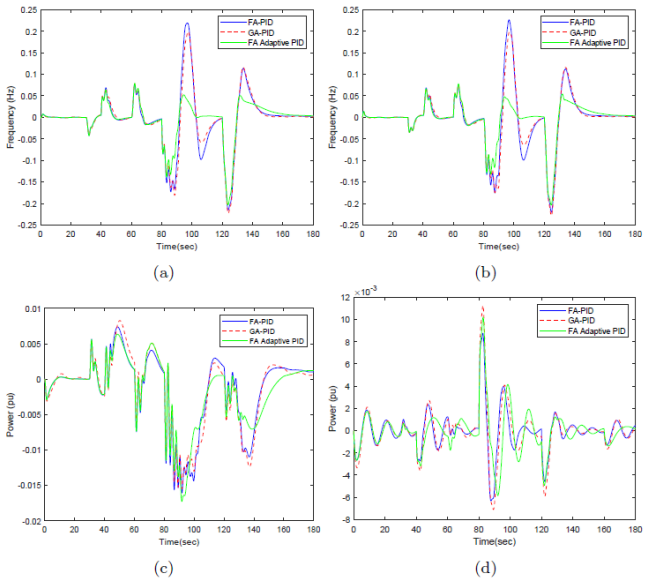

Figure 4. Comparison of the controllers under random input variations (a)Δf_1 (b)Δf_2 (c)ΔP_{tie} (d)ΔP_{gw}.

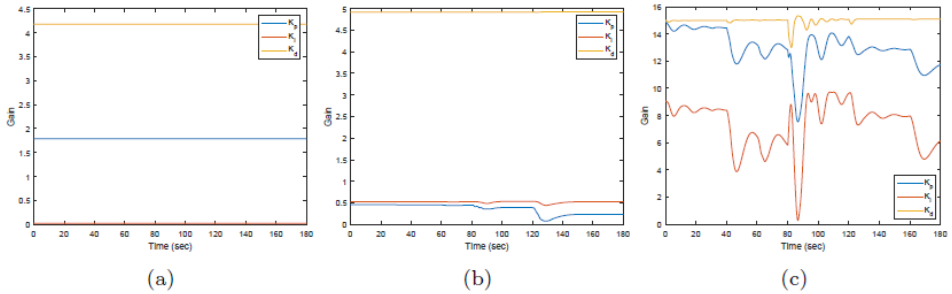

Figure 5. Variation of the adaptive PID coefficients (a)controller-1 (b)controller-2 (c)controller-3.

Table 2. Performance index of the controllers.

PID controller	IAE	ISE	ITAE
FA-PID	5.861	0.281	586.4
GA-PID	5.784	0.267	572.5
FA Adaptive PID	3.877	0.126	385.5

Conclusion

In this study, an ANN-based gradient descent PID controller has been applied to an interconnected power system for LFC with the integration of RES. The power system model incorporates GDB and GRC. For comparison, a PID controller optimized for only a single scenario and not re-optimized under varying conditions has been employed. The proposed method has exhibited superior and faster damping performance in frequency deviations, along with better results in performance indices. However, no noticeable improvement has been observed in the output power of the WTG. Consequently, it is suggested that the proposed method can be adapted to different control techniques to further enhance system performance.

Acknowledgements

This paper has been written based on the preliminary studies of my ongoing master's thesis under the supervision of Prof. Dr. Ayşen Demirören in Electrical Engineering Master Program at Istanbul Technical University.

References

Kundur, Prabha S., and Om P. Malik. (2022). "Active Power and Frequency Control." Chap. 11.1 in Power System Stability and Control. 2nd ed. New York: McGraw Hill.

Mahto, T., & Mukherjee, V. (2017). Fractional order fuzzy PID controller for wind energy-based hybrid power system using quasi-oppositional harmony search algorithm. IET Generation, Transmission and Distribution, 11(13), (3299–3309). https://doi.org/10.1049/iet-gtd.2016.1975

Masikana, S. B., Sharma, G., Sharma, S., & Çelik, E. (2024). Frequency regulation in solar PV-powered thermal power system using FPA-PID controller through UPFC and RFB. Electrical Engineering. https://doi.org/10.1007/s00202-024-02417-5

Nguyen, M., Toan, T., & Trung, N. (2019). Auto-tuning controllers of a class of plants using gradient descent algorithm.

Taşören, A. E., Gökçen, A., Soydemir, M. U., Şahin, S. (2020). Artificial Neural Network-Based Adaptive PID Controller Design for Vertical Takeoff and Landing Model. Avrupa Bilim Ve Teknoloji Dergisi (87-93).

Url-1 https://yarpiz.com/259/ypea112-firefly-algorithm, accessed: 11.12.2024.

ELECTRICAL ENGINEERING

Electric Power & Energy Systems

Electrical Machines

Electrical Vehicles

Power Electronics

Smart Grids

Contributions to the Determination of Optimized Driving Strategies with ML-Based Methods for Electric Vehicles

Ufuk Bolat[a], Gülcihan Özdemir[b], Derya Ahmet Kocabaş[c]

[a] Istanbul Technical University, Graduate School, Electrical Engineering Program, Türkiye
[b] Istanbul Technical University, Informatics Institute, Türkiye
[c] Istanbul Technical University, Faculty of Electrical and Electronics Engineering, Türkiye
bolat17@itu.edu.tr

Keywords: Eco-driving Strategies, Electric Vehicles, Energy Consumption Optimization, Machine Learning, Particle Swarm Optimization.

Aim

Electric vehicles (EVs) have emerged as a cornerstone of sustainable transportation, driven by efforts to reduce greenhouse gas emissions and dependence on nonrenewable energy resources. Their low-emission operation, combined with advancements in battery technology, makes them increasingly viable for both personal and commercial applications. However, two critical challenges, such as limited driving range and high energy consumption, continue to hinder their widespread adoption. To address these concerns, a growing body of research focuses on "eco-driving" strategies, which minimize energy usage through deliberate control of speed, acceleration, and braking.

Although much of the eco-driving literature focuses on optimizing acceleration and deceleration under varying road conditions, routes featuring uphill or downhill slopes present additional challenges, as power demand, battery usage, and regenerative braking potentials can shift dramatically (Recalde et al., 2024). While modest slopes may have negligible impact over short distances, these effects accumulate substantially over longer or more frequently sloped routes (Kamal et al., 2011). Consequently, slope-aware eco-driving has emerged as a specialized area, incorporating methods such as Model Predictive Control (MPC) or reinforcement learning to adapt vehicle speed in real time (Bakibillah et al., 2018; Wu et al., 2023). Yet, these techniques often require significant computational resources and repeated planning cycles to accommodate longer or multi-segment trips, posing challenges for deployment.

This study proposes a slope-aware hybrid eco-driving framework for EVs that balances the realism of high-fidelity simulations with the computational efficiency of machine learning (ML) and meta-heuristic optimization. The framework begins with an offline simulation phase, where a comprehensive dataset is generated by simulating various driving scenarios along a basic route composed of multiple segments, including uphill, downhill, and flat sections, with different boundary speeds. Based on this dataset, two surrogate ML models are trained to predict total travel time and total energy consumption for any given speed profile. These models act as fast approximators, replacing repeated calls to computationally expensive simulators during the optimization process. In the online phase, a Particle Swarm Optimization (PSO) algorithm leverages these surrogate models to identify the optimal speed trajectory that minimizes energy consumption while satisfying a user-defined travel time constraint. By decoupling the computational burden of simulation from the real-time optimization, the proposed method ensures scalability and adaptability to various road configurations and constraint sets, making it a practical solution for energy-efficient route planning in EVs.

The methodology is evaluated on a 700-meter route divided into nine segments, each with a known length and slope. Although this example focuses on slopes of ±3° and flat sections, the same procedure can be extended to longer routes, steeper inclines, or more restrictive speed constraints. The underlying principle is to explore local adjustments to segment entry and exit speeds, thereby distributing speed changes more intelligently across uphill and downhill portions of the route.

Material and Method

a. Overall Workflow

The proposed method is organized into three core stages. First, a high-fidelity simulation of the EV is performed offline to generate a large dataset of hypothetical speed profiles and their associated time and energy outcomes. Second, ML surrogates (one model for predicting total travel time, another for total energy consumption) are trained on this dataset. Finally, a PSO algorithm uses the surrogates to explore a range of potential speed profiles, identifying one that meets a specified travel time with minimized total energy. Figure 1 illustrates the complete workflow, from data generation to final performance validation.

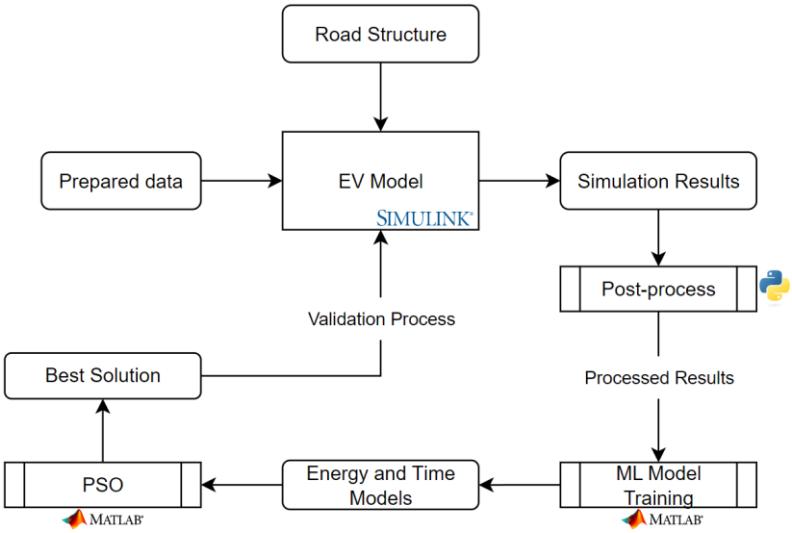

Figure 1. End-to-End Workflow.

b. Route Setup and Road Geometry

To evaluate the proposed methodology, a 700-meter test route composed of segments with varying slopes and lengths is used, as shown in Figure 2. The route includes flat, uphill (+3°), and downhill (−3°) segments, with lengths of 100 m and 50 m.

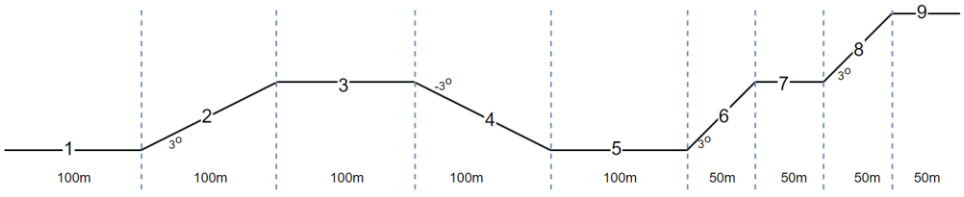

Figure 2. Road Structure.

A constraint enforces that the vehicle's speed at the start of segment 1 must match its speed at the end of segment 9, reflecting a realistic scenario where the vehicle enters and exits the entire route at a specified speed. Additionally, a maximum speed limit ensures that candidate solutions remain physically and legally acceptable. By dividing the route into distinct segments, slope effects are localized, and the optimization algorithm can tailor speed decisions to each individual segment.

c. Offline Simulation for Data Generation and Post-processing

The first step in developing the proposed eco-driving system is to generate an offline dataset that captures how different segment boundary speeds influence total travel time and energy consumption. For this purpose, a Simulink-based EV model is used. The model incorporates rolling resistance, aerodynamic drag, and motor-battery dynamics to ensure a realistic simulation behavior.

Following each simulation run, timestamped data are recorded, including the vehicle's speed, position, and both instantaneous and total energy consumption. From these records, the total travel time and total energy consumption required to complete the route are gathered, as illustrated in Figure 3. Each simulation input consists of systematically generated segment boundary speeds, ensuring that the exit speed of one segment becomes the entry speed of the next. This approach maintains a continuous speed profile along the route, allowing acceleration and deceleration dynamics to be realistically represented under varying slope conditions.

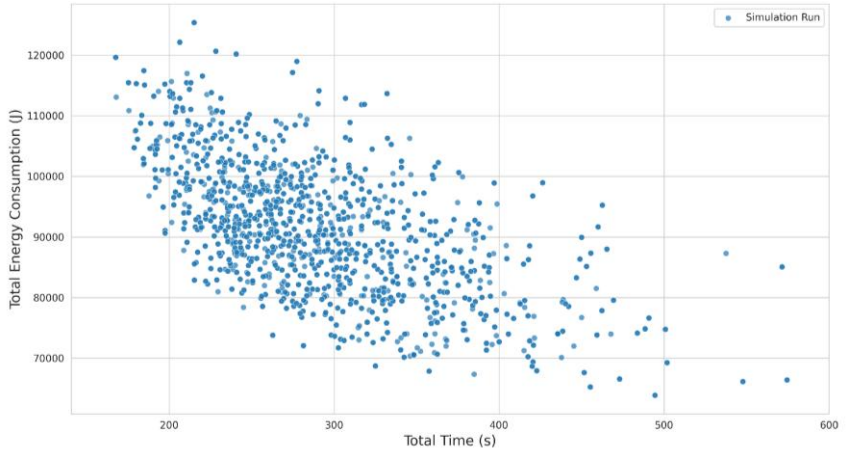

Figure 3. Offline Simulation Results.

A post-processing step compiles the simulation outputs into a structured dataset, associating each road segment with its entry and exit speeds, segment-level energy consumption, and time spent in that segment. This organized format, partially illustrated in Table 1, facilitates the subsequent training of ML models by providing clearly defined inputs and outputs for each simulated scenario.

Table 1. Post-Processed Data for ML.

Simulation No	Segment	Road Angle (°)	Distance (m)	V_{in} (km/h)	V_{out} (km/h)	Time (s)	Energy (J)
1	1	0	100	2.02	21.09	40.25	17136.10
1	2	3	100	21.09	10.32	23.75	20740.37
1	3	0	100	10.32	3.77	55.75	3018.52
1	4	-3	100	3.77	14.76	44.50	90.91

d. Machine Learning Surrogates

Once the offline dataset was compiled, it was randomly partitioned into training and test subsets using an 80–20 split. Several ML algorithms were then evaluated, including neural networks, gradient-boosted trees, and Gaussian process regressors, using each road segment's slope angle, length, entry speed, and exit speed as input features. Ultimately, a Gaussian process regressor with a Matérn 5/2 kernel achieved the lowest root mean square error (RMSE) on the test set for both the Time Model (predicting travel time) and the Energy Model (predicting energy consumption). This result highlights the regressor's capacity to capture the nonlinear relationships introduced by varying speeds and slopes. By adopting these final surrogate models, the time required to evaluate a new speed profile is reduced from a full physics-based simulation —which can take seconds to minutes— to a rapid inference step on the order of milliseconds, thereby enabling a more efficient search for optimal eco-driving strategies.

e. Particle Swarm Optimization

To identify the speed profile that satisfies a desired target travel time while minimizing energy consumption, a PSO algorithm is applied (Kennedy & Eberhart, 1995). Rather than enumerating possible speeds or exhaustively scanning a high-dimensional space, PSO maintains a "swarm" of candidate solutions, each representing a distinct set of nine boundary speeds.

During each iteration of the swarm:

- The Time and Energy surrogate models are queried for each candidate solution, yielding T' (predicted time) and E' (predicted energy).
- A cost function, defined in Equation 1, evaluates each solution's quality, where T_{target} denotes the user-defined travel time, and $\alpha \in [0, 1]$ controls how strictly the algorithm attempts to match that time versus minimize total energy.

$$cost = a\left|T' - T_{target}\right| + (1 - a)\, E' \qquad \text{(Eq. 1)}$$

- Boundary speeds for each candidate are updated according to both its local best performance and the global best solution found so far in the swarm.

After a predefined number of iterations or once the swarm's performance converges, the best-performing solution is selected. This final speed profile is then re-validated in the high-fidelity simulator to verify that the time and energy predictions align closely with the actual simulation results.

Findings

Tests conducted on the defined route demonstrate that the proposed method can significantly reduce energy consumption, even under stringent travel-time constraints. When the weighting factor α is relatively small, the algorithm prioritizes energy savings, often entering uphill segments at lower speeds to limit power demand. Conversely, under tighter time constraints (larger α), the optimizer raises speeds on flat and downhill segments to maintain a higher average speed and carry momentum into subsequent uphill sections.

Table 2. Optimized Segmented Speeds.

Segment No	V_{in} (km/h)	V_{out} (km/h)
1	2.00	12.64
2	12.64	4.33
3	4.33	6.22
4	6.22	17.85
5	17.85	6.82
6	6.82	4.83
7	4.83	12.12
8	12.12	5.47
9	5.47	2.00

In Table 2, the PSO-recommended segment speeds for a route completion time of 370 seconds are presented, along with the corresponding energy consumption estimates from the surrogate models. These predictions enable rapid assessment of candidate speed profiles without resorting to repeated high-fidelity simulations. To verify their accuracy, Figure 4 compares the surrogate-based estimates against results from a full Simulink run, revealing only minor differences between the predicted and actual travel times and energy usage. This close alignment highlights the reliability of the surrogate-driven optimization in meeting the user-specified travel time while still achieving substantial energy reductions. Furthermore, the offline–online structure of the framework provides a foundation for extension to longer routes or more complex slope distributions, requiring only additional simulation data and surrogate model retraining.

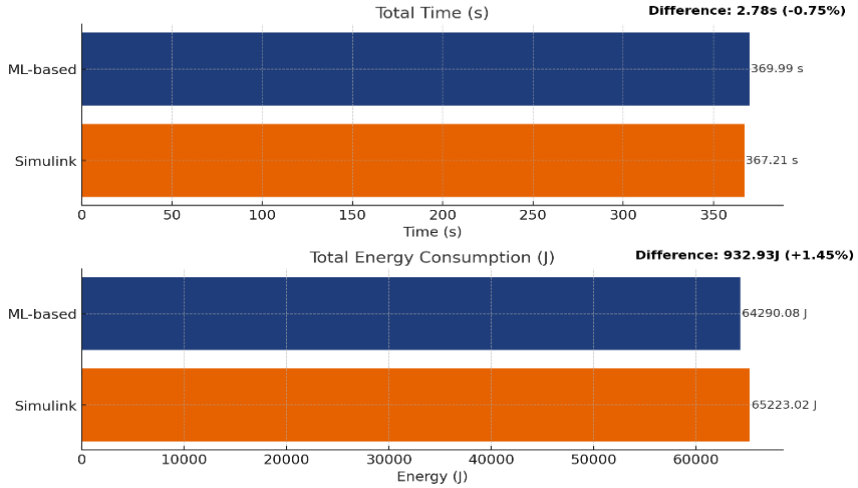

Figure 4. Validation Results.

Conclusion

This paper has presented a hybrid eco-driving framework for EVs on sloped, segmented roadways. By combining a one-time offline simulation with two ML models for travel time and energy consumption, and employing a PSO algorithm to identify an optimal speed profile, the method addresses key challenges in slope-aware driving without incurring excessive real-time computational costs.

The results from a 700-meter, nine-segment route demonstrate the system's capacity to balance energy minimization with a user-defined travel time. Boundary speeds are allocated intelligently, mitigating high power demands on uphill sections and leveraging efficient cruising where appropriate. The offline–online separation further ensures that once a robust dataset has been generated, adaptation to new constraints or route segments only requires re-running the optimization, not the entire high-fidelity simulation.

In principle, this framework can be generalized to larger or more intricate topographies by introducing additional simulation data, retraining the ML surrogates, and recalibrating the PSO. The methodology is also extensible by refining the offline model or road profile to account for further effects—such as curves or more complex geometries. Additionally, users can introduce extra constraints, for instance by specifying target speeds in certain segments, thus enabling the speed profile to meet more diverse operational requirements while still seeking minimum energy consumption. Overall, the proposed approach offers an effective, ML-based method of reducing energy costs for EVs and improving their operational viability in the face of range and efficiency concerns.

References

Bakibillah, A. S. M., Kamal, M. A. S., Tan, C. P., Hayakawa, T., & Imura, J. (2018, June). Eco-driving on hilly roads using model predictive control. In *2018 Joint 7th International Conference on Informatics, Electronics & Vision (ICIEV) and 2nd International Conference on Imaging, Vision & Pattern Recognition (icIVPR)* (pp. 476–480). IEEE.

Kamal, M. A. S., Mukai, M., Murata, J., & Kawabe, T. (2011). Ecological vehicle control on roads with up-down slopes. *IEEE Transactions on Intelligent Transportation Systems*, *12*(3), 783–794.

Kennedy, J., & Eberhart, R. (1995, November). Particle swarm optimization. In *Proceedings of ICNN'95 – International Conference on Neural Networks* (Vol. 4, pp. 1942–1948). IEEE.

Recalde, A., Cajo, R., Velasquez, W., & Alvarez-Alvarado, M. S. (2024). Machine learning and optimization in energy management systems for plug-in hybrid electric vehicles: A comprehensive review. *Energies*, *17*(13), 3059.

Wu, J., Song, Z., & Lv, C. (2023). Deep reinforcement learning-based energy-efficient decision-making for autonomous electric vehicle in dynamic traffic environments. *IEEE Transactions on Transportation Electrification*, *10*(1), 875–887.

ELECTRICAL ENGINEERING

Electric Power & Energy Systems

Electrical Machines

Electrical Vehicles

Power Electronics

Smart Grids

Conceptual Power Conversion Architecture for Unmanned Aerial Vehicles Utilizing BLDC Motor as Both Starter and Generator

Emel Timurkaynak Solak[a], Mehmet Onur Gülbahçe[a]

[a] Istanbul Technical University, Department of Electrical Engineering, Türkiye
timurkaynak@itu.edu.tr

Keywords: UAV Power Management, BLDC Starter-Generator, Four-Switch Buck-Boost Converter.

Unmanned Aerial Vehicles (UAVs) have become an essential component of various industries, including defense, logistics, agriculture, surveillance, and industrial automation. These applications require high efficiency, extended endurance, and lightweight design for optimal performance. One of the major challenges in UAV power systems is the inefficient energy management and weight constraints imposed by traditional architectures, which employ separate starting motors and generator systems. These conventional approaches lead to increased system and harness complexity, integration difficulties, and reduced energy recovery rates. The primary aim of this study is to develop an integrated BLDC motor-based power electronics system architecture that functions as both a generator and a starting motor, thereby reducing overall system weight and improving power efficiency. This dual-purpose system integrates a Four-Switch Buck-Boost Converter with a three-phase inverter to facilitate bidirectional power conversion. A Proportional-Integral (PI) control strategy is implemented to regulate power transitions and optimize energy recovery. The proposed approach is validated through extensive simulations in MATLAB/Simulink, demonstrating its feasibility in UAV applications.

The study focuses on designing and simulating a lightweight, efficient UAV power management system using a BLDC motor as a combined starter-generator unit. The key elements of the proposed system architecture are a Four-Switch Buck-Boost Converter (FSBBC) and a Three-Phase Inverter. FSBBC is a vital component that enables bidirectional energy transfer between the UAV power supply and the BLDC motor. Unlike traditional unidirectional converters, the FSBBC operates in both step-up (boost) and step-down (buck) modes, ensuring optimal power conversion efficiency in different UAV operational phases. During Startup, the converter operates in boost mode, supplying adequate voltage to the BLDC motor for rapid and efficient starting. During Generator Mode, the converter functions in buck mode, regulating the generated voltage and ensuring efficient energy recovery back to the UAV power system. The four-switch topology reduces switching losses and component count, leading to an overall reduction in system weight and complexity. Additionally, this design provides high dynamic response, making it well-suited for UAV applications that require real-time power management. Three-Phase Inverter is responsible for controlling the BLDC motor drive operation. It converts the DC power from the UAV battery into three-phase AC power required to drive the BLDC motor during start-up. Once the BLDC motor transitions into generator mode, the inverter performs the reverse operation, rectifying AC power back into DC and feeding it into the power management system for reuse. During the start-up phase, it operates as an inverter, converting DC battery power into AC to initiate motor rotation. In generator mode it operates as a synchronous rectifier, converting AC power generated by the BLDC motor into a regulated DC output. The inverter is designed with pulse-width modulation (PWM) control, ensuring precise speed and torque regulation of the BLDC motor while maintaining high conversion efficiency. To ensure stable operation, efficient energy transfer, and smooth mode transitions, a Proportional-Integral (PI) control strategy is implemented in the system. PI controllers are widely used in power electronics due to their simplicity, real-time computation efficiency, and robustness against disturbances. The control strategy is designed to regulate voltage and current levels, to ensure seamless mode transition and to enhance system stability. The PI controller dynamically adjusts the duty cycle of the FSBBC and switching sequence of the three-phase inverter to maintain optimal power levels. Smooth switching between starting and generator modes is critical to prevent voltage fluctuations that could affect UAV operation. The PI controller fine-tunes the system's response to avoid sudden spikes or dips in voltage and current. By continuously monitoring input voltage, output power, and system load, the PI controller maintains steady operation under various flight conditions.

The simulation results confirm that the proposed BLDC-based starter-generator system effectively operates in both generator and starting modes, demonstrating enhanced energy efficiency, weight reduction, and stable power regulation. The system integrates a Four-Switch Buck-Boost Converter (FSBBC) and a Three-Phase Inverter, enabling seamless bidirectional power flow. The PI control strategy ensures that voltage and current levels remain stable throughout mode transitions, avoiding unnecessary energy losses and disturbances. One of the primary advantages of the proposed system is its ability to recover and reuse energy more effectively than traditional UAV power architectures. The simulation results indicate that the system achieves a 15-20% higher energy recovery rate compared to conventional unidirectional power converters. This improvement is attributed to the bidirectional operation of the Four-Switch Buck-Boost Converter, which enables power to be efficiently transferred back to the UAV power supply during several flight phases. Another significant advantage of the proposed system is the reduction in overall UAV system weight, which directly impacts payload capacity and manoeuvrability. By integrating starter and generator functions into a single BLDC motor, the need for separate components is eliminated, leading to a weight reduction of 30% (to be determined based on hardware implementation). Traditional UAV power architectures require two separate electromechanical units: one for start-up and another for power generation. This increases weight and complexity, reducing available payload capacity. The proposed BLDC-based system consolidates these functions, significantly reducing the number of components and overall structural weight.

This study presents a novel integrated UAV power management system based on a BLDC motor-driven bidirectional power converter, offering substantial improvements over traditional dual-component architectures. Simulation results confirm that the proposed system enhances UAV energy efficiency by optimizing power conversion and energy recovery mechanisms. Additionally, by integrating the starter and generator functions into a single BLDC motor, the overall system weight is reduced, leading to increased payload capacity and operational flexibility. The PI control strategy ensures stable voltage and current regulation, contributing to smooth transitions between different modes. These findings suggest that the proposed power management system can play a significant role in next-generation UAV designs, improving operational efficiency and power autonomy. These findings suggest that the proposed power management system can significantly contribute to next-generation UAV designs, enhancing their operational efficiency and power independence. Future work may focus on experimental validation of the proposed system and exploring advanced control strategies for further efficiency improvements. While the simulation results confirm the effectiveness and feasibility of the proposed system, further research is necessary to validate its real-world performance and explore potential enhancements. One of the primary areas for future work involves experimental validation, where the system would be implemented in a real UAV prototype. This would allow for the assessment of its actual performance under practical operating conditions, considering environmental factors such as temperature variations, electromagnetic interference, and mechanical vibrations that are not fully captured in simulations. Additionally, hardware optimization could contribute to further improvements in power conversion efficiency and thermal performance. The use of emerging semiconductor technologies, such as Gallium Nitride (GaN) or Silicon Carbide (SiC) MOSFETs, could significantly reduce switching losses, improve power density, and enhance the system's overall reliability. These materials offer superior electrical and thermal characteristics compared to traditional silicon-based power devices, making them ideal for high-performance UAV power systems.

References

Bozhko, S., Yeoh, S. S., Gao, F., & Hill, C. (2014). *Aircraft starter-generator system based on permanent-magnet machine fed by active front-end rectifier*. In Proceedings of IECON 2014 – 40th Annual Conference of the IEEE Industrial Electronics Society (pp. 2958–2964). IEEE. Retrieved from https://doi.org/10.1109/IECON.2014.7048930

Degano, M., Arumugam, P., Fernando, W., Yang, T., Zhang, H., Borg Bartolo, J., Bozhko, S., Wheeler, P., & Gerada, C. (2014). *An optimized bi-directional, wide speed range electric starter-generator for aerospace application*. In 7th IET International Conference on Power Electronics, Machines and Drives (PEMD 2014) (pp. 1–6). IET. Retrieved from https://doi.org/10.1049/cp.2014.0483

Hasan, S. M. N., Husain, I., Veillette, R. J., & Carletta, J. E. (2007). *A PM brushless DC starter/generator system for a series-parallel 2×2 hybrid electric vehicle*. In Proceedings of the 2007 IEEE Industry Applications Annual Meeting (pp. 1686–1693). IEEE. Retrieved from https://doi.org/10.1109/07IAS.2007.259

[Okafor, E. G., Okafor, E., Ubadike, O. C., Abba, M. T., Jemitola, P. O., Shinkafi, A. A., Sule, G., Bonnet, M. U., & Udekwe, D. (2021). *Electric vehicle integrated with PMSM and regenerative braking system speed evaluation based on diverse control strategies*. Kaduna, Nigeria: Air Force Institute of Technology, Nigerian Air Force Base & Ahmadu Bello University.

Ubadike, O., Udekwe, D., Bonet, M. U., Momoh, M. O., Makinde, O. M., & Mohammed, A. (2022). *Development of a BLDC motor-based starter-generator for an experimental UAV*. Department of Aerospace and Mechatronics Engineering, Air Force Institute of Technology, Kaduna, Nigeria.

ENERGY SCIENCE AND TECHNOLOGY

Computational Fluid Dynamics

Computational Heat and Mass Transfer

Energy Conversion and Storage Technologies

Energy Conversion and Sustainability

Energy Management and Planning

Renewable Energy

Sustainable Energy

Comparative Analysis of LSTM and LightGBM for Short-Term Electricity Consumption Forecasting

Muhammet Furkan Baysal[a], Mustafa Berker Yurtseven[a]

[a]Istanbul Technical University/Energy Institute, Energy Science and Technology, Türkiye
baysalm16@itu.edu.tr

Keywords: Forecasting Accuracy, LightGBM, LSTM Model, Short-Term Electricity Consumption.

Aim

Electricity is a fundamental pillar of modern life, driving industries, powering households, and enabling emerging technologies such as electricity vehicles. With ongoing growth, rapid industrialization, and increasing electrification efforts across the globe, electricity demand has risen significantly in recent years (International Energy Agency, 2024). As a result, accurate electricity demand forecasting has become even more essential for the effective planning, management, and reliability of power systems. In particular, short-term electricity consumption forecasts play a crucial role in maintaining the delicate balance between supply and demand, ensuring operational efficiency, minimizing imbalance costs, and reducing price fluctuations in liberalized electricity markets (Bojnec & Križaj, 2021). This study focuses on forecasting short-term electricity consumption within a specific distribution region in Turkey. It aims to evaluate and compare the forecasting performances of two popular models: Long Short-Term Memory (LSTM), a type of deep learning model known for its ability to capture sequential patterns, and Light Gradient Boosting Machine (LightGBM), a decision tree-based gradient boosting algorithm recognized for its speed and scalability. The primary goal is to explore how these two models perform in forecasting hourly electricity demand for the next 24 hours, using historical data enriched with various features. Accurate short-term forecasting not only contributes to better operational decision-making for electricity providers and market participants but also supports strategic planning and the integration of renewable energy sources. Furthermore, it allows for more effective resource allocation and reduces the likelihood of energy imbalances, thereby contributing to a more stable and efficient electricity market.

Material and Method

In the model development process, a comprehensive dataset comprising three years of hourly electricity consumption data was used. This data was collected from transformer substations located in a specific distribution region of Turkey. In addition to consumption data, meteorological variables such as temperature, humidity, and wind speed were obtained from the Turkish State Meteorological Service. The dataset represents real consumer behavior and includes a wide range of consumption sectors: residential areas, industrial facilities, street lighting, agricultural activities, the public sector, and losses due to theft or transmission inefficiencies. To reflect real-world complexities and make the dataset more suitable for machine learning applications, the data underwent several preprocessing steps. These included cleaning, normalization, and the creation of additional variables. Derived features such as month, day, hour, day of the week, season, and a public holiday indicator were added to help capture temporal and cyclical patterns that influence electricity demand. Two models were selected for the analysis. The first, LSTM, is a type of recurrent neural network well-suited for time series data due to its ability to learn long-term dependencies. The second, LightGBM, is a gradient boosting framework that is efficient with large datasets and provides fast, interpretable results. Both models were trained to predict the electricity demand for the next 24 hours, based on historical input data. Model performance was assessed using three widely accepted error metrics: Mean Absolute Error (MAE), Root Mean Squared Error (RMSE), and Mean Absolute Percentage Error (MAPE) (Hyndman & Koehler, 2006). Additionally, a separate validation set was used to test how well each model could generalize to new, unseen data.

Findings

The results reveal that both the LSTM and LightGBM models can forecast short-term electricity consumption with a high degree of accuracy. Due to its deep neural network structure, the LSTM model was particularly successful at capturing time-based dependencies, which are often crucial in predicting electricity demand. Its sequential learning mechanism allowed it to detect complex patterns across consecutive time intervals, making it a powerful tool for time series forecasting.

On the other hand, the LightGBM model delivered strong performance with a significantly faster training time and greater interpretability. This made it especially advantageous for scenarios where quick results and transparency in model decisions are essential. Both models achieved commendable accuracy based on RMSE and MAPE scores. While LSTM was more effective in modeling complex temporal behaviors, LightGBM stood out in terms of computational efficiency and ease of deployment. Both models were also successful in capturing the influence of external variables such as public holidays and seasonal changes. The training and validation loss curves for the LSTM model (Figure 1) demonstrated that after a rapid decline in the early epochs, the validation loss stabilized, indicating that the model had learned the essential patterns without overfitting. This suggests that the LSTM model was able to maintain generalization capability and deliver consistent performance on new data. The performance metrics of the LSTM model are summarized in Table 1. The model achieved a Mean Squared Error (MSE) of 3220.27, a MAE of 42.79, an RMSE of 56.75, and a MAPE of 7.05%. These results indicate that the model effectively learned temporal dependencies and produced reliable forecasts. However, the LSTM's high computational complexity and longer training time could pose challenges in scalability and real-time applications.

In comparison, the LightGBM model achieved better error scores. As shown in Table 2, the model recorded an MSE of 381.52, a MAE of 13.48, an RMSE of 19.53, and a MAPE of 2.10%. These metrics suggest that LightGBM outperformed LSTM in terms of forecast accuracy and is particularly well-suited for real-time forecasting environments due to its speed and low resource consumption. While LightGBM may not capture long-term dependencies as effectively as LSTM, its ability to deliver accurate and rapid predictions makes it highly valuable in many operational contexts. Ultimately, the study demonstrates that both models are viable for short-term electricity demand forecasting. The decision to use one over the other should depend on the specific needs of the task, such as the required speed, computational resources, and the complexity of temporal patterns in the data.

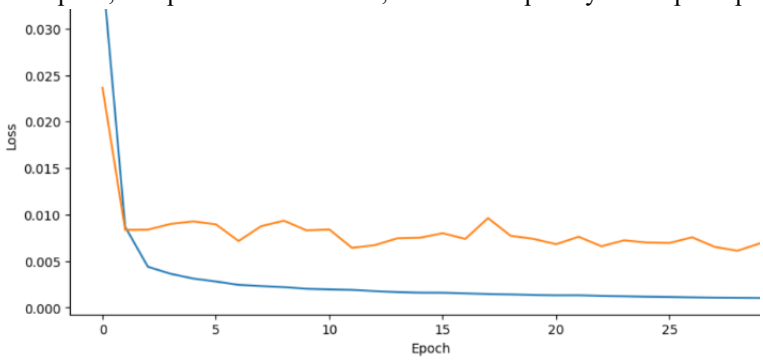

Figure 1. Training and validation loss graph for LSTM model.

Table 1. LSTM model performance metrics.

Metric	LSTM
MSE	3220.27
MAE	42.79
RMSE	56.75
MAPE, %	7.05

Table 2. LightGBM model performance metrics.

Metric	LightGBM
MSE	381.52
MAE	13.48
RMSE	19.53
MAPE, %	2.10

Conclusion

This research has demonstrated that both LSTM and LightGBM are effective modeling approaches for short-term electricity consumption forecasting in Turkey's liberalized electricity market. Each model brings unique strengths to the table. LSTM offers the advantage of learning complex time-dependent structures in electricity consumption, whereas LightGBM provides rapid and accurate forecasts with strong interpretability. These capabilities are valuable for market participants, such as distribution companies, suppliers, and large-scale consumers, in optimizing their strategic planning and bidding strategies, reducing imbalance costs, and enhancing operational efficiency. Moreover, reliable short-term forecasts contribute to the stability of market clearing prices, support grid reliability, and play a vital role in facilitating the integration of renewable energy sources. As energy systems become more dynamic and decentralized, accurate forecasting tools become even more critical. In this context, the selection of the forecasting model should be aligned with the operational requirements, data availability, and desired response time. LSTM might be more appropriate for complex forecasting scenarios that involve strong time dependencies, while LightGBM could be the preferred choice in environments requiring fast and explainable predictions. Future studies may consider developing hybrid or ensemble models that combine the strengths of both LSTM and LightGBM to further improve forecasting performance. In addition, evaluating the adaptability of these models to different regions or varying consumption profiles could offer insights into their scalability and robustness. Such advancements would not only benefit electricity market operations but also contribute to a more resilient and sustainable energy future.

References

Bojnec, Š., & Križaj, A. (2021). *Electricity markets during the liberalization: The case of a European Union country*. Energies, 14(14), 4317. https://doi.org/10.3390/en14144317

International Energy Agency (2024). *World Energy Investment 2024 Report*.

International Energy Agency (2024). *Electricity 2024: Analysis and Forecast to 2026 Report*.

Hyndman, R. J., & Koehler, A. B. (2006). Another look at measures of forecast accuracy. *International Journal of Forecasting*, 22(4), 679–688. https://doi.org/10.1016/j.ijforecast.2006.03.001

Building Energy Efficiency: A Data-Driven Machine Learning Approach for Energy Management and Planning

Ahmad Reza Darabi[a], Mustafa Berker Yurtseven[a]

[a] Istanbul Technical University, Energy Institute, Türkiye
darabi22@itu.edu.tr

Keywords: Building Energy Consumption, Building Energy Efficiency, Indoor Condition Prediction, Machine Learning, Thermal Comfort.

Aim

Between 1971 and 2019, the world's total energy supply has increased 2.6 times (International Energy Agency, 2020) (Figure 1). We are producing and consuming more and more energy. In recent years, there has been growing recognition of the importance of reducing energy consumption in buildings to address the urgent challenge of climate change. Buildings are responsible for a significant portion of greenhouse gas emissions, representing 35% of energy-related EU emissions (European Commission, 2022), and improving their energy efficiency is essential for achieving the targets set out in international climate agreements such as the Paris Agreement (United Nations Paris Agreement, 2015). The operations of buildings account for 30% of global final energy consumption (Figure 2) and 26% of global energy-related emissions (8% being direct emissions in buildings and 18% indirect emissions from the production of electricity and heat used in buildings). According to the IEA Energy Efficiency Indicators database, almost 50% of final energy consumption in residential buildings is used for heating (International Energy Agency, 2020) (Figure 3). This study aims to enhance energy efficiency in buildings while maintaining thermal comfort by leveraging machine learning (ML) techniques. This approach can help optimize resource usage, reduce operational costs, and mitigate the environmental impact by accurately forecasting and controlling energy consumption in real time. Ultimately, it supports sustainable development goals and promotes a healthier future for society through data-driven, intelligent building management.

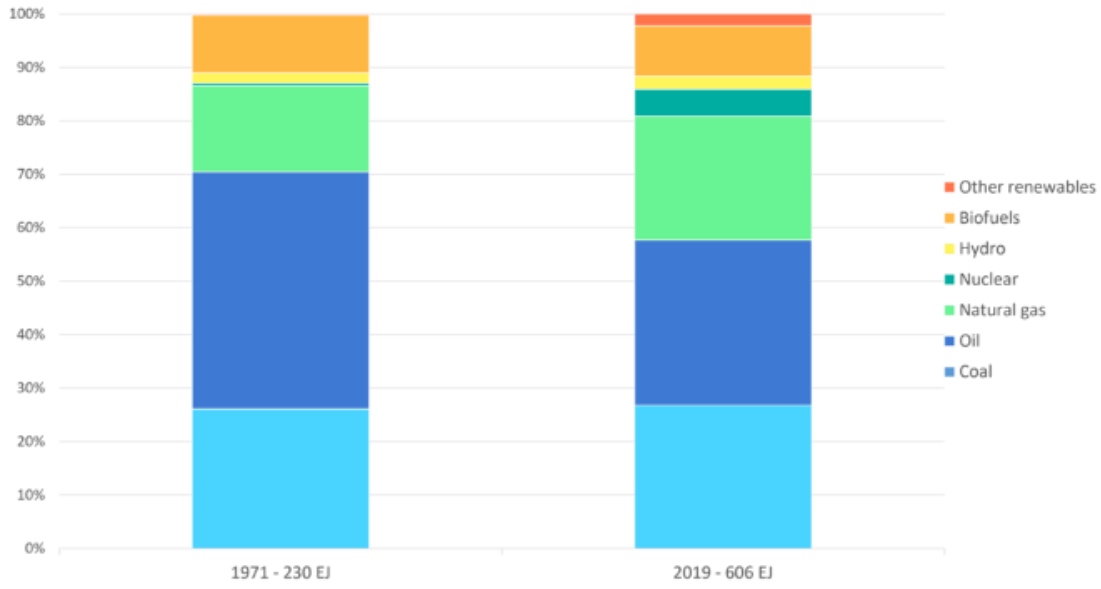

Figure 1: Total Energy Supply by Fuel.

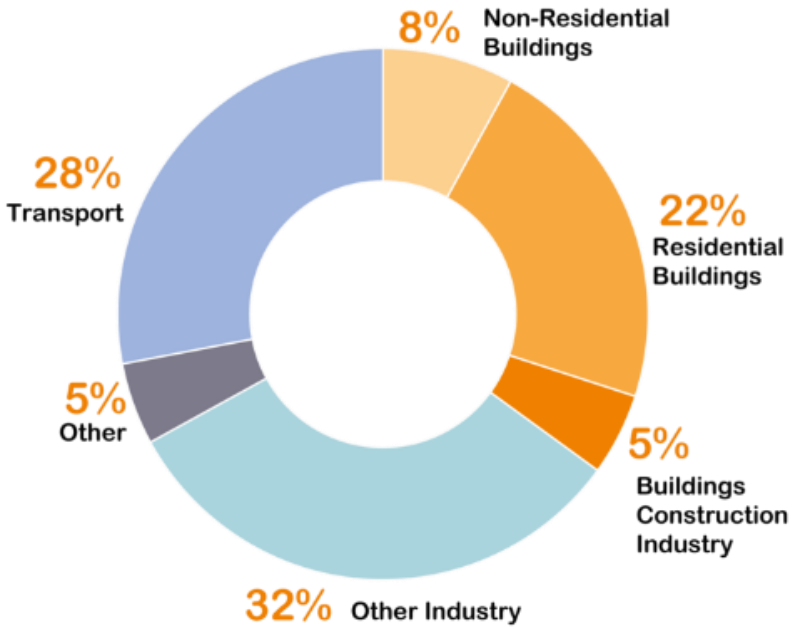

Figure 2: Global Share of Buildings and Construction.

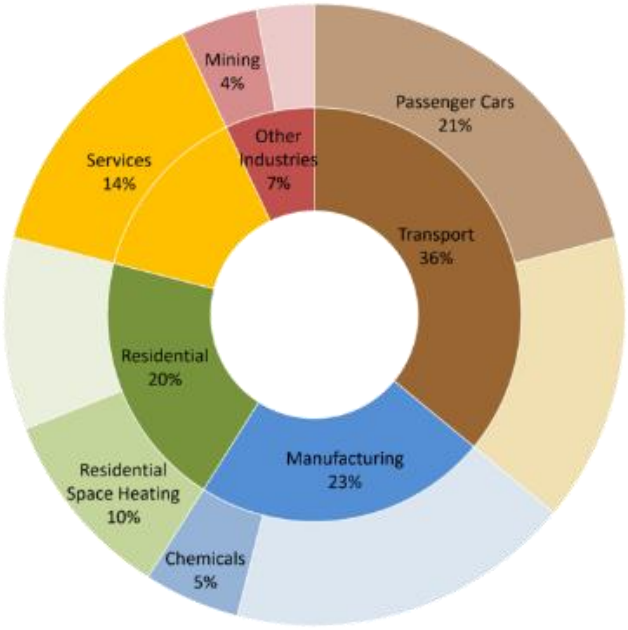

Figure 3. Largest End Uses of Energy by Sector.

Material and Method

This research integrates an internal condition dataset, collected via a Smart Thermostatic Radiator Valve, with an external environmental conditions dataset obtained from online sources based on the case study's location. The internal condition dataset (sampled every 30 minutes) includes features such as Room Temperature, Room Humidity, Target Temperature, Valve State, and Time as an ID number, which is very important for time series datasets. The www.visualcrossing.com website was used to gather external environmental conditions data (sampled every 60 minutes). The dataset for the study period was downloaded and includes many useful features such as External Temperature, External Humidity, Wind Speed, Solar Radiation, and so forth. The data cleaning

process for the integrated dataset involved steps such as removing or filling missing values (about 7% of the total records), and matching rows according to the time column. Furthermore, due to the use of Long Short-Term Memory (LSTM) models and the importance of numeric values, correlation analysis was performed on categorical features such as Atmospheric Condition, and only those with low correlation were removed. In cases where a categorical feature was essential for the research, it was converted to numeric features using Label Encoding.
The dataset was split into 80% for training and 20% for testing, and the final prediction was performed on one day of unseen data. Using an LSTM model, indoor temperature was predicted to determine the optimal times to turn on or turn off the Radiator Valve to control hot water flow to the radiators. The initial models achieved an R^2 value above 0.78. Through feature engineering, some features were removed and the impact of this was examined in the results. On the other hand, new features were created to utilize previous timestep data, which is useful for forecasting. Specifically, two previous timesteps were used as lag features. Hyperparameter tuning was performed on the LSTM parameters, and the most optimized values were used in the final version of the model. The hyperparameters considered in the tuning process included the number of LSTM layers, the number of units (neurons) per layer, the dropout rate, the learning rate, the batch size, the number of epochs, and the activation function. The final model was implemented using the TensorFlow library, and the Adam optimizer was applied with MSE as the loss function. After these steps, the model's performance improved, reaching an R^2 value of 0.95. (Table 1).

Table 1: Initial and Final Model Performance Comparison.

Measurement	Initial Model	Model after Tuning
R-squared	0.78	0.95
Mean Absolute Error	0.50	0.30
Mean Squared Error	0.75	0.17

Findings

Energy usage between the existing heating system and the proposed method was compared using heat transfer equations. Specifically, the fundamental relationship $Q=m\cdot c\cdot\Delta T$ was employed, where Q is the heat energy, m is the mass of the air in the room, c is the specific heat capacity of the air, and ΔT is the temperature difference (room temperature when valve is off - room temperature when valve is on). In this study, m and c remain constant for the same room, so focusing on ΔT and the duration over which hot water flows into the radiator allows for a straightforward comparison of energy transfers. By integrating this equation over time, we can account for the total heat delivered, making it an effective measure to compare the radiator's energy transfer in different heating scenarios. Our results indicate that by implementing this methodology, heating system energy consumption can be reduced by 33% while still maintaining indoor thermal comfort (Table 2).

Table 2: Energy Consumption Comparison between Baseline Model and Optimized Valve State Model.

Measurement	Baseline Model	Optimized Valve State Model	Improved Percent
Radiator Working Time (Hours)	6	4.5	25%
Total Energy Transferred ro Room (W)	23.55	15.67	33%
Energy Transferred by Radiator (W/h)	3.93	3.48	11%

Conclusion

Energy consumption is increasing worldwide, and building heating systems account for a large portion of it. This study aims to provide A Data-Driven Machine Learning Approach to Managing and Planning Energy and to improve energy efficiency in buildings. A smart thermostatic radiator valve and an internet-based source were used to collect data to train and test an LSTM model (Figure 4). Results show that the application of an LSTM model

with a high R^2 value enables us to predict indoor temperature based on the next hours' external conditions. This ability can be used to control the hot water flow to the radiator and optimize heating system operation to reduce energy consumption in buildings. The important point is that the proposed approach achieves energy efficiency while ensuring occupants' comfort remains at the same level as the original approach. These findings highlight the importance of using machine learning for building energy optimization.

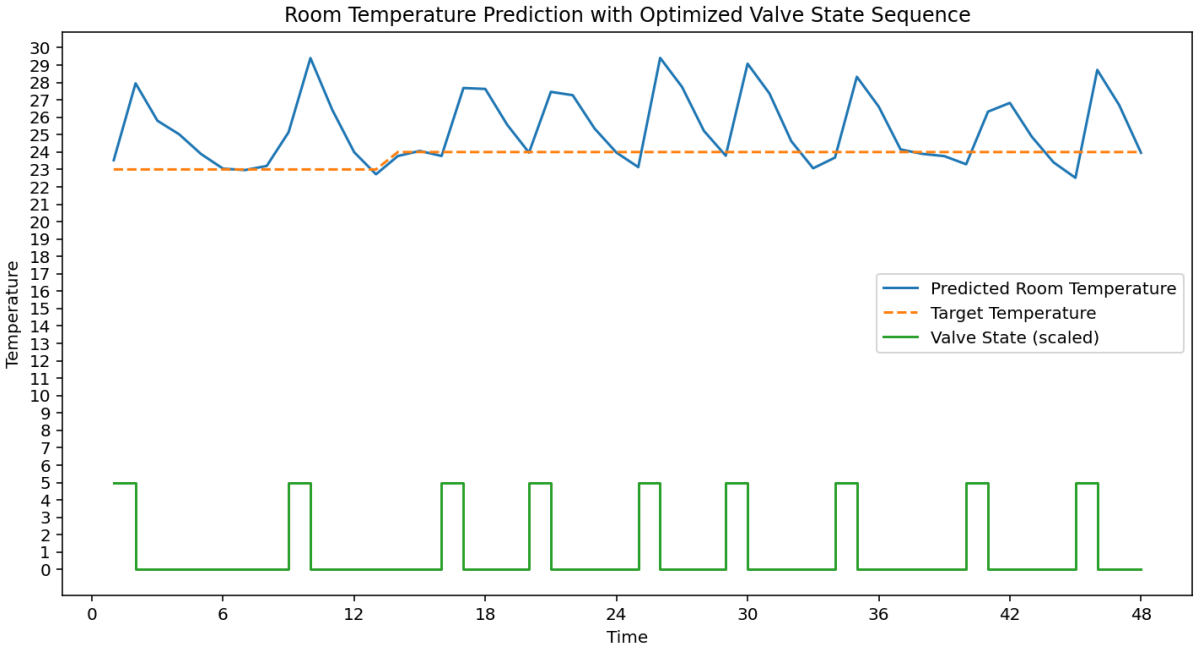

Figure 4: Final Model Operation.

References

Boegli, M., Stauffer, Y., Koch, N., Gorecki, T., Langou, R., & Hutter, A. (2022, May). Smart thermostatic valves-based heat generator control to cut heating bills. In CLIMA 2022 Conference.

European Commission. (2022). European environment agency (EEA)

Fabrizio, E., Ferrara, M., & Monetti, V. (2017). Smart heating systems for cost-effective retrofitting. In Cost-effective energy efficient building retrofitting (pp. 279–304). Woodhead Publishing.

International Energy Agency. (2020). Energy efficiency indicators database

Manfren, M., James, P. A., Aragon, V., & Tronchin, L. (2023). Lean and interpretable digital twins for building energy monitoring–A case study with smart thermostatic radiator valves and gas absorption heat pumps. Energy and AI, 14, 100304.

United Nations Paris Agreement. Paris, 12 December 2015.

Zhou, Z., Zhang, S., Wang, C., Zuo, J., He, Q., & Rameezdeen, R. (2016). Achieving energy-efficient buildings via retrofitting of existing buildings: A case study. Journal of Cleaner Production, 112, 3605–3615.

ENERGY SCIENCE AND TECHNOLOGY

Computational Fluid Dynamics

Computational Heat and Mass Transfer

Energy Conversion and Storage Technologies

Energy Conversion and Sustainability

Energy Management and Planning

Renewable Energy

Sustainable Energy

Optimization of Ground Heat Exchangers for Sustainable Heating Solutions: A Case Study Approach

Nurullah Yıldırım[a,b], Ece Asan[a], Z. Fatih Ozturk[a]

[a]Istanbul Technical University, Energy Institute, Türkiye
[b]TUBITAK Rail Transportation Technologies Institute, Türkiye
yildirimnur@itu.edu.tr

Keywords: Ground Heat Exchanger, Ground Source Heat Pump, Thermal Energy Demand.

Aim

Ground source heat pump systems provide efficient heating, because the underground temperature is higher than the outdoor temperature in cold climate. In this study, the ground heat exchanger length that meet all the thermal energy demand of the buildings throughout the heating season is calculated. Also, underground temperature profiles are investigated.

A significant portion of the energy consumption at homes is thermal energy [1]. Therefore, considering the thermal energy demands of buildings during the design phase, and using efficient energy systems both provides economical solutions and helps reduce environmental impacts. Especially in recent years, issues such as climate change and environmental pollution have been on the agenda of developed and developing countries. As a result, in line with the European Union's 2050 zero carbon targets [2], the use of renewable energy systems is encouraged both in electricity generation and in thermal energy production and storage. One of the renewable energy systems used to meet the thermal energy demands of buildings is heat pumps. Heat pumps are called as air, water or ground source depending on the environment where the heat exchangers are located [3]. The most commonly used heat pump type is air source heat pumps due to their low initial investment cost, but ground source heat pumps (GSHP) have also become widespread over time, especially in cold climates, due to their high coefficient of performance (COP) values [4,5]. GSHPs can be used for both heating and cooling purposes.

In this study, the length of ground heat exchangers (GHE) is calculated for a region (Ankara, Turkey) where the heating season is longer than the cooling season. The heat exchange of the GHEs with the underground is numerically calculated and underground temperature profiles investigated in five years of operation.

Material and Method

In the study, an underground heat pump system that meets the heat demand of five independent buildings, each of which is 100 m^2, is analyzed. For this purpose, the total heat load is investigated for five years by considering the instantaneous temperature change during the heating season of the region. When the seasonal temperature changes are in recent years examined, the October 15 - May 15 range is accepted as heating season. The comfort temperature of the buildings is taken as 22^0C. If the GHEs interact thermally, thermal shortcuts occur and the system efficiency decreases [6]. For this reason, the GHEs are positioned as far away from each other as possible so that they do not interact thermally. However, if there is not enough space for the proper configuration, either the GHE depths should be changed or GHEs configuration with less interaction should be tried. Of course, positioning them further away than necessary increases the piping costs. The GHEs with a depth of 75 m are used in the study. The unperturbed ground temperature of the field is accepted as the annual average temperature of the region, 11 ^{0}C [7]. This value was accepted as the initial temperature of the underground when performing numerical calculations. Because the changes resulting from the edge effects at the lower and upper points of the GHEs are observed to be around two percent in the numerical experiments, two-dimensional temperature profiles are used to reduce the numerical load. The design characteristics of the GSHP system are given in Table 1.

Table 1: The design and operational characteristics of the ground source heat pump systems.

Number of houses	N_A	5
Effective heat loss area of each houses	A_H	290m^2
Comfort temperature of houses	T_H	22°C
U value for heat loss	U_H	0.286 W/m^{2}K
Number of boreholes	N_B	4
Depth of boreholes	H_B	75m
Radius of boreholes	r_B	0.1m
Ground depth of the model	H_G	200m
Ground radius of the model	r_G	100m
Undisturbed ground temperature	T_∞	11°C
Ground thermal conductivity	k	3.2W/mK
Ground heat capacity	c_p	780J/kgK
Ground density	ρ	2750kg/m^3
Heating Season		15 Oct.-15 May
Standby Season		15 May-15 Oct.

The temperature profile of the GHE field is obtained using the time-dependent 2D heat conduction equation. If the GHEs do not interact, a single GHE can be modeled and the energy extracted during the heating season can be obtained by multiplying it by the number of GHEs. However, if the GHEs interact, all GHEs should be placed in the field and a common solution should be made. The heat transfer equation that gives the underground temperature change is given in equation 1.

$$\frac{1}{\alpha}\frac{\partial T}{\partial t} = \frac{1}{r}\frac{\partial T}{\partial r} + \frac{\partial^2 T}{\partial r^2} \#(\ SEQ\ Equation\ \backslash *\ ARABIC\ 1)$$

where; α is thermal diffusivity of the ground which depends on the conductivity (k), heat capacity (c_p) and the density (ρ) of the ground as $\alpha = \frac{k}{(\rho\, c_p)}$, T is the temperature, t is time and r is te distance from the GHE surface. Because the thermal demand of the houses changes continuously during the heating season, the heat energy extracted from the ground also changes continuously. Therefore, the transient thermal loads of the houses are calculated by using the hourly outdoor temperatures [8] and this value is defined as the transient heat flux boundary condition to the GHEs surface. The transient heat flux boundary condition on the GHEs is written in equation 2.

$$J_Q^{DC}(t) = \frac{\dot{Q}(t) n_H}{n_B A_B} \#(\ SEQ\ Equation\ \backslash *\ ARABIC\ 2)$$

where, $\dot{Q}(t)$ is the thermal energy demand of a single house, n_H is the number of the houses, n_B is the number of the boreholes and A_B is the surface heat transfer area of a single GHE. The heating energy demand of a single house is determined as in equation 3.

$$\dot{Q_D}(t) = U_H A_H \big(T_H - T_{out}(t)\big) \#(\ SEQ\ Equation\ \backslash *\ ARABIC\ 3)$$

where; U_H is the heat transfer coefficient of the house, A_H is the effective heat loss area of a single house, T_H is the comfort temperature of the houses, $T_{out}(t)$ is the time dependent outdoor temperature. The heat flux is coupled to the hourly averaged heat demand of the houses during heating. Furthermore, the underground is considered to be composed of dry rock, and underground flows or saturated environments are not considered. And the outside the heating season the soil temperature recover around the GHEs. This mode is called as the standby mode of the GSHP system. Furthermore, in this analysis the underground is considered as a single layer.

Findings

The thermal energy demand during the heating season is calculated separately for the years 2018-2023. During these years, the total thermal energy demand of a single building for heating varies between 7.13 MWh and 7.92 MWh. Figure 1 shows the five years hourly thermal energy demand of a building.

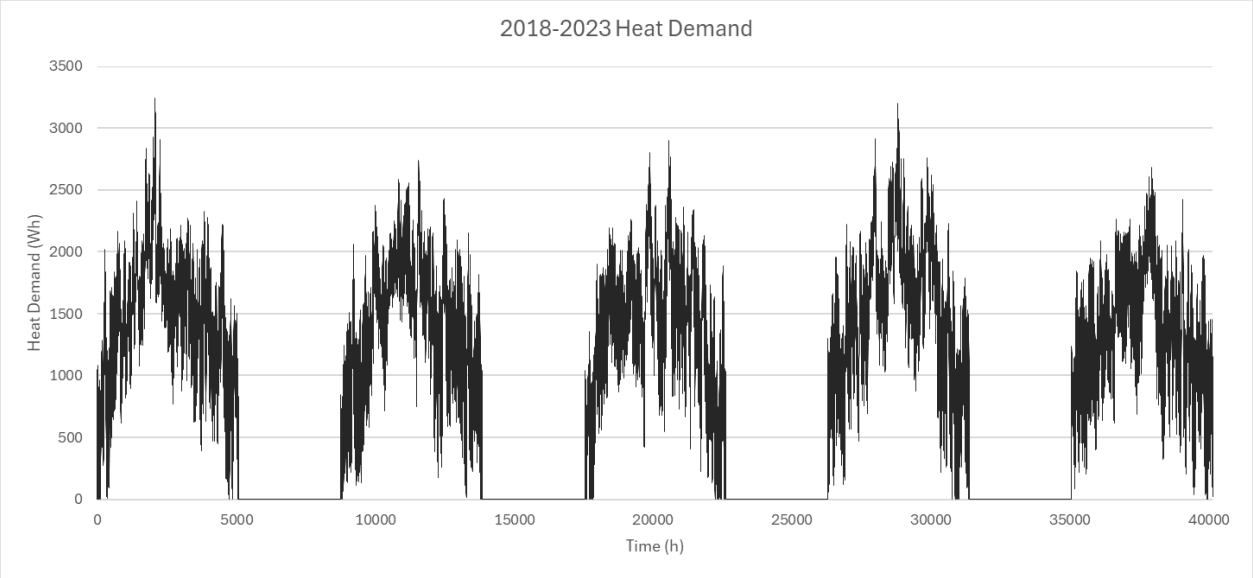

Figure 1: Five years thermal energy demand of a building (2018-2023).

In the numerical calculations, the heat exchangers are placed 6 meters away from each other to minimize thermal interaction. As a result of the analysis by using the different numbers of GHEs with a length of 75 meters, it is seen that four GHEs provides the thermal energy demand when the characteristics of the heat pump is considered. The temperature field at the end of the one and five years of operation is given in Figure 2. At the end of the first year, it is observed that the underground temperature does not fall below zero degrees even in areas close to the GHE surface and does not fall below the characteristic values of the heat pump. In the period after the discharge mode in the first year, it is clear that the GHE surface temperature almost completely increased by conduction heat transfer from the surroundings. At the end of the fifth year, it is also seen that the underground temperatures do not exceed the desired values and the thermal needs of the houses are met without interruption.

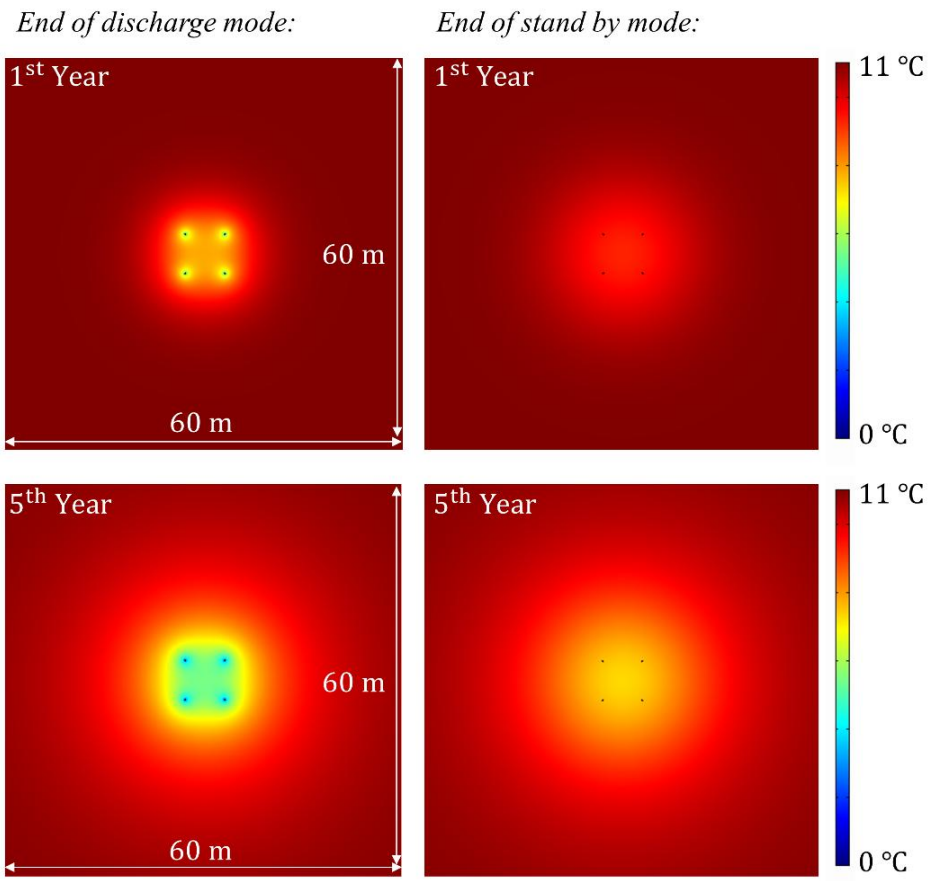

Figure 2: Underground temperature distribution at the end of the discharge and stand by modes for the first and fifth years of operation.

Conclusion

In the study, the underground heat pump system for the heating demand of five houses is analyzed and it is seen that four GHEs at a depth of 75 meters meet more than the thermal energy demand (7.92 MWh). In the next study, the system will be converted into a borehole thermal energy system (BTES) by charging solar thermal energy. Thus, the required heat exchanger length for the BTES system will be calculated and the economic analysis for the two systems will be compared.

References

Ürge-Vorsatz D, Cabeza LF, Serrano S, Barreneche C, Petrichenko K. Heating and cooling energy trends and drivers in buildings. Renew Sustain Energy Rev 2015;41:85–98. http://dx.doi.org/10.1016/j.rser.2014.08.039.
IEA. International energy agency, net zero by 2050. 2021, p. 224. http://dx.doi.org/10.1787/c8328405-en.
David B. Options and applications for ground source heat pumps. In: An introduction to thermogeology: ground source heating and cooling. John Wiley & Sons, Ltd; 2012, p. 150–201. http://dx.doi.org/10.1002/9781118447512.ch7.
Sarbu I, Sebarchievici C. General review of ground-source heat pump systems for heating and cooling of buildings. Energy Build 2014;70:441–54. http://dx.doi.org/10.1016/j.enbuild.2013.11.068.
Bae S, Nam Y. Economic and environmental analysis of ground source heat pump system according to operation methods. Geothermics 2022;101:102373. http://dx.doi.org/10.1016/j.geothermics.2022.102373.
Gultekin A, Aydin M, Sisman A. Effects of arrangement geometry and number of boreholes on thermal interaction coefficient of multi-borehole heat exchangers. Appl Energy 2019;237:163–70. http://dx.doi.org/10.1016/j.apenergy.2019.01. 027.

Rees S. Advances in ground source heat pump systems. Woodhead Publishing; 2016, http://dx.doi.org/10.1016/C2014-0-03840-3.
NASA. POWER data access viewer. 2023, URL https://power.larc.nasa.gov/dataaccess-viewer/, Last accessed 19 June 2023.

ENVIRONMENTAL ENGINEERING

Air Pollution and Control

Membrane Technologies

Carbon Capture and Utilization in the Cement Industry: Opportunities for Methanol and Urea Production from Process Emissions – A Systematic Literature Review

Gökçe Yalin[a]

[a] Istanbul Technical University, Faculty of Civil Engineering, Department of Environmental Engineering, Türkiye
yalin22@itu.edu.tr

Keywords: Carbon capture, Cement industry, CO_2 utilization, Methanol synthesis, Urea synthesis.

Aim

The cement industry is a significant source of global greenhouse gas emissions, responsible for nearly 7% of total anthropogenic CO_2 output (IEA, 2023; Andrew, 2019). A substantial portion of these emissions stems from the calcination of limestone during clinker production, where calcium carbonate ($CaCO_3$) is thermochemically converted into calcium oxide (CaO), releasing CO_2 as a by-product of the process. Since these process-related emissions are inherent to the chemistry of cement manufacturing, they cannot be effectively eliminated through conventional energy efficiency improvements or fuel switching alone (Habert et al., 2020). In response to increasing climate change concerns and regulatory pressures, Carbon Capture and Utilization (CCU) technologies are gaining traction as a promising industrial decarbonization strategy. These technologies offer the potential to capture CO_2 emissions directly from point sources such as cement kilns and enable their transformation into value-added products, thereby supporting both mitigation goals and resource circularity. Among various utilization pathways, methanol and urea production have emerged as particularly relevant due to their established industrial applications, global market demand, and potential to integrate captured carbon into existing chemical supply chains (Artz et al., 2018; Kätelhön et al., 2019). This study presents a systematic literature review on the application of CCU technologies in the cement sector, with a focus on evaluating their technological maturity (Technology Readiness Levels), integration potential with cement production infrastructure, and specific applicability to methanol and urea synthesis routes. Through this review, the study aims to highlight current research trends, identify existing gaps, and contribute to the discourse on feasible decarbonization pathways for the hard-to-abate cement industry.

Material and Method

This study employs a structured Systematic Literature Review (SLR) approach consisting of four integrated stages: article selection, classification scheme development, systematic mapping, and synthesis. Relevant studies were gathered through comprehensive searches in Scopus, Web of Science, and ScienceDirect databases, supplemented by references from selected venues and manual browsing. A total of 114 records were initially retrieved. Following the application of inclusion and exclusion criteria—based on study relevance, publication quality, and thematic fit—a refined pool of 79 articles was selected for full-text analysis. Following selection, attribute identification was performed to extract key classification categories such as capture technology type, utilization pathway, and TRL (Technology Readiness Level). These attributes were iteratively generalized and refined to ensure consistent application across studies of varied structure. The resulting classification framework enabled systematic mapping of the literature, allowing the visual distribution of studies by CCU technologies and application focus (e.g., methanol and urea synthesis). Insights derived from this mapping were then synthesized to identify prevailing research trends, technological challenges, and underexplored areas in the application of CCU in the cement industry. Special attention was given to the maturity and integration potential of CO_2-based methanol and urea production systems, given their dual relevance for emissions reduction and industrial value creation.

Findings

This systematic literature review evaluated current approaches for capturing CO_2 emissions from the cement industry and their subsequent utilization in chemical production. The cement sector, being one of the most carbon-intensive industries, has prompted a growing body of research into feasible Carbon Capture and Utilization (CCU) strategies that can address both environmental and industrial demands.

Among the carbon capture technologies identified in the literature, the most frequently studied are:

- Post-combustion capture, particularly using amine-based solvents like MEA (monoethanolamine) and solid looping systems such as Ca-looping, has been widely adopted at pilot and demonstration scales. These methods are compatible with existing cement kilns, making them attractive for retrofitting.
- Oxy-fuel combustion, which involves burning fuel in a pure oxygen environment, produces a flue gas with high CO_2 concentration that simplifies the separation process. However, the requirement for large-scale oxygen production introduces significant energy and cost barriers.
- Direct Air Capture (DAC) stands out as an emerging and flexible option that captures CO_2 directly from ambient air, enabling decentralized operation. Despite its novelty, DAC is still in early development stages due to the low atmospheric CO_2 concentration and high energy input required for sorbent regeneration and compression.

The Technology Readiness Levels (TRLs), capture efficiencies, and challenges of key CCU technologies are summarized in Table 1. MEA-based post-combustion systems show the highest TRL and efficiency, while DAC technologies face energy and cost barriers despite their potential. Two main CO_2 utilization pathways stand out:

methanol synthesis: $CO_2 + NH_3 \rightarrow CH_3OH$
especially when integrated with green hydrogen and,
urea synthesis: $CO_2 + NH_3 \rightarrow CO(NH_2)_2$

relevant for fertilizer production. These routes can reduce emissions and create value-added products. Successful deployment depends on access to renewable inputs, infrastructure readiness, and supportive policies. While technically promising, CCU in cement still requires scale-up and system-level integration for real impact.

Conclusion

This study systematically explored the current state of Carbon Capture and Utilization (CCU) technologies in the cement industry, with a particular emphasis on their applicability to methanol and urea production. The findings demonstrate that while post-combustion capture methods, especially MEA-based chemical absorption, are technologically mature and relatively well-studied, other methods such as Ca-looping and Direct Air Capture (DAC) remain in experimental or pilot stages. These latter technologies, although promising in terms of flexibility and long-term scalability, face significant obstacles related to high energy demand, infrastructure needs, and operational costs. The reviewed literature indicates that methanol synthesis from captured CO_2 is widely explored and offers integration opportunities with green hydrogen technologies, aligning well with broader decarbonization and Power-to-X strategies. On the other hand, urea synthesis, despite its large-scale industrial potential, remains underrepresented in academic research, suggesting a key knowledge gap that should be addressed through future investigations. Another critical insight from the review is the importance of technology readiness level (TRL) assessment and lifecycle analysis when evaluating CCU applicability. While some technologies appear technically viable, their environmental and economic performance across the full value chain must be further validated. Additionally, coupling CCU technologies with renewable energy inputs, such as green H_2 and sustainable NH_3, will be essential to ensure that CO_2 utilization pathways truly contribute to climate mitigation.
In conclusion, CCU technologies represent a vital tool in the decarbonization of hard-to-abate sectors like cement manufacturing. Their successful implementation, particularly for methanol and urea production—depends on continued interdisciplinary research, policy support, infrastructure development, and real-world pilot applications. Bridging the gap between academic innovation and industrial deployment will be key to unlocking the full potential of CCU within circular and low-carbon economy frameworks.

References

Andrew, R. M. (2019). Global CO_2 emissions from cement production. Earth System Science Data, 11(4), 1675–1710. https://doi.org/10.5194/essd-11-1675-2019

Artz, J., Müller, T. E., Thenert, K., Kleinekorte, J., Meys, R., Sternberg, A.& Bardow, A. (2018). Sustainable conversion of carbon dioxide: An integrated review of catalysis and life cycle assessment. Chemical Reviews, 118(2), 434–504. https://doi.org/10.1021/acs.chemrev.7b00435

Habert, G., d'Espinose de Lacaillerie, J. B., & Roussel, N. (2020). An environmental evaluation of geopolymer based concrete production: reviewing current research trends. Journal of Cleaner Production, 224, 957–972. https://doi.org/10.1016/j.jclepro.2019.03.019

IEA – International Energy Agency. (2023). Cement – Tracking Industry 2023. Retrieved from **Url-1** https://www.iea.org/reports/cement

Kätelhön, A., Meys, R., Deutz, S., Suh, S., & Bardow, A. (2019). Climate change mitigation potential of carbon capture and utilization in the chemical industry. Proceedings of the National Academy of Sciences, 116(23), 11187–11194. https://doi.org/10.1073/pnas.1821029116

FOOD ENGINEERING

Food Bioactive Compounds

Food Microbiology

Food Science

Functional Foods

Novel Food Processes

Sustainable Foods

Postharvest Application Of Cold Plasma On Fresh Spices And Evalution Of Major Changes

Emel Özdemir[a], Pervin Başaran[a], Sehban Kartal[b], Tamer Akan[c]

[a]Istanbul Technical University, Department of Food Engineering, Faculty of Chemical and Metallurgical Engineering, Turkey
[b] Istanbul University, Department of Physics, Faculty of Science, Turkey
[c] Eskisehir Osmangazi University, Department of Physics, Faculty of Science and Letters, Turkey
ozdemirem20@itu.edu.tr

Keywords: Atmospheric Cold Plasma, Fresh Spices, Food Quality, Food Safety

Aim

Cold plasma technology has been a technology that has been widely preferred in the food sector in recent years due to its nonthermal feature (Özdemir et al., 2023). Plasma is an ionized gas consisting of charged particles, electric fields, ultraviolet photons, and reactive oxygen and reactive nitrogen species (Ziuzina et al., 2020). In addition to gases such as helium and nitrogen, atmospheric air can also be used in cold plasma systems (Sudarsan & Keener, 2022). The use of atmospheric air is preferred because it is extremely economical and sustainable (Min et al., 2017). These systems are also called atmospheric cold plasma or dielectric barrier discharge (Bermúdez-Aguirre et al., 2013). The cold plasma produced in the system can be applied directly to samples or at a certain distance. In both applications, it can lead to the inactivation of various microorganisms that are important for food sterilization and does not have a negative effect on the sample surface (Ermis et al., 2021). Microbial inactivation can be explained by the fact that various reactive species released as a result of chemical reactions during cold plasma production create oxidative stress in the cell on the product surface and cause the destruction of the cell wall (Shah et al., 2019). Cold plasma can be preferred to kill possible pathogenic microorganisms after harvest, especially in products with short shelf lives such as fresh herbs, spices, and vegetables (Pankaj et al., 2018). This study aims to increase the shelf life of such fresh spices as bay leaf, basil, mint, rosemary, and thyme with short shelf lives but high economic value in foreign trade; to develop an alternative method to chemical disinfections used in the food industry; and to ensure that cold plasma application is spread to a wider area. For this purpose, a new system has been designed to perform atmospheric cold plasma production. This designed system is a highly effective system in terms of being scalable and applicable to many products.

Material and Method

For this purpose, various herbs and spices with different texture and surface properties were selected. The effect of direct application of atmospheric cold plasma to the product surface on quality properties, shelf life, and microbial inactivation was investigated for a certain shelf life. In order to observe the effect of atmospheric cold plasma on quality properties, physicochemical (color, pH, titratable acidity, moisture, and water activity), spectrophotometric (total phenolic, total flavonoid, total antioxidant, total anthocyanin, total chlorophyll, and essential oil composition) and scanning electron microscope (SEM) analyses were performed. A total viable count was performed to obtain information about the natural microflora of the samples. In addition, samples inoculated with microorganisms with different inoculation loads were exposed to atmospheric cold plasma for different durations, and the inactivation rate was determined.

Findings

When the physicochemical properties of the samples were examined, it was found that the effect of atmospheric cold plasma on pH was significantly lower than the control samples. In some samples, the total flavonoid content increased with the extension of the treatment time; moreover, it was observed that some monoterponoids preserved more than 50% and increased their amount. However, in some samples, a decrease in the total chlorophyll amount was observed after 3 minutes of treatment. Scanning electron microscopy (SEM) revealed that the tissue integrity

was affected by atmospheric cold plasma in some samples. However, atmospheric cold plasma extended the shelf life of samples stored at 4°C up to 8 days. It was observed that other analysis results were not affected by the increased atmospheric cold plasma exposure. The results were not found to be statistically significant. When the effect of atmospheric cold plasma on microbial inactivation of the samples was examined, it was determined that the greatest decrease was in the natural microflora load as a result of long-term exposure. When the samples were compared with the microorganisms inoculated at different concentrations, a higher inactivation was observed with the increase of the exposure time in the pathogenic species with higher concentrations. The results obtained showed that the selected system, plasma duration, initial concentration of the inoculation fluid, selected microorganism type, and storage period were effective on the samples. In addition, it was observed that the optimized conditions and selection of the appropriate system could increase the sample quality.

Conclusion

In our research, we compared the exposure time and investigated the suitability of the system parameters to observe the effect of atmospheric cold plasma application on microbiological decontamination and quality properties of fresh spices. Atmospheric cold plasma application showed a positive effect on the physicochemical properties of fresh spices and extended the shelf life. While the microbial loads of control samples increased rapidly during storage, the applied samples remained more stable in terms of physicochemical and microbial quality. Especially, the fact that it does not leave any chemical residue compared to other methods used today suggests that it can be used as an alternative method. However, the reliability of plasma sources and plasma composition are important concerns that should be evaluated in future studies in the development of post-harvest pretreatment technologies for agricultural products with short shelf lives in large industrial volumes. Our study shows that the variety of plasma systems and the direct exposure time affect general quality parameters and microbial inactivation, and this is confirmed by the analysis results. Although there are positive effects on the commercialization of products processed with atmospheric cold plasma, the interaction between plasma and the sample remains uncertain with the application. Therefore, more studies are needed on different samples and under different application conditions.

References

Bermúdez-Aguirre, D., Wemlinger, E., Pedrow, P., Barbosa-Cánovas, G., & Garcia-Perez, M. (2013). Effect of atmospheric pressure cold plasma (APCP) on the inactivation of *Escherichia coli* in fresh produce. *Food Control*, *34*(1), 149–157. https://doi.org/10.1016/j. foodcont.2013.04.022

Ermis, E., Yagci, M. O., & Durak, M. Z. (2021). Combination of vaporized ethyl pyruvate and non-thermal atmospheric pressure plasma for the inactivation of bacteria on lettuce surfaces. *Innovative Food Science & Emerging Technologies*, *73*, 102795. https://doi.org/10. 1016/j.ifset.2021.102795

Min, S. C., Roh, S. H., Niemira, B. A., Boyd, G., Sites, J. E., Uknalis, J., & Fan, X. (2017). In-package inhibition of *E. coli* O157: H7 on bulk Romaine lettuce using cold plasma. *Food Microbiology*, *65*, 1–6. https://doi.org/10.1016/j.fm.2017.01.010

Özdemir, E., Başaran, P., Kartal, S., & Akan, T. (2023). Cold plasma application to fresh green leafy vegetables: Impact on microbiology and product quality. *Comprehensive Reviews in Food Science and Food Safety*, *22*(6), 4484-4515. **https://doi.org/10.1111/1541-4337.13231**

Pankaj, S. K., Wan, Z., & Keener, K. M. (2018). Effects of cold plasma on food quality: A review. Foods, 7(1), 4. https://doi.org/10.3390/foods7010004

Shah, U., Ranieri, P., Zhou, Y., Schauer, C. L., Miller, V., Fridman, G., & Sekhon, J. K. (2019). Effects of cold plasma treatments on spot-inoculated *Escherichia coli* O157: H7 and quality of baby kale (*Brassica oleracea*) leaves. *Innovative Food Science & Emerging Technologies*, *57*, 102104. https://doi.org/10.1016/j.ifset.2018.12.010

Sudarsan, A., & Keener, K. M. (2022). Inactivation of *Salmonella enterica* serovars and *Escherichia coli* O157: H7 surrogate from baby spinach leaves using high voltage atmospheric cold plasma (HVACP). *LWT*, *155*, 112903. https://doi.org/10.1016/j.lwt.2021.112903

Ziuzina, D., Misra, N. N., Han, L., Cullen, P. J., Moiseev, T., Mosnier, J. P., Keener, K., Gaston, E., Vilaró, I., & Bourke, P. (2020). Investigation of a large gap cold plasma reactor for continuous in-package

decontamination of fresh strawberries and spinach. *Innovative Food Science & Emerging Technologies*, *59*, 102229. https://doi.org/ 10.1016/j.ifset.2019.102229.

FOOD ENGINEERING

Food Bioactive Compounds

Food Microbiology

Food Science

Functional Foods

Novel Food Processes

Sustainable Foods

Evaluation of Pasting and Rheological Properties of Modified Starches for Use in Plant-Based Products

Muhammed Harun Giray[a], Meral Kiliç Akyilmaz[a]

[a]Istanbul Technical University, Food Engineering, Türkiye
giraym22@itu.edu.tr

Keywords: Pasting, Rheological Proporties, Starch, Structure.

Aim

Starch is one of the major components in structure formation of plant-based products. Starch is traditionally used to regulate food texture and improve stability during shelf life of food products due to its pasting, thickening and gelling abilities. Therefore, it is an important structure forming and stabilizing ingredient in plant-based food products (Dobson & Marangoni, 2023). In this study, four different starches including three modified waxy corn starches and modified tapioca starch were evaluated for pasting and rheological properties.

Material and Method

Prepared aqueous solution of each starch was been prepared at a concentration of 6% by weight. Pasting properties were determined by monitoring viscosity in a temperature sweep test applying a controlled temperature program by using a rheometer with cone/plate geometry at a shear rate of 225 s^{-1}. A sample from the solution was placed on the plate of the rheometer and a temperature program was applied where the sample was held at 50 °C for 1 min, and then the temperature was increased to 95 °C linearly in 7.5 min. After reaching this temperature, the sample was kept at a temperature of 95 °C for 5 min and then it was cooled to 50 °C in 7.5 min and kept at this temperature for 2 min (Ishiwata et al., 2007). According to the data, onset temperature, peak viscosity, peak temperature, trough viscosity and final viscosity were determined for each starch. Rheological properties of gel form of starch samples were also measured. A gel was prepared using an aqueous solution of each starch at a concentration of 10% by heat treatment at 95 °C for 10 min and then cooling. Rheological properties of the gel were determined by using the rheometer with cone/plate geometry and changesin elastic (G') and viscous (G'') moduli were measured (Wang & Ren, 2020). Temperature and frequency sweep tests were carried out for determining changes in the gel structure by heating and application of constant strain at increasing frequency, respectively. Properties of starch samples were compared statistically by anova and Tukey's test.

Findings

Pasting measurements showed onset temperatures of modified tapioca starch and modified waxy corn starch 1 were lower than those of the modified waxy corn starch samples.Modified tapioca starch had the lowest peak viscosity among the other samples. Moreover, one of the modified waxy corn starch (1) samples had lower peak viscosity than the other two modified waxy corn starches. Peak temperature of the tapioca starch was lower than those of the modified waxy corn starch samples. While, trough viscosity of the modified tapioca starch was also the lowest, modified waxy corn starch 1 had the highest trough viscosity. In additon, final viscosity of the modified tapioca starch was the lowest among the starch samples. On the contrary, modified waxy corn starch 1 and 2 had the highest final viscosity.

In frequency sweep tests, the gel of the modified waxy corn starch sample 1 had the strongest structure at constant strain with increasing frequency. This sample was followed by the other modified waxy corn starch samples while modified tapioca starch sample had the weakest structure among the samples. In the temperature sweep tests, modified waxy corn starch samples 2 and 3 were found to have the highest initial G' value and the values were reduced by increasing temperature to 95 °C by 1.26-fold and 1.4-fold, respectively. On the other hand, the modified waxy corn starch sample 1 and modified tapioca starch sample had lower initial G' value. While G' values of modified waxy corn starch sample 1 declined by 1.2-fold, G' values of modified tapioca starch sample reduced by

3.4-fold by increasing temperature.All samples had higher G' values than G'' values during temperature sweep with no crossover.

The results showed that each starch had different pasting properties. In addition, they formed a viscoelastic gel with varying strength (Zhong et al., 2009). Moreover, tapioca starch is differentiated from the modified waxy corn starches clearly. In addition, some properties of tapioca starch were similar to those of modified waxy corn starch sample 1. The low onset temperatures of these starches indicate that they gelatinize at an early stage during heat treatment and potentially, they are less suitable for applications that require high cooking temperatures. Furthermore, these two starch samples had relatively low viscosity with a weak structure compared to those of the other starches. This shows that these two starches might not be suitable for application where a strong gel structure is required. However, they can be used for thickening of plant-based products. Pasting measurements exhibited that the modified waxy corn starch sample 2 and 3 had high peak viscosity and a stable gel structure. All starches have a weak gel structure with declining G' and G'' values with increasing frequency according to the frequency analyses. Temperature sweep analysis showed that the starch samples form thermoirrevesible gels with no clear liquefaction temperature. The modified corn starch sample 2 had a more elastic gel structure and the modified corn starch sample 2 had a hard gel structure which are suitable for use in plant-based products.

Conclusion

This study provide data for structure forming ability of different starches that will be beneficial in various food applications including plant-based products. Four different starches will have different potential in plant-based food applications. In light of the findings, combining starch as an ingredient with plant-based sources can pave the way for the development of new food products.

References

Ishiwata, T., Yamaguchi, Y., & Okamoto, T. (2007). Gelatinization and pasting properties of waxy and non-waxy rice starches. *Starch - Starke, 59*(7), 331-338.

Dobson, S., & Marangoni, A. G. (2023). Methodology and development of a high-protein plant-based cheese alternative. *Current Research in Food Science, 7,* 100632.

Wang, S., & Ren, F. (2020). Rheological, pasting, and textural properties of starch. In S. Wang & F. Ren (Eds.), *Starch structure, functionality and application in foods* (pp. 121–129).

Zhong, F., Li, Y., Ibáñez, A. M., Oh, M. H., McKenzie, K. S., & Shoemaker, C. (2009). The effect of rice variety and starch isolation method on the pasting and rheological properties of rice starch pastes. *Food Hydrocolloids, 23*(2), 406-414.

FOOD ENGINEERING

Food Bioactive Compounds

Food Microbiology

Food Science

Functional Foods

Novel Food Processes

Sustainable Foods

Use of Chlorella Vulgaris in Development of a Functional Ice Cream

Büşra Yalçın[a], Meral Kılıç Akyımaz[a]

[a] Istanbul Technical University, Department of Food Engineering, Türkiye
yalcin16@itu.edu.tr

Keywords: *Chlorella*, Clean label, Ice cream, Microalgae, Quality.

Aim

Ice cream is a dairy product that is produced by freezing a pasteurized mixture of milk, other dairy ingredients, emulsifiers, stabilizers, colorants, and flavorings while incorporating air. It is a popular dessert with high nutritional value for consumers of all ages. (Ozturk et al., 2018). Due to the high sugar and fat content of ice cream, along with the use of synthetic colorants, stabilizers, and emulsifiers, consumer preferences have shifted towards reduced fat, reduced sugar and functional ice cream with the market expected to grow rapidly. (Villaró-Cos et al., 2023). Microalgae have been used in human and animal nutrition since ancient times and recently gained popularity due to consumers' growing interest in healthy, nutritious, and clean-label food products. (Boukid and Castellari, 2021). Among microalgae, *Chlorella vulgaris* has attracted attention of food industry by its nutrient- and bioactive compound-rich composition with a potential to serve as a food ingredient. (Nurko et al., 2023) *Chlorella* is referred to as a "green health food" by the Food and Agriculture Organization (FAO). This study aimed to investigate the enrichment of ice cream with *Chlorella vulgaris* at different levels and its effect on product quality and stability. Additionally, the study examined effectiveness of *Chlorella vulgaris* as a stabilizer and emulsifier substitute in ice cream formulation.

Material and Method

Chlorella vulgaris was obtained from a local producer in powder form. The nutritional composition of the *Chlorella* used in this study was measured as containing 61.7% protein, 4.7% fat, 0.4% fiber, and 12.0% carbohydrates. Notably, 60% of protein content of *Chlorella* consists of amino acids allowing enrichment with essential amino acids. *Chlorella* powder was added to three different low-fat ice cream formulations, without stabilizers and emulsifiers, without stabilizers only, and without emulsifiers only, at concentrations of 1%, 3%, and 5%. According to the Turkish Food Codex, low-fat ice cream must contain at least 31% total dry matter, 3-8% milk fat, and a minimum of 10% non-fat milk solids by mass. The ice cream formulations used in this study were prepared in accordance with these standards, with a dry matter content of 37.1%, fat content of 5.3%, and non-fat milk solids of 10.1%. The composition, physical, chemical, and sensory properties of the ice creams were analyzed according to standard methods.

Findings

In the control mix without stabilizers and emulsifiers, the protein content was 3.76%, while formulations containing 1%, 3%, and 5% *Chlorella* showed protein levels of 4.65%, 5.33%, and 5.97%, respectively. The highest protein increase was obtained in the 5% *Chlorella* mix, representing approximately 58.7% more protein compared to the control. Compared to the control formulation with 5.3% fat, formulations with 1%, 3%, and 5% *Chlorella* showed fat contents of 5.2%, 5.5%, and 6.0%, respectively. Additionally, the dry matter content, which was 36.6% in the control mix, ranged between 36.7% and 38.9% in the algae-containing formulations. Since low-fat formulations require at least 31% dry matter by mass, the increase in dry matter from the algae mass could reduce the required sugar content, offering consumers a product with potentially lower sugar levels. The average pH of low-fat ice cream formulations ranges between 6.30 and 6.90. In the control sample, the pH was measured at 6.23, which increased to 6.58 in the formulation containing the highest *Chlorella* concentration without stabilizers and emulsifiers, indicating a pH increase with rising algae concentration.
The addition of *Chlorella* raised the freezing point from -2.60 °C in the control to -2.76 °C at a 5% concentration. The initial drip and complete melting times of the ice cream samples stored at -28 °C were measured on the first

day of storage at 24 °C, and the times for the first and last drips were recorded. Samples containing *Chlorella* exhibited greater resistance to melting. Hardness of the ice cream was reduced by microalgae addition. While the control formulation with stabilizers and emulsifiers achieved a 50% overrun, the overrun rates for ice creams containing 1%, 3%, and 5% *Chlorella* as stabilizer and emulsifier substitutes were measured at 25%, 25%, and 30%, respectively. Samples containing algae as a stabilizer substitute in emulsifier-only formulations exhibited overrun rates between 42% and 45%, closest to the control.

One major drawback is the color and aroma of microalgae which are foreign to food products. Overall, the color and sensory properties of the ice creams were significantly influenced by the *Chlorella* concentration, with samples containing lower percentages being preferred by the panelists. Furthermore, natural green color of *Chlorella* was darkened with the highest concentration of *Chlorella* added to the ice cream formulation.

Conclusion

This study demonstrated that *Chlorella* addition to ice cream formulation increased nutritional value with highly digestible proteins along with bioactive compounds, minerals, vitamins and dietary fiber. Effect of *Chlorella* on physical, chemical and sensory properties of ice cream was enhanced with the level of addition. The addition of *Chlorella* reduced overrun, freezing point and hardness while it increased melting resistance. Sensory properties and color of ice cream were significantly influenced by *Chlorella* addition at the highest level while lower levels were acceptable by the panelists. The findings of the study have shown that *Chlorella* can be used in ice cream formulations; however, optimum usage level that does not affect quality and stability should be determined.

The global demand for protein-rich and clean-label foods has increased by the health-concious consumers. Finding sustainable alternative protein sources is crucial due to the environmental impact of traditional protein sources. Microalgae such as *Chlorella* contain protein at levels up to twice as high as the traditional protein sources that make them promising alternative protein sources. While microalgae can be used to enhance the color and functional properties of ice cream, the optimization of their usage level is critical to minimize their sensory drawbacks.

References

Boukid, F., & Castellari, M. (2021). Food and beverages containing algae and derived ingredients launched in the market from 2015 to 2019: a front-of-pack labeling perspective with a special focus on Spain. Foods, 10(1), 173.

Nurko, E., Nakilcioglu, E., Otles, S. (2023). Geleceğin Gıdaları için Mikroalgler: *Spirulina spp.* ve *Chlorella spp.* Düzce Üniversitesi Bilim ve Teknoloji Dergisi, 11 (2023) 1655-1665.

Öztürk, H. İ., Demirci, T., & Akın, N. (2018). Production of functional probiotic ice creams with white and dark blue fruits of Myrtus communis: The comparison of the prebiotic potentials on *Lactobacillus casei* 431 and functional characteristics. LWT, 90, 339-345.

Turkish Food Codex (2023). Turkish Food Codex Regulation on food additives. Retrieved March 24, 2023 from: www.resmigazete.gov.tr, date retrieved 22.05.2025.

Villaró-Cos, S., Sánchez, J. L. G., Acién, G., & Lafarga, T. (2023). Research trends and current requirements and challenges in the industrial production of *Spirulina* as a food source. Trends in Food Science & Technology, 104280.

Novel Nutritional Yeast Formulation as a Functional Ingredient for Healthy Snacks

Aleyna Nur Karslı[a], Beyza Saricaoglu[a], Esra Capanoglu Guven[a]

[a] Istanbul Technical University, Faculty of Chemical and Metallurgical Engineering, Department of Food Engineering, Turkiye
karsli22@itu.edu.tr

Keywords: Utritional yeast, Healthy snacks, Bioaccessibility, Phenolic compounds.

Aim

In recent years, the increasing awareness of healthy living has driven consumers to prefer foods that not only provide basic nutrition but also offer functional benefits. In this context, natural compounds with biological activity such as phenolic compounds have gained prominence in the food industry due to their antioxidant properties, which support the immune system and help reduce the risk of chronic diseases (Czech et al., 2018; Karaman, 2021).

At the same time, the rising demand for clean-label and sustainable production practices has increased interest in foods rich in protein and phenolic compounds (Ma et al., 2023). This trend has encouraged the development of innovative and functional products, particularly in the category of healthy snacks. Nutritional yeast (*Saccharomyces cerevisiae*) has emerged as a valuable alternative in this context, offering a rich profile of proteins, B vitamins, and minerals. As a microbial protein source that is neither plant- nor animal-based, it represents a sustainable and unique ingredient with significant potential (Jach et al., 2022).

The purpose of this thesis is to investigate the potential of nutritional yeast enriched with phenolic-rich fruit and vegetable powders pecifically apple, beetroot, and black carrot as a functional food ingredient. The study aims to enhance the bioactivity, nutritional value, and sensory properties of nutritional yeast through natural enrichment.

Within this scope, total phenolic content, antioxidant capacity, and the bioaccessibility of phenolic compounds after in vitro digestion were analyzed. In addition, sensory evaluations were conducted to assess consumer acceptance in terms of taste, color, and texture. This study aims to contribute to the development of health-promoting and sensorially acceptable functional food products. Furthermore, it seeks to enrich the limited scientific literature on the enhancement of microbial proteins with plant-based bioactive compounds.

Material and Method

In this study, nutritional yeast with a minimum dry matter content of 17%, a gas production capacity of ≥700 mL CO_2/2 hours and a pH range of 4.5–7.0 was used. It was stored at +0 to +4 °C throughout the study to preserve its functional properties. For enrichment, apple, beetroot, and black carrot powders were used in their dried form. Each formulation was prepared by mixing 100 g of liquid yeast with 10 g of plant-based powder. The mixtures were homogenized, frozen at –20 °C for 12 hours, and then freeze-dried at –56,7 °C. The dried materials were ground into a fine powder for further analysis.

Phenolic compounds were extracted using an ultrasound-assisted ethanol method adapted from Zuo et al. (2021). Total phenolic content was determined by the Folin–Ciocalteu colorimetric method (Singleton & Rossi, 1965), and antioxidant capacities were measured using ABTS (Miller & Rice-Evans, 1996) and CUPRAC (Apak et al., 2004) assays. Results were expressed as mg gallic acid equivalent (GAE) or mg Trolox equivalent (TE) per gram of dry weight. In vitro digestion was simulated based on the standardized protocol of Minekus et al. (2014), which includes oral, gastric, and intestinal phases. At each stage, total phenolic content and antioxidant capacity were evaluated using Folin–Ciocalteu, ABTS, and CUPRAC assays.

Texture profile analysis (TPA) was performed to assess mechanical properties of the freeze-dried samples. A double compression cycle simulating mastication was applied to evaluate parameters such as hardness, cohesiveness, and springiness (Bourne, 2002). Descriptive sensory analysis was conducted using the Quantitative

Descriptive Analysis (QDA) method with 10 trained panelists (Stone & Sidel, 2004). Sensory attributes including taste, color intensity, acidity, and umami perception were evaluated using coded yoghurt samples under controlled conditions.

Gas production capacity of the samples was assessed by measuring CO_2 release over a 2-hour period at 30 °C, following a modified version of the method by Ktenioudaki et al. (2015).

All analyses were performed in triplicate, and the results were expressed as mean ± standard deviation. Statistical analysis was conducted using IBM SPSS Statistics 27.0. One-way ANOVA followed by Tukey's test was applied to determine significance. Additionally, independent sample t-tests and Pearson correlation coefficients were used to evaluate group differences and relationships. Statistical significance was set at $p < 0.05$.

Findings

In this study, formulations were developed by combining nutritional yeast (*Saccharomyces cerevisiae*) with apple, beetroot, and black carrot powders, and their performance was evaluated in terms of phenolic compound bioaccessibility, antioxidant capacity, textural and sensory properties, and gas production potential during in vitro digestion.

Phenolic compound analysis revealed that yeast enrichment significantly improved the intestinal bioaccessibility of phenolics in ingredients with low to moderate initial phenolic content, such as apple and beetroot. In the apple formulation, the phenolic content increased approximately 24-fold in the intestinal phase. In contrast, black carrot naturally rich in phenolics showed a lower bioaccessibility ratio when combined with yeast, suggesting that part of the phenolics may have been bound within the yeast matrix.

In terms of antioxidant capacity, a substantial increase was observed in ABTS radical scavenging activity in the apple formulation, whereas CUPRAC results showed only minor changes. Beetroot and black carrot formulations demonstrated a general decrease in antioxidant capacity after digestion. These findings indicate that the effect of yeast varies depending on the structural composition of the plant matrix.

Texture analysis showed that the addition of plant powders reduced the hardness and stickiness of the yeast matrix, resulting in a softer and more chewable product. Especially with beetroot and black carrot, the products were more elastic and consumer-friendly in texture. Sensory evaluation revealed that although plain yogurt was the most preferred in overall acceptability, yeast-enriched formulations enhanced umami perception and reduced sourness. The black carrot formulation stood out with its dark color, while the apple variant was rated highest for fruity aroma.

Gas production measurements showed low levels of CO_2 release in all samples, indicating that the freeze-drying process effectively inactivated the yeast cells and eliminated their fermentative potential.

Conclusion

Formulations developed by enriching nutritional yeast with apple, beetroot, and black carrot powders stand out as sustainable and functional food ingredients. Initially aimed at enhancing the nutritional and sensory properties of microbial proteins, this study demonstrated a significant improvement in the bioaccessibility of phenolic compounds, particularly in low phenolic matrices such as apple, along with notable textural enhancements and improved umami perception.

The consistently low CO_2 production across all samples indicates a digestion-friendly profile, making these products attractive to individuals seeking non-fermentative, gut-friendly food options. With its non-animal and non-plant origin, high protein content, and compatibility with phenolic-rich plant matrices, nutritional yeast emerges as a unique and scalable raw material for the development of healthy snacks (Jach et al., 2022; Karaman, 2021).

This work contributes to the advancement of next-generation functional products that combine microbial proteins with plant-based bioactives to deliver both health benefits and consumer satisfaction. Given the rising demand for clean-label products and the global shift toward plant-forward nutrition, these formulations show strong commercial potential, particularly in the rapidly growing healthy snack segment (Ma et al., 2023).

References

Apak, R., Güçlü, K., Özyürek, M., & Karademir, S. E. (2004). Novel total antioxidant capacity index for dietary polyphenols and vitamins C and E, using their cupric ion reducing capability in the presence of neocuproine: CUPRAC method. *Journal of Agricultural and Food Chemistry*, *52*(26), 7970–7981. **Url-1** https://pubmed.ncbi.nlm.nih.gov/15612784/

Bourne, M. C. (2002). *Food texture and viscosity: Concept and measurement* (2nd ed.). Academic Press. Erişim bağlantısı: **Url-1** https://www.sciencedirect.com/book/9780121190620/food-texture-and-viscosity

Czech, J., Zając, G., & Biernacka, B. (2018). Antioxidant properties of selected phenolic compounds. *Rocznik Ochrona Środowiska*, *20*, 1131–1145.

Jach, M. E., Serefko, A., Ziaja, M., & Kieliszek, M. (2022). Yeast protein as an easily accessible food source. *Metabolites*, *12*(1), 63. **Url-1** https://pmc.ncbi.nlm.nih.gov/articles/PMC8780597/

Karaman, Ş. (2021). Polyphenols in food systems and their health-promoting properties: A review. *Food and Health*, *7*(1), 1–15. **Url-1** https://dergipark.org.tr/en/pub/food

Ktenioudaki, A., O'Shea, N., & Gallagher, E. (2013). Rheological properties of wheat dough supplemented with functional by-products of food processing: Brewer's spent grain and apple pomace. *Journal of Food Engineering*, *116*(2), 362–368. **Url-1** https://www.sciencedirect.com/science/article/pii/S0260877412005894

Ma, Y., Wang, Y., Liu, X., & Zhang, H. (2023). Extraction of natural bioactive compounds using clean label technologies. *Frontiers in Sustainable Food Systems*, *7*, 1207704. **Url-1** https://www.frontiersin.org/journals/sustainable-food-systems/articles/10.3389/fsufs.2023.1207704/full

Miller, N. J., & Rice-Evans, C. A. (1996). Spectrophotometric determination of antioxidant activity. *Redox Report*, *2*(3), 161–171. **Url-1** https://www.tandfonline.com/doi/abs/10.1080/13510002.1996.11747044

Minekus, M., Alminger, M., Alvito, P., Ballance, S., Bohn, T., Bourlieu, C., ... & Brodkorb, A. (2014). A standardised static in vitro digestion method suitable for food – an international consensus. *Food & Function*, *5*(6), 1113–1124. **Url-1** https://pubs.rsc.org/en/content/articlelanding/2014/fo/c3fo60702j

Singleton, V. L., & Rossi, J. A. (1965). Colorimetry of total phenolics with phosphomolybdic–phosphotungstic acid reagents. *American Journal of Enology and Viticulture*, *16*(3), 144–158. **Url-1** https://www.ajevonline.org/content/16/3/144

Stone, H., & Sidel, J. L. (2004). *Sensory evaluation practices* (3rd ed.). Academic Press. **Url-1** https://www.sciencedirect.com/book/9780126726909/sensory-evaluation-practices

Zuo, T., Wu, A., Ding, Y., Li, Y., & Wang, J. (2021). Ultrasound-assisted extraction of polyphenols from plant materials: Mechanisms, optimization, and applications. *Food Reviews International*, *37*(2), 157–174. **Url-1** https://www.frontiersin.org/journals/nutrition/articles/10.3389/fnut.2023.1135712/full

FOOD ENGINEERING

Food Bioactive Compounds

Food Microbiology

Food Science

Functional Foods

Novel Food Processes

Sustainable Foods

Production and Characterization of a Functional Food Additive from Lemon Peel

Dilara Mercan[a], Erenay Erem[a], Meral Kılıç Akyılmaz[a]

[a]Istanbul Technical University, Faculty of Chemical and Metallurgical Engineering, Department of Food Engineering, Turkey
mercand21@itu.edu.tr

Keywords: Lemon Peel, Antioxidant, Antidiabetic, Emulsifying, Sustainability.

Aim

Lemon is an important citrus species widely appreciated for its refreshing aroma and high antioxidant activity. Antioxidant activity of lemon is due to its high vitamin C and phenolic compound contents. These attributes of lemon contribute not only to its appeal in food formulations but also health-promoting properties. However, approximately 50% of the fruit is wasted after processing to juice leading to loss of valuable nutritional and health-improving components. Currently, lemon waste is utilized as animal feed, dietary fiber source and feedstock for fermentations. Lemon waste is composed of flavedo, albedo, membranes and seeds. Among the by-products of lemon, the peel including flavedo and albedo, is particularly abundant and offers numerous components with techno-functionality and bioactivity. Biopolymers present in lemon peel can have techno-functionalities such as emulsification, gelling and foaming ability which are important in formation of different food structures (Magalhães et al., 2023). Other components like flavonoids, terpenes, vitamin C, and essential oil found in lemon peel and dietary fiber are known to enhance the positive health effects of this natural by-product, including antidiabetic, anti-inflammatory, anticancer, and antimicrobial properties (González-Molina et al., 2010; Figuerola et al., 2005). Valorization of lemon by-products has the potential to reduce waste, increase the efficiency of food production, and create revenue while supporting environmental sustainability. In this context, the lemon peel stands out as an unused resource of bioactive compounds with the potential to be transformed into valuable functional ingredients for various applications, including the food, pharmaceutical, and cosmetic industries. Therefore, this study aims to investigate valorization of lemon peel as a techno-functional and bioactive food additive.

Material and Method

Fresh lemons of Lamas cultivar were obtained from a local supplier. Peels were separated manually and then dried using an oven at a temperature of 50°C until constant weight. This temperature was chosen to avoid the degradation of sensitive bioactive compounds while efficiently removing moisture from the peels. After the drying process, the lemon peels were ground into a fine powder using a grinder. The powdered material was then sieved to obtain uniform particle size to obtain a natural additive. The proximate composition of lemon peel powder was determined. Moisture content was determined by infra-red moisture analyzer. Oil content was measured by Soxhelet extraction. Protein content was measured by Kjeldahl method. Ash content was detected by gravimetric methods. Total carbohydrate content was calculated by proximate analysis. Emulsifying capacity was measured by preparation of oil-in-water emulsion with and aqueous solution of lemon peel powder at a concentration of 1% and sunflower oil at a volume ratio of 3:1. Stability of the emulsion was determined by heat treatment. Foaming capacity was measured by whipping the aqueous solution of lemon peel powder. Oil binding and water binding capacity were measured by using one g of powder (Garau et al., 2007; Ghanem RomDhane et al., 2015). Antioxidant activity of lemon peel was determined by CUPRAC and DPPH antioxidant activity assays (Apak et al., 2005). Antidiabetic activity of lemon peel powder was measured by in vitro α-amylase and α-glucosidase inhibition assays (Esfandi et al., 2021).

Findings

Lemon peel powder from Lamas cultivar was found to contain 76% total carbohydrate, 8.0% protein 3.8% oil, 2.9% ash, and 9.3% moisture. Water binding capacity of lemon peel powder was measured as 4.99 g/g powder. Oil binding capacity of lemon peel powder was determined to be 4.29 g/g powder. In addition, lemon peel powder exhibited 100% emulsifying capacity and 68.8% emulsion stability in oil-in-water emulsion. The foaming capacity and foam stability were found to be 25% and 50%, respectively. Lemon peel powder showed antioxidant activity of 6.93 mg TE/g dry weight in the DPPH assay and 12.22 mg TE/g dry weight in the CUPRAC assay. In in vitro antidiabetic activity. assays, lemon peel powder was found to inhibit the activity of α-amylase and α-glucosidase enzymes at a level of 4% and 100%, respectively.

Conclusion

The compositional analysis showed that the lemon peel powder contained mostly carbohydrates which includes high amounts of polysaccharides along with some protein. These components can be responsible for the measured techno-functional properties of lemon peel powder. The antioxidant and antidiabetic properties of lemon peel powder are possibly due to these polymeric compounds, phenolic compounds and essential oil. Antioxidant activity is important in prevention of free radical-induced oxidative stress while antidiabetic activity can be beneficial in diet-induced glucose metabolism disorders. The obtained data also suggests that lemon peel powder can be evaluated as a tecno-functional additive to improve emulsifying properties in food systems. In addition, lemon peel powder can be utilized as a water or oil binding agent in food structures. On the other hand, foaming ability is not at a significant level for use solely as an additive in practice. However, it can contribute positively to other foaming agents in food systems.

Lemon peel from a local cultivar was used for development of a food additive with techno-functionality and bioactivity. The findings of this study will provide valuable insights into upcycling of lemon peel, ultimately highlighting its potential as a sustainable and functional food additive. This could not only contribute to reducing food waste but also offer a healthier, more natural alternative to synthetic additives in the food sector, aligning with current trends towards clean-label and health-improving ingredients. Future studies can examine other possible techno-functional and bioactive properties of lemon peel powder. In addition, improvement of techno-functional and bioactive properties of lemon peel powder by different novel techniques can be investigated. Moreover, the developed additive can be applied in formulations of various food products to demonstrate its effectiveness. Bioactivity of the lemon peel powder can also be evaluated in in vivo systems to determine its effectiveness in human body.

References

Apak, R., Güçlü, K., Ozyürek, M., Karademir, S. E., & Altun, M. (2005). Total antioxidant capacity assay of human serum using copper(II)-neocuproine as chromogenic oxidant: The CUPRAC method. *Free Radical Research, 39*(9), 949–961. https://doi.org/10.1080/10715760500201249

Esfandi, R., Seidu, I., Willmore, W., & Tsopmo, A. (2021). Antioxidant, pancreatic lipase, and α-amylase inhibitory properties of oat bran hydrolyzed proteins and peptides. *Journal of Food Biochemistry, 45*(8), e13762. https://doi.org/10.1111/jfbc.13762

Figuerola, F., Hurtado, M. L., Estévez, A. M., Chiffelle, I., & Asenjo, F. (2005). Fibre concentrates from apple pomace and citrus peel as potential fibre sources for food enrichment. *Food Chemistry, 91*(3), 395–401. https://doi.org/10.1016/j.foodchem.2004.06.049

González-Molina, E., Domínguez-Perles, R., Moreno, D. A., & García-Viguera, C. (2010). Natural bioactive compounds of *Citrus limon* for food and health. *Journal of Pharmaceutical and Biomedical Analysis, 51*(2), 327–345. https://doi.org/10.1016/j.jpba.2009.10.020

Garau, M. C., Simal, S., Rosselló, C., & Femenia, A. (2007). Effect of air-drying temperature on physico-chemical properties of dietary fibre and antioxidant capacity of orange (*Citrus aurantium* v. Canoneta) by-products. *Food Chemistry, 104*(3), 1014–1024. https://doi.org/10.1016/j.foodchem.2007.01.002

Ghanem RomDhane, N., Bonazzi, C., Kechaou, N., & Mihoubi, N. B. (2015). Effect of air-drying temperature on kinetics of quality attributes of lemon (*Citrus limon* cv. lunari) peels. *Drying Technology, 33*(13), 1581–1589. https://doi.org/10.1080/07373937.2015.1036287

Magalhães, D., Vilas-Boas, A. A., Teixeira, P., & Pintado, M. (2023). Functional ingredients and additives from lemon by-products and their applications in food preservation: A review. *Foods, 12*(5), 1095. https://doi.org/10.3390/foods12051095

From Waste to Packaging: Biodegradable Films from Artichoke Products Phenolics via Subcritical Water Extraction

İlayda Hızır Kadı[a], Beraat Özcelik[a]

[a]Istanbul Technical University, Food Engineering Department, Food Engineering Program, Türkiye
hizir17@itu.edu.tr

Keywords: Artichoke Waste, Biodegradable, Food Packaging, Sustainability.

Aim

The aim of this study, focusing was to the production of PVA-based films by solvent casting, with the incorporation of natural antioxidant artichoke waste extract phenolics to obtain biodegradable food packaging. The study successfully produced films comprising PVA and artichoke extracts, blended at varying ratios (1%, 2%, 3%), and characterized them. The findings indicated that the incorporation of extracts into PVA films has considerably improved the optical properties (colour-UV light blocking), thickness, and water vapor permeability of the prepared films. The elongation at the break of PVA-extract films was enhanced with rising extract concentration, which resulted in a decline of tensile strength. The composite films exhibited enhanced overall characteristics with increasing artichoke extract concentrations, primarily attributable to the presence of polyphenolic compounds. Similarly, the antibacterial activity of films including artichoke extracts was found to be superior to that of neat PVA and stretch film. It is proposed that a 3% artichoke waste extract concentration may be optimal.

Material and Method

Extraction of Artichoke Waste

Artichoke waste was subjected to subcritical water extraction at 200°C and 10 bar to separate the liquid and solid fractions. The liquid extract, which contained phenolic compounds with strong antioxidant and antimicrobial properties, was incorporated into the PVA film matrix to improve its functional properties (Kasapoglu et al., 2022).

Figure 1. The appearance of Artichoke Waste.

Film Preparation and Characterization

The solution casting method was employed to fabricate the biodegradable composite film, using PVA as the polymer matrix. To prepare the PVA solution, 5% PVA was heated in distilled water at 70°C for 1 hour. Subsequently, 1 ml of carboxymethyl cellulose (1%), 350 uL of glycerol as a plasticizer, and 850 uL of citric acid as a crosslinker (1%) were mixed into the warm PVA solution (Arun et al., 2022). Different concentrations were prepared for the PVA-AE composite films (1, 2, and 3% w/v PVA) Three replicates were prepared for each

concentration. Samples were coded with, control (neat PVA film), AE-I (1%), AE-II (2%), and AE-III (3%) (Fig 2). These mixtures were then poured onto a clean, smooth glass plate and left to dry overnight at room temperature. The prepared films were characterized in terms of mechanical strength (tensile strength, elongation at break), and optical properties (transparency, color). The optical properties of the films were analyzed using a UV-Vis spectrophotometer to determine light transmittance and opacity, which play a crucial role in food preservation by limiting exposure to harmful UV radiation (Rhim et al., 2009; Passareti et al., 2019).

The antioxidant activity of the artichoke extract was determined using TPC and CUPRAC assays to assess their potential to inhibit the oxidation processes (Table 1) Furthermore, the antimicrobial efficacy of the films was assessed against common foodborne pathogens, including *Escherichia coli* and *Staphylococcus aureus*, utilizing both agar diffusion and plate count methods. Additionally, the water vapor permeability (WVP) and moisture content of the films were evaluated, as these factors influence the ability of the packaging to maintain food quality by controlling moisture exchange (Suganthi et al., 2020).

Table 1. Total phenolic content (TPC) and total antioxidant activity (TAA) of AE.

Sample	TPC (mg GAE/g sample) FOLIN-CIOCALTEU	TAA (mg TE/ g sample) CUPRAC
Artichoke waste extract	30.02 ± 1.42^{a}	20.44 ± 1.42^{b}

*AE: Artichoke waste extract, GAE: Gallic acid equivalent, TE: Trolox equivalent, values are expressed as mean ± standard deviation
Different letters in the same column indicate significant differences in mean ($p<0.05$).

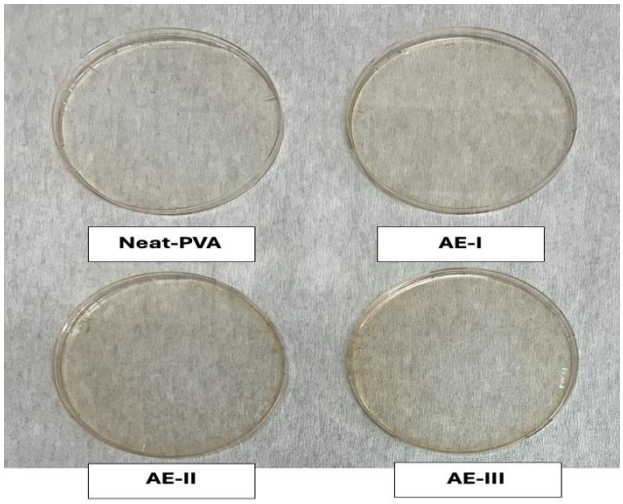

Figure 2. The physical appearance of prepared PVA-based film.

Applications of the Films on Fresh Cut Apple in storage life

An examination of the packaging properties of the prepared PVA films was conducted using fresh-cut apples. The samples were randomly divided into equal groups and sealed with prepared films. The storage containers were sealed with the prepared film samples (AE-I, AE-II, AE-III, neat PVA, and conventional stretch film. All samples were stored in the refrigerator.

Quality parameters of the stored fresh-cut apple were recorded after 0 and 7 days of storage. Following the designated period, the alterations (color, juiciness, appearance, and weight loss) in the quality of the samples were noted. The decay progression in fruits was monitored, documented, and photographed using a digital camera (Nkede et al., 2023).

Findings

The study successfully produced films comprising PVA and artichoke extracts phenolics blended at varying ratios (1%, 2%, 3%), and characterized them. The findings indicated that the incorporation of extracts into PVA films has considerably improved the optical properties (colour-UV light blocking), thickness, and water vapor permeability of the prepared films (Table 2&3). The elongation at the break of PVA-extract films was enhanced (24.87 %) with rising extract concentration, which resulted in a decline of tensile strength (8.02 mPa). (Fig 3). The composite films exhibited enhanced overall characteristics with increasing artichoke extract concentrations, primarily attributable to the presence of polyphenolic compounds. Similarly, the antibacterial activity of films including artichoke extracts was found to be superior to that of neat PVA and stretch film. It is proposed that a 3% artichoke waste extract concentration may be optimal (Fig 4).

Furthermore, the packaging films demonstrated effective preservation effects, slowing color changes, and minimizing weight loss during storage. The film with the highest extract (AE-III) ratio was found to offer optimal protection, resulting in a weight reduction of 4.3 % (Fig 5). The quality of this film is similar to that of a stretch film (4.4%). The water vapor permeability analysis suggested that the films maintained an optimal moisture barrier, which is essential for prolonging the freshness of perishable food (Fig 6).

Additionally, food storage trials revealed that packaged food items retained better color and texture compared to those stored in conventional plastic packaging or without any covering.

Table 2. Results of color, thickness, and WVP measurements of biodegradable films.

Sample Name	L*	a*	b*	ΔE	Thickness (mm)	WVP (g.mm/m^2.h.kPa)
Neat PVA	85.05	0.98	-1.39	10	0.060	$11.3*10^{-2}$
AE-I	65.50	0.32	1.78	12	0.082	$9.82*10^{-2}$
AE-II	74.22	0.35	1.28	13	0.087	$9.34*10^{-2}$
AE-III	75.28	0.38	1.007	14	0.095	$10.2*10^{-2}$

AE: Artichoke waste extract, L* (measurable in terms of white to black intensity), a* (measurable in terms of red and green intensity), and b* (measurable in terms of yellow and blue intensity) of the Hunter system, WVP: Water vapor permission

Table 3. UV absorbance spectrum of all films.

Light transmittance (%) at different wavelengths (nm)						
Sample name	**200**	**300**	**400**	**500**	**600**	**700**
Neat PVA	87.5	92	96.4	98.2	99.5	100.4
AE-I	62.3	65	70	73.5	79	81
AE-II	23	25.4	31.9	35	38	40
AE-III	21	23	28.5	31.6	34.3	38.2

AE: Artichoke waste extract

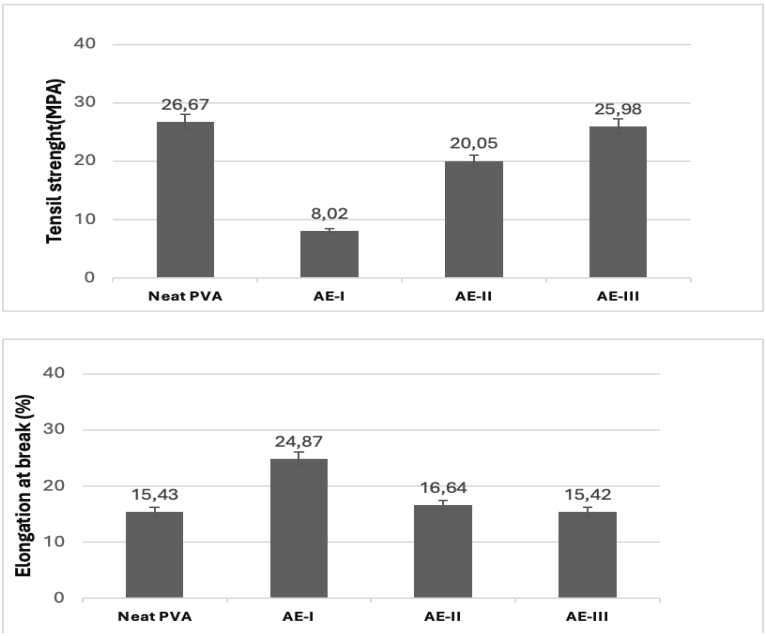

Figure 3. Tensile strength and elongation at break of neat PVA and composite films.

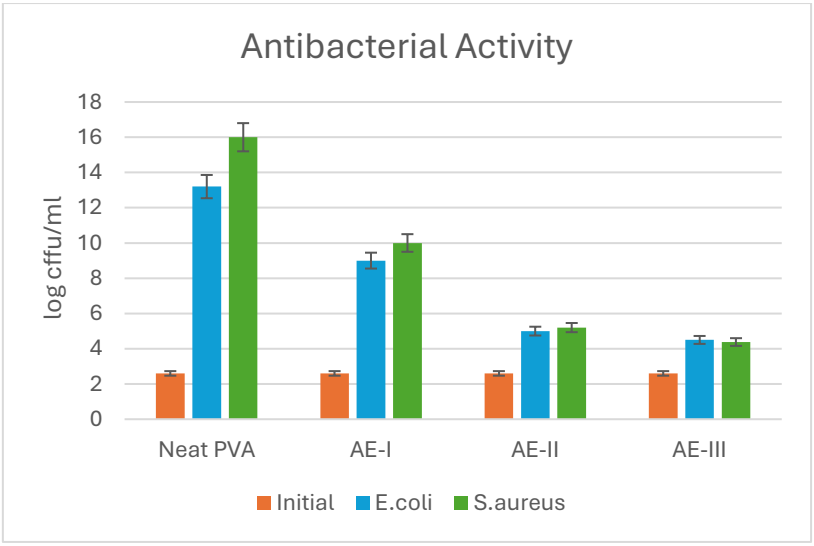

Figure 4. Antibacterial activity of films.

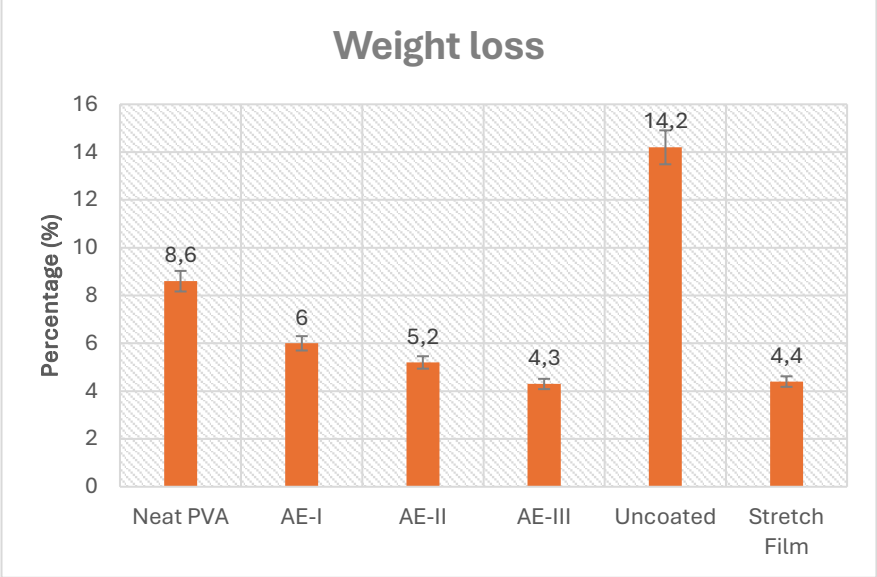

Figure 5. Weight loss of films after 1 week of storage in refrigerator.

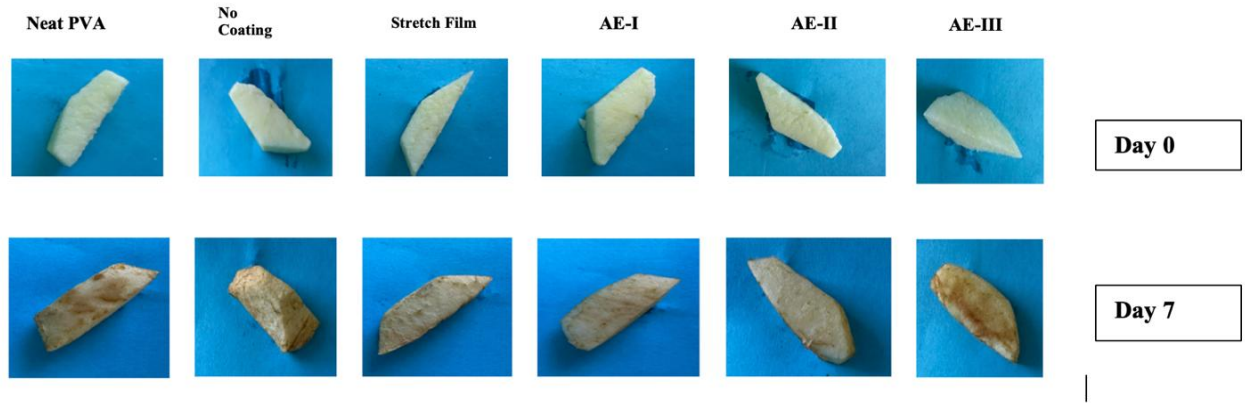

Figure 6. The shelf-life studies with fresh cut apples before and after 7 days of storage in the refrigerator.

Conclusion

This study successfully demonstrates the potential of artichoke waste-derived phenolic compounds as a sustainable bioactive additive for biodegradable food packaging. The developed films exhibit promising mechanical, antioxidant, and antimicrobial properties, making them suitable for extending the shelf life of fresh produce. Given their enhanced structural and functional properties, these films could serve as viable alternatives to synthetic food packaging materials, contributing to reducing plastic waste and promoting a circular economy. Future work will focus on the optimization of film formulations to enhance their functional properties, the scaling up of production for commercial applications, and extensive shelf-life studies to evaluate long-term performance.

References

Arun, R., Shruthy, R., Preetha, R., & Sreejit, V. (2022). Biodegradable nanocomposite reinforced with cellulose nanofiber from coconut industry waste for replacing synthetic plastic food packaging. *Chemosphere*, *291*, 132786.
Galanakis, C. M. (2012). Recovery of high added-value components from food wastes: Conventional, emerging technologies and commercialized applications. *Trends in Food Science & Technology*, *26*(2), 68-87.
Kanmaz, N., Uzer, A., Hizal, J., & Apak, R. (2020). Determination of total antioxidant capacity of Cynara Scolymus L.(globe artichoke) by using novel nanoparticle-based ferricyanide/Prussian blue assay. *Talanta*, *216*, 120960.

Kasapoğlu, K. N., Demircan, E., Gültekin-Özgüven, M., Kruger, J., Frank, J., Arslaner, A., & Özçelik, B. (2022). Recovery of polyphenols using pressurized hot water extraction (PHWE) from black rosehip followed by encapsulation for increased bioaccessibility and antioxidant activity. Molecules, 27(20), 6807

Khanifah, S., Legowo, A. D. K., Sholihun, S., & Nugraheni, A. D. (2023). Physical properties of polyvinyl alcohol/chitosan films with the addition of anthocyanin extract from butterfly pea for food packaging applications. *Indonesian Journal of Chemistry*, *23*(4), 1021-1031

Nkede, F. N., Wardana, A. A., Phuong, N. T. H., Takahashi, M., Koga, A., Wardak, M. H., ... & Tanaka, F. (2023). Preparation and characterization of chitosan/lemongrass oil/cellulose nanofiber Pickering emulsions active packaging and its application on tomato preservation. Journal of Polymers and the Environment, 31(11), 4930-4945.

Passaretti, M. G., Ninago, M. D., Villar, M. A., & López, O. V. (2019). Protective packaging for light-sensitive foods. In *Food Packaging* (pp. 1-31). CRC Press.

Rhim, J. W., Hong, S. I., & Ha, C. S. (2009). Tensile, water vapor barrier, and antimicrobial properties of PLA/nanoclay composite films. *LWT-Food Science and Technology*, *42*(2), 612-617.

Suganthi, S., Vignesh, S., Kalyana Sundar, J., 2020. Fabrication of PVA polymer films with improved antibacterial activity by fine-tuning via organic acids for food packaging applications. Appl Water Sci 10, 100. https://doi.org/10.1007/s13201- 020-1162-y.

GEOMATICS ENGINEERING

Geodesy

Geographic Information Systems

Natural Hazards

Photogrammetry

Remote Sensing

Earthquake Risk Analysis of Water Transmission Lines in Istanbul

Emir Ekrem Barutcu[a], Himmet Karaman[a]

[a] Istanbul Technical University, Department of Geomatics Engineering, Geomatics Engineering, Türkiye
barutcue17@itu.edu.tr

Keywords : Earthquake Hazard, GIS, Istanbul, Seismic Risk, Water Transmission Lines.

Aim

Water has been a decisive factor in the development of civilizations throughout history, encouraging agriculture, enabling the establishment of cities, and contributing to the shaping of trade routes. In particular, Middle Eastern civilizations developed on the shores of major water sources such as the Euphrates, Tigris, Nile, and Yellow River, discovering and developing water management systems over time. In terms of water resources, Istanbul also has historical significance; advanced infrastructure including arches, cisterns, and dykes was developed to satisfy water needs during the Roman, Byzantine, and Ottoman periods (Yoon et al., 2018). But given population growth, climate change, and rising water consumption today, the city's water security has become a progressively important concern. Furthermore, Istanbul's geological composition poses a significant risk. Historically, the city, which sits on the North Anatolian Fault Line and is highly prone to earthquakes, has suffered terrible shocks. The city's dense population, historical buildings, and old earthquake-unresistant building stock, combined with unplanned urbanization, aggravate the effects of a possible major earthquake. In this context, developing a sustainable and resilient urban model in terms of both water management and earthquake risk stands out as a vital necessity for the future of Istanbul (Istanbul Metropolitan Municipality, 2009).

The February 6, 2023, earthquake Turkey experienced revealed the shortcomings in disaster management and had terrible multi-dimensional effects. The effects of the disaster were worsened by elements including buildings not constructed in line with earthquake rules, defective interventions in the load-bearing systems of buildings, and insufficient emergency plans. In this regard, the state of transmission lines, a key component of infrastructure, also catches great interest for study. The Maraş earthquake seriously damaged the transmission lines, which were not built to withstand quakes or were not sufficiently reinforced, so disrupting water supply in the area for days. Moreover, the absence of efficient data backup systems for these units made emergency response challenging, and only one- to two-year-old backups could be applied (Alemdar, 2025).

Similar issues were noted during the Gölcük Earthquake on August 17, 1999, when widespread water shortages, particularly during the hottest time of the summer, were caused by damage to the water transmission systems in the affected areas (Istanbul Metropolitan Municipality Department of Earthquake and Soil Survey, 2002). These disturbances in the densely populated Marmara Region highlighted the urgency of efforts to improve the disaster resilience of these systems and exposed the susceptibility of vital infrastructure to earthquakes.

Therefore, the earthquake resilience of the transmission lines that supply water to about 16 million people in Istanbul is a major concern in the event of a major earthquake. To make Istanbul disaster-resistant, a seismic resilience analysis of the city's water management infrastructure is essential. This study aims to assess the seismic risk of Istanbul's water transmission lines using Geographic Information Systems (GIS) based risk mapping and structural vulnerability analysis. The primary objectives include identifying high-risk areas, evaluating pipeline weaknesses.

Material and Method

The methodology of this study consists of several basic steps. Firstly, the data of the transmission lines in Istanbul was obtained from Istanbul Water and Sewerage Administration (ISKI) together with the parameters such as material and diameter to be used in the analysis and calculations. Earthquake risk map and geological and geophysical data to be used in earthquake risk scenarios were collected from relevant institutions such as the Disaster and Emergency Management Presidency (AFAD) and Istanbul Metropolitan Municipality (IBB).

Using the collected data, an earthquake risk map was first created with the help of ArcGIS Pro software. In order to create an earthquake risk map, each of the data obtained for use in earthquake risk calculations was added in separate layers. After this stage, since the data to be used in earthquake risk calculation will be used in raster format, the remaining vector data were converted to raster format. In order to make the earthquake risk data more understandable and to create a standard, the datasets contained in the added layers were arranged probabilistically, and a normalization process was applied to take values from 1 to 5 (1 being the lowest, 5 being the highest risk). These normalized data were combined using the weights, and a raster with a single risk value was obtained. This raster was colored according to the risk value, and what is actually called the Earthquake Risk Map was obtained for Istanbul.

The purpose of this earthquake risk map in our study is to classify the transmission lines according to earthquake risk by integrating with the transmission lines data obtained from ISKI. This process was done as follows. The earthquake risk data in raster format created with the data used for the earthquake risk calculation was overlaid with the data of the transmission lines that provide water transfer to Istanbul in vector format. As a result of this overlapping process, an earthquake risk value was assigned for each line in the transmission lines data. What is obtained as a result of the above procedure is actually the data of the transmission lines classified according to earthquake risk from 1 to 5 (1 is the lowest risk, 5 is the highest risk), and the earthquake risk is known for each line.

Using the data of transmission lines with earthquake risk values, possible earthquake scenarios in Istanbul were simulated with HAZTURK software (Istanbul Metropolitan Municipality Department of Earthquake and Soil Survey, 2019). In line with these scenarios, HAZTURK software estimated the potential damages that may occur in the transmission lines carrying water to all across the city (Karaman, 2008).

Findings

The results of earthquake risk analysis try to shed light on how vulnerable the water transmission lines in Istanbul indeed are to an earthquake. The GIS-based earthquake risk analysis implied that quite a considerable area of the water infrastructures of the city lay within the high-risk zone. The risk classification of the transmission lines was 1 to 5, with 5 being associated with the highest risk. This translates to the fact that the older and more fragile a pipe, the more vulnerable it is to destruction.

The earthquake risk map, generated with ArcGIS Pro software, identified the areas where transmission lines may be exposed to the highest seismic hazard. Overlaying this data with the network of transmission pipelines in Istanbul confirmed that critical water supply lines also pass-through areas with a high probability of strong ground motion and soil liquefaction.

By HAZTURK simulation, different magnitudes and locations of earthquakes gave the potential scenarios of damage. The simulation output was that the transmission lines which were aligned over the fault zones and structurally unstable geological formations had the greatest risk of collapsing. In the results, major earthquakes could bring a sharp decline in water supply, mostly in urban areas. From the results, it can also be said that the material quality of the pipeline is fundamental in its resilience since older and more brittle pipework has a higher risk of failure.

Conclusion

The results of the study underline how urgently Istanbul's water network's seismic resilience has to be strengthened. Given the city's sensitivity to major earthquakes, deliberate interventions must be carried out to minimize possible disruptions of the water supply.

Among the key suggestions is to give high-risk locations top priority for infrastructure strengthening. Replacing or retrofitting existing pipes with materials resistant to earthquakes will significantly lower the possibility of damage and consequent disturbances. Moreover, early identification of transmission line defects will benefit from the network's real-time monitoring systems' integration. Faster reaction and repair will follow from this.

This study also underlines the need of incorporating seismic elements in urban planning and infrastructure development and advises that future transmission line planning should avoid locations with high liquefaction risk and as much as feasible active fault zones. Furthermore, backup water supply systems should be part of emergency ready plans to guarantee ongoing access to pure water following an earthquake.

Eventually, constant risk assessment and mitigating strategy planning depend on cooperation among government agencies, local authorities, and research facilities. Istanbul can provide sustainable and consistent water access even in the face of significant seismic occurrences by means of data-driven strategies and innovative technologies, hence strengthening the resilience of its water system.

References

Alemdar, K. D. (2025). Seismic risk assessment of transportation networks for the impending Istanbul earthquake with GIS-based MCDM approach. *Natural Hazards*.

Istanbul Metropolitan Municipality Department of Earthquake and Soil Survey. (2002). The Study on a Disaster Prevention/Mitigation Basic Plan in Istanbul Including Seismic Microzonation in the Republic of Turkey.

Istanbul Metropolitan Municipality Department of Earthquake and Soil Survey. (2019). Istanbul Province Probable Earthquake Loss Estimation Update Project.

Istanbul Metropolitan Municipality. (2009). Istanbul Potential Earthquake Loss Estimates October 2009.

Karaman, H. (2008). Sonuç bazlı risk yönetimi ve deprem kayıp tahmini analizi [Consequence-based risk management and earthquake loss estimation analysis]. PhD thesis, Istanbul Technical University.

Yoon, S., Lee, Y.-J., & Jung, H.-J. (2018). A comprehensive framework for seismic risk assessment of urban water transmission networks. International Journal of Disaster Risk Reduction, 31, 983-994.

Spatial Estimation of Potential Utilization Performance of Electric Vehicle Charging Stations in Türkiye Using Machine Learning

Serkan Tanrıverdi[a], Adalet Dervişoğlu[b]

[a] Istanbul Technical University, Graduate School, Geomatics Engineering Program, Türkiye
[b] Istanbul Technical University, Faculty of Civil Engineering, Department of Geomatics, Türkiye
tanriverdise@itu.edu.tr

Keywords : Electric Vehicles, Charging Stations, Machine Learning, Spatial Analysis, Regression Models.

Aim

Electric vehicles (EVs) are increasingly recognized as key solutions to environmental challenges and energy security concerns, occupying a central position in sustainable transportation policies (International Energy Agency [IEA], 2023; Zaino et al., 2024). Effective adoption of EVs necessitates strategically planned and adequately developed charging station infrastructure (T.C. Enerji ve Tabii Kaynaklar Bakanlığı [ETKB], 2023; T.C. Ulaştırma ve Altyapı Bakanlığı [UAB], 2023). Proper and efficient infrastructure facilitates hassle-free charging experiences, significantly enhancing the adoption rate of electric vehicles (Acar & Taşkın, 2024; Salari, 2022). Motivated by this necessity, this study employed extensive datasets derived from various socioeconomic factors and regions across Türkiye. The primary objective of this research is to estimate the future usage performance of potential EV charging station locations nationwide based on charging station usage data and various socioeconomic indicators obtained from selected regions of Türkiye (Kazempour et al., 2025; Soczówka et al., 2024).

Material and Method

The study utilized, datasets from the Turkish Statistical Institute (TÜİK), education statistics, EV charging station data, administrative boundaries of Türkiye, OpenStreetMap (OSM) road network data, Sentinel-2 satellite imagery, and shopping center locations.

Data from TÜİK were meticulously analyzed to understand household consumption expenditure, income distribution, and demographic structure. These datasets are critical for uncovering the economic and social disparities across countries. The regional distribution of household consumption expenditures and expenditure behaviors across different income levels has allowed a deeper understanding of regions with concentrated economic activities and consumer profiles. Income distribution analyses have provided valuable insights into the development of regional development policies and the mitigation of economic inequalities. Moreover, detailed demographic data, including population density, age group, and gender distribution, have facilitated more precise infrastructure planning, significantly improving public service efficiency.

Educational data have been extensively analyzed to assess education levels, graduation rates, and labor market participation of young populations. These analyses have clearly demonstrated the impact of educational attainment on labor market outcomes, providing the necessary insights to improve educational policies and address unemployment issues. Additionally, charging station data provided by Zorlu Energy Solutions (ZES), Türkiye's largest EV charging network provider, encompassing major cities such as Istanbul, Ankara, Izmir, Eskişehir, and Antalya, were integrated into the study. These cities were chosen because of their high economic activity and significant electric vehicle usage (Güray & Merdan, 2021). A detailed analysis of ZES data, including usage patterns, socket types, and user preferences, has provided valuable insights for future infrastructure planning (Jonas et al., 2023).

Another critical dataset used was OpenStreetMap (OSM). Comprehensive transportation infrastructure metrics were calculated for Türkiye at hexagonal levels 4, 5, 6, 7, and 8 using Python-based algorithms and the OSMNX library. These metrics include counts of motorways, trunk roads, primary, secondary, and tertiary roads, residential roads, service roads, unclassified roads, living streets, node counts, total roads, average graph level, streets per node average, intersection counts, total street lengths, street segment counts, and average street lengths. These

parameters critically influence the accessibility and usage of charging stations, serving as independent variables in the developed machine learning models, thus enabling robust and comprehensive infrastructure analyses (Cai et al., 2014; Shahraki et al., 2015).

Sentinel-2 satellite imagery, provided by the European Space Agency, constitutes a significant portion of the research and offers high-resolution and up-to-date remote sensing data. The 10-meter resolution facilitated clear differentiation between urban and rural areas, accurately determining settlement boundaries, densities, and spatial distributions. These detailed spatial data are essential for regional population estimations and prioritization of infrastructure investments. Additionally, the geographic locations of shopping centers provided critical insights into consumer mobility and regional economic activities, significantly influencing the selection of potential charging station locations (Soczówka et al., 2024).

In spatial analyses, administrative boundary data at the provincial, district, and neighborhood levels have enabled detailed regional evaluations, revealing the socioeconomic dynamics and enhancing the effectiveness of public policies. Furthermore, the H3 hexagonal indexing system, developed by Uber and internationally recognized, allows analyses at various spatial resolutions, providing coherent and precise insights into regional differences.

Machine learning techniques were chosen for data analysis, integrating multiple data sources into a unified spatial database to inform future strategic decisions regarding charging infrastructure investments. Additionally, data integration and modeling approaches used in this study aim to provide both scientific and practical contributions to addressing the challenges of transitioning to sustainable transportation.

All the datasets underwent extensive preprocessing and transformation processes suitable for machine learning. Missing data were corrected, inconsistencies were resolved, and data integrity was ensured. The datasets were integrated and aggregated at the neighborhood level, enhancing the consistency of the spatial database. This comprehensive database was analyzed primarily through regression analysis and various machine-learning methods. Regression analysis provides a powerful statistical approach to quantitatively evaluate the relationships between dependent variables (such as charging station usage, transmitted electricity in kW, and transaction counts) and independent variables (such as population density, income level, and infrastructure features).

Numerous linear and nonlinear regression models (e.g., random forest and gradient boosting) have been explored to achieve an optimal prediction performance. Model performance was assessed using statistical metrics, such as the Coefficient of Determination (R^2), Mean Absolute Error (MAE), and Mean Squared Error (MSE). The results indicated that some models achieved R^2 values above 0.6, demonstrating a satisfactory predictive capability. Detailed analyses of the MAE and MSE further enhanced the prediction accuracy by thoroughly evaluating the error magnitudes.

Findings

Research findings have underscored the significant relationships between socioeconomic indicators and EV charging station usage (Salari, 2022; Zaino et al., 2024). The charging infrastructure was found to be densely concentrated in major cities, displaying varying usage patterns across locations (Güray & Merdan, 2021; Jonas et al., 2023). Despite the geographical limitations of the analyzed data, general predictions applicable to Türkiye are possible. The findings provide a generalized model that is adaptable to regions with varying geographical and economic conditions.

This study highlights the vital importance of integrating spatial data, particularly transportation infrastructure and settlement data, for charging station planning (Erol, 2022; Karasu Asnaz & Özdemir, 2021). Variables such as shopping center locations have emerged as important indicators of potential charging station usage (Soczówka et al., 2024). Furthermore, population data enhanced by Sentinel-2 imagery significantly improved the accuracy of demographic and spatial analyses.

This study provides meaningful insights into the strategic planning of Türkiye's EV infrastructure, emphasizing the importance of socioeconomic and demographic indicators (Acar & Taşkın, 2024; Güray & Merdan, 2021). The high predictive performance achieved by machine learning-based regression models facilitates effective decision-

making for infrastructure investments (Hecht et al., 2021; Kazempour et al., 2025). High R^2 values further underscore the reliability and applicability of the model across different cities and regions.

In Figure 1, the hexagon-level map for western Türkiye reveals substantially higher predicted monthly kW consumption, with the darkest cells clustering around major urban and industrial centers—particularly the Marmara and Aegean regions—indicating strong demand for EV charging infrastructure. By contrast, Figure 2 shows eastern Türkiye's hexagons shaded in much lighter tones, reflecting lower population density, less developed EV networks, and correspondingly reduced predicted consumption. The clear east–west gradient in these visualizations underscores how socioeconomic and demographic factors drive regional variation in charging-station usage. Together, these maps highlight the necessity of tailoring infrastructure investments: prioritizing capacity expansions in the high-demand west while strategically developing charging networks in the understudied eastern provinces.

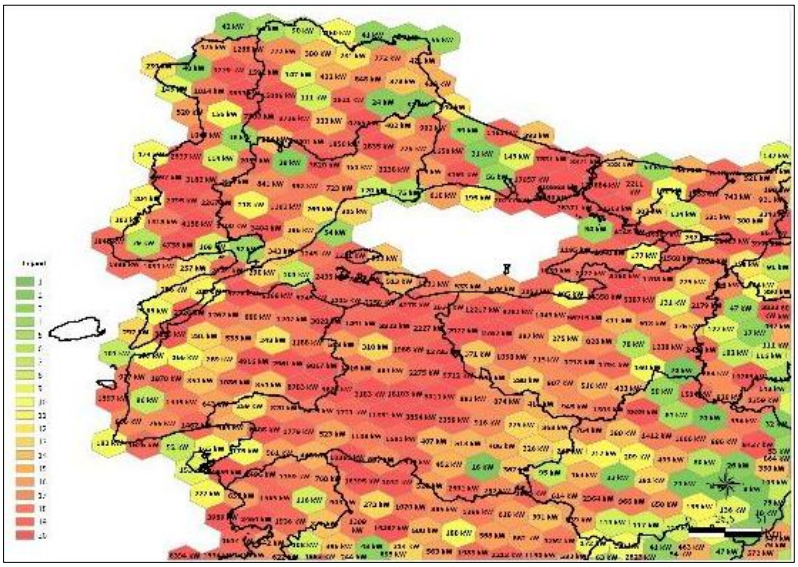

Figure 1. Western Regions of Türkiye.

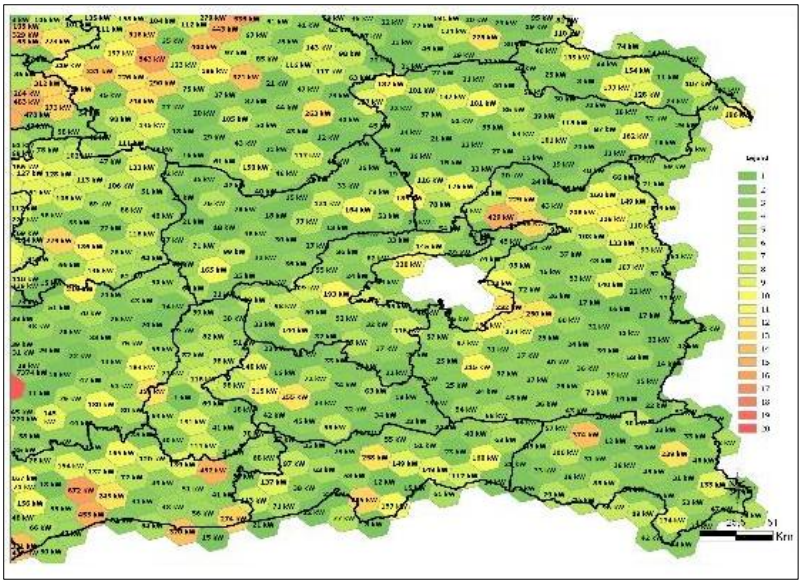

Figure 2. Eastern Regions of Türkiye.

Conclusion

Despite extensive analysis, this study has several limitations. First, charging station data are limited to certain major cities, which reduces generalizability across Türkiye. Second, the datasets focused solely on 2024, excluding temporal variations. Future studies should broaden the scope of geographic and temporal data to enhance model generalizability and predictive precision.

Future research may also investigate the impact of alternative energy policies and economic incentives on EV user behavior, enabling more effective public and private sector strategies (Salari, 2022; Zaino et al., 2024). This study offers significant academic contributions and practical recommendations for developing sustainable transportation policies (Banister, 2008).

In addition to the limitations noted, the present work undertook a systematic evaluation of multiple regression frameworks, combining several feature-selection strategies(Exhaustive Feature Selection, Sequantial Feature Selection) with parameterized cross-validation protocols (k = 2, 3, 5, and 10 folds) in order to identify the most robust modeling approach. By carefully tuning model complexity and validation parameters, the coefficient of determination (R^2) was established at approximately 0.60, demonstrating solid predictive accuracy without evidence of overfitting. Notably, demographic indicators collectively emerged as the most influential predictors of monthly kW consumption. Moreover, spatially disaggregated results uncovered a marked east–west divide: hexagon-level estimates of monthly energy use were consistently higher in western Türkiye, whereas eastern regions exhibited substantially lower consumption levels.

References

Soczówka, P., Lasota, M., Franke, P., & Żochowska, R. (2024). Method for determining new locations for electric vehicle charging stations using GIS tools. Energies, 17(18), 4546.

Kazempour, M., Sabboubeh, H., Moftakhari, K. P., Najafi, R., & Fusco, G. (2025). GIS-based geospatial analysis for identifying optimal locations of residential on-street electric vehicle charging points in Birmingham, UK. Sustainable Cities and Society, 120, 105988.

Karasu Asnaz, M. S., & Özdemir, B. (2021). Optimal placement of electric vehicle charging stations using multi-criteria decision-making methods. Akıllı Ulaşım Sistemleri ve Uygulamaları Dergisi, 4(2), 175–187.

Erol, Ü. N. (2022). GIS-based multi-criteria decision-making for EV charging station site selection (Master's thesis). Adana Alparslan Türkeş Science and Technology University.

Cai, H., Jia, X., Chiu, A. S. F., Hu, X., & Xu, M. (2014). Siting public electric vehicle charging stations in Beijing using big data informed travel patterns of the taxi fleet. Transportation Research Part D: Transport and Environment, 33, 39–49.

Shahraki, N., Cai, H., Turkay, M., & Xu, M. (2015). Optimal locations of electric public charging stations using real-world vehicle travel patterns. Transportation Research Part D: Transport and Environment, 41, 165–176.

Acar, O., & Taşkın, Ç. (2024). Türkiye'de elektrikli otomobillerin benimsenmesi sürecinin değerlendirilmesine yönelik nitel bir araştırma. Anadolu Üniversitesi İİBF Dergisi, 25(1), 205–241.

Salari, N. (2022). Electric vehicles adoption behavior: Synthesizing the technology readiness index with environmentalism values and instrumental attributes. Transportation Research Part A: Policy and Practice, 164, 60–81.

Jonas, T., Daniels, N., & Macht, G. (2023). Electric vehicle user behavior: An analysis of charging station utilization in Canada. Energies, 16(4), 1592.

Zaino, R., Ahmed, V., Alhammadi, A. M., Alghoush, M. (2024). Electric vehicle adoption: A comprehensive systematic review of technological, environmental, organizational, and policy impacts. World Electric Vehicle Journal, 15(8), 375.

International Energy Agency (IEA) (2023). Global EV Outlook 2023: Catching up with climate ambitions. Paris: IEA.

Güray, B. Ş., & Merdan, E. (2021). Türkiye Elektrikli Araçlar Görünümü 2021. Istanbul: Sabancı University, IICEC.

T.C. Enerji ve Tabii Kaynaklar Bakanlığı. (2023). Türkiye Ulusal Enerji Planı. Ankara: ETKB.

T.C. Ulaştırma ve Altyapı Bakanlığı. (2023). Elektrikli Araç Şarj İstasyonlarının Yer Seçiminin Belirlenmesi Projesi. Ankara: UAB.

Banister, D. (2008). The sustainable mobility paradigm. Transport Policy, 15(2), 73–80.

Hecht, C., Figgener, J., Sauer, D. U. (2021). Predicting electric vehicle charging station availability using ensemble machine learning. Energies, 14(23), 7834.

Geographic Information System-Based Accessibility Analysis of Disaster and Emergency Assembly Areas: The Case of Esenyurt District

Ezgi Şenol Tanrıverdi[a], Adalet Dervişoğlu[b]

[a] Istanbul Technical University, Graduate School, Geomatics Engineering Program, Türkiye
[b] Istanbul Technical University, Faculty of Civil Engineering, Department of Geomatics Engineering, Türkiye
senole21@itu.edu.tr

Keywords : Disaster Management, Disaster and Emergency Assembly Areas, Geographic Information Systems, Accessibility Analysis, Esenyurt District.

Aim

Disasters and emergencies occur unexpectedly, leading to substantial losses of life, property, and social structures. Historically, the severity of damage caused by such events has often been exacerbated by factors such as high population density, unplanned urbanization, structurally vulnerable buildings, and inadequate preventive measures (UNISDR, 2011; Aşıkoğlu, 2009). Additionally, ineffective implementation of disaster mitigation regulations and the lack of consistent monitoring of urban transformation processes have further increased these vulnerabilities (Aşıkoğlu, 2009).

In the aftermath of a disaster, it is crucial to designate safe assembly areas that are accessible to the public without disruption. Therefore, the accessibility of disaster and emergency assembly areas is a critical component of effective disaster management (Kırçın et al., 2017). Poorly planned assembly areas may cause confusion among both the public and emergency response teams, significantly delaying response operations and potentially escalating panic and chaos. Moreover, inadequate planning can lead to overcrowding at some assembly points, whereas others remain underutilized because of insufficient communication or poor location choices. This imbalance can reduce the overall effectiveness of emergency services, increase response times, and ultimately lead to greater risk. Furthermore, poorly accessible or distant assembly areas may discourage people from using them, causing them to seek unsafe alternatives and thus further complicating rescue efforts. To mitigate these risks, comprehensive analyses of assembly point accessibility—combined with clear communication strategies, regular drills, and community engagement—are integral components of disaster preparedness programs. By ensuring that assembly areas are strategically located, clearly marked, easily accessible via multiple safe routes, and effectively communicated to the public, communities can better manage disaster situations and minimize the potential loss of life and resources.

The selection criteria for disaster and emergency assembly areas include ground stability, accessibility, ease of evacuation, infrastructure availability, regional population density, and risk factors (Aman & Aytaç, 2022; Kırçın et al., 2017). In addition to ensuring a sufficient number of these areas, access time and route availability are equally vital considerations. Factors such as road capacity, potential road closures, and the availability of alternative routes significantly affect accessibility. The quality and adequacy of pedestrian infrastructure, including sidewalks and crosswalks, also play a crucial role. Thus, analyzing the accessibility of these assembly areas using Geographic Information Systems (GIS) contributes to the development of robust disaster management strategies, enhancing local preparedness and raising community awareness (Arca, 2012).

Istanbul is Turkey's most populous city, located near the North Anatolian Fault Line, which poses significant disaster risks, particularly from earthquakes. A major earthquake expected in the Marmara Sea region could cause catastrophic damage to Istanbul, potentially affecting millions of residents, disrupting vital infrastructure, and overwhelming emergency response systems (Parsons, 2004; Hürriyet Daily News, 2023). Following the devastating 1999 Gölcük earthquake, detailed investigations revealed that many structures across the city were insufficiently earthquake-resistant due to outdated construction practices, inadequate enforcement of building codes, and poor maintenance (Demirelli, 2001). Despite ongoing urban transformation efforts to reduce these vulnerabilities, the city's uncontrolled and rapid urbanization continues to pose severe challenges. High-density

development, informal (illegal) settlements, and structurally unsafe buildings all amplify existing earthquake risks, particularly in densely populated districts (Aşıkoğlu, 2009). Additionally, issues like heavy traffic congestion, thousands of narrow streets, inadequate road infrastructure capacity, and a lack of clearly defined evacuation routes exacerbate these problems. These logistical constraints hinder emergency service accessibility and reduce the speed and effectiveness of disaster-response operations (Hürriyet Daily News, 2023). Moreover, limited emergency response resources, inadequate training, and insufficient coordination among response agencies further complicate the effective management of disaster scenarios (Corbacioglu & Kapucu, 2006). To comprehensively address these issues, the city requires strengthened disaster preparedness initiatives, enhanced infrastructure resilience, expanded public awareness programs, and significant investments in emergency response capacity and planning.

Material and Method

GIS offers significant advantages in disaster management, including streamlined data sharing between institutions, the integration of diverse data formats, ease of regular updates, and rapid analytical capabilities. GIS also facilitates clear and effective communication of spatial data through visualizations such as maps, tables, and charts (Arca, 2012).

Within this research, the accessibility of disaster and emergency assembly areas in Esenyurt was analyzed using GIS techniques. Initially, the spatial and attribute data required for the analysis were collected, including road networks, existing buildings, population statistics, officially designated assembly areas (as identified by the Istanbul Metropolitan Municipality and AFAD), roads likely to be blocked during earthquakes, and high-risk disaster zones. These data were obtained from relevant institutions and integrated into the analysis.

Following data collection, ArcGIS (ArcMap) was used for data preparation, while ArcCatalog was utilized to organize data for analysis readiness. Detailed network topologies were established for the road network, and the entrance points to each assembly area were precisely identified using high-resolution satellite imagery. Additionally, building data were correlated with neighborhood population densities to incorporate demographic factors into the accessibility analysis. Data verification steps were implemented to ensure accuracy and reliability of all datasets.

Network analysis, a GIS-based analytical approach, examines the relationships and connections between points in a network. It is frequently used to determine the shortest or quickest routes, delineate service areas, locate nearest facilities, and perform logistical planning involving interconnected transportation networks. Network analysis is particularly beneficial in disaster management scenarios to establish emergency routes, facilitate access to critical locations, and identify alternative paths when primary roads are blocked.

Findings

For the Esenyurt District, we applied a suite of GIS-based network analyses to evaluate both spatial coverage and pedestrian accessibility of designated assembly areas. First, walking-distance catchments around each site were delineated and their service capacities quantified. We then executed closest-facility analyses from high-risk zones, deliberately excluding road segments predicted to be impassable during seismic events, in order to identify viable alternative evacuation routes.

These calculations revealed significant disparities in the distribution, capacity, and accessibility of existing assembly areas. In particular, several peripheral neighborhoods fall entirely outside any 250 m service buffer, while central zones exhibit overlapping coverage. Such insufficiencies threaten to impede orderly evacuation, risking delays, public confusion, and potentially greater loss of life and property.

Table 1 synthesizes these capacity imbalances by grouping all 40 neighborhoods into eight priority levels. Four "None" neighborhoods (0 % capacity) lack any permanent gathering points; six are "Very Insufficient" (> 0–10 %); eight each are "Insufficient" (> 10–50 %) and "Moderate" (> 50–100 %); six qualify as "Sufficient" (> 100–200 %); and a further eight exceed full demand by over 200 %. This tiered framework provides clear guidance on

interventions—from the urgent deployment of temporary units in "None" areas to routine maintenance and capacity-preservation measures in over-served sectors.

Table 1 and Figures 1–3 deliver a multidimensional portrait of Esenyurt's assembly-area landscape. They not only quantify capacity shortfalls but also trace the precise evacuation routes and service gaps that must be addressed. These empirical insights directly inform the intervention packages detailed in the Conclusion.

Table 1. Summary of Prioritization of Assembly Areas in Esenyurt Neighborhoods (Esenyurt Municipality Data, 2025).

Priority Level	Number of Neighborhoods	Capacity Range (%)	Recommended Interventions
1. None	4	0	Immediate establishment of temporary assembly units (schools, mosques, etc.)
2. Very Insufficient	6	>0–10	Implementation of modular, infrastructure-supported permanent assembly areas
3. Insufficient	8	>10–50	Expansion of existing areas; increase capacity
4. Moderate	8	>50–100	Regular maintenance, drills, and infrastructure improvements
5. Sufficient	6	>100–200	Focus on routine drills and maintenance programs
6. Excessive	4	>200–300	Implement capacity preservation and environmental regulation measures
7. Highly Excessive	1	>300–500	Provide additional support for extremely high usage potential
8. Extremely Excessive	6	>500	Subdivide space into smaller units to distribute demand

Figure 1 illustrates the spatial distribution of all existing assembly sites alongside their 250 m service radii. High-capacity clusters are concentrated in Esenyurt Merkez, Yeşilkent, and Talatpaşa, whereas Sultaniye, Güzelyurt, and other outlying neighborhoods lie almost entirely beyond these buffers.

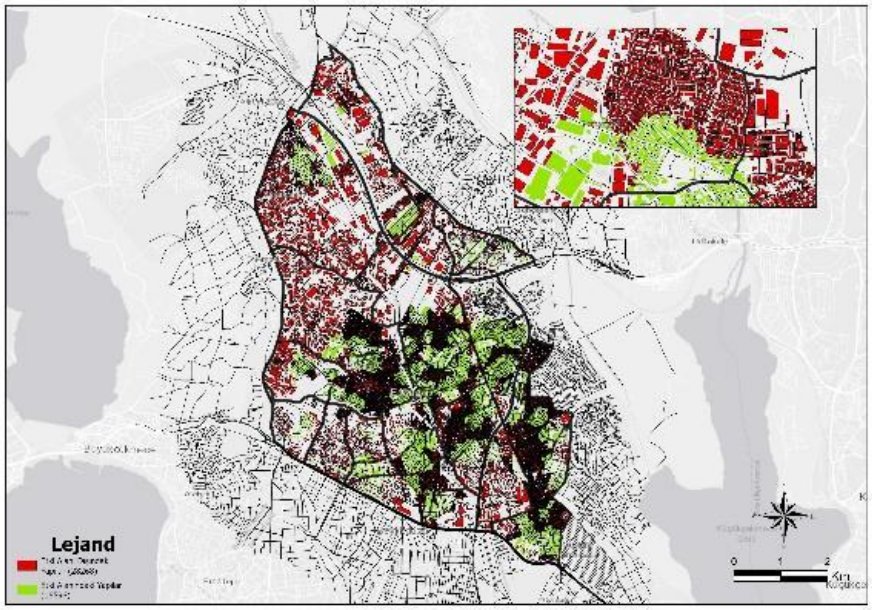

Figure 1. Distribution of Assembly and Service Areas in Esenyurt.

In Figure 2, the closest-facility routes depict the actual pedestrian pathways residents would use. Whereas corridors in Esenkent and Ardıçlı remain under 250 m (confirming their high-priority status), routes serving Soğanlı and Yayla exceed 500 m—well beyond recommended emergency planning standards.

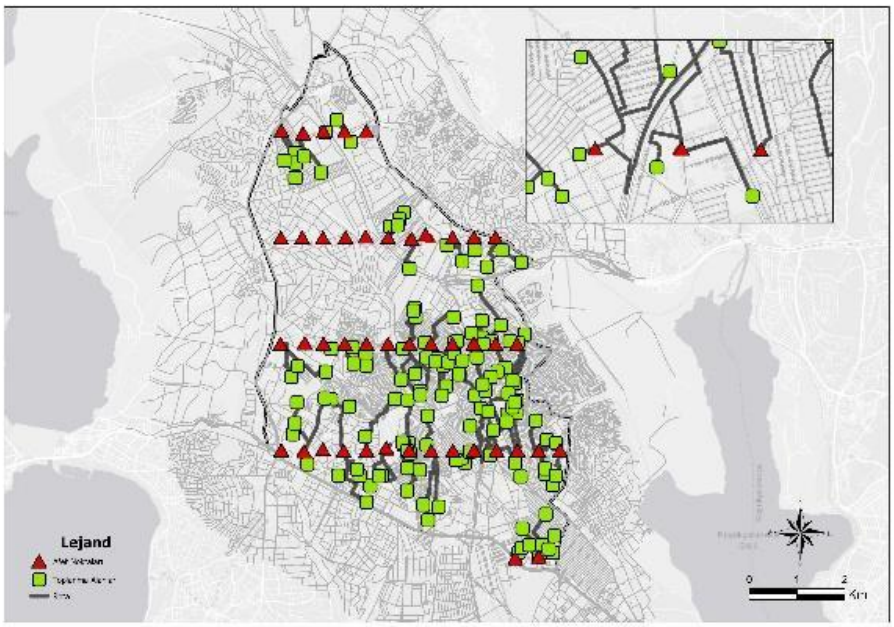

Figure 2. Closest Facility Analysis in Esenyurt.

Finally, Figure 3 overlays the service radii with a near-comparison buffer to highlight "dead zones" where neither proximity nor route quality meets minimal thresholds. These combined visualizations pinpoint exactly which corridors and intersections require new sidewalks, alternative paths, or interim gathering centers.

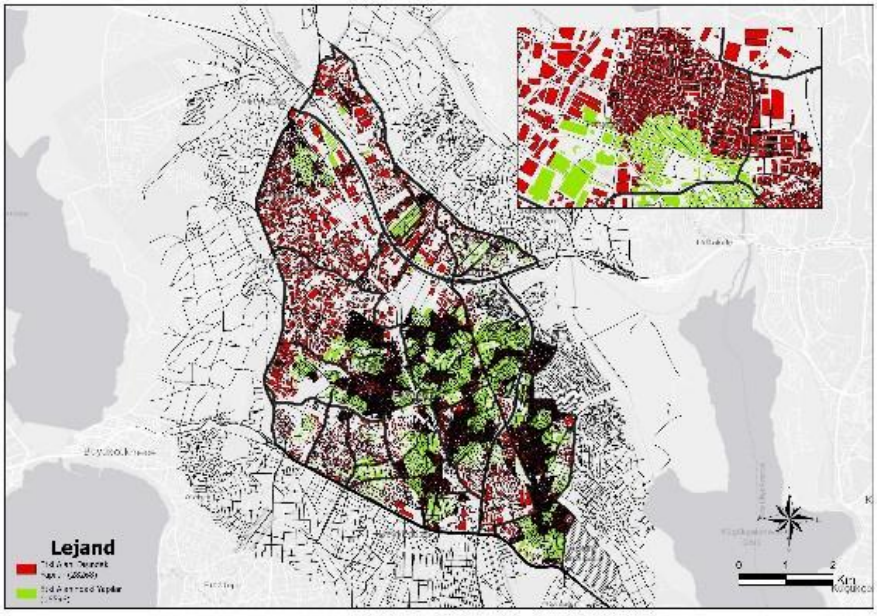

Figure 3. Closest Facility & Near Comparison in Esenyurt.

Conclusion

The study recommends increasing the number and capacity of assembly areas and establishing alternate evacuation routes in critical zones. Furthermore, key recommendations include enhancing public awareness through targeted educational campaigns and improving pedestrian infrastructure around assembly points. These measures are intended to help policymakers allocate resources more efficiently for disaster preparedness and to strengthen urban resilience. Ultimately, this work seeks to advance the scientific understanding of disaster management and urban planning in the Esenyurt District.

Our analyses reveal pronounced imbalances in both capacity and accessibility at the neighborhood level. Esenyurt Merkez, Yeşilkent, and Talatpaşa neighborhoods possess comparatively high person-capacity ratios, whereas Sultaniye and Güzelyurt exhibit critically low capacities that could render these areas severely underserved in the event of a major disaster. Examination of the 250 m service-radius building counts further underscores this spatial heterogeneity: Esenkent, Ardıçlı, and Pınar demonstrate high potential demand, while Soğanlı and Yayla fall well below average, confirming that physical accessibility issues are unevenly distributed across the district.

When classified by priority level, four neighborhoods with virtually no existing capacity ("None") require the immediate deployment of temporary assembly facilities. In the combined fourteen neighborhoods categorized as "Very Insufficient" and "Insufficient," the construction of modular, infrastructure-supported permanent assembly sites should be prioritized. In those ranked "Moderate" and "Sufficient," efforts should focus on expanding current areas and implementing regular maintenance and drill programs. Together, these targeted intervention packages will substantially elevate each neighborhood's preparedness for emergency scenarios.

Accordingly, Esenyurt Municipality and relevant agencies should adopt a dual strategy: first, prioritize both temporary and permanent solutions in the "None" and "Very Insufficient" neighborhoods; second, reinforce infrastructure, training, and drills in the "Insufficient," "Moderate," and "Sufficient" areas. Additionally, in neighborhoods with low building density within the 250 m service radius, investment in new pedestrian routes and improved sidewalks is essential. By aligning resource allocation with these prioritized actions, Esenyurt can achieve a more holistic and resilient urban framework against future disasters.

References

Aman, D. D., & Aytaç, G. (2022). *Multi-criteria decision making for city-scale infrastructure of post-earthquake assembly areas: Case study of Istanbul*. *International Journal of Disaster Risk Reduction, 81*, 103256.

Arca, D. (2012). *Geographic Information System and Remote Sensing in Disaster Management*. *Karaelmas Science and Engineering Journal, 2*(2), 53–61.

Aşıkoğlu Şahin, G. (2009). *Developing strategies for urban disaster risk mitigation* (Doctoral dissertation). Dokuz Eylül University, Institute of Science, İzmir.

Corbacioglu, S., & Kapucu, N. (2006). *Disaster management in Turkey: A need for a unified crisis management system*. *Disaster Prevention and Management, 15*(3), 451–460.

Demirelli, K. (2001). *Major earthquakes in Istanbul and a geotechnical examination of Istanbul* (Doctoral dissertation). Istanbul Technical University, Institute of Science, Istanbul.

Hürriyet Daily News. (2023, April 4). **Istanbul's narrow streets cause concern for emergency situations**. Retrieved from https://www.hurriyetdailynews.com/istanbuls-narrow-streets-cause-concern-for-emergency-situations-182081

Kırçın, P. N., Çabuk, S. N., Aksoy, K., & Çabuk, A. (2017). *A study on increasing the use of green spaces as post-disaster assembly areas in Turkey*. In *Proceedings of the 4th International Conference on Earthquake Engineering and Seismology*. Eskişehir, Turkey: Anadolu University.

Parsons, T. (2004). *Heightened odds of large earthquakes near Istanbul: An interaction-based probability calculation*. *Science, 306*(5695), 1088–1092.

United Nations International Strategy for Disaster Reduction (UNISDR). (2011, November 1). **Making cities resilient** [Magazine article]. World Meteorological Organization. Retrieved from https://public.wmo.int/en/resources/bulletin/making-cities-resilient

HISTORY OF SCIENCE AND TECHNOLOGY

History of Engineering

History of Mathematics

History of Physics

History of Sciences

The Impact of Gödel's Incompleteness Theorem on Artificial Intelligence: The Roger Penrose Approach

Fatma Nur Bilke[a]

[a]Istanbul Technical University, Faculty of Science and Letters, History of Science and Technology, Turkiye
bilke21@itu.edu.tr

Keywords: Artificial Intelligence, Gödel's Incompleteness Theorems, History of Science and Technology, Roger Penrose.

Aim

The primary objective of this study is to evaluate Kurt Gödel's Incompleteness Theorem not merely as a boundary-setting result in mathematics, but as a philosophical turning point that has shaped modern debates on knowledge, consciousness, and computability. In this context, the study aims to systematically analyze both the historical position of the theorem within the history of science and Roger Penrose's approach, which redefines the distinction between human cognition and artificial intelligence based on Gödel's insights. At the beginning of the 20th century, the formalist approach—shaped by Hilbert's program for absolute certainty and the logical positivism of the Vienna Circle—sought to reconstruct the language of mathematics and science through axiomatic systems. Within this intellectual climate, Gödel's publication of the Incompleteness Theorem in 1931 revealed the inherent limitations of such systems, creating not only a mathematical but also an epistemological and ontological rupture. Against this background, the study aims to revisit the question, "Is the human mind fully computable?", particularly in light of the debates on artificial intelligence that emerged in the postGödel era. This question gained significant depth through the arguments developed by Penrose within the framework of Gödel's theorem in his works The Emperor's New Mind (1989) and Shadows of the Mind (1994) (Penrose, 1989; Penrose, 1994). Penrose's assertion that conscious thought cannot be fully explained by algorithmic processes will be situated within the evolving conceptual frameworks of the history of science and technology. The human–machine distinction will thus be reopened for discussion within both historical and philosophical contexts. In doing so, this study aims not only to introduce a philosophical argument but also to reconsider the boundaries of modern knowledge on a historical plane.

Material and Method

This study is a qualitative research structured within a historical-conceptual framework. Its primary aim is to understand the rupture caused by Gödel's Incompleteness Theorem in the history of scientific thought and to reveal how this rupture has become an epistemological foundation in Roger Penrose's critique of artificial intelligence. Accordingly, the methodology adopted is based on textual analysis, historical contextualization, and conceptual comparison. The principal sources of this research include Gödel's Proof by Ernest Nagel and James R. Newman, which interprets Gödel's theorem from both mathematical and philosophical perspectives (Nagel & Newman, 2008); Penrose's own works—The Emperor's New Mind (1989) and Shadows of the Mind (1994)—which offer direct access to his ideas (Penrose, 1989; Penrose, 1994); and the Turkish translation Yapay Zekâya Karşı Doğal Zekâ (2023) (Penrose, 2023). These sources are treated as key references for understanding both the impact of Gödel's theory on the history of science and the debates on consciousness and computability that Penrose develops in its wake. The intellectual environment in which Gödel's theorem emerged is examined within the context of Hilbert's program for certainty and the logical positivist efforts of the Vienna Circle. The historical background of the belief in formal systems is clarified accordingly. Penrose's arguments are positioned not merely as technical critiques but as part of a broader historical discourse; through this lens, the study questions how the relationship between the human mind and

machines has been historically constructed. Within this framework, by employing literature-based analysis and historical reading methods, the study aims to contribute to the debates on computability in artificial intelligence from the perspective of the history of science and technology.

Findings

Kurt Gödel's Incompleteness Theorem, presented in 1931, opened up new avenues of discussion not only regarding the limits of mathematics but also concerning the nature of human reasoning. According to the theorem, any sufficiently powerful and consistent formal system will contain propositions that are both true and unprovable within that system (Nagel & Newman, 2008). Developed in the intellectual context of Hilbert's pursuit of absolute consistency and the formalist school, Gödel's theorem is not merely a technical delimitation—it represents a profound critique of the 20th-century ideal of the absoluteness of knowledge. In this regard, the theorem marks a pivotal moment in the history of science, challenging not only the scope of mathematical reasoning but also the nature of knowledge systems and the boundaries of the human mind. Building on this historical and theoretical context, Roger Penrose interpreted Gödel's theorem not solely as a mathematical discovery, but as a fundamental indication of how the human mind operates. According to Penrose, the human mind has an intuitive capacity to grasp truths that lie beyond formal systems (Penrose, 1989). This view evolves into a compelling argument that consciousness and the capacity for understanding cannot be fully explained through algorithmic structures. As Penrose asserts, machines may operate on symbols, but human beings generate meaning (Penrose, 1989). Penrose articulates this idea as follows: "If, as I believe, Gödel's argument does force us towards accepting view C, then we must also face up to the other consequences of this position. We shall find ourselves driven towards a Platonic viewpoint" (Penrose, 1989). The "view C" referenced here denotes the non-computational view, which maintains that the mind is not entirely a computable system. According to Penrose, conscious awareness and the ability to understand cannot be modeled by an algorithmic system akin to a Turing machine (Penrose, 1989; Penrose, 2023). In Shadows of the Mind, Penrose extends this argument to the physical domain by proposing that conscious experiences must be explained at the quantum level (Penrose, 1994). In his view, the laws of classical physics fall short of accounting for the phenomenon of consciousness: "I believe that certain quantum-level processes taking place in some microscopic structures of the brain play a role in the emergence of what we call consciousness" (Penrose, 1994). Penrose grounds this claim in the Orchestrated Objective Reduction (Orch-OR) theory, which he co-developed with Stuart Hameroff. According to this theory, conscious experiences can be explained through quantum processes. While the theory remains controversial within scientific circles, it is regarded as a distinctive example in the ongoing search for a physical explanation of consciousness (Penrose, 1994).

Conclusion

This study has examined, within a historical context, how the early 20th-century pursuit of grounding scientific knowledge gained momentum through the goal of achieving certainty via formal systems—and how Gödel's Incompleteness Theorem revealed the structural limitations of this ideal. The boundaries introduced by Gödel do not merely constitute a technical obstacle to the internal consistency of mathematical systems; they also serve as a profound critique of the representative epistemology that underlies modern science's conception of knowledge and the mind (Nagel & Newman, 2008). Following this epistemological rupture, Roger Penrose carried the notion of Gödelian limits into the domain of artificial intelligence, arguing that the human mind is too complex and profound to be reduced to a purely algorithmic framework (Penrose, 1989; Penrose, 1994). Penrose's approach characterizes the human mind through its capacity for meaning-making, intuitive understanding, and conscious experience—qualities that signify a qualitatively distinct cognitive domain inaccessible to machines. Thus, the link established between Gödel's theorem and the mind's capacity for meaning transcends the bounds of computation theory, evolving into a fundamental philosophical inquiry into the nature of mind. In the context of the history of science, this debate reflects not only the evolution of mathematical thought but also the paradigm shifts in modern science's approach to knowledge. The formalist ideal—embodied in Hilbert's program for certainty and aligned with positivist thought—was fundamentally disrupted by Gödel's theorem. With Penrose's intervention, this disruption was brought to the forefront of contemporary debates on consciousness, computability, and artificial intelligence. In conclusion, by bringing together the views of Gödel and Penrose within a framework

of historical continuity, this study has aimed to demonstrate that the concepts of knowledge, consciousness, and intelligence are shaped not only by technical or computable systems, but also by interpretation, meaning, and subjective experience. In this respect, the study reaffirms that the history of science is not merely a record of the past, but a dynamic framework for understanding today's intellectual crises.

References

Nagel, E., & Newman, J. R. (2008). Gödel's proof. New York University Press. (Not: Eserin orijinali 1958'dir; burada kullanılan baskı 2008 tarihli yeniden basımdır.)

Penrose, R. (1989). The emperor's new mind: Concerning computers, minds, and the laws of physics. Oxford University Press.

Penrose, R. (1994). Shadows of the mind: A search for the missing science of consciousness. Oxford University Press.

Penrose, R. (2023). Yapay zekâya karşı doğal zekâ (Çev. S. E. Yücel). Alfa Yayınları. (Orijinal eser: Shadows of the Mind, 1994).

INDUSTRIAL DESIGN

Historical, Cultural and Social Context of Design

Product Design

Theory and Methodology in Industrial Design

Manufacturability for Industrial Design: Mass Production and Design

Ecem Karabıyık Boyraz[a], Aysun Ateş Akdeniz[b]

[a] Istanbul Technical University, Graduate School, Industrial Design Program, Turkey
[b] Istanbul Technical University, Faculty of Architecture, Department of Industrial Design, Turkey
karabiyikec21@itu.edu.tr

Keywords: Industrial Design, Manufacturability, Mass Production, Design for Manufacturability.

Aim

Production is a multidisciplinary creation event. When mass production is considered, there are many subjects and objects that enable the realization of the object to be produced. These subjects can be defined as stakeholders. It is undeniable that the number and diversity of stakeholders will change depending on the type of product to be produced. These stakeholders are involved in many different stages of a product's development processes. The industrial designer is also one of the important stakeholders of a created product (Pedgley, 2009; Todić at al., 2012). This study aims to explore what the concept of manufacturability means to industrial designers by focusing on the stage of industrial design for mass production. he approaches of industrial designers who work or have worked professionally to the concept of manufacturability in the electrical appliances sector are investigated in this research.

Material and Method

The study began with a literature review and progressed by examining the framework of the concept of manufacturability in depth. In continuation of the research, interviews were conducted with industrial designers who previously worked or are still working in the electrical appliances sector. It is important that designers have different years of experience within the scope of the same sector and in different companies.
It aims to deeply understand how designers create a bridge between mass production, design and their experiences with the concept of manufacturability. In addition, after the interviews are completed, survey questions will be created, and a survey will be conducted and analyzed to reach more designers and support the outputs. The interview questions begin with the designers' professional background in the sector and include questions aimed at exploring their practices and experiences in their professional lives within the scope of the concept of manufacturability.

Findings

"Manufacturability" or "producibility," is described as the ease to realize an effective product with the lowest cost through the implementation of manufacturing technology. Nevertheless, the manufacturability of a design could not be measured quantitatively until the 1970s (Boothroyd et al., 2010; Lianos, 2020). Cong and Zhang defined the manufacturability of a product as a relative term, including whether the product meets the design requirements or not, in terms of concepts such as function, performance, cost, and quality (Cong & Zhang, 2012). According to Fabricius, manufacturability focuses on these three strategies: modular design, standardization and ease of assembly (Fabricius, 1994). On the other hand, Korol and Petrosyan accepted manufacturability as a combination of features that provide the highest performance with the least energy, materials and tools, using advanced technology and at the lowest cost (Korol & Petrosyan, 2020). It has been stated that manufacturability is not the accuracy but the degree of being able to be produced correctly. This degree may vary according to each variable (Todić et al., 2012).
In the literature the term manufacturability combines with many different terms to create new conceptual phenomena. One of the most common phenomena is design for manufacturability (DFM) which is a design philosophy that advocates the use of production inputs in the early stages of design so that the designed product can be produced more easily and more economically (Poli et al., 1992). Das et al. defined DFM as a "product

design approach" that can enable the design to be produced in a short time and at low cost, and the distribution of the product with low energy (Das et al., 2000).

Historically, designers have followed the mindset of "we create the design, and you handle the manufacturing.". This approach, referred to as the "over-the-wall approach" involves designers working independently and passing their designs along to manufacturing engineers, who must then address production challenges due to their lack of involvement in the design process. A solution to this issue is to involve manufacturing engineers early in the design phase and this involvement promotes teamwork, preventing numerous complications (Boothroyd, 1992). In the past, traditional production activities caused loss of energy and time as the design and production stages were carried out at different stages. Today the design and production phases were intertwined and started to be carried out together. This strategy resulted in an increase in the efficiency of the designed products, a decrease in the costs and a shortening of the time to market (Boothroyd et al., 2010).

The costs of the product design and manufacturing processes constitute a small portion of the total product price. However, the decisions made during these processes significantly affect the total costs of new product development and are crucial for market success. Therefore, it is necessary to consider the manufacturing task as early as possible, even in the product design phase, because the costs of changes are higher if they are implemented at a later stage of the product (Todić at al., 2012). Unfortunately, designers often lack the in-depth manufacturing experience necessary to determine the impact of various design features on manufacturing difficulty and cost. Therefore, collaboration between designers and manufacturers is crucial to share manufacturing experience when evaluating the product's structure, to modify the design or its components and receive prompt feedback regarding the impact of these changes (Geng, 2004). Conflicting perspectives on product development processes due to different levels of knowledge and differences of backgrounds often lead to inadequate integration of the industrial design profession within the industry (Svengren, 1995; Persson, 2004).

Creating multidisciplinary teams ensures industrial design competence by integrating industrial and engineering design roles and creating a more homogeneous unit. However, team members often have challenges in collaborating smoothly because each individual brings distinct responsibilities, perspectives, and experiences related to design tasks (Svengren, 1995). Industrial designers focus on social benefit values such as aesthetic concerns, trends and originality, while engineering designers focus on material benefit such as function performance (Muller, 2001). Industrial designers use an outside-in approach; however, engineering designers take an inside-out approach (Hubka & Eder, 1996). According to the research conducted by Kim and Lee, engineering designers stated that industrial designers are less knowledgeable about construction, manufacturing methods, materials and mold structure, thus industrial designers can often design things that cannot be manufactured (Kim & Lee, 2014).

In the interviews, industrial designers emphasized that they need to be familiar with production processes in order not to increase production costs, resource usage and production time. This research revealed that professional designers have limited awareness and priority for manufacturability, and designers apply manufacturability principles as a secondary priority in design practice. However, the production competence of the designer plays a key role in shortening the design process and reduces the need for revisions during the design phase. On the other hand, some of the participants stated that manufacturability concerns conflict with creativity and aesthetic perspectives. It was also reported that the aesthetic thought and creativity are more restricted when the knowledge and experience in terms of manufacturability increases. The balance between the manufacturability concerns and creativity of designers is critical for product creation.

Conclusion

This study demonstrated that the design product and the production process are directly related to each other. The more problem-free the production process is, the closer the designed product can be produced to what is desired and imagined. It is a fact that the product is in contact with the designer from the first stage when it starts to take shape. The participants emphasized that designers should be involved in the entire process until the last step of the product development. Considering the production process in every stage of a product design provides great savings in cost by reducing the revisions required. At this point, it is clear that the design must be imagined as manufacturable by the designer. On the other hand, what is important for the designer is that the designer's dream

turns into a real product with the least amount of change. The designer's experience plays a big role here and his/her success can also be measured in the form of time, material and cost savings that the designer can provide during the product development process. In this context, one of the critical elements for creating a manufacturable design is the designer's relationship with manufacturability. Three issues are highlighted in this research: the designer's lack of production knowledge, the designers' conflict of communication with multidisciplinary group members, and the resistance of the manufacturability concern to the designer's aesthetic concern.

In summary, the involvement of the designer in the production process has the potential to make a significant contribution to the change in production costs, time and resource usage. This research addresses the gaps in the literature by focusing on the understanding of manufacturability of industrial designers working in the electrical home appliances sector. It reveals the various approaches of industrial designers towards the concept of manufacturability and sheds light on their contribution and effects on the production process.

References

Boothroyd, G. (1992). Design for Assembly and Disassembly. Kynote Paper, 41, pp. 625-636.

Boothroyd, G., Dewhurst, P., & Knight, W. A. (2010). Product design for manufacture and assembly. CRC press.

Cong, J., & Zhang, B. (2012). Methodology for evaluating manufacturability of composite materials. Applied Composite Materials, 19(3), 189-201.

Das, S. K., Datla, V., & Gami, S. (2000). DFQM - an approach for improving the quality of assembled products. International Journal of Production Research, 38(2), 457–477.

Fabricius, F. (1994). A seven-step procedure for design for manufacture. World Class Design to Manufacture, 1(2), 23-30.

Geng, H. (2004). Manufacturing Engineering Handbook. Mcgraw-Hill.

Hubka, V., & Eder, W. E. (1996). Design science: introduction to needs, scope and organization of engineering design knowledge.

Kim, K., & Lee, K. P. (2014). Industrial designers and engineering designers; causes of conflicts, resolving strategies, and perceived image of each other.

Korol, E. A., & Petrosyan, R. S. (2020). Methodological approaches to the formation of the organizational and technological mechanism for improving the manufacturability of work during the overhaul of buildings. IOP Conference Series: Materials Science and Engineering, 753(3), 032057. IOP Publishing.

Lianos, A. K., Koutsoukos, S., Bikas, H., & Stavropoulos, P. (2020). Manufacturability Assessment and Design for AM. Procedia CIRP, 91, 290-294.

Muller, W., "Order and Meaning in Design", Lemma Publishers, Utrecht, the Netherlands, 2001.

Pedgley, O. F. (2009). Influence of stakeholders on industrial design materials and manufacturing selection. International Journal of Design, 3(1), 1-15.

Persson, S., & Wickman, C. (2004). Effects of industrial design and engineering design interplay: An empirical study on tolerance management in the automotive industry. In DS 32: Proceedings of DESIGN 2004, the 8th International Design Conference, Dubrovnik, Croatia.

Poli, C., Dastidar, P., & Graves, R. (1992). Design knowledge acquisition for DFM methodologies. Research in Engineering Design, 4(3), 131-145.

Svengren, L. (1995). Industriell design som strategisk resurs: En studie av designprocessens metoder och synsätt som del i företags strategiska utveckling [Industrial design as a strategic resource: A study of design process methods and approaches as part of companies' strategic development]. Lund Institute of Technology.

Todić, V., Lukić, D., Milošević, M., Jovičić, G., & Vukman, J. (2012). Manufacturability of product design regarding suitability for manufacturing and assembly (DfMA). Journal of production engineering, 16(1), 47-50.

INDUSTRIAL ENGINEERING

Decision Making

Engineering Management

Industrial Data Analytics

Knowledge Management

Manufacturing Management

Analysis of Organizational Capabilities of Companies in Construction Industry Using a Multi-Criteria Decision-Making Approach

Görkem Kayacıoğlu[a], Çiğdem Kadaifçi[a]

[a] Istanbul Technical University, Department of Industrial Engineering, Engineering Management Master's Program, Türkiye
kayacioglu21@itu.edu.tr

Keywords: Project Management, Organizational Capabilities, Turkish Construction Industry, Multi-Criteria Decision Making.

Aim

The construction industry has played a crucial role in global economic and social development from the past to the present. The broad scope of the industry, including urbanization, infrastructure, transportation, and establishment of communication networks, has ensured that the industry holds a large share of national economies, especially in Türkiye, by offering extensive employment opportunities. Given the industry's role in the national - and global- economy, adapting to change to survive, ensure sustainability, and grow in a dynamic environment characterized by intense competition and continuous transformation is essential. In this dynamic environment, due to the high level of competition, the complexity of project management activities, and rapid technological advancements, companies need to be aware of their organizational capabilities. These capabilities determine not only their current performance but also their ability to adapt to changes in the industry and market demands. Therefore, it is crucial for companies to continuously assess, develop, and enhance their organizational capabilities to preserve their competitiveness and achieve long-term success.

The sustainability of organizational success and competitive advantage depends on effectively utilizing and developing a firm's resources, capabilities, and competencies. Resources refer to all tangible and intangible assets "controlled by a firm that enable the firm to conceive of and implement strategies that improve its efficiency and effectiveness" (Barney, 1991). However, merely having resources does not guarantee success and competitive advantage. Firms must also be able to effectively allocate and coordinate these resources (Teece et al., 1997). Capabilities are the organization's ability to perform specific tasks and activities by integrating and utilizing its resources efficiently (O'Regan & Ghobadian, 2004). While capabilities define what a firm can do with its resources, competence arises when these capabilities are effectively combined and harmonized across different functions to create superior performance. Competence refers to the integration of capabilities from different disciplines and working together in harmony (Javidan, 1998). Core competency represents a firm's unique and strategically valuable competencies that provide a sustainable competitive advantage (Prahalad & Hamel, 1990). While the literature extensively discusses organizational competencies, this study primarily focuses on capabilities, as they form the foundation for firms to develop competitiveness, achieve project objectives, and respond to dynamic market conditions.

The first definitions of organizational competencies were given by researchers within the framework of the organization's ability to maintain its current performance and achieve goals by using existing resources and structuring its processes. With increasing competition and rapid advancements in technology, researchers have expanded the concept of organizational competence by including aspects such as achieving competitive advantage, adapting to changing market conditions, and developing new products and processes.

A detailed literature review reveals that numerous studies have evaluated organizational capabilities across various industries including the construction industry using methods such as performance measurement models and capability maturity models. However, there is a limited number of studies applying multi-criteria decision-making (MCDM) methods to organizational capabilities especially those specific to the construction industry in Türkiye. To address this gap, this study aims to examine the organizational capabilities that construction companies must recognize and develop to gain competitive advantage, achieve their growth targets, and adapt to market changes

using the MCDM approach. For this purpose, a capability model has been developed by reviewing the relevant literature to identify the key organizational capabilities in construction companies. Using the developed model, this study aims to prioritize organizational capabilities in construction companies with respect to their impact on project success.

Material and Method

The main contribution of this study is to develop an organizational capability model for companies in the construction industry. In developing this model, the first step was to examine studies and models in the literature related to organizational capabilities across various industries. Subsequently, the research was refined specifically for the construction industry analyzing industry-specific organizational capability models. The 21 capabilities identified through this analysis are functional capabilities, which are defined as "the technologies, abilities, and knowledge necessary to perform work-related tasks effectively and to produce specific desired outcomes within the functional domains of an organization." (McDermott 2003; Loufrani-Fedida and Missonier 2015 as cited in G. Tiruneh & Fayek, 2020).

These functional capabilities are categorized under three groups: General Administration, Technical, and Project Management Capabilities. This grouping will enable the evaluation of capabilities both in relation to each other and within the relevant capability groups through the analyses to be conducted. The complete list of capabilities is provided in Table 1.

Based on the established organizational capabilities model, data will be collected through an online survey administered to managers in the Turkish construction industry. The survey will include pairwise comparison questions aligned with the selected MCDM approach, and the results will be analyzed accordingly.

Table 1. Organizational Capabilities.

Capability Groups	Organizational Capabilities	References
General Administration	Employee Development	(Barney, 1991; Hawi et al., 2015; Kersiene & Savaneviciene, 2009; Lewis, 2003; Omar & Fayek, 2016; Pariafsai & Behzadan, 2021; G. Tiruneh & Fayek, 2020; G. G. Tiruneh & Fayek, 2017)
	Information Technology Management	(Hawi et al., 2015; Kersiene & Savaneviciene, 2009; Omar & Fayek, 2014; Pariafsai & Behzadan, 2021; Schienstock, 2009; G. Tiruneh & Fayek, 2020; G. G. Tiruneh & Fayek, 2017)
	Legal Framework Management	(Pariafsai & Behzadan, 2021; G. Tiruneh & Fayek, 2020; G. G. Tiruneh & Fayek, 2017)
	Strategic Planning	(Pariafsai & Behzadan, 2021; G. Tiruneh & Fayek, 2020; G. G. Tiruneh & Fayek, 2017)
	Innovation and R&D Capabilities	(Omar & Fayek, 2014, 2016; Pariafsai & Behzadan, 2021; G. Tiruneh & Fayek, 2020; G. G. Tiruneh & Fayek, 2017)
	Customer Relationship Management	(Hawi et al., 2015; Schienstock, 2009; G. Tiruneh & Fayek, 2020; G. G. Tiruneh & Fayek, 2017)
Technical	Technical and Operational Applications	(Pariafsai & Behzadan, 2021; G. Tiruneh & Fayek, 2020; G. G. Tiruneh & Fayek, 2017)

	Occupational Health and Safety Applications	(Omar & Fayek, 2016; Pariafsai & Behzadan, 2021; G. Tiruneh & Fayek, 2020; G. G. Tiruneh & Fayek, 2017)
	Materials Management	(Pariafsai & Behzadan, 2021; G. Tiruneh & Fayek, 2020; G. G. Tiruneh & Fayek, 2017)
	Operation and Maintenance	(Pariafsai & Behzadan, 2021; G. Tiruneh & Fayek, 2020; G. G. Tiruneh & Fayek, 2017)
	Construction Technology Infrastructure	(Omar & Fayek, 2014, 2016; Pariafsai & Behzadan, 2021; Schienstock, 2009; G. Tiruneh & Fayek, 2020; G. G. Tiruneh & Fayek, 2017)

Table 1 (continued). Organizational Capabilities.

Capability Groups	Organizational Capabilities	References
Project Management	Quality Management	(Omar & Fayek, 2016; Pariafsai & Behzadan, 2021; G. Tiruneh & Fayek, 2020; G. G. Tiruneh & Fayek, 2017)
	Schedule (Time) Management	(Omar & Fayek, 2016; Pariafsai & Behzadan, 2021; G. Tiruneh & Fayek, 2020; G. G. Tiruneh & Fayek, 2017)
	Change Management	(Omar & Fayek, 2014, 2016; Pariafsai & Behzadan, 2021; G. Tiruneh & Fayek, 2020; G. G. Tiruneh & Fayek, 2017)
	Cost Management	(Omar & Fayek, 2016; Pariafsai & Behzadan, 2021; G. Tiruneh & Fayek, 2020; G. G. Tiruneh & Fayek, 2017)
	Risk Management	(Omar & Fayek, 2014, 2016; Pariafsai & Behzadan, 2021; G. Tiruneh & Fayek, 2020; G. G. Tiruneh & Fayek, 2017)
	Team Management	(Hawi et al., 2015; Omar & Fayek, 2016; Pariafsai & Behzadan, 2021; G. Tiruneh & Fayek, 2020; G. G. Tiruneh & Fayek, 2017)
	Contract Administration	(Omar & Fayek, 2014, 2016; Pariafsai & Behzadan, 2021; G. Tiruneh & Fayek, 2020; G. G. Tiruneh & Fayek, 2017)
	Scope Management	(Omar & Fayek, 2014, 2016; Pariafsai & Behzadan, 2021; G. Tiruneh & Fayek, 2020)
	Resource Management	(Hawi et al., 2015; Omar & Fayek, 2016; Pariafsai & Behzadan, 2021; G. Tiruneh & Fayek, 2020; G. G. Tiruneh & Fayek, 2017)
	Procurement Management	(Omar & Fayek, 2016; Pariafsai & Behzadan, 2021; G. Tiruneh & Fayek, 2020; G. G. Tiruneh & Fayek, 2017)

Findings

The survey data collected from the participants will be analyzed using an MCDM approach suitable for the purpose of the study. The expected findings include determining the relative importance of different capability groups and prioritizing capabilities with respect to their contribution to the project success in the construction industry.
These findings will serve as a strategic guide for companies and provide valuable insights for both academic research and practical applications. By enabling companies to effectively allocate resources, this study will help them develop the most relevant capabilities based on their current circumstances and market position.

Conclusion

This study emphasizes the importance of organizational capabilities in preserving their competitiveness and achieving long-term success of companies in the Turkish construction industry. By addressing a gap in the existing literature, it provides a structured framework for evaluating the impact of organizational capabilities on project success using the MCDM approach. This model provides companies in the industry with a comprehensive tool to evaluate their performance and identify strategic areas for development.

The findings of the analyses are expected to provide valuable insights into which capabilities should be prioritized based on their impact on project success and offer companies a strategic foundation for improving their practices.

As a suggestion for future studies, considering the dynamic capabilities that enable companies to adapt to changing market conditions and innovative processes (Zollo & Winter, 1999) with an approach similar to this study may provide insights into which dynamic capabilities are effective in developing the existing organizational capabilities of companies.

Furthermore, including behavioral capabilities, such as managerial and individual skills, in the organizational capability model can help to understand how human factors contribute to project success and how they compare with functional capabilities.

References

Barney, J. (1991). Firm Resources and Sustained Competitive Advantage. *Journal of Management*, *17*(1), 99–120. https://doi.org/10.1177/014920639101700108

Hawi, R. O., Alkhodary, D., & Hashem, T. (2015). Managerial competencies and organizations performance. *International Journal of Management Sciences*, *5*(11), 723–735.

Javidan, M. (1998). Core competence: What does it mean in practice? *Long Range Planning*, *31*(1), 60–71. https://doi.org/10.1016/S0024-6301(97)00091-5

Kersiene, K., & Savaneviciene, A. (2009). The formation and management of organizational competence based on cross-cultural perspective. *WORK HUMANISM*, *5*.

Lewis, M. A. (2003). Analysing organisational competence: Implications for the management of operations. *International Journal of Operations & Production Management*, *23*(7), 731–756. https://doi.org/10.1108/01443570310481531

Omar, M. N., & Fayek, A. R. (2014). *A Framework for Identifying and Measuring Competencies and Performance Indicators for Construction Projects*. 2043–2052. https://doi.org/10.1061/9780784413517.208

Omar, M. N., & Fayek, A. R. (2016). Modeling and evaluating construction project competencies and their relationship to project performance. *Automation in Construction*, *69*, 115–130. https://doi.org/10.1016/j.autcon.2016.05.021

O'Regan, N., & Ghobadian, A. (2004). The Importance of Capabilities for Strategic Direction and Performance. *Management Decision*, *42*(2), 292–313. https://doi.org/10.1108/00251740410518525

Pariafsai, F., & Behzadan, A. H. (2021). Core Competencies for Construction Project Management: Literature Review and Content Analysis. *Journal of Civil Engineering Education*, *147*(4), 04021010. https://doi.org/10.1061/(ASCE)EI.2643-9115.0000051

Prahalad, C.K., & Hamel, G. (1990). The Core Competence of the Corporation. *Harvard Business Review, 68*, 275-292.

Schienstock, G. (2009). *Organizational Capabilities: Some reflections on the concept*.

Teece, D. J., Pisano, G., & Shuen, A. (1997). Dynamic capabilities and strategic management. *Strategic Management Journal*, *18*(7), 509–533. https://doi.org/10.1002/(SICI)1097-0266(199708)18:7<509::AID-SMJ882>3.0.CO;2-Z

Tiruneh, G., & Fayek, A. (2020). Competency and Performance Measures for Organizations in the Construction Industry. *Canadian Journal of Civil Engineering*, *48*. https://doi.org/10.1139/cjce-2019-0769

Tiruneh, G. G., & Fayek, A. R. (2017). Identifying construction organizational competency measures and performance indicator metrics. *6th CSCE Construction Specialty Conference*. https://legacy.csce.ca/elf/apps/CONFERENCEVIEWER/conferences/2017/pdfs/CONSPEC/FinalPaper_16.pdf

Zollo, M., & Winter, S. (1999). From Organizational Routines to Dynamic Capabilities. *Working Paper in the INSEAD Series*.

MANAGEMENT

Economics

Finance

Human Resource Management

Marketing

Organization

Production Management

Value Co-Creation in Banking: Service-Dominant Logic and Service Logic Perspectives via Electronic Wallets

Zübeyde Buket Aydın[a], Adnan Veysel Ertemel[a]

[a] Istanbul Technical University, Faculty of Management, Department of Management, Türkiye
aydinzu16@itu.edu.tr

Keywords: Customer Satisfaction, Electronic Wallets, Service Logic, Service-Dominant Logic, Value Co-Creation.

Aim

Today, the banking sector, propelled by the rapid pace of digital transformation and technological innovations, has shifted away from traditional service approaches toward customer-centric, interactive, and holistic service models. In this context, the value co-creation achieved through the collaboration between customers and banks has become a strategic element that enhances the competitive strength of banks and deepens customer experience. At the core of this thesis is an examination of how electronic wallet technologies strengthen the collaboration between customers and banks and contribute to the value creation process, and how this process can be explained through the perspectives of Service-Dominant Logic (SDL) and Service Logic.

Introduced by Vargo and Lusch (2004), Service-Dominant Logic argues that value is not created by a one-sided presentation of products; rather, it is generated through a dynamic process in which the resources of both the service provider and the customer are integrated and co-created. This approach enables a model in the banking sector where customers evolve from mere service consumers to active participants in the service process, thereby co-producing value with the enterprise. On the other hand, Service Logic emphasizes that customer relationships should not remain merely transactional but must evolve into sustainable value creation through mutual interaction and the restructuring of business processes. The Service Logic Business Model Canvas developed by Ojasalo and Ojasalo (2018) serves as a guide in developing customer-centric strategies in the increasingly digital banking environment, thereby underscoring the strategic importance of electronic wallet applications.

This thesis comprehensively analyzes how the collaboration between customers and banks in the Turkish banking sector, in the context of electronic wallet usage, transforms into value co-creation from the perspectives of SDL and Service Logic. The study aims to reveal the effects of electronic wallets on customer satisfaction, perceived value, and usage habits, while also discussing how banks can strategically position digital payment systems as tools to achieve competitive advantage.

Literature suggests that digital banking applications—especially mobile banking and digital payment systems—are transforming customer experience and value creation processes (Dabare, Hewapathirana, & Fernando, 2023). However, the effects of electronic wallets on the banking sector and their contribution to deepening the interaction between customers and banks, thereby enhancing value co-creation, have not yet been sufficiently examined. This gap highlights the significance of the thesis both academically and practically.

The scope of the research is supported by a quantitative data analysis conducted on individuals using electronic wallets across Türkiye; the survey data were analyzed in detail using SPSS 29.0 In this way, the usage habits, perceived benefits, and impacts on customer satisfaction of electronic wallet technologies are systematically evaluated.

In conclusion, this study aims to demonstrate how the innovative payment solutions brought about by digital transformation strengthen the collaboration between customers and banks and contribute to sustainable value creation. Additionally, it offers recommendations on how banks can strategically develop digital payment systems within the framework of SDL and Service Logic.

Material and Method

The data collection procedure in this study was carried out using quantitative research methods. Examining how electronic wallet technologies affect value co-creation through customer-bank collaboration in the Turkish banking industry is the main goal of the study. People that use electronic wallets all around Türkiye make up the sample, and information was gathered from 300 participants in total. Demographic traits including age, gender, income, and education are diverse among the participants, which improves the findings' generalizability.

A specifically created questionnaire that supports the study's objectives was employed as the data gathering tool. Three primary sectionsmake up the questionnaire: the first gathers demographic data about the participants; the second discusses their usage patterns, preferences, and experiences with electronic wallets; and the third uses Likert scale statements to gauge attitudes and perceptions regarding electronic wallets. Using Google Forms, the survey was distributed via LinkedIn and WhatsApp, with responses collected voluntarily and anonymously from December 22, 2024, to February 8, 2025. Data were analyzed using SPSS 29.0. Descriptive statistics, including frequency distributions, means, medians, and standard deviations, were first calculated. Then, using parametric and non-parametric techniques, such as the t-test, one-way ANOVA, Mann-Whitney U test, Pearson correlation, and Chi-Square test, the associations between the participants' attitudes and their electronic wallet usage patterns were investigated.

Furthermore, multiple regression analyses were performed to further investigate the relationships between the independent and dependent variables. The study hypotheses have been able to be meaningfully and consistently tested thanks to this methodological technique.

Findings

The results of the study are presented in this section, which also examines how electronic wallets affect customer-bank relationships from the viewpoints of service logic and service-dominant logic (SDL). The findings came from statistical analysis of survey information gathered from 306 individuals throughout Turkey, which covered e-wallet perceptions, usage patterns, and demographic characteristics. With regard to e-wallet acceptance, consumer satisfaction, and perceived value, the results provide important information that banks may use to strategically position digital payment systems. Significantly, 60.8% of respondents did not know the difference between an e-wallet and a digital wallet, indicating that there is a need for more financial literacy with relation to digital payment methods.

Given that respondents indicated a significant association between the frequency of e-wallet usage and the feeling of ease, the study validates that people believe e-wallets save time. Furthermore, it was discovered that e-wallet users had substantially higher customer satisfaction than those who used more conventional payment methods. With statistical analyses showing that consumers who believe e-wallets to be secure also report higher levels of overall satisfaction, security emerged as a critical issue. These results suggest that securityfeatures have a significant impact on adoption and confidence.

The study also looked at whether e-wallet features like discounts, promotions, and quick payment services raise the perceived worth of the product. The findings, however, revealed no connection between these variables and users' assessments of e-wallets, indicating that promotional incentives might not be enough on their own to improve consumer opinion. Rather, elements like ease and security seem to have a bigger influence on user happiness and retention.

Demographic trends indicate that younger users (18–35 years old) are significantly more likely to adopt e-walletscompared to older age groups. The results also show a positive trend between income level and e-wallet adoption, though the relationship was not statistically significant at the 5% level. This suggests that while higher-income individuals may be inclined to use e-wallets, other factors such as accessibility, awareness, and usability may also play a role in adoption.

All things considered, the results highlight how strategically significant electronic wallets are for raising customer satisfaction and building closer ties between banks and their clients. In order to increase adoption and confidence, banks should concentrate on improving the e-wallet technologies' dependability and user experience, given the importance of security and usability. Additionally, focused marketing campaigns and instructional programs that target various demographic groups may boost the uptake of digital payments even more. These findings highlight

how important digital financial tools are becoming for influencing consumer experiences and maintaining a competitive edge in the banking industry.

Conclusion

In conclusion, this study demonstrates that electronic wallet technologies make a significant contribution to value co-creation through the collaboration between customers and banks in the Turkish banking sector. The analyses reveal that the use of electronic wallets saves time for users, that customer satisfaction is higher compared to traditional payment methods, and that the security features have a positive impact on customer satisfaction. Notably, an increase in the adoption of this technology among young users has been observed, and similar trends have been detected among individuals in higher income groups. However, it has been concluded that the effects of demographic factors need to be subjected to more comprehensive analysis. These findings indicate that electronic wallets are a strategic element in enhancing competitive advantage in the banking sector and that future studies conducted across different demographic groups will contribute to a clearer understanding of this relationship.

References

Dabare, D., Hewapathirana, R., & Fernando, S. (2023). Digital banking applications and their impact on customer experience and value creation processes. *Journal of Digital Banking*, 5(2), 123–137.

Ojasalo, K., & Ojasalo, J. (2018). Service Logic Business Model Canvas. *Journal of Business Models*, 6(1), 1–13.

Pizzan-Tomanguillo, R., Martínez-Ruiz, M. P., & Izquierdo-Yusta, A. (2024). The growing importance and competitive power of electronic wallets in digital banking. *International Journal of Bank Marketing*, 42(3), 456–472.

Pula, J. S. (2022). The impact of electronic and digital wallets on customer satisfaction and perceived value. *Journal of Financial Services Marketing*, 27(1), 14–25.

Vargo, S. L., & Lusch, R. F. (2004). Evolving to a new dominant logic for marketing. *Journal of Marketing*, 68(1), 1–17.

MANAGEMENT ENGINEERING

Finance

Marketing

Quantitative Methods

Selection of an Electronic Marketplace for Micro-Exports by SMEs: A Hierarchical IFS-WASPAS Approach

Cidal Ustun[a], Cafer Erhan Bozdağ[a]

[a] Istanbul Technical University, Industrial Engineering, Engineering Management, Türkiye
ustunc21@itu.edu.tr

Keywords : E-Export, Electronic Marketplace Selection, Weighted Aggregated Sum Product Assessment (WASPAS), Intuitionistic Fuzzy Sets, IFS-WASPAS.

Aim

E-export create opportunities for SMEs by overcoming resource limitations and entry barriers, enabling them to compete not only in local but also in international markets. The correct selection of electronic marketplaces (EMP) is a vital strategic decision to enhance SMEs' export potential. To make this decision effectively, a structured approach is essential, as it must align with multiple objectives while considering various quantitative and qualitative factors. These include the platform's business model and expertise, technical aspects such as software and security, regulatory frameworks, cost implications, sales and marketing strategies, and the process of integrating with the platform. Despite the diversity of studies in the literature on customer perspectives and their choices regarding EMPs, research adopting the sellers' perspective on the same subject, as well as the variety of MCDM (Multi-Criteria Decision-Making) techniques, remains limited. The purpose of this study is to develop a decision model for determining the most suitable platform for micro-export among EMPs from the sellers' perspective for two SMEs operating in different sectors and possessing different organizational capabilities. The study seeks to answer the following questions: "What are the decision criteria affecting SME's selection of international digital marketplaces?" and "How do varying criterion weights – shaped by the SME's priorities- influence the result of the decision?"

Method

This research adopts a MCDM approach, employing the hierarchical Weighted Aggregated Sum Product Assessment (WASPAS) method, which is integrated with Intuitionistic Fuzzy Sets (IFS) as proposed by Koç and Bozdağ (2024). The solution process begins with the development of a two-layer hierarchical criteria structure and follows determination of criteria weight then a systematic progression from the lowest to the highest level, calculating weighted sums and weighted products of alternative performance evaluations at each stage. Ultimately, this process yields a single aggregated WASPAS score for each alternative in the final phase (Figure 1).

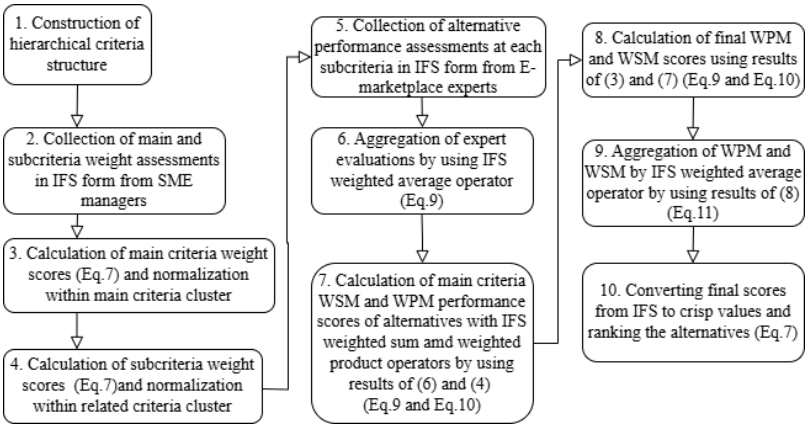

Figure 1. Flowchart of the Proposed Solution Model.

The decision criteria framework, comprising 10 main categories and 70 sub-criteria, was established through literature review, risk assessments, expert consultations, and evaluations of existing EMP seller interfaces. The

primary criteria encompass platform recognition (F1), usability and compatibility of EMP (F2), costs and payments (F3), store management within EMP (F4), order processing mechanisms (F5), reporting and analytics tools (F6), support programs (F7) , security and reliability of EMP (F8), advertising and marketing functionalities (F9) , and the localization of EMP (F10) (Figure 2).

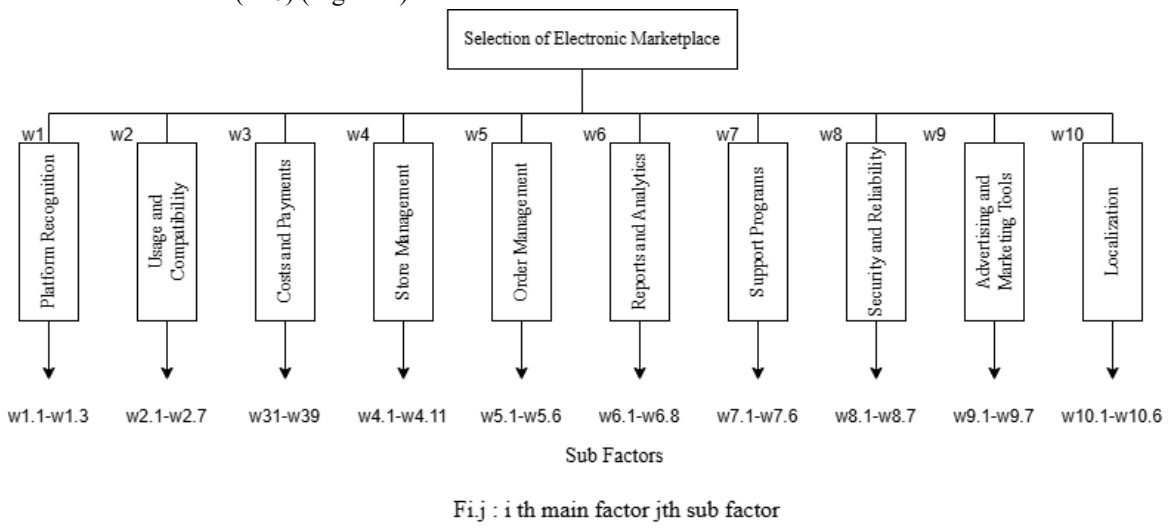

Figure 2. Hierarchical Structure of the Proposed Model.

To observe differences stemming from firm-specific characteristics and priorities, two distinct companies Firm1 and Firm 2 were analyzed separately. The alternative platforms are chosen among the marketplaces most frequently used for micro-exports by SMEs in Turkiye. In the performance evaluation of alternatives, assessments were conducted in collaboration with four independent EMP experts. The inclusion of four experts was intended to ensure a comprehensive and balanced evaluation by incorporating diverse perspectives and minimizing potential bias. It was assumed that all experts have equal weight of value 0.25. Their aggregated assessments provided a more robust and objective basis for decision-making. To ensure consistency in expert evaluations and maintain methodological reliability, it was prioritized that the experts had enough knowledge about all the three alternatives and the target markets of the two companies. This situation may lead into a limitation in the study in terms of EMP options, but the primary aim of the study is to demonstrate the applicability of the methodology and define the decision criteria. To ensure consensus on the terms used, maintain linguistic consistency, and provide immediate explanations when needed, face-to-face or telephone interviews were preferred during the data collection process. Company representatives evaluated the criteria based on their business models, organizational capabilities, and priorities using the linguistic expressions provided in Table 1. To ensure the impartiality of the study, avoid potential misguidance, and focus solely on the features of alternatives the names of the EMPs are referred to as EMP-A, EMP-B and EMP-C. The evaluation of EMPs' competencies regarding the sub-criteria was conducted by the experts, who are professionals at various consultancy firms specialized in e-export at the EMPs, by using the linguistic expressions given in Table 1.

Table 1. Intuitionistic Fuzzy Linguistic Scale (IFLS) (Adapted from Koç and Bozdağ (2024).

Linguistic variables (used by firm representatives)	IFLS	Linguistic variables (used by experts)
Extremely important	(0.99, 0.01)	Extremely Sufficient
Intermediate value	(0.9, 0.1)	Intermediate Value
Very important	(0.8, 0.1)	Very Sufficient
Intermediate value	(0.7, 0.2)	Intermediate Value

Quite important	(0.6, 0.3)	Quite Sufficient
Moderately important	(0.5, 0.4)	Moderately Sufficient
Relatively less important	(0.4, 0.5)	Relatively Less Sufficient
Intermediate value	(0.25, 0.6)	Intermediate Value
Very less important	(0.1, 0.75)	Very Insufficient
Intermediate value	(0.1, 0.9)	Intermediate Value
Extremely low importance	(0.01, 0.99)	Extremely Insufficient

Subjectivity and limited rationality in decision-makers' judgments can be significant sources of uncertainty in problem structuring. IFS, an extension of traditional fuzzy logic, provide comprehensive analysis by modeling not only the membership and non-membership degrees of an element but also the remaining hesitation caused by uncertainty (Atanassov, 1986). The foundational terms and operators that enable the understanding and application of the IFS-WASPAS method used in our study are as follows:

Definition 1 (Atanassov,1999): Let a (non-fuzzy) set E be fixed. An IFS A in E is defined as an object of the following form $A = \{x \epsilon E\}$ where the functions $\mu_A: E \rightarrow [0,1]$ and $v_A: E \rightarrow [0,1]$ define the degree of membership and the degree of non-membership of the element x ∈ E, respectively, and for every x ∈ E.

$$0 \leq \mu_A(x) + v_A(x) \leq 1 \quad \text{(Equation 1)}$$

Definition 2 (Atanassov, 1999) :The value of

$$\pi_A = 1 - \mu_A(x) - v_A(x) \quad \text{(Equation 2)}$$

is called the degree of non-determinacy of the element x ∈ E to the IFS A. For computational practicality, an intuitionistic fuzzy number (IFN) is represented as $\tilde{a} = (\mu_{\tilde{a}}, v_{\tilde{a}})$.

Definition 3 (Atanassov, 1999): Let A and B be two different IFS' defined in E, and let the function f_{A+B} map x ∈ E to the point f_{A+B} ϵ F with coordinates specified in Equation3.

$$\langle (\mu_A(x) + \mu_B(x) - \mu_A(x)\mu_B(x), v_A(x)v_B(x) \rangle \quad \text{(Equation 3)}$$

Definition 4 (Atanassov, 1999): Let A and B be two different IFS' defined in E, and let the function $f_{A\times B}$map x ∈ E to the point $f_{A\times B}$ ϵ F with coordinates specified Equation 4.

$$\langle (\mu_A(x)\mu_B(x), v_A(x) + v_B(x) - v_A(x)v_B(x), \rangle \quad \text{(Equation 4)}$$

Definition 5(Xu, 2007): Lets $\tilde{a} = (\mu_{\tilde{a}}, v_{\tilde{a}})$ be an IFN

$$\lambda\tilde{a} = \left(1 - \left(1 - \mu_{\tilde{a}}\right)^{\lambda}, v_{\tilde{a}}^{\lambda}\right), \lambda > 0 \quad \text{(Equation 5)}$$

$$\tilde{a}^{\lambda} = \left(\mu_{\tilde{a}}^{\lambda}, 1 - (1 - v_{\tilde{a}})^{\lambda}\right), \lambda > 0 \quad \text{(Equation 6)}$$

Definition 6 (Xu,2007): Let $\tilde{a} = (\mu_{\tilde{a}}, v_{\tilde{a}})$ and $\tilde{b} = (\mu_{\tilde{b}}, v_{\tilde{b}})$ be two IFNs. The normalized score function s(ã) and accuracy function h(ã) of ã are calculated using the formulas provided below:

$$s(\tilde{a}) = 0.5\ (1 + \mu_{\tilde{a}} - v_{\tilde{a}})\ ,\ 0 \le s(\tilde{a}) \le 1 \quad \text{(Equation 7)}$$

$$h(\tilde{a}) = \mu_{\tilde{a}} + v_{\tilde{a}}\ , 0 \le h(\tilde{a}) \le 1 \quad \text{(Equation 8)}$$

Using the normalized score and accuracy functions $\tilde{a}$ ve $\tilde{b}$ can be compared as follows:

1. If $s(\tilde{a}) < s(\tilde{b})$ then $\tilde{a} < \tilde{b}$
2. If $s(\tilde{a}) = s(\tilde{b})$ and
   a. If $h(\tilde{a}) = h(\tilde{b})$ then $\tilde{a}$ ve $\tilde{b}$ represent the same information.
   b. If $h(\tilde{a}) < h(\tilde{b})$ then $\tilde{a} < \tilde{b}$.

Definition 7 and 8: Let $\tilde{a}_i = (\mu_{\tilde{a}_i}, v_{\tilde{a}_i})$ represent different IFNs and w_is represent their corresponding weights. (i = 1,2,……,n) , $w_i \in [0,1]$ ve $\sum w_i = 1$. As Xu (2007) stated The IFWA (Intuitionistic Fuzzy Weighted Average) operator first weights all given arguments and then averages them into a single value. The aggregated weighted value obtained through the IFWA operator can be expressed using the Equation 9.

$$IFWA_w(\tilde{a}_1, \tilde{a}_2, \dots\dots, \tilde{a}_n) = (1 - \prod_{i=1}^{n} \left(1 - \mu_{\tilde{a}_i}\right)^{w_i}, \prod_{i=1}^{n} \left(v_{\tilde{a}_i}\right)^{w_i}) \quad \text{(Equation 9)}$$

As Xu and Yager (2006) stated The IFWG (Intuitionistic Fuzzy Weighted Geometric) operator first weights all given arguments and then calculates the geometric mean of them into a single value. . The geometric weighted value obtained through the IFWG operator can be expressed using the Equation 10.

$$IFWG_w(\tilde{a}_1, \tilde{a}_2, \dots\dots, \tilde{a}_n) = (\prod_{i=1}^{n} \left(\mu_{\tilde{a}_i}\right)^{w_i}, \prod_{i=1}^{n} \left(1 - v_{\tilde{a}_i}\right)^{w_i}) \quad \text{(Equation 10)}$$

The IFWA operator is applied for aggregation of expert evaluations and in the weighted sum (WSM) section, and the IFWG operator is employed in the weighted product (WPM) part of the WASPAS method to solve our problem. Since the weighted aggregated sum product assessment (WASPAS) method is the weighted combination of WSM and WPM methods , final scores for ranking of alternatives is calculated as by using the IFWA and IFWG values obtained at the top level of the hierarchy (Zavadskas et al, 2014) :

$$S = f_{0.5IFWA + 0.5IFWG} \quad \text{(Equation 11)}$$

Findings

For the determination of main factor weights first by using normalized score function given in Equation 7 all IFS formed assessments were transferred to crisp values and then normalized . The same procedure has been repeated for the subcriteria, and the subcriteria have been normalized within the cluster to which they belong. For Firm1 the most important criteria have been identified as F1,F8 and F9 whereas for Firm 2 most significant ones are F3, F1,F8 and F10. Comparison of the main criteria priorities for Firm 1 and Firm 2 are given in Figure 3.

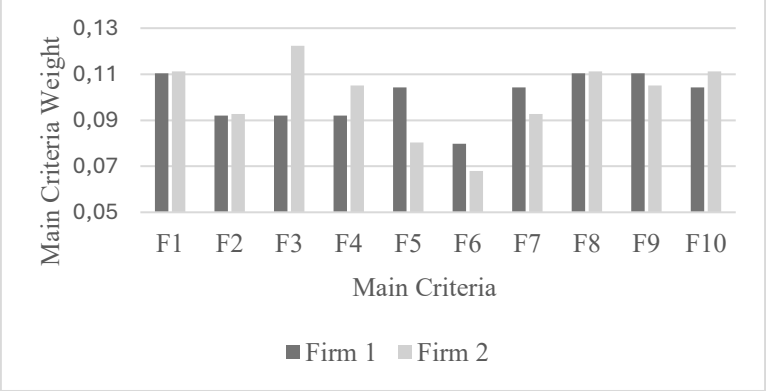

Figure 3. Comparison of Criteria Weights Assessed by Firm1 and Firm 2.

The final performance scores of alternatives obtained through weighted aggregation of WSM and WPM are given in Table 2.

Table 2. Final IFS-WASPAS Scores of EMPs.

	Firm1			**Firm 2**		
	EMP-A	**EMP-B**	**EMP-C**	**EMP-A**	**EMP-B**	**EMP-C**
Final IFWA	(0.906,0.076)	(0.859,0.107)	(0.782,0.162)	(0.916,0.069)	(0.834,0.124)	(0.789,0.155)
Final IFWG	(0.828,0.130)	(0.746,0.174)	(0.668,0.237)	(0.825,0.128)	(0.722,0.188)	(0.674,0.228)
WASPAS average	(0.873, 0.099)	(0.811,0.136)	(0.731, 0.195)	(0.879,0.094)	(0.785,0.153)	(0.738,0.188)
Final Score	0.8868	0.8374	0.7679	0.8925	0.8161	0.7750

Using the applied methodology, the ranking of alternatives for selecting the electronic marketplace for sales was determined based on the ranking criteria specified in Definition 6:

- For Firm 1: EMP-A > EMP-B > EMP-C
- For Firm 2: EMP-A > EMP-B > EMP-C

Conclusion

In this study, a hierarchical decision model integrating Intuitionistic Fuzzy Sets (IFS) and WASPAS was developed. With a properly designed questionnaire structure, IFS enable the evaluation of responses on a unified measurement scale thereby eliminating the necessity for data normalization. One of the key advantages of WASPAS is its computational efficiency, making it well-suited for structured decision problems involving multiple criteria. In cases where WSM and WPM yield different rankings, identifying the weight parameter at which the ranking changes is crucial for result interpretation.

SMEs tend to overcome resource gaps through tools offered by EMPs. Financial constraints affect the assessment of criteria weights. Platform recognition, security and reliability of EMP, advertising and marketing tools provided by EMP and localization skills of EMP are among the top priorities for sellers. Support programs and marketing tools are critical for firms with less digital expertise, while cost sensitivity varies based on financial structure. Reporting tools are undervalued unless directly enhancing competitive visibility and marketing performance. EMP-A ranked highest despite operational and financial burdens, demonstrating its overall market strength.The study highlights that EMP selection is not solely about customer alignment but also involves operational and technical factors.

Future research can expand the criteria set, considering regional differences in logistics and localization strategies for local EMPs. A broader sample size is necessary to statistically validate SMEs' decision-making criteria for selecting digital marketplaces. The WASPAS method proves efficient for objective data analysis but requires comparison with the Analytic Hierarchy Process (AHP) to assess its applicability in subjective decision-making scenarios.

References

Atanassov, K. (1986). Intuitionistic fuzzy sets. Fuzzy Sets System, 20(1), 87–96. https://doi.org/10.1016/S0165-0114(86)80034-3

Atanassov, K. T. (1999). *Intuitionistic fuzzy sets* (pp. 1-137). Physica-Verlag HD.

Koc, T., & Bozdag, E. (2024). Organizational Innovativeness: The Role of Innovation Adoption Capability. *Engineering Management Journal*, 1-15.

Xu, Z., & Yager, R. R. (2006). Some geometric aggregation operators based on intuitionistic fuzzy sets. *International journal of general systems*, *35*(4), 417-433.

Xu, Z. (2007). Intuitionistic fuzzy aggregation operators. *IEEE Transactions on fuzzy systems*, *15*(6), 1179-1187.

Zavadskas, E. K., Antucheviciene, J., Hajiagha, S. H. R., & Hashemi, S. S. (2014). Extension of weighted aggregated sum product assessment with interval-valued intuitionistic fuzzy numbers (WASPAS-IVIF). *Applied soft computing*, *24*, 1013-1021.

MARITIME STUDIES

Maritime Human Resources

Maritime Security

Advancing Maritime Security With Unmanned Maritime Systems

Deniz Çiçek[a], Bihter Erol[a]

[a]Istanbul Technical University, Faculty of Civil Engineering, Department of Geomatics Engineering, Türkiye
cicekd22@itu.edu.tr

Keywords: Maritime Security, Mine Countermeasures, NATO Naval Exercises, Precise Positioning Systems, Unmanned Maritime Systems.

Aim

Maritime security faces escalating challenges, including piracy, smuggling, illegal fishing, and underwater mine threats. These illicit activities not only disrupt international trade routes but also pose significant risks to national security and marine ecosystems. Traditional manned surveillance and intervention methods involve substantial risks to personnel and often lack the agility needed to counter these evolving threats effectively (Liu & Bucknall, 2015). Addressing these challenges requires innovative approaches and the integration of advanced technologies. Unmanned Maritime Systems (UMSs) have emerged as pivotal assets in this domain, offering versatility, resilience, and reduced risk to human operators. Their effectiveness critically depends on precise positioning, ensuring safe and efficient navigation in complex maritime environments. Given the growing role of autonomous systems in modern naval operations, NATO has prioritized UMS integration to enhance interoperability, strengthen coalition operations, improve joint maritime defense strategies, and support key missions such as mine countermeasures, surveillance, and threat deterrence (NATO, 2020).

The DACIA/TOMIS ROU OPEX 2024 (Romanian Operational Experimentation Exercise 2024) is an international, NATO-led maritime exercise focused on operational experimentation. Its inaugural edition, organized by the Romanian Naval Forces, took place in the Black Sea near Mangalia, Romania, from May 27 to May 31, 2024, aiming to evaluate and enhance UMS interoperability within a multi-domain operational environment (NATO Maritime GEOMETOC CoE, 2024). Figure 1 shows an international formal gathering of military and civilian personnel, highlighting international cooperation during the event.

By leveraging data from this exercise, this study examines the integration and operational impact of UMSs in contemporary multinational naval operations. It highlights their adaptability to dynamic maritime threats by analyzing their sensor systems, autonomous functionality in challenging conditions, and precision positioning capabilities.

Figure 1. Turkish Naval Officers Inspecting UMSs During The Exercise (Romanian Naval Forces, 2024).

Material and Method

The study will tackle the main UMSs outlined below.

1. Ocean Aero – Triton Autonomous Unmanned Surface Vehicle (AUSV)

The Triton AUSV, developed by Ocean Aero, is the world's first and only unmanned system capable of both sailing on the surface and diving below the ocean. Powered by wind and solar energy, Triton is designed for extended deployments and broad-scope operations, making it a versatile platform for various mission requirements. As shown in Figure 2, the exercise involved the deployment and handling of Triton by naval personnel, demonstrating the integration of unmanned systems into maritime operations. The key specifications of the Triton platform are summarized in Table 1 (Ocean Aero, n.d.).

Figure 2. Deployment of Ocean Aero – Triton (Romanian Naval Forces, 2024).

Table 1. Specifications of Triton AUSV.

Parameter	**Specification**
Length	4.4m
Weight	350 kg
Power Source	Electricity
Maximum Surface Speed	5 knots
Maximum Subsurface Speed	2 knots
Max Submergence Depth	100m
Solar collection	740W (peak)
Surface Endurance	14 + Days at sea
Subsurface Endurance	5 + Days at sea
Sensor Systems	Multi-beam sonar Side-scan sonar Radar Electro-optical camera
Comms	Silvus, Iridium and cell
Navigation	GPS, IMU (Inertial Measurement Unit), automatic route planning

2. Teledyne - Z Boat

Z-Boat has demonstrated its value in mine detection operations using its integrated sonar sensors. It is equipped with advanced navigation and telemetry systems, high-resolution sonar capabilities, and optional autonomous features. As shown in Figure 3, the Z-Boat platform was presented during a naval demonstration event, where its operational capabilities and onboard systems were introduced to Turkish military personnel. The key technical specifications of the Z-Boat are summarized in Table 2 (Teledyne Marine, n.d.).

Figure 3. Teledyne Z-Boat (Romanian Naval Forces, 2024).

Table 2. Specifications of Z-Boat.

Parameter	**Specification**
Boat Length	1.8 m
Boat Width	1.0 m
Boat Height	1.1 m
Weight of Base Boat	38 kg
Payload Weight	30 kg
Navigation System	Remote Hitec with Vessel Telemetry
Navigation Frequency	2.4 GHz FHSS
Navigation Range	Up to 1200 m
Battery Endurance	Up to 4.5 hours
Multibeam Echosounders	Teledyne Odom MB1, MB2
ADCPs	Teledyne RD Instruments
Sonars	Tritech Side Scan Sonars
Cameras	HD video cameras
Autonomous Features	Optional autonomous operation, on-board data logging, and waypoint navigation

3. YellowScan – Navigator

It is a high-performance LiDAR system designed for professional mapping and surveying applications. Known for its versatility and precision, the Navigator is equipped with cutting-edge technology, enabling accurate 3D point cloud generation for both aerial and ground-based operations. As shown in Figure 4, the system can be deployed via Unmanned Aerial Vehicles (UAVs) for bathymetric scanning and generates high-resolution data that

can be visualized in real-time. The key specifications of the Navigator LiDAR system are summarized in Table 3 (YellowScan, n.d.).

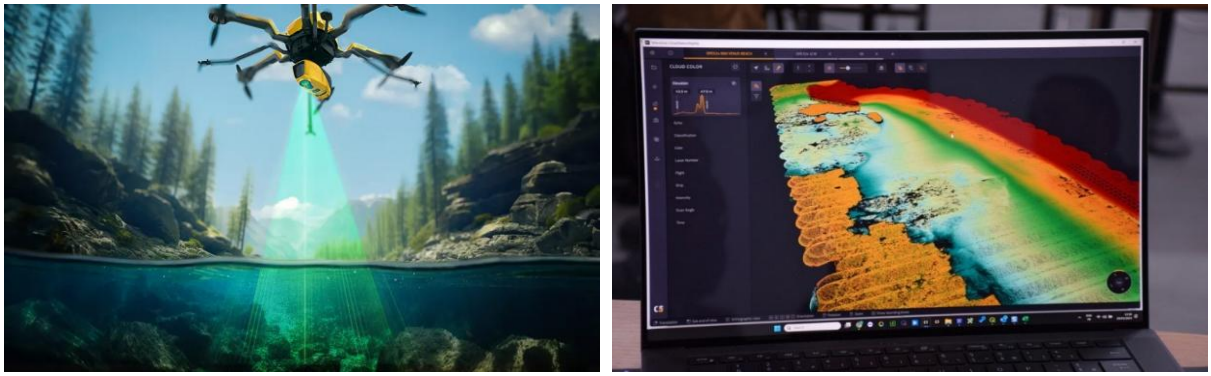

Figure 4. The Navigator and Collected Data During the Exercise (Romanian Naval Forces, 2024).

Table 3. Specifications of Navigator.

Parameter	**Specification**
Size	L 350 x W 160 x H 190 mm
Weight	3.7 kg (8.15 lbs) batt. excl
Laser class	Class 3B - Avoid direct exposure to beam
GNSS inertial solution	SBG Quanta Micro
Precision	3 cm
Accuracy	3 cm
Typ. flight speed	5 m/s
Typ. flying height	80 m
Laser range	Up to 120 m
Laser wavelength	532 nm
Min. Depth	0.30 m
Max. Depth	2 Secchi

4. Hydroid Inc. - REMUS 100 Unmanned Surface Vehicle (USV)

The REMUS 100 USV is a compact, lightweight, and highly versatile autonomous system designed to support a wide range of underwater missions. Its portability and modular structure enable rapid deployment in diverse environments—from shallow littoral zones to offshore operational theaters. As illustrated in Figure 5, two REMUS 100 units are securely housed in a rigid container onboard a support craft, demonstrating the system's ease of transportation and mission readiness. The color-coded handles and compact form factor emphasize the system's operational efficiency and modularity.

Engineered for high-resolution hydrographic surveys, the REMUS 100 also supports environmental monitoring, mine countermeasure operations, and scientific data collection. Table 4 provides a detailed overview of its performance specifications, including endurance, sensor payload capacity, and depth rating—underlining its utility in both defense and civilian applications (Aulinas et al., 2010).

Figure 5. Remus 100 USV (Romanian Naval Forces, 2024).

Table 4. Specifications of REMUS 100 USV.

Parameter	**Specification**
Depth Rating	100 meters (328 feet)
Diameter	19 cm (7.5 inches)
Length	1.6 meters (63 inches)
Weight	37 kg (80 lbs)
Speed	Up to 5 knots
Endurance	Up to 22 hours at 3 knots cruising speed
Navigation Systems	Long Baseline (LBL), Ultra-Short Baseline (USBL), Dead Reckoning, Inertial Navigation System (INS)
Communication	Acoustic modem, Wi-Fi, Iridium satellite (optional)
Sensors	Side-scan sonar, Conductivity-Temperature-Depth (CTD) sensor, Acoustic Doppler Current Profiler (ADCP), optional cameras and environmental sensors

UMS platforms are deployed in various maritime settings, including open seas, coastal regions, and areas with complex underwater terrains. These trials assess the systems' performance in real-world conditions, evaluating factors such as sensor accuracy, data latency, environmental influences (e.g., water salinity, temperature, turbidity), and the UMS's ability to execute mission-specific tasks. The primary sensors under evaluation include:

- **Inertial Measurement Units (IMUs):** These devices provide critical data on the UMS's orientation, acceleration, and angular velocity, enabling precise calculation of position and movement. IMUs are essential for dead reckoning navigation, especially in environments where Global Positioning System (GPS) signals may be degraded or unavailable, such as underwater or in areas with significant signal interference.
- **GPS Receivers:** They determine the UMSs' exact global position by receiving satellite signals. This information is crucial for mission planning, real-time navigation, and coordination with other assets. The integration of GPS data with IMU outputs allows for enhanced accuracy through sensor fusion techniques, mitigating the limitations of each individual system.
- **High-Resolution Sonar Systems:** High-Resolution Sonar Systems emit sound pulses and analyze echoes to create detailed images of the underwater environment. They are essential for seabed mapping, obstacle

avoidance, and detecting underwater mines and hazards, thereby enhancing situational awareness and safe navigation in uncharted waters.

- **Bathymetric LiDAR:** Bathymetric Light Detection and Ranging (LiDAR) systems, also known as airborne LiDAR bathymetry (ALB), use laser pulses to penetrate water and measure underwater topography. They offer rapid, high-resolution data for coastal mapping, shallow-water surveys, and environmental monitoring. By capturing both water surface and bottom reflections, these systems produce precise bathymetric maps essential for navigation, coastal engineering, and marine habitat assessment.
- **Data Integration and Sensor Fusion:** Advanced data fusion algorithms integrate inputs from IMUs, GPS receivers, and sonar systems. Techniques like Kalman filtering combine sensor data to enhance navigation accuracy and robustness. This fusion compensates for individual sensor shortcomings, such as GPS signal loss or IMU drift, by leveraging the strengths of each system to deliver a cohesive and reliable navigation solution.

Findings

The integration of advanced sensor systems such as Real-Time Kinematic GPS (RTK-GPS), enhanced IMUs, LiDAR, and sonar has significantly improved the capabilities of UMSs. These technologies enable precise navigation, improved environmental awareness, and greater mission autonomy. However, several key limitations still affect operational performance in real-world maritime conditions.

RTK-GPS delivers high-accuracy positioning under ideal conditions, but its effectiveness decreases in GPS-denied or obstructed environments such as ports or narrow straits. Signal disruptions — whether caused by physical obstructions or intentional interference such as GPS jamming — can lead to localization errors and reduced system reliability. Similarly, sonar and LiDAR systems perform well in calm, clear waters but become less effective in rough seas or turbid environments due to signal scattering and instability, which degrade data quality.

IMUs, despite technological advancements, remain prone to drift during long missions without GPS corrections. This makes accurate localization increasingly difficult in deep-sea or GPS-limited operations. Furthermore, communication between unmanned and manned systems is hindered by limited bandwidth, latency, and protocol incompatibilities, reducing interoperability and complicating real-time coordination during joint missions.

Although these integrated systems have expanded the operational scope and success rates of UMSs, performance still varies significantly based on environmental conditions and system hardware limitations. Complex sea states, weather variability, and mission duration all contribute to this operational uncertainty.

The study indicates that current sensor fusion methods are insufficient to fully overcome the weaknesses of individual navigation components in such complex conditions. Moreover, navigation and communication systems show performance degradation when exposed to GPS-denied or signal-obstructed maritime environments. These findings emphasize the urgent need for more robust sensor integration strategies and advanced communication frameworks to ensure the resilience and effectiveness of UMSs in critical applications such as maritime security, infrastructure monitoring, and environmental assessment.

Conclusion

The increasing reliance on UMSs highlights their transformative impact on modern naval operations. The findings from the DACIA/TOMIS ROU OPEX 2024 exercise demonstrate that UMSs not only enhance maritime security through precise positioning technologies and advanced sensor integration but also contribute to the seamless coordination between autonomous and manned assets. Their ability to operate in complex environments, execute critical tasks, conduct high-accuracy measurements, and integrate into NATO's strategic framework underscores their growing importance. Future research should focus on refining these technologies to overcome existing limitations, ensuring UMSs remain central to maritime security and coalition-based defense strategies.

References

Aulinas, J., Llado, X., Salvi, J., & Petillot, Y. R. (2010). Selective submap joining for underwater large scale 6-DOF SLAM. *Proceedings of the IEEE/RSJ International Conference on Intelligent Robots and Systems*, 2552–2557. https://doi.org/10.1109/IROS.2010.5650438

Liu, Y., & Bucknall, R. (2015). Path planning algorithm for unmanned surface vehicle formations in a practical maritime environment. *Ocean Engineering, 97*, 126–144. https://doi.org/10.1016/j.oceaneng.2015.01.008

NATO. (2020). *Maritime Unmanned Systems (Fact Sheet)*. Retrieved from https://www.nato.int/nato_static_fl2014/assets/pdf/2020/11/pdf/2011-factheet-mus.pdf, date retrieved 21.05.2025.

NATO Maritime Geospatial Meteorology and Oceanography Centre of Excellence. (2024). *NATO Maritime MGEOMETOC CoE participates in DACIA/TOMIS ROU OPEX 2024*. Retrieved from https://www.mgeometoc-coe.org/News/Pages/NATO-Maritime-MGEOMETOC-CoE-participates-in-DACIATOMIS-ROU-OPEX-2024.aspx, date retrieved 21.05.2025.

Ocean Aero. (n.d.). *The Triton: World's First Autonomous Surface and Underwater Vehicle*. Retrieved from https://www.oceanaero.com/the-triton, date retrieved 21.05.2025.

Romanian Naval Forces. (2024). *Dacia Tomis-24*. Retrieved from https://www.navy.ro/comunicat.php?id=821, date retrieved 05.03.2025.

Teledyne Marine. (n.d.). *Z-Boat 1800RP*. Retrieved from https://www.teledynemarine.com/en-us/products/Pages/z-boat-1800rp.aspx, date retrieved 20.01.2025.

YellowScan. (n.d.). *Bathymetric LiDAR*. Retrieved from https://www.yellowscan.com, date retrieved 22.01.2025.

MATERIAL SCIENCE AND ENGINEERING

Ceramics, Glass, Refractory Materials

Materials Synthesis and Processing

Nanomaterials

Structural and Mechanical Characterization of Repair Welded Steels

Berk Çakır[a], Faiz Muhaffel[a]

[a] Istanbul Technical University, Department of Metallurgical and Materials Engineering, Materials Engineering, Türkiye
cakirb17@itu.edu.tr

Keywords: 4130 Steel, Tungsten Inert Gas Welding, Mechanic Characterization, Repair Welding, Residual Stress.

Aim

High-strength low-alloy (HSLA) steels exhibit superior mechanical properties, including enhanced toughness and strength, along with improved corrosion resistance compared to carbon steels. Additionally, their high weldability makes them widely preferred in various industrial applications. These alloys are commonly used in pressure vessels, where high toughness is a critical requirement.

HSLA steels have a low carbon content like mild steel and contain small amounts of alloying elements such as copper, nickel, niobium, vanadium, chromium, molybdenum, and zirconium. Due to their relatively low alloying element concentrations, they are classified as micro-alloyed steels. The yield strength of HSLA steels ranges from 250 to 600 MPa, making them suitable for applications in industries such as automotive, trucking, and bridge construction (Cochrane, 2012). However, their use in aircraft is limited due to their low specific strength and poor corrosion resistance in harsh environments.

AISI 4130 is a low-alloy carbon steel that contains chromium and molybdenum as alloying elements. Due to its low carbon content, it is highly weldable. However, despite its good weldability, welding defects can still occur due to factors such as process parameters and operator errors. These defects create weak points in the weld areas of pressure vessels, potentially leading to structural failures at pressures lower than the intended levels (Antonini, 2014). The process of eliminating welding defects through an additional welding operation is known as repair welding. Some international standards limit the number of repair welding to one or two. Additionally, as the number of repair welding increases, residual stress in the metal also increases, which can cause structural deterioration, such as distortion, during the welding process (Salami et al., 2014).

Repair welding is a critical procedure in the manufacturing of certain structures. Properly executed repair welding can restore static strength, ductility, fracture toughness, and fatigue strength to levels comparable to the original, defect-free weld areas (Bailey, 1994). Repair welding can be carried out systematically to ensure the production of durable and reliable components, or they can be performed inconsistently. An alternative approach often leads to poor-quality workmanship, failure to fully correct defects, and noncompliance with quality standards, ultimately compromising the integrity of the repaired parts.

Repair welding can be classified into three main categories: the repair of weld defects, the repair of defective parts, and the repair of worn parts (Bailey, 1994). Most existing research on repeated repair welding focuses on the distribution of residual stresses, primarily using finite element simulations (Mallick, 2021). In contrast, studies examining the effects of repeated welding on the microstructure, mechanical properties, and corrosion behavior of steels are limited and primarily concern non-hardenable steels (Bouchard et al., 2005). To date, no detailed investigation into the impact of repeated welding on quenched and tempered steels has been reported in the literature.

In this study, the production process involved repeated weld thermal cycles applied to high-strength low-alloy (HSLA) steels. Subsequently, heat treatment processes were conducted. Mechanical characterizations such as tensile testing, cross-sectional hardness testing, and impact toughness testing were performed on the produced specimens. In addition, residual stress analyses were conducted to investigate the stress accumulation within the structure during repeated weld thermal cycling.

Material and Method

In this study, AISI 4130 plates were obtained and welded using the tungsten inert gas (TIG) welding method. The welded areas were then ground and re-welded under identical parameters to simulate the repair welding process. This process was repeated up to five times, resulting in six different sample groups: an unmodified welded plate and plates subjected to one to five repair welding. Following welding, the plates underwent oil cooling and tempering heat treatments to complete the production process. Additionally, non-heat-treated plates were produced to evaluate the structural effects of repeated welding on the material.

Mechanical test specimens and microstructural characterization samples were taken from both heat-treated and welded plates. Residual stress measurements using the X-ray diffraction (XRD) method were conducted on non-heat-treated plates. The study aims to evaluate the influence of repeated repair welding and increased heat input on the material's microstructure and mechanical properties while evaluating the structural effects of repeated welding. Furthermore, SEM, EDS, and XRD analyses will be used to examine the relationship between the microstructure and properties.

Table 1 provides details regarding sample naming. Each sample set included five tensile test specimens, four notch impact test specimens, two hardness test specimens, and one specimen for microstructural, macrostructural, and SEM/EDS analyses. Additionally, one welded plate without heat treatment was produced for each sample set for residual stress measurements. Mechanical test specimens, both with and without heat treatment, were taken from the same plate to determine base metal properties.

Table 1. Naming of Different Specimens and Welding Procedures.

Sample Name	Welding	1st Repair Welding	2nd Repair Welding	3rd Repair Welding	4th Repair Welding	5th Repair Welding
BM	-	-	-	-	-	-
0R	X	-	-	-	-	-
1R	X	X	-	-	-	-
2R	X	X	X	-	-	-
3R	X	X	X	X	-	-
4R	X	X	X	X	X	-
5R	X	X	X	X	X	X

Findings

The results of the mechanical tests (tensile and impact tests) are presented in Figure 1. The ultimate tensile strength and yield strength of the material are not significantly influenced by the repair welding process, showing only a slight increase. Fracture in all tensile specimens occurs within the heat-affected zone (HAZ). The heat treatment processes ensure uniform strength across all plates. Toughness values increase with multiple repair welding processes, and further studies on material characterization will help clarify the reasons for this increase.

The residual stresses of each repair-welded plate are presented in Figure 2. X-ray diffraction (XRD) has been used to measure residual stress with a portable XRD device that allows measurements to be made at a variety of distances from the weld region. For each specimen, Figure 2 only shows maximum stress values, which are all found near the area of welding. To isolate the effects of repair welding, measurements are carried out on non-heat-treated plates, eliminating residual stresses introduced by the heat-treatment process.

Tensile tests are performed on specimens machined from non-heat-treated plates to determine the threshold points of residual stress. The yield strength of the plates is 350 MPa. This means that if residual stresses form during

welding that exceed this strength, plastic deformation occurs. According to Figure 2, after the third repair, residual stress exceeds the yield strength. This indicates that performing three or more repair welding processes harms the structural properties of the material.

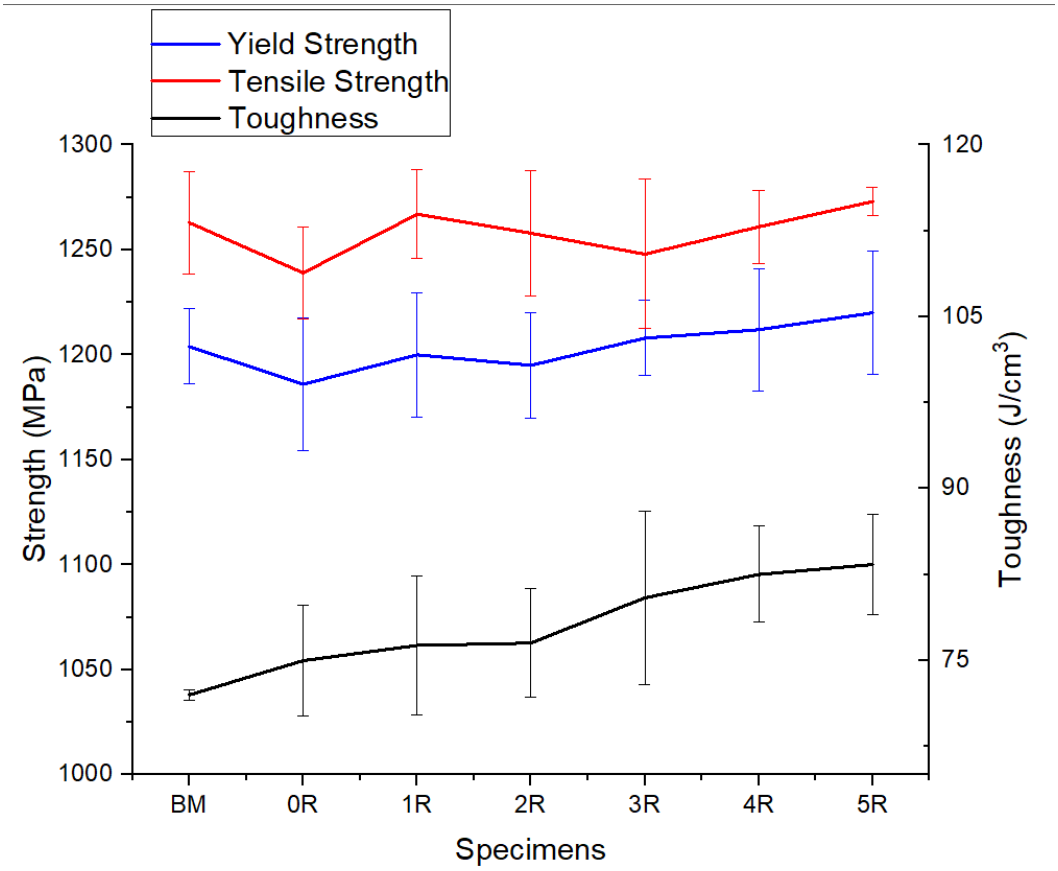

Figure 1. Average Tensile Strength, Yield Strength and Impact Toughness as a Function of Number of Repairs.

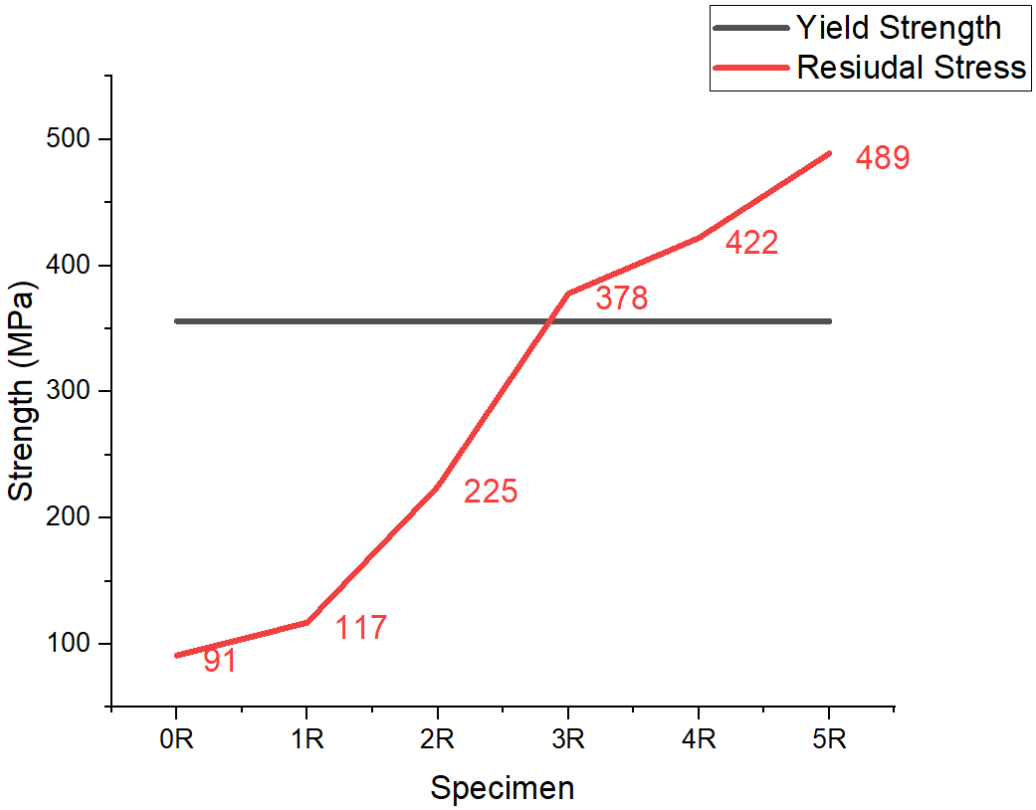

Figure 2. Maximum Residual Stresses as a Funciton of Number of Repairs and Yield Strength of Welded Plate.

Conclusion

In conclusion, the mechanical properties of the plates remain largely unchanged with an increasing number of repair welding. However, residual stress can negatively impact the structural integrity of the material. Future studies will focus on material characterization, including microstructural and macrostructural analyses as well as SEM/EDS examinations, to further investigate the effects of multiple repair welding on both mechanical and structural properties.

References

Antonini, J. M. (2014). 8.04—Health Effects Associated with Welding. In S. Hashmi, G. F. Batalha, C. J. Van Tyne, & B. Yilbas (Eds.), *Comprehensive Materials Processing* (pp. 49–70). Elsevier. https://doi.org/10.1016/B978-0-08-096532-1.00807-4

Bailey, N. (1994). 11—Repair. In N. Bailey (Ed.), *Weldability of Ferritic Steels* (pp. 224–235). Woodhead Publishing. https://doi.org/10.1533/9781845698935.224

Bouchard, P. J., George, D., Santisteban, J. R., Bruno, G., Dutta, M., Edwards, L., Kingston, E., & Smith, D. J. (2005). Measurement of the residual stresses in a stainless steel pipe girth weld containing long and short repairs. *International Journal of Pressure Vessels and Piping*, *82*(4), 299–310. https://doi.org/10.1016/j.ijpvp.2004.08.008

Cochrane, R. C. (2012). 6—Phase transformations in microalloyed high strength low alloy (HSLA) steels. In E. Pereloma & D. V. Edmonds (Eds.), *Phase Transformations in Steels* (Vol. 2, pp. 153–212). Woodhead Publishing. https://doi.org/10.1533/9780857096111.2.153

Mallick, P. K. (2021). Chapter 8—Joining for lightweight vehicles. In P. K. Mallick (Ed.), *Materials, Design and Manufacturing for Lightweight Vehicles (Second Edition)* (pp. 321–371). Woodhead Publishing. https://doi.org/10.1016/B978-0-12-818712-8.00008-2

Salami, P., Khandani, T., Asadi, P., & Besharati Givi, M. K. (2014). 10—Friction stir welding/processing as a repair welding. In M. K. B. Givi & P. Asadi (Eds.), *Advances in Friction-Stir Welding and Processing* (pp. 427–457). Woodhead Publishing. https://doi.org/10.1533/9780857094551.427

Synthesis of Boron Carbon Nitride Particles for Adsorptive Heavy Metal Removal

Sibel Şentürk[a], H. Enis Karahan[a,b], and Hale Gürbüz[a]

[a] Istanbul Technical University, Department of Chemical and Metallurgical Engineering, Chemical Engineering Program, Türkiye
[b] Istanbul Technical University, Synthetic Fuels & Chemicals Technology Center (ITU-SENTEK), Türkiye
senturks16@itu.edu.tr

Keywords: Thermolysis, Surface adsorption, Lead removal, Wastewater, Adsorbent.

Aim

Alternative adsorbents are being sought for various wastewater treatment applications to replace or complement activated carbon, the staple of the field (GadelHak et al., 2023). Among candidates, boron carbon nitride ($B_xC_yN_z$) materials (in short, BCNs) recently attracted growing attention with their tunable chemical and physical attributes akin to graphene and boron nitride materials (Bahadur et al., 2023; Liu et al., 2018; Panda et al., 2023; Portehault et al., 2010; Mighri et al., 2023). Also, BCNs can be synthesized through rather facile and poorly investigated methods, such as thermolysis, which is intriguing to make an exploratory investigation.

To test the potential utility of BCNs in common wastewater treatment problems, such as heavy metal removal, we primarily focused on existing synthesis conditions for preparing adsorbents. In a prominent study dealing with heavy metals removal (i.e., Hg^{2+} and Pb^{2+}), Peng et al. (2018) synthesized BCNs via thermolysis using melamine and boric acid as precursors (at a ratio of 3:0 and 3:5) and deionized water as the solvent. They tested the effect of temperature (in the range of 500-650 °C) at a holding duration of 4 hours. In another study, boron oxide and melamine were reacted at 550 °C (holding duration: 2 hours) using ethanol (Zhong et al., 2019). In a similar study, another group employed the same precursors and solvent for the thermolysis step at 500 °C by keeping the holding time the same (2 hours). However, these researchers subjected their BCN products to heat treatment at 520-600 °C for 2 hours before use (Yan, Li, & Zou, 2010).

Considering the experimental space summarized above, we decided to test the impact of solvent selection (i.e., deionized water and ethanol) and thermolysis temperature (in the range of 500°C to 600°) on the materials properties and performance of resulting BCN materials in adsorption-based Pb^{2+} removal. To analyze the structure and morphology of produced BCN materials, we employed various techniques for characterization, including scanning electron microscopy (SEM), X-ray diffractometry (XRD), energy-dispersive spectroscopy (EDS), and Fourier-transform infrared spectroscopy (FTIR). Lastly, we assessed the gas adsorption behavior and heavy metal removal potential of BCNs using Pb^{2+} as a model contaminant.

Material and Method

In this study, the precursor mixture was prepared by using melamine (MA) and boric acid (BA) in either deionized water or ethanol. The MA-BA mixture was prepared at a ratio of 3:5. Thermolysis experiments were carried out in a muffle furnace by placing the precursor mixtures inside lid-covered alumina crucibles to limit air exposure. The process duration was kept constant at 4 hours for all experiments, while the synthesis temperatures were set at 500 °C or 600 °C. SEM and XRD studies were performed to examine the overall morphology and structural characteristics of as-produced BCN materials. And the elemental and functional compositions of BCNs were evaluated by EDS and FTIR analyses. Finally, the adsorption behavior of the products was evaluated by using nitrogen gas as a probe and Pb^{2+} as a model contaminant. Heavy metal adsorption tests were carried out by exposing the as-produced BCNs (0.4 g/L solids) to 50 ppm Pb^{2+} solution for 24 hours in a thermostatic shaker bath (185 rpm) at 30 °C), and the amount of Pb^{2+} remaining in the solution was determined by inductively coupled plasma mass spectrometry (ICP-MS). The products prepared in deionized water at 500 and 600 °C were named BCN-W500 and BCN-W600, while the ethanol-based samples were named BCN-E500 and BCN-E600, again according to the holding temperatures (500 or 600 °C).

Findings

BCN materials were initially synthesized through thermolysis at 500 °C using different solvents (water or ethanol). Based on the SEM and EDS observations, both solvents (water and ethanol) gave morphologically irregular and agglomerated particles with no visibly large pores (Figure 1). EDS measurements, summarized in Table 1, confirmed the inclusion of B. XRD measurements revealed that those irregular and B-containing agglomerates are amorphous-like in nature with broad peaks belonging to BCN materials observed at around 26.3° and 41.3° (Figure 2). And increasing the synthesis temperature (600 °C) also resulted in similar patterns with minimal shifting (Kokulnathan & Wang, 2019; Yu et al., 2023), with the exception of superimposed sharp features in BCN-W600, which potentially comes for currently unidentified contaminants. FTIR analyses, on the other hand, showed the rich functional group profile of resulting materials, including $-NH_2$, $-NH-$, O−H, C−N, B−O, C−N−(C)−C or C−NH−C, and B−N−B bonds (Figure 3) (Shang et al., 2018). Thus, overall, the BCN synthesis was carried out successfully. Nevertheless, we could not modulate the structural or chemical characteristics of the samples substantially under the tested conditions. Yet still, the adsorption performances of produced materials differed noticeably. While the material synthesized using deionized water achieved virtually 100% Pb^{2+} removal, the ethanol-based samples exhibited much lower performance (Figure 4). Curiously, however, none of the produced BCN materials were highly porous at the (ultra)micropore level with specific surface area values ranging from ~9.2 to ~9.8 m2/g, based on nitrogen adsorption test results analyzed by Brunauer-Emmett-Teller (BET) analyses. As a result, we argue that the observed variations in the Pb^{2+} removal performances could be attributed to the surface charge variations of the synthesized materials. We plan to perform further studies to explore this possibility.

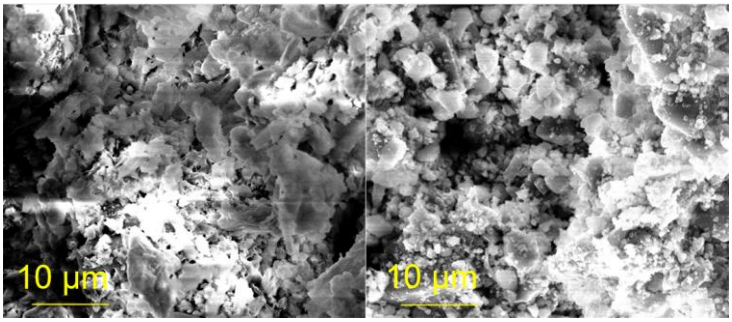

Figure 1. SEM images of BCN-W500 and BCN-E500. (Scale bars indicate 10 µm.).

Table 1. The EDS-based elemental compositions of the samples prepared at 500 °C.

Sample	B (at %)	C (at %)	N (at %)	O (at %)
BCN-W500	21.1	21.4	35.0	22.4
BCN-E500	15.8	33.0	40.6	10.7

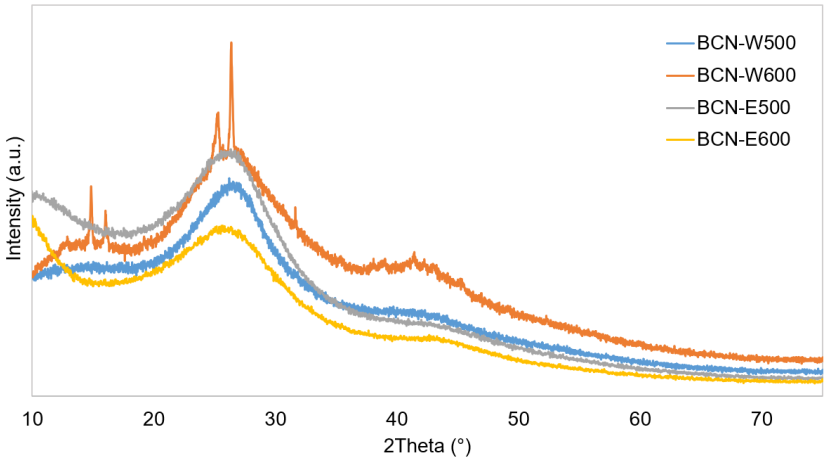

Figure 2. XRD patterns of water- and ethanol-based BCNs.

(Note that BCN-W600, which has not been repeated in this preliminary study.)

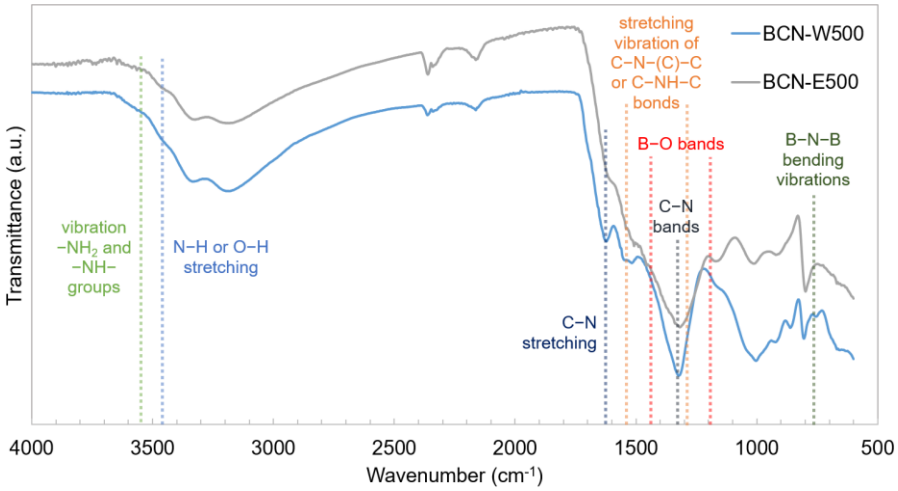

Figure 3. FTIR spectra of BCN-W500 and BCN-E500.

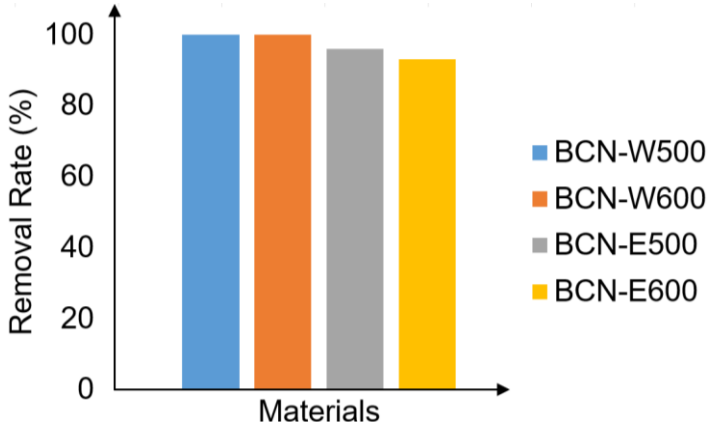

Figure 4. Pb^{2+} adsorption performances of all BCN materials produced.

Conclusion

In this preliminary exploration, we examined the effect of solvent selection and synthesis temperature on the materials' properties and Pb^{2+} removal performances of thermolysis-based BCN products. The produced materials exhibited similar structural characteristics. However, while the lead removal efficiencies of water-based samples were superior, we observed that all samples exhibited promising performances for heavy metal removal applications as adsorbents. Nevertheless, we could not yet explain the mechanism behind the lead removal behavior of produced BCNs as the overall (nitrogen-adsorption-based) porosity of the produced samples was much lower than typical activated carbons. Therefore, we plan to further explore the impact of thermolysis conditions on contaminant removal by employing additional modal contaminants and analytical tools.

References

Bahadur, R., Singh, G., Li, M., Chu, D., Yi, J., Karakoti, A., & Vinu, A. (2023). BCN nanostructures conjugated nanoporous carbon with oxygenated surface and high specific surface area for enhanced CO_2 capture and supercapacitance. *Chemical Engineering Journal*, *460*, 141793.

GadelHak, Y., El-Azazy, M., Shibl, M. F., & Mahmoud, R. K. (2023). Cost estimation of synthesis and utilization of nano-adsorbents on the laboratory and industrial scales: A detailed review. *Science of the Total Environment*, *875*, 162629.

Kokulnathan, T. and Wang, T.J. (2019). Synthesis and characterization of 3D flower-like nickel oxide entrapped on boron doped carbon nitride nanocomposite: An efficient catalyst for the electrochemical detection of nitrofurantoin, *Composites Part B: Engineering, 174*, 106914.

Liu, Z., Fang, Y., Jia, H., Wang, C., Song, Q., Li, L., Lin, J., Huang, Y., Yu, C., & Tang, C. (2018). Novel multifunctional cheese-like 3D carbon-BN as a highly efficient adsorbent for water purification. *Scientific Reports*, *8*(1), 1104.

Mighri, R., Demirci, U. B., & Alauzun, J. G. (2023). Microporous borocarbonitrides $B_XC_YN_Z$: Synthesis, characterization, and promises for CO_2 capture. *Nanomaterials*, *13*(4), 734.

Panda, P., Samanta, R., & Barman, S. (2023). Facile synthesis of Two-Dimensional (2D) boron carbonitride and 2D porous boron carbonitride for excellent energy storage and gas adsorption applications. *Energy & Fuels*, *37*(7), 5540–5555.

Peng, D., Jiang, W., Li, F., Zhang, L., Liang, R., & Qiu, J. (2018). One-pot synthesis of boron carbon nitride nanosheets for facile and efficient heavy metal ions removal. *ACS Sustainable Chemistry & Engineering*, *6*(9), 11685–11694.

Portehault, D., Giordano, C., Gervais, C., Senkovska, I., Kaskel, S., Sanchez, C., & Antonietti, M. (2010). High-surface-area nanoporous boron carbon nitrides for hydrogen storage. *Advanced Functional Materials*, *20*(11), 1827–1833.

Shang, S., Chen, P., Wang, L., Lv, Y., Li, W., & Gao, S. (2018). Metal-free nitrogen- and boron-codoped mesoporous carbons for primary amides synthesis from primary alcohols via direct oxidative dehydrogenation. *ACS Catalysis*, *8*(11), 9936–9944.

Yan, S. C., Li, Z. S., & Zou, Z. G. (2010). Photodegradation of Rhodamine B and methyl orange over boron-doped g-C_3N_4 under visible light irradiation. *Langmuir*, *26*(6), 3894–3901.

Yu, J., Xiong, S., Wang, B., Wang, R., He, B., Jin, J., Wang, H. and Gong, Y. (2023). Constructing boron-doped graphitic carbon nitride with 2D/1D porous hierarchical architecture and efficient N_2 photofixation, *Colloids and Surfaces A: Physicochemical and Engineering Aspects, 656*, 130481.

Zhong, Y., Lin, Y., Chen, Q., Sun, Y., & Fu, F. (2019). Rapid photo-degradation of various organic dyes with thin-layer boron-doped graphitic carbon nitride nano-sheets under visible light irradiation. *Journal of Environmental Chemical Engineering*, *8*(2), 103567.

MECHANICAL ENGINEERING

Additive Manufacturing

Automotive

Computational Fluid Dynamics

Computational Solid Mechanics

Fluid Mechanics

Industrial Data Analytics

Machine Design

Machine Dynamics, Vibration, and Acoustic

System Dynamics and Control

Combustion Simulation of HCNG Fueled Single-Cylinder Research Engine Using Fractal Combustion Model

Eren Özdemir[a], Alper Tolga Çalık[a]

[a] Istanbul Technical University, Faculty of Mechanical Engineering, Department of Automotive, Türkiye
ozdemire22@itu.edu.tr

Keywords: Engine Simulation, Fractal Combustion Model, CNG, HCNG, AVL Cruise M.

Aim

This study investigates the effects of hydrogen (H_2) addition to compressed natural gas (CNG) on combustion and performance in a single cylinder spark-ignition (SI) engine. Two combustion modeling methods are particularly emphasized: AVL Spark Ignited (SI) and Fractal-based models (Ma et al., 2008, 2012) by comparing simulation results with experimental measurements. The Fractal model is used for its ability to more accurately simulate turbulent flame propagation and combustion timing in hydrogen-rich fuel scenarios.

Material and Method

1. Engine Setup and Experimental Data

A diesel single-cylinder research engine was converted to CNG PFI mode, reducing the compression ratio from 17 to ~12 by replacing the injector with a spark plug (Doğan et al., 2019). The relevant specifications are:

Bore: 85 mm, Stroke: 80 mm, Conrod: 145 mm, Compression ratio: ~12.

Control: Spark timing and injection pulse width driven by a custom electronic control system.

Instrumentation: A 70-kW eddy-current dynamometer and AVL GU21D piezoelectric pressure sensor for in-cylinder pressure. Air flow rate is measured by a Dresser G65 flow meter, and the CNG flow rate is tracked by a digital scale.

Experimental runs were at 1500–2000 rpm, 3–5 bar BMEP and additional conditions shown in Table 1. Additional H_2 doping tests were conducted to evaluate the impacts on torque, BSFC, and IMEP (Khodamrezaee & Keshavarz, 2020).

Table 1. Experimental conditions.

Engine speed (rpm)	Lambda (-)	Air Flow Rate (kg/h)	Throttle Control (%)	Atm. Pressure (mbar)	Atm. Humidity (%)	Atm. Temperature ('C)	Fuel Mass (kg)	Fuel Measurement Duration (s)	Vol. Efficiency (%)
2000	1	18.24	23.70	1004	44.5	20	0.032	114	55.97

2. Modeling in AVL Cruise M

AVL Cruise M is a simulation platform for model-based vehicle system development.
The engine model used AVL Spark Ignited and Fractal combustion models, which are more sophisticated than the Wiebe model (Ayad et al., 2021), and was validated at 5 bar BMEP and 2000 rpm. Initially, CNG was used.
The engine model was initially built with AVL Spark Ignited (SI) combustion and 1D intake-exhaust components.

Then, due to its improved representation of turbulent flame propagation which is critical in hydrogen-enriched combustion (Ma et al., 2012), the Fractal model was selected. To ensure compatibility, the engine model was simplified to a zero-dimensional (0D) structure.

Model components included: Intake boundary → manifold → cylinder block → exhaust manifold → exhaust boundary.

Throttle valve to match the measured airflow.
Mass Flow Connection adjusts the fuel flow based on the air–fuel ratio.

3. Combustion Model Selection and Implementation

AVL Spark Ignited (SI) Model:

Quasi-dimensional approach regulates flame speed with parameters like flame speed multiplier (FSM), combustion multiplier (CM), ignition delay multiplier (IDM), swirl ratio, and heat transfer multipliers. It requires tuning CM and FSM to align PFP and crank angle.

Fractal-based Combustion Model:

A two-zone approach with fractal flame surface expansion was used (Ma et al., 2012). The model has a calibrated wall-combustion submodel for HCNG. It captures faster flame speeds and turbulence, especially in hydrogen-enriched cases (Ma et al., 2011, 2012). Fractal geometry improves combustion phasing in lean-burn and HCNG. The interaction between the flame front and turbulence is also modeled (Doğan et al., 2023; Ma et al., 2008, 2012). After CNG validation, the Fractal model was used for hydrogen addition due to its better suitability. The mass burning rate is defined by Equation 1.

$$\left(\frac{dm_b}{dt}\right)_{cfractals} = \rho_u \left(\frac{L_{max}}{L_{min}}\right)^{D_3-2} A_L S_L$$

Equation 1. Mass burning rate with fractal wrinkling.

Where

m_b: Mass of burned fuel
t: Time
ρ_u: Density of unburned fuel
S_L: Laminar flame speed
A_L: Laminar flame area
L: Length scale
D_3: Fractal dimension

Some critical parameters:
Fractal Dimension (D_3): Increases flame surface area → faster combustion, higher PFP, more NOx.

Turbulence Production Constant (C_t): Boosts turbulence → faster flame propagation, higher knock and NOx risk.
Turbulent Length Scale (c_l): Sets eddy sizes affecting flame wrinkling → controls flame surface and burning rate.

4. Hydrogen Addition

Fuel properties were updated, AFR was adjusted, laminar flame speed and turbulence parameters were adjusted to match the combustion dynamics to H_2 (Khodamrezaee & Keshavarz, 2020).

5. Manual Calibration and Global Optimization

There are three stages of calibration and optimization in the study:

First, manual parameter sweeps were performed to evaluate the sensitivity of key combustion variables and their effects on BMEP, torque, PFP, T_{exh}, and BSFC.

Second, Latin Hypercube sampling and discrete genetic algorithms were used as a multi-parameter optimization. The focus was minimizing the error between experiment and simulation (Kavathekar et al., 2021; Ma et al., 2011).

Third, fine-tuning was applied with PID controllers to improve convergence to target operation.

Findings

1. Baseline CNG Results (No H_2)

As shown in Table 2, baseline CNG simulations closely matched experimental data, with less than 5% error in BMEP, BSFC, torque, and PFP at 2000 rpm and 5 bar BMEP (Ma et al., 2012).
The Fractal model accurately reproduces pressure trace shape and combustion duration when it's tuned but requires complex calibration (Ma et al., 2012).
The simulated pressure and ROHR curves (Figure 1 and Figure 2) show an earlier start and broader peak compared to experiments which indicates calibration sensitivity in flame speed and ignition delay parameters.

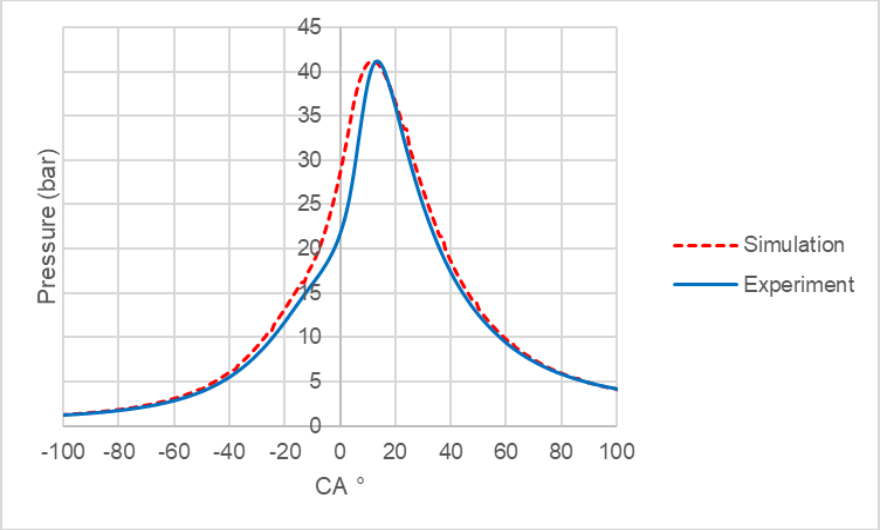

Figure 1. Comparison of experimental and simulated pressure vs. crank angle for CNG.

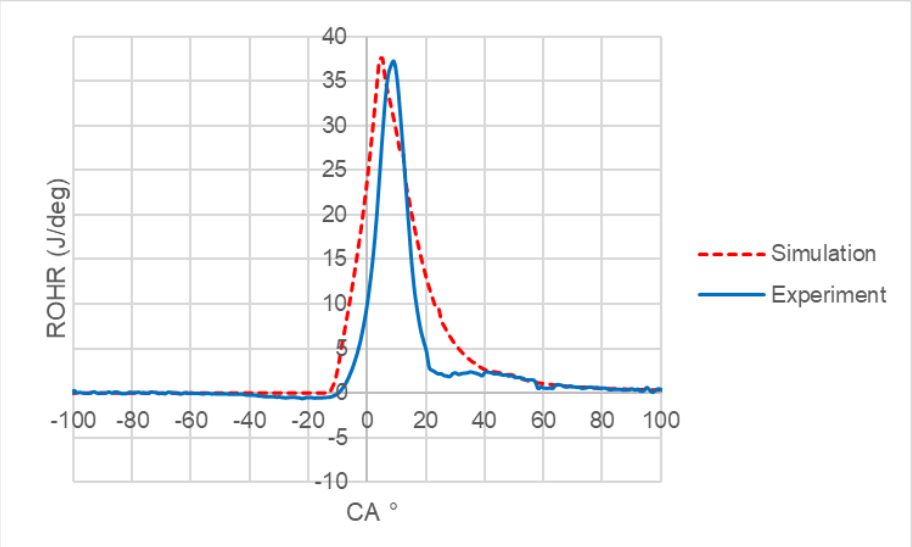

Figure 2. Comparison of experimental and simulated rate of heat release vs. crank angle for CNG.

Table 2. Engine performance metrics: Experimental vs. simulated data for CNG.

5 BMEP	Brake mean effective pressure	Brake specific fuel consumption	Power	Torque	Fuel Consumption Rate	Net indicated mean effective pressure	Peak Firing Pressure (PFP)	PFP Crank Angle	Exhaust Temperature

λ=1.0	BMEP	BSFC	N_e	M_e	$\dot{m}_f$	$IMEP_N$	P_{max}	CA@ P_{max}	T_{exh}
2000 rpm	bar	g/kWh	kW	Nm	kg/h	bar	bar	deg	°C
Simulation	5.22	252.525	3.96	18.85	1.00	6.11	41.37	12.00	498.00
Experiment	5.01	262.275	3.80	18.092	0.996	6.002	41.18	13.0	523.00
%Error	4.12	-3.72	4.24	4.19	0.37	1.80	0.46	-7.69	-4.78

2. Effects of Adding ~15% H_2

Literature reports that BMEP increases with hydrogen addition due to faster flame speeds (Khodamrezaee & Keshavarz, 2020; Park et al., 2020). The peak firing pressure (PFP) typically rises by 1–2 bar, BSFC improves by 2–4%, and optimum spark timing advances slightly (Kavathekar et al., 2021; Khodamrezaee & Keshavarz, 2020). The simulation results reflected similar trends as shown in Figure 3, with faster combustion and increased PFP (Khodamrezaee & Keshavarz, 2020) requiring adjustments in turbulence, laminar flame speed or swirl ratio parameters to prevent over-predictions and maintain combustion stability. Further effects can be seen in Table 3.

In general, these findings are consistent with previous observations in dual-fuel hydrogen-diesel engines as well (Ekin et al., 2022). In addition, the effect of swirl strategies for improving in-cylinder flow have been applied successfully in other studies (Calik et al., 2018). Exhaust temperature (T_{exh}) discrepancies were noted: experiments showed a minor rise, while simulations predicted a decrease. This can be corrected by adjusting the heat transfer multiplier (Khodamrezaee & Keshavarz, 2020).

In future studies, simulations with more than 35% hydrogen enrichment will be conducted as measured data becomes available. These studies will focus on combustion stability, feasibility, and performance impacts using the Fractal model (Ma et al., 2011).

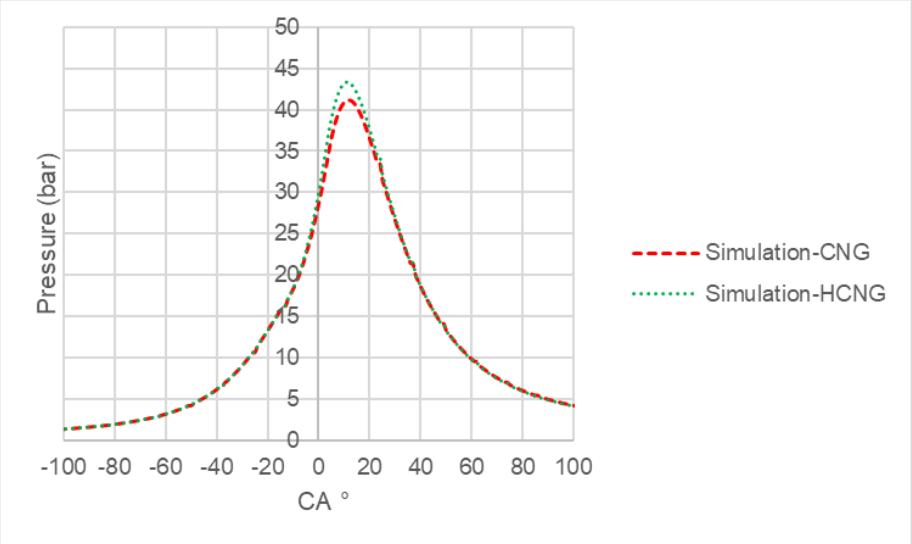

Figure 3. Comparison of simulated pressure vs. crank angle for CNG and HCNG.

Table 3. Engine performance metrics: Simulated data for CNG vs. HCNG.

5 BMEP	Brake mean effective pressure	Brake specific fuel consumption	Power	Torque	Fuel Consumption Rate	Net indicated mean effective pressure	Peak Firing Pressure (PFP)	PFP Crank Angle	Exhaust Temperature
λ=1.0	BMEP	BSFC	N_e	M_e	$\dot{m}_f$	$IMEP_N$	P_{max}	CA@ P_{max}	T_{exh}
2000 rpm	bar	g/kWh	kW	Nm	kg/h	bar	bar	deg	°C
CNG Simulation	5.22	252.53	3.96	18.85	1.00	6.11	41.37	12.00	498.00
HCNG Simulation	5.25	220.55	3.99	18.98	0.88	6.14	43.48	11.0	488.14
%Deviation	0.57	-12.66	0.76	0.69	-12	0.49	5.10	-8.33	-1.98

Conclusion

Both AVL Spark Ignited and Fractal combustion models can precisely predict key performance and combustion parameters in a single-cylinder CNG spark-ignition engine, with less than 5% deviation from experimental data under baseline conditions. Comparable accuracy has also been reported in the literature (Ma et al., 2008, 2011), supporting the modeling approach used. This study found that the Fractal model was more effective for hydrogen-enriched scenarios, particularly in representing turbulent flame propagation and combustion phasing, which aligns with previous findings (Ma et al., 2012).

Simulations with 15% hydrogen addition showed improvements in BMEP, combustion stability, and fuel efficiency, which are consistent with empirical trends and literature findings (Ma et al., 2011, 2012). However, the potential for increased peak firing pressures and NOx emissions requires careful optimization of ignition timing and combustion parameters to ensure stable operation (Khodamrezaee & Keshavarz, 2020).

The current 0D model configuration limits the analysis of transient behavior with exhaust gas characteristics. Combustion chamber designs, such as piston bowl modifications, can enhance turbulence and flame propagation in HCNG engines (Temizer & Cihan, 2021), and these aspects should be addressed in future studies.

Future studies will explore hydrogen enrichment beyond 35% for combustion stability and performance. EGR and advanced spark control may be needed to mitigate knock and NOx (Ma et al., 2008).

References

Ayad, S. M. M. E., Vago, C. L., Belchior, C. R. P., & Sodré, J. R. (2021). Cylinder pressure based calibration model for engines using ethanol, hydrogen and natural gas as alternative fuels. *Energy Reports*, *7*. https://doi.org/10.1016/j.egyr.2021.06.015

Calik, A. T., Taskiran, O. O., & Mehdiyev, R. (2018). Numerical investigation of twin swirl application in diesel engine combustion. *Fuel*, *224*. https://doi.org/10.1016/j.fuel.2018.03.049

Doğan, H. E., Demirci, A., Kutlar, O. A., Arslan, H., & Cihan, Ö. (2023). Prediction of the mean turbulence intensity with a thermodynamic model for CNG and gasoline fuels. *Fuel*, *348*. https://doi.org/10.1016/j.fuel.2023.128532

Doğan, H. E., Kutlar, O. A., Javadzadehkalkhoran, M., & Demirci, A. (2019). Investigation of burn duration and NO emission in lean mixture with CNG and gasoline. *Energies*, *12*(23). https://doi.org/10.3390/en12234432

Ekin, F., Ozsoysal, O. A., & Arslan, H. (2022). The effect of using hydrogen at partial load in a diesel-natural gas dual fuel engine. *International Journal of Hydrogen Energy*, *47*(42). https://doi.org/10.1016/j.ijhydene.2022.03.287

Kavathekar, K. P., Thipse, S. S., Rairikar, S. D., Sonawane, S. B., Sutar, P. S., & Bandyopadhyay, D. (2021). Study of Effect on Engine Performance Using 15% HCNG Blend Versus CNG Using a Simulation Approach. *Lecture Notes in Mechanical Engineering*. https://doi.org/10.1007/978-981-15-3639-7_25

Khodamrezaee, F., & Keshavarz, A. (2020). Thermodynamic and experimental analysis of hydrogen addition to CNG in a spark ignition engine for emission reduction. *Energy Sources, Part A: Recovery, Utilization and Environmental Effects*. https://doi.org/10.1080/15567036.2020.1743388

Ma, F., Deng, J., Qi, Z., Li, S., Chen, R., Yang, H., & Zhao, S. (2011). Study on the calibration coefficients of a quasi-dimensional model for HCNG engine. *International Journal of Hydrogen Energy*, *36*(15). https://doi.org/10.1016/j.ijhydene.2011.04.177

Ma, F., Li, S., Zhao, J., Qi, Z., Deng, J., Naeve, N., He, Y., & Zhao, S. (2012). A fractal-based quasi-dimensional combustion model for SI engines fuelled by hydrogen enriched compressed natural gas. *International Journal of Hydrogen Energy*, *37*(12). https://doi.org/10.1016/j.ijhydene.2012.03.045

Ma, F., Wang, Y., Wang, M., Liu, H., Wang, J., Ding, S., & Zhao, S. (2008). Development and validation of a quasi-dimensional combustion model for SI engines fuelled by HCNG with variable hydrogen fractions. *International Journal of Hydrogen Energy*, *33*(18). https://doi.org/10.1016/j.ijhydene.2008.06.068

Park, B. Y., Lee, K. H., & Park, J. (2020). Conceptual approach on feasible hydrogen contents for retrofit of CNG to HCNG under heavy-duty spark ignition engine at low-to-middle speed ranges. *Energies*, *13*(15). https://doi.org/10.3390/en13153861

Temizer, İ., & Cihan, Ö. (2021). Analysis of different combustion chamber geometries using hydrogen / diesel fuel in a diesel engine. *Energy Sources, Part A: Recovery, Utilization and Environmental Effects*, *43*(1). https://doi.org/10.1080/15567036.2020.1811808

CFD Analysis of The Effects Of Hydrogen Addition On The Performance And Emissions Of A Natural Gas-Fuelled Single-Cylinder Internal Combustion Engine

Barış Bingül[a], Hikmet Arslan[a]

[a] Istanbul Technical University, Mechanical Engineering, Automotive, Türkiye
bingul18@itu.edu.tr

Keywords: CFD, Hydrogen, ICE, Natural Gas.

Aim

The single-cylinder test engine, modified from original production of Anadolu Motor Production and Marketing Inc., located in the Automotive Laboratory of Istanbul Technical University, has been used for various academic studies. With the engine, which was converted from compression ignition to spark ignition, these studies have been conducted with gasoline and natural gas fuels on different combustion chambers. In this study, after validating the experimental data of the engine operated with natural gas fuel by using three-dimensional computational fluid dynamics, an emission and performance analysis will be conducted by adding hydrogen to the mixture in different ratios.

Along with the advancing technology, consumption habits, and production relations, the number of polluting gases released into nature has risen to critical levels throughout human history. As the concentration of these gases in the atmosphere increases, they contribute to the greenhouse effect. The primary greenhouse gases are carbon dioxide (CO_2), nitrogen oxides (NOx), and methane (CH_4). The excess of these polluting gases causes the greenhouse effect, raising the average global temperature over the years. 25% of the gases responsible for this problem come from the transportation sector, and 25% of this portion is released due to the use of internal combustion engines in automobiles (Al-Wreikat et al., 2021).

The hydrogen-natural gas mixture offers significant advantages in internal combustion engines, both environmentally and in terms of their performance. Natural gas is a fuel with a low combustion rate. When mixed with hydrogen, which has a wide combustion range and high combustion speed, a more homogeneous and efficient combustion process is achieved, providing stability even under low load conditions, thereby increasing fuel efficiency (Mariani et al., 2013; Park et al., 2011). Additionally, adding up to 20% hydrogen by volume can be applied without major changes to the existing engine structure, resulting in power increase while significantly reducing harmful emissions, particularly carbon monoxide (CO) and unburned hydrocarbons (HC). However, when hydrogen exceeds 20% by volume, thermal losses increase, leading to a decrease in efficiency (Bundele et al., 2022). Although hydrogen addition may sometimes cause an increase in NO_x emissions, this can be controlled with proper calibration and combustion strategies (Costa et al., 2021). Thus, hydrogen-natural gas fuel presents an innovative alternative for the future of internal combustion engines in a time when emission regulations are becoming stricter.

Material and Method

In this study, a single-cylinder spark-ignition internal combustion engine produced by Anadolu Motor will be used. The Antor 3LD 450 engine, originally manufactured as a diesel engine, has been converted to a spark-ignition engine (Kutlar, 1999). Various doctoral students have conducted experiments on this engine, which retains the construction of a diesel engine. The experiments with natural gas fuel in doctoral thesis (Doğan, 2019) will be used to validate the CFD analyses in this study. Table 1 shows the general specifications of the engine, while Table 2 presents the experimental information.

Table 1: Specifications of test engine.

Parameter	Value	Unit
Engine	Antor 3LD 450	-
Number of Cylinder	1	-
Stroke x Bore	80 x 85	mm
Compression Ratio	12	-
Stroke Volume	454	cm^3
Connecting Rod Length	145	mm
Crank radius/ connecting rod length	0.275	-
Dead Volume	7.9	cm^3
Intake valve opening	16	°CAD
Intake valve closing	40	°CAD
Exhaust valve opening	40	°CAD
Exhaust valve closing	16	°CAD
Power	7.35 (3000 rpm)	kW
Torque	28.5 (1700 rpm)	Nm

Table 2: Information of experiments.

Parameter	Value	Unit
Engine Speed	1501	rpm
BMEP	5.03	bar
Lambda	1.02	-
Fuel Mass Flow	0.7992	kg/h
Maximum Pressure	43.5	bar
Pmax Location	12.2	CAD
IMEPH	6.25	bar
IMEPN	5.95	bar
Spark Advance	15	CAD BTDC

The mass and mole ratios of the natural gas mixture used in the experiments conducted by Hüseyin Emre Doğan are provided in Table 3 below. Since butane (C_4H_{10}) fuel is not present in the combustion mechanism, it could not be included in the calculations. Since the engine operates with a homogeneous mixture, the fuel-air mixture will be introduced into the combustion chamber as the initial condition. In Figure 1 below, the mass ratios of the gas mixture at the initial conditions for different fuel-air mixtures are shown. The hydrogen ratio in the mixture was increased in such a way that the thermal energy of the fuels remained constant.

Table 3: Mole and Mass Fractions of Fuel.

Gas	Formula	Mole Fraction, %	Mass Fraction, %
Methane	CH_4	94.277	88.799
Ethane	C_2H_6	3.1889	5.6317
Propane	C_3H_8	0.796	2.0618
Butane	C_4H_{10}	0.2939	1.0035
Nitrogen	N_2	1.1655	1.9211
Carbon Dioxide	CO_2	0.2255	0.5833

Case 1	
0%	
H_2	0
CH_4	0.0489
C_2H_6	0.0031
C_3H_8	0.0015
CO_2	0.006
H_2O	0.0048
O_2	0.2114
N_2	0.7247

Case 2	
5%	
H_2	0.0011
CH_4	0.0465
C_2H_6	0.003
C_3H_8	0.0015
CO_2	0.006
H_2O	0.0048
O_2	0.2114
N_2	0.7247

Case 3	
10%	
H_2	0.0022
CH_4	0.044
C_2H_6	0.0029
C_3H_8	0.0014
CO_2	0.006
H_2O	0.0048
O_2	0.2114
N_2	0.7247

Case 4	
15%	
H_2	0.0033
CH_4	0.0416
C_2H_6	0.0027
C_3H_8	0.0014
CO_2	0.006
H_2O	0.0048
O_2	0.2114
N_2	0.7247

Case 5	
20%	
H_2	0.0044
CH_4	0.0391
C_2H_6	0.0025
C_3H_8	0.0012
CO_2	0.006
H_2O	0.0048
O_2	0.2114
N_2	0.7247

Figure 1: Initial Gas Mixture of Different Cases.

Ansys Forte was used for 3D computational fluid dynamics analysis. To reduce and simplify the computational time, a combustion chamber with a compression ratio of 12 was modelled as a quarter geometry, using Creo Parametric. The model imported into Ansys Forte was meshed using an adaptive mesh method, with finer mesh regions around the spark zone, walls, and areas of high velocity and pressure, while the remaining parts of the model were assigned a coarser mesh.

For the combustion model in Forte, the Grimech 3.0 model was selected. This model, whose characteristics are presented in Table 4, has been widely used in the literature for methane-hydrogen mixtures, yielding successful results (Cameretti et al., 2023; De Robbio et al., 2022; Halter et al., 2005). Subsequently, the initial and boundary conditions were determined based on experimental conditions and measurements. The parameters within the Flame Speed and Turbulence Model, as mentioned in the Ansys Forte Theory Manual, were manipulated to validate the calculations (Ansys Forte Theory Manual, 2023).

Table 4: Properties of Grimech 3.0 Mechanism.

Grimech 3.0 Mechanism	
Fuels	Hydrogen, Methane
Oxidizer	Air
Number of species	53
Number of reversible reactions	325

Findings

The comparison between the analysis results and experimental data is illustrated in the Pressure – Crankshaft Angle graph shown in Figure 2. During the compression phase, it is evident that the curves closely overlap, with only minor discrepancies that remain within acceptable limits. This alignment highlights the strong correlation between the simulation outcomes and the experimental measurements, providing a solid foundation for the reliability of the analysis.

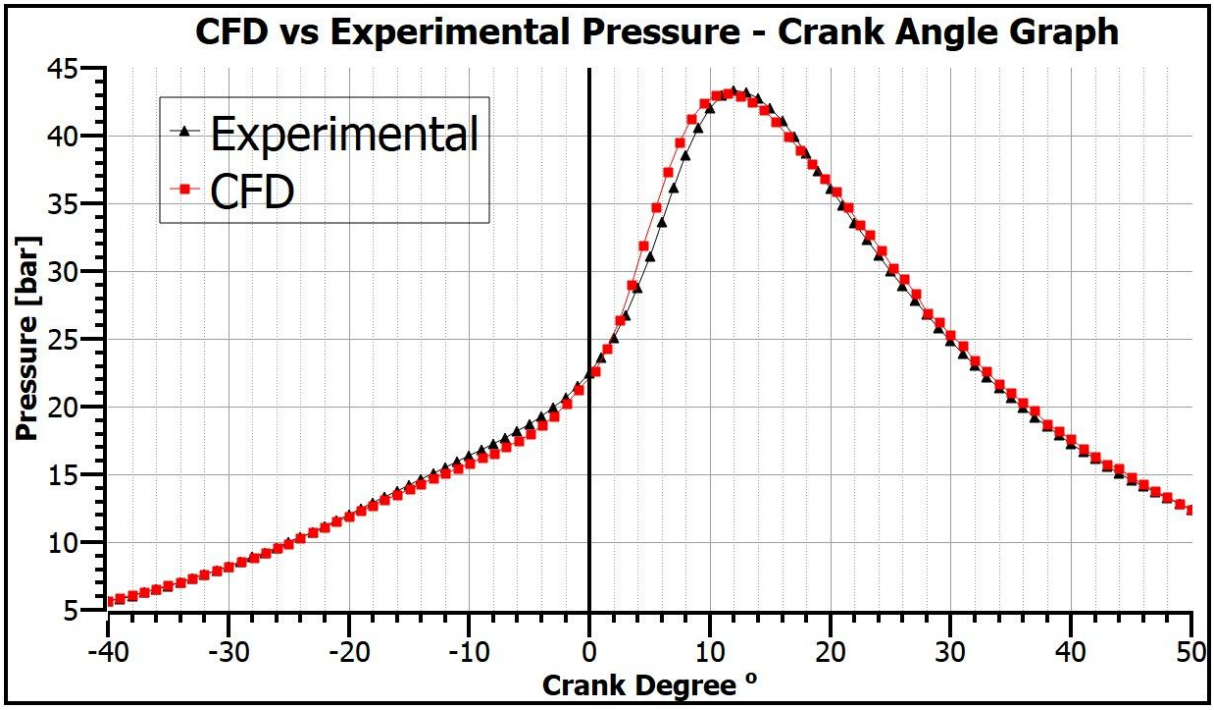

Figure 2: Graph of CFD vs Experimental Pressure – Crank Angle Degree.

After the validation process, results were obtained by adding hydrogen to the mixture in different ratios. As shown in Figure 3, as the amount of hydrogen added to the mixture increases, the combustion rate also increases, causing the peak pressure to occur at an earlier time. Additionally, it is observed that the maximum pressure value increases. Since the same spark advance value was used for all five models, the curves shift to the left as the hydrogen ratio increases. This shift indicates an early pressure rise, which results in a decrease in efficiency. To mitigate this, spark ignition advance values should be optimized. As the hydrogen ratio increases, without the optimization of spark advance, early pressure rise occurs, leading to a decrease in thermal efficiency, as shown in Figure 4. Consequently, due to the decrease in efficiency, the gross indicated power (GIP) value also decreases. Theoretically, when hydrogen is added, the combustion is faster, and an increase in thermal efficiency is expected. To observe this result, spark advance optimization, as previously mentioned, must be performed.

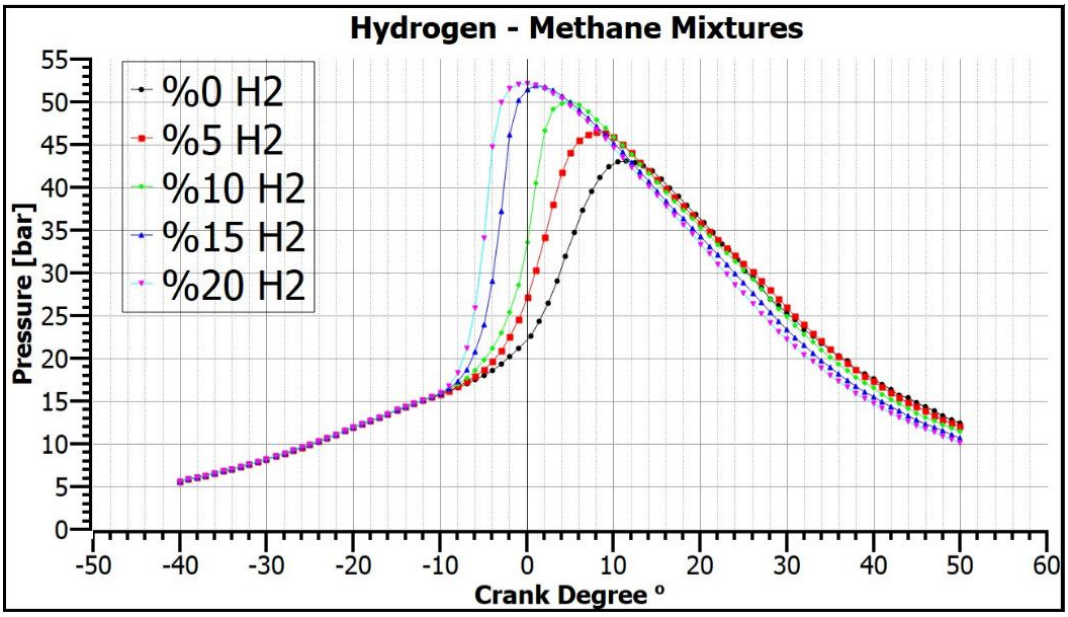

Figure 3: Graph of Pressure – Crank Angle Degree for Different Hydrogen-Methane Mixtures.

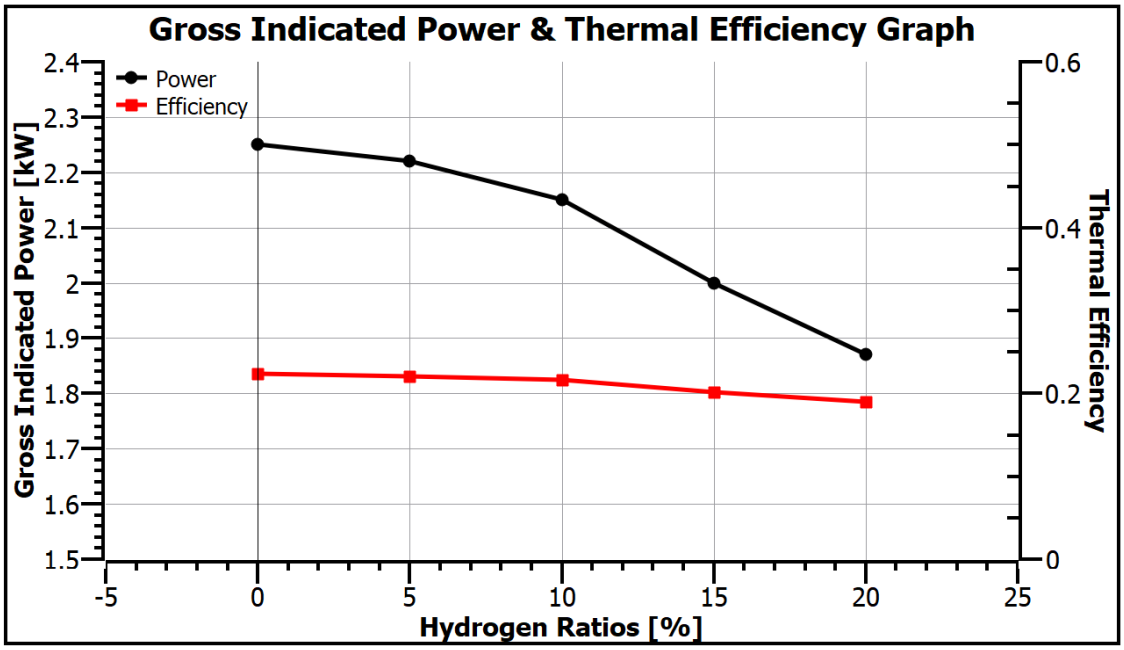

Figure 4: Graph of Gross Indicated Power & Thermal Efficiency for Different Hydrogen-Methane Mixtures.

Since hydrogen has a higher combustion temperature compared to other fuels, it is expected that the maximum temperature value will increase as the hydrogen ratio increases. However, when hydrogen is first added to the mixture, the maximum temperature value decreases, due to the previously mentioned reasons that lead to a reduction in thermal efficiency. As the hydrogen ratio in the mixture increases, the maximum temperature value also rises. In internal combustion engines, NO_X emissions are directly proportional to the temperature in the combustion chamber. As the combustion temperature increases, NO_X formation accelerates, and as shown in Figure 5, NO_X emissions also rise with the increasing hydrogen ratio in the mixture. The cause of this phenomenon is the increase in the maximum temperature value. On the other hand, CO emissions decrease as the hydrogen ratio increases. Since the amount of natural gas in the mixture decreases as the hydrogen ratio increases, a reduction in carbon-containing emissions is an expected outcome. However, as the hydrogen amount increases, the rate of CO emission reduction progressively decreases.

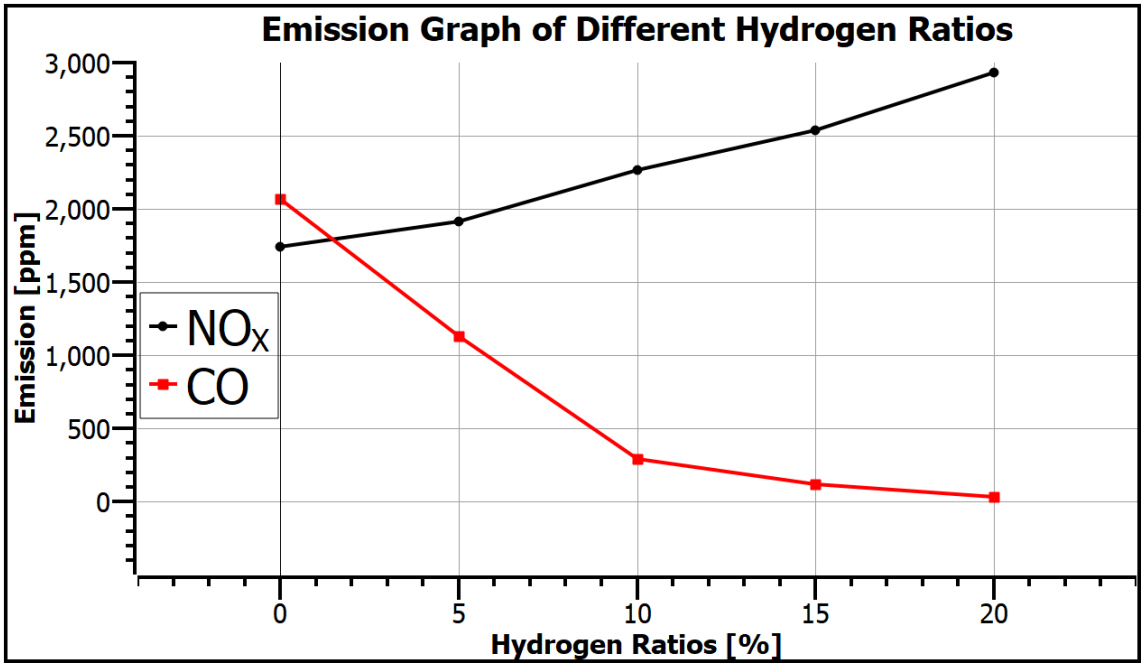

Figure 5: Graph of NOx and CO Emissions for Different Hydrogen-Methane Mixtures

Conclusion

In this study, the effects of hydrogen addition on the performance and emissions of a converted spark-ignition engine fuelled with natural gas were analysed using experimental data and computational fluid dynamics (CFD) simulations. The results showed that increasing the hydrogen ratio in the fuel mixture led to an earlier peak pressure due to the faster flame speed, which caused a reduction in thermal efficiency when the spark timing was not optimized. This indicates that spark advance optimization is necessary to fully utilize the benefits of hydrogen addition without sacrificing engine efficiency. Furthermore, while the initial introduction of hydrogen resulted in a slight decrease in peak temperature due to efficiency losses, further increases in hydrogen concentration led to a higher combustion temperature. This directly impacted NO_x emissions, which increased as the hydrogen ratio rose, confirming the strong correlation between combustion temperature and NO_x formation. In contrast, CO emissions decreased with higher hydrogen content due to the reduced presence of carbon-based fuel components. However, the reduction rate of CO emissions diminished as hydrogen concentration increased.

Overall, this study highlights the potential of hydrogen as a supplementary fuel to improve combustion characteristics while emphasizing the need for optimized engine parameters to mitigate efficiency losses and control emissions effectively. Future work should focus on refining spark timing and exploring exhaust gas recirculation (EGR) strategies to balance the trade-offs between performance and emissions.

References

Al-Wreikat, Y., Serrano, C., & Sodré, J. R. (2021). Driving behaviour and trip condition effects on the energy consumption of an electric vehicle under real-world driving. *Applied Energy*, *297*. doi: 10.1016/j.apenergy.2021.117096

Ansys Forte Theory Manual. (2023). Retrieved from http://www.ansys.com [Accessed 2025 May 23]

Bundele, H., Kurien, C., Varma, P. S., & Mittal, M. (2022). Experimental and computational study on the enhancement of engine characteristics by hydrogen enrichment in a biogas fuelled spark ignition engine. *International Journal of Hydrogen Energy*, *47*(71). doi: 10.1016/j.ijhydene.2022.07.029

Cameretti, M. C., De Robbio, R., & Palomba, M. (2023). Numerical Analysis of Dual Fuel Combustion in a Medium Speed Marine Engine Supplied with Methane/Hydrogen Blends. *Energies*, *16*(18). doi: 10.3390/en16186651

Costa, M., Piazzullo, D., & Dolce, A. (2021). Hydrogen Addition to Natural Gas in Cogeneration Engines: Optimization of Performances Through Numerical Modeling. *Frontiers in Mechanical Engineering*, *7*. doi: 10.3389/fmech.2021.680193

De Robbio, R., Cameretti, M. C., Mancaruso, E., Tuccillo, R., & Vaglieco, B. M. (2022). CFD Analysis of Different Methane/Hydrogen Blends in a CI Engine Operating in Dual Fuel Mode. *SAE Technical Papers*. doi: 10.4271/2022-01-1056

Doğan, H. E. (2019). *Farklı Yanma Odası Geometrilerinin Doğal Gaz Ve Benzin Yakıtı İle İncelenmesi*.

Halter, F., Chauveau, C., Djebaïli-Chaumeix, N., & Gökalp, I. (2005). Characterization of the effects of pressure and hydrogen concentration on laminar burning velocities of methane-hydrogen-air mixtures. *Proceedings of the Combustion Institute*, *30*(1). doi: 10.1016/j.proci.2004.08.195

Kutlar, O. A. (1999). *Dört Zamanlı Otto Çevrimli Motorlarda Kısmi Yakıt Tüketimini Azaltmak İçin Yeni Bir Yöntem (Periyot Atlatmalı Motor)*.

Mariani, A., Prati, M. V., Unich, A., & Morrone, B. (2013). Combustion analysis of a spark ignition i. c. engine fuelled alternatively with natural gas and hydrogen-natural gas blends. *International Journal of Hydrogen Energy*, *38*(3). doi: 10.1016/j.ijhydene.2012.11.051

Park, C., Kim, C., Choi, Y., Won, S., & Moriyoshi, Y. (2011). The influences of hydrogen on the performance and emission characteristics of a heavy duty natural gas engine. *International Journal of Hydrogen Energy*, *36*(5). doi: 10.1016/j.ijhydene.2010.12.021

MECHANICAL ENGINEERING

Additive Manufacturing

Automotive

Computational Fluid Dynamics

Computational Solid Mechanics

Fluid Mechanics

Industrial Data Analytics

Machine Design

Machine Dynamics, Vibration, and Acoustic

System Dynamics and Control

Design Optimization of Crane Hook by using Generative Design Approach

Cihat Sofracı[1], Eren Kalay[1], C. Erdem İmrak[1]

[1]Istanbul Technical University, Faculty of Mechanical Engineering, Department of Mechanical Engineering, Turkiye
sofraci20@itu.edu.tr

Keywords: Crane hook, Generative Design, Optimization, Weight Reduction.

Aim

The primary aim of this research is to conduct design optimization of NR025 crane load hook, which is manufactured according to the DIN15401 standard, by using a generative design methodology. Crane hooks are important mechanical components which are commonly used in various industries, such as construction and logistics[1]. While it is serving in the field, it should also meet safety and efficiency requirements[2]
Main motivation of proposed project is based on limitations that we had from past to the present [6]. Analytical approach (Equation 1) was conventional method to improve existent designs and to conduct design optimization related studies. Considering current capabilities, growing finite element methods and their solvers, on top of that, artificial intelligence based software being implemented to these methods, it is vital to engage with these methods and take advantage of these opportunities to improve current designs and re-think over the limitations that we had for years. In this direction, generative design offers a new solution to these challenges by integrating artificial intelligence-driven algorithms that simultaneously optimize material, geometry and manufacturability.

$$\sigma = \frac{F}{A} + \frac{My}{I}$$

Equation 1 – Analytical Approach

Where M is the maximum bending moment, Y is the distance from the centroid axis to the neutral axis, and I is the moment of inertia for different cross-sections

Material and Method

1.Crane Hook Modeling: Single crane hook is modeled in a computer-aided design (CAD) environment using industry-recognized software which is SolidWorks 2017 Student Edition. The standard dimensions have taken based on DIN15401 specifications, and the model has been analyzed under different loading conditions using finite element analysis (FEA). The stress distribution, deformation characteristics, and failure points have been identified through this simulation process. Special attention is given to stress concentration areas, as these are the primary indicators of structural weaknesses in the traditional crane hook design.
The most critical sections of the single hook are called A-B and C-D sections according to DIN15401 standard. These sections will be mentioned in the following parts of the extended abstract.

2.Finite Element Model: Mesh structure of analysis was created by using Ansys Structural 19.2 software. The element size was selected as 1mm. 511562 nodes and 147625 elements with hexagonal 3D shape were used. Large deformation has not been used since the expected maximum equivalent stress is below than yield strength of the material. Afterwards, hook model was loaded within the range of 0,5KN to 10KN. It has been fixed from all degree of freedooms from top of the hook in a way that it could reflect the test. Load direction is passed through the shaft axis as test is conducted. In this regard, stress and strain results were recevied as shown in Figure 1. below.

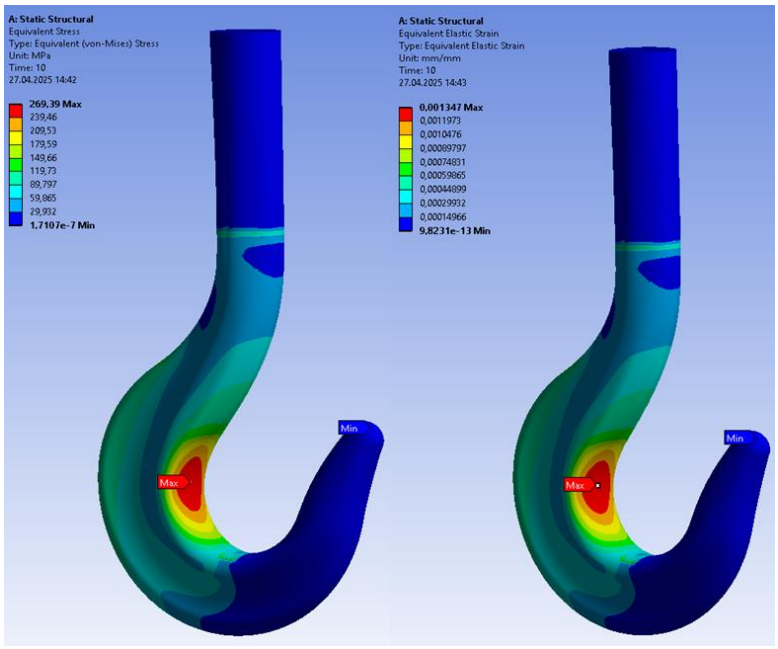

Figure 1. FEA Model Von-Mises Stress and Elastic Strain Results.

3.Experimental Validation: Accuracy of FEA model is verified through tensile testing, which is conducted under controlled laboratory conditions. To validate both the FEA model, CAD model and the material properties, bi-axial rosette types strain gauges which are able to measure the strain in both horizontal and vertical directions, were deployed on the inner and outer surfaces of Section A-B as shown in Figure 2. Sample hook was loaded within a specific load range between 0,5KN and 10KN, and the results of biaxial strain values were recorded. These values were compared with the corresponding results from the FEA model under the same load conditions.

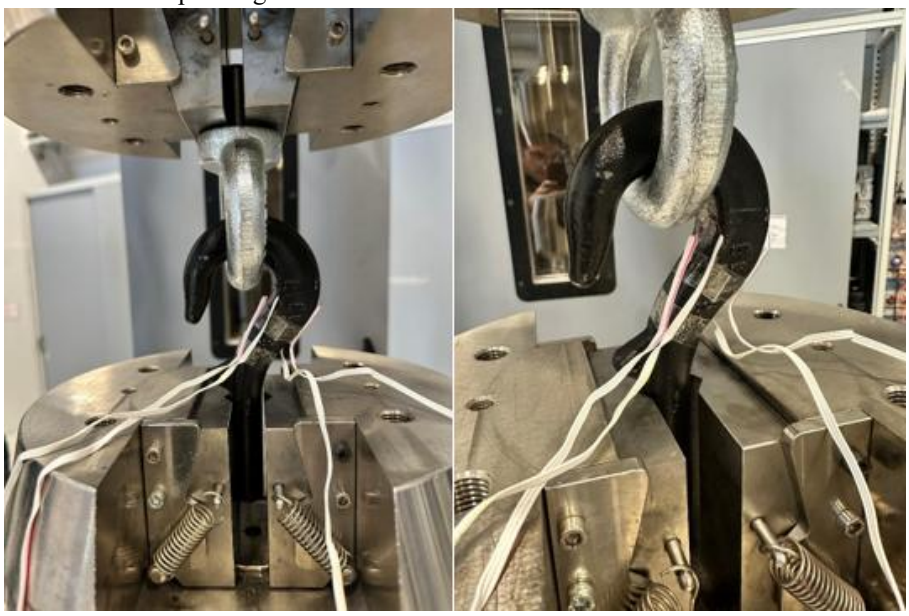

Figure 2. Test Instrumentation of single hook.

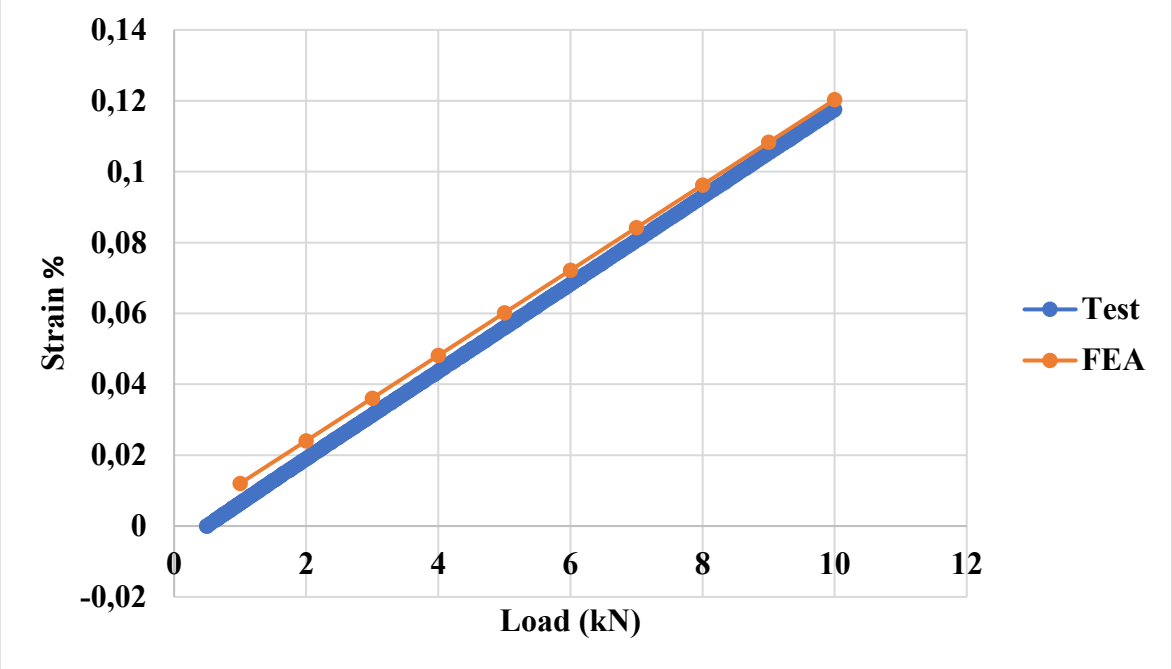

Figure 3. Test and FEA Model Comparison.

Deformation occured is within elastic limit of material since strain vs load graph shows the slope is lineer. Additionally, poisson ratio has been calculated by Equation 2. Results show that poisson ratio is between 0.3 and 0.34.

$$\upsilon = -\frac{\varepsilon_{horizontal}}{\varepsilon_{vertical}}$$

Equation 2 – Analytical Approach

Where υ is poisson's ratio, ε is strain.

In this comparison, the elastic modulus and Poisson's ratio were changed within the limits set by the Taguchi method (L9 orthogonal array) to identify the most consistent elasticity modulus and poisson ratio with experimental data. It is observed that 220GPa Elasticity modulus and 0,32 poisson's ratio are the best match with FEA model over other trials as it is shown in Figure 3. Besides, detailed comparison results with factors chosen is shown in Table 1.

Table 1. με (%ε x 1000) Delta Between FEA and Test.

E (Gpa)	Poisson's Ratio	Inner Surface		Outer Surface		Average Delta
		Vertical	Horizontal	Vertical	Horizontal	
200	0.3	14,44	1,849	5,944	0,597	5,7075
200	0.32	14,82	4,647	5,996	0,642	6,52625
200	0.34	15,2	7,479	6,046	1,883	7,652
220	0.3	2,44	1,581	0,309	2,269	1,64975
220	**0.32**	**2,79**	**0,963**	**0,355**	**1,142**	**1,3125**
220	0.34	3,14	3,537	0,401	0,014	1,773
240	0.3	7,55	4,44	4,388	3,661	5,00975
240	0.32	7,23	2,107	4,345	2,628	4,0775
240	0.34	6,92	0,253	4,303	1,594	3,2675

4. Generative Design: Using the validated CAD model and physical material properties, the process has proceeded with the generative design phase in Fusion 360 (version 2021). Based on the stress distribution of the hook, the volume with the highest potential for material reduction was identified. This volume with constraints and boundary conditions, entered as an input into the software.

As per catalog values of hook, maximum load that it can carry has been applied, passing through the shaft axis. Top area of the shaft of the hook has been fixed within all degrees of freedom. Factor of safety has been chosen as 1.5. As for material selection, Fusion 360 has wide range of materials. Choosing the right material is vital since it puts some limitations on the software. Physical properties of material, elasticity modulus, poisson's ratio and yield strength has been entered as 220GPa, 0,32 and 315MPa respectively. Yield strength of material data comes from DIN15400 standard for hook P-Grade material. The other ones received from test validation.

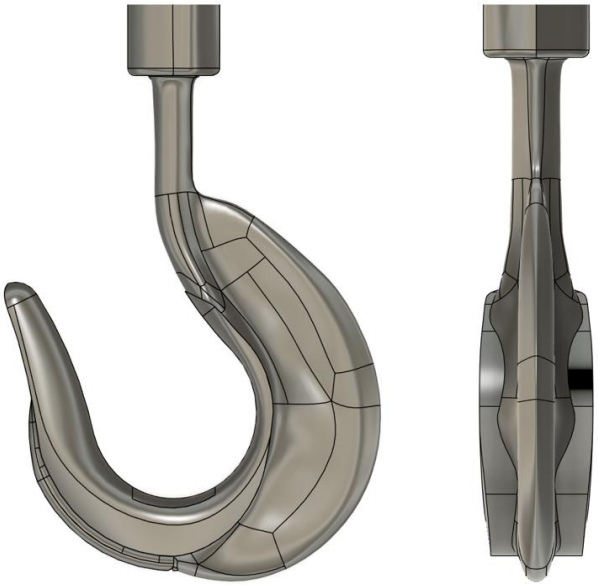

Figure 4. Final alternative front and side view.

Findings

The weights of the proposed designs were compared with the original hook's weight (640 gr). The third alternative achieved the lowest weight reduction at 38.1%, whereas, the second alternative achieved at 46.5% which is the highest.

Initially, four prominent alternatives among others have been identified and assessed in terms of durability, producibility and weight reduction. It was seen that up to 46.5% weight reduction was achieved with various

manufacturing methods. To validate the second design offering highest weight reduction, finite element model with fine mesh was created. It was noticed that maximum von-mises stress is 281MPa which is below yield strength of P-Grade material. However it is above from the value that Fusion 360 has given as maximum (210Mpa.)
After considering the stress concentration since there is sharp transition towards free tip of the hook, it was decided that an action is required to make this transition smoother. For this purpose, durability related improvement has been made between free tip of the hook and C-D section. In order to ensure material integrity and increase the safety in this section, preserved geometry has been revised and final alternative was created. In addition, this final alternative is the closest one to the original design in terms of manufacturability. It is symmetrical and does not have an undercut.
Based on these conditions, final alternative has been proposed in this study considering producibility, fit, form and function of the hardware. Figure 4 shows front and side views of proposed design of hook.
When we compare the weight reduction between the original model and the final alternative proposed, only in sections C-D and E-F, reduction was observed from 306.6 g to 139.8 gr. This reduction in this region constitutes 66% of the total weight reduction. In other words, the highest reduction occurred in this region.

Conclusion

This study indicates that considerable weight reduction is possible through generative design approach by re-designing mechanical components which were designed traditionally.
The weight of Crane hooks with higher load capacity such as NR250 can reach up to 4800kg. In this case, the weight reduction will naturally be much higher and meaningful. Figure 5 shows overlapping demonstration of single hooks growing in size gradually.
As future work, final proposed design could be subjected to detailed fatigue, fracture mechanics, creep related studies including test validation in these domains. Futhermore, other studies could focus on extending this methodology to other mechanical components, validating the feasibility of AI-driven design optimization.

Figure 5. Demonstration of single crane hooks growth in size [12].

References

V.D. Hiep, N.X. Quynh, T.T. Tung, (2024). A topology optimization design of a crane hook, Results Eng. 23, 102492. https://doi.org/10.1016/j.rineng.2024.102492.
N.R. Patel, N.S. Patel, (2015). Design and Analysis of 50 Tonne Crane Hook for Optimization, 3 581–584.
M.K. Panse, P.N. Nagayach, (2016). International journal of recent technology science & management, 1 (2016) 1–5.
H. Wang, W. Du, Y. Zhao, Y. Wang, R. Hao, M. Yang, (2021). Joints for treelike column structures based on generative design and additive manufacturing, J. Constr. Steel Res. 184 106794. https://doi.org/10.1016/j.jcsr.2021.106794.
E. Tyflopoulos, D.T. Flem, M. Steinert, A. Olsen, (2018). State of the art of generative design and topology optimization and potential research needs, Proc. Nord. Des. Era Digit. Nord. 2018 1–15.
A. Gabriel, V. Suganth, S. Velumani, (2020). Experimental Investigation of Stress Concentration in Cross Section of Crane Hook, Int. J. Trend Sci. Res. Dev. (2020).
Y. Torres, J.M. Gallardo, J. Domínguez, F.J. Jiménez E, (2008). Brittle fracture of a crane hook, Eng. Fail. Anal. 17 (2010) 38–47. https://doi.org/10.1016/j.engfailanal.2008.11.011.

K. Kishore, V. Sanjay Gujre, S. Choudhary, A. Sanjay Gujre, M. Vishwakarma, T. Thirumurgan, M. Choudhury, M. Adhikary, A. Kumar, (2020).Failure analysis of a 24 T crane hook using multi-disciplinary approach, Eng. Fail. Anal. 115 104666. https://doi.org/10.1016/j.engfailanal.2020.104666.
J. Plocher, A. Panesar, (2019). Review on design and structural optimisation in additive manufacturing: Towards next-generation lightweight structures, Mater. Des. 183. https://doi.org/10.1016/j.matdes.2019.108164.
A.N. Pilagatti, E. Atzeni, A. Salmi, (2023). Exploiting the generative design potential to select the best conceptual design of an aerospace component to be produced by additive manufacturing, Int. J. Adv. Manuf. Technol. 126 5597–5612. https://doi.org/10.1007/s00170-023-11259-7.
I.T. Teke, M. Akbulut, A.H. Ertas, (2021). Topology optimization and fatigue analysis of a lifting hook, Procedia Struct. Integr. 33 75–83. https://doi.org/10.1016/j.prostr.2021.10.011.
Url-1 Lifting Hook DIN 15401, https://grabcad.com/library/lifting-hook-din-15401-1, data retrieved: 18 May 2025.

Hyperelastic Characterization, Modeling and Testing Under Compression Stress Relaxation of a Sealing Component

Emre Öztürk[a,b], Alaeddin Burak İrez[a]

[a]Istanbul Technical University, Faculty of Mechanical Engineering, Department of Mechanical Engineering
[b]ASELSAN Inc., REHIS Section
emozturk@aselsan.com.tr, irez@itu.edu.tr

Keywords: Ethylene Propylene Diene Monomer, Hyperelastic Characterization, CSR (Compression Stress Relaxation), Sealing Setup.

Aim

Effective sealing is critical in defense industry projects, as aerospace, maritime, and land-based systems face harsh environmental conditions like humidity, pressure fluctuations, saltwater, precipitation, and chemical agents over their lifespan. Protecting sensitive internal electrical components from these factors is vital. Sealing components at connection points must withstand deformation and wear caused by such conditions, balancing flexibility to prevent damage and strength to endure external loads. They must also conform to surrounding contours and compress under specific reaction forces. Elastomers, known for their hyperelastic behavior, can recover after significant deformation, unlike metals. Their incompressibility results from strong bonds between overlapping carbon and hydrogen chains. In the automotive sector, elastomers are widely used as damping elements due to their physical and mechanical properties. In industries such as construction, electronics, and automotive, they are extensively employed as sealing elements, with their usage is consistently rising [1,2].

The mechanical properties of elastomers are evaluated through tests like uniaxial tensile, biaxial tensile, planar shear, and volumetric compression. Data from these tests help develop material models such as Yeoh, Ogden, and Mooney-Rivlin [3]. Their varying responses to strain and compression complicate the establishment of design standards. Accurate estimations require thorough material characterization and reliable finite element analysis (FEA) models. While companies like Parker Hannifin&Chomerics provide general guidelines for gasket applications, challenges remain in defining critical parameters like groove dimensions, positioning, bolt spacing, and material selection, all of which impact sealing efficiency [4]. However, due to the distinct characteristics of each design, generalization is not feasible; therefore, it must be both modelled and verified by experimentation for accuracy in material behaviour definition.

The main objective of this study is to analyze the material behaviour of a specific sealing element, validate the findings via FEA modelling, and reproduce the product-level assembly in a numerical setting. A leakage test is performed to determine the precision of the analytical model and to ascertain the occurrence of stress relaxation.

Material and Method

The research started by analyzing the material properties of a rubber-based sealing element. EPDM rubber with 70 Shore-A hardness was selected for its suitability in defense applications, considering its hardness, chemical and corrosion resistance, and optimal temperature range. Literature review revealed that EPDM, unlike NBR and FVMQ elastomers, operates effectively across a wider temperature range (-57 to 204°C). It also offers superior ozone resistance and higher tensile strength compared to silicone gaskets [4,5].

Considering literature review and commercial catalogues, two different EPDM 70 materials were purchased from 'Tombak Rubber LLC.' and 'Babacan Kauçuk'. The EPDM based sealing elements have a 1x1 meter square sheet gasket and a 'Hollow-O' type sealing gasket with an inner diameter of 2.29 mm and an outside diameter of 5.49 mm. The hardness of the supplied sheet gaskets was assessed according to the ASTM D2240 standard using a Shore A hardness measurement tool, as illustrated in Figure 1. The sample under measurement must possess adequate thickness to prevent interference from the hardness of the underlying table. These measurements confirm whether the sourced material adheres to the qualities delineated in the manufacturer reports.

Figure 1: 'Durometer Type A' Hardness Measurement [6].

Samples were extracted from the sheet gasket utilizing a die that adheres to ASTM D412 standards to assess the material's mechanical properties. Specimens of the dog bone type were manufactured utilizing 'Die C,' which ensures an appropriate aspect ratio of '>10:1,' as illustrated in Figure 2. Rubber materials exhibit lower tensile strength and higher elongation compared to metals, necessitating the use of precise tensile testing equipment. Testing was performed utilizing small force level, high-precision machines such as the 'Instron 5864'. which are fitted with 10 kN load cells. Gripping fixtures adhere to ASTM standards to mitigate slipping, excessive pressure, or damage in proximity to observation areas. Compression testing and product-level tensile testing were conducted at the METU Materials Laboratory. Additional tests are currently ongoing at Axel Products Inc., a recognized authority in elastomer testing [6,7]. The laser extensometer method was employed, with tensile speeds established in accordance with ASTM D412 (500±50 mm/min) or ISO 37 (100±10 mm/min). To obtain strain rate independent results, the tests were conducted at a rate of 1% strain per second.

Figure 2: ASTM D412 Die and Specimens [6].

The data from characterisation tests were included into the material modelling exhibiting optimal convergence by curve fitting techniques. Upon integrating the test data into finite element software (ANSYS_23R1), the material and incompressibility constants were ascertained. The curve fitting method will be selected based on the invariant it depends on, its extent, and the strain range where it performs best [3]. Yeoh proposed omitting I_2 term because strain energy is less sensitive to changes in I_2 than I_1. In cases where only limited test data is accessible, it has been demonstrated that disregarding the second invariant results in more accurate predictions of general deformation states [9,10]. This procedure determines the material's characteristics and mathematical framework, establishing the basis for commercial software.

This study used 'Hollow-O' type gaskets for compression testing at the product level. Two graphs delineating compression stress and deformation percentages for the seal are created based on compression testing and the 'Chomerics Design Guide' (Figure 3). The test data, although not intended for material characterization, was compared with the documentation from 'Chomerics.' The gasket response force was assessed in relation to these data within different analysis configurations.

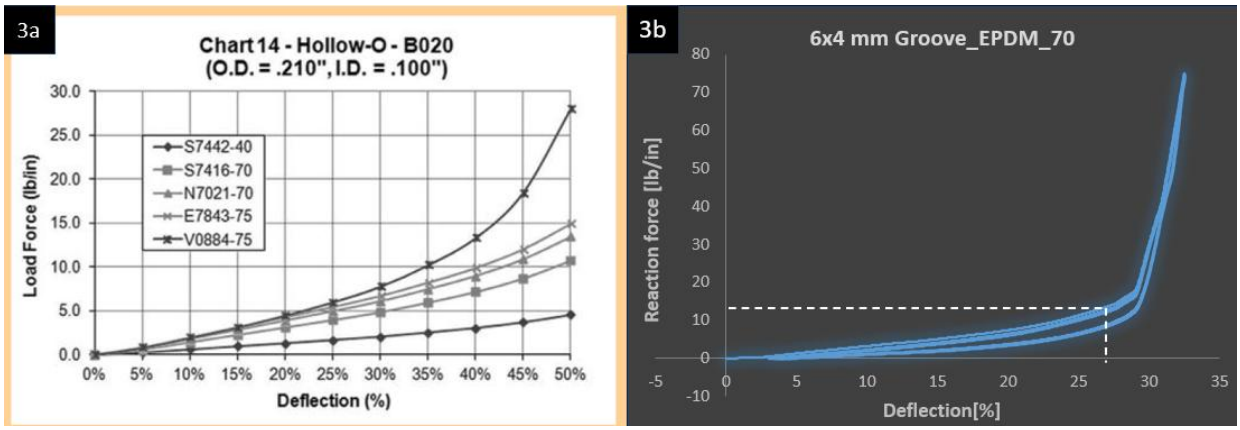

Figure 3: Reaction force of gasket and deflection percentage graphs: (3a) Chomerics, P. (2014). PARFABTM design guide deflection graph p.39; (3b) Our compression test results.

This research concentrates on finite element analysis modeling and evaluating the sealing efficiency of a 'Hollow-O' type seal. The sealing element is composed of 'Ethylene Propylene Diene Monomer' with a hardness grade of 'Shore-A 70'. A 'Sealing Test Setup' measuring 1m x 0.5m x 0.2m was constructed in accordance with the design criteria specified by the relevant authorities such as design guide of Chomerics Elastomer Handbook p. 4-17. The test configuration comprises a pressurized air inlet, a relief valve, and an observation manometer, as illustrated in Figure 4. The friction coefficient between the aluminum cover and the flange is considered to be 0.21. The bolt size is designated as metric 5 A4-70 grade, with a presumed bolt pretension of 4510 N.

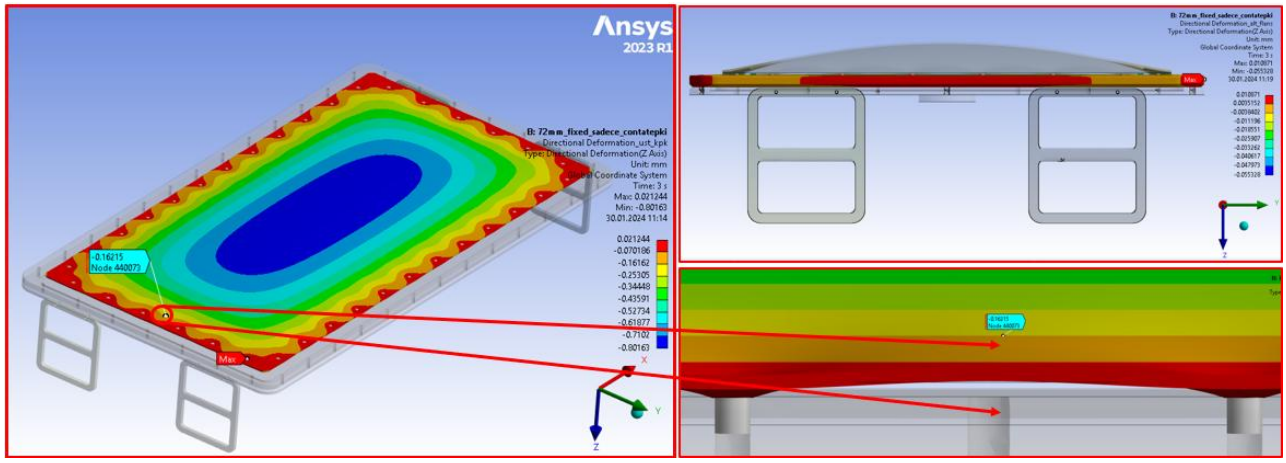

Figure 4: Sealing Setup FEA Model, directional deformation Al-6061 cover plate, 0.16 mm.

The gasket reaction force induces bending during the installation of the cover, referred to as 'Cover Bowing,' as illustrated in Figure 5. This phenomenon, increasing with internal pressure, is analyzed using analytical methods and finite element modeling. 'Cover Bowing' and gasket compression percentage are evaluated to identify the sealing failure threshold. The study also examines stress relaxation in the sealing component through controlled pressure monitoring. When an elastomer is held at constant strain, its polymer chains initially stretch and align, generating stress. Over time, these chains reorganize, break, or reform crosslinks, reducing stress. This process is influenced by temperature, chemical composition, crosslink density, and additives. After installation, the gasket experiences compressive stress, which relaxes over time due to its viscoelastic properties [8].

The stress relaxation testing of solid specimens is governed by ISO 3384 and ASTM D6147-97, which establish standards for times spanning from 10 to 168 hours. In accordance with these standards, this research evaluates the relaxation of the product-level (Hollow-O) gasket by monitoring internal pressure. Data on pressure fluctuations were gathered within identical timeframes and settings. Analytical methods, taking into account cover bowing and

gasket deflection force (GDF), established internal pressures (25 to 50 mbar) for bolt spacing of 72 mm and 110 mm, while considering groove dimensions, GDF, cover thickness, and material configuration.

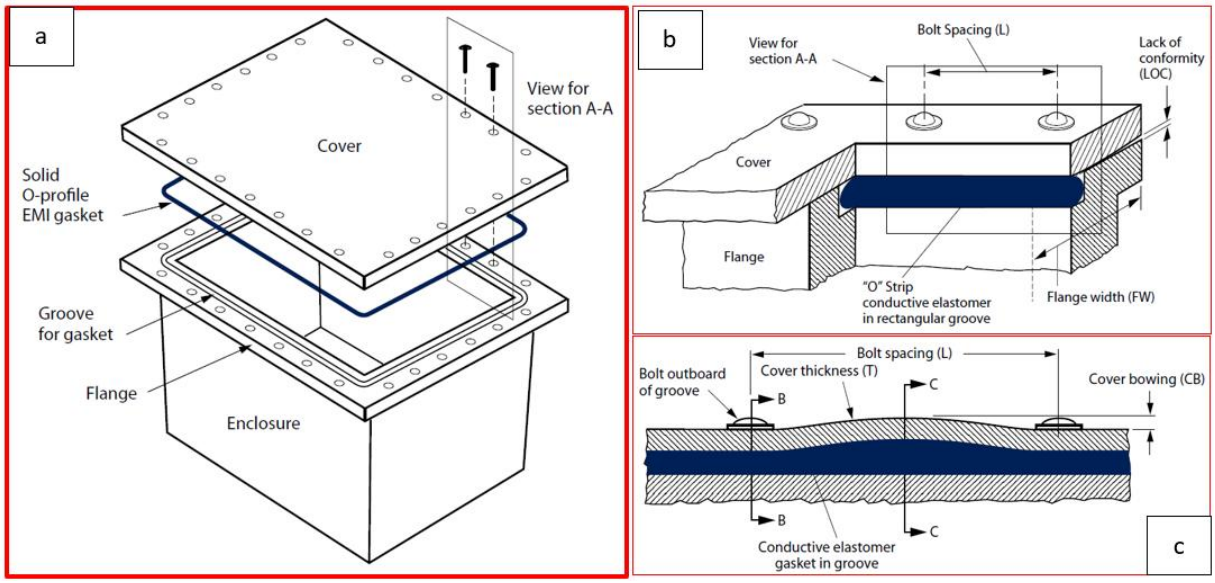

Figure 5: 'Cover Bowing' description, (a) assembly isometric view, (b) Cover, flange cut-away view, (c) section A-A of assembly, sectioned midway through gasket and groove [4].

$$CB_{min} = \frac{GDF\ X\ (L_{max})^4}{FW_{min}\ X\ (T)^3 X\ E\ X\ 32} \quad (1)$$

CB_{min}: Cover bowing (in)
GDF: Gasket deflection force (lb/in)
L_{max}: Max. bolt spacing (in)
FW_{min}: flange width (in)
T: Cover thickness (in)
E: Young's modulus (psi)

Findings

The material constants were determined from the curves obtained in the elastomer characterisation experiments, as seen in Table 1. The selected material model is the 'Third-order Yeoh' model.

Table 1: Hyperelastic curve fitting results, material constants, (W) strain energy density, $(\boldsymbol{I_1})$ first invariant of the Cauchy-Green deformation tensor, $(\boldsymbol{C_{i0}})$ material constants.

3-Parameter Yeoh Model		
C_{10}	C_{20}	C_{30}
0.7472	-0.0707	0.0397
$W = C_{10}(I_1 - 3) + C_{20}(I_1 - 3)^2 + C_{30}(I_1 - 3)^3$ (2)		

The squeeze percent of 'Hollow-O' gasket is 27.1 percent which decided and designed regarding gasket deflection recommendation table as shown in Figure 6. Since a 6x4 mm slot size is feasible to produce and the outer diameter of the gasket is 5.49 mm, it has been concluded that this design is the most reasonable and closest to the recommended value.

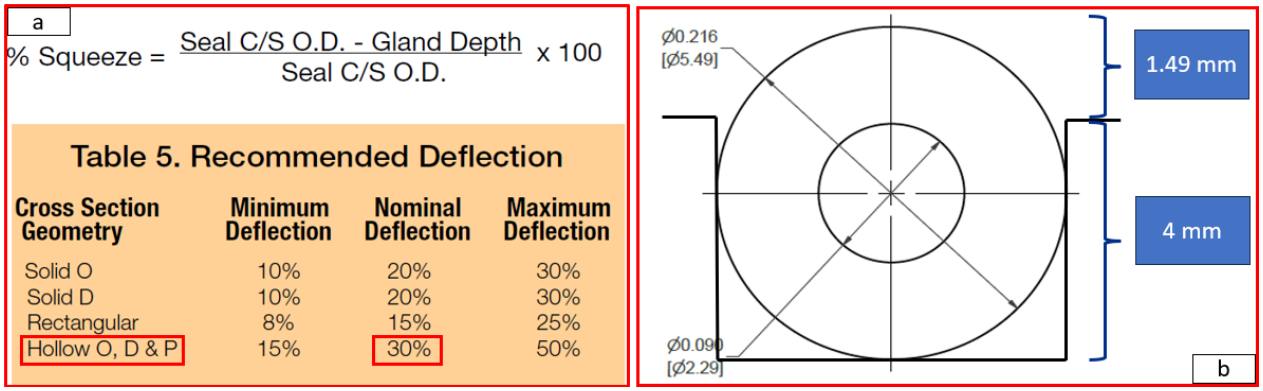

Figure 6: Groove size selection, (a) Chomerics gasket recommended deflection table p.7 [5], (b) Squeeze percent calculation.

$$\text{(b) } Squeeze\ Percent = \frac{1.49\ mm}{5.49\ mm} = \%27.1 \quad (3)$$

The gasket's reaction force was measured at 12.25 lb/in with a squeeze percent of 27.1, as illustrated in Figure 3 (3b). To determine the initial cover bowing during mounting, it was necessary to establish an assumption about the bolt spacing. A spacing of 72 mm was selected because of its high number common divisors, providing versatility in following design guidelines related to proximity, distance, and spacing.

GDF (at %27.1 squeeze) = 12.25 lb/in

$$CB_{min} = \frac{12.25\ X\ (2.83)^4}{1\ X\ (0.0787)^3 X\ 10^7 X\ 32} = 0.00504\ in = 0.128\ mm \quad (4)$$

The reaction force per unit length of the gasket, derived from compression tests, served as input for both analytical calculations and the FEA model. The total gasket groove length measures 2488 mm, and the reaction force of 2146 N/mm, converted from US units, results in an applied force of 5340 N on the aluminum cover plate during the initial mounting process. The 'Cover Bowing' was calculated to be 0.128 mm (4), whereas the FEA model estimated it at 0.16 mm under identical conditions, leading to a 25% error rate.

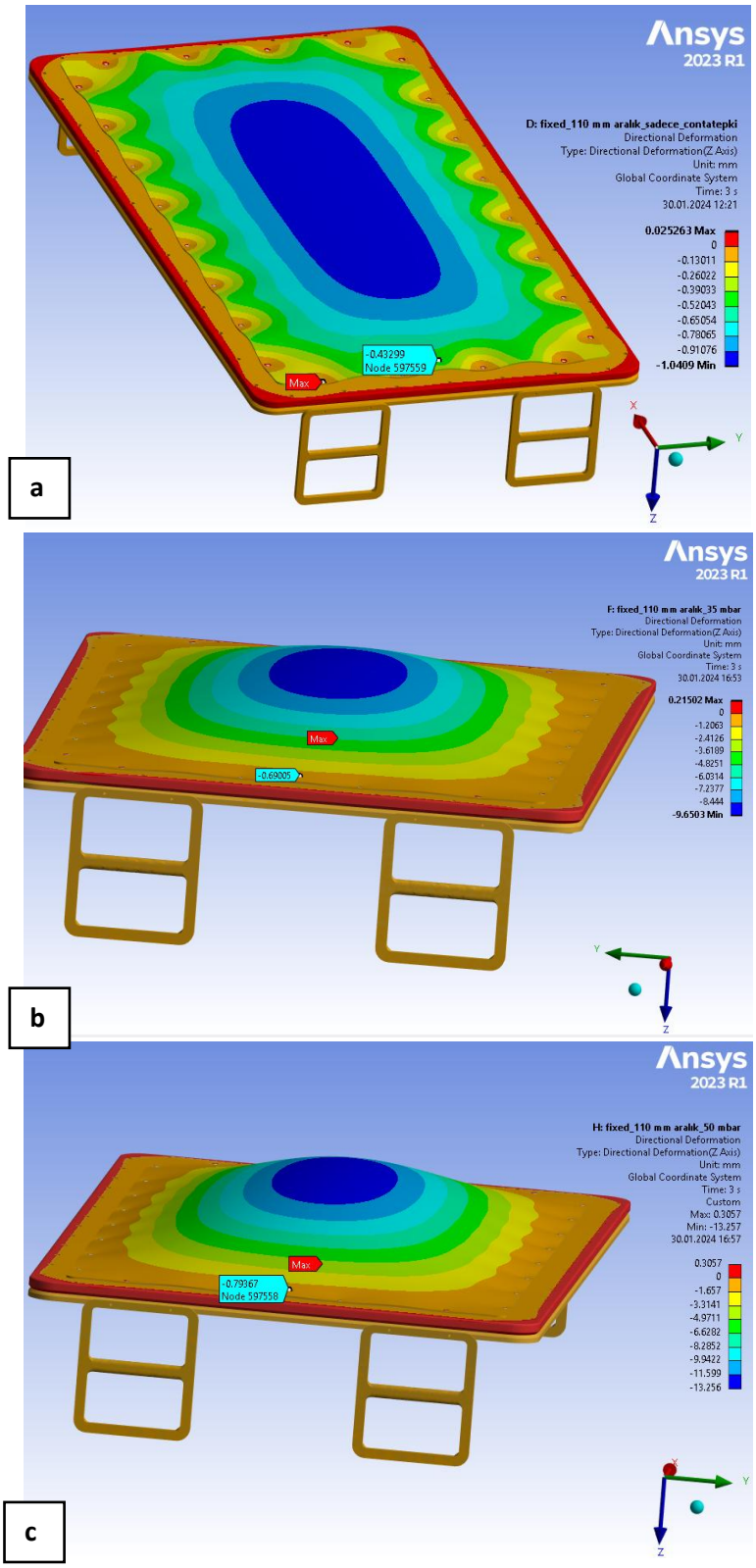

Figure 7: Directional deformation *z* axis under internal pressure (a) 0 mbar, 043mm, (b) 35 mbar, 0.69mm (c) 50 mbar, 0.79mm.

The minimum recommended squeeze percentage is 15 percent, suggesting that the designer may not observe a pressure drop even with increased internal pressure. A second configuration is established with a bolt spacing of

110 mm and begins operation with a 15 percent compression at cover bowing points, represents the threshold for seal failure. Analytical methods calculate 'Cover Bowing' at 0.66 mm, while the finite element analysis model shows a directional deflection of 0.43 mm, reflecting a 35% error rate. The FEA model's squeeze rate is 19%, closely matching the design guideline's critical minimum. At internal pressures of 35 mbar and 50 mbar, specific locations in the 110 mm configuration experience compressions of 14.5% and 12.75%, respectively. Both the FEA and analytical models suggest that the sealing configuration may fail within 35-40 mbar, with an estimated error margin of 30%.

In airtightness testing, defense sector standards require maintaining system pressure within ±2% of the target pressure. Errors may stem from compressor inaccuracies, manometer discrepancies, or human factors. Results are shown in Table 2. In Test Setup 1, 5.5 mbar pressure drop occurred at 40 mbar internal pressure, representing a 13.75% reduction, exceeding the 2% limit. These findings align with FEA results. As internal pressure approaches the critical threshold, gasket stress relaxation becomes more likely. The system with 72 mm bolt spacing showed no pressure loss at 45 mbar initially, but 12% drop was observed after 72 hours. Systems with initial pressure drops had already reached the gasket's tolerance limit, showing minimal variation over time, as detailed in Table 2.

Conclusion

The two sealing designs were subjected to incremental pressure via a compressor, with the observation manometer recording each pressure increment. A material model, based on uniaxial tensile test results, was included into an analytical model to estimate the leakage point. The research anticipated leakage at 35 mbar; however, testing indicated leakage at 40 mbar, yielding an error of around 12.5%. This technique established a material model for future systems and validated the reliability of the FEA model for predictive applications.

Table 2: Air tightness test at sealing setup.

Internal Pressure (mbar) - Pressure Drop Over Time				
Test Configuration	Int. Pressure (mbar)	Pressure Drop **(1 hour)**	Pressure Drop **(24 hours)**	Pressure Drop **(48 hours)**
1-EPDM Gasket 5.49-2.27 M5 Bolts: **110 mm** dist.	25	0.5	0.6	0.5
	30	0.6	0.6	0.6
	35	0.9	1	1.1
	40	**5.5**	**5.5**	**5.5**
	45	**8.5**	**8.5**	**9**
	50	**10.5**	**11**	**12.5**
2-EPDM Gasket 5.49-2.27 M5 Bolts: **72 mm** dist.	25	0.4	0.4	0.5
	30	0.5	0.5	0.5
	35	0.5	0.6	0.8
	40	0.8	0.9	1
	45	0.5	0.5	**5.5**
	50	0.5	**5.5**	**5**
	55	**7.5**	**9.5**	**15.5**

References

Statista Research Department. (2022, January 18). *Global synthetic rubber market size 2022*. Statista. Retrieved September 29, 2023, from https://www.statista.com/statistics/653788/global-market-size-of-synthetic-rubber/

Market Research Future. (n.d.). *Elastomer seal market*. Retrieved October 10, 2023, from https://www.marketresearchfuture.com/reports/elastomer-seal-market-24819

ANSYS, Inc. (2015). *ANSYS Mechanical experimental elastomers, Appendix 2A:*

Hyperelasticity (16.0 Release).
Parker Chomerics. (2022). *Conductive elastomer engineering handbook*. Parker Hannifin Corporation. https://www.parker.com/content/dam/Parker-com/Literature/Chomerics/Parker-Chomerics-Conductive-Elastomer-Engineering-Handbook.pdf
Chomerics, P. (2014). *PARFABTM design guide - Parker Hannifin Corporation*. Chomerics Sealing DesignGuide. https://www.parker.com/literature/TechSeal%20Division/Literature%20PDF%20Files/TSD%205420_ParFab%20Design%20Guide_2014.pdf (accessed Oct. 11, 2023)
A. P. Inc., "AXEL PRODUCTS Inc.," Axel Products Physical Testing Services, http://www.axelproducts.com/downloads.html (accessed Oct. 11, 2023)
A. Products, "Axel Products, Inc..," Axel Capabilties, http://www.axelproducts.com/downloads/Axel_Capabilities.pdf (accessed Oct. 11, 2023).
Mark, J. E., Erman, B., & Roland, M. (2013). *The science and technology of rubber*. Academic Press.
Yeoh, O. H. (1990). Characterization of elastic properties of carbon-black-filled rubber vulcanizates. *Rubber Chemistry and Technology, 63*(5), 792–805. https://doi.org/10.5254/1.3538289
Yeoh, O. H. (1993). Some forms of the strain energy function for rubber. *Rubber Chemistry and Technology, 66*(5), 754–771. https://doi.org/10.5254/1.3538343

Design and Analysis of the Drive System Prototype for a Wire Rope Fatigue Test Setup

Ardıl Adar Yalçın[a], Mohsen Seyyedi[a], Adem Candaş[a], C. Erdem İmrak[a]

[a] Faculty of Mechanical Engineering, Istanbul Technical University, Gumussuyu Istanbul, 34437, Türkiye
yalcin24@itu.edu.tr

Keywords: Drive System Design, Fatigue, Four Bar Mechanism, Wire rope.

Aim

Steel wire ropes are widely used in various industries due to their high axial strength and bending flexibility, making them essential components in lifts, cranes, bridges, and other structural applications. Effective use of steel wire ropes consists several must have components whose are rope drums, rope sheaves, rope wedges and clamps. In their operating conditions, ropes are subjected to cyclic bending over sheaves, leading to fatigue due to fluctuating loads and progressive structural degradation. In recent works, the fatigue and degradation processes were studied by many authors [1-10]. To ensure their durability and reliability in such demanding conditions, fatigue testing is important in the design and evaluation process.

Cyclic bending over sheaves (BoS) fatigue in steel wire ropes can be analysed using a specialized fatigue test setup, as discussed in studies [3,4,5,11,12], which replicates operational conditions through repeated bending cycles. The steel wire rope fatigue testing system for cyclic bending over sheaves has been specially designed and developed. The setup features a four-bar mechanism [12] powered by a permanent magnet synchronous motor. The primary bar of the mechanism generates an up-and-down motion, causing the steel wire rope to bend over a sheave continuously. To maintain the required tension in the rope, a weight carrier system has been integrated into the setup. Given the prolonged cyclic loading in this system, components within the drive mechanism are also prone to fatigue over time.

One of the bars in the four-bar mechanism is directly coupled with the synchronous motor shaft, making its fatigue resistance a critical factor in the performance of test suit. Additionally, the bar responsible for creating the up-and-down motion experiences the highest range of motion, making it a key component for fatigue and vibration analysis. Evaluating the long-term performance of these components is essential for ensuring the reliability of the entire system. The main aim of this study is to calculate and analyse the forces and stress distributions within the drive mechanism of the test setup under different operating conditions. The findings contribute to optimizing the system's design for improved durability and performance in long-term cyclic loading applications.

Material and Method

The proposed drive mechanism design has been developed to meet the requirements of a steel wire rope fatigue test as shown in Fig. 1. The performance of the four-bar mechanism was analysed through mathematical model generated in Python. The propsed model calculates the linear and rotational speeds, accelerations, and forces acting on the bars. These calculations serve as a basis for validating further design analysis. The Python code takes input parameters such as bar dimensions, motor specifications, pivot points, weight on the carrier mechanism, and the length of the steel wire rope.

In furthermore, Finite Element Analysis (FEA) is performed to simulate dynamic forces acting on the four-bar mechanism components. The analysis is conducted using ANSYS Mechanical software to evaluate stress distribution and deformation under cyclic loading conditions. To ensure the accuracy of the FEA results, they were validated using the mathematical model developed earlier. A comparison of directional forces on the bars helps assess the consistency between the two approaches. By analysing the results, the total deformations and stresses on critical parts are determined, helping to improve the system's durability and performance. The combined use of mathematical modelling and simulation ensures a comprehensive evaluation of the design.

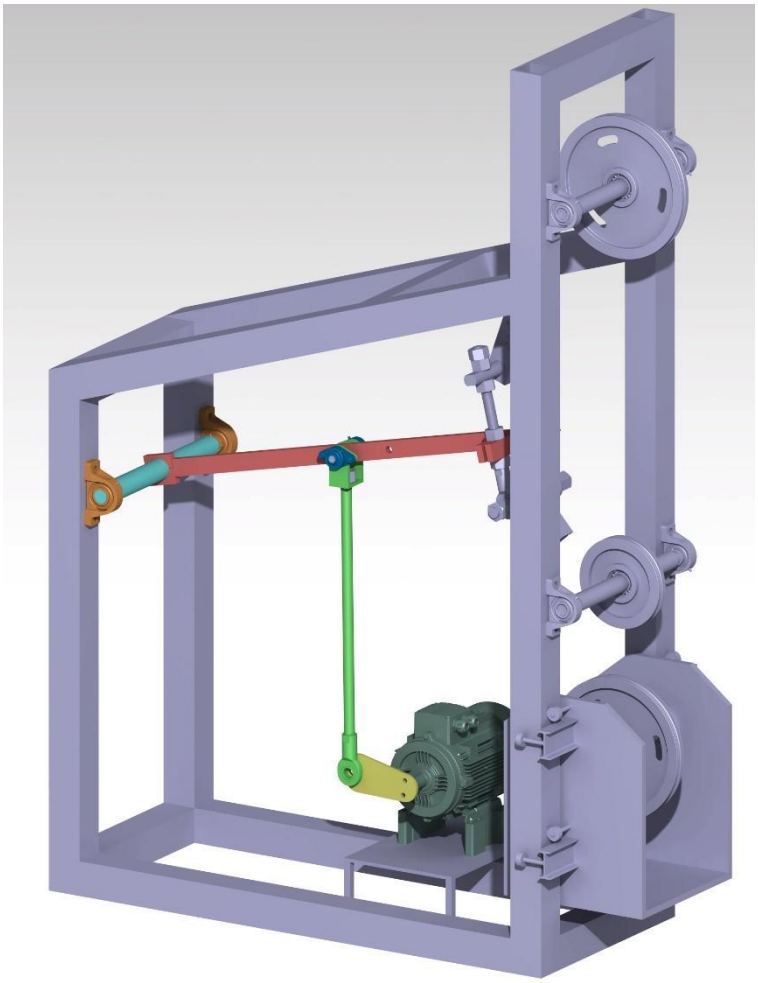

Figure 1. CAD model of the steel wire rope fatigue test setup's four-bar mechanism.

Findings

The four-bar mechanism ensures realistic operating conditions by producing the motion required for the fatigue testing setup for cyclic bending over sheaves. The mechanism's kinematic design allows controlled movement, which makes it easier to perform the cyclic loading required for the fatigue study. By utilizing this mechanism, the system enables the weight carrier to be pulled with variable acceleration, effectively simulating real-world conditions. The mechanism is driven by a permanent magnet synchronous motor, which guarantees accurate and steady action. A short bar that is mechanically connected to a connecting rod is rotated by the motor. The rotating motion is transferred to the primary bar via this rod, which transforms it into oscillatory up-and-down movement at its free end with respect to the ground. In order to enable controlled bending and unbending of the wire rope during the test cycles, the Primary Bar experiences an angular displacement of 32°. This angular displacement also creates a horizontal displacement. In this way the ropes pulled away the axis between the top and bottom sheaves, resulting in lifting the weight carrier. Fig. 2 shows the four-bar mechanism's schematic representation, highlighting the functional connections between its parts and how each one contributes to the intended movement pattern [13]. In Fig. 2, X and Y coordinates of the fixed points are, A (0,800) and B (780,0), in millimetres. The Connecting Rod is 920 mm, Crank is 170 mm. Primary Bar's length |AC| is 615 mm and |CE| is 580 mm.

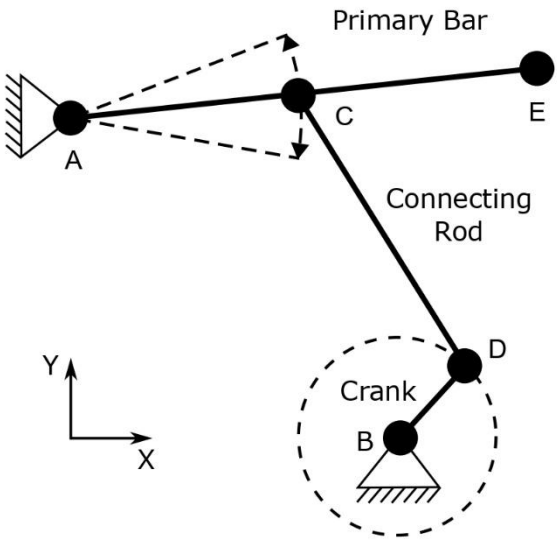

Figure 2. Four-bar mechanism schematic for the steel wire rope fatigue test setup.

Conclusion

This study successfully validates the design and functionality of the test setup for bending-over-sheave (BoS) fatigue testing. The proposed mechanism effectively replicates real-world operating conditions by incorporating a four-bar system that enables controlled cyclic loading on the steel wire rope. The design considerations ensure that the system can accommodate different test parameters, providing flexibility for various experimental conditions. In addition to the validation of the design, the dynamic analysis of the system will be conducted by comparing the results with analytical calculations performed using Python-based calculations. This step help refine the model and improve its accuracy in predicting real-world fatigue behaviour. In further studies, fatigue analysis will be carried out to evaluate the long-term durability of the fatigue testing setup under continuous loading. By integrating computational validation, this research contributes to the advancement of fatigue testing setup designs, providing valuable insights for future studies and industrial applications involving steel wire ropes and load-bearing structures. Dynamic analysis will be validated by comparing with the outputs from the mathematical model generated in Python. Then the results of the analysis can be utilized in the further studies. In the further studies fatigue analysis and developing different test mechanisms including variation of four-bar or similar mechanisms will be done.

References

D. Battini, L. Solazzi, A. M. Lezzi, F. Clerici, and G. Donzella (2020). Prediction of steel wire rope fatigue life based on thermal measurements, Int. J. Mech. Sci., vol. 182, doi: 10.1016/j.ijmecsci.2020.105761.

Z. Hu, E. Wang, and F. Jia (2022). Study on bending fatigue failure behaviors of end-fixed wire ropes, Eng. Fail. Anal., vol. 135, doi: 10.1016/j.engfailanal.2022.106172.

Y. A. Onur and C. E. Imrak (2011). The influence of rotation speed on the bending fatigue lifetime of steel wire ropes, Mechanical Engineering Science, vol. 225, no. 3, pp. 520–525, doi: 10.1243/09544062JMES2275.

Y. A. Onur and C. E. Imrak (2012). Experimental and theoretical investigation of bending over sheave fatigue life of stranded steel wire rope, Indian Journal of Engineering & Materials Sciences, vol. 19, pp. 189–195.

Y. A. Onur and C. E. Imrak (2013). Experimental determination of degradation influence on bending over sheave fatigue life of steel wire ropes, Indian Journal of Engineering & Materials Sciences, 20. 14-20.

I. M. L. Ridge, C. R. Chaplin, and J. Zheng (2001). Effect of degradation and impaired quality on wire rope bending over sheave fatigue endurance, Eng Fail Anal, vol. 8, no. 2, pp. 173–187.

O. Salman and C. E. Imrak (2020). Experimental investigation of corrosion effect on bending fatigue of the wire ropes, Indian Journal of Engineering & Materials Sciences, vol. 27, pp. 770–775.

O. Vennemann, R. Törnqvist, and I. Frazer (2008). Bending fatigue testing of large diameter steel wire rope for subsea deployment applications, International Society of Offshore and Polar Engineers.
O. Vennemann, R. Törnqvist, B. Ernst, S. Winter, and I. Frazer (2008). Bending fatigue tests using a suitable NDT method to determine lifetime of large diameter wire ropes for offshore lifting applications.
D. Zhang et al. (2013). Bending fatigue behaviour of bearing ropes working around pulleys of different materials, Eng Fail Anal, vol. 33, pp. 37–47, doi: 10.1016/j.engfailanal.2013.04.018.
K. Feyrer (2015). Wire ropes: Tension, endurance, reliability, Springer Berlin Heidelberg. doi: 10.1007/978-3-642-54996-0.
l. M. L. Ridge and C. R. Chaptlin (1995). A machine for interactive fatigue testing of wire rope.
Daniali, H.M., Varedi, S.M., Dardel, M. et al. (2015). A novel algorithm for kinematic and dynamic optimal synthesis of planar four-bar mechanisms with joint clearance. J Mech Sci Technol, 29, 2059–2065. doi: https://doi.org/10.1007/s12206-015-0426-1.
Url-1 https://github.com/alejo1630/4bar_mechanism?tab=readme-ov-file 17.03.2025.

Creep Behavior of Polyglass Band Used in Electrical Transformer Cores

Barış İşler[a], İbrahim Mehmet Palabıyık[b], Oğuzkan Şentürk[c], Hakan Özcan[c]

[a] Istanbul Technical University/Graduate School, Mechatronics Engineering, Türkiye
[b] Istanbul Technical University/Graduate School, Mechanical Engineering, Türkiye
[c] GE Vernova Grid Solutions, Türkiye
bisler@itu.edu.tr

Keywords: Composite, Creep, Transformer.

Aim

Power transformers and shunt reactors are indispensable components of electrical power system, playing a critical role in energy transmission and distribution networks. They are essential for minimizing energy losses, ensuring voltage regulation, and enhancing system stability. However, for these electrical machines to operate efficiently and have a long service life, several factors must be carefully considered during their design and manufacturing process. Some of the variables influencing the service life and performance of power transformers and shunt reactors include vibrations caused by Maxwell forces, Lorentz forces acting on current-carrying windings, and magnetostriction forces in electrical steel [1,4]. Additionally, the vibration and noise adversely affect human health and comfort, resulting from the increasing demand for electrical power, particularly in urban regions, has necessitated new high-capacity substations nearby to residential areas. This may lead to neighboring inhabitants experiencing uncomfortable noise levels [2,3].

The core, consisting of yokes, main limbs and vertical return flux limbs significantly influences the dynamic performance of power transformers and shunt reactors. The core is made of stacked silicon steel laminations, secured and tightened with bolts, together with continuous glass fiber reinforced polyesterimide resin composites (Polyglass) or polyethylene terephthalate (PET) bands to attain a specific lamination pressure to ensure its structural stability. Non-linear contact rigidity between laminations leads to complex dynamic behavior. Thus, it is important to understand the clamping performance of the components which ensure the structural integrity of the core.

Currently, the majority of research on power transformers and shunt reactors core vibration mostly concentrates on the magnetostrictive properties of materials, noise sources, vibration transfer paths etc. No specific investigations have been published on the evaluation of clamping components performance on lamination pressure and the influence of them on dynamic properties of power transformers and shunt reactors. Polyglass offer distinctive mechanical properties and used as an important core clamping component. Therefore, this study is extensively focus on to examine its influence.

One of the performance criteria expected from clamping elements is to be able to provide the desired clamping force continuously. Since the creep phenomenon is unavoidable in viscoelastic materials such as Polyglass, the creep performance of this material should be examined. Therefore, the creep properties of the Polyglass material were examined in accordance with the application practice. Moreover, a combination of experimental and numerical methodology was employed to determine the influence of lamination pressure, which was ensured by Polyglass. Experimental Modal Analysis (EMA) was conducted on a yoke mock-up to evaluate the non-linear contact stiffness between laminations. The data were subsequently employed in the modal analysis of the mock-up to examine the impact of core lamination pressure.

Material and Method

Test samples were prepared using Von Roll Polyglas® P30 B-stage banding tape, which is composed of parallel glass strands that have been pre-impregnated with a thermosetting polyesterimide resin.

The creep test samples were made from 50mm wide x 0.3mm thick tape. Each band had four turns of the Polyglass, with two in parallel, and therefore each sample composed of 8 layers in total. A pair of steel buckle clamp pins were used to tension each band assembly. The curing procedure was conducted under a complete vacuum. The

specimen was subjected to a temperature of 120 °C, with a heating rate of 0.8 °C per minute. The process involved a waiting period of 14 hours at a temperature of 120 °C. Subsequently, the temperature was reduced to 60°C at a cooling rate of 1.2°C per minute. Creep tests were conducted with the Instron 5982 universal testing machine and temperature-controlled chamber depicted in Figure 1. The tests were performed with 3 samples. To conduct the creep tests, the samples were initially maintained at room temperature for one hour after a displacement equivalent to 2000N was achieved at a constant crosshead speed of 0.5 mm. The chamber temperature was increased to 120°C, and the total time required for heating and sample conditioning was three hours. The chamber was subsequently cooled to ambient temperature, a process that lasted for 30 minutes. A constant force was maintained while measuring the corresponding elongation.

Figure 1. Positioning of the creep test specimen between the grips.

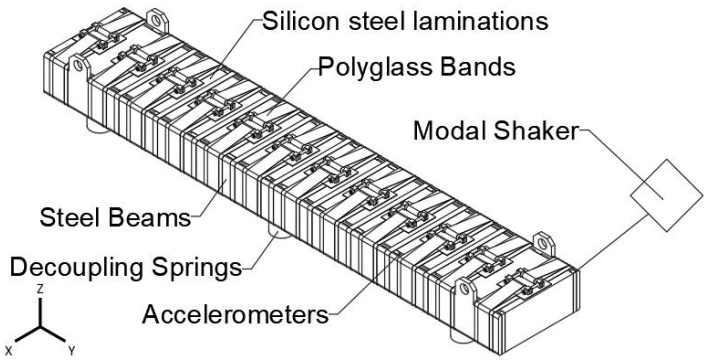

Figure 2. Mock-up with a modal testing setup.

Figure 2 illustrates the EMA, which contains the modal shaker equipment. The mock-up dimensions were 150 mm in height, 358 mm in width, and 2000 mm in length, with silicon steel laminations measuring 0.3 mm in thickness. The laminations were secured between nonmagnetic steel beams and fiberglass insulation using Polyglass. In modal analysis experiments, the bands were initially positioned to exert 1 MPa on the laminations, and this lamination pressure was subsequently reduced by incrementally cutting the bands to assess the impact of varying lamination pressures. A modal shaker was employed to stimulate the mock-up at an angle of 45° using sine sweep excitation ranging from 30 Hz to 1000 Hz. The mock-up was mounted to six decoupling springs to replicate free-free boundary conditions. Subsequently, initial hammer impacts were applied to the structure to verify that the supporting springs and the mock-up behaviors remained non-interactive. Thirty triaxial accelerometers were placed and structural responses recorded. The EMA was conducted for three lamination pressures: 1 MPa, 0.5 MPa, and 0.15 MPa. Eigenfrequencies, mode shapes, and structural damping ratios were quantified for each evaluated design.

Findings

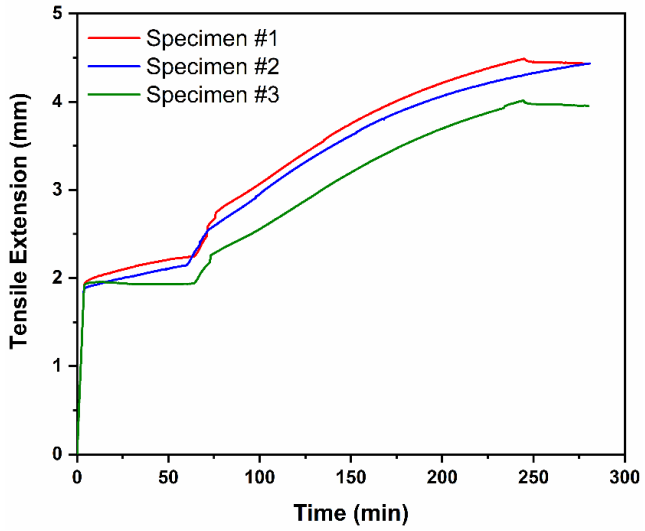

Figure 3. Creep test results for a constant force vs elongation.

The short-term creep results for a constant force was maintained while measuring the corresponding elongation, as shown in Figure 3. Examining Figure 3, elongation of about 2 mm was observed after applying the load, which remained constant. It was observed that after the 60th minute, when the temperature began to rise, there was a additional increase in elongation, which reached 4 mm after 3 hours.

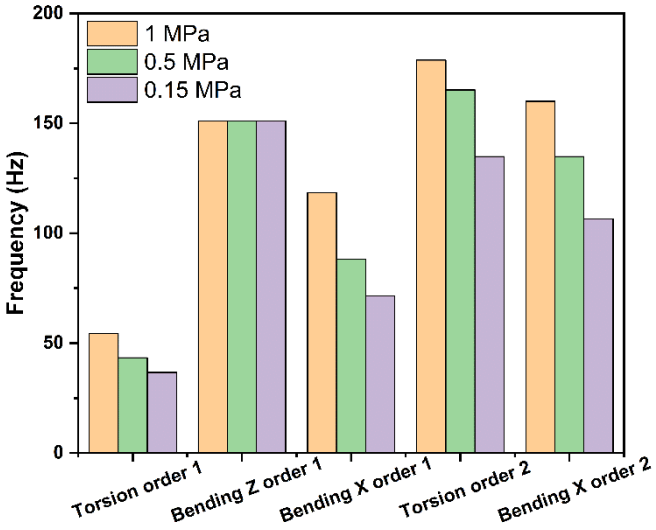

Figure 4. Modal frequency dependency with respect to core lamination pressure.

Figure 4. demonstrates the modal frequency dependency with respect to core lamination pressure. A distinct trend is observed for torsion mode orders 1 and 2, as well as for bending modes in the horizontal (X, Y) direction order 1 and 2. Modal frequencies decline when core lamination pressure drops. It is concluded that the friction among laminations significantly influences the dynamic behavior of the laminated structure in these modes. However, no alteration was seen in the first bending mode in the vertical (Z) direction, independent of lamination pressure. The initial bending mode is unaffected by the friction between laminations, thereby functioning as a homogeneous vibrating system only dictated by mass and elastic characteristics.

Conclusion

The creep behavior of Polyglass bands used in electrical transformer cores was experimentally examined to evaluate their structural response and explore the effects of the creep phenomena. Experimental results led to the following observations:

- After the forming and curing process of the Polyglass band, load loss due to heat effects are prominent and needs to be considered. Review of manufacturing process stages and retightening of Polyglass bands is recommended after the drying process of the power transformer or shunt reactor active part.

- The friction among laminations significantly influences the dynamic behavior of the laminated structure. The examination revealed that torsion orders 1 and 2, as well as horizontal bending modes 1 and 2, are affected by lamination friction. The modal frequency diminishes with a decrease in lamination pressure. But lamination friction exhibited no effect on the vertical bending modes.

References

CIGRE Working Group A2.48. (2016). Technology and utilization of oil-immersed shunt reactors (Technical Brochure No. 655).

Institute of Electrical and Electronics Engineers. (2001). IEEE guide for sound level abatement and determination for liquid-immersed power transformers and shunt reactors rated over 500 kVA (IEEE Std C57.136-2000).

International Electrotechnical Commission. (2005). Power transformers—Part 10: Determination of sound levels (IEC Standard No. 60076-10).

Senturk, O., Gillet, M., Boroomand, T., Ozcan, H., & Gupta, R. (2023). Influence of core lamination pressure on vibration of shunt reactors. In Proceedings of the 23rd International Symposium on High Voltage Engineering (ISH 2023) (pp. 581–586).

MECHATRONICS ENGINEERING

Autonomous Vehicles

Control Systems

Robotics

Vehicle Design

Development Of A Deep Reinforcement Learning-Based Flight Control System For F-16 Aircraft

Kerem Köm[a,c], Gülay Öke Günel[b]

[a] Istanbul Technical University, Mechatronics Engineering Program, Türkiye
[b] Istanbul Technical University, Control and Automation Engineering Program, Türkiye
[c] Turkish Aerospace Industries, Weapon Systems Engineering, Türkiye
kom22@itu.edu.tr

Keywords: Deep Reinforcement Learning, Flight Control, Intelligent Control, Nonlinear Control.

Aim

The primary goal of this study is to develop a mission-oriented flight control system for the F-16 aircraft, utilizing the Deep Reinforcement Learning (DRL) approach, specifically the Deep Deterministic Policy Gradient (DDPG) algorithm, to autonomously track commanded altitude and attitude parameters. The primary objective is to explore the applicability of DRL methodologies in military aviation, where executing high-precision tactical maneuvers is critical. The research focuses on how a reinforcement learning-based controller can effectively manage the complex, nonlinear dynamics inherent in fighter aircraft, ensuring stability and accuracy in altitude and attitude tracking under various operational conditions. Also, one of the objectives of this study is to show the performance of the trained DRL controller in different flight regimes.

Material and Method

The design of the flight control system is based on the DDPG algorithm, a DRL approach that combines the benefits of both value-based and policy-based reinforcement learning. The F-16 aircraft is represented in a simulation environment where the control inputs such as throttle, aileron, and elevator deflections are adjusted to track the commanded altitude and attitudes.

The proposed system utilizes a six-degree-of-freedom (6-DoF) flight dynamics model of the F-16, implemented in MATLAB/Simulink. The DDPG algorithm, an off-policy actor-critic method, is employed to learn a deterministic policy that maps observed states to continuous control actions [6]. This approach is particularly suited for environments with continuous action spaces, such as aircraft flight control systems.

The training process involves simulating various flight scenarios to enable the agent to learn optimal control strategies that minimize tracking errors in altitude and attitude. The reward function is carefully designed to penalize deviations from the desired flight parameters, promoting precise control behavior. The trained agent's performance is evaluated across different flight regimes, demonstrating its capability to maintain stable and accurate control in dynamic and unpredictable conditions. The model is implemented in MATLAB/Simulink environment shown in Figure 1.

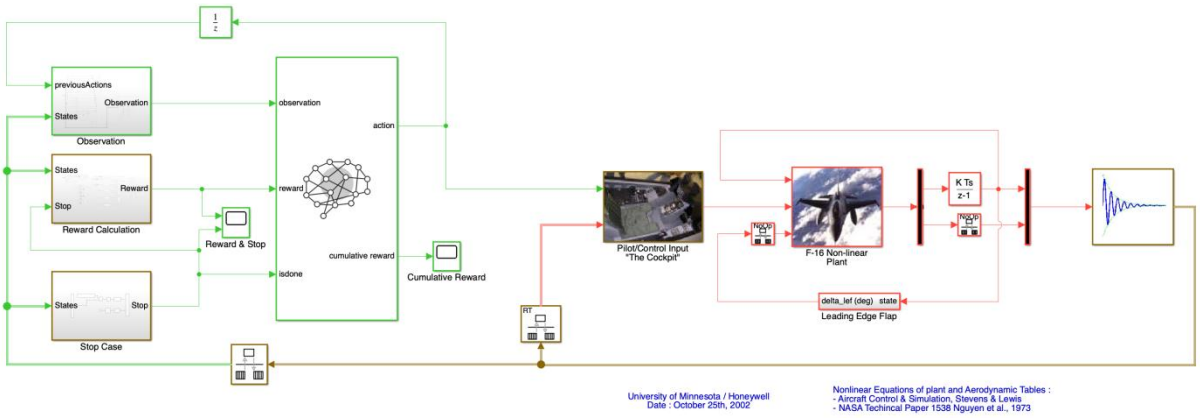

Figure 1. Deep Reinforcement Learning Controller MATLAB/Simulink Model.

Aircraft Dynamics Model

In this study, open-loop F-16 flight dynamics MATLAB/Simulink model which is known as Minnesota University model in the literature is used [3]. This model incorporates aerodynamics, control surface dynamics, and the non-linearities associated with aircraft behavior.

Flight Control System

The F-16 dynamics model is used in order to design Stability Augmentation System (SAS) and then Control Augmentation System (CAS) [5]. This flight control system (FCS) includes in Pitch-Rate (Longitudinal) and Lateral-Directional CAS. All FCS has been modeled on MATLAB/Simulink environment, and then integrated into the open-loop aircraft dynamics model.

Deep Reinforcement Learning Method

In the Deep Deterministic Policy Gradient (DDPG) algorithm, which is one of the DRL techniques, the Actor network is responsible for selecting actions based on the current state, effectively exploring the environment and making decisions. The Critic network, on the other hand, evaluates the chosen actions by estimating their expected long-term rewards, providing feedback to the Actor. This feedback guides the Actor's learning process, enabling it to improve its action selection strategy over time [4].
The DDPG framework operates in an off-policy manner, utilizing experience replay and target networks to stabilize training. The Actor and Critic networks are updated through back-propagation, with the Critic's evaluation influencing the Actor's policy gradient updates. The framework structures and the specific process of the DDPG algorithm are shown in Figure 2. This algorithm is modeled as DRL agent in Simulink model via Reinforcement Learning Toolbox of MATLAB.

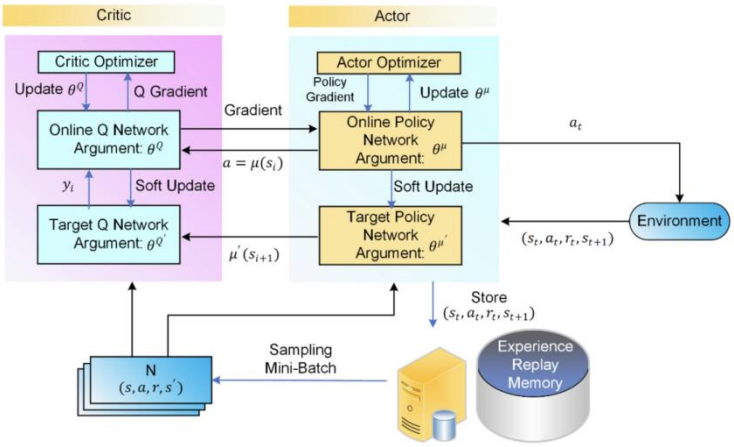

Figure 2. Block Scheme of Deep Deterministic Policy Gradient Method [2].

Reward Function

$$r(x) = \lambda(x - x_{min}) - \sqrt{\lambda^2(x - x_{min})^2 + \tau^2} + \lambda(x_{max} - x) - \sqrt{\lambda^2(x_{max} - x)^2 + \tau^2} \qquad (1)$$

In equation (1), τ and λ are non-negative shape parameters. The reward function employs a hyperbolic penalty function to quantify deviations from desired flight parameters, including altitude, roll angle, pitch angle, heading angle, roll rate, and pitch rate. These parameters have been used to calculate error between desired and current values by implementing as "x" in equation (1). This formulation ensures that the agent is penalized for deviations outside the specified range, promoting precise control. The total reward is the sum of individual rewards for each parameter [1].

Action Vector:

- The agent outputs commands for roll rate and pitch rate to the Flight Control System (FCS).
- Yaw rate is maintained at zero to act as a damper, enhancing stability.
- Throttle control is managed by a Proportional-Integral (PI) controller to maintain a constant true airspeed.

Observation Vector:

- The state vector comprises 16 parameters: Roll rate, pitch rate, yaw rate, roll angle, pitch angle, yaw angle, angle of attack (α), side-slip angle (β), altitude, error terms from the reward function, and previous actions.

This comprehensive observation set enables the agent to assess the aircraft's state and make informed control decisions.

Training Setup and Process

The agent is trained using a F-16 flight dynamics model implemented in MATLAB/Simulink Reinforcement Learning Toolbox. Training occurs over multiple episodes, each lasting 30 seconds, with a simulation time step of 0.2 seconds and a FCS sampling time of 0.01 seconds.
The actor's neural network has 16 observation inputs and 2 outputs. It has 3 hidden layer with 128 neurons. The critic's neural network has 18 inputs. It has 2 input paths. First is observations and the other is actions. These paths are concatenated and occur common path which has 3 hidden layers with 128 neurons.

Initial Conditions:

- Altitude: 25,000 ft
- Roll Angle: 0°
- Pitch Angle: 4.32°
- Heading Angle: Random between -180° and 180°
- True Airspeed: 600 ft/s

Target Conditions:

- Altitude: 22,000 ft
- Roll Angle: 0°
- Pitch Angle: 4.32°
- Heading Angle: 0°
- Roll Rate: 0°/s
- Pitch Rate: 0°/s

The agent learns to adapt its policy to achieve the target conditions, balancing control precision and smoothness. Training parameters, including learning rate, exploration strategy, and reward structure, are fine-tuned to optimize performance.

Findings

The trained agent was used for 2 different cases than training conditions scenario:

1. Start: 14,000 ft altitude and 120 deg heading >> Reach: 15,000 ft altitude and 0 deg heading
2. Start: 8,000 ft altitude and -90 deg heading >> Reach: 4,000 ft altitude and 0 deg heading

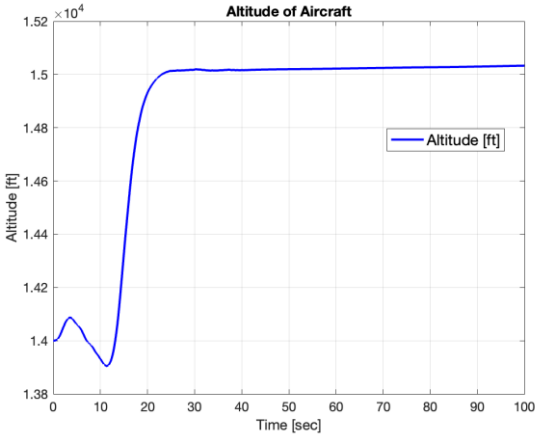

Figure 3. Altitude Tracking for The First Case.

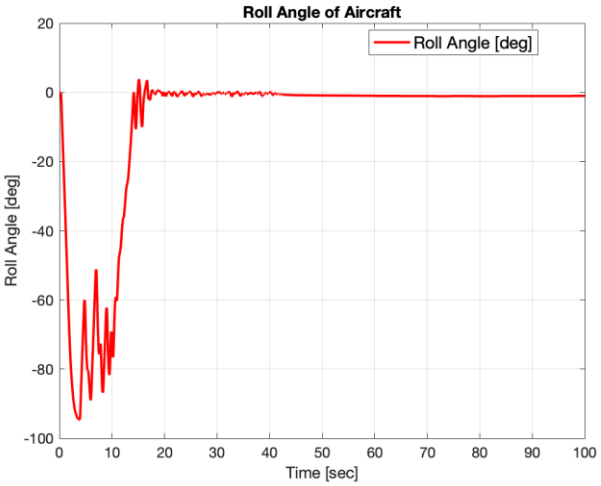

Figure 4. Roll Angle Tracking for The First Case.

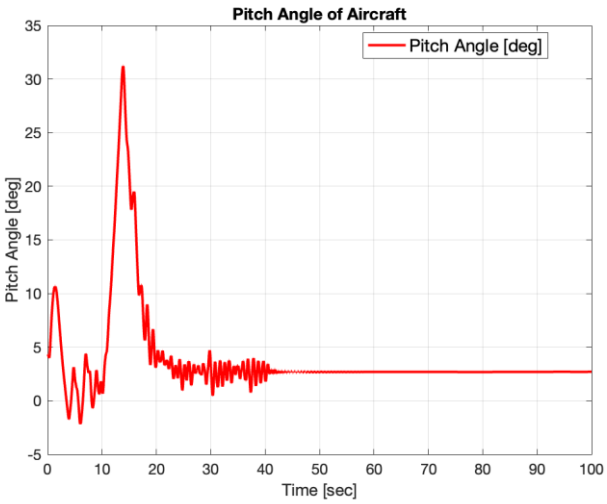

Figure 5. Pitch Angle Tracking for The First Case.

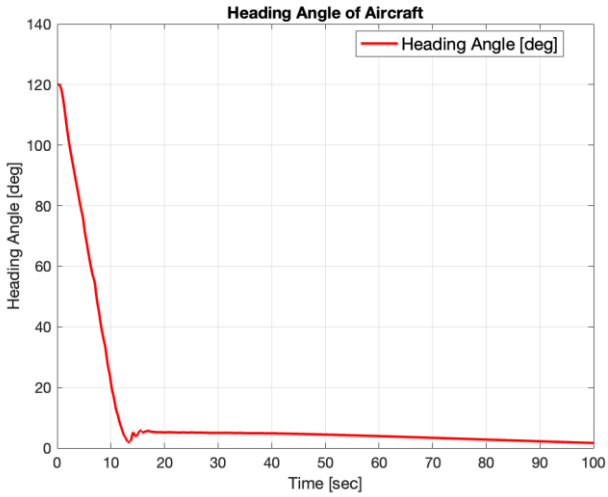

Figure 6. Heading Angle Tracking for The First Case.

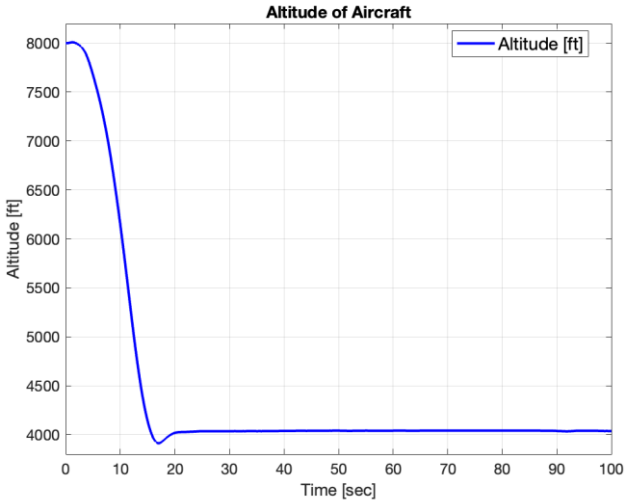

Figure 7. Altitude Tracking for The Second Case.

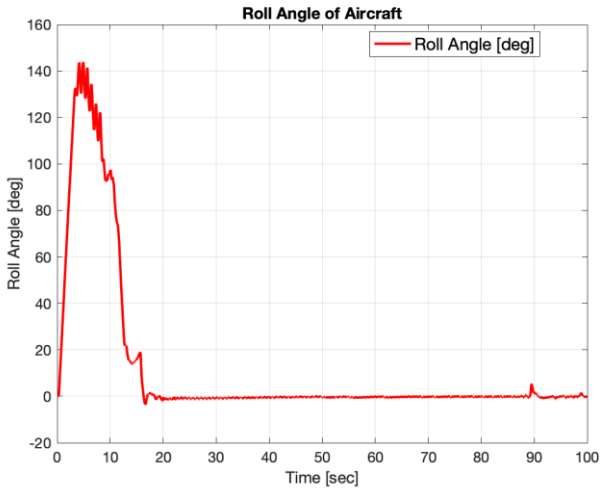

Figure 8. Roll Angle Tracking for The Second Case.

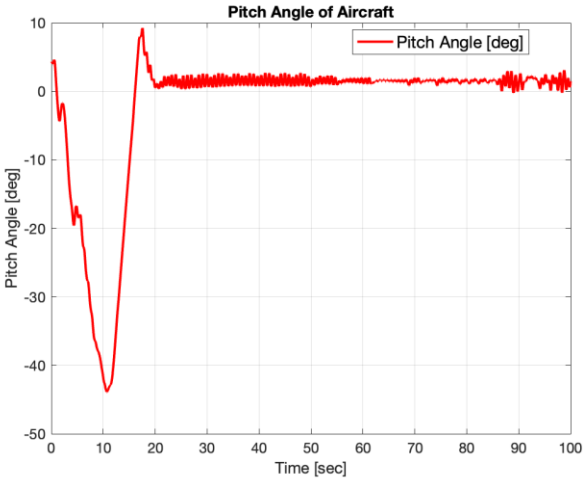

Figure 9. Pitch Angle Tracking for The Second Case.

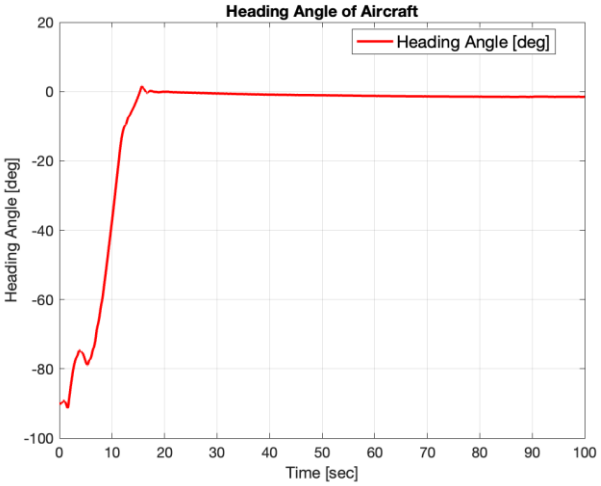

Figure 10. Heading Angle Tracking for The Second Case.

Conclusion

The results from this study demonstrate the potential of applying Deep Reinforcement Learning techniques, specifically the DDPG method, to the design of flight control systems for modern aircraft such as the F-16. The DDPG controller achieved high precision in tracking commanded altitude and heading while maintaining stability and smooth control actions.

The results underscore the potential of DRL methods in enhancing the performance of flight control systems, particularly for complex, high-performance aircraft like the F-16. By leveraging the DDPG algorithm, it is possible to create intelligent control systems that autonomously adapt to changing flight conditions and optimize aircraft performance. One of the future work will be enhancing precision of the responses and reducing the noisy behaviors. Another one of the future work is to focus on extending this approach to other aspects of intelligent flight control, such as implementing fuzzy logic structures into the system to improve learning and training processes.

References

De Marco, A., D'Onza, P. M., & Manfredi, S. (2023). *A deep reinforcement learning control approach for high-performance aircraft.* Nonlinear Dynamics, 111(18), 17037–17077. https://doi.org/10.1007/s11071-023-08725-y

Dong, R., Du, J., Liu, Y., Heidari, A. A., & Chen, H. (2023). *An enhanced deep deterministic policy gradient algorithm for intelligent control of robotic arms.* Frontiers in Neuroinformatics, 17, 1096053. https://doi.org/10.3389/fninf.2023.1096053

Russel, R. S. (2003). Non-linear F-16 simulation using Simulink and Matlab, Ver. 1.0. Technical Report, University of Minnesota, United States of America.

Silver, D., et al. (2014). *Deterministic policy gradient algorithms.* Proceedings of the 31st International Conference on Machine Learning (ICML 2014).

Stevens, B. L., & Lewis, F. L. (2003). Aircraft control and simulation (2nd ed.). John Wiley & Sons, Inc.

Sutton, R. S., & Barto, A. G. (2018). Reinforcement learning: An introduction. MIT Press.

METALLURGY AND MATERIALS ENGINEERING

Composite and Polymer Materials

Corrosion and Wear

Energy Materials

Extractive Metallurgy

Mechanical Metallurgy

Metals and Alloys

Surface Treatment and Coatings

The Impact of Different Dispersing Agents Used in Ball Milling onto The Electrochemical Performance of Spinel $LiNi_{0.5}Mn_{1.5}O_4$ Cathode Material

Yunus Emre Gul[a], Ozgul Keles[a], Billur Deniz Karahan[a]

[a]Istanbul Technical University, Department of Metallurgical and Materials Engineering, Istanbul, Maslak, 34469, Türkiye
bdkarahan@itu.edu.tr

Keywords: Lithium-Ion Battery, Spinel Lnmo, High Voltage Applications, Ball Milling.

Aim

Lithium ion batteries must meet today's challenging requirements of high energy and power densities, a long cycle life, low toxicity, and affordability. Therefore, new cathode materials must be designed since the cathode active material is a crucial factor in determining the lithium ion cell's overall performance. Among alternatives, spinel type cathode chemistries like lithium nickel manganese oxide ($LiNi_{0.5}Mn_{1.5}O_4$: here after named as 'LNMO') are one of the candidate for the high energy applications. Because, the spinel structure has three-dimensional Li^+ ion diffusion pathways that mitigate and increase the amount of Li^+ ions during charge and discharge. Given that the working voltage of a lithium manganese oxide spinel material is 4.2 V, its operational voltage is raised to 4.7 V by adding nickel to its structure. Recent studies have revealed that not only the chemistry but also the atomic arrangement affect the cycle performance of the spinel LNMO material. Therefore, an optimization is needed to arrange the atoms in LNMO in an ordered or disordered manner [1].

Even though LNMO has a high theoretical energy density, capacity fading has been a general problem due to possible electrolyte oxidation at high potentials, parasitic processes at the electrolyte-cathode interface, and its degradation by Jahn Teller distortion [2,3]. Knowing that accurate dopant element selection may create stronger bonds with oxygen in the lattice, doping has been used to increase the structural stability over cycles. Modifying electrolyte compositions to restrict HF formation has also been studied to enhance the electrochemical performance of LNMO at higher working voltages. Additionally, researchers have looked into coating LNMO surface with a more stable chemistries or adjusting the heat treatment process parameters to change the atoms' orientation, to restrict the capacity fading by reducing side reactions with the electrolyte.

There are numerous ways to create spinel LNMO cathode materials, including solid-state ball milling, spray drying, molten salt synthesis, combustion synthesis, and wet chemistry techniques including sol-gel and co-precipitation. A high-temperature heat treatment is used to modify the atoms' orientation and produce the final spinel structure. Although solid state ball milling is one of the most practical method and it may be used successfully in mass production, its parameters must be carefully adjusted to regulate the particle size distribution of the resulted powder [4].

In this study, spinel LNMO cathode powder is synthesized by typical 'one pot' solid state ball milling. All of the initial raw materials ($Mn(CH_3CO_2)_2.4H_2O$, $Ni(CH_3CO_2)_2.4H_2O$, $LiOH.H_2O$) are introduced to the vial along with dispersing agents i.e. ethanol and citric acid. Based on the structural and morphological investigations, a thorough analysis of the impact of the dispersing agent type on the final powder qualities is conducted. When utilized as cathode active material, the electrochemical performances of these resultant powders (LNMO-ETH and LNMO-CA) are evaluated both galvanostatically and potentiostatically.

The outcomes show that dispersing agent would interfere particle interaction in the vial during the synthesis leading to differentiation in the particle size distribution and the phase purity, which would lead cycle performance eventually.

Material and Method

In this work, two different cathode powders (LNMO-ETH and LNMO-CA) were synthesized by one pot solid state synthesis method where the dispersing agents were selected as ethanol and citric acid. In the synthesis of LNMO-ETH and LNMO-CA, firstly the stoichiometric amount of $Mn(CH_3CO_2)_2.4H_2O$, $Ni(CH_3CO_2)_2.4H_2O$, $LiOH.H_2O$ were added to the vial (Retsch PM100) along with the dispersing agent (10% wt. ethanol and 50% wt. citric acid), then after the ball milling, wet powders were separated from the zirconia balls and dried in vacuum furnace overnight. Then, the dried powder was heated in three steps: to 180°C for 2 hours, to 500°C for 2 hours and to 800°C for 12 hours with a heating rate of 2°C/min.

In both experiments, ball milling parameters were selected as follows: 400 RPM milling speed, 8 hours milling time, 5:1 ball to powder ratio.

For structural characterization and evaluation of atomic ordering in LNMO-ETH and LNMO-CA, XRD (Bruker D2 PHASER) and Raman Analyses (i-Raman Plus 785H that utilizes 785 nm laser source) were realized. SEM (Zeiss Gemini 500) analysis was done to identify the morphology of each powder.

Then, to make a cathode electrode, firstly a slurry made of 80%wt. cathode active material, 10%wt. carbon black and 10%wt. PVDF binder was formed, and Dr Blade method was applied to create a film of 150 micron thickness on aluminum foil. Once the film was vacuum dried, and rolled, then electrodes were punched in 14 mm size. Finally, CR2032 coin cells were produced where the fabricated electrodes were used as a cathode working electrode versus Lithium metal foil, Celgrad 2400 was utilized as separator, and a commercial solution made of 1M $LiPF_6$ salts in EC:DMC (1:1 as volume) was selected as an electrolyte. Once cells were assembled, they were galvanostatically tested at 1C rate between 3V-4.8V (1C = 147 mAh/g), and potentiostatically tested between 3V-4.8V vs Li, in the cyclic voltammetry testing conditions for 4 cycles with 0.1 mV/s scan rates.

Findings

XRD analyses of LNMO-CA and LNMO-ETH reveal that they both display peaks related to the spinel cubic structure with space group Fd$\underline{3}$m (Figure 1). In addition, due to oxygen deficiency in the high temperature calcination above 700°C, both samples have rock-salt impurity phases like NiO and $Li_xNi_{(1-x)}O$ which were noted at 37.5, 43.6 and 63.4 2θ values, with small intensities. A scrutiny look on the peak ratio of $I_{(311)}/I_{(400)}$ shows that LNMO-CA sample has higher ratio, which reveals that LNMO-CA has higher crystallinity compared to LNMO-ETH.

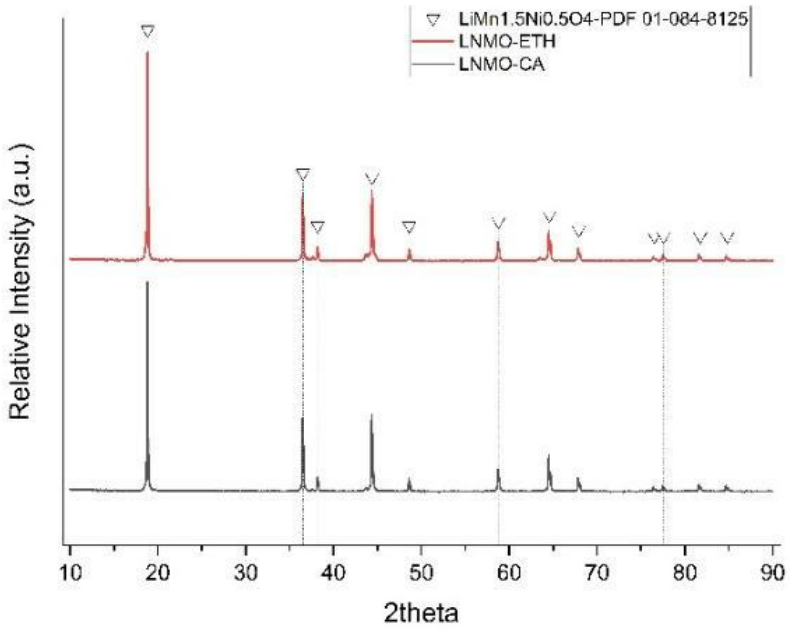

Figure 1. XRD diagram of LNMO-ETH and LNMO-CA.

SEM images taken from both samples, show the agglomeration of powder is less remarkable in LNMO-CA as citric acid forms cation complexes that repel one another electrostatically during ball milling [5]. Both samples have octahedron morphology with variable particle sizes at sub-micron level (Figures 2a-d).

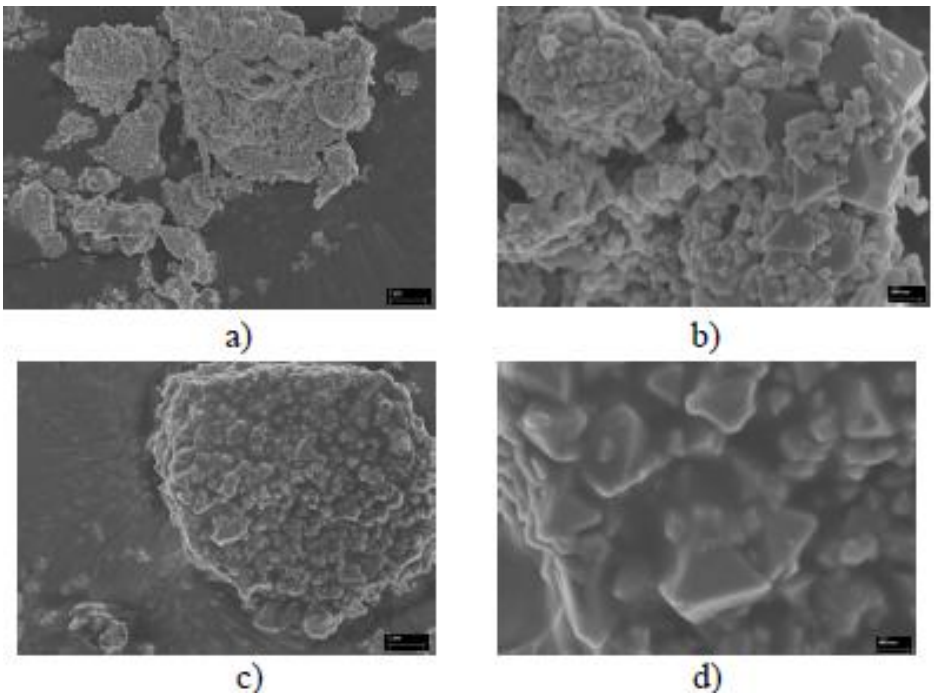

Figure 2. SEM images of LNMO-CA (a,b) and LNMO-ETH (c,d) at 5kX and 20kX magnifications.

In Raman analyses, both samples have shown disordered atomic arrangement as expected by the presence of broaden peeks at 590 and 612 cm^{-1} which is account for vibration of Mn-O_6 bonds (Figure 3) [6].

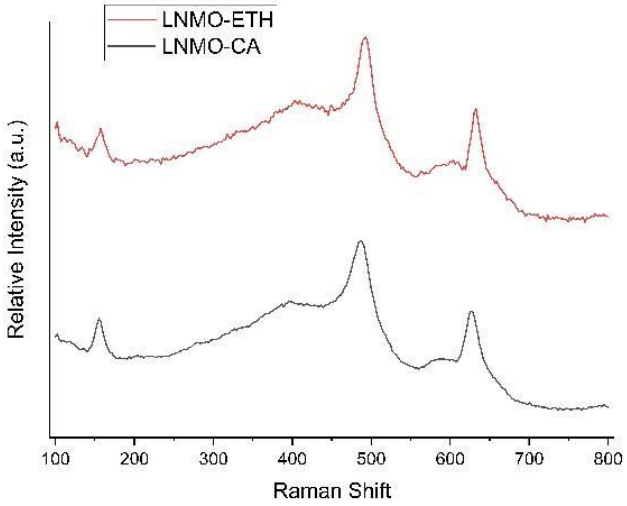

Figure 3. Raman shifts of LNMO-ETH and LNMO-CA.

In the cycling tests of both samples, they reveal low 1st cycle Coulombic efficiency due to the unstable cathode electrolyte interface formation. Moreover, the existence of rock salt structure and partial agglomeration in the powder prevent lithium ions to take their places back easily in cycling which causes a progressive capacity degradation. The comparison of the cycle performances of both electrodes (Figures 4a-b) shows that the improved electrode active surface area accessible for Li^+ ion transportation as a result of less agglomerated and smaller particle size is the reason why LNMO-CA offers superior cycle performance even at different C-rates.

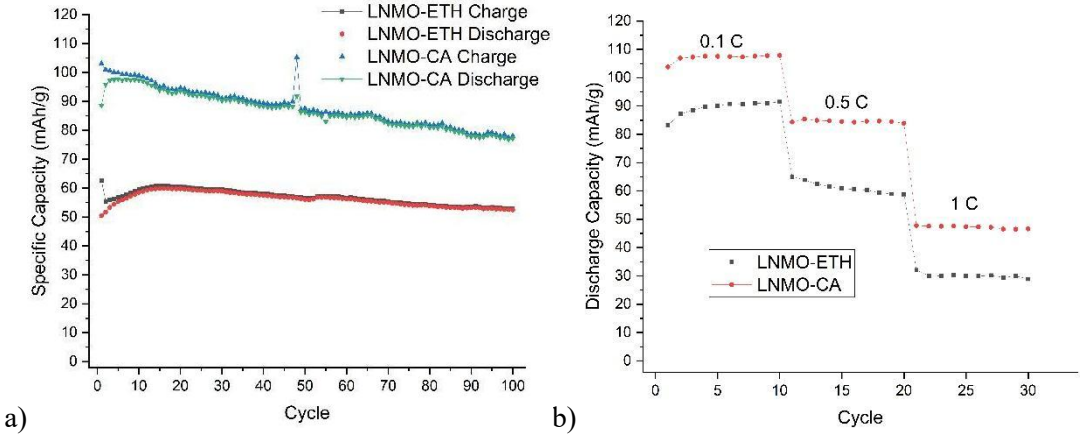

Figure 4. a) Galvanostatic test at 0.1C rate for 100 cycles, b) Rate tests performances.

Then, to study the electrode/electrolyte interface in detail, the potentiostatic test results of both electrodes (LNMO-ETH and LNMO-CA) are analyzed (Figures 5a-b). CV curves clearly demonstrate a lot of similarities, with two redox peaks in the 4.7–4.8 V range and a tiny peak at 4 V. At around 4.7 V and 4.75 V, the two redox peaks indicate the existences of redox couples $Ni^{2+}/Ni^{3+}$and Ni^{3+}/Ni^{4+}. Knowing that the oxidation peak in the Fd3m spinel is separated into two distinct peaks due to the larger voltage difference between the $Ni^{2+}/Ni^{3+}$and Ni^{3+}/Ni^{4+} redox couplings in the nonstoichiometric spinel, both samples have revealed a dominant Fd3m space group atomic arrangement, which is consistent with the Raman results above (Figure 3). Moreover, as the minor redox peak near 4 V is assigned to the Mn^{3+}/Mn^{4+} redox couple, LNMO-CA displays lower peak intensity at about 4 V, indicating lower Mn^{3+} content within the product. When the peak positions and intensities are compared, they are overlapped in LNMO-CA as opposed to LNMO-ETH, where they fluctuate from the 1st to the 4th cycle, indicating an unstable electrode/electrolyte interface formation.

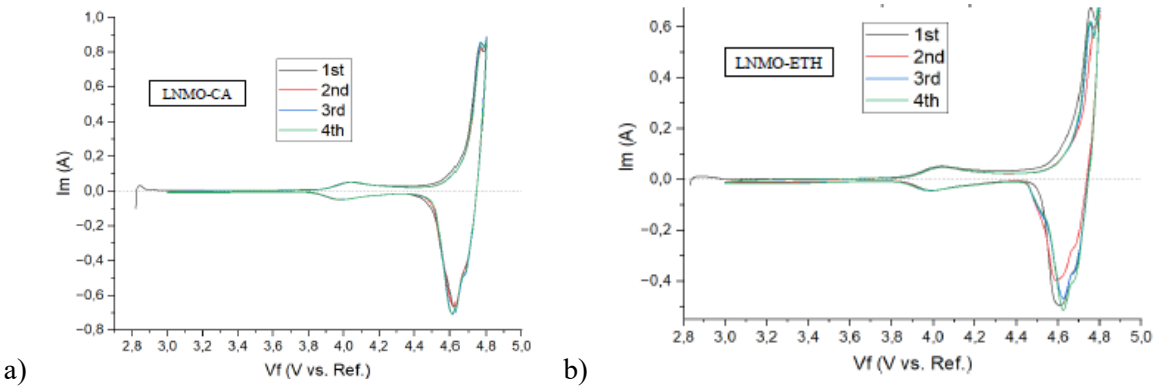

Figure 5. a) Cyclic voltammetry test result of LNMO-CA, b) Cyclic voltammetry test result of LNMO-ETH.

Conclusion

This work fabricates spinel structured LNMO via one pot solid state synthesis. Using citric acid as a dispersant agent in ball milling can form more uniformly distributed submicron sized powders with less agglomeration, which results in better electrochemical performance when used as cathode, even at high C-rates. This is in line with the understanding that controlling the particle size, morphology, and atomic arrangement would perform better cycle performance.

Acknowledgements

The authors would like to greatly acknowledge Istanbul Technical University Scientific Research Prog. (Project No: MYL-2023 45208) for the financial support. The authors thank Humza Ashraf and Istanbul Medipol University REMER Research Center and Metrohm for their supports in the characterization.

References

Okudur, F. U., Mylavarapu, S. K., Safari, M., De Sloovere, D., D'Haen, J., Joos, B., ... & Hardy, A. (2022). LiNi0. 5Mn1. 5O4-δ (LNMO) as Co-free cathode for lithium ion batteries via solution-gel synthesis: particle size and morphology investigation. *Journal of alloys and compounds, 892*, 162175.

Zhang, Y., Zhang, W., Zhou, J., Li, X., Zhou, W., Xie, Y., ... & Dai, K. (2023). Research development on spinel lithium manganese oxides cathode materials for lithium-ion batteries. *Journal of The Electrochemical Society*, *170*(9), 090532.

Mokhtar, N., & Idris, N. H. (2016). Comparison on electrochemical performancesofLiNi0. 5Mn1. 5O4cathodematerials synthesizedusing differentprecursors.MaterialsToday:Proceedings,3,S129-S135.

Kozawa, T. (2019). Lattice deformation of LiNi0. 5Mn1. 5O4 spinel cathode for Li-ion batteries by ball milling. *Journal of power sources*, *419*, 52-57.

Song, J., Wu, H., Xu, D., Guo, J. B., Yan, W., Lin, F., & Chen, T. (2022). The choice of organic acids as complexing agent affecting on the electrochemical properties of spinel LiNi0. 5Mn1. 5O4. *Journal of Materials Science: Materials in Electronics*, *33*(28), 22217-22229.

Kaur, G., Nesvaderani, F., Hadidi, L., Dunn, D., Campbell, S., & Gates, B. D. (2022). Unraveling the role of composite Li3PO4/ZrO2 coatings prepared by dry milling on high voltage spinel cathodes for lithium-ion batteries: Insights into lattice strain, thermal behavior, material compatibility, and electrochemical performance. *ACS Applied Energy Materials*, *5*(11), 14335-14352.

Efficient Leaching of Valuable Metals from NMC Cathodes of Li-Ion Batteries with Green Deep Eutectic Solvents

Gizem Burcu Bilgin[a], Ozgul Keles[a], Billur Deniz Karahan[a]

[a] Istanbul Technical University, Department of Metallurgical and Materials Engineering, Turkiye
bdkarahan@itu.edu.tr

Keywords: Lithium-Ion Battery, Cathode, Leaching, Deep Eutectic Solvent, Recycling.

Aim

The quantity of used batteries and process scrap-electrodes are increased as a result of the growing use of lithium-ion batteries (LIB) in the energy storage industry. The growing need for essential minerals necessitates recycling spent LIBs and process scrap-electrodes. Strategic metals like lithium, nickel, cobalt, and manganese can be recovered, which has benefits for the economy and sustainability. Among alternative recycling methods, deep eutectic solvents (DESs) used in the leaching of metals has shown promising results in terms of high metal recovery rates and low environmental impact. DESs are solvents formed by mixing two or more solids in a certain ratio to obtain a liquid. The melting point of the mixture is lower than the constituents due to hydrogen bond interactions (Abbott et al., 2004). DESs are also biodegradable, reusable and nearly non-toxic (Zhang et al., 2012).

Up to now, various DES combinations have been studied to leach Ni, Mn, Co and Li from NMC cathode. Among alternatives, DES with choline chloride (ChCl) stands forward due to the biocompatibility of ChCl referred to as vitamin B4. However, recent DES experiments with ChCl need higher leaching temperatures or longer leaching times to increase leaching efficiency. Therefore, usability of DESs in milder leaching conditions must be developed to enhance the practical applications of DES in the recovery of valuable metals of cathode active materials.

Previous studies reveal that the choice of DES composition is determined based on the cathode chemistry and structure. $LiNi_xMn_yCo_{1-x-y}O_2$ has a layered structure consisting of lithium, oxygen, and transition metals. Leaching is obtained by destroying the covalent bonds of metal oxides to form a metal(II)-chlorine complexes (Lu et al., 2022). Also, in order to increase the dissolution of metal ions, hydrogen ions are needed to destroy the structure by removing oxygen from it (Luo et al., 2023). Ethylene glyocol (EG) and urea being utilized in previous studies of DES are neutral compounds and need high temperatures for leaching. For high-yield leaching under mild conditions, DES made of ChCl and reducing acids could be a suitable option for metal extraction.

In this study, to form DES, 5-sulfosalicylic acid (SSA) is chosen uniquely for cathode recovery to be used along with ChCl due to its environmentally friendly behaviors (Xu et al., 2021). 5-sulfosalcylic acid (SSA) is a potent organic acid with three functional groups: a carboxyl group, a sulfonic acid group, and a phenolic OH group. Deprotonation, or the separation of protons, will occur in these groups, potentially generating acceptor sites for hydrogen bonding (De Vries et al., 2016). Additionally, it is possible to generate sulfonic acids as hydrogen bond donors (HBD) because of their high metal oxide solubility properties. This results from the presence of protons that function as oxide acceptors and are supplied by the high acidity of sulfonic acids (Liao et al., 2022).

Literature review reveals that the intermolecular interactions between compounds of DES have an impact on the DES properties, thus the molar ratios of DES need to be studied carefully. The optimum molar ratios vary depending on the hydrogen-binding ability of the components (Sazali et al., 2023). A change in the molar ratio can affect the intermolecular hydrogen bond network within DES, altering the ability to complex with metal ions and thus the leaching activity. High hydrogen bond donor (HBD) ratios can increase proton activity, while extreme ratios can inhibit the formation of DES or increase the viscosity, making mass transfer difficult. For example, in a DES system based on ChCl:DL-malic acid:Glycerol, a molar ratio of 1:1:3 was found to keep viscosity in equilibrium while providing high leaching efficiencies (Zheng et al., 2024).

Therefore, in this work, first time in the open literature, DES made of ChCl and SSA is firstly proposed to leach NMC cathode active material. Then, this study will examine the impact of altering the molar ratio in the ChCl:SSA

mixture on the leaching efficiency.After recovery of metals with leaching, oxalate precipitation of Ni, Co and Mn is conducted to exemplify the circular behavior of the process.

Material and Method

The process flowchart used in this work is given in Figure 1. In this research, firstly the process scrap cathodes are heated to 500ºC and 600ºC for 1 hour with 5ºC/min heating rate in air atmosphere to peel off the cathode layer from the aluminum foil, current collector. Then, the recovered black mass' composition, structure and morphology is characterized by means of inductively coupled plasma–mass spectrometry (ICP-MS, X-ray diffraction (XRD; Bruker D2 Phaser) and scanning electron microscopy (SEM, Zeiss Gemini 500) techniques. Then two different mixtures of ChCl:SSA solvent (1:1, 2:3) is prepared (see Table 1) and the effects of leaching temperature (25ºC, 50ºC) and solid/liquid ratio (20g/L, 200g/L) are optimized for each DES mixture. After leaching, Ni, Mn and Co ions are co-precipitated with oxalic acid at pH 2 to form metal oxalates to be used in cathode synthesis.

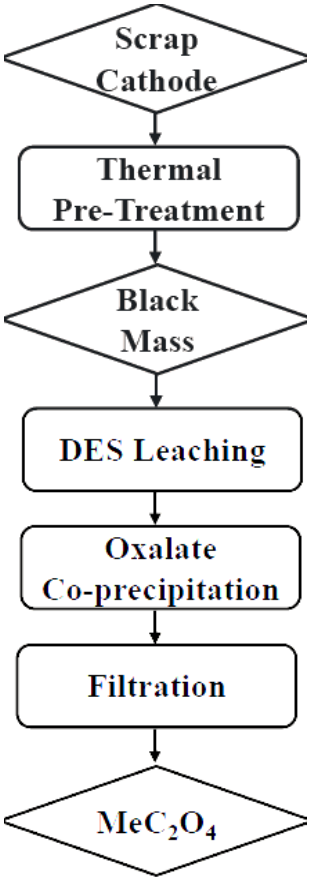

Figure 1. Process flowchart of this study.

Table 1. Leaching experiment parameters.

HBA:HBD	Temperature (ºC)	S/L Ratio (g/L)
1:1	25	20
	50	20
	50	200
2:3	25	20
	50	20
	50	200

Findings

SEM images of cathode powders without thermal pretreatment (Figure 2a-b), pretreatment at 500°C for 1h (Figure 2c-d), and pretreatment at 500°C for 1h followed by 600°C for 1h (Figure 2e-f) are given.

SEM images demonstrate that the average particle size and their spherical morphology of the cathode active material (NMC) are similar for each case, independent on the heat treatment temperature, as expected. The comparison of images shows that heat treatment enables to remove PVDF and carbon black residues while faciling the removal of the black mass from Aluminum foil.

XRD analysis of the black mass (with no Al current collector) after being heat treated at 500°C and 600°C reveals that in each case, no additional peak related to any impurities is detected. XRD patterns of the heat-treated samples show that both samples exhibit well-defined diffraction peaks of the hexagonal structure of α-$NaFeO_2$ with the $R\bar{3}m$ space group. Crystallinity is maintained in both samples with no impurity phases. Diffraction peaks of CAM-600 are slightly weaker than CAM-500 diffraction peaks, which indicates a lower degree of crystallization (Figure 3).Therefore, choosing 500 °C as heat treatment temperature is the best option to lower energy input of the process without compromising material integrity.

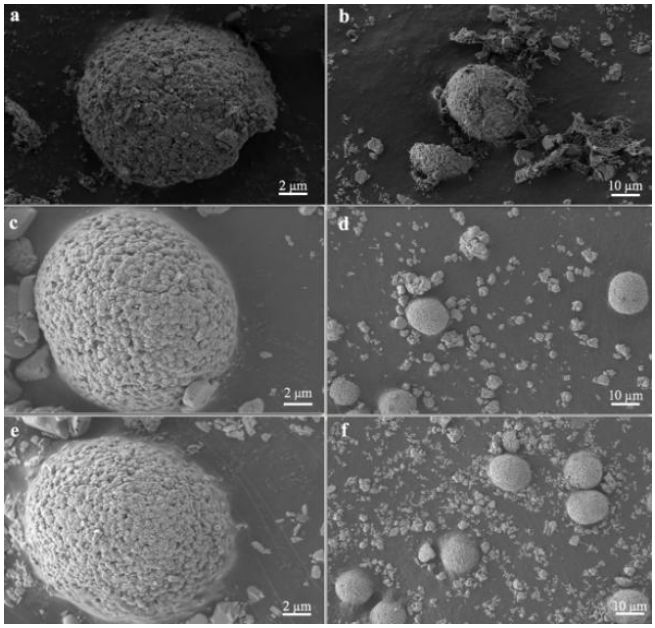

Figure 2. SEM images of cathode powders (a-b) without thermal pretreatment, (c-d) pretreatment at 500°C for 1h: CAM-500 , (e-f) pretreatment at 500°C for 1h followed by 600°C for 1h : CAM-600 .

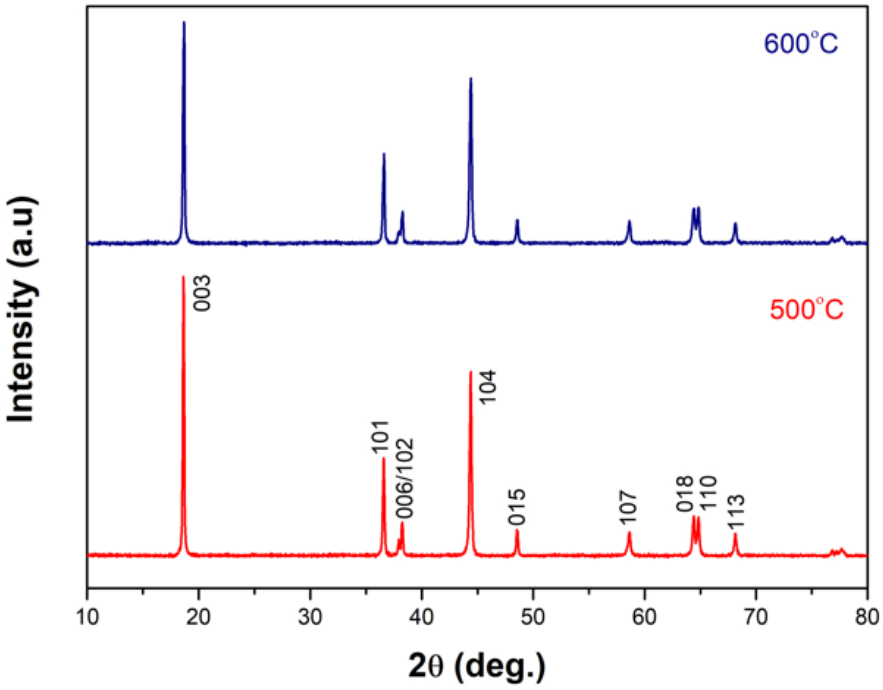

Figure 3. XRD patterns of heat-treated samples.

After peeling off the black mass from the Al foil at 500ºC, ICP-MS analysis is used to obtain the composition of the powder. ICP-MS results from Table 2 indicate that cathode powder stoichiometry is close to NMC811 with exception of a less amount of Mn.

Table 2. ICP-MS results of the black mass.

Sample	Li%	Ni%	Mn%	Co%	Al%
Black Mass	98.25	81.00	5.68	10.89	0.09

Figure 4 shows changes in solution's color after leaching at different conditions, presented in Table 2. DES leaching conducted based on the parameters given in Table 1 indicate that dark, poorly dissolved liquid at 25°C turns clear green at 50°C, indicating a higher metal dissolution. Also, with the increasing S/L ratio it is seen that dissolution remains incomplete and undissolved residues remain in the solution since high S/L ratios lead to slower Ni/Co/Mn dissolution, decreasing overall recovery. Following leaching, with the oxalic-acid precipitation step, targeted ions were effectively removed from solution and converted into an insoluble oxalate product, settled at the bottom of the beaker. The oxalate ion acts as a precipitating agent because of it coordinates with metal ions, such as Ni^{2+}, Co^{2+}, or Mn^{2+}, to form a five-membered ring structure oxalate complex (Choi et. al, 2022). These metal ions precipitate as solids due to their limited solubility. In this precipitation process, due to the solubility of $Li_2C_2O_4$ is much greater than the transition metal oxalate compounds, Li is not precipitated (Sidiq et. al, 2022). The obtained precipitate is suitable for calcination to form oxides for the regeneration of the new cathode material.

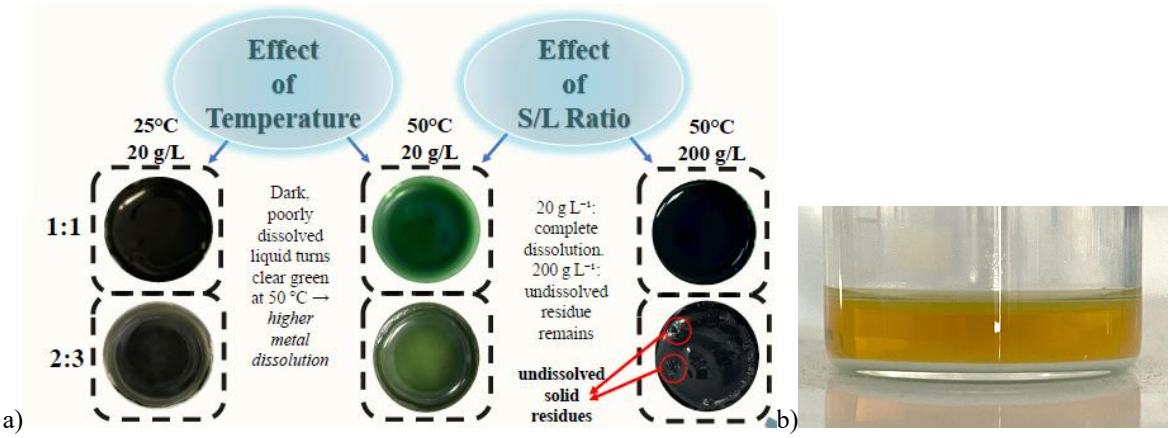

Figure 4. (a) Results of leaching experiments at different parameters (b) Image of the solution and precipitate after oxalic acid precipitation.

Conclusion

In this work, 2 different heat treatments then 6 different leaching experiments are realized to optimize NMC cathode recycling process parameters by DES. Herein first time in the open literature SSA:ChCl mixrture is proposed to be used in NMC leaching. The results show that black cathode layer is peeled off from aluminum current collector when the cathode is heat treated at 500°C for 1 hour at air atmosphere. without destructing the CAM structure. Then the highest efficiency in leaching with SSA:ChCl is achieved with a 1:1 ratio at 50°C and 20 g L^{-1} solid load. The outcomes demonstrate that raising temperature decreases DES viscosity and accelerates diffusion, leading to higher metal dissolution. Higher ChCl in the DES promotes more free Cl^- existence in the solution to form stable M-Cl complexes while keeping viscosity moderate; excess HBD in 2:3 reinforces H-bond network, raising viscosity and slowing mass transfer. Finally, by means of chemical precipitation at pH 2 Ni, Co and Mn are coprecipitated effictively which exemplifies the circularity of the designed process in the synthesis of CAM.

Acknowledgements

This work is financially supported by the Istanbul Technical University Scientific Research Prog. (Project no: MYL-2025-46787). The authors acknowledge Humza Ashraf and Istanbul Medipol University REMER Research Center for supporting in characterizations. The authors also thank Aspilsan A.Ş. for supplying the raw material used in the experiments.

References

Abbott, A. P., Boothby, D., Capper, G., Davies, D. L., & Rasheed, R. K. (2004). Deep Eutectic Solvents Formed between Choline Chloride and Carboxylic Acids: Versatile Alternatives to Ionic Liquids. Journal of the American Chemical Society, 126(29), 9142–9147.

Choi, J., Kim, J., Kim, S., & Yun, Y. (2021). Simple, green organic acid-based hydrometallurgy for waste-to-energy storage devices: Recovery of NiMnCoC2O4 as an electrode material for pseudocapacitor from spent LiNiMnCoO2 batteries. Journal of Hazardous Materials, 424, 127481.

De Vries, E. J. C., Kantengwa, S., Ayamine, A., & Báthori, N. B. (2016). Testing the limits of synthon engineering: salts of salicylic and sulfosalicylic acid with nucleobases and derivatives. CrystEngComm, 18(39), 7573–7579.

Liao, Y., Gong, S., Wang, G., Wu, T., Meng, X., Huang, Q., Su, Y., Wu, F., & Kelly, R. M. (2022). A novel ternary deep eutectic solvent for efficient recovery of critical metals from spent lithium-ion batteries under mild conditions. Journal of Environmental Chemical Engineering, 10(6), 108627.

Lu, B., Du, R., Wang, G., Wang, Y., Dong, S., Zhou, D., Wang, S., & Li, C. (2022). High-efficiency leaching of valuable metals from waste Li-ion batteries using deep eutectic solvents. Environmental Research, 212, 113286.

Luo, Y., Ou, L., & Yin, C. (2023). A green and efficient combination process for recycling spent lithium-ion batteries. Journal of Cleaner Production, 396, 136552.

Sazali, A. L., AlMasoud, N., Amran, S. K., Alomar, T. S., Pa'ee, K. F., El-Bahy, Z. M., Yong, T. K., Dailin, D. J., & Chuah, L. F. (2023). Physicochemical and thermal characteristics of choline chloride-based deep eutectic solvents. Chemosphere, 338, 139485.

Sidiq, A. L., Floweri, O., Karunawan, J., Abdillah, O. B., Santosa, S. P., & Iskandar, F. (2022). NCM cathode active materials reproduced from end-of-life Li-ion batteries using a simple and green hydrometallurgical recycling process. Materials Research Bulletin, 153, 111901.

Xu, M., Kang, S., Jiang, F., Yan, X., Zhu, Z., Zhao, Q., Teng, Y., & Wang, Y. (2021). A process of leaching recovery for cobalt and lithium from spent lithium-ion batteries by citric acid and salicylic acid. RSC Advances, 11(44), 27689–27700.

Zhang, Q., De Oliveira Vigier, K., Royer, S., & Jérôme, F. (2012). Deep eutectic solvents: syntheses, properties and applications. Chemical Society Reviews, 41(21), 7108.

Zheng, S., Xu, S., Wang, Z., Duan, H., Chen, D., Long, M., & Li, Y. (2024). Efficient Leaching of Valuable Metals from Spent Lithium-Ion Batteries Using Green Deep Eutectic Solvents: Process Optimization, Mechanistic Analysis, and Environmental Impact Assessment. Journal of Cleaner Production, 144128.

METALLURGY AND MATERIALS ENGINEERING

Composite and Polymer Materials

Corrosion and Wear

Energy Materials

Extractive Metallurgy

Mechanical Metallurgy

Metals and Alloys

Surface Treatment and Coatings

Development of NiCoCrTiAl Alloy's High Temperature Deformation Resistance With Refractory Alloying

Emin Yiğit Taşdelen[a], Cevat Bora Derin[a]

[a]Istanbul Technical University/Graduate School, Metallurgical and Materials Engineering, Materials Engineering, Turkey
tasdelene18@itu.edu.tr

Keywords : Aerospace Materials, Computational Modeling, High-Entropy Alloys, High-Temperature Mechanical Properties.

Aim

The primary aim of this study is to develop a high-entropy NiCoCrTiAl-based alloy with enhanced high-temperature mechanical properties and thermal stability for aerospace applications with additions of refractory metals. By incorporating refractory elements such as W, Nb, and Mo in small molar percentages (1% and 2%), with the helps of their solubility in Ni3(Ti,Al) phase which also can be seen on Figure 1., the objective is to optimize the microstructure, improve high-temperature deformation strength and enhance the overall mechanical performance of the alloy. These refractory elements are deeply discussed in literature whether they are beneficial in aspect of strengthening the material or not, as stated by Grudzień, Loomis, Maniar, Manriquez et al.. This study aims to design and validate an alternative material to traditional nickel-based superalloys, utilizing computational thermodynamics to guide experimental processes, heat treatments, and similar to the main reference work, which is done by Zhang et. al., whose simulation results can be seen on Figure 2. Lastly, the second aim of the study is to increase the solvus temperature of the strength increasing phases such as gamma prime and gamma double prime without too much addition of given refractory metals which can make the material heavier.

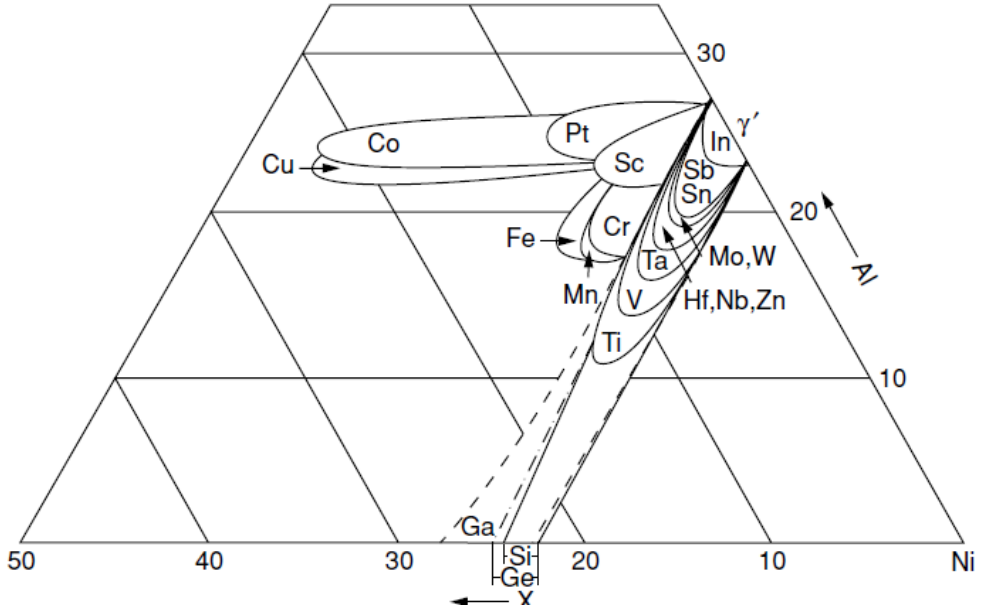

Figure 1. Solubility Values of Different Elements in Gamma Prime Phase
Donachie, M. J., & Donachie, S. J. (2002). *Superalloys: a technical guide*. ASM international.

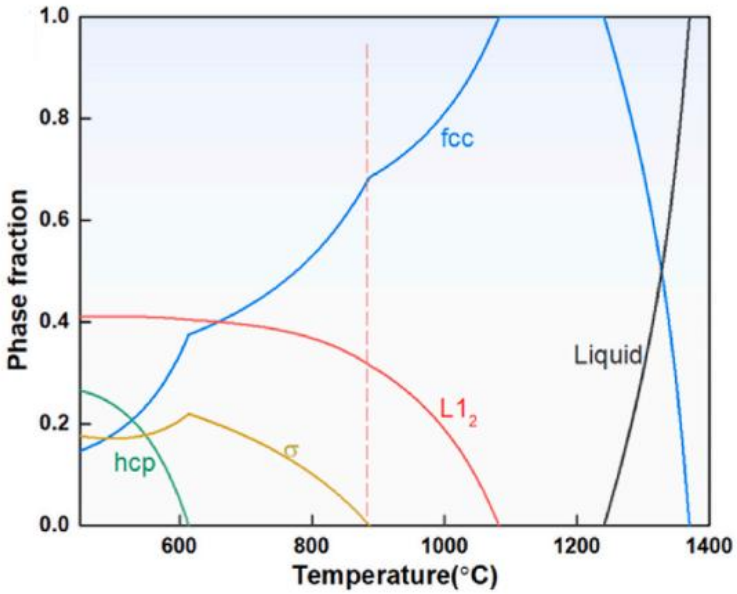

Figure 2. An Example ThermoCalc Modelling For the Given High Entropy Alloy, NiCoCrTiAl
Zhang, H., Meng, H., Meng, F., Tong, Y., Liaw, P. K., Yang, X., ... & Chen, S. (2024). Magnificent tensile strength and ductility synergy in a NiCoCrAlTi high-entropy alloy at elevated temperature. *Journal of Materials Research and Technology*, *28*, 522-532.

Material and Method

The NiCoCrTiAl alloy system with a fixed composition of 33.3Ni-33.3Co-23.4Cr-5Ti-5Al (at. %) will be produced using vacuum arc melting (VAM) to ensure homogeneity and minimize contamination. Small additions of W, Nb, and Mo (1% and 2% molar) will be introduced to analyze their impact on the alloy's microstructure and mechanical properties. Instead of trial-and-error heat treatment optimization, FactSage thermo-chemical software will be used to determine the most effective homogenization and aging parameters, allowing for precise phase stability predictions. Right after obtaining different alloy compositions for each refractory metal added to the high-entropy alloy system, tensile test specimens and ingots that have rectangular cross sections will be cast with the helps of suction casting unit in the vacuum arc remelting device. The most optimized factsage modelling heat treatment conditions which are made up of 2 stages, homogenization and aging, will be experimentally implemented to verify their effectiveness. The characterization process will involve X-ray diffraction (XRD) for the detection of the solid solution matrix gamma and gamma prime phase as a precipitation phase and scanning electron microscopy (SEM) to examine phase distribution, grain morphology, and elemental dispersion. Transmission electron microscopy (TEM) will provide more reliable insights into atomic-scale structural features, while differential scanning calorimetry (DSC) will determine phase transformation behavior and thermal stability of the precipitation and different phases of interest with changing temperature. Mechanical properties will be assessed through tensile, hardness, and wear tests at both room temperatures, along with high-temperature rolling and tensile test experiments to evaluate workability and deformation response at elevated temperatures. Fractography using SEM will be conducted to analyze failure mechanisms and crack propagation patterns after tensile tests which will determine the principle of the failure.

Findings

Expected results include an improvement in high-temperature mechanical properties due to the incorporation of refractory metals, which are anticipated to enhance creep resistance and refine the microstructure due to their lattice distortion and contribution to precipitation of specific phase effects. The computational thermodynamics approach is expected to optimize the gamma prime precipitation process, leading to a more stable microstructure under prolonged exposure to high temperatures and to prevent over-aging, homogenization stages so that poor mechanical properties and high-cost heat treatment procedures will not be involved. The characterization studies

will provide detailed insights into phase evolution and strengthening mechanisms, helping identify the most effective alloy composition for potential industrial application. Mechanical testing will reveal the alloy's ability to withstand operational stresses and deformation experiments will determine its feasibility for industrial-scale manufacture which has a possibility to be proved from the Figure 3. in the main reference article[6]. Consequently, alloy design with its advanced operation conditions will be experimentally calculated and interpreted if they are compatible with real-life results so that more precise and accurate works will be performed in further metallic alloying studies.

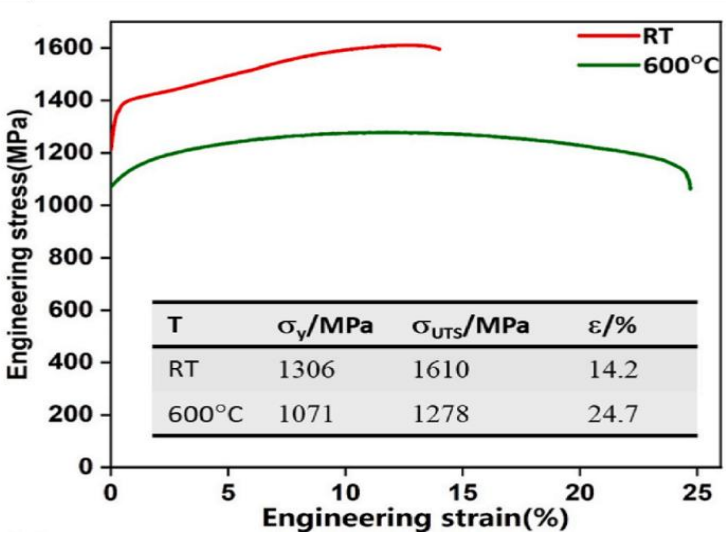

Figure 3. Tensile Test Result of NiCoCrTiAl Alloy Performed at Room and High Temperature

Zhang, H., Meng, H., Meng, F., Tong, Y., Liaw, P. K., Yang, X., ... & Chen, S. (2024). Magnificent tensile strength and ductility synergy in a NiCoCrAlTi high-entropy alloy at elevated temperature. *Journal of Materials Research and Technology*, *28*, 522-532.

Conclusion

This study aims to establish a new class of high-entropy nickel-based superalloys that can serve as a viable alternative to conventional aerospace materials in aspect of high-temperature strength, long-life usability and lower cost. The integration of computational modeling with experimental validation will provide a systematic approach to alloy development, reducing energy waste by helping the estimation of the homogenization and aging conditions in heat treatment procedure as well as improving process efficiency by impeding excessively long heat treatment operations which will eventually decrease the strength of the material at both ambient and high temperatures. By leveraging refractory metal additions, the alloy is expected to exhibit superior thermal stability, improved high-temperature deformation resistance and enhanced other mechanical performance such as hardness, fracture toughness, wear resistance when it is compared with the unalloyed state of the high-entropy alloy. The insights gained will contribute to the broader understanding of high-entropy and nickel or cobalt based alloys' behavior in high temperature environments and lay the foundation for further material optimization and industrial applications in aerospace and other high-temperature engineering sectors where these highly similar alloys systems are continuously developed .

References

Grudzień-Rakoczy, M., Rakoczy, Ł., Cygan, R., Chrzan, K., Milkovič, O., & Pirowski, Z. (2022). Influence of Al/Ti ratio and ta concentration on the as-cast microstructure, phase composition, and phase transformation temperatures of lost-wax Ni-based superalloy castings. Materials, 15(9), 3296.

Maniar, G. N., & Bridge, J. E. (1971). Effect of gamma-gamma prime mismatch, volume fraction gamma prime, and gamma prime morphology on elevated temperature properties of Ni, 20 Cr, 5.5 Mo, Ti, Al alloys. Metallurgical Transactions, 2, 95-102.

Manriquez-Frayre, J. A. (1993). The effect of high aluminum and niobium levels on the coarsening behavior of gamma double prime and gamma prime phases and on the precipitation of delta phase in nickel-iron-chromium-base alloys (Doctoral dissertation, The University of Texas at Austin).

Smith, G. D., & Patel, S. J. (2005). The role of niobium in wrought precipitation-hardened nickel-base alloys. Superalloys, 718(625), 135-154.

Loomis, W. T., Freeman, J. W., & Sponseller, D. L. (1972). The influence of molybdenum on the γ/'phase in experimental nickel-base superalloys. Metallurgical and Materials Transactions B, 3, 989-1000.

Zhang, H., Meng, H., Meng, F., Tong, Y., Liaw, P. K., Yang, X., ... & Chen, S. (2024). Magnificent tensile strength and ductility synergy in a NiCoCrAlTi high-entropy alloy at elevated temperature. *Journal of Materials Research and Technology*, *28*, 522-532.

METALLURGY AND MATERIALS ENGINEERING

Composite and Polymer Materials

Corrosion and Wear

Energy Materials

Extractive Metallurgy

Mechanical Metallurgy

Metals and Alloys

Surface Treatment and Coatings

Investigation of the Properties of Micro-Arc Oxidation Coating on Selective Laser Melted AlSi10Mg Alloy

Aysima Güzel[a], Murat Baydoğan[a]

[a]Istanbul Technical University, Department of Metallurgy and Materials Engineering, Türkiye
guzela18@itu.edu.tr

Keywords: Alsi10mg, Selective Laser Melting, Micro-Arc Oxidation, Additive Manufacturing.

Aim

Aluminum and aluminum alloys are widely used in various industries, particularly in the aerospace sector, due to their lightweight nature, high corrosion resistance, and excellent thermal and electrical conductivity. With the advancement of additive manufacturing technology, the production of these alloys has become feasible, making the investigation of the effects of additive manufacturing methods on these alloys a highly intriguing topic for researchers.

Aluminum alloys produced by additive manufacturing generally exhibit relatively lower hardness and wear resistance due to the challenges in precisely controlling their surface properties during the manufacturing process. Surface coating is one of the most used methods to enhance surface quality and improve surface mechanical properties.

Micro-arc oxidation (MAO) is an efficient coating technology used for aluminum alloys. In this method, a ceramic oxide layer is formed on the surface of the alloy. The properties of the resulting layer can be controlled by adjusting the electrical parameters applied during the coating process, such as coating duration and applied voltage. One of the most significant advantages of using Micro Arc Oxidation (MAO) is its ability to reduce the porosity of the substrate material's surface. Relatively more ductile materials produced by the Selective Laser Melting (SLM) process, surface roughness issues such as keyhole defects are highly likely to occur [1]. Therefore, AlSi10Mg alloys produced by SLM are highly suitable materials for the MAO process.

MAO enhances surface quality by forming a homogeneous and less porous oxide layer, which improves the mechanical properties of the material [2]. Additionally, MAO coatings provide high-temperature and corrosion resistance, making AlSi10Mg alloys more useful in aerospace, automotive, and biomedical applications. Thus, MAO is considered a highly suitable surface treatment method for AlSi10Mg alloys produced by SLM.

The MAO coating consists of three distinct layers. The outermost layer is highly porous and brittle, predominantly composed of metastable gamma-alumina (γ-Al_2O_3), which accounts for approximately 5-30% of the total coating thickness. Below this layer, a dense and hard alpha-alumina (α-Al_2O_3) layer forms due to the high-temperature transformation of gamma-alumina into alpha-alumina. This phase constitutes 70-95% of the coating thickness and is responsible for its high wear and corrosion resistance. The interface region between the coating and the substrate can be further divided into three sublayers, where the first sublayer displays an amorphous structure, and the crystallization level increases towards the substrate. These sublayers function as a diffusion barrier, enhancing the material's anti-corrosion properties .

In this study, the properties of the ceramic oxide coating formed under different electrical parameters were investigated. The applied voltage values and duration caused variations in surface roughness, coating thickness, and surface properties of the material. The coating thickness and surface roughness were analyzed. SEM, XRD and optical microscope analyses were done.

Material and Method

The material and method section should be written in Times New Roman font, justified-alignment and in 10-point size. Selective Laser Melting (SLM) method was used to produce AlSi10Mg samples. To better observe the surface

effects, the samples were first sanded with 800, 1200, and 2500-micron sandpapers. After sanding, the surfaces were coated using the Micro-Arc Oxidation (MAO) method.

The MAO method operates with a bipolar power source. While stainless steel was used as the cathode, the samples were placed in the anode. Due to the electrical arcs generated on the surface of the samples immersed in a conductive electrolytic solution, a ceramic-oxide coating layer was formed. A mixer was placed at the bottom of the system to ensure homogeneous mixing of the electrolyte. A cooling system was also used to control the system temperature.

The parameters used to control the properties of the coatings are shown in Table 1. The first four samples were coated in a solution containing 10 g/L $NaAlO_3$, 2 g/L NaOH, and 2 g/L Na_3PO_4, whereas the 5th and 6th samples were coated in a solution with 20 g/L $NaAlO_3$, 2 g/L NaOH, and 2 g/L Na_3PO_4. After the Micro-Arc Oxidation (MAO) process, the surface thickness and roughness of the samples were measured, followed by Scanning Electron Microscopy (SEM) and X-ray Diffraction (XRD) analyses. Subsequently, the samples were sectioned in half, and the cross-sectional area was examined using an optical microscope.

Table 1. Applied Voltage Parameters and Solutions**.**

Sample	Positive Pulse Duration (µs)	Negative Pulse Duration (µs)	Off time (µs)	Positive Voltage (V)	Negative Voltage (V)	Duration (minute)
1	600	1200	400	480	80	3
2	600	900	400	480	80	4
3	600	600	400	480	90	5
4	400	400	600	480	90	5
5	400	400	600	450	100	5
6	400	400	600	450	100	5

Findings

The surface coating thicknesses of the samples were measured as 6, 8, 11, 10, 38, and 37 microns, respectively. Considering the coating thickness, we can conclude that the increase in negative voltage values and voltage duration leads to an increase in coating thickness.

The surface roughness (Ra, Rz) values of the samples were measured before and after the MAO process. The results are presented in Table 2.

In the As-Built samples, the Ra and Rz values appear to be quite low, indicating a relatively smooth surface. Due to the increased surface thickness and the formation of a ceramic coating after the MAO process, the surface became rougher in all samples. The highest surface roughness was observed in Samples 5 and 6. This is likely explained by the fact that the coating was most prominent in these samples.

When examining the SEM surfaces, the presence of micropores on the coating is observed. This phenomenon occurs when the released energy exceeds the dielectric breakdown strength of the substrate material, leading to the formation of an electric arc between the substrate and the coating surface. [4] Consequently, this results in the development of cracks and pancake-like morphology on the coating.

As the coating thickness increases, ceramic particles generated during the process progressively fill the existing pores, thereby reducing porosity. However, this also leads to an increase in surface crack formation. Excessive coating thickness can negatively impact the uniformity of the coating and contribute to an increase in surface roughness.

The examination of the cross-sectional area shows that the coating thickness increases in direct relation to the processing duration and applied voltage. As the coating becomes thicker, surface roughness also increases, leading

to a less uniform surface morphology. This suggests that excessive coating growth may negatively affect surface homogeneity.

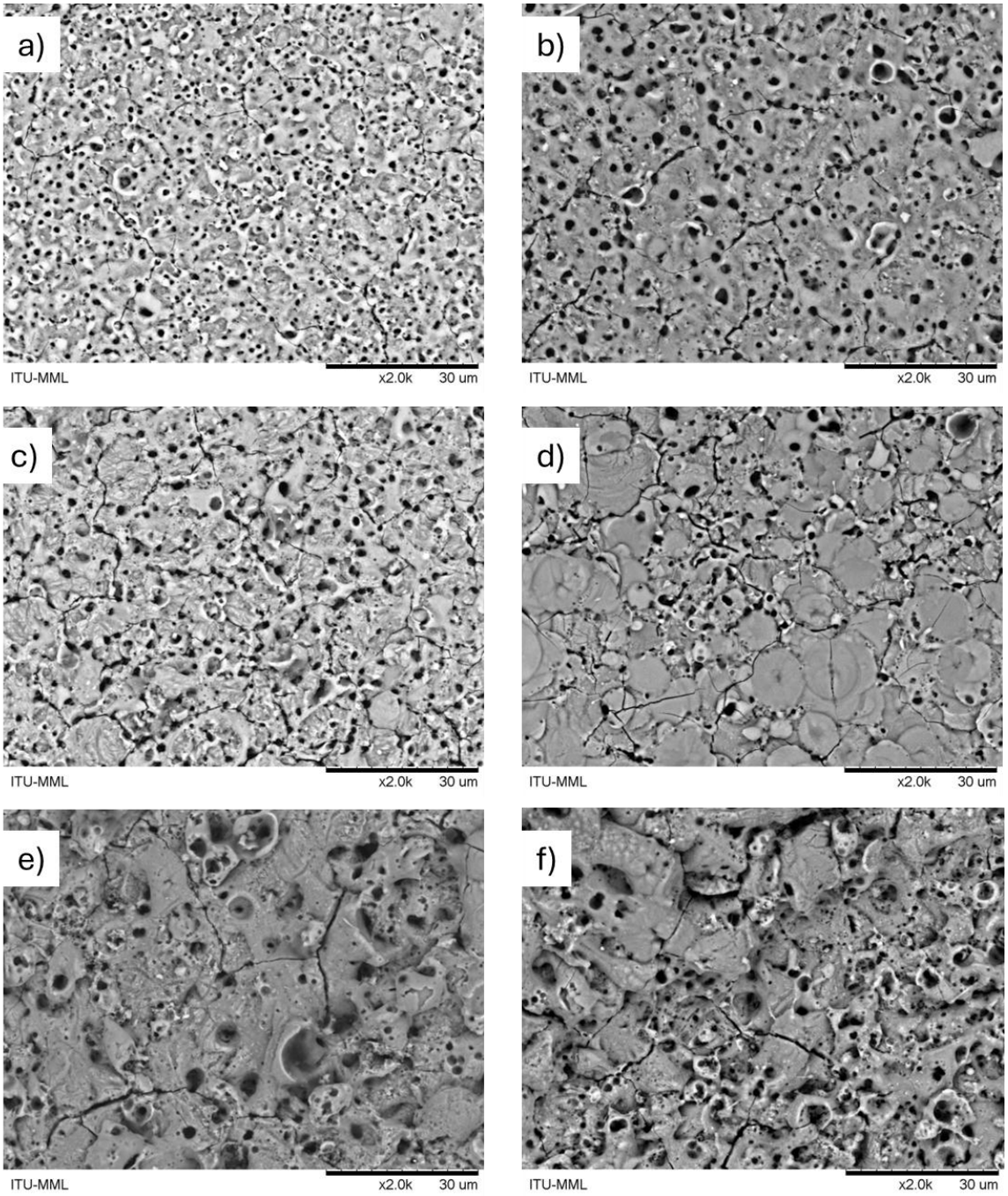

Figure 2. SEM surface images of Samples (a) Sample 1, (b) Sample 2, (c) Sample 3, (d) Sample 4, (e) Sample 5, (f) Sample 6.

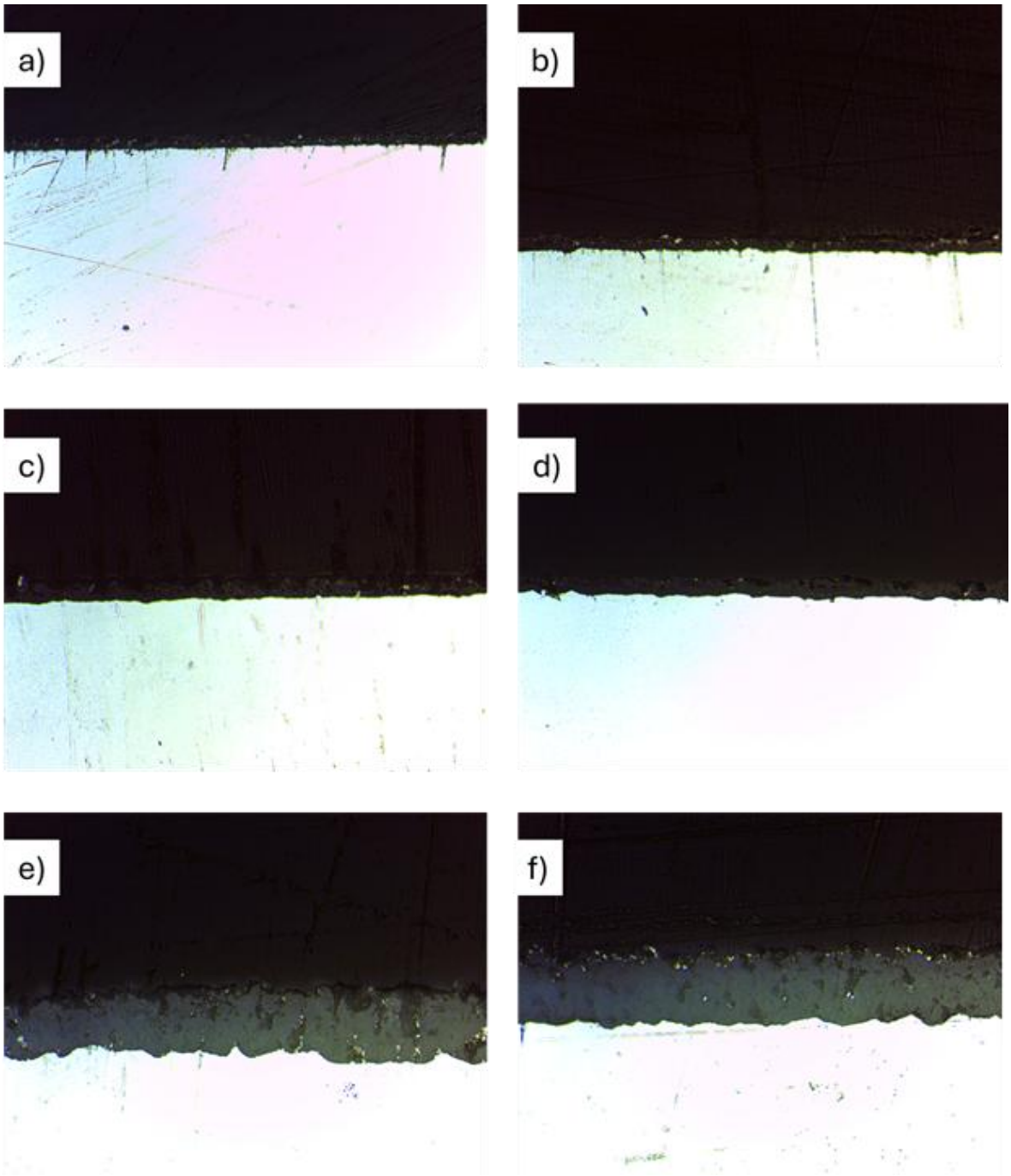

Figure 3. Cross sectional SEM micrographs of the coatings of Samples (a) Sample 1, (b) Sample 2, (c) Sample 3, (d) Sample 4, (e) Sample 5, (f) Sample 6.

The analysis of the XRD results indicates that the Al and Si phases originate from the substrate material. Initially, neither the gamma nor the alpha phases are present; however, these phases emerge as the coating duration increases. In samples 5 and 6, a higher number of peaks corresponding to alpha-alumina and gamma-alumina are observed, suggesting that the $NaAlO_3$ solution positively influences alumina phase formation.

Conclusion

This study demonstrated that micro-arc oxidation (MAO) effectively enhances the surface properties of SLM-produced AlSi10Mg alloys. Increasing the applied voltage duration significantly increased coating thickness. While MAO improved surface durability, it also increased surface roughness, particularly in thicker coatings. SEM

and optical microscope analyses revealed that micropores and cracks, with excessive coating thickness compromising uniformity. XRD analysis indicates that the $NaAlO_3$ solution promotes alumina phase formation and that gamma-alumina and alpha-alumina phases develop more prominently as the coating duration increases. Overall, MAO is a promising surface treatment for AlSi10Mg alloys, but optimizing electrical parameters is essential to balance thickness, porosity, and roughness.

References

Dong, G., Wang, W., Guo, L., Yang, H., Li, H., & Zhao, D. (2024). *Properties of micro-arc oxidation coating of selective laser melting AlSi10Mg alloy.* Materials Science and Technology, 02670836241288976.

Guo, Y., Wei, Z., Lu, X., Xu, R., Fei, Y., Chen, D., & Ding, H. (2021*). Growth characteristics and properties of micro-arc oxidation coatings on AlSi10Mg selective laser-melted components.* Surface and Coatings Technology, 426, 127765.

Guo, Y., Yuan, X., Li, X., Li, G., Lu, X., Wang, Z., & Zhang, S. (2021). *Investigation of the addition of (NaPO3) 6 to Al2O3 ceramic coatings prepared on AlSi10Mg selective laser melted components via micro-arc oxidation.* Journal of Materials Engineering and Performance, 30(10), 7117-7127.

METEOROLOGICAL ENGINEERING

Atmosphere, Meteorology

Aviation Meteorology

Renewable Energy

Batman Airport Fog Analysis and The Relationship of Long-Term Fog With Low-Level Jets

Rozerin Koyuncu[a,b], Ali Deniz[a]

[a] İstanbul Technical University, Department of Meteorology, Turkey.
[b] Turkish State Meteorological Service, Batman Airport Meteorology Office, Turkey.
koyuncu15@itu.edu.tr

Keywords : Fog, Metar, Aviation, Low Level Jet, Radiation, Wind.

Aim

This study thesis presents a detailed analysis of fog events observed at Batman Airport between 2010 and 2024 in terms of frequency, duration, and types, and examines the relationship between long-lasting fog events and low-level jets (LLJs), a phenomenon of the atmospheric boundary layer.

Material and Method

In this study, 8,285 observations were evaluated using METAR and SPECI meteorological reports and upper-air radiosonde data. The data were obtained from the Turkish State Meteorological Service (MGM) and the Iowa State University's IEM database.

Findings

A total of 750 foggy days were detected in the 15-year period. The annual average was 50 foggy days. A total of 3829.02 hours of fog occurred. In the 15-year period, prevailing visibility dropped below 1000 meters in 8270 METAR observations. It was detected that fog continued for 24 hours on December 31, 2013, January 1, 2014, December 26, 2014, February 8, 2017 and January 11, 2023 in the 15-year period. The prevailing visibility dropped to 400 meters in 61% of the METAR observations, to 300 meters in 43.63%, to 200 meters in 16.86%, and to 100 meters in 2.28%. Wind directions and speeds of the observations were determined in the 15-year period. The observation frequency of wind blowing from variable directions (VRB) was determined as 29.32%, south-southwest wind (from 180-240 degrees) as 21.15% and north-northeast wind (from 360-060 degrees) as 21.9%. Wind frequency over a 15-year period was determined and in 97.03% of the observations, the wind intensity was between 0-5 knots, and in 2.97% the wind frequency was between 6-10 knots. In 18.4% of the fogs that occurred, pressure values occurred between 1016-1020 hPa, in 47.7% the pressure values occurred between 1021-1025 hPa and in 25.9% the pressure values occurred between 1026-1030 hPa. Fog type was determined according to temperature in the 15-year period by years and months; 67.4% warm fog and 32.6% cold fog were detected. These fogs were classified as radiation fog, cloud base lowering, precipitation fog, advection fog, and unknown fog. It was determined that fog continued for 24 hours on 31 December 2013, 1 January 2014, 26 December 2014, 8 February 2017, and 11 January 2023 within the 15-year period.

Fog classification was made for Batman Airport using the fog classification of Tardif and Rasmussen (2007). These fogs were classified as radiation fog, cloud base lowering, precipitation fog, advection fog and unknown fog. According to their formation types, 52.27% radiation fog, 30.56% cloud base lowering, 2.8% precipitation fog, 3.47% advection fog and 11.07% unknown fog were classified. In addition, fog types and the durations during which they occurred were determined. Radiation fog occurred for 2234.4 hours (%58.35), cloud base lowering for 1170 hours (%30.56), precipitation fog for 140.6 hours (%3.67), advection fog for 95.5 hours (%2.49) and unknown fog for 188.5 hours (%4.92). The dispersion conditions of the fogs differed according to the fog types. Radiation fog generally lost its effect with sunrise, temperature increase and wind. Precipitation fog generally lost its effect with the cessation of rain, decrease in precipitation intensity or change in fog type. The dominant visibility, which decreases with the lowering of the cloud base, lost its effect with the rise of the cloud base. It was observed that radiation fog generally started to form at night.

Low-level jets (LLJs) are wind speed maxima occurring within the boundary layer and can indirectly affect fog formation mechanisms. It was found that LLJs from the southwest transported moisture into fog-prone areas, enhancing fog development and duration, whereas strong northerly LLJs contributed to fog dissipation through turbulence and mixing. In this context, the synoptic analyses of long-duration fog events on January 21, 2013, December 18, 2013, December 28, 2013, and February 8, 2017, were conducted and the effects of LLJs were evaluated with concrete data.

The synoptic analyses identified strong relationships between the direction and altitude of LLJs and fog intensity. Southwesterly jets transported the water vapor required for fog development, increasing its persistence, while strong northerly jets rapidly dissipated fog. Weaker northerly jets could also help maintain fog presence. These findings indicate that LLJs influence not only the formation of fog but also its distribution and duration.

In light of these findings, it is recommended that the effects of LLJs be integrated into operational planning at Batman Airport to enable more accurate forecasting of long-lasting fog events and to prevent disruptions in air traffic. The thesis offers both academic and practical contributions to aviation meteorology, boundary layer meteorology, and synoptic analysis methods.

Figure 1: Batman Airport.

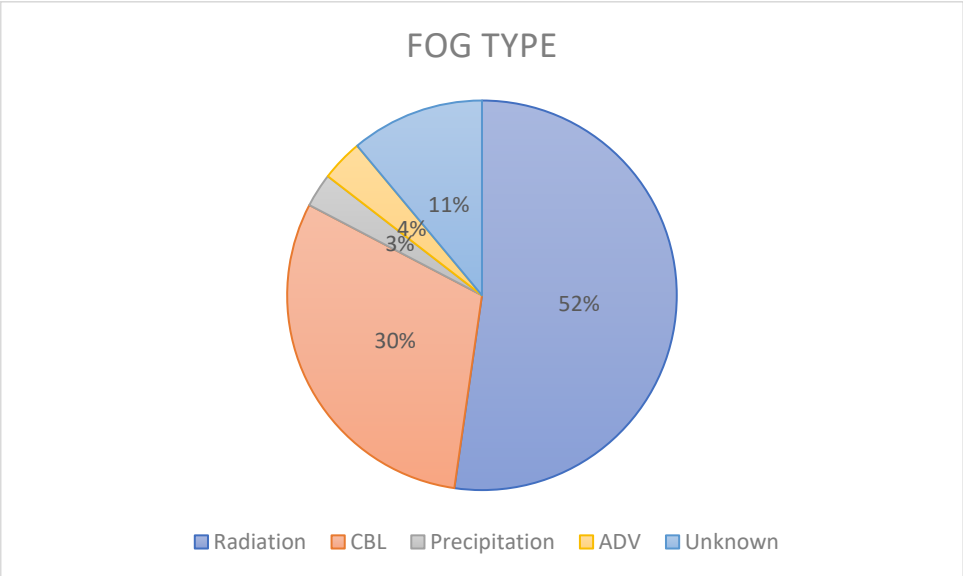

Figure 2: Distribution of fog durations according to formation types in Batman Airport 2010-2024 period.

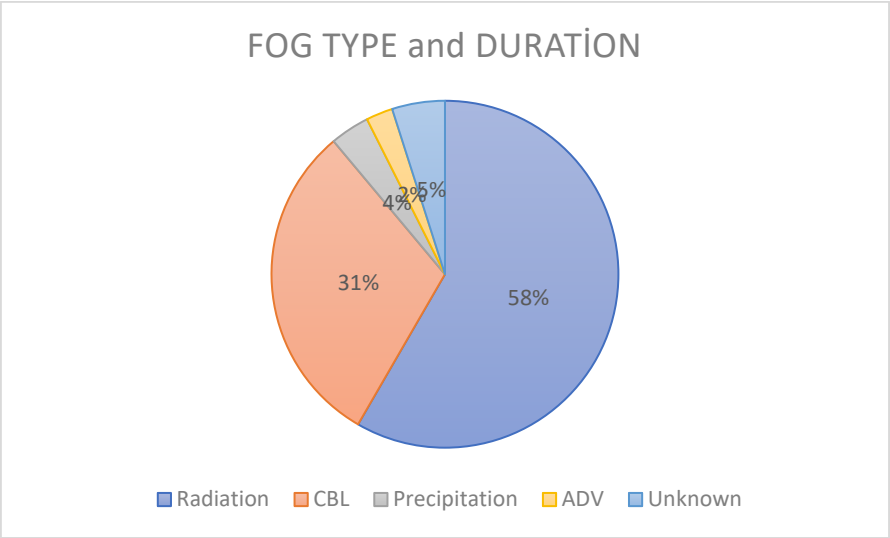

Figure 3: Distribution of fog durations according to formation types and duration in Batman Airport 2010-2024 period.

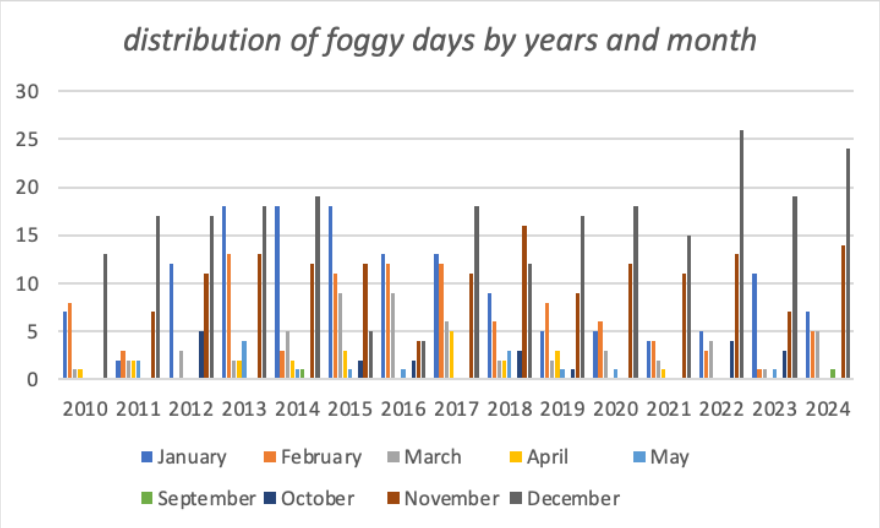

Figure 4: Distribution of fog according to montly and year in Batman Airport 2010-2024 period.

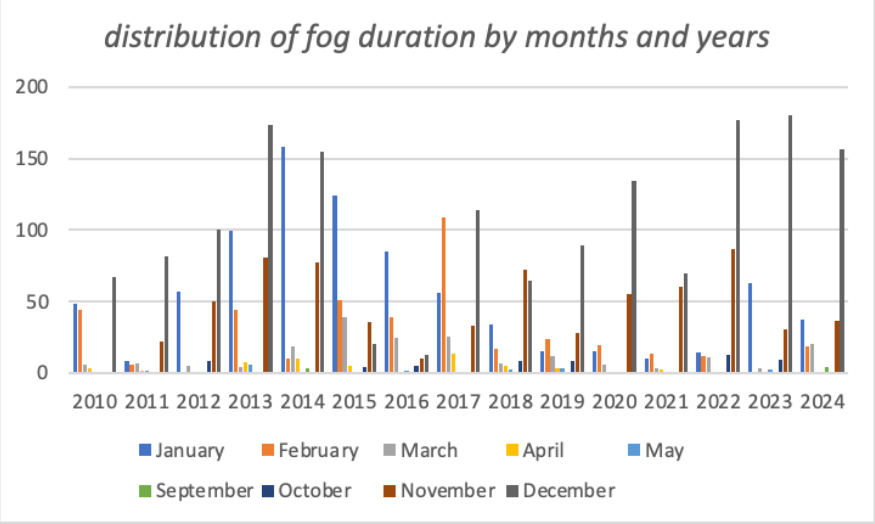

Figure 5: Distribution of fog durations according to montly and year in Batman Airport 2010-2024 period.

Table 1: Inversion hourly data.

Station No	Date	Time(Z)	Env_start_lev mb	Env_start_ height m	Env_start temperature	Env_start_ Wind_direc	Env_start_wind_ speed Knot	Env_end_level mb	Env_end_level _height m	Env_end_ temp	Env_end_wind_ direction	Env_end_wind_speed _Knot
17281	21 Jan2013	0	943	679	0,8	270	60	926	826	4,9	235	22
17281	21 Jan 2013	0	810	1904	-1,5	304	88	789	2114	0,0	307	142
17281	12 Nov 2013	12	651	3677	-5,9	24	54	629	3939	-5,0	3	68
17281	18 Dec 2013	0	886	1185	1,2	52	117	865	1383	1,4	72	117
17281	18 Dec 2013	0	908	994	-0,4	47	66	886	1185	1,2	52	117
17281	18 Dec 2013	12	745	2565	-4,2	131	175	725	2779	-4,1	133	142
17281	28 Dec 2013	0	947	678	-3,9	250	19	918	929	2,6	0	0
17281	28 Dec 2013	0	918	929	2,6	0	0	870	1366	5,5	35	17
17281	28 Dec 2013	12	896	1118	4,5	89	52	862	1432	6,0	93	37
17281	28 Dec 2013	12	938	744	0,2	192	37	913	958	4,7	74	27
17281	3 Jan 2014	0	937	743	1,0	139	12	900	1067	3,8	59	29
17281	4 Jan 2014	12	702	3036	-10,1	234	35	681	3272	-8,9	348	93
17281	26 Dec 2014	0	789	2157	0,1	251	103	755	2512	1,4	225	90
17281	26 Dec 2014	0	947	681	6,0	0	0	918	936	4,5	75	26
17281	8 Feb 2017	0	753	2517	-2,5	217	54	722	2849	-1,1	237	66
17281	8 Feb 2017	0	946	681	-2,8	200	10	834	1698	2,1	141	43
17281	8 Feb 2017	12	935	756	2,8	228	56	911	965	3,5	264	179
17281	2 Dec 2017	0	946	681	1,9	90	10	807	1992	8,1	62	35
17281	17 Dec 2020	0	941	681	0,5	50	1	921	861	0,8	289	1
17281	19 Dec 2020	12	945	681	0,3	100	2	918	917	0,6		

Table 2: Atmospheric boundary layer properties during fog formation process.

Fog Type	Date	Durarion (sa)	Min. Pre. Vis (m)	Ground Level							Fog Top*				
				Wind (knot)					Temperature(°C)		Height (m)			Temperature(°C)	
				BRY	DRY	DRH	ORH	Mean	Mean	Range	Mean	Range	Thickness	Mean	Range
CBL	21 January 2013	22,42	100	SE	3	VRB	3	2	1	-1/4	662	204/835	631	3.45	0.8/4.8
CBL	12 November 2013	18,2	100	NE	4	VRB	2	2	9.4	7/11	655	172/840	668	10.3	7/11.4
CBL	13 November 2013	20,17	150	VRB	1	VRB	2	-	8.9	8/11	861	773/1085	312	10.06	6.8/12.6
CBL	18 December 2013	21	400	SW	4	VRB-SSW	2	2.4	-8.3	-7/-10	988	830/1382	552	-4.5	-11.1/1.2
RAD	28 December 2013	22,5	100	SSW	3	VRB	2	2.7	-8.7	-6/-12	1057	232/1570	1338	1.3	-8/5.2
PRCP	31 December 2013	24	200	SSW	2	CALM-NNE	0-2	1.8	1.3	0/2	605	171/770	599	3.4	2/4.3
PRCP	1 January 2014	24	200	VRB	2	VRB	2-3	2.7	0.8	-1/1	660	136/886	750	3.1	1/5.4
PRCP	3 January 2014	23	100	SW	2	VRB	2	2.7	0.2	-1/3	708	210/1069	859	1.4	0/3.6
RAD	4 January 2014	19,87	200	VRB	1	VRB	3	2.7	-0.3	-1/2	680	218/863	645	0.8	-2/2,8
RAD	26 December 2014	24	200	CALM	2	VRB	2-3	2.6	-0.2	-3/2	726	239/932	693	2.3	-2/4.6
RAD	8 February 2017	24	100	NE	3	NNE-VRB	2	2.2	-4.3	-2/-8	901	239/1431	1192	-4	-4/2.6
RAD	2 December 2017	18	250	VRB	1	VRB	2-3	3.2	2.7	2/4	1009	234/1991	1757	5	-1/8
RAD	17 December 2020	20,5	100	NNE	3	CALM-VRB	0-3	1.9	5	1/7	712	181/903	722	6.5	1/8.1
CBL	19 December 2020	18,23	300	NE	4	CALM-VRB	0	2.1	2.4	2/3	782	223/1124	901	4	-2/7.8
CBL	11 January 2023	24	100	SW	3	VRB	2	2.6	-1.7	1/-3	-	-	-	-	-
CBL	16 December 2023	21	250	SW	0	VRB	2	1.4	5.3	3/7	-	-	-	-	-

*AGL Data
Initial Wind Direction(BRY),Initial Wind Speed(BRH), dominant wind speed(DRH), mean wind speed(ORH),

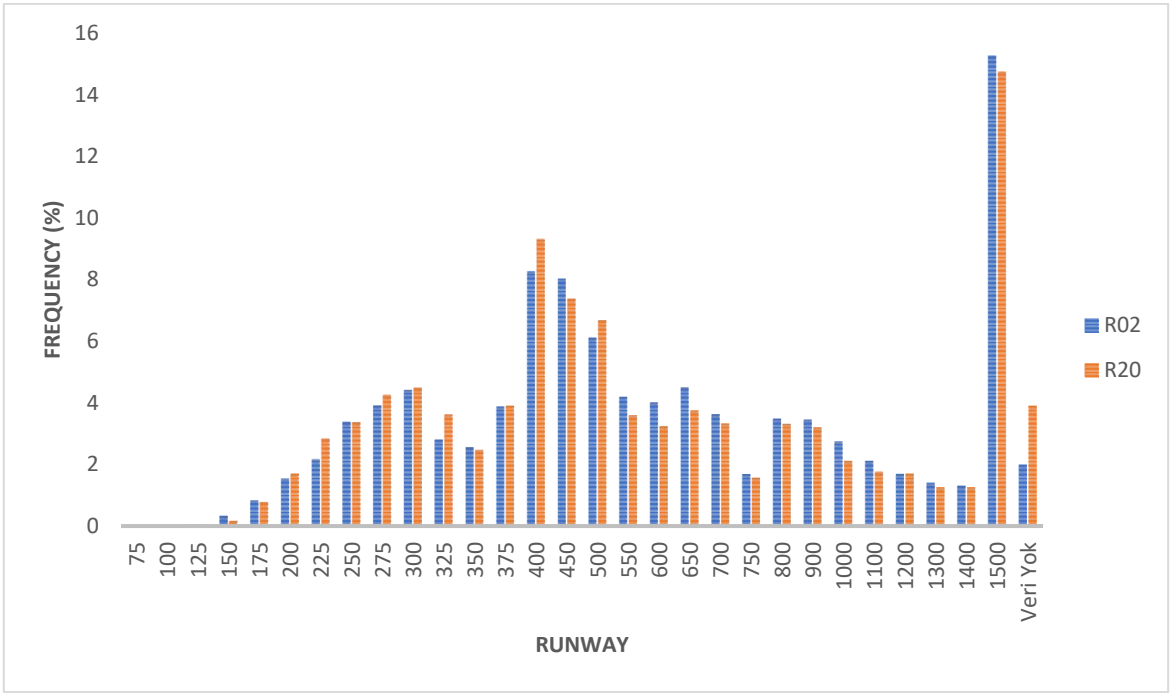

Figure 6: Distribution of fog observations in Batman Airport 2010-2024 period according to runway head RVR values.

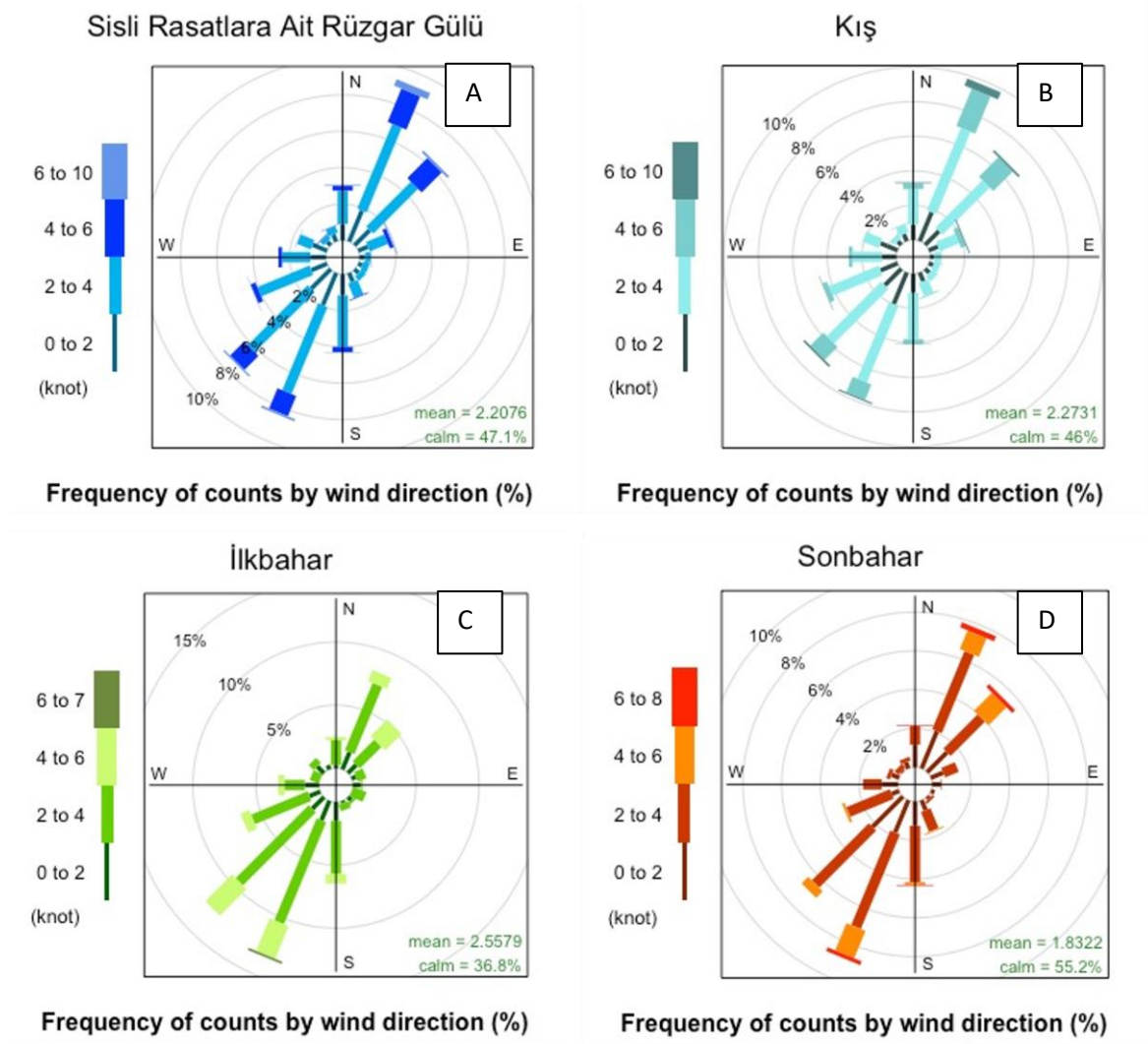

Figure 7: Batman Airport wind roses of foggy observations for the period 2010-2024 according to seasons (A)General (B) Winter, (C) Spring, (D) Autmum.

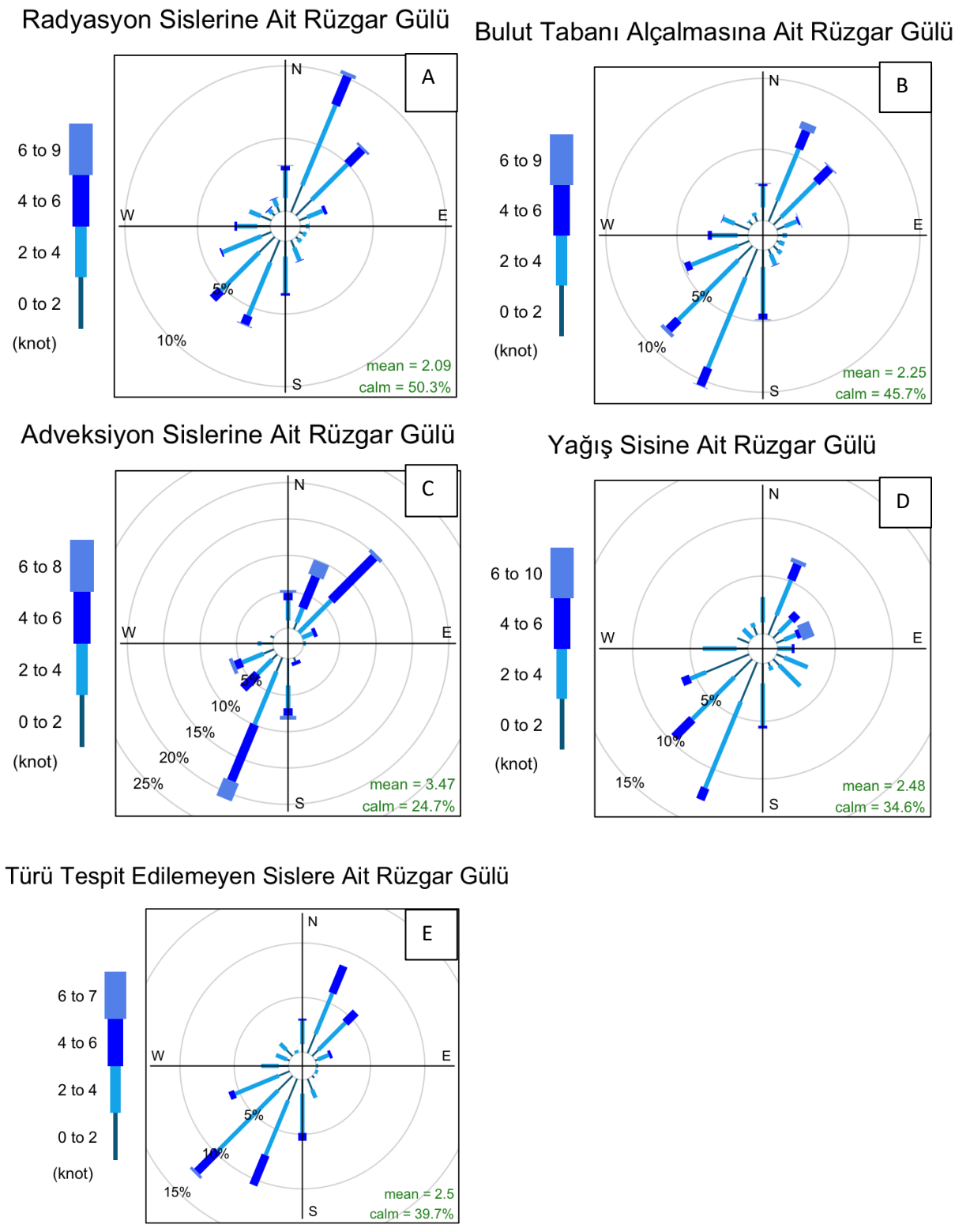

Figure 8: Batman Airport wind roses according to fog types in the period 2010-2024 (A) Radiation fog, (B) CBL, (C) Advection fog, (D) Precipitation Fog, (E) Unknown.

Table 3: Fog Classification algorithm flow chart (Tardif and Rasmussen, 2007; Koyuncu et al., 2022).

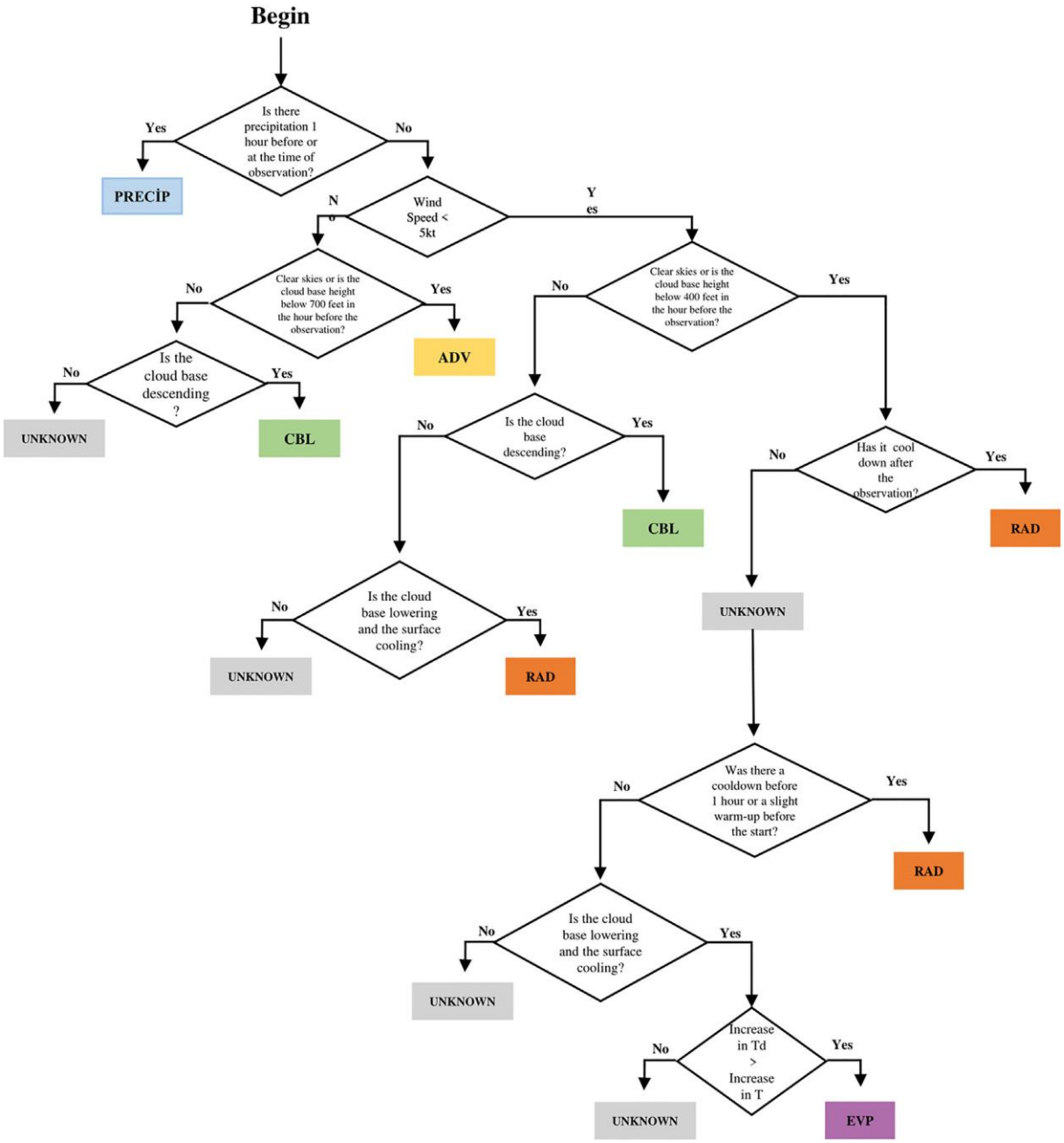

Conclusion

One of the most important findings of the study is the identification of 751 foggy days over the 15-year period, corresponding to a total duration of 3,834.85 hours. The year with the highest number of foggy days was 2013, while the longest-lasting fog event occurred in 2014. The year with the least fog was 2010. Approximately 75% of fog events occurred during nighttime hours (22:00–06:00 UTC). Winter was by far the season with the most intense fog formation. Fog types were classified as radiation fog, advection fog, low cloud base, precipitation fog, and morning evaporation fog, with radiation fog being the most commonly observed.

Low-level jets (LLJs), which are wind speed maxima within the boundary layer, play an indirect role in fog formation processes. Observations revealed that southwesterly LLJs transported moisture into areas prone to fog, thereby promoting its development and extending its duration. In contrast, strong northerly LLJs contributed to fog dissipation through enhanced turbulence and mixing. In this context, synoptic analyses were carried out for

prolonged fog events on January 21, 2013; December 18, 2013; December 28, 2013; and February 8, 2017, to assess the impacts of LLJs using concrete data.

The synoptic evaluations revealed a strong correlation between the direction and altitude of LLJs and the intensity of fog. Southwesterly jets facilitated the transport of moisture necessary for fog formation, leading to greater persistence, while strong northerly jets dispersed fog more rapidly. Interestingly, weaker northerly jets were also found to contribute to the maintenance of fog under certain conditions. These results demonstrate that LLJs significantly influence not only the initiation of fog but also its spatial extent and duration.

References

Akbayır, İ., & Yavuz, V., & Deniz, A., & Özdemir, E.T. (2018). *"Türkiye'deki Havalimanlarında Meydana Gelen Sis Hadisesinin Zamansal Analizi"* El-Cezerî Fen ve Mühendislik Dergisi, 5(2); 327-330.

Annex, ICAO (International Civil Aviation Organization). (2013) *"Annex3– Meteorological Service for International Air Navigation" Seventeenth Edition, July 2010, APP 3-9.* Retrieved from https://www.icao.int/airnavigation/IMP/Documents/Annex%203%20-%2075.pdf

Avşar, E. (n.d.). *"İzmir Adnan Menderes Havalimanı'nın Kümülonimbüs (Cb), Oraj Ve Sis Analizi"*. Adnan Menderes Havalimanı Meteoroloji Müdürlüğü, İzmir.

Byers, H.R. (1959). "*General Meteorology"*. Third Ed., (McGraw Hill, New York).

Çamalan, G., & Yağan, S., & Akgün, N. (2010). TC Çevre ve Orman Bakanlığı, Meteoroloji işleri Genel Müdürlüğü*, "Esenboğa Havalimanı Sis Etüdü"* Uluslararası Katılımlı 1. Meteoroloji Sempozyumu, 27-28 Mayıs 2010 Sempozyum Bildiri Kitabı, 317-327.

Deniz, A., & Yavuz, V. & Özdemir, E.T. (2018). *"İstanbul Sabiha Gökçen Uluslararası Havalimanı'na Ait Sis Oluşumu İle İlgili Sinoptik Durum Araştırması"* Türkiye Ulusal Jeodezi ve Jeofizik Birliği: 30 Mayıs - 2 Haziran 2018, İzmir. Retrieved from: https://www.researchgate.net/publication/327303954.

Duynkerke, P. G., and P. Hignett. (1993). *"Simulation of Diurnal Variation in a Stratocumulus-capped Marine Boundary Layer during FIRE". Mon. Wea. Rev.*, **121**, 3291–3300, https://doi.org/10.1175/1520-0493(1993)121<3291:SODVIA>2.0.CO;2.

Fathalli, M., Lac, C., Burnet, F. & Vié, B. (2022). *"Formation of fog due to stratus lowering: An observational and modelling case study". Quarterly Journal of the Royal Meteorological Society*, 148(746), 2299–2324. Retrieved from: **https://doi.org/10.1002/qj.4304**.

Gultepe, I., Tardif, R., Michaelides, S. *et al.* (2007). *"Fog Research: A Review of Past Achievements and Future Perspectives". Pure appl. geophys.* **164**, 1121–1159. Retrieved from: https://doi.org/10.1007/s00024-007-0211-x.

Haby, J. (n.d.*). "The Low Level Jets"*. Retrieved from: https://www.weather.gov/source/zhu/ZHU_Training_Page/Miscellaneous/lowleveljet/lowleveljet.html. Alıntılanma tarihi: Mart 2025.

Ju, T., Wu, B., Wang, Z., Liu, J., Chen, D., & Zhang, H. (2020). *"Relationships between Low-Level Jet and Low Visibility Associated with Precipitation, Air Pollution, and Fog in Tianjin". Atmosphere*, *11*(11), 1197. Retrieved from: https://doi.org/10.3390/atmos11111197.

Kim, C. K., & Yum S. S. (2010). *"Local Meteorological and Synoptic Characteristics of Fogs Formed Over Incheon International Airport in The West Coast of Korea"* Advances In Atmospherıc Scıences, 27(4), 761–776, Retrieved from: doi: 10.1007/s00376-009-9090-7.

Koyuncu, R., A. Deniz, and E. T. Özdemir. (2022). *"Ankara Esenboga International Airport (Turkey) fog Analysis and Synoptical Investigation of the Fog Event Dated 17–19 December 2019." International Journal of Climatology* **42**: 8368–8389. Retrieved from: **https://doi.org/10.1002/joc.7728**.

Li, P., G. Fu, C. Lu, D. Fu, and S. Wang. (2012). *"The Formation Mechanism of a Spring Sea Fog Event over the Yellow Sea Associated with a Low-Level Jet".* Wea. Forecasting, 27, 1538–1553. Retrieved from: https://doi.org/10.1175/WAF-D-11-00152.1.

Liu, D.Y., Niu, S.J., Yang, J. *et al.* (2012). *"Summary of a 4-Year Fog Field Study in Northern Nanjing, Part 1: Fog Boundary Layer". Pure Appl. Geophys.* **169**, 809–819. Retrieved from: https://doi.org/10.1007/s00024-011-0343-x

Luiz, E. W., & Fiedler, S. (2024). *"Global Climatology of Low-Level-Jets: Occurrence, Characteristics, and Meteorological Drivers".* Journal of Geophysical Research: Atmospheres, 129(9), e2023JD040262. Retrieved from: https://doi.org/10.1029/2023JD040262.

Mazon, J., Rojas, J.I., Lozano, M., Pino, D., Prats, X. and Miglietta, M.M. (2018). *"Influence of meteorological phenomena on worldwide aircraft accidents, 1967–2010".* Met. Apps, 25: 236-245. Retrieved from: https://doi.org/10.1002/met.1686.

Meteoroloji Genel Müdürlüğü. (2023). *"Köppen-Trewartha İklim Siniflandirmasina Göre Türkiye İklimi".* Erişim linki: https://www.mgm.gov.tr/FILES/iklim/iklim_siniflandirmalari/K%C3%B6ppen-Trewatha.pdf

Meteoroloji Genel Müdürlüğü. (n.d.). *"İklim Sınıflandırmaları".* Retrieved from: https://www.mgm.gov.tr/files/iklim/yayinlar/iklim_siniflandirmalari.pdf.

Meteoroloji Genel Müdürlüğü. (n.d.). *"Sis (FOG)".* Erişim linki: https://www.mgm.gov.tr/genel/meteorolojisozlugu.aspx?.

Meyer, M. B., & Lala, G. G. (1990). *Climatological Aspects of Radiation Fog Occurrence at Albany,* New York, Journal of Climate, 3(5), 577-586. Retrieved from: https://journals.ametsoc.org/view/journals/clim/3/5/1520-0442_1990_003_0577_caorfo_2_0_co_2.xml.

National Oceanic and Atmospheric Administration Services. (2021). *Glosary, "Fog".* Retrieved from: https://w1.weather.gov/glossary/index.php?word=Fog.

Oliver, D. A., W. S. Lewellen, and G. G. Williamson. (1978). *"The Interaction between Turbulent and Radiative Transport in the Development of Fog and Low-Level Stratus".* J. Atmos. Sci., 35, 301–316. Retrieved from: https://doi.org/10.1175/1520-0469(1978)035<0301:TIBTAR>2.0.CO;2.

Özdemir, E. T., Deniz, A., Sezen, İ., Menteş, Ş. S., & Yavuz, V. (2016). *"Fog Analysis at Istanbul Ataturk International Airport".* Royal Meteorology Society, doi:10.1002/wea.2794. Weather – November 2016, Vol. 71, No. 11. Retrieved from: https://rmets.onlinelibrary.wiley.com/doi/abs/10.1002/wea.2747

Özdemir, E.T., & Sezen, İ., vd. (2014). *"Atatürk Havalimanı Sis Analizi".* 3th Ulusal Havacılıkta İleri Teknolojiler Konferansı. 18-19 Haziran 2014, Hava Harp Okulu, İstanbul.

Özdemir, E.T., Deniz, A., Yavuz, V., Doğan, N., Akbayır, İ., (2018*). "Investigation of Fog-Air Quality Relationship in Istanbul"*, Fresenius Environmental Bulletin, 27(1), 30-36.

Pedro M. P. Guerreiro, & Pedro M. M. Soares, & Rita M. Cardoso & Alexandre M. Ramos. (2020). *"An Analysis of Fog in the Mainland Portuguese International Airports".* Atmosphere 2020, 11, 1239; Retrieved from: doi:10.3390/atmos11111239

Román-Cascón, C., Yagüe, C., Steeneveld, G., Morales, G., Arrillaga, J. A., Sastre, M., & Maqueda, G. (2019). *"Radiation and cloud-base lowering fog events: Observational analysis and evaluation of WRF and HARMONIE". Atmospheric Research*, *229*, 190-207. Retrieved from: https://doi.org/10.1016/j.atmosres.2019.06.018

Roquelaure S., & Tardif R., & Remy S., vd. (2009). *"Skill of a ceiling and visibility local ensemble prediction system (LEPS) according to fog-type prediction at Paris-Charles de Gaulle Airport".* DOI: https://doi.org/10.1175/2009WAF2222213.1 Weather and Forecasting 24(6): 1511–1523.

Stolaki S.N., & Kazadzis S.A., & Foris D.V., vd. (2009). *"Fog characteristics at the airport of Thessaloniki, Greece"*. Natural Hazards & Earth System Sciences. 9(5): 1541–1549.

T.C. Tarım ve Orman Bakanlığı, Meteoroloji Genel Müdürlüğü. (2018). *"Havacılık Meteorolojisi"*. Ankara. Retrieved from https://www.mgm.gov.tr/FILES/genel/kitaplar/havacilikmeteorolojisi.pdf

Tardif R., & Rasmussen R.M. (2007). *"Event- based Climatology and Typology of Fog in the New York City Region".* J. Appl. Meteorol. Climatol. 46(8): 1141–1168.

van Schalkwyk, L., & Dyson, L. L. (2013). "Climatological Characteristics of Fog at Cape Town International Airport", Weather and Forecasting, 28(3), 631-646. Retrieved from: https://journals.ametsoc.org/view/journals/wefo/28/3/waf-d-12-00028_1.xml

Wu, B., Li, Z., Ju, T., & Zhang, H. (2020). *"Characteristics of Low-level jets during 2015–2016 and the effect on fog in Tianjin". Atmospheric Research*, *245*, 105102. Retrieved from: https://doi.org/10.1016/j.atmosres.2020.105102.

Yan, S., Wang, H., Liu, X., Zu, F., and Liu, D. (2023). *"Effect of the boundary layer low-level jet on fast fog spatial propagation"*. Atmos. Chem. Phys., 23, 13987–14002. Retrieved from: https://doi.org/10.5194/acp-23-13987-2023.

MINERAL PROCESSING ENGINEERING

Critical and Strategic Raw Materials

Industrial Raw Materials

Li Recovery from Clayey Boron Plant Tailings Through Mechanical Activation and Saline Water Leaching

Gülsen Obuz Teker [a], Feridun Boylu [a]

[a] Istanbul Technical University, Faculty of Mines, Mineral Processing Engineering Department, Türkiye
obuz19@itu.edu.tr

Keywords: Mechanical Activation, Lithium Recovery, Salt Leaching, Clay Mineral.

Aim

In this study the recovery of lithium from clayey wastes from Kırka Boron Plant was investigated. As an alternative method proposing selective, economic and environmentally friendly process "mechanical activation followed by saline water" proposed and patented by Tesla was applied on Kırka Boron Plant tailings. Optimizing the mechanical activation and leaching conditions resulted in 60-70 % lithium recovery and 115 ppm lithium concentration in leach solution.

Introduction

The increasing world population, new requirements and technologies developed to meet these, naturally accelerate the studies on the production of new technological raw materials. In particular, the supply or production of these raw materials is extremely important for the economic/technological development of countries. The production of electric vehicle batteries, the production of which has been rapidly increasing in the world and in our country recently, is a very good example of this situation, with minerals such as Lithium, Nickel, Cobalt and Aluminum coming to the forefront as important and critical raw materials. Among these critical minerals, Lithium in particular is of vital importance as an indispensable component/raw material in the production of rechargeable batteries, fuel cells and electronic devices. The interest in electric vehicles in terms of preventing environmental pollution and reducing CO2 emissions and the increasing production of electric vehicles indicate that the demand for lithium resources will potentially increase in the next 10-30 years. For this reason, lithium is included in the critical raw material class for many countries. Lithium is traditionally obtained from salt water (brine), pegmatite lithium mines and sedimentary lithium mines. As a potential lithium source, lithium-containing clay minerals have recently attracted great attention and are of strategic importance to meet lithium demand. There are also lithium-containing resources in our country, and especially the smectite/hectorite clays in Boron wastes appear to have significant potential with their high lithium content. As stated in ETİ Mine reports, the solid waste generated in Kırka Borax facilities within ETİ Mine generally contains lithium-containing clay, marl, calcite and dolomite, and the lithium content varies between 1200-2150 ppm.

Today, direct leaching, chlorination-sulfuration and supported roasting leaching are among the lithium extraction methods from lithium-containing clay minerals. In these conventional methods, high-temperature roasting and acid use are involved, creating significant problems in terms of both economic and environmental impacts. Therefore, it has become essential to develop other alternative methods that are more economical and environmentally friendly.

As stated in the 2020 "Tesla Battery Day" organization, Tesla claims in its patent for the process it developed that lithium-containing clays can be mechanically activated in high-energy mills and the resulting activated powder, referred to as extraction powder, can be selectively taken into solution with high efficiency (70-80%) in hot water (65 °C) with a low-cost agent such as table salt (10% of the clay by weight). Tesla's process is based on the recovery of lithium from lithium-containing clays; (i) taking the lithium between the layers into solution based on the cation exchange principle, (ii) taking the lithium in the cage structure out of the cage using high-energy mills and taking it into solution with mechanical activation (mechano-chemical methods). Although it enables selective lithium recovery with high efficiency without the application of acid and high temperature (roasting), no industrial application of the patent in question or an article confirming the findings has been found in the literature so far. In addition, it has not been stated or presented how the high-energy equipment in the patent in question can be applied

in an industrial sense, what the mechano-chemical activation conditions are, how the possible problems that may be experienced in the discharge of mechano-chemically activated clays from the system will be overcome.
In this study, the applicability of the patent in question to Kırka Boron Plant clayey wastes and the applicability of the Tesla Patented process on this sample were investigated.

Material and Method

The material used in this study is taken from Boron Plant (Penta 4) tailings. The sample was homogenized, dried and crushed down to 2 mm for mechanical activation followed by saline water leaching. The chemical analysis of the used material is given in Table 1.

Table 1. Chemical analysis results of the sample.

Element	Value	Element	Value
Al, %	0.69	Mg, %	10.16
SiO_2, %	16.34	K, %	0.62
Fe, %	0.25	Na, %	2.15
S, %	0.21	Ca, %	11.16
Li, ppm	**900**	**LOI, %**	**34.08**

The mineralogical analysis was carried out through XRD analysis given in Figure 1. XRD analysis illustrated that the tested sample contains dominantly dolomite (>85 %), totally less than 15 % of Illıte, Clinoclor, montmorillonite, clinoptinolite, tincalcoite etc. The existence of dolomite was also highlighted with the Table 1 pointing out the high amounts of Ca and Mg.

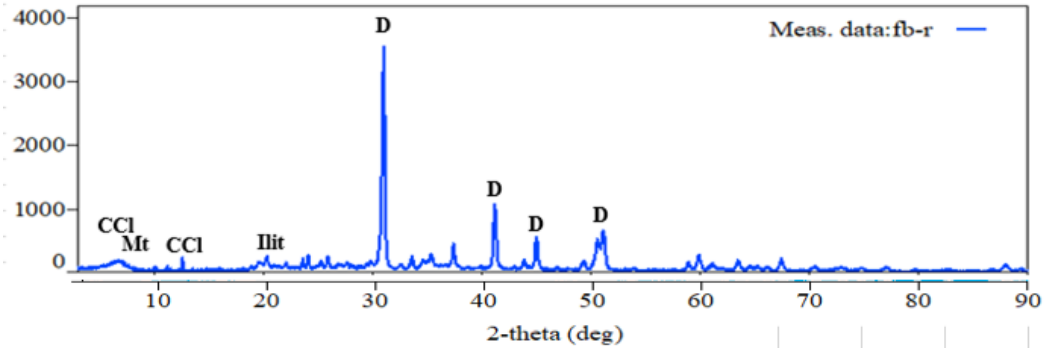

Figure 1. XRD Analysis of Kırka Boron Plant Tailings (Tested Sample) (D: Dolomit, CCI: Clinochlore, Mt: Montmorillonit, Ilit: Illit).

Representative samples in small amounts were used at mechanical activation test through Stirred mill (Fig 2) which is actually an attritor having cell including shaft for mixing and zirconium balls in size of 3 mm.

Figure 2. Stirred Mill used for mechanical activation tests.

The operational parameters for both mechanical activation and leaching process chosen as; Grinding media (ball) volume, cc, Material (Sample) weight, gr, Mechanical activation period, min, Shaft speed, rpm, Salt Addition, %, Leach time, min., Leach Temp., oC and Water/solid ratio.

Findings

In mechanical activation experiments, the grinding conditions were set as a shaft speed of 700 rpm, a liquid/solid ratio of 5, a salt concentration of 10%, a leaching duration of 60 minutes, a leaching temperature of 80°C, and an agitation speed of 520 rpm. In the mechanical activation experiments, the optimum ball amount was found to be 1100 g in a grinding medium ranging between 700 and 1200 g, and the lithium recovery efficiency was 24.00%. As the sample amount decreased, the mechanical activation rate increased, leading to higher lithium recovery efficiencies. When the ground amount was 52 g, the lithium recovery efficiency was 16.94%, whereas it increased to 44.28% when the amount was reduced to 16 g. The effect of the changing grinder shaft speed was observed to increase the recovery efficiency to 51.67% at a rotation speed of 550 rpm. When the grinding duration was 150 minutes, a recovery efficiency of 56.67% was achieved. Figure 3 presents the lithium recoveries (%) and lithium amounts (ppm) obtained with varying activation conditions.

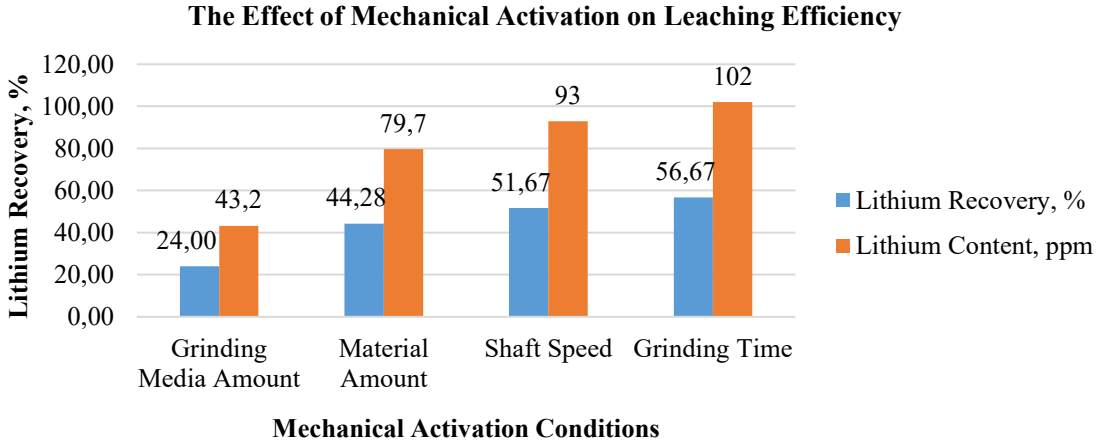

Figure 3. Effects of mechanical activation on lithium recovery.

In mechanical activation experiments, the grinding duration was set to 150 minutes, the grinding medium amount to 1100 g, the shaft speed to 550 rpm, and the sample amount to 16 g. Under these grinding conditions, leaching parameters were studied. The extension of the leaching duration did not have a positive effect on lithium recovery. The values varied approximately between 103 and 109 ppm within a leaching duration range of 5 to 180 minutes, and a 20-minute leaching duration was deemed sufficient, yielding an efficiency of 60.72% with a lithium

concentration of 109.3 ppm. When the temperature ranged between 60 and 80°C, lithium recovery varied between 58% and 61%. At temperatures above and below this range, the efficiency dropped to as low as 44%. The optimum temperature was determined to be 80°C, achieving a recovery efficiency of 60.72%. As the salt concentration increased, the recovery efficiency also improved, reaching 63.67% at a 25% salt concentration. However, when no salt was added to the system, the efficiency was observed to be 54.11%. When the liquid/solid ratio was 100%, the efficiency reached 69.67%. Figure 4 presents the leaching efficiency percentages and lithium ppm contents. Figure 5 illustrates the variation of lithium dissolution efficiency with temperature and time. The highest efficiency was obtained at 50°C, while lower values were observed at 80°C and 25°C.

- At 50°C, lithium recovery started at 59.44%, reaching its maximum at 66.28% at 90 minutes, before slightly decreasing to 60.11%.
- At 80°C, recovery started at 60.22% and remained relatively stable, around 59.78%.
- At 25°C, the initial recovery was 35.67%, increasing over time to 47.33%, before slightly decreasing to 46.22%.

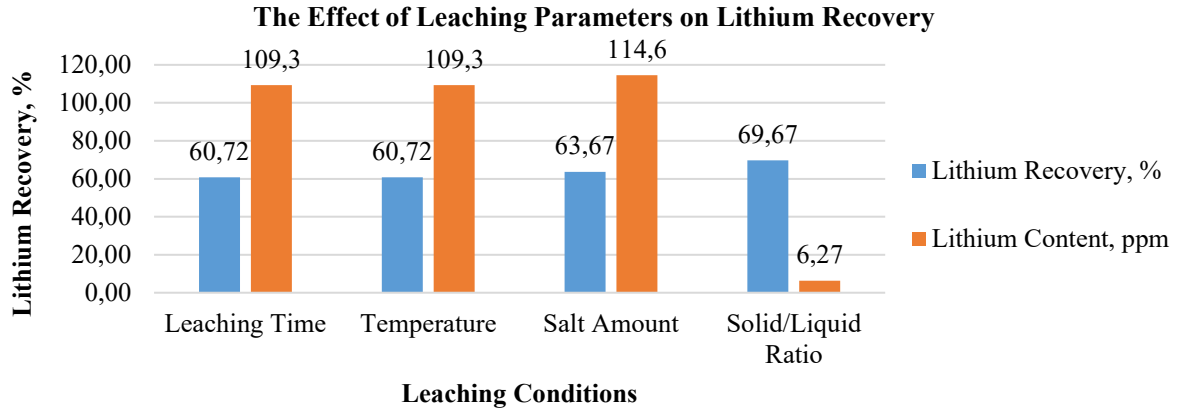

Figure 4. Effects of varying leaching conditions on lithium recovery.

As the leaching time increases, lithium recovery initially rises rapidly, but after a certain point, it reaches a plateau and stabilizes. Although higher temperatures generally enhance reaction rates, the fact that 50°C resulted in the highest efficiency could be related to factors such as solubility equilibrium, re-precipitation, surface passivation, and chemical reaction kinetics. At high temperatures, certain lithium compounds may precipitate instead of remaining in solution, leading to a decrease in efficiency. Additionally, passive layers forming on the surface could hinder further reactions. Furthermore, at 80°C, water evaporation may alter the solution concentration, affecting reaction equilibrium, while the decomposition of some reactive species could further reduce efficiency. Considering these results, 50°C appears to be the optimal temperature for lithium dissolution and effective interaction with the mineral structure. Therefore, chemical equilibrium, surface reactions, and energy efficiency should be considered when selecting the optimum temperature.

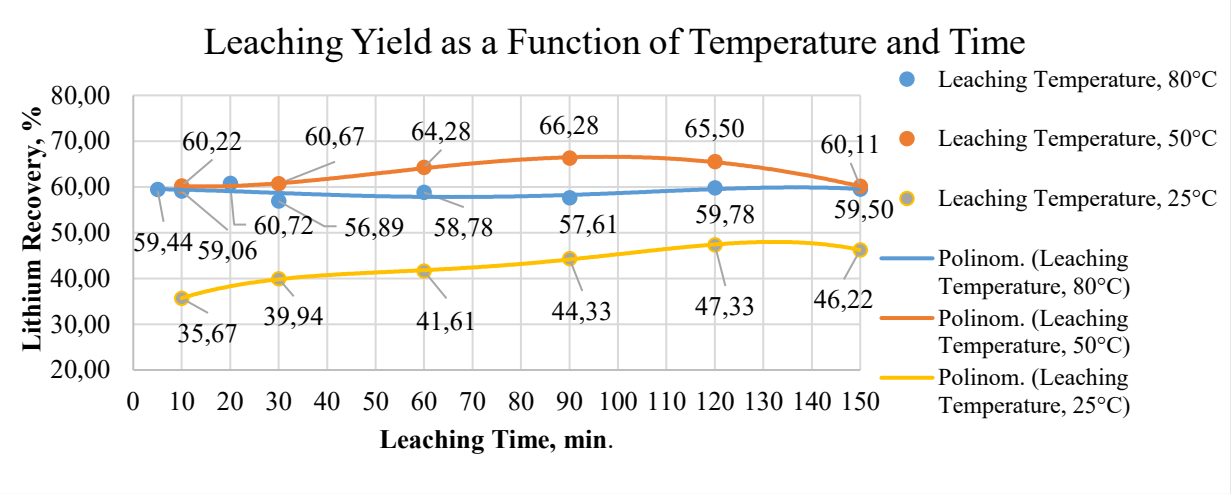

Figure 5. Influence of Temperature on Leaching Kinetics Over Time.

Conclusion

In mechanical activation, the greatest impact was observed with the sample amount and grinding duration. When the sample amount was reduced from 52 g to 16 g, the recovery increased by 27%, while extending the grinding duration from 30 minutes to 150 minutes resulted in a 25% increase in recovery. When the shaft speed was increased from 400 rpm to 700 rpm, the change in recovery was 8%, whereas variations in the grinding medium led to only a 2% difference in recovery.

Among the leaching parameters, salt concentration, temperature, and liquid/solid ratio influenced the leaching kinetics, but the leaching duration had no positive effect. The lithium recovery was 59.44% with a 5-minute leaching time and 60.44% with a 180-minute leaching time. This clearly indicates that with effective mechanical activation, lithium can be easily recovered from the sample in a short time. Another striking result is that due to the presence of dolomite in the sample, lithium can be recovered with approximately 54.11% efficiency without the need for additional salt, thanks to the Mg and Na elements it contains.

Effect of Temperature (Room Temperature-25°C, 50°C, and 80°C) on Leaching Kinetics - Time-Based (from 10 minutes to 150 minutes) has been examined. No significant difference was observed between 50°C and 80°C; however, 50°C yielded more efficient results compared to 80°C. Although an increase in temperature was expected to positively affect the leaching kinetics, the opposite was observed. At 50°C, the recovery reached up to 66%, whereas at 80°C, it could not exceed 66% and only reached a maximum of 60.72%. These results show that temperature increase does not always have a positive effect on solubility and recovery. The optimum temperature at 50°C ensures better dissolution by balancing the reaction rate and preventing surface passivation, providing a more efficient leaching process.

References

Bediroğlu, G. ve Gençer, YG. (2024). Elektrikli araç satışları, karbon emisyonu ve elektrik tüketimi arasındaki ilişkinin incelenmesi. Elektronik Sosyal Bilimler Dergisi, 23 (91), 1192-1209. https://doi.org/10.17755/esosder.1452405

Gülcan, M. F., Alkan, E., Çotuker, O., Yuca Doğdu, N. (2024). Lityum İyon Batarya Üretiminde Kullanılan Hammaddelerin İncelemesi ve Türkiye'nin Batarya Üretim Potansiyelinin İrdelenmesi. Bilecik Şeyh Edebali Üniversitesi Fen Bilimleri Dergisi, 11(1), 204-217. https://doi.org/10.35193/bseufbd.12940

Sun, Z., Chen, H., Caldwell, T. B., & Thurston, A. M. (2021). Selective extraction of lithium from clay minerals (U.S. Patent Application No. 2021/0207243 A1). U.S. Patent and Trademark Office.

Zhao, H., Wang, Y., & Cheng, H. (2023). Recent advances in lithium extraction from lithium-bearing clay minerals. Hydrometallurgy, 217, 106025.

MINERAL PROCESSING ENGINEERING

Critical and Strategic Raw Materials

Industrial Raw Materials

Effect of Particle Size on Obtaining High-Quality Silica by Flotation Method

Yuşa Şahin[a], Gülay Bulut[a]

[a]Istanbul Technical University, Faculty of Mines, Department of Mineral Processing Engineering, Türkiye
sahinyu17@itu.edu.tr

Keywords: Flotation, Impurity, Mineral Processing, Particle Size, Silica Sand.

Aim

This study aims to produce high-quality glass sand using the reverse flotation method in different size ranges with flotation. In addition to the size of the material, the effects of various parameters and methods such as flotation reagents and mechanical scrubbing are also examined in the research. It aims to obtain high-quality silica sand with low iron oxide content and thus reduce the import of silica sand required for areas of use such as solar sand, thus reducing the use of domestic products in the industry and foreign dependency.

Material and Method

In the experimental studies conducted for this thesis, a sample of silica sand from the flotation unit feed of the sand preparation plant was utilized. Following the crushing processes, grinding, and sizing, the material is fed to the flotation unit at the plant. The sieve analysis results of the silica sand sample are presented in Table 1, showing that the portion of the material less than 106 micrometers (µm) constitutes 46.6%. In glass production, a low percentage of the -106 µm particle size is desired because it negatively impacts the furnace operation and increases costs [1]. For instance, in photovoltaic glass production furnaces, the amount of this size should be less than 5%. Therefore, flotation experiments were not conducted on the -106 µm particle size. After sieving the flotation feed sample, which was entirely below 500 microns, flotation test studies were performed on three size groups; (-500+300), (-300+212), and (-212+106) micrometers.

Table 1. Sieve Analysis Results of Silica Sand Sample**.**

Size Fractions	Quantity	Σ Under Screen
(µm)	(%)	(%)
-500+300	7,6	100,0
-300+212	7,6	92,4
-212+150	13,0	84,8
-150+106	25,1	71,7
-106+75	22,0	46,6
-75+53	18,8	24,7
-53+38	4,9	5,8
-38	0,9	0,9
Total	100,0	-

The chemical analysis results for this sample are shown in Table 2. Upon examining these results, it is evident that there is a significant increase in the levels of impurity components such as Al_2O_3, Fe_2O_3, TiO_2, CaO, MgO, Na_2O, and K_2O as the grain size decreases. In the -38 µm size fraction, the impurity levels are as follows: Al_2O_3 1.33%, Fe_2O_3 0.231%, and TiO_2 0.858%. This represents a significant increase compared to coarse size fractions. This trend can be attributed to the finer fractions containing a higher amount of clay minerals, iron oxides, and other impurities.

Table 2. Chemical Analysis Results of Silica Sand Sample.

Size Fractions	SiO_2	Al_2O_3	Fe_2O_3	TiO_2	CaO	MgO	Na_2O	K_2O
(µm)	(%)	(%)	(%)	(%)	(%)	(%)	(%)	(%)
Flotation Feed	99,48	0,30	0,045	0,099	0,01	0,00	0,00	0,07
-500+300	99,20	0,48	0,067	0,095	0,02	0,01	0,00	0,13
-300+212	99,29	0,40	0,073	0,109	0,02	0,01	0,00	0,10
-212+106	99,59	0,22	0,043	0,077	0,01	0,00	0,00	0,06
-106+38	99,54	0,24	0,047	0,097	0,01	0,01	0,00	0,06
-38	96,93	1,33	0,231	0,858	0,13	0,03	0,16	0,33

May apply mechanical scrubbing to the material, to remove the clay minerals found in the fine size fractions [2]. The values for CaO (0.13%), MgO (0.03%), Na_2O (0.16%), and K_2O (0.33%) also peak in the finest fraction, indicating that alkali and alkaline earth oxides tend to accumulate as the grain size decreases. Conversely, in the -500 µm fraction, which was not subjected to the sieving process in the experiments, the levels of Fe_2O_3 are at 0.045%, TiO_2 at 0.099%, and Al_2O_3 at 0.30%. This analysis highlights that to achieve high-purity silica, it is essential to either remove the fine fractions or subject them to purification processes. The increase in iron, titanium, and alkali oxides, in particular, may limit the direct application of the material in glass and solar panel industries. Therefore, flotation or acid leaching processes would be necessary [3].

Literature research predicted that the amount of material and impurities transitioning to fine size would increase by applying mechanical scrubbing processes. Experiments on mechanical scrubbing were conducted in 10, 20, and 30 minutes, and the results of the sieve tests performed on the material are shown in Table 3. Contrary to expectations, the sieve analysis results indicated no transition to fine material.

Table 3. Sieve Analysis Results of Mechanical Scrubbing Applied Material.

Time	10 min	20 min	30 min
Size (µm)	Quantity, %	Quantity, %	Quantity, %
-500+300	8,6	8,1	8,4
-300+212	9,1	10,0	10,0
-212+106	38,1	37,4	37,9
-106+38	42,7	42,7	42,4
-38	1,6	1,9	1,3
Total	100,0	100,0	100,0

Flotation experiments were carried out in the flotation laboratory of the Mineral Processing Engineering Department of Istanbul Technical University, Faculty of Mines. In the experimental studies, the reverse flotation method was utilized to remove iron oxide minerals, such as magnetite and hematite, along with other impurities from silica sand. In the reverse flotation method, iron oxides and other impurities in silica sand are separated using selective reagents. In experiments conducted with different particle sizes, the anionic type collector, which has a

high selectivity to provide a reduction in iron oxide content, was kept constant and the effects of 2 different frothers were investigated. As collector anionic chemical Collector1, Frother1 and Frother2 were used as frothers. In the first experiments, the effect of the parameters was investigated by keeping the number of stages and reagent dosages high to increase the efficiency of the flotation process. The experiments were carried out by adding reactants in 5 stages. A laboratory-type Denver flotation machine was used in the flotation experiments. The machine rotation speed was kept constant at 1150 rpm, the solid ratio in the pulp was 23%, the conditioning time was 5 minutes for the collector, 2 minutes for the frothers, and the flotation time was 2 minutes for each stage. The experiments were carried out in the natural pH range. The obtained products were made using XRF (X-Ray Fluorescence) in the laboratory. Optimization studies were carried out to increase the success of flotation to higher levels in line with the analysis results. Flotation experiments were applied again to optimum conditions.

Findings

In the experiments conducted using Frother2 as a frother, a more selective flotation process was performed compared to the experiments conducted using Frother1, and impurities were collected in the floating product, resulting in both a higher quality product and a higher final product quantity in the sinking product. The images of the products obtained from the experiments conducted at the same size on the microscope are given in Figure 1 and Figure 2. Images A-E are images of products floated using Frother1, and image F is of the sinking final product. In the images of the other experiment, image G is of the floating product using Frother2, and image H is of the sinking product. It was determined that the mechanical scrubbing process also had a no positive effect on the product obtained at the end of the flotation. As a result of the experiments, in studies conducted within the size range of 212-106 microns, the SiO2 content of the obtained material increased to 99.75%, while the Fe2O3 content was reduced to levels of 200 ppm. The high silica content obtained increases the marketable value of the material and makes it suitable for use as a main material in many sectors.

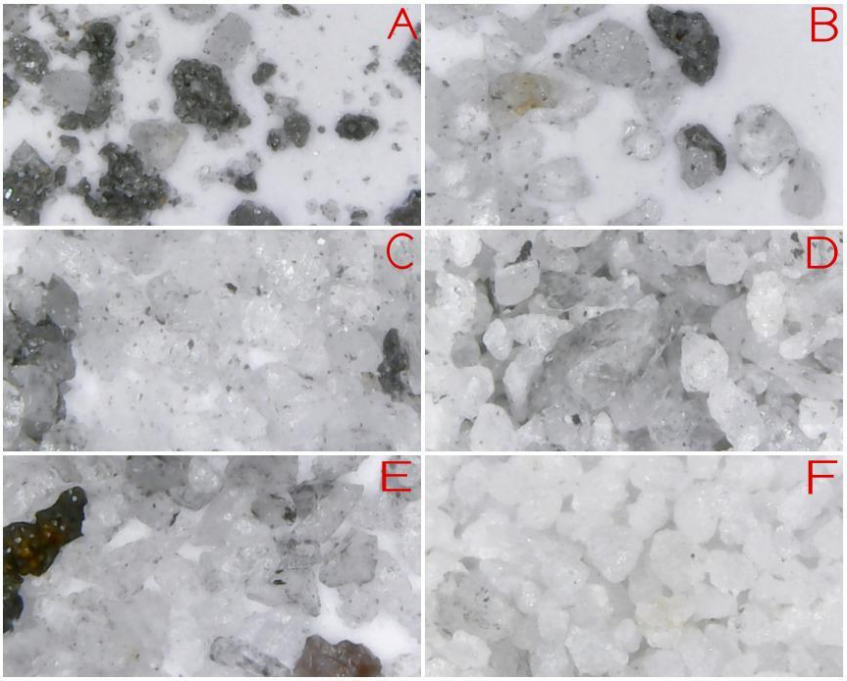

Figure 1. Microscope Image of the Products in the Different stages of the Experiment Performed Using Frother1.

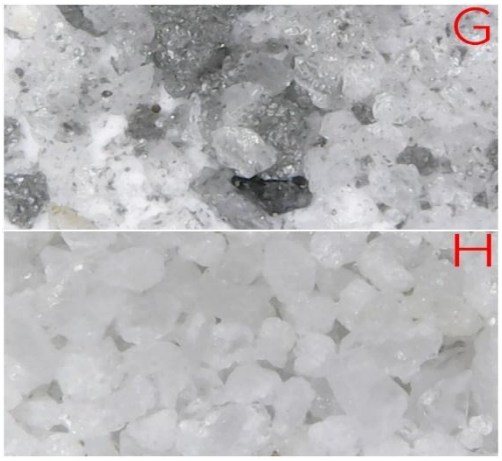

Figure 2. Microscope Image of the Products the Experiment Performed Using Frother2.

Conclusion

As a result, the reverse flotation method stands out as an effective technique for purifying silica sand from impurities and improving quality. This method provides high-purity silica, especially by removing iron oxides and other undesirable components. Thus, its usability in the glass and solar panel industry is increasing.

References

Keser, B. Y. (2010). *Kaliteli cam üretiminde küçük boyutlu silis kumu kullanımının araştırılması, İstanbul Teknik Üniversitesi, Yüksek Lisans Tezi, h*ttp://hdl.handle.net/11527/8378

Hacıfazlıoğlu, H. (2011). Methods Used In The Beneficiation Of Silica Sand And Comparison Of Flotation And Magnetic Separation In Terms Of Iron Removal. *Bilimsel Madencilik Dergisi, 50*(3), 35-48.

Aydın, Ş. B., Oğuz, C., & Gül, A. (2021). Beneficiation Of Low Quality Quartz Sand By Flotation And Oxalic Acid Leaching. *Bilimsel Madencilik Dergisi*, *60*(1), 7–20. Https://Doi.Org/10.30797/Madencilik.803383.

MOLECULAR BIOLOGY - GENETICS AND BIOTECHNOLOGY

Bioimaging

Drug and Vaccine Development

Metabolic and Evolutionary Engineering

Metagenomics and Protein Engineering

Microbial Biotechnology and Genetics

Nanobiotechnology

Characterization of Cell Features and Trajectories Using Adaptive Tracking Integrated with Learning-based Segmentation Method

Kübra Ateş[a], Halil Bayraktar[a]

[a] Istanbul Technical University/Graduate Education Institute, Molecular Biology-Genetics and Biotechnology, Molecular Biology-Genetics and Biotechnology Program, Turkey
atesku19@itu.edu.tr

Keywords: Cells, Deep-learning, Segmentation, Tracking.

Aim

The motility of cells is fundamental for the establishment of organs, the immune system and tissue regeneration [1,2]. Many internal and external factors can affect the pathways that control cell motility. To uncover the regulation of these key elements in detail and their impact on directional changes, state-of-the-art microscopy methods have been applied for high-throughput acquisition of images [3,4]. Despite the recent advances, the lack of automated analysis tools remains as a challenge for the characterization of cell movement [5]. The demand for dynamic programs imposes novel approaches for computing cell tracks and their motility features [6]. While open-source tools are available for the analysis of image data, [7,8] many of the proposed techniques to determine cell paths and lineages are composed of multiple sections. The major weaknesses are the use of various parameters and manual curation, although they are applied to determine the dynamics of cell movement. Additionally, the signal-to-noise ratio (SNR), and confluency of cells lead to a variety of image data. The lack of tuning of these methods reduces the efficiency of the linkage step. There is a need for automated methods to segment cells and find corresponding linkages, thus addressing the current limitations of advanced imaging applications. We introduced the integration of learning-based segmentation with the adaptive tracking [9] and determined the tracking performance for fluorescently labeled cells. This combined approach resulted in improved segmentation efficiency compared to the manual methods based on thresholding/pixel linkage. Moreover, the accuracy of cell association was enhanced when compared to the initial version of the adaptive tracking method. Furthermore, the motility parameters were computed and used to characterize the motility modes of single cells. Briefly, the persistence distribution was computed by using the cell paths obtained by adaptive tracking process. HeLa cells exhibited a random migratory pattern, whereas RPE cells displayed directional movement. In conclusion, the integration of adaptive cell tracking with watershed-based segmentation allowed for the computation of cell tracks and motility parameters.

Material and Method

Preparation of cells and imaging.
For HeLa and RPE cells, they were transfected with GFP plasmid by using FuGENE reagent. They were seeded in tissue culture plates. The epifluorescence imaging was performed on an Olympus inverted microscope. Time-lapse images were captured with 10× air objective.
Segmentation of cells.
We have used a modified version of U-net architecture [10] that is composed of encoder and decoder network sections. All convolution layers use a kernel size of 3x3 with a layer depth from 128 to 16. We used Adam as the optimizer with a learning rate of 0.0005. The annotated images including raw and mask data were prepared and used for the model to learn the output. To increase the variability of annotated image pool, images with different signal-to-noise ratios were inserted into dataset. For the model training, randomly selected 1000 of 256x256 images as a train set. A total of 20 epochs were used in all studies. All codes were implemented through Keras API. To separate the touching cells, watershed method was finally applied to binary images. The centroids and other

features were saved for each cell and transferred as an input for the tracking step. To evaluate the training performance, we used a mean squared error loss function. The cell identity was finally achieved by watershed.

Computation of cell paths with adaptive tracking.

The adaptive tracking method [9] was primarily composed of two sections named node and coupling sections that were used to compute the optimum distance and predict all plausible matches respectively. The workflow of the segmentation and adaptive tracking was shown in Figure 1. Briefly, the lowest distance between cells was determined by computing the Euclidean distance in a given frame. Additionally, the closest distance between cells identified in two consecutive frames was estimated and used to determine the step length. To reduce the mismatch ratio, these values were evaluated to compute the optimum threshold distance. Minimum track length and maximum gap time were 25 and 5 frames respectively.

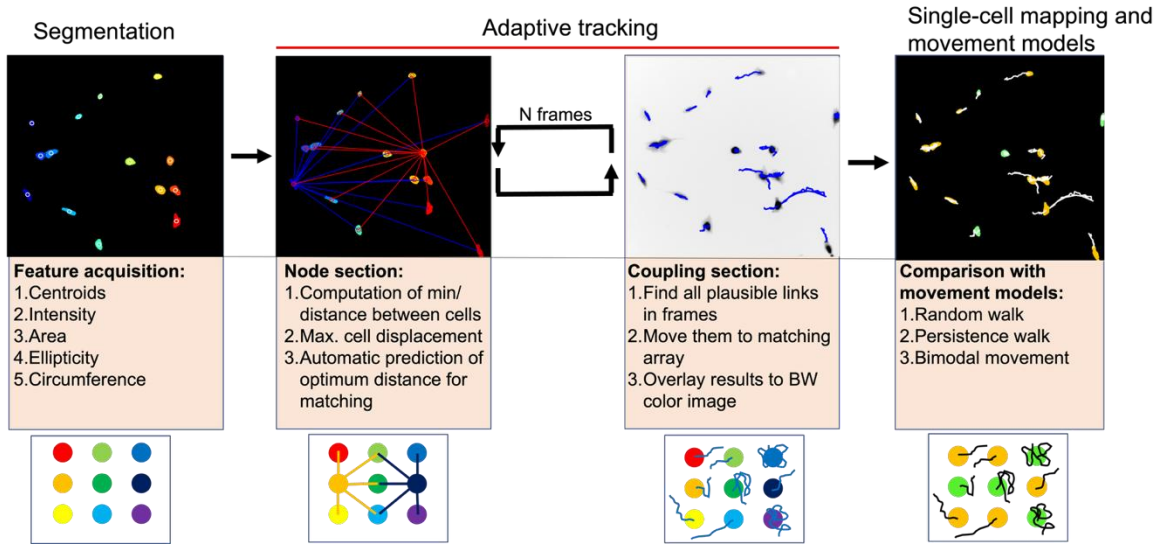

Figure 1. Workflow of adaptive tracking method with CNN based segmentation and characterization of motility dynamics. All raw images were preprocessed before segmentation. The masks of images were prepared for training sample and used to compute the model parameters of U-net. By following the model development, the regions in each image were classified with CNN and later segmented with watershed (First panel). Adaptive tracking modes composed of node and coupling sections were used to determine the optimum matching distance and used to find the cell path (second and third panel). After the trajectories are imported to analysis section, the movement pattern of cells was determined by using the persistence distribution and angular changes of cells.

Computation of persistence.

The descriptors of cell motility such as total displacement, persistence, angular changes were computed and used to determine movement characteristics of each cell type. The module present in adaptive tracking can also overlay each property to the computed trajectories. After reconstructing the cell tracks, the centroids were used to determine the average speed that was computed by the ratio of total distance to elapsed time. The persistence ratio was measured by dividing the ratio of line distance to total cumulative displacement.

Findings

Segmentation with deep learning and comparison with nPixel method

We have used two data sets that demonstrate the HeLa and RPE cells (Fig. 2A). To remove the pixel noise, each video was initially convoluted by using a band-pass filter before segmentation (Fig. 2B). Then, the data sets were separately processed either pixel-based method or U-net-based methods, where the cell and other attributes centroid positions were finally computed. The deep learning with watershed method yielded higher separation efficiency for cells whose boundaries were overlapping. As compared to nPixel, areas of some touching cells in the videos were clearly identified when the watershed transform was applied at the segmentation step (Fig. 2C and Fig. 2D). When the nPixel method was applied, cells with attached boundaries were not completely separated, a

single cell center rather than two was registered at this section. In the presence of high confluency, learning method yielded increased segmentation scores. To evaluate the segmentation efficiency, the results were compared with those obtained from manually annotated images (Fig. 2E). The Jaccard values were high for all sets of segmented images obtained from both methods (Table 1). Although similar scores were observed for all cell types, low number of undersegmented images were obtained when the learning approach was applied. The centroids of touching cells were correctly labeled before the tracking analysis. The learning-based method scored higher than traditional techniques. The increased ratio of true positive cell count can be attributed to the integration of U-Net with watershed segmentation. As a result, a higher separation efficiency was obtained for the cell borders in most videos.

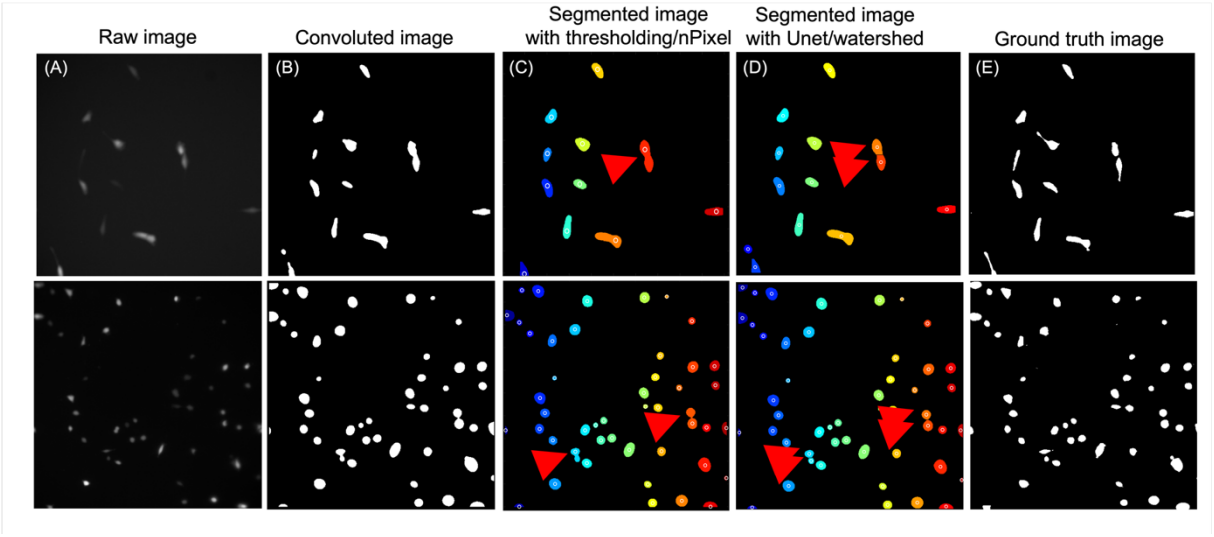

Figure 2. Segmented images for comparison of U-Net like segmentation and pixel linkage methods. Side-by-side comparison of segmentation steps and ground truth images. The representative pictures from left to right represent (A) raw images of RPE and HeLa, (B) convoluted images after background subtraction and band pass filtering, (C) segmentation results obtained from nPixel linkage methods, (D) segmented image with deep-learning/watershed method, (E) manually annotated ground truth images. The color-coded regions represent the total area of each cell. The red arrows indicate the cells whose centroids were correctly labeled when watershed was applied. The cell number was higher for the watershed methods compared to previous method (red arrow).

Table 1. The comparison of thresholding/nPixel linkage and watershed-based segmentation results by using the Jaccard index value. The tracking efficiency is reported in the table.

Name of data set after thresh./Pixel	a. Thresholding with nPixel segmentation	b. DeepLearning segmentation	c. Adaptive tracking	d. Adaptive tracking after DeepLearning segmentation
HeLa	0.7575	0.7732	0.8742	0.9046
RPE	0.8024	0.8195	0.8546	0.8947

The comparison of thresholding/nPixel linkage and watershed-based segmentation results by using the Jaccard index value. Tracking efficiency was reported in the table. A total of 10 video data sets for each cell type were recorded by a live-cell inverted microscope (Olympus IX71). A. The values represent the average Jaccard index values. B. The centroids computed with nPixel or watershed-based method were used for adaptive tracking. C. Tracking efficiency of Adaptive Tracking method. D. Tracking efficiency of Adaptive tracking after Deep-Learning segmentation.

Evaluation of trajectories obtained from adaptive tracking.

The representative trajectories were overlaid over fluorescence images of cells (Fig. 3A). The incomplete trajectories were observed when the areas and centroids obtained from nPixel were used at the tracking section. As described previously, adaptive tracking automatically computes the optimum matching distance for consecutive frames. Threshold distances computed at the node section of the adaptive tracking to match cells were computed

for all cell types (Fig. 3B). The algorithm initially computes the minimum distance between cells (Fig. 3B, black-circles) and maximum displacement (Fig. 3B, black- diamonds). The optimum distance was then determined and used to identify plausible matches of cells in consecutive frames (Fig. 3B, red-square). For most frames, the mean value of adaptive distance was smaller than the minimum distance between cells (Fig. 3B, green-triangle), indicating that the threshold distance was dynamically computed and used to determine the cell trajectories. To evaluate the efficiency, tracked cell ratios compared to total cells were computed by using the centroids and attributes from segmentation section (Fig. 3C). The ratio of tracked to total cells was computed as 0.80 when the centroids from watershed were used at the tracking section. When the centroids from the nPixel method were applied for tracking, the ratio of total tracked cells to all identified cells was computed as 0.71. Total track time was also longer when the centroids from watershed were used at the tracking section. We obtained an average track frame of 38 when the centroids from the watershed were applied at the segmentation section (Fig. 3D). Although we have used a low number of input values, Adtari can correctly determine the cell linkages for most videos.

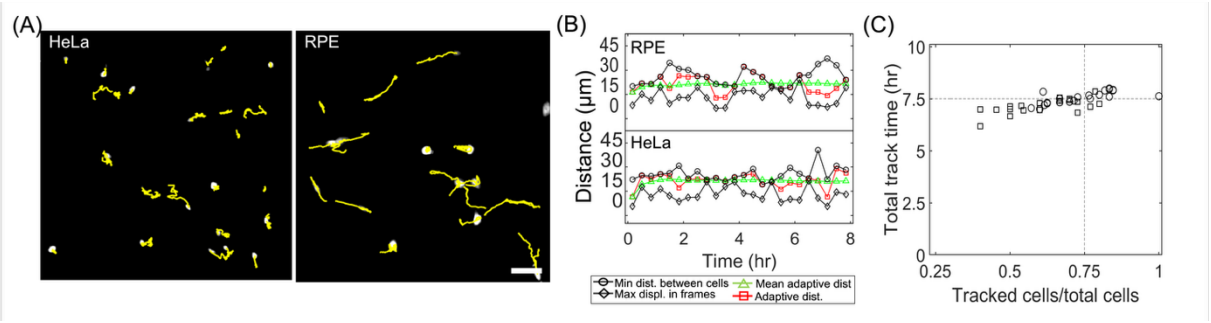

Figure 3. Cell trajectories and evaluation of tracking efficiency. The centroids computed by using nPixel or watershed methods were used to determine the cell paths. (A) Representative cell trajectories of Hela, and RPE and (yellow line). A higher tracking ration was obtained due to the high efficiency of watershed-based segmentation that yields highly accurate centroids. A total of 40 frames were evaluated using both methods. (B) The dynamic computation of threshold distance (red squares) as a function of time. Distance represents the limit of the threshold to determine all plausible matches. Maximum displacement (black diamonds) remained below the threshold distance. The average adaptive distance (green triangles) was lower than the minimum distance between cells (black circles). The overlap of adaptive distance and minimum distance resulted from an increased displacement of cells in frames.

Characterization of RPE, and HeLa cells.

The normalized persistence was computed with an interval of 16 frames for each cell type. The computation of persistence depends on the measurement of centroid positions, however the segmentation methods used to determine cell centers are subject to different errors. Frame rate, distribution of cell intensity, and small displacements between frames affect the accurate estimation of cell centers. Since the tracks can be highly noisy, the total distance was measured at 2-frame intervals. HeLa cells demonstrated low values of persistence ratio (Fig. 4A, left panel), while the RPE cells had high values of persistence, indicating their tendency to move linearly on the substrate (Fig. 4A, right panel). We concluded that these cells demonstrate distinct persistence patterns. To determine peaks and average values of persistence for different states, their distributions were fitted by a single or double Gaussian distribution. The average (Pave) and PL for HeLa cell demonstrating a wide distribution were 0.31 and 0.24 respectively (Fig. 4B). We concluded that HeLa cell movement can be described as random movement. The persistence distribution of RPE cells demonstrates a right-shifted peak with high amplitude and was fitted with the double Gaussian function by using MLE (Fig. 4B). The abundance of a high persistence value (Pave=0.66) with a strong occurrence was an indicator for directional movement for RPE cells. We concluded that both HeLa and RPE cells exhibited different motility patterns, which can therefore be characterized either random or directional.

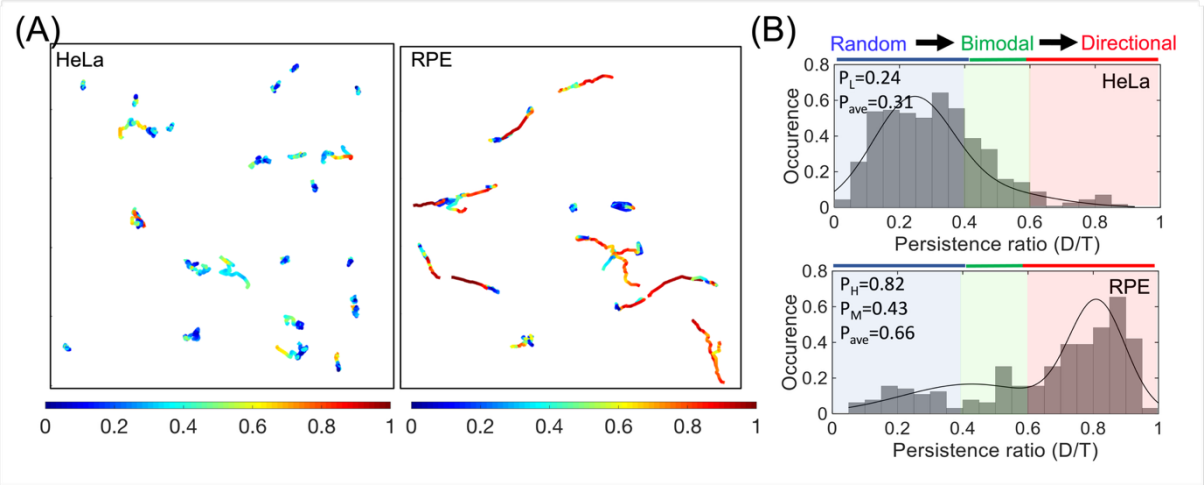

Figure 4. Computation of persistence distribution for different cell types. (A) The collection of representative cell trajectories demonstrating the instant persistence changes for HeLa (left panel), and RPE (right panel). (B) The distribution of persistence was obtained at an interval of 16 frames for HeLa cells (left panel) and RPE cells (right panel). The data was fitted to Gaussian functions (black line) to determine the peak values for different regions. Average persistence (P) values were given for each plot.

Conclusion

As a conclusion, we integrated the adaptive tracking method with CNN-based segmentation. Notably, segmentation errors decreased compared to the previous iteration. We successfully identified the borders of adjacent cells and determined their centroid positions. As a result, our method, which autonomously determines the optimal search radius for identifying potential cell linkages, achieved higher tracking scores across various video datasets. Adtari excels in determining the majority of tracks [5,11–13]. When employing centroids from watershed in the tracking phase, the average tracked time and the ratio of successfully tracked cells to the total were high for different video sets. Our proposed method still has certain limitations, particularly when cell displacement surpasses the minimum distance between cells. These challenges can be addressed either by incorporating more cell features or by modifying the weight of matching parameters.

References

Emami, N., Sedaei, Z., & Ferdousi, R. (2021). Computerized cell tracking: Current methods, tools and challenges. *Visual Informatics, 5*(1), 1–13. https://doi.org/10.1016/j.visinf.2021.01.001.

Falk, T., Mai, D., Bensch, R., Çiçek, Ö., Abdulkadir, A., Marrakchi, Y., Böhm, A., Deubner, J., Jäckel, Z., Seiwald, K., Dovzhenko, A., Tietz, O., Dal Bosco, C., Walther, P., Cremers, D., Buhmann, J. M., & Hamprecht, F. A. (2019). U-Net: Deep learning for cell counting, detection, and morphometry. *Nature Methods, 16*, 67–70. https://doi.org/10.1038/s41592-018-0261-2.

Löffler, K., Scherr, T., & Mikut, R. (2021). A graph-based cell tracking algorithm with few manually tunable parameters and automated segmentation error correction. *PLoS ONE, 16*(7), e0254680. https://doi.org/10.1371/journal.pone.0254680.

Maddalena, L., Antonelli, L., Albu, A., Hada, A., & Guarracino, M. R. (2022). Artificial intelligence for cell segmentation, event detection, and tracking for label-free microscopy imaging. *Algorithms, 15*(2), 48. https://doi.org/10.3390/a15020048.

Matula, P., Maška, M., Sorokin, D. V., Matula, P., Ortiz-de-Solórzano, C., & Kozubek, M. (2015). Cell tracking accuracy measurement based on comparison of acyclic oriented graphs. *PLoS ONE, 10*(12), e0144959. https://doi.org/10.1371/journal.pone.0144959.

Nketia, T. A., Sailem, H., Rohde, G., Machiraju, R., & Rittscher, J. (2017). Analysis of live cell images: Methods, tools and opportunities. *Methods, 115*, 65–79. https://doi.org/10.1016/j.ymeth.2016.11.008.

Padfield, D., Rittscher, J., & Roysam, B. (2011). Coupled minimum-cost flow cell tracking for high-throughput quantitative analysis. *Medical Image Analysis, 15*(4), 650–668. https://doi.org/10.1016/j.media.2011.03.001.

Qureshi, H., Ozlu, N., & Bayraktar, H. (2022). Adaptive tracking algorithm for trajectory analysis of cells and layer-by-layer assessment of motility dynamics. *Computers in Biology and Medicine, 150*, 106109. https://doi.org/10.1016/j.compbiomed.2022.106109.

Scarpa, E., & Mayor, R. (2016). Collective cell migration in development. *Journal of Cell Biology, 212*(2), 143–155. https://doi.org/10.1083/jcb.201508047.

SenGupta, S., Parent, C. A., & Bear, J. E. (2021). The principles of directed cell migration. *Nature Reviews Molecular Cell Biology, 22*(8), 529–547. https://doi.org/10.1038/s41580-021-00353-3.

Taïeb, H. M., Bertinetti, L., Robinson, T., & Cipitria, A. (2022). FUCCItrack: An all-in-one software for single cell tracking and cell cycle analysis. *PLoS ONE, 17*(5), e0267978. https://doi.org/10.1371/journal.pone.0267978.

Ulman, V., Maška, M., Magnusson, K. E. G., Ronneberger, O., Haubold, C., Harder, N., Matula, P., Svoboda, D., Radojevic, M., Smal, I., Rohr, K., Jalden, J., Blau, H. M., Dzyubachyk, O., Le Guyader, S., Kervrann, C., Cheezum, M. K., Cohen, A. R., Godinez, W. J., ... & Ortiz-de-Solórzano, C. (2017). An objective comparison of cell-tracking algorithms. *Nature Methods, 14*, 1141–1152. https://doi.org/10.1038/nmeth.4473.

Wolf, S., Wan, Y., & McDole, K. (2021). Current approaches to fate mapping and lineage tracing using image data. *Development, 148*(8), dev191213. https://doi.org/10.1242/dev.191213.

MOLECULAR BIOLOGY - GENETICS AND BIOTECHNOLOGY

Bioimaging

Drug and Vaccine Development

Metabolic and Evolutionary Engineering

Metagenomics and Protein Engineering

Microbial Biotechnology and Genetics

Nanobiotechnology

Vaccinomics to Design Chimeric Vaccine Candidate Against Four *Bordetella* Species

Beyza Uslu[a], Çiğdem Yılmaz Çolak[a]

[a] Istanbul Technical University, Molecular Biology-Genetics & Biotechnology, Türkiye
uslube17@itu.edu.tr

Keywords: Bordetella, Chimeric vaccine, Immunoinformatics, Multi-epitope Vaccine, Vaccinomics.

Aim

Various *Bordetella* species are known to cause respiratory diseases across a range of hosts, affecting both animal and human populations. Besides human pathogens including *B. pertussis* and *B. parapertussis*, animal pathogens such as *B. avium*, *B. hinzii*, *B. bronchiseptica*, and *B. holmesii* have critical importance as they can cause disease in economically important animals and can also be transferred to immunocompromised patients. Using a vaccinomics-based strategy, this study attempts to create a chimeric vaccine that targets conserved antigenic areas across these four species to effectively elicit an immune response.

Members of the *Bordetella* genus are Gram-negative, aerobic coccobacilli that predominantly target the respiratory system.[1] Birds, especially turkeys, are the primary host of *Bordetella avium*, which causes avian bordetellosis, which costs the poultry business money.[2] Because of its great adaptability, *Bordetella bronchiseptica* can infect a variety of species, such as dogs, cats, and pigs, and can linger in the environment. In people with compromised immune systems, it can occasionally result in respiratory infections.[3] Once thought to be a harmless commensal in birds, *Bordetella hinzii* has become an opportunistic pathogen, causing sepsis and bacteremia in immunocompromised people.[4] An emerging pathogen called *Bordetella holmesii* is associated with systemic and respiratory diseases that might be mistaken for pertussis.[5] The virulence, host specificity, and environmental persistence of these *Bordetella* species vary, presenting problems for public health as well as the economy. Their zoonotic potential highlights the necessity of a vaccine to lower the danger of transmission. This work intends to create a chimeric vaccine that can elicit a robust immune response, ultimately assisting in disease control and prevention, by identifying conserved antigenic areas and using a methodical *in silico* methodology.

Material and Method

Proteome Data Retrieval

The complete proteomic datasets of the four *Bordetella* species were downloaded from public repositories such as UniProt and NCBI. In selecting the proteomes, priority was given to sequences from the reference strains of each species to ensure data consistency and reliability.

Sequence Alignment and Homology Analysis

The multiple sequence alignment was performed using Clustal Omega, MEGA, and NCBI BLASTp to identify conserved proteins across the species by aligning entire protein sequences. Four proteins (LolA, LptA, OmpA, and LapB) demonstrating high conservation were marked for further analysis, ensuring the potential for cross-protection.

Subcellular Localization and Transmembrane Domain Analysis

The cellular localization of candidate proteins was determined using the TargetP program. This step was critical as proteins secreted or located on the cell surface are more likely to be immunogenic. The presence of transmembrane domains was evaluated using the TMHMM program. This analysis was performed to determine whether any part of the selected proteins remained intracellular, which could hinder epitope accessibility.

Epitope Prediction and Selection

Both MHC-I and B-cell epitopes were predicted using the IEDB analysis resource. For the MHC epitope predictions, the source species was set to dog to reflect the specific MHC allele data pertinent to the host of interest. Epitopes were selected based on stringent criteria including high binding affinity (evaluated by scoring metrics and percentage rank), robust immunogenicity, and favorable antigenicity. Additional filters, such as toxicity and allergenicity assessments, were applied to eliminate any candidates that might induce adverse reactions.

Multi-Epitope Vaccine Construction and Structural Analysis

The selected epitopes were concatenated to form several multi-epitope vaccine constructs. Various adjuvant sequences, known to enhance immune responses, were appended at the N-terminal of the constructs. Flexible linker sequences were inserted between epitopes to maintain proper folding and optimal epitope presentation. Different configurations were explored to optimize the overall antigenicity and structural integrity of the vaccine construct. The antigenicity scores, solubility, and physicochemical properties of each construct were predicted using VaxiJen, Protein-Sol, and ProtParam servers, respectively, and compared to guide the selection of the most promising candidate.

A three-dimensional structural model of the selected construct was generated using both homology modeling and *ab initio* techniques. The model was then refined using GalaxyRefine server. The ProSA and SAVES tools was used to provide insight into the overall quality of the refined model.

Molecular Docking Analysis

Molecular docking was performed using ClusPro to assess the interaction between the vaccine construct and immune receptors TLR2 and TLR4. The best binding pose was selected based on the lowest energy score. Docking results indicated strong and stable interactions, supporting the potential of the designed construct to activate immune pathways.

Findings

Four conserved proteins, LolA, LptA, OmpA, and LapB were identified across the four *Bordetella* species by looking at multiple sequence alignment results with Clustal Omega and MEGA. After homology analysis, a refined set of epitopes was chosen based on high antigenicity, strong binding affinity, and favorable percentage rank values with IEDB tools. Toxicity and allergenicity filters were applied to ensure immunological safety. 20 selected epitopes were then used to design multiple multi-epitope vaccine constructs with different adjuvant and linker combinations, resulting in 10 different designs. After antigenicity analysis, an about 30-kDa multi-epitope vaccine construct with the highest antigenic profile was obtained. The final vaccine construct was subjected to 3D structural modeling using I-TASSER, generating multiple structural models ranked by confidence scores (C-score, TM-score, and RMSD values). The best model was selected for further refinement. Structural validation was further performed using Ramachandran plot analysis, Ramachandran analysis showed that 92.3% of residues are in the most favored regions, indicating good stereochemical quality. The ProSA tool was used to calculate the Z-score, ensuring that the final selected model was within the range of native proteins and had a realistic 3D conformation. The ProSA Z-score (–2.52) indicates a reliable overall model quality within the range of native protein structures. The physicochemical properties of the vaccine constructs including molecular weight, isoelectric point (pI), instability index, and half-life were evaluated using ProtParam, ensuring the selected construct met the required stability criteria. The physicochemical properties of the vaccine construct including molecular weight, isoelectric point (pI), instability index, and half-life were evaluated using ProtParam, ensuring the selected construct met the required stability criteria. The designed protein is stable (instability index: 39.42), hydrophilic (GRAVY: –0.441), and moderately thermostable (aliphatic index: 49.87). It is suitable for expression in E. coli (half-life >10 h) and shows a high extinction coefficient (14,285 $M^{-1}cm^{-1}$), facilitating purification. After using Cluspro for molecular docking, as seen in figure below, the vaccine construct shows binding interaction with both TLR2 and TLR4.

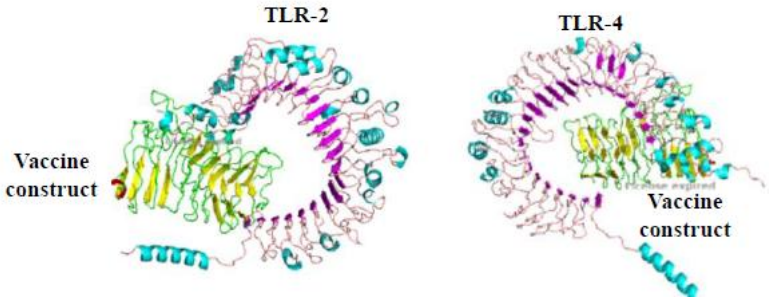

Figure 1. Predicted binding interaction between the vaccine construct and TLR2/TLR4 based on ClusPro docking.

Conclusion

This study presents the computational design of a chimeric multi-epitope vaccine candidate targeting four *Bordetella* species. Immunoinformatics tools were used to select highly immunogenic epitopes while minimizing potential adverse responses. The results indicate promising immunogenic potential. Further validation through in vitro and in vivo studies is needed. Future work may include plasmid-based expression and molecular dynamics simulations to assess structural stability and receptor interactions.

References

Finger, H., & von Koenig, C. H. W. (1996). Bordetella. In S. Baron (Ed.), *Medical Microbiology* (4th ed., Chap. 31). University of Texas Medical Branch at Galveston. Retrieved from https://www.ncbi.nlm.nih.gov/books/NBK7813/.

Temple, L. M., Weiss, A. A., Walker, K. E., Barnes, H. J., Christensen, V. L., Miyamoto, D. M., Shelton, C. B., & Orndorff, P. E. (1998). Bordetella avium virulence measured in vivo and in vitro. *Infection and Immunity, 66*(11), 5244–5251. https://doi.org/10.1128/IAI.66.11.5244-5251.1998.

Chan, K. H., Ajao, S. O., Farouji, I., & Slim, J. (2021). A case of Bordetella bronchiseptica bacteremia in a patient with decompensated liver cirrhosis. *Cureus, 13*(3), e13938. https://doi.org/10.7759/cureus.13938.

Sparks, R., Painter, A., Callum, J., Swan, C., Polkinghorne, A., Fong, W., Gall, M., Sintchenko, V., & Branley, J. (2023). Detection and characterisation of Bordetella hinzii in line-related bacteraemia and respiratory tract infection in Australia. *Pathology, 55*(1), 117–122. https://doi.org/10.1016/j.pathol.2022.06.004.

Elgarini, M., Mennane, Z., Sobh, M., & Hammoumi, A. (2024). Bordetella holmesii: Causative agent of pertussis. *Archives de Pédiatrie, 31*(3), 172–17 https://doi.org/10.1016/j.arcped.2023.10.012.

MOLECULAR BIOLOGY - GENETICS AND BIOTECHNOLOGY

Bioimaging

Drug and Vaccine Development

Metabolic and Evolutionary Engineering

Metagenomics and Protein Engineering

Microbial Biotechnology and Genetics

Nanobiotechnology

Analysis of Oxidative Stress Response of Stress-Resistant Saccharomyces cerevisiae Strains Obtained by Evolutionary Engineering

Gürkan Bozkurt[a,b,c], Furkan Fıçıcı[a,b,c], Tarık Öztürk[c], Alican Topaloğlu[a,b], Zeynep Petek Çakar[a,b]

[a] Istanbul Technical University, Molecular Biology-Genetics and Biotechnology Master of Science Program, Turkiye
[b] Dr. Orhan Öcalgiray Molecular Biology-Biotechnology and Genetics Research Center (ITU-MOBGAM), Turkiye
[c] TUBITAK Marmara Research Center, Türkiye
bozkurtg18@itu.edu.tr

Keywords: *Saccharomyces cerevisiae*, Metabolic Engineering, Evolutionary Engineering, Stress Resistance, Oxidative Stress, Antioxidant, Secondary Metabolites.

Aim

Metabolic engineering involves the improvement of cellular activities by manipulating the enzymatic, transport, and regulatory functions of the cell using recombinant DNA technology (Bailey, 1991). Rational metabolic engineering involves designing a targeted genetic manipulation for the genetic makeup of industrially important microorganisms based on existing knowledge of their metabolic pathways (Bailey, 1999). However, this method faces several limitations. Firstly, extensive biochemical and genetic knowledge of the metabolism or metabolic pathways of the target organism is required. Moreover, cellular responses to interventions are typically complex and unpredictable. For instance, when an existing metabolic pathway is inhibited, cells may activate an alternative metabolic pathway. Consequently, a large number of stimulus-response experiments are necessary to realistically assess the effects of such perturbations. Additionally, the genetic manipulation of industrial strains is considerably challenging due to their complex genetic makeup, such as polyploidy. Furthermore, regulatory issues related to the use of genetically modified organisms in the food industry complicate this process even more. Lastly, the limited availability of suitable vectors and methodologies for genetic modification presents a significant obstacle (Bailey, 1991; Bailey et al., 1996). To overcome all these limitations, a bottom-up approach to metabolic engineering has been developed, called inverse metabolic engineering. This approach begins by first identifying or designing the desired phenotype. The genetic or environmental factors responsible for this phenotype are then identified. Finally, these factors are transferred to the target organism, thereby reproducing the desired phenotype (Bailey et al., 1996). Evolutionary engineering, an inverse metabolic engineering approach, involves the application of continuous cycles of mutation and selection to obtain a desired phenotype in successive generations. Selection pressures may favor the utilization of a particular substrate, the production of a particular product, or resistance to a specific stress factor. Due to its industrial importance, the yeast *Saccharomyces cerevisiae* has been widely used for the improvement and study of stress resistance through evolutionary engineering (Cakar et al., 2012). It is also suitable for studying oxidative stress responses since oxidative stress plays a critical role in various industrial fermentation processes, affecting cellular viability and product yield (Toledano et al., 2002; de Fátima Alves et al., 2023). Secondary metabolites, which are often involved in stress responses, contribute to oxidative stress resistance through their antioxidant activity (Clarkson et al., 1991).

The aim of this study was to investigate the oxidative stress response mechanism of genetically stable and stress-resistant *S. cerevisiae* strains that had been previously developed through evolutionary engineering. The findings of this study are expected to provide insights into the oxidative stress response mechanisms of stress-resistant *S. cerevisiae* strains and elucidate the role of secondary metabolites in these processes.

Material and Method

Strains: In this study, *Saccharomyces cerevisiae* CEN.PK 113-7D was used as the reference strain (provided by Prof. Dr. Jean Marie François and Dr. Laurent Benbadis from the University of Toulouse, France), along with mutant strains developed from this reference strain through evolutionary engineering technique to confer resistance to various stress factors. Previously developed *S. cerevisiae* mutant strains, their characteristics, and sources are given in Table 1.

Table 1. Previously developed *S. cerevisiae* mutant strains, their characteristics, and sources.

Strains	Characteristics	Source
REF (Reference strain)	CEN.PK 113-7D (haploid)	Entian and Kötter (2007)
SRM11	Chronologically long-lived	Çakar's Lab collection
FD11	Propolis-resistant	Çakar's Lab collection
8C	Iron-resistant	Çakar's Lab collection
B2	Ethanol-tolerant	Çakar's Lab collection
R12	Rapamycin-resistant	Çakar's Lab collection
F1	Freeze thaw-resistant	Çakar's Lab collection
ALU10	Aluminum-resistant	Çakar's Lab collection
K1	KCl-resistant	Çakar's Lab collection
H7	Hydrogen peroxide-resistant	Çakar's Lab collection
ANT	Antimycin A-resistant	Çakar's Lab collection
FT9	Freeze thaw-resistant	Çakar's Lab collection
K9	KCl-resistant	Çakar's Lab collection
C9	2-phenylethanol-resistant	Çakar's Lab collection
CAF	Caffeine-resistant	Çakar's Lab collection
B8	Ethanol-resistant	Çakar's Lab collection
2E	Silver-resistant	Çakar's Lab collection

Yeast Culture Conditions: Initially, the reference and mutant strains were revived by inoculating 100 µL from stock cultures into 10 mL of YPD medium (1% w/v yeast extract, 1% w/v peptone, 2.2% w/v glucose monohydrate) in 50 mL culture tubes, followed by overnight incubation at 30 °C and 150 rpm. Subsequently, the reference and mutant strains were pre-cultured in YMM medium (0.67% w/v yeast nitrogen base w/o amino acids, 2.2% glucose monohydrate) at an initial OD_{600} of 0.2 (~2.8 x 10^6 cells/mL) and incubated overnight at 30 °C and 150 rpm. Afterward, the cultures were inoculated into fresh YMM medium at an initial OD_{600} of 0.2 and incubated at 30 °C and 150 rpm for 5 hours and 18 hours.

Secondary Metabolite Extraction: Following incubation for 5 hours and 18 hours, ethyl acetate extraction was performed at a 1:1 ratio on the liquid cultures to isolate secondary metabolites via phase separation. The solvent phase was collected in glass tubes and evaporated at 45 °C under a nitrogen blowdown. After solvent evaporation, the purified extract of secondary metabolites, appearing as an orange-brown residue, was recovered from the bottom of the tubes by dissolving with 70% methanol.

Determination of Antioxidant Activity: The antioxidant activities of the secondary metabolite extracts were evaluated using the 2,2-diphenyl-1-picrylhydrazyl (DPPH) assay and total phenolic content (TPC) assay. The DPPH assay results were expressed as Trolox equivalent antioxidant capacity (TEAC) per gram of cell dry weight. The TPC assay results were expressed as milligrams of gallic acid equivalents per gram of cell dry weight (mg GAE/g cell dry weight).

A schematic representation of the methodology is provided in Figure 1.

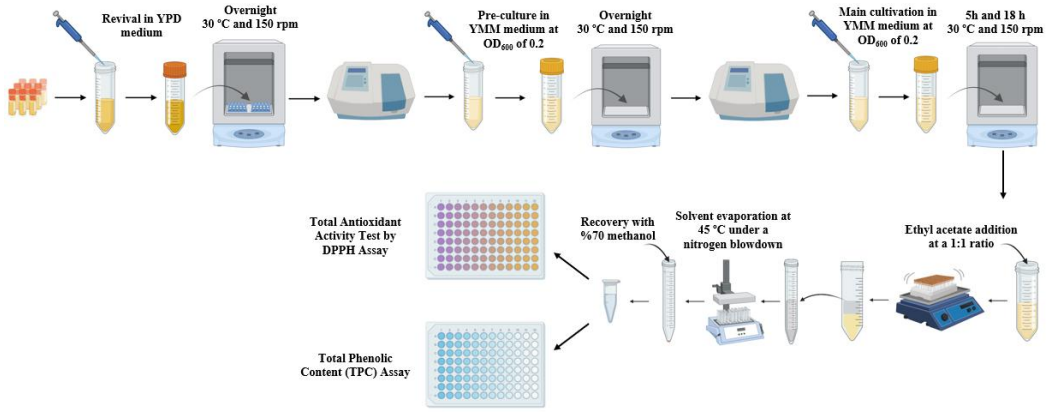

Figure 1. Schematic representation of the methodology.

Findings

The antioxidant capacity of secondary metabolites derived from *S. cerevisiae* strains was assessed at both the exponential and stationary growth phases using the DPPH assay (Figure 2). Some of the stress-resistant *S. cerevisiae* strains tested in this study exhibited higher antioxidant activity than the reference strain.

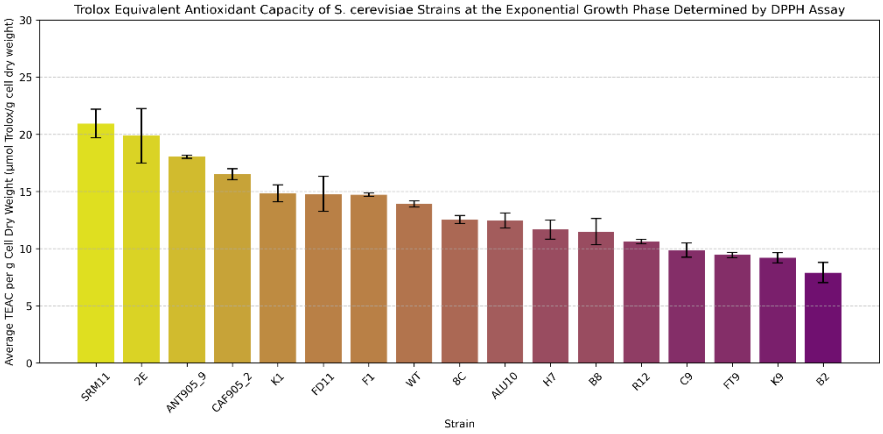

(a)

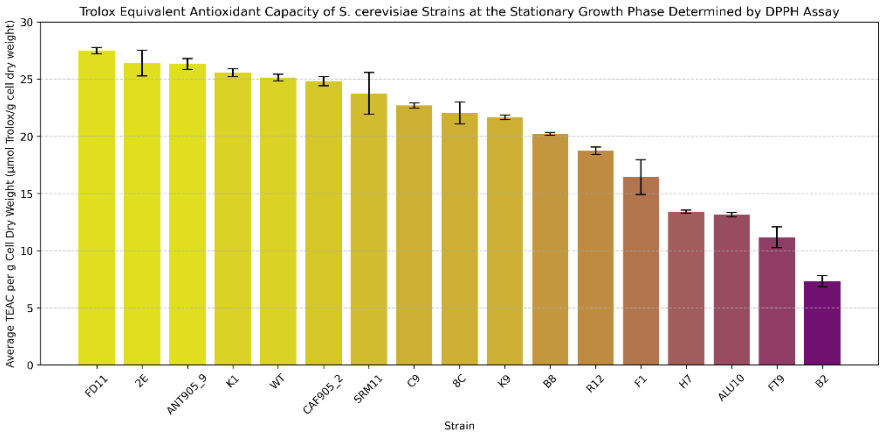

(b)

Figure 2. Trolox equivalent antioxidant capacity (TEAC) per gram of cell dry weight. **(a)** Total antioxidant capacity of *S. cerevisiae* strains measured during the exponential growth phase (5 hours incubation). **(b)** Total antioxidant capacity of *S. cerevisiae* strains measured during the stationary growth phase (18 hours incubation).

The total phenolic content of secondary metabolites derived from *S. cerevisiae* strains was assessed at both the exponential and stationary growth phases using the TPC assay (Figure 3). A few stress-resistant *S. cerevisiae* strains tested in this study exhibited higher phenolic content than the reference strain during the stationary growth phase.

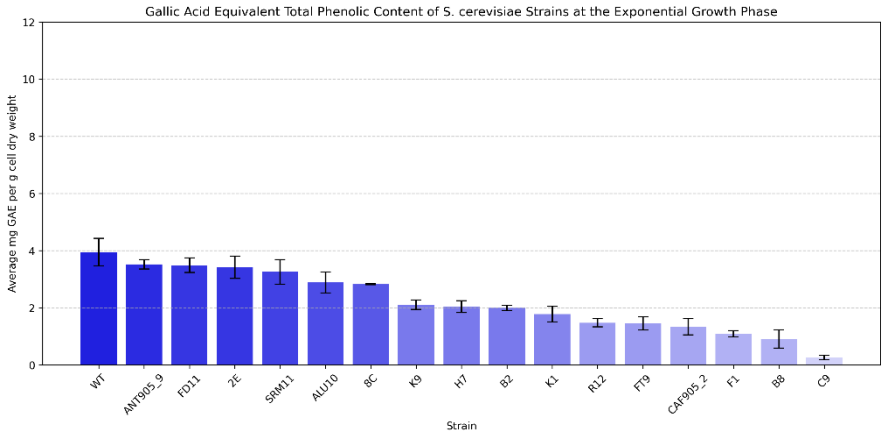

(a)

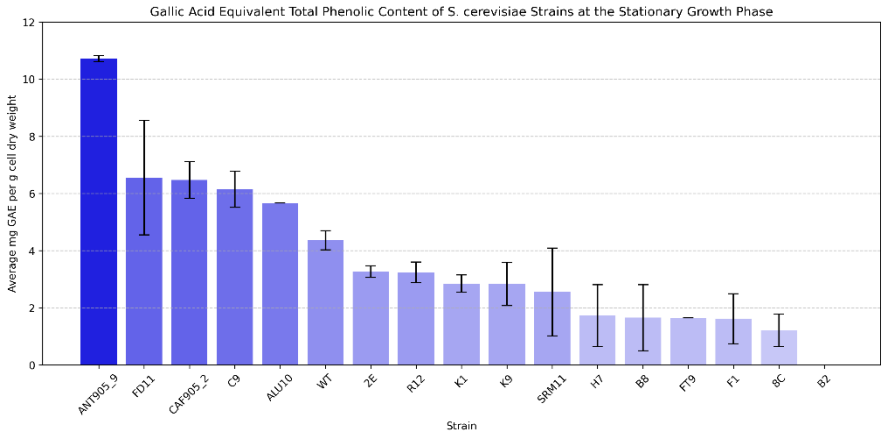

(b)

Figure 3. Total phenolic content (TPC) expressed as milligrams of gallic acid equivalents per gram of cell dry weight (mg GAE/g cell dry weight). **(a)** TPC of *S. cerevisiae* strains measured during the exponential growth phase (5 hours incubation). **(b)** TPC of *S. cerevisiae* strains measured during the stationary growth phase (18 hours incubation).

Conclusion

Overall, the results indicate that the antioxidant activity of both the stress-resistant *S. cerevisiae* strains and the reference strain was generally higher during the stationary growth phase compared to the exponential growth phase. This suggests that the accumulation of antioxidant metabolites is more prominent as cells undergo a transition into the stationary growth phase. Among the stress-resistant strains tested, only the antimycin A-resistant strain (ANT905_9) exhibited consistently higher antioxidant capacity than the reference strain in both the exponential and stationary growth phases, suggesting that its adaptation mechanism may contribute to its increased antioxidant capacity. In contrast, the ethanol-tolerant strain (B2) showed the lowest antioxidant capacity, implying that its tolerance mechanism is likely independent of oxidative stress pathways. Furthermore, ANT905_9 also showed elevated phenolic content during the stationary growth phase compared to the other strains. The findings of this study highlight potential candidates for further molecular and biochemical characterization of oxidative stress resistance mechanisms in *S. cerevisiae*.

Acknowledgement

This research was supported by Scientific Research Projects Department of Istanbul Technical University, Project Number: TYL-2025-46843. All of the experiments during this research was conducted in TUBITAK (The Scientific and Technological Research Council of Turkey) Marmara Research Center.

References

Bailey J. E. (1991). Toward a science of metabolic engineering. *Science (New York, N.Y.)*, *252*(5013), 1668–1675. https://doi.org/10.1126/science.2047876.

Bailey, J. E. (1999). Lessons from metabolic engineering for functional genomics and drug discovery. *Nature biotechnology*, *17*(7), 616-618.

Bailey, J. E., Sburlati, A., Hatzimanikatis, V., Lee, K., Renner, W. A., & Tsai, P. S. (1996). Inverse metabolic engineering: A strategy for directed genetic engineering of useful phenotypes. *Biotechnology and Bioengineering*, *52*(1), 109–121. https://doi.org/10.1002/(SICI)1097-0290(19961005)52:1<109::AID-BIT11>3.0.CO;2-J.

Cakar, Z. P., Turanli-Yildiz, B., Alkim, C., & Yilmaz, U. (2012). Evolutionary engineering of *Saccharomyces cerevisiae* for improved industrially important properties. *FEMS Yeast Research*, *12*(2), 171–182. https://doi.org/10.1111/j.1567-1364.2011.00775.x.

Clarkson, S. P., Large, P. J., Boulton, C. A., & Bamforth, C. W. (1991). Synthesis of superoxide dismutase, catalase and other enzymes and oxygen and superoxide toxicity during changes in oxygen concentration in cultures of brewing yeast. *Yeast*, *7*(2), 91-103.

de Fátima Alves, L., Bortolucci, J., Reginatto, V., Guazzaroni, M. E., & Mussatto, S. I. (2023). Improving *Saccharomyces cerevisiae* acid and oxidative stress resistance using a prokaryotic gene identified by functional metagenomics. *Heliyon*, *9*(4), e14838.

Toledano, M. B., Delaunay, A., Biteau, B., Spector, D., & Azevedo, D. (2002). Oxidative stress responses in yeast. In *Yeast stress responses* (pp. 241-303). Berlin, Heidelberg: Springer Berlin Heidelberg.

Investigation of Caffeine Metabolism in Saccharomyces cerevisiae

Furkan Fıçıcı[a,b,c], Gürkan Bozkurt[a,b,c], Alican Topaloğlu[a,b], Tarık Öztürk[c], Zeynep Petek Çakar[a,b]

[a] Istanbul Technical University, Molecular Biology-Genetics and Biotechnology Master of Science Program, Turkiye
[b] Dr. Orhan Öcalgiray Molecular Biology-Biotechnology and Genetics Research Center (ITU-MOBGAM), Turkiye
[c] TUBITAK Marmara Research Center, Turkiye
ficici17@itu.edu.tr

Keywords: Caffeine stress resistance , Evolutionary engineering , High-Performance Liquid Chromatography (HPLC) , Metabolic engineering , *Saccharomyces cerevisiae.*

Aim

Caffeine, a widely consumed alkaloid, is primarily known for its antioxidant properties and stimulant effects, making it a crucial component in the food and pharmaceutical industries. However, its biological activity is not limited to beneficial effects, as caffeine has been documented to exert toxic effects on microorganisms. While certain microorganisms exhibit susceptibility to caffeine-induced stress, others have evolved metabolic pathways or resistance mechanisms that enable them to tolerate or even utilize caffeine. Understanding these mechanisms is of significant interest, particularly in eukaryotic systems, as it provides insights into stress adaptation and cellular detoxification pathways that may be relevant to higher organisms, including humans.

Saccharomyces cerevisiae, a eukaryotic model organism, has been extensively used to study genetic and metabolic responses to various stressors. The investigation of caffeine resistance and metabolism in this yeast species not only enhances our comprehension of microbial adaptation but also serves as a model for understanding caffeine metabolism in more complex eukaryotic systems. Furthermore, caffeine metabolism in yeast could offer potential applications in biotransformation and bioremediation strategies, particularly for the degradation and detoxification of caffeine in environmental and industrial settings. Given the widespread presence of caffeine in nature and its impact on microbial ecology, deciphering these mechanisms in *S. cerevisiae* is crucial. Moreover, insights gained from such studies can contribute to biomedical research, as caffeine is known to interact with various metabolic pathways in mammalian systems.

The primary aim of this study was to investigate the metabolism of caffeine in caffeine-resistant *S. cerevisiae* strains CAF905-2, CAF906-11, and CAF906-12 that have been previously developed using an evolutionary engineering approach. By analyzing their growth kinetics and intracellular caffeine accumulation profiles, this research aimed to elucidate the relationship between caffeine metabolism and resistance mechanisms. Another aim of this study was to compare the obtained results with the existing literature to assess similarities, variations, and potential novel findings regarding caffeine metabolism in eukaryotic microorganisms. Understanding these dynamics could provide valuable information on how cells adapt to caffeine exposure over successive generations and whether resistance confers any selective advantage in different environmental conditions.

Material and Method

In this study, previously developed caffeine-resistant *S. cerevisiae* strains CAF905-2, CAF906-11, and CAF906-12 obtained by evolutionary engineering and their reference strain CEN.PK 113-7D were used. The strains were cultivated in both caffeine-containing and caffeine-free yeast minimal media (YMM). In order to compare caffeine response at different growth phases, samples were collected at exponential and stationary phases. The growth kinetics of the strains were monitored using optical density measurements at 600 nm wavelength (OD600) at regular time intervals. Samples were centrifuged at 10,000 g for 5 min to separate cell pellets from the culture

media. Supernatants were collected as an extracellular fraction, and pellets were collected and lysed to analyze the intracellular fraction. The lysis step was performed with an ultrasonic homogenizer.

High-performance liquid chromatography (HPLC) was employed for caffeine quantification in both intracellular and extracellular fractions. C18 reverse-phase column was used, and 3% acetonitrile was used as the mobile phase. Both intracellular and extracellular caffeine amounts were assessed to determine whether resistance mechanisms involved altered uptake, efflux, or degradation of caffeine to its three main metabolites: paraxanthine, theophylline, and theobromine.. The caffeine degradation potential of the strains was analyzed, and comparisons were made to understand how resistance influences caffeine metabolism. Additionally, stress response markers and possible genetic adaptations in resistant strains were considered to further characterize their physiological and metabolic responses.

A schematic representation of the methodology is provided in Figure 1.

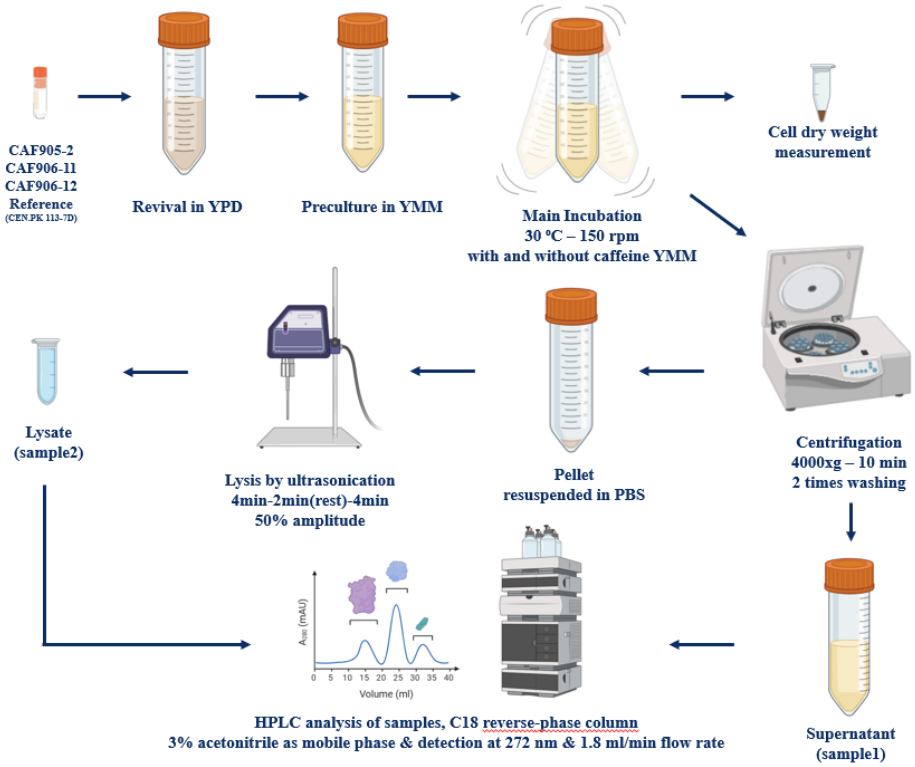

Figure 1. Schematic representation of the methodology.

Findings

Both intracellular and extracellular caffeine accumulation of the mutant strains CAF905-2, CAF906-11 and CAF906-12 were compared against the reference strain (wild type) in Figure 2 and Figure 3. Intracellular levels of caffeine were significantly higher in the mutant strains compared to the reference strain in the exponential phase, while this difference decreased in the stationary phase. Moreover, intracellular levels of caffeine decreased from the exponential phase to the stationary phase for all three mutant strains.

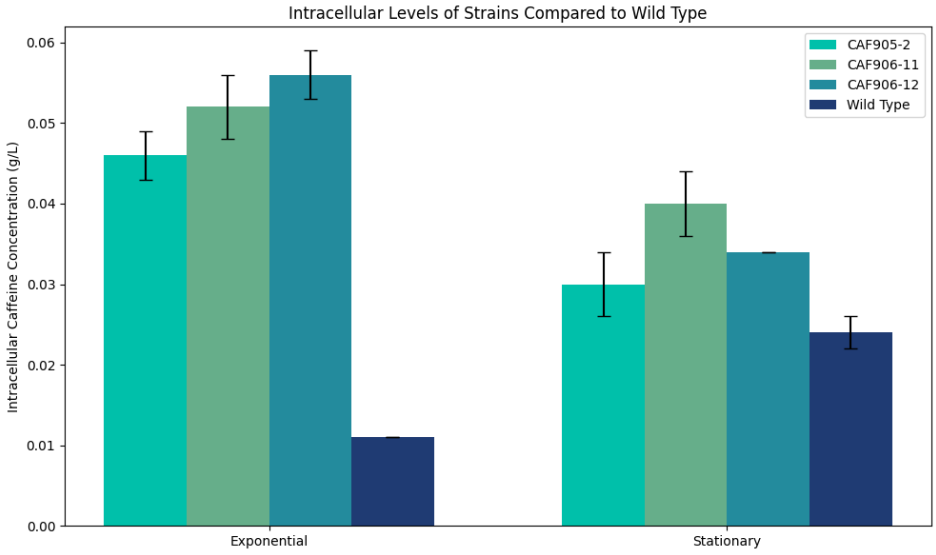

Figure 1. Differences between intracellular level of caffeine for CAF905-2, CAF906-11, CAF906-12 and reference strain in both exponential and stationary phases.

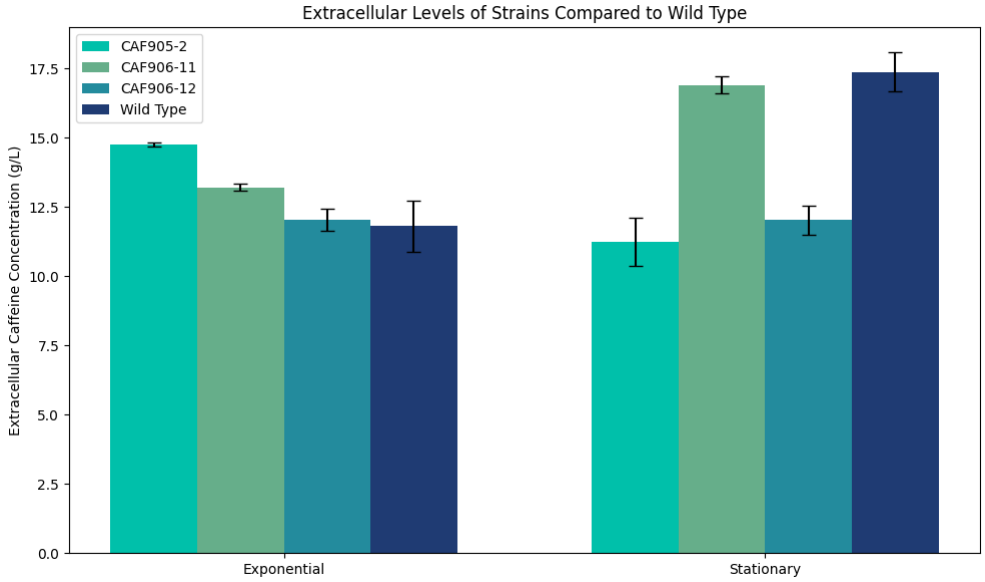

Figure 2. Differences between extracellular level of caffeine for CAF905-2, CAF906-11, CAF906-12 and reference strain in both exponential and stationary phases.

Conclusion

Increase in the extracellular levels of caffeine from the exponential to the stationary phase of growth could imply efflux or pumping out of caffeine. Decrease in both intracellular and extracellular levels of caffeine from the exponential to the stationary phase of growth could be interpreted as metabolizing of caffeine by the cells. Increase in the intracellular levels of caffeine could indicate that cells could tolerate caffeine toxicity by diverse intracellular processes. Further research should be conducted by also analyzing the main metabolites of caffeine, to obtain more detailed results. As a conclusion, all mutant strains could tolerate intracellular caffeine during the exponential phase of growth stronger than the reference strain. During the stationary phase of growth, the caffeine-resistant mutant strains possibly removed intracellular caffeine by metabolizing it or pumping it out of the cell.

Acknowledgement

We thank İlkay Yurdaer, for her technical assistance and contribution on HPLC analysis experiments. This research was supported by Scientific Research Projects Department of Istanbul Technical University, Project Number: TYL-2025-46832. All of the experiments during this research was conducted in TUBITAK (The Scientific and Technological Research Council of Turkey) Marmara Research Center.

References

Ashihara, H., Sano, H., & Crozier, A. (2008). Caffeine and related purine alkaloids: biosynthesis, catabolism, function and genetic engineering. *Phytochemistry*, *69*(4), 841-856.

Yu, C. L., Summers, R. M., Li, Y., Mohanty, S. K., Subramanian, M., & Pope, R. M. (2015). Rapid identification and quantitative validation of a caffeine-degrading pathway in Pseudomonas sp. CES. *Journal of proteome research*, *14*(1), 95-106.

Mock, M. B., & Summers, R. M. (2024). Microbial metabolism of caffeine and potential applications in bioremediation. *Journal of Applied Microbiology*, *135*(4), lxae080.

Ibrahim, S., Shukor, M. Y., Syed, M. A., Ab Rahman, N. A., Khalil, K. A., Khalid, A., & Ahmad, S. A. (2014). Bacterial degradation of caffeine: a review. *Asian Journal of Plant Biology*, *2*(1), 19-28.

Geck, R. C., Moresi, N. G., Anderson, L. M., Brewer, R., Renz, T. R., Taylor, M. B., & Dunham, M. J. (2024). Experimental evolution of *Saccharomyces cerevisiae* for caffeine tolerance alters multidrug resistance and target of rapamycin signaling pathways. *G3: Genes, Genomes, Genetics*, *14*(9), jkae148.

Kuranda, K., Leberre, V., Sokol, S., Palamarczyk, G., & François, J. (2006). Investigating the caffeine effects in the yeast *Saccharomyces cerevisiae* brings new insights into the connection between TOR, PKC and Ras/cAMP signalling pathways. *Molecular microbiology*, *61*(5), 1147-1166.

Kuzu, G. (2009). Effects of rapamycin and caffeine on tor signaling pathway in *Saccharomyces cerevisiae*. *Master's thesis*, Boğaziçi Üniversitesi Fen Bilimleri Enstitüsü.

Dereli, E. (2013). An integrated approach to investigate tor signaling mechanism in *Saccharomyces cerevisiae*. *PhD's thesis*, Boğaziçi Üniversitesi Fen Bilimleri Enstitüsü.

Sürmeli, Y., Holyavkin, C., Topaloğlu, A., Arslan, M., Kısakesen, H. İ., & Çakar, Z. P. (2019). Evolutionary engineering and molecular characterization of a caffeine-resistant *Saccharomyces cerevisiae* strain. *World Journal of Microbiology and Biotechnology*, *35*, 1-16.

Zhao, F., Wang, Z., & Huang, H. (2024). Physical cell disruption technologies for intracellular compound extraction from microorganisms. *Processes*, *12*(10), 2059.

Comparative Whole Genome Sequencing and Bioinformatic Analysis of an Aluminum-Resistant, Industrial *Saccharomyces cerevisiae* Strain

Alya Emanet[a,c], Naciye Durmuş[a,c], Can Holyavkin[a,c], Alican Topaloğlu[a,b,c], Zeynep Petek Çakar[a,b,c]

[a] Istanbul Technical University, Graduate School, Department of Molecular Biology – Genetics and Biotechnology, Turkiye
[b] Istanbul Technical University, Faculty of Science & Letters, Department of Molecular Biology and Genetics, Turkiye
[c] Istanbul Technical University, Dr. Orhan Öcalgiray Molecular Biology, Biotechnology and Genetics Research Center (ITU-MOBGAM), Turkiye
emanet19@itu.edu.tr

Keywords: Saccharomyces Cerevisiae, Metabolic Engineering, Evolutionary Engineering, Stress Resistance, Aluminum Stress, Next-Generation Sequencing.

Aim

Saccharomyces cerevisiae is a widely used eukaryotic model organism in both basic and industrial research due to its genetic tractability and resilience to environmental stressors (Vanderwaeren et al., 2022; Walker, 2009). Aluminum, though abundant, is a toxic and non-essential metal that disrupts key cellular processes, induces oxidative stress, and interferes with DNA and protein function (Kakimoto et al., 2005; Walton, 2013). Evolutionary engineering—based on the principle of adaptive selection under controlled stress—has proven effective for improving microbial tolerance to such toxic compounds (Çakar et al., 2011; Parapouli et al., 2020).

This study aimed to investigate the molecular mechanisms of aluminum-stress-resistance in *S. cerevisiae* by comparative genomic analysis of an aluminum-stress-resistant *S. cerevisiae* strain that was previously obtained by evolutionary engineering which involved chemical mutagenesis by ethyl methane sulfonate followed by 43 successive batch passages at gradually increasing AlCl3 levels. The results of this study may be useful for potential industrial applications that involve aluminum, aluminum bioremediation, and for a better understanding of aluminum-related health issues, including some neurodegenerative diseases. This research was supported by Scientific Research Projects Department of Istanbul Technical University, Project No: TYL-2025-46840.

Material and Method

Strain and Growth Media: The reference strain used was *Saccharomyces cerevisiae* CEN.PK113-7D (named as strain 905), kindly provided by Prof. Dr. Jean-Marie François and Dr. Laurent Benbadis (University of Toulouse, France). Chemical mutagenesis was performed using ethyl methane sulfonate (EMS). Yeast Minimal Medium (YMM) was used during selection experiments.

Mutagenesis and Selection of Aluminum-Resistant Mutants: The reference strain 905 was subjected to EMS mutagenesis to obtain a genetically diverse initial population called 906. Aluminum tolerance was assessed at concentrations ranging from 0.05 to 50 mM $AlCl_3$. Batch selection involved 43 successive passages, by gradually increasing aluminum chloride ($AlCl_3$) concentration to 21.5 mM. After plating, 12 resistant mutants were isolated, with four (Alu9, Alu10, Alu11, Alu12) showing high aluminum resistance. Spot assay and Most Probable Number (MPN) methods confirmed their resistance, and their genetic stability was verified. Cross-resistance tests against various stressors such as lithium chloride, gallium nitrate, ethanol, and silver nitrate were also performed, as described previously (Durmuş-İşleyen, 2015).

DNA Isolation and Whole Genome Sequencing: Yeast cells (the reference strain 905 and the highly aluminum-resistant and genetically stable evolved strain Alu10) were cultured overnight in YMM. Genomic DNA was extracted using the MasterPure DNA Purification Kit (Epicentre) and evaluated using a NanoDrop 2000

spectrophotometer. Whole genome sequencing was conducted using the Illumina NextSeq 550 platform at Gen ERA Diagnostics Laboratory.

Bioinformatics Analysis: The Galaxy Europe platform facilitated sequence data processing. Quality control (using FastQC software), trimming (using Trimmomatic software), genome mapping (BWA-MEM), and variant calling (DeepVariant, BCFtools) steps were performed, as described previously (Demir-Yılmaz et al., 2025). BAM files were visualized using Golden Helix Genome Browser to assess mutation types and genomic positions. VCF filtering was used to isolate strain-specific variants for further analysis.

Data Annotation and Functional Analysis: Mutations specific to the evolved strain Alu10 were classified using the Microsoft Excel software. The Ensembl Fungi Variant Effect Predictor (VEP) tool annotated genetic variants, focusing on EMS-induced point mutations, predominantly missense mutations. The Saccharomyces Genome Database (SGD) was used to investigate phenotypic effects and functional consequences of identified mutations. Cross-referencing with external databases was used for the evaluation of aluminum resistance-related genetic modifications.

Findings

The comparative genomic analysis between the reference strain and the aluminum-resistant evolved strain Alu10 revealed specific genetic alterations associated with the Alu10 strain. When compared to the reference strain, Alu10 exhibited 69 unique genetic variants. Out of a total of 69 observed variants, 67 were GC to AT transitions, a mutation type commonly induced by ethyl methane sulfonate (EMS). These variants were further analyzed using the Ensembl Fungi Portal to assess their functional consequences.

The Variant Effect Predictor (VEP) analysis identified 345 variant consequences specific to the Alu10 strain. Among the coding consequences:

- 70% were missense variants
- 24% were synonymous variants
- 4% were stop-gained mutations
- 2% were start-loss mutations

Missense variants, which result in amino acid substitutions, were the most prevalent. These substitutions are of particular interest as they can impact protein function. Stop-gained and start-loss mutations, though less frequent, may have significant effects by truncating proteins or preventing translation initiation, potentially altering gene expression and cellular function.

Given the known mutagenic properties of EMS, the focus was placed on missense mutations for further analysis. To determine the functional relevance of these variants, the Saccharomyces Genome Database (SGD) was utilized to assess their potential roles in gene function, protein interactions, and cellular pathways.

From this analysis, several genes with mutations were identified as potential contributors to aluminum resistance due to their involvement in oxidative stress and cellular response pathways. The following genes were selected as potential contributors to aluminum resistance:

Oxidative Stress Response:

- *MSH6*: DNA mismatch repair of oxidative lesions
- *ADR1*: Transcriptional activator of antioxidant genes
- *BMH1:* Stress signaling regulator
- *BRO1*: Vacuolar metal detoxification

Cell Wall/Membrane Integrity:

- *BEM2:* Rho1-PKC1 cell integrity pathway
- *IPT1:* Sphingolipid biosynthesis

Metal Ion Homeostasis:

- *PMR1:* Golgi ion transporter (direct Al^{3+} resistance evidence)

Chemical Stress Adaptation:

- *MDS3, PCL8, SRL4:* Stress-responsive regulators

These findings suggest that specific genetic variants within these genes may contribute to the Alu10 strain's enhanced aluminum resistance. The integration of VEP results with functional genomic databases has provided a strong foundation for identifying candidate genes for experimental validation and further research into the mechanisms underlying aluminum resistance in yeast.

Conclusion

Understanding microbial aluminum resistance is critical for industrial and environmental applications. This study explored the molecular mechanisms of aluminum resistance in *Saccharomyces cerevisiae* by analyzing the evolved Alu10 strain. Through comparative genomics, key mutations in genes like *PMR1*, *BEM2*, *MDS3*, *PCL8*, and *SRL4* were identified, linking aluminum tolerance to enhanced cell wall integrity, ion detoxification, stress signaling, and DNA repair. Additional genes (*IPT1*, *MSH6*, *BMH1*, *BRO1* and *ADR1*) further supported resistance via oxidative defense, vacuolar function, and sphingolipid metabolism. The findings reveal a multifactorial adaptation strategy, offering insights for industrial biotechnology (e.g., robust yeast strains) and bioremediation. Future work should validate these targets experimentally. This research highlights the power of evolutionary engineering combined with genomics to decode complex stress resistances.

References

Çakar, Z. P., Turanlı-Yıldız, B., Alkım, C., & Yılmaz, Ü. (2011). Evolutionary engineering of saccharomyces cerevisiae for improved industrially important properties. *FEMS Yeast Research*, *12*(2), 171–182. https://doi.org/10.1111/j.1567-1364.2011.00775.x.

Demir-Yılmaz, F., Arslan, M., Holyavkin, C., Topaloğlu, A., Kısakesen, H. İ., Sürmeli, Y., & Çakar, Z. P. (2025). Molecular characterization of propolis-resistant saccharomyces cerevisiae obtained by evolutionary engineering. *Fermentation*, *11*(2), 47. https://doi.org/10.3390/fermentation11020047.

Durmuş-İşleyen, N. (2015). Inverse metabolic engineering of aluminium-resistant *Saccharomyces cerevisiae*. *M.Sc. Thesis*, Istanbul Technical University, Graduate School of Science Engineering and Technology.

Kakimoto, M., Kobayashi, A., Fukuda, R., Ono, Y., Ohta, A., & Yoshimura, E. (2005). Genome-wide screening of aluminum tolerance in saccharomyces cerevisiae. *BioMetals*, *18*(5), 467–474. https://doi.org/10.1007/s10534-005-4663-0.

Parapouli, M., Vasileiadi, A., Afendra, A.-S., & Hatziloukas, E. (2020). saccharomyces cerevisiae and its industrial applications. *AIMS Microbiology*, *6*(1), 1–32. https://doi.org/10.3934/microbiol.2020001.

Vanderwaeren, L., Dok, R., Voordeckers, K., Nuyts, S., & Verstrepen, K. J. (2022). Saccharomyces cerevisiae as a model system for eukaryotic cell biology, from cell cycle control to DNA damage response. *International Journal of Molecular Sciences*, *23*(19), 11665. https://doi.org/10.3390/ijms231911665

Walker, G. M. (2009). Yeasts. *Encyclopedia of Microbiology*, 478–491. https://doi.org/10.1016/b978-012373944-5.00335-7.

Walton, J. R. (2013). Aluminum involvement in the progression of alzheimer's disease. *Journal of Alzheimer's Disease*, *35*(1), 7–43. https://doi.org/10.3233/jad-121909.

MOLECULAR BIOLOGY - GENETICS AND BIOTECHNOLOGY

Bioimaging

Drug and Vaccine Development

Metabolic and Evolutionary Engineering

Metagenomics and Protein Engineering

Microbial Biotechnology and Genetics

Nanobiotechnology

Saccharomyces cerevisiae-Based Silver Nanoparticle Biosynthesis

Ayşenur Kalfa[a], Alican Topaloğlu[a,b,c], Zeynep Petek Çakar[a,b,c], Abdulhalim Kılıç[a,b,c]

[a]Istanbul Technical University, Graduate School, Molecular Biology - Genetics and Biotechnology Program, Türkiye
[b]Istanbul Technical University, Faculty of Science and Letters, Department of Molecular Biology and Genetics, Türkiye
[c]Istanbul Technical University, Dr. Orhan Öcalgiray Molecular Biology, Biotechnology and Genetics Research Center (ITU-MOBGAM), Türkiye
kalfaa18@itu.edu.tr

Keywords: *Saccharomyces Cerevisiae*, Silver Nanoparticles, Green Synthesis, Biosynthesis Optimization.

Aim

Silver nanoparticles (AgNPs) have garnered extensive attention in recent years due to their distinctive physicochemical properties and broad-spectrum antimicrobial activity. These nanostructures possess unique optical, electrical, and thermal characteristics that make them particularly valuable in biomedical, environmental, and industrial applications. Their utility spans a wide range of sectors, including drug delivery, diagnostic imaging, water purification, textile engineering, and food packaging (Rai et al., 2014; Ahmed et al., 2016). However, the conventional methods for synthesizing AgNPs typically rely on chemical and physical processes, which often involve toxic chemicals, high temperatures, and non-renewable energy sources. Such drawbacks pose significant environmental and safety concerns, thereby creating a demand for greener, more sustainable alternatives (Iravani, 2011). In this context, biological or green synthesis has emerged as an eco-friendly and cost-effective method for nanoparticle production. Among biological systems, microorganisms such as bacteria, fungi, and yeast have demonstrated considerable potential in nanoparticle biosynthesis. These organisms can reduce metal ions to their corresponding nanoparticles through enzymatic and non-enzymatic mechanisms. The advantages of microbial synthesis include scalability, low toxicity, mild reaction conditions, and the possibility of precise control over particle size and morphology (Durán et al., 2011; Singh et al., 2015). Among the diverse microbial agents, *Saccharomyces cerevisiae*, commonly known as baker's yeast, represents a promising platform for nanoparticle biosynthesis due to its well-established genetic background, biosafety (GRAS status), and ability to tolerate and interact with metal ions. S. cerevisiae is a eukaryotic model organism that has been widely used in biotechnology, particularly in the production of ethanol, enzymes, and biopharmaceuticals. Its cell wall, composed of polysaccharides and proteins with functional groups such as hydroxyl, amino, and carboxyl moieties, provides a reactive interface for metal ion binding and reduction. Moreover, its intracellular enzymes and metabolites can facilitate the bioreduction of silver ions (Ag^{+}) to elemental silver (Ag^{0}), enabling the formation of stable AgNPs (Bhainsa & D'Souza, 2006; Shahzad et al., 2019).

This study investigates the biosynthetic potential of *S. cerevisiae* for AgNP production under varying experimental conditions, specifically focusing on the influence of yeast cell density and silver nitrate ($AgNO_3$) concentration. The aim was to optimize these parameters to achieve efficient, rapid, and reproducible nanoparticle formation, thereby enhancing the feasibility of yeast-mediated nanoparticle synthesis for practical applications.

Material and Method

S. cerevisiae cells were initially grown in yeast extract peptone dextrose (YPD) medium at 30°C for 18 hours with constant shaking. Then, cells were harvested by centrifugation and washed a few times with sterile deionized water to remove any residual media components that might interfere with nanoparticle formation. Firstly, a set of yeast suspensions were prepared at varying concentrations to assess the effect of cell density on AgNP formation. The washed cells were resuspended in deionized water to achieve different optical densities (OD_{600}) ranging from 0.5 to 5.0, with increments of 0.5. Each suspension (1.5 mL) was transferred into a sterile 2 mL microcentrifuge tube. $AgNO_3$ was added to each tube to a final concentration of 1 mM. To evaluate the impact of $AgNO_3$ concentration,

a separate set of yeast suspensions at a fixed OD_{600} of 2.0 was prepared, and varying concentrations of $AgNO_3$ were added (0.5–5 mM, in 0.5 mM increments). In both experimental sets, 50 mM $AgNO_3$ freshly prepared in deionized water was used. The tubes were incubated in the dark at 30°C for 72 hours to minimize photo-induced reactions. The formation of silver nanoparticles was detected by using a microplate reader, measuring absorbance in the range of 300–700 nm. The presence of a characteristic surface plasmon resonance (SPR) peak around 420–450 nm confirmed the synthesis of AgNPs (Song & Kim, 2009).

Findings

The biosynthesis of AgNPs was found to be significantly influenced by the density of *S. cerevisiae* cells. The most efficient nanoparticle formation, characterized by a strong SPR peak at ~430 nm was observed at an OD_{600} of 2.0. Lower cell densities resulted in weaker SPR signals, likely due to insufficient reducing agents or reactive groups to convert silver ions effectively. Conversely, at higher cell densities, a decline in nanoparticle yield was noted, possibly due to aggregation of particles or metabolic inhibition caused by overaccumulation of silver ions (Gurunathan et al., 2009). These findings highlight the importance of maintaining an optimal biomass concentration to ensure efficient nanoparticle biosynthesis. Varying the concentration of $AgNO_3$ revealed that 1 mM was optimal for AgNP synthesis at OD_{600} = 2.0. At lower concentrations, AgNP formation was slow and incomplete, indicating a threshold concentration is necessary to drive the reduction process. High $AgNO_3$ concentration beyond a limit led to diminished nanoparticle production, possibly due to the cytotoxic effects of silver ions, which interfere with yeast metabolism and viability (Khan et al., 2017). Time-course analysis demonstrated that most nanoparticle synthesis occurred within the first 24 hours of incubation. Absorbance values generally peaked at 24 or 48 hours and plateaued or slightly decreased by 72 hours, indicating a saturation point beyond which no significant synthesis occurred. This observation aligns with previous studies that suggest AgNP formation is typically a rapid process in microbial systems (Ghaffari-Moghaddam & Hadi-Dabanlou, 2014). Extended incubation periods may also promote agglomeration or oxidative dissolution of nanoparticles. The biosynthesis of AgNPs by *S. cerevisiae* likely involves multiple mechanisms. Extracellular enzymes such as reductases may play a role in reducing Ag^+ to Ag^0, while functional groups on the yeast cell surface bind and nucleate the formation of nanoparticles (Kumar et al., 2007). Glutathione, a key antioxidant present in yeast, has also been implicated in redox processes involved in nanoparticle synthesis. The resulting nanoparticles are often stabilized by capping agents derived from cellular proteins or polysaccharides, which prevent aggregation and improve colloidal stability. The interplay between cell wall chemistry, metabolic activity, and environmental conditions determines the size, shape, and dispersion of the synthesized nanoparticles. Understanding and optimizing these variables can lead to more uniform nanoparticle characteristics, which is critical for applications in biomedicine where particle size directly influences cellular uptake and cytotoxicity (Singh et al., 2015).

Conclusion

In conclusion, *Saccharomyces cerevisiae* represents a promising green nanofactory for the synthesis of silver nanoparticles. Our findings demonstrate that both yeast cell density and silver nitrate concentration are critical factors influencing the efficiency of AgNP biosynthesis. Optimal nanoparticle formation was achieved at an OD_{600} of 2.0 and 1 mM $AgNO_3$ concentration after 24 hours of incubation. These results contribute valuable insights into the development of sustainable microbial synthesis protocols and lay the groundwork for further research into the mechanistic and functional properties of biologically synthesized AgNPs. Future works can be done to determine detailed physicochemical characteristics of the synthesized nanoparticles using electron microscopy (TEM/SEM), zeta potential analysis, and X-ray diffraction (XRD).

Acknowledgments

This study was supported by the Scientific Research Projects Commission of Istanbul Technical University (Grant no: TYL-2025-46727).

References

Ahmed, S., Ahmad, M., Swami, B. L., & Ikram, S. (2016). A review on plants extract mediated synthesis of silver nanoparticles for antimicrobial applications: A green expertise. *Journal of Advanced Research, 7*(1), 17–28.
Bhainsa, K. C., & D'Souza, S. F. (2006). Extracellular biosynthesis of silver nanoparticles using the fungus Aspergillus fumigatus. *Colloids and Surfaces B: Biointerfaces, 47*(2), 160–164.
Durán, N., Marcato, P. D., De Souza, G. I. H., Alves, O. L., & Esposito, E. (2011). Mechanistic aspects of biosynthesis of silver nanoparticles by several Fusarium oxysporum strains. Journal of Nanobiotechnology, 9(1), 1–8.
Ghaffari-Moghaddam, M., & Hadi-Dabanlou, R. (2014). Plant mediated green synthesis and antibacterial activity of silver nanoparticles using Crataegus douglasii fruit extract. *Journal of Industrial and Engineering Chemistry, 20*(2), 739–744.
Gurunathan, S., Kalishwaralal, K., Vaidyanathan, R., Venkataraman, D., Pandian, S. R. K., Muniyandi, J., ... & Eom, S. H. (2009). Biosynthesis, purification and characterization of silver nanoparticles using Escherichia coli. *Colloids and Surfaces B: Biointerfaces, 74*(1), 328–335.
Iravani, S. (2011). Green synthesis of metal nanoparticles using plants. Green Chemistry, 13(10), 2638–2650.
Khan, S. A., Shahid, S., & Khan, M. (2017). Green synthesis of silver nanoparticles using plant extracts and their antimicrobial activities: A review. *Green and Sustainable Chemistry, 7*(1), 34–56.
Kumar, V., Yadav, S. K., & Yadav, S. C. (2007). Biodegradable nanoparticles synthesized using plant extracts. *Journal of Biomedical Nanotechnology, 3*(3), 190–197.
Rai, M., Yadav, A., & Gade, A. (2014). Silver nanoparticles as a new generation of antimicrobials. *Biotechnology Advances, 27*(1), 76–83.
Shahzad, A., Khan, M. I., Ahmad, T., & Mushtaq, M. (2019). Biological synthesis of metallic nanoparticles using yeast and their applications. *Micron, 124*, 102681.
Singh, P., Kim, Y. J., Zhang, D., & Yang, D. C. (2015). Biological synthesis of nanoparticles from plants and microorganisms. *Trends in Biotechnology, 34*(7), 588–599.
Song, J. Y., & Kim, B. S. (2009). Rapid biological synthesis of silver nanoparticles using plant leaf extracts. *Bioprocess and Biosystems Engineering, 32*(1), 79–84.

Production of Silver Nanoparticles by Green Synthesis

Ekin Deren Gürtekin[a,c], Abdulhalim Kılıç[a,b]

[a] Istanbul Technical University, Graduate School, Molecular Biology - Genetics and Biotechnology Program, Turkiye

[b] Istanbul Technical University, Faculty of Science and Letters, Department of Molecular Biology and Genetics, Turkiye

[c]Istanbul Technical University, Dr. Orhan Öcalgiray Molecular Biology, Biotechnology and Genetics Research Center (ITU-MOBGAM)

gurtekin23@itu.edu.tr, kilicabd@itu.edu.tr

Keywords: Silver Nanoparticles, Green Synthesis, Antimicrobial Activity, Nanobiotechnology.

Aim

The aim of this project is to systematically investigate the green synthesis of silver nanoparticles (AgNPs) using cinnamon (Cinnamomum zeylanicum), hibiscus (Hibiscus sabdariffa), and green tea (Camellia sinensis) extracts and to evaluate the antimicrobial potential of the synthesized AgNPs. By comparing the reduction and stabilization capacities of these plant extracts, the project seeks to optimize the synthesis parameters, including silver ion concentration and extract type, to obtain the most efficient and stable AgNPs. Furthermore, the study aims to characterize the synthesized AgNPs in terms of size, shape, crystal structure, and surface properties, while assessing their antimicrobial activities against various bacterial strains, including Escherichia coli, Staphylococcus aureus, and Pseudomonas aeruginosa. The project also aims to explore the unique antimicrobial mechanisms of cinnamon AgNPs, particularly those linked to cinnamaldehyde, and to uncover the potential applications of cinnamon, hibiscus and green tea AgNPs in fields such as food safety, sustainable energy, wound healing, and targeted drug delivery. By addressing the gaps in the literature, the results will contribute to the development of plant-based AgNPs as novel antimicrobial agents in the fight against antimicrobial resistance.

Materials and Method

Synthesis process was started with the preparation of plant extracts. First, cinnamon, hibiscus and green tea plant extracts were prepared with the coffee grinder. Solutions of the extract were obtained by mixing the powdered forms of the extracts with distilled water at the specified temperatures and times. Cinnamon was mixed at 100° for 20 minutes; hibiscus and green tea were mixed at 60° for 20 minutes. After that, they were sterilized by filtering with filtration papers and stored at +4°C for use.

Silver nitrate ($AgNO_3$) solutions were prepared at different concentrations (5 mM and 10 mM) for making the synthesis of silver nanoparticles. Extracts from plants and $AgNO_3$ solutions were reacted at the specified temperatures and times in the specified ratios of 1:5 and 1:10 plant solution-silver nitrate. To synthesize the cinnamon-AgNps 90° for an hour was selected. For hibiscus and green tea process were done at 70° for 2 hours. Then, the extracts waited for 24 hours in a dark room. After the waiting process; the progress of the reaction was followed by color change and UV-Vis spectroscopy. The obtained AgNPs were purified again by passing through filtration paper. Then dialysis processes were done to make more stable AgNPs. Measurements were taken for plant extract, silver nanoparticles without dialysis, and silver nanoparticles after the dialysis with UV-Vis. With this application, the purity of the silver nanoparticles was checked. Finally, the antimicrobial activity of the synthesized AgNPs will be evaluated against Escherichia coli bacteria by disk diffusion method, minimum inhibitory concentration (MIC) and minimum bactericidal concentration (MBC) tests. As a result of the antimicrobial tests, the activities of AgNPs synthesized from different plant extracts will be compared.

To control the optical properties and surface plasmon resonance (SPR) peak of the AgNP's UV-Vis spectroscopy is used. Also, to check whether the purification process was successful, SDS-Page method was used. To check the functional groups inside the silver nanoparticles which synthesized from plant extracts, FTIR process was done.

However, there are other techniques and analysis methods that will be planned to be used in this study for the characterization and optimization of the synthesized nanoparticles. The XRD analysis will be used to determine the crystal structure of the nanoparticles. SEM (Scanning Electron Microscope) imaging will be performed to examine the morphology and size distribution of AgNPs (Ahmad et al., 2023). DLS (Dynamic Light Scattering) analysis will be applied to determine the hydrodynamic diameter and stability of the nanoparticles.

Findings

Green synthesis of silver nanoparticles was successfully conducted using cinnamon, hibiscus, and green tea extracts. UV-Vis spectroscopy confirmed silver nanoparticle formation, with 1:5 and 1:10 $AgNO_3$ ratios. Dialysis improved nanoparticle purification, sharpening UV-Vis absorption peaks. After the measurement was taken with UV-VIS and the production of silver nanoparticles was proven, the SDS-Page process was performed for the dialyzed silver nanoparticles. The purpose of this process was to see if the plant extract still remained after dialysis. For every solution, 1:5 and 1:10 ratios' dialysis results are used respectively. No protein from the plant extracts was observed in the SDS-Page result. This shows that the filtration processes were successful. FTIR analyses demonstrate the presence of functional groups on the surface of silver nanoparticles synthesized using Hibiscus, Cinnamon, and Green Tea extracts. The observed –OH, C=O, C–O, and C–N bands indicate that phytochemicals in the extracts acted as reducing and stabilizing agents. Signals detected in the 500–600 cm^{-1} region suggest possible Ag–O or Ag–N bonding on the nanoparticle surfaces

To see the antimicrobial activity of AgNPs Agar Diffusion Test is going to be done with Escherichia coli, Staphylococcus aureus, and Pseudomonas aeruginosa. For characterizing the produced AgNPs; DLS, XRD, SEM tests are also going to be done.

Conclusion

To make a sum up; in this research the aimed silver nanoparticles (AgNPs) were victoriously produced with the use of plant-based extracts from cinnamon, hibiscus, and green tea. Plant-based extracts help to force an eco-friendly green synthesis method. The green synthesis technique escapes the apply of detrimental and hazardous chemicals by depending on organic reducing and stabilizing agents inherent in plant materials (Gudikandula & Charya Maringanti, 2016). The production of AgNPs was established through UV-Vis spectroscopy analysis, where sharp and unique absorption peaks were marked. These results specified that the great fabrication of nanoparticles. Between the three distinct plant extracts chosed in the fabrication of AgNp operation, green tea extract manufactured the nanoparticles with the highest absorbance numbers, proposing that green tea is especially effective in assist the nanoparticle formation.

This study contributes to the area of sustainable nanotechnology by focusing the attention on the utilize of organic resources in nanoparticle production. With the replacement of hazardous chemicals with plant extracts, the technique transforms both safer and more environmentally production (Nasrollahzadeh et al., 2019). More extensive characterization researches utilizing methods such as Dynamic Light Scattering (DLS), X-ray Diffraction (XRD), and Scanning Electron Microscope (SEM) are designed to superior acknowledge the size, shape, and morphology of the produced silver nanoparticles. Later researches will also goal to optimize manufacturing factors and evaluate the antimicrobial effects of these nanoparticles operating the agar diffusion technique. With this research study silver nanoparticles' implementations in the different industries, such as biomedical devices, wound healing and drug delivery applications may be explored in depth (Sahu et al., 2021). Some agricultral and food packaging applications can be done with antimicrobial coating (Herrera-Rivera et al., 2024; RL Manjunatha et al., 2019). In addition, bioenergy production can be done with the nanotechnological processes because of the nanomaterial's specific qualities such as higher surface area and catalytic properties (Kamla et al., 2021).

References

Abass Sofi, M., Sunitha, S., Ashaq Sofi, M., Khadheer Pasha, S. K., & Choi, D. (2022). An overview of antimicrobial and anticancer potential of silver nanoparticles. In *Journal of King Saud University - Science* (Vol. 34, Issue 2). Elsevier B.V. https://doi.org/10.1016/j.jksus.2021.101791.

Ahmad, A., Mushtaq, Z., Saeed, F., Afzaal, M., & Al Jbawi, E. (2023). Ultrasonic-assisted green synthesis of silver nanoparticles through cinnamon extract: biochemical, structural, and antimicrobial properties. *International Journal of Food Properties*, *26*(1), 1984–1994. https://doi.org/10.1080/10942912.2023.2238920

Gong, X., Jadhav, N. D., Lonikar, V. V., Kulkarni, A. N., Zhang, H., Sankapal, B. R., Ren, J., Xu, B. Bin, Pathan, H. M., Ma, Y., Lin, Z., Witherspoon, E., Wang, Z., & Guo, Z. (2024). An overview of green synthesized silver nanoparticles towards bioactive antibacterial, antimicrobial and antifungal applications. In *Advances in Colloid and Interface Science* (Vol. 323). Elsevier B.V. https://doi.org/10.1016/j.cis.2023.103053

Gudikandula, K., & Charya Maringanti, S. (2016). Synthesis of silver nanoparticles by chemical and biological methods and their antimicrobial properties. *Journal of Experimental Nanoscience*, *11*(9), 714–721. https://doi.org/10.1080/17458080.2016.1139196

Herrera-Rivera, M. del R., Torres-Arellanes, S. P., Cortés-Martínez, C. I., Navarro-Ibarra, D. C., Hernández-Sánchez, L., Solis-Pomar, F., Pérez-Tijerina, E., & Román-Doval, R. (2024). Nanotechnology in food packaging materials: role and application of nanoparticles. *RSC Advances*, *14*(30), 21832–21858. https://doi.org/10.1039/D4RA03711A

Kamla, M., Sushil, A., Karmal, M., Shweta, & Yadvika. (2021). Nanotechnology: A Sustainable Solution for Bioenergy and Biofuel Production. *Journal of Nanoscience and Nanotechnology*, *21*(6), 3481–3494. https://doi.org/10.1166/JNN.2021.19001

Nasrollahzadeh, M., Sajadi, S. M., Sajjadi, M., & Issaabadi, Z. (2019). An Introduction to Nanotechnology. In *Interface Science and Technology* (Vol. 28, pp. 1–27). Elsevier B.V. https://doi.org/10.1016/B978-0-12-813586-0.00001-8

RL Manjunatha, Dhananjay Naik, & KV Usharani. (2019). *Nanotechnology application in agriculture: A review*.

Sahu, T., Ratre, Y. K., Chauhan, S., Bhaskar, L. V. K. S., Nair, M. P., & Verma, H. K. (2021). Nanotechnology based drug delivery system: Current strategies and emerging therapeutic potential for medical science. In *Journal of Drug Delivery Science and Technology* (Vol. 63). Editions de Sante. https://doi.org/10.1016/j.jddst.2021.102487

Vanlalveni, C., Lallianrawna, S., Biswas, A., Selvaraj, M., Changmai, B., & Rokhum, S. L. (2021). Green synthesis of silver nanoparticles using plant extracts and their antimicrobial activities: a review of recent literature. In *RSC Advances* (Vol. 11, Issue 5, pp. 2804–2837). Royal Society of Chemistry. https://doi.org/10.1039/d0ra09941d.

NANOSCIENCE AND NANOENGINEERING

Nanoparticles

Nanotechnology for Energy Systems

Polymer and Nano Composites

A Comparative Evaluation of Copper-Based Electrocatalysts as Potential Candidates for Effective and Selective Electrochemical Conversion of CO_2

Buse Nur Şimşek[a], Mehmet Suha Yazıcı[a, b]

[1] Istanbul Technical University, Graduate School, Nanoscience and Nanoengineering, Türkiye
[2] Istanbul Technical University, Graduate School, Energy Science and Technology, Türkiye
simsekbu24@itu.edu.tr

Keywords: CO2 Reduction, Copper, Phthalocyanine.

Aim

Climate change and global warming are among the biggest problems in ensuring a sustainable world life. CO2 emissions, which increased after the industrial revolution, are one of the main reasons for these problems. For this reason, every step that will reduce emissions is important today.

Although various strategies such as carbon capture and storage have been developed on the subject, these strategies also include various disadvantages such as pollution of groundwater and leaks [1, 2]. For this reason, Electrochemical Conversion of CO2 (CO2RR) is a promising process for a carbon-neutral future. The conversion of CO2 into various liquid and gaseous products such as carbon monoxide, formic acid, ethylene, ethanol and methanol as a result of the reduction reaction not only reduces emissions but also provides economic benefits [3, 4].

CO2RR starts with the absorption of CO2 into the electrocatalysts surface. Firstly, CO2 molecules are converted into HCOO- intermediates, then CO- and H2O through some proton-electron transfers. Further reactions keep happening on the surface of catalysts to create abundant forms of atomic carbon. Controlling intermediate products is a must to control product selectivity. Common intermediate is CO- to produce various products up to C2+ hydrocarbons. Efforts are focusing on adjusting adsorption parameters and modifying surface properties to determine key intermediates like *CO, *COH, and *CH2O to achieve C2+ products [5].

Electrocatalysts are the fundamental factor of reduction selectivity and efficiency. They provide active reaction sites for the adsorption of CO2 and the desorption of the products. Vacant sites on the surface of catalysts facilitate CO2 reduction by stronger bonding [5]. Different pathways for different products require large energy input, mainly activation of CO2. For this reason, design and characterization of exceptional catalysts are one of the important topics. Copper (Cu) is known as the most effective metal catalysts for producing C2+ products with high faradaic efficiency (FE). It has negative adsorption energy for *CO, making it easier to reach a balance with hydrogenation of *CO to enhance hydrocarbon products [6].

To improve catalytic performance and faradaic efficiency of electrocatalysts, molecular catalysts are investigating in addition to bulk form of Cu. For a molecular catalyst, it is important to achieve defined structure and tunable ligands for optimizing structure to enhance catalytic activity. Copper phthalocyanine (CuPc) is one of the molecular Cu-based catalysts that is studied in the literature [7]. For instance, Wang et al. found out that CuPc exhibits good selectivity for methane production [8].

In this study, the electrochemical performances of various copper-based electrocatalysts were tested to determine the best candidate for further studies to be carried out for the electrochemical conversion of CO2.

Material and Method

Cu-foil, Cu-foam and CuPc used in the studies were purchased commercially. Tetrahydrofuran (THF, 99.9%) is used as solvent. Support materials were 300 micron stainless steel fiber, 150 micron %56 porosity titanium fiber, and 200 micron %83 porosity nickel fiber, purchased commercially.

Electrode ink is prepared by 100 mg of CuPc, 202.4 mg of Nafion, 1 ml of DI water and 1399.9 mg of THF. All chemicals added in a container and mixed in an ultrasonic bath. Surface of the support materials (nickel, titanium and stainless steel) were painted. The dyed electrodes were kept at 130°C for 10 minutes, then they were cooled to room temperature and weighed. Support amounts of CuPc electrocatalysts were provided in Table 1.

Table 1. Amount of supports on copper phthalocyanines (CuPc).

Support Materials	CuPc loading (mg/cm^2)
Stainless Steel (SS)	1.3975
Titanium (Ti)	1.1488
Nickel (Ni)	1.1863

All electrochemical tests were carried out in conventional three-electrode cells using Gamry 5000 potentiostat. Cu-foam, Cu-foil, CuPc@Ni, CuPc@SS and CuPc@Ti were used as working electrodes (WE), SCE as reference electrode (RE) and Pt wire as counter electrode (CE). 0.5 M KHCO3 solution was used as electrolyte. Linear sweep voltammetry (LSV) and cyclic voltammetry (CV) tests were carried out at a scan rate of 50 mV/s in the potential range of -0.3 V to -1.3 V vs SCE. For each working electrode, the system was purged with CO2 for 30 min before starting the tests. After each test, gas purging was repeated for 5 min.

Findings

Electrochemical performance of different copper-based electrocatalysts (Cu-foam, Cu-foil, CuPc@SS, CuPc@Ti, and CuPc@Ni) were investigated using Linear Sweep Voltammetry (LSV) and Cyclic Voltammetry (CV) measurements at a scan rate of 50 mV/s within a potential range of -0.3 V to -1.3 V vs. SCE shown in Figure 1 and Figure 2, respectively.

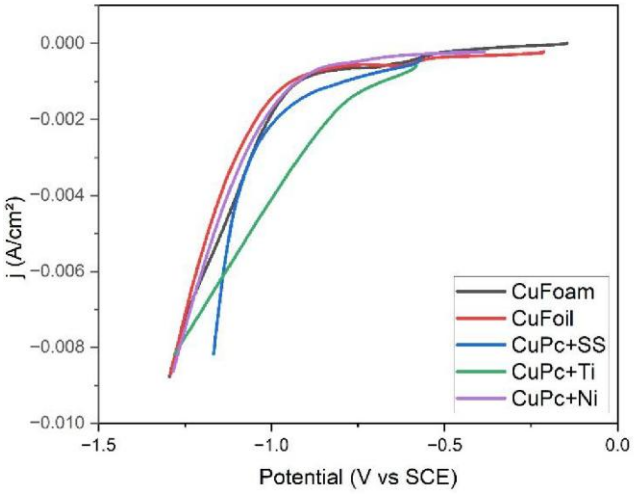

Figure 1. LSV measurements of copper-based catalysts in 0.5 M KHCO3.

As shown in Figure 1, LSV analysis exhibits that foam and foil form of Cu have similar current density trends while foam form shows slightly higher current density values in the more negative potential range (beyond -0.8 V vs. SCE). It can be a result of the porous structure of foam, which improves electrochemical activity by enhancing surface area.

The molecular catalysts, including CuPc@SS, CuPc@Ti and CuPc@Ni displayed different electrochemical behaviors than the bulk forms. While CuPc@SS showed average current densities, CuPc@Ni had the highest current density, particularly at potentials more negative than -0.8 V vs. SCE. CuPc@Ti achieved high current densities at low applied potentials, making it a highly promising candidate for further studies which will be conducted.

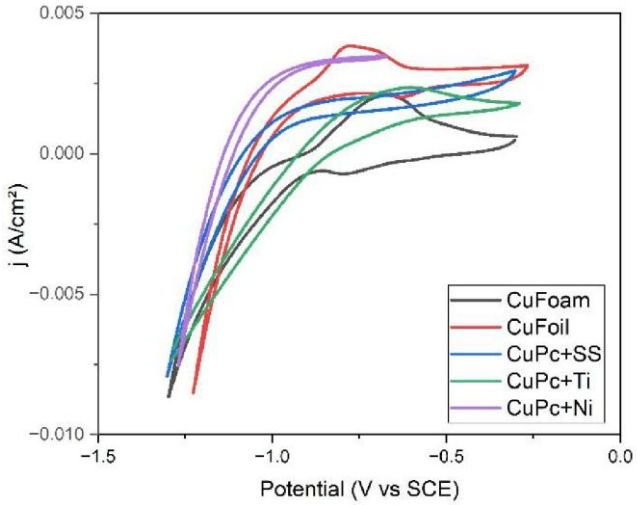

Figure 2. CV measurements of copper-based catalysts in 0.5 M KHCO3.

In Figure 2, CV measurements exhibit that Cu foam shows a superior electrocatalytic performance than foil form with relatively high current density and defined redox peaks. Among the CuPc forms, CuPc@SS and CuPc@Ni displayed less observable peaks than CuPc@Ti, which reveals their slower reaction kinetics.
In summary, CV results showed that foam and CuPc@Ti demonstrated better catalytic performance in CO2 reduction reactions by having high current densities at relatively low potentials in addition to observable well-defined reduction peaks.

Conclusion

Electrochemical performances of bulk and molecular catalysts forms of copper were evaluated by using LSV and CV measurements at 50 mV/s scan rate within -0.3 V to -1.3 V/SCE. Among the tested catalysts, Cu-foam and CuPc@Ti exhibited highest electrochemical activity at relatively low potentials and well-defined peaks in relatively low potentials, which is required for an effective CO2RR electrocatalyst. Therefore, Cu-foam and CuPc@Ti are the most promising candidates for further studies.

Acknowledgement

This study was financially supported by the Scientific and Technological Research Council of Turkey (TUBITAK) ARDEB 1001 Grant No 123M380.

References

Leung DYC et al (2014) An overview of current status of carbon dioxide capture and storage technologies. Renew Sustain Energy Rev 39:426–443. https://doi.org/10.1016/j.rser.2014.07.093
Rabiu KO et al (2020) Geoelectrical characterization of CO2–water systems in porous media: application to carbon sequestration. Environ Earth Sci 79:1–12. https://doi.org/10.1007/ s12665-020-09059-3
Sivula K (2013) Metal oxide photoelectrodes for solar fuel production, surface traps, and catalysis. J Phys Chem Lett 4:1624–1633. https://doi.org/10.1021/jz4002983
Lu X et al (2016b) Highly selective and stable reduction of CO2 to CO by a graphitic carbon nitride/carbon nanotube composite electrocatalyst. Chem A Eur J 22:11991–11996. https://doi.org/ 10.1002/chem.201601674
Kumar, A., Aeshala, L. M., & Palai, T. (2023). Electrochemical reduction of CO2 to useful fuel: Recent advances and prospects. Journal of Applied Electrochemistry, 53(7), 1295–1319.
Tabassum, H., Yang, X., Zou, R., & Wu, G. (2022). Surface engineering of Cu catalysts for electrochemical reduction of CO2 to value-added multi-carbon products. Chem Catalysis, 2(7), 1561–1593. https://doi.org/10.1016/j.checat.2022.04.012
Chen, J., Xie, W., Yang, Z., & He, L. (2024). Molecular Engineering of Copper Phthalocyanine for CO2 Electroreduction to Methane. ChemSusChem, 17(6), e202301634. https://doi.org/10.1002/cssc.202301634 **Weng,**

Z., Wu, Y., Wang, M., Jiang, J., Yang, K., Huo, S., Wang, X., Ma, Q., Brudvig, G. W., Batista, V. S., Liang, Y., Feng, Z., & Wang, H. (2018). Active sites of copper-complex catalytic materials for electrochemical carbon dioxide reduction. Nature Communications, 9(1). https://doi.org/10.1038/s41467-018-02819-7

NUCLEAR RESEARCH

Radiation Detection and Measurement

Neutron Reflection Method for Element Analysis Using GEANT4

Zehra Güzel[a]

[a] Istanbul Technical University/Energy Institute, Nuclear Researches Division, Radiation Science and Technology, Turkey
guzelz15@itu.edu.tr

Keywords: GEANT4, Neutron Reflection Method, Reflection Cross-Section, Elemental Analysis.

Aim

The study was conducted to investigate the interaction of thermal neutrons with various materials and to develop a material characterization method. The focus is on the concept of the reflection cross-section, a fundamental parameter that defines the neutron reflection properties of different substances. The neutron reflection method can be used for the non-destructive characterization of materials(Csikai & Buczkó, 1999). The aim of applying this method is to improve the analysis of compounds containing elements such as hydrogen, which are difficult to detect. Hydrogen has a high neutron scattering cross-section and a low atomic number. Detecting and quantifying this element is relatively grueling. In this study, the neutron reflection method was also employed to determine the amount of hydrogen in different hydrogen-containing compounds. It is anticipated that this approach could contribute to quality control processes, scientific research, and industrial applications. In this study, analyses were conducted in different experimental geometries and various materials using GEANT4 simulation. The simulation results were compared with experimental data from the literature. The aim of the study was to develop a method in the simulation environment that would increase the accuracy rate in determining the type and quantity of the contents of materials with unknown compositions.

Material and Method

In this study, the dimensions of the experimental setup established in the Csikai and Buczko (1998) paper were used as a reference when defining the geometry in the Geant4 (GEneration ANd Tracking) simulation program, which was employed to apply the neutron reflection method. The simulation setup includes a Pu-Be neutron source and a BF3 proportional counter to detect thermal neutrons. A moderator was used in the geometry to thermalize the neutrons before interacting with the sample, providing an optimal environment for interaction(Csikai, 2001). Polyethylene was chosen as the moderator material. In the simulation developed in Geant4, the interactions of neutrons with various materials have been modeled for this setup. A point-source, isotropic neutron source has been defined in the particle source class of the simulation. Neutrons reaching the experimental geometry from this source are tracked. Nuclear interactions were examined and analyzed using particle tracking methods. The analyses for each event were carried out with ROOT. The neutron reflection method is based on obtaining the relative neutron counting rate measured with (I) and without (I_0) the target sample present. This ratio (R) is related to the composition of the material:

$$R = \frac{(I - I_0)}{I_0} \tag{1}$$

$$R = \sigma_\beta CNd \tag{2}$$

Here, σ_β represents the reflection cross-section, C= 10^{-24} cm2, d is thickness, S is the surface area of the sample, and N is the number of atoms per cm3 (Csikai & Buczkó, 1999).The reflection cross-sections (σ) were determined based on the relationship between neutron counts obtained with the sample, considering material thickness, atomic density, and scattering properties. The neutron reflection method enabled materials to be distinguished based on the reflected neutrons. Additionally, simulations were designed for different target materials to ensure the reliability of the results. The experimental findings from the Csikai and Buczko (1998) study were compared with the simulation data. The Geant4 simulation played a critical role in optimizing the experimental design and interpreting

the neutron reflection data. Thus, performing an initial representation of any experimental setup through simulation will save time and increase accuracy.

The simulation of neutron reflection was carried out using GEANT4 to validate the experimental methodology and characterize neutron-material interactions. By simulating 14 different elements and 16 compounds, the reflection behavior under varying material compositions was analyzed. Furthermore, the average neutron reflection cross section of hydrogen was derived from the reflection cross sections of the compounds. The results were compared with experimental data to validate the approach. The GEANT4 source code includes a plutonium-beryllium source spectrum constructed with literature data, CH2 moderator, samples, and BF3 proportional counter by defining all detailed physical quantities(Figure 1). The meshbox consists of 10 bins along each axis for measuring physical quantities such as neutron flux(Figure 2). Figure 3 presents the simulation output for 50 events, showing neutrons emitted from below the cadmium material within the setup. Geometry involves defining the particle source code with parameters such as the location and type of the neutron source (e.g., angular, point, etc.), the physical parameters of the moderator materials, and the effects of changes in sample thickness on the cross-section. Figure 1 contains a visual of the 3D drawing of the GEANT4 geometry created to apply the neutron reflection method. Figure 3 is an image of 50 neutrons with an energy of 3.25 MeV scattering from the bottom of the Cadmium material. The geometry a cadmium layer around the detector to absorb thermal neutrons. These images are created by using OpenGL.

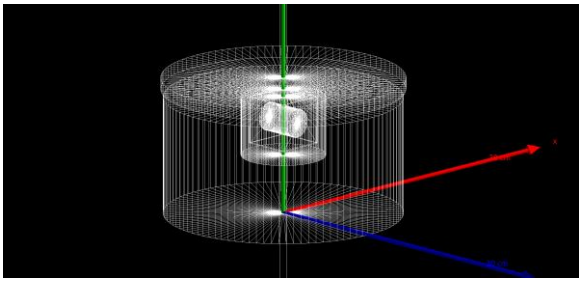

Figure 1. 3D view of the GEANT4 simulation geometry, visualized via Qt.

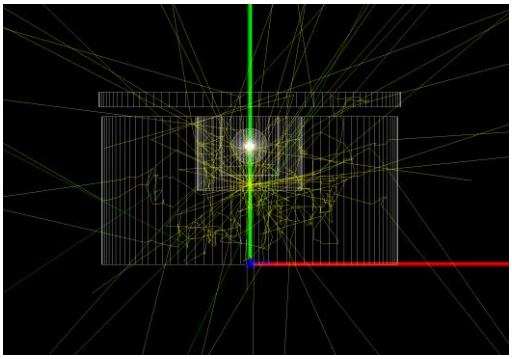

Figure 2. Visualization of the 50 events of 2.5 MeV neutron(yellow), visualized via Qt.

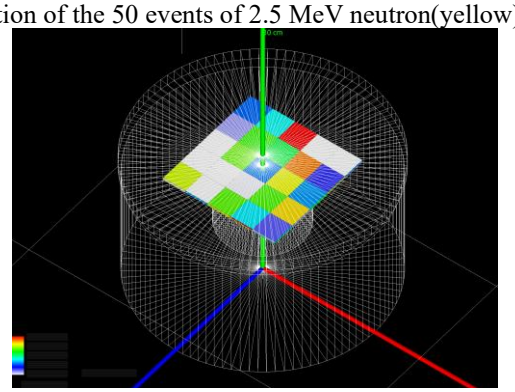

Figure 3. Scoring mesh geometry with thermal filter for counting thermal neutrons (10x10x10), visualized via Qt.

Findings

By simulating neutron reflection for various elements and compounds, the experimental approach was validated, and neutron-material interactions were effectively characterized. Geant4 simulations also allowed the determination of neutron reflection behavior under different experimental conditions, such as changes in material composition or sample geometry. The interaction of 14 different elements and 32 compounds(organics and inorganics) with thermal neutrons was observed, and the reflection behavior under varying material compositions was analyzed. The proposed methodology provided a successful framework for analyzing hydrogen content and other difficult-to-detect elements in complex matrices through Geant4 simulations. The reflection cross-sections calculated from the analyses of different compounds and elements were compared with the experimental reflection cross-section values reported in the literature. For the compounds, this comparison was first made to determine the cross-sections of their elements. The simulation results were also compared with theoretical calculations based on known neutron scattering cross-sections from nuclear data libraries. The combination of simulation and experimental data helped refine the methodology, providing a more robust foundation for future neutron reflection studies. The simulations confirmed that materials with high hydrogen content exhibited strong neutron reflection properties, while metals such as aluminum and lead showed significantly lower reflection cross-sections. To validate the simulation approach, the results were compared with experimental data, yielding a strong correlation coefficient of 0.98, which indicates high reliability(see Figure 4). In the simulation, both elements and molecules were explicitly defined as materials. For molecules, it was assumed that the cross sections are additive—i.e., the total cross section of a compound was calculated as the sum of the cross sections of its constituent elements. This approach produced consistent results, with an overall deviation of 9.09%. However, certain discrepancies were observed in specific compounds such as $Ca(OH)_2$, Fe_2O_3, and CF_2. These deviations may be attributed to uncertainties or inconsistencies in the nuclear data libraries used, or to the sensitivity of these materials to the energy range considered. The simulation exhibited higher accuracy for elemental materials, whereas systematic deviations were more pronounced in organic compounds. When investigating neutron reflection across elements from hydrogen to metals, the reflection cross-section values were found to be reliable. This Geant4 geometry, which produced consistent results, is expected to be particularly useful for evaluating hydrogen content in materials, conducting structural integrity analyses, supporting quality control applications, and detecting hidden substances in security applications. Furthermore, the methodology could be applied to quality control in material production, monitoring moisture content in geological and agricultural samples, and optimizing neutron shielding materials for nuclear reactors.

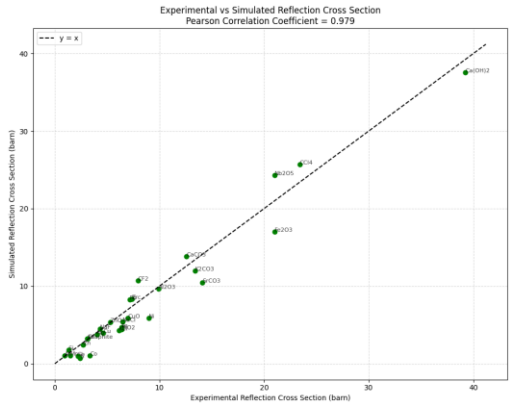

Figure 3. Simulated vs Experimental reflection cross section as a result of 10^6 events.

Conclusion

This study highlights the importance of reflection cross sections in neutron-based material analysis, especially for hydrogen detection and broader compositional studies. The integration of experimental and simulation techniques increases the reliability and applicability of neutron reflection methods. Future work will focus on improving the methodology for greater sensitivity, developing simulation models, and working on a wider range of materials, including elements with high absorption coefficients and complex composite structures.

References

Csikai, J., & Buczkó, C. M. (1999). The concept of the reflection cross section of thermal neutrons. Applied Radiation and Isotopes, 50(3), 487–490. https://doi.org/10.1016/S0969-8043(98)00077-3
Csikai, J. (2001). Handbook of Fast Neutron Generators.

PHYSICS ENGINEERING

Condensed Matter Physics

High Energy and Particle Physics

Mathematical Physics

Optics and Photonics

Two-Body Problem In a Periodic Potential with a Complex Interaction

Koray Hurma[a], Ahmet Levent Subaşı[a]

[a] Istanbul Technical University, Faculty of Science and Letters, Physics Engineering, Istanbul, Türkiye

hurma@itu.edu.tr

Keywords: Bound States, Non-Hermitian Physics, Periodic Potential, Two-Body Problem.

Aim

The formation of Cooper pairs, which are bound-states in the presence of a Fermi sea, is crucial for Bardeen-Cooper-Schrieffer type fermionic superfluidity and superconductivity. In particular, the condensed phase in the strongly interacting limit can be described by the Bose-Einstein condensation of Cooper pairs which behave like tightly-bound dimers. The behavior of such a system in the presence of a periodic potential, which can be realized in the laboratory with ultracold atomic gases in optical lattices, leads to a large effective mass among other effects. [7] The peculiar band structure of the quasiparticle energy spectrum in the lattice can reduce the effects of pair-breaking excitations. [5] Similarly, when the pairing gap is large compared to the strength of the lattice, the effects of the band structure can be suppressed which can play an important role for neutron superfluid density in the inner crust of neutron stars. [8] Therefore, the effects of the periodic potential in superfluid systems are significant for various physical systems with vast differences in their properties such as densities and absolute temperatures. In the presence of inelastic collisions, it has been suggested that the superfluidity in ultracold atoms can show reentrant behavior with increasing dissipation for weak attractive interactions and should be enhanced by dissipation due to an interplay between the BCS-BEC crossover and the quantum Zeno effect. [9] Models with non-Hermitian dynamics on the two particle problem can host bound states in continuum. [2,5,10]

The aim of this work is to investigate the simultaneous effects of a periodic potential and a complex-valued interaction for the two-body problem in a periodic potential. With the gained understanding of the bound-state formation in this problem and the established computational approach, we will be able to attack the Cooper problem in the context described above. This will improve the understanding of superfluid systems in a periodic potential with particle losses.

Material and Method

The standard approach to two-body problems is to use the so-called center-of-mass and relative coordinates instead of the individual particle coordinates. When the problem is separable, the equations decouple and the relative coordinate involving the interaction becomes effectively a one-body problem which is independent of the center-of-mass motion. However, unlike the textbook examples, the two-body problem in a periodic potential is not separable in the center-of-mass and relative coordinates. In addition, the periodic potential leads to a band structure for the one-body problem where stationary states can be labeled by their quasi-momentum k and band index n. In order to simplify the calculations, one can further make a single-band approximation where only one energy band is considered. This allows one to describe the system in terms of a tight-binding Hamiltonian where each unit cell has one orbital. Such a model is described by a hopping matrix element between nearest-neighbor unit-cells and an on-site interaction term on a lattice. The two-body problem within a single-band approximation has been studied. [4] The Cooper problem in a one-dimensional lattice has also been studied with a single band tight-binding approximation. [3] In the lattice, a center-of-mass quasi-momentum K can still be defined as a conserved quantity. It appears in the eigenvalue equation for the relative coordinate in the solution of the energy eigenstates as a constant term. This symmetry consideration leads to smaller problems for each K and all solutions can be obtained in this way avoiding the larger Hilbert space to two-particles. The interaction leads to bound states with both

repulsive and attractive interactions. In this case, the Schrödinger equation for the relative coordinate has to be solved for each value of the center-of-mass momentum.
Our numerical approach involves constructing the Hamiltonian matrix in both position and momentum bases and diagonalizing it. We consider fermionic particles in a spin singlet state so that the spatial wave functions are symmetric under the exchange of particle coordinates. Following the above references, we consider the same problem with a complex-valued interaction. The non-Hermitian Hamiltonian is studied by following the treatment in [1]. Here, we focus on the binding energy of two-particles with an attractive interaction. The complex-valued interaction models the inelastic collision with particle losses. The mechanism for non-Hermiticiy enters in the two-particle problem as opposed to non-Hermitian mechanism acting the on the single particles. [2,5,10]

Findings

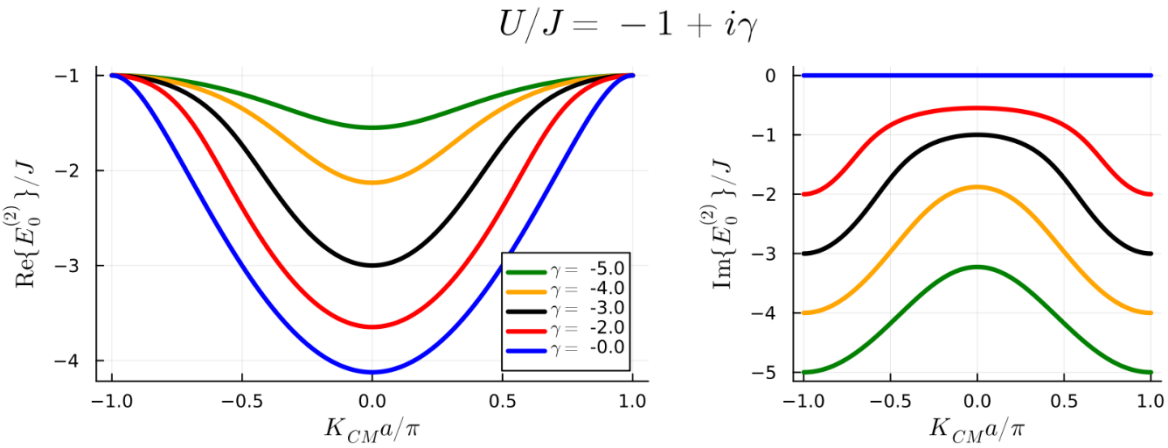

Figure 1. The real (left panel) and the imaginary (right panel) parts of the two-body ground state energies as a function of the center-of-mass momentum of the pair for different values of the collision loss rate.

We study the effects of dissipation on the binding energy as shown in Fig 1. The figure shows the bound state energy as a function of the center-of-mass quasi-momentum for a single band model. The real part of the interaction is negative for attractive interactions. The imaginary part is increased from zero and the results are shown for four non-zero values. It is seen that the global effect of the imaginary part of the interaction increases the (negative) bound state energy which thus decreases the binding energy. In addition, the imaginary part shown on the right panel implies that non-zero values correspond to a finite-lifetime for the bound state. From the shape of the three curves it is seen that the bound state with zero center-of-mass momentum has the longest lifetime and the states with maximum center-of-mass quasi-momentum have the largest decay rate for a given interaction. Finally, looking at the curvature of the real part of the bound state energy curves it is seen that the effective mass of the bound state increases with dissipation. The behavior of the dependence of these quantities on the imaginary part of the interaction is non-monotonic for weak interactions when the bound state band is partly within the continuum of extended two particle states.

Conclusion

The effects of a complex-valued interaction on the bound state energies of two-particles in a periodic potential has been studied within a single band approximation. It is found that the imaginary part of the interaction leads to lower binding energies, finite life-times and increased effective masses for the bound states. The preliminary results indicate a possible non-monotonic dependence on the imaginary part of the interaction, i.e. dissipation. We are ready to study the Cooper problem in a periodic potential with a complex-valued interaction. The inclusion of additional single-particle bands is also possible but becomes numerically more challenging as the number of single-particle bands increases.

References

Brody, D. C. (2014). Biorthogonal quantum mechanics. Journal of Physics A: Mathematical and Theoretical, 47(3):035305.

Liu, Y., & Chen, S. (2024). Fate of Two-Particle Bound States in the Continuum in Non-Hermitian Systems. *Physical Review Letters*, *133*(19), 193001.

Martikainen, J.-P. (2008). Cooper problem in a lattice. Physical Review A, 78(3):035602.

Valiente, M. and Petrosyan, D. (2008). Two-particle states in the Hubbard model. Journal of Physics B: Atomic, Molecular and Optical Physics, 41(16):161002. arXiv:0805.1812 [math-ph, physics:quant-ph].

Wang, Q., Zhu, C., Zheng, X., Xue, H., Zhang, B., & Chong, Y. D. (2023). Continuum of Bound States in a Non-Hermitian Model. *Physical Review Letters*, *130*(10), 103602.

Watanabe, G., Dalfovo, F., Pitaevskii, L. P., and Stringari, S. (2011). Effects of periodic potentials on the critical velocity of superfluid Fermi gases in the BCS-BEC crossover. Physical Review A, 83(3):033621. **Watanabe, G., Orso, G., Dalfovo, F., Pitaevskii, L. P., and Stringari, S.** (2008). Equation of state and effective mass of the unitary Fermi gas in a one-dimensional periodic potential. Physical Review A, 78(6):063619. **Watanabe, G. and Pethick, C.** (2017). Superfluid Density of Neutrons in the Inner Crust of Neutron Stars: New Life for Pulsar Glitch Models. Physical Review Letters, 119(6):062701.

Yamamoto, K., Nakagawa, M., Adachi, K., Takasan, K., Ueda, M., and Kawakami, N. (2019). Theory of non-hermitian fermionic superfluidity with a complex-valued interaction. Phys. Rev. Lett., 123:123601.

Zelenayova, M., & Bergholtz, E. J. (2024). Non-Hermitian extended midgap states and bound states in the continuum. *Applied Physics Letters*, *124*(4), 041105.

PHYSICS ENGINEERING

Condensed Matter Physics

High Energy and Particle Physics

Mathematical Physics

Optics and Photonics

Neutrino Particle Direction Estimation Using Transformer-Based Deep Learning

Şevval Coşkun[a], Emre Onur Kahya[a]

[a] Istanbul Technical University, Faculty of Science and Letters, Department of Physics Engineering, Türkiye
coskun21@itu.edu.tr

Keywords: Deep Learning, Neutrino, Transformer.

Aim

Neutrino events come from various processes, including astrophysical and atmospheric neutrinos, and, when studied scientifically, they provide valuable insights into the mechanisms that generate them. In particular, detecting and analyzing neutrinos produced by high energy cosmic phenomena, such as supernova explosions, gamma-ray bursts, and events in active galactic nuclei, offer crucial information about these extreme astrophysical processes [1]. Determining the direction of neutrino events presents a significant opportunity to investigate associated astrophysical phenomena through targeted observations rapidly. Neutrino direction estimation is fundamentally a parameter inference problem, where traditional approaches either struggle to achieve sufficient accuracy or demand significant computational resources [2]. Artificial intelligence offers promising prospects for processing complex event structures, enabling direct parameter estimation, and facilitating rapid inference. The aim of this study is to determine the direction of neutrino arrival by applying deep learning techniques to neutrino event data.

Material and Method

In this study, a Transformer-based deep learning approach is employed to estimate the direction of neutrinos. The study utilizes 117 GB of simulated neutrino event data provided within the IceCube – Neutrinos in Deep Ice competition, hosted by the IceCube Neutrino Observatory on the Kaggle platform from January 19, 2023, to April 20, 2023 [3]. The estimation process focuses on predicting the azimuth and zenith angles of neutrinos using a Transformer-based approach, drawing on the architecture first introduced in the 2017 paper "Attention Is All You Need"[4]. By leveraging the capabilities of deep learning, this study aims to enhance the accuracy of neutrino direction estimation while improving computational efficiency. The IceCube detector at the IceCube Neutrino Observatory is a cubic detection system consisting of a total of 5160 Digital Optical Modules (DOMs) installed in 86 boreholes drilled 2.5 km deep at the South Pole [5]. These DOMs detect the Cherenkov radiation caused by neutrinos, convert it into digital signals, and generate the dataset. The dataset used in the study consists of simulated data generated in parallel with the real data and consists of a train folder with a total of 660 Parquet files named in batch_id format, a sensor_geometry file containing the locations of the sensors in the IceCube detector, and a train_meta file. Due to resource constraints, training was conducted on randomly selected subsets of the dataset using the sub-sample method. As shown in Table 1 with the shared sample data, the train folder's Parquet files contain the event_id representing each neutrino event, the time parameter indicating the relative time in nanoseconds of any neutrino pulse within the event, the sensor_id specifying which sensor the pulse hit, the pulse charge, and an auxiliary flag indicating the fully digitized state with values true or false. The sensor_geometry file, which contains example data as shown in Table 2, provides the x, y, and z coordinates in meters of the DOMs in the IceCube detector. As shown in Table 3, the train_meta file contains the batch_id values of the batch files in the train folder, event_id information, the first and last pulse indices for the respective event, and the azimuth and zenith values used to determine the direction of the neutrinos. The azimuth and zenith values are used as target variables in the training process. A classical transformer architecture was used in the study. Transformer is a deep learning model with high prediction performance despite long training times, which is preferred in many problems today [4]. Python was used as the coding language, and pytorch as the library. The computations were performed as part of a graduate student project on machines provided by the National High Performance Computing Application and Research Center (UHeM) at Istanbul Technical University, which is supported by the Presidency of the Republic of Turkey, Presidency Strategy and Budget Directorate [6]. During data preprocessing, the sensor

position values, time values, and charge values were normalized. Positional encoding was added to the input data to transfer sequential information, and padding was applied to stabilize the sequence length value. The model architecture is a 2-layer Transformer encoder. There are 4 multi-head attention mechanisms in each layer. Different experiments were conducted with various sub-set sizes, evaluating two loss functions: the classical Mean Squared Error (MSE) loss and a custom DirectionMSELoss. While the classical MSE loss computes the squared differences directly between the predicted and target values, the DirectionMSELoss first converts the azimuth and zenith angles into 3D vectors using sine and cosine functions before calculating the MSE, thereby accounting for the spherical nature of the data. The optimizer was chosen as Adam, and the learning parameter value was set to 1e-4. The data set is randomly divided into 70% train, 15% validation, and 15% test.

Table 1. Presents a sample of the parquet data structure read from the train folder.

Event_id	Sensor_id	Time	Charge	Auxiliary
1829379101	3736	6541	0.975	True
1829379101	2727	6879	1.375	True
1829379101	510	7211	1.075	True

Table 2. Presents a sample of the sensor geometry data.

Sensor_id	X	Y	Z
0	-256.14	-521.08	496.03
1	-256.14	-521.08	479.01
2	-256.14	-521.08	461.99

Table 3. Presents a sample from the train_meta parquet file.

Batch_id	Event_id	First_pulse_index	Last_pulse_index	Azimuth	Zenith
1	24	0	60	5.029555	2.087498
1	41	61	111	0.417742	1.549686
1	59	112	147	1.160466	2.401942

Findings

The model's performance was evaluated using two main metrics: the Mean Squared Error (MSE) and the R^2 score, as defined in Equation (1) and Equation (2), respectively.

$$MSE = \frac{1}{n}\sum_{i=1}^{n} \quad (y_i - \hat{y}_i)^2 \tag{1}$$

$$R^2 = 1 - \frac{\sum_{i=1}^{n} \quad (y_i - \hat{y}_i)^2}{\sum_{i=1}^{n} \quad (y_i - \bar{y}_i)^2} \tag{2}$$

In some experiments, the MSE and R^2 were computed directly from the predicted and actual values (classical MSE), while in others, the azimuth and zenith angles were first transformed into 3D vectors before calculating the MSE and R^2 (3D MSE), thereby accounting for the spherical nature of the data. The classical MSE represents the mean square of the differences between the predicted values and the actual values, whereas the 3D MSE considers the spatial orientation of the data. The R^2 score is a statistic that measures the ratio of the difference between the

model's predicted values and the actual values to the total variance in the actual data. For different experiments, the model training durations, the loss function used, batch size, number of epochs, and findings are summarized in Table 4 using abbreviations such as Exp1, Exp2, etc. Additionally, the model outputs for each experiment are visualized in 3D in Figure 1, 2, 3, 4, and 5, where the predicted and actual direction vectors are displayed, as referenced in the table.

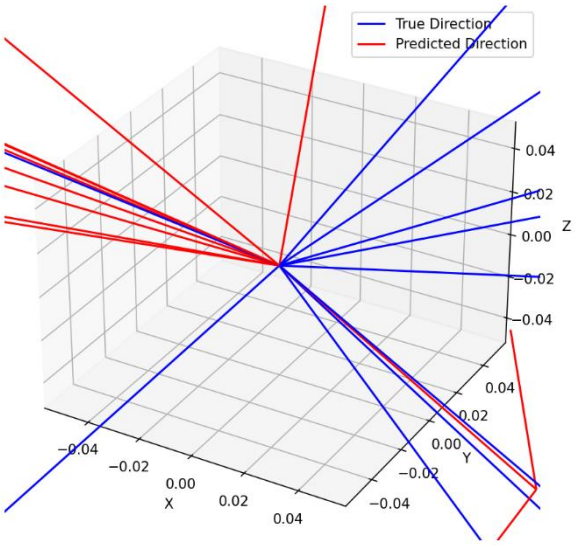

Figure 1. 3D visualization of the model outputs for Exp1, displaying the predicted and actual direction vectors.

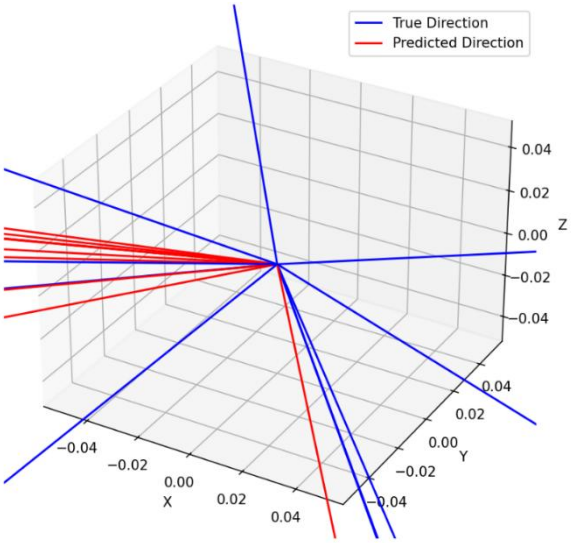

Figure 2. 3D visualization of the model outputs for Exp2, displaying the predicted and actual direction vectors.

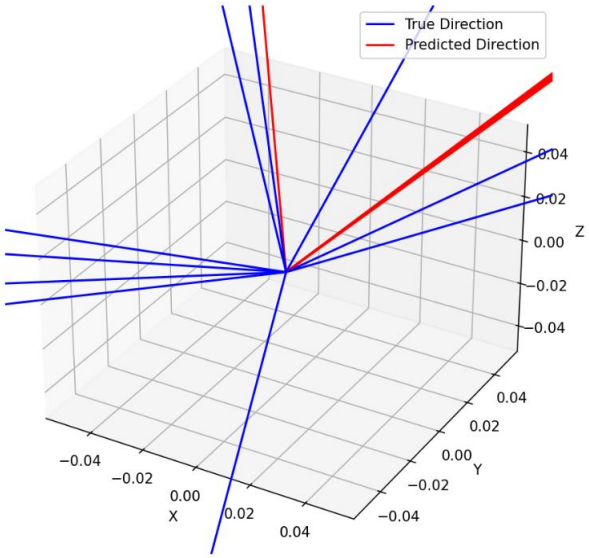

Figure 3. 3D visualization of the model outputs for Exp3, displaying the predicted and actual direction vectors.

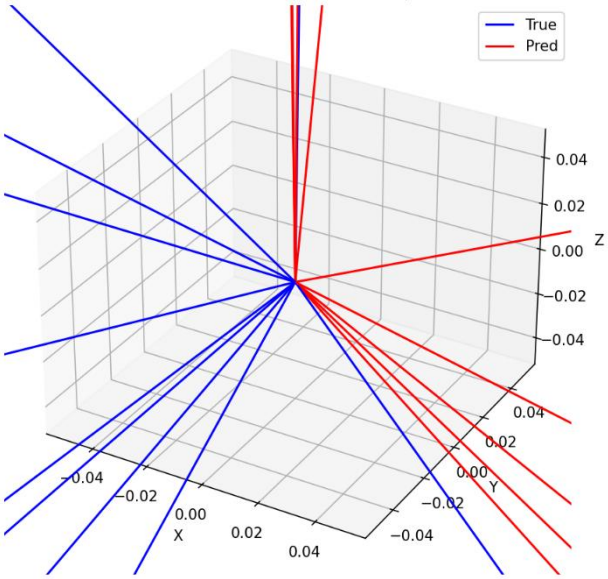

Figure 4. 3D visualization of the model outputs for Exp4, displaying the predicted and actual direction vectors.

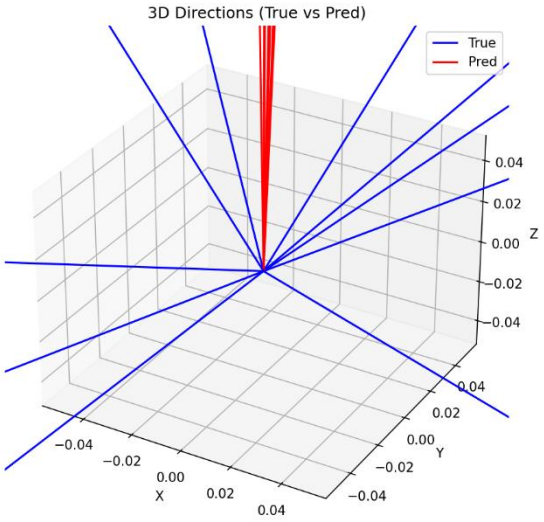

Figure 5. 3D visualization of the model outputs for Exp5, displaying the predicted and actual direction vectors.

Table 4. Results table containing various parameter values and findings.

Experiment Name	Training Duration(min.)	Average Training Loss	Batch Size	Epoch Number	Sub-Sample Size	MSE	R^2	Figure Name
Exp1	79.38	1.71 (MSELoss)	1	2	90000	1.70 (MSE)	0.32	Figure 1
Exp2	742.91	1.64 (MSELoss)	1	2	900000	1.66 (MSE)	0.34	Figure 2
Exp3	650.52	0.68(DirectionMSE Loss)	1	25	1000	0.67 (3D MSE)	-1.02	Figure 3
Exp4	804.85	0.65(DirectionMSE Loss)	1	5	1000	0.64 (3D MSE)	- 0.95	Figure 4
Exp5	742.59	0.65(DirectionMSE Loss)	1	5	1000	0.61 (3D MSE)	-0.87	Figure 5

Conclusion

In this study, a Transformer-based deep learning approach was employed to estimate neutrino directions using a simulated dataset from the IceCube – Neutrinos in Deep Ice competition. An examination of the results presented in Table 4 indicates that, in experiments Exp1 and Exp2, increasing the sub-sample size had a positive impact on the loss and evaluation metrics (MSE, R^2). However, due to resource limitations, the batch size could not be increased, leading to longer training times and higher computational costs when dealing with larger datasets. This finding highlights the importance of optimizing data loading and preprocessing strategies. Furthermore, in

experiment Exp3, Exp4, and Exp5 which utilizes a specialized loss function (DirectionMSELoss) that converts azimuth and zenith angles into 3D vectors, promising loss and MSE values were achieved even with fewer data points. Exp 4 and 5 improved the data-loading pipeline and enhanced efficiency by limiting the maximum sequence length. In Exp 5, unlike Exp 4, masking was also applied to the padding positions within each sequence in order to prevent the model from processing the padded elements, thereby aiming to improve performance. On the other hand, although R^2 showed an upward trend in Exp1 and Exp2 as the sub-sample size increased, it did not reach the expected level in Exp3, Exp4, and Exp5. This outcome underlines the need for further research and additional experiments. Overall, these findings underscore the significance of striking a careful balance between model configuration, data preprocessing, and computational resources in neutrino direction estimation. Future work will enhance preprocessing methods, explore various parameter settings, and broaden experimental conditions to achieve more robust and accurate results.

References

Niederhausen, H. (2018). Measurement of the High Energy Astrophysical Neutrino Flux Using Electron and Tau Neutrinos Observed in Four Years of IceCube Data (Doctoral dissertation). State University of New York at Stony Brook. ProQuest Dissertations & Theses, 10823307.

IceCube Collaboration (2022). Graph Neural Networks for low-energy event classification & reconstruction in IceCube, Journal of Instrumentation, 17(11), P11003.

Url-1 https://www.kaggle.com/competitions/icecube-neutrinos-in-deep-ice, date retrieved 23.03.2025.

Vaswani, A., Shazeer, N., Parmar, N., Uszkoreit, J., Jones, L., Gomez, A. N., Kaiser, Ł., & Polosukhin, I. (2017). Attention is all you need. Advances in Neural Information Processing Systems, 30, 5998–6008.

Url-2 https://icecube.wisc.edu/, date retrieved 23.03.2025.

Url-3 https://www.uhem.itu.edu.tr/, date retrieved 23.03.2025.

POLITICAL STUDIES

Political and Social Thought

Political Philosophy

Understanding Epistemic Injustice Through Speech Act Theory

Berfin Eroğlu[a]

[a] Istanbul Technical University Department of Political Studies, Political Studies Program, Türkiye
eroglub21@itu.edu.tr

Keywords: Epistemic Injustice, J. L. Austin, Miranda Fricker, Perlocutionary Silencing, Speech Act Theory.

Aim

This thesis will attempt to establish a connection between Miranda Fricker's epistemic injustice and J. L. Austin's speech act theory. Although the connection between testimonial injustice and non-assertoric speech acts has been made by David C. Spewak (2017, 2021, 2023), I wish to argue that the relationship between hermeneutical injustice and non-assertoric speech acts, especially perlocutionary acts, has been overlooked.

Material and Method

In her book titled Epistemic Injustice: Power and Ethics of Knowing (2007), Miranda Fricker formed a link between social epistemology, virtue ethics and theories of justice. She coined the key term ''epistemic injustice'' in order to illustrate how a person can be epistemically harmed in their capacity as a knower. The term has two sub-categories such as testimonial injustice and hermeneutical injustice. While the former refers to dismissed assertions, not only in testimonial exchanges but also in any sort of action involving telling, the latter is related to the inability of a speaker making themselves intelligible to a hearer due to a gap in the collective hermeneutical resources as a result of the speaker to being hermeneutically marginalised on a systematic basis and excluded from meaning-making and knowledge production process. While the large portion of the book revolves around a detailed discussion on testimonial injustice, taking precisely six chapters, the discussion about hermeneutical injustice is discussed only in the final chapter of the book. For this reason, even though the concept seems intriguing and has piqued the interest of some scholars, there seems to be a need for further exploration. Since Fricker's theory is directly related to language and epistemology, there have been attempts by some scholars such as David Spewak Jr. to correlate epistemic injustice to J. L. Austin's (Austin, 1962) speech act theory in order to gain a better insight on the practical aspect of Fricker's theory. Challenging Fricker's assumption that testimonial injustice involves only assertions, David Spewak Jr. argued that the cases of testimonial injustice are not exclusive to assertions but can also include other speech acts. In his papers, Spewak uses Austin's speech act theory as well as the notion of 'conversational scoreboard' by David Lewis (1979), which is a contextual account of meaning and reference in philosophy of language. With this notion, Lewis argues that conversational dynamics are akin to a baseball game in the sense that each move in the game is recorded, thus, the score of the game/conversation is influenced by what happens within the game/conversation.

Similar to Spewak, I will also take the Lewisian account and argue that if the aim of a conversation is to update its scoreboard by making use of shared meanings and concepts, then the speaker contributes to the conversation in order to influence the scoreboard. A similar idealisation has been made by Rae Langton and Jennifer Hornsby (Hornsby & Langton, 1998) regarding silencing, though their focus was on the illocutionary acts involving assertions. Similarly, Fricker's own notion of testimonial injustice is linked directly to assertions even though Fricker objects to Hornsby and Langton's model of silencing due to the claim that it is not a sufficient account of exploring the epistemic harm as Fricker envisages with her own theory. Correspondingly, Spewak also rejects Langton and Hornby's account on illocutionary silencing as a model to explain testimonial injustice due to his belief that it only illustrates linguistic harm and fails to offer the epistemic harms of dismissed assertions. Thus, this leads Spewak to challenge both Fricker on the grounds that testimonial injustice does not only involve assertions, but also other speech acts such as perlocutionary acts which include directives, commissives, expressives and exercitives. In Austin's theory, perlocutionary acts refer to utterances that are made to influence the hearer whereas illocutionary acts, as argued by Langton and Hornsby, are mainly related to performatives which refers to 'doing by saying' in Austinian terms. To illustrate, a speaker may promise to do a certain act and

by uttering "I promise", he/she performs the very act of promising. Other examples of performatives given by Austin are christening, apologising, warning, declaring and refusing. Thus, Langton and Hornby's model of illocutionary silencing focuses on especially the acts of refusal in the context of women's sexual encounters with men who are misled by pornography and fail to perceive the refusal of real-life women. In this case, since women's capacity as knowers is not harmed on an epistemic level, both Fricker and Spewak reject applying this model of silencing to cases of testimonial injustice.

Findings

As argued above the main difference between Fricker and Spewak is related to which speech acts they believe to be involved in cases of testimonial injustice. It is the purpose of this thesis to add another dimension to this matter and argue that although Spewak's account of non-assertoric speech acts is significant for providing a better understanding of non-assertoric cases of testimonial injustice, both Fricker and Spewak overlook the connection between perlocutionary acts and hermeneutical injustice and how those acts can provide a better understanding of testimonial injustice. For this reason, I aim to offer a theoretical contribution to the issue at hand. In order to link this to both speech act theory and epistemic injustice, I will argue that there are cases of hermeneutical injustice that do not only involve assertions and can directly lead to testimonial injustice. Even though silencing has been equated to illocutionary silencing (assertions) thus far, Spewak's concept of perlocutionary silencing is a step forward in understanding the notion of epistemic injustice. However, Spewak connects perlocutionary silencing to the cases of testimonial injustice, I will argue that perlocutionary silencing can also be connected to hermeneutical injustice which has not been thoroughly discussed by Fricker herself in terms of the speech acts it may involve. The main idea behind my thesis is that if we take the Lewisian account of conversational dynamics, then a speaker uses common meanings and concepts while engaging in a conversation with the aim of updating the scoreboard. This would require the hearer to accept the conversational moves made by the speaker to update the conversational scoreboard. This means that the speaker intends to have the perlocutionary effects on the hearer to accept the moves made. If the speaker's meaning in their utterance is not shared by the hearer, then the speaker is rendered unintelligible and is silenced by the hearer, which leads the speaker to become hermeneutically marginalised. If the speaker is hermeneutically marginalised, they cannot contribute to the meaning-making and knowledge production processes due to failing to achieve their perlocutionary goals and to update the conversational scoreboard. Thus, if there is a case of perlocutionary silencing, then hermeneutical injustice occurs. Even though this argument may seem flawed to some, I will argue that it helps explain what kind of prejudicial dynamics take place even before testimonial injustice occurs. Since conversation revolves around common concepts, the subject of hermeneutical injustice, by definition, is rendered unintelligible due to a gap in common hermeneutical resources. When this is the case, it leads to bias in understanding the subject of hermeneutical injustice in their testimonial exchanges. This means that hermeneutical injustice takes place before testimonial injustice due to the prejudice created by the assumed unintelligibility of the speaker which usually follows certain groups in other aspects of their lives.

Conclusion

As this thesis offers a sequentialist account of epistemic injustice with the integration of speech act theory, it might be argued by some readers that the link between hermeneutical injustice and perlocutionary acts seems to be based on shaky grounds in the sense that hermeneutical injustice may not involve any speech acts at all. Even though this may be a valid concern, Fricker's own gaps in the exploration of the concept and her previous adamancy on assertions in the cases of testimonial injustice point to another assertoric assumption. Furthermore, as I will argue, taking a Lewisian account would require the need for common concepts and when this account is added to Fricker's own argument that hermeneutical injustice takes place before testimonial injustice does, it creates a sequentialist account between the types of epistemic injustice. Therefore, there has to be a previous conversation between two groups/individuals involved in the conversations before testimonial injustice takes place due to identity prejudice. Since Fricker's account fails to explain how this identity prejudice is formed and leads to testimonial injustice, taking hermeneutical injustice proves useful, for in the cases of testimonial injustice that are by definition always based on identity prejudice, there is always a previous stage of hermeneutical injustice that lays the groundwork

for identity prejudice that leads to testimonial injustice. By taking hermeneutical injustice as a preliminary stage, wherein the absence of common concepts leads to the unintelligibility of the speaker and consequently perlocutionarily silencing the speaker who fails to make the conversational moves based on perlocutionary goals that require the hearer to accept the made moves and to be influenced by those moves, the subject of hermeneutical injustice becomes hermeneutically marginalised and cannot contribute to the common meaning-making and knowledge production process, thus becoming a subject of identity prejudice as someone who cannot make what they are and what they know to be heard. By following this logic, before testimonial injustice takes place due to identity prejudice, we can argue that one first becomes hermeneutically marginalised which then leads to the identity prejudice and the testimonial injustice that they face.

References

Austin, J. L. (1962). How to do things with words. Oxford university press.
Fricker, M. (2007). Epistemic injustice: Power and the ethics of knowing. OUP Oxford.
Hornsby, J., & Langton, R. (1998). Free speech and illocution. Legal Theory, 4(1), 21-37.
Lewis, D. (1979). Scorekeeping in a language game. Journal of philosophical logic, 8, 339-359.
Spewak, D. C. (2017). Understanding assertion to understand silencing: Finding an account of assertion that explains silencing arising from testimonial injustice. Episteme, 14(4), 423-440.
Spewak, D. C. (2021). Conversational epistemic injustice: Extending the insight from testimonial injustice to speech acts beyond assertion. Social Epistemology, 35(6), 593-607.
Spewak, D. C. (2023). Perlocutionary Silencing: A Linguistic Harm That Prevents Discursive Influence. Hypatia, 38(1), 86-104.

POLYMER SCIENCE AND TECHNOLOGY

Porous Materials

Material Science

Adsorption Performance of Hydrophilic PolyHIPE on Removal of Methylene Blue Dye

Bora Işılgan[a], Büşra Akın Özmen[a], Erdem Yavuz[a]

[a]Istanbul Technical University, Department of Polymer Science and Technology, Polymer Science and Technology Programme, Türkiye
isilgan23@itu.edu.tr

Keywords: Electrostatic Interaction , Emulsion Template , Langmuir Isotherms , PolyHIPE , Pseudo-Second Order Kinetic.

Aim

Methylene blue with environmentally persistent and harmful, toxic, and carcinogenic is one of the widely used cationic dyes that dyeing fabrics in textile industries and also for dyeing papers and leathers are applied in large amount as synthetic dye. That is why, leakage of methylene blue with not biodegradable into the environment as waste necessitates solutions for its removal. Adsorption process is a useful technique for elimination of dyes from wastewater. Thus, by making use of emulsion templating method, which is the polymerized of high internal phase emulsion abbreviated as polyHIPE, for synthesizing adsorbent, methylene blue has been captured from dye solution in a remarkable amount, constituted of the main reason of this study.

This work ascribed to the two properties that electrostatic interaction between methylene blue contained quaternary amine group with porous polymeric material including the potassium salt of sulfonic acid and swelling degree was assessed by terms of the two fundamental approach involved the kinetics and isotherms. The various parameters like pH, ionic strength, dye concentration and adsorbent amount on adsorption kinetics were evaluated as well.

Material and Method

Chemicals;

All starting chemicals utilized for the synthesis of adsorbent and adsorption study were used without any pre-purification. 3-Sulfopropyl methacrylate potassium salt (SPMA), N,N′-Methylene bis(acrylamide) (MBAM), potassium persulfate (KPS), N,N,N′,N′-Tetramethyl ethylenediamine, Toluene, Poly (ethylene oxide)-block-poly(propylene oxide)-block-poly(ethylene oxide), (Pluronic F-127, MW = 12,500 g/mol) provided from Sigma-Aldrich. were used for synthesis of polyhipe. Diethyl ether purchased from Sigma- Aldrich and ethanol with of analytical grade were handled for the purpose of soxhlet extraction. Methylene blue, Rodamine B and Malachite Green Carbinol supplied from Sigma- Aldrich were used to realize the adsorption process.

Synthesis of Sulfonated Based PolyHIPE;

The oil in water (o/w) emulsion composed of 80 % volume fraction oil droplets was prepared as following steps. Initially, surfactant Pluronic F-127 (1g), monomer SPMA (6,12g) cross-linker MBAM (0.154 g), the initiator KPS (0.120 g) were dissolved in water in three neck flask. After that toluene was added drop by drop in a period of two hour. An Overhead stirrer operating at 450 rpm was used to obtain a homogenous emulsion. After the addition of toluene, stable emulsion was achieved and with the addition of the catalyst TEMED(0,1ml), further mixing with approximately one minute was continued. Subsequently, the emulsion was transferred to polypropylene vial and polymerization occurred in a convection oven at 40°C for 24 h. The resulting monolith was purified via Soxhlet extraction with ethanol and diethyl ether, each for 24 h. The polyHIPE was dried under convection oven at 60°C for at least 24 h.

Characterization;

The Attenuated Total Reflectance Fourier Transform Infrared (ATR FT-IR) spectra of samples were recorded on a Thermo Scientific, Nicolet iS20 FT-IR spectrometer equipped with the Platinum diamond ATR module in the range

of 400-4000 cm-1 with a resolution of 4 cm-1.By a double beam UV−vis spectrophotometer (PerkinElmer, Lambda 25) was used to determined for dye concentrations in the adsorption experiments.

Findings

The preparation of polyHIPEs which incorporate the ionically charged functionalities along with the inherent hydrophilic properties and low crosslinking degree that contributes to the improvement of adsorption capacity by swelling in water and thus to the highly effective removal of dyes.

Adsorption Kinetics of Metyhlene Blue

All of the adsorption assays were carried out with plastic vials in magnetic bar and 500, 1000, 2000, 3000, 4000 and 5000 ppm dye solutions, i.e., approximately 7 ml, were used for kinetic experiments. The maximum adsorption capacity was reached to 1483 mg/g after 180 min. A highly efficient adsorption is reflected with in a very rapid decrease of methylene blue dye concentration in aqueous solution during the first 10 min, which is reprepented with Figure 1.

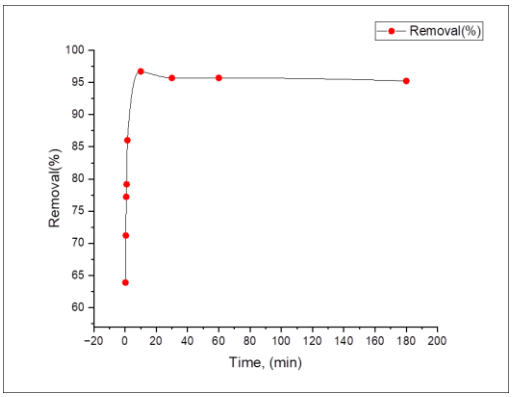

Figure 1. The removal percentage of 5000 ppm methylene blue versus time.

Adsorption kinetics and isotherms demonstrated that the hydrophilic polyHIPE is an effective adsorbent toward methylene blue. Maximum adsorption capacity of this material reached to 1483 mg/g, is intriguing value compared to other scientific articles. Another interesting point is that other cationic dyes, Malachite Green Carbinol and Rodamine B, were removed to 99,15 % and 98,35 % from 1000 ppm dye solution. Evaluating the kinetics and isotherms, as shown Table 1, Table 2 and Figure 2, Pseudo-second order kinetic and Langmuir isotherms are agreed well with experimental datasets which is situation shows that electrostatic interaction are more dominant than other intermolecular forces.

Table 1. The parameters of pseudo-first-order and second-order kinetics models for adsorption of methylene blue on adsorbents.

	First Order				Second Order		
Methylene Blue (mg/L)	$q_{eq,}exp$ (mg g^{-1})	k_1*10^2 (min^{-1})	q_e (mg g^{-1})	R^2	k_2 (g $mg^{-1}min^{-1}$)	q_e (mg g^{-1})	R^2
500 ppm	139.74	57.5	0.0982	0.3960	36.14	139.66	1
1000 ppm	279.49	110.9	2.07	0.8921	2.29	279.33	1
2000 ppm	559.03	520.2	25.17	0.9491	0.56	561.79	0.999
3000 ppm	837.32	203.7	235.18	0.9441	0.0162	862.06	0.999
4000 ppm	1115.84	146.0	503.70	0.8622	0.0063	1138.85	0.991
5000 ppm	1354.33	87.4	558.91	0.9865	0.0055	1296.84	0.997
2,5-20 ppm (ref5)	417.12	22.7	131.61	0.8327	0.0763	405.22	0.996
10 ppm (ref6)	3.66	26	1.22	0.9843	0.66803	0.461	0.999

Table 2. Isotherm parameters and correlation coefficients for hydrophilic polyHIPE.

Langmuir				Freundlich			D-R		
q_{exp} (mg g^{-1})	K_d (mg L^{-1})	q_m (mg g^{-1})	R^2	K_f (L g^{-1})	n	R^2	q_m (mg g^{-1})	E (kcal mol^{-1})	R^2
1483	0.1562	1409.39	0.999	238.82	2.36	0.7805	957.72	$7{,}16*10^{-7}$	0.899
- (ref 5)	1.40	417.12	0.998	15.62	3.108	0.913	418.17	0.8011	0.804

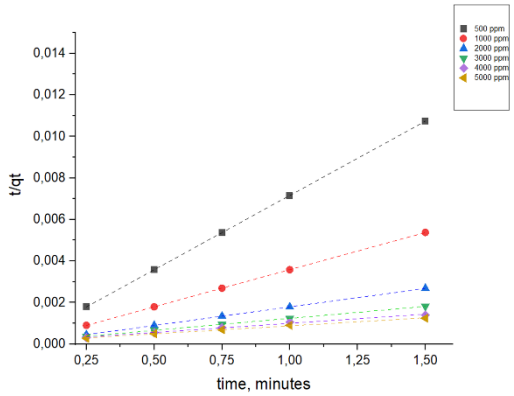

Figure 2. The pseudo-second Order kinetics for different dye concentration.

Water Uptake and Swelling Ratio

Evaluating the kinetics of water uptake, the rapid uptake reaching the equilibrium value in 20 min proved that the high degree of capillary action within the void structure and void expansion of polyHIPE is the main factor. The maximum water uptake was reached to 34,2 g. In other words, as seen in Figure 3, the adsorbent held ,approximately, 3400 percent of its own weight in water.

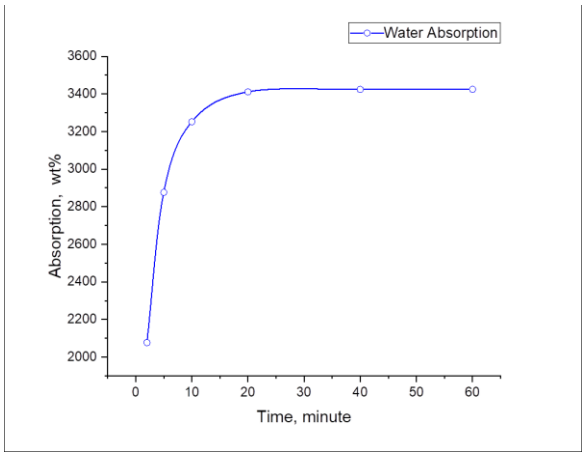

Figure 3. Variation of water absorption with time.

The equilibrium water uptake was calculated with according to the formula shown in Equation 1. The equilibrium water uptake (Ai) was obtained by placing with a known dry mass (m_D) into a sintered glass filter funnel filled with the water until a constant swollen mass (m_{SW}) was reached.

$$A_i = \frac{m_{sw} - m_D}{m_D} \quad \text{(Equation 1)}$$

The Maximum Adsorption Capacity of Adsorbent

To determine of maximum adsorption capacity of adsorbent, dye solutions prepared at various concentrations ranging from 100 ppm to 10000 ppm were adsorbed with adsorbent quantity remained constant. The results show that an adsorption capacity of 1483 mg of dye per 1 gram of adsorbent was achieved.

Demonstration of The Ionic Effect on Adsorption Capacity

The effect on adsorption capacity of ionic strength was determined with 100 ppm dye solution prepared with 0.1, 0.2 and 0.3 M sodium chloride. As can be seen from the Figure 4, the higher salt concentration found in dye solution, the lower adsorption capacity was obtained.

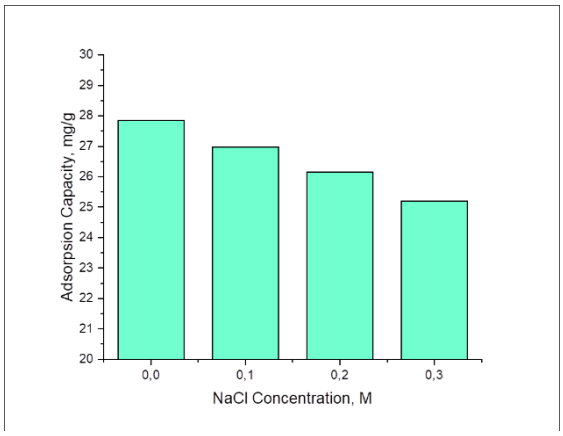

Figure 4. The ionic effect on adsorption capacity.

The Effect on Adsorption Capacity of Buffer Solution

To understand the effect of pH on the adsorption capacity, adsorption assays were taken place in acidic medium prepared with acetate buffer and basic medium obtained from phosphate buffer. As observed in Figure 5, the adsorbent is suitable for dye adsorption in a wide pH range.

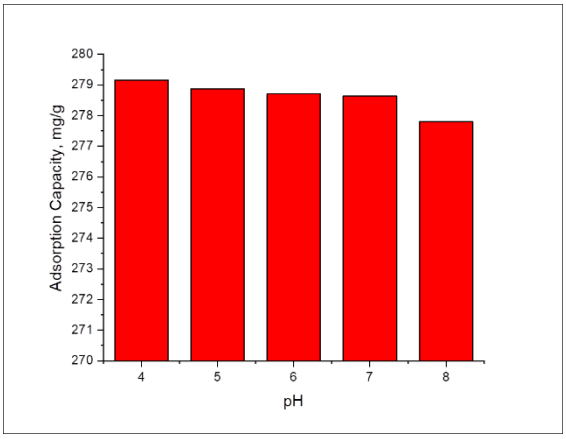

Figure 5. The effect of buffer solutions with different pH values on adsorption capacity.

Conclusion

PolyHIPE based adsorbent bearing sulfonic acid salts which imparts its hydrophilic characters possesses low-crosslinking, which made its good candidate for removing the cationic dyes.

References

Oladoye, P, O., Ajiboye, T, O., Omotola, E, O. & Oyewola, O, J. (2022). Methylene blue dye: Toxicity and potential elimination technology from wastewater, Results in Engineering, 16**,** 100678.

Kovacic, S., Drasinac, N., Pintar, A. & Zagar, E. (2018). Highly Porous Cationic Polyelectrolytes via Oil-in-Water Concentrated Emulsions: Synthesis and Adsorption Kinetic Study, Langmuir 2018, 34, 10353−10362.
Üzüm, G., Özmen, B, A., Akgül, E, T. & Yavuz, E. (2022). Emulsion-Templated Porous Polymers for Efficient Dye Removal, ACS Omega 2022, 7, 16127−16140.
Makrygianni, M., Christofili, A. and Deimede, V. (2021). Emulsion-templated macroporous ammonium based polymers: Synthesis and dye adsorption study, Colloids and Surfaces A: Physicochemical and Engineering Aspects, 610, 125634.
Choi, H-J. and Yu, S-W. (2019). Biosorption of methylene blue from aqueous solution by agricultural bioadsorbent corncob, Environmental Engineering Research, 24(1): 99-106.
Ozyaman, M, N., Cagsirli, S. and Ozudogru, Y. (2023). Adsorption and Kinetic Studies of Methylene Blue from Aqueous Solution Using Modified Spent Tea Leaves, Hittite Journal of Science and Engineering, 10 (2) 145–151.

POLYMER SCIENCE AND TECHNOLOGY

Porous Materials

Material Science

Preparation of Novel Lignin-Based Hydrogels, Properties, and Adhesive Application

Ali Asgharian[a], Öykünaz Duranlar[b], Ayda Yari-Ilkhchi[b,c], F. Seniha Güner[b,d]

[a]Istanbul Technical University, Faculty of Chemical and Metallurgical Engineering, Department of Materials Science and Engineering, Türkiye
[b]Istanbul Technical University, Faculty of Chemical and Metallurgical Engineering, Department of Chemical Engineering, Türkiye
[c]Sabanci University, Faculty of Engineering and Natural Sciences, Türkiye
[d]Sabanci University, Nanotechnology Research and Application Center (SUNUM), Türkiye
asgharian21@itu.edu.tr

Keywords: Hydrogels, Eco-Friendly Adhesives, Lignin, Polyvinyl Alcohol, Bio-Based Adhesives.

Aim

Adhesives, as an essential supplementary material in several industries, are widely used in medicine, packaging, fabrication, transportation, construction, and renewable energy. Current adhesives, due to their toxicity, negative environmental effects, and non-renewable raw ingredients, have led to attempts to synthesize environmentally friendly and renewable adhesives from bio-based materials and have attracted increasing attention (Huang et al., 2022). Lignin (Lig) is one of the most abundant renewable natural polymers on the planet(Shah et al., 2023). As the only non-petroleum source of renewable aryl compounds in nature, it is an appropriate alternative for phenol because of its phenylpropane units, which are similar to phenol(Gong et al., 2022). Because of their low manufacturing costs, biocompatibility, and biodegradability, as well as their numerous functional groups such as hydroxyl, carboxyl, and aldehyde, Lig can be cross-linked with other polymers, giving them a high potential for use in the synthesis of biodegradable hydrogels and adhesives(Kai Dan et al., 2016).

Tannic acid (TA) is a natural polyphenol, that exists in a wide variety of plants as a colorless to pale yellow solid with an astringent taste. It is also known as a main component of mussel-inspired adhesives(Trimble, 1892),(Yang et al., 2022). TA is composed of pyrogallol and catechol groups with antioxidant, antibacterial, and anti-inflammatory characteristics when interacting with other materials(Trimble, 1892). Polyvinyl alcohol (PVA) is a water-soluble, synthetic, inexpensive, and nontoxic polymer(Ben Halima, 2016). The hydroxyl groups (-OH) on the PVA can connect with multiple functional groups, leading to the formation of crosslinked and water-resistant networks with good mechanical stability(Nagarkar & Patel, 2019),(Pingan et al., 2017). Polyethyleneimine (PEI) is a positively charged hydrophilic polymer with an abundance of amine groups. This crosslinking agent creates a three-dimensional, hydrophobic structure by hydrogen bonding and electrostatic processes (Wang et al., 2022).

According to the mentioned toxicity and limitations in the adhesives sector, lignin-based hydrogels with the adhesion ability to attach to different surfaces are highly required in the modern world. For this aim, we synthesized eco-friendly bioadhesives using Lig, PVA, TA, and PEI by mixing and investigating Lig's effects on characteristics and adhesion properties in both dry and wet environments.

Material and Method

Briefly, the solution of PVA (30% w/v), TA (0.66 w/v), and Lig (15% w/v) was prepared. Then, the determined amounts of PVA, PEI, and TA were added respectively and mixed at room temperature to reach a homogenous mixture. By the addition of 0, 0.4, 0.8, and 1.6 g of Lig in the prepared compound and mixing for another 40 min, the PTPL(PVA+TA+PEI+Lig)0, PTPL0.4, PTPL0.8, and PTPL1.6 formulations were achieved, respectively.

The synthesized hydrogels were characterized by Fourier Transform Infrared (FTIR), scanning electron microscopy (SEM), contact angle, and adhesion strength tests. In order to study the adhesion strength of PTPL hydrogels, the lap shear test was performed on steel substrate under dry and wet conditions using the ASTM (F2255-05) standard method on a Devotrans tensile machine (DVT UZMK).

Findings

The obtained results displayed the successful synthesis of coacervate hydrogels. FTIR spectra indicated resulted functional groups formed through the various interactions between compounds. As shown in Figure 1, the peak at around 1700 cm^{-1} is related to the stretching vibration of aromatic C=O groups in TA, which is seen in all formulas(Mobaraki & Hemmateenejad, 2011). The asymmetric stretching bond of C-H groups of PVA can be seen at 2917cm^{-1} (Hong et al., 2018). The broad peak at 3307 cm^{-1} is attributed to O-H stretching vibrations of Lig, TA, PVA, and all formulas and hydrogen bonding (C. Chen et al., 1998). This peak overlapped with the N-H stretching vibration peak of PEI at 3277cm^{-1} in the prepared adhesives spectra (Z. Chen et al., 2020).

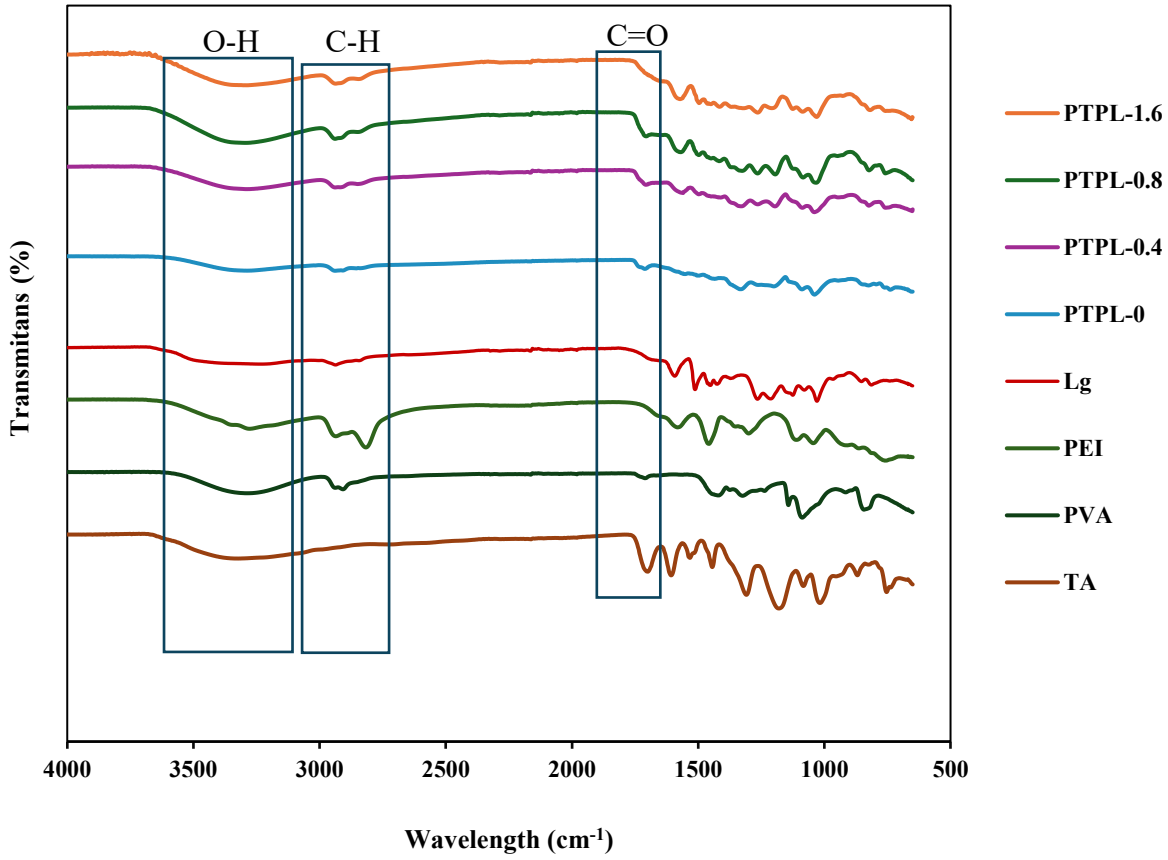

Figure1: FTIR spectra components and prepared hydrogels

The lap shear adhesion test demonstrated a remarkable enhancement in adhesion strength under both dry and wet conditions by the addition of Lig in the formulation. As we can see in Figure 2a and b, the PTPL0.8 adhesive hydrogel showed the highest amount of adhesion strength in both dry and wet conditions with 1753±417 and 2719±634 kPa, respectively, which was attributed to the increase in Lig concentration and strong crosslinking via hydrogen bonding, electrostatic, π-π, and ionic interactions (Benítez-Mateos et al., 2021)·(Xie et al., 2021)·(Qin et al., 2022).

Conclusion

In conclusion, this study successfully synthesized novel, environmentally friendly bioadhesives utilizing Lig, PVA, TA, and PEI. Considering the growing demand for eco-friendly alternatives to traditional toxic adhesives, this research explored the potential of Lig, an available and renewable resource, to enhance adhesive properties. The successful formation of coacervate hydrogels was confirmed through characterization tests, which revealed the presence of functional groups indicative of interactions between the constituent polymers. The lap shear adhesion

test findings suggest that this adhesive holds great promise in dry and underwater applications with increasing Lig concentration. Notably, the PTPL0.8 formulation exhibited the highest adhesion strength, which facilitated effective crosslinking. Future research focuses on optimizing the adhesion strength and rheological properties of lignin-based hydrogels on various substrates, wet environments with acidic and basic pHs, and long-term environmental impact assessment.

References

Ben Halima, N. (2016). Poly(vinyl alcohol): review of its promising applications and insights into biodegradation. *RSC Advances*, *6*(46), 39823–39832. https://doi.org/10.1039/C6RA05742J

Benítez-Mateos, A. I., Bertella, S., Behaghel de Bueren, J., Luterbacher, J. S., & Paradisi, F. (2021). Dual Valorization of Lignin as a Versatile and Renewable Matrix for Enzyme Immobilization and (Flow) Bioprocess Engineering. *ChemSusChem*, *14*(15), 3198–3207. https://doi.org/10.1002/cssc.202100926

Chen, C., Gao, J., & Yan, Y. (1998). Observation of the Type of Hydrogen Bonds in Coal by FTIR. *Energy & Fuels*, *12*(3), 446–449. https://doi.org/10.1021/ef970100z

Chen, Z., Lv, Z., Sun, Y., Chi, Z., & Qing, G. (2020). Recent advancements in polyethyleneimine-based materials and their biomedical, biotechnology, and biomaterial applications. *Journal of Materials Chemistry B*, *8*(15), 2951–2973. https://doi.org/10.1039/C9TB02271F

Gong, X., Meng, Y., Lu, J., Tao, Y., Cheng, Y., & Wang, H. (2022). A Review on Lignin-Based Phenolic Resin Adhesive. *Macromolecular Chemistry and Physics*, *223*(4), 2100434. https://doi.org/https://doi.org/10.1002/macp.202100434

Hong, W., Meng, M., Xie, J., Gao, D., Xian, M., Wen, S., Huang, S., & Kang, C. (2018). Properties and thermal analysis study of modified polyvinyl acetate (PVA) adhesive. *Journal of Adhesion Science and Technology*, *32*(19), 2180–2194. https://doi.org/10.1080/01694243.2018.1465687

Huang, C., Peng, Z., Li, J., Li, X., Jiang, X., & Dong, Y. (2022). Unlocking the role of lignin for preparing the lignin-based wood adhesive: A review. *Industrial Crops and Products*, *187*, 115388. https://doi.org/https://doi.org/10.1016/j.indcrop.2022.115388

Kai Dan, K. D., Tan MeinJin, T. M., Chee PeiLin, C. P., Chua YunKhim, C. Y., Yap YongLiang, Y. Y., & Loh XianJun, L. X. (2016). *Towards lignin-based functional materials in a sustainable world.*

Mobaraki, N., & Hemmateenejad, B. (2011). Structural characterization of carbonyl compounds by IR spectroscopy and chemometrics data analysis. *Chemometrics and Intelligent Laboratory Systems*, *109*(2), 171–177. https://doi.org/https://doi.org/10.1016/j.chemolab.2011.08.011

Nagarkar, R., & Patel, J. (2019). Polyvinyl alcohol: a comprehensive study. *Acta Sci. Pharm. Sci*, *3*(4), 34–44.

Pingan, H., Mengjun, J., Yanyan, Z., & Ling, H. (2017). A silica/PVA adhesive hybrid material with high transparency, thermostability and mechanical strength. *RSC Advances*, *7*(5), 2450–2459.

Qin, Z., Huang, Y., Xiao, S., Zhang, H., Lu, Y., & Xu, K. (2022). Preparation and Characterization of High Mechanical Strength Chitosan/Oxidized Tannic Acid Composite Film with Schiff Base and Hydrogen Bond Crosslinking. In *International Journal of Molecular Sciences* (Vol. 23, Issue 16). https://doi.org/10.3390/ijms23169284

Shah, S. W. A., Xu, Q., Ullah, M. W., Zahoor, Sethupathy, S., Morales, G. M., Sun, J., & Zhu, D. (2023). Lignin-based additive materials: A review of current status, challenges, and future perspectives. *Additive Manufacturing*, *74*, 103711. https://doi.org/https://doi.org/10.1016/j.addma.2023.103711

Trimble, H. (1892). *The tannins: A monograph on the history, preparation, properties, methods of estimation, and uses of the vegetable astringents, with an index to the literature of the subject* (Vol. 1). JB Lippincott Company.

Wang, N., Liu, Q., Xie, B., Huang, X., & Xiao, D. (2022). Tannin-coated PVA/PVP/PEI nanofibrous membrane as a highly effective adsorbent and detoxifier for Cr(VI) contamination in water. *Separation and Purification Technology*, *303*, 122164. https://doi.org/https://doi.org/10.1016/j.seppur.2022.122164

Xie, Z., Hu, B.-L., Li, R.-W., & Zhang, Q. (2021). Hydrogen Bonding in Self-Healing Elastomers. *ACS Omega*, *6*(14), 9319–9333. https://doi.org/10.1021/acsomega.1c00462

Yang, N., Yuan, R., You, D., Zhang, Q., Wang, J., Xuan, H., & Ge, L. (2022). Gallol-based constant

underwater coating adhesives for severe aqueous conditions. *Colloids and Surfaces A: Physicochemical and Engineering Aspects*, *634*, 127948. https://doi.org/https://doi.org/10.1016/j.colsurfa.2021.127948

Effect of Talc on Carbon Black Reinforced Natural Rubber Compound

Hatay Cöcen[a], Nilgün Kızılcan[b]

[a] Istanbul Technical University, Graduate School of Science Engineering and Technology, Department of Polymer Science and Technology, Türkiye
[b] Istanbul Technical University, Faculty of Science, Department of Chemistry, Türkiye
cocen@itu.edu.tr

Keywords: Carbon Black, Hybrid Filler, Natural Rubber, Talc.

Aim

The unique mechanical properties of rubbers make them suitable for applications in which cyclic loadings are involved. However, due to the high hysteretic losses present in such materials, a significant heat generation occurs. This effect in combination with the low thermal conductivity, leads to a considerable increase in the temperature in the rubber components, which is commonly referred to as heat build-up. (Scihieppati, 2019) High temperatures accelerate the fatigue of rubbers, so it is very important to find proper ways to reduce the heat buildup of rubbers in dynamic applications. Therefore, the formation of thermal conductive pathways in a rubber matrix with a high thermal conductivity can be helpful to attenuate heat build-up. (Weng, 2010)

To improve the thermal conductivity of polymers, fillers with a higher thermal conductivity than the matrix, such as aluminium nitride (AlN), boron nitride (BN), aluminium oxide (Al_2O_3), silicon dioxide (SiO_2), silicon carbide (SiC), silicon nitride (Si_3N_4), carbon nanotubes and nano-diamond, are used to create polymer-based composites with improved thermal conduction (Kochetov, 2011). Using two or more different fillers in the same composite material provides higher enhancements in thermal conductivity. It is caused by the synergetic effect between the particles. (Suplicz, 2012)

The purpose of this research study is to investigate the potential for the use of hybrid fillers by exploiting their various properties, especially thermal conductivity, particle size and shape. With this aim, into the carbon black reinforced natural rubber (NR) based compounds; talc, which is a natural mineral composed of hydrated magnesium silicate with the chemical formula $Mg_3(Si4O_{10})(OH)_2$ (Rothon, 2017), will be added as a second filler. The use of NR as rubber matrix in this research is attributed to its inherent properties making it suitable for dynamic applications, which are excellent mechanical properties and high resilience (lower hysteresis (heat build-up)) compared to other rubber materials (Mathew, 2001). As the main filler, carbon black is chosen due to its high reinforcement, low cost and thermally conductive properties. As a second filler, talc is preferred because of its thermally conductive nature and platelet particle shape in addition to the advantageous price. Moreover, there has been very little previous research on the performance of carbon black and talc filled natural rubber compounds so far. With this aim, carbon black reinforced natural rubber compounds without and with different amounts of talc will be produced keeping other parameters constant at the predetermined values, and the effect of talc amount on mechanical and dynamic properties of compound will be examined. In addition, the effects on their morphological, rheological, physical, and thermal resistance properties will be also analyzed and correlated with the used formulations.

Material and Method

5 different recipes were prepared containing different amounts of carbon black and talc, as seen in Table 1. Imerflex T10C product with median diameter 4.7µ from Imerys was preferred for talc whereas N330 grade carbon black, whose particle size is 28-36nm, from the producer, Kremenchug was used. SEM images of these two filler materials can be seen in Figure 1, showing the spherical shape of carbon black and platelet shape of talc.

Table 1. Recipes of the natural rubber compounds produced.

Materials	CB50	CB50+T5	CB50+T10	CB55+T5	CB60
NR	100	100	100	100	100
Peptizer	0,25	0,25	0,25	0,25	0,25
N330	50	50	50	55	60
Talc	-	5	10	5	-
ZnO	5	5	5	5	5
Stearic acid	2	2	2	2	2
6PPD	2	2	2	2	2
TMQ	2	2	2	2	2
S-80	2	2	2	2	2
TBBS-75	2	2	2	2	2

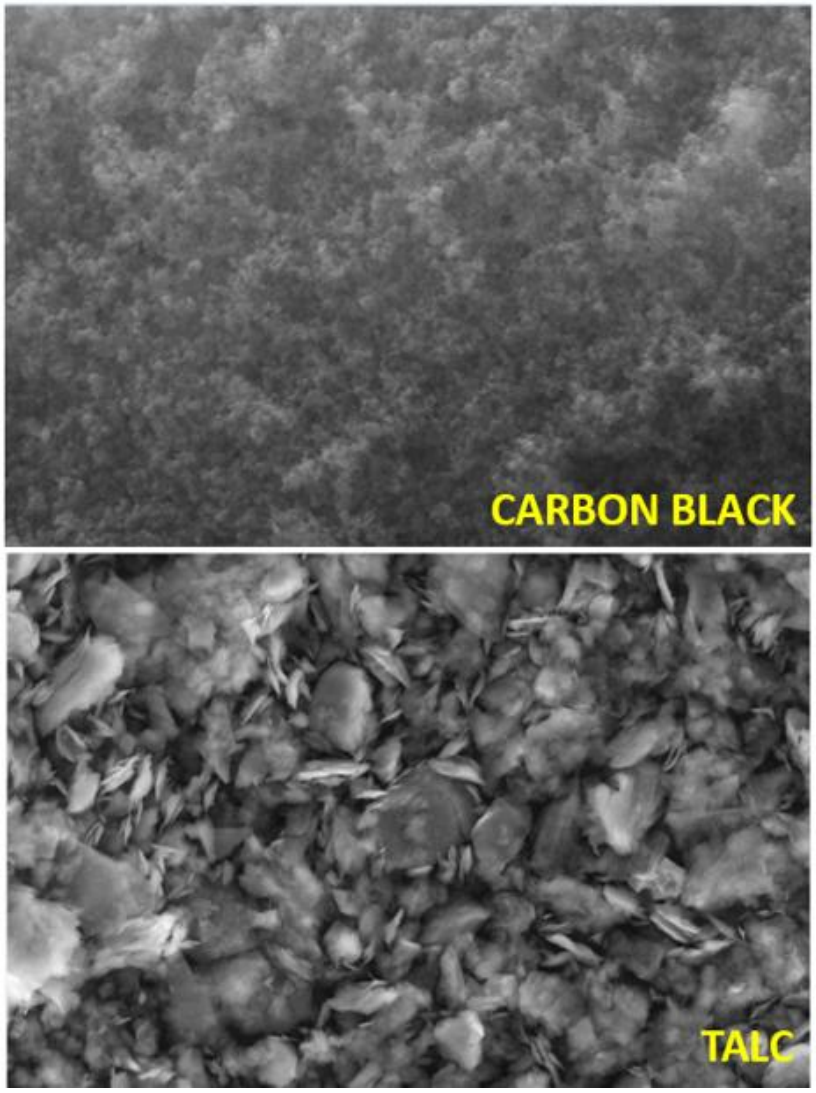

Figure 1. SEM images of carbon black and talc.

The weighed raw materials according to the formulation were mixed, and rubber compounds were produced using a laboratory type mixer and a two-roll mill. All the compounds were prepared by 2-stage mixing. The 1st stage is masterbatch preparation, in which rubbers, fillers, and all chemicals are mixed. The 2nd stage is final mix, where vulcanization agents (sulphur and accelerators) are added.

Findings

Rheological properties:

When the ts_2 (scorch time, the time for the viscosity to increase 2 units above minimum torque) and t_{90} (time at which 90% of crosslinking has been completed) values of the CB50, CB50+T5, and CB50+T10 compounds; in which talc was added as extra amounts to the carbon black, are compared, it can be seen that the results are scattered in a narrow range, as seen in Figure 2. In other words, it can be concluded that talc does not affect the scorch and vulcanization time much. On the other hand, comparison of CB50+T10, CB55+T5, and CB60 compounds shows us that partial replacement of carbon black with talc increases both the scorch and vulcanization time, directly proportional to the talc amount. Also, as realized in Figure 2, the addition of talc decreases CRI (curing rate index, which is equal to $100/(t_{90}-ts_2)$) in both cases, but is more dominant in the partial replacement.

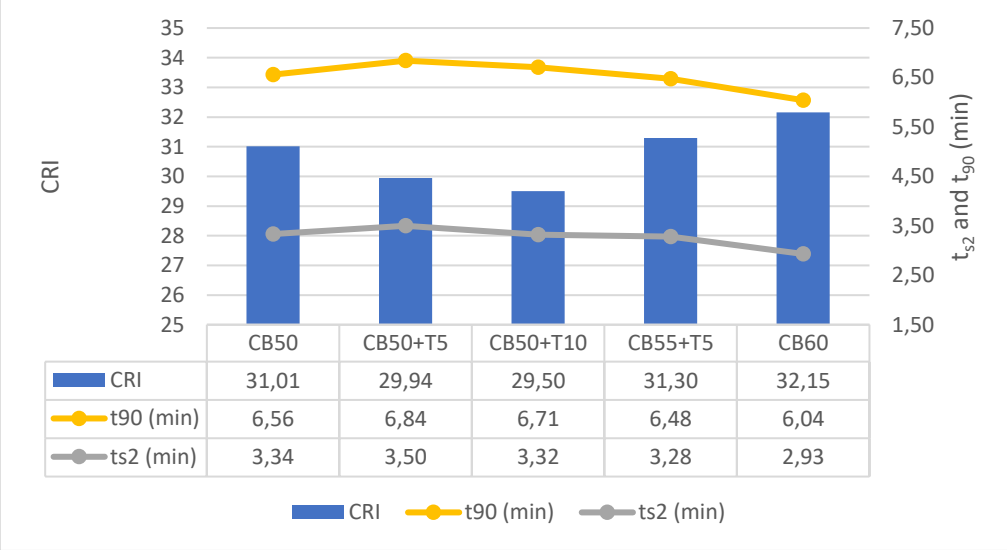

Figure 2. Effect of talc on the curing rate of the compounds.

It is observed in Figure 3, ML (minimum torque), which gives insight into the viscosity, increases as the amount of talc in the compounds increases from CB50 to CB50+T10 because of the reinforcement effect of the talc. On the other hand, while talc amount goes up in the carbon black-replaced compounds, ML goes down because of the higher particle size of the talc than carbon black; as a result less interfacial area and less friction between the rubber and filler. In Figure 3, ML values are also correlated with ML (1+4) values obtained in the Mooney viscosity test at 100˚C. It is observed that the results from both tests are aligned perfectly.

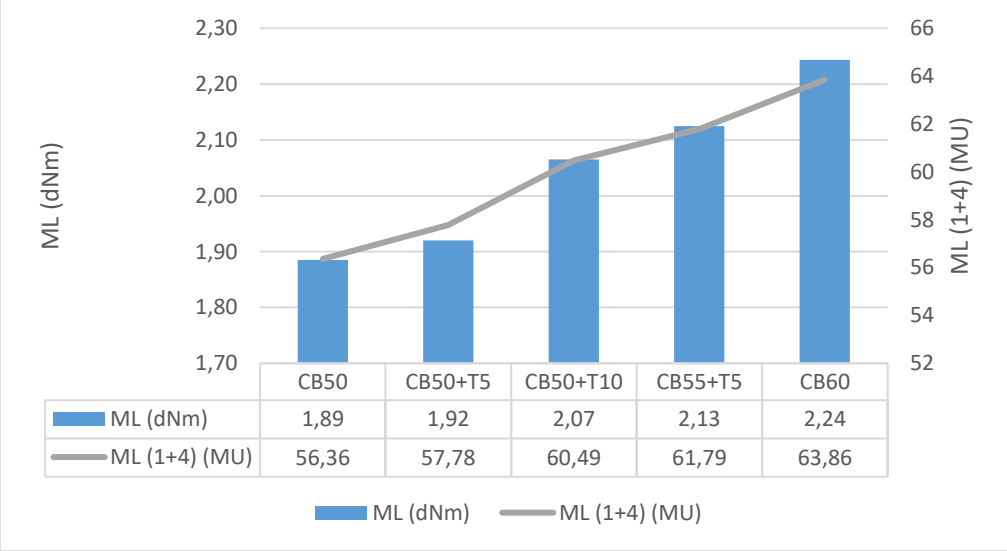

Figure 3. Effect of talc on the viscosity of the compounds.

Morphological properties:

It is seen in Table 2, addition of talc to the compound improves dispersion (X) of carbon black and decreases average agglomerate diameter (AAD) while partial replacement of carbon black does not affect the filler dispersion, which can be concluded from the similar X and AAD values of the CB60, CB55+T5 and CB50+T10 compounds.

Table 2. Morphological properties of the compounds.

	CB50	CB50+T5	CB50+T10	CB55+T5	CB60
X	5,99	6,23	6,63	6,66	6,66
AAD (μ)	10,1	9,65	9,09	9,07	9,14

Physical and mechanical properties:

Physical and mechanical properties of the compounds are summarized in Table 3. The density of the compounds increases with increasing talc amount as expected since talc density is higher than both natural rubber and carbon black. Moreover, the hardness of the compounds, increases with the addition of the talc and decreases with the partial replacement of the carbon black because of its lower reinforcing effect, which stems from both its inorganic structure and higher particle size. In the terms of mechanical properties, it can be concluded that tensile strength and elongation at break values are very close to each other (see Table 3) whereas modulus values of the compounds increase depending on the increasing amount and reinforcement effect of the two fillers, which is in line with hardness results (see Table 3).

Table 3. Physical and mechanical properties of the compounds.

	CB50	CB50+T5	CB50+T10	CB55+T5	CB60
Density (gr/cm_3)	1,1191	1,1388	1,1580	1,1505	1,1431
Hardness (Shore A)	67,0	68,3	69,3	70,3	71,5
Tensile strength (MPa)	27,4	26,9	26,2	26,2	25,4
Elongation at break (%)	483,2	483,2	468,8	466,6	448,2
Modulus 100% (MPa)	3,05	3,28	3,58	3,57	4,03
Modulus 200% (MPa)	8,32	8,42	8,73	9,19	10,72
Modulus 300% (MPa)	14,98	14,98	15,30	15,89	17,40

Thermal aging properties:

In Table 4, change in properties after aging for 72h at 100˚C shows us that compounds containing talc have slightly higher aging resistance, especially when the talc is added as extra like in the compounds CB50+T5 and CB50+T10.

Table 4. Thermal aging performance of the compounds.

Change in properties (%)	Tensile strength	Elongation at break
CB50	-23,46	-30,46
CB50+T5	-20,51	-28,56
CB50+T10	-19,25	-28,71
CB55+T5	-19,16	-28,20
CB60	-16,47	-30,39

Dynamic properties:

In the heat build-up test, it is seen that as the filler amount increases, the heat build-up (temperature rise) increases because of the friction between the rubber and filler, as seen in Figure 4. The results at different loads align well and confirm each other. It is also observed that, although carbon black has a lower particle size and so a higher surface area, it increases the temperature rise less than talc. This is most probably caused by interfacial resistance between organic rubber and inorganic talc.

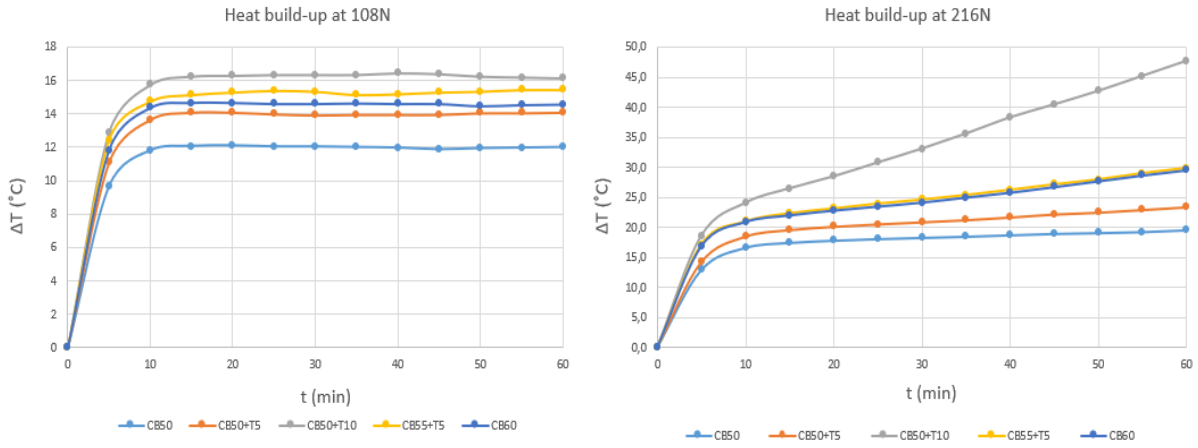

Figure 4. Temperature rise of the compounds at different loadings.

In the tension fatigue test, it is realized that the amount and reinforcement effect of filler impact the fatigue performance negatively (see Figure 5). In other words, the addition of talc or carbon black decreases the fatigue life; however, partial replacement of the carbon black with talc, as in the case of CB55+T5 and CB50+T10 samples improves the compound performance. This result can be attributed to the higher stiffness of the compounds and so lower crack growth resistance with increasing reinforcement.

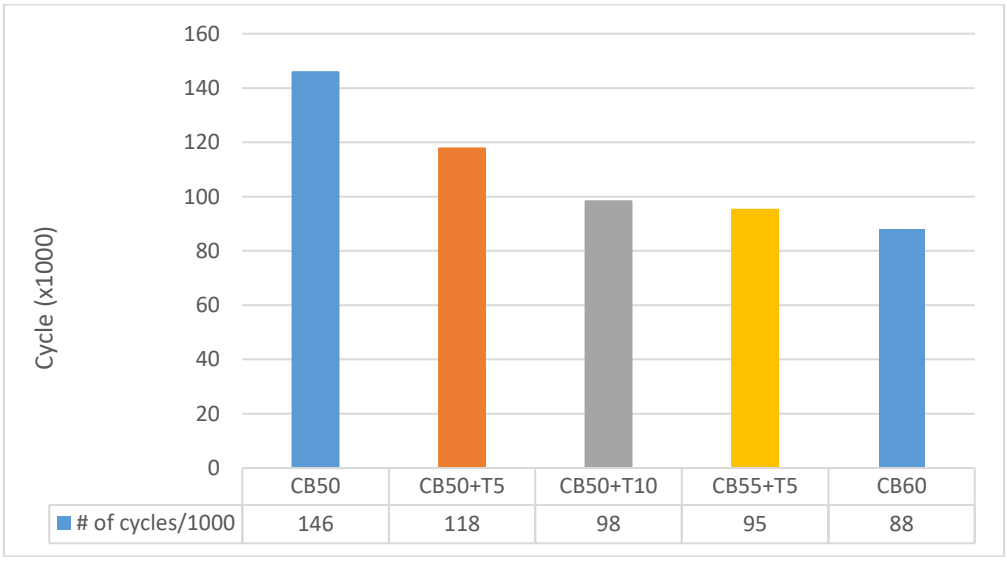

Figure 5. Fatigue lives of the compounds.

Conclusion

To conclude, talc increases the hardness and stiffness of the compounds, but its reinforcing effect is less than carbon black, as expected. It also increases heat aging resistance. When used as a partial replacement of carbon black, it improves tension fatigue performance. On the other hand, talc increases heat build-up of the compounds, even more than carbon black. This negative effect of talc is because of weak physical bonds formed with natural rubber and interfacial resistance at the rubber-filler interface, which are the results of its inorganic nature. It is estimated that this disadvantage will be eliminated via interface functionalization by forming covalent bonds using the silane coupling agent in the next part of the research.

References

Kochetov, R., Korobko, A.V., Andritsch, T., Morshuis, P.H.F., Picken, S.J., Smit, J.J. (2011). Modelling of the thermal conductivity in polymer nanocomposites and the impact of the interface between filler and matrix. Journal of Physics D: Applied Physics, 44, 39.

Mathew, M. N. (2001). Natural Rubber. In J. R. White, S. K. De (Eds.), Rubber Technologist's Handbook (1st ed., Vol. 1, pp.11-46). UK: Rapra Technology Limited.

Rothon, R. (2017). Talcs. In R. Rothon (Ed.) Fillers for Polymer Applications (pp.195-202). Switzerland: Springer International Publishing.

Schieppati, J., Schrittesser, B., Wondracek, A., Robin, S., Holzner, A., Pinter, G. (2019). Heat build-up of rubbers during cyclic loading, Proceedings of the 11th European Conference on Constitutive Models for Rubber – ECCMR, Nantes, France, June 25-27.

Suplicz, A., Kovacs, J. G. (2012). Development of Thermal Conductive Hybrid Composites, 15th European Conference on Composite Materials, Venice, Italy, June 24-28.

Weng, G., Huang, G., Qu, L., Zhang, P.,Nie, Y., Wu, J. (2010). Natural Rubber with Low Heat Generation Achieved by the Inclusion of Boron Carbide. Journal of Applied Polymer Science, 118, 2050–2055.

RAILWAY SYSTEMS ENGINEERING

Railway Systems Engineering

Signaling Systems in Railways

Traction Systems in Railways

Railway Positioning and Fiber Optic Sensor Fusion: Integrating GNSS, IMU, and FOS for Enhanced Train Localization

Serhat Boynukalın[a], Neslinur Kalkan[b]

[a] Istanbul Technical University, Graduate Education Institute, Department of Railway Systems Engineering, Turkiye
[b] Istanbul Technical University, Faculty of Electrical and Electronics, Department of Electronics and Communication Engineering, Turkiye
boynukalin@itu.edu.tr, kalkann21@itu.edu.tr

Keywords: Train Localization, Sensor Fusion, FOS (Fiber Optic Sensors), GNSS/IMU Integration, FDI.

Aim

Railway systems are indispensable for modern urban and intercity transportation, offering high capacity, energy efficiency, and robust sustainability (Heirich, 2020; Özgüner et al., 2011). However, guaranteeing operational safety and reliability in these systems requires continuous monitoring of trains and tracks—an endeavor challenged by issues such as electromagnetic interference and GNSS (Global Navigation Satellite System) signal dropouts (Zhou et al., 2022; Emirler et al., 2013).

This document focuses on improving the accuracy, reliability, and safety of railway system localization by leveraging a combination of GNSS, IMU (Inertial Measurement Unit), Radar, LiDAR (Light Detection and Ranging), camera, and other sensor technologies, in addition to more specialized methods such as indoor positioning (IPS) and fiber optic sensing (Özgüner et al., 2011; Heirich, 2020).

Finally, this study explores the strengths and limitations of various sensor types and advanced techniques—such as sensor fusion, machine learning-based fault detection (FDI), and track irregularity-based localization—to address environmental challenges like electromagnetic interference and GNSS signal loss (Akleylek et al., 2021; Emirler et al., 2013). It also evaluates the potential of fiber optic methods such as DOFS (Distributed Optical Fiber Sensors) and FBG (Fiber Bragg Grating) for real-time rail deformity detection and improved train positioning (Sasy Chan et al., 2021). Furthermore, novel approaches like CNN–LSTM (Convolutional Neural Network–Long Short-Term Memory) are considered for enhancing accuracy, lowering maintenance costs, and strengthening early warning systems (Sun et al., 2024; Garramiola et al., 2018). Ultimately, the study proposes an integrated framework that combines GNSS–IMU with next-generation sensing and analytics for precise and reliable train localization.

Material & Method

2.1. Sensor Suite Configuration

An advanced sensor suite provides global position information with GNSS (GPS, GLONASS, Galileo, etc.) but can be affected by signal obstructions and low-signal areas (Akleylek et al., 2021). However, methods like RTK (Real-Time Kinematic) or DGPS (Differential Global Positioning System) enable centimeter-level accuracy (Özgüner et al., 2011). The IMU uses inertial data for position and movement tracking but relies on GNSS corrections to minimize drift (Emirler et al., 2013). Radar offers reliable detection even under poor visibility conditions, while LiDAR facilitates high-resolution 3D mapping (Göhring et al., 2011). Camera-based systems provide detailed scene recognition but are sensitive to varying lighting conditions. In indoor environments, IPS (Indoor Positioning System) technologies using Wi-Fi (RSSI – Received Signal Strength Indicator), BLE (Bluetooth Low Energy), RFID (Radio-Frequency Identification), or UWB (Ultra-Wideband) complement GNSS for positioning when satellite signals are insufficient (Akleylek et al., 2021; Gao et al., 2024).

2.2. Sensor Fusion & Estimation

Combining multiple sensor data enhances system accuracy and robustness. For instance, ETCS (European Train Control System)–level systems use GNSS, IMU, odometer, and balise signals together for train localization (Heirich, 2020; Lundquist, 2011). Variants of the Kalman Filter (standard and extended) reduce noise and compensate for drift. Particle-based or Monte Carlo methods sample possible states, providing estimates resilient to uncertainties (Fox et al., 1999). By merging radar, LiDAR, and camera data, the shortcomings of each sensor are addressed, resulting in a more comprehensive scene perception (Göhring et al., 2011).

2.3. Fiber Optic Integration

Fiber optic solutions, particularly DOFS and FBG technologies, are considered powerful alternatives or complements to conventional sensors. DOFS, which uses Rayleigh/Brillouin scattering, enables wide-area monitoring of temperature, strain, and vibration (Sasy Chan et al., 2021). FBG sensors, capable of detecting local temperature or strain changes while remaining immune to electromagnetic interference, offer advantages in railway safety applications (Zhou et al., 2022). Their insensitivity to electromagnetic noise makes these sensors highly effective for real-time detection of track deformations and anomalies in harsh environments.

2.4. Indoor & GNSS-Denied Environments

In tunnels or environments where GNSS signals are inadequate, indoor positioning methods like Wi-Fi, BLE, and RFID rely on RSSI or fingerprinting, though calibration variability can pose challenges (Akleylek et al., 2021). UWB, which transmits short radio pulses across a wide frequency band, offers centimeter-level accuracy but entails higher infrastructure costs (Gao et al., 2024). Additionally, recording rail geometry deviations (gauge, cross-level, alignment) with an IMU and matching them to a known map helps mitigate drift in the absence of GNSS (Zhou et al., 2022).

2.5. Machine Learning (ML) & Fault Detection (FDI)

FDI: Systems track sensor data in real time, isolating faulty measurements to maintain performance (Garramiola et al., 2018).

Deep Learning (CNN–LSTM): Dynamically updates noise parameters in GNSS–INS (Inertial Navigation System) or multi-sensor scenarios, improving localization resilience when signals degrade (Sun et al., 2024).

2.6. Simulation & Performance Evaluation

To validate system reliability, simulation-based experiments evaluate sensor fusion, Kalman filtering, and advanced ML algorithms on representative datasets before field deployment (Lauer & Stein, 2014). Key metrics include accuracy (deviation from ground truth), error margins (impact of sensor noise), transition times (rate of track segment changes), and uncertainty rate (speed of model convergence under sensor or environment fluctuations). By iteratively refining sensor architecture, data integration, and state estimation, the system targets continuous, high-precision train localization, offering both safety and operational benefits.

Findings

3.1. GNSS and IMU Integration

GNSS systems (GPS, GLONASS, Galileo, etc.) combined with IMU sensors (accelerometers, gyroscopes) provide highly accurate positioning and velocity information for vehicles (Özgüner et al., 2011).

In indoor or tunnel environments where GNSS signals are weak, IMU-based dead reckoning can estimate position but may accumulate bias and drift errors. Therefore, it is important to periodically correct IMU outputs using GNSS data via Kalman filtering or its extended variants (Emirler et al., 2013).

3.2. Indoor (IPS) and Alternative Positioning

Wi-Fi (RSSI) and BLE infrastructures, RFID-tag systems, camera-based SLAM (Simultaneous Localization and Mapping), and UWB technologies provide supplementary positioning data where GNSS is inadequate, both indoors and outdoors (Akleylek et al., 2021; Gao et al., 2024).
Camera-based approaches benefit from low cost and rich data, though performance is directly impacted by lighting conditions and line-of-sight constraints.
Radar and LiDAR offer valuable long-range or high-resolution scans for environment detection and obstacle recognition, yet both face limitations related to cost and field of view (Göhring et al., 2011).

3.3. Sensor Fusion and Error Types

In advanced railway systems such as ETCS, IMU, odometry, balise, and GNSS data are combined to provide reliable train localization (Heirich, 2020).
Errors such as "random noise," "drift," "calibration error," and "multipath effect" are widespread in sensor readings and can be minimized via Kalman filtering, RLS, or machine learning-based corrections (Lundquist, 2011).

3.4. Vision-Based and UWB Positioning

Camera systems are becoming more widespread for detecting environmental markers and recognizing traffic signs, but lighting conditions and occlusions directly affect performance. UWB achieves centimeter-level precision through interference mitigation, though at the expense of higher infrastructure costs (Gao et al., 2024).

3.5. FDI and Machine Learning Applications

By comparing multiple odometers or IMU sensors, faulty data can be swiftly identified (Garramiola et al., 2018). Additionally, CNN–LSTM deep learning models dynamically adjust noise parameters in GNSS–INS fusion, significantly boosting accuracy when GNSS signals are unavailable (Sun et al., 2024). In this way, both sensor failures and environmental challenges (signal outages, wheel slip, etc.) can be more effectively addressed through machine learning techniques.

3.6. Fiber Optic Sensor (FOS) Approaches

Distributed Optical Fiber Sensors (DOFS) exploit Rayleigh/Brillouin scattering techniques to track temperature, strain, and vibration changes over distances of 100–150 km, reducing maintenance costs and improving track safety (Sasy Chan et al., 2021).
Fiber Bragg Grating (FBG) accurately measures local strain and temperature changes, with immunity to electromagnetic interference, making it favorable for track monitoring and train localization systems (Sasy Chan et al., 2021).
FOS methods show promise for continuous monitoring—potentially lessening the need for guide locomotives—and offer early warnings for earthquakes or landslides.

3.7. Track Irregularity–Based Localization

Geometric deviations in track design (e.g., gauge, cross-level, alignment) produce repeated signals during train operation, forming a positioning "fingerprint" (Zhou et al., 2022).
Integrating this approach with INS data enables sufficient accuracy with a low-cost IMU even in the absence of GNSS signals.It proactively enhances track safety, especially in tunnels and other enclosed environments.

Conclusion

Fiber optic-based methods are increasingly important for enhancing positioning and track safety in railway systems. Alongside GNSS, IMU, LiDAR, radar, camera, and UWB, FBG and DOFS provide robust, high-precision alternatives. Their long service life, resistance to electromagnetic interference, and reliable operation in harsh environments make FBG sensors especially promising for improving operational safety and efficiency (Sasy Chan et al., 2021).

Integrating fiber optic sensor data with INS readings mitigates positioning errors in GNSS-denied areas, enabling precise localization and early detection of anomalies like track deformation or vibration. Even a low-cost IMU can achieve high accuracy without GNSS through track irregularity approaches, cutting maintenance costs and preventing accidents (Zhou et al., 2022).

Sensor fusion and FDI (Fault Detection and Isolation) ensure uninterrupted reliability despite faulty measurements, while machine learning and deep learning address noise and modeling limitations beyond those of traditional Kalman filter methods. As a result, continuous monitoring solutions can potentially replace guide locomotives, issue alerts for natural disasters, and detect subtle track issues.

In summary, fortifying GNSS, IMU, and other sensors with FBG technology offers significant potential for proactive safety, lower maintenance costs, and precise localization in railway systems. Ongoing advances in signal processing and sensor design will likely make fiber optic-based solutions a cornerstone of both railway and broader industrial applications.

References

Akleylek, S., Kılıç, E., Söylemez, B., Aruk, T. E., & Çavuş Yıldırım, A. (2020). A research on indoor positioning systems. *Journal of Engineering Sciences and Design, 8*(5), 90–105. https://doi.org/10.21923/jesd.773123

Emirler, M. T., Uygan, İ. M. C., Altay, İ., Acar, O. U., Keleş, T., Aksun Güvenç, B., & Güvenç, L. (2013, September 16–17). *A cooperating autonomous road vehicle platform*. IFAC Workshop on Advances in Control and Automation Theory for Transportation Applications, İstanbul, Türkiye. https://doi.org/10.3182/20130916-4-TR-4042.00028

Fox, D., Burgard, W., Dellaert, F., & Thrun, S. (1999). Monte Carlo localization: Efficient position estimation for mobile robots. *Proceedings of the Sixteenth National Conference on Artificial Intelligence (AAAI-99)*, 343–349. http://robots.stanford.edu/papers/fox.aaai99.pdf

Gao, H.; Li, X.; Song, X. (2024). *A Fusion Strategy for Vehicle Positioning at Intersections Utilizing UWB and Onboard Sensors*. Sensors 24, 476. https://doi.org/10.3390/s24020476

Garramiola, F., Del Olmo, J., Poza, J., Madina, P., & Almandoz, G. (2018). Integral Sensor Fault Detection and Isolation for Railway Traction Drive. *Sensors*, *18*(5), 1543. https://doi.org/10.3390/s18051543

Göhring, D., Wang, M., Schnürmacher, M., & Ganjineh, T. (2011). Radar/Lidar sensor fusion for car-following on highways. In *Proceedings of the 5th IEEE International Conference on Automation, Robotics and Applications* (pp. 407–412). IEEE. https://doi.org/10.1109/ICARA.2011.6144866

Heirich, O. (2020). *Localization of trains and mapping of railway tracks*. Technische Universität München.

Lauer, M., & Stein, D. (2014). A train localization algorithm for train protection systems of the future. *IEEE Transactions on Intelligent Transportation Systems*, 1–10. https://doi.org/10.1109/tits.2014.2345498

Lundquist, C. (2011). *Sensor fusion for automotive applications* (Doctoral dissertation). Linköping University, Department of Electrical Engineering.

Sasy Chan, Y. W., Wang, H.-P., & Xiang, P. (2021). *Optical Fiber Sensors for Monitoring Railway Infrastructures: A Review towards Smart Concept*. Symmetry, 13(12), 2251. https://doi.org/10.3390/sym13122251

Sun, Z., Song, H., Zhou, M., Yin, H., & Dong, H. (2024). *Integrating GNSS and INS data with deep learning-enhanced invariant extended Kalman filter for train localization.* Proceedings of the 43rd Chinese Control Conference, 8975-8980. https://doi.org/10.1109/TIM.2024.3144207

Ü. Özgüner, T. Acarman, K. Redmill, *Autonomus Ground Vehicles*, Artech House, 2011

Zhou, Y., Chen, Q., Wang, R., Jia, G., & Niu, X. (2022). *Onboard train localization based on railway track irregularity matching.* IEEE Transactions on Instrumentation and Measurement, 71, 1–13. https://doi.org/10.1109/tim.2022.3144207

RAILWAY SYSTEMS ENGINEERING

Railway Systems Engineering

Signaling Systems in Railways

Traction Systems in Railways

Development of a Control System for Enhanced Safety and Efficiency in a Two-Switch Railway Station Area

Mehmet Zahit Kırdemir[a], Serhat Boynukalın[b]

[a]Istanbul Technical University, Faculty of Electrical and Electronics, Department of Control and Automation Engineering, Turkey
[b]Istanbul Technical University, Graduate Education Institute, Department of Railway Systems Engineering, Turkey
kirdemir18@itu.edu.tr

Keywords: .NET, Interlocking, MODBUS, PLC, Route.

Aim

Railway systems play a crucial role in contemporary transportation infrastructure, necessitating robust control mechanisms to ensure both safety and operational efficiency (Pachl, 2021). The station areas, particularly those incorporating switch mechanisms, are essential for directing train movements across various tracks (Theeg & Vlasenko, 2017**)**. This project endeavors to enhance safety and operational effectiveness within railway operations by developing a control system specifically designed for a two-switch station area. The proposed system utilizes HIMA Programmable Logic Controllers (PLCs) and integrates them with a .NET-based user interface via the MODBUS protocol. The primary objectives of this project are as follows:

- Design and implement the operational logic for a two-switch station area utilizing both SILworX and .NET development environments.
- Establish reliable communication pathways between HIMA PLCs and the .NET application through MODBUS/TCP protocols.
- Develop an intuitive, user-friendly interface that enables operators to remotely monitor and control the operational status of the station area.
- Create and integrate a routing algorithm specifically tailored to the unique configuration of the two-switch system, thereby ensuring the safe and efficient passage of trains.

This research builds upon the existing single-switch infrastructure at the ITÜ Railway Systems Laboratory, transitioning it to accommodate the complexities associated with a two-switch configuration. By addressing the increasing demands of modern railway operations—characterized by heightened traffic volumes and stringent safety requirements—this project aims to offer a scalable and reliable solution that can serve as a foundation for future advancements in railway automation. The emphasis on safety is aligned with international standards (such as TS EN 50126 and TS EN 50129) (Durmuş et al., 2011), while the focus on efficiency aims to optimize train routing and minimize operational delays. By integrating these elements, the project seeks to contribute significantly to the advancement of railway systems, ultimately enhancing both safety and operational performance within the sector.

Material and Method

1. Materials

The project encompasses a comprehensive integration of hardware and software tools to accomplish its defined objectives:

1.1. Hardware:

The experimental infrastructure is provided by the ITÜ Railway Systems Laboratory, incorporating essential components such as two switches, signaling devices, and an Ethernet network to facilitate effective communication.

- HIMA PLCs: The selection includes two models, specifically HIMatrix F20 01 and HIMatrix F2 DO 16 01, chosen for their reliability and adherence to safety-critical standards pertinent to industrial automation,
- Physical Setup: The ITÜ Railway Systems Laboratory provides the experimental infrastructure, which incorporates essential components such as two switches, signaling devices, and an Ethernet network to facilitate effective communication.

1.2. Software:

SILworX: This programming environment serves as a platform for designing and configuring PLC logic, ensuring compliance with safety regulations.

- .NET Framework: Utilized for the development and integration of the user interface in conjunction with MODBUS communication. The development process leverages Visual Studio as the primary development environment.
- MODBUS/TCP: An open and reliable protocol implemented for data exchange between the PLCs and the .NET application (Swales, 1999).
- Anklaşmatik V2: An existing software application that has been updated to support the functionalities of the dual-switch system.

2. Methods

The methodology adopted for this project adheres to a systematic approach in designing, implementing, and evaluating the control system:

2.1. Logic Design:

The interlocking logic for the dual-switch station area is meticulously developed utilizing SILworX. This process entails creating interlocking tables and safety mechanisms to prevent conflicting routes or hazardous conditions (Dincel & Kurtulan, 2012). The design is structured to ensure compliance with relevant standards such as TS EN 50129 (Durmuş et al., 2011), with an emphasis on fail-safe operations.

2.2. Communication Configuration:

The implementation of MODBUS/TCP facilitates real-time data exchange between the HIMA PLCs and the .NET application. This critical step ensures accurate transmission and reception of switch positions, signal states, and control commands.

2.3. User Interface Development:

A .NET-based application has been meticulously designed to furnish operators with a graphical interface that depicts the operational status of the station area, including switch positions and train locations. This interface supports remote monitoring and control capabilities, thereby enhancing operational flexibility.

2.4. Route Algorithm Development:

A route algorithm has been crafted to manage train movements through the dual-switch system. This algorithm diligently verifies route availability, switch alignments, and signal states prior to authorizing train passage, with a paramount focus on safety and operational efficiency.

2.5. Testing and Validation:

The system undergoes thorough testing within the ITÜ Railway Systems Laboratory using simulated scenarios. The testing protocols are designed to evaluate system functionality, assess safety under fault conditions, and measure performance during the management of simultaneous train movements.

Collectively, these methodologies aim to evolve the existing single-switch system within the laboratory into a dual-switch configuration, ensuring that it fulfills the contemporary operational requirements in railway systems.

Findings

As this project continues to develop, the findings presented herein are preliminary and reflective of current progress. Notably, several significant outcomes have been identified:

1. Communication Success:

The establishment of MODBUS/TCP communication between the HIMA Programmable Logic Controllers (PLCs) and the .NET application has been successfully achieved. Initial testing indicates reliable data transfer, with the application effectively displaying switch states and signal conditions in real time.

2. Logic Implementation:

The interlocking logic for the two-switch system, designed utilizing SILworX, has undergone partial implementation. Simulation results demonstrate the system's capacity to prevent conflicting routes and ensure safe switch operations under standard conditions. However, further testing is imperative to validate the system's behavior during edge cases, such as simultaneous route requests.

3. Route Algorithm Progress:

A prototype route algorithm has been developed and integrated into the Anklaşmatik V2 program. Preliminary tests suggest that the algorithm can effectively manage train movements; however, optimization is necessary to address complex scenarios and mitigate processing delays.

4. User Interface Development:

The .NET interface clearly visualizes the station area, enabling operators to monitor and control switches remotely. Feedback from initial usability assessments indicates that further refinements are required to enhance system responsiveness and operator intuitiveness.

5. Challenges Identified:

Several critical challenges have been recognized, including the necessity of ensuring system scalability for larger station areas and maintaining safety during high-traffic scenarios. Additionally, the integration of fault detection mechanisms is currently being developed to improve overall system reliability.

These findings suggest that the project is progressing toward its goals, with the system showing potential as a safe and efficient solution for two-switch station control. Ongoing work focuses on completing the implementation and conducting comprehensive tests to refine the system further.

Conclusion

This project explores the integration of HIMA PLCs, MODBUS/TCP, and a .NET application to facilitate the effective control of a dual-switch railway station area. Preliminary findings suggest that the proposed system significantly enhances safety by mitigating unsafe conditions and increasing operational efficiency through real-time monitoring and automated route management. The successful establishment of MODBUS communication and the partial implementation of interlocking logic and route algorithms represent substantial progress in this endeavor.

Upon completion, the system is anticipated to minimize human error, enhance response times to operational changes, and provide a scalable framework suitable for managing increasingly complex railway scenarios. Its implications may extend beyond experimental settings, offering a contemporary model for modernizing railway control systems in practical applications. Additionally, this project contributes to academic and industrial advancements in railway automation by demonstrating the effective integration of safety-critical hardware and software solutions. Future efforts will concentrate on the finalization of the system, the resolution of identified challenges, and the validation of its performance across a range of operational conditions. This project demonstrates the potential of integrating HIMA PLCs, MODBUS/TCP, and a .NET application to control a two-switch railway station area effectively. Preliminary results indicate that the system can enhance safety by preventing unsafe conditions and improving efficiency through real-time monitoring and automated route management. The successful establishment of MODBUS communication and the partial implementation of the interlocking logic and route algorithm mark significant steps forward.

Once completed, the system is expected to reduce human error, improve response times to operational changes, and provide a scalable framework for managing more complex railway scenarios. Its impact could extend beyond

the laboratory, offering a model for modernizing railway control systems in real-world applications. The project also contributes to academic and industrial advancements in railway automation by showcasing the integration of safety-critical hardware and software solutions. Future work will focus on finalizing the system, addressing identified challenges, and validating its performance under diverse operational conditions.

References

Dincel, E., & Kurtulan, S. (2012). Interlocking and Automatic Operating System Design with Automaton Method. *13th IFAC Symposium on Control in Transportation Systems*, Sofia.
(2nd ed., Vol. 1, pp.19-40). New York: Wiley.
Durmuş, M. S., Yıldırım, U., & Söylemez, M. T. (2011). Application of Functional Safety on Railways Part I: Modelling & Design. *8th Asian Control Conference*.
Pachl, J. (2021). *Railway Signalling Principles*. Braunschweig: Publications of TU Braunschweig.
Swales, A. (1999). *Open MODBUS/TCP Specification*. Schneider Electric.
Theeg, G., & Vlasenko, S. (Eds.). (2017). *Railway Signalling and Interlocking: International Compendium*. Eurailpress.

RAILWAY SYSTEMS ENGINEERING

Railway Systems Engineering

Signaling Systems in Railways

Traction Systems in Railways

Fiber Optic Sensing Applications in Railway Systems

Serhat Boynukalın[a], Cem Şengül[b]

[a] Istanbul Technical University, Graduate Education Institute, Department of Railway Systems Engineering, Türkiye
[b] Istanbul Technical University, Faculty of Electrical and Electronics, Department of Control and Automation Engineering, Türkiye
boynukalin@itu.edu.tr

Keywords: Fiber Bragg Gratings (FBG), Fiber Optic Sensors (FOS), Railway Monitoring, Signal Processing, Clearance Train.

Aim

Railway systems are essential for urban and intercity transportation, offering high capacity, energy efficiency, and sustainability. Ensuring safety and efficiency requires continuous train and track monitoring. Traditional electronic sensing faces challenges like electromagnetic interference, making fiber optic sensor (FOS) technologies a promising alternative for reliable real-time detection (Hartog, 2017).

This research aims to demonstrate how Fiber Optic Sensors (FOS), particularly Distributed Acoustic Sensing (DAS) and Fiber Bragg Gratings (FBG), can track train positions and assess infrastructure integrity in rail systems. While current implementations operate within 20-50 km, the goal is to extend detection to 75 km and ultimately 500 km, using advanced signal processing and noise suppression to enable early-warning functions and multi-faceted monitoring without electromagnetic or environmental vulnerabilities (Boynukalin et al., 2023).

Furthermore, the aim is to demonstrate the feasibility of replacing or enhancing existing electronic-based secondary warning systems with fiber optic solutions, despite the absence of higher-level safety certifications. This approach supports hybrid applications by enabling real-time detection of track hazards, moving objects, and clearance train functionalities, ultimately encouraging further research and investment in fiber optic-based railway technologies to reduce manual intervention, improve reaction times, and enhance safety and efficiency (Sun et al., 2022).

Material and Method

FOS technologies rely on changes in light signals transmitted through optical fibers to detect external influences such as temperature, stress, and vibration (Agrawal, 2012). The primary advantage is immunity to electromagnetic interference, a key concern in rail environments where traction motors and power lines can disrupt conventional electronic sensors (Asawa & Yao, 1983). Two main FOS approaches are explored:

Distributed Acoustic Sensing (DAS) uses standard single-mode or multimode fibers, which are also common in communication networks; a laser source injects pulses, and variations in Rayleigh backscattering along the fiber reveal acoustic or vibrational changes, which are then processed to locate events (e.g., train wheels passing, track deformation) with a resolution dependent on pulse width, scattering intensity, and signal processing algorithms (He & Liu, 2021; Xiong et al., 2020).

Fiber Bragg Gratings (FBG) incorporate mirror-like gratings inside the fiber core, where mechanical strain, vibration, or temperature shifts alter the fiber's refractive index at the grating locations and change the reflected wavelength, offering higher localized sensitivity and making it suitable for detecting low-intensity events (e.g., minor track cracks) (Werneck et al., 2013; Kinet et al., 2014).

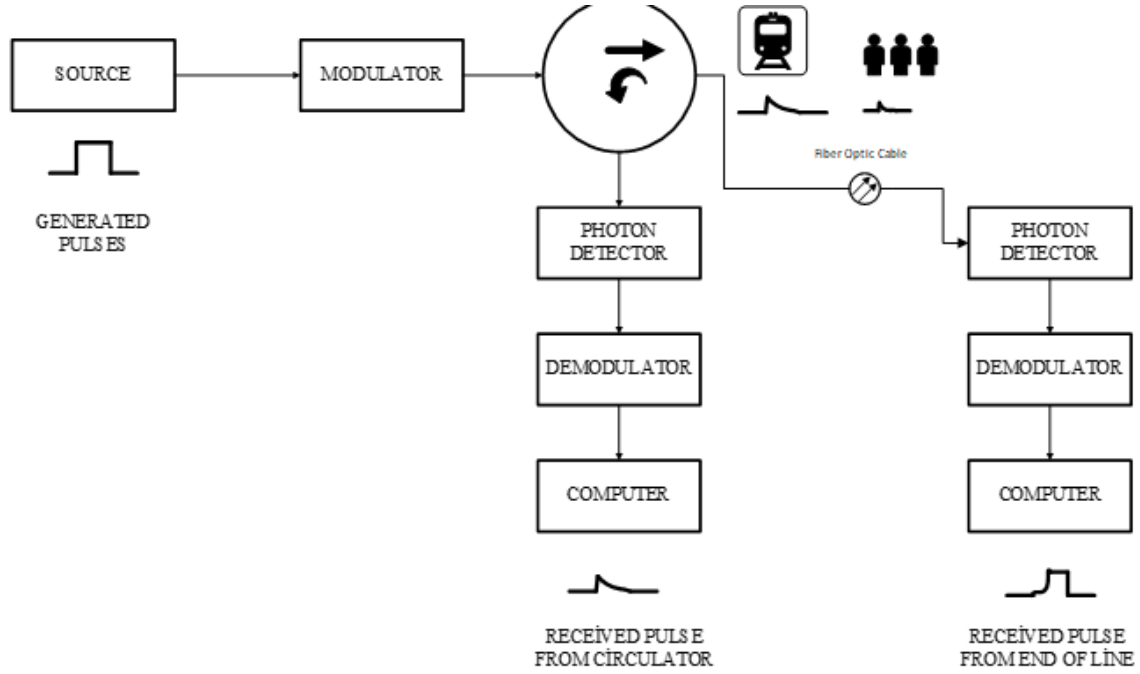

Figure 1: General block diagram of FOS system Adapted from Boynukalin et al. (2023). Copyright 2023 by the authors. Reprinted with permission.

Figure 1 presents a fundamental diagram of a fiber optic sensor application, where enhancements in the source, modulator, fiber link, demodulator, and sensor improve vibration detection, while analyzing transmitted or backscattered signals at specific power and wavelength enables scattering location identification and event detection (Boynukalin et al., 2023).

This work is designed to extend the 20 km detection range of existing systems to 50 km initially, then 75 km, and ultimately 500 km, by optimizing Fiber Bragg Grating (FBG) design, employing Advanced SNR Enhancement techniques such as PN-Codes and cross-correlation, and reducing signal attenuation by operating in the 1550 nm band, where absorption and scattering are minimized. Patent applications have been filed for innovative signal processing and sensor configurations to address randomness in DAS and localized reflection in FBG, ensuring accurate detection of event location, intensity, and direction through a modulated light source and signal analysis (Boynukalin et al., 2023).

Three primary rail categories in Turkey guide the optimal FOS installation:

a.) Intercity High-Speed Trains (YHT): YHT typically has fiber cables running near the ballast or in protective conduits, which provides direct access to track vibrations and anomalies while being crucial for real-time train positioning and early detection of rail deformation (Boynukalin et al., 2023).

b.) Urban Light Rail (Tramway): Urban Light Rail (Tramway) operates at street level, sharing space with vehicles and pedestrians, where fiber optic cables are less common due to minimal dedicated communication ducts, requiring special integration or localized segments for key intersection monitoring, with the potential to improve traffic safety and track boundary detection (Hartog, 2017).

c.) Urban Metro Systems: Urban Metro Systems are typically installed in tunnels with cable trays on the ceiling or walls, offering stable conditions for fiber placement but demanding higher resolution (under 1 meter) for precise position feedback, making them well-suited for continuous structural health monitoring, including tunnel movement and water ingress detection (Kinet et al., 2014).

Fiber optic sensors must contend with Thermal Noise and Shot Noise (inherent in optical sources and detectors), Environmental Noise (mechanical vibrations, temperature fluctuations), and System Noise from splices, connectors, or cable imperfections (Sun et al., 2022).

Filtering is accomplished via High-pass, Low-pass, or Band-pass approaches, depending on target event frequency, Median and Wavelet Filters to suppress outliers and separate noise from actual events, and Cross-correlation using PN-coded signals to boost sensitivity in high-noise conditions (Xiong et al., 2020). A key outcome mentioned is the ability to detect movement with around 1.2 cm accuracy at 50 km, even under significant noise.

Findings

1.) Hybrid System Demonstration: Moving Objects and Track State

A fiber optic system can simultaneously handle vehicle tracking by identifying trains and unauthorized objects on the track and infrastructure monitoring by detecting structural faults such as cracks, ballast shifts, and temperature-induced stress, surpassing the limitations of traditional electronic systems through amplitude and frequency shift analysis in backscattered signals. This approach provides early warnings despite lacking Safety Integrity Level (SIL) certifications, while holding strong potential as a critical secondary safety system to enhance railway monitoring and operational security.

2.) Clearance Train Feature

After maintenance or following a natural disaster, a track may appear structurally intact while still concealing hidden defects. Traditionally, a clearance train is used to verify track integrity; however, the risks associated with this method were highlighted in 2023, when a guide locomotive derailed on the Ankara-Sivas line, emphasizing the need for more advanced and reliable inspection technologies (Boynukalin et al., 2023). Fiber optic–based clearance train approach would provide:

2.a.) Automatic, Real-Time Track Assessment: The FOS continuously monitors the track. If the locomotive encounters a defect or if foreign material is present, the sensor data flags abnormal reflections or frequency shifts (He & Liu, 2021).

2.b.) Reduced Human Dependency: Minimizing the need for personnel to physically inspect the line (Boynukalin et al., 2023).

2.c.) Immediate Feedback: If a section is compromised, the system promptly triggers alarms for remedial action line (Boynukalin et al., 2023).

Simulations show that FBG arrays, placed at intervals along the track, detect variations in reflection levels. Even small anomalies manifest as measurable frequency shifts in the backscattered spectrum (Griffiths, 1987).

3.) Multi-FBG Modeling and Frequency Shift Analysis

Each Fiber Bragg Grating (FBG) reflects a portion of transmitted light at a specific wavelength, and when a train wheel or an external force applies pressure to the rail, the resulting strain alters the reflection profile (Kinet et al., 2014). As the train approaches, the spectrum shifts toward the red or blue range depending on whether the fiber undergoes tension or compression, while as it departs, the spectrum shifts back with a drop in amplitude once beyond the FBG detection zone. Multiple FBG sensors along the track generate distinct signals, allowing precise speed and direction calculations by analyzing frequency shifts. If shifts occur sequentially in consecutive gratings, the train is moving forward, whereas a reversed sequence indicates backward motion. The train's exact location is determined by evaluating the time differences between FBG responses, ensuring accurate real-time monitoring.

4.) Ray Damage Tracking and Early Warning Potential

Another critical finding is the ability to detect rail defects such as cracks or broken rails. Traditional methods may miss sub-millimeter cracks until they become hazardous. Fiber optic cables register the changes in mechanical coupling or acoustic signatures, thereby identifying problems:
4.a.) Micro-Cracks: Cause subtle but detectable shifts in the backscattered signal amplitude and frequency.

4.b.) Ballast Issues: Sinking or washouts generate abnormal vibrations, easily identified under the FOS system's filter algorithms (He & Liu, 2021).

4.c.) Earthquakes or Flash Floods: Instantly produce large spectral anomalies, offering an early warning mechanism (Sun et al., 2022).

Conclusion

The fiber optic sensor (FOS) approach addresses key limitations in rail monitoring by providing long-range, high-resolution detection across 75 km and beyond, with enhanced sensitivity to vibrations, cracks, and structural deformations. It ensures versatility across rail environments, offering tailored solutions for high-speed intercity lines, urban tramways, and metro systems, with adaptable sensor placement in ballast zones, cable trays, or embedded installations.

Robust signal processing against noise is achieved through wavelet transforms, median filters, PN-coded signal transmission, and cross-correlation, enabling precise localization in challenging conditions. The system also supports clearance train automation and disaster preparedness, reducing reliance on manual inspections while providing real-time track assessment and early warnings for natural disasters such as washouts, landslides, and earthquakes, minimizing derailments and disruptions.

This technology lays the groundwork for future SIL (Safety Integrity Level) certifications, as its performance and reliability indicate strong potential for becoming primary safety instruments or secondary warning systems in rail infrastructure. Additionally, FOS developments significantly reduce operational costs by integrating real-time train tracking, infrastructure health monitoring, and environmental impact assessment, with minimal electromagnetic interference, making them superior to traditional electronic solutions.

In conclusion, fiber optic sensors are a transformative technology that can reshape railway safety, maintenance, and operations. The research and prototypes demonstrate how Fiber Bragg Gratings (FBG) and Distributed Acoustic Sensing (DAS), combined with advanced signal processing techniques, overcome range limitations while ensuring high precision and reliability, paving the way for early track anomaly detection, continuous train positioning, and improved clearance train operations, ultimately contributing to a safer, more efficient, and more reliable railway system.

References

Agrawal, K. S. P. (2012). *Fiber-optic communication systems* (3rd ed.). John Wiley & Sons.

Asawa, C. K., & Yao, S. K. (1983). Microbending fiber optic sensing. *1983 Technical Symposium East*, 9–13. SPIE.

Boynukalin, S., Atieh, A., & Paker, S. (2023). Investigation of hybrid remote fiber optic sensing solutions for railway applications. *Photonics, 10*(864). https://doi.org/10.3390/photonics10080864

Boynukalin, S., Atieh, A., & Paker, S. (2023). Raylı sistemlerde fiber Bragg ızgaralar ile hareketli obje ve hat durumu takibi. *Proceedings of the Conference on Railway Systems and Optical Sensing Technologies*. https://www.researchgate.net/publication/374545995

Griffiths, R. W. (1987). Structural monitoring system using fiber optics (U.S. Patent No. 4,654,520). United States Patent and Trademark Office.

Hartog, A. H. (2017). *An introduction to distributed optical fibre sensors* (pp. 6–38). CRC Press.

He, Z., & Liu, Q. (2021). Optical fiber distributed acoustic sensors: A review. *Journal of Lightwave Technology, 39*(11), 3671–3686. https://doi.org/10.1109/JLT.2021.3059771

IEEE Std 1698-2009. (2009). *IEEE guide for the calculation of braking distances for rail transit vehicles* (pp. 1–41). IEEE. https://doi.org/10.1109/IEEESTD.2009.5332051

Kinet, D., Mégret, P., Goossen, K. W., Qiu, L., Heider, D., & Caucheteur, C. (2014). Fiber Bragg grating sensors toward structural health monitoring in composite materials: Challenges and solutions. *Sensors, 14*(4), 7394–7419. https://doi.org/10.3390/s140407394

Sun, Y., Li, H., Fan, C., Yan, B., Chen, J., Yan, Z., & Sun, Q. (2022). Review of a specialty fiber for distributed acoustic sensing technology. *Photonics, 9*(277). https://doi.org/10.3390/photonics9050277

Werneck, M., Allil, R., Ribeiro, B., & de Nazaré, F. (2013). *A guide to fiber Bragg grating sensors*. Intec Open Science. http://dx.doi.org/10.5772/54682

Xiong, J., Wang, Z., Wu, Y., Wu, H., & Rao, Y. (2020). Long-distance distributed acoustic sensing utilizing negative frequency band. *Optics Express, 28*(24), 35844–35856. https://doi.org/10.1364/OE.403951

SHIPBUILDING AND OCEAN ENGINEERING

Hydrodynamics of Marine and Offshore Structures

Marine Environmental Impact and Pollution Control

Numerical and Experimental Study of The Effect of The Hull Vane on The Total Resistance of The Catamaran

Rahmi Murat Dural[a], Devrim Bülent Danışman[a]

[a] Istanbul Technical University, Department of Naval Architecture and Marine Engineering, Naval Architecture and Ocean Engineering Program, Turkey
dural22@itu.edu.tr

Keywords: Computational Fluid Dynamics (CFD), Experimental Study, Hull Vane, Hydrodynamics.

Aim

The development of technology affects all branches of industry. The maritime industry is a vital and major sector fueled by advanced technological developments implemented to improve safety, efficiency, cost, etc., on the operating ships. Since the early efforts of sailing, humankind has desired to build less resistant, highly efficient ships. As a result, various innovations have been developed to reach the current level of technological advancement in the maritime industry. One of the innovations to increase the efficiency of the ship by lowering resistance is the Hull Vane technology. A Hull Vane (HV) is a submerged wing (hydrofoil) appendage that is transversely fixed at the vessel's transom. Accelerated flow passing through the suction side of the foil creates negative pressure on the stern of the hull, resulting in reduced stern wave and lifting force created from the foil. This lifting force results in trim correction and additional thrust force. This study aims to study the effect of Hull Vane on total ship resistance of a catamaran after the addition of the Hull Vane by performing an experimental study and computational fluid dynamic (CFD) analysis on OpenFOAM (Open Source Field Operation and Manipulation).

Material and Method

There are two methods used in this research: the experimental method and the CFD method. Foil profile of the Hull Vane is chosen as optimized foil profile of NACA 4412 from the study of (Çelik et al., 2021) for both numerical and experimental study. In this work, the Hull Vane is investigated at different locations with different angles of attack to fully look into the importance of the location of the Hull Vane on the total resistance of the model catamaran. Hull Vane's chord and span lengths are kept constant throughout the study. The Hull Vane chord length ratio is kept the same as the study of (Çelik et al., 2021), which is 2.9% of the waterline length, and the span length is the same as the model breadth. The initial location of the hydrofoil's leading edge is located at a horizontal and vertical distance of 2.33% (LWL/43) and 1.87% (LWL/53) of the transom bottom corner. The position of the Hull Vane is shifted horizontally and vertically. Hull Vane's leading edge is positioned horizontally at 3.23% (LWL/31) and vertically at 2.44% (LWL/41). In addition, the Hull Vane is positioned with a 0-degree and 5-degree angle of attack with respect to the calm waterline. Hence, 8 different configurations are created, as given in Table 1. In addition to the eight Hull Vane configurations, the bare hull is also tested at five different speeds from 1.715 m/s (Fr=0.327) to 4.115 m/s (Fr=0.784). CFD analysis and experimental work are conducted with a scale of 1/9 catamaran model. The main dimensions of the catamaran model are given in Table 2. A wooden model is manufactured at the workshop of İTÜ Ata Nutku Ship Model Testing Laboratory (see Image 1.). The model is CFD analyzed and tested at the towing tank for a loading condition of T = 1.235 meters. For the experimental study, 3D printing is concluded to be a cost-efficient manufacturing method that can fulfill the Hull Vane profile sensitivity. Therefore, two sets of the Hull Vane are printed for 0-degree angle of attack configurations and 5-degree angle of attack configurations. 3D printed 0-degree angle of attack Hull Vane is given with the connection part in Image 2. The connection part is supplementary to the printed Hull Vane to attach the Hull Vane to the transom of the model. The connector part is designed to change the vertical and horizontal locations of the Hull Vane according to the studied configuration. The location of the Hull Vane is fixed by bolts attached to the connection part. For 3D printing parts, PLA material is used. PLA is a cost-effective option for the ABS material. PLA has a very low thermal shrinkage value and does not cause problems when in contact with water. For numerical study, Open FOAM, which is a free, open source CFD software program is used. OpenFOAM can be

used effectively to solve fluid dynamics problems such as laminar, turbulent, multi-phase flows, etc (Url-1). To calculate the hydrodynamic forces acting on the model scale for bare vessel and Hull Vane installed versions, incompressible Navier-Stokes equations are solved by performing the finite volume discretization. Domain dimensions and boundary conditions for the CFD analysis are determined according to the ITTC Practical Guidelines for Ship CFD Applications (Url-2). Inlet, side, and bottom boundaries are located at 2 LBP away, while the top boundary is 1.5 LBP and the outlet boundary is 4.1 LBP away (downstream direction) from the ship model. The boundary condition of the model hull and Hull Vane were stated as a wall function. The sides and bottom boundaries were specified as symmetry conditions. Inlet, outlet, and atmosphere boundary conditions were separately defined in compliance with flow characteristics and turbulence parameters. Around 1.1 million number of mesh is used in the domain, and detailed mesh views are given in Figure 1.

Table 1. Hull Vane configuration table.

HV No.	Angle of Attack	HV Trailing Edge AP (TEAP)	HV Trailing Edge Draft (TED)
1	0	LWL/43	LWL/53
2	0	LWL/31	LWL/53
3	0	LWL/43	LWL/41
4	0	LWL/31	LWL/41
5	5	LWL/43	LWL/53
6	5	LWL/31	LWL/53
7	5	LWL/43	LWL/41
8	5	LWL/31	LWL/41

Table 2. Main Dimensions of the catamaran.

Scale (α)	9	Model	Ship
Length between perp.	LBP (m)	2.778	25.00
Waterline Length	LWL (m)	2.811	25.301
Breadth (at wl)	B (m)	0.783	7.049
Hull separation	Sc (m)	0.546	4.914
Draught (midship)	T (m)	0.137	1.235
Displacement volume	∇ (m^3)	0.101	3.642
Displacement	Δ (ton)	0.101	75.550
Block coefficient	CB	0.334	0.334
Service speed	V_S	4.115 m/s	24 knot
Froude number	Fr	0.78	0.78

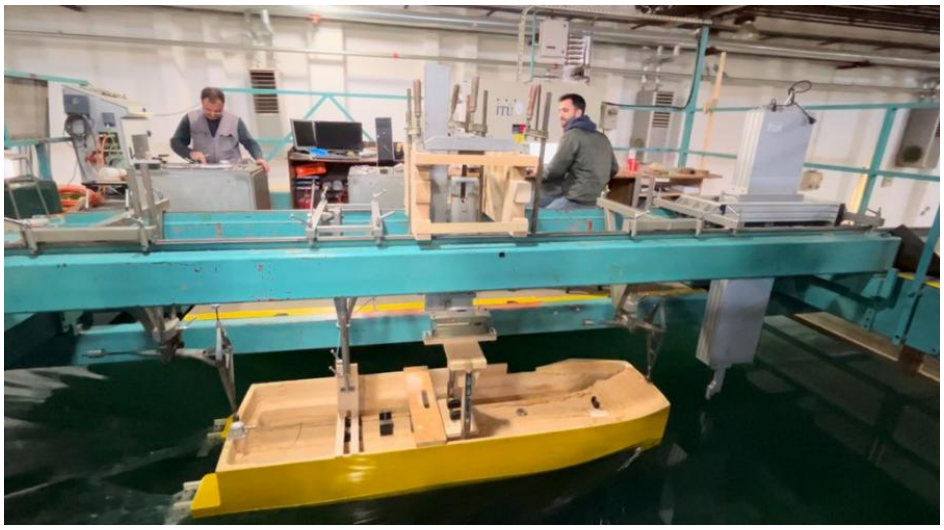

Image 1. ITU Ata Nutku Ship Model Testing Laboratory towing carriage.

Image 2. 3D printed Hull Vane model.

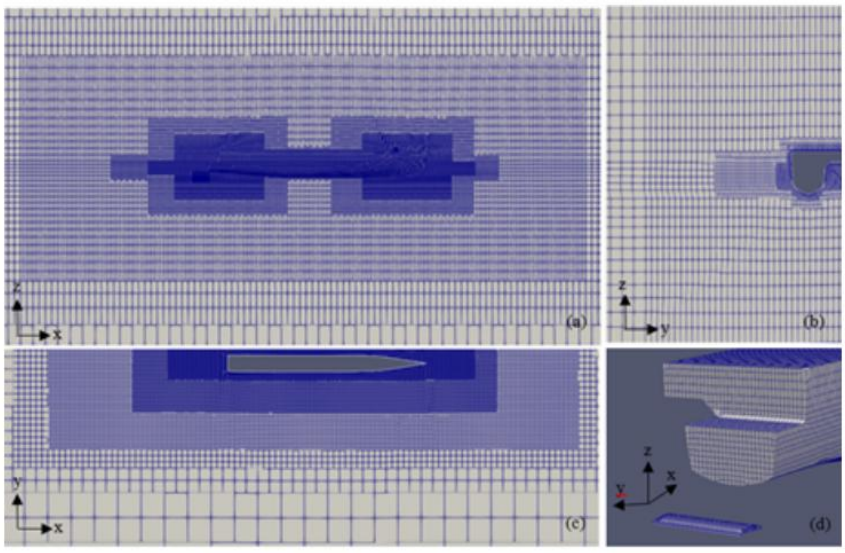

Figure 1. Detailed mesh views of the ship model from (a) profile, (b) section, (c) top, and (d) stern.

Findings

Findings of the experimental and numerical analysis show that the Hull Vane attachment is advantageous on the catamaran around 0.35-0.63 Fr, which is in line with the previous studies. It is also found that the Hull Vane provides extra resistance and becomes a disadvantage outside this range. Sinkage data show that when the speed of the model passes around 0.65 Fr, the sinkage of the vessel increases for all Hull Vane appended configurations. Thus, resulting in increased total resistance compared to the bare hull. Among the Hull Vane configurations, the designs with the 0-degree angle of attack gave better results than the designs with the 5-degree angle of attack. In Figure 2., a comparison of the numerical and experimental C_T differences for bare hull vs 0-degree angle of attack HV configurations are given. In Figure 3., a comparison of the numerical and experimental C_T differences for bare hull vs 5-degree angle of attack HV configurations are given. Comparing Figure 2. and Figure 3., the advantage of 0-degree angle of attack HV configurations over 5-degree ones can be seen, and the performance of HV with comparison to the bare hull relative to the speed of the model can be observed. Trim data shows that Hull Vane configurations with a 5-degree angle of attack cause excessive trim compared to the bare hull, causing disadvantages. This occurs because the excessive z-component of the lifting force causes the x-component, which causes thrust to decrease, causing drag and decreased total resistance. Also, it is observed that the configuration named HV3 with a 0-degree angle of attack with LWL/43 vertical and LWL/41 horizontal distance from the trailing edge is found to be the most advantageous design, providing total resistance reduction for a wider speed range with higher percentages (around 0.32-0.62 Fr). HV3 total resistance coefficient reduction peaks at 7.8 % at 2.401 m/s (0.457 Fr) compared to the bare hull total resistance coefficient at the same speed.

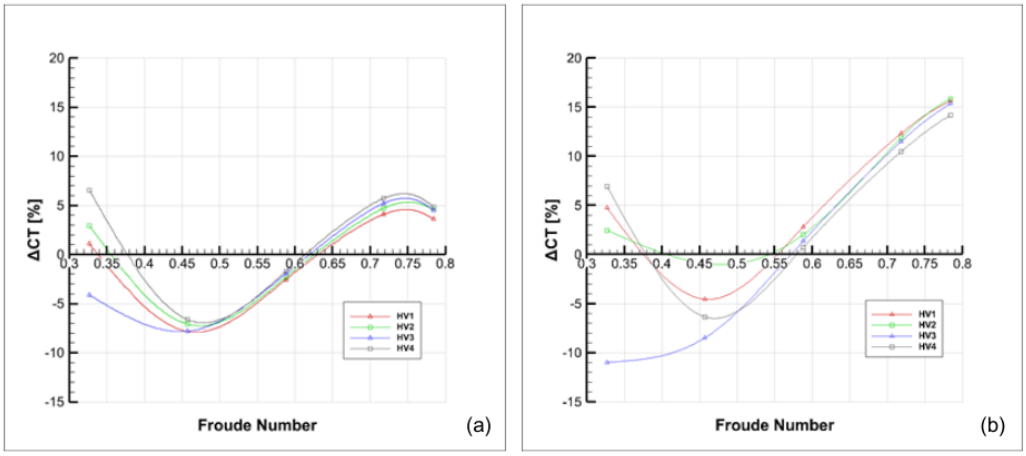

Figure 2. Comparison of the experimental (a) and numerical (b) C_T Differences for Bare Hull (BH) vs Hull Vane Configurations (HV1-HV4).

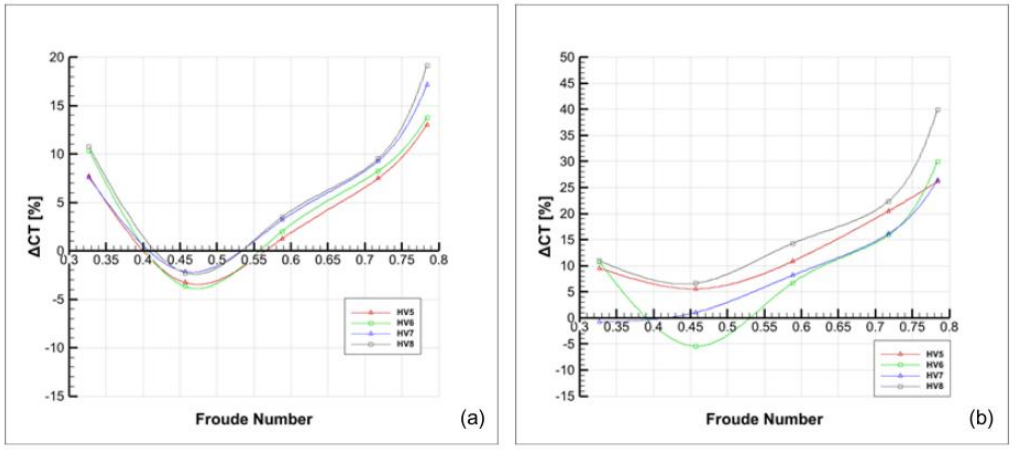

Figure 3. Comparison of the experimental (a) and numerical (b) C_T Differences for Bare Hull (BH) vs Hull Vane Configurations (HV5-HV8).

Conclusion

It is concluded that the Hull Vane is an advantageous appendage for ship operators who want to reduce their ship's fuel consumption by reducing the total resistance of the ship, thus resulting in decreased cost and carbon emission levels that comply with the International Maritime Organization (IMO) regulations. However, this innovation is interesting for vessels that operate at a moderate to high non-planing speed, it is not optimal for all ships and all operating speeds. Therefore, a detailed experimental and numerical investigation should be conducted for the specific ship to better evaluate the applicability of the Hull Vane. This work exhibits that for the studied catamaran vessel, the Hull Vane appendage achieves total resistance reduction at lower speeds (around 0.3-0.6 Fr) and up to around 8 % total resistance reduction. For future work, it is necessary to find the optimal values of the Hull Vane position and the angle of attack by using data-driven optimization techniques applied to an expanded dataset to further increase the advantage of the Hull Vane on the total resistance of the catamaran.

References

Çelik, C., Danışman, D. B., Khan, S., & Kaklis, P. (2021). A reduced order data-driven method for resistance prediction and shape optimization of hull vane. Ocean Engineering, 235, 109406. https://doi.org/10.1016/j.oceaneng.2021.109406

Url-1 https://doc.cfd.direct/openfoam/user-guide-v12/index, data retrieved 08.03.2025

Url-2 https://ittc.info/media/1357/75-03-02-03.pdf, data retrieved 08.03.2025

SOIL MECHANICS AND GEOTECHNICAL ENGINEERING

Environmental Geotechnics

Foundation Engineering

Geotechnical Earthquake Engineering

Geotechnics

Comparison of Different Methods for Dynamic Earth Pressures on a Retaining Wall

Perim Kılıç[a], Recep İyisan[a]

[a]Istanbul Technical University, Department of Civil Engineering, Soil Mechanics and Geotechnical Engineering, Türkiye
kilicp22@itu.edu.tr

Keywords: Retaining Walls, Lateral Earth Pressures, Dynamic Earth Pressures.

Aim

Retaining walls, like many other structures, have been damaged or destroyed due to devastating earthquakes throughout history. Retaining walls that support important structures such as roads, buildings, bridges and slopes can affect the damage that may occur in these structures. Therefore, the design of retaining walls in earthquake zones is of great importance in terms of usability and safety of the environment (Singh et al., 2023). The seismic behavior of retaining structures is a widely studied topic in geotechnical engineering due to its effects on the safety and stability of structures in earthquake zones. Retaining structures are important because they provide structural support and prevent the movement of the soil mass, especially when the ground elevation or slope geometry changes (Thottoth et al., 2024). Retaining walls are generally under the effect of lateral earth pressures. These earth pressures are static pressures due to gravity and dynamic pressures due to earthquake loads. Dynamic earth pressures acting on retaining walls in earthquake zones differ from static pressures in distribution and magnitude (Kramer & Stewart, 1996). It is observed that a lot of damage occurs in retaining structures as a result of ground movements caused by pressure increases during earthquakes. When designing a retaining wall, the structure must resist static and dynamic lateral earth pressures. At the same time, when constructing a safe retaining wall, care should be taken to design the structure economically. For these reasons, the necessary static and dynamic analyses must be performed to design an optimum retaining wall. To properly design and construct retaining structures, the lateral earth pressures between retaining structures and soil masses must be known in detail. The magnitude and distribution of the lateral earth pressure depend on factors such as the shear strength parameters of the soil, the slope of the backfill surface, the slope and height of the retaining wall on the surface between the wall and backfill, the angle of adhesion and friction on the surface between the wall and backfill (Das, 2010).
This study aims to determine the dynamic earth pressures on retaining walls using different methods and compare the results obtained. It is desired to determine the differences between the methods and their effects on dynamic earth pressures. Lateral dynamic earth pressures will be analyzed for a retaining wall in the same model. In the study, the effects of distributed load and backfill soil properties on dynamic soil pressures will also be investigated. It is aimed to contribute to engineering applications by determining and comparing dynamic earth pressures according to the methods.

Material and Method

This study will determine dynamic lateral earth pressure on the retaining wall according to Mononobe Okabe, Seed & Whitman methods and Türkiye Building Earthquake Code (TBDY-2018). Some parameters were selected as variables to analyze this study in more detail. The shear strength angle (φ), retaining wall length (H) and the distributed load (q) of the backfill soil behind the retaining wall were selected as variables In the calculations, the effects of different methods and the selected variable parameters on the earth pressures were investigated. The selected parameters and their values are given in the Table 1.

Table 1. Selected parameters and their values.

H (m)	ϕ (˚)	q (kPa)
4	25.0	15
5	27.5	30
6	30.0	
7	32.5	
8	35.0	

Findings

As a result of the detailed literature review, it is revealed that there are many studies to determine the earth pressures on retaining walls. Rankine and Coulomb Theory are the most widely used basic methods for determining static earth pressures. It is seen that later-developed methods are based on these theories. In the event of an earthquake, retaining walls are affected by static earth pressures as well as dynamic earth pressures due to ground movements. Dynamic earth pressures can be determined using Mononobe-Okabe, Prakash-Saran, Seed & Whitman, and Steedman-Zeng methods. Together with these methods, there are earthquake codes that countries have created according to their conditions. The methods developed to find dynamic earth pressures are generally based on the Mononobe Okabe method. In the Mononobe-Okabe method, in addition to the forces existing in the static state, lateral and vertical inertial forces due to the earthquake effect are applied to the Coulomb active (or passive) wedge mass. With these forces acting on the wedge, a force polygon is created, and dynamic earth pressure is obtained. Maximum active force is found by drawing different force polygons. TBDY is based on the Mononobe-Okabe method with some differences while determining the earth pressures acting on the retaining structures under earthquake ground motion. In TBDY, the vertical seismic coefficient k_v is acting both downward and upward. Seed and Whitman (1969) use the formulas in the Mononobe-Okabe analysis when determining the active earth pressure coefficient. The Mononobe-Okabe method assumes that the total dynamic earth pressure acts at H/3 from the base of the wall of height H (Kramer & Stewart, 1996). However, Seed and Whitman calculate the point of action of the active earth pressure differently than the Mononobe-Okabe method. In Figure 1. the distribution of earth pressures acting on the retaining wall is shown for static and dynamic lateral loads.

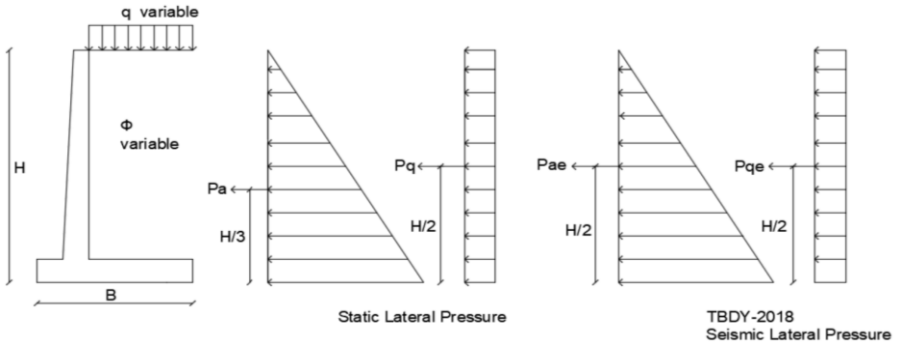

Figure 1. The load distribution of static and dynamic earth pressures on the retaining wall.

The changes in dynamic soil pressures according to the shear strength angle, wall length and distributed load values for three methods are given in Figures 2. 3. and 4.

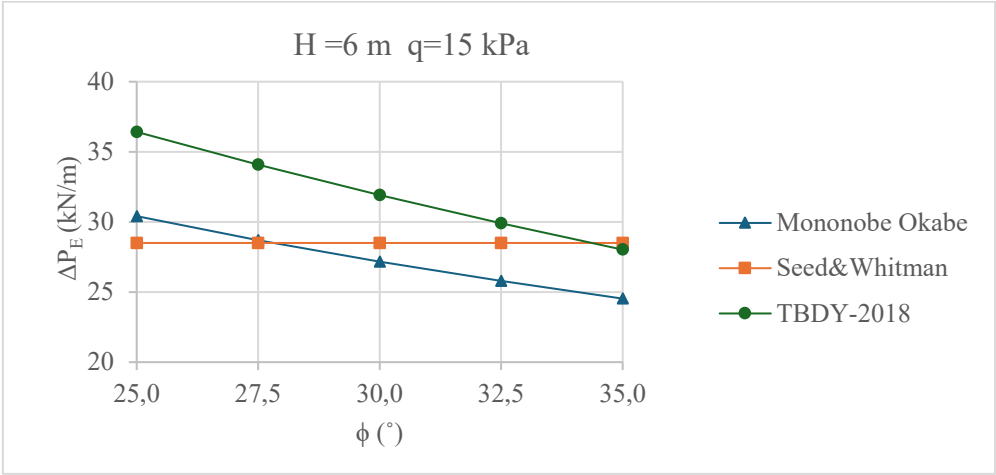

Figure 2. Variation of additional dynamic earth pressure with shear strength angle.

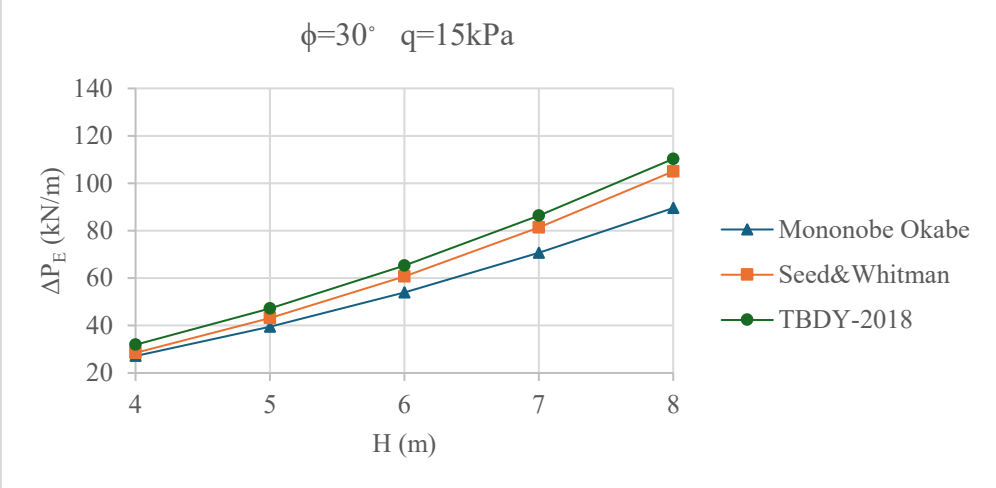

Figure 3. Variation of additional dynamic earth pressure with wall height.

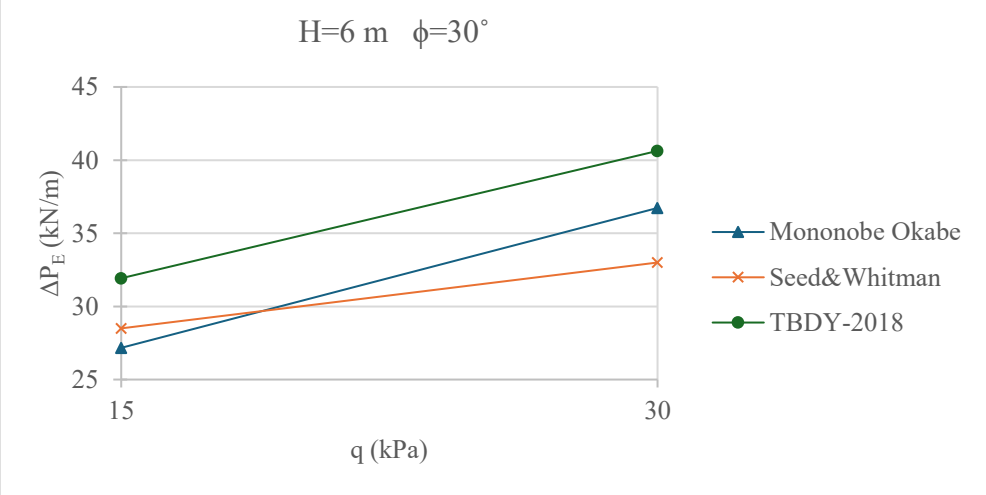

Figure 4. Variation of additional dynamic earth pressure with the distributed load value.

Conclusion

In this study, dynamic soil pressures on the retaining wall were calculated according to Mononobe Okabe, Seed and Whitman and TBDY-2018. The effect of the obtained results on dynamic earth pressures was investigated. The Mononobe-Okabe and Seed-Whitman methods provide simplified approaches. While both are practical for preliminary analyses, they do not fully capture dynamic earth pressures. TBDY-2018 based on current seismic data, considers soil classes and structural response. For this reason, it can be said that it gives more comprehensive results. TBDY-2018 represents a more advanced and regulated methodology aligned with current engineering standards.

References

Das, B. M. (2010). Principles of Geotechnical Engineering (7. ed.).

Kramer, S. L., & Stewart, J. P. (1996). *Geotechnical earthquake engineering*. CRC Press.

Singh, P., Bhartiya, P., Chakraborty, T., & Basu, D. (2023). Numerical investigation and estimation of active earth thrust on gravity retaining walls under seismic excitation. *Soil Dynamics and Earthquake Engineering*, *167*, 107798.

TBDY, (2018) *Türkiye Bina Deprem Yönetmeliği*, Afet ve Acil Durum Yönetimi Başkanlığı, Ankara.

Thottoth, S. R., Khatri, V. N., Kolathayar, S., Keawsawasvong, S., & Lai, V. Q. (2024). *Optimizing seismic earth pressure estimates for battered retaining walls using numerical methods and ANN*. Geotechnical and Geological Engineering, *42*(5), 3307-3329.

STRUCTURAL ENGINEERING

Bridges

Finite Element Methods

Reinforced Concrete Structures

Seismic Performance

Steel Structures

Structural Damages

Effect of Fly Ash on Chloride Permeability and Sulfate Resistence of Concrete

Hüsnü Kadir Özcan[a], Hasan Yıldırım[a]

[a] Istanbul Technical University, Structural Engineering Program, Türkiye
ozcanhusn@itu.edu.tr

Keywords: Fly Ash, Chloride Permeability, Sulfate Resistance, Concrete Durability, Ultrasonic Pulse Velocity.

Aim

This study aims to investigate the effects of high-volume fly ash (HVFA) usage in concrete production on chloride permeability and sulfate resistance. Portland cement, commonly used in traditional concrete production, is an important topic in the search for sustainable building materials due to its high carbon footprint and environmental impact (Malhotra and Mehta, 2002). Fly ash is a pozzolanic additive used as a replacement for cement, with the potential to improve the mechanical properties and durability of concrete (Bilodeau et al., 1994; Bouzoubaa et al., 2000). In this context, the main objective of the study is to perform a comparative analysis of concrete mixes containing different proportions of HVFA in terms of chloride ion penetration, sulfate resistance, and general mechanical properties. Research by Malhotra (1986) showed that the inclusion of fly ash significantly improved the permeability characteristics of concrete. Similarly, Ramezanianpour and Malhotra (1995) found that fly ash-containing concretes were more resistant to chloride ion penetration, and curing conditions directly influenced this durability. When examining the sulfate resistance of concrete, it was determined that mixes with high-volume fly ash showed resistance to sulfate attack (Sivasundaram et al., 1992). The study aims to improve the long-term durability of concrete by evaluating the potential of fly ash to reduce chloride permeability and increase sulfate resistance.

Material and Method

The materials used in this study include CEM I 42.5 R type cement produced at the Nuh Cement's Hereke factory and fly ash sourced from a single supplier. Concrete samples were prepared by using different amounts of fly ash in the mixtures. The fly ash amounts were determined as K250+70 and K250+90, with 70 kg and 90 kg of fly ash used, respectively. Additionally, a control sample (R001) without fly ash was included in the experiments. The chemical and physical properties of the fly ash, including SiO2, Al2O3, and Fe2O3 contents, are classified as Class C according to ASTM C 618 standard. Experimental methods include the evaluation of the physical and chemical properties of the concrete mixtures, such as chloride permeability, compressive strength, and ultrasonic pulse velocity. The chloride permeability of the concrete samples was measured using the Rapid Chloride Permeability Test (ASTM 1202-10), and the compressive strength of the concrete was tested using the Hardened Concrete Compressive Strength Test (TS EN 12390-3). Additionally, the Ultrasonic Pulse Velocity Test was conducted to assess the internal structure and durability of the concrete samples. These experiments were performed to determine the effects of fly ash on the concrete mixtures and their durability.

Findings

In this study, the performance of different concrete mixtures was examined in terms of compressive strength and chloride permeability. While compressive strength determines the load-bearing capacity of concrete, chloride permeability is a critical factor affecting the structure's resistance to corrosion. Comparisons made by considering various aging processes (7-day, 28-day, and post-sulfate exposure) revealed the performance differences among different concrete codes.

As a result of the experiment, the chloride ion permeability of the reference concrete R300, which does not contain fly ash, was measured as 1402.1 Coulombs, placing it in the high permeability category. Among the mixtures containing fly ash, the K250+70 sample showed a slight reduction in permeability with a value of 1151.4 Coulombs, while the lowest permeability was observed in the K250+90 sample with 621.5 Coulombs. These

results indicate that increasing the amount of fly ash improves the pore structure of the concrete, thereby limiting ion penetration and enhancing resistance to chloride ions. In particular, the K250+90 mixture demonstrated the best performance with its low permeability level (See Table 1).

Table 1. Rapid Chloride Permeability Test Results.

Concrete Code	Passed Charge (Coulomb)
R300	1402.1
K250+70	1151.4
K250+90	621.5

As a result of the experiment, the sulfate resistance compressive strength of the reference concrete R300 was measured as 46.4 N/mm², while this value reached 54.0 N/mm² in the fly ash-containing mixtures K250+70 and K250+90 (See Table 2).

Table 2. Compressive Strengths of Reference and Fly Ash-Containing Concretes (N/mm²).

Concrete Code	7-Day	28-Day	After Sulfate Exposure
R300	33.4	43.0	46.4
K250+70	31.4	42.8	54.0
K250+90	34.3	44.9	54.0

The results obtained from the study demonstrate that the use of fly ash significantly enhances the strength and durability properties of concrete. Notably, the K250+70 and K250+90 specimens exhibited clear improvements in both chloride ion permeability and resistance to sulfate attack with increasing amounts of fly ash. In terms of compressive strength at 7 and 28 days, the mixtures containing fly ash performed similarly to, or even better than, the reference concrete (R300), indicating that fly ash does not negatively affect early or long-term strength and may even improve it under certain conditions (See Figure 1).

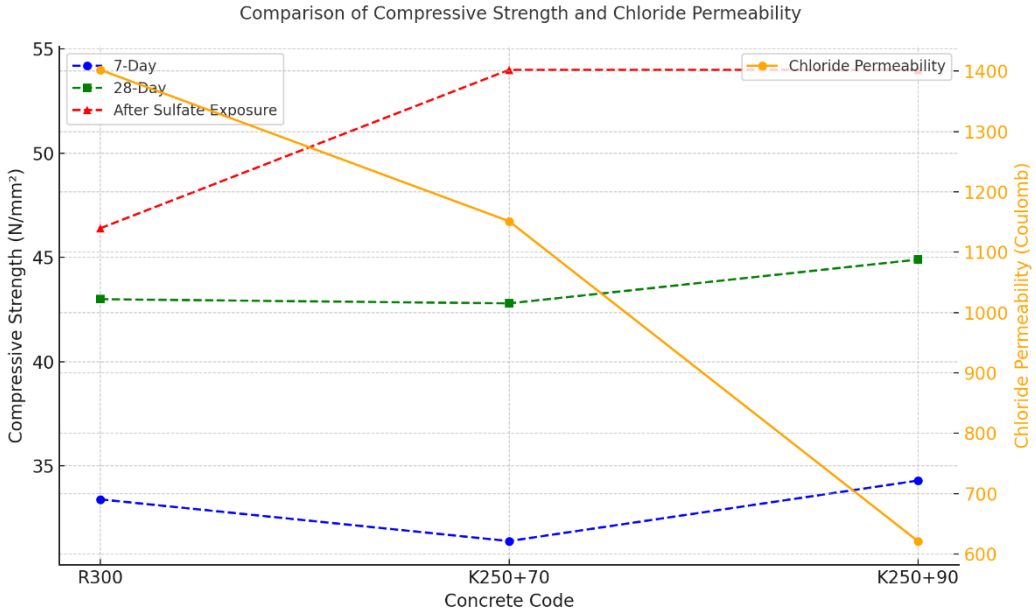

Figure 1. Comparison Of Concrete Strength and Chloride Permeability.

With regard to chloride permeability, the reference sample R300 exhibited a charge passed of 1402.1 Coulombs, whereas the K250+90 sample showed a significant reduction to 621.5 Coulombs. This result indicates that fly ash refines the pore structure of concrete, effectively reducing permeability and enhancing resistance to external

agents. A similar trend was observed in sulfate resistance. While the compressive strength of R300 after sulfate exposure was 46.4 N/mm², this value increased to 54.0 N/mm² in both K250+70 and K250+90 samples. These findings suggest that fly ash forms a protective matrix within the concrete, enhancing long-term durability against sulfate attack. In summary, the inclusion of fly ash in concrete mixtures proves to be an effective strategy for improving durability by reducing permeability and increasing chemical resistance. Among the samples, K250+90 demonstrated the best performance with the lowest chloride permeability and highest sulfate resistance. These findings clearly highlight the potential of fly ash as a strategic additive for producing sustainable, durable, and environmentally friendly concrete.

Table 3 presents the results of the ultrasonic velocity test for the concrete samples. This test is an important parameter for assessing the structural integrity and durability of concrete, and an increase in ultrasonic velocity indicates that the concrete is stronger and more durable. Below are the ultrasonic velocities (in km/s) of each concrete mixture over time:

Table 3. Ultrasonic Velocity Measurements (km/s) for Concrete Samples at Different Ages.

Concrete Code	15 Days	30 Days	45 Days	60 Days	90 Days	156 Days	387 Days	402 Days
R300	4.77	5.11	4.90	5.15	5.00	4.90	5.20	5.05
K250+70	4.87	5.13	4.85	5.23	5.45	4.99	5.27	5.14
K250+90	4.95	5.13	5.01	5.29	5.36	5.09	5.24	5.17

Ultrasonic velocity is an important test used to understand the internal integrity and durability of concrete. An increase in ultrasonic velocity indicates that the concrete is harder and more durable. According to the test results, the ultrasonic velocity of the K250+90 mixture remains more stable and at higher levels compared to the other mixtures. This indicates that with an increase in fly ash content, the structural integrity of the concrete is better preserved and it is more resistant to sulfate effects. Notably, the higher and more stable ultrasonic velocities of the K250+90 mixture after the 90th day demonstrate that fly ash contributes to enhancing the durability of the concrete. In the case of the K250+70 mixture, the ultrasonic velocity shows lower values compared to the K250+90 mixture, and a decline over time is observed. This indicates that the sulfate effect has a greater impact on the K250+70 mixture, and as the fly ash content increases, this effect diminishes. In the R300 mixture, the fluctuation in ultrasonic velocity and generally lower levels suggest that the concrete without fly ash has weaker structural integrity and is less resistant to sulfate effects.The durability and long-term performance of concrete are evaluated using parameters such as chloride permeability and ultrasonic velocity. Chloride permeability indicates the concrete's resistance to harmful ions, while ultrasonic velocity measurements help determine the integrity and density of the concrete's internal structure. In this study, the chloride permeability and ultrasonic velocity values of different concrete mixtures were examined to assess the material's durability (See Figure 2).

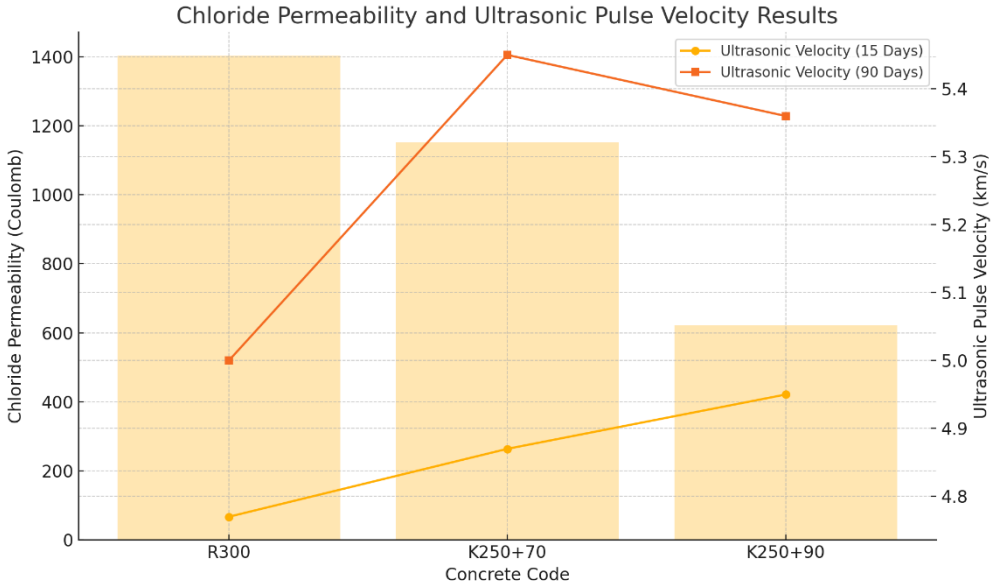

Figure 2. Chloride Permeability and Ultrasonic Pulse Velocity Results.

Conclusion

The increase in fly ash content significantly enhances the chemical durability of concrete. In chloride permeability tests, as the amount of fly ash increases, the chloride permeability of the concrete decreases noticeably. This results in reduced water permeability, making the concrete more resistant to chemical attacks. Fly ash decreases the porosity of the concrete, preventing the passage of water and chloride ions, and thereby contributing to the long lifespan of the concrete. The durability and long-term performance of concrete are evaluated using parameters such as chloride permeability and ultrasonic velocity. Chloride permeability shows the concrete's resistance to harmful ions, while ultrasonic velocity measurements help determine the integrity and density of the concrete's internal structure. In this study, the chloride permeability and ultrasonic velocity values of different concrete mixtures were examined to assess the material's durability. The following findings compare the ultrasonic velocity values and chloride permeability levels of samples with different concrete codes at 15 and 90 days. Under sulfate exposure, the stability of the ultrasonic velocity is an important parameter indicating the concrete's resistance to sulfates. The more stable ultrasonic velocity in the K250+90 mixture indicates that the concrete is more resistant to sulfates. These findings show that fly ash is a factor that enhances the concrete's resistance to sulfates. By maintaining the structural integrity of the concrete, fly ash makes it more resistant to the damage caused by sulfate reactions within the concrete. In conclusion, the addition of fly ash to concrete mixtures increases the concrete's resistance to sulfates, resulting in stronger and more durable structures. Therefore, high fly ash content concrete mixtures should be preferred for constructing structures that are particularly resistant to chemical attacks.

References

Bilodeau, A., Sivasundaram, V., Painter, K. E., & Malhotra, V. M. (1994). Durability of concrete incorporating high volume fly ash from sources in the U.S. ACI Materials Journal, 91, 3-12.

Bouzoubaa, N., Zhang, M. H., & Malhotra, V. M. (2000). Laboratory produced high-volume fly ash blended cements: Compressive strength and resistance to chloride-ion penetration of concrete. Cement and Concrete Research, 30, 1037-1046.

Bouzoubaa, N., Zhang, M. H., & Malhotra, V. M. (2001). Mechanical properties and durability of concrete made with high-volume fly ash blended cements using a coarse fly ash. Cement and Concrete Research, 31, 1393-1402.

Malhotra, V. M. (1986). Superplasticized fly ash concrete for structural concrete application. Concrete International, 8(28), 28-31.

Malhotra, V. M., & Mehta, P. K. (2002). High performance, high volume fly ash concrete. Supplementary Cementing Materials for Sustainable Development Inc.

Ramezanianpour, A. A., & Malhotra, V. M. (1995). Effect of curing on the compressive strength, resistance to chloride-ion penetration, and porosity of concretes incorporating slag, fly ash, or silica fume. Cement and Concrete Composites, 17, 125-133.

Sivasundaram, V., Carette, G. G., & Malhotra, V. M. (1992). Concrete incorporating high volumes of ASTM Class F fly ashes: Mechanical properties and resistance to deicing salt-scaling and chloride-ion penetration. American Concrete Institute SP, 132(1), 319-349.

STRUCTURAL ENGINEERING

Bridges

Finite Element Methods

Reinforced Concrete Structures

Seismic Performance

Steel Structures

Structural Damages

High-Temperature Performance of Concrete Containing Calcium Aluminate and Portland Cements

Halil Gençoğlu[a], Muhammet Tekingündüz[a], Hasan Yıldırım[a]
[a] Istanbul Technical University, Faculty of Civil Engineering, Türkiye
gencoglu19@itu.edu.tr

Keywords: Aggregate, Calcium Aluminate Cement, High-Temperature Resistant Concrete, Mechanical Properties Of Concrete, Portland Cement.

Aim

In today's world, the performance of building material at high temperatures is crucial for both the safety of occupants and the structural integrity of buildings. To avoid the deterimental effects of this environment, many materials have been designed and produced. Concrete is one of them-a material that can be durable at elevated temperatures. However, concrete produced with Portland cement (PC) has some drawbacks in maintaining its mechanical properties at these levels. The compressive strength and other mechanical properties of concrete produced with Portland cement (PC) decline sharply above 400–600°C because the CH ($Ca(OH)_2$) in hydrated Portland cement begins to decompose at these temperature levels. Due to the shortcomings of concrete containing Portland cement (PC), calcium aluminate cement (CAC) was explored as a potential replacement. In contrast to Portland cement, CAC does not contain CH ($Ca(OH)_2$) in its hydrated phase. For this reason, it is considered a more favorable cement type for producing concrete with a service temperature above these levels and is often associated with the refractory concrete— a type of high-temperature-resistant concrete made with calcium aluminate cement (CAC) [1][2]. Despite its superior advantages, concrete containing CAC undergoes a conversion mechanism— a type of recrystallization of certain hydrated compounds — which leads to noticeable proportional decreases in strength. As a result, it is often considered a less preferable material for use in building construction [3].

In spite of the sheer amount of research regarding the performance of building materials, especially concrete, at high temperatures, their scopes and contents resemble one another and do not differ significantly, leading to a deficiency in literature. In the modern academic field and codes, most research discussing the performance of concrete elements at high temperatures involves the aggregates that can withold high temperatures and are conducted at temperatures below 800 ºC. Moreover, although the amount of research related to refractory concrete has significantly increased in recent years, knowledge about calcium aluminate cement (CAC) and the comparison of its performance with Portland cement (PC) at high temperatures is still very limited and most of them are not prepared in detail [4]. In light of these factors, there should be new research in this field. In this research, the main goal is to contribute new and accurate knowledge and data about the high-temperature performance of concrete to the academic field by properly conducting relevant experiments and analyses.

Material and Method

In the research, there are a total of six different types of concrete which will be separated into two main types: those produced with portland cement (PC) and those made with calcium aluminate cement (CAC), resulting in three concrete types for each group. The three types of concrete will be separately produced with three types of aggregates: sandstone, basalt and limestone. The water-to-binder ratio is 0.45 and cement dosage is 400 kg, and both parameters remain same for all concrete.

In the first phase, the concrete was produced and cast into 10x20 cm cylindrical specimens. The fresh state tests such as workability and unit weight will be conducted on the produced concretes. In the end of this phase, standard curing with water will be applied for 28 days to the samples, which will be demolded the day after casting.

Secondly, after 28 days curing of specimens in curing pools, the specimens will be exposed to high temperatures ranging from 200°C to 1000°C for at least two hours, and each specimen will be ovendried at only one temperature level. When the temperature at the core of the specimens reaches the target degree, they will be removed and left

to cool until their temperature equilibrates with the ambient temperature. The central temperature will be measured by using high-temperature resistant thermocouples.

Figure 1. Heating process of specimens made with calcium aluminate cement (CAC) at 800 °C.

Figure 2. Mortars produced with CAC after being held at 800 °C for one hour.

This experiment type is the residual test which is one of the three main types of high-temperature experiments: 'stressed', 'unstressed' and 'residual'. For all methods, the specimen is taken out from the furnace when the temperature at its the center reaches the target temperature. However, there are other factors that vary from one another. In the 'stressed' test, the specimen is subjected to 0.4 f_c stress in the furnace and is immediately subjected to relevant mechanical test upon removal from the furnace. In contrast, there is no such a thing that applying forces to specimen during heating in the 'unstressed' test. For 'residual' test, the specimen needs to be cooled after heating until its core temperature drops to ambient temperature: this process typically takes 24 hours [5].
Finally, the mechanical experiments will be conducted on the cooled samples to measure changes in compressive strength, elasticity modulus and mass. Based on the data obtained at different high-temperature values, the various statistical models will be developed to compare the behavior of these mixtures at ambient temperatures (approximately 23-25°C) with their behavior at high temperatures.

Figure 3. Compression test of unheated sandstone specimen containing CAC.

Figure 4. Cube specimen made with limestone and CAC under compression test after being held at 400 °C.

Findings

So far, the production of all concrete mixtures for this study has been completed, and the heating and mechanical experiments will be performed after the curing of the concrete is complete.
However, as a preliminary preparation for this study, mortars were produced using exactly the same materials as in the main study. There are some differences between the produced concrete and mortars. Instead of using a 0.45 water/binder ratio and casting into cylindrical specimens, the mortars were made with a 0.35 water/binder ratio and poured into prism molds with dimensions of 40×40×160 mm. Later, 40x40x40 mm cube mortars were made by slicing those prisms into cubes. After 14 and 28 days curing, those specimens were exposed to separately exposed at 400°C and 800°C for a hour each. At 400°C, the average relative compressive strength compared to ambient temperature strength for mortars containing fine sandstone, limestone, and basalt is %60.41, %73.45, and %74.18 respectively for those made with Portland cement (PC), and %55.39, %70.11, and %56.69 for those made with calcium aluminate cement (CAC). At 800°C, the results are %26.81, %17.42, and %30.36 for mortars produced with Portland cement (PC), and %50.56, %62.01, and %65.03 for those made with calcium aluminate cement (CAC), following the same aggregate order. Assumptions and conclusions can be drawn from this mortar research, both for general insights and for guiding the ongoing main study.

Firstly, there is a significant decrease in the compressive strength of mortars produced with Portland cement (PC) at 800°C compared to that at 400°C. This phenomenon was also studied for three types of aggregates—gravel, ilmenite, and baryte—by Sakr and El-Hakim [6], showing that concrete containing Portland cement (PC) dramatically loses its strength after 500°C.

In addition, mortar containing calcium aluminate cement (CAC) performed better at 800°C—a high temperature—than those produced with Portland cement (PC). The work by Khan and Khaliq [7] reported similar results at 400°C and 800°C for concrete aggregate produced with separately Portland cement (PC) and calcium aluminate cement (CAC), both containing limestone aggregate. It was stated that the compressive strength of concrete at 400°C, relative to its strength at ambient temperature, was %77 and %76 for mixtures with Portland cement (PC) and calcium aluminate cement (CAC), respectively; and at 800°C, the values were %22 and %29, in the same order of cement types. Furthermore, Koksal et al. [8] studied a similar effect, and their research observed that mortars made from calcium aluminate cement (CAC) withstood further than those with Portland cement (PC) above 600°C.

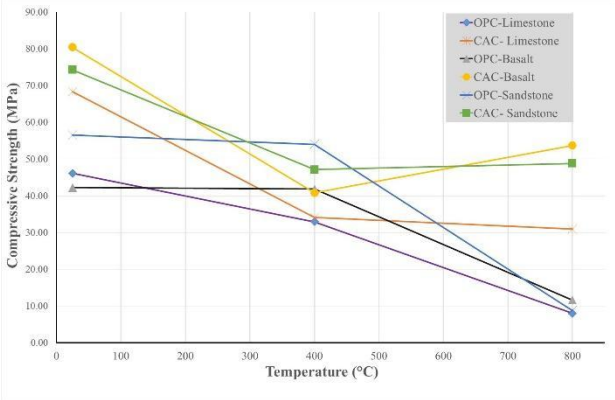

Figure 5. Compressive strength of mortars cured for 14 days as a function of target temperature.

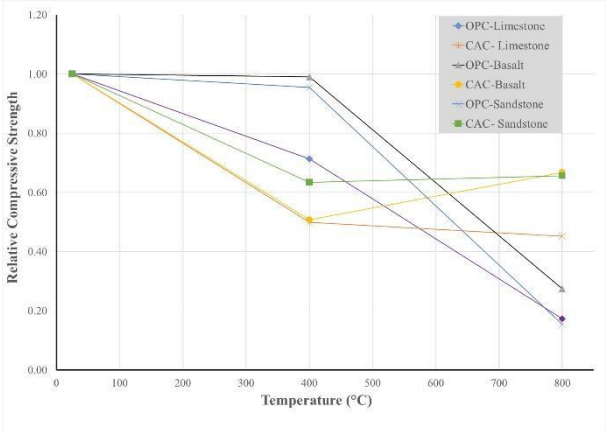

Figure 6. Relative compressive strength of mortars cured for 14 days as a function of target temperature.

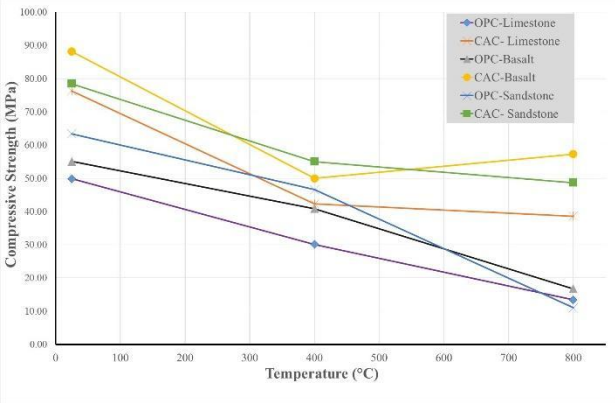

Figure 7. Compressive strength of mortars cured for 28 days as a function of target temperature.

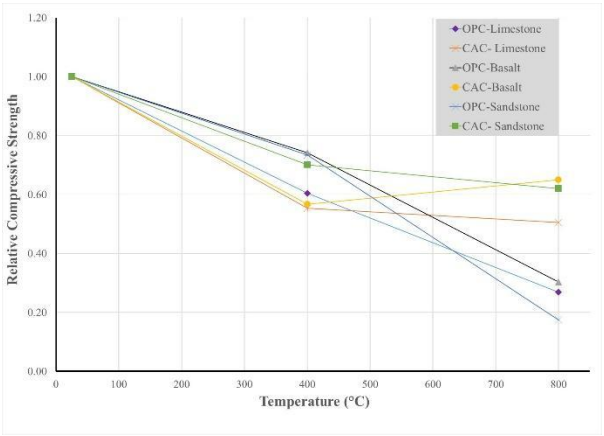

Figure 8. Relative compressive strength of mortars cured for 28 days as a function of target temperature.

Moreover, as shown in our mortar research, the slight decrease—and even increase, as observed in Koksal's study [8]—in the strength of concrete and mortar containing calcium aluminate cement (CAC) above 700°C is likely due to the development of a ceramic bond between the hydrated cement paste and fine aggregates in this type of binder [3]. It was observed that at 600°C and 900°C some mortar produced with calcium aluminate cement (CAC) gained strength ranging from %1.7 to %12.3, depending on the amount of cement and fine aggregate in the mixture [3][9].

Additionally, up to the 400–600°C range—where a dramatic reduction in the strength of concrete produced with Portland cement (PC) begins—concrete containing calcium aluminate cement (CAC) does not retain its strength as well as concrete with Portland cement (PC). In the mortar research, at 400°C, all mixtures with Portland cement (PC) retained more of their strength compared to those made with calcium aluminate cement (CAC). This observation was similarly noted by Newey [3].

Conclusion

In conclusion, at the high temperatures, the performance of concrete can vary depending on the type of cement that concrete contains. With the produced concrete mixtures, the aim is to determine the mechanical and elastic properties of these concretes in their hardened state when exposed to high-temperature.

This study can be beneficial for dealing with certain problems and improving conditions in the construction industry. There are two main area where this research can come in handy.

Firstly, with the infrastructure investments rapidly increasing, a large number of the tunnels are being constructed for railway and highway projects worldwide. When these structures are exposed to fire, the temperature of concrete elements forming the tunnels can swiftly increase. This is because extinguishing the fire could take long time, and the intensity of fire could quickly grow, often causing to structural damages and economic losses. Furthermore, except the tunnels, there is also need high-temperature resistant concrete for the industrial furnaces. As in the tunnels, formal regulations does not present suitable solutions for those furnaces. Since the service temperature is too high in those ovens, the structural elements making up the furnace need to endure these temperature levels. For such situations, modern codes and regulations may be insufficient to overcome them. Therefore, during the construction of these concrete elements, the findings and analyses from this research can help to construct durable and resilient structures.

References

Montgomery, R. (2003). " Heat-resisting and refractory concretes", https://doi.org/10.1016/B978-075065686-3/50290-1

Lhopitallier, P. (Washington DC, 1960). "Calcium aluminates and high-alumina cement", *Proc. 4th Int. Symp. on the Chemistry of Cement*, pp.1007–33

Neville, A. M. (1996). "Properties of Concrete", 4 th ed., USA, New York: John Wiley and Sons.

ElKhatib, L.W., Khatib, J., Assaad, J.J., Elkordi, A., Ghanem, H. (2024). "Refractory Concrete Properties—A Review", https://doi.org/10.3390/infrastructures9080137

Phan, L.T., Carino, N.J. (2002). "Effects of Test Conditions and Mixture Proportions on Behavior of High-Strength Concrete Exposed to High Temperatures", https://www.researchgate.net/publication/279888137_Effects_of_Test_Conditions_and_Mixture_Proportions_on_Behavior_of_High-Strength_Concrete_Exposed_to_High_Temperatures

Sakr, K., EL-Hakim, E. (2005). " Effect of high temperature or fire on heavy weight concrete properties", https://doi.org/10.1016/j.cemconres.2004.05.023

Khaliq, W., Khan, H.A. (2015). "High temperature material properties of calcium aluminate cement concrete", https://doi.org/10.1016/j.conbuildmat.2015.07.023

Koksal, F., Cosar, K., Dener, M., Benli, A., Gencel, O. (2023). "Insulating and fire-resistance performance of calcium aluminate cement based lightweight mortars", https://doi.org/10.1016/j.conbuildmat.2022.129759

Zoldners, N.G., Malhotra,V.M. (May 1964). "Discussion of reference" 2.33, Proc. Inst. Civ. Engrs, 28, pp. 72–3

SUSTAINABILITY

Biodiversity

Climate Change Mitigation

Life Cycle Assessment

Reinforced Concrete Structures

Smart and Sustainable Cities

Sustainable Development Goals

Water and Waste Management

A Multidisciplinary Approach to Sustainable Agriculture: The Impact of Microbial and Organomineral Fertilization on Soil Bacteria, Crop Yield, and Farmer Adoption

Ceyda Alat Doruk[a], Bülent Arıkan[a]

[a]Istanbul Technical University, Eurasia Institute of Earth Secience, Departmant of Ecology and Evolution, Geoanthropology Program, Türkiye
doruk21@itu.edu.tr

Keywords: Microbial Diversity, Microbial Fertilizer, Organomineral Fertilizer, Sustainable Agriculture.

Aim

Agriculture has long been a cornerstone of human survival, influencing economic and social frameworks of civilizations (Altieri, 1999). Modern challenges like increasing populations, climate change, and soil degradation make achieving agricultural sustainability difficult (Tilman et al., 2011). Soil microbiota plays a crucial role in nutrient availability, organic matter decomposition, carbon storage, and disease resistance (van der Heijden et al., 2008). A diverse microbial community is essential for soil health, as beneficial microbes aid nutrient cycling, suppress diseases, and enhance soil structure (Philippot et al., 2023). Excessive synthetic fertilizer use leads to soil acidification, salinization, and nutrient depletion, affecting microbial communities and diminishing productivity (Vitousek et al., 2009). Alternatives include microbial and organomineral fertilizers. Microbial fertilizers contain beneficial microorganisms promoting plant growth (Rehman et al., 2022). Organomineral fertilizers combine mineral nutrients with organic matter, improving soil structure and microbial activity while supplying nutrients; boost soil fertility by releasing nutrients gradually, reducing leaching losses, and increasing nutrient-use efficiency (Uddin et al., 2025). Despite proven benefits, their use remains limited. Farmers often prefer traditional methods due to economic concerns, market uncertainties, and existing policies (Aghabeygi et al., 2024).

This study hypothesizes that combined microbial and organomineral fertilizers will have a more pronounced impact on soil microbial diversity, plant growth, crop yield, and soil quality than either type alone. It aimed to assess effects of microbial, organomineral, and combined fertilization on soil microbial diversity and composition; evaluate changes in soil physicochemical properties; analyze plant growth and crop yield under different treatments; and explore socioeconomic and policy-related barriers to adoption of these fertilization methods by farmers.

Material and Method

The research occurred in Apa Village, Çumra, Konya, on a 23,394 m^2 plot uncultivated for nearly a decade. The field was divided into three 7,000 m^2 areas, separated by one-acre buffer zones. Beans (*Phaseolus vulgaris L.*) were sown using microbial, combined microbial and organomineral, and organomineral fertilizers. Comprehensive soil physicochemical and metagenomic analyses were conducted pre-planting and post-harvest for each area. Soil samples from a neighboring cultivated field served as a control. Plant parameters were measured monthly on 10 random samples per area. Post-harvest, bean samples' physical properties were examined in triplicate. The study ran from 20.05.2023 to 20.09.2023. Amplicon sequencing of the 16S rRNA gene was performed on the Illumina platform. Raw sequences were filtered using DADA2 package (v1.34.0) (Callahan et al., 2016). OTUs were created and classified using SILVA genus database (v138.2) and Naïve Bayes classifier (99% similarity threshold). Mitochondrial, chloroplastic, and undetermined sequences were removed. Soil microbial community structure was assessed using alpha diversity (Shannon, Chao1, Simpson indices) and beta diversity (NMDS based on Bray-Curtis distance). Relationships between soil properties and microbial diversity were examined using Spearman correlation. Statistical differences were determined by PERMANOVA, Wilcoxon, and Kruskal-Wallis tests. Principal Component Analysis (PCA) visualized major microbial genera distribution. Analyses and visualizations were performed in R (v4.2.2). One-way ANOVA determined significance of differences between treatments.

Multiple comparisons used Tukey's HSD test ($p < 0.05$). Pearson correlation analysis determined relationships between soil properties, microbial activity, and plant growth parameters.

Findings

The soil's organic matter content peaked at 1.90% in areas treated with microbial and organomineral fertilizers, while it was lowest at 1.06% where only organomineral fertilizer was used. Soil pH values varied slightly, ranging from 7.48 to 7.78. There were no notable changes in electrical conductivity and phosphorus levels. Potassium content was highest with microbial fertilizer, whereas lime content was highest with organomineral fertilizer.

Beta diversity analysis using NMDS and PERMANOVA based on Bray-Curtis distance showed that fertilization significantly influenced microbial community composition. PERMANOVA indicated phosphorus concentration significantly impacted microbial community differences ($F=2.086$, $R^2=0.294$, $p=0.0023$) (Delgado- Baquerizo et al., 2017). Considering fertilizer applications and soil pH, 45.8% of microbial community variation was explained ($F=1.69$, $R^2=0.458$, $p=0.033$). However, pH alone was not significant ($p=0.090$) due to the limited pH range. The NMDS graph (Figure 1) showed distinct pre-planting and post-harvest microbial communities, indicating plant growth and fertilizers altered microbial composition over time. Microbial fertilizer and microbial-organomineral treatments showed similarities, while organomineral fertilizer alone resulted in a distinct microbial community. The control group was markedly different from other treatments.

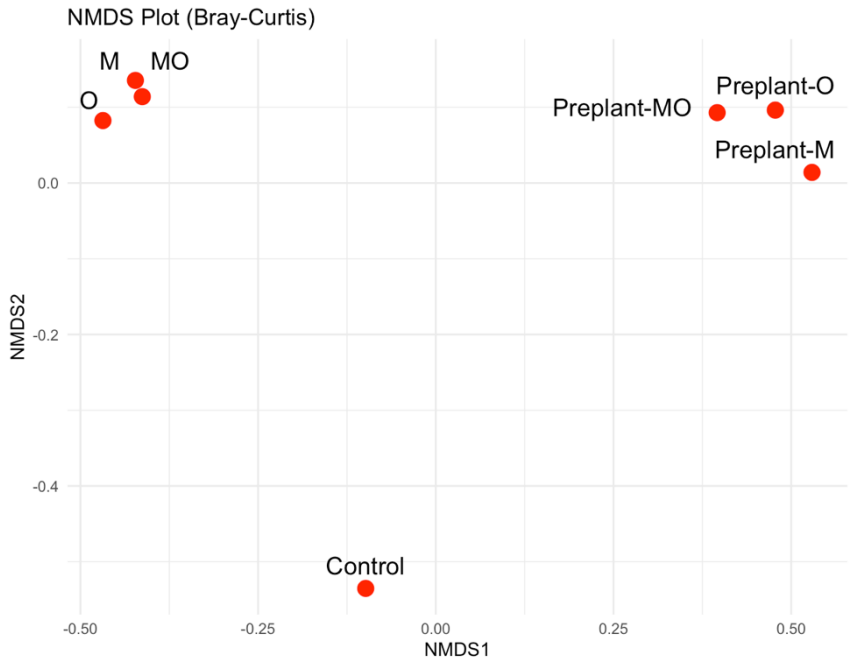

Figure 1. Non-metric Multidimensional Scaling (NMDS) analysis based on Bray-Curtis distances illustrating the impact of different fertilization treatments on soil bacterial community composition.

In alpha diversity analyses, Shannon index values ranged from 3.62 to 4.60, and Simpson index values varied from 0.93 to 0.98, reflecting generally high diversity and balanced species distribution. Chao1 estimated species richness values were between 140 and 395.6. The Kruskal-Wallis test showed no statistically significant differences between treatments in Shannon ($p=0.423$), Simpson ($p=0.512$), and Chao1 ($p=0.297$) indexes. Spearman correlation analysis (Figure 2) evaluated the relationships between alpha diversity indices and soil properties. The Shannon index showed no significant relationship with soil pH ($r=0.037$, $p=0.94$). Although the Chao1 index was negatively correlated with potassium levels, it was not statistically significant ($r=-0.56$, $p=0.19$). The Simpson index had a high positive correlation with phosphorus levels, but this was not statistically significant ($r=0.90$, $p=0.90$). These findings suggest that the observed relationships were not statistically significant, preventing clear biological conclusions. A significant positive correlation was found between potassium and phosphorus levels ($r=0.95$, $p<0.01$), indicating that these elements may jointly influence microbial diversity.

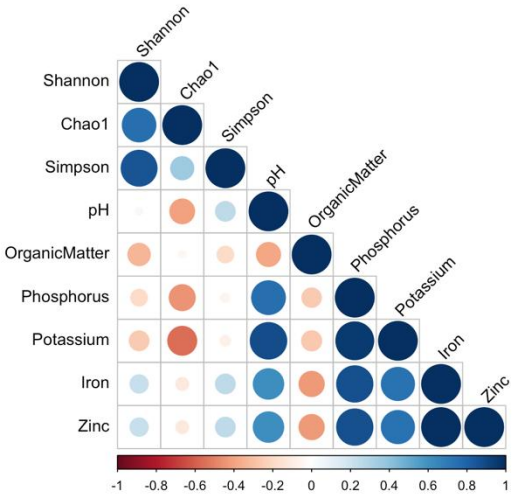

Figure 2. Spearman correlation matrix illustrating the relationships between alpha diversity indices (Shannon, Chao1, Simpson) and environmental factors.

The effects of different fertilization practices on microbial diversity were analyzed at the genus level using 16S rRNA sequencing. In the control area with ongoing agriculture and post-harvest soil samples, *Vibrio* (22.7%) was prevalent, while *Rhizobium* and *Bradyrhizobium* were absent, suggesting long-term cropping may have negatively selected against these symbiotic taxa (Hartmann et al., 2015; Vitousek et al., 2009). In the field with only microbial fertilizer, *Rubrobacter* (25%) and *Microvirga* (12.5%) initially dominated, but post-harvest, *Vibrio* rose (25.4%), and *Rubrobacter* fell to 1.6%. In the field with a microbial-organomineral fertilizer mix, *Rubrobacter* was initially low (10.3%), while *Afipia*, *Microvirga*, and *Pseudomonas* were high. Post-harvest, *Rubrobacter* vanished, *Vibrio* (18.1%) rose, and *Microvirga* and *Pseudomonas* declined. With only organomineral fertilizer, *Rubrobacter* and *Pseudonocardia* (9.4%) initially dominated, but post-harvest, *Vibrio* (11.9%) increased, *Rubrobacter* decreased, *Peredibacter* and *Sandaracinus* rose. PCA results (Figure 3) showed the first component (PC1), accounting for 99.93% of microbial community variation, was marked by aquatic environment-related genera like *Vibrio* and *Catenococcus*. PCA and Wilcoxon tests indicated irrigation impacted microbial composition more than fertilization and pH. Post-irrigation, aquatic genera like *Vibrio*, *Pseudocitrobacter*, and *Catenococcus* increased , while drought-resistant *Rubrobacter* decreased. These results highlight irrigation's greater influence on soil microbial communities than fertilization, underscoring its importance in agricultural management (Naylor et al., 2023).

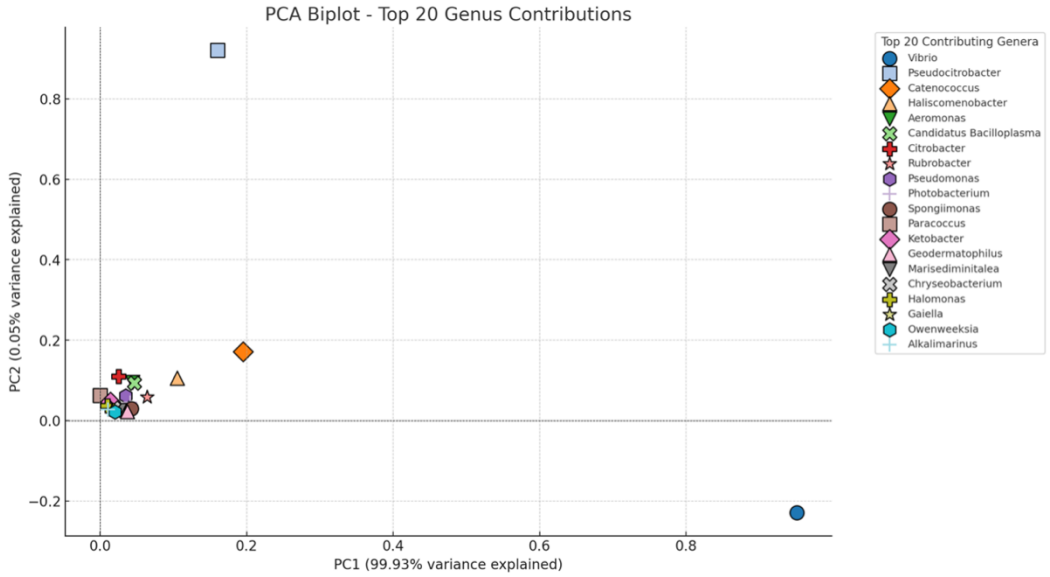

Figure 3. Principal Component Analysis (PCA) biplot of bacterial genus contributions in soil.

The microbial-organomineral fertilizer combination resulted in the most balanced microbial structure, controlling *Vibrio* more effectively than microbial fertilizer alone and ensuring high initial levels of beneficial bacteria (*Afipia*, *Microvirga*, *Pseudomonas*). In the organomineral fertilizer application alone, although *Vibrio* levels were lower, beneficial bacteria were limited. Thus, the microbial-organomineral fertilizer combination is a more sustainable approach supporting beneficial microbial groups. However, optimizing fertilizer application and inoculation strategies is crucial to maintaining beneficial microorganisms (Hartmann et al, 2015).

Although no statistically significant differences were observed in plant growth, plants treated with the microbial and organomineral fertilizer combination showed the highest root length and overall development. Different fertilization strategies did not significantly affect the physical properties of beans, such as wet and dry grain weights and water uptake capacities. ANOVA analysis revealed that plots with a combination of microbial and organomineral fertilizers had significantly higher yields compared to other applications ($p<0.05$) (Silva et al., 2022).

The study identified economic and psychological barriers as the main challenges farmers face in transitioning to sustainable fertilization methods, with economic concerns and uncertainties arising from moving away from familiar chemical fertilizers to alternative options (Aghabeygi et al., 2024). The current situation arises from the elevated costs of biofertilizers and the fact that their anticipated benefits are not immediately apparent. Additionally, farmers' unfamiliarity and lack of experience with these new methods lead them to maintain a psychological distance from adopting them. It has been noted that Türkiye's existing agricultural policies and publication services have a direct impact on farmers' willingness to adopt these practices. Due to insufficient state support and limited access to agricultural publication services, farmers are unable to fully utilize the information and incentives for sustainable practices. Consequently, to enhance the use of microbial and organomineral fertilizers, it is necessary to bolster educational programs, increase economic support, and tailor policies to meet farmers' needs.

Conclusion

This study evaluated the effects of microbial and organomineral fertilizers, both individually and in combination, on soil microbial composition, plant growth, and crop yield. The results indicated that the combination of microbial and organomineral fertilizers led to a more balanced microbial structure in the soil compared to single-type fertilizer applications and significantly boosted crop yield. However, irrigation was found to be a more influential factor in shaping microbial communities than fertilizer applications. It is stressed that reducing economic uncertainties, strengthening comprehensive education programs, and enhancing policy support are crucial to

increasing farmers' adoption of biofertilizers and organomineral fertilizers. Future research should focus on optimizing application methods and ensuring the long-term sustainability of microbial communities.

References

Aghabeygi, M., Strauss, V., Paul, C., & Helming, K. (2024). Barriers of adopting sustainable soil management practices for organic and conventional farming systems. Discover Soil, 1 (1), 11. https://doi.org/10.1007/s44378-024-00008-1

Altieri, M. A. (1999). The ecological role of biodiversity in agroecosystems. In Ecosystems and Environment (Vol. 74). https://doi.org/10.1016/S0167-8809(99)00028-6

Callahan, B. J., McMurdie, P. J., Rosen, M. J., Han, A. W., Johnson, A. J. A., & Holmes, S. P. (2016). DADA2: High-resolution sample inference from Illumina amplicon data. Nature Methods, 13 (7), 581–583. https://doi.org/10.1038/nmeth.3869

Delgado-Baquerizo, M., Reich, P. B., Khachane, A. N., Campbell, C. D., Thomas, N., Freitag, T. E., Abu Al-Soud, W., Sørensen, S., Bardgett, R. D., & Singh, B. K. (2017). It is elemental: soil nutrient stoichiometry drives bacterial diversity. Environmental Microbiology, 19 (3), 1176–1188. https://doi.org/10.1111/1462-2920.13642

Hartmann, M., Frey, B., Mayer, J., Mäder, P., & Widmer, F. (2015). Distinct soil microbial diversity under long-term organic and conventional farming. ISME Journal, 9 (5), 1177–1194. https://doi.org/10.1038/ismej.2014.210

Naylor, D., Naasko, K., Smith, M., Couvillion, S., Nicora, C., Trejo, J., Fransen, S., Danczak, R., McClure, R., Hofmockel, K. S., & Jansson, J. K. (2023). Interactive effects of depth and differential irrigation on soil microbiome composition and functioning. Frontiers in Microbiomes, 2. https://doi.org/10.3389/frmbi.2023.1078024

Philippot, L., Chenu, C., Kappler, A., Rillig, M. C., & Fierer, N. (2023). The interplay between microbial communities and soil properties. In Nature Reviews Microbiology. Nature Research. https://doi.org/10.1038/s41579-023-00980-5

Rehman, I. U., Islam, T., Wani, A. H., Rashid, I., Sheergojri, I. A., Bandh, M. M., & Rehman, S. (2022). Biofertilizers: The Role in Sustainable Agriculture. In S. A. Bandh (Ed.), Sustainable Agriculture: Technical Progressions and Transitions (pp. 25–38). Springer. https://doi.org/10.1007/978-3-030-83066-3

Silva, A. M. M., Estrada-Bonilla, G. A., Lopes, C. M., Matteoli, F. P., Cotta, S. R., Feiler, H. P., Rodrigues, Y. F., & Cardoso, E. J. B. N. (2022). Does Organomineral Fertilizer Combined with Phosphate-Solubilizing Bacteria in Sugarcane Modulate Soil Microbial Community and Functions? Microbial Ecology, 84 (2), 539–555. https://doi.org/10.1007/s00248-021-01855-z

Tilman, D., Balzer, C., Hill, J., & Befort, B. L. (2011). Global food demand and the sustainable intensification of agriculture. Proceedings of the National Academy of Sciences of the United States of America, 108 (50), 20260–20264. https://doi.org/10.1073/pnas.1116437108

Uddin, Md. K., Saha, B. K., Wong, V. N. L., & Patti, A. F. (2025). Organo-mineral fertilizer to sustain soil health and crop yield for reducing environmental impact: A comprehensive review. European Journal of Agronomy, 162, 127433. https://doi.org/10.1016/j.eja.2024.127433

van der Heijden, M. G. A., Bardgett, R. D., & van Straalen, N. M. (2008). The unseen majority: Soil microbes as drivers of plant diversity and productivity in terrestrial ecosystems. In Ecology Letters (Vol. 11, Issue 3, pp. 296–310). https://doi.org/10.1111/j.1461-0248.2007.01139.x

Vitousek, P. M., Naylor, R., Crews, T., David, M. B., Drinkwater, L. E., Holland, E., Johnes, P. J., Katzenberger, J., Martinelli, L. A., Matson, P. A., Nziguheba, G., Ojima, D., Palm, C. A., Robertson, G. P., Sanchez, P. A., Townsend, A. R., & Zhang, F. S. (2009). Nutrient imbalances in agricultural development. In Science (Vol. 324, Issue 5934, pp. 1519–1520). https://doi.org/10.1126/science.1170261

SUSTAINABILITY

Biodiversity

Climate Change Mitigation

Life Cycle Assessment

Reinforced Concrete Structures

Smart and Sustainable Cities

Sustainable Development Goals

Water and Waste Management

Life Cycle Assessment in a Zinc Oxide Recovery Plant Using the Waelz Process: Evaluation of Environmental Impacts from a Sustainability Perspective

Cansu Gunes[a], Orhan Ince[b]

[a] Istanbul Technical University/Graduate School, Environmental Sciences, Engineering and Management Program, Türkiye
[b] Istanbul Technical University / Civil Engineering Faculty, Engineering Department, Türkiye
gunesc22@itu.edu.tr

Keywords: Life Cycle Analysis (LCA), Waste Recovery, Waelz Process, Zinc Production, Electric Arc Furnace Dust (EAFD).

The iron and steel industry plays a pivotal role, particularly in developing countries, and is expected to maintain its influence across multiple sectors, including construction, automotive, and machinery manufacturing. The primary inputs of this industry are iron ore or scrap, while its main output is crude steel (Ersöz et al., 2016). Currently, steel production is carried out using various methods, with the Electric Arc Furnace (EAF) and Blast Furnace (BF) being the most commonly employed techniques (Bıyık & Özkale, 2017). According to 2021 data, steel production in facilities utilizing the Electric Arc Furnace method increased by 16.6% compared to previous years (Iron and Steel Sector Report, 2021). In EAF-based steel production, in addition to sludge and slag, Electric Arc Furnace Dust (EAFD) is generated as a by-product (Iron and Steel Industry Waste Management Report, 2014). Due to its zinc content, EAF dust adversely affects the refractory lining of the Electric Arc Furnace and reduces the economic efficiency of the process, thereby preventing its direct recycling into steel production. Consequently, this waste is collected via filtration systems. Approximately 10–15 kilograms of EAFD are generated per ton of steel produced. Owing to its content of heavy metals such as zinc (Zn), cadmium (Cd), lead (Pb), and chromium (Cr), it is classified as hazardous waste by the U.S. Environmental Protection Agency (EPA) (Kalpaklı et al., 2020). In Turkey, EAF dust is likewise regulated as hazardous waste (Iron and Steel Industry Sectoral Waste Guide). Due to the high costs of landfilling, the challenges of managing leachate resulting from heavy metal contamination, and the valuable zinc content of EAF dust, the recovery of zinc from EAFD has gained increasing importance (Kalpaklı et al., 2020). The zinc content of EAF dust varies depending on the quality of the scrap used in the process and generally ranges between 23–26% Zn. This high zinc content is primarily attributed to the presence of galvanized steel scrap in the EAF charge (Antuñano et al., 2019).

Globally, zinc production is carried out through both primary and secondary sources. While primary zinc production involves extraction from ores, secondary production refers to zinc recovery from waste materials. Both approaches employ pyrometallurgical and hydrometallurgical methods (Kania & Saternus, 2023). In hydrometallurgical zinc production, zinc is separated using various leaching solutions, whereas pyrometallurgical production is based on the high volatility of zinc at elevated temperatures (Nair et al., 2022). The most commonly used and historically established pyrometallurgical method for zinc recovery is the Waelz Process. This German-patented method was first implemented in 1925 in Lünen, Germany (Ruetten, 2006). The Waelz Process is recognized as a Best Available Technology (BAT) (Best Available Techniques (BAT) Reference Document for the Non-Ferrous Metals Industries, 2017). In this process, zinc recovery is based on reduction-oxidation principles and involves the use of raw materials (EAF dust), auxiliary substances, and coal (TÜBİTAK, 2023). The output of this process is a Waelz Zinc Oxide Concentrate with a minimum zinc content of 55% (Wang et al., 2021).

The concept of Life Cycle Analysis (LCA) emerged in the 1960s and, with its widespread application beginning in the 1990s, necessitated the establishment of standardized frameworks. Currently, ISO 14040 defines the principles and framework of LCA, while ISO 14044 provides detailed requirements and guidelines (Yıldız & Atış, 2023). Since the industrial advancements of the 19th century, global environmental concerns have intensified. In response, international conferences and agreements have been convened since the 1970s to address these issues.

One of the most significant contributors to environmental degradation is climate change. To ensure a sustainable future and reduce carbon emissions, the Paris Agreement was signed in 2015, with the goal of limiting global temperature rise relative to pre-industrial levels. This agreement necessitates a reduction in fossil fuel consumption and a shift toward renewable energy sources (Ministry of Environment, Urbanization, and Climate Change).

Life Cycle Analysis allows for the identification of the key environmental aspects of a product, the discovery of improvement opportunities, the quantification of the overall environmental burden, and the establishment of fundamental performance indicators. This study aims to conduct a Life Cycle Analysis of Waelz Zinc Oxide Concentrate. The research will evaluate the environmental impacts of replacing fossil fuels with renewable energy sources during production and examine the influence of different renewable energy types on the process and product life cycle. Moreover, the study seeks to explore sustainable and environmentally friendly production strategies and provide recommendations based on these finding.

Aim

Adopting the life cycle methodology within the scope of ISO 14040 and ISO 14044 standards, this study aims to conduct a Life Cycle Analysis of Waelz Zinc Oxide Concentrate, a product of a hazardous waste recovery facility in Turkey. The study will identify key environmental impact points in the life cycle of raw material procurement and production (cradle-to-gate).

Material and Method

Life cycle assessment calculations were conducted using SimaPro 9.5 software and Ecoinvent LCA Database. It

was developed by PRé Sustainability, a Netherlands based company.Under the ISO 14040 and ISO 14044 standards, the Life Cycle Assessment (methodology primarily consists of four main phases. These standards are internationally recognized references for environmental impact assessment, and the phases are outlined as follows

Goal and Scope Definition: This study aims to identify the environmentally significant aspects of Waelz zinc oxide concentrate through a comprehensive life cycle assessment and to explore potential process improvement opportunities The scope of the study has been defined as cradle to gate.

Table 1: System Boundaries.

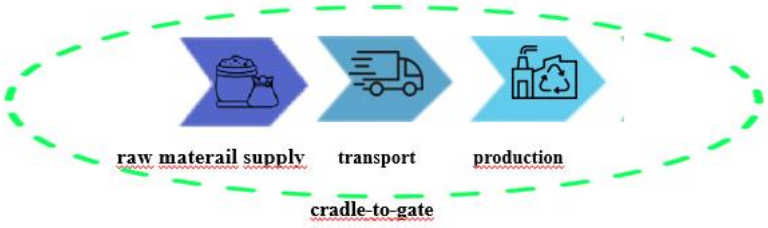

Inventory Analysis: Inventory refers to the set of data collection and computation procedures used to quantify the inputs and outputs associated with a product system.

Impact Assessment: The impact assessment was conducted using the Environmental Footprint 3.1 (EF 3.1) method with the Normalization and Weighting Set V 1 01.

Interpretation: This study encompasses a life cycle assessment based on data from a hazardous waste recovery

facility located in Turkey.

Findings

The life cycle assessment of Waelz zinc oxide concentrate was conducted using a cradle to gate approach and the

SimaPro 9.5 software, in accordance with ISO 14040 and 14044 standards A total of 27 impact categories were assessed (Table 2).

Table 2: Impact Categories Distribution according to Stage of LCA.

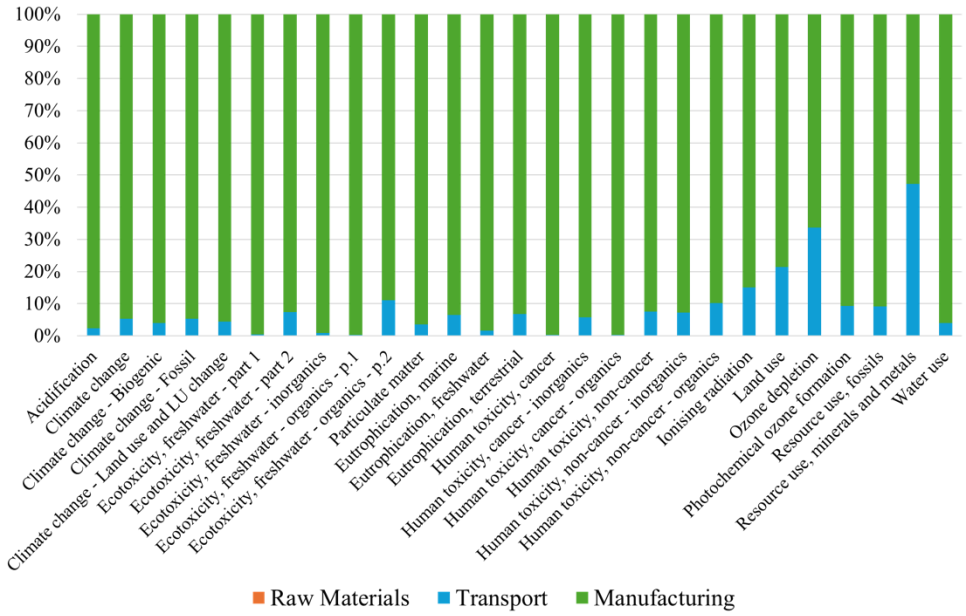

The manufacturing phase has been identified as the dominant contributor across the majority of minimal Greenhouse gas emissions, particularly carbon dioxide are observed to originate predominantly from the manufacturing process This suggests that the energy sources utilized during production are primarily fossil fuel based and/or that the manufacturing operations are highly energy intensive (Table 3).

Table 3: Percentage Distribution of Climate Change Category according to Phases.

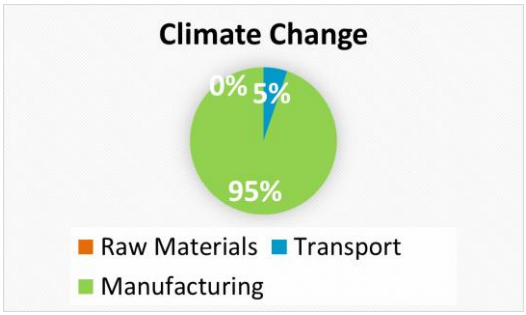

Conclusion

The life cycle assessment of Waelz Zinc Oxide production from Electric Arc Furnace Dust reveals that the majority of environmental impact (>90%) is concentrated in the manufacturing phase.This is primarily due to the high energy demand of the Waelz Process and emissions related to heavy metals. To mitigate these impacts, the use of low carbon energy sources and emission control technologies is recommended WZO recovery contributes to resource efficiency and reduces the environmental risks associated with hazardous waste. For more sustainable production, process improvements and alternative methods should be explored.

Acknowledgement

This study was financially supported by the Istanbul Technical University, Scientific Research Projects Coordination Division (ID:46770, Project Code:MYL-2025-46770).

References

Abhilash T. Nair, Aneesh Mathew, Archana A R, M Abdul Akbar,Use of hazardous electric arc furnace dust in the construction industry: A cleaner production approach,Journal of Cleaner Production,Volume 377,2022

Biyik, Yasin. (2017). DEMİR ÇELİK ENDÜSTRİSİ ÜRETİM YÖNTEMLERİ İLE İHRACAT, KATMA DEĞER VE KARBON EMİSYONU AZALTMA POLİTİKALARI ARASINDAKİ İLİŞKİ. International Journal of Management Economics and Business. 13. 10.17130/ijmeb.2017ICMEB1735485.

Ersoz, Taner & DÜĞENCİ, Muharrem & Ünver, Muharrem & EYİOL, Berkay. (2016). Demir Çelik Sektörüne Genel Bir Bakış ve Beş Milyon Ton Üstü Demir Çelik İhracatı Yapan Ülkelerin Kümeleme Analizi ile İncelenmesi. Nevşehir Bilim ve Teknoloji Dergisi. 4. 75-75. 10.17100/nevbiltek.210941.

Henryk Kania and Mariola Saternus, Evaluation and Current State of Primary and Secondary Zinc Production—A Review, 2023

Best Available Techniques (BAT) Reference Document for the Non-Ferrous Metals Industries(2017). Erişim Tarihi:04.01.2025
URL:https://eippcb.jrc.ec.europa.eu/sites/default/files/2020-01/JRC107041_NFM_bref2017.pdf

T.C. Çevre, Şehircilik ve İklim Değişikliği Bakanlığı, İklim Değişikliği Başkanlığı, Paris Antlaşması. Erişim Tarihi:04.01.2025
URL:https://iklim.gov.tr/paris-anlasmasi-i-34

TÜBİTAK, Yeşil Büyüme Teknoloji Yol Haritası Demir-Çelik Sektörü (2023).Erişim Tarihi:07.01.2025
URL:https://tubitak.gov.tr/sites/default/files/2023-12/yesil_tyh_demir-celik_19072023.pdf

T.C. Çevre ve Şehircilik Bakanlığı, Çevre Yönetimi Genel Müdürlüğü, Sektörel Atık Kılavuzları, Demir Çelik Sanayi. Erişim Tarihi:05.01.2025
URL:https://webdosya.csb.gov.tr/db/cygm/editordosya/Demir_celik_Sanayi_Kilavuzu.pdf

T.C. Sanayi ve Teknoloji Bakanlığı Demir-Çelik Sektör Raporu (2021). Erişim Tarihi:10.01.2025
URL:https://www.sanayi.gov.tr/assets/pdf/plan-program/DemirCelikSektorRaporu2021.pdf

T.C. Kalkınma Bakanlığı, İktisadi Sektörler ve Koordinasyon Genel Müdürlüğü, Demir Çelik Sektöründe Atık Yönetimi (2014). Erişim Tarihi:10.01.2025
URL:https://www.sbb.gov.tr/wp-content/uploads/2022/08/Demir-Celik-Sektorunde-Atik-Yonetimi-Yasin-Ocal.pdf

Jie Wang, Yingyi Zhang, Kunkun Cui, Tao Fu, Jianjun Gao, Shahid Hussain, Tahani Saad AlGarni, Pyrometallurgical recovery of zinc and valuable metals from electric arc furnace dust – A review, Journal of Cleaner Production, Volume 298, 2021

Kalpaklı, A., Ayaz, Ş., İlhan, S., Zorağa, M. (2020). Tehlikeli Atık Sınıfında Olan Elektrik Ark Fırını Baca Tozlarından Hidrometalurjik Yöntemler Kullanılarak Çinkonun Geri Kazanılması: Güncel Değerlendirmeler. Journal of Anatolian Environmental and Animal Sciences, 5(3), 274-282.

N. Antuñano, J.F. Cambra, P.L. Arias,Hydrometallurgical processes for Waelz oxide valorisation – An overview,Process Safety and Environmental Protection,Volume 129,2019,

Ruetten, Dr. (2006). APPLICATION OF THE WAELZ TECHNOLOGY ON RESOURCE RECYCLING OF STEEL MILL DUST BY. 35.

Von Der Assen, N. V., Lafuente, A. M. L., Peters, M., & Bardow, A. (2015a). Environmental assessment of CO2 capture and utilisation. In Elsevier eBooks (pp. 45–56). https://doi.org/10.1016/b978-0-444-62746-9.00004-9

Yıldız, M., & Atış, E. (2023). Yaşam döngüsü analizi: teorik çerçeve ve tarıma uygulanması. Journal of Agriculture Faculty of Ege University, 60(2), 363-374. https://doi.org/10.20289/zfdergi.1126540.

TEXTILE ENGINEERING

Smart and Functional Textiles

Sustainability in Textile and Fashion Industries

Textile Clothing and Fashion Design

The Impact of Ski Jumping Suit Aerodynamics on Flight and Performance

Katja Ravnjak[a], BAS Textile engineering[a], Selin Hanife Eryuruk[b], Pelin Altay[b]

[a]University of Maribor, Faculty of Mechanical Engineering, Textile Engineering, Slovenia
[b]Istanbul Technical University, Faculty of Textile Technologies and Design, Textile Engineering, Turkey
katja.ravnjak@student.um.si

Keywords: Ski Jumping Suits, Aerodynamics, Air Permeability, Drag Coefficient.

Aim

Ski jumping is a highly demanding winter sport that is gaining increasing popularity over the years. In this discipline, athletes are judged based on the distance traveled and the form maintained during flight and landing. To achieve optimal performance, several important factors regarding the quality of one's performance must be taken into account, as they play a crucial role. Among them, one of the most important factors is the aerodynamic properties of an athlete's equipment and their posture during flight. While numerous studies have examined the aerodynamic effects of jump technique and ski design, relatively little research has focused on the role of ski jumping suits, even though these suits must meet strict regulations. Therefore, the aim of this research is to investigate how different fabric properties, such as air permeability and surface roughness, impact aerodynamic behavior and the overall performance of the athlete.

Material and Method

Ski jumping suits must meet strict regulations according to the International Ski and Snowboard Federation (FIS). All portions of the ski jumping suit must be made of the same material and must exhibit the same air permeability from the outside in and from the inside out. The construction of the suit must be a five-layer laminated fabric, consisting of an outer fabric layer, foam layers, an elastic membrane, and a lining fabric. The outer fabric is a bi-elastic warp-knit fabric, made of 81% Polyamid gloss and 19% Elasthane (Lycra), which weighs 180-190 g/m^2 and has the elasticity 150-160% in length and approx. 85-95% in width. The controlled air permeability of the suit must be a minimum of 40 liters per m^2/sec under 10 mm water pressure, achieved through perforation (FIS Rules). The thickness of the suit may not exceed 6.0 mm nor be less than 4.0 mm. The suit must be close-fitting on any part of the body and must close with a zipper placed at the center of the front part of the suit (Figure 1). No additional chemical or mechanical treatment of the material or suit is allowed. All seams must be inside the suit. (FIS, 2024)

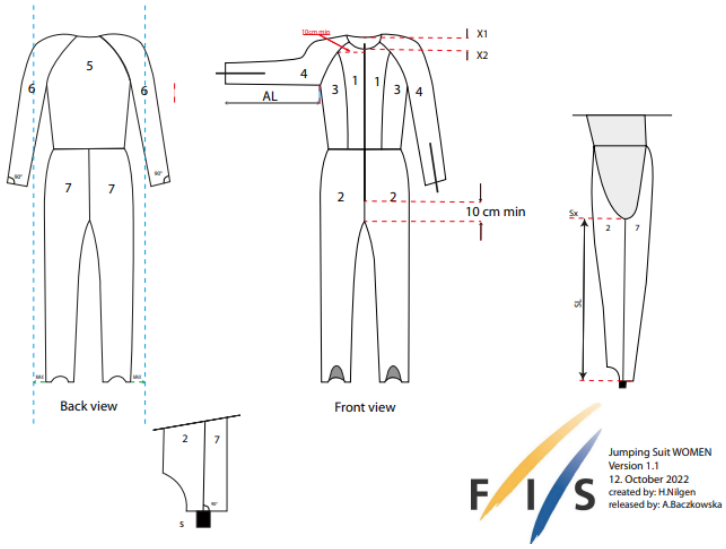

Figure 1. Jumping Suit Women Version 1.1 (FIS, 2024).

Air permeability, which is an important factor in ski jumping suit regulations, is measured using different systems. According to Hasegawa et al., the measurement system used in their study consists of a vacuum pump to provide a constant supply of air through the fabric, a differential pressure gauge, a valve, a measuring cylinder, and a water tank (Figure 2). To measure the flow rate of air passing through the fabric, the differential pressure gauge was used. The air permeability is then calculated based on the pressure difference between the points upstream and downstream of the fabric (Hasegawa, Kawabata, Murakami, Seo, & Obayashi, 2018).

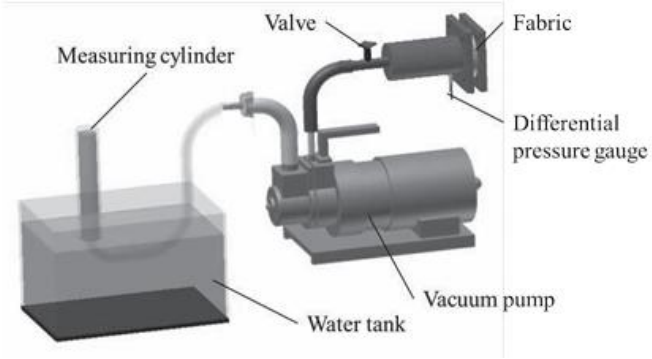

Figure 2. Schematic of air permeability measuring system (Hasegawa, Kawabata, Murakami, Seo, & Obayashi, 2018).

Another important method for investigating aerodynamic properties is wind tunnel testing. According to Chowdhury et al., fabrics are evaluated on various cylindrical arrangements, which are first tested without any fabric covering and then with fabrics wrapped around them (Figure 3). The wind tunnel used in their study is a closed-return circuit with a maximum airspeed of approximately 150 km/h. The drag and lift forces and their moments are computed via purpose-made computer software. The measured aerodynamic forces are later converted to non-dimensional drag and lift coefficients. (Chowdhury, Alam, & Subic, Aerodynamic performance evaluation of sports textile, 2010)

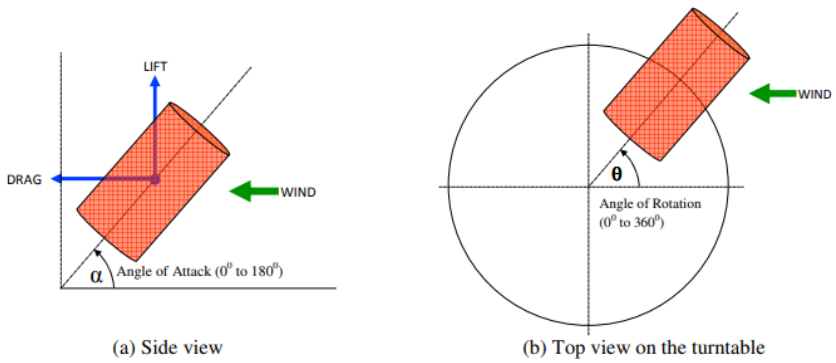

Figure 3. Standard cylinder arrangement for wind tunnel studies (Chowdhury, Alam, & Subic, Aerodynamic performance evaluation of sports textile, 2010).

Chowdhury et al. also designed a robust and safe experimental setup to better investigate aerodynamic properties with minimal interference. This setup can be used to examine a mannequin or athlete with full ski gear, covering most possible variations of an athlete's position in a real ski jump (Figure 4). The system allows adjustments in ski angle relative to the horizontal plane, body position angle, hip angle, and the angle between two skis. The experimental setup was designed to accommodate the athlete/mannequin with all associated equipment (skis, suit, boots, goggles, helmet, gloves, etc.). The mounting device consists of six adjustable circular steel pipe stands connected to a six-component force sensor. This force sensor is linked to a wind tunnel data acquisition computer port, where specialized software captures all six-component forces and moments simultaneously. (Chowdhury, Alam, & Mainwaring, Aerodynamic study of ski jumping suits, 2011)

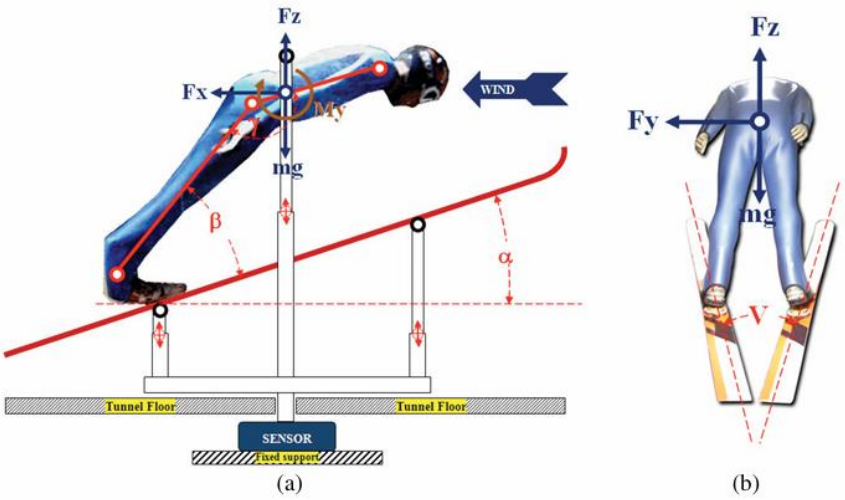

Figure 4. A schematic of experimental setup: (a) side view; (b) rear view (Chowdhury, Alam, & Mainwaring, Aerodynamic study of ski jumping suits, 2011)

More recent studies have also included Computational Fluid Dynamics (CFD) simulations. Liu et al. used a special turbulence model and simulation software to analyze airflow. They set the flight velocity at 29 m/s based on field measurements and tested how different surface roughness values of the suit affect aerodynamic properties. They then calculated lift, drag, and pitching moments and conducted flow field visualizations. Additionally, they examined the effect of surface roughness on different body parts (Figure 5). (Liu, Wang, & Liu, 2025)

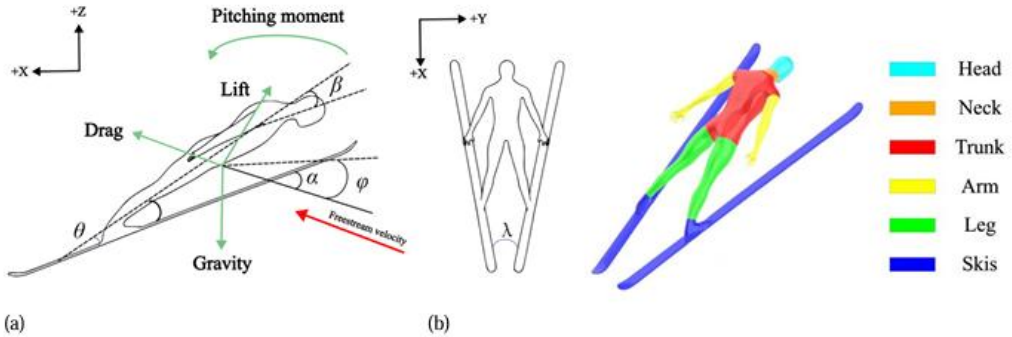

Figure 5. (a) Schematic diagram of posture parameters and force directions during flight; (b) different parts of the multibody system (Liu, Wang, & Liu, 2025).

There is also a growing use of sensor technology to measure aerodynamic forces acting on ski jumpers in real time. These sensors allow the calculation of drag and lift coefficients as well as the lift-to-drag ratio.

Findings

Air permeability is an important factor affecting the aerodynamic properties of ski jumping suits. Hasegawa et al. found that increasing air permeability raises the stall angle and decreases the drag coefficient (Hasegawa, Kawabata, Murakami, Seo, & Obayashi, 2018). Kataoka et. al. carried out wind tunnel experiments to investigate the aerodynamic performances of an elliptic cylinder clothed with fabrics of differing air permeabilities and figured that the stall was delayed by the fabrics with higher air permeabilities. (Kataoka, Hasegawa, Murakami, Seo, & Obayashi, 2020) According to limited studies, jump length can be increased when lift is increased by 1%, whereas jump length decreases when drag is increased by 1%. (Chowdhury, Alam, & Mainwaring, Aerodynamic study of ski jumping suits, 2011)

There is limited information available on full-scale aerodynamic testing methodologies for ski jumping suits. However, Chowdhury et al. developed a reliable full-scale experimental setup, allowing for experimental

evaluation of drag and lift for all types of ski gear, as well as for real athletes and mannequins. Their research concluded that a tight-fitting ski jumping suit provides an aerodynamic advantage over a loose suit. (Chowdhury, Alam, & Mainwaring, Aerodynamic study of ski jumping suits, 2011)

Liu et al. discovered that surface roughness impacts aerodynamic characteristics during the stable flight phase. Their research found that the lift-to-drag ratio peaks at a roughness of 28 μm, making it optimal for maximizing aerodynamic efficiency. However, this roughness also induces significant forward pitching moments. Considering this, roughness values of 8 μm and 11 μm were found to offer commendable aerodynamic performance along with better flight stability. Additionally, the study showed that trunk roughness has the greatest impact on aerodynamic performance, while arm roughness influences the backward shift of the airflow separation point, reducing pressure drag. For leg roughness, when it is small, aerodynamic performance is primarily affected by the position of the separation point, whereas when roughness is higher, frictional drag becomes the dominant factor. (Liu, Wang, & Liu, 2025)

Conclusion

The drag coefficient decreases with an increase in air permeability near the stall angle of attack. Flight distance can be extended by wearing a ski jumping suit made of fabric with higher air permeability.

Wind tunnel testing, with the addition of specialized experimental setups and software, provides a robust method for evaluating drag and lift on various ski gear types.

A tight-fitting suit provides aerodynamic advantages, and in addition, surface roughness plays a significant role in aerodynamic performance, ultimately affecting jump distance and flight stability.

References

Chowdhury, H., Alam, F., Mainwaring, D. (2011). Aerodynamic study of ski jumping suits, Procedia Engineering (Vol. 13, pp.376-381). 5th Asia-Pacific Congress on Sports Technology (APCST).

Chowdhury, H., Alam, F., Subic, A. (2010). Aerodynamic performance evaluation of sports textile, Procedia Engineering (Vol. 2, iss. 2, pp.2517-2522). 8th Conference of the International Sports Engineering Association (ISEA).

Hasegawa, H., Kawabata, Y., Murakami, M., Seo, K., Obayashi, S. (2018). Effect of Air Permeability on the Aerodynamic Characteristics of Ski Jumping Suits, Advanced Experimental Mechanics (Vol. 3, pp.118-122). The Proceedings of the Symposium on sports and human dynamics.

Kataoka, Y., Hasegawa, H., Murakami, M., Seo, K., Obayashi, S. (2020). Flow Behavior Caused by Air Permeability of Ski Jumping Suit Fabric, Proceedings (49(1), 109). The 13th Conference of the International Sports Engineering Association.

Liu, K., Wang, Z., Liu, Q. (2025). Numerical Study of the Aerodynamic Effect of Ski Suit Surface Roughness on Ski Jumping Athletes During the Flight Phase, Journal of Applied Fluid Mechanics (Vol. 18, no. 3, pp.710-727). Isfahan University of Technology.

Url-1 https://assets.fis-ski.com/f/252177/x/c999db9348/specifications-for-cc_jp_nc_competiton-equipment_2024_25-marked-up.pdf, date retrieved 20.03.2025.

TEXTILE ENGINEERING

Smart and Functional Textiles

Sustainability in Textile and Fashion Industries

Textile Clothing and Fashion Design

Simple And Timeless Woven Fabrics Design

Rasim Çırak[a], Aynur Şahin[a], Aslı Sevinç[a], Veli Kaya[a], Burcu Yılmaz[b]

[a]Almodo Altunlar Textile Design Centre, Türkiye
[b]Marmara University, Faculty of Technology, Department of Textile Engineering, Türkiye
rasim.cirak@almodo.com.tr

Keywords: Timeless Woven Fabric, Simple Woven Design, Woven Fabric Design, Basic And Timeless.

Aim

The textile industry, which is an important part of people's daily lives, has an important place in the global economy. In recent years, the concepts of sustainability and slow fashion have become the agenda of textile designers in order to prevent these industrial processes from posing a threat to the ecosystem [1]. Designers all over the world have turned to different design approaches in order to stop or slow down the rapid pollution of the planet with the fast fashion concept. One of the most important reasons for this is that textiles that are consumed rapidly along with the fast fashion trend create a huge waste burden on the environment. In order to prevent the formation of this waste load, intensive studies are carried out on sustainable approaches such as the use of renewable and environmentally friendly raw materials, reduction of carbon emissions, durability and long life of products. These studies reveal that more than 80% of a product's environmental impact is determined by the design process. For these reason, one of the approaches that should be implemented to achieve sustainable fashion for the consumer and the producer is timeless designs [1-2]. Timeless textiles are the workhorse of slow fashion. Similar to concept of slow fashion, designers work on timeless models with quality materials, in small numbers, and without using current fashion data [3-4]. As the level of awareness of consumers increases, it is seen that their tendency to purchase a design that will never lose its value increases. In this case, they both prefer permanent textiles that will not stand the test of time and also exhibit a more environmentally friendly approach [1,5]. In some of the exemplary studies on these subjects, it is seen that fabrics that have existed throughout history are reinterpreted by taking inspiration from their own historical processes. With vibrant colours and tones that will attract attention, designs that can liberate personal expressions, go beyond time, and have a two dimensional appearance and feel with use of different weaving types and yarn counts together can contribute to the creation of original and distinct styles [6].

The aim of this study was to design woven fabrics by reinterpreting timelessness with a minimalist approach. Thus with timeless designs that were realized, it was tried to obtain fabrics that were both high in design qualities and simple yet functional. The designs, which will bring effortless elegance in every season, are aimed to be woven fabrics that can be worn at any time the day and the year.

Material and Method

Weight, weaving type and blend ratios of the fabric designs are summarized in Table 1. These parameters were determined according to the fabric properties of upper garments that can be basic and timeless.

Table 1. Parameters of designs.

Fabrics	Fabric Weight (g/m²)	Weaving Type	Blend Ratio
Design 1	285	Twill	100 % CO
Design 2	125	Plain	54/40/6 % CO/PA/EL
Design 3	235	Twill	73/25/2 % CO/PES/EL
Design 4	315	Twill	52/46/2 % Organic CO/CO/EL
Design 5	315	Special Dobby	97/3 % CO/EL
Design 6	275	Twill	60/34/4/2 % Recycled PES/CV/PES/EL
Design 7	260	Twill	97/3 % CO/EL
Design 8	285	Special Dobby	56/32/10/2 CV/PES/PAN/EL

The process of realizing designs is divided into two: designing woven fabrics and weaving the designs. In the first step of designing woven fabrics, the screening method, which is a qualitative research method, was used to examine past comments on basic and timeless fabrics. Trend analysis was conducted by following seasonal fashion shows and fashion sites such as WGSN. The findings were reinterpreted according to today's fashion sense using the brainstorming method. The theme is 'timelessness'. Studies have been carried out on the overlap of theme and trend. Drawings, stories and storyboards were created within the scope pf the theme. To ensure consistency and repeatability when making colour selections, eight neutral tones were selected from PANTONE Colour Chart: 14-1217 TCX, 18-0430 TCX, 18-0513 TCX, 19-1034 TCX, 18-4215 TCX, 19-3922 TCX, 19-4122 TCX and 19-3902 TCX. The theme of the study was the main factor in determining the colours. In the weaving process of the designs, plain, twill and special dobby were used as the weave structure. All fabric designs were produced as samples on an eccentric air weaving machine. After additional work on cost and production details, the necessary design revisions were made and the designs were finalized.

Findings

Sample production images of eight designed basic and timeless woven fabrics are presented in Figure 1. Basic and timeless designs were achieved in the works with vague thin or thick lines, denim look and linen look. The fact that the colours chosen were predominantly dark tones supported the timeless design element. At the same time, their combinability has made the designs usable in the production of key textile pieces.

Figure 1. Fabric samples.

The colour fastness to washing test results of the fabrics were carried out in accordance with the method described in ISO 105-C06 (A2S test conditions; 40°C), the colour fastness to rubbing tests were carried out in accordance with ISO 105-X12 and the colour fastness to perspiration tests were carried out in accordance with ISO 105-E04. The Martindale Pilling Tendency tests were applied according to BS EN ISO 12945-2 standard test method for 2000 cycles. When all the test results were evaluated in general, colour fastness washing was staining 4, colour change ¾, colour fastness to rubbing was dry 4, wet 2/3 +, colour fastness to perspiration was acid and alkaline staining 4, acid colour change 4, alkaline colour change ¾ and pilling was 3 +.

Conclusion

In this work, eight basic and timeless woven fabrics were designed. Thanks to the seasonless colour palette and minimalist patterns of the designs, they will appeal to a wide target audience and will be included in both women's and men's collection, regardless of gender. Patterns that are far from sparkle and exaggeration may appeal to those who love the minimal style. In addition, that can also find a place in the quiet luxury trend.

When the technical findings of the designs were evaluated, it was seen that colour fastness and pilling tendencies were generally at acceptable values.

The designs are found to be timeless and minimalist in these aspects, as they enable elegance, comfort and aesthetics to be achieved simultaneously business or social life, depending on the season. It is expected that these woven fabric designs, which will continue to be trendy especially for stylish women in SS25 and 26 globally, will find a response in the fashion industry, with pieces supported by palazzo trousers, midi skirts, tweed jackets and details that can be combined with the quiet luxury trend.

This paper includes the outputs of the project titled '23-24 Simple and Timeless' completed at the Almodo Altunlar Textile Design Center.

References

Gabriel, M. and Loundes Delgedo, M. (2020). Sustainable development goal 12 and its relationship with the textile industry, The UN Sustainable Development Goals for the Textile and Fashion Industry, 21-46.
Bilen, U. (2024). Investigation of the role of sustainable fashion on sustainable development goals, EJEAS, 7(1), 6-20.
Elbeyoğlu, S. Avar, S. (2022). An example of textile heritage approaches in slow fashion: carpet applications in fabric and garment design, yedi: Journal of Art, Design & Science, 28, 83-98.
Fletcher, K. (2010). A slow fashion: an invitation for systems change, Fashion Practise, 2(2), 259-265.
Türkmen, N. (2011). 'Slowness' and alternative production models for a sustainable textile industry, Akdeniz Sanat, 4 (8), 59-61.
Kaya, V., Uca, L., Şahin, A., Çırak, R. and Yılmaz, B. (2024). Timeless Gingham Fabric Designs, UÇTEK 2024, 16-17 September, Adana, Türkiye, 353-361.

BOOK OF

EXTENDED ABSTRACTS

www.igrs2025.com

/itulisansustu
/itulisansustu
/itulisansustu
/itulisansustu
/company/itulisansustu